SB³C

biomechanics.
bioengineering.
biotransport.

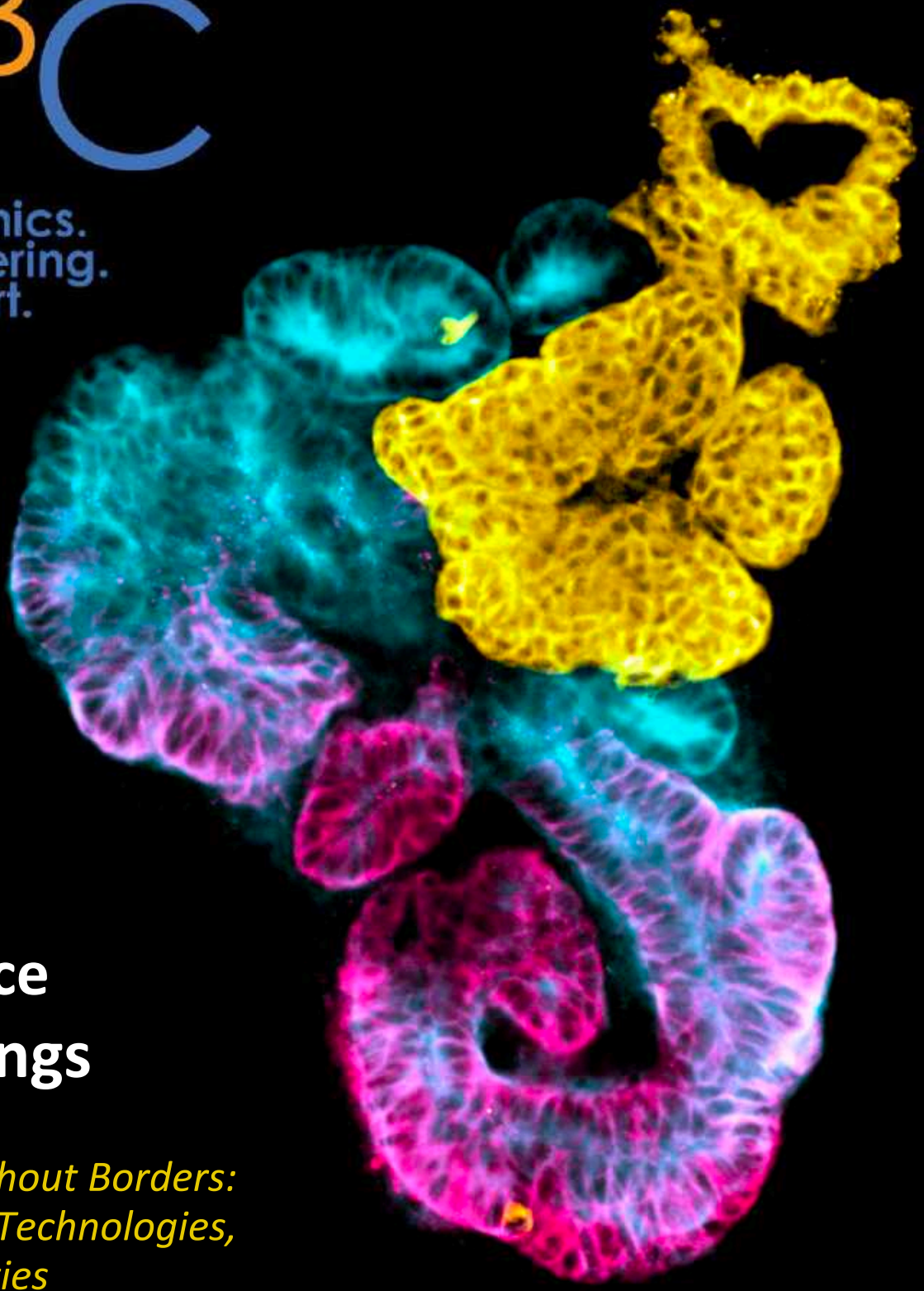

Conference Proceedings

Innovation without Borders: Uniting Ideas, Technologies, and Communities

2024 Summer Biomechanics, Bioengineering, and Biotransport Conference

June 11–14, Lake Geneva, Wisconsin

This conference was supported by the National Science Foundation's Civil, Mechanical, and Manufacturing Innovation Division (Biomechanics and Mechanobiology) under award number 2413182, and by award number R13EB033191A from the National Institute of Biomedical Imaging and Bioengineering. The views expressed in written conference materials or publications and by speakers and moderators do not necessarily reflect the official policies of National Science Foundation nor those of the Department of Health and Human Services; nor does mention of trade names, commercial practices, or organizations imply endorsement by the U.S. Government.

Congratulations to the 2023 Cover Art Contest Winner:

Catherine M. Porter and Alex J. Hughes, University of Pennsylvania
Title: Highly Parallel Production of Designer Organoids by Mosaic Patterning of Progenitors

Description: Proximal-to-distal segmentation in an immunostained human kidney organoid. The midplane from a confocal z-stack of an induced pluripotent stem cell-derived kidney organoid shows nephron segmentation. Nephrin (yellow) marks the boundaries of podocytes, the cells in glomeruli that initially filter blood in vivo. Lotus tetragonolobus lectin (cyan) delineates proximal tubule cells, and membranous E-cadherin (bright pink) outlines distal tubule cells. This kidney organoid was grown in suspension using a novel culture device, which integrates transient 2D cell patterning technology with microwell arrays.

ISBN 978-1-7351808-6-1

SB^{3}C 2024 Meeting Scientific Podium Sessions

Tuesday, June 11	4:15PM–5:45PM CDT

AI & Machine Learning in Biofluids

Session Chairs: **Amir Arzani**, *University of Utah*
Hoda Hatoum, *Michigan Technological University*

Loramoor C

4:15PM **Generative Modeling of Congenital Heart Defect Anatomies for Surrogate Cardiac Flow Simulations**
Fanwei Kong, Alison Marsden
Stanford University

4:30PM **Towards 3D-3C Velocity Maps From Single Camera 2D-2C PTV Using Physics-Informed Neural Networks**
Amin Pashai Kalajahi, Zayeed Bin Mamun, Forouzan Naderi, Sangeeta Yadav, Roshan D'Souza
University of Wisconsin-Milwaukee

4:45PM **Modeling Pharyngeal Airway Pressure Distributions With Neural Networks**
Jun Tao Cui[1], Kok Ren Choy[1], Sanghun Sin[2], Mark E. Wagshul[3], Jayaram K. Udupa[4], Raanan Arens[2], David M. Wootton[1]
[1]Cooper Union, [2]Children's Hospital at Montefiore, [3]Albert Einstein College of Medicine, [4]University of Pennsylvania

5:00PM **Automated Bladder Segmentation of 3D Dynamic MRI for Urodynamic Analysis Using Deep Learning**
Labib Shahid, Juan Pablo Gonzalez-Pereira, Jennifer Franck, Alejandro Roldán-Alzate
University of Wisconsin-Madison

5:15PM **Synthesizing Multi-Branch Aortic Vessels Using Diffusion Model**
Pan Du, Xiaozhi Zhu, Jian-xun Wang
University of Notre Dame

5:30PM **Accuracy of Physics-Informed Neural Networks Under Laminar and Turbulent-Like Aortic Flow Conditions**
Arman Aghaee, M. Owais Khan
Toronto Metropolitan University

Tuesday, June 11	4:15PM–5:45PM CDT

Cartilage Structure, Lubrication & Mechanics

Session Chairs: **Corinne Henak**, *University of Wisconsin-Madison*
Matthew Fisher, *NC State and UNC Chapel Hill*

Maple Lawn B

4:15PM **Distinct Molecular and Structural Traits of Permanent Versus Transient Cartilage in Early Development**

Jiaqi Xiang[1], Bryan Kwok[1], Mingyue Fan[1], Meghan Kupratis[2], Sara Tufa[3], Douglas Keene[3], Robert Mauck[2], Nathaniel Dyment[2], Eiki Koyama[4], Lin Han[1]

[1]Drexel University, [2]University of Pennsylvania, [3]Shriners Hospital for Children, [4]Children's Hospital of Philadelphia

4:30PM **Sustained Structural and Functional Deficits in the Porcine Knee Six Months Following Meniscus Destabilization**

Brendan Stoeckl[1,2], Stephen Ching[1], Veridiana Nadruz[1], Kyle Meadows[3], John Peloquin[3], Owen McGroary[1], Madeline Boyes[1], Lorielle Laforest[1,2], Tim Teinturier[1], Miltiadis Zgonis[1,2], Dawn Elliott[3], Robert Mauck[1,2], Michael Hast[1], Thomas Schaer[1], David Steinberg[1,2]

[1]University of Pennsylvania, [2]CMC VA Medical Center, [3]University of Delaware

4:45PM **Impact of Lubricant Properties on the Synergistic Lubrication of Articular Cartilage**

Emily Lambeth, Brooklyn Tyndall, Sean Farrington, David Burris, Norman Wagner, Christopher Price

University of Delaware

5:00PM **The Protective Effect of Synovial Fluid Against Cartilage Fatigue Wear Is Concentration Dependent**

C.V. Sise, Courtney Petersen, Anna Ashford, Sinisa Vukelic, Clark Hung, Gerard Ateshian

Columbia University

5:15PM **Cartilage Strain Predicts Patient-Reported Outcomes Six Months Post-ACL Reconstruction**

Emily Miller[1], Timothy Lowe[1], Hongtian Zhu[1], Woowon Lee[1], Daniel Stokes[2], Rachel Frank[2], Jonathan Bravman[2], Eric McCarty[2], Nancy Emery[1], Corey Neu[1] *[1]University of Colorado, Boulder, [2]University of Colorado, Anschutz*

5:30PM **Influence of Labrum Size and Material Parameters on Cartilage Mechanics in Hips With Cam FAIS**

Luke Hudson[1,2], Travis Maak[1], Andrew Anderson[1,2], Gerard Ateshian[3], Jeffrey Weiss[1,2]

[1]University of Utah, [2]Scientific Computing and Imaging Institute, [3]Columbia University

Tuesday, June 11	4:15PM–5:45PM CDT

Fiber Mechanics Symposium

Session Chairs: Ian Sigal, *University of Pittsburgh* **Maple Lawn C**
Jason Hua, *University of Mississippi*

4:15PM **Displacement Propagation in Prestressed Two-Dimensional Fibrous Networks**
Ashutosh Mishra, Hamed Hatami-Marbini
University of Illinois at Chicago

4:30PM **A Continuum Model May Artefactually Homogenize Local Strains While Also Artefactually Disrupting Long Distance Strain Transmission**
Xuehuan He[1], Mohammad Islam[2], Bingrui Wang[1], Ian Sigal[1]
[1]University of Pittsburgh, [2]University of Texas Rio at Grande Valley

4:45PM **Effect of Collagen Fiber Tortuosity Distribution on the Mechanical Response of Arterial Tissue**
Yamnesh Agrawal, Ronald N Fortunato, Alireza Asadbeygi, Mehdi Ramezanpour, Michael R Hill, Anne M. Robertson, Spandan Maiti
University of Pittsburgh

5:00PM **Physics Based Machine Learned Constitutive Models for Fibrous Materials**
Jacob Merson, Nishan Parvez
Rensselaer Polytechnic Institute

5:15PM **An Interpenetrating-Network Theory of the Cytoskeletal Networks in Living Cells**
Haiqian Yang, Ming Guo
Massachusetts Institute of Technology

5:30PM **Fiber Alignment and Tortuosity Influence the Load-Carrying Performance of the Lamina Cribrosa Collagen Beams**
Yi Hua[1], Lindee Wilson[1], Ian Sigal[2]
[1]University of Mississippi, [2]University of Pittsburgh

Tuesday, June 11	4:15PM–5:45PM CDT

Mechanobiology in Cancer

Session Chairs: **Alisa Morss Clyne**, *University of Maryland*
M. K. Sewell-Loftin, *University of Alabama at Birmingham*

Maple Lawn A

4:15PM **YAP/TAZ Activity Regulates a Mechano-Metabolic Crosstalk During 3D Breast Cancer Invasion**
Haider Ali[1], Hrishika Rai[1], Adil Khan[1], Jacopo Ferruzzi[1,2]
[1]University of Texas at Dallas, [2]University of Texas Southwestern Medical Center

4:30PM **Mechanical Stimulation and Hyaluronic Acid Alter Ovarian Cancer Cell Behaviors**
Maranda Kramer, Allyson Criswell, Kamari Marzette, M.K. Sewell-Loftin
University of Alabama at Birmingham

4:45PM **A Cell-Based and AI-Accelerated Computational Framework for the Prediction of Mechanosensitive Tumour Growth**
Irish Senthilkumar, Enda Howley, Eoin McEvoy
University of Galway

5:00PM **Decoding the Quantitative Relationship Between Mechanical Forces on Cell Nucleus and YAP Protein Translocation**
Miao Huang[1,2], Maedeh Lotfi[1], Kevin Connell[1], Malisa Sarntinoranont[1], Xin Tang[1,2]
[1]University of Florida, [2]UF Health Cancer Center

5:15PM **Intratumoral Compression Promotes Proneural to Mesenchymal Transitions in Glioblastoma**
Allison McKenzie Johnson, Lylah Cox, Joseph Chen
University of Louisville

Tuesday, June 11	4:15PM–5:45PM CDT

Modeling Cardiac and Coronary Artery Flow and Physiology

Session Chairs: Hannah Cebull, *Emory University*
Vitaliy Rayz, *Purdue University*

Loramoor A

4:15PM **Synthesis of Coronary Arterial Networks From Myocardial Blood Volume Maps**
Mostafa Mahmoudi[1,2], Amirhossein Arzani[3,4], Kim-Lien Nguyen[1,2]
[1]University of California, Los Angeles, [2]VA Greater Los Angeles Healthcare System, [3]University of Utah, [4]Scientific Computing and Imaging Institute

4:30PM **Hemodynamic Assessment of Coronary Atherosclerotic Lesions in Elderly Patients With Myocardial Infarction: a Longitudinal Study**
Diego Gallo[1], Maurizio Lodi Rizzini[1], Alessandro Candreva[1,2], Jean Paul Aben[3], Claudio Chiastra[1], Barbara Stähli[2], Simone Biscaglia[4], Gianluca Campo[4], Umberto Morbiducci[1]
[1]Politecnico di Torino, [2]University Hospital Zurich, [3]Pie Medical Imaging, [4]University of Ferrara

4:45PM **A Multi-Physics Model of Contrast Injection in the Coronary Arteries to Assess Index of Microcirculatory Resistance**
Haizhou Yang[1], Jiyang Zhang[2], Ismael Assi[3], Brahmajee Nallamothu[1], Krishna Garikipati[4], C. Alberto Figueroa[1]
[1]University of Michigan, [2]Sichuan University, [3]University of Cincinnati, [4]University of Southern California

5:00PM **Personalized and Uncertainty-Aware Virtual Planning for Coronary Artery Bypass Graft Surgery Informed by CT Myocardial Perfusion Imaging**
Karthik Menon[1], Zachary Sexton[1], Owais Khan[2], Daniele Schiavazzi[3], Koen Nieman[1], Alison Marsden[1]
[1]Stanford University, [2]Toronto Metropolitan University, [3]University of Notre Dame

5:15PM **The Importance of the Left Atrial Appendage on the Flow in the Atrium** Ahmad Bshennaty[1], Brennan Vogl[1], Alessandra Bravo[2], Agata Sularz[3], Anders Kramer[4], Jens Nielsen-Kudsk[4], Yuheng Jia[5], Ole De Backer[5], Matthieu De Beule[2], Mohamad Alkhouli[3], Hoda Hatoum[1]
[1]Michigan Technological University, [2]FEops, [3]Mayo Clinic, [4]Aarhus University Hospital, [5]Copenhagen University Hospital

5:30PM **Evaluation of Flow Dynamics in the Left Atrium After Hybrid Ablation for Atrial Fibrillation**
Brennan Vogl[1], Grace Hoeppner[1], Hailey LaBonte[1], Emily Vitale[1], Agata Sularz[2], Alejandra Chavez-Ponce[2], Ammar Killu[2], Mohamad Alkhouli[2], Hoda Hatoum[1]
[1]Michigan Technological University, [2]Mayo Clinic

Spine & Disc

Session Chairs: **Deva Chan**, *Purdue University* **Linwood**
Daniel Cortes, *Pennsylvania State University*

4:15PM **Low Back Pain Treatment Options Based on Statistical Shape Models: Spinal Decompression Surgery Versus Non-Operative**
Mary Foltz, Alexandra Seidenstein, Amit Jain, Jill Middendorf
Johns Hopkins University

4:30PM **A Novel Approach to Create the Mean Lumbar Spine Model Using Statistical Shape Modeling for Finite Element Analysis**
Faris Almalki[1,2], Daniel Cortes[2]
[1]University of Jeddah, [2]Penn State University

4:45PM **Correlation of Pain Symptoms in Military Fighter Pilots With Spinal Morphology Obtained Using Supine and Upright MRI Scans**
Rachel Cutlan[1], Vaibhav Porwal[2], Riley McCarty[2], Cory Everts[2,3], Alok Shah[2], Amy Nader[2], Keeley Hamill[2], Narayan Yoganandan[2,4], Keri Hainsworth[2], L. Tugan Muftuler[2], Timothy Meier[2], Hershel Raff[2], Peter Le[5], Chris Dooley[5], Benjamin Gerds[3], Brian Stemper[1,2,4]
[1]Marquette University and Medical College of Wisconsin, [2]Medical College of Wisconsin, [3]115th Fighter Wing, Wisconsin Air National Guard, [4]Zablocki Veterans Affairs Medical Center, [5]Air Force Research Laboratory

5:00PM **In Vivo Lumbar Intervertebral Disc Strain in Flexion, Extension, and Diurnal Motions: Variation With Age in Healthy Adults**
John Peloquin, Harrah Newman, Edward Vresilovic, Dawn Elliott
University of Delaware

5:15PM **Mechanical and Structural Changes to the Annulus Fibrosus in Response to Cyclic Loading: an I-PREDICT Study**
Jack Seifert[1,2,3], Lance Frazer[4], Dennis Maiman[2], Alok Shah[2,3], Narayan Yoganandan[2,3], Keith King[5], James Sheehy[5], Glenn Paskoff[5], Timothy Bentley[6], Daniel Nicolella[4], Brian Stemper[1,2,3]
[1]Marquette University, [2]Medical College of Wisconsin, [3]Zablocki Veterans Affairs Medical Center, [4]Southwest Research Institute, [5]Naval Air Warfare Center, [6]Office of Naval Research

5:30PM **Biomechanicnal Comparison of Commonly Used Three Different Material Composition Used in Cervical Disc Arthroplasty**
Yuvaraj Purushothaman[1], Resetar Ethan[2], Hoon Choi[1], Abdulbaki Kozan[1], Narayan Yoganandan[3]
[1]Cleveland Clinic Florida, [2]University Of Michigan, [3]Medical College Of Wisconsin

Tuesday, June 11	4:15PM–5:45PM CDT

Valvular Biomechanics

Session Chairs: **Rana Zakerzadeh**, *Duquesne University*
Rouzbeh Amini, *Northeastern University*

Loramoor B

4:15PM **Patient-Specific Long-Term Prediction of Transcatheter Edge-to-Edge Mitral Valve Repair**
Natalie Simonian[1], Sneha Vakamudi[2], Mark Pirwitz[2], Michael Sacks[1]
[1]University of Texas at Austin, [2]Ascension Texas Cardiovascular

4:30PM **The Impact of Sex and Hormone-Differences on Heart Valve Disease**
Colton Kostelnik[1], Chien-Yu Lin[1], Magda Piekarska[2], Gaweda Boguslaw[2], Austin Goodyke[2], Tomasz Timek[2], Manuel Rausch[1]
[1]University of Texas at Austin, [2]Corewell Health

4:45PM **Device Deployment and the Onset of Structural Valve Degeneration: Simulation of Transcatheter Aortic Valve Implantation In Vitro**
Sam Boxwell[1], Dylan Armfield[2], William Hickey[3], Scott Cook[3], Patricia Kelly[3], Philip Cardiff[2], Laoise McNamara[1]
[1]University of Galway, [2]University College Dublin, [3]Boston Scientific Corporation

5:00PM **A Parametric Analysis of Chordae Tendineae Density and Branching in Finite Element Simulations of Mitral Valve Closure**
Nicolas Mangine[1], Patricia Sabin[1], Devin Laurance[1], Wensi Wu[1], Christian Herz[1], Christopher Zelonis[1], Csaba Pinter[2], Andras Lasso[3], Stephen Ching[1], Steve Maas[4], Jeff Weiss[4], Metthew Joley[1]
[1]Children's Hospital of Philadelphia, [2]EBATINCA, [3]Queens University, [4]University of Utah

5:15PM **Biomechanical Impact of Neochordoplasty and Leaflet Resection for Mitral Valve Prolapse Repair**
Gediminas Gaidulis[1], Muralidhar Padala[2], Lakshmi Dasi[1]
[1]Georgia Institute of Technology, [2]Nyra Medical Inc.

5:30PM **A Neural-Network Finite-Element Approach to Modeling of Multibody Contact of Trileaflet Heart Valves**
Kenneth Meyer, Christian Goodbrake, Shruti Motiwale, Michael Sacks
Oden Institute for Computational Engineering and Sciences

Biomedical Devices and Materials for Global Health Solutions

Session Chairs: **Byron D. Erath**, *Clarkson University*
Mahsa Dabagh, *University of Wisconsin-Milwaukee*

Maple Lawn C

8:00AM **A Soft 3D Microarchitected Pressure Sensor for Urethral Monitoring**
Nakhiah Goulbourne
University of Michigan

8:15AM **Development and In-Vitro Validation of a Simple 1D Mechanical Model for Pediatric Vascular Patch Planning**
Shannen Kizilski[1,2], Dominic Recco[1,2], Jocelyn Davee[1], Patrick Earley[1], Nicholas Kneier[1], Lauren Marshall[1], Peter Hammer[1,2], David Hoganson[1,2]
[1]Boston Children's Hospital, [2]Harvard Medical School

8:30AM **Machining Living Osteochondral Allografts for Joint ResurfacingIn A Canine Patellofemoral Joint Model**
Katherine Spack[1], Chantelle Bozynski[2], Courtney Petersen[1], Joseph Viola[1], Peter Shyu[1], Edward Guo[1], Clark Hung[1], James Cook[2], Gerard Ateshian[1]
[1]Columbia University, [2]University of Missouri

8:45AM **Detecting Cardiac States With Photoplethysmography Wearables: Implications for Out-of-Hospital Cardiac Arrest Detection**
Mahsa Khalili, Saud Lingawi, Jacob Hutton, Babak Shadgan, Jim Christenson, Brian Grunau, Calvin Kuo
University of British Columbia

9:00AM **Refined Endovascular Solutions: Leveraging 3D Printing in Shape Memory Polymer-Based Embolization for Intracranial Aneurysm Rupture Prevention**
Tanner Cabaniss[1], Yingtao Liu[1], Bradley Bohnstedt[2], Chung-Hao Lee[3]
[1]University of Oklahoma, [2]Indiana University School of Medicine, [3]University of California, Riverside

9:15AM **Assessment of Clot Adhesion Strength on Endothelial Cells and Biocompatible Materials**
Vikas Kannojiya[1], Sara Almasy[1], Ian Goetz[1], Jose Monclova[1], Francesco Costanzo[1], Keefe Manning[1,2]
[1]Pennsylvania State University, [2]Penn State Hershey Medical Center

Cancer Mechanics I

Session Chairs: **Meenal Datta**, *University of Notre Dame*
Jacopo Ferruzzi, *University of Texas at Dallas*

Loramoor A

8:00AM **Towards Cancer Mechano-Therapy: Yap as an Emerging Mechanical Target to Eradicate Tumors**
Miao Huang[1,2], Mu Yu[1,2], Chase Stallings[1], HeYang Wang[3], Lu Li[1], Conner Traugot[1], Mingyi Xie[1,2], Youhua Tan[4], Franziska Haderk[5], Juan Guan[6], Lizi Wu[1,2], Xin Tang[1,2]
[1]University of Florida, [2]UF Health Cancer Center (UFHCC), [3]Northwestern University, [4]Hong Kong Polytechnic University, [5]University of California, San Francisco, [6]University of Texas at Austin

8:15AM **Multiscale Mechanoimmunology: From Molecular Mechanisms to Precision Therapies**
Kolade Adebowale
Harvard University

8:30AM **Reverse-Engineering Cancer Mechanics: Piezo Regulates Epithelial Topology and Promotes Precision in Organ Size Control**
Nilay Kumar, Mayesha Mim, Megan Levis, Maria Unger, Gabriel Miranda, Trent Robinett, Jeremiah Zartman
University of Notre Dame

8:45AM **Development of a High-Throughput Drug Screening Platform Via Pipetting Gel Droplet Micro-Organoids Models**
Daniel Montes Pinzon, Angela Taglione, Fei Fan, Liao Chen, Xin Lu, Sharon Stack, Donny Hanjaya-Putra, Hsueh-Chia Chang
University of Notre Dame

9:00AM **A 3D Model for the Study of Macrophage-Induced Solid Stress**
Alice Burchett, Saeed Siri, Meenal Datta
University of Notre Dame

9:15AM **Chronic Off-Target Cardiotoxicity of Doxorubicin Is Mediated by Pathological Changes in Paracrine Signaling and miRNA Prevalence**
George Ronan[1], Frank Ketchum[1], Nicole Kowalczyk[1], Noor Behnam[1], Lara Çelebi[1], Pinar Zorlutuna[1,2]
[1]University of Notre Dame, [2]Harper Cancer Research Institute

Cardiovascular Devices and Design

Session Chairs: **Noelia Grande Gutiérrez**, *Carnegie Mellon University*
David Bark, *Washington University in St. Louis*

Loramoor C

8:00AM **Digital Twin Development and Fatigue Optimization of Novel Polymeric TAVR Devices Tailored for Patient-Specific Needs**
Brandon Kovarovic[1], Kyle Baylous[1], Ryan Helbock[1], Oren Rotman[1], Marvin Slepian[2], Danny Bluestein[1]
[1]Stony Brook University, [2]University of Arizona

8:15AM **Stent Retriever Removal Forces in an Experimental Stroke Model With Porcine Carotid Arteries**
Demitria Poulos[1], Michael Froehler[2], Bryan Good[1]
[1]University of Tennessee, [2]Vanderbilt University Medical Center

8:30AM **TomoPINNs: Computed Tomography Enriched Physics-Informed Neural Networks for Hemodynamic Descriptors**
Sangeeta Yadav[1,2], Forouzan Naderi[1], Amin Pashaei Kalajahi[1], Zayeed Bin Mamun[1], Roshan M. Dsouza[1]
[1]University of Wisconsin, [2]Indian Institute of Science

8:45AM **Efficient Shape Optimization of the Total Cavopulmonary Connection Via Hyper-Reduced Order Models and Free Form Deformation**
Imran Shah[1,2], Francesco Ballarin[3], Lakshmi Dasi[1], Alessandro Veneziani[2]
[1]Georgia Institute of Technology, [2]Emory University, [3]Università Cattolica del Sacro Cuore

9:00AM **Impacts of Tears Size and Location on Blood Flow Dynamics in Type-B Aortic Dissection**
Khalil Khanafer, Shaun Scofield, Yasser Aboelkassem
University of Michigan

9:15AM **Dynamic Patient-Specific Computer Simulation of Transcatheter Aortic Valve Replacement Using the Evolut R and SApien3**
Masod Sadipour[1], Jordan Brown[2,3], David Wells[2], Boyce Eugene Griffith[1,2]
[1]University of North Carolina, [2]University of North Carolina, Chapel Hill, University of North Carolina, [3]College of Sciences and Mathematics, Belmont University

Wednesday, June 12	8:00AM–9:30AM CDT

Emerging Topics in Biomechanics and Mechanobiology

Session Chairs: **Arina Korneva**, *Virginia Tech*
Lei Shi, *Kennesaw State University*

Maple Lawn A

8:00AM **Human Airway Tissue Biaxial Tensile Mechanics**
Crystal Mariano, Mona Eskandari
University of California, Riverside

8:15AM ***WITHDRAWN*** **Non-Injurious Impact Loading to Explanted Cartilage Results in DNA Damage Within Chondrocytes**
Katie Gallagher[1], Stephanie Schnieder[1], David Pierce[2], Corey Neu[1]
[1]University of Colorado, Boulder, [2]University of Connecticut

8:30AM **Investigating the Range of Cell Cluster Biomechanical Behavior With Cluster Size**
Sara Ghanbarpour Mamaghani, Ethan Wagner, Jonathan P. Celli, Joanna B. Dahl
University of Massachusetts Boston

8:45AM **Dietary Cholesterol Stiffens the Steatotic Liver**
David Li, Abigail Loneker, Paul Janmey, Rebecca Wells
University of Pennsylvania

9:00AM **The Role of Early Life (Psychological) Stress on Central Artery Aging and Remodeling**
Brooks Lane[1], Nazli Gharraee[1], Gabrielle Lohrenz[1], Abigail Polter[2], Paul Marvar[2], John Eberth[1]
[1]Drexel University, [2]George Washington University, Pharmacology and Physiology

9:15AM **Stiffening or Softening? Deciphering the Role of Multiple Contracting Inclusions in Modulating the Stiffness of a Fibrous Matrix**
Mainak Sarkar, Brian M. Burkel, Suzanne M. Ponik, Jacob Notbohm
University of Wisconsin-Madison

Engineered In Vitro Models

Session Chairs: Spencer Szczesny, *Pennsylvania State University*
Yubing Sun, *University of Massachusetts Amherst*

Loramoor B

8:00AM **Development and Analysis of Scaffold-Free Adipose Spheroids**
Jesse Liszewski, Riley Behan-Bush, Michael Schrodt, Aloysius Klingelhutz, Ed Sander, James Ankrum
University of Iowa

8:15AM **A Bioreactor Platform Designed to Estimate Cell Generated Stresses Within Uniaxially Constrained Tissue Equivalents**
Andrew V. Glick[1], Daniel Paukner[2], Christian J. Cyron[2], Jacopo Ferruzzi[1,3]
[1]University of Texas at Dallas, [2]Institute for Continuum and Material Mechanics, Hamburg University of Technology, [3]University of Texas Southwestern Medical Center

8:30AM **Development of Engineered Tendon Tissue Micro-Gauges (TENTUGS) for Investigating Tendon Organization and Mechanobiology**
Stephanie Steltzer, Seung-Ho Bae, Nicole Migotsky, Henry Yu, Charlie Mentzer, Syeda Lamia, Brendon Baker, Megan Killian, Adam Abraham
University of Michigan

8:45AM **A Novel Millifluidic Dual-Flow Bioreactor for Recapitulating Shear Stress In Vitro**
Fariha Ahmad, Katrina Cao, Jane Grande-Allen
Rice University

9:00AM **A 3D In-Vitro Neuro-Vascular Human Brain Model With Meningeal Lymphatics for Studying Alzheimer's Disease**
Xun Wang[1], Seunggyu Kim[1], Maria Proestaki[1], Shun Zhang[1], Georgios Pavlou[1], Se Hoon Choi[2,3], Rudolph Tanzi[2,3], Roger Kamm[1]
[1]Massachusetts Institute of Technology, [2]Massachusetts General Hospital, [3]Harvard Medical School

9:15AM **Strain, Stiffness, and Composition Effects on Lung Fibroblasts and Their Implications in Pulmonary Fibrosis**
Qi Wang, Kristan Worthington, Ed Sander
University of Iowa

Ligament & Tendon Mechanics & Imaging

Session Chairs: **Stephanie Cone**, *University of Delaware* **Linwood**

Zachary G. Davis, *DoD-VA Extremity Trauma and Amputation Center of Excellence*

8:00AM **Connexin-43 Positive Cell Ratio Is Not Modulated by Severity of Damage or Change in Cycle Number in Tendon Fatigue Injury Model**
Benjamin Johnston[1], Nelly Andarawis-Puri[1,2]
[1]Cornell University, [2]Hospital for Special Surgery

8:15AM **Elastin Alters Fatigue Mechanics of Functionally Distinct Tendon Fascicles in Murine Model of Elastin Knockdown**
Shawn Pavey, Nathan Xu, Spencer Lake
Washington University in St. Louis

8:30AM **Tendon Impingement Produces Differential Regional Profiles of Intact and Fragmented Aggrecan**
Brian Wise, Whasil Lee, Mark Buckley
University of Rochester

8:45AM **Aged Tendons Have a Higher Strain Threshold for Stimulation From Dynamic Compression Than Young Tendons**
Samuel Mlawer, Brianne Connizzo
Boston University

9:00AM **Estrogen Receptor Expression Is Greater Than Progesterone Receptor Expression in the Porcine Anterior Cruciate Ligament and Varies Across Age and Animal**
Jacob D. Thompson[1], Matthew B. Fisher[1,2]
[1]North Carolina State University and University of North Carolina at Chapel Hill, [2]University of North Carolina at Chapel Hill

9:15AM **Effects of Soaking Solution on Anterior Cruciate Ligament Hydration, Mechanics, and Magnetic Resonance Imaging**
Charlotte Andreasen[1], Peter Kuetzing[1], Hassan Siddiqui[2], Audrey McManus[1], Ulrich Scheven[1], Ellen Arruda[1]
[1]University of Michigan, [2]Pennsylvania State University

Nano, Micro, Tissue & Multiscale Mechanics

Session Chairs: **Camilo Duarte Cordon**, *Columbia University*
Kristin Myers, *Columbia University*

Maple Lawn B

8:00AM **Does Tissue Composition Alter Strain-Based or Stress-Based Susceptibility to Injury?**
Callan Luetkemeyer
University of Illinois Urbana-Champaign

8:15AM **Anisotropic Mechanical Properties in Scaled Lattice Composites Estimated by Magnetic Resonance Elastography**
Kevin Eckstein[1], Daniel Yoon[1], Margrethe Ruding[1], Ramin Balouchzadeh[1], Aaliyah Thompson-Mazzeo[1], Ruth Okamoto[1], Curtis Johnson[2], Matthew McGarry[3], Philip Bayly[1]
[1]Washington University in St. Louis, [2]University of Delaware, [3]Dartmouth College

8:30AM **Influence of Glenohumeral Joint Angle on in Situ Supraspinatus Strain Behavior**
Aaron Hellem, John Liffrig, Allison Rao, Matthew MacEwen, Victor Barocas, Paula Ludewig, Arin Ellingson
University of Minnesota

8:45AM **A Tale of Two Tissues: Effects of Collagen III Dysyfunction on Determinants of Mechanical Properties in Tendon and Cervix**
Amir Moghaddam[1], Matthew Confer[2], Roberto Pineda Guzman[3], Kelechi Uhegbu[4], Rohit Bhargava[2], Bruce Damon[3,2], Sanmi Koyejo[4], Christina Laukaitis[3,2], Amy Wagoner Johnson[2], Mariana Kersh[2]
[1]University of Nebraska-Lincoln, [2]University of Illinois at Urbana-Champaign, [3]Carle Health, [4]Stanford University

9:00AM **Flexible Carbon Nanotubes (CNT)-Polydimethylsiloxane (PDMS) Force Sensors for the Rate-Dependent Characterization of Compliant Biomaterials** Sinan Candan, Vanessa Barton, Joseph Andrewas, Jacob Notbohm, Christian Franck
University of Wisconsin-Madison

9:15AM **Evaluating Adaptation of Amputee Skin Due to Prosthesis Use**
Jack Hayes[1], Jennifer Andrews[2], Tomas Andriuskevicius[1], Omar Abdelwahab[3], Ralph Gordon[3], Tom Briggs[1], Peter Worsley[3], Claire Higgins[1], Marc Masen[1] *[1]Imperial College London, [2]University of Salford, [3]University of Southampton*

Cancer Mechanics II

Session Chairs: Meenal Datta, *University of Notre Dame* **Loramoor A**
Jacopo Ferruzzi, *University of Texas at Dallas*

11:30AM **Structural and Biomechanical Hallmarks of Early-Onset Colorectal Cancer**
Nicole Huning[1], Munir Buhaya[2], Adil Khan[1], Haider Ali[1], Sara Roccabianca[3], Emina Huang[2], Jacopo Ferruzzi[1,2]
[1]University of Texas at Dallas, [2]University of Texas Southwestern Medical Center, [3]Michigan State University

11:45AM **Interplay Between Interstitial Flow and Extracellular Matrix Physical Properties in the Initiation and Control of Angiogenesis and Lymphangiogenesis**
Jonathan W. Song, Jacob C. Holter, Shashwat S. Agarwal, Joseph W Tinapple, Marcos G. Cortes-Medina, Travis H. Jones, Joseph Barlage
Ohio State University

12:00PM **Quantifying Enzymatic Small Extracellular Vesicles (SEVs) for Cancer Companion Diagnostics Using Magnetic Nanoporous Membrane (MNM)-Based Activity Assay**
Tiger Shi[1], Chenguang Zhang[1], Youwen Zhang[1], Xuemin Lu[1], Gaeun Kim[1], Sonu Kumar[1], Ceming Wang[2], Nan Su[2], Yichun Wang[1], Xin Lu[1], Satyajyoti Senapati[1], Hsueh-Chia Chang[1,2]
[1]University of Notre Dame, [2]Aopia Biosciences, Inc.

12:15PM **Investigating the Paracrine Effects of Breast Cancer Cells on Osteoblast Differentiation, Proliferation, and Mineral Deposition**
Sarah Nano[1], Laurie Littlepage[1], Laoise McNamara[2], Glen Niebur[1]
[1]University of Notre Dame, [2]University of Galway

12:30PM **Investigating the Effects of an Increased Adipocyte Density on A 3D Human Breast Tumor Spheroid Model**
Jensen Amens, Gokhan Bacecioglu, Pinar Zorlutuna
University of Notre Dame

12:45PM **Oscillatory Shear Stress Modulates Lymphatic Progenitor Cells Maturation Into Lymphatic Vessels With Anti-Cancer Phenotypes**
Nancy Keilany Lightsey, Eva Hall, Sanjoy Saha, Donghyun Paul Jeong, Donny Hanjaya-Putra
University of Notre Dame

Wednesday, June 12	11:30AM–1:00PM CDT

Cardiovascular Patient-Specific Modeling in the Setting of Disease

Session Chairs: Stephanie George, *East Carolina University* **Loramoor C**
Noelia Grande Gutiérrez, *Carnegie Mellon University*

11:30AM **Computational Modeling of a Human Placentone**
Armita Najmi, Noelia Grande Gutiérrez
Carnegie Mellon University

11:45AM **In Situ Robotic Mechanical Testing of Rat Tibiofemoral Joints**
Karol Calò[1], Andrea Guala[2], Valentina Mazzi[1], Maurizio Lodi Rizzini[1], Lydia Dux-Santoy[2], Jose Rodriguez-Palomares[2], Stefania Scarsoglio[1], Luca Ridolfi[1], Diego Gallo[1], Umberto Morbiducci[1]
[1]Politecnico di Torino, [2]Vall d'Hebron Institut de recerca

12:00PM **Wall Shear Stress in Intracranial Aneurysms Computed From CFD and 4D Flow MRI Augmented With Flow Physics Principles**
Farshid Goudarzian, Mohammadreza Balouchestani Asl, Neal Patel, Abhishek Singh, Jiacheng Zhang, Pavlos Vlachos, Vitaliy Rayz
Purdue University

12:15PM **Analysis of Regional Hemodynamic Changes in Type A Aortic Dissection Repair Using 4D Flow MRI**
Hannah Cebull[1], Hai Dong[2], Minliang Liu[2], Rudy Gleason[2], John Elefteriades[3], John Oshinski[1,2], Marina Piccinelli[1], Bradley Leshnower[1]
[1]Emory University, [2]Georgia Institute of Technology, [3]Yale University

12:30PM **A Case Study: Computational Modeling of Hemodynamics in a Patient With End Stage Renal Disease Under Hemodialysis Via Arteriovenous Fistula With Pulmonary Hypertension**
Fatemeh Bahmani, Kaitlin Southern, Alex Vadati, Veeranna Maddipati, Stephanie George
East Carolina University

12:45PM **Patient-Specific Modeling of Hemodynamics During Splenic Artery Embolization**
Younes Tatari[1], Tyler Andrew Smith[1], Jingjie Hu[2], Amirhossein Arzani[1]
[1]University of Utah, [2]North Carolina State University

Wednesday, June 12	11:30AM–1:00PM CDT

Digital Health and Computational Modeling to Improve Health Outcomes

Session Chairs: **Antonis P. Stylianou**, *University of Missouri-Kansas City*
Lyndia C. Wu, *University of British Columbia*

Maple Lawn C

11:30AM **Real-Time Segmentation, Virtual Image Modification, Surgical Intervention Modeling and 3D Printing (REVISIT-3D): A Treatment Planning Workflow for Congenital Heart Disease**
Robert McCarthy[1], Kasey Chaszczewski[2,3], John LaDisa[1,2,3,4]
[1]Marquette University and the Medical College of Wisconsin, [2]Pediatric Cardiology, Medical College of Wisconsin, [3]Herma Heart Institute, Children's Wisconsin, [4]Cardiovascular Medicine

11:45AM **Vascular Model Generation With the Space Colonization Algorithm**
Daniel Emerson, Yoed Rabin, Levent Burak Kara
Carnegie Mellon University

12:00PM **Optimal Lattice Geometry for Implementation in Scoliotic Braces**
Robert Rizza[1], Xue-Cheng Liu[2], Vince Anewenter[1]
[1]Milwaukee School of Engineering, [2]Medical College of Wisconsin

12:15PM **Virtual Prostate Cancer Biopsies Using Adc Targeted Lesions Shows Superior Performance Than T2 and Non-Mr Guided Surgical Sampling**
Savannah Duenweg[1], Samuel Bobholz[1], Allison Lowman[1], Aleksandra Winiarz[1], Biprojit Nath[1], Kenneth Iczkowski[2], Kenneth Jacobsohn[1], Peter LaViolette[1]
[1]Medical College of Wisconsin, [2]University of California, Davis

12:30PM **Perfusion Optimization in Engineered Microvessel Network Design**
Elbert Heng, Lazaros Papamanolis, Alyssa Garrison, Daniel Alnasir, Weiguang Yang, Zachary Sexton, Aravind Krishnan, Alison Marsden, John MacArthur
Stanford University

12:45PM **Comparison of Computational Models for Predicting Leaching From Implanted Medical Devices**
Martin L. Tanaka[1], David M. Saylor[2], Robert M. Elder[2]
[1]Western Carolina University, [2]US Food and Drug Administration

Emerging Topics in Soft Tissue Mechanics

Session Chairs: **Sara Roccabianca**, *Michigan State University*
Mona Eskandari, *University of California*

Maple Lawn B

11:30AM **High-Speed Cardiac Pressure Volume Simulations Using A Novel Neural Network Finite Element Approach**
Shruti Motiwale, Michael Sacks
University of Texas at Austin

11:45AM **Mouse Lung Emphysematous Mechanical Strains Under Positive Versus Negative Pressure Ventilation**
Talyah Nelson, Kathrine Quiros, Mona Eskandari
University of California, Riverside

12:00PM **Artificial Intelligence Assisted Multiscale Lung Modeling to Predict Alveolar Septal Wall Stress**
Sunder Neelakantan[1], Raza Mehdi[1], Bradford Smith[2], Kyle Myers[1], Rahim Rizi[3], Reza Avazmohmammadi[1]
[1]Texas A&M University, [2]University of Colorado Denver, [3]University of Pennsylvania

12:15PM **Concentric Contraction During Unloading Prevents Strain Softening in the Mouse Urinary Bladder**
Tyler Tuttle[1], Daniel Deuel[1], Sara Roccabianca[2], Sarah Calve[1]
[1]University of Colorado, [2]Michigan State University

12:30PM **Employing Micro-Computed Tomography to Elucidate Hypoxanthine-Induced Alterations in Bladder Wall Geometry**
Fatemeh Azari[1], Lori Ann Birder[2,^], Amanda Sue Wolf-Johnston[2], Ricardo Cardozo[1], Anne M. Robertson[1,*]
[1]University of Pittsburgh, [2]University of Pittsburgh,

12:45PM **Infants Sucking Patterns Identification Using Machine Learning**
Abdullahi Olapojoye, Fatemeh Hassanipour, Abishek Pratap Singh
University of Texas at Dallas

Wednesday, June 12	11:30AM–1:00PM CDT

Emerging Topics in Tissue & Cellular Engineering

Session Chairs: **Victor Varner**, *University of Texas at Dallas*
Soham Ghosh, *Colorado State University*

Loramoor B

11:30AM **Characterization of Biomaterial Interfaces for Cranial Phantoms to Investigate Traumatic Brain Injury**
Anthony Baker[1], Natalie Smith[2], Suhas Vidhate[3], Ricardo Mejia-Alvarez[3], Zane Lybrand[2], Tony Yuan[4], Adam Willis[3,5], Michaelann Tartis[1]
[1]New Mexico Institute of Mining and Technology, [2]Texas Woman's University, [3]Michigan State University, [4]Uniformed Services University of Health Sciences, [5]59th Medical Wing

11:45AM **Assessment of DNA Motility Within Local Nuclear Area Through Telomere Motion Analysis**
Masashi Yamazaki[1,2], Bansei Andoshiro[2], Hiromi Miyoshi[1,2], Satoshi Ii[1,2], Naoya Sakamoto[1,2]
[1]Faculty of Systems Design, Tokyo Metropolitan University, [2]Tokyo Metropolitan University

12:00PM **Characteristics of Resolvable Polymers Used for Developing in Utero Fetal Valve Replacements**
Sanchita Bhat, Julia Toma, Lakshmi Prasad Dasi
Georgia Institute of Technology

12:15PM **Lympho-Vascularized Breast-Skin Platform for Modeling Lymphovascular Space Invasion in Advanced Breast Cancer**
Melika Mehrabi Dehdezi, Marissa Nichole Rylander
University of Texas at Austin

12:30PM **Profibrotic and Myofibroblast Activation Gene Expression in Right Ventricular Cardiac Fibroblasts in Pulmonary Arterial Hypertension**
Giuditta Monti, Yufan Lin, Daniela Valdez-Jasso
University of California San Diego

12:45PM **Incubation in Physiologically Relevant Oxygen Conditions Changes Lymphatic Endothelial Cell Gene Expression and Vessel Morphology**
Ellie Johandes, Donny Hanjaya-Putra
University of Notre Dame

Growth, Remodeling, and Repair

Session Chairs: **Pat Alford**, *University of Minnesota*
Adrian Buganza Tepole, *Purdue University*

Maple Lawn A

11:30AM **Multiscale Model Predicts Modulation of Cardiac Remodeling by Intrinsic Ventricular Contractility Before and After Mitral Valve Repair**
Johane Bracamonte[1], Lamario Williams[1], Brett Cooke[1], Rongbing Xie[1], Panayotis Vardas[1], Betty Pat[1], Louis Dell'Italia[1], Lionel Watkins[2], Jeffrey Saucerman[2], Jeffrey Holmes[1]
[1]University of Alabama at Birmingham, [2]University of Virginia

11:45AM **Biomechanical and Compositional Changes in the Murine Uterus With Age**
Mari Domingo[1], Triniti Vanoven[1,2], Raffaella De Vita[3], Maria Florian-Rodriguez[2], Isaac Pence[1,2], Kristin Miller[1,2]
[1]University of Texas at Dallas, [2]University of Texas Southwestern Medical Center, [3]Virginia Tech

12:00PM **Micromechanics and Mechanoresponsivity of the Developing Porcine Meniscus**
Meghan E. Kupratis[1], Yuqi Zhang[1], Jiaqi Xiang[2], Byan Kwok[1], Elisabeth A. Lemmon[1], Karen Xu[1], Nathaniel A. Dyment[1], Lin Han[2], Eiki Koyama[3], Robert L. Mauck[1]
[1]University of Pennsylvania, [2]Drexel University, [3]Children's Hospital of Philadelphia

12:15PM **Localized Growth Rate Analysis on a Global Ensemble Averaging of Abdominal Aortic Aneurysm Growth**
Pratik Mitra[1], Juan C. Restrepo[1], Merjulah Roby[1], Satish C. Muluk[2], Mark K. Eskandari[3], Seungik Baek[4], Ender A. Finol[1]
[1]University of Texas at San Antonio, [2]Allegheny Health Network, [3]Northwestern University School of Medicine, [4]Michigan State University

12:30PM **Coupling Systems Biology and Kinematic Growth in Open-Source Finite Element Software**
Steven LaBelle[1], Mohammadreza Sadrabadi[2], Seungik Baek[3], Mohammad Mofrad[4,5], Jeffrey Weiss[1], Amirhossein Arzani[1]
[1]University of Utah, [2]Northern Arizona University, [3]Michigan State University, [4]University of California, Berkley, [5]University of California, Riverside

12:45PM **Influence of In-Vitro Tissue Culturing Conditions on the Properties of Tissue-Engineered Heart Valves - A Computational Analysis**
Elmer Middendorp[1], Justina Ghebryal[1], Valery Visser[2], Polina Zaytseva[2], Sarah Motta[2], Simon Hoerstrup[2,3], Max Emmert[2,3,4], Frank Baaijens[1], Sandra Loerakker[1]
[1]Eindhoven University, [2]Institute for Regenerative Medicine (IREM), University of Zurich, [3]ETH Zurich, [4]German Heart Center Berlin

Wednesday, June 12	11:30AM–1:00PM CDT

Novel Approaches to Bioengineering Education and Outreach

Session Chairs: **Alan Eberhardt**, *University of Alabama at Birmingham*
Jifu Tan, *Northern Illinois University*

Linwood

11:30AM **Students' Perceptions on Using Generative Artificial Intelligence (GAI) in Engineering Courses**
Victor Lai
University of Minnesota - Duluth

11:45AM **Increasing Students' Exposure to Research Via Applied Homework Problems Integrated in Research Manuscripts**
Sean Harrington, Turner Jennings, Ana Vargas, Frederick Sebastian, Rouzbeh Amini
Northeastern University

12:00PM **Fostering STEM Engagement: Building a Collaborative Partnership Between a Research University and Local High School**
Ryan Castile[1], Jamie Jobe[2], Leanne Iannucci[1], Rebecca Reals[1], Shawn Pavey[1], Jon Fitzgerald[2], Spencer Lake[1]
[1]Washington University, [2]Pattonville High School

12:15PM **Immersion, Innovation, Design & Development (I2D2): A 9-Week Summer Experience in Biomedical Bngineering**
Alan Eberhardt
University of Alabama at Birmingham

12:30PM **A 'Dinner Party' Themed Approach to Constructing Equitable and Exciting Literature Reviews**
Daniel Pearce, Corinne Henak
University of Wisconsin-Madison

12:45PM **Establishing a Comprehensive Collection of Ethics Resources for BMES at the Online Ethics Center: Assessing and Structuring Mentoring Resources**
Anjelyka Fasci[1], Sanjana Prashanth[2], Andrew Brightman[2], Lyle Hood[1]
[1]University of Texas at San Antonio, [2]Purdue University

Wednesday, June 12	3:45PM–5:00PM CDT

Translational Technology Pitch Competition

Session Chair: Lyle Hood, *University of Texas, San Antonio* **Maple Lawn C**

3:45PM **A Rapid Novel Assay for Measuring Hemoglobin-Oxygen Affinity**
Rucha Natu[1], Zoe Sekyonda[1], Yuxuan Du[1], John Hinshaw[2], Peter Galen[2], Umut Gurkan[1,2]
[1]Case Western Reserve University, [2]Hemex Health Inc

4:00PM **From Light to Relief: Revolutionizing Pain Management With Optical Blood-Spinal Cord Barrier Modulation**
Harsh Dave[1], Tiffany Leong[1], Eric David[1], Theodore Price[1,1], Zhenpeng Qin[1,1]
[1]University of Texas at Dallas

4:15PM **YoungHeartValve - Next Generation Heart Valve Technology**
Lakshmi Dasi[1], Srujana Joshi[1], Justin Gangwish[2], Nipa Khair[2], Susan James[2]
[1]Georgia Institute of Technology, [2]Colorado State University

4:30PM **Pulse Electric Field Treatment Induced Angiogenesis as a Promising Therapy for Diabetic Foot Ulcers**
Neeraj Raghuraman Rajagopalan, Govindarajan Srimathveeravalli
University of Massachusetts Amherst

4:45PM **Tapping Into Ligament Tension With Our Ligament Tensiometer to Enhance Outcomes Following Total Knee Arthroplasty**
Lesley Arant, Josh Roth
University of Wisconsin - Madison

Emerging Topics in Computational Modeling and Imaging in Soft Tissue Mechanics

Session Chairs: **Maria Holland**, *University of Notre Dame*
Emma Lejeune, *Boston University*

Linwood

8:00AM **The Mechanical Loading of the Murine Uterus and Cervix in Early Pregnancy**
Abigail Laughlin[1], Joy Vink[2], Steven Abramowitch[3], Kristin Miller[4], Raffaella De Vita[5], Kristin Myers[1]
[1]Columbia University, [2]University of Hawaii, [3]University of Pittsburgh, [4]University of Texas at Dallas, [5]Virginia Tech

8:15AM **Automated Full-Field Mechanical Analysis of Cardiac Microbundles**
Hiba Kobeissi, Emma Lejeune
Boston University

8:30AM **Low-Energy Impact Induced Damage in Cartilage: A Multiscale Modeling Study Using FE2M**
Kosar Safari, Ashkan Almasi, Phoebe Szarek, David M. Pierce
University of Connecticut

8:45AM **Lamina Cribrosa Vascular Network Analysis: Associations Between Structural and Functional Parameters**
Yuankai Lu[1], Hua Yi[2], Ruhani Gill[1], Andrew Theophanous[1], Po-Yi Lee[1], Ian Sigal[1,1]
[1]University of Pittsburgh, [2]University of Mississippi

9:00AM **Image-Based Patient-Specific Modeling of Human Stomach Electromechanics**
Lei Shi[1], Qi Zhao[2], Yurui Chen[3]
[1]Kennesaw State University, [2]Shandong Provincial Hospital, [3]Columbia University

Joint Biomechanics

Session Chairs: **Brianne Connizzo**, *Boston University*
Ken Fischer, *University of Kansas*

Maple Lawn B

8:00AM **Functional-Aggregate Method for Objective Determination of Vertebral Coordinate Systems**
Tara Nagle, Jeremy Loss, Rob Colbrunn
Cleveland Clinic Foundation

8:15AM **Sensor Fusion Algorithm to Improve Accuracy of Robotic Superposition Testing Using a 6-DOF Position Sensor**
Callan Gillespie[1], Lesley Arant[2], Tara Nagle[1], Joshua Roth[2], Robb Colbrunn[1]
[1]Cleveland Clinic, [2]University of Wisconsin-Madison

8:30AM **Characterization of the Mechanical and Compositional Effects of MMP-9 Exposure on Neuron-Collagen Constructs: Implications for Joint Degeneration**
Chang Wang, Michelle Meyers, Prabesh Ghimire, Mistica Lozano Perez, Beth Winkelstein
University of Pennsylvania

8:45AM **A Biomechanical Evaluation of Two Internal Fixation Methods With Different Screw Directions for Capitellum Fractures**
Hui Zhang, Justin Hellwinkel, Kiran Agarwal-Harding, Thomas Gardner, Susanne Roberts
Columbia University

9:00AM **Biomechanical Analysis of Dual Mobility Intraprosthetic Dissociation**
Joshua Bland, Alexander Hooke, Allison Tanner, Katherine Mallett, Sergio Gaurin-Perez, James Fitzsimmons, Chunfeng Zhao, Michael Taunton, Rafael Sierra
Mayo Clinic

9:15AM **In Situ Robotic Mechanical Testing of Rat Tibiofemoral Joints**
Olivia Dyer, Stephanie Cone
University of Delaware

Machine Learning: Computational Modeling & Predicting Patient Outcomes

Session Chairs: **Luke Mattar**, *University of Pittsburgh*
Jeremy Warren, *University of Texas at Dallas*

Maple Lawn C

8:00AM **Machine Learning Mediated Prognosis of Major Adverse Cardiac Event (MACE) for Patients With Coronary Artery Dysfunction Using Pressure Drop Coefficient**
Israel Ajiboye, Rao Marepalli, Rupak Banerjee
University of Cincinnati

8:15AM **A Novel Diffusion Tensor Myocardial Material Model Using Neural Networks for Form Determination**
Benjamin Thomas, Christian Goodbrake, Michael Sacks
Oden Institute for Computational Engineering and Sciences

8:30AM **Advancing 3D Organ Geometric Reconstruction From MRI: A Hybird Framework With Deep Learning and Iterative Optimization**
Hui Wang[1,2], Xiaowei Li[3], Chenxin Zhang[1,2], Jianwei Zuo[1,2], Xiuli Sun[3], Jianliu Wang[3], Jiajia Luo[1,2]
[1]Peking University Health Science Center, [2]Peking University, [3]Peking University People's Hospital

8:45AM **Computational Modeling and Machine Learning Methods to Predict Patient-Specific Healing Following Breast-Conserving Surgery**
Zachary Harbin[1], Alexander Argyros[1], Carla Fisher[2], Sherry Voytik-Harbin[1], Adrian Buganza Tepole[1]
[1]Purdue University, [2]Indiana University

9:00AM **Role of Physics-Informed Constraints in Real-Time Assessment of 3D Vascular Fluid Dynamics Via Multi-Case Deep Learning Neural Network**
Wei Xuan Chan, Wenhao Ding, Binghuan Li, Hong Shen Wong, Choon Hwai Yap
Imperial College London

9:15AM **Super-Resolving and Denoising 4D Flow MRI of CSF Using a Physics-Guided Temporally Coherent Neural Network**
Neal Patel, Sriram Baireddy, A.J. Schwichtenberg, Edward Delp, Vitaliy Rayz
Purdue University

Mechanobiology and Engineering of Musculoskeletal Soft Tissues

Session Chairs: **Deva Chan**, *Purdue University*
Ed Sander, *University of Iowa*

Maple Lawn A

8:00AM **Effects of Spontaneous Calcium Signaling on Cartilage Anabolic Activities**
Ying Peng, Annie Porter, Steven DiStefano, X. Lucas Lu
University of Delaware

8:15AM **Female Anterior Cruciate Ligaments Exhibit A Minimal Mechanobiological Response to Mechanical Loading**
Lauren Paschall, Maxwell Konnaris, Aman Dhawan, Erdem Tabdanov, Ilias Georgakopoulos-Soares, Spencer Szczesny
Pennsylvania State University

8:30AM **In Vitro Assessment of Metformin Treatments for Cartilage Injury**
Hessam Noori-Dokht[1,2], Taylor Williams[1], Sogol Younesi[2], Diane Wagner[1]
[1]Indiana University, [2]Purdue University

8:45AM **The Effect of Hyaluronic Acid and Proteoglycan on the Centrifugally Compressed Cell-Collagen Combined Construct (C6)**
Kazuki Moribe, Xu Ye, Masashi Yamazaki, Hiromichi Fujie
Tokyo Metropolitan University

9:00AM **An Engineered In VitroModel of the Human Myotendinous Junction** Mitchell Josvai, Erzsebet Polyak, Meghana Kalluri, Samantha Robertson, Wendy Crone, Masatoshi Suzuki
University of Wisconsin-Madison

9:15AM **Neocartilage Cellular Morphology and Strain Profiles Are Improved by Physiologic TGF-β Doses**
Yifan Peng, Tianbai Wang, Sedat Dogru, Celina Maldonado, Michael Albro
Boston University

Thursday, June 13	8:00AM–9:30AM CDT

Mechanobiology and Fluid Mechanics in the Setting of Disease

Session Chairs: **Ruihang (Rita) Zhang**, *University of Minnesota*
Colleen Witzenburg, *University of Wisconsin-Madison*

Loramoor C

8:00AM **Uniform Growth Laws Recapitulate Some Aspects of Ascending Aortic Aneurysm Progression in the FbInSMKO Mouse**
Marisa Bazzi, Hadi Wiputra, Victor Barocas
University of Minnesota

8:15AM **Morphological and Hemodynamic Changes to the Right Ventricular Microvascular Network in Response to Chronic Pressure Overload**
Ilham Essafri[1], Kenzo Ichimura[2], Kurt Stenmark[1], Edda Spiekerkoetter[2], Vitaly Kheyfets[1]
[1]University of Colorado, Anschutz Medical Campus, [2]Stanford University

8:30AM **Co-Mapping of Smooth Muscle Cell Actin and Hemodynamics in Intact Human Intracranial Aneurysm**
Yasutaka Tobe[1], Anne Robertson[1], Mehdi Ramezanpour[1], Juan Cebral[2], Simon Watkins[1], Fady Charbel[3], Sepideh Amin-Hanjani[4], Alexander Yu[5], Boyle Cheng[6], Henry Woo[7]
[1]University of Pittsburgh, [2]George Mason University, [3]University of Illinois at Chicago, [4]University Hospital Cleveland Medical Center, [5]Allegheny Health Network, [6]Director of Translational Research, Neuroscience and Orthopedic Institutes, Allegheny Health Network, [7]Donald and Barbara Zucker School of Medicine at Hofstra Northwell

8:45AM **Elevated VWF Levels Drive Thrombus Instability**
Ava Obenaus[1], Dang Truong[1], Derek Macatangay[1], Annie Ke[1], Junmei Chen[2], José López[2], Nathan Sniadecki[1]
[1]University of Washington, [2]Bloodworks Northwest Research Institute

9:00AM **Presence of Red Blood Cells Promotes Stretching and Cleavage of Von Willebrand Factor in Whole Blood Under High Shear**
Rukiye Tuna[1], Alice Liu[2], David Bark[2], Z. Leonardo Liu[1]
[1]FAMU-FSU College of Engineering, [2]Washington University School of Medicine

9:15AM **Coronary Height and Peak Systolic Velocity as Main Predictors of Post-TAVR Thrombosis**
Fateme Esmailie[1], Aniket Venkatesh[2], Hoda Hatoum[3], Huang Chen[4], Breandan Yeats[2], BeomJun Lee[2], Philipp Ruile[5], Franz-Josef Neumann[5], Lakshmi Prasad Dasi[2]
[1]University of North Texas, Denton, [2]Georgia Institute of Technology, [3]Michigan Technological University, [4]University of Nevada, [5]Medical Center - University of Freiburg

Mineralized & Soft Tissue Mechanics & Modeling

Session Chairs: **Jacqueline Cole**, *NC State and UNC Chapel Hill*
Megan Killian, *University of Michigan*

Loramoor A

8:00AM **Probable Relation Between Structure & Composition of the Dentin-Enamel Junction (DEJ) & Dentinogenesis Imperfecta (DGI)**
Sobhan Katebifar[1,1], Kai Clark[1], Bradley Rosenberg[1], Michael Truhlar[1], Alix Deymier[1,1]
[1]UConn Health

8:15AM **Ovine Fracture Healing Is Robust to High Gap Strain: A Virtual Mechanical Testing and Image Colocalization Analysis**
Maham Tanveer, Hannah Dailey
Lehigh University

8:30AM **Cam Morphology and Sex-Based Differences in the Proximal Femur Anatomy of Collegiate Athletes Without Hip Pain: A Three-Dimensional Statistical Shape Modeling Analysis**
Bergen Braun, Andrew Anderson
University of Utah

8:45AM **Medial Iliofemoral Ligament Strain and Orientation Following THA Implantation Correlate With Its Ability to Contribute to Hip Stability**
Clarisse Zigan, Jennifer Bido, Kathleen Meyers, Jose Rodriguez, Timothy Wright, Fernando Quevedo Gonazalez
Hospital for Special Surgery

9:00AM **Physeal-Sparing ACL Reconstruction Provides Better Initial Joint Stability and Function Than Complete Transphyseal ACL Reconstruction in an Early Adolescent Porcine Model**
Yukun Zhang[1], Kaan Gurbuz[2], Jeffrey Spang[3], Matthew Fisher[1,3]
[1]North Carolina State University and University of North Carolina at Chapel Hill, [2]Kayseri State Education & Research Hospital, [3]University of North Carolina at Chapel Hill

9:15AM **Investigating Nonlinear Intrinsic Viscoelasticity of Collagen Type II in Immature Bovine Articular Cartilage**
Kimberly Kroupa[1], Jeffrey Weiss[2], Gerard Ateshian[1]
[1]Columbia University, [2]University of Utah

Thrombosis, Hemolysis & Mechanical Circulatory Support

Session Chairs: Bryan Good, *University of Tennessee* **Loramoor B**
John LaDisa, *Marquette University and the Medical College of Wisconsin*

8:00AM **In Vitro Fluid Mechanics and Blood Study to Evaluate Catheter-Related Thrombosis**
Hannah Palahnuk[1], Boyang Su[1], Thaddeus Harbaugh[2], Elias Rizk[2], Sprague Hazard[2], Jonathan Bernstein[3], Keefe Manning[1,2]
[1]Pennsylvania State University, [2]Penn State Hershey Medical Center, [3]Penn State Hershey Children's Hospital

8:15AM **Micro-Channels Maintain Endothelial Cell Adhesion Under Physiologic Wall Shear Stress**
Alexander Armstrong[1], Patrick McCarthy[1,2], Alexander Raskin[1], John LaDisa[1,2,3], Brandon Tefft[1]
[1]Medical College of Wisconsin, [2]Marquette University, [3]Herma Heart Institute, Children's Wisconsin

8:30AM **Plaque Length and Stenosis Influence Instantaneous Wave-Free Ratio and Wall Shear Stress**
Arnav Garcha, Noelia Grande Gutiérrez
Carnegie Mellon University

8:45AM **The Balance of Von Willebrand Factor and Platelet Activation in Causing Bleeding in an Aortic Stenosis**
Alice Liu, Katrina Ashworth, Nina Lasky, Yi Qiao, Kimsey Platten, Jorge Di Paola, David Bark
Washington University in St. Louis

9:00AM **Post-TAVR Thrombogenic Risk Comparisons for Bicuspid Aortic Valve Patients Using Novel Fluid-Structure Interaction Approach**
Kyle Baylous[1], Brandon Kovarovic[1], Salwa Anam[1], Ryan Helbock[1], Marvin Slepian[2], Danny Bluestein[1]
[1]Stony Brook University, [2]University of Arizona

9:15AM **Flow and Turbulence Quantification Using 4D Flow Magnetic Resonance Imaging in a Pulsatile Total Artificial Heart**
Twan Bakker[1], Azad Najar[1,2], Thomas Finocchiaro[3], Ina Laura Perkins[3], Jonas Lantz[1], Tino Ebbers[1]
[1]Linköping University, [2]Scandinavian Real Heart AB, [3]Scandinavian Realheart AB

Thursday, June 13	11:00AM–12:30PM CDT

PhD SPC: Biotransport, Human Motion, Reproductive, and Other Emerging Topics

Session Chairs: **Ottman Teruliano**, *University of Pennsylvania*
Alix Deymier, *UConn Health*

Loramoor A

11:00AM **Enzyme- and Compartment-Free Single Protein Detection by Digital Plasmonic Nanobubble**
Tingting Zhang[1], Ye Gao[1], Yaning Liu[1], Zhenpeng Qin[1,2]
[1]University of Texas at Dallas, [2]University of Texas at Southwestern Medical Center

11:15AM **The Fate of Ultrasmall Fluorescent Silica Nanoparticles as Drug Delivery Vehicles in Cartilage Explants: Differential Retention Kinetics Between Matrix and Chondrocytes**
Aiyana Fortin, Antonio Garces, Ulrich Wiesner, Lawrence Bonassar
Cornell University

11:30AM **Generic Versus Personalized Foot-Ground Contact Models- Is Personalization Worth the Effort?**
Spencer Williams, Kayla Pariser, Claire Hammond, Benjamin Fregly
Rice University

11:45AM **Ex Vivo Minoxidil Treatment Increases Elastic Fiber Deposition in the Murine Vaginal Wall**
Niyousha Karbasion[1], John Caleb Snider[1], Savannah Chatman[1], Kristin Miller[2], Matthew Bersi[1]
[1]Washington University in St. Louis, [2]University of Texas at Dallas

12:00PM **Mechanistic Model of Biochemical-Biomechanical Crosstalk in Vascular Endothelial Cell Alignment**
Shannon Flanary, Victor Barocas
University of Minnesota

12:15PM **Deep Learning-Based Biomechanical Characterization of Infarcted Myocardium From Strain Imaging**
Rana Raza Mehdi, Tanmay Mukherjee, Emilio Agustin Mendiola, Sunder Neelakantan, Reza Avazmohammadi
Texas A&M University

Thursday, June 13	11:00AM–12:30PM CDT

PhD SPC: Heart Valves, Devices, and Computational Fluid Mechanics

Session Chairs: **Alejandro Roldán-Alzate**, *University of Wisconsin-Madison*
Marisa Bazzi, *University of Minnesota*

Loramoor C

11:00AM **Changes in Gene Spatial Expression, Structure, and Function in Response to Altered Mechanical Stress in a Murine Model of Bicuspid Aortic Valve**
Hail Kazik, Julie Kessler, Carol Mattern, Joy Lincoln, John LaDisa
Medical College of Wisconsin

11:15AM **Feasibility and Post-Procedural Risk Analysis of Redo-Transcatheter Aortic Valve Replacement: A Patient-Specific Fluid-Structure Interaction Based Study**
Symon Reza, Brandon Kovarovic, Danny Bluestein
Stony Brook University

11:30AM **Assessment of Aortic Valve Stenosis Using a Novel Functional Index: a Pilot Prospective Study for Trans-Catheter Aortic Valve Replacement Patients**
Shreyash M. Manegaonkar[1], Mohamed A. Effat[1], Marepalli Rao[2], Rishi Sukhija[1], Rupak K. Banerjee[3]
[1]University of Cincinnati, [2]Environmental & Public Health Sciences, University of Cincinnati, [3]University of Cincinnati, Veterans Affairs Medical Center

11:45AM **Parametric Investigation of a Bioprinted Pulsatile Fontan Conduit**
Zinan Hu[1], Jessica Herrmann[1], Erica Schwarz[2], Fannie Gerosa[1], Nir Emuna[2], Jay Humphrey[2], Tain-Yen Hsia[3], Mark Skylar-Scott[1], Alison Marsden[1]
[1]Stanford University, [2]Yale University, [3]Arnold Palmer Hospital for Children

12:00PM **Prediction of Pressure Drop Across Aortic Coarctation During Exercise Using a Hybrid Mock Circulatory Loop**
Priya Nair[1], Emanuele Perra[2], Doff McElhinney[1], Alison Marsden[1], Daniel Ennis[1], Seraina Dual[2]
[1]Stanford University, [2]KTH Royal Institute of Technology

12:15PM **Enhancing 4D-Flow MRI With Input-Parametrized Physics-Informed Neural Network (IP-PINN)**
Amin Pashaei Kalajahi[1], Omid Amili[2], Amirhossein Arzani[3], Roshan D'Souza[1]
[1]University of Wisconsin-Milwaukee, [2]University of Toledo, [3]University of Utah

PhD SPC: Musculoskeletal, Joint, and Spine Solid Mechanics

Session Chairs: **Daniel Cortes**, *Penn State University*
Caitlyn Collins, *Virginia Tech*

Maple Lawn B

11:00AM **Benefits of Using Functional Joint Coordinate Systems in In Vitro Knee Testing**
Tara Nagle[1,2], Jeremy Loss[1], Callan Gillespie[1,2], Robb Colbrunn[1,2]
[1]Cleveland Clinic Foundation, [2]Cleveland State University

11:15AM **Direct Quantification of Errors in Bone Positions and Ligament Tensions Using the Superposition Technique With a Robotic Testing System**
Lesley Arant, Joshua Roth
University of Wisconsin - Madison

11:30AM **Raman Arthrotomy for IN Vivo Quantitative Monitoring of Cartilage Defect Repair in Equine Stifle Joint**
Erik Ersland[1], Madeline Boyes[2], Keming Yan[1], Li-Hsin Han[3], J. Todd Lawrence[4], Thomas Schaer[2], Mark Grinstaff[1], Brian Snyder[5], Mads Bergholt[6], Michael Albro[1]
[1]Boston University, [2]University of Pennsylvania, [3]Drexel University, [4]Children's Hospital of Philadelphia, [5]Beth Israel Deaconess Medical Center, [6]King's College London

11:45AM **Immobilization and Soft Tissue Injury Are Necessary to Cause Persistent Disability in a Rat Model of Elbow Contracture**
Rebecca Reals[1], Alex Reiter[1,2], Ryan Castile[1], Sophia Miller[1], Spencer Lake[1]
[1]Washington University in St. Louis, [2]Saint Louis University

12:00PM **Loss of Decorin Accelerates Cartilage Surface Damage and Aberrant Fibrous Remodeling During Aging**
Mingyue Fan[1], Bryan Kwok[1], Aanya Mohan[2], Michael Newton[2], Jiaqi Xiang[1], Yuchen Liu[1], Ling Qin[3], David Birk[4], Renato Iozzo[5], Tristan Maerz[2], Robert Mauck[3], Lin Han[1]
[1]Drexel University, [2]University of Michigan, [3]University of Pennsylvania, [4]University of South Florida, [5]Thomas Jefferson University

12:15PM **Influence of Sex and Sex Hormones on Skeletal Responses to Intermittent Parathyroid Hormone (PTH) Treatment and Discontinuation**
Y. Vincent Jin, Wonsae Lee, Tala Azar, Xiaoyu Xu, Kruti Desai, Wei-Ju Tseng, X. Sherry Liu
University of Pennsylvania

PhD SPC: Platelets and Cardiovascular Biomechanics

Session Chairs: **Noelia Gutierrez**, *Carnegie Mellon University*
Bryan Good, *University of Tennessee*

Loramoor B

11:00AM **Shear-Induced Platelet Aggregation Is Mediated by vWF-Binding Receptors in A Stenotic Model**
Connor Watson[1], Christopher Siedlecki[1,2], Keefe Manning[1,2]
[1]Pennsylvania State University, [2]Penn State Hershey Medical Center

11:15AM **A Micromechanics Based Multiscale Model for Platelet-Driven Clot Contraction**
Chayut Teeraratkul, Debanjan Mukherjee
University of Colorado, Boulder

11:30AM **The Biomechanics of Radiation-Induced Cardiotoxicity in Mice**
Tanmay Mukherjee[1], Sarah Elliott[2], Prasanna Alluri[2], Reza Avazmohammadi[1]
[1]Texas A&M University, [2]University of Texas Southwestern Medical Center

11:45AM **Investigating the Influence of Lactation on Murine Heart Growth Through Ultrasound and Computational Analysis**
Molly Kaissar[1], Arden Shen[2], Jennifer Anderson[2,3], Elnaz Ghajar-Rahimi[2], Adalyn Meeks[2], Craig Goergen[2], Kyoko Yoshida[1]
[1]University of Minnesota, [2]Purdue University, [3]University of Vermont

12:00PM **Dynamic Imaging of the Collagenous Myocardial Extracellular Matrix During Post-Infarction Inflammation**
Daniel Pearce, Colleen Witzenburg
University of Wisconsin-Madison

12:15PM **Microstructural Alterations in the Murine Thoracic Aorta: Unveiling a Mechanism for Biomechanical Remodeling in Late-Gestation Pregnancy**
Ana Vargas, Turner Jennings, Rouzbeh Amini, Chiara Bellini
Northeastern University

PhD SPC: Tissue Engineering, Development, Mechanobiology, and Other Emerging Topics

Session Chairs: **Meghan Kupratis**, *University of Pennsylvania*
Jason Szafron, *Carnegie Mellon University*

Linwood

11:00AM **Rhythmic Nephron Progenitor Renewal and Differentiation Informs Kidney Tissue Engineering Strategies**
Samuel Grindel, Sachin Davis, John Viola, Grace Liu, Jiageng Liu, Grace Qian, Catherine Porter, Alex Hughes
University of Pennsylvania

11:15AM **Tailored Delivery of A Small Molecule Agonist for Hedgehog Signaling Activation in Tendon-to-Bone Integration**
Jonathan Marcelin, Rashad Madi, Timur Kamalitdinov, Xi Jiang, Dong Hwa Kim, Robert Mauck, Andrew Kuntz, Nathaniel Dyment
University of Pennsylvania

11:30AM **Scleraxis-Targeted Deletion of Non-Muscle Myosin Leads to Tendon Degeneration**
Mary Kate Evans[1], Ellie Bernstein[1], Tonia Tsinman[1], Ellie Ferguson[1], Xi Jiang[1], Joel Boerckel[1], Lin Han[2], Eiki Koyama[3], Robert Mauck[1], Nathaniel Dyment[1]
[1]University of Pennsylvania, [2]Drexel University, [3]Orthopaedic Biomedical Research, Children's Hospital of Philadelphia

11:45AM **Reduced Loading After Sciatic Nerve Resection Impairs Hindlimb Growth and Maturation**
Talayah Johnson[1], Natalie Fogarty[1], Alisia Lin[1], Xi Jiang[1], Eiki Koyama[2], Lin Han[3], Josh Baxter[1], Joel Boerckel[1], Robert Mauck[1], Nathaniel Dyment[1]
[1]University of Pennsylvania, [2]Children Hospital of Philadelphia, [3]Drexel University

12:00PM **Cell-Extracellular Matrix Feedback Results in Spontaneous Cellular Orientation and Contact Guidance Behavior in 3D Discrete Fiber Models of Cell Compaction**
Adam Ley, Lauren Bersie-Larson, Ryan Collanton, Sabin Adhikari, Robert Tranquillo, Kevin Dorfman, Victor Barocas
University of Minnesota, Twin Cities

12:15PM **Logic-Based Cell Signaling Model for Predicting Vascular Smooth Muscle Cell Contractility During Pregnancy**
Paige Nielsen, Yusheng Wu, Kyoko Yoshida
University of Minnesota

Thursday, June 13	11:00AM–12:30PM CDT

PhD SPC: Neural, Lung, and Developmental Solid Mechanics

Session Chairs: **Sara Moshage**, *University of Illinois at Urbana-Champaign*
Ryan Pedrigi, *University of Nebraska-Lincoln*

Maple Lawn A

11:00AM **Cross-Correlation of Biomechanical, Connectomic, and Pathologic Markers in Neurodegeneration at 7T MRI**
Em Triolo[1], Mackenzie Langan[2], Oleksandr Khegai[2], Sarah Binder[2], Trey Hedden[2], Priti Balchandani[2], Mehmet Kurt[1,2]
[1]University of Washington, [2]Icahn School of Medicine at Mount Sinai

11:15AM **Comparison of Head Impact Biomechanics Across Multiple Sports**
Zaryan Masood, David Luke, Rebecca Kenny, Daniel Bondi, Adam Clansey, Lyndia Wu
University of British Columbia

11:30AM **Associations Between Cerebrovascular Remodeling and Neuropathological Changes in the Brain During Alzheimer's Disease Progression**
Samuel Halvorsen[1], Raymond Nicks[2], Thor Stein[2,3], Katherine Zhang[1]
[1]Boston University, [2]Boston University School of Medicine, [3]US Department of Veterans Affairs

11:45AM **Surfactant Depleted Rat Lungs: A Global to Local Study of the Impact of Positive Versus Negative Pressure Ventilation**
Matthew Shankel, Mona Eskandari
University of California, Riverside

12:00PM **Towards Improved Surgical Sealants by Investigating Human Visceral Pleura Mechanics**
Gustavo Ramirez, Mona Eskandari
University of California, Riverside

12:15PM **Lung Lobar Sliding Reduces Parenchymal Distortion in the Left and Right Lungs**
Adam Galloy, Joseph Reinhardt, Suresh M. L. Raghavan
University of Iowa

Friday, June 14	10:00AM–11:30AM CDT

Undergraduate Design Competition

Session Chair: Anita Singh, *Temple University* **Maple Lawn B**

10:00AM **Soft Robotics for Progressive Vertebrae Rehabilitation**
Rachel Yu, Charmaine Tan, Michelle Haung, Thomas Ho, Jesse Kimie-Brylka, Nathan Ou, Amber Kashay, Ian Morales, Allison Cheng, Sina Ghadimi, Carissa Ott, Evan Zhao
University of California, Los Angeles

10:15AM **Preventing and Detecting Nasogastric Tube Dislodgement in Infant Patients**
Jeffrey Huang, Katherine Han, Stephanie Yoon, Dahin Song
University of Pennsylvania

10:30AM **Reinforcing Safe Walker Use: A Universal 2-Wheel Walker Monitoring Device**
Ashwin Gadiraju, Pradnesh Kolluru, Cecelia Rodriguez, Nick Tsintolas
Duke University

10:45AM **LAPPI: Lip and Palate Prosthetic Interface**
Camilla Whitesel, Serena Carson, Andrea Urdaneta, Ryan Lim, Ravikiran Ramjee
University of Pennsylvania

11:00AM **Sistance: A Two-Way Base Communication System for Deaf-Blind Students**
Mackenzie Hunt, Maxim Hansen, Souleymane Cissokho, Timothy Johnson
Rose-Hulman Institute of Technology

11:15AM **Adaptive Sport Solutions: Assistive Kayak Mount Device for Mobility Impaired Users**
Alex Britton, Megan Parker, Douglas Wingert, Christine Walck
Embry-Riddle Aeronautical University

Friday, June 14	12:45PM–2:15PM CDT

Cardiac Biomechanics

Session Chairs: Lei Fan, *Marquette University*
Colleen Witzenburg, *University of Wisconsin-Madison*

Evergreen I

12:45PM **Right Ventricular Myocardium Remodeling in Pulmonary Arterial Hypertension Is Sex-Specific and Ovarian-Hormone Dependent**
Becky Hardie, Jessica Huberts, Daniela Valdez-Jasso
University of California San Diego

1:00PM **Estrogen, Testosterone, and Mechanics : Modeling Sex-Specific Left Ventricular Remodeling in Heart Failure**
Adhithi Lakshmikanthan[1], Minnie Kay[1], Kenneth Bilchick[2], Anya Grosberg[1], Pim Oomen[1]
[1]University of California, Irvine, [2]University of Virginia

1:15PM **Identifying the Role of the Septum Wall in Right Ventricular Remodeling**
Kristen Garcia, Becky Hardie, Jessica Huberts, Daniela Valdez-Jasso
University of California San Diego

1:30PM **Comparative Analysis of Myocardial Wall Thickness: Insights From MRI-Derived Models and Biomechanical Simulations Across the Cardiac Cycle**
Mohsen Darayi[1], Mary Robakowski[1,2], Yiling Fan[3], Danielle Kara[1], Ojas Potdar[4], Christopher Nguyen[1], Debkalpa Goswami[1]
[1]Cleveland Clinic, [2]Cleveland State University, [3]Massachusetts Institute of Technology, [4]Case Western Reserve University

1:45PM **Patient-Specific Modeling of Left Atrial Electromechanics**
Lei Shi[1], Aaron Brown[2], Fanwei Kong[2], Chen Zhang[3], Hannah Haider[3], Vijay Vedula[3]
[1]Kennesaw State University, [2]Stanford University, [3]Columbia University

2:00PM **A Personalized Multiscale Model of Biventricular Cardiac Electromechanics**
Aaron Brown[1,2], Lei Shi[3], Matteo Salvador[1,2], Fanwei Kong[1,2], Vijay Vedula[4], Alison Marsden[1,2]
[1]Stanford University, [2]Stanford Cardiovascular Institute, [3]Kennesaw State University, [4]Columbia University

Emerging In Vitro, Experimental, and Computational Methods in Fluid Mechanics I

Session Chairs: Grace McIlvain, *Emory University*
Melissa Brindise, *Pennsylvania State University*

Maple Lawn A

12:45PM **Eulerian-Lagrangian Framework for Simulations of Particle-Laden Biological Flows in Complex Geometries**
Abhilash Reddy Malipeddi, Jesse Capecelatro, C. Alberto Figueroa
University of Michigan

1:00PM **Computational Analysis of the Effect of Type B Aortic Dissection on Pulse Wave Velocity and Pulse Waveform Shape**
Marisa Bazzi[1], Hadi Wiputra[2], Rumi Faizer[3], Victor Barocas[2]
[1], University of Minnesota, [2]University of Minnesota, [3]UP Medical

1:15PM **Experimental Validation of 3D Dynamic MRI Using an Ex-Vivo Porcine Model of the Bladder**
James Rice, Michael Stellon, Wade Bushman, Alejandro Roldán-Alzate
University of Wisconsin-Madison

1:30PM **Biphasic Modeling of 9L Glioma: Radiation Treated Versus Untreated**
Isabel Rivera Santiago[1], Malisa Sarntinoranont[1], James R. Ewing[2,3,4,5], Prabhu Acharya[2,4], Glauber Cabral[2], Tavarekere N. Nagaraja[2,3], Stephen L. Brown[3,2]
[1]University of Florida, [2]Henry Ford Hospital, [3]Michigan State University, [4]Oakland University, [5]Wayne State University

1:45PM **Experimental and Computational Modeling of Brain Shunt Performance**
Bryan Good, Ashley Handy, Alyson Matushek, Stephanie TerMaath
University of Tennessee

2:00PM **Spatiotemporal Variations in Blood Velocity and Hematocrit in A Microfluidic Capillary Network**
Solomon Oshabaheebwa, Christopher Delianides, Michael Suster, Pedram Mohseni, Umut Gurkan
Case Western Reserve University

Friday, June 14	12:45PM–2:15PM CDT

Head & Injury Mechanics I

Session Chairs: **Maria Holland**, *University of Notre Dame*
Ken Monson, *University of Utah*

Loramoor C

12:45PM **Strain-Based Cellular Injury Thresholds in a 3D In Vitro Model of Traumatic Brain Injury**
Jessica Park, Annalise Daul, Jing Zhang, Christian Franck
UW-Madison

1:00PM **A Human Organoid Model of Traumatic Brain Injury**
Shahrzad Shiravi[1], Alexandra Yufa[2], Maria Jose Quezada Valladares[3], Colin Franz[3], John Finan[2]
[1]Chicago, [2]University of Illinois at Chicago, [3]Northwestern University

1:15PM **Bridging Gaps in Traumatic Brain Injury Modeling: A Multiscale Approach to Unifying Global and Axonal Injury Models**
Chaokai Zhang[1], Lara Bartels[2], Adam Clansey[2], Julian Kloiber[2], Daniel Bondi[2], Paul van Donkelaar[2], Lyndia Wu[2], Alexander Rauscher[2], Songbai Ji[1]
[1]Worcester Polytechnic Institute, [2]University of British Columbia

1:30PM **Mapping Nonlinear Mechanical Properties of Ex VivoBrain Tissue Using MR Elastography With Applied Pre-Strain**
Olivia Bailey, Alexa Diano, Ali Lateef, Elise Corbin, Curtis Johnson
University of Delaware

1:45PM **Improving Glioma Segmentation Fairness in Low-Resolution Domains With Transfer Learning**
Juampablo Heras Rivera[1], Tianyi Ren[1], Ethan Honey[1], Harshitha Rebala[2], Abhishek Sharma[1], Mehmet Kurt[1]
[1]University of Washington, [2]Computer Science- University of Washington

2:00PM **Exploring the Potential Role of Sex-Based Brain Structural Variations in Susceptibility to Traumatic Brain Injury From a Biomechanics Perspective**
Bahram Jafari, Marzieh Memar
University of Texas at San Antonio

Friday, June 14	12:45PM–2:15PM CDT

Knee Biomechanics

Session Chairs: **Jacob Merson**, *Rensselaer Polytechnic Institute*
Tara Nagle, *Cleveland Clinic Foundation*

Maple Lawn C

12:45PM **Study of the Structures That Limit Combined Abnormal Hyperextension and Abnormal Varus of the Knee**
Rebekah Deardurff[1,2,3], Edward Grood[1,2], Frank Noyes[2,3,4]
[1]University of Cincinnati, [2]Cincinnati SportsMedicine Research and Education Foundation, [3]Cincinnati Sports Medicine and Orthopedic Research, The Jewish Hospital, Mercy Health, [4]Noyes Knee Institute

1:00PM **Towards Validation of Knee-Specific Finite Element Models in A Loaded MRI Condition**
Sean Letendre[1], Kalle Chastain[1], Joshua Leadem[2], Manuela Montes de Oca[2], Lila Pender[2], Madison Lang[2], Erin Leatherman[3], Thomas Santner[4], Kate Lindsey[2], Erin Argentieri[1], Amanda Wach[1], Ashley Pekmezian[1], Sara Sacher[1], Matthew Koff[1], Amy Lerner[2], Scott Rodeo[1], Suzanne Maher[1], Brett Steineman[1]
[1]Hospital for Special Surgery, [2]University of Rochester, [3]Kenyon College, [4]Ohio State University

1:15PM **Longitudinal MRI Analysis of Intratissue Cartilage Strain and Relaxometry in the ACL Reconstructed Knee: A Case Study**
Hongtian Zhu[1], Emily Miller[2], Woowon Lee[1], Timothy Lowe[1], Corey Neu[1,2]
[1]Paul M. Rady University of Colorado, Boulder, [2]University of Colorado, Boulder

1:30PM **Tibial Slope Affects ACL Force and Coupled Internal Tibial Rotation Under A Simulated Clinical Pivot Shift Exam: A Computational Study**
Reza Pourmodheji[1], Mitchell Wheatley[1], Julien Lulec[2], Jacob Hirth[1], Mark Amirtharaj[1], Thomas Wickiewicz[1], Matthieu Olivier[2], Andrew Pearle[1], Danyal Nawabi[1], Carl Imhauser[1]
[1]Hospital for Special Surgery, [2]Aix-Marseille University

1:45PM **Higher Percent Load Through the Intact Meniscus Results in Higher Reduction in Meniscal Loading After Partial Meniscectomy at Heel Strike in Simulated Gait**
Kalle Chastain, Sean Letendre, Heath Gould, Ian Hutchinson, Joshua Wright-Chisem, Arden Wach, Anil Ranawat, Scott Rodeo, Suzanne Maher
Hospital for Special Surgery

2:00PM **Biomechanical Consequences of Ligament Releases During Total Knee Arthroplasty**
Matthew Blomquist, Dylan Schmitz, Joshua Roth
University of Wisconsin-Madison

Friday, June 14	12:45PM–2:15PM CDT

Mechanobiology in Tissue & Cellular Engineering

Session Chairs: **Eno Ebong**, *Northeastern University*
Daniela Valdez-Jasso, *University of California, San Diego*

Maple Lawn B

12:45PM **An Optogenetic Platform for Controlled Release of Nucleocytoplasmic Shuttling Proteins**
Erin Berlew, Paula Camacho Sierra, Joel Boerckel
University of Pennsylvania

1:00PM **TRPV4 Integrates Matrix Mechanosensing to Modulate Calcium Signaling and Mechanobiology in Schlemm'S Canal Cells**
Haiyan Li[1], Seyed Siadat[2], Kristin Perkumas[3], Jacques Bertrand[4], Darryl Overby[4], Todd Sulchek[5], W. Daniel Stamer[3], C.Ross Ethier[1]
[1]Georgia Institute of Technology/Emory University, [2]Northeastern University, [3]Duke University, [4]Imperial College London, [5]Georgia Institute of Technology

1:15PM **Functional Expression of Mechanosensitive Ion Channels in Regenerating Axolotl Limbs**
Vineel Kondiboyina, Melissa Miller, James Monaghan, Sandra Shefelbine
Northeastern University

1:30PM **Pharmaceutical Interrogation of Podocyte Biomechanics Through Kinome Screening**
Jonathan Haydak[1], Anika Hudson[1], Stefanie DeFronzo[2], Yibang Chen[1], Nanditha Anandakrishnan[1], Alan Stern[1], Evren Azeloglu[1]
[1]Icahn School of Medicine at Mount Sinai, [2]Northeastern University

1:45PM **Interaction With Endothelial Cells Induces Vascular Smooth Muscle Cell Orientation Under Wall Shear Stress Condition**
Kaoru Sawasaki[1], Masanori Nakamura[2], Naoyuki Kimura[3], Koji Kawahito[3], Masashi Yamazaki[1], Hiromichi Fujie[1], Naoya Sakamoto[1]
[1]Tokyo Metropolitan University, [2]Nagoya Institute of Technology, [3]Jichi Medical University

2:00PM **Collagen Type-Dependent Extracellular Defect Sensing Driven by Actin Protrusions and Membrane Tension**
Hannah Zmuda, Christopher Walter, Amit Pathak
Washington University in St. Louis

Special Session Honoring Ken Diller

Session Chairs: **Sihong Wang**, *City College of New York*
Chris Rylander, *University of Texas at Austin*

Loramoor A

12:45PM **Thermal Control of Circadian Function for Enhanced Sleep Onset and Blood Pressure Modulation**
Kenneth Diller, Laura Namisnak, Sepideh Khoshnevis
University of Texas

1:00PM **Professor Ken Diller's Impact in Cryobiology and Biomedical Engineering**
Mehmet Toner
Massachusetts General Hospital

1:15PM **Ken Diller and Bioheat Transfer**
John Bischof
University of Minnesota

1:30PM **In Vitro Platforms to Assess the Spatial Response to Burn Injury and Thermoembolization**
S. Brocklehurst, A. Sabaghan, M.N. Rylander
University of Texas, Austin

1:45PM **Rapid Thermal Control of Liquids (RealCooL): Development of a Four-Compartment Transient Heat Transfer Model**
Nadia Hannon, Marissa Rylander, Chris Rylander
University of Texas at Austin

2:00PM **Synergistic Effects of Periodically Mild Hyperthermia and Ultrasound Treatment on Osteogenesis in Aged Human Mesenchymal Stem Cells**
D. Dawkins, Sihong Wong
City College of New York

Friday, June 14	12:45PM–2:15PM CDT

Speech Biomechanics

Session Chairs: **Rana Zakerzadeh**, *Duquesne University*
Byron Erath, *Clarkson University*

Loramoor B

12:45PM **The Influence of Blunt Force Laryngeal Trauma on Phonation: Aerodynamic, Kinematic, and Acoustic Effects**
Md Roknujjaman, Molly E. Stewart, Byron D. Erath
Clarkson University

1:00PM **Insights Into Curved and Incomplete Glottal Closure Patterns: an Euler-Bernoulli Approach**
Mohamed Serry[1], Gabriel Alzamendi[2], Matias Zanartu[3], Sean Peterson[1]
[1]University of Waterloo, [2]CONICET-UNER, [3]Universidad Tecnica Federico Santa Maria

1:15PM **Effect of Type I Thyroplasty Implant Location and Stiffness on Voice Production**
Weili Jiang[1], Mahdi Sangbori[1], Liran Oren[2], Charles de Luzan[2], Ephraim Gutmark[2], Xudong Zheng[1], Qian Xue[1]
[1]Rochester Institute of Technology, [2]University of Cincinnati

1:30PM **Building a Numerical Framework for Energy Budget Analysis of Phonation**
Lucy Zhang
National Science Foundataion

1:45PM **Effects of Semi-Occluded Vocal Tract Exercise on Vocal Fold Biomechanics as Observed During High-Speed Videoendoscopy**
David Ford[1], Dimitar Deliyski[2]
[1]Duquesne University, [2]Michigan State University

2:00PM **Multiphysics Simulation of Flow and Oxygen Transport in a Poroelastic Vocal Fold Model**
Isabella McCollum, Manoela Neves, Rana Zakerzadeh
Duquesne University

Friday, June 14	2:30PM–4:00PM CDT

Biotech and Drug Delivery

Session Chairs: **Marissa Rylander**, *University of Texas at Austin*
Lyle Hood, *University of Texas at San Antonio*

Loramoor A

2:30PM **Evaluation of the Effects of PFAS on Pancreatic Cancer Using A Microfluidic Pancreas Model**
Tarun Singh[1], Sae Choi[1], Barbara Hocevar[2], Lisa Kamendulis[2], Bumsoo Han[1]
[1]Purdue University, [2]Indiana University

2:45PM **Compensating for the Simulated Foreign Body Response to Medical Implants Using Local Fluid Flow**
Lesley Trask[1], Niamh A. Ward[1], Ruth Tarpey[1], Rachel Beatty[1,2], Eimear Wallace[1], Joanne O'Dwyer[1], William Ronan[1], Garry P. Duffy[1,2], Eimear B. Dolan[1]
[1]University of Galway, [2]Trinity College Dublin

3:00PM **A Multiphasic Model for Determination of Mouse Ascending Thoracic Aorta Mass Transport Properties With and Without Aneurysms**
Keshav Kailash, Jessica Wagenseil
Washington University in St. Louis

3:15PM **Pulse-Driven Microfluidic Infusion Pumps With Constant and Heart Rate-Sensitive Flow Rates**
Shuyu Zhang[1], Rafael Davalos[2], Anne Staples[1]
[1]Virginia Tech, [2]Georgia Institute of Technology

3:30PM **Sex Differences in Placenta Villous Structure in Low- and High-Risk Pregnancies**
Adrienne Scott, Patrick Yang, Abigail Arter, Caroline Fosher, Ulugbek Kamilov, Anthony Odibo, Michelle Oyen
Washington University in St. Louis

3:45PM **Characterization of a Polymeric Device for Localized and Controlled Drug Delivery to Cervical Cancer**
Jacob Provencio[1], Monica Elbjorn[1], Paige Phillips[1], David Di Rocco[1], Lyle Hood[1,2]
[1]University of Texas at San Antonio, [2]University of Texas Health Science Center at San Antonio

Friday, June 14	2:30PM–4:00PM CDT

Bone and Cartilage Mechanobiology & Tissue Engineering

Session Chairs: **Alejandro Almarza**, *University of Pittsburgh*
Arun Nair, *University of Arkansas*

Loramoor B

2:30PM **Wnt-11 and SOST Are Regulated by Different Mechanical Stimuli in Loaded Bone**
Meghana Machireddy, Sara Cole, Lucas DeBiase, Jun Li, Glen Niebur
University of Notre Dame

2:45PM **Dynamic Micromechanical Characterization of 3D Printed Bone In Vitro Models Manufactured Via Vat Photopolymerization**
Elizabeth Hunt, Sera Choi, Edward Shangin, Emma Nguyen, Abby Whittington, Caitlyn Collins
Virginia Tech

3:00PM **Magnetic Actuation of Piezo1 Functionalized Superparamagnetic Iron Oxide-Gold Nanoparticles: A Novel Dual Acting Osteogenesis and Anti-Osteopenia Nanomedicine**
Elias Georgas[1], Muzhaozi Yuan[2], Ya Wang[2], Yi-Xian Qin[1]
[1]Stony Brook University, [2]Texas A&M University

3:15PM **Bone Formation Dependance on Microsphere Size in 3D Printed PLGA Microsphere Scaffolds**
Roland Klar, James Cox, Naren Raja, Stefan Lohfeld
University of Missouri-Kansas City

3:30PM **Raman Monitoring of Engineered Cartilage Development Across Different Hydrogel Scaffolds**
Dev Mehrotra[1], Carolina Cordova[1], Erik Ersland[1], Thomas Schaer[2], Mark Grinstaff[1], Brian Snyder[3], Mads Bergholt[4], Michael Albro[1]
[1]Boston University, [2]New Bolton Center, [3]Beth Israel Deaconess Medical Center, [4]King's College London

3:45PM **Investigating Dynamic Loading-Induced Fluid Effects on Bone Cells in 3D**
Kailin Chen[1], Alessandro Maggi[2], Alexander Bolanos-Campos[1], Mistica Perez[1], Michael Abrams[2], Julia Greer[2], Ottman Tertuliano[1]
[1]University of Pennsylvania, [2]California Institute of Technology

Emerging In Vitro, Experimental, and Computational Methods in Fluid Mechanics II

Session Chairs: **Anne Staples**, *Virginia Tech*
Alejandro Roldán-Alzate, *University of Wisconsin-Madison*

Maple Lawn A

2:30PM **Development and Implementation of Novel Framework for Thermofluid Analyses in FEBio**
Raphael Kepecs[1], Steve Maas[2], Jeffrey Weiss[2], Gerard Ateshian[1]
[1]Columbia University, [2]University of Utah

2:45PM **SeqSeg: Automatic Image-Based Vascular Model Construction Using Sequential Segmentations**
Numi Sveinsson Cepero, Shawn C. Shadden
University of California Berkeley

3:00PM **Pre-Surgical Assessments of CSF Flow and Brain Motion Are Indicative of Improved Cerebral Dynamics Following Surgery in Chiari Malformation I**
Grace McIlvain[1], Saeed Mohsenian[2], Mohamad Motaz Al Samman[2], Brice Williams[1], Daniel Barrow[1], Francis Loth[2], John Oshinski[1]
[1]Emory University, [2]Northeastern University

3:15PM **Negative Effort Dependence in Obstructive Sleep Apnea: Insights From a Mathematical Model**
Guilherme Garcia[1,2], B. Tucker Woodson[1]
[1]Medical College of Wisconsin, [2]Marquette University

3:30PM **Temperature Effect on In-Vitro Sinus Flow After Aortic Valve Replacement**
Ahmad Bshennaty[1], Brennan Vogl[1], Agata Sularz[2], Mohamad Alkhouli[2], Hoda Hatoum[1,1]
[1]Michigan Technological University, [2]Mayo Clinic

3:45PM **In Vitro Flow Study of the Penn State Pediatric Total Artificial Heart**
Cody Kubicki[1], Emma Raich[1], Peter Selinsky[1], Sailahari Ponnaluri[1], Steven Deutsch[1], William Weiss[2], Keefe Manning[1,2]
[1]Penn State University, [2]Penn State College of Medicine

Friday, June 14	2:30PM–4:00PM CDT

Emerging Tools for Cell Mechanics

Session Chairs: **Guy Genin**, *Washington University in St. Louis*
Ming Guo, *Massachusetts Institute of Technology*

Maple Lawn C

2:30PM **Myosin-Free Molecular Clutch Model Predicting Myosin-Independent Stiffness Sensing**
Sangyoon Han, Nikhil Mittal
Michigan Technological University

2:45PM **Optimal Design of Experiments for Nuclear Membrane Stiffness Estimation**
Emilio Mendiola[1], Rana Raza Mehdi[1], Jacques Ohayon[2,3], Roderic Pettigrew[1,3], Reza Avazmohammadi[1,3]
[1]Texas A&M University, [2]Savoie Mont-Blanc University, [3]Houston Methodist Research Institute

3:00PM **FRET Measurement of Cellular Tension in Tissues Using Conventional Confocal Microscopy in Newly Established Transgenic Mice Expressing Actinin Tension Sensor**
Takeo Matsumoto[1], Junfeng Wang[1], Eijiro Maeda[1], Yuki Tsujimura[2], Takaya Abe[3], Hiroshi Kiyonari[3], Hideo Yokota[2], Tetsuya Kitaguchi[4]
[1]Nagoya University, [2]RIKEN Center for Advanced Photonics, [3]RIKEN Center for Biosystems Dynamics Research, [4]Tokyo Institute of Technology

3:15PM ***WITHDRAWN*** **Uncovering Electro-Mechano-Physiological Rules of Life: A New 2D/3D All-Optical Interrogation Technology**
Chenyu Liang[1], Erica Hengartner[2], Abygale Cochrane[3], Bruna Balbino de Paula[4], Basak Ayaz[4], Robert Caudle[5], Allison Campbell[6], Eleana Manousiouthakis[6], Christine Schmidt[6], Tian He[7], Christopher Werley[8], Xin Tang[1,6,9]
[1]Mechanical and Aerospace Engineering, University of Florida, [2]Biochemistry, University of Florida, [3]Physics, University of Florida, [4]Neuroscience, University of Florida, [5]Dentistry, University of Florida, [6]University of Florida, [7]BioNTech SE, [8]Vertex Pharmaceuticals, [9]UF Health Cancer Center

3:30PM **Non-Contact Biomechanical Imaging of Cell and Tissue Using Optical Brillouin Microscopy**
Jitao Zhang
Wayne State University

3:45PM **Controlling Cellular Rearrangements in an Epithelial Monolayer Through Micropatterning Techniques**
Molly McCord, Jacob Notbohm
University of Wisconsin - Madison

Friday, June 14	2:30PM–4:00PM CDT

Head & Injury Mechanics II

Session Chairs: **Lyndia Wu**, *University of British Columbia*
Mehmet Kurt, *University of Washington*

Loramoor C

2:30PM **Population-Specific Biomechanical Response of the Brain by Age and Sex**
Ahmed A. Alshareef[1], Aaron Carass[2], Yuan-Chiao Lu[3], Joy Mojumder[4], Ruth J. Okamoto[5], Alexa M. Diano[6], Curtis L. Johnson[6], Dzung L. Pham[3,7], Jerry L. Prince[2], Philip V. Bayly[5]
[1]University of South Carolina, [2]Johns Hopkins University, [3]Henry M. Jackson Foundation, [4]National Institutes of Health (NIH), [5]Washington University in St. Louis, [6]University of Delaware, [7]Uniformed Services University

2:45PM **Sex-Related Variations in Head Impact Kinematics During Controlled Soccer Heading**
Alireza Abbasi Ghiri, Morteza Seidi, Kelly Cheever, Marzieh Memar
University of Texas at San Antonio

3:00PM **A Computational Modeling Approach for the Forensic Analysis of Infant Short Height Falls**
Keith Button, Yun Cai, Luis Nolasco, Brian Weaver
Explico

3:15PM **Detection of Intracranial Cavitation in Polyacrylamide Brain Phantoms Under Blunt Impacts Using Shadowgraph and Acoustic Plane Wave Imaging**
Eric Galindo[1], Ricardo Mejia-Alvarez[2], Michaelann Tartis[1], Adam Willis[2,3]
[1]New Mexico Institute of Mining and Technology, [2]Michigan State University, [3](3) 59th Medical Wing, Office of the Chief Scientist, Lackland AFB

3:30PM **Liver Injuries in Porcine Due to Behind Armor Blunt Trauma**
Parker Berthelson[1], Justin McMahon[1], Alexander Stotka[1], Barney McEntire[2], Robert Salzar[1]
[1]University of Virginia, [2]U.S. Army Aeromedical Laboratory

3:45PM **The Structural and Mechanical Behavior of Skin During Puncture for Different Impactor Sizes and Loading Rates**
Joseph LeSueur[1,2], Carolyn Hampton[3], Jared Koser[1], William Dzwierzynski[1], Michael Kleinberger[3], Frank Pintar[1,2]
[1]Medical College of Wisconsin, [2]Marquette University, [3]Army Research Laboratory

Friday, June 14	2:30PM–4:00PM CDT

Reproductive Biomechanics

Session Chairs: **Matthew Bersi**, *Washington University in St. Louis*
Kyoko Yoshida, *University of Minnesota*

Evergreen I

2:30PM **Impact of Novel Elastomeric Membrane on Vaginal Smooth Muscle Structure and Function**
Sophya Breedlove[1], Gabrielle King[2], Pamela Moalli[1,2], Katrina Knight[1]
[1]University of Pittsburgh, [2]Magee-Womens Research Institute

2:45PM **Evaluating Mechanical Properties and Extracellular Matrix Composition of Anterior and Posterior Murine Vaginal Walls**
Qinhan Zhou[1], Triniti Vanoven[2,3], Maria Florian-Rodriguez[3], Isaac Pence[3,2], Kristin Miller[2,3]
[1]Univerity of Texas at Dallas, [2]University of Texas at Dallas, [3]University of Texas Southwestern Medical Center

3:00PM **Finite Deformations of the Entire Murine Reproductive Tract Under Inflation**
Aileen Suarez[1], Steven Abramowitch[2], Kristin Myers[3], Kristin Miller[4], Raffaella De Vita[1]
[1]Virginia Tech, [2]University of Pittsburgh, [3]Columbia University, [4]University of Texas Dallas

3:15PM **Three-Dimensional Shape Analysis of the Pelvic Floor: Identifying Defects in Cystocele Development**
Liam Martin[1], Alireza Hadizadeh[2], Henry Chill[2], Ghazaleh Rostaminia[2], Steven Abramowitch[1]
[1]University of Pittsburgh, [2]University of Chicago

3:30PM **The Effects of Growth and Remodeling on the Contractile Function of the Pregnant Murine Uterus**
Emily Hoffmann, Kyoko Yoshida
University of Minnesota

3:45PM **A Reactive Viscoelastic Model of the Macaque Rhesus Cervix to Quantify Cervical Remodeling**
Camilo Duarte-Cordon[1], Shuyang Fang[2], Ivan Rosado-Mendez[3], Timothy Hall[3], Helen Feltovich[4], Kristin Myers[2]
[1]New York, [2]Columbia University, [3]University of Wisconsin-Madison, [4]Mount Sinai

Friday, June 14	2:30PM–4:00PM CDT

Vascular Biomechanics & Pathology I

Session Chairs: **Jacopo Ferruzzi**, *University of Texas at Dallas*
Rebecca Vanderpool, *University of Arizona*

Maple Lawn B

2:30PM **Numerical Analysis of Pulmonary Artery Behavior: Investigating the Effects of Wall Complexity, Model Parameters, and Prestrain**
Seda Aslan[1], Tianyi Xu[1], Enze Chen[1], Miya Mese-Jones[2], Xiaolong Liu[3], Bryan Gonzalez[4], Ryan O'Hara[4], Yue-Hin Loke[4], Narutoshi Hibino[5], Laura Olivieri[6], Axel Krieger[1], Thao Nguyen[1]
[1]Johns Hopkins University, [2]Baltimore Polytechnic Institute, [3]Texas Tech University, [4]Children's National Hospital, [5]University of Chicago, [6]University of Pittsburgh Medical Center

2:45PM **Comparing Regional Variations in Radiodensity With Stiffness in an Atherosclerotic Human Aorta**
Carly Donahue, Victor Barocas
University of Minnesota

3:00PM **Alterations of the Mechanical and Failure Properties of Aging Human Descending Thoracic Aorta With Type-II Diabetes**
Ruizhi Wang, Katherine Zhang
Boston University

3:15PM **A Sex-Based Biomechanical Analysis and Normalization for Improved Prediction of Abdominal Aortic Aneurysm Rupture**
Katherine Kerr[1], Pete Gueldner[1], Indrani Sen[2], Tiziano Tallarita[2], Joseph Wildenberg[2], Nathan Liang[3], David Vorp[1], Timothy Chung[1]
[1]University of Pittsburgh, [2]Mayo Clinic Health Systems, [3]University of Pittsburgh Medical Center

3:30PM **Impact of Elastin Fragmentation on the Mechanical Dissection Properties of the Human Descending Thoracic Aorta**
Ramin Shahbad, Majid Jadidi, Sayed Ahmadreza Razian, Anastasia Desyatova
University of Nebraska Omaha

3:45PM **The Stiffness of False Lumen Wall Increased in Chronic Type B Aortic Dissection Vs. Normal Tissue Based on the Unified-Fiber-Distribution (UFD) Model**
Hai Dong[1,2], Minliang Liu[3,2], Hannah Cebull[1], Marina Piccinelli[1], John Oshinski[1], John Elefteriades[4], Rudolph Gleason[2], Bradley Leshnower[1]
[1]Emory University, [2]Georgia Institute of Technology, [3]Texas Tech University, [4]Yale University

Friday, June 14	4:15PM–5:45PM CDT

Cell-Microstructure Interactions in Cardiovascular Mechanics

Session Chairs: **Chiara Bellini**, *Northeastern University*
Matthew Bersi, *Washington University in St. Louis*

Evergreen I

4:15PM **Cellular Micro-Biaxial Stretching for Characterizing Stress-Strain Relations for Single Cardiomyocytes Exposed to Complex Deformations**
Taylor Rothermel[1], Anna Grosberg[2], Patrick Alford[1]
[1]University of Minnesota, [2]University of California, Irvine

4:30PM **Mechanical Characterization of Calcified Clot Analogs**
Jose Jose Monclova[1], Daniel Walsh[1], Vikas Kannojiya[1], Scott Simon[2], Francesco Costanzo[1,1], Keefe Manning[1,2]
[1]Pennsylvania State University, [2]Penn State Hershey Medical Center

4:45PM **Adipose-Driven Hypertension Impacts 3rd Order Mesenteric Artery Contractile Behavior in a Sex-Dependent Manner**
Dillon McClintock, Osvaldo Vega Rodríguez, Nathan Tykocki, Sara Roccabianca
Michigan State University

5:00PM **Mechanical Heterogeneity in Human Cerebral Aneurysms: Exploring the Role of Tissue Microstructure and Inflammation**
Sergio A. Pineda-Castillo, Elizabeth D. Shih, Andrew W. Grande, Patrick W. Alford
University of Minnesota

5:15PM **Effects of Mechanical Dyssynchrony on Myocardial Contractility**
Lei Fan[1], Jenny Choy[2], Chenghan Cai[1], Ghassan Kassab[2], Lik Chuan Lee[3]
[1]Marquette University and Medical College of Wisconsin, [2]California Medical Innovations Institute, [3]Michigan State University

5:30PM **Smooth Muscle Cell Mechanoadaptation Is Chronically Disrupted by High-Velocity Stretching**
Samuel Boland, Patrick Alford
University of Minnesota

Friday, June 14	4:15PM–5:45PM CDT

Emerging Topics in Extracellular Matrix Adaption, Alterations, and Therapy in Soft Tissue Mechanics

Session Chairs: **Michelle Oyen**, *Washington University in St. Louis*
Xun Wang, *Massachusetts Institute of Technology*

Maple Lawn C

4:15PM ***WITHDRAWN***

Evidence of Highly Localized Mechanical Adaptation in the Lamina Cribrosa: Within Beam Regional Variations in Collagen Crimp and Stretch-Induced Uncrimping

Qi Tian, Po-Yi Lee, Juana Yang, Ian Sigal

[1]*University of Pittsburgh*

4:30PM

Differentiating Between the Effect of Damage to Tenocytes and Extracellular Matrix Using Precise Laser Ablation

Diane Stonestreet[1], Robert Hawkins[1], Nozomi Nishimura[1], Nelly Andarawis-Puri[1,2]

[1]*Cornell University,* [2]*Hospital for Special Surgery*

4:45PM

Photosensitizer-Mediated Low-Level Light Exposure Alters the Stiffness of Nonpregnant and Pregnant Human Cervix Tissue

Daniella Fodera[1], Jiashuai Fan[1], Aidan Therien[1], Serena Russell[1], Christine Hendon[1], Joy Vink[2], Kristin Myers[1]

[1]*Columbia University,* [2]*University of Hawaii*

5:00PM

Impact of GAGs Removal and CXL Therapy on Corneal Stromal Properties

Hamed Hatami-Marbini, M.E Emu

University of Illinois Chicago

5:15PM

Exploring the Possible Relationship Between Lost Elastin Integrity and Glycosaminoglycan Buildup in Elastic Arteries Using Computational Modelling

Yousof Abdel-Raouf[1], Lauranne Maes[2], Mathias Peirlinck[3], Nele Famaey[2], Patrick Sips[1], Julie De Backer[1,4], Patrick Segers[1], Jay Humphrey[5,6]

[1]*Ghent University,* [2]*KU Leuven,* [3]*Delft University of Technology,* [4]*Ghent University Hospital,* [5]*Yale University,* [6]*Yale School of Medicine*

5:30PM

The Influence of Pectinate Ligaments on the Patency of the Murine Aqueous Humor Outflow Pathway: a Finite Element Study

Babak N. Safa[1,2], Nina Sara Fraticelli Guzmán[1,2], Guorong Li[3], W. Daniel Stamer[3], Andrew J. Feola[1,2,4], C. Ross Ethier[1,2]

[1]*Georgia Institute of Technology,* [2]*Emory University,* [3]*Duke University,* [4]*Atlanta VA Center for Visual and Noncognitive Rehabilitation*

Engineering Tissue Regeneration and Wound Healing

Session Chairs: **Kristan Worthington**, *University of Iowa*
Kyoko Yoshida, *University of Minnesota*

Loramoor B

4:15PM **The Effects of Preeclamptic Milieu on Cord Blood Derived Endothelial Colony-Forming Cells**
Eva Hall[1], Laura Alderfer[1], Sanjoy Saha[1], Ellie Johandes[1], Laura Haneline[2], Donny Hanjaya-Putra[1]
[1]University of Notre Dame, [2]Indiana University School of Medicine

4:30PM **Injectable Synthetic Platelet-Based Therapy Enhances Clot Formation in Synovial Fluid Joint Injury Model**
Melika Osareh, Grant Scull, Jacob D. Thompson, Ashley C. Brown, Matthew B. Fisher
North Carolina State University and University of North Carolina at Chapel Hill

4:45PM **Can Pattern Recognition Receptor Agonists Modulate Tendon Healing In Vitro?**
Sam Winston, Amelia Stoner, Jade Kurihara, Lyndah Chow, Lynn Pezzanite, Steven Dow, Kirk McGilvray
Colorado State University

5:00PM **IL-1β Increases Mitochondrial Transfer From Mesenchymal Stromal Cells to Annulus Fibrosus Cells**
Ashley Cardenas, Lawrence Bonassar
Cornell University

5:15PM **Optimization of iPSC Differentiation to Lymphatic Endothelial Cells Through Metabolites and Machine Learning**
Donghyun Jeong, Sanjoy Saha, Maksym Zarodniuk, Donny Hanjaya-Putra
University of Notre Dame

5:30PM **Fibroblast-Adipocyte Interactions Alter Extracellular Matrix Production**
Ed Sander[1], Mariam El-Hattab[1], Kathryn Jacobson[2]
[1]University of Iowa, [2]University of Colorado

Friday, June 14	4:15PM–5:45PM CDT

Head & Injury Mechanics III

Session Chairs: **John Finan**, *University of Illinois at Chicago*
Corinne Henak, *University of Wisconsin-Madison*

Loramoor C

4:15PM **Mechanical Covariance Networks of the Cortex Regions as Identified by Magnetic Resonance Elastography**
Kyra Twohy, Alexa Diano, Olivia Bailey, Mary Kramer, Curtis Johnson
University of Delaware

4:30PM **Effect of Cortical Folds on Head Acceleration-Induced Brain Deformation: A Computational Study**
Anu Tripathi[1], Jose Gonzalez[2], Peter Ferrazzano[2], Christian Franck[2], Rika Carlsen[1]
[1]Robert Morris University, [2]University of Wisconsin Madison

4:45PM **Regional Correlation of Stiffness and Perfusion in the Human Brain at 7T MRI Through MR Elastography and Arterial Spin Labeling Techniques**
Caitlin Neher, Em Triolo, Mehmet Kurt
University of Washington

5:00PM **Incremental Overstretch Increases Failure Values of Cerebral Blood Vessels**
Farshid Shojaeianforoud, Brittany Coats, Ken Monson
University of Utah

5:15PM **Microstructural Damage Progression in the Pia-Arachnoid Complex**
Leonardo Marin, Tim Dixon, Brittany Coats
University of Utah

5:30PM **Novel MRI Phantoms for Investigating Skull-Brain Mechanics Using Magnetic Resonance Elastography**
Joy Mojumder[1], Suhas Vidhate[2], Yuan-Chiao Lu[1,3], Alexa Diano[4], Ahmed Alshareef[5], Curtis Johnson[4], Michaelann Tartis[6], John Butman[1], Dzung Pham[1,7]
[1]National Institutes of Health, [2]Intuitive Surgical Inc, [3]The Henry M. Jackson Foundation, [4]University of Delaware, [5]University of South Carolina, [6]New Mexico Institute of Mining and Technology, [7]Uniformed Services University

Friday, June 14	4:15PM–5:45PM CDT

Heart Valve and Ventricular Fluid Mechanics

Session Chairs: Hoda Hatoum, *Michigan Technological University* **Maple Lawn A**
John LaDisa, *Marquette University and the Medical College of Wisconsin*

4:15PM **Post-Transcatheter Edge-to-Edge Repair Pressure Gradient Prediction After Mitraclip in Functional Mitral Regurgitation Patients**
Shelley Gooden[1], Mani Vannan[2], Konstantinos Boudoulas[3], Vinod Thourani[2], Pradeep Yadav[2], Lakshmi Dasi[1]
[1]Georgia Institute of Technology, [2]Piedmont Heart Institute, [3]Wexner Medical Center

4:30PM **Computational Construction and Optimization of A Novel Tri-Tube Heart Valve Design**
Jirong Li, Yijiang Yu, Robert Tranquillo
University of Minnesota, Twin Cities

4:45PM **Patient-Specific Fluid-Structure Interaction Simulations of Young Bicuspid Aortic Valve Patients**
Hail Kazik[1,2], Harkamaljot Kandail[3], Joy Lincoln[1,4], John LaDisa[1,2,4]
[1]Medical College of Wisconsin, [2]Marquette University, [3]Medtronic Neurovascular, [4]Children's Wisconsin

5:00PM **Intraventricular Fluid Dynamics Study Using an In VitroModel of Mitral Valve Regurgitation and Edge-to-Edge Therapy**
Cody Kubicki[1], Michael Sacks[2], Keefe Manning[1,3]
[1]Pennsylvania State University, [2]University of Texas, [3]Penn State College of Medicine

5:15PM **Analysis of Energy and Pressure in the Sinus Under Different Blood Pressures After Aortic Valve Replacement**
Brennan Vogl[1], Agata Sularz[2], Scott Lilly[3], Vinod Thourani[4], Mohamad Alkhouli[2], Hoda Hatoum[1]
[1]Michigan Technological University, [2]Mayo Clinic, [3]Ohio State University, [4]Piedmont Heart Institute

5:30PM **Effect of Patient-Specific Ascending Aortic Curvature on Flow in the Vicinity of TAVR**
Jae Hyun Kim[1], Vahid Sadri[1], Huang Chen[1], Sanchita Bhat[1], Keshav Kohli[1], Raj Makkar[2], Vasilis Babaliaros[3], Rahul Sharma[4], Ajit Yoganathan[1]
[1]Georgia Institute of Technology, [2]Smidt Heart Institute, [3]Emory University Hospital, [4]Stanford University

Nanotechnology and Microfluidics

Session Chairs: **Jing Fan**, *City College of New York*
Khalil Khanafer, *University of Michigan*

Loramoor A

4:15PM **On the Margination of White Blood Cells**
Tam Nguyen, Trung Le
North Dakota State University

4:30PM **Development of a Microfluidic Dual-Gel Cell Culture Model**
Malgorzata Dwulat, Sihong Wang, Jing Fan
City College of New York

4:45PM **Design of a µ-Fluidic Chip for in Situ Quantification of Traumatic Brain Injury Biomarker Release**
Mauricio Araiza Canizales[1], Alexander McGhee[2], Rafael González-Cruz[3], Diane Hoffman-Kim[3], Christian Franck[1]
[1]University of Wisconsin-Madison, [2]University of Arizona, [3]Brown University

5:00PM **Prototyping of a Microfluidic Mechanochemical Gradient Chip by 3D Printed Molding for In Vitro Drug Testing**
Milad Fathi, Ali Mehrasa, Altuğ Özçelikkale
Middle East Technical University

5:15PM **Enhancing the Target Efficacy of Endothelial Colony Forming Cells for Renal Regeneration Via Kidney-Targeted Liposomal Nanoparticles**
Brenda Cruz Gonzalez[1], Fei Fan[2], Eva Hall[1], Sanjoy Saha[1]
[1]University of Notre Dame, [2]Michigan State University

5:30PM **Radiofrequency Ablation Facilitated by Microchannel Jetting**
Bo Cao, Hongying Wang, Ruizhe Hou, Shiqing Zhao, Aili Zhang
Shanghai Jiao Tong University

Friday, June 14	4:15PM–5:45PM CDT

Vascular Biomechanics & Pathology II

Session Chairs: **Abhay Ramachandra**, *Iowa State University* **Maple Lawn B**
Luke Timmins, *Texas A&M University*

4:15PM **Relation Between Cyclic Convection Fluid Filtration (CCFF) and Atherosclerosis**
Bruce Simon[1], Paul Rigby[2], Paul Howard[3], Jonathan Vande Geest[4]
[1]University of Arizona, [2]Raytheon Technologies, [3]Midwest Cardiovascular Specialists Indiana University, [4]University of Pittsburgh

4:30PM **Differential Effects of Hypertension on the Morphological, Mechanical, and Physiologic Characteristics of Male and Female Human Femoropopliteal Arteries**
Sayed Ahmadreza Razian, Majid Jadidi, Alexey Kamenskiy
University of Nebraska at Omaha

4:45PM **Effects of the Loading Rate on the Mechanical Behavior of Proximal Superficial Femoral Artery**
Ali Zolfaghari Sichani, Majid Jadidi
University of Nebraska at Omaha

5:00PM **Age and Sex Specific Biomechanics and Extracellular Matrix Remodeling of the Ascending Aorta in A Mouse Model of Marfan Syndrome**
Krashn Dwivedi, Jacob Rother, Jessica E. Wagenseil
Washington University in St. Louis

5:15PM **Effect of Collagen Accumulation on Right Ventricular Passive Viscoelasticity With Pulmonary Hypertension Development**
Yuecheng Wang, Kristen LeBar, Zhijie Wang
Colorado State University

5:30PM **Accelerated Stent Deployment Simulations Via Model Order Reduction for Predictive Modeling of Transcatheter Aortic Valve Replacement**
Imran Shah[1,2], Sri Krishna Sivakumar[1], Francesco Ballarin[3], Vinod Thourani[4], Alessandro Veneziani[2], Lakshmi Dasi[1]
[1]Georgia Institute of Technology, [2]Emory University, [3]Università Cattolica del Sacro Cuore, [4]Piedmont Heart Institute

Poster Sessions

Posters will be presented in two sessions as listed below. See the Instructions for Poster Presenters section on page 8 for additional information. All poster sessions will take place in the **Forum** exhibition hall.

Poster Session I	**Wednesday, June 12, 1:00 - 2:30 PM CDT**
Poster Session II	**Thursday, June 13, 12:30 - 2:00 PM CDT**

Poster Session I

BS SPC: Experimental Methods in Biomechanics and Mechanobiology

P1 **Building ASGR1-Overexpressed Fluorescent Reporter Cell Model for Optimization of CRISPR Delivery**
Yun-I Sang, Morgan Clay, Chun-Wei Chi, Yeh-Hsing Lao
University at Buffalo

P2 **Impact of a Cognitive Dual Task on Older Adult Motor Performance and Strategies**
Erin Kreis, Mitchell Tillman, Jun Liu, Zahava Hirsch, Antonia Zaferiou
Stevens Institute of Technology

P3 **Measuring Limb Loads Using A Novel Prosthetic Pylon Force Sensor**
Hanna Armstrong, Kaleb Burch, Amit Chaudhari, Sagar Doshi, Erik Thostenson, Jill Higginson
University of Delaware

P4 **Comprehensive Assessment of Community Mobility and Participation of Wheelchair Users Using Wearables.**
Madisyn R. Adelman[1], Maja Goršič[1,2], Grace Fasipe[1], Jacob R. Rammer[1]
[1]University of Wisconsin-Milwaukee, [2]Marquette University

P5 **Collaborative Pathways: Empowering Pregnant and Parenting Teens Through STEM Engagement**
Oluwatomisin Ajayi[1], Emily Hoffmann[1], Paige Nielsen[1], Lauren Tolbert[2], Kyoko Yoshida[1]
[1]University of Minnesota, [2]Longfellow Alternative High School

P6 **Development of a Benchtop Model for Cerebral Collateral Circulation**
Argudit Chauhan, Alena Tucker, Debanjan Mukherjee
University of Colorado Boulder

P7 **Full-Field Comparison of Porcine Pulmonary and Aortic Valve Leaflet Collagenous Architecture Using Quantitative Polarized Light Imaging**
Shreya Sreedhar, Daniel Pearce, Connor Link, Colleen Witzenburg
University of Wisconsin-Madison

P8 **Mechanical and Damage Properties of Preterm and Adult Sheep Middle Cerebral Arteries Following Mechanical Damage**
Kerrigan Denham, Joseph Bail, Andrew Rebentisch, Kurt Albertine, Kenneth Monson
University of Utah

P9 **In Vitro Stretch Injury Affects Mitochondrial Membrane Potential, Calcium Concentration, and Nuclear Morphology in Rat Astrocytes**
Citlally Santacruz, Shahrzad Shiravi, Alexandra Yufa, John Finan
University of Illinois Chicago

P10 **Design and Optimization of a 3D-Printed Testing Platform for Evaluating the Effects of Voluntary Wheel Running on the Biomechanical Properties of Murine Achilles Tendons**
Elsa Lecaj, Samantha Muscat, Nolan Sparks, Mark Buckley, Anne Nichols
University of Rochester

P11 **Regional Mechanical Properties on the Macroscale and Microscale Are Not Associated for the Equine Superficial Digital Flexor Tendon**
Samantha Watson[1], Zachary Davis[1,2], Shannon Connard[2], Lauren Schnabel[2], Matthew Fisher[1,2,3]
[1]NC State and UNC Chapel Hill, [2]North Carolina State University, [3]University of North Carolina - Chapel Hill

P12 **Effect of Intermolecular Crosslinking on the Multiscale Mechanical Behavior of Tendons**
Madeline Wagner[1], Rachel Klink[1], Steven Eppell[2], Allen Lin[3], Jeffrey Weiss[1]
[1]University of Utah, [2]Case Western Reserve University, [3]Revvity

P13 **Mechanical Response to Compression of the Pig Optic Nerve**
Katherine Metrey, Arina Korneva
Virginia Tech

P14 **Combined Effects of Proteoglycan and Collagen on the Lubrication Properties of a Polyvinyl Alcohol Hydrogel**
Monika Maeda, Heitaro Chiba, Hiromichi Fujie
Tokyo Metropolitan University

P15 **Controlling Neural Culture Density and Orientation for Enhanced Analysis of Traumatic Brain Injury Electrophysiology**
Griffin Radtke, Jamie Sergay, Jessica Park, Jing Zhang, Christian Franck
University of Wisconsin-Madison

P16 **Investigating the Effects of Surface Stiffness and Viscoelasticity on Human Mesenchymal Stem Cell Immunomodulation**
Sara Olsen, Rose Leader, Bethany Almeida
Clarkson University

P17 **Effects of Detrusor Contraction on Urinary Bladder Extracellular Matrix Organization**
Daniel Deuel[1,2], Tyler Tuttle[3], Sara Roccabianca[4], Sarah Calve[3]
[1]University of Colorado, Boulder, [2]University of Colorado Boulder, [3]Paul M. Rady University of Colorado Boulder, [4]Michigan State University

P18 **Biomedical Applications of Novel Magnetostrictive Composite**
Aaron Brandner[1], Chui Law[2], Rani Elhajjar[2], Priyatha Premnath[2]
[1]University of Wisconsin-Madison, [2]University of Wisconsin-Milwaukee

P19 **Compliance Matching A Polyurethane and PLCL Biohybrid Tissue Engineered Vascular Graft**
Trin Murphy[1,2], David Maestas[1,2], Katarina Martinet[1,2], William Wagner[1,2], Sang-Ho Ye[1,2], Jonathan Vande Geest[1,2,3]
[1]University of Pittsburgh, [2]McGowan Institute for Regenerative Medicine, [3]Vascular Medicine Insitute

BS SPC: Image-Based Measurement, Analysis, and Modeling

P20 **Kinematic Sensitivity Study of Total Knee Replacement FEA Model to Ligament Attachment Site**
Elizabeth Wynn[1,2], Takayuki Koya[1,3], Markus Wimmer[1], Hannah Lundberg[1], Steven Mell[1]
[1]Rush University, [2]University of Illinois at Chicago, [3]Showa University Koto Toyosu Hospital

P21 **VIGOR4D: Vascular Idealized Geometry Open-Source Repository for 4D Flow MRI Denoising and Super-Resolution**
Moses Hamm, Neal Patel, Vitaliy Rayz
Purdue University

P22 **A Machine Learning Approach to Mining Hemodynamics Data From Pulmonary Arterial Hypertension Rats**
Jingwen Hui, Ethan Kwan, Daniela Valdez-Jasso
University of California, San Diego

P23 **4D Flow MRI Reveals That Carotid Artery Bifurcation Geometry Impacts Hemodynamics Associated With Atherosclerosis**
Carissa Lucas[1], Brennen Anderson[2], Retta El Sayed[1,3], Jason Allen[3,4], John Oshinski[1,3]
[1]Georgia Institute of Technology, [2]Augusta University, [3]Emory University, [4]Indiana University

P24 **Advancing Cardiac Metrics: Computational CMR Methods for Ejection Fraction Evaluation**
Ella Lyon[1,2], Ilham Essafri[2], Mengqian Zhang[2], Melissa Lucero[2], Kenzo Ichimura[3], Kurt Stenmark[2], Edda Spiekerkoetter[3], Vitaly Kheyfets[2]
[1]Colorado School of Mines, [2]University of Colorado Anschutz Medical Campus, [3]Stanford University

P25 **Comparative Study of Image-Based Modeling Using a Novel Medical-Image-to-Reduced-Order-Simulation Framework**
Boyang Gan, Numi Sveinsson, Shawn Shadden
University of California, Berkeley

P26 **Multimodal Study of Ischemic Cardiac Remodeling: Murine 4D Ultrasound and Mass Spectrometry Imaging**

WITHDRAWN

Amelya Fox[1], Luke Schepers[2], Conner Earl[2], Craig Goergen[2], Colleen Crouch[1]
[1]University of Tennessee, Knoxville, [2]Purdue University

P27 **MRI-Based Measurements of Strain in the Aorta: Does Cardiac Disease Impact Aortic Deformation?**

Petra Alsahwi, Alice Guest, Rylan Marianchuk, Dina Labib, James White, Elena Di Martino
University of Calgary

P28 **Personalized Finite Element Models of Tissue Expansion for Breast Reconstruction After Mastectomy**

Joel Laudo[1], Tianhong Han[1], Ariel Figueroa Baker[2], Arun Gosain[2], Taeksang Lee[3], Adrian Buganza Tepole[1]
[1]Purdue University, [2]Northwestern University, [3]Myongji University

P29 **Development of Tailored Finite Element Head Models for Free Vibrational Analysis Across Subject Specific Geometry**

Diego Acosta, Turner Jennings, Sinan Müftü, Rouzbeh Amini
Northeastern University

P30 **Optimization of Objective Measurements for Evaluating Sagittal Synostosis Detection and Treatment Efficacy**

Tim Dixon[1], Jason Ramsey[2], Philip Stevens[2], Brittany Coats[1]
[1]University of Utah, [2]Hanger Clinic

P31 **Toward the Detection of Cerebral Vessel Softening Using Magnetic Resonance Elastography**

Lucas Bolster, Henrik Odeen, Allison Payne, Ken Monson
University of Utah

P32 **A Framework for Slice-Wise Motion Correction in Magnetic Resonance Elastography of the Human Brain**

Tyson Lam, Emily Triolo, Mehmet Kurt
University of Washington

P33 **Sensitivity of Contact Mechanics to FE Model Generation Decisions Compared to Variations Between Knees and Due to Partial Meniscectomy**

Joshua Leadem
University of Rochester

P34 **3D Geometric Reconstruction of Electrospun Fibers**

Evan He, Shruti Motiwale, Elizabeth Cosgriff-Hernandez, Michael Sacks
University of Texas at Austin

P35 Sex Differences in Iris Stiffness With a History of Angle-Closure Glaucoma: An In-Vivo Image-Based Inverse Modeling Analysis
Hayden DelCiello[1], Frederick Sebastian[2], Anup Pant[3], Vanita Pathak-Ray[4], Syril Dorairaj[5], Rouzbeh Amini[2,2]
[1]Khoury Northeastern University, [2]Northeastern University, [3]University of Akron, [4]LV Prasad Eye Institute, [5]Mayo Clinic

P36 In-Silico Models of In-Vivo Cervical Stiffness Measurements for Improving Preterm Birth Prediction
Adriana Delagarza[1], Erin Louwagie[1], Abigail Laughlin[1], Jacqueline Hairston[1], Mirella Mourad[1], Michael House[2], Kristin Myers[1]
[1]Columbia University, [2]Tufts University

P37 Development of In-Silico Model of Cancerous Tissue
Nathanael Sovitzky
University of Wisconsin-Milwaukee

P38 Assessment of a Tumor's Malignancy Using In Silico Model of Breast Tumor Tissue
Hannah Vincent[1], Morgan Connaughton[1], Kianoush Falahkheirkhah[2], Erik Robert Hansen[1], Rohit Bhargava[2], Mahsa Dabagh[1]
[1]University of Wisconsin Milwaukee, [2]University of Illinois at Urbana-Champaign

Design, Dynamics, Rehabilitation, and Regulations

P80 Exploration of the Full-Field Biomechanics of the Human Spine
Emma C. Coltoff, Benjamin S. Hezrony, Philip J. Brown
Wake Forest School of Medicine

P81 Comparison of OpenSim and AnyBody Modeling System Predictions in Biomechanical Modeling of Upper Extremities
kamal Gautam, Mohamed Samir Hefzy, Abdul A Mustapha, Behrens Kyle
University of Toledo

P82 Stability of the C2-C3/C3-C4 Level During C4-C6 Laminoplasty With and Without C3 Laminectomy in Cadaveric Biomechanical Models
John Francis[1], Jeremy Loss[2], Derrick Obiri-Yeboah[3], Orlando Martinez[1], Bilal Butt[2], Michael Steinmetz[2]
[1]Case Western Reserve University School of Medicine, [2]Cleveland Clinic Foundation, [3]Cleveland Clinic Lerner College of Medicine

P83 Evaluating the Performance of Extended Kalman Filter Vs. Unscented Kalman Filter for Displacement Estimation
Nafiseh Mohammadianaftah[1], Sara Wilson[1], Neena Sharma[2]
[1]University of Kansas, [2]University of Kansas Medical Center

P84 Novel Stent Design and Prototyping Method
Kaitlyn Elmer[1], Barry Uretsky[2], Adib Chaus[3], Morten Jensen[1]
[1]University of Arkansas, [2]University of Arkansas for Medical Sciences, [3]Lutheran General Hospital

P85 In Vitro Clot Trapping Efficiency of the FDA Generic Inferior Vena Cava Filter in the Supine Position
Ian Goetz[1], Ryan Frasca[1], Garrett Campbell[1], Terrell Barraclough[1], Kenneth Aycock[2], Brent Craven[2], Keefe Manning[1,3]
[1]Pennsylvania State University, [2]US Food and Drug Administration, [3]Penn State College of Medicine

P86 Bubbler System Design for Removal of Oxygen From Media in an Open Testing Environment
Margaret Capalbo, Spencer Szczesny
Pennsylvania State University

P87 Uncovering Electro-Mechano-Physiological Rules of Life: A New 2D/3D All-Optical Interrogation Technology
Chenyu Liang[1], Erica Hengartner[1], Abygale Cochrane[1], Bruna Balbino de Paula[1], Basak Ayaz[1], Robert Caudle[1], Allison Campbell[1], Eleana Manousiouthakis[1], Christine Schmidt[1], Tian He[2], Christopher Werley[3], Xin Tang[1]
[1]University of Florida, [2]Harvard University, [3]Q-State Biosciences

P88 Ocular Hypothermia, In-Vitro Validation of A Novel Therapeutic Apparatus Using Non Perfused Porcine Eye Model
Luigi Mecacci, Yukinari Nakamura, John R. Hetling
University of Illinois at Chicago

P89 The Pomelo Peel as Impact Protection From Fall-Related Femur Fracture: Mechanical and Biological Property Investigation
Stacey Zeigler, Benjamin Ellis, Daniel Fuller, Laurel Kuxhaus
Clarkson University

P90 Validation of FEA Models for Design of Engineered Foam for Scoliotic Braces
Robert Rizza[1], Xue-Cheng Liu[2], Vince Anewenter[1]
[1]Milwaukee School of Engineering, [2]medical College of Wisconsin

Fluid Mechanics

P91 Geometry and Physics-Informed Neural Network Modeling of Flows Inside Y-Shaped Bifurcated Ducts
Abdullahi Olapojoye, Fatemeh Hassanipour
University of Texas at Dallas

P92 Enhancing Predictive Accuracy in Cerebral Aneurysm Hemodynamics: Insights From Machine-Learning Evaluation and Parameter Influence Analysis
Narges Kamaei Asl[1], Mahkame Sharbatdar[2]
[1]University of Tehran, [2]K. N. Toosi University of Technology

P93 Automatic Segmentation of Abdominal Aortic Aneurysm From Computed Tomography Angiography Using A Patch-Based Dilated U-Net Model
Merjulah Roby[1], Juan Restrepo[1], Haehwan Park[1], Satish Muluk[2], Mark Eskandari[3], Ender Finol[1]
[1]University of Texas at San Antonio, [2]Allegheny Health Network, [3]Northwestern University School of Medicine

P94 Experimental Evaluation of the 'Plunger Technique' for Manual Cyclic Aspiration Treatment of Acute Ischemic Stroke
Demitria Poulos[1], James Keith[1], Michael Froehler[2], Bryan Good[1]
[1]University of Tennessee, [2]Vanderbilt University Medical Center

P95 Impact of Particle Seeding on the Rheological Characteristics of Blood Analog Fluid Used in Laser Doppler Velocimetry
Shreyash M Manegaonkar[1], Israel Ajiboye[1], Gavin A. D'Souza[2], Rupak K Banerjee[1]
[1]University of Cincinnati, [2]US Food and Drug Administration

P96 Clinical Validation of the PSCOPE Hybrid Framework for Cardiovascular Predictive Modeling
Abraham Umo[1], Brett Welch[2], Armand Kilic[2], Ethan Kung[1]
[1]Clemson University, [2]Medical University of South Carolina

P97 A 3D Tissue Model of the Endothelial Glycocalyx Post-Pneumonectomy
Camden Holm, Jacob Elliot, Mia Long, Solomon Mensah
Worcester Polytechnic Institute

P98 A Computational Model to Simulate the Roughness of Narrowed Coronary and Cerebral Arteries in Diabetes Mellitus Patients and to Design Effective Treatment Strategies
Senol Piskin
Istinye University

P99 A Simple Model of Angiotensin Converting Enzyme Hub Capacity on Peptide Flux and Renin Influence
Brian Westwood, Mark Chappell
Wake Forest School of Medicine

P100 Comparison of Lumped, Distributive and 1D Navier-Stokes Model of Coronary Blood Flow
Chenghan Cai[1], Lik Chuan Lee[2], Lei Fan[3]
[1]Medical College of Wisconsin, [2]Michigan State University, [3]Marquette University

P101 Development and Application of On-Site Velocity Boundary
Reza Bozorgpour, Mahsa Dabaghmeshin
University of Wisconsin-Milwaukee

P102 Numerical Simulation of Multi-Frequency Ventilation Within the Central Airways of a Porcine Lung
Bing Han[1,2], Emmanuel A. Akor[3], Mingchao Cai[4], David W. Kaczka[2,3,2]
[1]University of North Carolina, Chapel Hill and Morgan State University, [2]University of Iowa, [3]Roy J. Carver University of Iowa, [4]University of North Carolina, Chapel Hill, Morgan State University

P103 Modeling Heat Sink Effects of Cerebrospinal Fluid (CSF) During Thermal Therapies for Treatment of Glioblastoma (GBM)
Yash Lad, Omar Abdulqader, Shreeniket Pawar, Anilchandra Attaluri
Pennsylvania State University

P104 Proportional Integral Derivative (PID) Controller Applied to Magnetic Nanoparticle Hyperthermia Therapy (MNHT)
Nageshwar Arepally, Yash Lad, Shreeniket Pawar, Ma'Moun Abu-Ayyad, Anilchandra Attaluri
Pennsylvania State University

P105 Heat Sink Effects of Large Blood Vessel During Thermal Therapies
Shreeniket Pawar, Naveen Kondreddy, Yash Lad, Anilchandra Attaluri
Pennsylvania State University Harrisburg

P106 Computational Analysis of Stroke Risk During Cardiopulmonary Bypass in Adult and Pediatric Anatomies
Nafis Arefin, Bryan Good
University of Tennessee

P107 Flow Dynamic Factors Correlated With Device-Related Thrombosis After Left Atrial Appendage Occlusion
Brennan Vogl[1], Agata Sularz[2], Alessandra Bavo[3], Matthieu De Beule[3], Jens Erik Nielsen-Kudsk[4], Ole De Backer[5], Mohamad Alkhouli[2], Hoda Hatoum[1]
[1]Michigan Technological University, [2]Mayo Clinic, [3]FEops, [4]Aarhus University Hospital, [5]Copenhagen Univerrsity Hospital

P108 Computational Modeling of Carotid Artery Stenosis and Fibromuscular Dysplasia for Prediction of Biomechanical Platelet Activation
J. Scott Malloy[1], Suman Guntupalli[2], Scott Cameron[2], Vitaliy Rayz[1]
[1]Purdue University, [2]Cleveland Clinic

P109 Flexible Rotor Blades in LVADs: Investigating Implications for Hemocompatibility
Shweta Karnik, Shobana Santhanam, Charles Federico, Huang Chen, Lakshmi Prasad Dasi
Georgia Institute of Technology

P110 Simulation of the Viscoelasticity of Clots Considering Red Blood Cells and Fibrin Network
Ryan Mueller, Jifu Tan
Northern Illinois University

P111 Hemodynamic Evaluation of the Sensitivity of Graft Morphology on Direct Vascular Surgery for Moyamoya Disease: An In Vitro and In Silico Study
Cheng Peng[1], Ephraim Church[2], Melissa Brindise[1]
[1]Pennsylvania State University, [2]Hershey Medical Center

P112 The Influence of Echocardiographic and Computed Tomography Phases on the Resulting Flow Dynamics in the Left Atrium
Ahmad Bshennaty[1], Brennan Vogl[1], Agata Sularz[2], Mohamad Alkhouli[2], Hoda Hatoum[1]
[1]Michigan Technological University, [2]Mayo Clinic

Solid Mechanics

P127 Anisotropic Porous Hydroxyapatite/Gelatin Implants for Trabecular Structure Reconstruction
Anton Pavlov, Jimmy Johnson, Ben Gadomski
Colorado State University

P128 Radiation Induces Fibrosis in Skin, but This Injury Is Mitigated in Expanded Skin
Laura Nunez[1], Joanna Ledwon[2], Vahid Tac[1], Arun Gosain[2], Adrian Buganza[1]
[1]Purdue University, [2]Northwestern University

P129 Creation of a Multi-Scale Model of Skin Growth to Understand the Effect of Microstructure and Tissue Heterogeneities on Skin Mechanobiology
Omar Moreno Flores[1], Maria Holland[2], Adrian Buganza Tepole[1]
[1]Purdue University, [2]University of Notre Dame

P130 Selection of Loading Conditions for Reliable Virtual Mechanical Testing of Bone Fracture Healing in Sheep and Humans
Mehran Bahrami, Kylie Frew, Hannah Dailey
Mechanical Engineering & Mechanics, Lehigh University

P131 Automatic Boundary Detection and Meshing for Virtual Mechanical Testing of Tibial Fracture Healing
Alireza Ariyanfar, Mehran Bahrami, Hannah Dailey
Lehigh University

P132 Modelling Vascularization in the Healing Callus After Fracture
Joseph Soldenwagner, Priyatha Premnath, Mahsa Dabagh
University of Wisconsin Milwaukee

P133 Adaptation of a Multiscale Model of Heart Growth in Pregnancy for Use in Canines
Tiffany Corlin, Molly Kaissar, Kyoko Yoshida
University of Minnesota

P134 Measurement of the Population Distribution of Helmet-to-Head Contact Forces
Turner Jennings, Aidan Tillman, D'Mitra Mukasa, Michael Marchev, Rouzbeh Amini, Sinan Müftü
Northeastern University

P135 Is Synthetic Clear Gelatin a Validated Surrogate for Biological Tissue in Low-Velocity Penetrating Impacts?
Joseph LeSueur[1,2], Jared Koser[1], Stephen Hargarten[1], Frank Pintar[1,2]
[1]Medical College of Wisconsin, [2]Marquette University

P136 Infant Skull Anatomical Standards for Use in Head Trauma Modeling
Yousef Alsanea, Tagrid Ruiz-Maldonado, Brittany Coats
University of Utah

P137 A Numerical Study on the Effect of Cortical Diffusivity on Brain Tissue Gyrification
Karan Taneja, Maria Holland
University of Notre Dame

P138 Effect of Impact Magnitude and Direction on the Injury Risk of Neural Cells
Raisa Akhtaruzzaman, Arthur Koster, Kamal Awad, Venu Varanasi, Marco Brotto, Ashfaq Adnan
University of Texas at Arlington

P139 Method for Extracting Intact Skull-Brain Samples for Ex-Vivo Mechanical Testing
Brandon Chelstrom, Corinne Henak
University of Wisconsin-Madison

P140 Numerical Modelling of Low-Level Blast Scenarios to Quantify Likelihood of Cavitation-Induced Traumatic Brain Injury
Manik Bansal[1], Baudouin Fonkwa[2], Eric Johnsen[2], Christian Franck[3], Rika Carlsen[1]
[1]Robert Morris University, [2]University of Michigan, [3]University of Wisconsin-Madison

P141 Modification of Polyacrylamide Using Dextran and Linear Acrylamide Chains to Mimic Human Brain Tissue
James Angelos[1], Adam Willis[2,3], Michaelann Tartis[1]
[1]New Mexico Institute of Mining and Technology, [2]Michigan State University, [3]59th Medical Wing

P142 Re-DiffiNet: Modeling Discrepancy in Tumor Segmentation Using Diffusion Models
Tianyi Ren, Abhishek Sharma, Juampablo Heras Rivera, Harshitha Rebala, Agamdeep Chopra, Ethan Honey, Mehmet Kurt
University of Washington

P143 Estimating Severe Injury Risk to Human Cervical Spine Using Scaled Head Kinematic Response From Non-Human Primate
Jesse Gerringer, Karthik Somasundaram, Frank Pintar
Medical College of Wisconsin and Marquette University

P144 Effect of Rear Impact on the Instrumented Spine: A Finite Element Study
Balaji Harinathan[1,2], Karthik Devaraj[3], Aditya Vedantam[3], Narayan Yoganandan[3]
[1]Medical College of Wisconsin, [2]Vellore Institute of Technology, [3]Medical College Wisconsin

P145 Cervical Neck Muscle Morphology Under Load-Bearing Conditions and Its Impact on Spinal Alignment: An Upright Magnetic Resonance Imaging Study
Mahmudur Rahman[1], Ali Warraich[2], Vicky Varghese[3], Aditya Vedantam[1], Narayan Yoganandan[1]
[1]Medical College of Wisconsin, [2]University of Chicago, [3]American International University

P146 Neck Strength and Endurance After 1-Hour Exposure to Vertical Whole-Body Vibration
Ana I. Lorente, Robert S. Salzar
University of Virginia

P147 Quantitative Analysis of the Compressive Force Applied to the ACL Tibial Enthesis
Daichi Ishii, Shiho Sato, Hiromichi Fujie
Tokyo Metropolitan University

P148 The Effect of Cam Morphology of the Hip on Sacroiliac Motion During Functional Hip Biomechanics
Alexander Hooke, Mason Uvodich, Joshua Bland, Allison Tanner, Zachary Braig, Micah Nieboer, Evan Dugdale, William Cross, Chunfeng Zhao, Aaron Krych, Mario Hevesi
Mayo Clinic

P149 The Importance of the Meniscus Inner Segment on the Mechanical Function of the Meniscus
Satoshi Yamakawa, Toshitaka Tsunematsu, Issei Ogasawara, Tomoki Ohori, Akira Tsujii, Shoji Kondo, Seira Sato, Takashi Kanamoto, Ken Nakata
Osaka University

P150 Compression Stability of Three Fixation Modes for Intraoperative Femoral Condyle Fractures During Knee Replacement
Timothy Eastep[1], Brady Killham[1], Yi Hong[1], Cheng-Jen Chuong[1], Dane Wukich[2], Jun Liao[1], Senthil Sambandam[3]
[1]University of Texas at Arlington, [2]University of Texas Southwestern Medical Center, [3]Dallas VA Medical Center

P151 Biomechanical Variability in Composite Lumbar Spine Surrogates During Multi-Laboratory Collaborative Testing
Emma Coltoff[1], Jeremy Loss[2], Siril Dukkipati[3], Jenna Wahbeh[4], Kalle Chastain[5], Matthew Pelletier[6], Tian Wang[6], Philip Brown[1], Mark Driscoll[7], Sophia Sangiorgio[4], Edward Ebramzadeh[4], Kathleen Meyers[5], William Walsh[6], Bryan Cornwall[6,8], Brian Kelly[9], Robb Colbrunn[2]
[1]Wake Forest School of Medicine, [2]Cleveland Clinic, [3]McGill University, [4]University of California, Los Angeles, [5]Hospital for Special Surgery, [6]University of New South Wales, [7]McGill University,, [8]University of San Diego, [9]Barrow Neurological Institute

P152 Temporal Variability in Composite Lumbar Spine Surrogates During Multi-Laboratory Collaborative Testing

Emma Coltoff[1], Jeremy Loss[2], Siril Dukkipati[3], Jenna Wahbeh[4], Kalle Chastain[5], Matthew Pelletier[6], Tian Wang[6], Philip Brown[1], Mark Driscoll[3], Sophia Sangiorgio[4], Edward Ebramzadeh[4], Kathleen Meyers[5], William Walsh[6], Bryan Cornwall[6,7], Brian Kelly[8], Robb Colbrunn[2]

[1]Wake Forest School of Medicine, [2]Cleveland Clinic, [3]McGill University, [4]University of California, Los Angeles, [5]Hospital for Special Surgery, [6]University of New South Wales, [7]University of San Diego, [8]Barrow Neurological Institute

P153 Walking Recovers Cartilage Strain: An Analysis of Measurement Repeatability

JiYeon Hong[1], Tejus Surendran[1], Shu-Jin Kust[2], Dana Voinier[3], Kyle Meadows[3], Dawn Elliott[3], Daniel White[3], Axel Moore[1]

[1]Carnegie Mellon University, [2]Temple University, [3]University of Delaware

P154 Rotary Pivot Shift: A New Loading Profile for Quantifying Rotational Stability in the Knee

Elizabeth Pace, Robb Colbrunn, Vincent Lizzio, Paul Saluan, Tara Nagle

Cleveland Clinic Foundation

P155 Evaluation of Spine Biomechanics Using Micro-Computed Tomography

Hutomo Tanoto, Yuxiao Zhou

Texas A&M University

P156 Extent of Vascular Damage at Varying Degrees of Stretch in Hypoxic Neonatal Brachial Plexus

Sanjna Srinivasan[1], Virginia Orozco[1], Smriti Nair[2], Mitali Sahni[3], Sriram Balasubramanian[1], Anita Singh[2]

[1]Drexel University, [2]Temple University, [3]Sunrise Children's Hospital

P157 Collagen Denaturation Quantification in Bone Using Collagen Hybridizing Peptide.

William Woolley[1], Katy Martin[2], Seungju Yu[2], Claire Acevedo[1,2]

[1]University of California, San Diego, [2]University of Utah

P158 Resolving Nanoscale Deformations of Mineralized Collagen Fibrils in 3D

Riti Sharma, Luc Capaldi, Kailin Chen, Ottman A. Tertuliano

University of Pennsylvania

P159 Investigating the Effect of Co and Cr Substitutions on Biomimetic Apatite Maturation

Kennedy Drake[1], Julianna DeSantis-Raymond[2], Stephanie Wong[1], Alix Deymier[1]

[1]University of Connecticut Health Center, [2]University of Connecticut

P160 Osteotomy Has Variable Effects on Construct Stiffness of Cadaveric Tibiae: Implications for Functional Evaluations

Luke Mattar[1], M. Enes Kayaalp[2], Tianyu Chen[1], Ron Curelaru[1], Volker Musahl[1], Richard Debski[1]

[1]University of Pittsburgh, [2]Istanbul Kartal Dr. Lutfi Kirdar Training and Research Hospital

P161 Mechanics of Cobalt Substitution in Biommetic Apatites
Abigail Eaton[1], Stephanie Wong[2], Kennedy Drake[2], Arun Nair[1]
[1]University of Arkansas, [2]University of Connecticut

P162 Correlation Between Loading-Induced Changes in Optical Redox Metrics and Mitochondrial Depolarization Varies by Strain Rate and Cartilage Zone
Jingyi Wang, Greta Scheidt, Corinne Henak
University of Wisconsin-Madison

P163 Quantifying Soleus Muscle Structure Through Diffuse Tensor Imaging (DTI) in Individuals With Achilles Tendon Rupture
Shabnam Rahimnezhad Baghche Jooghi[1], Xiaoxiao Bai[1], Tanzil Arefin[1], Thomas Neuberger[1], Morgan Voulo[2], Daniel Cortes[1]
[1]Pennsylvania State University, [2]Milton Hershey Medical Center

P164 Investigating the Mechanisms of Patella Osteochondral Allograft Transplant Failure Using Finite Element Methods
Michael Hernández Lamberty, John Grant, Rhima Coleman, Ellen Arruda
University of Michigan

P165 Postural Stability in Helicopter Aircrew With and Without Neck and Back Pain: the Medical College of Wisconsin Military Aircrew Neck and Back Pain Study
Rachel Cutlan[1], Cory Everts[2,3], Alok Shah[2], Amy Nader[2], Keeley Hamill[2], Narayan Yoganandan[2,4], Lance Frazer[5], Barry Shender[6], James Sheehy[6], Glenn Paskoff[6], Daniel Nicolella[5], Timothy Bentley[7], Brian Stemper[1,2,4]
[1]Marquette University and Medical College of Wisconsin, [2]Medical College of Wisconsin, [3]115th Fighter Wing, Wisconsin Air National Guard, [4]Zablocki Veterans Affairs Medical Center, [5]Southwest Research Institute, [6]Naval Air Warfare Center Aircraft Division, [7]Office of Naval Research

P166 Multiscale Correlations Between, Joint and Tissue Biomechanics and Morphology in Ovine Stifles
Aritra Chatterjee[1,2], Zachary Davis[2], Timothy Lescun[2], Deva Chan[2]
[1]Birla Institute of Science and Technology, [2]Purdue University

P167 Selective Bundle ACL Reconstruction Does Not Initially Restore the Normal ACL Force Distribution in an Adolescent Porcine Model: Implications for Treatment of Partial ACL Injuries
Yukun Zhang[1], Kaan Gurbuz[2], Jeffrey Spang[3], Matthew Fisher[1,3]
[1]NC State and UNC Chapel Hill, [2]Kayseri State Education & Research Hospital, [3]University of North Carolina at Chapel Hill

P168 Tackling Heterogeneity in Canine Osteosarcoma- A Biomechanical Analysis of Histotripsy-Treated and Untreated Bone
Preeya Achari[1], Elliana Vickers[1], Lauren Ruger[1], Eli Vslaisavljevich[1], Joanne Tuohy[2], Caitlyn Collins[1]
[1]Virginia Tech, [2]Virginia-Maryland College of Veterinary Medicine

P169 Growth Plate and Its Role in Pediatric ACL Injuries
Isaac Woodward, Antonis Stylianou
University of Missouri-Kansas City

Special Session: Cancer Mechanics

P66 Single Cell Mechanical Analysis Reveals Viscoelastic Similarities Between Astrocytes and Glioblastoma Cells
Julian Najera, Killian Onwudiwe, Luke Holen, Alice Burchett, Dorielis Rodriguez, Maksym Zarodniuk, Saeed Siri, Meenal Datta
University of Notre Dame

P67 Long-Distance Symphony Among Human Cancer Cells: an Underappreciated Mechano-Regulated Process in Tumor Progression
Chenyu Liang[1,2], Mai Tanaka[2], Dietmar Siemann[2], Bo Zeng[3], Xin Tang[1,2]
[1]University of Florida, [2]UF Health Cancer Center, [3]Southwest Medical University

P68 Perivascular CNS Fibroblasts Are Associated With Increased Tumor Stiffness and Poor Immunotherapy Response in Glioblastoma Patients
Maksym Zarodniuk, Megna Panchbhavi, Alexander Steele, Xin Lu, Jun Li, Meenal Datta
University of Notre Dame

P69 Simulating the Impact of Tumor Mechanical Forces on Glymphatic Networks in the Brain Parenchyma
Saeed Siri, Alice Burchett, Meenal Datta
University of Notre Dame

P70 Biophysical Characterization of Increased Prostate Cancer Cell Survival in Muscle Tissue
Jonah Spencer[1], Anne Cress[2], Jacob Notbohm[1]
[1]University of Wisconsin-Madison, [2]University of Arizona

P71 Direct Quantification of Cancer-Associated Exosomes in Plasma Enables Rapid Identification of Cancer Using Rotational Diffusometry of Janus Particles
John Sinclair[1], Sonu Kumar[1], Tiger Shi[1], Satyajyoti Senapati[1], Han-Sheng Chuang[2], Chia Chang[1]
[1]Notre Dame, [2]National Cheng Kung University

P72 Towards the Estimation of Tumor Stiffness Using B-Mode Ultrasound Imaging
Tanmay Mukherjee, Adarsh Shree, Reza Avazmohammadi
Texas A&M University

Special Session: Emerging Tools for Cell Mechanics

P73 A Novel Method for Studying Mechanotransduction: Complex Force Frequency Application Using Magnetic Vortex Microdiscs
Matthew Holler[1], Elena Rozhkova[2], Valentine Novosad[2], Scott Wood[1]
[1]South Dakota School of Mines, [2]Argonne National Laboratory

P74 Building Homemade Optical Tweezers to Study the Mechanical Forces of the Chondrocyte Cytoskeleton in the Context of Osteoarthritis
Samantha Smith, Scott Wood
South Dakota School of Mines

Special Session: Fiber Mechanics

P75 3D Printing Patient-Specific Left-Heart Models for Surgical Planning
Jakari Harris, Scott Hollister, Lakshmi Dasi
Georgia Institute of Technology

P76 Assessing the Impact of Hyaluronic Acid on the Rheological Properties of Collagen Hydrogels
Nicholas Gigliotti, Vivian Su, Mitra Taheri
Johns Hopkins University

P77 Femtosecond Laser Generated Micro-Cuts in Partially Recruited Collagen Fibers Show Micro-Forces Relevant on the Microscale
Miriam Bohlmann Kunz, Hannah Schilpp, Po-Yi Lee, Ian Sigal
University of Pittsburgh

P78 Using Fiber Modeling to Understand the Effects of Modulating Tissue Mechanical Properties as A Preventative Treatment for Glaucoma
Yingzhe Han, Bingrui Wang, Xuehuan He, Yuankai Lu, Ian Sigal
University of Pittsburgh

P79 Low Strain Rate Cyclic Loading and Recovery Effect on the Fatigue Properties of the Anterior Cruciate Ligament
Peter Kuetzing, Ulrich Scheven, Ellen Arruda
University of Michigan

Tissue & Cellular Engineering

P113 Developing a Scaffold With Gradient Mechanical Properties for Rotator Cuff Repair: A Parametric Finite Element Study
Sam Winston[1], Lynn Pezzanite[1], Ted Schlegel[2], Anthony Romeo[3], Steven Dow[1], Kirk McGilvray[1]
[1]Colorado State University, [2]University of Colorado School of Medicine, [3]Rothman Orthopedic Institute

P114 Role of Obese-Like Adipocytes in the Pathophysiology of Atrial Fibrillation Using 3D Bioprinted Models
Lara Celebi, Pinar Zorlutuna
University of Notre Dame

P115 Shining Light on Calcium-Mediated Morphogenesis: Forward Engineering Organ Development With Optogenetics and Mechanosensation
David Gazzo, Mayesha Sahir Mim, Nilay Kumar, Megan Levis, Maria Unger, Gabriel Miranda, Jeremiah Zartman
University of Notre Dame

P116 In Vitro Regionalization of Early Midbrain and Hindbrain Tissues Derived From Micropatterned Human Pluripotent Stem Cells
Tianfa Xie, Han Jiang, Lauren Brown, ChangHui Pak, Yubing Sun
University of Massachusetts Amherst

P117 Balancing Competing Effects of Epithelial Tissue Growth and Cytoskeletal Regulation During Organogenesis
Nilay Kumar[1], Jennifer Ambriz[2], Kevin Tsai[2], Mayesha Mim[1], Marycruz Flores-Flores[1], Weitao Chen[2], Mark Alber[2], Jeremiah Zartman[1]
[1]University of Notre Dame, [2]University of California

P118 Spatiotemporal Analysis for Hypertrophic Chondrocyte Differentiation in Spheroid Culture
Jeonghyun Kim[1], Kosei Tomida[1], Eijiro Maeda[1], Taiji Adachi[2], Takeo Matsumoto[1]
[1]Nagoya University, [2]Kyoto University

P119 Developing Mouse-Tumor Model for High Intensity Foucsed Ultrasound (HIFU) Ablation Procedures
Nabin Khanal[1], Victoria Summey[2], Jeffrey Bailey[2], Xin Duan[2], Rupak K. Banerjee[1]
[1]University of Cincinnati, [2]Cincinnati Children's Hospital Medical Center

P120 A Click Chemistry Method to Evaluate Glycosaminoglycan Composition and Metabolism in Articular Cartilage
Annie Porter, Steven DiStefano, Emily Newcomb, Michael Axe, X. Lucas Lu
University of Delaware

P121 Polychlorinated Biphenyls Alter Macrophage Polarization and Plasticity
Riley Behan-Bush, Jesse Liszewski, Michael Schrodt, Aloysius Klingelhutz, James Ankrum
University of Iowa

P122 A Novel Explant-in-A-Chip Perfusion Platform for Ex Vivo Preservation of Tissue Viability Applied to Both Healthy and Cancerous Tissues
WITHDRAWN
Eva Zeringa[1], Saverio Charalambous[1,2], Kinga Suba[1], Avirup Chowdhury[1,2], Ester Reina-Torres[1], Larry O'Connell[1], Foivos Chatzidimitriou[1], Joseph van Batenburg-Sherwood[1], Olivier Pardo[1], Alan Melcher[1,2], Paul Huang[2], Darryl Overby[1]
[1]Imperial College, [2]Institute of Cancer Research

P123 p21 Suppression to Improve Osteogenic Capacity of MSCs
Sina Jafari, Aaron Brandner, Julie Sandria, Priyatha Premnath
University of Wisconsin Milwaukee

P124 Assessing Pattern Recognition Receptor Agonist Loaded Hydrogels as A Potential Rotator Cuff Repair Augment
Sam Winston, Devin von Stade, Cody Plaisance, Renata Impastato, Lynn Pezzanite, Steven Dow, Kirk McGilvray
Colorado State University

P125 The Effect of Tissue Engineered Heart Valve Design on Remodeling: Optimizing Valve Functionality and Collagen Organization
Valery Visser[1], Sarah Motta[1], Simon Hoerstrup[1,2], Frank Baaijens[3,4], Sandra Loerakker[3,4], Maximilian Emmert[1,2,5,6]
[1]Institute for Regenerative Medicine, [2]Wyss Translational Center, [3]Eindhoven University of Technology, [4]Institute for Complex Molecular Systems, [5]German Heart Center, [6]Charité Universitätsmedizin

P126 Synthetic Hyaluronic Acid Coating Preserves the Phenotypes of Lymphatic Endothelial Cells
Sanjoy Saha, Fei Fan, Laura Alderfer, Francine Graham, Eva Hall, Donny Hanjaya-Putra
University of Notre Dame

Translational Technology Pitch Competition

P64 Integrating Autopsy-Based Radio-Pathomic Maps of Tumor Probability for Guiding Surgical Biopsies in Glioblastoma
Samuel Bobholz, Allison Lowman, Aleksandra Winiarz, Savannah Duenweg, Michael Flatley, Biprojit Nath, Jennifer Connelly, Dylan Coss, Max Krucoff, Anjishnu Banerjee, Peter LaViolette
Medical College of Wisconsin

P65 Delta Cuff
Cyrus Darvish[1], Pete Gueldner[1], Rabih Chaer[2], David Vorp[1], Timothy Chung[1]
[1]University of Pittsburgh, [2]University of Pittsburgh Medical Center

Poster Session II — Biotransport

P64 Hydrogel Wound Healing in Palliative Care
Tre Welch, Jamie Wright, Vanini Pimpalwar, Kelley Newcomer, Matteo Ligorio
University of Texas Southwestern Medical Center of Dallas

P65 Characterization of Microstructural Changes on Biglycan/Decorin Induced Mouse Bone by Low-Field NMR
Qingwen Ni
Texas A&M International University

P66 Comparative Liquid Flow Analysis in Battery-Powered Suction Devices for Advanced Airway Management
Maria J. Londono[1], Saketh R. Peri[1,2], Zach Fallon[1], David DiRocco[1], David Restrepo[1], Robert A. De Lorenzo[2,1], R. Lyle Hood[1,2]
[1]University of Texas at San Antonio, [2]University of Texas Health Science Center at San Antonio

P67 **Significantly Amplified Photoacoustic Effect for Silica-Coated Gold Nanoparticles by Interface Heat Transfer Mechanisms**
Chen Xie[1], Peiyuan Kang[1], Jonghae Youn[1], Blake Wilson[1], Lokesh Basavarajappa[1], Qingxiao Wang[1,2], Moon Kim[1], Kenneth Hoyt[1], Zhenpeng Qin[1,3]
[1]University of Texas at Dallas, [2]King Abdullah University of Science and Technology, [3]University of Texas at Southwestern Medical Center

P68 **Development of a Non-Invasive Imaging Approach for Assessing Radiation-Induced Changes in Intestinal Barrier Function**
Austen Nissen, Christopher Hansen, Guru Sharma, Brian Fish, Dana Veley, Amit Joshi, Heather Himburg
Medical College of Wisconsin

P69 **Effect of Breathing Technique for Targeted Laryngopharyngeal Drug Delivery**
Shamudra Dey[1], Guilherme J.M. Garcia[1,2]
[1]Marquette University and Medical College of Wisconsin, [2]Medical College of Wisconsin

P70 **A New Strategy to Enhance Radiofrequency Ablation Within the Low Electrical Conductivity Region of Atherosclerotic Plaque: A Mathematical Modeling**
Ruizhe Hou, Hongying Wang, Shiqing Zhao, Aili Zhang
Shanghai JiaoTong University

P71 **Enhancing Fluid Infusion via Introduction and Enlargement of Microcracks in Tumors – Theoretical Simulations**
Md Jawed Naseem, Ronghui Ma, Liang Zhu
University of Maryland Baltimore County

P72 **Accelerating Hydrodynamic Fabrication of Microstructure Using Deep Neural Networks**
WITHDRAWN
Nicholus Clinkinbeard, Reza Montazami, Nicole Hashemi
Iowa State University

P73 **Measuring Flow Resistivity in Microfluidic-Based Medical Devices**
Ali Bozorgnezhad, Luke Herbertson, Suvajyoti Guha
US Food and Drug Administration

P74 **Computational Analysis of the Contribution of Paracrine Chemotaxis to Spatial Distribution of Leukocytes in Cerebral Aneurysms**
Ruskin Shi, Hadi Wiputra, Victor Barocas
University of Minnesota-Twin Cities

Fluid Mechanics

P75 **The Hemodynamics of Mechanical Heart Valves: A Comparison of Numerical Simulations Against Experimental Measurements**
Syed Samar Abbas[1], Lorenzo Ferrari[2], Dominik Obrist[2], Iman Borazjani[1]
[1]Texas A&M University, [2]University of Bern

P76 A Parametric Model of the Mitral Valve From Multimodal Imaging Data
André Da Luz Moreira, Anders Persson, Farkas Vanky, Matts Karlsson, Jonas Lantz, Tino Ebbers
Linköping University

P77 Non-Newtonian Effects on Sinus Flow After Aortic Valve Replacement
Ahmad Bshennaty[1], Brennan Vogl[1], Zhongtian Zhang[1], Agata Sularz[2], Bruce Lee[1], Mohamad Alkhouli[2], Hoda Hatoum[1,1]
[1]Michigan Technological University, [2]Mayo Clinic

P78 Image-Based 3D Reconstruction Analysis of Regional Thrombosis After Transcatheter Aortic Valve Replacement
Katelynne Berland[1], Breandan Yeats[1], Taylor Becker[2], Marco Moscarelli[3], Khalil Fattouch[3], Lakshmi Dasi[1]
[1]Georgia Institute of Technology, [2]Ohio State University, [3]Maria Eleonora Hospital

P79 Transcatheter Aortic Valve Hemodynamics in HALT Positive and Negative Patient Cohorts: An FSI Study
Thangam Natarajan[1], Aniket Venkatesh[1], Stephanie Sellers[2], Janarthanan Sathananthan[2], Lakshmi Dasi[1]
[1]Georgia Institute of Technology, [2]University of British Columbia

P80 Virtual Stenting of Patient-Specific Vascular Stenoses
Jonathan Pham, Fanwei Kong, Doug James, Jeffrey Feinstein, Alison Marsden
Stanford University

P81 Impact of Boundary Conditions and Blood Rheology on Indices of Wall Shear Stress From IVUS-Based Patient-Specific Stented Coronary Artery Simulations
Robert McCarthy[1], Peter Mason[2], David Marks[3], John LaDisa[1,3,4,5]
[1]Marquette University and the Medical College of Wisconsin, [2]Medical College of Wisconsin, [3]Cardiovascular Medicine, Medical College of Wisconsin, [4]Pediatric Cardiology, Medical College of Wisconsin, [5]Children's Wisconsin

P82 Fluid-Structure Interaction Model of the Human Heart With a Closed-Loop Model of the Circulation
Masod Sadipour[1], Marshall Davey[2], David Wells[3], Charles Puelz[4], Boyce Griffith[1,5]
[1]University of North Carolina, [2]Curriculum in Bioinformatics and Computational Biology,University of North Carolina, [3]University of North Carolina at Chapel Hill, [4]Baylor College of Medicine and Texas Children's Hospital, [5]University of North Carolina, Chapel Hill

P83 Cardiac-Induced Brain Tissue Motion in Chiari Malformation Type 1 and Its Relationship to: Surgery, Crowding, and Symptomatology
Mahsa Karamzadeh[1], Mohamad Motaz Al Samman[1], Christopher Maclellan[2,3], Rafeeque Bhadelia[2,3], Amir Ebrahimzadeh[2,3], John Oshinski[4], Francis Loth[1]
[1]Northeastern University, [2]Beth Israel Deaconess Medical Center, [3]Harvard Medical School, [4]Emory University School of Medicine

P84 Characterization of Failure in Cerebral Aneurysm Stenting

Reza Bozorgpour[1], Pilhwan Kim[1], Peter Tze Man Kan[2], Mahsa Dabaghmeshin[1]
[1]University of Wisconsin-Milwaukee, [2]University of Texas Medical Branch

P85 Using CFD to Assess Tracheal Work of Breathing in Neonates With Tracheoesophageal Defects Pre and Post Surgical Repair

Christopher Boles[1,2], Chamindu Gunatilaka[1], Qiwei Xiao[1], Jason Woods[1], Paul Kingma[1], Alister Bates[1,2]
[1]Cincinnati Children's Hospital Medical Center, [2]University of Cincinnati

P86 Multiscale Modeling of Blood Flow in Aortic Root Aneurysm

Yurui Chen[1], Hannah Zhai[1], Hiroo Takayama[2], Vijay Vedula[1]
[1]Columbia University, [2]Columbia University Irving Medical Center

P87 Bladder Biomechanics and Shape Characterization: Comparison Study of Healthy vs BPH Using Uro-Dynamic MRI

Juan P. Gonzalez-Pereira, Shane Wells, Matthew Grimes, Wade Bushman, Alejandro Roldan-Alzate
University of Wisconsin-Madison

P88 Extension of Murray's Law to Three Dimensions With Multiple Daughter Vessels

Seth Street[1], David Dierker[1], Mark Johnson[1], Samer Hoz[2], James Castiglione[3], Charles Prestigiacomo[1]
[1]University of Cincinnati College of Medicine, [2]University of Pittsburgh, [3]Thomas Jefferson University

P89 Comparison Between Vessel Wall Models to Estimate Hemodynamics in Coronary Artery Bypass Graft Patients

Nhien Tran-Nguyen[1], Andrew Yan[1,2], Stephen Fremes[1,3,4], Laura Jimenez-Juan[1,2,4], Piero Triverio[1]
[1]University of Toronto, [2]St. Michael's Hospital, [3]Sunnybrook Health Sciences Centre, [4]Sunnybrook Research Institute

P90 Longitudinal Changes in Mechanical Properties of Aorta From Angiotensin-II Infused Mice Obtained by an Inverse Finite Element Method

Hadi Wiputra[1], Sydney Clark[2], Craig Goergen[2], Victor Barocas[1], Matthew Bersi[3]
[1]University of Minnesota, [2]Purdue University, [3]Washington University in St. Louis

P91 Differences in Flow Dynamics Between Coronary Artery Aneurysms and Ectasia

Brennan Vogl[1], Emily Vitale[1], Simon Lee[2], John Kovalchin[3], Hoda Hatoum[1]
[1]Michigan Technological University, [2]Lurie Children's Hospital of Chicago, [3]Nationwide Children's Hospital

P92 Medical Imaging Based Patient-Specific Blood Flow Modelling of Cerebrovasculature

Amar Shrivastava[1], Ashish Suri[2], Sitikantha Roy[1]
[1]Indian Institute of Technology Delhi, [2]AIIMS New Delhi

P93 **Revisiting Murray's Law Pulmonary Arteries: Exploring Branching Patterns and Principles**
Sofia Altieri Correa, Amirreza Kachabi, Mitchel J. Colebank, Naomi C. Chesler
University of California, Irvine

P94 **Hemodynamic Analysis of Sinotubular Junction Plication Techniques During Ascending Aortic Replacement**
Hannah Zhai[1], Yurui Chen[1], Yu Hohri[2], Hiroo Takayama[2], Vijay Vedula[1]
[1]Columbia University, [2]Columbia University Medical Center

P95 **A Thermodynamics-Based Approach for Estimating Ventricular Efficiency: Application in Patients With Single Ventricle Physiology**
Sanjib Gurung, Arutyun Pogosyan, Gregory S. Perens, Kim-Lien Nguyen, John Paul Finn
University of California, Los Angeles

MS SPC: Cardiovascular

P39 **Development of Coarctation of the Aorta Software to Combat Hypertension**
Shahd Sawalhi[1], Arash Ghorbannia[1,2,3], Andrew Spearman[2], Robert Cooper[1], John LaDisa[1,2,4]
[1]Marquette University and the Medical College of Wisconsin, [2]Children's Wisconsin and the Medical College of Wisconsin, [3]Duke University, [4]Medical College of Wisconsin

P40 **Computational Study on the Hemodynamics of Bioprosthetic Pulmonary Valves in Patients With Repaired Tetralogy of Fallot**
Kwang-Bem Ko[1], Jung-Hee Seo[1], Ashish Doshi[2], Danielle Gottlieb-Sen[2], Rajat Mittal[1]
[1]Johns Hopkins University, [2]Johns Hopkins Medicine

P41 **Estimation of Flow Rates From Clinical Pressure Measurements for Individualized CFD of Cerebral Venous Stenotic Disease**
Gurnish Sidora[1], Anna Haley[1], Nicole Cancelliere[2], Vitor Pereirav[2,1], David Steinman[1]
[1]University of Toronto, [2]St. Michael's Hospital

P42 **The Impact of Natural Estrogen and Progesterone Cycling on Cardiac Function in Mice**
Thaotho Nguyen, Cassandra Conway-O'Donnell, Naomi Chesler
University of California, Irvine

P43 **Computational Modeling of Left Ventricular Flow Using MRI-Derived Four-Dimensional Wall Motion**
Seyed Babak Peighambari[1], Tanmay Mukherjee[1], Amr Darwish[2], Roderic Pettigrew[1,3], Dipan Shah[2], Reza Avazmohammadi[1,3]
[1]Texas A&M University, [2]Houston Methodist DeBakey Heart & Vascular Center, [3]School of Engineering Medicine

P44 **Marginal Chordae Force Data in a Physiological In Vitro Mitral Valve Setup**
Mads Ancker[1], Sam Stephens[1], Neil Ingels[1], Jonathan Wenk[2], Morten Jensen[1]
[1]University of Arkansas, [2]University of Kentucky

P45 **Structural and Mechanical Analysis of Treated and Untreated Aortic Coarctation**
Matt Culver, Colleen Witzenburg, Alejandro Roldan-Alzate, Luke Lamers, Michael Stellon, Leah Gober
University of Wisconsin-Madison

P46 **Porcine Thoracic Aortic Tissue Failure Strength Is Associated With Bulk Density Which May Be Detectable From Diffusion Tensor Imaging**
Pete Gueldner[1], Cyrus Darvish[1], Timothy Chung[1], Chandler Benjamin[2], Keshava Rajagopal[3], Kevin Hitchens[1], Spandan Maiti[1], Kumbakonam Rajagopal[2], David Vorp[1]
[1]University of Pittsburgh, [2]Texas A&M University, [3]Thomas Jefferson University

MS SPC: Solid Mechanics

P47 **The Mechanicalization of Locomotor Training for Gait Rehabilitation Due to Damage Caused by Partial Spinal Injuries: Defing Parameter of Knee Jerk Relex Stimulation Device.**
Hannah Khelfa, Mohammed Sbai, Sanford Meek
University of Utah

P48 **A Finite Element Model for Simulating Closed-Head Impact Injury in a Mouse Model: Implications for Tau Pathology in Traumatic Brain Injury**
Ruiyuan Chi, Patrick Alford
University of Minnesota Twin Cities

P49 **The Material Tuning of Annealing PVA Hydrogels for the Application of TMJ Disc Replacement**
Hassan Mahmoud, Christian Puttlitz, Kevin Labus
Colorado State University

P50 **3D Assessment of Rat Knee Joint Anatomy Using High Field MRI**
Olivia Dyer, Mackenzie Conner, Stephanie Cone
University of Delaware

P51 **Microscale Shear Wave Tensiometry Tracks Axial Stress in Tendon Fascicles**
Shreya Kotha[1], Samantha Kahr[1], Darryl Thelen[1], Jonathon Blank[2], Alex Reiter[3]
[1]University of Wisconsin-Madison, [2]University of Pennsylvania, [3]St. Louis University

P52 **A Systematic Analysis Confirmed That Mechanical and Structural Anisotropies Do Not Concur in 37 percent of Equatorial Sclera Samples**
Bangquan Liao[1], Yi Hua[2], Fengting Ji[1], Frederick Sebastian[3], Rouzbeh Amini[3], Ian Sigal[1]
[1]University of Pittsburgh, [2]University of Mississippi, [3]Northeastern University

P53 **Development and Validation of a Vehicle Front Profile Finite Element Model to Evaluate Pedestrian Impacts**
James Wolf, Karthik Somasundaram, Frank Pintar
Marquette University and Medical College of Wisconsin

P54 Pregnancy and Age Differentially Affect Stiffness, Collagen Microdamage Susceptibility, and Composition of Uterosacral Ligaments
Catalina Bastias[1,2], Lea Savard[2], Kathleen Connell[3], Kathryn Jacobson[2], Sarah Calve[2], Virginia Ferguson[2], Callan Luetkemeyer[1]
[1]University of Illinois Urbana-Champaign, [2]University of Colorado Boulder, [3]University of Colorado Anschutz

P55 Uniaxial Biomechanical Response of Murine Uterine Tissue After Surgery-Induced Scarring
Savannah Chatman, Niyousha Karbasion, Abigail Fisk, Matthew Bersi, Perry Ann Brody
Washington University in St. Louis

MS SPC: Tissue Engineering, Biotransport, Mechanobiology

P56 Functionalized Nanoparticles Mediated High Intensity Focused Ultrasound (HIFU) Ablation in Mice
Nabin Khanal[1], Michael Marciniak[2], Marie-Christine Daniel[2], Liang Zhu[2], Matthew Lanier[3], Charles Dumoulin[3,1], Rupak K. Banerjee[1]
[1]University of Cincinnati, [2]University of Maryland Baltimore County, [3]Cincinnati Children's Hospital Medical Center

P57 Mechanical Characterization of Human Mesenchymal Stem Cell-Derived Osteocytic Spheroids by Uniaxial Compression Testing
Takashi Inagaki, Jeonghyun Kim, Eijiro Maeda, Takeo Matsumoto
Nagoya University

P58 Pressure Overload During Murine Pregnancy and Its Effects on Acute Cardiac Remodeling
Adalyn Meeks[1], Elnaz Ghajar-Rahimi[1], Molly Kaissar[2], Kyoko Yoshida[2], Craig Goergen[1]
[1]Purdue University, [2]University of Minnesota

P59 Evaluating the Biomechanical Response of 3D Printed Synthetic Tissue-Mimicking Materials for Cardiovascular Applications.
Vivian Tan[1], Daniella Eliathamby[2], Craig Simmons[2], Jennifer Chung[3], M. Owais Khan[1]
[1]Toronto Metropolitan University, [2]University of Toronto, [3]University Health Network

P60 Induced Pluripotent Stem-Cell Derived Cardiomyocyte Aged Tissue Model
Hatice Emanet, Frances Dipietro, Sneha Philip, Aylin Acun
Widener University

P61 The Impacts of Estrogen and Progesterone on Extracellular Matrix Remodeling in Female Mice Are Strain-Dependent
Allison Sander, Brianne Connizzo
Boston University

P62 A Pre-Chondrogenic Stem Cell Niche Facilitating Articular Cartilage Formation via Improving Chondrogenic Phenotype via Changing Stiffness and Cell Seeding Density

Yuqian Yang[1], Ruxin Yang[1], Kiera Downey[1], Samuel Oh[1], Erika Noel[2], Cheri Deng[1], Rhima Coleman[1]

[1]University of Michigan, [2]Florida International University

P63 Modulating In Vivo Compliance and Remodeling of a Polyurethane Based, Antithrombogenic Tissue Engineered Vascular Graft via Gelatin Incorporation

Katarina Martinet[1], David Maestas[1], Keishi Kohyama[1], William Wagner[1,2], Jonathan Vande Geest[1,2,3]

[1]University of Pittsburgh, [2]McGowan Institute of Regenerative Medicine, [3]Vascular Medicine Institute

Solid Mechanics

P112 Rapid Estimation of Left Ventricular Contractility With a Physics-Informed Neural Network Inverse Modeling Approach

Ehsan Naghavi[1], Haifeng Wang[1], Lei Fan[2,3], Jenny S. Choy[4], Ghassan Kassab[4], Seungik Baek[1], Lik-Chuan Lee[1]

[1]Michigan State University, [2]Marquette University, [3]Medical College of Wisconsin, [4]California Medical Innovations Institute

P113 iPSC-Derived Endothelial Multi-Cell Networks Synergistically Modify Their Basal Contractility and Extracellular Matrix in 3D

Toni West, Jiwan Han, Gabriel Peery, Robin Tuscher, Janet Zoldan, Michael Sacks

University of Texas

P114 Unravelling the Structural Mechanisms Underlying Aging-Augmented Risk of Aortic Dissection

Ruizhi Wang, Xunjie Yu, Bela Suki, Katherine Zhang

Boston University

P115 Deciphering Cardiac Allograft Vasculopathy: A Multiscale Computational Approach to Improve Heart Transplant Outcomes

Elisa Serafini[1,2], Anna Corti[3], Enrico Sangiorgio[4], Maddalena Bovetti[4], Diego Gallo[4], Carly S. Filgueira[1], Xian C. Li[1,5], Claudio Chiastra[4], Stefano Casarin[1,2,5]

[1]Houston Methodist Research Institute, [2]La Rochelle University, [3]Politecnico di Milano, [4]Politecnico di Torino, [5]Houston Methodist Hospital

P116 Mechanism of the Developed Pressure – Preload Relationship in Ex-Vivo Beating Heart

Lei Fan[1], Vahid Ziaei-Rad[2], Jason Bazil[2], Lik Chuan Lee[2]

[1]Marquette University and Medical College of Wisconsin, [2]Michigan State University

P117 Mechanical Stress in Atherosclerotic Coronary Arteries Are Associated With Plaque Growth

Jeremy Warren, Clark Meyer, Heather Hayenga

University of Texas at Dallas

P118 AI-Based Quantification of Vascular Calcifications for Enhanced Risk Evaluation
Mehdi Ramezanpour[1], Anne M. Robertson[1], Xiaowei Jia[1], Juan R. Cebral[2]
[1]University of Pittsburgh, [2]George Mason University

P119 Biomechanics Parameter Predicts Outcome of Fetal Heart Intervention Better Than Clinical Scan Parameters
Laura Green[1], Wei Xuan Chan[1], Andreas Tulzer[2], Gerald Tulzer[2], Choon Hwai Yap[1]
[1]Imperial College London, [2]Children's Heart Center Linz

P120 Multiscale Cardiac Modeling of Preterm Neonates
Salla Kim[1], Mitchel Colebank[1], Filip Jezek[2], Kara Goss[3], Pim Oomen[1], Dan Beard[2], Naomi Chesler[1]
[1]University of California, Irvine, [2]University of Michigan, [3]University of Texas Southwestern Medical Center

P121 A Random Forest Classification Method to Estimate Rupture Risk of Abdominal Aortic Aneurysms Based on Biomechanical and Geometric Surrogates
Juan C. Restrepo[1], Merjulah Roby[1], Pratik Mitra[1], Satish C. Muluk[2], Mark Eskandari[3], Ender A. Finol[1]
[1]University of Texas at San Antonio, [2]Allegheny Health Network, [3]Northwestern University School of Medicine

P122 Computational Insights on the Correlation of Myofiber Contractility With the Developed Pressure-Preload Dynamics in Ex-Vivo Beating Hearts
Vahid Ziaei-Rad[1], Lei Fan[2], Jason Bazil[1], Lik Chuan Lee[1]
[1]Michigan State University, [2]Marquette University and Medical College of Wisconsin

P123 Computational Modeling of the Aorta in a Mouse Model of Marfan Syndrome to Determine Temporal Changes in Geometric Biomarkers and Wall Shear Stress
Yufan Wu, Krashn Dwivedi, Jessica Wagenseil
Washington University in St. Louis

P124 Investigating the Role of Wall Stress in Aortic Growth of Acute Uncomplicated Type B Aortic Dissection Using Fluid-Structure Interaction Analysis
Minliang Liu[1], Yuxuan Wu[2], Adam Mazlout[2], Yuhang Du[1], Rishika Agarwal[2], Hannah Cebull[3], Marina Piccinelli[3], John Elefteriades[4], Rudolph Gleason[2], Bradley Leshnower[3]
[1]Texas Tech University, [2]Georgia Institute of Technology, [3]Emory University, [4]Yale University

P125 Microstructural Abnormalities in Human Hypertrophic Septal Tissues
Duc Khang Chung[1], Milad Almasian[2], Houjia Chen[1], Katherine Copeland[1], Kytai Nguyen[1], Matthias Peltz[3], Pietro Bajona[3], Yi Hong[1], Yichen Ding[2], Jun Liao[1]
[1]University of Texas at Arlington, [2]University of Texas at Dallas, [3]University of Texas Southwestern Medical Center

P126 Finite Element Simulations of Heart Valve Function With Shape Enforcement in FEBio
Devin Laurence[1], Patricia Sabin[1], Steve Maas[2], Jeffrey Weiss[2], Matthew Jolley[1]
[1]Children's Hospital of Philadelphia, [2]University of Utah

P127 The Impact of Right Ventricular Fiber Re-Orientation on Left Ventricular Contraction: A Numerical Studay
Mengqian Zhang[1], Kenzo Ichimura[2], Kurt Stenmark[1], Edda Spiekerkoetter[2], Vitaly Kheyfets[1]
[1]University of Colorado Anschutz Medical Campus, [2]Stanford University

P128 Novel Computational Model for Planning Patent Ductus Arteriosus Stenting Procedure
Luis René Mata Quiñonez[1,2], Srujana Joshi[1,2], Shweta Karnik[1,2], Leon Cheng[1,2], Andrew Marini[1,2], Shobana Santhanam[1,2], Rahav Kothuri[1], Charles Federico[1,2], Suhaas Bonkur[1,2], Lakshmi Dasi[1,2], Holly Bauser-Heaton[1,2,3]
[1]Georgia Institute of Technology, [2]Emory University, [3]Children's Healthcare of Atlanta

P129 Structure and Function of the Murine Greater Thoracic Vessels
Abhay Ramachandra[1], Cristina Cavinato[2], Jay Humphrey[3]
[1]Iowa State University, [2]Université Montpellier, [3]Yale University

P130 Evaluation of Transcatheter Edge-to-Edge Repair Clip Selection via an Open-Source Finite Element Simulation Framework
Patricia Sabin[1], Devin Laurence[1], Wensi Wu[1], Christian Herz[1], Steve Maas[2], Jeffrey Weiss[2], Matthew Jolley[1]
[1]Children's Hospital of Philadelphia, [2]University of Utah

P131 Fiber Shortening and Laminar Thickening Strain Attributes Reveal Greater Transmural Heterogeneity in Myocardial Deformation than Green Strains via DENSE MRI
Tawfik Hussein, John Oshinski
Georgia Institute of Technology

P132 Effects of Residual Stress on the Buckling and Twisting Behavior of Arteries
Qin Liu[1,2], Alejandro Cisneros[1], Hai-Chao Han[1]
[1]University of Texas at San Antonio, [2]New York Institute of Technology

P133 Simulated TAVR Lifetime Management to Assess Coronary Obstruction Risk for Varied Deployments of Balloon-Expandable and Self-Expanding Valves
Courtney Ream[1], Taylor Becker[2], Venkateshwar Polsani[3], Pradeep Yadav[3], Vinod Thourani[3], Lakshmi Dasi[1]
[1]Georgia Institute of Technology, [2]Ohio State University, [3]Piedmont Hospital

P134 Simulation of Self-Expanding Transcatheter Pulmonary Valve Deployment in the Right Ventricular Outflow Tract
Christopher Zelonis[1], Nicolas Mangine[1], Kyle Sunderland[2], Steve Maas[3], Stephen Ching[1], Yuval Barak-Corren[1], Devin Laurence[1], Wensi Wu[1], Patricia Sabin[1], Andras Lasso[2], Matthew Gillespie[1], Jeff Weiss[3], Matthew Jolley[1]
[1]Children's Hospital of Philadelphia, [2]Queen's University, [3]University of Utah

P135 Aortic Location and Sex Specific Alterations in Mechanics and Wall Remodeling in a Mouse Model of Marfan Syndrome
Krashn Dwivedi, Jacob Rother, Jessica E Wagenseil
Washington University in St. Louis

P136 Developing an Experimentally Informed Structurally Representative Human Lung Model
Arif Badrou, Crystal Mariano, Gustavo Ramirez, Matthew Shankel, Talyah Nelson, Mona Eskandari
University of California, Riverside

P137 In Vivo Pulmonary and Thoracic Wall Injury Risk From Behind Armor Blunt Trauma
Justin McMahon[1], Parker Berthelson[1], Alexander Stotka[1], Barney McEntire[2], Robert Salzar[1]
[1]University of Virginia, [2]US Army Aeromedical Laboratory

P138 Mechanical Characterization of the Fibrosed Lung Surface via Spherical Indentation
Kathrine Quiros[1], Talyah Nelson[1], Mona Eskandari[2,1]
[1]University of California, [2]University of California, Riverside

P139 Shear Strains as a Tear Growth Mechanism for High-Grade Partial-Thickness Rotator Cuff Tendon Tears
Carla Nathaly Villacis Nunez[1], Ulrich Scheven[1], Asheesh Bedi[2], Ellen Arruda[1]
[1]University of Michigan, [2]NorthShore Orthopedic and Spine Institute

P140 Microscale Remodeling of Arterial Wall Leads to Macroscopic Pressure-Independent Axial Force
Ruturaj Badal, Ryan Mahutga, Patrick Alford, Victor Barocas
University of Minnesota

P141 Determining High Strain Rate Porcine Brain Material Properties Using Inertial Microcavitation
Elizabeth Bremer-Sai[1], Anastasia Tzoumaka[2], Surya Kolluri[2], David Henann[2], Christian Franck[1]
[1]University of Wisconsin-Madison, [2]Brown University

P142 In-Situ and In-Vitro Heterogeneity of Porcine Meninges: Insights From 2-Photon Microscopy and Correlated Micro-Indentation
Seyed Mohammad Tabatabaei, Lakiesha N. Williams
J. Crayton Pruitt Family University of Florida

P143 Functions of Prolyl Hydroxylation in Elastin
Chengeng Yang, Anna Tarakanova
University of Connecticut

P144 Validation of a Platform to Quantify Corneal Endothelial Cell Damage Due to Indentation
Alex J. McMullen[1], Aldo Tecse[1], Paul D. Funkenbusch[1], Naveen Mysore[2], Yousuf M. Khalifa[3], Mark R. Buckley[1]
[1]University of Rochester, [2]University of Rochester Medical Center, [3]Emory University School of Medicine

P145 IOP-Induced Lamina Cribrosa Astrocyte Deformations Measured Directly From the Astrocytes Are Larger Than Those Estimated From the Deformations of the Collagen Beams
Bingrui Wang, Susannah Waxman, Sofia Lusvardi, Hannah Schilpp, Ashley Linton, Yuankai Lu, Ian Sigal
[1]*University of Pittsburgh*

P146 Investigating the Influence of GAG Digestion and Corneal Crosslinking on Collagen Fibril Organization
M.E. Emu, H. Hatami-Marbini
University of Illinois Chicago

P147 Preconditioning Impact on Porcine Corneal Biomechanics
Md Esharuzzaman Emu, Hamed Hatami-Marbini
University of Illinois Chicago

P148 Predicting Failure Locations in Heterogeneous Soft Materials
Catherine Eberman, Colleen Witzenburg
University of Wisconsin Madison

P149 A Multiscale and Multimodal Computational Framework Towards Understanding Mechanotransduction in the Distal Colon and Rectum
Amirhossein Shokrani, Bin Feng, David M. Pierce
University of Connecticut

P150 AI in B3: Artificial Intelligence in Biomechanics, Bioengineering, and Biotransport
Chester Jar, Lindsey Westover, Gail Thornton
University of Alberta

P151 Probing the Rat Urinary Bladder During Isotonic Active Contraction Using Multiphoton Microscopy
Alireza Asadbeygi[1], Yasutaka Tobe[1], Sean Stocker[1], Simon Watkins[1], Paul Watton[1,2], Christopher Hardin[3], Naoki Yoshimura[1], Anne Robertson[1]
[1]*University of Pittsburgh,* [2]*University of Sheffield,* [3]*University of Missouri*

P152 Y-Shaped Cutting of Soft Solids: Potential for Soft Biological Material Characterization
Shaobo Zhan, Amy Wagoner Johnson, Shelby Hutchens
University of Illinois at Urbana-Champaign

P153 Finite Element Modeling of Behind Armor Blunt Trauma From Indentor Impacts to the Lung and Liver
Karthik Banurekha Devaraj[1,2], Balaji Harinathan[1,2], Alok Shah[2], Jared Koser[2], Karthik Somasundaram[2], Brian Stemper[2], Narayan Yoganandan[2]
[1]*Vellore Institute of Technology,* [2]*Medical College of Wisconsin*

P154 Computational and Multi-Scale Mechanical Analysis of Soy Gel Extrusion Process
Marco Fielder, Arun Nair
University of Arkansas

P155 Optical Coherence Elastography Measurement of Cerebral Artery Stiffness
Mykyta Ananchenko[1], Xu Feng[2], Samuel Halvorsen[1], Guoyang Li[3], Seok-Hyun Yun[2,4], Yanhang Zhang[1]
[1]Boston University, [2]Massachusetts General Hospital, [3]Peking University, [4]Harvard University

P156 Development of an Acoustically Augmented Uniaxial Extension Testing Apparatus to Detect the Proportional Limit in Biological Soft Tissues
Cyrus Darvish[1], Peter Jacobs[2], Elias Mignonga[2], Yuqi Cai[2], Pete Gueldner[2], David Vorp[2], Timothy Chung[2]
[1]Univeristy of Pittsburgh, [2]University of Pittsburgh

P157 Morphological Analysis of Hindfoot Osteoarthritis via Statistical Shape Modeling of the Foot and Ankle
Elana Renae Lapins[1,1], Shireen Elhabian[1,1], Charles Saltzman[1], Amy Lenz[1,1]
[1]University of Utah

P158 Propylparaben Exposure Alters Uterine Microstructure and Indentation Modulus
Mahmuda Arshee, Indrani Bagchi, Ayelet Ziv-Gal, Amy Wagoner Johnson
University of Illinois at Urbana-Champaign

P159 Hydrogel Phantom System as Mechanical Placental Tissue Mimics
Samyuktha Kolluru[1], Adrienne Scott[2], Patrick Yang[2], Michelle Oyen[1,2]
[1]Washington University in St. Louis, [2]Washington University in St Louis

P160 Umbilical Arterial Development and Mechanics in Gestational Diabetes Mellitus
Kara Peak, Sarah Wernimont, Victor Barocas
University of Minnesota

P161 MRC2 Is Necessary for Typical Cervical Remodeling in Rodent Pregnancy
Serena Russell[1], Bex Pendrak[1], Mariano Colon-Caraballo[2], Mala Mahendroo[2], Kristin Myers[1]
[1]Columbia University, [2]University of Texas Southwestern Medical Center

P162 Prediction of Tearing in Vaginal Tissue Using Machine Learning
Mostafa Zakeri, William Snyder, Justin Krometis, Traian Iliescu, Raffaella De Vita
Virginia Tech

P163 Characterizing the Influence of Proteoglycans on Passive and Viscoelastic Material Properties of Female Pelvic Floor Skeletal Muscles
Megan Routzong[1], Francesca Sesillo[1], John Rudell[1], Marianna Alperin[1,2]
[1]University of California, San Diego, [2]Sanford Consortium for Regenerative Medicine

P164 Spatially Mapping the Time-Dependent Material Properties of the Nonhuman Primate Cervix Through Gestation
Echo Xu[1], Camilo Duarte-Cordon[1], Daniella Fodera[1], Shuyang Fang[1], Ivan Rosado-Mendez[2], Timothy Hall[2], Helen Feltovich[3], Kristin Myers[1]
[1]Columbia University, [2]University of Wisconsin-Madison, [3]Mount Sinai

Tissue & Cellular Engineering

P96 3D Age-Related Breast Cancer Model With Aged and Young Collagen Extracts for Drug Screening
Jun Yang, Gokhan Bahcecioglu, Aktar Ali, Brian Blagg, Pinar Zorlutuna
University of Notre Dame

P97 Spatial Heterogeneity in Engineered Heart Tissue Mechanics Following In Vitro Infarction
Michael Potter[1], Samuel Coeyman[1], Jonathan Heywood[1], William Richardson[2]
[1]Clemson University, [2]University of Arkansas

P98 Development of Hormonally Responsive Tunable Hydrogel
Vivian Su[1], Nicholas Gigliotti[1], Juan Diego Carrizo[2], Mitra Taheri[1]
[1]Johns Hopkins University, [2]University of Pennsylvania

P99 Microfluidic Dual-Gel Cell Culture Model: Studying Cell Migration Under Controlled Interstitial Flow
Rossana Iturbide, Alimohammad Anbari, Jing Fan, Sihong Wang
City College of New York

P100 Role of Sex and Sex Hormones in Pulmonary Artery Adventitial Fibroblast Mechanosignaling
Yufan Lin, Giuditta Monti, Daniela Valdez-Jasso
University of California, San Diego

P101 Engineering Mesenchymal Stromal/Stem Cells Into an Anti-Oxidative Agent by a Mechanically Dynamic Hydrogel System Sensitive to Oxidative Stress
Nicholas Serio, Thomas Leahman, Sing-Wan Wong
Colorado State University

P102 Quantifying Changes in Morphological and Biochemical Properties of Senescent Cells
Amarnath Singam[1], Kimberly Ramirez[1], Deok-Ho Kim[2], Jingchun Chen[1], Seungman Park[1]
[1]University of Nevada, Las Vegas, [2]Johns Hopkins University

P103 The Compound Stimulation of Matrix Stiffness and Collagen Concentration on Tumor Organoid Migration
Bo-Jiang Lin, Hiromichi Fujie, Masashi Yamazaki, Koji Takahashi, Naoya Sakamoto
Tokyo Metropolitan University

P104 Alterations in Microglia Morphology and Viability Following In Vitro Traumatic Brain Injury
Emily Blick, Christian Franck, Aviad Hai
University of Wisconsin-Madison

P105 Role of Calcium in Regulating Mechanical Phenotype of Cells in A 3D Microtissue
Vaishali Bala, M.K. Sewell-Loftin
University of Alabama at Birmingham

P106 In Vitro, Network-Wide Excitotoxic Disruption Following Traumatic Brain Injury Model to Assess Critical Injury Thresholds
Jamie Sergay[1], Natalie Schick[2], Emily Blick[1], Aviad Hai[1], Christian Franck[1]
[1]University of Wisconsin Madison, [2]Rutgers

P107 Endothelial Cells Exhibit a Similar Temporal Response to Ultrasound as Normal Flow
Ian McCue, Adam Johnson, Joseph Turner, Ryan Pedrigi
University of Nebraska-Lincoln

P108 Characterization of the Basal Endothelial Glycocalyx
Zoe Vittum, Solomon Mensah
Worcester Polytechnic Institute

P109 Dissecting YAP/TAZ Mechanotransductive Mechanisms in Vascular Morphogenesis
Paula Camacho[1], Brendan Tobin[2], Devon Mason[1], Jason Burdick[3], Amber Stratman[4], Levi Wood[2], Joel Boerckel[1]
[1]University of Pennsylvania, [2]Georgia Institute of Technology, [3]University of Colorado Boulder, [4]Washington University in St. Louis

P110 LIM-Nebulette Regulates Podocyte Mechanoresponse and Focal Adhesion Remodeling
Jacob Wright[1], Yixin Hu[1], Anthony Mendoza[1], Nanditha Anandakrishnan[1], Anika Hudson[1], Alan Stern[1], Eric Lima[2], Evren Azeloglu[1]
[1]Icahn School of Medicine at Mount Sinai, [2]Cooper Union

P111 Assessing the Effect of Dimethyl Sulfoxide on the Properties of Regulatory Enzyme Fructose 1,6-Bisphosphatase in Gluconeogenesis Conditions
Amin Sabaghan, Neda Ghousifam, Mahboobeh Rezaeeyazdi, Christopher Riley, Dwight Romanovicz, Marissa Nichole Rylander, Matthew Uden
University of Texas at Austin

Undergraduate Design Competition

P165 Exoskeleton for Surgery Training
Moved to Poster Session I: P170
Jeremy Varughese, Andres Miramontes, Jesse Gomez, Andrew Gonzales Alayo, Anissa Cantu, Luis Morales
University of Texas at Dallas

P166 Epilog: Rapid EEG Detection of Status Epilepticus
Rohan Chhaya, Carly Flynn, Elena Grajales, Priya Shah, Dori Xu
University of Pennsylvania

P167 Erias: A Bluetooth Cardiac Monitoring System for Pediatric Inpatient Use Erias: A Bluetooth Cardiac Monitoring System for Pediatric Inpatient Use
Alexandra Dumas, Angela Song, Samir Maarouf, Daphne Nie, Georgia Georgostathi
University of Pennsylvania

P168 Region Adjustable Prosthetic Socket
Camilo Rodriguez Rozas, Kristin Bindas, Katie LeClaire, Maddi Viteri, Savannah Waymer
University of Pittsburgh

P169 Easy-O: Low-Cost Oxygen Therapy Unit
Emma Kim, Kaito Hara-Lee, Alina Gammage, Darien Gaw, Sabrina Packer, Michael Jones, Amanda Donoso, Xian Wang
Queen's University

P170 See-Rynge: A Visually Accessible Liquid Measurement Device
Chiadika Eleh, Liam Pharr, Venkatesh Shenoy, Joey Wei, Isaac Kim
University of Pennsylvania

P171 IV Tutor: IV Insertion Training Module
Kaito Hara-Lee, Maya Goodman, Nathan Duncan, Andrew Kim, Gavin Nyhof, Rebecca Hisey, Xian Wang
Queen's University

P172 Non-Invasive, Quantitative Anterior Cruciate Ligament Integrity Measurement System
Lindsay Phillips, Daniel Lounsbery, Jake Ritchie, Alex Ropars
Binghamton University

P173 SmartSleeve+: A Post-Operation Solution for Detecting Infections Underneath Casts for Patients With Open Fractures
Jamie Moni, Gautham Nair, Ajit Saran, Pavan Raghupathy
University of Pennsylvania

P174 Home Unweighting Exercise Device for Patients With Diabetic Foot Ulcers
MOVED TO SESSION I, POSTER 171
Victoria Moore, Miles Yoshinobu, Mirabella Herrera, Tanveer Ahmed, Rachel Porter
University of Texas at Dallas

P175 KneeVive: At-Home Osteoarthritis Symptom Mitigation
Aaryan Chaudhary, Anitez Gautam, Yennifer Lemus, Devan Yarberry, Zeeshan Haque, Anna Maria Kuraszkiewicz, Aryan Kulkarni, Ian Miller, Anna Lin, Benjamin Goldblatt, Brooke Oberlee, Caroline Gerety, Diya Asawa, Dylan Yee, Juliette Tao, Kavyon Touserkani, Kush Gami, Liam Morrison, Michael Leacoma, Nare Parseghian, Shafeena Uddin, Sofia Goryachev, Victoria Villalonga, Wesley Hanson, Zainab Khalil
University of Massachusetts Amherst

P176 Enhancing Labor Comfort: Development of an Adaptive Pressure Clamp for Double Hip Squeeze
Connor Beck[1], Noah Kibler[2], Sheryl Korah[1], Osman Sayginer[1]
[1]Temple University, [2]Drexel University

P177 CARDIOFORECASTER - An AI-Driven Cardiovascular Disease Forecasting Platform
Valerie Balas, Krysta Bernold, Mathieu Colon, James Evangelisto III, Kylie Herbert, Daniel Roozbahani, Ria Mazumder
Widener University

P178 TrueDose, An Adolescent Medication Compliance iOS Application
Nicolette Cilenti, Matthew Jester, Skylar Ford, Elle Ferguson
University of Pennsylvania

P179 Neuragame: Integrating App-Based & Physical Therapy for at Home Stroke Rehabilitation
Jishnu Basu, Samarth Kabbur, Arnav Nair, Deeya Kaneria, Ryan Virkar, Reshmitha Muppala
University of Texas at Austin

P180 OASIS: Oxygen Auto-Titrating System for Increased Sustainability
WITHDRAWN
Srish Chenna, Kira Lu, Sylvia Mihailescu, Karan Shah, Kalen Truong
University of Pennsylvania

P181 Engineering Mesenchymal Stromal Cells to Facilitate Muscle Regeneration by Correcting Oxidative Stress
Ali Eldeiry, Sing-Wan Wong
Colorado State University

P182 Universal Hitch Attachment for Blind Veteran
Alexa Warren, Anna Sasse, Joshua Perry, Bailey Erickson, Marvin Aguilera, Christopher Luliucci, Erik Brewer
Rowan University

P183 VITAFLOW - The Future of Heart Preservation
Jimin Jung, Nigel Newby, Spencer Tuohy, Tyler McGoldrick
University of Pennsylvania

P184 Tracheostomy Humidification Device
Estefania Enciso Pelayo, Jonathan Balsano, Michael Fong
University of California, San Diego

P185 Firefighter Cooling Device
Emanuel Guzman, Wade Coons, Brady Killham
University of Texas at Arlington

P186 Goniotape: Creating a Wearable Alert System for Post Operative Patients and Communication to Healthcare Professionals
Vikas Addanki, Caeley Shorr, Madison Plone, Erik Brewer
Rowan University

P187 ExoFlex: An Accessible Exoskeleton Glove for Gross Hand Function Rehabilitation
Nova Meng, Haley Morgenstern, Anthony Saldutti, Sharon Zheng
University of Pennsylvania

P188 RoboGripper: EMG-Controlled, Wrist Brace-Mounted, Robotic Manipulator for Hand Paralysis Patients
WITHDRAWN
Shaiv Mehra, Tyler Merrill
Purdue University

P189 Optical Coherence Tomography and Vibrometry Endoscope
Christopher Clark, Sofia Gandarilla, Briana Marquez, Minh-Huy Tran, Alexis Valencia
University of Riverside, California

P190 The Future of Intravenous Therapy Insertions by Using Vein Finder Technology in Emergency Scenarios to Improve Patient Safety

Ugochukwu Akpati, Ramiro Flores, Thai Pham, Baohong Yuan
University of Texas at Arlington

P191 A Benchtop Study of Physiological Response for the Novel Self-Powered Fontan Circulation

Clayton Purdy[1], Anthony Damon[1], Levi Blumer[1], Keyu Vadaliya[1], Martin Cinelli[1], Megan Parker[1], Dr. Ray Prather[1,2], Dr. Arka Das[1], Dr. Eduardo Divo[1], Dr. Alain Kassab[2], Dr. William DeCampli[3]
[1]Embry-Riddle Aeronautical University, [2]University of Central Florida, [3]Orlando Health Arnold Palmer Hospital for Children

P192 Development of an Automated Bone Transport Device for Use in Distraction Osteogenesis

Chloe Brekhus, Ben Gadomski, Christian Puttlitz
Colorado State University

CONFERENCE PROCEEDINGS

SB³C2024
Summer Biomechanics, Bioengineering and Biotransport Conference
June 11-14, Lake Geneva, WI, USA

IMMERSION, INNOVATION, DESIGN & DEVELOPMENT (I2D2): A 9-WEEK SUMMER EXPERIENCE IN BIOMEDICAL ENGINEERING

Alan W. Eberhardt

Department of Biomedical Engineering
University of Alabama at Birmingham
Birmingham, Alabama, USA

INTRODUCTION

The past fifty years has seen tremendous growth in the healthcare industry, constituting 20% of the gross domestic product of the United States (U.S.) by 2020 [1]. With a medical device market size of $155 billion in 2017, the U.S. was considered the largest market in the world [2]. Engineered solutions produced game-changing medical innovations including MRI/CT scanning, angioplasty and stents, hip and knee replacement [3]. Clinical and rehabilitation needs present golden opportunities for biomedical engineering (BME) students to be trained in medical device design and commercialization.

The National Institute for Biomedical Imaging and Bioengineering (NIBIB) has long been a strong advocate for interdisciplinary approaches to STEM education that apply knowledge and employ innovative technologies. Interdisciplinary education that brings together biomedical engineering and business/entrepreneurship is key to bolstering innovation. The present abstract describes an 8-week summer program aimed at providing rising juniors in biomedical engineering at the University of Alabama at Birmingham (UAB) an opportunity to gain an introductory experience in clinical immersion, innovation, design, and development (I2D2).

METHODS

This program was designed to provide rising juniors from the UAB BME undergraduate program an opportunity to engage in an 8-week innovation experience based on clinical immersion. Six Summer Innovation Fellowships of $3,000 were awarded competitively that were intended to defray expenses incurred by students living on campus during the summer. An additional $250 was available for prototyping expenses. As a recipient of the award, students were expected to invest at least 30 hours per week to their project, performing background research, engaging in design and prototyping, and interacting extensively with clinicians and other project mentors. Projects emphasized improving outcomes for hospitalized patients and patients living with disabilities. No outside employment was permitted for the duration of the fellowship.

The program began with discussions on empathy, where students familiarized themselves with the areas they would encounter during their clinical rotations (advanced endoscopy, minimally invasive surgery, endovascular/vascular surgery, colo/rectal/GI surgery, endocrine surgery, and melanoma surgery). Shadowing was completed over one week, including clinicians from the UAB School of Medicine. Two additional days of shadowing were done at Lakeshore Foundation (a fitness facility and hospital for people with disabilities, where students were exposed to rehab engineering and various needs for assistive technologies. The students returned to the classroom and defined the problem(s) and articulated the challenges clinicians faced with respect to a particular process or device for treating a specific disorder.

The next two weeks were spent on classroom lectures, provided by the author, on the following topics:

1. Disease State Fundamentals, Existing Solutions
2. Working in teams – DISC, Need Statements
3. From Need Specs to Design Constraints
4. Stakeholder & Market Analyses
5. Intellectual Property & Regulatory Pathways
6. Best Design Practices, User-centered Design
7. Ideation & Evaluation
8. Early- and Late-Stage Prototyping

To better prepare students to be successful with their early design planning, lectures on “Best Practices in Design” were presented using excerpts from Biodesign [4]. A lecture was given on Design for Manufacture/Assembly (DFMA), where students were instructed to minimize and standardize parts and subassemblies, and determine what is commercially available (e.g., motors, bearings) vs. custom-made components. The ideation portion of the class tasked the students with generating multiple ideas. A Pugh matrix approach was used to identify

the leading solution candidate based upon the established design requirements. Prototyping of leading design candidates was enabled through multiple fabricating facilities for conventional machining, forming, and 3D printing of prototypes. Solutions were expressed in written and oral form through team-based reports and presentations. Highlights are shown in Figure 1.

At the completion of the I2D2 program, students were asked to

Figure 1. (left) early prototyping; (center) machine shop work; (right) final presentation day with surgeons.

rank the following concepts with a 1 (no knowledge/skill) to 5 (knowledgeable/ skilled), according to their experiences (before vs. after completing I2D2.

1. How to perform clinical needs finding
2. Ability to formulate design constraints
3. How to determine a medical device class
4. How to determine the market associated with a device
5. How to use machine shop tools to build a device
6. How to perform a Risk Analysis

They were also asked to provide comments concerning the time spent performing clinical rotations; in the classroom; and building and testing prototypes (too short, too long, just about right), as well as what recommendations would you provide to make the overall experience better for the students next summer?

RESULTS

All students agreed that the time spent in the classroom was too long, while the time spent prototyping was too short. Time spent shadowing clinicians/therapists was about right, though the students reported feeling a bit lost.

Figure 2 shows the survey results comparing the students' opinions of their own knowledge/skill levels regarding the lecture portion of the course. There are clear increases across the board – the experience was valuable in helping students to work with clinicians to identify needs and to establish the relevant design constraints. The identification of medical device class was a topic where students were initially very ignorant but learned easily how to use the FDA website to identify relevant predicate devices to establish the likely device class of their design. Interesting, students felt the most confident and there was the least change in knowledge/skill related to market analysis. The experience gained in the UAB Design & Fabrication Facility proved invaluable to the students and the topic of Risk Analysis was one that they had never seen and after the experience, still felt a bit uncertain.

Students were encouraged to submit their work to the 2023 BMES Annual Meeting. One student did so and traveled to Seattle where her work was accepted for the undergraduate student poster session.

DISCUSSION

Improvements planned for Summer, 2024 include reducing the overall number of days in the classroom by increasing the hours/day during the initial lectures. The mix of hospital/rehab projects was good. Overall, the complexities of the hospital projects, along with the regulatory hurdles involved in bringing a device into the clinic, preclude most hospital projects from making it beyond initial prototypes. Rehab/assistive technologies, on the other hand, commonly result in devices that can be delivered to the client, which increases the overall satisfaction of both client and the students. Prototyping will be extended allowing the students more time to iterate on designs based on feedback from clients.

One addition will be to have the students better familiarize themselves with the problem and disease state through a review of peer-reviewed journal articles related to the clinical problems.

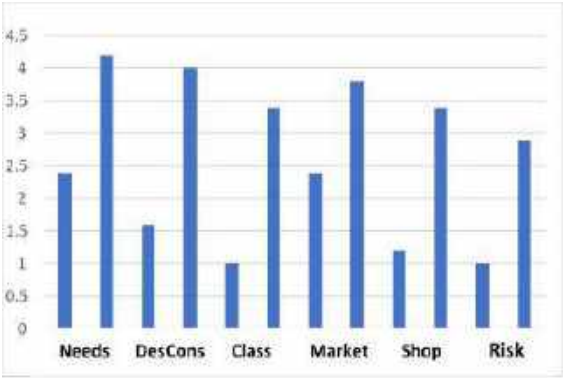

Figure 2. Pre/post student survey results for I2D2 experience.

ACKNOWLEDGEMENTS

The author gratefully acknowledges financial support from the National Institutes of Health Grant No. R25EB032762. A hearty shout-out to Mr. Steven Thompson at the UAB Design and Fabrication Facility for training and assisting students in "the reality zone" of the machine shop. Thank you to Dr. Herb Chen (UAB Dept. of Surgery) and all the surgeons who participated in the shadowing experiences, especially Drs. Wong, Kennedy, Bateni, and Gillis. Special thanks to Rebecca Rogers, Stephanie Ward, John Franks and Karyn Sullivan at Lakeshore Foundation.

REFERENCES

[1] Keehan, S.P., et al., Health Affairs, 30(8), pp. 1594–1605
[2] https://www.selectusa.gov/medical-technology-industry-united-states.
[3] Lee, J.-S., 2010 "Biomedical Engineering Entrepreneurship," World Scientific Publishing Co, Inc.
[4] Yock, P et al., Biodesign, 2nd ed., 2015.
[5] Norma, D, The Design of Everyday Things, 2013.
[6] ideaedu.org

COMPARISON OF COMPUTATIONAL MODELS FOR PREDICTING LEACHING FROM IMPLANTED MEDICAL DEVICES

Martin L. Tanaka (1), David M. Saylor (2), Robert M. Elder (2)

(1) College of Engineering and Technology, Western Carolina University, Cullowhee, NC, USA
(2) US Food and Drug Administration (DBCMS – OSEL – CDRH), Silver Spring, MD, USA

INTRODUCTION

Utilization of computational modeling and simulation in medical device development can enable faster development of new products, lower research and development costs, and decrease animal usage. The engineering standard ASME V&V40, "Assessing Credibility of Computational Modeling through Verification and Validation: Application to Medical Devices" released in 2018 has made the use of computational modeling more accessible for companies seeking approval or clearance from the US Food and Drug Administration (FDA). Moreover, Regulatory Science Tools (RSTs) and Medical Device Development Tools (MDDTs) approved by the FDA include new computational approaches to aid with submissions that did not exist only a few years ago.

An important aspect of any implanted medical device is biocompatibility, an attribute of which is the need for a device not to release hazardous materials into the body at a level above the safe limit (toxicological threshold). The rate that polymeric components within medical devices leach potentially hazardous materials can be estimated using computational modeling.

In this research, two computational models are developed and compared. The first is a one-component model that predicts the rate that materials are leached from an implanted polymeric medical device using Fickian diffusion equations and a sink boundary condition at the polymer tissue interface. The second model contains two components and adds complexity and clinical relevance by accounting for migration across the polymer tissue interface and diffusion through peri-implant tissue. Differences in the modeling results are compared and the advantages of each approach are identified.

METHODS

Physics based models were developed to calculate the diffusion rate of leachables using Fick's law [1],

$$\frac{\partial C(x,t)}{\partial t} = D_p \nabla^2 C(x,t) \tag{1}$$

where, the concentration of the leachable substance, C, is a function of the position within the polymer, x, and time, t. D_p is the effective (macroscopic) diffusion coefficient of the leachable in the polymer. D_p is scalar and independent of C, x, and t.

The one-component model for the mass release $M(\tau)$ as a fraction of the initial mass of leachable contained within the device M_0 is given by,

$$\frac{M(\tau)}{M_0} = \begin{cases} 2\sqrt{\frac{\tau}{\pi}} & \tau \le 0.2 \\ 1 - \frac{8}{\pi^2} exp\left(-\frac{\tau \pi^2}{4}\right) & \tau > 0.2 \end{cases} \tag{2}$$

$$\tau = \frac{D_p\, t}{L^2} \tag{3}$$

where τ, is a dimensionless time parameter that is scaled by D_p, and half the implant thickness, L.

Leaching from the two-component model is characterized by the equation below [2],

$$\frac{M(\tau,\beta)}{M_0} = \left(\frac{\beta}{1+\beta}\right) 2\sqrt{\tau}\left(\frac{1}{\sqrt{\pi}} - \left(\frac{\beta}{1+\beta}\right) 2 \sum_{n=1}^{\infty}\left[\left(\frac{1-\beta}{1+\beta}\right)^{n-1} ierfc\left(\frac{n}{\sqrt{\tau}}\right)\right]\right) \tag{4}$$

$$\beta = \frac{1}{K_{p:t}} \sqrt{\frac{D_t}{D_p}} \tag{5}$$

where, β, is a dimensionless parameter associated with migration across the polymer-tissue interface and the relative migration rate within the polymer, $K_{p:t}$, is the polymer tissue partition coefficient, and D_t, is the diffusion rate of the leachable within the tissue.

Numerical solutions were developed using custom MATLAB code to characterize a "general medical device". Thus, the solutions presented are applicable to any implanted device that contains polymeric material. Two cases were used as an example 1) the release of Bisphenol A (BPA) from a silicone device and 2) the release of Irganox 1010 from a device made from high density polyethylene (HDPE). The first case is representative of small molecules diffusing through a high diffusivity polymer where $\log_{10}\beta$ = - 1.27. The second case represents the other extreme, a large molecule diffusing through a low diffusivity polymer where $\log_{10}\beta$ = 2.40.

RESULTS

For BPA in silicone the one-component model estimated complete mass release (M/M_0 = 100%) within about 8 hours, but the more complex two-component model only predicted 35.3% mass release in 24 hours (Figure 1a). For Irganox 1010 in HDPE the one-component model and two-component model have visibly identical results with the first line being totally covered by the second (Figure 1b). Both models predict a mass release of 0.15% of the total mass in the first 24 hours.

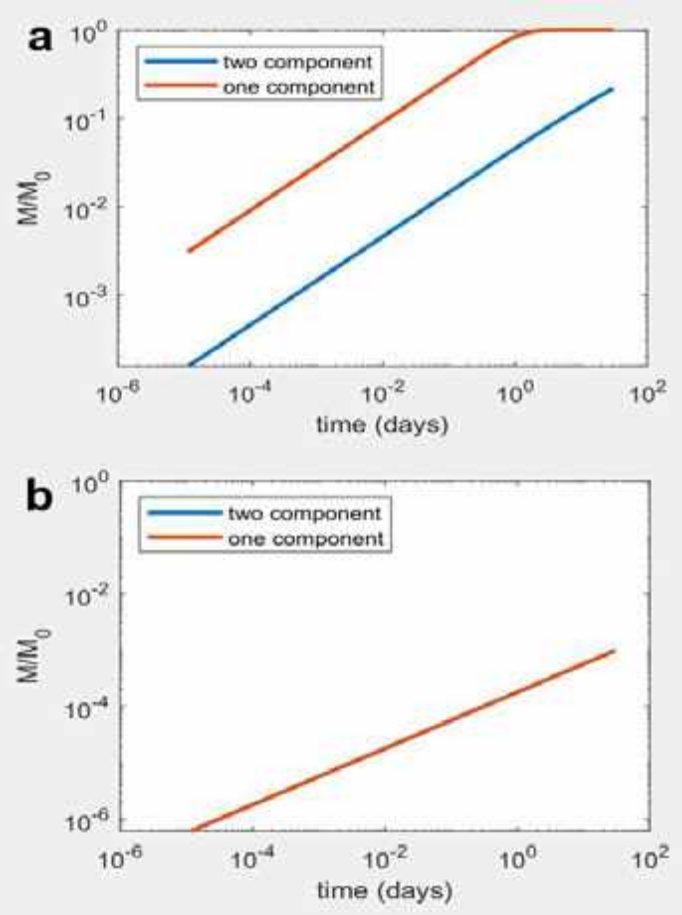

Figure 1: Comparison of model results for cumulative mass release of BPA in silicone (a) and Irganox 1010 in HDPE (b).

Figure 2 shows the difference in predicted mass release using the two models to be indistinguishable over much of the clinically relevant input parameter range (Deep blue area on the top portion). However, when the value of β was small, large differences were observed in the predicted mass release, exceeding four orders of magnitude in some instances.

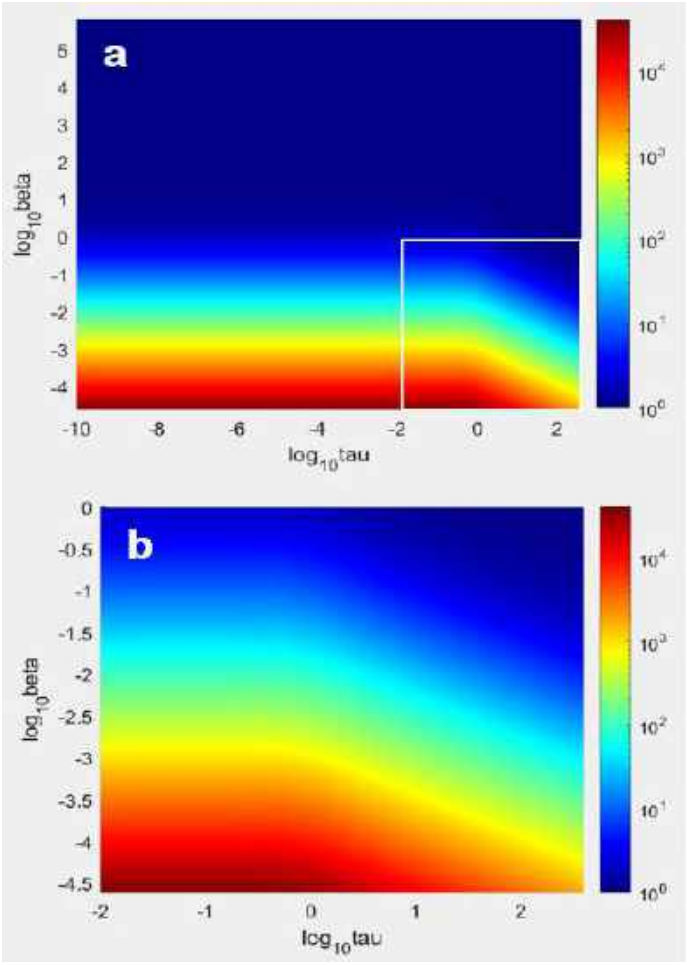

Figure 2: The ratio of predicted mass release (one-component model / two-component model) is shown over the typical range of input parameter values (a) and in a close-up section (b).

DISCUSSION

The findings imply that the one-component model may be sufficient to predict the mass release in cases like Irganox 1010 in HDPE because the two models yield essentially the same result. This effect was also observed in general for other cases where values of β are high. Thus, in these cases, it may not be beneficial to apply the more complex model when the simpler model predicts the same outcome.

However, in the case of BPA in silicone, mass release predicted by the one-component model exceeded the two-component model by an order of magnitude. When clinically relevant predictions of mass release are desired, use of the more complex two-component model may be warranted.

ACKNOWLEDGEMENTS

This research was supported by a grant from the National Science Foundation, Award #2149517.

REFERENCES

[1] Crank, J., 1975, The mathematics of diffusion. (2nd ed.), Claredon Press, Oxford.

[2] Tanaka, M., Saylor, D., and Elder, R., (in review), "Polymer-Interface-Tissue Model to Estimate Leachable Release from Medical Devices," Mathematical Medicine and Biology: A Journal of the IMA

SINGLE CELL MECHANICAL ANALYSIS REVEALS VISCOELASTIC SIMILARITIES BETWEEN ASTROCYTES AND GLIOBLASTOMA CELLS

J. Najera (1), K. Onwudiwe (1), L. Holen (2) A. Burchett (1), D. Rodriguez (1), M. Zarodniuk (1), S. Siri (1), and M. Datta (1)

(1) Department of Aerospace and Mechanical Engineering, University of Notre Dame, Notre Dame, IN, USA
(2) Department of Biological Sciences, University of Notre Dame, Notre Dame, IN, USA

INTRODUCTION

In malignant tumors, the physical attributes of the host organ can significantly affect cancer spread. For tumors outside of the brain, it has been previously reported that cancer cells become softer and more mobile than normal cells in response to local mechanical forces, promoting their migration and metastasis away from the primary tumor [1]. However, these mechanobiological phenomena are vastly unexplored in the brain. In this study, we aimed to compare the viscoelastic properties of human U87 glioblastoma (GBM) cells and their normal counterpart, immortalized human astrocytes (IHAs) using a parallel-plate flow chamber. We also used fluorescence microscopy to quantify actin density and alignment in both cell types given the essential role of actin in cellular mechanical behavior. Indeed, an understanding of GBM cell mechanics may lead to the identification of novel disease mechanisms, biomarkers, and therapeutic strategies to improve treatment outcomes.

METHODS

Cell Culture. IHAs and U87 GBM cells were cultured at 37 °C and 5% CO_2. GBM cells were cultured in DMEM + 10% FBS + 1% penicillin/streptomycin, and IHAs were cultured in SuperCult IHA Media + 1% IHA growth supplement + 2% FBS + 1% penicillin/streptomycin. Both cell types were seeded in 35 mm Petri plates at a density of 5,000 cells/plate.

Shear Assay. The viscoelastic properties of IHAs and U87 cells were evaluated by employing our previously established modified shear assay technique [2]. Briefly, IHAs and U87 cells were exposed to physiological levels of fluid shear stress (FSS) experienced in the brain (4 Pa). The amount of stress applied (σ) was calculated using the formula for a parallel-plate flow chamber (Eqn. 1).

$$\sigma = \frac{6\mu Q}{wh^2} \tag{1}$$

Here, μ is the viscosity of the infused fluid (serum-free DMEM + 0.5 wt% methylcellulose), Q is the volumetric flow rate, and w and h are the width and height of the rubber gasket placed on the flow chamber, respectively. Phase-contrast video recordings were taken of cells while exposed to FSS for subsequent digital image correlation (DIC) analysis.

Digital Image Correlation Analysis. The Davis 10.1.2 software was used to perform DIC analysis on individual cells exposed to FSS using the phase-contrast recordings taken. Nuclear and cytoplasmic deformation within a cell was tracked by adding strain gauges to randomly selected areas of the nucleus and cytoplasm and using the sum of the differential track option. The output of the DIC analysis is a strain-time profile that can be further analyzed for mechanical characterization of the cell's subcellular components.

Modeling and Computation. Strain (ε)-time (t) profiles were fitted with a three-parameter generalized Maxwell model (Eqn. 2 and 3) using MATLAB's curve-fitting tool to quantify the viscoelastic properties (stiffness [E], viscosity [η_1], and stress-relaxation time [τ]) of the nucleus and cytoplasm of individual cells.

$$\varepsilon = \left(\frac{\sigma}{\eta_1}\right)t + \frac{\sigma}{E}\left(1 - \exp\left(\frac{-t}{\tau}\right)\right) \tag{2}$$

$$\tau = \frac{\eta_2}{E} \tag{3}$$

Statistical Analysis. T-tests were performed using the IBM SPSS statistical software. We adopted a 95% confidence level and considered means as being statistically significantly different at $p < 0.05$. Bar plots display the mean ± standard error of the mean (SEM).

Actin Density Quantification and Fiber Alignment Analysis. The actin fibers of IHAs and U87 GBM cells were stained with phalloidin to evaluate actin organization and alignment. The stained cells were imaged using a Keyence BZ-X810 widefield microscope. The Leica

fluorescence image processing software, LAS X, was used to quantify mean actin stain intensity for individual cells from each cell type as a measure of cellular actin density. Fiber alignment analysis was conducted using the MATLAB-based software CT-FIRE. Fiber angles were normalized to the circular mean angle for each cell and combined for statistical analysis.

RESULTS

A total of 84 U87 cells and 96 IHAs were analyzed for mechanical characterization. Our analysis of the strain-time profiles showed that the nuclear and cytoplasmic viscoelastic properties quantified were not statistically significantly different ($p > 0.05$) between U87 cells and IHAs (Fig. 1). Thus, there are no distinct mechanical differences between the normal and malignant brain cells. Comparing nuclear and cytoplasmic viscoelastic properties within each cell type, however, revealed that there are statistically significant differences ($p < 0.05$) in the stiffness and relaxation time in IHAs, but not in U87 GBM cells (Fig. 2). The difference between the nuclear and cytoplasmic viscosity in both cell types was statistically insignificant.

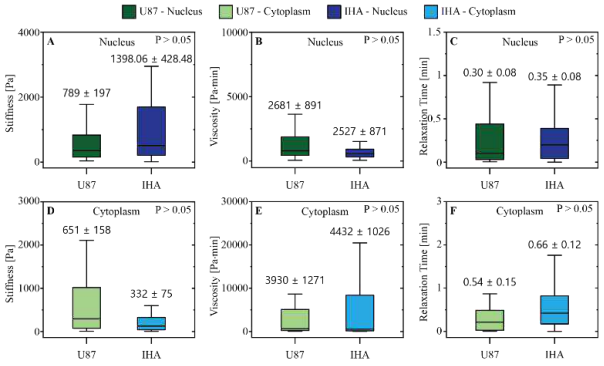

Figure 1: Comparison of the (A) nuclear stiffness, (B) nuclear viscosity, (C) nuclear relaxation time, (D) cytoplasmic stiffness, (E) cytoplasmic viscosity, and (F) cytoplasmic relaxation time between IHAs and U87 GBM cells.

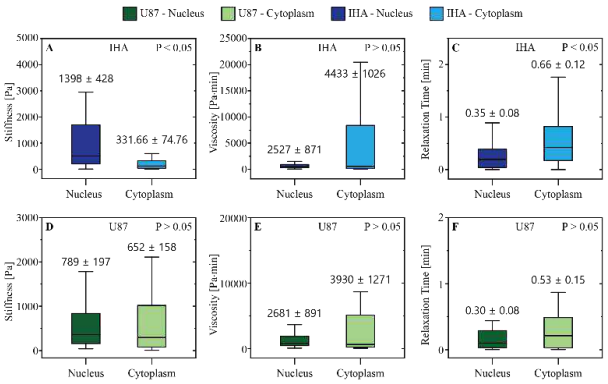

Figure 2: Comparison of nuclear and cytoplasmic stiffness, viscosity, and relaxation time of IHAs (A-C) and of U87 cells (D-F)

The actin density and alignment of 29 U87 cells and 32 IHAs was analyzed via fluorescent microscopy and is presented in Fig. 3. Fluorescent intensity analysis revealed that IHAs and GBM cells have similar levels of actin density as there were no statistically significant differences between the fluorescent intensity per cell area of both cell types. On the other hand, analysis of the actin fibers showed that the actin fibers of IHAs are typically more organized and aligned relative to U87 cells.

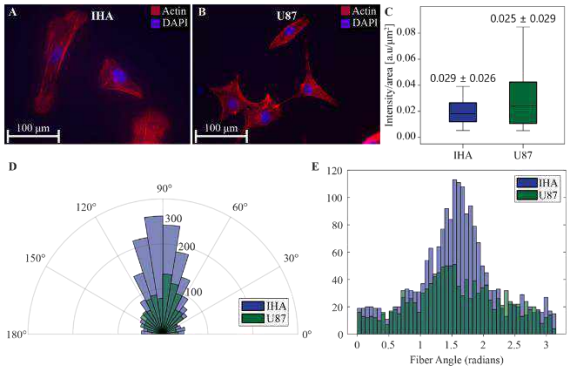

Figure 3: Representative images of phalloidin-stained (A) GBM cells and (B) IHAs. (C) Comparison of actin stain intensity between GBM cells and IHAs. (D) Angular representation of fiber orientation in GBM cells and IHAs. (E) Distribution of fiber angles relative to the average angle in each cell type investigated.

DISCUSSION

Our study sought to compare the mechanical properties between normal astrocytes and malignant brain cancer cells. Surprisingly, our results showed that, contrary to cancer cells originating from outside of the brain [1], the viscoelastic properties of GBM cells are similar to their normal counterpart. Moreover, our findings showed that, unlike the GBM cells, the differences between the stiffness and relaxation time of the nucleus and cytoplasm of IHAs are statistically significant. We also found that the actin density between both cell types did not differ significantly; this aligns with our mechanical analysis of IHAs and GBM cells discussed earlier. However, we did notice that the actin fibers of IHAs were more aligned and organized compared to the U87 cells. This feature may contribute to cell-type specific physiological and mechanical behaviors not captured in this study.

Overall, our results suggest that GBM cells may exhibit unique behaviors not seen in other extracranial cancer cell types. Notably, given the important role cellular mechanics plays in cancer cell migration, as well as the low mechanical demands and high fluid content in the brain [3], malignant cells may adopt unique brain-specific mechanical properties via inherent (genetic) and externally-driven (microenvironmental) mechanisms. This may explain why metastasis in GBM patients is rare [4] and conventional treatment options are unsuccessful [5], although future studies directly evaluating this connection are required. The impact of experimental parameters such as substrate stiffness is also a subject of future studies as tuning them may reveal mechanical differences not captured in this study.

ACKNOWLEDGEMENTS

This work was supported by the National Cancer Institute (NIH/NCI K22-CA258410 to M. Datta).

REFERENCES

[1] Alibert, C et al., *Biol. Cell*, 109:167-189, 2017.
[2] Holen, L et al., *J. Vis. Exp.*, 195:1-14, 2023.
[3] Kashani, AS et al., *R. Soc. Open Sci.*, 7:1-16, 2020.
[4] Mourad, PD et al., *Surg. Neurol.*, 63:511-519, 2005.
[5] Yalamart, SSK et al., *Cancers*, 15:1-37, 2023.

IMPACTS OF TEARS SIZE AND LOCATION ON BLOOD FLOW DYNAMICS IN TYPE-B AORTIC DISSECTION

K. Khanafer (1), S. Scofield (1), Y. Aboelkassem (1)

(1) Engineering/Technology Division, University of Michigan, Flint, Michigan, USA

INTRODUCTION

Acute type B aortic dissection (TBAD) is a critical cardiac condition with a high mortality rate that increases by 1-2% per hour after symptom onset [1]. This condition leads to tears in the inner layer of the aorta, resulting in the development of a flap tissue and the separation of aortic wall layers. The thin, weak outer aortic wall and a flexible, curved flap are significant consequences of acute dissection [2, 3]. Clinical interventions, such as grafting methods, surgery, and medications, are employed to restore normal aortic blood flow and prevent complications. Studies have investigated risk factors, including anatomical features (e.g., maximum aorta diameter, false lumen patency) and hemodynamic parameters (e.g., flow velocities through tears, pressure difference across the flap), influencing aortic dilation post-aortic dissection repair to mitigate the risk of complications.

Computational fluid dynamics (CFD) is considered a potential modeling tool to assist clinicians in provide valuable information on the hemodynamics of TBAD. The mechanism of some vascular illnesses, such aortic dissection, can be better understood and their course can be predicted using CFD. Previous research has shown that hemodynamic factors such flow velocity, wall pressure, and wall shear stress (WSS) strongly correlate with rupture. The development of a dissecting aneurysm is subject to a number of phenomena that CFD helps to understand and anticipate. There have been many studies on tears of aortic dissection. However, the majority of these studies assumed rigid wall model [8-11]. For example, Shi et al. [12] studied the effect of hemodynamics on Stanford type-A aortic dissection with various tear sizes and location. Their results illustrated that entry tear can significantly change the hemodynamics of aortic dissection. Further, their numerical results showed that the velocity in the true lumen was lower when the entry tear size was larger, and inversely, the velocity in the false lumen was higher.

The objective of this study is to develop in-silico numerical simulations using fluid structure interaction technique to study the effect of changing tear size and location on false lumen pressure of type-B aortic dissection.

METHODS

The numerical model of the aorta dissection used in this investigation is shown in Figure 1. Blood flow is governed by the incompressible Naiver-Stokes and continuity equations in a moving domain described by an arbitrary Lagrangian-Eulerian (ALE). The Navier–Stokes equations were solved numerically with a commercial finite-volume fluid dynamics solver (ANSYS Fluent 2023R1). Transient analysis was adopted to investigate the pulsatility of blood flow. The SST *k*-ω model was used in this investigation to describe turbulent flow.

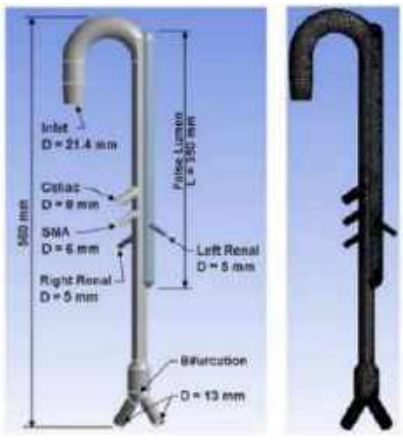

(a) (b)

Figure 1: (a) Schematic diagram of the model, (b) Mesh

Time-dependent pressure waveforms and velocities obtained from ex-vitro experiments [13] were applied at the inlet and outlet branches of the fluid domain. Total pressure was applied at the inlet of the numerical model while static pressures were applied at renal, celiac, superior mesenteric artery and iliac arteries. In this work, the false lumen, flap, and branches were assigned an elastic modulus of 9 MPa (PTFE) to mimic the physical model in [13].

RESULTS

In this section, we compare our numerical predictions with the experimental data reported in [13]. To arrive at a periodic solution, simulations for four cardiac cycles were run. The information output from the final cycle served as the foundation for the results shown below. Our numerical model was first validated against the ex-vitro experimental results for 65 mm^2 proximal tear and 20 mm^2 distal tear [13]. Pressure was measured in true and false lumens of the ex-vitro experimental model and was used to validate the values predicted by the numerical model in the same location. An excellent comparison was found between numerical and experimental results as depicted in Figure 2.

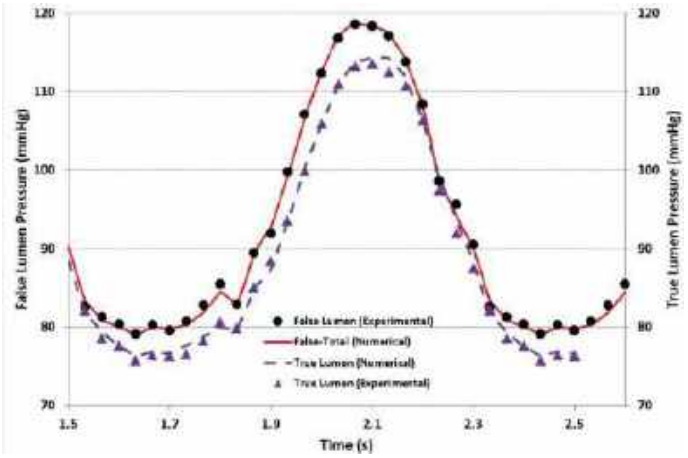

Figure 2: Comparison of the pressures in the true lumen and false lumen between experimental and numerical results (65 mm^2 proximal tear and 20 mm^2 distal tear).

The effect of varying the tear size on the pressure in false and true lumens was analyzed using FSI model. The results indicated that as the size of the distal tear increased, the peak systolic pressure decreased in both true and false lumens (Figure 3). Moreover, the pressure observed in both false and true lumens was significantly higher in the scenario with only a proximal tear compared to a situation involving both proximal and distal tears. In this context, the distal tear serves as a mechanism to diminish the pressure within the false lumen, subsequently lowering the risk of aneurysm development. These findings indicate that enlarging the distal tear size further will lead to a reduction in pressure disparity across the flap, eventually equalizing the pressure.

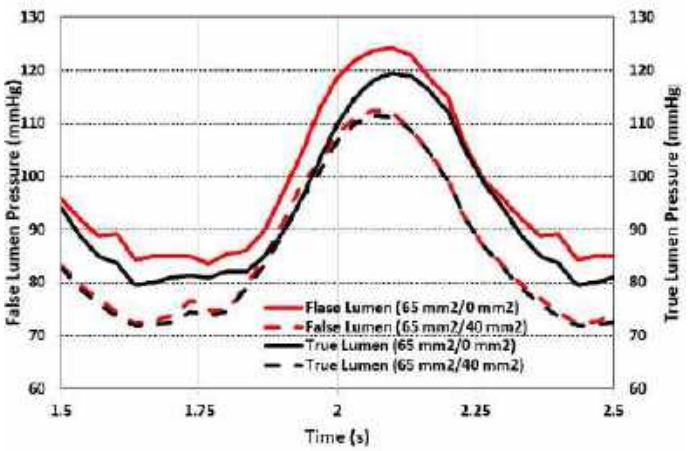

Figure 3: Effect of varying the tear size on the pressure in true lumen and false lumen.

ACKNOWLEDGEMENTS

The authors express their gratitude to the University of Michigan-Flint's Office of Research for their support through the Undergraduate Research Opportunity Program (UROP) and to the College of Innovation and Technology for their support through the START grant.

REFERENCES

[1] Fann, JI et al., *Ann. Vascular Surg*., 9: 311-23, 1995.
[2] Czermak, BV et al., *Radiology*, 217: 544-50, 2000.
[3] Tsai, TT et al., *Circulation*, 112: 3802-13, 2005.
[4] Zhu, Y. et al., *Sci. Rep*. 11, 1–13, 2021.
[5] Zhu, Y. et al., *JTCVS Open*, 9: 11–27, 2022.
[6] Cheng, C. et al., *Med Eng Phys*. 36:1176-84, 2014.
[7] Shad, R. et al., *Semin. Thorac. Cardiovasc. Surg*. 3: S1043–S0679, 2021.
[8] Rudenick, PA et al., *J Vasc Surg*. 57:464–74, 2013.
[9] Cheng, Z et al., *J Vasc Surg*. 57:35S–43S, 2013.
[10] Tse, KM et al., *J Biomech*. 44:827–36, 2011.
[11] Chen, D et al., *Med Eng Phys*. 35:1321–30, 2013
[12] Shi, Y. et al., BioMedical Engineering OnLine , 15, 2016.
[13] Khanafer, K. et al., *J. Biomedical Engineering and Informatics*. 2: 82-90, 2016.

SB³C2024
Summer Biomechanics, Bioengineering and Biotransport Conference
June 11-14, Lake Geneva, WI, USA

IN VITRO FLOW STUDY OF THE PENN STATE PEDIATRIC TOTAL ARTIFICIAL HEART

Cody Kubicki (1), Emma Raich (1), Peter Selinsky (1), Sailahari Ponnaluri (1), Steven Deutsch (1), William Weiss (2), Keefe B. Manning (1,2)

(1) Department of Biomedical Engineering, The Pennsylvania State University, University Park, PA, United States
(2) Department of Surgery, Penn State College of Medicine, Hershey, PA, United States

INTRODUCTION

Congenital heart disease (CHD) has an incidence rate of 1.79% worldwide and affects about 40,000 births annually in the United States [1,2]. Approximately 8% of CHD patients have single ventricle anomalies (SVAs), which require surgical palliation or heart transplantation. However, donor scarcity has resulted in high waitlist mortality rates. According to the US Organ Procurement and Transplantation Network (OPTN), 592 infants < 1 year of age and 496 children aged 1-5 years received heart transplants in the US over the last 5 years (2019-2023). Of the 703 new pediatric patients added to the waiting list in 2021, 21.3% were under 1 year of age, and 26.4% were 1-5 years of age. Infants younger than 1 year of age had the highest waitlist mortality in 2021 at 29.8 deaths per 100 patient-years. In addition, biventricular failure, often associated with CHD, is not uncommon in pediatrics. Biventricular assist devices (BiVADs) were used in 37.3% of Berlin Heart EXCOR patients in a review by Rohde *et al.* [3]. However, BiVAD patients had higher overall mortality (45.9%) compared to left ventricular assist device (LVAD) patients (19.6%). Stroke remains one of the prevalent adverse events experienced by pediatric patients receiving biventricular support with the EXCOR device. To address current pediatric mechanical circulatory support device (MCSD) complications and donor scarcity, Penn State is developing a pediatric total artificial heart (pTAH) to support infants and small children with SVAs or biventricular heart failure. The design intends to reduce thromboembolic complication incidence by minimizing regions of flow stasis, increasing high wall shear rate (WSR) exposure, and promoting efficient pump filling and ejection.

In the present study, we characterize flow experimentally within the pTAH using particle image velocimetry (PIV) and identify potential thrombogenic regions of flow stasis and low WSR. Results are compared to the Penn State ventricular assist device (PVAD), which has been studied extensively [4-7].

METHODS

To study the pump fluid mechanics, acrylic models of the right side (RpTAH) and left side (LpTAH) of the Penn State pTAH were manufactured to provide a clear visualization surface and to mimic the internal geometry of the pump sac and blood contacting surface. The LpTAH and RpTAH were studied independently in a mock circulatory loop, which replicated physiological hemodynamic conditions. A non-Newtonian blood analog was created to mimic the viscoelastic behavior of pediatric blood by matching the kinematic viscosity and elasticity of pediatric whole blood [8]. The blood analog was primarily composed of sodium iodide, de-ionized water, glycerin, and Xanthan gum. Pressure transducers (Utah Medical Products, Inc.) and ultrasonic flow probes (Transonic, Inc.) measured pressure and flow rate, respectively.

Two dimensional-planar PIV was used to quantify the flow. The system included a camera (TSI, Inc.) mounted orthogonally to a laser (Quantel, Inc.), which illuminated an ~800 μm thick plane within the acrylic pump model. A frame straddling technique was used to capture images with a frame capture time difference of 200 μs and a laser exposure time of 405 μs. The camera and laser synchronizer (TSI, Inc.) was triggered by the outlet pressure waveform. End of systole and beginning of diastole were defined as the time point of peak outlet pressure. Two hundred image pairs were collected every 50 ms, ranging from 50 to 700 ms into the cardiac cycle. PIV images were masked along the wall using an in-house MATLAB® (The MathWorks, Inc.) code that defined the fluid boundary and improved near-wall image quality. Masked images were processed using Insight 4G™ (TSI, Inc.). Velocity fields at each plane were averaged for each time point, and the vorticity field was calculated using a least squares finite difference approximation approach appropriate for oversampled PIV data [9]. Velocity and vorticity data were postprocessed to generate contour plots using TECPLOT Focus (TECPLOT, Inc.).

WSRs were determined using an in-house MATLAB® code developed by Hochareon *et al.* [10], which calculated the WSR based

on the tangential velocity and distance from the wall. Navitsky *et al.* established a minimum threshold value of 500 s^{-1} for reduction of platelet adhesion and thrombus deposition onto polyurethane materials, such as the material used to make the pTAH pump sac [11]. WSR magnitude and high WSR exposure time were combined into a thrombus susceptibility potential (TSP) metric, given by

$$\mathrm{TSP} = 1 - \sum_0^N \left(\frac{\Delta t \gamma_w}{\gamma_c t_{crit}}\right)\left(\frac{e^{[(\gamma_w-\gamma_p)/(\gamma_c-\gamma_p)]}-1}{e^1-1}\right) \quad (1)$$

Where N was the number of PIV data collection time points, γ_w was the WSR, Δt was the portion of each time step that $\gamma_w > \gamma_{peak}$, γ_{peak} was the threshold for thrombus deposition (500 s^{-1}), γ_{cutoff} was the threshold for platelet deposition inhibition (1000 s^{-1}), and t_{crit} was double the time interval between PIV collection times. TSP ranges from zero (reduced thrombus risk) to one (elevated thrombus risk).

RESULTS

Diastole was characterized by a strong jet through the inlet valve. The jet was observed in all three parallel planes and in the normal inlet planes in the RpTAH (Figure 1). The jets corresponded to the inlet valve major and minor orifice locations and orientations. Rotational flow in the central body of the pump was initiated by the inlet jet during diastole. However, rotational flow fully developed 100 ms later in the LpTAH compared to the RpTAH. The rotation aligned flow near the outlet side in the direction of the outlet port prior to systolic ejection.

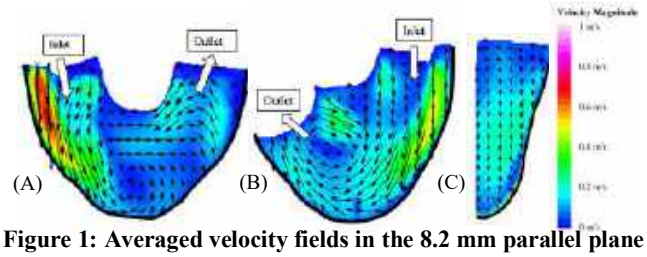

Figure 1: Averaged velocity fields in the 8.2 mm parallel plane of the (A) LpTAH and (B) RpTAH at 400 ms (87% diastole), and (C) RpTAH inlet centerline normal plane.

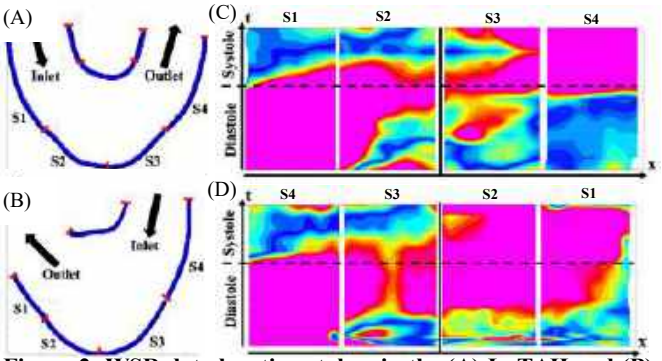

Figure 2: WSR data locations taken in the (A) LpTAH and (B) RpTAH. Normalized WSR contour plots along the bottom wall in the 8.2 mm parallel plane of the (C) LpTAH and (D) RpTAH.

The systolic characteristic flow pattern was the rapid formation of the outlet jet while rotational flow decayed. The RpTAH and LpTAH outlet jets encompassed the entire outlet port diameter and were skewed toward the outer wall of the device, leading to a rapid ejection of fluid. Flow patterns through the RpTAH during systole were more complex than those of the LpTAH due to the three dimensionality of the outlet port. Rotational flow in the RpTAH was maintained longer than in the LpTAH. The outlet jet also began to converge toward the center of the outlet port to orient flow with the outlet valve major orifice.

Most regions near the inlet and outlet had consistently high WSRs (Figure 2) and a low TSP. Some regions near the LpTAH apex failed to sustain WSRs above the threshold for sufficient wall washing, resulting in elevated TSP. Despite increased flow complexity in the RpTAH resulting from the modified geometry, the TSP values were mostly consistent with the LpTAH, showing low TSP near the inlet and outlet and elevated TSP along the apex wall (Figure 3).

The LpTAH and Penn State PVAD had many common flow characteristics and similar WSR trends. However, TSP in the LpTAH was slightly elevated near the pump apex compared to the PVAD due to reduced strength of the rotational flow in the LpTAH.

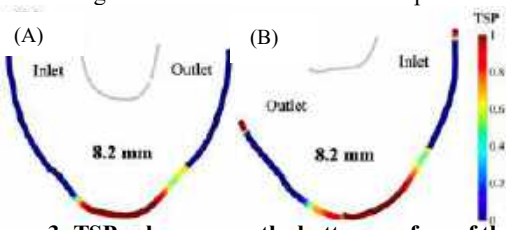

Figure 3: TSP values across the bottom surface of the (A) LpTAH and (B) RpTAH in the 8.2 mm parallel plane.

DISCUSSION

Previous studies show that the flow inside similar pulsatile MCSDs directly impacts thrombus formation on blood contacting surfaces. Scaled down pediatric MCSDs have complex flow compared to larger adult devices due to increased levels of curvature along the surfaces. Currently, no PIV studies exist that assess the fluid mechanics in a pTAH. Flow characterization can identify regions of flow stasis and low WSR, which provides guidance for optimizing device design and operation to reduce the thrombogenic risk potential that plagues similar circulatory support devices. The pTAH design generates three-dimensional flow due to the angling of the inlet and outlet ports, particularly in the RpTAH, compared to the PVAD whose inlet and outlet are aligned on a single plane with the pump body [12]. Overall, this study shows that the Penn State pTAH design experiences low thrombus deposition potential along much of the pump surface, similar to the PVAD. The primary area of concern is in the apical region of the pump, which is consistent with observations in other pulsatile MCSDs. These results suggest the Penn State pTAH may have comparable thrombogenic potential to other available pulsatile MCSDs despite its reduced size. Thus, making this device a viable option to support pediatric patients with severe biventricular failure as a bridge-to-transplant therapy.

ACKNOWLEDGEMENTS

The research reported in this publication was supported, in part, by the National Institutes of Health grant R01HL131921.

REFERENCES

[1] Wu, W et al., *Medicine*, 99(23):e20593, 2020.
[2] Reller, M et al., *J Pediatrics*, 153(6):807-813, 2008.
[3] Rohde, S et al., *Euro J Cardio-Thorac Surg*, 56(5):830-839, 2019.
[4] Roszelle, B et al., *Cardiovasc Eng Technol*, 2(4):224-252, 2011.
[5] Schonberger, M et al., *ASAIO Journal*, 58(5):481-493, 2012.
[6] Cooper, B et al., *J Biomech Eng*, 130(4):041019, 2008.
[7] Roszelle, B et al., *ASAIO Journal*, 56(4):356-363, 2010.
[8] Long, J et al., *ASAIO Journal*, 51(5):563-566, 2005.
[9] Raffel, M et al., *Particle Image Velocimetry Practical Guide*, 2007.
[10] Hochareon, P et al., *J Biomech Eng*, 126(4):430-437, 2004.
[11] Navitsky, M et al., *Artif Organs*, 38(12):1046-1053, 2014.
[12] Roszelle, B et al., *Ann Biomed Eng*, 38(2):439-455, 2010.

SB³C2024
Summer Biomechanics, Bioengineering and Biotransport Conference
June 11-14, Lake Geneva, WI, USA

A SIMPLE MODEL OF ANGIOTENSIN CONVERTING ENZYME HUB CAPACITY ON PEPTIDE FLUX AND RENIN INFLUENCE

Brian M. Westwood, Mark C. Chappell

Department of Surgery/Hypertension and Vascular Research, Cardiovascular Sciences Center
Wake Forest School of Medicine, Winston-Salem, North Carolina, United States

INTRODUCTION

Under classical physiologic conditions, angiotensin converting enzyme (ACE, EC 3.4.15.1) is a critical hub node for the Renin-Angiotensin-Aldosterone System (RAAS) and the conservation of the precursor angiotensinogen (Ao) consumption for a direct chain of conversions to angiotensin-(1-5) [Ang-(1-5)]. Angiotensin I [Ang-(1-10) or Ang I] is generated by renin [EC 3.4.23.15] from Ao, then ACE yields the first N-terminally intact bioactive peptide (with direct receptor action, B) in this cascade, angiotensin II [Ang-(1-8) or Ang II], which is converted to the next B, angiotensin-(1-7) [Ang-(1-7)], then ACE generates Ang-(1-5) [1] (Fig. 1).

We recently completed a post-hoc analysis of the RAAS in a subset of patients from the VICTAS septic shock trial that revealed a strong association of renin to mortality [2]. However, plasma samples were not collected with a renin inhibitor, so Ang I or intact Ao levels were not assessed in the study. To determine these components, we developed a conservation model that utilized the RAAS data from the VICTAS trial, which may be applied to other situations to calculate an unknown member of the RAAS [3].

METHODS

If we consider ACE and its substrates and products from Fig. 1 as a hub control volume extended (ACE hub, gray arrows) from Ang-(1-7), we can write the conservation equation 1 [this model assumes essentially all Ang I generated by renin is converted to Ang II by ACE, then directly converted to Ang-(1-7) by ACE2 [EC 3.4.17.23] and is acted upon by ACE to generate Ang-(1-5)]. There is an egress construct in the ACE hub linear model for bioactive peptides with rate B* acting on Ang II (encompassing direct receptor binding or conversion to Ang-(1-7) with receptor binding and/or any other non-ACE hub flux), which we modeled as equivalent to that of ACE [Q0, Q1, Q2 and Q3]. Under the pseudo-steady state hypothesis (PSSH), we can set the accumulation term to zero, and solve for Ao (equation 2).

Given the ACE hub (Fig. 1), the conservation of Ang-(1-7) can be described:

$$\frac{dAng-(1-7)}{dt} = Renin[Ao] - ACE[Ang-(1-7)] - B*[Ang\ II] = 0 \quad (1)$$

Enzyme concentrations were used as proxy for rate constants. The PSSH yields the key to estimating intact Ao level:

$$[Ao]_{calc} = \frac{ACE[Ang-(1-7)]+B*[AngII]}{Renin} \quad (2)$$

Calculated Ao values were evaluated to find 'far out' extreme outliers (outer fence) [4]. These 'wild shots' were Winsorized (W) by setting them to the outer fence value [5].

Area under the curve (AUC) for receiver operating characteristic (ROC) curves [6] were calculated by renin concentration percentile divisible by 5 (%ile/5) vs. whether Ao_{calc}, AngII and Ang-(1-7) concentrations were in normal range or not [1] (Fig. 2).

All calculations were performed in Excel (Microsoft Corp., WA), Prism (GraphPad Software, MA) was used for plotting data in figures and statistical analyses.

RESULTS

Using ACE quartiles as a surrogate for B* yielded output values with a correlation matrix for the four sets of calculations with all coefficients being greater than 0.995. The field solution was repeated for 20 control subjects, with $Q1_{ACE}$ yielding an interquartile range of Ao_{ctrl} calculated values matching the range of normal range values for Ao [1]. For all subsequent plots B* = $Q1_{ACE}$. Ao_{calc}, Ang II and Ang-(1-7) [r^2= (0.64, 0.04 and 0.24) log-log line (with 95% CI bands), respectively; n=84; Ao_{ctrl}, r^2=0.59, n=20; Fig. 3] concentrations were

plotted against renin. W signal clipping only effected the uppermost [Ao] values ($r^2_{noW\text{-}Ao}$ = 0.67).

ROC curves were plotted relative to renin %ile/5 for Ao_{calc}, Ang II and Ang-(1-7) in Fig. 4. W had no effect on ROC analysis.

The three AUC values were 0.65±0.032 ($\bar{x}$ ±SD). To achieve an FP rate = 0 and TP rate = 1 would result in an AUC = 1 yielding a perfect positive performance [6].

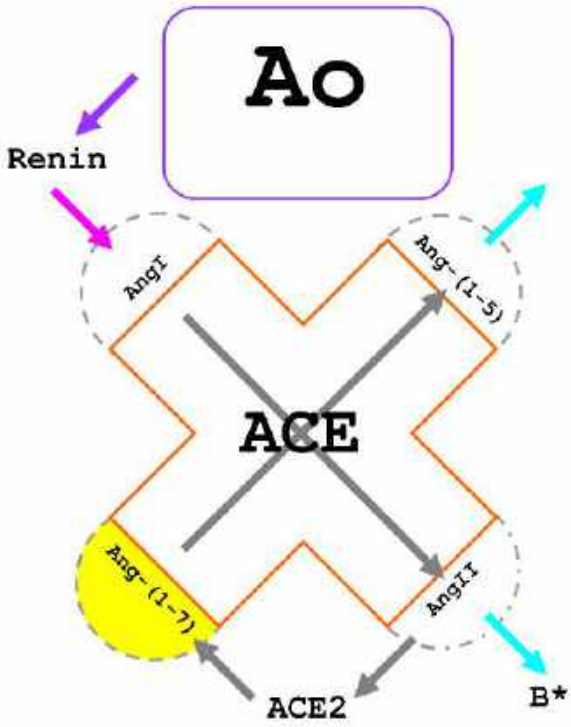

Figure 1: Simple model for ACE hub with the control volume extended to substrates and products, for development of conservation equation mathematical model for RAAS components. Graphic shows the mostly linear path of major angiotensin peptides under classical physiologic conditions.

For each **[renin]** %ile/5	Are **[Ao]**, **[AngII]** and **[Ang-(1-7)]** in normal range?		
		Yes	No
[renin] %ile	below	TP	FP
	above	FN	TN

Figure 2: Receiver operating characteristics for renin, relative to the two major bioactive RAS peptides and the system precursor protein. Contingency used to analyze data shown in Figure 4.

DISCUSSION

While the correlations between renin concentrations vs. Ao_{calc}, Ang-(1-7) and Ang II concentrations denote rank logarithmic decay {[Ao_{calc}, Ang-(1-7), Ang II], [0.64, 0.24, 0.04]; r^2 = 1}, the receiver operating characteristic AUC values have a small rank slope {[Ang-(1-7), Ao_{calc}, Ang II], [0.69,0.64,0.63]; equation 3, r^2 = 0.87}.

$$AUC = -0.03(rank) + 0.71 \qquad (3)$$

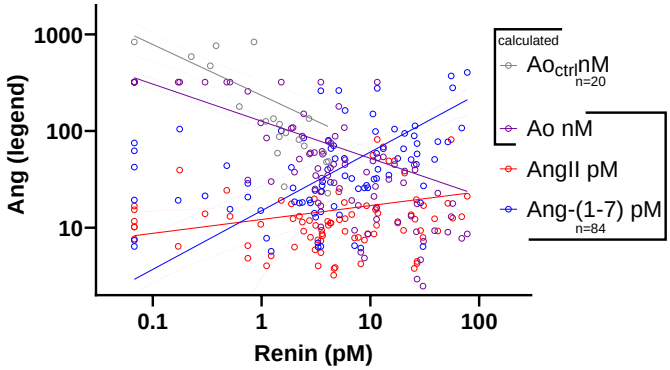

Figure 3: Log-log plot of Ao_{ctrl}, Ao_{calc}, Ang II and Ang-(1-7) concentrations vs. renin concentration.

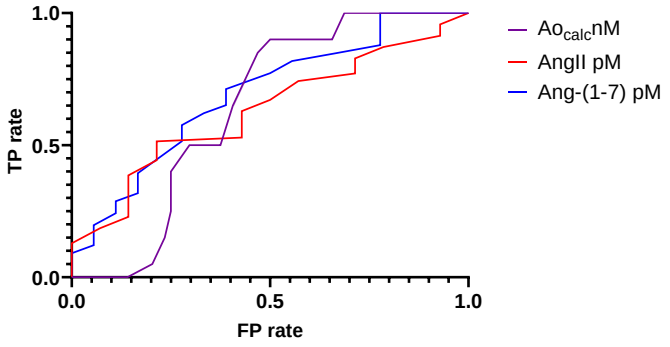

Figure 4: ROC curves for Ao_{calc}, Ang II and Ang-(1-7) concentration contingency with renin concentration as described in Figure 2.

This model may represent a seed method for the description of the complex interplay between not only this select catalog of RAAS components, but also may be generalized as a paradigm to explore greater utility in more complex systems.

ACKNOWLEDGEMENTS

The authors acknowledge support from the National Heart, Lung, and Blood Institute (R01HL146818) and the Cardiovascular Sciences Center (pilot award).

REFERENCES

[1] Chappell, M *AJP Heart Circ. Physiol.*, 310(2):H137-52, 2016.
[2] Busse, L et al. *Crit Care Med.*, 2023.
[3] Westwood, B et al. *SBC2008-190990*:181-182, 2008.
[4] Tukey, J *Exploratory Data Analysis*, 1977.
[5] Tukey, J *The Annals of Mathematical Statistics* 33:1-67, 1962.
[6] Fawcett, T *Pattern Recogn. Lett.* 27:861-874, 2006.

IMMOBILIZATION AND SOFT TISSUE INJURY ARE NECESSARY TO CAUSE PERSISTENT DISABILITY IN A RAT MODEL OF ELBOW CONTRACTURE

Rebecca F. Reals (1), Alex J. Reiter (2,3), Ryan M. Castile (2), Sophia D. Miller (2), Spencer P. Lake (1,2,4)

(1) Department of Biomedical Engineering, Washington University in St. Louis, St. Louis, MO, USA
(2) Department of Mechanical Engineering and Materials Science, Washington University in St. Louis, St. Louis, MO, USA
(3) Department of Biomedical Engineering, Saint Louis University, St. Louis, MO, USA
(4) Department of Orthopaedic Surgery, Washington University in St. Louis, St. Louis, MO, USA

INTRODUCTION

Post-traumatic joint contracture (PTJC) is a debilitating condition that occurs in up to 50% of elbow injuries, causing pain, stiffness, and reduced range of motion (ROM) [1]. Physical therapy is a common nonsurgical treatment strategy, and early joint use limits ROM loss and tissue pathology [2]. Immobilization (IM) is known to contribute to joint stiffness and reduced ROM, but clinical practice typically requires a period of joint IM after injury to prevent re-injury and limit joint instability [2]. Thus, identifying the contribution of IM to stiffness and decreased ROM will help to optimize physical therapy protocols to maximize ROM while sufficiently stabilizing the joint.

Other groups have investigated animal models of IM in the shoulder [3-5], hip [6], knee [7-15], and ankle [16,17], reporting muscle atrophy, joint contracture, capsule fibrosis, and inflammatory cell infiltration. However, to our knowledge the effect of IM without injury in the elbow joint has not yet been evaluated.

Previously, our group established the first animal model of elbow contracture [18], wherein we replicate soft tissue injuries seen in a simple elbow dislocation through anterior capsule puncture and lateral collateral ligament transection, which when combined with IM of the injured limb results in characteristic traits of PTJC such as persistent motion loss and anterior capsule fibrosis [2,18]. Past studies using this model have shown that early motion initiated soon after injury improves ROM in the joint [2]. Here, we investigated the contributors to PTJC to determine if IM without injury is sufficient for persistent ROM loss or whether soft tissue damage is also necessary to produce contracture. We hypothesized that animals receiving IM only in the absence of soft tissue injury would develop joint contracture, but that it would be less severe than the contracture seen in animals with both IM and soft tissue injury.

METHODS

In this IACUC approved study, male Long-Evans rats underwent unilateral IM of one forelimb with stretch netting and Vetrap bandages as previously described [18] (IM-Only group, n=6). IM limbs received no injury or surgical procedure, and contralateral (CL) limbs received neither injury nor IM. After 21 days of IM, bandages were removed and animals were allowed 21 days of free mobilization (FM) via unrestricted cage activity (Figure 1). Animals were sacrificed at the end of the FM period. Past data from an injured group with 21 days IM and 21 days FM [2] (Injury+IM; n=8 for mechanics; n=2 for functional testing) were included for comparison.

Functional testing was performed during the FM period. Forelimb strength was measured weekly beginning on day 21 using a custom-built device as previously described [19] to obtain maximum left and right forelimb strength measurements simultaneously. Gait analysis was performed weekly beginning on day 28 as previously described [19] using an open source, fully automated rodent gait system.

After sacrifice, both forelimbs were prepared as previously described [18] and mechanically tested in flexion-extension. Torque vs. angular position curves were analyzed to obtain total ROM, maximum extension/flexion, and extension/flexion stiffness.

Past data from a group with no injury or IM [19] (Control, n=9-10), which had functional testing at six different time points and mechanical testing after sacrifice were included for comparison. Mechanical testing parameters from all three groups were compared using one-way ANOVA with post-hoc Bonferroni correction. Forelimb strength and gait parameters from IM-Only group were compared to Injury+IM group using linear mixed models as previously described [19]. Control functional testing data were averaged and included as a reference line for comparison, but not statistically evaluated.

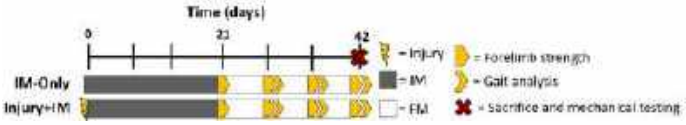

Figure 1: Timeline for immobilized groups. Control group with no injury or immobilization was also included from past data.

RESULTS

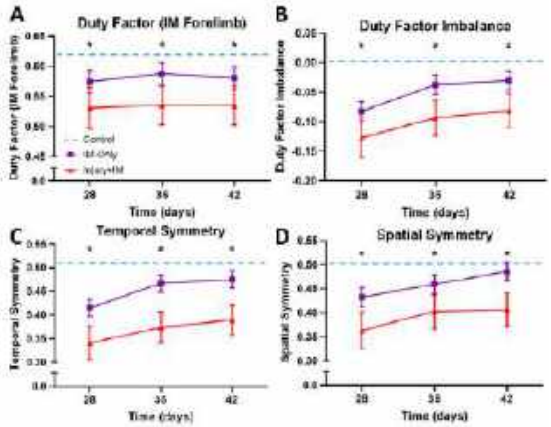

Figure 2: Gait analysis: (A) IM duty factor, (B) duty factor imbalance between forelimbs, (C) temporal symmetry, and (D) spatial symmetry were significantly different between IM-Only and Injury+IM (* for $p<0.05$); while IM-Only values approximated Control levels (dashed lines) over time, Injury+IM values remained decreased compared to Control (data are model predictions for rats of average weight/velocity with 95% CI).

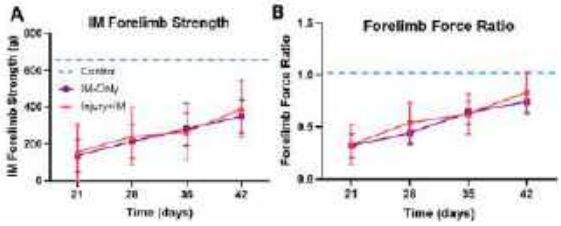

Figure 3: (A) IM forelimb strength and (B) force ratio between forelimbs increased towards Control levels (dashed lines) over time but were not different between groups (data are model predictions for rats of average weight with 95% CI).

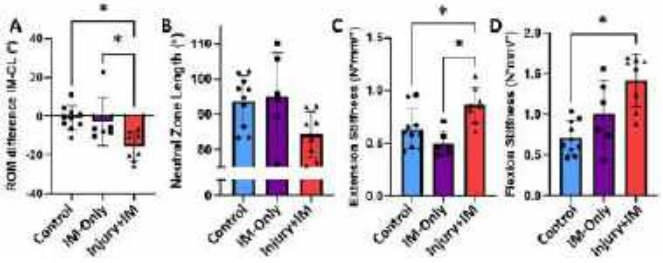

Figure 4: Joint mechanics: (A) ROM difference between forelimbs, (B) neutral zone length, (C) extension stiffness, and (D) flexion stiffness showed some differences between IM-Only and Injury+IM, but only Injury+IM values were different from Control (mean ± std; * for $p < 0.05$).

Gait analysis showed that duty factor (i.e., percent stance time) in the IM forelimb (Fig. 2A), duty factor imbalance between forelimbs (Fig. 2B), temporal symmetry between forelimbs (Fig. 2C), and spatial symmetry between forelimbs (Fig. 2D) were all significantly reduced for Injury+IM compared to IM-Only at all time points.

Forelimb strength in the IM forelimb (Fig. 3A) and the ratio between IM forelimb and CL forelimb (Fig. 3B) were not significantly different between IM-Only and Injury+IM at any time point. Both parameters increased over time in both groups.

Joint ROM difference (Fig. 4A) was significantly different in Injury+IM versus both IM-Only and Control; however, IM-Only ROM was not different from control. Neutral zone length (Fig. 4B) was not significantly different between groups. Extension stiffness (Fig. 4C) for Injury+IM was significantly different than Control and IM-Only, while Control values were not different from IM-Only. Flexion stiffness (Fig. 4D) was only significantly different between Control and Injury+IM.

DISCUSSION

Results show that IM alone in the rat elbow induces some features of PTJC (reduced forelimb strength, altered gait parameters, slightly reduced ROM, and slightly increased flexion stiffness compared to Control). However, most parameters were not as severe as Injury+IM and many functional outcomes returned to Control levels after FM.

Gait analysis demonstrated that the IM-Only group exhibited a lower magnitude than Control at the beginning of the FM period, but these differences were less severe than the differences between Control and Injury+IM. All gait parameters in the IM-Only group were significantly different from Injury+IM at all time points, but duty factor imbalance and spatial symmetry of IM-Only nearly returned to Control levels at later time points. Data at time points beyond 42 days would show whether all IM-Only gait parameters eventually return to Control.

Forelimb strength measurements in both IM-Only and Injury+IM exhibited a lower magnitude than control, which may be due to muscle atrophy caused by IM affecting both groups equally. However, forelimb strength improved during FM and previous work showed muscle does not play a significant role in contracture in this preclinical model [20].

No metrics of joint mechanics were significantly different between IM-Only and Control. Conversely, several measures were significantly different between Injury+IM and IM-Only (ROM difference, extension stiffness) and between Injury+IM and Control (ROM difference, extension/flexion stiffness).

Taken together, these results confirm in the elbow what has been demonstrated in other joints, specifically that IM alone causes some stiffness and contracture without injury. The method of IM may affect results; whereas some studies use external methods such as casting [4,13,15,16,17,21-23] or the bandages described here, other studies use surgical IM via Kirschner wires, plates, screws, and/or sutures that are drilled into the bone adjacent to the joint [3,5-12,14]. Although not designed to injure the joint tissues directly, such surgical methods of IM likely cause an inflammatory or foreign body response that could aggravate stiffness and contracture beyond the effect of IM alone.

In conclusion, this work demonstrates that IM alone induces some deficits in forelimb strength and gait parameters, but FM allows these parameters to recover and nearly return to Control levels. Both injury and IM are necessary to replicate the persistent effects of PTJC seen clinically. Future work will assess histological markers of PTJC such as anterior capsule thickness, adhesions, cellularity, and vascularity to investigate the cell and tissue level effects of elbow IM.

ACKNOWLEDGEMENTS

Funding from NIH (R01 AR71444, T32 AR060719) and Spencer T. and Ann W. Olin Fellowship at Washington University in St. Louis.

REFERENCES

[1] Anakwe+ JBJS 2011. [2] Reiter+ JBJS 2022. [3] Blessing+ PNAS 2019. [4] Kim+ J. Orthop Surg Res 2016. [5] Oki+ J Orthop Res 2015. [6] Minamimoto+ Clin Biomech 2021. [7] Kaneguchi+ J Appl Physiol 2018. [8] Lee+ Connect Tissue Res 2010. [9] Maimaiti+ J Orthop Surg Res 2023. [10] Matsuzaki+ J Phys Ther Sci 2013. [11] Nagai+ BMC Musculoskelet Disord 2014. [12] Ohtera+ J Appl Physiol 2002. [13] Sasabe+ J Orthop Res 2017. [14] Trudel+ Arch Phys Med Rehabil 2003. [15] Watanabe+ J Phys Ther Sci 2012. [16] Kunz+ Braz J Med Biol Res 2014. [17] Ono+ J Phys Ther Sci 2014. [18] Lake+ J Orthop Res 2016. [19] Reiter+ J Biomech Eng 2019. [20] Dunham+ JBJS 2019. [21] Aihara+ J Phys Ther Sci 2017. [22] Hayashi+ Physiol Res 2020. [23] Moore+ J Orthop Res 2022.

FRET MEASUREMENT OF CELLULAR TENSION IN TISSUES USING CONVENTIONAL CONFOCAL MICROSCOPY IN NEWLY ESTABLISHED TRANSGENIC MICE EXPRESSING ACTININ TENSION SENSOR

Takeo Matsumoto (1), Junfeng Wang (1), Eijiro Maeda (1), Yuki Tsujimura (2), Takaya Abe (3), Hiroshi Kiyonari (3), Hideo Yokota (2), Tetsuya Kitaguchi (4)

(1) Department of Mechanical Systems Engineering, Nagoya University, Nagoya, Aichi, Japan
(2) RIKEN Center for Advanced Photonics, Wako, Saitama, Japan
(3) RIKEN Center for Biosystems Dynamics Research, Kobe, Hyogo, Japan
(4) Institute of Innovative Research, Tokyo Institute of Technology, Yokohama, Kanagawa, Japan

INTRODUCTION

Mechanical forces play crucial roles in many biological phenomena such as embryonic development and etiology of critical diseases. Many research groups study how cells sense and respond to extrinsic mechanical loading, and how cells generate mechanical force to regulate the extracellular environment. To monitor the intracellular mechanical environment, several tension sensors using Förster resonance energy transfer (FRET) have been developed to visualize intracellular forces [1-2]. However, it is extremely difficult to introduce these sensors into tissues using conventional methods such as electrophoresis, and thus visualization of tension in biological tissues at cellular level was practically impossible. Recently, Tao *et al*. [3] developed transgenic mice expressing a tension sensor to visualize forces at the tissue level. Their results were obtained with a high-cost FLIM (Fluorescence Lifetime Imaging Microscopy) but not with a widely-used CLSM (confocal laser scanning microscope), possibly because the response of their sensor to tension is not clear enough. Furthermore, the combination of the fluorophores used in their sensor, mTFP1 and Venus, cannot be observed with the widely used 488-nm laser system. In a previous study, a group including one of the co-authors developed a tension sensor by inserting a FRET cassette made of two fluorophores, EGFP and mCherry, connected with spider flagelliform silk protein into actinin [4]. The response of this sensor to tension can be evaluated with a FRET ratio that is the ratio of the acceptor (mCherry) to the donor (EGFP) fluorescence using a conventional 488 nm CLSM system. In this study, we introduced the gene of this sensor into C57BL/6N mice to obtain mice expressing the tension sensor [5].

METHODS

We introduced our tension sensor gene engineered with the Cre/loxP system into the ROSA26 locus of C57BL/6N mice (Figure 1) and crossbred them with Cre mice to obtain animals expressing the tension sensor. We excised various tissues including the aorta, tail tendon, heart, and skin, and isolated cells from the tissues with enzymes. The isolated tissues and cells were stretched with a tensile tester (STB 150W NK, Strex, Japan) under a conventional CLSM (LSM880, Carl Zeiss, Germany) with a 63× oil immersion objective at room temperature in phosphate-buffered saline (PBS) (Figure 2). The fluorescence signals of EGFP and mCherry were obtained under excitation with a 488 nm wavelength laser at each stretch step to calculate the FRET ratio.

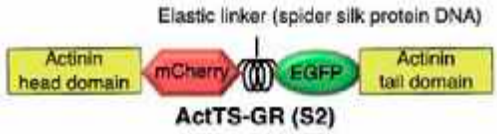

(a) Basic structure of actinin FRET tension sensor

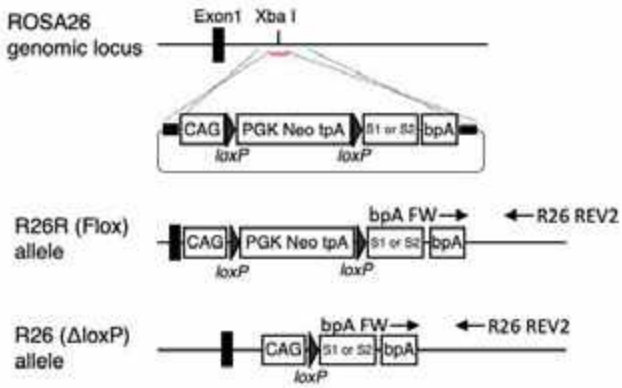

(b) Strategy for the expression of the sensor

Figure 1: Structure of the tension sensor ActTS-GR[5].

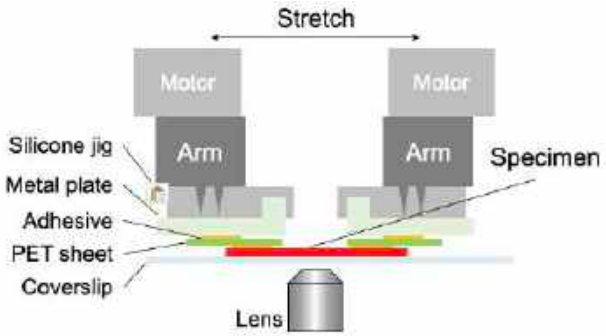

Figure 2: Tensile stretching apparatus and custom-made jigs for application of tensile strain to tissue explants and isolated cells.

RESULTS

The expression of the sensor was clearly observed in all excised tissues (Figure 3) and cells. The fluorescence intensity was high enough to observe the change in the FRET ratio with the confocal microscope. We performed tensile tests of the aortic tissues, tail tendons, and smooth muscle cells (SMCs) isolated from the aortic tissue and confirmed that the FRET ratio decreased in response to stretch, as expected (Figure 4). The FRET ratio decreased linearly in aortic tissues and SMCs. For tendons, it did not change until collagen fibers became straight, and then began to decrease beyond this point. The sensitivity of the FRET sensor was dependent on tissue types and cells. It was -0.63, -1.39, and -2.78 (%FRET/%strain) for aortic tissues, SMCs, and tendons, respectively.

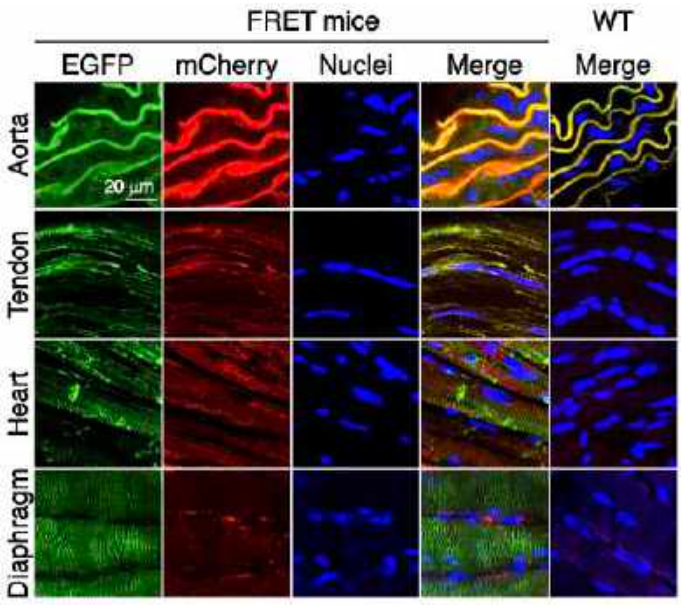

Figure 3: FRET sensors expressed in various tissues [5].

DISCUSSION

Sugita *et al.* have reported that strain in actin stress fibers in SMCs in the direction of the fiber axis was half of the strain in the smooth muscle layers in the circumferential direction of the aorta [6]. The relatively low FRET ratio variation in aortic tissues than SMCs observed in this study may support this observation.

We have developed a transgenic mouse line expressing an actinin tension sensor. The present mouse may become a powerful tool in mechanobiology.

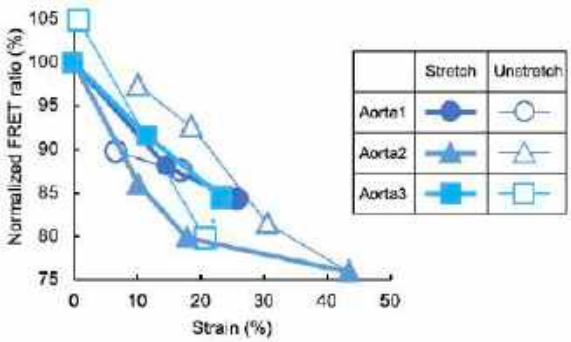

(a) Aorta

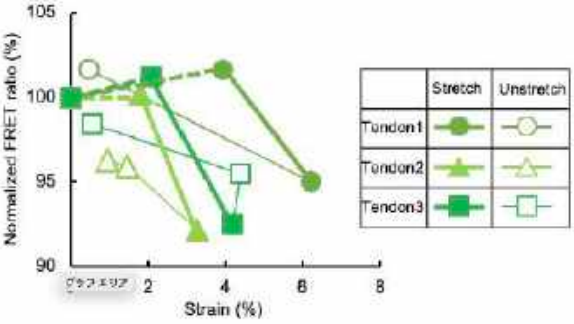

(b) Tendon fascicles

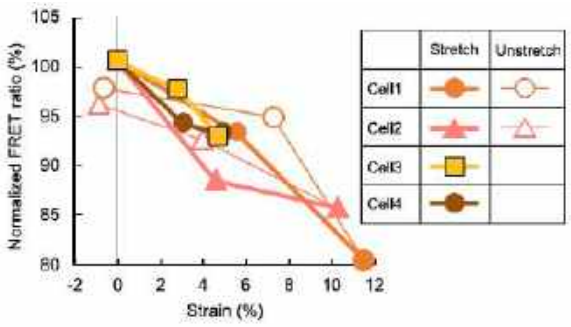

(c) Aortic smooth muscle cells

Figure 4: FRET ratio changes in smooth muscle cells in aorta (a), tenocytes in tail tendon fascicle (b), and isolated aortic smooth muscle cells in response to macroscopic stretching.

ACKNOWLEDGEMENTS

We thank Ms. Satomi Tsuruga for her technical contributions. This work was supported in part by AMED-CREST (JP19gm0810005), JSPS KAKENHIs (Nos. 21H04533, 21K19902, and 23K17194), and the NAKATANI Foundation.

REFERENCES

[1] Grashoff C et al. *Nature* **466**: 263-266, 2010.
[2] Meng F, Sachs F. *J Cell Sci* **124**: 261-269, 2011.
[3] Tao H et al. *Nat Commun* **10**: 1703, 2019.
[4] Yamashita S, Tsuboi T, Ishinabe N, Kitaguchi T, Michiue T. *Sci Rep* **6**: 28535, 2016.
[5] Wang, JF, Maeda E, Tsujimura Y, Abe T, Kiyonari H, Kitaguchi T, Yokota H, Matsumoto T. *Sci Rep*, **13**: 22729, 2023.
[6] Sugita S et al. *Biomech Model Mechanobiol* **20**: 1003-11, 2021.

PRESENCE OF RED BLOOD CELLS PROMOTES STRETCHING AND CLEAVAGE OF VON WILLEBRAND FACTOR IN WHOLE BLOOD UNDER HIGH SHEAR

Rukiye Tuna (1), Alice Liu (2), David Bark (2), Z. Leonardo Liu (1)

(1) Department of Chemical & Biomedical Engineering, FAMU-FSU College of Engineering, Tallahassee, FL, USA
(2) Department of Pediatrics, Hematology and Oncology, Washington University School of Medicine, St. Louis, MO, USA

INTRODUCTION

Von Willebrand factor (VWF) is a mechanosensitive plasma glycoprotein that controls hemostasis and thrombosis, with its hemostatic capacity/function directly related to the multimer size/length. Excessive high molecular weight multimer (HMWM) VWF can lead to harmful thrombosis, while the opposite can cause bleeding. The latter occurs in acquired von Willebrand syndrome (aVWS). To maintain healthy hemostasis/homeostasis, HMWM VWF needs to be cleaved by ADAMTS13 in circulation, which requires unfolding of the A2 subdomain on VWF, occurring through stretching beyond a critical tension threshold (∼20 pN) [1]. Although studies have demonstrated VWF cleavage through fluid shear, the loss of HMWM is modest from shear applied to plasma or to recombinant VWF in the presence of ADAMTS13, whereas aVWS involves excessive cleavage and substantial loss of HMWM, creating a gap in knowledge for how aVWS occurs in patients [2]. Combining the state-of-the-art computational and experimental rheometry approaches, we show that the presence of red blood cells (RBCs) creates a complex flow environment leading to elevated instantaneous stretching and tension on VWF in shear that promotes cleavage, elucidating a potential key cofactor to ADMAMTS13 and shear, causing excessive cleavage in aVWS.

METHODS

The study synergistically employs *in vitro* and *in silico* rheometer techniques (Figure 1) to unravel the biophysical mechanisms of shear-mediated activation and cleavage of VWF multimers. **Experiment** Citrated blood was centrifuged in two steps to collect platelet-poor plasma (PPP), which was then resupsended with 3x washed RBCs to a chosen hematocrit. Samples were exposed to a constant shear rate in a Rheostress 1 cone-and-plate rheometer with passivated surfaces. Sodium dodecyl sulphate-agarose discontinuous gel electrophoresis was performed on PPP separated from the RBCs in a western blot. **Computation** A multiscale computational method for simulating cellular and molecular blood flow has been developed to simulate VWF multimer conformation dynamics in concentrated RBC suspensions. The method has been validated to capture realistic hemorheology, cell mechanics and VWF multimer biophysics [3–5].

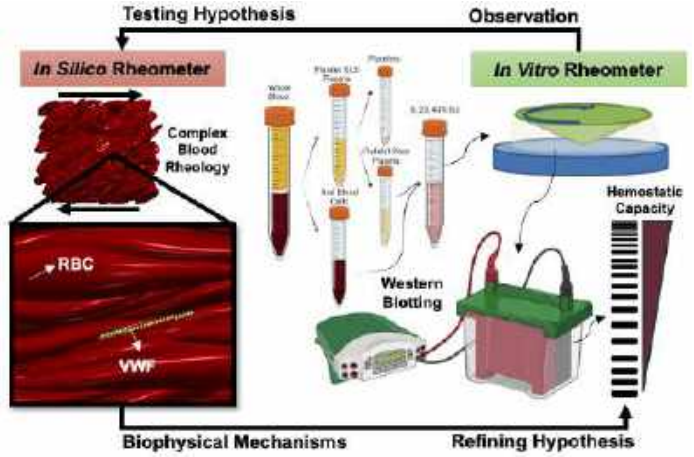

Figure 1: A research engine combining multiscale computational modelling with experimental multimer analysis for understanding the shear-mediated stretching and cleavage of VWF in whole blood.

RESULTS

In vitro exposure of PPP to a constant shear rate of 5000 1/s leads to little or no VWF cleavage, yet when combined with RBCs, there is a loss of HMWM, as seen in Figure 2. Band density in the figure is indicative of the amount of protein found at a specific size, with each band essentially adding another dimer of VWF from the bottom to the top of the gel. A physiological Hct of 40% leads to the most cleavage. Comparatively little to no cleavage is seen at other Hcts, even when samples are supplemented with dextran to increase viscosity of the sample to the levels expected for 40% Hct blood. These results indicate that increasing Hct, increases the potential for VWF cleavage at a specific shear rate through a mechanism related to the RBCs, themselves, as opposed to changes in bulk viscosity (and shear stress).

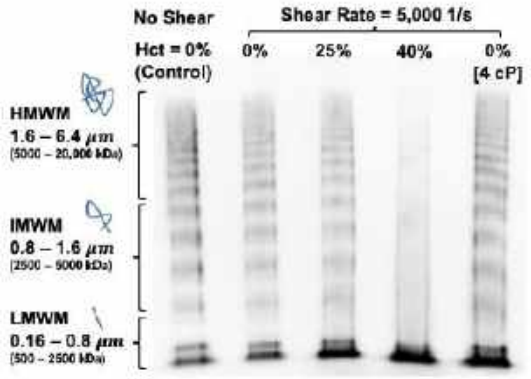

Figure 2: VWF length (molecular weight) distribution demonstrated through Western Blotting. The bands span from low molecular weight multimer (LMWM) through intermediate MWM (IMWM), up to HMWM. The left column is a sample not exposed to shear, while other columns were samples exposed to a shear of 5000 1/s with different amounts of Hct or with the addition of Dextran to elevate viscosity.

In parallel, *in silico* rheometry tests (Figure 1) are performed in a Lees-Edwards shear cell [3] under the same conditions as Figure 2 to investigate the potential biophysical mechanism leading to VWF conformational stretching and subdomain unfolding. Figure 3 shows representative time-lapse snapshots of VWF conformation over a complete folding-elongation cycle. Both of the Hct = 0% cases (with or without elevated bulk viscosity) show typical multimer coil-stretch conformational change under high shear, where the local tensile force on the multimer strand remains consistently below 5 pN. In contrast, the Hct = 40% case under high shear shows much-extended conformation during unfolding, where the instantaneous tensile force can significantly surpass the 20 pN threshold for A2 unfolding, particularly at the middle of the multimer strand.

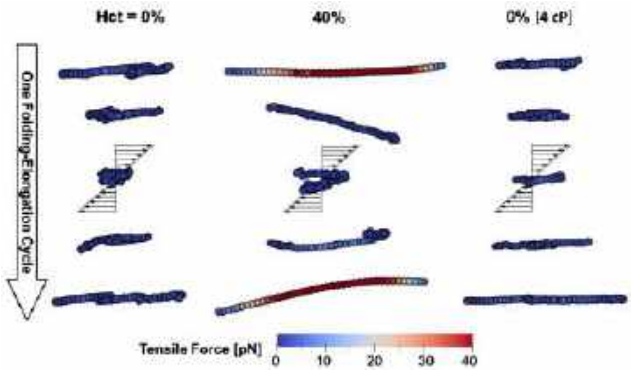

Figure 3: Time-lapse snapshots of VWF folding-elongation cycle with (Hct > 0%) or without (Hct = 0%) added RBCs. During stretching, the 40% Hct case features elevated tensile force (> 40 pN) along the VWF strand. The 0% Hct case consistently shows low tensile force (< 10 pN), even when the plasma viscosity is elevated to the bulk viscosity of whole blood or the 40% Hct RBC suspension (4 cP). The multimer has a contour length 6.4 μm. The shear rate is set to 5000 1/s.

Figure 4 shows the time change of VWF elongation (a), VWF average tension (b) and their statistics corresponding to the HMWM% (c, d, and e). Adding RBCs (25–40% Hct) leads to more frequent and severe VWF elongation than cases without RBCs (Figure 4a), while the 0% Hct with 4 cP viscosity does not significantly enhance VWF elongation. Correspondingly, VWF tension evolution shows that adding Hct to 25–40% can elevate the peak VWF tension by 1–2 orders of magnitude, surpassing the A2 unfolding threshold, even though the bulk viscosity has only been elevated by up to 4×. In addition, increasing the bulk viscosity to 4 cP without adding RBCs only linearly increases the VWF tension. Overall, the presence of RBCs seems to enhance VWF stretching through RBC-VWF micro-hydrodynamic interactions, not through linear increase of macroscopic viscosity. Box plots in Figure 4c confirm that elongation is enhanced significantly in the presence of RBCs. Figure 4d shows that 25-40% Hct leads to ultra-high tension beyond 20 pN (A2 unfolding threshold), making VWF susceptible to cleavage. In contrast, VWF tension with 0% Hct remains well below the A2 unfolding threshold, suggesting cleavage is unlikely. Both VWF stretching and tension statistics predicted *in silico* show strong inverse correlation with the HMWM% data quantified from the *in vitro* western blotting data (Figure 2), suggesting the elevated VWF stretching in the presence of RBCs under shear is likely the mechanistic reason for excessive VWF cleavage.

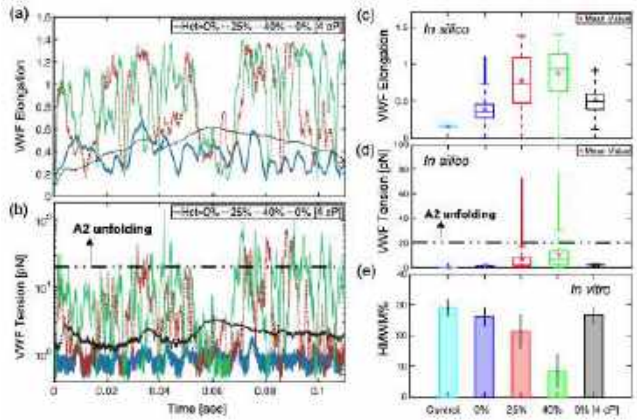

Figure 4: Instantaneous (ab) and average (cd) behavior of VWF elongation and tension. With RBCs (Hct > 0%), VWF tensile force can reach 10–100 pN levels, 1–2 orders of magnitude higher than those without RBCs. Presence of such high-tension events correlates well with the loss of HMWMs% (e). The shear rate is set to 5000 1/s.

DISCUSSION

The presence of RBCs promotes stretching and tension-dependent cleavage of VWF in whole blood under high shear through instantaneous RBC-VWF microhydrodynamic interactions. RBC is found to be a co-factor to high shear to cause VWF cleavage, providing a potential resolution to the controversy that pathological high shear-alone is insufficient to cause excessive VWF cleavage seen in aVWS. Furthermore, this work aligns with previous studies that show turbulence can enhance VWF cleavage, where turbulence also features instantaneous changes in microscale stresses [6]. This work also appears to provide a clue to the natural multimer distributions in circulation, which reaches only a peak shear of 3000 1/s and may allow us to identify better treatment for patients at-risk of aVWS, especially for abnormal hematocrit in high shear situations, e.g. aortic stenosis and patients on mechanical circulatory support.

ACKNOWLEDGEMENTS

Z. L. Liu and R. Tuna acknowledge the start-up fund from FAMU-FSU and HPC resources supported by FSU Research Computing Center (RCC). D. Bark and A. Liu acknowledge funding support from National Institutes of Health, National Heart, Lung, and Blood Institute (R01HL164424).

REFERENCES

[1] Ying J et al. *Biophysical journal* 98.8 (2010).

[2] Bortot M et al. *Cellular and Molecular Bioengineering* 13 (2020).

[3] Liu Z et al. *Journal of Fluid Mechanics* 871 (2019).

[4] Liu ZL et al. *Biophysical Journal* 120.21 (2021).

[5] Liu ZL et al. *Blood Advances* 6.8 (2022).

[6] Bortot M et al. *Arteriosclerosis, thrombosis, and vascular biology* 39.9 (2019).

SB³C2024
Summer Biomechanics, Bioengineering and Biotransport Conference
June 11-14, Lake Geneva, WI, USA

ACCURACY OF PHYSICS-INFORMED NEURAL NETWORKS UNDER LAMINAR AND TURBULENT-LIKE AORTIC FLOW CONDITIONS

Arman Aghaee(1), M. Owais Khan (1)

(1) Department of Electrical, Computer and Biomedical Engineering, Toronto Metropolitan University, Toronto, Ontario, Canada

INTRODUCTION

Physics-informed neural networks (PINNs) have emerged as a powerful approach to encode governing partial differential equations (PDEs) and training data to model complex engineering problems. One potential application of PINNs includes inverse solutions to the Navier-Stokes equations, with important implications for modelling blood flow in the cardiovascular system. Given the flexibility of PINNs, additional losses from the training data, such as those obtained experimentally or from in-vivo imaging, can be added to the loss function to further regularize the minimization process during the training.

While PINNs has shown tremendous potential, the utility of PINNs in cardiovascular biofluids is still debatable. One of the primary reasons is that the accuracy and convergence of PINNs is dependent on the complexity of the flow due to "spectral bias" that is inherent in neural networks [1]. Due to spectral bias, neural networks can learn low-frequency data much more easily while high-frequency data may be challenging or, in some cases, impossible to learn. Although recent studies have proposed methodological advancements to reduce spectral bias in benchmark problems [2,3], their utility for practical and real-world applications remain unknown. In particular, there is a lack of data available that shows systematically the accuracy of PINNs under physiological and pathological blood flow conditions in patient-specific geometries. Hence, the primary goal of this work was to establish the accuracy of PINNs under a range of a range of patient-specific blood flow conditions using our previously-developed Fourier-based PINNs architecture that has shown higher performance compared to traditional activation functions (e.g., *tanh, swish*) [4].

METHODS

PINNs Model: The solution $u(\boldsymbol{x}, t)$ was approximated with a deep learning network $f(\boldsymbol{x}, t; \theta)$, where θ represents the trainable parameters of the neural network. The loss function is defined as:

$$\mathcal{L}_{\text{total}}(\theta) = \mathcal{L}_{PDE} + \lambda_{BC}\mathcal{L}_{BC} + \lambda_{data}\mathcal{L}_{data} \quad (1)$$

where $\mathcal{L}_{PDE}$, $\mathcal{L}_{BC}$ and $\mathcal{L}_{data}$ correspond to the loss term for the Navier-Stokes equation, boundary conditions, and known sensor data, respectively. The parameters λ_{BC} and λ_{data} aim to balance the interplay of the different terms in the loss function. The training parameter θ is optimized by minimizing the total training loss, $\mathcal{L}_{\text{total}}(\theta)$ via a standard gradient descent optimization (i.e., ADAM).

The weighting coefficients in the loss function, λ_{BC} and λ_{data}, are problem-specific and tedious to choose for complex flow cases. Hence, we applied the strategy of dynamic weights that adaptively update the coefficients by utilizing the back-propagated gradient statistics during training. The iterative formulation for the adaptive weight is:

$$\theta^{k+1} = \theta^{k} - \eta\,\nabla_\theta\mathcal{L}_{PDE} - \eta\lambda_{BC}\nabla_\theta\mathcal{L}_{BC} - \eta\lambda_{data}\nabla_\theta\mathcal{L}_{data} \quad (2)$$

where k is the iteration step, and η is the learning rate. The coefficients λ_{BC} and λ_{data} can be estimated using the following relation [2]:

$$\lambda_{BC} = \frac{max_\theta(|\nabla_\theta\mathcal{L}_{PDE}(\theta_n)|)}{\overline{(|\nabla_\theta\mathcal{L}_{BC}(\theta_n)|)}}, \lambda_{data} = \frac{max_\theta(|\nabla_\theta\mathcal{L}_{PDE}(\theta_n)|)}{\overline{(|\nabla_\theta\mathcal{L}_{data}(\theta_n)|)}} \quad (3)$$

A Fourier-based, ω_o-scaled *sine* activation function (SIREN [5]) was used due to better convergence and differentiability for high-frequency signals. The PINNs architecture consisted of 4 layers with 128 neurons/layer. Boundary conditions and the velocity field at the mesh nodes were treated as unknown quantities. A total of 1600 sensor data points, corresponding to sensor point density of 360 L/D were used.

CFD Simulations: A 3D patient-specific aortic geometry was obtained from a public repository (www.vascularmodel.com, patient ID: 01750000). The patient had a flow rate of 108mL/s, corresponding to a cardiac-averaged Reynolds number of 823. In order to systematically vary the flow complexity, a stenosis was virtually introduced into the thoracic segment of the aorta and varied from 0%-70% severity in increments of 5% (i.e., total 15 cases) (code: https://github.com/Owais-Khan/ImageAnalysisTools). Boundary conditions were assigned such that 25% of the flow was fed to the head and neck vessels while 75% of the flow was fed to the descending aorta.

The model was meshed into ~7 million tetrahedral elements. CFD simulations were performed using the SimVascular package (www.simvascular.github.io) with 10,000 time-steps for four cardiac cycles. The last cycle was used for in all subsequent analyses.

Data Processing: Spectral Power Index (SPI), a normalized parameter that quantifies the power >25 Hz in the velocity signal, was computed for all time-velocity signals to highlight the extent and intensity of turbulent-like flow features. L_2 errors of the velocity magnitude for CFD vs. PINNs was computed using the equation below:

$$L_2 - error = \sqrt{\frac{\sum_{i=1}^{N} |u_{PINNs}(x_i, t_i) - U_{CFD}(x_i, t_i)|^2}{\sum_{i=1}^{N} |U_{CFD}(x_i, t_i)|^2}} \quad (4)$$

where $u_{PINNs}(x,t)$ is the trained approximation, $U_{CFD}(x,t)$ is the ground-truth obtained from CFD, and N is the number of mesh points.

RESULTS

Flow Complexity with Increasing Stenosis Severity: Figure 1 highlights the intensity of turbulent-like flow with increasing stenosis severity in 8 (out of 15) cases simulated. Low-frequency fluctuations are present in 0% stenosis (i.e., healthy) case which increases in intensity with increasing stenosis severity, ultimately covering the entire post-stenotic descending aorta in the 70% stenosis case.

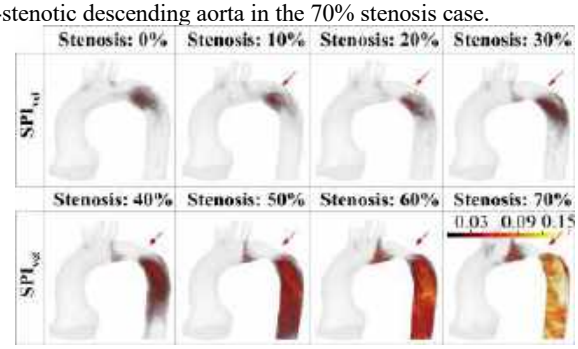

Figure 1: Spectral Power Index (SPI) intensity with increasing stenosis severity. Red arrow: stenosis location

PINNs Errors: Figure 2A shows qualitative comparison of the velocity maps for CFD vs. PINNs in two representative cases. In the highest stenosis severity case of 70%, notable differences are observed within and distal to the stenosis, such as limited penetration and intensity of the stenosis jet. For an intermediate stenosis severity of 40%, the gross velocity patterns predicted by PINNs are similar to those of CFD. Figure 2B shows qualitative contour maps of L_2 errors over the length of the aorta and for all stenosis severities. Errors were limited to 0.1-0.2 within the ascending aorta and increased to 0.2-0.3 in the stenosis region. The highest variability was found in the post-stenotic region. For stenosis severity <30%, errors were ~0.2. However, with increase in stenosis severity, ranging from 30% to 70%, the errors increased from ~0.3 to a maximum of 0.55.

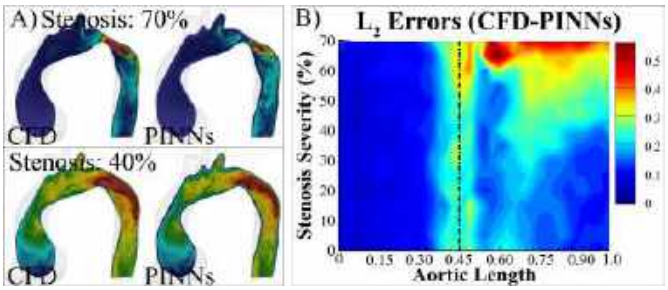

Figure 2: A) Time-averaged CFD vs. PINNs velocity magnitude for two representative cases. Color range is from min to max velocity. B) L_2 errors along the centerline of the Aorta for all 15 cases. The dashed-dotted line corresponds to the location of the stenosis.

POD Eigen-spectra: Figure 3 shows POD eigen-spectra of CFD vs. PINNs for three representative cases. For modes <20, both CFD and PINNs had similar eigen-spectra but deviated beyond >20 modes. More specifically, CFD eigen-spectra contained more kinetic energy in higher modes while PINNs showed reduced kinetic energy, indicating lack of high frequency spatial features in the learned velocity field.

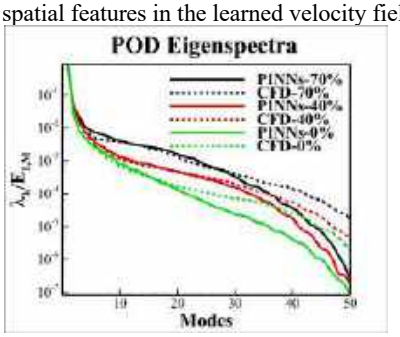

Figure 3: POD Eigen-spectra of CFD vs. PINNs for three representative cases.

DISCUSSION

By systematically increasing stenosis severity and consequently, flow complexity in a 3D patient-specific aorta, we have demonstrated that the accuracy of PINNs is highly dependent on the flow regime. Interestingly, the errors were limited to 0.1-0.2 in models with no stenosis or with stenosis of low severity but increased substantially in cases with pathological flow conditions, such as in patients with intermediate to high stenosis severity (>30%). In addition, we have demonstrated that PINNs was able to capture the kinetic energy within the lower modes, which represents large-scale gross flow features, but deviated substantially at higher modes, which represent high-frequency spatial features.

Our findings highlight that fully-connected neural networks – such as the ones used in PINNs – suffer from spectral bias, which make it incapable of learning functions with high-frequencies both in theory and practice. Our previous work has demonstrated that using Fourier-based activation functions, such as the ones used in this study, compared to conventional activation functions (e.g., *swish*, *tanh*) showed improved accuracy across a range of physical problems [4]. Despite such approaches, no method has shown to completely eliminate spectral bias. Recent findings, such as the use of neural tangent kernel to adaptively calibrate the weights of the neural network, has shown to reduce spectral bias in benchmark test cases; however, the practical utility of such techniques, for example in patient-specific blood flow applications, remain unknown. Future studies should focus on adopting approaches that can reduce such errors in cardiovascular flow applications.

ACKNOWLEDGEMENTS

M.O.K funding support from the Natural Sciences and Engineering Research Council (NSERC) of Canada and computing resources from SciNet funded by the Digital Research Alliance of Canada.

REFERENCES

[1] Rahaman et al., 36th Int. Conference on Machine Learning, 2019.
[2] Tanick et al., Adv. in Neural Information Processing Sys., 2020
[3] Wang, S., Journal of Computational Physics, 2022.
[4] Aghaee et al., Comp. Methods Programs Biomed, 2024 (in revision).
[5] Snitzman et al., Adv. in Neural Information Processing Sys., 2020.

BIOMECHANICS PARAMETER PREDICTS OUTCOME OF FETAL HEART INTERVENTION BETTER THAN CLINICAL SCAN PARAMETERS

L. Green (1), W. X. Chan (1), I. Prakash (1), A. Tulzer (2), G. Tulzer (2), C. H. Yap (1)

(1) Department of Bioengineering, Imperial College London, London, UK
(2) Department of Pediatric Cardiology, Children's Heart Center Linz, Kepler University Hospital, Linz, Austria

INTRODUCTION

Some mid-gestational cardiac abnormalities can progress in severity, causing irreversible damage or hypoplasia to the heart, leading to malformations at birth. Catheter-based fetal heart interventions showed promise in resolving abnormalities preventing the progression.

We study one such intervention: fetal aortic valvuloplasty (FAV), which is performed on fetal hearts with critical aortic stenosis and evolving hypoplastic left heart syndrome (CAS-eHLHS). During CAS-eHLHS, outflow obstruction causes high left ventricular (LV) pressure, diminished LV strains and stroke volume (SV), and mitral regurgitation (MR), leading to underdevelopment of the LV. Most such cases (~73%) progress to hypoplastic left heart syndrome (HLHS) at birth [1], but FAV can reduce the likelihood of a HLHS outcome, to 27-45% [2,3].

However, a considerable number of cases do continue to a HLHS birth outcome despite FAV, suggesting that current selection criteria based on clinical scans alone lacks sufficient predictive capabilities and cannot accurately select suitable patients for the intervention. This exposes inappropriately chosen fetal patients to unnecessary procedural risks, and some who are suitable but not chosen may miss the benefits.

Since the fetal heart is known to respond and develop to mechanical forces, and both CAS disease and FAV involves significant changes to cardiac biomechanics, we hypothesize that biomechanical parameters can indicate how strong the heart is and whether it will respond well to the intervention. We investigate this hypothesis via image-based, patient-specific cardiac finite element (FE) modelling.

METHODS

4D STIC fetal echocardiography is obtained for 9 CAS-eHLHS cases (4 with univentricular (UV) outcomes and 5 with biventricular (BV) outcomes) and 6 healthy cases, with ethics approvals and informed consent. Image-based LV Finite Element (FE) simulations are performed using our previous methods [4] (codes available at [5]), coupled with an age scalable lumped parameter model [6]. FE is iteratively performed while adjusting contractility and valve flow resistances to ensure patient-specific match with imaged data in terms of stroke volume, valve velocities, and expected LV pressures (literature values for healthy hearts and Doppler gradients for diseased cases). The biomechanics parameters are compared to a wide range of echo image measurements to investigate which parameters can best distinguish between UV and BV outcomes in the diseased cohort.

To enable rapid computations of myocardial stress, we derive a simple empirical equation to calculate stress from echo parameters best correlated to it (LV dimensions, volumes, and valve velocities), via principal component analysis (PCA). Myocardial stress calculated this way from pre-FAV data is compared to various pre-FAV echo image parameters, for their ability to predict UV versus BV birth outcomes, via receiver operating characteristic (ROC) analysis, using a cohort of 37 CAS-eHLHS patients undergoing FAV.

RESULTS

Echocardiography measurements show that CAS-eHLHS results in high aortic valve (AV) velocities, reduced circumferential and longitudinal strains and stroke volume, and the presence ofMR. Pre-FAV echo parameters such as valvular velocities, morphometrics, myocardial strain, stroke volume and end diastolic volume (EDV) do not statistically distinguish between cases with UV or BV outcomes (sample plots in Figure 1 top row), although LV inner diameter (LVID) and LV longitudinal length Z score have mild statistical differences between UV and BV ($p=0.0635$). On the other hand, several biomechanics parameters from FE modelling distinguish BV versus UV outcomes well. Cases with BV outcomes showed significantly elevated LV work done ($p=0.0635$), peak systolic myofiber stress (stress in the myofiber direction, $p=0.0159$) and the back-computed myocardial contractility ($p=0.0317$), compared to those with UV outcomes (Figure 1 bottom row). All FE biomechanics parameters are normalized to age-variations.

Using Cohen's D to compare the effect size of all these parameters (in terms of how different they are in BV versus UV groups), we find that peak systolic myocardial stress had an exceptionally high effect size (Figure 2), suggesting that it could distinguish BV versus UV cases much better than all other parameters.

From PCA analysis, the equation for calculating peak systolic myofiber stress is:

$$Stress = -24.924 + 0.9550V_1 + 4.2687V_2 - 0.1952V_3 + 1.1530V_4 + 0.1677V_5 - 1.4611V_6 - 0.004771V_7 + 4.8968V_8$$

Where V1 is aortic valve velocity, V2 is MR velocity, V3 and V4 are LV and RV longitudinal lengths, V5 is LV internal diameter, V6 is relative wall thickness, V7 is LV end-diastolic volume and V8 is LV stroke volume.

ROC analysis showed that myofiber stress has the largest area under the curve (AUC) of 0.91, while the next best performing parameters were LV longitudinal length Z Score (AUC=0.84), and EDV Z score (AUC=0.83).

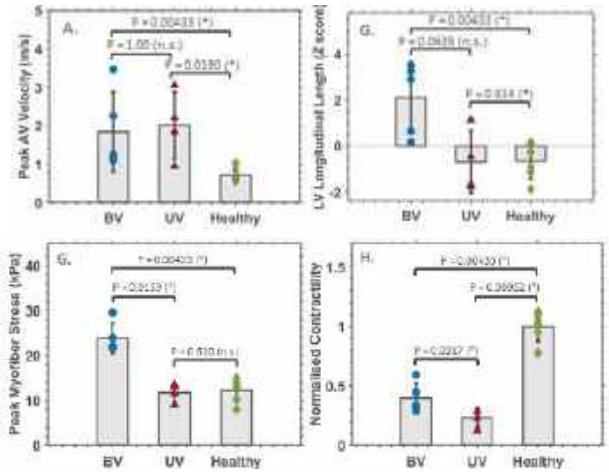

Figure 1: Bar charts (mean±std) of some examples of (top row) clinical echo measurements and (bottom row) FE biomechanics parameters that we investigated, for CAS diseased feal hearts with BV or UV birth outcomes and normal healthy fetal hearts.

DISCUSSION

In our study, we find that biomechanics parameters such as backcomputed active tension magnitude and peak myofiber stress, computed before FAV, have robust abilities to distinguish between UV and BV intervention outcomes, and can do so better than a wide range of echo measured parameters. Our ROC analysis confirms that myofiber stress has stronger predictive power than echo parameters. Our results thus suggest that biomechanics analysis is useful for predicting outcomes of FAV and can be used to improve patient selection, such as by incorporating them into clinical scoring system [2].

On our results that high myofiber stress of CAS-eHLHS diseased hearts can predict BV outcomes, we interpret this to suggest that CAS-eHLHS hearts that respond well to intervention with the ability to develop into functionally BV hearts at birth (as opposed to being UV) tend to be the ones that are biomechanically "stronger". This is where the heart has a stronger contractility to cause higher myocardial stresses, and at the same time, has an ability to withstand the higher myocardial stresses without becoming hypertrophic (which reduces stress).

To achieve clinical adoption, tests on a larger prospective cohort will be necessary. In this sense, our proposed approach to use the empirical equation to compute myocardial stress is useful, as it is fast and can be easily applied to a large cohort, while FE simulations are time consuming and therefore difficult to use on a large cohort.

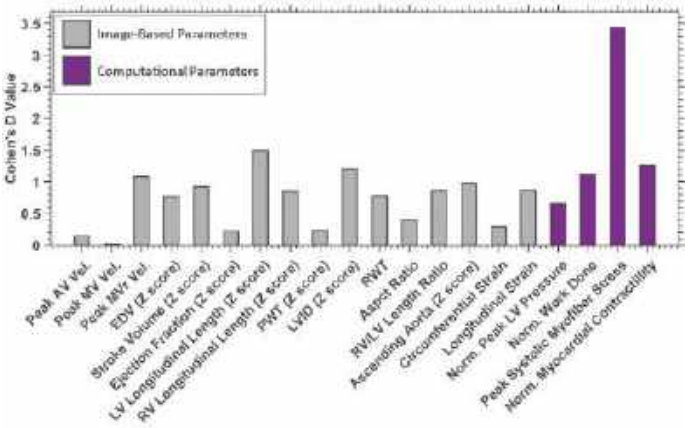

Figure 2: Cohen's D value showing the effect size of various echo (gray) and biomechanics (purple) parameters in their ability to distinguish between UV and BV outcomes for CAS hearts undergoing FAV.

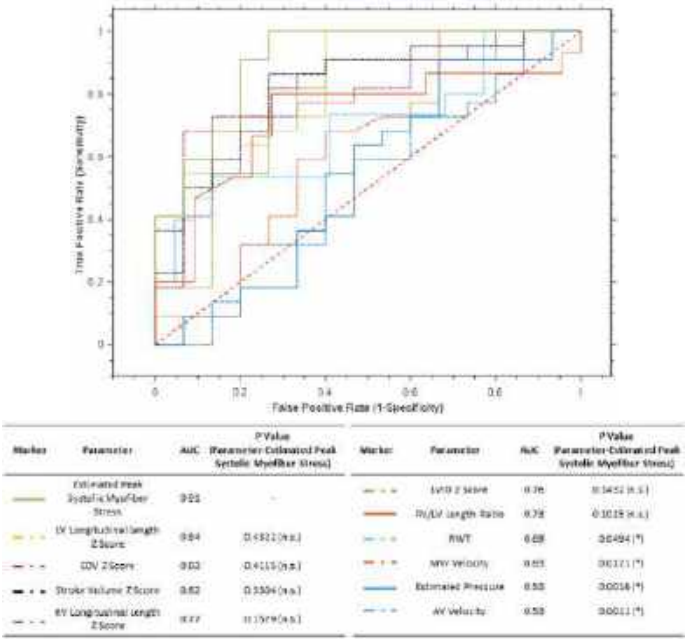

Figure 3: ROC analysis showing that peak systolic myofiber stress, estimated via empirical equation from routine clinical measurements, is the best for predicting UV versus BV outcomes.

ACKNOWLEDGEMENTS

The Study was supported by Imperial College PhD scholarship (Green), and BHF Centre of Research Excellence grant (RE/18/4/34215, Chan).

REFERENCES

[1] Mäkikallio. 2006, Circulation 113,1401.
[2] Tulzer. Ultrasound Obstet Gynecol. 2022 May;59(5):633-641.
[3] Friedman. 2018, Ultrasound Obstet Gynecol 52,212.
[4] Green. Biomech Model Mechanobiol . 2023 Apr;22(2):629-643.
[5] https://github.com/WeiXuanChan/heartFEM
[6] Wong. Ann Biomed Eng. 2023; 51(7): 1485–1498.

DEVELOPING A SCAFFOLD WITH GRADIENT MECHANICAL PROPERTIES FOR ROTATOR CUFF REPAIR: A PARAMETRIC FINITE ELEMENT STUDY

S. Winston (1), L. Pezzanite (2), T. Schlegal (3), A. Romeo (4), S. Dow (2), K. McGilvray (1)

(1) Department of Mechanical Engineering, Colorado State University, Fort Collins, Colorado, USA
(2) Department of Clinical Sciences, Colorado State University, Fort Collins, Colorado, USA
(3) Department of Orthopedics, University of Colorado School of Medicine, Aurora, Colorado, USA
(4) Rothman Orthopedic Institute, New York, New York, USA

INTRODUCTION

In the United States, >250,000 rotator cuff repair surgeries occur annually. These repairs are currently failing at high rates, typically around 20-94% [1,2], resulting in socioeconomic costs to the US population of roughly $3.44B [3]. Current clinical approaches in rotator cuff repair typically use "patches" that attempt first to augment the acute strength of the repair and second result in a strengthening at the bone-tendon junction following healing to make it stronger. However, retrospective examinations of these repaired tissues indicate that the native biomechanical transition between bone and tendon, the enthesis, is not regenerated using current surgical interventions [4]. Instead, scar tissue forms over the enthesis, leading to a weaker junction and higher retear rates. The poor clinical performance of current devices is thought to stem from the fact that these patches still struggle to recapitulate the native transition from bone to mineralized fibrocartilage to the tendon at the enthesis.

Advances in additive manufacturing have created a potential avenue to create patches that are more effective. Melt electrowriting (MEW) specifically can print precise structure with highly tunable mechanical properties with 'cellularly instructive' fiber diameters. MEW has allowed our group to fabricate a novel scaffold geometry that demonstrates a gradient in the local stiffness across the length of the scaffold using a single material on a length scale similar to those observed across the enthesis.

With this novel structure, little is known about how the critical print parameters play a role in the graded mechanics, so our group aims to probe how the central radius of curvature, the fiber spacing, and the fiber diameter of our scaffold affect the local biomechanical properties of these scaffold geometries (Figure 1) using parametric finite element analysis (FEA). **We hypothesize that our novel architecture will recapitulate the biomimetic gradient of stiffness seen across the rotator cuff enthesis, resulting in a biomechanically robust enthesis formation at the repair site.**

METHODS

Using a custom-built MEW printer, scaffold architectures were printed with 45 kDa polycaprolactone (PCL) (Polysciences) at 5.5 kV, 100 °C, 2.2 psi, and at a 4 mm collector distance. Printed scaffolds (N=4) were loaded to 4% global tensile strain at 0.1% strain • s^{-1}. Regional strain during the test was calculated using digital image correlation (MATLAB 2022b). The mechanical testing data was then utilized to validate a fully converged 2D, linear elastic, beam FEA model of the scaffold geometry (Abaqus 2021). Models were validated based on regional-specific strain levels in the "bony region" and "tendon region" of the scaffolds.

These validated and converged models then underwent a parametric study where the radius of curvature (R), fiber spacing (FS), and fiber diameter (FD) were varied across the printability spectrum of our MEW printer (Figure 1). For each simulation, the ratio between the tendon region and the bony region of the scaffold was calculated and dubbed the "Strain Gradient Factor" (SGF). The SGF gives a unitless metric to how much the geometry parameters affect the regional-specific mechanical properties. Spearman rank correlations were run to determine the

correlation between the varied geometric parameters and the SGF.

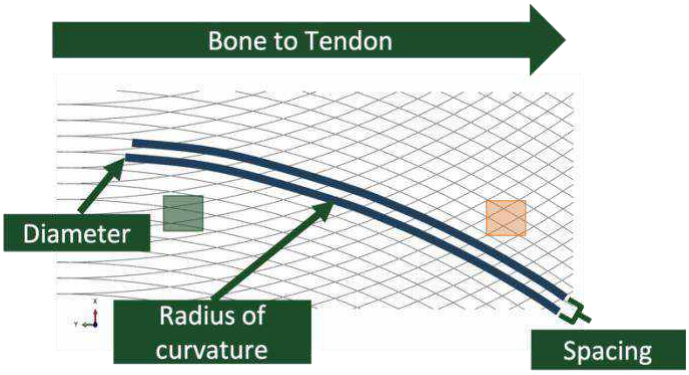

Figure 1: FEA model displaying parameters perturbed in study

RESULTS

The SGF was most correlated with alterations in the scaffold's radius of curvature. For R, FD, and FS The spearman correlation coefficients were -0.12, -0.25, and -0.85 respectively (Figure 2). This indicates that there is a slight inverse relationship between SGF and fiber spacing, a moderate inverse relationship with fiber diameter, and a strong inverse relationship with radius of curvature (figure 2).

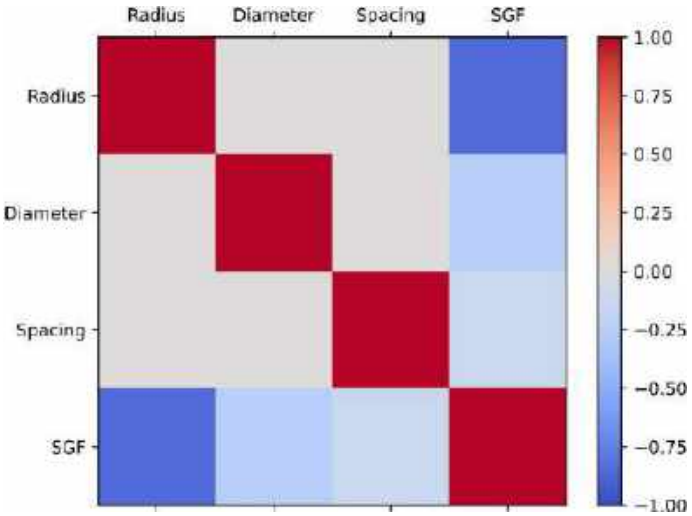

Figure 2: Spearman correlation matrix of each parameter

At R = 50mm and FS = 200 µm, SGF ranged from 48.9 to 8.78 as diameter ranged from 15 µm to 70 µm, and at FS = 200µm and FD = 15 µm SGF ranged from 48.9 to 1.7 as R ranged from 50 to 150 mm. These data clearly illustrate that the SGF can be tuned by selecting specific MEW scaffold geometries.

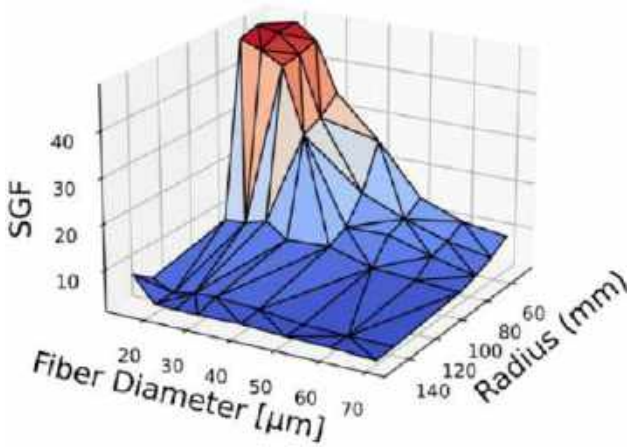

Figure 3: Representative 3D plot of SGF with respect to radius and fiber diameter at fiber spacing = 200 µm

DISCUSSION

The SGF of the scaffold varied the most as the radius of curvature and fiber diameter were parameterized. As the radius of curvature is increased, the rate at which the fiber angle changed decreased leading to a decreased change in local mechanics. As diameter decreased, the SGF increased moderately due to the decreased bending stability of curved fibers loading in bending.

This novel geometry has created a tunable, single material, fibrous scaffold with gradation levels approaching that of the human enthesis (50-100x). Future work will be focused on creating a predictive tissue healing finite element model to determine the optimal scaffold geometry that provides the strain levels that best caters to both bone and tendon regeneration on either side of these scaffolds.

ACKNOWLEDGEMENTS

We would like to acknowledge Colorado State University's College of Engineering Walter Scott Jr. 'High Impact' Grant mechanism for funding this research.

REFERENCES

[1] Cole, B et al., *J of Shoulder and Elbow Surgery*, 16:579-585, 2007.
[2] Galatz, L et al., *J of Bone and Joint Surgery*, 86:219-224, 2004.
[3] Mather, R et al., *J bone and Joint Surgery*, 95:1993-2000, 2013.
[4] Zumstein, M. et al., *Orthopaedics and Traumatology: Surgery and Research*, 103:S1-S10, 2017.

SB³C2024
Summer Biomechanics, Bioengineering and Biotransport Conference
June 11-14, Lake Geneva, WI, USA

FUNCTIONS OF PROLYL HYDROXYLATION IN ELASTIN

C. Yang (1), A. Tarakanova (1,2)

(1) Department of Biomedical Engineering, University of Connecticut, Storrs, CT, USA
(2) School of Mechanical, Aerospace, and Manufacturing Engineering, University of Connecticut, Storrs, CT, USA

INTRODUCTION

Elastin is a key extracellular matrix protein responsible for elasticity, resilience, and mechanical strength in connective tissues. During elastogenesis, the hierarchical elastic fiber assembly process, elastin is subject to an understudied post-translational modification, prolyl hydroxylation, where, mediated by prolyl-4-hydroxylase, a hydroxyl group replaces one of the hydrogen atoms at the C-γ position in proline residues. While prolyl hydroxylation is known to mediate the structural stability in collagen, a related structural connective tissue protein, the role of prolyl hydroxylation in native elastin remains vague at the molecular scale. According to recent experimental studies, elastin-like peptides with hydroxyproline modifications are more resistant to enzymatic digestion, and subject to abnormal elastogenesis. We hypothesize that hydroxylation alters elastin behavior by modulating protein-solvent interactions. To substantiate our hypothesis, we use existing mass spectrometry data of human elastin samples to build representative molecular models with naturally occurring prolyl hydroxylation patterns and perform extensive molecular dynamics simulations. As a starting point, we employ our recently developed fully atomistic model of the elastin precursor, tropoelastin. Our findings suggest that compared to proline, hydroxyproline increases hydrogen bonding with water and thereby supports adjacent hydrophilic hydration. Such enhanced protein-solvent interactions reduce the number of a residue's local configurations, thereby negatively impacting elastin's global dynamics required for essential biological processes, potentially act to shield the molecule from targeted degradation and modulate canonical hierarchical assembly. Overall, our study results provide insights into the role of hydroxylation in native elastin structure, function, and the process of elastogenesis, as well as offer design consideration for subtle tuning of engineered elastin-based materials.

METHODS

We propose three elastin-based models to study how prolyl hydroxylation impacts elastin function at different scales. We begin with short representative motifs where prolyl hydroxylation often occurs natively to study the fundamental mechanism of how prolyl hydroxylation alters the protein's activity at the scale of unit building blocks. We also consider domain 18 because of its intrinsic flexibility and the high occurrence of prolyl hydroxylation associated with this domain. Finally, we study the full-length tropoelastin molecule as it is the fundamental monomeric building block of elastic fibers.

We employ the hydroxylation degree of a Pro site as one of the criteria to select hydroxylation positions, using mass spectrometry data as our guide to select residues for modification [1]. For example, among 20 hydroxylation sites, Pro 190 and Pro 360 are determined to be hydroxylated in over 70% of the elastin samples, so these two positions are always hydroxylated in the models. In addition, Pro 615 is found 50% hydroxylated among all elastin samples, so half of our models exhibit this position in the unchanged state and half exhibit this position in the hydroxylated state. The hydroxylation degree of the remaining potential sites, however, remains unavailable from experimental studies. Therefore, we select the remaining hydroxylation positions randomly from all the potential sites. We also include a non-hydroxylated native model without any prolyl hydroxylation and an overhydroxylated model that includes all potential hydroxylated sites.

We use the Gromacs simulation package version 2018 for our simulations, with the CHARMM36m protein parameter set for topology and force field parameters for elastin, and TIP3P for water molecules. We implement the Particle Mesh Ewald method to compute electrostatic forces with grid spacing of 1.6 Å. We set the cut-off radius as 12 Å for short-range electrostatic interactions and Lennard-Jones interactions. We first restrain the bonding connecting hydrogen with protein backbone and apply the steepest descent algorithm to minimize the energy of the system for at most 50,000 steps. We then equilibrate the

system for 100 ps respectively in NVT and NPT ensembles. For temperature equilibration, we adopt the V-rescale thermostat to couple protein and non-protein groups to separate temperature baths of 300 K with 0.1 ps as the time constant. We use the Parrinello Rahman barostat for pressure coupling, with 2 ps as the time constant for isotropic pressure coupling, 1 bar as the reference pressure, and 4.5e-5 bar-1 as compressibility. Upon the end of equilibration stages, we remove position restraints and initiate 1000 ns production runs using the NPT ensemble. Across the stages of equilibration and MD production run, we harness the LINCS algorithm to constrain covalent bonds with hydrogen atoms and the leap-frog algorithm for integration every 1 fs during equilibration and every 2 fs during MD production runs. Tropoelastin models are based on our original model in [2]. All measurements are performed as an average over the last 500 ns of the production runs from all replicates. The statistical significance of analysis results is indicated in all figures as, * $p < 0.05$, ** $p < 0.01$, *** $p < 0.001$.

RESULTS

We find that the introduction of hydroxyproline results in dissimilar structural ensembles in the models. The full-length tropoelastin models reveal remarkable variations in their representative structural ensembles, some of which adopt an elongated structure with a longer end-to-end length, such as model 5hyp-2, 8hyp-2, 9hyp-1 and 17hyp-1, while some favor a wider molecular shape with a shorter end-to-end length, as model 17hyp-2. Owing to the high number of degrees of freedom in highly disordered molecules as tropoelastin, Hyp-containing models undergo substantial conformational changes and consequently display distinct structural ensembles at equilibrium, where localized changes propagate widely across the whole molecule (Fig 1).

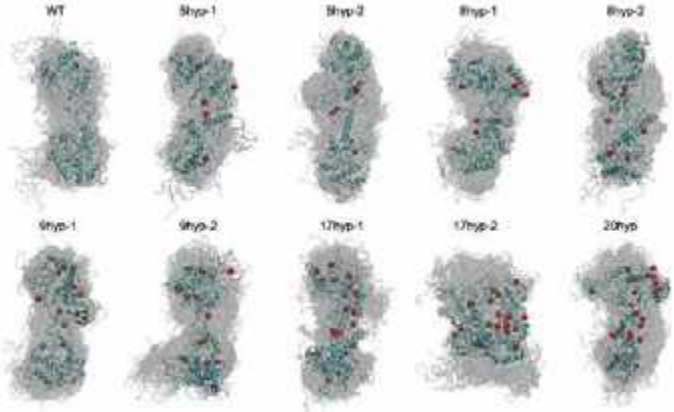

Figure 1: Tropoelastin ensembles with different hydroxylation patters. Hyp shown in red. Peptides and domains not shown.

Comparing the number of hydrogen bonds formed between proline and hydroxyproline residues and their surrounding water molecules, our results indicate that hydroxyproline residues have a greater propensity to form hydrogen bonds with water than proline residues (Fig 2). In the motif models, hydroxyproline forms two more hydrogen bonds with water on average compared to proline. Analogously, hydroxyproline residues in the domain 18 models and the full-length tropoelastin models form twice as many hydrogen bonds with water as proline residues do. Fig 2D shows representative snapshots of the hydrogen bond network within a cut-off distance of 5 Å of Pro vs. Hyp.

We also evaluate the water distribution locally and globally. The local water density around the modification site across different sequence lengths reveals a sharper peak in the first hydration shell (~ 2 Å) of Hyp compared to that of Pro, corresponding to enhanced hydrophilic hydration (not shown). In addition, locally, we observe more hydration waters surrounding Hyp residues compared to Pro residues in the motif models. This finding can be attributed to a higher proportion of hydrophilic hydration in relation to total hydration for Hyp as compared to Pro. We observe similar trends in the domain 18 models and the full-length tropoelastin models. We observe similar global hydration water distribution patterns in the motifs, and domain 18 models; for the full-length tropoelastin models, however, no clear trends are apparent. For each mutation site, Hyp still manifests its affinity to water, as evidenced by a rise in hydrophilic hydration. Based on the close proximity among Hyp sites in the ensembles, we infer that these Hyp residues may form a hydrogen bonding network during structural rearrangement, which is consistent with tropoelastin's flexible nature. Such rearrangement may thereby result in shared hydration waters, leading to a decrease in total hydration water content.

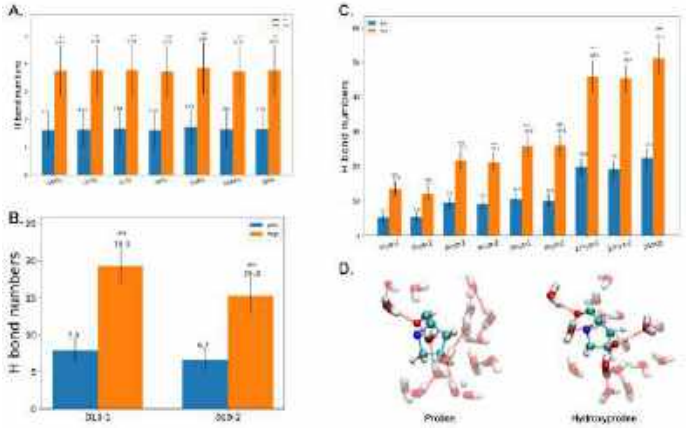

Figure 2: Local hydrogen bonding patterns in (A) motifs, (B) domain 18, (C) tropoelastin, and (D) cartoon representations.

DISCUSSION

We perform molecular dynamics simulations on elastin models of different length, originating from the tropoelastin monomer, namely, short elastin motifs, domain 18, and full-length tropoelastin, in the presence of various combinations of hydroxyproline in place of proline residues, to study the effects of hydroxylation in elastin. We find that prolyl hydroxylation strengthens local hydration effects, specifically, by enhancing protein-water hydrogen bonding, which gives rise to local rigidity characterized by reduced accessible conformational states and reduced local fluctuations. Consequently, the structural ensembles of the elastin molecules are altered, and the protein dynamics are dampened, which together serves as a possible mechanism for reduced enzymatic degradation and abnormal assembly and crosslinking behavior of elastin-like proteins, as observed in experimental studies. These findings shed light on native elastin assembly, and contribute insights into the possible role of hydroxylation in the degeneration of elastin in aging and disease. On this basis, we further propose that strategically placed hydroxyproline residues may be useful for engineering elastin-based materials with desired properties.

ACKNOWLEDGEMENTS

This research was supported by NSF CAREER 2145759, NIH 1R56AG075690, 1R01AG084715, 5U01HL146188, and ACCESS, supported by NSF.

REFERENCES

[1] Schmelzer CH et al., *Biochim Biophys Acta* 10:2169-77, 2016.
[2] Tarakanova, A et al., *PNAS* 115:7338-7343, 2018.

SB³C2024
Summer Biomechanics, Bioengineering and Biotransport Conference
June 11-14, Lake Geneva, WI, USA

A CLICK CHEMISTRY METHOD TO EVALUATE GLYCOSAMINOGLYCAN COMPOSITION AND METABOLISM IN ARTICULAR CARTILAGE

Annie Porter, Steven DiStefano, Emily Newcomb, Michael Axe, X. Lucas Lu

Mechanical Engineering, University of Delaware, Newark, DE, USA

INTRODUCTION

Proteoglycan is a primary component of cartilage extracellular matrix (ECM). Quantity and composition of proteoglycan plays an essential role in cartilage's mechanical function and the pathology of osteoarthritis [1]. The most abundant proteoglycan in cartilage is aggrecan, on which glycosaminoglycan (GAG) chains covalently attach along a protein core. The two dominant GAG chains are chondroitin sulfate (CS) and keratan sulfate (KS) [2]. Aggrecans can bind to another GAG chain, hyaluronan (HA), to form aggrecan aggregates (Fig. 1a) [3]. GAG chains are composed of repeating disaccharide units. CS chains contain N-acetylgalactosamine (GalNAc) as part of the repeating unit, whereas both KS&HA chains contain N-acetylglucosamine (GlcNAc) (Fig. 1b left) [4]. This study developed a novel click chemistry-based technique to quantify the synthesis and degradation of CS and KS&HA GAG chains separately in articular cartilage.

METHODS

Cartilage samples were harvested either from healthy juvenile bovine (1-2 months) knees or from regions of osteoarthritic senior human (average age 62 yrs) knees which lacked visible degeneration.

GAG Labeling via Click Chemistry. Newly synthesized CS or KS&HA GAG chains in cartilage were labeled using a copper-free click chemistry-based technique [5]. Cartilage was cultured in media supplemented with either GalNAz or GlcNAz, azide modified GalNAc and GlcNAc, respectively. Chondrocyte biosynthetic pathways can incorporate GalNAz into CS chains, and GlcNAz into KS&HA chains. New GAG chains were fluorescently labeled by "clicking" a fluorophore onto the azide groups (Fig. 1b Right). GAG synthesis was quantified by reading the fluorescent intensity of enzymatically digested samples on a plate reader. The click chemistry labelled cartilage can also be cultured afterwards, and the loss of fluorescent GAGs from cartilage into the culture media was longitudinally tracked by reading the fluorescent intensity of culture medium every other day.

GAG Composition by Anatomic Region. The ratio of newly synthesized KS&HA to CS was evaluated in cartilage from four regions of bovine knees: medial and lateral condyles (MC and LC), patellar groove (PG), and tibial plateau (TP) (n=10) (Fig. 2a).

Synthesis Response to Inflammation. The synthesis of CS and KS&HA was quantified after an inflammatory challenge. Bovine cartilage was treated for 72 hrs with IL-1β (10 ng/ml). Senior human

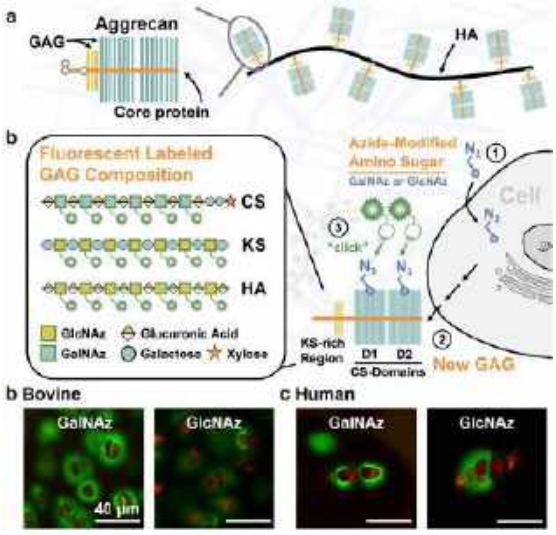

Figure 1. Glycosaminoglycan (GAG) synthesis. (a) Proteoglycan structure. (b) Click chemistry method to label CS (GalNAz) or KS&HA (GlcNAz) GAG chains. Newly synthesized GalNAz or GlcNAz labeled GAGs (green) surrounding (c) juvenile bovine or (d) senior human chondrocytes (red).

cartilage was treated for 96 hrs with a pro-inflammatory cytokine cocktail (5 ng/ml IL-1α, 5 ng/ml IL-1β, 50 ng/ml IL-6, and 20 ng/ml TNF-α) (n=10) (Fig. 3a).

Degradative Response to Inflammation. New CS or KS&HA synthesis was labeled in juvenile bovine (48 hrs) and senior human cartilage (96 hrs). Samples were then treated with pro-inflammatory cytokines as above, and the longitudinal loss of CS or KS&HA was tracked during a 10-day (bovine) or 18-day (human) culture (n=10). The total amount of GAG lost in each group was normalized to the amount of GalNAz lost from control samples.

RESULTS

Newly synthesized CS and KS&HA chains were both localized around the chondrocytes (red), forming a cell halo (green). Chondrocytes from juvenile bovine cartilage synthesized more GAGs in 48 hrs (Fig. 1c) than senior human chondrocytes in 96 hrs (Fig. 1d).

GAG Composition by Anatomic Region. The amount of newly synthesized CS chains (GalNAz) did not vary by anatomic region, but KS&HA synthesis was significantly lower in the medial condyle compared to the lateral condyle and patellar groove ($p<0.05$) (Fig. 2b). The total amount of GAG synthesis (CS+KS&HA) did not vary between regions (Fig. 2c). The ratio of KS&HA to CS was significantly lower in the medial condyle compared to the lateral condyle ($p<0.001$), patellar groove ($p=0.006$) and tibial plateau ($p=0.015$) (Fig. 2d).

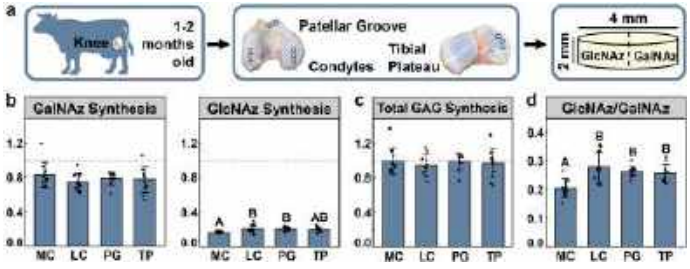

Figure 2. GAG composition by anatomic region. (a) Experimental design. (b) Separately quantified CS (GalNAz) and KS&HA (GlcNAz) GAG chain synthesis. (c) Total GAG (CS+KS&HA) synthesis. (d) Ratio of KS&HA to CS GAG chain synthesis. Different letters indicate significant differences ($p < 0.05$).

Synthesis Response to Inflammation. The ratio of new KS&HA to CS chains was much higher in senior human cartilage (0.42±0.11) than in juvenile bovine cartilage (0.16±0.04, $p<0.001$). In juvenile bovine cartilage, inflammation significantly reduced both CS and KS&HA chain synthesis. However, CS chain synthesis was reduced by a greater amount, increasing the KS&HA to CS ratio (0.22±0.05, $p=0.003$) (Fig. 3b). In senior human cartilage, inflammation only reduced CS chain synthesis, not KS&HA. KS&HA to CS ratio was increased to 0.69±0.10 ($p<0.001$) (Fig. 3c).

Degradative Response to Inflammation. In untreated cartilage, GAG loss in senior human samples had a higher ratio of KS&HA to CS chains (0.63±0.13) compared to juvenile bovine samples (0.50±0.13, $p=0.025$). In juvenile bovine cartilage, inflammation induced seven times more CS chain loss compared to untreated cartilage (7.09±2.96 vs 1.00±0.19, $p<0.001$). Inflammation also increased KS&HA chain loss, although not as drastically (1.32±0.44 vs 0.49±0.10, $p<0.001$), reducing the ratio of KS&HA to CS chains lost (0.19±0.03, $p<0.001$) (Fig. 4a). In senior human cartilage, inflammation increased both CS and KS&HA chain loss, but in lesser amounts compared to healthy bovine cartilage. The loss of CS chains doubled (1.96±0.53 vs 1.00±0.16, $p<0.001$), whereas the loss of KS&HA only increased by ~50% (0.95±0.31 vs 0.62±0.11, $p=0.001$). Thus, the ratio of lost KS&HA to CS chains decreased (0.49±0.13, $p=0.004$) (Fig. 4b).

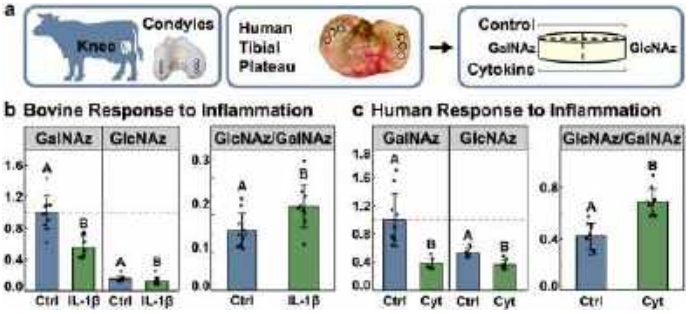

Figure 3. GAG synthesis under inflammation. (a) Experimental design. Separately quantified CS (GalNAz) and KS&HA (GlcNAz) chain synthesis and the ratio of KS&HA to CS chain synthesis for (b) juvenile bovine and (c) senior human cartilage. Different letters indicate significant differences ($p < 0.05$).

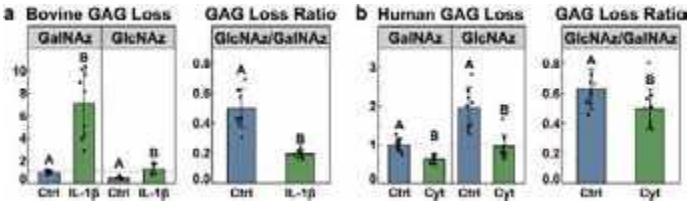

Figure 4. Degradative response to inflammation. Separately quantified CS (GalNAz) and KS&HA (GlcNAz) GAG loss and the ratio of KS&HA to CS chain loss from (a) juvenile bovine and (b) senior human cartilage under inflammation. Different letters indicate significant differences ($p < 0.05$).

DISCUSSION

We presented a novel technique to conveniently quantify the synthesis and degradation of different GAG chains in articular cartilage. The method detected differences in CS and KS&HA synthesis in different species of cartilage, different anatomic regions, and cartilage with/without inflammatory challenge. In confocal images, both GalNAz and GlcNAz labeled GAGs had similar spatial distributions around chondrocytes but differed in fluorescent intensity. This distribution is consistent with aggrecan having attachment domains for both CS and KS along its protein core (Fig. 1a,b bottom).

Inflammation is known to inhibit chondrocyte anabolic activities. For the first time, we showed that it also caused juvenile cartilage to transition to a more aged state, in which the percentage of keratan sulfate increased [6]. Mechanical environment may also regulate GAG composition. The medial femoral condyle, which undergoes the highest loading in the knee, had the lowest KS&HA:CS ratio. Little is known about the function of keratan sulfate in cartilage, or how changes in GAG composition are related to the development of osteoarthritis. Our new technique can help to further our understanding of proteoglycan metabolism in cartilage and its role in osteoarthritis processes.

ACKNOWLEDGEMENTS

This work was supported by NIH R01AR074472 (Lu) and NSF GRFP (Porter).

REFERENCES

[1] Roughley, P and Mort, J, *J Exp Orthop*, 1:8, 2014. [2] Sharma, A et al., *Arthritis Res Ther,* 9(4):1-10, 2007. [3] Garanziotis and Savani, *Matrix Biol*, 78-79:1-10, 2019. [4] Li, L et al., *Mol Biosyst*, 8(6):1613-1625, 2012. [5] Porter, A et al., *ACS Biomat Sci Eng*, 8(6):2564-2573, 2022. [6] Roughley, P et al., *J Biol Chem*, 256(24):12699-12704, 1981.

SB³C2024
Summer Biomechanics, Bioengineering and Biotransport Conference
June 11-14, Lake Geneva, WI, USA

INTRAVENTRICULAR FLUID DYNAMICS STUDY USING AN *IN VITRO* MODEL OF MITRAL VALVE REGURGITATION AND EDGE-TO-EDGE THERAPY

C. Kubicki (1), M.S. Sacks (2), K.B. Manning (1,3)

(1) Department of Biomedical Engineering, The Pennsylvania State University, University Park, PA, United States
(2) Department of Biomedical Engineering, James T. Willerson Center for Cardiovascular Modeling and Simulation, Oden Institute for Computational Engineering Sciences, University of Texas, Austin, TX, United States
(3) Department of Surgery, Penn State College of Medicine, Hershey, PA, United States

INTRODUCTION

Degenerative mitral valve disease is one of the most common cardiac valvulopathies, with an estimated 24.2 million cases resulting in over 34,000 deaths globally in 2019 [1]. Mitral valve disease is associated with mitral regurgitation (MR), which is attributed to excess heart failure and mortality in all subsets of patients experiencing MR [2]. The prevalence of this pathology and its increasing global burden due to an aging population has driven recent advances in surgical repair strategies and technologies. Recently, focus has shifted toward minimally invasive catheter-based interventions due to the risks associated with surgery in elderly patients [3]. Of these burgeoning treatment options, edge-to-edge repair is the most common, with more than 200,000 patients treated globally over the past 20 years as reported by Abbott, the manufacturer of the clinical standard MitraClip for edge-to-edge repair. Despite its prevalence, there have been no publications related to quantifying the impacts of clipped valve edge-to-edge repair on intraventricular hemodynamics. This therapy creates a two-orifice inlet to the left ventricle (LV), which is anticipated to drastically change the fluid dynamics. Change from native, healthy flow could result in previously unforeseen comorbidities in patients with edge-to-edge repair and worsen patient long-term outcomes.

In the present study, we construct a LV duplicator with flow visualization capabilities and characterize flow experimentally within the LV experiencing MR using particle image velocimetry (PIV). The study explores how flow is impacted by edge-to-edge repair of the mitral valve using a MitraClip compared to complete valve replacement with a mechanical valve. The goal is to better understand how edge-to-edge mitral valve repair impacts blood flow within the LV.

METHODS

An optically transparent ventricle duplicator was used to perform intraventricular flow visualization studies. The duplicator consisted of an external hydraulic pressure chamber attached to a pulsatile pump (Vivitro Labs, Inc.) and a silicone ventricle model placed inside the hydraulic chamber. The silicone ventricle was attached to a flow loop with a reservoir and resistance clamp (see Fig. 1A). Piston head motion in the pulsatile pump controlled pressure in the hydraulic chamber, which drove flow through the loop by causing ventricle compression. The pump operated at a beat rate of 75 bpm with a 35% systolic duration, producing an average flow rate of roughly 3 L/min through the ventricle. The aortic valve in the system was a Bjork-Shiley monostrut (BSM) tilting disk valve and the mitral valve was either another BSM valve or a custom bileaflet tissue valve.

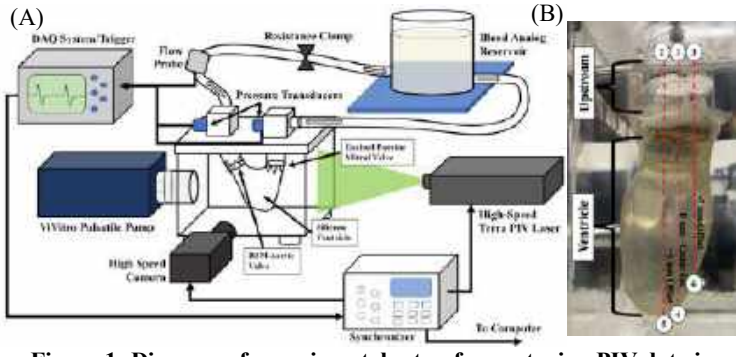

Figure 1: Diagram of experimental setup for capturing PIV data in the ventricle duplicator.

Bileaflet tissue valves were created by extracting the mitral valve from porcine hearts ordered from Lampire Biologics (Lampire Biological Labs, Inc.) and sewing the excised leaflet tissue onto a stent. The valve was secured into the mitral location in the silicone ventricle using internal retaining rings and gaskets. Two conditions were observed in the flow visualization studies: first with no MR treatment and second simulating edge-to-edge repair using a MitraClip (Abbott).

High-speed 2D planar particle image velocimetry (HSPIV) was

used to quantify flow in the silicone ventricle duplicator for the clipped and unclipped mitral valve conditions. The HSPIV setup included a high-speed camera (Vision Research, Inc.) and a high-speed PIV laser (Continuum, Inc.) coupled to lenses to produce a 1 mm thick light sheet mounted orthogonally (see Fig. 1A). The laser sheet was adjusted to image the centerline of the mitral valve stent and two positions offset ±5 mm from the centerline position (see Fig. 1B). Camera position and magnification were adjusted to collect images inside the ventricle and upstream of the mitral valve. Images were collected at 25 Hz to collect images at 21 time points across the 800 ms cardiac cycle for 200 cycles. A blood analog composed of saline and glycerin was made to match the kinematic viscosity of whole blood (3.5 cSt) and seeded with 7 µm fluorescent polymer microspheres (Thermo Fisher Scientific, Inc.). Fluorescent PIV particles coupled with a 546/612 nm camera lens filter reduced reflections from the ventricle, MitraClip, and valve housing. PIV data were processed in Insight4G (TSI, Inc.). Intraventricular viscous energy dissipation (VED) was calculated by (1). VED was used as a metric to quantify reduced pumping efficiency in the LV because of suboptimal flow in the presence of MR [4].

$$VED = \frac{\mu}{2}\int_A \sum_{\forall\, i,j}\left(\frac{\partial u_i}{\partial x_j}+\frac{\partial u_j}{\partial x_i}\right)^2 dA \qquad (1)$$

Where μ was the fluid dynamic viscosity and u_i was the velocity in the i^{th} direction. Equation (1) was integrated over the ventricle plane where PIV data were collected. Spatial derivatives were calculated from the discrete PIV data using a least squares finite difference approach for oversampled data [5]. Velocity and vorticity fields and contour plots were generated in post-processing using Tecplot 360 (Tecplot, Inc.).

RESULTS

Each of the three cases had unique intraventricular flow characteristics (see Fig. 2). The MR case did not produce any significant rotational flow during the cardiac cycle. The case with the BSM valve implanted in the mitral location had a major and minor orifice jet that combined directly beneath the valve occluder to form a single coherent inlet jet. This inlet jet produced fully developed rotational flow through the central body of the ventricle. The valve simulating edge-to-edge mitral repair with the MitraClip produced two distinct inlet jets from the two orifices created by the clipped valve. Unlike the major and minor orifice jets in the BSM case, these jets did not combine and remained separate through the ventricle body. These parallel jets produced multiple vortical structures in the ventricle.

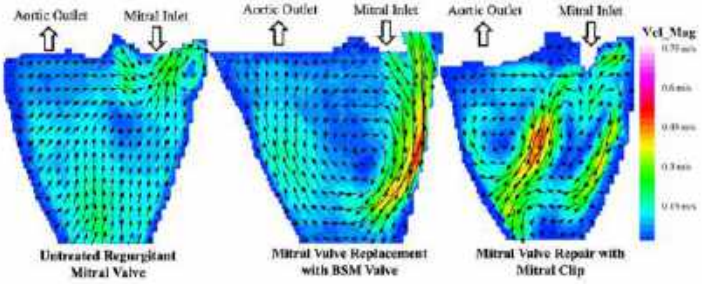

Figure 2: Intraventricular velocity fields from PIV data taken during late diastole for all three mitral valve types in this study.

The flow structures for the three valve types resulted in different levels of VED during the cardiac cycle (see Fig. 3). The VED increased at the beginning of diastole as the LV filled and the inlet jet generated viscous forces. The VED was lower in the BSM case compared to both the clipped and unclipped porcine valve cases. The clipped case had the highest peak and total VED, but the unclipped regurgitant case had a higher sustained VED during late diastole into systole.

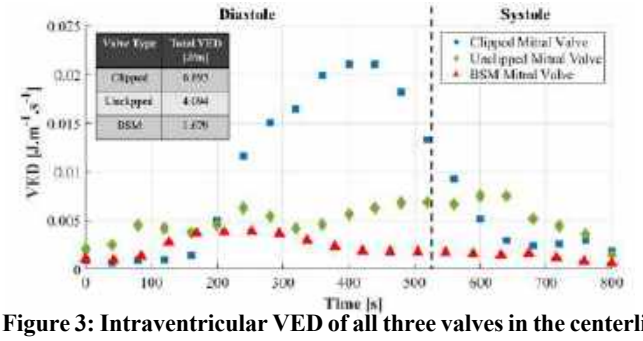

Figure 3: Intraventricular VED of all three valves in the centerline plane integrated over the cardiac cycle in overlapped table.

MR was observed upstream of the mitral valve in both the clipped and unclipped mitral valves (see Fig. 4). The unclipped case produced regurgitant flow that encompassed the entire valve diameter. The clipped case produced two small regurgitant jets at the locations of the two valve orifices created by the attached MitraClip.

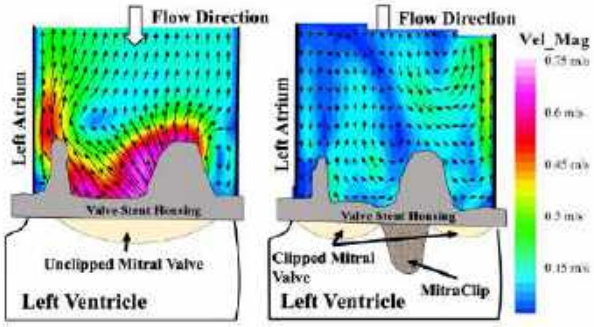

Figure 4: Velocity fields upstream of the valve in the unclipped (left) versus clipped (right) custom bioprosthetic mitral valve.

DISCUSSION

The rising prevalence of transcatheter percutaneous edge-to-edge mitral valve repair as a treatment for MR has increased the importance of improving our understanding of its impact on LV hemodynamics. Characterizing flow changes can help elucidate potential comorbidities associated with edge-to-edge valve repair, advance the development of new surgical therapies, and improve future MR patient outcomes. Currently, no studies exist that have quantified flow in the LV following mitral valve clipping. This study showed that the dual-orifice mitral valve post-treatment resulted in suboptimal flow for efficient ventricle filling and ejection. The two jets resulted in multiple interacting vortices and produced a less coherent diastolic rotational flow structure that is a characteristic of healthy ventricular flow. These changes caused elevated VED, which indicates less efficient intraventricular flow and an elevated workload on the ventricle to maintain healthy cardiac output. These results may indicate the development of comorbidities such as ventricular hypertrophy or reduced ejection fraction resulting in heart failure in patients receiving edge-to-edge repair as a long-term treatment option for MR.

ACKNOWLEDGEMENTS

No funding acknowledgments.

REFERENCES

[1] Roth, G et al., *J Amer College of Cardiol*, 76(25):2982-3021, 2020.
[2] Dziadzko, V et al., *Lancet*, 391:960-969, 2018.
[3] Del Forno, B et al., *Nature Rev Cardiology*, 17(12):807-827, 2020.
[4] Papolla, C et al., *Cardiovasc Eng and Tech*, 11(6):708-718, 2020.
[5] Raffel, M et al., *Particle Image Velocimetry Practical Guide*, 2007.

RAPID ESTIMATION OF LEFT VENTRICULAR CONTRACTILITY WITH A PHYSICS-INFORMED NEURAL NETWORK INVERSE MODELING APPROACH

Ehsan Naghavi (1), Haifeng Wang (1), Lei Fan (2), Jenny S. Choy (3), Ghassan Kassab (3), Seungik Baek (1), Lik-Chuan Lee (1)

(1) Department of Mechanical Engineering, Michigan State University, East Lansing, MI
(2) Joint Department of Biomedical Engineering, Marquette University and Medical College of Wisconsin, Milwaukee, WI
(3) California Medical Innovations Institute, San Diego, CA

INTRODUCTION

A pressing need exists for a clinical tool capable of rapid assessing and closely monitoring alterations in heart function through the cardiovascular blood circulation. To address this need, we developed a neural network model [1] that encodes the physics of a closed-loop blood circulation system embedding a left ventricle (LV). The physics-informed neural network (PINN) model is trained to satisfy a system of ordinary differential equations (ODEs) associated with a lumped parameter description of the circulatory system [2]. Then, we enhanced and implemented an inverse modeling approach utilizing the trained PINN model, enabling rapid estimation of key model parameters from single-beat LV pressure and volume waveforms, including the end-systolic elastance (E_{es}). This framework was tested with an in vivo animal model where we show that it can potentially be used in the clinic to simultaneously estimate LV contractility and other physiological parameters from single-beat measurements.

METHODS

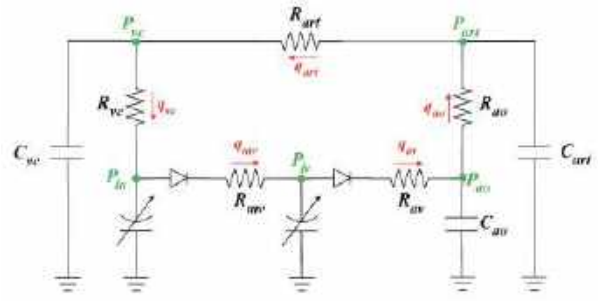

Figure 1: The electrical equivalent diagram of the closed-loop blood circulation. lv, left ventricle; ao, aorta; art, peripheral artery; vc, vena cava; la, left atrium; av, aortic valve; mv, mitral valve.

The closed-loop circulatory model is comprised of five compartments (Fig. 1). The volume change of each compartment is governed by inflow and outflow rates as described by the following system of ODEs

$$\frac{dV_{lv}}{dt} = q_{mv} - q_{av}, \quad \frac{dV_{ao}}{dt} = q_{av} - q_{ao}, \quad \frac{dV_{art}}{dt} = q_{ao} - q_{art}, \quad \frac{dV_{vc}}{dt} = q_{art} - q_{vc}, \quad \frac{dV_{la}}{dt} = q_{vc} - q_{mv}, \tag{1}$$

Flow rates q_{ao}, q_{art}, q_{vc}, q_{mv}, q_{av} are determined by corresponding resistances and pressure differences. Pressure in the blood vessels is governed based on the vessel's volume and compliance. Left ventricle and atrium contraction is modeled using a time-varying elastance model.

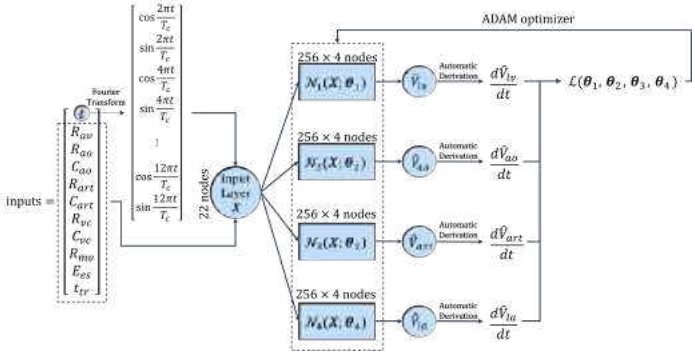

Figure 2: Model architecture: Input layer size is 22, comprising 12 Fourier terms and 10 input parameters. Four separate neural networks, each characterized by its set of weights and biases (θ_i).

The PINN model uses time t and 10 physiological parameters, including E_{es}, as inputs. Volume waveforms are represented by the first twelve terms of the Fourier series of time t to enforce the periodic boundary conditions. Four neural networks (Fig. 2) represent the volume of each indi-

vidual compartments in the system (Fig. 1). The volume of the fifth component (vena cava) is calculated using mass conservation, i.e.,

$$\hat{V}_{vc} = V_{total} - (\hat{V}_{lv} + \hat{V}_{ao} + \hat{V}_{art} + \hat{V}_{la}). \quad (2)$$

A dataset comprising 100 000 cases was generated for the training using Latin Hypercube Sampling (LHS) to sample the parameter space. Each case has 400 timepoints. In total, we have 40 000 000 collocation points for training. The loss function is defined as the mean square error of the sum of the residuals (of Eq. 1) computed at all the collocation points.

The trained PINN model is used to estimate parameters from experimental measurements of 11 Yorkshire swine, including 3 with administration of an inotropic drug (Dobutamine). The goal here is to use given left ventricle pressure and volume waveforms to estimate an optimal combination of input parameters that maximizes the coefficient of determination R^2 between the PINN model predicted waveforms and the given waveforms. Optimization is performed using the differential evolution method. Parameter estimation is also performed on synthetic waveforms generated by the PINN model for 100 cases with distinct parameters to determine whether the same parameters used for generating the waveforms are recovered with inverse modeling.

RESULTS

To assess the trained PINN model's accuracy relative to the numerical solution, the relative mean absolute error (RMAE) for the volume state variables (Eq. 1) was calculated in 1000 cases, with a maximum error below 5%. In inverse modeling, RMAE between parameters estimated based on the synthetic waveforms and their ground truth was below 1% for all parameters in the 100 cases (Fig. 3).

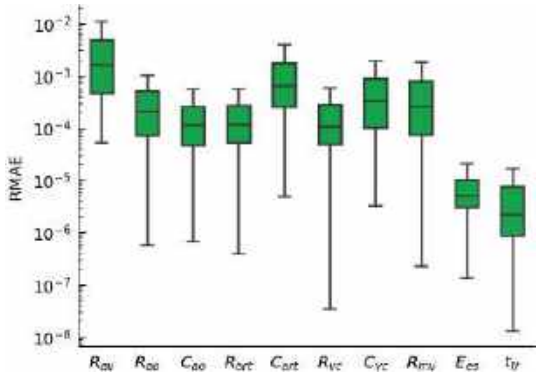

Figure 3: RMAE between the estimated input parameters and their ground truth for 100 synthetic cases

Results of inverse modeling performed using measurements of the swine subjects is shown in Fig. 4. Table 1 shows some of the estimated parameters. For the 3 animal data in which measurements before and after dobutamine administration were available, the inverse modeling is able to predict an increase in contractility (E_{es}). The fitted LV pressure and volume waveforms agree well with the experimental measurements, as reflected by the large R^2 value.

DISCUSSION

We have developed and trained a PINN model that is based on the mathematical ODE formulation of a closed-loop lumped parameter model of the cardiovascular system. The trained PINN model can be used for inverse modeling to estimate parameters reflecting the heart function in less than 3 minutes, which could take up to 6 hours if numerical methods were used. Inverse modeling performed on synthetic LV volume and pressure waveforms successfully recovered the original model inputs, which implies the uniqueness of these parameters (Fig. 3). Correspondingly, parameters estimated from inverse modeling using experimental measurements of the volume and pressure waveforms are likely to be also unique (Fig. 4 and Table 1). We also validated the inverse PINN modeling approach using experimental measurements acquired from a swine model with and without the administration of an inotropic agent. These results suggest that the PINN model can potentially be further developed as a clinical tool to simultaneously estimate ventricular contractility and other physiological parameters using single-beat measurements from patients.

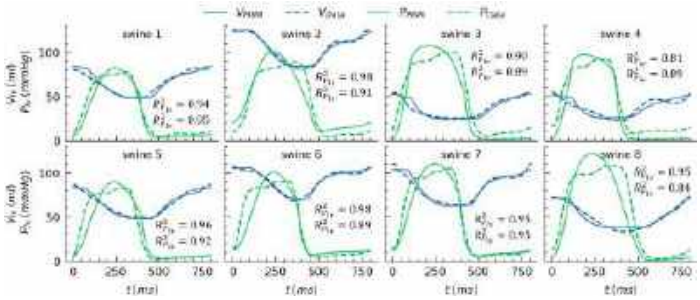

(a) Inverse modeling for eight swine subjects at their baseline

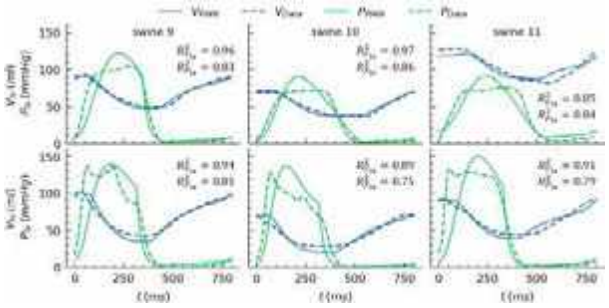

(b) Inverse modeling for three swine subjects before (top panel) and after (bottom) Dobutamine administration

Figure 4: The results of inverse modeling for eleven swine subjects

Table 1: Estimated parameters for each swine case.

Swine Number	State	$mmHg\,\frac{ms}{ml}$	$\frac{ml}{mmHg}$		$\frac{mmHg}{ml}$	ms
		R_{art}	C_{art}	C_{vc}	E_{es}	t_{tr}
1	baseline	389.2	1.7	370.4	1.96	389
2	baseline	655.7	10.0	42.8	1.22	453
3	baseline	3167.0	10.0	400.0	7.09	420
4	baseline	3375.0	10.0	400.0	5.82	366
5	baseline	353.8	3.9	336.4	2.10	398
6	baseline	546.5	7.6	114.8	1.44	376
7	baseline	563.4	8.0	125.3	2.03	393
8	baseline	1862.5	1.0	400.0	3.98	567
9	baseline	817.1	1.0	181.0	2.73	345
	dobutamine	865.2	1.0	128.4	4.34	314
10	baseline	834.4	10.0	274.8	2.50	567
	dobutamine	1111.9	1.0	316.1	7.82	316
11	baseline	728.8	10.0	59.4	1.00	567
	dobutamine	1092.9	1.0	162.2	3.84	328

ACKNOWLEDGEMENTS

This work is supported by HL160997, HL163977 and HL166508.

REFERENCES

[1] Raissi M et al. *Journal of Computational Physics* 378 (2019). ISSN: 0021-9991. DOI: https://doi.org/10.1016/j.jcp.2018.10.045.

[2] Zambrano BA et al. *Frontiers in Bioengineering and Biotechnology* 8 (2021). ISSN: 2296-4185. DOI: 10.3389/fbioe.2020.611149.

DECODING OF QUANTITATIVE RELATIONSHIP BETWEEN MECHANICAL FORCES ON CELL NUCLEUS AND YAP PROTEIN TRANSLOCATION

Miao Huang (1,2), Maedeh Lotfi (1), Kevin Connell (1), Malisa Sarntinoranont (1), Xin Tang (1,2)

(1) Department of Mechanical & Aerospace Engineering (MAE), University of Florida (UF), Gainesville, FL 32611, USA
(2) UF Health Cancer Center (UFHCC), University of Florida (UF), Gainesville, FL 32611, USA

INTRODUCTION

Mechanotransduction, i.e., living cells sense and transduce mechanical forces into intracellular biochemical signaling and gene expression, is ubiquitous across diverse organisms. Increasing evidence suggests that mechanotransduction significantly influences cell functions and its mis-regulation is at the heart of various pathologies. A quantitative characterization of the relationship between mechanical forces and resulted mechanotransduction is pivotal in understanding the rules of life and innovating new therapeutic strategies [1][2][3]. However, while such relationship on the cell surface membrane and cytoskeleton have been well studied, little is known about whether/how mechanical forces applied on the cell interior nucleus ("headquarter of the cell") quantitatively trigger mechanotransduction. This is because conventional techniques cannot simultaneously access, manipulate, and record the mechano-chemo-genetic dynamics inside the cell nucleus. In this presentation, we will present our new results on (1) the experimental characterization of the translocation of YAP (Yes-associated protein) induced by quantitative force applied directly on the nucleus; and (2) computation-guided quantification of applied mechanical forces.

As a critical mechano-sensitive transcription coactivator, YAP regulates downstream gene transcription to promote tumor progression at different key stages of cancer development: neoplasm initiation, growth, metastasis, and drug-resistance [4][5]. Overexpression and nuclear translocation of YAP are observed in multiple tumor types [6]. Independent of conventional Hippo pathway, physiological mechanical force can also induce nuclear translocation of YAP in parallel. In solid tumors, abnormal microenvironment applies elevated mechanical stimuli (tissue stiffness, solid stress, interstitial fluid stress, etc.) to tumor cells, which also show abnormal mechanosensing mechanisms [7]. Therefore, understanding of the YAP-associated mechanism of tumor mechanotransduction is needed for the development of new mechanotherapy.

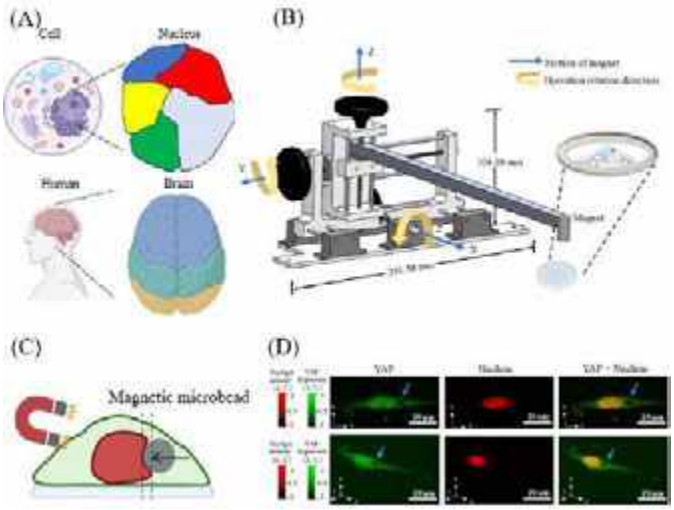

Figure 1: Direct manipulation of nucleus by magnetic microbeads. (A) Nucleus as the central control system of cell. (B) Three-dimensional schematic of device implemented to hold the magnet and move it in x, y, and z directions. The magnet will be lowered to the dish to apply magnetic on magnetic microbeads (C) Schematic of magnetic microbead applying indentation on the nucleus. (D) Representative images showing magnetic microbead (black hollow pointed by blue arrow) is internalized into the cell (indicated by YAP) and outside the nucleus. Top: X-Y cross-section of cell of YAP (green), nucleus (red) and bright-field. Bottom: 3D reconstruction of the cell.

Similar to the function-compartmentalized brain in the human body, the nucleus also has compartmentalized functional regions to perform both central control and multi-task coordination in the cell **(Fig.**

1A). Recent results show that extracellular mechanical signals need to be transmitted through cytoskeleton to the nucleus to induce translocation of YAP. Despite the emerging evidence of LINC complex and nuclear Lamins are involved in nuclear mechanotransduction, multiple critical knowledge gaps remain [8][9][10]. First, how the YAP translocation changes with respect to the magnitude and direction of the force applied to the nucleus remains unclear. Second, how to directly apply the force to the nucleus to regulate YAP translocation without interrupting the normal function of cytoskeleton. To our knowledge, our result is the first to bypass cell membrane and cytoskeleton and directly manipulate cell nucleus to regulate YAP translocation.

METHODS

To quantify the real-time translocation of YAP, we use CRISPR/Cas9-engineered human normal Beas-2B (B2B) cells that highlight endogenous YAP tagged by fluorescence protein mNeonGreen21-10/11. B2B cells are cultured in 35-mm glass-bottom petri dish with RPMI 1640 culture medium and 10% fetal bovine serum for confocal fluorescence imaging. 0.2 g of 7-μm mean diameter carbonyl iron microbeads are cultured with B2B cells for 12 hours to allow internalization of the microbeads into the cytoplasm. An XYZ-manipulator **(Fig. 1B)** is used to move the magnet to attract the intracellular microbeads and apply indentation on the cell nucleus **(Fig. 1C)** [11]. Nuclear/cytoplasmic translocation of YAP is quantified by high-resolution confocal fluorescence imaging throughout the manipulation of the nucleus. Cells are treated with CytoD (2.5 μM; 1 hour) to dissolve the actin cytoskeleton. Nucleus is stained by incubating with 1X NucSpot live-cell nuclear stain for 2 hours.

RESULTS

First, we directly manipulate the nucleus and confirm that nuclear indentation can induce YAP translocation. A set of representative images of increased YAP fluorescence images and corresponding YAP N/C ratio quantification are shown in **Fig. 2A and B**. We observed both increase and decrease of the YAP nucleus to cytoplasm (N/C) ratio when the force is applied to the nucleus because of variance of force magnitude and direction.

Next, we confirm that the force is applied directly to the nucleus. To make sure the magnetic microbead can indent the nucleus from the cytoplasm side, we confirm that the microbeads are internalized by the B2B cells into the cytoplasm while outside the nucleus (after 12 hours of culturing) shown by fluorescence imaging of whole-cell YAP and cell nucleus (**Fig. 1D**). To exclude the possibility that the indentation is induced by deformation of cytoskeleton, we manipulate the nucleus with dissolved actin cytoskeleton (**Fig. 2C**) and observe similar nuclear deformation.

To quantify the force directly applied to the nucleus, we use atomic force microscopy (AFM) to indent cell nucleus with deformation similar to the magnetic indentation. 3D fluorescence imaging shows a representative image that nucleus is indented by 1.5 μm (**Fig. 2D**) and 0.8 μm with two force magnitude. The force magnitude of a single microbead is calibrated as 0.8 nN and 1.4 nN, respectively, when the magnet is 13 mm and 120 mm above the bottom of the petri dish.

Finally, based on the AFM-calibrated force, we develop a finite element model of the cell nucleus to simulate the force magnitude and direction for each cell during the manipulation. The YAP N/C ratio is quantified and recorded during the nuclear manipulation process of each cell. We map the change of the YAP N/C ratio and force applied to the nucleus to generate a mathematical model of how direct manipulation of nucleus induces YAP translocation.

DISCUSSION

To our knowledge, this research is the first attempt to directly manipulate cell nucleus to induce YAP translocation without force transmission through cell membrane or cytoskeleton.

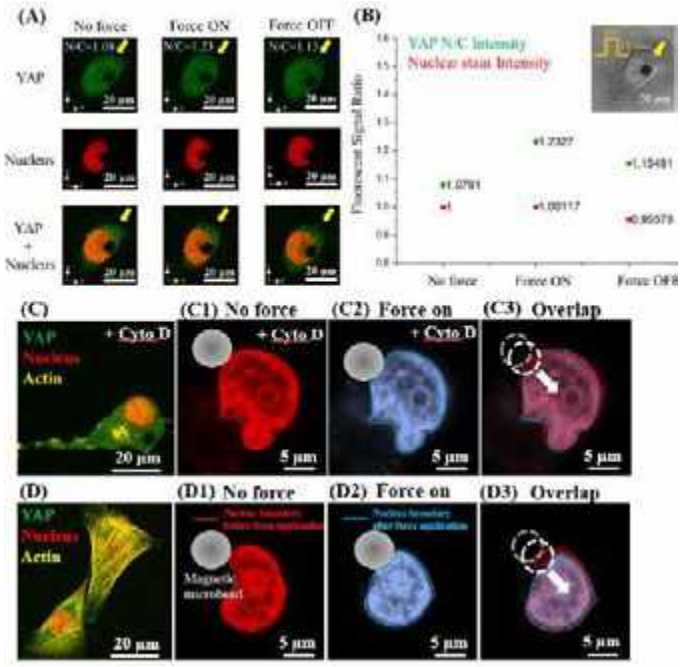

Figure 2: Direct manipulation of nucleus induces translocation of YAP. (A) X-Y cross-section of YAP (green) and nucleus (red) fluorescent image of the cell at no force, force on, and force off. (B) YAP N/C ratio increases when force on (from 1.0791 to 1.2327) and decreases when force off (from 1.2327 to 1.1548). Normalized nuclear stain intensity shows minor change with force application (1.00117) and releasing (0.95578). (C) Cells show disrupted actin filaments (yellow) after Cyto D treatment (2.5 μM, 1 h). Nucleus is indented by magnetic microbead. (D) Nucleus is indented by 1.5 μm with 1.4 nN force.

Our results suggest that magnetic microbeads can regulate the YAP translocation and downstream gene transcription while avoiding the interruption of cytoskeleton and corresponding important cell functions. Our results advance the understanding of the mechanisms of nuclear mechanotransduction and potentially contribute to the development of new therapies for tumor suppression targeting YAP.

ACKNOWLEDGEMENTS

This project is financially supported by the National Institute of General Medical Sciences of the National Institutes of Health under award number R35GM150812 (X. T.), the National Science Foundation under grant number 2308574 (X. T.), the Air Force Office of Scientific Research under award number FA9550-23-1-0393 (X. T.), the UFHCC Pilot Award (X. T. and Dr. Dietmar Siemann), UFHCC University Scholars Program (H. Y. Wang), UF Research Opportunity Seed Fund (X. T.), and the Gatorade Award (X. T.).

REFERENCES

[1] Jaalouk, D. E et al., *Nat Rev Mol Cell Biol*, *10*(1), 63-73. 2009
[2] Liang, C et al., *Biomaterials*, *290*, 121823 2022
[3] Liang, C et al., *Soft Matter*, *18*(6), 1112-1148, 2022
[4] Zhao, B et al., *Genes & development*, *22*(14), 1962-1971, 2008
[5] Zanconato, F et al., *Cancer cell*, *29*(6), 783-803, 2016
[6] Xin, Y et al., *Oncogene*, 1-34, 2023
[7] Huang, M et al. *Int. J. Mol. Sci.* 24.15, 12491, 2023
[8] Elosegui-Artola, A et al. *Cell*, *171*(6), 1397-1410, 2017
[9] Kalukula, Y et al. *Nat Rev Mol Cell Biol*, *23*(9), 583-602, 2022
[10] Driscoll, T. P et al. *Biophysical journal*, *108*(12), 2783-2793, 2015
[11] Huang, M et al. *JoVE*, (185), e64098, 2022

LONG-DISTANCE SYMPHONY AMONG HUMAN CANCER CELLS: AN UNDERAPPRECIATED MECHANO-REGULATED PROCESS IN TUMOR PROGRESSION

Chenyu Liang (1,2), Mai Tanaka (2,3), Dietmar W. Siemann (2,3), Bo Zeng (4), Xin Tang (1,2)

(1) Department of Mechanical & Aerospace Engineering (MAE), University of Florida (UF), Gainesville, FL 32611, USA
(2) UF Health Cancer Center (UFHCC), University of Florida (UF), Gainesville, FL 32611, USA
(3) Department of Radiation Oncology, University of Florida (UF), Gainesville, FL 32611, USA
(4) Key Laboratory of Medical Electrophysiology, Southwest Medical University (SMU), Luzhou, Sichuan, PR China

INTRODUCTION

Electrically excitable cells such as neurons and cardiomyocytes transmit long-distance calcium (Ca^{2+}) or electrical signals to regulate their physiological functions.[1–3] While the molecular underpinnings and down-stream effects of these intercellular communications in electrically excitable cells have been well appreciated, little is known about whether and how electrically non-excitable cancer cells spontaneously initiate and transmit long-distance intercellular signals.[4–6] Recently we discovered that human cancer cells from different organs, e.g., colon and prostate, can initiate and transmit previously "invisible" long-distance (~100s μm) biochemical Ca^{2+} waves in a substrate-mechanics-regulated manner (**Fig. 1**).[7,8] In this presentation, we will present our new results on (1) the characterization of the long-distance and the intra-/inter-cellular Ca^{2+} signals; (2) the functional influences of mechanical microenvironment on the spatial-temporal properties of Ca^{2+} symphony; and (3) the molecular mechanisms and biological consequences of the Ca^{2+} dynamics during tumor progression *in vivo*.

Ca^{2+} signals offer regulatory functions at different key cancer development stages: tumor initiation, growth, angiogenesis, and metastasis, highlighting their critical role in tumor progression.[5,9] In human colorectal cancer cells, expression of Ca^{2+} channels and transporters has been either abnormally elevated or reduced, which remodels the network of Ca^{2+} signaling and functionally suppress or promote tumor progression.[10,11]

Despite of the significance of Ca^{2+} signals in cancer development, multiple critical knowledge gaps remain. First, spontaneous intercellular Ca^{2+} waves have never been identified in non-excitable tumor cells from organs other than brain and heart. To our knowledge, only one publication to date specifically reported the existence of spontaneous Ca^{2+} transients (not wave) in colon cancer cells.[12] Second, how the physiologically relevant microenvironmental mechanics mechanistically influences the intra-/inter-cellular Ca^{2+} signals in cancer cells remains unclear.

METHODS

GCaMP5G (a genetically-encoded Ca^{2+} sensor)-expressing HCT-8 human colon cancer cells and DU145 human prostate cancer cells, respectively, were cultured on two types of two-dimensional (2D) substrates with different mechanical properties: (1) polyacrylamide (PAA) hydrogels that have elastic Young's moduli of 250 Pa, 10 kPa, 20 kPa, and 40 kPa; and (2) polystyrene (PS) substrates in tissue-culture petri dishes that have an elastic Young's modulus of 3 GPa (**Fig. 1A**).

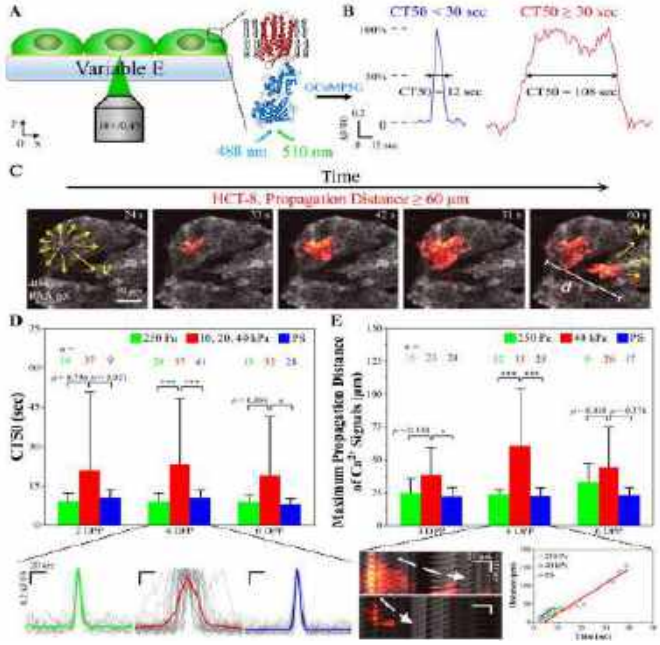

Figure 1: Substrate-stiffness-dependent spatial-temporal characteristics of spontaneous Ca^{2+} signals in HCT-8 cells. (A)

Experimental setup for Ca^{2+} imaging of cancer cells cultured on mechanical-stiffness-variable substrates. (B) Time traces of GCaMP5G fluorescence intensity ($\Delta F/F_0$) for short-duration (left) and long-lasting (right) Ca^{2+} transients. (C) Long-distance propagation of Ca^{2+} waves (hot map) among HCT-8 cells on 40-kPa PAA gels. (D) Top: Mean+SD data for the CT50 of HCT-8 cells cultured on 2D substrates with different Young's moduli. Bottom: Averaged time traces of GCaMP5G fluorescence intensity showing the waveform differences of Ca^{2+} transients in HCT-8 cells on different substrates. (E) Top: Mean+SD data for the propagation distance of Ca^{2+} signals in HCT-8 cells cultured on 2D substrates with different moduli. Bottom left: Kymographs of representative Ca^{2+} wave propagations among HCT-8 cells on 40-kPa (upper) and 250-Pa (lower) PAA gels. Bottom right: Distances of Ca^{2+} wave propagations vs. time in HCT-8 cells on the different substrates.

Time-lapse fluorescent imaging recorded the spatial-temporal dynamics of $[Ca^{2+}]_{cyt}$ daily from the 1st to the 6th day post-plating (DPP). Xenograft model and *ex vivo* Ca^{2+} imaging were performed to investigate Ca^{2+} dynamics in tissues. The spatial-temporal properties of the $[Ca^{2+}]_{cyt}$ signals, including (1) the lasting duration of Ca^{2+} transients at 50% of peak intensity (CT50; **Fig. 1B**) and (2) the maximum spatial propagation distance of Ca^{2+} waves (**Fig. 1C**), were analyzed using customized MATLAB algorithms. Patch-clamp electrophysiology, high-resolution imaging, and pharmacological modulation were integrated to dissect the molecular mechanisms of the Ca^{2+} transient. IP_3 sponges that inhibit Ca^{2+} signals and xenograft model were integrated to elucidate the *in vivo* Ca^{2+} functions on tumor progression.

RESULTS

We found that, starting from the 1st DPP on, non-excitable HCT-8 cells constitutively showed spontaneous intracellular Ca^{2+} transients on both PS substrates and 40-kPa PAA gels (**Fig. 1B–C**). Of note, HCT-8 cells showed a myriad of long-distance, radial intercellular propagations of Ca^{2+} waves in multiple regions of cell colonies cultured on 40-kPa PAA gels (**Fig. 1C**). DU145 human prostate cancer cells also showed spontaneous Ca^{2+} transients and Ca^{2+} waves. Moreover, evident $[Ca^{2+}]_{cyt}$ transients and waves occur in HCT-8 tumor slices *ex vivo*.

Interestingly, regarding to the temporal characteristics, on 10–40-kPa PAA gels, a sub-group of the HCT-8 cells constitutively generated Ca^{2+} transients with CT50 higher than 30 s from the 1st DPP on (**Fig. 1B&D**). In contrast, on 250-Pa PAA gels and 3-GPa PS substrates, all the CT50s of the same batch of HCT-8 cells were less than 30 s (**Fig. 1B&D**). Regarding the spatial characteristics, on 40-kPa PAA gels, the HCT-8 cells constitutively generated radial intercellular Ca^{2+} waves with propagation distance longer than 60 μm at a propagation speed of 6.98 ± 2.45 μm/s in multiple regions of large cell colonies from the 3rd DPP on (**Fig. 1C&E**). In contrast, on 250-Pa PAA gels and 3-GPa PS substrates, all the propagation distances of Ca^{2+} signals were less than 60 μm (**Fig. 1E**). The results suggest that the spatial-temporal characteristics of Ca^{2+} waves can be tuned by the mechanical stiffnesses of culture substrates.

Our mechanistic dissections suggest that the spontaneous Ca^{2+} transient initiation in HCT-8 cells is caused by inositol trisphosphate receptor (IP_3R)-regulated Ca^{2+} release from endoplasmic reticulum (ER), with the G_q-PLC-IP_3R pathway be the upstream signaling. We applied IP_3 sponge, a hyper-affinity IP_3 absorbent that deactivates IP_3R,[13] to inhibit Ca^{2+} transients in HCT-8 cells *in vitro* (**Fig. 2A**) and *ex vivo* (**Fig. 2B–C**). In a xenograft model, the tumors grown from IP_3-sponge-transduced HCT-8 cells possessed 1.6 times lower weight compared to those from control cells, whereas the body weights of the tumor-bearing mice were similar between the two groups (**Fig. 2D–E**). These data suggest that the inhibition of Ca^{2+} signals in HCT-8 cells suppresses *in vivo* tumor growth.

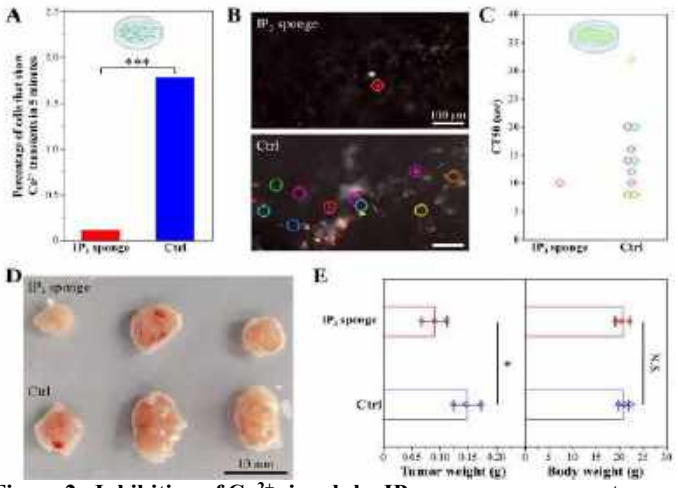

Figure 2: Inhibition of Ca^{2+} signals by IP_3 sponge suppresses tumor growth *in vivo*. (A) The percentages of IP_3-sponge-transduced and control (Ctrl) HCT-8 cells that showed spontaneous Ca^{2+} transients when cultured in petri dishes. (B) Spontaneous Ca^{2+} transients in the tumor slices of the IP_3 sponge and control groups. Ca^{2+} flashing spots during the 5-min recording are circled. (C) The CT50 of Ca^{2+} flashing spots circled in (B). (D) Dissected tumors two weeks after inoculation. (E) The effect of IP_3 sponge on the weight of tumors and the body weight of tumor-bearing mice.

DISCUSSION

To our knowledge, this research is the first attempt to fill several knowledge gaps in the field. Our results suggest that IP_3R-induced Ca^{2+} transients in human colon cancer cells could be regulated by the mechanical microenvironment. These results indicate a possible crosstalk between the G_q-PLC-IP_3R pathway[14,15] and the mechanotransduction process.[16,17] We hypothesize that substrate stiffness could influence the spatial-temporal characteristics of Ca^{2+} signals in HCT-8 cells possibly via regulation of (1) mechanosensitive GPCRs,[18,19] (2) interaction between PIP2 and PLC,[20,21] and (3) IP_3R activities[22,23] in a cytoskeleton-dependent manner. Although we found that HCT-8 cells uniquely show the IP_3 signaling and ER Ca^{2+}-release-based mechanism in comparison to other reported colon cancer cell lines,[12] this mechanism is widely found in many other cell types.[14,15]

This study is the 1st report that shows the long-distance Ca^{2+} waves in human cancer cells (**Fig. 1C**) and tumors derived from xenografts (**Fig. 2B**). Our results advance the understanding of the mechano-regulated functions/mechanisms of Ca^{2+} signals in cancer and potentially contribute to the development of new therapies for tumor suppression.

ACKNOWLEDGEMENTS This project is supported by the National Institute of General Medical Sciences of the National Institutes of Health under award number R35GM150812 (X.T.), the National Science Foundation under grant number 2308574 (X.T.), the Cancer Pilot Award from UF Health Cancer Center and the state of Florida through the Casey DeSantis Cancer Research Act (Fla. Stat. § 381.915) (X. T. and D. S.), UF Research Opportunity Seed Fund (X. T.), and the Gatorade Award (X. T.).

REFERENCES [1]Izu, LT et al., *JMCC*, 58:118–124, 2013. [2]Curran, J et al., *JMCC*, 49:25–32, 2010. [3]Hoogland, TM et al., *PNAS*, 106:3496–3501, 2009. [4]Xin, Y et al., *Oncogene*, 42:3457–3490, 2023. [5]Liang, C et al., *Soft Matter*, 18:1112–1148, 2022. [6]Huang, M et al., *IJMS*, 24(15):12491, 2023. [7]Liang, C et al., *Biomaterials*, 290:121823, 2022. [8]Liang, C et al., *Methods Mol Biol*, 2679:95–125, 2023. [9]Monteith, GR et al., *Nat Rev Cancer*, 17:367–380, 2017. [10]Parkash, J et al., *Life Sci*, 87:587–595, 2010. [11]Monteith, GR et al., *Nat Rev Cancer*, 7:519–530, 2007. [12]Jiang, M et al., *Nat Commun*, 11:19, 2020. [13]Uchiyama, T et al., *JBC*, 277:8106–8113, 2002. [14]Karagas, NE et al., *Cells*, 8:1232, 2019. [15]Berridge, MJ, *Physiol Rev*, 96:1261–1296, 2016. [16]Janmey, PA et al., *Physiol Rev*, 100:695–724, 2020. [17]Tang, X et al., *Mol Cancer*, 13:1–15, 2014. [18]Wei, WC et al., *Curr Biol*, 28:3815–3823, 2018. [19]Xu, J et al., *Cell*, 173:762–775, 2018. [20]Vasilev, F et al., *Cell Physiol Biochem*, 48:2011-2034, 2018. [21]Kovacevic, I et al., *PLoS Genet*, 9:e1003510, 2013. [22]Kim, TJ et al., *eLife*, 4:e04876, 2015. [23]Fukatsu, K et al., *J Neurochem*, 114:1720–1733, 2010.

UNCOVERING ELECTRO-MECHANO-PHYSIOLOGICAL RULES OF LIFE: A NEW 2D/3D ALL-OPTICAL INTERROGATION TECHNOLOGY

Chenyu Liang (1,2), Erica Hengartner (1), Abygale Cochrane (3), Bruna Balbino de Paula (4), Basak Ayaz (4), Robert Caudle (4), Allison Campbell (5), Eleana Manousiouthakis (5), Christine Schmidt (5), Tian He (6), Christopher Werley (7), Xin Tang (1,2)

(1) Department of Mechanical & Aerospace Engineering (MAE), University of Florida (UF), Gainesville, FL 32611, USA
(2) UF Health Cancer Center (UFHCC), University of Florida (UF), Gainesville, FL 32611, USA
(3) Department of Physics, University of Florida (UF), Gainesville, FL 32611, USA
(4) Department of Oral and Maxillofacial Surgery, University of Florida (UF), Gainesville, FL 32610, USA
(5) J. Crayton Pruitt Department of Biomedical Engineering, University of Florida (UF), Gainesville, FL 32611, USA
(6) Department of Chemistry and Chemical Biology, Harvard University (HU), Cambridge, MA 02138, USA
(7) Q-State Biosciences, Cambridge, MA 02139, USA

INTRODUCTION

Biological systems can modulate their electrical membrane potential and apply mechanical forces simultaneously to regulate key physiological functions including proliferation, communication, computation, and migration.[1–4] However, the 4D spatial-temporal dynamics of the electro-mechano-physiological signals in most multi-cellular systems remains unknown, mainly because of the limitation of current technologies to elucidate the coupled signals. To fill this gap and reveal the general rules of life, we created a wide-area 2D/3D optical interrogation system to visualize and control the electro-mechano-physiological signals in > 50 cells simultaneously within 5 min across conditions of *in vitro*, *ex vivo*, and *in vivo*. Our new technologies enable mechanistic study of both electrical and mechanobiological nature of biological systems in a high-throughput, non-invasive, high-speed (> 1 kHz), high signal-to-noise ratio (SNR), cell-type-specific, and long-term (from milli-seconds to months) manner.

Neurological diseases remain a significant unmet societal need today, affecting millions of patients worldwide.[5–7] However, due to the low throughput of traditional drug screening approaches (e.g., up to 200 cells per day for automated patch-clamp)[8,9] and the complexity of the human nervous system (e.g., 100s of neuronal cell types and 100 billion nerve cells),[10,11] neurological drugs have a much longer development time than other-organ-targeting drugs. Hence, we are in dire need of innovative approaches that can improve the throughput to discover new drugs and advance integrative understanding of neurological diseases.

Electrical activities are the "finger-printer" and "regulator" of cell states, especially in neurons.[12,13] In parallel, mechanical stimuli including substrates' mechanical stiffness,[14–17] compression,[18,19] and tension[20,21] are demonstrated to regulate the electrical properties of neurons. However, existing publications show opposite influence of mechanics on the electrical behavior of neurons,[14,17] partially due to the inconsistent methods of the measurement and control for the coupled signals. Moreover, the causal links, i.e., molecular mechanisms, among electrical, mechanical, and physiological signals in neurons are not clear, triggering the development of multidimensional systems to acquire the omics data.

METHODS

Optopatch (optical patch-clamp) imaging was performed via a customized all-optical electrophysiology interrogation (AOEI) system (**Fig. 1A−B**).

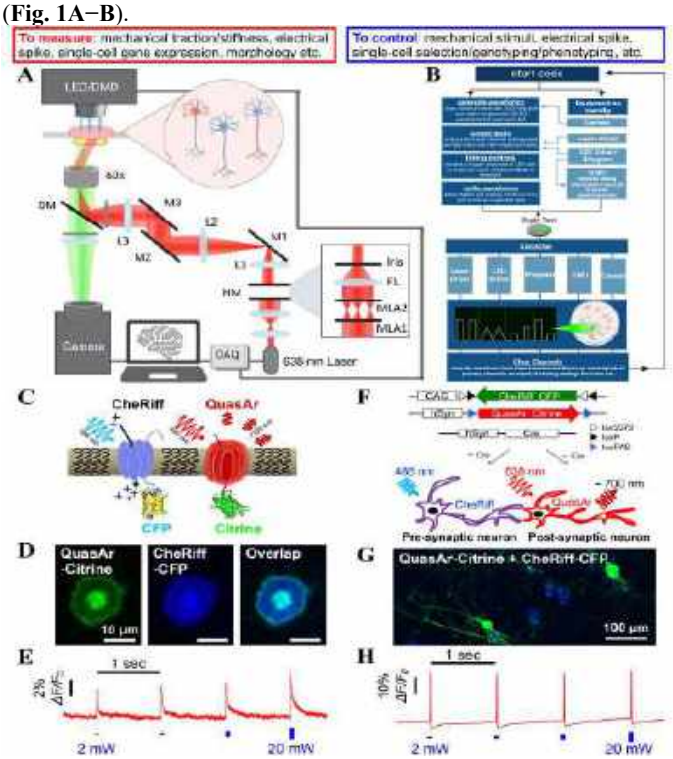

Figure 1: All-optical electrophysiology interrogation (AOEI) system enabling optical recording and control of single action potential (Optopatch) and synaptic transmission (SynOptopatch). (A) Optical path diagram. (B) Synchronization of hardware via precise signals produced by our LabVIEW code. (C) Optopatch molecular tools (QuasAr + CheRiff) in the same neuron. (D) Expression and distribution of QuasAr-Citrine and CheRiff-CFP. (E) Single spike readout (Red) under optogenetic stimulation (Blue) in a single neuron. (F) SynOptopatch molecular tools: Cre-recombinase-mediated exclusive expression of CheRiff and QuasAr. (G) Pre-synaptic neurons expressing CheRiff-CFP and post-synaptic neurons expressing QuasAr-Citrine. (H) Post-synaptic potential readout (Red) under optogenetic stimulation (Blue) including both inhibition and excitation.

For large field-of-view (FOV) voltage imaging, a 4X objective (NA 0.28) and a 0.5-kHz camera sampling rate were used. For high-resolution voltage imaging, a 60X objective (NA 1.5) and a 1-kHz sampling rate were used. The rat primary trigeminal ganglion (TG) and dorsal root ganglion (DRG) neurons were cultured on: (1) polyacrylamide (PAA) hydrogels with elastic Young's moduli of 0.1 kPa and 100 kPa; and (2) glass substrates with a Young's modulus of 70 GPa. The raw data were post-processed and analyzed using ImageJ software and custom MATLAB programs.

RESULTS

To investigate intrinsic neuronal excitability using our AOEI system, we expressed the Optopatch molecular tools (QuasAr for voltage readout[22] + CheRiff for voltage actuation) in the same neuron using lentivirus (**Fig. 1C**). The expression and membrane trafficking of QuasAr and CheRiff were confirmed by confocal imaging of their tagged proteins, Citrine and cyan fluorescent protein (CFP), respectively (**Fig. 1D**). 5-msec stimuli of blue (488 nm) light triggered single action potentials (APs) in multiple Optopatch-expressing primary TG and DRG neurons (**Fig. 1E**). The blue light with increasing intensities triggered APs with increasing peak voltage.

To investigate synaptic transmission using our AOEI system, we expressed the synaptic Optopatch (SynOptopatch) molecular tools,[23] i.e., CheRiff and QuasAr exclusively in the pre-synaptic and post-synaptic neurons using a Cre-recombinase-mediated system (**Fig. 1F**). A multiplicity of infection (MOI) of 1 for AAV-Cre was applied to have approximately equal numbers of neurons expressed CheRiff or QuasAr (**Fig. 1G**). We found that, 5-msec stimuli of blue LED light at the whole FOV triggered post-synaptic potentials in multiple QuasAr-expressing primary TG and DRG neurons (**Fig. 1H**). The post-synaptic potentials reveal both inhibition and excitation in the same post-synaptic neuron.

To increase the FOV of the imaging system for high-throughput AOEI, we expanded the QuasAr illumination area to 4.6×0.7 mm^2 while maintaining the illumination power density at 1 W/mm^2 to compensate for the short exposure time.[24–26] To examine the imaging capability of the whole illumination area, we located the same group of neurons at the middle, right edge, and left edge of the FOV and performed Optopatch imaging in sequence (**Fig. 2A**). We found that, our AOEI system recorded single-spike-resolved AP firing from neurons at all three locations under multiple 500-msec optogenetic stimulation trials (**Fig. 2A**). The blue light with increasing intensities triggered APs with increasing firing frequency in a subgroup of neurons.

To investigate the influence of mechanical microenvironment on the AP firing patterns of neurons, we cultured the rat primary TG neurons on 0.1-kPa PAA, 100-kPa PAA and glass substrates and performed Optopatch imaging (**Fig. 2B**). We found that, primary TG neurons cultured on soft PAA gels started to fire multiple APs at lower intensities of the 500-msec optogenetic stimuli than those cultured on stiff glass (**Fig. 2B**).

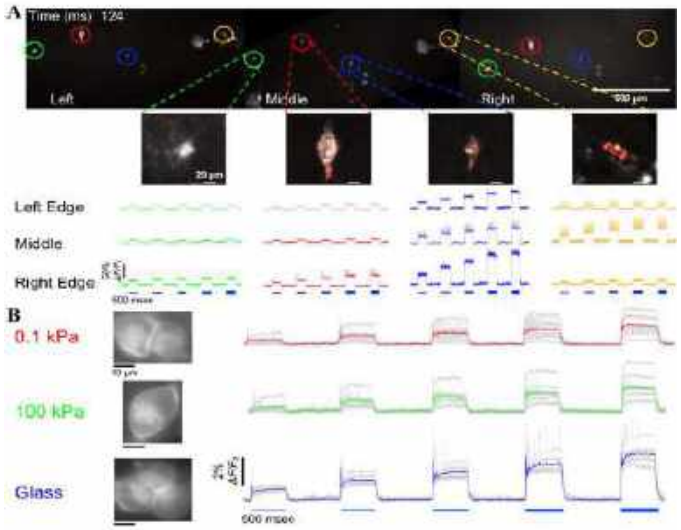

Figure 2: (A) Wide-FOV (4.6×0.7 mm^2, 4X) excitability recordings of primary TG neurons. Top: QuasAr fluorescence (hot map) image of Optopatch-expressing neurons. Middle: Magnified views of spiking neurons circled in the top image. Bottom: AP readout under optogenetic stimulation in neurons at different locations of the whole FOV. (B) High-resolution (60X) excitability recordings of primary TG neurons cultured on mechanical-stiffness-variable substrates. Left: QuasAr expression in spiking neurons. Right: Averaged AP waveforms of neurons under optogenetic stimulation on different substrates.

DISCUSSION

To our knowledge, this research is the first attempt to fill several knowledge gaps in the field, by recruiting 2D substrates with tunable mechanical properties and all-optical interrogation to study the mechano-electrophysiology of primary neurons (**Fig. 2**). Our results suggest that neurons cultured on physiologically relevant soft substrates could be more easily excited compared to those cultured on glass-bottom petri dishes. These data are in the same trend with several previous publications.[16,17] However, those previous results were measured by conventional patch-clamp in a cell-by-cell manner, and our wide-area AOEI system could increase the throughput by > 500-fold.

Our AOEI technologies enable high-throughput investigation of intrinsic neuronal excitability and synaptic transmission under different mechanical microenvironments. More functions are to be added, including compressive/tensile stimuli, traction force measurement, and single-cell-resolved selection/genotyping/phenotyping. The integrated multidimensional system potentially contributes to the mechanistic studies of the omics among electrical/mechanical/physiological signals in neurons and to the drug screening for neurological diseases.

ACKNOWLEDGEMENTS This project is supported by the National Institute of General Medical Sciences of the National Institutes of Health under award number R35GM150812 (X.T.), the National Science Foundation under grant number 2308574 (X.T.), the Air Force Office of Scientific Research under award number FA9550-23-1-0393 (X. T.), the Cancer Pilot Award from UF Health Cancer Center and the state of Florida through the Casey DeSantis Cancer Research Act (Fla. Stat. § 381.915) (X. T. and D. S.), UF Research Opportunity Seed Fund (X. T.), and the Gatorade Award (X. T.).

REFERENCES [1]Liang, C et al., *Biomaterials*, 290:121823, 2022. [2]Liang, C et al., *Methods Mol Biol*, 2679:95–125, 2023. [3]Liang, C et al., *Soft Matter*, 18:1112–1148, 2022. [4]Xin, Y et al., *Oncogene*, 42:3457–3490, 2023. [5]Schulte, F et al., *Cancer*, 127:35-44, 2020. [6]Tracy, H, *Cerebrum*, 8, 2016. [7]Panagiotoglou, D et al., *BMJ Open*, 11:e053191, 2021. [8]Ghovanloo, MR et al., *Cell Rep Methods*, 3:100385, 2023. [9]Seibertz, F et al., *Commun Biol*, 5:969, 2022. [10]Sousa, AMM et al., *Cell*, 170:226-247, 2017. [11]Herculano-Houzel, S, *Front Hum Neurosci*, 3:31, 2009. [12]Zeng, H et al., *Nat Rev Neurosci*, 18:530–546, 2017. [13]Farhi, S et al., *J Neurosci*, 39:4889–4908, 2019. [14]Lantoine, J et al., *Biomaterials*, 89:14-24, 2016. [15]Zhang, QY et al., *Sci Rep*, 4:6215, 2014. [16]Evans, MG et al., *Integr Biol (Camb)*, 11:395-403, 2019. [17]Karahuseyinoglu, S et al., *J Neurochem*, 156:848-866, 2021. [18]Kunze, WA et al., *J Physiol*, 526:375-85, 2000. [19]Kugler, EM et al., *Front Cell Neurosci*, 9:342, 2015. [20]Kang, WH et al., *Biomech Model Mechanobiol*, 14:561-75, 2015. [21]Kang, WH et al., *J Neurotrauma*, 32:1011-9, 2015. [22]Tian, H et al., *Nat Methods*, 20:1082-1094, 2023. [23]Fan, L et al., *Nat Methods*, 15:823–831, 2018. [24]Werley, CA et al., *Biomed Opt Express*, 8:5794-5813, 2017. [25]Werley, CA et al., *Curr Protoc Pharmacol*, 78:1–24, 2017. [26]Borja, GB et al., *Methods Mol Biol*, 2191:109-134, 2021.

FUNCTIONAL EXPRESSION OF MECHANOSENSITIVE ION CHANNELS IN REGENERATING AXOLOTL LIMBS

Vineel Kondiboyina (1), Melissa Miller (2), James R. Monaghan (2), Sandra J. Shefelbine (1,3)

(1) Dept. of Bioengineering, Northeastern University, Boston, MA, USA
(2) Dept. of Biology, Northeastern University, Boston, MA, USA
(3) Dept of Mechanical and Industrial Engineering, Northeastern University, Boston, MA, USA

INTRODUCTION

The role of mechanics in skeletal development is pivotal, with extensive research elucidating the significance of mechanical factors in this process[1–3]. Stem cells, which are fundamental for skeletal development, perceive their mechanical surroundings through cell–cell and cell–extracellular matrix adhesion, mechanosensitive ion channels, and primary cilia[4]. The role of mechanosensitive ion channels, TRPV4 and PIEZO are pivotal to mesenchymal stem cell behavior. Volume expansion mediated by TRPV4 activation, has been shown to regulate osteogenesis in stem cells embedded in 3D hydrogels[5]. Similarly, PIEZO1 has been shown to regulate osteoblast differentiation in mesenchymal stem cells[6]. While the in-vitro manipulation of stem cell differentiation by mechanical cues holds promise in tissue engineering and regenerative medicine[4], the specific impact of stresses and strains during regeneration in-vivo remains relatively unexplored.

Even though the gene expression and pattern formation between regeneration and embryonic development are similar[7], there are a few critical differences. Notably, regenerating tissues source their cells from pre-existing mature structures, in contrast to the de novo formation of tissues during development[8]. The blastema, a heterogeneous pool of restricted progenitor cells, is the initial stage of regeneration[9]. Mechanosensitive channels are important in the context of cellular movement during limb regeneration in axolotls.

While several studies have elucidated the critical role of calcium dynamics in skeletal development and maintenance[10], such studies are limited in the context of regeneration. A recent study showed that inhibiting L, N, and T-type calcium channels in regenerating axolotl tail, inhibits regeneration, emphasizing the significance of calcium ion kinetics in regeneration[11]. However, the functional expression of mechanosensitive calcium ion channels, particularly TRPV4 and PIEZO channels, in blastemal cells during axolotl limb regeneration has yet to be studied.

This study aims to bridge this knowledge gap by employing single nuclear RNA sequencing and immunofluorescence to delineate the expression patterns of TRPV4 and PIEZO channels at different stages of axolotl limb regeneration. This will enable us to further elucidate the roles of the channels in blastemal cells, shedding light on their contributions to the regenerative capabilities of axolotl limbs.

METHODS

Single Nuclear RNA Sequencing: Limb tissues from 4 different animals at early and late blastema stage of regeneration were pooled and dissociated for single nuclear RNA sequencing on a Chromium platform. Reads were aligned to the axolotl v6 genome, counted, and normalized using 10X Genomics Cellranger software. Counts matrices were filtered for high quality cells and re-clustered using the 10X Genomics Loupe browser to produce UMAP visualizations with broad tissue type annotation.

Immunostaining: Both forelimbs of fully developed axolotls were amputated mid-humerus. Amputated, fully grown limbs served as the fully-grown time point as well as the positive controls since TRPV4 and PIEZO1/2 ion channels are known to be expressed in skeletal tissues[12]. Tissue from regenerating forelimbs were harvested at early and late blastema stages of regeneration, (3 limbs at each time point). The samples were fixed in 4% paraformaldehyde over night at 4˚C, cryopreserved in Optimal Cutting Temperature Solution and stored at -80˚C. The samples were cryosectioned and baked at 65˚C. The slides were blocked with goat serum and incubated with 1:200 Rabbit Anti-TRPV4 polyclonal antibodies and 1:300 Rabbit Anti- PIEZO2 polyclonal antibodies, followed by staining with 1:400 Goat Anti-Rabbit Alexa Fluor® 647 secondary antibodies. Negative controls were incubated with just the secondary antibodies. The sections were washed and then stained with 1:5000 DAPI nuclear stain. The samples were washed and then mounted with coverslips. The sections were imaged using a confocal microscope.

RESULTS

TRPV4, PIEZO1 and PIEZO2 mechanosensitive ion channel genes are expressed at early and late stages of blastemal growth but with higher expression occurring in the later stage. PIEZO1 has fairly nonspecific expression in both early and late blastema, but moderately increases in the late-blastema stage. PIEZO2 is highly upregulated in fibroblasts at both timepoints. It is also the most highly expressed out of these three genes. TRPV4 is expressed at both stages but appears upregulated in the late-blastema stage and shows moderately higher expression in epithelial populations and macrophages (Figure 1).

Immunofluorescence study confirmed the presence of TRPV4 and PIEZO2 ion channels in early and late stage blastema and as well as in the fully grown cartilage samples as expected (Figure 2).

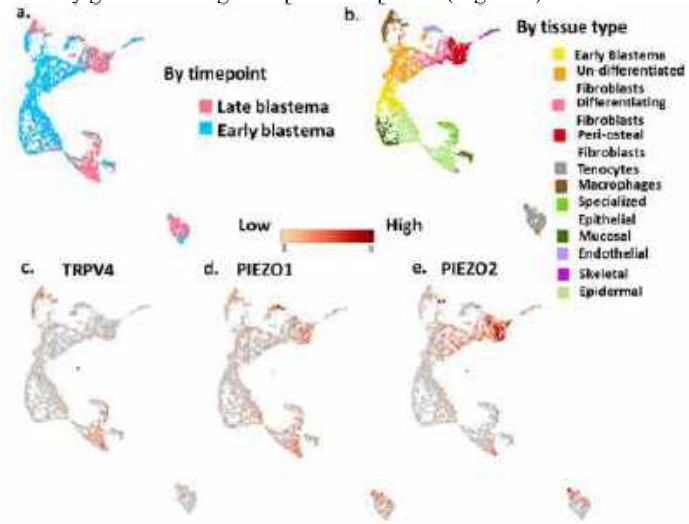

Figure 1: Single Nuclear RNA data (a) Clusters organized by regeneration timepoint (b) Clusters organized by tissue type (c) TRPV4 expression (d) PIEZO1 expression (e) PIEZO2 expression

DISCUSSION

In this study, we have shown that regenerating limb blastemas express mechanosensitive ion channels TRPV4 and PIEZO2 beginning in the early stages of regeneration using immunostaining. Further we showed the differential gene expression of the ion channels in the different populations of the blastemal cells during regeneration using single nuclear RNA sequencing.

Expression of TRPV4 and PIEZO channels in mature chondrocytes align well with published literature[12]. Further, it confirms that the primary antibodies have good target specificity to axolotl tissues.

In our study, we showed that macrophages in the limb blastema highly express TRPV4 genes along with epithelial cells. This is consistent with previous studies that showed the transcriptional presence of TRPV4 in macrophages[13]. Macrophages are known to be pivotal for limb regeneration. Depletion of macrophages results in failure of limb regeneration[14]. Further, activation of PIEZO1 ion channel in macrophages has been shown to inhibit wound healing in-vitro[15]. However, the functional role of TRPV4 channels on macrophage activity in limb blastema is yet to be studied.

We further show that the mesenchyme begins to condense in a proximo-distal direction which aligns well with our previous results where we showed that the stiffness of late stage blastema has a proximo-distal gradient in stiffness with proximal parts having a higher stiffness compared to the distal tissue[16]. The robust expression of TRPV4 and PIEZO channels in the condensate aligns well with studies on limb development that show that cartilage differentiation and proliferation are mediated via the mechanosensitive channels[5].

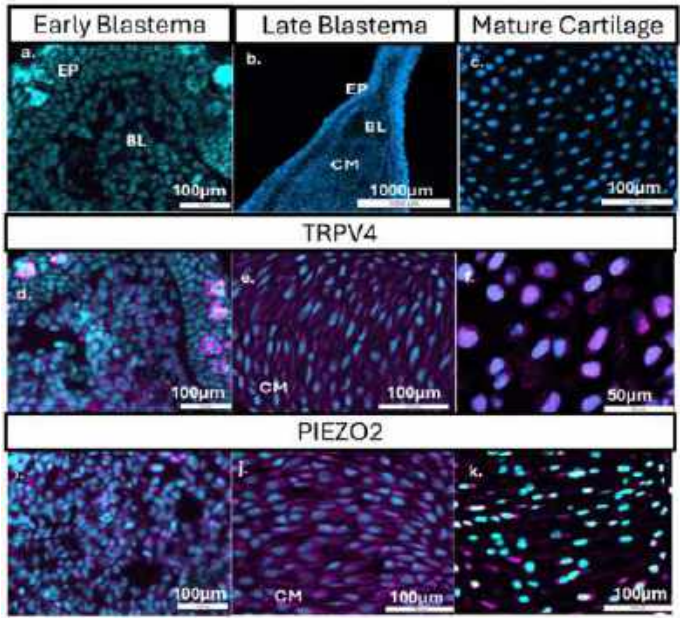

Figure 2: (a-c). Negative controls (d-f) TRPV4 expression (g-i) PIEZO2 expression in early and late blastema, and mature axolotl cartilage. Cyan stains for the nucleus and magenta stains for the presence of TRPV4/ PIEZO2 ion channels. EP: Epithelium, BL : De-differentiated Blastemal cells, CM: Condensed Mesenchyme

Our data shows that blastemal fibroblasts express PIEZO genes. PIEZO1 activation is known to suppress migration of dermal fibroblasts in-vitro[17]. Its role in cell migration and recruitment in blastemal cells needs further investigation.

Future studies will study calcium signaling response mediated by TRPV4 and PIEZO mechanosensitive ion channels in regenerating limbs to evaluate the functionality of the channels in mechanotransduction.

ACKNOWLEDGEMENTS

This project was funded by NSF grant # 2318594. Imaging was performed at the Center for Imaging Living Systems (CILS), Northeastern University.

REFERENCES

1. Sermeus Y et al, *Cells*. 2022;11(3):420
2. Shea CA et al, *Bone Jt Res*. 2015;4(7):105-116
3. Nowlan NC et al, *Ann N Y Acad Sci*. 2007;1101(1):389-411.
4. Vining KH et al, *Nat Rev Mol Cell Biol*. 2017;18(12):728-742.
5. Lee H pyo et al, *Nat Commun*. 2019;10(1):529.
6. Sugimoto A et al,*Sci Rep*. 2017;7(1):17696
7. Monaghan JR et al, *Biol Open*. 2012;1(10):937-948.
8. Chiou K et al, *Dev Biol*. 2018;433(2):155-165
9. Kragl M et al, *Nature*. 2009;460(7251):60-65
10. Khatib NS et al, *Sci Adv*. 2023;9(4):eade2155
11. Franklin BM et al, *Mech Dev*. 2017;146:42-54
12. Du G et al, *Exp Biol Med*. 2020;245(3):180-189
13. Groot-Kormelink PJ, *BMC Immunol*. 2012;13(1):57
14. Godwin JW et al, *Proc Natl Acad Sci*. 2013;110(23):9415-9420
15. Atcha H et al, *Nat Commun*. 2021;12(1):3256.
16. Kondiboyina V et al, *J Mech Behav Bio Mater*. 2024;150:106341
17. He J et al, *Cell Death Dis*. 2021;12(3):1-13

DYNAMIC IMAGING OF THE COLLAGENOUS MYOCARDIAL EXTRACELLULAR MATRIX DURING POST-INFARCTION INFLAMMATION

Daniel P. Pearce (1) and Colleen M. Witzenburg (1)

(1) Cardiovascular Biomechanics Lab, Department of Biomedical Engineering, UW-Madison, Madison, WI, USA

INTRODUCTION

Coronary artery occlusion leads to myocardial infarction (MI), irreparable cardiomyocyte damage, and impaired left ventricle (LV) function for nearly a million Americans each year.[1] During the first week post-MI, an intense inflammatory response occurs in the myocardium that contributes to notable extracellular matrix (ECM) degradation.[2–4] While the destruction of the innate ECM is necessary for the removal of necrotic cardiomyocytes and long-term healing, it weakens the myocardium, leaving it vulnerable to rising volumes and pressures, and raising the risk of ventricular rupture and death.[5,6] While some prior descriptions of the inflammatory post-MI environment have been reported, they relied on one-dimensional measures of stiffness and collagen content.[3,7,8] There remains a need for full-field quantifications of the myocardium's mechanical properties, as well as depictions of the fibrous ECM architecture giving rise to these complex properties during this critical healing phase.

Quantitative polarized light imaging (QPLI) is a novel and affordable imaging modality enabling macroscopic, full-field descriptions of collagen fiber alignment in thin soft tissues. QPLI has been used to examine fiber rotation/alignment in mouse skin,[9] bovine flexor tendons,[10] human ulnar collateral liagments,[11] and pulmonary valve leaflets.[12] To our knowledge, however, it has not been applied to the myocardium. When combined with our Generalized Anisotropic Inverse Mechanics (GAIM) method, these two approaches can capture a soft tissue's dynamic mechanical and structural behavior.[13]

The objective of our study was to leverage both QPLI and GAIM to quantify the full-field anisotropy and stiffness of healthy and infarcted rodent myocardium at one day post-MI, an important, but woefully understudied timepoint in the MI healing process. We hypothesized that post-MI inflammation[2,3,14] would lead to depressed stiffnesses and levels of anisotropy in the affected myocardium,[3,7,8] resulting in a stark borderzone between the infarcted and remote myocardium.

METHODS

Animal Model. Adult male Sprague Dawley rats underwent either permanent occlusion (PO) of their left anterior descending coronary artery through ligation or sham surgery, where their chest was opened but the heart was not disturbed. MI was confirmed by blanching of myocardium downstream of the suture, which remained present until hearts were harvested 1 day after the PO or sham surgery.

Decellularization. Hearts were decellularized by retrograde perfusion of sodium dodecyl sulfate (SDS) and Triton X-100 (Figure 1).[13,15] Briefly, the heart was perfused with SDS via constant pressure, then constant flow at 2 mL/min. Next, it was perfused with deionized water and Triton-X 100 for 30 minutes at constant pressure, followed by PBS for 72 hours. Isolation of the ECM results in thinning of the LV wall enabling plane stress characterizations of the myocardium's passive mechanics.

Figure 1. (Top) Native rodent heart with a clear MI (arrow). **(Bottom)** Decellularized rodent heart with MI (arrow).

Laser Micrometry. Decellularized myocardium samples were trimmed to a cruciform shape[16] and scanned by a LJ-V7080 class II laser micrometer (Keyence; Itasca, IL) operating at 200 Hz to capture their full-field thickness. A custom MATLAB script (shared in our previous publication) generated 3D profiles from the raw CSV files.[17]

Biaxial Testing. Samples were then clamped and secured to a biaxial testing machine using a custom clamping system.[17] After preloading,[18] samples were preconditioned via ten rounds of equibiaxial extension at 20% strain. Each sample was then subjected twice to a series of unique and asymmetric planar biaxial loading patterns to generate a broad strain space, aiding detection of mechanical

heterogeneity.[17] QPLI was captured during the first series, then a speckle pattern was applied to the sample and standard imaging was conducted for GAIM.

GAIM. Images from each extension were exported for digital image correlation (DIC), generating a series of full-field displacements for each test. GAIM combines these displacements with corresponding normal and shear arm forces to estimate the full-field stiffness of each sample[13,19] by assuming a linear relationship between the second Piola-Kirchoff stress and the Green-Lagrange strain. Thickness profiles were also incorporated into GAIM, a step we and others have found crucial for determining mechanics of complex soft tissues.[17,20]

DQPLI. QPLI capitalizes on the birefringent properties of collagen fibers. Full-field QPLI results include *AoP*, the angle of linear polarization which is a measure of preferred collagen fiber angle, and *DoLP*, the degree of linear polarization which is a measure of strength of fiber alignment. DoLP ranges from 0 (indicating no alignment) to 1 (indicating total alignment). QPLI results were then mapped to the GAIM mesh using the location of the grips in each image. Successful mapping allowed for the inference of full-field displacements during polarized light imaging and subsequent determination of full-field QPLI parameters in a particular region of the tissue as that region deforms – i.e., mapping captured the DoLP of the top boundary throughout the test as it moved upwards (Figure 2).

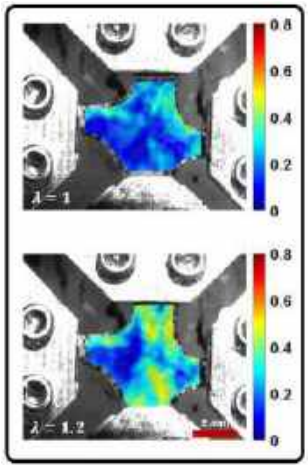

Figure 2. Strength of fiber alignment in an unloaded (**top**) and fully loaded (**bottom**) PO sample during an equibiaxial stretch (λ = 1.2).

Data Analysis. Visual comparisons were made between sham and PO groups and summary statistics were computed. Unpaired, one-sided T-tests were used to detect statistically significant group differences.

RESULTS

Figure 3 depicts the geometrical (thickness), mechanical (stiffness), and structural (DoLP) differences between representative sham and infarcted myocardium samples. The infarct region of two PO samples exhibited much larger thickness than the periphery or sham sample. Despite this notably higher thickness, the infarct regions of both PO samples also exhibited depressed stiffness and low collagen fiber alignment. The sham sample had a remarkably homogeneous thickness (SHAM1: 0.91 ± 0.07 mm, CoV = 0.08) compared to the two PO samples (PO1: 1.56 ± 0.37 mm, CoV = 0.24; PO2: 1.71 ± 0.26 mm, CoV = 0.15, not shown). A similar trend was observed in stiffness (SHAM1: 371 ± 98.4 kPa, CoV = 0.27; PO1: 378 ± 181 kPa, CoV = 0.48; PO2: 155 ± 66.1 kPa, CoV = 0.43). However, DoLP distributions were comparable between the two groups (SHAM1: 0.237 ± 0.12, CoV = 0.52; PO1: 0.245 ± 0.12, CoV = 0.48; PO2: 0.281 ± 0.11, CoV = 0.37).

DISCUSSION

In this study, we applied QPLI, an imaging approach that offers insight into collagen fiber alignment, and GAIM, an inverse method for measuring heterogeneous soft tissue mechanics, to infarcted myocardium at one day post-MI. Although traditionally understudied compared to long-term scar formation, the inflammatory phase of the post-MI healing response is associated with drastic ECM degradation, stiffness reduction, and increased rates of rupture.[2–4] PO samples exhibited high thickness but low stiffness in the infarct region. The thickness and stiffness distributions were also much more heterogeneous (~140% and ~69% increase in CoVs, respectively, compared to sham). Similar DoLP distributions were observed between groups. However, both PO samples exhibited strong collagen fiber alignment at the border surrounding the less aligned infarct core, suggesting a sudden transition in structure that could accentuate stress concentrations in the vulnerable myocardium. Additional samples are necessary to confirm these observations. In the future, we will also include a reperfusion therapy group, which is a more clinically relevant model of MI. We anticipate this work will highlight mechanical and structural properties altered during post-MI inflammation, allowing for the development of therapies to further safeguard the heart against catastrophic ventricular rupture.

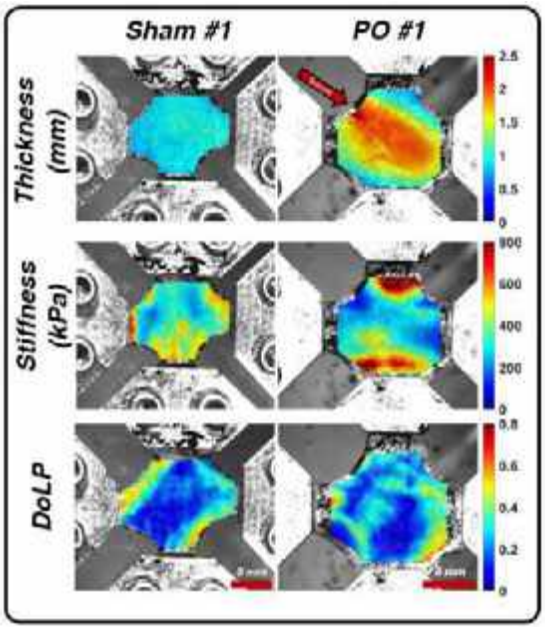

Figure 3. Representative sham (**left**) and PO (**right**; arrow: suture) samples showing full-field thickness from laser micrometry (**top**), stiffness from GAIM (**middle**), and DoLP from QPLI (**bottom**).

ACKNOWLEDGEMENTS

This study was funded by a grant from the NSF to CMW (2030173). We would like to also thank Michael Chiariello, Elizabeth Gunderson, Mark Nemcek, Shreya Sreedhar, Rhea Nagori, and the rest of the CBL for their assistance.

REFERENCES

[1] Tsao, C. W. et al. *Circulation* 145 (2022). [2] O'Rourke, S. A., et al. *Front. Cardiovasc. Med*. 6 (2019). [3] Gao, X., et al. *Cardiovasc. Res.* 65 (2005). [4] Etoh, T. et al. *Am. J. Physiol. Heart Circ. Physiol*. 281, (2001). [5] Helpap, B. et al. *DMW* 105 (2008). [6] Roberts, W. et al. *Am. J. Cardiol*. 115 (2015). [7] Connelly, C. et al. *Circ. Res.* 71 (1992). [8] Pearce, D. P., Nemcek, M. T. & Witzenburg, C. M. *Biophys. Rev*. 15 (2023). [9] Blair, M. J. & Quinn, K. P. *Front. Bioeng. Biotechnol.* (2022). [10] York, T. et al. *J Biomed Opt* (2014). [11] Smith, M. V. et al. *Am. J. Sports Med*. 47 (2019). [12] Sreedhar, S., Link, C., Pearce, D. & Witzenburg, C. *SB3C* (2023). [13] Witzenburg, C. et al. *J. Biomech.* 45 (2012). [14] DeLeon-Pennell, K. Y et al. *Prog. Mol. Biol. Transl. Sci*. 147 (2017). [15] Ott, H. C. et al. *Nat. Med.* 14 (2008). [16] Mönch, E. & Galster, D. *Br. J. Appl. Phys.* 14 (1963). [17] Pearce, D., Nemcek, M. & Witzenburg, C. *Curr. Protoc.* 2 (2022). [18] Debes, J. & Fung, Y. *Am. J. Physiol.* 269 (1995). [19] Raghupathy, R. & Barocas, V. H. *J. Biomech. Eng.* 132 (2010). [20] Lin, C. Y. et al. *Biomech. Model. Mechanobiol*. (2022).

SB^{3}C2024
Summer Biomechanics, Bioengineering and Biotransport Conference
June 11-14, Lake Geneva, WI, USA

AUTOMATED FULL–FIELD MECHANICAL ANALYSIS OF CARDIAC MICROBUNDLES

H. Kobeissi (1,2), E. Lejeune (1,2)

(1) Department of Mechanical Engineering, Boston University, Boston, MA, USA
(2) Center for Multiscale and Translational Mechanobiology, Boston University, Boston, MA, USA

INTRODUCTION

With the heart's poor capability of self-regeneration [1], any damage to the heart muscle is not only irreversible but can lead to debilitating effects on the organ's overall function. Cardiac tissue engineering, in particular human induced pluripotent stem cell derived cardiomyocyte (hiPSC-CM) based technology [2], offers a promising approach to understanding heart disease and alleviating its fatal consequences via disease modeling, drug discovery, and regenerative tissue engineering [1, 3]. However, a key limitation of hiPSC-CM technology is that these induced cardiomyocytes resemble fetal CMs and are morphologically and functionally distinct from the cells in mature cardiac tissue [4].

At present, there are multiple techniques to promote maturity of hiPSC-CMs including different physical platform designs (Fig 1) and cell culture protocols. With this variability in the applied techniques, performing quantitative comparisons of functional behavior between different systems becomes a major challenge, especially because there are limited available options for reliably and reproducibly extracting mechanics-based quantitative information from these platforms. Furthermore, available tools to obtain such metrics from time-lapse images of cardiac microbundles mainly provide averaged results, such as post forces and average tissue stress, that lump the spatially heterogeneous tissue behavior into a single value per frame [5–7]. On the other hand, available tools that can output full-field results, such as full-field tissue displacements and strains [8, 9], lack automation and are not readily adaptable to function on new platform designs out of the box.

In this context, we present here our work on "MicroBundleCompute," a computational framework for automatic quantification of morphology-based mechanical metrics from movies of cardiac microbundles subjected to extensive validation against synthetic examples. We further showcase the adaptability of the software to a diverse pool of input examples and highlight the valuable insight about the heterogeneous mechanical behavior of cardiac tissue gained from the extracted full-field metrics such as full-field displacements, subdomain-averaged strains, and displacement and strain-derived outputs. Finally, we make our software available under open-source MIT License on GitHub (https://github.com/HibaKob/MicroBundleCompute).

METHODS

We briefly describe here the underlying code behind "MicroBundleCompute" workflow as well as the data used for testing and validating the software.

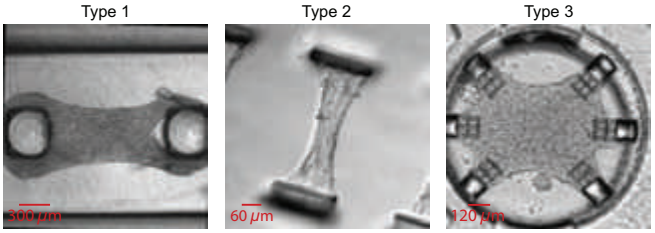

Figure 1: Examples of 3 different microbundle experimental testbeds.

Code. "MicroBundleCompute" is mainly built on OpenCV's implementation of the Lucas-Kanade sparse optical flow algorithm [15]. In our implementation, the tracking points are Shi-Tomasi corner points (points at which a slight shift in location leads to "large" changes in intensity along both main horizontal and vertical axes) [16] computed on the first frame. Notably, our approach relies solely on the natural contrast of brightfield microbundle textures and the resulting intensity gradients which makes it straightforward to implement in the experimental setting. From tracking these points across consecutive frames, we can compute full-field displacement, strain, and strain derived metrics to quantitatively capture mechanical function. Critically, for strain outputs, we avoid differentiating the displacements. Instead, we automatically perform subdomain spatial segmentation and compute a mean deformation gradient, and likewise, an average strain within each subdomain. We mainly adopt this approach to reduce the influence of imaging artifacts and noise on strain results.

Data. Our complete dataset is comprised of two general categories: 1) experimental data comprising of time-lapse videos of brightfield and phase contrast movies of cardiac microbundles and 2) synthetic data with a known ground truth for software validation.

The experimental dataset can be divided into 3 different types (Fig 1).

"Type 1" includes movies obtained from standard experimental microbundle strain gauge devices where cardiac microbundles are seeded between two poly(dimethylsiloxane) (PDMS) pillars, as described in more detail in [10]. "Type 2" is comprised of data collected from non-standard platforms termed FibroTUGs [11]. In these systems, differentiated iPSC-CMs are seeded onto electrospun dextran vinyl sulfone (DVS) fiber matrices suspended between a pair of PDMS cantilevers. As for "Type 3," they represent data obtained from highly versatile PDMS devices with embedded microfluidic channels and deformable seeding wells [12]. A more detailed description of the 3 data types can be found in [13]. We share the whole dataset on Dryad [14] under Creative Commons Zero (CC0) waiver.

Realistic synthetic data of beating cardiac microbundles were generated based on examples from "Type 1." Briefly, we first isolate the microbundle component of a real frame and use the extracted region to obtain both microbundle geometry and image texture. We then run simplified Finite Element (FE) simulations where the microbundle model is defined as nearly-incompressible transversely isotropic hyperelastic material with periodic activation and extract displacement and Green-Lagrange strain results. Based on the obtained FE displacements, we estimate projective transformations and warp the image texture accordingly. Finally, to render this data more challenging, we add Perlin noise of different magnitudes and number of octaves. A more detailed description of the synthetic data generation pipeline can be found in [13] and on GitHub (https://github.com/HibaKob/SyntheticMicroBundle).

RESULTS

We test our computational pipeline on a total of 416 synthetic validation examples and showcase its performance and versatility on 24 experimental time-lapse images of beating cardiac microbundles. A major advantage of "MicroBundleCompute" over similar tools [8, 9] that are available lies in the fact that we can run all 440 examples without the need for any parameter tuning. Furthermore, all software functionality is implemented in a test-driven development framework with 100% code coverage and automatic testing on ubuntu, windows, and macOS platforms.

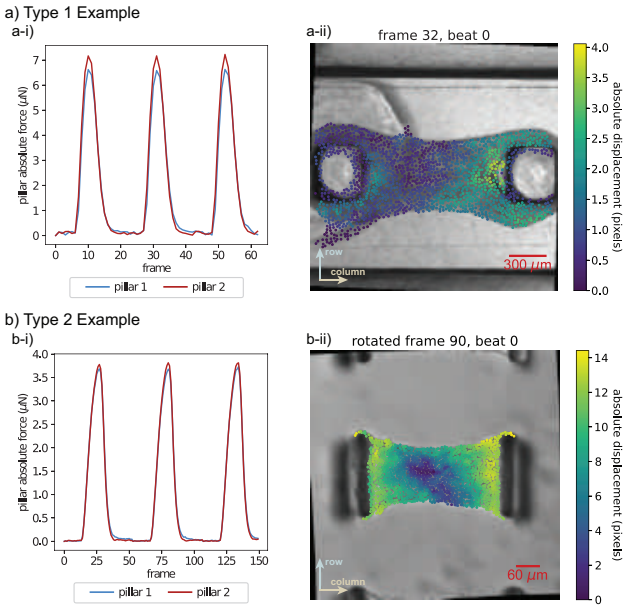

Figure 2: Direct comparison of pillar tracking and tissue tracking.

Experimental Data Examples. In Fig. 2, we show, side by side, the outputs obtained via pillar tracking (a-i and b-i) and via tracking the entire tissue domain (a-ii and b-ii) for an example from "Type 1" and "Type 2" data respectively. While pillar tracking enables the calculation of an average pillar displacement-based tissue force or stress given approximate tissue width and thickness, tissue tracking reveals abundant information regarding the inherent heterogeneous nature of microbundle beating, where for example, full-field displacement fields show regions where maximum or minimum tissue contractions are taking place. Furthermore, subdomain-averaged strains also underline the spatial heterogeneity of the tissue contractions (Fig 3a), and visualizing them with respect to time (or frame number) (Fig 3b) reveals the nature of temporal synchrony across the different subdivisions of the beating microbundle. For the particular example of "Type 3" shown in Fig. 3, the column-column direction (i.e., horizontal) Green-Lagrange strain (E_{cc}) clearly indicates that the microbundle is experiencing positive strains at the center, suggesting that a necking instability is forming on this tissue over time. This observation is further supported by the thinning tissue width at the center. Accordingly, the ability to extract and examine full-field strains enables further investigations into understanding and determining the factors, such as pillar stiffness and ECM density, that play a major role in influencing the behavior of microbundles.

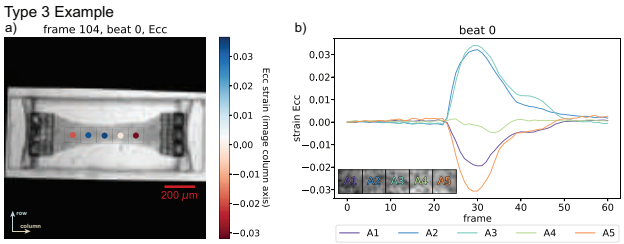

Figure 3: Example strain outputs of "MicroBundleCompute."

Synthetic Data Examples. Validation studies reveal that our software is quite robust to all tested cases with super-pixel displacements and Perlin noise of realistic parameters that result in artifacts found in experimental settings. In these cases, errors on displacements are below 10%.

DISCUSSION

Based on the results, we have demonstrated that complementing conventional metrics (i.e. pillar force and tissue stress) obtained via basic pillar tracking with reliable and reproducible full-field data, such as displacement distributions and subdomain-averaged strains, obtained via "MicroBundleCompute" allows for a better assessment of highly heterogeneous cardiac tissue behavior and a better understanding of the complex underlying mechanisms driving this behavior. Looking forward, our plan is to grow our dataset and build on this approach to develop appropriate statistical models of these tissue.

ACKNOWLEDGEMENTS

This work was supported by the CELL-MET Engineering Research Center NSF ECC-1647837, the Boston University Hariri Junior Faculty Fellowship and Graduate Student Fellowship, the David R. Dalton Career Development Professorship, and an American Heart Association Career Development Award #856354.

REFERENCES

[1] Bursill CA et al. *Heart, Lung and Circulation* (2022).
[2] Takahashi K et al. *cell* 131.5 (2007).
[3] Dou W et al. *Microsystems & Nanoengineering* 8.1 (2022).
[4] Batalov I et al. *Scientific Reports* 11.1 (2021).
[5] Sala L et al. *Circulation research* 122.3 (2018).
[6] Tamargo MA et al. *ACS Biomater. Sci. Eng.* 7.11 (2021).
[7] Rivera-Arbeláez JM et al. *Plos one* 17.4 (2022).
[8] Huebsch N et al. *Tissue Engineering Part C: Methods* 21.5 (2015).
[9] Méry A et al. *Nature Communications* 14.1 (2023).
[10] Das SL et al. *Am J Physiol Heart Circ Physiol* 323.4 (2022).
[11] DePalma SJ et al. *Biomater. Sci.* 9 (1 2021).
[12] Jayne RK et al. *Lab on a Chip* 21.9 (2021).
[13] Kobeissi H et al. *arXiv* (2023). DOI: `arXiv:2308.04610`.
[14] Kobeissi H et al. 2023. DOI: `https://doi.org/10.5061/dryad.5x69p8d8g`.
[15] Lucas BD et al. *Proceedings of the 7th IJCAI*. 1981.
[16] Shi J et al. *CVPR*. IEEE. 1994.

EFFECTS OF SPONTANEOUS CALCIUM SIGNALING ON CARTILAGE ANABOLIC ACTIVITIES

Ying Peng, Annie Porter, Steven DiStefano, X. Lucas Lu

Department of Mechanical Engineering, University of Delaware, Newark, Delaware, USA

INTRODUCTION

Intracellular calcium, $[Ca^{2+}]_i$, signaling is a crucial mechano-transduction response in chondrocytes and regulates cartilage metabolism [1]. We discovered that chondrocytes in cartilage exhibit spontaneous $[Ca^{2+}]_i$ signaling, similar to active cells such as neurons and cardiomyocytes. A spontaneous $[Ca^{2+}]_i$ peak is initiated by the influx of extracellular Ca^{2+} and can be amplified by the release of Ca^{2+} stored in the endoplasmic reticulum (ER). Additional Ca^{2+} influx may occur through the gap junctions connecting adjacent cells [2]. The roles of spontaneous $[Ca^{2+}]_i$ signaling in chondrocyte metabolism are not well understood. In this study, we investigate: (1) the roles of extracellular Ca^{2+} source, PLC-IP_3 pathway, ER Ca^{2+} store, and gap junctions in spontaneous $[Ca^{2+}]_i$ signaling in human cartilage, and 2) the effects of these pathways on the synthesis rates of proteoglycan and collagen using a novel click chemistry technique.

METHODS

Tissue preparation and treatment: Cylindrical cartilage samples (diameter = 3 mm, thickness = 2 mm) were harvested from human knee joints (n = 5, avg. age = 60 years old) from total knee arthroplasty (Fig. 1a) or from the femoral condyles of calf knees (n = 5, 1 to 2 months old) (Fig. 1d). Cartilage samples were incubated in chondrogenic medium for two days before experiments [2]. Samples were bisected axially into two halves and dyed with 5 μM Calbryte-520 (AAT Bioquest) to label $[Ca^{2+}]_i$. One half of each sample was used as the control; the other half was treated with one of the following antagonists for 30 min (n ≥ 3/group): 1) 10 mM EGTA to chelate all extracellular Ca^{2+}, 2) 11 μM neomycin to inhibit the phospholipase C (PLC) activity that is required for the Ca^{2+} release of ER store, 3) 1 μM thapsigargin (TG) to deplete ER store, or 4) 75 μM 18α-glycyrrhetinic acid (18α-GA) to block the gap junctions (Fig. 3).

Calcium signaling imaging and analysis: Cartilage was imaged on a confocal microscope (Zeiss LSM 510) for 30 min at a frequency of 2 s/frame (Fig. 1b). Calcium videos were processed with an established protocol to extract the $[Ca^{2+}]_i$ transient of each cell. The responsive rate was defined as the ratio of the number of cells with ≥ 1 $[Ca^{2+}]_i$ peak to the total number of cells. Spatiotemporal parameters of the $[Ca^{2+}]_i$ peaks, including the number of multiple peaks, time to reach a peak, time for a peak to relax, magnitude of peaks, and time between two neighboring peaks, were obtained from a custom-built software (Fig. 1c).

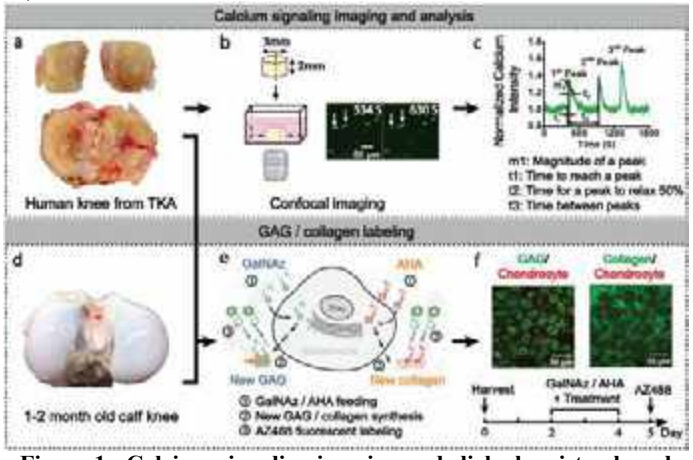

Figure 1: Calcium signaling imaging and click chemistry-based GAG and Collagen labeling.

Fluorescent labeling of new GAG/collagen with click chemistry technique: Samples (n = 12/group) were first cultured in medium containing an azide-modified monosaccharide (GalNAz) or azide-modified analog of methionine (AHA), building blocks for the GAG disaccharide units and collagen molecules, respectively. During the 24-hour incubation for bovine cartilage or 48-hour incubation for human

cartilage, GalNAz was taken up by chondrocytes and incorporated into the newly synthesized chondroitin sulfate in GAG. Similarly, AHA was incorporated into newly synthesized collagen molecules. The antagonists for the pathway study were added to the GalNAz or AHA incubation medium. Afterwards, a fluorescent dye, AZ488, was "clicked" to the azide groups on the new GAG chains and new collagen fibrils (Fig. 1e,f).

Quantification of GAG and collagen content: To quantify the newly synthesized GAG and collagen content, click chemistry labeled cartilage was enzymatically digested, and the fluorescent intensity of the digestion medium was read with a plate reader.

RESULTS

In senior human cartilage, the $[Ca^{2+}]_i$ responsive rate and number of calcium peaks of chondrocytes in cartilage explants decreased with the treatment of EGTA (Ca^{2+} chelator), neomycin (PLC inhibitor), and thapsigargin (ER Ca^{2+} remover) (Fig. 2a,d,g). No differences in responsive rate or number of calcium peaks were observed under 18α-GA (gap junction blocker) treatment (Fig. 2j). The results are consistent with our previous study on juvenile bovine cartilage [2]. $[Ca^{2+}]_i$ peaks took longer to reach apex and to return to the baseline with the treatment of EGTA, neomycin, thapsigargin, and 18α-GA. The magnitude of $[Ca^{2+}]_i$ peaks was reduced in all four treated groups compared to the control (figures not shown).

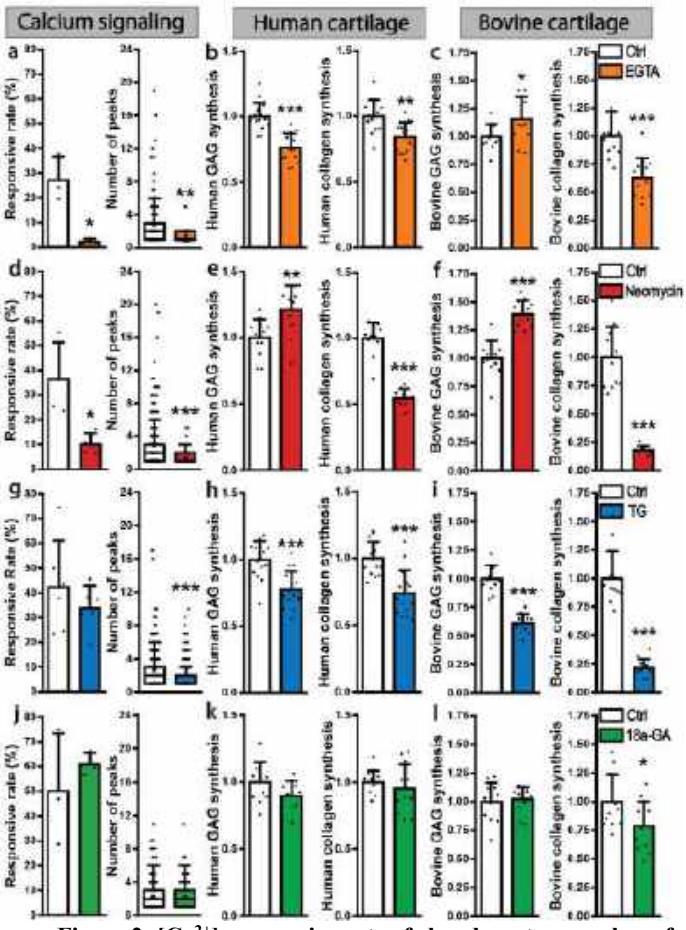

Figure 2: $[Ca^{2+}]_i$ responsive rate of chondrocytes, number of peaks, human GAG and collagen synthesis, bovine GAG and collagen synthesis with the treatment of (a,b,c) EGTA, (d,e,f) neomycin, (g,h,i) thapsigargin, and (j,k,l) 18α-GA.

For the anabolic activities of senior human cartilage, full depletion of extracellular Ca^{2+} with EGTA and emptying of the ER Ca^{2+} store with thapsigargin suppressed both GAG and collagen synthesis (Fig. 2b,h). Inhibition of the PLC-IP_3 pathway with neomycin promoted GAG synthesis but diminished collagen synthesis (Fig. 2e). No differences were noted in GAG and collagen synthesis with the block of gap junctions (Fig. 2k).

In young bovine cartilage, depletion of extracellular Ca^{2+} and blockage of the PLC-IP_3 pathway increased GAG synthesis, but decreased collagen synthesis (Fig. 2c,f). Depletion of the ER Ca^{2+} store inhibited both GAG and collagen synthesis (Fig. 2i). Blocking gap junctions showed no significant impact on GAG synthesis but inhibited collagen synthesis (Fig. 2l).

DISCUSSION

In this study, we have revealed that spontaneous calcium signaling is important for proteoglycan and collagen synthesis rates in both young bovine and senior human cartilage. The blockage of the extracellular Ca^{2+} source, PLC-IP_3 pathway, ER Ca^{2+} store, and gap junctions all inhibited the synthesis of collagen, indicating the necessity of spontaneous calcium signaling for collagen synthesis. This is consistent with the previous study, in which the blockage of Ca^{2+} influx and ER Ca^{2+} release inhibited collagen synthesis in porcine chondrocytes, measured by immunofluorescent staining [3]. In contrast, the synthesis of proteoglycan was regulated in a different manner by calcium signaling. The clearance of extracellular Ca^{2+} source increased GAG synthesis in bovine cartilage but inhibited it in senior human cartilage. The different trends could be related to the difference between young bovine cartilage and senior human cartilage [4]. Inhibition of the PLC-IP_3 pathway promoted GAG synthesis, but removal of the ER Ca^{2+} store impeded GAG synthesis. Blocking gap junctions showed no effect on GAG synthesis in both bovine and human cartilage. Our data brings new insights into the connections between spontaneous calcium signaling in chondrocytes and cartilage metabolism.

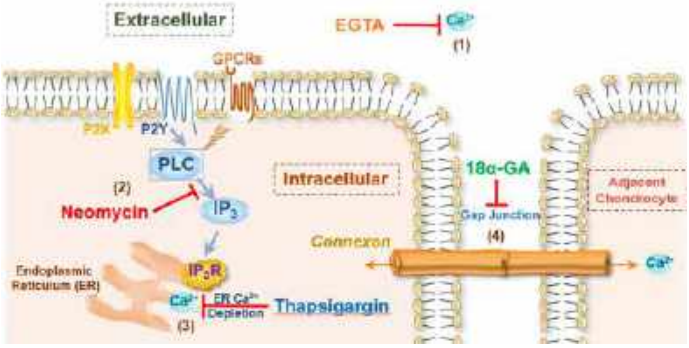

Figure 3: Calcium signaling pathways. (1) Extracellular $[Ca^{2+}]_i$ chelator, EGTA; (2) PLC-IP_3 inhibitor, neomycin; (3) ER $[Ca^{2+}]_i$ remover, thapsigargin; (4) Gap junction blocker, 18α-GA.

ACKNOWLEDGEMENTS

This work was supported by NIH R01AR074472 (Lu) and NIH COBRE P20GM139760 (Elliott).

REFERENCES

[1] Huser, C et al., *Arthritis Rheum.*, 56(7):2322-34, 2007.
[2] Zhou, Y et al., *FASEB J.*, 33(4):4675-4687, 2019.
[3] Gong, X et al., *J Cell Physiol.*, 234:9711-9722, 2019.
[4] DeGroot, J et al., *Arthritis Rheum.,* 42(5): 1003-1009, 1999.

EXPERIMENTAL EVALUATION OF THE 'PLUNGER TECHNIQUE' FOR MANUAL CYCLIC ASPIRATION TREATMENT OF ACUTE ISCHEMIC STROKE

Demitria A. Poulos (1), James S. Keith (1), Michael T. Froehler (2), Bryan C. Good (1)

(1) Mechanical, Aerospace, and Biomedical Engineering
University of Tennessee
Knoxville, TN, USA

(2) Vanderbilt Cerebrovascular Program
Vanderbilt University Medical Center
Nashville, TN, USA

INTRODUCTION

Approximately 87% of all strokes in the United States are classified as acute ischemic strokes (AIS), the result of sudden blood loss to areas of the brain [1]. The standard treatment for AIS is a mechanical thrombectomy (MT), which requires the use of either an aspiration or stent retriever (SR) technique. Some studies indicate that aspiration MT leads to faster reperfusion, which correlates to improved patient outcomes [2], when compared to SR MT [3]. Attempts to optimize aspiration MT so that complete reperfusion is achieved on the first aspiration pass have been made by incorporating cyclic aspiration into MT protocols [4-6]. In these cases, cyclic aspiration was shown to outperform static aspiration in terms of overall MT success. However, these results have only been demonstrated using electromechanical vacuum pumps, which are not always used by neuro interventionalists. A manual method to apply cyclic aspiration is needed, therefore the *'plunger technique'* [7] for direct aspiration thrombectomy is evaluated in this study. The 'plunger technique' generates cyclic aspiration using a large syringe and will be compared to manual static aspiration within an experimental benchtop model of AIS. Both aspiration techniques will be applied to embolus analogs (EAs) of varying hematocrit, and the rate of complete clot digestion and/or the percent of partial clot ingestion for each method will be analyzed. We hypothesize that the plunger technique will result in greater clot ingestion compared to static aspiration.

METHODS

Whole bovine blood (Lampire Biologic) was obtained in CPDA-1 anticoagulated bags and centrifuged to separate red blood cells (RBCs) and platelet rich plasma (PRP). The blood was reconstituted to 0% and 50% hematocrits, and recalcified with calcium chloride to promote coagulation. The reconstituted and recalcified blood was then injected into 5.5 mm diameter tubes and placed in a Chandler loop system, where they rotated at 30 RPM for approximately 2 hours while submerged in a 37ºC water bath to mimic *in vivo* conditions. After the clotting period, the EAs were removed from the Chandler loop and stored in PBS at 4 ºC until testing.

A benchtop circulatory flow loop (**Fig. 1**) consisting of a peristaltic pump, fluid reservoir, pressure transducers, and an arterial model was developed to mimic AIS and experimentally study MT techniques. The arterial model was tapered from 5.5 to 3.3mm in diameter to represent a constricting cerebral artery and to ensure the EA lodged within this segment of the flow loop.

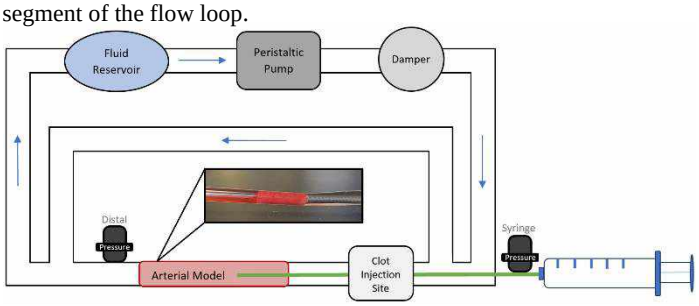

Figure 1: Schematic of benchtop AIS flow loop.

To mimic AIS, an EA was injected upstream into the flow loop and was allowed to lodge downstream within the arterial model for 5 minutes. After this waiting period, a React 71 (Medtronic) large bore catheter connected to a 60 mL VacLock syringe was passed through a hemostatic valve into the flow loop and guided to the proximal face of the EA. Static or plunger technique protocols were then performed to dislodge the EA.

For manual static aspiration, the syringe was fully opened to 60 mL and the plunger was locked so that a constant vacuum was applied to the EA for 60 seconds. For cyclic aspiration, the syringe was opened to 60 mL and then carefully released back to 0 mL. This oscillation between 0 and 60 mL was repeated for 30 seconds, after which the syringe was locked in the fully open position at 60 mL for an additional 30 seconds. Following each aspiration period, the catheter with the

attached EA was removed from the flow loop, and the length of the EA remaining outside the catheter lumen was measured and normalized by the initial EA length, resulting in a % clot ingestion measurement.

RESULTS

Examples of the pressures measured during both static (**Fig. 2A**) and plunger (**Fig. 2B**) aspiration are shown below. An immediate drop in pressure to approximately -670 mmHg is observed during static aspiration and is held constant after the syringe is locked. For cyclic aspiration, a similar drop in pressure is observed as the syringe is opened, followed by oscillations in pressure (between -400 and -710 mmHg) as cyclic aspiration is applied. After the final cycle the syringe is locked, and a constant vacuum is maintained.

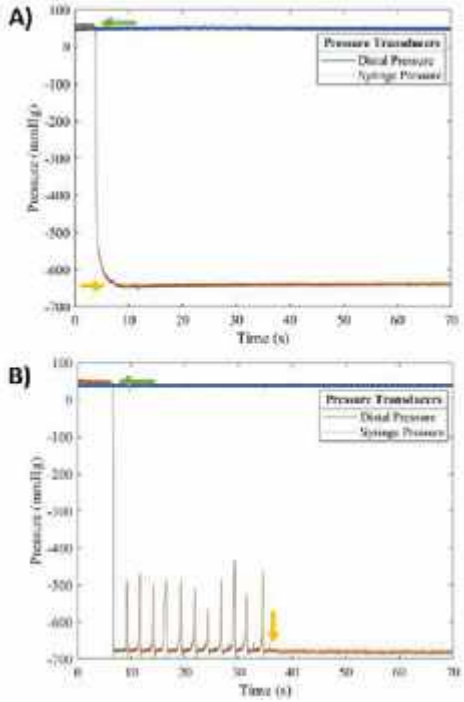

Figure 2. Examples of A) static and B) cyclic aspiration pressure measurements. Green arrows indicate opening and yellow arrows indicate closing of the syringe.

The plunger technique resulted in higher rates of complete clot ingestion (10% of the static and 30% of the plunger cases for 50% hematocrit EAs), as well as greater %'s of partial ingestion for both 0% and 50% hematocrit EAs (examples of EA ingestion shown in **Fig.3**).

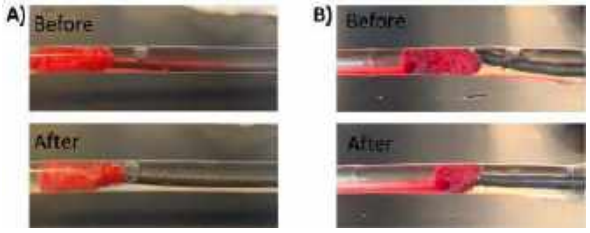

Figure 3. Before and after ingestion images of A) static and B) cyclic aspiration for 50% hematocrit EAs.

The average % ingestion (**Fig. 4**) for the 50% hematocrit EAs was measured to be 15.1±10.0% in the static cases and 34.4±19.5% in the plunger technique cases. An increase in average % ingestion was also observed for the 0% hematocrit EAs, 12.8± 4.6% for static compared to 15.8±7.3% for cyclic aspiration. A one-way ANOVA indicated a statistical difference between the two aspiration techniques for the 50% hematocrit EAs ($p=0.048$). A Tukey-Kramer post hoc test performed on the 50% hematocrit data excluding the complete ingestion cases also indicated significance.

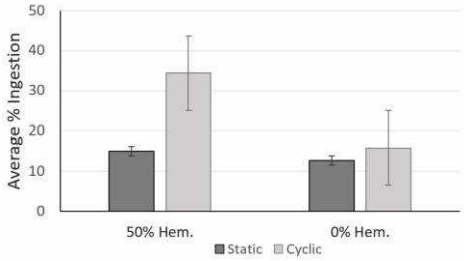

Figure 4. Comparison of average % ingestion (excluding complete ingestion cases) for static and cyclic aspiration techniques.

DISCUSSION

Using Newton's 2nd Law, force equals mass times acceleration, the effect of cyclic aspiration can be predicted. In addition, 'jerk', the time derivative of acceleration, is associated with a change in force with respect to time, and can lead to the deformation of an elastic material. Therefore, by varying the vacuum pressure through cyclic aspiration on the clot, the applied force is altered over time and jerk is generated.

The results of this study indicated that the plunger technique for manual cyclic aspiration, when compared to static aspiration, yielded overall greater levels of ingestion for both 0% and 50% hematocrit EAs (**Fig. 4**). A greater ingestion can minimize the risk of clot detachment from the catheter during the retrieval process, and thus limit the likelihood of multiple aspiration attempts. **Figure 2B** highlights that a negative vacuum pressure is maintained throughout the duration of the cyclic aspiration procedure and confirms that positive pressure does not occur. This suggests that the EA is no more likely to detach from the catheter during this procedure compared to standard techniques and will not lead to an increased risk of embolization. A comparison of the pressures in **Figs. 2A, B** indicate that an increase in maximum vacuum pressure can also be achieved through manual cyclic aspiration (-710 mmHg using plunger compared to -670 mm Hg using static).

Cyclic aspiration takes advantage of the mechanical properties of the clot and an increase in % ingestion may be due to initial clot softening under dynamic loading. A greater % ingestion for the 50% hematocrit EAs (34.4±19.5%) was found compared to the 0% EAs (15.8±7.3%) during cyclic aspiration. RBC-rich EAs exhibit decreased stiffness under compression [8], which may lead to their incremental ingestion through each aspiration cycle. Fibrin-rich EAs exhibit stiffening under cycles of compression and decompression [8], which leads us to the hypothesis that cyclic aspiration may result in a stronger cork (i.e., occlusion of the catheter tip) with fibrin-rich clots. Future work will focus on quantifying the 'corking' of the catheter tip by measuring the force needed to remove the EA from the catheter following both cyclic and static aspiration removal. Plunger technique parameters, including cyclic frequency and duration, will also be the focus of future studies to optimize this technique for a range of clinical scenarios.

REFERENCES

[1] Phipps MS, Cronin CA, *BMJ* 2020; 368
[2] Pabhakaran S, et al., *JAMA* 2015;313:1451-1462.
[3] Turk AS, et al., *Lancet* 2019 ;393 :998-1008.
[4] Simon S, et al., *J Neurointerv Surg* 2014; 6:677-683.
[5] Arslanian RA, et al., *J Neurointerv Surg* 2019;11:931-936.
[6] Kalousek V, et al., *J Neuroimaging* 2021;31:912-924.
[7] Froehler MT. J NeuroIntervent Surg. DOI: 10.1136/jnis-2023-021067.
[8] Liang X, et al., *Acta Biomaterialia* 2017;60:275-290.

SB³C2024
Summer Biomechanics, Bioengineering and Biotransport Conference
June 11-14, Lake Geneva, WI, USA

EXPLORATION OF THE FULL-FIELD BIOMECHANICS OF THE HUMAN SPINE

Emma C. Coltoff (1), Benjamin S. Hezrony (1), Philip J. Brown, PhD (1)

(1) Department of Biomedical Engineering, Wake Forest School of Medicine, Winston-Salem, North Carolina, USA

INTRODUCTION

Finite element models of the spine have significantly contributed to the study of the spinal biomechanics and the effects of implants and surgical procedures on patient wellness. Yet these models are often based solely on ligamentous behavior in uniplanar loading, in part due to the computational cost of musculoskeletal modeling, but also as a result of available experimental data on which to base the simulation. The biomechanics of the spine is understood to be naturally multidimensional, yet standard single bending moment characterizations developed from the seminal work of Panjabi et al[1] leave motion-loading space in-between planes untested and unknown, leading to incomplete validation of spinal finite element models. Accurate simulation of *in vivo* spinal loads is best supported by experimental loading that is sensitive to 1) the multiplanar behavior of the spine itself[2] and 2) the multidimensional spinal stiffness response and its dependency on the directionality of the loading path. To address this gap, we developed a novel testing protocol using six-degree-of-freedom trajectories to produce complex motion paths which map the spine's multiplanar behavior and visualize its multidimensional bending stiffness in all directions within its physiological limits.

METHODS

One L2-L5 synthetic lumbar surrogate specimen from Sawbones (Washington, USA) was mounted to custom fixtures on a 6 DOF KR 300 R2500 Ultra Robot (KUKA Robotics, Germany). The specimen's moment-displacement behavior was captured by a Delta IP68 SI-330-30 (ATI Industrial Automation Inc, USA) load cell, Optotrak (Northern Digital Inc, Canada) sensors, and simVITRO (Cleveland Clinic BioRobotics, USA) software. A geometric combined FE and LB loading scheme (**Figure 1a**) was designed as a combination of three different loading trajectories which can be run clockwise/counter-clockwise about the craniocaudal axis: circles, angled "petals", and medially/distally moving "rays" which pass through the spine's neutral zone. This pattern is designed with a scalable quantity of intersection points within the spine's physiologic space at which the three trajectories overlap. This series of experiments resulted in 930 distinct intersection points (**Figure 1b**) at each of the three trajectories and their two variants (clockwise/counterclockwise), resulting in eight distinct angles at which the intersection point can be approached during a specimen loading trajectory. The specimen was first tested in moment-controlled loading of combined Flexion-Extension (FE) and Lateral Bending (LB) circles with no axial preload in increasing combined moments up to 7.5 Nm, the standard maximum loading for the lumbar spine[2]. This testing captured the organic shape of the spine's physiologic boundary under maximal combined FE and LB loading. The geometric trajectory was then cropped to match the output of the boundary capture testing, but to maintain the spacing between intersection points. The specimen was then loaded by the cropped trajectory in displacement-controlled loading, to maintain the spacing of the intersection points.

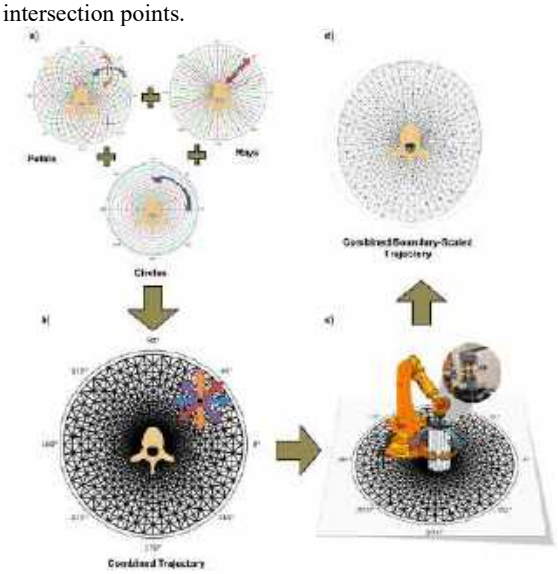

Figure 1: Combination of the ray, petal, and circle trajectories (a,b), test setup (c), and the boundary-scaled output (d).

RESULTS

Displacement measurements from the Optotrak system were transformed through simVITRO into anatomical bending measures in Anterior, Lateral, and Superior translations (mm) and Flexion-Extension, Lateral Bending, and Axial Rotation bending (deg) relative to the joint coordinate system of the spine. The ATI load cell measures were processed through simVITRO to determine the Anterior, Lateral, and Superior forces (N) and Flexion-Extension, Lateral Bending, and Axial Rotation bending moments (Nm) on the spine segment in response to the loading trajectory. The displacements and loads were combined into a resultant stiffness value of the spine throughout the loading trajectory. The data were then sliced to visualize the corresponding FE and LB planar and 45° off-axis stiffness behaviors for each trajectory type in response to the multiplanar loading.

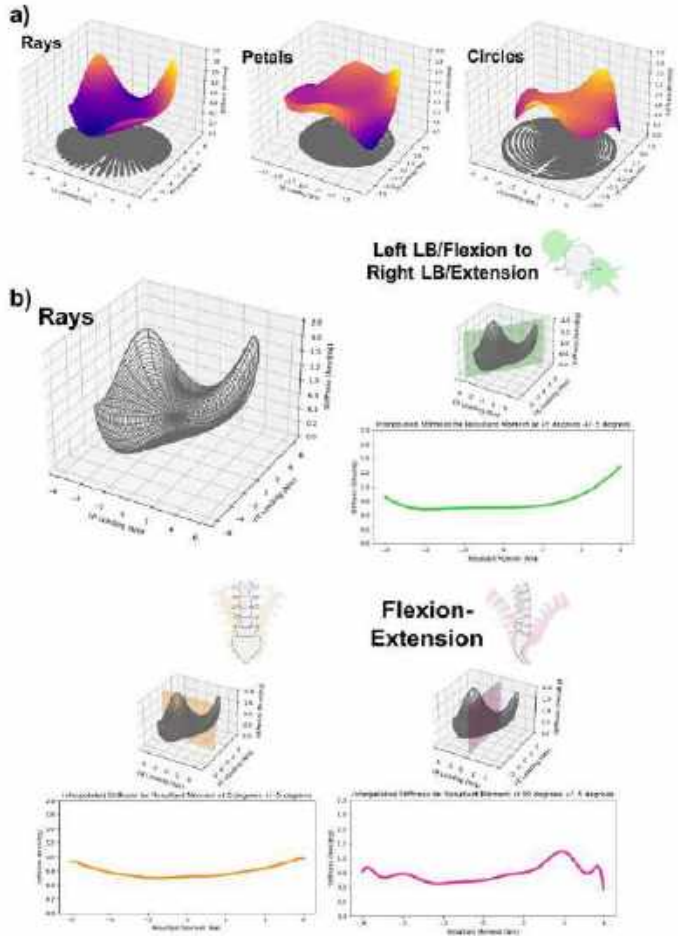

Figure 2. (a) Stiffness surfaces for three trajectories. (b) Slices through stiffness surface for rays trajectory in planar Lateral-Bending and Flexion-Extension and Negative 45° (Left LB/Flexion to Right LB/Extension).

The spinal surrogate stiffness creates vastly different surface shapes shown in the 3D plots in **Figure 2a**. Peak stiffness (1.4 Nm/deg) in the circular trajectory was 0.35 Nm/deg lower than in the petals or rays trajectories (1.75 Nm/deg). The circular trajectory produces peak stiffness measures where LB is minimized and FE is maximized. By contrast, the rays trajectory enables visualization of peak stiffness at the maximum combination of left and right LB and extension. The planar slices (**Figure 2b**) facilitate visualization of distinct behaviors of the spine's stiffness in planar FE and LB for comparison to uniplanar behaviors. The spine had similar peak LB planar stiffness measures (1.09 Nm/deg) under the petal and circle trajectories but a peak of only 0.95 Nm/deg under the rays trajectory.

This testing is unique in that it enables assessment of stiffness of the spine as it passes from combined full Flexion and left LB through the neutral zone to full Extension and right LB (**Figure 3, green**), during which it sees a peak stiffnesses of 0.6-1.2 Nm/deg and 0.9-1.5 Nm/deg at the extrema of the path, respectively, depending on trajectory. The complementary path from full Flexion and right LB through the neutral zone to full Extension and right LB (**Figure 3, blue**), saw different peaks in stiffness values of 1.0-1.1 Nm/deg and 0.75-1.2 Nm/deg. These paths can be compared with a moving average of the stiffness in planar LB and FE (**Figure 3, black dashed**) across the same range of resultant moment values. Focusing just on the circular trajectory, this was calculated to be 1.25 Nm/deg and 1.15 Nm/deg at the extrema. The differences in behavior between the two off-axis slices and the calculated average planar stiffness suggests that multiplanar spinal stiffness cannot be inferred exclusively from planar testing.

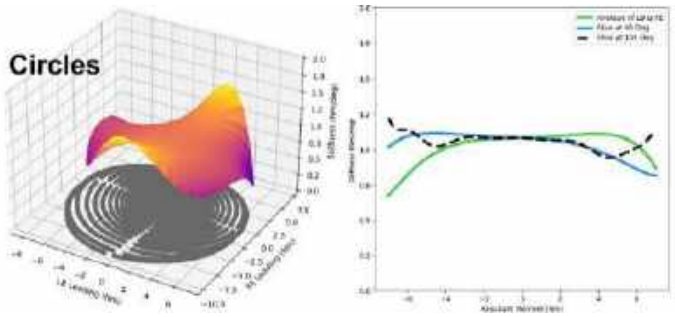

Figure 3: Left LB/Flexion to Right LB/Extension & Right LB/Flexion to Left LB/Extension compared to average planar LB & FE stiffness.

DISCUSSION

Comparing the slice behaviors by their peak and range values helps to establish a range of expected values of spinal stiffness during experimental loading. Integrating the intersection points into the trajectory design affords an opportunity to determine a range of potential stiffness measures of the spine at a specific location in its physiologic space and consequently, to parameterize the expected stiffness behavior of the spine depending on the applied loading behavior. This information can be incorporated into spine finite element models to produce more accurate predictions.

The interpretation of this data is in and of itself, a part of the objective of this study. Mapping the changes in stiffness of the spine across its physiologic spaces enables improved visualization of healthy and injurious spinal behavior. This in turn, informs more nuanced diagnosis, assessment of treatment modalities, and differentiation between movement patterns which may otherwise not be visible in uniplanar testing. Future work will explore the spine's response in various surgical states to inform treatment predictions for patients based on pre-surgical and desired post-surgical biomechanics of the spine.

ACKNOWLEDGEMENTS

The authors would like to acknowledge the support of the simVITRO team from Cleveland Clinic for their guidance.

REFERENCES

[1] Panjabi MM, et al. Spine (Phila Pa 1976). 2000 Nov 1;25(21):2748–54. [2] Costi, J. J., et al. (2021). JOR Spine, 4(1), e1138. https://doi.org/10.1002/JSP2.1138

BENEFITS OF USING FUNCTIONAL JOINT COORDINATE SYSTEMS IN *IN VITRO* KNEE TESTING

Tara F. Nagle (1,2), Jeremy G. Loss (1), Callan M. Gillespie (1,2), Robb W. Colbrunn (1,2)

(1) Lerner Research Institute, Cleveland Clinic Foundation, Cleveland, Ohio, USA
(2) Dept. of Applied Biomedical Engineering, Cleveland State University, Cleveland, Ohio, USA

INTRODUCTION

When measuring knee joint kinematics to assess the effects surgical/pathological conditions have on knee biomechanics, coordinate systems (CS) must be assigned to the tibia and femur. Typically, this step is executed by selecting anatomical landmarks on the knee and using standard definitions for defining Anatomical CS based on landmark locations [1]. Variability in landmark selection can result in varying CS definitions and subsequent representation or interpretation of kinematic responses [2,3].

A previous work [4] utilized a generalized framework incorporating a Linear-Least-Square optimization to redefine the tibia and femur origins, the femur flexion (FE) axis, and the tibia internal rotation (IR) axis based on low-resistance motion profiles. The authors found this approach for establishing Functional CS to significantly reduce CS variability and resulting off-axis translations and rotations during passive motion [4].

In this study, we aimed to quantify the effects landmark selection variability can have on reported kinematic response during loaded states. We hypothesize that regardless of anatomical landmark selection, compared to Anatomical CS, the use of Functional CS will reduce kinematic cross-talk (coupling of DOFs where loads in one direction generate motion in a different direction), which will reduce the variation in kinematic response throughout various loading conditions and flexion angles. Ultimately, use of Functional CS will result in more similar kinematic responses between knee specimens than what has been observed historically, enabling higher fidelity 6 DOF kinematic characterization of knee populations within studies and across different laboratories.

METHODS

Seven (7) fresh-frozen, cadaveric leg specimens were utilized in this study. Specimens were tested using a simVITRO® Universal Musculoskeletal Simulator (Cleveland Clinic, Cleveland, OH) and a 6-axis force/torque sensor (Omega160, ATI, Apex, NC). Each specimen was mounted to the robot and positioned in full extension. A single observer digitized anatomical landmarks to establish Anatomical local CS. Spatial relationships between the specimen, robot, and force/torque sensor were established. Kinematics were calculated based on spatial relationships and robot positions. Kinetics were calculated at the joint coordinate system based on spatial relationships, kinematic measurements, and force/torque sensor measurements. Functional CS were obtained by optimizing the Anatomical CS using the passive motion methodology outlined previously [4].

Quasistatic laxity loading was performed across Anatomical and Functional CS sets at 45° flexion with 20 N compression and all remaining loads minimized, unless specified (Table 1). Kinematic cross-talk was evaluated by performing a paired t-test comparing off-axis range of motion during Anterior-Posterior (AP), Varus-Valgus (VV) and Internal-External Rotation (IRER) laxity loading between Anatomical and Functional CS.

Table 1: Laxity Loading Profiles

Loading Profile	Anterior Force (N)	Valgus Torque (Nm)	IR Torque (Nm)
Anterior	100	0	0
Posterior	-100	0	0
Valgus	0	5	0
Varus	0	-5	0
IR	0	0	5
ER	0	0	-5

A dynamic ISO gait profile (ISO 14243-3) was executed across Anatomical and Functional CS sets with loads scaled to 25% over a 120 second duration. Kinematic response was resampled to 100 data points and the standard deviation of kinematic response was calculated for each data point across Anatomical and Functional CS. Inter-Knee

kinematic variation was evaluated by performing a paired t-test comparing the standard deviation between Anatomical and Functional CS throughout the ISO gait profile.

RESULTS

During laxity loading, significant reductions in off-axis translations and rotations (i.e. kinematic cross-talk) were observed for Functional CS compared to Anatomical. During AP laxity tests, superior, valgus, and IR motion were significantly reduced by 1.38 ± 0.91 mm (P=0.007), 1.04 ± 1.05° (P=0.039), and 12.41 ± 10.99° (P=0.024), respectively (Figure 1a). During IRER laxity tests, medial, posterior, and valgus motion were significantly reduced by 12.48 ± 4.23 mm (P<0.001), 4.59 ± 4.81 mm (P=0.045), and 3.12 ± 2.11° (P=0.008), respectively (Figure 1b). During VV laxity tests, medial, superior, and IR motion were significantly reduced by 3.43 ± 2.97 mm (P=0.022), 0.90 ± 0.65 mm (P=0.011), and 7.40 ± 7.48° (P=0.040), respectively (Figure 1c).

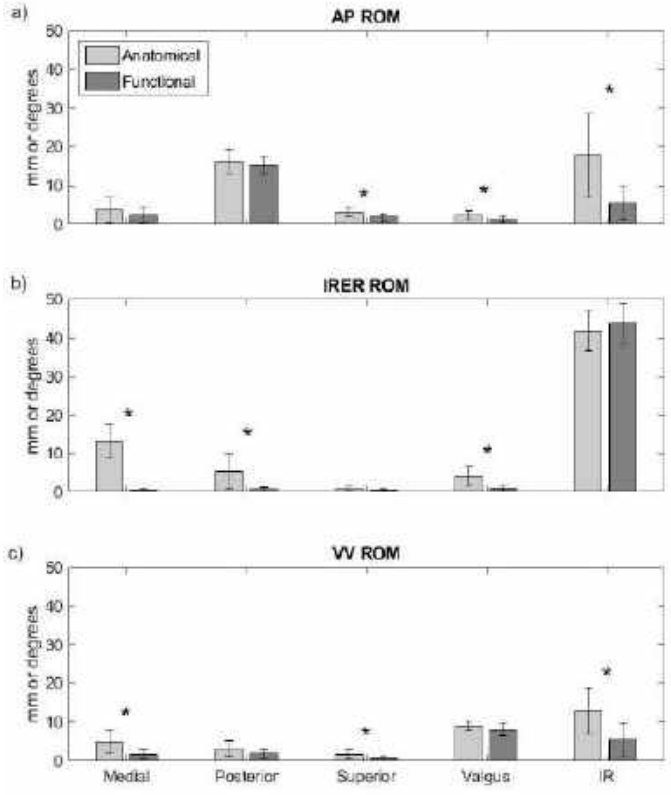

Figure 1: Off-Axis Range of Motion during Laxity Style Loading, *Significance determined for p-value < 0.05

The average and standard deviation of the kinematic responses (and extension torque response) over the 100 resampled points in the ISO Gait profile were calculated using Anatomical and Functional CS. Figure 2 displays the results with the average values represented as lines, and the shaded regions as standard deviation ranges. Significant overall reductions in the standard deviation range were observed using Functional CS compared to Anatomical for each DOF throughout the ISO Gait profile. Average reductions were 0.94 ± 0.67 mm (P<0.001) in medial translation, 0.84 ± 1.07 mm (P<0.001) in posterior translation, 1.94 ± 1.50 mm (P<0.001) in superior translation, 1.14 ± 0.98 Nm (P<0.001) in extension torque, 1.15 ± 1.05° (P<0.001) in valgus rotation and 0.78 ± 1.20° (P<0.001) in internal rotation.

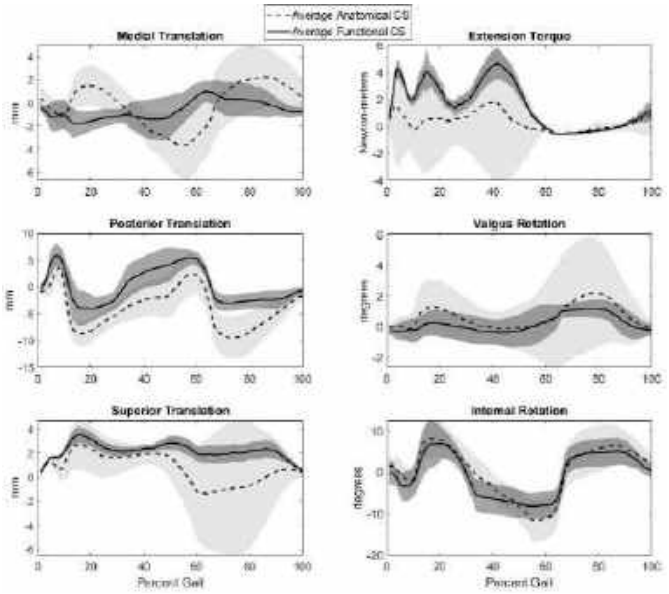

Figure 2: Average and Standard Deviation of Kinematic Response for Anatomical (dotted line with light shading) and Functional (solid line with dark shading) Coordinate Systems

DISCUSSION

Joint kinematics are a common outcome measurement from *in vitro* studies where *in situ* loads are controlled and applied to a joint. It is important that these measurements are objective and minimally influenced by observer decisions, like anatomical landmark selection. If the measurements are objective, then testing the same specimen should generate similar output data, regardless of the operator. Data in Figure 2 compares the kinematic response of the *same* seven knee specimens undergoing the *same* loading profile, with the only difference being how CS systems are defined, which is an experimental setup variable. This data demonstrates that with Anatomical CS, variation in kinematic response throughout a common loading profile is significantly greater compared to Functional CS. Large kinematic variation observed with Anatomical CS makes it difficult to characterize the kinematic response of a population of knees undergoing a complex loading profile. However, kinematic responses with Functional CS yield trending motion paths common to all included specimens.

The reduction in kinematic response variation with Functional CS is, in part, attributed to the significant reduction in kinematic cross-talk compared to Anatomical CS (Figure 1). Functional CS are designed to minimize kinematic cross-talk by optimizing the axes of the joint to be better aligned with the joint's natural passive motion path. If kinematic cross-talk is successfully reduced, then the joint's motion should predominantly be in the direction loads are applied and reduced in all other DOFs (i.e. an applied IR torque would produce an IR rotation with minimal motion in other DOF), which is demonstrated for Functional CS in Figure 1.

In this study, we have demonstrated that using Functional CS significantly reduces kinematic response variation across multiple loading conditions and flexion angles. For this reason, we recommend that Functional CS be used in *in vitro* knee testing.

REFERENCES

[1] Grood, E & Suntay, W, *J Biomech Eng*, 105(2):136-44, 1983.
[2] Morton, N et al., *J Bone Joint Surg Br*, 87(6):804-8, 2007.
[3] Yau, W et al., *J Arthroplasty*, 22(8):1150-61, 2007.
[4] Nagle, T et al., *J Biomech*, 127:110664, 2021.

IMPACT OF ELASTIN FRAGMENTATION ON THE MECHANICAL DISSECTION PROPERTIES OF THE HUMAN DESCENDING THORACIC AORTA

Ramin Shahbad (1), Majid Jadidi (1), Sayed Ahmadreza Razian (1), Anastasia Desyatova (1)

(1) Department of Biomechanics, University of Nebraska Omaha, Omaha, Nebraska, USA

INTRODUCTION

Aortic dissection is a severe and life-threatening condition that involves delamination of the aortic wall layers and primarily occurs in the thoracic segment of the aorta [1]. Aging, aortic aneurysm and atherosclerosis induce significant arterial remodeling, weakening the aortic wall and elevating the risk of dissection up to three-fold when exposed to pulsatile pressure during the cardiac cycle[2]. Understanding the interplay between the wall's structure and mechanical strength is crucial for comprehending dissection onset and progression.

While numerous studies have explored the delamination strength of the arterial wall to unravel the link between heightened aortic dissection risk and structural irregularities [3], quantitative analyses of the impact of elastin fragmentation on the mechanisms underlying aortic dissection in the human population of sufficient age range remain insufficiently understood. Furthermore, current research has not thoroughly addressed the influence of aging on aortic dissections. Therefore, through peeling tests and microstructural analysis, this study aims to address these gaps by investigating how aging and elastin fragmentation contribute to the underlying damage behavior in the context of aortic dissections.

METHODS

Specimen Preparation. Human aorta samples from 35 tissue donors aged 13-76 (average age 38 ±15 years, 31% female) were acquired after the consent of the next of kin. Tubular segments from the descending thoracic aorta were excised and cut lengthwise into flat rectangular sheets. Multiple samples were obtained from each sheet, both longitudinally and circumferentially. An initial incision in the medial layer was created with a scalpel.

Peeling Test Procedure. Peeling tests were conducted utilizing the CellScale biaxial testing device. The two tongues of the sample were securely mounted on custom-designed 3D-printed clamps, which moved in opposite directions while maintaining the sample's center in a fixed position. Aorta samples were fully immersed in a 0.9% phosphate-buffered saline solution at a controlled temperature of 37±1°C throughout the testing process. The peeling force, representing the force required to delaminate the two tongues along the longer side of the sample, was recorded continuously. As shown in Figure 1, the delamination strength of the aorta's media was characterized as Force/Width (F/W), computed by dividing the average force recorded during the stable plateau phase of the force-displacement curve by the sample width.

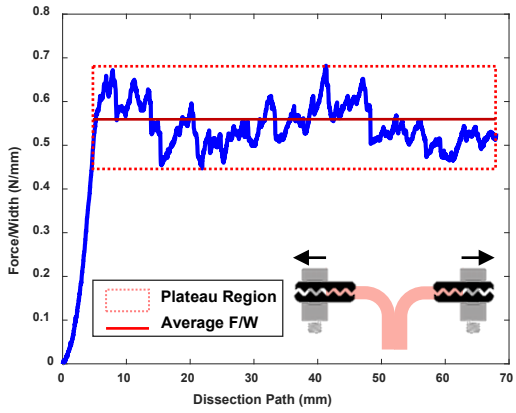

Figure 1. A schematic illustration of the peeling test procedure and the changes in force/width with dissection growth.

Structural Analysis. Structural analysis was conducted using bidirectional histology on the same aorta samples utilized for the peeling tests immediately following the mechanical testing phase. Aorta samples were subjected to Verhoeff-Van Gieson (VVG), which stained the elastin fibers black. A semi-automated, custom-built software was

developed in Visual Studio C# utilizing the .Net 4.6.2 framework, which enabled us to select distinct layers of the arterial wall and perform RGB thresholding to quantify elastin density within each arterial layer individually.

RESULTS

Changes in dissection properties and structural characteristics with aging are presented in Figure 2. As individuals age, delamination strength exhibited a statistically significant decline in both directions (r=-0.7 for longitudinal, r=-0.629 for circumferential, p<0.001). Delamination strength was higher in the longitudinal direction (49.95±17.66 N/mm) than in the circumferential direction (35.13±9.51 N/mm), p < 0.001. The rate of strength decline was more pronounced in the longitudinal direction (-7.744 N/mm per decade) than in the circumferential direction (-3.898 N/mm per decade).

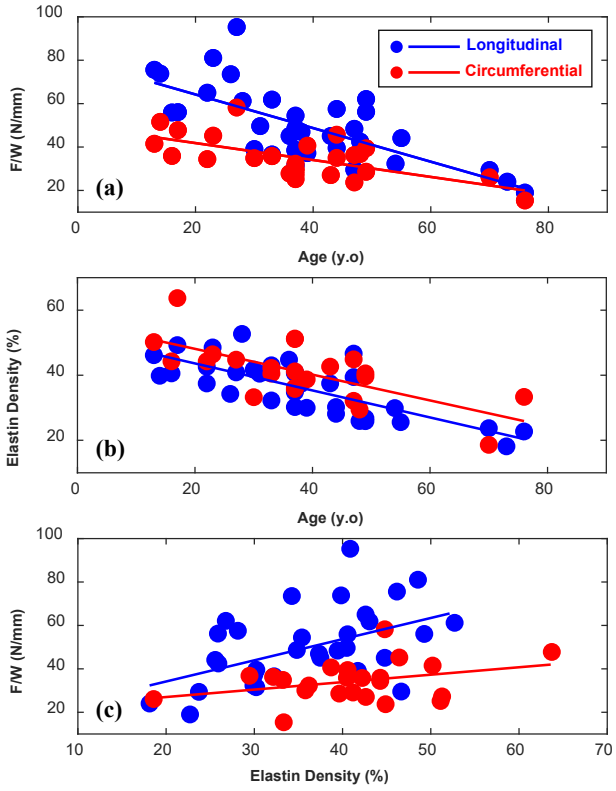

Figure 2. Changes in dissection properties and structural characteristic of descending thoracic aorta with aging.

Quantitative measurements indicated a significant reduction in the density of the media's elastin with aging in both directions (r=-0.762 for axial, r=-0.681 for circumferential, both p<0.001). The elastin density was shown to be significantly higher in the circumferential direction (41.09±9.00) compared to the axial direction (36.54±8.07), p=0.009. Figure 3 demonstrates a comparison of histological images of the aorta's media between young and elderly individuals, illustrating that older arteries tend to exhibit more degraded and fragmented elastin fibers.

Our results demonstrate that samples with higher elastin density exhibit better delamination resistance. The correlation between the strength and elastin density is statistically significant in the longitudinal direction (r=0.487 and p=0.003). However, this correlation is not statistically significant in the circumferential direction (r=0.340 and p=0.112).

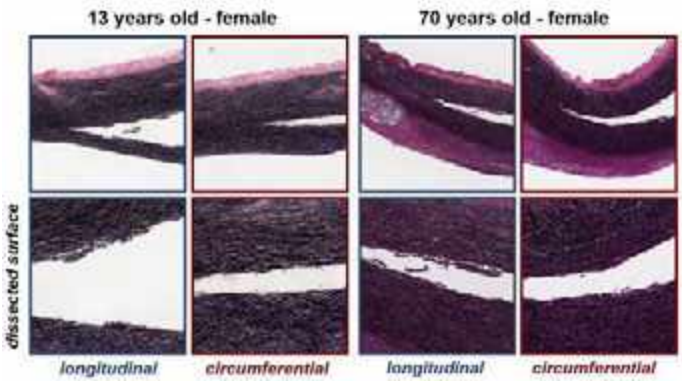

Figure 3. Longitudinal and circumferential VVG-stained images of the descending thoracic aorta in 16-year-old and 76-year-old subjects, highlighting elastin (black) content differences.

DISCUSSION

Quantitative analysis and histology observations revealed an elevated breakdown and fragmentation of interlaminar fibers attributed to aging. The pronounced loss of the framework-like structure is particularly notable in components such as elastin struts, which function as critical connections between laminae within the arterial wall. This breakdown disrupts architectural integrity between laminae, leading to weakened connective fibers and lower resistance to microstructural layer delamination. This explanation bolsters our current findings and aligns with previous research [4], further substantiating the heightened susceptibility of elderly patients to aortic dissection.

The aorta's delamination strength significantly differs when the tear propagates longitudinally versus circumferentially, which is consistent with prior studies indicating strength anisotropies in arterial tissues [5]. This observation is supported by smoother dissection surfaces in the circumferential direction seen in the histology images. These differences seem to be linked to the unique orientation and alignment of fibers in these two distinct directions. In the circumferential direction, both collagen fibers and smooth muscle cells (SMCs) tend to align preferentially in the circumferential orientation. Given that interlamellar connections serve as the link between SMCs and the extracellular matrix, they also exhibit a preference for circumferential alignment. This partial tendency of the fibers to align in the circumferential direction facilitates a smoother and more favorable trajectory for crack propagation. In contrast, the fibers responsible for withstanding delamination forces are predominantly radially oriented in the axial direction. These radial fibers can offer superior resistance to peeling compared with the obliquely oriented bonds in the circumferential direction. This observation aligns with computational findings that indicate fewer interlamellar connections are engaged in processes related to circumferential stretching resistance [6].

ACKNOWLEDGEMENTS

This work was supported by the NHLBI HL147128.

REFERENCES

[1] Criado, FJ., *Texas Heart Institute Journal*, 38.6 (2011): 694.
[2] Hibino, M, et al., *Circulation*, 145.9 (2022): 633-644.
[3] Tong, J, et al., *J of biomechanics*, 49.12 (2016): 2366-2373.
[4] Horný, L, et al., *J of the Mechanical Behavior of Biomedical Materials*, 133 (2022): 105340.
[5] Sommer, G, et al., *J of Biomechanical Engineering*, (2008): 021007.
[6] Witzenburg, CM., et al., *J of Biomechanical Engineering*, 139.3 (2017): 031005.

SB^{3}C2024
Summer Biomechanics, Bioengineering and Biotransport Conference
June 11-14, Lake Geneva, WI, USA

ENHANCING 4D-FLOW MRI WITH INPUT-PARAMETRIZED PHYSICS-INFORMED NEURAL NETWORK (IP-PINN)

Amin Pashaei Kalajahi (1), Omid Amili (2), Amirhossein Arzani (3), Roshan M D'Souza (1)

(1) Department of Mechanical Engineering, University of Wisconsin-Milwaukee, Milwaukee, Wisconsin, USA
(2) Department of Mechanical Engineering, University of Toledo, Toledo, Ohio, USA
(3) Mechanical Engineering Department and Scientific Computing and Imaging Institute, University of Utah, Salt Lake City, Utah, USA

INTRODUCTION

Cardiovascular diseases such as aneurysms and arteriovenous malformations present significant health challenges, where understanding hemodynamics is key for effective diagnosis and treatment. 4D-Flow MRI (Magnetic Resonance Imaging) [1], a non-invasive imaging technique, providing in-vivo volumetric time-resolved 3D velocity maps plays a crucial role for estimating hemodynamic parameters but faces limitations like low spatio-temporal resolution, velocity aliasing, acquisition noise, and phase offset errors.

Recent advancements in Computational Fluid Dynamics (CFD) simulations, along with data assimilation techniques and deep learning frameworks have aimed to enhance the resolution and accuracy of hemodynamic estimations. Despite these advancements, challenges remain in accurately representing anatomical characteristics and flow parameters, geometry segmentation, image registration, and processing time [2–4].

Addressing the limitations of 4D-Flow MRI data processing, we introduce the Input Parameterized Physics-Informed Neural Network (IP-PINN), tailored for time-resolved phase-contrast MRI. This novel framework merges Convolutional Neural Networks (CNN)-based method's generalizability with PINNs' continuous field representation, effectively tackling challenges such as low spatio-temporal resolution, noise, phase offset errors, and velocity aliasing. The IP-PINN enhances both the velocity maps reconstruction accuracy and processing time, with experimental validations showing significant improvements over current methods.

PROPOSED METHOD

Our study introduces an algorithm to enhance 4D Flow MRI processing, using 3-directional velocity-encoded complex Cartesian images which is selected from the larger domain of 4D Flow MRI velocity-encoded complex Cartesian scans. At its core, the algorithm employs a hybrid neural network that combines CNNs and Multi layer perceptrons (MLPs). It encodes features from input images into a latent vector $\mathbf{C}$ and then generates high-resolution images using MLPs.

As shown in fig. 1, the CNN component processes the input data to extract pivotal features. This encoder encodes essential information from the input images into a latent vector. The MLPs then use this latent vector, along with normalized spatio-temporal coordinates, to produce high-resolution velocity and magnitude images. IP-PINN approximates two continuous functions: $\mathbf{f}$ and $\mathbf{\Phi}$. Function $\mathbf{f}$ maps the 4D spatio-temporal velocity-encoded complex Cartesian data to the normalized velocities, relative pressure, and image magnitude. Meanwhile, $\mathbf{\Phi}$ predicts phase offset errors in three dimensions. These functions are expressed as:

$$\mathbf{f}(\mathcal{U}^\dagger, \mathbf{x}^\dagger, t^\dagger) = \begin{bmatrix} u^\dagger(\mathbf{x}^\dagger, t^\dagger) \\ v^\dagger(\mathbf{x}^\dagger, t^\dagger) \\ w^\dagger(\mathbf{x}^\dagger, t^\dagger) \\ p^\dagger(\mathbf{x}^\dagger, t^\dagger) \\ |M_o(\mathbf{x}^\dagger, t^\dagger)| \end{bmatrix}, \mathbf{\Phi}_B(\mathcal{U}^\dagger, \mathbf{x}^\dagger, t^\dagger) = \begin{bmatrix} \phi_B^x(\mathbf{x}^\dagger, t^\dagger) \\ \phi_B^y(\mathbf{x}^\dagger, t^\dagger) \\ \phi_B^z(\mathbf{x}^\dagger, t^\dagger) \end{bmatrix} \tag{1}$$

Here, $u^\dagger(\cdot)$, $v^\dagger(\cdot)$, $w^\dagger(\cdot)$, $p^\dagger(\cdot)$, and $|M_o(\cdot)|$ are the dimensionless normalized velocities in the x, y and z directions, relative pressure, and magnitude of the image, respectively and $\phi_B^x(\cdot)$, $\phi_B^y(\cdot)$, and $\phi_B^z(\cdot)$ are the predicted composite phase along the the x, y and z directions, respectively. These functions are approximated using the latent vector $\mathbf{C}$, generated by the CNN from processing $\mathcal{U}^\dagger$, the velocity-encoded scans of the region of interest (ROI). This is further combined with normalized spatio-temporal coordinates, processed by the MLPs, to generate the final outputs:

$$\mathbf{f}^* = \mathcal{M}_{\Theta_2}(\mathbf{C}, \mathbf{x}^\dagger, t^\dagger) = \mathcal{M}_{\Theta_2}(\mathcal{G}_{\Theta_1}(\mathcal{U}^\dagger), \mathbf{x}^\dagger, t^\dagger) \tag{2}$$

$$\mathbf{\Phi}^* = \mathcal{M}_{\Theta_3}(\mathbf{C}, \mathbf{x}^\dagger, t^\dagger) = \mathcal{M}_{\Theta_3}(\mathcal{G}_{\Theta_1}(\mathcal{U}^\dagger), \mathbf{x}^\dagger, t^\dagger) \tag{3}$$

Our training methodology employs a composite loss function, comprising of a data fidelity and physics regularization term. Data fidelity is done with respect to the complex Cartesian image data of the three velocity-encoding scans.

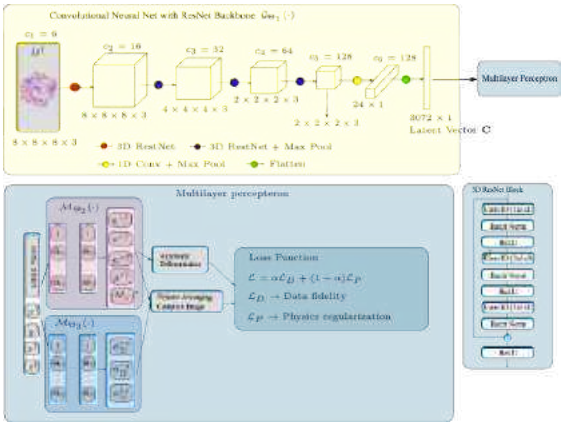

Figure 1: Schematic representation of the proposed IP-PINN architecture.

RESULTS

We tested the IP-PINN algorithm using synthetic 4D-Flow MRI datasets derived from two patient-specific 3D CFD simulations: a posterior cerebral artery (PCA) aneurysm for pre-training and a middle cerebral artery (MCA) aneurysm for testing. Both datasets were downsampled and modified with phase offset errors, using first-order and second-order polynomials for the PCA and MCA simulations, respectively. After pre-training, we fine-tuned IP-PINN for an unseen ROI in the MCA dataset. Figures 2 and 3 show the predicted velocity maps for ROIs at 40 dB and 20 dB noise levels, respectively, for a specific y-direction slice at a given temporal snapshot.

We compared the performance of IP-PINN with a physics-informed neural network (PINN) [3] in terms of accuracy and processing time. By using a pre-trained IP-PINN model on a new dataset, we significantly reduced processing time to 1.5 minutes, compared to 30 minutes with the PINN model. For a fair comparison, both models were trained on the same region of interest. Table 1 summarizes their performance, listing accuracy metrics including root mean squared error (RMSE), coefficient of determination (R^2), and median absolute percentage error for u^*, v^*, and w^*. These results demonstrate the enhanced efficacy of the IP-PINN algorithm over the conventional PINN in terms of both accuracy and processing time.

Our approach uniquely predicts high-resolution velocity and magnitude images from time-resolved phase contrast MRI velocity-encoded images, removing the need for separate MRI reference scans. Figure 4 illustrates this, displaying the luminal boundary in a selected ROI and the corresponding ground truth. It also shows low-resolution MRI magnitude images, generated from overlapping blocks of flow-encoded scan data, demonstrating the IP-PINN model's effective boundary delineation.

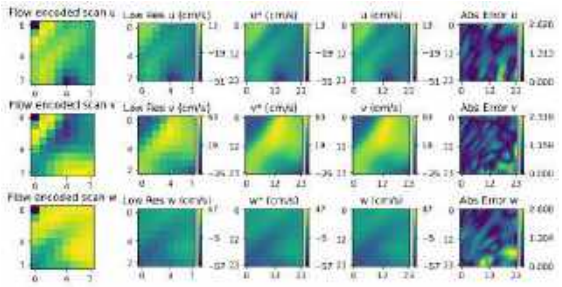

Figure 2: Predicted velocity maps from IP-PINN for a ROI in the MCA aneurysm dataset with a noise level of 40 dB.

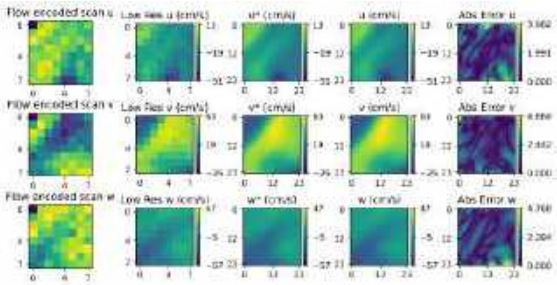

Figure 3: Predicted velocity maps from IP-PINN for a ROI in the MCA aneurysm dataset with a noise level of 20 dB.

Table 1: A comparison of error metrics attained by the PINN models and the proposed IP-PINN model when processing noisy input data.

Method	SNR	RMSE	R^2	MDAPE$_u$	MDAPE$_v$	MDAPE$_w$
IP-PINN	40 dB	1.064	0.997	3.747	1.222	6.522
	20 dB	1.818	0.992	6.178	2.267	8.360
PINN	40 dB	4.508	0.947	12.622	7.604	20.035
	20 dB	5.789	0.913	13.066	8.626	21.144

Figure 4: Luminal boundary prediction.

DISCUSSION

We introduced a novel deep learning method, Input-Parameterized Physics-informed Neural Network (IP-PINN), for enhancing 4D-Flow MRI data, including super-resolution, phase offset corrections, and noise reduction. IP-PINN merges the fast execution and generalizability of traditional image super-resolution frameworks with PINNs' continuous representation capability. It employs a CNN to encode an MRI region of interest into parameters and an MLP for generating high-resolution images. Notably, IP-PINN eliminates the need for ground truth labeling, allows for ongoing training with new data, and significantly reduces processing time – a twentyfold decrease compared to traditional PINNs. This makes IP-PINN a valuable tool for hemodynamic analysis in clinical settings, potentially reducing 4D-Flow MRI scan time by 25% and improving lumen boundary segmentation. While currently validated only on simulated datasets, future work involves in-vitro validation and incorporating actual 4D-Flow MRI acquisition mechanics for further refinement.

ACKNOWLEDGEMENTS

This work was supported by a collaborative National Science Foundation (NSF) award under Grant No. 2103560 and 2246916. The views expressed in this article are those of the authors alone and may not necessarily be endorsed by the NSF.

REFERENCES

[1] Markl M et al. *Journal of Magnetic Resonance Imaging: An Official Journal of the International Society for Magnetic Resonance in Medicine* 17.4 (2003).

[2] Berg P et al. *Neurosurgical Focus* 47.1 (2019).

[3] Fathi MF et al. *Computer Methods and Programs in Biomedicine* 197 (2020).

[4] Ferdian E et al. *Frontiers in Physics* (2020).

REFINED ENDOVASCULAR SOLUTIONS: LEVERAGING 3D PRINTING IN SHAPE MEMORY POLYMER-BASED EMBOLIZATION FOR INTRACRANIAL ANEURYSM RUPTURE PREVENTION

Tanner L. Cabaniss (1), Yingtao Liu (1), Bradley N. Bohnstedt (2), Chung-Hao Lee (3)

(1) School of Aerospace and Mechanical Engineering, University of Oklahoma, Norman, OK, USA
(2) Department of Neurological Surgery, Indiana University School of Medicine, Indianapolis, IN, USA
(3) Department of Bioengineering, University of California Riverside, Riverside, CA, USA

INTRODUCTION

Saccular intracranial aneurysms (ICAs), affecting an estimated 4% of the American populace, manifest as protuberances resulting from localized arterial wall attenuation [1]. The primary concern with ICAs revolves around their propensity to rupture (an estimated annual rate of 2.1-7.2% [2]). This rupture often triggers a chain of severe and life-threatening conditions such as subarachnoid hemorrhage (SAH) that bears a daunting 50% fatality rate, with only 6-17% of survivors regaining full cognitive function [3].

Efforts to reduce the risk of aneurysm rupture have driven the development of therapeutic options. While surgical clipping remains effective, advancements have been made in endovascular methods. However, widely used techniques, such as Guglielmi Detachable Coils (GDCs) introduced in 1991, still face limitations including incomplete occlusion rates of ~40% that induces subsequent rebleeding, diminishing its efficacy [4]. Arterial stents, integrated into endovascular therapeutics, pose risks of delayed occlusion post-intervention due to their deployment location [5]. The WEB devices represent a modern alternative addressing limitations of GDCs and stents. However, the challenge lies in inadequate conformity to irregular patient's aneurysm geometries, potentially leading to protrusion complications [6], elevating the risk of rupture by 3-fold compared to regular shapes [2].

Recognizing these limitations, this study aims to address critical shortcomings in current endovascular approaches for treating ICAs. Our focus centers on *three pivotal aspects*: (i) mitigating compaction via anisotropic materials, (ii) enhancing occlusion speed through a dense internal scaffolding network, and (iii) ensuring adaptability to intricate geometries via additive manufacturing technologies.

METHODS

SMP Foam Fabrication: First, sacrificial polyvinyl alcohol (PVA) templates were fabricated via FDM additive manufacturing (Ender 5 printer). Next, polyurethane-based shape memory polymer (SMP) solution comprised of hexamethylene isocyanate (HDI), N,N,N0,N0-tetrakis (hydroxypropyl) ethylenediamine (HPED), and triethanolamine (TEA) in a molar ratio of 1:0.18:0.42, was prepared as previously reported [7]. The PVA templates were coated with the liquidous SMP solution, followed by meticulous removal of excess SMP employing a drying mat. Then, the coated templates underwent a three-stage curing procedure within a vacuum oven: 3 h at 45°C, followed by 1 h at 70°C, and finally, 1 h at 130°C. Dissolution of the foam construct occurred within a circulating water bath, leaving the porous SMP foam.

Scaffold Characterization: PVA templates and SMP foams were acquired, featuring three distinct line distances between rectilinear internal scaffolds (2.0, 1.5, 1.0 mm). Utilizing an ultramicroscope (Keyence VHX-7000), images were captured for PVA templates and SMP foams (n=3 for each of the rectilinear internal scaffolds and analyzed via ImageJ software to quantify the pore size/facet diameter and porosity. Further, the SMP scaffold thickness was assessed using scanning electron microscopy (Quattro S ESEM), followed by quantitative analysis in ImageJ.

Porous Media Quantification & Patient-Specific CFD Analysis: CAD models representing the internal scaffolds were crafted using SolidWorks. These scaffolds were subsequently positioned within a hollow cylinder (10 mm in diameter and 40 mm in length). The evaluation process involved subjecting the three experimental samples, alongside a control, to a spectrum of inlet velocities and measuring the respective outlet pressure drop using CFD analysis in ANSYS Fluent. The inertial and viscous resistances were determined by:

$$\Delta p = C_0 v^2 + C_1 v\,, \frac{1}{\alpha} = \frac{C_1}{\mu \Delta n}, C_2 = \frac{2C_0}{\rho \Delta n} \quad (1)$$

where Δp is the pressure drop for the velocity, v, and C_0/C_1 are the coefficients of the 2nd order polynomial trendline, μ is the dynamic viscosity, $1/\alpha$ is the viscous resistance, Δn is the thickness of the scaffold section, C_2 is the inertial resistance, and ρ is the fluid density.

Next, a personalized 3D model was constructed in Amira software and finite element mesh was generated via Meshmixer (Autodesk).

Boundary conditions were prescribed to mimic standard hemodynamics observed in the middle cerebral artery [8], with fluid properties configured to match established specifications for intracranial blood. Specifically, the aneurysm sac was designated as a porous zone, its properties determined via porous media evaluation. Post-processing was performed in ParaView software for comprehensive analysis.

Thermal and Mechanical Characterizations: Differential scanning calorimetry (DSC) was employed to analyze solid and porous SMP specimens (n=3) for quantifying the glass transition temperature (T_g) of the specimens. In addition, uniaxial compression within a controlled heated chamber (T_g + 20°C) was performed on the SMP samples (n=3) along both the *X*- and *Z*-axes, with a compression rate of 5 mm/min.

Shape Recovery Evaluation: The shape recovery (SR) properties of dry and wet samples were assessed as follows. Briefly, the samples (10x10x 10 mm) were subjected to 80% compressive strain at T_g+20°C. Next, the samples were placed in a -20°C freezer to set in this reprogrammed configuration and the samples were heated to restore their to original shape. For the wet samples, following saturation in a water bath, samples underwent a 15-minute air-drying period before radial compression and determination of volumetric compression limit.

RESULTS

Scaffold Characterization: The deliberate removal of surplus SMP during the fabrication process enhanced the precision in replicating the structures from PVA templates to SMP foams (**Fig. 1a-f**). The consistency in facet pore diameter translation from PVA templates to SMP foams was observed, and a marginal improvement in precision was noted in 1.5 and 1.0 mm infill line distances (ILDs), **Fig. 1g**.

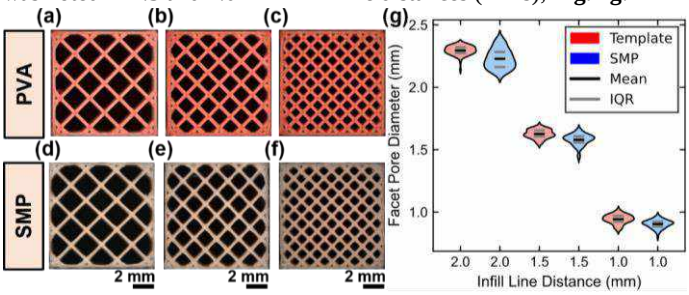

Figure 1: Top view of **(a,b,c)** PVA templates and **(d,e,f)** SMP specimens for 2.0, 1.5, and 1.0 mm infill line distance (ILD), with the corresponding facet pore diameter in **(g)**. Representative scale bars are given at the bottom of each column of images.

Porous Media Quantification & Patient-Specific CFD: Noticeable increases were observed in the porous media as the densities of internal scaffolds increased: 462.8, 724.7, and 1575.0 for the 2.0 mm, 1.5 mm, and 1.0 mm ILDs, respectively. Similarly, the calculated viscous resistances were 9.01×10^6, 1.46×10^7, and 3.22×10^7, respectively. Application of the device yielded noteworthy reductions in both the wall shear stress and the fluid velocities within the aneurysm sac (CFD plots not shown here). These reductions were particularly pronounced in regions distanced farther from the arterial interface (**Fig. 2**), indicating that the impact was more pronounced deeper within the aneurysm sac.

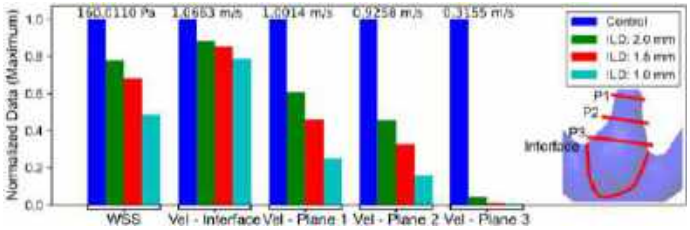

Figure 2: Comparison of the normalized maximum wall shear stress and fluid velocity across surfaces denoted by inscribed image.

Thermal & Mechanical Characterizations: DSC revealed a T_g of 41°C for the porous SMP samples composed of the 1:0.18:0.42 (HDI:HPED:TEA) molar ratio utilized for successively reported tests. In addition, the stress-strain analyses displayed minimal cyclic reduction along the *X*-axis, while the *Z*-axis testing exhibited noticeable effects of cyclic deformation and stress reduction (**Fig. 3a,b**). Uniaxial compression tests unveiled the anisotropic nature of the SMP foams, showcasing up to a 40% increase in maximum stresses for the *Z*-axis compared to the *X*-axis compression evaluations (**Fig. 3c,d**).

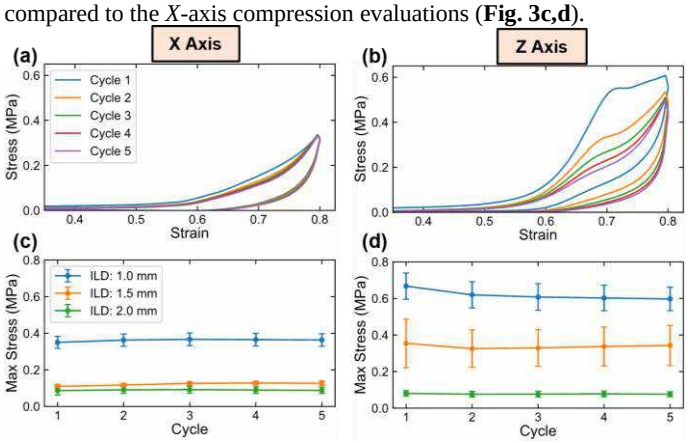

Figure 3: (a,b) Representative stress-strain behaviors of 1.5 mm ILD samples, and **(c,d)** cyclic maximum stress (MPa) for SMP foams under uniaxial compression along the *X*- and *Z*-axes.

Shape Recovery Evaluation: The assessment of shape recovery (SR) under dry conditions demonstrated no substantial variance in SR rate or completeness across the evaluated groups with all groups achieving greater than 95% SR. Under wet conditions, an immediate SR response was observed, accompanied by volumetric compression ratios of 9.61, 7.59, and 5.91 for the three experimental groups, respectively.

DISCUSSION

This study aims to enhance endovascular embolization techniques for ICAs by addressing three key clinical and technological challenges: (i) mitigating compaction tendencies, (ii) improving the occlusion rates, and (iii) optimizing device fitment. Anisotropic mechanical behavior reveals a promising avenue to reduce material displacement within embolized aneurysms, potentially lowering reoccurrence rates. Our CFD findings highlight a localized reduction in blood flow within the aneurysm cavity, suggesting more effective treatment outcomes without impeding essential intracranial/arterial circulation. In addition, the improved precision in replicating patient's 3D geometry is expected to minimize procedural complications. Yet, limitations include porosity constraints for larger aneurysms and a time-intensive fabrication process. Future studies involve refining our 3D printing for larger ICAs, exploring alternative scaffolding patterns, and incorporating carbon nanotubes to enhance conductivity and structural integrity. Collectively, these efforts render a transformative shift in ICA therapeutic paradigms.

ACKNOWLEDGEMENTS

This study is supported by the National Heart, Lung, and Blood Institute of the National Institute of Health (NIH R01 HL159475).

REFERENCES

[1] Keedy, A. *et al., Mcgill J Med*, 9:141-146, 2006. [2] van der Kamp, L. T. *et al., JAMA Neurol*, 78:1-8, 2021. [3] Al-Khindi, T. *et al., Stroke*, 41:519-536, 2010. [4] Gonzalez, N. *et al., Am J Neuroradiol* 25:577-583, 2004. [5] Vanninen, R. *et al., Am J Neuroradiol* 24:263-266, 2003. [6] Goertz, L. *et al., Sci Rep* 12:11467, 2022. [7] Wang, J. *et al., Polymers*, 11:631, 2019. [8] Kofke, A. *et al., Stroke*, 26:1603-1606, 1995.

MORPHOLOGICAL ANALYSIS OF HINDFOOT OSTEOARTHRITIS VIA STATISTICAL SHAPE MODELING OF THE FOOT AND ANKLE

Elana R. Lapins (1,2), Shireen Y. Elhabian (3,4), Charles L. Saltzman (1), Amy L. Lenz (1,2)

(1) Department of Orthopaedics, University of Utah, Salt Lake City, UT, United States
(2) Department of Biomedical Engineering, University of Utah, Salt Lake City, UT, United States
(3) School of Computing, University of Utah, Salt Lake City, UT, United States
(4) Scientific Computing and Imaging Institute, University of Utah, Salt Lake City, UT, United States

INTRODUCTION

Patients with advanced foot and ankle osteoarthritis (OA) experience limited function, severe pain, and reduced quality of life [1,2]. There is no direct cause of foot and ankle OA, however, 75-80% of cases arise secondary to a traumatic event, such as an ankle bone fracture [3]. Isolated subtalar OA (STOA) and isolated tibiotalar OA (TTOA) affect the talocalcaneal and tibiotalar joints, respectively. These joints in the ankle play crucial roles in the movement and biomechanics of the human foot and affect younger populations [1,3,4]. The connection between foot deformities and these two types of OA has not been thoroughly investigated, and a comprehensive understanding could potentially lead to more targeted interventions, enhanced patient care, and informed preventative measures. This gap in knowledge is because foot and ankle OA diagnoses have historically only been used with 2D radiographs. However, with the introduction of three-dimensional weightbearing computed tomography (WBCT), we are now able to capture a complete anatomical view of the foot from a single scan. Morphological analysis can be performed on weightbearing computed tomography (WBCT) data via statistical shape modeling (SSM) to quantify and compare foot shape models between different patient groups [5]. The objective of this study was to create a 19-bone SSM project to investigate the morphology of patients experiencing STOA and TTOA and compare them with healthy control models. We hypothesized that multi-bone SSM would indicate significant and unique morphological differences between the two OA groups and the healthy controls – encompassing significant variation not only within the subtalar and tibiotalar joints, but also in other bones.

METHODS

In this study, WBCT (0.37x0.37x0.37 mm voxel) data from 45 total participants (15 healthy, 15 STOA, 15 TTOA) was acquired with IRB approval. Patients were grouped as STOA or TTOA based on evaluations from a musculoskeletal radiologist and an orthopaedic surgeon. Semi-automatic segmentation software (DISIOR v2, *Bonelogic*) was used to generate preliminary bone segmentations for 19 bones in the ankle: tibia, fibula, talus, calcaneus, navicular, cuboid, cuneiforms (medial, intermediate, lateral), metatarsals, and proximal phalanges. These initial segmentations were verified and revised, if necessary, using Mimics 24.0 (*Materilise*). 3-Matic (*Materialise*) was used to smooth and decimate all segmented bones, then a global plane cut was performed across all patient models based on the shortest tibia and fibula. All 19 bones from each patient were used to create a multidomain SSM project in ShapeWorks 6.4.2 (*SCI Institute*) to determine the mean shape and quantify morphological differences between STOA, TTOA, and healthy patients [5]. Principal Component Analysis (PCA) was utilized to assess the modes of variation from the SSM model, and MATLAB R2023a (*MathWorks Inc.*) parallel analysis determined significant PCA modes. To identify localized regions with notable disparities in both overall morphology and alignment, a Hotelling's T^2 test was employed with a false discovery rate p-value correction. Additionally, PCA scores from each mode were exported from ShapeWorks and compared to another using a t-test or Wilcoxon rank sum test with a Holm-Sidak correction (α=0.05). ShapeWorks 6.4.2 built-in Linear Discriminant Analysis (LDA) was also applied to investigate shape variation between the healthy and OA groups [5].

RESULTS

Figure 1 illustrates the results from Hotelling's T^2 test comparing the healthy, STOA, and TTOA groups. Blue indicates areas that have significantly different morphology and alignment (α=0.05). The two types of OA compared to the healthy controls (top and middle rows) show expected results, where the subtalar or tibiotalar joints are visually different from the healthy group, as areas around those affected joints are blue. Additionally, the p-values suggest that bones distal from the cuneiforms experience less deformity than more proximal bones. The bottom row shows several blue areas in the tibia, fibula, and talus that

indicate variation in morphology and alignment between the two OA groups. Parallel analysis of the PCA scores indicated 7 significant modes of variation among the 3 groups, where 26 total modes accounted for 95% of the overall variation. An ANOVA test of the 3 groups determined two modes that were significantly different (α=0.05) from another: mode 1 of STOA vs. Healthy and mode 1 of TTOA vs. Healthy. PCA mode results are shown in Figure 2 for the first three significant modes comparing all three groups. Mode 1 distributions indicate that STOA appears to align more closely with minus two standard deviation results, and TTOA similarly with plus two standard deviations. Mode 1 contains 30.8% variation and presents cuneiform movement in the radial direction, tibia/fibula movement from posterior to anterior, and subtalar joint movement in the anterior direction. Additionally, this mode appears to represent variants in the specific foot type, ranging from planus to cavus (while standing). Mode 2 accounts for 17.8% of the cumulative variance and demonstrates apparent twisting of the lamina pedis in the direction opposite of the subtalar joint rotation. Lastly, the third mode (10.6% explained variance) represents midfoot bending in the sagittal plane, which alters the subtalar, calcaneal, and talonavicular orientations.

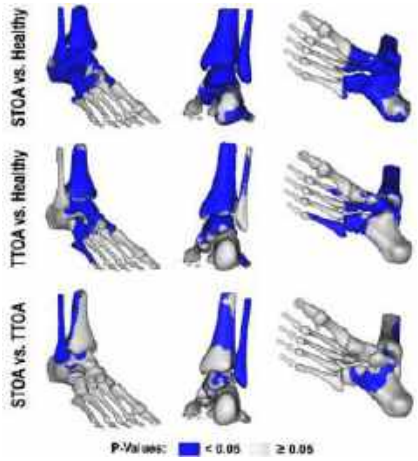

Figure 1: Dorsolateral, posterior, and ventrolateral views of the mean foot shape obtained from SSM. The data illustrates Hotelling's T^2 test with false discovery rate correction that compares the STOA group with the healthy group (Row 1), the TTOA group with the healthy group (Row 2), and the STOA group with the TTOA group (Row 3). Blue indicates significantly different areas with p-values less than α=0.05. Grey areas show non-significant differences in morphology and alignment.

DISCUSSION

The 19-bone SSM model indicated significant differences between the morphology and alignment of patients with STOA, TTOA, and the healthy control group. This type of model is the first three-dimensional 19-bone model that investigates different presentations of hindfoot OA based on patient WBCT data. Information from this type of modeling will have a great impact on clinical diagnoses and treatment planning for patients experiencing hindfoot OA. As mentioned, the SSM model identified 7 significant PCA modes of variation out of the 26. These modes, capturing substantial variability, provide valuable insights into the distinct patterns and trends of joint deformity and structural changes associated with STOA and TTOA. Specifically, information in Figure 2 may be useful for physicians to identify associated deformities such as planus/cavus in Mode 1 (30.7% variance) or anticipate potential restoration of the lamina pedis in cases of midfoot twisting opposing the direction of the subtalar joint rotation seen in Mode 2 (17.8% variance). The persistence of specific foot types (planus/cavus) in patients over time raises questions about the attainability of a neutral position through surgical intervention in affected joints. Addressing solely the affected joint may limit the overall improvement of the foot, as the entire foot structure is not being considered. An isolated focus on realigning a single joint disregards the potential impact of its prolonged diseased state of

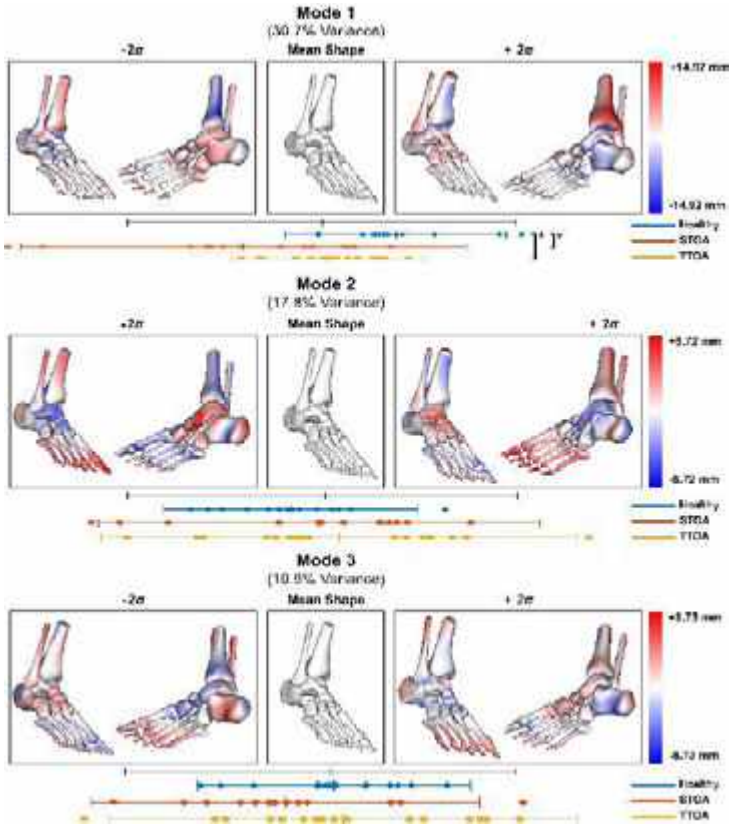

Figure 2: PCA mode analysis across all three subgroups: Healthy, STOA, and TTOA. The top row indicates changes through mode 1 and includes two statistically significant differences in morphology and alignment between the healthy group and both types of OA. The middle and bottom rows show modes 2 and 3, respectively. The left and right columns represent two different views of two standard deviations below and above the mean shape. Blue regions are smaller than the mean, and red regions are larger.

the surrounding structures, potentially triggering further changes in the foot. Understanding these adaptations through three-dimensional modeling highlights the importance of holistic foot joint treatments to attain the most favorable clinical results for patients with hindfoot OA. This work serves as a valuable guide for identifying necessary foot adjustments that are essential for the restoration of normal foot alignment and treatment of pain associated with OA.

Ultimately, the comprehensive understanding gained from SSM and WBCT enables surgeons to make well-informed decisions about full-foot treatment options. The potential impact of this work is vast, offering orthopaedic physicians and surgeons advanced knowledge about different presentations of OA in the foot and ankle. Armed with this depth of understanding, clinicians can formulate patient-specific treatment plans and treat OA in the foot and ankle before the deformities become too severe for intervention.

ACKNOWLEDGEMENTS

National Institutes of Health (1K01AR080221) and the University of Utah BME Department. *ShapeWorks* Funding: NIBIB-U24EB029011, NIAMS-R01AR076120, NIBIB-R01EB016701.

REFERENCES

[1] Glazebrook, M et al., *J Bone Joint Surg Am*, 90(3):499-505, 2008. [2] Hintermann, B et al., *J Am Acad Ortho Surg*, 24(7):424-432, 2016. [3] Herrera-Perez, M et al., *J Clin Med*, 10(19), 2021. [4] Krahenbuhl, N et al., *Foot Ankle Int*, 38(2):124-132, 2017. [5] Cates, J et al., *Statistical Shape and Deformation Analysis*, p.257-298, 2017.

SURFACTANT DEPLETED RAT LUNGS: A GLOBAL TO LOCAL STUDY OF THE IMPACT OF POSITIVE VERSUS NEGATIVE PRESSURE VENTILATION

M. Shankel (1), M. Eskandari (1,2,3)

(1) Department of Mechanical Engineering, University of California, Riverside CA, USA
(2) BREATHE Center, School of Medicine University of California, Riverside CA, USA
(3) Department of Bioengineering, University of California, Riverside CA, USA

INTRODUCTION

Lung diseases can necessitate mechanical ventilation and are often linked to insufficient surfactant levels, resulting in greater surface tension and therefore, increased work of breathing [1]. Ultimately, surfactant loss can lead to atelectasis (partial lung collapse), which increases the risk and severity of ventilator induced lung injury (VILI) due to excessive distension of the remaining aerated lung regions [2]. Prior work utilizing magnetic resonance imaging (MRI) confirms surfactant depletion results in increasing lung distension and finds that improved alveolar recruitment reduces this local overdistension [3]. Furthermore, recent work reports mechanical differences between lungs subjected to negative pressure ventilation (NPV) and positive pressure ventilation (PPV), where NPV results in decreased hysteresis (work of breathing), suggesting that NPV may provide more homogeneous alveolar recruitment [4]. However, past surfactant studies have been limited by the extended imaging acquisition times, where the highly viscoelastic nature of the lung is greatly affected by such time lapses; and the overinflation and heterogeneity due to surfactant depletion has yet to be characterized over the continuous breathing cycle to understand the role of PPV and NPV in surfactant depleted lungs.

To address these knowledge gaps, this current study analyzes the mechanics of surfactant-depleted lungs under both NPV and PPV using a custom-designed apparatus in conjunction with high spatiotemporal digital image correlation (DIC) techniques to facilitate simultaneously linked global inflation behavior and local surface strain patterns characterization [4,5]. We hypothesize NPV results in decreased hysteresis, strains, and heterogeneity compared to PPV in surfactant depleted lungs, indicative of more homogenously recruited alveoli.

METHODS

Eight male Sprague-Dawley rats, weighing 250-320g, were anesthetized and sacrificed, where the lungs were excised and cannulated according to approved IACUC protocol (KUALI #132). Four lungs were established as the control group, while the remaining four underwent a warm internal saline wash via the trachea (37°C, 30mL/kg) three times to remove the native surfactant according to prior methods [2,3]. Subsequently, lungs were prepared for DIC measurements and speckled, as established previously [5]. The lungs were placed in an airtight chamber and attached to our previously validated custom-designed dual piston electro-mechanical ventilation system adapted for rat lungs to acquire the global pressure and volume measurements [4].

To establish a common volume history before the test inflation cycle, lungs were subjected to a driving pressure of 20 cmH_2O with stepwise increments of 3 cmH_2O positive-end expiratory pressure for 30 s each up to 15 cmH_2O, performed at 60 BPM, as used in similar rat studies [3]. Tests applied 6mL of air either by direct inflation via the trachea (PPV) or by removing air from the tank (NPV), where the resulting change in lung volume was matched within 10%. Sequential PPV/NPV tests were applied at 10BPM, enabling quasi-static tissue assessments and DIC measurements, and where the sequence has been demonstrated to not impact the lung response [6,7].

Pressure-volume curves and DIC major strain contour maps were generated (Figure 1-i and 1-ii), where the reduced Jacobian confirmed similar DIC surface areas analyzed across all specimens [4]. Hysteresis was measured as the area between the loading and unloading curve of the pressure-volume cycle (Figure 2-i) [6]. Distributions of the major strain across each lung specimen were analyzed as an average kernel density plot with standard deviation, where the strain distribution peaks represent an increase in the surface fraction exhibiting the measured tissue strains. (Figure 2-ii) [8]. The average major strain and 75th percentile major strain values were calculated (Figure 2-iii and iv).

Statistical analysis between groups was compared using a paired and unpaired t-test, for PPV versus NPV and control versus surfactant

depleted groups respectively, with normality verified via the Shapiro-Wilk test and a significance threshold of $p<0.05$ [9].

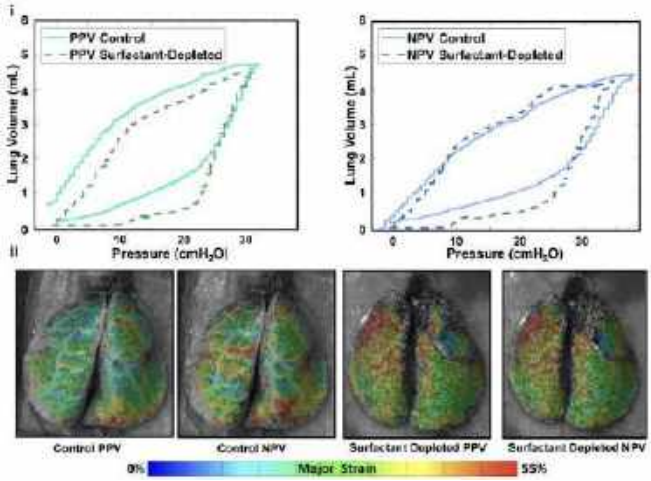

Figure 1: Representative (i) pressure-volume hysteresis curves, and (ii) DIC contour maps of major strain over the pleural surface for contrasted PPV/NPV control/surfactant groups.

RESULTS

Pressure-volume curves exhibited varying hysteresis between groups (Figure 1-i). DIC qualitatively saw an increase in control NPV strains compared to PPV, and similar strain contours for PPV and NPV surfactant depleted groups, where blue indicates 0% strain and red as high as 55% strain (Figure 1-ii). Surfactant depleted groups tended to result in increased hysteresis compared to control PPV and NPV (significant for NPV, Figure 2-i), where NPV trended lower than PPV group counterparts. The relative local strain behavior of PPV to NPV appears to alternate depending on control or surfactant depleted groups: for the control groups, NPV tended to show an increase in strain distribution peak compared to PPV (Figure 2-ii). Contrarily, for the surfactant depleted groups, NPV shifted towards decreased strains compared to the PPV counterpart (Figure 2-ii). The average strain and 75th percentile strain trended higher for the surfactant depleted group compared to the control group, (significant for PPV, Figures 2-iii, 2-iv).

DISCUSSION

In this study, we observe that surfactant depletion leads to increased hysteresis and increased lung surface strains, indicating greater work of breathing and localized overdistension, respectively, confirming prior studies [3-5,10]. Hysteresis is associated with the collapse/re-opening of alveolar groups and with surfactant molecules, where surfactant depletion increases surface tension, thus explaining our findings of greater hysteresis with surfactant depletion; further, the reduced hysteresis in NPV suggests NPV recruitment of alveolar groups may occur more homogeneously than PPV; however, exact mechanisms are unknown currently and warrant further study [4,10].

Although prior work with MRI utilizes longer image acquisition times, and thus cannot capture the mechanics before viscoelastic effects set in, they find increasing distension from surfactant loss [3]. Our study, conducted with high-speed and high-resolution imaging, allows us to substantiate these claims of surfactant loss resulting in increased distension, indicated here by increased regional strains [5]. In the surfactant depletion group, NPV results in notably (albeit insignificantly) lower surface strains compared to PPV, these lower strains may indicate NPV to be a useful method for decreasing overdistension to improve aeration and recruitment in surfactant depleted lungs [3]. Further, we find NPV strains to vary insignificantly

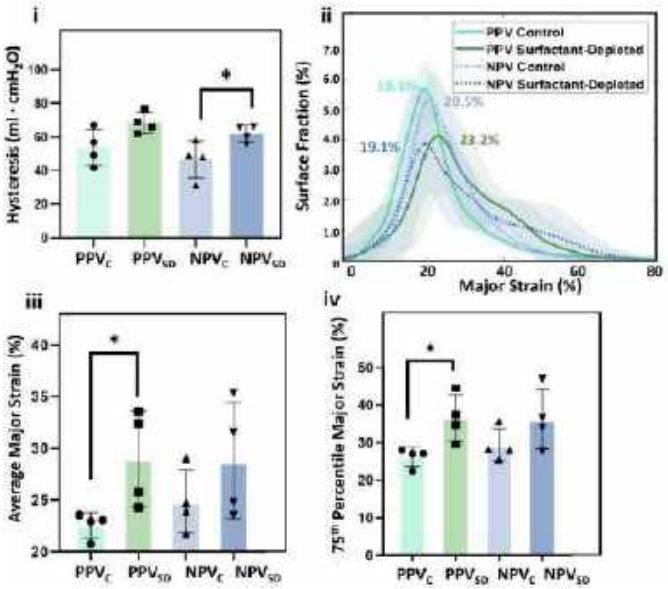

Figure 2: (i) Reported values and significance for hysteresis, (C, control; SD, surfactant depletion). (ii) Kernel density plot demonstrated major strain distribution over the pleural surface. (iii, iv) Reported values and significance for the average and 75th percentile major strain values.

between its surfactant depletion and control groups, in contrast to significant differences in PPV; this is an intriguing implication given ventilators utilize PPV and the compromised surfactant may cause greater overdistension in comparison to NPV. Notably, the non-significant average strain increase between the control NPV compared to PPV contradicts previous findings for pig lungs [4]; this may be attributable to differences in species (e.g., collateral ventilation effects observed in mice rodents but not pigs [11]).

While this study provides evidence of the local effect of surfactant depletion and the impact of NPV, quantified analysis throughout the inflation and deflation cycle will enable improved insights regarding the differences between PPV and NPV. Furthermore, this study was performed ex-vivo, and therefore without the presence of the chest cavity; however, recent studies have suggested surface strains to represent internal strains [12]. Despite these limitations, this study is the first of its kind to evaluate the adverse effect of severe lung disease and injury in the form of surfactant depletion on localized PPV/NPV tissue strains in order to help better probe the mechanics in recruiting damaged lungs and understanding VILI.

ACKNOWLEDGEMENTS

Supported in part by the Opportunity to Advance Sustainability Innovation and Social Inclusion (OASIS) UCR and State of California Climate Action Through Resilience Program Grant.

REFERENCES

[1] Calkovska, A et al., *Physiol Res*, 2021. [2] Tsuchida, S et al., *AJRCCM* 174 (3): 279–89.. 2006. [3] Cereda, M et al., *Crit Care Med* 41 (2): 527–35. 2013. [4] Sattari, S et al., *AJRCCM*. 2023. [5] Nelson, T.M et al., *Sci Rep* 13 (1): 4564. 2023. [6] Quiros, KAM et al., *Ann Biomed Eng.*, 2023. [7] Dong, S et al., *Am J Physiol Lung Cell Mol Physiol* 322 (5): L673–82. 2022. [8] Rodriguez, A et al *Med. Phys.* 44 (6): 2267–80. 2017. [9] Korstanje, J. *Medium*, 2020. [10] Yoshida, S. *Am. J. Physiol.* 203 (October): 725–30. 1962. [11] Eskandari, M et al., *ATS*. A5776. 2023. [12] Arora, H et al., *Materials* 14 (2). 2021.

ELASTIN ALTERS FATIGUE MECHANICS OF FUNCTIONALLY DISTINCT TENDON FASCICLES IN MURINE MODEL OF ELASTIN KNOCKDOWN

Shawn N. Pavey (1), Nathan L. Xu (2), Spencer P. Lake (1,3,4)

(1) Department of Mechanical Engineering and Materials Science, Washington University in St. Louis, St. Louis, MO, United States
(2) Department of Biology, Washington University in St. Louis, St. Louis, MO, United States
(3) Department of Biomedical Engineering and Materials Science, Washington University in St. Louis, St. Louis, MO, United States
(4) Department of Orthopaedic Surgery, Washington University in St. Louis School of Medicine, St. Louis, MO, United States

INTRODUCTION

Elastin-based elastic fibers are the second most abundant fibrous structural material in tendons after collagen fibrils [1], yet their role in dynamic tendon mechanics is poorly understood [1]. Elastin is known to provide fatigue resistance and recoil properties in soft tissues [1], such as seen in the aorta, and may also reduce strains during tendon repair [2]. We hypothesize that elastin may limit damage accumulation and rupture in tendons, especially in the energy-storing Achilles tendon (AT). Studies have shown significant contributions of the dense mesh-like interfascicular elastin matrix to tendon mechanics, as elastase treatment of the interfascicular matrix drastically reduces fatigue life [3]. The mechanical contribution of axially-aligned elastin within fascicles is less understood; however, uni-fascicular mouse tendons are well suited to addressing their role.

Ramp-to-failure testing of functionally distinct tendons from elastin knockdown (*Prx1Cre*$^{+}$*/Eln*$^{fl/fl}$) mice revealed a trending increase in linear modulus in ATs with elastin knockdown, but a decrease in positional tibialis anterior tendon (TBAT) linear modulus values [4]. Tendon-specific mechanical results agreed with dynamic structural changes measured with quantitative polarized light imaging (QPLI). Thus, elastin's role may change with tendon function, perhaps providing a gradual fiber-recruitment function in wild type (WT) ATs which have a lower linear modulus, and a more direct structural function in TBATs where elastin increases the linear modulus instead.

Building upon previous results, the present study sought to determine the role of fascicular elastic fibers in fatigue mechanics of tendon. We hypothesized that elastin knockdown would reduce the fatigue life of tendons, especially in ATs compared to TBATs. We further expected to observe altered peak strain through the three phases of fatigue: (1) initial steep phase, (2) linear region with constant rate of peak strain increase, and (3) exponential strain increase before rupture. Finally, elastin deficient tendons were expected to show more damage accumulation (collagen denaturation and fiber kinking) during testing.

METHODS

Mechanical Testing: ATs and TBATs (n=55/tendon type; WT and *Prx1Cre*$^{+}$*/Eln*$^{fl/fl}$; ~split male/female) were harvested at 20 weeks and stored in PBS-soaked gauze at -20° C until ready for testing. Thawed samples were clamped and stretched until just taut, at which point gauge length and cross-sectional area were measured. Samples were preloaded to 0.1 N then cyclically loaded at 1 Hz to a percentage of previously determined average ultimate stress for each tendon type. ATs were tested between 0.68 and 34 MPa (1-50%), while TBATs were tested between 2.4 and 81 MPa (1-35%). Stress levels were selected to avoid slippage and optimize test duration. While testing, QPLI videos were acquired to determine ROI average degree of linear polarization (i.e., strength of collagen alignment) and standard deviation of the angle of polarization (i.e., spread of collagen distribution).

Data Analysis: Custom MATLAB code was used to analyze and synchronize mechanical and QPLI data. Six points of interest were determined from the three-phase strain-time plot (Fig. 1): (1) first cycle, (2) beginning of linear region (second phase), (3) middle of linear region, (4) end of linear region, (5) transition point in third phase (based on global optimized fitting of peak strains throughout test), and (6) last cycle before failure. QPLI data was analyzed at twelve frames: one for each peak and trough of the six points of interest.

Multiphoton Imaging: Tendons were flash frozen after mechanical testing failure and stored at -20° C. Samples were stained with Alexa Fluor 633 hydrazide and blocked with bovine serum

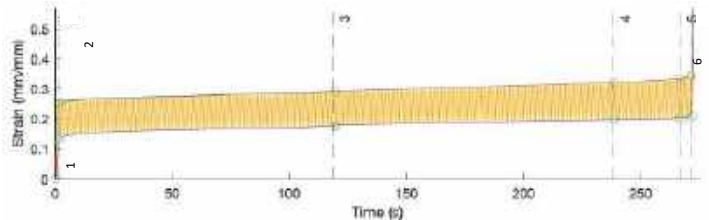

Figure 1: Fatigue curve and calculated points of interest.

albumin and 0.05% Triton-X in 0.1X PBS for two hours, then optically cleared using the SeeDB protocol [5]. Longitudinal image stacks ~150-µm-deep were acquired on an inverted multiphoton microscope with acquisition of SHG/fluorescence for collagen/elastin, respectively. Images were acquired near the break site and mid-substance of the larger fragments post-rupture. Collagen fiber kinking was visualized with a 10x1-µm-deep median Z-projection. Elastic fiber integrity was qualitatively evaluated near break sites and tendon midsubstance.

Statistical Analysis: All statistical outcomes were determined with linear mixed models (JMP, SAS Institute), where genotype, sex, genotype*sex, and a random variable based on mouse of origin were used as model inputs. A standardized effect size parameter, Cohen's *d* [6], was calculated for each parameter, where values of 0.2, 0.5, and 0.8 indicate mild, moderate, and strong effects, respectively. For mechanical testing, exclusion criteria were determined before analysis: any test lasting less than 10 cycles or more than 8000 was excluded. Remaining samples were analyzed in Prism using a ROUT outlier test with Q = 1%. After exclusion, 21 ATs per genotype, 12 *Prx1Cre*$^{+}$*/Eln*$^{fl/fl}$ TBATs and 20 WT TBATs were included (evenly-pooled sex).

RESULTS

Mechanical testing results (Fig.2) show that hysteresis (green) is increased in both *Prx1Cre*$^{+}$*/Eln*$^{fl/fl}$ tendon types early in the fatigue test (roughly time points 1-3), though this difference disappeared by the end of the test. Also, though not significant, the effect sizes for various time points in the test including cycles to failure were substantial (gray), and effect sizes show the range of possibility for the true mean of these effects being mostly negative. The main genotype-specific difference between ATs and TBATs was that only ATs had increased peak and trough strain accumulation (blue) and a decreased dynamic modulus

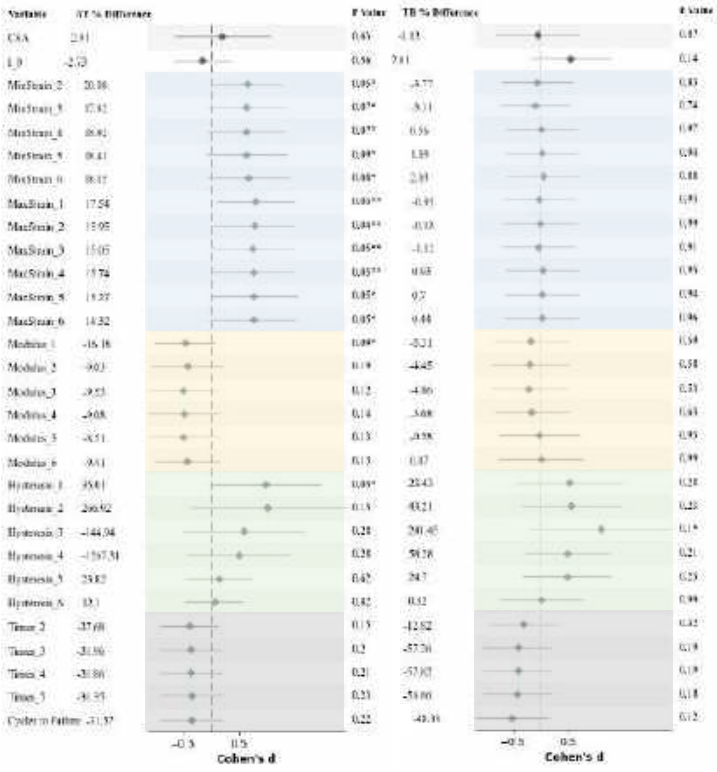

Figure 2: Fatigue mechanical data for ATs (left) and TBATs (right) including percent differences of *Prx1Cre*$^{+}$*/Eln*$^{fl/fl}$ from WT values, *p* values, and Cohen's *d* standardized effect size with 95% CI. Numbers indicate interest points on the fatigue curve.

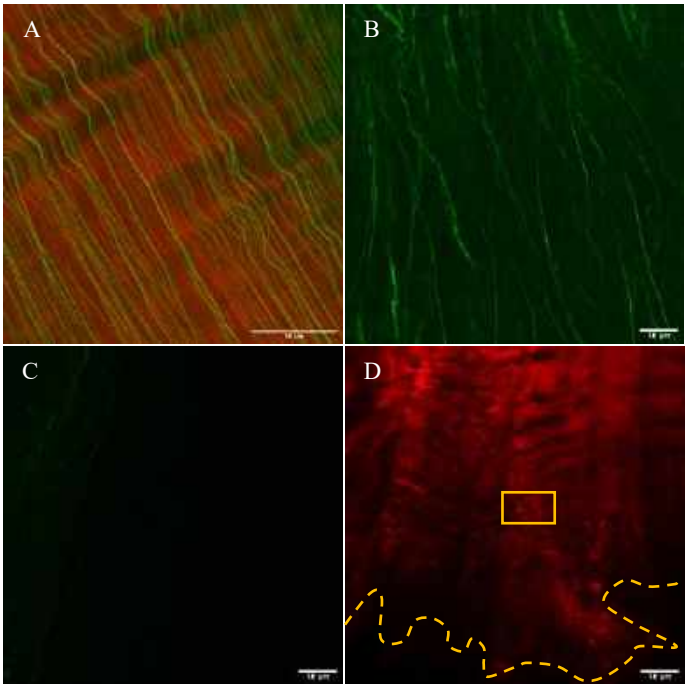

Figure 3: Two photon images of ATs. A: Composite (collagen in red and elastin in green) image of undamaged sample. B: Elastic fibers in damaged WT sample. C: Lack of elastic fibers in damaged Prx1Cre^{+}/Eln$^{fl/fl}$ sample. D: Collagen kinking (rectangle) in WT near fatigue rupture site (dotted line).

(yellow) with elastin knockdown (note this dynamic modulus is different from the linear modulus, it conventionally assumes linearity).

Multiphoton images show uniformly aligned elastic fibers in undamaged WT ATs (Fig.3A) versus frayed, mildly kinked, and less organized fibers after tendon rupture (Fig.3B). There were no visible fibers in *Prx1Cre*$^{+}$*/Eln*$^{fl/fl}$ tendons (Fig.3C). The collagen matrix near the break site was markedly crimped, which seemed to increase in frequency nearer the break site (Fig.3D).

DISCUSSION

Elastic fiber knockdown has significant effects on tendon fatigue dynamics, especially in ATs where increased peak and trough strain values were measured at all time points, potentially pointing to elastin sustained elastic recoil in healthy tendon loading. Though our hypothesis that elastin increases fatigue life was not confirmed by reported p values, Cohen's *d* and confidence intervals for the timing of all points of interest (including cycles to failure) show a possible mild effect of elastin on the timing of the fatigue curve in both tendon types. Multiphoton images unveiled, perhaps for the first time, the morphology of a fascicular elastic fiber networks near a fatigue-induced break site. These fibers are less organized, show mild kinking behavior, and expose branching sites not previously observed. Further quantitative analysis will evaluate elastin and collagen fiber networks farther away from the break site, CHP-based damage assays of collagen denaturation, and analysis of sex dependent. Future work will evaluate pre-failure to determine whether elastin alters damage accumulation kinetics.

ACKNOWLEDGEMENTS

We thank the NSF for supporting this work (BMMB 1562107).

REFERENCES

[1] Thorpe, CT+ *I J Exp Path*, 94:248-259, 2013; [2] Svärd, A+ *FASEB*, 34:13409-13418, 2020; [3] Godinho, MS, Acta Biomat, 123, 187-196, 2021; [4] Pavey, S+, ORS, 2271, 2023; [5] Ke, MT+, Nat Neurosci, 16, 1154-1161, 2013; [6] Lee, DK, Kor J Anesth, 69, 555-562, 2016.

ADVANCING 3D ORGAN GEOMETRIC RECONSTRUCTION FROM MRI: A HYBIRD FRAMEWORK WITH DEEP LEARNING AND ITERATIVE OPTIMIZATION

Hui Wang (1)(2), Xiaowei Li (3), Chenxin Zhang (1)(2), Jianwei Zuo (1)(2), Xiuli Sun (3), Jianliu Wang (3), Jiajia Luo (1)(2)

(1) Institute of Medical Technology, Peking University Health Science Center, Beijing, China
(2) Biomedical Engineering Department, Peking University, Beijing, China
(3) Department of Obstetrics and Gynecology, Peking University People's Hospital, Beijing, China

INTRODUCTION

Reconstructing 3D organ geometric models from magnetic resonance imaging (MRI) is essential in numerous fields, such as patient-specific solid biomechanical numerical simulations [1], computer-aided diagnosis, treatment and prognosis, and virtual surgical planning. Using high-quality 3D geometric models precisely depicts organ spatial architecture, crucial for finite element analysis. Typically, conventional methods involve either manual or automatic segmentation of 2D MRI slices, followed by several post-processing steps such as reconstructing 3D geometric models, repairing complex geometries, and manually partitioning meshes [2]. The shapes of many organs are complex and diverse, often requiring a significant amount of effort to create high-quality 3D geometric models. The reconstruction process is complicated, tedious, and time-consuming, taking several hours or even days. Furthermore, the consistency of reconstruction results varies with different technicians, limiting its practicality for large-scale analysis.

As an alternative to traditional reconstruction methods, deep learning approaches exhibit great potential in reconstructing 3D geometric models, demonstrating fast execution time and desirable geometric quality. These techniques are categorized into implicit and explicit methods. Implicit methods achieve indirect reconstruction of 3D models by predicting the implicit surface using the signed distance function (SDF) [3], but still necessitate laborious post-processing steps like iso-surface extraction and mesh correction. Explicit methods, which include direct shape prediction and deformable shape modeling, tackle various challenges. The first approach, dependent on loss functions for quality control [4], struggles with training and is limited to simpler geometries. The second, focusing on template geometry deformation to fit the target [5], solves some of these difficulties. However, it presents challenges in designing adaptable templates for different organs and ensuring uniform application across diverse organ reconstructions.

In this work, our aim was to develop a unique hybrid framework for deformable shape modeling. This framework integrates deep learning with iterative optimization to streamline the reconstruction of high-quality 3D organ models from 3D MRI, enabling a flexible tradeoff between reconstruction time and model quality.

METHODS

Figure 1 illustrates our framework's architecture, showcasing inputs and outputs. For instance, 3D MRIs are processed to predict the organ model. Initially, the MRIs undergo segmentation, either manually or automatically. The resulting segmentations are converted into point clouds, which represent the organ boundaries. These points are then normalized within a -1 to 1 range. The deep learning module then processes these point clouds, predicting displacements for spherical template deformation. These displacements serve as initial inputs for the

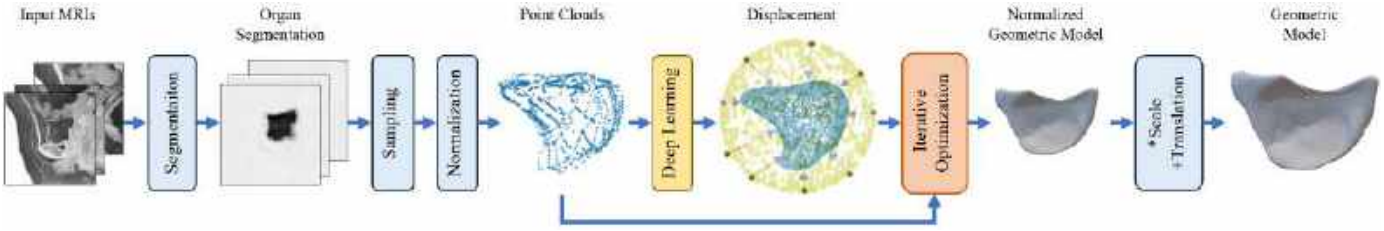

Figure 1: Our framework's architecture

iterative optimization module, refining the organ models. Finally, the resulting model is scaled and positioned by reversing normalization process to form the final 3D organ geometric model.

Algorithm 1: Training

Input: $Pointcloud_{train}, Mesh_{sphere}$
$Displacement_{train} = 0\ (Zero\ Matrix)$
for $iter = 1 \rightarrow T$ **do**
  $Mesh_{train} = Mesh_{sphere} + Displacement_{train}$
  $Displacement'_{train} = \underset{Displacement_{train}}{\operatorname{argmin}} [Loss_{CD}(Pointcloud_{train}, Mesh_{train}) + Loss_{ENL}(Mesh_{train})]$
end for
$\theta_{train} = \theta_0$
repeat
  $Displacement_{train} = NN_{\theta_{train}}(Pointcloud_{train}, Mesh_{sphere})$
  $\theta'_{train} = \underset{\theta_{train}}{\operatorname{argmin}} [\mathbb{E}_{training\_set}[Loss_{MSE}(Displacement'_{train}, Displacement_{train})]]$
until converged
Output: θ'_{train}

Algorithm 2: Inference

Input: $Pointcloud_{infer}, Mesh_{sphere}, \theta'_{train}$
$\theta_{infer} = \theta'_{train}$
$Displacement_{infer} = NN_{\theta_{infer}}(Pointcloud_{infer}, Mesh_{sphere})$
for $iter = 1 \rightarrow T$ **do**
  $Mesh_{infer} = Mesh_{sphere} + Displacement_{infer}$
  $Displacement'_{infer} = \underset{Displacement_{infer}}{\operatorname{argmin}} [Loss_{CD}(Pointcloud_{infer}, Mesh_{infer}) + Loss_{ENL}(Mesh_{infer})]$
end for
$Mesh_{infer} = Mesh_{sphere} + Displacement'_{infer}$
Output: $Mesh_{infer}$

NN represents the deep learning network. The symbol θ denotes the network's parameters. The minimum value of the variable post-iteration is identified with an asterisk (*). $\mathbb{E}_{training\_set}[]$ signifies the expected outcome of the enclosed expression within the training set.

Figure 2: The algorithm of the training and inference pipeline.

Figure 2 depicts the algorithm of the deep learning and the iterative optimization modules for both training and inference. In training, the iterative optimization module searches for optimal displacement, aiming to minimize the Chamfer Distance (CD) between deformed geometry and input point clouds, augmented with loss function ENL (Edge Loss, Normal Loss, and Laplacian Loss [1]) for geometric model quality. These optimal values are the ground-truth for deep learning training. During inference, the trained deep learning model predicts displacement, initializing the optimization module's further refinement, resulting in the final organ geometric model.

Figure 3 shows the deep learning module's structure. Initially, EdgeConv [6] extracts features from the input point clouds and spherical template individually. These features are combined using a multi-head cross-attention module, followed by spatial feature transformation through EdgeConv. An alternating structure of convolutional neural network (CNN) and self-attention modules is then used for encoding and decoding. Ultimately, EdgeConv is used to perform spatial transformation on the output features, yielding the final displacement values.

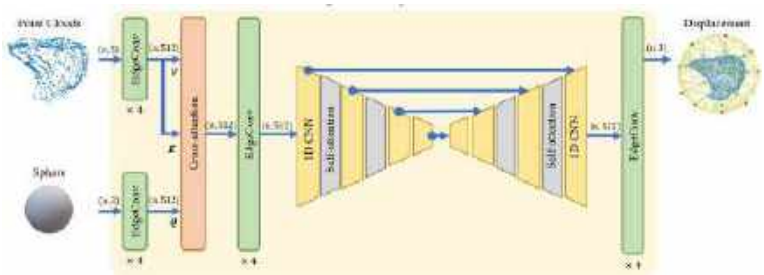

Figure 3: The structure of the deep learning module.

We utilized the Mean Squared Error (MSE) loss function for predicting deep learning displacement. Both CD and Hausdorff Distance (HD) are used as the evaluation metrics.

For training, we adopted the Adam optimizer with a learning rate $1e^{-4}$ and a batch size of 1 across all experiments. The network was implemented using Python 3.8.8, and Pytorch 1.12.0, and executed on an Nvidia Titan RTX graphic card with 24GB of computational memory.

We constructed a 3D MRI dataset of 100 subjects from Peking University People's Hospital. Specifically, the T2 3D sagittal MR data of each subject at rest were used. The MR images had a 2 mm spacing and slice thickness. The dataset was randomly divided into training, validation, and testing sets at a 6:2:2 ratio by subject. During training, we ran 10,000 iterations to ensure optimal reconstruction for each organ. To prove the effectiveness of our approach, we compared it with three other advanced 3D organ reconstruction deep learning methods, including Voxel2mesh [5], MR-net [1], and MeshDeform-Net [7]. To address the significant size discrepancies among individuals and their organs, we adopted a normalized geometric model for quantitative assessments.

RESULTS

Table 1: 3D reconstruction performance on the testing set.

Methods	Bladder		Uterus		Rectum		Levator	
	CD(mm)	HD(mm)	CD(mm)	HD(mm)	CD(mm)	HD(mm)	CD(mm)	HD(mm)
Voxel2mesh	0.0574	0.7469	0.0887	0.8462	0.0356	0.6227	0.0281	0.5936
MR-net	0.0535	0.7609	0.0875	0.8580	0.0383	0.6052	0.0226	0.5869
MeshDeformNet	0.0467	**0.6647**	0.0732	0.8949	0.0348	0.7189	0.0235	0.5364
Ours	**0.0399**	0.7005	**0.0705**	**0.8287**	**0.0263**	**0.5210**	**0.0190**	**0.5036**

The testing results of the 3D reconstruction, along with comparative analysis, are summarized in Table 1, where smaller metrics indicate better results. Additionally, Figure 4 displays the 3D reconstruction and runtime results for four organs (bladder, uterus, rectum, and levator) of a subject from the testing set. These results suggest that our 3D reconstruction closely matches the ground-truth, and the iterative optimization module improves reconstruction quality without the lengthy runtime typical of traditional methods.

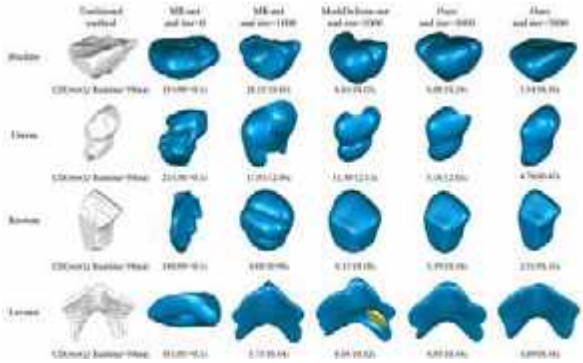

Figure 4: A visual comparison of 3D reconstruction results. The yellow area in the result signifies the bad self-intersection issue.

DISCUSSION

This study introduces a unique hybrid framework for deformable shape modeling, combining deep learning with an iterative optimization module to streamline the reconstruction of high-quality 3D organ models from 3D MRI. The experimental results demonstrate that our framework effectively balances reconstruction speed and quality, proving versatile for various complex organs. Looking ahead, expanding the training dataset is anticipated to further enhance the reconstruction process.

ACKNOWLEDGEMENTS

National Key R&D Program of China 2023YFC2411201, NSFC Grant 31870942, Peking University Clinical Medicine Plus X-Young Scholars Project PKU2020LCXQ017 and PKU2021LCXQ028, PKU-Baidu Fund 2020BD039.

REFERENCES

[1] Chen et al., *Med Image Anal 2021*, 74, 2021.
[2] Luo et al., *J Biomech*, 48(9):1580-1586, 2015.
[3] Cruz et al., *IEEE/CVF WACV 2021*, 806–815, 2021
[4] Beetz et al., *Med Image Anal 2023*, 90, 2023.
[5] Wickramasinghe et al. *MICCAI 2020*, 299-308,2020
[6] Wang et al., *Acm T Graphic*, 38(5), 2019.
[7] Kong et al., *Med Image Anal 2021,74,2021*,

DEVELOPMENT OF ENGINEERED TENDON TISSUE MICRO-GAUGES (TENTUGS) FOR INVESTIGATING TENDON ORGANIZATION AND MECHANOBIOLOGY

S. S. Steltzer (1,2), S. Bae (1,3), N. Migotsky (1), H. Yu (1), C. Mentzer (1,4), S.N. Lamia (5), B. A. Baker (4), M. L. Killian (1), A. C. Abraham (1)

(1) Orthopaedic Surgery, University of Michigan, Ann Arbor, MI, U.S.A.
(2) Molecular and Integrative Physiology, University of Michigan, Ann Arbor, MI, U.S.A.
(3) Medical School, University of Michigan, Ann Arbor, MI, U.S.A.
(4) Biomedical Engineering, University of Michigan, Ann Arbor, MI, U.S.A.
(5) Mechanical Engineering, University of Michigan, Ann Arbor, MI, U.S.A.

INTRODUCTION

The cellular and extracellular mechanisms underlying tendon disease are not well understood thereby limiting the development of effective therapies.[1,2] The *status quo* as it pertains to *in vitro* tendon biology are monolayer 2D tissue culture plastic or 3D systems with fixed geometry that typically do not provide quantitative biomechanical measures, are relatively large constructs resulting in diffusion gradients, and are incompatible with high-throughput/content microscopy.[3–6] Micro-physiological systems (MPS) have emerged as an invaluable tool for disease modeling and for understanding cell-extracellular matrix (ECM) interactions, which is currently challenging *in vivo*.[7] In this study, we established a tendon-specific MPS to monitor tissue contractility and compared the gene expression of tendon fibroblasts (TFs) in an engineered 3D tendon tissue micro-gauge (tenTμG) to native mouse Achilles and tail tendons.

METHODS

The tenTμG platform was generated by casting polydimethylsiloxane (PDMS) from 3D stereolithography printed resin molds (Phrozen Sonic Mini 8k).[8] Tissue dimensions were 2 mm long x 0.2 mm width tethered between 1 mm long cantilevers with tapered heads (Fig1A). We maintained an aspect ratio of 1:10 for tendon constructs, mimicking the aspect ratio of human Achilles tendon while reducing diffusion gradient issues that arise in larger 3D culture systems.[9] Tail TFs were isolated from N=12 2-month-old C57BL6/J wildtype mice (n=6 male, n=6 female; 2 animals/device). From the same animals, Achilles tendons (AT) and additional tail tendons (TT) were flash frozen for tissue-level RNA isolation. To isolate TFs, tail tendon was embedded in collagen-I hydrogel (PureCol®-S, Millipore) for 10 days. TFs were passaged once to collagen-I-coated tissue culture plastic before being embedded with collagen-I (FibriCol, Advanced BioMatrix) in the tenTμG device. Each device contained 21 micro-gauges (two cylindrical silicone pillars spaced 2-mm apart) in individual wells (Fig1A).

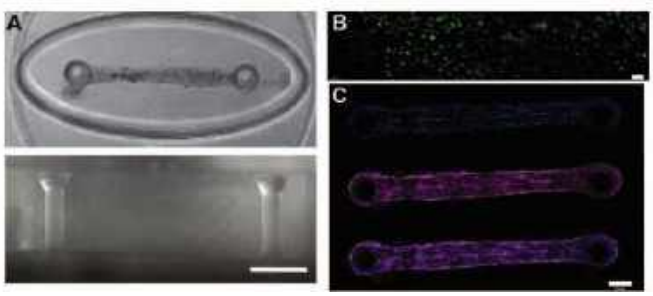

Figure 1: Mouse TFs embedded in tenTμG devices can be maintained for at least 4 weeks. (A) Visualization of the tenTμG molds from top and side. Pillars are 2mm apart (scale bar = 0.5mm). (B) Cell Viability (Live, calcein in green; Dead, ethidium-1 in red) staining shows high cell survival in constructs after 7 days in culture (scale bar = 0.8mm). (C) Nuclear (blue) and phalloidin (purple) staining showed dense, aligned constructs after 4 weeks in culture; scale bar = 0.2mm.

Each tenTμG tissue was formed from 4μL of 2.5mg/mL collagen-I mixed with 1.5 million TFs/mL and cultured in Advanced DMEM/F12 containing 4% FBS, 1% pen/strep. The number of intact gauges, tissue length (distance between the center of the two pillars), and tissue width were assessed on 0-, 1-, 3-, 7- and 10-days using 10x phase contrast imaging (LionHeart, Agilent). Pillar displacement was converted to contractile force using Hooke's law and the pillar's bending stiffness (0.6037 μN/μm, FEBio model simulation; data not shown). Statistical comparisons of tissue survival, force, and width were performed using Prism (GraphPad v10; 2-way ANOVA for time/device). RNA was

isolated from TFs after 10 days in culture or from flash-frozen tissues (AT and TT) for cDNA synthesis for SYBR-based quantitative PCR (qPCR). Expression of matrix-associated genes (*Col1a1, Col1a2, Col3a1, Tnc, Tnmd)* and progenitor markers (*Scx, Mkx)* were quantified from flash frozen tissues and cultured mouse tail TFs and data were normalized to AT from the same animals (Pfaffl-based; $2^{-\Delta\Delta Cq}$; reference = *Rplp0* and *Polr2a*). Statistical comparisons of ΔCqs were made using Prism (GraphPad v10; two-way ANOVA for sex/tissue). Additional devices were treated with either 10ng/mL hTGFβ2 or 0.1% bovine serum albumin (BSA) control at time of seeding (supplemented media was refreshed every 48h) and imaged at 1-, 3-, 7- and 9-days. Treated tenTμGs were imaged on day 9 using brightfield and quantitative polarized light imaging (qPLI, ThorLabs, Inc) on an epifluorescent microscope (Leica).

RESULTS

TFs survived in tenTμG constructs after 1-week in culture (Fig1B). A preliminary study with TFs isolated from 6-month-old female mice (n=2) demonstrated long-term survival (4-week) of TFs in tenTμGs (Fig1C). Over a 10-day period in vitro, tissue tension increased, and tissue width decreased (Fig2A'). The majority of tenTμGs were intact after 1-day in culture and remained intact through the 10-day experiment (Fig2). However, with TGFβ2 treatment, tissue tension increased rapidly and more than half of the tenTμGs failed by 7-days (Fig2B). Prior to failure, collagen alignment increased in TGFβ2-treated tissues as compared to BSA-treated controls (Fig2C).

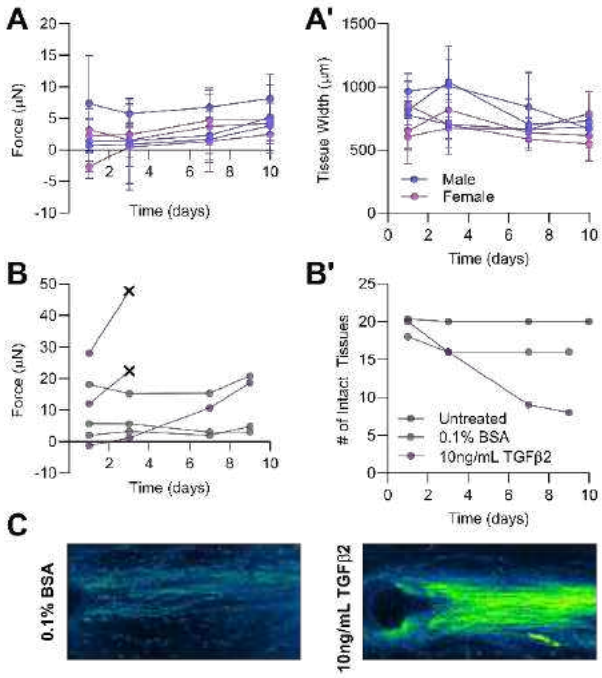

Figure 2: TFs cultured in collagen on tenTμGs devices exhibit mechanical and structural changes including (A) increased tissue force (decreased distance between pillars) and (A') increased compaction (i.e., decreased tissue width) over time in culture. (B) Treatment of tenTμG constructs with TGFβ2 leads to increased contractility and (B') premature construct failure after 3 days in culture compared to untreated or BSA-treated tenTμGs. (C) Collagen organization of remaining intact tenTμGs was increased with TGFβ2 treatment compared to BSA only after 10 days in culture.

In 3D tenTμGs and 2D culture, *Scx* was downregulated compared to native tissues, and *Tnc* was upregulated in 3D tenTμGs compared to 2D culture and native tissue (Fig 3). Additionally, *Col1a1* and *Col3a1* (Fig 3) were upregulated in 3D culture compared to 2D culture and AT (for *Col3a1* only).

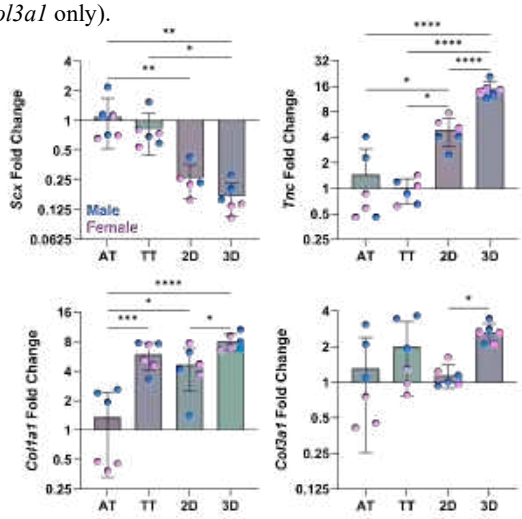

Figure 3: TFs elicit environment-dependent transcriptional responses. Gene expression of native tissues (AT and TT) compared to primary TFs isolated from TT in 2D and 3D tenTμGs culture after 7 days. * p<0.05; **p<0.01; ***p<0.001; ****p<0.0001 (of ΔCq for gene expression). Individual dots represent biological replicates of male (blue) and female (pink) mice.

DISCUSSION

Our findings support the utility of MPS fabrication for developing an *in vitro* platform for measuring TF contractility *in vitro* in 3D. We successfully demonstrated the ability to generate and maintain TF viability and contractility with increased expression of matrix-associated genes in 3D conditions. Previously, TGFβ2 has been shown to enhance tenogenesis (e.g., increase *Scx* expression) in mesenchymal and embryonic stem cells.[4] In agreement, when TGFβ2 was added to tenTμGs, we observed increased contractility and more organized collagen. Although several constructs were lost due to the increased contractility, our pillar geometry can be re-designed to withstand larger contractile forces to prevent failure. Surprisingly, expression of tenogenic transcription factors (e.g., *Scx*) *in vitro* in our tenTμGs did not mimic that of native (adult) tendon. Future studies will compare the expression of genes in developing (e.g., neonatal) tendon. Additionally, this tunable tenTμG platform will allow us examine if and how cellular contractility and pillar stiffness influences nascent matrix deposition. This platform will allow us to investigate mechanisms by which tendon extracellular matrix can be reorganized or regenerated in 3D, as well as test druggable targets that have potential to promote matrix deposition mimicking that of native tendon.

ACKNOWLEDGEMENTS

NIH NIAMS (R01AR079367, MLK; P30AR069620), NSF (CAREER 1944448, MLK).

REFERENCES

[1] Nourissat, G., et al. *Nat. Rev. Rheumatol.* 2015. [2] Andarawis-Puri, N., et al. *J. Orthop. Res.* 2015. [3] Abraham, A. C. *et al. Sci. Transl. Med.* 2019. [4] Chien, C., et al. *Connect. Tissue Res.* 2018. [5] Bayer, M. L. *et al. Biomaterials* 2010. [6] Breidenbach, A. P. *et al. Tissue Eng. Part A* 2015. [7] Grubb, M. L. & Caliari, S. R. *Acta Biomater.* 2021. [8] Legant, W. R. *et al. Proc. Natl. Acad. Sci.* 2009. [9] Baker, B. M. & Chen, C. S. *J. Cell Sci.* 2012.

COMPUTATIONAL ANALYSIS OF STROKE RISK DURING CARDIOPULMONARY BYPASS IN ADULT AND PEDIATRIC ANATOMIES

Nafis M. Arefin (1), Bryan C. Good (1)

(1) Department of Mechanical, Aerospace, and Biomedical Engineering, University of Tennessee Knoxville, TN, USA

INTRODUCTION

Neurological complexities resulting from surgery requiring cardiopulmonary bypass (CPB) remain a major concern, encompassing a spectrum of complications including thromboembolic stroke [1]. Surgical manipulation during CPB is considered the primary cause of these neurological complications [2]. This study addresses the overall lack of knowledge concerning CPB hemodynamics within the aorta, employing a combined experimental and computational modeling approach, featuring CFD simulations validated with a realistic *in vitro* CPB circuit [3]. Parametric studies were systematically performed, varying critical CPB parameters including patient-specific aorta anatomy, pump flow rate, hemodiluted blood viscosity, and emboli size and density. This study represents the first comprehensive investigation of the individual and combined effects of these factors on the risk of embolic stroke associated with CPB.

METHODS

For the *in vitro* study, an experimental mock circulatory flow loop (MCFL) (**Fig. 1**) was used to observe emboli distribution through the aorta with varying hemodiluted blood viscosities [3]. This experimental dataset was then used to successfully validate computational simulations of emboli transport in the same patient-specific aorta model of a 26-year-old healthy male [3]. Building upon that work, the study was expanded to investigate the role of emboli density, pump flow rate, and aortic anatomy, specifically focusing on a 7-month-old pediatric patient (acquired from the Vascular Model Repository [4]). Utilizing the Lagrangian particle transport capability of *OpenFOAM*, we observed emboli distribution through the aortic arch branches (**Fig. 3**), replicating the experimental study.

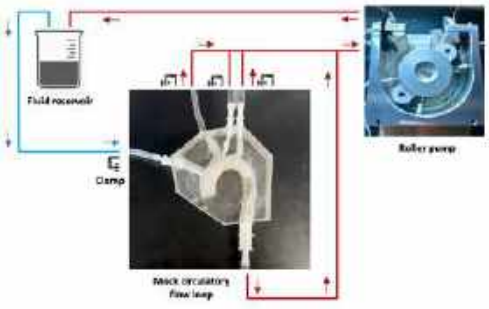

Figure 1: CPB mock flow loop for *in vitro* embolus tracking [3].

Hemodilution: Incorporating hemodilution during CPB is known to improve peripheral perfusion, increase blood flow to tissues, and facilitate venous return [5]. In the CFD simulations, three distinct fluids with viscosities of 1.5, 2.5, and 3.5 cP were used, aligning with the viscosities employed in our *in vitro* study [3].

Pump Flow Rate: Optimal CPB pump flow rate can be determined by calculating the product of an individual's body surface area (BSA) and a constant of 2.2-2.4 [6]. BSA can also be approximated using the Du Bois formula [7]: $BSA[m^2] = Weight\ [kg] \times height\ (cm) \times 0.007184$

This equation was used to estimate BSA, and subsequent pump flow rate and cannula size, for each patient case. For the adult patient, flow rates of 3 LPM and 5 LPM, representing patients with lower BSA and those with higher BSA, respectively, were employed. For the pediatric patient, a pump flow rate of 0.75 LPM was used [7].

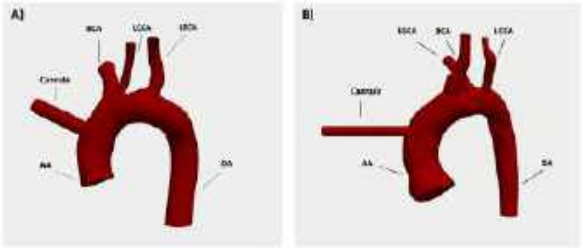

Figure 2: CAD models of patient-specific aorta anatomies: A) 26-year-old male and B) 7-month-old female.

Emboli Size: Prior research established that smaller-sized emboli travel proportionally to the flow, prompting us to exclude micro-emboli from our study. Additionally, it has been found that aortic emboli can range in diameter from 0.3-2.9 mm [8]. Therefore, we chose to employ two emboli sizes in this study: 2.4 mm (1/16 in) and 1.6 mm (3/32 in).

Emboli Density: Simulations were performed using emboli of three different densities: one to match the density of the hemodiluted blood in which they were suspended, one to match the density of whole blood (1092 kg/m³), and one to match the emboli from the *in vitro* study (1134 kg/m³).

RESULTS

In **Fig. 3**, emboli transport is shown over time as the injected particles flow in through the CPB pump cannula and are distributed to one of the aortic outlets. The particles were tracked until they exited through one of the aortic outlets. In phase (i), the injection of the emboli into the aorta model is observed. The particles begin exiting through the outlets of the model in phase (ii) until nearly all have been transported out of the fluid domain by phase (iv).

In **Fig. 4**, the % of emboli exiting through the aortic branches during CPB is shown for two different pump flow rates in the adult aorta model. For all hemodiluted blood viscosities, a marked increase in emboli exit was observed through the aortic branches at the higher 5 LPM flow rate. An increase in emboli transport was also observed, ranging from 12% to 42%, during the transition from 3 to 5 LPM pump flow rate for different blood viscosities.

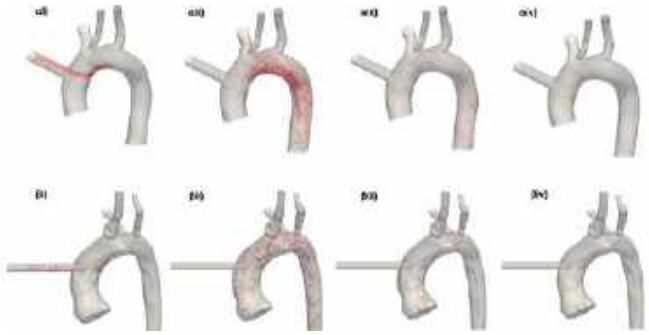

Figure 3: Visualization of emboli trajectories over time in computational simulations in the aortic arch adult (α) and pediatric (β) anatomies.

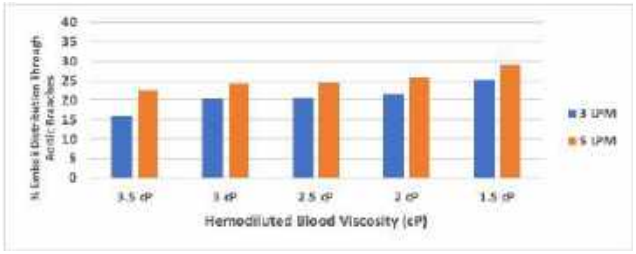

Figure 4: Emboli transport into the aortic branches of the adult anatomy at varying CPB pump flow rates.

Figs. 5 and **6** illustrate the relationship between emboli density and hemodiluted blood viscosity in terms of the % of emboli that exited through the aortic branches for the adult and pediatric anatomies, respectively. It was observed that, across all cases, a higher proportion of emboli exited through the aortic branches as their density decreased. This observation indicates that emboli density plays an important role in their transport in the aorta. Reduced emboli density leads to a notable increase in emboli exiting through the aortic branches, subsequently directing them toward the cerebral vasculature.

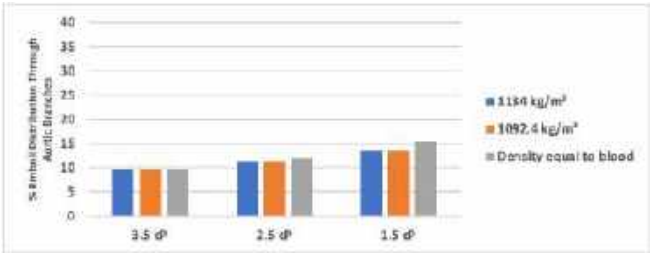

Figure 5: Emboli transport into the aortic branches of the adult anatomy with varying emboli densities.

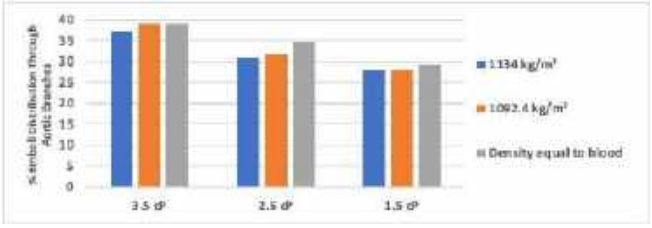

Figure 6: Emboli transport into the aortic branches of the pediatric anatomy with varying emboli densities.

However, with varying blood viscosity, the two aortic models exhibited opposite trends. For the adult case (**Fig. 5**), an inverse relationship was observed, with increased emboli distribution through the aortic branches with decreasing blood viscosity. Conversely, the pediatric case (**Fig. 6**) demonstrated the opposite tendency.

Figure 7 displays the % of large (2.4 mm) and small (1.6 mm) emboli exiting through the aortic branches. It illustrates that, for both patient anatomies, larger emboli exit through the aortic branches at higher rates. Also, the % increase between emboli sizes is similar for both adult (27%) and pediatric (28%) cases.

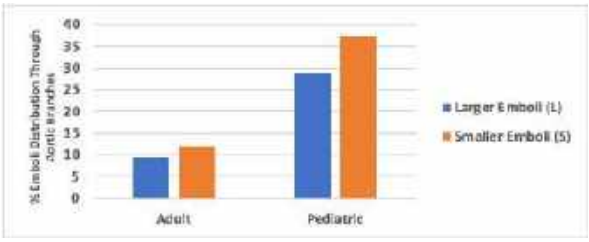

Figure 7: Influence of embolus size on their aortic transport.

DISCUSSION

This study provides critical insights into the interplay of different CPB parameters, employing validated CFD models [3] to compare emboli transport in the human aorta. Further CFD simulations showed that smaller emboli generated during CPB have a higher tendency to exit through the aortic branches compared to larger emboli (**Fig. 7**). Also, irrespective of their size, emboli with lower density have a greater tendency to exit through the aortic branches (**Fig. 6**). Additionally, it was observed that a greater number of emboli exit through the aortic branches at higher pump flow rates. Consequently, emboli tend to follow the fluid streamlines and exit through the descending aorta at lower pump flow rates (**Fig. 4**). This behavior could be attributed to the turbulent nature of the flow exiting the cannula at high pump flow rates, causing emboli to deviate from the streamlines and preferentially exit through the aortic branches. These findings highlight the critical role that high pump flow rate, small emboli size, and lower emboli density play on emboli distribution in the aorta.

The present study has certain limitations, and our future work will involve simulating emboli transport in patient-specific aortas for two additional age groups (adolescent and geriatric). Further, we plan to vary the cannula orientation to comprehensively understand its influence on emboli transport. Through these additional studies, we aim to arrive at a more robust conclusion regarding the reasons behind higher rates of emboli transport to the cerebral vasculature. Additionally, emboli were modeled as rigid spheres. In reality, emboli exhibit irregular shapes, and their viscoelastic mechanical properties may prove critical when simulating larger-sized emboli and their interactions with the vessel walls. Furthermore, the CFD simulations did not account for the pulsatile blood flow, assuming constant CPB pump flow with a cross-clamped ascending aorta.

The computational approach and findings hold significant implications for understanding stroke biomechanics and treatment planning during CPB. This study can make meaningful contributions to the field by reducing the risk of stroke and complications associated with CPB, enhancing the overall safety of cardiovascular surgery.

REFERENCES

[1] Berger, M et al., *Anesthesiology,* 829-851, 2018.
[2] M. Ono *et al.*, *British journal of anaesthesia,* 391-398, 2012.
[3] Arefin N and Good B., In review at *BMMB*.
[4] Wilson, N et al., *Journal of Medical Devices*, 2013.
[5] Messmer, K et al., *Surgical Clinics of North America,*659-678, 1975.
[6] Starr, A et al., *Journal of Thoracic & Cardiovascular Surgery*, 1959.
[7] Bois, D., *Nutrition,* 303, 1989.
[8] Barbut, D *et al.*, *The Annals of Thoracic Surgery,* 1262-1265, 1997.

SB³C2024
Summer Biomechanics, Bioengineering and Biotransport Conference
June 11-14, Lake Geneva, WI, USA

EVALUATING ADAPTATION OF AMPUTEE SKIN DUE TO PROSTHESIS USE

J. Hayes (1), J. Andrews (2), T. Andriuskevicius (3), O. Abdelwahab (4), R. Gordon (4), T. Briggs (1), P. Worsley (4), C. Higgins (3) and M. Masen (1)

(1) Mechanical Engineering, Imperial College London, London, UK
(2) Podiatry, University of Salford, Manchester, UK
(3) Bioengineering, Imperial College London, London, UK
(4) Health Sciences, University of Southampton, Southampton, UK

INTRODUCTION

Skin plays an important role in how we perceive and interface with our environment. Our skin is constantly in mechanical contact with our environment, yet when skin interacts with surfaces or medical devices for long periods of time the contacting skin may break down and develop blisters, ulcers and other lesions. One such group that suffers with persistent skin breakdown is lower limb amputees. Prosthetics have proven to be a very successful medical device, providing users with improved mobility, a factor which is essential for independence and social inclusion, so preventing skin breakdown is critical.

Research into skin injury mechanics has shown that when normal loading is combined with shear, skin breakdown is more severe [1], a common loading scenario in a prosthetic socket. We know that this relationship is site specific, for example the foot can withstand 50 times more loading than skin on the sacrum [2] and foot skin responds positively to mechanical load by forming a thicker stratum corneum [3].

However, it is not well understood what adaptations occur in amputee skin and if they are beneficial to resist mechanical load, despite a clinical belief that the skin of the residuum can be trained to be load bearing [4]. It has not been well explored how the stratum corneum architecture of lower limb amputees is altered compared to the intact contralateral limb and if skin health is altered through inflammatory response to repeated mechanical loading. Previous research has found lower transcutaneous oxygen tension and reduced skin barrier function [5].

Here we address this gap in knowledge by characterizing at multiple scales, the mechanics, microstructure and Raman spectra of amputee and contralateral limb skin. We aim to bridge understanding on how the skin on the residuum adapts to a new role of load bearing skin. We aim to discover how skin barrier composition, cytokine response, morphology, hydration, topography, apparent stiffness and coefficient of friction all vary in the amputated limb compared to the intact contralateral limb. Quantifying these parameters will highlight how changes to residuum skin improve or deteriorate the contact situation and inform adaptations in skin biology from prosthesis use.

METHODS

In this study we analysed the skin of 12 lower limb amputees, results were taken on the surface of the residuum and the contralateral intact limb for comparison. After an initial acclimitisation period (20-minutes), photographs are taken of the skin sites using a Visioscan VC 98 to analyse skin surface roughness. In-vivo skin Raman spectra is then taken using a RiverDiagnostics Gen2-SCA Raman confocal spectroscope. Raman spectra are collected from the skin surface to 53 µm into the tissue. Raman spectra are separated into principal components using the RiverDiagnostics SkinTools software, namely protein, ceramides & fatty acids, cholesterol, natural moisturising factor and water. Depth profiles of each component are then compared between skin sites and tested for statistical significance using the Mann-Whitney test. Raman spectra water depth profiles were used to determine stratum corneum thickness using an indirect method [6]. Sebutapes were applied on both skin sites for 2-minutes and analysed using a recently proposed method [7], with a chemiluminescent multi-analyte V-PLEX kit for inflammatory cytokines (IFN-γ, IL-10, IL-12p70, IL-13, IL-1β, IL-2, IL-4, IL-6, IL-8 and TNF-α).

Coefficient of friction was recorded using a handheld tribometer covered with prosthetic liner material to mimic the contact situation in the prosthetic socket. The tribometer features two load cells perpendicular to measure normal and friction force during motion, the contacting wheel rotates in both directions, friction force is divided by the normal force to calculate coefficient of friction. Here we analyse the middle 50% of the forward motion only. Mechanics in indentation was recorded using a custom-built indenter, that recorded the force applied to a 10 mm steel indenter when applying 5 mm of indentation. Each participant had 5 indentation curves taken from each site. Linear

regression was applied to the indentation portion of the force curve and gradients of the fit were compared as a measure of stiffness.

Results relating to roughness, stratum corneum thickness, coefficient of friction, inflammatory cytokines and stiffness were analysed using a two-tailed unpaired t-test

RESULTS

Stratum corneum thickness was recorded using Raman spectroscopy, the average stratum corneum thickness of the contralateral limb and amputation site was found to be 19.5 (SD = 5.05) µm and 21.1 (SD = 4.96) µm respectively ($p>0.05$).

When analysing the Raman spectra of the epidermis we find lower levels of ceramides and fatty acids, cholesterol and natural moisturising factor content in the stratum corneum of amputee skin compared to intact limbs ($p<0.05$) as a result higher water content is found at superficial layers in amputee skin compared to intact skin ($p<0.05$).

We find that IFN-γ, IL-10, IL-12p70, IL-13, IL-1β, IL-2, IL-4, IL-6, IL-8 and TNF-α levels are all increased in baseline amputee skin than the baseline contralateral control but not significantly ($p>0.05$).

Coefficient of friction is higher ($p<0.05$) at the amputation site at 0.7 (SD = 0.76) compared to 0.6 (SD = 0.58) on the contralateral limb respectively (figure 1A).

We find that the stiffness of the amputation site was significantly lower than the contralateral limb ($p<0.05$) where the stiffness was 0.18 N/mm (SD = 0.13) and 0.49 N/mm (SD = 0.24) respectively (figure 1B).

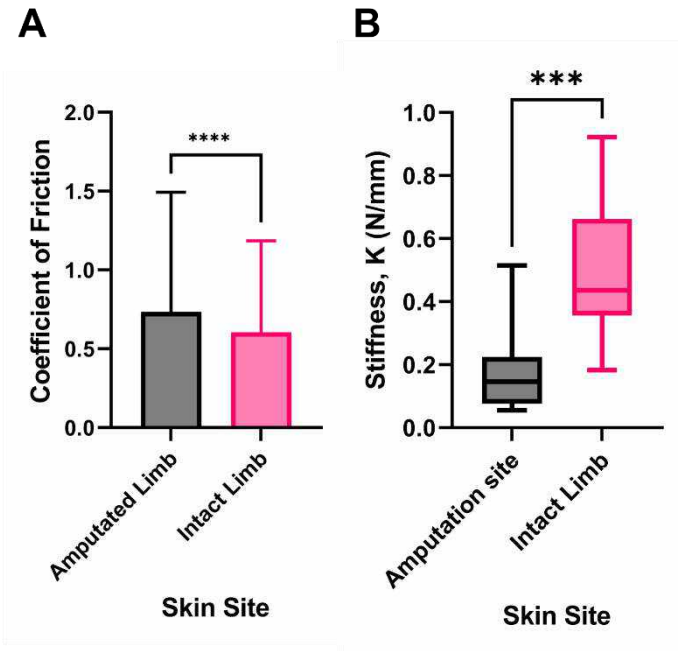

Figure 1: (A) Coefficient of friction in the forward direction for amputated limb (n=9) (black) and intact limb (n=9) (pink), whiskers indicate SD, an asterisk(s) above graph indicates level of significance. (B) Stiffness recorded in indentation only for amputated limb (n=12) (black) and intact limb (n=12) (pink), whiskers indicate min and max data, an asterisk(s) above the graph indicates level of significance.

DISCUSSION

Here we take a multiscale approach to interrogate how skin at the amputation interface has adapted to perform a new load bearing role. We have gained new insights into molecular composition of amputee skin as an outcome of prosthesis use. We found that as a result of prosthesis use, we see adaptation in stratum corneum thickness, allowing amputee skin to mediate mechanical load with a thicker stratum corneum, however these changes are minimal compared to the intact limb. We see adaptation in mechanics as shown by a 64% reduction in stiffness in the amputation limb compared to the contralateral limb (figure 1B). In addition, we record a 17% increase in friction at the amputation site compared to the contralateral limb (figure 1A), suggesting the adapted mechanics of the stump leave skin more susceptible to deformation and friction injuries. Our findings show altered biological function, more specifically, microstructural changes in the skin at the amputation site indicate impaired barrier function, suggesting skin would be more prone to infection, delayed wound healing and impaired desquamation. Altered biological function is also supported by higher baseline inflammatory cytokines at the amputation site compared to the contralateral limb.

While we gained new insights into the in-vivo state of lower limb amputee skin, our recruitment was not exhaustive and would require a larger study population for stronger conclusions.

In conclusion, the work presented shows the adaptation of amputee skin to be minimal. We find reduced stratum corneum thickness and softer contact of the limb, increased friction and reduced skin barrier function. Challenging the notion that amputee skin can be trained to be load bearing. The observations of increased water content and reduced natural moisturising factor content at the superficial layers could lead to higher friction, suggesting a secondary role of a naturally occurring lubricant that protects skin. However, this could be more heavily influenced by the softness of the skin leading to high pile up.

This finding highlights the need for improved therapies as well as product solutions that directly relate to improving load bearing capacity on the skin of the stump.

ACKNOWLEDGEMENTS

This work was supported by the UK Engineering and Physical Sciences Research Council (EPSRC) grant EP/S02249X/1 for the Centre for Doctoral Training in Prosthetics and Orthotics.

REFERENCES

[1] Hoogendoorn, I et al, *Journal of tissue viability*, *26*(3), pp.157-171, 2017.
[2] Boyle, C.J et al, *Science advances*, *5*(10), p.eaay0244, 2019.
[3] Holowka, N.B et al, *Nature*, *571*(7764), pp.261-264, 2019.
[4] Wang, Y and Sanders, J, *Medical hypotheses*, *61(1), pp.29-35 2003.*
[5] Rink, C.L et al, *Advances in wound care*, *6*(7), pp.225-232, 2017
[6] Egawa, M et al, *Acta dermato-venereologica*, *87*(1), pp.4-8, 2017.
[7] Jayabal, H et al, *Skin Pharmacology and Physiology*, *36*(1), pp.38-50, 2023.

MEASUREMENT OF THE POPULATION DISTRIBUTION OF HELMET-TO-HEAD CONTACT FORCES

Turner Jennings (1), Aidan Tillman (2), D'Mitra Mukasa (2), Michael Marchev (2), Rouzbeh Amini (1,2), Sinan Müftü (1)

(1) Department of Mechanical and Industrial Engineering, Northeastern University, Boston, MA, USA
(2) Department of Bioengineering, Northeastern University, Boston, MA, USA

INTRODUCTION

Research on improving the protective performance of helmets has mainly focused on the development of new and improved materials [1]. However, the effect of helmet ergonomics on protective performance remains understudied. It is well known that in many helmet applications, well-fitting helmets in a reduced risk of brain injury [2-4]. Although we know that good fit is correlated with performance, quantitative descriptions of what constitutes good helmet fit remain scarce. Existing studies on helmet fit in military helmets have not provided sufficient spatial resolution to properly describe the way the helmet rests on the head [5]. Additionally, we hypothesize that helmet fit will vary significantly across the population, and previous work in this area has lacked a representative volunteer population to capture such a distribution [5,6].

A lack of robust data has led to varying assumptions about helmet fit being made. The level of pre-compression in the helmet lining created by the user who wears the helmet, which constitutes the deformed initial condition for any subsequent impact analysis, has not been characterized. As a result, researchers in previous studies of helmet performance have arbitrarily selected initial compression conditions [7,8], or assumed a zero-stress state prior to impact or blast analysis [9]. The wide variety in the assumptions being made demonstrates a *clear need* for a comprehensive description of the appropriate helmet fitting conditions, and how those conditions vary across the population.

In this study, we have developed a method to quantitatively describe helmet fit and addressed the clear need for fit data in the specific case of military helmet systems. We have defined the spatial and population distribution of helmet-to-head contact forces, as well as chinstrap tension, in the Advanced Combat Helmet (ACH) system. We have also evaluated the relationship between head dimensions and the observed force distribution. Finally, we have examined the relationship between population demographics and the resultant helmet fit. We hypothesize that head size and user demographics will change the resultant helmet fit.

METHODS

To evaluate helmet fit, four sizes of the ACH (S, M, L, XL) were fitted with an aftermarket foam padding system. Each pad was instrumented with a force sensitive resistor (FSR), enabling measurement of the contact force between the pads and the head at seven areas around the inside of the helmet, as shown in Figure 1A. Custom mechanical force gauges, shown in Figure 1B, were incorporated into the helmet, replacing the existing tensioning buckles.

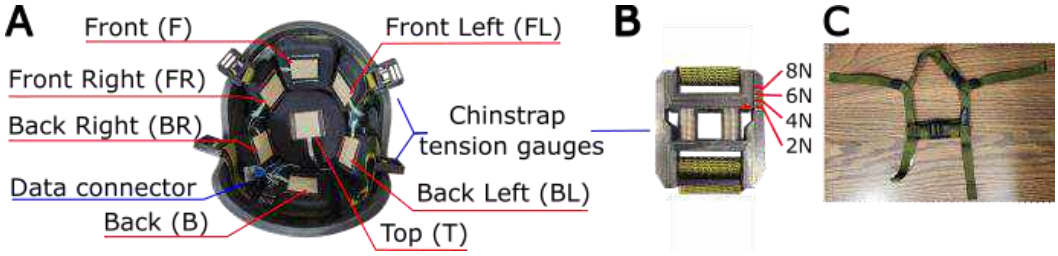

Figure 1. Measurement system diagram. (A) Helmet padding configuration with position notation. (B) Chinstrap tension gauge detail. (C) Helmet chinstrap system.

The force gauges enabled measurement of the chinstrap tension at the four connection points to the helmet, shown in Figure 1A and 1C.

Helmet fit testing was performed on 89 volunteers (25 female, 64 male) with varying levels of prior experience using combat helmet systems. The volunteer study was conducted with official exemption from the Northeastern University Institutional Review Board. The age, biological sex, and experience level of each volunteer were recorded, and their head length, width, and circumference were measured. The correct size helmet was selected for the volunteer based on their head measurements and guidelines prescribed by the helmet manufacturer. Volunteers were asked to wear the helmet in three configurations: Without the chinstrap fastened (No Chinstrap/NC configuration), with the chinstrap tightened to the volunteer's preference (User Comfort/UC configuration), and with the chinstrap tightened to a fixed value by the facilitator (Fixed Tension/FT Configuration). For each configuration, the head/helmet contact force was measured at the seven FSR positions. Chinstrap tension was also recorded for the UC and FT configurations.

RESULTS

We observed contact forces between 0 N and 30 N, with most falling between 0 N and 10 N, as shown in Figure 2. The highest contact forces were found on the front pad and the back left and right pads with some load also carried by the top pad, indicating that the helmet did not sit uniformly on the head. The contact force data followed a skewed distribution with many high outliers.

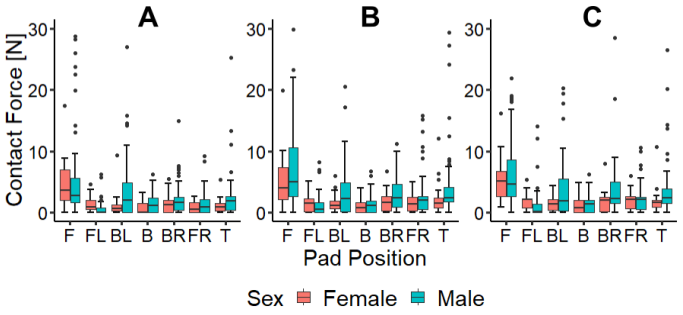

Figure 2. Contact force distribution for (A) NC configuration, (B) UC configuration, (C) FT configuration, measured at each of the seven positions, see Figure 1A for notation.

When the contact force was averaged across the seven interior pads, as shown in Figure 3, most of the outliers disappeared, indicating that high forces in one area of the helmet were compensated by a low force somewhere else and highlighting the role of head shape in the way the helmet sits on the head. We observed a statistically significant difference in contact pressures between male and female volunteers for the two configurations in which they adjusted their own helmet fit, as shown in Figure 3.

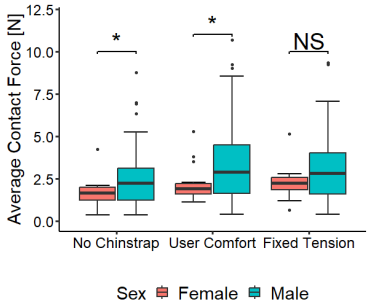

Figure 3. Average contact force in different test configurations comparing male and female volunteers.

Figure 4 shows the relationship between the volunteer head dimensions, normalized as a ratio to the corresponding dimension of the helmet, and the head-to-helmet contact forces observed. We found no correlation between the head dimensions and the resultant contact forces.

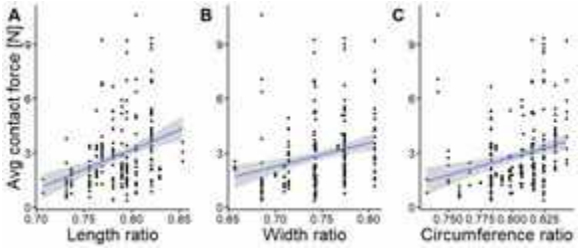

Figure 4. Average contact force vs head / helmet (A) length ratio, R^2=0.10 (B) width ratio, R^2=0.06 (C) circumference ratio, R^2=0.06

DISCUSSION

The experimental fit data shown in Figure 4 highlights the variation in helmet fit between subjects with similar head dimensions. Head length, width, and circumference collected during the study did not show a correlation to the observed contact forces, indicating that head shape, not just size, played a significant role in determining interface forces. The measured head dimensions were selected since they were the measures used to select the correct helmet size. Further evaluation is necessary to determine if there are head dimensions that better correlate with contact forces, and if there may be better dimensions for selecting the appropriate helmet size.

Differences observed between male and female volunteers may be due to different scalp profiles, padding from more hair, different preferences on how to wear the helmet, or some combination of the above. Given that the differences between male and female volunteers became negligible when the study facilitator adjusted the helmet for the volunteer, it is likely that differing comfort levels partially contribute to the observed difference. It is important to note that no conclusions can be drawn from these results as to whether higher or lower contact forces are inherently "better". Additional research is necessary to determine whether the differences observed correspond to a protection difference.

Our study has established—for the first time—a broad, quantitative, and population-inclusive description of the forces at the head/helmet interface for military helmet systems. Although our study focuses on military helmets, the methodology we have established is applicable to a variety of different types of helmets. The framework we have established is critical to establish accurate initial conditions for the evaluation of the protective performance of helmet systems.

ACKNOWLEDGEMENTS

We would like to thank the Northeastern University Young Scholars Program for their generous support of the authors. Funding for this project was provided by the United States Army Research Lab Soldier Protection Program Cooperative Agreement #W911NF2120208. The views presented in this paper are those of the authors and do not necessarily represent the views of the sponsor.

REFERENCES

[1] Li, Y. et al., *Compos B : Engrg*, 238, 2022
[2] Romanow, N. et al., *Chronic Dis Inj Canada*, 34, 2014
[3] Gamble, A. et al., *J Athl Trng*, 56 :845-850, 2021
[4] Greenhill, D. et al., *Sports Health*, 8, 238-243, 2016
[5] Kuo, C. et al., *Proc HCII2020*, 145-154, 2020
[6] Samil, F., et al., *Procedia Engrg*, 41:1660-1666, 2012
[7] Tse, K. et al., *Med Biol Engrg Comp*, 55(4):641-662, 2017
[8] Li, X. et al., *Compos Struct*, 91 :56-67, 2016
[9] Tan. L et al., *Int J Impact Engrg*, 50:99-112, 2012

COMPENSATING FOR THE SIMULATED FOREIGN BODY RESPONSE TO MEDICAL IMPLANTS USING LOCAL FLUID FLOW

Lesley Trask (1), Niamh A. Ward (1), Ruth Tarpey (1,2), Rachel Beatty (2,3), Eimear Wallace (2), Joanne O'Dwyer (2), William Ronan (1), Garry P. Duffy (2,3,4), Eimear B. Dolan (1,4)

(1) Biomedical Engineering, School of Engineering, College of Science and Engineering, University of Galway, Galway, Ireland.
(2) Anatomy and Regenerative Medicine Institute (REMEDI), University of Galway, Galway, Ireland.
(3) Advanced Materials and BioEngineering Research Centre (AMBER), Trinity College Dublin, Dublin, Ireland
(4) CÚRAM, Centre for Research in Medical Devices, University of Galway, Galway, Ireland

INTRODUCTION

Medical implants are being developed to facilitate the delivery of therapy in the form of drugs, proteins, cells, and bioactive agents, to localized sites[1]. Despite having shown some success, many have limited long term performance, in part due to the diffusion barrier they pose which is exacerbated by the foreign body response (FBR) following implantation[2]. This results in the formation of a dense hypo-permeable fibrous capsule (FC) around the device, leading to failure of many implantable technologies[3]. One potential method for overcoming the FBR is to enhance therapy transport through the incorporation of local fluid flow[4-6]. In this work, we used experimental inputs to characterize the change in the FC over time and quantified how it impacts therapy release using computational methods. For this purpose, insulin was used as a representative therapy as encapsulation devices for Type 1 diabetes are among the most-well characterized[7]. We then explored how local fluid flow may be used to counteract the FBR. Achieving continuous flow in a clinically relevant setting may prove challenging as a steady external supply of fluid is required. However, pulsatile flow can be driven by the displacement of interstitial fluid and therefore does not require an external fluid supply. As such, the impacts of both continuous and pulsatile flow were investigated. We aimed to combine computational and experimental methods to better understand the temporally dynamic impacts of the FBR on therapy delivery, and how local fluid flow may be implemented to reduce or eliminate them.

METHODS

The implant modelled in this study was redesigned from previous work[5,6]. The implant consists of a central therapy reservoir with laser cut semi-permeable membranes (0.15 mm thick, 10 µm pores, 3.5 % porosity) on either side. This therapy reservoir (0.5 mm x 10 mm) is surrounded by an actuation reservoir which can be cyclically inflated and deflated to drive interstitial fluid flow (Fig 1A). The implant is made entirely of thermoplastic polyurethane (TPU).

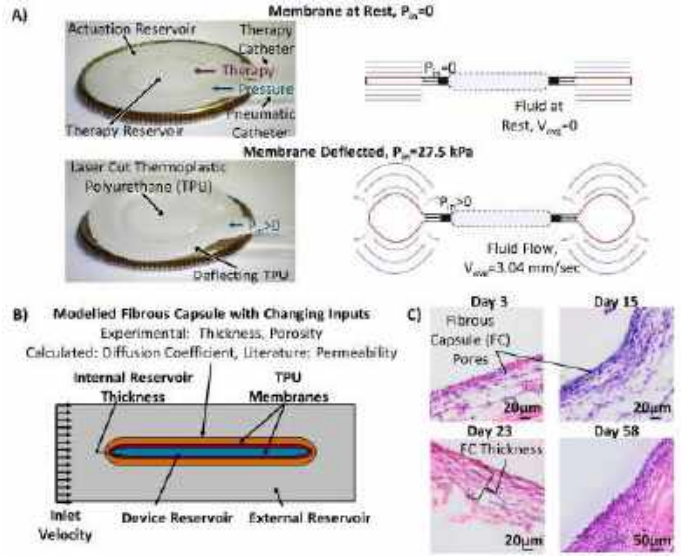

Figure 1: A) Actuating device prototype. B) Model set-up diagram. C) Representative H&E images of the fibrous capsule.

A simplified 2D model of the therapy reservoir and FC at days 15 and 58 post-implantation were constructed in COMSOL Multiphysics® using the Transport of Diluted Species and flow through porous media (Brinkman) modules. The impact of the actuation reservoir on local fluid was captured by idealized flow over the implant (Fig 1B). Two velocities achievable by existing device designs (0.25, 3.04 mm/sec) and two pulsatile regimens (0.1, 1 Hz) were used. The initial therapy reservoir concentration was 9.5×10^{-13} mol/mm^3. Membrane transport properties were obtained using Franz cell apparatus. FC thickness and porosity were taken from previous *in vivo* studies in our group[6,8],

diffusion coefficients were approximated from the porosity (Fig 1C) and a simplified version of Maxwell's model[9], while permeability was taken from literature[8,10].

RESULTS

We first captured the impacts of the FBR on insulin release at days 15 and 58 post-implantation (no flow). This showed reduced therapy diffusion after 15 minutes, the approximate time for first phase insulin secretion (Fig 2A). This is a major contributor to control of postprandial hyperglycaemia and later blood glucose levels in individuals with impaired glucose tolerance[11,12]. This impaired release persisted over 60 minutes with near two-fold reduction by day 58 (Fig 2B). At the clinically relevant 15 minute time point this correlated to drops in area under the curve (AUC) of 35.8% and 64.2% (day 15 and 58) relative to baseline (No FC) (Fig 2C).

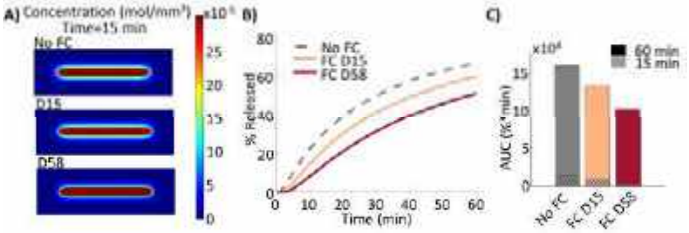

Figure 2: A) Model concentration profiles (15 min). B) Therapy release over 60 min. C) AUC values (15 and 60 min).

Continuous local fluid velocity was incorporated with simulated day 58 FC. There was minimal insulin accumulation outside the implants with fluid flow at 0.25 and 3.04 mm/sec (Fig 3A) and release was restored to baseline levels after 46 and 58 minutes respectively (Fig 3B). However, AUC values did not reach baseline (Fig 3C).

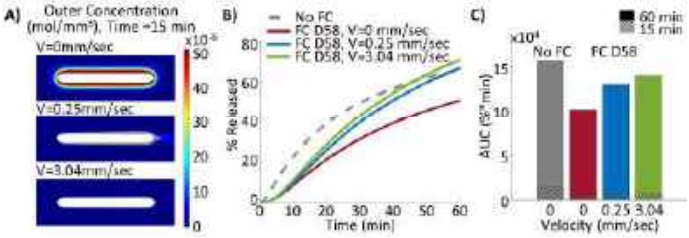

Figure 3: A) Model concentration profiles (15 min). B) Therapy release over 60 min. C) AUC values (15 and 60 min).

Pulsatile flow regimens were then implemented in the model. During the 'pulse' the idealized inlet velocity was cyclically ramped up to the maximum velocity of 3.04 mm/sec (Fig 4A). The resulting release profiles over a 60 minute period showed that a frequency of 1 Hz was sufficient to nearly match that of continuous flow (Fig 4B) with a relative difference in AUC of only 1.8% (Fig 4C).

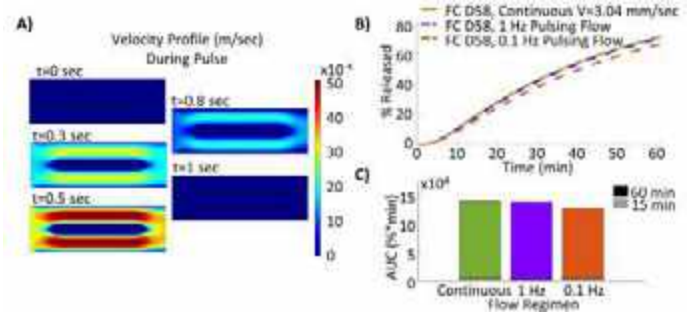

Figure 4: A) Model velocity profiles during pulse. B) Therapy release over 60 min. C) AUC values (15 and 60 min).

DISCUSSION

In this study, we describe a simplified implantable encapsulation device model informed by experimental inputs. It can be used to investigate how therapy release is impacted by the FBR, and the implementation of local continuous and pulsatile fluid flow around the implant. This allows us to evaluate how we expect the implant to perform *in vivo* under a variety of conditions and tune our design accordingly.

Our model is able to capture the expected decrease in therapy release that would result from the FBR at two critical time points, days 15 and 58. Although factors such as glucose uptake by the FC tissue were not considered in this model, the expected deficits in insulin release at days 15 and 58 (35.8% and 64.2% drop in AUC compared to baseline after 15 minutes) correlate reasonably well with the percentage reduction in the maximum percentage blood glucose drop at 3 and 8 weeks seen *in vivo* (43% and 71%, respectively)[5]. Though these values cannot be directly equated, they show a similar trend and magnitude of change, as expected given the intrinsic links between insulin release and circulating blood glucose levels.

We then demonstrate how the implementation of idealized local fluid flow achievable by existing designs may be used to help improve therapy transport and overcome the FBR. We show an improvement in insulin release at the clinically relevant time point of 15 minutes, and a return to baseline (no FC) within 60 minutes using both continuous and more clinically achievable pulsatile flow regimens. Additionally, although not explored herein, previous studies have shown that local mechanical stimuli around implants, such as those induced by fluid flow, can decrease the magnitude of the FBR and resulting FC[,9]. As such, local flow may induce a dual improvement in therapy release through the combined reduction in FBR and advantageous convective transport elements, further improving the 15 minute response captured by the model.

Incorporating local fluid flow may hold the key to overcoming the FBR, which currently leads to consistent implant failure *in vivo*. This model can be used as a method to test and optimize simulated flow regimens readily achievable by existing designs that are suitable for a clinical setting. Although this model was generated using insulin as a representative therapy, these findings are also highly applicable to the delivery of other drugs or cell therapies which rely on timely and accurate transport which can be inhibited by the FBR. Overall, the computational model outlined herein may serve as a valuable means to investigate the impacts of the FBR and how they may be overcome.

ACKNOWLEDGEMENTS

L.T & E.B.D: Irish Research Council (GOIPG/2022/984). R.T.: Science Foundation Ireland (SFI) & CÚRAM (13/RC/2073_P2, C2C-GCMP:19/US-C2C/3633). N.A.W. & E.B.D.: SFI (URF\R1\191335). E.B.D.: IRC (IRCLA/2022/2766). G.P.D & E.B.D: CÚRAM, SFI (SFI/13/RC/2073_P, SFI/12/RC/2278_P22). G.P.D; AMBER.

REFERENCES

[1] Pons-Faudoa FP et al., *Biomed Microdevices*, 21(2):47, 2019. [2] Veiseh O et al., *Adv Drug Deliv Rev*. 144:148–161, 2019. [3] Coulter FB et al., *Adv Healthc Mater*, 10(14):2100229, 2021. [4] Yang K et al., *Proc Natl Acad Sci USA*. 118(37): e2101258118, 2021. [5] Whyte W et al., *Nat Commun*. 13:4496, 2022. [6] Dolan EB et al., *Sci Robot*. 4(33): eaax7043, 2019. [7] Zhang D et al., *Adv Funct Mater*. 31(6):2007226, 2021. [8] Beatty R et al., *Sci Robot*. 8(81):eabq4821, 2023. [9] Sharkawy AA et al., *J Biomed Mater Res.* 37:401–12, 1997. [10] Gardiner BS et al., PLOS ONE. 5(10):e13178, 2010. [11] Del Prato S. *Diabetologia*, 46(1):M2–8, 2003 [12] Di Giuseppe G et al., *Trends Endocrinol Metab*, 34(4):216–230, 2023.

VIRTUAL PROSTATE CANCER BIOPSIES USING ADC TARGETED LESIONS SHOWS SUPERIOR PERFORMANCE THAN T2 AND NON-MR GUIDED SURGICAL SAMPLING

Savannah R. Duenweg (1), Samuel A. Bobholz (2), Allison K. Lowman (2), Aleksandra Winiarz (1), Biprojit Nath (1), Kenneth A. Iczkowski (3,4), Kenneth A. Jacobsohn (5), and Peter S. LaViolette (1,2,6)

(1) Department of Biophysics, Medical College of Wisconsin, Milwaukee, WI, USA
(2) Department of Radiology, Medical College of Wisconsin, Milwaukee, WI, USA
(3) Department of Pathology and Laboratory Medicine, University of California – Davis, Davis, California, USA
(4) Department of Urologic Surgery, University of California – Davis, Davis, California, USA
(5) Department of Urology, Medical College of Wisconsin, Milwaukee, WI, USA
(6) Department of Biomedical Engineering, Medical College of Wisconsin, Milwaukee, WI, USA

INTRODUCTION

Prostate cancer (PCa) is the leading new male cancer diagnosis in the United States, accounting for 1 in 8 new male cancer diagnoses[1]. Improved screening, including multi-parametric magnetic resonance imaging (MP-MRI)-based risk assessment, and treatments have led to a high five-year overall survival rate; however, PCa still accounted for an estimated 35,000 deaths in 2023. Conventionally, PCa diagnosis relies on prostate-specific antigen (PSA) testing and multi-core needle transrectal ultrasound (TRUS)-guided biopsies; however, these biopsies carry risks such as missing significant cancer and infection. The Prostate Imaging Reporting and Data System (PI-RADS) has standardized acquisition, interpretation, and reporting of prostate MRI, as well as aided in the accurate detection of cancerous lesions[2], and recently, MRI-guided biopsies have emerged as a promising alternative, demonstrating the ability to detect higher-risk cancers, requiring fewer biopsy cores, and thus minimizing associated risks. This study, therefore, investigates the potential superiority of simulated MRI-guided biopsies over traditional simulated zone-sampling 12-core needle biopsies using prostate cancer digital twins.

METHODS

This study prospectively recruited 109 patients with pathologically confirmed prostate cancer undergoing radical prostatectomy, whose demographic information can be found in **Table 1**. Patients underwent MP-MRI prior to radical prostatectomy on a 3T MRI scanner using an endorectal coil, including T2 (T2WI) and diffusion weighted imaging (DWI). Apparent diffusion coefficient (ADC) maps calculated from DWI were manually aligned to the T2WI using FreeSurfer's *tkregister2*. After surgery, tissue was sliced using a custom patient-specific, 3D-printed slicing jig modeled after the patient's T2WI. Tissue slices were processed, hematoxylin and eosin (H&E) stained, and digitized at 40x resolution (0.2 microns per pixel) on a sliding stage microscope (**Figure 1**). A board-certified genitourinary pathologist annotated lesions by Gleason patterns on a total of 327 digitized slides (n = 3 per patient). The slides were then nonlinearly aligned to each patient's T2WI using custom in-house control-point based MATLAB software[3, 4].

Table 1: Patient demographic information.

Age, years (mean, SD)	60.1 (6.3)
Preoperative PSA, ng/mL (n, %)	
< 6	57 (52)
≥ 6 – 10	33 (30)
≥ 10 – 20	17 (16)
≥ 20	2 (2)
Grade Group at RP (n, %)	
6	22 (20)
3+4	55 (50)
4+3	15 (14)
8	4 (4)
≥ 9	13 (12)

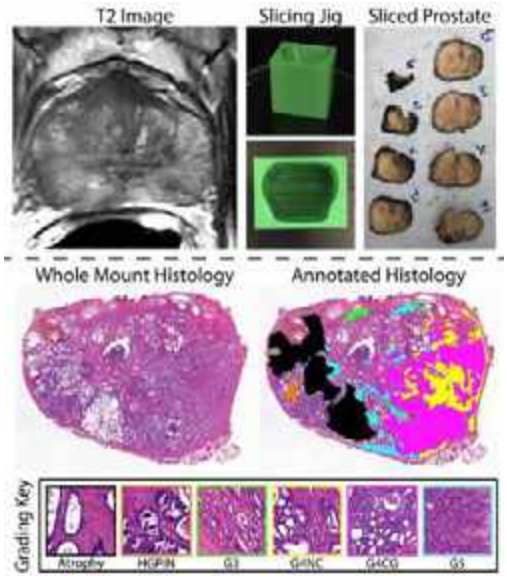

Figure 1: Tissue processing steps (top) and example Gleason pattern annotations (bottom).

Figure 2 illustrates the virtual biopsy simulation process on an example prostate digital twin. Each patient's first aligned slide was divided into twelve equally sized "quadrants" to simulate a 12-core prostate biopsy. Histology within each quadrant was masked and coordinates corresponding to the mask were generated. A random point was selected as the central location of the simulated needle biopsy and was radially expanded by one voxel, for an estimated 1.2mm region (i.e., the standard biopsy needle size). This needle location was translated to the remaining slides and simulated biopsy results (i.e., cancer presence and highest Gleason grade found) were recorded.

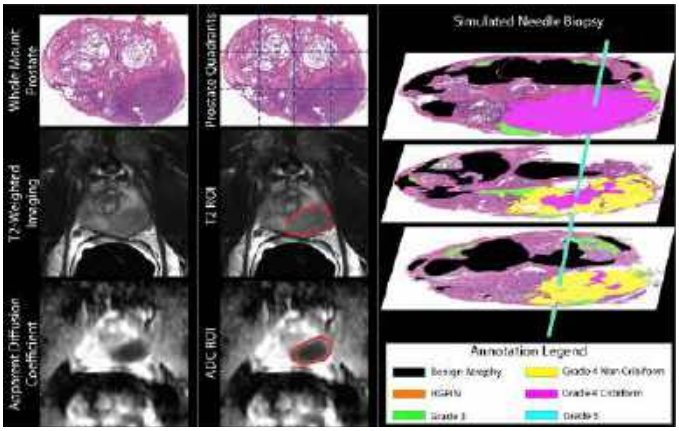

Figure 2: Graphical representation of a virtual biopsy performed on a digital twin.

To test MRI-guided biopsies, a PCa expert annotated 1-3 regions of hypointensity on the T2WI corresponding to the first aligned slide. The coordinates within these regions were translated to histology slides, and four random points were selected as T2-guided needle points. ADC maps were segmented using the 5th percentile of intensity to determine regions of increased hypointensity. Similarly, four randomly selected points within these regions were translated to the histology as ADC-guided needle points. As with the histology-based biopsy needle, the T2 and ADC-derived points were translated into a simulated biopsy needle, and the results were recorded. The entire simulated biopsy process was repeated 100 times per patient for robust predictions. Histograms of biopsies that detected the highest tumor grade present were plotted for each of the simulated procedures, and the average number of successful biopsies were calculated to compare biopsy accuracies.

RESULTS

Simulated ADC-guided prostate biopsies detected the highest tumor grade present on a slide in 81% of simulated biopsies. T2-guided biopsies detected the highest tumor grade in 65% of biopsies, followed by the simulated 12-core histology-based biopsies only capturing the highest tumor grade in 26% of biopsies (**Figure 3**).

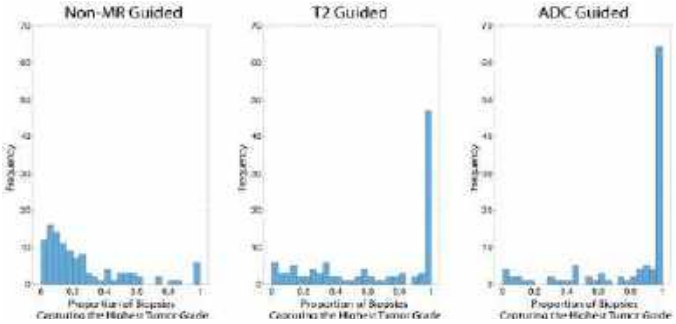

Figure 3: Results of the virtual biopsy analyses. ADC-guided biopsies best captured clinically significant cancers compared to unguided biopsies.

DISCUSSION

While the simulated histology based prostate biopsy used three times as many needles across the entire prostate, simple four needle MRI-guided biopsies more frequently detect high risk cancers. Specifically, ADC-guided biopsy with regions defined by increased hypointensity can detect the highest tumor grade present within patient more frequently with minimal biopsy needles.

ACKNOWLEDGEMENTS

This research was funded by NIH/NCI R01CA218144, R21CA231892, R01CA249882, and the State of Wisconsin Tax Check Off Program for Prostate Cancer Research. We would like to thank our patients for their participation in this study.

REFERENCES

[1] R. L. Siegel, *et al.*, *CA Cancer J Clin,* vol. 73, no. 1, pp. 17-48, Jan 2023, doi: 10.3322/caac.21763.

[2] J. C. Weinreb *et al.*, *Eur Urol,* vol. 69, no. 1, pp. 16-40, Jan 2016, doi: 10.1016/j.eururo.2015.08.052.

[3] S. D. McGarry *et al.*, *Tomography,* vol. 5, no. 1, 2019, doi: 10.18383/j.tom.2018.00033.

[4] S. R. Duenweg *et al.*, *Cancers (Basel),* vol. 15, no. 18, Sep 06 2023, doi: 10.3390/cancers15184437.

SHEAR STRAINS AS A TEAR GROWTH MECHANISM FOR HIGH-GRADE PARTIAL-THICKNESS ROTATOR CUFF TENDON TEARS

Carla N. Villacís Núñez (1), Ulrich Scheven (1),
Asheesh Bedi (4), Ellen M. Arruda (1,2,3)

(1) Mechanical Engineering, University of Michigan, Ann Arbor, MI, USA
(2) Biomedical Engineering, University of Michigan, Ann Arbor, MI, USA
(3) Macromolecular Science and Engineering, University of Michigan, Ann Arbor, MI, USA
(4) NorthShore Orthopedic and Spine Institute, Chicago, IL, USA

INTRODUCTION

Rotator cuff tendon tears are one of the most frequent causes of shoulder dysfunction and pain, with a prevalence between 13% to 32% in the general population and 40% in overhead athletes [1]. Of these, the subset of high-grade partial-thickness rotator cuff tendon tears (type III, 50% of footprint detachment) do not have definite criteria regarding when to surgically repair, as there has been a paucity of biomechanical studies which predict risk of tear progression and the natural history of these tears remains unclear from clinical cases. Consequently, the repair decision is based on anecdotal findings, and not a thorough examination of the likelihood of progression based on the tear's original characteristics.

One of the main metrics to predict tear growth and propagation directions in full-thickness tendon tears has been maximum principal strain concentrations in tear edges [2, 3]. Given that these strains are typically measured with surface probing methods and tear edges are on internal surfaces in partial-thickness tendon tears, examining the strain patterns on these injuries becomes prohibitive with these techniques. Moreover, the effect of the hierarchical and three-dimensional nature of the rotator cuff tendons on strains cannot be evaluated with surface strain measurement methods.

Considering the above, our goal was to obtain full-field displacement and strain patterns in intact and partially torn rotator cuff tendons (type III tear) to evaluate significant changes that could elucidate tear progression mechanisms. Based on our previous studies in type I and II partial-thickness tears, where large shear strains were observed, we hypothesized that delamination (mode II failure) would be a potential tear progression mechanism in type III injuries.

METHODS

The sheep infraspinatus tendon was selected as our animal model to study tear progression, as it has been previously validated as a proxy for the human supraspinatus tendon due to their similar shape and size [4].

The infraspinatus tendon with its intramuscular portion and humeral attachment was isolated from seven fresh ovine shoulders (n=7). Each bony attachment was shaped into a truncated pyramid for fixture fitting, preserving the curved part of the footprint (Figure 1-a). The tendon's intramuscular portion was gripped between interlocked truncated pyramidal teeth, while aligning the sample at a neutral position of $\sim$0 degrees abduction and rotation (Figure 1-a). A wedge was inserted between the anterior part of the bone and the fixture to counteract mechanical moment.

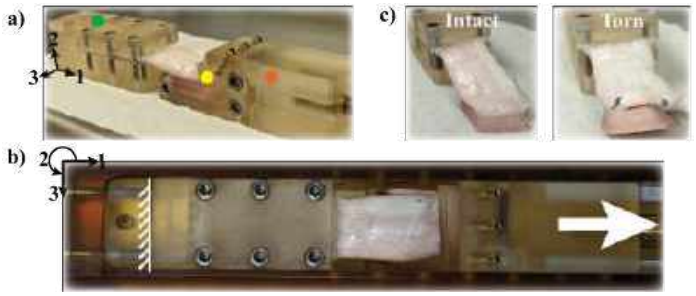

Figure 1: Experimental setup: a) Sample holder with tendon's gripper (green circle), humerus fixture (orange circle), and wedge (yellow circle), b) MRI compatible apparatus with sample holder inside, showing pull direction (white arrow), c) Intact and torn configurations.

Fixtures were mounted to a magnetic resonance imaging (MRI)-compatible apparatus (Figure 1-b) and placed inside a 7 Tesla MRI unit, positioning the region of interest in the center of the magnet. Once in place, samples underwent cyclic uniaxial tension in the main fiber direction. The load-unload cycles were synchronized to a displacement encoding protocol [5], which captured voxel-wise phase variation between loaded and un-

loaded configurations. Full-field displacements, Lagrangian strains, and maximum shear strains were obtained from these phase differences.

We tested two clinically relevant configurations per tendon: i) intact tendon, followed by ii) 75% bursal footprint detachment (type III tear with ∼75% width) with inverted U-shape, surgically cut with a #10 scalpel blade (Figure 1-c). Each configuration underwent two physiologically relevant displacements of 1 mm and 2 mm, which had been shown to represent submaximal and supramaximal human shoulder force ranges in preliminary studies. In total, we ran four experiments per tendon, each with a conditioning cycle of 10 minutes for force stabilization.

Binary masks were obtained from high resolution images of the samples in MATLAB to isolate tendon from bone in the intact and torn configurations. Displacements and strains were evaluated in these regions of interest. Then, each mask was transformed into a smooth high-quality mesh and full-field displacements and strains were interpolated to match these meshes. Quantitative differences were calculated in the interpolated maps.

RESULTS

Non-homogeneous full-field displacement maps in all directions were visualized for both intact and torn tendons (Figures 2-a, 2-b, and 2-c). In the torn configurations, larger displacements in the longitudinal direction were registered in the detached band of fibers (Figure 2-a) as compared to corresponding intact counterparts. In particular, we observed displacements 4 times higher than those of the intact condition close to the detached bursal surface. In the remaining attached portion of fibers in the torn configurations, displacement increases went beyond 1.5 times those of the intact configurations. Lower degree of tendon wrapping around the humeral head appeared to have a lower level of sliding in the detached tissue portion with respect to the attached region, as compared to tendons with higher degree of wrapping (Figure 2-d).

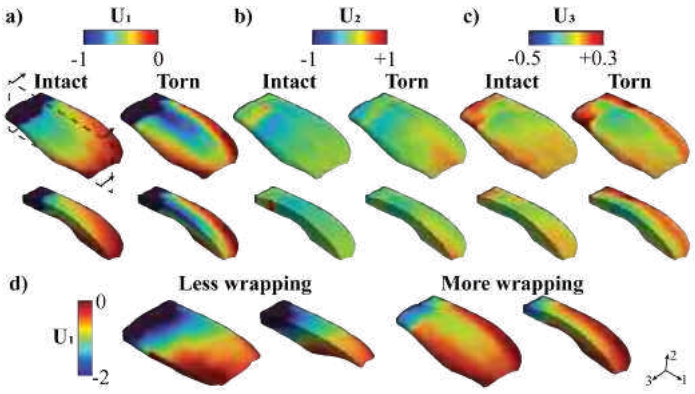

Figure 2: Displacements of intact and torn conditions (representative tendon) in the a) longitudinal, b) vertical, and c) transverse directions. Tendon sections (second row) are obtained from a longitudinal cut, as indicated by the dashed lines and arrows in the first 3D section. d) Displacement in the longitudinal direction for torn tendons with different degrees of wrapping around the bone.

Torn tendons showed absolute shear strain differences larger than 0.10 compared to the intact tendons for all shear strain components. This was a result of the gradient of longitudinal and transverse displacements between the detached band of fibers and the remaining portion of fibers. Shear strain magnitudes were above 0.10 for both the 1-2 and 1-3 components, and 0.05 for the 2-3 component (Figure 3-a, 3-b and 3-c). Maximum shear strain concentrations appeared in the articular surface, the remaining footprint of the tendon, the tendon's mid-substance, and the boundaries between attached and detached tissue bands in torn tendons (Figure 3-d). More than 0.08 maximum shear strains were registered in the regions close to the enthesis, which represented an absolute difference larger than 0.05 compared to the intact configurations. We report values for the 2 mm cyclic displacement; corresponding results for the submaximal force followed a similar trend.

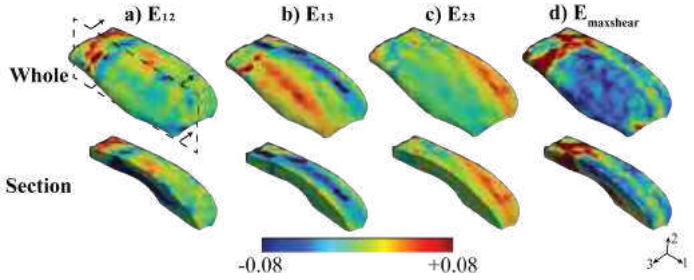

Figure 3: Shear strain maps for a representative torn tendon: a) 1-2 component, b) 1-3 component, c) 2-3 component, d) maximum shear. The dashed lines and arrows indicate the section plane and directions.

DISCUSSION

Our complex displacement maps show material heterogeneity and three-dimensional structure effects in this animal model of the rotator cuff, which implies that surface strain probing methods provide an incomplete picture of the mechanical behavior of the tendon. In high-grade bursal-sided partial-thickness tears, the detached band of tissue appears to slide on top of the remaining portion of fibers, developing larger longitudinal displacements and shear strains as compared to the intact condition. Sliding is a failure mechanism that appears in composite materials with one fiber family and has been visualized in tendons with transverse tears [6]. Hence, a thorough analysis of tendon tear progression should include fiber-matrix debonding or matrix failure mechanisms. Contrary to previous studies [2], we did not observe the largest increase of strain in tear edges, potentially because we examined different tear types. Also, in injured tendons, we observed more than 60% increases for maximum shear strains in the articular-sided region close to the enthesis, suggesting that tear progression could occur in this area even at neutral position with supramaximal forces.

These results support our hypothesis that delamination could be a potential tear growth inducing mechanism in type III bursal-sided tears. However, the progression threshold has not been defined yet, and we could not ascertain tear growth occurrence. Although one of the limitations of our study includes our small sample size, we observed sliding behavior and shear strains larger than 0.10 in all tendons, which should persist in studies with a larger sample size. Also, our animal model of the rotator cuff has a single fiber family and no load sharing as opposed to the human rotator cuff tendons. However, our full-field strain measurement technique is suitable for human cadaveric specimens and could be combined with finite element models for the study of all kinds of tears.

In brief, our full-field data provide quantifiable evidence that high-grade bursal-sided partial-thickness tears produce shear strains between the articular and bursal regions, suggesting that delamination could be a mechanism for tear growth. Accurate measurement of three-dimensional shear strains and damage thresholds in different tear types could inform surgical decisions, tears at high risk of progression, and the natural history of tears.

ACKNOWLEDGEMENTS

This study was conducted thanks to internal funding through the University of Michigan.

REFERENCES

[1] Sayampanathan AA et al. *Journal of Orthopaedic Surgery* 25.1 (2017). DOI: 10.1177/2309499016684318.

[2] Andarawis-Puri N et al. *Journal of Biomechanics* 42.2 (2009). DOI: 10.1016/j.jbiomech.2008.10.020.

[3] Miller RM et al. *Journal of Orthopaedic Research* 32.10 (2014).

[4] Gerber C et al. *JBJS* 86.9 (2004).

[5] Scheven UM et al. *Journal of Magnetic Resonance* 310 (2020). DOI: 10.1016/j.jmr.2019.106620.

[6] Szczesny SE et al. *Scientific reports* 5.1 (2015).

ROLE OF SEX AND SEX HORMONES IN PULMONARY ARTERY ADVENTITIAL FIBROBLAST MECHANOSIGNALING

Yufan Lin (1), Giuditta Monti (1), Daniela Valdez-Jasso (1)

(1) Department of Bioengineering, University of California, San Diego, La Jolla, California, United States

INTRODUCTION

Pulmonary arterial hypertension (PAH) is a progressive disease driven by pathological activities of mechanosensitive cells in pulmonary arteries (PAs) [1]. PAH is more prevalent in women than men, but pre-menopause females have better outcomes than man and post-menopausal women [2]. As PAH differentially affects men and women, and there is no cure, we are studying the mechanosignaling of pulmonary artery adventitial fibroblasts (PAAFs), the cell type that is attributed for vasculature stiffening in PAH, and how they are regulated by the chromosomal sex and sex hormone in rats. By combining *in-vitro* cell experiments with *in-silico* model simulations, we seek to develop and validate a sex-specific PAAF signaling network model.

METHODS

PAAFs isolated from healthy male, female, and ovariectomized (OVX) female rats are cultured in polyacrylamide gels. These scaffolds are built with different stiffness levels to represent healthy conditions (0.5 kPa), and mild (3 kPa) and severe (10 kPa) disease stages of PAH [3]. To mimic changes in strain due to increase in pulmonary blood pressures, we exposed the gels to 10% biaxial stretch for 24 hours [3]. Cells are then collected and lysed for RNA isolation, which is followed by cDNA synthesis and quantitative PCR (qPCR). qPCR targets were selected to be profibrotic genes shown previously to be upregulated in PAs from animals treated with sugen-hypoxia (SuHx), a well-established animal model of PAH. The gene expressions are normalized against the housekeeping gene *18S*, and analyzed with 2-way ANOVA with the two factors being stretch and stiffness, which is followed by Dunnett's *post-hoc* multiple comparisons test.

The cell signaling model is composed of mechano- and biochemical inputs, receptors, kinases, transcription factors, mRNA, and protein or cell phenotype outputs. The dynamical system is modeled as a logic-based differential equation model, where:

$$\frac{dy_i}{dt} = \frac{1}{\tau_i}\left(\sum_j \omega_j f_j y_i^{max} - y_i\right) \quad (1)$$

where y_i is the activation level of species i, τ_i and y_i^{max} are the time constant and maximal fractional activation, while f_j and ω_j are the associated Hill activation/inhibition functions and corresponding reaction weights, respectively [4].

PAAF signaling model simulations were iteratively conducted with varying mechanical input weight ($\omega_{stiffness}$ and $\omega_{stretch}$) within the normalized interval between 0 and 1 [5]. To recapitulated female signaling, we conducted separate simulations with knockdown of biochemical nodes – including PDGFR, p38 and NFAT - based on literature data [6-7]. In the model, this is implemented by reducing parameters y_{PDGFR}^{max}, y_{p38}^{max}, and y_{NFAT}^{max} to 0.25 from default value of 1.

RESULTS

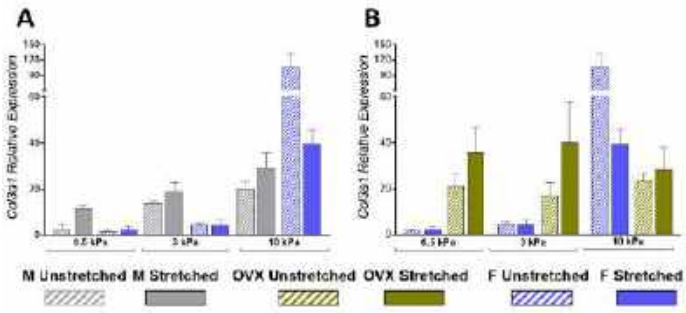

Figure 1: Effect of substrate stiffness and stretch on *Col3a1* expression in PAAFs derived from male rats and female rats (A), and intact vs. OVX female rats (B). Note that female cells have a higher stiffness response threshold than male (A), and OVX cells are more resistant to the up-regulation of substrate stiffness increase compared to intact female (B).

Profibrotic gene expressions in PAAFs derived from male, female, and OVX female animals show an upregulation due to stretch and substrate stiffness (**Figure 1B & D)**. Specifically, intact female-derived PAAFs exhibits a higher substrate stiffness response threshold compared to male **(Figure 1A).** Meanwhile, OVX female-derived cells show higher baseline expression but lower sensitivity to an increase in substrate stiffness when compared to intact female **(Figure 1.B)**.

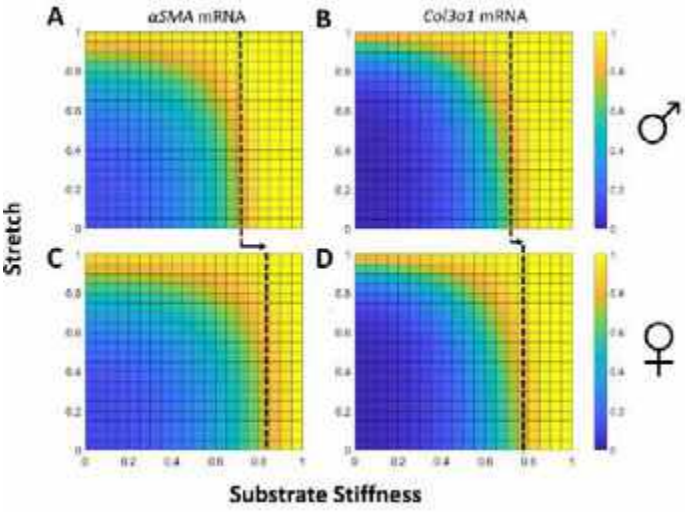

Figure 2: Model simulation ranging from none (0) to fully activated (1) stretch and degrees of substrate stiffness recapitulating male- (A-B) and female-derived (C-D) PAAFs. Dashed lines indicate the stiffness level for expression to reach 0.8 at a low stretch level. In the gene expression of *Acta2* (A, C) and *Col1a1* (B-D), increasing stretch and stiffness levels generally upregulate the expression levels in a non-linear manner. Note that the drastic increase in expression levels occurs at higher stiffness levels in the simulations recapitulating females (C, D).

By simulating the normalized Hill-based computational model of our established PAAF mechanosignaling network iteratively across various mechanical stimuli levels, we obtained the prediction of mechano-induced PAAF profibrotic gene expression dynamics, with parameters tuned to specifically recapitulate male versus female signaling networks (**Figure 2**). Qualitatively, the female-representing simulations – featuring knockdowns of nodes including PDGFR, p38, and NFAT (**Figure 2.C-D**) – show higher stiffness response thresholds for genes including *Acta2* and *Col3a1* than the analogous simulations for male PAAFs (**Figure 2.A-B**).

DISCUSSION

Based on the *in-vitro* cell experiment results, we observe that increased substrate stiffness and stretch generally lead to activation of profibrotic gene expressions. Moreover, the measured levels of these genes - including *Acta2* and *Col3a1* - show differential response patterns between male and female-derive PAAFs; specifically, being female appears to increase the threshold for stiffness-induced response in fibrotic gene expressions, while male cells show a lower threshold when exposed to stretched. In summary, these results demonstrate differential mechanical stimuli thresholds at the cellular level between male and female PAAFs. Similar differences are also observed between intact and OVX female groups. Compared to male, OVX derived cells respond to changes in mechanical stimuli in a similar manner, namely low threshold for stiffness and high sensitivity for stretch, but they also show higher baseline expression levels than male cells. This suggests that the presence of ovarian hormones is also a significant factor to consider during PAH development.

Since our PAAF mechanosignaling model was informed with and validated against exclusively male-derived data, its predictions align well with the male-derived PAAF *in vitro* experiment results. However, the observed sex-dependent phenotype differentiation motivates the incorporation of sex specificity in this network. Studies focusing on cardiac fibroblasts have found key biochemical components to be differentially expressed between cells from male versus female [6-7]. Among these components, the ones involved in profibrotic mechanosignaling activities include PDGFR, p38, and NFAT, all found to be less active in female. Assuming high level similarities between cardiac fibroblasts and PAAF, we conducted simulated knockdowns of these three nodes and thus granted the network female features. Simulating this female-recapitulating network, we observe that mechano-induced activation dynamics for ECM genes (including *Col1a1* and *Col3a1*) and the myofibroblast marker *Acta2* are qualitatively like the male-version simulations, where higher stretch or stiffness levels generally induce greater responses; however, the thresholds for the drastic increase in expression due to substrate stiffness increase are higher in the female simulations. This agrees with the *in vitro* experiment results where female PAAFs are activated only at a relatively high stiffness level. No difference in terms of stretch response thresholds is predicted by the simulations. This network does not yet describe the role of sex hormones, and thus it cannot discriminate OVX versus female-derived cells, while ovarian hormone presence is observed to differentiate PAAF phenotypes *in vitro*. Hence, model expansion and parameter adjustment based on sex hormone presence will be the future direction of the improvement. This computational model will assist in hypothesis generation, response prediction, and results validation for future sex-dependent PAH development studies.

In summary, the *in-vitro* experiments suggest that both chromosomal sex and the presence of ovarian hormones dictate PAAF mechanosignaling by altering the response thresholds and intensities under increasing stretch and substrate stiffness. Upon further expansion and incorporation of sex hormone in the training of the model, we will use this as a tool for signaling mechanism validation, examination target selection, and *in silico* experimentation for more efficient investigation of sex-specific PAAF mechanosignaling activities.

ACKNOWLEDGEMENTS

This work was funded by National Heart, Lung, and Blood Institute Grants 1R01HL155945-01 (to D. Valdez-Jasso) and 1T32HL160507-01A1 (to Y. Lin); and National Science Foundation CAREER Award 2046259 (to D. Valdez-Jasso).

REFERENCES

[1] Maron, BA et al., *Global Cadiol Sci*, vol.2020,1 e202003 (2020).
[2] Umar, S et al., *Am J Respir Crit Care Med*, 186(2):125-131, 2012.
[3] Wang, A et al., *Cells*, 10(5):1000, 2021.
[4] Kraeutler, MJ et al., *BMC Syst Biol*, 4:157, 2010.
[5] Wang, A et al., *Phil Trans R Soc A*, 378:20190338, 2020.
[6] Achkar, A et al., *Oxid Med Cell Longev*, 2020: 8282157, 2020
[7] Watts, K et al, *Cells*, 10(10):2564, 2021

FEMALE ANTERIOR CRUCIATE LIGAMENTS EXHIBIT A MINIMAL MECHANOBIOLOGICAL RESPONSE TO MECHANICAL LOADING

L. Paschall (1), M. Konnaris (1), A. Dhawan (2), E. Tabdanov (2), I. Georgakopoulos-Sores (2), S. Szczesny (1,2)

(1) The Pennsylvania State University, University Park, PA, USA
(2) The Pennsylvania State University, Hershey, PA, USA

INTRODUCTION

Anterior cruciate ligament (ACL) tears are one of the most common knee injuries affecting over 200,000 people a year. This is particularly true for female athletes, who are 2-8 times more likely to suffer an ACL tear compared to their male counterparts[1,2]. The reason for this phenomenon remains unclear; however, it is possible that exposure to sex hormones make ACLs less capable of repairing tissue damage from repetitive loading. Recent studies suggest that ACL injuries occur from fatigue failure, where repetitive loading causes an accumulation of tissue damage predisposing the ACL to injury[3]. Prevention of ACL fatigue rupture requires successful remodeling of tissue damage, and estrogen has been shown to regulate genes involved in tissue remodeling (collagen, collagen crosslinking, MMPs, and MMP inhibitors)[4,5]. Furthermore, prior data on tendon and bone suggest that estrogen is a key modulator of the biological response of musculoskeletal tissues to mechanical loading[6,7]. Despite these data, the sex-specific response of ACLs to load is unknown. Therefore, the objective of this study was to investigate the sex-specific mechanobiological response of ACLs to cyclic loading. We **hypothesized** that in response to load, female ACLs will exhibit an increased catabolic response and have an impaired activation of mechanotransduction pathways that will be accompanied by activation of the estrogen signaling pathway.

METHODS

Following IACUC approval, ACLs were harvested from both knees of 7 male and 8 female New Zealand white rabbits and placed in a tensile bioreactor with culture media kept at 37°C and 5% CO_2. After 18 h of accumulating the ACLs to explant culture, the bioreactor cyclically loaded the samples to 2, 4, or 8 MPa at 0.5 Hz for 8 h. These stress levels encompass the full range of physiologic ACL loading[8]. Control samples were placed in the bioreactor under the same duration but under a minimal (0.1 MPa) static load. ACLs were immediately removed after loading, rinsed with ice cold RNase-free water and flash frozen in liquid nitrogen. Total RNA was extracted with RNeasy minicolumns, cDNA was synthesized from 10 ng of the total RNA, and real time-PCR was performed using Taqman probes to measure expression of anabolic (*COL1A1, COL1A2, LOX, COL3A1, TGFβ1 ACTA2*), catabolic (*MMP1. MMP2, MMP10, MMP13, TIMP1, TIMP3*), and inflammatory (*IL-1β, PTSG2*) genes with *GAPDH* and *ACTB* as reference genes. Quantification of gene expression was performed via the delta-delta Cq method correcting for primer efficiencies and using the genomic mean of the two reference genes. To determine the effect of mechanical loading on both male and female ACL explants, the male and female cyclically loaded samples were compared to their sex-matched statically loaded control. To determine baseline sex-specific gene expression differences, the statically loaded female samples were compared to male statically loaded samples. Mann-Whitney tests were used to determine differential expression and to compare gene expression response between sexes. Statistical significance was set at $p < 0.05$ with statistical trends set at $p < 0.10$. A subset of the samples was sent to GENEWIZ for RNA-sequencing. Sequence reads were trimmed and mapped to the OryCun 2.0 reference genome. DESeq2 was used to determine differentially expressed genes between the 4 MPa and static load samples for both sexes. The Wald test was used to generate p-values of all the differentially expressed genes. Genes with an adjusted p-value < 0.05 and absolute log2 fold change > 1 were selected as differentially expressed genes. Pathway enrichment analysis was performed using DAVID.

RESULTS

Female ACLs have impaired remodeling response to load: Minimal changes in gene expression were observed at low (2 MPa) and high (8 MPa) loading for both sexes (data not shown). In response to cyclic loading at 4 MPa, male ACLs (n = 5) significantly upregulated anabolic genes (*COL3A1, TIMP1, TIMP3*) ($p < 0.05$) with additional anabolic

genes (*COL1A1, LOX*) trending toward upregulation ($p < 0.1$) (**Fig. 1**). In contrast, when female ACLs were cyclically loaded to 4 MPa (n = 7), there was only significant upregulation of one anabolic gene (*ACTA2*) ($p < 0.05$) (**Fig. 1**). When directly comparing the load-induced gene expression between male and female ACLs, multiple anabolic genes (*COL3A1, TIMP1, TIMP3*) were upregulated in males compared to females, while the anabolic gene *ACTA2* and the catabolic gene *MMP10* were downregulated in male samples ($p < 0.05$) (**Fig. 1**). There was no differential expression of any genes between male and female control samples under static load (data not shown).

Female ACLs have reduced mechanotransduction signaling to load:

In response to 4 MPa load, male ACLs had 760 differentially expressed genes and 80% of those genes were upregulated (**Fig 2A**). In contrast, female ACLs had only 98 differentially expressed genes with 59% of those genes upregulated (**Fig 2A**). In contrast, only 44 genes were differentially expressed between freshly harvested female and male ACLs (**Fig 2A**). Pathway analysis found that male ACLs had 41 signaling pathways enriched in response to load while female ACLs only had 3 enriched pathways (TNF, IL17, PPAR). Of the pathways uniquely enriched in males, 16 of them are mechanotransduction pathways and/or pathways associated with cell-matrix interactions (**Fig. 2B**).

DISCUSSION

This study investigated how female ACLs respond to mechanical loading compared to males in a tissue explant model. Overall, female ACLs had a muted response to mechanical loading. While male ACLs were able to upregulate multiple anabolic genes in response to load, female ACLs were only able to upregulate one. Furthermore, female ACLs had substantially less differentially expressed genes in response to load compared to males (98 and 760 respectively). These differences are despite the fact that there weren't differences in gene expression between male and female ACLs prior to loading. This muted mechanobiological response to load in female ACLs could be partially due to an impaired mechnaotransduction response. While male ACLs had 16 unique pathways enriched associated with mechanotransduction pathways, female ACLs only exhibited one unique pathway associated with mechanotransduction. While we did not observe the estrogen pathway being enriched (as we hypothesized), we did observe pathways involving ERK as/MAPK) and YAP (Hippo) pathways which have been shown to interact with estrogen receptor signaling[9,10]. Together, this study demonstrates that female ACLs have an impaired mechanobiological response to load compared to males, which may help explain the increased rate of ACL tears in women. Future work will directly investigate the role of estrogen in the mechanobiological response of ACLs by treating male ACLs with estrogen and inhibiting estrogen in female studies. Furthermore, future studies will investigate the mechanistic influence of ERK and YAP on ACL tissue remodeling by performing pharmacological perturbations.

ACKNOWLEDGEMENTS

We would like to the Genomics Core Facility at Penn State for their assistance. Funding for this project was provided by the Orthopaedic Research and Education Foundation (234995) and the Congressionally Directed Medical Research Program (W81XWH2110152).

REFERENCES

[1] Garrett, W. et al., *J Bone Joint Surg. Am*, 88:660-667, 2006.
[2] Ardent, E.. et al., *Am. J. Sports Med.* 23:694-701, 1995.
[3] Chen, J. et al., *Am J Sports Med*, 47:2067-2076, 2019.
[4] Chidi-Ogbolu, N. et al., *Front Physiol*. 9:1834, 2018.
[5] Salamonsen, L. et al., *Hum R*eprod. 2:124-33, 1996.
[6] Damien, E. et al., *J Bone Miner Res*. 13(8):1275-82, 1998.
[7] Lee, C. et al., *Matrix Biol*. 23(5):323-329, 2004.
[8] Holden, J. et al., *J Biomech*. 27(5):517-526, 1994.
[9] Fuentes, N. et al., *Adv Protein Chem Struct Biol*. 116:135-170. 2019.
[10] Ma, S. et al., *Nat Commun*. 13:1061, 2022.

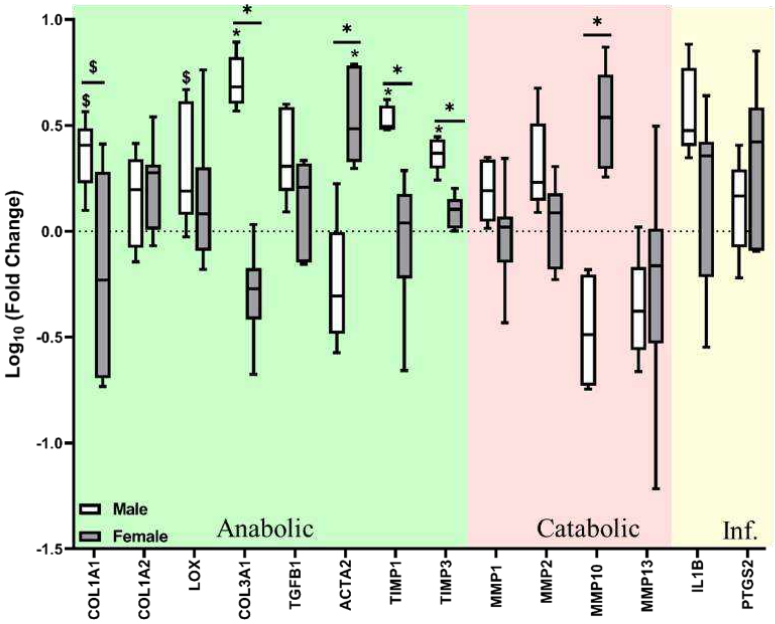

Fig 1. Change in gene expression of male and female ACLs cyclically loaded to 4 MPa relative to sex-matched static control. * : $p < 0.05$, $: $p < 0.10$.

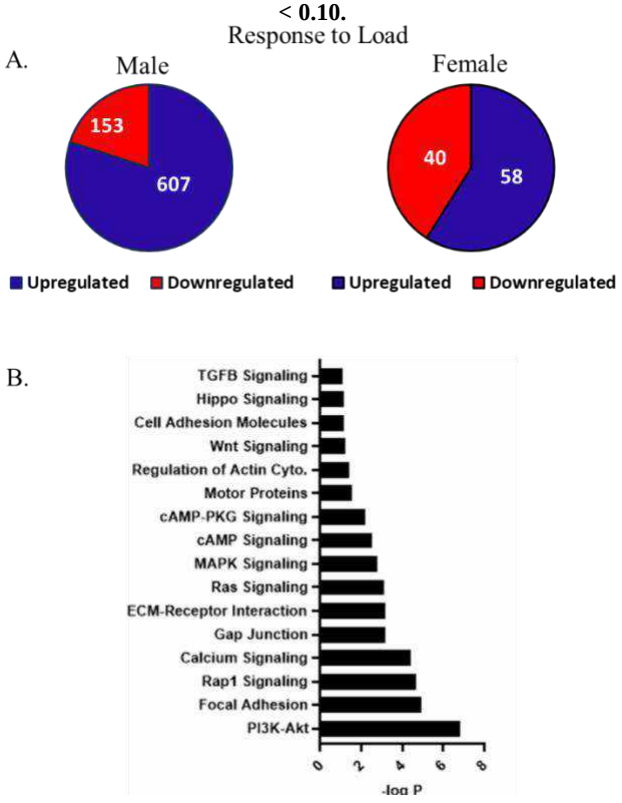

Fig 2. ACLs mechanobiological response to load. A) Differentially expressed genes in response to loading. B) Selected unique enriched pathways in male samples.

IPSC-DERIVED ENDOTHELIAL MULTI-CELL NETWORKS SYNERGISTICALLY MODIFY THEIR BASAL CONTRACTILITY AND EXTRACELLULAR MATRIX IN 3D

Toni M. West (1, 2), Jiwan Han (1), Gabriel Peery (1,2), Robin Tuscher (1,2), Janet Zoldan (1), Michael S. Sacks (1, 2)

(1) Biomedical Engineering, University of Texas, Austin, TX, USA
(2) Oden Institute for Computational Engineering and Science, University of Texas, Austin, TX, USA

INTRODUCTION

Cells modify the local micromechanical environment that they live in. Indeed, we have seen within 3D matrices that newly differentiated endothelial cells (ECs) from induced pluripotent stem cells (iPSCs) migrate towards each other and form networks of connected cells which configure into hollow tubes that resemble capillary networks. [1] Understanding how the mechanical attributes of these cell networks change and affect their microenvironment is key to developing efficacious stem cell therapies for microvascular disease, myocardial infarction repair, and embolism. In our current work, we hypothesize that measurements from 3D traction force microscopy (3D-TFM) experiments can be implemented to develop inverse models to determine how networks of endothelial cells differentially affect their 3D microenvironment (through degradation and collagen deposition) and how their cytoskeletal structure organization is distinct compared to individual cells.

METHODS

We have developed a method for differentiating iPSCs into endothelial cells, which depending on seeding density within 3D gels form into networks composed of single cells, small groups of cells, or large groups of cells that form microvascular-type structures. [2] These cells were seeded into Norbornene-functionalized hyaluronic acid 3D gels at densities that produce single cell distributions and small clusters of cells (Fig 1A). We have previously developed a Gaussian process model to determine how basal cell contractility (the contractile state of the cell when it is in its resting metabolic state) affects displacement of the surrounding 3D gel by implementing traction force microscopy (3D-TFM) [3]. 3D TFM was performed on a Leica laser scanning confocal microscope by imaging cells in their basal state and after treatment with the actin depolymerization agent, cytochalasin-D. In brief, fluorescent microspheres are placed homogenously in the gel and the nearest neighbors principle is applied to track the displacement of the beads, while a live cell stain detects the cell membrane and Hoechst detects the nuclei. This method produced rich 3D displacement fields and cell morphologies.

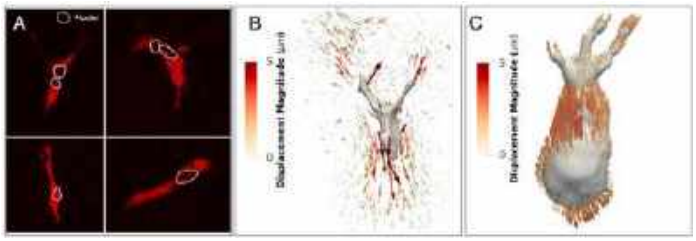

Figure 1: 3D-TFM. A) Maximum intensity for each pixel projected into a flat z-slice. Circles indicate areas of sparse staining at the loci of nuclei. Both single cell and multi-cell networks were analyzed. B) Experimental displacement field of fiducial markers in the local vicinity of the iPSC as measured with FMT. The iPSC surface is reconstructed and shown in white. C) Gaussian-process model interpolation of displacement field onto the cell surface.

To extract the cellular forces, the mechanical properties of the gel need to be accurately known. However, most studies assume the embedded cells do not affect the gel, which is typically not the case. To address this limitation, we have developed an inverse computational model that computes local cell-induced modification of the gel modulus [4]. Using these cell-specific gel mechanical properties, we are then able to utilize an inverse computational continuum model of the internal stress fiber structure of single cells [5] to be able to analyze multi-cell

networks. Eq. 1 delineates our inverse model for extracellular matrix modulus determination:

$$\Psi = \alpha(\boldsymbol{x}_0) * \left[\frac{\mu}{2}(I_1 - 3) - \mu\, ln(J) + \frac{\lambda}{2} ln(J)^2\right] \quad (1)$$

Where $\alpha(\boldsymbol{x}_0)$ is applied to a neo-hookean model, where μ is the homogenous shear modulus, I_1 is the first invariant of the isochoric part of the Right Cauchy Green deformation tensor, J is $det(\mathbf{F})$, and λ is Lame's first parameter. $\alpha(\boldsymbol{x}_0)$ is a scaling parameter that varies spatially over $\boldsymbol{x}_0$ which converges the measured bead displacement to the expected bead displacement if the gel modulus was homogenous. The calculated total strain energy of the system is then divided by the volume of the cell(s) present in the system to determine the amount of strain energy per unit volume.

Eq. 2 defines our inverse continuum model of the internal actin fiber structure of the cell, which accounts for both active and passive contributions of stress fibers:

$$\boldsymbol{T}^{sf} = H(I_4 - 1) * \boldsymbol{T}^p + \boldsymbol{T}^a \quad (2)$$

The Passive stress that arises when fibers are stretched is modeled as

$$\boldsymbol{T}^P = 2\frac{I_4}{J}\frac{\partial \Psi_p^{sf}}{\partial I_4}\boldsymbol{m}\otimes\boldsymbol{m} \quad (3)$$

Where

$$\Psi_p^{sf} = \frac{\mu_{sf}\varphi_{sf}}{2}(I_4 - 1)^2 \quad (4)$$

Application of the Heaviside step function, H, ensures passive stress only from fiber stretch and not compression. The active stress that arises when fibers actively contract is modeled as

$$\boldsymbol{T}^a = f_{sf}\varphi_{sf}\frac{I_4}{J}\boldsymbol{m}\otimes\boldsymbol{m} \quad (5)$$

An objective function combined with the adjoint method is then implemented to fit the model to the data.

Our models therefore account for localized differences in matrix modulus that previous 3D-TFM models assumed were homogenous. Since cells degrade extracellular matrices to grow and move in them while also depositing stiff matrix substances such as collagen, factoring the variation in matrix modulus into our calculations allows us to determine the cell-generated traction forces with much less error. Herein our improved models were implemented to determine the mechanical properties of nuclei, cells, and the microenvironment of 3D multi-cell networks from experimentally measured displacements that occur because of basal contractility (Figure 1B-C).

RESULTS

From our computational models, we found that multi-EC networks, when compared to individual ECs, have roughly four times the strain energy per unit cell volume, an increase in extracellular matrix modification per cell volume, and differing stress fiber orientation that affects basal nuclear shape (Figure 2).

DISCUSSION

These results suggest that networks of iPSC-EC cells work together mechanically in a synergistic manner to form mechanically robust tissues such as capillary beds. The increase in strain energy per unit volume indicates that the cells are more energy dense as clusters. As we have seen here (Fig 3) and previously [1, 2], the number of iPSC-derived ECs in network correlates non-linearly with the amount of matrix modification they produce. In a large enough network, this can even lead to a hollow-space lumen on the inside of the tube of cells, with a high-modulus layer of collagen laid down by the ECs on the exterior of the tube of cells. Further research into the mechanical properties of iPSC-derived ECs will enable us to understand how these cells are able to maintain structural integrity as they highly modify the environment in which they live. This will pave the way for development of stem cell therapies for a variety of diseases where microvascular repair is beneficial.

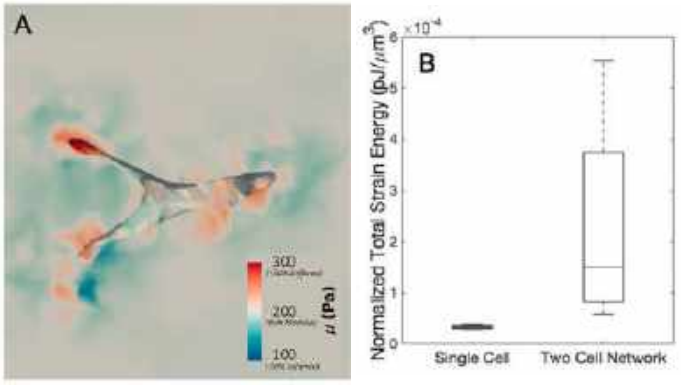

Figure 3: Gel modulus variation and strain energy per unit volume increases greatly in networks of cells. A) Simulated modulus field local to the iPSC. Regions in red are stiffened regions, peaking at around 1.5 times the bulk modulus. Regions in blue show simulated softened hydrogel, which is as soft as 0.5 times the bulk modulus. B) The volume-normalized total strain energy (E_gel) for single and two cell networks increases by a factor of 4 in two-cell networks.

ACKNOWLEDGEMENTS

TMW is an NIH F32 post-doctoral fellow (1F32HL167570). This work is funded by the following grant awards: NIH-1R01HL142504, NIH-2R01HL073021, NIH-1R01HL157829, MDACC-AWD 00000078, UTAUS-FA00000461.

REFERENCES

[1] Crosby et. al. 2019 Tiss Eng Part A
[2] Crosby et. al. 2021 Acta Biomat
[3] Khang et. al. 2019 Acta Biomat
[4] Khang et. al. 2023 Acta Biomat
[5] Khang et. al. 2023 J Biomech Eng

A NOVEL APPROACH TO CREATE THE MEAN LUMBAR SPINE MODEL USING STATISTICAL SHAPE MODELING FOR FINITE ELEMENT ANALYSIS

Faris A. Almalki (1) (2), Daniel H. Cortes (2)

(1) Mechanical Engineering Department, University of Jeddah, Jeddah, Saudi Arabia
(2) Mechanical Engineering Department, Penn State University, University Park, PA, USA

INTRODUCTION

Low back pain (LBP) significantly affects individuals' ability to perform daily life activities [1]. LBP can be caused by facet joint problems [2], [3]. Radiofrequency ablation (RFA) is one of the standard methods to treat this condition [4]. However, the RFA procedure may cause denervation of the multifidus muscle (MF) [5]. In our previous study [6], a musculoskeletal model from AnyBody software was used to evaluate the biomechanics of the spine during different movements. The model simulated the denervation of MF. The results showed that changes occur in the kinematics of the lumbar spine, which may affect the biology of the spine and the strain on the intervertebral disc. This alteration in the mechanobiology can lead to disc degeneration.

To further investigate the effect of the RFA procedure on the intervertebral disc, an anatomical model representing several samples of the lumbar spine would be essential. This model can be provided by statistical shape modeling (SSM), which helps in understanding the spinal mechanics. This investigation aims to create a three-dimensional model that represents the lumbar spine accounting for the average of several samples to be used in finite element analysis (FEA). The purpose of this FEA is to examine the strains of the intervertebral disc under different loads when MF is denervated.

METHODS

In this study, publicly available CT images and 3D lumbar segmentations from the Vertebrae Segmentation Challenge (VerSe) 2020 were utilized [7-9]. A total of 138 lumbar vertebrae from 46 patients were carefully selected. The study ensured a balanced gender representation, with an equal number of male and female patients. The inclusion criteria were centered around CT scans that clearly depicted the L3 to L5 lumbar vertebrae. In contrast, scans were excluded if they showed anomalies such as the lumbar spine terminating at L4 or L6, presence of implants, or inaccuracies in the L5/S1 segmentations.

The VerSe dataset included the original CT scans and the segmented vertebrae (*.nii file type). Using Slicer software and SlicerMorph extension [10], [11], the 3D vertebral segmentations were overlayed onto the corresponding CT scan. This resulted in a combined 3D model containing all the vertebrae as a single object. Using the 'split volume tool' from the 'segmentation editor' module, the model was divided into separate vertebrae and exported (*.nrrd file type).

In the SSM procedure, the segmentations were then processed in ShapeWorks software [12], where they underwent a grooming step to be converted into isotropic meshes (Fig. 1), followed by an optimization step to compute point-based shape models (Fig. 2). These steps were crucial for preparing the data to create the mean of the sample for detailed analysis.

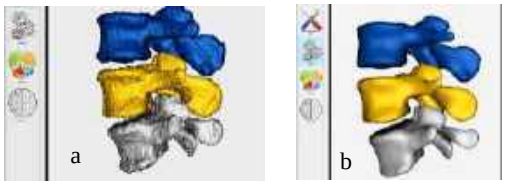

Fig. 1: Lumbar spine model after loading into software (a), and after grooming (b).

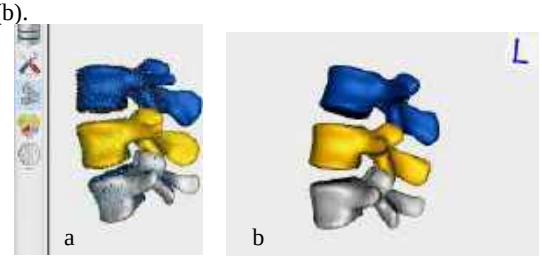

Fig. 2: Optimized lumbar spine model (a), and final mean model (b).

To create the FEA model, the STL files of the vertebrae were imported into a 3D modeling software to create the discs' geometry in between the bones (Fig. 3a). Then, they were imported into Fusion 360 to convert them into BRep models. Next, a 'Boolean cut' operation was performed on the discs to create the interface surface between them and the bone (Fig. 3b). To create the FEA model, Abaqus software was used to partition the discs' internal layers and cartilage endplate inside the disc model and cleaned using 'virtual topology' feature (Fig. 4).

Fig. 3: Creating the disc geometry (a), and performing Boolean cut operation (b)

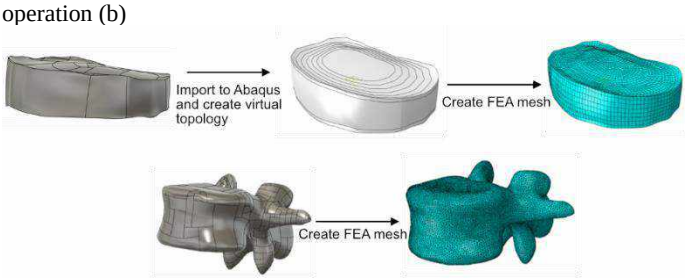

Fig. 4: Generation of FEA mesh in Abaqus

RESULTS

Using this method, 46 statistical shape models (23 per gender) were created for the lumbar spine containing each of the L3, L4, and L5 vertebrae. Each vertebrae represented the mean of the male, female, and combined samples (Fig. 5a). Upon preparing the vertebrae for FEA, two intervertebral discs were created in the joints between each of the L3-L4 and L4-L5 vertebrae. The discs comprised of hexahedral elements. Meanwhile, the vertebrae were made of tetrahedral elements due to their complexity. On the other hand, the resulting endplates were made of shell elements. The final model contained the vertebrae and discs connected by tie constraints. (Fig. 5b)

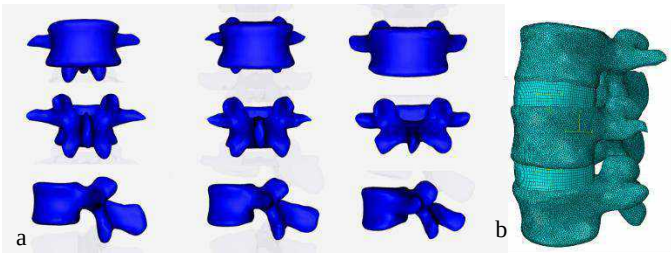

Fig. 5: The lumbar vertebrae SSM of the combined overall sample (a), meshed FEA model of discs and vertebrae.

DISCUSSION

The creation of 3D models representing the spine has been used in several fields. For example, previous research used CT scans and 3D models of the lumbar spine to 3D-print vertebrae [13]. Also, these models were used for visualization of human biomechanical simulations [14]. Moreover, 3D models have been utilized and built for FEA [15]. This study demonstrated how to achieve the average of lumbar vertebrae for usage in applications such as FEA.

The mean of L3L4L5 vertebrae was used to build an FEA model to study the stresses and strains on the intervertebral disc. The advantage of this method, compared to studies that used numerous samples for analysis [16], [17], is the efficiency and simplicity of analyzing a single 3D model. Moreover, the single model represents the average of different samples; thereby, it contains information on the vertebral morphology concisely. The mean model was also visualized clearly to identify the general morphological patterns of the lumbar vertebrae. This method utilized multiple 'domains' analysis so each of the L3L4L5 vertebrae is analyzed separately from other vertebrae. Therefore, the final results do not combine the L3, L4, or L5 vertebrae for more accurate evaluation.

CONCLUSION

This method illustrates the steps to utilize segmentations from CT scans and lumbar vertebrae SSM to create the mean of a sample of L3L4L5 vertebrae for use in FEA. Using this technique can exploit the simplicity and efficiency of 3D software to achieve the best representative average 3D model of other anatomical human parts for further concise yet comprehensive evaluation.

ACKNOWLEDGEMENTS

This work is funded by the Saudi Cultural Mission, SACM and University of Jeddah, Jeddah, Kingdom of Saudi Arabia.

REFERENCES

[1] Hurwitz, Eric L. et al., *European Spine Journal*, 27:796-801, 2018.
[2] Yu, Li Peng et al., *PLoS ONE*, Vol. 7 No. 12, 2012.
[3] Knezevic NN et al., *The Lancet (British edition)*, 398(10294):78–92, 2021
[4] Maher CP et al., *The Lancet (British edition)*, 389(10070):736–47, 2017
[5] Sadeghi S et al., *J Eng Sci Med Diagnostics Ther*, 3(4), 2020.
[6] Almalki, F. A., & Cortes, D. H., *Journal of applied biomechanics*, 39(6), 414-420, 2023
[7] Liebl, Hans et al., *Scientific Data*, 8(1):284, 2021.
[8] Löffler, Maximilian T. et al., *Radiology: Artificial Intelligence*, 2(4):e190138, 2020.
[91] Sekuboyina, Anjany, et al. *Medical Image Analysis*, 73:102166, 2021.
[10] Fedorov, Andriy et al., *Magnetic Resonance Imaging*, 30(9), 1323-1341, (2012).
[11] Rolfe, Sara, et al., *Methods in Ecology and Evolution*, 12(10), 1816-1825, 2021.
[12] Cates, Joshua et al., *In Statistical Shape and Deformation Analysis: Methods, Implementation and Applications*, (pp. 257-298). Academic Press., 2017.
[13] Cramer J. et al., *Journal of digital imaging*, 30:296-300, 2017
[14] Eulzer P. et al., *IEEE Transactions on Visualization and Computer Graphics*, *27*(2):700-710, 2020
[15] Tyndyk M.A. et al., *Acta of bioengineering and biomechanics*, 9(1):35, 2007
[16] Kanawati A. et al., *Acad Radiol*, 28(6):e172-e181, 2021.
[17] Sugisaki K. et al., *Spine* 2009 Nov 15;34(24):2599-604.

SB³C2024
Summer Biomechanics, Bioengineering and Biotransport Conference
June 11-14, Lake Geneva, WI, USA

VIRTUAL STENTING OF PATIENT-SPECIFIC VASCULAR STENOSES

J. Pham (1), F. Kong (2), D. James (3), J. Feinstein (2), A. Marsden (2,4)

(1) Department of Mechanical Engineering, Stanford University, Stanford, CA, USA
(2) Department of Pediatrics, Stanford University, Stanford, CA, USA
(3) Department of Computer Science, Stanford University, Stanford, CA, USA
(4) Department of Bioengineering, Stanford University, Stanford, CA, USA

INTRODUCTION

Computational modeling and simulations of patient-specific vascular anatomies are increasingly used to support personalized interventional treatment planning [1]. In angioplasty applications, these tools allow clinicians to non-invasively test different stent and ballooning configurations and simulate the resulting hemodynamics to design optimal treatment strategies [2]. Computational models are not yet routinely used in clinical practice, however, despite these predictive advantages. One of the key bottlenecks preventing routine application is the difficulty of editing the geometry of the anatomical models to reflect the pre-operative and post-operative shapes of the vessels.

In traditional image-based modeling pipelines, a patient-specific vascular anatomical model is created by segmenting 2D contours of the vessels from CT or MRI scans [3]. To perform virtual interventions on the model, segmentations are often edited to produce the post-interventional shape. Segmentation-editing, however, is generally a manual and laborious process, as the segmentations must be carefully updated to prevent intersections between different contours on a single vessel branch, while ensuring that segmentations of daughter branches are fully encapsulated within the segmentations of the parent branch. This makes automated segmentation-editing particularly challenging. In scenarios where multiple stenting configurations need to be explored, such as in treatment planning for patients with multiple peripheral pulmonary stenoses, a common abnormality in patients with Alagille and Williams syndrome, this segmentation-editing procedure must be painstakingly reperformed for each intervention.

We propose a novel framework for automated stenting of virtual vascular anatomies via physics-informed simulations to overcome these challenges. Algorithm 1 shows a high-level overview of our framework. Our framework directly deforms the mesh of the models and enables us to obtain the post-operative vessel shape without segmentation-editing.

METHODS

We morph the stenosed geometry of an input model into its stented shape by simulating the stenting process using Extended Position Based Dynamics (XPBD) [4]. XPBD is a physics-based technique commonly used by the computer graphics community for simulating deformable objects. XPBD represents the objects as particle systems and simulates their motions according to Newton's 2nd law. The vertices of the meshes correspond to the particles in our framework. XPBD begins by applying external forces, such as gravity, to the particles to update their positions (lines 2–3 of Algorithm 1). Internal forces are then applied via an iterative "constraint projection" step (lines 7–8). In XPBD, constraints are functions that govern the material properties of the deformable objects. The velocities of the particles are updated afterwards.

```
(1) For each timestep:
(2)   For all particles:
(3)     Update positions from external forces
(4)   Inflate stent and update SDF
(5)   Find collisions between SDF and vessel mesh
(6)   Add collision constraints
(7)   For each constraint:
(8)     Project constraint and update positions
(9)   For all particles:
(10)    Update velocities from updated positions
```

Algorithm 1: Overview of the virtual stenting framework

We model the internal mechanical behavior of vasculature using geometric constraints. Namely, we use distance and bending constraints, two constraints commonly employed for simulating thin, membranous materials in XPBD [5, 6]. Distance constraints control the amount of stretching of edges in a mesh, while bending constraints govern the degree of bending between adjacent triangle elements.

As stenting is naturally a collision-based process, in which a stent collides with and interacts with a blood vessel, we also include collision

constraints. We model the stent, which has a cylindrical shape, using a signed distance field (SDF). Representing the stent as an SDF, rather than as a mesh, reduces the cost of collision detection. At each time step in the simulation, we radially inflate the stent and search for collisions between the SDF and mesh of the vascular anatomy. Found collisions are then applied using vertex-normal constraints [5].

RESULTS

We illustrate the results of our stenting framework in Figure 1. This figure illustrates stenting in three distinct patient-specific models: an aortic coarctation model and two pulmonary models with peripheral arterial stenoses. The pulmonary models correspond to patients with Alagille syndrome [2]. These models were obtained from the Vascular Model Repository, an open-source collection of patient-specific cardiovascular models [7].

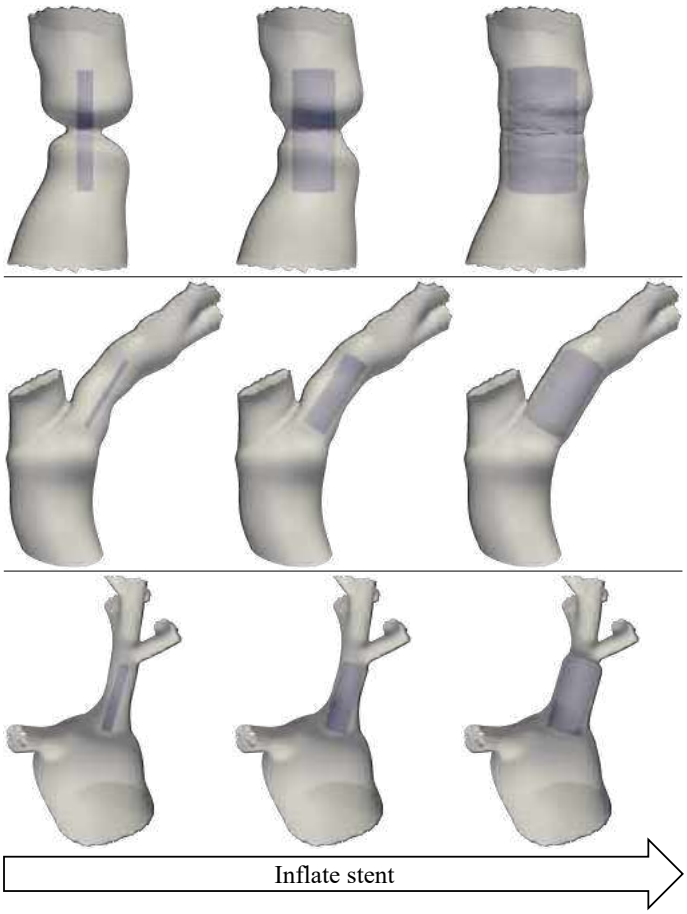

Figure 1: Stents (blue) are placed in the stenosed regions of a patient-specific aortic coarctation model (top) and two pulmonary models (middle and bottom). As the stents inflate to a user-specific diameter, as shown from left to right, they collide with the vascular walls and deform the vessels to relieve the stenoses.

Before applying our framework, we remeshed each model to obtain a uniform mesh resolution, clipped the models to the regions neighboring the stenoses, and applied fixed boundary conditions at the clipped boundaries. We limit our simulations to these sites, which are the regions where the stenting deformations would occur, to reduce their computational expense. With this, each simulation takes only several minutes to run on a standard desktop computer with a single processor.

As we observe Figure 1, the stenosed, pre-operative vessels deform with inflation of the stents and expand to their alleviated, post-operative shapes. We note that the final, deformed meshes do not exhibit any issues with mesh self-intersection.

DISCUSSION

Our methods enable stenting of patient-specific blood vessels using simulation-driven techniques. Such capabilities will enable users to circumvent the need for laborious, manual editing of segmentations. Our framework works well across a wide range of vascular anatomies, as illustrated for the aortic and pulmonary vessels (Figure 1).

One primary advantage of our framework is the ability to parameterize the angle, length, and diameter of the deployed stent. This feature, when coupled with computational fluid dynamics simulations, will allow interventional cardiologists to parametrically and automatically alter stent configurations and quantify the resulting hemodynamic impact. In the example of Alagille and Williams patients with multiple stenoses, such automation will make it significantly easier to create numerous models reflecting different stent designs. This will ultimately help clinicians better optimize treatments for their patients.

The parameterizability of the stent configuration also enables uncertainty-aware planning. By connecting our virtual stenting framework to a robust uncertainty quantification platform [8], uncertainties in the final deployed stent diameter, for example, can be analyzed and used to obtain confidence intervals in the resulting hemodynamics. These confidence intervals will help clinicians assess the viability and success rates of their interventional strategies.

A limitation of our stenting framework, however, is that it can only simulate "rigid" stents, stents that maintain their original orientation and curvature in their fully inflated state. Such rigid mechanical behavior is commonly found in closed-cell stents [9]. Two-way coupled interaction between the stent and the vessel is needed to increase the longitudinal flexibility of the stent and allow it to conform to the curvature of its corresponding vessel, as is commonly characteristic of open-cell stents. To achieve this, we will represent the stent as a mesh and apply collision constraints between vertices and triangle elements of the stent and vessel meshes [5] in future work.

ACKNOWLEDGEMENTS

This study was supported by NIH grants R01EB029362, R01LM013120, R01HL141712, and R01HL167516 and NSF grants 1663671 and 2105345.

REFERENCES

[1] Taylor C and Figueroa C, *Annual Review of Biomedical Engineering*, 11(1):109–134, 2009.
[2] Lan, I et al., *Journal of the American Heart Association*, e023532, 2022.
[3] Updegrove, A et al., *Annals of Biomedical Engineering*, 45:525–541, 2017.
[4] Macklin, M et al., *Proceedings of the 9th International Conference on Motion in Games*, MIG '16, 49–54, 2017.
[5] Müller, M et al., *Journal of Visual Communication and Image Representation*, 18(2):109–118, 2007.
[6] Bender, J et al., *European Association for Computer Graphics: Tutorials*, 1–31, 2017.
[7] Wilson, N et al., *Journal of Medical Devices*, 7(4): 040923, 2013.
[8] Fleeter, C et al., *Computer Methods in Applied Mechanics and Engineering*, 365, 113030, 2020.
[9] Müller-Hülsbeck S et al., *Journal of Endovascular Therapy*, 16(2):168–177, 2009.

UNRAVELLING THE STRUCTURAL MECHANISMS UNDERLYING AGING-AUGMENTED RISK OF AORTIC DISSECTION

Ruizhi Wang (1), Xunjie Yu (1), Béla Suki (2,3), Katherine Yanhang Zhang (1,2,3)

(1) Department of Mechanical Engineering, Boston University, Boston, MA, USA
(2) Department of Biomedical Engineering, Boston University, Boston, MA, USA
(3) Division of Material Science and Engineering, Boston University, Boston, MA, USA

INTRODUCTION

Understanding of the risk factors and underlying mechanisms of aortic dissection (AD) is critical for improved clinical management of the disease. Aging is a prominent risk factor for AD as it increases the incidence and mortality [1] due to impaired aortic interlamellar bonding [2]. However, structural mechanisms of the compromised dissection resistance capabilities in the aging aorta have not been elucidated. Given the dominant role of collagen fibers in maintaining aortic interlamellar integrity [3], we hypothesize that aging-associated structural rearrangement of interlamellar collagen dictates the elevated AD propensity. AD propagates with avalanche-like failure of interlamellar fibers and exhibits a power-law distribution of force drops with an exponent that is closely associated with the mechanical and structural properties of interlamellar fibers [5]. However, quantitative imaging assessment of interlamellar collagen structure is challenging due to the inhomogeneity of interlamellar collagen distribution [3] as well as the obliqueness, dispersion and undulation of collagen orientation [4]. Our previous study using an innovative finite element (FE) model of dissection propagation that captures the rupture of discrete collagen fibers recapitulated the power-law behavior and revealed that the inhomogeneous distribution of interlamellar collagen fibers is the origin of such phenomena [5]. Furthermore, the power-law behavior and exponent could serve as a novel indicator of interlamellar structural characteristics. By recapitulating the power-law behavior observed from experimental testing with FE modeling, this study aims to delineate the structural mechanisms of aging-augmented risk of AD.

METHODS

Human descending thoracic aortas (DTAs) ranging from 24 to 92 years of age were divided into three age groups: <40 years (n=4), 40-60 years (n=6), and >60 years (n=7). Peeling test was performed on samples obtained from each aorta with a rate of 0.2 mm/s in both the circumferential and longitudinal directions. Figure 1a shows a representative curve of peeling force/width versus displacement and the mean peeling force/width (F_m/W). The energy release rate (G_c) was calculated by subtracting the elastic energy stored in each sample from the total work done by the peeling force [6]. Magnitudes of drops of peeling force/width ($\Delta F/W$) were collected. The probability density distribution of $\Delta F/W$ of each age group was analyzed to assess the power-law behavior and corresponding exponent β.

A two-dimensional (2D) FE model in which adjacent elastic lamellae were connected by discrete interlamellar collagen fibers [5], was used to simulate dissection propagation (Figure 1b). The elastic lamellae were meshed with four-node 2D elements and described by a neo-Hookean constitutive law. Interlamellar fibers were modeled with Timoshenko beam elements and followed an exponential stress-strain relation [7] with failure strain uniformly ranging between 0.107 and 0.207 [8]. AD was simulated by prescribing opposite horizontal displacement for the top ends of the lamellae, and the sum of nodal forces at the right top end was taken as the simulated peeling force. For each age group, the interlamellar distance (d) was obtained by dividing the difference between total media thickness [9] and total lamellae thickness by the number of interlamellar spaces [10], while the lamellar stiffness (μ) was obtained by matching the neo-Hookean strain energy density to the elastic energy storage per unit tissue volume during peeling. The density and degree of angular dispersion (θ) of interlamellar collagen fibers were tuned to fit the power-law exponent β from simulations to that of the experimental results. Within each age group, equal number of interlamellar fibers was assumed for the circumferential and longitudinal directions, while θ was independently tuned for each direction.

RESULTS

The mean F_m/W and G_c decreased with aging (Figures 2a and 2b). Power-law behavior was identified in all age groups in both the circumferential and longitudinal directions, as shown by the prominent

linear decrease on a log-log plot of the probability density distribution spanning almost two decades of ΔF/W (Figure 2c). In the circumferential direction, β increased from 1.35 to 1.55 and then to 1.74 for the <40, 40-60, and >60 years groups, respectively. In the longitudinal direction, β decreased from 1.49 to 1.46 and then to 1.17.

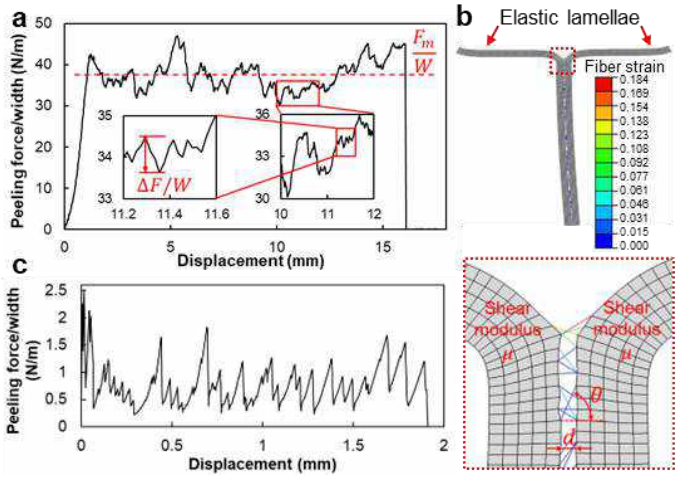

Figure 1: (a) A presentative curve of peeling force/width - displacement and zoom-in graphs showing peeling force oscillation and ΔF/W. (b) FE model of AD with contour plot of fiber strain in the interlamellar fibers. (c) A representative peeling force/width - displacement curve obtained from FE simulation.

The fluctuations of peeling force were reproduced by the FE simulations (Figure 1c), in which both the power-law behavior and associated exponent β of dissection propagation were also recapitulated for all age groups (Figure 2c). The estimated number of interlamellar fibers decreased with aging from 450 to 350 and then to 250 for the <40, 40-60 and >60 years groups, respectively. In the circumferential direction, θ increased from 27° to 56° and then to 68° for the three groups, respectively; in the longitudinal direction, θ remained 27° from the <40 to the 40-60 years groups and increased to 68° for the >60 years group. For both directions, a strong and positive correlation was found between the number of interlamellar fibers and G_c ($p<0.05$), see Figure 2d. No significant correlation was found between θ and G_c.

DISCUSSION

Aging diminishes the dissection resistance capabilities of the lamellar layers within the media of human DTA, in accordance with previous clinical [1] and biomechanical [2] results. The significant decrease of F_m/W and G_c in the >60 years group (Figure 2a and 2b) also agrees well with the mean age of 63 years of AD patients [1]. Therefore, age is a critical factor for AD risk stratification.

Power-law behavior was identified in aortas of all age groups. Interestingly, the corresponding exponents are within the range of avalanche behavior of self-organized criticality [11]. Avalanches occur when a group of fibers at the dissection front transfers accumulated strain energy to subtended fibers which immediately reach their failure strain and break instantaneously. This explains the rapid propagation of AD. The power-law behavior and exponent are a powerful tool toward a quantitative evaluation of interlamellar fiber structure and an in-depth understanding of aortic pathology.

The reduction of interlamellar collagen density in the >60 years group is largely responsible for the higher risk of AD in the elderly population based on the strong correlation between the number of interlamellar fibers and G_c (Figure 2d). Aging-induced extracellular matrix remodeling may impair collagen recruitment to the interlamellar space. The decrease of collagen undulation with aging could reduce the length of radially running segments along a wavy fiber that is oriented in the circumferential-longitudinal plane and thus reduce its chance of being recruited under transmural tension. Also, elastin fragmentation with aging could decrease the connectivity between collagen and elastic lamellae and reduce the number of load bearing interlamellar collagen.

Interlamellar collagen dispersion triggers the power-law behavior in AD propagation [5], which is enhanced by aging. Although such effect has not been demonstrated before, as a major predisposing factor for AD, aneurysm significantly increases interlamellar collagen dispersion [12]. Further investigations into interlamellar fiber dispersion are needed given its fundamental role in AD propagation and a potential marker for aortic health assessment. In conclusion, a prominent aortic interlamellar structural rearrangement of collagen occurs with aging, including lower density and higher dispersion, of which the former diminishes interlamellar bonding while the later is vital in triggering the fast propagating avalanche behavior of AD.

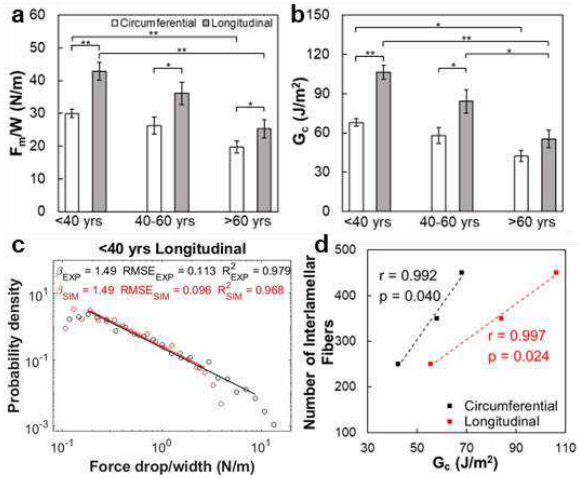

Figure 2: (a) Changes of F_m/W and (b) G_c of DTA media with aging. Error bars represent standard error of the mean ($^{*}p<0.05$, $^{**}p<0.01$). (c) A representative log-log plot (<40 circumferential) of the probability density distribution of ΔF/W from experiment (EXP) and simulation (SIM). The lines represent the power-law fit to the data. The goodness of fit is assessed by the root mean square error (RMSE) and coefficient of determination (R^2). (d) Correlation between the number of interlamellar collagen fibers and G_c. The linear fit is shown with the Pearson's correlation coefficient r and p-value of the correlation.

ACKNOWLEDGEMENTS

National Institute of Health (2R01HL098028).

REFERENCES

[1] Hagan, PG et al., *JAMA*, 283:897-903, 2000.
[2] Sokolis, DP and Papadodima, SA, *J Biomech*, 141:111174, 2022.
[3] Wang, R et al., *Biomech Model Mechanobiol*, 20:93-106, 2021.
[4] Tsamis, A et al., *J Biomech*, 46:2787-2794, 2013.
[5] Yu, X et al., *Sci Adv*, 6(21):eaaz1173, 2020.
[6] Sommer, G et al., *J Biomech Eng*, 130:021007, 2008.
[7] Hadi, MF et al., *J Biomech Eng*, 134(9):091005, 2012.
[8] Miyazaki, H and Hayashi, K, *Biomed Microdevices*, 2:151-157, 1999.
[9] Dingemans, KP et al., *Anat Rec*, 258(1):1-14, 2000.
[10] Jadidi, M et al., *Acta Biomater*, 103:172-188, 2020.
[11] Bak, P et al., Phys Rev Lett, 59(4):381, 1987.
[12] Niestrawska, JA et al., *J R Soc Interface*, 13:20160620, 2016.

PRECONDITIONING IMPACT ON PORCINE CORNEAL BIOMECHANICS

M.E. Emu (1), H. Hatami-Marbini (1)

(1) Mechanical and Industrial Engineering, University of Illinois Chicago, Chicago, IL USA
Email: hatami@uic.edu

INTRODUCTION

The eye, an intricately designed organ, undergoes continuous rotational and translational motion within its orbital gimbal suspension, facilitated by multiple extraocular muscles. The cornea, a vital component, maintains structural integrity and optical properties, with its stromal layer constituting 90% of its thickness, comprising collagen fibrils, proteoglycans, and a cellular matrix [1, 2]. Previous studies visualized corneal microstructure, revealing collagen fibril orientations. While uniaxial tensile loading assessed biomechanical properties, biaxial loading and whole-globe inflation offered a more realistic representation of tissue behavior [3].

Preconditioning, releasing residual stress, is essential in biomaterial characterization [4]. Its significance in corneal biomechanics, especially under biaxial loading, is largely unknown. The cornea, associated with the sclera and optic nerve, undergoes deformation and mechanical loading, with repetitive strain injuries and myopia-induced changes [5]. Understanding preconditioning's influence on corneal biomechanics is crucial for managing myopia-related corneal changes.

Our study aims to examine preconditioning's impact on porcine corneal biomechanics using biaxial tests. We seek a comprehensive understanding of how preconditioning influences the cornea's mechanical response in multiple directions, evaluating its anisotropic nature under physiological loading scenarios.

METHODS

Fresh porcine eye globes, obtained from a local abattoir, were carefully transported to the laboratory. After tissue removal, a 2 mm scleral-corneal ring was excised from each globe, resulting in 20 samples. These were divided into preconditioned and nonpreconditioned groups. Using a double-blade cutter, samples were transformed into mm squares for planar biaxial testing (Figure 1). After soaking in a PBS solution to achieve the desired thickness, measured with a pachymeter to ensure similar thickness for preconditioned and non-preconditioned specimens.

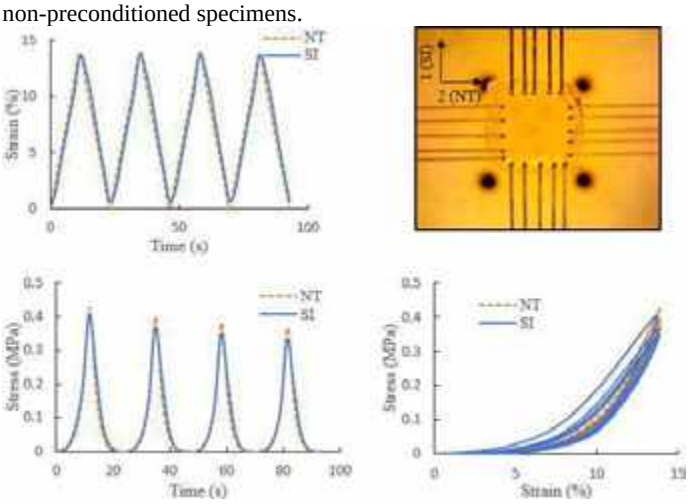

Figure 1: Preconditioning curve and biaxial test setup with Bio-Rakes for secure sample fixation.

Mechanical tests utilized the "ElectroForce TestBench" system, with modified grips for secure fixation of square corneal strips using bio-rakes. These grips, preferred for their speed and moisture preservation, facilitated secure sample attachment. Strain measurement relied on grip position or Digital Image Correlation (DIC), showing comparable results. Displacement control tests were chosen over load control tests, performed at various stretch ratios and displacement rates. Preconditioning involved four loading-unloading cycles, maintaining tissue integrity and reproducible responses. Strain rates and levels, relaxation time, and cycle counts were carefully selected to prevent tissue damage while ensuring accuracy. Samples were pre-stressed at

0.02N and underwent preconditioning cycles before equibiaxial strain at 2 mm/min. Non-preconditioned samples followed a similar process without preconditioning cycles. Continuous hydration using a PBS spray, maintained sample thickness for consistent testing conditions and reliable mechanical property measurements.

Data analysis encompassed meticulous processing in Microsoft Excel and statistical analysis using SAS Analytic Software. Normality of specimen groups was assessed via the Shapiro-Wilk test. Subsequent t-tests and ANOVA tests, with a significance level of α=0.05, determined statistical differences between groups.

RESULTS

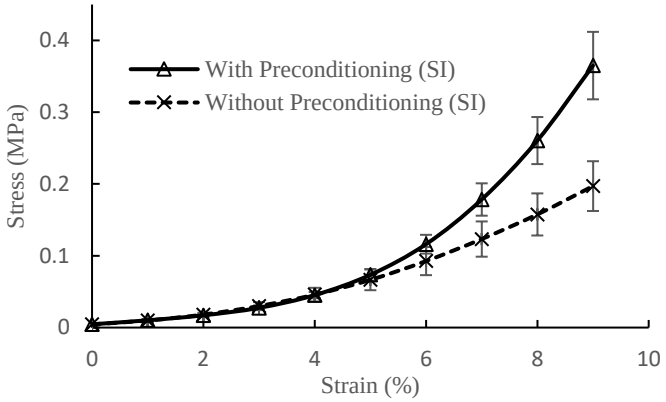

Figure 2: Stress-strain curve comparison of preconditioned and non-preconditioned porcine corneal stroma at equibiaxial strain ratio. The vertical error bars represent the standard deviation.

Our focus was on preconditioning's impact on corneal biomechanics, particularly elasticity and extensibility. Figure 2 showcases stress-strain curves of the porcine cornea in the superior-inferior direction under equibiaxial loading. It was seen that the stress increased nonlinearly with tensile strain in both preconditioned and non-preconditioned corneal specimens. We also observed no directional anisotropy in the tensile behavior of the cornea, and stress-strain behavior in the SI and NT directions was almost similar.

Peak stress values for superior-inferior (SI) and nasal-temporal (NT) directions were determined. For example, with preconditioning, the SI direction had 0.37±0.05 MPa peak stress and without preconditioning, it showed 0.20±0.04 MPa.

The tangent moduli were also determined from Figure 2 across different strain levels. At lower strains (3%), preconditioning showed no significant effect. However, at higher strains (>3%), preconditioning significantly influenced the cornea's mechanical response.

DISCUSSION

Our study aimed to explore how preconditioning affects corneal biomechanics, focusing on elasticity and extensibility. Analyzing stress-strain behavior in equibiaxial-loaded porcine corneas, we found a distinct nonlinear stress increase, revealing no directional anisotropy. Peak stress values for different directions showed significantly higher levels with preconditioning, aligning with previous ocular tissue studies [6]. This consistency underscores preconditioning's crucial role in understanding these tissues' biomechanics. Additionally, our analysis revealed higher stress and modulus due to preconditioning, particularly at higher strain levels. However, at lower strains, the effect on the modulus was not statistically significant. These findings enhance our understanding of corneal biomechanics, emphasizing preconditioning's role in its mechanical response.

Preconditioning ensures consistent results in biological material testing, but its impact on corneal tissue remains unclear. Our study investigated this using equibiaxial testing at varying strain levels. At lower strains, preconditioning didn't significantly affect corneal tissue, but at higher strains, it notably altered the tissue's behavior, potentially impacting overall biomechanics. This aligns with previous research on human sclera [6]. Collagen fiber features, observed in Transmission Electron Microscopy (TEM) images (Figure 3), might explain preconditioning effects. Crimped collagen fibers transitioned to an uncrimped state during loading cycles, impacting strains at higher levels. However, at lower strains, this transition may not occur fully, explaining the lack of significant effect on corneal strength. These findings highlight the intricate relationship between preconditioning, collagen organization, and corneal biomechanics, urging further research for implications in surgeries and biomaterials.

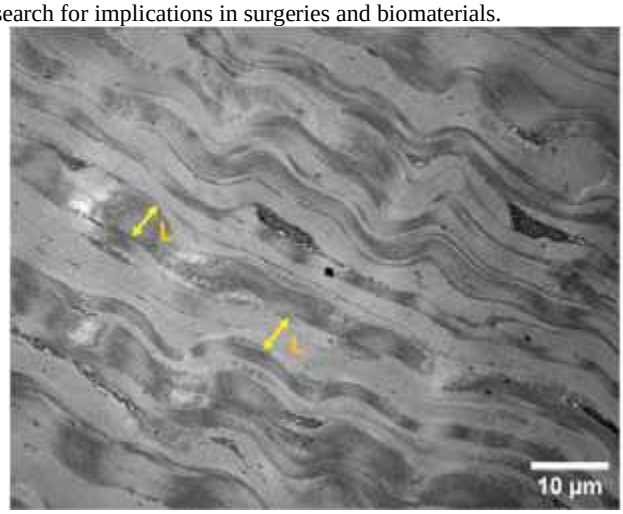

Figure 3: TEM analysis of porcine cornea reveals lamellar (L) structural features in NT (out-of-plane) and SI (in-plane).

While effective, our biaxial loading system has limitations. Unlike studies using digital image correlation (DIC), we prioritized grip position for strain calculation, leveraging a rigid gripping system for comparable results. A limitation includes the lack of control over porcine age and breed, introducing variability. Preload discrepancies due to corneal curvature were addressed by focusing on elastic modulus comparisons in each direction. A large sample size aimed to minimize individual variations. Despite peak strains of 9-11%, considered low for soft tissues, our study captured the corneal stress-strain curve trend. Though limited, our findings offer valuable insights into corneal biomechanics, emphasizing preconditioning's role in ocular tissue characterization.

ACKNOWLEDGEMENTS

This work has been supported in part by grants from the National Institutes of Health (R21EY030264).

REFERENCES

[1] Hatami-Marbini, H. and M.E. Emu, Experimental Eye Research, 2023: p. 109476.
[2] Meek, K.M., et al., Prog Retin Eye Res, 2009. **28**(5): p. 369-92.
[3] Eilaghi, A., et al., J Biomech, 2010. **43**(9): p. 1696-701.
[4] Lanir, Y., Journal of Biomechanical Engineering, 2009. **131**(4).
[5] Sedaghat, M.R., et al., Front Bioeng Biotechnol, 2020. **8**: p. 595330.
[6] Park, J., et al., Biomechanics and Modeling in Mechanobiology, 2021. **20**(4): p. 1353-1363.

THE HEMODYNAMICS OF MECHANICAL HEART VALVES: A COMPARISON OF NUMERICAL SIMULATIONS AGAINST EXPERIMENTAL MEASUREMENTS

S.S. Abbas (1), L. Ferrari (2), D. Obrist (2) and I. Borazjani (1)

(1) J. Mike Walker '66 Department of Mechanical Engineering, Texas A&M University, College Station, Texas, USA
(2) ARTORG Center for Biomedical Engineering Research, University of Bern, Bern, Switzerland

INTRODUCTION

Mechanical Heart Valves (MHVs) have undergone tremendous design improvements in the past few decades. Their current commercially most preferred designs are termed Bileaflet MHVs (BMHVs), being used in about 20% of the total aortic heart valve replacement surgeries every year [1]. The use of BMHVs has been widely associated with platelet activation [1-2] and thrombotic complications. Consequently, the valve's recipient is necessarily required to undergo life-long anticoagulation therapy [3].

In efforts to reduce the thrombogenic potential of MHVs, several designs of Trileaflet MHVs (TMHVs) have been proposed that offer an inherently improved hemodynamics owing to their design [4]. To the best of our knowledge, however, there are no published studies on the comparison of the cardiac mechanics and hemodynamics of a TMHV and a BMHV, carried out under similar numerical and experimental conditions. Such studies are needed to provide a validation of the employed numerical methodology, so that it could be extended to obtain further highly resolved, unprecedented insights into the cardiac performance of the two MHVs. In this research, we present a comparison of the numerical simulations and experimental measurements of a TMHV and a BMHV under similar conditions.

METHODS

The TRIFLO Valve (Novostia, Switzerland) and the On-X Valve (Cryolife Inc., USA) have been respectively modelled as the TMHV (Figure 1a) and the BMHV (Figure 1b) in this study.

For the numerical assessment, the continuity equation and the Navier Stokes equations constitute the set of governing equations. The Curvilinear Immersed Boundary (CURVIB) method has been used as a flow solver [1,3], strongly coupled to a Fluid-Structure Interaction (FSI) algorithm for calculating the leaflet kinematics of the MHVs. The *In-Vitro* measurements of the MHV flow fields have been performed in a validated pulse duplicator with a multi-view imaging system for Tomographic Particle Image Velocimetry (Tomo-PIV) [5]. The flow is computed as an ensemble-average over 200 consecutive beats. The Refractive Index Matched (RIM) fluid for the Tomo-PIV experiment has been obtained by mixing a water/glycerol/NaCl solution, with a respective weight ratio of 0.494:0.340:0.166. The dynamic viscosity 5.6 of mPa/s and the density of 1200 kg/m^3 in experiments match the fluid parameters in the numerical simulations.

Figure 1: (a) the TMHV (b) the BMHV

RESULTS

Figure 2 compares the projected areas of the TMHV and the BMHV, which is an indicative parameter of their leaflets' kinematics.

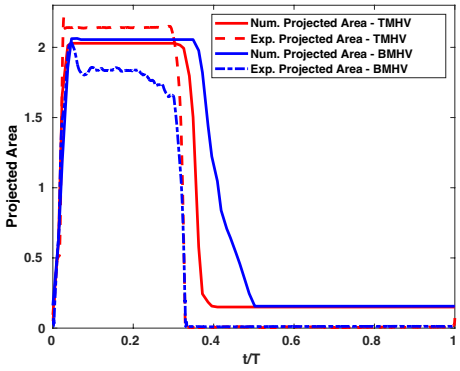

Figure 2: Comparison of the projected areas

An excellent agreement is observed between the numerical and experimental projected areas for the TMHV and BMHV during the valves' opening phase (t/T < 0.05). Numerically, upon fully opening, the TMHV and BMHV demonstrate a constant projected area of 2.0290 cm^2 and 2.0634 cm^2, respectively. Experimentally, while the TMHV has a constant projected area of 2.215 cm^2 after fully opening, a decline in that is observed for the BMHV. The fractional difference between the numerical and experimental maximum projected areas of the TMHV is 8.2945%, whereas that for BMHV is 11.32%. While both valves start to close simultaneously during the forward deceleration phase of the cardiac cycle in experiments, numerically we observe a subtle difference. The TMHV leaflets in numerical simulations start to close during late systole whereas the BMHV leaflets begin their closing excursion at the onset of regurgitation. In addition, the projected areas of the two valves reduce to zero in experiments, while to a minimum of 0.15 cm^2 in the numerical simulations. This difference could be attributed to a limitation of the employed numerical method, i.e., the upstream and downstream regions of the valves must be simply connected for the Pressure Poisson solver to converge. Therefore, a small opening must be provided in the numerical TMHV and BMHV models while they realistically should be 'fully closed'.

Figures 3 and 4 respectively compare the streamwise velocities for the TMHV and BMHV at peak systole, plotted at three different lines (as shown on the contours) to facilitate a quantitative comparison.

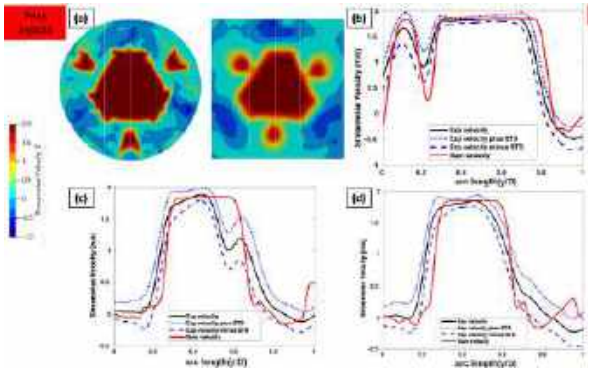

Figure 3: Comparison of velocity profile for the TMHV

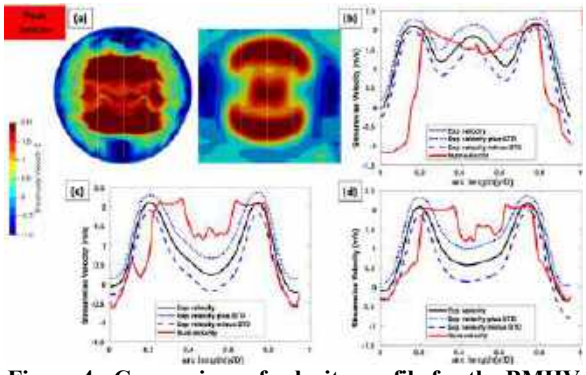

Figure 4: Comparison of velocity profile for the BMHV

The TMHV demonstrates a strong central jet, that dominantly covers the arc lengths of the three lines, alongside three narrower lateral jets. For the central (Figure 3b) and the right line (Figure 3d), we observe that the numerically calculated streamwise velocity is in excellent agreement with the averaged, experimentally measured streamwise velocity for the central jet ($0.25 < y/D < 0.85$), whereas lies mostly within the Root Mean Square (RMS) of the experimental velocity fluctuations for the lateral jet ($y/D < 0.25$ or $y/D > 0.85$). The differences on the left line (Figure 3c) could be attributed to the slight misorientation of TMHV in experiments relative to simulations.

For the BMHV, from the contours at the peak systole (Figure 4a), we numerically observe that the central jet has a diffused shape in comparison to the side jets. Similarly, the central jet seems to be narrower and weaker than the side jets, and only extends to the central lumen region in experiments. For the central line (Figure 4b), both numerical simulations and experimental measurements demonstrate higher streamwise velocities in the side jets relative to the central jet. The numerical simulations also predict higher adverse streamwise velocity compared to experiments in the region encompassing the aortic sinuses as the end points of the central line extend to regions of high adverse velocity. For the left line (Figure 4c) and the right line (Figure 4d), although the numerically predicted maximum streamwise velocities in the side jets are in good agreement with the experimental measurements, the numerical velocities exceed the RMS fluctuations of the experiments in the middle region of the two lines ($0.2 < y/D < 0.7$). This discrepancy could be explained based on the previously discussed lesser/reduced extension of the central jet in the experiments compared to the numerical simulations, not extending to the points covered by the left and the right lines.

DISCUSSION

We compare the numerical simulations and experimental measurements of leaflet kinematics and hemodynamics of a novel TMHV design against a BMHV. While we obtain a good agreement in the numerical and experimental predictions of opening kinematics of the two valves, striking differences exist during the closing phase. Numerically, the TMHV leaflets start to close during forward deceleration while the BMHV leaflets wait for the reversed flow to begin their closing excursion. The delayed closure of BMHV has been previously reported by several studies [1-4] and can have adverse effects on the performance of the heart. Experimentally, both valves start to close simultaneously by late systole, which is in contradiction with previous findings on other BMHVs. The early closure of the TMHV, observed both numerically and experimentally, is a desirable feature.

The flow field of the TMHV is dominated by a strong central jet, resembling that of natural/tissue valve [3]. The magnitudes of the numerical streamwise velocities are either in excellent agreement over the arc lengths or deviate while staying within the RMS fluctuations of experiment. For the BMHV, the qualitative trends look similar in numerical simulations and experiments, such as generation of tri-orifical jets and a weaker extension of central jet compared to side jets. The trends on the streamwise velocities plotted over lines slightly differ between the numerical simulations and experiments for the BMHV, likely due to the misorientation of the valve in two setups. The validated numerical setup could now be employed to quantify parameters that are difficult to be experimentally measured, for instance, clotting potential.

ACKNOWLEDGEMENTS

The authors acknowledge Novostia, Switzerland for partially funding this research, and the High-Performance Research Computing (HPRC) group at Texas A&M University for computational resources.

REFERENCES

[1] Asadi, H et al., *J. Biomech. Eng.*, 144:101008, 2022.
[2] Abbas, SA et al., Artif. Organs., 44: E20-E39, 2020.
[3] Borazjani, I et al., *Ann. Biomed. Eng.*, 38:326-344, 2010.
[4] Li, Chi-Pei et al., ASAIO Journal., 57(3): 188-196.
[5] Pietrasanta, L et al., Front. Cardiovasc. Med., 8: 804565

POST-TAVR THROMBOGENIC RISK COMPARISONS FOR BICUSPID AORTIC VALVE PATIENTS USING NOVEL FLUID-STRUCTURE INTERACTION APPROACH

Kyle J. Baylous (1), Brandon J. Kovarovic (1), Salwa B. Anam (1), Ryan T. Helbock (1), Marvin J. Slepian (2), Danny Bluestein (1)

(1) Department of Biomedical Engineering, Stony Brook University, Stony Brook, NY, USA
(2) Department of Medicine and Biomedical Engineering, Sarver Heart Center, University of Arizona, Tucson, AZ, USA

INTRODUCTION

Transcatheter aortic valve replacement (TAVR) is a well-established, minimally invasive treatment for severe aortic stenosis. The number of TAVR procedures has surpassed surgical aortic valve replacement (SAVR). TAVR is now expanding to younger patient cohorts and is being used to treat patients with bicuspid aortic valve (BAV) [1,2]. However, TAVR is associated with several clinical complications, including long-term, life-threatening thrombotic events that may be a consequence of prolonged exposure of platelets to elevated cyclic stresses. These risk factors may be exacerbated in BAV patients due to the complexity of bicuspid anatomy that often leads to improper deployment of TAVR device stent frames and leaflets in an elliptical annulus, as opposed to circular annuli in conventional trileaflet aortic valve (TAV) patients. Under-expansion of the device can cause the leaflets to perform poorly, as the opening orifice area is greatly reduced along with excessive leaflet flutter during systole. During diastole, paravalvular leaks occur due to poor device sealing post-deployment which is largely affected by calcium deposits on the native BAV leaflets. All these factors cause elevated flow velocity profiles and jets that can cause shear stress on platelets, leading to stress accumulation and subsequent activation [3].

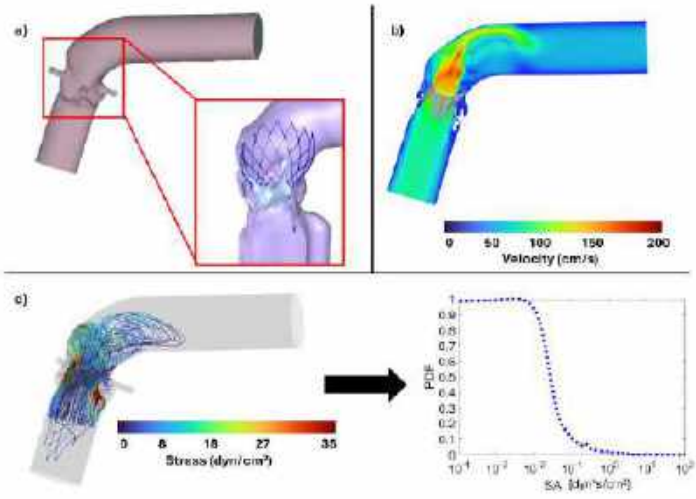

Figure 1. a) Patient-specific FSI geometry with deployed TAVR device shown. b) Flow results showing a contour plot for flow velocity. c) Contours of virtual platelet stresses plotted on the trajectories (left) along with the respective PDF profile (right).

Flow-induced thrombogenicity increases the risk of platelet activation, and microthromboemboli formation can lead to a range of complications, from prosthetic leaflet thrombosis to embolism and stroke [1,2,3]. The rapid expansion of TAVR in BAV patients highlights the importance of developing alternatives to current tissue-based TAVR devices that suffer from structural deterioration and thrombus formation – leading to poor functionality and efficacy for the long-term in these patients, which is evident after just 30 days from reports of significantly higher occurrence of stroke in BAV patients [4]. Here we examine and compare thrombogenicity of a current commercial TAVR device deployed in three BAV patients with varying degrees of eccentricity and anatomical complexity, demonstrating the utility of our novel fluid-structure interaction (FSI) workflow for detecting thrombogenic risk. This also further motivates designing a novel BAV-specific device.

METHODS

The patient-specific *in silico* models used in this study for FSI were reconstructed from three type 1 BAV patients that received a 29-mm self-expandable TAVR [5]. De-identified preoperative CT scans of these patients were obtained from Rabin Medical Center (Petah Tikva, Israel) under Stony Brook IRB approved protocol (522113). ScanIP

(Synopsys, Mountain View, CA) was used for segmentation of the relevant patient geometries (Fig. 1a). To validate the FSI models, a 3D printed replica of one BAV patient was created and the TAVR device was deployed inside following the clinical procedures performed in these patients [6]. Flow data was collected *in vitro* using a left heart simulator (VivitroLabs, Inc., Victoria, BC). The patient-specific TAVR device deployment was then modeled *in silico* (ABAQUS Explicit v2022, Dassault Systèmes, Vélizy-Villacoublay, France) and FSI simulations were created and run using LS-Dyna (ANSYS, Canonsburg, PA) such that the *in vitro* and *in silico* flow rates could be compared. The thrombogenic risk analysis was then conducted by taking the three post-TAVR deployment (29-mm Evolut R) patient models and configuring each with a physiological pressure gradient waveform. Each FSI simulation was conducted for three beat cycles and the flow data was collected (Fig. 1b). Each FSI simulation was then post-processed using EnSight (ANSYS, Canonsburg, PA) in which ~50,000 virtual platelets were seeded in the flow (Fig. 1c). Stress accumulation (SA) was calculated and tracked for all the seeded platelets. Continuous seeding was done to accurately model new platelets introduced into the flow [7]. The probability density function (PDF) of the accumulated stresses of the large population of flowing platelets was then computed for each patient, which represents the unique "thrombogenic footprint" for the TAVR device in the respective patient [7]. To analyze the thrombogenic potential of the device in the different BAV patients, PDFs were compared amongst each other - along with tabulated SA data – with Hellum's criterion considered.

RESULTS

The flow velocity profiles showed peak systolic jet velocities over 200 cm/s. The highest velocities were found near the centerline of the flow in addition to near the wall of the upper aortic arch, where the flow was directed (Fig. 2). Recirculation zones were observed near the

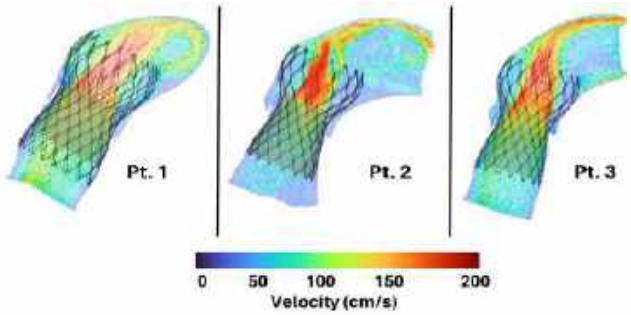

Figure 2. Peak systolic flow velocity in each patient model.

sinuses of the patient models and at the initial bend of the aortic arch. Paravalvular leak (PVL) was observed in all patients, with velocities reaching over 250 cm/s through these gaps. Based on the flow results, thrombogenic risk simulations were then performed. The virtual platelets experienced the largest stress values near the surfaces of the leaflets and while traveling through PVL gaps (Fig. 3). Upon comparison of the PDFs and top 100 stress accumulation platelet trajectories, or "hotspots", in each of the patient models, it was evident that platelet activation thresholds were surpassed in each patient. However, the performance of the Evolut R device varied since patient #1 had the highest median stress accumulation of 1.193 Pa-s (Table 1), while patient #2 showed a much lower median stress accumulation of 0.687 Pa-s. Patients with higher anatomic eccentricity showed higher thrombogenic risk due to excessive leaflet fluttering, irregular GOA shapes and larger PVL gaps.

Table 1. Median SA from top 100 platelet hotspots for patients #1-3.

BAV Patient No.	Pt. 1	Pt. 2	Pt. 3
Median SA (Pa-s)	1.193	0.6870	0.7574

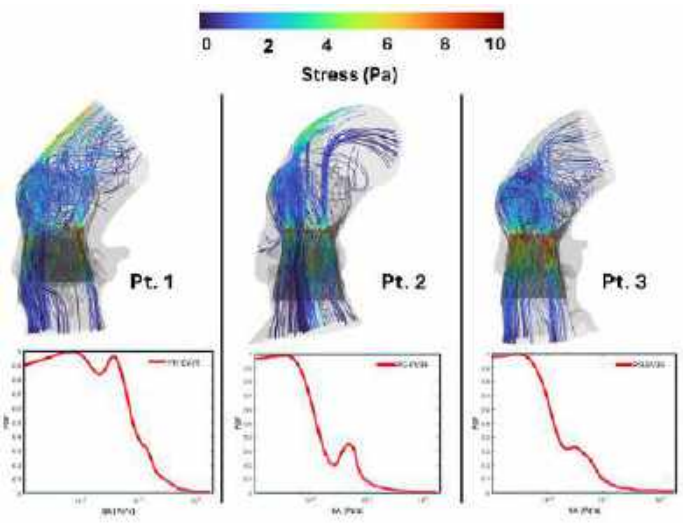

Figure 3. Visualized platelet trajectories with contour plot of stress (top) and respective PDF profiles (bottom) for patients #1-3.

DISCUSSION

This study demonstrates the ability to analyze and compare post-TAVR thrombogenic risk by studying hemodynamics of prosthetic devices via a fully integrated TAVR FSI approach. More specifically, our workflow allows us to take patient CT scans and create fully coupled FSI models for thrombogenic risk analysis where we can analyze the performance of TAVR devices in a patient-specific manner. From this study, we see that more complex and eccentric BAV patient anatomies can lead to poorer TAVR device performance and increased risk of platelet activation. This highlights the importance of developing novel TAVR devices that may outperform current ones on the market with special attention paid to reducing thrombogenicity and enhancing durability for new patient cohorts such as BAV [5]. This analysis can be applied to the optimization of a BAV-specific TAVR device in addition to understanding what specific patients would benefit most from such a device. Limitations of this study include the inability to use patient-specific flow conditions due to the lack of catheterization data. In the future, we wish to compare thrombogenic risk between current TAVR devices and our own BAV-specific design, PolyV-B. Additionally, we plan to perform our own *in vitro* hemodynamics testing with TAVR devices that we are developing.

ACKNOWLEDGEMENTS

Funding provided by NIH-NIBIB Phase II-U01EB012487 (DB); NIH-NIBIB 1U01EB026414-01 (DB). Industry Partners: ANSYS, Dassault Systèmes.

REFERENCES

[1] Al-Asad, KS et al., American J Cardiology, 203 (2023): 105-112
[2] Gupta, R et al., Cath and Cardio Interv, 102(4): 721-730 (2023)
[3] Bluestein, D et al., J Biomechanics, 46(2) (2013): 338-344
[4] Improta, R et al., J Clinical Med, 12(23) (2023): 7371
[5] Helbock, R et al., Annals of Biomed Eng, 51(1) (2023): 58-70
[6] Anam, S et al., Cardio Eng Tech, 13(6) (2022): 840-856
[7] Xenos, M et al., J Biomech, 43(12): 2400-2409 (2010)

COMPUTATIONAL ANALYSIS OF THE CONTRIBUTION OF PARACRINE CHEMOTAXIS TO SPATIAL DISTRIBUTION OF LEUKOCYTES IN CEREBRAL ANEURYSMS

Zhitian "Ruskin" Shi (1), Hadi Wiputra (1), Victor H. Barocas (1)

(1) Department of Biomedical Engineering,
University of Minnesota-Twin Cities,
Minneapolis, MN, USA

INTRODUCTION

As much as 3% [1] of the general population is affected by cerebral aneurysms (CAs). CA rupture is rare, but its consequences are severe, with a mortality rate of 25-50% [1]. Surgical repair also carries inherent risk of mortality, ranging from 0.6% to 2% [2]. To improve risk evaluation (rupture vs. surgery risk), there is a need for computational tools to help understand CA growth, remodeling, and rupture.

Leukocyte secretion of matrix metalloproteinases [3] in the aneurysm wall can weaken the wall and increase rupture risk., and leukocyte deposition in aneurysmal wall has been linked experimentally to CA rupture [4]. The reported distribution of leukocytes in CA walls varies widely: leukocytes can concentrate in the apex, neck, or body of CA [4], or they can distribute diffusely [5]. Despite the leukocytes' role in CA remodeling, and despite the many computational models of CAs, to our knowledge, no model of the leukocyte distribution has been proposed. We tested the hypothesis that ***leukocyte chemotaxis and chemokine secretion lead to spontaneous inhomogeneity within the aneurysm wall***. In this study, we hypothesized that non-uniform distributions of leukocytes can arise due to a feedback loop between chemotactic movement and chemokine production and transport. Further, we explored how different magnitudes of chemokine kinetics can lead to different of leukocyte distributions.

METHODS

A bidomain model (Figure 1) of leukocyte distribution was constructed, consisting of a discrete leukocyte domain and a continuous chemokine domain. The discrete domain is described by an agent-based model (ABM) for leukocyte chemotactic movement, informed by the (continuous) chemokine concentration distribution. The continuous domain is described by a partial differential equation for chemokine transport within the vessel wall, treating a subset of leukocytes as discrete chemokine sources. The two model domains are described in more detail below.

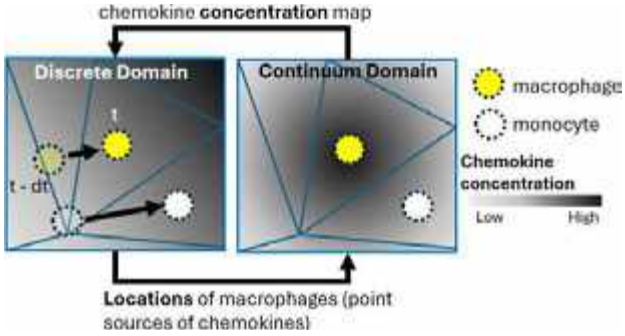

Figure 1: Schematic of the mathematical model.

Discrete (Leukocyte) Domain: Leukocyte recruitment into the vessel wall is a multi-step process that involves a series of phenotypic transitions. Three classes of leukocytes were simulated:

- **Monocytes**, which have been captured by the vessel wall, roll and/or crawl on its luminal surface. Extravasation into the wall and the transition to macrophages are triggered if surrounding chemokine concentration > 0.3 mmol/um^3. Monocytes are highly motile and do not secrete chemokine.
- **Macrophages** are less motile but still motile. They transition into the foamy phenotype if surrounding chemokine concentration > 3 mmol/um^3. Macrophages secrete chemokine at a moderate level.
- **Foamy macrophages** have low motility but secrete larger amounts of chemokine than macrophages.

Leukocyte movement was discretized into steps of uniform length and was made chemotactic via direction control. Specifically, the direction of each leukocyte step was determined as a biased random variable drawn from a Von Mises distribution [6], with the distribution parameters based on the chemokine concentration field around the cell.

Continuum (chemokine) Domain: Because leukocytes' chemotactic movements are significantly slower than chemokine diffusion, the transport of chemokine was assumed to reach steady state at the end of every time step, as given by the equation

$$D\nabla^2 c - kc + p\delta^3\left(\vec{x} - \vec{x}_{secreting\ cell(s)}\right) = 0 \qquad (1)$$

where D is the diffusivity; p is the production rate of chemokine by each leukocyte as point source; and δ^3 is the three-dimensional Dirac delta function. The clearance of chemokine from the aneurysmal tissue was assumed to be first order with rate constant k [7]. Assuming that the surrounding tissue is not inflamed, the chemokine concentration was set to zero at the domain boundary. Chemokine diffusivity was set to 150 um^2/s [8]. The chemokine production rate p was set to 1 mmol/s for macrophages and 3 mmol/s for foamy macrophages. Eq (1) was solved in a custom MATLAB Finite Element code.

The second Damköhler Number (Da_{II}) was introduced to normalize the chemokine clearance rate with respect to diffusivity:

$$Da_{II} = \frac{kL^2}{D} \qquad (2)$$

where k and D are as defined above, and L is a characteristic length.

RESULTS

Leukocyte clustering results fell into four broad, roughly defined regimes, as demonstrated in Figure 2a, which shows final results for four different Damköhler numbers.

$Da_{II} < 1$: Chemokine concentration is high throughout the domain because of rapid diffusion, driving monocytes to differentiate into macrophages and then foamy macrophages quickly upon entering the vessel wall. Macrophages have low motility, leading to minimal clustering. Nearly all macrophages are foamy.

$Da_{II} \in (1, 40]$: Leukocytes form large clusters. Chemokine level is not high enough to trigger the macrophage phenotypic switch to foamy, but the chemokine concentration is high enough to sustain a paracrine chemotactic feedback loop in which macrophages secrete chemokine → more macrophages recruited → more chemokine secretion. No foamy macrophages are present.

$Da_{II} \in (40, 500]$: Leukocytes form small clusters. The same feedback loop exists as previously, but the chemotactic range is smaller as chemokine clearance (k) begins to outweigh diffusion (D). No foamy macrophages are present.

$Da_{II} > 500$: Chemokine clearance is so fast that the chemotactic gradient does not extend significantly out from the cell, so secreting macrophages do not attract monocytes, and thus no clusters form. No foamy macrophages are present, and most cells are monocytes.

These effects can be quantified by plotting the number of clusters, cluster diameter, and % foamy macrophages vs. Da_{II}. As can be seen in Figure 2b and 2c, both the number and the diameter of clusters rises with Da_{II} and then falls, with few clusters forming at either extreme Da_{II} value. Almost all of the macrophages are foamy for small Da_{II}, with a sharp shift to almost no foamy macrophages at about $Da_{II} = 1$.

DISCUSSION

The key conclusion of this work was that there is a window of Damköhler number values for which the combination of phenotypic transitions and chemokine dynamics lead to clusters. For the conditions we studied, this window generally did not include transition to foamy macrophages, although changes in the phenotypic transition parameters or the leukocyte motility parameters could lead to different results.

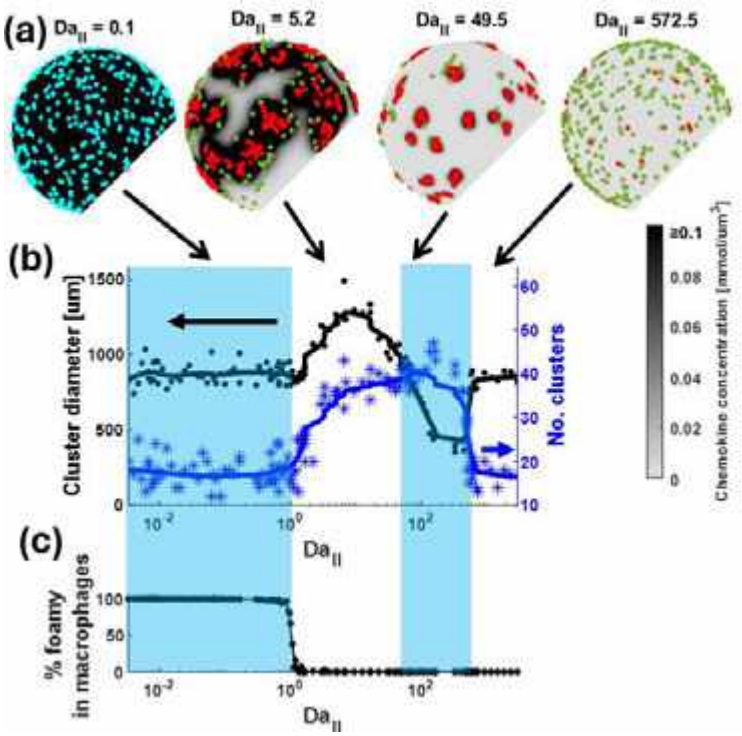

Figure 2: (a, b) Cluster diameter, number of clusters, & percentage of foamy macrophages in all macrophages were used to quantify clustering states. Each dot represents one simulation; solid lines are moving average fits of the dots. (c) one simulation output from each range of Damköhler number. Cyan dot = foamy macrophage, red dot = macrophage, green dot = monocyte.

Both leukocyte and chemokine dynamics were simplified in this model. Leukocyte migration, a complex process that involves many signaling molecules, was represented by a single chemokine, and both chemokinesis or contact guidance were ignored. Similarly, multiple factors were lumped into the chemokine clearance parameter k, including the thickness of vessel wall, chemokine mass transfer to the bloodstream, and natural decay of chemokine. Despite these simplifications, the model showed different clustering regimes and provides a tool to evaluate the interaction among different mechanisms.

Macrophage activation has been identified as a surrogate marker distinguishing between rupture-prone and lower risk aneurysms [9]. In our model, we observed correlated behavior between the leukocyte clustering and phenotype (Fig. 2b,c), which may help guide future studies into the biological difference between the walls of rupture-prone aneurysm and lower risk aneurysm.

ACKNOWLEDGEMENTS

This work was supported by the National Institutes of Health through grant R01 NS126762.

REFERENCES

[1] Etminan, N et al., *Transl. Stroke Res.* 2014; 5:167–173. [2] Thompson, B. et al., *Stroke,* 2015; 46:2368–2400. [3] Signorelli, F et al., *World Neurosurg*, 2018; 115:234-244. [4] Crompton, M.R., *Br Med J*, 1966; 1:1138 [5] Kanematsu, Y et al., *Stroke*. 2011; 42:173–178 [6] Best, D. J. et al., *J. R. Stat. Soc*. Series C, 28, No. 2 (1979), 152-57 [7] Su, B et al*., Comput Math Methods in Medicine*, vol. 10, Article ID 537013, 30 pages, 2009. [8] Cynthia Hajal et al., *Sci. Adv.*7, eabg8139 (2021). [9] Tomohiro Aoki et al., *Sci. Signal*.10, eaah6037 (2017).

SB^{3}C2024
Summer Biomechanics, Bioengineering and Biotransport Conference
June 11-14, Lake Geneva, WI, USA

PERSONALIZED AND UNCERTAINTY-AWARE VIRTUAL PLANNING FOR CORONARY ARTERY BYPASS GRAFT SURGERY INFORMED BY CT MYOCARDIAL PERFUSION IMAGING

Karthik Menon[*1], **Zachary Sexton**[2], **Owais Khan**[3], **Daniele Schiavazzi**[4], **Koen Nieman**[5] **and Alison Marsden**[1,2]

(1) Department of Pediatrics (Cardiology), Institute for Computational and Mathematical Engineering, and Stanford Cardiovascular Institute, Stanford University, Stanford, CA, USA
(2) Department of Bioengineering, Stanford University, Stanford, CA, USA
(3) Department of Electrical, Computer, and Biomedical Engineering, Toronto Metropolitan University, Toronto, Ontario, Canada
(4) Department of Applied and Computational Mathematics and Statistics, University of Notre Dame, Notre Dame, IN, USA
(5) Department of Medicine (Cardiovascular Medicine), Stanford University, Stanford, CA, USA

INTRODUCTION

Coronary artery disease (CAD) is the leading cause of death globally. While coronary artery bypass graft (CABG) surgery improves mortality in patients with severe CAD, long-term outcomes remain a challenge, with 24% of patients reporting chest pain within a year [1]. This is because revascularization is often guided by anatomical risk, which has worse outcomes than treatment based on hemodynamic severity [2]. To address this, personalized computational fluid dynamics (CFD) simulations can improve CAD treatment outcomes via non-invasive hemodynamic risk assessment and virtual treatment planning.

CFD can non-invasively calculate clinically relevant hemodynamics by simulating blood flow in patient-specific anatomies based on non-invasive clinical imaging. However, while current CFD tools are mostly diagnostic, predictive surgical planning requires personalized and multi-scale models that recapitulate pre-treatment hemodynamics for each patient and link clinical interventions in epicardial vessels with downstream myocardial blood flow. This is a challenge with image-based models because clinical imaging cannot resolve arteries below the image resolution, thus resulting in models that omit small vasculature and do not reflect true patient-specific coronary flow. These image-based models distribute flow among arteries empirically [3], which ignores patient variability, disease and model uncertainty. In addition, while current models are usually deterministic, robust clinical application requires rigorous uncertainty quantification to be incorporated into these virtual diagnosis and treatment planning tools.

To address these issues, we demonstrates a framework for more accurate, personalized and uncertainty-aware coronary hemodynamics models that are informed by clinical data. In particular, the focus is on personalized models for virtual CABG surgical planning that include novel methods to (1) combine conventional image-based models with synthetic vascular trees to represent arteries that are under-resolved in clinical imaging; (2) estimate more accurate and personalized model parameters and boundary conditions based on clinical data; (3) incorporate uncertainty in model parameters as well as clinically relevant hemodynamic metrics. We demonstrate the utility of these data-informed models both in disease diagnosis and CABG treatment planning.

METHODS

We used patient-specific coronary anatomical models based on CT angiography (CTA). The models were constructed using the the open-source *SimVascular* software and 3D flow simulations were performed using the finite element solver *svSolver* within *SimVascular*. We used 0D lumped-parameter models of flow in distal vasculature as well as for parameter estimation.

We augmented the image-based models with synthetic vascular trees generated using Constrained Constructive Optimization (CCO) [4] to represent vessels that are under-resolved in CTA. CCO can generate multiple non-intersecting trees in concave ventricle-like volumes that are constrained by hemodynamics and vascular scaling laws while minimizing vascular volume. This allowed us to create realistic vascular trees beyond the limits of CTA resolution.

We used closed-loop lumped parameter network (LPN) boundary conditions at inlets and outlets of the aorta and coronary arteries in the 3D simulations to capture the coupling with downstream systemic circulation. This included blocks to model each heart chamber, the intramyocardial pressure in coronary arteries, and resistance of vascular beds distal to each coronary artery which determines the distribution of flow amongst coronary arteries [5].

We enforced patient-specific flow distributions in the coronary tree based on clinical dynamic CT myocardial perfusion imaging (MPI_{CT}) [6]. MPI_{CT} is a non-invasive contrast-based imaging modality that quantifies the spatial distribution of blood flow perfusing the left ventricle (LV). From clinical MPI_{CT}, we extracted patient-specific LV volumes and myocardial blood flow (MBF) distributions. Using co-registered 3D models of each patient's coronary anatomy from CTA and the MBF distribution in the LV

from MPI_{CT}, we estimated the LV perfusion regions and MBF corresponding to each coronary artery.

The models described above consisted of several parameters governing the hemodynamics of upstream coronary arteries as well as the distal closed-loop circulation model. Personalized parameters were estimated using MPI_{CT} and measurements of cardiac function for each patient so that the resulting simulations reproduced clinically measured coronary flows, heart rate, aortic pressure, cardiac output and ejection fraction for each patient. This parameter estimation was performed in two ways - (1) using deterministic gradient-free Nelder Mead optimization; (2) using uncertainty-aware Bayesian estimation based on an adaptive Markov Chain Monte Carlo method [7].

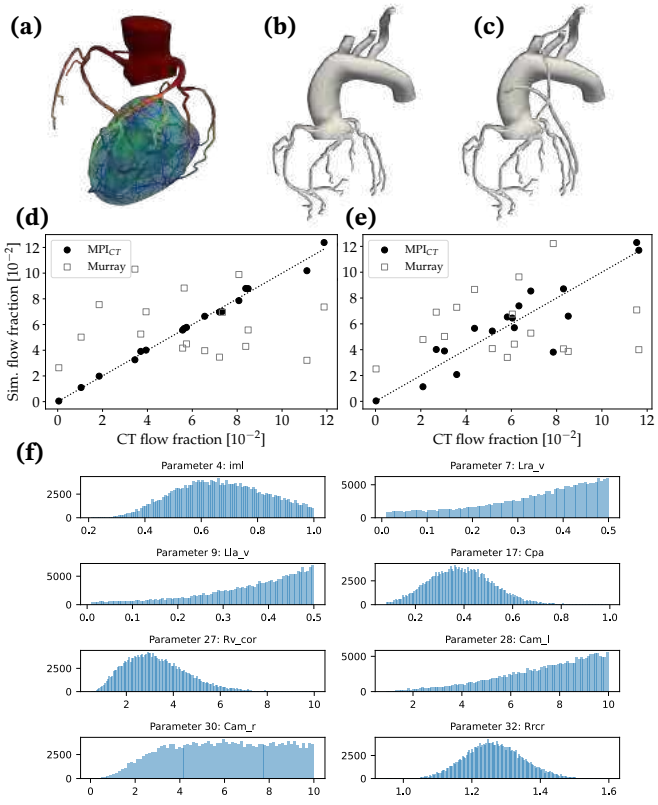

Figure 1: (a) Sample case with synthetic vascular trees. (b) Pre-CABG model (c) Post-CABG model. (d) Simulated pre-CABG flow in each coronary compared with flow from MPI_{CT}. (e) Simulated post-CABG flow in each coronary compared with flow from MPI_{CT}. (f) Posterior distributions for a subset of model paramaters.

RESULTS

We compared the framework proposed here for the estimation of personalized coronary flow distributions with the conventionally used Murray's law method for assigning coronary flow distributions [3] with an exponent of 2.6. We performed this comparison for hemodynamics simulated pre-CABG as well as post-CABG. Figure 1(a) shows a sample image-based anatomical model augmented with synthetic vascular trees that are constrained to grow in the patient-specific LV volume. Figures 1(b)-(c) show the patient's pre-CABG and post-CABG coronary anatomy.

Preliminary results indicate that our automated framework to personalize coronary hemodynamics models accurately recapitulates patient-specific clinical measurements both pre-CABG and post-CABG. Figures 1(d)-(e) compare the clinically measured flow in each branch of the coronary tree, estimated from MPI_{CT}, with simulation results based on the novel MPI_{CT}-informed technique and conventional Murray's law. In the pre-CABG scenario, figure 1(d) shows that the MPI_{CT}-informed model is significantly more accurate in capturing coronary flow fractions than the Murray's law-based model, with errors of 4.04% and 391.23% respectively. Importantly, when these personalized pre-CABG models are used to predict post-CABG outcomes, the models based on MPI_{CT} continue to be more accurate than the models based on Murray's law, with errors of 23.82% and 692.37% respectively. Although not show here, this automated personalization framework also produces good agreement between simulations and clinically measured metrics of cardiac function.

We have also incorporated uncertainty quantification into this parameter estimation framework using Bayesian methods to estimate posterior distributions for model parameters based on physiologically informed priors and patient-specific clinical measurements. Figure 1(f) shows the posterior distribution of a subset of the model parameters for a sample patient.

DISCUSSION

This work presents a novel framework for personalized and uncertainty-aware CABG treatment planning that is informed by non-invasive myocardial perfusion imaging and augmented with synthetic vascular trees. We seek to address three challenges in current coronary hemodynamics CFD models; (1) the exclusion of anatomical features of the coronary tree that cannot be resolved from clinical imaging; (2) the use of empirical flow splits amongst arteries that are not patient-specific; (3) the incorporation of novel uncertainty quantification techniques. Preliminary results indicate good success with the automated framework for tuning simulation parameters to reproduce patient-specific clinical measurements of coronary flow distributions as well as cardiac function. Importantly, our results indicate that such patient-specific flows are beneficial to recapitulate accurate hemodynamics pre-CABG as well as for the prediction of post-CABG outcomes.

Previous work has highlighted the inaccuracies introduced in coronary hemodynamics simulations due to inaccuracies in anatomy as well as outflow boundary conditions [5, 8]. We expect that this model personalization framework will aid in producing more personalized flow distributions as well as provide rigorous uncertainty estimates in pre-treatment disease diagnosis as well as in predictive virtual treatment planning. Moreover, the incorporation of non-invasive perfusion imaging into the tuning of coronary flow boundary conditions is a novel method to obtain personalized flow distributions in the coronary tree, which in turn leads to more accurate estimates of clinically relevant hemodynamic metrics such as fractional flow reserve.

ACKNOWLEDGEMENTS

This work is supported by NIH grant 5R01HL141712.

REFERENCES

[1] Cameron AA et al. *Journal of the American College of Cardiology* 26.4 (1995). DOI: 10.1016/0735-1097(95)00280-4.

[2] Tonino PA et al. *New England Journal of Medicine* 360.3 (2009). DOI: 10.1056/nejmoa0807611.

[3] Zhou Y et al. *Physics in Medicine and Biology* 44.12 (1999). DOI: 10.1088/0031-9155/44/12/306.

[4] Schreiner W et al. *IEEE Transactions on Biomedical Engineering* 40.5 (1993). DOI: 10.1109/10.243413.

[5] Menon K et al. *medRxiv* (2023). DOI: 10.1101/2023.08.17.23294242.

[6] Giordano M et al. *Medical Physics* 44.4 (2017). DOI: 10.1002/mp.12126.

[7] Vrugt JA et al. *International Journal of Nonlinear Sciences and Numerical Simulation* 10.3 (2009). ISSN: 15651339. DOI: 10.1515/IJNSNS.2009.10.3.273.

[8] Wellnhofer E et al. *Atherosclerosis* 213.2 (2010). DOI: 10.1016/j.atherosclerosis.2010.09.007.

SB³C2024
Summer Biomechanics, Bioengineering and Biotransport Conference
June 11-14, Lake Geneva, WI, USA

NON-CONTACT BIOMECHANICAL IMAGING OF CELL AND TISSUE USING OPTICAL BRILLOUIN MICROSCOPY

Jitao Zhang

Department of Biomedical Engineering, Wayne State University, Detroit, MI, USA

INTRODUCTION

Biomechanical interactions play crucial roles in regulating many cellular functions and system-level behaviors. To understand the mechanical interplay within cells and tissue, we need tools to identify mechanically related pathways, measure deformations and forces, and quantify the mechanical properties (e.g., elasticity) of materials. Many important techniques have been developed to assess material mechanical properties and can be loosely classified into three categories [1]. The first is contact-based techniques, including atomic force microscopy (AFM) and other cantilever-based indentation methods, micropipette aspiration, parallel-plate rheometer, and stretching substrate. Contact-based techniques can provide direct quantification of elasticity and are considered the gold standard. However, they need to physically touch and apply force to the sample during experiment, making the measurement invasive and mostly limited to the superficial layer of material. The second is bead-based techniques, including optical tweezer, magnetic tweezer, magnetic twisting cytometry, passive microrheology, and microdroplet-based sensors. These techniques have been extensively used to extract the localized mechanical properties of the sample, mostly at the cellular and subcellular scales. However, the injection of beads or droplets is required for experiments. The third is elastography techniques, where the application of an external force is coupled with imaging technologies to measure force-induced deformation and back calculate the strain. These include optical stretching, optical coherence elastography (OCE), and microfluidics-based deformers. OCE is powerful to characterize and map the mechanical properties of biological tissue in large scale, and the microfluidics-based techniques can assess cell biomechanics in medium with high throughput. In short, each of these techniques has strengths and limitations, leading to a specialization of their use for particular applications.

Here, we would like to introduce a new technology named optical Brillouin microscopy [2-4], which utilizes an entirely different approach to probing material mechanical properties. Brillouin microscopy is based on the physical principle of spontaneous Brillouin light scattering, where the incident light undergoes a frequency shift (i.e., Brillouin shift) after interaction with the sample being tested. The Brillouin shift Ω is proportional to the local longitudinal elastic modulus M' of the sample by $M' = K \cdot \Omega^2$, where the coefficient $K = \lambda\rho/(4n^2)$ for backward scattered light. λ is the known laser wavelength in air, ρ and n is the mass density and refractive index of the sample, respectively. With a known value of ρ/n^2, the longitudinal modulus M' can be computed from the Brillouin shift Ω measured by a Brillouin spectrometer. A confocal Brillouin microscope is built by integrating a Brillouin spectrometer and a standard optical confocal microscope [4], allowing the mechanical mapping of material with diffraction-limited resolution in 3D. Brillouin microscopy only uses a laser beam to probe the mechanical modulus, making it a non-contact, non-invasive, and label-free mechanical testing tool.

The unique features of the Brillouin microscopy provide new opportunities for probing cell and tissue biomechanics in physiologically relevant conditions that are not easily accessible to conventional technologies, such as the nuclear mechanics in an intact cell, subcellular mechanics during confined migrations and in 3D *in vitro* microenvironments (e.g., 3D culture, spheroid, and organoid), and tissue mechanics of early-stage embryo. In this work, we will first talk about the innovation and instrumentation of several Brillouin technologies, including confocal Brillouin microscopy [4], line-scanning Brillouin microscopy [5], and Brillouin flow cytometry [6]. We will then show several biomedical research that is enabled by Brillouin technology, with a focus on cancer related research and embryo development.

METHODS

Figure 1a shows the schematic setup of a confocal Brillouin microscope. To excite Brillouin signal, the beam of a laser source

(single mode, continuous wave laser) is guided into a standard optical microscope by several optical components and focused into a spot by an objective lens. The backward-scattered Brillouin signal generated from the beam voxel is collected by the same objective lens and analyzed by a Brillouin spectrometer, which quantifies the optical Brillouin frequency shift by using a specific optical etalon. A single-mode fiber is used for both delivering Brillouin signal and serving as a confocal pinhole. Therefore, the spatial resolution of Brillouin microscope is mainly determined by the size of the focused beam spot, which is usually less than 1μm laterally when using an objective lens with moderate numerical aperture (e.g., 0.6). Therefore, a high-resolution 2D mechanical Brillouin image of a cell can be acquired by scanning the sample using a translational stage. By adding Brillouin microscopy to a fluorescence microscope, the co-registered mechanical and molecular image could allow comprehensive understanding of biological processes (**Figure 1b**).

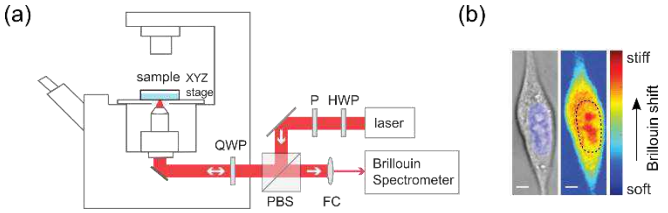

Figure 1: Confocal Brillouin microscopy. (a) Optical setup of a confocal Brillouin microscope. HWP: half-wave plate, P: polarizer, PBS: polarized beam splitter, QWP: quarter-wave plate, FC: fiber coupler. (b) Brightfield/fluorescence and Brillouin image of a NIH 3T3 fibroblast cell. Color map represents Brillouin shift. Dash line indicates the nucleus. Scale bar: 5 μm.

RESULTS

A. Cellular nuclear biomechanics and their role in cancer metastasis.

Cellular nucleus has been identified as a critical mechanosensory and regulates many cell functions including migration, immune cell trafficking and cancer metastasis. However, nucleus in an intact cell is not directly accessible to conventional contact-based technologies because it is enclosed by, and mechanically interacts with, the surrounding cytoplasm. In our recent work [7], we directly quantified intact nuclear mechanics using the non-contact Brillouin microscopy. The technological advantage of Brillouin further enabled us to reveal the role of cytoskeletal modulation in nuclear mechanics (**Figure 2a**), which is confirmed by chemomechanical modeling.

In addition, we employed Brillouin microscopy to probe nuclear modulus of metastatic cancer cells as they are migrating inside the confined microchannel [8]. We observed that cells in vertical confinement have slower migration speed and higher nuclear modulus than their counterpart in lateral confinement (**Figure 2b**). This work leads to the new finding that cancer cells respond to external confinement by adjusting nuclear stiffness regulated via a crosstalk between myosin II and lamin-A.

During the process of cancer metastasis, tumor cells experience substantial changes in shape to pass through the junctions between endothelial cells in blood vessel walls. As the gap is usually narrower than the size of nucleus, the nuclear stiffness could be an important limiting factor for transendothelial migration, yet no studies has been conducted to understand whether cancer cells mediate nuclear stiffness to facilitate this process. Using the Brillouin microscopy, for the first time, we observed that cancer cells soften their body and nuclei upon extravasation (**Figure 2c**) [9]. Collectively, these works suggest that adjusting stiffness could be a common strategy employed by cancer cells during metastasis.

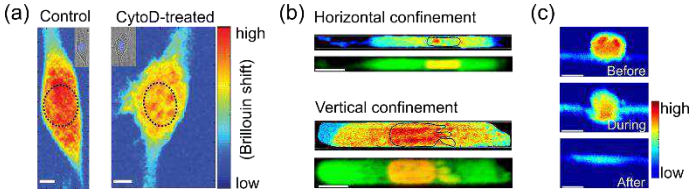

Figure 2: (a) Brillouin shift of nucleus decreases upon disruption of actin filament. Inset: brightfield image. Scale: 5μm. (b) Co-registered Brillouin and fluorescence images. Brillouin shift of nucleus is higher in vertical confinement than in horizontal confinement. (c) Cancer cells show decreased Brillouin shift during transendothelial migration. Scale in (b) and (c) is 10μm. Color bar: Brillouin shift. Dashed line highlights nucleus.

B. Evolution of tissue mechanics during embryo development.

Tissue biomechanics, together with genetic factors and molecular signaling, coordinates morphogenesis in embryonic development. However, mapping tissue mechanics *in situ* is highly challenging because of 3D mechanical interactions inside the embryo body. Using optical coherence tomography-guided Brillouin microscopy, we acquired 2D mechanical maps of mouse embryonic tissue, confirming that the Brillouin technology has cellular spatial resolution and sufficient mechanical sensitivity for early-stage embryo. Very recently, our lab devised a time-lapse Brillouin microscopy that can conduct longitudinal mechanical imaging when a live embryo is developing, enabling real-time quantification of tissue biomechanics during neural tube closure (**Figure 3**).

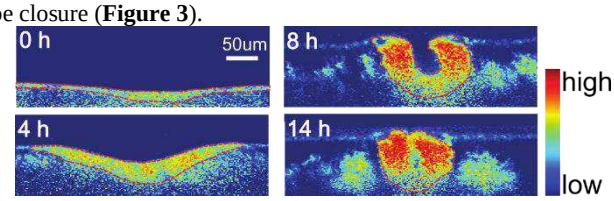

Figure 3: Time-lapse mechanical imaging of neural plate tissue (highlighted by red dashed line) of a live chick embryo.

DISCUSSION

As an emerging technology, Brillouin microscopy is currently far from mature and has limitations and challenges [10], including the acquisition speed, penetration depth, potential phototoxicity, and data interpretation and validation. While the technology itself is rapidly growing to address these challenges, we expect this new technology can serve as a unique complement to existing mechanical testing tools and promote research in a broad range of fields where the understanding of biomechanics is urgently needed but currently remains in accessible, such as cancer metastasis and tumorigenesis, organogenesis, congenital defects, regenerative medicine, tissue engineering, and biomaterials.

REFERENCES

[1] Bao, G et al., *Nature Materials*, 2: 715-725, 2003.
[2] Scarcelli, G et al., *Nature Photonics*, 2: 39-43, 2008.
[3] Scarcelli, G et al., *Nature Methods*, 12: 1132-1134, 2015.
[4] Zhang, J et al., *Nature Protocols*, 16: 1251-1275, 2021.
[5] Zhang, J et al., *Nature Methods*, 20: 677-681, 2023.
[6] Zhang, J et al., *Lab Chip*, 17: 663-670, 2017.
[7] Zhang, J et al., *Small*, 1907688, 2020.
[8] Wisniewski, E et al., *Science Advances*, 6: eabas6506, 2020.
[9] Roberts, A et al., *J Biomechanics*, 121: 110400, 2021.
[10] Prevedel, R et al., *Nature Methods*, 16: 969-977, 2019.

SB³C2024
Summer Biomechanics, Bioengineering and Biotransport Conference
June 11-14, Lake Geneva, WI, USA

p21 SUPPRESSION TO IMPROVE OSTEOGENIC CAPACITY OF MSCS

Sina Jafari (1), Aaron Levi Brandner (1), Julie Sandria (1) Priyatha Premnath (1)

(1) Department of Biomedical Engineering, University of Wisconsin Milwaukee, WI, USA

INTRODUCTION

The recovery process following a fracture is contingent upon several variables, including the nature of the fracture (comminuted or non-comminuted) [1], smoking [2] history, and the presence of diabetes. Generally, individuals who are young and in optimal health often exhibit favorable healing outcomes, particularly with non-comminuted fractures. Conversely, individuals facing more intricate fractures, advanced age [3], or conditions like osteoporosis [4] that disrupt the natural healing process may require external interventions to facilitate a successful recovery. When a bone is fractured, the body naturally recruits mesenchymal stem cells (MSCs) to the fracture site. MSCs then differentiate into bone (osteoblasts) or cartilage cells (chondrocytes), release growth factors, and exhibit anti-inflammatory properties. These actions promote bone healing by supporting tissue repair, angiogenesis, and extracellular matrix production [5]. The immunomodulatory effects of MSCs also contribute to a balanced immune response, enhancing the overall regenerative process.

One way of enhancing bone regeneration after a fracture is through gene therapy, where specific genes can be targeted to improve outcomes [6]. p21, a cyclin-dependent kinase inhibitor (CDKN1A), is a pivotal gene that regulates various aspects of the cell cycle, such as inducing cycle arrest, apoptosis, senescence, and facilitating DNA repair. Studies have demonstrated that inhibiting p21 can enhance bone healing and regeneration following an injury [7]. A small molecule inhibitor of p21 is UC2288. UC2288 is a derivative of Sorafenib, a multikinase inhibitor renowned for its ability to decrease p21 [8]. Sorafenib, an FDA-approved and extensively studied multiple kinase inhibitor, is utilized for treating various cancer types, particularly hepatocellular carcinoma (HCC). Sorafenib can impede angiogenesis, curb tumor cell proliferation, and facilitate apoptosis in HCC [9]. In contrast to Sorafenib, UC2288 does not impact the levels of p-ERK protein or hinder the activity of Raf kinases [8]. Instead, UC2288 diminishes the p21 protein at the transcriptional or post-transcriptional level without involving protein degradation. It significantly reduces cytosolic p21 protein levels while leaving nuclear p21 unaffected and operates independently of p53 [10].

In this research project, our objective is to investigate the efficiency of UC2288 in reducing p21. The underlying hypothesis is that reducing p21 levels will amplify the osteogenic potential within mesenchymal stem cells (MSCs). To investigate this hypothesis, we tested human umbilical cord derived MSCs (HU UCMSCs) with various concentrations of UC2288. The subsequent analysis focused on assessing any discernible improvement in their osteogenic capabilities.

METHODS

Cell viability was assessed via an MTT assay in HU UCMSCs. 2.5 μM, 5 μM, and 10 μM concentrations of UC2288 were tested with 5k cells of HU UCMSCs in a 96-well plate for 24, 48, and 72 hours. To determine transcriptional changes in the osteogenic capacity of the cells, RT-qPCR in a 24-well plate was performed with 30k cells at 2.5 μM, 5 μM, and 10 μM concentrations of UC2288 for 7,14 and 21 days to quantify the expression of osteogenic genes of interest that included Sp7, RUNX2, Bglap, Col1a1, and p21. Data was normalized against endogenous control gene 18s. Results were analyzed using the ΔΔCt method of analysis. Results were analyzed via a 2way ANOVA. Alizarin red staining was performed on a 24-well plate with cells seeded at a density of 30,000 cells per well to visualize the extracellular release of calcium. The cells were treated with UC2288 at concentrations of 2.5 μM, 5 μM, and 10 μM for 21 days.

RESULTS

MTT assay indicates that 2.5 μM and 5 μM UC2288 is not cytotoxic to Hu UCMSCs, while at 72 hours 10 μM decreases cell viability.

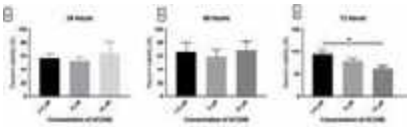

Figure 1: Percent viability of Hu UCMSCs when incubated with UC2288 at 24, 48 and 72 hours. n=3, *p<0.5.

For Alizarin red staining, 2.5 µM resulted in more intense staining of Alizarin red compared to the control (Figures 2(a-b). 10 µM of UC2288 resulted in reduced viability of cells as evidenced by the absence of cells (Figures 2d).

Figure 2. Alizarin red staining of Hu UCMSC incubated with different concentrations of UC2288 for 21 days.

RT-qPCR shows that 2.5µM of UC2288 increased osteogenic expression at transcriptional level when cultured with Hu UCMSCs for 7 and 14 days (figure a, b). At 21 days however there was no significant change between the osteogenic genes expect at concentration of 10µM for Sp7 and Bglap which were significantly higher (figure c).

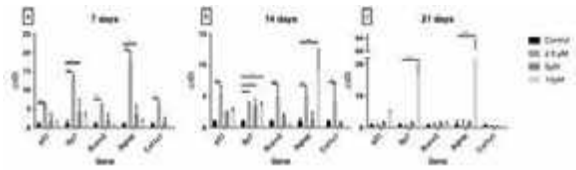

Figure 3. Relative expression of osteogenic genes and p21 after Hu UCMSCs were treated with UC2288.

DISCUSSION

Previous studies in mice showed that inhibition of p21 can increase rate at which bone heals after an injury [8]. It was hypothesized that MSCs were recruited to the site of injury and aided in healing of the fracture by differentiating into bone cells. Therefore, in this study, we focused on MSCs. When Hu UCMSC were treated with UC2288 to decrease p21, a transcriptional increase in osteogenic activity was observed through RT-qPCR at 7 and 14 days compared to control but not at 21 days. At 21 days' time point it could be that the cells are becoming drug tolerant. While we observed overall positive results with HUMSCs, bone marrow MSCs present a more accessible alternative to clinical applications where a patient's own MSCs can be used to increase osteogenic capacity. In this case, either cells can be isolated and cultured ex-vivo with UC2288, or UC2288 can be delivered to the fracture site. Once the nature of UC2288-cell interaction is further understood, a delivery mechanism will be determined to deliver the drug locally to the site of interest. Eventually, the therapeutics targeting p21 could pave new pathways for bone healing. This is especially important in the aging population, and this line of study could ultimately lead to clinical applications.

ACKNOWLEDGEMENTS

This project was partially funded by a UWMRF Catalyst Grant and an NSF I-Corps grant.

REFERENCES

[1] L. Chen, L. Yang, M. Yao, X. Cui, C. Xue, Y. Wanget al., "Biomechanical characteristics of osteoporotic fracture healing in ovariectomized rats: a systematic review", Plos One, vol. 11, no. 4, p. e0153120, 2016. https://doi.org/10.1371/journal.pone.0153120

[2] A. Mahajan, N. Kumar, & B. Gupta, "Delayed tibial shaft fracture healing associated with smoking: a systematic review and meta-analysis of observational studies conducted worldwide", International Journal of Environmental Research and Public Health, vol. 18, no. 19, p. 10228, 2021. https://doi.org/10.3390/ijerph181910228

[3] D. Clark, M. Nakamura, T. Miclau, & R. Marcucio, "Effects of aging on fracture healing", Current Osteoporosis Reports, vol. 15, no. 6, p. 601-608, 2017. https://doi.org/10.1007/s11914-017-0413-9

[4] G. Rußow, D. Jahn, J. Appelt, S. Märdian, S. Tsitsilonis, & J. Keller, "Anabolic therapies in osteoporosis and bone regeneration", International Journal of Molecular Sciences, vol. 20, no. 1, p. 83, 2018. https://doi.org/10.3390/ijms20010083

[5] Z. Ouyang, T. Tan, X. Zhang, J. Wan, Y. Zhou, G. Jianget al., "Circrna hsa_circ_0074834 promotes the osteogenesis-angiogenesis coupling process in bone mesenchymal stem cells (bmscs) by acting as a cerna for mir-942-5p", Cell Death &Amp; Disease, vol. 10, no. 12, 2019. https://doi.org/10.1038/s41419-019-2161-5

[6] R. Dimitriou, E. Jones, D. McGonagle, & P. Giannoudis, "Bone regeneration: current concepts and future directions", BMC Medicine, vol. 9, no. 1, 2011. https://doi.org/10.1186/1741-7015-9-66

[7] P. Premnath, B. Jorgenson, R. Hess, P. Tailor, D. Louie, J. Taianiet al., "P21−/− mice exhibit enhanced bone regeneration after injury", BMC Musculoskeletal Disorders, vol. 18, no. 1, 2017. https://doi.org/10.1186/s12891-017-1790-z

[8] H. Wettersten, S. Hwang, C. Li, E. Shiu, A. Wecksler, B. Hammocket al., "A novel p21 attenuator which is structurally related to sorafenib", Cancer Biology &Amp; Therapy, vol. 14, no. 3, p. 278-285, 2013. https://doi.org/10.4161/cbt.23374

[9] W. Tang, Z. Chen, W. Zhang, Y. Cheng, B. Zhang, F. Wuet al., "The mechanisms of sorafenib resistance in hepatocellular carcinoma: theoretical basis and therapeutic aspects", Signal Transduction and Targeted Therapy, vol. 5, no. 1, 2020. https://doi.org/10.1038/s41392-020-0187-x

[10] R. Liu, H. Wettersten, S. Park, & R. Weiss, "Small-molecule inhibitors of p21 as novel therapeutics for chemotherapy-resistant kidney cancer", Future Medicinal Chemistry, vol. 5, no. 9, p. 991-994, 2013. https://doi.org/10.4155/fmc.13.56

HYDROGEL WOUND HEALING IN PALLIATIVE CARE

T. Welch (1), J. Wright (1), V. Pimpalwar(1), K. Newcomer (2), M. Ligorio (3)

(1) Cardiovascular and Thoracic Surgery, UT Southwestern Medical Center, Dallas, TX, USA
(2) Internal Medicine, UT Southwestern Medical Center, Dallas, TX, USA
(3) Surgery, UT Southwestern Medical Center, Dallas, TX, USA

INTRODUCTION

Palliative care patients often undergo an aggressive oral regimen for adequate pain management due to cancer dissemination in multiple (non-skin) organs. Chronic wounds affect 5 – 7 million patients and cost more than $30 billion annually in the US. As a result, topical solutions are synergistically added to the oral administrations of other analgesic compounds, which unfortunately limits their pain control in skin and mucosa ulcerated tissues. In addition, high doses of systemic administered opioids can trigger a state of hyperalgesia, worsening the pain from neoplastic ulcers. Moreover, several studies have indicated a decrease in the utilization of oral opiates when topical formulations are co-administered to mitigate the current opioid abuse crisis. In further support of this, the World Health Organization recommends trying adjuvants such as topical analgesics before systemic medications in its Analgesic Ladder. The objective is to develop a topical hydrogel to effectively deliver pharmaceuticals to patients.

METHODS

We developed a hydrogel through a design of experiments to determine concentrations of polyvinyl alcohol and poloxymer and used dexamethasone as a proof-of-principle drug for the experimental work. We analyzed the hydrogels' polymer peak identification by Fourier transform infrared spectroscopy (FTIR), rheological properties, drug release, and thermal properties. The hydrogels were fabricated by placing PVA (10% wt/wt), water and Poloxymer (10% wt/wt), and Dexamethasone (3% wt/wt) at 90 °C bath with continuous mixing for 3 hours. The samples (n=3 per group) were placed into separate circular glass plates and freeze thawed at -80 °C for 12 hours 2 times (2X), 4 times (4X) and 6 times (6X). For drug saturation limit determination, 4 films per drug loading group, 20%, 30%, 40% and 50% were analyzed on differential scanning calorimetry. Fourier Transform Infrared Spectroscopy (FTIR) was used to characterize the presence of specific chemical groups in the materials that were obtained as 1–2 mm thick films and analyzed by FTIR using Transmittance Mode in the range of wavenumber from 4000 to 650 cm^{-1} during 64 scans, with 2 cm^{-1} resolution (Nicolet iS5, Thermoscientific, USA).

Rheological properties such as storage modulus and loss modulus were measured on a parallel plate rheometer (AR G2, TA Instruments, Newcastle, DE) with a gap size of 1000 μm. For strain rate dependence experiments, the temperature was held at room temperature, while the strain rate was varied continuously from 0.1 to 100 s^{-1}. For stress dependence, the temperature was held at room temperature, and the stress was varied from 1 to 1000 (Pa). Next, thermal properties were determined by differential scanning calorimetry (Q20, TA Instruments, Newcastle, DE). Three samples from each group were equilibrated at 20 °C and ramped to 250 C at a rate of 10 °C / min and held constant for 3 minutes and cooled by to 20 °C at 50 °C / min. Heat curves were analyzed for heat of enthalpy, H_m, using TA Universal Analysis Software. The percent crystallinity was determined by equation (1) with H_0 = 138.6 J/g for 100% crystalline PVA measured at the equilibrium point T_m. [1]. The drug saturation limit was determined by linear regression analysis using the measured enthalpy of fusion for each drug loaded hydrogel and graphing the enthalpy of fusion vs the dexamethasone amount loaded per hydrogel.

The last experiment was determining the drug release curve for a 2x freeze thaw cycle and a control of Solosite (S1), a commonly used hydrogel in wound healing, mixed with 3 % (wt/wt) dexamethasone compared to a 2x freeze thaw film (H1). Using three PermeGear Franz Cells fitted with an Ultracel 10 kDa membrane in each one and Phosphate Buffered Saline at 37 °C in the 12 ml receptor chamber with a 37 °C circulating heated water jacket. Drug release was measured each hour up to 12 hours and one at 24, 36, 48, 60, 72 hours with a Dionex Ultimate 3000 HPLC with an acclaim C-30 column. The mobile phase was 50:50 Water / Acetonitrile / 0.001% Trifluoroacetic acid with a pH of 2.0 at a flow rate of 0.5 ml / min. The cumulative drug release was plotted and analyzed using power law equation (2) curve fitting.

All data sets were analyzed using GraphPad Prism version 10.0.0 for Windows, GraphPad Software, Boston, Massachusetts USA. The rheology data was analyzed using One-Way ANOVA per cross-linking group followed by a *post hoc* Bonferroni test ($p < 0.05$). For DSC, all cross-linking groups were analyzed using a One-Way ANOVA followed by a post hoc Bonferroni test ($p < 0.05$). The saturation limit was determined by a linear regression analysis where the y-intercept is the saturation limit.

Equation

$$X\,(\%) = \frac{H_m}{H_0} \times 100 \qquad (1)$$

$$\frac{M_t}{M_\infty} = kt^n \qquad (2)$$

RESULTS

The drug release curve of these films showed a dexamethasone release of approximately 50% in 24 hours and 67% within 72 hours. On the contrary, the hydrogel control, solosite, showed a (linear) dexamethasone release of less than 5% in 24 hours. The hydrogels were fitted to the Korsmeyer-Peppas Power Law, equation (2) [1] since only one equation does not fit the data across the entire time range. The zero-order kinetics model, Higuchi, gave us a correlation coefficient of 0.96; therefore, we fitted the data piecewise to the first 12 hours and then 13–72 hours. The corresponding equations shown have an "n" value of 0.87, which relates closely to a zero-order function where the drug release depends on the polymer relaxation and swelling with a correlation coefficient of 0.99. The second equation, 16–72 hours, has an "n" value of 0.37. The Peppas Power Law equation without piecewise fitting shows the drug release as non-fickian diffusion with an n = 0.53 (**Figure 1A**). Based on this, we believe the piecewise curve fitting better explains the drug release being linear due to polymer swelling and forcing the drug out of the polymer matrix with an n = 0.87 for the first 12 hours and quasi-fickian release with an n = 0.37 for the later times of drug release (**Figure 2B**). This lower value corresponds to a diffusion model where the drug release depends on diffusion.

The FTIR results showed we can make hydrogels with dexamethasone entrapped within the polymer. The dexamethasone aromatic stretches (-C=O) are shown at v1615 cm^{-1}, v1657 cm^{-1} and v1705 cm^{-1}. PVA is shown at (C-H) v2939 cm^{-1}, (-C=O) 1742 cm^{-1}, CH_2 s 1455 cm^{-1}, C-O v1141 cm^{-1}, C-O-C v1057 cm^{-1}, and poloxamer at (C-H) s2877 cm^{-1}, (O-H) b1345 cm^{-1} and (C-O) s1111 cm^{-1} stretches.

The rheology results showed that as the frequency increases, so does the storage modulus and loss modulus up to 100 Hz. No crossover between the storage and loss modulus was observed on the frequency sweep. The storage modulus shows an increasing trend with more freeze-thaw cycles from 5652±629 Pa to 7842±84 Pa, but none was statistically different. The yield stress of the polymer shows an increase from 283±12 kPa to 432±26 kPa with an increase in the number of freeze-thaw cycles, but they are not statistically different. At high oscillating strains above 10% we saw a crossover between the storage and loss modulus. At high oscillating stresses above 100 Pa we observed a crossover between the storage and loss modulus.

The DSC results showed the percent crystallinity increases with degree of freeze thaw cycles from 10% - 17 %. The distinct enthalpy peaks show up for poloxamer at 54.6±0.3 °C, PVA at 190.8±0.3 °C and dexamethasone at 252.6±1.7 °C for 2X group; poloxamer at 51.5 ±0.5 °C, PVA at 190.6±0.2 °C and dexamethasone at 249±0.6 °C for 4X group, 53.4±0.3 °C, PVA at 191.5±0.5 °C and dexamethasone at 253.3±1.1 °C for 6X group. The drug saturation was determined to be 10.06%. The scatter data was plotted for each drug loaded amount of dexamethasone and fit to a linear regression curve with a $R^2 = 0.89$.

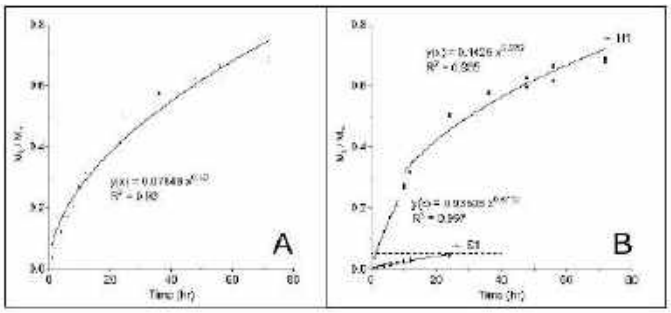

Figure 1: (A) Showing Power Law fit and (B) piece-wise Power Law fit with control sample S1 and H1 films.

DISCUSSION

Using the Korsmeyer-Peppas power law model in a piecewise model fits the drug release profile with higher correlation coefficients of 0.99 compared to other methods, such as Higuchi of 0.96. The synthetic hydrogel we have formulated has a drug release curve that is mostly linear for the first 12 hours at a 35% drug release and then asymptotically changes to plateau around 60% drug release. In comparison to control, solosite, or S1, we showed a higher drug release. Hydrogel formulation usually occurs by cross-linking with UV, physical entanglement, hydrogen bonding, and ion cross-linking. There are several hydrogels, such as chitosan, a natural hydrogel with strong strength and stability. Others have used carboxy methylcellulose and modified the formulation with essential oils to increase their drug release with curcumin. They showed a drug release range of 20% without any modification to 80% using different essential oils to modulate their drug release. Others have used chemical crosslinkers to modulate their drug release, such as glutaraldehyde with PVA, creating a sustained drug release over 35 days. In comparison, our model showed that we could achieve a high release of the drug within 24 hours without chemical crosslinking or the use of other oils or ointments. The limitations of the study show a one-way diffusion model for topical treatment and the use of a membrane instead of skin as a filter. The implications of this work are to advance treatment options for patients in palliative care for wound management.

Although much progress has been made in early diagnostic and therapeutics, many cancer remain a deadly disease. Virtually all patients with uncurable metastatic conditions undergo palliate treatments, including oral or intravenous (IV) administration of opioids. Recent studies showed that a better control of cancer-related pain and discomfort for cancer patients with skin or mucosal lesions can be achieved by using the local administration of pain-control compounds. Local vs. systemic drug administration has several benefits, spanning from fewer drugs needed to superior control of the local pain/discomfort to largely limit systemic side effects. Our hydrogel has the potential to outperform all the current topical-delivery methodologies as shown herein by a 50% drug released compared to 5% of a commonly used hydrogel, solosite, in current palliative care practice. This 10-fold enrichment in drug release has also the potential, if it proved efficacious in prospective clinical trials, to mitigate the current opioid crisis determined by an abuse of the systemic administration (e.g., oral or IV) of opioids, which our society has experienced in the last decade.

ACKNOWLEDGEMENTS

Acknowledge grant or other funding support or the assistance of others as appropriate.

REFERENCES

[1] Peppas, N.A, Merril, E. J. Appl. Polym. Sci., 20:1457-1465, 1976.
[2] Lee Pl. Kinetics of drug release from hydrogel matrices. J. Contr. Rel., 2:277-288, 1985.

THE STRUCTURAL AND MECHANICAL BEHAVIOR OF SKIN DURING PUNCTURE FOR DIFFERENT IMPACTOR SIZES AND LOADING RATES

Joseph LeSueur (1), Carolyn Hampton (2), Jared Koser (3), William Dzwierzynski (4), Michael Kleinberger (2), Frank A. Pintar (1,3)

(1) Joint Department of Biomedical Engineering, Marquette University & Medical College of Wisconsin, Milwaukee, WI, USA
(2) US DEVCOM Army Research Laboratory, Aberdeen Proving Ground, MD, USA
(3) Department of Neurosurgery, Medical College of Wisconsin, Milwaukee, WI, USA
(4) Department of Surgery, Division of Plastic Surgery, Medical College of Wisconsin, Milwaukee, WI, USA

INTRODUCTION

Violent crimes using knives or other sharp objects account for 22% of all global homicides [1] in addition to thousands of non-fatal sharp force injuries treated daily in the United States [2]. In court, forensic experts have assessed the alleged assailant's level of intent by comparing it to force thresholds. However, blunter instruments with varying tip radii and geometry, such as screwdrivers, glass shards, scissors, and sharpened metal rods [2], lack quantified force data and are more difficult to determine when excessive force is used [3,4].

Forensic studies have investigated the high-rate, traumatic failure of skin during puncture and stabbings from screwdrivers and knives [3,5]. However, many studies have used skin simulants rather than biological tissue to reduce variability [3–5], but synthetic materials do not account for anisotropy and viscoelasticity of skin with natural pre-tension. Based on impactor size and geometry, sharp and blunt punctures have differences in failure mechanisms [6], but damage to the microstructure of skin from puncture has not been examined.

To account for the multivariate nature of puncture incidents, finite element models have been developed to simulate puncture of fruit [7] and skin simulants [8]. Mechanical behavior of skin may be validated with experimental surface deformations measured using 3D digital image correlation (DIC). 3D-DIC also allows analysis of localized strains during puncture to validate anisotropy of strain distribution.

The purpose of this study was to investigate the structure and mechanical behavior of skin in isolated puncture through histological analyses, strain distribution using 3D-DIC, and statistical effects of skin thickness, loading rate, and impactor diameter. Experimental results may be used to develop a computational model of puncture, capable of predicting failure thresholds for various impactor sizes and geometries.

METHODS

Frozen porcine tissue was thawed, excised into discs, and subjected to physiological initial tension [9]. Initial tension was quantified by measuring biaxial strain of the sample, and skin thickness was measured at the puncture site after testing using calipers (1-4 mm inclusion).

An electrohydraulic piston actuator (MTS) with an attached uniaxial accelerometer (DTS) loaded the skin and recorded force, displacement, and acceleration at 20 kHz. A steel impactor with a 3, 5, or 8 mm stainless steel sphere was fixed to the load cell. Skin was pre-conditioned while unclamped and sub-failure trials were conducted to a displacement of 15 mm at 50 and 500 mm/s while clamped, allowing the sample to recover between runs. A failure trial was performed at a rate of 5, 50, 500, or 1000 mm/s. Inertial effects were minimized by subtracting forces due to acceleration. Trials were excluded when failure occurred at displacements less than 15 mm or strain energy of sub-failure 2 decreased by more than a conservative 12% from sub-failure 1 determined from sample inspection, however, "damaging" pre-failure loads have shown to not affect ultimate strength of skin [10].

3D digital image correlation (DIC) was performed using two high-speed cameras (NX-Air series, IDT) at sampling rates up to 5250 Hz for failure runs to measure local surface strains during puncture. A speckle pattern was randomly applied to the adipose surface of the specimen. Displacement and major strain were calculated with a median spatial filter of 5 pixels (GOM Correlate Pro, Trilion). DIC data was imported into MATLAB and interpolated to create a continuous surface. For wounds of samples punctured at 5 mm/s, the elliptical area of disrupted tissue was quantified using Image J and statistically compared between the three impactor sizes with ANOVA.

A generalized linear mixed model with random effects (of pig) was used to determine significance of loading rate, skin thickness, and impactor diameter for displacement, stiffness, force, and strain energy at failure (SAS Studio). A generalized linear model with repeated measures and a logit link function was used to predict probability of puncture by normalized force and impactor diameter.

To investigate histological changes, twelve samples from 3 pigs were tested in puncture with the 5 mm impactor. Skin samples were

grossed at the area of impact, fixed, processed, sliced cross-sectionally and parallel to the epidermis about 100 μm deep, and stained with H&E after each step in the puncture protocol (Untested, Pre-Conditioned (PC), Sub 1, Sub 2, and Failure). PC samples were sliced near and away from the impactor site to analyze fiber re-orientation. Quantitative analysis of gaps between collagen bundles, previously reported as damage [11], were determined using the Color Threshold tool on ImageJ for 8 encompassing areas at 10x. Collagen fiber orientation was analyzed using the Distribution tool at 20x to calculate the percentage of fibers aligned with ± 15° of the preferred collagen orientation. ANOVA was used to determine significant differences.

RESULTS

After exclusion of 15 samples, 218 puncture trials were analyzed for 3 impactor diameters impacting at 4 various rates (n>18 for each impactor diameter and rate). Force at failure and skin thickness demonstrated a strong linear correlation and force was normalized by thickness for analysis. Increased impactor diameter resulted in greater normalized force, displacement, and strain energy, whereas increased rate resulted in increased normalized force and stiffness but decreased displacement (**Figure 1**). Normalized force and impactor diameter were significant (p<0.001) in predicting probability of penetration (**Figure 1**), but impact rate between 50 and 500 mm/s was insignificant (p=0.58).

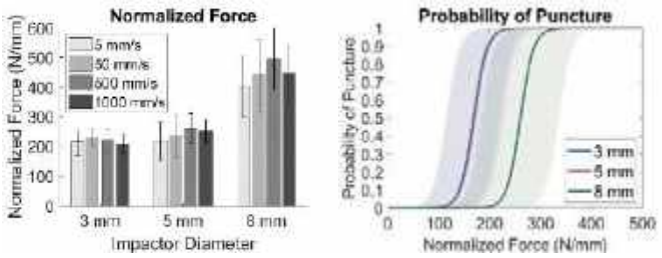

Figure 1: Effect of rate and impactor diameter in normalized force (left) and probability of puncture by normalized force (right)

The generalized linear model resulted in significant dependency of thickness, loading rate, and impactor diameter at failure (**Table 1**).

Table 1: p-values in failure metrics (* indicates significance)

	Displacement	Stiffness	Force	Strain Energy
Rate	<.0001*	<.0001*	.0011*	.1122
Thickness	.0018*	<.0001*	<.0001*	.0019*
Impactor Size	.0329*	.0695	.0164*	.0114*

Prior to puncture, the skin expressed conically distributed displacement (**Figure 2a-b**) but directionally in major (principal) strain (**Figure 2c**), which confirmed the presence of anisotropy at failure. The major strain distribution and resulting wound (**Figure 2d**) formed an ellipse-like shape, assumed parallel to natural skin tension lines and independent of the applied tension direction. The major axis length of wounded tissue was significantly greater from 8 mm punctures (p<0.001) with no differences between 3 mm and 5 mm impactor wounds (p=0.88).

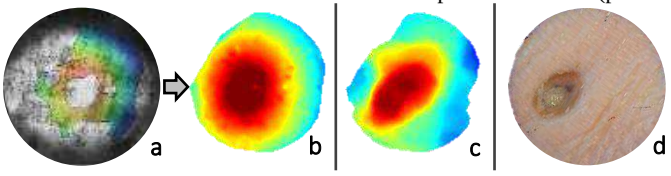

Figure 2: a) 3D-DIC displacement map of skin before failure (subcutaneous view), b) interpolation in MATLAB, c) elliptical strain profile, and d) zoomed-in wound orientation (surface view)

Natural gaps (white area) between collagen fiber families (up to 12%) were observed in untested skin (**Figure 3**). Gaps between collagen fibers significantly increased after Sub 2 and Failure (p<0.01). Collagen fibers were significantly more aligned after PC near center compared to PC away trials (p<0.001). With parallel slices, only Failure resulted in significantly more gaps than Untested, PC, and Sub 1 (p<0.01).

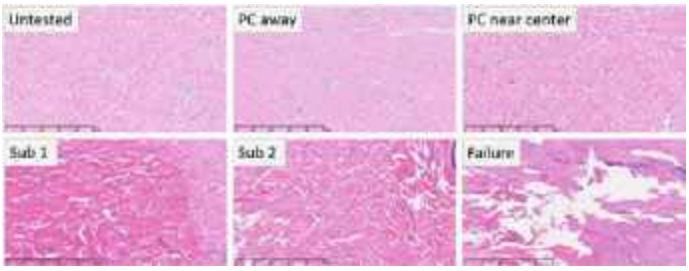

Figure 3: H&E cross-sectional stain of the dermis after Pre-conditioning (PC), Subfailure (Sub 1 and Sub 2), and Failure tests with white area showing gaps between collagen fiber families

DISCUSSION

Rate-dependency was observed in displacement, stiffness, and force during dynamic puncture of skin, which similar trends have been observed in uniaxial tension of skin [12,13]. Significantly greater failure thresholds and wound sizes were observed with the 8 mm impactor, which was also reported with increased screwdriver cross-sectional area [3], due to increased contact area and simultaneous blunt loading of the dermis and epidermis [6]. Expressing probability of puncture based on normalized force and impactor diameter allows forensic experts to quantify the likelihood of puncture with a specific instrument.

From the histological analyses, we can conclude alignment of collagen fibers near the impactor from pre-conditioning, sub-failure trials caused minimal structural damage with consistent mechanical behavior [11], and the failure mechanism of skin during puncture occurred first in the reticular dermis followed by subsequent failure of the papillary dermis and epidermis.

For accurate simulation of puncture, a material model of skin should account for the viscoelastic nature of skin with rate effects. Furthermore, this model should account for the anisotropic behavior of skin with a directionally dependent strain distribution at failure, which was measured with 3D-DIC. Ultimately, this study lays the foundation for development of a finite element model of skin during puncture to quantitatively assess failure thresholds of skin with various impactor sizes, geometries, rates, and skin thicknesses, which may aid in determining level of intent during unique stabbing incidents.

ACKNOWLEDGEMENTS

This research was supported by resources at the Zablocki VA Medical Center, Milwaukee, Wisconsin. This research was funded by DEVCOM ARL Cooperative Agreement W911NF-21–2-0004.

REFERENCES

[1] Kabir, R., et al., 2022, Nepal J Epidemiol, **12**(4), pp. 1242–1247.
[2] Burke, M. P., et al., 2018, For Sci Med Pathol, **14**(3), pp. 295–300.
[3] Parmar, K., et al., 2012, Int J Legal Med, **126**(1), pp. 43–53.
[4] Hainsworth, S., et al., 2008, Int J Legal Med, **122**(4), pp. 281–291.
[5] Gilchrist, M. D., et al., 2008, Forensic Sci Int, **177**(1), pp. 52–65.
[6] Shergold, O., et al., 2005, J Biomech Eng, **127**(5), pp. 838–848.
[7] Zulkifli, N., et al., 2021, Foods, **10**(442).
[8] McCarthy, C. T., et al., 2010, Eng Fract Mech, **77**(3), pp. 437–451.
[9] LeSueur, J, et al., (in review), *Medical Engineering and Physics*
[10] Sree, V. D., et al., 2023, Ann Biomed Eng, **51**(9), pp. 2056–2069.
[11] Lakhani, P., et al., 2020, J Mech Behav Biomed Mater, **104**.
[12] Ottenio, M., et al., 2015, J Mech Behav Bio Mat, **41**, pp. 241–250.
[13] Trotta, A. & Ní Annaidh, A., 2019, J Mech Behav Bio Mat, **100**.

IS SYNTHETIC CLEAR GELATIN A VALIDATED SURROGATE FOR BIOLOGICAL TISSUE IN LOW-VELOCITY PENETRATING IMPACTS?

Joseph LeSueur (1), Jared Koser (2), Stephen Hargarten (3), Frank A. Pintar (1,2)

(1) Joint Department of Biomedical Engineering, Marquette University & Medical College of Wisconsin, Milwaukee, WI, USA
(2) Department of Neurosurgery, Medical College of Wisconsin, Milwaukee, WI, USA
(3) Department of Emergency Medicine, Medical College of Wisconsin, Milwaukee, WI, USA

INTRODUCTION

Biological tissue is variable and difficult to access large sample sizes. Ballistic gelatin provides a repeatable, biofidelic surrogate to simulate the mechanical response of biological tissues in which 10% ordnance gelatin at 4°C has been adopted as the best surrogate for muscle [1]. Historically, calibration tests were conducted by launching a .177 steel BB at 181 meters per second (m/s) and the measured depth of penetration (DoP) must be 85 ± 5 millimeters (mm) in 10% gelatin at 4°C to verify the biofidelity [1,2]. This standard to calibrate gelatin was based on ballistic experiments into *one* porcine leg (n=10) by Dr Fackler in the late 1980s [2,3]. To assess DoP at varying velocities, empirical relationships have also been developed to establish calibration boundaries for 10% ordnance gelatin at varying temperatures [4,5].

Recent studies have compiled substantially larger datasets of DoP measurements into animals and post-mortem human subjects (PMHS) from ballistic impact of spheres and fragment simulating projectiles at velocities up to 1200 m/s [5–7]. Surprisingly, these DoP measurements were substantially less than values reported by Fackler, in which the 10% ordnance gelatin calibration standard was established. Better biofidelity was observed in 20% ordnance gelatin at 10°C. Although the 20% gelatin was adopted as the "NATO standard" for testing of small arms [8], there is no standard to verify its calibration [9,10].

One attempt to calibrate 20% gelatin used the same experimental procedure that was performed on 10% ballistic gelatin and measured the DoP, which a synthetic gelatin manufacturer claimed as 1.50 ± 0.25 inches (38.1 ± 6.35 mm) (Clear Ballistics, Greenville, SC). Since this "NATO standard" was developed based on extrapolation from 10% ordnance gelatin performance rather than biological DoP data, there is no verification that "calibrated" 20% gelatin represents a biofidelic response, especially with larger DoP data sets that contradict early, limited findings of Fackler [5].

Ordnance gelatin has been commonly used for decades but has some limitations including sensitivity to temperature and considerable variability during formation of the gelatin [1,9,10]. Synthetic gelatin has been introduced to overcome these limitations with better temperature-independence, simpler formation, increased transparency for high speed video, and the ability to re-melt multiple times. Several studies have compared the DoP, energy absorption, and cavity mechanics between ordnance and synthetic gelatins [5,11,12]. Most researchers have dismissed the opportunity to utilize synthetic gelatin in ballistic testing due to differences in these metrics. However, very few studies have compared synthetic gelatin to the actual medium researchers are attempting to simulate: biological tissue.

The purpose of this study was to investigate the validity of synthetic clear gelatin as an acceptable surrogate of biological tissue by comparing measured DoP at the low-velocity calibration range.

METHODS

90 whole porcine legs from 30 post-mortem Yorkshire pigs were frozen thawed according to previous studies, shown to not significantly affect impact behavior [13]. Shaved legs were suspended from the most proximal bone and oriented perpendicular from the projectile path. Multiple trials were conducted on each leg, but erroneous impacts to skin with underlying bone and impacts within 4 cm of a previous impact were excluded [13]. The internal and external tissue temperatures were measured at the impact site prior to each trial.

Impact velocities were targeted so that approximately half of the projectiles penetrated the skin; only penetrating impacts were used for analysis in this study. Thirteen spherical ball bearings (BBs) of stainless steel, silicon nitride, or Delrin acetal plastic ranging from 1.59 mm (1/16") to 9.53 mm (3/8") were chosen to create a spectrum of sectional densities from 0.3 to 5 g/cm^2. High-speed videography was captured laterally up to 40 kHz (nac Image Technology, Simi Valley, CA), and projectile motion (velocity and displacement) was quantified using a physics-based video analysis software (Tracker, Aptos, CA). 2D video

analysis was calibrated using the known distance of the test label, which was taped to the barrel in the plane of projectile motion.

Two blocks of 20% synthetic NATO Clear Ballistics gelatin were received from the manufacturer that claimed a calibrated DoP of 1.41 inches. The gelatin block was unbounded on a metal stand and oriented perpendicular to the projectile path at 20°C. Forty-three impacts with .177 (n=10) and 3/16" (n=33) steel BBs were conducted into gelatin spaced at least 4 cm apart. To re-test the manufacture's calibration, .177 steel BBs were launched into two blocks at a range of velocities around 590 fps. The DoP was measured and compared to the NATO "standard" using linear regression to predict the DoP at 590 fps. Additionally, 3/16" stainless steel BBs were launched into the same two gelatin blocks at velocities consistent with penetrating impacts into porcine legs. The gelatin temperature was measured at the impact site prior to each trial.

DoP was measured by inserting a probe into the tissue/gelatin until contacting the BB and adding the diameter of the BB. CT scans of the porcine legs were captured to measure DoP on RadiAnt DICOM Viewer for projectiles that were unable to be located with manual dissection. Measurements of DoP were verified using 2D video analysis.

A literature search was performed to add DoP data for low velocity ($\leq$ 250 m/s) impacts into pigs and post-mortem human subjects (PMHS). To compare DoP between projectiles of different sizes and materials, DoP was normalized by dividing by projectile diameter and material density [5]. Analysis of covariance (ANCOVA) was performed (SPSS, IBM) to determine differences in DoP (dependent variable) over velocity (covariate) between pig, PMHS, and gelatin (categorical independent variables).

RESULTS

A total of 264 penetrating ballistic trials on pig (n=192, 36 from literature), PMHS (n=29 from literature), and synthetic gel (n=43) were used for DoP analysis. At 590 fps (180 m/s) the .177 steel BB was predicted to penetrate 1.50 inches (38.10 mm) with linear regression (**Figure 1**), which was consistent with the manufacturer's calibration of 1.41 inches and the NATO standard between 1.25 in (31.75 mm) and 1.75 in (44.45 mm). Due to a larger diameter, the 3/16" steel BBs resulted in a similar linear regression slope with slightly greater DoP.

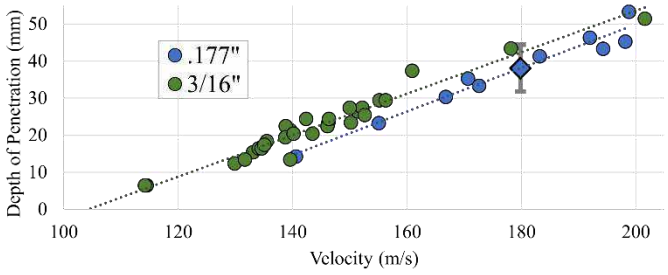

Figure 1: DoP versus velocity into 20% clear synthetic gel at 20°C with a 3/16" and .177 stainless steel BB. The calibration bounds according to the NATO standard (error bar) and the predicted velocity (diamond) at the fixed velocity of 180 m/s are shown.

Linear regression of normalized DoP over density and velocity resulted in similar equations for combined pig ($y = 0.26v - 2.16$, R^2=0.40), PMHS ($y = 0.19v - 1.28$, R^2=0.61), and clear gelatin ($y = 0.36v - 3.88$, R^2=0.96) (**Figure 2**). The synthetic gelatin demonstrated the least variability in DoP and sufficiently achieved a "calibrated" normalized DoP over density at 180 m/s, according to NATO standards. From the One-way ANCOVA, velocity was a significant covariate ($p<0.001$), and there were insignificant differences ($p=0.22$) between medium type (pig, PMHS, and gelatin).

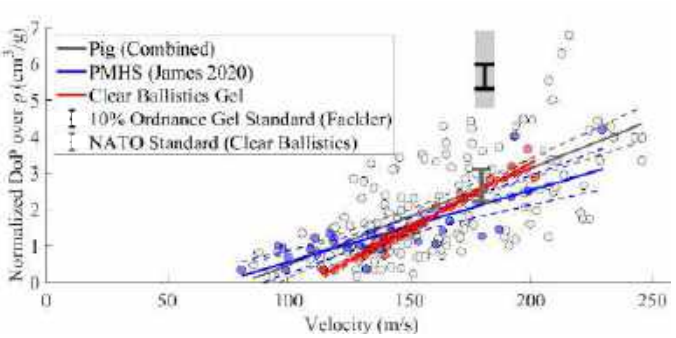

Figure 2: Linear regression of normalized DoP over density and velocity for pig, PMHS, and synthetic gelatin. The original Fackler average DoP and standard deviation into porcine leg that established the 10% ordnance gelatin standard at 4°C is shaded in gray.

DISCUSSION

Previous studies have dismissed the use of synthetic gelatin due to significantly smaller temporary cavities and greater DoP in the Clear Ballistics gel (10%) than 10% ordnance gel [12]. Unsurprisingly, differences in mechanic behavior between ordnance gelatin and synthetic gelatin have been reported. However, a larger dataset of DoP in biological tissue suggests that the original 10% gelatin standard based on experimental work by Fackler [3] may not have been infallible. These discrepancies may be due to limited sample size (1 porcine leg, 10 impacts) and small size and weight (40 kg) of the pig [3].

The results from this study and the doctoral work by James in 2020 suggest that 20% ballistic gelatin (synthetic and organic) is a better surrogate than 10% gelatin at 4°C for biological muscle tissue based on DoP [5]. Furthermore, Humphrey et al found that clear gel (10%) at 16°C was not significantly different in energy loss compared to lung, liver, kidney, heart, and 10% ordnance gel at 4°C for medium velocity impacts of 450 m/s [11], suggesting that 10% gelatin at 4°C better simulates organs rather than muscle tissue.

Ultimately, this study lays the foundation for using synthetic gelatin in ballistic research of firearms. The establishment of ordnance gelatin standards seemed to be blindly accepted based on an underwhelming sample size, but recent studies with abundant sample sizes have contradicted this DoP "standard." The authors of this study recognize the longevity of knowledge from 10% ordnance gelatin and believe the surrogate should not be entirely replaced, but that synthetic gelatin may also be used as a repeatable surrogate of biological tissue.

ACKNOWLEDGEMENTS

This research was supported by resources at Zablocki VA Medical Center, Milwaukee, Wisconsin and partially funded by DEVCOM ARL Cooperative Agreement W911NF-21–2-0004.

REFERENCES

[1] Jussila, J., 2004, Forensic Sci Int, **141**(2–3), pp. 91–98.
[2] Fackler, M. L., et al., 1988, Am J Forensic Med Pathol, **9**(3)
[3] Fackler, M. L., et al., 1990, J Trauma (China), **6**(2), pp. 32–37.
[4] Jussila, J., 2005, Forensic Sci Int, **150**(1), pp. 53–62.
[5] James, G., 2020, PhD Thesis, Cranfield University.
[6] Bourget, D., et al., 2012, Personal Armor Systems Symposium.
[7] Breeze, J., et al., 2013, J Forensic Leg Med, **20**(4), pp. 296–299.
[8] Neades, D. N., et al., 1984, U.S. Army Ballistic Research Lab, **2**.
[9] Maiden, N. R., et al., 2015, J Forensic Leg Med, **34**, pp. 145–150.
[10] Post, S. M., et al., 1995, J Int Wound Ballistics Assoc, **2**(1)
[11] Humphrey, C., et al., 2018, Forensic Sci Int, **288**, pp. 123–130.
[12] Courtney, E., et al., 2017, *30th Int Symp Ballistics*, DEStech
[13] Koser, J., et al., 2022, J Forensic Leg Med, **90**.

MECHANICAL AND STRUCTUAL CHANGES TO THE ANNULUS FIBROSUS IN RESPONSE TO CYCLIC LOADING: AN I-PREDICT STUDY

J. Seifert (1,3), L.L. Frazer (5), D. Maiman (2), A. Shah (2,3), N. Yoganandan (2,3), K. King (4), J.B. Sheehy (4), G. Paskoff (4), T. Bentley (6), D.P. Nicolella (5), B.D. Stemper (1,2,3)

(1) Department of Biomedical Engineering, Marquette University & Medical College of Wisconsin, Milwaukee, Wisconsin, USA
(2) Department of Neurosurgery, Medical College of Wisconsin, Milwaukee, Wisconsin, USA
(3) Zablocki Veterans Affairs Medical Center, Milwaukee, Wisconsin, USA
(4) Naval Air Warfare Center, Aircraft Division, Patuxent River, Maryland, USA
(5) Southwest Research Institute, San Antonio, Texas, USA
(6) Office of Naval Research, Arlington, Virginia, USA

INTRODUCTION

Low back pain (LBP) is prevalent in military helicopter pilots [1], influenced by the unique combination of high frequency whole body vibration and the duration/frequency of missions. Whole body vibration was shown to increase mechanical loading on the spine [2], which likely contributes to annulus fibrosus (AF) degradation [3], a known contributor to LBP [4]. To prevent or limit AF degradation in these populations, protocols and technologies can be developed to reduce the mechanical burden individual pilots endure. However, to properly design these mitigation strategies it is necessary to understand how the structure and mechanical properties of AF tissue change in response to elevated mechanical loading conditions. Thus, we aimed to quantify how repetitive loads, relevant to the military environment, alter AF mechanics and understand structural changes to the tissue associated with damage. We hypothesized that structural changes would occur in response to elevated mechanical loads and the elastic response, viscoelastic response, and ultimate strength of the AF would degrade relative to the magnitude and duration of applied loads.

METHODS

Fresh porcine cervical spines were acquired from a local abattoir and AF specimens were dissected with a scalpel from the outermost layers of the anterior AF region from C3/4 to C6/7 intervertebral discs (IVDs). Test specimens were oriented in the circumferential direction and hydrated in a bath of physiologic saline for approximately one hour prior to testing to ensure uniform hydration levels. Specimen length, width, and thickness were measured using ImageJ Software (Version 1.53). A fine metal mesh was secured to each end of the specimen to prevent slippage during tensile testing and the specimen was mounted in the load frame (ElectroForce 3200, TA Instruments) using grips with knurled contact surfaces. Specimens were submerged during testing in a saline bath heated to a constant temperature (37°C). Force and displacement were measured via a 45-N loadcell (TA Instruments, New Castle, DE) and a linear variable differential transformer (LVDT) internally within the load frame. Force was converted into stress using the mid-length specimen cross sectional area as measured prior to the initiation of testing. Displacement was converted to strain based on specimen length at the 0.1-N pre-load step in the loading protocol.

Mechanical changes from cyclic loading were assessed with a 3-step experimental protocol: (1) Pre-Damage: (1A) Pre-load specimen to 0.1 N; (1B) Precondition; (1C) Incremental strain step and hold for 20 minutes at four discrete strain magnitudes (4%, 8%, 12%, 16%); and (1D) 100 tensile cycles to 11% strain at 5 Hz. (2) Damage: Specimens were exposed to one damage protocol with a constant strain magnitude (11%, 20%, 28%, 44%) for a set number of loading cycles (400, 1600, 6400, 12800 cycles) tensile loading cycles at 1.3-5 Hz. Sixteen total damage protocols were created, each with n=5, to quantify damage induced by each combination of strains and cycle count. (3) Post-Damage: (3A) Incremental strain step and hold for 20 minutes at four discrete strain magnitudes (4%, 8%, 12%, 16%); (3B) 100 tensile cycles to 11% strain at 5Hz; (3C) Quasi-static distraction to failure. All cyclic loading steps (1D, 2, 3B) were strain rate matched at 1.12 s^{-1}. Specimens were allowed to recover between each loading step. Average change in strain energy density (SED) from pre- to post-damage was calculated to quantify changes in the elastic response of the tissue. Strain energy density for each loading hysteresis was the difference between the area under the loading and unloading stress strain curve for each loading cycle (100 pre-damage, 100 post-damage). Relaxation stress delta (delta = maximum stress – minimum stress) of each incremental strain hold was calculated and compared pre- to post-damage to quantify changes in the viscoelastic response of the tissue. Finally, the linear modulus of each specimen was calculated as the slope of the linear region of the stress-strain curve during quasi-static distraction to failure. The ultimate stress and strain for each specimen were calculated to be the point at which peak stress before failure was reached, and the SED of the failure curve was calculated as the area under the stress-strain curve. To

determine what effects the assigned damage strain magnitude and number of damage loading cycles had on the mechanical properties, two factor ANOVAs were performed using (1) strain magnitude and (2) number of cycles during the damage protocol as factors.

Structural change from cyclic loading was assessed with a 2-step experimental protocol: mechanical loading followed by histologic analysis. Cyclic loading consisted of preloading AF specimens to 0.1N to remove slack from the tissue followed by 6400 cycles of cyclic loading to each of the four strain magnitudes outlined in step (2) of the aforementioned protocol. One control group was created that underwent all the same experimental steps excluding any mechanical loading. Following cyclic loading, specimens were fixed, processed, sliced parallel to the AF lamella, and stained with Verhoeff-van Gieson (VVG) stain.

RESULTS

No changes in SED and relaxation stress delta were present between Steps 1 and 3 in the baseline group, indicating their elastic and viscoelastic properties were not altered by the pre-damage and post-damage loading protocols. Ultimate properties from the baseline group were comparable with findings from our previous study measuring the elastic and ultimate properties in healthy AF tissue. Specimens exposed to damage cycles had dose dependent changes in the elastic and viscoelastic response that were each significantly dependent on strain magnitude ($p<0.001$) and number of damage cycles ($p<0.001$). Interestingly, during quasi-static distraction to failure, the linear modulus (16.6±6.5 MPa) (p strain=0.4, p cycles = 0.6), ultimate stress (5.0±2.1 MPa) (p strain=0.9, p cycles = 0.6), ultimate strain (0.58±0.2) (p strain= 0.5, p cycles = 0.9), and SED to failure (1.2±0.8 MPa) (p strain= 0.3, p cycles = 0.4) were not significantly affected by damage protocol. These findings indicate that the mechanical response during low strain magnitudes is significantly affected, while the high strain mechanical response remains relatively unaffected. This statement is further supported by the stress response in the toe and transition regions (0-30% strain) of the stress-strain curve during quasi-static distraction to failure (Figure 1). It was determined that the SED of the toe and transition regions was significantly dependent on both the strain magnitude ($p<0.001$) and number of damage cycles ($p=0.003$). Specimens exposed to 44% strain for 12800 cycles were affected the most and had a SED of 0.017±0.01 MPa, 95.2% less than the baseline group.

Histologic analysis of the AF tissue following cyclic loading shows cleft formation between collagen bundles as well as uncrimping of individual fibers (Figure 2). Damage to the elastic fiber matrix is under preliminary analysis.

DISCUSSION

This study characterized mechanical and structural changes in AF associated with sub-failure damage from repetitive loading. It was determined that increasing the number and strain magnitude of damage cycles significantly affected the mechanical response at low strain magnitudes (0-30%). However, the linear modulus and ultimate stress and strain were unaffected, regardless of the damage protocol, suggesting the mechanical response at high strain magnitudes is maintained. Prior studies reported similar changes in the low strain regime after cyclic loading. Gregory et al. cyclically loaded porcine functional spinal units at 5hz, finding a diminished toe region in the stress-strain response [5]. They hypothesized this change occurred because of elastin damage, a fiber which influences the low strain response of collagenous tissue [6].

In addition to elastin damage, collagen uncrimping found during histological examination of damaged AF tissue correlate with the mechanical changes reported from cyclic loading. Uncrimped collagen fibers, like damaged elastin fibers, decrease the response of tissues at low strain magnitudes [7]. However, despite the altered toe region mechanics, the collagen fibers are likely intact as the ultimate properties of the AF were not affected by our damage protocol, which was consistent with prior studies [8].

Mechanical and structural changes within the AF would contribute to instability of the IVD after cyclic loading, as shown by the reduced elastic, viscoelastic response, and uncrimping of collagen fibers. Due to segmental load sharing between the disc and facet joints, IVD instability can cause higher stresses in the facet joints that would contribute to accelerated facet arthropathy and may be one contributing factor to the acute back pain many helicopter pilots experience post-flight [9]. Despite these structural and mechanical changes, the overall integrity of the IVD appears to be maintained as the ultimate stress and strain in all damage groups are equivalent to un-damaged tissue. These findings can be used to better inform the design of future technologies and exposure protocols aimed at reducing the mechanical load on the lumbar spine to prevent or limit LBP and AF degeneration.

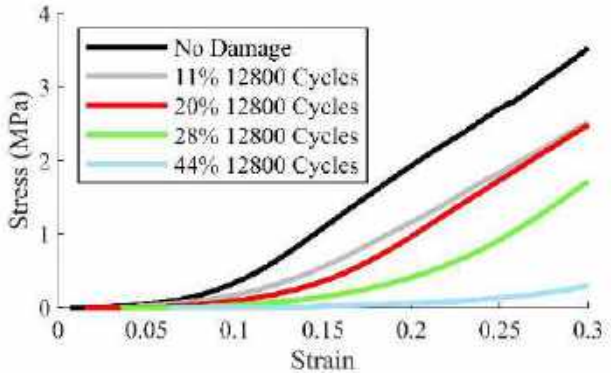

Figure 1: Average stress-strain curves (0-0.3 strain) for high cycle count groups during quasi-static distraction.

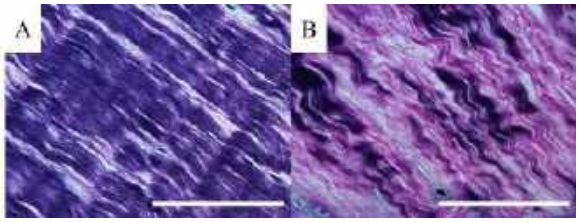

Figure 2: Control (A) and damaged (28% strain) (B) AF tissue stained with VVG. Scale bar = 100 µm.

ACKNOWLEDGEMENTS

This study was supported by the Office of Naval Research (ONR) through the Medical Technology Enterprise Corporation (MTEC) and Southwest Research Institute (SwRI). Support was also provided by Department of Veterans Affairs Medical Research.

REFERENCES

[1] Yang et al., *Front Public Health*, 9:1-10.2022.
[2] Amiri et al., *Comp. in Biology and Medicine*, 107:292-301.2019.
[3] Patterson et al., *Anim. Models Exp Med*.,4:77–86. 2021.
[4] Adams et al., *Spine*, 31(18):2151-2161.2006.
[5] Gregory et al., *Med Eng & Phys*, 34:472-477.2012.
[6] Henninger et al., *JOR*, 31(8):1226-1233. 2019.
[7] Sharabi, M., Sec. *Mechanics of Materials*, 8:1-28.2022.
[8] Isaacs et al., *J. Mech. Behav. Biomed. Mat*., 40:75-84.2014.
[9] Gaydos et al., *Aviat. Sp. Environ. Med*., 83(9):879-889. 2012

INFANT SKULL ANATOMICAL STANDARDS FOR USE IN HEAD TRAUMA MODELING

Y. Alsanea (1), T. Ruiz-Maldonado (2), B. Coats (1)

(1) Mechanical Engineering, University of Utah, Salt Lake City, Utah, USA
(2) Pediatrics, University of Utah, Salt Lake City, UT, USA

INTRODUCTION

Child abuse and neglect is a long-standing global problem. Infants under the age of one are particularly vulnerable as they have the highest risk of fatality and recurrence if not detected [1]. Low-height falls are the most common etiology reported in cases of suspected abusive head trauma, but it is also the most common cause of accidental head trauma in the same age group [2]. The paucity of biomechanical data in this vulnerable age group makes it challenging for medical professionals and legal teams to differentiate between accidental and inflicted trauma.

Computational modeling is an effective tool for investigating the mechanics of pediatric head trauma and predicting the likelihood of injury in accidental scenarios [3]. However, many models still face uncertainties and limitations, particularly when it comes to accounting for natural anatomical variability in infants. Typically, computational models of the infant skull are derived from a single infant and used to represent an entire infant population without justification. The objective of this study was to evaluate the similarity of infant skull thickness distribution within data-driven age and sex groups and identify the skull most representative of all infants in each age/sex group.

METHODS

CT images of 273 infants (<15 months of age) without any evidence of abnormality were collected from Primary Children's Hospital with approval from the Institutional Review Boards of Primary Children's Hospital and the University of Utah. Previously, we quantified skull thickness at over 12,000 locations for each infant CT image dataset [4]. In this study, these data were averaged for each infant and used in a Jenks Natural Breaks (JNB) optimization algorithm that identified potential divisions in the skull thickness data by minimizing in-class variance with a specified number of groups. We varied the number of groups from 1 to 10, and the goodness of variance fit was calculated for each number of groups. The appropriate number of groups was chosen to be the point where diminishing returns in goodness of fit were observed.

The JNB optimization does not consider the age dependence of the data. Therefore, a Receiver Operating Characteristic (ROC) analysis was employed after the JNB optimization to identify appropriate age divisions based on the JNB thickness groups. For each thickness group, we systematically examined all possible age ranges containing that thickness group. For each age range, we defined a predicted positive region as the interval between the lower and upper age limit. The true positive region was defined as thickness values in the predicted positive region that belonged to the thickness group being evaluated. Other groups within the predicted positive region were false positive predictions. True and false negatives were evaluated in a similar manner, focused on the predicted negative regions outside of the limits.

For each pair of age limits, a single sensitivity and specificity were calculated based on the true/false positive/negative calculations. The pair of limits associated with the best sensitivity and specificity (i.e. closest Euclidean distance to 0,1 when plotting 1-specificity vs specificity) were chosen as the ideal age limits for that thickness group. Each thickness group was evaluated independently of the limits defined by other thickness groups because this would introduce a bias based on the order in which the groups were evaluated. The independent analysis thus naturally resulted in overlapping upper and lower bounds for the age groups because thickness groups shared age ranges. To remove overlap, we created a variance optimization algorithm that maximized the between-group variance and minimized the sum of the within-group variance. Groups were optimized in consecutive pairs by shifting the lower limit of the subsequent group towards the upper limit of the former group until the variance optimization requirements were met.

Once age groups were found, a similarity metric was developed to identify similar patterns of skull thickness distribution within each age/sex group. For this analysis, the 12,000 thickness data points were divided and averaged across 132 locations on the skull. The similarity

metric calculated and summed distances between rank-ordered thickness at these locations for pairwise comparisons of all subjects. Data were normalized by a spatial weight matrix dictated by a negative exponential function. A similarity score of 1 indicated perfect similarity between regions of high and low thickness across the skull, while a score of 0 indicated no similarity. The subject with the highest similarity metric in each age/sex group was selected to act as the anatomical standard for that group.

RESULTS

The JNB optimization resulted in diminishing returns in goodness of fit after 5 thickness groups (**Fig. 1A**). The 5 thickness groups (**Fig. 1B**) had overlapping age ranges due to natural variability in an infant population. Using these 5 thickness groups in the ROC analysis and subsequent variance optimization, the optimal age divisions for infants under 15 months of age were 0-1.8 months, 1.9-5.4 months, 5.5-8.3 months, 8.4-10.3 months, and 10.4-15 months (**Fig. 2**).

Table 1 provides a summary of similarity metric descriptive statistics for each age and sex group. Infants in the Male 1.9-5.4-month age group had the lowest variability, while infants in the Male 10.4-15-month age group had the highest variability. While some differences are seen in skull thickness between the selected skull standard and other calvaria in the age/sex group (**Fig. 3**), thickness distribution trends are similar

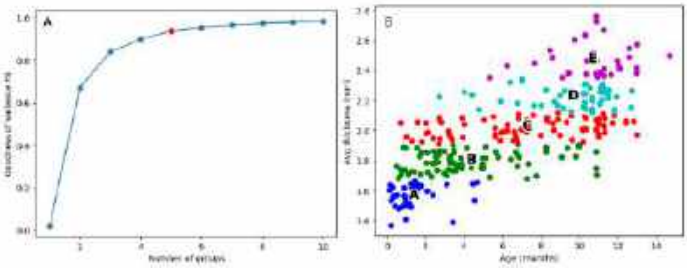

Figure 1. (A) Goodness of variance fits to find the best number of groups based on the Jenks Natural Breaks optimization on skull thickness data. The chosen number of groups was 5, which is shown as a red circle. (B) This resulted in 5 groups represented by blue dots (Group A), green dots (Group B), red dots (Group C), cyan dots (Group D), and magenta dots (Group E).

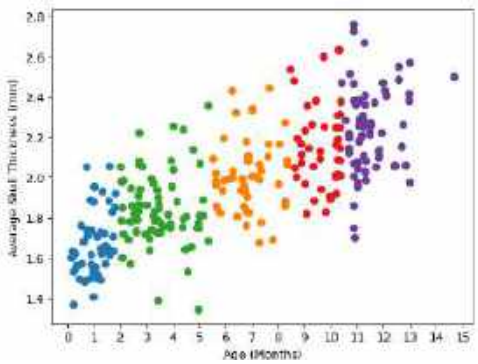

Figure 2. The optimal age groups in the clinical data set were 0-1.8 months (blue), 1.9-5.4 months (green), 5.5-8.3 months (orange), 8.4-10.3 months (red), and 10.4-15 months (purple).

Table 1: Subject pool size and similarity for each age/sex group

Sex	Age group (months)	Count	Max Similarity	Minimum Similarity	Average Similarity
F	0-1.8	22	0.7011	0.6882	0.6947
	1.9-5.4	33	0.7099	0.6871	0.7002
	5.5-8.3	18	0.7089	0.6864	0.6999
	8.4-10.3	12	0.7030	0.6855	0.6947
	10.4-15	35	0.7048	0.6887	0.6961
M	0-1.8	24	0.7085	0.6862	0.6999
	1.9-5.4	39	0.7127	0.6868	0.7037
	5.5-8.3	27	0.7039	0.6870	0.6957
	8.4-10.3	18	0.7036	0.6856	0.6961
	10.4-15	53	0.7001	0.6845	0.6930

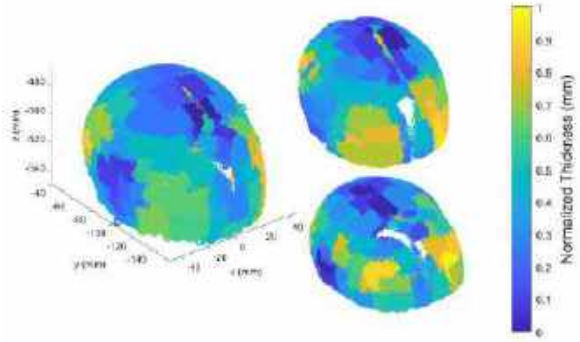

Figure 3. Thickness contour map of most similar male infant skull 1mo (left) and other male infant skulls in age group <1.8 months old (right).

DISCUSSION

Typically, age groups are defined *a priori* for a study and data is binned accordingly. To our knowledge, this study is the first to determine infant age bins based on the data itself. Our findings suggest that splitting up ages less than 15 months into 5 groups is optimal. Other studies have previously split similar age ranges into 2 or 3 groups. Utilization of 5 age groups improves the identification of anatomical changes in the rapidly developing cranium in early infancy.

We then calculated similarity metrics based on pairwise Euclidean distances between ranked thickness locations across each skull. The variation of the similarity metric within each age/sex group was small because groups were defined by minimizing variance, and ideally, they should be small. The anatomical standards for each age/sex group were chosen as the skull with the highest average similarity score. A previous study also created anatomical standards for 0-3, 3-6, and 10–12 month-old infants but only used 24 locations of comparison on each skull and had n=4, 3, and 6 infants per age group, respectively [5]. Our previous work found significant age-dependent differences in skull thickness between males and females that were also not considered in the above study. The developed age- and sex-based anatomical standards and similarity metrics methodology will improve consistency and accuracy for predicting infant head trauma through early development.

ACKNOWLEDGEMENTS

This research was supported by 2016-DN-BX-0160 and 2020-75-CX-0014 provided by the National Institute of Justice. The opinions, findings, and conclusions are those of the authors and do not necessarily reflect those of the Department of Justice.

REFERENCES

[1]. U.S. DHHS. Child Maltreatment 2020. 2022
[2] Reece R, Sege R. *Arch Pediatr Adolesc Med*. 2000
[3] Roth, S et al. *Comptr Meth Prog in Biomed*. 2010
[4] Alsanea, Y et al. SB^{3}C 2023
[5] Li, Z et al. *PLoS One*. 2015

INFANTS SUCKING PATTERNS IDENTIFICATION USING MACHINE LEARNING

Abdullahi O. Olapojoye (1), Fatemeh Hassanipour (1), Abishek P. Singh (1)

(1) Department of Mechanical Engineering, University of Texas at Dallas, Richardson, TX, USA

INTRODUCTION

Breastfeeding is a complex process that demands the synchronized coordination of swallowing, breathing, and sucking. The efficiency of nutrient delivery to an infant during breastfeeding depends on the child's sucking proficiency. Evaluating in real-time whether a baby is receiving the required amount of milk is challenging, often leading to the identification of signs of inadequate sucking after the infant has already faced a nutrient deficiency.

Newborns possess primal reflexes, such as grasping, searching, sucking, and swallowing, which enable them to initiate feeding shortly after birth. The intricate sucking mechanism involves the elevation of the jaw, pressing the tongue against the nipple's front tip, and subsequent peristaltic action that effectively extracts milk. This roller-like tongue movement, reminiscent of peristalsis, facilitates the efficient expression of milk from the nipple [1]. However, infants may encounter feeding challenges due to underdeveloped primitive reflexes.

Addressing these challenges necessitates a deep understanding of infant feeding behavior. Various scientific methodologies, including ultrasonic tomography and intraoral video cameras, have been employed in research to comprehend the actions of the tongue during feeding [2–5]. The gradual integration of Machine Learning (ML) techniques into healthcare is evident, with studies focusing on assessing and intervening in various aspects of infant care [6, 7]. This exploration not only enhances our understanding of infant feeding patterns but also opens avenues for tailored interventions to support the unique needs of infants.

Traditionally, assessments of an infant's sucking potential are performed by medical professionals relying on subjective judgments, introducing variability into the evaluation process. Our approach involves the utilization of an artificial nipple-based sensor to capture tongue forces exerted by infants during breastfeeding sessions. We leverage this clinical data to develop a robust system that identifies the sucking potential of an infant. By integrating ML into clinical practice, our goal is to enhance real-time assessments and early identification of unhealthy sucking patterns, enabling timely interventions and proactive healthcare management of infants.

METHODS

To comprehend the intricate dynamics of infant feeding, a specialized measurement sensor device embedded in an artificial nipple was devised to capture the peristaltic-like movement of an infant's tongue during sucking. This innovative device features two sensors attached to a baby bottle nipple, providing insights into the forces generated during the sucking activity [8].

The force sensor integrated into the artificial nipple employs a cantilever structure, utilizing a thin stainless-steel plate as a beam. A strategically affixed strain gauge on its surface enables precise force measurement. The two sensor channels are positioned at the tip and base of the nipple, measuring forces at the root and tip of the tongue, respectively. The workflow for the proposed system is illustrated (Figure 1).

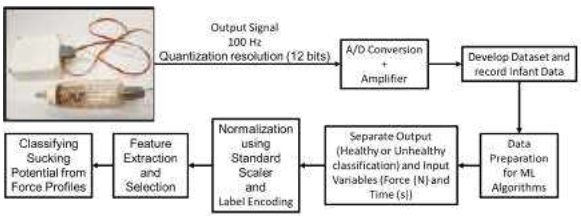

Figure 1: Sucking Pattern Classification Workflow.

During the clinical experiment, each subject was held, and the sensor device was inserted into their oral cavity, simulating the position used during normal breastfeeding. To translate these force measurements into usable data, the output signal undergoes A/D conversion through a bridge circuit and an amplifier before being transmitted to a PC via USB. Operating at a sampling frequency of 100 Hz with a 12 bits quantization resolution, this system ensures a detailed and accurate representation of peristaltic-like tongue movements.

To enhance data quality, a Low-Pass Filter was applied to mitigate noise and emphasize essential signal components in the force data. The force data involved a total of 40 subjects, categorized into unhealthy sucking (18 infants) and healthy sucking (22 infants).

In the present investigation, we developed two traditional ML and two

Deep Learning (DL) models with the aim of identifying infant sucking patterns using time series force data. The four models employed in this study are the Support Vector Classifier (SVC), Gradient Boosting Classifier (GBC), one-dimensional Convolutional Neural Network (1D-CNN), and Long Short-Term Memory (LSTM). We also conducted hyperparameter optimization to enhance the performance of our models.

RESULTS

Ten subjects' data were allocated for testing, while the remaining thirty were designated for training and cross-validation purposes. A summary of the results obtained from the five-fold cross-validation experiment is presented (Table 1). Concerning accuracy, the 1D-CNN model exhibited superior performance with approximately 90% accuracy for training, cross-validation, and testing, surpassing all other models. Following closely, the LSTM model demonstrated commendable accuracy levels of around 80%, 83%, and 90% for training, cross-validation, and testing, respectively. The noteworthy performance of CNNs and LSTM models in uncovering intricate relationships within our data can be attributed to their capability to automatically extract relevant features and capture local patterns and dependencies, and handle noise inherent in clinical data.

Table 1: Cross-Validation(CV) Experiment Results(Accuracy)

Model	Training(%)	CV(%)	Testing(%)
SVC	76.7	60.0	70.4
GBC	100.0	75.6	80.0
LSTM	80.0	83.3	90.0
1D-CNN	90.0	90.0	90.0

Evaluating the performance of a classification model based solely on accuracy may not provide a comprehensive assessment. Consequently, we extended our analysis to include precision, recall, and F1 score, along with the corresponding confusion matrix. The confusion matrix and ROC curve for the best performing model (1D-CNN) is shown (Figure 2).

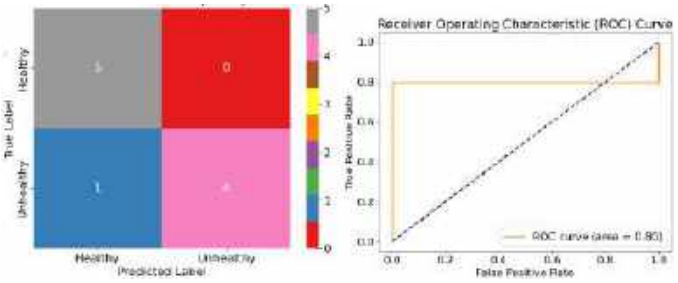

Figure 2: Confusion matrix and ROC curve for 1D-CNN model.

The confusion matrix revealed that all four models achieved a precision score of 100%. A high precision score signifies minimal false positives, implying that when the model predicts an unhealthy sucking pattern, it is typically correct. However, only the CNN and LSTM models attained the highest recall score of 80%. A high recall score indicates few false negatives, suggesting that the models excel at capturing actual positives.

In a medical diagnosis scenario, where false positives and false negatives carry distinct implications, the F1-score serves as a valuable metric to assess the overall effectiveness of the model. A high F1-score, approaching 1, signifies both high precision and high recall, indicating a well-balanced and effective model. In our study, the 1D-CNN and LSTM models shared the top position with an F1-score of 0.90, showcasing a harmonious blend of precision and recall. Following closely, the GBC model achieved an F1-score of 0.79, while the SVC model obtained a score of 0.67. We present comprehensive details regarding recall, precision, and F1-score (Table 2).

Table 2: Classification Report

Model	Recall(%)	Precision(%)	F1-score
SVC	40.0	100.0	0.67
GBC	60.0	100.0	0.79
LSTM	80.0	100.0	0.90
1D-CNN	80.0	100.0	0.90

Additionally, the analysis of Receiver Operating Characteristics (ROC) curves and the computation of the Area Under Curve (AUC) provided valuable insights into the performance of the models at different sensitivity and specificity levels. The AUC ranges from 0 to 1, where 0.5 indicates random guessing and 1 signifies a flawless model. Notably, the AUC values obtained for the SVC (0.84), GBC (0.80), 1D-CNN (0.80), and LSTM (0.80) models indicate the discriminatory power of each model.

Our results highlights the ability of the proposed system to identify infants unhealthy sucking patterns in real-time. As far as our understanding goes, this represents the pioneering application of machine learning to classify infants' sucking potential based on the force exerted by the infant during breastfeeding. This approach is readily applicable to new datasets in a clinical setting, thus serving as a significant decision-support system in infant care.

DISCUSSION

Our study has introduced a robust classification system for infant sucking patterns, leveraging artificial nipple-based sensors to capture tongue forces exerted by infants and generating valuable clinical data. Analyzing the collected time-series data involved the application of machine learning algorithms to extract pertinent features and identify distinctive sucking patterns. The emphasis on identifying unhealthy sucking patterns is paramount for timely intervention. Both LSTM and 1D-CNN models excelled in this aspect, achieving 90% accuracy, 80% recall, a perfect precision score of 100%, a 0.9 f1-score, and an AUC of 0.80.

In practical terms, the high precision score assures us that when the model predicts a sucking pattern to be unhealthy, it is highly likely to be correct, minimizing instances where it falsely identifies an unhealthy pattern when it's not the case. Simultaneously, the recall score assures that the model is adept at capturing the majority of actual unhealthy pattern instances, ensuring a robust performance in identifying the true positives while keeping false negatives at a lower rate.

This classification system, driven by advanced machine learning techniques, holds promise for providing valuable insights into infant health by accurately identifying and distinguishing sucking patterns associated with both health and potential concerns. The findings suggest that leveraging these models in clinical settings could significantly contribute to early detection and intervention, ultimately improving infant care and well-being.

ACKNOWLEDGEMENTS

This work was supported by the National Science Foundation under grant number 2121075.

REFERENCES

[1] Weiss PP. *A report written for MAM Babyartikel GesmbH* (2003).

[2] McClellan HL et al. *Ultrasound in medicine & biology* 36.11 (2010).

[3] Burton P et al. *Early human development* 89.9 (2013).

[4] Geddes DT et al. *Early human development* 84.7 (2008).

[5] Stone M et al. *Dysphagia* 1 (1986).

[6] Elgersma KM et al. *The Journal of Pediatrics* (2023).

[7] Oyebode O et al. *IEEE Access* 9 (2021).

[8] Nishi E et al. *2016 38th Annual International Conference of the IEEE Engineering in Medicine and Biology Society (EMBC)*. IEEE. 2016.

INTEGRATING AUTOPSY-BASED RADIO-PATHOMIC MAPS OF TUMOR PROBABILITY FOR GUIDING SURGICAL BIOPSIES IN GLIOBLASTOMA

Samuel A. Bobholz (1), Allison K. Lowman (1), Aleksandra Winiarz (2), Savannah R. Duenweg (2), Michael Flatley (1), Biprojit Nath (2), Jennifer Connelly (3), Dylan Coss (4), Max Krucoff (5), Anjishnu Banerjee (6), Peter S. LaViolette (1,7)

(1) Department of Radiology, Medical College of Wisconsin, Milwaukee, WI, USA
(2) Department of Biophysics, Medical College of Wisconsin, Milwaukee, WI, USA
(3) Department of Neurology, Medical College of Wisconsin, Milwaukee, WI, USA
(4) Department of Pathology, Medical College of Wisconsin, Milwaukee, WI, USA
(5) Department of Neurosurgery, Medical College of Wisconsin, Milwaukee, WI, USA
(6) Department of Biostatistics, Medical College of Wisconsin, Milwaukee, WI, USA
(7) Department of Biomedical Engineering, Medical College of Wisconsin, Milwaukee, WI, USA

INTRODUCTION

Glioblastoma is a unilaterally lethal form of primary brain tumor expected to affect more than 14,000 persons in the US in 2023. Maximally safe surgical resection is critical to improving patient survival, with gross total resection showing the largest impact on prognosis across disease factors. Following surgery, targeted radiation is used to treat residual tumor. Both critical treatments require precise localization of the tumor to maximize efficacy, which is primarily based on MRI. Contrast-enhanced T1-weighted images show a bright lesion where tumor-associated blood vessel formation is occurring and is typically used to define the surgical margin. It is, however, well known that areas of non-vascular tumor invasion exist well-beyond the enhancing margin, leading to distant areas of tumor ultimately being spared treatment. Radio-pathomic mapping of tumor probability (TPMs) has demonstrated the ability to detect these areas of non-enhancing tumor using current standard clinical imaging merged with autopsy tissue data. The algorithm allows for expanded surgical margins to more fully remove non-enhancing infiltrative tumor. As gross total resection is the primary driving factor for patient survival, it is likely that extending this margin further to encompass both enhancing and non-enhancing tumor portions will further improve survival outcomes. This study presents the first test cases for clinical implementation, where we tested the hypothesis that tumor probability maps identify areas of non-enhancing tumor for biopsy during both first surgery and recurrence.

METHODS

Autopsy tissue and clinical imaging was acquired from 65 patients with a pathologically confirmed glioma diagnosis. A schematic representation of the data collection process and analytic framework is presented in **Figure 1**.

A total of 159 tissue samples were collected across all patients at autopsy, which were then processed and stained for hematoxylin and eosin (H&E). Following staining, slides were digitized using a sliding stage microscope at 40X magnification (0.2 microns per pixel). Images were then segmented to compute cell density, extracellular fluid density (ECF) and cytoplasm density (Cyt) using a color deconvolution algorithm. A subset of 33 tissue samples from 9 patients were also annotated for tumor presence by our pathologist-trained technician. T1,

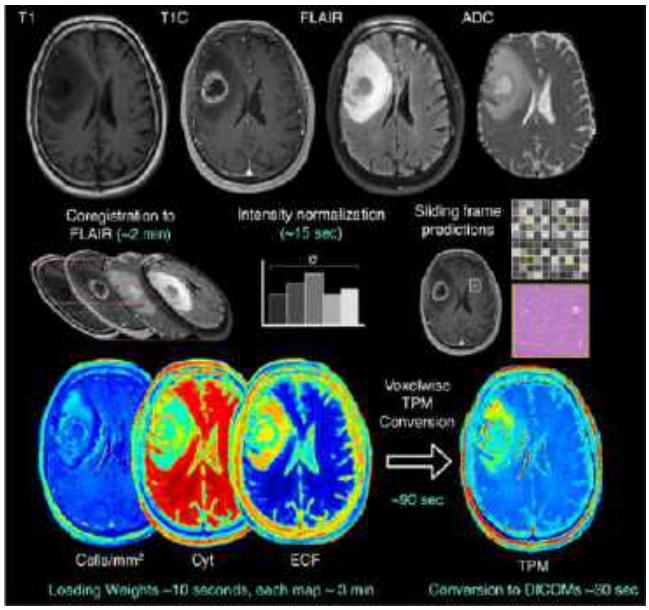

Figure 1: Overview of TPM generation process.

T1C, FLAIR, and ADC images from each patient's last clinical imaging session prior to death were used for this study. All images were aligned to the FLAIR image, and all images (T1, T1C, FLAIR) were intensity normalized. Histology samples were then aligned to the MRI using a custom in-house software that applies a nonlinear transform to match tissue data to the FLAIR image from manually defined control points[8–11]. Separate bootstrap aggregated ("bagged") ensemble algorithms were trained to predict voxel-wise ECF, Cyt, and cell density using 5 by 5 voxel tiles from each MRI. Models were trained on 2/3s of the full data set (43 subjects) and tested on a held out set to assess generalizability (22 subjects). An RUSBoost algorithm was then used to identify tumor presence using the pathological annotations as ground truth and the tissue segmentations for Cell, ECF, and Cyt as input (train size: 6 subjects, test size: 3 subjects). The training and development of this model is presented in full in a previously published study, with an example of the model's potential to identify non-enhancing tumor presented in **Figure 2**[1,2].

For prospective clinical integration, we applied our model to pre-surgical imaging for two patients with a primary glioblastoma, one prior to first surgery and one following radiographic recurrence. Regions of interest were defined based on hotspots of non-enhancing tumor presence on TPM and cellularity radio-pathomic maps, which were then used as biopsy targets prior to surgical resection in addition to standard biopsy procedures. Both surgeries were conducted using 5-aminolevulinic acid (5-ALA) staining for fluorescence-based guidance, as well as compared to our TPM-based predictions for tumor presence. Biopsy tissue was then stained for H&E and immunohistochemical markers, including SOX2 as a measure of pluripotency, and were examined by a board-certified pathologist for tumor presence.

RESULTS

A total of 2 TPM-guided biopsies were taken from prospectively identified regions of interest for each patient **(Figure 3)**. For the first surgery case, both biopsies were collected from 5-ALA negative areas,

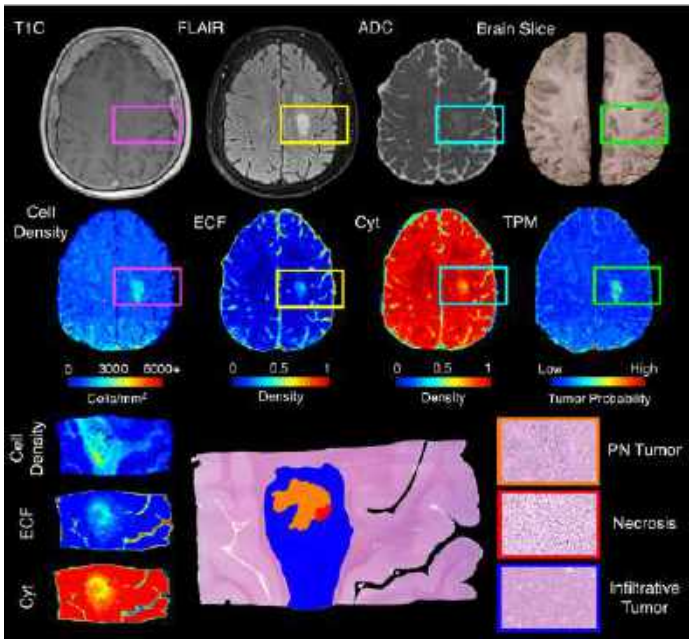

Figure 2: Example TPM accurately identifying an area of non-enhancing tumor, as well as a high ECF area of pseudopalisading necrosis (PN) within the tumor.

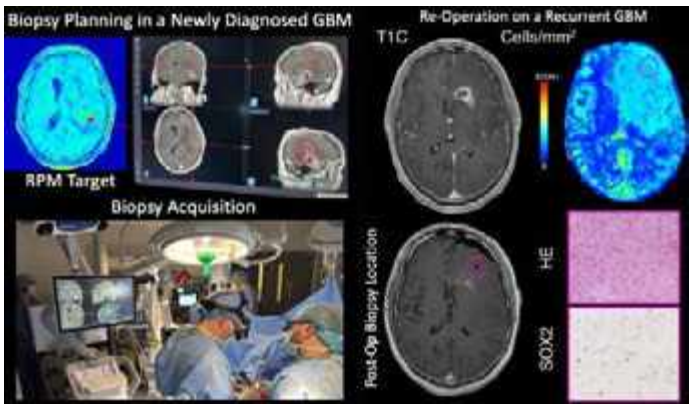

Figure 3: (left) Images from biopsy planning for a prospective newly diagnosed GBM using TPMs to identify non-enhancing tumor areas for sampling. (left) Imaging, TPM, and pathology from a recurrent surgery where TPM-guided biopsy found SOX2-positive tumor from beyond the enhancing region.

indicating an absence of tumor on both radiological and fluorescence-based guidance. Both biopsies were found to contain pathological tumor presence, indicating tumor presence identified by TPMs that failed to present on other visualization methods. For the recurring patient, prior follow-up surgeries had failed to identify tumor presence despite radiographic progression, suggesting pseudoprogression. Both of the TPM-guided samples were 5-ALA positive, potentially indicating tumor presence, and both showed moderately increased cellularity and positive SOX2 staining, supporting tumor presence. No other biopsies collected from this surgery showed signs of tumor presence from traditionally identified regions.

DISCUSSION

This preliminary study provides a framework and initial evidence for the surgical integration of radio-pathomic TPMs to identify occult tumor missed by other forms of surgical guidance, such as traditional MRI and intraoperative fluorescence. These maps are rapidly generated using traditional MRI as input, allowing for non-enhancing tumor identification without impacting scanner time or slowing down clinical workflows. This tool has also been undergoing extensive external validation, where high-quality maps have been generated for over 1000 external cases from publicly available datasets in addition to external studies comparing high tumor probability regions to advanced imaging signatures such as perfusion imaging, APT-CEST based pH-weighted imaging, and MR spectroscopy for measuring tumor metabolism. While this small prospective sample will require a larger sample size to fully validate the use of TPMs for guiding surgery, the results from this study suggest this technique has the potential to non-invasively expand the treatable tumor margin for glial tumors.

ACKNOWLEDGEMENTS

Funding: PSL: American Brain Tumor Association Grant DG160004, Froedtert Foundation, Strain for the Brain 5K Run, Milwaukee, WI, NIH/NCI R01CA218144, R01CA218144-02S1, R21CA231892, and R01CA249882. BME: NIH/NCI R01CA270027, NIH/NCI P50CA211015, DoD CA20029. JML: NCI P01CA118816

REFERENCES

[1] Bobholz et al., *AJNR*, DOI: 10.3174/ajnr.A7477
[2] Bobholz et al. medRxiv, doi: 10.1101/2022.08.17.22278910

MOUSE LUNG EMPHYSEMATOUS MECHANICAL STRAINS UNDER POSITIVE VERSUS NEGATIVE PRESSURE VENTILATION

T.M. Nelson (1), K.A.M. Quiros (1), M. Eskandari (1,2,3)

(1) Department of Mechanical Engineering, University of California, Riverside CA, USA
(2) BREATHE Center, School of Medicine University of California, Riverside CA, USA
(3) Department of Bioengineering, University of California, Riverside CA, USA

INTRODUCTION

Chronic obstructive pulmonary disease (COPD) is one of the world's most prevalent morbidities, often requiring ventilatory support [1]. However, this may lead to ventilator induced lung injury (VILI), as devices commonly employ non-physiological positive pressure ventilation (PPV) which pushes air directly into the lung [2]. Negative pressure ventilation (NPV) devices are more akin to physiological breathing which induces an external pressure drop, causing an inrush of air to the lung to balance pressure. NPV devices are not widely used, and the deviation from natural breathing in clinical PPV may contribute to VILI [3,4,5]. Specifically, studies link VILI to elevated lung heterogeneity, using this metric to investigate ventilatory methods [6,7]. Yet, most PPV versus NPV literature addresses global pressure-volume measures and cannot explore nuanced local attributes, such as heterogeneity, and how they differ between schemes [3]. While current local studies exist, they are limited to healthy states [5], underscoring the need to examine PPV versus NPV for pathological lungs.

Herein, we examine healthy control versus emphysematous murine local lung strains by pairing digital image correlation (DIC) with interchangeable PPV and NPV loads. DIC allows full-field spatial and temporally continuous deformation quantification; thus, we examine lung expansion over the inflation profile to quantify heterogeneity, anisotropy, and evolution of these strains, which is central to divulging potential pathways to VILI [8,9]. By analyzing elastase exposed lungs, we explore how emphysema, a clinically relevant pathology, affects the local pulmonary response to PPV versus NPV [10]. We hypothesize NPV strains will be less heterogenous and of lower magnitude (i.e., less stretch) than PPV—reducing potential for VILI [4,5].

METHODS

Ten 8-12 week-old male C57BL/6J mice were procured (Jackson Laboratory, Bar Harbor, ME, USA; Institutional Animal Care and Use Committee approved). Five mice were intranasally exposed to porcine pancreatic elastase (single dose, 0.9 ul) to induce emphysematous COPD, while the five healthy controls received 1X phosphate-buffered saline, according to established protocols [10]. After four weeks, mice were anesthetized and sacrificed, then lungs were extracted, cannulated, inflated to 0.5 ml, and speckled for DIC as in previous methods [11].

Lungs were placed in an airtight clear tank attached to our custom electromechanical dual-piston breathing mimicry device, facilitating inflation testing via both PPV and NPV on each specimen consecutively (albeit the response is not PPV/NPV mode sequence dependent [12]). Briefly, a piston either pushed air (PPV) into the lung, or increased tank volume to prompt air entrainment (NPV) into the lung. Simultaneously, a compensatory piston accounted for real-time air compression, and reported resultant global lung pressure [13]. Lungs were tested at 0.7 ml applied volume at 10 breaths/minute, in accordance with past studies [14]. The test sequence included a 5 cmH_2O preload, followed by three inflation-deflation preconditioning cycles, and a fourth test inflation cycle wherein overhead DIC cameras captured surface deformation (Trilion Quality Systems, King of Prussia, PA, USA), as extensively validated in past works [9,11]. Collected DIC data was analyzed for principal strains

Average pressure-strain curves reported the lung local response (analogous to global pressure-volume curves) [9] (Fig. 1). Slopes were fitted (R^2>0.95) to assess bilinear compliance where applicable, (C_1=lower slope associated with initial recruitment, C_2=final steeper slope; Fig. 1b) [5,9,15]. Moreover, correlated surface strain histograms exhibit the evolutionary strain response at select inflation volumes (0.2, 0.5, and 0.7 ml maximum air delivery); averaged mean strain values (ε_{avg}) and interquartile range (IQR, used to assess heterogeneity [16]) are listed with each histogram. The anisotropic ratio (AR, major to minor stretch ratio) was assessed at 0.7 ml, where a value of 1 is isotropic [5,9,11]. Strain metrics were compared between PPV and NPV within control and exposed groups using a paired two-tailed t-test with $p<0.05$ for significance (GraphPad Prism 9 for Windows) [17].

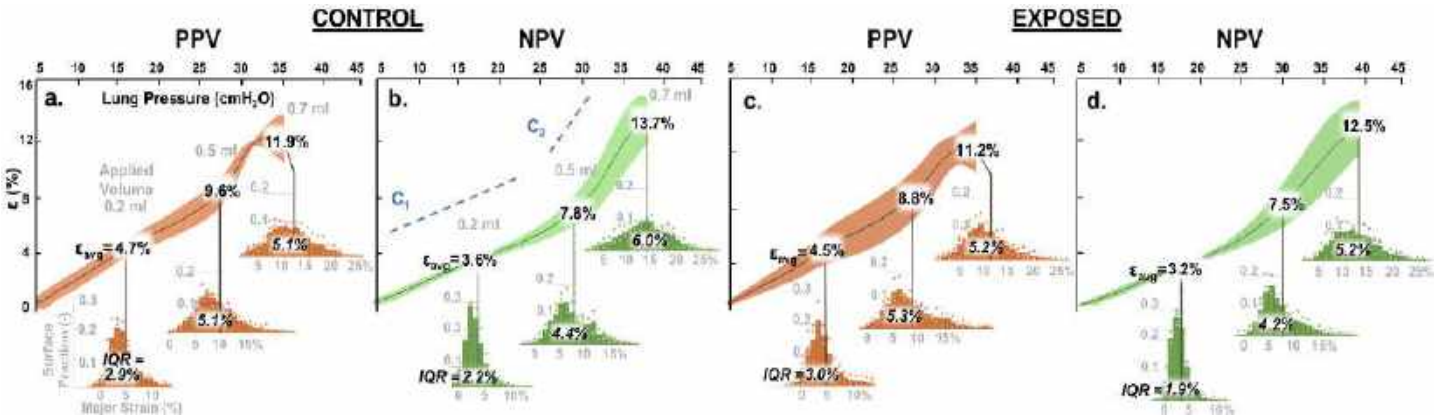

Fig. 1. Murine lung PPV (orange) and NPV (green) pressure-strain curves (average ± standard deviation; shadows) for control (a, b) and elastase-exposed emphysematous (c, d) lungs. Representative compliance slopes are shown (dotted blue lines; b). Histograms of average strain ± standard deviation (dots) are shown at 0.2, 0.5, and 0.7 ml, with averaged mean strain (ε_{avg}) and interquartile range (IQR; italicized).

RESULTS

The local pressure-strain response for PPV curves (orange) were not consistently bilinear, rendering C_2 occasionally immeasurable (Fig. 1); average C_1 slopes were 0.35 and 0.27 %/cmH_2O for control (Fig. 1a) and exposed (Fig. 1c) emphysema groups, respectively. NPV curves (green) were notably bilinear, with average C_1 slopes of 0.25 %/cmH_2O for both control and exposed specimens, and C_2 slopes of 0.81 and 0.65 %/cmH_2O for control (Fig. 1b) and exposed (Fig. 1d), respectively. Thus, PPV tended to yield steeper C_1 slopes than NPV, albeit statistically insignificant.

Histograms associated with low- to mid-volume (i.e., 0.2 and 0.5 ml) tended to show higher ε_{avg} and IQR in PPV compared to NPV. Conversely, ε_{avg} and IQR trended greater for NPV at 0.7 ml (control group IQR: $p<0.05$).

AR values were 0.93 (PPV) and 0.94 (NPV), for both control and exposed lungs. This greater anisotropy for PPV compared to NPV was significant for the exposed group ($p<0.05$).

DISCUSSION

We find strain magnitude trends greater in PPV at 0.2 and 0.5 ml, suggesting greater stretch and therefore more potential for VILI, compared to NPV [2,4,5]; however, we observe decreased strain in PPV compared to NPV at maximum volume in contrast to previous porcine studies, possibly due to physiological discrepancies between species [5,18]. Moreover, elevated mechanical heterogeneity is correlated with injury and disease [6,7], and we find strain heterogeneity increases in PPV (0.2 and 0.5 ml), in agreement with porcine lungs—thus indicative of VILI tendencies.

Anisotropic ratio assesses tissue stretch distortions [5], which can indicate injury or pathologies (e.g., COPD) [19]. We find lungs are generally isotropic, but show more anisotropy with PPV, as in previous studies [5]. Notably, this is significant for exposed lungs, suggesting that VILI induced by PPV may be exacerbated by emphysema.

We also observe disparate pressure-strain inflation profiles between the schemes: C_1 tends to be greater in PPV, and curves are not always bilinear in PPV contrary to NPV. Previous studies claim that the recruitment of secondary peripheral airways (indicated by C_2 [9,15]) may be delayed in PPV [12]. Our findings may also reflect such an altered secondary recruitment phase in PPV.

Elastase-induced emphysema in mice affects centrilobular regions [20]. Thus, highly compliant (fenestrated) central regions, combined with PPV and its lessened ability to distend peripheral secondary airways, may render PPV-emphysematous lungs susceptible to centrally-located regional overdistension. This may be why we observe greater heterogeneity trends (i.e., IQR regional variability) in PPV compared to NPV for exposed lungs (0.2 and 0.5 ml, Fig. 1c and Fig. 1d), while IQR values tend to be more similar between PPV and NPV for controls (0.2 and 0.5 ml, Fig. 1a and Fig. 1b). Interestingly, this behavior does not carry through to maximum inflation at 0.7 ml, which motivates further investigation.

Herein, we assess murine lungs' local mechanical response to PPV versus NPV. DIC methods are used to characterize continuous local strains, which are nascent despite providing nuanced insights that global metrics cannot. Notably, we provide localized comparisons of ventilatory schemes for lungs with induced emphysema, offering new perspectives on how artificial ventilation (PPV) deviates from natural breathing (NPV). Ultimately, this may help reveal how VILI develops in lung states which necessitate ventilatory support. Future work will characterize other pathologies, such as fibrosis, to further catalog clinically relevant lung diseases under the ventilation schemes.

ACKNOWLEDGEMENTS

This study is supported in part by the NSF Graduate Research Fellowship, as well as the California Climate Action Through Resilience Program UCR Opportunity to Advance Sustainability, Innovation, and Social Inclusion (OASIS) grant, and the NASA California Space Grant Consortium Fellowship.

REFERENCES

[1] Hogg, JC & Timens, W, *Annu Rev Pathol* 4, 435–459 (2009). [2] Slutsky, AS *Chest* 104, 1833–1859 (1993). [3] Grasso, F et al. *AJRCCM* 177, 412–418 (2008). [4] Eskandari, M et al. *ATS Conf*: A4671 (2021). [5] Sattari, S et al. *AJRCCM* 207(5), 577–586 (2023). [6] Kaczka, DW et al. *Ann Biomed Eng* 39, 1112–1124 (2011). [7] Hurtado, DE et al. *Ann Intensive Care* 10, 107 (2020). [8] Rizzuto, E et al. *Exp Tech* 40, 743–753 (2016). [9] Nelson, TM et al. *Sci Rep* 13, 1–14 (2023). [10] Suki, B et al. *Alpha-1 Antitrypsin Deficiency: Methods and Protocols*, 67–75 (Springer New York, 2017). [11] Mariano, CA et al. *Front Physiol* 11, 600492 (2020). [12] Dong, S et al. *AJP Lung Cell Mol Physiol* 322(5), 673–682 (2022). [13] Sattari, S et al. *Front in Bioeng & Biotech* 8, 1183 (2020). [14] Quiros, KAM et al. *Ann Biomed Eng* (2023). [15] Harris, RS *Respir Care* 50, 78–98; (2005). [16] Tomaszewski, MR et al. *NMR Biomed* 34, e4454 (2021). [17] de Winter, JCF *PARE* 18, 10 (2019). [18] Eskandari, M et al. *ATS Conf*: A5776 (2023). [19] Chaudhary, MFA et al. *Thoracic Image Analysis* 143–154 (2020). [20] Valentine, R et al. *Toxicol Appl Pharmacol* 68, 451–461 (1983)

ROLE OF PHYSICS-INFORMED CONSTRAINTS IN REAL-TIME ASSESSMENT OF 3D VASCULAR FLUID DYNAMICS VIA MULTI-CASE DEEP LEARNING NEURAL NETWORK

W. X. Chan (1), W. H. Ding (1), B. H. Li (2), H. S. Wong (1), C. H. Yap (1)

(1) Department of Bioengineering, Imperial College London, London, United Kingdom
(2) Department of Chemical Engineering, Imperial College London, London, United Kingdom

INTRODUCTION

Computational fluid dynamics (CFD) simulations have emerged as a powerful tool in biomedical and clinical applications, for e.g., it is used for determining vascular fractional flow reserves to guide coronary interventions, for sizing bypass grafts, and for identification regions of abnormal flow during atherosclerosis and aneurysms for predicting disease progression. However, traditional simulations are slow, and cannot generate large data to show utility of biomechanics parameters, which is needed before clinical adoption. Here, we investigate the use of deep learning [1] to enable real-time computation of vascular fluid mechanics. We propose to use multi-case networks, which are networks pre-trained across a range of vascular geometries, such that they can give real-time fluid dynamics results. We tested an unsupervised Physics-Informed Neural Network (PINN) [2] and a fully supervised network trained by CFD without physics constraints. We compare these two networks to understand the utility of physics-informed training, and investigate associated strategies to achieve accuracy.

METHODS

We train networks to calculate full 3D flow fields over an arbitrary range of vascular geometries. Geometric variations are controlled by three geometric shape parameters, "S1" and "S2" control the half-sinusoidal curvature in the y- and z-axis respectively, and "A" controls the stenotic extent in the middle of the vessel (Figure 1). The centerline c, defined over $x = [-0.15m, 0.15m]$ follows the equation,

$$c_y = S_1 \sin(x\pi/0.15) - \sin(2x\pi/0.15) \quad (1)$$

$$c_z = S_2 \sin(x\pi/0.15) + \sin(2x\pi/0.15) \quad (2)$$

while the radius of the vessel as a function of x is,

$$r = 0.006\,[1 - A\,exp(-x^2/0.045)] \quad (3)$$

A parabolic profile with max velocity of 0.12m/s at the inlet, zero reference pressure at the outlet via boundary condition loss functions (**BC**). For **PINN**, the incompressibility and steady-state Navier-stokes Equations are applied as loss terms. For the fully supervised network (**SN**), instead of fluid physics equations, constraints enforce a similarity to CFD velocity and pressure results for a range of geometries.

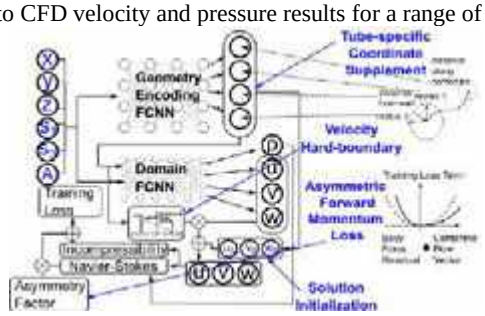

Figure 1: Illustration of Neural network structure with dependent techniques.

WE further tested several ancillary strategies: **(1) Geometric Encoding (GE):** a side network, the GE network is trained separately and used to compute tube-specific coordinates (centerline distance, distance from wall, etc.) of any point in the flow field. These are used as additional input to the main network on top of the cartesian coordinates and geometric shape parameters to improve results (Fig 1). **(2) Hard Wall Boundary Constraint (HB):** The no slip wall boundary conditions better enforced via a hard constraint rather than a loss term, by multiplying network velocity results with a power law function that dips to zero at the walls, guided by the distance to wall parameter. **(3) Volume Flow Rate Constraint (QC):** a loss term enforces the same volume flow rate at the inlet and outlet to mitigate difficulty in spatial propagation of PINN convergence. **(4) Asymmetric loss function (ASYM):** The Navier Stokes momentum equation loss was biased to favor forward flow momentum, to mitigate the optimizer's tendency to move towards the zero-velocity solution. We used NVIDIA Modulus v22.09 with additional codes [3]. Training is performed for 64 geometries, along a regular grid (4 by 4 by 4) of shape parameters.

RESULTS

From training PINN for a single geometry, we find that QC, GE,

HB and ASYM strategies all improved accuracy (Fig 2), with GE being the most important. Our PINN is reasonably optimized with GE, HB and ASYM, having low errors. This is then used for multi-case training. Fig 3 can show that PINN results closely resemble CFD results in 3D.

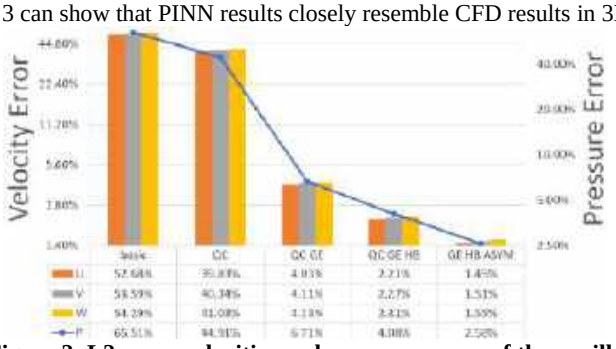

Figure 2: L2 norm velocities and pressure errors of the vanilla PINN and PINN in combinations with various strategies.

Figure 3: Comparison of PINN results to CFD results.

After the multi-case training, both PINN and SN can rapidly produce flow field results in real-time (~15ms inference time per 1000 data points) even for previously unseen geometries. Accuracy testing is conducted using 279 geometries unseen by the networks, spaced regularly across the 3 shape parameters, and errors are quantified by comparing deep learning outputs to CFD outputs. When we compared the accuracy of PINN to SN, surprisingly, SN performed better in terms of velocity and pressure errors (Table 1). We further tested a network that combines PINN and SN, where some CFD results are used to help the training in PINN, at geometries where errors are high (PINN+TC). Results are still not as good as SN. This surprising result suggests that physics-informed training is not as robust as CFD-guided training in the network. However, PINN has lower errors when quantifying wall shear stresses (WSS) than SN (Table 2).

type	BC	HB	GE	Relative L2 error (%) (Average/Maximum value)			
				U	v	w	p
SN	√	√	√	0.55 / 1.61	0.63 / 1.87	0.54 / 1.60	0.64 / 2.51
SN		√	√	0.76 / 2.75	0.90 / 3.05	0.84 / 2.84	1.31 / 5.86
SN			√	0.79 / 2.64	0.88 / 2.80	0.91 / 3.33	1.38 / 3.67
SN				0.72 / 2.14	0.83 / 2.20	0.72 / 2.41	1.16 / 4.50
SN	√			0.75 / 1.44	0.86 / 1.64	0.67 / 1.26	0.57 / 0.92
PINN	√	√	√	2.11 / 8.62	2.43 / 8.88	2.17 / 8.70	2.52 / 12.5
PINN+TC	√	√	√	1.70 / 3.61	2.14 / 4.20	1.75 / 3.85	2.41 / 6.50

Table 1: Errors in u, v, w velocities and pressure (p) when testing the multi-case networks, average or maximum of 279 test cases.

type	BC	HB	GE	Relative L2 error of WSS (%)	
				Average	Maximum
SN	√	√	√	8.29	10.86
SN		√	√	6.86	8.95
SN			√	8.85	12.11
SN				8.71	16.58
PINN	√	√	√	4.61	14.59
PINN+TC	√	√	√	4.32	7.46

Table 2: Average and maximum testing errors of wall shear stress within range of case parametric.

Interestingly, even with SN, the additional strategies of BC, HB and GE are still important, as they can reduce velocity and pressure errors substantially (table 1). For wall shear stress, having HB and GE are helpful but not BC in reducing errors.

DISCUSSION

Our vision is for flow details to be available to clinicians, including flow velocities, pressure drops and wall shear stresses, immediately after scans are performed. Having very fast processing can enable large sample clinical investigations to robustly demonstrate the clinical utility of biomechanics parameters, and can enable adoption into clinical practices. Our study shows that it is feasible to develop networks that can instantaneously yield flow simulation results with low errors, even for geometries that are not yet seen by the network, by pretraining the network over a range of geometric shapes. However, currently, our implementation is limited to steady and laminar flow, and we have only trained for 3 shape parameters. Much future work is thus needed to achieve this vision.

Our results show that to achieve good accuracy, it is important to use tube specific coordinates, obtained via GE network. This is likely because fluid dynamics in a tube is highly dependent on these coordinates, eg., velocities are highly dependent on distance to wall, while pressure is highly dependent on centerline distance. This approach is somewhat similar to Oldenburg et al's Geometric-Aware PINN [4], but we have used tube-specific coordinates rather unidentified shape parameters. On the hard boundary constraint (HB) strategy, our results that HB improves accuracy is in agreement with previous implementations [4]. One challenge that PINN has, is the spatial propagation of convergence through the tube. For example, convergence on the continuity equation is difficult to spread from the inlet to the outlet, resulting in the PINN favoring solutions with lower velocities. For this reason, the QC and ASYM strategies were effective in reducing errors. We believe that this is likely related to PINN's use of the fully connected network structure, and enhancements such as graph network may be able to improve this.

Surprisingly, the CFD supervised network (SN) outperformed PINN in velocity and pressure errors. This suggests that the physics equations constraints in PINN are not effective in enabling a convergence to the truth. Again, this is likely related to the weak ability of PINN in achieving convergence and minimization of losses. On top of accuracy, SN also trains and converges faster than PINN. As such, unless PINN's convergence abilities are enhanced, the CFD-supervised approach seems to be a better way for multi-geometry deep learning fluid mechanics inferences. Although PINN has better WSS accuracy than SN, it is possible to train SN with WSS details, on top of velocity and pressure details, to close the gap.

Thus, Overall, our results unexpectedly suggest that CFD-supervised network is superior to PINN for deep learning vascular fluid mechanics estimations. When using such fully supervised networks, our proposed strategies of geometric encoding (GE), providing boundary conditions (BC), and imposing a hard wall boundary constraint can significantly reduce errors.

ACKNOWLEDGEMENTS

The Study was supported by Imperial College PhD scholarship (Wong), and BHF Centre of Research Excellence grant (RE/18/4/34215, Chan).

REFERENCES

[1] Tompson J. et al., *Proc. 34th Intl. Conf. on Machine Learning*, 70: 3424-3433, 2017.
[2] Raissi M. et al., *Science*, 367(6481): 1026-1030, 2020.
[3] Chan W. X., Github https://github.com/WeiXuanChan/ModulusVascularFlow, 2023.
[4] Oldenburg J. et al., Adv. Model. Simul. Eng. Sci., 9(1): 8, 2022.

CORRELATION BETWEEN LOADING-INDUCED CHANGES IN OPTICAL REDOX METRICS AND MITOCHONDRIAL DEPOLARIZATION VARIES BY STRAIN RATE AND CARTILAGE ZONE

Jingyi Wang (1), Greta E. Scheidt (2), Corinne R. Henak (1,2,3)

(1) Mechanical Engineering, UW-Madison, Madison, WI, US
(2) Biomedical Engineering, UW-Madison, Madison, WI, US
(3) Orthopedics & Rehabilitation, UW-Madison, Madison, WI, US

INTRODUCTION

Redox balance, the balance between oxidative and reductive reactions, is crucial for cartilage health. Accumulation of reactive oxygen species (ROS) disrupts redox balance and plays a role in osteoarthritis (OA) progression [1] [2]. Monitoring redox balance is a potential way to evaluate cartilage health and screen therapeutics.

Given that mitochondria are the main site of ROS production, monitoring mitochondrial membrane potential, an indicator of mitochondria function, can indicate redox imbalance. Mitochondrial depolarization in cartilage induced by impact injury has been shown using polarity-sensitive fluorescent dye [3]. Although fluorescent dye is a well-established way to evaluate redox balance, clinical usage and translational potential of exogenous dye are limited.

Optical redox imaging (ORI) is a label-free and real-time method to monitor redox balance in living tissue [4]. It utilizes the autofluorescence of flavin adenine dinucleotide (FAD), nicotinamide adenine dinucleotide and nicotinamide adenine dinucleotide phosphate (together termed NAD(P)H), which are cofactors in cellular redox reactions. The fluorescence intensity correlates with accumulation of the corresponding compound, and the optical redox ratio (ORR) calculated using their intensities reflects their relative concentration. A previous study from our lab showed that ORI metrics (fluorescent intensity of FAD, fluorescent intensity of NAD(P)H, and ORR) were mechanoresponsive [5].

Although ORI provides a promising way to quantify cellular redox balance, there is a knowledge gap between measured ORI metrics and commonly used ways to monitor redox balance such as mitochondrial depolarization. The objective of this study is to establish correlations between ORI metrics and mitochondrial depolarization in response to mechanical stimuli.

METHODS

Twenty full-thickness cartilage strips were collected from the patella of one 4-5-month-old pig (sex unknown). The dimensions of the strips were at least 10 mm long by 0.65±0.17 mm thick (Figure 1A). Ten randomly selected strips underwent tensile loading at either 10%/s or 100%/s, while the other ten served as unloaded controls. A custom microscope-top loading device (Figure 1B) was manufactured so that loaded and unloaded samples were exposed to the same environment throughout the test.

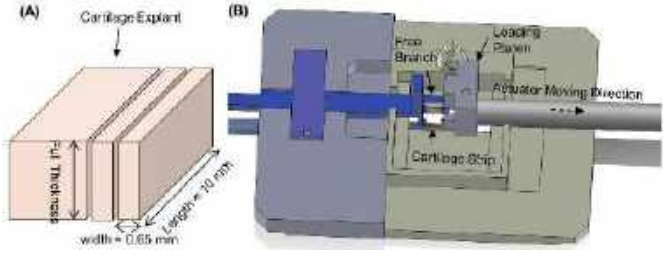

Figure 1: (A) Schematic of cartilage strip collection; (B) Microscope-top loading device.

ORI was performed [5] on 24 regions of interest (ROI) through the superficial, middle, and deep zones (Figure 2). Images in each ROI were taken in green and DAPI channels, corresponding to the spectrum of FAD and NAD(P)H, respectively. Before loading, images were captured in two regions in each zone. At 0 and 30 minutes after loading, images were taken in one region in each zone.

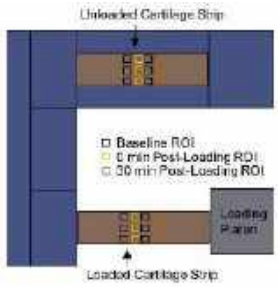

Figure 2: ROIs in microscope view of loading device, articular surface is up.

Five loaded-control pairs were subject to mitochondrial depolarization staining. Both loaded and unloaded samples were removed from the device and incubated with 1x JC-1 mitochondrial membrane potential detection dye (Biotium, Hayward, CA, USA) at 37°C for 15 minutes. Images were then taken in green and red channels, for depolarized and polarized mitochondria, respectively.

Image intensity was measured using Image J. ORR was calculated using equation (1). Post-loading autofluorescent intensity in green channel, post-loading autofluorescent intensity in DAPI channel, and post-loading ORR were normalized to the averaged pre-loading value of each sample in each zone. For JC-1 images, fluorescent intensity in the red channel was divided by that in green channel in the same ROI [6]. Linear regression analysis was conducted on scatter plots between normalized ORI metrics and mitochondrial depolarization (weak correlation at $0.10 < R^2 < 0.20$; no p-values reported because of the small sample size and weak correlations).

$$ORR = \frac{FAD\ intensity}{FAD\ intensity + NAD(P)H\ intensity} \quad (1)$$

RESULTS

When considering all data collected in both loading conditions and all zones together, mitochondrial depolarization was not correlated with either autofluorescent intensity or ORR (Figures 3A). However, weak correlations were observed by loading rate (Figures 3B,C). Also, the superficial zone showed weak correlations (Figure 4A).

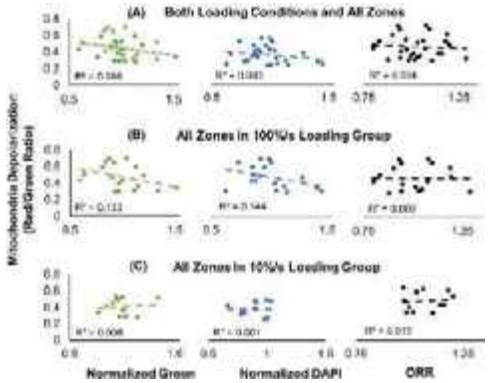

Figure 3: Mitochondrial depolarization versus ORI metrics for (A) all data; (B) 100%/s data; (C) 10%/s data.

Samples loaded at 100%/s and their unloaded counterparts showed a weak correlation between mitochondrial depolarization with normalized autofluorescent intensity in both green and DAPI channels, but there was no correlation between mitochondrial depolarization and ORR (Figure 3B). Mitochondrial depolarization was not correlated with any of the ORI metrics in the 10%/s group (Figure 3C).

For data collected in superficial zone, mitochondrial depolarization correlated with normalized autofluorescent intensity in both green and DAPI channels, but did not correlate with ORR (Figure 4A). There was no correlation between mitochondrial depolarization and any of the ORI metrics in the middle and deep zones (Figure 4B,C).

DISCUSSION

In this study, we induced changes in ORI metrics and mitochondrial membrane potential in cartilage using tensile loading, and showed there were zonal differences in cartilage mechanobiological response. The superficial zone was more responsive than middle or deep zone, demonstrating a weak correlation between post-loading mitochondrial depolarization and ORI metrics. This observation is

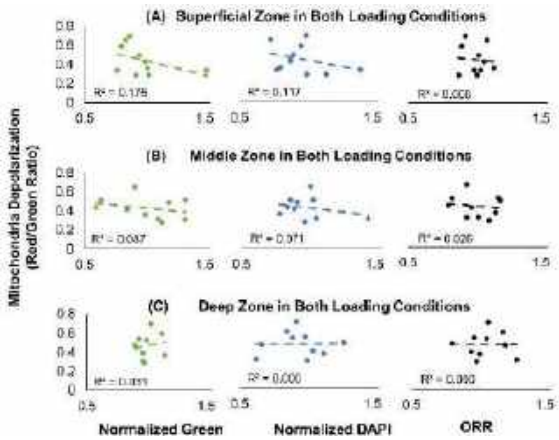

Figure 4: Mitochondrial depolarization versus ORI metrics for (A) superficial zone; (B) middle zone; (C) deep zone.

consistent with the roles of the superficial zone as highly dissipative and compliant [7] and with higher chondrocyte density [8].

Our results also showed that the cartilage mechanobiological response to tensile loading is strain-rate dependent. Samples in 10%/s loading group showed no correlation between post-loading mitochondrial depolarization level and ORI metrics, while samples in 100%/s loading group showed weak correlation between mitochondrial depolarization and autofluorescence in both channels. It is well-known that cartilage is responsive to mechanical stimuli, and its response is dependent on loading parameters such as stress magnitude, frequency, and strain rate. Specifically, a previous study showed the percentage of chondrocytes exhibiting calcium signaling was significantly increased by cyclic compression at a strain rate of 100%/s, but the effect was not observed at 25%/s or 50%/s [9]. Our findings aligned with their observation that cartilage was more responsive to higher strain rates.

The main limitations of this study are the relatively small sample size, the collection from one animal, and the noise inherent in both ORI data and mitochondrial depolarization measures. Only five pairs of samples were subject to JC-1 dye staining (n = 3 for 100%/s loading group, n = 2 for 10%/s loading group). Future research will aim to increase these numbers as well as explore the effects of other stimuli on ORI metrics and mitochondrial depolarization.

Although more data are necessary to complete the story, current findings of the study demonstrated the potential of using autofluorescent intensity to evaluate cartilage redox balance and implied its correlation with mitochondrial depolarization. The variation of correlation by strain rate and zone was consistent with previous knowledge and would be helpful in further study of cartilage redox balance in response to mechanical stimuli.

ACKNOWLEDGEMENTS: Funding from NSF CMMI BMMB 2237707 is gratefully acknowledged.

REFERENCES [1] Henrotin, Y. et al., *Osteoarthritis and Cartilage*, 13:643-654, 2005; [2] Li, D. et al., *The American Journal of the Medical Sciences*, 34:486-490, 2012; [3] Delco, M. L. et al., *Journal of Orthopaedic Research*, 36:739-750, 2018; [4] Skala, M. et al., *Methods in Molecular Biology*, 594:155-162, 2010; [5] Walsh, S. K. et al., *Osteoarthritis and Cartilage*, 27:1841-1850, 2019; [6] Rang Im, A. et al., *Cellular and Molecular Neurobiology*, 33: 625-635, 2013; [7] Buckley, M. Et al., *Journal of Biomechanical Engineeering*, 135: 0310021–0310029, 2013; [8] Quinn, T. M. et al., *Osteoarthritis and Cartilage*, 21:1904-1912, 2013; [9] Pingguan-Murphy, B. et al., *Journal of Cellular Physiology*, 209:389-397, 2006

ENGINEERING MESENCHYMAL STROMAL/STEM CELLS INTO AN ANTI-OXIDATIVE AGENT BY A MECHANICALLY DYNAMIC HYDROGEL SYSTEM SENSITIVE TO OXIDATIVE STRESS

Nicholas J. Serio (1), Thomas B. Leachman (2), Sing-Wan Wong (1,2)

(1) School of Biomedical Engineering, Colorado State University, Fort Collins, Colorado, USA
(2) Department of Mechanical Engineering, Colorado State University, Fort Collins, Colorado, USA

INTRODUCTION

Oxidative stress is a biochemical stress resulting from the overproduction of reactive oxygen species (ROS)[1]. The accumulation of ROS can damage nucleic acids, proteins, and lipids[2]. It has been reported that oxidative stress has a strong association to some irreversible disease conditions such as fibrosis and cancer[3,4]. Normally, the human body removes ROS by the action of antioxidative enzymes. Unfortunately, there is always redox imbalance in fibrotic or cancerous tissue, as well as post-injury conditions, because the generation of ROS outpaces the removal of it. One logical way to counter excessive oxidative stress is to provide additional antioxidative support to patients. A common way to fulfill the antioxidative demand is to intake antioxidative supplements. But multiple antioxidants are necessary to provide a full spectrum antioxidation because oxidative stress is a result of a collection of varied ROS and different antioxidants are required to neutralize specific ROS. Since consistently taking numerous supplements is not favorable, a solution that can offer multiple antioxidative actions in one shot would be ideal. In this notion, mesenchymal stromal/stem cells (MSCs) can serve as a suitable candidate for this purpose because of their multiaxial regulatory role[5]. Although there has been some success in MSCs therapy, the therapeutic effect of MSCs remains unpredictable in most of the applications[6]. We, therefore, have designed a novel hydrogel system that can control the production of antioxidative enzymes of MSCs through a mechanobiology approach, as it has been shown that the secretome profile of MSCs is sensitive to the mechanical properties of the microenvironment they reside in[7]. Our goal is to develop a mechanically dynamics hydrogel that specifically responds to oxidative stress and then triggers the extra production of antioxidative enzymes from MSCs. We believe the success of this work will offer a new management approach for oxidative stress.

METHODS

To make ROS responsive hydrogels, 3-aminophenylboric acid (PBA) was first conjugated to sodium alginate (Alg) via a reaction with 1-ethyl-(3-dimethylaminopropyl) carbodiimide hydrochloride (EDC-HCl) using a 1:1.26:2.73 molar ratio of Alg:PBA:EDC-HCl. The reaction was stirred at room temperature for 24hr, then dialyzed against DI water for 3 days and freeze dried, yielding Alg-PBA (Figure 1)[8].

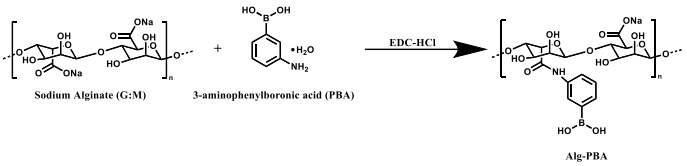

Figure 1: Alg-PBA conjugation.

Dried Alg-PBA was then dissolved in FlouroBrite DMEM (FDMEM) to make a 5%(w/v) solution. The Alg-PBA hydrogel was then formed by a dual crosslinking method: covalent easter bonds between PBA and PVA (polyvinyl alcohol) + ionic bonds between Ca^{2+} ions and the carboxylic groups on the alginate chains that were not conjugated with PBA (Figure 2). The PBA-PVA bonds are expected to cleave in the presence of ROS, while the ionic bonds remain intact. With this partial cleavage of crosslinking bonds, the hydrogel will become mechanically softer in the presence of ROS.

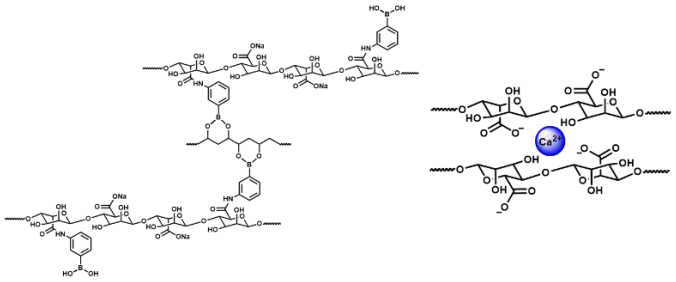

Figure 2: PBA-PVA covalent bonding (left) and ionic bonding between carboxylic groups on the alginate and Ca^{2+} ion (right).

The ROS responsive hydrogels were mechanically characterized using an axial compression test on HR 20 Rheometer (TA Instruments). An 8mm diameter gel disc was compressed with a 25mm diameter indenter. The test was performed in a submerge chamber filled with 10mL of culture media (DMEM +10% fetal bovine serum, +1% GlutaMax, +1% penicillin-streptomycin) and warmed to 37°C. The compression test was conducted with 10% strain, at a 5µm/s strain rate. The Young's Modulus was then calculated by Hertz Model by assuming the Poisson's ratio of the hydrogel was 0.5. To characterize the ROS response of the gel, 2 identical tests were performed on the same gel disc with 1µM H_2O_2 added in between the 2 tests.

Then, to evaluate the effect of the mechanical properties of the culture environment on the anti-oxidative properties of MSCs, one million D1 cells, marine bone marrow derived MSCs, were cultured in the hydrogel, followed by 1µM H_2O_2 treatment for 3 days. The MSC-gel cultures were then digested using alginate lyase and the RNA was extracted and purified from the cells for reverse transcription then qPCR analysis. The expression of antioxidative enzyme genes *sod1*, *gpx1 and cat1* were analyzed and normalized to housekeeping gene *gapdh.*

RESULTS

Rheometer analysis indicates that the Young's modulus of the ROS responsive hydrogel reduced by ~ 43% in the presence of H_2O_2 (Figure 3). This data aligns with our hypothesis that the Alg-PBA-PVA gel will become softer under an oxidative environment. The ROS sensitive hydrogel (+/- H_2O_2) is defined as a "soft gel" and a "stiff gel" respectively onward.

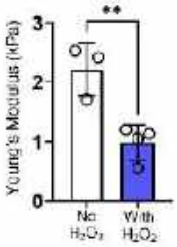

Figure 3: Young's modulus of ROS responsive hydrogel (+/- H_2O_2) where each data point represents one gel disc, **: P <0.01, student T-test

The expression of antioxidative enzymes *sod1*, *gpx1* and *cat1* were analyzed by qPCR (Figure 4). The results reveal there is a significant increase in expression of *sod1* and *gpx1* when the MSCs reside in a softer hydrogel while the expression of *cat1*, in contrast, shows a significant decrease in a softer environment. These data suggest that the anti-oxidative properties of MSCs can be controlled by varying the Young's Modulus of the microenvironment.

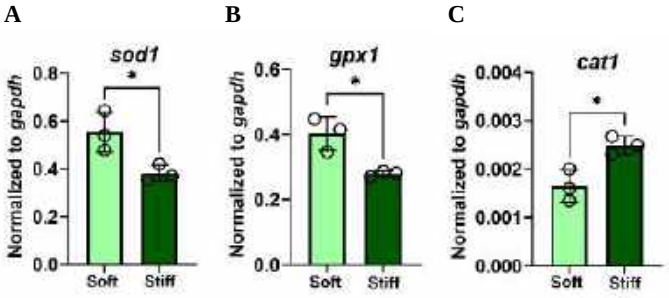

Figure 4. Gene expression of anti-oxidative enzymes (A) *sod1*, (B) *gpx1* and (C) *cat1* as a function of hydrogel stiffness. Technical triplicates, *: P<0.05 in student t-test.

DISCUSSION

With the preliminary data reported here, we developed a novel mechanically dynamic hydrogel system that is sensitive to oxidative stress. We also successfully demonstrated the control of expression of antioxidative enzymes in MSCs with the novel hydrogel. These data reveal the possibility to engineer MSCs, through a mechanobiology approach, to become an antioxidative agent to counteract oxidative stress.

Building on these findings, we will continue to test different compositions of Alg-PBA, the crosslinking protocol, and evaluate the change of mechanical properties of this ROS responsive hydrogel under different strengths of oxidative stress, since oxidative stress is varied between patients depending on their respective disease status.

The central premise of this study is to maximize the dynamic range of mechanical properties of the hydrogel and to investigate the changes in stiffness of the hydrogel as a function of oxidative strength. Followed by the mechanical control of the hydrogel, we will also study the production of anti-oxidative enzymes from MSCs cultured in varied Alg-PBA gels, to provide optimum support to suppress oxidative stress.

We believe this technology can facilitate the personalization of MSCs-based therapy for patients suffering from oxidative stress related diseases such as fibrosis or cancer.

ACKNOWLEDGEMENTS

Funding support: Colorado State University Start-up Fund, NIH R00AR079561. We acknowledge Dr. Herrera-Alonso's Lab of the School of Advanced Materials Discovery at Colorado State University for her support in lyophilization of the hydrogel materials.

REFERENCES

1. Kozakowska, M., at al., *J. Muscle Res. Cell Motil.* **36**, 377–393, 2015.
2. Sies, H. et al., *Nat. Rev. Mol. Cell Biol.* **23**, 499–515, 2022.
3. Anathy, V. et al., *Nat. Med.* **24**, 1128–1135, 2018.
4. Hayes, J. D., et al., *Cancer Cell* **38**, 167–197, 2020.
5. Kumar, S., at al., *Hum. Cell* **35**, 37–50, 2022.
6. Baranovskii, D. S. et al., *Stem Cell Investig.* **9**, 7–7, 2022.
7. Zonderland, J. & Moroni, L., *Biomaterials* **268**, 120572, 2021.
8. Rui, J.-Z., at al. *J. Supercrit. Fluids* **188**, 105682, 2022.

MECHANICAL CHARACTERIZATION OF THE FIBROSED LUNG SURFACE VIA SPHERICAL INDENTATION

K.A.M. Quiros (1), T.M. Nelson (1), M. Eskandari (1, 2, 3)

1. Department of Mechanical Engineering, University of California, Riverside, CA, USA
2. BREATHE Center, School of Medicine, University of California, Riverside, CA, USA
3. Department of Bioengineering, University of California, Riverside, CA, USA

INTRODUCTION

Emerging studies are developing computer-aided tumor detection devices for use in minimally invasive surgery. These devices utilize finger-like indentation to palpate organs and locate stiffer tumors within the healthy tissue [1]. Extraordinarily, the feasibility of this type of device for the lung has already been demonstrated [2]. Baseline mechanical data of healthy lung samples is needed to calibrate detection capabilities and improve the accuracy of these devices. While there is an abundance of tissue characterization studies that utilize tensile tests, results between tensile and compression studies are incongruous [3]; therefore, applying data acquired from tensile experiments does not accurately reflect measures from compressive palpation devices. Currently, data on the compression mechanics of the lung are absent from the literature, particularly for pulmonary tissue and investigations focusing on compressive pulmonary mechanics which are critical to the development of tumor detection, as well as for providing foundational knowledge to advance computational and surgical simulation models.

To address this need, we determine the compressive mechanics of pulmonary tissue using spherical indentation. The Hertz model, as is often used for small strain spherical indentation of biological tissues [4], is employed to calculate the Young's modulus and peak stresses. We perform tests on healthy and fibrotic samples to explore potential effects of known heterogeneous fibrotic stiffening on compressive results. This heterogeneity has recently been demonstrated across the lung surface during inflation testing [5, 6], but is unexplored in indentation studies. We conjecture that demonstrated surface heterogeneity in fibrotic lungs – particularly significant surface stiffening – may interfere with cancerous-tumor detection during robotic palpation. This is important as lung cancer is a common comorbidity of idiopathic pulmonary fibrosis [7]. As such, herein we report baseline compressive data of healthy and fibrosed lungs that can be used for future calibration of tumor-detection devices and used to help develop predictive models (e.g., computational and surgical simulation).

METHODS

Two groups of mice were studied where mice intranasally received 1X phosphate buffered saline (PBS) (n=5) to serve as a control or 12.5% hog dust extract (vol/vol) (n=5) to induce fibrosis, both with an exposure duration of 21 weeks, as previously established for a larger study [3, 5, 8]. Subsequently, animals were sacrificed, and the lungs were removed, inflated, and frozen slowly in PBS to -80 °C to preserve mechanics for this study [9]. Lungs were then thawed at 4 °C on the day of testing. Left lobes were occluded and attached to a metal platform with Cyanoacrylate glue to avoid motion and submerged in PBS (37 °C) for indentation testing. Displacement-controlled micro-indentation was performed on three equidistant regions across the lung's surface using a cantilever indentation apparatus (Figure 1, MicroTester G2, CellScale). A spherical glass tip (diameter = 2 mm) was attached to the tungsten beam (diameter = 0.2032 mm) to probe the sample surface. The indentation protocol included a small (1 μN) preload and four indentation cycles (5% deformation, $0.01\%s^{-1}$). The small strain restriction ($\varepsilon < 0.08$) in this study allowed application of the Hertz model to analyze the fourth cycle [10]. Hertz's theory was used to model the force-displacement and calculate the effective Young's modulus (eqn. 1) and generate stress-strain data (eqn. 2) as follows:

$$F = \frac{4E\sqrt{R}\delta^{3/2}}{3(1-\nu^2)} \quad (1)$$

$$\sigma = \frac{F}{\pi a^2}, \qquad \varepsilon = 0.2\frac{a}{R}, \qquad a = \sqrt{R\delta} \quad (2)$$

where δ is the applied indentation depth, F is the resultant load, E is the calculated Young's modulus, and σ & ε are the calculated indentation stress and strain, respectively. With known values: ν (Poisson's ratio, 0.34, [11]), R (indenter tip radius, 1 mm), and a (contact area) [10]. E & peak σ at all three regions were averaged and analyzed for significance to compare control and exposed groups (student's t-test, $p<0.05$, GraphPad Prism 9), similar to previous analyses [12]. The small

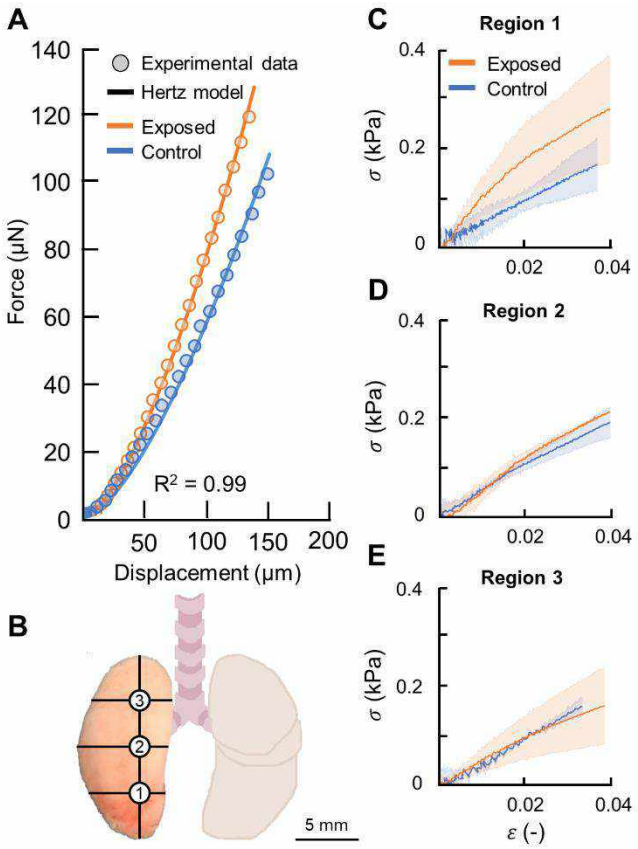

Figure 1: (A) Representative experimental force-displacement loading curves fitted with the Hertz model. Mean ± SD of stress-strain loading curves for control (blue) & fibrotic (orange) specimens. Regional testing performed according to (B). Regional data presented for (C) region 1, (D) region 2, and (E) region 3.

sample size inhibited statistical comparisons between exposed and control groups within each region.

RESULTS

In this study the stiffness associated with fibrosis was evaluated across the lung surface using micro-indentation at three regions. Analysis was completed using the Hertz model which demonstrated an excellent fit of 0.98-0.99 for all tests (Figure 1A).

When tests from all regions were averaged, the Young's modulus (calculated from force-displacement data, eqn. 1) reflected that the exposed group (1.46 ± 0.57 kPa) was slightly stiffer than the control group (1.40 ± 0.24 kPa) but was not statistically significantly stiffer. Stress-strain curves calculated from the force-displacement data were used to analyze the peak stress (Figure 1C-E). Although preliminary, results demonstrated a stiffening of the fibrosis group compared to the control in region 1 alone, the lower region (Figure 1C); neither regions 2 nor 3 (middle and upper regions) exhibited stiffening tendency (Figure 1D & E), albeit regions could not be robustly analyzed for statistical significance.

The peak stress averaged across all test regions reflected no statistical difference between the exposed and control groups despite the potential stiffening seen in region 1 (0.24 ± 0.04 kPa for control versus 0.28 ± 0.08 kPa for exposed groups respectively).

DISCUSSION

In this study, we investigated the compressive mechanics of the surface of the murine left lobe. We find that the heterogenous nature of lung fibrosis results in a single region with seemingly increased stiffness compared to the control, while the average stiffness of the entire surface does not significantly differ between fibrotic and control samples. Specifically, the average mechanics of the total surface – both Young's modulus and peak stress – do not differ between control and fibrotic specimens in this study.

The tendency of region 1 to be stiffer aligns with measurements of low strain from a study employing digital image correlation to analyze the surface of the lung during inflation [5]. This response is anticipated as dense fibrotic tissue manifests in lower and peripheral regions of the lung, as is characteristic of pulmonary fibrosis [6]. This pattern of peripheral and basal scarring is identified on CT scans in the process of diagnosing fibrosis [6]. Interestingly, this study in conjunction with Nelson et al. indicates that dense interior stiffening is also observed in measurements acquired from the lung surface as reported here.

This current pilot study of the lobe heterogeneity suggests that future work should characterize the entire lung surface with finer regional resolution to map fibrotic stiffening with greater accuracy.

As compressive mechanics are sought as baseline data to calibrate tumor detection devices, the probable heterogeneous surface stiffening identified here indicates caution should be taken when characterizing lung tissue of diseased lungs for use in tumor detection. This will be important if fibrosis and tumor stiffnesses are similar as detectable heterogeneous stiffening of the fibrosed lung surface could lead to inaccurate tumor detection. Fortunately, tumors in other organs are known to be ten times stiffer than healthy tissue and if this ratio is similar for the lung, fibrotic regions may be comparably negligible [1].

The limited literature on compressive mechanics reports the Young's modulus of healthy lung tissue to be 1.3-1.4 kPa, which is in excellent agreement with the results of this study [13]. Additionally, the expansive literature reporting the Young's modulus of lung tissue from tensile tests (1.91-7.6 kPa) are greater than that reported here from compressive data [11,13]. Further, as demonstrated here, compressive investigations also allow for the characterization of the intact lung surface heterogeneity unlike destructive tensile tests. Hence, underscoring the pressing need to investigate compressive mechanical parameters to inform accurate surgical probing applications and surgical simulation models.

ACKNOWLEDGEMENTS

Authors thank funding support in part from the NASA California Space Grant Consortium Fellowship to K.A.M.Q., the NSF GRFP (DGE-1840991) to T.M.N., and the State of California Climate Action Through Resilience Program Opportunity to Advance Sustainability, Innovation, and Social Inclusion (OASIS) UCR grant to M.E.

REFERENCES

[1] Konstantinova, J., *et al.* IEEE Sens. J. 14, 2490–2501 (2014) [2] S. Joung, *et al*. WCMPB, 39,1405-1407. (2013) [3] McKee, C. T., *et al.* Tissue Eng. Part B Rev. 17, 155–164 (2011) [4] Lin, D. C., *et al*. Biomech. Model. Mechanobiol. 8, 345–358 (2009) [5] Nelson, T. M. *et al.* Sci. Rep. 13, 4564 (2023) [6] Noth, I. & Martinez, F. J. Chest 132, 637–650 (2007) [7] Cano-Jiménez, E., *et al.* Med Sci (Basel) 6, (2018) [8] Dominguez EC, *et al.* Cancers (2022) [9] Polio, S. R. *et al*. PLoS One 13, e0204765 (2018) [10] Pathak, S. *et al.* Mater. Sci. Eng. R Rep. 91, 1–36 (2015) [11] Birzle, A. M., *et al*. J. Mech. Behav. Biomed. Mater. 94, 126–143 (2019) [12] De Winter, J. C. F., PARE (2019) [13] Polio, S. R. *et al*. PLoS One 13, e0204765 (2018)

SB³C2024
Summer Biomechanics, Bioengineering and Biotransport Conference
June 11-14, Lake Geneva, WI, USA

THE INFLUENCE OF BLUNT FORCE LARYNGEAL TRAUMA ON PHONATION: AERODYNAMIC, KINEMATIC, AND ACOUSTIC EFFECTS

Md. Roknujjaman[1], Molly E. Stewart[1], Byron D. Erath[1]

[1]Department of Mechanical and Aerospace Engineering, Clarkson University, Potsdam, NY, United states

INTRODUCTION

Blunt force laryngeal trauma, while infrequent can pose significant, life-threatening consequences due to the airway being compromised [1]. Common causes of laryngeal trauma include endotracheal intubation, motor vehicle accidents, strangulation, falls, sports activate, etc., The primary injuries resulting from blunt laryngeal trauma are, typically, (1) displaced fractures of the laryngeal cartilage, (2) paralysis affecting at least one vocal fold (VF), and (3) subsequent scar formation in the VF tissue [2]. In addition to the immediate threat posed by airway obstruction, laryngeal trauma also usually results in significantly comprised vocal outcomes due to damage to the larynx and the VFs.

The effect of vertical VF misalignment and vocal fold scarring, as occurs with acute laryngeal trauma, have each been investigated individually [3] [4] [5] [6]. However, it is unclear how VF scarring, in tandem with vertical misalignment, influences phonation. Because most surgical interventions for laryngeal trauma are focused on restoring airway function, restoration of vocal function is a secondary consideration at best. This work aims to address that deficiency by providing insight into how concurrent scarring and vertical displacement of the VFs influence both the kinematics and acoustics of phonation.

EXPERIMENTAL METHOD

An experimental facility with synthetic, self-oscillating VFs was employed for the investigations. The facility consisted of a flow channel representative of the human airway and subglottal tract, which is shown schematically in Figure 1. The geometry of the vocal fold models, and the corresponding layers are shown in Figure 2 (a). Details regarding the facility and VF composition and fabrication are described in previous work [4]. Inferior-superior vertical displacement of the VFs was achieved by inserting 1.0 mm thick shims between the VF mounting bracket and the tracheal flow channel, as shown in Figure 2(b). The vertical displacement (d) was reported as a ratio relative to the length of the VF medial surface in the inferior-superior axis (t_{VF}). The length of the medial surface of the VF models was measured as 2.88 mm. Vocal fold oscillation was initiated by regulating shop air to specify the subglottal pressure, measured via a Dwyer series 1227 flow pressure manometer. The mean flow rate was recorded with a Dwyer RMC 103-SSV flow meter. The VF kinematics were measured from a superior view (see Figure 1) with a Photron AX200 high-speed camera at 20,000 frames per second. Details of the data acquisition can be found in [4].

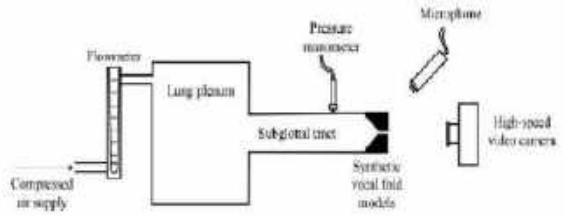

Figure 1. Schematic of the experimental flow facility.

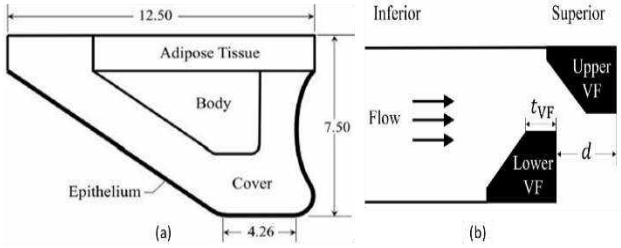

Figure 2. (a) The synthetic VF model geometry. All dimensions are in mm. (b) Inferior-superior thickness of the medial VF surface (t_{VF}) and vertical displacement, d, which was introduced to the upper VF in increments of 1.0 mm.

To mimic VF scarring, three different stiffnesses of the VF cover layer were considered. Table 1 displays the silicone ratios used to fabricate the cover layers and the resultant moduli of elasticity for the three cases of interest. The E_{1x} VF model represented a healthy, unscarred VF and acted as the baseline stiffness model. The E_{3x} and E_{10x} VF models had cover layers that were 3 times and 10 times as stiff as the baseline model, respectively. A stiffness asymmetry between the

opposing VFs was introduced by pairing the E_{1x} VF model with both a E_{3x} and E_{10x} VF model. Vertical displacement in the inferior-superior direction was also introduced to these VF models. A total of four cases were investigated with the two groupings of VF models. The first case was the E_{3x} superior case, denoted as $E_{3x,sup}$ in which the E_{3x} model was displaced superiorly relative to the E_{1x} model. The second case was the E_{3x} inferior case, denoted as $E_{3x,inf}$ where the E_{3x} model was displaced inferiorly with respect to the E_{10x} model. The $E_{10x,sup}$ and $E_{10x,inf}$ cases followed the same approach, but included the $E_{10x,}$ model instead of the E_{3x} model.

Table 1. Modulus of elasticity of the cover layer resulting from different silicone mixtures to achieve three different stiffnesses.

VF model	Silicone ratio	Cover layer stiffness (kPa)
E_{1x}	E1:1:6	1.12
E_{3x}	E1:1:4	3.43
E_{10x}	E1:1:2	10.34

RESULTS AND DISCUSSION

Data were collected at six displacement levels, such that d/t_{VF} = 0.0, 0.35, 0.69, 1.04, 1.39, and 1.74. Figure 3 represents the kymograms for the baseline case of symmetric VF stiffness, with vertical displacement. Figure 4 presents the kymograms for the $E_{3x,sup}$. Even with no vertical displacement, the asymmetric VF cover stiffness resulted in diminished VF closure and an increased open quotient. As the vertical displacement increased, the motion of the stiffer VF model on top also became irregular and began to exhibit an oscillation pattern that was indicative of the emergence of biphonation with period-doubling.; behavior not observed in Figure 3.

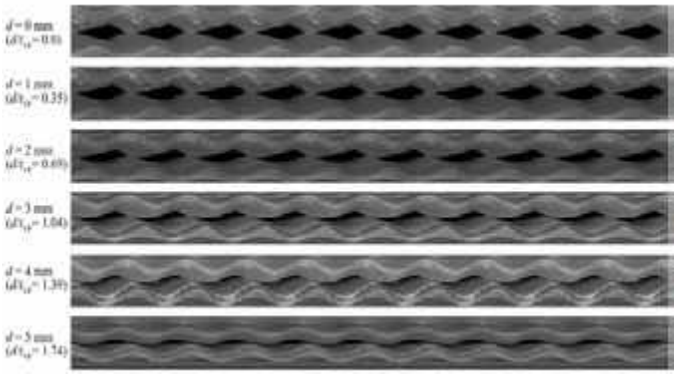

Figure 3. Kymograms consisting of 10 cycles for 6 different displacement levels of d/t_{VF} for symmetric E_{1x} VFs.

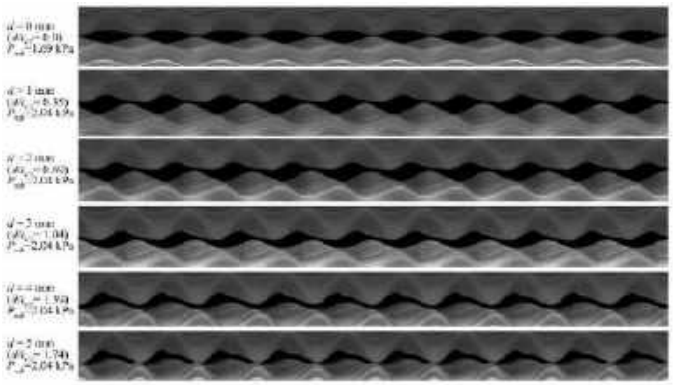

Figure 4. Kymograms consisting of 10 cycles for 6 different displacement levels for the $E_{3x,sup}$ case.

The emergence of higher oscillation modes in asymmetrically tensioned VFs with increasing subglottal pressure is a well-known instability [7]. However, the current results indicate that this instability is more likely to occur as vertical misalignment increases. Interestingly, the E_{3x} case, displacing the stiffer VF in the inferior, as opposed to superior, direction resulted in much more irregular and pathological VF motion, which was also reflected in the acoustic measures of H1-H2, jitter, shimmer, and cepstral peak prominence, which are not reported for brevity. The $E_{10x,inf}$ and $E_{10x,sup}$ investigations exhibited the same, but even more pronounced, behavior. These findings indicate that, importantly, the position of the stiff VF relative to the normal VF influences the emergence of irregular oscillation patterns, and that if the stiffer VF is in a more inferior position, poor phonatory quality is more likely to occur.

CONCLUSION

The effect of blunt force laryngeal trauma to the larynx was modeled by introducing both VF cover stiffness and inferior-posterior positional asymmetries. Kinematic and acoustic measures were more irregular than for vertical misalignment in VFs with symmetric cover stiffnesses. Asymmetric VF cover stiffness produced asymmetric oscillations in both amplitude and phase. These became more pronounced as vertical displacement increased. Positioning a stiffer VF inferior to a normal stiffness model was more likely to result in biphonation and pathological motion.

ACKNOWLEDGEMENTS

This work was funded in part by the National Institutes of Health (NIH) National Institute on Deafness and other Communication Disorders Grant P50 DC015446

REFERENCES

[1]. Schaefer, N., Griffin, A., Gerhardy, B. and Gochee, P., 2014. Early recognition and management of laryngeal fracture: a case report. *Ochsner Journal*, *14*(2), pp.264-265.

[2]. Becker, M., Leuchter, I., Platon, A., Becker, C. D., Dulguerov, P., & Varoquaux, A. (2014). Imaging of Laryngeal Trauma. *European Journal of Radiology, 83*(1), 142-154.

[3]. Bouvet, A., Tokuda, I., Pelorson, X., & Van Hirtum, A. (2020). Influence of Level Difference due to Vocal Folds Angular Asymmetry on Auto-Oscillating Replicas. *The Journal of the Acoustical Society of America, 147*, 1136-1145.

[4]. Stewart, Molly E., and Byron D. Erath. "Investigating blunt force trauma to the larynx: The role of inferior-superior vocal fold displacement on phonation." *Journal of biomechanics* 121 (2021): 110377.

[5]. Murugappan, S., Khosla, S., Casper, K., Oren, L., & Gutmark, E. (2009). Flow Fields and Acoustics in a Unilateral Scarred Vocal Fold Model. *Annals of Otology, Rhinology & Laryngology, 118*(1), 44-50.

[6]. Pickup, B. A., & Thomson, S. L. (2009). Influence of Asymmetric Stiffness on the Structural and Aerodynamic Response of Synthetic Vocal Fold Models. *Journal of biomechanics, 42*(14), 2219-2225.

[7]. Erath, B. D., Zañartu, M., Peterson, S. D., & Plesniak, M. W. (2011). Nonlinear Vocal Fold Dynamics Resulting from Asymmetric Fluid Loading on a Two-Mass Model of Speech. *Chaos: An Interdisciplinary Journal of Nonlinear Science 21*(3), 03311

NOVEL STENT DESIGN AND PROTOTYPING METHOD

KM Elmer (1), BF Uretsky (2), A Chaus (3) MO Jensen (1)

(1) Department of Biomedical Engineering, University of Arkansas, Fayetteville, AR, USA
(2) Department of Internal Medicine, University of Arkansas for Medical Sciences, Little Rock, AR,
(3) Advocate Heart Institute, Lutheran General Hospital, Park Ridge, IL, USA

INTRODUCTION

Coronary artery disease (CAD) often manifests as lesions in the vessel that obstruct blood flow. Invasive treatment for CAD involves balloon angioplasty followed by stent placement. Bifurcation lesions, 20% of all interventions, are notoriously complex to treat [1-2]. The theme of our work is to create stenting devices and methodologies that reduce stent malapposition and other poor procedure outcomes.

A single stent spanning the bifurcation core, with optional second stent placement in distal branches, has been proposed [3-4] (Figure 1).

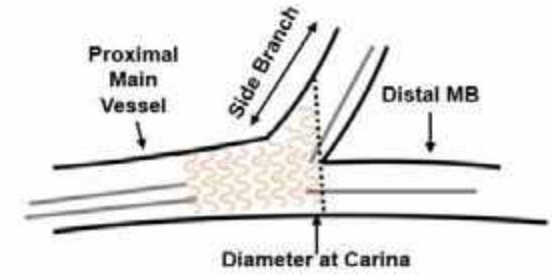

Figure 1: Tapered stent shown within bifurcation core. Carina diameter shown in dashed line.

However, this has not been widely adopted. Recent work has suggested that this 'proximal-to-distal' approach is limited by the change in vessel diameter occurring within the bifurcation core [5]. We propose a tapered stent design, along with novel balloon designs and methodologies, as a solution for proximal-to-distal approaches. Additionally, we anticipate an 'elliptical' shape in the bifurcation core, with chords defined by the diameter at the carina (CD) and proximal main vessel diameter (pMVD). In this study, a tapered stent prototype was designed, constructed, and tested. We also hypothesized that the stents can be expanded into elliptical shapes of equivalent perimeter to the designed distal stent diameter.

METHODS

Design: The stent was designed using a generic stent pattern consisting of sinusoidally-shaped rings connected by connecting struts. The proportions of the sinusoid shape were adapted from commercially-available stents (Xience everolimus-eluting stent; Abbott), in an effort to keep a similar ratio of stent to vessel surface area. The stent was scaled to have a proximal diameter of 16 mm, for ease of prototype creation and handling. The distal diameter was designed to be 21 mm, giving a CD that is 1.3x the pMVD. Amplitude and periodicity of the stent rings were 5.4 mm and 6.5 mm respectively. For the two proximal rings of the stent, 8 periods of the sinusoid shape were used. To create the taper, 9 and 10 periods were used for the distal end, keeping the same sinusoidal shape. Two evenly-spaced connecting struts were placed between each ring, with each row of stents offset between adjacent layers.

Previous work from clinical patient data indicates that most coronary bifurcation have a CD 1.5-2x larger than the pMVD [5]. To approximate an ellipse of 'equivalent expansion' to a 21mm diameter circle, the perimeter of a 21 mm diameter circle was calculated. Using this as the perimeter for an ellipse, with one axis equal to the pMVD (16 mm), the second axis was calculated to be 26 mm.

Ramanujan's Perimeter of Ellipse

$$p = \pi\left\{(a+b) + \frac{3*(a-b)^2}{10*(a+b)\sqrt{a^2+14ab+b^2}}\right\} \quad (1)$$

The long axis (26 mm) was taken as the elliptical carina length (eCD), and is 1.6x the pMVD.

Fabrication: The stent was formed from 0.02" diameter 316L stainless steel wire. The individual layers of the stent were formed into the intended sinusoidal shape. The stent layers were laser-welded to the

connecting struts, forming a flat sheet. The sheet was then wrapped around a mandrel, trimmed, and the seam laser-welded to form the stent.

Testing: The goal of the initial prototype was to determine the feasibility of manufacturing a tapered stent and confirm the stent expands as desired. To show this, the stent was crimped and expanded to the desired shapes (Figure 2).

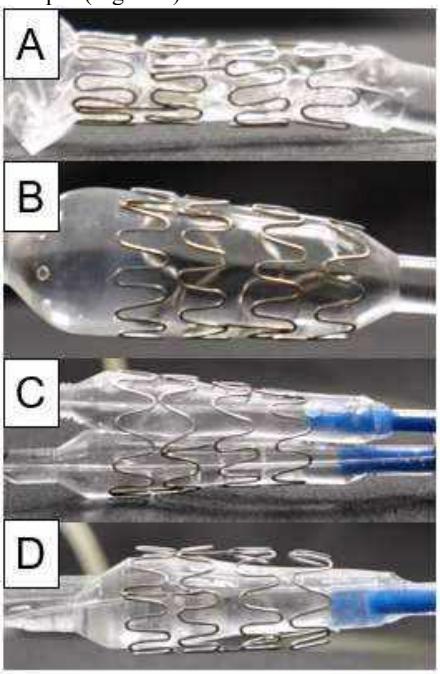

Figure 2: Stent prototype. A) Stent crimped onto deflated balloon. B) Stent expanded on tapered balloon. C) Stent expanded with kissing balloon inflation (KBI) (long axis) D) Stent expanded with KBI (short axis)

Metrics for success were that the stent could be crimped at least 25% without fracture, the stent could be re-expanded to 1.3x pMVD, and then re-expanded again to an ellipse with long axis 1.6x pMVD. Qualitatively, for each test success required no observable stent fracture, particularly at weld points, during each test. For the expansion tests, Percent Elastic Recoil (PER) of the stent should be minimal, ideally ≤10%.

Procedure: For test 1, the stent was crimped onto a deflated tapered balloon. The stent was expanded using the tapered balloon. Tests 2 and 3 used two 'kissing balloons.' Balloon diameters are summarized in Table 1:

Table 1: Balloon Diameters for Inflation Tests

	Proximal Diameter (mm)	Distal Diameter (mm)
Test 1	16	21
Test 2	8	11
Test 3	8	13

All balloons were manufactured using our lab's custom balloon forming machine [6]. The kissing balloons were designed to sum to the desired diameter. For each test, the stents were photographed and measured before and after balloon inflation, and following balloon deflation. The PER was calculated from the after inflation and after deflation measurements.

RESULTS

A prototype stent was designed, fabricated, and tested. The stent was crimped onto a balloon to 11mm, and re-expanded to a 26 mm CD with no observed fracture. The PER of the proximal and distal rings for each expansion of the stent is shown in Table 2. Three additional prototypes are in production to be presented at the conference. PER will be presented as Mean +/- standard deviation.

Table 2: Percent Elastic Recoil for Stent

	Proximal End	Distal End
Test 1: 16-21 mm	11%	10%
Test 2: 8-11 mm KBI		
Long Axis	5%	8%
Short Axis	3%	-5%
Test 3: 8-13 mm KBI		
Long Axis	5%	9%
Short Axis	8%	7%

,During Test 1, the stent was observed to slide proximally along the balloon. Figure 1B shows the distance between the distal end of the balloon and distal end of the stent.

DISCUSSION

This study focused on the feasibility of tapered stent design and expansion capacity. There were no observed fractures in the stent, and it expanded to the desired shape. This indicates that our prototyping methods and tapered stent design are feasible for further study.

The stent expanded to an elliptical distal shape, with the long axis 1.6x the pMVD. This confirms that the stent can expand to elliptical configurations with equivalent perimeter to the circular diameter. This indicates that for use in 'elliptical' bifurcation cores, tapered stents will need to specify the eCD limits for tapered stent sizing. Future work will explore additional tapering ratios. As the change in diameter increases, stent strut location and design may require modification.

The PER for the stent was within reasonable limits, with the recoil decreasing as the stent was expanded to elliptical shapes. The short axis for the first KBI increased slightly (negative recoil), which indicates that the elliptical shape may put stress on the vessel perpendicular to the short axis. Future work will seek to understand and quantify these forces, as well as PER of the stent when under forces that mimic *in-vivo* conditions.

Additional testing will use benchtop bifurcation vessel models in tissue mimicking gel to confirm deliverability and expandability of the stents in environments closer to *in-vivo* conditions. The stent slipping that occurred during the initial stent expansion on a unilaterally tapering balloon may be resolved when the stent is deployed within a blood vessel model.

This study is limited because the stent prototype was scaled up and created using 316L stainless steel rather than alloys such as cobalt chromium. However, we believe that the geometry of the stent design greatly impacts the stent's ability to expand.

ACKNOWLEDGEMENTS

This work was supported by the American Heart Association grants # 18AIREA33960590 and 24AIREA1241655. The authors thank Amelie Wise for help with data collection.

REFERENCES

[1] Lassen, JL, et al., *EuroIntervention,* 13: 1540-54, 2018.
[2] Rizik, D, et al., *J Invasive Cardiology* 20: 82-90, 2008.
[3] Uretsky, BF (2014) Apparatus and method for treatment of bifurcation lesions. In S. United (Ed.): Barry F. Uretsky.
[4] Elabbassi, W, et al., *Cardiovasc Revasc Med* 18: 281-8, 2017.
[5] Elmer, KM, et al., *JCIMCR*, 4: 1-8, 2023.
[6] Elmer, KM, et al., *JCTR,* 15: 1119-28, 2022.

COMPARISON OF LUMPED, DISTRIBUTIVE AND 1D NAVIER-STOKES MODEL OF CORONARY BLOOD FLOW

Chenghan Cai (1), Lik Chuan Lee (2), Lei Fan (1)

(1) Joint Department of Biomedical Engineering, Marquette University and Medical College of Wisconsin, Milwaukee, WI, USA
(2) Department of Mechanical Engineering, Michigan State University, East Lansing, MI, USA

INTRODUCTION

Coronary artery disease (CAD) is a cardiovascular disease which has been found to be the leading cause of death in the U.S. Although the development of some clinical indices has helped improve the prognosis of patients suffering from CAD, the underlying mechanisms that cause CAD remain unclear. The lack of understanding of these mechanisms arises largely because of the complicated mechanisms that control blood flow in the coronary vessels, and difficulties/challenges of measuring blood flow and pressures in the coronary vessels embedded in deep layer of the myocardium (**Fig. 1A**). Computational modeling of the coronary vascular system thus provides an alternative approach to understand the pressure-flow relationship in coronary circulation as well as their interaction with cardiac function. The 0D lumped parameter model (LM) and distributive model (DM) based on mass conservation of each vessel, have been applied to predict the pressure and flow rate in coronary vessels. Compared to LM, DM can provide spatial distribution of pressures and blood flow within each vessel, but at a higher computational cost. The 1D Naiver-Stokes (NS) equation based on conservation of both mass and momentum considers the wave propagation in the elastic vessels, and thus provides more physiological predictions of pressure and flow rate. The goal of this work is to develop DM and 1D NS model to predict the spatial distribution of coronary flow and pressure waveform information, which can be potentially applied to understand the mechanisms of CAD.

METHODS

The three-element Windkessel LM has been developed in our previous work [1-2] where each vessel is represented by a proximal resistor (R_1), distal resistor (R_2), and capacitor (C). The mass conservation is imposed as

$$\frac{P_{in}-P_{mid}}{R_1}+\frac{P_{out}-P_{mid}}{R_2}=C\frac{d(P_{mid}-P_T)}{dt} \quad (1)$$

where P_{in} and P_{out} are inlet and outlet pressures, respectively, P_T is intramyocardial pressure (IMP), and P_{mid} is the unknown pressure at the middle of each vessel. Then, the vessel radius, r , is calculated based on P_{mid} as

$$r = = B_P \times \frac{A_P-B_P}{\pi}\left[\frac{\pi}{2}+\arctan\left(\frac{P_{mid}-P_T-\varphi_p}{C_P}\right)\right] \quad (2)$$

where A_P and B_P are the highest and lowest radius, respectively, C_P is the passive response bandwidth of the vessel, φ_p is the transvsacular pressure corresponding to the mean of A_P and B_P. These parameters are the same as used in our previous work [1-2].

In DM, the conservation of mass is given as

$$\frac{\partial A}{\partial t}+\frac{\partial Q}{\partial x}=0. \quad (3)$$

In Eq (3), A is the cross-sectional area of the vessel, which is a function of unknown vessel radius, and Q is the flow rate which can be written

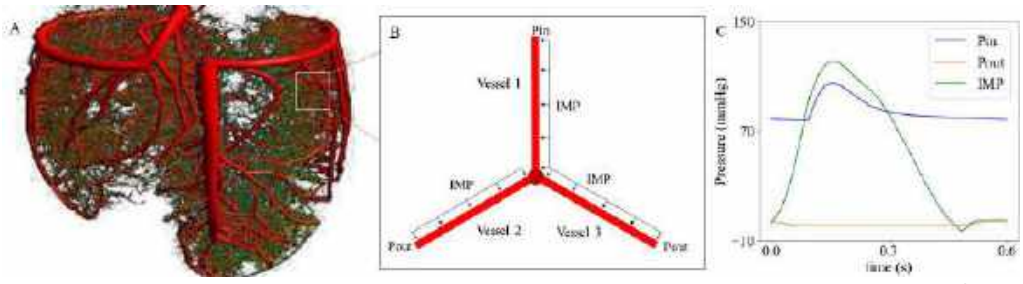

Fig. 1: A. Coronary vessel network; B. Three-vessel network; C. Inlet, outlet pressure waveforms and IMP waveforms used for the three-vessel network.

as a function of unknown vessel radius and pressure as $Q = \frac{\pi r^4}{8\mu}\frac{\partial P}{\partial x}$. The relationship between pressure and radius used in DM is that same as that used in LM (Eq. (2)). Then, Eq. (3) can be rewritten as a function of unknown radius, which will be solved.

The governing equation of 1D NS model based on momentum conservation is given as

$$\rho * \frac{\partial v}{\partial t} + \alpha * \rho * v\nabla v + \nabla P + \beta * \mu\nabla^2 v = 0 \quad (4)$$

where v is the velocity along the vessel direction, μ and ρ are the dynamic viscosity and density of blood inside the vessel, respectively. The parameters α and β are the momentum flux correction factor and viscosity friction coefficient, respectively [3], both of which are affected by the flow velocity in the vessel [4]. The weak form of the governing equation is derived by multiplying a test function (w) as

$$\int \rho * \frac{\partial v}{\partial t} * w * dx + \int \alpha * \rho * v\nabla v * w * dx + \int \nabla P * w * dx + \int \beta * \mu\nabla^2 v * w * dx = 0 \quad (5)$$

where v and P are unknown values. In 1D NS model, the unknown P and v are solved by mass conservation (Eq. (3)), and momentum conservation (Eq. (4)) using a staggered method.

These three methods are used to solve the pressure and coronary flow rate in a three-vessel network (**Fig. 1B**) using hemodynamics measurments of a swine model. Perfusion presssure and IMP in the model are imposed using the difference between arterial and venous pressure waveforms, and the left ventricular pressure, respectively (**Fig. 1C**). LM is implemented in MATLAB to compare agaisnt the developed DM and 1D NS model that are implemented using finite element method in FEniCS. In DM and NS model, each vessel is discretized using 32 elements.

RESULTS

Fig. 2 shows the comparison of model predicted pressure and radius at the middle of each vessel, inlet and outlet flow rate of each vessel, and the flow conservation at the junction of the three-vessel network, using the three methods. It is shown that P_{mid} is smaller in the downstream vessels 2 and 3 compared to vessel 1 in the three models (**Fig. 2A**). Model predicted P_{mid} waveform using DM and 1D NS models shows the similar trend as that predicted by LM. The relative percentage difference is 7% between DM and LM, and 7% between 1D NS model and LM. The largest difference occurs when the IMP gradient is the largest. The model predicted vessel radius shows the same trend using three models and the radius in vessels 2 and 3 reduces are smaller than that in vessel 1 (**Fig. 2B**). The percentage difference is 4% between DM and LM, and 5% between 1D NS model and LM. The model predicted inlet and outlet flow rates shows the same trend using the three models where flow rate reduces during systole as IMP increases to impede flow rate (**Fig. 2C-D**). The diastolic flow rate is higher in vessel 1 than that in vessel 2 and 3 due to the higher perfusion pressure in vessel 1. The percentage difference is 5% between DM and LM, and 6% between LM and 1D NS model for both inlet and outlet flow rates (**Fig. 2C-D**). Three model predictions show that mass conservation is satisfied at the junction of the three-vessel network since the difference between outlet flow rate from vessel 1 and inlet flow rate from vessel 2 and 3 is close to 0 (**Fig. 2E**).

DISCUSSION

In this project, we compared the LM, DM and 1D NS models in a three-vessel coronary network. The model predictions in terms of pressure in the middle of each vessel, radius in the middle of each vessel, inlet flow rate and outlet flow rate using DM and 1D NS are comparable with those predicted by LM. Compared to LM, the DM and 1D NS models can provide pressure and flow rate at any point of the vessel. In the future, we will extend the coronary vessel network and apply the developed model to investigate the pressure and flow rate distribution under physiological and pathological conditions.

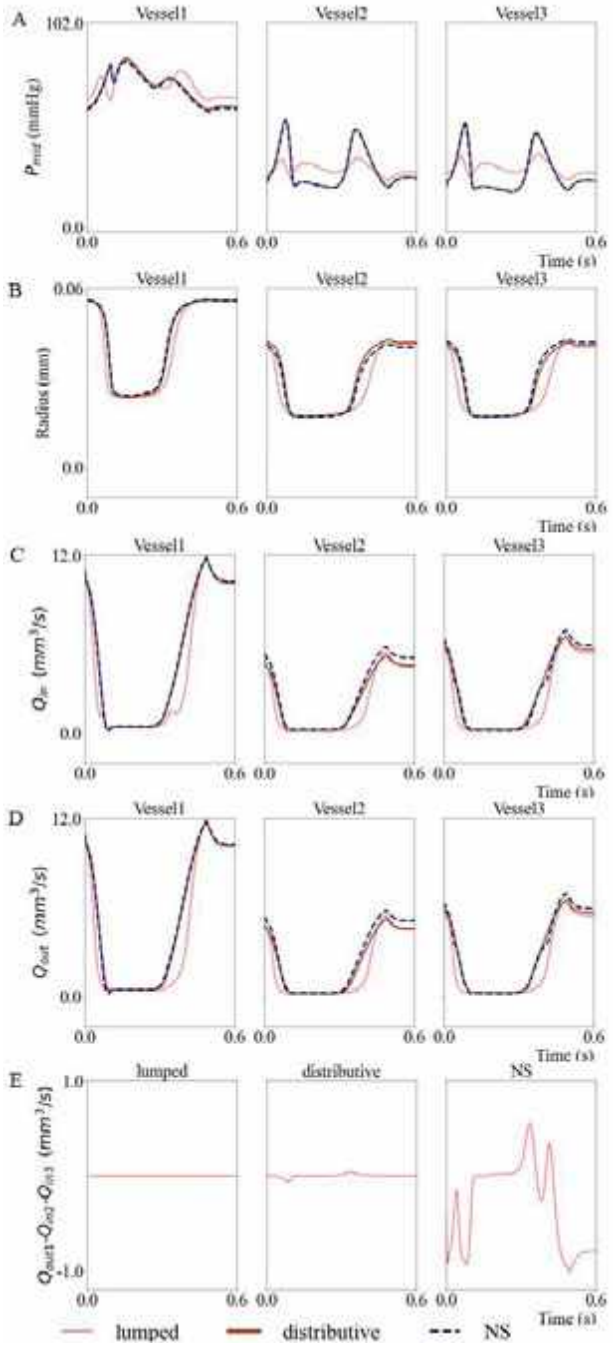

Fig. 2: Comparison of A. pressure in the middle of each vessel; B. radius in the middle of each vessel; C. inlet flow rate; D. outlet flow rate; E. mass conservation at junction, predicted by LM, DM and 1D NS model.

REFERENCES

[1] Fan, L. et al., Am. J. -*Mec. Of Exe*., 12, 2202

[2] Fan, L. et al., Front. Physiol., -*Eff. Of Mec*.., 14, 08, 2020

[3] Sochi T., R, arXiv, -*One-Dim. Nai*., 9,2013

[4] Bessems D., et al, CUP, -*A Wav. Pro*., 5,2007

DEEP LEARNING-BASED BIOMECHANICAL CHARACTERAZION OF INFARCTED MYOCARDIUM FROM STRAIN IMAGING.

RR. Mehdi (1), T. Mukherjee (1), EA. Mendiola (1), S. Neelakantan (1), R. Avazmohammadi (1)

(1) Department of Biomedical Engineering, Texas A&M University, College Station, TX, USA

INTRODUCTION

Myocardial infarction (MI), resulting from blockage of the coronary artery, is a leading cause of death in the US and worldwide [1]. The loss of functional cardiac myocytes due to MI induces multiscale remodeling of the myocardium, including alterations in the properties and structure of cellular and extracellular components, degrading the overall heart function in a complex manner [2]. The emerging invasive cardiac interventions for MI patients, such as cardiac sleeves and patches, aim to alleviate post-MI remodeling effects. However, the personalized design of these interventions relies heavily on the basic characteristics of the infarct (scar) regions, including size and stiffness. Late gadolinium enhancement (LGE)-based cardiac magnetic resonance (CMR) imaging remains the state-of-the-art technique to delineate scar regions in MI patients [3]. However, LGE has downsides, including complications with gadolinium injection, safety issues for patients with kidney diseases, reliance on CMR, and prolonged scanning time, which overall limit its scope and safety in time-sensitive clinical applications.

We hypothesize that integrated modeling-strain imaging can accurately predict the heterogeneous tissue stiffness in the MI heart. In this work, we have developed a deep learning (DL)-assisted method that can identify scar regions and their stiffness from cardiac strains attainable from four-dimensional (4D) imaging. We successfully validated the predictions of our model for the size and location of tissue scars against the estimation of cine CMR with LGE. To broaden the applicability of our model and further evaluate its predictions, we sought the validation of our model in rodent models of MI where the rats were imaged by echocardiography (and not CMR), and the infarct regions were characterized using histology and mechanical testing. Our approach thus offers a promising avenue for accurate infarct characterization without subjecting patients to invasive procedures or gadolinium-related concerns and provides an affordable alternative to LGE-CMR by the possibility of needing only echocardiography (echo) instead of CMR.

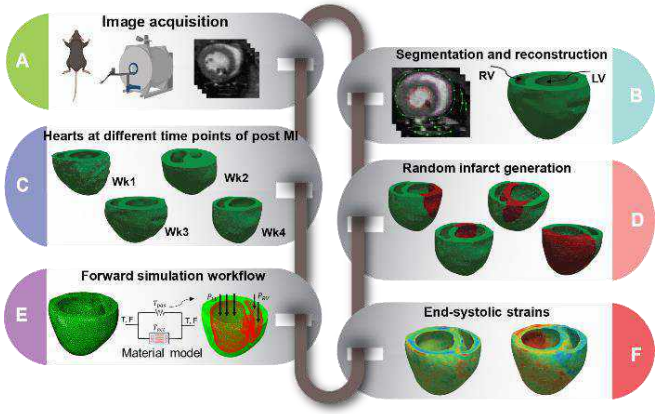

Fig 1: Development of simulated cardiac strains using computational rodent heart models.

METHODS

MI Rodents. The male Wistar-Kyoto rats, aged 8 weeks underwent anteriobasal infarct induction and were sacrificed at four time points post-MI (1-, 2-, 3-, and 4 weeks). *Cardiac simulation.* These subjects were employed for the development of finite-element rodent cardiovascular computational models (Fig. 1). The 3-D biventricular hearts were reconstructed from CMR scans truncated under the valve plane, and a tetrahedral mesh was generated in each heart. We utilized an additive stress decomposition constitutive model [4] to represent the passive and active behaviors of the myocardium, expressed by

$$\mathbf{T} = \underbrace{\frac{1}{J}\bar{\mathbf{F}}\frac{\partial W^{dev}}{\partial \bar{\mathbf{E}}}\bar{\mathbf{F}}^{T} + \frac{\partial W^{vol}}{\partial J}}_{Passive} + \underbrace{\frac{1}{J}\mathbf{F}\mathbf{S}^{\mathbf{act}}\mathbf{F}^{\mathbf{T}}}_{Active}.$$

An inverse problem was set up to estimate the passive material properties and active tension by replicating the biaxial test result and pressure-volume measurements, respectively. The Green Lagrangian strains, including circumferential, radial, and longitudinal (CRL) strains, were obtained for the entire heart, described in detail in [4]. This process was repeated to create 600 examples by infarct sizes, locations, and stiffness levels to obtain a large dataset to train the DL model.

Preprocessing steps of DL. Left ventricle (LV) strain data was translated into standard American Heart Association (AHA) bullseye maps for each CRL strain. These individual CRL maps were then compiled into a single image, followed by rotation for data augmentation. The resulting images were inputs for the UNet DL model, trained with a binary cross-entropy loss function. The evaluation metrics included the dice similarity coefficient metric (DSC), with corresponding binary infarct masks serving as outputs, as illustrated in Fig. 2.

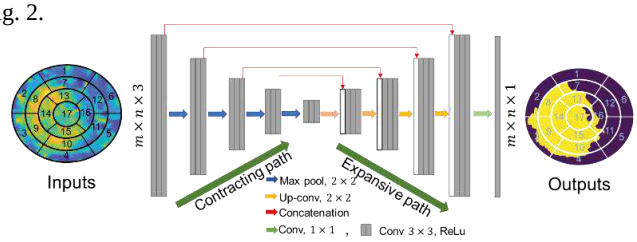

Fig 2: UNet model employing cardiac strains as input and generating the corresponding infarct mask as output.

Validation by human LGE-CMR. Slice deformations were assessed during the end-systole (ES) timeframe, with the end-diastolic frame serving as the reference point using $\mathbf{E} = \frac{1}{2}[\mathbf{F}^{\mathbf{T}}\mathbf{F} - \mathbf{I}]$ expression. The resulting strains were transformed into the widely accepted CRL axes using $\mathbf{E}_{[\mathbf{C},\mathbf{R},\mathbf{L}]} = \mathbf{QEQ}^{\mathbf{T}}$, where **E**, **F**, **I, and Q** represent strain, deformation gradient, identity matrix, and transformation matrix, respectively. *Validation in rodents with echo, biaxial test, and histology*. MI rats were imaged using Vevo 2100 at four timepoints post-MI. LV tissues were mounted on the biaxial tensile machine to obtain a force-displacement plot to measure stiffness. After biaxial testing, LV slices were stained with picrosirius red, and prepared slides were imaged using Olympus VS120 at 20x.

RESULTS

The UNet model predictions for infarct regions in the FE test data examples are illustrated in Fig. 3. The results highlight infarct regions with the highest and lowest DSC metric scores, demonstrating minimal variation between the predicted infarct regions and the ground truth masks even in examples with the lowest DSC scores. The overall performance of the DL model was assessed using the DSC score, resulting in a value of 0.9837. Additionally, we obtained an accuracy of 98.35%, along with sensitivity, precision, and intersection over union-score values of 0.9737, 0.994, and 0.968, respectively.

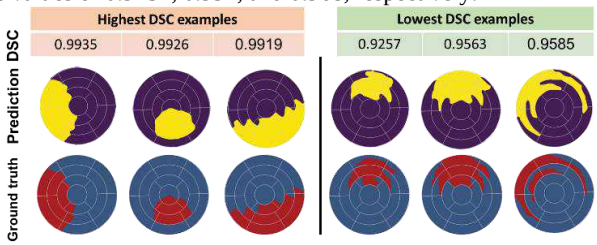

Fig 3: Visual comparison of finite element (FE) ground truth against UNet predictions.

Human LGE-CMR. We validated our proposed model by comparing the DL predictions with measurements by LGE imaging in two MI human patients (Fig. 4). We used our in-house diffeomorphic image registration to calculate 4D strains (3D + time) using only short-axis (SA) slices. End-systolic strains at each segment of AHA segmentation were provided to the DL model to classify the infarcted region. Very good agreement (DSC >0.8) was obtained compared to the estimation by LGE in both patients.

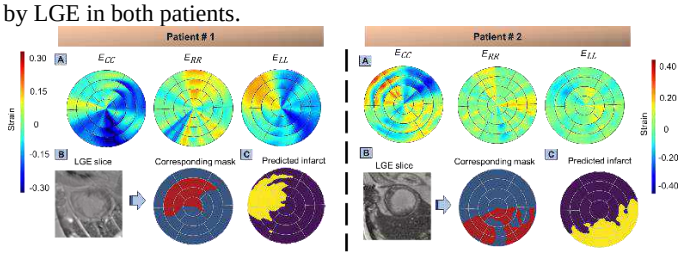

Fig 4: Cardiac CRL strains alongside DL predictions of infarct regions, compared with gadolinium contrast agent. Dice similarity coefficient (DSC) scores for the first and second patients are 0.8084 and 0.8149.

Validation in rodents using echo. The possibility of estimating scar properties from echo strains (Fig. 5a,b) significantly broadens the applicability of our approach due to the ubiquity and affordability of echo compared to CMR. In addition, biaxial testing and histology images in rodents provide the ground truth for the scar tissue stiffness and scar location in contrast to human LGE-CMR (Fig. 5c,d). We have obtained echo strains and infarcted LV myocardium properties (Fig. 5) in 30 rats (6 rats per timepoint plus controls) and are in the process of validating the prediction of our DL model for scar location and stiffness against ex-vivo measurements serving as ground truth.

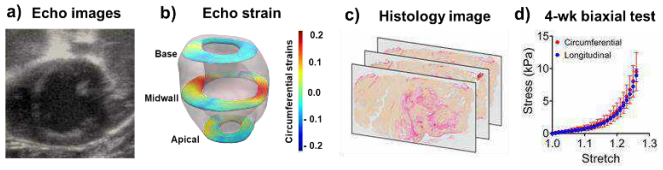

Fig. 5: Integrated validation of infarct characterization in rodent myocardium.

DISCUSSION

In this work, we developed a UNet-based DL model that capitalized exclusively on cardiac strain data as input features. The use of strains eliminated the requirement for pressure values, obviating the need for invasive procedures like catheterization to record patient pressure data. Additionally, our methodology leveraged the concept of impaired deformation at infarct locations. By seamlessly integrating cardiac strain images with DL techniques, we enabled the precise identification of infarct tissue by extracting image features. This innovative framework obviates the need for LGE.

Moreover, our approach used cardiac strains, which can be obtained from more ubiquitous and affordable imaging modalities than CMR, such as echocardiography, reinforcing cardiac strain approach generality in clinical settings. Furthermore, the comprehensive use of strain data enables the characterization of "border" zones with compromised contractility compared to the LGE-CMR approach, which can primarily locate mature scar regions, overall improving the prognostication in MI.

ACKNOWLEDGEMENTS

RA was supported by the NIH, under grant No. R00HL138288.

REFERENCES

[1] Bui, A. L. et al., *Nature Reviews Cardiology*, 8(1), pp.30-41, 2011.
[2] Wu, M.-T., et al., *Circulation*, 2(1) p. 32-40, 2009.
[3] Lintingre, P. F., et al., *Cardiovascular Imaging*, 13(5), 2020.
[4] Mendiola, EA et al., *Annals of Biomedical Engineering*, 1-18, 2022.
[5] Fox, C. S. et al., *Circulation*, 121(3), pp.357-365, 2010.

DECIPHERING CARDIAC ALLOGRAFT VASCULOPATHY: A MULTISCALE COMPUTATIONAL APPROACH TO IMPROVE HEART TRANSPLANT OUTCOMES

Elisa Serafini[1,2], Anna Corti[3*], Enrico Sangiorgio[4*], Maddalena Bovetti[4*], Diego Gallo[4], Carly S. Filgueira[5], Xian C. Li[6,7], Claudio Chiastra[4], Stefano Casarin[1,2,7]

(1) LaSIE, UMR 7356 CNRS, La Rochelle Université, La Rochelle, France

(2) Center for Precision Surgery, Houston Methodist Research Institute, Houston, Texas, USA

(3) LaBS, Politecnico di Milano, Milan, Italy

(4) PolitoBIOMed Lab, Department of Mechanical and Aerospace Engineering, Politecnico di Torino, Turin, Italy

(5) Nanomedicine, Houston Methodist Research Institute, Houston, Texas

(6) Immunobiology and Transplant Science Center, Houston Methodist Hospital, Houston, Texas

(7) Department of Surgery, Houston Methodist Hospital, Houston, Texas

*These authors contributed equally to the work

INTRODUCTION

Cardiac Allograft Vasculopathy (CAV) is a coronary artery disease affecting 50% of heart transplant (HTx) recipients, it is the major cause of graft chronic rejection [1], and it is associated with a 30% 5-year mortality [2]. CAV is characterized by a strong inflammatory response triggering a cascade of vascular remodeling processes that ultimately lead to coronary arteries' narrowing, impaired blood flow and graft failure [3]. The poor long-term outcome in CAV management results from an incomplete understanding of the disease initiation mechanisms, making CAV prevention challenging and impairing treatments' effectiveness. The morphology of coronary arteries has been identified as a critical factor influencing vascular response and, consequently, HTx long-term outcome [4]. However, a detailed morphometric characterization of coronary geometry and a comprehensive understanding of how morphology quantitatively affects vessel fate during CAV is lacking. So far, animal studies, mainly based on mouse models, have been extensively used to investigate CAV [2], and have identified inflammation and hemodynamics as the main triggering stimuli. Although informative, *in vivo* studies have limitations such as high time and resource consumption, animal welfare concerns, paucity of investigation time points, and challenges in addressing the pathology multiscale nature. Integrating *in vivo* with *in silico* approaches can overcome these drawbacks and generate more informative models, thus enhancing *in vivo* studies' efficacy. We, therefore, hypothesize that an integrated *in vivo – in silico* approach will optimize anti-chronic rejection research pipeline. Additionally, a thorough morphological measurements' portfolio from mouse model is currently missing in literature, although pivotal to understand how morphology impacts post-transplant follow-up and to feed ad hoc computational models focused on pre-clinical research. Accordingly, we i) generated a portfolio of morphological measurements from mice's coronary artery trees to enrich our understanding of how geometry influences CAV development, and ii) developed a mouse-specific multiscale computational model of CAV formation and progression to study in real time the pathology progression and predict long-term vascular outcome.

METHODS

The project workflow is illustrated in Figure 1. Via *ex vivo* protocol on C57BL/6 mouse models (5-8 weeks, 16.5 g weight), the hearts were perfused with Microfil and fixed in 10% formalin, making the coronary vessels suitable for visualization through µCT-imaging. The µCT technique (SkyScan1276 at 55kV, 200µA, pixel size 10 µm) allowed imaging the hearts (*n = 10*) including both cardiac tissue and microfilled-coronary vessels. The left coronary artery (LCA) was 3D reconstructed through 3 semi-automatic steps: i) segmentation of cardiac tissue in ITK-SNAP software; ii) segmentation of coronary tree via filtering, thresholding and binarization, and iii) retention of the first-K largest volumes in Bruker CTAn Micro-CT software (K spans between 5 and 7 depending on the initial number of volumes). Once reconstructed, LCA geometries were freed from artifacts and smoothened by shrink-wrap technique developed in Ansys SpaceClaim. Subsequently, geometries were subjected to centerline-based morphometric analysis (i.e., branches' and bifurcations' angles, cross-sectional area, curvature, and torsion) and to preliminary simplified CFD simulations. The latter required initialization of mouse-specific blood properties, LCA inlet-velocity profile and the application of intraspecific flow-diameter scaling-laws to properly provide flow partition through the coronary tree [5]. In parallel, an idealized 2D Agent-Based Model (ABM) of CAV [6] was developed to simulate

arterial wall response to inflammation (i.e., leukocyte infiltration, chemoattractant release) and hemodynamic disturbances (i.e., low wall shear stress (WSS)) over 4-weeks of follow-up. Through the implementation of probabilistic rules, these stimuli triggered inflammatory cell activation and exacerbated vascular cell activities. Moreover, an extensive analysis was performed to investigate the ABM sensitivity to the driving parameters (i.e., Latin hypercube sampling based-sensitivity analysis), inputs (i.e., test scenarios with single stimulus, combined stimuli, and stimuli along with main events) and to gain insights into the ABM working mechanisms (i.e., CAV manifestations).

RESULTS

The Microfil perfusion and 3D geometrical reconstruction showed that the same line of mice presents visible different coronary tree structures and degree of complexity. However, the preliminary intra- and inter-sample morphometric analysis reported a consistency in i) branches' angles ([61.9922º ± 11.5532º]) (ii) bifurcation angles ([49.9430º ± 14.0852º]); and iii) decreasing cross-sectional areas from the main inlet toward the outlet's artery (max: 0.0470 ± 0.0050 mm^2, min: 0.0015 ± 0.0002 mm^2) (Figure 2a).

The *solo* 2D ABM was able to effectively replicate a 4-week CAV initiation and progression, characterized by symmetric and non-symmetric lumen area decrease due to progressive intimal thickening in regions exposed to high inflammation and low WSS. Both the scenario testing and CAV manifestations identified three classes of artery response characterized by a slight lumen area decrease (<20%), a moderate lumen area decrease (20%–40%), and a severe lumen area decrease (>50%) (Figure 2b). Moreover, the parameter and input sensitivity analysis highlighted that the inflammatory-related events rather than the WSS predominantly drive CAV, corroborating the inflammatory nature of vasculopathy.

DISCUSSION

The preliminary results of the morphometric analysis performed on mouse coronary tree, along with the ABM insights, fill a fundamental gap of knowledge in CAV literature. Furthermore, these findings pave the way to justify why CAV manifests with different severity in vessels close to each other, since different morphological features (e.g., branches' and bifurcations' angles, or cross-sectional area) can explain different vessel fates. In conclusion, our ABM, scaled-up to a quasi-3D level, and enriched with realistic cross-sectional geometry, mouse-specific blood properties and CFD-derived hemodynamic profiles, represents a versatile tool to elucidate CAV onset and progression on a multiscale perspective, ultimately optimizing preventive pathology research.

ACKNOWLEDGEMENTS

We acknowledge Carly Filgueira's Lab (Antonio Martino, Blake Fallon) from the Department of Nanomedicine, Houston Methodist Research Institute (Houston, Texas) for their contribution in the animal studies.

REFERENCES

[1] Khush, K. et al., *J. Hear. Lung Transpl.*, 2019
[2] Agarwal, Shikhar et al., *JACC.*, 2014
[3] Pober, J. S. et al., *Cardiovascular research.*, 2021
[4] Ciri, U., Bennett, R.L., Bhui, R. et al., *Sci Rep*, 2021
[5] Huo and Kassab, *J.R. Soc. Interface*, 2012
[6] Serafini, E. et al., *Front. Bioeng. Biotechnol.*, 2023

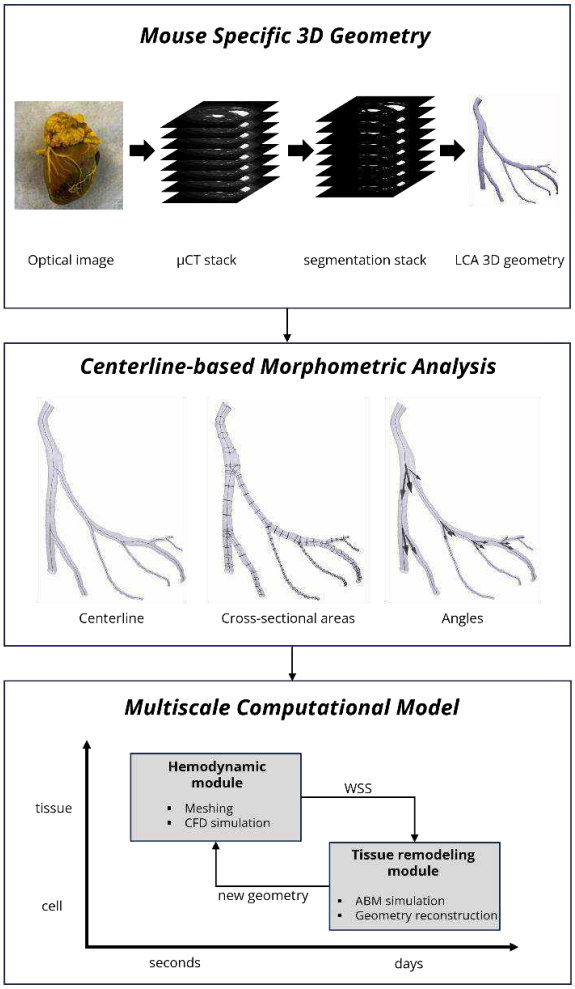

Figure 1: Mouse-specific 3D geometry reconstruction, centerline-based morphometric analysis, multiscale computational model.

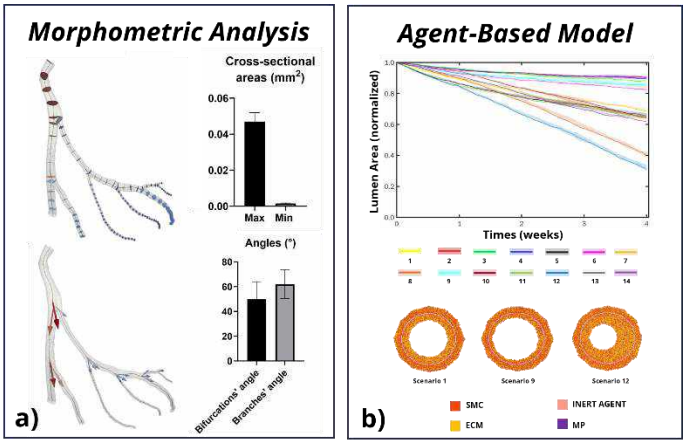

Figure 2: a) cross-sectional areas and angles, b) normalized lumen area over 4-week of the 14 explored ABM scenarios and three representative outcomes for three specific scenarios (i.e, scenarios 1,9,12).

Characterization of microstructural changes on biglycan/decorin induced mouse bone by low-field NMR

Q. Ni (1), A. Tinajeor (1), R. Hura (2), J X. Jiang (2) and X Wang (3)

(1)Texas A&M International University, Laredo, TX, USA
(2)The University of Texas Health Science Center, San Antonio, TX, USA
(3)The University of Texas at San Antonio, San Antonio, TX USA

INTRODUCTION

Previous study has revealed that water in bone is present in three different conformations; namely freely mobile water in pores; bound water at surfaces and/or within the mineral and collagen phases; and structural water as part of collagen and mineral molecules [1]. Evidence shows that water may also play a major role in viscous response of bone, most likely *via* the so-called sacrificial bonding mechanism. In fact, hydration status significantly affects the toughness of bone, and bound water has been considered as a biomarker for prediction of bone fragility fractures. In addition to the collagen phase, recent evidence shows that glycosaminoglycans (GAGs) of proteoglycans (PGs) in the extracellular matrix also play a pivotal role in regulating the tissue-level hydration status of bone, there by affecting the tissue-level toughness of bone. And biglycan and decorin are two major types of PGs in bone reports. Biglycan/decorin knockout induced changes in GAGs, bound water, as well as bone tissue toughness. Among all subtypes of PGs, biglycan and decorin are identified as a major subtype in the bone mineral matrix [3]. In this study, we used a biglycan/decorin knockout mouse model and the obtained bone samples were measured by low-field nuclear magnetic resonance (NMR) to determine the bone porosity and bound water changes and used to predict if knockout of biglycan/decorin may affect the amount of bound water and subsequently lead to reduce toughness of bone. The technique of low-field pulsed proton NMR spin relaxation is described for assessment of structural changes of normal and disuse (biglycan/decorin knockout) mice bone in situ. This technique involves spin-spin relaxation measurement and inversion spin-spin relaxation spectral analysis methods [2].

METHODS

A total of 24 mouse leg bone specimens with 6 in control (WT), 6 in biglycan knockout, 6 in decorin knockout, and 6 in biglycan/decorin double knockout were obtained from 6 month-old male and the samples were prepared by UTSA/UTHSCSA. The animals were sacrificed at the age of 6 months and the bone soft tissues were dissected and stored in -80 ^{o}C; and prior to NMR measurements, the samples were completely thawed at room temperature. A low-field NMR spectrometer (Bruker 20 MHz) was set up at a proton frequency of 20 MHz for these measurements. ^{1}H spin-spin (T_2) relaxation profiles were obtained by using NMR CPMG $\{90^0 [-\tau- 180^0 -\tau- (\text{echo})]_n - T_R\}$ spin echo method with a 6.5 s wide 90^{o} pulse, τ of 500 μs for mouse bone and T_R (sequences repetition rate) of 15 s. Each T_2 profile, one thousand echoes (one scan with n = 1000) were acquired and sixty-four scans were used. Thus, one scan will have repeated 1000 echoes in the window. For each FID profile, 1000 data points were acquired in one scan (an approximate 2 ms delay window). The data was measured on fresh frozen leg tissues after complete thawing in the room temperature (21 ± 1^{o}C). The full water saturated bone tissues were used for CPMG measurements, and free air dried (mobile water removed) bone tissues were used for FID measurements.

RESULTS

Comparison of disuse mouse leg bone group with control leg bone group, the significant differences are found. For example, in Figure 1, from the inversion NMR CPMG relaxation data spectra (samples are full saturated) the porosity, and the

pore size differences for samples between the control WT and the disuse KO are clearly observed. From the example of inversion FID spectrum, after the mobile water was removed by free air dry, only two water peaks are observed with left first is solid-like component and second is bound water component in Figure 2. From low-field NMR measurement, the relative amount of bound water was then estimated as the ratio of the total intensity of bound water signal with respect to the total intensity of the solid-like from water signal (representative of bone mass because in these sample measurements, the solid form proton signal intensities were correlated with the sample mass weights) of each sample.

The estimated results for ratio of the bound water to solid-like water were calculated. In addition, our previous results showed that the number of GAGs and bound water in bone matrix was significantly reduced in KO mice compared with WT mice [4]. These *in situ* results indicate that coupling with water biglycan/decorin is apparently one of PGs in bone mineral matrix that plays a key role in sustaining the toughness of bone. Our recent study demonstrates that loss of GAGs may significantly reduce the tissue-level toughness of bone and such effects are most likely induced by the associated loss of bound water in bone matrix [5], and the results show the similarity as that among the age-related ultrastructural changes, the loss of bound water in bone matrix with significant reduction of the toughness of bone. Based on the aforementioned evidence, it could be conjectured that changes in matrix GAGs may contribute to the deterioration of bone quality. Studying mice with targeted Bgn/Dcn disruption has revealed the involvement of Bgn/Dec in the regulation of postnatal skeletal growth. Bgn/Dcn deficiency may lead to bone porosity increase, bone bound water decrease and bone biomechanical strength changes.

From these mice groups study, the average of the porosity in control group is 27.27% (±4.64%), the average of the porosity in biglycan knockout group is 33.93% (±8.16%), the average of the porosity in decorin knockout group is 36.36% (±12.3%), the average of the porosity in biglycan/decorin deficient group is 34.46% (±10.6%).

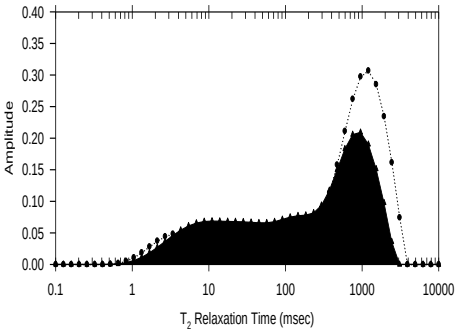

Figure 1. Inversion CPMG T_2 relaxation time spectra for mouse WT and KO leg bones. The high intensity is for KO (●), with porosity 37.7%, and the low intensity (▲) is for WT, with porosity 21.33%, respectively, measured by low-field NMR.

Fig. 2 shows the example of inversion FID spectrum, after the mobile water is removed by free air dry. It is because in mice bone tissues the mobile water signal is overwhelming than the bound water signal, and the mobile water is not the interesting at this moment. Therefore, only two water peaks are observed with left first is solid-like component and second is bound water component. From low-field NMR measurement, the relative amount of bound water is then estimated as the ratio of the total intensity of bound water signal with respect to the total intensity of the solid-like water signal (representative of bone mass because in these sample measurements, the solid form proton signal intensities are correlated with the sample mass weights) of each sample.

As the results, the average of the ratio of bound water to solid-like water in control group is 2.662 (±0.548), the average of bound water to solid-like water in biglycan knockout group is 1.897 (±0.528), the average of bound water to solid-like water in decorin knockout group is 2.005 (±0.324), and the average of the bound water to solid-like water in biglycan/decorin deficient group is 1.883 (±0.476). And the samples mechanical test is planned underway.

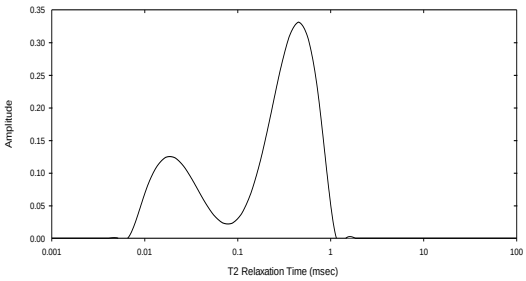

Figure 2. Example of inversion FID T_2 relaxation time spectra for mouse, measured by low-field NMR. The peaks from left to right are solid-like water and bound water, respectively.

ACKNOWLEDGEMENTS

Supported by TAMIU internal grant and NIH R01 grant AR076190 (JXJ, QN, XW) and Welch Foundation Grant AQ-1507 (JXJ); NSF Major research instrument grant 0820919 (QN) for low-field NMR system.

REFERENCES

[1] Horch, et a (2010), Magn Reson Med 64 (3)
[2] Ni et al (2007) Measurement Science and Technology 18, 715-723.
[3] Morgan et al, (2015) Calcif Tissue Int. 97(3).
[4] Hua R, Ni Q, Eliason T. D., Han Y, Gu S, Nicolella D, Wang X, Jiang J. Biglycan and chondroitin sulfate play pivotal roles in bone toughness via retaining bound water in bone mineral matrix. Matrix Biology. 2020: 94:95-109.
[5] Wang X., Xu, H., Huang Y., Gu S., Jiang J. X. Coupling effect of water and proteoglycans on the in situ toughness of bone, J Bone Miner. Res 2016 31(5): 1026-1029.

ASSESSMENT OF AORTIC VALVE STENOSIS USING A NOVEL FUNCTIONAL INDEX: A PILOT PROSPECTIVE STUDY FOR TRANS-CATHETER AORTIC VALVE REPLACEMENT PATIENTS

Shreyash M Manegaonkar (1), Mohamed A. Effat (2), , Marepalli Rao (3), Rishi Sukhija (2), Rupak K. Banerjee (4)

(1) Department of Mechanical and Materials Engineering, University of Cincinnati, Cincinnati, Oh, USA
(2) Division of Cardiovascular Health and Disease, University of Cincinnati, Cincinnati, Ohio, USA
(3) Environmental & Public Health Sciences, University of Cincinnati, Cincinnati, Ohio, USA
(4) Department of Biomedical Engineering, University of Cincinnati, Veterans Affairs Medical Center, Cincinnati, Ohio, USA

INTRODUCTION

Cardiovascular disease emerges as the predominant cause of mortality in the United States reported by AHA [1], and on a global scale reported by WHO [1]. Aortic stenosis (AS) is a form of valvular heart ailment arising from the abnormal constriction of the aortic valve opening. AS is usually caused by gradual degeneration of the aortic valve, leading to an elevated occurrence of calcific aortic disease with advancing age [2]. Therefore, accurate assessment of AS severity is critical. The uncertainties and lack of precision associated with existing diagnostic parameters may lead to less-than-optimal clinical decision-making. This is particularly true for patients with low gradient (LG, $\Delta p < 40$ mmHg) AS, for whom evaluating AS can be challenging.

Benefits and drawbacks of echocardiography and cardiac catheterization has been extensively documented in the literature [3, 4]. Pressure drop across the aortic valve can be exaggerated in elevated circulatory conditions, such as those observed in sepsis, anemia, AV fistula, hyperthyroidism, liver failure and aortic regurgitation, which leads to an overestimation of the degree of stenosis.

In particular, for 'paradoxical low-flow, low-gradient (LFLG) severe AS,' the pressure drop and peak velocities remain low, despite a normal left ventricular ejection fraction (LVEF ≥ 50%). This condition underestimates the true AS severity. The *objective* of this study is to improve the accuracy of AS severity assessment, using a novel functional diagnostic parameter, Aortic Valve Coefficient (AVC: the ratio of the total transvalvular pressure drop (Δp) to the proximal dynamic pressure (1/2×blood density×V_{LVOT}^2;V_{LVOT}: left ventricular outflow peak velocity)). The *hypothesis* is that the AVC, developed from the fundamental fluid dynamics principles, will better delineate the level of AS severity, as it includes square of V_{LVOT} and downstream pressure recovery. This involves assessing the correlation and comparison with established diagnostic parameters aortic valve area (AVA) and transvalvular pressure gradient (Δp).

METHODS

This prospective study consists of 47 patients undergoing transcatheter aortic valve replacement (TAVR) procedure for AS. The study protocol was approved by the Institutional Review Board at University of Cincinnati. The consented patients were aged 65-86 years. The values of jet velocity, V_{LVOT}, and AVA were obtained from the standard Doppler echocardiography reports. Whereas Δp was obtained through catheterization. Pressure-velocity measurements were obtained pre- and post- TAVR, resulting in a total of 78 data points, with 32 of them corresponding to LG AS. The proposed diagnostic index, AVC, was calculated using mean transvalvular Δp and Doppler-derived V_{LVOT} using the following equation [5]:

$$AVC = \frac{\Delta p}{\frac{1}{2}\times\rho\times V_{LVOT}^2}$$, ρ is the density of blood (1050kg/m^3) (1)

A regression analysis was performed on the data set to correlate AVC with AVA. The correlation analysis was carried out for both LG ($\Delta p < 40$ mmHg) and for HG ($\Delta p > 40$ mmHg). Welch 2 sample t-test was performed to compare the mean values of AVC against AVA. A probability value of $p < 0.05$ was considered statistically significant. Statistical data analysis was performed using R markdown software RStudio Team (2022; RStudio: Integrated Development Environment for R. RStudio, PBC, Boston, MA).

RESULTS

Figure 1 shows the linear correlation of AVC with AVA for pre- and post-TAVR data points. The AVC, when correlated with AVA, had a moderately significant correlation ($r = 0.75$, $p < 0.001$), suggesting the feasibility of AVC as a prospective index.

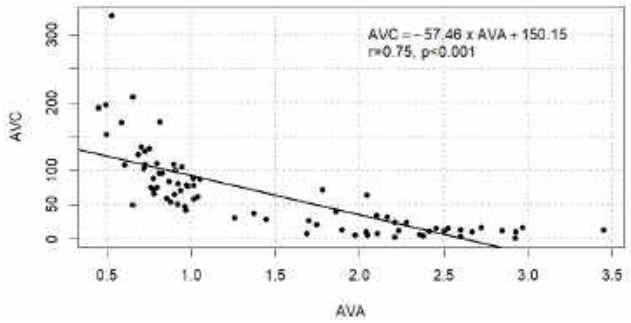

Figure 1: Correlation of AVC with AVA

Figure 2 shows the linear correlation of AVC with AVA for A) low pressure gradient (Δp < 40 mmHg) patients, and B) high pressure gradient (Δp > 40 mmHg) patients. The correlation between AVC and AVA decreased (r = 65, p < 0.001, Fig. 2A) for LG (Δp < 40 mmHg) AS patients, indicating the increased discordancy. However, AVC had a moderately significant correlation (r = 0.74, p < 0.001, Fig. 2B) with AVA for HG (Δp ≥ 40 mmHg) AS patients.

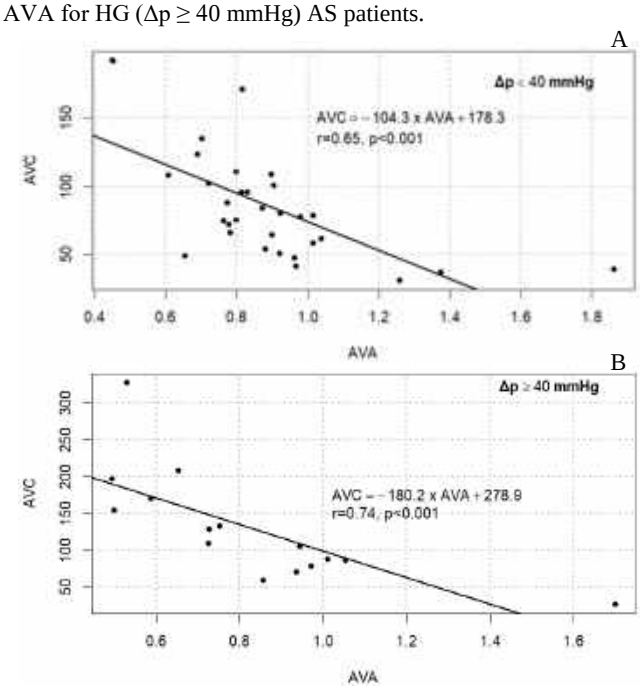

Figure 2: Correlation of AVC with AVA for A) low pressure gradient (Δp < 40 mmHg) cases, and B) high pressure gradient (Δp > 40 mmHg) cases

Comparing AVC and AVA in patients with LGAS with LVEF < 50% and LVEF ≥ 50% (Table 1), the t-test results revealed statistical significance for AVC (*p < 0.05*). In contrast, AVA demonstrated insignificant differences (p = 0.44). The 95% CI for mean values of AVA for LGAS with LVEF < 50% has a *significant overlap* with LVEF ≥ 50%. Therefore, AVC delineates LG AS better than AVA.

DISCUSSION

Misclassification commonly arises due to the pressure-recovery phenomenon in the ascending aorta [3]. The degree of pressure recovery depends on the ratio of *vena contracta area* relative to the cross-sectional area of the ascending aorta. A relatively larger pressure recovery is seen in patients with mild to moderate stenosis and smaller aortas in relation to the overall pressure gradient. Doppler measurements are taken at the *vena contracta* just distal to the aortic valve orifice, neglecting the aortic pressure recovery. In contrast, catheterization measures the pressure difference between the left ventricle and a point in the aorta well beyond the aortic valve, where pressure is generally fully recovered. Consequently, significant disparities exist between Doppler-derived and catheterization-derived pressure gradients. While Δp derived from Doppler often overestimates AS severity, the Δp measured from catheterization is typically recorded after pressure recovery, representing the net pressure drop due to AS. Therefore, AVC derived from Δp measured from catheterization is expected to be superior to AVC obtained from Doppler derived Δp.

	Welch 2 Sample t test			
	LG AS			
	AVC		AVA	
	LVEF < 50%	LVEF >= 50%	LVEF < 50%	LVEF >= 50%
MV ± SD	116.9 ± 11.9	72.2 ± 5.5	0.83 ± 0.06	0.91 ± 0.05
95% CI	93.1 – 140.8	61.2 - 83.2	0.71 - 0.9	0.81 – 1.0
p value	**p* < 0.05**		p = 0.44	

Table 1: Comparison of mean values of AVC and AVA

It is commonly known through the literature that the mean pressure gradient (Δp) and flow rate relationship is non-linear: $\Delta p = A \times V + B \times V^2$ for the flow through constrictions such as arterial lesions and valvular stenosis, Here, A represents the linear coefficient of viscous (frictional) loss, and B is the nonlinear coefficient of pressure loss attributable to momentum change resulting from area reduction [6].The flow becomes transitional (laminar to turbulent) at higher Reynolds number values, ~ 5000, which are frequently observed in the human ascending aorta [7]. When the flow is transitional to turbulent, the nonlinear pressure loss resulting from the aortic stenosis-induced momentum change usually exceeds the linear pressure loss resulting from viscous effects.

Hence, it is important to note that the AVC, a non-dimensional diagnostic parameter, better accounts for the non-linear pressure loss due to having V_{LVOT}^2 in denominator. Furthermore, AVC can enhance assessment of AS severity assessment and aid in clinical decision-making for AS patients.

Study Limitations. The primary limitation of this pilot study was the unavailability of directly measured V_{LVOT} from the cardiac catheterization. Hence, AVC was calculated using Doppler measured V_{LVOT}. Furthermore, the measure of non-linearity can be better evaluated by using the log-transformation; thereby, improving the correlation between AVC and AVA.

REFERENCES

[1] Santulli, G. et al., JCvD. 2013;1(1):1-2.
[2] Manenti A. et al., JCvD. 2015;3(2): 316-319.
[3] Bonow RO et al., J Am Coll Cardiol. 2006; 48(3):e1-148.
[4]Baumgartner H et al., Journal of the American Society of Echocardiography. 2009; 22(1):1-23.
[5] K. Paul, A. et al., Journal of Advances in Medicine and Medical Research, 8(2), pp. 177-191.
[6] K. L. Gould et al., Circulation Research, vol. 43, no. 2, pp.242–253, 1978.
[7] P.D. Steinand, et al., CirculationResearch,vol.39,no.1,pp.58–65,1976

TOWARDS CANCER MECHANO-THERAPY: YAP AS AN EMERGING MECHANICAL TARGET TO ERADICATE TUMORS

Miao Huang (1,2), Mu Yu (2,3), Chase Stallings (4), Heyang Wang (5), Lu Li (2,6), Conner M. Traugot (2,6), Mingyi Xie (2,6), Youhua Tan (7), Franziska Haderk (8), Juan Guan (9), Lizi Wu (2,3), Xin Tang (1,2)

(1) Department of Mechanical & Aerospace Engineering (MAE), University of Florida (UF), Gainesville, FL 32611, USA
(2) UF Health Cancer Center (UFHCC), University of Florida (UF), Gainesville, FL 32611, USA
(3) Department of Molecular Genetics and Microbiology, University of Florida (UF), Gainesville, FL 32611, USA
(4) Department of Biology, University of Florida (UF), Gainesville, FL 32611, USA
(5) Department of Mechanical Engineering, Northwestern University, Evanston, IL 60201, USA.
(6) Department of Biochemistry and Molecular Biology, University of Florida (UF), Gainesville, FL 32611, USA
(7) Department of Biomedical Engineering, The Hong Kong Polytechnic University, Hong Kong, China
(8) Department of Medicine, University of California, San Francisco; San Francisco, CA, USA
(9) Department of Chemical Biology & Medicinal Chemistry, University of Texas at Austin, Austin, TX 78712, USA

INTRODUCTION

A grand challenge in human cancer therapies is to eliminate the drug resistance of cancer cells. To date, even the most effective targeted therapies are not able to completely eradicate the entire tumor, mainly because a subpopulation of cancer cells persistently acquires drug resistance and tirelessly re-develops diseases after the treatments. As a result, high cancer mortality rates have been causing societal burdens worldwide. Hence, we are in dire need of innovative approaches that can eliminate drug resistance. In this talk, I will introduce our recent findings that multiple types of human lung cancer cells, especially EGFR-mutated non-small cell lung cancer (NSCLC) subtypes, dramatically alter their sensitivity and response to mechanical force indicated by Yes-associated protein (YAP) throughout the process of drug treatments. I will discuss our newly developed mechanobiology strategies to apply forces in cancer cells and to promote death of drug-resistant cancer cells.

Human lung cancer contributes to the highest morbidity (22%) within all cancer types, with NSCLC as the most common subtype (85%). EGFR mutation occurs in 50% of Asian NSCLC patients and 10%–16.6% of Caucasian NSCLC patients [1]. Pharmacological targeted therapies including EGFR tyrosine kinase inhibitors (TKI) have been applied in clinical and show enhanced survival (from 29.77 months to 22.97 months) [2]. However, for all generations of EGFR TKI from 1st to 3rd generation, patients gain drug-resistance after a median period of 10–18.9 months [3]. During the acquirement of drug-resistance, YAP nuclear translocation and activation are necessary [4]. Unfortunately, none of the current YAP inhibitors are clinically effective due to their high required dosage and poor selectivity [5]. Therefore, besides pharmacological approach, new methods are needed to reduce YAP-mediated drug-resistance. Independent of conventional Hippo pathway, abnormal tumor microenvironment applies elevated mechanical stimuli to tumor cells and alters YAP nuclear translocation and activities [6,7].

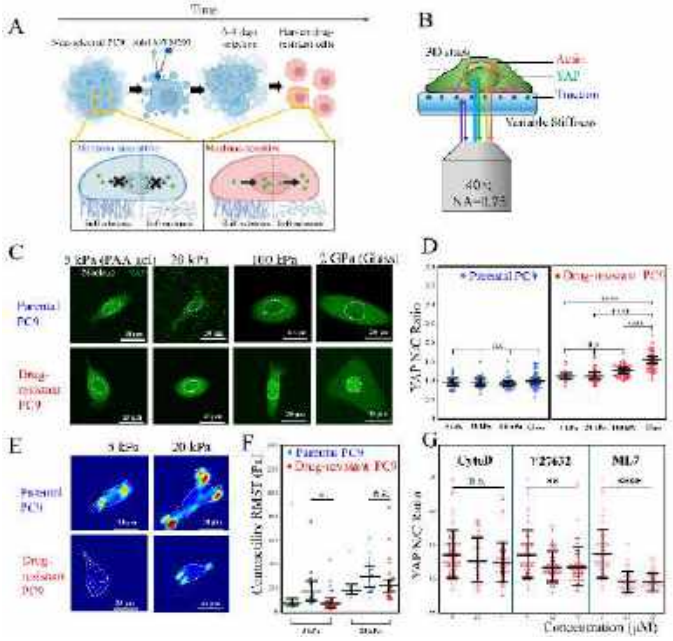

Figure 1: Drug-resistance NSCLC (PC9) cells show increased YAP mechanosensitivity. (A) Schematic of EGFR-TKI selection process and differential YAP mechanosensitivity in drug-resistant cells. (B) Schematic of multi-channel imaging to quantify YAP translocation, actin cytoskeleton structure and contractility. (C) Representative image of YAP translocation in parental and drug-resistant PC9 cells. (D) Quantification of YAP N/C ratio shows no YAP translocation on various substrate stiffness in parental PC9 and significantly increased YAP nuclear translocation in drug-resistant PC9 (YAP N/C ratio = 1.12 on 5 kPa, YAP N/C Ratio = 1.54 on glass,

p = **). (E) Representative image of contractility in parental and drug-resistant PC9 cells. (F) Quantification of root mean square of traction shows decreased (p = *) and similar contractility (p = non-significant) in drug-resistant cells on 5 kPa and 20 kPa substrate, respectively. (G) Pharmacological inhibition of contractility inhibits YAP nuclear translocation in drug-resistant PC9 cells.**

Therefore, mechanical regulation of YAP provides new potential in inhibition of drug-resistance. However, how drug-resistant cancer cells uniquely sense and respond to mechanical signals remains unclear. Our result is the first data that show (1) altered YAP mechanosensitivity of drug-resistant cancer cells; (2) mechanical cyclical stretching can kill 50% of the drug-resistant cancer cells.

METHODS

To quantify the real-time translocation of YAP, we use CRISPR/Cas9-engineered human NSCLC PC9 cells that enable endogenous YAP be tagged by fluorescence protein mNeonGreen21-10/11. PC9 cells are cultured in 35-mm glass-bottom petri dish. Drug-resistant PC9 cells are selected by culturing with 3rd generation of EGFR TKI Osimertinib (AZD9291; 2 μM) for 6–9 days **(Fig. 1A)**. Nuclear/cytoplasmic translocation of YAP is quantified by high-resolution confocal fluorescence imaging throughout the manipulation of the nucleus [8,9,10]. Quantification of mechanical contractility is conducted by traction force microscopy (TFM) on polyacrylamide hydrogels (5 kPa and 20 kPa). YAP imaging with inhibition of contractility is done after 72 hours of application of CytoD, Y27632 and ML7. Uniaxial cyclical stretching of cells is performed on customized PDMS membrane by stretching machine at 0.5 Hz and 13% strain for 20 hours **(Fig. 2A)**. Viability is quantified by flow cytometry with EthD-1 and Propidium Iodide as dead markers.

RESULTS

First, we quantify the mechanosensitivity of YAP in both parental and drug-resistant PC9 cells **(Fig. 1B)**. Different from the conventional findings in most cell types [6,11,12], our results show that, in parental PC9, YAP shows no mechanosensitivity on different substrate stiffness from 5 kPa to glass (~3 GPa). In contrast, drug-resistant PC9 cells show upregulated YAP nuclear translocation on stiffer substrate **(Fig. 1C and D)**. This is the first data showing increased mechanosensitivity of YAP in drug-resistant cancer cells.

Next, to investigate the reason for the increased YAP mechanosensitivity, we measure the cytoskeleton contractility which is considered as an upstream mechanical regulator of YAP **(Fig. 1B)** [11,12,13,14]. On 5 kPa and 20 kPa substrate, drug-resistant PC9 shows significantly lower (p = 0.029) and similar contractility, respectively **(Fig. 1E and F)**. However, in drug-resistant PC9 cells, pharmacological inhibition of contractility (by CytoD, Y27632 and ML7) still can inhibit the YAP translocation **(Fig. 1G)**. This indicates that although contractility is the mechanical regulator of YAP in drug-resistant PC9 cells but is not responsible for the increased YAP mechanosensitivity after AZD9291 treatment.

Finally, based on the increased YAP mechanosensitivity in drug-resistant PC9, we use mechanical cyclical stretching to inhibit YAP and kill the drug-resistant cells. By applying uniaxial cyclical stretching (0.5 Hz, 13% strain) to drug-resistant cells for 20 hours **(Fig. 2A)**, we observe decreased YAP nuclear translocation, decreased viability and a positive correlation (correlation coefficient = 0.82) between YAP N/C ratio and viability **(Fig. 2B)**. Specifically, cell viability and YAP N/C ratio are the lowest with cyclical stretching only **(Fig. 2C–F)**.

DISCUSSION

To our knowledge, this research is the first investigation to show increased YAP mechanosensitivity in drug-resistant cancer cells. Importantly, our data show that the drug-resistant NSCLC cells, which are not sensitive to EGFR TKI, can be mechanical killed up to 50%. Our results suggest that cyclical stretching, and other mechano-based therapies may help eradicate the drug-resistant cancer cells in clinical. Note that whether/which chemotherapy should be applied with mechanotherapy needs to be determined carefully **(Fig. 2D)**.

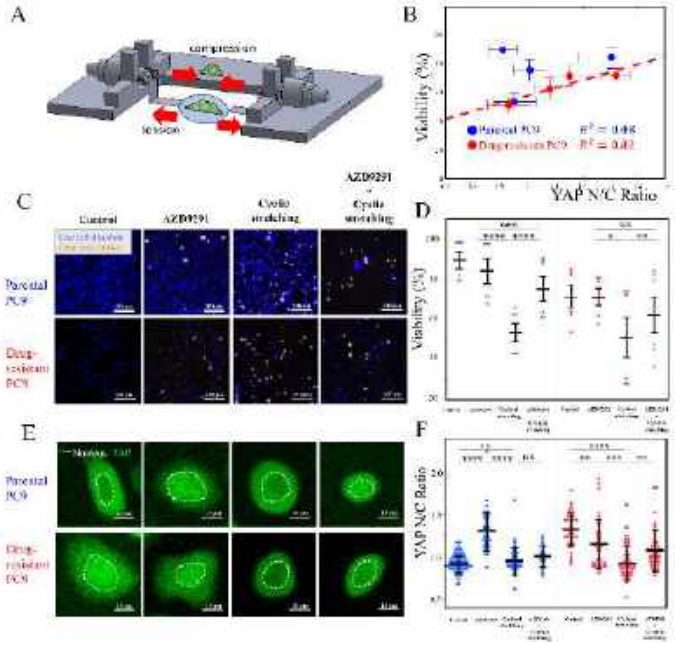

Figure 2: Mechanical cyclical stretching kills drug-resistant NSCLC cells. (A) Customized stretching machine applies uniaxial cyclical stretching on cells. (B) Positive correlation (R^2 = 0.82) between viability and YAP N/C ratio in drug-resistant cells. (C) Viability (51%) is significantly lower with only cyclical stretching applied (p=* compared with AZD9291 only, p= compared with combination of AZD9291 and cyclical stretching). (C) YAP N/C ratio (0.93) is significantly lower with only stretching applied (p=*** compared with AZD9291 only, p=** compared with combination of AZD9291 and cyclical stretching).**

ACKNOWLEDGEMENTS

This project is financially supported by the National Institute of General Medical Sciences of the National Institutes of Health under award number R35GM150812 (X. T.), the National Science Foundation under grant number 2308574 (X. T.), the Air Force Office of Scientific Research under award number FA9550-23-1-0393 (X. T.), the UFHCC Pilot Award (X. T. and Dr. Dietmar Siemann), UFHCC University Scholars Program (H. Y. Wang), UF Research Opportunity Seed Fund (X. T.), and the Gatorade Award (X. T.).

REFERENCES

[1] Siegel, R. L et al., *Ca Cancer J Clin*, *71*(1), 7-33. 2021
[2] Yu, X et al., *Cancer Medicine*, *12*(5), 5630-5638.
[3] Wu, L et al., *Frontiers in Oncology*, *10*, 602762. 2020
[4] Lee, J. E et al., *Biochem Bioph Res Co*, *474*(1), 154-160. 2016
[5] Liu-Chittenden, Y et al., *Genes Dev*, *26*(12), 1300-1305. 2012
[6] Zhao, B et al., *Genes & development*, *22*(14), 1962-1971, 2008
[7] Zanconato, F et al., *Cancer cell*, *29*(6), 783-803, 2016
[8] Luo, Q et al., *J Vis Exp*, (178), e62934. 2021
[9] Liang, C et al., *Biomaterials*, *290*, 121823 2022
[10] Luo, Q et al., *Plos one*, *17*(7), e0266098. 2022
[11] Xin, Y et al., *Oncogene*, 1-34, 2023
[12] Liang, C et al., *Soft Matter*, *18*(6), 1112-1148, 2022
[13] Huang, M et al. *Int. J. Mol. Sci.* 24.15, 12491, 2023
[14] Elosegui-Artola, A et al., *Cell*, *171*(6), 1397-1410, 2017

ESTIMATING SEVERE INJURY RISK TO HUMAN CERVICAL SPINE USING SCALED HEAD KINEMATIC RESPONSE FROM NON-HUMAN PRIMATE

Jesse W. Gerringer (1,2), Karthik Somasundaram (1,2), Frank A. Pintar (1,2)

(1) Joint Department of Biomedical Engineering, Medical College of Wisconsin and Marquette University, Milwaukee, WI, USA
(2) Neuroscience Research Facility, VA Medical Center, Milwaukee, WI, USA

INTRODUCTION

Not much is known about the dynamic limits of survivability of humans during frontal impact [1]. However, severe, yet survivable cervical spine injuries are rare, and recovery is extensive [2]. To date, anecdotal cases of survivable, and not survivable, frontal impacts provide only limited information on the potential c-spine dynamics of injury with many variables to consider [3,4]. Historical non-human primate (NHP) frontal impact experiments provide detailed experimental results, spanning from non-injury to severe injury and fatality [5]. It is crucial that the injury risk as a function of head kinematics is assessed, as has been done previously as a function of peak sled acceleration (PSA) and be scaled to a relative human injury risk.

Therefore, the objective of this study was to further develop and validate a ligamentous NHP head-neck model [6] and derive scaling factors from output head kinematics of the NHP model and a previously developed human head-neck model [7]. The scaling factors can then be applied to injury risk curves for respective head kinematic outputs from historical experimental frontal impact data in NHP for an initial estimate of human cervical spine injury risk.

METHODS

The first iteration of the NHP model was developed and described in full in the literature [6], but briefly described below. Model geometry was obtained from CT image data of a NHP skeleton, then meshed, and the head-neck were aligned under the assumption of a neutral head position. Ligaments of the c-spine were attached as 1D elastic spring beam elements with force vs deformation curves imported from a previously developed human head-neck model, the Global Human Body Model Consortium (GHBMC) M50 HN (50th percentile male, head-neck) [7]. These failure curves were scaled to NHP values using the ratio of NHP to human magnitudes at failure [8].

To improve the movement head-neck from the previously published model, 2D discs were constructed between the vertebral bodies from C2-T1. The discs were assigned an estimated Poisson's ratio and Young's modulus adapted from the literature to simplify the discs [9]. Additionally, the cruciate ligament was added as 1D beam elements between the skull-C2 and connected to a 2D shell transverse ligament part allowing the ligaments to interact anatomically. The 2D transverse ligament part was assigned a simplified elastic fabric material type, like the GHBMC model [7].

NHP frontal impact studies from the literature were used to validate the head-neck model [5,10]. In the original NHP experiments, their torsos were restrained to a sled, allowing the head-neck to move freely. Subjects faced the +X lab direction and were fired in the -X direction to simulate an inertial frontal impact. A six-accelerometer package was fixed directly to each subject's skull to record the acceleration in all three planes and calculate the rotational accelerations around each axis. Peak linear and angular accelerations were published publicly [10]. To assess injury threshold risk in NHPs, injury risk as a function of local head kinematics, linear head X (HeadX) and Z (HeadZ) accelerations, was computed using left and right censoring and a weibull statistical fit, as was done previously for injury risk in NHPs as a function of PSA [11]. A total of 40 animal subjects were considered, with 18 total injuries. 12 of these injuries were immediately fatal and 6 ranged from moderate to severe.

For NHP model validation, individual runs were considered for the sample sizes for a total of 57 runs between 10 G and 70 G PSA, at 10 G increments. The NHP model was driven in the -X direction at T1 using a sled pulse from the literature scaled to each PSA [11]. Peak HeadX from the model output was compared to the experimental values since peak HeadX acceleration was the most consistent head kinematic metric. The GHBMC head-neck model was simulated using the same T1 acceleration as for the NHP to replicate the same conditions for theoretical human research volunteers (HRVs). The output peak HeadX and HeadZ from GHBMC were compared to the NHP outputs to obtain

linear scaling equations to then scale the NHP injury risk curves to obtain theoretical HRV injury risk.

RESULTS

Figure 1 demonstrates the model HeadX was close to the experimental measurements for the NHP subjects. Experimental HeadX was the most consistent kinematic metric, with an overall linear behavior and R^2=0.97. For each corridor of PSA, the model output was within the standard deviation or within 15% of the lower bound with respect to the mean, except for 50 G. Model validation was limited to the reported peak kinematic data and would benefit from the full, raw data curves to perform correlative analysis. Additionally, for each corridor, sample sizes are inconsistent and range from n=3 to n=15, with an average of n=8. Nevertheless, for a simplified, ligamentous model the results are sufficient.

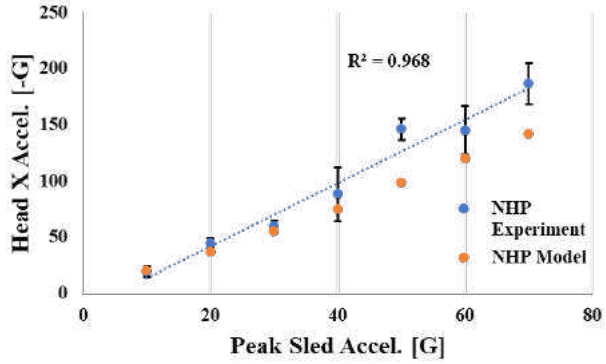

Figure 1: HeadX of the NHP model vs experimental.

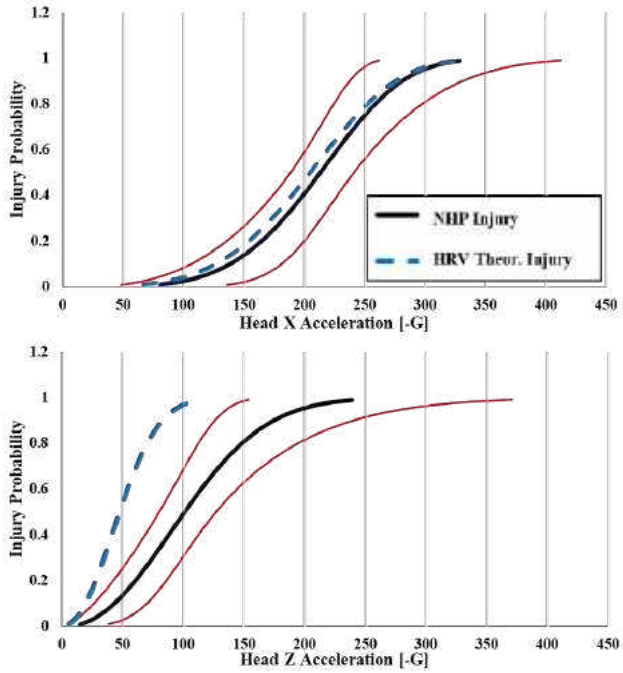

Figure 2: Injury risk probability curves for NHP and theoretical HRV as a function HeadX (top) and HeadZ (bottom).

Injury risk curves with scaled, theoretical human risk are shown in Figure 2 as a function of local head kinematics. For linear HeadX of the NHP, 50% injury risk was at 213 G, ranging from 189 to 241 G. When scaling from NHP to human, the theoretical HRV injury risk as a function of HeadX was almost matching that of the NHP. For HeadZ of the NHP, 50% injury risk was at 101 G, ranging from 80 to 127 G. When scaling from NHP to human, the theoretical HRV injury risk as a function of HeadZ was much lower at 48 G.

DISCUSSION

The scaled injury risk curve demonstrates that for a theoretical HRV subject, the 50% risk of severe injury during frontal impact occurs when the head accelerates at almost half the acceleration of a NHP in the Z direction. Using the head mass of the GHBMC M50 model [7], 4.376 kg, the total load in tension on the neck at 48 G is 2061. N. Yoga et al. reported quasistatic structural failure for isolated head-neck at a load of 1555 N ± 459 and for a human cadaver subject at 3373 N ± 464 [1]. Therefore, the 50% threshold of 48 G for a theoretical HRV injury risk is reasonable as it is between the isolated head-neck and full cadaver maximum tension forces.

A limitation of the scaled results is the lack of raw kinematic data, as stated above and therefore these results should be taken as initial estimates. Raw data would help in fine tuning the material properties to better match the model and experimental kinematic outputs. In particular, the HeadZ is overestimated in the model, ranging between 10-40 G. However, HeadZ had a larger standard deviation for each corridor and the mean peak values were inconsistent with rising PSA, making it difficult to trust the data. If the theoretical HRV simulation results are compared directly the peak HeadZ, the 50% injury risk rises to 69 G, meaning the tension on the neck would be 2962 N, which is just within the standard deviation of the maximum forces a human cadaver neck can withstand [1]. Additionally, the lack of active musculature is a limitation in the NHP ligamentous model. However, the GHBMC model kinematic outputs and ligament strains were almost identical at simulated PSA of 30 G or higher for passive and active musculature indicating the muscles do not dampen the response once the acceleration is higher enough. Muscles were activated in accordance with the authors' previous study on GHBMC muscle activation [12].

The initial scaled injury risk curves shown provide the best estimate of severe injury threshold in humans during frontal impact. With further development of the simplified NHP head-neck model, more analysis on ligament and tissue strains can yield insight into injury mechanisms and help safety system engineers create new injury prevention systems for protection at high acceleration impacts.

ACKNOWLEDGEMENTS

The simulation was completed in part with computational resources and technical support provided by the Research Computing Center at the Medical College of Wisconsin. This work was partially supported by the Department of Veterans Affairs research service and the Dr. Robert D. and Dr. Patricia E. Kern Professorship in Biomedical Engineering.

REFERENCES

[1] Yoganandan, N et al., *Med Eng Phys*, 18(4): 289-294, 1996.
[2] Freeman, MD et al., *Accid. Anal. Prev.*, 142:105571, 2020.
[3] Hall, GC et al., *World J Orthop.*, 6(3):236-243, 2015.
[4] Joaquim, AF et al., *J Spinal Cord Med.*, 37(2): 139-151, 2014.
[5] Thomas, DJ et al., *Impact Injury of the Head and Spine*, Book, 1983.
[6] Gerringer, JW et al., *J Med. Diag. and Ther.*, 7:031003-1—5, 2024.
[7] Panzer, MB et al., *Med Eng Phys*, 37:1147-1159, 2011.
[8] Pintar, FA, PhD Dissertation, *Marquette University*, 1986.
[9] Yang, H et al., *J Biomech*, 49(7): 1134-1140, 2017.
[10] Mauro, CA et al., Technical Report, *ADA173720*, 1986.
[11] Olszko, AV et al., *Traffic Inj. Prev.*, 19:S44-S49, 2018.
[12] Gerringer, JW et al., *Accid. Anal. Prev.*, 190:107157, 2023.

DIFFERENTIAL EFFECTS OF HYPERTENSION ON THE MORPHOLOGICAL, MECHANICAL, AND PHYSIOLOGIC CHARACTERISTICS OF MALE AND FEMALE HUMAN FEMOROPOPLITEAL ARTERIES

Sayed Ahmadreza Razian (1), Majid Jadidi (1), Alexey Kamenskiy (1)

(1) Department of Biomechanics, University of Nebraska at Omaha, Omaha, NE, USA

INTRODUCTION

Peripheral Artery Disease (PAD) commonly refers to the atherosclerotic blockage of the femoropopliteal artery (FPA) in the lower extremities. It manifests as leg pain, cramping, and numbness during physical exertion, and, in advanced stages, may escalate to critical limb ischemia, potentially leading to limb amputation. Hypertension (HTN) is a primary risk factor for PAD, affecting an estimated 50-90% of individuals with this condition[1].

Both HTN and PAD impact men and women but exhibit notable sex-specific differences in prevalence, pathophysiological development, clinical presentation, and treatment outcomes. Typically, PAD is diagnosed more frequently in younger men, who also tend to experience an earlier onset of HTN, compared to women[2]. Conversely, women often display atypical symptoms or may remain asymptomatic, and they face a higher likelihood of adverse outcomes, including critical limb ischemia or stroke[3].

Despite these epidemiological distinctions between PAD and HTN across sexes, the influence of sex on the morphological, mechanical, and physiologic properties of the FPAs is not well understood. Investigating these aspects could shed light on the varied impacts of HTN on PAD pathogenesis in males and females, but such analysis demands a detailed biomechanical evaluation of FPA tissues, which are seldom available. Our study aimed to compare the biomechanics of the FPA in both healthy and hypertensive conditions across matched male and female subjects, to discern their similarities and differences.

METHODS

The cardiovascular biomechanics research team at the University of Nebraska Omaha, Department of Biomechanics, performed multi-ratio planar biaxial mechanical characterizations of human FPAs from a large group of 463 donors, spanning an age range of 12 to 99 years (average age 51±18 years, 65% males)[4]. Tissues were evaluated fresh within 24 hours of procurement after obtaining consent from their next of kin. Data on age, sex, and risk factors (including HTN) were recorded, and morphological characteristics that included diameter, wall thickness, and circumferential and longitudinal opening angles were measured for each specimen (Figure 1). A total of 176 subjects were devoid of any risk factors, while 82 had only HTN (no diabetes, dyslipidemia, coronary artery disease, or smoking). Constitutive parameters for the invariant-based four-fiber-family model that accurately portrays the behavior of human FPAs in all ages[4], were determined through minimization, and a kinematics framework was used to assess the physiologic arterial characteristics that accounted for the *in situ* longitudinal pre-stretch, circumferential and longitudinal opening angles, and the internal pressures of 120/80 mmHg[5].

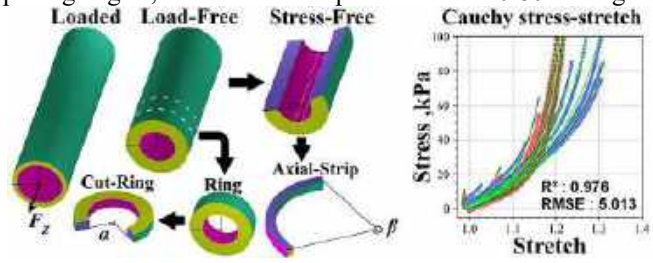

Figure 1. FPA kinematics and biaxial mechanical properties.

The initial phase of the analysis focused on comparing male and female specimens without risk factors. To ensure comparability, male and female arteries were age-matched, with a maximum age difference of 4 years between each pair. In total, 62 pairs were selected for this comparison. The average age in both groups was 36±16 years, indicating no significant age difference (p=0.97). The second phase of the analysis focused on age-matching male and female specimens each presenting a single risk factor – HTN. This process resulted in 28 matched pairs, with an average age of 54±8 years in both groups (p=0.99).

Normality and homogeneity assessments were conducted for all variables. The primary statistical analysis involved conducting an independent t-test for variables that met the normality assumptions. For data not normally distributed, the Mann-Whitney U test was utilized to compare the groups.

RESULTS

In the comparison of healthy pairs (Figure 2), men had arteries that were 12% larger in diameter (6.8mm) compared to women (p<0.01), but there was no significant difference in wall thickness (p=0.05, 1.56mm vs 1.45mm for males and females, respectively). Additionally, no significant differences were noted in either the circumferential or longitudinal opening angles between male and female FPAs (p=0.78 and p=0.85). The intrinsic mechanical properties, assessed as stretches at equibiaxial Cauchy stresses ranging from 40 to 120 kPa in 10kPa increments in both longitudinal and circumferential directions, also showed no notable differences. However, under physiologic conditions, female arteries exhibited a 40% lower axial tethering force associated with the *in situ* pre-stretch (p=0.04). Despite this, there were no differences observed in circumferential stiffness as the artery deformed from diastole to systole (p=0.21), in the elastic strain energy during both systole and diastole (p=0.21 and p=0.22), the *in situ* longitudinal pre-stretch (p=0.44), longitudinal or circumferential physiologic Cauchy stresses (p=0.21, p=0.40), circumferential cardiac cycle stretch (p=0.40), or in the circumferential physiologic stretch between diastole and systole (p=0.49).

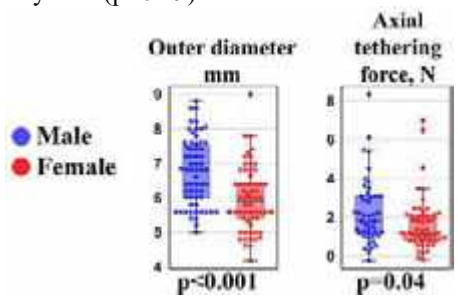

Figure 2. Differences between healthy male and female FPAs.

When comparing male and female subjects with HTN (Figure 3), the arterial diameter was 18% larger in men (7.9mm) than in women (p<0.01), but there were no significant differences in wall thickness (p=0.05), or either circumferential (p=0.24) or longitudinal opening angles (p=0.14). In terms of the intrinsic mechanical properties, FPAs from men with HTN exhibited greater circumferential stiffness compared to those from women with HTN (p<0.02), but there were no differences longitudinally (p>0.43). Physiologically, men with HTN had a 30% higher circumferential arterial stiffness compared to women with HTN (p=0.03). Nevertheless, no significant differences were found in the *in situ* longitudinal pre-stretch (p=0.44), axial tethering force (p=0.97), elastic strain energy at both systole and diastole (p=0.57 and p=0.48), longitudinal or circumferential physiologic Cauchy stresses (p=0.66, p=0.83), circumferential cardiac cycle stretch (p=0.69), or the circumferential stretch across the cardiac cycle (p=0.76).

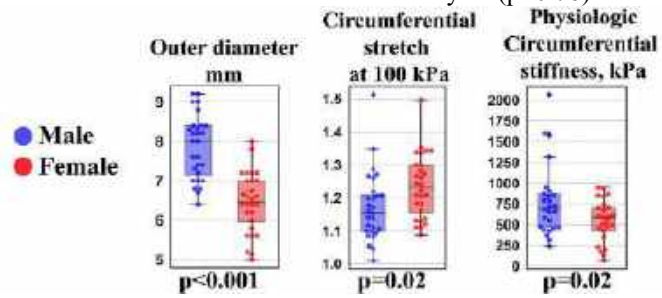

Figure 3. Differences between male and female FPAs with HTN.

DISCUSSION

Healthy males have larger FPAs compared to females, yet most other biomechanical characteristics, including intrinsic mechanical properties and physiologic features, are similar between the sexes. The notable exception is the axial tethering force associated with *in situ* pre-stretch, which is lower in females. HTN impacts male and female FPAs differently, leading to a more pronounced difference in arterial diameter and increased circumferential stiffness in male arteries. This is evident in both intrinsic mechanical properties and physiologic conditions, which take into account axial pre-stretch, opening angles, and internal pressure.

These findings enhance our understanding of the differences and similarities in vascular biomechanics of male and female arteries. This knowledge could be instrumental in developing more effective materials and devices for sex-specific treatment. Furthermore, our data elucidate the distinct effects of HTN on male and female FPAs, which could refine diagnostic methods and improve therapeutic strategies for hypertensive PAD patients of both sexes.

ACKNOWLEDGEMENTS

This work was supported in part by the NHLBI HL125736 and NIGMS P20GM152301. The authors would also like to acknowledge Live On Nebraska for their help and support, and thank tissue donors and their families for making this study possible.

REFERENCES

[1] Emdin,C et al., *Bmj*,351, 2015.
[2] Aday,A et al., *Circulation Res*, 128-12:1818-1832,2021.
[3] Jelani,Q et al., *Current Atherosclerosis Rep*,20:1-11,2018.
[4] Kamenskiy,A et al., *Biomechanics and modeling in mechanobiology*, 16:681-692,2017.
[5] Jadidi,M et al.,*Biomechics and modeling in mechanobiology*, 18:1591-1605,2019.

IMPACT OF BOUNDARY CONDITIONS AND BLOOD RHEOLOGY ON INDICES OF WALL SHEAR STRESS FROM IVUS-BASED PATIENT-SPECIFIC STENTED CORONARY ARTERY SIMULATIONS

Robert P. McCarthy (1), Peter Mason (2), David S. Marks (2), John F. LaDisa, Jr. (1,2,3,4)

(1) Biomedical Engineering, Marquette University and the Medical College of Wisconsin, Milwaukee, WI, USA
(2) Cardiovascular Medicine, Medical College of Wisconsin, Milwaukee, Wisconsin, USA
(3) Pediatric Cardiology, Medical College of Wisconsin, Milwaukee, WI, USA
(4) Herma Heart Institute, Children's Wisconsin, Milwaukee, WI, USA

INTRODUCTION

Drug-eluting and bare-metal stents have led to percutaneous coronary intervention (PCI) being the most common form of revascularization. The success of stents is limited by restenosis, resulting in >200,000 repeat PCI procedures in the US annually[1]. Late stent thrombosis (LST) may also lead to morbidity and mortality, but is less common[2]. The factors contributing to restenosis are not fully understood, but wall shear stress (WSS) indices have been implicated since stenting alters artery geometry, which may result in adverse wall shear stress (WSS)[3]. Adverse WSS also correlates with neointimal hyperplasia (NH; the main component of restenosis) and inhibits endothelialization that protects against LST.

Computational fluid dynamics (CFD) has become a valuable tool for assessment of WSS indices due to its noninvasive nature and potential for results with high spatiotemporal resolution. This is particularly important in the setting of stents with local geometric perturbations on the order of ~50 microns. CFD models employ assumptions regarding boundary conditions and rheologic properties that influence WSS indices. It is therefore important to understand the implications of these assumptions and the manner in which they manifest themselves in stent-induced coronary blood flow patterns, and to better interpret the range of WSS results in the literature. The object of this work is to assess differences in WSS indices as a result of assumptions commonly applied with CFD models of stented coronary arteries, focusing on inlet velocity profile, outlet boundary conditions, and the viscosity model.

METHODS

After IRB approval, computed tomography angiography (CTA) and intravascular imaging patient data were acquired after stenting (3.0 x 24.0 mm Synergy, Boston Scientific) of a right coronary artery (RCA) and used to create a patient-specific reconstruction. The workflow described by Ellwein *et al.*[4] for use with optical coherence tomography data was applied to the intravascular ultrasound (IVUS) data obtained in the current case (Fig 1).

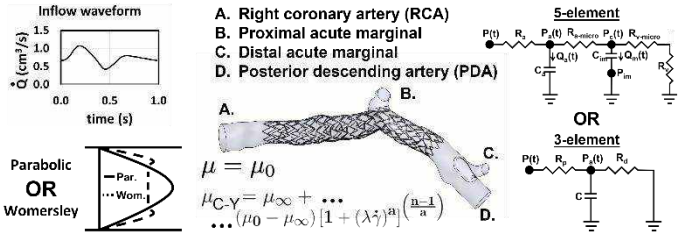

Figure 1: Overview of RCA model and assumptions applied.

Inlet and outlet boundary conditions were individually varied to measure and compare differences in WSS indices. For the inlet, the velocity flow profile was modeled as parabolic or Womersley ($\alpha = 2.5$). The inflow waveform is adopted from healthy RCA flow at rest studied by Ghorbannia *et al.*[5]. For the outlets, lumped parameter networks (LPN) were applied using electrical circuit analogs[6,7]. All outlets for a given simulation were conducted using a 3-element Windkessel model that has been applied for simplicity by ignoring the impact of ventricular contraction[8], or an open loop 5-element coronary model[9]. The resistance and compliance parameters of the 3-element LPN were initially approximated based on patient-specific clinical data and the CTA-derived geometric model, and then iteratively adjusted to yield physiologic outlet pressure and flow waveforms. Parameters for the 5-element LPN were adapted using the approach of Kim *et al.*[6] and Mantero *et al.*[7] while applying the same iterative adjustments employed for the 3-element LPN to achieve physiologic outlet pressure and flow waveforms within the constraints of each approach.

An isometric mesh composed of ~16.8 million elements was created with MeshSim™ (www.simmetrix.com) to resolve complex

flow features around stent struts. Simulations were conducting using SimVascular (simvascular.github.io), where blood was assumed to have a density of 1.06 g/cm^3 and viscosity of 4 cP. Common WSS indices of time-averaged WSS (TAWSS) and oscillatory shear index (OSI) were evaluated for the combination of inlet and outlet boundary conditions studied as shown in Fig 1. To account for the non-Newtonian behavior of blood, results were processed to compare TAWSS from simulations conducted under a Newtonian fluid assumption to those calculated using non-Newtonian viscosity based on the Carreau-Yasuda model[10].

RESULTS

Percent differences in TAWSS between the 3-element and 5-element outlet boundary conditions for a Womersley inlet profile revealed elevated values adjacent to stent struts, often exceeding 5% when coupled with perturbations in the local RCA geometry (Fig 2). This was particularly true in two locations: one along the angled inner portion of the main curve, and one where the stent intersects with the proximal branch. Percent differences in OSI were elevated throughout and proximal to the stented region with values exceeding 100% on ~50% of the lumen surface (Fig 2) with one stented region proximal to the first branch showing values of ~200%.

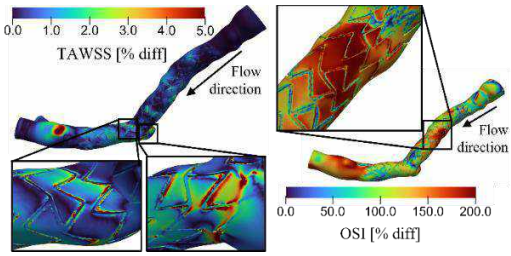

Figure 2: Percent difference in TAWSS (left) and OSI (right) between simulations employing a Womersley inlet flow profile with 3-element vs 5-element outlet boundary conditions.

Local plots of velocity magnitude in these locations shows changes in velocity profiles resulting from different outlet boundary conditions (Fig 3, left). Differences in velocity magnitude between the two inlet velocity profiles employing coronary outlet boundary conditions coincide with the time of greatest pressure difference between the two simulations (Fig 3, right). Cross-sectional slices one and two diameters downstream of the inlet show pronounced differences near the wall. Farther downstream, flow patterns emerge far from the wall distal to the proximal branch, midway into the stented region. Differences in this region persist throughout the entire cardiac cycle.

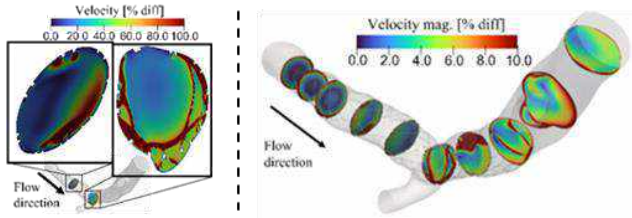

Figure 3: End systolic differences in velocity magnitude due to outlet boundary conditions (left) and inlet velocity profiles (right).

TAWSS calculated using non-Newtonian versus Newtonian viscosities show the greatest percent difference (often exceeding 100%) adjacent to stents struts (Fig 4). Differences at locations greater than one strut width away from the stent rarely exceeded 10%.

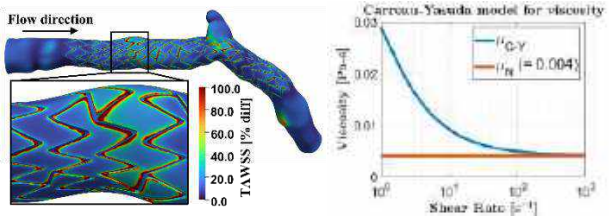

Figure 4: TAWSS percent difference (left) from the viscosity models applied with Womersley inlet flow profile and 5-element outlet boundary conditions.

DISCUSSION

Our IVUS-based patient-specific stented RCA study reveals the importance in choosing appropriate assumptions when conducting CFD simulations of stented coronary arteries. Given the relationship of WSS indices in predicting regions susceptible to restenosis, it is somewhat concerning that model results for TAWSS or OSI can differ by as much as 100-200% from a single assumption. Of note are the differences stemming from the choice of outlet boundary conditions. The 3-element LPN model adapted from literature, although simple to implement, cannot replicate the out-of-phase nature between pressure and flow in the coronary arteries since it ignores intramyocardial pressure. Differences in WSS indices presented in Figure 2 are due to changes in velocity profiles in the model, and are a manifestation of neglecting ventricular contraction, resulting in different pressure gradients during the cardiac cycle. Differences near the inlet due to the prescribed velocity profile were expected and consistent with prior literature[11] since the two types of velocity profiles impose different velocity gradients at the wall thereby resulting in different WSS values. Analysis of differences in velocity between subsequent cycles for a given inlet profile shows that the downstream differences are likely due to turbulent kinetic energy rather than the inlet profile. They can be minimized to some degree with highly resolved meshes and additional cardiac cycles, but are nonetheless an inherent part of flow features developing under complex flow conditions. The choice of viscosity model also affects the WSS indices in the stented region, which agrees with the established literature[12]. This highlights a need for flow solvers to include non-Newtonian models, particularly when characterizing stent-induced differences in WSS indices. Collectively these results suggest that certain assumptions commonly applied for simulations of stented coronary arteries have a greater impact on TAWSS and OSI than others, with outlet boundary conditions being paramount, followed by viscosity model and inlet velocity profile.

ACKNOWLEDGEMENTS

The authors gratefully acknowledge the clinical support of Mary Wexler, Shelley Schultz, Sue Cotey and Nicole Lohr.

REFERENCES

[1] Bønaa, K, et al., *N Engl J Med* 375.13:1242-1252, 2016.
[2] Yeo K et al., *Cath Cardiovasc Int*. 79:550-6, 2012.
[3] Koskinas, K et al., J Am Coll Cardiol . 59.15:1337-1349, 2012.
[4] Ellwein, L et al. *Cardiovasc Eng Techn* 2:212-227, 2011.
[5] Ghorbannia, A et al. *J Biomech Eng* 143.5:051011, 2021.
[6] Kim, H et al. *Ann Biomech Eng* 38:3195-3209, 2010.
[7] Mantero, S, et al. *J Biomech Eng* 14.2:109-116, 1992.
[8] Chiastra, C et al. *J Biomech* 49.11:2102-2111, 2016.
[9] Razavi et al. *Semin. Thorac. Cardiovasc. Surg*., 33.1:155-167, 2021.
[10] Cho, Y, and Kensey, K, *Biorheology* 28.3-4:241-262, 1991.
[11] Myers, J et al. *Ann Biomech Eng* 29:109-120, 2001.
[12] Benard, N et al., *Ann Biomech Eng* 34:1259-1271, 2006.

SB³C2024
Summer Biomechanics, Bioengineering and Biotransport Conference
June 11-14, Lake Geneva, WI, USA

GENERIC VERSUS PERSONALIZED FOOT-GROUND CONTACT MODELS- IS PERSONALIZATION WORTH THE EFFORT?

Spencer T. Williams, Kayla M. Pariser, Claire V. Hammond, Benjamin J. Fregly

Mechanical Engineering Department, Rice University, Houston, Texas, United States

INTRODUCTION

Musculoskeletal modeling researchers seek to use predictive simulations to design optimized, personalized treatments for patients with movement impairments [1, 2]. Direct collocation optimal control has become the computational method of choice for developing these predictive simulations [3], ideally using personalized neuromusculoskeletal models of individual subjects [1]. For predictions of post-treatment walking function, an important component in these personalized models is the foot-ground contact (FGC) model. FGC models account for changes in interactions between the subject's feet and the ground as the subject's gait pattern is altered during the optimization, estimating updated ground reaction forces and moments to preserve dynamic consistency.

Despite the goal of designing personalized treatments, nearly all optimal control simulations of walking use generic FGC models that have not been calibrated using experimental ground reaction data collected from the subject being modeled. This study investigated the extent to which personalization of FGC model parameters in a two-segment three-dimensional foot model affects the model's ability to reproduce experimental ground reaction and foot kinematic data collected from a single subject post-stroke. Three different FGC models were investigated: 1) a generic model that uses a sparse non-uniform grid of nonlinear springs [4], 2) a personalized version of this generic model, and 3) a personalized FGC model that uses a dense uniform grid of linear spring contact elements [1, 5].

METHODS

The FGC Model Personalization Tool within the MATLAB-based Neuromusculoskeletal Modeling (NMSM) Pipeline software [6] developed by the authors was used to perform the present study. The software uses two-segment, three-dimensional foot models from full-body OpenSim [2] models and adds viscoelastic frictional contact elements to the bottom of the feet. MATLAB's nonlinear least squares optimization algorithm is used to find FGC model parameter values and minimal kinematic changes such that experimental ground reaction and foot kinematic data are matched as closely as possible. Design variables available within the tool include deviations from spline-fitted hindfoot and toes kinematics, spring stiffness coefficients, a damping coefficient, a dynamic friction coefficient, a viscous friction coefficient, and a spring resting length. The cost function penalizes errors in experimental foot kinematics (four marker positions, four hindfoot and toes orientations) and ground reactions (three forces, three moments). It can also penalize a Gaussian weighted average of each contact element's stiffness deviation relative to its neighbors, designed to prevent discontinuities in the identified stiffness profile. The software can calibrate one foot independently or both feet together using a common set of FGC model parameter values as done in the present study.

The experimental ground reaction and foot kinematic data used for this study were collected from a single subject post-stroke. Two walking trials were included in this analysis; the first involved walking at a self-selected speed of 0.35 m/s, and the second involved walking at a fastest comfortable speed of 0.65 m/s. The 0.35 m/s walking trial was used for calibration and testing, and the 0.65 m/s trial was used only for testing.

Three personalized FGC models were investigated in this study in addition to a generic FGC model used in OpenSim Moco optimal control simulations of walking [4]. The generic model uses a sparse non-uniform grid of six spherical contact elements on each foot, where each contact element exerts a Hertzian nonlinear spring force with Hunt and Crossley nonlinear damping [7] in the vertical direction and dynamic and viscous friction in the horizontal direction. Model 1 was a manually personalized version of the generic model. Since the generic model represents a barefoot subject, Model 1 manual personalization involved changing the vertical location of the contact elements in the feet to account for the height of the subject's shoe. For this model and the generic model, the FGC Model Personalization Tool adjusted only foot kinematics while seeking to reproduce the experimental ground reaction

and foot kinematic data. Model 2 was a fully personalized version of Model 1. For this model, the FGC Model Personalization Tool adjusted stiffness coefficients common to both feet, friction coefficients, and the common radius of the spherical contact elements along with foot kinematics. Model 3 was a personalized FGC model used for GPOPS-II [8] optimal control simulations of walking [1]. This contact model uses a dense uniform grid of 55 contact elements on each foot, where each contact element exerts a linear spring force with linear damping in the vertical direction and dynamic and viscous friction in the horizontal direction. For this model, the FGC Model Personalization Tool adjusted individual stiffness coefficients shared by both feet, common friction coefficients a spring resting length along with foot kinematics.

The three personalized FGC models were calibrated using a single cycle of 0.35 m/s gait data and tested using the 0.35 m/s cycle and a second cycle of 0.65 m/s gait data. Testing involved adjusting only foot kinematics and keeping all model parameter values fixed while seeking to match experimental ground reaction and foot kinematic data.

RESULTS

While the generic model was unable to reproduce experimental ground reactions forces and moments for the 0.35 m/s calibration cycle, all three personalized models reproduced them closely while also reproducing experimental foot kinematics closely (Table 1). When the personalized models were tested using the 0.35 m/s and 0.65 m/s cycles, all three reproduced experimental ground reaction and foot kinematic data with comparable accuracy to the calibration cycle (Tables 2 and 3). Though Model 3 generally had the lowest errors, the differences from Model 1 and 2 results were small.

Table 1: RMS error in matching experimental kinematics and ground reactions for calibration with 0.35 m/s gait trial.

Model	Generic	Model 1	Model 2	Model 3
GRF (N)	311.88	9.95	10.16	8.51
Moment (Nm)	21.06	3.13	2.98	2.50
Rotation (°)	0.35	0.73	0.74	0.50
Trans (mm)	5.44	6.30	5.34	3.02

Table 2: RMS error in matching experimental kinematics and ground reactions for testing with 0.35 m/s gait trial. Model 1 is included again for comparison.

Model	Model 1	Model 2	Model 3
GRF (N)	9.95	10.37	8.51
Moment (Nm)	3.13	3.05	2.49
Rotation (°)	0.73	0.74	0.50
Trans (mm)	6.30	5.30	3.02

Table 3: RMS error in matching experimental kinematics and ground reactions for testing with 0.65 m/s gait trial.

Model	Model 1	Model 2	Model 3
GRF (N)	12.05	13.84	12.63
Moment (Nm)	3.72	3.69	3.12
Rotation (°)	0.73	0.74	0.46
Trans (mm)	5.40	5.15	3.44

DISCUSSION

Our results indicate that FGC models may be sufficiently personalized for walking simulations by simply modifying the vertical locations of the contact elements in the feet, and thus calibrating FGC model parameter values may be unnecessary for generating accurate full-body predictive simulations of walking. Without changing parameter values in the generic FGC model, Model 1 accurately reproduced experimental ground reaction and foot kinematic data, though changing the height of the contact elements in the feet was essential, as shown by the failure of the generic model in Table 1. For full-body predictive simulations of walking, the main potential benefit of Model 3 is the smaller vertical translation error, which may make it easier to produce an initial dynamically consistent walking simulation.

Though model personalization was performed using a single 0.35 m/s calibration cycle, all three personalized models also produced accurate results for 0.35 and 0.65 m/s gait data in testing. Thus, the personalized models remained accurate under new testing conditions despite the facts that model parameter values were the same for both feet and the two feet interacted with the ground in a very different manner due to the subject's stroke. These findings support the generalizability of the personalized FGC models to new simulated walking motions produced during the optimal control solution process.

Despite how well Model 1 reproduced experimental ground reaction data with minimal changes to foot kinematics, other situations may necessitate the more extensive personalization performed for Models 2 and 3. First, movements other than straight level walking at constant speed may require a more personalized FGC model. For example, walking up or down an incline or stairs, turning, running, or squatting may require a more highly personalized model. Second, foot models possessing more than two segments may also require a more personalized FGC model. While two-segment foot models are sufficient for optimal control simulations of walking [1], researchers interested in predicting detailed foot kinematics and kinetics may want to include more segments in their foot models. The limited set of spherical contact elements used in Models 1 and 2 may not work for foot models with more segments, and the denser grid of springs used in Model 3 may be useful. Third, walking simulations intended to predict the pressure distribution under the foot may require the denser grid of contact elements used by Model 3. However, pressure maps predicted by Model 3 have not yet been validated. Fourth, modeling different types of shoes may require more extensive model personalization. The subject in the present study wore Adidas Samba sneakers, which possess a uniform neutral sole. It is unknown whether a higher level of personalization would be needed to model more complex shoe designs, such as those with variable stiffness or thickness soles.

This study was limited by the fact that only one subject was included. Nonetheless, the fact that the three personalized FGC models worked well for different walking speeds and both feet of a subject with an asymmetrical gait pattern suggests that similar results are likely to be found for other subjects.

MATLAB source code for the FGC Model Personalization Tool is available on SimTK.org as a part of the NMSM Pipeline. The data used in this study will also be made available on SimTK.org as part of the first Stroke Grand Challenge Competition.

ACKNOWLEDGEMENTS

This research was supported by a National Science Foundation Graduate Research Fellowship under Grant No. 1842494 and by the National Institutes of Health under grant R01 EB030520.

REFERENCES

[1] Meyer, A et al., *Front Bioeng Biotech*, 4, 2016.
[2] Seth, A et al., *PLoS Comput Biol*, 14(7), 2018.
[3] van den Bogert, A J et al., *Procedia IUTAM*, 2: 297-316, 2011.
[4] Bianco, N et al., *PLoS Comput Biol*, 19(8), 2023.
[5] Jackson, J et al., *J Biomech Eng*, 138(9), 2016.
[6] Fregly, B J et al., *Int Sym Comput Sim Biomech*, 2023.
[7] Hunt, K H et al., *ASME. J. Appl. Mech*, 42(2): 440–445, 1975.
[8] Patterson, M A et al., *ACM Trans. Math. Softw.*, 41(1), 2014.

MECHANISTIC MODEL OF BIOCHEMICAL-BIOMECHANICAL CROSSTALK IN VASCULAR ENDOTHELIAL CELL ALIGNMENT

Shannon M. Flanary M.S.E. (1), and Victor H. Barocas Ph.D. (2)

(1) Chemical Engineering & Materials Science, University of Minnesota, Minneapolis, MN, USA
(2) Biomedical Engineering, University of Minnesota, Minneapolis, MN, USA

INTRODUCTION

Vascular endothelial cells (ECs) are highly responsive to mechanical[1] and biochemical[2] stimuli. When exposed to fluid flow *in vitro*, ECs align along the flow direction, mimicking their axial alignment *in vivo*.[3] Seminal work by Nerem and co-workers demonstrated that EC alignment is dependent on magnitude of shear stress stimulus and proper cellular mechanosensing,[3,4] but the exact mechanobiological mechanisms involved remain undetermined.

EC alignment is vital for vascular barrier integrity. In regions with low shear stress or perturbed flow patterns such as arterial bifurcation points, alignment is decreased, and this structural change is paired with alterations in surface protein expression, leading to an increased propensity for atherosclerotic plaque formation.[5]

Diabetes is a major cardiovascular disease risk factor and is strongly associated with endothelial dysfunction.[6] In non-diabetic individuals, atherosclerotic plaques occur mainly in regions of disturbed flow, but diabetic patients also develop diffuse plaques in laminar flow regions.[6] Alterations in endothelial biochemical signaling due to hyperglycemia have been proposed; the interplay between these alterations and cellular mechanics, however, is unknown.[2]

While *in vitro* experiments have provided valuable insight into mechanical[1] and biological[2] regulation of EC alignment, computational modeling techniques can examine the interconnected mechanisms in complementary ways. The objective of this study was to create a model of the structural EC response to mechanical and biochemical stimuli by connecting intracellular signaling to the mechanical stress fiber response and cellular repositioning. We hypothesized that ECs require actin-myosin motor engagement, which is dampened by hyperglycemia, for stress fibers to respond to a flow stimulus and for the cells to align.

METHODS

Model Formulation. The model (Fig. 1) consists of (1) biochemical signaling, (2) single-actin-filament mechanics in response to biochemical activation, (3) cell-substrate mechanical coupling, and (4) a cellular Potts model of EC shape change. Each component is described in turn below.

Biochemical Signaling Model. The signaling network was constructed from published vascular endothelial responses to glucose, mechanical stretch, and shear stress (Fig. 1). Each reaction "edge" was supported by one publication, and each species' response to perturbations in input species (blue nodes) by a minimum of two publications. The species reactions were defined using established methods,[7] with node activations represented by a system of ordinary differential equations and connected by Boolean logic. The hyperglycemic condition was simulated by increasing the "Glucose" node input from 0.4 to 0.9. The "Intracellular Tension" node input was determined by the normalized mean fiber stress.

Actomyosin Contraction. The steady-state level of the "Actomyosin" node within the biochemical network was passed to the fiber-level component, triggering stress fiber activation.[8] The stress fiber activations were converted into an active fiber stress described by

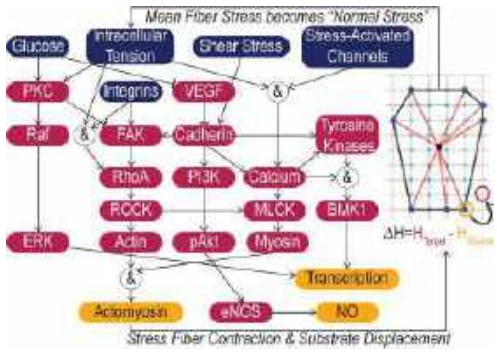

Figure 1: Model Schematic. (a) Signaling model responds to various stimuli and computes an actomyosin activation signal. (b) The cell moves in accordance with that signal.

a Hill-type model that depended on strain rate. The passive fiber stress depended exponentially on fiber strain.[8]

Elastic Substrate Response. The deformation due to focal adhesion-applied traction force was found by assuming that the substrate was an 10 kPa, elastic half-space.[9] Mechanical equilibrium was enforced at each time step to determine each node's position.

Cellular Potts Model (CPM). At each time step, the CPM iteratively attempted a number of moves equal to the number of lattice sites. For each move, a random source and neighboring target were selected (Fig. 1). The pseudo-energy of the system was represented by a Hamiltonian that combined the effects of area and perimeter changes, local substrate strain-stiffening, and fiber stress avoidance. The energy associated with cellular area and perimeter was quantified as

$$H_{Geom} = \sum_{i \in cells} \lambda_A (a_i - A)^8 + \lambda_P \left(p_i - p_{i,0}\right)^4$$

where λ_A and λ_P were weighting parameters for area and perimeter change contributions, a_i and p_i were the cell area and perimeter, A was a target resting area, and $p_{i,0}$ was the target perimeter. Elastic substrate deformation lead to local stiffening,[10] represented in the model as

$$\Delta H_{Strain} = -g(\vec{x}, \vec{x}')\lambda_S \left(h\left(E(\varepsilon_1)\right)(\vec{v}_1 \cdot \vec{v}_m)^2 + h\left(E(\varepsilon_2)\right)(\vec{v}_2 \cdot \vec{v}_m)^2\right)$$

where $g = 1$ for extension and -1 for retraction, λ_S was a weighting parameter, $h\left(E(\varepsilon_1)\right)$ was a sigmoidal focal adhesion maturation function, $\vec{v}_m$ was a unit vector of the movement direction, and $\vec{v}_1$, $\vec{v}_2$, ε_1, and ε_2 were the eigenvectors and eigenvalues of the local substrate strain. The energy associated with fiber shear stress avoidance was quantified as

$$H_{Shear} = \sum_{j \in fibers} \tau_F \eta_j \frac{l_j}{L} \left(\tan^{-1}\left(\frac{\pi^2}{64}\right) - \tan^{-1}\left(\left(\theta_j - \frac{\pi}{2}\right)^2\right)\right)$$

where τ_F was normalized shear stress magnitude, η_j was the fiber activation, l_j/L was the ratio of fiber length to lattice spacing, and θ_j was the angle of the fiber with respect to the fluid flow. The sum of all Hamiltonian components was converted into an acceptance probability to determine whether the proposed move occurred.

Cell Alignment. The alignment tensor was calculated as

$$A_{ij} = \frac{\sum_{k \in fibers} l^k n_i^k n_j^k}{\sum_{k \in fibers} l^k}$$

where for fiber *k*, *l* was the length and *n* was a unit vector of its direction. The degree of cell alignment was defined as the difference between the two eigenvalues of *A* (1 is perfectly aligned, 0 is isotropic). The model was run 10 times with 4 cells per replicate for each condition (shear stress input in increments of 0.1 between 0 and 1, ± hyperglycemia) for 1000 simulated seconds.

RESULTS

ECs respond to many stimuli by altering their structure and preferred alignment. In the absence of exterior stimuli, the simulated ECs were mostly isotropic (Fig. 2a). In response to shear, the cells aligned with the flow (Fig. 2b). With or without flow, stress fibers activated and equilibrated at 91% of max activation (Fig. 2c). When a flow stimulus was present, the fiber activation was conferred into EC realignment parallel to the direction of flow (Fig. 2d).

When the glucose levels were increased to mimic hyperglycemia,

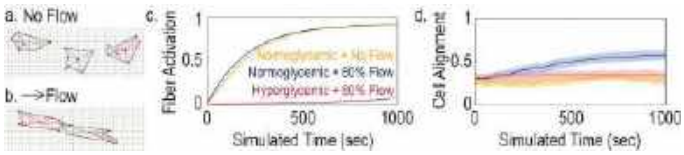

Figure 2. Representative normoglycemic cells without (a) and with (b) flow stimulation. (c) Stress fiber activation and (d) cell alignment in normoglycemic cells with (blue) and without (yellow) flow and hyperglycemic cells with flow (pink). Shaded regions are 95% CI (n=40). Fiber activation error is $\sigma(10^{-3})$.

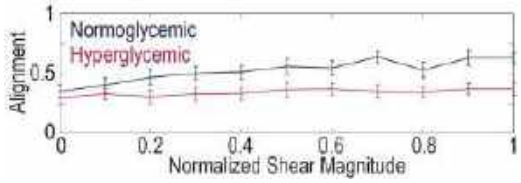

Figure 3. ECs align with increasing shear. Error is 95% CI (n=40).

the flow-mediated cadherin signaling was partially blocked by inhibition of FAK by PKC (Fig. 1), and the stress fibers did not activate beyond 7% of max activation (Fig. 2c), and the cells did not align in response to the flow (Fig. 2d).

The normoglycemic cell response was dependent on the magnitude of shear stress. With increasing normalized shear magnitude, the model endothelial cells achieved greater alignment (Fig. 3). The degree of cell alignment saturated at ~50% normalized shear, with a mean degree of alignment of roughly 0.63.

DISCUSSION

These results demonstrate the capability of our model to describe the complex biochemical and mechanical signaling events that drive EC structural alignment. To our knowledge, this model is the first to connect knowledge of the biochemical signaling of ECs to a structural mechanical response to normal and shear stress. Previous computational models have been employed to predict single fiber[11] and cellular[12] alignment responses to cyclic stretch, but there was no consideration for biochemical signaling events. A more recent model by Hardin *et al*. incorporates the mechanical effects of intercellular communication, but not disease-perturbed behaviors.[13]

Since Nerem's seminal work, numerous *in vitro* studies have observed that ECs respond to both mechanical stimuli, e.g. cyclic stretch or fluid flow, and biochemical stimuli, e.g. changes in glucose levels or pharmacological interventions. The power of our model is demonstrated in its recapitulation of perturbed EC alignment in hyperglycemic systems (Fig. 2, 3). Biochemically, our model connects previous findings[2] of glucose-mediated PKC inhibition of actomyosin (Fig. 1); mechanisms that can now be more fully explored computationally than was previously possible in an *in vitro* system. Our model suggests that the mechanical, stress-avoidant response of stress fibers is prevented in hyperglycemic systems by a lack of actin-myosin activation (Fig. 2).

In its current form, our model employs a simplified fiber network to represent the cytoskeleton, so there is no consideration of actin monomer retrograde flow nor a stiff nuclear body. Actively migrating cells or those undergoing external stretching utilize actin retrograde flow to coordinate stress fiber alignment and cell polarization.[11,14] Even without these features, however, our model offers a tool to quantify and interpret experimentally-observed biophysical mechanisms of EC alignment.

ACKNOWLEDGEMENTS

Support was provided by an American Heart Association Predoctoral Fellowship (SMF) and NIH grant R01 HL164800.

REFERENCES

[1] Sinha, R et al., *Sci Rep*, 6:29510, 2016. [2] Kemeny, S.F. et al., *PLoS ONE*, 8:e66176, 2013. [3] Levesque, M.J. et al., *J Biomech*, 107:341-347. 1985. [4] Girard, P.R. et al., *J Cell Physiol*, 163:179-193, 1995. [5] Fallon, M.E. et al., *BBRC*, 555:160-167, 2021. [6] Nicholls, S.J. et al., *J Am Coll Cardiol*, 47:1967-1975, 2006. [7] Kraeutler, M.J. et al., *BMC Syst Biol*, 4:157, 2010. [8] Flanary, S.M. et al., *BMMB*, 22:1221-1238, 2023. [9] Menga, N et al., *Eur J Mech A Solids*, 73:137-143, 2019. [10] van Oers, R.F.M. et al., *PLoS Comput Biol*, 10:e1003774, 2014. [11] Suciu, A et al., *Bull Math Biol*, 59:1029-1046, 1997. [12] Wei, Z et al., *J Biomech*, 130:031009, 2008. [13] Hardin, C.C. et al., *BBRC*, 495:749-754, 2018. [14] Xu, G.K. et al., *Biophys J*, 114:701-710, 2018.

SHEAR-INDUCED PLATELET AGGREGATION IS MEDIATED BY vWF-BINDING RECEPTORS IN A STENOTIC MODEL

C. Watson (1), C.A. Siedlecki (1,2), K. B. Manning (1,2)

(1) Department of Biomedical Engineering, The Pennsylvania State University, University Park, PA, USA
(2) Department of Surgery, Penn State Hershey Medical Center, Hershey, PA, USA

INTRODUCTION

Atherosclerosis and mechanical circulatory support (MCS) devices perturb healthy blood flow, demonstrating supraphysiological shear rates (>1-2,000 s^{-1}) [1] that induce platelet activation, amplify unfurling of the von Willebrand factor (vWF), and increase platelet adhesion [2]. vWF is an ultralarge, mechanically sensitive glycoprotein that circulates within plasma as a coiled multimer, acting to temporarily tether platelets prior to firm clot stabilization by other adhesive receptors. These multimers unfurl in response to arterial or supraphysiological shear stresses, upregulating vWF-mediated platelet capture.

MCS devices apply supraphysiological shear stresses, often resulting in device-induced thrombosis. Recent studies have highlighted the vWF-rich composition of these blood clots [3]. Device-induced thrombosis can occur within blood-contacting pumps or the arterial circulation as a result of systemically elevated prothrombotic factors and platelet activity [1]. The physical forces experienced by blood in MCS devices prime vWF and platelets to a hyper adhesive state, driving the incidence of thrombosis in these patients.

Due to the clinical severity of arterial thrombosis-associated pathology, it is crucial that the factors contributing to vWF-mediated platelet adhesion are further mapped to improve predictive modeling and inform the development of novel anticoagulant and antiplatelet agents. Elevated shear rates and shear rate gradients have been demonstrated to play a role in vWF-mediated platelet aggregation [4]. Local shear rates and shear rate gradients induced by flow-perturbing geometries drive an increase in both vWF adhesion and effective platelet capture by the unfurling of adherent vWF multimers [5]. Recent studies highlight vWF-binding GPIb as the major receptor involved in shear-induced platelet aggregation (SIPA) [6] and collagen-binding GPVI as a potential target for antiplatelet therapy [7]. The primary objective of this study was to observe the effect of variable shear rate as a means to understand the contributions of different platelet receptors to platelet deposition in a stenotic model.

METHODS

Using established methods of soft lithography [8], polydimethylsiloxane (PDMS) microchannels were fabricated to act as a testing platform for shear-altered deposition. Four stenotic geometries were fabricated to induce rapid shear rate gradients, with contractions of 0, 25, 50, and 75% **(Figure 1)**. Microchannels had a cross-section of 200 x 50 µm in the upstream region. PDMS chips and glass microslides were cleaned in 70% ethanol and sealed by air-plasma treatment in a plasma cleaner (Harrick Plasma, Ithaca NY). Shear rates were calculated in ANSYS FLUENT (ANSYS, Canonsburg PA) and verified by velocity data using a micro-PIV system (TSI Inc., Shoreview MN).

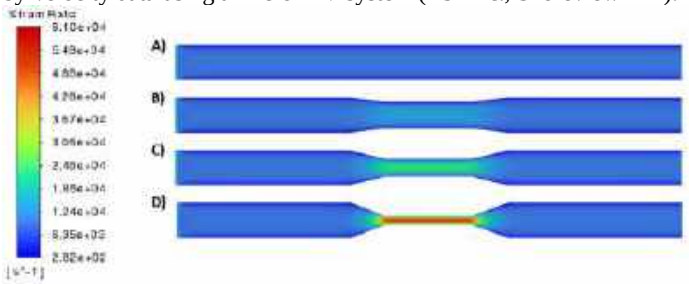

Figure 1: Numerical calculation of shear rates at 50 µL/min flow (upstream shear rate of 10,000 s^{-1}) for A) 0% B) 25% C) 50% and D) 75% stenotic channels with diameters ranging from 50-200 µm. Contour plane is 2 µm from the channel bottom wall.

Prior to experiments, channels were coated with human type I collagen at 100 µg/mL to create an adherent surface. Human blood was acquired via a Penn State IRB approved protocol and anticoagulated with sodium citrate at a final concentration of 0.32%. Blood was centrifuged at 300g for 30 min to obtain separated platelet rich plasma (PRP), which was used to quantify platelet concentration. Platelets were stained with $DiOC_6$ and incubated for 30 min at 37˚C. To determine the

contributions of platelet binding receptors, GPIb and $\alpha_{IIb}\beta_{III}$ function was inhibited by incubation with monoclonal blocking antibodies (Biolegend, San Diego CA), while GPVI was blocked by D-dimer (Abcam, Cambridge UK). Blood was then reconstituted to 40% HCT with PRP, maintaining native platelet concentration (367±93 x 10^6 /mL). Blood was not recalcified to avoid triggering the coagulation cascade. Blood was then perfused for 5 min through microchannels with a Harvard syringe pump (Kd Scientific, MA) at 5, 25, or 50 µL/min to achieve upstream wall shear rates of 1,000, 5,000, and 10,000 s^{-1}, correlating to arteriolar, pathological, and mechanical device-relevant shear rates, respectively. Throat shear rates (up to 40000 s^{-1}) within the stenoses were dependent on both the aforementioned prescribed flow rate and degree of stenotic contraction **(Figure 1).** Real-time immunofluorescence images were acquired at 1 frame per second with an Olympus IX71 inverted microscope and DP74 4MP CMOS camera (Olympus, Tokyo Japan). Pixel resolution was 0.586 µm/pixel. Images were converted to binary and processed in ImageJ (NIH, Bethesda MD) and MATLAB (Mathworks, Natick MA). Significance was assessed by a two-way ANOVA followed by Dunnett's multiple comparisons test.

RESULTS

Control samples exhibited SIPA as a result of increasing shear rate and increasing stenotic contraction **(Figure 2)**. Platelet adhesion (measured by % surface area coverage) and aggregation (measured by mean thrombus area) increased proportionally with increasing shear rate and stenotic contraction. Inhibition of $\alpha_{IIb}\beta_{III}$ and GPIb receptors caused rapid reduction in both platelet adhesion and a loss of aggregation at >1,000 s^{-1}. GPVI inhibition did not notably reduce platelet adhesion at 1,000 s^{-1} but affected microthrombus stability at 5-10,000 s^{-1}. While adhesion and aggregation were modestly reduced, embolization notably occurred as shear rates and stenotic grade increased. At an upstream shear rate of 10,000 s^{-1}, adhesion of unblocked samples (n=6-8) increased as stenotic grade increased, while GPIb-inhibited and $\alpha_{IIb}\beta_{III}$-inhibited samples displayed minimal platelet adhesion, and no shear-induced aggregation. GPVI-inhibited samples (n=6-7) displayed reduced surface area coverage (SAC), but this effect was more pronounced in 50 and 75% stenotic channels.

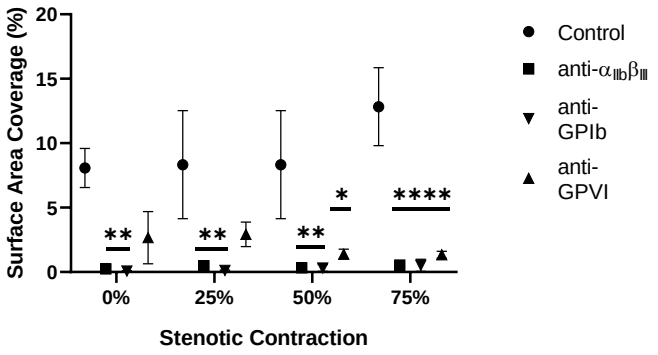

Figure 2: Surface area coverage (SAC) measuring platelet adhesion at 50 µL/min (upstream shear rate of 10,000 s^{-1}) for 0-75% stenoses. Data are presented as mean±SEM. Significance denotes the effect of receptor inhibition vs unblocked (control) samples.

Platelet aggregation followed similar trends to overall adhesion. Mean thrombus area (MTA) was dramatically reduced in $\alpha_{IIb}\beta_{III}$- and GPIb-inhibited samples as throat shear rates exceeded 1-2,000 s^{-1} **(Figure 3)**. GPVI-inhibited samples did not display significantly reduced MTA until throat shear rates exceeded 10,000 s^{-1}. This reduction was not due to a loss of aggregability from GPVI inhibition but frequent embolization of large (>100 µm^2) thrombi as throat shear rates reached 2-40,000 s^{-1} within the 50 and 75% stenotic channels.

DISCUSSION

SIPA of unblocked blood samples was observed at supraphysiological shear rates, influenced by both upstream shear rate and stenotic contraction. Inhibition of the vWF-binding receptors $\alpha_{IIb}\beta_{III}$ and GPIb completely blocked platelet adhesion and aggregation at shear rates exceeding 1-2,000 s^{-1}. The lack of any platelet adhesion at these shear rates further supports the need for an initial vWF-bound platelet layer to facilitate arterial, pathological, or device-mediated thrombosis within the acute time scale investigated here.

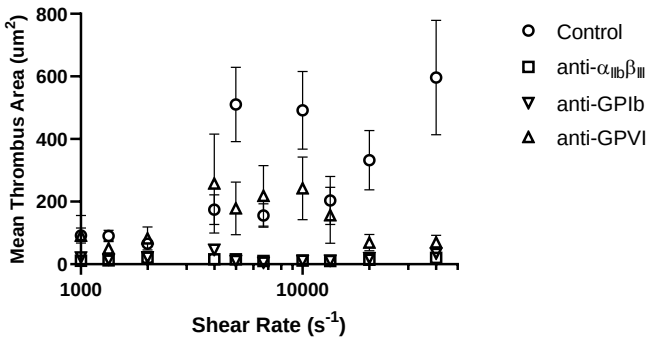

Figure 3: Mean thrombus area (MTA) measuring platelet aggregation for all flow rates (5-50 µL/min). Shear rate is the wall shear rate within the throat of each channel, based on flow rate and stenotic grade (0-75%). Data are presented as mean±SEM.

Alternatively, inhibition of GPVI only modestly decreased platelet adhesion at upstream shear rates of 5-10,000 s^{-1} but made larger microthrombi more susceptible to embolization at 20-40000 s^{-1}. Prior to embolization, larger microthrombi formed as a result of platelet aggregation in GPVI-inhibited samples. This suggests that the collagen-binding function of GPVI serves primarily as a method of stabilization as thrombi grow into the freestream and experience stronger hydrodynamic drag. This does not prohibit SIPA in a thrombogenic geometry such as a severe stenosis and may not be an effective target for the regulation of arterial thrombosis.

This study yields further insight into mechanisms regulating rapid growth of arterial thrombi at supraphysiological shear rates. Three major platelet adhesion receptors were investigated in a study of shear-induced platelet aggregation. Stenotic geometries created shear rate gradients that increased platelet adhesion in unblocked blood samples, yet increased embolization in GPVI-blocked samples. Inhibition of $\alpha_{IIb}\beta_{III}$ and GPIb prohibited platelet adhesion and aggregation, indicating a reliance on vWF-mediated adhesion to precipitate SIPA.

ACKNOWLEDGEMENTS

This work is supported by NIH HL136369.

REFERENCES

[1] Manning, K. B., et al., Curr Opin Biomed, 2021.
[2] Sadler JE., Annual Review of Biochemistry, 1998, 67.1: 395-424.
[3] Kreuziger, LB., ASAIO, 2018, 64.6: 754.
[4] Receveur, N., Haematologica, 2020, 105.10: 2471.
[5] Westein, E., Proc Natl Acad., 2013, 110.4: 1357-1362.
[6] Liu Z.L., Blood Advances. 2022, 26;6(8):2453-65.
[7] Billiald P., Blood Advances, 2023, 11;7(7):1258-68.
[8] Jamiolkowski, MA., Biomaterials, 2016, 96: 72-83.

FLUID-STRUCTURE INTERACTION MODEL OF THE HUMAN HEART WITH A CLOSED-LOOP MODEL OF THE CIRCULATION

M. Sadipour (1), M. R. Davey (2), D. R. Wells (3), C. Puelz (4), B. E. Griffith (1,3)

(1) Department of Biomedical Engineering, University of North Carolina, Chapel Hill, NC, USA
(2) Curriculum in Bioinformatics and Computational Biology, University of North Carolina, Chapel Hill, NC, USA
(3) Department of Mathematics, University of North Carolina, Chapel Hill, NC, USA
(4) Department of Pediatrics, Section of Cardiology, Baylor College of Medicine and Texas Children's Hospital, Houston, TX, USA

INTRODUCTION

Cardiovascular disease stands as the primary cause of mortality in the United States [1]. Severe valvular heart disease induces pressure or volume overload on the cardiac chambers, impairing myocardial contraction and ultimately impacting the overall function of the heart [2]. The prevailing approaches for in vivo cardiovascular research and diagnosis involve catheterization and imaging. However, these methods present drawbacks–imaging tends to be costly, and catheterization is invasive [3]. To address these limitations, computational modeling, especially fluid structure interaction (FSI) simulations of the whole heart, emerges as a valuable tool for researchers and clinicians. Previous whole-heart fluid-structure interaction models either lack physiologic valves [4] or fail to capture the nuanced stresses and strains within the myocardium [5]. We propose instead to construct a model utilizing the immersed finite element/finite difference (IFED) technique [6], which has been successfully used in previous work to simulate heart chambers and valves [7,8]. This approach is employed to develop a model of the entire heart, serving as a foundation for future studies on valve replacement and repair. Furthermore, it is demonstrated that our model captures the Frank-Starling mechanism, which is a fundamental response of the heart in which increased diastolic filling results in increased systolic ejection.

METHODS

Anatomical structures were derived from cardiac computed tomography (CT) imaging, capturing detailed three-dimensional representations of major cardiac components (Figure 1). Biomechanical models of the heart and its valves were parameterized using experimental tensile test data sourced exclusively from human tissue specimens. These models incorporated established approaches describing the heart's fiber architecture based on prior experimental work. FSI simulations utilized the IFED version [6,9] of the immersed boundary method, enabling automatic handling of contact between structures, including valve leaflets.

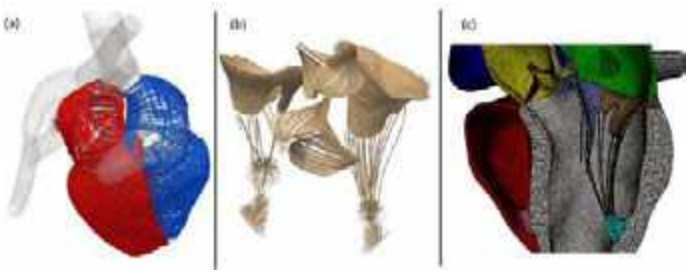

Figure 1. (a) The main myocardial fibers within the right heart and left heart depicted in blue and red, respectively. (b) A visualization of the main fiber orientation on the valve leaflet, chordae, and papillary muscles. (c) A visualization of the heart mesh with a focus on the left side and mitral valve apparatus. The colors denote different subdomains within the mesh [10].

In this study, the circulation model employed is a closed system, where the flows and pressures originating from the left and right sides of the heart are coupled, unlike previous iterations of the model.

RESULTS

Preliminary dynamic simulation results using a decoupled circulation model illustrated crucial aspects of the cardiac cycle for the left heart (Fig. 2). Blood velocity magnitudes and pressures depicted fluid dynamics within the heart, providing insights into blood flow patterns during various phases of the cardiac cycle. These

representations underscore essential dynamics, showcasing the model's ability to simulate key aspects of cardiac function.

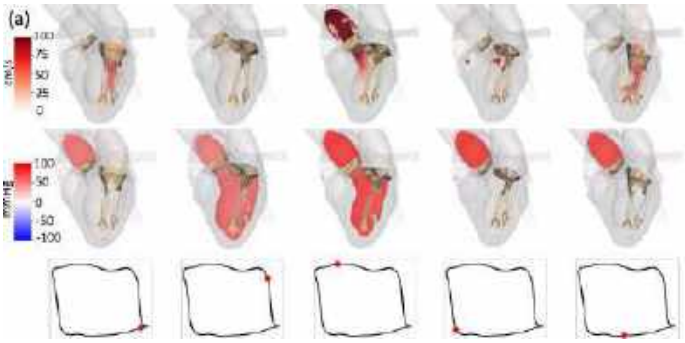

Figure 2. Blood flow dynamics within the heart: Visual representations of both blood velocity magnitude and pressure across a plane dividing the aortic and mitral valves, depicted alongside semi-transparent views of the heart chambers at five distinct time intervals throughout the cardiac cycle. The lowest panels display the pressure-volume loop generated by the model.

To demonstrate the satisfaction of the Frank-Starling mechanism, in Fig. 3(a), our model effectively captures the expected trend, showing that a larger end-diastolic volume (ventricular preload) corresponds to a larger stroke volume. This relationship is quantified in the ventricular function curve depicted in Fig. 3(c). While approaching a non-linear response, as seen in Fig. 3(c) with larger loads [11 -13], additional data points at higher loads will help confirm this observation. Although ventricular preload (end-diastolic volume) is not a perfect indicator of cellular length [12], it remains adequate for capturing overall trends in the Frank-Starling mechanism. The consistency of the end-diastolic filling section of the pressure-volume relation across different loads is highlighted in Fig. 3(b). This observation aligns with in vivo findings [11, 14].

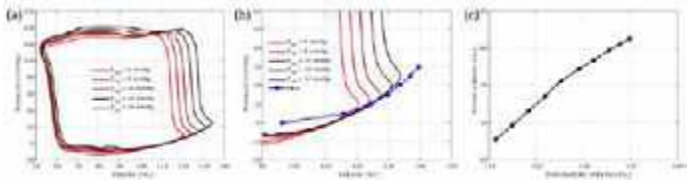

Figure 3. (a) The overlaid pressure-volume relations from multiple cycles (b) Comparison of the diastolic filling portion of the pressure-volume relations to the static end-diastolic pressure-volume relationship [15] (c) Plot of the left ventricular end-diastolic volume load values against the resultant stroke volumes to generate the left ventricular function curve for atrial loading pressures of 6-15 mmHg.

DISCUSSION

Our model showcases nuanced dynamics of the cardiac cycle, capturing distinct features like the mitral valve closing transient and aortic valve closure, aligning qualitatively with clinical and experimental data. While our pressure-volume relationships do not replicate textbook curves or idealized valve models, they mirror clinical measurements, emphasizing the model's realism in representing physiological cardiac function. The discrepancies observed, such as differences in volume losses and left ventricular pressure during isovolumetric contraction compared to in vivo examples, highlight areas for further refinement. However, our model's ability to replicate clinical features, such as regurgitant flow volumes and mitral flow rate waveforms, showcases its potential in simulating and understanding complex cardiac dynamics. These findings underscore the model's strength in capturing realistic pressure-flow relations and its relevance in studying various cardiac dysfunctions, particularly valvular disorders. By providing direct access to crucial metrics like flows and pressures, our model holds promise for advancing simulation-based studies aimed at improving the understanding and treatment of a wide spectrum of cardiac pathologies.

ACKNOWLEDGEMENTS

We acknowledge research support from NIH award R01HL157631 and NSF award OAC 1931516.

REFERENCES

[1] https://www.cdc.gov/heartdisease/facts.htm. 2021.
[2] Ajmone, N et al., *European Heart Journal*, 44, 1: 28-40, 2023.
[3] Di Carli, MF et al., *Circulation*, 133(25):2640-2661, 2016.
[4] Kariya, T et al., *Ann Biomed Eng*, 48(6):1740-1750, 2020.
[5] McQueen, DM et al., *Mechanics for a New Mellennium*, 2002.
[6] Griffith, BE et al., *Int J Numer Method Biomed Eng*, 0:1-32, 2017.
[7] Liuyang, F et al.,*Int J Numer Method Biomed Eng*, 35:e3254, 2019.
[8] Gao, H et al., *Med Eng Phys*, 47:128-136, 2017.
[9] Wells, D et al., *J Comput Phys*, 477:111890, 2023.
[10] arXiv:2307.02680
[11] Jacob, R. et al., *Eur Heart J*, 13:7-14 (1992).
[12] Kosta, S. et al., *PLoS Comput Biol*, 17: e1009469 (2021).
[13] Han, J. et al., *Prog Biophys Mol Biol*, 159:10-21 2021.
[14] Bastos, M. et al., *Eur Heart J*, 41:1286-1297 (2020).
[15] Klotz, S. et al., *Am J Physiol Heart Circ Physiol*, 291.H:403-416 (2006).

EXPLORING THE POSSIBLE RELATIONSHIP BETWEEN LOST ELASTIN INTEGRITY AND GLYCOSAMINOGLYCAN BUILDUP IN ELASTIC ARTERIES USING COMPUTATIONAL MODELLING

Yousof MA. Abdel-Raouf (1), Lauranne Maes (2), Mathias Peirlinck (3), Nele Famaey (2), Patrick Sips (4), Julie De Backer (4,5), Patrick Segers (1), Jay D. Humphrey (6,7)

(1) Institute of Biomedical Engineering and Technology (IBiTech), Ghent University, Ghent, Belgium
(2) Department of Mechanical Engineering, KU Leuven, Leuven, Belgium
(3) Department of Biomechanical Engineering, Delft University of Technology, Delft, Netherlands
(4) Center of Medical Genetics (CMGG), Ghent University, Ghent, Belgium
(5) Department of Cardiology, Ghent University Hospital, Ghent, Belgium
(6) Department of Biomedical Engineering, Yale University, New Haven, CT, USA
(7) Vascular Biology and Therapeutics Program, Yale School of Medicine, New Haven, CT, USA

INTRODUCTION

The extracellular matrix (ECM) represents the vast scaffolding and framework of microstructural elements that lend soft tissues their mechanical properties, as well as protein molecules that facilitate signaling and sensing of cells to their environment. A confluence of this physicochemical signaling and sensing provides cells with a myriad of sophisticated adaptive mechanisms to respond to changes in their homeostatic environment, and understanding the ECM as a constantly evolving environment has recontextualized the importance of mechanobiology in the larger scale of biomechanics [1].

More specifically, recent advances in microscopy and imaging have allowed us a closer look at the ECM of elastic arteries, and attention has been drawn to the sensing and remodeling undertaken by the stress sensing smooth muscle cells (SMC) which predominantly occupies the media of these arteries. SMCs are predominantly oriented circumferentially, and reside within elastin lamellae organized concentrically around the axis of flow. There is evidence to suggest that the spacing between these lamellae is conserved in aging [2], which is typically associated with progressive elastin degradation. SMCs differentially deposit glycosaminoglycans (GAGs) -which in turn generates Donnan Swelling- in response to change in their mechanical environment [3, 4]. In a more extreme model for advanced ageing, Murtada and Kawamura et al. [5] shows that SMCs in the media of Hutchinson-Guilford Progeria mice modulate their phenotype to an osteochondrogenic phenotype that produces pathological amounts of GAGs as a response to medial degeneration of elastin in advanced ageing.

Since the correlation between elastin damage, GAG deposition and aortic dilatation is of importance, we seek to describe these relationships in a mathematical framework. To that end, we revisit work presented by Roccabianca et al. [6,7] previously developed to describe the mechanics of swollen arteries. We utilize this framework in an attempt to simulate the behavior of arteries undergoing elastin damage and Donnan Swelling. First, we observe the behavior of the model in the context of elastin integrity loss. Additionally, we attempt to characterize the swelling that would take place during this elastin loss. Since [2] and [4] suggest that interlamellar distance and medial thickness are somewhat conserved with elastin damage and dilatation (to maintain radially sensed stresses by SMCs), we attempt to reflect this in our model. Finally, a simple coupling between damage and swelling is directly imposed, and subsequent biomechanical change is reported.

METHODS

Identical to [7], the framework of the constrained mixture model is used to describe the constitutive behavior of the bilayered modelled arteries. The cylindrically shaped layers are an inner layer (comprising approximately 38% of the total thickness) representing the media, and an outer one representing the adventitia. Relevant to our investigation are two configurations that deviate from homeostatically hydrated (swollen) homeostatic conditions ($\kappa_h{}^*$) conditions previously reported in [7]. These configurations are shown in **Fig. 1**. The first configuration (κ_γ^*) corresponds to the carotid artery dimensions at the homeostatic load but with a compromised elastin integrity, that we implement by multiplying the neo-Hookean constant c^e by a gain parameter ranging between 0 % and 100 % integrity. As elastin degrades, the artery must dilate to accommodate the homeostatic load, leading to a decrease in the interlamellar distance. The second configuration (κ_{γ,ν^*}^*) corresponds to the swelling that takes place in the medial layer due to that elastin loss. While in [7] the swelling was applied onto excised sample tissue, we wish to understand what swelling would take place to satisfy the hypothesis derived from [2] and [4].

The deformation gradient describing the change from a swollen homeostatic configuration to a new configuration with elastin compromise is given by $\mathbf{F}_\gamma{}^* = \mathrm{diag}[\frac{dr_\gamma}{dr_h}, \frac{r_\gamma}{r_h}, \lambda_\gamma]$. The kinematic constraint between configurations is given by the following radius change in cylindrical coordinates $r_\gamma = \sqrt{{r_{\gamma i}}^2 + \frac{{r_h}^2 - {r_{hi}}^2}{\lambda_\gamma}}$. Similarly, the deformation gradient mapping from this damaged configuration to one with damage and swelling adapted to damage is given by $\mathbf{F}_{\nu^*,\gamma}{}^* = \mathrm{diag}[\nu_\gamma^* \frac{dr_{\gamma,\nu}}{dr_\gamma}, \frac{r_{\gamma,\nu}}{r_\gamma}, 1]$ and the radius change is dictated by $r_{\gamma,\nu} = \sqrt{{r_{\gamma,\nu i}}^2 + \frac{\int \nu_\gamma^* r_\gamma \, dr_\gamma}{2}}$. The swelling formulation corresponds to a volume change, and is directly applied axisymmetrically on the domain according to the following scalar analytical relationship to the radius r_γ

$$\nu_\gamma^* = \frac{\nu_a + \nu_i}{2} + \frac{\alpha(r_\gamma - r_{\gamma m})}{\sqrt{1 + \frac{4\alpha^2 (r_\gamma - r_{\gamma m})^2}{(\nu_a - \nu_i)^2}}} \quad (1)$$

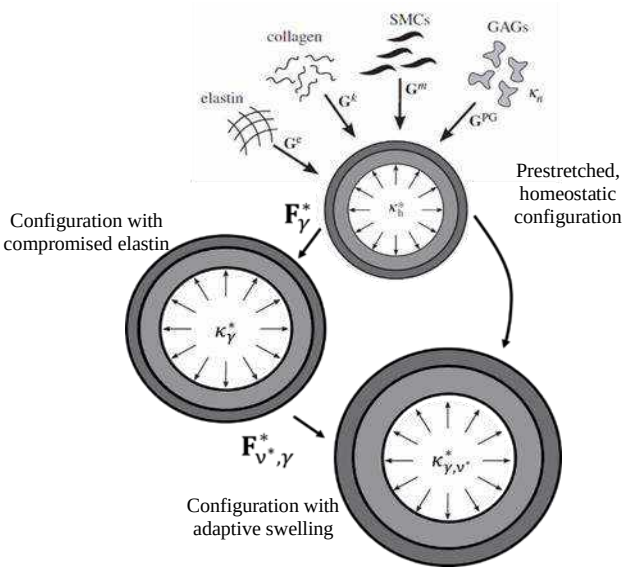

Figure 1 Illustration of configurations of interest

where ν_a and ν_i corresponds to the volume change at the adventitia (outer radius) and the intima (inner radius) respectively. r_{ym} here corresponds to the radial position from the inner radius at the border where the media and adventitia meet. Since this analytical relationship creates a sigmoidal shape, the parameter α enforces the steepness of the sigmoid. In our investigations, we always apply the boundary condition where $\nu_a = 1$ meaning that the volume change at the adventitia does not take place, and a large value of α therefore means that the adventitial volume change can entirely and uniformly be given a value of 1 and the entire volume change of the intima takes a value of $\int_i^a \nu_i dr$. In our effort to investigate swelling as a function of damage, and subsequent modification of the swelling profile, we optimize for the value of ν_i at 93.33 mmHg with the conservation of medial thickness being the objective function to minimize. In other words, loss of medial thickness due to dilatation and elastin loss is counteracted by swelling which aims to maintain medial thickness.

RESULTS

Our simulation demonstrates that the loss of elastin at differing luminal pressures (and in the absence of compensatory swelling in the media $\mathbf{F}_{\nu^*,\gamma}{}^* = \mathbf{I}$) leads to dilatation (**Fig. 2**). This behavior is asymptotic as elastin loss at different stresses tends to dilate to a diameter at which full collagen and SMC recruitment bear the elastic load, i.e., the model emulates the phenomenon of adventitial rescue. Additionally, we show that the presence of swelling that maintains medial thickness (confirmed in **Fig. 3(a)** solid line) implies logarithmic correlation (**Fig. 3(b)**) between swelling and elastin degradation. The consequence of this adjustment or adaptation on the transmural stress is the decrease of stress attributed to less elastic load bearing and increased fluid (swelling) load-bearing (**Fig. 3(d)**).

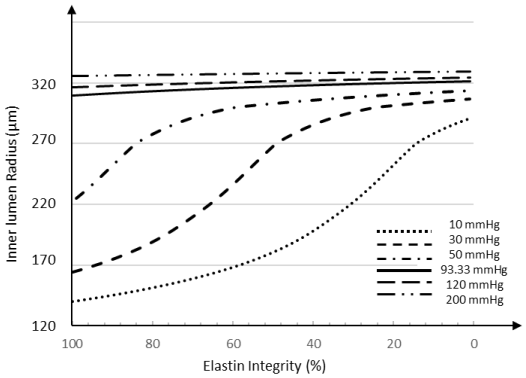

Figure 2 Lumen radius in elastin integrity loss ($\mathbf{F}_{\nu^*,\gamma}{}^* = \mathbf{I}$)

DISCUSSION

Given the importance of incorporating mechanobiological phenomena in soft tissue biomechanics, integrating additional microstructurally and mechanobiologically relevant components of the ECM is significant. We show that the model proposed in [6,7] adopted here can effectively demonstrate adventitial rescue in absence of elastin (**Fig. 2**) which was suggested to explain the absence of dilatation in compromised elastin [8], and why dilatation and excessive GAG production appears when elastin degradation happens in conjunction with adventitial (collagen crosslinking) compromise [9]. Recently published work by Li et al. [10] highlights two forms of failure related to mechanosensing with the first being a linear relationship between elastin loss and tissue damage, and the second being a saturation relationship when mechanosensing is compromised. The latter is heavily correlated with the anchoring of cells in the media, and is sensitive to interlamellar spacing, therefore **Fig. 3(b)** solid line reflects that maintained mechanosensing follows the same trend. We therefore hope to utilize this modelling approach in future numerical studies on evolving GAG content as an adaptive mechanism in response to elastin damage.

ACKNOWLEDGEMENTS

This research was funded by the Concerted Action Program of Ghent University Special Research Fund (GOA019-21BOF). We would also like to thank Dr. Sara Roccabianca for sharing relevant material with us

REFERENCES

[1] Humphrey, J et al., Nat Rev Mol Cell Biol 15, 802–812, 2014.
[2] Cavinato, C et al., Mech Age Dev 196, 2021.
[3] Glagov, S et al. Atherosclerosis IV, 362-366, 1977.
[4] Yousef, S et al., Sci Rep 11, 13185 2021.
[5] Murtada, S et al., Biomech & Mod in Mechanobiol 22, 1333–1347 2023.
[6] Sorrentino, T et al., J Biomech Eng 137, 2015.
[7] Roccabianca, S et al., J R Soc Interface 11, 2014.
[8] Kawamura, Y et al., J Mech Behavior Biomed Mat 116, 2021.
[9] Weiss, D et al., Acta Biomat 132, 422-434, 2021.
[10] Li, D et al., Proc. R. Soc. A 479, 2023.

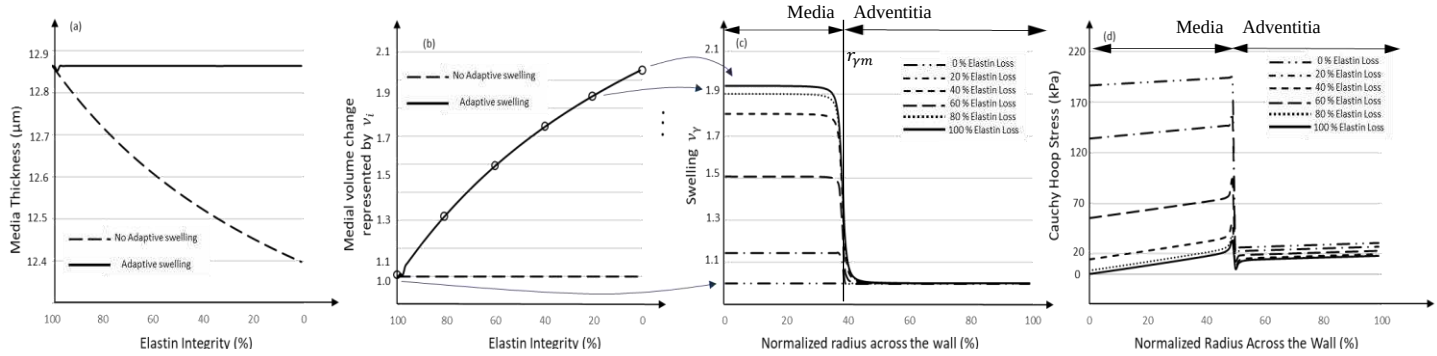

Figure 3 The relationship between interlamellar spacing (media thickness) and loss of elastin integrity as well as adaptive swelling

NEGATIVE EFFORT DEPENDENCE IN OBSTRUCTIVE SLEEP APNEA: INSIGHTS FROM A MATHEMATICAL MODEL

Guilherme J.M. Garcia (1,2), B. Tucker Woodson (2)

(1) Department of Biomedical Engineering, Marquette University and The Medical College of Wisconsin, Milwaukee, WI, USA

(2) Department of Otolaryngology and Communication Sciences, The Medical College of Wisconsin, Milwaukee, WI, USA

INTRODUCTION

Obstructive sleep apnea (OSA) is a disease characterized by recurrent episodes of airflow limitation during sleep due to upper airway (UA) collapse. OSA pathophysiology is complex, but increased UA collapsibility is a major risk factor [1]. The anatomical and physiological factors that regulate UA collapsibility remain incompletely understood. A better understanding of UA biomechanics may lead to the development of more effective methods to diagnose and treat OSA.

The Starling Resistor (i.e., a collapsible tube between two rigid tubes) has been the archetype model of UA collapse in OSA for the last 35 years as it explains many observations [2]. For example, snoring is similar to oscillations that arise in collapsible tubes during flow limitation [2]. However, the observation of negative effort dependence (NED) in OSA patients led researchers to question if the human UA really behaves like a Starling Resistor [3,4]. NED is a reduction in flowrate with increasing breathing effort. The observation of NED contradicts the leading theory of flow limitation in collapsible tubes (i.e., the wave speed flow limitation theory [5]), which predicts that flowrate remains constant and independent of the downstream pressure after the onset of flow limitation. A mathematical model to explain the occurrence of NED in collapsible tubes is lacking. Here, we present a simple mathematical model to explain NED in OSA. Our model predicts that NED is a consequence of the coupling between the fluid mechanics of airflow in a constricted tube and the solid mechanics of how UA soft tissues respond to negative intraluminal pressure.

METHODS

Our solid mechanics model is the area-pressure relationship (tube law) of the pharynx in OSA patients [6] (**Fig. 1**)

$$A = A_{max}\left[1 - e^{-\frac{C_0}{A_{max}}(P_{pharynx} - P_{close})}\right]$$

where A is the airspace cross-sectional area of the pharyngeal choke point, $P_{pharynx}$ is the air pressure at the choke point, P_{close} is the pharyngeal closing pressure (i.e., $A = 0$ at $P_{pharynx} = P_{close}$), A_{max} is the maximal area of the choke point (observed when $P_{pharynx} \gg P_{close}$), and C_0 is the pharyngeal compliance (slope of the area-pressure relationship) at the closing pressure, namely

$$C_0 = \left(\frac{dA}{dP_{pharynx}}\right)_{P_{pharynx}=P_{close}}$$

The tube law is illustrated in **Fig. 1** for a patient with A_{max} = 1 cm^2, P_{close} = 2 cmH$_2$O, and C_0 = 0.15 cm^2/cmH$_2$O.

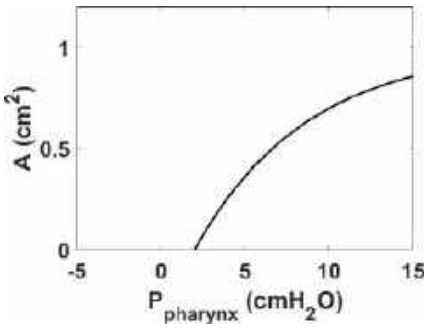

Figure 1: Area-pressure relationship of the human pharynx in an OSA patient with A_{max} = 1 cm^2, P_{close} = 2 cmH$_2$O, and C_0 = 0.15 cm^2/cmH$_2$O.

Our fluid mechanics model consists of equations describing the flow upstream and downstream of the choking point. First, we apply the Bernoulli equation (i.e., conservation of energy) between an upstream point and the pharyngeal choke point to obtain an equation that relates the flowrate (Q) to the choke point cross-sectional area (A)

$$Q = A\sqrt{\frac{2(P_{UP} - P_{pharynx})}{\rho(1-\beta^2)}}$$

where P_{UP} is the upstream pressure, ρ = 1.2 kg/m^3 is air density, and $\beta = A/A_{max}$. Next, we assume that the pressure loss downstream of the choke point is a combination of major losses and minor losses due to a sudden expansion, so that the downstream pressure (P_{DOWN}) is

$$P_{DOWN} = P_{pharynx} - (\Delta P)_{MAJOR} - (\Delta P)_{MINOR}$$

The major losses $(\Delta P)_{MAJOR}$ are computed from the Darcy friction factor in the standard fashion [7] assuming a circular tube with length of 10 cm, while the minor losses are

$$(\Delta P)_{MINOR} = K_L \frac{\rho V^2}{2}$$

where $V = Q/A$ is the air velocity at the pharyngeal choke point and K_L is the loss coefficient of a sudden expansion

$$K_L = \alpha(1-\beta)^2$$

where $\alpha = 1.05$ is the kinetic energy correction factor for turbulent flow [7].

We define negative effort dependence (NED) as the percent reduction in flowrate from the peak flowrate (Q_{max}) to the flowrate Q^* at a downstream pressure of -5 cmH$_2$O (**Fig. 2**)

$$NED = 100\frac{(Q_{max} - Q^*)}{Q_{max}}$$

RESULTS

The model predicts that as the downstream pressure decreases (i.e., breathing effort increases) the flowrate increases, reaches a maximum value (Q_{max}), and then decreases to zero due to UA collapse (**Fig. 2**).

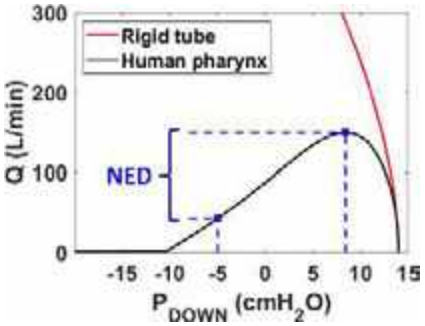

Figure 2: Pressure-flow curve of the human pharynx (A_{max} = 1 cm^2, P_{close} = 2 cmH$_2$O, C_0 = 0.15 cm^2/cmH$_2$O, and P_{UP} = 14 cmH$_2$O) compared to a rigid tube. Abbreviation: NED = negative effort dependence.

For an OSA patient with A_{max} = 1 cm^2, P_{close} = 2 cmH$_2$O, and C_0 = 0.15 cm^2/cmH$_2$O assuming an upstream pressure P_{UP} = 14 cmH$_2$O, the model predicts that NED = 72%, i.e., a 72% reduction in flow from its peak of 149.9 L/min to 42.4 L/min at a downstream pressure of -5 cmH$_2$O (**Fig. 2**). When pharyngeal compliance at the closing pressure was increased from C_0 = 0.05 to 0.25 cm^2/cmH$_2$O while keeping A_{max}, P_{close}, and P_{UP} constant, NED increased from 58.6% to 80.3% (**Fig. 3**). NED depended on the values of A_{max}, P_{close}, and P_{UP}, but higher pharyngeal compliance produced greater NED.

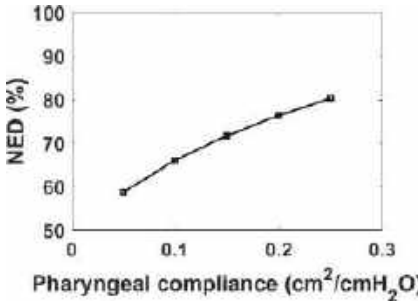

Figure 3: The mathematical model predicts that negative effort dependence (NED) increases as pharyngeal compliance increases.

DISCUSSION

To our knowledge, this is the first biomechanical model to explain the occurrence of NED in OSA patients. Our model predicts that collapsible tubes can also display NED (not shown), which supports the view that the human UA behaves like a Starling Resistor. Importantly, the model predicts that NED increases as pharyngeal compliance increases (**Fig. 3**). This prediction supports the hypothesis by Wellman and collaborators that NED can be used to identify the anatomical structure causing airflow limitation in OSA patients [8]. Specifically, four anatomical structures can cause airflow limitation in OSA, namely the tongue, epiglottis, soft palate, and lateral pharyngeal walls. Our model suggests that the collapse of highly compliant structures that flap quickly (e.g., epiglottis and soft palate) will produce more NED than the collapse of low-compliance structures that move more slowly (e.g., tongue). This prediction is consistent with the in vivo observation that isolated epiglottic collapse and isolated soft palate collapse have greater NED than tongue collapse [8]. We acknowledge that our model is a simplification of the complex fluid-structure interactions involved. Experimental studies are needed to test the validity of our assumptions and to verify our predictions. Future studies will help refine our model and lead to a better understanding of the biomechanics of UA collapse in OSA.

ACKNOWLEDGEMENTS

The authors gratefully acknowledge funding by the Advancing a Healthier Wisconsin Endowment (grant number AHW REP 5520494) and by the National Center for Advancing Translational Sciences, National Institutes of Health (grant number 8KL2TR000056).

REFERENCES

[1] Eckert DJ, Wellman A. *ERS Monograph* 9781849840606:9-23, 2015.
[2] Schwartz AR, Smith PL. *J Physiol*, 591:2229-2232, 2013.
[3] Butler JP, Owens RL, Malhotra A, Wellman A. *J Physiol*, 591:2233 -2234, 2013.
[4] Wellman A, et al. *J Appl Physiol,* 117:1478-1485, 2014.
[5] Dawson SV, Elliott EA. *J Appl Physiol,* 43:498-515, 1977.
[6] Isono S. *J Appl Physiol*, 75:148-154, 1993.
[7] White, FM. *Fluid Mechanics*, McGraw-Hill, 2008.
[8] Genta PR, et al. *Chest* 152:537-546, 2017.

PREDICTING FAILURE LOCATIONS IN HETEROGENEOUS SOFT MATERIALS

Catherine C. Eberman (1), Colleen M. Witzenburg (1,2)

(1) Department of Mechanical Engineering, University of Wisconsin – Madison, Madison, WI, USA
(2) Department of Biomedical Engineering, University of Wisconsin – Madison, Madison, WI, USA

INTRODUCTION

Identifying the risk of rupture in soft tissues, such as aortic or cerebral aneurysms, myocardial infarct tissue, or ligament or tendon following repair, poses a significant clinical challenge [1-4]. Mitigating rupture risk often involves surgical or percutaneous intervention. Current research in failure modeling and prediction often involves complex finite element modeling and damage modeling [5-8], while clinical risk prediction is often limited to geometry (e.g., aneurysms [1]). Predicting failure risk is particularly challenging in pathologic soft tissues since (1) spatial differences in both geometry and material properties contribute to the creation of stress concentration zones and material failure and (2) soft tissues are mechanosensitive and remodel their extracellular matrix in response to disease or injury. The objective of our study was to create an algorithm that predicts failure initiation location from pre-failure biaxial testing data. To test the algorithm, we created spatially variable soft tissue analog samples from PDMS. The algorithm combined full-field deformation, loading direction, and sample geometry from sub failure tests to predict regions at high risk for failure. These locations corresponded well with the actual failure locations in equibiaxial mechanical testing.

METHODS

Sample Preparation and Testing. PDMS (Sylgard) was cast, and silicone sealant or desiccant beads were added to create heterogeneity. Samples were cut into cruciform shapes and speckled using black spray paint (Fig. 1) to enable full-field strain tracking via digital image correlation (DIC). Samples were attached to a biaxial testing machine (574E2, TestResources) and underwent 15 extensions to 10% strain, including equibiaxial, two-arm, three-arm, strip uniaxial, and single arm extension extensions [9]. Samples were then pulled to failure equibiaxially at a rate of 0.15% strain/s. Images of the sample were captured at 4k at a minimum of 24fps for all protocols.

Failure Prediction. DIC was applied to all extensions to determine full-field displacement. Briefly, the tissue boundary was sketched on top of the reference image, meshed with quadrilateral elements, and tracked. The deformation gradient tensor, **F**, was computed at each element edge (i) and compared to the neighboring element (j) [10]:

$$Def = \left(F_{11}^{i} - F_{11}^{j}\right)^2 + \left(F_{12}^{i} - F_{12}^{j}\right)^2 + (F_{21}^{i} - F_{21}^{j})^2 + (F_{22}^{i} - F_{22}^{j})^2 \quad (1)$$

This enables identification of regions with large spatial differences in deformation, *Def*.

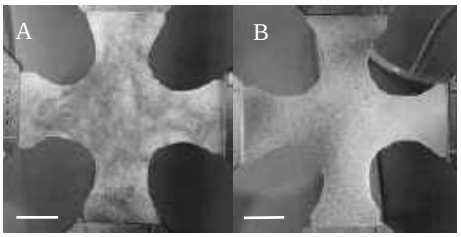

Figure 1: PDMS with silicone sealant (A) or desiccant beads (B) added to produce a heterogeneous sample, scale bar = 0.875 in.

To account for the direction of the deformation, *Dir*, the dot product of the nodal connection direction, N_c, and the local principal strain direction, E_p, from the 10% equibiaxial subfailure test was computed.

$$Dir = \frac{E_p}{|E_p|} \cdot \frac{Nc}{|N_c|} \quad (2)$$

A connectivity matrix, *A*, was generated for the mesh such that if two mesh elements shared an edge, their corresponding centroids were considered connected. The deformation and direction were then used to weight the connectivity matrix.

$$A_w = A * Def * Dir / \max(Dir) \quad (3)$$

The weighted connectivity of shared edges below a certain threshold were reduced to near zero, eliminating the impact of connections with low weight on predicted failure location.

$$A_{threshold} = \begin{matrix} A_w \geq threshold & A_w \\ A_w < threshold & A_w * 10^{-10} \end{matrix} \quad (4)$$

The threshold value was calibrated by fitting the means of the nonzero values of A_w and the effective threshold range for each sample.

$$threshold = -3.40 * mean(A_w) + 3.55 \quad (5)$$

Lastly, following Witzenburg et al. [9] the betweenness of the weighted mesh was computed and the sample was segmented into two distinct regions by removing mesh edges with the largest betweenness.

RESULTS

Fig. 2 shows the spatial variation in *Def* (A), E_p (B), A_w (C) and betweenness (D) for the PDMS sample with silicone sealant. The map of *Def* identifies edges with large differences in the deformation gradient, shown in brighter red, from 15 asymmetric extensions. The map of *Dir* identifies the principal strain directions in the subfailure equibiaxial extension as edges perpendicular to the principal direction are more likely to break. Lastly, betweenness incorporates the geometry of the mesh, favoring more central elements over more remote.

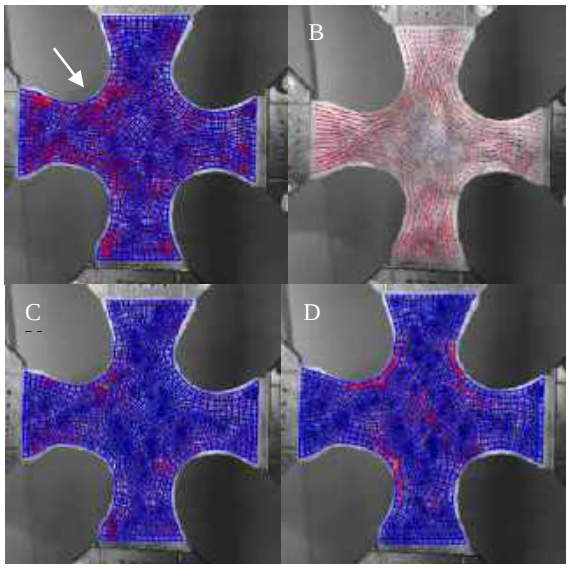

Figure 2: Difference in deformation gradient (A), principal strain for biaxial extension (B), weighted connectivity (C) and betweenness (D) for the heterogeneous PDMS sample with silicone sealant. The arrow in (A) indicates the location where the difference in deformation was largest.

The predicted failure locations for the PDMS samples were very close to the location of experimental failure (Fig. 3). Note that the predicted failure location did not necessarily correspond to the location of largest deformation gradient difference. For the PDMS sample with silicone sealant, *Def* was largest on the interior curve of the sample (arrow in Fig. 2A), while the failure location was across the left arm (Fig. 3C, E).

DISCUSSION

Failure prediction in heterogeneous soft materials is important clinically as disease and damage induces local extracellular matrix variations in tissues and puts them at high rupture risk [1,8]. Unfortunately, local spatial variations in structure can lead to unexpected failure location and mechanics. Our novel algorithm was able to predict failure locations for two heterogeneous PDMS samples, from full field subfailure deformation measurements. In an initial test we were also able to predict the corner where the grip failure initiated in a specimen of decellularized rat myocardium (Fig. 4). Notably this did not require alternation of the algorithm or the threshold value. Thus, this algorithm shows promise for predicting soft tissue failure, however further testing and validation is needed.

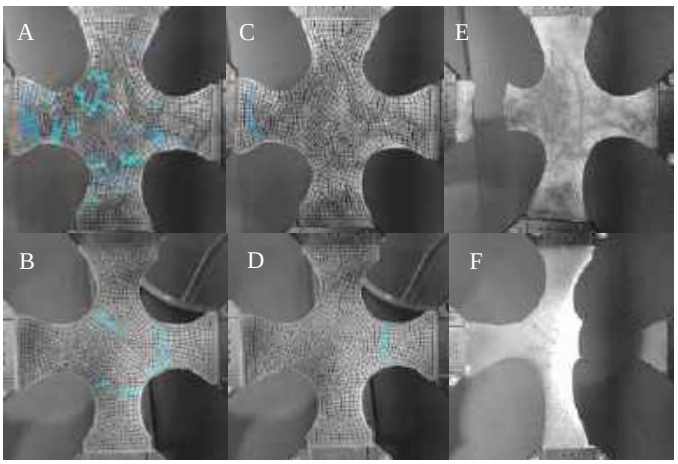

Figure 3: All edges removed prior to predicted failure for the PDMS with silicone sealant (A) or desiccant beads (B). Brighter blue edges were removed first and darker blue were removed later. Edges that were removed corresponding to predicted failure location (C, D). Experimental equibiaxial failure location (E, F).

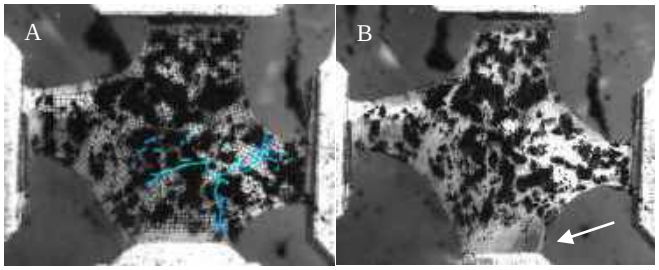

Figure 4: Decellularized myocardial tissue with myocardial infarction showing edges removed prior to predicted failure (A). Grip failure occurred at location of arrow (B).

ACKNOWLEDGEMENTS

This study was funded by a grant from the NSF (2030173).

REFERENCES

[1] Baliyan, V. et al., *Cardiovasc Diagn Ther*, 2018. [2] Perumal, V. et al., *Clinical Anatomy*, 2020. [3] Pearson, R. et al., *Euro J of Cardio-thoracic Surg*, 2008. [4] Wagner, P. et al., *Foot & Ankle Intl*, 2019. [5] Chittajallu, S. et al., *Bioeng*, 2022. [6] Rausch, M. et al., *Biomech Model Mechanobiol*, 2017. [7] Migueis, G. et al., *Clinical Biomech*, 2019. [8] Hadi, M. et al., *J of Biomech Eng*, 2012. [9] Pearce, D. et al., *Current Protocols*, 2022. [10] Witzenburg, C. et al., *Trans Med Img*, 2016.

INFLUENCE OF SEX AND SEX HORMONES ON SKELETAL RESPONSES TO INTERMITTENT PARATHYROID HORMONE (PTH) TREATMENT AND DISCONTINUATION

Y. Vincent Jin (1,2), Wonsae Lee (1), Tala Azar (1,2), Xiaoyu Xu (1), Kruti Desai (1), Wei-Ju Tseng (1), X. Sherry Liu (1,2)

(1) Department of Orthopaedic Surgery, University of Pennsylvania, Philadelphia, PA, U.S.
(2) Department of Bioengineering, University of Pennsylvania, Philadelphia, PA, U.S.

INTRODUCTION

Intermittent parathyroid hormone (PTH) is an FDA approved treatment for osteoporosis that rapidly elicits new bone formation. Our recent study unexpectedly discovered that intact female and estrogen-deficient female rats had distinct responses to the discontinuation of PTH treatment [1]. No adverse effect was observed in intact female rats, which sustained treatment benefit after PTH discontinuation [1], in contrast to the significant bone loss and bone microarchitecture deterioration observed in estrogen-deficient rats [1-3] and pre-pubertal male rats [4]. However, osteoporosis is a chronic disease that not only affects postmenopausal women, but also aged men. Moreover, though rare, young adults may also suffer from osteoporosis and require treatment. These motivate the objective of the current study to elucidate the influence of sex and gonadal function on skeletal responses to anabolic treatment (such as PTH) and discontinuation. We hypothesized that skeletal responses to PTH treatment and discontinuation are influenced by both sex and sex hormones. To test this hypothesis, ovariectomized (OVX) rats were used to simulate post-menopausal osteoporosis and orchiectomized (ORX) rats were used to simulate hypogonadism in aged men. Age-matched, intact female and male rats were used as young adults with intact gonadal function. Elucidation of the potential sexual dimorphisms associated with PTH treatment and discontinuation may help guide the novel design of anabolic treatment regimens to achieve the greatest treatment benefit by considering patient sex and gonadal function.

METHODS

Animals and treatments: Ten male Sprague-Dawley (SD) rats received bilateral ORX surgery at the age of 4 months and developed osteopenia for 4 weeks before being divided into ORX-PTH (n=5) and ORX-VEH (n=5) groups. Eleven age-matched male, intact SD rats were divided into two groups, Male-PTH (n=5) and Male-VEH (n=6). PTH 1-34 (40 μg/kg/day, 5x/week) was administered for three weeks while saline (VEH) was administered following the same injection plan as in the PTH groups. Data of intact and OVX female rats were from our previously published study [1]. Briefly, 18 female rats received bilateral OVX surgery at the age of 4 months and developed osteopenia for four weeks, before being assigned to groups of OVX-VEH (n=9) and OVX-PTH (n=9). Twelve age-matched female intact rats were divided into Female-PTH (n=6) and Female-VEH (n=6) groups. All animals and procedures were approved by UPenn's IACUC.

In vivo micro computed tomography (μCT) imaging: The right tibiae of male rats were scanned using *in vivo* μCT (Scanco vivaCT80, 11.6 μm voxel size) before ORX surgery (week -4), after osteopenia development (week 0, baseline), after PTH/VEH treatment (week 3), and during treatment discontinuation (weeks 4, 5, 8, 10, and 12). A landmark-initialized mutual information based registration toolkit [5] was employed to identify the corresponding volume of interest (VOI) at different timepoints (Fig. 1A). Bone volume fraction (BV/TV), trabecular thickness (Tb.Th), and trabecular number (Tb.N) were computed in the VOIs. Similar imaging and analysis protocols were used for female rats, with a voxel size of 10.5 μm [1].

Statistics: A two-way ANOVA with repeated measures was performed to compare treatment groups over time with adjustment for baseline. Bonferroni corrections were used for the multiple comparisons. The significance level was set at 0.05.

RESULTS

Skeletal responses in intact and ORX male rats:

Compared to the Male-VEH group (Fig. 1B), BV/TV decreased by 40% in the ORX-VEH group 4 weeks after ORX surgery and then remained stable for 12 weeks (Fig. 1C). In the Male-PTH group, BV/TV improved by 46% after 3-week PTH treatment and continued to increase for one week after the treatment discontinuation, which we defined as the extended anabolic period (EAP), followed by a continuous decrease from weeks 4 to 12 (Fig. 1B). Similarly, in the ORX-PTH group, 3-

week PTH treatment yielded a 97% increase in BV/TV, followed by a 1-week EAP, and decreased continuously after week 4 (Fig. 1C). In both intact and ORX male groups, the benefit in BV/TV from PTH treatment diminished after 9-week treatment discontinuation, as there was no difference in BV/TV between PTH- and VEH-treated bone in either the intact or ORX male groups.

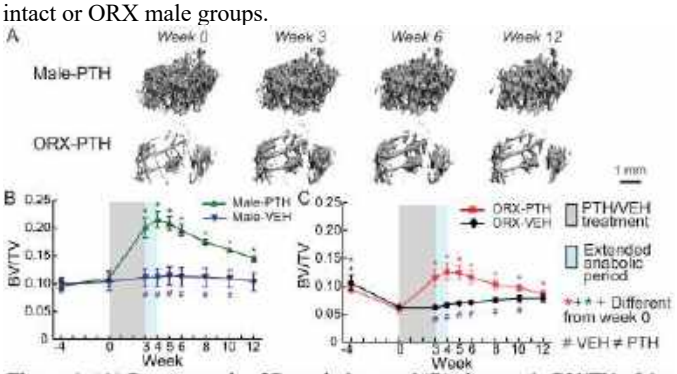

Figure 1. (A) Representative 3D renderings and (B) changes in BV/TV of the registered trabecular bone of the proximal tibiae of Male and ORX groups in response to PTH treatment and discontinuation.

Comparisons between intact male and female rats:

Although VEH treatments had minimal impacts on the BV/TV of intact males and females, there were significant differences between them starting at week 3 (Fig. 2A). These differences were due to the significant trabecular thickening in the males (Fig. 2B). Unexpectedly, there was a similar decline of Tb.N in both intact males and females (Fig. 2C). On the other hand, PTH treatment led to a 2.5-fold greater percentage increase of BV/TV in intact males than in intact females (Fig. 2D). The increased BV/TV in intact females was sustained stably during PTH discontinuation; however, BV/TV continued to decline from weeks 6 to 12 in intact males (Fig. 2D). Significant trabecular thickening occurred in both groups in response to PTH treatment, and the improvement in Tb.Th was maintained during the treatment discontinuation (Fig. 2E). In contrast, while Tb.N stabilized in females, it decreased continuously in males during treatment discontinuation (Fig. 2F).

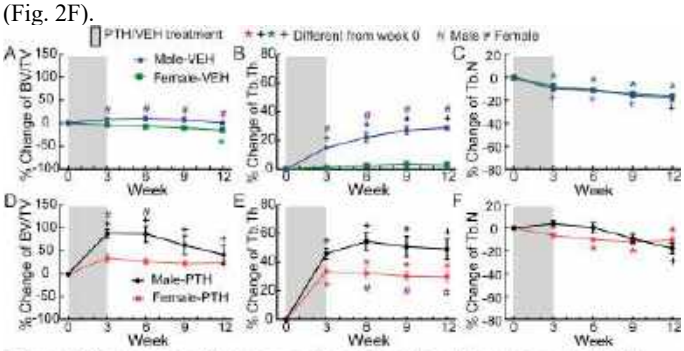

Figure 2. Comparisons between male and female rats in response to (A-C) VEH and (D-F) PTH treatements.

Comparisons between OVX and ORX rats:

There was a significant decline in BV/TV in OVX rats while no change in BV/TV was found in ORX rats (Fig. 3A). Intriguingly, trabecular thickening occurred in both ORX and OVX rats, with a greater extent (58% *vs.* 32%) of thickening in ORX *vs.* OVX rats. (Fig. 3B). Moreover, Tb.N decreased in both groups, but the rate of decrease was greater in OVX *vs.* ORX rats. PTH treatments led to improvements in BV/TV (104% *vs.* 31%) and Tb.Th (55% *vs.* 39%) in both groups, with a greater percent increase in ORX *vs.* OVX rats. Upon treatment discontinuation, BV/TV and Tb.Th continued to increase during the 1-week EAP in both groups. After the EAP, BV/TV started to decline and Tb.Th and Tb.N both reached a plateau in ORX rats (Fig. 3D-E). In contrast, BV/TV, Tb.Th, and Tb.N declined rapidly following the 1-week EAP (Fig. 3D-F).

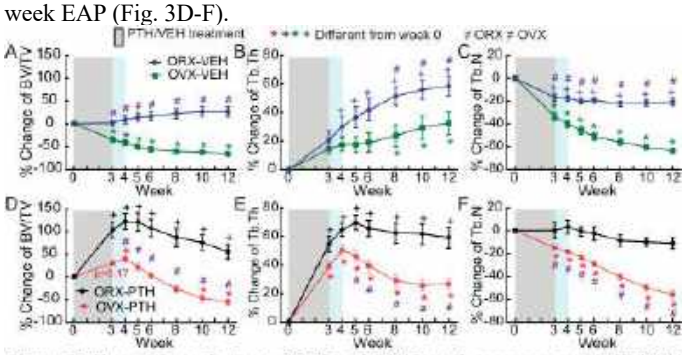

Figure 3. Comparisons between ORX and OVX rats in response to (A-C) VEH and (D-F) PTH treatements.

DISCUSSION

Understanding skeletal responses to the discontinuation of anabolic treatment is crucial to optimize osteoporosis treatment regimens. Significant bone loss after discontinuation of PTH treatment has been reported for postmenopausal women [6-8]. In contrast, there is limited yet conflicting clinical data on premenopausal women [9, 10] and limited data on young men. Similarly, although data are available for estrogen-deficient animals [1, 11], limited data are available regarding the PTH withdrawal effect in intact male or female animals.

Our current study suggested that skeletal responses to the discontinuation of PTH are sex dependent. PTH treatment led to increased bone mass by trabecular thickening in both intact males and females, with greater efficacy in males. However, upon withdrawal from PTH, a reduced number of trabeculae led to a decreased bone mass in male rats, in contrast to female rats, where no adverse effect was found. When comparing ORX and OVX rats that received VEH treatments, surprisingly, no significant bone loss was found in ORX rats, while in contrast, there was substantial bone loss in OVX rats. Our results indicated that trabecular thickening may be an adaptive mechanism to protect excessive bone loss from OVX/ORX conditions, with a greater thickening effect in ORX rats. Similar to intact rats, PTH treatment had greater efficacy in ORX *vs.* OVX rats. However, both ORX and OVX rats showed a significant withdrawal effect in response to PTH discontinuation.

Overall, our current work exhibited a sexual dimorphism in the skeletal responses to PTH treatment and discontinuation in rats. Our results indicated that intact male rats, ORX male rats, and OVX female rats all had significant withdrawal effects in response to PTH discontinuation. In contrast, no adverse effect was observed in intact female rats, which sustained treatment benefit even after 9 weeks of discontinuation. Given that OVX rats, intact male rats, and ORX rats all had substantially lower levels of estradiol than intact female rats, we suspect that skeletal responses to PTH discontinuation may be estradiol level-dependent, which will be a focus of our future studies.

ACKNOWLEDGEMENTS

Our work is supported by NIH/NIAMS R01-AR077598.

REFERENCES

[1] Tseng, W. et al, *JBMR*, 37:616-628, 2022. [2] Iwaniec, U. T. et al, *Bone*, 29:352-360, 2001. [3] Shahnazari, M. et al, *JBMR*, 26:569-581, 2011. [4] Gunness-Hey, M. and Hock, J. M., *Bone*, 10:447-452, 1989. [5] Lan, S. et al, *Bone*, 56:83-90, 2013. [6] Black, D. M. et al, *NEJM*, 353:555-65, 2005. [7] Leder, B. Z. et al, *JCEM*, 94:2915-2921, 2009. [8] Eastell, R. et al, *JBMR*, 24:726-736, 2009. [9] Finkelstein, J. S. et al, *JCEM*, 84:1214-9, 1999. [10] Cohen, A. et al, *JCEM*, 100:4208-14, 2015. [11] Duong, L. T. et al, *Bone*, 93:86-96, 2016.

MAGNETIC ACTUATION OF PIEZO1 FUNCTIONALIZED SUPERPARAMAGNETIC IRON OXIDE-GOLD NANOPARTICLES: A NOVEL DUAL ACTING OSTEOGENESIS AND ANTI-OSTEOPENIA NANOMEDICINE

Elias Georgas (1), Muzhaozi Yuan (2), Ya Wang (2, 3, 4), Yi-Xian Qin (1)

(1) Department of Biomedical Engineering, The State University of New York at Stony Brook, Stony Brook, NY, United States
(2) J. Mike Walker '66 Department of Mechanical Engineering, Texas A&M University, College Station, TX, United States
(3) Department of Biomedical Engineering, Texas A&M University, College Station, TX, United States
(4) Department of Electrical and Computer Engineering, Texas A&M University, College Station, TX, United States

INTRODUCTION

Osteoporosis is a debilitating disease that results in excessive bone loss that can lead to fragility fractures, which can increase mortality, especially in the spine, pelvic, and hip. This disease affects over 200 million patients worldwide and is set to increase further due to the increased life expectancy of the population.[1] Current osteoporosis treatments target osteoclast or osteoblast activity, specifically and very few can simultaneously target both cell types. Treatments that target osteoclasts result in an impairment of osteoblast recruitment, which leads to bone quality reduction and slight improvement in fracture risk.[2] In addition, targeting osteoblast activity has a limited effect over time, which hinders the bone mineral density improvement. Therefore, there is a clear need to develop novel dual-acting osteoporosis treatments.

Nanomaterials, especially nanoparticles that are less than 100 nm, have been attractive in bone and cartilage tissue engineering due to their ability to regulate cell differentiation, maintain tissue stability and promote tissue regeneration. Of the various nanomaterials, gold (Au) and superparamagnetic iron oxide (SPIO) nanoparticles (NPs) have gained significant attention. Au NPs allow for outstanding biocompatibility, high stability and tunable surface function. The ease of surface functionalization makes AuNPs more widely used due to the ability to modify drugs, proteins, peptides and DNA through thiol-Au linkage. SPIO-NPs are easy to synthesize and have good chemical stability, magnetic properties, and biocompatibility, making their use the most promising magnetic nanomaterial in clinical practice.[3] Furthermore, combining the properties of both Au and SPIO by creating Au-SPIO core-shell NPs, can protect the SPIO core and simultaneously enhance both the plasmonic and magnetic properties of Au and SPIO.

Bone is a highly mechanosensitive tissue that requires mechanical stimulation to maintain homeostasis. Localized targeting of mechanosensitive ion channels is a novel approach to enhance the cellular activity of bone cells. Piezo1 (P1), a newly discovered mechanosensitive ion channel, proves to play a critical role in responding to mechanical signals and bone formation. P1 deficiency in osteoblasts leads to loss of bone mass and fractures with increased bone resorption while P1 deficiency in osteoclasts has no effect on bone mass and bone resorption.[4] Interestingly, expression of P1 was significantly upregulated upon exposure to static magnetic field (SMF) in osteoblast cells on SPIO NP doped nanocomposites and only had small changes in expression with no SMF.[5] Our previous research has shown that dynamic magnetic fields (DMF) outperform SMF in enhancing cellular activity and differentiation when combined with SPIO-Au NPs.[6] Therefore, we hypothesized that DMF stimulation of P1 antibody functionalized SPIO-Au NPs will increase activity of P1 and calcium (Ca^{2+}) influx in osteoblasts, which will enhance differentiation and osteogenesis. Furthermore, since Au NPs and magnetic fields mitigate osteoclastogenesis,[7,8] separately, we hypothesized that DMF stimulation of P1-SPIO-Au NPs will also reduce osteoclast formation and function to further mitigate bone loss.

METHODS

The SPIO-Au NPs (20 nm diameter) were synthesized according to our previous work using the seed growth method.[6] P1 antibody was then functionalized to the Au surface using carbodiimide cross linker chemistry. The hydrodynamic diameter and zeta potential of the SPIO-Au NPs were measured after each conjugation step to confirm attachment.

In order to visualize the successful targeting of the P1 ion channel, Alexa Fluor 674 conjugated P1 antibodies were functionalized to SPIO-Au NPs. MC3T3-E1 osteoblast precursor cells were fixed, permeabilized, and stained with either P1-SPIO-Au NPs (20 μg/ml) or P1 antibodies alone. The cells were counterstained with DAPI and visualized using confocal microscopy.

DMF was created by rotating a Halbach array of magnets (0.5T) around a 35-mm petri dish using a DC motor as shown in our previous work.[6] Four groups were evaluated for Ca^{2+} influx: (1) Control, (2)

Control+P1-SPIO-Au NPs, (3) 0.5Hz DMF, (4) 0.5Hz DMF+P1-SPIO-Au NPs. MC3T3-E1 cells were subjected to 30 min of DMF stimulation and Ca^{2+} influx was measured using Fluo-4 3 min following the treatment via confocal microscopy. The baseline fluorescence was determined by averaging the first 10s after stimulation (F_0) and this value was used to normalize the fluorescence for each cell over time ($\Delta F/F_0$). The total fluorescence was determined through area under curve (AUC) analysis using the trapezoidal method.

Pre-osteoclast RAW 264.7 cells were differentiated using receptor activator of nuclear factor κ-β ligand (RANKL) and subjected to the same groups as the Ca^{2+} imaging described previously. DMF treatment was given for 30 min/day for 5 days and then cells were stained for tartrate-resistant acid phosphatase (TRAP) activity. The amount of osteoclasts formed was determined by counting the number of TRAP-positive cells containing ≥3 nuclei (MNCs).

All results were analyzed based on at least 3 independent experiments and differences between groups were compared using one-way ANOVA. Statistical significance was noted for $p<0.05$.

RESULTS

The hydrodynamic diameter and zeta potential of the SPIO-Au NPs were 54.7 ± 0.4 nm and -55.8 ± 0.5 mV, respectively. Attachment of SH-PEG-COOH to the surface increased the hydrodynamic diameter to 68.2 ± 1.8 nm and decreased the zeta potential to -69.15 ± 1.8 mV. The addition of PEG increased the size of the NPs and the addition of COOH created a highly negatively charged surface. After the addition of P1 antibody, the hydrodynamic diameter further increased to 114.7 ± 2.0 nm and the zeta potential increased to -47.9 ± 1.5 mV, indicating the successful conjugation of P1 to SPIO-Au NPs.

The immunofluorescence staining of MC3T3-E1 cells shows that P1 is expressed on the membrane (Fig. 1(a)) and that fluorescently conjugated P1-SPIO-Au NPs were located in the same areas as the antibodies alone (Fig. 1(b)). This demonstrates that P1-SPIO-Au NPs can effectively target P1 in osteoblast cells.

To demonstrate whether DMF can enhance the opening of P1 channels using P1-SPIO-Au NPs, the Ca^{2+} signal in the cell body was visualized using confocal microscopy. Results showed that calcium fluorescence increased 3 min following 30 min of DMF stimulation, but the combination with P1-SPIO-Au NPs resulted in a sustained effect (Fig. 1(c)). Incubation with P1-SPIO-Au NPs alone had no effect on Ca^{2+} fluorescence, while control cells had a decrease in Ca^{2+} fluorescence (Fig. 1(c)). Further quantification using AUC analysis revealed that DMF stimulated P1-SPIO-Au NPs significantly increased Ca^{2+} influx compared to DMF and P1-SPIO-Au NPs alone, and control ($p<0.05$, $p<0.01$, and $p<0.001$, respectively). DMF and P1-SPIO-Au NPs also had significantly greater Ca^{2+} influx compared to control ($p<0.01$), while DMF had a slight more increase in Ca^{2+} influx compared to P1-SPIO-Au NP, but was not significantly different.

To determine the effect of DMF stimulation on osteoclast activity, the amount of osteoclasts, TRAP+ MNCs, were counted. The results showed P1-SPIO-Au NPs, DMF, and DMF + P1-SPIO-Au NPs significantly reduced the formation of osteoclasts compared to the control (Fig. 1(e)) ($p<0.0001$). DMF + P1-SPIO-Au NPs resulted in the greatest inhibition of osteoclast formation, but this reduction was not significant compared to DMF alone.

DISCUSSION

In this work, we demonstrated the ability to magnetically activate P1 functionalized SPIO-Au NPs to enhance the mechanosensitive nature of osteoblasts. Changes in Ca^{2+} intracellular concentration are key secondary messengers in signaling pathways that regulate gene transcription, mRNA translation, and post-translation protein modifications. Here, we show that DMF stimulation of P1-SPIO-Au NPs greatly increases the Ca^{2+} influx in osteoblast cells, which may further regulate proliferation and differentiation. Our previous study investigating DMF stimulated SPIO-Au NPs on neuronal cells found that increased Ca^{2+} influx resulted in enhanced neuronal gene expression, which is in accordance with these results.[6] In addition, magnetic actuation of P1-graphene oxide NPs has been shown to greatly enhance osteogenic gene expression.[9] Further evaluation on osteogenic activity is needed to confirm the potential of DMF stimulated P1-SPIO-Au NPs to increase bone formation, which is ongoing.

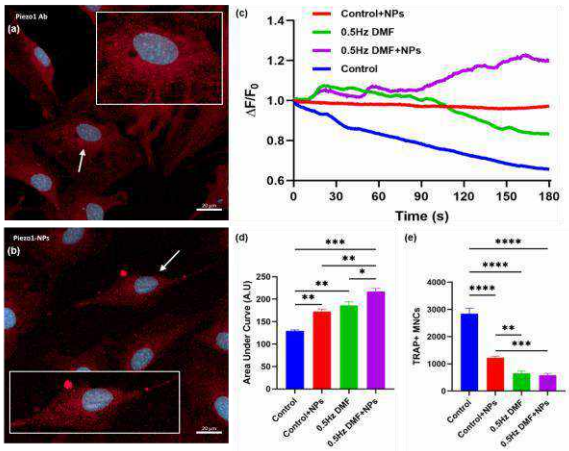

Figure 1: Representative MC3T3-E1 P1 immunofluorescence images after incubation with (a) P1 antibody or (b) P1-SPIO-Au NPs (Red: Piezo1, Blue: Nucleus, Arrow: Zoomed insert, Scale bar: 20 µm). DMF stimulation of P1-SPIO-Au NPs results in an increase in average change in intracellular Ca^{2+} fluorescence (c), and an increase in total intracellular Ca^{2+} fluorescence (d) in osteoblasts, while inhibiting osteoclast formation (e). *p<0.05, **p<0.01, ***p<0.001, ****p<0.0001

Interestingly, we showed that DMF stimulation of P1-SPIO-Au NPs resulted in reduced osteoclast formation. Au NPs have been shown to inhibit osteoclast formation by attenuating reactive oxygen species production, which leads to suppression of osteoclast fusion.[7] Furthermore, SMF attenuates the nuclear factor-κβ pathway in osteoclasts,[8] which may explain the combined effect seen in our results.

In summary, this study demonstrated the potential for a novel non-invasive bone regeneration approach using DMF stimulation integrated with P1-SPIO-Au NPs by simultaneously activating osteoblasts and inhibiting osteoclasts, which may pave the way for future osteoporosis treatments.

ACKNOWLEDGEMENTS

The authors would like to acknowledge the United States Nation Science Foundation (NSF) GCR awards ECCS 2021081 (Y.W.) and ECCS 2020867 (Y-X.Q.) for funding this work.

REFERENCES

[1] Ström, O et al., *Arch Osteoporos*, 6:59-155, 2011.[2] Eastell, R et al., *Osteoporos Int*, 21:1277-1285, 2010.[3]Yuan, M et al., *Nanomaterial*s, 12(13):2242, 2022.[4] Wang, L et al., *Nat Commun*, 11:282, 2020.[5] Hao, L et al., *Nanoscale*, 11:23423-23437, 2019.[6] Georgas, E et al., *Bioact Mater*, 26:478-489, 2023.[7] Shi, Y et al., *Front Chem*, 9:724188, 2021.[8] Kim, EC et al., *Bioelectromagnetics*, 39(5):394-404, 2018. [9] Unnithan, AR et al., *Adv Funct Mater*, 32:50, 2022.

PHARMACEUTICAL INTERROGATION OF PODOCYTE BIOMECHANICS THROUGH KINOME SCREENING

Jonathan C. Haydak (1,2), Anika Hudson (1), Stefanie DeFronzo (3), Yibang Chen (1), Nanditha Anandakrishnan (1), Alan D. Stern (1), Evren U. Azeloglu (1,2)

(1) Department of Nephrology, Icahn School of Medicine at Mount Sinai, New York, NY, USA
(2) Department of Pharmacological Sciences, Icahn School of Medicine at Mount Sinai, New York, NY, USA
(3) Department of Bioengineering, Northeastern University, Boston, USA

INTRODUCTION

Podocytes are highly specialized, terminally differentiated epithelial cells with an arborized morphology that wrap around the glomerular endothelial capillaries and interdigitate with each other to serve as the final component of the glomerular filtration barrier. In proteinuric kidney diseases, such as hypertensive and diabetic nephropathy, podocytes undergo pathologic cytoskeletal rearrangement called foot process effacement (FPE) resulting in a simplification of their morphology and altered biomechanics[1, 2]. Although alterations to the podocyte cytoskeleton and biophysics are a key driver of disease progression, a full mechanistic model driving this phenomenon remains elusive. Here we sought to gain insight into pathways underpinning foot process effacement in podocytes by integrating results from an *in vivo* model of FPE with *in vitro* drug screening. Sprague-Dawley rats injected with puromycin aminonucleoside (PAN), a nephrotoxin, induces temporary and reversible massive proteinuria and FPE in rats [3]. Unbiased proteomics from isolated glomeruli of the PAN-treated rats showed an altered kinome expression that returned to baseline upon resolution of proteinuria. To probe the relative contributions of different kinases on podocyte biomechanics, we performed high content image analysis on iPSC-derived human podocytes treated with various tyrosine kinase inhibitors (TKIs). Although TKIs are clinically used for specific inhibition of one or several kinases, we leveraged their entire inhibition profile obtained from KinomeScans [4, 5] to computationally resolve individual kinase contributions to cytoskeletal and focal adhesion phenotype (Fig. 1). Finally, we identified the Hippo pathway as a key determinant of podocyte biomechanics.

METHODS

6-week-old male Sprague-Dawley rats were injected with 100mg/kg puromycin aminonucleoside (Sigma Aldrich) or phosphate buffered saline (PBS) as control. Rats were euthanized according to approved IACUC protocols, and the kidneys harvested for glomerular isolation using serial sieving at post-injection days 7, 14, 21, and 28. Quantitative isobaric TMT proteomics was then performed on the isolated glomeruli.

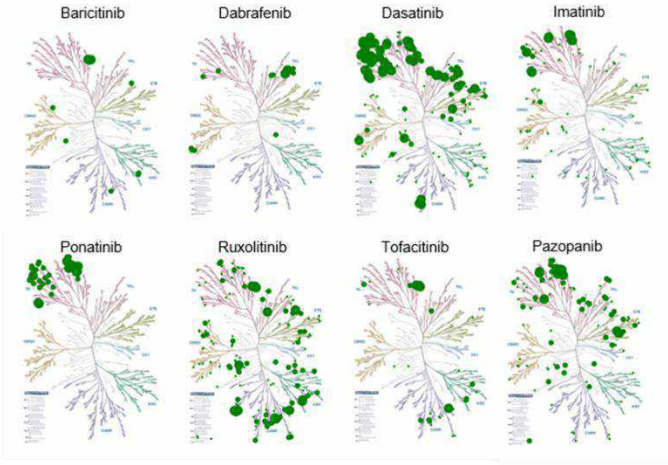

Figure 1: Inhibitory profile of select TKIs used in this study.

For high content imaging, iPSC-derived podocytes were plated onto a 96 well plate (Corning Incorporated) coated with Matrigel. Wells were treated with 12 different TKIs at a concentration of 2 µM for 24 hours and then fixed and stained for nuclei, paxillin, synaptopodin, and YAP. Imaging was performed on an InCell Analyzer 2200 (GE Healthcare) using a 40x air objective. To generate cell and nuclear masks, segmentation with Cellpose was carried out on combined synaptopodin/YAP and the nuclear channel respectively. The raw images and labelled masks were imported into Matlab and run through

an in-house script to generate intensity and morphological based features.

The high content image analysis results and publicly available TKI inhibition profiles from LINCS [5] were run through an in-house SVD-based feature analysis script to calculate individual kinase contributions on cell, focal adhesion, and nuclear morphology and features. Enrichment analysis of top ranking kinases was performed using Enrichr [6] and interconnectivity using Genes2Networks [7].

RESULTS

Male Sprague-Dawley rats (n=3, each group) were injected with a single dose of 100 mg/kg PAN or PBS and monitored for 4 weeks. Rats treated with PAN developed significant albuminuria that peaked at day 7 and achieved near complete resolution by day 28 (Fig. 2A). The rats were euthanized on days 7, 14, 21, and 28 and the kidneys harvested for glomerular isolation. Unbiased isobaric TMT proteomics of the isolated glomeruli revealed significant alterations in kinase expression, correlating with the degree of albuminuria (Fig. 2B).

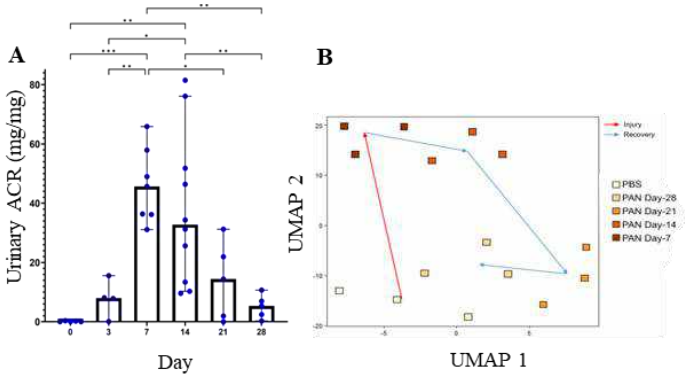

Figure 2: Kidney dysfunction in PAN rats corresponds with altered kinome expression. (A) Urine Albumin-Creatinine ratio over 28 days. (B) UMAP of kinome obtained from proteomics.

We next hypothesized that altered kinase activity is sufficient to drive podocyte cytoskeletal rearrangement and sought to quantify the relative contributions of individual kinases in maintaining podocyte cytoskeletal integrity. To this end, we performed high content image analysis of iPSC-derived human podocytes treated with 12 clinically used TKIs to assess cytoskeletal and focal adhesion organization, obtaining a unique feature signature for each TKI (Fig. 3).

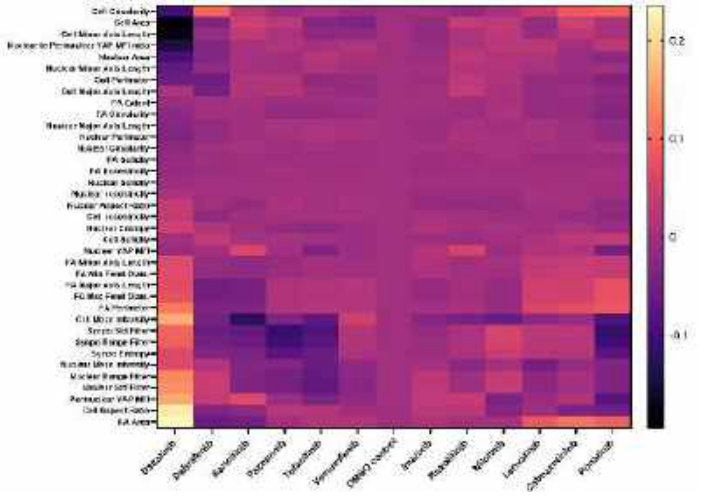

Figure 3: High content image analysis of cytoskeletal and focal adhesion related features of TKI-treated podocytes.

By using the kinome inhibitory profile of each drug (obtained from LINCS), we performed feature analysis to quantify the impact of inhibiting each kinase on each assessed metric. From here, a list of kinases ranked by fold change in the PAN rats at day 7 and a list kinases ranked by cumulative impact on all high content imaging metrics was consolidated to generate a final ranked list of kinases. The top 20 consolidated kinases showed high interconnectivity and overrepresentation analysis identified the Hippo pathway as significantly enriched (adjusted p-value 2.3e-8) (Fig. 4).

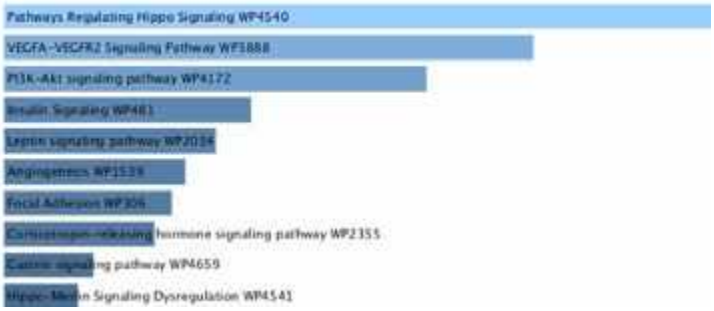

Figure 4: Overrepresentation analysis of the top 20 consolidated kinases on WikiPathways.

DISCUSSION

In this study we integrated proteomics from an *in vivo* kidney disease model to an *in vitro* drug screening assay to identify key kinases that regulate and maintain the podocyte cytoskeleton. The top candidate kinases identify enrich for the Hippo pathway, a signaling pathway whose dysfunction is both sufficient to cause glomerular disease and observed in human kidney disease [8, 9].

In addition to the identification of kinases regulating podocyte biomechanics, this study also provides a means of screening TKIs for potential nephrotoxicity. This framework of using TKIs to deconvolve relative kinase contributions can be applied to virtually cells of any type for any high content metric.

ACKNOWLEDGEMENTS

This study was funded by NIH grant R01 DK118222. J. Haydak was partially funded by T32 HD075735. We would like to acknowledge Dr. Ravi Iyengar for generously sharing his laboratory resources for the rat experiments.

REFERENCES

1. Faul, C., et al., Trends Cell Biol, 2007. **17**(9): p. 428-37.
2. Kriz, W., et al., American Journal of Physiology-Renal Physiology, 2012. **304**(4): p. F333-F347.
3. Ge, X., et al., J Am Soc Nephrol, 2020. **31**(10): p. 2372-2391.
4. Anastassiadis, T., et al., Nat Biotechnol, 2011. **29**(11): p. 1039-45.
5. Davis, M.I., et al., Nat Biotechnol, 2011. **29**(11): p. 1046-51.
6. Xie, Z., et al., Current Protocols, 2021. **1**(3): p. e90.
7. Berger, S.I., J.M. Posner, and A. Ma'ayan, BMC Bioinformatics, 2007. **8**: p. 372.
8. Meliambro, K., et al., JCI insight, 2023. **8**(7).
9. Meliambro, K., et al.. Journal of Biological Chemistry, 2017. **292**(51): p. 21137-21148.

AUTOMATED BLADDER SEGMENTATION OF 3D DYNAMIC MRI FOR URODYNAMIC ANALYSIS USING DEEP LEARNING

Labib A. Shahid (1), Juan Pablo Gonzalez-Pereira (1), Jennifer A. Franck (1), Alejandro Roldan-Alzate (1,2,3)

(1) Department of Mechanical Engineering, University of Wisconsin-Madison, Madison, WI, USA
(2) Department of Radiology, University of Wisconsin-Madison, Madison, WI, USA
(3) Department of Biomedical Engineering, University of Wisconsin-Madison, Madison, WI, USA

INTRODUCTION

Bladder voiding dysfunction is common among aging men and is often associated with benign prostatic hyperplasia (BPH) and lower urinary tract symptoms (LUTS) [1]. Over 50% of men over 60 years of age suffer from BPH, and 15%-30% of these men have LUTS [2]. Multichannel urodynamic studies are the most common diagnostic method to assess BPH/LUTS [3,4]. These procedures are highly invasive, requiring urethral and rectal catheterization, and provide insufficient information on biomechanical properties, bladder anatomy, and detrusor muscle function [5,6]. Our research group recently published the feasibility of using 3D dynamic MRI to calculate various urodynamic nomograms non-invasively [7]. However, manually segmenting the bladder is a time-consuming step and is a bottleneck for increasing the study cohort. The objective of this study is to implement a deep learning approach that automatically segments the bladder from 3D dynamic images of voiding. This will significantly accelerate our MRI urodynamic workflow.

METHODS

Male subjects were recruited following an IRB-approved HIPAA-compliant protocol. Subjects underwent pelvic MRI on a clinical 3T scanner (Premier, GE Healthcare, Waukesha, WI, USA). The pulse sequence used was either 3D Differential Subsampling with Cartesian Ordering (DISCO) Flex where patients received 1/3 of a single weight-based (0.1 mmol/kg) of gadolinium-based contrast which was slowly hand injected intravenously 15 minutes prior to the start of the imaging session, or balanced steady state free precession (bSSFP) that did not require contrast. Subjects that received contrast were asked to walk around to ensure contrast mixing and homogenous enhancement of the urine in the bladder. Immediately before the scan, the subjects were equipped with a condom catheter to allow micturition and urine collection while scanning. Subjects were scanned in supine position and volumetric dynamic images of the bladder and urethra were acquired throughout the voiding event. The spatial resolution was 1 mm × 1 mm isotropic in the sagittal plane, with a slice thickness of 2 mm.

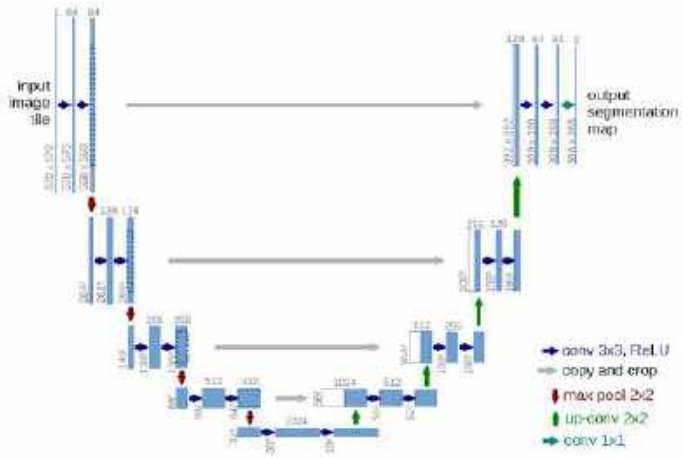

Figure 1: U-Net architecture from Ronneberger et al. [8]

The 3D image datasets were loaded into semiautomatic segmentation software Mimics (Materialise NV, Leuven, Belgium). The bladder was manually segmented such that there were separate 3D masks at each time point of the voiding event. These manually segmented masks served as the ground truth. The U-Net [8] convolutional neural network (CNN) was used to automatically detect the bladder geometry and generate binary masks. The input image undergoes a series of convolutions, rectified linear units, and max pooling operations. The number of channels increase in the contracting path, then decrease in the expansive path. There are 23 convolutional layers in the U-Net architecture. Figure 1 shows the details of the U-Net

architecture that we implemented. We used augmentation (rotations and flips) to quadruple the dataset size. The CNN was implemented using PyTorch (The Linux Foundation, San Francisco, CA, USA) inside a Docker container, and the source code is publicly available (https://github.com/lshahid/Pytorch-UNet). All training and testing were performed on an Intel Core i7-9800X processor and Nvidia Titan RTX GPU on a desktop workstation. Dice score was used to compare manual and automated segmentations.

RESULTS

Five subjects underwent pelvic MR scans and 3D dynamic images were successfully acquired while they voided during scanning. Table 1 provides the subject and scan information. Figure 2 visualizes the bladder for all five subjects. Subject 5's images exhibited significant artifact due to eddy currents that led to poor image quality. 8702 2D sagittal images (256 × 256 pixels) from 3D dynamic MRI were used, with 10% used for validation. After augmentation, the total number of images was 34808. The total training time was 14 hours. The final Dice score was 0.99. Time to manually segment one 3D bladder at one time point was 20 minutes, compared to < 3 minutes using the automated approach.

Table 1: Subject and scan information

Subject	Age	BPH/LUTS?	Pulse Sequence	Temporal Resolution	Void Time
1	29	No	3D DISCO Flex	3.8	111
2	55	No	3D DISCO Flex	4.7	156
3	56	Yes	3D DISCO Flex	4.8	77
4	70	Yes	3D DISCO Flex	5.0	64
5	35	No	bSSFP	1.7	53

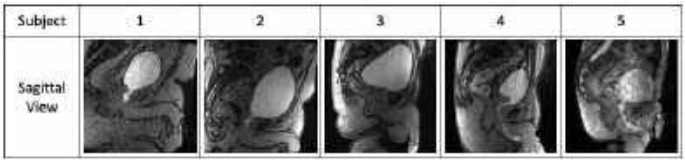

Figure 2: MRI of bladder in the sagittal plane in the middle of voiding

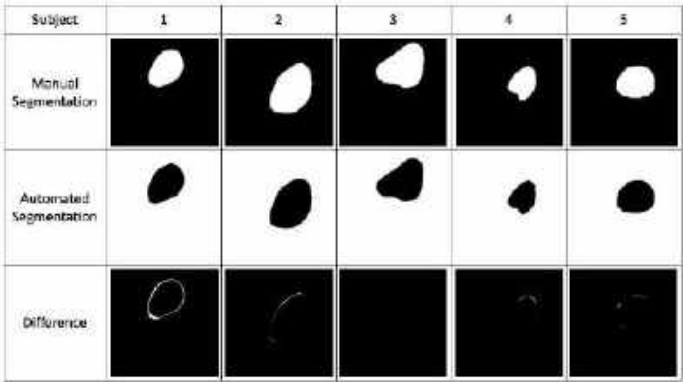

Figure 3: Manual, automated segmentation, and their difference, at the middle of voiding

DISCUSSION

Using 3D dynamic MRI of only five patients, we implemented a deep learning-based automated segmentation of the bladder during voiding. The main findings of the study are that the CNN segments a 3D bladder at one time point in < 3 minutes, produces excellent segmentation, and performs well over a range of subject ages, phenotypes, and two different sequences. Figure 3 shows that the difference in segmentations is about 1-3 pixel wide around the bladder wall, which is in the range of spatial resolution. We chose the U-Net architecture due to its popularity in the image segmentation field. We also prioritized portability of the CNN by using a container which will allow easier scaling to high-performance computing clusters and sharing with the scientific community. The segmented masks can be used to calculate urodynamic metrics including flow rate, post-void residual volume, and bladder neck angle. Future studies would investigate spatio-temporal interconnectivity of the images, increase the number of subjects, explore the effects of interobserver variability and scan parameters, and compare the urodynamic metrics from manual segmentation with automated. We previously introduced MRI urodynamics using 3D dynamic imaging to enhance information from UDS while being non-invasive. Segmentation is the most tedious step in our workflow, and this automated process significantly reduces operator time. This acceleration in the workflow paves the path for MRI urodynamics to increase cohort size including women, diabetes patients, and patients with overactive bladder.

ACKNOWLEDGEMENTS

NIH R01 DK126850-01A1 and Wisconsin Partnership Program WPP AAM3497. GE Healthcare, which provides research support to the University of Wisconsin-Madison.

REFERENCES

[1] Roehrborn CG. Benign prostatic hyperplasia: an overview. Rev Urol. 2005;7 Suppl 9(Suppl 9):S3-S14.

[2] Thorpe A, Neal D. Benign prostatic hyperplasia. Lancet. 2003 Apr 19;361(9366):1359-67. Erratum in: Lancet. 2003 Aug 9;362(9382):496.

[3] Nitti VW. Pressure flow urodynamic studies: the gold standard for diagnosing bladder outlet obstruction. Rev Urol. 2005;7 Suppl 6(Suppl 6):S14-21.

[4] Blaivas J. Multichannel urodynamic studies. Urology. 1984 May;23(5):421-38.

[5] Bushman W. Etiology, epidemiology, and natural history of benign prostatic hyperplasia. Urol Clin North Am. 2009 Nov;36(4):403-15.

[6] Pewowaruk R, Rutkowski D, Hernando D, Kumapayi BB, Bushman W, Roldán-Alzate A. A pilot study of bladder voiding with real-time MRI and computational fluid dynamics. PLoS One. 2020 Nov 19;15(11):e0238404.

[7] Gonzalez-Pereira JP, Johnson CJ, Wells S, Bushman W, Roldan-Alzate A. Technical feasibility of uro-dynamic MRI study of voiding biomechanics: a pilot study. Int Urol Nephrol. 2023 Oct 12.

A 'DINNER PARTY' THEMED APPROACH TO CONSTRUCTING EQUITABLE AND EXCITING LITERATURE REVIEWS

D.P. Pearce (1) and C.R. Henak (1,2)

(1) Department of Biomedical Engineering, UW-Madison, Madison, WI, USA
(2) Department of Mechanical Engineering, UW-Madison, Madison, WI, USA

INTRODUCTION

Citations in peer-reviewed articles help solidify the influence and value of the cited studies, but have traditionally contained biases against women and people of color (PoC).[1,2] This results in a lack of citations and recognition for these individuals, and may influence decisions regarding hiring and funding applications. Past work has shown black and Latinx men to be notoriously underrepresented in health and biomedical research, while black, Latinx, and white women were all underrepresented in fields such as engineering and technology, mathematics, and physics.[3] Although citational patterns vary from field to field, many of these biases are still present today despite a growing increase in awareness.[3]

Techniques to visualize and organize citations for a manuscript, such as the *dinner party* strategy,[4] may help promote more equitable citational patterns. The dinner party strategy, first proposed by Kamler and Thomson,[4] transforms the lead author's role to that of a host of a generous and elaborate dinner party, in which each cited author is invited and present at the party. The lead author, or host, then arranges guests based on shared interests, experimental designs, or findings, grouping cited studies in a way that fosters clear connections between studies and promotes a valuable discussion focused on synthesis of ideas and proposed 'next steps' for the field.[4] This technique is employed in literature reviews to promote higher-quality, interwoven narratives, but may also be used as a resource to help reduce student's writing anxiety.[5,6] Additionally, the dinner party technique could be used to promote more equitable citational patterns. By including pictures of cited authors, the lead author is given information regarding the demographics of their bibliography. Should they find their citational patterns to be exclusive, they may go back and add new studies to promote more equitable citational patterns.

Here, we studied graduate student awareness of citational justice in a Tissue Mechanics course at UW-Madison. We hypothesized that students would be generally unaware of citational justice prior to the new instructional material, and that the requirements of this assignment would result in more equitable citational patterns compared to the student's initial submissions. Through this work, we hope to share strategies to aid students learning to write literature reviews and to highlight the importance of being intentionally inclusive when conducting literature searches.

METHODS

Survey Design and Distribution. A survey (MRR IRB 2023-1411) was developed to assess student's awareness of citational justice prior to the delivery of our new lecture material and to help quantify the effectiveness of this material. The survey was distributed digitally to graduate students in BME/ME 615: Tissue Mechanics, a split undergraduate/graduate technical elective course offered at UW-Madison. A total of 8 graduate students were enrolled in the course. The survey, discussed in more detail in the subsequent section, was sent out to students one week prior to the delivery of content material, then one week after the submission of the first draft of their literature review assignment. Responses to the survey, which offered participants the opportunity to use a unique study identifier to log their before-and-after answers, were not accessed until the end of the Fall 2023 semester according to IRB guidelines.

Quantifying Impact of Material and Student Awareness. Our survey first explained the objectives of our study, the accompanying instructional material, and offered participants the chance to grant waived consent. Participants were asked to create a unique identifier using the following scheme: (Birth Month XX) + (First two letters of mother's name) + (First two numbers from current mailing address), taking the form of 12RE72, for example. We then asked participants to select their sex assigned at birth, then the gender with which they identified the most.[7] Next, we asked students a series of questions about their ability to define and explain the concept of citational justice, their perception of its significance and its impact, and strategies for

improving the equitability of citational patterns. For all questions regarding citational justice, participants were presented with multiple-choice answers ranging from Strongly Disagree (-10) to Neither Agree nor Disagree (0) to Strongly Agree (10). These questions were formatted similar to questions presented during end-of-class surveys for ABET accreditation processes.[8,9]

Instructional Material and Delivery. A self-directed literature review assignment is the course project for graduate students in BME/ME 615: Tissue Mechanics. A portion of the assignment is the annotated bibliographies of the studies they plan to use for their literature review. We introduced the dinner party technique and citational justice with a 23-minute asynchronous lecture (available upon request). For their annotated bibliographies, students were required to find pictures of the first and last authors for their cited studies, submit a dinner party for their bibliography, discuss the equitability of their citational patterns, then address any gaps in their citational patterns they may have observed. All assignments were submitted digitally via Canvas.

Quantifying Equitability of Citational Patterns. An example assignment was given to students (and elaborated on during the asynchronous lecture) to demonstrate the dinner party technique. In this example assignment, the most glaring inequities were a lack of women and PoC authors in both first and last author positions. We reported the mean ± st. dev. years for the example assignment, as well as the Man:Woman (M:W) and White:PoC (W:PoC) splits, resulting in similar analyses by many students. For this study, we manually checked the mean year, M:W, and W:PoC splits reported by our students by reviewing headshots, lab webpages, and/or LinkedIn profiles for the first and last authors of each study, and completed this analysis for reviews with different approaches. It is worth noting here that these metrics both reduce identity to a binary state, an inaccurate simplification, but reflects limitations of quantitative tools that may be used in the future to more systematically perform this kind of analysis.[10,11]

Statistical Analysis. Before-and-after survey results, as well as M:W and W:PoC splits before and after our required assignment, were compared statistically using a Wilcoxon signed-rank test. Analyses were performed using GraphPad Prism 10 (Dotmatics; Boston, MA).

RESULTS

M:W and W:PoC splits trended towards a more equitable distribution following the dinner party assignment (Figure 1). For each split, a value of 1 was considered desirable. It is worth nothing that a split of 1 may not be realistic, especially for the W:PoC metric. Following the dinner party assignment, each of these splits displayed a trend towards 1, suggesting improvements in the equitability of the student's citational patterns. Wilcoxon signed-rank tests revealed statistically significant improvements for only the W:PoC split for the first author position, which is likely due to a small sample size and the limited additions (2 – 3 studies) required of students.

We observed positive increases for each survey question, particularly regarding the ability of students to identify strategies to improve the equitability of their citations (Figure 2). These observations were limited by a small number of survey responses and only one true before-after completion (indicated with a *square marker*), so no statistical analysis was included.

DISCUSSION

Despite initial unawareness regarding citational justice, we found that our dinner party assignment and the accompanying lecture promoted more equitable citational patterns and offered students techniques they could use to improve the fairness of their work.

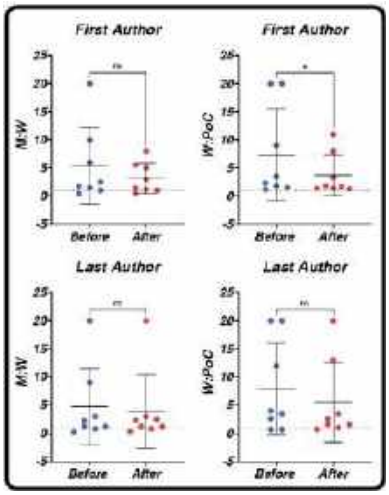

Figure 1. M:W and W:PoC splits for the first and last author positions *before* and *after* the dinner party assignment (*$p < 0.05$).

Citations establish the influence and impact of a study, but are given to women and authors of color at lower rates than men and white authors.[1,2] We found that requiring students to be intentionally inclusive with their references did, in fact, promote more equitable citational patterns. Although we received a limited number of survey responses, we saw encouraging trends in student awareness of citational justice. This was most evident in the ability of students to identify and implement strategies to improve the equitability of their citational patterns. This study was limited by the small sample size and lack of before-after survey responses, which we hope to improve in future iterations of the class. We also hope to compare this semester's citational patterns to those from past semesters to determine the effectiveness of the intervention for promoting more equitable bibliographies. We anticipate this work has improved students' awareness of citational justice, and hope future efforts will be made to actively and intentionally improve the equitability of bibliographies published in peer-reviewed journals.

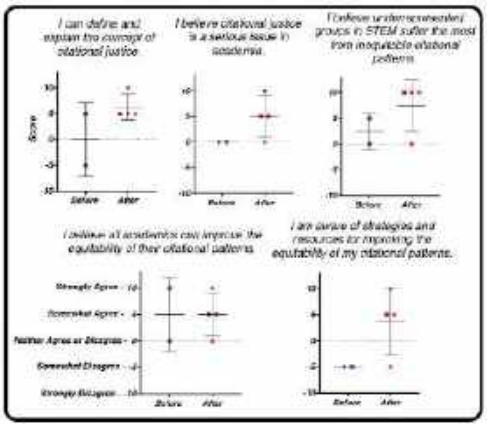

Figure 2. Student opinions of citational justice *before* and *after* delivery of new instructional material.

ACKNOWLEDGEMENTS

The authors would like to thank Dr. Alejandro Roldán-Alzate for his help with participant recruitment; Dr. Rouzbeh Amini and Frederick Sebastian for their encouragement and guidance while designing this study; the Delta Program in Research, Teaching, and Learning; and the graduate students who completed our surveys and put together excellent reviews.

REFERENCES

[1] Kwon, D. *Nature* 603 (2022). [2] Rossiter, M. W. *Soc. Stud. Sci*. 23 (1993). [3] Kozlowski, D. et al. *Proc. Natl. Acad. Sci*. 119 (2022). [4] Kamler, B. & Thomson, P. (2014). [5] Huerta, M. et al. *High. Educ. Res. Dev*. 36 (2017). [6] Zhang, X. *Int. J. Educ. Technol. High. Educ*. 16 (2019). [7] GenIUSS. (2014). [8] He, Y. et al. *J. Chem. Educ*. 89 (2012). [9] Liu, Y. & Baker, F. *Int. J. Mech. Eng. Educ*. 46 (2018). [10] Elmas, F. https://pypi.org/project/SexMachine/. [11] Zhou, D. https://github.com/dalejn/cleanBib (2023).

TRPV4 INTEGRATES MATRIX MECHANOSENSING TO MODULATE CALCIUM SIGNALING AND MECHANOBIOLOGY IN SCHLEMM'S CANAL CELLS

Haiyan Li (1), Seyed Mohammad Siadat (2), Kristin M. Perkumas (3), Jacques A. Bertrand (4), Darryl R. Overby (4), Todd Sulchek (5), W. Daniel Stamer (4), C. Ross Ethier (1,5)

(1) Biomedical Engineering, Georgia Institute of Technology/Emory University, Atlanta, GA, United States
(2) Bioengineering, Northeastern University, Boston, MA, United States
(3) Department of Ophthalmology, Duke University, Durham, NC, United States
(4) Bioengineering, Imperial College London, London, United Kingdom
(5) Mechanical Engineering, Georgia Institute of Technology, Atlanta, GA, United States

INTRODUCTION

Glaucoma is the leading cause of irreversible vision loss worldwide, and elevated intraocular pressure (IOP) is the only modifiable risk factor [1-3]. Elevated IOP results from increased resistance to aqueous humor (AH) outflow in the juxtacanalicular region of the conventional outflow pathway where the trabecular meshwork (TM) and Schlemm's canal (SC) inner wall cells interact [4].

The SC inner wall experiences a basal-to-apical pressure gradient which deforms SC cells to create giant vacuoles and pores that facilitate fluid drainage from the eye [5]. This deformation may also trigger mechanosensitive ion channels, such as transient receptor potential vanilloid 4 (TRPV4). These cationic channels open in response to physical deformation (i.e., cell membrane strain) to allow calcium influx and thus initiate downstream signaling [6]. However, the precise role of TRPV4 in SC cells remains unclear.

The substrate of the SC inner wall, known as the trabecular meshwork (TM), is stiffer in glaucoma [7-9]. Here we investigate how TRPV4 activity and substrate (matrix) stiffness modulate SC cell mechanobiology, with a focus on actin cytoskeletal structure, cell stiffness, and pore formation.

METHODS

Primary SC cells were isolated from healthy and glaucomatous human eyes, and characterized using established protocols [10]. Five normal (nSC) and three glaucomatous (gSC) SC cell strains were used in this study, with donor demographics as follows: nSC75: Male/10-years-old; nSC74: M/0.67; nSC82: na/56; nSC87: M/62; nSC89: M/68; gSC57: M/78; gSC64: M/78; gSC90: F/71. Soft substrates were fabricated by UV crosslinking gelatin methacryloyl (GelMA; 6% + 0.075% (w/v) LAP photoinitiator), whereas stiff substrates incorporated methacrylate-conjugated hyaluronic acid (MA-HA; 0.25%). Substrates were coated with fibronectin (5 μg/cm^2) to mimic the native basal lamina of SC inner wall cells. SC cells were plated on substrates and exposed to the TRPV4 inhibitor HC067047 (10 μM) or activator GSK1016790A (100 nM) for 2 days. TRPV4 transcript levels were assessed by qRT-PCR. F-actin was visualized by phalloidin staining. To assess intracellular Ca^{2+} levels, the SC cells were loaded with Fluo-4 and imaged using a Zeiss LSM 700 confocal microscope. Substrate and cell stiffnesses were measured by atomic force microscopy (AFM) using a 10 μm spherical tip.

Pore formation by SC cells was assessed by a well-developed *in vitro* assay for inducing pores that subjects SC cells to localized cellular stretching [11]. Briefly, carboxyl microspheres (~5 μm dia) were seeded on a biotinylated gelatin substrate, followed by over seeding with SC cells. SC cells were treated +/- ROCK inhibitor (Y27632; 10 μM) for 30 minutes. Subsequently, fluorescently-tagged streptavidin was introduced into the culture medium. The fluorescently-tagged streptavidin traversed the SC cell monolayer at locations where pores or gaps between cells existed, irreversibly adhering to the biotinylated substrate and thereby generating an observable persistent fluorescent signal (**Fig. 1A**). The number of fluorescently-tagged streptavidin spots that associated with microspheres in each well of the plate was quantified. Subsequently, the percentage of pores induced by microspheres was calculated.

RESULTS

The soft and stiff substrates had elastic moduli of 2.36 and 8 kPa, as measured by AFM, similar to the stiffness of the substrate of SC inner wall cells in healthy and glaucomatous eyes, respectively. nSC cells on the stiff substrate exhibited elevated TRPV4 transcript levels (1.31-fold, $p<0.01$), steady-state intracellular Ca^{2+} (1.76-fold, $p<0.001$), and F-actin (2.17-fold, $p<0.0001$) vs. nSC cells on the soft substrate. TRPV4 activation increased F-actin stress fibers in nSC cells grown on the soft substrate (1.85-fold, $p<0.01$) and induced cell stiffening (2.48-fold, $p<0.05$), but not on the stiff substrate. In nSC cells grown on the stiff substrate, TRPV4 inhibition decreased F-actin (0.60-fold, $p<0.0001$)

and cell stiffness ($p<0.05$), but not on the soft substrate. Effects of TRPV4 modulation were damped in gSC cells.

Cellular stretching imparted by microspheres underlying SC cells induced formation of pores (**Fig. 1B**). In normal SC cells, 10.89% of microspheres had an associated pore, which was significantly higher than the frequency observed in glaucomatous cells (7.02%, $p<0.001$; **Fig. 1C**). Importantly, we observed that pore formation in SC cells induced by microspheres correlated strongly with cell stiffness (**Fig. 1D**); softer cells formed more pores and vice versa. Rho-associated kinase (ROCK) inhibitors have been shown to lower IOP, soften SC cells and enhance outflow facility [12]. In our assay, ROCK inhibition of cultured nSC cells for 30 minutes led to a marked increase in pore formation, with noticeable variability between cell strains.

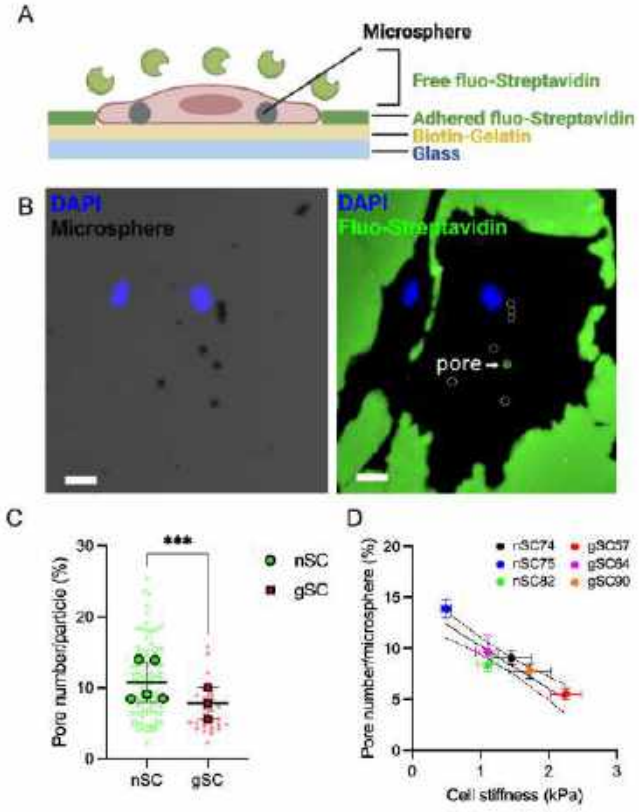

Figure 1. *In vitro* pore induction and detection in SC cells. (A) Schematic showing microspheres for inducing, and fluorescence assay for detecting, pores in SC cells. (B) Fluorescent micrograph showing spots where fluorescently-tagged streptavidin (green) has reacted with biotin substrate under cultured SC cells (at sites of intracellular pores) as well as surrounding regions not covered by cells. White circles outline microspheres. Scale bar: 20 µm. (C) Pore number induced by microspheres in nSC and gSC cell strains (*$p < 0.001$; small symbols = one experimental replicate, large symbols = mean of each cell strain). (D) Correlations (black line) of pore formation rate vs. cell stiffness. Bars = SEM. Light curves = 95% CIs on the linear regression ($p<0.0001$).**

DISCUSSION

SC inner wall cells experience substantial biomechanical stresses and strains, resulting in stretching of the plasma membrane and likely activation of mechanosensitive ion channels (e.g., TRPV4) to induce Ca^{2+} influx. Previous studies have shown that TRPV4 can affect AH outflow facility and IOP [13-16]. However, the detailed mechanisms underlying TRPV4 activity in SC cells under glaucomatous conditions (i.e., increased substrate stiffness) remain to be elucidated. To model this, we used GelMA and HA hydrogels to investigate how TRPV4 integrates matrix mechanosensing to modulate SC cell mechanobiology, including Ca^{2+} signaling. Our data suggest that TRPV4 plays a crucial role in SC cell mechanosensing of substrate stiffness by modulating actin cytoskeletal structure and cell stiffness. This conclusion is supported by the findings that: (i) matrix stiffening upregulated TRPV4 transcript levels, steady-state intracellular Ca^{2+}, and F-actin labeling; (ii) TRPV4 activation in SC cells on the soft substrate increased F-actin and cell stiffness; (iii) TRPV4 inhibition counteracted the effects of matrix stiffening, leading to a decrease in F-actin levels and cell stiffness.

The inner wall of the SC undergoes a basal-to-apical cellular stretch that creates micron-sized pores to regulate AH outflow [5]. To mimic this process, we utilized microspheres to induce a similar basal-to-apical stretch in SC cells, leading to the formation of pores that closely resemble those found naturally. Notably, nSC cells exhibited a higher pore formation rate compared to gSC cells, consistent with previously observed differences in pore formation between normal vs. glaucomatous SC cells, both in native tissues and in an *in vitro* assay inducing pore formation by a membrane stretching device [17, 18].

We observed a strong correlation between the formation of pores induced by microspheres and cell stiffness, with softer cells demonstrating a higher capacity for pore formation. Furthermore, a ROCK inhibitor, a cell-softening agent, increased pore formation, suggesting that SC cell stiffness could be a promising target for IOP reduction. Since we have found a connection between TRPV4 activity and SC cell stiffness, we hypothesize that altering TRPV4 activity may influence SC cell pore formation and thus fluid conductivity via modulating SC cell actin remodeling and cell stiffness.

In conclusion, our findings highlight the importance of TRPV4 in SC cell mechanobiology and suggest that targeting this ion channel could be a promising strategy for the treatment of glaucoma. Future studies are needed to further elucidate the molecular mechanisms underlying TRPV4-mediated cellular responses and to explore the therapeutic potential of TRPV4 in glaucoma treatment.

ACKNOWLEDGEMENTS

This project was supported by grants NIH 5R21EY033142, BrightFocus Foundation CG2020001, and the Georgia Research Alliance (CRE).

REFERENCES

[1] Quigley, H.A. et al., *N Engl J Med*, 328(15): p. 1097-106, 1992.
[2] Quigley, H.A. et al., *Br J Ophthalmol*, 90(3): p. 262-7, 2006.
[3] Tamm, E.R. et al., *Prog Mol Biol Transl Sci*, 134: p. 301-14, 2015.
[4] Brubaker, R.F., *IOVS*, 32(13): p. 3145-66, 1991.
[5] HOLMBERG, A., Archives of Ophthalmology, p. 956-958,1959.
[6] Martinac, B., Channels (Austin), 2012. 6(4): p. 211-3.
[7] Wang, K., et al., *IOVS*, 2017. 58(11): p. 4809-4817.
[8] Last, J.A., et al., *IOVS*, 2011. 52(5): p. 2147-2152.
[9] Vahabikashi, A., et al., *PNAS*, 2019. 116(52): p. 26555-26563.
[10] Stamer, W.D., et al., *IOVS*, 1998. 39(10): p. 1804-12.
[11] Siadat, S.M., et al., *IOVS*, 2023. 64(8): p. 50-50.
[12] Serle, J.B., et al., *Am J Ophthalmol*, 2018. 186: p. 116-127.
[13] Ryskamp, D.A., et al., *Sci Rep*, 2016. 6: p. 30583.
[14] Luo, N., et al., *PNAS*, 2014. 111(35): p. 12871-6.
[15] Uchida, T., et al., *PLoS One*, 2021. 16(10): p. e0258911.
[16] Patel, P.D., et al., *PNAS*, 2021. 118(16).
[17] Overby, D.R., et al., *PNAS*, 2014. 111(38): p. 13876-81.
[18] Johnson, M., et al., *IOVS*, 2002. 43(9): p. 2950-5.

MACHINE LEARNING MEDIATED PROGNOSIS OF MAJOR ADVERSE CARDIAC EVENT (MACE) FOR PATIENTS WITH CORONARY ARTERY DYSFUNCTION USING PRESSURE DROP COEFFICIENT

Israel O. Ajiboye (1), Rao B. Marepalli (2), Rupak K. Banerjee (3)

(1) Department of Mechanical and Materials Engineering, College of Engineering and Applied Science, University of Cincinnati, Cincinnati, OH, USA
(2) Department of Environmental & Public Health Sciences, College of Medicine, University of Cincinnati, Cincinnati, OH, USA
(3) Department of Biomedical Engineering, College of Engineering and Applied Science, University of Cincinnati, Cincinnati, OH, USA

INTRODUCTION

While the cardiovascular diagnostics is a data-rich area, cardiologists may inadvertently miss important information for predicting, diagnosing and treating coronary artery disease. One of the way this problem can be mitigated is by adopting machine learning-based techniques, which have been employed in different areas of the health care field [1]. Traditionally, doctor's intuition, knowledge, and experience coupled with standard statistical methods have been used for prognosis/prediction of disease risk. However, this practice often leads to unwanted biases, negatively influencing the quality of service provided to patients. With the increasing availability of electronic health data, machine learning has become a more practical approach in the field of disease prediction [2]. Several studies have utilized machine learning algorithms to predict and diagnose diseases such as hepatitis C [1], prostate cancer [3], stroke [4], and diabetes [5]. However, very few studies have applied machine learning techniques to predict % major adverse cardiac events (MACE) such as myocardial infarction, revascularization, and death of patients.

In the field of coronary artery diagnosis, the severity of intermediate epicardial stenosis is determined using the current gold-standard, a pressure-based coronary diagnostic index: fractional flow reverse (FFR, a ratio of distal to proximal pressures across stenosis). It often leads to inaccuracies in the presence of microvascular diseases (MVD). Pressure drop coefficient (CDP), a fundamental fluid dynamics-based combined pressure-flow index, was recently developed to solve this constraint. Specifically, CDP is the ratio of the trans-stenotic pressure drop to the proximal dynamic pressure (1/2 x blood density x APV^2; where APV is average peak velocity). The combined approach of assessing both coronary pressure and flow has been reported as the improved basis to assess coronary physiology [6]. In particular, the CDP was tested *in vitro* [7] as well as *in vivo* in animal studies [8] and was able to delineate between epicardial stenosis and MVD. In addition, CDP has been recognized as possible alternate coronary diagnostic parameters by other researchers [9,10].

The primary *objective* of this study is to use several machine learning algorithms to predict %MACE and survival of patients after five years using FFR and CDP data. The early identification and improved prediction of coronary stenosis prior to the onset of MACE may direct earlier clinical management. The *hypothesis* is that CDP will have a better prognosis of MACE outcome than FFR.

METHODS

Three steps have been employed in this study. First, the description of the datasets, preprocessing, and cleaning of the data by identifying and correcting errors in the dataset, such as missing or inconsistent data, removing duplicates, and handling outliers were conducted. Subsequently, the machine learning algorithms were developed. Lastly, the performance of each algorithm was evaluated, and the best algorithm for the prediction was selected after comparing the performance of each algorithm. The algorithms were developed with Python programming on Google Colab. Figure 1 shows the steps adopted for the study.

Four machine learning algorithms: logistic regression (LGR), support vector machine (SVM), k-nearest neighbors (KNN), and artificial neural networks (ANN) were adopted in this study for training the 5-year MACE outcome data (n = 122). These algorithms were selected based on their proven effectiveness in medical diagnosis. FFR and CDP were used as input, and the outcome was the presence of MACE or survival after five years. The input data was split into 80% training and 20% testing sets. The average accuracy, precision, recall, receiver operating characteristics (ROC), and area under the curve (AUC) for each algorithm was calculated implementing 500 seeding iterations. For the algorithm, this study used solvers 'lbfgs' for Logistic Regression, radial basis kernel function for SVM and n_neighbors being

4 for KNN. Similarly, the activation function 'relu' and hidden layer of 4 for ANN were employed.

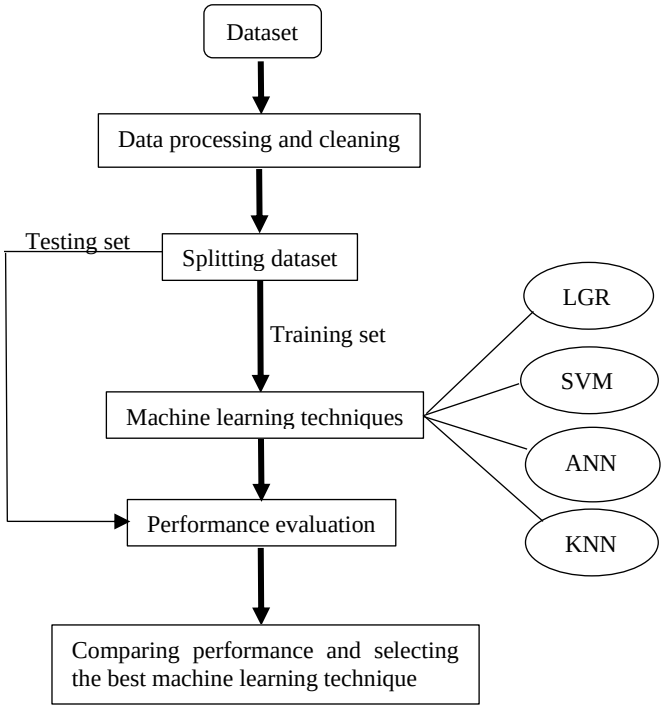

Figure 1: Machine learning steps for prognosis of MACE outcome using FFR and CDP.

RESULTS

Table 1A and 1B below display the output of the algorithms that were used for training the dataset. The SVM had accuracy of 0.50 and precision of 0.51 for FFR whereas accuracy of 0.56 and prediction of 0.57 for CDP. Similarly, the KNN had accuracy of 0.49 and precision of 0.50 for FFR whereas accuracy of 0.55 and prediction of 0.57 for CDP. SVM and KNN provided the best predictions for the two datasets for accuracy and precision. Further, SVM (FFR: recall = 0.65; CDP: recall = 0.62) performed better compared to KNN (FFR: recall = 0.37, CDP: recall = 0.46) for recall value. Importantly, CDP having accuracy = 0.56 and AUC = 0.57 predicts MACE more accurately than FFR having accuracy = 0.50 and AUC = 0.53 for SVM.

DISCUSSION

This study shows that the machine learning-based prognosis of MACE outcome can be better achieved for patients with coronary artery dysfunction using CDP because it incorporates the square of APV in the denominator. This is corroborated by the results of the 5-year outcome (MACE and event-free survival) analysis reported by Banerjee et al [11]. They showed that a clinical decision made on the basis of CDP relative to FFR would reduce MACE and significantly increase event-free survival. The advantages of combining both pressure and flow measurements within a single parameter is well supported by several published studies in the literature.

In particular, results from this study shows that SVM can be an effective tool for medical professionals to predict %MACE and patient survival at five years with the highest accuracy (>50%) and AUC among the test models. This finding is similar to the results of Alizargar et al. [1], where six machine learning algorithms were utilized on NHANES and UCI datasets to predict hepatitis C based on the blood test data of early-stage patients. SVM and XGBoost outperforms other algorithms. SVM has also been reported as the best prediction in some other literatures [12,13] for heart diseases. Nandipati et al. [14] in 2020 reported KNN model as the highest accuracy (51.06 %) in their study using an Egyptian hepatitis C dataset. This present study corroborates this study [14]. One of the strengths of current study is that the data used are for patients whose medical record was followed for 5 years.

It is expected that the accuracy and precision of these algorithms can be improved with larger training datasets of MACE outcomes. This study could serve as a reference for future researchers in the field of machine learning. Furthermore, using current findings patients at risk of MACE can be identified a prior for targeted treatment.

Table 1: Comparative results of the four machine learning algorithms on a) FFR, and b) CDP data.

FFR **A**

	LGR	SVM	ANN	KNN
Accuracy	0.43	**0.50**	0.48	**0.49**
Precision	0.32	**0.51**	0.45	**0.50**
Recall	0.51	**0.65**	0.56	0.37
AUC	0.50	0.53	0.51	0.50

CDP **B**

	LGR	SVM	ANN	KNN
Accuracy	0.49	**0.56**	0.48	**0.55**
Precision	0.55	**0.57**	0.47	**0.57**
Recall	0.42	**0.62**	0.49	0.46
AUC	0.53	0.57	0.53	0.56

ACKNOWLEDGEMENTS

This work was partly funded by the Cincinnati Children's Hospital Medical Center (CCHMC) (grant no. 16814) and the department of mechanical engineering, university of Cincinnati.

REFERENCES

[1] Alizargar et al. *Bioengineering*, *10*(4), 481. [2] Uddin et al. *BMC medical informatics and decision making*, *19*(1), 1-16. [3] Hussain et al. Cancer Biomarkers. 2018;21(2):393–413. [4] Hung et al. 39th Annual International Conference of the IEEE, vol. 1; 2017. p. 3110–3. IEEE. [5] Malik et al. SpringerPlus. 2016;5(1):701. [6] van de Hoef et al. *J. Mol. Cell Cardiol.* 52, 786–793. [7] Peelukhana et al. *J. Biomech.* 42, 2753–2759. [8] Peelukhana et al. *Heart Vessels* 29, 97–109. [9] Govindaraju et al. *Atherosclerosis* 233, 630–635. [10] Garcia et al. *PLoS One* 14:e0208612. [11] Banerjee et al. *Frontiers in Physiology*, *12*, 689517. [12] Alonso et al. J Nucl Cardiol. 2018;1:1–9. [13] Lu et al. J Healthc Eng. 2018;2018:1–9. [14] Nandipati et al. Appl. Model. Simul. 2020, 4, 89–100.

MICROSCALE REMODELING OF ARTERIAL WALL LEADS TO MACROSCOPIC PRESSURE-INDEPENDENT AXIAL FORCE

Ruturaj M. Badal (1), Ryan R. Mahutga (2), Patrick W. Alford (2), and Victor H. Barocas (2)

(1) Department of Mechanical Engineering, University of Minnesota, Minneapolis, Minnesota, USA
(2) Department of Biomedical Engineering, University of Minnesota, Minneapolis, Minnesota, USA

INTRODUCTION

The aorta, which is the body's largest artery and carries blood flow from the heart, exhibits diverse material properties and dimensions along its length [1]. These variations are influenced by in vivo axial stretch, a crucial factor determining arterial wall behavior and influencing the growth and remodeling processes [2]. A key observation, exemplified by the Pressure-Force experiment [3], is that under healthy conditions, the axial force on the vessel remains remarkably constant despite fluctuating pressure, hinting at a specific optimal in vivo axial stretch. It has been further argued [4] that the flat pressure-axial-force response is energetically advantageous and thus an attractive state for the vessel. Despite its importance, however, there is limited understanding of how an artery reaches the point at which the pressure-axial-force is flat.

This study delves into the microscopic remodeling processes within arterial walls, focusing on how changes in individual fiber dimensions to attain a target fiber stress influence tissue restructuring as a whole. By doing so, this study explores the connection between microscale tissue remodeling and the observed pressure-axial-force behavior. Specifically, we tested the hypothesis that **fiber-level adaptations collectively lead to a consistent axial force response by the tissue in the Pressure-Force experiment at in vivo loading levels**.

METHODS

To investigate this phenomenon, we model the aorta as a thin-walled cylinder, capturing its essential geometric characteristics. Calculations are performed on a single element representing a section of the vessel wall using the Non-affine Fiber Network Solver (NaFNS) plugin for the FEBio software [5]. This approach allows us to employ discrete microstructural fiber networks as a representation of the tissue. The initial network comprises actomyosin (actin), collagen, and elastin fibers, with actin exhibiting an isotropic distribution while elastin and collagen are characterized as transversely isotropic in the axial and circumferential directions. The detailed structure of a representative network element is depicted in (Fig. 1(a)). The properties and governing equations for each fiber type are based on established literature [5-6].

To simulate physiological conditions for remodeling, we apply controlled stretch to the vessel in axial direction and a circumferential stretch representing pressure, while allowing for free expansion in the radial direction. The vessel then undergoes remodeling while maintaining a constant axial stretch and pressure (Fig. 1(b)). Using the NaFNS plugin, we calculate individual fiber stresses. Each fiber in the network then remodels independently based on its specific stress, driven by the core concept of localized tensional homeostasis, under which each fiber seeks to achieve a predefined target stress, ultimately leading to an overall tissue equilibrium state. The remodeling laws and properties in this study are drawn from existing literature [6]. Briefly, elastin does not remodel, but collagen and actin fibers lengthen and thicken if their stress is above the target stress, and they shorten and thin if their stress is below the target stress. The model parameters are the

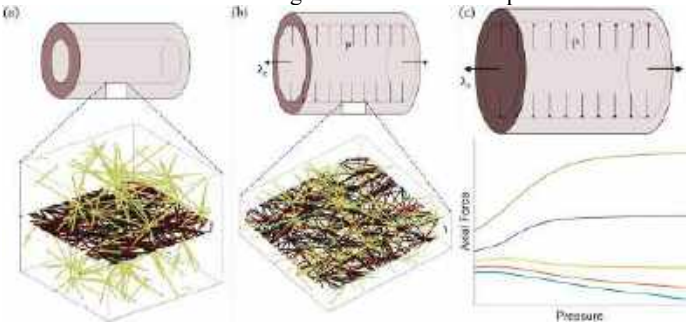

Figure 1: (a) Initial arterial vessel state, with vessel thickness illustrated by a single element in NaFNS plugin. (b) The vessel's remodeled state under the influence of imposed axial stretch (λ_z) of 1.72 and a pressure of 100 mmHg (P), showcasing alterations in the network. (c) Presents a typical outcome from the Pressure-Force test conducted on the sample post-remodeling.

specified target stresses and time constants for collagen and actin. Upon remodeling, the final discrete network representation of the remodeled material is saved for further analysis.

After remodeling, we replace our constraints with free boundaries, and the remodeled tissue moves to an unloaded configuration, thereby defining the growth stretch. Next, we perform a simulated planar biaxial extension test on the remodeled tissue. Finally, we subject the remodeled vessel to a simulated Pressure-Force experiment (Fig. 1(c)). In this experiment, a cylindrical tissue segment that has been subjected to an applied axial stretch is capped at both ends and pressurized. The force at the capped ends is measured for different pressures and axial stretches. On an element level, the axial and circumferential stretch are varied, and the force and pressure are calculated using stresses and stretches. Under the assumption of a thin-walled vessel and the Law of Laplace, the following formulas result:

$$\mathrm{P} = \frac{\mathrm{h}}{\mathrm{r}}\sigma_{\theta\theta} = \frac{\lambda_r h_0 \sigma_{\theta\theta}}{\lambda_\theta R_0} \quad (1)$$

$$\mathrm{F} = 2\pi \mathrm{r h}\left(\sigma_{zz} - \frac{\mathrm{Pr}}{2\mathrm{h}}\right) = \pi R_0 h_0 \lambda_\theta \lambda_r (2\sigma_{zz} - \sigma_{\theta\theta}) \quad (2)$$

where, h_0 is the ex vivo wall thickness, R_0 is the ex vivo radius, λ_θ is circumferential stretch and λ_r is radial stretch. The quantities $\sigma_{\theta\theta}$ and σ_{zz} are circumferential and axial stresses respectively.

We applied the protocol to remodeling at initial in vivo stretches of 1.2 to 1.9 with the remodeling pressure held constant at 100 mmHg. The initial wall thickness and vessel radius were set at 84 μm and 197 μm [7]. For the simulated Pressure-Force test, pressure was varied over the range 0 to 140mmHg, and stretch was varied from 1.1 to 1.95.

RESULTS

In presenting and discussing the results, we employ three different measures of axial stretch. The *imposed* axial stretch (λ_z) is the amount that the vessel is stretched from its initial (unremodeled) configuration. The growth stretch (λ_z^g) is the length of the remodeled vessel relative to that of the initial, and the in vivo stretch (λ_z^*) is the stretch at the in vivo length relative to the remodeled/grown tissue. Thus, $\lambda_z = \lambda_z^* \lambda_z^g$.

As a representative example, we begin with the case of $\lambda_z = 1.72$ and a remodeling pressure of 100 mmHg. For this case, λ_z^g was found to be 1.11. Thus, the in vivo axial stretch λ_z^* using the above formula was found to be 1.72/1.11 = 1.54. Simulated biaxial testing showed the remodeled tissue to be anisotropic, with greater stiffness in the circumferential direction than in the axial (Fig. 2(a)). Under varying pressures, the vessel diameter increased monotonically with applied pressure. At a given pressure, vessel diameter was higher at lower axial stretch (Fig. 2(b)).

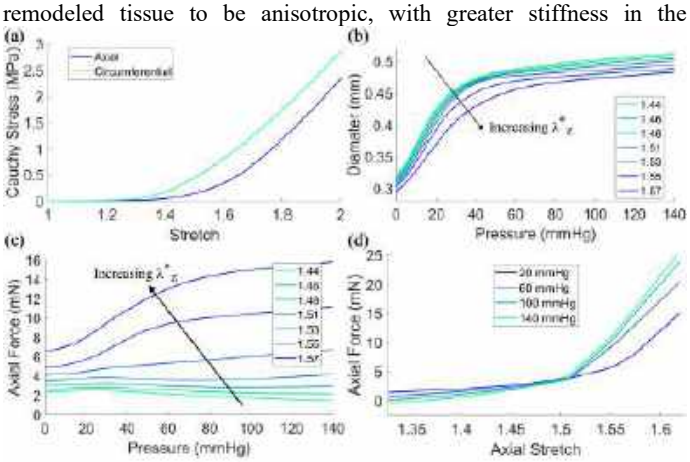

Figure 2: Results for imposed initial axial stretch of 1.72, which resulted in λ_z^g = 1.11 and λ_z^* = 1.54. (a) Biaxial extension test results and (b) alterations in vessel diameter with pressure in the Pressure-Force test. (c) Axial force in a Pressure-Force test decreases for low λ_z^* and increases for high λ_z^*. (d) Axial force rises monotonically with axial stretch, with all curves intersecting at one point.

For axial stretches 1.48 or below, axial force decreased as pressure increased (Fig. 2(c)), meaning that increasing the pressure caused a larger outward force on the end caps. Conversely, for stretches 1.53 or above, the forces exhibited an upward trend with increasing pressure. At an axial stretch of 1.51, the force remained relatively constant over the imposed pressure range, as depicted in Fig. 2(c). Plotting the axial force against the axial stretch across different pressures revealed a compelling trend: all curves converged at a singular point of intersection between 1.5 and 1.55 axial stretch (Fig. 2(d)). These results are all consistent with both classical [4] and recent [7] experimental observations.

Repeating simulations with imposed axial stretch λ_z of 1.2 and 1.9 while maintaining a pressure of 100 mmHg confirmed the observed trends. The λ_z^* for these cases is found to be 1.16 and 1.68 respectively. As in Fig. 2(c), for each case, there was an in vitro stretch ratio for which the pressure-force curve was relatively flat (Fig. 3(a-b)). For all three cases, the stretch associated with the flat pressure-force curve was very close to the in vivo stretch. The effect is illustrated in a plot of the difference in axial force for pressures of 60 and 120 mmHg versus the ratio of the applied axial stretch λ_z^{exp} to the in vivo axial stretch λ_z^* (Fig. 3(c)). For each case, the zero force difference is observed for a ratio close to 1. This finding supports the hypothesis that the force is invariant with pressure at in-vivo axial stretch.

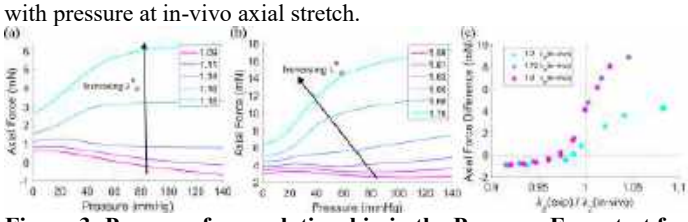

Figure 3: Pressure-force relationship in the Pressure-Force test for λ_z^* of (a) 1.16 and (b) 1.68. (c) Axial force difference between p=60 and p=120 mmHg vs. the ratio of experimental to in vivo axial stretch.

DISCUSSION

We found that the simulated remodeled vessel through the application of local tensional homeostasis had a specific axial stretch at which the force remained roughly invariant with pressure in a pressure-force test, *and that stretch was nearly the same as the in vivo stretch in all cases*. This observation agrees with the experimental observation that the flat pressure-axial-force curve occurs at the in vivo stretch [2,4,7]. The in vivo stretch effect ***arose with no specification of the effect in the model, and without any macroscopic target in the remodeling.*** Rather, the combined effect of all fibers remodeling individually was to produce the flat pressure-axial-force curve at the in vivo remodeling stretch.

ACKNOWLEDGMENTS

This work was supported by the NIH grant R01 HL164800and R01 NS126762.

REFERENCES

[1] Kassab, G., *J. R. Soc. Interface.3719–740*, 2006. [2] Humphrey, JD et al., *J Biomech.*, 42(1):1-8, 2009. [3] Van Loon P et al., *Biorheology*, 14(4):181-201, 1977. [4] Weizsäcker, HW et al., *J Biomech*, 16(9):703-15., 1983. [5] Mahutga, RR et al., *J Mech Behav Biomed Mater*, 144:105967, 2023. [6] Gacek, E et al., *Acta Biomater*, 163:7-24, 2023. [7] Ferruzzi, J et al., *Ann Biomed Eng.*, 41(7):1311-30, 2013.

AN ENGINEERED IN VITRO MODEL OF THE HUMAN MYOTENDINOUS JUNCTION

Mitchell Josvai (1,2), Erzsebet Polyak (3), Meghana Kalluri (1,2), Samantha Robertson (3), Wendy C. Crone (1,2,4,5,6), Masatoshi Suzuki (1,3,4)

(1) Department of Biomedical Engineering, University of Wisconsin-Madison, Madison, WI, USA
(2) Wisconsin Institute for Discovery, University of Wisconsin-Madison, Madison, WI, USA
(3) Department of Comparative Biosciences, University of Wisconsin-Madison, Madison, WI, USA
(4) The Stem Cell and Regenerative Medicine Center, University of Wisconsin-Madison, Madison, WI, USA
(5) Department of Nuclear Engineering and Engineering Physics, University of Wisconsin-Madison, Madison, WI, USA
(6) Department of Mechanical Engineering, University of Wisconsin-Madison, Madison, WI, USA

INTRODUCTION

The myotendinous junction (MTJ) is a specialized region at the interface of muscle and tendon tissues. The complex architecture forms an integrated mechanical unit capable of transducing forces through the tissue to enable musculoskeletal movement [1]. The MTJ is a common site of injury due to the cyclic nature of tissue loading and the resulting storage and release of energy [2]. While the MTJ represents the transition from muscle to tendon, the microstructure reveals that this is not a discrete boundary between tissues, but rather overlapping interdigitations of the two cell types [3]. At the interface, muscle fibers integrate with tendons through extracellular matrix (ECM) interactions and surface proteins, allowing for functional integration and mechanical transduction without tissue damage [4].

The bidirectional chemical and mechanical crosstalk between myocytes and tenocytes in the developing MTJ occur within a limited spatial and temporal window [5]. However, the architecture and mechanical complexity of the MTJ has made it a difficult tissue to model and study *in vitro* [6]. In this work, we present a novel technique for the spatially restrictive coculture of myocytes and tenocytes for two-dimensional (2D) modeling of the human MTJ.

METHODS

Micropatterned lanes of Cultrex ECM were deposited on 10 kPa polydimethylsiloxane (PDMS) substrates. A 2-well culture chamber defined the initial regions of occupation for each cell line, for a total of approximately 38,500 primary tenocytes (1,750 cells/mm^2) and 67,000 human embryonic stem cell (hESC)-derived myogenic progenitors (3050 cells/mm^2) (**Fig. 1A**). Brightfield live cell imaging for migration and contractile analysis was performed with samples maintained at 37 °C. Samples were immunolabeled to identify proteins of interest and corrected total cell fluorescence was used to quantify their expression [7,8]. On day 24, electrical stimulation (1 Hz, 5 ms, 0.6 – 1.6 V/mm) was provided to induce global full-field contractions for analysis. Digital image correlation (DIC) was used to quantify induced strain behavior [9].

RESULTS

On day 1 after seeding, both lines occupied less than 20% of the initially vacant interstitial zone, referred to henceforth as the junction. Myocyte-tenocyte contact was observed by day 7 when both cell types had undergone a significant increase in area at the junction (**Fig. 1B**).

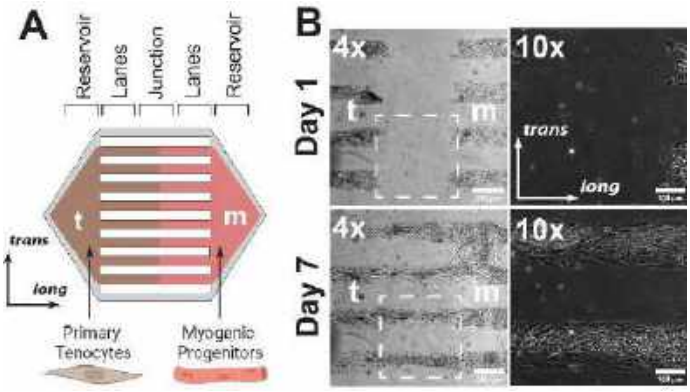

Figure 1: (A) Schematic of the micropatterned design. **(B)** By Day 7, a myocyte-tenocyte interface develops. Scale bars: 250 µm (4x) and 100 µm (10x).

Myocytes within reservoirs exhibit myofibrillar disarray, with fewer myofibers and poor organization in comparison to myocytes within lanes (**Fig. 2A**). By day 24, tenocytes in lanes had secreted an organized network of Collagen Type I (COL1A), while reservoir matrix deposition appears more disorganized (**Fig. 2B**). Tenocytes in lanes

were also found to have increased nuclei area and alignment in the longitudinal orientation in comparison to tenocytes in the reservoir.

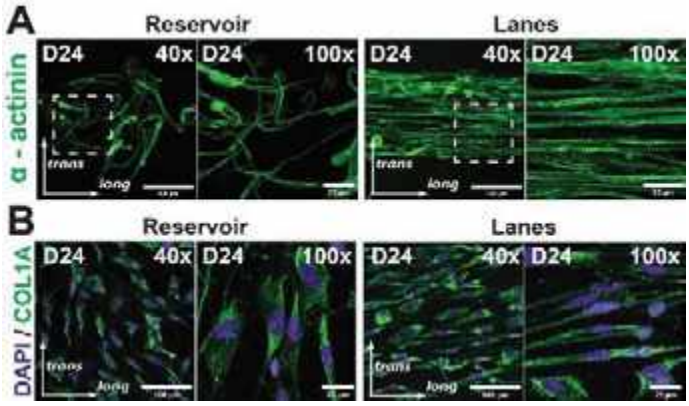

Figure 2: (A) Myofibrillar organization was enhanced in lane regions. **(B)** Tenocytes in lanes orient in the longitudinal direction, parallel to patterned lanes. Scale bars: 100 µm (40x) and 25 µm (100x).

Immunolabeling demonstrated that myocytes and tenocytes at the junction express reported MTJ protein markers and develop integrated structures resembling native MTJ interdigitations. To probe the mechanical integrity of these structures, electric stimulation was provided. Stimulation induced coordinated contractile behavior in the electrically and mechanically active myocytes but did not directly affect the behavior of the passive tenocytes. DIC was used to quantify strains in the longitudinal, transverse, and shear directions relative to the alignment of patterned lanes (**Fig. 3**).

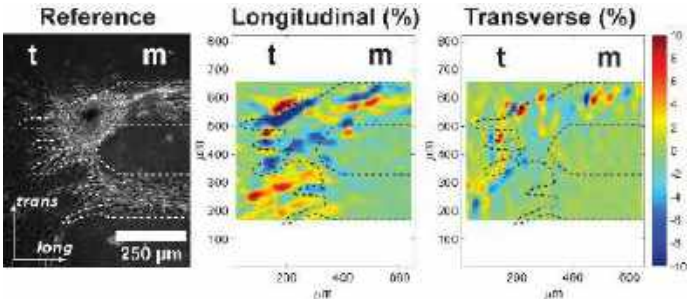

Figure 3: A representative image of the junction in a relaxed state (left), with heat map plots of the same junction in a contracted state, showing the longitudinal (center) and transverse strains (right).

At the junction and within patterned lanes, myocytes demonstrated enhanced contractility and an increased maximum magnitude of strain compared to unpatterned myocytes within the reservoir. No difference existed in the maximum magnitude of strain between myocytes at the junction and myocytes within patterned lanes. The maximum magnitude of tenocyte strain was tensile, or positive, at all regions of interest, and decreased with increased distance from the junction (**Fig. 4**). Tenocytes at the junction experienced the largest magnitude of positive strain in response to the external force of myocyte contraction. Tenocytes within lanes, but not at the junction, experienced significantly decreased magnitudes of strain in comparison to junction cells, as did tenocytes in unpatterned reservoir regions. A positive correlation existed between the maximum magnitude of myocyte strain and the corresponding maximum magnitude of tenocyte strain at the junction (R^2 = .6207). These data demonstrate that the electrically induced myocyte contraction behavior was transferred in part across the phenotypic boundary of the MTJ model, and that myocyte-tenocyte mechanical integrity was achieved.

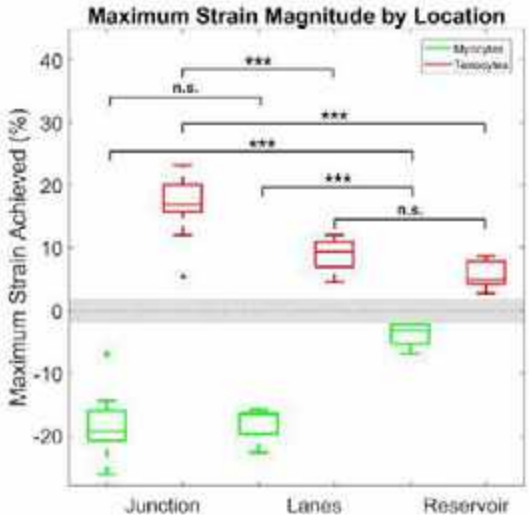

Figure 4: The maximum magnitude of strain in myocytes (green) and tenocytes (red) by region. Dotted line represents zero strain, the shaded area represents the noise limit of DIC detection. ***p < 0.001.

DISCUSSION

Due to the intricate architecture and the necessity that models contain structural and mechanical accuracy, the MTJ has become a difficult area of human anatomy to model *in vitro* [10]. The significance of our study was to engineer a novel 2D micropatterned model of the human MTJ, which aims to mimic cellular structure and mechanics of the native tissue. The model expressed reported MTJ protein markers and developed myocyte-tenocyte integrations capable of transducing forces and strains originating in contracting myocytes across the cell-cell interface to be experienced by tenocytes.

While this system is capable of modeling the 2D architecture and biomechanics of the human MTJ at early developmental timepoints, it also represents a platform capable of investigating injury and disease progression at later stages. We anticipate that the platform will have applications in disease modelling of an assortment of myogenic and tenogenic disorders that manifest at the junction [11, 12].

ACKNOWLEDGEMENTS

Funded by the National Institutes of Health [R01AR077191 (M.S. and W.C.C.)], the Good Food Institute, the University of Wisconsin Foundation, and UW Stem Cell & Regenerative Medicine Center. This material is based upon work supported by (while serving at) the National Science Foundation (W.C.C.).

REFERENCES

[1] Jakobsen, JR et al, *Front Physiol*, 12:635561, 2021.
[2] Knudsen, A et al, *Transl Sports Med*, 4:431-438, 2021.
[3] Curzi, D et al, *J Musc Lig Tend*, 3:275-280, 2013.
[4] Yaseen, W et al, *Nat Commun*, 12:3852, 2021.
[5] Subramanian, A et al, *Development*, 142:4191-4204, 2007.
[6] Bayrak, E et al, *Front Mater*, 5:24, 2018.
[7] Hosoyama, T et al, *Stem Cell Trans Med*, 3:564-574, 2014.
[8] McCloy, RA et al, *Cell Cycle*, 13:1400-1412, 2014.
[9] Bar-Kochba, E et al, *Exp Mech*, 55:261-274, 2015.
[10] Arrigoni, C et al, *Biofabrication*, 11:032004, 2019.
[11] Rovina, D et al, *Stem Cell Res*, 45:101941, 2020.
[12] Yue, F et al, *Genes*, 68:103050, 2023.

RAMAN ARTHROTOMY FOR IN VIVO QUANTITATIVE MONITORING OF CARTILAGE DEFECT REPAIR IN EQUINE STIFLE JOINT

Erik E Ersland(1), Madeline Boyes(2), Keming Yan(1), Hsin Han(3), J. Todd Lawrence(4), Thomas P Schaer(2), Mark W Grinstaff(1), Brian D Snyder(5), Mads S Bergholt(6), Michael B Albro(1)

(1) Boston University, MA, USA
(2) University of Pennsylvania Department of Clinical Studies New Bolton Center, PA, USA
(3) Drexel University, PA, USA
(4) The Children's Hospital of Philadelphia, PA, USA
(5) Beth Israel Deaconess Medical Center, and Boston Children's Hospital MA, USA
(6) King's College London, UK

INTRODUCTION

Hyaline cartilage is a viscoelastic, biphasic, composite material optimized for its mechanical performance, comprised of a type-II collagen (COL) fibril network (5-20% wet weight) that affords structure and tensile strength to constrain a negatively charged sulfated glycosaminoglycan (GAG) hydrogel matrix (<15% wet weight) that retains interstitial water imparting interstitial fluid load support (IFLS). These components act synergistically, bestowing the compressive, rheological and tribological material properties essential to cartilage function. Osteoarthritis (OA) is an incapacitating condition in which hyaline cartilage progressively breaks down as a consequence of mechanical overloading that promulgates structural failure (fissuring/ fibrillation/ superficial zone delamination), tissue swelling, GAG depletion and COL network derangement. GAG depletion reduces IFLS, transferring load to the COL fibril network, which subsequently breaks down, culminating in increased hydraulic permeability, decreased cartilage stiffness and lubricity. Development of disease-modifying OA therapies is impeded by a lack of non-destructive clinical assessments of cartilage composition and mechanical properties germane to tissue function. Quantitative MRI (T1ρ, T2*) and arthroscopic-based cartilage grading (Outerbridge) are only moderately correlated with metrics characterizing cartilage composition and material properties[1]. Raman spectroscopy is an inelastic optical light scattering technique that provides an optical fingerprint of a tissue's molecular building blocks, allowing quantification of the predominant molecular constituents of cartilage (GAG, COL, H_2O) that contribute to the material properties intrinsic to its function. We developed a novel Raman spectroscopy needle probe and real-time spectral analysis platform capable of performing both *ex-vivo* and *in-vivo* measurement of ECM-specific compositional biomarkers for cartilage with a high degree of accuracy[2] (R^2=0.8-0.94). Absolute measures of cartilage content can be derived from the Raman spectra using phantoms comprised of prescribed proportions of GAG, COL and H_2O that serve as biochemical standards.[3] Here we demonstrate that *in-vivo*, real-time Raman spectroscopy performed on the equine stifle joint using a needle probe to measure cartilage composition at discrete anatomical sites along the equine trochlear groove can track changes in cartilage composition after an induced chondral injury and repair (microfracture, autologous chondrocyte implantation).

METHODS

Raman Probe: A custom Raman probe (In Photonics) comprised of a threaded needle tip (2.75mm diam.) with a distal 2mm diam. sapphire ball lens (AWI) was fiber-coupled to a battery powered 785nm laser (100mW output; IPS), and high-performance spectrometer (Eagle; Ibsen), allowing for portability. **Raman Spectra:** High SNR spectra in the fingerprint (800-1800cm^{-1}) and high wavenumber (2700-3800cm^{-1}) ranges were acquired. Spectra were preprocessed by background subtraction and area-under-curve normalization. The cartilage spectra (800-1800cm^{-1}) was fit to a multivariate linear regression model:

$$\mathbf{Cartilage_{spectra}} = GAG_{score}*(\mathbf{GAG_{REF}}) + COL_{score}*(\mathbf{COL_{REF}}) + H_2O_{score}*(\mathbf{H_2O_{REF}}) + Bone_{score}*(\mathbf{Bone_{REF}})$$

where: GAG_{REF}, COL_{REF}, H_2O_{REF}, and $Bone_{REF}$ are reference spectra of purified chemicals comprising each ECM constituent; the "scores" are the "fit" regression coefficients reflecting the relative contribution of each ECM constituent and subchondral bone to the composite spectra (**Fig.1A-C**). The high-wavenumber range spectra (2700-3800cm^{-1}) was used to compute the area under the CH_2 and OH peak, reflecting tissue hydration[4]. Raman spectral analysis was performed in real time, with ECM biomarker scores and quality metrics displayed to the operator via a custom GUI. The fit Raman biomarker scores derived from the cartilage spectra (**Fig1A**) were converted to absolute content measures (%w/v) using tissue phantoms comprised of prescribed ratios of GAG (chondroitin sulfate [0-10%w/v]), COL (gelatin [0-20%w/v]), and H_2O [70-100%w/v] by fitting a 2nd order polynomial to express the known %w/v of the tissue phantoms as a function of the measured Raman scores.[3] ***Ex- Vivo* Validation**: from a 5-y/o equine stifle joint, 3mm full thickness cartilage plugs were harvested at 169 discrete locations over the surface of the femoral trochlear groove. The composition of each

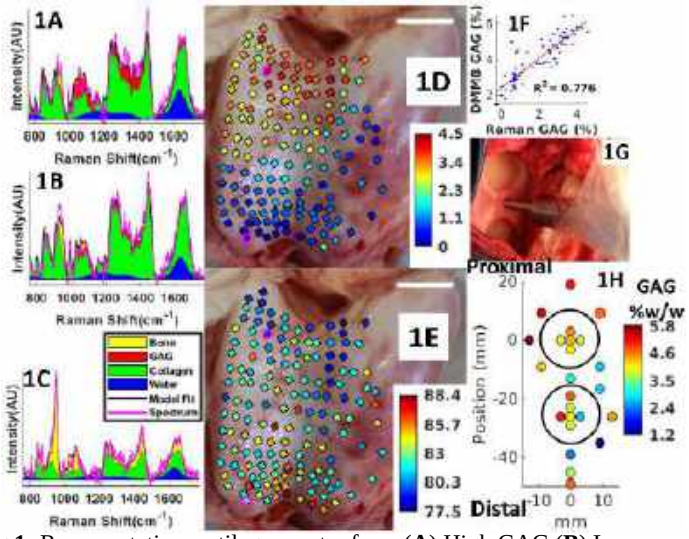

Fig 1: Representative cartilage spectra from (**A**) High GAG (**B**) Low GAG, (**C**) Thin cartilage (high bone signal) specimens. *Ex-vivo* mapping of cartilage composition derived via phantom-corrected Raman measures (%w/v) of (**D**) GAG and (**E**) H_2O. (**F**) Correlation Raman GAG vs. DMMB assay *ex-vivo*. (**G**) Intra-op Raman probe measuring tissue composition adjacent 2 circular excised chondral defects (**H**) *In vivo* phantom corrected Raman GAG content of cartilage prior to chondral defects (represented as circles)

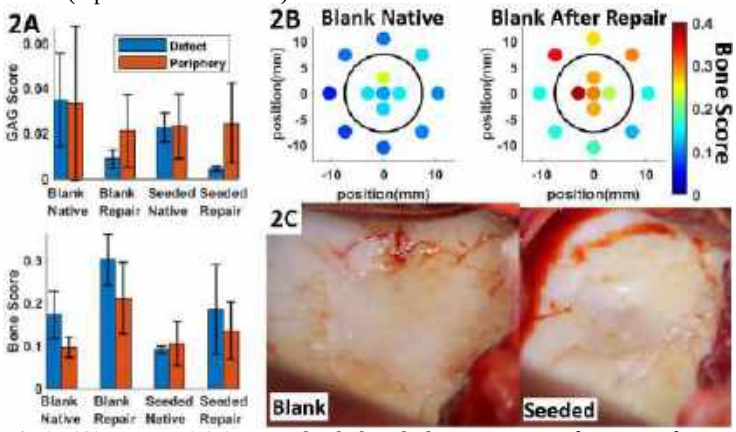

Fig 2: (A) Raman GAG_{score} and subchondral $Bone_{score}$ as a function of location, repair type, and time (before defect or 3month after repair). (**B)** $Bone_{score}$ anatomic site map before defect and 3 months after repair. (**D)** Photographs of neocartilage repair tissue at 3 months

plug was measured by Raman spectral analysis and confirmed by DMMB GAG assay (**Fig 1F**).

***In Vivo* Spectra Analysis**: The needle tip was autoclaved, and optics draped in sterile plastic film. Through a parapatellar arthrotomy between the middle and lateral patellar ligaments, Raman needle probe spectral analysis was performed at multiple sites along the lateral trochlear groove of a 5-year-old thoroughbred horse to measure cartilage composition at defined anatomical sites within the footprint of two planned 15mm diam. focal chondral defects to the subchondral bone (**Fig.1G**) and sites peripheral to the defect (**Fig.1H, 2B**). At each site, the probe lens contacted the surface with minimal force to prevent slipping; spectra were acquired for 5 seconds. **Cartilage Repair:** Defects were repaired by one of two treatments: 1) unseeded collagen scaffold placed on top of micro-fractured subchondral bone (Blank), 2) collagen scaffold seeded with equine chondrocytes (Seeded) covered by a thin collagen membrane sutured to the peripheral cartilage. Raman spectra of the neocartilage repair tissue was performed at the same locations within the defect and peripheral sites 3 months after the defects were created and repaired using a similar surgical approach.

RESULTS

Ex-vivo: Raman derived biochemical estimates accounted for 78% of the variance in DMMB measured GAG content (**Fig.1F**) and depicted a biochemical spatial gradient along the length of the trochlear groove, with GAG content increasing and H_2O content decreasing from distal to proximal (**Fig. 1D,E**). The Raman derived GAG %w/v underestimated the GAG content by ~20%, which is attributable to disparately between the regions of Raman probe interrogation (~300µm depth of penetration) vs. the full thickness cartilage plug used for the DMMB assay. ***In-vivo:*** Using the needle probe, real time Raman analysis achieved high quality spectral acquisition of cartilage, as evidenced by a high SNR and ability of the multivariate regression model to account for 93% of the variation of the "fingerprint" cartilage spectra (R^2=0.93±0.03). *In-vivo* Raman GAG measures of cartilage exhibited a similar range and spatial distribution as the *ex-vivo* phantom converted analysis (**Fig 1H**). For both repair groups, GAG_{score} trended lower in neocartilage, and $Bone_{score}$ was elevated in the neocartilage and peripheral sites around the defect compared to native cartilage (**Fig.2A**).

DISCUSSION

This study establishes the capability of our Raman needle probe spectroscopy platform to achieve accurate quantitative *in-vivo* measures of the biochemical content of native cartilage and neocartilage repair tissue in real time, allowing diagnostic assessments of tissue quality at defined anatomic sites. The accuracy of ECM composition calculated from the *in-vivo* Raman spectral analysis is supported by *ex-vivo* measures of tissue composition at discrete anatomical sites along the trochlea of the equine stifle joint, where Raman derived GAG wt% accounted for 78% of the variation in GAG content. *In-vivo* assessment demonstrated lowered Raman GAG_{score} in the neocartilage for both repair groups at 3 months after repair relative to native cartilage. The higher contribution of subchondral bone to the neocartilage spectra at both the defect + periphery sites, manifest by an elevated Raman $Bone_{score}$, indicates that the repair tissue is thinner than the native cartilage at the same anatomic locations assessed prior to creation of the defect, demonstrating that adjacent cartilage is also degraded as part of the overall inflammatory response to the surgically induced joint trauma. The elevated $Bone_{score}$ also reflects softening of the cartilage, with more compressive tissue strain under the same contact tare force produced by the probe during Raman measures. The elevated $Bone_{score}$ precluded phantom conversion of neocartilage Raman ECM biomarker scores to absolute wt% measures, but we will adopt biochemical phantoms with subchondral bone to allow for fully quantitative Raman-derived biochemical wt% measures of the neocartilage repair tissue.

Significance: This work supports the use of Raman spectroscopy acquired through needle probes as a clinical tool to perform comprehensive diagnostics of the composition of articular cartilage in health and disease and as a non-destructive tool to monitor the tissue response to chondroprotective and chondroregenerative therapies *ex-vivo*, *in-vivo* and clinically using Raman arthrotomy. This is the first longitudinal *in-vivo* Raman assessment of tissue response to a chondroregenerative therapy.

ACKNOWLEDGEMENTS

Supported by NIAMS AR081393, the Arthritis Foundation, MTF Biologics, Coulter—Drexel Translational Research Partnership Program, Institute for Medical Translation New Bolton Center, and the Boston University MSE Innovation Award.

REFERENCES

[1] Li X+ 2011, Magn Res Imag. 29(3). [2] Kroupa KR+ 2021 JOR. [3] Ersland E+ 2023 SB3C (No.461) [4] Unal M+ 2018 Osteoarthritis Cartilage; 27(2):304-313.[5]Kazemi et. al. 2023 ORS Ann. Mtg (#339)..

A PERSONALIZED MULTISCALE MODEL OF BIVENTRICULAR CARDIAC ELECTROMECHANICS

Aaron L. Brown (1,2), Lei Shi (4), Matteo Salvador (2,3), Fanwei Kong (2,3), Vijay Vedula (5), Alison L. Marsden (1,2,3)

(1) Department of Mechanical Engineering, Stanford University, Stanford, CA, USA
(2) Stanford Cardiovascular Institute, Stanford, CA, USA
(3) Department of Pediatrics (Cardiology), Stanford University, Stanford, CA, USA
(4) Department of Mechanical Engineering, Kennesaw State University, Marietta, GA, USA
(5) Department of Mechanical Engineering, Columbia University, New York, NY, USA

INTRODUCTION

Numerical simulations of the biomechanics of the heart tissue (myocardium) are useful for non-invasive investigations of cardiovascular disease mechanisms and treatments. In such simulations, modeling the circulatory system is essential for capturing physiological cardiac behavior. To reduce the computational cost, blood circulation is typically represented with a zero-dimensional (0D) lumped-parameter network (LPN). Recently, we described a novel scheme to couple three-dimensional (3D) cardiac mechanics models with 0D circulatory models, demonstrating the method with an idealized left ventricle coupled to an open-loop LPN. Here, we extend the coupling scheme to an image-derived, electromechanical model of the left and right ventricles (LV, RV) coupled to a closed-loop LPN. We also present a workflow to personalize the multiscale biventricular model based on clinical measurements of cardiovascular function.

METHODS

We construct a biventricular cardiac model for a healthy adult male. Phase-resolved (3D+t) computerized tomography (CT) images were obtained at 10 time points during the cardiac cycle. We then apply a deep-learning whole-heart mesh reconstruction approach to segment the images [1]. From this, we calculate time-dependent cardiac chamber volumes. Other clinical measurements, including cuff blood pressures and electrocardiogram (ECG) waveforms, were also obtained for this individual (Fig. 1).

The computational model is composed of a 3D biventricular model, obtained from the segmented CT data at end-diastole, coupled to a closed-loop LPN of the circulatory system, borrowed from [2] (see Fig. 2). The LPN contains capacitor-resistance-inductor assemblies to model four basic compartments of the circulatory system – systemic/pulmonary arterial/venous – as well as time-varying elastance elements for the left and right atria (LA, RA). In addition, diodes are used to represent the cardiac valves.

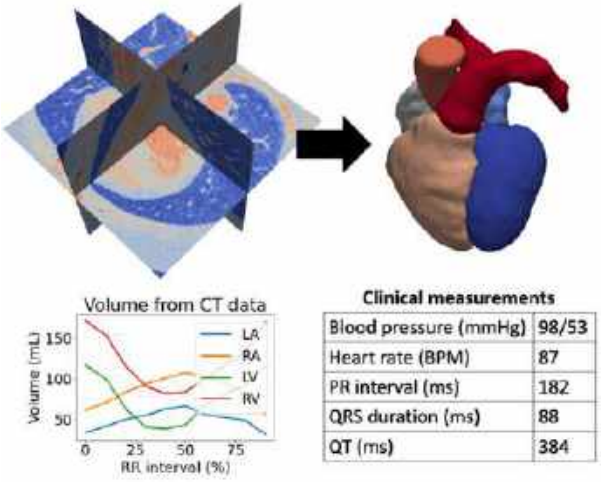

Figure 1: Summary of clinical data used to inform the model. Top: CT image data is automatically segmented using the deep-learning method of [1]. Bottom: Chamber volumes are computed from segmentations, and clinical measurements are obtained.

For the biventricular model, we generate myocardial fiber directions using a rule-based Laplace-Dirichlet method [3]. To model tissue support on epicardial and basal surfaces, we apply Robin boundary conditions, indicated by the spring-dashpot assemblies in Fig. 2. The equations of hyperelastodynamics, with the fiber-based Holzapfel-Ogden material law for myocardium, are solved using a recently developed variational multiscale finite element (FE) method

suitable for incompressible finite deformations [4]. Electrophysiology is simulated using the monodomain equation for the transmembrane potential and the ten Tusscher-Panfilov ionic model [5]. We use a fractal-tree-based Purkinje network [6], crucial for realistic electrical activation patterns and cardiac contraction. Simulations are performed with the open-source multiphysics code *svFSI* [7].

The two submodels – 3D biventricular electromechanics and 0D blood circulation – are coupled using our recently published method [8]. Briefly, in our coupling scheme, flowrate and pressure are passed iteratively between the 3D and 0D solvers, until both are converged in each timestep. In addition, we numerically calculate the resistance experienced by the 3D cardiac model due to the 0D fluid, computed as the derivative of pressure with respect to flowrate. This is used to modify the tangent matrix of the 3D solver, significantly improving the convergence robustness, particularly during the isovolumic cardiac phases.

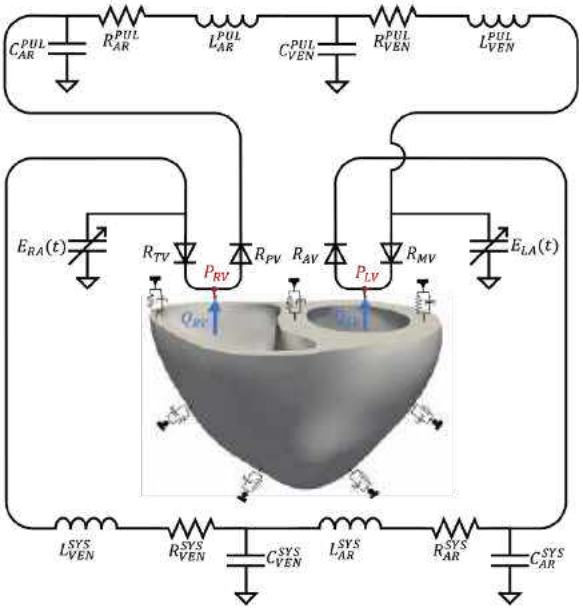

Figure 2: Image-derived biventricular model coupled to closed-loop LPN model of [2].

Our combined 3D-0D model has many parameters that must be tuned to match clinical measurements. This is achieved in multiple steps. First, we employ a full LPN model of the cardiovascular system, in effect replacing the 3D FE model of the ventricles with time-varying elastances. Using a combination of manual tuning and Nelder-Mead optimization, we determine parameters of the LPN that yield the observed patient-specific metrics, within a specified tolerance. Second, we perform an inverse FE analysis to determine the stress-free configuration and passive material parameters of the myocardium using a novel optimization framework [9]. Finally, we again apply Nelder-Mead optimization to determine the parameters of the active cardiac contraction model.

RESULTS

Fig. 3 shows preliminary results, in which we simulate the coupled biventricular model for five cardiac cycles. On the left, we show the biventricular model at end-systole, colored by von Mises stress. Comparing the deformed configuration to the reference configuration, shown in gray and semi-transparent, we see that much of the decrease in volume is obtained by the downward movement of the basal plane. Also, stress is concentrated at the basal plane, owing to stiff Robin boundary conditions imposed here.

On the right, we plot the pressure-volume (PV) loops. For the LV PV loop, we see clear delineation of the four cardiac phases – isovolumic contraction, ejection, isovolumic relaxation, and filling. These phases are less defined for the RV. We also note that LV and RV stroke volumes are initially different but equalize by the fifth cardiac cycle.

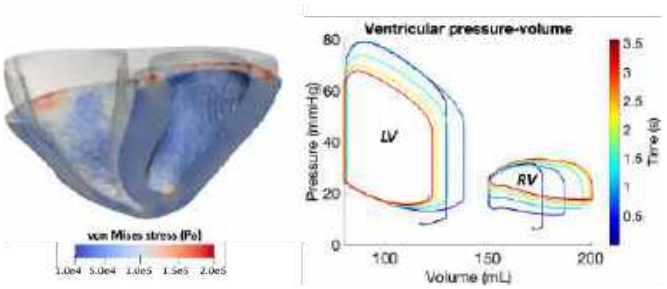

Figure 3: The simulation was run for five cardiac cycles. Left: Biventricular model at end-systole in cut view colored by stress magnitude, with reference configuration in gray and semi-transparent. Right: Pressure volume loops for the LV and RV.

DISCUSSION

This work provides a methodology and a baseline model for simulating personalized biventricular electromechanics, accounting for the entire cardiovascular system. Using a high-fidelity 3D model for the myocardium, but a simplified 0D model for blood circulation, permits a physiological yet computationally tractable simulation of the heart function. Indeed, our preliminary results exhibit important features of physiological cardiovascular behavior, including the downward motion of the basal plane, reasonable PV loops, and equalization of stroke volumes. The isovolumic phases of the cardiac cycle, which traditionally pose numerical challenges, are well captured by our coupling method without any *ad hoc* special treatment [2,8]. One can modify this model to investigate the effect of congenital heart defects (CHDs), including arrhythmia, ventricular dyssynchrony, septal defects, and transposition of the great arteries, as well as surgical interventions to address such diseases. The method may also be extended to four-chamber heart models to simulate whole-heart cardiac electromechanics.

ACKNOWLEDGEMENTS

The authors would like to thank National Institutes of Health (R01HL129727) and the National Science Foundation (1663671) for grant funding for this project, and the members of the Cardiovascular Biomechanics Computation Lab at Stanford for many helpful discussions.

REFERENCES

[1] Kong F., et al., *Med Im Ana* 74, 102222 (2021)
[2] Regazzoni F., et al., *J Comp Phys* 457, 111083 (2022)
[3] Bayer J.D., et al., *Ann Biomed Eng* 40, 2243-2254 (2012)
[4] Liu J., et al., *CMAME*, (2018)
[5] Niederer S.A., et al., *Phil Trans R Soc A* 369, 4331-4351 (2011)
[6] Costabal F.S., et al., *J Biomech* 12, 2455-2465 (2016)
[7] Zhu C., et al., *JOSS* 7(78), 4118, (2022)
[8] Brown A., et al., *CMAME*, (2024)
[9] Shi L., et al., (2024), manuscript in preparation

A PARAMETRIC MODEL OF THE MITRAL VALVE FROM MULTIMODAL IMAGING DATA

André Da Luz Moreira (1,2), Anders Persson (2,3) , Farkas Vanky (4), Matts Karlsson (2,5), Jonas Lantz (1,2), Tino Ebbers (1,2)

(1) Unit of Cardiovascular Sciences, Department of Health, Medicine and Caring Sciences, Linköping University, Linköping, Sweden
(2) Center for Medical Image Science and Visualization (CMIV), Linköping University, Linköping, Sweden
(3) Department of Radiology, and Department of Health, Medicine and Caring Sciences, Linköping University, Linköping, Sweden
(4) Department of Cardiothoracic and Vascular Surgery, Heart Centre, Department of Health, Medicine and Caring Sciences, Linköping University, Linköping, Sweden
(5) Department of Management and Engineering, Linköping university, Linköping University, Linköping, Sweden

INTRODUCTION

Understanding the motion and geometry of the mitral valve (MV) in a beating heart is a complex and often impractical task with normal medical imaging. Most clinical evaluations of valves are performed using two-dimensional trans-thoracic echocardiography images, which allow for some evaluations of function, lesions and diseases. Some more advanced non-invasive evaluations are performed using transesophageal echocardiography, Cardiac Magnetic Resonance (CMR) and Cardiac Computed Tomography (CCT). These techniques are capable of three-dimensional time-resolved images [1], but still cannot easily produce a clear geometrical representation of the MV. This, however, is of great importance for simulations of cardiac hemodynamics, with blood flow calculated from time-resolved CT using geometrical information of a subject's heart and computational fluid dynamics (CFD) [2]. As detailed valve geometry and their motion cannot be directly extracted from CT data, these simulations utilise approximate open and closed shapes for cardiac valves with motion and dynamics of the valves.

This study presents a method for calculating subject-specific dynamic geometrical models for the mitral valve from either CCT or CMR. The model should be simple enough, while allowing for sufficient agreement with valvular geometries and dynamics. The shapes of the MV annulus and leaflets were parametrised, while the the *chordæ tendinæ* were neglected. The MV geometries included the valve translations and rotations following the cardiac motion.

METHODS

Image data and mitral valve tracking

CT images were obtained from 2 patients with no reported mitral valve disease, subjected to preoperative aortic valve evaluations. Images were obtained either with a 3rd generation energy-integrating dual-source CT scanner (Somatom Force, Siemens Healthineers, Forchheim, Germany) or with a photon-counting detector dual-source CT scanner (NAEOTOM Force, Siemens Healthineers, Forchheim, Germany). Time-resolved images were acquired during an end-inspiration breath hold with full heart beat reconstructed to 20 time instants. Each 3D volume consisted of slices of in-plane resolutions 512×512 pixels, with spacings from 0.309×0.309 mm^2 to 0.391×0.391 mm^2, 0.6 mm thickness, 0.3 mm or 0.4 mm spacing between slices. For MV evaluation, a three-chamber long-axis view was manually defined for each subject using a slice in ParaView v5.11. This cross-sectional view, utilised in clinical echocardiography and CMR, allows for visualisation of cardiac anatomy showing the left atrium, left ventricle and part of the ascending aorta. CT data were interpolated to this plane and to 9 additional evenly rotated planes around an axis from the MV to the ventricular apex, used for mitral valve segmentation.

Cine balanced steady-state free precession (bSSFP) CMR data were obtained from three control subjects in a study investigating MV function and blood flow in postoperative mitral valve repair surgery. The bSSFP images were acquired at end-expiratory breath holds for MV visualisation at a 1.5 T MRI system (Philips Healthcare, Best, the Netherlands). These consisted of a three-chamber view and 7 to 10 additional planes parallel to it. At each of these locations, 40 time frames representing a full cardiac cycle were reconstructed, with slices' in-plane resolutions of 256×256 pixels, spacing of 1.25×1.25 mm^2 and thicknesses and slice spacings of 5 mm. To match the temporal resolution of CCT, only half of the CMR time frames were utilised for tracking.

The studies were approved by the Swedish Ethical Review Authority.

The mitral valve annulus and leaflets, as well and the ventricular apex

and papillary muscles, were manually tracked in the CCT and CMR data, as exemplified in Fig. 1. All steps of data management, interpolation and point tracking were performed using custom developed software implemented in Python 3.11.

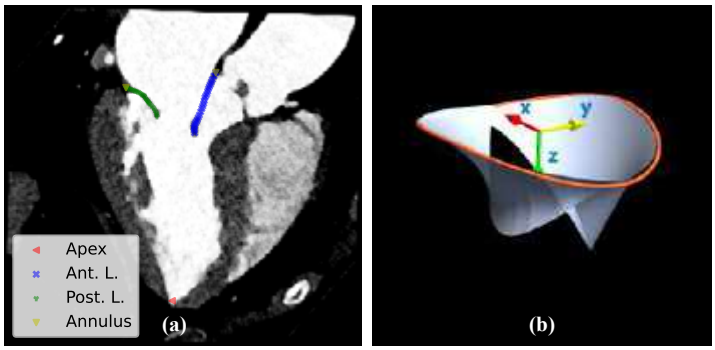

Figure 1: (a) Segmented MV points on three-chamber view from interpolated CCT. (b) Modelled MV geometry in local coordinates.

Mitral valve model

Transformation matrices for the point data were first determined using the MV annulus points at each time step to transform tracked MV points from global coordinates to valve-centric coordinate systems. A translation vector was calculated as the mean coordinate of the annulus points. For standardisation, local coordinate systems' orientations were defined with z-axes from MV to ventricle apex and x-axes lying in a plane perpendicular plane to the three-chamber view in an approximate posteroanterior orientation, as seen in Fig. 2 (a) and (c).

The adoption of a combination of elliptical and hyperbolic paraboloid equations for the mitral annulus has been described extensively in generalised models of the MV geometry [3] , but their use with the tracked points showed poor agreement. To improve the results, the original equations were modified. The two-dimensional elliptical equation in cylindrical coordinates of the MV in local xy-planes was altered with values for the semi-axes depending on each quadrant, while also allowing for displacements in x and y-directions, so the centre of the ellipses may not overlap with the origin of the coordinate system. While the true hyperbolic paraboloid equations have constant parameters, the modified HP used had coefficients changing smoothly as functions of the angle ϕ in cylindrical coordinates. Such changes made it possible to account for asymmetries in the annular shape, improving the agreement between predicted and measure annulus coordinates.

The anterior and posterior MV leaflets were approximated to fourth order polynomial functions in cylindrical coordinates, with the radius ρ as a function of ϕ and z. For each leaflet a displaced coordinate system along the local y-axis was used, to mitigate problems caused by leaflet segments intersecting the coordinate system origin.

The coefficients of the MV annulus and leaflet functions were calculated by minimising the difference from the tracked point coordinates to the outputs of these functions. The transformation displacements and rotations, as well as the coefficients for the annulus and leaflet functions, were smoothed in time to assure continuity between cardiac cycles, used to produce MV geometries at all 20 analysed time steps.

RESULTS

The resulting mitral valve geometries were calculated for the subjects at all analysed time frames using subject-specific input parameters as well as the mean values from the six subjects analysed. Figure 2 shows example MV annulus and leaflet geometries produced using the model approach described, corresponding to the same instant seen in Fig. 1.

Using the parametric model results, the projected annulus area from the modified ellipse equations. The projected leaflet opening area during diastole was also computed using the leaflet parametric models. The results of these area calculations are presented in Figure 3.

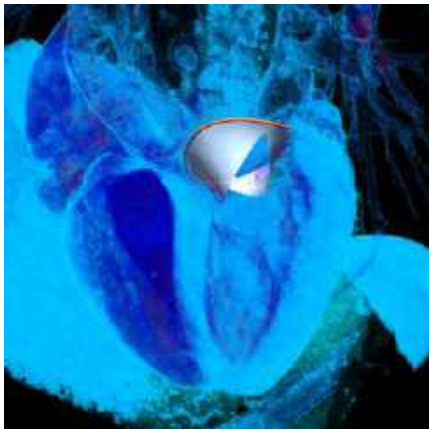

Figure 2: Modelled MV geometry with CCT data.

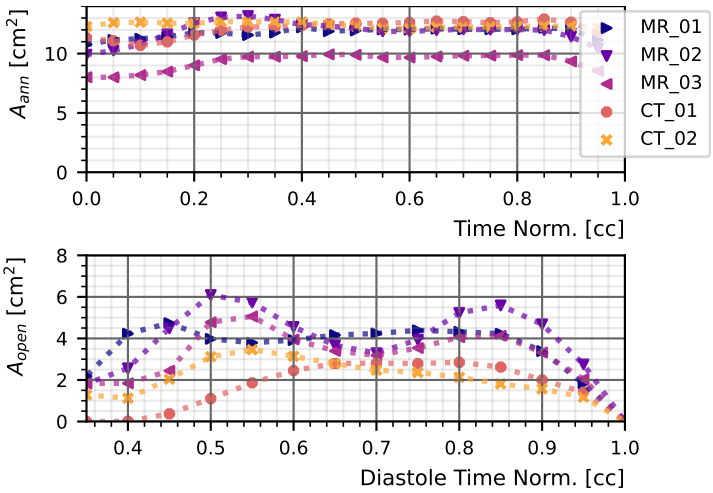

Figure 3: (a) MV annulus projected area and (b) MV opening projected area during diastole.

DISCUSSION

In this study, a method for producing subject-specific geometric models of the mitral valve based on multimodal medical images has been described. The model presents a trade-off between simplicity and accuracy. This method utilises segmentation information for the MV annulus and leaflets, which after data processing produce a parameter-based approach for calculating the valve's position and shape along a cardiac cycle, and the agreement between the calculated geometries and the tracked point coordinates indicates good similarities. As shown in Fig 3, the presented parametric method may potentially be used for assessment of MV annulus and leaflet geometries and function. Additionally, the mitral valve motion is affected by both the left ventricle and atrium, so the the translation and rotations obtained from the transformation parameters may be used for further assessment. This geometrical modelling can also facilitate and increase accuracy of CFD simulation of blood flow, producing dynamic and more realistic representations of the mitral valve geometry.

ACKNOWLEDGEMENTS

The authors acknowledge funding from the Swedish Research Council and Swedish Heart Lung Foundation.

REFERENCES

[1] Vahanian A et al. *European Heart Journal* 43.7 (2022). ISSN: 0195-668X. DOI: 10.1093/eurheartj/ehab395.

[2] Lantz J et al. *Journal of Biomechanical Engineering* 138.12 (2016). ISSN: 0148-0731. DOI: 10.1115/1.4034652.

[3] Oliveira D et al. *Journal of Anatomy* 237.2 (2020). DOI: 10.1111/joa.13196.

THE EFFECTS OF GROWTH AND REMODELING ON THE CONTRACTILE FUNCTION OF THE PREGNANT MURINE UTERUS

Emily A. Hoffmann (1), Kyoko Yoshida (1)

(1) Department of Biomedical Engineering, University of Minnesota, Minneapolis, MN, U.S.A.

INTRODUCTION

The uterus changes dramatically during pregnancy. Significant uterine growth (mass and cavity volume change) and remodeling (mechanical property changes) occur to support a healthy, term pregnancy. Abnormal uterine growth and remodeling (G&R) are implicated in compromised uterine mechanical function, potentially leading to preterm birth (< 37 weeks gestation), a condition that affects over 10% of births worldwide and is the leading cause of newborn mortality [1]. One avenue of preterm birth is a premature increase in uterine contractility [1], but little is known about the mechanical and biological factors that direct the timing and magnitude of contractions.

Soft tissue G&R typically maintains mechanical homeostasis: cells grow or remodel their extracellular matrix to optimize the stress or stretch they experience, helping preserve their function [2]. Unlike in other soft tissues, the mechanical function of the uterus evolves during pregnancy: first remaining relaxed while experiencing large amount of stretch, then increasing its contractility for labor at term [3]. Because stretch determines the active stress that smooth muscle cells (SMCs) generate, we hypothesize that the stretches uterine SMCs experience is an important driver of organ-level uterine function during pregnancy.

Changes in the *in vivo* mechanical environment that uterine SMCs experience, however, are challenging to characterize. Imaging modalities like ultrasound can track changes in total deformation of the tissue, confounding uterine growth (changes in undeformed geometry) with mechanical stretch from the growing fetus. Additionally, uterine tissues are known to remodel, potentially altering *in vivo* stretch or stress [4]. In other soft tissues, the kinematic growth framework has been used to account for growth, remodeling, and mechanical loading in solving for the *in vivo* mechanical environment of muscle cells [5]. Here, we apply the same framework with the goal of elucidating the effects of uterine growth, remodeling, and mechanical loading on the *in vivo* mechanical environment of uterine SMCs. Towards this goal, the objectives of this study were to 1) quantify uterine remodeling by fitting a constitutive model to published passive and active tensile data, and 2) create a finite element (FE) G&R model of the pregnant mouse uterus to investigate the effects of growth, remodeling, and mechanical loading on uterine stress and contractility. We hypothesized that growth would decrease stress in the uterus and that G& R would reduce contractility.

METHODS

Here, we investigate uterine remodeling in mice, a common animal of pregnancy [6]. First, we quantified passive uterine remodeling by fitting a coupled transversely isotropic Mooney-Rivlin (TIMR) constitutive equation (Eq. 1) to published passive uniaxial tensile data from nonpregnant and pregnant mouse uterine tissues on gestation days (d) 7, 13, 15, 17, and 19 of a 19-day gestation [7]. In this constitutive relationship, the strain energy density function (W) depends on fiber stretch (λ), the invariants and Jacobian of the deformation tensor (I_1, I_2, J), material parameters $c_{1\text{-}4}$, and bulk modulus k (Eq. 2).

$$W = c_1(I_1 - 3) + c_2(I_2 - 3) - 2(c_1 + 2c_2)\ln J + F(\lambda) + \frac{1}{2}k(\ln J)^2 \quad (1)$$

$$F(\lambda) = \begin{cases} 0, & \lambda \le 1 \\ c_3\left(e^{-c_4}\left(\mathrm{Ei}(c_4\lambda) - \mathrm{Ei}(c_4)\right) - \ln\lambda\right), & 1 < \lambda \end{cases} \quad (2)$$

where Ei() is the exponential integration function. We determined optimal parameters by simulating the tensile tests with FEBio (v4.0). To prevent overfitting, we set c_2=0 and c_4=1.4 for all gestation days and iterated values of c_1 and c_3 to minimize the R^2 value between the simulated and experimental stretch-stress curves. We incorporated active contraction by prescribing published stretch-active stress curves for each timepoint using the "active fiber stress" model in FEBio [6].

Next, we developed a FE G&R model of the murine uterus (FIG. 1). We idealized the nonpregnant uterus as a thick-walled cylinder based on gross anatomy measurements and modeled a quarter section for computational efficiency. We simulated two myometrial layers to mimic known uterine architecture [7]. Here, we simulated d7 and d13 of pregnancy, each with gestation day specific TIMR and active

contraction parameters. To simulate uterine growth, we assumed constant mass density throughout pregnancy and used the kinematic growth model to prescribe fiber growth ($F_{g,ff}$) based on published uterine weight measurements (d7: $F_{g,ff}$ =1.15[-], d13: $F_{g,ff}$ =1.5[-]) [6]. Fixed boundary conditions enforced symmetry and a coplanar constraint allowed the upper end of the uterus to displace freely in the z-direction (FIG. 1). To simulate mechanical loading, we idealized two pups as spheres (with a sliding facet-on-facet contact between the pups and the inner uterine wall) and used the "cell growth" model to simulate pup growth according to published pup weight data [6,9].

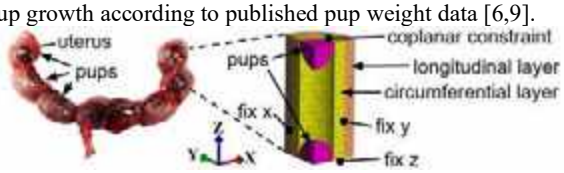

Figure 1: Image of a pregnant mouse uterus with two horns. The FE model simulated a segment with two pups.

We simulated three cases for d7 and d13: 1) remodeling only (R-only), where we changed TIMR properties but not fiber growth ($F_{g,ff}$ =1), 2) growth only (G-only), where we allowed fiber growth but kept TIMR properties unchanged, and 3) growth and remodeling (G+R), where both TIMR parameters and $F_{g,ff}$ changed over time. In each simulation, we allowed the uterus to passively stretch due to pup growth, then simulated contraction. We compared the 1st principal stresses in the three adaptation cases, then before and after contraction, to understand the effects of G&R on uterine stress and contractility.

RESULTS

The TIMR constitutive model successfully captured the passive experimental stretch-stress curves (FIG. 2A). The c_1 and c_3 parameters decreased to capture the elongation and lower slope of the toe region in the experimental stretch-stretch curve (FIG. 2B).

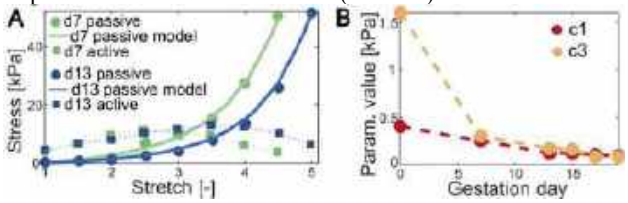

Figure 2: A) Representative material model fits at d7 and d13 demonstrate agreement between model and experimental results. The dotted lines show stretch-dependent active stress curves at d7 and d13. B) TIMR parameters c_1 and c_3 decreased with gestation.

We incorporated these changes in c_1 and c_3 into our organ-level FE models. In the d13 models, the contracted 1st principal stresses were highest when accounting for R-only (av. 1.24kPa, max. 4.97kPa), followed by G-only (0.98, 2.55kPa) then the G+R case (0.53, 1.40kPa) (FIG. 3A). The difference between stress before and after contraction (i.e., the active stress) was highest in the R-only case (0.22kPa) compared to the G-only (0.10kPa) and G+R (0.11kPa) cases.

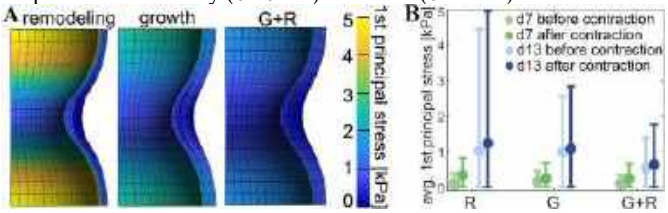

Figure 3: A) 1st principal stresses were different in the three d13 adaptation cases (after contraction). B) Max. and avg. stress were lowest with G+R (error bars: max and min) at both d7 and d13.

The d7 model had similar trends (R: av. 0.10kPa, max. 0.38kPa; G: 0.15, 0.45kPa; G+R: 0.10, 0.32kPa). Comparing across gestation days, stresses were lower at d7 compared to d13, and d7 contractile stresses were similar to those at d13 (R: 0.22, G: 0.08, G+R: 0.14kPa).

DISCUSSION

The objectives of this study were to quantify uterine remodeling during pregnancy and investigate the effects of uterine G&R on stress and contractile function. To this end, we fit a constitutive model to passive tensile data and developed a FE G&R model of the murine uterus, incorporating realistic G&R changes during pregnancy.

By changing the c_1 and c_3 parameters, we were able to capture the elongated toe region and decreased toe region slope in the tensile stress-stretch curve with progressing pregnancy. This result indicates that the TIMR model is appropriate for quantifying uterine remodeling.

In our d13 G&R FE model, passive stresses were highest when accounting for remodeling only, followed closely by the growth-only case. The lowest stresses occurred in the G+R case, indicating that both adaptations are important for maintaining the optimal mechanical environment during pregnancy. R-only and G-only stresses were 94% and 87% higher than stress in the G+R case, respectively. Thus, our simulations demonstrate that the mechanical consequences of G&R, particularly growth, have an important effect on reducing uterine SMC stress during pregnancy. These results support the notion that uterine G&R occurs to help uterine SMCs maintain homeostasis as the fetus grows; this is potentially an important mechanism for protecting uterine SMCs from experiencing too much stretch early in the pregnancy and preventing premature contractions. This idea is also consistent with the higher risk of preterm birth in cases of excess stretch [1].

Interestingly, the ability of the uterus to contract was similar when comparing G-only to G+R. These results suggest that the passive curve can affect the active stress of the uterus. Higher active stress in the R-only case compared to the G-only case agree with literature in which increased substrate stiffness results in higher SMC traction forces [2]. Overall, our results highlight the importance of accounting for mechanical G&R history when developing computational models that simulate pregnancy and labor contractions.

In conclusion, we demonstrate the mechanical consequences of tissue-level uterine G&R on organ-level stress and contractility. Future work will improve model assumptions, including those of identical material properties in the two uterine layers and homogenous properties and growth throughout the tissue. We are currently simulating additional gestation days to understand how the *in vivo* mechanical state of the uterus evolves during pregnancy. In the future, we will integrate this model with biological signaling models to provide a comprehensive multiscale computational platform to elucidate the biological and mechanical interactions that underly preterm birth.

ACKNOWLEDGEMENTS

This work was supported in part by the NSF Graduate Research Fellowship and the NSF CAREER award.

REFERENCES

[1] Romero, R et al., *Science*, 345, no.6198:760–765, 2014.
[2] Karkhaneh Yousefi, A et al., *JMBBM,* 144:105990, 2023.
[3] Cunningham, GF et al., Williams Obstetrics 26e, 2022.
[4] Myers, M and Elad, D, *WIREs Sys Bio and Med*, 9:1388, 2017.
[5] Rodrieguez, EK et al., *J Biomech*, 27:455-467, 1994.
[6] Mahendroo, M. et al., *Reprod. Camb. Engl*, 143:429–438, 2012.
[7] Wu, X et al., *JCMM*, 12:1360-1373, 2008.
[8] Ouellette, A et al., *Biol. of Repro*., 104:741-751, 2022.
[9] Mu, J et al., *Repro. Bio. And Endo.*, 6:34, 2008.

ASSOCIATIONS BETWEEN CEREBROVASCULAR REMODELING AND NEUROPATHOLOGICAL CHANGES IN THE BRAIN DURING ALZHEIMER'S DISEASE PROGRESSION

Samuel C. Halvorsen (1), Raymond Nicks (2), Thor D. Stein (2,3,4), Katherine Yanhang Zhang (1,5,6)

(1) Mechanical Engineering, Boston University, Boston, Massachusetts, United States
(2) Alzheimer's Disease and CTE Center, Boston University School of Medicine, Boston, Massachusetts, United States
(3) United States Department of Veterans Affairs, VA Boston Healthcare System, Boston, Massachusetts, United States
(4) Pathology and Laboratory Medicine, Boston University, Boston, Massachusetts, United States
(5) Biomedical Engineering, Boston University School of Medicine, Boston, Massachusetts, United States
(6) Division of Materials Science & Engineering, Boston University, Boston, Massachusetts, United States

INTRODUCTION

Alzheimer's Disease (AD) is a debilitating neurodegenerative disease and the most common form of dementia, affecting over 6.5 million Americans [1]. AD progression leads to various forms of cognitive decline, most notably memory impairment. Cerebrovascular integrity is essential for proper brain perfusion and metabolism. The ability of cerebral arteries to dampen the pulsatile blood flow is important to prevent damage to the brain. Cerebrovascular remodeling and degradation of artery wall constituents including elastic fibers, collagen, and smooth muscle cells (SMCs) may lead to decreased compliance and impact its ability to remove neurotoxic materials from the brain. This includes amyloid-β (Aβ) deposits and the protein tau in the form of neurofibrillary tangles (NFT), the two proteins established as the primary indicators of preclinical AD [2,3].

In this study, neuropathological AD progression in the form of neuritic Aβ deposition and NFT formation in brain tissue was compared with changes to the mechanical behavior and microstructure of human anterior cerebral arteries (ACAs) from patients diagnosed at various stages of AD. Our findings showed that the presence of NFTs and neuritic Aβ plaques in the regions of the brain supplied by the ACA corresponded with decreased ACA compliance and microstructural changes.

METHODS

Sample Preparation and Mechanical Testing: Human ACAs (n = 49) obtained from the BU Alzheimer Disease Center were delivered to the laboratory on dry ice and stored in a -80°C freezer before experiments. ACA sections roughly 15mm in length and 2mm in diameter were gently cleared of connective tissue and blood was flushed before mechanical testing. ACA samples were mounted on metal cannula in a pressure myograph (DMT 110P, Denmark). Arteries were stretched to their *in vivo* stretch ratio λ_z and inflated to 120mmHg at 2.5mmHg/s for preconditioning and testing. Four inflation-deflation cycles were performed to ensure repeatability. Transmural pressure P, axial force f, and outer radius r_o were measured during the experiment. After testing, an artery ring was carefully excised from the sample to measure the undeformed inner (R_i) and outer (R_o) radii. Circumferential stretch (λ_θ) as well as circumferential (σ_θ) and axial (σ_z) Cauchy stresses were calculated as:

$$\lambda_\theta = \frac{r_o+r_i}{R_o+R_i},\ \sigma_\theta = \frac{Pr_i}{r_o-r_i}, \sigma_z = \frac{f+P\pi r_i^2}{\pi(r_o-r_i)(r_o+r_i)} \qquad (1,2,3)$$

where r_i is the deformed inner radius calculated based on the soft-tissue incompressibility assumption [4]. Circumferential tangent stiffness was calculated as the slope of the stress-stretch curve for the low-pressure region (0-20 mmHg). Mechanical testing data was grouped by age (≤65, 66-79, and ≥80) along with NFT and Aβ pathology levels to study the age dependency and association with brain pathology. AD neuropathological development is quantified by its spread throughout the brain and scored from 0 (control) to 3 (whole brain is afflicted) [5]. In this study, samples were grouped based on NFT (0-1 and 2-3) and Aβ scores (0 and 1-3).

Histology and Multiphoton Microscopy: Sections ~3mm in length were cut from mechanically tested ACAs and fixed in 4% paraformaldehyde overnight. Fixed samples were embedded in paraffin and cut in 5μm thick sections then stained with Movat's pentachrome to view elastic fibers (black), collagen fibers (yellow), cellular material (red), and ground substance (blue). Stained sections were imaged at 40× to examine for structural changes.

ACA microstructures were further examined using multiphoton microscopy using an excitation wavelength of 805 nm with a 20× water immersion objective lens. Signals from elastic fibers (495-540nm) and collagen bundles (390-420nm) were isolated using two-photon excitation and second harmonic generation, respectively. Images of the ACA cross-section and the adventitia were obtained to analyze changes in the abundance and organization of these two structural constituents.

RESULTS

Averaged circumferential stress-stretch responses for the three age groups were plotted in Fig. 1a, with corresponding average tangent stiffness of the low-pressure region in Fig. 1d. The left-ward shift in the curves indicates a progressive stiffening of the ACAs, with a significant decrease in the circumferential stretch and increase in the circumferential stress in the ≥80 age group. A stiffening trend is consistently present in the low-pressure region (Fig. 1d), although the changes are not significant.

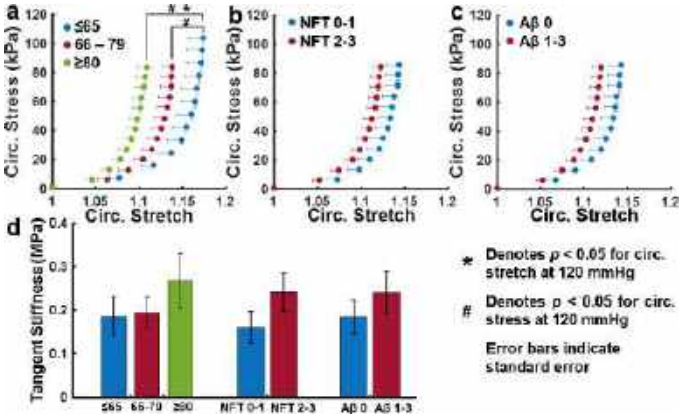

Figure 1. (a)-(c) Circumferential stress-stretch responses of ACAs, grouped by (a) age, (b) NFT formation, and (c) neuritic Aβ deposition. (d) Circumferential tangential stiffness for low-pressure region (0-20mmHg) of the stress-stretch curves in (a)-(c).

To reduce the effects of aging, mechanical testing data for samples above age 65 (n = 31) were grouped by NFT formation (Fig. 1b) and neuritic Aβ deposition (Fig. 1c). In both cases, the presence of NFTs and neuritic Aβ corresponded with decreased maximum circumferential stretch (Figs. 1b,c) and increased tangential stiffness (Fig. 1d).

Representative histological stains of the ACAs with different AD-associated neuropathological stages in Fig. 2 show the multilayered structure of the ACA consisted of the internal elastic lamina (IEL), media, and adventitia. Thinning of the media occurs due to smooth muscle cell atrophy at the media-adventitia interface, and collagen disorganization is present in the adventitia.

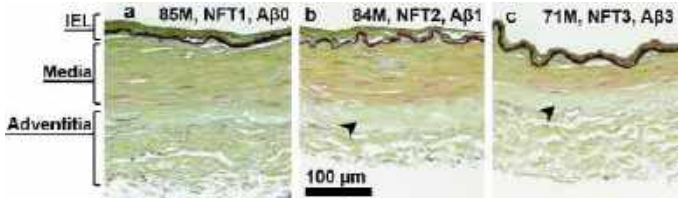

Figure 2. Histological sections of human ACAs from different neuropathological disease stages. Arrow indicates SMC atrophy.

Multiphoton images in Figs. 3a,b show the elastic (green) and collagen (red) fibers in the ACAs from a sample with moderate NFT formation and an older sample with severe deposition of NFTs and Aβ. The IEL (top) exhibits strong elastic signal while the medial elastin content is sparse. Circumferentially oriented elastic fibers populate the media-adventitia border. Adventitial collagen in Figs. 3c,d is primarily aligned in the axial direction with noticeable straightening of the collagen fiber bundles in the old and diseased sample.

DISCUSSION

This study offers new insights into the structure-function relationship of the human cerebrovasculature in neurodegenerative diseases. Our findings suggest the presence of NFTs and Aβ plaques in the frontal cortex corresponds with decreased compliance (Figs. 1b,c) and microstructural changes (Figs. 2,3) in the ACA. Effect of aging on the stiffness of the ACAs (Fig. 1a) should be carefully considered when exploring associations between the progression of AD and cerebrovascular remodeling.

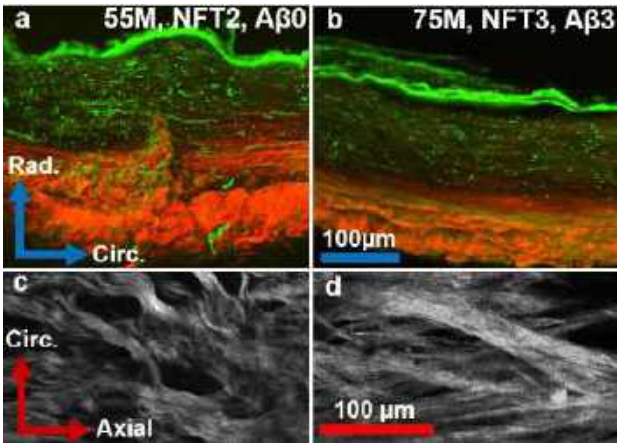

Figure 3. (a)-(b) Max. intensity projections of cross-sectional multiphoton images from ACAs of different age and disease state, showing elastic (green) and collagen (red) fibers. (c)-(d) 1μm thick multiphoton images depicting collagen fiber bundles in the adventitia, matched to samples from (a)-(b), respectively.

The stress-stretch response shows a stiffening trend for ACAs from subjects exhibiting high levels of NFT formation (Figs. 1b,d) or Aβ deposits (Figs. 1c,d). It is important to note that the frontal lobe, in part supplied by the ACA, experiences deposition of Aβ plaques during early AD development (score of 1 out of maximum 3), while NFT formation generally begins in later stages (score of 2). The different deposition patterns of Aβ plaques and NFTs was accounted for when determining the grouping methods for statistical comparisons of mechanical data.

The stiffer circumferential response of the older and diseased samples is evidenced by the shorter toe regions (Figs. 1a-c) and increased stiffness (Fig. 1d). These changes in mechanical properties are corroborated by the straighter collagen fibers seen in the multiphoton images (Fig. 3d), which would be recruited earlier to bear mechanical load than the crimped collagen fibers seen in Fig. 3c.

Changes in the medial thickness due to SMC atrophy (Fig. 2) may also affect the mechanical response of the ACAs. Decreases in perivascular innervation in cerebral arteries has been reported during AD progression [6]. Perivascular innervation provides physiological stimulus for proper blood flow control [7]. Degradation of the neurons and SMC atrophy may be associated with the subsequent microstructural and functional changes in ACA.

The findings of this study provide new insights into the mechanical response of human ACAs and the relationship between their structural remodeling and neuropathological AD development. The complex mechanisms between aging, AD progression, neurodegeneration, and cerebral arterial mechanics requires further investigation.

ACKNOWLEDGEMENTS

National Institutes of Health (R01AG075876).

REFERENCES

[1] Alzheimer's Association, 2023.
[2] Govindpani, K et al., *Neural Regen Res*, 15(6):1030–1032, 2020.
[3] Tan, CC et al., *J Alzheimers Dis.*, 42(4):1051-69, 2014.
[4] Carew, TE et al., *Circulation Res,* 23:61-68, 1968.
[5] Hyman, BT et al., *Alzheimers Dement*, 8(1):1-13, 2012.
[6] Bleys, R et al., *J. Cereb. Blood Flow Metab.*, 16(5):1034-47, 1996.
[7] Westcott & Segal, *Microcirculation*, 20(3):217–238, 2014.

MECHANISM OF THE DEVELOPED PRESSURE – PRELOAD RELATIONSHIP IN EX-VIVO BEATING HEART

Lei Fan (1), Vahid Ziaei-Rad (2), Jason Bazil (3), Lik Chuan Lee (2)

(1) Joint Department of Biomedical Engineering, Marquette University and Medical College of Wisconsin, Milwaukee, Wisconsin, US
(2) Department of Mechanical Engineering, Michigan State University, East Lansing, Michigan, US
(3) Department of Physiology, Michigan State University, East Lansing, Michigan, US

INTRODUCTION

The heart's developed pressure is determined primarily based on the myocardial contractile force that is dependent on the preload (or equivalently the degree of inflation) via the Frank-Starling mechanism. There is a critical transition at which developed pressure starts to decrease with increasing preload. At the myocardial tissue level, this length-dependent property is reflected by an increase in the peak twitch force with increasing muscle stretch [1]. At the cellular level, it is found that modulation of the responsiveness of the cardiac contractile apparatus to activating calcium is largely responsible for the Frank-Starling property, a regulatory mechanism that is termed myofilament length dependent activation [2]. While these studies have demonstrated the pressure-volume or force-sarcomere length relationships across different spatial scales, it still remains unclear whether these observations (at the organ and cell levels) can be directly correlated or connected [3]. This issue largely arises because it is not possible to directly measure forces developed locally by the myocytes in the beating heart. To address this issue, we developed a computational framework consisting of a left ventricular finite element (FE) model based on our previous work [4-6] to connect cellular to organ mechanics found in the *ex-vivo* beating rat heart. *We hypothesis that the saturation of developed pressure at higher preload in the heart at the organ level can be directly connected to the length-dependency of the myocyte contractile force occurring at the cellular level.*

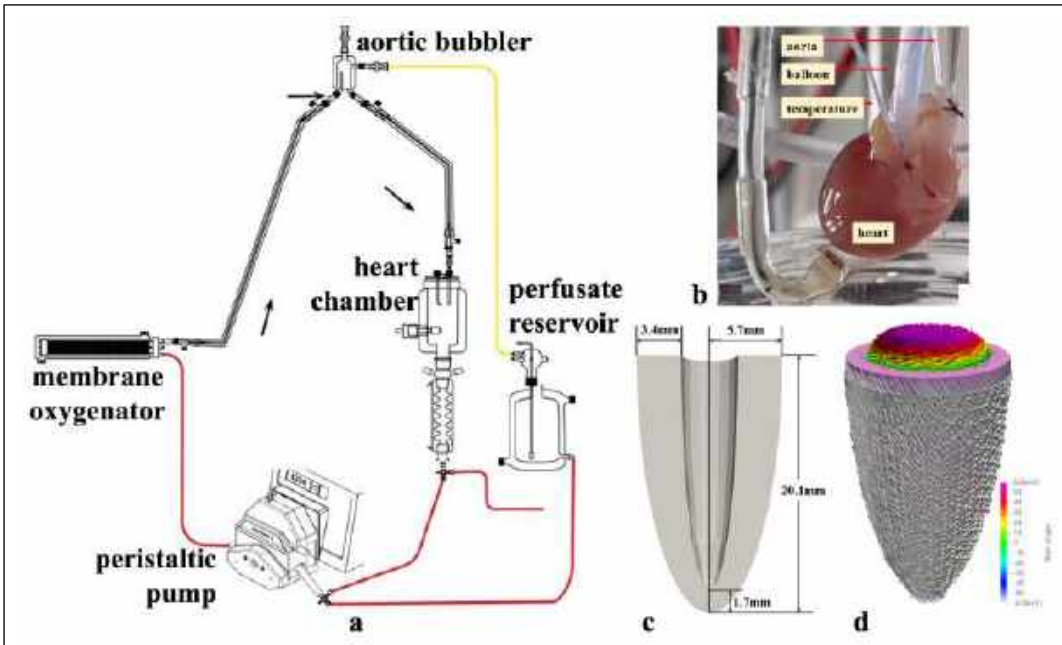

Fig 1: **a**. Schematic of Langendorff perfusion system; **b**. Configuration of the *ex-vivo* beating rat heart experiments; **c.** Idealized left ventricular geometry of a rat with its dimension; **d.** Left ventricular geometry of a rat with myofiber distribution.

METHODS

***Ex-vivo* beating heart experiments**: Approval for conducting the animal experiments using male Sprague-Dawley rat weighting 300-350 g was granted by the Institutional Animal Care and Use Committee of Michigan State University and all animal procedures were conducted in accordance with the Guiding Principles in the Care and Use of Animals.

The animals (n = 5) were first deeply anesthetized with 4-5% isoflurane after 15mins of heparin injection (100 U, i.p.). The animals were then decapitated when they were unresponsive to noxious stimuli, and their chest were opened. The heart was excised immediately from the animals and submerged in cold Krebs-Henseleit bicarbonate (KH) buffer. Then the aorta was rapidly attached to aortic cannula that is connected to an 80mmHg perfusion pressure in Langendorff perfusion system (Radnoti, US) and perfused via the Langendorff constant flow mode at a flow rate of 10 ml/min with oxygenated KH buffer at 37°C with PH 7.14 (**Fig. 1a**). The aorta root was then carefully sutured to the aortic cannula without leaking.

The heart was paced at 4 Hz by a pair of electrodes placed on the surface of the right atrium and connected to an isolated stimulator (AD Instrument). A size 6 latex balloon was inserted into the LV via the pulmonary vein that was exposed to air. A baseline case was established by inflating the balloon until the LVEDP (preload) is between to 5-15 mmHg. The heart was then stabilized for 15-20 mins. Thereafter, the preload was varied by inflating or deflating the balloon. After the heart was stabilized in each preload, the LV pressure and aortic pressure were each continuously recorded by a pressure transducer connected to the isovolumic beating heart (**Fig. 1b**). In addition to these signals, the right pressure product, temperature, and ECG were also continuously recorded in LabChart Pro (AD Instruments).

Computational Modeling: The length, wall thickness, basal inner and outer diameters measured from the rat LV were used to construct a prolate ellipsoid geometry in a finite element (FE) model of the LV (**Fig. 1c**). Myofiber orientation in the LV FE model was prescribed to vary transmurally from -60° at the epicardium to 60° at the endocardium (**Fig. 1d**). The relationship between LV pressure and volume is prescribed as $P_{LV}(t) = f(V_{LV}(t))$, where P_{LV} is decomposed to passive and active components [4]. The LV FE model was applied to simulate the *ex-vivo* beating heart under isovolumic contraction in the Langendorff preparation.

RESULTS

A representative LV pressure waveform measured during isovolumic contraction is shown in **Fig. 2a**. The measured developed pressure (DP) in the LV chamber is greater than 50 mmHg in all the rat hearts. With an increase in preload from 0 to above 65 mmHg, LVESP increases from close to 0 to 118 mmHg at the highest preload. The corresponding LV pressure waveforms were recoreded. By connecting the end-diastolic (ED) and end-systolic (ES) points at different preloads, respectively, the model predicted EDP-t and ESP-t relationships agree with the experimental measurements by increasing the preload that is controlled by inflating the balloon volume in the experiments.

The LV DP, which is the difference between LV ESP and LV EDP, varies non-monotonically with an increase in preload. Specifically, LV DP increases with preload and then decreases with preload beyond a transition point. This transition occurs when the balloon volume is between 280-340 μm (**Fig. 2c**). The computed sarcomere length at the transition point is close to 2.11 μm. The model-predicted contractile force varies similarly with preload as the LV DP with a similar transition point (**Fig. 2d**).

DISCUSSION

The mechanism of this length-tension relationship rests on the degree of overlap between the thick and thin filaments at different sarcomere lengths during cross-bridge cycling. However, it is challenging to directly connect them because of the difficulty in measuring myofiber strain and sarcomere length in the deep myocardial wall in the Langendorff preparation. To circumvent this issue, we developed an LV FE model to simulate isovolumic contraction based on the *ex-vivo* beating rat heart experiments and estimate these two quantities. The model predicted EDPVR and ESPVR at various preloads agree with the measurements from the *ex-vivo* beating rat heart experiments by varying balloon volumes (n = 5). With an increase in preload, DP increases first and then start to decrease at a critical point. At this critical value of preload, the average sarcomere length is 2.11 μm, which is close to the sarcomere length corresponding to the highest force generated by myofiber. With an increase in preload, myocardial contractility increases first and then start to decrease at the same critical point, where DP starts to reduce. This result corroborated that the DP-preload relationship is controlled by the length-tension relationship of the myocytes.

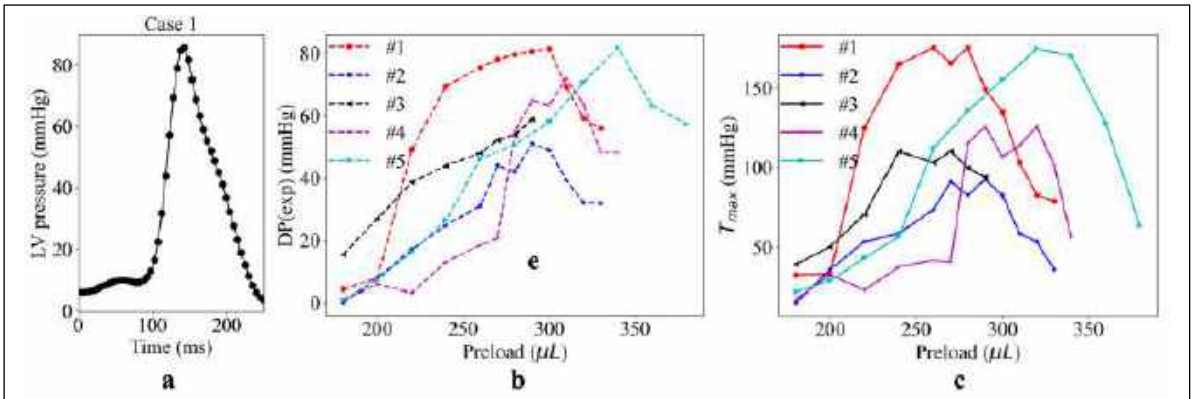

Fig 2: **a**. Experimentally measured LV pressure waveform from the *ex-vivo* beating heart experiments in a representative case; **b.** LV DP-preload relationship; **c.** LV contractility-preload relationship.

ACKNOWLEDGEMENTS

This work was supported by the National Institute of Health (R01 HL134841 and R01 HL163977).

REFERENCES

[1] Ter Keurs, H., *Circ. Res*., 46, 703-714, 1980.
[2] Kentish, J. C., *Circ. Res*., 58, 755-768, 1986.
[3] Wannenburg, T., Am. J. Physiol. – Hear. Circ. Physiol., 273, 2428-2435, 1997.
[4] Fan, L., Comput. Biol. Med., 105050, 2021.
[5] Fan, L., Front. Physiol., 12, 1-20, 2021.
[6] Fan, L., Artif. Organs, 1-17, 2023.

ANISOTROPIC POROUS HYDROXYAPATITE/GELATIN IMPLANTS FOR TRABECULAR STRUCTURE RECONSTRUCTION

A. Pavlov (1), J. Johnson (1), B. Gadomski (1)

(1) Orthopedic Bioengineering Research Laboratory, Colorado State University, Fort Collins, Colorado, USA

INTRODUCTION

Within the United States, it is estimated that 40% of the population suffers from foot related conditions [1]. Specifically, osteoarthritis is one of the most common with more than three million cases reported annually. This condition is most frequently reported in the first metatarsophalangeal (MTP) joint and leads to degenerative joint disease and patient pain and discomfort. In some cases, this can lead to irregularities within the toe orientation (i.e., hallux valgus). Both conditions can lead to loss of mobility [1] and severe discomfort during walking if left unchecked.

For patients who are unresponsive to non-invasive treatments for this condition, the standard of care is arthrodesis. First MTP arthrodesis is a joint fusion approach that entails removal of both articular cartilage surfaces with preparation of the bony surfaces into appropriate opposing geometries (e.g., cup and cone reaming) [2], followed by fixation of the joint using various hardware to eliminate subsequent joint motion. While the removal of cartilage and preparation of the opposing boney surfaces is requisite for successful fusion outcomes [3], it will invariably induce loss of joint length. To maintain anatomical symmetry and unaltered gait, there exists a need for a graft material capable of replacing the lost material and fusing to the bone without significantly lengthening the surgical or recovery process.

To promote cellular infiltration and rapid boney remodeling, a resorbable candidate graft material must be conducive to the design and manufacturing of a tailorable porosity, similar to the trabecular bone underlying these joint/arthrodesis surfaces. Researchers have long investigated hydroxyapatite/collagen for use in bone fusion applications (e.g., coatings for total hip replacements) as collagen has been proven to generate a structurally sound scaffold around which hydroxyapatite crystals can form [4]. These tend to be expensive, however, due to collagen availability and degeneration. Gelatin has emerged as a potential alternative, offering the same ability to create structures of controlled porosity within hydroxyapatite at a fraction of the cost. This allows for a material with mechanical properties comparable with cancellous bone, and anisotropically porous to stimulate quick bone ingrowth for arthrodesis purposes.

This work details the development of a novel biomaterial processing methodology aimed to generate a graft material suitable for use in joint fusion situations such as first MTP arthrodesis. Specifically, this work sought to determine the optimal processing techniques to produce a graft material with similar porosity and mechanical properties to human trabecular bone using a gelatin-hydroxyapatite compound.

METHODS

GEL:HAP Ratio Selection: Commercial hydroxyapatite powder was mixed with a 10% W/V solution of microbiology grade gelatin [5] in decadal concentrations ranging from 30:70 to 70:30 and stirred at 45°C for 20 minutes. After this the slurry was cast into a cylindrical silicon mold with dimensions r=0.5cm, h=0.5cm. The molds were then placed into a freezer at -20°C and left for 24 hours to solidify. From here the samples were immersed in liquid N_2 for 1 minute and lyophilized for 24 hours.

MicroCT Analysis: Micro–computed tomography (microCT) analysis was performed on the specimens using the following parameters: isotropic resolution, 37 µm; voltage, 70 kVp; current, 114 µA; and integration time, 500 ms (Scanco µCT 80; Scanco USA Inc). Following the scans, a bone trabecular morphometry analysis was performed and the density, bone volume/total volume fraction as well as pore size values were recorded.

Gelatin Crosslinking: To crosslink gelatin a solution of 1% Glutaraldehyde was made, and samples were submerged for 24 hours [5]. However, this led to over crosslinking and samples ended up brittle and cracked. To correct for this, 8 test groups of n=5 samples were created. Crosslinking was performed at 2-hour intervals, ranging from 2 to 16 hours with a 24-hour batch being used as a control. After the crosslinking was done, samples were rinsed 3 times in deionized (DI)

water before being fully submerged in DI water. After 10 minutes of soaking a compression test was run to determine mechanical toughness.

Mechanical Testing: Unconfined compression testing was performed using an MTS landmark hydraulic tester at a rate of 1mm/min up to 60% strain. Force-displacement data were utilized to generate stress-strain curves for all samples. Ultimate compressive stress and young's modulus for the 8 different crosslinking times groups were calculated.

Statistical Analysis: A one-way ANOVA with Tukey HSD post hoc test was performed using alpha = 0.05.

RESULTS

MicroCT analysis of samples revealed a linear relationship between Gel:HAp ratio and density and pore size (**Table 1**). In contrast, these data illustrate the logarithmic relationship between Gel:HAp ratio and bone volume fraction (BV/TV) and porosity (**Table 1**). Representative three-dimensional reconstruction images from microCT analysis illustrate the alterations to pore size and distribution at the extreme ends of the tested Gel:HAp ratios (60:40 **Figure 1B**, 30:70 **Figure 1C**). The 60:40 Gel:HAp samples exhibited porosity values of 0.62 most closely replicating porosity noted in human trabecular bone; as such, this group was chosen to proceed to mechanical testing/assessment of crosslinking on mechanical properties.

Mechanical testing of samples revealed a non-monotonic relationship between crosslinking time and ultimate compressive strength, with a maximum at 8-hours (**Figure 3A**). Specifically, the 8-hour group exhibited a 2-fold increase in ultimate compressive strength as compared to the 2-hour time ($p=0.0038$, **Figure 3A**). Compressive modulus was inversely proportional to crosslinking time (**Figure 3B**). A significant decrease in compressive modulus was not found between the 2- and 8-hour groups ($p=0.243$, **Figure 3B**); however, the compressive modulus significantly decreased in all groups with >10-hours crosslinking time ($p\leq0.0001$ **Figure 3B**).

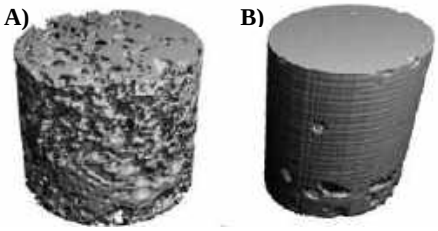

Figure 1: uCT Visualization of Pore distribution. A) 60:40 Gel:HAp ratio. **B)** 30:70 Gel:HAp Ratio

Table 1: Comparison of Gel:HAp ratio to porous properties

Gel:HAp ratio	Density (mg/mL)	BV/TV	Porosity	Pore Size (mm)
30/70	445.6	0.99	0.02	0.08
40/60	430.6	0.96	0.04	0.098
50/50	425.5	0.9	0.1	0.107
60/40	333.5	0.38	0.62	0.205
70/30	320.1	0.2	0.8	0.312

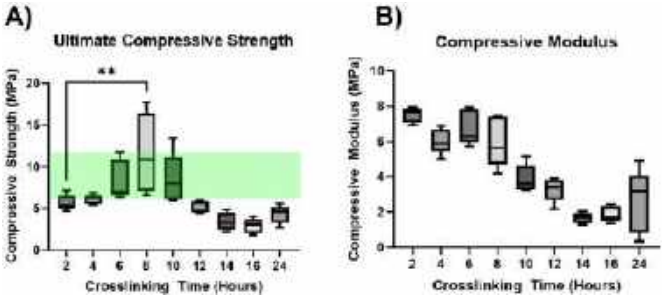

Figure 3: A) Ultimate compressive strength of 60:40 Gel:HAp samples produced with varying crosslinking times. Green band indicates reported compressive strength values of human trabecular bone [5]. **B)** Compressive modulus of 60:40 Gel:HAp samples produced with varying crosslinking times. Boxes indicate lower to upper quartile with mean, whiskers indicate minimum to maximum.

DISCUSSION

These data illustrate that by controlling compound ratio and crosslinking time, a physiologically comparable cancellous bone replacement can be created using a gelatin and hydroxyapatite slurry. This material has porous properties to allow for cellular infiltration possible through the lyophilization of the gelatin solution and crosslinking of the remaining gelatin chains within the hydroxyapatite structure.

Of important consideration is the ratio of Gel:HAp. While a higher concentration of gelatin (≥70%) yielded bigger pores, the pore distribution was uneven. Specifically, pores were located exclusively at the top of the sample and higher concentrations of HAp yielded pores that were too small (<100 μm) and lacked interconnectivity. For these reasons, a ratio of 60:40 Gel:HAp was selected to best mimic human cancellous bone conditions.

To achieve a comparable modulus and ultimate compressive strength to native cancellous bone, a crosslinking time of 8-hours produced peak compressive strength values that fell within the range of reported human cancellous bone [5]. These data also clearly indicate the potential for over-crosslinking, wherein samples became brittle and exhibited decreased strength and modulus values.

In conclusion, the current research delineates a substantial advancement in the synthesis of a Gel:HAp graft material that closely emulates the porosity and mechanical attributes of human trabecular bone. By regulating the Gel:HAp ratio and optimizing crosslinking time, we have successfully engineered a material with potential applicability as a bone surrogate in arthrodesis procedures. This innovation presents a significant step towards enhancing osteoconductivity and mechanical stability in joint fusion procedures, which may ultimately contribute to improved surgical outcomes and patient quality of life. Future explorations are anticipated to refine the fabrication process, augmenting the consistency of the graft material, while further biocompatibility assessments are poised to validate the material's efficacy in promoting osteogenic cell activity and integration within the host tissue.

REFERENCES

[1] Long, H et al., *Arthritis Rheumatol*, 74(7):1172-1183, 2022.
[2] Hunter, D et al., *Rheumatic Disease Clinics of North America*, 34(3):623-643, 2008.
[3] Smith, N et al., *Foot & Ankle Specialist*, 14(4):366-371, 2021.
[4] Antebi, B et al, *Tissue Eng Part C Methods*, 19(7):487–496, 2013.
[5] Azami, M et al, I*nt J Artif Organs*, 33(2):86-95, 2010
[6] David M, et al., *European Journal of Orthopedic Surgery and Traumatology*, 15:264-269, 2005

A SOFT 3D MICROARCHITECTED PRESSURE SENSOR FOR URETHRAL MONITORING

N. C. Goulbourne

Aerospace Engineering, University of Michigan, Ann Arbor, MI, USA

INTRODUCTION

Urethral function in women has received little scientific attention in the past, in part due to the lack of tools to understand its function. Recent studies challenge the long held belief that urethral failure is not clinically important in stress and urge incontinence in women. For decades, urethral pressure and function has been determined using a rigid pressure probe, which fails to isolate urethral closing pressure from kinematic events due to patient-specific movement (for example, coughing). Recent advances in soft materials could enable real-time in situ monitoring of urethral muscle function and move the field forward by providing new approaches where treatment (and success rates) has been stagnant for decades. A soft sensor monitoring urethral wall activity could be the key to achieving real-time, spatially mapped recordings of urethral pressure and muscle function under physiological conditions.

We developed a novel 3D microarchitected dielectric elastomer sensor based on micropillar arrays, which has significant advantages over monolithic sensor designs explored in prior work [1]. The elastomer array is fabricated via soft nanolithography and 3D compliant electrodes are patterned directly via sputter-coating. The sensor generates projected electric fields externally and nonuniform fields within the material itself. Disturbances to these fields as well as deforming the embedded micro-architecture are the two primary mechanisms altering the capacitance of the device. Parasitic capacitance is undesirable and as such the sensor must be designed to eliminate its effects. Design flexibility exists by way of suitable selection of the electrode and dielectric materials, their macroscopic geometry and configuration, and the pillar microarchitecture. A wide range of pillar structures can be designed and fabricated whereby pillar geometry is used to tune the mechanical stiffness of the overall sensor as well as sensor sensitivity. Micropillar structures have been shown to increase response times and reduce viscoelastic effects as compared to monolithic sensors. These are two important aspects in developing soft pressure sensors.

METHODS

We developed micropillar arrays for spatio-temporal pressure sensing over extended contact areas. Our method combines soft elastomeric dielectrics with soft 3D-electrodes to create electromechanical architectures that can be tuned for different sensitivities and mechanical stiffness. Our method is based on existing soft nanolithography processes (Fig. 1) and MEMS electroding techniques making it amenable to a range of soft elastomeric materials and electrodes (from metallic powders to ionic conducting liquids and gels) [2]. The technique creates opportunities for design flexibility in material selection, device geometry, and sensor performance. Previous work on microstructured PDMS has shown its utility for pressure sensing using monolithic flat plate rigid electrodes for pressures above 1 kPa. The current work focuses on a lower pressure regime as would be experienced in evaluating urethral function.

We fabricated soft stretchable sensors based on 3D micro-architected structures of polydimethylsiloxane (PDMS) elastomers with 3D compliant electrodes deposited using a masking technique (Fig. 2). The proof of concept sensor is demonstrated using a 5 x 5 cross-grid array of overlapping 5mm x 5mm gold electrode areas. Different micropillar geometries are fabricated with dimensions on the order of 100 microns.

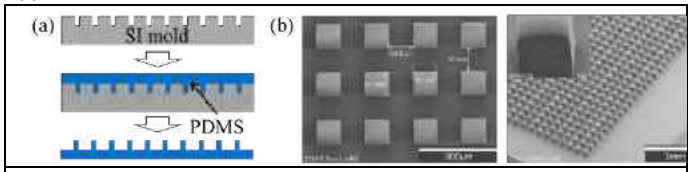

Figure 1: (a) Schematic of the PDMS molding process by replica molding. (b) SEM images of the micropillar array.

The bottom layer of the assembly is a PDMS micropillar array. Buckled metallic electrodes are deposited by sputter coating gold over the individual pillars and between the pillar gaps in a parallel line pattern using a shadow mask on the mm scale. A top monolithic PDMS film is placed on top of the Au micropillar array and is subsequently electroded (lines are orthogonal to the bottom Au layer) using a shadow mask. The electroded lines form a grid pattern.

Micropillars of various designs were fabricated: low aspect ratio pillars, high aspect ratio pillars, C-shaped pillars, and a hybrid design. These structural features influence the deformation mechanisms of the pillars and the overall sensor characteristics. The base design is a square cross-section micropillar array with a 1:1 aspect ratio. The microstructured electrode morphologies locally pattern nonuniform electric fields that amplify electrostatic phenomena. In other words, the pillar geometry can be used to tune sensor sensitivity and mechano-sensitivity. For example, we designed high aspect ratio pillars and exploit their mechanical instabilities to increase sensor sensitivity at low pressures. The integrated microstructures form a network of soft microcapacitor arrays. Future designs can be driven by rational combinations of liquid electronic conductors, ionic conducting gels, ionic conducting liquids, and stretchable metallic films.

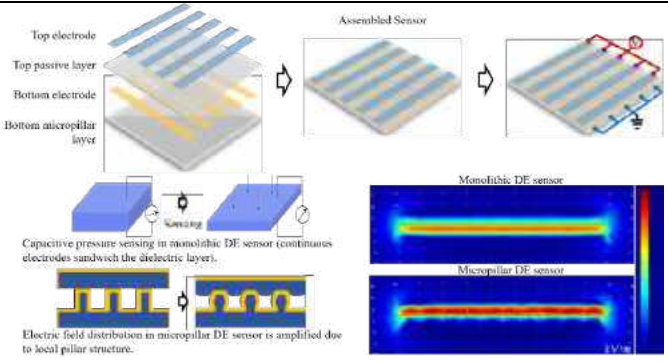

Figure 2: Microarchitected pressure sensor assembly process, capactive sensing mechanism, and electric field simulation using COMSOL.

RESULTS

Sensor performance was evaluated over a range of pressures 100 Pa – 10 kPa for several sensor designs. The base design is a square cross-section micropillar array with a 1:1 aspect ratio. High aspect ratio pillars are designed for bending, C shaped pillars are designed for elastic buckling at low pressures, and a hybrid pillar array composed of multi-level pillars is designed to maximize sensitivity using multiple contact levels through a combination of 3 high aspect ratio pillar designs. The hybrid design has the highest sensitivity over all the pressure ranges tested followed by the high aspect ratio C-shaped pillar arrays.

Precise capacitance measurements were made with a table-top capacitance meter (Model 3000, GLK instruments, 7.4 Hz). The response time of the sensor was measured using a capacitance to digital converter (EVAL-AD7746EBZ, Analog Devices) with a 90 Hz sampling rate. Figure 3 shows the cyclic off and on response of a square cross-section micropillar array due to pressure. Figure 3 shows the typical input/output traces between the applied force and the measured capacitance change. The time scale characteristics of the micropillar array was measured using a digital converter (EVAL-AD7746EBZ, Analog Devices) circuit. For a typical sensor of square geometry and 1:1 aspect ratio, the sensor response time is 60.8 ms. The response time is defined as the time interval between 10% and 90% of the steady state values. We studied the influence of gap distance, cross-section shape, and aspect ratio. Based on these studies, a novel hybrid design was proposed with over 300% increased sensitivity of 0.34 kPa^{-1} and a broad pressure sensing range up to 10kPa with a single sensor platform (i.e. without modifying the structure).

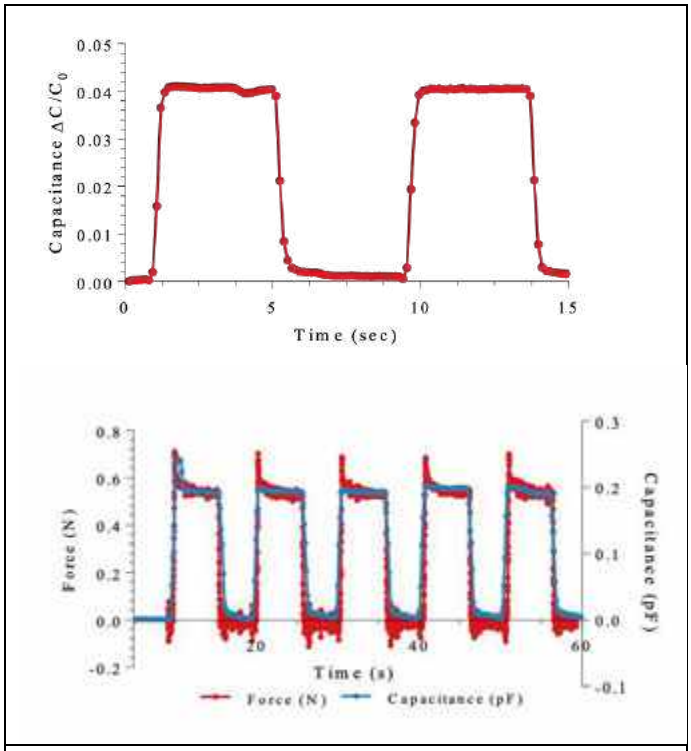

Figure 3: Results for (1:1 aspect ratio, square cross-section, 200µm gap) sensor: (top) Capacitance versus time graph. (bottom) Capacitance and force versus time graph. The response time is 60.8ms.

DISCUSSION

A 3D microarchitected pressure sensor for functional monitoring was developed using well-established fabrication techniques. As a proof of concept, soft Au/PDMS micropillar arrays were fabricated using soft nanolithography and electro-sputtering methods. The sensing response is repeatable and the response time (60.8ms) is comparably fast for capacitive sensors. Also, the resulting system is both flexible and stretchable. These preliminary results highlight this sensor technology as a promising candidate for continuous biomedical monitoring.

ACKNOWLEDGEMENTS

Early support for this work was provided by the National Science Foundation.

REFERENCES

[1] S. Son and N.C. Goulbourne, *Journal of Intelligent Material Systems and Structures,* Vol. 23, *5,* p. 575-586, 2012.

[2] Kim, P., W.E. Adorno-Martinez, M. Khan, and J. Aizenberg, *Nature Protocols*, 2012. 7(2): p. 311-327.

ARTIFICIAL INTELLIGENCE ASSISTED MULTISCALE LUNG MODELING TO PREDICT ALVEOLAR SEPTAL WALL STRESS

Sunder Neelakantan (1), Rana Raza Mehdi (1), Bradford J Smith (2), Kyle Myers (3), Rahim Rizi (4), Reza Avazmohammadi (1)

(1) Department of Biomedical Engineering, Texas A&M University, College Station, TX, USA

(2) Department of Bioengineering, University of Colorado Denver | Anschutz Medical Campus, Aurora, CO, USA

(3) Hagler Institute for Advanced Study, Texas A&M University, College Station, TX 77843, USA

(3) Department of Radiology, Perelman School of Medicine, University of Pennsylvania, Philadelphia, PA, USA

INTRODUCTION

Lung injuries such as ventilator-induced lung injury (VILI) and radiation-induced lung injury (RILI) can lead to heterogeneous alterations in the biomechanical behavior of the lungs [1]. For clinical applications, organ-level biomarkers such as X-ray imaging and plethysmography are the most commonly used methods for diagnosing lung injuries and estimating lung function. However, plethysmography measurements represent average metrics across both lungs (global lung function). X-ray imaging may fall short of providing mechanistic and prognostic insights into local lung injuries, especially given their heterogeneous nature. Thus, there remains a need for a regional biomarker to predict the onset and progression of lung injuries due to injury-induced factors such as mechanical ventilation and radiation.

We hypothesize that alveolar septal wall stress (SWS), as a regional biomechanical factor in lung function, plays a key role in the onset and progression of lung injuries. In this study, we aim to estimate SWS from dynamic imaging. Dynamic imaging (or imaging at end-inspiration, EI, and end-expiration, EE) processed by image registration, can provide regional strains at a mesoscale in the lung. Multiscale modeling, incorporating parenchymal microstructure, constitutive tissue models, and mesoscale strains, can estimate SWS accurately [2]. To overcome the challenges of computationally prohibitive multiscale full lung modeling and offer a translational tool for SWS estimation, we propose to use machine learning to both enhance the alveolar architecture databases and estimate SWS directly from strains without the need for finite-element modeling.

METHODS

The lungs of a healthy Sprague-Dawley (SD) rat were fixed, and X-ray microtomography (μCT) imaging was performed to reconstruct the parenchymal microstructure. Cubes of side ~1mm were isolated to serve as the representative tissue element (RTE), for in-silico simulations and training of the ML model. Several RTEs were used for in-silico simulations and to train the ML model. For each simulation, the stretch values were specified on the surface boundaries of the RTE (Fig. 2A). The stretch values were set through Latin hypercube sampling, and 200 simulations were performed for each RTE. The alveolar skeleton in parenchymal tissue was modeled as an incompressible Neo Hookean material.

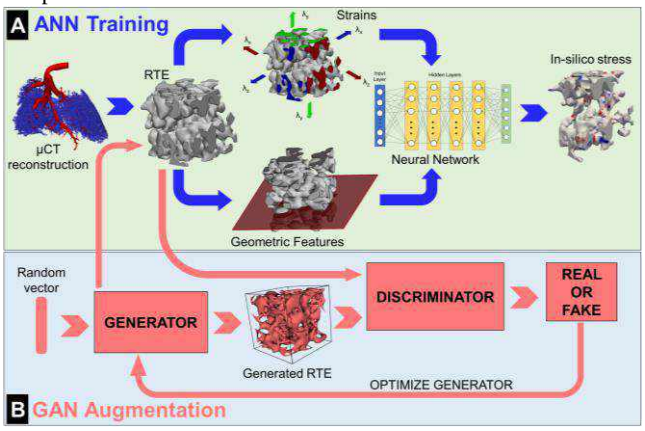

Figure 1: Training of neural network and GAN augmentation of RTE geometry.

Since there is a non-linear relationship between the stresses and strains, we used a multi-layer perceptron (MLP) for this work (Fig. 1A). The input features for the ML model consisted of stretch values and geometric features such as volumetric and cross-sectional area porosity. The output features were the six unique stress values in the stress tensor. The model was trained for 500 epochs with the loss function set to mean absolute error (MAE).

The knowledge of parenchymal microstructure remains a limitation of this approach. To mitigate this limitation, we have used generative networks to create a large synthetic parenchymal microstructure based on realistic inputs. We used a generative

adversarial network (GAN) to generate synthetic RTE geometries based on segmented RTE cubes (Fig. 1B). The components of the GAN were based on a study by Kwon et al [3]. To determine the quality of the RTEs generated by the GAN generator, we performed principal component analysis on the synthetic and actual RTEs.

We used dynamic imaging and image registration from our previous work [4] to calculate strains. Briefly, four-dimensional (4D) computed tomography (CT) scans were obtained for a healthy SD rat placed under isoflurane anesthesia. We used non-linear non-rigid image registration to obtain voxel-based displacement during respiration and, subsequently, the strain. The strains, along with geometric features estimated from voxel intensity, were used as inputs to the trained MLP to estimate SWS across the lungs during inspiration.

RESULTS

The maximum stress occurred in thinner regions and parts of the alveolus prone to stress concentration (Fig. 2B). When training the MLP, the loss function plateaued around 200 epochs (Fig. 2C). The accuracy of the ML was 75.3% for the average normal stress (Fig. 2D). However, training accuracy was increased to 84% when considering only RTE2 and RTE3.

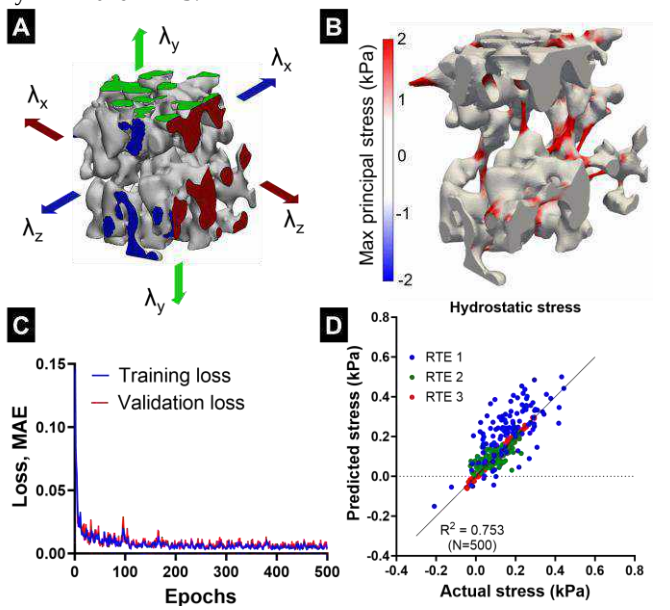

Figure 2: (A) Triaxial stretching of RTE resembling RTE deformation during inspiration. (B) Maximum principal stress in RTE from representative simulation. (C) Training and validation loss during training. (D) Comparison between predicted and actual average normal stress.

When the first two principal components were plotted against each other, the actual and synthetic data occupied the same region (Fig. 3A), indicating that the GAN model can produce RTEs that are quantitatively similar to the actual RTEs obtained from segmentation (Fig. 3B). At end-inspiration, the hydrostatic strain in the lungs was ε=0.15 (Fig. 3C) and the corresponding average stress value was σ=0.32 kPa (Fig. 3D).

DISCUSSION

Through the in-silico simulations, we observed that the maximum stress is two orders of magnitude larger than the average stress in the RTE. This indicates that the parenchymal microstructure is essential to accurately estimate regional SWS in the lungs during respiration. Hence, generating a wide variety of physiologically realistic RTEs becomes a crucial step towards accurately estimating SWS. Towards this end, the GAN method, generating a large number of synthetic but realistic RTEs, serves as a tool to augment the quality and quantity of the training data used in the MLP. This effectively overcomes the difficulty of reconstructing parenchymal microstructure from μCT imaging and potentially increases the quality of generated RTEs.

Lung injuries, such as VILI and RILI, can cause significant heterogeneities in ventilation, leading to additional injuries in the healthy regions. The combination of SWS and kinematic biomarkers, such as strain, can enable an improved understanding of the progression of lung injury. In addition, the method presented in this study has the potential to be applied to optimize mechanical ventilation settings and clinical intervention strategies in humans. We note that while dynamic CT scans are commonly avoided in human patients due to excessive radiation, lung strains can be obtained through static CT scans taken at EE and EI and our method can certainly be extended to accommodate this limitation.

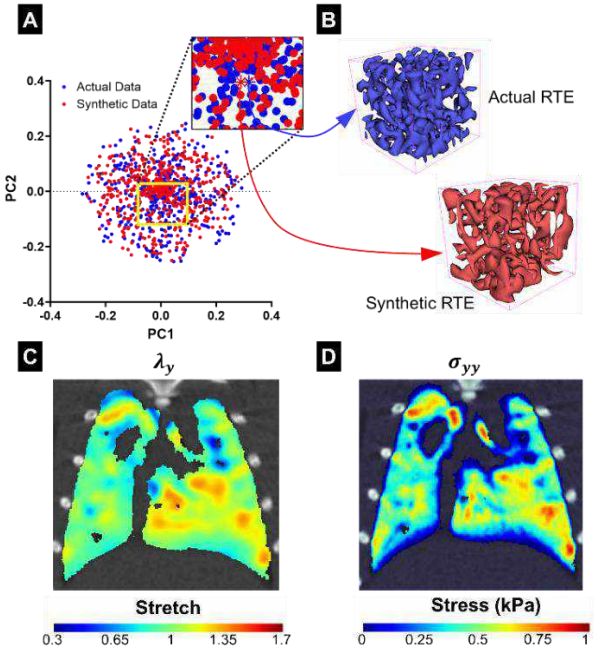

Figure 3: (A) Principal components for segmented and synthetically generated RTEs show excellent agreement. (B) Representative RTEs from each group. (C) Stretch estimated from 4D image registration. (D) Representative stress contour estimated from the MLP model.

In this study, we have presented an integrated ML-imaging-based method to estimate septal wall stress as a critical, but overlooked, regional biomechanical marker to understand and predict the heterogeneous nature of lung injuries. The machine learning model was trained using synthetic data from in-silico simulations of RTEs obtained from μCT imaging. In addition to the RTEs obtained through segmentation and reconstruction, we have presented a method to augment the number of RTE geometries through GAN to enhance the application potential of our ML model. We expect SWS to serve as an important biomarker to identify lung regions at risk of injuries in VILI and RILI.

ACKNOWLEDGEMENTS

This work was supported by the NIH (R00HL138288 to R.A)

REFERENCES

[1] Cereda, M. et al. Crit. Care Med., 41(2), 2013. ISSN 0090=3493
[2] Neelakantan, S. et al. J R Soc Interface. 2022 Jun; 19: 20220062.
[3] Kwon, G. et al. Medical Image Computing and Computer Assisted Intervention–MICCAI 2019, pages 118–126.
[4] Neelakantan S. et al. Medical Imaging 2023: Image-Guided Procedures, Robotic Interventions, and Modeling volume 12466.

COLLAGEN DENATURATION QUANTIFICATION IN BONE USING COLLAGEN HYBRIDIZING PEPTIDE.

William Woolley (1), Katy Martin (2), Seungju M. Yu (2), Claire Acevedo (1,2)

(1) Department of Mechanical & Aerospace Engineering, University of California San Diego, La Jolla, CA, 92093
(2) Department of Biomedical Engineering, University of Utah, Salt Lake City, UT, 84112

INTRODUCTION

Denatured collagen is prevalent in various conditions, including age, cancer, osteogenesis imperfecta, osteoarthritis, osteoporosis, and diabetes or mechanical damage [1]. In these conditions, denatured collagen molecules usually result in a local unfolding or unwinding of the collagen triple helix. This unfolding might be caused by breaking a small number of consecutive hydrogen bonds. Collagen denaturation increases the fracture risk and reduces bone's resistance to fracture [2]. The primary approach for determining fracture risk involves evaluating bone mineral density and comparing it to a reference population. However, to thoroughly assess the risk of fractures, it is essential to consider bone mineral density and examine collagen integrity. Ex vivo, collagen denaturation can be measured by a destructive, time-consuming technique called trypsin-hydroxyproline assay. This technique is the gold standard for measuring a quantity but does not allow localization of denatured collagen. This study investigates a novel method to quantify and localize collagen denaturation in bone using collagen hybridizing peptide (CHP). CHP has been used in soft tissues such as tendons, arteries, etc. It is a peptide that specifically binds to denatured collagen and is labeled with a fluorescent head. This study aims to prove that R-CHP can be used in mineralized tissue, such as bone, and that this method can be applied to quantify denatured collagen in a heat treatment model that mimics collagen unfolding in several conditions, such as diabetes or aging.

METHODS

Sample preparation: Bovine bone was cut and polished to 0.5 x 1.5 x 15 mm beams. Samples (n=5/group) were placed in a furnace heated at 150°C for 15 min, 30 min, 1 h, and 2 h to denature mineralized collagen. Samples were rehydrated after the heat treatment.
CHP staining: Samples were stained in 5μM R-CHP solution for 24 h, then rinsed five times for 10 min each.
Confocal imaging: Samples were imaged using a Leica SP8 confocal microscope. Captured images were thresholded using ImageJ to obtain mean pixel intensity values.
CHP microplate assay: After imaging, R-CHP fluorescence was measured in a microplate assay.
Trypsin-hydroxyproline assay: Samples were digested by proteinase K, and the percentage of denatured collagen was measured by absorbance.

RESULTS

Mineralized collagen undergoes denaturation at temperatures around 150°C. The trypsin-hydroxyproline assay revealed that samples subjected to heat treatment at this specific temperature for durations of 15 minutes, 30 minutes, 1 hour, and 2 hours exhibited a statistically significant increase in collagen denaturation (+2495% increase for 2 h vs control) (figure: 1). When employing R-CHP, a peptide that binds to denatured collagen, we observed an increased fluorescence through confocal imaging (+100.8%) (figure: 2). This finding was subsequently validated through a microplate assay that measured the fluorescence of digested samples (+96.3%) (figure: 3). Finally, a calibration curve showing the relationship between trypsin-hydroxyproline collagen denaturation and CHP microplate fluorescence showed a positive correlation (R^2=0.90) (figure: 4).

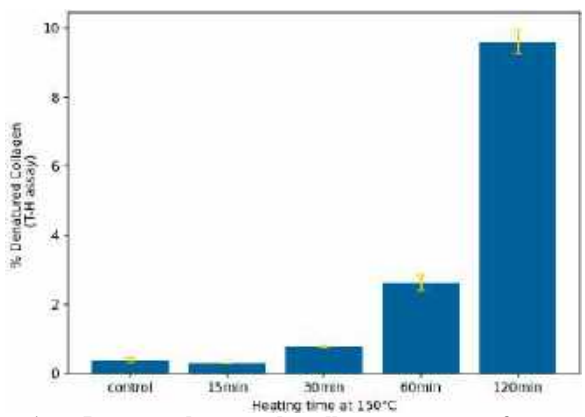

Figure 1: Percent denatured collagen content from trypsin-hydroxyproline assay

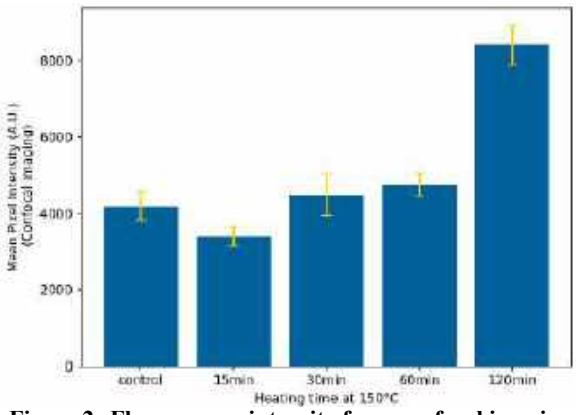

Figure 2: Fluorescence intensity from confocal imaging

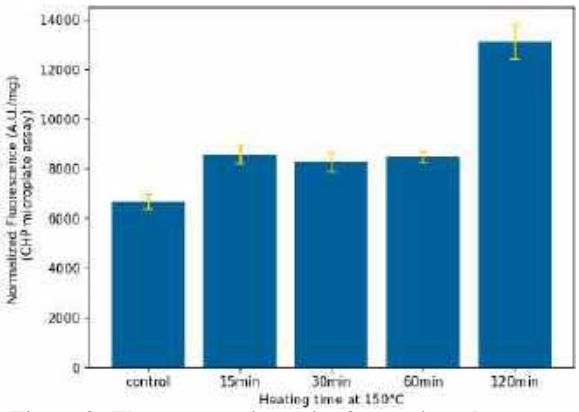

Figure 3: Fluorescence intensity from microplate assay

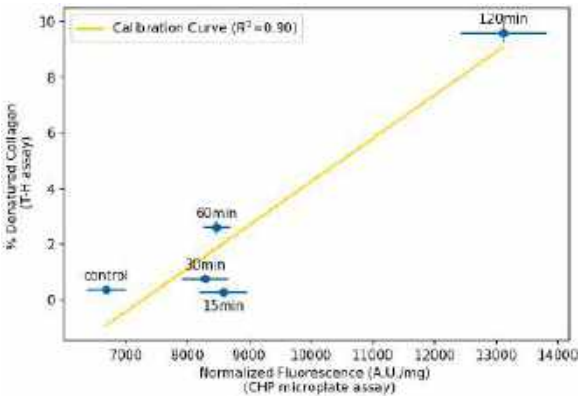

Figure 4: Correlation between percent denatured collagen and fluorescence intensity

DISCUSSION

We showed that R-CHP can be used in mineralized tissues to quantify collagen denaturation. R-CHP was shown to be able to be used in soft tissues such as tendons, ligaments, arteries, etc, but opening this method to hard tissues such as bone is promising for future research. The increase in mineralized collagen denaturation measured by the gold standard, destructive technique – trypsin-hydroxyproline assay – positively correlates with the fluorescence intensity from bone samples stained with R-CHP (R^2=0.90). The heat treatment model used in this study increased the denaturation content in every group except at 15 minutes. This could be due to the time for the oven to stabilize at 150°C after loading the samples and the time for the samples to reach the set temperature. We chose 150°C because denaturation of mineralized collagen in cortical bone has been shown at temperatures between 150°C and 160°C. Having a non-destructive method that can quantify and localize collagen denaturation in bone is an important result. Localizing regions of high denaturation will be compared with other bone quality factors. Studying the effect of diseases, such as diabetes, on collagen denaturation is important for understanding the mechanisms related to reduced toughness in diabetic bones. Future studies will evaluate collagen denaturation under various loading conditions, aiming to uncover the influence of strain on the denaturation process. Finding a non-destructive way to quantify and localize collagen denaturation in bone, and hence an indicator of bone quality, would be beneficial to assess the fracture risk in patients affected by diseases such as diabetes.

ACKNOWLEDGEMENTS

The authors would like to thank Dr. Yu for his expertise in using CHP. In addition, image acquisition was possible thanks to the HSC Cell Imaging Core from the University of Utah.

REFERENCES

[1] Li Y et al. *Collagen: Methods and Protocols* (2019).

[2] Wang X et al. *Annals of Biomedical Engineering* 31 (2003).

INCREMENTAL OVERSTRETCH INCREASES FAILURE VALUES OF CEREBRAL BLOOD VESSELS

F. Shojaeianforoud (1), B. Coats (1,2), K. Monson (1,2)

(1) Department of Mechanical Engineering, University of Utah, Salt Lake City, Utah, United States
(2) Department of Biomedical Engineering, University of Utah, Salt Lake City, Utah, United States

INTRODUCTION

Blood vessels play an important role in maintaining the health of the body, but their function can be compromised by injury. A deeper understanding of vessel damage mechanics is critical to defining mechanisms of injury in and recovery from events like traumatic brain injury and procedures like balloon angioplasty. The development of damage models is particularly important to the prediction of injury processes.

Experiments in our laboratory show that overstretching of cerebral blood vessels results in softening, a persistent change in mechanical properties that likely alters subsequent vessel performance. These experiments show that softening increases with overstretch [1,2]. However, previous experiments also showed that overstretch did not reduce failure properties when samples were stretched to failure following an overstretch [1].

Incremental creep experiments have been used to define the contributions of both discontinuous and continuous softening mechanisms in tendon damage [3]. Using a similar incremental protocol, we subjected cerebral vessels to various amounts of incremental axial overstretch, with the goal of defining how such loading influenced vessel mechanical response, including at failure. Based on our previous research, we expected significant changes in sub-failure stress-stretch behavior but that failure values would be unchanged.

METHODS

Tissue and sample preparation:

Six sections of middle cerebral arteries (MCA) were dissected from 2 adult sheep heads based on the rules established by the Institutional Animal Care and Use Committee at the University of Utah. Immediately after removing the brains from heads, the MCA sections were dissected and placed in phosphate-buffered saline (PBS) until testing. Any side branches were ligated with unwound 6-0 silk suture. Cross-sectional rings cut from the ends of each sample were imaged to provide reference wall dimensions.

Testing apparatus:

The arteries were mounted and attached to two cannulas made of hypodermic needles using 6-0 silk sutures. Cyanoacrylate glue was applied on the distal sides of the sutures to secure the vessels to the cannulas. The specimens were bathed in PBS during testing. One of the cannulas was mounted to a 50-g capacity load cell on the fixed end of the tester, and the other cannula was attached to a voice coil linear actuator with a built-in encoder to monitor displacements. The tester was equipped with a camera mounted on a light microscope to record images during the test. A pressure transducer at each end of the artery monitored the luminal pressure of the vessel. Target pressures were maintained via a syringe pump operating on a closed-loop feedback controller for preconditioning and then changed to a simple PBS column at the desired pressure for the uniaxial tests. Test control and data acquisition were performed with a custom LabVIEW program.

Testing protocol:

Vessels were preconditioned by oscillating the luminal pressure between 6.7 and 20 kPa for five cycles while the vessel length was held constant. Pressure cycles were repeated at gradually increasing lengths until the *in vivo* length (IVL) was identified [4]. The final preconditioning process was conducted at a stretch of 1.05 times IVL.

After preconditioning, vessels were tested using one of two axial-stretch protocols. In Protocol 1, a vessel was cyclically stretched from a slightly buckled configuration to the IVL five times. It was then similarly stretched to 1.05 times IVL for five cycles, then to 1.10 times IVL five times, and so forth, until the vessel ruptured.

In Protocol 2, we applied the same incremental cyclic overstretch procedure described in Protocol 1 but only up to a stretch of 1.2, 1.3, 1.4, 1.5, 1.6, or 1.7. Samples were then stretched to failure.

Data analysis:

Data were collected from the encoders, the load cell, and pressure transducers at a sampling rate of 500 Hz. Load cell data were smoothed using a phaseless, fourth-order Butterworth filter. Stretch was measured using suture-to-suture distances. Reference outer (D_e) and inner diameter (D_i) were measured from cross-section images. The camera mounted on the tester recorded images at a frequency of 3 Hz. The collected data were used to determine stretch – referencing IVL – and first Piola-Kirchhoff stress.

RESULTS

Protocol 1 produced a set of stress-stretch curves with gradually increasing stress and stretch values up to the point of vessel rupture (Figure 1). As is true of our recent findings on vessel softening, the slope of the curve at the IVL consistently decreased with overstretch. However, the maximum slope of the curve increased with overstretch up to 1.65 times IVL and then started to decrease. Also, ultimate failure did not occur until stretch and stress values of 1.9 and 4 MPa, respectively. Previous research characterizing failure values of sheep cerebral arteries [5] reported that the average stretch values at maximum stiffness for juvenile and adult sheep were 1.42 to 1.53, respectively, and that failure stretches and stresses were 1.8 and 1.6, and 3.5 and 2.5 MPa, respectively. Though tested in a single specimen only, these relatively high values led us to revise our hypothesis to state that incremental overstretch increases vessel failure stress and stretch values.

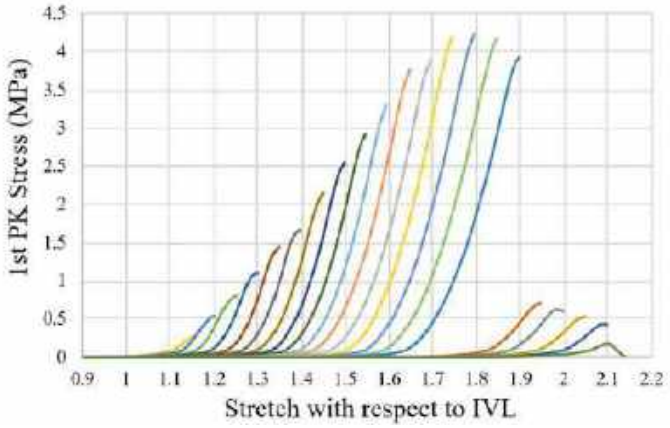

Figure 1: Stress-stretch of the first loading ramp of each set of loading cycles during incremental overstretch in Protocol 1 (stretch is referencing the IVL: 1 on the x-axis shows the IVL).

Protocol 2 resulted in similar sets of stress-stretch curves, though only up to the targeted overstretch values, followed by stretch to failure (only the failure curves are shown in Figure 2). As shown, more extensive incremental overstretch led to larger ultimate stretch values, except for the test with a 1.2 times IVL overstretch. A similar increase in failure stress was also observed in some of the specimens, especially considering that the 1.7 case had been stretched beyond its point of ultimate stress.

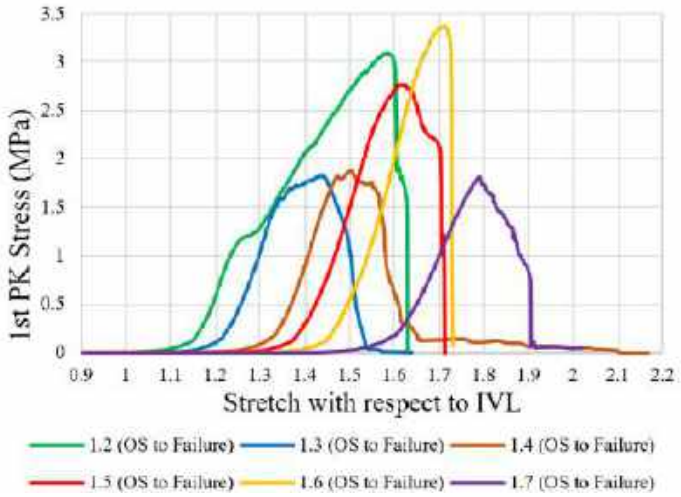

Figure 2: Failure stretch curves following incremental overstretch to 1.2, 1.3, 1.4, 1.5, 1.6, and 1.7 × IVL using Protocol 2

DISCUSSION

This preliminary study aimed to define how incremental loading influences cerebral artery mechanical response. While additional data clearly need to be collected and considered, these preliminary findings suggest that failure values increase with incremental overstretch. This was unexpected, primarily because it seems logical that tissue that has been previously damaged would be more susceptible to further damage and failure, rather than less so. Our previous experiments also showed that a single overstretch did not change failure properties, so we did not expect repeated, and incrementally increasing, overstretch to improve failure properties.

Reasons for this observation are currently unknown, but it seems that repeated, subtle increases in overstretch may serve to reorganize extracellular matrix fibers such that they are more efficiently recruited during loading, perhaps by reducing dispersion of fibers. If this is the case, the mechanical softening observed at lower stretch values may be a manifestation of reorganization rather than structural disruption. As such, this process may be similar to preconditioning, though preconditioning is not typically performed to levels of deformation that significantly exceed typical physiological loads. In any case, these preliminary results provide interesting insights into soft tissue response to overstretch, but additional experiments are clearly needed to confirm these findings and to investigate their associated mechanisms.

ACKNOWLEDGEMENTS

This material is based upon work supported by the National Science Foundation under Grant No. 2140373.

REFERENCES

[1] Bell, ED et al. *Front Bioeng Biotechnol.* 2015 Jan 28;3:2. PMID: 25674561.

[2] Converse, M.I. et al. *J. Mech. Behav. Biomed. Mater.* 2021. 118, 104447.

[3] Allan, AN et al. *J Mech Behav Biomed Mater.* 2022 Nov;135:105342. PMID: 36055109.

[4] Weizsacker, H. W. et al. *J. Biomech.*, 16(9), 1983. pp. 703–715.10.1016/0021-9290(83)90080-5.

[5] Nye, KS et al. *Ann Biomed Eng.* 2017 Apr;45(4):1101-1110. Epub 2016 Sep 27. PMID: 27679444; PMCID: PMC5364047.

AN INTERPENETRATING-NETWORK THEORY OF THE CYTOSKELETAL NETWORKS IN LIVING CELLS

Haiqian Yang (1), Ming Guo (1)

(1) Department of Mechanical Engineering, Massachusetts Institute of Technology, Cambridge, MA, USA

INTRODUCTION

Under many physiological and pathological conditions such as division and migration, cells undergo dramatic deformations, and their mechanical integrity is supported by cytoskeletal networks (i.e. intermediate filaments, F-actin, and microtubules). Recent observations of cytoplasmic microstructure indicate interpenetration among different cytoskeletal networks, and micromechanical experiments have shown evidence of complex characteristics in the mechanical response of the interpenetrating cytoskeletal networks of living cells, including viscoelastic, nonlinear stiffening, microdamage, and healing characteristics [1]. However, a theoretical framework describing such a response is missing, and thus it is not clear how different cytoskeletal components with distinct mechanical properties come together to build the overall complex mechanical features of the cytoskeletal networks.

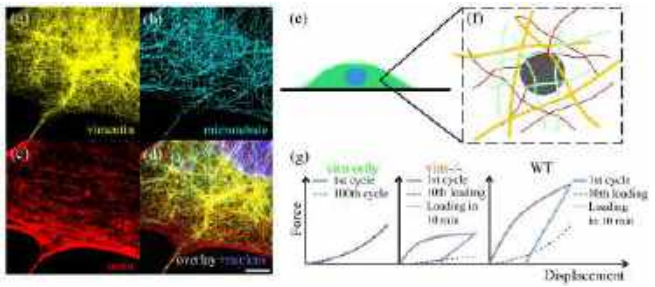

Figure 1: Confocal image of (a) vimentin intermediate filament, (b) microtubule, (c) F-actin, and (d) overlay of a mouse embryonic fibroblast [1]. (Scale bar, $5\,\mu$m). Schematics: (e) A cell. (f) Interpenetrating cytoskeletal fibers. Intermediate filaments (green), F-actin (red), and microtubule (yellow). In an optical-tweezers measurement, a micron-size particle (grey) is perturbed within the cytoplasm. (g) Force-displacement response of vim only, vim-/-, and WT. Multiple cycles are applied. After 10 cycles, the particle stays in its original position for 10 minutes before another loading is applied.

In this work, we address this gap by developing a finite-deformation continuum-mechanical theory with a multi-branch visco-hyperelastic constitutive relation coupled with phase-field damage and healing. The governing equations are derived from the principle of virtual power and free-energy imbalance [2, 3]. Here a summary of the theory is provided.

METHODS

We identify a body B with the region of space it occupies in a fixed reference configuration, and denote by $\mathbf{X}$ an arbitrary material point of B. A motion of B to the deformed body $\mathcal{B}$ is then a smooth one-to-one mapping $\mathbf{x} = \boldsymbol{\chi}(\mathbf{X}, t)$ with the deformation gradient given by $\mathbf{F} = \nabla\boldsymbol{\chi}$. The force balance is

$$\operatorname{Div}\mathbf{P} = \mathbf{0}, \tag{1}$$

where the Piola stress $\mathbf{P}$ is given by $\mathbf{P} = 2\mathbf{F}\frac{\partial\Psi_{\mathrm{R}}}{\partial\mathbf{C}}$, where Ψ_{R} is the free energy per unit reference volume and $\mathbf{C} = \mathbf{F}^{\top}\mathbf{F}$ is the right Cauchy-Green tensor.

To account for the combined effects of nonlinear elasticity, visco-relaxation, damage, and healing in the interpenetrating networks of vimentin intermediate filaments with F-actin and microtubules, we propose the following form of the free energy

$$\Psi_{\mathrm{R}} = \underbrace{\Psi_{\mathrm{R}}^{eq}(\bar{\mathbf{C}})}_{\text{vimentin}} + \underbrace{g(\mathsf{d})}_{\text{damage}}\ \underbrace{\Psi_{\mathrm{R}}^{neq}(\bar{\mathbf{C}}, \{\mathbf{A}^{(i)}\})}_{\text{F-actin/microtubule}} + \Psi_{\mathrm{R}}^{vol}(J) + \Psi_{\mathrm{R}}^{nonlocal}(\nabla\mathsf{d}), \tag{2}$$

with $J = \det\mathbf{F}$ the volumetric deformation, $\bar{\mathbf{C}} = J^{-2/3}\mathbf{C}$ the distortional deformation tensor, $\{\mathbf{A}^{(i)}\}$ $(i = 1, 2)$ two tensorial symmetric and positive definite internal variables that quantify a long-time and a short-time visco-relaxation, d a positive scalar damage variable ($\mathsf{d} = 0$ intact; $\mathsf{d} > 0$ damaged), and $\nabla\mathsf{d}$ the gradient of the damage field. The degradation function $g(\mathsf{d})$ progressively damages the energy-carrying capacity of the F-actin/microtubule networks as the damage variable d increases, and in this work takes the form of an exponential decay function $g(\mathsf{d}) = e^{-\mathsf{d}}$.

The equilibrium energy $\Psi_{\mathrm{R}}^{eq}(\bar{\mathbf{C}})$ accounts for the nonlinear stiffening of the elastic vimentin intermediate filaments, and is given by $\Psi_{\mathrm{R}}^{eq} =$

$\frac{G_{eq}}{2b}\exp\left(b(\bar{I}_1-3)\right)$ [4], with G_{eq} the equilibrium shear modulus b a nonlinear stiffening coefficient, and $\bar{I}_1 = \mathrm{tr}\bar{\mathbf{C}}$.

The non-equilibrium energy $\Psi_{\mathrm{R}}^{neq}(\bar{\mathbf{C}}, \{\mathbf{A}^{(i)}\})$ accounts for the viscoelasticity of F-actin and microtubule, and is given by $\Psi_{\mathrm{R}}^{neq} = \sum_{i=1}^{2} \frac{1}{2} G_{neq}^{(i)} \left(\left(\mathbf{A}^{(i)} : \bar{\mathbf{C}} - 3 \right) - \ln \left(\det \mathbf{A}^{(i)} \right) \right)$ [5], where $G_{neq}^{(i)}$ is the non-equilibrium shear modulus of the ith viscoelastic branch.

The volumetric energy $\Psi_{\mathrm{R}}^{vol}(J)$ accounts for the compressibility of the whole material, and is given by $\Psi_{\mathrm{R}}^{vol} = \frac{1}{2}\kappa(J-1)^2$, with κ the bulk modulus.

The damage gradient energy $\Psi_{\mathrm{R}}^{nonlocal}(\nabla \mathsf{d})$ accounts for energy stored in the process zone of the damaged F-actin and microtubule filaments, and is given by $\Psi_{\mathrm{R}}^{nonlocal} = \frac{1}{2}\psi^* \ell^2 |\nabla \mathsf{d}|^2$ [2], where ψ^* is the energy density stored in the damage process zone and ℓ is the length scale associated with the damage process zone.

The visco-relaxation internal variable $\mathbf{A}^{(i)}$ evolves according to

$$\dot{\mathbf{A}}^{(i)} = \frac{1}{\tau^{(i)}}(\bar{\mathbf{C}}^{-1} - \mathbf{A}^{(i)}), \qquad (i = 1, 2), \tag{3}$$

where $\tau^{(i)}$ is the relaxation time scale of the ith viscoelastic branch.

To account for the damage and healing process of F-actin and microtubule networks, we propose the following form of the evolution equation for the damage variable d

$$\underbrace{\zeta \dot{\mathsf{d}}}_{\text{dissipative}} = \underbrace{e^{-\mathsf{d}} \Psi_{\mathrm{R}}^{neq}(\bar{\mathbf{C}}, \{\mathbf{A}^{(i)}\}) + \psi^* \ell^2 \triangle \mathsf{d}}_{\text{energetic}} - \underbrace{\frac{\zeta}{\tau_H}\mathsf{d}}_{\text{heal}}, \tag{4}$$

where ζ is a material parameter controlling the rate of damage and τ_H is the healing time scale. This evolution equation states that damage d in the non-equilibrium branch increases due to mechanical deformation and gradient effects, and decreases due to healing.

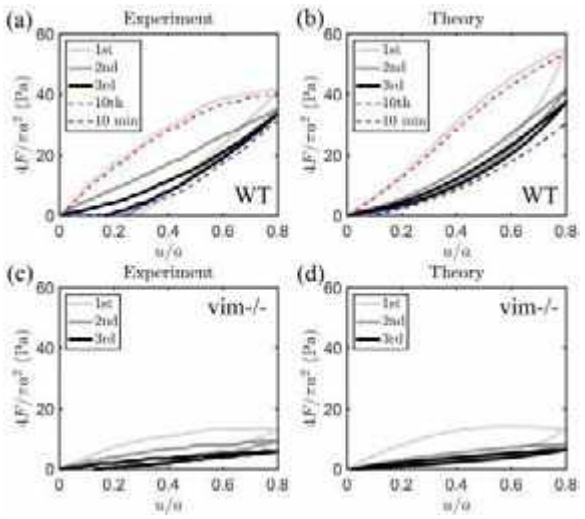

Figure 2: Damage and healing of interpenetrating cytoskeletal networks in the WT cells and the cytoskeletal networks in the vimentin knock-out cells. Cyclic loading damages the viscoelastic network and reveals the elastic-stiffening network, in both (a) experiment and (b) theoretical prediction. The non-equilibrium network is damaged with 10 cycles of loading, while it almost fully heals in 10 minutes, in both (a) experiment and (b) theoretical prediction. 1st, 2nd, 3rd: the first, second, and third loading-unloading cycle; 10th: the tenth loading; 10 min: loading in 10 minutes after the initial ten cycles are finished. Multiple-cycle damage of vim-/- cytoskeletal networks in (c) experiment and (d) theoretical prediction. Experimental data from [1].

We implemented our theory in the finite element program FEniCS [6, 7]. In our simulations, a rigid spherical particle (diameter $a = 1\,\mu\mathrm{m}$) within a cylindrical matrix (diameter and height both $20\,\mu\mathrm{m}$) is displaced in the axial direction to a maximum distance of $0.8\,\mu\mathrm{m}$ at a constant speed $1\,\mu\mathrm{m/s}$, then unloaded at the same speed to the initial position. Multiple-cycle loading-unloading is applied. Our simulations predict the force F on the particle as a function of displacement u, which we then compare with experimental force-displacement data of eukaryotic cytoskeletal networks using optical tweezers in [1].

RESULTS

We explore the damage and healing of WT cells with interpenetrating cytoskeletal networks. We find that the model is capable of describing multiple-cycle hysteresis as well as healing of WT interpenetrating cytoskeletal networks. We demonstrate that cyclic loading-unloading reduces the load-carrying capacity of the cytoskeletal network, and the force-displacement cycle gradually degrades from a viscous-dominated cycle to a hyperelastic-dominated cycle (Fig. 2(b)), consistent with experiments shown in Fig. 2(a). For the healing test, we hold the particle at the initial position for 10 minutes at the end of the 10-cycle loading-unloading, before another loading is applied. Remarkably, the cytoskeletal network restores its load-carrying capacity in 10 minutes, which is captured by the model (Fig. 2(b)) and consistent with the experiment (Fig. 2(a)).

We further test the predictive capabilities of the model by numerically "knocking out" the vimentin intermediate filament network. To do so, we use exactly the same material parameters of the WT and remove the hyperelastic branch. The numerical results nicely capture the behavior of the experimental results measured in vim-/- cells (Fig. 2(c&d)). Consistent with experimental observations, the load-carrying capacity is dramatically reduced after removing the hyperelastic vimentin network (Fig. 2(c&d)).

DISCUSSION

We have idealized the microstructure of the cytoskeletal networks in living cells as an interpenetrating network of intermediate filaments, F-actin, and microtubules. Motivated by this physical picture, we then formulated a finite-deformation continuum-mechanical theory for the cytoskeletal networks which comprises a tough, stretchable, and stiffening primary network in combination with a viscoelastic, damageable, and healable secondary network. We demonstrated that the theory and accompanying numerical implementation capture the micromechanical response, damage and healing of eukaryotic cytoskeletal networks within living cells undergoing mechanical deformation via optical tweezers. These results help to interpret the interactions between the individual networks and explore the contributions from viscous relaxation, elastic stiffening, damage, and healing. The theory and accompanying numerical implementation represent significant advances in understanding and predicting the complex mechanical behavior of the cytoskeletal networks in living cells under large deformations. More generally, the theoretical framework holds great potential for modeling cellular mechanical behaviors under large deformations involved in many other biological processes.

ACKNOWLEDGEMENTS

We would like to acknowledge the support from the NIH (1R01GM140108).

REFERENCES

[1] Hu J et al. *Proceedings of the national Academy of Sciences* 116.35 (2019).

[2] Mao Y et al. *Journal of the Mechanics and Physics of Solids* 115 (2018).

[3] Gurtin ME et al. Cambridge University Press, 2010.

[4] Fung Y. *American Journal of Physiology-Legacy Content* 213.6 (1967).

[5] Linder C et al. *Journal of the Mechanics and Physics of Solids* 59.10 (2011).

[6] Alnæs M et al. *Archive of Numerical Software* 3.100 (2015).

[7] Logg A et al. Vol. 84. Springer Science & Business Media, 2012.

CHANGES IN GENE SPATIAL EXPRESSION, STRUCTURE AND FUNCTION IN RESPONSE TO ALTERED MECHANICAL STRESS IN A MURINE MODEL OF BICUSPID AORTIC VALVE

Hail B. Kazik (1), Julie Kessler (2), Carol Mattern (2), Joy Lincoln (2,3), John F. LaDisa, Jr. (1, 2, 3).

(1) Biomedical Engineering, Marquette University & Medical College of Wisconsin, Milwaukee, WI, USA
(2) Pediatrics, Section of Pediatric Cardiology, Medical College of Wisconsin, Milwaukee, WI, USA
(3) Herma Heart Institute, Children's Wisconsin, Milwaukee, WI, USA

INTRODUCTION

Bicuspid aortic valve (BAV) is the most common congenital cardiovascular defect and is characterized by formation of two, rather than three, leaflets.[1] Approximately 50% of BAV patients prematurely develop calcification and aortic stenosis (AS) by the age of 35, which is more severe with fusion of the right and noncoronary (R/NC) leaflets.[2] This holds true for a cohort of 117 patients with R/NC BAV at the Herma Heart Institute (HHI) where 60% developed AS by age 20. Importantly, not all R/NC BAV patients develop AS since some patients maintain a normal peak gradient into early adulthood (Fig 1).

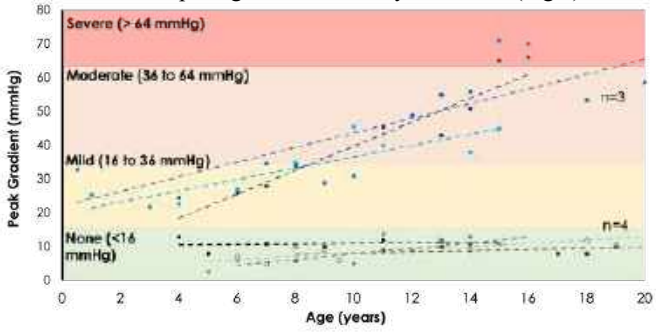

Figure 1. The evolution of peak aortic valve gradients from R/NC BAV patients at our center.

The mechanisms underlying premature AS induced by calcification in BAV patients are unknown, but it has been suggested that abnormal mechanical stimuli induced by the bicuspid anatomy plays a role. While our group is actively conducting computational and ex vivo studies from a BAV patient cohort at the HHI, we are unable to comprehensively study the interplay between changes in gene expression, structure, and function specific to BAV-induced changes in mechanical stress due to limited availability of patient samples preceding the advanced stages of the disease. To address this limitation, we use multi-disciplinary approaches in a murine BAV model that mimics the human disease process and allows us to characterize the anatomical, mechanical, and molecular environment during the progression of calcification in BAV. We hypothesize that in BAV, structure-driven, regionalized adverse mechanical stimuli leads to localized activation of mechanosensitive pro-calcific signaling pathways.

METHODS

Conditional heterozygous knockout of the *exocyst 5* gene (*Nfatc1cre;Exoc5*$^{fl/+}$) leads to formation of the more severely affected configuration (R/NC) of BAV in mice with a penetrance of ~45% in addition to tricuspid aortic valve (TAV) controls.[3] This model was implemented after IACUC approval, resulting in 3 experimental groups: (1) *Cre*+ BAV, (2) *Cre*+ TAV, and (3) *Cre*- TAV. All groups underwent echocardiography at 5 and 10 weeks, followed by valve collection at 10 or 18 weeks. These time points were determined considering the onset of calcification seen in BAV patients in our clinic and murine-to-human age equivalencies.[4] Tissue samples were paraffin-embedded and sectioned at 5 □m. Prior to staining, paraffin sections were serially imaged under autofluorescence using an EVOS M7000 (ThermoFisher). This allowed for 3D reconstruction of the aortic valve leaflets using Amira (ThermoFisher) and subsequent quantification of leaflet thickness and volume. Sections were then stained for Alizarin Red for detection of calcification. Spatial Transcriptomics was performed on *Cre*(+) BAV (n=3), *Cre*(+) TAV (n=3) and *Cre*(-) TAV (n=4) using the Visium Protocol (10X Genomics). Immunofluorescent staining of remaining tissue sections was performed to validate high priority hits from spatial transcriptomics. To conduct fluid-structure interaction (FSI) simulations, subject-informed 3D models were created based on averaged dimensions from echocardiography and Amira 3D leaflet reconstructions of individual mice in each group and time point (Fig 2A, B). Physiologic boundary conditions were implemented

including subject-informed left ventricular pressure at the inlet, a lumped-parameter model of downstream physiology at the aortic outlet, and flow imposed at coronary artery outlets (Fig 2C,D).

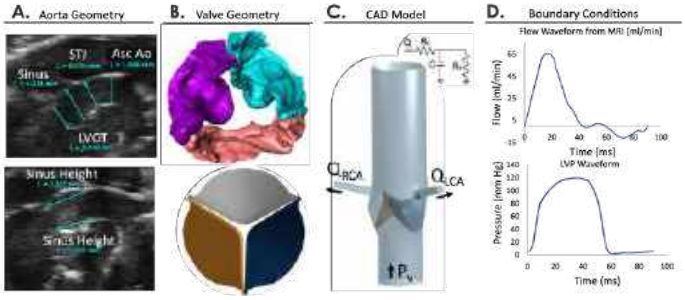

Figure 2. Computational modeling in *Cre*(-) TAV controls.

RESULTS

At 18 weeks, *Cre*(+) BAV mice have structurally different aortic valves, with only two distinct leaflets as opposed to three (Fig 3A). Average leaflet thickness is also significantly increased in *Cre*(+) BAV mice vs *Cre*(+) TAV and *Cre*(-) TAV (Fig 3B; $p < 0.05$, Kruskal-Wallis one-way ANOVA). Alizarin red staining was negative in *Cre*(+) BAV mice at this timepoint, suggesting this is a pre-calcific stage (Fig 3A).

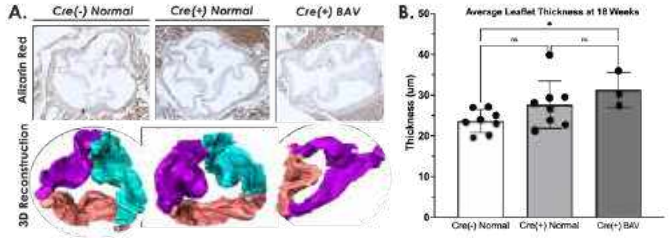

Figure 3. Morphology and Alizarin red staining in *Cre*(+) BAV mice vs. *Cre* (+) TAV and *Cre*(-) TAV controls.

By 5 weeks, *Cre*(+) BAV mice have a significantly higher peak aortic velocity vs *Cre*(+) TAV and *Cre*(-) TAV (Fig 4A; $p<0.05$, repeated measures two-way ANOVA). Between 5 and 10 weeks, *Cre*(+) BAV mice experience a 23% increase in peak aortic velocity vs controls (<10% increase), indicating more rapid progression of peak aortic velocity than that due to physiologic growth over time (Fig 4B).

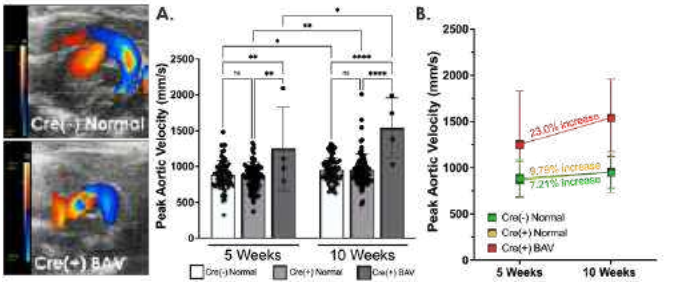

Figure 4. Functional changes in peak aortic velocity in *Cre*(+) BAV mice vs. *Cre* (+) TAV and *Cre*(-) TAV controls.

Despite no Alizarin red positivity, spatial transcriptomics at 18 weeks revealed pathway enrichment for osteogenic processes and mechanosensitive genes. Particularly, there was a 5.4-fold increase in expression of a calcification marker, Secreted Phosphoprotein 1 (*Spp1*) in the attachment and coaptation regions of *Cre*(+) BAV compared to *Cre*(-) TAV (Fig 5B).[5] This was validated through immunostaining of Osteopontin (OPN) which is the protein encoded by *Spp1* (Fig 5C).

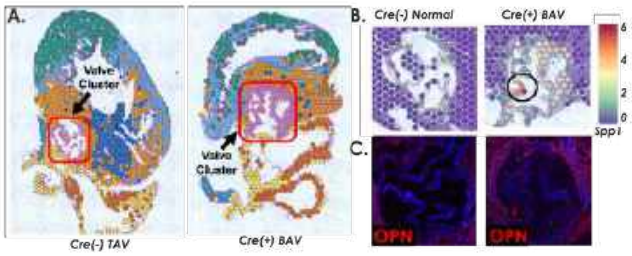

Figure 5. Spatial transcriptomics in *Cre*(+) BAV mice at 18 weeks shows increase in *Spp1* expression in the valve vs. TAV controls.

DISCUSSION

At an early timepoint (5 weeks), *Cre*(+) BAV mice have a significantly higher peak aortic velocity that more rapidly progresses by 10 weeks compared to normal TAV controls. These functional differences contribute to adverse changes in mechanical stress along the valve leaflets and ongoing work to be presented will characterize these changes with fluid structure interaction (FSI) simulations. While there is no detectable calcium deposition at 18 weeks, spatial transcriptomics revealed pre-calcific changes occurring in *Cre*(+) BAV leaflets as evidenced by the increase in *spp1*.[5] Expression of these markers were localized to the attachment and coaptation regions, which are also more likely to develop calcification in the patient population.[6] Additionally, based our group's FSI simulations of BAV in the human population, we expect to see the same increase in mechanical stress indices such as wall shear stress and von Mises stress in those regions in our proposed FSI simulations in the murine model. Our goal is to identify predictive indicators for calcification risk in young BAV patients and determine novel targets for molecular therapies for premature calcification in BAV.

ACKNOWLEDGEMENTS

This work was supported by NIH/NHLBI R01HL132801 and R01HL127033 (JL), 1R01HL142955 (JFL), Advancing a Healthier Wisconsin (9520519) (JL), Herma Heart Institute Innovation Award (JL), Children's Research Institute Pilot Award Project (JL), Project Bubaloo Research Grant (JL). A special thanks to Dr. Harkamaljot Kandail for guidance with FSI simulations (Cardio Consulting, LLC), Chris Wright & Jenny Dernovich for Spatial Transcriptomics Analysis (University of Illinois Urbana-Champaign), and Dr. El-Sayed Ibrahim for performing MRI of our mice.

REFERENCES

[1] Menon V, Lincoln J, Frontiers in Cardiovascular Medicine, 5, 2018.
[2] Tzemos N et al., JAMA, 300(11), 2008.
[3] Fulmer D, et al., Circulation, 140(16):1331–41, 2019.
[4] Flurkey, K et al., Elsevier, 2nd Ed.*pp. 637–72,2007.*
[5] Mazur, P et al., Circulation, 81(7), 1043-50, 2017.
[6] Thubrikar et al., American Journal of Cardiology, 58:304-8, 1986.

DYNAMIC PATIENT-SPECIFIC COMPUTER SIMULATION OF TRANSCATHETER AORTIC VALVE REPLACEMENT USING THE EVOLUT R AND SAPIEN3

M. Sadipour (1), J. A. Brown (2,3), D. R. Wells (2), B. E. Griffith (1,2)

(1) Department of Biomedical Engineering, University of North Carolina, Chapel Hill, NC, USA
(2) Department of Mathematics, University of North Carolina, Chapel Hill, NC, USA
(3) College of Sciences and Mathematics, Belmont University, Nashville, TN, USA

INTRODUCTION

Valvular heart diseases, such as aortic valve stenosis, are becoming more common as the global population's average age rises [1]. Transcatheter aortic valve replacement (TAVR), a less invasive alternative to conventional surgical valve replacement, involves implanting a bioprosthetic valve through arteries. TAVR is now the primary method for aortic valve replacement [2]. Computer modeling can aid in device design, approval, and personalized patient care [3]. This study uses dynamic computer simulations to compare the dynamics of two FDA-approved TAVR devices, the CoreValve Evolut R and the SAPIEN 3. Our models extend prior patient specific TAVR simulations [4] by considering aortic root flexibility, which can have a substantial impact on simulation outcomes [5]. This project, using advanced numerical methods for fluid-structure interaction, incorporates realistic clinical conditions and biomechanics, predicting detailed device performance and interactions within the patient's anatomy.

METHODS

This work utilizes the immersed finite element-difference (IFED) method [6] to simulate the fluid-structure interaction among the transcatheter aortic valve (TAV), native aortic valve, and the aortic root with the surrounding blood. The patient-specific model anatomy (Figure 1(a,c)) is based on pre-procedural CTA images obtained from a female patient scheduled for TAVR using a 26 mm Medtronic CoreValve Evolut R (Figure 1 (b)). As the patient's native valve leaflets weren't clearly visible in the images, idealized representations were created based on measurements from previous research [7].

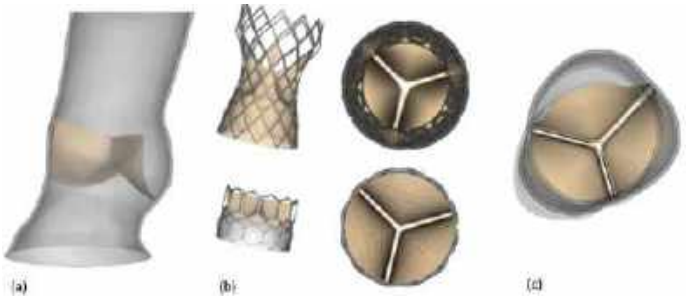

Figure 1: (a) Reconstructed aortic root geometry, (b) Top. CoreValve Evolut R, Bottom. Sapian 3, (c) Native aortic valve geometry.

These artificial valves leaflets were adjusted using SOLIDWORKS to fit the reconstructed anatomy. Both sets of valve leaflets (native valve, porcine and bovine pericardial tissue) and the sealing skirt were modeled as hyperplastic materials. For our leaflets and sealing skirts, we employ the modified Holzapfel–Gasser–Ogden (HGO) model as described by Murdock et al. [8, 9],

$$W = C_{10}\{\exp[C_{01}(\overline{I}_1 - 3)] - 1\} + \frac{k_1}{2k_2}\sum_i\{\exp[k_2(I^*_{4,i} - 1)^2 - 1\} \quad (4)$$

$\overline{I}_1 = \mathrm{tr}(\overline{C})$ is the first invariant of the modified right Cauchy–Green strain tensor $\overline{C}=\overline{F}^{\mathrm{T}}\overline{F}$ and $I^*_{4,i}$= max ($\mathrm{I}_{4,i}$,1) = max ($f_i^0.\overline{C}f_i^0$, 1) where f_i^0 denotes a unit vector aligned with the ith fiber direction, referring to the reference configuration.

Fiber arrangements and model parameters follow those detailed previously [4,8,10]. In addition, we model the vessel wall as a hyperplastic material model based on our vessel wall deformation optimization.

We characterize blood as a viscous incompressible fluid using the Navier-Stokes equations, with density of 1.0 g cm^{-3} and dynamic viscosity $\mu = 3.5$ cP. To set afterload conditions, at the outlet we use a three-element Windkessel model, and at the inlet we employ a time-dependent elastance-based left heart model. The period of the cardiac cycle is T=0.8512s.

RESULTS

Figure 2 displays detailed flow patterns within and downstream of the Evolut R (Fig. 2a) and SAPIEN 3 (Fig. 2b) across the cardiac cycle. The model generates physiological flow rates and yields effective orifice areas that are in good agreement with clinical data. The model can also predict fine-scale flow features. Specifically, in the final frame of Figure 2a, the model captures the nuanced flow dynamics indicative of a minor paravalvular leak, visible behind the native leaflet on the left side of the Evolut R's sealing skirt. Conversely, our intentional over-expansion of the SAPIEN 3 stent frame results in a secure seal within the native leaflets, preventing any occurrence of paravalvular leakage.

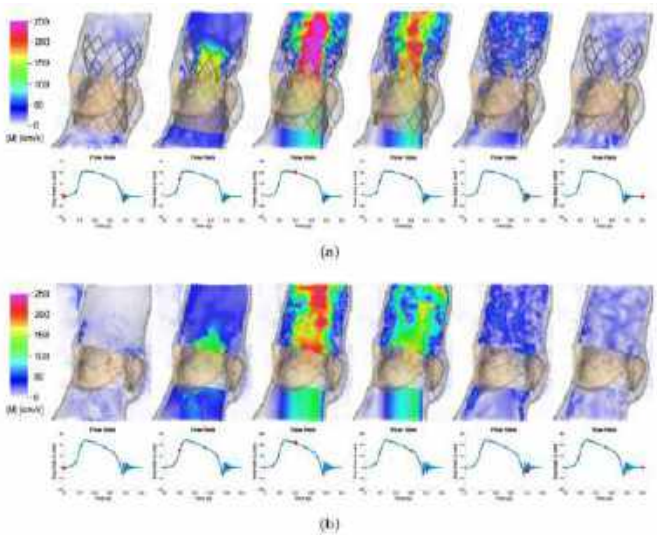

Figure 2: Cross-sectional representations reveal flow patterns for both the (a) Evolut R and (b) SAPIEN models, simulated under driving conditions derived from the time-dependent elastance-based left heart model. Each frame is separated by a time increment of 0.1 seconds.

DISCUSSION

This study introduces a computational modeling framework for fluid-structure interaction in transcatheter aortic valve replacement (TAVR) devices within patient-specific anatomies. It compares two prominent TAVR devices: Medtronic's CoreValve Evolut R and Edwards Lifesciences' SAPIEN 3. Employing a flexible aortic root model and comprehensive three-dimensional representations of the device stent frames, our simulations offer enhanced realism in capturing device interactions with the patient's native anatomy compared to our earlier model. Specifically, our improved model shows a reduction in paravalvular leakage (PVL) compared to a model featuring a stationary aortic root and a discrete device stent frame representation.

ACKNOWLEDGEMENTS

We acknowledge research support from NIH award R01HL157631 and NSF award OAC 1931516.

REFERENCES

[1] Yacoub M. H. et al., *Nat Clin Pract Cardiovasc Med*, 2: 60–61, 2005.

[2] Mentias A. et al., *Am Heart J*, 234:23–30, 2021.

[3] Morrison T. M. et al., *J Med Device*, 11:024503, 2017.

[4] Brown. J.A. et al., *Ann Biomed Eng*, 51, 103-116 (2023).

[5] Bonfanti, M. et al., *Med. Eng. Phys*, 58:72-79, 2018.

[6] Griffith B. E. et al., *Int J Numer Method Biomed Eng*, 33: 2888, 2017.

[7] Sahasakul Y. et al., *Am J Cardiol*, 62.7, 424-430, 1988.

[8] Murdock K. et al., *J Mech Behav Biomed Mater*, 77:148–156, 2018.

[9] Lee J. H. et al., *Ann Biomed Eng*, 48:1475-1490, 2020.

[10] Yudi M. B. et al., *J Am Coll Cardiol*, 71.12:1360-1378, 2018.

INVESTIGATING THE INFLUENCE OF LACTATION ON MURINE HEART GROWTH THROUGH ULTRASOUND AND COMPUTATIONAL ANALYSIS

Molly S. Kaissar (1), Arden C. Shen (2), Jennifer L. Anderson (2,3), Elnaz Ghajar-Rahimi (2), Adalyn Meeks (2), Craig J. Goergen (2), Kyoko Yoshida (1)

(1) Department of Biomedical Engineering, University of Minnesota, Minneapolis, MN, USA
(2) Weldon School of Biomedical Engineering, Purdue University, West Lafayette, IN, USA
(3) Larner College of Medicine, University of Vermont, Burlington, VT, USA

INTRODUCTION

The pregnant body adapts to accommodate the growing fetus. For example, the cardiovascular system meets rising physiological demands by expanding blood volume, reducing systemic vascular resistance, and increasing cardiac output.[1] Throughout pregnancy, the left ventricle (LV) grows to support this increased workload.[2] After delivery, these adaptations are thought to reverse. However, whether the heart returns to its pre-pregnant size, shape, and function after delivery is unclear.[2,3] Moreover, postpartum-specific behaviors like lactation are known to affect hemodynamics in rodents, which are common animal models of pregnancy and postpartum. For example, cardiac outputs in lactating rats remain elevated, whereas non-lactating rats return their cardiac outputs to pre-pregnant values.[4] While increased cardiac outputs are implicated in LV growth, direct comparisons of LV growth between lactating and non-lactating animals are lacking.

Thus, the objectives of this study are to (1) measure postpartum changes in LV morphometry, (2) investigate how lactation affects these changes, and (3) use a computational model to analyze the mechanisms driving heart growth after delivery. We hypothesize that LV growth (1) increases to meet the elevated hemodynamic demand of lactation, (2) reverses to its pre-pregnant size, shape, and function without lactation, and (3) that this difference in growth is driven by mechanical loading.

METHODS

Animals: We assessed cardiac hypertrophy longitudinally in mice throughout a 19-day pregnancy and 21-day postpartum period. Female nulliparous C56Bl/6J mice (n = 10) were randomized into Lactating (*L*, n=5) and Non-Lactating (*NL*, n=5) groups to study the effect of nursing on postpartum LV growth. *L* mice were allowed to nurse their pups and *NL* mice were immediately removed from their litter after delivery.

Cardiac ultrasound imaging and processing: To track cardiac growth, we collected four-dimensional cardiac ultrasound (4DUS) images. Baseline measurements were taken before pairing (day 0: D0), and mice were scanned on days 6, 12, 15, and 18 of gestation (GD6, GD12, GD15, GD18) and days 1, 4, 7, 14, and 21 postpartum (PPD1, PPD4, PPD7, PPD14, PPD21) using a high-frequency ultrasound system (Vevo 3100, Fujifilm VisualSonics).[5] Tail cuff blood pressure was monitored throughout the study (CODA, Kent Scientific).

Using our previously established methods, we segmented the 4DUS images by outlining the epicardial and endocardial boundaries to trace local wall motion throughout the cardiac cycle.[5] The epicardial and endocardial meshes were used to calculate heart size (LV mass: *LVM*), shape (end-diastolic volume: *EDV*, end-diastolic wall thickness: *WT*), and function (stroke volume: *SV*, ejection fraction: *EF*).

Multiscale model simulations: To test the hypothesis that hemodynamic changes drive postpartum heart growth, we simulated LV growth in *L* and *NL* animals using our previously published multiscale model.[6] This model, which accounts for cell-signaling and hemodynamic interactions during pregnancy, correctly captures heart growth in pregnant rats. We assume the same mechanisms drive pregnancy-induced heart growth across all species; thus, we assume our model can be used to observe relative changes in both rats and mice. To simulate our experiment, we input gestation-appropriate changes in hemodynamics by incorporating relative change in group-averaged systemic vascular resistance (*SVR*) changes based on measured *SV* and mean arterial pressure and optimizing stressed blood volume to match the average changes in *EDV*. We included time-appropriate relative changes in hormones (estrogen, progesterone, angiotensin II) reported in rats. Based on previous research, we assumed that hormonal changes are comparable between rodents during pregnancy and values return to pre-pregnant levels postpartum regardless of lactation status.[7,8]

Statistical Analysis: Metric differences between groups and on selected days (D0, GD18, PPD21) were assessed with a student's t-test ($P < 0.05$ for significance). Raw data are presented as mean ± standard error of the mean (SEM). Relative changes are reported as percent change of the mean ± relative standard deviation (RSD).

RESULTS

Pregnancy induced heart growth: As there were no noteworthy differences in average metrics between the *L* and *NL* groups during pregnancy (Table 1), we compared metrics at D0 and GD18 across all 10 mice. Before pairing (D0), *LVM* measured 68.5±4.4 mg. Throughout gestation, *LVM* grew to 81.7±1.0 mg at GD18 ($P = 0.01$ vs. D0). This growth was facilitated by an increase in *EDV* (D0: 36.3±2.1 µL, GD18: 50.0 ± 2.6 µL, $P = 0.002$) while myocardial *WT* was largely maintained (D0: 1.00±0.04 mm, GD18: 0.99±0.04 mm, $P = 0.60$), suggesting eccentric hypertrophy consistent with volume overload. These changes aligned with increased *SV* (D0: 20.0±2.7 µL, GD18: 30.7±2.7 µL, $P \leq 0.001$) and *EF* (D0: 59.1±2.9%, GD18: 65.3±2.9%, $P = 0.03$), indicating enhanced cardiac function.

Growth continued throughout lactation: *L* mice carried an average litter size of 6.4±0.3 pups, which they nursed for 21 days postpartum. At PPD21, *LVM* increased significantly compared to the end of pregnancy (Table 1, $P = 0.008$ vs. GD18). This additional growth corresponded with further chamber enlargement (*EDV*: $P = 0.02$ vs. GD18) and an upward trend in *SV*, agreeing with reported changes in cardiac output in Wistar rats.[4] However, the average increase in *SV* was not significant compared to the end of pregnancy ($P = 0.12$ vs. GD18). Moreover, *EF* remained consistent with the end of pregnancy ($P = 0.78$ vs. GD18). Together, these results suggest cardiac function was maintained, but not enhanced, during lactation compared to GD18.

Growth partially reversed after pups removed: *NL* mice carried an average litter of 6.8±0.4 pups ($P = 0.62$ vs. *L*), which were removed from the cage after delivery. By PPD21, *LVM* decreased slightly from the end of pregnancy (Table 1, $P = 0.28$ vs. GD18). Interestingly, cavity dilation persisted at the end of the study (*EDV*, $P = 0.04$ vs. D0). While *SV* decreased from the end of pregnancy ($P = 0.02$ vs. GD18), it remained marginally elevated above pre-pregnant levels ($P = 0.06$ vs. D0). Together, these results suggest that the heart does not return to its pre-pregnant shape or function in the first three weeks postpartum.

Lactation status impacted postpartum growth: At PPD21, *L* mice had significantly larger hearts than their *NL* counterparts (*LVM*, Table 1, $P = 0.04$ vs. *NL* at PPD21). Similarly, *L* mice had elevated *SV* ($P = 0.046$ vs. *NL* at PPD21) and *EF* ($P = 0.04$ vs. *NL* at PPD21). As these animals experienced otherwise identical study conditions, these results suggest lactation directly impacts LV growth after delivery.

Table 1: Ultrasound estimations of LV size, shape, and function before pairing (D0), during pregnancy (GD18), and postpartum (PPD21) in *L* and *NL* mice. Values are mean ± SEM. n = 5/group. * $P < 0.05$ vs. D0. $^{+}$ $P < 0.05$ vs. GD18. $^{\$}$ $P < 0.05$ vs. NL.

			D0	*GD18*	*PPD21*
Size	*LVM (mg)*	*L*	65.1 ± 2.2	82.1 ± 1.8 *	102.5±6.1 *$^{+\$}$
		NL	72.0 ± 8.8	81.2 ± 1.0	76.9±6.1
Shape	*WT (mm)*	*L*	0.96 ± 0.06	1.02 ± 0.07*	1.10±0.09*
		NL	1.03 ± 0.06	0.96 ± 0.04	0.93±0.01
	EDV (µL)	*L*	39.2 ± 1.9	51.3 ± 3.9 *	63.5±4.7 *$^{+}$
		NL	33.4 ± 3.5	48.8 ± 3.8 *	48.0±5.0 *
Function	*SV (µL)*	*L*	22.8 ± 1.2	34.7 ± 3.5 *	40.9±4.3 *$^{\$}$
		NL	20.0 ± 2.7	30.7 ± 2.7 *	26.6±3.1 $^{+}$
	EF (%)	*L*	58.6 ± 4.2	67.6 ± 4.6 *	64.0±3.0 *$^{\$}$
		NL	59.7 ± 4.3	63.0 ± 3.9	55.3±3.0 $^{+}$

Model predictions differentiate postpartum growth: Since there were no significant differences in *EDV* (Fig 1A) and *SVR* ($\propto 1/SV$, not pictured) between the *L* and *NL* groups during pregnancy, our model predicted similar changes in *LVM* (*L*: +24%, *NL*: +25% vs. D0, Fig 1B) and *WT* (*L*: +5%, *NL*: ±0% vs. D0, Fig 1C) by GD18. These predictions were on par with observed growth in all mice (*LVM*: +19±4% vs. D0, Fig 1B; *WT*: -1±13% vs. D0, Fig 1C).

Postpartum, the higher *EDV* (Fig 1A) and lower *SVR* in the *L* group resulted in the prediction that *LVM* would increase an additional +9% above GD18 by PPD21 (Fig 1B). While this continued growth agreed with the experimental data, our model notably underpredicted the lactation-induced changes in mass (+25±12% vs. GD18, Fig 1B). Yet, the predicted minimal change in *WT* after 21 days of lactation (-5% vs. GD18, Fig 1C) agreed with our experimental results in *L* mice (*WT*: +8±24% vs. GD18, Fig 1C). Given the lower *EDV* (Fig 1A) and higher *SVR* in the *NL* group, our model predicted a slight decrease in *LVM* (-5% vs. GD18, Fig 1B) and *WT* (-5% vs. GD18, Fig 1C), which agrees with our data in the *NL* mice (*LVM*: -5±16% vs. GD18, Fig 1B; *WT*: -3±11% vs. GD18, Fig 1C). Collectively, our predictions suggest that our model can accurately capture organ-level cardiac shape changes.

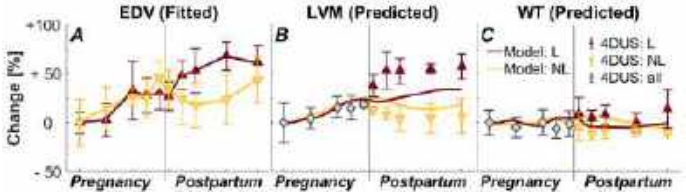

Figure 1: Multiscale model optimized (A) *EDV* to predict (B) *LVM* and (C) *WT*, compared here to relative changes in ultrasound estimations. Symbols are percent change of the mean ± RSD.

DISCUSSION

Here, we explored how the murine heart changes in size, shape, and function following pregnancy-induced hypertrophy. We show that heart growth continued in *L* mice and regressed in *NL* mice after delivery. However, our results suggest the heart does not return completely to its pre-pregnant state in the *NL* mice, disagreeing with our hypothesis. Alternatively, these results imply full recovery may take longer than pregnancy and should be examined in an extended study.

We employed a computational model to interpret our experimentally observed heart growth. We illustrated that changes in postpartum hemodynamics drive continued growth in *L* mice and regression in *NL* mice. However, our model underpredicted *LVM* in the *L* group, suggesting additional (i.e., hormonal) mechanisms may play a role. While these discrepancies may stem from our current model being calibrated to rat anatomy and physiology, it is important to highlight that our rat model successfully captured heart growth during mouse pregnancy. Regardless, we are currently developing a mouse-specific model, which will allow us to simulate animal-specific hemodynamics.

To our knowledge, this murine study is the first to investigate the effects of lactation on LV morphometry following a healthy pregnancy. Our findings demonstrate lactation's significant impact on postpartum heart growth. Unsurprisingly, lactation is integral to transgenic mouse models of new-onset heart failure during pregnancy,[9] which is the leading cause of pregnancy-related deaths after delivery in the United States.[10] Our findings, along with these models, underscore the importance of considering lactation status, which is often not reported, in postpartum-related cardiovascular research.

ACKNOWLEDGEMENTS

This work was supported by the UMN Cardiovascular Engineering Training Program (T32-HL139431), an AHA Career Development Award, and the Purdue University Women's Global Health Institute.

REFERENCES [1]Hunter S et al. *Br Heart J* 68(1992). [2]Savu O et al. *Circ Cardiovasc Imaging* 5(2012). [3]Clapp J & Capeless E *Am J Card* 80(1997). [4]Hanwell A & Linzell J *J Physiol*, 233(1973). [5] Damen F et al. *AJP Heart Circ*, 321.1(2021). [6]Yoshida K et al. *JMMB* 21(2022). [7]Hackwell E et al. *Endocrinology* 164(2023). [8]Mitchell B & Taggart M *AJP Regul Integr Comp Physiol* 297(2009). [9]Ricke-Hoch M et al. *Cardiovasc Res* 101(2014). [10]Petersen E et al. *MMWR Morb Mortal Wkly Rep* 68(2019).

OCULAR HYPOTHERMIA, IN-VITRO VALIDATION OF A NOVEL THERAPEUTIC APPARATUS USING NON PERFUSED PORCINE EYE MODEL

Luigi Mecacci (1), Yukinari Nakamura (1), John R. Hetling (1,2)

(1) Department of BioEngineering, University of Illinois at Chicago, Chicago, Illinois, USA
(2) Department of Ophthalmology and Visual Sciences, University of Illinois at Chicago, Illinois, USA

INTRODUCTION

Hypothermia has been widely used in the heart and brain thanks to its therapeutic effects to people suffering from certain conditions, such as cardiac arrest [1, 2], traumatic brain injury and strokes [3, 4]. Similarly, this technique has been proven to be effective in the ophthalmic field to preserve retinal tissue vitality in the diseased eye [5, 6] and in rat models it prevented adverse effects when applied prior to the onset of an ischemic condition (hypothermic preconditioning) [7, 8].

The physiological effects of hypothermia in the eye, many of which are thought to be neuroprotective, include decrease in the metabolic activity of the cells, reduced release of neurotransmitters, and induce the breakdown of the blood-aqueous barrier as reviewed by Xi [6]. Lactate production levels and glucose utilization levels were lowered in eyes treated with moderate hypothermia when compared to eyes kept at a physiological temperature, while, they also showed a return to normal rates for these two parameters when the hypothermic eyes were brought back to normal temperatures [6].

Current commercially available solutions to deliver therapeutic hypothermia to the eye (i.e. cold packs, cold saline irrigation) present passive heat removal, with an uncontrolled heat removal rate and inconsistent contact areas with the eye decreasing the efficacy of such cooling. As of now, the most used cooling technique is contact cooling using cold packs, in which cooling rate is dependent on the temperature of the pack and the contact area with the eye and surrounding tissues, which changes with time. Thus cooling is not regulated. A second method uses irrigation of the eye with cooled saline which is also not regulated and is only practical in a clinical or laboratory setting. A technology gap exits where the desire is to deliver therapeutic hypothermia to the eye that is regulated and targeted.

METHODS

The Eye Cooler System (ECS) was designed to address the technology gap described above. The ECS is comprised of three main components as shown in Figure 1. An eye contact ring is shaped to conform to the sclera of a typical adult human eye and to be held in place by the eyelids; this ring allows viewing of the cornea and pupil during use. A thermoelectric heat pump actively moves heat from the eye contact ring in a regulated manner (i.e. with feedback). An active convection heat sink (water block) uses chilled fluid to absorb and transport heat away from the heat pump. The viewing port extending through the device is left unobstructed to allow viewing of the cornea and pupil during use. A temperature sensor at the eye surface integrated inside of the eye contact ring provides feedback.

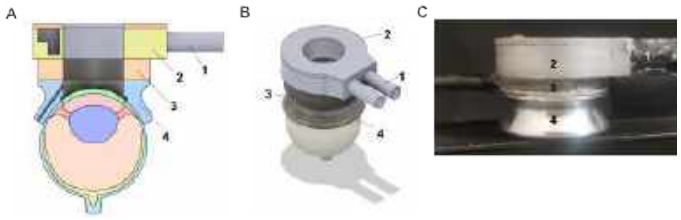

Figure 1: Overall design and components of the Eye Cooler System. (A) Cross-section of the CAD model of the eye cooler set on an eye. The main components of the system are numbered: 1) convection fluid ports, 2) active convection heat sink, 3) thermoelectric heat pump, 4) eye contact ring (B) CAD model of the eye cooler set on an eye, panorama view. The reference numbers are the same as panel A. (C) Side view photograph of the assembled Eye Cooler System; numbered components the same as in panel A.

Fresh pig eyes (n = 5) were obtained and cleaned of extraocular tissue, placed in a custom holder and imaged using MRI to document the gross anatomy.

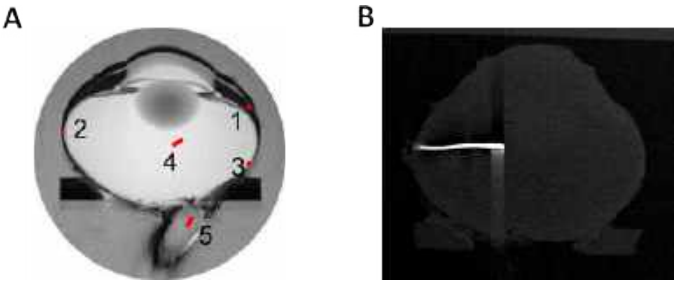

Figure 2: (A) Target position of the implanted thermistors (0.5mm diameter) in the eye, shown in red: 1 anterior sclera, 2 equatorial sclera, 3 posterior sclera, 4 vitreous, 5 optic nerve. (B) CT image showing actual position of an implanted thermistor at Vitreous.

Following MRI imaging, each eye was implanted with temperature sensors (NTC thermistors) at five key locations, as illustrated in Figure 2.

The ECS was then positioned to contact the sclera. The (eye + ECS) was the lowered to the level of the lowest edge of the ECS (approximately 4mm peripheral to the limbus) into a 37°C oil bath (used to simulated naturally found fat tissues surrounding the eye globe) and the eye was allowed to reach equilibrium at typical physiological temperature (34.5°C).
The ECS was turned on, initiating the cooling, and the temperatures monitored as a function of time. The ECS sensor/feedback ensured the sclera was never below 4°C. After 20 minutes of ECS cooling, the device was turned off and the eye was removed from the system. Each eye was then placed back in the custom holder and imaged using micro-CT to document the precise location of each implanted temperature sensor. The position of the sensors was then analysed for consistency across the five eyes.

RESULTS

Each experiment resulted in temperature vs time curves for each of the five sensor positions in the eye plus one curve for the eye contact ring temperature. Temperature vs time curves for each sensors location across the five eyes are summarized in Figure 3.

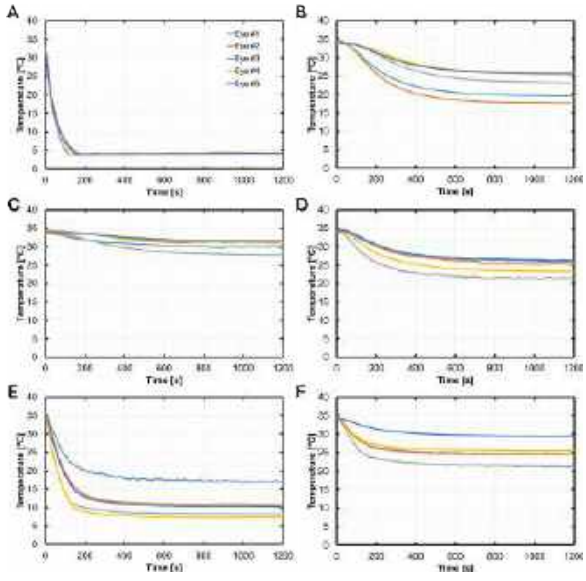

Figure 3: Temperature observed at each thermistor position for all five eyes as a function of time after onset of current through the TEC (at t = 0 s). Each plot shows the temperature data for one of the six sensor locations: (A) eye contact ring, (B) anterior sclera, (C) equatorial sclera, (D) posterior sclera, (E) vitreous, (F) optic nerve. In each plot, the five coloured curves plot the temperatures obtained at that location for the five eyes used in this study.

On average, the temperature at the ECS sensor, located adjacent to the sclera, reached 4°C within three minutes of turning the system on (Figure 4).

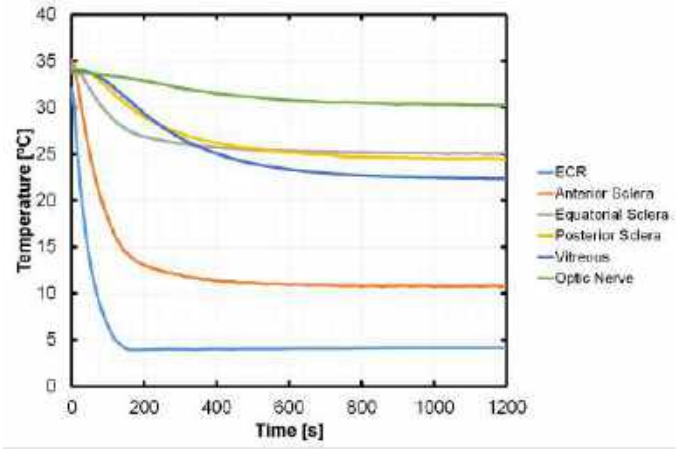

Figure 4: Temperature observed at each of six thermistor positions is plotted versus time following onset of current through the TEC (at t = 0 s). Curves are averages across the five eyes shown in Figure 3

Final equilibrium temperatures, and the times to reach 90% of the final change in temperature at each sensor location (mean across 5 eyes), were: anterior sclera, 10.7°C, 194 sec; equatorial sclera, 25.0°C, 338 sec; posterior sclera, 24.4°C, 532 sec; vitreous, 22.4°C, 569 sec; proximal optic nerve, 30.2°C, 703 sec. Temperature vs time profiles were similar across eyes, with root mean squared differences from the mean profile of 11-29%, depending on sensor location.

DISCUSSION

In the non-perfused eye model, the ECS was able to achieve therapeutically relevant temperatures throughout the eye, including the proximal optic nerve. Equilibrium temperatures could be maintained for as long as the system was powered. Next steps include measuring ECS-induced temperature changes in a human eye model.

ACKNOWLEDGEMENTS

Unrestricted grant from anonymous source.

REFERENCES

[1] Bernard SA et al. *New England Journal of Medicine* 346 (8 2002). ISSN: 0028-4793. DOI: 10.1056/NEJMoa003289.

[2] Silverman MG et al. *Trends in Cardiovascular Medicine* 26 (4 2016). ISSN: 10501738. DOI: 10.1016/j.tcm.2015.10.002.

[3] Kurisu K et al. *Neuropharmacology* 134 (2018). Cerebral Ischemia. ISSN: 0028-3908. DOI: https://doi.org/10.1016/j.neuropharm.2017.08.025.

[4] Kim JH et al. *Recent Patents on Inflammation and Allergy Drug Discovery* 5 (2 2011). ISSN: 1872213X. DOI: 10.2174/187221311795399219.

[5] Reinhard K et al. *Investigative Ophthalmology and Visual Science* 57 (2 2016). ISSN: 15525783. DOI: 10.1167/iovs.15-17751.

[6] Xi L. *Oxidative Medicine and Cellular Longevity* 2020 (2020). ISSN: 19420994. DOI: 10.1155/2020/3897168.

[7] Salido EM et al. *PLoS ONE* 8 (4 2013). ISSN: 19326203. DOI: 10.1371/journal.pone.0061656.

[8] Faberowski N et al. *Investigative Ophthalmology and Visual Science* 30 (11 1989).

VALIDATION OF A PLATFORM TO QUANTIFY CORNEAL ENDOTHELIAL CELL DAMAGE DUE TO INDENTATION

Alex J. McMullen (1,2), Aldo Tecse (1,2), Paul D. Funkenbusch (3), Naveen Mysore (4), Yousuf M. Khalifa (5), Mark R. Buckley (1,2)

(1) Department of Biomedical Engineering, University of Rochester, Rochester, NY, USA
(2) Center for Visual Science, University of Rochester, Rochester, NY, USA
(3) Department of Mechanical Engineering, University of Rochester, Rochester, NY, USA
(4) Flaum Eye Institute, University of Rochester Medical Center, Rochester, NY, USA
(5) Department of Ophthalmology, Emory University School of Medicine, Atlanta, GA, USA

INTRODUCTION

The non-proliferative corneal endothelial cells (CEC) located on the posterior side of the cornea are vital for maintaining central corneal transparency by regulating the hydration and thickness of the corneal stroma through a "pump-leak" mechanism [1]. When the endothelial cell density decreases ~80% from healthy adulthood levels, an individual is at risk of developing corneal decompensation [2], which results in blurred vision, pain, and even blindness if untreated [3,4].

A leading etiology for corneal decompensation is CEC damage during intraocular surgeries [2-4]. For instance, CEC losses of 23-42% have been observed at 1 year after corneal transplant surgeries [5,6]. An argument can be made that mechanical loading plays a big role in acute CEC loss, as the mechanical environment CECs experience during corneal transplantation is much different than physiological conditions.

Our lab has previously shown that CECs are highly susceptible to mechanical trauma via indentation [7]. However, further investigation is needed to understand which of the numerous parameters that influence contact mechanics during indentation can be controlled to mitigate acute CEC damage during surgery. Thus, we designed the "CECure Mechanical Testing Platform" (**Fig. 1**).

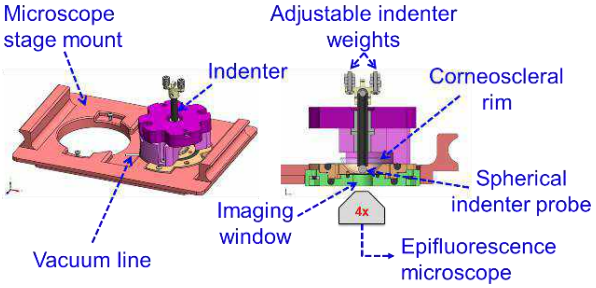

Figure 1: SolidWorks 3-D rendering of the CECure platform, highlighting some important features.

The CECure platform facilitates improved visualization of the endothelium before, during, and after indentation, with less manipulation of the corneal sample to isolate CEC damage as a result of indentation from damage caused by experimental handling.

The objective of this study was to demonstrate the CECure platform's ability to detect differences in CEC viability during different indentation loading conditions. A design of experiments (DOE) approach was used that allowed us to efficiently test the effects of multiple parameters (control factors) simultaneously.

METHODS

Indentation Experiments: Corneoscleral rims were carefully dissected from porcine eyes within 72 hours after euthanasia. For each sample, a solution of PBS and Hexidium Iodide was applied to the endothelium to stain all CEC nuclei. The corneoscleral rim was then rinsed with PBS and placed in the CECure platform endothelial-side-up. A solution of either PBS or ophthalmic viscosurgical device (OVD) and SYTOX Green was placed onto the endothelium, where it remained for the rest of the experiment to stain injured CEC nuclei. Prior to indentation, the baseline z-position was measured and a 3-D z-stack image was acquired of the endothelium using an inverted fluorescence microscope (**Fig. 2A**).

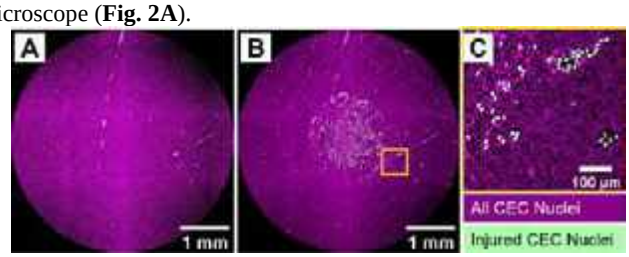

Figure 2: Representative images of the corneal endothelium (A) before and (B) after indentation, as well as a (C) zoomed in view where individual CEC nuclei are visible.

The endothelium was then indented under varying conditions with prescribed values of different control factors, and the z-position of the indenter was measured through the microscope. The indenter was then lifted from the endothelium, and a final fluorescence z-stack image was taken of the endothelium (**Fig. 2B**).

DOE Strategy: A full factorial array design was used to test five different control factors (**Table 1**). This resulted in 32 treatment conditions (TC), or 32 different combinations of control factors.

Table 1: DOE control factors.

Control Factor	Level	
	-1	+1
A. OVD application	Ocu+ 1%	No OVD
B. Indenter diameter	3 mm	4 mm
C. Indent load	~16 mN	~36 mN
D. Indent duration	5 sec	30 min
E. Death-to-Experiment (DTE) time	24-48 hrs	48-72 hrs

Three characteristic responses (outcomes) of CEC damage were measured for each TC: percent CEC injury (PCI), percent CEC detachment (PCD), and total CEC loss (TCL). The effect of each control factor, and their interactions, on each characteristic response was measured using analysis of means (ANOM). Significance of each effect was determined using analysis of variance (ANOVA).

Image Processing & Analysis: Custom image processing/analysis algorithms (ImageJ and MATLAB) were used to flatten and correct the z-stack images, measure indentation depths, and count CEC nuclei to obtain both baseline total and injured CEC counts (TC_1 and IC_1, respectively), and final total and injured CEC counts (TC_2 and IC_2, respectively). These counts were used to calculate PCI and PCD, which were summed together to compute TCL:

$$TCL = PCI + PCD = \left[\left(\frac{IC_2}{TC_2} - \frac{IC_1}{TC_1}\right) \times 100\right] + \left[\frac{TC_1 - TC_2}{TC_1} \times 100\right] \quad (1)$$

RESULTS

As expected, the +1 level for each control factor resulted in more CEC damage than the -1 level, although not all effects were statistically significant (**Fig. 3**). Notice that indent duration had the largest effect on TCL, followed by indent load. There were also several factor interactions that had statistically significant effects (not shown).

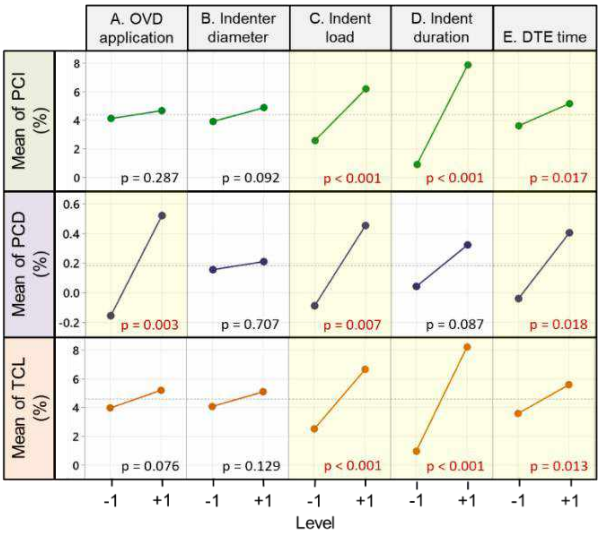

Figure 3: DOE main effects plots from ANOM for PCI (top row), PCD (middle row), and TCL (bottom row), including p-values obtained from ANOVA (significant effects highlighted in yellow).

A linear regression analysis showed that a moderate and significant correlation exists between indentation depth and TCL (**Fig. 4**).

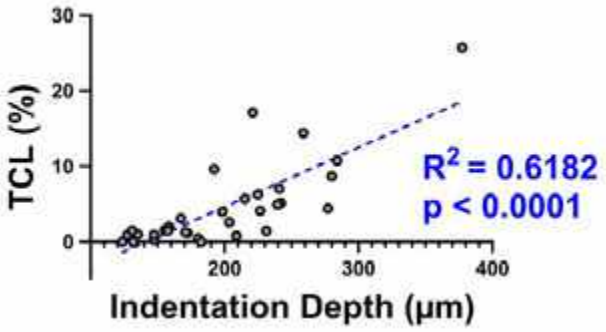

Figure 4: Correlation between indentation depth and TCL.

DISCUSSION

We successfully validated our custom test platform's ability to detect differences in CEC viability under different indentation loading conditions by showing statistically significant effects of multiple parameters that were expected to influence CEC damage. Indent duration had the most notable effect on CEC damage, suggesting that how long CECs are subjected to mechanical loading is just as, if not more, important than the magnitude of the load. More work is needed to better understand if CEC damage at longer durations is due to the poroelastic response of the cornea (time-dependent strain) or a contact surface interaction, such as adhesion.

We also identified an exciting relationship between indentation depth and CEC damage, which suggests corneal mechanical properties could serve as a predictor of CEC loss during surgery. For example, if a surgical maneuver requires application of a given load onto the endothelium of a transplanted corneal graft, our findings suggest a stiff graft will experience less CEC loss than a more compliant graft because it will deform less under the same load.

A limitation of this study was that the levels used for the DOE control factors were meant to test the device rather than represent surgical conditions. However, the CECure platform design is amenable to accommodating more surgically-relevant conditions (e.g. the indenter probe geometry can be changed to match surgical forceps).

Collectively, the findings of this study validate our experimental platform and pave the way for future work investigating how different surgical tools, corneal treatments, and corneal mechanical properties affect the tolerance of CECs to mechanical loading.

ACKNOWLEDGEMENTS

This work was partially supported by the NEI of the NIH under Award Number T32EY007125. The content is solely the responsibility of the authors and does not necessarily represent the official views of the NIH.

REFERENCES

[1] Bonanno, JA, *Exp Eye Res*, 95(1):2-7, 2012.
[2] Dawson, DG et al., *Adler's Physiology of the Eye*, 11:71-130, 2011.
[3] Feizi, S, *Ther Adv Ophthalmol*, 10:2515841418815802, 2018.
[4] Price, MO et al., *Prog Retin Eye Res*, 82:100904, 2021.
[5] Acar, BT et al., *Int J Ophthalmol*, 4(6):644-7, 2011.
[6] Lee, WB et al., *Ophthalmology*, 116(9):1818-30, 2009.
[7] Ramirez-Garcia, MA et al., *Exp Eye Res*, 175:73-82, 2018.

MECHANICAL STIMULATION AND HYALURONIC ACID ALTER OVARIAN CANCER CELL BEHAVIORS

Maranda E. Kramer (1), Allyson Criswell (2), Kamari Marzette (1), MK Sewell-Loftin (1,3)

(1) Department of Biomedical Engineering, University of Alabama at Birmingham, Birmingham, AL, USA
(2) Department of Clinical and Diagnostic Sciences, University of Alabama at Birmingham, Birmingham, AL, USA
(3) O'Neal Comprehensive Cancer Center, University of Alabama at Birmingham, Birmingham, AL, USA

INTRODUCTION

Ovarian cancer is both the most common and lethal gynecological cancer[1]. Despite being such a devastating disease, the effects that the tumor microenvironment (TME) play on ovarian cancer cell behavior are not well characterized. Different features of the ovarian TME that can alter cell behaviors include forces such as strains, interstitial flow, or compression; stromal cell interactions; and extracellular matrix (ECM) remodeling[2]. Specifically, this work focuses on tensile strains in the ovarian TME and how strain interacts with changes in ECM composition. Cancer-associated fibroblasts (CAFs) are stromal cells responsible for secreting and remodeling ECM proteins; CAFs also have increased contractility compared to normal fibroblasts[3]. These increases in contractility allow CAFs to exert tensile strains through the matrix components onto the ovarian cancer cells.

Hyaluronic acid (HA) is a matrix component secreted by CAFs commonly found in the ovarian TME, although the role HA plays in the mechanobiology of ovarian cancer is poorly defined. HA can interact with ovarian cancer cells *in vivo* as a stromal or serum component. While stromal HA has been shown to be associated with a worse prognosis and lower 5-year survival rate, serum HA has been shown to not be a predictor of disease stage or progression[4, 5]. HA signals through the cell surface receptor, CD44 which is ubiquitously expressed in a variety of cancers including ovarian, breast, prostate, head, and neck cancers to name a few. The intracellular region of CD44 connects to the cytoskeletal components through ankyrin and ERM proteins (ezrin, radixin, and moesin), which regulate mechanotransduction. There are proteins, including Src and the Rho/ROCK pathway, that associate with CD44 and are known to be mechanosensitive[6]. Through these cytoskeletal proteins, CD44 can alter cancer cell behaviors including proliferation, migration, and drug resistance[7]. However, it is unclear if mechanical stimulation of CD44 alters its signaling pathways. I hypothesize that mechanical stimulation and interaction between HA and CD44 alters downstream signaling and ultimately causes differences in proliferation and migration.

METHODS

All studies utilized the ovarian cancer OVCAR-8 model cell line. A CD44 knock down in the OVCAR-8 line (shCD44) and scramble control (shSCR), both with an RFP reporter, were created using a lentiviral vector. Cells received a No Strain or tensile Strain treatment for 24h at 0.3 Hz and 9% elongation using a FlexCell system before being harvested for use in further experiments. Both 3D disk and 3D microfluidic device models were utilized to elucidate how Strain and HA altered ovarian cancer cell behaviors through CD44 signaling. . OVCAR-8 unmodified (Wild-type, WT), shSCR, and shCD44 cells were used in the disk studies. HA was introduced to the cells either as a matrix component (F+GEL HA) which mimics stromal HA or as a soluble component (F+SOL HA) which mimics serum HA. Fibrin only gels (F only) were used as controls. After Strain treatment, samples were cultured for 48h before being fixed and stained for proliferation marker Ki67 and DAPI. The second model was a microfluidic device that consisted of 3 chambers that were loaded independently to study ovarian cancer cell migration[8]. Cells were loaded into the middle chamber while blank F only gels were loaded into the left side chambers and F+GEL HA were loaded into the right-side chambers. Samples were fed everyday using the outward flow set-up, where media is only provided to the middle chamber and flows equally into the side chambers[8]. Devices were cultured for 7 days before being fixed and stained for DAPI to determine migration between chambers. All images were analyzed using the FIJI Analyze Particle plugin and positive count (Ki67) or positive area (migration) normalized to total cell count or area via DAPI staining was collected for analysis.

RESULTS

Our results show that a Strain pre-treatment followed by F+GEL HA treatment significantly increases the percent of proliferating

cells in the OVCAR-8 WT cells compared to strain F only samples (Figure 1a,b). However, the Strain pre-treatment plus SOL HA does not increase Ki67 staining compared to the F only samples (Figure 1a.b). OVCAR-8 shSCR samples demonstrate a significant increase in proliferation in the F+GEL HA environment with both No Strain and Strain pre-treatment compared to their respective F only samples (Figure 1a,b). The shCD44 cells show no significant changes in proliferation with Strain pre-treatment, F+SOL HA, or F+GEL HA (Figure 1b). After 7 days in the microfluidic devices, our data indicate that the OVCAR-8 WT cells preferentially migrate towards the side chambers containing F+GEL HA compared to the F only side (Figure 2b,c). Pre-treatment with Strain did not influence the ability of the cells to migrate.

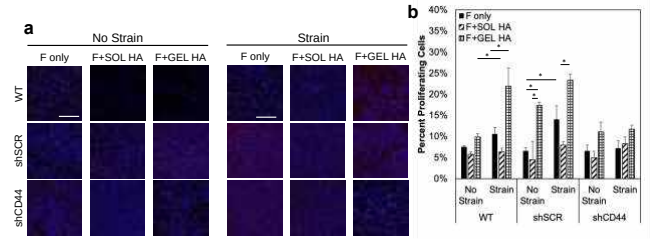

Figure 1: Ovarian Cancer Cell Proliferation is Increased with HA Treatment. (a) Representative images of OVCAR-8 WT, shSCR, and shCD44 cells treated with a 24h Strain pre-treatment before being grown in 3D disk models with F+SOL HA or F+GEL HA Scale bar = 500 µm. (b) Quantification of Ki67 cell count normalized to DAPI cell count in immunofluorescence samples. Data shown as average + SEM, n=3 samples, * p <0.05. Samples were compared using ANOVA followed by post-hoc Tukey HSD.

DISCUSSION

Our studies looked to quantify changes in ovarian cancer behaviors associated with disease progression. Specifically, we looked at proliferation as a stand-in for tumor growth and migration as a model of metastatic potential. HA and CD44 have been associated with both migratory and proliferative behaviors in a variety of cell types, though previous studies have not reported strain-sensitivity of the receptor. The OVCAR-8 WT cells exhibited higher levels of Ki67 positive staining after Strain pre-treatment with the F+GEL HA treatment, while the shSCR cells demonstrated increased proliferation with F+GEL HA treatment both with and without the Strain pre-treatment (Figure 1b). Even without HA, Strain treated OVCAR-8 WT and shSCR cells exhibited some increases in Ki67 staining, indicating that strain can induce proliferation; this was not observed in the shCD44 samples. These results highlight that HA presentations that mimic the stromal HA (F+GEL HA) can increase ovarian cancer cell proliferation while models mimicking serum HA (F+SOL HA) do not. Furthermore, the studies indicate that active tensile strains can enhance the effect of stromal HA on CD44 signaling to increase proliferation of ovarian tumor cells.

Our studies also utilized an advanced 3D TME model to investigate the interactions of strain and HA on ovarian cancer cell migratory behaviors as a readout of metastatic potential. The microfluidic device design was chosen due to the 3 chambers that could be loaded independently, allowing for cellular components to be loaded into the middle while acellular gels with F only or F+HA gels were loaded into the side chambers. The media flow pattern was chosen so that media was fed only into the middle chamber and allowed to diffuse into the side chambers; this resulted in a system where any secreted factors from cells loaded into the middle chamber were equally diffused into the side chambers. This feeding regime creates an equal magnitude of interstitial fluid flows towards the side chambers. Taken together, this means our studies controlled for both secreted factors and shear forces that could affect ovarian cancer cell migration and proliferation in the side chambers, solely focusing the studies on how Strain pre-treatment and HA in the TME drive cell migration. After 7 days, the OVCAR-8 WT cells preferentially migrated into the side chambers containing the F+HA gel regardless of Strain pre-treatment (Figure 2c).

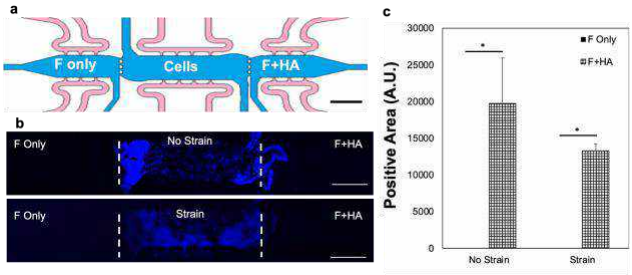

Figure 2: Stromal HA Promotes Migration in 3D Ovarian TME Models. (a) Microfluidic device design showing tissue chambers (blue) connected via communication ports (20µm) and independent fluidic lines (pink). Experimental set up with F-only in left chamber, Cells in F-only in the middle chamber, and F+HA matrix in the right chamber (b) Representative images for DAPI staining of OVCAR-8 WT cells in microfluidic devices. Samples either received Strain pre-treatment (24h) or No Strain prior to loading in F only gels in the middle chamber. Insets indicate side chamber matrix composition. White dashed lines indicate interfaces of adjacent chambers. Scale bars = 500µm. (c) Quantification of DAPI positive area in side chambers. Data presented as average + SEM, n=3 samples, * p < 0.05. Samples were compared using Kruskal-Wallis followed by post-hoc Dunn's tests.

In conclusion, ovarian cancer cells with high levels of CD44 have increased proliferation and migration with HA treatments that model stromal HA but not those that model serum HA. Cells with lower levels of CD44 do not show the same changes in cell behavior. These results suggest a unique interaction between mechanical stimulation and HA-binding that creates mechanosignaling through the CD44 receptor to drive ovarian cancer cell proliferation and migration. With CD44 expression noted in a variety of cancers, these results may translate to other cancers including breast, prostate, head and neck cancers, and glioblastomas. Future studies will focus on uncovering the specific mechanism of mechanosignaling in the CD44 pathway.

ACKNOWLEDGEMENTS

We wish to thank the following funding sources: R00-CA230202 (M.K.S.L.), IMPACT Award (O'Neal Comprehensive Cancer Center, M.K.S.L.), the Fine Family Philanthropic Grant (M.K.S.L), UAB Blazer Fellowship (M.K.) and T32-EB023872 (M.K.).

REFERENCES

[1] Penny, S et al., *Radiol Technol*, 91:561-75, 2020. [2] Kramer, M et al., *Frontiers in Materials*, 10, 2023. [3] Sewell-Loftin, M et al., *Sci Rep*, 7(1):12574, 2017. [4] Anttila, M et al., Cancer Res, 60(1):150-5, 2000. [5] Ricciardelli, C et al., *BMC Cancer*, 13:476, 2013. [6] Cortes-Dericks, L et al., *Respir Res*, 18(1):58, 2017. [7] Gao, Y et al., *Oncotarget*, 11:9313-26, 2015. [8] Sewell-Loftin, M et al., *Lab Chip*, 20(15):2776-87, 2020.

THE FATE OF ULTRASMALL FLUORESCENT SILICA NANOPARTICLES AS DRUG DELIVERY VEHICLES IN CARTILAGE EXPLANTS: DIFFERENTIAL RETENTION KINETICS BETWEEN MATRIX AND CHONDROCYTES

Aiyana G. Fortin (1), Antonio T. Garces (1), Ulrich B. Wiesner (2), Lawrence J. Bonassar (1,3)

(1) Biomedical Engineering, Cornell University, Ithaca, NY, US
(2) Materials Science and Engineering, Cornell University, Ithaca, NY, US
(3) Mechanical and Aerospace Engineering, Cornell University, Ithaca, NY, US

INTRODUCTION

The effectiveness of intra-articular (IA) drug delivery approaches for osteoarthritis (OA) is hindered by the dense, avascular extra-cellular matrix (ECM) of cartilage and the rapid synovial fluid clearance time on the order of hours[1]. Due to these diffusion and clearance constraints, there are no available IA-injectable therapeutics that prevent cartilage loss – the hallmark of this irreversible disease[1,2]. Injectable nano- and micro-particle systems have been engineered to deliver therapeutic payloads, yielding modest improvements in cartilage penetration and joint residence time compared to free therapeutics[3,4,5]. However, little is known regarding the fate of these vehicles within joint tissues.

Ultrasmall (d_h ~ 6 nm) fluorescent poly(ethylene glycol) coated core-shell silica nanoparticles (Cornell Prime Dots, or C' Dots) have been used in multiple investigational new drug (IND) FDA-approved diagnostic and therapeutic human clinical trials in oncology[6,7]. Locally or systemically injected C' Dots exhibit favorable biodistribution and pharmacokinetics (PK) in humans due to their small size which enables renal clearance[6]. Our work aims to translate this promising nanotechnology to applications in OA. We have shown previously that C' Dots penetrate the articular surface of healthy cartilage within 2 hours (D_{eff} = 2 μm²/s) to reach tissue-resident chondrocytes *in vitro*[8]. Separately, we characterized the clearance of IA-injected C' Dots in rat knees as a biexponential decay ($t_{1/2,\,1}$ ~ 0.5 days; $t_{1/2,\,2}$ ~ 2 weeks) and observed joint retention for 3+ months after a single injection[9].

Therapeutic nanoparticles are typically characterized for bulk cartilage penetration or biocompatibility and targeting in 2D chondrocyte cultures, but few studies have reported on the role of tissue-resident chondrocytes as part of a delivery strategy[3,4,5]. To our knowledge, there are no data describing the fate of nanoparticles in intra-tissue and intra-cellular compartments in 3D whole tissue. Understanding and leveraging these biological and transport phenomena may inform the design of future OA therapeutics.

The objective of this study was to utilize C' Dots as an ultrabright and photostable fluorescent tracker to probe their processing dynamics and retention kinetics in chondrocytes by assessing whole cartilage explants over 6 days *in vitro*. We hypothesized that internalized C' Dots (e.g. loading explants for 24 hours) would be released from chondrocytes and ECM by 5 days after removal of C' Dots from the media.

METHODS

C' Dot Synthesis: Cyanine 5 fluorophore-encapsulating C' Dots were synthesized following previously established methods[10,11]. *Cellular Internalization:* Cylindrical cartilage plugs (d = 6 mm, h = 2 mm, n = 3 per group) were cut from the patellofemoral groove of 1-3 day old bovine stifle joints and randomly assigned to C' Dot (EXP) or Control (CTRL) groups. C' dots in media (2 μM) passively diffused through the articular surface and radial edges of submerged cartilage plugs[12]. After 24 hours, EXP plugs were moved to fresh media and washed once per day until imaging. *Imaging:* Cartilage plugs were bisected with a lubricated blade for staining (30 minutes Calcein, AM & Sytox Blue nucleic acid stain, 30 minutes lysosome stain, or 24 hours endosome transfection). Tissue penetration and cellular internalization of C' Dots were assessed at the bisected plane using a Zeiss 710 inverted confocal microscope and the following excitation wavelengths: Sytox Blue (405 nm), Calcein, AM (461 nm), Endosome-GFP (488 nm), LysoView 540 (540 nm), tissue reflectance (561 nm), and Cyanine-5 (633 nm). *Image Analysis:* A custom MATLAB code created logical masks for each sample compartment. Sample viability was calculated from Calcein and Sytox Blue cell counts (samples with < 1000 total cells were excluded from further analysis). *Statistical Analysis:* Viabilities and Mean Pixel Intensities were compared using a linear mixed-effects model

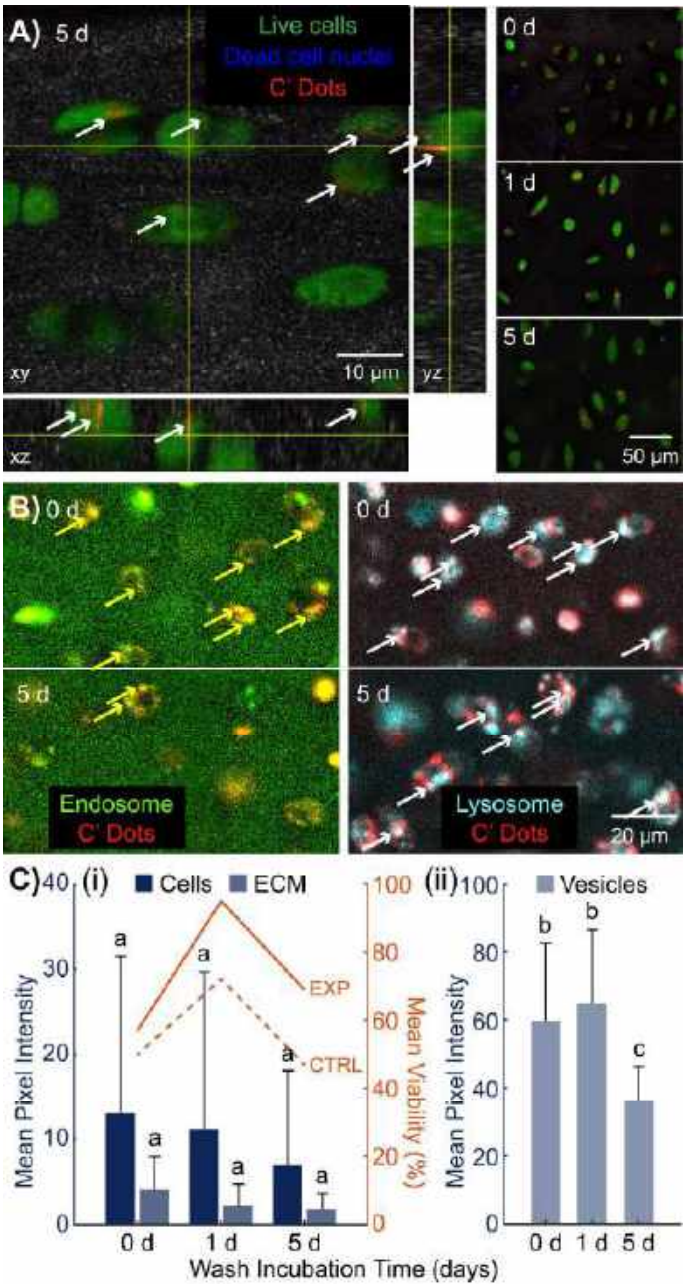

Figure 1. C' Dots are internalized by native chondrocytes in whole cartilage and retained intracellularly for 5 days after removal from the media. A) Merged confocal fluorescence micrographs showing internalized C' Dots (z-stack spans 10 µm; green – Calcein, AM, red – Cyanine 5). Orthogonal views highlight intracellular localization of C' Dots. Arrows indicate C' Dot fluorescence. **B)** Merged confocal micrographs showing internalized C' Dots at 0d (i.e. 24 hours loading) and 5d with co-staining of *(left)* endosomes and *(right)* lysosomes. Arrows indicate colocalized C' Dots & stain. Notably, C' Dots are present in endosomes, lysosomes, and unlabeled vesicular structures. **C) (i)** Quantified mean pixel intensity of C' Dot fluorescence within live cells and within ECM (left axis) and mean viabilities (right axis). **(ii)** Quantified mean pixel intensity of C' Dot fluorescence within vesicular structures (r = 1.5 µm) in live cells. Shared letters denote no significant difference between groups (α = 0.05).

with Kenward-Roger approximation (α = 0.05).

RESULTS

Fluorescent C' Dot puncta were observed within live cell cytoplasm after 24 hours of incubation and 5 subsequent days of washing (**Fig. 1A** *(left)*). C' Dot signal remained detectable intracellularly and in ECM from 0 to 5 days after C' Dots were removed from the media (**Fig. 1A** *(right)*). C' Dot signal was co-localized with endosomal and lysosomal fluorescent markers (arrows), but unlabeled C' Dot-containing vesicular structures were also present (diameter ~ 0.5 – 4 µm) (**Fig. 1B**).

Mean C' Dot signal in the Cell and ECM compartments trended towards decreasing with longer washing, with ~50% reductions observed from 0 d to 5 d (**Fig. 1C (i)**, p = 0.79, p = 0.97, respectively). C' Dot signal is highly heterogeneous within cells; this organization into subcellular vesicular structures contributes to the observed variation in Cell pixel intensity. Vesicle C' Dot signal decreased from 1d to 5d (p = 0.036) and is distinct from total Cell and ECM compartments at 5 d (**Fig. 1C (ii)**, p = 0.037, p = 0.014, respectively). Viabilities were not different between groups (**Fig. 1C (i)**, p > 0.05).

DISCUSSION

C' Dots were internalized within 24 hours by chondrocytes in 3D cartilage explants and remained detectable in Cell, ECM, and Vesicle compartments over 5 days of washing. While we expect that C' Dots will be released from chondrocytes at later timepoints, these processing dynamics and unexpected retention kinetics observed on this timescale offers insight into chondrocyte dynamics for possible applications in drug delivery.

In other studies, chondrocytes in 2D cultures robustly endocytose fluorescent particles as the primary (but not exclusive) uptake mechanism[4,5]. Particles are internalized within 3-6 hours and retained for up to 48 hours[4,5]. To our knowledge, this study is the first to examine compartmental retention of nanoparticles for longer than 48 hours, and the first to use whole tissue explants to investigate chondrocyte processing dynamics.

The role of chondrocytes in processing injected particles may offer a previously unexplored mechanism for increasing joint retention of OA therapeutics. The exceptionally long joint residence of untargeted, unfunctionalized C' Dots observed in our previous *in vivo* study may be due in part to particle interactions with tissue-resident cells[4,5,9]. Further investigation of not only bulk tissue transport kinetics, but complex cell-mediated sink/source modeling on the timescale of days to weeks is necessary to bridge the gap in timescale between *in vitro* studies (e.g. hours-days) and preclinical models (e.g. months-years).

This study highlights the active role of chondrocytes in mediating nanoparticle presence in whole cartilage tissue and yields important insights into chondrocyte-mediated mechanisms to extend particle joint residence and deliver therapeutics with subcellular precision.

ACKNOWLEDGMENTS

This work was funded by the Cornell IGNITE program and the NSF GRFP and made use of the Cornell Biotechnology Resource Center which is supported through the NYSTEM CO29155 and NIH S10OD018516.

REFERENCES

[1]DiDomenico+ *Nat Rev Rheum* 2018; [2]Doan+ *Acta* 2019; [3]He+ *J Contr Rel* 2020; [4]Pontes+ *Front Bioeng Biotech* 2023; [5]Aldrich+ *ORS* 2023; [6]Phillips+ *Sci Transl Med* 2014; [7]Zanoni *JAMA* 2021; [8]Fortin+ *ORS* 2023; [9]Fortin+ *BMES* 2023; [10]Ma+ *Chem Mat* 2015; [11]Ma+ *Chem Mat* 2017; [12]DiDomenico+ *J Biomech* 2017.

LUNG LOBAR SLIDING REDUCES PARENCHYMAL DISTORTION IN THE LEFT AND RIGHT LUNGS

Adam E. Galloy (1), Joseph M. Reinhardt (1), Suresh M. L. Raghavan (1)

(1) Roy J. Carver Department of Biomedical Engineering, University of Iowa, Iowa City, Iowa, United States of America

INTRODUCTION

Lung lobar sliding is an often-overlooked aspect of lung mechanics. Human lungs are typically divided into five lobes (two on the left and three on the right) separated by lobar fissures that allow sliding between lobes. However, some people have incomplete, missing, or auxiliary lobar fissures which may affect lung mechanics through the intermediate mechanism of lobar sliding. During their study of the deformation of dog lungs, Hubmayr et al. [1] hypothesized that lung lobar sliding "provides the means to reduce parenchymal distortion". This hypothesis is difficult to test with controlled in vivo experiments since a method would need to be developed that can prevent sliding between complete lobes without otherwise impacting the deformation of the lung tissue.

The goal of this study was to test the hypothesis that lung lobar sliding reduces parenchymal distortion by performing paired comparisons between subject-specific contact mechanics models of the lung that do and do not allow lobar sliding.

METHODS

Six healthy subjects (ages 22-37) underwent CT scans following a procedure approved by our institutional review board. Scans were obtained with the subjects in the supine position during breath holds at total lung capacity (TLC) and functional residual capacity (FRC). The lobes of the lungs and the left and right thoracic cavities (defined here as the outline of the full lung) were segmented from the images. From the segmentations at TLC, solid meshes representing the lung lobes were generated along with a surface mesh of the thoracic cavity. Left and right lungs were meshed and analyzed separately.

Subject-specific contact mechanics models of lobar sliding were implemented in FEBio using the procedure described in Galloy et al. [2]. Briefly, the lung parenchyma was modeled as a homogenous, hyperelastic solid using the neo-Hookean constitutive law ($\lambda = 1.73$ kPa, $\mu = 1.15$ kPa). Nonzero displacements were prescribed to the thoracic cavity surface to drive deformation of the lobar tissue with frictionless sliding contact constraints between the lung lobes and thoracic cavity. Thoracic cavity displacements were derived by non-rigid registration of the thoracic cavity mask at FRC to the mask at TLC. For the lobe-lobe contact interfaces two different models were made for each subject: a sliding model where frictionless sliding was allowed between lobes, and a non-sliding model where a high Coulomb friction coefficient ($f = 1.5$) effectively eliminated sliding. Boundary conditions for both models are schematically illustrated in Figure 1. Simulations were quasi-static and assumed no viscoelasticity in the lung tissue.

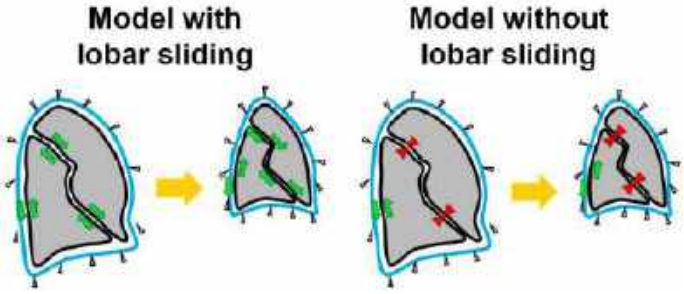

Figure 1: Subject-specific thoracic cavity surface displacements were applied to drive deformation of the lobe volumes through sliding contact constraints. To delineate the effect of lobar sliding a model was made with frictionless sliding between lobes (left) and another with a large friction coefficient to prevent sliding (right).

Parenchymal distortion was quantified by computing the anisotropic deformation index (ADI) in each element of the model [3]:

$$\mathrm{ADI} = \sqrt{\left(\frac{\lambda_1 - \lambda_2}{\lambda_2}\right)^2 + \left(\frac{\lambda_2 - \lambda_3}{\lambda_3}\right)^2} \quad (1)$$

Where λ_i are the principal stretches sorted from greatest to least. The ADI quantifies the anisotropy of deformation independent of volume change making it an appropriate metric for quantifying lung parenchymal distortion. The spatial mean ADI was computed for both the sliding and non-sliding model of each subject for paired intra-subject comparison. Wilcoxon signed rank tests were performed to determine statistical significance ($p < 0.05$).

RESULTS

Mean ADI and its difference between the sliding and non-sliding models for each subject is displayed in Figure 2 to demonstrate the effect of lobar sliding on parenchymal distortion. Results for the left lung are adapted from [4], with the right lung results novel to this work. Examining the lungs in their entirety, the mean ADI was lesser in the sliding models than the non-sliding models with median percent differences across the subjects ($n = 6$) of 3.2% ($p = 0.03$) and 19.6% ($p = 0.03$) for the left and right lung respectively indicating a reduction in distortion with lobar sliding. Notably, lobar sliding had a more pronounced effect on the right lung than the left lung. Examining individual lobes, the reduction in distortion primarily occurred in the left lower, right lower, and right middle lobes with median percent differences of 8.0% ($p = 0.03$), 19.6% ($p = 0.03$), and 40.7% ($p = 0.03$) respectively. On the other hand, in the upper lobes of the lungs the difference in mean ADI between sliding and non-sliding models was insignificant with the median percent difference having the reverse trend of 1.9% ($p = 0.06$) and 1.1% ($p = 0.84$) greater mean ADI in the sliding model for the left and right upper lobes respectively.

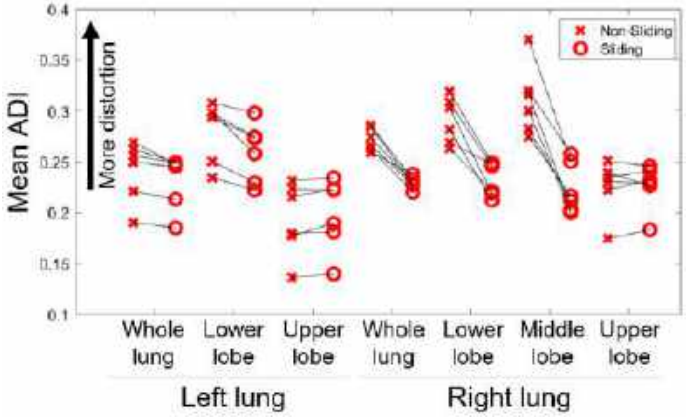

Figure 2: Consistent with the hypothesis that lung lobar sliding reduces parenchymal distortion, the spatial mean ADI for both lungs was lower in simulations that allowed lobar sliding than paired simulations that did not. The difference primarily occurred in the lower and middle lobes with no significant difference in the upper lobe of both lungs.

Contour plots of ADI in a representative subject's right lung (Figure 3a & b) further illustrate the regional differences in lobar sliding's effect on distortion. In the non-sliding model, parenchymal distortion is most densely concentrated towards the base of the lung near the lobar fissure between the left and middle lobes, but this distortion is significantly relieved in the sliding model. The denser concentration of distortion at the base of the lung could explain the greater reduction in distortion with lobar sliding in the lower and middle lobes than the upper lobes. Furthermore, plots of ADI vs. distance from the fissures (Figure 3c) for each right lung lobe in both models demonstrate that the distortion-reducing effect of lobar sliding is most pronounced near the fissure of the lower and middle lobe. The upper lobe is not as affected by lobar sliding regardless of distance from the fissure.

DISCUSSION

The lesser amount of mean ADI in sliding models when compared to non-sliding models is consistent with the hypothesis of Hubmayr et al. [1] that lung lobar sliding reduces parenchymal distortion. This result suggests subjects with incomplete or missing fissures may require more mechanical work to breathe. The need to reduce parenchymal distortion (or the lack of such need) may help explain differences in lobar anatomy between animal species. For example, Hoffman and Ritman noted pronounced lobar fissures in the relatively shape-dynamic lungs of dogs, but fibrosed fissures in the more inert lungs of sloths [5].

The effect of lobar sliding on parenchymal distortion varied with location. The right lung had a significantly larger reduction in distortion with lobar sliding than the left lung did. This is likely because the right lung's three lobes provide more degrees of freedom to reduce the impact of thoracic cavity shape changes on parenchymal distortion. Lobar sliding also had a greater effect on the lower and middle lobes than it did the upper lobes. This seems to be because of the larger amounts of distortion near the base lung where diaphragm motion causes some of the largest shape changes of the thoracic cavity.

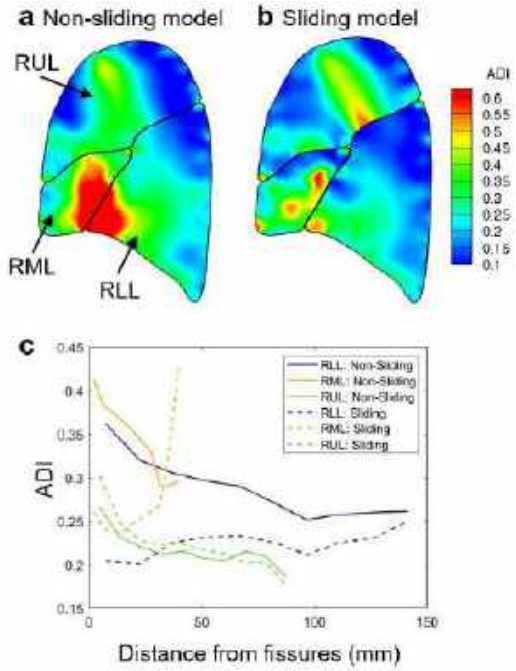

Figure 3: ADI contour plots for both right lung models of a representative subject (a & b) suggest lobar sliding affects the lower and middle lobes more than the upper lobe because of the higher concentration of distortion near the base of the lung. Lobar sliding's effect is greatest near the lobar fissures for the lower and middle lobes, but the upper lobe was largely unaffected by lobar sliding regardless of location as seen in plots of ADI vs. distance from lobar fissures (c).

ACKNOWLEDGEMENTS

This research was supported by training grant T32 HL144461 and research grant R01 HL142625 from the National Institutes of Health.

REFERENCES

[1] Hubmayr et al., *J. Appl. Physiol.*, 63:2467-2475, 1987.
[2] Galloy et al., *Appl. Eng. Sci.*, 10:100098, 2022.
[3] Amelon et al., *J. Biomech.* 44:2489-2495, 2011.
[4] Galloy et al., *J. Appl. Physiol*., 135:534-541, 2023.
[5] Hoffman, E and Ritman E, *J. Appl. Physiol.*, 59:481-491, 1985.

THE INFLUENCE OF PECTINATE LIGAMENTS ON THE PATENCY OF THE MURINE AQUEOUS HUMOR OUTFLOW PATHWAY: A FINITE ELEMENT STUDY

Babak N. Safa[1], Nina Sara Fraticelli Guzmán[2,3], Guorong Li[4]
W. Daniel Stamer[4], Andrew J. Feola[1,3,5], C. Ross Ethier[1,2,3]

(1) Dept. of Biomedical Engineering, Georgia Institute of Technology/Emory University, Atlanta, GA, USA
(2) School of Mechanical Engineering, Georgia Institute of Technology, Atlanta, GA, USA
(3) Dept. of Ophthalmology, Emory University, Atlanta, GA, USA
(4) Dept. of Ophthalmology, Duke University, Durham, NC, USA
(5) Atlanta VA Center for Visual and Neurocognitive Rehabilitation, Decatur, GA, USA

INTRODUCTION

Glaucoma is the leading cause of irreversible blindness worldwide and is commonly associated with elevated intraocular pressure (IOP). The trabecular meshwork (TM) and Schlemm's canal (SC) – together forming the aqueous outflow pathway – are the primary tissues controlling aqueous humor outflow and IOP. Mice are often used to study these tissues' role in glaucoma; however, mouse eyes have anatomical differences vs. humans that need to be considered. Notably, the murine eye's aqueous humor outflow pathway contains prominent pectinate ligaments (PLs) that connect the iris to the TM (Fig 1). The PLs can exert mechanical traction on the TM, deforming TM and SC, thus affecting aqueous humor outflow [1], which may confound the translation of results obtained in mice to humans. In addition, PLs have developed differentially across species, indicating a potential evolutionary significance [2]. However, much is unknown about the PLs' biomechanics and function, thus motivating this study.

We hypothesized that PL biomechanics directly influences the patency of the murine outflow pathway, including the lumen of SC. We therefore investigated the role of PLs in a common model used in glaucoma research, namely C57BL/6 mice. Specifically, we used image-based finite element (FE) modeling of the murine outflow pathway, based on histomorphometric and optical coherence tomography (OCT) images. We also conducted parametric numerical simulations to elucidate how outflow pathway patency changed with IOP.

METHODS

We summarize experimental procedures described in detail elsewhere [3], [4]. In brief, we conducted OCT imaging of the mouse anterior eye during ocular perfusion tests to capture IOP-induced iris and outflow pathway tissue deformations. Further, we histomorphometrically determined the dimensions of TM region tissues, which are not generally visible in OCT. By combining OCT images and histomorphometric measurements, we then created age-specific finite element (FE) models and evaluated the effects of changing IOP and tissue stiffness on outflow pathway patency, especially SC canal lumen area (SCLA).

Animals: We used wild-type C57BL/6 mice from three age groups: 'young' (2-6 mo), 'middle-aged' (11-16 mo), and 'elderly' (25-32 mo). All procedures received IACUC approval at Duke University.

OCT imaging: Anesthetized mice underwent ocular perfusion at IOP levels of 10, 15, and 20 mmHg [4]. Two types of OCT images were acquired from different mice during perfusions: High resolution (TM-OCT) and low resolution (Iris-OCT), enabling evaluation of SC and iris deformations, respectively.

Histomorphometric analysis: Since the detailed structure of the TM region was not visible by OCT, we augmented OCT images with 0.5 µm

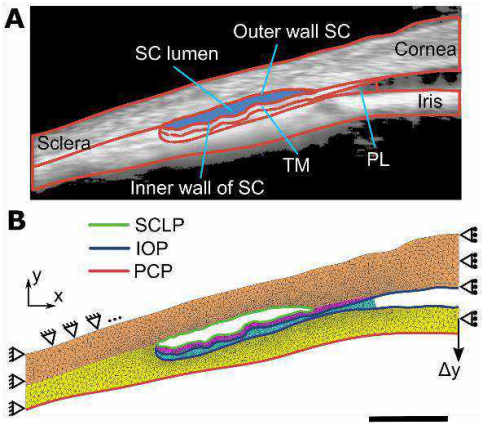

Fig. 1: (A) TM-OCT image used for creating the young model. The boundaries of different regions are shown in red and annotated (SC= Schlemm's canal, TM = trabecular meshwork, and PL = pectinate ligament). (B) The corresponding FE mesh and its associated boundary conditions. SCLP = SC lumenal pressure, IOP= intraocular pressure, PCP = posterior chamber pressure. Scale bar = 100 µm

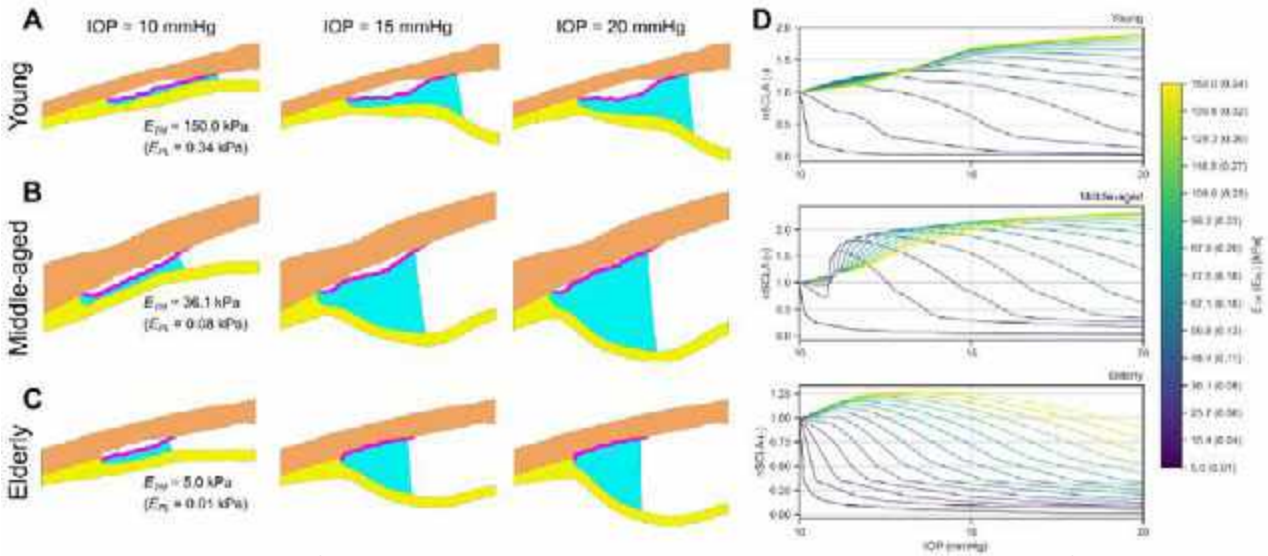

Fig. 2: Representative simulation results from (A) young. (B) middle-aged and (C) elderly models, and (D) detailed graphs of nSCLA dependence to IOP at different TM/PL stiffness (colored lines). Our results indicated that SC collapse was not guaranteed at elevated IOP, where, for instance, in the young models (A and D), the higher TM/PL stiffness case showed expansion of SCLA with elevation of IOP.

thick sagittal histologic sections from age-matched eyes, stained with methylene blue. Key features of the TM region were manually annotated (e.g., TM cross-sectional area and length). These values were used in the creation of age-specific FE meshes.

FE modeling: We used the TM-OCT images to delineate the boundaries of the cornea, sclera, iris, and SC (Fig. 1A). TM and PL regions were added based on the histomorphometric analysis. We then extruded the 2D boundaries by 10 μm to create a plane-strain model, justified based on the small size of the TM region relative to the distance from the eye's axis of symmetry. As a simplifying assumption, the PLs were modeled as a homogenized region. We used TET10 elements for meshing.

The boundary conditions were based on the pressures during the perfusion test ([4]; Fig. 1B), and the deformations of the iris were specified based on the data from the Iris-OCT images (Fig. 1B).

An incompressible, neo-Hookean model was used for all the tissues, except PLs, which were modeled as compressible (Poisson ratio = 0) to account for their fibrous structure. Young's modulus (E) was set to 2700 kPa for cornea/sclera [5] and 96.1 kPa for iris [6]. We varied E_{TM} over a physiological range (5-150 kPa). Finally, we estimated the PL region's effective stiffness as E_{TM} multiplied by a fixed percentage (0.23%), based on the solid fraction of the PL beams.

Data analysis: For each age model, we simulated 15 cases with different TM/PL stiffness using FEBio [7]. We calculated the normalized SC lumen area (nSCLA) as:

$$nSCLA = \frac{SCLA}{SCLA_{@10\ \mathrm{mmHg}}} \quad (1)$$

To quantify SC patency, we defined SC collapse as the nSCLA value becoming less than 33%.

RESULTS

In all age models, we observed SC lumen collapse at elevated IOP (Fig. 2), consistent with experimental observations [4]. Further, SCLA was strongly dependent on TM/PL stiffness, and showed a non-linear dependence on IOP (Fig. 2C). However, SC collapse did not happen in all cases; for example, it only occurred at low TM/PL stiffnesses (lower than E_{TM}/E_{PL}=25.7/0.06 kPa in the young and middle-aged models, and 87.9/0.20 kPa in the elderly model). In all age models, when TM/PL-stiffness was large and IOP was elevated, we were surprised to observe a non-physiological opening of the SC lumen (Fig. 2A). Overall, the elderly model showed a higher susceptibility to IOP-induced SC collapse compared to the younger models.

DISCUSSION

This study provides an analysis of the PLs' role in influencing patency of the outflow pathway, in particular the IOP-induced changes in SC lumen area (SCLA). Our results indicated that the SCLA is sensitive to PLs' biomechanical properties. We also observed that the PLs can exert mechanical traction opposite to that of the physiological trans-TM pressure, thereby inhibiting SC collapse. We also showed age-specific differences in the role of PL in IOP-induced SCLA changes, with younger eyes being less susceptible to SC collapse than older ones.

Our study had some limitations. For instance, since no experimental PL biomechanical properties have been reported, we estimated the PL stiffness from that of TM, an adjacent tissue of similar developmental origin. Further, we modeled the PLs as a homogenized material; in reality, PLs are a complex fibrous structure. Future studies should focus on the characterization of the PL structure and biomechanics to better elucidate the potentially crucial role of PLs in outflow pathway patency and ultimately IOP dynamics in animal models of glaucoma.

ACKNOWLEDGEMENTS

The BrightFocus Foundation (G2021005F, BNS), NIH (K99EY035360 [BNS], T32EY007092 [NSFG], R01EY030871 [AJF], P30EY006360, P30EY005722, R01EY031710 [CRE and WDS], and R01EY030124 [WDS]), the Alfred P. Sloan Foundation G-2019-11435 (NSFG), the Georgia Research Alliance (CRE), and VA (AJF; CDA-2; RX002342).

REFERENCES

[1] Johnson and Kamm, *IOVS*, 24: 320–325, 1983.
[2] Simones *et al.*, *J Vet Med Sci*, 58: 977–982, 1996.
[3] Safa & Fraticelli Guzmán *et al.*, *bioRxiv*, 2023.10.17.562754, 2023.
[4] Li *et al.*, *bioRxiv*, 2023.10.17.562768, 2023.
[5] Li *et al.*, *PNAS*, 116: 1714–1722, 2019.
[6] Lee *et al.*, *Exp Eye Res*, 202: 108374, 2021.
[7] Maas *et al.*, *J Biomech Eng*, 134: 011005–011005, 2012.

THE BIOMECHANICS OF RADIATION-INDUCED CARDIOTOXICITY IN MICE

Tanmay Mukherjee (1), Sarah Elliott (2), Prasanna Alluri (2), Reza Avazmohammadi (1)

(1) Department of Biomedical Engineering, Texas A&M University, College Station, TX, USA
(2) Department of Radiation Oncology, University of Texas Southwestern Medical Center, Dallas, TX, USA

INTRODUCTION

Cancer remains a leading source of mortality, with an estimated incidence of 17.5 million cases worldwide. The suggested treatment protocol for many thoracic and breast cancer patients involves radiation therapy (RT), which accounts for significant reduction in malignancy [1]. The risks associated with RT limit its benefits as a long-term therapeutic measure, and are a major health concern. The increasing prevalence of thoracic RT has been associated with the development of radiation-induced cardiotoxicity (RIC). RIC-related myocardial injuries have been identified as precursors to cardiac dysfunction in the form of fibrosis and metabolic impairments that could restrict myocardial contractility. However, despite the benefits of standard functional indices such as the ejection fraction (EF) in diagnosing advanced cases, they fall short in detecting the early-stage development of RIC [2,3]. In contrast to the poor efficacy of functional indices, which are insensitive to subclinical dysfunction, structural indices such as cardiac strains are strong determinants of early-stage cardiac diseases. However, current strain metrics are limited to the anatomical axes, i.e., radial-circumferential-longitudinal (RCL) axes, which may confound the representation of RIC-related myofiber impairment. We propose the investigation of three-dimensional principal strains as an approximation of myofiber contraction to improve the assessment of early-stage RIC.

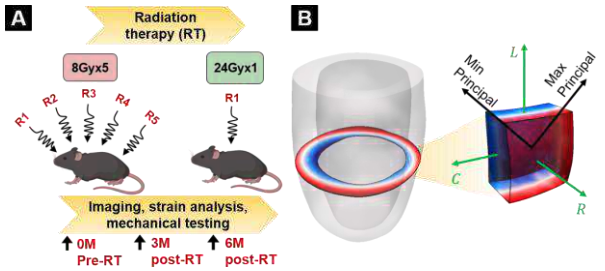

Figure 1: Schematic representation of (A) the longitudinal study to investigate the incidence of radiation-induced cardiotoxicity and (B) strain analysis in the left ventricle (LV)

METHODS

We implemented a longitudinal study in two cohorts of C57BL mice subjected to RT and a pre-RT control group (Control; n = 5; Fig. 1). The first RT group was subjected to five doses of 8 Gy radiation (8Gyx5; n= 5) and the second group was administered a single dose of 24 Gy radiation (24Gyx1; n = 5) via whole heart irradiation using a small animal irradiator (X-RAD 225Cx- Precision X-ray Inc). *In-vivo investigation:* Cardiac magnetic resonance imaging was performed for all mice pre-RT (0M), and three- (3M) and size-months (6M) post-RT. Short-axis (SA) images of the left ventricle (LV) were acquired using a 7T Bruker Avance III HD scanner with a 72 mm quadrature proton volume coil. All mice were anesthetized prior to the procedure, with anesthesia administered via 1-5% isoflurane. An in-house non-rigid image registration framework was used to estimate cardiac motion in terms of cartesian displacements. The resulting displacement vectors and cartesian strain tensor ($\boldsymbol{E}$) were subsequently used to derive strains at end-systole in the RCL axes.

$$\boldsymbol{E}_{RCL} = \boldsymbol{Q}\boldsymbol{E}\boldsymbol{Q}^T = \begin{bmatrix} E_{RR} & E_{RC} & E_{RL} \\ E_{CR} & E_{CC} & E_{CL} \\ E_{LR} & E_{LC} & E_{LL} \end{bmatrix}; \; \boldsymbol{Q} = \begin{bmatrix} cos\theta & -sin\theta & 0 \\ sin\theta & cos\theta & 0 \\ 0 & 0 & 1 \end{bmatrix}.$$

In contrast to the anatomical strains (E_{RR}, E_{CC}, E_{LL}) that ignore all three components of shear and offer confounded measures in describing myofiber contraction, principal strains incorporating both normal and shear strains represent the maximum deformation. The maximum (E_1) and minimum principal (E_3) strains were calculated using an eigenvalue decomposition of $\boldsymbol{E}$. A single global organ-level value averaging the regional distribution of normal or principal strains was calculated to obtain the global circumferential strain (GCS) and the global E_3 strain. *Ex-vivo investigation*: In addition to in-vivo strain analysis, we also

employed ex-vivo mechanical testing to determine the effects of RIC on the biomechanics of the LV myocardium. Hearts were harvested pre-RT and 3M post-RT for five control and 8Gyx5 mice, and the left ventricular free wall (LVFW) was excised. Fresh LVFW specimens were equibiaxially stretched at a rate of 1% per second to a maximum stretch of 30%.

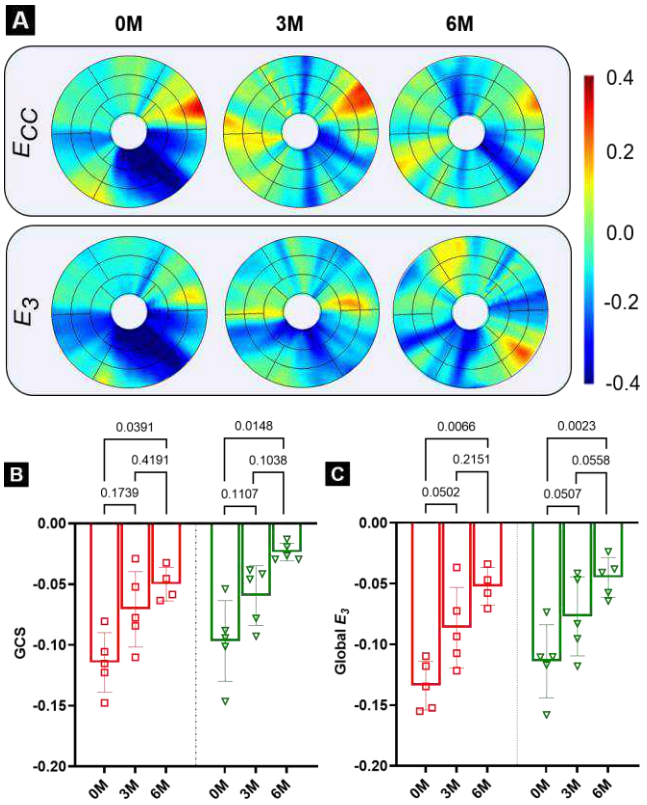

Figure 2: Representative heat maps of end-systolic strain calculations in AHA segmentation plots along the (top) circumferential (E_{CC}) and (bottom) minimum (E_3) principal axes for 8Gyx5 mice. (B) Estimation of the global circumferential (GCS) and minimum principal strains (global E_3) for □ 8Gyx5, and ▽ 24Gyx1 groups at pre-RT (0M, Control), three- (3M) and six-months (6M) post-RT.

RESULTS

Strain analysis showed stark variations in the contractile function of the LV between pre- and post-RT (Fig. 2A). Similar trends in the time-course changes in contractility were noted between GCS and the global E_3 metric (Figs. 2B, C). A near 50% drop in the GCS was observed between 0M and 6M post-RT (-0.09685 ± 0.0332 vs. -0.0594 ± 0.0245). Principal strain markers presented improvements in confidence intervals for both radiation groups, with marked reductions in contractility along the minimum principal axis from 0M to 6M post-RT for all mice in both groups (8Gyx5: -0.1178 ± 0.0252 vs. -0.0506 ± 0.0130; 24Gyx1: -0.1079 ± 0.0337 vs. -0.0450 ± 0.0162 (Fig. 2B). Moreover, the principal strain marker offered improvements in the statistical confidence in the early stages of RIC, with marked reductions between 0M and 3M post-RT. In contrast, measurements of EF at all timepoints presented minimal changes, indicating preserved cardiac function in both groups (Fig. 3A). In addition to the statistical confidence in varying contractile behavior between the control and 8Gyx5 mice evidenced via the in-vivo strains, an increase in the ensemble LVFW stress, measured as the sum of circumferential and longitudinal stresses, was noted at 3M post-RT suggesting RIC-related myocardial stiffening (Fig. 3B).

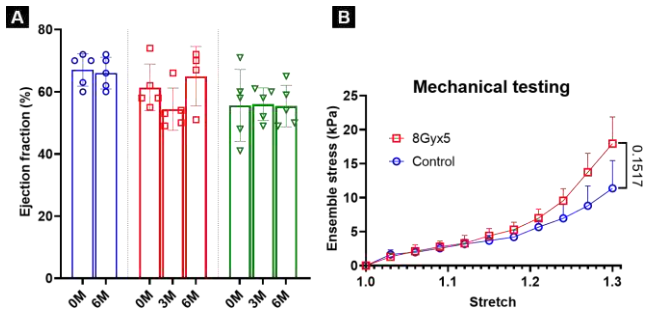

Figure 3: (A) Left ventricular ejection fraction for o Control, □ 8Gyx5, and ▽ 24Gyx1 groups at all timepoints. (D) Ensemble LVFW stress for Control and 8Gyx5 mice at 3M post-RT.

DISCUSSION

Despite the merits of traditional measurements of the EF in advanced-stage RIC, they have shown little promise as an early-stage biomarker. The strain indices proposed in this study aim to provide a more sensitive link between subclinical LV dysfunction and myofiber impairments, thus improving the detection of early-stage RIC. Our findings revealed a rapid decline in LV contractility not evidenced via the EF measurements, suggesting the presence of subclinical LV dysfunction. This is supported by the progressive reduction in both anatomical and principal strain values, with the global E_3 metric offering better delineation of the potential time-course impairments in the LV. Despite comparable magnitudes, E_3 provided a more precise estimation of RIC than GCS while providing greater statistical confidence between all the timepoints. A possible explanation could be the torsional mechanics exhibited by the LV during contraction, and underlying transverse CL shear. Since LV torsion is widely attributed to the helical arrangement of myofibers leading to a counter-rotational twist, principal strain analyses that account for both normal and shear strains may show greater association with the resulting myofiber shortening. Moreover, ex-vivo mechanical testing highlighted potential stiffening of the myocardial tissue, with further investigations required to quantify the associated fiber-level adaptations. A histological examination quantifying the helicity of myofibers will provide further insight into the sensitivity of principal strains to myofiber impairments. Specifically, fiber-level contributors to organ function have been experimentally validated for small animal models [4], and we expect our proposed strain markers to be strong determinants of organ- and fiber-level dysfunction. Additionally, both strain markers provided high levels of statistical significance ($p < 0.05$) 6M post-RT, thus highlighting the utility of structural indices in detecting RIC. Moreover, the alignment of the principal strains with the LV microstructure carries the potential to improve the early-stage diagnostic efficacy of strain analysis. Our findings through a comprehensive strain analysis and mechanical testing offered insight into the debilitating effects of RT on cardiac function. The quantification of contractility and its association with fiber-level dysfunction holds great promise in the characterization of remodeling before the manifestation of LV global decompensation.

ACKNOWLEDGEMENTS

This work was supported by the NIH (R00HL138288 to R.A).

REFERENCES

[1] Begg, A. C. et al. Nat Rev Cancer, 2011. 11(4)
[2] Walker, V. et al. Radiation Oncology, 2019. 14(1).
[3] Russo, C. et al. European J. of Heart Failure, 2014. 16(12)
[4] Neelakantan, et al. Acta Biomaterialia, 2023. 162

PROBABLE RELATION BETWEEN STRUCTURE & COMPOSITION OF THE DENTIN-ENAMEL JUNCTION (DEJ) & DENTINOGENESIS IMPERFECTA (DGI)

Sobhan Katebifar (1), Kai Clark (1), Bradley S. Rosenberg (2), Michael Truhlar (2), Alix C. Deymier (1)

(1) Biomedical Engineering, UConn Health, Farmington, CT, USA
(2) School of Dental Medicine, UConn Health, Farmington, CT, USA

INTRODUCTION

Dentinogenesis Imperfecta (DGI) is an inherited disorder affecting dentin and enamel [1]. DGI type I, associated with COL1A1 or COL1A2 mutations, leads to collagen type I disruption. Individuals with DGI type I exhibit translucent or discolored teeth, rapid enamel loss, and increased tooth wear due to softer dentin [2]. All types of DGI cause tooth discoloration, dentin weaknesses, and enamel defects [3]. Understanding of the structural and mechanical causes of tooth attrition in DGI, particularly at the Dentin-Enamel Junction (DEJ), is limited. The DEJ, the interface which connects dissimilar dentin and enamel tissues, has a graded structural design that minimizes stress concentrations in healthy teeth, making it fracture-resistant [4]. Enamel loss in DGI is suggested to originate from or near the compromised DEJ [5]. This study aims to elucidate the murine DEJ's structure and composition in relation to DGI type I, utilizing Micro-Computed Tomography, high-resolution Raman Spectroscopy mapping and Scanning Electron Microscopy for analysis.

METHODS

Tooth acquisition & Sample Preparation: The Col1a2oim mouse (OIM) was used as a model for Dentinogenesis Imperfecta (DGI). The mice were bred from heterozygous pairs. Genotyping was done through ear notching and DNA extraction, followed by polymerase chain reaction (PCR) and Sanger sequencing. Age-matched Wild type (WT) littermates served as controls. At 12 weeks of age, 20 OIM and 20 WT mice were sacrificed for analysis of their upper and lower incisors through various assessments (Fig. 1). The lower right incisors (n=5 per group) underwent micro-CT scanning without additional preparation. Meanwhile, the left lower incisors (n=5 per group) were embedded, polished for Raman spectroscopy, and coated with Au/Pd for SEM imaging to minimize charging. A subset of embedded samples (n=3 per group) also underwent acid etching before SEM imaging.

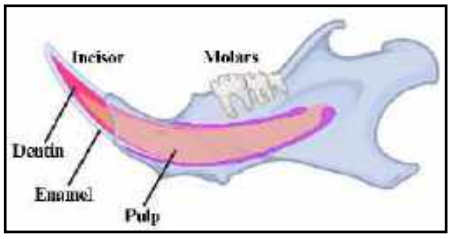

Fig. 1: Schematic of a mouse incisor

Micro-Computed Tomography: The thawed tooth samples were examined with Scanco 50 microcomputed tomography with a resolution of 3.4 µm. Attentuation coefficients across the DEJ of all teeth were determined using CTAn software. Gradients in the attenuation coefficient, which is correlated to tissue density, were fit with a logistic function. The full width half max (FWHM) of the derivative of the logistic function was used to determine the gradient width.

Raman spectroscopy: Raman spectra were acquired over a 15x15 µm area across the DEJ with a 0.5 µm resolution using a Witec Alpha 300 Raman Spectrometer. The 960 cm^{-1} PO_4^{3-} peak FWHM and intensity were determined using Lorentzian fitting and plotted as a function of position. Gradients in peak FWHM, which inversely correlates to crystallinity, and peak intensity, which correlates to mineral content, were fit with logistic functions. Gradients widths and locations were determined from the FWHM and peak center of the logistic function derivative.

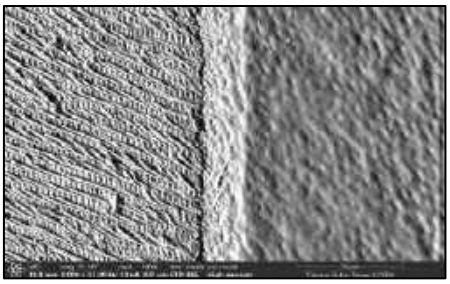
Fig. 2: SEM image from a DGI sample

Scanning electron microscopy (SEM) imaging: After gold sputtering, SEM imaging was conducted on acid-etched (n=3) and unethced samples (n=3) using the

TENEO LVSEM device (Fig. 2). Operating at 15-30 kV, 3.2-13 nA, and high vacuum mode, images were scanned by ETD detector with magnification between ×500 and ×10000. Using ImageJ software, DEJ widths were measured for normal samples, while acid-etched samples were used for mantle dentin width. SEM images were filtered and thresholded for tubule analysis (0.5 to 15 microns) using the ImageJ "Analyze Particle" tool, and porosity was calculated based on tubule count and diameter.

Statistics

For all quantitative data values were compared using 2-way ANOVA followed by Tukey's multiple comparisons test to determine significance using GraphPad Prism software with the factors of condition (DGI and WT) and Sex (male or female). Results are expressed as means ± standard deviation (SD). A value of $p < 0.05$ was considered significant.

RESULTS

Width of the density and compositional gradient across the DEJ: The average density gradient between enamel and dentin was similar for DGI (16.45±3.6 µm) and WT (15.48±2.7 µm) samples, with slight variations between groups. Although DGI females had the widest gradient (17.24±3.4 µm) and WT females the smallest (13.98±2.6 µm), there was no statistical difference overall.

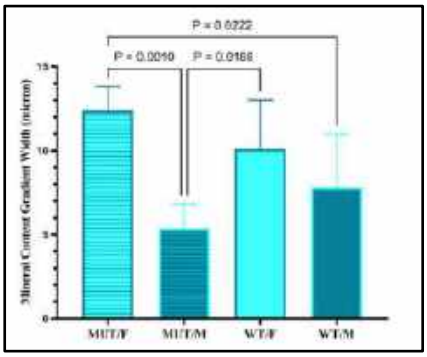

Fig. 3: Mineral content gradient measured by Raman

Raman spectroscopy revealed a larger mineral content gradient in females (11.2±2.5 µm) compared to males (6.6±2.6 µm), irrespective of DGI status. DGI females also exhibited a significantly wider mineral content gradient compared to both DGI and WT males (Fig. 3). The mineral crystallinity gradient (inverse FWHM of PO_4^{3-} ν_1 peak) averaged 9.3±2.7 µm, with no significant differences based on sex or DGI status. The shift in gradient centers between mineral content and mineral crystallinity was similar in DGI and WT mice. However, the mineral content gradient center was significantly shifted towards dentin in females compared to males. The location and width of the PO_4^{3-} ν_1 peak, indicating mineral maturity and crystallinity, remained unchanged in dentin and enamel across sexes and DGI status.

Structural properties (DEJ width, tubule number and size, mantle dentin width) in DGI and WT: In polished samples, the Dentin-Enamel Junction (DEJ) appeared as a single line, but etching revealed a wider zone termed the structural DEJ. DGI mice showed a broader structural DEJ compared to WT, with the widest in DGI females (8± 0.9 µm) and the narrowest in WT males (5±0.7 µm). The DEJ width in female DGI samples is significantly higher than WT males (Fig.4). In SEM examination, DGI mice showed a significant increase in the number of dentinal tubules compared to WT, with mutant females having the highest count (60 per 0.01 mm^2) and WT females having a lower count (30 per 0.01 mm^2). Conversely, the mean diameter of dentinal tubules was significantly smaller in WT compared to DGI, with the largest diameter in WT females and the smallest in DGI females. Despite more tubules in DGI mice, their smaller diameter maintained a consistent total porosity of around 2% to 2.5%. Mantle dentin width significantly decreased in DGI mice compared to WT, with the smallest width in mutant males (43±1.1 µm) and the largest in WT males (around 85 µm).

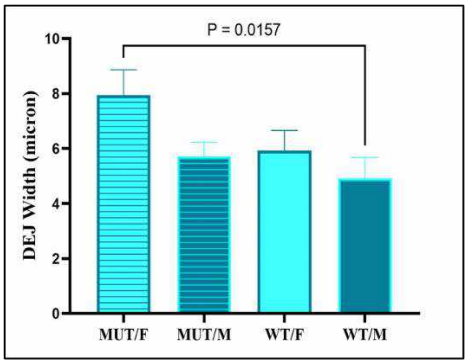

Fig. 4: DEJ width comparison measured by SEM

DISCUSSION

This study shows that the DEJ structure and composition is affected both by DGI and sexual dimorphism. Density gradient widths were unaffected by either factor but agreed with other studies [6]. However, Raman and SEM indicated that the gradients in crystallinity, mineral content, and structural features were significantly smaller, suggesting that the DEJ exhibits multiple overlapping graded structures. The DEJ width as measured by SEM or mineral content was significantly lower in the male mice than the females. This could possibly contribute to the higher occurrence of DGI in men. Although DGI had minimal effects on DEJ width, it had significant effects on the dentin. We found significantly more dentinal tubules in DGI teeth compared to wild types; however, the size of the tubules was reduced in the DGI mice. Although this lead a constant porosity between the DGI and WT enamel, hydrodynamic theory explains that the smaller diameter and greater number of tubules in DGI mice will impact fluid flow and pressure possibly explaining some of the hypersensitivity seen with DGI [7,8]. Finally, the mantle dentin, a thin layer found between the DEJ and the dentin, was significantly thinner in DGI mice compared to WT. This drastic change may be responsible for the higher mechanical failure of DGI teeth; however, little is known about the mechanical role of mantle dentin [9]. This provides an entirely new insight into the compositional and strucutral features that may be critical to controlling tooth mechanics in conditions such as DGI.

ACKNOWLEDGEMENTS

Funded by an NIH R03 GRANT13319573. µCT was performed at the UConn Health Imaging Core by Renata Rydzik.

REFERENCES

[1] Barron, M.J., et al., *Orph. J. of rare diseases* 3: 1-10, 2008.
[2] Andersson, K., et al. *PLoS One*, 12(5), 2017.
[3] De Coster, P. J., et al., *Endodontic Topics* 21(1): 41-61, 2009.
[4] Imbeni, V., et al., *Nature materials*, 4(3): 229-232, 2005.
[5] Verdelis, K., et al., *Matrix Biology*, 52: 246-259, 2016.
[6] Fong, H et al., *Mater. Sci. Eng. C*, 7(2):119–128, 1999.
[7] Davari, A. R., et al., *Journal of Dentistry*, 14(3):136, 2013.
[8] Sasaki, K. et al., *Interface oral health science 2011*, Springer, 2012.
[9] Goldberg, M. et al., *Frontiers in bioscience (Elite edition)* 3:711, 2011.

MECHANICAL STRESSES IN ATHEROSCLEROTIC CORONARY ARTERIES ARE ASSOCIATED WITH PLAQUE GROWTH

Jeremy L. Warren (1), Clark A. Meyer (1), Heather N. Hayenga (1)

(1) Department of Bioengineering, University of Texas at Dallas, Richardson, TX, United States

INTRODUCTION

Previous research has established that the growth of plaque in atherosclerotic coronary arteries is significantly influenced by low or fluctuating wall shear stress at the luminal surface [1]. However, the role of solid mechanics within the plaque in driving the progression of atherosclerosis remains less understood. To gain insight into this relationship, this study explores how the mechanics of the artery wall affect plaque growth. Using longitudinal patient-specific data and in-silico analyses, we examined correlations between the biomechanics of patient arteries and morphological changes in plaque over a six-month period. The findings from this investigation are expected to enhance our understanding of the mechanical factors influencing plaque growth, offering valuable insights for personalized treatment strategies aimed at slowing disease progression.

METHODS

Our previously published automated meshing algorithm was used to generate volumetric 3D meshes of coronary arteries for finite element analysis (FEA) [2]. A 16-patient dataset of paired VH-IVUS images at baseline (BL) and 6-month follow-up (FU) images were used. Each artery was broken into segments for high fidelity FEA simulations. Volumetric meshes comprised quadratic 10-node tetrahedral elements with a mean edge length of 0.15 mm. A Neo-Hookean material model was utilized for each plaque type [**Table 1**].

Material Type	Young's modulus	Poisson's ratio
Artery	0.3 MPa	0.48
Calcium	10 MPa	0.48
Necrotic Core	0.02 MPa	0.48
Fibrotic	0.6 MPa	0.48
Fibrofatty	0.5 MPa	0.48

Table 1. Neo-Hookean material properties for each plaque type.

Two studies were conducted: (i) an image-to-image comparison study and (ii) a volumetric comparison study.

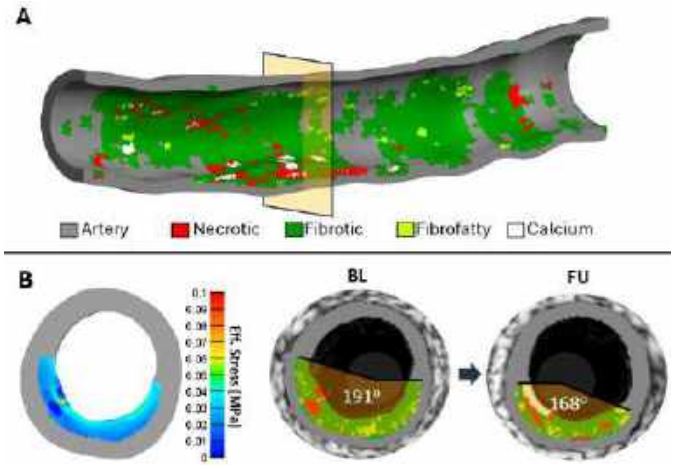

Figure 1. Image-to-image comparison study. A) Volumetric coronary artery mesh. B) FEA analysis and BL to FU images.

Image-to-image Comparison Study. We used our reconstruction algorithm to generate straight meshes of the patient's artery at BL [**Figure 1A**]. Subsequent FEA simulations were performed using the open-source FEBio software [3]. Patient-specific blood pressures were applied to the and the ends of the artery were fixed in space. Heterogenous materials were applied throughout the mesh with literature-derived material properties for each plaque type. Mean elemental effective stress and strain corresponding to each pair of BL and FU VH-IVUS image was calculated from FEA results [**Figure 1B**].

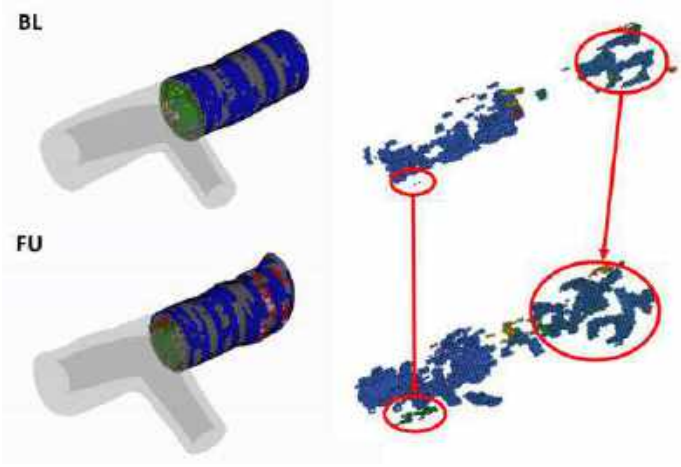

Figure 2. Matching groups of calcium elements in BL to FU volumetric co-registration. Red circles and arrows show co-registered groups of calcium elements.

Volumetric Comparison Study. This study was applied only to severely stenosed, calcified regions of the arteries. The nodes of all calcium elements were combined into a single point cloud. A separate automated script analyzed the point cloud and spatially co-registered groups of calcium elements using a 3D DBSCAN clustering algorithm [**Figure 2**]. Correspondingly, the mean stress of each group of clusters was used to determine correlations between elemental effective stress and changes in calcium volume between BL and FU.

RESULTS

Preliminary results using the 16 patient datasets (1482 total images) showed that larger changes in plaque area between BL and FU occur at low-mid eff. stresses. In the image-to-image study, effective stress was stratified into low (< 35kPa), intermediate (35kPa ≤ σ < 70kPa), and high (>70 kPa) ranges. We saw a high statistical correlation between low stresses and increases in size for calcium and necrotic core plaque types whereas fibrotic and fibrofatty exhibited decreases in size in the same stress range [**Figure 3**]. Similarly in the volumetric comparison study, larger increases in the volume of calcium element clusters corresponded with lower mean effective stresses of those clusters.

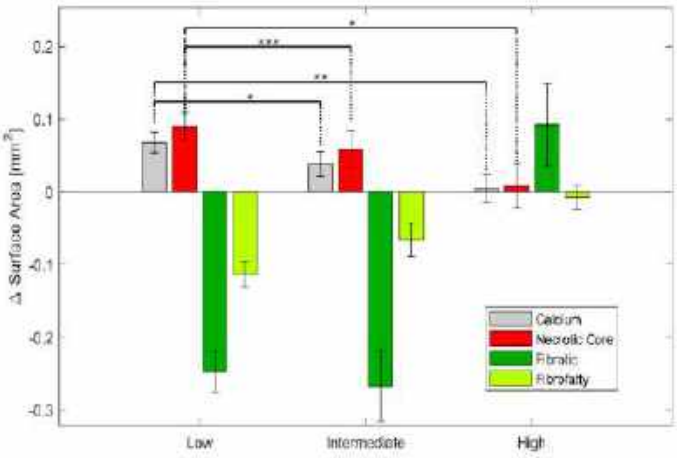

Figure 3. Low stress corresponds with significant increases in plaque size. Calcium and necrotic core exhibit increased size when stratified into low, intermediate, and high stress ranges.

DISCUSSION

Our preliminary results revealed trends similar to those found in the work by Samady et al. which established a correlation between low hemodynamical wall shear stress and increased plaque volume over a 6-month period [1]. Additionally, our results corroborate the work of Tziotziou et. al. which revealed trends that correlated low mechanical wall stress regions with large increase in lipid-rich necrotic core size [4]. The outcomes of our work innovate on both findings, yielding fresh and insightful information regarding the trends of mechanically mediated patient-specific plaque growth in coronary arteries, yet the presented studies are not without limitations. Factors such as mesh resolution, material properties, and boundary conditions can augment stress calculations within the plaque causing discrepancies when comparing results. To this end, both studies utilized the same meshing parameters, material properties, and boundary conditions in the FEA models to ensure comparability of the stress results. We hope the outcomes of these studies set a solid foundation for future research aimed at enhancing our understanding of coronary artery disease.

ACKNOWLEDGEMENTS

Authors gratefully acknowledge funding for this work provided by the American Heart Association (17SDG33400239), the National Heart, Lung, And Blood Institute of the National Institutes of Health (NIH) under Award Number R01HL136776, and the Louis Stokes Alliances for Minority Participation program. The content is solely the responsibility of the authors and does not necessarily represent the official views of the NIH. Emory University (ClinicalTrials.gov; Identifier: NCT00576576) for the data set used in this study. Vascular Mechanobiology Lab at UTD for providing opportunity to work on this research through the guidance of Dr. Hayenga, the lab director.

REFERENCES

[1] H. Samady *et al.*, "Coronary Artery Wall Shear Stress Is Associated With Progression and Transformation of Atherosclerotic Plaque and Arterial Remodeling in Patients With Coronary Artery Disease," *Circulation*, vol. 124, no. 7, pp. 779–788, Aug. 2011, doi: 10.1161/CIRCULATIONAHA.111.021824.

[2] J. L. Warren, J. E. Yoo, C. A. Meyer, D. S. Molony, H. Samady, and H. N. Hayenga, "Automated finite element approach to generate anatomical patient-specific biomechanical models of atherosclerotic arteries from virtual histology-intravascular ultrasound," *Front Med Technol*, vol. 4, Nov. 2022, doi: 10.3389/fmedt.2022.1008540.

[3] S. A. Maas, B. J. Ellis, G. A. Ateshian, and J. A. Weiss, "FEBio: finite elements for biomechanics.," *J Biomech Eng*, vol. 134, no. 1, p. 011005, Jan. 2012, doi: 10.1115/1.4005694.

[4] A. Tziotziou *et al.*, "Mechanical wall stress and wall shear stress are associated with atherosclerosis development in non-calcified coronary segments," *Atherosclerosis*, vol. 387, p. 117387, Dec. 2023, doi: 10.1016/j.atherosclerosis.2023.117387.

LOGIC-BASED CELL SIGNALING MODEL FOR PREDICTING VASCULAR SMOOTH MUSCLE CELL CONTRACTILITY DURING PREGNANCY

P. Nielsen (1), Y. Wu (1), K. Yoshida (1)

(1) Department of Biomedical Engineering, University of Minnesota – Twin Cities, Minneapolis, Minnesota, U.S.A.

INTRODUCTION

Adequate flow through maternal arteries is essential for maintaining fetal and maternal health throughout gestation. During normal human pregnancy, uteroplacental blood flow reaches levels near 1 L/min accompanied by an astounding decrease in downstream vascular resistance near the placenta [1]. In response, arteries undergo significant changes in contractile properties and passive mechanics driven by a delicate balance of chemical and mechanical cues. This process is hypothesized to be crucial to prevent adverse pregnancy outcomes such as pre-eclampsia, a leading cause of maternal mortality. Despite our knowledge of the role perturbed artery mechanics plays in hypertensive disorders, little is known about the specific mechanisms that drive mechanical adaptation of arteries during pregnancy. Blood pressure, wall shear stress, and hormonal signaling are all implicated in the growth and remodeling of arteries and vascular smooth muscle cells (VSMCs) [2]. Untangling signal crosstalk during pregnancy is difficult, but important for understanding how a healthy gestation progresses.

Computational modeling is a valuable platform for understanding how chemical and mechanical cues translate through signaling mechanisms to physiologically relevant VSMC function. While pathological arterial signaling and remodeling have been explored extensively using modeling [3], the effects of pregnancy hormones on VSMCs have remained unexplored. Experimentally, researchers are particularly interested in hormonal effects on contractility, but existing work has shown little consistency in contractility measurement and hormonal dose. Importantly, most of these studies are performed at short time scales [C] making it difficult to apply those results to pregnancy. Therefore, the goals of this work are to 1) adapt and validate a signaling network (SN) model of a VSMC from Irons *et al* [3] for pregnancy by incorporating estrogen (E2) and progesterone (P4), and 2) qualitatively compare model predictions to traction force microscopy (TFM) data of VSMCs after long-term exposure to E2 and P4.

METHODS

The model by Irons et al is a generalized arterial VSMC SN model with fibroblast and endothelial signaling, which translates mechanical stresses and biological inputs into matrix production, proliferation, and contractility activation [3]. We added relevant signaling pathways for E2 and P4 through literature review across 23 papers. Our final SN consists of 113 activation/inhibition reactions and 58 species modeled by a system of logic-based normalized Hill differential equations with uniform time constants, EC50, and Hill coefficients (Fig. 1).

Once the reactions were set, we swept for optimal model parameters and baseline inputs for wall shear stress (blood flow), stress (blood pressure), E2, and P4. The parameter combination that yielded the most qualitative agreement of outputs and interior nodes with experimental data from literature was chosen as the optimal parameter set. We validated the model by comparing the absolute difference in baseline and perturbed species to experimental outcomes using separate publications than those used to build the model.

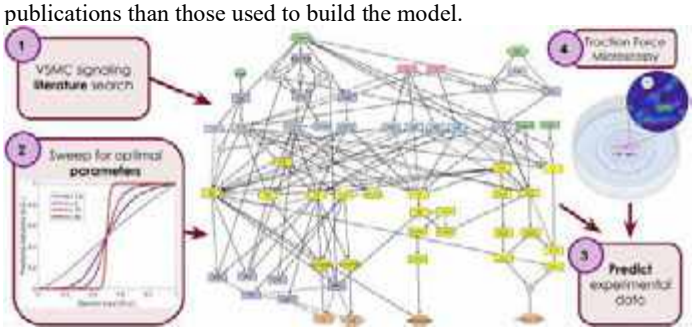

Figure 1: Model structure with mechanical and hormonal inputs.

To simulate an *in vitro* environment, model reactions involving endothelial/nitric oxide signaling were set to zero and stress inputs were decreased to 0.01. E2 and P4 were incrementally increased to evaluate

these dose-dependent hormonal effects on the 'ActomyosinActivity' output. Sensitivity sweeps at high and low integrin inputs were included to evaluate the role of cell adherence on *in vitro* contractility. To validate our model predictions, we conducted TFM experiments by plating human umbilical artery VSMCs on a deformable layer of a 13.5 kPa polyacrylamide gel embedded with fluorescent beads. The cells were incubated with 10 nM E2 and P4, then imaged at 0 and 72 hours to examine long-term traction force. After lysing the cells and comparing the final images with the cell-free state, the tracked displacements were converted to force [4]. The change in the sum of the force magnitudes for a single cell were qualitatively compared to the model output.

RESULTS

The final model parameters chosen correctly predicted 81% of validation paper experimental outcomes; nodes evaluated included interior and output species mediating matrix production, proliferation, and contractility (Fig. 2). Notably, the model failed to predict decrease of the ActomyosinActivity node in response to E2 and P4 increase.

Figure 2: Absolute difference between baseline and perturbed input results and node qualitative agreement with literature data.

In our TFM experiments, treating cells with E2 had no significant effect on traction force (Fig. 3B). This result disagrees with literature (Fig. 2), but agrees with our model (Fig. 3A, left), showing qualitative downregulation but at negligible values, particularly at low integrin activation levels. Treating cells with P4 caused a decrease in traction force, which agrees with literature but disagrees with our model (Fig. 3A, middle). After exposure to the combination of E2+P4, our TFM results show that traction forces are decreased relative to the control; at low doses, our model instead shows contractility upregulation, and at high doses, it shows contractility downregulation (Fig. 3A, right).

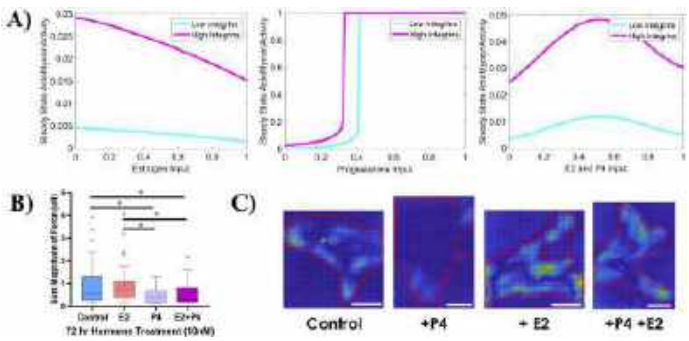

Figure 3: A) SN model results. B) Traction force of VSMCs (* = p < 0.05) exposed to E2 (n = 49), P4 (n = 28), and E2+P4 (n = 46) after 72 hours. C) Representative micrographs of TFM vector fields.

DISCUSSION

The goal of this study was to explore VSMC contractile behavior during pregnancy using modeling and traction force microscopy. While the common consensus is that E2 and P4 relax arteries at the tissue scale [5] and therefore suggest a decrease in VSMC contractility, some tissue myograph studies show no effect of E2 on contraction [6]. Further, our TFM experimental and modeling results show that more information is needed to further elucidate endocrinological effects on contractility.

There are a few possible sources of discrepancies between our modeling results, our TFM data, and literature reports. For example, we did not account for hypertrophy when calculating traction forces; since we define a change in contractility as the sum of the magnitude of the force, 3-D increase in cell volume is lost in translation. We will characterize cell growth in future experiments because pregnancy hormones have been shown to have a hypertrophic effect on other cardiovascular cell types [7]. Additionally, connections in the contraction pathway may still be missing from the model. Research on sex differences has been historically lagging, and information on E2 and P4 pathways is limited. To address this, we'll continue to update the model with new information from our lab or other publications.

An intriguing source of error may be how "contractility" itself is defined. While TFM allows direct force measurements, many studies report indirect measures of VSMC contraction, such as cytoplasmic calcium flux, tissue-scale myograph measurements, and *in vivo* angiographs [6]. Additionally, there is little consistency to the time scales, length scales, and hormonal doses arterial cell and tissue samples are exposed to in these reports. This is particularly important to standardize when modeling active mechanics of cardiovascular cells, as it has been shown that high and low E2/P4 doses have differential effects on cardiomyocyte behavior [7]. While our model failed to capture P4-induced relaxation through the ActomyosinActivity output, it can exhibit time-dependent progesterone-induced dampening of the calcium node (Fig. 4), suggesting that our model can capture short-term, but not long-term, mechanical changes in VSMCs. Long time-scales are crucial for understanding cellular behavior in a pregnancy context, so future work will focus on potential mechanisms of mechanical memory.

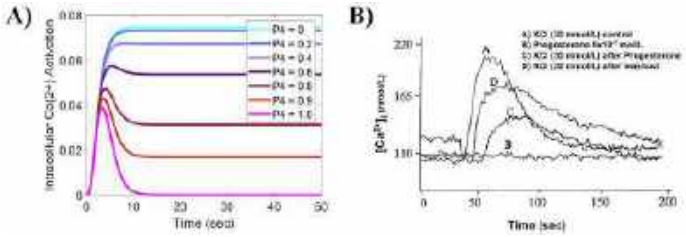

Figure 4: A) Fractional activation of intracellular calcium in response to increasing P4. B) Transient VSMC cytoplasmic calcium dampened by P4 in response to induced contraction [6].

In conclusion, this work uncovers the importance of time-scale, dose, and environment when testing and modeling smooth muscle cell mechanics during pregnancy. In the future, we hope to use this work to develop novel predictive modeling and treatments of pregnancy-induced hypertension and reduce maternal and fetal mortality in the U.S.

ACKNOWLEDGEMENTS

Thank you to the Patrick Alford Lab, the ARCS Foundation and the AHA Career Development Award for supporting this work.

REFERENCES

[1] Ko, NL et al., *Am J Phys Heart Circ Phys*, 315:709-717, 2018.
[2] Osol, G & Mandala, M, *Physiology*, 24:59-71, 2009.
[3] Irons, L & Humphrey, J, *PLoS Compu Bio*, 16, no. 8, 2020.
[4] Wheelwright et al., *PLoS One*, 13, no. 4, 2018.
[5] Freay, A et al., *Circulation Research*, 81:242-248, 1997.
[6] Minshall, R et al., *J App Physiology*, 92: 701-709, 2002.
[7] Kilić, A et al., *J Molec Cell Cardiology*, 46: 360-369, 2009.

LOSS OF DECORIN ACCELERATES CARTILAGE SURFACE DAMAGE AND ABERRANT FIBROUS REMODELING DURING AGING

M. Fan (1), B. Kwok (1), A. Mohan (2), M. Newton (2), J. Xiang (1), Y. Liu (1), L. Qin (3), D. E. Birk (4), R. V. Iozzo (5), T. Maerz (2), R. L. Mauck (3), L. Han (1)

(1) School of Biomedical Engineering, Science and Health Systems, Drexel University, Philadelphia, PA, United States
(2) Department of Orthopaedic Surgery and Biomedical Engineering, University of Michigan, Ann Arbor, MI, United States
(3) McKay Orthopaedic Research Laboratory, University of Pennsylvania, Philadelphia, PA, United States
(4) Department of Molecular Pharmacology and Physiology, University of South Florida, Tampa, FL, United States
(5) Department of Pathology, Anatomy and cell Biology, Thomas Jefferson University, Philadelphia, PA, United States

INTRODUCTION

Aging is the leading risk factor for osteoarthritis (OA), with more than 10% of the adults over 60 years of age presenting with symptomatic disease [1]. While considerable efforts have been made to understand the cellular hallmarks of aging [2], there is limited knowledge on how changes in cartilage extracellular matrix (ECM) contribute to the onset of aging-related spontaneous OA [3]. Our recent studies found that decorin, a small proteoglycan, plays a crucial role in regulating the retention of aggrecan during post-natal growth [4] and in injury-induced OA [5]. In post-traumatic OA, up-regulation of decorin delays loss of fragmented aggrecan and thus attenuates surface fibrillation [5]. Decorin is actively expressed in human cartilage from both young and old donors [6], indicating a potentially active role of decorin in regulating cartilage maintenance during aging. This study sought to investigate how decorin regulates cartilage matrix integrity and associated cell phenotypic changes via evaluating the phenotypic changes of knee cartilage resulted from targeted, cartilage-specific decorin deletion in an aging murine model.

METHODS

Cartilage-specific knockout of *Dcn* was induced by i.p. injection of tamoxifen to $Dcn^{f/f}/AcanCre^{ER}$ (Dcn^{cKO}) mice at 3 months of age [7], and the joints were evaluated at 9 and 18 months (9M and 18M). Safranin-O/Fast Green histology and Picrosirius Red staining were applied to sagittal paraffin sections to assess joint morphology and collagen fiber alignment. RNAscope in situ hybridization of collagen I (*Col1a1*) and decorin (*Dcn*) was applied to evaluate corresponding spatial gene expression profiles and to validate the knockout of *Dcn* gene. Single-cell RNA-sequencing (scRNA-seq, 10X) was applied to 18M femoral condyle cartilage, following pronase and collagenase II enzyme-based cell isolation [8]. High-quality cells were selected with quality control and used for further analysis with the cell numbers of 6,654 for the control and 5,165 for Dcn^{cKO} from 2 mice each. Seurat was used to identify cellular subsets and the PANTHER database to identify biological pathways impacted by *Dcn* deletion via statistical enrichment [9]. SEM was applied to assess the collagen fibril alignment, following established procedures [3]. Distributions of the fibril orientation were plotted after offsetting the mediolateral direction as 0° for each joint.

RESULTS

We validated the reduction of *Dcn* expression as the result of effective knockout in 9M via RNAscope imaging (Fig. 1a). At 9M, Dcn^{cKO} femoral surface already developed highly aligned collagen fibrils, evidencing surface fibrillation (Fig. 2a). At 18M, Dcn^{cKO} femoral cartilage surface formed a layer of highly aligned, thick collagen fibers along the mediolateral direction, which were devoid of sGAGs (Fig. 1b, 2b), highlighting aberrant fibrous remodeling (Fig. 2). In addition to these pronounced matrix phenotypic changes, a new cell group with elongated morphology was noted within this fibrous layer. These cells actively express *Col1a1* (Fig. 1b), indicating the formation of fibrous tissue. They also showed active *Dcn* expression (Fig. 1b), suggesting that these cells were not originated from cartilage, but may have migrated from adjacent tissues that did not express *Acan* at 3M.

In support, scRNA-seq identified a new cell cluster in Dcn^{cKO} cartilage (cluster 2, Fig. 3a,b). These cells were highly metabolic, with high expression of collagens, proteoglycans, lysyl oxidases and MMPs, as well as altered biological pathways (Fig. 3c,d). In contrast, in other cell clusters, including articular chondrocytes (cluster 4), loss of decorin resulted in only mild changes in matrix organization genes, suggesting that decorin may not directly impact chondrocyte biological signaling.

DISCUSSION

This study highlights an unexpected emergent phenotype marked by aberrant fibrous remodeling on the femoral surface of aged cartilage

caused by the loss of decorin. The presence of *Col1a1* and *Dcn*-expressing cells indicates the fibrous character of this surface remodeling and suggests infiltration of cells from adjacent tissues. This fibrous layer consists of thick collagen fibers that are aligned in a mediolateral direction (Fig. 2), and this layer becomes gradually more pronounced from 9M to 18M. The fibrillated cartilage lacks the sGAG-rich hyaline traits, and thus, does not possess the poroelastic energy dissipation functions of cartilage [4]. These changes represent accelerated, severe degradation of femoral condyle cartilage with the deletion of decorin.

Given the observed degenerating of femoral cartilage and aligned fibrils pattern on cartilage surface at 9M (Fig. 2a), it is possible that the continuous physiologic loading on the cartilage with already impaired force dissipation leads to progressive cartilage erosion and cell infiltration. The aligned fibrils on femoral surface formed due to decorin loss at 9M may also facilitate the cell migration and infiltration with the local structural and mechanical environment [10]. These metabolically active cells could originate from adjacent tissues, possibly synovial lining and fat pad, forming this aberrant layer covering the damaged surface by 18M.

As cartilage erosion and fibrillation are common symptoms in advanced OA patients [11], these results point to a crucial role of decorin in inhibiting cartilage damage and OA progression in aged individuals. Notably, such role is primarily manifested through decorin's direct impacts on ECM integrity, rather than chondrocyte signaling, as supported by the mild changes in *Dcn*^{cKO} chondrocyte signaling pathways (cluster 4, Fig. 3c,d). Thus, this study establishes decorin as a novel target for enhancing cartilage maintenance and ameliorating aging-related degeneration.

ACKNOWLEDGEMENTS

This work was supported by NIH R01AR074490, NSF CMMI-1751898 and UPenn PCMD NIH P30AR069619.

REFERENCES

[1] Zhang, Y. et al, Clin Geriatr Med, **26**(3): p. 355-69, 2010
[2] Loeser, R.F., Nat Rev Rheumatol, **12**(7): p. 412-20, 2016.
[3] Fan, M., et al., Journal of Biomechanics, 144: p. 111336, 2022.
[4] Han, B., et al., ACS Nano, **13**(10): p. 11320-11333, 2019.
[5] Li, Q., et al., Arthritis Rheumatol, **72**(8): p. 1266-1277, 2020.
[6] McAlinden, A., et al., Osteoarthritis Cartilage, **9**(1): p. 33-41, 2001.
[7] Henry, S.P., et al., Genesis, **47**(12): p. 805-14, 2009.
[8] Collins, J.M., et al., bioRxiv, 2023.
[9] Knights, A.J., et al., Ann Rheum Dis, **82**(2): p. 272-282, 2023.
[10] Wolf, K., et al., Trends Cell Biol, **21**(12): p. 736-44, 2011.
[11] Pritzker, K.P., et al., Osteoarthritis Cartilage, **14**(1): p. 13-29, 2006.

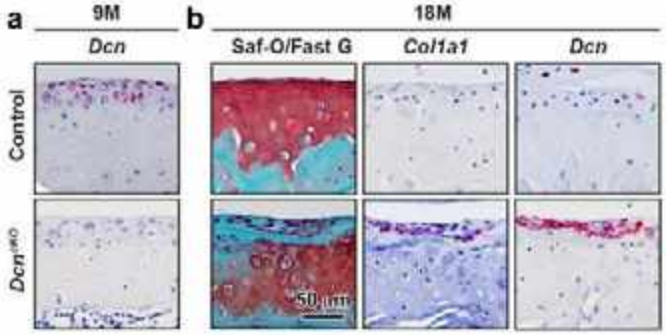

Fig. 1: a) RNAscope of decorin at 9M confirms the knockout of *Dcn* expression. b) Safranin-O/Fast Green histology and RNAscope of collagen I and decorin of control vs *Dcn*^{cKO} femur cartilage at 18M. ($n \geq 6$ animals for each age and genotype).

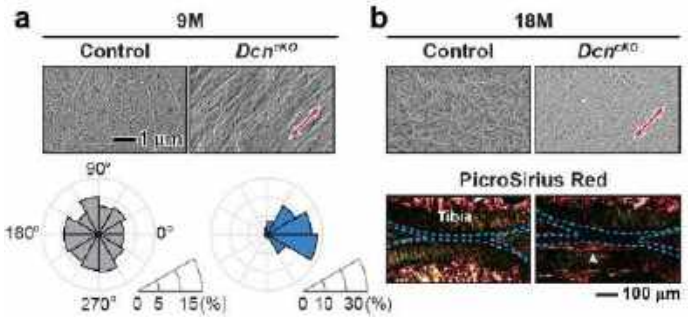

Fig. 2: a) SEM images of medial femoral condylar cartilage surfaces at 9M. Distributions of the fibril orientation following offsetting the mediolateral direction as 0° for each joint of measurement (from ⩾ 400 fibrils pooled from $n = 4$ animals per group). b) SEM images on femoral cartilage surface and PicroSirius Red staining on sagittal joint sections at 18M. Red arrow: mediolateral direction. Blue dash lines indicate the borders of femur, tibia cartilage and meniscus.

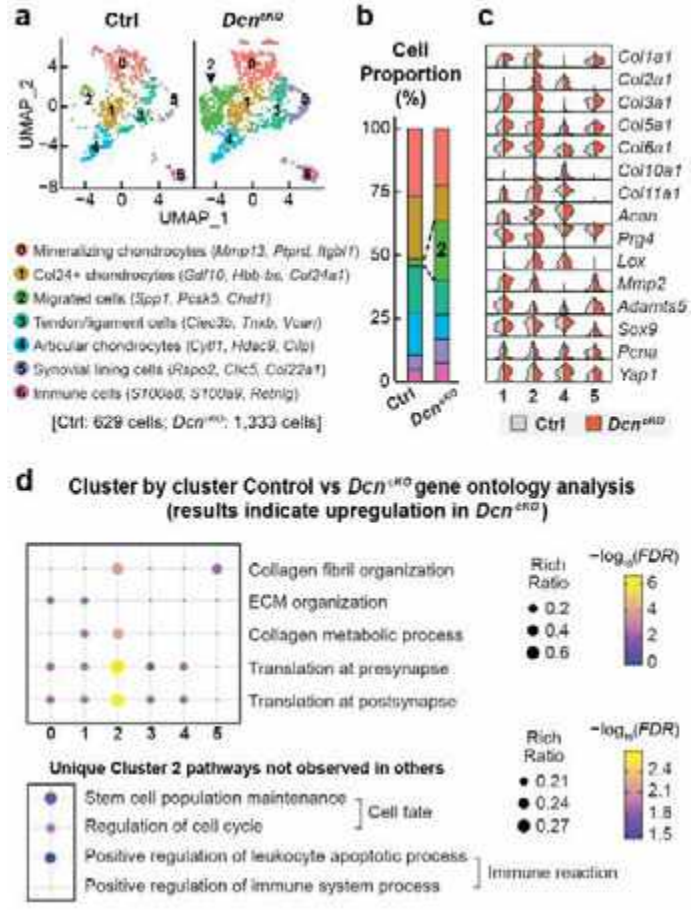

Fig. 3: ScRNA-seq of 18M femur cartilage. a) UMAP shows a new cell Cluster 2 for *Dcn*^{cKO} group (arrowhead) after excluding irrelevant cells. Top 3 gene markers are listed after filtering by pct. 1 > 0.5 and sorted by average $\log_2$-fold comparison between *Dcn*^{cKO} and control. b) Comparison of cell proportions highlights the infiltration of Cluster 2 cells. c) Violin plots of genes of interest related to extracellular matrix organization. d) Gene enrichment analysis of altered biological pathways. (cell numbers in UMAP: 629 for the control, 1,333 for *Dcn*^{cKO}).

AI-BASED QUANTIFICATION OF VASCULAR CALCIFICATIONS FOR ENHANCED RISK EVALUATION

Mehdi. Ramezanpour (1), Anne M. Robertson (1), Xiaowei Jia (2), Juan R. Cebral (3)

(1) Department of Mechanical Engineering and Materials Science, University of Pittsburgh, PA, USA
(2) Department of Computer Science, University of Pittsburgh, PA, USA
(3) Department of Mechanical Engineering, George Mason University, Fairfax, Virginia, USA

INTRODUCTION

Vascular calcifications are associated with significant cardiovascular events, such as heart attacks and strokes [1]. These particles exhibit different phenotypes that can significantly influence their effects on diseased tissues. For example, the size of calcifications plays a crucial role, with microcalcifications being reported to contribute to tissue failure, while macrocalcifications may have a protective effect [1]. Another study suggests that macrocalcifications with sharp edges can create stress concentration in tissues, potentially promoting tissue failure [2]. Additionally, the spatial distribution of microcalcifications is highlighted as a factor that can greatly amplify their harmful impact on tissue stability. Specifically, a single microcalcification situated in the fibrous caps of arterial plaques is reported to increase abnormal intramural stresses fourfold [3], and the presence of two closely positioned microcalcifications, regardless of their location within the tissue, can cause substantial elevations in intramural stresses [4]. Furthermore, the impact of calcifications on tissue stresses can be significantly influenced by the surrounding environment in which they are present [2]. For example, it is shown that when calcifications are covered by lipid pools, lipid pools can significantly attenuate stress concentrations caused by calcifications.

Calcifications in an atherosclerotic artery can exhibit various phenotypes whose collective impact on tissue strength is not well understood. Reliable assessment of diseased tissue strength is crucial for enhancing risk evaluation tools for major adverse cardiovascular events (MACE). Current approaches, like calcium scoring (CAC), assume a positive correlation between overall calcification burden and risk, overlooking the protective or deleterious roles of calcification phenotypes in the failure process. This oversight has led to inconsistent outcomes with CAC. Fundamental scientific studies are needed to sophisticate calcium related risk assessment for MACE. Such studies necessarily must include objective and efficient classification of calcification particles in large numbers of arteries (both atherosclerotic and non-atherosclerotic), along with experimental or computational analyses of wall failure in these specimens. Currently lacking are a comprehensive classification system and a high-throughput tool for accurately assessing calcification phenotypes in these tissues.
In this study, we present a novel comprehensive system to classify calcification in vascular tissues based on phenotype and a high-throughput artificial intelligence-based quantification tool capable of performing this classification for thousands of calcification particles in dissected arterial samples in less than seven hours.

METHODS

Figure 1 A depicts the proposed classification system for calcifications in vascular tissues. The 24 identified groups encompass a range of potential phenotypes motivated by prior research. Initially, calcifications are divided by size (micro and macro). Macrocalcifications are then subcategorized by surface topology (sparse or dense), and microcalcifications are grouped by spatial distribution (clustered or isolated). Moving to the next tier, each phenotype is classified based on colocation with lipid pools as atherosclerotic or non-atherosclerotic. Finally, the eight distinct phenotypes are further classified according to their distribution across the wall as innermost, middle, and outermost layers of the wall, denoted as I, M, and O.

Figure 1 B illustrates a semi-automated deep-learning framework. This tool, utilizing transfer learning, accurately segments sample and lipid pools in thousands of high-resolution micro-CT images. Manual annotations are required for less than 1% of the total images. The tool is evaluated on five samples, achieving a mean dice similarity coefficient of 97% and 85% for sample and lipid pool segmentation compared to human expert ground truth.

To create 3D models of calcifications, lipid pools, and samples, we employ an in-house code for segmentation (Figure 2). Subsequently, a

different in-house code is used to calculate the volume of each calcified particle, categorizing them as macro or microcalcifications based on a predefined volume threshold. Microcalcifications are then analyzed for spatial distribution using a density-based clustering algorithm, detecting local elevations in density. This algorithm is then applied to the space occupied by each macrocalcification, classifying them as dense or sparse based on surface topology.

Next, the colocation of each of the calcified particles with lipid pools is determined and applied to classify calcification based on their type as atherosclerotic and non-atherosclerotic. In the final step, to classify calcifications based on their location within arterial walls, an in-house code is applied to the reconstructed 3D model of the samples to split their wall thickness into three distinct layers, including the innermost, middle, and outermost layers. Finally, the colocation of calcifications with each of these layers is determined to classify them based on their location within the tissue wall.

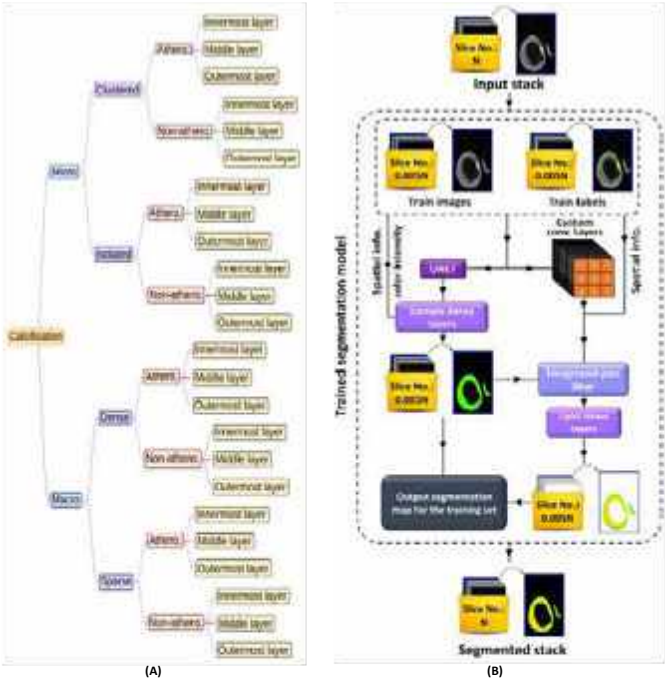

Figure 1: The proposed calcification classification system (A) and the developed semantic segmentation framework.

Figure 2: The reconstructed 3D model for an arterial sample.

RESULTS

The developed quantification tool is applied to a representative dissected sample of atherosclerotic cerebral arteries, and the results are presented in Figure 3. In Figure 3 A, the volumetric ratios of lipid pool to tissue and calcification to tissue are presented, which are measures of atherosclerosis and calcification, respectively. The ratios of atherosclerotic calcification, macrocalcifications, and clustered microcalcifications to overall calcifications are presented, which, based on statistical results, are significant predictors of failure [5].

Figure 3B shows the microcalcification phenotype proportions, crucial for studying correlations between lipid pool presence and microcalcification density, as well as exploring relationships between microcalcification location and spatial distributions. Figure 3C quantifies sparse and dense parts in atherosclerotic and non-atherosclerotic macrocalcifications.

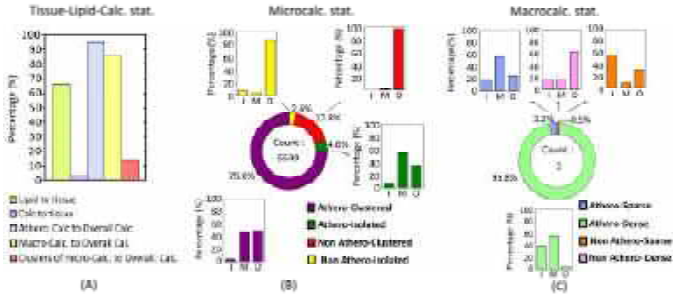

Figure 3: Quantification based on calcification phenotypes.

DISCUSSION

Vascular calcifications are widely acknowledged as a primary contributor to tissue failure in MACE. The impact of calcifications on tissue failure varies depending on their phenotypic characteristics. A thorough understanding of these phenotypes and their intricate interactions is essential for enhancing risk assessment tools for MACE. This study aims to facilitate such understanding by introducing a comprehensive classification system for phenotyping calcification, complemented by a high-throughput quantification tool for assessing samples based on their calcification phenotypes. The evaluation of tissue strength across a sufficiently extensive number of arterial samples, coupled with an exploration of their associations with calcification phenotypes, is pivotal for achieving a more precise risk assessment of MACE.

The classification system includes phenotypes like size, type, spatial distribution, surface topology, and location. Atherosclerotic calcifications are suggested to form in the intima layer, while non-atherosclerotic ones accumulate in the media layer. Our quantification tool allows a detailed investigation of associations between calcification type, location, and tissue origin in various arterial systems. Regarding the size phenotype, studies indicate microcalcifications tend to aggregate into macrocalcifications in locations of fibrous tissues with lower collagen densities [4]. With respect to the surface topology phenotype, it is shown that sharp edges of macrocalcifications can induce stress concentrations, compromising stability [2]. Our tool, equipped with ML-based clustering frameworks, detects local increases in microcalcification distribution and sharp irregularities on macrocalcification surfaces. Understanding the association between microcalcification clusters, macrocalcification surfaces, and the initiation of tissue failure during mechanical testing is crucial for enhancing risk assessment tools that currently overlook these calcification phenotypes.

ACKNOWLEDGEMENTS

NIH funded:1S10OD025041, 2R01NS097457.

REFERENCES

[1] Ruiz, J. et al., The Journal of Physiology 594, 2915-2927, 2016.
[2] Fortunato, R. et al., Exp Mech 61, 5-18, 2021.
[3] Corti, A. et al., Frontiers in Cardiovascular Medicine 9, 2022.
[4] Kelly-Arnold, A. et al., Proc Natl Acad Sci, 110, 10741-746, 2013.
[5] Gade, P. et al., ATVB 39, 2157-2167, 2019.

COMPARISON OF HEAD IMPACT BIOMECHANICS ACROSS MULTIPLE SPORTS

Zaryan Z. Masood (1), David S. Luke (2), Rebecca A. Kenny (3), Daniel R. Bondi (2), Adam C. Clansey (1), Lyndia C. Wu (1,2)

(1) Mechanical Engineering, University of British Columbia, Vancouver, BC, Canada
(2) School of Biomedical Engineering, University of British Columbia, Vancouver, BC, Canada
(3) Faculty of Medicine, University of British Columbia, Vancouver, BC, Canada

INTRODUCTION

Sports head impact exposure have been associated with acute and chronic neurological consequences [1]. Wearable head impact sensors have enabled collection of real-world data from multiple sports, with instrumented mouthguards becoming a standard validated technology [2]. Despite increasing application of sensors, most studies focus on investigating single sports, and there has been no quantitative analysis of impact biomechanics across sports using field data. Some studies have introduced potential sport-specific impact characteristics, including American football and rugby, exhibiting high magnitude player-to-player collisions [3], while soccer displaying lower magnitude heading impacts [4]. Since head impact biomechanics have been associated with brain injury risk, further investigation would enable insight into sport-specific injury mechanisms.

Numerous factors contribute to the biomechanical variability in head impacts between sports, including playing style [5], game speed [6], sex differences [7], and the presence of protective equipment, such as helmets [8]. Uniquely, we have gathered head impact data across multiple sports using similar sensors and methodologies that enable comparison of impact biomechanics between ice hockey, American football, soccer, and rugby. With this dataset, we aim to (i) determine biomechanical differences between sports by comparing peak kinematics and impulse duration, and (ii) characterize and compare head impact directionality across sports.

METHODS

A head impact database was curated from previously collected instrumented mouthguard data from university-level men's American football (MF), men's ice hockey (MH), women's rugby (WR), and women's soccer (WS) teams. Both MH and WR teams wore Prevent Biometrics [9] instrumented mouthguards during practices and games. The WS team wore instrumented mouthpieces from Wake Forest Center for Injury Biomechanics [10], while MF wore Stanford University instrumented mouthguards [11]. All instrumented mouthguards were custom-fit and recorded 6 degrees of freedom head linear acceleration and angular velocity. The Prevent and Wake Forest devices had a 5g trigger for recording head impacts while the Stanford mouthguard had a 10g trigger. To account for this difference, we removed all impacts below 10g prior to comparison. Data were sampled at a minimum of 1000Hz, filtered using a low-pass 4th order Butterworth filter at 200Hz for linear accelerations and 180Hz for angular velocity, then transformed to the head center of gravity. Only video-verified head impacts were included in the analysis. Processed signals were used to compute metrics of interest such as peak linear acceleration (PLA), peak angular velocity (PAV), and peak angular acceleration (PAA) in all three planes of motion. Impulse durations were extracted by calculating the width of the impulse at half the maximum value of both linear and angular accelerations. All features were then compared across sports using pairwise Mann-Whitney U test with $\alpha = 0.05$ and Bonferroni correction for multiple comparisons. Dominant planes of head rotation were characterized by determining if PAA in any anatomical plane (coronal - x, sagittal - y, or transverse - z) was greater than 90% of the resultant PAA.

RESULTS

Our database consisted of 1838 video-verified total head impacts, where 463 were from MH, 411 from WR, 1056 from WS, and 275 from MF. Comparing across sports, we observed MF to have the highest median peak linear acceleration (24.6 g), peak angular velocity (11.7 rad/s), and angular acceleration (1996 rad/s^2) compared to MH, WR, WS (Figure 1). We also observed WS to have the lowest median peak kinematics compared to the other sports (14.4 g, 6.9 rad/s, 1269 rad/s^2) (Figure 1). Pairwise comparisons resultant PLA, PAV, and PAA showed statistically significant differences between sports for all combinations except resultant PAA between WR and WS.

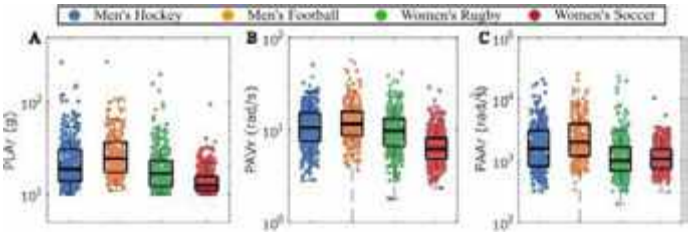

Figure 1: Resultant PLA (A), PAV (B), and PAA (C) for all head impacts across sports.

Figure 2 shows example comparisons of resultant linear acceleration impulse durations, with similar trends observed for each anatomical axis and angular acceleration. While the unhelmeted sports (WR and WS) had slightly higher median impulse durations (11 ms) compared with helmeted sports (MH and MF, 10 ms), pairwise comparisons revealed no significant differences (Figure 2B). Notably, MH and WR show higher variance in impulse duration distributions than MF and WS.

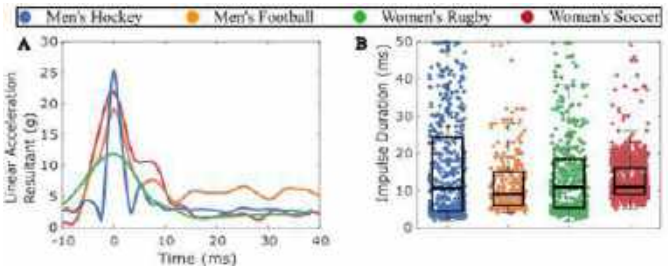

Figure 2: Resultant linear accelerations for one impact used to compute impulse duration (A). Impulse duration across all sports (B).

Examining impact directionality, WS involved more impacts with dominant sagittal plane (y-axis) rotation (50%), MH showed more transverse plane (z-axis) dominance (31%), MF showed more coronal plane (x-axis) dominance (33.4%), while WR involved multi-directional head rotations with no particular directional dominance.

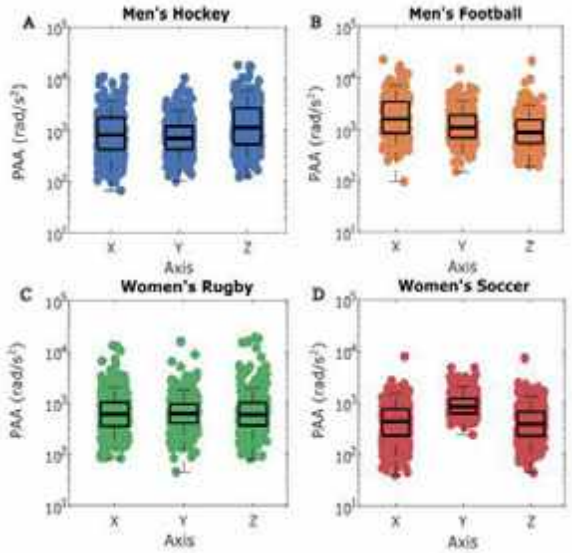

Figure 3: Per axis comparison of PAA for all head impacts.

DISCUSSION

Cross-sport comparisons of peak kinematics highlights MF to exhibit the largest peak linear and angular accelerations, which may be associated with high concussion incidence found in football [3]. MH also exhibited comparable high peak kinematics to MF. Reasons for high kinematics in MF and MH can be multivariable and could be attributed to greater body mass and higher speed collisions [3].

While it was expected that the presence of helmets and padding would attenuate impacts and increase the impact duration, helmeted sports (MH and MF) showed slightly shorter impulse duration than unhelmeted sports (WR and WS), and this duration difference was found to be statistically significant. Contrary to expectations, the helmet does not seem to have any substantial effect on impulse duration based on our findings. Further examination of helmet effects on impact biomechanics may be needed to confirm the effectiveness of helmets.

Furthermore, every sport displayed unique directionality patterns in our study. Most head impacts in soccer occur during frontal heading [4] and indeed our results show sagittal plane linear and angular components to dominate in WS. Past helmet sensor studies have reported inconsistent findings in impact location for American football and ice hockey [12,13], while our study shows preliminary evidence of some dominant planes of head rotation during impact. Animal and modeling studies have shown potential directional-dependence in brain injury risk, with the coronal [14] and transverse [15] planes proposed as more vulnerable.

Given our sample, it is difficult to speculate main factors leading to biomechanical differences between sports, since sex and sport factors cannot be isolated. Previous literature has found sex-differences in impact severity [16]. In the future, we aim to expand our dataset to better match sports for further understanding of the influence of sex, equipment, and playstyle on head impact biomechanics.

In summary, our study is one of the first to compare head impact biomechanics across multiple sports using real-world head impact data. We observed impact magnitude and direction differences between-sports with injury risk implications, as well as unexpected impulse duration findings that call for further investigation of helmet effects on impact biomechanics.

ACKNOWLEDGEMENTS

We would like to thank the CIHR, CFI, and NSERC for funding of this study. We would also like to thank all the Varsity teams involved, along with Prevent Biometrics, Wake Forest Center for Injury Biomechanics, and Stanford CamLab for their support.

REFERENCES

[1] Bailes, J et al., *J Neurosurgery*, 119:1235-1245, 2013.
[2] Kuo, C et al., *Annals of Biomedical Eng*, 50: 1372-1388, 2022.
[3] Broglio, S et al., *J Athletic Training*, 44:342-349, 2009.
[4] Kenny, R et al., *Annals of Biomedical Eng*, 50: 1461-1472, 2022.
[5] Mihalik, J et al., *J Sports Engineering and Tech*, 222: 45-52, 2008.S
[6] Bailes, J et al., *J Neurosurgery*, 48: 26-46, 2001.
[7] Withnall, C et al., *BJSM*, 39: 49-57, 2005.
[8] Lewis, L et al., *Academic Emergency Med*, 8: 604-609, 2001.
[9] Bartsch, A et al., *Annu Int Conf IEEE*, 2068-2072, 2019.
[10] Rich, A et al., *Annals of Biomedical Eng*, 47:2109-2121, 2019.
[11] Wu, L et al., *IEEE Transactions on BME*, 61: 2659-2688, 2014.
[12] Pellman, E et al., *Neurosurgery*, 53 : 1328-1341, 2003.
[13] Gwin, J et al., *ASTM*, 6 : 1-8, 2009.
[14] Gennarelli, T et al., *Annals of Neurology*, 12 : 564-574, 1982.
[15] Weaver, A et al., *Annals of Biomedical Eng*, 40 : 2005-2018, 2012.
[16] Saunders, T et al., Clinical Biomechanics, 74:14-20, 2020.

SEQSEG: AUTOMATIC IMAGE-BASED VASCULAR MODEL CONSTRUCTION USING SEQUENTIAL SEGMENTATIONS

Numi Sveinsson Cepero (1), Shawn C. Shadden (1)

(1) Department of Mechanical Engineering, University of California Berkeley, Berkeley, California, USA.

INTRODUCTION

Image-based computer modeling of vasculature has become an important aspect of patient care and cardiovascular research [1]. These modeling approaches use medical images to construct an anatomically accurate geometry of patient's blood vessels to be used for simulation-based modeling. Despite its wide range of applications, constructing anatomically correct geometries of blood vessels from medical images remains challenging and involves multiple steps and a combination of approaches, including ones reliant on labour intensive manual inputs.

Segmenting blood vessels from other nearby tissue is challenging because of limited resolution, unclear boundaries and image artifacts. To simplify the task, a "centerline" path is often constructed along vessels of interest, which is then traversed to perform 2D segmentations of the vessel lumen at discrete steps along the path. These 2D segmentations can then be lofted using spline interpolations to form a unified 3D surface representing the blood vessel domain[2]. Until now, these two steps (centerline generation and lumen segmentations) have been viewed as separate, resulting in methods to either accurately construct centerlines [3] or accurately determine lumen boundaries around centerlines [4]. We present a novel method to do both at once automatically, utilizing local deep-learning based segmentation with a tracing algorithm to construct a global vascular segmentation piece-wise while taking steps.

METHODS

Our approach tackles blood vessel segmentation by operating locally around a particular blood vessel segment. Local 3D segmentations are processed to determine vessel direction and size in order to take steps.

Algorithm. Figure 1 shows an overview of the algorithm steps. The algorithm is initialized using a given seed point and radius estimate, which is used to extract the first subvolume. The subvolume is segmented using a 3D U-Net neural network, where pixels are classified in a binary manner; either belonging to blood vessel or not. The segmentation is converted into surface mesh representation using the marching cubes algorithm, and a centerline is extracted using the open-source Vascular Modeling Tool Kit library. The resulting centerline is then post processed to estimate the size of the vessel and choose the next point to move to. If the centerline includes two or more branches, the largest branch is chosen for immediate stepping and the others are stored in a bifurcation queue for subsequent tracing. During step-taking, we save the local segmentations and assemble them in a single global model as the final output.

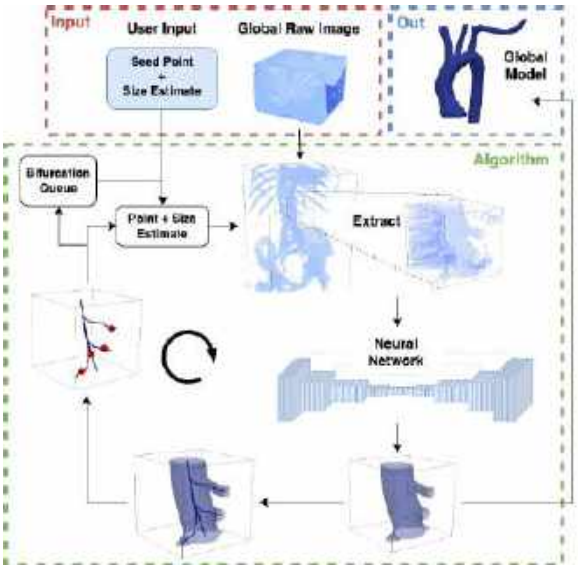

Figure 1: The different steps in the SeqSeg algorithm from initialization with inputs of seed point, radius estimate and global raw image, to subvolume extraction, 3D U-Net segmentation, surface and centerline calculation and stepping. Bifurcation points are saved in queue for subsequent tracing.

Datasets and Sampling. The datasets used are aortic and aortofemoral models from CT, and MR image data, see Table 1, acquired from the open and free Vascular Model Repository, accessible at *vascularmodel.com*[5].

Each case in a dataset has a medical image scan (CT/MR) with corresponding segmentation and centerline, see inputs in Figure 2. For neural network training, the global 3D medical image volume is sampled along the centerline of its corresponding vasculature model, see Fig. 2 for reference. Two subvolumes are extracted at each instance: 1) raw medical image data, and 2) binary segmentation of blood vessel. The samples vary in centering and size; some centered along the centerline while others shifted perpendicular to its tangent, and sizes vary from barely capturing the vessel lumen, to others including more nearby tissue. This variance is purposefully added to represent the variance that the tracing algorithm encounters in practice and is intended to increase the neural network's robustness. Approximately 15% of subvolumes are used for validation and 20% of cases are kept aside for testing, see further details in Table 1.

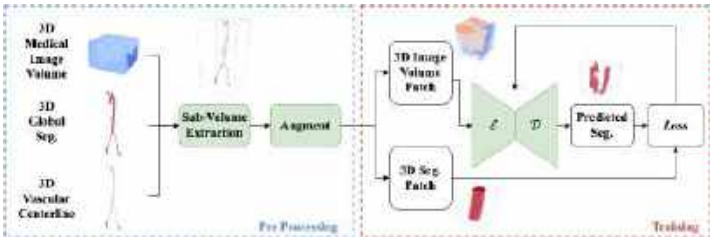

Figure 2: The pre processing of data for neural network training. Samples are extracted along vasculature centerline and augmented, and ground truth segmentations are used for loss calculation.

Table 1: The number of cases used for training and testing.

Dataset	Modality	Train/Val	Test
VMR Aortic / Aortofemoral[5]	CT	33	8
VMR Aortic / Aortofemoral[5]	MR	37	7

Neural Network Architecture and Training. The U-Net architecture is used for the segmentation task, and a 3D-version is chosen. The nnU-Net framework is used for hyperparameter choice and training[6]. The loss function used is a combination of Dice loss and binary cross entropy:

$$l = 1 - \mathcal{D} - \mathcal{CE} \tag{1}$$

where $\mathcal{D}$, $\mathcal{CE}$ are Dice score and binary cross entropy, respectively. Training took place using two GPUs, an NVIDIA k80 dual-GPU, on the Savio High Performance Computing cluster at UC, Berkeley.

Global Assembly. The local segmentations are gathered globally by calculating the mean prediction for each voxel. The final segmentation is then converted to a surface mesh using marching cubes and smoothed to remove voxel artifacts.

RESULTS

We tested our method (SeqSeg) on two different datasets as shown in Table 1, and compare to results from a benchmark model. A global nnU-Net model is chosen as benchmark because of its state-of-the-art performance on medical image segmentation tasks[6]. We compare using Dice score and avg. Hausdorff distance, see Table 2 for the avg. scores across both test datasets. As the results show, SeqSeg, on average, outperforms the benchmark using both metrics. Figure 3 shows a qualitative comparison between the ground truth and predictions from SeqSeg and the benchmark model on six aortic/aortofemoral models, three CT, and three MR. The method, SeqSeg, manages to capture all the branches present in the ground truth model. It also manages to extend the branches further than that was segmented in the ground truth.

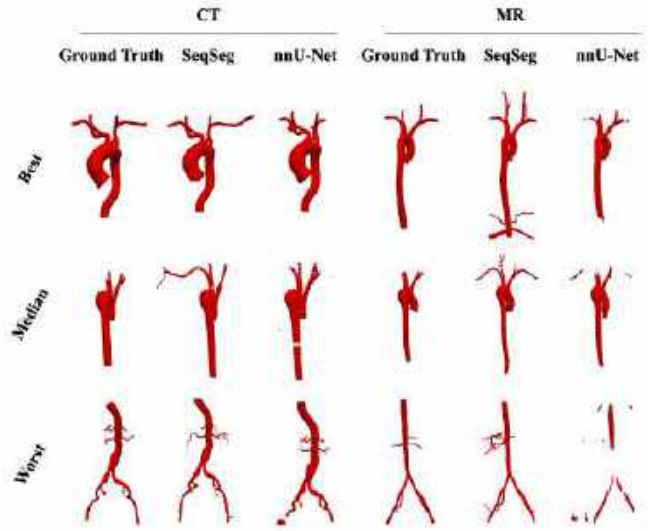

Figure 3: Comparison between ground truth model (left), prediction results from SeqSeg (middle) and nnU-Net benchmark model (right), for CT, and MR data. The cases shown are the best, median, and worst ranking Dice score results for the nnU-Net benchmark model.

Table 2: Avg. Dice score ($\mathcal{D}$) and Avg. Hausdorff distance ($\mathcal{H}$) score results on testing data, comparing SeqSeg (our) and nnU-Net benchmark model.

	$\mathcal{D}\uparrow$		$\mathcal{H}\downarrow$	
Dataset	SeqSeg	nnU-Net	SeqSeg	nnU-Net
CT Aorta VMR	**0.927**	0.901	**0.023**	0.071
MR Aorta VMR	**0.877**	0.844	**0.0335**	0.114

DISCUSSION

We present a novel model construction method, SeqSeg, based on local step taking, which uses deep learning to predict vascular segments instead of the whole vasculature at once. With only a single seed point, SeqSeg is capable of automatically constructing expansive vasculature. As a result of the neural network training strategy, the machine learning model manages to adequately capture bifurcations and generalize to new vessel branches not present in the training data. The results show the method works both for CT, and MR, image data. Additionally, by assembling vascular models piece-wise, the method ensures connectivity of the final segmentation, a necessity if the final purpose is simulation.

ACKNOWLEDGEMENTS

This work has benefited from support of the NIH, Award No. 5R01LM013120 and the NSF, Award No. 1663747.

REFERENCES

[1] Gray RA et al. 2018. DOI: 10.1007/s12265-018-9792-2.

[2] Updegrove A et al. 2017. DOI: 10.1007/s10439-016-1762-8.

[3] Wolterink JM et al. *Medical Image Analysis* 51 (2019). ISSN: 13618423. DOI: 10.1016/j.media.2018.10.005.

[4] Maher G et al. *Cardiovascular Engineering and Technology* 11.6 (2020). ISSN: 18694098. DOI: 10.1007/s13239-020-00497-5.

[5] Wilson NM et al. *Journal of Medical Devices, Transactions of the ASME* 7.4 (2013). ISSN: 1932619X. DOI: 10.1115/1.4025983.

[6] Isensee F et al. *Nature Methods* 18.2 (2021). ISSN: 1548-7105. DOI: 10.1038/s41592-020-01008-z.

BRIDGING GAPS IN TRAUMATIC BRAIN INJURY MODELING: A MULTISCALE APPROACH TO UNIFYING GLOBAL AND AXONAL INJURY MODELS

C. Zhang (1), L. Bartels (2), A. Clansey (3), J. Kloiber (2), D. Bondi (3), P. van Donkelaar (4), L. Wu (3), A. Rauscher (2), S. Ji (1,5)

(1) Department of Biomedical Engineering, Worcester Polytechnic Institute, Worcester, MA, USA
(2) Department of Pediatrics, University of British Columbia, Vancouver, BC
(2) Department of Mechanical Engineering, University of British Columbia, Vancouver, BC
(3) School of Health and Exercise Sciences, University of British Columbia, Kelowna, BC
(5) Department of Mechanical Engineering, Worcester Polytechnic Institute, Worcester, MA, USA

INTRODUCTION

Sixty-night million people suffer from traumatic brain injury (TBI) each year [1], with most incidents mild TBI (mTBI) or concussion. It is common to use a global brain model or microscale axonal model to study the mechanisms of TBI. The latter uses strains from the global model as input to study cytoskeletal behaviors to investigate the triggering mechanisms of "traumatic axonal injury (TAI)" [3,4]. Nevertheless, a significant gap exists between a global and a microscale model: a global model provides detailed brain strain responses but the spatial resolution is limited and insufficient to inform damage at the cellular level. While a microscale model is capable of estimating cytoskeletal damage, often it lacks real-world input for simulation.

This study unifies a global model and a microscale axonal injury model in a multimodal analysis pipeline to study the mechanism of TAI. It employs a unique subject-specific multimodal dataset, including on-field head impact kinematics and subject-specific neuroimages to provide anatomy and detailed white matter tractography. The computational pipeline employs a displacement voxelization scheme with adjustable spatial resolution to balancing accuracy and efficiency. The structured data format easily allows multimodal analysis with neuroimages and white matter tractography. The pipeline generates a diverse range of fiber strain profiles, which is important to facilitate future development of a deep learning axonal injury model. This will be critical to allow for large-scale and multiscale biomechanical modeling of TAI to uncover the mechanism of axonal damage at the microscale.

METHODS

The subject-specific multimodal dataset from the University of British Columbia is from a 21-year-old male varsity ice hockey player who suffered a concussion. The study was approved by the Research Ethics Board (ID: H21-00400). Biomechanical data were collected using an instrumented mouthguard. The subject's concussive impact was identified and verified with multi-angle video recordings. Neuroimages were acquired before and after the concussion on a 3T MRI scanner, including 3D T1-weighted scans and diffusion-weighted imaging. A subject specific model [5] was developed based on the anisotropic Worcester Head Injury Model (WHIM) Version 1.0 *via* mesh warping (Figure 1.). The WHIM has been extensively validated for brain responses across a large-range of impact conditions [7].

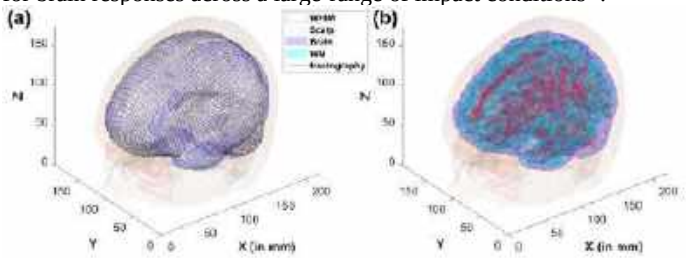

Figure 1: (a) The subject-specific WHIM for the concussed athlete. (b) Randomly selected tractography streamlines overlaid against surface renderings of the white matter.

The subject-specific WHIM model was used to analyze voxel wise strains through a displacement voxelization scheme [6]. Displacement field is utilized to calculate the voxel wise maximum principal strain (MPS) and fiber strain in white matter region. For voxel wise fiber strain, the fiber strain at each white matter fiber sampling point was calculated, and voxel wise weighted averages of peak fiber strains were determined. By resampling impact-induced relative brain-skull displacement at different resolutions, diverse fiber strain profiles in the white matter could be identified. The study's computational pipeline allowed for the processing of simulated biomechanical data at various

spatial resolutions. The ensuing multimodal analysis allows convenient identification of vulnerable brain regions, such as the corpus callosum and gray-white matter interface, to traumatic axonal injury (TAI).

Data analysis includes comparing computational efficiency and accuracy of fiber strains across different displacement resampling resolutions. This also included analyzing representative fiber strain profiles in areas prone to TAI and diverse fiber strain profiles across the white matter. The simulations were conducted in SIMULIA Abaqus with the explicit FEA solver (28 cores, 256GB). While all data analyses were conducted in MATLAB (R2020a; Mathworks, Natick, MA) on a desktop computer (16 cores, 64GB).

RESULTS

Figure 2 shows voxelized relative brain-skull displacement, captured at the moment of peak fiber strain in the corpus callosum. This is illustrated across three neuroimaging planes – coronal, axial, and para-sagittal. Accompanying these are the corresponding voxelwise peak Maximum Principal Strain (MPS) and peak fiber strains.

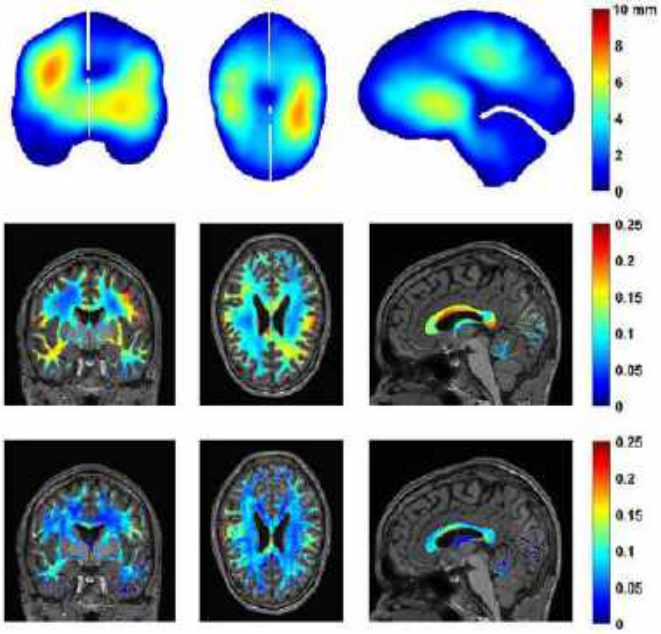

Figure 2: Voxelized magnitude of relative brain-skull displacement from impact simulation (top row) at the time when corpus callosum fiber strain reached its first major peak in coronal (left), axial (middle column) and para-sagittal (right) planes, along with the corresponding voxel wise peak MPS (second row) and fiber strains (bottom row).

In exploring the effects of voxel resampling resolutions on brain-skull displacement and strain measures, we compared fiber train accuracy and efficiency at three different resolutions (1 mm, 2 mm, and 4 mm), using results at the isotropic resolution of 1 mm as the baseline. The results show a direct correlation between the increase of the resampling voxel size and the increase in fiber strain error (6.4% for 2 mm and 14.2% for 4 mm) and the decrease in computational time (83.4% and 96.9% reduction in time for the 2 mm and 4 mm resolutions, respectively). To balance accuracy and efficiency, an isotropic resolution of 2 mm seems to offer an optimal trade-off between response accuracy and computational efficiency.

To illustrate multimodal analysis, representative fiber strain profiles near the gray-white matter interface and in the corpus callosum are shown (Figure 3). They were identified based on subject-specific neuroimage segmentation. It was observed that the left and right hemispherical regions experienced tension and compression in opposite phases, which was expected given the nearly incompressible brain to maintain a nearly constant volume.

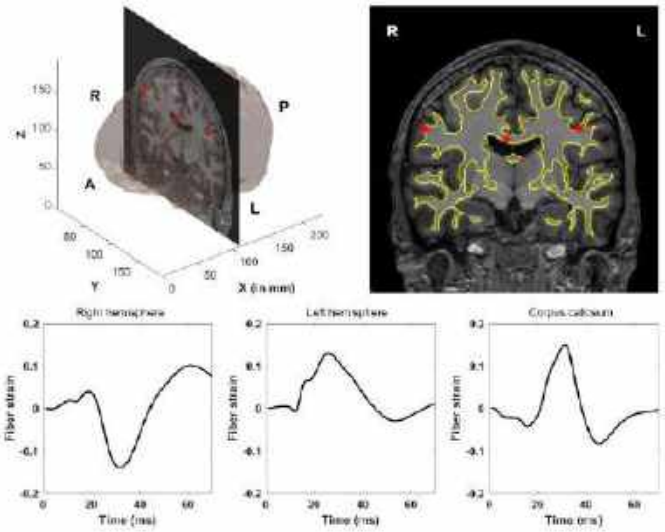

Figure 3: Representative fiber strain profiles near the gray-white matter interface in two contralateral regions and in the corpus callosum for a concussive head impact recorded for a male ice-hockey player.

Finally, the voxelized displacement field over time also enables convenient determination of white matter fiber strains at arbitrary locations. Pearson correlation was calculated between pairs of fiber strain profiles, from which the most diverse set with the lowest Pearson correlation scores were identified. They will be used to develop a deep learning axonal injury model in the future, which will rapidly provide cytoskeletal responses rapidly without a costly direct model simulation, critical for large-scale axonal injury modeling.

DISCUSSION

We have established a computational pipeline to unify a global and a microscale brain injury model. The voxelized displacement field allows accurate and efficient determine voxelwise maximum principal strains and white matter fiber strains. This pipeline is crucial for identifying a diverse set of fiber strain profiles necessary for developing a deep learning model for axonal injury. The framework established in this work is critical for enabling large-scale (i.e., across the entire white matter region, head impacts, and individuals) and multiscale (i.e., from organ to cell length scales) modeling for the investigation of traumatic axonal injury triggering mechanisms. Ultimately, these efforts could enhance the assessment of concussion risks and design of protective headgear. Therefore, this work contributes to improved strategies for concussion detection, mitigation, and prevention.

ACKNOWLEDGEMENTS

Funding is provided by the National Science Foundation (NSF) under Grant No. 2114697 and the Canadian Institutes of Health Research (CIHR) Project No. 436806.

REFERENCES

[1] Yana, N. et al., Heliyon 23, 109 (2023)
[2] Gavin, F. B. et al., Acta Neurochir. 163, 31 (2021)
[3] Montanino, A. et al., Front. Neurol. 9, 1–12 (2020).
[4] Ahmadzadeh, H. et al., Biophys. J. 106, 1123–1133 (2014).
[5] S, Ji. et al., J. Neurotrauma. 32, 441–454 (2015).
[6] S, Ji. et al., Comput. Methods Programs Biomed. 213 (2022).
[7] W. Zhao. Et al., J. Neurotrauma. 36, 250–263 (2019).

TENDON IMPINGEMENT PRODUCES DIFFERENTIAL REGIONAL PROFILES OF INTACT AND FRAGMENTED AGGRECAN

Brian C. Wise (1,2), Whasil Lee (1,2,3), Mark R. Buckley (1,2)

(1) Department of Biomedical Engineering, University of Rochester, Rochester, NY, USA
(2) Center for Musculoskeletal Research, University of Rochester Medical Center, Rochester, NY, USA
(3) Department of Pharmacology and Physiology, University of Rochester, Rochester, NY, USA

INTRODUCTION

Tendon impingement generates a unique mechanical strain environment distinguished by elevated transverse compressive strains[1] that sustain a localized fibrocartilage phenotype enriched with glycosaminoglycans (GAGs)[2] (**Fig 1A**). While fibrocartilage is a normal feature in impinged regions of healthy tendon, excess GAG content is a hallmark feature of tendinopathy, a degenerative disease that disproportionately affects impinged tendons[3,4]. As such, impingement is clinically recognized as an important extrinsic factor in tendinopathy pathogenesis. Despite this, the cellular and molecular basis of impingement mechanobiology is poorly described, in part due to a lack of experimental models. To fill this void, our lab has developed a novel murine hind limb explant model for studying the mechanobiology of Achilles tendon impingement[5] (**Fig 1B**). By preserving anatomical structures of the impinged region *in situ*, this model allows for controlled prescription of impingement via passive ankle dorsiflexion to reproduce multiaxial strain patterns that are measurable and well-characterized[1] (**Fig 1C**). Moreover, we have demonstrated that impingement produces significant change in GAG staining, consistent with fibrocartilage formation[5] (**Fig 1D**). Here, we utilize this model of impingement to study aggrecan: a large, GAG-rich proteoglycan upregulated in regions of fibrocartilage. Notably, prior studies have explicated dynamic aggrecan turnover in tendon fibrocartilage via constitutive ADAMTS catabolism, with evidence that simple uniaxial compression regulates both aggrecan biosynthesis and turnover[6-9]. Nevertheless, aggrecan turnover within complex, spatially heterogeneous patterns of mechanical strain generated by impingement has yet to be described. We hypothesize that impingement elicits differential regional profiles of intact and fragmented aggrecan across the Achilles tendon insertion.

METHODS

Explant Culture: Hind limbs (C57BL/6, <1 year) were dissected and pretreated in culture media with 100 nM of dexamethasone at 37°C

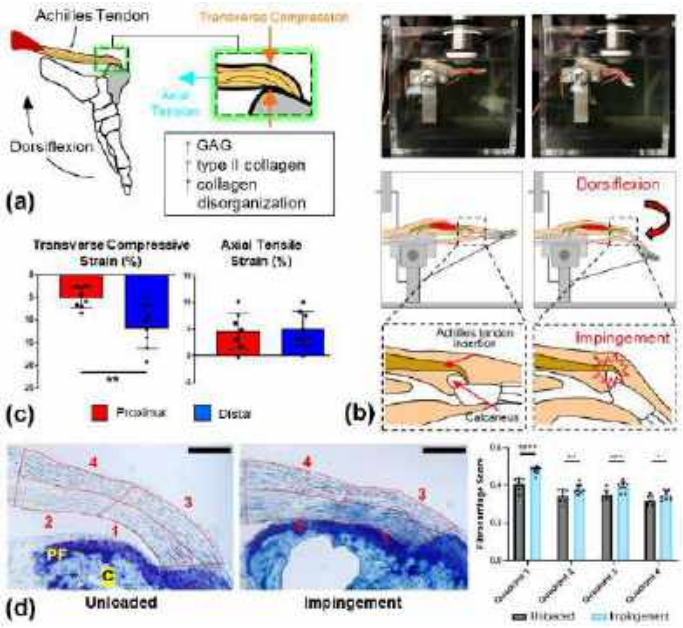

Figure 1: (a) Schematic depicting local fibrocartilage and transverse compressive strains sustained by impingement of the Achilles tendon insertion upon the calcaneus (gray) during ankle dorsiflexion. **(b)** (Top) Hind limb explant in our experimental platform before (left) and after (right) passive dorsiflexion to impinge the Achilles tendon insertion, as shown schematically (bottom)[1]. **(c)** Impingement produces significantly elevated transverse compressive strain (left) at the distal Achilles tendon insertion of hind limb explants measured via ultrasound elastography, but no change in axial tensile strain (right)[1]. **(d)** GAG staining (Toluidine blue) across quadrants dividing the

Achilles tendon insertion after 7 days of impingement (middle) appears enriched in distal quadrant 1 compared to unloaded tendons (left)[5]. (Right) Color image analysis indicates significantly elevated fibrocartilage score (quadrant color normalized to PF color) across all regions[5], most pronounced in distal quadrants 1 and 3. PF: Periosteal fibrocartilage. C: Calcaneus. Scale bar: 200μm.

for 48 hours. After 48 hours, dexamethasone was no longer supplemented in media. From each mouse, one hind limb was cultured for an additional 7 days in the absence of externally applied load, while the contralateral limb was positioned into our experimental platform to place the Achilles tendon insertion under static impingement[5].

Immunofluorescence: Level-matched formalin fixed, paraffin embedded tissue sections (10μm, sagittal) from contralateral pairs of limbs (unloaded vs. static impingement, n=7 pairs) were incubated pairwise (i.e. simultaneously using the same antibody solutions) with rabbit polyclonal anti-Aggrecan antibodies targeting either the G2 domain or the chondroitin sulfate-2 (CS) domain followed by secondary antibodies conjugated with AlexaFluor 555, with DAPI counterstaining. Given the structure of aggrecan and landscape of aggrecan fragments isolated from fresh and cultured tendon tissue[6-9], we expect the G2 antibodies to label intact aggrecan and most prominent fragments, serving as a proxy for total aggrecan content (**Fig 2**). The CS antibodies target a region spanning a high affinity site of ADAMTS-4,5 proteolysis[10] that drives constitutive aggrecan turnover[6-9] and are expected to label only intact aggrecan (**Fig 2**). 60X confocal microscopy images were analyzed to quantify average fluorescence intensity within spatial quadrants subdividing the tendon insertion (**Fig. 3**).

Statistics: Data were compared using repeated measures two-way ANOVA with Šídák's multiple comparison test. *$p \leq 0.05$. **$p \leq 0.01$. ***$p \leq 0.005$. ****$p \leq 0.001$.

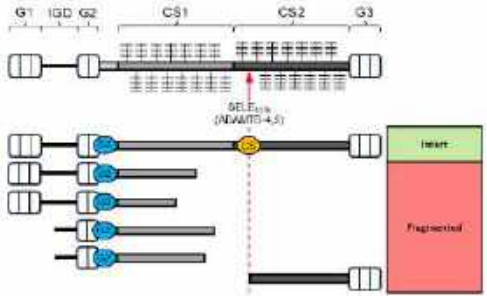

Figure 2: (Top) Schematic of aggrecan structure. Red arrowhead indicates a high affinity site of ADAMTS-4,5 proteolysis[10] that drives constitutive aggrecan turnover in tendon fibrocartilage. (Bottom) Landscape of aggrecan structure in tendon[9]. G2 antibodies serve as a proxy for total aggrecan. CS antibodies label intact aggrecan only.

RESULTS

Significant increases in G2 labeling intensity were detected in quadrant 1 of impinged tendons (**Fig 3A** – insets, data) without any change in CS labeling intensity (**Fig 3B** – insets, data), indicating an increase in total aggrecan with no change in intact aggrecan. This is reflected by a significant decrease in aggrecan integrity score (**Fig 3C**), suggesting lower relative proportions of intact/total aggrecan. Alternatively, no change in G2 labeling intensity was detected in quadrants 2-4 of impinged tendons (**Fig 3A**) despite significantly elevated CS labeling intensity (**Fig 3B**), indicating no change in total aggrecan but an increase in intact aggrecan. This is reflected by significantly elevated aggrecan integrity score in quadrants 3 and 4, suggesting increase in the relative proportions of intact/total aggrecan.

DISCUSSION

The results of this study indicate that impingement produces an

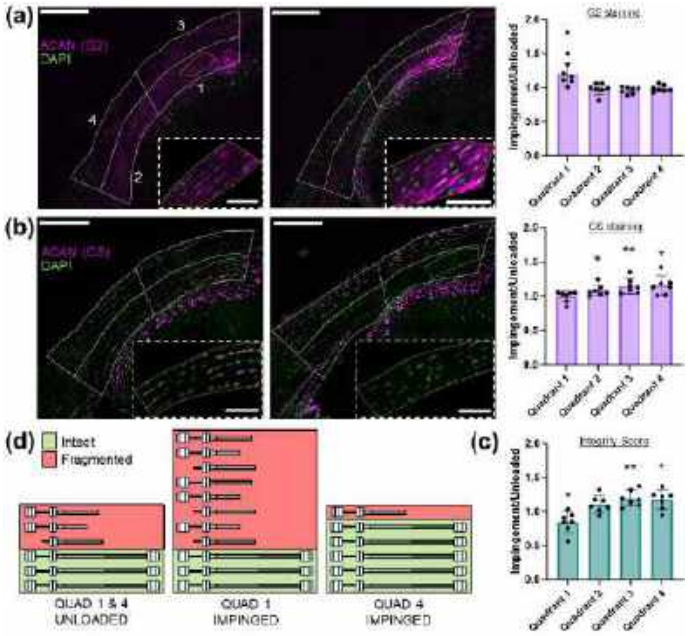

Figure 3: Immunofluorescent labeling of unloaded (left) and impinged (middle) tendons with **(a)** G2 antibodies for total aggrecan and **(b)** CS antibodies for intact aggrecan. (Right) Quadrant intensity data for impinged tendons normalized to contralateral unloaded tendons. Insets highlight change in distal quadrant 1. **(c)** Aggrecan integrity score for impinged tendons normalized to contralateral unloaded tendons, where higher scores represent higher relative proportions of intact/total aggrecan. **(d)** Schematic interpretation of impingement-driven change in aggrecan turnover within compressed (quadrant 1) and tensile (quadrant 4) regions. Scale bars: 200μm (main), 50μm (inset). Significant differences between impinged and unloaded indicated by *$p \leq 0.05$. **$p \leq 0.01$. ***$p \leq 0.005$. ****$p \leq 0.001$.

increase in total aggrecan in quadrant 1 with no change in intact aggrecan, suggesting accumulation of aggrecan fragments (**Fig 3D**). Previously, we measured significantly elevated transverse compressive strain at the distal insertion secondary to impingement despite uniform magnitude of axial tensile strain (**Fig 1C**). Our interpretation of these data is that compressive strains distally drive increased aggrecan turnover in parallel to increased production. Conversely, predominantly tensile strains proximally drive down aggrecan turnover yielding an increase in intact aggrecan with no change in total aggrecan, as described in quadrant 4 (**Fig 3D**). Together, these data support the hypothesis that spatial patterns of mechanical strain elicit differential regional patterns of aggrecan turnover at the impinged Achilles tendon insertion. In the future, we plan to relate these molecular-level changes in aggrecan turnover and structure to microscale change in compressive mechanical properties with atomic force microscopy (AFM).

ACKNOWLEDGEMENTS

This research was supported by the National Institutes of Health R01AR070765, R01AR082349, and R35GM147054.

REFERENCES

[1] Mora, KE et al., *J Biomech*, 132:110920, 2022. [2] Malaviya, P et al., *J Orth Res*, 18:116-125, 2000. [3] Cook, JL et al., *Br J Sp Med*, 46(3): 163-168, 2012. [4] Bah, I et al., *J Mech Beh Biomed Matl*, 112:104031, 2020. [5] Wise, BC et al., *JoVE*, 202: 2023. [6] Vogel, KG et al., *Mat Bio*, 14(2):171-9, 1994. [7] Rees, SG et al. *J Biochem*, 350: 181-188, 2000. [8] Robbins, JR et al. *Eur J Cell Bio*, 64(2):264-270, 1997. [9] Samiric, T et al., *Mat Bio*, 23(2):127-40, 2004. [10] Tortorella, MD et al., *Mat Bio*, 21(6):499-511, 2002.

PERIVASCULAR CNS FIBROBLASTS ARE ASSOCIATED WITH INCREASED TUMOR STIFFNESS AND POOR IMMUNOTHERAPY RESPONSE IN GLIOBLASTOMA PATIENTS

M. Zarodniuk (1), M. Panchbhavi (3), A. Steele (2), X. Lu (4), J. Li (3), M. Datta (1)

(1) Department of Aerospace and Mechanical Engineering, University of Notre Dame, Notre Dame, IN, USA
(2) Department of Electrical Engineering, University of Notre Dame, Notre Dame, IN, USA
(3) Department of Applied and Computational Mathematics and Statistics, University of Notre Dame, Notre Dame, IN, USA
(4) Department of Biological Sciences, University of Notre Dame, Notre Dame, IN, USA

INTRODUCTION

Glioblastoma (GBM) is the most common type of glioma accounting for more than 60% of all brain tumors in adults. GBM is highly aggressive and carries a profoundly poor prognosis with a median survival (OS) of <2 years [1]. Modern therapies have allowed for a modest increase in average survival time; however, GBM remains a terminal diagnosis with poor outcomes due to resistance to approved treatment modalities. Poor therapeutic response is mediated in part by the tumor microenvironment (TME) that harbors aberrant vasculature that promotes hypoxia and immunosuppression, and limits the entry of drugs and effector immune cells [2]. Although much is known about GBM endothelial cells, pericytes, and perivascular immune cells, it is unknown whether other mural cell types, such as fibroblasts, can be similarly reprogrammed by the tumor to promote its growth and treatment resistance.

Recent studies have uncovered the presence of fibroblasts in the meninges, choroid plexus, and perivascular spaces of the brain. Although the origins and functions of these central nervous system (CNS) fibroblasts are still being elucidated, recent data indicate that these cells play vital roles in fibrotic scarring in the CNS following injury and inflammation. In various CNS malignancies, however, particularly GBM, fibrotic scar formation by fibroblasts has been largely overlooked due to paucity of these cells within the CNS.

In some extracranial cancers, local tissue-resident fibroblasts can be reprogrammed by the tumor into cancer-associated fibroblasts (CAFs) that can remodel extracellular matrix (ECM), thereby accelerating tumor growth and impairing response to immunotherapies [3]. Understanding whether this mechanism is also conserved within the CNS can reveal novel insights into therapeutic resistance and guide the design of new strategies to improve outcomes in brain tumor patients.

To this end, we used publicly available single cell and bulk RNA sequencing (RNA-seq) datasets to identify CNS fibroblasts in glioblastoma and characterize their gene expression profiles, as well as their clinical correlates. In particular, we sought to answer (1) whether CNS fibroblasts may be responsible for ECM remodeling and tumor stiffening (1), and (2) whether CNS fibroblasts may hinder response to immune checkpoint blockade (ICB) immunotherapy in GBM patients.

METHODS

The scRNA-seq data (GSE182109, GSE163577) were obtained from Gene Expression Omnibus [4]. Individual samples were log-normalized and integrated using Seurat's (v4.3.0.1) reciprocal PCA [5]. Doublets were identified and removed using Scrublet (v0.2.3) algorithm [6]. Next, cells were clustered and annotated based on previously reported marker genes [4] as well as copy number alterations (CNAs) inferred using CopyKat (v1.1.0) algorithm [7]. To exclude poor quality cells within each cell type, we applied median absolute deviation (MAD)-based outlier detection approach, as described previously [8]. Clusters characterized by low UMI counts, high fraction of mitochondrial reads, and uninformative marker genes were removed. scRNA-seq datasets were integrated using anchor-based Seurat (v3) integration [9].

Publicly available RNA-seq data were downloaded from TCGA and CGGA databases. Magnetic resonance elastography (MRE) data as well as biopsy-matched RNA-seq data were obtained from GitHub repository (SkabbiVML/stiffR) [10]. TCGA and CGGA datasets were were TMM-normalized (edgeR v3.40.2), and logCPM values were used for all downstream analyses. Signature scoring was performed using ssGSEA (GSVA v1.50.0). Cell type deconvolution was performed using MuSiC (c.1.0.0).

RESULTS

In order to identify CNS fibroblasts as well as other perivascular cell types in scRNA-seq data [4], we first undertook a marker-based approach by subclustering *PDGFRβ+ ACTA2+* mural cells. Based on

previously identified gene expression markers [11], we found distinct clusters of perivascular fibroblasts (P-FB; *FBLN1*, *LAMA2*), meningeal fibroblasts (M-FB; *SLC4A4*, *KCNMA1*), pericytes (PC; *PDGFRB*, *COL4A1*), and smooth muscle cells (SMC; *ACTA2*) (**Fig. 1a**). Integration of GBM mural cells with those from a human brain vascular atlas [11] resulted in alignment of respective subpopulations in the UMAP space (**Fig. 1b**). Notably, the P-FB cluster expressed several classical CAF markers such as *PDGFRA*, *PDGFRB*, *COL1A1*, and *FAP* [12]–[14] (**Fig. 1a**), suggesting that perivascular fibroblasts may assume a CAF-like phenotype in GBM.

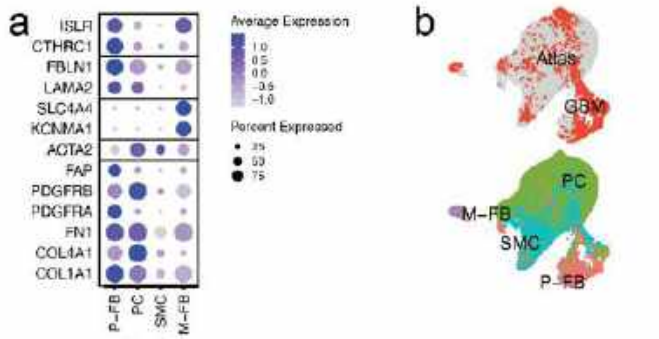

Figure 1: Identification of mural cell populations in GBM. **a** Marker genes identifying subpopulations of mural cells in GBM. P-FB – perivascular fibroblast; PC – pericyte; SMC – smooth muscle cell; M-FB – meningeal fibroblast. **b** Joint UMAP embedding of mural cells from a human brain vascular atlas (grey) and GBM mural cells (red).

Next, we sought to determine whether perivascular fibroblasts may be responsible for deposition of ECM and increased tumor stiffness by analyzing magnetic resonance elastography (MRE) and biopsy-matched RNA-seq data from eight GBM patients [10]. Using single-sample GSEA, we found an enrichment of perivascular fibroblast and pericyte gene signatures in stiff biopsies (**Fig. 2a**). Similarly, we found a higher estimated proportion of perivascular fibroblasts in stiff biopsies using single-cell deconvolution (**Fig. 2b**).

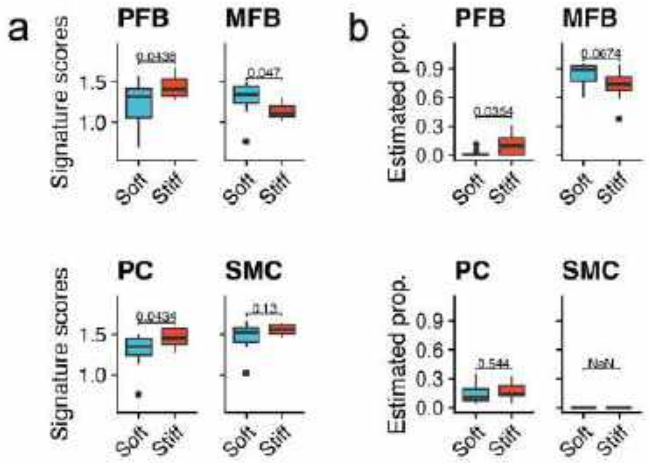

Figure 2: Perivascular fibroblasts are associated with increased GBM stiffness. **a** Marker genes identifying subpopulations of mural cells in GBM. P-FB – perivascular fibroblast; PC – pericyte; SMC – smooth muscle cell; M-FB – meningeal fibroblast. **b** Joint UMAP embedding of mural cells from a human brain vascular atlas (grey) and GBM mural cells (red) (P values were calculated using t-test).

These findings suggest that fibrotic scarring observed in glioblastoma multiforme (GBM) can have common mechanisms with other neuropathologic conditions where fibrogenic cells originate from perivascular fibroblasts in response to inflammatory stimuli.

Next, to determine whether perivascular fibroblasts play a role in response to immunotherapy in GBM, we interrogated retrospective data from two recent anti-PD1 immunotherapy trials [15], [16]. In both cohorts, we found a significant reduction in overall survival for patients whose tumors were enriched in perivascular fibroblasts (**Fig. 3a-b**), suggesting that the presence of perivascular fibroblasts may be prognostic of a poor immunotherapeutic response.

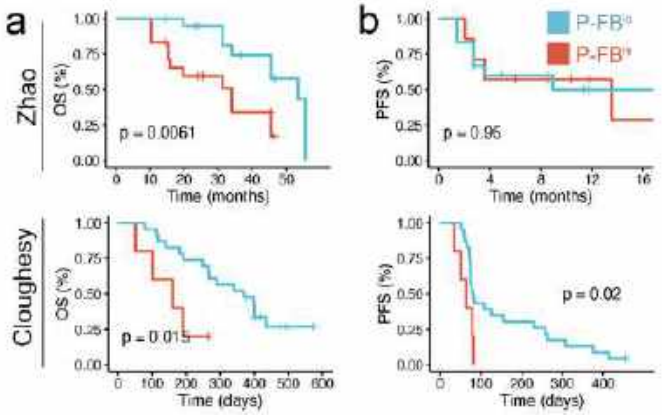

Figure 3: Perivascular fiborblasts predict response to PD-1 immunotherapy. Kaplan–Meier plots of overall (**a**) and progression free (**b**) survival for patients with high (red) or low (blue) presence of perivascular fibroblasts in Cloughesy ($n = 28$) and Zhao ($n = 38$) cohorts treated with anti-PD1 therapy (P values were calculated using log-rank test).

DISCUSSION

A previous study has shown that GBM stiffness is associated with ECM reorganization, particularly fibrillar collagens [10]. However, it was previously unknown which cell type(s) are responsible for this phenomenon. In this study, we used publicly available MRE and gene expression data to show that perivascular fibroblasts are associated with increased tumor stiffness. In contrast, a recent study of human glioblastoma identified pericytes as the cellular source of ECM [17]. However, the reliance of this study on cell surface markers without comprehensive gene expression profiling raises the possibility that the identified cells could represent a different cell type such as fibroblasts or smooth muscle cells, which share overlapping cell surface markers with pericytes [18].

Therapeutically reducing ECM deposition can alleviate immunosuppression across various cancer models, including GBM [19]–[21]. In our study, we further show that perivascular fibroblasts hinder response to PD-1 ICB therapy; however, the mechanisms by which perivascular fibroblasts thwart immunotherapy efficacy remains to be established.

Taken together, our results suggest that perivascular fibroblasts actively remodel ECM, leading to increased tumor stiffness and therapy resistance, and may therefore act as analogs of CAFs in peripheral tumors.

ACKNOWLEDGEMENTS

This work was supported in part by NIH K22CA258410 (to M.D.); X.L. is supported by NIH grant R01CA248033 and DoD grants W81XWH2010312 and W81XWH2010332; Part of the analysis was performed on the high performance computing clusters provided by the Notre Dame Center for Research Computing. We thank J. Najera, L. Celebi, and R. Rumbach for their input on the manuscript. We thank K. E. Emblem, R. M. Prins, and R. Rabadan for kindly providing their data.

REFERENCES

[1] R. Stupp *et al.*, "Effect of Tumor-Treating Fields Plus Maintenance Temozolomide vs Maintenance Temozolomide Alone on Survival in Patients With Glioblastoma: A Randomized Clinical Trial," *JAMA*, vol. 318, no. 23, pp. 2306–2316, Dec. 2017.

[2] R. K. Jain, "Antiangiogenesis strategies revisited: from starving tumors to alleviating hypoxia," *Cancer Cell*, vol. 26, no. 5, pp. 605–622, Nov. 2014.

[3] J. M. Houthuijzen *et al.*, "CD26-negative and CD26-positive tissue-resident fibroblasts contribute to functionally distinct CAF subpopulations in breast cancer," *Nat. Commun.*, vol. 14, no. 1, p. 183, Jan. 2023.

[4] N. Abdelfattah *et al.*, "Single-cell analysis of human glioma and immune cells identifies S100A4 as an immunotherapy target," *Nat. Commun.*, vol. 13, no. 1, p. 767, Feb. 2022.

[5] Y. Hao *et al.*, "Integrated analysis of multimodal single-cell data," *Cell*, vol. 184, no. 13, pp. 3573-3587.e29, Jun. 2021.

[6] S. L. Wolock, R. Lopez, and A. M. Klein, "Scrublet: Computational Identification of Cell Doublets in Single-Cell Transcriptomic Data," *Cell Syst*, vol. 8, no. 4, pp. 281-291.e9, Apr. 2019.

[7] R. Gao *et al.*, "Delineating copy number and clonal substructure in human tumors from single-cell transcriptomes," *Nat. Biotechnol.*, vol. 39, no. 5, pp. 599–608, May 2021.

[8] P.-L. Germain, A. Sonrel, and M. D. Robinson, "pipeComp, a general framework for the evaluation of computational pipelines, reveals performant single cell RNA-seq preprocessing tools," *Genome Biol.*, vol. 21, no. 1, p. 227, Sep. 2020.

[9] T. Stuart *et al.*, "Comprehensive integration of single-cell data," *Cell*, vol. 177, no. 7, pp. 1888-1902.e21, Jun. 2019.

[10] S. F. Svensson *et al.*, "MR elastography identifies regions of extracellular matrix reorganization associated with shorter survival in glioblastoma patients," *Neuro Oncol Adv*, vol. 5, no. 1, Jan. 2023.

[11] A. C. Yang *et al.*, "A human brain vascular atlas reveals diverse mediators of Alzheimer's risk," *Nature*, vol. 603, no. 7903, pp. 885–892, Mar. 2022.

[12] Y. Sharon, L. Alon, S. Glanz, C. Servais, and N. Erez, "Isolation of normal and cancer-associated fibroblasts from fresh tissues by Fluorescence Activated Cell Sorting (FACS)," *J. Vis. Exp.*, no. 71, p. e4425, Jan. 2013.

[13] N. Erez, M. Truitt, P. Olson, S. T. Arron, and D. Hanahan, "Cancer-Associated Fibroblasts Are Activated in Incipient Neoplasia to Orchestrate Tumor-Promoting Inflammation in an NF-kappaB-Dependent Manner," *Cancer Cell*, vol. 17, no. 2, pp. 135–147, Feb. 2010.

[14] M. Nurmik, P. Ullmann, F. Rodriguez, S. Haan, and E. Letellier, "In search of definitions: Cancer-associated fibroblasts and their markers," *Int. J. Cancer*, vol. 146, no. 4, pp. 895–905, Feb. 2020.

[15] T. F. Cloughesy *et al.*, "Neoadjuvant anti-PD-1 immunotherapy promotes a survival benefit with intratumoral and systemic immune responses in recurrent glioblastoma," *Nat. Med.*, vol. 25, no. 3, pp. 477–486, Mar. 2019.

[16] J. Zhao *et al.*, "Immune and genomic correlates of response to anti-PD-1 immunotherapy in glioblastoma," *Nat. Med.*, vol. 25, no. 3, pp. 462–469, Mar. 2019.

[17] Y. Hoogstrate *et al.*, "Transcriptome analysis reveals tumor microenvironment changes in glioblastoma," *Cancer Cell*, vol. 41, no. 4, pp. 678-692.e7, Apr. 2023.

[18] C. E. Dorrier, H. E. Jones, L. Pintarić, J. A. Siegenthaler, and R. Daneman, "Emerging roles for CNS fibroblasts in health, injury and disease," *Nat. Rev. Neurosci.*, vol. 23, no. 1, pp. 23–34, Jan. 2022.

[19] M. Datta *et al.*, "Losartan controls immune checkpoint blocker-induced edema and improves survival in glioblastoma mouse models," *Proc. Natl. Acad. Sci. U. S. A.*, vol. 120, no. 6, p. e2219199120, Feb. 2023.

[20] Y. Zhao *et al.*, "Losartan treatment enhances chemotherapy efficacy and reduces ascites in ovarian cancer models by normalizing the tumor stroma," *Proc. Natl. Acad. Sci. U. S. A.*, vol. 116, no. 6, pp. 2210–2219, Feb. 2019.

[21] V. P. Chauhan *et al.*, "Reprogramming the microenvironment with tumor-selective angiotensin blockers enhances cancer immunotherapy," *Proc. Natl. Acad. Sci. U. S. A.*, vol. 116, no. 22, pp. 10674–10680, May 2019.

SIGNIFICANTLY AMPLIFIED PHOTOACOUSTIC EFFECT FOR SILICA-COATED GOLD NANOPARTICLES BY INTERFACE HEAT TRANSFER MECHANISMS

C. Xie(1), P. Kang(1), J. Youn(1), B. A. Wilson(1), L. Basavarajappa(2), Q. Wang(3,4), M. Kim(3), K. Hoyt(2), Z. Qin(1,2,5,6)

(1) Department of Mechanical Engineering, University of Texas at Dallas, Richardson, Texas, USA
(2) Department of Bioengineering, University of Texas at Dallas, Richardson, Texas, USA
(3) Department of Material Science and Engineering, University of Texas at Dallas, Richardson, Texas, USA
(4) King Abdullah University of Science and Technology, Thuwal, Makkah, Saudi Arabia
(5) Department of Biomedical Engineering, University of Texas at Southwestern Medical Center, Dallas, Texas, USA
(6) Center for Advanced Pain Studies, University of Texas at Dallas, Richardson, Texas, USA

INTRODUCTION

Gold nanoparticles (AuNPs) can efficiently convert laser energy into heat, emitting thermal acoustic waves, making them valuable agents for photoacoustic (PA) signaling in biomedical applications.[1,2] Recently, studies have shown that silica-coated AuNP (SiO_2-AuNP) can enhance the laser-acoustic conversion compared with that of AuNP.[3] However, debate surrounds the mechanism behind this PA enhancement. Hu et al.'s experiments suggest improved thermal transport at the particle-water interface due to silica coating, potentially explaining the enhancement.[4] Conversely, modeling suggests a reduced PA signal due to limited heat conduction through the silica layer.[5] The conflicting results leave the SiO2-AuNP's PA enhancement mechanism uncertain.

Here, we systematically explored the impact of silica coating on PA generation with SiO_2-AuNP under ps and ns pulsed lasers. We observed substantial PA enhancement (up to 400%) with silica coating and ps laser excitation. Our proposed theoretical model highlights two key factors contributing to this amplification: improved interface thermal conductance at the silica-water interface and efficient electron-phonon coupling at the gold-silica interface. This study discovers a regime of large PA amplification and provides a new rationale for plasmonic nanoparticle design to achieve better PA efficiency.

METHODS

Nanoparticle preparation: AuNP was prepared by following the Frens' as previously reported.[6] SiO_2-AuNP preparation were followed by the procedures reported by Luis et al. (**Fig. 1A**).[7]

PA signal reading: Fig. 1B shows the experimental setup: a flow system with dialysis tubing installed in water bath. The laser beam (532 nm) was aligned on tubing. PA signal is detected by a transducer. PA enhancement (%) was calculated from PA signal intensity from sample (P), from bare AuNP (P_{Au}) and from water (P_{H_2O}):

$$PA\ enhancement\ (\%) = \frac{P - P_{Au}}{P_{Au} - P_{H_2O}} \times 100 \quad (1)$$

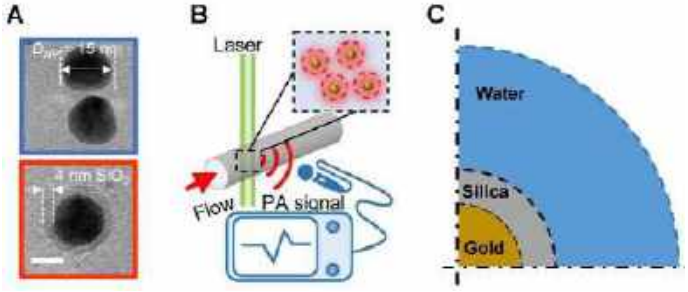

Figure 1. (A) TEM image of AuNP and SiO_2-AuNP, scale bar: 20 nm. (B) Schematic illustration of experimental setup. (C) Schematic illustration of PA modeling setup.

PA modeling: Fig. 1C demonstrates the setup for PA modeling. The plasmonic heating is modeled with two-temperature model:[8]

$$\rho_{Au} C_e \frac{\partial T_e}{\partial t} - \nabla \cdot \mathrm{k}_e \nabla T_e = Q_v(t) - G_{ep}(T_e - T_p) \quad (2)$$

$$\rho_{Au} C_{p\_Au} \frac{\partial T_p}{\partial t} - \nabla \cdot \mathrm{k}_p \nabla T_p = G_{ep}(T_e - T_p) \quad (3)$$

The thermal acoustic emission is estimated with wave function:

$$\frac{1}{\rho_m {c_s}^2} \frac{\partial^2 p_w}{\partial t^2} - \nabla \cdot \left(-\frac{1}{\rho_m} \nabla p_w\right) = \frac{\partial}{\partial t}\left(\beta \frac{\partial T_m}{\partial t}\right) \quad (4)$$

To analyze the laser-acoustic conversion efficiency, we define the PA quantum yield efficiency (Φ_{PA}) as the ratio between acoustic energy ($E_{acoustic}$) and laser energy ($E_{optical}$):

$$\Phi_{PA} = \frac{E_{acoustic}}{E_{optical}} = \frac{4\pi {r_m}^2}{z} \frac{\int p^2 dt}{F C_{abs}} \quad (5)$$

RESULTS

First, we determined the effect of laser pulse duration on the PA signal from AuNP and SiO_2-AuNP (**Fig. 1A**). As shown in **Fig. 2**, upon the ps pulsed laser (28 ps) irradiation, PA signal amplitude from SiO_2-AuNP is larger than that from AuNP. However, no noticeable PA signal enhancement was observed under ns pulsed (6 ns) laser. We further

analyzed the peak-to-peak (P2P) amplitude of PA signal with different laser fluence. With the ps laser excitation, the slope of P2P amplitude for both 15 nm and 45 nm SiO_2-AuNP is significantly higher than that for the bare AuNP (**Fig. 2B&C**), while there is no significant enhancement for the ns laser cases (**Fig. 2E&F**).

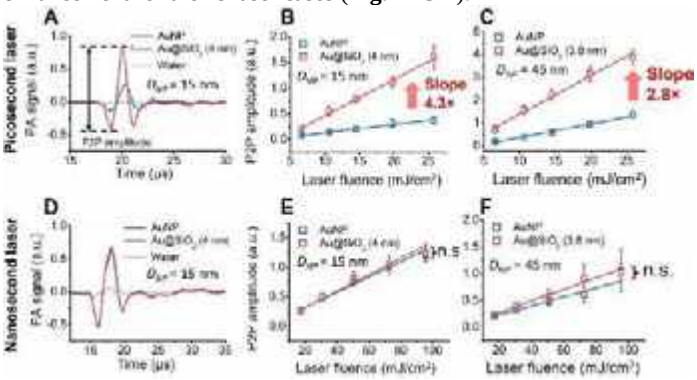

Figure 2. (A) PA wavefunctions of AuNPs and SiO_2-AuNP (15 nm Au core) with ps laser (19.7 mJ/cm^2). Amplitude of PA signals with ps laser (B) 15 nm Au core and (C) 45 nm Au core. (D) PA wavefunctions of AuNPs and SiO_2-AuNP (15 nm Au core) with ns laser (72.5 mJ/cm^2). Amplitude of PA signals with ns laser (E) 15 nm Au core and (F) 45 nm Au core.

Next, we investigated the effect of the thickness of silica coating on PA enhancement with ps laser. SiO_2-AuNP with 2 nm to 16 nm thickness silica coatings are prepared (**Fig. 3A**). As shown in **Fig. 3B**, for the 15 nm Au core, notable PA enhancement (Eq. 1) is observed with thin coatings (2.5 ± 0.5 to 3.9 ± 0.7 nm). Similar for 45 nm Au core (**Fig. 3C**), thin silica coating (2.0 ± 0.4 to 4.9 ± 1.2 nm) leads to PA enhancement. Among these, maximum enhancement around 400% (300%) with 4.6 nm silica (4.9 nm silica) for 15 nm Au core (45 nm Au core) is observed. Additionally, PA enhancement was only observed with a thin silica coating (thickness < 5 nm).

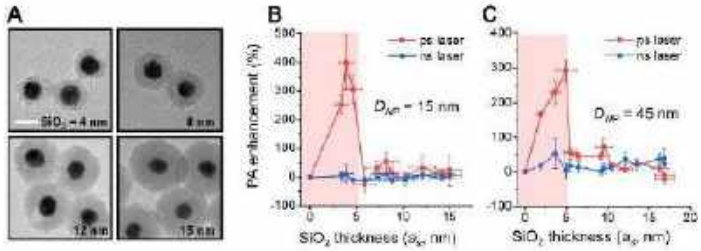

Figure 3. (A) TEM image of SiO_2-AuNP with different thickness of silica coating, scale bar: 20 nm. (B&C) Effects of silica coating thickness (ps laser: 19.8 mJ/cm^2, ns laser: 72.5 mJ/cm^2) on PA signal generation from (B) 15 nm Au core and (C) 45 nm Au core.

Lastly, we proposed a theoretical model for the mechanism of PA enhancement with SiO_2-AuNP. The energy transforms from hot electrons in gold (T_e) to heating in water (T_m) are the key issues in the model. In the traditional two temperature model for AuNP heating (**Fig. 4A**), heat transportation starts from T_e to gold lattice heating (T_p) through electron-phonon (*e-ph*) coupling, and further transfer to T_m through phonon-phonon (*ph-ph*) coupling. In contrary, an extra energy transfer channel from T_e to T_m in the SiO_2-AuNP scenario is considered in our model: 1) Heat transfer from T_e to T_p and then to silica through *ph-ph* coupling (R_{ps}); 2) Energy from T_e directly deposite to silica phonons through *e-ph* coupling at the gold-silica interface (R_{es}, **Fig. 4B**, marked as red). Based on this model, we estimated Φ_{PA} (Eq. 5) and only found Φ_{PA} enhancement with ps laser and thin silica coating (< 5.7 nm) (**Fig. 4C**). This laser duration and silica thickness dependent PA enhancement qualitatively agrees with our experimental findings. Further analysis of the model shows that synergistic heat transfer enhancements on gold-silica interface (*e-ph* coupling) and silica-water interface (h_{sw}) leads to the PA enhancement observed in the experiment (**Fig. 4D**). This study is an important step towards a better understanding of PA signal generation from plasmonic nanoparticles by providing a clear mechanism to account for the PA enhancement by silica coating.

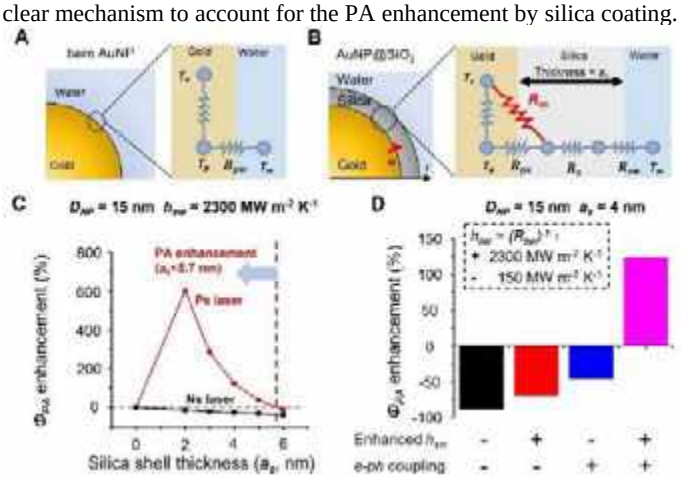

Figure 4. (A&B) Heat transfer model for (A) AuNP and (B) SiO_2-AuNP. (C) The silica shell thickness effect for PA quantum yield efficiency (Φ_{PA}) under ps and ns laser. (D) Enhanced Φ_{PA} is only observed with *e-ph* coupling at gold-silica and enhanced thermal transport at silica-water interface (h_{sw}).

DISCUSSION

In this work, we experimentally investigated the PA enhancement with SiO_2-AuNP and proposed a theoretical model for the mechanism. The theoretical model qualititatively explains the experimental findings. There may be additional factors which can contribute to the observed PA enhancement not captured by the current model, including the silica porosity and the presence of water in silica. Water can decrease silica's thermal conductivity, potentially reducing PA enhancement. However, water confined in narrow nanopores within silica could boost thermal expansion, potentially elevating the PA signal. Further investigation is crucial to unveil the role of silica porosity and the presence of water.

ACKNOWLEDGEMENTS

This work was supported by National Institutes of Health (R35GM133653), by the National Science Foundation (1631910), and by funds from a Eugene McDermott Professorship.

REFERENCES

[1] Beard, P, *Interface Focus*, 1:602–631, 2011.

[2] Lin, L et al., *Nat Commun*, 9:2352, 2018.

[3] Moon, H et al., *ACS Nano*,9: 2711–2719, 2015.

[4] Hu, M et al., *Chem Phys Lett*, 372:767-772, 2003.

[5] Shahbazi, K et al., *Commun Phys*, 2:119, 2019.

[6] FRENS, G et al., *Nat Phys Sci*, 241:20–22, 1973.

[7] Liz-Marzán, L et al., *Langmuir*, 12:4329-4335, 1996.

[8] Chen, Y S et al., *Nano Lett*, 11:348_354, 2011.

IDENTIFYING THE ROLE OF THE SEPTUM WALL IN RIGHT VENTRICULAR REMODELING

Kristen M. Garcia (1), Becky A. Hardie (1), Jessica Huberts (1), Daniela Valdez-Jasso (1)

(1) Department of Bioengineering, University of California San Diego, La Jolla, CA, US

INTRODUCTION

Pulmonary arterial hypertension (PAH) is a vasculopathy of the arteries of the lungs that is four times more prevalent in women than men. PAH is associated with vasoconstriction, stiffening, and *in-situ* thrombosis, raising the mean pulmonary arterial pressure.[1] This pressure overload induces right ventricle (RV) remodeling. The RV can adapt, however, when left untreated, RV remodeling can become maladaptive and lead to right heart failure and premature death.[2]

Studies of the RV free wall mechanical properties have shown myocardium stiffening and changes in contractility, leading to overall diastolic dysfunction in PAH. However how and what the role of the interventricular septal (IVS) wall has in this remodeling process is understudied.[3] The healthy IVS is softer, with a lower collagen content than the ventricular walls, suggesting a lower stiffness compared to the RV free-wall.[3] It is hypothesized that the increased RV pressures with an unaltered left ventricle can lead to changes in transeptal pressure gradient, increasing septal wall stress, and inducing possible septal flattening. Previous septum studies have included working with slices of canine tissue. Here we seek to characterize the full thickness of the IVS and understand how the properties change during PAH.[4]

METHODS

All protocols were carried out in accordance with the Institutional Animal Care and Use Committee at the University of California San Diego. Septal walls were harvested from 5 male and 4 female Sprague-Dawley rats weighing ~250-300 grams. Rats were anesthetized with 5% isoflurane in 100% oxygen. After exsanguination, the heart is flushed with cold phosphate-buffered saline (PBS) and heparin. Once the heart was harvested, the IVS was isolated from the ventricles, and a rectangle sample region of the tissue was cut with one axis aligned along the apex-to-base (longitudinal direction X_1) and the perpendicular axis aligned circumferentially (X_2) as shown in Figure 1.

PAH was induced in one male rat by a single injection of a vascular endothelial growth factor receptor inhibitor (SU5416,S8442 MilliporeSigma, CAS Number 204005-46-9, PubChemSubstance ID 24278606 Sigma-Aldrich, MO) followed by 3 weeks in hypoxia (10% oxygen levels). The rat was kept in normoxia for an additional 9 weeks. PAH was confirmed by invasive measurements of blood pressure at the inlet of the pulmonary artery with a mean pulmonary arterial pressure of 48 mmHg.

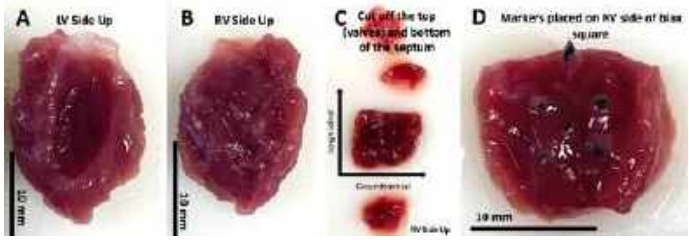

Figure 1. The isolated septum facing the left ventricle (A) and the right ventricle (B). The apical and basal borders of the septum were trimmed to obtain a rectangular sample for biaxial testing (C). Markers were placed on the middle region of the RV side to track displacement during planar biaxial testing.

Planar Biaxial Testing: All protocols for the septum followed the previously used RV planar biaxial protocols described by Vélez-Rendón et al.[5] Sample tissue length along both axes were measured with a digital caliper. Wall thickness was determined by the average of five thickness measurements throughout the sample. Tissue mass was recorded, five graphite markers were placed on the middle region of the RV side of the tissue sample, and the tissue was placed in the Bose Electro Force planar biaxial device attached via hooks placed on a pulley system. The tissue was submersed in temperature-controlled PBS

(37 °C) and the pixel positions of the markers were tracked throughout the test. One preconditioning trial was performed with the tissue being stretched to 8%, 10%, and 12% of the ex-vivo tissue side length. After preconditioning, the sample was preloaded and stretched 10% of the ex vivo side length for multiple trials, following the X_1:X_2 ratios: 1:1, 1:0.5, 1:0.25, 1:1, 0.5:1, 0.25:1, and 1:1.

Constitutive Equations: The septum wall is modeled as a hyperelastic, anisotropic, incompressible material with axes aligned along the longitudinal and circumferential directions (Figure 1). We used a Fung-type exponential strain-energy function to relate stress and strain. The Limited Memory BFGS algorithm is used to optimize the parameters (C, α_1, α_2, and α_3) which are then used to compute the strain-energy surface for each individual animal. The two-dimensional strain-energy density function (per unit area) is described as:

$$W(\boldsymbol{E}) = C(e^{Q(\boldsymbol{E})} - 1) \quad (1)$$
$$\text{where } Q(\boldsymbol{E}) = \alpha_1 \boldsymbol{E}_{11}^2 + \alpha_2 \boldsymbol{E}_{22}^2 + \alpha_3 \boldsymbol{E}_{11}\boldsymbol{E}_{22}$$

where shear strains are negligible. The strain-energy surfaces are averaged across the Green-strain space bounded by experimentally measured strain. The equibiaxial stress-strain curves from the averaged surface +/- standard error curves are plotted to represent a group.

RESULTS

IVS from male and female rats exhibited an isotropic response (Figure 2). When comparing the response between male and female IVS, female tissues are significantly stiffer than the male tissues (Figure 3). Finally, when comparing the normotensive group with a hypertensive male septum, there is a difference in material stiffness (Figure 4).

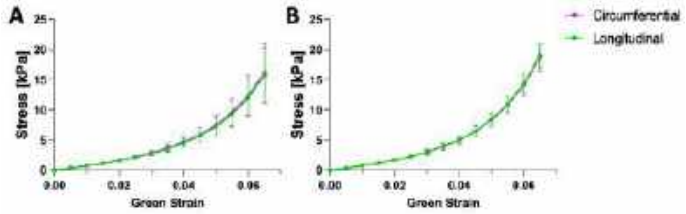

Figure 2. Equibiaxial stress-strain curves of the septum, with RV side facing up exhibit an isotropic tissue response in male (A) and female (B) hearts.

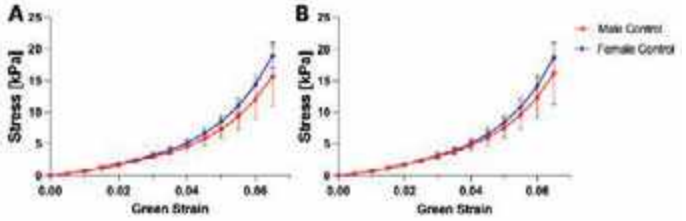

Figure 3. When comparing the male and female control septum tissue responses, we note that female septa are stiffer than the males in both longitudinal (A) and circumferential (B) directions.

DISCUSSION

IVS research with respect to RV remodeling during PAH is limited. Our initial findings indicate feasibility and reproducibility even though the morphology of the septum is more challenging than that of the ventricular walls. Findings of the septum being isotropic has only been found at high strain values in adult sheep hearts by Nguyen-Truong et al.[5] It is noteworthy that at small strains, Nguyen-Truong et al. reported the septum to be anisotropic.[5] Differences in orientation of the tissue and levels of stretch can lead to differences in behavior of the tissue. Some of the discrepancy in these results might be a resultant of testing slices of the septum versus our full-thickness septum samples.

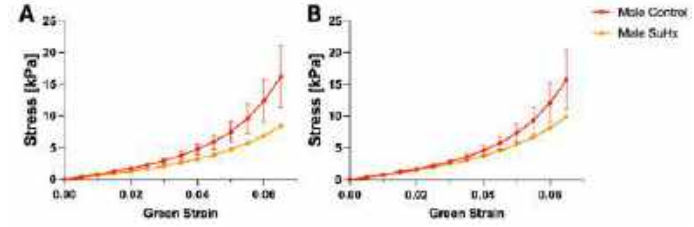

Figure 4. Initial results of comparing the septum from normotensive animals to a pulmonary hypertensive animal septum. We find that in both the circumferential (A) and the longitudinal (B) directions, the male control septa are stiffer.

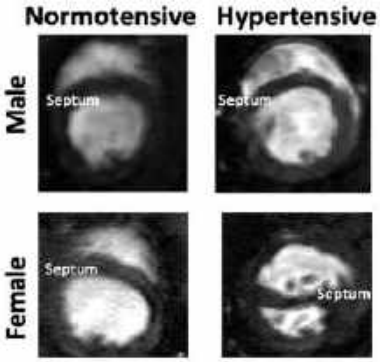

Figure 2. Cardiac magnetic resonance imaging of a female and male rat at the normotensive state and then again at a hypertensive state.

When testing the septa of normotensive male and female animals we found the female septa to be significantly stiffer than the males. When comparing the mechanical properties of male normotensive (n=5) and hypertensive (n=1) septa there appeared to be no significant stiffening from one state to the next. This could explain what we have seen in the cardiac magnetic resonance imaging (Figure 5) of normotensive and hypertensive male rats, where the septum geometry does not change between states. A major limitation of this study is the lack of female hypertensive septum samples. To understand how the female septum responds to progressive pressure overload, future samples are needed. Further investigation is needed for both male and female hypertensive septum. The goal of our work is to understand the mechanics of the IVS and to determine how RV pressure overload changes the properties of the septum wall.

ACKNOWLEDGEMENTS

We would like to thank Michael Megally, Andrew Harris, and Parisa Shahabi for assistance with experiments. Funding was provided by NHLBI 1R01HL155945-01, 1R25HL145817-01, 1T32HL160507-01A1, NSF CAREER Award 2046259, and the University of California San Diego Graduate Interfaces Program under the T32 EB 009380 training grant.

REFERENCES

[1] Lai, Y.-C. et al. *Circ. Res.* **115**, 115–130 (2014).
[2] Franco, V. *Pulm. Hypertens.* **8**, 403–412 (2012).
[3] Triposkiadis, F. *et al. J. Clin. Med.* **11,** 3227 (2022).
[4] Vélez-Rendón, D. *et al. J. Biomech. Eng.* **141**, 091011 (2019).
[5] Nguyen-Truong, M. *et al. Bioengineering.* 8(12): 216 (2021).

CROSS-CORRELATION OF BIOMECHANICAL, CONNECTOMIC, AND PATHOLOGIC MARKERS IN NEURODEGENERATION AT 7T MRI

E. Triolo (1), M. Langan (2), O. Khegai (2), S. Binder (3), T. Hedden (3), P. Balchandani (2), M. Kurt (1,2)

(1) Department of Mechanical Engineering, University of Washington, Seattle, WA, USA
(2) The Biomedical Engineering and Imaging Institute, Icahn School of Medicine at Mount Sinai, New York City, NY, USA
(3) Department of Neurology, Icahn School of Medicine at Mount Sinai, New York City, NY, USA

INTRODUCTION

Alzheimer's disease (AD), a progressive neurodegenerative disease thought to be caused by abnormal deposits of amyloid plaques in the cortical gray matter in the brain, is the leading cause of dementia, having an immense impact on the aging population worldwide[1]. Over the progression of AD, damage spreads throughout the brain, shrinking the volume of the overall brain tissue[2]. Early diagnosis of AD is still challenging due to subtle microstructural changes, which is particularly troubling, as most treatments for AD can only be used to slow its progression, not reverse it, and are often far more successful when started early. β-amyloid can be detected through the utility of positron emission tomography (PET) with aid of a radioactive, but this procedure is invasive, leading to a profound need to identify non-invasive correlates of AD pathologies.

MR Elastography (MRE) is a technique for determining the mechanical response of tissues using applied harmonic deformation and motion-sensitive MRI. Performing MRE on human brain can provide information on different structures within brain tissue based on their mechanical properties, and pivotal studies applying MRE have shown a progressive softening of white and gray matter tissue in AD patients in regions in line with the known topography of AD pathology[3,4]. Another potential non-invasive diagnostic tool is diffusion tensor magnetic resonance imaging (DTI), which provides a metric for understanding the integrity of microstructure[5]. In addition to changes in signal intensity in the white matter due to aging, previous DTI studies have also identified changes in DTI signal intensity in gray matter regions[6,7], making it a region of interest to study in aging and neurodegeneration.

Additionally, studies at 3T have found correlations between MR Elastography (MRE) and DTI metrics in small white matter structures in young, healthy individuals[8,9], but low imaging resolution limited the specificity of the results in small regions due to partial volume effects.

Leveraging non-invasive ultra-high field (UHF), 7 Tesla (7T) MRI, with increased signal-to-noise ratio and improved soft tissue contrast afforded by UHF allows us to accurately map tissue microstructure. *In this study we aim to use 7T MRE, 7T DTI, 3T amyloid-PET, and cognitive testing results to determine the relationships between these metrics in a cohort of older individuals with either normal cognition, mild cognitive impairment (MCI), or AD.*

METHODS

Two scanning sessions (7T MRI and 3T PET, Fig 1A) and the Preclinical Alzheimer Cognitive Composite (PACC) test were performed on 14 subjects (Avg. age 70.3±5.2 years) determined to be cognitively normal (CN), and 6 subjects (Avg. age 70.0±9.4 years) determined to have MCI or AD. All MCI/AD patients had a consensus diagnosis of cognitive impairment and a Clinical Dementia Rating >4.0 in the Clinical Dementia Rating Scale Sum of Boxes.

Full brain coverage MRE (using a custom SE-2D-EPI-based sequence[10]) was performed at 1.1mm isotropic resolution and 50Hz vibration frequency[11], using a 32-channel head coil (Nova Medical) on a 7T Siemens Magnetom MRI scanner (TR/slice=140ms, TE=65ms, GRAPPA=3, Partial Fourier 7/8). Raw data were collected and analyzed as described in Triolo, *et al.*[12] to calculate the absolute value of the complex shear modulus (|G*|).

A high-angular-resolved diffusion MRI sequence was acquired with 1.05 mm isotropic resolution (b=1500 s/mm2, reversed-phase encoding in anteroposterior and posteroanterior directions for paired acquisition in 68 directions). The Diffusion pre-processing was performed using the human connectome project (HCP) pipelines, adjusted to account for significant eddy currents.[13]. This allowed us to estimate whole brain maps of mean diffusivity (MD) and fractional anisotropy (FA). Segmentation of brain regions was performed on an MP2RAGE T1scans (0.7mm^3) using Freesurfer[14] and regional masks were co-registered to the MRE space and DTI space using SPM[15]. SPM was also used to estimate the percentage area of CSF for each region.

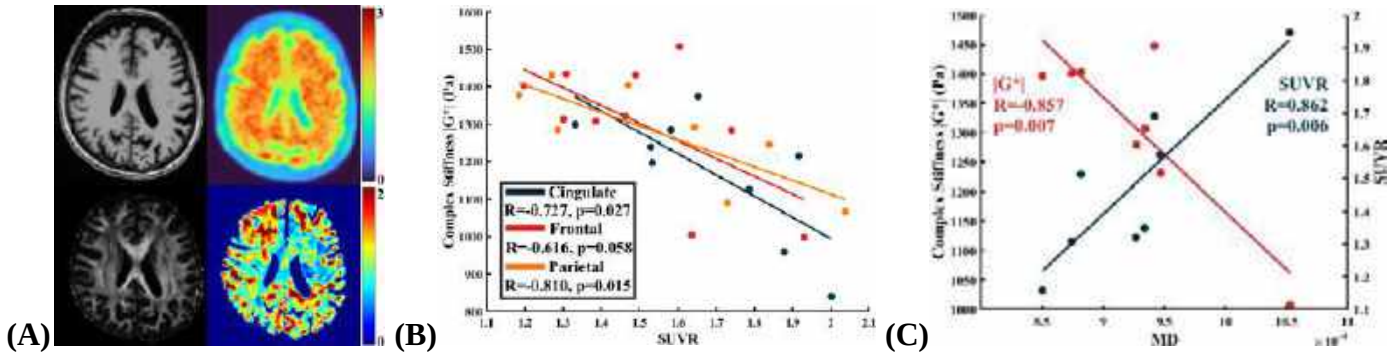

Figure 1: (A) Top: *T1 (left), PET (right), Bottom: FA (left), and |G*| (right) maps for one subject with MCI,* ***(B)*** *Linear correlations between |G*| and SUVR in three cortical brain regions, and* ***(C)*** *The linear correlations between |G*| and MD, and SUVR and MD in the temporal cortex.*

Subjects also underwent a Siemens Biograph mMR simultaneous PET-MR scan to measure Aβ burden using F18-labeled florbetaben using FDA standardize protocols. Average selective uptake value ratio (SUVR), FA, MD, and |G*| were calculated per cortical region of interest as specified in Palmqvist, *et al.*[16]. All MCI/AD subjects and one CN subject were determined to be Aβ-positive. We performed multiple Shapley Regressions in subjects with amyloidosis (subjects whose average SUVR are above the region threshold as described in Bullich, *et al.*)[17] in five PET-relevant brain regions (cingulate, frontal, parietal, temporal, and palmqvist-early)[16] with combinations of the different imaging metrics and PACC that were acquired for each subject.

RESULTS

We found significant differences (one-tailed, unequal variance t-test, $p<0.05$) between the CN and AD/MCI groups in |G*| of the hippocampus and frontal lobe, and SUVR of all brain regions investigated. A significant negative correlation was found between average SUVR and |G*| in the cingulate and parietal cortical regions in the Aβ-positive subjects, with a trending correlation in frontal (Fig 1B). We also found a significant positive correlation between SUVR and MD, and a negative correlation between |G*| and MD in the temporal gray matter (Fig 1C). There was a significant negative correlation between SUVR and PACC, and positive correlation between |G*| and PACC, in all regions.

From the Shapley Regressions (Fig 2 A,B), excluding PACC, |G*| was the best predictor of SUVR in subjects with amyloidosis in all brain regions tested, apart from the temporal and parietal lobes, where MD was a better predictor. Once again, excluding PACC, SUVR was the best predictor of |G*| in subjects in all brain regions tested, apart from the temporal lobe, where MD was a better predictor.

DISCUSSION

The negative correlation between |G*| and SUVR in brain regions initially impacted in MCI/AD progression is consistent with a previous investigation, supporting the hypothesis that tissue degeneration caused by Aβ accumulation results in tissue softening. The Shapley regression analyses demonstrated that SUVR and |G*| were the most important imaging covariates in their corresponding multi-regression analyses for multiple brain regions, which is promising for finding correlates of PET through MRE.

MD being the best predictor of SUVR and G* in the temporal and parietal cortexes is consistent with previous investigations of neurodegenerative and age-related brain changes in gray matter. Specifically, correlations between SUVR or |G*| and MD, but not SUVR and |G*| in the temporal cortex may be indicative of cascades which contribute to Aβ deposition, microstructural damage, and tissue softening and degradation. Additionally, similar correlation coefficients between PACC and |G*|, and PACC and SUVR in all brain regions has interesting implications about use of MRE and DTI instead of PET for diagnosing amyloidosis with cognitive impairment.

One limitation of this study is that a more robust MRE inversion algorithm would benefit the high-resolution allowed by 7T, resulting in even more detail. This study is limited by a small sample size, limiting statistical power, so future studies should look to include larger cohort of subjects diagnosed with MCI/AD. Despite these challenges, our multi-modal biomechanical imaging and analysis framework has promise to determine relationships between a multitude of MRI and PET measures for AD and MCI subjects, providing a physical understanding between tissue mechanics and AD pathophysiology.

ACKNOWLEDGEMENTS

We acknowledge funding support from NSF CMMI 1953323, NIH R21AG071179, NIH P30AG066514, and the Sanford Grossman Interdisciplinary Center in Neural Circuitry and Immune Function.

REFERENCES

[1] Double, *et al.*, *Neurobiol. Aging*, 1996 [2] Blinkouskaya, *et al.*, *IMECE*, 2021 [3] Murphy, *et al.*, *NeuroImage Clin.*, 2016 [4] Hiscox, et al., *Brain Commun.*, 2019 [5] O'Donnell, *et al.*, *Neurosurgery Clinics of North America*, 2011 [6] Pfefferbaum, *et al.*, *Neurobiol Aging*, 2010 [7] Lee, *et al.*, *BMC Neurology*, 2020 [8] Johnson, *et al.*, *NeuroImage*, 2013 [9] Anderson, *et al.*, *JMBBM*, 2016 [10] Triolo, *et al.*, *SB3C*, 2021 [11] Triolo, *et al.*, *Curr. Protoc.*, 2022 [12] Triolo, *et al.*, *SB3C*, 2023 [13] Fischl, *et al.*, *Med Phys.* 2001 [14] Reuter, *et al.*, *NeuroImage*, 2019 [15] SPM12 [16] Palmqvist, *et al.*, *Nat. Commun.*, 2017 [17] Bullich, *et al.*, *Alzheimer's Research & Therapy*, 2021

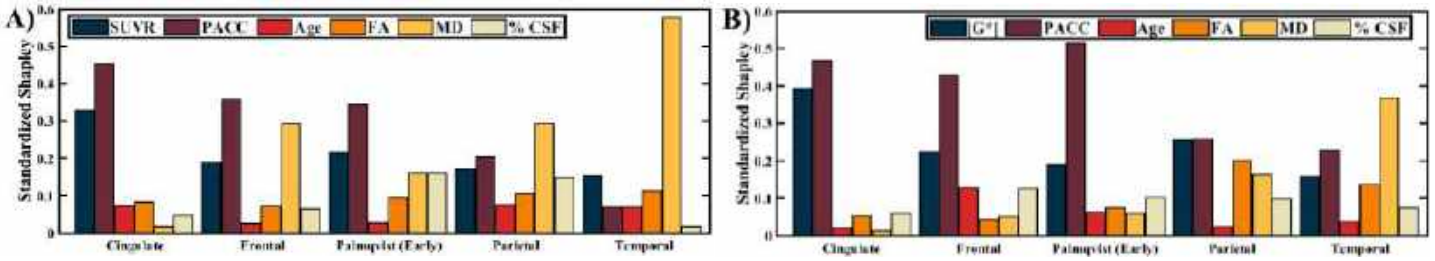

Figure 2: Results of the Shapley Regressions, *calculating the importance of* ***(A)*** *SUVR, Age, FA, RD, % CSF, and PACC in the results of MRE, and* ***(B)*** *the importance of Age, FA, RD, % CFS, and |G*| from MRE in the results of SUVR in multiple brain regions.*

ESTROGEN, TESTOSTERONE, AND MECHANICS: MODELING SEX-SPECIFIC LEFT VENTRICULAR REMODELING IN HEART FAILURE

Adhithi Lakshmikanthan (1,2), Minnie Kay (1,2), Kenneth C. Bilchick (3), Anya Grosberg (1,2), Pim Oomen (1,2)

(1) Biomedical Engineering, University of California, Irvine, California, USA
(2) UCI Edwards Lifesciences Foundation Cardiovascular Innovation and Research Center, University of California, Irvine, California, USA
(3) Department of Medicine, University of Virginia, Charlottesville, VA, USA

INTRODUCTION

Health inequities like sex-differences cost the USA $320 billion today and could reach $1 trillion by 2040 if left unaddressed[1]. In particular, heart failure is a deadly cardiovascular disease that exhibits sex inequities. Women are at lower risk of developing heart failure, with "only" 2.6 million females versus 3.4 million males in the USA suffering from this deadly disease[2]. Premenopausal women are initially at a lower risk of developing heart failure than men, however, after entering menopause the risk for women increases significantly. The phenotype of heart failure is also related to sex: females are predisposed to develop heart failure with preserved ejection fraction (HFpEF) whereas males are more likely to develop heart failure with reduced ejection fraction (HFrEF)[3].

Sex differences in cardiac remodeling play an important role in both the onset and treatment of heart failure[5]. However, the underlying mechanisms are still poorly understood[6]. Estrogen and testosterone are known to strongly affect cardiomyocyte hypertrophy through intracellular signaling pathways[7]. Estrogen has protective effects on the heart (but not on the vasculature), whereas testosterone is considered to be pro-hypertrophic. Since female and male heart failure patients express different levels of sex hormones, we hypothesize that these hormones in combination with changes in mechanics are largely responsible for sex differences in cardiac remodeling.

Our group has previously generated growth models to predict changes in left ventricular structure and function after cardiac resynchronization therapy (CRT), which is implemented through a pacemaker or implantable cardioverter defibrillator to correct electromechanical abnormalities in heart failure. In the present study, we extend these biophysical models to incorporate sex-specific effects of estrogen and testosterone in the prediction of left ventricular growth and remodeling after CRT. Specifically, we develop and validate models of post-CRT remodeling for male sex, female sex in the premenopausal state, and female sex in the postmenopausal state.

METHODS

Multiscale model of Cardiac Growth

We developed a multiscale model of cardiac growth consisting of an organ-level model of cardiac mechanics and cell-level model of cardiomyocyte hypertrophy.

Organ-level cardiac mechanics were modeled using our recently published model[8]. The heart was modeled as three spherical walls using the TriSeg method (Fig 1)[9], where the left ventricular walls were functionally divided into segments according to the 16-segment AHA model to enable modeling of cardiac dyssynchrony. We used a lumped parameter circuit to model the hemodynamic circulation.

Cell-level hypertrophy was modeled using an intracellular signaling network model that we developed using Netflux[10]. The model has 3 inputs: estrogen (E2), testosterone (T), and stretch (Fig 1). The output is captured as a change in cardiomyocyte cell area. The signaling pathways were informed by in-vitro studies and include Calcineurin, CamKII, eNOS, IP3, PI3K and NFkB[7]. Reactions were modeled using normalized Hill-type ordinary differential equations.

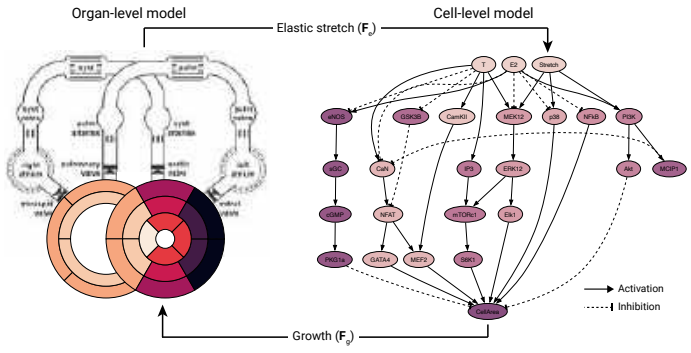

Figure 1: Overview of the multiscale model framework.

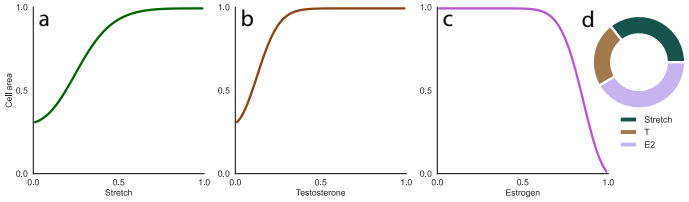

Figure 2: Cell-level model sensitivity to sex hormones and stretch.

The organ-level and cell-level models were coupled using the kinematic growth framework, where the total deformation gradient tensor for each wall segment is decomposed into an elastic and growth part: $\boldsymbol{F} = \boldsymbol{F}_{\mathrm{e}} \cdot \boldsymbol{F}_{\mathrm{g}}$. The growth tensor (we assumed isotropic growth) was determined by the cell-level model's predicted change in cell area. Conversely, the maximum elastic stretch tensor for each wall segment from the organ-level model was used as input into the cell-level model to close the loop (Fig 1).

Sensitivity and response of the signaling network model

Sobol global sensitivity analysis was conducted on the intracellular signaling network to show the impact of inputs on downstream species and cell area change. The model's response to input upregulation and downregulation was tested to compare with literature trends.

Model validation

To test our model's capability of predicting sex-specific cardiac remodeling in patients, we simulated 6 months of remodeling for three individual patients suffering from dyssynchronous heart failure that were treated with CRT. We specifically chose to simulate a premenopausal female, postmenopausal female, and male patient to test different concentrations of sex hormones. We calibrated the organ-level model to match clinical data including blood pressure, wall mass, and ventricular cavity volumes. We then simulated 6 months of post-CRT remodeling. Sex hormone (E2 and T) concentrations were adjusted to match the clinically observed 6-month change in left ventricular end-diastolic volume (LVEDV) and end-systolic volume (LVESV).

RESULTS

The global sensitivity analysis of our cell-level model confirmed that T, E2, as well as stretch significantly influence cell area change (Fig 2d). The signaling model's response to input upregulation and downregulation matches with literature data: a higher concentration of E2 decreased cell area, and higher concentrations of T and stretch increased cell area (Fig 2a-c). For the three patients we simulated, our multiscale model matched post-CRT change in LVESV and LVEDV to within ±2 percent of the measured value (shown for post-menopausal female in Fig 3, dashed lines). We were only able to match the clinically observed 6-month post-CRT remodeling when the hormone concentrations of E2 and T were tuned for each patient. Most excitingly, in each case, the tuned hormone concentrations to match clinically observed remodeling fell within the reported literature range of estrogen and testosterone of each sex and age (Table 1)[11,12]. Higher concentrations of E2 led to better post-CRT remodeling (lower LVESV), while higher concentrations of T exacerbated remodeling for all 3 patients (shown in Fig 3 for the postmenopausal female patient).

DISCUSSION

Purely mechanics-based growth models have in the past successfully predicted changes in ventricular mass or size, however these were unable to discern between outcomes in men and women. We were able to overcome this crucial shortcoming by using a combined mechanics and systems biology approach. To the best of our knowledge, this is the first model that incorporates sex-specific signaling pathways to predict cardiac remodeling.

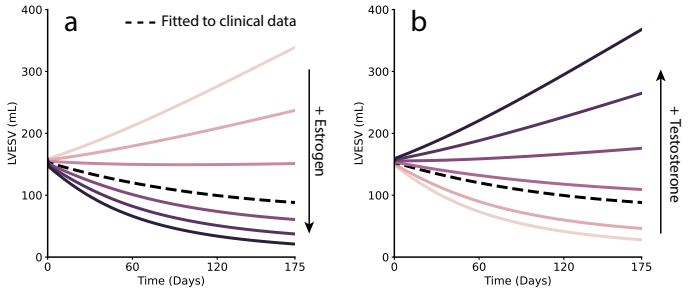

Figure 3: Validation of the multiscale model, predicted cardiac remodeling in postmenopausal female patient.

	Male	Postmenopausal female	Premenopausal female
E2 literature	10-40	0-30	30-400
E2 validated	29.96	**21.09**	314.8
T literature	265-923	2-41	15-70
T validated	278.5	**3.00**	17.00

Table 1: Literature and prediction sex hormone concentrations. E2 in pg/ml, T in ng/dl. Fitted data shown in Fig 3 in bold.

Our multiscale model still has several limitations. Some crosstalk with other connected pathways and feedback loops were not considered in this version of our signaling model. We have currently included hormone concentrations as a fitting parameter because the true concentration in our patients is unknown. Even though all fitted hormone concentrations agreed with literature values, some were towards the outer limits of the reported ranges. However, we here only tested our model for three individual patients; more (female and male) patients will be included in the future.

In conclusion, we developed a multi-scale model and validated cardiac remodeling in response to CRT in three patients: male, postmenopausal and premenopausal females by tuning sex hormones to match measured clinical remodeling volumes (within ±2 percent of measured). As heart failure patients exhibit both mechanical and sex-specific hormonal changes, and receive drugs that alter sex-specific pathways, our multi-scale model has the potential to lead to advancements in heart failure therapies for both women and men.

ACKNOWLEDGEMENTS

This work was supported by funding from the National Institutes of Health (R01HL159945).

REFERENCES

[1] Davis et al., *Deloitte Insights*, 2022.
[2] DeFilippis et al., Circulation Research 130: 436–54, 2022.
[3] Arcopinto et al., *Internl Emergency Medicine* 17: 1589–98 2022.
[4] Ryczkowska et al., *Archives Medical Science* 19: 458–66, 2023.
[5] Lam et al., *European Heart Journal* 40: 3859–68, 2019.
[6] Mackall et al., JACC: Clinical Electrophysiology 7: 716–18, 2021.
[7] Wu et al., *Journl Cardiovas Transll Research* 13, 73–84, 2020.
[8] Oomen et al., *Biomech Model Mechanobiol*, 21: 231–47, 2022.
[9] Walmsley et al., *PLoS Comput. Biol.* 11, e1004284, 2015.
[10] Clark et al., *bioRxiv*, 2024.
[11] Varma. *Medical News Today*, December 2023.
[12] Jacobson, Zieve. Mount Sinai, July 2021.

DEVELOPMENT AND APPLICATION OF ON-SITE VELOCITY BOUNDARY

Reza Bozorgpour (1), Mahsa Dabagh (2)

(1,2) Department of Biomedical Engineering, University of Wisconsin-Milwaukee, WI, Milwaukee, USA

INTRODUCTION

Lattice Boltzmann simulations of fluid flow in complex geometries, like patient-specific cerebro/cardio-vasculature often require on-site boundary conditions. These conditions enable the precise positioning of the boundary, simplifying system analysis independently of other simulation parameters. In practical applications, the ability to freely specify inlet fluid flow direction and easy three-dimensional implementation are crucial. Additionally, for parallelized solvers, locally applicable boundary conditions that involve only the information on the current lattice site offer significant advantages. This study details the adaptation of Zou and He's approach to a D3Q27 lattice, ensuring local application, independence from collision relaxation, and absence of artificial slip. The on-site no-slip boundary condition is seamlessly incorporated. Through various setups, we validate the effectiveness of the proposed boundary condition, demonstrating its accurate modeling of the velocity field up to the second order without any numerical slip.

Simulation Method

The lattice Boltzmann method solves the Boltzmann equation on a discrete lattice, capturing the microscopic dynamics of gas particles, collisions, and momentum exchange. Ideal collisions conserve total momentum and energy. This equation expresses the evolution of the probability function f(x, v, t) over time (t) for finding a particle with velocity v at position x.

$$\boldsymbol{V}.\nabla_x f + \boldsymbol{F}.\nabla_p f + \frac{\partial f}{\partial t} = \hat{\Omega}(f) \quad (1)$$

F is the external force, $\nabla_{x,p}$ is the gradient, and $\hat{\Omega}(f)$ is the collision operator. BGK dynamics, proposed by Bhatnagar, Gross, and Krook [1], uses Ω with a relaxation time τ towards the equilibrium distribution $f^{eq}(v,p)$.

$$\hat{\Omega}(f) = -\frac{1}{\tau}(f - f^{eq}) \quad (2)$$

The lattice Boltzmann method discretizes probability density in space and time for athermal models. Using a D3Q27 lattice in 3D LB simulations, it stores 27 values on each lattice site $f_i(\boldsymbol{X}, t)$, corresponding to lattice vectors c_i. The equilibrium distribution function f^{eq} and discretization depend on the lattice type [2, 3].

$$c_i = \begin{bmatrix} 0 & 1 & -1 & 0 & 0 & 0 & 0 & 1 & -1 & 1 & -1 & 1 & -1 & 1 & -1 & 0 & 0 & 0 & 0 & 1 & -1 & 1 & -1 & 1 & -1 & 1 & -1 \\ 0 & 0 & 0 & 1 & -1 & 0 & 0 & 1 & 1 & -1 & -1 & 0 & 0 & 0 & 0 & 1 & -1 & 1 & -1 & 1 & 1 & -1 & -1 & 1 & 1 & -1 & -1 \\ 0 & 0 & 0 & 0 & 0 & 1 & -1 & 0 & 0 & 0 & 0 & 1 & 1 & -1 & -1 & 1 & 1 & -1 & -1 & 1 & 1 & 1 & 1 & -1 & -1 & -1 & -1 \end{bmatrix}$$

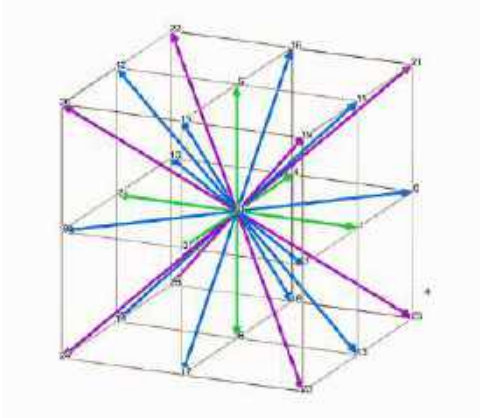

Figure 1. The lattice structure of D3Q27

The sum of all fi yields the local density at a lattice point.

$$\rho(\boldsymbol{X},t) = \sum_1^{27} f_i(\boldsymbol{X},t) \quad (3)$$

The sum of all fi yields the local density at a lattice point.

$$V(\boldsymbol{X},t) = \frac{1}{\rho(\boldsymbol{X},t)} \sum_1^{27} f_i(\boldsymbol{X},t) c_i \quad (4)$$

Discretizing the Boltzmann distribution yields the equilibrium value f^{eq}. We adopt a widely used form involving velocity terms up to the second order, as proposed in various expressions [4-6]

$$f_i^{eq} = \omega_i \rho (1 + 3\frac{c_i.V}{c_s} + \frac{9}{2}\frac{(c_i V)^2}{{c_s}^2} - \frac{3}{2}\frac{V^2}{{c_s}^2}) \quad (5)$$

During each iteration, the lattice Boltzmann method involves two pivotal procedures: streaming and collision. Streaming involves particle movement along discrete velocities to adjacent nodes determined by the lattice discretization. On the other hand, collision entails the relaxation of particle distribution towards the Maxwell-Boltzmann equilibrium distribution, often approximated as f_i^{eq}

$$f_i^{eq} = \omega_i \rho (1 + \frac{\boldsymbol{c_i}.\boldsymbol{u}}{c_s^2} + \frac{\boldsymbol{uu}:(\boldsymbol{c_i c_i} - c_s^2 I)}{2c_s^4}) \quad (6)$$

In our code implementation, we employ a single relaxation time Bhatnagar-Gross-Krook (BGK) collision operator [1] for lattice weights ω_i and a lattice speed of sound $c_s = 1/\sqrt{3}$.

The general on-site velocity boundary condition

Extending Zou and He's [4] boundary condition to a D3Q27 lattice, we provide a detailed derivation for the bottom plane (z = 0). The derivation utilizes the set of equations composed of equation (3) and the components of equation (4).

$$\rho v_x = f_3 + f_7 + f_8 + f_{15} + f_{17} + f_{19} + f_{20} + f_{23} + f_{24} - (f_4 + f_9 + f_{10} + f_{16} + f_{18} + f_{21} + f_{22} + f_{25} + f_{26}) \quad (7)$$

$$\rho v_y = f_1 + f_7 + f_9 + f_{11} + f_{13} + f_{19} + f_{21} + f_{23} + f_{25} - (f_2 + f_8 + f_{10} + f_{12} + f_{14} + f_{20} + f_{22} + f_{24} + f_{26}) \quad (8)$$

$$\rho v_z = f_5 + f_{11} + f_{12} + f_{15} + f_{16} + f_{19} + f_{20} + f_{21} + f_{22} - (f_6 + f_{13} + f_{14} + f_{17} + f_{18} + f_{23} + f_{24} + f_{25} + f_{26}) \quad (9)$$

From (3) and 9

$$v_z = 1 - \frac{1}{\rho}[f_1 + f_2 + f_3 + f_4 + f_7 + f_8 + f_9 + f_{10} + f_{27} + 2(f_{13} + f_{14} + f_{17} + f_{18} + f_{23} + f_{24} + f_{25} + f_{26} + f_{27}) \quad (10)$$

In line with Zou and He's approach, we presume that the bounce-back condition remains valid for the non-equilibrium part f_i^* of the single-particle distribution f_i at the boundary.

$$f_i^* = f_i - f_i^{(eq)} \quad (11)$$

The unknown distribution functions after streaming will be $f_5, f_{11}, f_{12}, f_{15}, f_{16}, f_{19}, f_{20}, f_{21}$ and f_{22}. Using the Zou and He's method,

$$f_5 = f_6 + \frac{2\omega_5}{c_s^2}\rho v_z \quad (12)$$

$$f_{11} = f_{14} + \frac{2\omega_{11}}{c_s^2}\rho(v_y + v_z) \quad (13)$$

$$f_{12} = f_{13} + \frac{2\omega_{12}}{c_s^2}\rho(-v_x + v_z) \quad (14)$$

$$f_{15} = f_{18} + \frac{2\omega_{15}}{c_s^2}\rho(-v_y + v_z) \quad (15)$$

$$f_{16} = f_{17} + \frac{2\omega_{16}}{c_s^2}\rho(v_y + v_z) \quad (16)$$

$$f_{19} = f_{26} + \frac{2\omega_{19}}{c_s^2}\rho(v_x - v_y + v_z) \quad (17)$$

$$f_{20} = f_{25} + \frac{2\omega_{20}}{c_s^2}\rho(-v_x - v_y + v_z) \quad (18)$$

$$f_{21} = f_{24} + \frac{2\omega_{21}}{c_s^2}\rho(v_x + v_y + v_z) \quad (19)$$

$$f_{22} = f_{23} + \frac{2\omega_{22}}{c_s^2}\rho(-v_x + v_y + v_z) \quad (20)$$

Results

In our initial and elementary test case, we replicated the flow dynamics around an elliptic cylinder. We applied the Zou-He boundary condition at the inlet, utilized bounce-back for the wall, and maintained a constant pressure at the outlet. The simulation was conducted for Reynolds numbers of 30, 50, and 60.

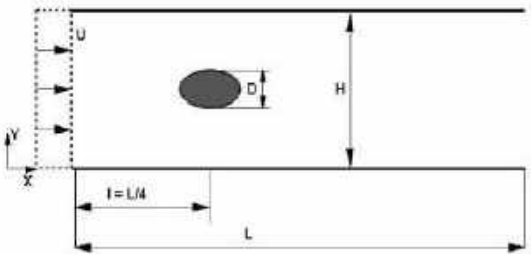

Figure 2. Schematic diagram of the flow past an elliptical cylinder confined in a channel

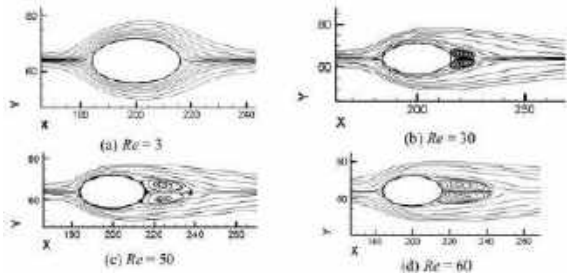

Figure 3. Streamline patterns for steady flows past an elliptical cylinder at different Reynolds

DISCUSSION

An explicit local on-site flux boundary condition was developed for LB simulations on a D3Q27 lattice, integrating velocity terms up to second order to ensure accuracy, validated through numerical tests. Unrestricted influx and outflux velocities in all directions were established. Comparisons between simulation results and theoretical expectations for flow through a tilted channel, specifically a Poiseuille flow, demonstrated numerical accuracy. Testing this boundary condition in Poiseuille flow between planar walls and shear flow revealed exact alignment with analytical solutions, independent of BGK relaxation time and without requiring slip parameters, while incorporating no-slip boundary conditions. Our next step is to simulate flow through different complex vasculatures and validate our results.

ACKNOWLEDGEMENTS

Authors would like to thank UWM-College of Engineering and Applied Science for CEAS Dean's fellow which has been provided for author R.B.

REFERENCES

1. Bhatnagar, P.L., E.P. Gross, and M. Krook, *A model for collision processes in gases. I. Small amplitude processes in charged and neutral one-component systems.* Physical review, 1954. **94**(3): p. 511.
2. Kadanoff, L.P., G.R. McNamara, and G. Zanetti, *From automata to fluid flow: Comparisons of simulation and theory.* Physical Review A, 1989. **40**(8): p. 4527.
3. He, X. and L.-S. Luo, *Theory of the lattice Boltzmann method: From the Boltzmann equation to the lattice Boltzmann equation.* Physical review E, 1997. **56**(6): p. 6811.
4. Zou, Q. and X. He, *On pressure and velocity boundary conditions for the lattice Boltzmann BGK model.* Physics of fluids, 1997. **9**(6): p. 1591-1598.
5. Qian, Y.-H., D. d'Humières, and P. Lallemand, *Lattice BGK models for Navier-Stokes equation.* Europhysics letters, 1992. **17**(6): p. 479.
6. Chen, S., D. Martinez, and R. Mei, *On boundary conditions in lattice Boltzmann methods.* Physics of fluids, 1996. **8**(9): p. 2527-2536.

SB³C 2024
Summer Biomechanics, Bioengineering and Biotransport Conference
June 11-14, Lake Geneva, WI, USA

MEASURING FLOW RESISTIVITY IN MICROFLUIDIC-BASED MEDICAL DEVICES

Ali Bozorgnezhad (1), Luke Herbertson (1), Suvajyoti Guha (1)

(1) Division of Applied Mechanics, Office of Science and Engineering Laboratories, Center for Devices and Radiological Health, U.S. Food and Drug Administration, Silver Spring, Maryland, United States

INTRODUCTION

An increasing number of medical device manufacturers are integrating microfluidic technologies into their products [1]. However, failure modes such as leakage and bubbles commonly occur for this technology. While flow resistivity information has largely been used in fundamental fluid mechanics research, it can also be used to evaluate the functionality and overall performance of microfluidic medical devices. In the medical device field, flow resistivity measurements can serve two primary purposes for early device developers. Firstly, developers can use flow resisivity measurements to ensure that the device has low flow resistivity, as higher flow resistivity can lead to higher pressures and an increased risk of mechanical integrity issues. High resistivity may also induce higher shear stress on the biological molecules and materials, which can compromise their viability and functionality. Secondly, the flow resistivity of a new design can also be compared to validated benchmark models to confirm that the new system under investigation, along with its flow and pressure controllers and sensors, is adequate over its entire intended operating range.

To date no standard test methods have been developed to accurately measure flow resistivity in a microfluidic device. There are inherent difficulties associated with accurately measuring very low flow rates and pressure differentials in microfluidics. This study presents an experimental protocol to evaluate flow resistivity and a comparison with theoretical predictions. The microfluidics community can use this protocol to measure the flow resistivity of the presented standard geometry as a benchmark to evaluate their capacity to measure the flow resistivity of their flow sensors with acceptable precision.

METHODS

Flow resistivity measurements are made to find the corresponding flow rate of a given pressure difference between the inlet and outlet of the microfluidic device. We used the setup illustrated in Figure 1(a) to conduct the tests. The microchip is made of cyclic olefin copolymer (COC) consisting of a straight microchannel with a 100 µm x 100 µm square cross-section and a length of 17.5 mm. The fluid (ultrapure deionized water) is introduced into the system via the pressure controller, which regulates the pressure within the pressurized reservoir. The 1/16" OD x 1/32" ID PTFE tubings were connected via ¼"-28 Swivel compression fittings to the sensors and the pressurized reservoir. The gas tubing from the pressure controller to the reservoir is reinforced tubing with dimensions of 4 mm OD and 2.4 mm ID, and it was connected to the tank via ¼-28 Swivel to Barbed 3/32" ID Adapter.

The Hagen-Poiseuille equation describes the relationship between the pressure and the flow rate for a laminar steady-state flow in a cross-section where the fluid is incompressible and Newtonian. When rearranged, the following equation can be used to calculate the experimental flow resistivity in a microfluidic channel [3]

$$R_H = \frac{\Delta P}{Q} \tag{1}$$

Where R_H, ΔP and Q are the flow resistivity, pressure difference between the inlet and outlet of the microchip and the flow rate, respectively. The theoretical value of the flow resistivity for a straight microchannel with a rectangular cross-section can be calculated by equation (2) [3]

$$R_{H,sq} = \frac{12\,\mu L}{1-0{,}63\times\left(\frac{h}{w}\right)}\left(\frac{1}{h^3 W}\right) \tag{2}$$

Where the L, w and h are the length, width and height of microchannel, respectively. The μ is the dynamic viscosity which is estimated to be 0.001 Pa·s for water at 23 °C. Given the input parameters above, the theoretical flow resistivity is calculated to be 4.97 x 10^{12} Pa·s/m^3, which is the reference value in this study used for calculating accuracy. Three flow sensors—brand A and B from one manufacturer and brand C from a second manufacturer—were used. Their nominal flow ranges are provided in Figure 1(b). Flow rates were

carefully selected to cover the range of flow rates likely to be encountered for common microfluidic medical device applications [1]. The lower limit for the flow sensor was typically represented as 10% of the maximum labeled flow rate [4].

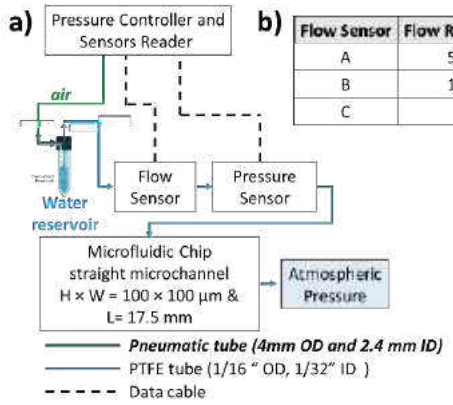

Figure 1: (a) Schematic of the flow resistivity measurement setup (b) Operating ranges for flow sensors.

RESULTS

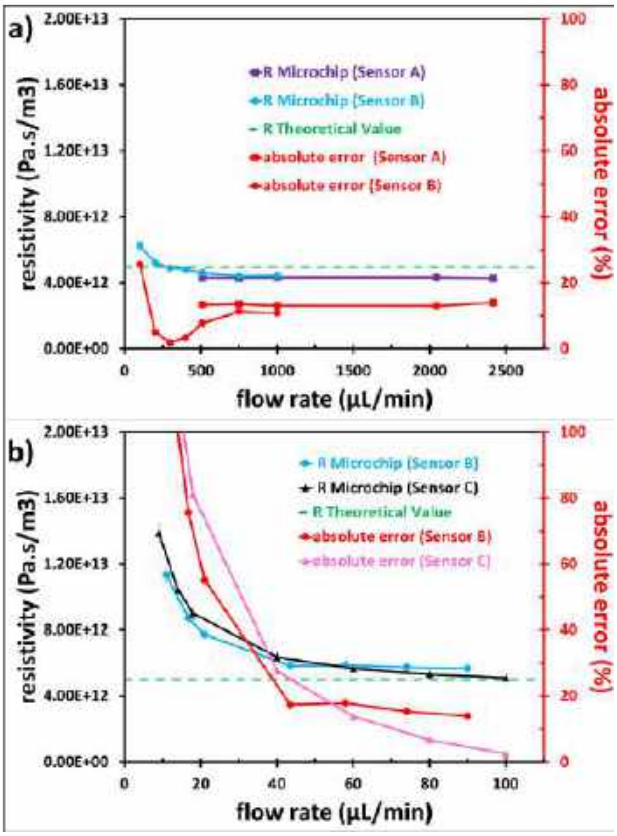

Figure 2: Flow resistivity and absolute error over a range of flow rates for (a) Sensors A and B (≥ 100 µL/min), and, (b) Sensors B and C (≥ 8 µL/min).

Figure 2 reports the flow resistivity for all three sensors. Error bars (not visually apparent) were based on n=3 replicate measurements. We calculated the relative error of resistivity between these experimental data and the theoretical values calculated by Equation 2 and reported the average of the absolute values (used to eliminate the potential of the relative errors with differing positive and negative signs cancelling each other out) of these errors for each flow sensor. The maximum average absolute error of resistivity determined using flow sensor A was ± 13.4 %, using sensor B was +9.54%/-4.54% when in range, and, +46.2%/-60.12% when outside range, and C was ±60.12%.

DISCUSSION

As seen in Figure 2 (a) - (b), sensors A and B had an acceptable performance when used in their nominal flow rate ranges up to 1000 and 2500 µL/min, respectively. While sensor C was used in its nominal flow rate range, sensor B was deliberately used outside its nominal flow rate range to assess sensor measurement errors outside the labeled flow rate range. While the lower limit of the nominal flow rate of sensor B is 100 µL/min, it yielded less than 20% error when used at a flow rate as low as 40 µL/min. However, under 40 µL/min, sensor B reported much higher values of error (55.1% at 21 µL/min, 75.7% at 16 µL/min and 128.3% at 11 µL/min). This underscores the need to operate sensors within their specified, labeled operating ranges. We also observed that although Sensor C was tested within its nominal flow rate range, it generated errors greater than 40%. Therefore, this study shows that while some sensors may provide accurate measurements of resistivity within their nominal range, other sensors may be inaccurate even within nominal range of operation. For device manufacturers embarking on developing a new device that uses microfluidics, this finding emphasizes the need for verifying the flow sensors against a protocol and chip with known resistivity values before using them for complex device development. It can also be used for failure mode studies to assess device performance in presence of bubbles or leakages. Moreover, it is useful for reliability and verification purposes, or as part of quality control process.

Further interlaboratory studies on resistivity based on multiple channel designs may also foster the development of standardized protocols that can be adapted by the community. Our studies were limited to flow rates ≥9 µL/min and ≤2500 µL/min because of limits of our flow and or pressure sensors. The current study was limited to only one design of a simple straight channel with a square cross-sectional area and hence cannot be extraplated to other geometries.

ACKNOWLEDGMENTS

The contents of this article do not necessarily represent policy or current thinking of the U.S. Food and Drug Administration or the Department of Health and Human Services. Dr. Ali Bozorgnezhad is currently an ORISE postdoctoral research fellow at the U.S. Food and Drug Administration funded through the Oak Ridge Associated Universities. We also thank MFMET, a consortium or metrology laboratories and its members for the helpful discussions on flow resistivity. We would like to thank Mr. Alex Herman for reviewing the contents of this abstract and providing constructive comments.

REFERENCES

[1] Natu R, Herbertson L, Sena G, Strachan K and Guha S, "*A Systematic Analysis of Recent Technology Trends of Microfluidic Medical Devices in the United States*" *Micromachines*, 14:1293, 2023. https://doi.org/10.3390/mi14071293

[2] Reyes D, Heeren H, Guha S, Herbertson L, Tzannis A, Ducrée J, Bissig H and Becker H, " Accelerating innovation and commercialization through standardization of microfluidic-based medical devices" *Lab on a Chip*, 21:9-21, 2021

[3] Bruus, H, *Theoretical Microfluidics*, Oxfor University Press, 1:288, 2007.

[4] Copeland M., Ogheard F., Batista E., and Heeren H. "*Whitepaper flow resistivity testing" MFMET*, 1:5, 2023. DOI: 10.5281/zenodo.7919134

COMPUTATIONAL MODELING AND MACHINE LEARNING METHODS TO PREDICT PATIENT-SPECIFIC HEALING FOLLOWING BREAST-CONSERVING SURGERY

Zachary J. Harbin (1), Alexander E. Argyros (1), Carla S. Fisher (2), Sherry L. Voytik-Harbin (3,4), Adrian Buganza Tepole (1,3)

(1) School of Mechanical Engineering, Purdue University, West Lafayette, IN, USA
(2) Indiana University School of Medicine, Indianapolis, IN, USA
(3) Weldon School of Biomedical Engineering, Purdue University, West Lafayette, IN, USA
(4) Department of Basic Medical Sciences, Purdue University, West Lafayette, IN, USA

INTRODUCTION

Breast cancer is the one of the most commonly diagnosed cancer in women across the world, with annual reports of new cases estimated at roughly 300,000 in the United States and 2.3 million worldwide [1]. Breast-conserving surgery (BCS; also known as lumpectomy) is now recognized as the preferred treatment for early-stage breast cancer, provided that the surgery maintains adequate breast volume [2]. The goal of BCS is complete removal of the tumor while preserving, as much as possible, healthy breast tissue and breast appearance. The resulting surgical cavity undergoes a healing process resulting in variable levels of tissue contraction, scar tissue formation, and breast deformation. However, the complexity of the breast cavity healing process along with patient-to-patient variability in breast characteristics (e.g., breast and tumor geometry, tumor location, breast density) make it extremely challenging for surgeons to predict post-surgical healing, oncologic, and cosmetic outcomes.

To address this gap, we developed a computational mechanobiology model that simulates breast healing and deformation following BCS. Our previous work focused on the calibration of an initial coupled biochemical-biomechanical model, with model parameters being fit to histopathological data obtained from an experimental porcine study and available human clinical data evaluating cavity contraction [3]. An investigation was also performed to identify how patient-specific characteristics, such as cavity size and breast density, affected breast healing and cosmetic outcomes, with simulation results aligning with clinical findings [3].

Given our initial computational model implemented a generalized human breast geometry, next model iterations aim to use relevant retrospective and prospective human clinical data to obtain a deeper understanding of how patient-specific characteristics affect post-operative healing and deformation outcomes. Here, we utilize the computational mechanobiological model to simulate patient-specific breast and tumor characteristics to predict individual breast healing and deformation outcomes following BCS. Furthermore, these simulations will be applied as training data for machine learning applications, such as Gaussian Process surrogate models, to further understand the complex interplay between patient-specific characteristics and their effect on cavity healing, contraction, and breast deformation. Such patient-specific computational models have potential to assist breast surgeons and their patients in surgical decision-making and treatment planning, addressing the goals for improved predictability of surgical outcomes, reduced complications, and improved patient satisfaction and quality of life.

METHODS

Pre-operative magnetic resonance images (MRIs) of breast cancer patients were obtained through a data repository collected by Duke University Hospital in collaboration with The Cancer Imaging Archive [4]. Patients (n = 103) were randomly selected, with patients with bilateral breast cancer or multiple tumors in one breast excluded. Table 1 summarizes patient and tumor characteristics. Tumor location frequency for the patient population was consistent with other clinical studies, with 41.7% of tumors located in the upper outer quadrant [5].

Table 1: Patient and Tumor Characteristics

Characteristic	Median	Range
Age (years)	51.9	29.3 – 81.6
Breast Density (%)	25.9	4.4 – 71.1
Tumor Volume (mm^3)	1485.3	33.4 – 35096.6
Tumor Major Axis Length (mm)	19.1	2.0 – 59.9
Tumor-to-Breast Volume (%)	0.20	0.0015 – 3.86

Given that MRIs were obtained in the prone position, it was necessary to process images to incorporate gravitational deformation of patient breasts prior to computational model simulations as depicted in Fig. 1. Image tissue segmentation was first performed by applying thresholds in 3D Slicer to approximate volumes of adipose and fibroglandular tissue (depicted as yellow and blue in Fig. 1) [6].

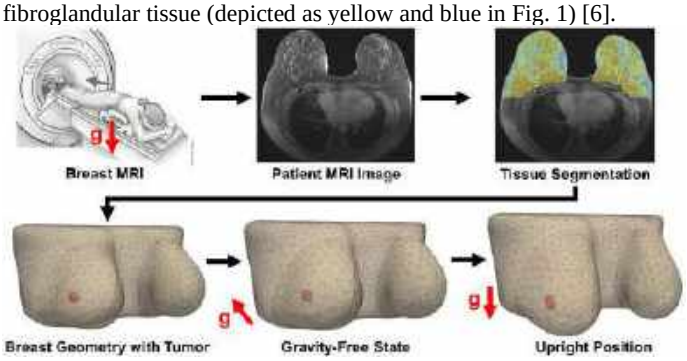

Figure 1: Gravity deformation procedure implemented for each patient MRI. Adapted from [7].

Breast density was then calculated for each patient and used to estimate breast Young's modulus using the rule of mixture. Evaluation of literature [8], along with testing a broad range of values, supported 1.5 kPa and 6 kPa as assumed Young's modulus values for adipose and fibroglandular tissue, respectively.

3D Slicer was used to identify tumor location in MRIs. Tumors were assumed to be ellipsoidal in shape, with patient-specific volumes and dimensions provided in MRI repository datasheets [4]. The BCS cavity was assumed to have the same volume and shape as the tumor. Material properties were assumed to be consistent with the buildup of serous fluid inside the cavity space (low shear modulus; high bulk modulus), which is common after BCS [9].

Patient-specific breast geometries were created and meshed in Slicer 3D based on the MRI acquired in the prone position. Using the established patient-specific characteristics, finite element analysis was performed to simulate breast and cavity deformation due to gravity from the prone position to the upright position (Fig. 1). Simulations were executed in COMSOL (COMSOL Multiphysics, Burlington, MA) with the breast and cavity defined using their respective parameters values as hyperelastic materials under the neo-Hookean model. Processed breast geometries in the upright position were then able to be simulated in the computational mechanobiological model, which is a custom C++ solver used to predict the breast healing response following BCS. The model framework and parameters were established in previous work [3].

RESULTS

MRI segmentation and gravity deformation simulations were performed for all 103 patient MRIs. The mechanobiological model was utilized to predict the breast healing response following BCS over a four-week period for each processed geometry. Exemplary simulation results for two patients are displayed in Fig. 2.

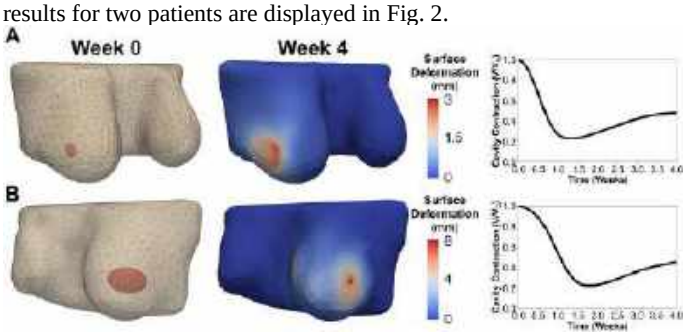

Figure 2: Mechanobiological model outcomes for patient-specific simulations (A and B) displaying post-surgical surface deformation and cavity contraction.

For Patient A, the breast cavity contracted substantially in the first nine days following surgery to 22.8% of its original cavity volume (Fig. 2A). A modest increase in cavity volume was shown by week 4, with the cavity being 48.1% of the excised volume (Fig. 2A). This permanent contracture led to minor deformations visible on the breast surface (Fig. 2A). The maximum point of deformation on the breast surface was found to be 2.71 mm four weeks post-surgery, with an area of 5715 mm^2 being affected by at least 1 mm surface deformation (Fig. 2A).

Patient B saw similar levels of cavity contraction compared to Patient A, as the breast cavity contracted to 22.6% of its original volume 12.5 days after surgery and was 45.3% of the excised volume by week 4 (Fig. 2B). However, Patient B was predicted to have a suboptimal post-surgical cosmetic outcome, as the maximum breast surface deformation was 7.55 mm with an area of 15459 mm^2 being affected by at least 1 mm surface deformation (Fig. 2B). The severity of the deformation led to the formation of a visible divot on the surface of the breast (Fig. 2B). Since breast density and tumor depth were very similar for both patients, the difference in cosmetic result can be attributed to differences in tumor-to-breast volume percentage (TVBP), with values for Patient A and Patient B being 0.36% and 3.86%, respectively. These results, which suggest that TVBP is an important prognostic indicator, are consistent with previous reported clinical outcomes [10].

A summary of the post-operative predictive breast healing and deformation results for the selected patients is shown in Fig. 3. The average patient breast cavity contracted to a minimum of 25.7% of the original excision volume in just nine days post-surgery (Fig. 3A). By week 4, the cavity moderately increased in volume to reach 52.6% of the excised volume (Fig. 3A). Maximum surface deformation range across the patient population was found to be 0.22 – 8.44 mm with an average and median of 1.92 mm and 1.44 mm, respectively (Fig. 3B).

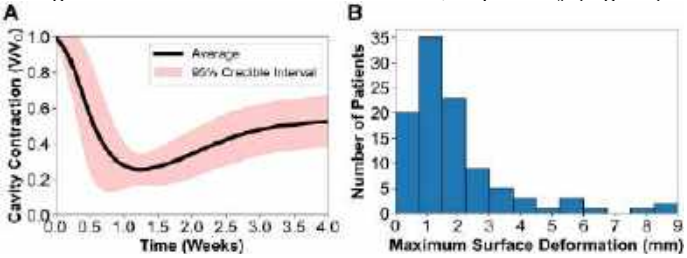

Figure 3: Predicted (A) cavity contraction over time and (B) maximum breast surface deformation for the patient population 4 weeks post-surgery.

DISCUSSION

The accessibility to the breast cancer patient MRI repository allowed for successful acquisition of patient-specific breast and tumor characteristics. This allowed for patient geometries to be utilized for the computational model to simulate breast healing outcomes such as cavity contraction and breast surface deformation following BCS. These simulations will be incorporated as training data for future machine learning applications, replacing the high-fidelity mechanobiological model with inexpensive and accurate surrogate models. Such surrogates can be employed to more efficiently understand the relationship between patient-specific breast characteristics and their effect on BCS outcomes, which will be explored in future work.

The study is not without limitations. The data repository used to obtain patient MRIs does not have additional scans or images following the patient post-surgery, with only pre-operative MRIs being available. Future model iterations will include the necessary data to track individual post-operative outcomes that can be compared to model predictions to further validate the computational mechanobiological model framework and parameters along with any machine learning surrogate models. With this work providing deeper insight into individual healing outcomes, future efforts can be shifted to focus on the addition of radiation therapy effects and the design of therapeutic approaches (e.g., regenerative breast fillers).

ACKNOWLEDGEMENTS

This work was supported by NSF CMMI grant (A.B.T.; 1911346).

REFERENCES

[1] Cancer Facts & Figures, *American Cancer Society*, 2023.
[2] Boughey J. et al., *J. Clin. Oncol.*, 41(17), 3184-93, 2023.
[3] Harbin, Z. et al., *Comput. Biol. Med.*, 165, 107342, 2023.
[4] Harowicz, S. et al., *Br. J. Cancer*, 119(4), 508-516, 2018.
[5] Kroman, N. et al., *Int. J. Cancer*, 105(4), 542-545, 2003.
[6] Fedorov, A. et al., *J. Magn. Reason. Imaging*, 30(9), 1323-41, 2012.
[7] Breast MRI, *American Cancer Society*, 2022.
[8] Eder, M. et al., *Ann. Biomed. Eng.*, 42, 843-857, 2014.
[9] Puls, T.J. et al., *Scientific Reports*, 11(1), 1-17, 2021.
[10] Dahlbäck, C. et al., *World J. Surg. Oncol.*, 14, 1-11, 2016.

RIGHT VENTRICULAR MYOCARDIUM REMODELING IN PULMONARY ARTERIAL HYPERTENSION IS SEX-SPECIFIC AND OVARIAN-HORMONE DEPENDENT

Becky A. Hardie (1), Jessica Huberts (1), Daniela Valdez-Jasso (1)

(1) Department of Bioengineering, University of California San Diego, La Jolla, CA, USA

INTRODUCTION

Pulmonary arterial hypertension (PAH) is a progressive vasculopathy of the pulmonary arteries that frequently results in right-heart failure and death.[1] PAH manifests as sustained elevation of pulmonary arterial pressures exceeding 20 mmHg and irreversible vascular remodeling that leads, and later exacerbates, pressure overload on the right ventricle (RV).[1,2] Previous studies with male animal models have shown that elevated RV pressures are associated with increased myocardial stiffness, tissue fibrosis, and disorganized collagen structure.[2–4] In particular, stiffening of the RV myocardial tissue is thought to be a significant contributor to overall RV chamber stiffness and function, a good prognostic indicator of PAH.[3,4]

PAH is significantly more predominant in women; however, despite the 2-4 times higher incidence in women, pre-menopausal women maintain better cardiac function.[5] Previous studies have shown that administration of 17-β estradiol (E2), the primary female sex hormone in non-pregnant women, improves RV function in rats and that E2 levels correlate with RV function in healthy post-menopausal women undergoing hormone replacement therapy.[5] Due to the less severe phenotype seen in pre-menopausal women, we hypothesize that the RV myocardium remodels in a sex and ovarian-hormone dependent manner in PAH. To investigate the tissue-level properties that may lead to sex or ovarian hormone-dependent remodeling, we designed a study using the well-established sugen-hypoxia (SuHx) rat model of PAH in male, intact female, and ovariectomized female (OVX) rats.

METHODS

Animal model. PAH is induced in male, intact-female, and ovariectomized-female (OVX) Sprague-Dawley rats by a 20 mg/kg injection of Sugen 5416, a vascular endothelial growth factor receptor blocker, followed by 3 weeks of hypoxia at 10% oxygen and a further 1-15 weeks of normoxia. Control animals are kept at normoxia. Hypertension is confirmed by invasive measurements of blood pressure at the inlet of the pulmonary artery. A 1.9Fr admittance pressure-volume catheter is inserted into the RV to obtain pressure-volume time series.

Tissue preparation. Immediately after hemodynamic measurements, the heart is harvested and flushed with saline. The RV free wall is excised and weighed. A square sample aligned along the apex-to-outflow (AOT) direction is cut from the mid-wall. Side lengths and tissue thickness measurements are taken with calipers prior to testing. Five graphite markers are glued on the epicardium in the center of the tissue to track displacement. The sample is attached to a Bose Electro-Force planar biaxial testing device with 4 custom-made hooks on each side and submerged in 37°C phosphate buffered saline.

Mechanical testing. RV samples are pre-stretched with a 3g load to ensure planar motion and preconditioned with two series of an 8%, a 10%, and a 12% *ex vivo* side length stretch at 0.2 Hz. Samples are subjected to displacement-controlled biaxial testing with 7 blocks of 15 loading-unloading cycles at 0.5 Hz. The AOT: circumferential stretch ratios are 1:1, 1:0.5, 1:0.25, 1:1, 0.5:1, 0.25:1, 1:1, with a maximum stretch of 10% of the *ex vivo* side-length. The last 3 cycles of blocks 2-6 are point-wise averaged and used for analysis. Pixel positions of the markers are recorded at 200 Hz throughout the test.

Constitutive equations. The locations of the four outer pixels are used to calculate the deformation gradient tensor $\boldsymbol{F}$ through isoparametric mapping. The Green strain tensor $\boldsymbol{E}$ is defined with respect to the pre-loaded reference configuration β_1, and the second Piola-Kirchhoff stress tensor $\boldsymbol{S}$ is calculated with the deformation gradient tensor. The myocardium is assumed to be a planar hyperelastic material with the loading curve described by a Fung-type exponential strain-energy function.

$$\mathrm{W}(\boldsymbol{E}) = C\left(e^{Q(\boldsymbol{E})} - 1\right) \tag{1}$$

where

$$Q(\boldsymbol{E}) = a_1\boldsymbol{E}_{11}^2 + a_2\boldsymbol{E}_{22}^2 + a_3\boldsymbol{E}_{11}\boldsymbol{E}_{22}. \tag{2}$$

Numerical implementation. Pre-stretch values $\{f_1, f_2\}$ are estimated in terms of the experimental stretches Λ_i as:

$$f_1 = \sqrt{\frac{E_{11}\Lambda_2}{\Lambda_1} + 1},\ f_2 = \sqrt{\frac{E_{22}\Lambda_1}{\Lambda_2} + 1} \quad (3)$$

and used to map from the stress-free reference state β_0 to the pre-loaded configuration β_1 at the beginning of the test. The model equations are fit to the experimental data using the Limited Memory BFGS algorithm by modifying the model parameters {C, a_1, a_2, a_3} in Python. A strain-energy surface is generated for each animal using the optimized set of parameters and within each group, the set of strain-energy surfaces are point-wise averaged over the range of experimentally measured strains. This averaged surface is used to generate a representative set of parameters for each group and the stress and strain relations from an equibiaxial stretch of 8% is computed.

Statistics. All values are presented as mean ± standard error of the mean and the significance level was set at 0.05 for all statistical tests. Two-factor ANOVA is used to compare RV thickness, mass, and hemodynamic measures, with the factors being group and treatment/week, followed by the Tukey *post-hoc* test for group. Stress-strain relations are compared using three-factor analysis of covariance (ANCOVA) with a log transformation in JMP, with the factors being strain, treatment, and group. When the interaction effects are significant, two-factor ANCOVA is performed within each group.

RESULTS

SuHx-treatment significantly increases RV thickness and mass ($p<0.0001$), with intact female RVs significantly thinner than male RVs ($p=0.0097$) and less massive than either male ($p<0.0001$) or OVX ($p=0.0002$) RVs (**Figure 1**). In each individual RV sample, the equibiaxial stress-strain response is isotropic (data not shown), thus only results in the AOT direction are shown.

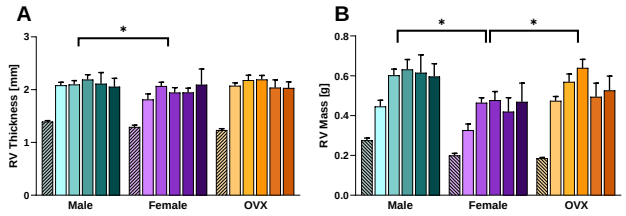

Figure 1: Morphological measurements of normotensive (patterned) and hypertensive (solid) male (green), female (purple), and OVX (orange) rats. RV thickness (A) and mass (B) increase with SuHx treatment in all groups and there is a significant difference between males and females. RV mass is significantly different between intact and OVX females. Data are presented as mean ± standard error and dark colors are later SuHx weeks.

There are significant interaction effects between strain, group, and weeks of treatment on the second Piola-Kirchhoff stress (**Figure 2**), indicating that sex and ovarian hormones impact the RV tissue-level remodeling seen in the SuHx groups. In males, 4 weeks of SuHx-treatment significantly increases RV stiffness (**Figure 2a**). The RV continues to stiffen over the next 4 weeks of treatment, before showing a slight reduction in stiffness at weeks 12 and 15 and a further increase in stiffness at week 18. In intact and ovariectomized females (**Figures 2b and 2c**), RV stiffness increases by week 4, but is then largely maintained at a similar level despite additional weeks of treatment.

DISCUSSION

Detailed studies of RV remodeling in PAH, particularly at the tissue level, have previously been conducted with only male animals. This is despite studies from Frump *et al.* and others that have shown sex-dependent RV remodeling at the organ, cell, and molecular levels and clinical evidence that pre-menopausal women have better cardiac function in PAH.[1,5] This study provides the first reported evidence that sex and ovarian hormones impact tissue-level RV remodeling in PAH.

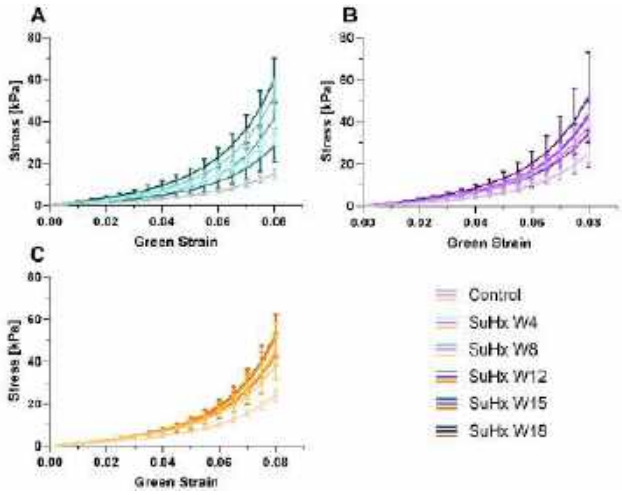

Figure 2: Average AOT stress-strain relations measured during biaxial testing. SuHx treatment increase RV stiffness in male (A), intact female (B), and OVX (C) rats. Data are presented as mean ± standard error and darker colors represent later SuHx weeks.

At baseline, there are significant differences in RV tissue thickness and mass, as well as myocardium stiffness between male and female rats. More specifically, normotensive male RVs are thicker, more massive, and less stiff than female or OVX RVs. SuHx-treatment results in similar pressure-overload in all groups (data not shown), yet the tissue-level response is sex-specific and ovarian hormone dependent. Significant RV myocardial thickening and mass increases with SuHx-treatment in males are consistent with previous studies.[2–4] Female RVs also increase in mass and thickness, but are thinner and less massive than those from males. The lack of ovarian hormones in the OVX rats results in a significant increase in RV mass compared to intact females.

Although the stress-strain relations after SuHx-treatment are show an increase in stiffness in all groups, the significance may lie in the degree of stiffening relative to the groups' normotensive stiffness. After 4 weeks of SuHx-treatment male RVs have approximately doubled in stiffness from control. This compares to the 1.5 times stiffness increase in the female and OVX RVs. By SuHx week 8, the male RV is more than 3.5 times as stiff as the normotensive male RV, whereas the stiffness of the female and OVX RVs still hasn't reached double that of their respective controls. Significant stiffening of the male RV in PAH has been previously reported,[2,4] however, this is the first study reporting a smaller increases in stiffness in female RVs, despite similar overall stiffnesses. In future studies, we will investigate how stiffening of the collagen extracellular matrix contributes to the comparatively large increase in RV stiffness seen in males.

ACKNOWLEDGEMENTS

This work was funded by NHLBI 1R25HL145817-01, 1R01HL155945-0, T32 HL 105373, and NSF CAREER 2046259.

REFERENCES

[1] Lai, YC et al., *Circ. Res.*, 115:115–130, 2014.
[2] Vélez-Rendón, D et al., *J Biomech Eng*, 141:1–8, 2019.
[3] Kwan, ED et al., *Am. J. Physiol*, 321:H702-H715, 2021.
[4] Kakaletis, S et al., *Acta Biomater*, 171:155-165, 2023.
[5] Frump, AL et al., *J Clin Invest*, 131:e129433, 2021.

DETECTION OF INTRACRANIAL CAVITATION IN POLYACRYLAMIDE BRAIN PHANTOMS UNDER BLUNT IMPACTS USING SHADOWGRAPH AND ACOUSTIC PLANE WAVE IMAGING

Eric J. Galindo (1), Ricardo Mejia-Alvarez (2), Michaelann S. Tartis (1), Adam M. Willis (2,3)

(1) Department of Chemical Engineering, New Mexico Institute of Mining and Technology, Socorro, NM, USA
(2) Department of Mechanical Engineering, Michigan State University, East Lansing, MI 48824
(3) 59th Medical Wing, Office of the Chief Scientist, Lackland AFB, TX 78236

INTRODUCTION

Traumatic brain injuries (TBIs) are a common source of disability and death worldwide, typically however damage mechanisms from an external force vary widely and are still not understood [1]. In civilian life, brain injuries can result from blunt impacts when performing daily activities. Similarly, military personnel encounter TBIs from blunt trauma but in combination with blast waves originating from explosives [2]. Cavitation is a suspected injury mechanism predicted to occur during blunt and blast impacts, where bubbles are expected to rapidly form, grow, and violently collapse in the cerebral spinal fluid (CSF) as a result of the pressure differential [3]. However, whether CSF cavitates during blunt and blast exposure is highly debated because there is no visual evidence due to the inability to monitor *in vivo* brain deformation and pressure profiles during collisions [3].

High-speed optical and acoustic imaging techniques are common approaches to acquire and visualize cavitation and shockwave behavior. Shadowgraph imaging visualizes phase changes through density variances, leading to differences in refractive index [4]. Ultrasound (US) can detect and form cavitation based on pressure differentials, one example being targeted drug delivery applications [5]. Acoustic plane wave imaging (PWI) differs by being able to capture events at high frame rates (max 10,000 FPS), compared to clinical US imaging techniques (10-30 FPS) without a focused transmit wave or varying pressure cycles [6].

This work aims to create a stand-alone tool from acoustic PWI as a unique approach to interpreting intracranial cavitation events at depths during blunt impacts. Therefore, a polyacrylamide (PAA) human head model was fabricated with optical transparency. Also, with similar shear rheological properties and simplified anatomical features present in the human brain. Cavitation was induced in head models under blunt impact via a drop tower setup in different orientations. Lastly, high-speed optical imaging was implemented to visualize and compare cavitation bubble dynamics with acoustic PWI.

METHODS

A drop tower was designed in Autodesk Inventor and fabricated to induce blunt impacts on PAA human head models. The drop tower is composed of aluminum T-slot railings held together by T-slot L-brackets, as presented in **Figure 1**. A 3-D printed impactor has an internal hollow structure that is filled with a mass of 4 kg. A trigger system allows synchronous imaging between acoustic and optical image modalities. The triggering system relies on manually pressing a mechanical button integrated into an Arduino UNO R3 microcontroller. Once pressed, a mechanical actuator retracts and releases the impactor from a height of 60 cm held together by a rope and anchor hook, breaking the continuity of a 36 AWG nichrome wire and sending a trigger voltage to the imaging hardware.

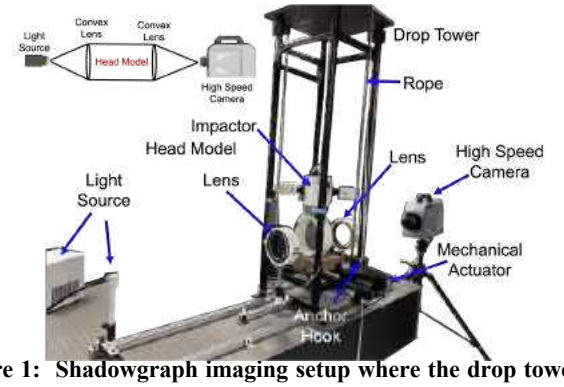

Figure 1: Shadowgraph imaging setup where the drop tower and head model are placed within the parallel light field.

A PAA composition of 10% (w/v) 60:1 (monomer:crosslinker) was chosen to construct a brain phantom. The steps for fabricating a brain phantom are previously reported [7]. Briefly, degassed DI water is mixed with a monomer (acrylamide (purity 98.0%, gas

chromatography)), crosslinker (N'-Methylenebis(acrylamide) (MBA, purity 99%)), initiator (ammonium persulfate (ACS Reagent, 98%)), and catalyst (N,N,N',N'-tetramethylethylenediamine (TEMED, ReagentPlus, 99%)). The homogenized solution is left to polymerize in a mold (**Figure 2a**), and the phantom (**Figure 2b**) is left to swell in an isotonic solution (ISOTON® II Diluent, Beckman Coulter) for 24 hours and is then sealed in a head model (**Figures 2c**) at room temperature (21C). All chemicals were purchased from Sigma-Aldrich, USA. These PAA hydrogels were previously characterized to determine mechanical properties for their applicability to simulate brain tissue [7].

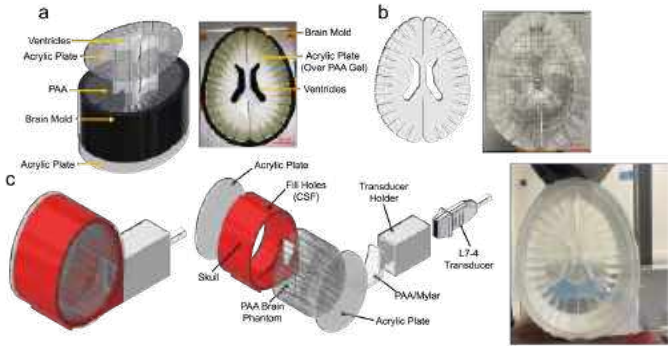

Figure 2: PAA brain phantom (a) fabrication process displaying the creation of the transparent (b) brain phantom. The brain phantom is then extracted from the mold and (c) sealed in a 3-D printed PLA skull to construct a head model. Fabricated head model incorporating a brain phantom with the inclusion of an L7-4 linear array transducer.

Shadowgraph imaging was performed under a parallel light field constructed by two Wollensak MTD telescope objective lenses (D=127 mm, FL =700 mm), as presented in **Figure 1**. A SugarCUBE Ultra LED illuminator light source illuminated the parallel field where the drop tower and head model were placed between both lenses. A Photron SA-Z high-speed camera recording at 100,000 FPS with a 0.16 µsec shutter speed captured events within the parallel light field. A Verasonics (VSX) US research scanner performed acoustic PWI by transmitting a plane wave with all 128 elements and receiving spatial information with the central 64 channels (**Figure 3**). The PWI frames had a 67 x 38 mm axial and lateral resolution, transit voltage of +17 V, and acquisition frame rate of 8620 FPS (Δt =116 µsec).

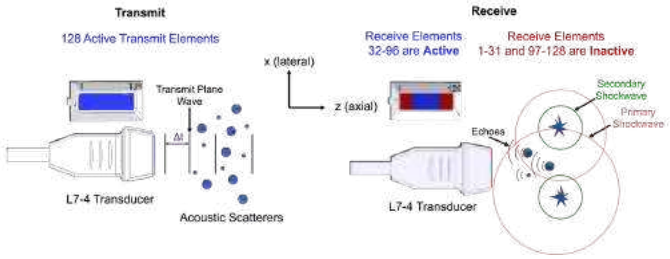

Figure 3: VSX PWI data acquisition sequence.

RESULTS

Shadowgraph imaging illustrated cavitation (yellow arrows) behavior and shockwave (magenta arrows) presence, especially in DI water (**Figures 4 a,e,c, and g**). Brain phantoms (**Figures 4 b,f,d, and h**) showed limited qualitative observations; however, cavitation was observed in the contrecoup region. Rotating the head model 90 degrees prior to impact (**Figure 4 c,g,d, and h**) produced less cavitation but increased material strain. US revealed high contrast regions (**Figure 4i**) during impact and spectra indicative of cavitation growth (**Figure 4j**) and collapse (**Figure 4k**) through broadband and harmonic behavior.

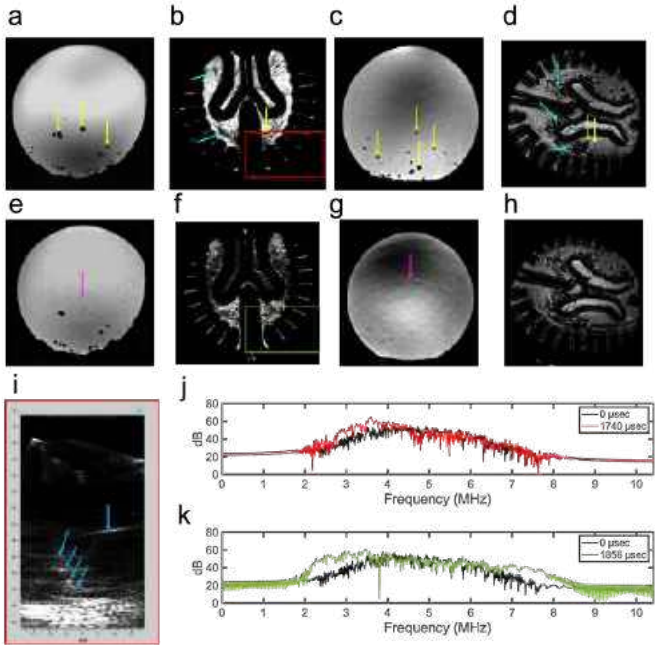

Figure 4: Shadowgraph frames of head models filled with (a,e) DI water and (b,f) brain phantom in the upright orientation. Similarly, head models rotated 90 degrees filled with (c,g) DI water and a (d,h) brain phantom. A representative (i) acoustic frame reveals an area of high contrast (blue arrows) with its corresponding power spectra revealing (j) harmonic and (k) broadband behavior. Yellow, magenta, and cyan-colored arrows reveal cavitation, shockwaves, and surface aberrations in the phantom, respectively.

DISCUSSION

A simplified PAA head model underwent blunt impacts for optical and acoustic data acquisition of cavitation events. Acoustic PWI assisted in detecting intracranial cavitation in the bulk CSF through reconstruction and signal processing techniques but lacks accuracy in spatial location and is the focus of future work. The degree of cavitation is affected by the change in orientation of the head models where the pressure profiles differ. Ultimately, this approach will allow the study of many TBI cases under various impact scenarios.

ACKNOWLEDGEMENTS

We want to thank Kevin Wedeward and the senior NMT electrical engineering student design team for fabricating the acoustic and optical triggering system. This research was funded by ONR DURIP N00014-19-1-2677, Department of Defense - Defense Health Program CDMRP award W81XWH2211117, and NNSA Minority Serving Institution Partnership Program (MSIPP) award DE-NA0003988.

REFERENCES

[1] Barlow, K. M. *Han. of Clin. Neuro.*, *112*, 891–904, 2000
[2] Santiago, L. A. et al., *Brain Injury*, *26*(2), 107–125, 2012
[3] Marsh, J. L. et al., *Frontiers in Neurology*, *12*, 1–14, 2021
[4] Castrejón-García, R. et al, *Rev. Mex. de Fis., 57*(3), 266–275, 2011
[5] Izadifar, Z. et al., *J of Med. and Biol. Eng*, *39*(3), 259–276, 2019
[6] Tanter, M. et al., *IEEE T. U. F., and F.Con.*, *61*(1), 102–119, 2014
[7] Knutsen, A et al., J of Mec Beh of Bio Mat, V138, 2023

INFLUENCE OF LABRUM SIZE AND MATERIAL PARAMETERS ON CARTILAGE MECHANICS IN HIPS WITH CAM FAIS

Luke T. Hudson[1, 2], Travis G. Maak[3], Andrew E. Anderson[1,2,3], Gerard A. Ateshian[4], Jeffrey A. Weiss[1,2,3]

(1) Department of Biomedical Engineering, University of Utah, Salt Lake City, UT, USA
(2) Scientific Computing and Imaging Institute, Salt Lake City, UT, USA
(3) Department of Orthopaedics, University of Utah, Salt Lake City, UT, USA
(4) Department of Mechanical Engineering, Columbia University, New York City NY, USA

INTRODUCTION

The acetabular labrum acts as a mechanical boundary in the hip and a load sharing mechanism with acetabular cartilage. In the presence of cam-type femoroacetabular impingement syndrome (FAIS), secondary labral tears are common and can disrupt these functions, potentially leading to overload of the articular cartilage. Labral tears are often repaired during arthroscopic surgery for FAIS through suture anchor fixation techniques, and labral augmentation and reconstruction are common in cases of hypertrophic and hypotrophic labra[1]. Currently, the role of labrum size in cartilage mechanics and femoroacetabular biomechanics is largely unknown, despite the relatively common use of surgical techniques to address variations in labral size. The objective of this study was to assess the influence of labral size on the mechanical environment of the cam-type hip during walking and squatting using finite element (FE) modeling. We hypothesized that a variation in labral size will not further alter the already deleterious contact stresses and strains in cam-type hips, therefore mechanical indices reflecting the likelihood of cartilage damage would be unchanged.

METHODS

A volunteer diagnosed with cam FAIS was selected from a previous cohort[2]. A FE model was created from closed surfaces of the labrum, cartilage, pelvis, and proximal femur obtained via CT arthrography (CTA). The anatomically normal labrum was modified to reflect a hypotrophic labrum (width $\leq$ 3mm) and a hypertrophic labrum (width $\geq$ 6mm) (Fig. 1)[3,4]. The labrum, cartilage, and pelvis were discretized using quadratic elements.

The acetabular and femoral cartilage were represented as inhomogenous, anisotropic, hyperelastic materials by embedding a continuous ellipsoidal fiber distribution of tension-only collagen fibers within an isotropic matrix[5]. The primary orientation of collagen fibers was varied transmurally to reflect the mechanical contribution and physiological distribution of fibers *in vivo*. The acetabular labrum was represented as transversely isotropic hyperelastic, with collagen fibers oriented circumferentially around the acetabular rim[5]. The pelvis was modeled as a neo-Hookean material with patient-specific material properties derived from the CTA voxel intensity[6].

Patient-specific skin-marker kinematics for both a full gait cycle and deep squat in combination with joint reaction forces from Bergmann et al. were used to drive the FE models[7]. Models analyzed using FEBio (www.febio.org). Modeling outcomes

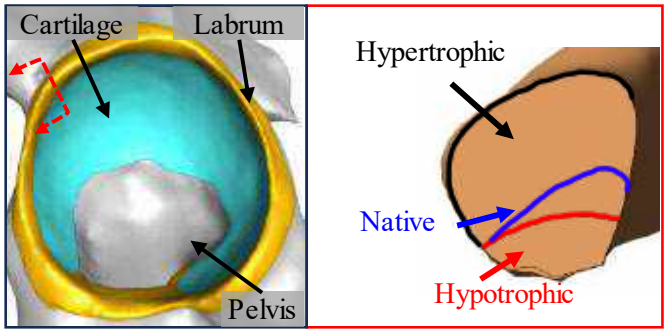

Fig. 1: (Left) Surfaces from a volunteer with cam-type FAIS were used for FE model creation. (Right) The anatomically normal labrum was modified to reflect the hypotrophic and hypertrophic cases.

were analyzed at heel-strike (level walking) and deep flexion (squat), corresponding to the highest amount of hip flexion and peak joint reaction force, where cam impingement traditionally occurs. Labral load support and labrum fiber stretch were evaluated to elucidate potential differences in load transfer and deformation between different sized labra. Contact pressure, 1st principal (tensile) strain on the articular surface, and maximum shear stress at the osteochondral interface (MSS) were also evaluated to compare the distribution of load.

Uncertainty quantification was performed using UncertainSCI[8]. Gamma distributions were defined for cartilage shear modulus, cartilage fiber modulus and labrum fiber modulus, and UncertainSCI generated sampling points in the parameter space. A quasi-static FE model simulating heel-strike was constructed analyzed repeatedly using the sampling points (N=20 models). The results were used in UncertainSCI to generate a statistical emulation model based on a polynomial chaos expansion, facilitating direct quantification of modeling sensitivity.

RESULTS

A larger labrum resulted in greater load transferred to the labrum during the gait cycle (Normal – 5.46%; Hypotrophic – 4.18%; Hypertrophic – 6.68%). Labral load support increased for all three cases during the squat and was greatest for the hypertrophic labrum (7.76%) compared to the hypotrophic (6.21%) and normal (6.93%) labra. Maximum circumferential labrum fiber strain varied from 7.0% to 7.5% during heel-strike, and between 11.0% to 12.6% at deep flexion across the three models. Contact pressure across the articular cartilage was unaffected by labral size (Fig 2). Additionally, there were minimal differences in tensile strain and maximum shear stress during heel-strike and deep flexion across the three labrum morphologies. Sensitivity analysis indicated that the modulus of the cartilage collagen fibers had the greatest contribution to variance in cartilage contact pressure, 1st principal strain, and max shear stress. For the labrum fiber stretch, variations in model outputs were equally sensitive to labrum fiber modulus and cartilage fiber modulus during heel-strike (Fig. 3).

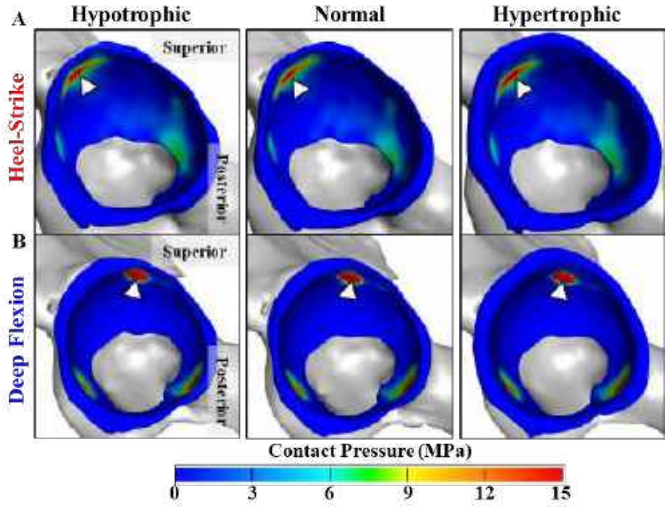

Fig. 2: There was no effect of labrum morphology on contact pressure across the three labrum morphologies during (A) heel-strike for gait or (B) deep flexion for the squat.

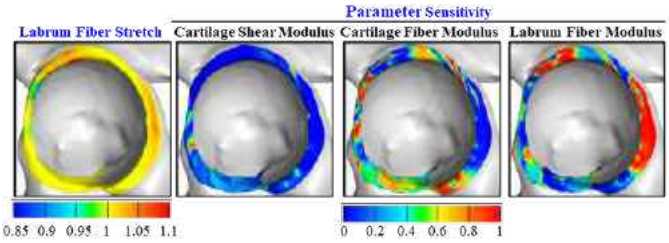

Fig. 3: Variations in the predicted labrum fiber stretch were both primarily sensitive to the cartilage fiber modulus (sensitivity = 0.48) and the labrum fiber modulus (sensitivity = 0.52).

DISCUSSION

The variability in labral load support observed between hypertrophic, normal, and hypotrophic morphologies implies that labral size exerts a discernible influence on load distribution across the joint during walking and squatting. This aligns with existing literature for dysplastic hips, where larger labral dimensions were associated with increased labral load support[9]. Sensitivity analysis revealed that uncertainty in the cartilage fiber modulus parameter directly influences the FE-predicted labral fiber stretch during heel-strike. This observation underscores an important mechanical interplay between the cartilage material properties and labrum deformation.

Despite the differences in labral mechanics among the three labral morphologies, differences in predicted cartilage contact pressure, tensile strain, and maximum shear stress were minimal. These measures fell within previously reported ranges for cam-type hips during both activities[5,10]. These FE results indicate that labrum size does not alter the cartilage stresses and strains in cam-type hips, leaving the cartilage susceptibility to similar levels of damage.

The results of this study likely have implications for surgical management of the labrum during arthroscopic surgery for cam-type FAIS. In particular, if the goal of labrum reconstruction is to reduce cartilage stress and deformation, it may be unnecessary since cartilage stresses and strains did not vary with changes in labrum size. Further, repair of the labrum with native labrum fibers may suffice in restoring hip functionality post-operatively, regardless of patient morphology. Future studies could evaluate the effect of labrum size using more advanced approaches to scale the dimensions of the tissue and incorporate statistical shape modeling to represent anatomical variation in size and shape that occurs across this population.

ACKNOWLEDGEMENTS: NIH #R01AR077636

REFERENCES [1] Ejnisman, L et al., *Clin Sports Med*, 30:317-329, 2011. [2] Atkins, P.R. et al., *J Orthop Res*, 38:823-833, 2020. [3] Drager, J et al., *Arthoscopy,* 36:2614-2620, 2020. [4] Walker, M et al., *Knee Surg Sports Traumatol Arthrosc.,*15:27-37, 2021. [5] Todd, J.N. et al., *Clin Orthop Relat Res,* 480:602-615, 2022. [6] Anderson, A.E. et al., *J Biomech Eng,* 127:364-373, 2005. [7] Bergmann, G et al., *J Biomech*, 34:859-871, 2001. [8] Narayan, A et al., *Comput Biol Med,* 106407, 2022. [9] Henak, C.R. et al., *J Biomech*, 44:2210-2206, 2011. [10] Ng, K.C. et al., *HSS J*, 8:206-212, 2012

ASSESSING PATTERN RECOGNITION RECEPTOR AGONIST LOADED HYDROGELS AS A POTENTIAL ROTATOR CUFF REPAIR AUGMENT

S. Winston (1), D. von Stade (2), C. Plaisance (3), L. Pezzanite (3), L. Chow (3), S. Dow (3) K. McGilvray (1)

(1) Department of Mechanical Engineering, Colorado State University, Fort Collins, CO, USA
(2) Department of Immunology, Microbiology, and Pathology, Colorado State University, Fort Collins, CO, USA
(3) Department of Clinical Sciences, Colorado State University, Fort Collins, CO, USA

INTRODUCTION

Over 250,000 rotator cuff (RC) repair surgeries occur annually in the United States. These surgeries are failing at rates ranging from 20-94% [1,2] depending on the age, weight, and other comorbidities of the patient [1,2]. Current estimates suggest that the number of surgeries will only increase subsequently, followed by a larger financial burden and pain on patients. Analysis of tissues after surgery suggests that the healthy transition region from calcified bone to non-calcified tendon vanishes, and the junction becomes scar tissue [4]. Scarring itself in the tendon is a very complex process, but it is known that the immune cell milieu's response to the wound is the primary driver of whether a tissue repairs or scars.

Modulating the immune response to repair tissues has been of significant interest recently. Pattern Recognition Receptor Agonists (PRRAs) are a class of molecules that have been used as vaccine adjuvants and anti-tumor treatment [4,5]. These agonists activate the innate immune response through receptor classes such as nod-like and toll-like receptors (NLRs & TLRs), respectively. **We aim to investigate the effects of NLR-3 and TLR-3 agonist-loaded hydrogels and determine if there are differential effects on an injured tendon healing in a rat model through histopathological means and functional outcomes.**

METHODS

Sprague Dawley Rats (N=32) were injured bilaterally through a partial RC release model and immediately received perilesional injections of a methylcellulose/hyaluronic acid (1.5wt%/0.5wt%) blend hydrogel with NLR3 agonist Aluminum Hydroxide (Invivogen) (ALOH) or TLR3 agonist Poly (I:C) (Invivogen) at concentrations of 50 ng/mL. In addition, select rats also received a melt electrowritten polycaprolactone (PCL) mesh. After surgery, rats voluntarily walked on a Tekscan Rodent Walkway System to analyze gait and weight bearing parameters. Rats were acclimated the week to surgery and were walked 1,2,3,4,6,8,10, and 12 weeks post-surgery.

Rats were euthanized at 1-, 4-, and 12-weeks post-surgery. Shoulders were embedded in paraffin, and 5 µm sections were cut and stained with Hematoxylin and Eosin (H&E). Slides were blindly scored on a 5pt 0-4 scale according to ISO 10993-06, as well as signs for tendon-specific markers such as tenocyte activity, tendon vascularity, and collagen disorganization.

RESULTS

Histology showed that after 4 weeks, the ALOH, ALOH+Mesh, and Poly(I:C) groups had lower levels of collagen disorganization compared to the Injured Control (Figure 1).

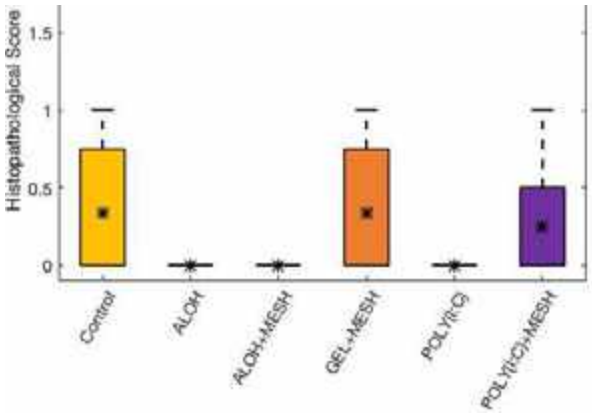

Figure 1: Collagen disorganization levels of each group after 4 weeks. A score of Zero is indicates a more organized, healthier collagen bundle, while a score of 1.5 can be considered to indicate increased disorganization or weaker tendon.

After 4 weeks post-surgery, Poly(I:C) treated rats had significantly higher stride length than ALOH treated rats (Figure 2; p = 0.0021). At 6 weeks, the Poly(I:C) treatment was significantly higher than ALOH+Mesh and ALOH groups (p = 0.0195 and 0.0090, respectively). Poly(I:C) also had markedly higher stride lengths than the injured control at weeks 4 and 6 as well. Finally, at 8 weeks, ALOH was significantly lower than the Injured Control, Poly(I:C), and Poly(I:C)+Mesh groups (p = 0.0460 Injured Control; 0.043 Poly(I:C); and 0.0031 Poly(I:C)+Mesh).

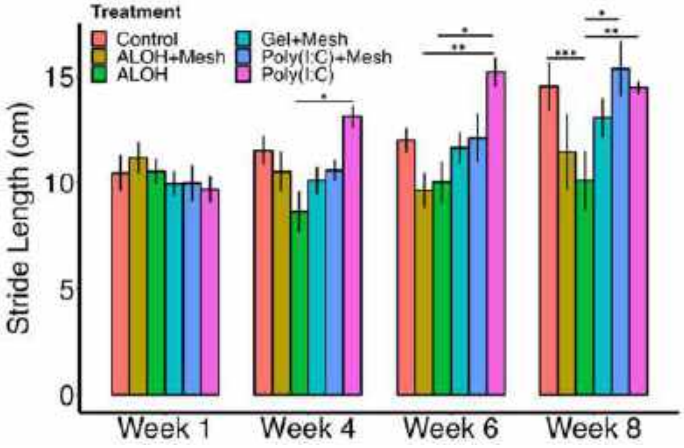

Figure 2: Bar chart of stride length of each rat group in weeks 1, 4, 6, and 8 with significance bars. Significance threshold was set to ($p<0.05$)

DISCUSSION

The Poly(I:C) and ALOH groups had different responses compared to the Control and the Gel+Mesh groups histologically, illustrating that stimulating the immune system through TLR and NLR activation have differential effects on tendon healing, possibly leading the way for a different tendon therapy.

The ALOH group had signs of increased tendon healing histologically, but these signs were not seen in the functional outcome of stride length. ALOH groups did not increase stride length temporally and even fell behind its starting after week 4, indicating less joint function than injured control groups. Poly(I:C) however, had marked increases compared to the injured controls at week 4 and 6, possibly leading to a faster healing response compared to the rat's native healing response. Poly(I:C) also had larger stride lengths compared to the ALOH groups starting at week 4, conveying that Poly(I:C) induced stimulation could be healing the shoulder better than the ALOH stimulated shoulders.

These data serve as an initial investigation of NLR and TLR stimulation in wound healing showing that there are functional level differences in gait after injections of NLR3 and TLR3 agonists ALOH and Poly(I:C) respectively.

ACKNOWLEDGEMENTS

We would like to acknowledge Colorado State University's College of Engineering Walter Scott Jr. 'High Impact' Grant mechanism for funding this research.

REFERENCES

[1] Cole, B et al., *J of Shoulder and Elbow Surgery,* 16:579-585, 2007.
[2] Galatz, L et al., *J of Bone and Joint Surgery,* 86:219-224, 2004.
[3] Zumstein, M. et al., *Orthopaedics and Traumatology: Surgery and Research,* 103:S1-S10, 2017.
[4] Chakroborty, S., et al., *Frintiers in Immunology*, 14, 2023
[5] Kaczanowska S., et al, J Leukocyte Biology, 93:847-863

SCLERAXIS-TARGETED DELETION OF NON-MUSCLE MYOSIN LEADS TO TENDON DEGENERATION

Mary Kate Evans (1), Ellie Bernstein (1), Tonia K. Tsinman (1), Ellie J. Ferguson (1), Xi Jiang (1), Joel D. Boerckel (1), Lin Han (2), Eiki Koyama (3), Robert L. Mauck (1), Nathaniel A. Dyment (1)

(1) Department of Orthopaedic Surgery, University of Pennsylvania, Philadelphia, PA, USA
(2) School of Biomedical Engineering, Drexel University, Philadelphia, PA, USA
(3) Orthopaedic Biomedical Research, Children's Hospital of Philadelphia, Philadelphia, PA, USA

INTRODUCTION

The specific signaling events by which tendon cells respond to mechanical cues are largely unknown [1]. Therefore, designing rehabilitation strategies to treat tendon pathologies that produce consistent outcomes is an unmet clinical need. To better understand the cell-intrinsic mechanisms that regulate tendon adaptation to applied loads, we investigated actomyosin contractility, the major force-generating machinery of mesenchymal cells. Actomyosin contractility relies on the fundamental motor protein, non-muscle myosin (NM-II), which binds actin filaments to generate contractile force and transduce signals from applied loads to the nucleus [2]. Prior *ex vivo* studies demonstrated that NM-II mediated contractility can regulate matrix remodeling [3-4] via YAP/TAZ signaling [5]. Yet, the importance of actomyosin contractility in tendon formation and maintenance *in vivo* is unknown. Therefore, we deleted NM-II proteins in tendons throughout growth and development. We hypothesized that NM-II is required to maintain tissue homeostasis.

METHODS

All animal work was IACUC approved. Mouse Model: To preferentially delete NM-II in tendons, we targeted the predominant NM-II isoforms, NM-IIA (*Myh9* gene) and NM-IIB (*Myh10* gene) using the Scleraxis (Scx) Cre driver to generate ScxCre;Myh9$^{f/f}$;Myh10$^{f/f}$ mice (myosin dKO) and Cre-negative littermate controls (WT). Cryohistology: Knees and ankles from P2, P28, and P112 myosin dKO and WT mice were fixed and sectioned in the sagittal plane. *In Situ* Hybridization (ISH): P2 patellar and Achilles tendon sections (n=4/group) were stained for *Myh9* (C1) and *Myh10* (C2) RNA using the BaseScope Duplex Assay. Tendon Morphology: P28 and P112 sections (n=4-7/group) were stained and imaged in two rounds: (1) calcein blue (CB), alkaline phosphatase (ALP), and TO-PRO-3 (nuclei), (2) Toluidine Blue, and were used to determine patellar tendon length and nuclear aspect ratio. Tendon Mechanics: P112 Patellar and Achilles tendon cross-sectional area (CSA) was measured before tendons were subjected to a testing protocol consisting of preconditioning and ramp to failure (0.1%/sec). Cytoskeletal Organization: F-actin (phalloidin staining) and cell nuclei were visualized via confocal z-stacks in P28 patellar tendon sections (n=4/group). Gene Expression: Patellar and Achilles tendon tissue sections (n=4-5/group) were collected for qPCR using a Standard BioTools Dynamic Array for 96 genes of interest. Statistics: Groups were compared via one-way ANOVA with Tukey post-hoc tests (α=0.05).

RESULTS

NM-II deletion in tendons. *Myh9* and *Myh10* expression was deleted from the vast majority of tendon cells. Interestingly, a subset of non-deleted cells in the dKO tendons exhibited elevated expression (**Fig. 1A-B**). Myosin dKO tendons progressively degenerate with age. NM-II deletion caused tendon degeneration by P112, characterized by tendon elongation (**Fig. 2C**), reduced nuclear aspect ratio (**Fig. 2D**), and disorganized matrix with increased proteoglycan staining (**Fig. 2A-B**). In fact, ectopic mineralization was evident in 4/6 patellar and 5/5 Achilles tendons in myosin dKO mice, compared to 0% in WT tendons. When P112 tendons were dissected for mechanical testing, there was a striking visual difference in myosin dKO tendons compared to WT, with patellar tendons presenting with abundant adipose deposits and decreased birefringence, while Achilles tendons appeared significantly smaller (**Fig 3A**). CSA measurements confirmed a decrease in Achilles but not patellar tendon CSA (**Fig 3B**), and both tendons displayed a marked decrease in tissue stiffness (**Fig 3C**). Expression profile of myosin dKO tendons suggest increased tissue remodeling. Gene expression analyses and hierarchical clustering revealed a marked difference in gene expression between WT and myosin dKO mice at both P28 and P112, with increased expression of both anabolic (e.g., *Col1a1*, *Col3a1*, *Lox*) and catabolic markers (e.g., *Mmp13*, *Mmp14*, *Timp1*) in myosin dKO tendons, with these changes being more

pronounced in the patellar tendon than the Achilles (**Fig. 4**). Aberrant cytoskeletal architecture and increased cellularity. Finally, to further probe the events that led to tendon degeneration in the absence of NM-II, we imaged the actin cytoskeletal network in P28 patellar tendons and found regions of disorganized actin cytoarchitecture and increased cellularity in the tendon midsubstance (**Fig. 5**).

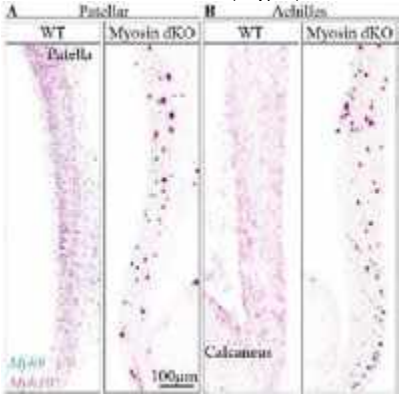

Figure 1: *Myh9* (green) and *Myh10* (red) deletion in (A) Patellar and (B) Achilles tendons of Myosin dKO mice. ISH shows deletion and surprisingly the presence of high-expressing cells in dKO tendons.

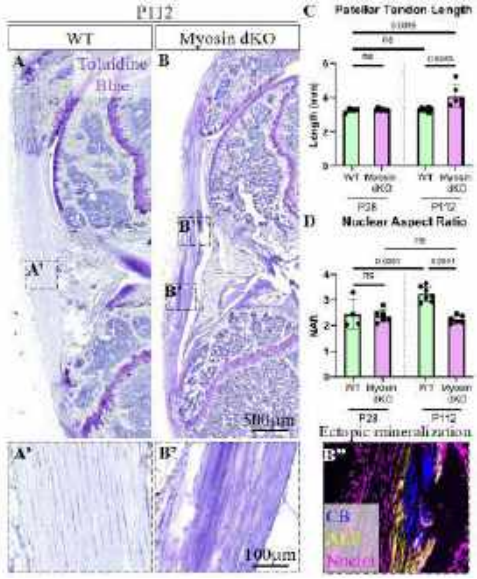

Figure 2: Degenerative dKO tendons at P112. Toluidine Blue (A-B), calcein blue (CB, B'') for mineral, and alkaline phosphatase (ALP, B'') staining. Elongated PTs (C) with decreased nuclear aspect ratio (D) in P112 myosin dKO tendons that is not present at P28.

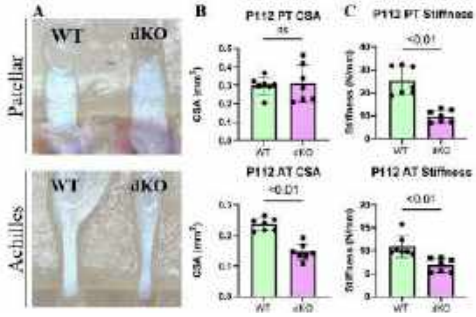

Figure 3: P112 Myosin dKO tendons have decreased structural properties. (A) gross dissection, (B) cross-sectional area measurements, and (C) tendon stiffness.

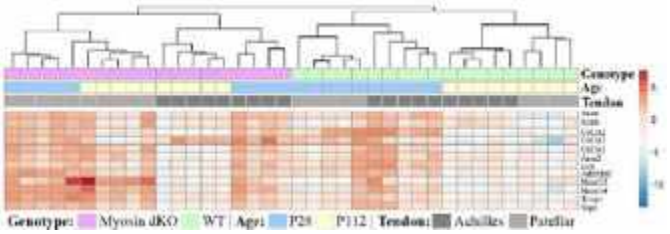

Figure 4: Increased anabolic/catabolic expression in dKO tendons. Heatmap and hierarchical clustering for subset of genes (12 from 91 total) from qPCR array.

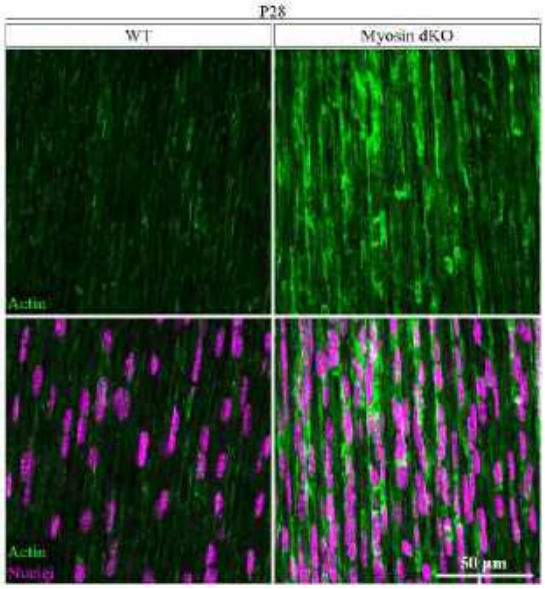

Figure 5: Aberrant actin cyto-architecture and increased cellularity at P28.

DISCUSSION

This study highlights the progressive onset of tendon degeneration following sustained deletion of *Myh9* and *Myh10* throughout tendon growth and development. Although P28 myosin dKO tendons display differences in actin organization and gene expression, they do not yet display the patellar tendon elongation and decreased nuclear aspect ratio present at P112. This progressive onset of tendon degeneration may parallel what has been shown *ex vivo*, where a disruption in tensional homeostasis can trigger a catabolic response and aberrant matrix remodeling [3-5]. Additionally, it is possible that disrupted actomyosin contractility impairs the ability of tenocytes to sustain the increased loading demands leading into adulthood. Alternatively, it may be that, once tendon cells mature and establish a tensional homeostatic set point required for proper tissue maintenance, the cells are less capable of responding appropriately to altered loading. Interestingly, a subset of non-deleted cells in myosin dKO tendons exhibited elevated expression, suggesting compensation. These data highlight the critical importance of NMII-mediated actomyosin contractility in maintaining tendon growth and homeostasis.

ACKNOWLEDGEMENTS

Work was supported by NIH P50 AR080581, P30 AR069619, R01 AR075418, T32 AR007132, and VA IK6 RX003416.

REFERENCES

1. Galloway, *J Bone Joint Surg*, 2013; 2. Franke, *Curr Biol*, 2005; 3. Schiele, *JOR*, 2015; 4. Arnoczky, *JOR,* 2004; 5. Jones, *PNAS*, 2023.

A MULTISCALE AND MULTIMODAL COMPUTATIONAL FRAMEWORK TOWARDS UNDERSTANDING MECHANOTRANSDUCTION IN THE DISTAL COLON AND RECTUM

Amirhossein Shokrani (1), Bin Feng (2), David M. Pierce (1,2)

(1) School of Mechanical, Aerospace, and Manufacturing Engineering, University of Connecticut, Storrs, CT, USA
(2) Department of Biomedical Engineering, University of Connecticut, Storrs, CT, USA

INTRODUCTION

Individuals suffering from irritable bowel syndrome (IBS) report severe chronic discomfort arising from visceral pain, a symptom that impacts their quality of life [1]. Mechanotransduction transforms mechanical stimulation of the colon and rectum (colorectum) into neural action potentials (APs) by sensory afferents and plays a crucial role in bowel pain associated with IBS [2]. Mechanical distension of the colorectum initiates visceral pain in IBS patients. Thus, a broader understanding of colorectal mechanotransduction will likely contribute significantly to the introduction of more effective therapeutic approaches for controlling visceral pain associated with IBS.

Recent experiments on the mouse colorectum have uncovered considerable mechanical heterogeneity across the longitudinal, circumferential, and radial directions [3,4]. Researchers have also captured the responses of sensory afferents to mechanical stimuli using single-fiber recordings to investigate colorectal afferent neural encoding [5]. Molecular-scale characterization also revealed the composition and function of ion channels in afferents of the colorectum, cf. Fig. 1 [6].

In this study, we established a multiscale computational framework to advance our understanding of colorectal mechanotransduction. We designed our multiscale framework to predict neural encoding by individual colorectal afferent endings in response to macroscopic mechanical stimuli applied to the colorectum. First, we model the macroscale biomechanics of the mouse colorectum using an experimentally validated finite element model to predict intra-tissue stresses. We then integrate a neural membrane model, informed by experimental data on the composition of ion channels, to simulate the generation of action potentials in response to local mechanical stress and strain acting on the afferent endings. We aim to apply our computational framework to: (1) evaluate and contrast three hypotheses on mechanical gating of the generation of APs and (2) investigate the effect of orientations of afferent endings on the encoding function.

METHODS

Experimental evidence. We utilized previous evidence from our experiments on mouse colorectums including the biomechanics [3,7], the encoding function [5], and the intra-tissue morphology of colorectal afferents [4] to establish our multiscale computational framework.

Finite element model. We developed a macroscopic FE model that considers mechanical heterogeneity of colorectal tissues in the longitudinal, radial, and circumferential directions using FEBio [8].

Morphology of nerve fibers. We quantified the morphology of nerve fibers within submucosa using our second harmonic generation (SHG) images [9] and custom image processing tools. To study the sensitivity of the generated APs to the orientation of the nerve fibers within the submucosa layer, we employed seven analytical neural afferent endings, each embedded within the colorectum with distinct

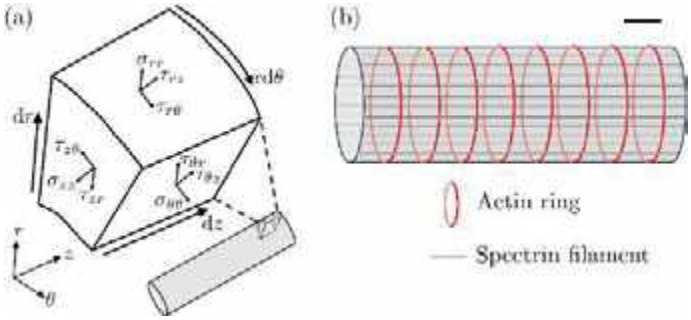

Figure 1: Analysis of afferent membrane tension as the gating parameter for the mechanosensititve (MS) channels. (a) Schematic of the stress components along with the axonal membrane skeleton. (b) Representation of the axon membrane skeleton demonstrating actin rings connected by spectrin filaments that provide structural sustainability of afferent axon. The scale bar is 115 nm.

orientations. For each analytical orientation we calculated the effective stress (in-plane stress) acting on the surface of the embedded fiber to compute the tension applied to the corresponding MS channels.

Micromechanics of nerve fibers. We calculated the local mechanical stress/strain profile along the length of each analytical fiber embedded in the colorectal wall using our custom program [8].

Generation of action potentials. We used our unique, mechanosensitive neural membrane simulation to replicate how local membrane tension along the afferent ending's surface encodes afferent stress/strain into APs. We calibrated our neural membrane simulations to generate results consistent with the experimental data from single fibers recordings considering the rule of NaV1.6 ion channels and mechanosensitive ion channels in spike initiation using NEURON [5,8].

Sensitivity of mechanotransduction using three hypotheses. Recent molecular-level studies have revealed that the cytoskeleton of nerve axons consist of ring-shaped actin filaments evenly spaced by 0.2-0.4 µm, see Fig. 1(b). Thus, we proposed three hypotheses to determine the in-plane stress acting on the membrane of the afferent ending to initiate and propagate the generation of APs: 1) axial stress dictates mechanical gating of mechanosensitive channels, 2) both axial and circumferential stresses contribute, and 3) membrane shear stress dictates, see Fig. 1(a).

RESULTS

In Fig. 2(a) we show the Cauchy stresses at regions surrounding the afferent endings derived from FE analyses. We then derived the stresses along the afferent endings using one of three hypotheses, shown in Figs. 2(b), (c), and (d), respectively.

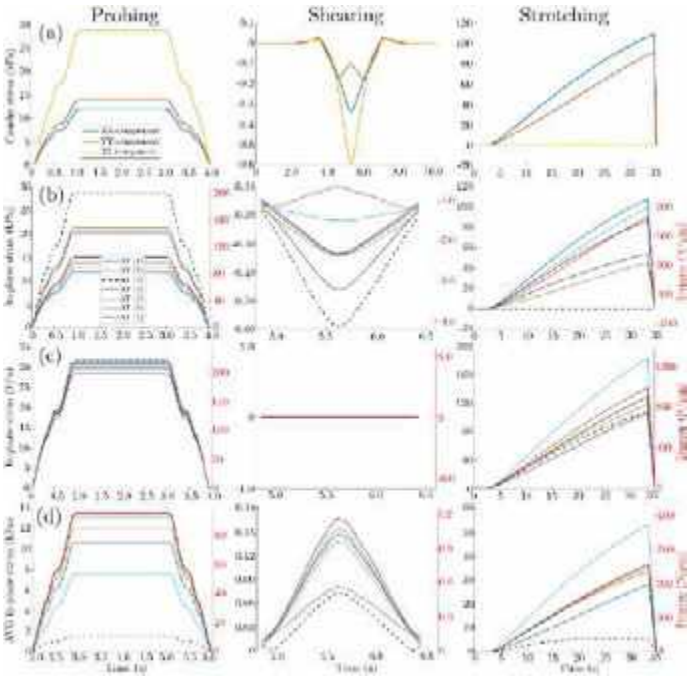

Figure 2: Microscopic stress profiles as a function of time acting on the afferent nerve fibers in response to three different mechanical stimuli to the colorectum: (a) Cauchy stresses at the region of the afferent ending within the colorectum, and membrane stresses and tensions acting on the afferent endings based on the (b) first, (c) second, and (d) third hypotheses.

In Fig. 3 we show APs generated and propagated from analytical fiber 7 (AF(7)) under three hypothesis for the relevant in-plane stresses and due to the three mechanical stimuli to the colorectum.

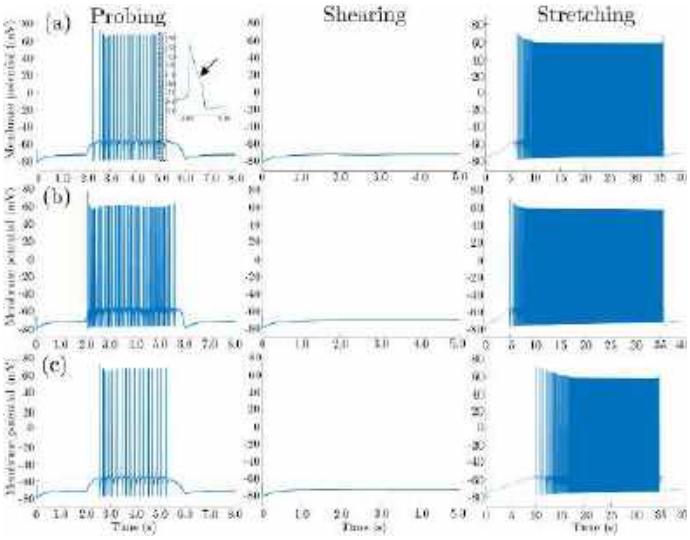

Figure 3: Representative action potentials generated from AF(7) using the membrane tensions calculated using (a) first, (b) second, and (c) third hypotheses for probing, shearing, and stretching.

In Table 1 we demonstrate the responses (or lack thereof) of each of the analytical fibers to each of the mechanical stimulations according to the three hypotheses used for deriving the membrane tension.

Table 1: Activation of action potentials from AF(1) through AF(7) under each stimuli for each of the three hypotheses (Active: A).

Hypothesis	Stimulation	AF(1)	AF(2)	AF(3)	AF(4)	AF(5)	AF(6)	AF(7)
1	Probing	A	A	A	A	A	A	A
	Shearing	-	-	-	-	-	-	-
	Stretching	A	A	-	A	A	A	A
2	Probing	A	A	A	A	A	A	A
	Shearing	-	-	-	-	-	-	-
	Stretching	A	A	A	A	A	A	A
3	Probing	A	A	-	A	A	-	A
	Shearing	-	-	-	-	-	-	-
	Stretching	A	A	-	A	A	A	A

DISCUSSION

We leveraged our experimental results to establish a novel multiscale computational framework enabling us to investigate mechanotransduction in the distal colon and rectum. Each component of our framework is driven by experimental data. Our multiscale modeling framework provides an innovative investigative tool bridging the gap between colorectal biomechanics and sensory afferent neural encoding. This research not only expands our understanding of colorectal mechanonociception but also sheds light on potential non-pharmacological interventions for colorectal diseases.

ACKNOWLEDGEMENTS

National Institutes of Health 1R01DK120824-01.

REFERENCES

[1] Feng *et al*., *Am J Physiol Gastrointest Liver Physiol*, **302**, G1085, 2012. [2] Pasricha *et al*., *Chronic Abdominal and Visceral Pain: Theory and Practice*. CRC Press: 2006. [3] Siri *et al.*, *Am J Physiol Gastrointest Liver Physiol*, **317**, G349, 2019. [4] Maier *et al.*, *J Mech Behav Biomed Mater*, **113**, 104116, 2021. [5] Feng, *Am J Physiol Gastrointest Liver Physiol*, **300**, G170, 2011. [6] Feng, *J Neural Transm*, **127**, 415-429, 2020. [7] Siri *et al.*, *Am J Physiol Gastrointest Liver Physiol*, **316**, G473, 2019. [8] Shokrani et al., *SSRN*, 4624852, 2023. [9] Guo *et al*., *Am J Physiol Gastrointest Liver Physiol*, **32**, G644, 2021.

EX VIVO MINOXIDIL TREATMENT INCREASES ELASTIC FIBER DEPOSITION IN THE MURINE VAGINAL WALL

N. Karbasion (1), J.C. Snider (1), S. Chatman (2), K.S. Miller (3), M.R. Bersi (1)

(1) Department of Mechanical Engineering & Material Science, Washington University in St. Louis, St. Louis, MO, USA
(2) Department of Biomedical Engineering, Washington University in St. Louis, St. Louis, MO, USA
(3) Department of Bioengineering, The University of Texas at Dallas, Dallas, TX, USA

INTRODUCTION

Female reproductive tissues are a set of dynamic organs, including the uterus, cervix, and vagina. These organs play a crucial role in maintaining hormonal balance and supporting fetal growth. The uterus and vagina undergo significant shape and size changes due to natural processes such as pregnancy, postpartum involution, and aging.

A recent study on the structure of the murine female vaginal wall has indicated that the biochemical composition of the aging vaginal wall, and consequently its mechanical properties such as stiffness, undergo changes due to a decrease in smooth muscle cell contractility and the loss of elastic fibers [1]. The elastin network's role in supporting the proper structure and functionality of vaginal tissues is not only affected by aging but also by different diseases such as pelvic organ prolapse (POP), which is known to be associated with the disruption of the vaginal elastin network in humans [2].

POP is characterized by the gradual descent of the uterus, bladder, or cervix into or through the vaginal canal. Examination of human vaginal samples from patients at different POP severity levels has revealed an inverse relationship between the severity of POP and elastin protein levels [3]. Unfortunately, recent studies have indicated that more than 40 percent of women are diagnosed with some level of POP in their lifetime [4]. Consequently, we hypothesize that strategies for increasing elastin synthesis in vaginal tissue could counteract the disruption of the elastin network resulting from aging and other associated diseases.

Given the significant number of women impacted by POP and the lack of current pharmaceutical intervention, we aimed to use a targeted drug therapy approach. To this end, we investigated the ability of minoxidil sulfate to promote elastic fiber deposition in the vaginal wall. Minoxidil is a potassium channel opener initially developed as an anti-hypertensive drug that has been shown to promote elastic fiber deposition in the cardiovascular system [5,6]. However, the potential for minoxidil to stimulate elastin synthesis in tissues outside of the cardiovascular system has not been explored.

METHODS

Animals. Intact pelvic organs of 10-12 weeks old adult female mice were extracted following anesthetization using isoflurane. The isolated tissues were randomly assigned to untreated control or minoxidil-treated groups. The tissues then were placed in phenol red-free DMEM media containing 10% fetal bovine serum (FBS) and 1% antibiotic-antimycotic solution (100x). The treatment group also received 0.24 mM minoxidil sulfate in the cell culture media. Extracted tissues were incubated at 37°C and 5% CO_2 for 7 days with culture media being replenished every 24 hours.

***Elastin Protein Measurements*.** In order to evaluate the changes in elastic fibers in the vaginal due to ex vivo minoxidil treatment, the total amount of soluble and insoluble elastin protein was measured using a Fastin elastin assay (Biocolor). Measurements were made in both vaginal tissue explants and cell culture media. Changes in the vaginal elastin fiber network were also visualized by sectioning and immuno-fluorescence staining of the tissue. Using an antibody specific to elastin, the stained tissue was imaged and analyzed using ImageJ [7] and CT-Fire (MATLAB) [8] to determine the normalized elastin area in the vaginal wall as well as number, length, and width of elastic fibers.

***Biaxial Mechanical Testing*.** The biaxial mechanical properties of control and minoxidil-treated vaginal tissue were assessed using an established extension-inflation technique [1]. After 7 days of ex vivo treatment, vaginal tissues were cannulated onto 8G and 21G blunt needles, and the unloaded geometry (length and outer diameter) was estimated. Following estimation of an in vivo length based on the axial force-pressure relationship, vaginal tissues were then preconditioned to reduce hysteresis. After preconditioning, the tissues were subjected to 3 cycles of 5-80 mmHg pressurization at the physiological length and ±5% of physiological length. The outer diameter was tracked throughout testing using an in-line camera while axial stretch and force were directly recorded during testing. After testing, vaginal wall

thickness was measured from an Optical Coherence Tomography (OCT) scan of a vaginal ring. Quantification of the wall thickness and average wall stresses were calculated using MATLAB.

Statistical Analysis. Changes in vaginal elastin protein levels (Fastin elastin and immunofluorescence image quantification) were assessed using the nonparametric Mann-Whitney U test. Group comparisons with $p < 0.05$ were considered significantly different.

RESULTS

In order to visualize the elastic fiber network in control and minoxidil-treated vaginas, tissue explants were cryosectioned and stained using an elastin-specific antibody. Interestingly, the number of elastin fibers (**Fig. 1A, B**) and the normalized elastin area fraction (**Fig. 1C)** increased in the minoxidil treated tissues, relative to control. Measuring the amount of insoluble and soluble elastin using a Fastin elastin assay also showed an increase in the amount of elastin in the minoxidil-treated vaginal tissues in comparison to control (**Fig. 1D** and **E**, respectively). We also measured 3.8-fold higher levels of soluble elastin in the culture media of minoxidil-treated samples, suggesting the tissues are producing more elastic fibers following minoxidil treatment.

Biaxial analysis of the untreated and treated tissue indicated changes in tissue geometry and mechanical response. Although the control and minoxidil-treated tissues were subjected to the same range of pressures, the treated tissue exhibited roughly 25 percent greater outer diameter in response to pressurization (**Fig. 2A).** Interestingly**,** the axial stretch of treated tissue was also increased (**Fig. 2B**). Minoxidil treatment not only changed composition and geometry of the tissue, but it also showed marginal increases in the distensibility (circumferential stretch range; **Fig. 2C**) and extensibility (axial stretch range; **Fig. 2D**).

Calculating the tissue stiffness at low (5-20 mmHg) and high pressures (60-80 mmHg) indicated that minoxidil treatment increases vaginal stiffness in both the circumferential and axial directions. Interestingly, the increase in vaginal stiffness was greater in the circumferential direction at both low pressures (89.4% vs. 38.8%) and high pressures (37.6% vs. 9.86%) relative to the axial direction.

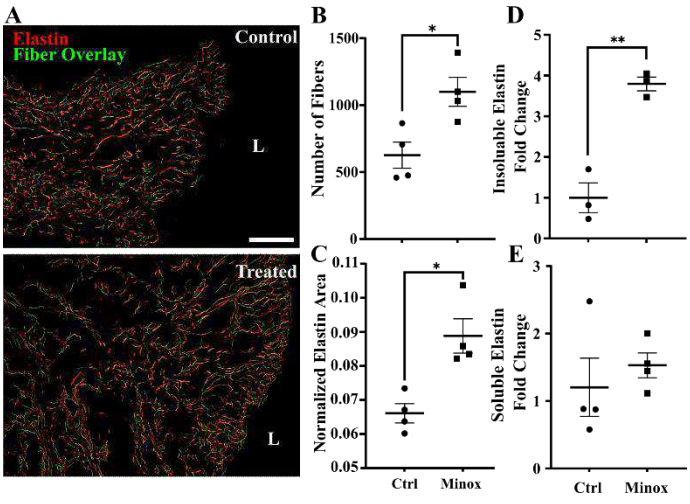

Figure 1: Comparison of elastin protein measurements in response to minoxidil treatment. Representative analysis showing overlaid elastic fibers in control (top) and minoxidil-treated (bottom) vaginal tissue (A). The vaginal lumen is indicated by L and the scale bar indicates 100 µm. Measurement of elastin protein was achieved by immunofluorescence staining (B and C) and a Fastin elastin biochemical assay (D and E). *, ** $p < 0.05, 0.01$; Mann-Whitney U test. n=3-4 biological replicates per group.

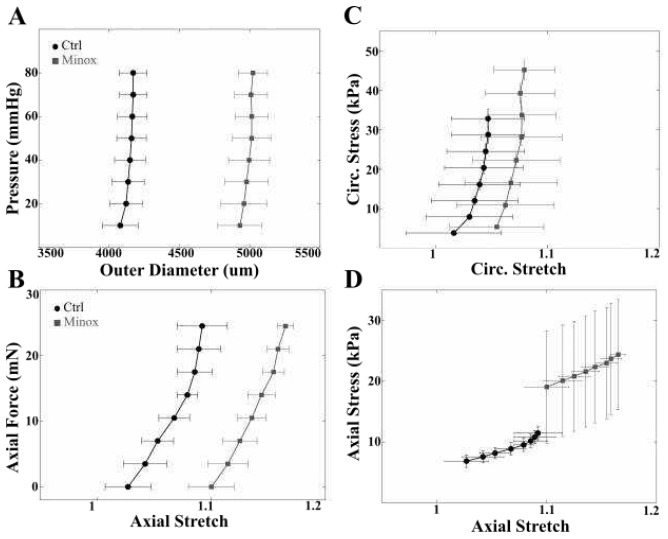

Figure 2: Comparison of tissue geometry and biaxial mechanical response of vaginal tissue following minoxidil treatment. Changes in outer diameter (A) and axial stretch (B) of control (black curves) and minoxidil-treated (gray curves) vaginal tissues exposed to the same range of pressure and force, respectively. Minoxidil treatment resulted in an increase in circumferential (C) and axial stress (D) and stretch. n=2-3 biological replicates per group.

DISCUSSION

In the current study, we have demonstrated for the first time that ex vivo treatment of vaginal tissue with minoxidil sulfate has the potential to alter the elastin network by increasing the number and area fraction of elastic fibers in the tissue. We found that in addition to increasing the amount of elastin in vaginal tissue, minoxidil treatment also led to measurable changes in the tissue geometry as shown by increases in the outer diameter and axial stretch. We also observed a right-ward shift of the biaxial stress-stretch response after minoxidil treatment, as well as increases in tissue stiffness both axially and circumferentially. The increase in elastin content of treated vaginal tissue is significant as it provides evidence for a first pharmaceutical treatment to potentially combat the loss of elastin fiber network associated with aging and other pelvic floor disorders such as POP. Here we have focused on changes in the elastic fiber network of the vaginal wall, however changes in other tissues of the pelvic floor, such as the uterus, cervix, and skeletal muscle, has not been investigated. During the next steps, we will focus on evaluating the potential for minoxidil treatment to effectively induce elastin synthesis in murine vaginal tissue when the drug is administered in an in vivo setting.

ACKNOWLEDGEMENTS

This work was funded by internal startup funds provided by Washington University in St. Louis.

REFERENCES

[1] White, SE et al, *Acta Biomaterialia*, 1742-7061, 2023. [2] Zong, W et al, *Obstet Gynecol*, 115(5), 953-961, 2010. [3] Budatha, M et al. *J. Clinical Investigation*, 121(5), 2048-2059, 2011. [4] Wang, B et al, *Front. Public Health*, 10, 2022. [5] Knutsen, R et al, *J. Physiol. - Hear. Circ. Physiol.* (315), H18-H32, 2018. [6] Slove, S et al. *Hypertension*, 62(4), 794-801, 2013. [7] Scheindlin, J et al, *Nature Methods*, 9(7), 676-682, 2012. [8] Liu, Y et al, *Methods Mol. Biol*, 1627, 429-451, 2017.

EVALUATION OF THE EFFECTS OF PFAS ON PANCREATIC CANCER USING A MICROFLUIDIC PANCREAS MODEL

Tarun Singh (1), Sae Rome Choi (1), Barbara Hocevar (2), Lisa Kamendulis (2), Bumsoo Han (1)

(1) School of Mechanical Engineering, Purdue University, West Lafayette, IN, USA
(2) Department of Environmental and Occupational Heath, Indiana University, Bloomington, IN, USA

INTRODUCTION

Pancreatic ductal adenocarcinoma (PDAC) is one of the most lethal cancer types with a dismal 5-year 12% survival rate [1]. Current therapeutic strategies to treat this ailment have shown minimal improvements in survival rates of patients over the past several years. Previously, most of the scientific research has been conducted around the genetic aspects of the disease and different approaches to target them. However, minimal attention has been given to the role that environmental toxicants might contribute to the promotion and progression of pancreatic cancer.

Per and polyfluoroalkyl substances (PFAS), also referred to as "Forever chemicals", are a hot research topic because of their non-reacting, non-degrading, and biologically interfering nature [2]. Their natural reservoirs include drinking water (several contamination sites have been identified in USA), and in general all surfaces where non-stick properties are necessary. In some human cohorts, the PFAS concentration in blood serum (95th percentile) reach as high as 23.87 ng/ml [3]. One of the family members of PFAS, perfluorooctanoic acid (PFOA, CAS 335-67-1), has previously been under class action lawsuits due to ground water contamination and has since been under investigation [4]. From previous studies conducted on animal models, PFOA has been reported to as a key factor in aggravating testicular, renal and breast cancers [5, 6]. Additionally, it is known to increase endoplasmic reticulum (ER) stress, which is often a characteristic of oncogenic cells [7]. Nevertheless, most research involving PFAS has been conducted on animal models and from human standpoint the data is often sparse.

In this research, we established a microfluidic model which recapitulates human pancreatic acini, and we tested the carcinogenic effects that PFOA has on acinar cells. Acinar cells form the backbone of secretory exocrine pancreas and is a common initiation site of PDAC [8]. Due to their high metabolic rates, acinar cells encounter PFOA dissolved in the serum more often. It is hypothesized that PFOA elevates the ER stress in the healthy acinar cells which in turn activates unfolded protein response (UPR). After persistent insult, cells accumulate oncogenic characteristics and initiate invasion into the surrounding tissue. In this regard, this study visualized the extracellular matrix (ECM) invading characteristics of the pancreas cells and later correlated the genetic changes induced by PFOA. The reported microfluidic model addresses the major knowledge gap of scarcity of human models by mimicking the human physiology and genetic profile, hence gathering the PFOA toxicological data in human subjects. The data presents a previously overlooked aspect of the carcinogenesis of the human pancreas i.e. the contribution of environmental toxicants.

METHODS

Microfluidic model fabrication

The Pancreatic acini-on-a-chip model used in the study was fabricated according to previously published research from our lab [9].

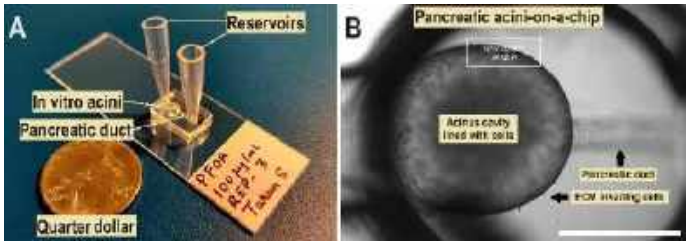

Figure 1: (A) The Pancreatic acini-on-a-chip microfluidic platform and its components (B) The *in vitro* acini with cellular invasion in the ECM. The dimension bar in the image is 500µm.

The theoretical background of the model is a fluid mechanical phenomenon known as viscous fingering, where a low viscosity fluid displaces a higher one to create hollow channel. The hollow channel is later lined with Panc1-Tet-PTF1a inducible cells to create a human acini

analog. Previously, it has been shown that Doxycycline hyclate (1µg/ml) induces PTF1a gene in the cells which creates a more normal like pancreatic cell line [10]. The PTF1a gene has been established as a master regulator of acinar gene program and pathways and keep the cells differentiated.

Toxicant delivery in 2D cultures and microfluidic device

PFOA was added to the cell culture media for the toxicant treatment. The cell culture media was comprised of DMEM supplemented with 10% Tet-free FBS, 1% P/S and 1% Glu. PFOA was tested at concentrations of 1, 10 and 100µg/ml. To reconstitute *in vivo* effects within a short span of days we utilized elevated concentrations. The media was also supplemented with 1µg/ml Dox to induce PTF1a gene expression. The experiment was run for 20 days with culture media changed at 24 hr intervals.

Data acquisition and processing

Images were obtained every 24 hrs using Olympus IX71 under brightfield settings with appropriate exposure times. The data was processed using WEKA segmentation module in ImageJ (NIH). The WEKA was trained over a sample image to identify the translucent cells invading the ECM and the program converted the brightfield image into a binary classified images using thresholding procedure. Once trained machine learning was used to process all the images in the data set. The average invasion was measured by finding the total area WEKA generated and later diving it by the base width. This method gave us an average invasion length. In Figure 1B, the interrogation window is represented by a small white box in which the above data processing procedure was performed.

RESULTS

The hypothesis of the experiment was to test whether PFOA increases invasiveness of the cells and also to verify the findings with molecular tools like PCR. PFOA clearly increased the invasive tendency as depicted in the micrographs (Figure 2A) as shown with marked black arrows.

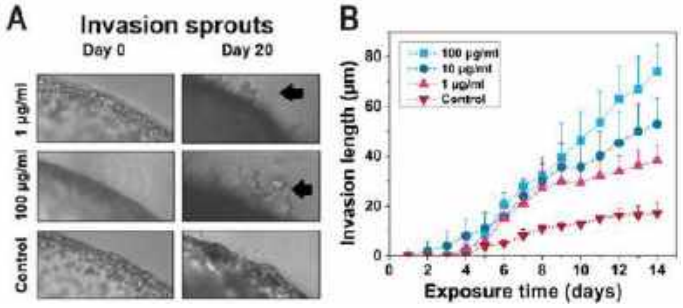

Figure 2: (A) The invasion sprouts seen for multiple PFOA concentrations (B) The average length of invasion for each PFOA treatment case

The protrusions are the group of cells invading the ECM. They were situated on the acini surface at the start and subsequently migrated to ECM compartment upon PFOA treatment. It is evident that upon treatment with PFOA, the average length of invasion increased in a dose dependent manner. The invasion in 1µg/ml was very similar to that of the control in which no PFOA was present. However, for the 100µg/ml PFOA, the invasions were much more prominent. They were both higher in number and thicker compared with those of the other concentrations. This is also reflected as the increase in length in the graph (Figure 1B). This experiment clearly demonstrates the rise in invasive tendency of the cells upon PFOA treatment. It is likely that PFOA could be altering gene expressions associated with higher migratory properties. The data is reported for the first 14 days of the experiment as no appreciable rise was observed in successive days.

To validate our earlier finding of increased invasive of the cells, we performed a set of PCR experiments with gene markers commonly associated cell migration (Epithelial to Mesenchymal Transition- EMT) markers, E-cadherin and vimentin. From Figure 3A , it is evident that E-cadherin expression decreases and vimentin expression increases. E-cadherin is a marker of cells with epithelial lineage and vimentin a marker of mesenchymal lineage.

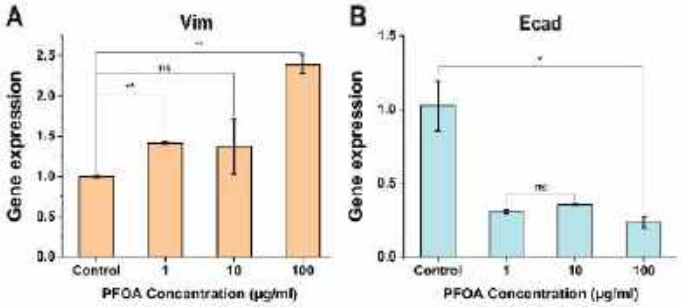

Figure 3: (A) PCR gene expression data for Vimentin (B) Gene expression data for E-cadherin

Taken together, data presented suggest that cell migration characteristics are elevated when exposed to PFOA in a dose dependent manner.

DISCUSSION

Our study establishes a link between pancreatic cancer and exposure to the environmental toxicant, PFOA. Researchers have often overlooked environmental toxicants like PFAS as molecules of concern. Animal studies in this area often use rats and mice which are physiologically and genetically different from humans and hence the translation of PFAS studies into humans are often difficult. Our study provides strong evidence that PFOA is a significant contributor to the progression of pancreatic cancer.

ACKNOWLEDGEMENTS

This study was supported by grants from NIH (Nos. U01 HL143403, R61 HL159948, R01 CA254110, and U01 CA274304), and the Purdue University Institute for Cancer Research (No. P30 CA023168). I deeply appreciate the support from Sae Rome Choi. I am grateful to Dr. Hocevar and Dr. Kamendulis for proving me with the PCR data. And I am grateful to Prof. Han for the guidance.

REFERENCES

[1] Siegel et al. *A Cancer Journal for Clinicians,* vol. 73, no. 1, pp. 17 48, 2023

[2] Rogers et al. *Journal of Exposure Science & Environmental Epidemiology,* vol. 31, no. 6, pp. 961-971, 2021.

[3] Bogdan et al. *Environmental Health Perspectives,* vol. 131, no. 6, p. 067701, 2023

[4] Shapira et al. National Bureau of Economic Research, 2017

[5] Bartell et al. *J Air Waste Manag Assoc,* vol. 71, no. 6, pp. 663-679, Jun 2021

[6] Pierozan et al, *Archives of Toxicology,* vol. 92, pp. 1729-1739, 2018.

[7] Oakes et al, *Am J Pathol,* vol. 190, no. 5, pp. 934-946, May 2020,

[8] Logsdon et al, *Nat Rev Gastroenterol Hepatol,* vol. 10, no. 6, pp. 362-70, Jun 2013

[9] Venis et al., *Lab on a Chip,* vol. 21, no. 19, pp. 3675-3685, 2021

[10] Jakubison *et al, Molecular Oncology,* vol. 12, no. 7, pp. 1104-1124, 2018

MICROSTRUCTURAL DAMAGE PROGRESSION IN THE PIA-ARACHNOID COMPLEX

L. Marin (1), T. Dixon (1), B. Coats (1)

(1) Mechanical Engineering, University of Utah, Salt Lake City, Utah,

INTRODUCTION

Traumatic brain injury (TBI) affects approximately 1.5 million individuals in the U.S. annually [1]. The majority of TBI research is focused on single-event impacts, neglecting the cumulative biomechanical effects of repeated trauma seen in military, sports, and abusive etiologies. This oversight impedes the development of accurate, comprehensive computational models and analysis, particularly in assessing cumulative strain damage.

When repeated loading has been considered, progressive damage and injury to the brain have been assessed. However, the connections between the brain and skull dictate how force is distributed to the brain. Damage from repeated loading to these connecting structures will alter what the brain experiences and will be critical to characterize before repeated loading to the brain in experimental settings can be defined. This study aims to start filling this knowledge gap by examining the progressive mechanical damage in the pia-arachnoid complex (PAC), a central mechanical interface between the brain and skull.

METHODS

All work in this study was approved by the University of Utah Institutional Animal Care and Use Committee. Sheep brains were extracted from calvaria within 24 hours post-mortem with all dural tissues intact. Following extraction, the dura was gently reflected to expose the PAC. Each brain was positioned in a stereotactic frame for optical coherence tomography (OCT) imaging, employing a Bioptigen R2200 spectral scanner (Leica, USA) with a 12 mm telecentric lens. This system provided a depth resolution of 12.5 µm and a lateral resolution of 6.25 µm.

A 22-gauge needle was inserted through the arachnoid membrane to inflate the subarachnoid space, utilizing a NE-300 New Era syringe pump. A fiber optic micro-catheter pressure transducer (FISO-LS Series, 0.9 Fr tip diameter) was placed in the subarachnoid space in proximity to the imaging location. Inflations were pressure-controlled using an Arduino circuit board to 0.2-0.4 mmHg for low-pressure 'characterization' cycles and 0.8-1.2 mmHg for high-pressure 'injury' cycles. Characterization cycles had low flow rates (0.3 ml/min) to ensure no injury or damage was induced. Injury cycles had higher flow rates (1 ml/min) to create higher strain rates in the system. Maximum pressures were constant within the same test but different across locations. This was because spaces with a greater number of structural connections required more pressure to induce similar amounts of strain. Each location was exposed to 11 inflation cycles, including 3 preconditioning cycles and then 4 injury exposures, which consisted of an injury cycle followed by a characterization cycle (**Fig. 1A**). The last preconditioning cycle was used as the baseline characterization cycle.

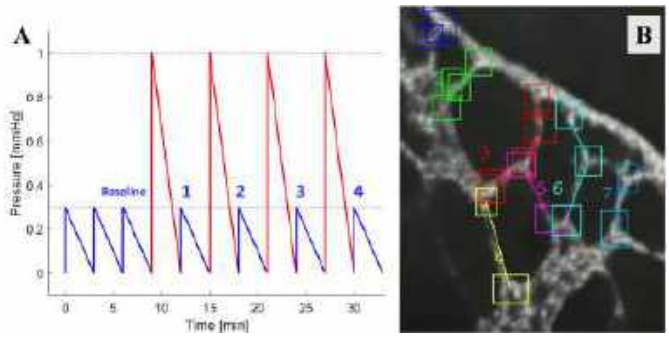

Fig. 1. (A) Ideal test protocol, with low-pressure 'characterization' cycles (blue) and high-pressure 'injury' cycles (red). The third preconditioning cycle (baseline) was used as a reference for damage characterization. (B) Detailed view of the pia-arachnoid space, featuring overlaid polylines for tracking trabeculae length changes during inflation cycles.

Damage to the PAC microstructures was defined by increases in arachnoid membrane displacement and in trabeculae strain. Arachnoid membrane displacement was tracked with a custom Python script and synchronized to pressure data to calculate an equivalent stiffness (peak pressure divided by peak membrane displacement). The lengths of single trabeculae fibers were tracked and quantified throughout all inflation cycles (**Fig. 1B**). Strain for each cycle was calculated as the change in length divided by the fiber length at the beginning of the baseline characterization cycle. Trabeculae that underwent significant shape changes, were excessively short, or moved outside the imaging plane were excluded from the analysis. A linear regression was used to assess progressive damage with each cycle. A Pearson's correlation was used to statistically evaluate the relationship between the magnitude of the injury cycles to the change from baseline in the characterization cycles.

RESULTS

Eight locations in two brains were evaluated. Both membrane equivalent stiffness and trabecular strain experienced progressive softening with each injury cycle, suggesting progressive damage to the microstructures of the PAC (**Fig. 2**). This softening was consistent across all measurements except for one measurement of membrane stiffness in one location which was unchanged (dark red line in **Fig. 2A**), The average decrease in stiffness for the remaining locations was 27.8 ± 19.9% (4.6%-66.6%). There was no significant relationship between the change in membrane stiffness and the magnitude of the injury applied.

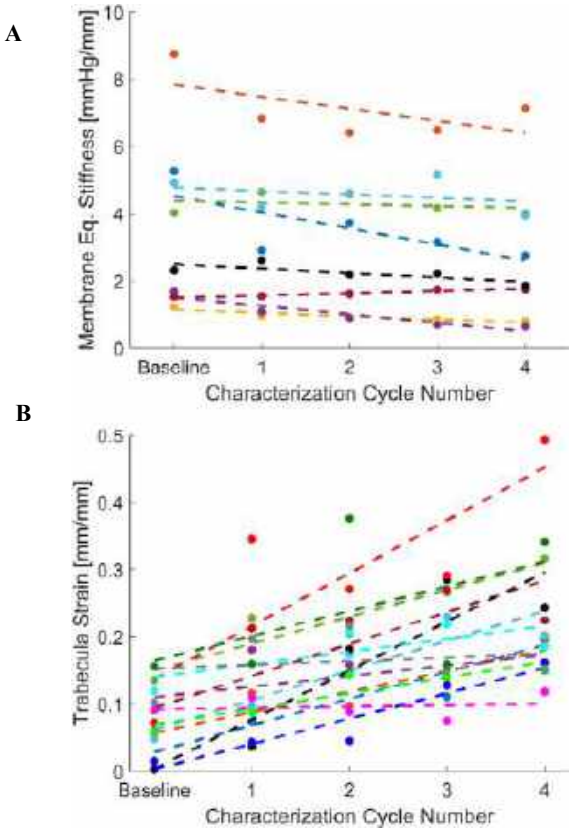

Fig 2. (A) Equivalent stiffness of the arachnoid membrane displays a softening (negative slope) across characterization cycles in 7 out of 8 locations. (B) Trabeculae strain also showed a consistent softening with each cycle (positive slope).

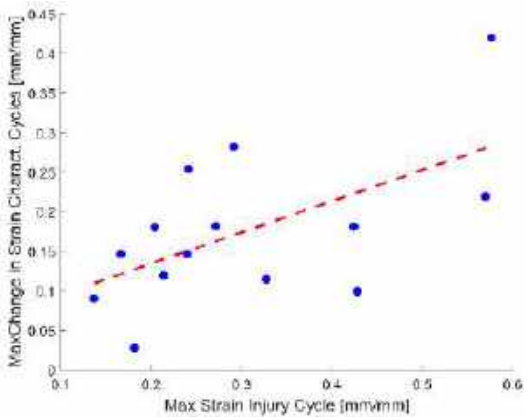

Fig. 3. Maximum change in strain from the baseline cycle to a subsequent characterization cycle was greater for trabeculae experiencing greater strain during the injury cycle.

The same trend was observed when analyzing individual trabeculae (14 trabeculae across the 8 locations, **Fig. 2B**). All trabeculae displayed an increase in strain between the baseline cycle and subsequent characterization cycles. The average increase in strain was 0.17 ± 0.09 (0.03-0.42). A significant correlation (p=0.02) was found between the level of injury and the increase in trabeculae strain (**Fig. 3**). As expected, a higher strain value during injury cycles led to a greater increase in strain during characterization cycles.

DISCUSSION

For the first time, this study demonstrates damage within the subarachnoid space both globally (measurements at the level of the arachnoid membrane) and locally (analysis of individual trabeculae) in an *ex vivo* configuration. This dual-focused approach reveals that global analyses (membrane displacement) may be able to capture overall damage, but they are unable to provide mechanistic correlations to the applied loading. One reason for this may be that we performed a 2D analysis of a single slice of the subarachnoid space in a highly complex 3D structure. Such a simplification may not fully capture the intricacies of spatial relationships and dynamic interactions within the subarachnoid space. Local measurements of trabeculae, however, provided a more direct measurement of deformation and, therefore, better correlated with the applied load. While this analysis was still a 2D analysis, it represents a significant advancement over other approaches in the literature, which have predominantly analyzed the arachnoid space at a macroscopic level [2],[3].

Both metrics in the study identified softening of the PAC microstructures with repeated loading. As a key mechanical connection between the brain and the skull, a reduction in localized structural integrity of the PAC microstructures may alter how force is distributed to the brain. Therefore, characterizing this damage will be paramount to the accuracy of computational simulations investigating repeated loading, and to the prediction of brain injury from repetitive head trauma.

ACKNOWLEDGEMENTS

This material is based upon work supported by the National Science Foundation under Grant No. 2140373.

REFERENCES

[1] Faul, M. et al., *NCICP-CDC,* 2010
[2] Jin, X., et al., Stapp Car Crash Journal, 2007
[3] Benko, N et al., J Mech Beh of Biomed Matls, 2021

AI IN B3: ARTIFICIAL INTELLIGENCE IN BIOMECHANICS, BIOENGINEERING, AND BIOTRANSPORT

Chester Jar (1), Lindsey Westover (1,2), Gail M. Thornton (1)

(1) Department of Mechanical Engineering, University of Alberta, Edmonton, Alberta, Canada
(2) Department of Biomedical Engineering, University of Alberta, Edmonton, Alberta, Canada

INTRODUCTION

The term 'artificial intelligence' (AI) was first coined in 1955 [1], and the significant development of AI-based technology over the recent years has given rise to the consideration of its potential applications in research. As a continuously advancing interdisciplinary field, the growth of biomedical engineering may be further facilitated by implementing AI-based solutions to areas such as data analysis and interpretation, model generation, and imaging analysis [2]. Given that the theme of the 2024 SB³C conference is Innovation without Borders: Uniting Ideas, Technologies, and Communities, how has AI been used over time, which areas have received the most attention, and how widespread is its application in biomedical research? To answer this question, a text analysis of the literature was conducted to identify trends in research involving AI and the "three B's" of SB³C: biomechanics, bioengineering, and biotransport.

METHODS

A total of 97 biomedical engineering journals indexed in the Web of Science were found by filtering Journal Citation Reports from Clarivate for the year 2022 under the category "Engineering, Biomedical" [2]. Of these journals, 96 were listed in MEDLINE (1946-present via Ovid) and were searched for articles containing the specific term of interest "artificial intelligence" with one or more of the three B's of SB³C: "biomechanics OR bioengineering OR biotransport". The search employed multi-purpose (.mp) fields, including the title, abstract, or subject heading, for each search term. The full texts of relevant articles (excluding tables, figures, and their respective captions) were extracted and compiled into an XML file. The file was then imported into Voyant Tools [4], which is an open-source application for text analysis.

To determine how AI has been applied to biomedical engineering research, article texts were analyzed using the built-in functions of Voyant Tools. Text analysis was performed with respect to publication year, article type (original, editorial, review), and topic (biomechanics, bioengineering, biotransport). Common words (e.g. the, a) were omitted using the default stopwords list with additional terms such as "et" and "al". The Terms tool was used to determine keywords with the highest absolute frequencies. For each keyword, the Collocates tool was used to determine terms with the highest frequency in which they appeared within 5 leading or trailing words. The Trends tool was used to determine the overall frequency of each combination of keyword and term identified by the Collocates tool. The results of the Collocates tool are reported as (number of articles categorized as biomechanics/bioengineering/both in which the collocate appears; year(s) with highest article count-number of articles). Correspondence Analysis was also performed using the ScatterPlot tool, using the top 50 terms with the highest relative frequencies.

RESULTS

Current to January 2, 2024, our search retrieved 28 articles from 2004 to 2023 in 16 different journals across 14 countries (of the first corresponding author's or interviewee's institution) (Table 1). This consisted of 17 original articles, 4 editorials, and 7 reviews, where two letters to the editor and one interview were classified as editorials. Over half of the 28 articles were published in the past three years, with 10 being published in 2023 (Figure 1). With respect to topic, 19 articles were related to biomechanics, 8 were related to bioengineering, and one discussed both. However, the search returned no articles containing the term "biotransport" in conjunction with "artificial intelligence".

Across all articles, "model" was the most frequent term (581) when considered together with "models" (388), followed by "data" (821), "gait" (499), and "analysis" (426). The Collocates and Trends tools found that "model*" was commonly associated with terms such as "training" (7/0/0; 2023-3), "emg" (4/0/0; 2004/2017/2020/2021-1), and "biomechanics" (3/1/0; 2011/2017/2020/2021-1). "Data" was associated with "medical" (5/2/1; 2023-3), "learning" (8/1/0,

2021/2023-3), and "classification" (6/0/0; 2023-2). "Gait" was associated with "patterns" (8/1/0; 2023-3), "classification" (6/1/0; 2023-2), and "kinematic(s)" (10/1/0; 2023-4). "Analysis" was associated with terms such as "data" (5/3/1; 2021/2022-2) and "clinical" (10/1/0; 2023-6).

Results of the Correspondence Analysis are shown in Figure 2. "Classification", "knee", "gait", and "musculoskeletal" were common terms in articles applying AI in biomechanics, while bioengineering articles were more general and frequently used terms such as "systems", "human", "models", and "clinical". Articles classified under both categories commonly used terms such as "applications", "medical", "tissue", and "engineering".

Table 1: Article count and country by journal.

Journal Abbreviation	Count	Country
Bioengineering (Basel)	5	CHN, DEU, ITA, USA
J Biomech	4	CAN, FIN, USA
Ann Biomed Eng	3	CHN, IND, USA
Clin Biomech	3	DEU, USA
Acta Bioeng Biomech	2	CZE, POL
Adv Healthc Mater	1	DEU
Appl Bionics Biomech	1	USA
Biodes Manuf	1	USA
Biomech Model Mechanobiol	1	AUS
Comput Biol Med	1	CAN
Comput Methods Programs Biomed	1	ESP
IEEE Pulse	1	NZL
IEEE Trans Neural Syst Rehabil Eng	1	GBR
J Mech Behav Biomed Mater	1	AUS
Proc Inst Mech Eng H	1	MEX
Sports Biomech	1	AUS

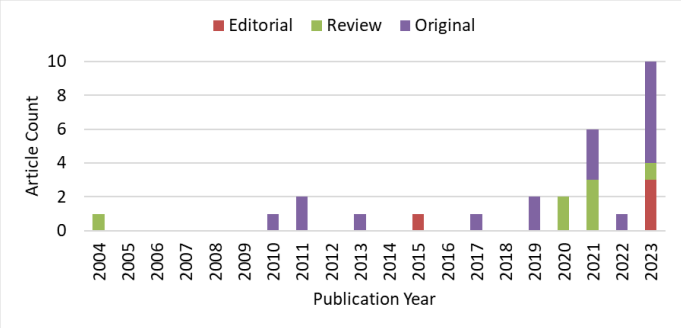

Figure 1: Article count and article type by year.

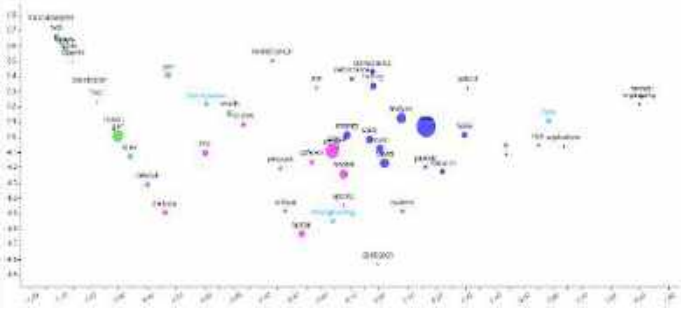

Figure 2: Correspondence Analysis by topic (biomechanics, bioengineering, or both).

DISCUSSION

Despite being coined in 1955 [1], the first occurrence of artificial intelligence detected by our search was in 2004. A larger proportion of original articles being published within the past three years (Figure 1) implies that an increasing number of authors have incorporated AI-based technologies in their research. Additionally, the use of AI appears to be widespread, as the articles are diverse with regards to the country of the first corresponding author/interviewee (Table 1). As an emerging technology however, there are ongoing discussions associated with its implementation, as shown by the three editorial articles published in 2023.

The results of the Correspondence Analysis (Figure 2) and Collocates tool both suggest similar trends in research involving AI in biomechanics and bioengineering. Studies using AI in biomechanics research involved kinetic or kinematic analysis of motion and gait, while bioengineering research comprised a broader, general topic involving artificial models and systems. Although no biotransport articles were found, one article [5] discussed the implementation of AI in lung models for drug development; this was not classified as biotransport since that term was not mentioned anywhere in the text. Across all articles, the most common application of AI was towards gait analysis, such as improving the accuracy of markerless motion capture systems [6-8] and kinematic analysis or algorithms [7-12].

The relatively small number of identified articles was likely, in part, because equivalent search terms were not considered. However, we purposely limited our search terms to (1) look at how the use of the specific term "artificial intelligence" has progressed over time, and (2) adhere to the "three B's" of SB^{3}C (biomechanics, bioengineering, and biotransport). While the reason for the decrease in 2022 remains unclear, part of the increase in 2023 was due to two editorial articles on GPT [2][13]. Overall, the results support the conclusion regarding the growing popularity of AI-based technologies in biomedical research globally, with its current usage mainly revolving around gait analysis, modeling, and data processing/analysis. Further developments in AI should facilitate its application in other areas, in addition to increased discussions surrounding its implementation and use in biomedical research.

ACKNOWLEDGEMENTS

Natural Sciences and Engineering Research Council of Canada (NSERC).

REFERENCES

[1] McCarthy, J et al. *AI Mag*, 27:12, 1955.
[2] Cheng, K et al. *Ann Biomed Eng*, 51: 1645-1653, 2023.
[3] Clarivate (2023). Journal Citation Reports.
[4] Sinclair, S and Rockwell, G. *Voyant Tools*. Web. http://voyant-tools.org
[5] Sun, A et al. *Biodes Manuf*, 4: 757-775, 2021.
[6] Ripic, Z et al. *J Biomech*, 159: 111793, 2023.
[7] Ripic, Z et al. *J Biomech*, 157: 111712, 2023.
[8] Cronin, N et al. *J Biomech*, 87: 75-82, 2019.
[9] Bernal-Torres, M et al. *Proc Inst Mech Eng H*, 237: 628-641, 2023.
[10] Aung, M et al. *IEEE Trans Neural Syst Rehabil Eng*, 21: 908-916, 2013.
[11] Kutilek, P and Farkasova, B. *Acta Bioeng Biomech*, 13: 57-65, 2011.
[12] Fukuchi, R et al. *J Biomech*, 44: 540-542, 2011.
[13] Ray, P and Majumder, P. *Ann Biomed Eng*, 51: 1904-1905, 2023.

RHYTHMIC NEPHRON PROGENITOR RENEWAL AND DIFFERENTIATION INFORMS KIDNEY TISSUE ENGINEERING STRATEGIES

Samuel H. Grindel[1,2], Sachin N. Davis[1,2], John M. Viola[1,2], Grace Y. Liu[1,2], Jiageng Liu[1,2], Grace Qian[1,2], Catherine M. Porter[1,2], Alex J. Hughes[1,2]

(1) Department of Bioengineering, University of Pennsylvania, Philadelphia, 19104, PA, USA
(2) Bioengineering Graduate Group, University of Pennsylvania, Philadelphia, 19104, PA, USA

INTRODUCTION

Nephrons are the blood filtering unit of the kidney, removing waste to the ureteric bud (UB)-derived collecting ducts. The kidney has limited endogenous nephron regeneration, leaving millions of people each year prone to pathologies like chronic kidney disease (CKD)[1,2]. However, dialysis and organ transplantation treatments affect quality of life and are associated with adverse health outcomes[3]. Engineering autologous kidney replacement tissue is an emerging alternative strategy, which requires control over nephron induction, maturation, and connection to a urinary collecting duct network. Bioengineering efforts are beginning to meet these demands, but current protocols generate substantially fewer nephrons than are required for tissue replacement.

Nephron organoid protocols currently lack the repeated nephron induction that occurs during kidney organogenesis. *In vitro*, nephrogenesis occurs as a single event leaving remaining NPs with reduced competency for future induction[4]. *In vivo*, nephron progenitor (NP) pools sit in the cap mesenchyme (CM) adjacent to UB tips[5]. A portion of the CM undergoes nephrogenesis approximately every UB tip branching cycle while remaining NPs expand and divide among the daughter UB tips for future nephrogenesis[5]. Cycles of UB branching morphogenesis exponentially duplicate nephrogenic niches and the delicate balance between NP renewal and differentiation is a critical determinant of final nephron number. The mechanisms regulating the balance of NP renewal and differentiation as well as its apparent synchronization with UB branching remain unknown.

Here, we used spatial transcriptomics to evaluate the correlation between NP transcriptional state and UB branching lifecycle. Then, we used human induced pluripotent stem cell (iPSC)-derived nephron organoids to assess how perturbation with phase-specific pathways impacts the balance of nephron progenitor differentiation and renewal. Engineering control over this balance may enable rhythmic nephron production in kidney replacement tissues and devices, finally contributing a third arm to therapy beyond dialysis and transplantation.

METHODS

Spatial transcriptomics: We used the NanoString GeoMx Digital Spatial Profiler (DSP) to profile 47 disparate CM from a mouse embryonic day (E)17 kidney. CM connectedness and UB branch point were used to qualitatively pseudo-aged CM relative to UB lifecycle (pre-, mid-, and post-branching) for comparison. GeoMx data were analyzed in R using code modified from Bioconductor and NanoStringNCTools, GeomxTools, and GeoMxWorkflows libraries.

Organoid culture: Nephron progenitor cells were generated according to a published protocol[4]. Briefly, iPSCs were plated at 5,200 cells/cm^2 in mTeSR plus supplements, then media was switched to TeSR-E6 plus supplements (TeSR-E6+) with 7 uM CHIR99021 from D0 to D5, and finally media was switched to TeSR-E6+ with 1 ug/mL heparin and 200 ng/mL FGF9 from D5 to D10. On D10, NPs were lifted and spotted in 1 µl aliquots (~0.3x10^6 cells/µL) onto 6-well 0.4 µm polyester transwell membranes overlying TeSR-E6+ and 7µM CHIR99021 'pulse' media for 2 hr. This was exchanged for 'chase' media consisting of TeSR-E6+, 1 µg/ml heparin, and 200 ng/ml FGF9 for 2 hr. The pulse or chase media included 0.1 µM TTNPB, 4 µM TRULI, or equivolume DMSO. Following the chase, media was switched to TeSR-E6+ with 1 ug/mL heparin and 200 ng/mL FGF9. Media was switched to TeSRE6+ (basal media) from D12 to D25.

Immunofluorescence: Organoids were fixed with 4% paraformaldehyde, permeabilized with 0.5% Triton-X-100, and blocked with IF Wash (DPBS + 1g/l Bovine Serum Albumin + 0.2% Triton-X-100 + 0.04% Tween-20) + 10% donkey serum. Primary and secondary antibody solutions were incubated overnight at 4°C at appropriate dilution in blocking solution. Following antibody incubations, organoids were washed with IF wash. D12 organoids were counterstained with 1ug/mL DAPI.

Imaging and data analysis: Z-stacks were acquired at 4x,10x, and 20x magnifications on a spinning-disk confocal microscope. Analyses were performed on a single, central z-plane for each organoid. Percent area relative to DAPI area or organoid area (determined by manual annotation of background signal) was determined by thresholding in FIJI. Statistical significance was determined using R to perform one-way ANOVA and Tukey's post-hoc tests.

RESULTS

Using the Nanostring GeoMx DSP (GeoMx), we profiled 47 CM regions of interest (ROI) from an E17 mouse kidney (Fig 1A). Each ROI was pseudo-aged relative to the UB branching lifecycle (pre-, mid-, or post-branching) for differential gene expression analysis. Pre-/mid-branching CM showed GeoMx hits associated with WNT, retinoic acid (RA), JAK-STAT, and TGFβ signaling, while post-branching CM showed GeoMx hits associated with YAP, FGF, and NOTCH signaling. Whole mount immunofluorescence of E17 kidneys showed similar trends at the protein level. Transient elevation in WNT signaling is required for nephron induction, while FGF signaling contributes to NP renewal[6,7]. We turned to a published embryonic whole kidney single cell (sc)RNA-seq datasets to evaluate how the rhythmic NP phases associate with NP and early nephron cell type clusters[8]. Intriguingly, mean normalized expression of post-branching GeoMx hits largely associated with uncommitted and cell cycle associated NP clusters, while pre/mid-branching GeoMx hits associated with committing NP and early nephron clusters. Together, our *in vivo* and scRNA-seq analyses suggest that NPs rhythmically fluctuate between phases of renewal and differentiation synchronized with the UB branching lifecycle (Fig 1B).

We then turned to iPSC-derived NP organoids to determine changes to the nephron formation vs. cell renewal balance conferred by perturbation with phase specific pathways *in vitro*. We promoted nephron induction in NP organoids with transient WNT/β-catenin activation ('pulse') using a GSK3β inhibitor, CHIR99021 (CHIR). CHIR pulses were either overlapped with or followed by ('chased') transient activation of YAP signaling using a LATS kinase inhibitor, TRULI, or RA signaling using an all-trans RA analog, TTNPB (Fig 1C). To evaluate NP balance, we fixed organoids two days after pulse/chase stimulation and performed immunofluorescence for the NP marker SIX2 and early nephron marker JAG1 (Fig 1D). YAP activation overlapped with the CHIR pulse significantly increased the NP population, while overlapping or chasing with YAP activation reduced early nephron populations (Fig 1E). Consistent with reduced early nephron populations, both overlapping or chasing with YAP activation reduced mature nephron area in prolonged culture (Fig 1E). Conversely, both overlapped and chased RA activation significantly reduced NP area but had no change in early nephron area by two days post stimulation (Fig 1E). Similarly, chasing the CHIR pulse with RA activation showed no reduction in mature nephron area in prolonged cultures (Fig 1E). However, RA activation altered nephron morphology in the organoids. Both overlapped and chased conditions showed distinct nephrons with anatomically correct proximal to distal polarization, while control nephrons were largely clustered together with less clear segment connectivity (Fig 1D).

DISCUSSION

How the kidney balances NP renewal and differentiation is an open question in the field with important implications for tissue engineering. We performed spatial transcriptomics with the GeoMx DSP platform, which revealed offset, rhythmic NP phases in synchrony with UB branching. We previously reported that the rate of nephrogenesis in non-uniform during UB branching. Our previous work suggests that UB branching induced mechanical stress in the nephrogenic niche is highest prior to the completion of branching[9], and our current work points to active YAP signaling, a central mechanosensitive pathway, in the post-branching phase. YAP activation also influenced the response of iPSC-derived NPs to WNT signaling. Together, this suggests that cycles of UB branching derived mechanical stress may promote rhythmic YAP signaling in the CM that can reduce NP sensitivity to inductive cues.
Less is known about the role of RA signaling in NPs, but neighboring CM are separated by a stromal progenitor population that actively secrete RA[10]. Here, we found that RA activation increased iPSC-derived NP sensitivity to WNT signaling.

This work provides new insight into the regulation balancing NP renewal and differentiation *in vivo*. Our work points to the potential for rhythmic activation of ancillary pathways to promote iPSC-derived nephron cultures capable of repeated nephron induction and co-existence of nephrons at differing maturities. This would massively increase nephron-forming potential for kidney replacement tissue applications.

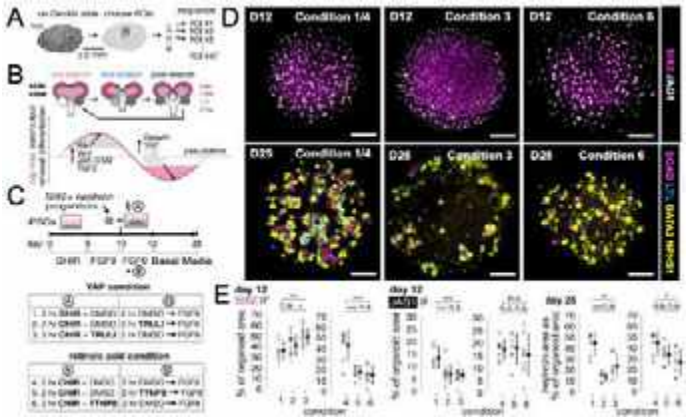

Figure 1: Rhythmic Nephron Progenitor State Influences Differentiation Outcomes *in vitro*. A) Schematic of GeoMx spatial sequencing. B) Schematic of rhythmic nephron progenitor states synchronized to ureteric bud branching. C) *S*chematic of iPSC-derived nephron progenitor culture (*top*). D10 pulse/chase media conditions for YAP activation using TRULI (*middle*) or for retinoic acid activation using TTNPB (*bottom*). Controls had equivolume DMSO and basal media was TeSR-E6. D) Representative max projections of nephron organoids fixed at D12 and stained for nephron progenitor (SIX2+) and early nephron (JAG1+) markers (*left*) or fixed at D25 and stained for mature nephron markers (*right*). Condition refers to tables in C. E) Quantification of organoid percent area for the following: D12 nephron progenitor area (*left*), D12 early nephron area (*middle*), and D25 total nephron area (*right*). Condition refers to table in C. * = $p < 0.05$, ** = $p < 0.01$, *** = $p < 0.001$.

ACKNOWLEDGEMENTS

We thank members of the Hughes laboratory for helpful discussions and assistance with experimental protocols.

REFERENCES

[1] Bikbov, B. et al. *Lancet*.395(10225):709-733, 2020.
[2] Naved, B.A. et al. *Kidney International* 101(5):845-853, 2022.
[3] Valderrábano, F. et al. *Am J Kidney Dis*. 38(3):443-64, 2001.
[4] Howden, S. et al. *EMBO Rep*. 20(4):e47483, 2019.
[5] Nagalakshmi, V.K. and Yu, J. *Mol Reprod Dev*.82(3):151-66, 2015.
[6] Barak, H., et al. *Dev. Cell* 22, 1191–1207, 2012.
[7] Park, J.S., et al. *Development* 134, 2533–2539, 2007.
[8] Combes, A.N. et al. *Development* 146, dev178673, 2019.
[9] Viola, J. et al. BioRxiv, 2023.
[10] Rosselot, C. et al. *Development* 137, 283–292, 2010.

SUSTAINED STRUCTURAL AND FUNCTIONAL DEFICITS IN THE PORCINE KNEE SIX MONTHS FOLLOWING MENISCUS DESTABILIZATION

Brendan D. Stoeckl[1,2], Stephen Ching[1], Veridiana Nadruz[3], Kyle D. Meadows[4], John M. Peloquin[4], Owen McGroary[1], Madeline Boyes[3], Lorielle G. Laforest[1,2], Tim Teinturier[1], Miltiadis H. Zgonis[1,2], Dawn M. Elliott[4], Robert L. Mauck[1,2], Michael W. Hast[1], Thomas P. Schaer[3], David R. Steinberg[1,2]

(1) Department of Orthopaedic Surgery, University of Pennsylvania, Philadelphia, PA, USA
(2) CMC VA Medical Center, Philadelphia, PA, USA
(3) School of Veterinary Medicine, University of Pennsylvania, Kennett Square, PA, USA
(4) Department of Biomedical Engineering, University of Delaware, Newark, DE, USA

INTRODUCTION

To better understand the progression of OA pathology, and to establish a test bed for assessing interventions in the context of an OA phenotype, effective large animal, human scale models of joint injury are necessary. Our previous work developed a porcine destabilization of the medial meniscus (DMM) model, where transection of the anterior horn of the medial meniscus resulted in deleterious changes in the knee at an early time point. However, these changes resolved at later time points, as the anterior attachment scarred back into place and the knee resumed normal biomechanics. [1] In a second iteration of this model, a 6mm portion of the medial meniscus anterior horn was resected en bloc, resulting in more severe joint pathology at a six-week time point [2]. The aim of the current study was to assess the progression of this OA phenotype over a six-month period and to assess changes in gait.

METHODS

Sixteen skeletally mature (12-month-old) Yucatan minipigs underwent mini-arthrotomy of the right stifle, and a 6mm portion of the medial meniscus anterior horn was resected en bloc. Animals were sacrificed at either 6 weeks or 6 months post-operatively (N=8 for both), with contralateral limbs serving as intact controls. Four of the animals in the six-month group were used for gait analysis. Videos of walking pigs were captured at 30 fps both preoperatively and four months post-op. Using DeepLabCut markerless tracking software [3], the hip, knee, ankle, and hind hoof of each pig were tracked across the gait cycle (Fig 3A). Landmark positions were used to compute knee flexion angles. Further analysis was conducted using the GAITFour® walkway system, six months post-operatively. The pigs walked across a sensor-embedded mat, and the contact pressure of each hoof-strike was recorded. A model which normalized by velocity and trial number was used to measure differences between left (intact) and right (DMM) limbs. After sacrifice, stifle joints were dissected, and osteochondral segments of both the medial femoral condyle and medial tibial plateau were isolated. Indentation creep tests were performed, and the resulting deformation

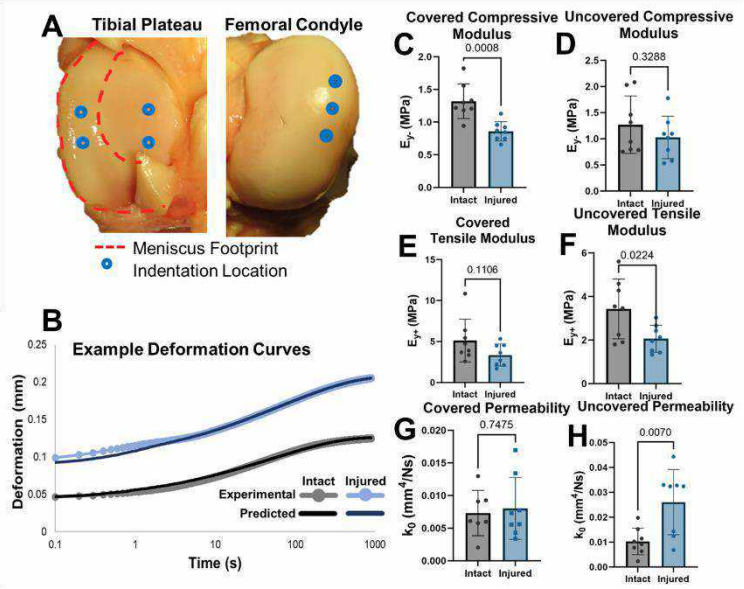

Figure 1: (A) Indentation testing locations on the medial tibial plateau and medial femoral condyle. For each subject, results were averaged for the uncovered and covered tibial plateau, and femoral condyle. (B) Example deformation curves. (C) Covered and (D) uncovered tibial plateau compressive moduli. (E) Covered and (F) uncovered tibial plateau tensile moduli. (G) Covered and (H) uncovered tibial plateau permeability. C-H are all at the 6-month endpoint.

curves fit to a model outputting compressive and tensile moduli and permeability (**Fig 1**). [4] Specimens were then scanned via microCT before and after contrast enhancement with Lugol's solution (I2 and KI

in water). Cylindrical regions of bone were defined superficial and deep to the cartilage interface, and bone volume fraction was calculated for each. For histologic analysis, osteochondral sections were stained with Safranin O/ Fast Green, and synovium sections were stained with Hematoxylin/Eosin. Statistics were performed in Graphpad.

RESULTS

Quantitative tissue analyses were performed at three regions per timepoint—on the medial tibial plateau in areas previously uncovered and covered by the meniscus, and on the medial femoral condyle (**Fig 2**). At 6 weeks, the cartilage was softer across regions of interest, with statistically significant differences in all regions, except for the uncovered tibial plateau. This mechanical weakening persisted at 6 months with statistical differences detected in the compressive modulus in the covered tibia and in the tensile modulus in the uncovered tibia region (**Fig 1)**. Bone volume fraction increased in the covered tibia and superficial femoral condyle regions in DMM knees, but these subchondral changes were attenuated by the 6 month time point. (**Fig 2**). Histologically, osteochondral sections of DMM knees showed some degree of surface fibrillation and roughening at 6 weeks, and mild loss of proteoglycan by 6 months. (**Fig 3A**) At 6 weeks, the synovium of DMM knees showed hyperplasia and signs of fibrosis, but little difference was detectable by 6 months. (**Fig 3B**). For gait analysis, graphical representations of post-op DMM knee flexion revealed a 'double-hump' signature during stance, which was not observed in the other groups (**Fig 4B**). Pigs exhibited greater maximal knee flexion in their post-op intact knee compared to pre-operative and post-op DMM knees (**Fig 4C**). Further, time spent in stance was shorter in both knees post-op compared to preoperatively (**Fig 4D**). When normalized for velocity and trial number, total pressure index percentage was significantly lower on the right hind limb when compared to the left hind limb (model adjusted effect: -0.5 , 95% CI: [-0.9, -0.1], p = 0.005; **Fig 4E**) Similarly, the total scale pressure (the sum of peak pressure values recorded from each activated sensor by a hoof during mat contact) showed significantly less pressure in the right hind limb compared with the left hind limb (model adjusted effect: -1.4, 95% CI: [-2.4, -0.5], p = 0.004; **Fig 4F**).

DISCUSSION

This study showed that a more aggressive medial meniscus destabilization involving a partial anterior horn resection (as opposed to a simple transection) results in a durable osteoarthritic phenotype in a porcine model. We showed persistent cartilage weakening as well as histologic evidence of degenerative changes six months after surgery. Most importantly, functional assays of animal gait showed detectable abnormalities at four and six months after surgery. Animals displayed decreased range of motion during stride in the affected limb, as well as a reduction in time spent in the stance phase, indicating that animals were favoring the unoperated limb. Further, the kinematic parameters assayed during the gait analysis showed a significant and consistent decrease in weight distribution on the affected limb post-surgery. Joint pain alters normal function, particularly locomotion, and is one of the clinical signs of osteoarthritis. The alterations in gait and loadbearing in pigs 6 months postoperatively may reflect painful ambulation secondary to OA changes as a result of DMM. This study developed a clinically relevant large animal model of OA leading to both structural and functional deficits of the knee and changes in pig gait patterns.

ACKNOWLEDGEMENTS

This work was supported by the Department of Veterans Affairs and the National Institutes of Health.

REFERENCES

[1] Bansal+ OJSM, 2021. [2] Stoeckl+ ORS, 2022. [3] Mathis+ Nature Neuroscience, 2018. [4] Moore+ J. Tribol. 2016.

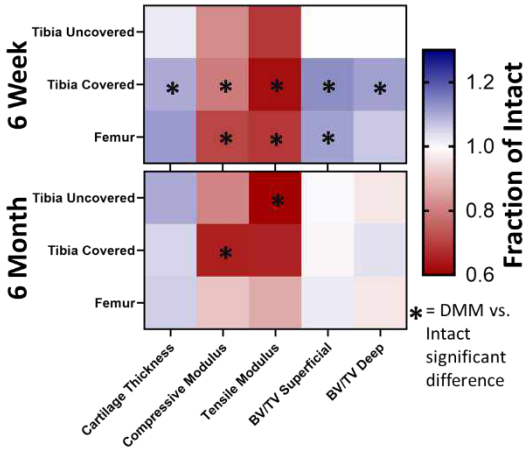

Figure 2: Tissue-scale quantitative outcomes of the operative limb after DMM for medial tibial plateau regions previously covered by the meniscus or uncovered, and for the medial femoral condyle, expressed as a fraction of intact control.

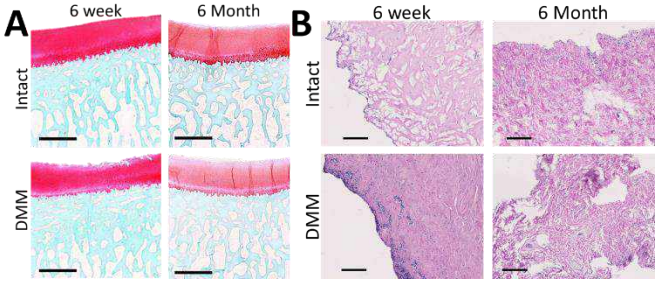

Figure 3: A) Safranin O / Fast Green-stained osteochondral sections of the medial tibial plateau (scale =1mm) B) Hematoxylin and Eosin stained synovium sections (scale = 100µm)

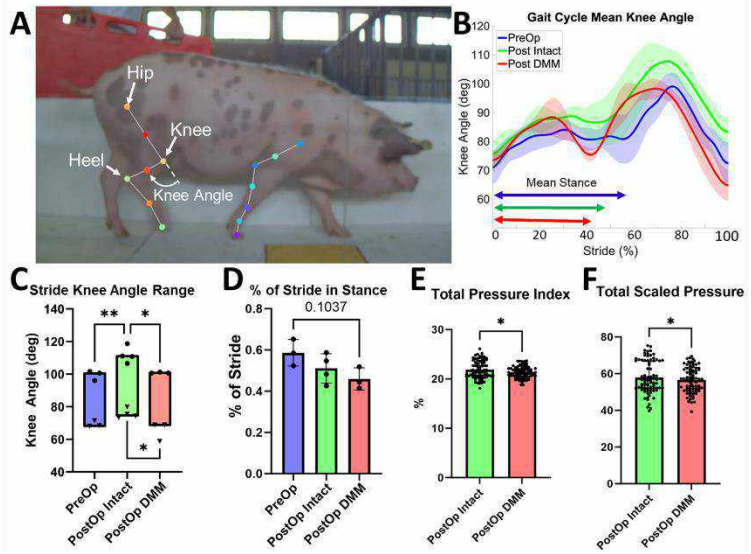

Figure 4: A) Still from motion tracking showing tracked landmarks. B) Average knee angle during gait cycle preoperatively, post-op on intact control limb, and post-op on DMM limb. C) Average minimum and maximum knee angle during stride. D) Average % of each stride spent in the stance phase. E) Total Pressure Index and F) Total Scaled Pressure, of each hoof strike as measured with the GAITFour system. *p<0.05, **p<0.01.

A CELL-BASED AND AI-ACCELERATED COMPUTATIONAL FRAMEWORK FOR THE PREDICTION OF MECHANOSENSITIVE TUMOUR GROWTH

Irish Senthilkumar (1,2,3), Enda Howley (1,2), Eoin McEvoy (3)

(1) School of Computer Science, University of Galway, Galway, Ireland
(2) Data Science Institute, University of Galway, Galway, Ireland
(3) Discipline of Biomedical Engineering, University of Galway, Galway, Ireland

INTRODUCTION

Tumour growth is a mechanosensitive process regulated in part by mechanical feedback between cell and the matrix. Sensitivity to mechanical cues can influence tumour progression and ultimately impact disease outcomes. As an example, stresses generated during the expansion of stiff extracellular matrix (ECM) leads to a suppression of proliferation markers [1] and a reduction in tumour spheroid size.

Critically, the underlying biomechanisms by which external loading impacts cellular growth and proliferation have not yet been uncovered. In this study, we propose a novel hydro-mechanical model for tumour cell growth and division, which we implement in a highly scalable agent-based (AB) framework and integrate with a custom neural network (NN) accelerated finite element (FE) solver to simulate stress-dependent growth.

MODEL DEVELOPMENT

Single-Cell Growth

Cell growth is regulated by competition between hydrostatic pressure ΔP arising from active cell stress and external loading, and osmotic pressure $\Delta\Pi$ arising from ion fluxes, such that:

$$dV/dt = -L_{p,m}(\Delta P - \Delta\Pi). \quad (1)$$

This competition is driven by several passive and active biomechanisms including mechanosensitive channels, active ion pumps, leak channels, and cytosolic proteins [2] (Fig. 1A). We consider that cell growth induced electro-osmotic fluxes $d(\phi)/dt$ can be driven by the synthesis of impermeable biomolecules dX/dt during the cell cycle. The osmotic pressure difference across the membrane can then be given by:

$$\Delta\Pi = RT\left(\Sigma\Delta c + \frac{X}{V}\right). \quad (2)$$

Multi-Cellular Simulation

We integrate our cell growth model with PhysiCell, a highly-scalable open-source AB modelling framework [3] which can describe forces associated with contact interactions (F_{ij}^{con}) and adhesion (F_{ij}^{adh}) between discrete cells. Migration is further driven by a motility force F_{ij}^{mot}. As the ECM cannot be explicitly represented within PhysiCell, we developed a custom linear FE solver to simulate continuum-level behavior of the ECM and cell-matrix interactions. Stresses generated from cell deformation are mapped to the matrix nodes through shape functions, and the matrix in turn imposes a point force F_{ij}^{mat} on individual cells. The total force acting on a given cell i is:

$$F_i = \sum_{j\in N(i)} F_{ij}^{adh} - F_{ij}^{con} - F_i^{mat} - F_i^{mot}. \quad (3)$$

We further consider that cell division is subject to a critical volume checkpoint V_{crit} [4]. As division is stochastic in nature, the probability of mitosis for a cell with volume V is then described by:

$$P_d(V) = 1/\left(1 + \exp\left(-k(V/V_{crit} - 1)\right)\right). \quad (4)$$

NN-FE Acceleration

Experimental observations demonstrate that the ECM exhibits nonlinear material behaviour [5]. To efficiently simulate such an anisotropic and hyperelastic matrix response, the deformation of the matrix is predicted using a neural network framework. Synthetic training data for a diverse range of load scenarios is generated using a novel data collection framework for FE software Abaqus. This data is subsequently provided to a fully connected deep neural network, comprised of four layers with 2,500 neurons per layer. This novel NN-FE framework is

extremely computationally efficient, arising from high-speed inference through TensorRT [6].

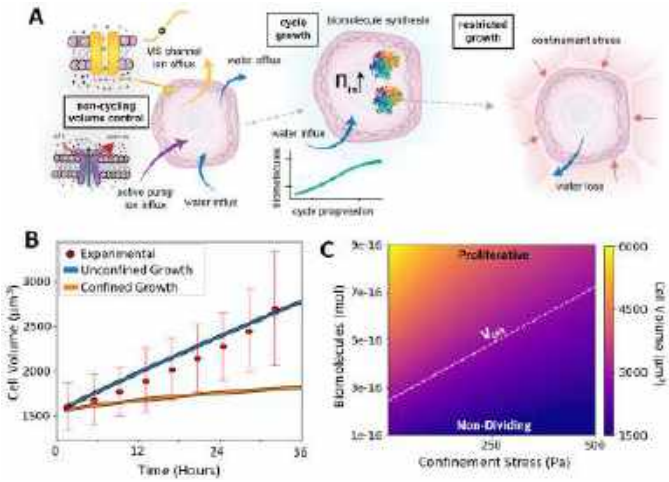

Figure 1: (A) Cell osmolarity and growth is regulated by a complex interplay between active and passive transport phenomena; (B) Cell growth arises from the synthesis of impermeable biomolecules, and mechanical confinement leads to a reduction in cell volume; (C) Phase diagram demonstrating how cell division is driven by high biomolecule concentration and low confinement stress.

RESULTS

At a cellular level, growth is driven by the synthesis of impermeable biomolecules and the associated increase in osmotic pressure. Cell confinement and associated loading can lead to an increase in hydrostatic pressure, which promotes fluid loss (via eqn 1) and ultimately reduces the rate of cell growth (Fig. 1B). This reduction in volume can prevent a cell from surpassing the critical volume checkpoint V_{crit} for division (Fig. 1C). Further, the model suggests that the associated stress to inhibit growth depends on biomolecule and ion concentrations.

Analysis of multicellular growth in a tumour spheroid with deformable matrix contact carries a significant computational cost (203 s per FE increment). Although the one-time up-front computational cost of synthetic training data generation and model training is relatively high, trained NN models can predict highly non-linear anisotropic material behaviour with a negligible computational cost (133 μs per FE increment, Fig. 2A) and near-perfect accuracy (Fig. 2B). Our fully coupled AB-NN-FE model allows for a deep insight into the mechanics of tumour growth at the cellular level (Fig. 2C).

4T1 tumour spheroid growth simulations using our fully coupled model suggests that cells at the tumour core experience greater stresses than cells at the periphery in agreement with data from excised tumours [7]. This promotes a reduction in cell volume at the spheroid core. These cells are also predicted to exhibit higher levels of biomolecule crowding, arising from the combined effects of the growth restriction and suppressed proliferation. Importantly, our simulations indicate that tumour spheroid size reduces with increasing matrix stiffness in a stress-dependent manner (Fig 2D), in agreement with our experimental data (Fig 2E) [8].

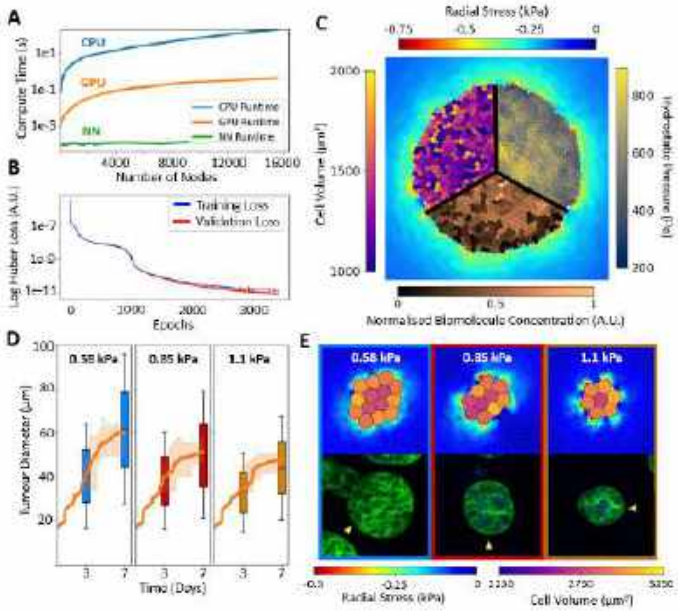

Figure 2: (A) The novel AI-FE framework is 1.5Mx faster than equivalent CPU-based computations, (B) while maintaining 99.95% prediction accuracy; (C) Coupled AB-BP-FE simulations allow for detailed analysis of tumour growth at the cellular level; (D, E) 4T1 spheroid size decreases due to mechanosensitive feedback between the cells and the matrix.

DISCUSSION

Our novel AB-BP-FE model provides a new and fundamental understanding of stress-dependent tissue and tumour growth, which is predicted to arise from a constraint on osmotically-driven growth at the cellular level. Biomolecule synthesis increases the cellular osmolarity, leading to an increase in cell volume and enabling cells to exceed a critical mitotic volume. Conversely, mechanical loading from cell-cell and cell-matrix interactions increases cellular hydrostatic pressure, giving rise to a water and ion efflux. This drives a reduction in cell volume and, subsequently, proliferation. Simulation of multicellular proliferation using NN-accelerated finite element and agent-based models provides critical insight into the evolution of tissue behavior and mechanosensitive growth, with broad applications to patient-specific cancer diagnosis.

ACKNOWLEDGEMENTS

This work was supported by the Irish Research Council (GOIPG/2022/910), DISC and DSI at University of Galway.

REFERENCES

[1] Curtis, K et al., *Journal of the Royal Society Interface*, 17, 2020.
[2] McEvoy, E et al. *Nature Communications*. 11, 2020.
[3] Ghaffarizadeh, A et al. *PLOS Computational Biology*. 14.2, 2018.
[4] Varsano, G et al., *Cell Reports*, 20.2:397-410, 2017.
[5] Chaudhuri, O et al., *Nature*, 584:535-546, 2020.
[6] Nvidia, *developer.nvidia.com/tensorrt*, 2024.
[7] Nia, H et al., *Nature Biomedical Engineering*, 1, 2017.
[8] Kumar, V et al. BioRxiv, 2023.

ADIPOSE-DRIVEN HYPERTENSION IMPACTS 3RD ORDER MESENTERIC ARTERY CONTRACTILE BEHAVIOR IN A SEX-DEPENDENT MANNER

Dillon McClintock (1), Osvaldo J. Vega Rodríguez (2), Nathan R. Tykocki (2), Sara Roccabianca (1)

(1) Mechanical Engineering, Michigan State University, East Lansing, MI, USA
(2) Pharmacology and Toxicology, Michigan State University, East Lansing, MI, USA

INTRODUCTION

Central and peripheral arteries share similar functions, that is to carry oxygenated blood from the heart and lungs to the rest of the body. Despite these common functions, they have many microstructural, biomechanical, and physiological differences. In addition, while aging and hypertension affect all arteries, elastic (central) and muscular (peripheral) arteries are affected in significantly different ways. Previous research has highlighted the importance of remodeling in muscular arteries, particularly mesenteric arteries, within an angiotensin II murine model of hypertension [1]. It is also recognized that mesenteric arteries play a crucial role in regulating peripheral resistance and, consequently, systemic blood pressure [2]. These findings suggest a need to better understand the biomechanical contribution of peripheral arteries to the progression of cardiovascular disease broadly and hypertension specifically. Nevertheless, there is a scarcity of research quantifying the mechanical, physiological, and microstructural changes in muscular arteries in response to hypertension, and especially in an adipose-driven model of hypertension. One single previous paper reported some limited effects of high-fat diet on sympathetic neurotransmission in mesenteric arteries [3]. Furthermore, sex-differences in the biomechanical behavior of muscular arteries remain virtually unexplored, both in health and disease.

In this study, we investigate the contrasting passive and active changes in peripheral arteries, specifically third-order mesenteric arteries, in male and female adult Dahl salt-sensitive rats fed a high fat diet.

METHODS

Experimental methods. The mechanical behavior of third-order mesenteric arteries in male and female Dahl Salt Sensitive (Dahl SS) rats fed a control diet (CD, F=5, M=5) or a high-fat diet (HFD, F=5, M=5) for 24 weeks, was assessed. The Dahl SS rat fed a high fat diet is an established model of adipose-driven hypertension [3]. The systolic arterial pressure of the animals was collected via tail-cuff before sacrifice. Following tissue isolation, the vessels were cannulated in a pressure arteriograph chamber and we estimated the *in-vivo* axial length as that required to prevent buckling at an inner pressure of 60 mmHg was determined (l_{iv}). Pictures were taken of the vessel before and after setting the axial length to measure *in-vivo* axial stretch as

$$\lambda_{iv} = \frac{l_{iv}}{l_o}, \tag{1}$$

where l_o is the axial length of the vessel after cannulation.

The arteries were then exposed to calcium-containing PSS buffer heated to ~37°C, and luminal pressures were incrementally increased from 20 to 120 mmHg in 20 mmHg steps. Luminal pressure was held at 20 mmHg for 20 minutes followed by a KCl contraction to allow for equilibration. At each subsequent step the luminal pressure was held until the vessel diameter plateaued. For each value of pressure, the vessels were subjected to a contraction with phenylephrine (PE). At the end of the experiment, passive diameter was measured at identical decreasing pressure increments from 120 to 20 mmHg in the absence of calcium and at room temperature. Throughout the pressurization protocol, the inner and outer diameter were tracked.

Mechanical metrics. Hoop stress in the arterial wall (σ_h) was calculated at mid-wall using the Laplace law for a thin-walled, cylindrical, pressurized vessel as

$$\sigma_h = \frac{Pd_m}{2h} \quad (2)$$

where d_m and h represent the mid-wall diameter and thickness at a pressure of P, respectively. Percent active diameter change was calculated as

$$\Delta\, diameter = \frac{d_{l,max} - d_l}{d_{l,max}} \times 100 \quad (3)$$

where $d_{l,max}$ is the passive luminal diameter at 120mmHg in and d_l is the active luminal diameter at each pressure P. Finally, wall distensibility at the mid-wall was defined as

$$D_i = \frac{d_{m,i+1} - d_{m,i}}{(P_{i+1} - P_i) d_{m,i}} \quad (4)$$

where i represents a set value of pressure and $i + 1$ the following value in the pressurization protocol (all active diameters). Parameters labelled as active refer to measurements from the portion of the test in calcium containing PSS at ~37°C without PE, while passive refer to absence of calcium.

RESULTS

Table 1. Body weight (mass), systolic blood pressure, in vivo axial stretch, and hoop stress for a pressure of 100 mmHg for all groups. † p<0.05 when comparing between diets. * p<0.05 when comparing between sexes.

	Control Diet	High Fat Diet
Body mass [g]		
Male	461.60±34.63	490.80±22.34
Female	276.60±11.06 *	292.40±19.03 *
Systolic blood pressure [mmHg]		
Male	162.22±10.74	182.98±10.28 †
Female	154.78±14.28	203.02±22.41 †
In vivo axial stretch		
Male	1.49±0.03	1.54±0.01
Female	1.54±0.05	1.61±0.05
Hoop stress [kPa] @100 mmHg		
Male	76.63±10.45	70.61±9.15
Female	74.80±11.25	80.26±9.72

Female animals weighted less when compared to males, independently of diet. Systolic blood pressure was higher in animals fed a high fat diet, independently of sex. We observed no difference in in vivo axial stretch and hoop stress (**Table 1**). Males presented a larger active diameter percent change than females for higher values of pressure on a high-fat diet, but not on a control diet (**Fig. 1**, p=0.0175 at 100 mmHg, and p=0.0113 at 120 mmHg). In addition, the mesenteric arteries of males on a high-fat diet were significantly less distensible than females on in the same pressure range (**Fig. 2**, p=0.0144 at 100-120mmHg).

DISCUSSION

Mean arterial pressure increased as a result of high fat diet in both male and female rats. Somewhat surprisingly, the mean arterial pressure in female animals was significantly higher compared to males fed a high fat diet but not control diet. While most mechanical metrics were unaffected by diet, mesenteric

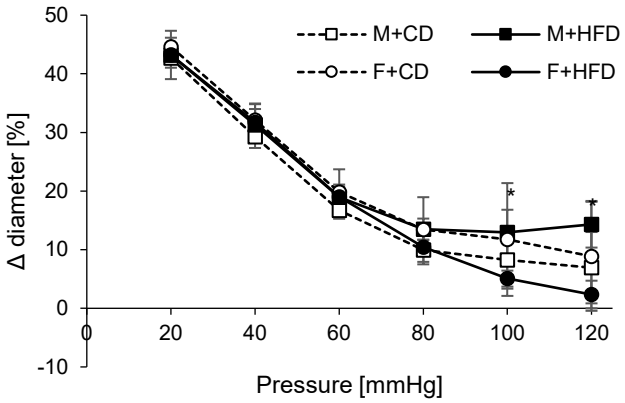

Figure 1: Active percent constriction (Δ *diameter*) of males (squares) vs females (circles) fed a control (open symbols) and high fat (closed symbols) diet. * p<0.05 between sexes in the high fat diet fed groups.

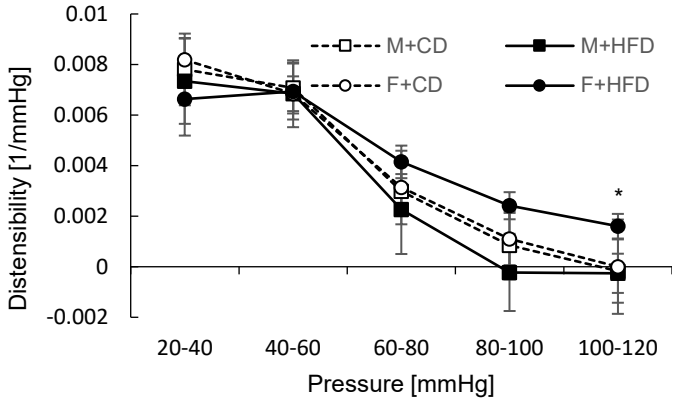

Figure 2: Active distensibility of males (squares) vs females (circles) fed a control (open symbols) and high fat (closed symbols) diet. * p<0.05 between sexes in the high fat diet fed groups.

arteries from high-fat male rats developed significantly more myogenic tone as compared to matched females as shown by the decreased active percent change in males. This resulted in a decreased distensibility in male animals compared to females. In comparison to Murtada [1], we did not see an increase in PE response in the mesenteric artery as a response to hypertension. Notably, the means of hypertension, order of mesenteric artery, and amount of PE used for contraction differed between our experiments. This study suggests, for the first time, that myogenic tone may play a different role in the development of adipose-driven hypertension in male and female animals.

ACKNOWLEDGEMENTS

This research was supported by grant number P01HL15951 from the NHLBI, National Institutes of Health.

REFERENCES

[1] Murtada, SI et al., *J Biomech*, 119:110297, 2021.
[2] Christensen, KL et al., *J. Vasc. Res.* 30.2:73-79, 1993.
[3] Alula, KM et al., *Auton Neurosci*, 222:102599, 2019.

SHINING LIGHT ON CALCIUM-MEDIATED MORPHOGENESIS: FORWARD ENGINEERING ORGAN DEVELOPMENT WITH OPTOGENETICS AND MECHANOSENSATION

(1) Mayesha Sahir Mim, (1) Nilay Kumar, (1) Megan Levis, (1) Maria Unger, (1) Gabriel Miranda (1) Jeremiah Zartman

(1) Chemical and Biomolecular Engineering, University of Notre Dame, Notre Dame, IN, USA

INTRODUCTION

Cells communicate to coordinate cellular processes across tissues, and calcium (Ca^{2+}) ions are second messengers facilitating such multiscale coordination. Ca^{2+} selective cation channels mediate Ca^{2+} influx from the extracellular environment into the cytosol upon activation. However, current understanding of the biological mechanisms precludes direct control of Ca^{2+}-mediated processes. Here, optogenetic[1] and mechanosensitive channels, CsChrimson and Piezo[2], respectively, are utilized as tools to investigate how Ca^{2+} dynamics impact epithelial growth and morphogenesis. *Drosophila melanogaster* was used as an in vivo system whose wing is acutely sensitive to changes in developmental pathways. We outline the phenotypic results of controlled stimulation of CsChrimson and Piezo in *Drosophila*. Optogenetics has emerged as a rapidly expanding solution to better decipher biological processes as it leverages engineered light-sensitive protein constructs to control cells and their governing biomolecular processes and signaling pathways. Hence, an artificial plasma-membrane embedded channelrhodopsin, CsChrimson, was used in transgenic fruit flies. Next, we used an endogenous mechanosensitive channel, Piezo. It can be activated through genetic overexpression, controlled mechanical force, or its specific agonist, Yoda1. We demonstrate that these channels regulate cytosolic Ca^{2+} dynamics, which impacts the activities of downstream proteins and growth-related biological pathways. As a bottom-up approach toward tissue engineering, we used optogenetic and mechanosensitive channels to forward engineer growth control in epithelia. These findings regarding how Ca^{2+} signaling dynamics tune the robustness of organ growth and cellular processes provide scope for future applications related to phenotypic drug screening assays and innovation in treatments of human diseases.

METHODS

GAL4-UAS, a bipartite method of activating gene expression in *Drosophila*, was used to express the genes of interest. To ensure more extended periods of viability during ex vivo imaging and allow the addition of a constant flow of media, a hybrid polyethylene terephthalate laminate (PETL) microfluidic device[3] was used for live imaging. The wing imaginal discs were imaged using a Nikon A1R-MP laser scanning confocal microscope. Wing discs were imaged throughout the entire depth of z-planes with a step size of 0.8 μm, depending on sample thickness, with a 40x and 60x oil objective with 200 ms exposure time, and 50 nW, 405 nm, 488 nm, 561 nm, and 640 nm laser exposure at 44% laser intensity.

For optogenetic experimentation, 1 mM All-Trans-Retinal was supplemented for the functional generation of CsChrimson in *Drosophila* (Fig. 1). The crosses were set up in darkness since white light can desensitize and deactivate the optogenetic channels. The dark condition was maintained by wrapping the vials in aluminum foil. On collecting the embryos in darkness, red light (~600 nm) LED strips were used to activate CsChrimson starting at the 1st instar larval stage. An Arduino microcontroller appended with transistors for amplification and resistors for dimming light was powered by a 9 V DC battery and programmed to manipulate the period of illuminance. A digital illuminance meter was used to measure the level of light in lux.

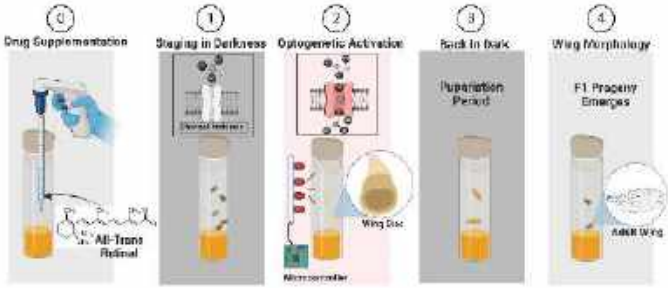

Figure 1: Schematic of Optogenetic Experimental Set-up.

RESULTS

We discovered that CsChrimson and Piezo modulate cellular processes involved in morphogenesis. We first confirmed that these channels transport Ca^{2+} using the GCaMP6f Ca^{2+} indicator in the wing discs and observed increased Ca^{2+} spiking dynamics to activate both channels through light and Yoda1-mediated activations (Fig.2).

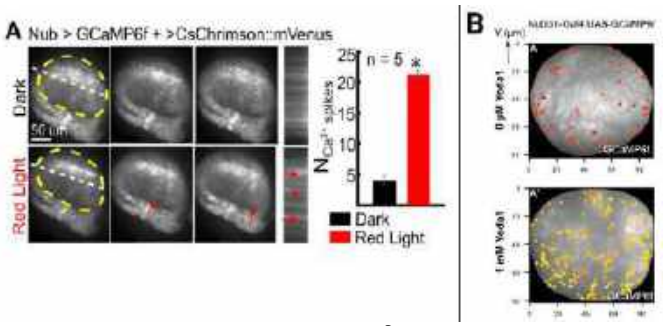

Figure 2: Emergence of elevated Ca^{2+} spiking dynamics on (A) optogenetic and (B) Piezo activation.

This confirmed that CsChrimson or Piezo can regulate Ca^{2+} dynamics in the tissue. Next, to investigate the effect of Ca^{2+} on terminal organ morphology, we discovered severe defects in the final shape and size of the wing for overexpression of CsChrimson or downregulation of Piezo in the wing disc, while overexpression of Piezo also resulted in smaller wings compared to control (Fig.3,4).

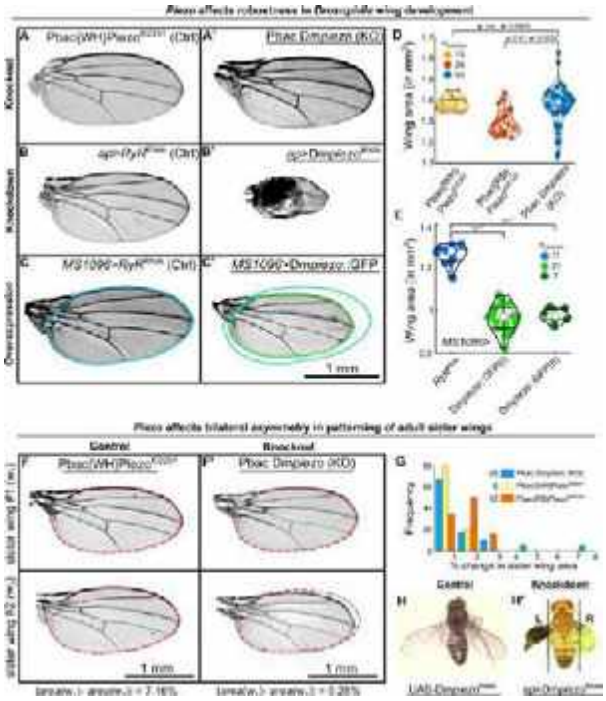

Figure 3: Divergent and spatial effects of Piezo expression in regulating size precision in bilateral organs.

For CsChrimson, the adult wing phenotypes were qualitatively and quantitatively correlated with the gradual increase in the intensity of light (Fig. 4A). Surprisingly, on quantifying the area of wings for different intensities of light activation, we found that at 5 lux of light, the size of the wings was larger compared to other intensities indicating an optimum level of light and Ca^{2+} level that induces growth (Fig. 4B). Different phenotypes for Piezo expression levels also point to similar regulation of morphogenetic processes (Fig. 3).

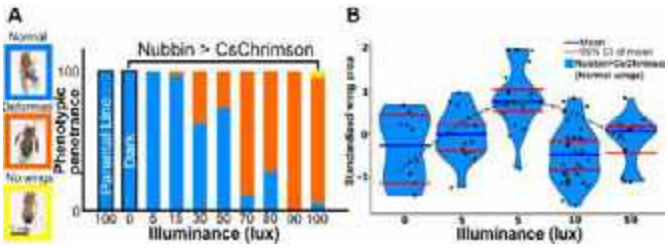

Figure 4: Optogenetic control of Ca^{2+} regulates organ shape and size. (A) Increase in phenotypic severity with the increasing Ca^{2+} levels. (B) Distribution of wing area for different light intensities.

We followed up these results by investigating subcellular processes and found increased cell death in wing discs for long periods of optogenetic activation and genetic misexpression of Piezo. Interestingly, we also observed higher proliferation for overexpression of Piezo or a lower frequency of light activation (1 min on/off period), indicating a probable apoptosis-induced compensatory proliferation phenomenon (Fig.5).

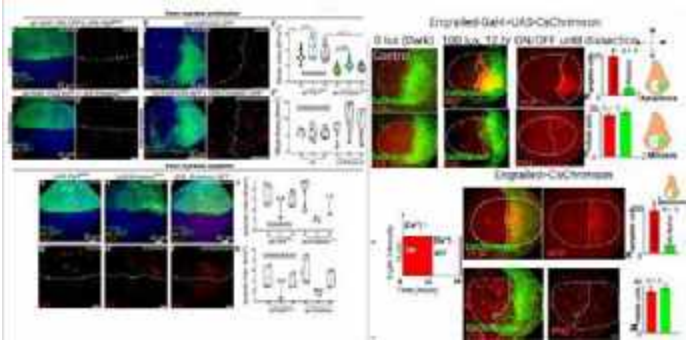

Figure 5: Piezo and Optogenetic mediated control of Ca^{2+} levels regulate cell proliferation and cell death.

Based on our results, we hypothesize that by controlling Ca^{2+}, tissue growth can be directly controlled, and an optimum level of cytosolic Ca^{2+} to promote growth can be established. Systematically varying the width of half max of optogenetic activation, e.g., by using a lower intensity of light or a faster optogenetic activation cycle, or by changing the mechanical activation level of Piezo using a microfluidic device will determine such "Goldilocks zone" of Ca^{2+} level.

DISCUSSION

In this work, we studied Ca^{2+} facilitated cellular communication and its role in shaping the growth of organs. We employed optogenetics and Piezo to program Ca^{2+} to elucidate the multi-layered steps and the general design principles that spatiotemporally govern morphogenesis. Cumulatively, these in vivo and ex vivo findings provide insights into practical applications for improving developmental research.

Through the manipulation of Ca^{2+} channels, we have gained novel insights into Ca^{2+} regulation of organ development and cellular processes while raising new questions regarding downstream growth-regulating pathways. We have also started investigating how these results affect cellular mechanics and developed a vertex model based on our results. Such an in silico model will help us better design our experiment to discover the "Goldilocks Zone" of cytosolic Ca^{2+} and how programming Ca^{2+} signaling may affect subcellular processes, tissue, and organ growth. Eventually, a new avenue of therapeutic discovery can be explored via activation period or activation level-based screening using light or mechanical activation of channels like CsChrimson or Piezo for Ca^{2+} channelopathies.

ACKNOWLEDGEMENTS

Multiple figures were created with BioRender.com. Thanks to Dr. Sara Cole from Notre Dame Integrated Imaging Facility for helping with imaging. The work was supported by NIH 1R35GM124935-01, NSF CBET-2225601, and NSF EMBRIO Institute, contract #2120200.

REFERENCES

[1] Mim, M. S., Knight, C., & Zartman, J. J. (2023). Quantitative insights in tissue growth and morphogenesis with optogenetics. *Physical Biology*, *20*(6), 061001.

[2] Kumar, N., Mim, M. S., Levis, M., Unger, M., Miranda, G., Robinett, T., & Zartman, J. J. (2023). Piezo regulates epithelial topology and promotes precision in organ size control. *bioRxiv*, 2023-08.

[3] Levis, M., et al. (2019). Microfluidics on the fly: Inexpensive, rapid fabrication of thermally laminated microfluidic devices for live imaging and multimodal perturbations of multicellular systems. *Biomicrofluidics*, *13*(2).

QUANTIFYING SOLEUS MUSCLE STRUCTURE THROUGH DIFFUSE TENSOR IMAGING (DTI) IN INDIVIDUALS WITH ACHILLES TENDON RUPTURE

Shabnam Rahimnezhad (1), Xiaoxiao Bai (2), Tanzil Arefin (3, 4), Thomas Neuberger (5), Morgan Alyssa Voulo (6), Daniel H. Cortes (1)

(1) Department of Mechanical Engineering, Penn State University, State College, PA, USA

(2) Social Science Research Institute, Penn State University, State College, PA, USA

(3) Department of Biomedical Engineering, Penn State University, State College, PA, USA

(4) Center for Neurotechnology in Mental Health Research (CNMHR), Penn State University, State College, PA, USA

(5) Huck Institute of the Life Sciences, Penn State University, State College, PA, USA

(6) Penn State College of Medicine, Milton Hershey Medical Center, Hershey, PA, USA

INTRODUCTION

Recovery from an Achilles tendon rupture (ATR) typically extends over several months. Patients often experience enduring deficits in functional performance. These deficits are characterized by weakness in calf muscle performance[1] and the activation of compensatory mechanisms[2] to overcome the weaknesses of the calf muscle. Functional deficiencies of the lower limb after surgery are intricately tied to the changes in the morphological and mechanical properties that are happening in both calf muscles[3] and the Achilles tendon[4].

Changes in the Achilles tendon include increased length of the free tendon[4], increased cross-sectional area[5], and changes in its mechanical properties [6]. On the other hand, common calf muscle changes include reduced cross-sectional area and volume of the Gastrocnemius and Soleus muscles [7], coupled with increased fat infiltration. Notably, Gastrocnemius muscle atrophy and heightened fat infiltration [7] emphasize the persistent nature of these changes.

Beyond assessing morphological and volume changes in calf muscles, examining alterations at the fascicular level in both the tendon and muscles provides insights into the negative consequences of ATR. Ultrasound, a common imaging modality for studying muscle fascicles [8], can be complemented by other imaging modalities, such as Diffuse Tensor Imaging (DTI)[9]. DTI quantifies tissue properties such as diffusion coefficients and fractional anisotropy [10]. Furthermore, fiber tracking methods using DTI data offer information about fascicle length, pennation angle, and fascicle curvature [11]. Despite investigations into the use of DTI techniques to understand the impact of diseases like Diabetes [12] and anterior interosseous nerve syndrome[13] on muscle structure, there is a noticeable absence of studies considering DTI as a technique for studying post-surgery changes in calf muscles, presenting an opportunity for further exploration and a more comprehensive understanding of the intricate changes occurring at both macro and micro levels in individuals recovering from ATR.

The current study aims to benefit from the DTI technique to comprehensively understand alterations in the Soleus muscle among individuals who have undergone surgical treatment for ATR. By examining the fascicular level changes, particularly in the context of DTI, this research seeks to contribute valuable insights into the intricacies of muscle transformations post-surgery.

METHODS

This study obtained approval and followed the Institutional Review Board (IRB) guidelines at the Pennsylvania State University (Study ID: STUDY00019121). Five participants who recovered from ATR in one leg (2 females and three males, with an average age of 45.6 ± 16.5 years, weight of 85.6 ± 17.6 kg, and height of 174.8 ± 3.4 cm) were included in the study. All participants underwent a 3T MRI system (Siemens Prima Fit) examination to obtain anatomical axial T1 and DTI images of the soleus muscle near the Achilles tendon, utilizing a 15-channel knee coil. For the anatomical scan, the following parameters were applied: coronal T1-weighted, TR/TE=650/8ms, FOV=160x160x144 mm, resolution=320x288x262, scan time= 3 min 35sec. The DTI scans were conducted using the following settings: an axial SE-EPI sequence, TR/TE=6500/70ms,FOV=160x160x144mm, resolution=128x128x192, gradient directions = 64, signal averages = 2, b values ≈ 0 and 600 s/mm^2, scan time = 14 min 26sec. Eddy's current distortions and possible motion during the DTI-EPI scan were corrected using DSI Studio[14]. The ROIEditor in DTI_Studio [15] created a mask for the muscle. Finally, the data was analyzed in MRtrix [16] as described in our former studies[17],[18]. Using MRtrix, we extracted several DTI indices to probe the diffusion integrity in the muscles. However, we have focused on indices, the mean diffusivity (MD) and fractional anisotropy (FA) in soleus. A comparison of each parameter map between the recovered ATR leg and its contralateral healthy counterpart (in the soleus muscle) was conducted to identify the best-suited measure for identifying the effects of the injury.

RESULTS

Key parameters in Diffusion Tensor Imaging (DTI) include the primary eigenvalues (λ_1, λ_2, λ_3), mean diffusivity (MD), and fractional anisotropy (FA). Calf muscle atrophy, involving both the Gastrocnemius and Soleus muscles and increased fat infiltration were

observed in all subjects. Figure 1 illustrates the anatomical, colored fractional anisotropy, and first eigenvalue for subject 2, comparing the right and left legs at the same height. Despite undergoing a total knee replacement on the right knee and Achilles tendon surgery on the left leg, this subject exhibited more pronounced calf muscle atrophy and increased fat infiltration (white tissues in the soleus) in the left leg, which had repaired Achilles tendon rupture. Increased fat filtration was absorbed to some extent in all the subjects.

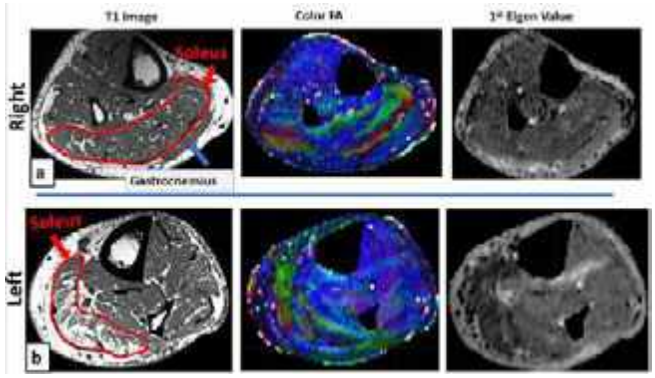

Figure 1: T1 image, color Fa map, 1st Eigenvalue for a) right leg, b) Left Leg

To examine variations in specific parameters (FA, MD, eigenvalues) within the healed leg after an Achilles tendon rupture, we assessed the volume around the musculotendon junction of the Soleus muscle. This analysis will be performed on both the injured and healthy legs, with the chosen volume's height being consistent for both legs. We calculated the mean FA, MD, and eigenvalues in the recovered leg after Achilles tendon rupture and the corresponding contralateral leg for all subjects (Table 2) using statistical analysis of ROIEditor. Figure 2 shows the bar chart of these parameters. Interestingly, the mean values of these parameters across participants do not show consistent trends. However, a compelling observation is the higher standard deviations of measured parameters over the region of interest (ROI) in the injured legs compared to the healthy legs across all subjects. This highlights a discernible alteration in the fascicles and a loss of their arrangement to some extent in the injured legs within the considered ROI. Further statistical analysis, specifically t-test calculations (for example, 0.085 for λ_1 and 0.049 for λ_2**)** underscores that the average standard deviation over the ROI for all participants is a robust indicator of the differences between healthy and injured leg. When contrasted with their healthy counterparts, it effectively demonstrates the inhomogeneity of fascicles in injured legs.

Table 2: Parameters values for different subjects

ID, gender, age, time after injury (Y)	leg		MD (e-3)	FA	λ_1 (e-3)	λ_2 (e-3)	λ_3 (e-3)
ATR1, F, 41, 1.5	R (ATR)	avg	1.54	0.177	1.75	1.33	1.75
		Std (ROI)	0.792	0.165	0.875	0.738	0.875
	L	avg	1.67	0.146	1.92	1.63	1.45
		Std (ROI)	0.397	0.063	0.453	0.412	0.358
ATR2, M, 73, 3.5	R	avg	1.61	0.164	1.58	1.86	1.37
		Std (ROI)	0.358	0.082	0.369	0.396	0.340
	L(ATR)	avg	1.54	0.183	1.80	1.51	1.30
		Std (ROI)	0.604	0.122	0.667	0.614	0.563
ATR3, M, 23, 5.5	R	avg	1.40	0.206	1.68	1.35	1.16
		Std (ROI)	0.345	0.112	0.385	0.344	0.333
	L	avg	1.38	0.216	1.66	1.35	1.13
	(ATR)	Std (ROI)	0.564	0.151	0.618	0.569	0.538
ATR4, F, 52, 3.5	R (ATR)	avg	1.48	0.195	1.77	1.43	1.24
		Std (ROI)	0.405	0.102	0.464	0.405	0.376
	L	avg	1.57	0.204	1.92	1.47	1.31
		Std (ROI)	0.263	0.052	0.305	0.275	0.239
ATR5, M, 39, 8	R (ATR)	avg	1.57	0.1663	1.84	1.53	1.35
		Std (ROI)	0.378	0.0857	0.425	0.377	0.356
	L	avg	1.67	0.1435	1.93	1.62	1.47
		Std (ROI)	0.336	0.056	0.381	0.343	0.310

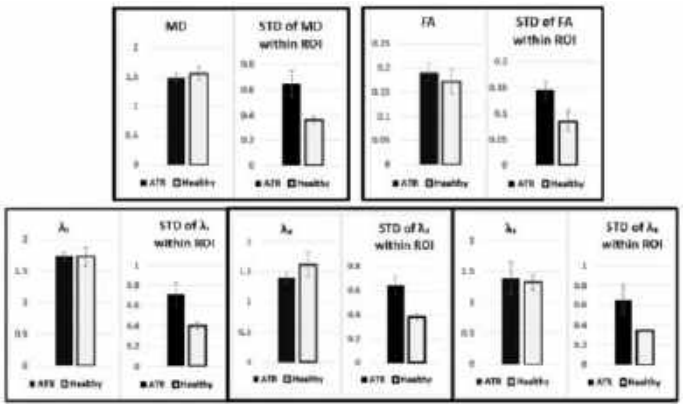

Figure 2. Chart of the changes in the specified parameters (MD, FA, λ_1, λ_2, λ_3)

DISCUSSION

This study utilized the DTI technique's potential to investigate the structural integrity changes in the soleus muscle after ATR and the contralateral healthy legs. From the anatomical images, we observed fat infiltration and muscle atrophy in the soleus muscle of all subjects. DTI results indicated alterations in the fascicle arrangement and inhomogeneity, evidenced by increased standard deviations over ROI of interest in various measured parameters. Despite the higher standard deviation values over ROI in the injured leg, the average values of parameters did not exhibit specific trends between the injured leg and contralateral legs. Given the complexity of the soleus muscle, this study focused on average values over the musculotendon junction volume. Further investigation through tractography-based analysis is recommended to understand the changes in each division of the soleus muscle.

ACKNOWLEDGMENTS: The research reported here was supported by NIAMS of the NIH under award number R21 AR077282. The Authors would like to thank **Debra Weston** and **Glenda Palmer**, MRI technicians.

REFERENCES

[1]A. Brorsson, et al., *Sports Med.*, 46(2), 470–477, 2018. [2]S. M. Suydam, et al., *Knee Surgery, Sport.* 23(3), 868–874, 2015. [3]G. P. Bostick, et al., *Orthop. Sports Phys. Ther.*, 40(6), 345–351, 2010. [4] J. Kangas, et al., *Am. J. Sports Med.*, 35(1), 59–64, 2007. [5]R. R. Bleakney, et al., *Clin. J. Sport Med.*, 12(5), 273–278, 2002. [6]L. N. Zhang *et al.*, *Med. Sci. Monit.*, 22, 1186–1191, 2016. [7]G. Eken,et al., *Foot Ankle Surg.*, 27(7), 730–735, 2021. [8]W. C. Peng *et al.*, *Clin. Biomech.*, 43, 50–57, 2017. [9]B. Bolsterlee, et al.," *PeerJ*, 6(4), 2018. [10]E. Kermarrec, et al., *Am. J. Roentgenol.*, 195(5), 352–356, 2010. [11]B. Bolsterlee, et al., *J. Appl. Physiol.*, 122(4), 727–738, 2017. [12]A. Stouge *et al.*, *Radiology*, 297(3), 608–619, 2020. [13]T. Godel *et al.*, *NeuroImage Clin.*, 21, 2019.[14]https://dsi-studio.labsolver.org/.[15]https://www.mristudio.org/.[16]https://www.mrtrix.org/. [17]T. M. Arefin *et al.*, *Neuroimage*, vol. 273, 2023. [18] T. M. Arefin, et al., *Bio-protocol*, 11(22), 1–17, 2021.

COLLAGEN TYPE-DEPENDENT EXTRACELLULAR DEFECT SENSING DRIVEN BY ACTIN PROTRUSIONS AND MEMBRANE TENSION

H. Zmuda (1), C. Walter (2), A. Pathak (2)

(1) Department of Biomedical Engineering, Washington University in St. Louis, St. Louis, MO, USA
(2) Department of Mechanical Engineering and Material Science, Washington University in St. Louis, St. Louis, MO, USA

INTRODUCTION

Migrating cell collectives interact with biochemically and mechanically heterogeneous environments. To sense and navigate such an environment, cells bind integrin receptors to extracellular matrix (ECM) proteins to form focal adhesions that connect to actin stress fibers. As epithelial collectives migrate forward and form leading-edge protrusions, the actin network continues to branch out, increasing plasma membrane tension and forming focal adhesions to adherent surfaces. On non-adherent surfaces, cells utilize multicellular actin stress fibers formed along adjacent cells, a purse-string mechanic, to close the gap [1]. However, much of the current work focuses on collagen type-I or fibronectin-laden substrates, or non-adherent substrates. Although classic wound healing assays focus on filling gaps created within epithelia, it remains unclear how cells sense wounds or defects in the ECMs of varying proteins and stiffnesses. Here we investigate how a laser-ablated defect on polyacrylamide gels coated in collagen type-I (col1) or collagen type-IV (col4) can affect collective cell migration.

METHODS

To better understand how collagen type can affect epithelial sensing of ECM defects, human mammary epithelial cells (MCF10A) were seeded on either 0.08, 0.5, or 20kPa polyacrylamide (PA) gels functionalized with either col1 or col4 [2]. After 24hr culture, a portion of the underlying PA gel was ablated perpendicular to the leading edge of the cell cluster using a laser, creating a micro-defect (µ-defect) (Fig. 1A). Subsequently, time-lapse imaging was performed (Zeiss Cell Observer) at 10min intervals for 24hr. Cell migration was measured using Matlab's PIV and manual tracking (ImageJ) of the leading edge on brightfield images. Time spent at the defect was measured by calculating the time difference from when the leading edge was first contacted, and the last leader cell crossed the µ-defect. The following were chemically inhibited or induced (drug): myosin ATPase (10µM Blebbistatin), protein phosphatases PP1 and PP2A (1nM calyculin-A), Arp2/3 (150µM CK666), hyperosmotic (3mM methyl-β-cyclodextrin), and hyposmotic (50% water/50% cell media). For fixed imaging, samples were fixed in 4% PFA after cells contacted the µ-defect. The following antibodies were used: phalloidin, anti-paxillin, and anti-T-plastin. Images were taken on a 63x oil objective on a Zeiss LSM 880 FAST Airyscan confocal. AFM was done with a Bruker Nanoscope Resolve atomic force microscope, and custom silicon nitride cantilever probes (4.5µm-diameter, 0.01N/m polystyrene bead).

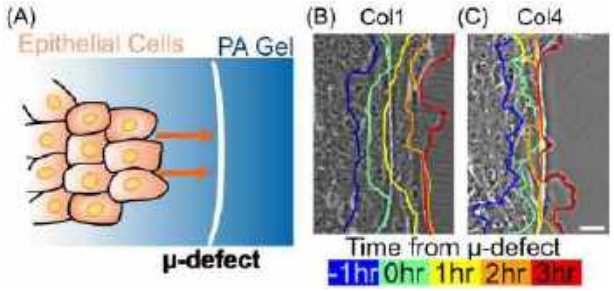

Figure 1. (A) MCF10A are seeded in a cluster on col1 or col4 PA gels. A portion of the PA gel is ablated using a laser (µ-defect). A brightfield image 3hr after the leading edge contacted the µ-defect on (B) col1 and (C) col4. Lines are color-coded based on the time relative to when the leading edge contacted the µ-defect. Scale bar: 25µm

RESULTS

Cells on col1 migrated over the µ-defect (defect) with little effect on migration distance (Fig. 1B). However, cells on col4 gels stalled at the defect site and took longer to migrate over (Fig. 1C). No matter the collagen type, cells migrated over a similar distance in control (non-defect) samples (Fig. 2A). When a defect was introduced, cells on col4 stalled and reduced the distance traveled while the leading edge on col1 traveled at a similar distance to the non-defect samples (Fig. 2A). To

understand whether such defect-sensing is also mechanosensitive, we varied PA stiffness and found that cells on even softer gels (~0.08kPa) sensed defects with both col1 and col4, showing similar times spent at the defect (Fig. 2B). By contrast, on stiffer substrates (~20kPa), cells overcame defects on both col1 and col4, showing negligible stall times in both cases (Fig. 2B).

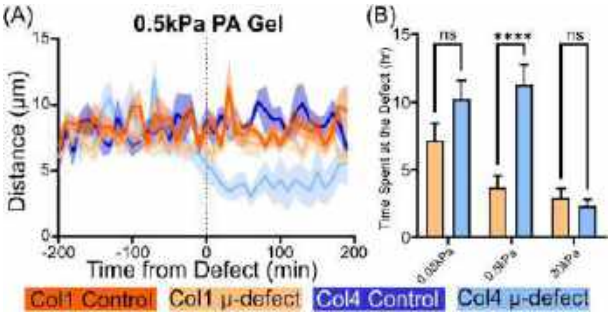

Figure 2. (A) The distance traveled by the leading edge over time. The vertical dashed line represents when the leading edge contacted the defect. (B) The average±SEM of time spent at the defect on different substrate stiffnesses. N≥3; statistical analysis: one-way ANOVA with Tukey's multiple comparisons ****P<0.0001, ns=not significant.

As cells migrate into the defect (Fig. 1C), their protrusions collapse and stall. We wondered if actin branching was critical for col4-dependent stalling. When actin branching was inhibited via CK666, the leading edge further stalled on col4 μ-defect compared to the control, supporting the regulatory function of actin branching of leading edge cells in collagen-dependent defect-sensing. To observe F-actin architecture at the μ-defect, we imaged the leading edge at the defect using Airyscan microscopy. On col1, the leading cell overcame the defect, but the F-actin built up at the μ-defect (Fig. 3Ai). On the other hand, cells on col4 form very short actin fibers at the defect and large actin bundles across adjacent cells parallel with the defect (Fig. 3Bi). Adhesion structures connect the cell cytoskeleton to the ECM. To visualize the adhesions, we imaged for paxillin. Images of paxillin illustrate distinct, individual puncta in the leading cell around the defect on col1 substrates (Fig. 3Aii). However, on col4, there are few distinct paxillin puncta; instead, smaller paxillin fibers at the leading edge and larger paxillin fibers form along the actin fibers (Fig. 3Bii). Cells near the col4 defect exert lower traction forces than those near the col1 defect (data not shown). Along these lines, cells are stiffer (measured via AFM) near col4 compared to col1 defects (data not shown). We also found that myosin activation through calyculin-A and RhoA activation increases defect-based stalling, while myosin inhibition via Blebbistatin allows cells to migrate over the defect (data now shown). These results indicate that leader cells are unable to form protrusions, and instead form long paxillin fibers and exert lower traction forces, all of which cause stalling near col4 defects.

To understand the role of cell protrusions in response to μ-defects, we imaged T-plastin, a calcium-sensitive conserved linker protein for actin branching [3]. We found T-plastin highly expressed in cells on col1 defects (Fig. 3Aiii), indicating a high amount of actin branching, while cells near col4 defects had lower T-plastin expression (Fig. 3Biii). The actin branching on col4 could potentially reduce membrane tension, and thus lower T-plastin in response. We hypothesized that externally lowering membrane tension could enhance protrusions and enable cells to cross the gap. To test this, we pharmacologically created hyperosmotic or hyposmotic media conditions to increase and decrease membrane tension, respectively. Here, cells in hyposmotic conditions were able to reach across the μ-defect more effectively than in hyperosmotic conditions, no matter the collagen type (Fig. 4A, 4B).

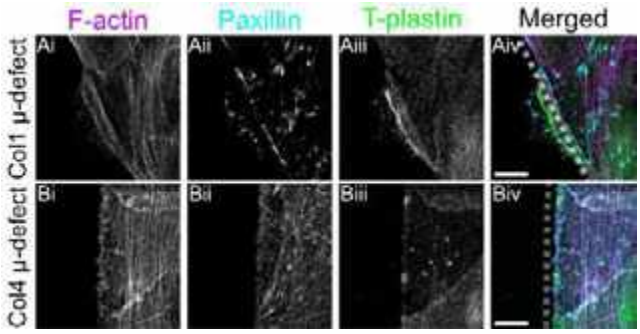

Figure 3. Max z-projection of leader cells at the μ-defect on (A) col1 or (B) col4 coated 0.5kPa PA-gels. (i-iii) Representative grey-scale images of (i) F-actin, (ii) paxillin, and (iii) T-plastin. μ-defects are represented by the gray dashed lines in the merged images. Scale bar: 10μm

DISCUSSION

Collective cells migrate through heterogeneous environments, including ECM gaps, such as wound healing. Much of the previous work utilizes fibronectin as the underlying ECM and focuses on wounds created in the epithelial layers and not the ECM wounds [1,4,5]. Our work reveals that epithelial sensitivities of ECM wounds or defects depend on matrix stiffness and collagen type (col1 vs col4). We further demonstrate that such defect-dependent mechanosensing in epithelia is regulated by actin-based protrusions wherein a rise in cell membrane tension stalls protrusions and slows collective cell migration across ECM defects. One limitation of the study is understanding how collagen structure changes in the presence of defects. Col4 is a dense, sheet-like structure. The fibers may shred during the ablation process while the fibrous col1 fibers remain intact, causing cells to unadhere. Future experiments focus on scanning electron microscopy (SEM) to visualize fiber architecture near the defects. This research helps answer a fundamental question of how differing ECM proteins and their defects can physically and biochemically affect cellular signaling.

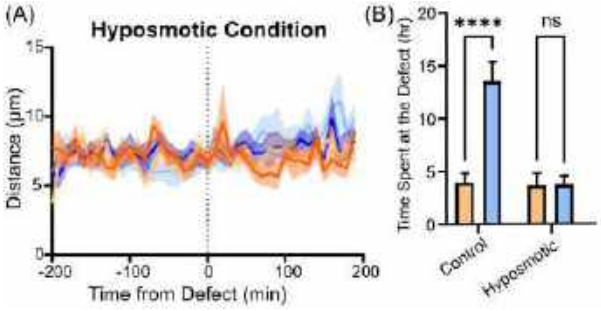

Figure 4. (A) The distance traveled by the leading edge over time in a hyperosmotic condition is similar no matter the collagen type. (B) The average±SEM time spent at the defect is less in hyperosmotic conditions no matter the collagen type. Control represents samples in normal osmotic conditions. . N=2; statistical analysis: one-way ANOVA with Tukey's multiple comparisons ****P<0.0001, ns=not significant

ACKNOWLEDGEMENTS

The authors would like to acknowledge the following funding source: NIGMS R35GM128764 to A.P.

REFERENCES

[1] Vedula, S et al., *Nat Commun*, 6:6111, 2015. [2] Almeida, J et al., *MBoC*, 34, 2023. [3] Delanote, V et al., *Acta Pharmacol. Sin.*, 26: 769-779, 2005. [4] Garbett, D et al., *Nat Commun*, 11:4818, 2020. [5] Ajeti, V et al., *Nat Phys*, 15:696-705, 2019.

RESOLVING NANOSCALE DEFORMATIONS OF MINERALIZED COLLAGEN FIBRILS IN 3D

Riti Sharma, Luc Capaldi, Kailin Chen, Ottman A. Tertuliano

Mechanical Engineering and Applied Mechanics, University of Pennsylvania, Pennsylvania, USA

INTRODUCTION

Bone is a hierarchical material that exhibits a complex multi-level organizational structure. This hierarchical structure is critical to bone tissue properties and depends on the arrangement and interaction of organic (collagen and proteins) and inorganic (hydroxyapatite) components of the tissue (4). At the nanoscale, the collagen molecules within bone tissue form a twisted and cross-linked structure. These structures have hydroxyapatite mineral crystals embedded in them, thus forming an individual mineralized collagen fibril (~100 nm). Mineralized collagen fibrils are the fundamental building blocks of bone tissue (4).

We have limited knowledge of the fundamental response mechanisms of mineralized collagen fibrils to physiological loads. Especially during cyclic loading, injury, and repair, where the bone tissue is exposed to large strains and dynamic loads presenting a drastic departure from quasi-static and macroscale conditions (5). This necessitates the probing of nanoscale tissue adaptation under dynamic failure processes.

The orientation and arrangement of mineralized collagen fibrils visualized using various imaging techniques have been a matter of interest for some time now (3). However, not all these techniques can be combined with mechanical testing. Electron-based techniques such as in-situ SEM cannot currently provide the spatial resolution to assess the bone's mineralized collagen fibrils and are destructive for 3D imaging (1). X-ray-based in-situ SAXS and WAXS can be useful for measuring strain fields in fibrils but are limited to discrete points in space and cannot provide quantitative data about the 3D orientation of fibrils (6).

Previous work using TEM suggests a reorientation of fibrils near cracks, but fundamental mechanisms remain unclear (Fig. 1) (1). Our overarching aim is to isolate and quantify nanoscale mechanisms facilitating bone fracture and understand how much of the change in mechanical properties of the bone is due to the fundamental building blocks – mineralized collagen fibrils.

Our objectives are to experimentally answer the following: 1. How do mineralized collagen fibrils deform or adapt under cyclic loading in the presence of a crack? 2. What nano and micro-scale mechanisms dictate dynamic fracture in bone?

To answer these questions, we introduce a novel 3D imaging technique using synchrotron X-ray tomography to visualize individual nanoscale mineralized collagen fibrils in bone.

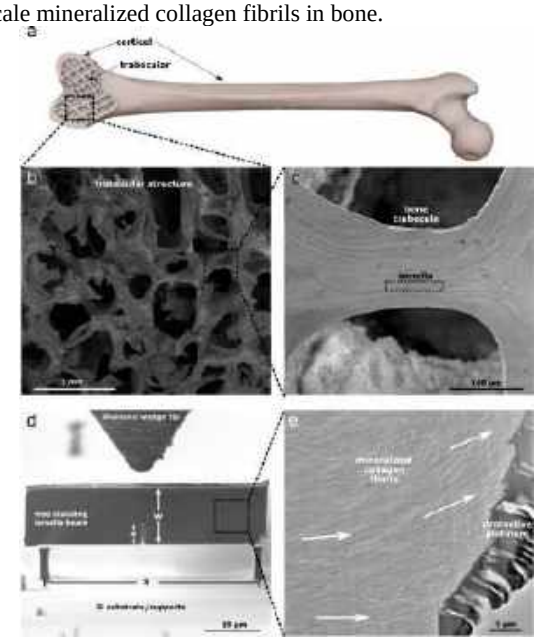

Fig. 1. Preliminary work suggests a reorientation of fibrils along the crack, but mechanisms are still unclear (1)

METHODS

Sample Preparation: Bulk human trabecular bone samples are purchased from healthy human donors with no history of bone disease via a tissue harvesting consortium (Articular Engineering, Inc.). These bulk samples are cleaned, polished, and coated before putting in the Focused Ion Beam – Scanning Electron Microscope (FIB-SEM) at Drexel University. We fabricate microscale (10x10x50 μm^3) beams using the FIB-SEM and introduce a small notch to induce an initial flaw in the bone. These beams are then lifted out and glued onto fabricated silicon supports etched on 2x2 mm^2 wafers. The final setup creates a

microscale three-point bending geometry. This beam setup is ready for X-ray tomography and radiography experiments at the Brookhaven National Laboratory.

In-situ X-ray imaging: First, we perform X-ray tomography of the microscale beams to observe the volumetric arrangement of mineralized collagen fibrils in 3D relative to the introduced notch. After tomography, we perform nanomechanical experiments using an in-situ testing apparatus (KLA NanoFlip) available in our lab at Penn. We use a spherical tip to load the beams to a stress less than 75% of failure stress and then apply a low amplitude cyclic load to propagate a crack. Radiography during this experiment gives us spatial and temporal information about any changes in mineralized collagen fibril arrangement due to applied stresses. After loading, we took another tomography scan to get 3D information about the changes that occurred during the experiment.

Tomography Data Processing: Tomography data was reconstructed using TXM_Sandbox and visualized in Dragonfly. We segmented two regions of interest - mineralized collagen fibrils and nanoscale pores- using histographic segmentation in Dragonfly. This type of segmentation creates a two-dimensional histogram with absorption contrast and domain boundaries. With these two masks, we select clustered data values to create the mentioned regions of interest. 3D orientation of the fibrils in beams with and without cracks can be visualized after segmentation.

Radiography Data Processing Radiography images from nanomechanical experiments were visualized and processed in Fiji. Next, we use Digital Image Correlation (DIC) (2) to quantify the strain and displacement fields of the deformed mineralized collagen fibrils. This processing technique provides full-field information on damage observed using in-situ radiography.

RESULTS

We introduced a novel 3D imaging technique using synchrotron X-ray tomography to visualize individual nanoscale mineralized collagen fibrils in bone with 30 nm voxel resolution (Fig. 2(a)). We found the mineralized collagen fibrils to be of the order of ~100 nm which aligns with previous measurements done using electron microscopy (4). Further, this technique uniquely allows us to capture the crack trajectory in 3D along with nanoscale deformations of fibrils (Fig. 2(b)).

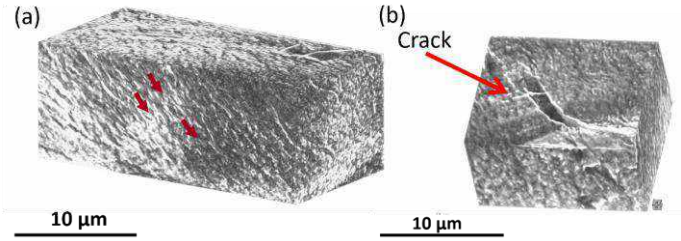

Fig. 2. (a) X-ray tomography reveals individual mineralized collagen fibril alignment and (b) crack trajectory in 3D.

We demonstrate for the first time the ability to successfully conduct in-situ nanomechanical dynamic loading experiments for bone in a synchrotron facility. These experiments have traditionally been done in an SEM to obtain 2D information at micron resolutions (1). Our technique has allowed us unprecedented 30 nm volume resolutions. This method not only gives us information on crack growth but can visualize real-time fibril deformation as well. We found in-situ radiography to be a robust technique for observing real-time nanoscale deformations and adaptation of fibrils under applied loads and near cracks.

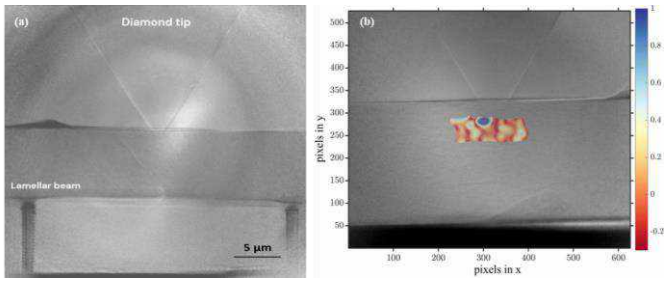

Fig. 3. (a) In-situ x-ray radiography nanomechanical experiments resolve nanoscale fibril deformation. (b) Preliminary data from the use of DIC on in-situ x-ray radiography images.

Data processing techniques like digital image and volume correlation are becoming more prevalent in quantitatively measuring deformation characteristics. This is due to the relative ease and ability to provide full-field displacement and strain fields under applied loads. DIC tracks surface speckle patterns to measure the local heterogeneity of the deforming fibrils using our radiography data. This speckle pattern serves as a marker for deformation information. For cyclic testing, DIC can help monitor the overall strain with loading cycles, along with local damage development of the fibrils. Our ongoing work includes preliminary processing of radiography data and the use of DIC to obtain quantitative information on displacement and strain fields (Fig. 3(b)).

DISCUSSION

The ability to quantitatively analyze the 3D organization and damage of the mineralized collagen fibrils is key to understanding structure-function relationships in bone. Previous attempts at isolating and visualizing deformations experimentally at these small length scales have been using electron microscopes where sample preparation for 3D imaging is destructive. We presented a non-destructive 3D imaging technique that can allow us to tackle these problems and open new paths toward ultrastructure organization investigations of whole sample volumes. Some studies have demonstrated the use of SRµCT to obtain high-resolution (~600 nm) images (7), but this does not allow the resolution of mineralized collagen fibril deformations (~100 nm). We note that the cost of our technique is a higher X-ray dose but generates a vast amount of acquired deformation data per sample (~200 Gb/sample).

Since isolating and quantifying nanoscale mechanisms is critical to understanding disease progression, this technique can help us resolve the changes occurring in bone tissue due to various diseases like osteoarthritis, osteoporosis, etc. We have the opportunity to approach understanding these diseases from a mechanics perspective and fundamentally resolve the role of the building blocks – mineralized collagen fibrils – in disease progression.

ACKNOWLEDGEMENTS

We thank Drexel University for their FIB-SEM system and the Brookhaven National Laboratory for their synchrotron facility.

REFERENCES

(1) Tertuliano et al. 2021 *Bioinspir. Biomim.*
(2) Yang, J. Et al. 2018 *Exp.Mech.*
(3) Georgiadis M. et al, 2016 *J. R. Soc. Interface*
(4) Weiner S. et al. 1998 *Annu. Rev. Mater. Sci.*
(5) Acevedo, C. Et al. 2018 *Nat Biomed Eng*
(6) Zimmermann, E. 2011 *PNAS USA*
(7) Obata Y., 2020 *J. Mech. Biomed. Mat.*

BIOMECHANICAL CONSEQUENCES OF LIGAMENT RELEASES DURING TOTAL KNEE ARTHROPLASTY

Matthew B. Blomquist (1), Dylan G. Schmitz (2), Joshua D. Roth (2,3)

(1) Department of Biomedical Engineering, University of Wisconsin-Madison, Madison, WI, USA
(2) Department of Mechanical Engineering, University of Wisconsin-Madison, Madison, WI, USA
(3) Department of Orthopedics and Rehabilitation, University of Wisconsin-Madison, Madison, WI, USA

INTRODUCTION

The traditional alignment goal for total knee arthroplasty (TKA) is to align the femoral and tibial implants to achieve a neutral mechanical alignment. However, altering the native joint alignment often overstuffs the medial and/or lateral compartment [1], which increases the tension in the soft tissue restraints (e.g., ligaments) of the tibiofemoral joint. To reduce excessive tension(s), surgeons routinely perform soft tissue releases [2]. They most often assess whether they have adequately released soft tissue restraints based on the joint gaps and/or varus-valgus (V-V) laxities [3]. Although soft tissue releases reduce tension, they also have been shown to increase the slacklength and decrease the stiffness of the released ligament [4]. Because the ligament properties are key determinants of the biomechanics of the knee, these ligament changes could cause unintended biomechanical changes to the joint (e.g., altered laxity or joint contact forces).

Accordingly, the two objectives of the present study were (1) to characterize the coupled changes in slack length and stiffness due to releases of the superficial medial collateral ligament (sMCL) and lateral collateral ligament (LCL) and (2) to determine how these coupled changes in ligament properties alter important biomechanical variables of knee function (i.e., V-V laxity, contact forces, and ligament tensions).

METHODS

Ex Vivo Mechanical Testing: To characterize the coupled changes in slack length and stiffness due to ligament releases, we isolated five MCLs and five LCLs from a crossbreed of large white, landrace, and red duroc pigs (age: 6 months, weight: 131.8 ± 18.9 kg) for mechanical testing. Following preconditioning, we computed baseline and post-release slacklengths and stiffnesses from the force-deformation data during a loading ramp. On each ligament, we performed ten release iterations consisting of 5 punctures each with a 16-gauge needle. After each release, we cyclically loaded the ligament and then allowed the ligament to recover.

Computational Simulations: To determine how coupled changes in ligament properties alter V-V laxities and tibial forces, we created four sets of TKA models (**Figure 1**). First, we performed 1000 virtual reference TKAs on a validated multi-body model of the knee consisting of 12 degrees of freedom [5]. To account for patient-to-patient variability in the ligament properties, we randomly sampled the stiffness and slacklength of each ligament [5] (*Reference TKA Set*, **Figure 1**).

Second, we created two additional sets of 1000 virtual TKAs with medial or lateral overstuffing by randomly introducing up to 2° of valgus and internal malrotation to the femoral component and up to 2° of valgus malrotation to the tibial component (*Medial Overstuff Set*,

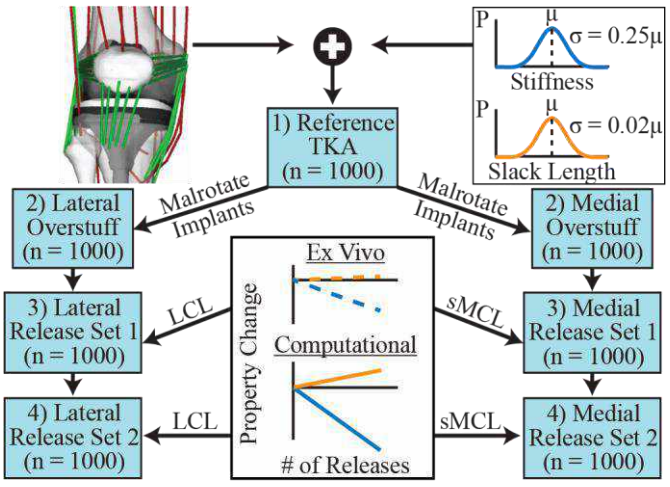

Figure 1: We generated four sets of musculoskeletal models to characterize the effects that implant overstuffing and subsequent releases have on knee biomechanics. In each model, we simulated passive flexion and varus-valgus laxity to compute laxities, contact forces, and ligament tensions.

Figure 1), or by randomly introducing up to 2° of varus and external malrotation to the femoral component and up to 2° of varus malrotation to the tibial component (*Lateral Overstuff Set*, **Figure 1**), respectively.

Third, we performed virtual releases to each overstuffed model by applying coupled reductions in stiffness and increases in slack length to the sMCL and LCL in the medially and laterally overstuffed TKAs, respectively, to reduce the ligament tensions back to those of the *Reference TKA Set* based on the linear regressions of the coupled changes determined in the ex vivo study (*Release Set 1*, **Figure 1**).

Fourth, because the patient-to-patient variability we introduced in the virtual ligament properties lead to different properties than those of the ex vivo ligaments, we performed an additional release set tuned to each of the overstuffed models (*Release Set 2*, **Figure 1**). To tune these releases, we computed the achieved tension change in either the sMCL or LCL between the *Overstuff Set* and *Release Set 1*. We then used the difference between the intended tension changes (*Overstuff Set* - *Reference TKA Set*) and achieved tension changes to inform how many releases iterations *Release Set 2* should have. For example, if an overstuffed model had 60 N of excessive tension and the released model now had 40 N of excessive tension (i.e., 20 N reduction), we determined we would need three times as many releases for *Release Set 2*.

Finally, in each model set, we performed forward dynamic simulations (OpenSim JAM) of passive flexion from 0° to 90° of knee flexion and clinical V-V laxity exams (±10 Nm) at 0°, 45°, and 90° of knee flexion. We computed the differences in compressive contact forces, V-V laxities, and ligament tensions between the four model sets.

RESULTS

In the experimental portion, the slack length of both the MCL and LCL increased linearly with increasing numbers of punctures (0.5 ± 0.2% and 1.0 ± 0.7% after 50 punctures, respectively) (**Figure 2a**). Additionally, the stiffness of both the MCL and LCL decreased linearly with increasing numbers of punctures (-50.4 ± 18.4% and -48.0 ± 28.1% after 50 punctures, respectively) (**Figure 2b**).

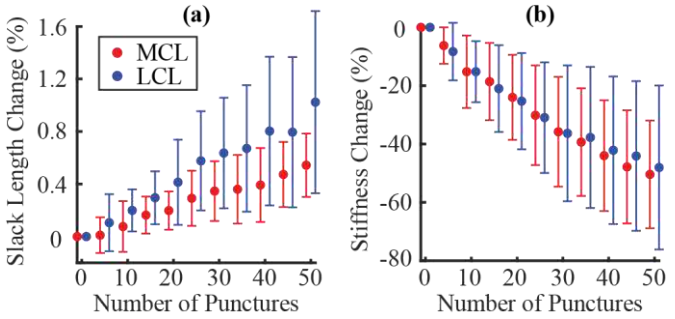

Figure 2: Mean (points) and standard deviation (error bars) show the ex vivo changes in (a) slack length and (b) stiffness.

Computationally, ligament releases decreased the median contact forces by as much as 42% in the medial overstuffed models and 24% in the lateral overstuffed models (**Figure 3a-b**). Additionally, ligament releases increased the median laxity up to 88% in the medial models and 54% in the lateral models (**Figure 3c-d**).

DISCUSSION

The ***key finding of the experimental portion*** of this study was that releases of the MCL and LCL caused coupled increases in slack length and decreases in stiffness. These results agree with a previous study that found similar trends in the MCL of human cadaveric knees [4]. Therefore, these property changes of ligaments should be considered in studies consisting of modeling TKA since releases are routinely performed. In addition, similar to the previous study, we found large

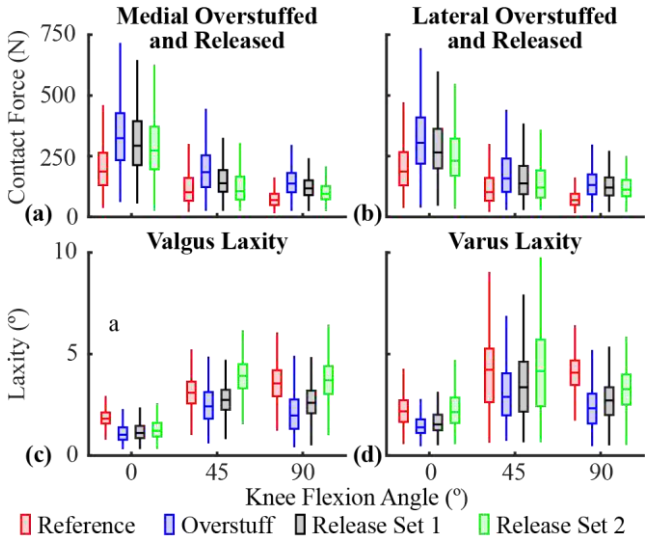

Figure 3: Boxplots show modeling results for (a) medial and (b) lateral contact forces and (c) valgus and (d) varus laxity.

variability in the property changes due to releases. Thus, the number of punctures needed to balance a particular knee is highly patient-specific.

The ***key finding of the computational portion*** of the study was that ligament releases decreased contact forces and increased laxity. However, even though the excessive ligament tension was reduced to approximately zero (median LCL and sMCL tensions were within -6.3 to 10.4 N of reference tensions during passive flexion after *Release Set 2*), contact forces and laxities were not necessarily restored back to the reference values (**Figure 3c-d**). Thus, if surgeons are using laxity assessments to determine the optimal balance of the knee [3], achieving a desired laxity may leave ligament tensions and/or contact forces too high. For example, *Release Set 2* restored varus laxity at 0° of knee flexion (median laxity difference of 0.04° compared to reference), but did not restore the compressive contact force, with a median excess of 44 N. This may lead to residual stiffness or pain in the joint, causing discomfort for the TKA patient. Therefore, laxity assessments alone may not be sufficient to identify overly tight ligaments or elevated contact forces in a TKA knee. Additional measures of biomechanics (e.g., ligament tension measured by a tensiometer [6]) may be necessary to achieve optimal soft tissue balance.

One main limitation of our study is that we did not account for the variability in ligament property changes due to releases (**Figure 2**) in our computational study. However, accounting for this variability was unnecessary to show how coupled changes in the ligament properties due to releases affected laxities, contact forces, and ligament tensions.

In conclusion, this study integrated experimental and computational approaches to show that assessments of ligament balance using V-V laxities might not identify overly tight ligaments and elevated contact forces. Therefore, assessments more specific to the ligaments being released [6] may be necessary to achieve optimal soft tissue balance, and in turn, high patient satisfaction and function.

ACKNOWLEDGEMENTS

NIH (R21 EB024957), UW-Madison Department of Orthopedics

REFERENCES

[1] Gu, Y et al., *JBJS*, 96: e101, 2014. **[2]** Whiteside, L et al., *J Arthroplasty*, 17: 23-27, 2002. **[3]** Elmasry, S et al., *Clin Orthop Relat Res*, 480: 1604-1615, 2022. **[4]** Amundsen, S et al., *J Arthroplasty*, 33: 2636-2639, 2018. **[5]** Smith, C et al., *J Biomech Eng*, 138: 2016. **[6]** Blomquist, M et al., *JOR*, 41: 524-533, 2021.

PARAMETRIC INVESTIGATION OF A BIOPRINTED PULSATILE FONTAN CONDUIT

Zinan Hu (1), Jessica E. Herrmann (2), Erica L. Schwarz (3), Fannie M. Gerosa(4) ,Nir Emuna (3), Jay Humphrey (3), Tain-Yen Hsia (5), Mark A. Skylar-Scott (6), Alison L. Marsden (1,4,6)

(1) Department of Mechanical Engineering, Stanford University, Stanford, CA, USA
(2) School of Medicine, Stanford University, Stanford, CA, USA
(3) Department of Biomedical Engineering, Yale University, New Haven, USA
(4) Department of Pediatrics, Stanford University, Stanford, CA, US
(5) Arnold Palmer Hospital for Children, Orlando, USA
(6) Department of Bioengineering, Stanford University, Stanford, USA

INTRODUCTION

The Fontan operation has become a standard surgical palliation for patients born with functionally univentricular hearts, enabling them to live with a unique circulatory configuration where systemic and pulmonary circulations are arranged in series [1]. As of 2020, it was estimated that around 50,000 patients worldwide live with a Fontan circulation [2]. While short-term outcomes following the Fontan surgery have improved over time, long-term outcomes remain less favorable, with a survival rate of only 74% over a 20-year period [3]. The absence of a subpulmonary pump in this circulation leads to increased central venous pressures in the range of 10 to 15 mm Hg — up to three times the normal range —and a decrease in cardiac output, which are associated with numerous morbidities including exercise intolerance, protein-losing enteropathy, liver fibrosis, and heart failure [4]. The introduction of an additional power source to the pulmonary circulation may be necessary to alleviate the elevated central venous pressure and improve long-term outcomes for Fontan patients.

With rapid recent advancements in three-dimensional bioprinting technology, we propose a bioprinted pulsatile conduit, constructed from induced pluripotent stem cells, as a promising functional power source. This approach offers significant advantages over traditional mechanical devices, particularly for pediatric patients, as it could potentially grow with the patient and circumvent complications associated with blood-contacting foreign materials. However, bioprinting large-scale tissues remains an expensive and complex process. Computational modeling emerges as a vital tool in this context, providing an efficient pathway for performance evaluation and design space exploration. Using a multiphysics computational framework that integrates active stress and fluid-structure interaction, coupled with a 0D closed-loop Lumped Parameter Network (LPN) representing the Fontan circulation, we evaluate the efficiency of the pulsatile conduit by investigating variations in contraction duration, fiber direction, pumping mechanisms, and valve placement. This approach aims to discern the respective impacts and identify the most favorable design configuration.

METHODS

Based on the standard Gore-Tex graft used in the Fontan surgery, our baseline design is a straight cylinder with a height of 75 mm, an inner radius of 10 mm, and a thickness of 4.4 mm. The fluid-structure interaction simulation of the conduit considers both the structural domain of the cylinder and the fluid domain contained within. All simulations are performed using the svFSI finite element solver provided by the open-source software SimVascular [5].

For the structural wall, Holzapfel's orthotropic material model is used to represent the anisotropic nonlinear material behavior [6] and fiber directions are generated. We approximate the time-resolved active fiber stress function τ (t) along the fiber direction using a linear model [7]. This profile resembles a triangular shape, where the ascending phase encompasses 60% of the total duration time T_d and the descending phase takes up the remaining 40%. The equation for τ (t) is

$$\tau(t) = \begin{cases} \frac{5}{3} \cdot \sigma_{peak} \cdot \frac{t - t_s}{T_d}, & if\ t_s \le t \le t_s + 0.6T_d; \\ \frac{5}{2} \cdot \sigma_{peak} \cdot \frac{t_s + T_d - t}{T_d}, & if\ t_s + 0.6T_d \le t \le t_s + T_d; \\ 0, & otherwise. \end{cases} \quad (1)$$

The parameter σ_{peak} is the maximum active tension and t_s denotes the starting time of contraction. We have set σ_{peak} at 65 kPa to reflect the contractility of an adult left ventricle [7]. At the inlet and outlet of the structural domain, homogeneous Dirichlet boundary conditions are applied, ensuring that the ring-shaped outlets can expand within their planes while being restricted in their axial motion. On the outer wall, a Robin-type boundary condition is employed to simulate the support provided by external tissues.

In the fluid domain, the blood is modeled as an incompressible, Newtonian fluid with density and viscosity given by 1060 kg/m^3 and 0.004Pa · s, respectively. A 0D closed-loop LPN is implicitly coupled to the 3D fluid domain as boundary conditions to model the whole

Fontan circulation [8]. The parameters in the LPN were tuned to match the clinical data from a Fontan patient with elevated central venous pressure elevated of 16.2 mmHg. To promote unidirectional blood flow, we incorporate valves with a 0D resistive immersed surfaces valve model at the outlet and a 0D valve at the inlet.

In this study, our baseline model features fibers with a 30° helix angle, and the contraction duration, T_d, spanning 60% of the cardiac cycle. We then modify this model by shortening the contraction duration to 20% for the fast case, adjusting the helix angles to 0° to simulate a purely circumferential contraction, and varying the starting time spatially, t_s, to create a peristaltic-like compression wave. Additionally, the impact of incorporating valves at both the inlet and outlet is assessed. Through exploring these design parameters, we identify a favorable design that can significantly lower the central venous pressure.

RESULTS

The performance of the conduit was primarily evaluated by the reduction in liver (central venous) pressure obtained from the LPN, and we found this metric to be comprehensive, as a decrease in liver pressure correlates with elevated pulmonary artery pressure, enhanced stroke volume, and improved cardiac output. Table 1 summarizes the simulation results for each design parameter.

Table 1. Simulation results highlighting the hemodynamic of various contraction durations, fiber directions, pumping mechanisms, and valve placements. (Pliver = mean liver pressure [mmHg], Psvc = mean SVC pressure [mmHg], Ppul = mean pulmonary artery pressure [mmHg], SV = Stroke Volume [mL], CO = Cardiac Output [L/min]).

	Pliver	Ppul	Psvc	SV	CO
Contraction Duration					
Normal	7.2	18.4	20.7	13.2	2.9
Fast	5.0	20	22.4	15.8	3.2
Fiber Direction					
Torsional	7.2	18.4	20.7	13.2	2.9
Circumferential	6.2	19.2	21.5	13.5	3.0
Pumping Mechanism					
Peristaltic	10	16.7	18.8	13.5	2.7
Favorable Design					
Fast+Circumferential	3.3	21.2	23.6	14.5	3.4
Valve Placement					
No Inlet Valve	12.2	14.7	12.2	18.2	2.3
No Outlet Valve	14.5	13.6	15.6	29.6	2.3
No Valve	16.5	11.0	13.0	25.6	1.8

Reducing the contraction duration from 60% to 20% of the cardiac cycle, while keeping the shape and contractility constant, significantly lowers the liver pressure to 5.0 mmHg. Since the SVC connects to the pulmonary artery, the SVC pressure is correspondingly increased to 20.7 mmHg. For fiber orientations, the circumferential contraction proves to be more effective, reducing liver pressure by an extra 1 mmHg with a similar stroke volume. Contraction patterns within the conduit can be non-uniform. A common approach is peristalsis, initiating contraction at the bottom and progressing to the top, with other parameters matching the baseline model. Compared to uniform contraction, the peristaltic pump produces a less pronounced pressure gradient, but it exhibits a more gradual increase and sustains over an extended duration. It reduces liver pressure to 10 mmHg, which is less effective than the uniform pumping mechanism.

The results from exploring various design factors indicate that the most favorable conduit design combines a fast contraction profile with circumferential fiber orientation. This configuration notably reduces liver pressure to 3.3 mmHg, increases cardiac output by 59%, raises pulmonary pressure to 21.2 mmHg, and elevates SVC pressure to 23.6 mmHg.

In all valve scenarios, removing valves leads to worsened hemodynamics. Without the inlet valve, significant backflow hinders forward flow. The removal of the outlet valve further reduces performance, dropping liver pressure to just 14.5 mmHg. Removing both valves adversely impacts hemodynamics, causing recirculation near the inlet and outlet, increasing blood volume in the conduit, and significantly enlarging stroke volume.

Overall, our results show a linear inverse relationship between increases in SVC pressure and decreases in liver pressure, primarily influenced by the conduit's geometry. With a consistent geometry, any design changes that keep SVC pressure below 20 mmHg result in a liver pressure around 8.8 mmHg.

DISCUSSION

Using a computational framework, we investigate the impact of different pulsatile conduit designs on Fontan patients' hemodynamics. The favorable design identified can successfully reduce the liver pressure to 3.3 mmHg and increase the cardiac output by 59%. Our study highlights the positive pressure gradient across the conduit as a key indicator of energy transfer efficiency from the structural wall to blood flow. Due to the straight tube design, any pressure increase causes the outlet valve to open, so that blood flows downstream before contraction is fully developed. Shortening contraction duration from 60% to 20% proves beneficial in this context. In this design, the limited time available for a pressure gradient to develop may be attributed to the straight tube geometry; this underscores the importance of exploring alternative geometries in future studies.

The efficiency of pumping is also influenced by the fiber orientation. We found that the conduit with circumferential fiber orientation performs better, which contrasts with the twisting motion seen in the human ventricle. This twist is vital that enables to expel 60-70% of its volume with only 10-20% shortening of myocardial fibers. This difference may stem from boundary conditions that restrict length change. Since torsional motion inherently involves length shortening, our study may not fully capture the associated volume changes. Another important factor is the difference in geometry. The ventricle is cone-shaped, with both inlet and outlet on the same side, necessitating a 180-degree turn of blood flow within the chamber. In contrast, the cylindrical conduit has no angle change between inlet and outlet, making circumferential contraction potentially more efficient. Future studies should include a comprehensive analysis of fiber directions to determine optimal structures.

A potential limitation of the proposed design is the elevation of SVC pressure. While SVC hypertension is generally regarded as more tolerable than central venous hypertension, its long-term clinical implications are yet not fully understood. Our study indicates that using a cylindrical geometry inevitably leads to SVC hypertension. Future research should explore the placement of a valve between the SVC and pulmonary artery, as well as alternative connection configurations, to address this issue.

ACKNOWLEDGEMENTS

The authors would like to thank the Additional Ventures Foundation Cures Collaborative Grant for support of this research.

REFERENCES

[1] F. Fontan and E. Baudet, *Thorax*, 1971.
[2] L. Plappert, et al., *Advances in Therapy*, 2022.
[3] T.E. Downing, et al., *The J of thorax and cardiovascular surg*, 2017.
[4] M. Gewillig, et al., *Heart,* 2016.
[5] A. Updegrove, et al. *Annals of biomedical engineering*, 2017.
[6] G.A. Holzapfel, et al., *Phil Transactions of the Royal Society A*, 2009
[7] F. Regazzoni, et al., *PLoS computational biology*, 2020.
[8] E. L. Schwarz, et al., *NPJ Regenerative Medicine*, 2021.

CARDIAC-INDUCED BRAIN TISSUE MOTION IN CHIARI MALFORMATION TYPE 1 AND ITS RELATIONSHIP TO: SURGERY, CROWDING, AND SYMPTOMATOLOGY

M. Karamzadeh (1), M. Al Samman (1), C. MacLellan (2), R. Bhadelia (2), A. Ebrahimzadeh (2), J. Oshinski (3), F. Loth (1)

(1) Bioengineering, Northeastern University, Boston, MA, USA
(2) Radiology, Beth Israel Deaconess Medical Center & Harvard Medical School, Boston, MA, USA
(3) Radiology & Imaging Sciences, Emory University School of Medicine, Atlanta, GA, USA

INTRODUCTION

Chiari Malformation type 1 (CMI) is radiologically defined as the decent of the cerebellar tonsil below the McRea line by more than 5mm [1]. The problem with this definition is that it poorly correlates with symptoms and is not predictive posterior fossa decompression (PFD) surgery outcomes [2]. Previous studies have shown that biomechanical parameters such as tissue motion differ between CMI and controls, and that brain tissue motion is more pronounced in CMI compared to healthy controls [3, 4].

In this study, we calculated brain tissue motion during a cardiac cycle for CMI subjects, assessed the displacement of patients after surgery, and compared it with their pre-surgical motion. Furthermore, we examined the relationship between brain tissue motion, specific symptomatology, and tonsillar descent.The goal of this study is to assess the relationship between tissue motion and CMI severity.

METHODS

The study participants, 48 adult CMI subjects (9 males and 39 females), had Phase Contrast Magnetic Resonance Imaging (PCMRI) at Beth Israel Deaconess Medical Center, Boston. 22 out of 48 patients underwent PFD surgery. Among the patients who underwent surgery, only eight had PCMRI scans after the procedure. All patients completed a questionnaire about their symptoms before surgery. These symptoms included cough-associated headache (CAH) (with vs. without = 34:17), neck pain (25:23), paresthesia (26:22), muscle weakness (5:43), dizziness (22:26), vomiting (8:40), problems with coordination and fine motor skills (7:41), hearing problems or tinnitus (6:42), vision problems (14:34), insomnia (5:43), and depression (7:41).

PCMRI scans were conducted using 1.5 or 3T MRI scanner (GE HDxT). These scans provided data about cerebrospinal fluid (CSF) and brain tissue motion during one cardiac cycle, acquired by ensemble averaging over many heartbeats. The images were retrospectively gated with a velocity encoding (VENC) set to 2 cm/s. For each patient, there were 31 phases during the cardiac cycle, with each phase consisting of one-component of velocity (superior-inferior direction) of 512×512 pixels in the midsagittal plane.

A MATLAB-written code was used to analyze the velocity data. Three different brain regions were investigated. These regions are: the cerebellum, the pons, and the medulla (Figure 1).

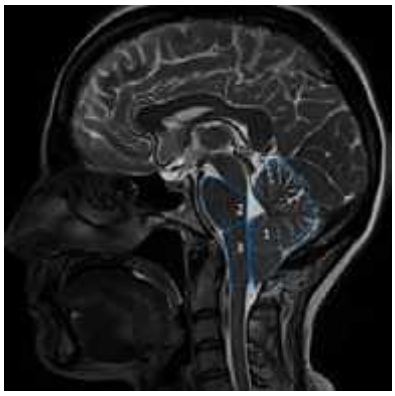

Figure 1. Three regions of interest (ROI) for displacement analysis: 1) cerebellum, 2) pons, 3) medulla

A mask was generated to segment the ROI to include brain tissue only. The velocity over the cardiac cycle for that mask was obtained. Figure 2 is an example of segmentation of the ROI.

By integrating the velocity on each ROI, the spatialy average displacement over the cardiac cycle was derived. Maximum displacement was calculated by subtracting the minimum position from the maximum position. Moreover, the spatially averaged tissue motion within a circle of diameter 5 mm was used to represent the maximum displacement within an ROI of each structure.

Cerebellar tonsillar position (TP) was measured and compared with the motion of the brain tissue. Furthermore, the displacement of the brain tissue was compared with the symptoms of the patients to identify any potential relationship between the motion and the symptoms.

Figure 2. Each region was segmented on the PCMRI image. Cerebellum is shown here

RESULTS

The displacement of brain tissue in eight patients was measured both pre-and post-surgery. There was a significant decrease in the maximum displacement in the cerebellum and medulla after surgery, 337 to 171 µm, p = 0.012 and 363 to 202 µm, p = 0.038, respectively. Figure 2 illustrates the distribution of displacement in the brainstem and cerebellum of one example CMI patient before (a and b) and after (c and d) surgery.

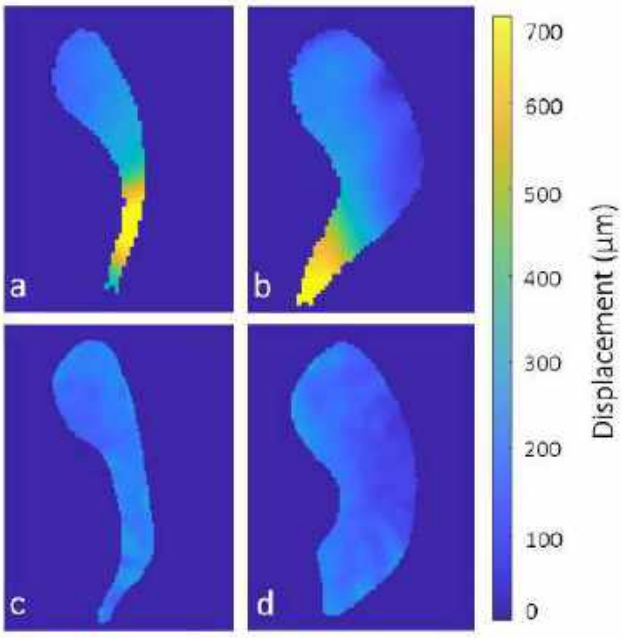

Figure 3. Example of displacement in a CMI subject before and after surgery: (a) brainstem before, (b) cerebellum before, (c) brainstem after, and (d) cerebellum after.

TP for all the patients (n=48) was measured and correlated with the brain tissue motion. TP exhibited a positive correlation with displacement in the cerebellum (r=0.52, p=0.004) and medulla (r=0.49, p=0.009).

No significant relationship was found between any of the examined symptoms. Although the CAH group has a greater motion on average, p-values comparing the two groups were not significant.

The displacement between the group that underwent surgery and the group that did not undergo surgery was compared, but no significant difference was observed.

DISCUSSION

Many researchers have examined brain tissue motion in CMI patients [2, 4-6]. Eppelheimer et al. and Radmanesh et al. demonstrated a significant decrease in tissue displacement in the cerebellum and brainstem after surgery [7, 8]. Eppelheimer et al. use Displacement Encoding with Stimulated Echoes (DENSE) MRI while Radmanesh et al. used trueFISP (fast imaging with steady-state free precession) to measurement brain tissue displacement. Our results demonstrated a similar pattern in decreasing displacement after surgery using PCMRI for the measurement. Our results showed that PCMRI can identify similar trends compared to DENSE and trueFISP which is interesting given the wider accessibility of PCMRI. It should noted that the displacement in the pons did not show statistically signficanant difference after surgery, only the medulla showed this difference. Considering that the increasing herniation of the cerebellar tonsil results in crowdedness at the foramen magnum, cerebellar and medullary motion increases with greater neural crowdedness. This result matching the finding by Mohsenian et al. which showed good correction between resistance to CSF motion and brain tissue displacement [5].

Our results also indicate that there is no relationship between the brain tissue motion and symptoms examined. Similarly, Eppelheimer et al., Al Samman et al., and Dawes et al. did not find a relationship between brain tissue motion and CMI symptomatology [4, 6, 7]. A study by Collin's et al. did find a significant different in tonsillar motion and snoring [9]. Our study did not examine snoring. However, Collin's et al. did not find a significant difference for balance and neck pain which were examined in the present study. Our findings in addition to previous work by others using different methodology and CMI subjects implies that tissue motion is not related to CMI symptomatology which is an important finding towards understanding the pathophysiology of CMI.

No significant difference was observed in the displacement between the surgical and non-surgical groups for any of the examined brain regions. It is important to note that the decision to have surgery or not depends on the patient's choice and factors like pain tolerance which explain the lack of difference between these two groups.

ACKNOWLEDGEMENTS

This work has been funded by Conquer Chiari, the National Institutes of Health, NINDS R15 (Grant No. 1R15NS109957-01A1), and National Center for Advancing Translational Sciences of the National Institutes of Health under award number UL1TR002378.

REFERENCES

[1] A. Elster et al. Radiology, 183, no. 2, pp. 347-353, 1992.
[2] C. Huang, et al. Neuroradiology, 62, no. 5, pp. 593-599, 2020.
[3] B. Lawrence et al. World Neurosurgery,116, pp. E298-E307, 2018.
[4] B. Dawes et al. World Neurosurgery, 130, pp. E74-E81, 2019.
[5] S.Mohsenian et al. Neuroradiology, 65, no. 10, pp.1535-1543, 2023.
[6] M. Al Samman et al. Cerebellum, Nov 7, 2023.
[7] M. Eppelheimer et al. Radiology, 301, no. 1, pp. 187-194, 2021.
[8] A. Radmanesh, et al. Neuroradiology, 57, no. 4, pp. 387-393, 2015.
[9] R. Collins et al. World Neurosurg, 168, pp. e518-e529, 2022.

CHARACTERIZATION OF FAILURE IN CEREBRAL ANEURYSM STENTING

Reza Bozorgpour (1), Pilhwan Kim (1), Peter Tze Man Kan (2), Mahsa Dabagh (1)

(1) Department of Biomedical Engineering, University of Wisconsin-Milwaukee, WI, USA
(2) Department of Neurosurgery, The University of Texas Medical Branch, TX, USA

INTRODUCTION

Intracranial aneurysms involve weakened areas of brain blood vessels that can form sacs filled with blood. When these aneurysms rupture, they cause subarachnoid hemorrhages, a life-threatening condition affecting around 30,000 individuals annually in the United States. Common treatments include surgical clipping and endovascular coiling, while flow diversion devices (FDD) offer a newer alternative. FDDs are fine-mesh tubular stents that restrict blood flow into an aneurysm, potentially altering blood flow patterns. Analyzing the blood flow's hemodynamics inside aneurysms can identify specific parameters, aiding in predicting favorable patient responses to stenting and understanding why some aneurysms grow, an undesirable outcome. This research examines eight patients post-stenting, analyzing fluid simulations using Lattice Boltzmann Method (LBM) D3Q27 via C++ programming in conjunction with Paraview software for visual hemodynamic analysis. By comparing hemodynamics and treatment response, crucial parameters such as wall shear stress and blood flow velocity distribution within aneurysms can be identified to predict stenting success in patients. The aim is to establish new criteria by monitoring aneurysm growth over time, distinguishing between stable and growing aneurysms. Approximately 6.5 million Americans have unruptured brain aneurysms, and annually, 30,000 experience rupture. Early detection is challenging due to lack of symptoms, making it difficult for clinicians to anticipate aneurysm stability or growth. Hence, monitoring aneurysm growth becomes vital for preventing rupture. This study involves reconstructing 3D geometries of aneurysms and parent arteries from patient-specific CT-scans. Pulsatile blood flow simulations within these 3D models quantify hemodynamic characteristics.

METHODS

The methodologies employed encompass several key elements:

Lattice Boltzmann Method (LBM)

LBM simulations progress based on the lattice Boltzmann equation [1]. Expressed with the LBM particle distribution function f and employing the single relaxation time (BGK) collision operator, the equation can be formulated separately for each distribution component f_i.

$$f_i(\boldsymbol{X} + \boldsymbol{c}_i, t+1) = f_i(\boldsymbol{X}, t) - \frac{1}{\tau}(f_i(\boldsymbol{X}, t) - f_i^{eq}(\boldsymbol{X}, t)) \quad (1)$$

$$f_i(\boldsymbol{X} + \boldsymbol{c}_i, t+1) = f_i^{eq}(\boldsymbol{X}, t) + (1 - \frac{1}{\tau}) f_i^{neq}(\boldsymbol{X}, t) \quad (2)$$

$$f_i^{neq} = f - f_i^{eq} \quad (3)$$

$$f_i^*(\boldsymbol{X}, t) = f_i^{eq}(\boldsymbol{X}, t) + (1 - \frac{1}{\tau}) f_i^{neq}(\boldsymbol{X}, t) \quad (4)$$

$$f_i(\boldsymbol{X} + \boldsymbol{c}_i, t+1) = f_i^*(\boldsymbol{X}, t) \quad (5)$$

Complex Geometry Handling

Generating uniformly spaced points within complex geometries, as represented by STL files, demands significant time and memory resources due to their intricate nature. The nature of this task entails considerable computational complexity. Additionally, within the LBM, the collision and streaming steps further highlight the need for efficient computational strategies, making MPI (Message Passing Interface) a crucial choice.

In our simulation, the STL file, which serves as a triangulated representation of the complex geometry, is divided across multiple processors to facilitate two distinct yet interrelated processes. Firstly, this distribution aids in efficient collision detection [2] within the

complex geometry. The utilization of MPI optimizes this computation, recognizing the challenge of identifying points within the intricate geometry. To further optimize this process, an Octree [3, 4] data structure is incorporated. This data structure efficiently partitions computations based on spatial hierarchy, significantly improving the collision-detection efficiency within the LBM context.

Post-division, each processor handles its allocated portion of the geometry, conducting collision and streaming operations. The utilization of MPI across various simulation stages, encompassing point generation within complex geometries and the collision and streaming processes in the LBM, yields a unified and highly efficient computational framework. This strategic use of MPI optimizes communication and workload distribution among processors, resulting in enhanced scalability, performance, and overall simulation efficiency. Its application at critical stages significantly accelerates computations while efficiently handling intricate geometries, collision detection, and LBM steps.

Boundary Conditions Implementation

In our simulation, we applied specific boundary conditions to accurately model fluid behavior. The inlet velocity used the Zou-He condition [5], while the walls were set with a bounce-back condition ensuring no-slip behavior. At the outlet, a constant pressure boundary condition was applied. These conditions collectively ensure precise representation of fluid flow dynamics within the computational domain.

Numerical Results

Reconstructed Geometry

In the subsequent section, we implemented the methodology outlined in the preceding section to reconstruct the vasculature and generate the LBM grid points.

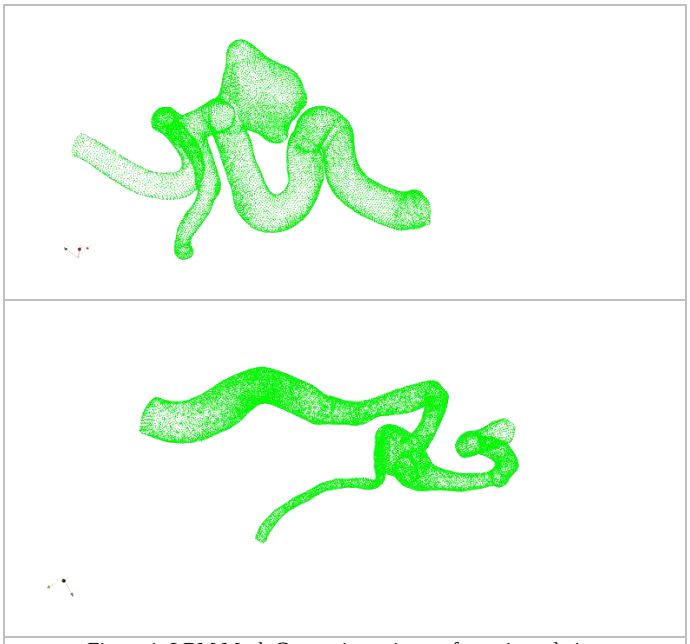

Figure 1. LBM Mesh Generation using surface triangulation

Parabolic Inlet Velocity and Boundary Conditions

In our first test case using cylindrical geometry, we utilized a parabolic velocity profile at the inlet. To accurately represent the inlet flow conditions, we applied the Zou-He boundary condition. This combination enabled precise simulation of fluid flow dynamics within the cylindrical domain.

Pulsatile Flow Simulation

In the subsequent phase, we introduced pulsatile flow within the complex geometry to analyze fluid dynamics. Our focus was on extracting the velocity field and assessing wall shear stress distribution. The aim is to correlate fluctuations in wall shear stress to potential implications for aneurysm growth or post-treatment conditions. This investigation aims to establish connections between fluid-induced mechanical forces, specifically wall shear stress variations, and their possible influence on the progression or alteration of aneurysms, contributing valuable insights into their pathophysiology and treatment outcomes.

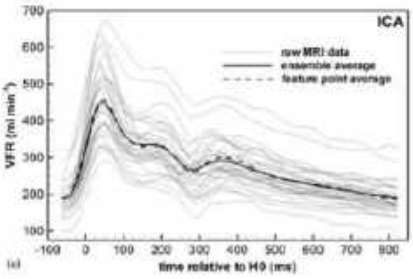

Figure 2. Temporal Profile of Pulsatile Flow: Volumetric flow rate variations over time relative to reference point H0, illustrating the pulsatile nature of fluid dynamics.

Results

In Figure 3, we showcase MPI domain decomposition for collision and streaming steps, with each color denoting a processor. Figure 4 illustrates initial and boundary conditions. Subsequent drafts will feature velocity and WSS distribution.

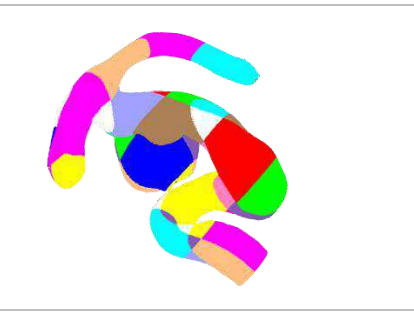

Figure 3. MPI domain decomposition

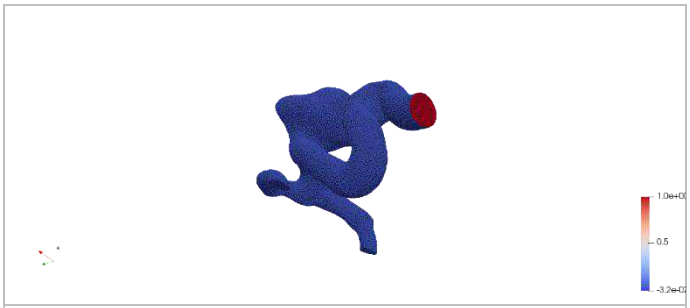

Figure 4: Initial and Boundary Conditions

DISCUSSION

Our study aims to explore the relationship between wall shear stress (WSS) fluctuations and post-stenting aneurysm behavior. Evidence indicates that changes in WSS levels within aneurysms may indicate alterations in their stability or growth after treatment. Elevated or fluctuating WSS has been linked to aneurysm development, while effective treatments seek to reduce WSS by modifying blood flow patterns. Using computational simulations through the Lattice Boltzmann Method (LBM), our objective is to uncover the link between WSS changes and aneurysm response post-stenting. This understanding could assist in predicting treatment outcomes and distinguishing between stable and potentially growing aneurysms. While WSS is crucial, considering other hemodynamic parameters, like flow velocity distribution, will offer a more comprehensive prognosis.

ACKNOWLEDGEMENTS

Acknowledge grant or other funding support or the assistance of others as appropriate.

REFERENCES

1. Krüger, T., et al., *The lattice Boltzmann method*. Springer International Publishing, 2017. **10**(978-3): p. 4-15.
2. Möller, T. and B. Trumbore, *Fast, minimum storage ray/triangle intersection*, in *ACM SIGGRAPH 2005 Courses*. 2005. p. 7-es.
3. Meagher, D.J., *Octree encoding: A new technique for the representation, manipulation and display of arbitrary 3-d objects by computer*. 1980: Electrical and Systems Engineering Department Rensseiaer Polytechnic ….
4. Meagher, D.J., *High-speed image generation of complex solid objects using octree encoding*. 1987, Google Patents.
5. Zou, Q. and X. He, *On pressure and velocity boundary conditions for the lattice Boltzmann BGK model*. Physics of fluids, 1997. **9**(6): p. 1591-1598.

WNT-11 AND SOST ARE REGULATED BY DIFFERENT MECHANICAL STIMULI IN LOADED BONE

Meghana Machireddy[1], Sara Cole[3], Lucas DeBiase[2], Jun Li[4], Sarah Nano[1], Glen L. Niebur[1]

[1]Bioengineering Program, University of Notre Dame, South Bend, Indiana
[2]Aerospace and Mechanical Engineering, University of Notre Dame, South Bend, Indiana
[3]Notre Dame Integrated Imaging Facility, University of Notre Dame, South Bend, Indiana
[4]Department of Applied and Computational Mathematics and Statistics, University of Notre Dame, South Bend, Indiana

INTRODUCTION

Osteoporosis is the most common metabolic bone disease characterized by the degradation of trabecular bone in the spine, proximal femur, and distal radius. Bone adaptation, particularly in response to mechanical loading, is primarily directed by osteocytes, which differentially express several genes in response to mechanical loading [1]. However, the specific mechanical cues osteocytes respond to are unknown. To determine the immediate response of osteocytes to mechanical loading, it is necessary to study the transcriptomic response of osteocytes. We found that SOST is downregulated, and Wnt-11 is upregulated following loading using bulk RNA sequencing [2]. SOST codes for the protein sclerostin which is an antagonist of the Wnt/β-catenin signaling pathway, a major driver of osteoblastogenesis and osteoblast differentiation [3]. Wnt-11 is involved in both canonical and non-canonical Wnt signaling and is necessary for osteoblastogenesis [4]. Trabecular bone is mechanically heterogeneous and there are regions of the bone that experience no strain while other regions experience relatively high strain. Hence, bulk sequencing aggregates the transcriptional response and cannot provide insight into the tissue strains that affect osteocyte gene expression. The goal of this study is to quantify the relationship between gene expression and local tissue strain by spatially mapping expression of Wnt-11 and SOST and finding the strains at the locations of cells that both express and do not express these genes.

METHODS

Cylindrical bone explants (N=8) from the cervical vertebra of mature female pigs were cultured in a bioreactor. Male pigs were excluded because they are typically castrated which could confound result interpretation. After 48h, the explants were subjected to two bouts of 1200 cycles of compressive loading to 196 N with 1 hour between bouts daily for 3 d. In addition, four control samples were cultured without loading. Samples were fixed 6 h after the final load, and were demineralized and embedded in paraffin, and 5 μm thick sections were prepared. The sections were stained using RNAScope Multiplex Kit (ACD, Newark, CA) for SOST and Wnt-11 using custom probes designed by ACD. Random areas covering 15% of the stained sections were imaged at 20x magnification using confocal microscopy (Nikon AXR) (Fig 1A.). Osteocytes were identified using a custom workflow and the intensity of the signal for each probe was measured. Approximately 1000 osteocytes were counted in each sample.

Samples were μ-CT scanned immediately after being removed from the bioreactor and finite element models were created to determine the deviatoric tissue strain corresponding to the measured displacement during loading. The tissue modulus was assigned based on the tissue mineral density [5].

The stained RNAScope labeled sections were aligned to the finite element results (Fig. 1B) to provide a mapping of the locations of the osteocytes and strain at all locations in the bone. We then calculated the mean strain within 10 μm of cells expressing or not expressing each gene in the loaded bone.

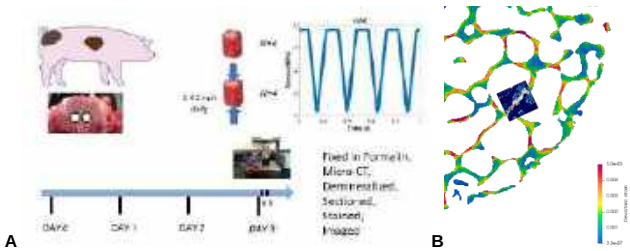

Fig. 1. A) Cervical bone explants were cultured in a bioreactor for 48 h after which samples were compressively loaded to 196 N. 6h after the final load, samples were fixed, μ-CT scanner, demineralized, sectioned, stained, and imaged. B) Histological sections for each gene were aligned to the corresponding location on the finite element model.

RESULTS

Using RNAScope, the intensity of the signal increases with the number of RNA molecules in each cell. The fraction of cells expressing less than

a specified threshold intensity was calculated, and a logistic curve was fit (Fig. 2). More osteocytes expressed SOST at high levels in the unloaded than in the loaded samples. In contrast, more cells expressed Wnt-11 at high levels in the loaded bones (Fig. 2). In order to quantify the difference between the loaded and unloaded groups across all thresholds, we fit a logistic curve to each sample and measured the difference in the characteristics of the curve. For SOST, the symmetric inflection point was significantly different between the loaded and unloaded samples (p=0.017). On the other hand, the threshold decay rate was significantly different for Wnt-11 expression (p=0.042).

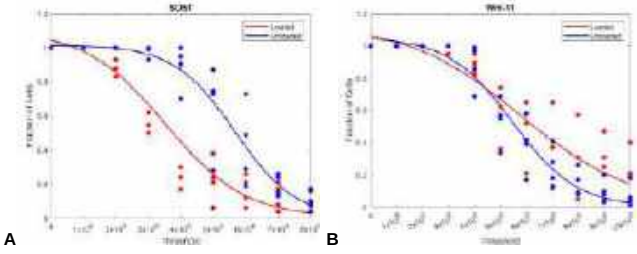

Fig. 2. A) More osteocytes expressed SOST at higher levels in the unloaded compared to loaded samples. B) More osteocytes expressed high levels of Wnt-11 in loaded vs. unloaded samples.

We chose intensity thresholds of $3x10^6$ for SOST and $9x10^6$ for Wnt-11 to differentiate high (+) and low (-) expression. For SOST, this threshold was where the number of cells in the unloaded bone starts to decrease from 100% positive. For Wnt-11, the loaded and unloaded groups did not differ until higher thresholds. We chose a level near the maximum threshold. We first looked at how the expressions of these genes relate to each other. We found that differential expression of Wnt-11 and SOST following loading occurred in different cell populations.

Approximately 80% of the cells that were Wnt-11+ were also SOST+, suggesting that Wnt-11 upregulation is not coincident with SOST suppression. However, 92% and 68% of the SOST+ cells were Wnt11- in the unloaded and loaded bone, respectively (Fig. 3). As such neither upregulated nor downregulated SOST expression implied Wnt-11 upregulation.

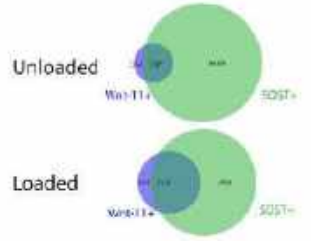

Fig. 3. The Venn diagrams show the fraction of all the cells that highly express Wnt-11 only, SOST only, or both Wnt-11 and SOST.

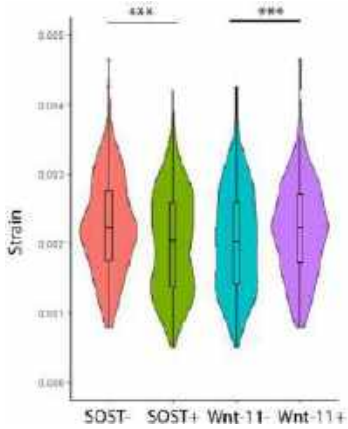

Fig. 4. The average strain near SOST- cells was higher than the strain near SOST+ cells while the average strain near Wnt-11+ cells was higher than the average strain near Wnt-11- cells (*** p<0.0005).

Lastly, we found the mean strain within 10 μm of each osteocyte (Fig. 4). The average strain near SOST- cells was 2254 ±689 με vs. 2009 ±731 με (mean ± S.D.) in SOST+ cells ($p < 0.0005$). In contrast, the average strain near Wnt-11- cells (2037±742 με) was lower than that near Wnt-11+ cells (2181±659 με) ($p < 0.0005$). The strain near SOST- cells was also significantly greater than the strains near Wnt-11+ cells ($p = 0.015$), while there was no difference in the average strain surrounding SOST+ and Wnt-11- cells.

DISCUSSION

The goal of this study was to investigate the spatial heterogeneity of the transcriptional response of osteocytes during mechanical loading. We identified subsets of osteocytes where the differential expression of SOST and Wnt-11 was consistent with bulk sequencing results [2]. However, the differential gene expression was not uniform. We found that most Wnt-11+ cells are also SOST+, but the majority of SOST+ cells are not Wnt-11+. However, the strain associated with Wnt-11+ cells was higher than that surrounding SOST+ osteocytes, on average (p=0.015), yet lower than SOST- osteocytes. This suggests that the conditions for Wnt-11 upregulation in response to mechanical loading differ from those for SOST downregulation. For example, Wnt-11 regulation may depend on the volumetric strain or combinations of strain measures. Indeed, the heterogeneity of the strain surrounding both SOST- and Wnt-11+ cells suggests that deviatoric strain is a weak indicator of osteocyte response.

Our study is unique in that we quantified the range of gene expression in individual cells and identified the strain in the tissue surrounding our cells of interest. This allowed us to capture strain and location dependence of gene expression that cannot be detected by bulk sequencing. However, our results may be sensitive to the threshold chosen for differential expression. RNAscope probes tag individual molecules, resulting in a gradient of fluorescence as the number of transcripts increases. We chose thresholds based on levels that ensured a difference in the fraction of positive cells between the loaded and unloaded bone. For SOST, this occurred at a low threshold and most cells were SOST+ in both loaded and unloaded bone. On the other hand, Wnt-11 expression only differed between loaded and unloaded bone at high thresholds. Further analysis with different thresholds is important to quantify the sensitivity.

Our study complements a recent study that measured the spatial expression of SOST and CTSK in cortical bone [6]. They found that the largest changes in the expression of these genes occurred in the regions of bone with the highest deformation. We similarly found that strain was higher surrounding osteocytes with differential SOST and Wnt-11 expression relative to unloaded bone.

Mechanical loading does not result in a uniform differential expression of all genes in osteocytes. Rather, differential gene expression varies based on the local mechanical environment, which in turn could drive spatially heterogeneous bone adaptation and paracrine effects in the local marrow resident cells.

ACKNOWLEDGEMENTS

This research was supported by the U.S. NIH AR075937

REFERENCES

[1] Schaffler MB, et. al, Calcif Tissue Int, 2014 94(1):5-24;
[2] Machireddy M, et. al, Bone, 2024 (accepted)
[3] Delgado-Calle J, et. al, Bone. 2017 96:29-37
[4] Caetano da Silva C, et. al. Hum Mol Genet. 2022 31(10): 1622-1634
[5] Hernandez CJ, et. al. Bone. 2001 29(1):74-8
[6] Chlebek C, et al. J Bone Miner Res. 2022 37(11):2277-2287

A HUMAN ORGANOID MODEL OF TRAUMATIC BRAIN INJURY

S. Shiravi (1), A. Yufa (1), M. Quezada Valladares (2), C. K. Franz (3, 4), J. D. Finan (1)

(1) Department of Mechanical and Industrial Engineering, University of Illinois at Chicago, Chicago, Illinois, USA
(2) Department of Biomedical Engineering, Northwestern University, Chicago, Illinois, USA
(3) Shirley Ryan Ability Lab, Northwestern University, Chicago, Illinois, USA
(4) Departments of Physical Medicine and Rehabilitation, and The Ken & Ruth Davee Department of Neurology, Northwestern University Feinberg School of Medicine, Chicago, IL, USA

INTRODUCTION

Traumatic brain injury (TBI) is a major cause of death and disability worldwide. In 2014, 2.53 million emergency visits, 288,000 hospitalizations, and 56,800 deaths related to TBI were documented in the United States by the Center for Disease Control [1]. Even mild TBI increases the risk of neurodegenerative disorders such as Parkinson's [2] and Alzheimer's disease [3]. Some important questions about species-specific and genotype-specific pathology in TBI are difficult to address with conventional rodent models. Human induced pluripotent stem cell (hiPSC) derived brain organoids have the potential to address these questions because they reproduce human pathophysiology and allow precise manipulation of the genotype [4]. Here we mechanically compressed brain organoids at strain magnitudes and rates relevant to clinical TBI and measured the resulting pathology.

METHODS

Cortical organoids were cultured from WTC11 hiPSCs (GM25256, Coriell) for 83 days before injury. Organoids from the same batch were fixed using 4% PFA on day 60 and sectioned for quality control purposes. Sections were mounted on glass slides and stained with MAP2 and S100B to identify mature neurons and glial cells, respectively. The custom injury device includes a stainless-steel indenter mounted on a vertically moving stage driven by a voice coil under closed-loop feedback control (Fig. 1). The injury device was used to measure organoid heights. The zero position was defined as the position at which the indenter was directly in contact with an empty chamber's bottom surface. Organoids were then placed in the chambers and their heights were calculated as the difference between the zero position and the position at which the indenter contacted the organoid. After height measurement, organoids were dynamically compressed between a fixed stage and the indenter. Organoids were compressed by 15, 25, 35 or 45% of their initial height and released in a period of 30 milliseconds. For the sham injury procedure, organoids were contacted but not compressed. Mitochondrial membrane potential was assayed using 3D confocal microscopy and tetramethylrhodamine methyl ester perchlorate (TMRM) staining. TMRM is a cell-permeable, positively charged small molecule stain that accumulates in healthy mitochondria. Injured and sham organoids were stained with 100nM TMRM 3 hours after trauma and incubated at 37°C for 1 hour. A series of fluorescence images were acquired using the 3D Z-stack feature of an Olympus FV3000 confocal microscope. Captured images were projected into a single plane for analysis. Projected images were segmented and analyzed using CellProfiler software to measure the mean intensity of TMRM fluorescence in each organoid.

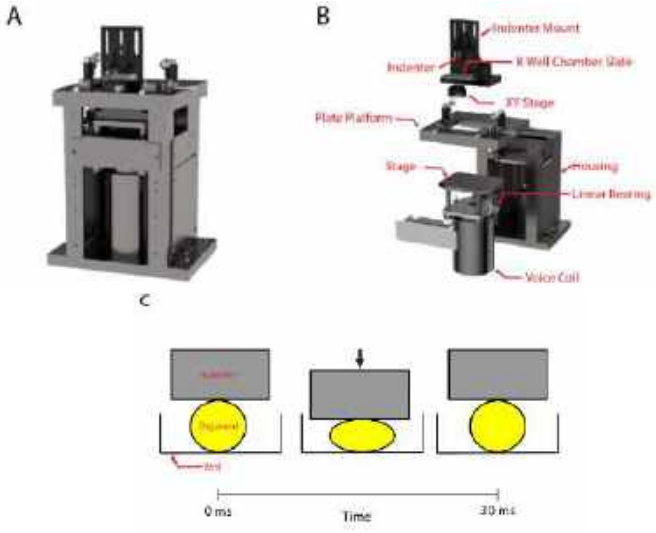

Figure 1: (A) Custom-built injury device. (B) Exploded view of custom-built injury device. (C) Schematic of the sequence of events during injury.

Supernatant was collected from individual organoid-containing wells and NF-L concentration was measured using an ELISA assay.

RESULTS

Organoids stained positive for MAP2 and S100B, indicating the presence of mature neurons and glial cells. (Fig. 2)

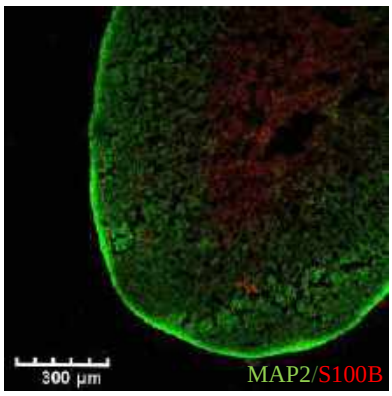

Fig.2: Organoid section stained positive for MAP2 and S100B.

The fluorescent TMRM signal declined steadily with increasing trauma severity (Fig. 3).

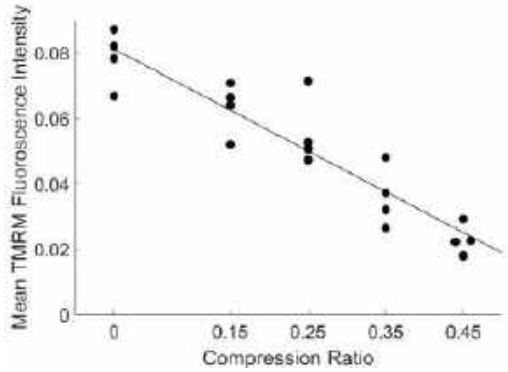

Fig. 3: Linear regression of the effect of various levels of trauma on TMRM fluorescence intensity (R^2=0.856). Compression ratio represents the percentage reduction in the initial height of organoids subjected to compression.

The injury protocol increased the concentration of NF-L in the culture media (Fig. 4). However, there was no clear dependence of NF-L concentration on trauma severity. The absolute concentration of NF-L was low and close to the bottom end of the standard curve used for quantification, suggesting that the volume of cell culture media was greater than the ideal value.

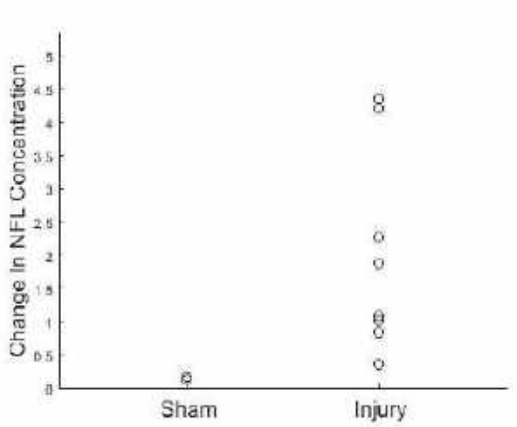

Fig.4: The effect of trauma on NF-L concentration.

DISCUSSION

Dynamic compression of organoids *in vitro* reproduced several important phenotypes of clinical TBI. It disrupted mitochondrial function in a dose-dependent manner (see Fig. 2), consistent with prior studies in other *in vitro* models [5], small animal models [6], and in human subjects [7]. Mitochondrial dysfunction appears to mediate vulnerability to subsequent head impacts after TBI [8]. We also observed post-traumatic mitochondrial dysfunction in an earlier version of the model that did not normalize compression to the initial height of the organoid. However, the data was more variable in that case [4], suggesting that normalizing the compression to the height improves consistency. Although we did not observe a linear relationship between NF-L concentration and trauma severity, the increased NF-L concentration in the trauma group raises the exciting possibility of using clinically validated TBI biomarkers [8, 9] as outcomes in drug discovery studies employing traumatized human cortical organoids.

ACKNOWLEDGEMENTS

This work was supported by the National Institutes of Health (R01NS113935).

REFERENCES

1. Capizzi, A., et al, M. Traumatic Brain Injury. Med. Clin. North Am. 104, 213–238 (2020)
2. GARDNER, R, et al., Ann Neurol, 77, 987-95, 2015.
3. BARNES, D. E et al., JAMA Neurol, 75, 1055-1061.
4. Shoemaker, A. R. et al.. Dis. Model. Mech. 14, dmm048916 (2021).
5. ELLIS, E. F et al., 1995. J Neurotrauma, 12, 325-39.
6. REN, Y. Z et al., 2020. J Neurochem, 154, 530-546.
7. AYGOK, G. A et al., 2008. Acta Neurochir Suppl, 102, 57-61.
8. Reed G. Selwyn, Sean J et al., http ://doi.org/10.1089/neu.2015.4129
8. DEWITT, D. S et al., 2018. 35, 2737-2754
9. SHAHIM, P et al., 2017. Neurology, 88, 1788-1794.

A HUMAN ORGANOID MODEL OF TRAUMATIC BRAIN INJURY

S. Shiravi (1), A. Yufa (1), M. Quezada Valladares (2), C. K. Franz (3, 4), J. D. Finan (1)

(1) Department of Mechanical and Industrial Engineering, University of Illinois at Chicago, Chicago, Illinois, USA
(2) Department of Biomedical Engineering, Northwestern University, Chicago, Illinois, USA
(3) Shirley Ryan Ability Lab, Northwestern University, Chicago, Illinois, USA
(4) Departments of Physical Medicine and Rehabilitation, and The Ken & Ruth Davee Department of Neurology, Northwestern University Feinberg School of Medicine, Chicago, IL, USA

INTRODUCTION

Traumatic brain injury (TBI) is a major cause of death and disability worldwide. In 2014, 2.53 million emergency visits, 288,000 hospitalizations, and 56,800 deaths related to TBI were documented in the United States by the Center for Disease Control [1]. Even mild TBI increases the risk of neurodegenerative disorders such as Parkinson's [2] and Alzheimer's disease [3]. Some important questions about species-specific and genotype-specific pathology in TBI are difficult to address with conventional rodent models. Human induced pluripotent stem cell (hiPSC) derived brain organoids have the potential to address these questions because they reproduce human pathophysiology and allow precise manipulation of the genotype [4]. Here we mechanically compressed brain organoids at strain magnitudes and rates relevant to clinical TBI and measured the resulting pathology.

METHODS

Cortical organoids were cultured from WTC11 hiPSCs (GM25256, Coriell) for 83 days before injury. Organoids from the same batch were fixed using 4% PFA on day 60 and sectioned for quality control purposes. Sections were mounted on glass slides and stained with MAP2 and S100B to identify mature neurons and glial cells, respectively. The custom injury device includes a stainless-steel indenter mounted on a vertically moving stage driven by a voice coil under closed-loop feedback control (Fig. 1). The injury device was used to measure organoid heights. The zero position was defined as the position at which the indenter was directly in contact with an empty chamber's bottom surface. Organoids were then placed in the chambers and their heights were calculated as the difference between the zero position and the position at which the indenter contacted the organoid. After height measurement, organoids were dynamically compressed between a fixed stage and the indenter. Organoids were compressed by 15, 25, 35 or 45% of their initial height and released in a period of 30 milliseconds. For the sham injury procedure, organoids were contacted but not compressed. Mitochondrial membrane potential was assayed using 3D confocal microscopy and tetramethylrhodamine methyl ester perchlorate (TMRM) staining. TMRM is a cell-permeable, positively charged small molecule stain that accumulates in healthy mitochondria. Injured and sham organoids were stained with 100nM TMRM 3 hours after trauma and incubated at 37°C for 1 hour. A series of fluorescence images were acquired using the 3D Z-stack feature of an Olympus FV3000 confocal microscope. Captured images were projected into a single plane for analysis. Projected images were segmented and analyzed using CellProfiler software to measure the mean intensity of TMRM fluorescence in each organoid.

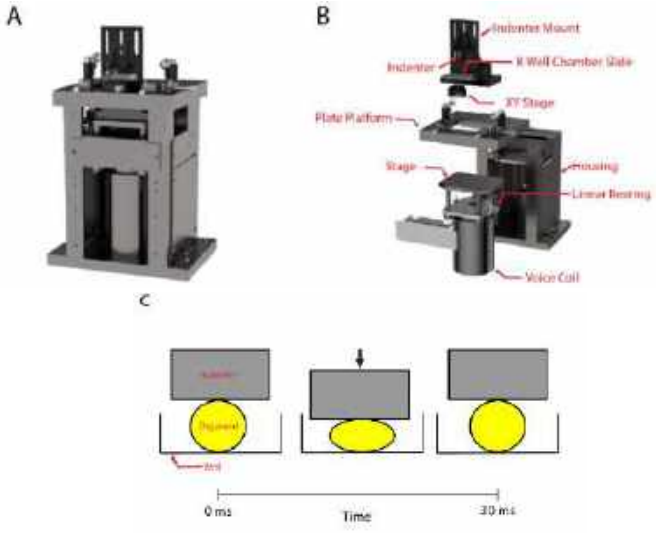

Figure 1: (A) Custom-built injury device. (B) Exploded view of custom-built injury device. (C) Schematic of the sequence of events during injury.

Supernatant was collected from individual organoid-containing wells and NF-L concentration was measured using an ELISA assay.

RESULTS

Organoids stained positive for MAP2 and S100B, indicating the presence of mature neurons and glial cells. (Fig. 2)

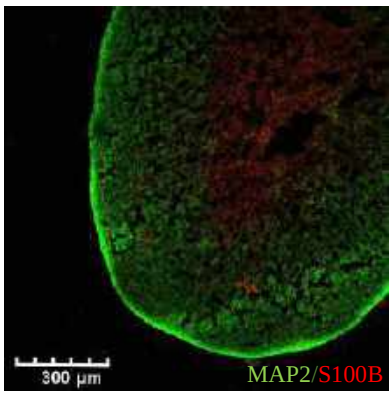

Fig.2: Organoid section stained positive for MAP2 and S100B.

The fluorescent TMRM signal declined steadily with increasing trauma severity (Fig. 3).

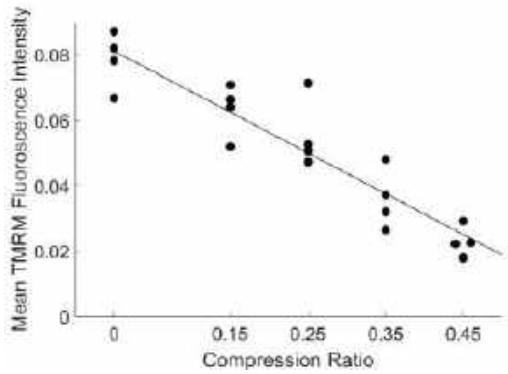

Fig. 3: Linear regression of the effect of various levels of trauma on TMRM fluorescence intensity (R^2=0.856). Compression ratio represents the percentage reduction in the initial height of organoids subjected to compression.

The injury protocol increased the concentration of NF-L in the culture media (Fig. 4). However, there was no clear dependence of NF-L concentration on trauma severity. The absolute concentration of NF-L was low and close to the bottom end of the standard curve used for quantification, suggesting that the volume of cell culture media was greater than the ideal value.

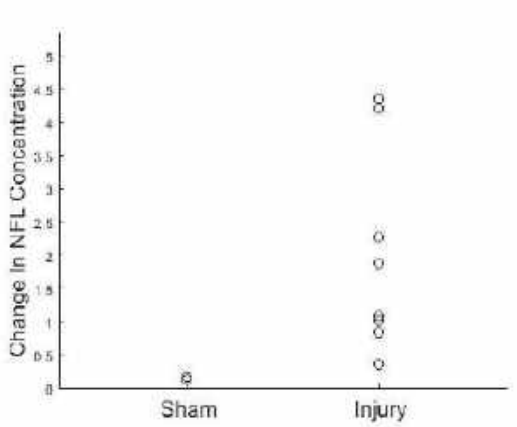

Fig.4: The effect of trauma on NF-L concentration.

DISCUSSION

Dynamic compression of organoids *in vitro* reproduced several important phenotypes of clinical TBI. It disrupted mitochondrial function in a dose-dependent manner (see Fig. 2), consistent with prior studies in other *in vitro* models [5], small animal models [6], and in human subjects [7]. Mitochondrial dysfunction appears to mediate vulnerability to subsequent head impacts after TBI [8]. We also observed post-traumatic mitochondrial dysfunction in an earlier version of the model that did not normalize compression to the initial height of the organoid. However, the data was more variable in that case [4], suggesting that normalizing the compression to the height improves consistency. Although we did not observe a linear relationship between NF-L concentration and trauma severity, the increased NF-L concentration in the trauma group raises the exciting possibility of using clinically validated TBI biomarkers [8, 9] as outcomes in drug discovery studies employing traumatized human cortical organoids.

ACKNOWLEDGEMENTS

This work was supported by the National Institutes of Health (R01NS113935).

REFERENCES

1. Capizzi, A., et al, M. Traumatic Brain Injury. Med. Clin. North Am. 104, 213–238 (2020)
2. GARDNER, R, et al., Ann Neurol, 77, 987-95, 2015.
3. BARNES, D. E et al., JAMA Neurol, 75, 1055-1061.
4. Shoemaker, A. R. et al.. Dis. Model. Mech. 14, dmm048916 (2021).
5. ELLIS, E. F et al., 1995. J Neurotrauma, 12, 325-39.
6. REN, Y. Z et al., 2020. J Neurochem, 154, 530-546.
7. AYGOK, G. A et al., 2008. Acta Neurochir Suppl, 102, 57-61.
8. Reed G. Selwyn, Sean J et al., http ://doi.org/10.1089/neu.2015.4129
8. DEWITT, D. S et al., 2018. 35, 2737-2754
9. SHAHIM, P et al., 2017. Neurology, 88, 1788-1794.

THE POMELO PEEL AS IMPACT PROTECTION FROM FALL-RELATED FEMUR FRACTURE: MECHANICAL AND BIOLOGICAL PROPERTY INVESTIGATION

Stacey L. Zeigler (1), Benjamin J. Ellis (2), Daniel T. Fuller (3), Laurel Kuxhaus (2)

(1) Biology Department, Clarkson University, Potsdam, NY, USA
(2) Mechanical and Aerospace Engineering, Clarkson University, Potsdam, NY, USA
(3) Mathematics Department, Clarkson University, Potsdam, NY, USA

INTRODUCTION

Falls from a standing height are the most common mechanisms of injury for the older adult population with hip fracture from fall being a leading cause of morbidity and mortality [1,2]. Wearable hip pad protection has been recommended to prevent fracture from falls [3] but use has been limited due to wearability and efficacy issues [4]. There is a need to do better. Natural materials may offer properties that can overcome the barriers of current hip protection. The pomelo (*citrus maxima*) peel is a naturally available foam-like material that is renowned for its ability to dissipate large amounts of energy from impact [5]. The purpose of our work is to examine natural and synthetic impact resistant materials through cross-disciplinary experimentation to establish material characteristics most valuable for hip fracture prevention from a fall.

METHODS

Testing included two mechanical (drop weight impact testing, compression creep testing) and two biological (scanning electron microscopy, proteomic analysis) assessments of the pomelo peel, with comparison to select market-available hip impact protectors.

Impact testing: A customized Dynatup 8250 Drop Weight Impact Tester was calibrated to meet the Canadian Standards Association Hip Protector Z325:20 testing standard (CSA, 2020) [6], designed to meet the impact force and velocity specifications expected from a sideways ground level fall of an older adult (2500-3000 N, 2.9-3.2 m/s). The assembly was used to test 16 materials (fall-related hip protectors, sport hip protectors, and pomelo peel). The attenuated peak force (APF) was calculated through equation (1) [6]:

$$APF = (1-(Fp/Fb)) \times 100 \quad (1)$$

[Where Fp = average over the three trials in peak recorded force for a given specimen; Fb = average over the two confirmatory trials in the peak recorded force with no specimen]

Creep testing: Uniaxial, direct load compression creep testing was performed utilizing a Bourns Series 3048 linear potentiometer, a flat 7 mm diameter indenter stabilized by linear bearings, and a voice coil actuator applying a 1N constant force at 20 Hz sampling rate. A single exponential model of analysis was applied to the creep testing data to establish the elastic deformation, viscous deformation, and a time constant. From these variables, viscous stiffness (2) and viscosity (3) were calculated:

$$k = f/\delta \quad (2)$$

[Where k = stiffness (N/m); f = force (N); δ = deformation of the test specimen (m)]

$$\eta = \tau \cdot \kappa_2 \quad (3)$$

[Where η = viscosity (Ns/m); τ = time constant (s); κ_2 = viscous stiffness (N/m)]

Scanning electron microscopy: Finite element scanning electron microscopy (FESEM) imaging was performed on samples of the surface, internal, and cross sections of each experimental material with a JEOL JSM-7900 FESEM. Pomelo samples were chemically dried prior to imaging. Quantitative comparison of surface and internal cell number fraction with micropores, mean cell size, and cell volume fraction for each material was established with ImageJ software. Correlation analyses and t-tests were performed.

Proteomic analysis: Consistent with a bottom-up proteomics approach [7], protein isolation, gel electrophoresis, and mass spectrometry (MS) were used to isolate and identify proteins in the pomelo peels of two pomelo. These methods established the pomelo proteome, with specific examination for the presence of elastomeric proteins within the peel.

RESULTS

Force Attenuation: Peak force reductions of 32.7%, 28.5%, and 20.1% were achieved by the best performing fall hip pad, sport hip pad, and pomelo peel, respectively. As a biologic material, pomelo peel was

expected to, and did, demonstrate considerable within-category standard deviation, although synthetic material categories of fall and sport hip padding showed variances within the same range as pomelo (Figure 1).

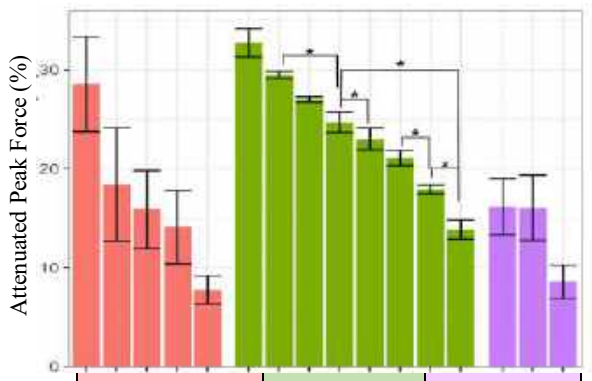

Category	Sport Padding	Fall Padding	Pomelo Peel
Variety (count)	Fig. skate (2), Jr. Hockey(2), Jr. Football(1)	Soft shell hip pads (8)	All red, source (3)
Samples	10	22	9
APF (%)	17.24	24.04	10.78
St. Dev. (%)	7.86	5.77	4.37

Figure 1: Attenuated peak force comparison by category. Error bars indicate APF standard deviation (%). Significance within category materials noted by '*' for $p<0.05$.

As the fall hip padding category had the greatest number of materials with high APF capacity, investigation for viscoelastic properties and cell structure characteristics preceded inclusion of that from other material categories (Table 1).

Table 1: Top APF fall hip padding multiple variable examination. Pearson correlation statistic (r=coefficient; p=significance)

n=6	Stiffness (N/m)	Viscosity (N*s/m)	Cells with micro-pores (%)	Mean cell size (µm)	Cell volume fraction (%)
r	-0.280	0.853	0.708	0.577	0.625
p	0.591	0.031	0.116	0.231	0.185

Stiffness/Viscosity: Viscous stiffness of fall hip padding materials demonstrated a weak inverse correlation to APF but a strong and significant direct correlation with viscosity (Table 1.) Within pomelo peel samples, both viscosity and stiffness have strong and significant correlations to APF (r=-0.99,p=0.04; r=0.99,p=0.05, respectively). Using t-testing to compare the highest APF pomelo peel and fall hip pads, a significantly higher stiffness in the pomelo material is demonstrated ($p<0.001$) while viscosity difference is not significant (p=0.15, power =.84).

Cell Morphology: Internal SEM imaging of synthetic fall hip padding samples demonstrated moderate positive correlations between cell fraction with micropores, mean cell size, and cell volume fractures compared with APF material performance (Table 1). Observational comparison of a pomelo peel with a fall hip pad sample revealed substantial differences in overall morphology and cell variability (Figure 2). The pomelo demonstrates a highly porous, strut laden structure while the hip pad provides a typical image of a compact open cell foam structure with observable micropores.

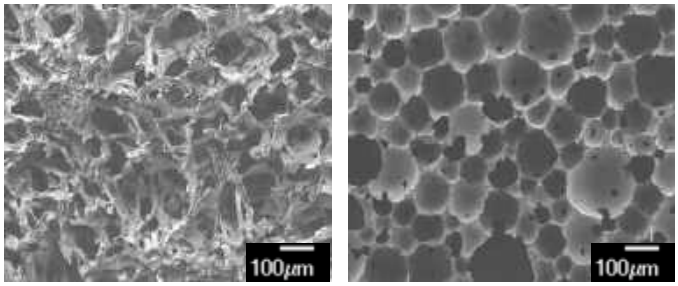

Figure 2: SEM micrographs of internal samples of pomelo peel (*left)* and a fall hip pad (*right)*.

Proteomics: SDS-PAGE gel with Coomassie staining of two domestic (U.S.) pomelo peels yielded generalized visualization of proteins including protein existence in the range for elastomeric proteins (11.5-60 kDa). There was no evidence of elastomeric proteins within the pomelo peel when run against the citrus database nor with specific search for known elastomeric protein sequencing.

DISCUSSION

This work demonstrated that the pomelo peel performs comparably to currently available synthetic hip padding. The biologic and structural reasons for its impact resistance are informative for their differences from existing materials. For example, while viscous stiffness was only very weakly correlated with hip pad APF, it was strongly correlated for pomelo peel. This suggests that there are structures of the pomelo that are designed to manage stiffness for an impact resistance advantage. Further, while all materials examined in this study are porous, pomelo differs substantially demonstrating 'struts' (similar to trabeculae in cancellous bone) suggestive of another potentially advantageous padding advancement.

This work reveals that the differences between biologic and synthetic materials may be the key to a superior material design for impact resistance. The pomelo peel could inform hip fracture prevention from falls and thereby be lifesaving by preventing injury.

Further work includes full analysis of the pomelo peel from SEM imaging, optical microscopy to examine the pomelo peel in its natural, hydrated form, and detailed characterization of the pomelo peel's strut framework.

ACKNOWLEDGEMENTS

The authors acknowledge the support of the NIH (NIBIB, Award Number R25EB033080.) Many thanks to Drs. Arthur Michalek and Costel Darie, along with Danielle Whitman and Kimberly Collins, for their expertise and support.

REFERENCES

[1] Spaniolas K, et al., *J Trauma*. 2010;69(4):821-825.
[2] Bhattacharya B, et al., *Injury*. 2016;47(9):1955-1959.
[3] CDC. *Home and Recreational Safety.* 2017.
[4] Santesso N, et al., *Cochrane Database.* Issue 3, 2014.
[5] Fischer SF et al. 2010. *Adv. Eng. Mater*. 12:B658-6.
[6] National Standard of Canada: *Hip Protectors – CSA Z325:20*. CSA Group, Ontario Canada. 2020.
[7] Darie, C.C., & Woods, A.G. *Advancements of mass spectrometry in biomedical research* (2nd ed.). Springer Publishers. 2019.

REDUCED LOADING AFTER SCIATIC NERVE RESECTION IMPAIRS HINDLIMB GROWTH AND MATURATION

Talayah A. Johnson (1), Natalie Fogarty (1), Alisia Lin (1), Tonia K. Tsinman (1), Xi Jiang (1), Eiki Koyama (3), Lin Han (2), Josh R. Baxter (1), Joel D. Boerckel (1), Robert L. Mauck (1), Nathaniel A. Dyment (1).

(1) McKay Orthopaedic Research Laboratory, University of Pennsylvania, Philadelphia, PA, USA
(2) Drexel University, Philadelphia, PA, USA
(3) Children's Hospital of Philadelphia, Philadelphia, PA, USA

INTRODUCTION

Mechanical forces during growth and development are vital for musculoskeletal tissue formation and maturation. Load bearing tissues such as tendons respond to mechanical cues to maintain "tensional homeostasis." For example, tenocytes respond to altered loading by fine tuning the formation and degradation of extracellular matrix proteins [1]. Similarly, reduced loading can increase bone resorption while decreasing formation [2]. Both excessive and insufficient loading are implicated in the disease etiology of musculoskeletal tissue. Manipulation of mechanical loads through implementation of rehabilitative loading exercises promotes repair processes that may culminate in improved restoration of normal structure and function [3]. Understanding the role of mechanical loading on developmental processes of load bearing tissues can improve our understanding the mechanosignaling events that drive tissue formation and maturation while potentially providing insights to guide new therapies.

Growth of load bearing tissues is predominantly governed by cell proliferation and extracellular matrix (ECM) production. For instance, rapid tissue growth occurs in early postnatal stages and this period is when growth can shift from cell proliferation dominant to matrix production dominant, especially in tendons. Here, we performed sciatic nerve resection (SNR) in both neonatal mice (surgery performed on postnatal day 1) and adult mice (surgery performed at 22 weeks of age) (**Fig. 1)** to explore how reduction in loading impacts the growth and maintenance of hindlimb load bearing tissues. Performing SNR in neonates and adults allows us to explore the age-related differences in response to mechanical loads and investigate the mechanisms behind these differences.

We hypothesized that reduced mechanical loading of the hindlimb after SNR would impair both the growth and maintenance of load bearing tissues. The reduced input in neonates will lead to attenuated growth whereas reduced loading in adults will lead to tissue resorption.

METHODS

All animals and procedures were approved by UPenn's IACUC. Unilateral left sciatic nerve resection (SNR) was performed as previously reported by our group [4] in neonate (postnatal day 1, P1) and adult (22-week-old) male and female mice. Gait Analysis. Video gait analysis was used to measure gait parameters at P14 in the neonate group and 14 days after injury (D14) in the adult group. MicroCT. Excised hindlimbs from each group of mice were scanned on a Scanco μCT45 scanner to measure tibial bone parameters. Because of difficulty in measuring bone parameters in P14 mice, limbs from the neonate group were scanned at only P42 whereas adult limbs were scanned at both D14 and D42. Cryohistology. Hindlimbs were harvested, formalin-fixed, embedded in OCT, and cryosectioned (8 μm) in the transverse plane using Cryofilm 2C. Fluorescent imaging with a nuclear counterstain followed by brightfield imaging with toluidine blue staining was performed. Image Analysis. Achilles tendon cross-sectional area and cell density were quantified using Fiji. Statistics. Gait parameters between SNR and control groups were compared via one-way ANOVA with Tukey's HSD post-hoc comparisons ($p<0.05$). SNR limb vs. contralateral limb were compared via paired t-tests for all other assays ($p<0.05$).

RESULTS

Neonatal and Adult SNR impaired gait. Video gait analysis 14 days after SNR (P14 and D14) was used to assess changes in gait parameters that would inform hindlimb loading patterns. SNR limbs exhibited sustained gait perturbations compared to contralateral limbs, including reduced paw print width (a hallmark of sciatic denervation) reduced ankle angle at both paw strike and lift off, and reduced distance from the hock to the ground (hock height) at lift off ($p < 0.01$, **Fig. 2**). These impairments persisted to later time points as well (data not shown).

Neonatal SNR altered Achilles tendon morphometry and mechanical properties. Neonatal SNR significantly decreased Achilles

tendon cross sectional area (CSA) at P14 and P42 ($p<0.05$, $p<0.01$, **Fig. 3A**) with reduced the total number of cells per cross section ($p<0.05$) and an increasing trend in cell density ($p=0.08$). SNR had much less of an effect in adults with only decreasing trends in cells per cross section and cell density at D42 ($p=0.07$, $p=0.09$, **Fig. 3B**).

Neonatal and Adult SNR altered bone morphogenesis. As SNR has been shown previously to affect bone growth, we quantified both trabecular and cortical bone morphometry in the tibia [5]. Neonatal SNR reduced trabecular bone volume fraction (BV/TV) and trabecular thickness ($p<0.05$, **Fig. 4A**) in the proximal metaphysis and reduced cortical polar moment of inertia (**Fig. 4B**) at P42. These data correspond with reduced tibia lengths reported by our group previously [4].

Adult SNR reduced BV/TV, BMD, trabecular number, and trabecular thickness, at both D14 and D42 ($p<0.05$, **Fig. 5A**). Adult SNR did not alter cortical bone parameters at D14, but significantly reduced cortical area and cortical thickness by D42 ($p<0.05$, **Fig. 5B**).

DISCUSSION

Here, we demonstrate that disruption of ambulatory mechanical loading by sciatic nerve resection alters tendon and bone morphogenesis in both neonatal and adult mice. The reduced hindlimb loading affected postnatal growth and adult tissue maintenance in the Achilles tendon and tibia. Neonatal SNR reduced Achilles tendon cross-sectional area and cells per cross section within 14 days, indicating that mechanical loading directs postnatal tendon growth. However, SNR in adults only led to trends in these parameters, suggesting that adult tendons may be less sensitive to the decreased loading from SNR compared to the rapidly growing neonates. As de-tensioning can lead to a catabolic tissue response [6], future work will investigate this mechanism at both ages. The differential effects of loading on tissues were also exemplified in the micro CT data. The reduced trabecular and cortical properties in the Neonate SNR group was likely a result of reduced growth. While the reduced bone volume in the Adult SNR group was likely a result of bone resorption, which we are in the process of analyzing via dynamic histomorphometry. We found differences in the onset of bone loss between trabecular and cortical bone, as trabecular bone is typically more sensitive to altered loading.

Given the results of this study, there are open questions related to the differential response between neonate and adult tissues. The matrix turnover rates are known to be different in both tissues between postnatal growth and adult homeostasis, which may contribute to the ability of these tissues to respond to the altered loading. In addition, the required mechanical inputs required for growth may be quite different than those in homeostasis. Future work will investigate the mechanosignaling events that regulate matrix assembly/turnover in this model system as elucidating these specific mechanisms can provide insights into rehabilitation strategies to treat injuries and disease.

ACKNOWLEDGEMENTS

This work was supported by NIH R01 AR075418 and P30 AR069619.

REFERENCES

[1] Wang JH, *J Biomech*. 2006; [2] Weinreb M, *Bone*, 1989; [3] Langberg H, *J Phys*. 1999; [4] Fogarty NL, *JOR*, 2023; [5] Killion CH, *Mol. Biol. Cell*. 2017; [6] Jones D, *Proc Natl Acad Sci*, 2023.

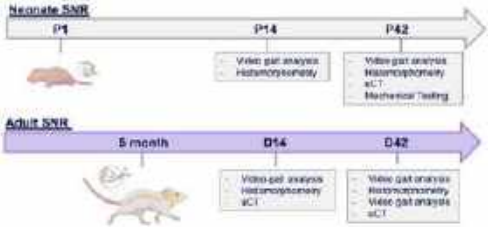

Figure 1: Experimental design

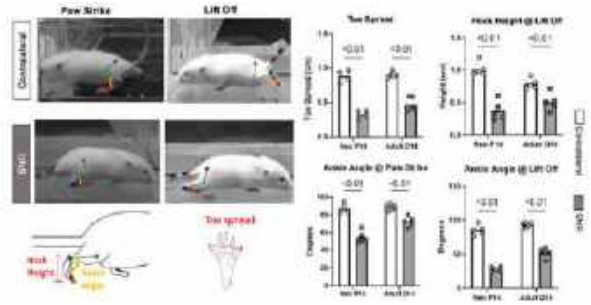

Figure 2: Video gait analysis at P14 and D14 comparing SNR operated limbs to contralateral controls. SNR yielded reduced toe spread and altered ankle flexion, resulting in the hock being closer to the ground at lift off.

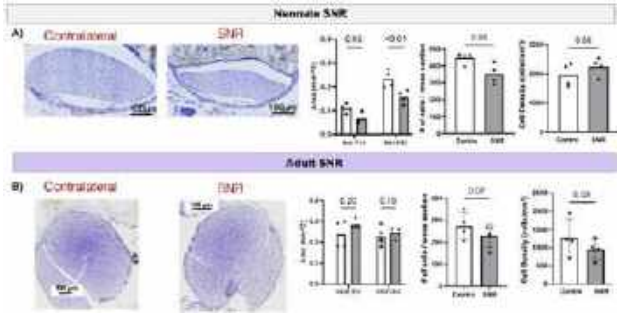

Figure 3: Toluidine blue staining of AT cross sections and corresponding analysis of cross-sectional area, cell count, and cell density following neonatal SNR (A) and (B) Adult SNR groups.

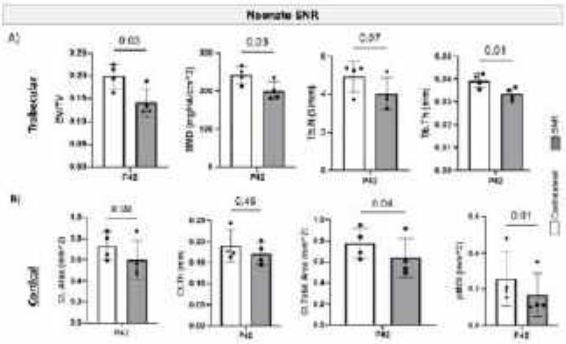

Figure 4: MicroCT tibial analysis following Neonatal SNR demonstrating reductions in trabecular (A) and (B) cortical bone parameters.

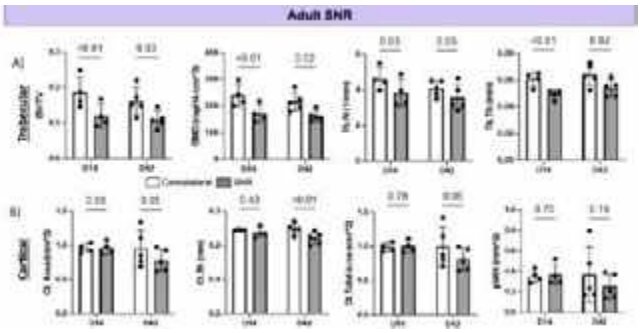

Figure 5: MicroCT analysis at D14 and D42 from Adult SNR group showing reduction in trabecular (A) and B) cortical bone parameters.

RADIATION INDUCES FIBROSIS IN SKIN, BUT THIS INJURY IS MITIGATED IN EXPANDED SKIN

L. Nunez-Alvarez (1), J. Ledwon (2), V. Tac (3), A. Gosain (2), A. Buganza (1,3)

(1) Weldon School of Biomedical Engineering, Purdue University, West Lafayette, Indiana, USA
(2) Feinberg Medical School, Northwestern University, Chicago, Illinois, USA
(3) School of Mechanical Engineering, Purdue University, West Lafayette, Indiana, USA

INTRODUCTION

In the US, breast cancer is the most common new cancer diagnosis among women [1], with approximately 50% undergoing mastectomy [1]. Breast reconstruction surgery (BRS) often involves tissue expansion (TE), where a silicon expander is gradually inflated under the skin, promoting tissue growth. However, when combined with radiotherapy (RT), patients may develop radiation-induced fibrosis (RIF), characterized by increased collagen deposition and tissue stiffening [2]. Unfortunately, there is only superficial knowledge of how dermal collagen architecture and skin mechanical properties change in vivo in the presence of RT and TE. Here, we use the preeminent large animal model for human skin, the swine, to measure skin deformation, growth, change in collagen architecture, and change in mechanical properties in three different skin study groups: control (CTRL), radiated (XR) and radiated and expanded (XRTE) skin.

METHODS

Porcine model

We used three 2-month-old Yucatan pigs for the study. Four grids were tattooed on their backs, and then tissue expanders were inserted underneath each grid (Fig.1A). The expanders were filled twice with 45 cc of a saline solution over 10 weeks. Out of the total 12 grids, 8 were exposed to radiation. We analyzed 3 expanded radiated patches (XRTE), 4 control radiated patches (XR), and 4 control non-radiated patches (CTRL). For radiation protocol, 20 Gy was administered on day 14 after the first inflation in the XR and XRTE groups. The experiment concluded at week 10, the expected RIF timeline for human patients [3].

Mechanical characterization

Upon excision, we tested the skin under biaxial stretching in the Biotester (CellScale, Waterloo, Canada). From these tests, we got characteristic stress-stretch curves of hyperelastic materials (Fig. 1B). In these curves, we defined two stages for a simpler analysis: an initial linear response and the non-linear part of the curve in which the stress increases rapidly. The value in the x-axis that divides both phases is termed the transition stretch (l_T). The tangent modulus for the linear response, "low modulus," and an approximate tangent modulus for the nonlinear response, "high modulus," were also quantified on the stress-stretch data.

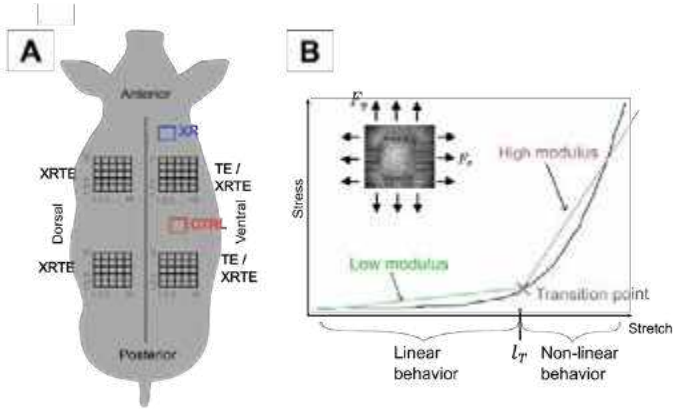

Figure 1: Skin extraction and testing. A) Porcine model. B) Stress-Stretch curve from biaxial mechanical testing.

Image analysis

Histology images of the three different skin groups from two pigs were obtained with Masson's Trichrome technique in which collagen is stained in blue and epithelial cells in red (Fig. 2A). OrientationJ plugin in ImageJ / Fiji software was used to compute orientation distributions of the collagen fibers of each histological image (Fig. 2B). Additionally, we measured coherency with the same plugin, which provided information about the strength of the fiber alignment. Coherency ranges from 0, meaning the fibers are dispersed, to 1, meaning all the fibers nearby follow the same angle [4].

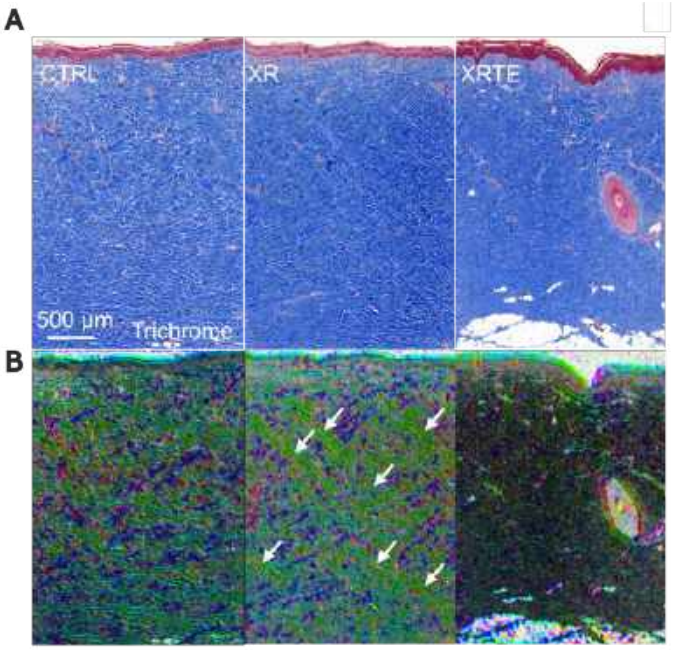

Figure 2: Histological analysis. A) Examples of stained samples with the Masson Trichrome technique. B) Different fiber orientations colored with the OrientationJ plugin of ImageJ / Fiji. Collagen fibers form bundles in XR skin, as shown with arrows.

Model fitting

A hierarchical Bayesian framework was used to estimate the Gasser Ogden Holzapfel (GOH) model parameters [5]. The second Piola Kirchhoff stress fitted was

$$\boldsymbol{S} = -p\boldsymbol{C}^{-1} + \mu\boldsymbol{I} + 2k_{1i}e^{k_{2i}E^2}\boldsymbol{E}[\kappa_i\mathbf{I} + (1-3\kappa_i)\mathbf{M_i}] \quad (1)$$

Where $i = 1,2$, assuming it comprises two groups of fibers distributed in two main orientations. Furthermore, $\mathbf{M_i} = \boldsymbol{a_{Oi}} \otimes \boldsymbol{a_{Oi}}$, with $\boldsymbol{a_{Oi}}$ being the unit vector determined by the angle α_i. Here $\mu, k_{1i}, k_{2i}, \kappa_i$ and α_i were the estimated parameters. We put a prior on the nine parameters and use the experimental stress-stretch data to define a likelihood function. After that, we derive the posteriors of the distributions of the model parameters using Markov-Chain Monte Carlo sampling.

RESULTS

Mechanical characterization

Transition stretch (l_T) was the highest in CTRL skin, considering both test directions (anterior–posterior and dorsal–ventral). In particular, l_T was significantly different between CTRL and both radiated groups, but only in the anterior–posterior direction ($p<0.05$, Dunn test) (Fig. 3A). This means that radiated skin transitions into the nonlinear stiffness regime at smaller stretches in comparison to controls.

Coherency and orientation analysis of histology images

When comparing the mean coherency values between groups, we found a significant difference between CTRL–XR and XR–XRTE ($p<0.05$, ANOVA) (Fig. 3B). When computing the orientation distribution, we found a significant difference between CTRL–XR and XR–XRTE ($p<0.05$, Kolmogorov-Smirnov test). On the other hand, no difference was found between CTRL and XRTE groups (Fig. 3C).

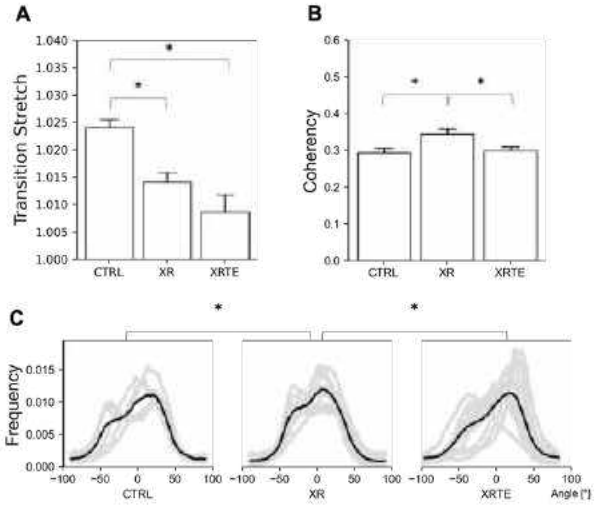

Figure 3: Results from mechanical testing and histological analysis. A) Transition stretch in the anterior-posterior direction (* = $p < 0.05$). B) Coherency (* = $p < 0.05$). C) Orientation distribution of all groups (* = $p < 0.05$).

GOH fitting

We obtained the posterior distribution of the nine parameters for all samples from the Bayesian fitting procedure. The median of each distribution was adjusted to fit the raw data (Fig. 4). The model captures the high modulus with an average error of 5.43%. This is particularly relevant for modeling TE at large stretch values that induce growth.

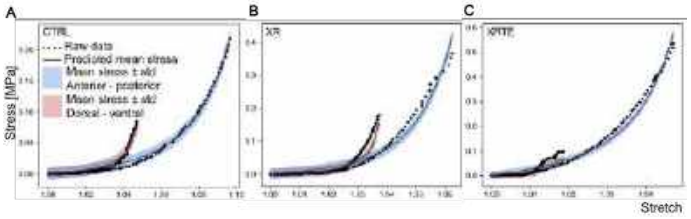

Figure 4: Model fitting for all groups. A) CTRL, B) XR, C) XRTE.

DISCUSSION

Radiated groups XR and XRTE exhibit lower transition stretch l_T, indicating increased skin stiffness due to collagen structural changes, such as bundle formation from cross-linking. This is reflected in high coherency values and less dispersed orientation distributions in radiated skin compared to CTRL and XRTE. Interestingly, CTRL and XRTE show no significant fiber distribution difference, suggesting TE induces fibril disorganization, making collagen structure more akin to normal skin. Unlike previous ones on radiation effects in rats [4], TE-induced changes in porcine models [6], or TE and RT on mouse skin [7], this study uniquely explores the combined effect of TE and RT on an in-vivo model resembling human skin during BRS.

ACKNOWLEDGEMENTS

This work was supported by NIAMS award R01AR074525.

REFERENCES

[1] Fahad, M., *Adv Exp Med Biol*, 1152:51–64, 2019.
[2] Maslennikova, A *et al.*, *Int J Radiat Biol*, 91: 240–247, 2015
[3] Müller, K et al., *Exp Hematol*, 35: 96–104, 2007
[4] Clemons, D et al., *RSC Adv*, 8:9661–9669, 2018.
[5] Gasser, T et al., *Journal of the royal society interface*, *3*:15-35, 2006.
[6] Ledwon, J et al., *Inter Journal of Mol Sciences, 23:13091*, 2022.
[7] Luby, A et al., *Ann Plast Surg*, 85:546, 2020.

POLYCHLORINATED BIPHENLYS ALTER MACROPHAGE POLARIZATION AND PLASTICITY

Riley M. Behan-Bush (1), Jesse N. Liszewski (1), Michael V. Schrodt (1), Aloysius J. Klingelhutz (2), James A. Ankrum (1)

(1) Roy J. Carver Department of Biomedical Engineering, University of Iowa, Iowa City, Iowa, USA
(2) Microbiology and Immunology, University of Iowa, Iowa City, Iowa, USA

INTRODUCTION

Despite being banned, polychlorinated biphenyl (PCB) mixtures produced before 1979, such as Aroclor 1254, can still be found at high levels in the environment and in building materials such as capacitors, transformers, caulk, and more making PCBs ubiquitous in public spaces. Human exposure to PCBs has been linked to an increased risk of heart disease, stroke, and cancer, as well as the development of metabolic syndromes such as obesity, hyperlipidemia, and type II diabetes [1]. Metabolic syndromes are characterized by insulin resistance, dyslipidemia, increased adiposity, as well as systemic and local inflammation [2]. Adipose tissue is comprised of many cell types including adipocytes, adipose mesenchymal stem cells, endothelial cells, and immune cells such as macrophages. Although adipocytes are often the focus of attention, adipose tissue macrophages (ATMs) play an integral role in regulating the inflammatory state of adipose tissue and influencing adipocyte function. During metabolic disease, ATMs shift from an anti-inflammatory, M2-like phenotype toward an inflammatory, M1-like phenotype. This shift initiates a cascade resulting in local and systemic inflammatory responses that exacerbate metabolic disease [3].

Despite the essential role of ATMs in the regulation of adipocyte function and the known accumulation of PCBs in adipose tissue, little is known about how PCBs directly or indirectly affect macrophages. Previous work suggests PCBs increase adipose tissue inflammation [4]. However, this work only investigated whole adipose tissue cytokines and did not elucidate which cells were responsible. Here, we've expanded on these prior studies to assess the effects of the PCB mixture, Aroclor 1254, on macrophages. Since macrophage phenotype is so vital to the health of adipose tissue, we sought to understand whether PCBs impact the polarization and plasticity of M2 macrophages resulting in shift toward a more inflammatory phenotype.

METHODS

Human Monocyte-Derived Macrophage Isolation and Differentiation All macrophages were derived from human monocytes isolated from peripheral blood mononuclear cells (PBMCs). Briefly, PBMCs were isolated from leukocyte reduction cones (LRCs) using Ficoll-gradient centrifugation. Then, the monocytes were isolated from the PBMCs using a MojoSort negative selection kit. Once monocytes were isolated, they were differentiated into macrophages by culturing them in complete RPMI supplemented with 10 ng/mL M-CSF. After 6 days, monocytes were fully differentiated into naïve macrophages.

Macrophage Polarization Naïve macrophages were polarized toward two different M2 macrophage phenotypes – M(IL-4) or M(dex). To polarize macrophages toward an M(IL-4) phenotype, they were cultured in complete RPMI supplemented with 20 ng/mL IL-4 for 48 hours. To polarize macrophages toward an M(dex) phenotype, they were cultured in complete RPMI supplemented with 100 nM dexamethasone for 48 hours.

Macrophage Exposure to PCBs The PCB mixture, Aroclor 1254, was used for all exposures. Briefly, macrophages were exposed to Aroclor 1254 dissolved in DMSO and mixed with low serum RPMI (0.5% FBS) at a nominal concentration of 10 μM. Macrophages exposed to the vehicle, DMSO (1 μL/mL), were used as a vehicle control (VC).

Surface Marker Analysis Macrophage surface markers CD14, CD16, CD86, CD163, and CD206 were analyzed using flow cytometry. Briefly, the macrophages were lifted using a 5 mM EDTA solution with cells on ice. Once collected, the macrophages were stained for cell death using Zombie B550. After cell death staining, the cells were stained with the following anti-human antibodies: CD14-Alexa Fluor 488, CD16-PE-Fire 640, CD86-PerCP-Cy5.5, CD163-PE-Cy7, CD206-PE-Dazzle. After surface marker staining, the cells were washed and resuspended in cell staining buffer before being analyzed by flow cytometry. Cells were gated based on singlet discrimination and negative cell death stain. The median fluorescent intensity (MFI) for each surface marker was used to compare PCB- vs VC-exposed groups.

ELISA The concentration of IL-8 and IL-10 was analyzed using enzyme-linked immunosorbent assays (ELISA). To perform the assay,

media was collected at the end of each experiment. Analysis was performed with Biolegend ELISA kits as described by manufacturer protocols.

RESULTS

PCBs inhibit M(IL-4) and M(dex) polarization In healthy adipose tissue, newly migrated, naïve macrophages polarize toward M2 phenotypes such as M(IL-4) and M(dex). However, it is unknown whether the accumulation of PCBs in adipose tissue would affect this process. Therefore, we wanted to know whether PCBs disrupt M2 macrophage polarization. To do this, we isolated and differentiated naïve monocyte-derived macrophages. Then, we exposed the naïve macrophages to PCBs for 24 hours. After PCB exposure, we differentiated the PCB-exposed macrophages toward an M(IL-4) or M(dex) phenotype. After 48 hours, the macrophages were collected for flow cytometry and the media was collected for cytokine analysis. We found that PCBs altered both M(IL-4) and M(dex) polarization resulting in more inflammatory macrophages. PCB exposure before M(IL-4) polarization resulted in decreased expression of both anti-inflammatory surface markers, CD163 (Fig 1A) and CD206 (Fig 1B). However, there was no change in the inflammatory marker, CD86 suggesting that PCBs do not globally reduce surface marker expression (Fig 1C). Additionally, there was a small, albeit non-statistically significant increase in the inflammatory cytokine, IL-8 (Fig 1D), as well as a statistically significant decrease in IL-10 (Fig 1E). Exposure of M(dex) macrophages to PCBs resulted in a similar fate. M(dex) macrophages had no change in CD86 (1F) but decreased CD163 (Fig 1G) and CD206 (Fig 1H) expression. Additionally, compared to PCB effects on M(IL-4), PCBs resulted in a much larger increase in IL-8 (Fig 1I) as well as a larger decrease in IL-10 (Fig 1J) for the M(dex) cells. These results suggest that PCBs inhibit M2 polarization resulting in a more inflammatory macrophage niche.

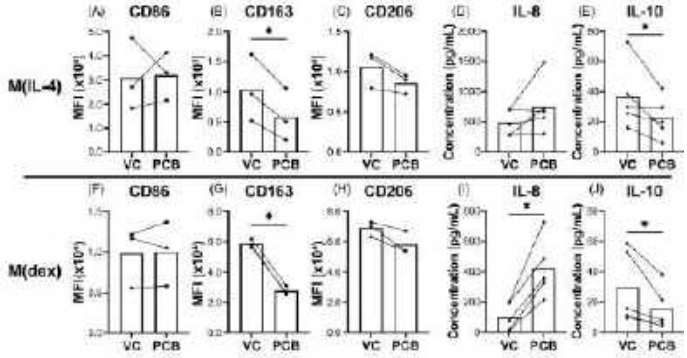

Figure 1: Surface marker and cytokine analysis for PCB exposure before M(IL-4) (A-E) and M(dex) (F-J) polarization. Surface marker analysis: Mean, N=3 donors, paired t-test, * p<0.05. Cytokine analysis: Mean, N=5 donors, paired t-test *p<0.05.

PCBs induce phenotypic plasticity of M(IL-4) and M(dex) macrophages Healthy adipose tissue contains a high number of M2 macrophages. However, macrophages are incredibly plastic. Therefore, they can alter their phenotype in response to environmental stimuli. PCBs can be liberated from adipocytes during lipolysis where they will then encounter mature adipose macrophages. Thus, we wanted to assess whether PCBs will induce phenotypic plasticity of mature M2 macrophages. To do this, we first polarized our monocyte-derived macrophages toward either an M(IL-4) or M(dex) phenotype for 48 hours. Then, we exposed the pre-polarized macrophages to PCBs for 48 hours. Then, we collected the macrophages for flow cytometry and the media for cytokine analysis. We again found that PCBs pushed the macrophages toward a more inflammatory phenotype. M(IL-4) macrophages exposed to PCBs had limited changes in surface marker expression of CD86 (Fig 2A), CD163 (Fig 2B), and CD206 (Fig 1C). However, PCB exposure resulted in a staggering 400X increase in IL-8 secretion (Fig 2D) as well as a significant decrease in IL-10 (Fig 2E). M(dex) macrophages were even more impacted by PCB exposure. Although M(dex) cells didn't have much change in CD86 (Fig 2F), they had a significant change in CD163 (Fig 2G) and CD206 (Fig 2H). Surprisingly, PCB-exposed M(dex) had an even larger change in cytokines with a 1000x increase in IL-8 (Fig 2I) as well as a significant decrease in IL-10 (Fig 2J). These results show that PCBs induce macrophage plasticity and flip anti-inflammatory M2 cells toward an inflammatory phenotype.

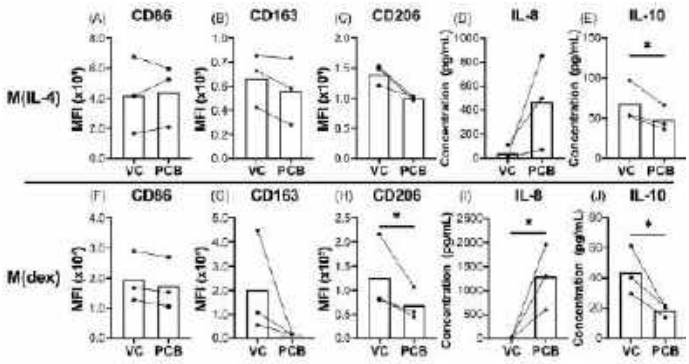

Figure 2: Surface marker and cytokine analysis for M(IL-4) (A-E) and M(dex) (F-J) exposed to PCBs after polarization. Surface marker analysis: Mean, N=3 donors, paired t-test, * p<0.05. Cytokine analysis: Mean, N=5 donors, paired t-test *p<0.05.

DISCUSSION

Our work shows that PCB exposure pushes macrophage toward a more inflammatory phenotype. Previously, Wang et al. showed that PCB 126 induces the polarization of naïve THP-1 macrophages toward an inflammatory, M1-like state [5]. Our results expand on this study to show that PCBs will also inhibit the polarization of anti-inflammatory, M2 macrophages, and more surprisingly, will induce plasticity resulting in a phenotypic switch.

A PCB-induced shift toward more inflammatory macrophages would have profound impacts on adipose tissue. Inflammatory ATMs drive adipocyte dysfunction and insulin resistance by communicating with adipocytes through paracrine signaling [3]. Furthermore, inflammatory macrophages disrupt adipogenesis, leading to improper turnover of mature adipocytes which has been linked to hypertrophic obesity and ectopic lipid accumulation in other tissues [6]. Future work will be needed to understand how PCB exposure alters macrophage-adipocyte crosstalk to influence the development of metabolic syndrome.

ACKNOWLEDGEMENTS

Support for this work was provided by NIEHS Grant #2P42ES013661-15 (PI: Keri Hornbuckle).

REFERENCES

[1] Herrick, R et al., *Environ Health Persp*, 112:1051–1053, 2004.
[2] Huang, P et al., *Dis Model Mech*, 2:231–237, 2009.
[3] Catrysse, L et al., *Cell Immunol*, 330:114–119, 2018.
[4] Baker, N et al., *Environ Health Persp*, 123:944–950, 2015.
[5] Wang, C et al., *Toxicol Appl Pharm* 367:71–81, 2019.
[6] Bilkovski, R et al., *Int J Obesity*, 35:1450–1454, 2011.

HIGH-SPEED CARDIAC PRESSURE-VOLUME SIMULATIONS USING A NOVEL NEURAL NETWORK FINITE ELEMENT APPROACH

Shruti Motiwale (1,2), Michael S. Sacks (1,2,3)

(1) James T. Willerson Center for Cardiovascular Modeling and Simulation, Oden Institute, University of Texas at Austin, Austin, TX, USA
(2) Department of Mechanical Engineering, University of Texas at Austin, Austin, TX, USA
(3) Department of Biomedical Engineering, University of Texas at Austin, Austin, TX, USA

INTRODUCTION

With advances in computational modeling as well as imaging techniques, patient-specific cardiovascular modeling for disease modeling and treatment is being widely explored as a means to improve patient outcomes. However, the slow computational speed for accurately simulating the complex physiology of the heart using traditional finite-element based methods still limits their practical clinical application. Moreover, patient-specific clinical applications require rapid evaluation of a large number of clinical scenarios. While reduced order models are commonly used to speed up simulations in many domains at a small loss of accuracy, the associated risk due to this is unacceptable in clinical applications.

We have previously demonstrated the efficacy of the neural network finite element (NNFE) [1] approach for predicting cardiac mechanics of an idealized left ventricle geometry [2] within clinically relevant timeframes without compromising accuracy. In this work, we extend this approach to predict cardiac mechanics using a realistic left ventricle model developed using data obtained from an ovine heart [3].

METHODS

The left-ventricular model utilized in this study is a part of a previously published biventricular ovine model and is described in extensive detail in Liu et al. [3]. Briefly, this model was based on a comprehensive experimental dataset, including ex-vivo MRI data, diffusion tensor MRI imaging data for the local fiber directions as well as in-vivo heart cavity pressures and volumes, all obtained from a single heart (Fig 1). The finite element mesh was created by segmenting the MRI scans and principal myofiber directions were prescribed using DT-MRI data to capture anisotropy and active contraction.

We modeled the passive mechanical properties of the myocardium using an incompressible transversely isotropic Fung-based hyperelastic material model, and the active contraction using an additive stress based on the Hunter-McCulloch-Ter Keurs model with minor modifications

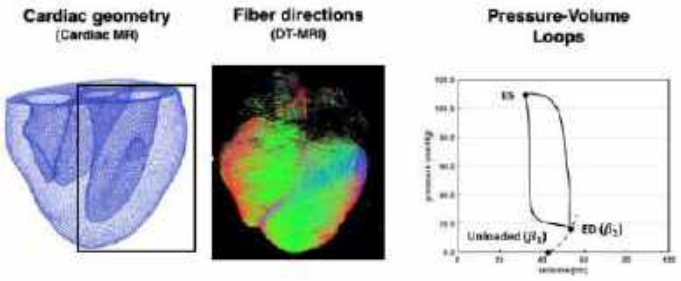

Figure 1: Cardiac geometry, fiber direction and PV loop data collected from a single ovine heart. In this work, we focus on modeling the left ventricle.

with material constants taken from a previous publication [3]. Briefly, the weak form of the governing PDE is

$$\delta W(\boldsymbol{u},\ \delta\boldsymbol{u}) = \int_{\Omega_0} \left(\frac{\partial \Psi}{\partial \mathbf{E}} + \mathbf{S}_{act}\right) : \delta\mathbf{E}\, d\Omega - \int_{\Gamma_0} \mathbf{T}.\,\delta\boldsymbol{u}\, d\Gamma = 0 \qquad (1)$$

where, $\boldsymbol{u} = \mathbf{UN}$ is the displacement field over the domain Ω, **U** are the nodal displacements and **N** are the basis functions, $\delta\boldsymbol{u} = \mathbf{VN}$ is the virtual displacement field and **V** are the virtual nodal displacements, Ψ is the strain energy density function describing the passive behavior of myocardium, **E** is the Green-Lagrange strain tensor, $\mathbf{S}_{act}$ is the 2nd Piola-Kirchhoff active contraction stress and **T** is the traction vector.

The NNFE model utilized a neural network (NN) to represent the nodal displacements, and conventional finite elements (FE) to map the NN output to the problem domain, as well as to specify the boundary conditions and perform numerical integrations (Fig. 2). The NN took pressure p and active contraction T_{Ca} as inputs and predicted nodal displacements **U** in the output layer, from which the myocardial volume (V) was determined.

The NN was trained with a physics-based training scheme by minimizing the residual force vectors of the governing PDE. This

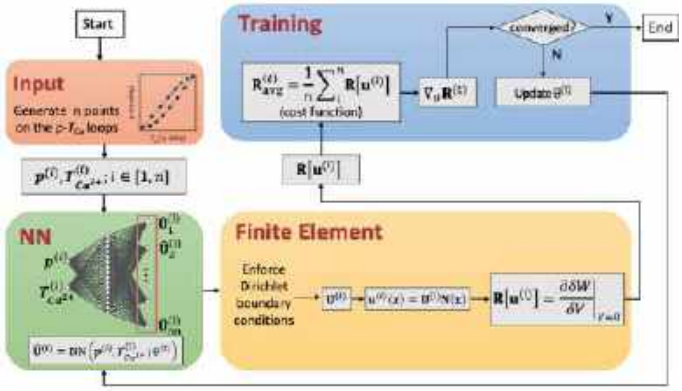

Figure 2: The NN took pressure p and active contraction T_{Ca} as inputs and predicted nodal displacements U in the output layer, from which the myocardial volume (V) was determined. Conventional finite elements were used to map the output on the problem domain. Note that finite element simulations were <u>not</u> run to generate training data for this model. The model was trained by minimizing the residual force vectors of the governing PDE using variational principles.

approach relies on variational principles, and thus, does not rely on the existence of a potential energy formulation of the PDE. The residual of the governing PDE is

$$R = \frac{\partial \delta W}{\partial V} = 0 \qquad (2)$$

where, **V** are the virtual nodal displacements. We designed the NN with five hidden layers and 256 neurons and trained it using the first-order gradient-based optimization algorithm Adam [4] with learning rate scheduling. Unique to this model was that we trained the model over the entire functional training space of pressures, volumes and T_{Ca} at once (Fig. 3). We compared model results against the results of the pre-established model run in Abaqus.

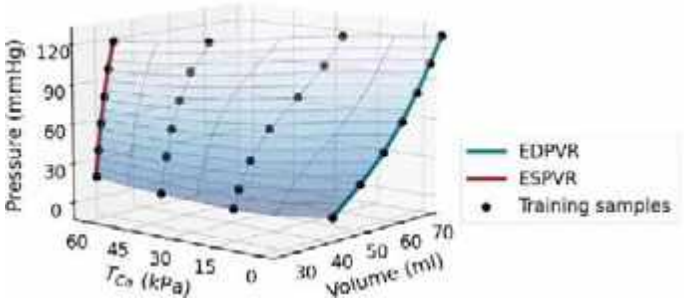

Figure 3: The functional space of the cardiac model is visualized as a 3D space of pressure, volumes and T_{Ca}. The training space consists of the variables p and T_{Ca}, which is space is discretized into a training grid. The model is trained over the entire functional p-T_{Ca} range simultaneously.

RESULTS

The NNFE model predicted the displacement field for any P-V loop in the physiological training space with a max nodal error <1% (Fig. 4). The trained NNFE model could accurately produce the twisting experienced by the left ventricle under active contraction. The NNFE model took 12 hours for training, but a trained NNFE model took 3 seconds for producing the results for any loading, whereas the Abaqus model required ~2.5 hours on average for a single loading path.

Table 1: Comparison of simulation times

Loading path	FEM (Abaqus)	NNFE
Single point	10 min	200 milliseconds
One PV loop	2.5 hours	3 seconds

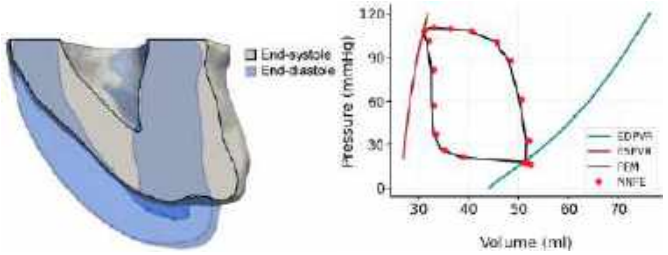

Figure 4: Deformed left ventricle and the pressure-volume loop predicted by the NNFE approach. The NNFE model took 12 hours for training, but a trained NNFE model took 3 seconds for producing the results for any loading path, whereas the Abaqus model required ~2.5 hours on average. Note that the NNFE model is trained only once, and the trained model can predict results for any loading path in the training range.

DISCUSSION

We presented a high-speed NNFE approach to produce the active contractile behavior of a left ventricle for any pressure-volume path within the functional range. Although the NNFE method does take longer to train, this is not a limitation, as the NN only needs to be trained once over a range of boundary conditions. Moreover, the NNFE model was trained over the entire functional space at once and can produce results for any loading path without need for retraining. Consequentially, the NNFE approach is well-suited for many-query problems, such as patient-specific disease modeling and treatment planning, where one needs to solve very similar problems repeatedly with only small changes to the inputs. For such applications, the training can be done in advance, and when presented with the patient-specific data, rapid simulation results can be produced with the trained model.

This approach is different from data-driven machine learning approaches as it does not rely on experimental data or any simulation-generated data for training the model. Instead, it utilizes the weak form of the PDE to train the neural network. However, it is also different from many other physics-based training approaches, as it does not require the existence of a potential energy formulation, and can thus capture a wider range of phenomenon such as non-conservative pressure loading and path-dependent active contraction.

Our results demonstrate the first application of the NNFE approach for a biomedical application at an organ level. We are working on extending this method to study the effects of inotropy on cardiac behavior by varying the slope of the end systolic P-V relationship. Our results represent a small but an important first step towards a digital twin. In the future, geometry and material property variations will be included. While still in its early stages, this approach paves the pathway for high-speed patient-specific clinical simulations.

ACKNOWLEDGEMENTS

NIH R01 HL073021 and Platform for Advanced Scientific Computing (Swiss Federation).

REFERENCES

[1] Sacks M, et al., J Biomech Eng 144.12 (2022).
[2] Motiwale S, et al., FIMH 2023: 537-544.
[3] Liu H, et al., Scientific Reports 11.1 (2021): 1-15.
[4] Kingma DP and Ba J, arXiv:1412.6980 (2014).

SB³C2024
Summer Biomechanics, Bioengineering and Biotransport Conference
June 11-14, Lake Geneva, WI, USA

EFFECT OF COLLAGEN FIBER TORTUOSITY DISTRIBUTION ON THE MECHANICAL RESPOSNE OF ARTERIAL TISSUE

Y. Agrawal (1), R. N. Fortunato (1), A. Asadbeygi (1), M. Ramezanpour (1), M. R. Hill (1), A. M. Robertson (1,2), S. Maiti (1,2,3)

(1) Mechanical Engineering & Materials Science, University of Pittsburgh, Pittsburgh, PA, USA
(2) Bioengineering, University of Pittsburgh, Pittsburgh, PA, USA
(3) Chemical and Petroleum Engineering, University of Pittsburgh, Pittsburgh, PA, USA

INTRODUCTION

The structural integrity of arteries is crucial for proper functioning of the cardiovascular system. Vascular diseases such as aneurysms and arteriosclerosis can compromise this integrity, leading to major cardiovascular events and even death. There is a pressing need to understand the structure-biomechanical property-function relationship of the arterial wall tissue in health and disease in order to improve diagnosis and treatment of vascular disease. The primary load-bearing component in the arterial wall is the collagen fiber network. Therefore, the structural role of the diverse features of this network must be elucidated to gain a mechanistic understanding of sources of tissue strength and failure. Previous studies have detailed the influence of fiber density and orientation distribution on the tissue's pre-failure and failure mechanical behavior [1]. While the effect of tortuosity distribution of the collagen fibers on the biomechanical properties of the arterial wall in the elastic regime have been evaluated [2], the impact on failure remains largely unknown.

In this context, we hypothesized that the distribution of collagen fiber tortuosity is a pivotal factor influencing the failure properties of arterial wall tissue. To investigate this hypothesis, we adopted a comprehensive approach combining advanced imaging techniques, experimental testing, and computational modeling to develop a generalized image-based in-silico model of rabbit carotid arterial wall tissue. We refined our tissue model with data from multiphoton microscopy imaging of artery samples and uniaxial tensile tests to characterize the material properties of the tissues. The computational model featured a representative volume element (RVE) that incorporated layer-specific collagen fiber architecture and was validated against experimental data to determine the material properties. Subsequently, a multi-variable parametric study was undertaken, involving finite element analysis on the RVE model and post-processing of simulation data. Our results demonstrated that variations in fiber tortuosity distribution indeed have a significant impact on the biomechanical failure properties of arterial wall tissue, a finding that has the potential to understand the relationship between pathological changes to the arterial wall and deleterious changes to tissue strength.

METHODS

In this study, we utilized the raw experimental data derived from the carotid arteries of six white New Zealand rabbits, obtained from a previous study performed by our research group [2]. The previous study integrated multiphoton microscopy (MPM) with uniaxial tensile (UT) testing to examine the fiber properties at different tissue stretches across the thickness. Moreover, uniaxial tensile test also generated the stress-stretch (SS) curves of each specimen experimentally. These methods are described in detail in [2] and are not repeated here.

To simulate the arterial wall's intricate behavior, we constructed a RVE model of the tissue which encompasses three distinct thickness regions—Adventitia, Media, and the Internal Elastic Lamina (IEL)—with layer dependent composition of the three material components: collagen, elastin, and ground substance. Collagen fibers were modeled as discrete anisotropic elements, while elastin and ground substance were modeled as homogeneous isotropic components. The RVE dimensions were determined based on the MPM scans and the individual layer thicknesses. Densities of elastin and collagen within each layer were quantified using image thresholding techniques applied to MPM scans, and the residual volumetric density was attributed to the ground substance. Collagen fiber diameter and orientation were also obtained from the image analysis of the MPM scans.

The collagen fibers within the arterial tissue demonstrate a crimp behavior, whereby a fiber only begins to bear load after it has been completely straightened. The tissue stretch at which a fiber starts engaging in the load bearing process is termed as the recruitment (or activation) stretch. Due to the natural variability among fibers having different tortuosity, we defined a probability density function of the

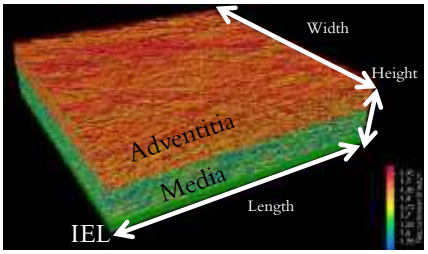

Figure 1: RVE model of the arterial wall tissue

recruitment stretch distribution as shown in Equation 1 where λ_{a1} is the activation stretch of the first recruited fiber. R_a is the range between first and last fiber activation stretches. We have used a Beta probability distribution for defining the shape of the tortuosity distribution function for data from [2]. The distribution function parameter values for the media of each specimen were calculated by obtaining the percentage of recruited fibers at different tissue stretches measured from our combined MPM-UT imaging data.

$$d(\lambda_a) = \lambda_{a1} + R_a \times \text{Beta}(\alpha, \beta) \quad (1)$$

For the adventitial collagen fibers, recruitment stretches were estimated from mapping the tortuous adventitial fibers back to an unloaded configuration, accounting for their angle. Subsequent to the RVE modeling as shown in Figure 1, we performed a finite element (FE) analysis by employing a fiber-reinforced method. In this model, fibers were rendered as 1D tensile rod elements within a 3D continuum, capable of stretching up to 1.2 times before failure [3]. The continuum components were homogeneously modeled using nearly-incompressible neo-Hookean material model. A fixed boundary conditions were applied to one face in the circumferential direction while the displacement load was applied to its opposite face in FE analysis to obtain the SS curve. Material properties of collagen and elastin were calibrated for each specimen by regressing the FE-generated SS curve to align with the experimental UT data. The RVE model for the arterial wall was then validated by comparing the confidence intervals of the material properties obtained from the model calibration and ensuring the SS curve of a random specimen fell within the range of SS curves generated by these intervals. Upon validation, we conducted a parametric study on each of the tortuosity distribution parameters outlined in Equation 1.

RESULTS

A comprehensive parametric study was performed to discern the influence of tortuosity parameters on the stress-stretch behavior of the arterial tissue and the SS curves obtained from the parametric studies of each tortuosity distribution parameter are shown in Figure 2. This investigation focused on key characteristics of the stress-stretch curve: failure stretch and failure stress (or strength). Our study revealed that variations in the value of λ_{a1} significantly affect the tissue's mechanical response. As the value of λ_{a1} increased, there was a notable rise in the tissue's failure stretch from 1.85 ± 0.01 to 2.49 ± 0.005 and strength from 4.64 ± 0.14 to 7.03 ± 0.23 MPa (Figure 2a). Conversely, increasing the range over which fibers were recruited (R_a) led to an increase in failure stretch from 2.035 ± 0.01 to 2.27 ± 0.01 and a slight decrease in failure stress from 5.89 ± 0.15 to 5.61 ± 0.20 MPa, indicating a linear but inverse sensitivity to these parameters (Figure 2b).

Additionally, changing the tortuosity distribution shape function parameters α and β altered the stress-stretch curve's properties in a complex manner, suggesting monotonic and non-monotonic dependencies for failure stretch and stress respectively (Figure 2c-d). An increase in α parameter of the shape function resulted in the increment of failure stretches from 1.96 ± 0.005 to 2.23 ± 0.003. In contrast to α, the parametric study of β displayed an inverse effect: failure stretch decreased from 2.28 ± 0.005 to 2.05 ± 0.006.

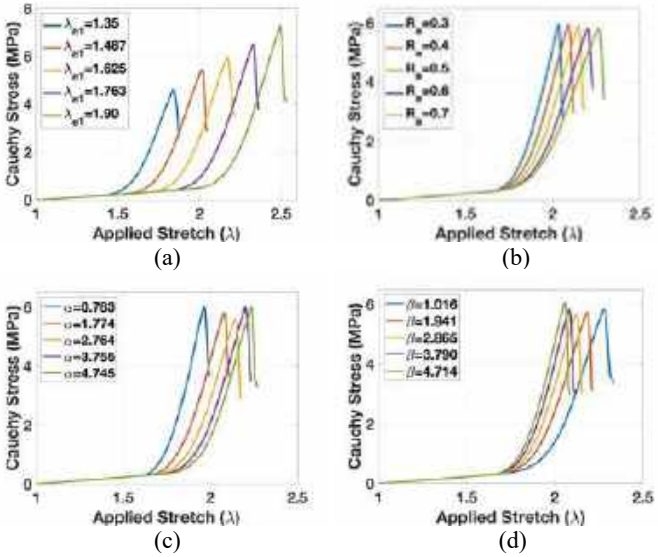

Figure 2: **SS curves generated from parametric study of (a) λ_{a1}, (b) R_a, (c) α and (d) β parameters of Beta probability density function while keeping all other tortuosity distribution parameters fixed.**

DISCUSSION

Our study elucidates the impact of the shape of the tortuosity distribution on the stress-stretch behavior of arterial wall tissue. This relationship is difficult, if not impossible to investigate during physical experiments. Here, we develop a high-fidelity model of a representative multi-layered fiber model of arterial tissue driven by collagen fiber data obtained from multiphoton imaging simultaneous with mechanical testing. The aggregate stress experienced by the tissue arises from the combined stress in both fibers and the surrounding matrix. If the fibers have higher tortuosity, then the overall stress in the tissue will be amplified due to the higher matrix stress. Moreover, if all fibers have identical tortuosity, they all will engage and bear the load simultaneously leading to higher overall stress. Conversely, higher variability in fiber tortuosity in the tissue leads to a scenario where, at any stretch point, some fibers are bearing load while other fibers are either not recruited yet or have already failed, resulting in relatively less overall stress. Taken together, our results suggest that fiber tortuosity plays an important role in failure behavior of the arterial tissues. This knowledge motivates further investigations into fiber distribution in other tissues to provide a better understanding of biomechanical behavior of arterial wall though failure. Ultimately such knowledge will provide a better understanding of how structural changes in arterial pathologies influence tissue failure properties. It is expected that such knowledge will improve treatment of arterial diseases.

ACKNOWLEDGEMENTS

Support from NIH grant 2R01NS097457 is gratefully acknowledged.

REFERENCES

[1] Qi, Nan, et al. *J mechanical behavior of biomedical materials* 52:108-119, 2015.
[2] Hill, M R., et al. *J Biomech,* 45.5:762-771, 2012.
[3] Fortunato, R N, et al. *Biomech and modeling in mechanobiology*, 18:1791-1807, 2019.

USING CFD TO ASSESS TRACHEAL WORK OF BREATHING IN NEONATES WITH TRACHEOESOPHAGEAL DEFECTS PRE AND POST SURGICAL REPAIR

Christopher R. Boles (1,2), Chamindu C. Gunatilaka (1), Qiwei Xiao (1), Jason C. Woods (1,3,4), Paul S. Kingma (3), Alister J. Bates (1,2,3)

(1) Center for Pulmonary Imaging Research, Cincinnati Children's Hospital Medical Center, Cincinnati, OH, USA
(2) Department of Biomedical Engineering, University of Cincinnati, Cincinnati, OH, USA
(3) Department of Pediatrics, Cincinnati Children's Hospital Medical Center, Cincinnati, OH, USA
(4) Department of Radiology, Cincinnati Children's Hospital Medical Center, Cincinnati, OH, USA

INTRODUCTION

The trachea and esophagus begin development as one single tube and separate at about four to eight weeks after conception. If the trachea and esophagus fail to separate, it causes a tracheoesophageal defect/fistula (TED/TEF) and can be life-threatening to neonates. TED/TEF is a connection at one or more places between the trachea and esophagus. As shown in Figure 1, where the esophagus is attached to the bottom of the trachea between the main bronchi. As a result, food or liquids swallowed by a child can be inhaled into their lungs. This rare disease is fixed by a surgical repair that closes the connection. Surgical repair can lead to other complications such as dynamic collapse during breathing, which is known as tracheomalacia and may require further surgical correction. These abnormalities and complications can increase breathing effort. Currently, the effects of TED/TEF and repairs to treat TED/TEF on breathing effort are not known nor whether breathing effort is in the normal range pre and post-surgery.

Computational Fluid Dynamics (CFD) can be used to generate patient specific modeling of respiratory airflow and quantify the effect of TED/TEFs on resistive components of breathing effort. To model patient-specific respiratory aerodynamics, three inputs are needed: respiratory flow rates, airway geometry, and airway motion, including tracheal collapse. These inputs can be captured non-invasively using ultrashort echo time (UTE) MRI. This method of imaging allows reconstruction of respiratory gated images during multiple phases of breathing and is used to create an accurate airway motion model via registration [1,2]. These tracheal component work of breathing (TR-WOB) values are compared to neonates in a healthy population that were previously calculated. We used patient specific CFD simulations to study the effect of TED/TEF on the TR-WOB in neonates. If the TR-WOB calculations are abnormal post-surgery, this would indicate that further surgery and treatment of tracheomalacia is required at the same time as the TED/TEF repair. The purpose of this study was to quantify the pre and post-surgery TR-WOB on the trachea of neonates with TED/TEF and compare it to results previously found in healthy neonates using the same methods.

Figure 1: Coronal slice through an MR image of a neonate with TED/TEF. The slice shows the distal trachea bifurcating at the carina, with a pathological connection to the esophagus occurring at the carina. The esophagus then terminates in a pouch.

METHODS

In this study, three neonatal intensive care unit subjects diagnosed with TED/TEF at Cincinnati Children's Medical Center were imaged using a neonatal MRI scanner before and after surgery. The gestational ages were between 35 and 40 weeks. MR raw k-space data received from the k_0 waveform throughout the breathing cycle were gated into 4 bins representing different respiratory cycles and reconstructed in 4 images [3,4,5]. From the MR Images, 3D segmentations were created from peak expiration, peak inhalation, end inhalation, and end expiration, extending from the nasopharynx to the main bronchi.

Surface registration was used to calculate the airway movement between each of these phases of the respiratory cycle, resulting in a model that moves as the real airway does *in vivo*. The tidal volume was determined from lung segmentations and the k_0 waveform in these MR images was used to calculate the airflow into the left and right bronchi of each subject [3]. For each patient pre- and post-surgery, a CFD simulation was performed utilizing the airway surfaces, motion, and airway flow to model airflow from the upper airway to the main bronchi as shown in figure 2.

CFD package STAR-CCM+ 14.06.012-R8 was utilized for the CFD simulations. Airway motion was included in the simulation by applying prescribed motion obtained from the registration of the airway surface at different timepoints. This technique ensures the CFD airway surface moves as the airway moves *in vivo*, without the necessity for a structural model which would require knowing material properties on the neonatal thorax. The mesh was between 3 million and 5 million polyhedral cells in the airway interior and 9 prism layers on the wall [6] based on previous convergence studies in neonates. The Large-Eddy Simulation turbulence model and no-slip conditions were applied. The CFD simulations for each patient's breathing cycle were unsteady and had a temporal resolution of 0.8 ms [6].

The tracheal component of the resistive TR-WOB was derived from calculating the difference in kinetic energy flux between planes located at the glottis, and carina.

RESULTS

The average tracheal component of the resistive TR-WOB was 1299 J/day in subjects before surgery and 341 J/day in subjects after surgery, as shown in Figure 3. There was a 74% decrease, which demonstrates that surgery aimed at treating TED/TEF significantly reduces the tracheal component of breathing effort.

However, normal values of the TR-WOB range from 24.7 to 96.1 J/day [3]. Therefore, even following the significant decrease due to surgery, patients with TED/TEF have breathing effort approximately 3-fold elevated breathing effort compared with healthy neonates.

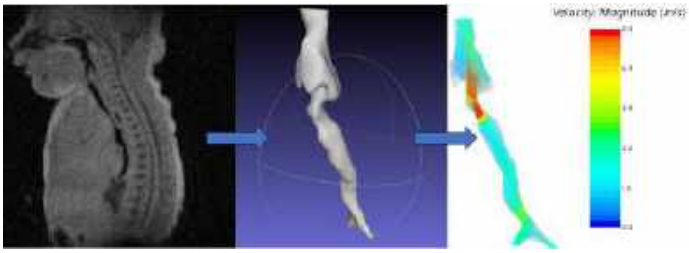

Figure 2: A MR Image is segmented to create a 3D surface of the airway. A surface is created for four timepoints during the respiratory cycle. Surface registration between these surfaces provides the movement of the airway between these timepoints, resulting in a moving airway surface. Using this moving surface, CFD simulations calculate the velocity and pressure fields throughout the airway and duration of the breath.

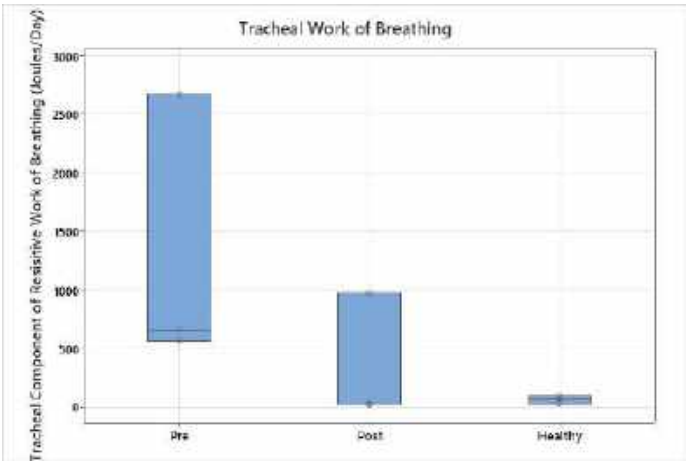

Figure 3: The tracheal component of resistive TR-WOB pre- and post- surgery (left and central boxes, respectively) compared to the normal range, calculated previously [3].

DISCUSSION

This study analyzed how effective surgical repair of TED/TEF is in terms of the reduction in the tracheal component of the TR-WOB due to surgery. Figure 3 indicates that there is a significant 74% decrease in the amount of energy used to breathe post-surgery. This finding demonstrates the positive effect surgery has on respiratory effort, in addition to the primary effect of the surgery which is to correct the tracheoesophageal defect and remove any fistulae between the airway and esophagus. Prior to surgery, the average TR-WOB of a TED patient is 22 times higher than the average for a healthy neonate. While surgery greatly reduces this value, post-surgery, subjects still have a TR-WOB that is 5.5 times higher than the average for controls. Whether this 5.5 higher TR-WOB compared to controls has a significant impact on patients' health will depend on factors outside the scope of this study such as the capacity of the neonate's respiratory system to cope with this increased effort. Patients who are unable to cope with large respiratory effort may require additional surgical interventions, such as aortopexy or tracheopexy to prevent tracheal collapse and further reduce breathing effort. Future studies may be able to predict the post-surgery TR-WOB prior to surgery and therefore, in patients considered unable to support increased respiratory load, will indicate additional surgical repairs to be performed.

Patient-specific simulations of respiratory aerodynamics quantify respiratory effort pre- and post-treatment. This allows the success of surgery to be measured. In neonatal medicine, the ability to quantify respiratory effort is particularly valuable since determining normal respiratory function can be extremely challenging, and the consequence of untreated increased breathing effort is reduced growth and development of the neonate. Therefore, this work demonstrates the value of respiratory CFD in providing an objective assessment of each individual's respiratory health.

REFERENCES

[1] Hahn, A D et al., J Magn Reason Imaging, 45: 463-471, (2017).
[2] Bates, A J et al., Int j numer method biomed eng, 34:e3144, (2018).
[3] Gunatilaka, C C et al., Ann Ann Thorac Soc, 17:1247-1256, (2020).
[4] Higano, N S et al., Magn Reason Med, 77:1284-1295, (2017).
[5] Bates, A J et al., J Magn Reason Imaging, 49:659-667, (2019).
[6] Gunatilaka, C C et al. Comput Biol Med, 127:104099, (2020).

PULSE-DRIVEN MICROFLUIDIC INFUSION PUMPS WITH CONSTANT AND HEART RATE-SENSITIVE FLOW RATES

Shuyu Zhang (1,2), Rafael V. Davalos (3), Anne E. Staples (1,2)

(1) Department of Biomedical Engineering and Mechanics, Virginia Tech, Blacksburg, Virginia, United States
(2) Virginia Tech-Wake Forest School of Biomedical Engineering and Sciences, Blacksburg, Virginia, United States
(3) Wallace H. Coulter Department of Biomedical Engineering, Georgia Institute of Technology, Atlanta, Georgia, United States

INTRODUCTION

Tethered infusion pumps and syringes have been used nearly as the sole means for the delivery of liquid pharmaceuticals across the skin. These pharmaceuticals include insulin, chemotherapy, analgesia, and vaccines. Tethered infusion pumps pose a wide range of limitations, including pump bulkiness, compromised patient mobility, and technical failures [1-3]. Moreover, both tethered infusion pumps and syringe-driven injections involve the insertion of sharp cannulas and needles, which is reported to be painful and can potentially cause infections, erythema, and fear of needles [4,5]. All these limitations can result in patient non-adherence, which in turn causes morbidity and mortality [6-7].

There is a critical need to develop drug infusion technologies that address these limitations. Here we present a slim, unpowered, minimally invasive alternative to syringes and tethered infusion pumps for the transdermal delivery of liquid drugs. Inspired by the insect respiratory system, we have invented featherweight, *pulse-driven* microfluidic pumps whose flow rate can vary with the driving heart rate and blood pressure. We have evaluated the flow rate of these pumps at different heart rates and blood pressures using a pressurized air-driven pulse simulator and developed device designs with ideal performance profiles.

METHODS

The pulse-driven microfluidic pumps were fabricated using soft lithography and stereolithographic (SLA) 3D printing. Briefly, pump-layer and actuation-layer channels were modified from the tapered channel design (S2) from our previous study [8] and further varied over six design generations. Negative master molds were CAD designed with SOLIDWORKS® and COMSOL Multiphysics® and fabricated with SLA 3D printing using a Formlabs printer. The bottom (pump/flow channel) and top (actuation) device layers were fabricated by cast molding polydimethylsiloxane (PDMS) against the master mold. A flexible membrane was fabricated by spin-coating a thin layer of PDMS onto a silicon wafer. The three PDMS layers were bonded together using a plasma cleaner into a multi-layer device (see Figure 1(a)).

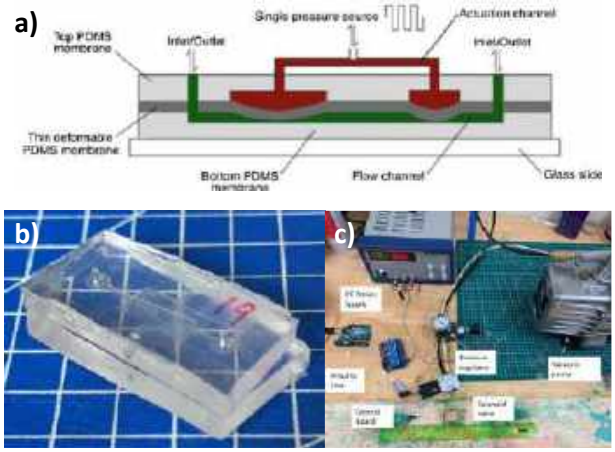

Figure 1: The insect-mimetic, pulse-driven microfluidic pump. (a) Schematic of the original 3-layer insect-mimetic pump from Chatterjee et al. [8]. (b) A prototype 3-layer drug-delivery device. (c) Pulse simulator for device actuation and testing.

To evaluate the performance of the microfluidic pumps, we actuated them using a pressurized air-driven pulse simulator (shown in Figure 1(c)). The pulse simulator was controlled by a solenoid valve that switched periodically between a pressurized air inlet and a vacuum inlet. The modeled heart rate and blood pressure were controlled using an Arduino program and a pressure regulator, respectively. The flow rate was measured by manual video tracking and Elveflow flow sensors.

RESULTS

Testing with the pulse simulator revealed that small changes in device design parameters like the flow channel width could lead to non-continuous changes in the flow rate produced for a given heart rate and sometimes even a change in the sign of the correlation with the driving heart rate. After six generations of device design refinement, we developed families of devices with negative and no correlation with the driving heart rate. The device in Figure 2(a) is in the first category. It is ideal for insulin delivery because it exhibits a sharp, negative correlation between the heart rate and the flow rate. In diabetic patients, elevated heart rates in exercise generally correlates to a reduced need for insulin due to a reduced glucose level in the blood [9]. On the other hand, the three devices in Figure 2(b) are in the second category. They show a constant flow rate across the physiological range of driving heart rates. These devices are ideal for applications other than insulin delivery because the flow rate generated is expected to be unaffected by the heart rate and other patient parameters. For example, Device 18 (teal curve in Figure 2(b)) generated a constant flow rate of 0.5 μL/min (1.8 mL/hr), which is suitable for the delivery of patient-controlled analgesia and chemotherapy [10,11]. Device 21 (magenta curve in Figure 2(b)) generated a flow rate of 2.5 μL/min (9 mL/hr), which is suitable for chemotherapy [11]. Device 25 (black cueve in Figure 2(b)), on the other hand, showed a flow rate of 0.05 μL/min (0.18 mL/hr) and is expected to support insulin delivery without a heart rate-driven feedback loop [12]. Most devices were tested under a simulated blood pressure of 100 mmHg, which approximately corresponds to the blood pressure in the radial artery of a healthy person [13].

We also evaluated the inter-device reproducibility by fabricating three identical replicate prototypes of the devices in the sixth and final design generation. The flow rates exhibited a maximum inter-device variability higher than 100% in each of the two device designs, as shown in Figures 2(c) and 2(d). This indicates that improvements to the device fabrication protocol are needed to reduce the flow rate variability and increase the fidelity of our devices.

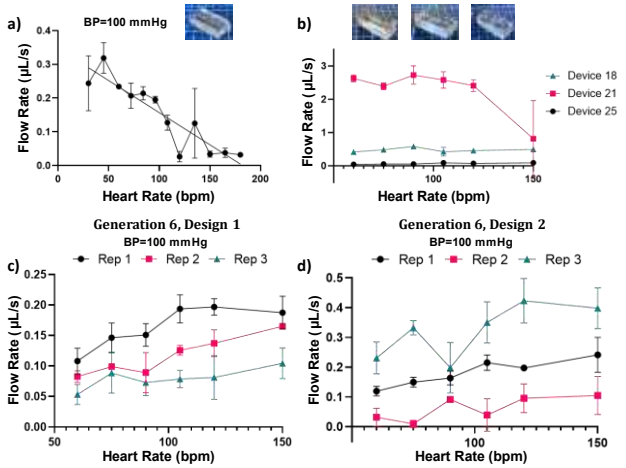

Figure 2: Microfluidic pump performance. (a) Flow rate vs. heart rate data for a prototype Device 19 (fifth design generation). (b) Flow rate vs. heart rate data for three prototype devices from the sixth/final design generation (Devices 18, 21, and 25). (c)(d) Flow rate vs. heart rate data for three replicates for two device prototype devices from the sixth/final design generation.

DISCUSSION

In this study, we have designed and fabricated insect-mimetic, pulse-driven microfluidic pumps for the transdermal infusion of liquid drugs. We evaluated the flow rates generated by more than 100 pump designs over six design generations. We found four ideally behaving prototype pump designs. One of the pumps exhibits a sharply decreasing flow rate with increasing heart rate, which is suitable for insulin delivery, as discussed in the previous section. The other three pumps, in comparison, generate a constant flow rate regardless of the driving heart rate and are suitable for the delivery of chemotherapy, analgesia, and insulin without the closed-loop feedback behavior that the first pump exhibits [10-12]. In the aspect of flow rate variability between prototype pumps of identical design, however, the pumps currently exhibit inconsistent performance compared to commercially available powered infusion pumps. For instance, commercially available insulin pumps typically have a flow rate variation of ±5% [14]. Other infusion pumps, although less stringent on the flow rate accuracy, typically only allow a flow rate variation within ±15% [11,15]. Therefore, it is critical for us to improve upon the device fabrication protocol to improve inter-device flow rate accuracy.

Since our device is intended to deliver liquid drugs across the skin, we are currently working on incorporating hollow microneedle arrays with the devices, which are known to inject drugs across the skin with minimal pain [16]. Other components we are integrating into the system include fluid reservoirs and medical-grade adhesives. Additionally, we plan to use genetic algorithms to optimize each of the four final device designs to provide specific flow rates for a given heart rate, thus tailoring the device designs to the precise needs of a large range of patients.

ACKNOWLEDGEMENTS

This work was supported by the Interdisciplinary Graduate Education Program in Regenerative Medicine and the Student Engineers' Council at Virginia Tech. We thank Mrigank Dhingra, Aleksandra Grodski, Zachary Vaday, Adaliah Dunya, Julia Frederick, Cayla Katz, Jessica Prisbe, Vedant Shah, Afreen Khoja, Tyler Kwak, Isabelle Mehochko, Demitria Poulos, Jenna Sims, and Ryan Zolovick for their contributions to the project.

REFERENCES

[1] Payne, F et al., *J Diabetes Sci Technol*, 13(1):49-54, 2019.
[2] Chefchaouni, A et al., *J Oncol Pharm Pract*, 29(1):125-129, 2023.
[3] Palmer, P et al. *Anesthesio Clinics*, 28(4):587-599, 2010.
[4] Noel, M et al. *Clin J Pain*, 31(Suppl 10):S124, 2015.
[5] Zhou C-P et al. *Int J Pharm*, 392:127-133, 2010.
[6] Davies, M. et al. *Diabet Med* 30(5):512-524, 2013.
[7] Etzioni-Friedman, T et al. *Acta Haematol*, 144(4):413-417, 2021.
[8] Chatterjee, K et al. *Bioinspir Biomim*, 16(3):036004, 2021.
[9] Colberg, S et al. *Diabetes Care*, 36(10): e177, 2013.
[10] Oh, S et al. *Perioper Med*, 11(1):52, 2022.
[11] Mohseni, M et al. *Anesthesiol Pain Med*, 4(2), 2014.
[12] Zhang, S et al. *Bull Am Phys Soc*, 2022.
[13] Scolletta, S et al. *BMC Anesthesiol*, 19:1-8, 2019.
[14] U. S. Food & Drug Administration. Retrieved from https://www.accessdata.fda.gov/cdrh_docs/pdf16/P160017b.pdf, 2016.
[15] Hwang, B et al. *Korean J Anesthesiol*, 57(5):610-614, 2009.
[16] Economidou, S et al. *Addit Manuf*, 38:101815, 2021.

PREDICTION OF PRESSURE DROP ACROSS AORTIC COARCTATION DURING EXERCISE USING A HYBRID MOCK CIRCULATORY LOOP

Priya J. Nair (1,2), Emanuele Perra (3), Doff B. McElhinney (2,4), Alison L. Marsden (1,2,5), Daniel B. Ennis (2,6), Seraina A. Dual (2)

(1) Bioengineering, Stanford University, Stanford, CA, USA
(2) Stanford Cardiovascular Institute, Stanford University, Stanford, CA, USA
(3) Biomedical Engineering and Health Systems, KTH Royal Institute of Technology, Stockholm, Sweden
(4) Cardiothoracic Surgery, Stanford University, Stanford, CA, USA
(5) Pediatric Cardiology, Stanford University, Stanford, CA, USA
(6) Radiology, Stanford University, Stanford, CA, USA

INTRODUCTION

Coarctation of the aorta (CoA) is a congenital heart defect characterized by a constriction of the aorta, and with an estimated incidence of 3 per 10,000 births.[1] The narrowing causes a drop in blood pressure (ΔP) across the CoA which can be alleviated using surgical and catheter-based treatments. In the current standard of care, only ΔP at rest (during catheterization) is used when determining whether a patient undergoes a corrective intervention. Since ΔP increases during exercise due to the increased cardiac output (CO), patients with ΔP below the threshold for intervention at rest can develop pathologically high ΔP during exercise, but this varies on a patient-specific basis.[2] In such cases, the catheterization at rest underestimates the actual disease burden. Adrenergic drug (dobutamine) infusion can be used during catheterization to simulate exercise and provoke any exercise-induced gradient, but studies have shown that the hemodynamic response during pharmacological stress does not accurately represent the responses to physical exercise.[3,4]

The aim of this study was to predict ΔP across the CoA in exercise state in a heterogeneous patient cohort (N=5) through *in vitro* measurements acquired in compliant aortic phantoms incorporated in a hybrid mock circulatory loop (HMCL).

METHODS

Acquisition of Patient Data: 4D-Flow MRI datasets (obtained with consent as part of the standard clinical care for CoA patients and approved by the IRB) were acquired from the Lucile Packard Children's Hospital for patients with CoA (N=5, age = 31 ± 16.8 years, 4 male/1 female) prior to their undergoing an invasive catheterization and stent placement. Patients were chosen from a larger patient cohort to represent a variety of CoA anatomies and ΔP at rest. Invasive blood pressure (BP) measurements were obtained via *in vivo* cardiac catheterization in the ascending and descending aorta (AAo and DAo) and in the chambers of the heart. Measurements of CO and heart rate (HR) were available from the catheterization report. Systemic vascular resistance (SVR) and pulmonary vascular resistance (PVR) were then calculated.

Anatomic Model Generation: Anatomic images were imported into SimVascular and manually segmented to generate 3D geometries of the aorta and branches arising from the aortic arch. A photopolymerization 3D printer (J735 PolyJet, Stratasys) with novel printing materials (Agilus30 and VeroClear, Stratasys) was used to manufacture compliant wall phantoms of patient-specific geometries with an elastic modulus matching that of a human aorta with CoA (Figure 1).[5] The printed models were coated with a thin conformal coating (DOWSIL 3-1953) to prevent fluid absorption.

Figure 1. 3D-printed patient-specific models of CoA with compliant walls.

Hybrid Mock Circulatory Loop (HMCL): Hemodynamics in the aortic phantoms at rest and exercise were evaluated using an HMCL (Figure 2).[6,7] HMCLs incorporate elements of both *in vitro* and *in silico* modeling allowing for rapid changes in boundary conditions to be mimicked in a closed loop circulation. The compliant aortic phantom was physically integrated into the HMCL *in vitro* while the remainder of the cardiovascular system was represented through a closed-loop lumped parameter numerical model *in silico*. The computer-controlled pressure reservoirs in the HMCL, which are the main hardware parts of the system, form the physical interface between the numerical model and the aortic phantom, by converting the simulated pressure waveforms into controlled actuation with real-time precision. The

parameters of the numerical model were tuned to match patient-specific flows and pressures in the HMCL. The working fluid was a mixture of water and glycerol (volume ratio 5:3) with viscosity matching that of blood. Pressure transducers (SPR-350S, Millar) were used to measure BP in the AAo and DAo (p_{AAo} and p_{DAo}) to determine ΔP during rest and in three different exercise states. An ultrasonic flow probe (Sonoflow CO.55/190, Sonotec GmbH) provided flow measurements at the AAo and DAo. The catheter signals were filtered using a low-pass filter with cutoff frequency between 5 and 10 Hz on a patient-specific basis. Mean pressure drop (ΔP_{mean}) was estimated as the difference in mean p_{AAo} and mean p_{DAo}. The average of the mean pressure drop across 5 cardiac cycles is reported.

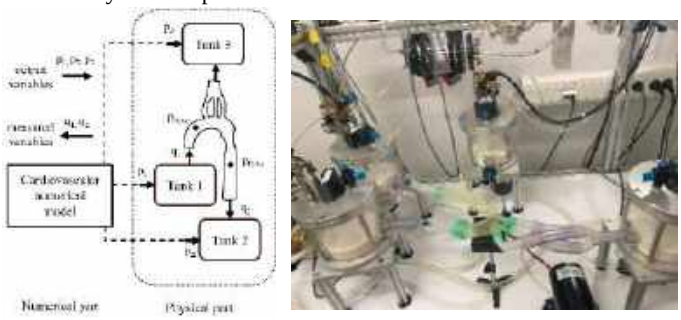

Figure 2. HMCL used for *in vitro* testing.

Simulating Rest and Exercise: *In vitro* pressure measurements were acquired in four patient-specific hemodynamic states: rest (1.00×CO), 1.25×CO, 1.5×CO, and 2×CO. First, for the resting state, the target HR, SVR and PVR were imposed in the numerical model. The simulation's Young's modulus of the systemic and pulmonary artery vessel walls and the maximum elastance of both ventricles were tuned to achieve the target resting CO as well as the target systolic and diastolic blood pressures (SBP, DBP) with a 5 mmHg tolerance. For the exercise states, target HR, SVR and PVR were extrapolated based on literature. For a 50% increase in CO with exercise, HR was increased by 50%, SVR decreased by 20%, and PVR decreased by 15% in accordance with a previous study performed in patients with CoA undergoing MRI-ergometry.[8] Again, Young's modulus of the vessel walls and elastance of the heart chambers were tuned to achieve the target CO, leaving SBP and DBP as dependent variables. For the remaining exercise states, since clinical data was unavailable, the target HR, SVR and PVR were linearly interpolated for 1.25×CO and linearly extrapolated for 2×CO.

RESULTS

Simulated pressures from the patient-specific numerical model were well matched with measured pressures in the HMCL (Figure 3).

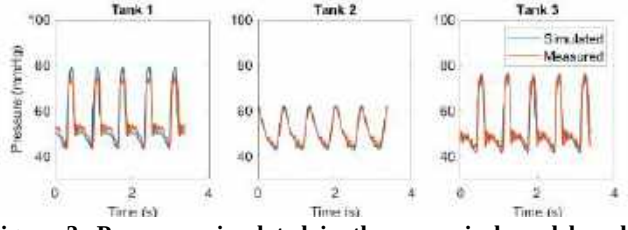

Figure 3. Pressures simulated in the numerical model and measured in the HMCL's reservoirs at rest. Tanks are shown in Figure 2.

simulation and measurement. However, the experimental systolic peak flow differed from the simulated one and did not increase as much as in simulation (Figure 4). As matching of peak systolic flow proved challenging, we report the drop in mean pressure (ΔP_{mean}) between AAo and DAo measured using the catheter (Figure 5).

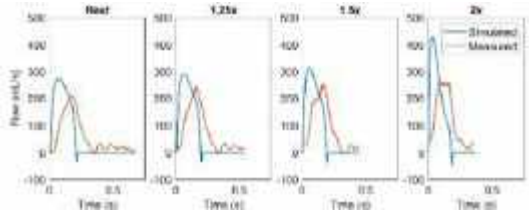

Figure 4. Simulated and measured flow waveforms at different hemodynamic states.

We observe that ΔP_{mean} changes non-linearly with an increase in CO and the changes vary on a patient-specific basis. For example, P2 experiences a linear increase in ΔP_{mean} from rest to 1.5×CO which stabilizes at 2×CO, whereas P4 has a relatively stable ΔP_{mean} from rest to 2×CO.

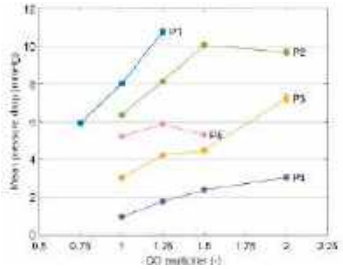

Figure 5. Drop in mean pressure between AAo and DAo at different hemodynamic states in five CoA patients.

DISCUSSION

This study demonstrates the capability of using an HMCL to estimate pressure drops in patients with CoA at rest and states of exercise unattainable in clinical practice. The patient-specific non-linear increase in the mean pressure drop with increasing CO indicates the importance of this study in estimating pressure drops at exercise. These estimates lay the foundation for further research into the factors that influence the non-linearity of pressure drop increase during exercise. The HMCL combined both *in vitro* and *in silico* components, with a numerical representation of the cardiovascular system and incorporation of 3D-printed patient-specific compliant aortic phantoms. The numerical cardiovascular model allowed efficient tuning of the system to achieve patient-specific flows and pressures. Limitations of the current study include mismatched peak flows between simulation and measured aortic flow, and instabilities introduced in the numerical model at high COs. Future studies can validate the findings from this study using CFD simulations in patient-specific CoA models.

ACKNOWLEDGEMENTS

The authors acknowledge technical expertise from Peter Arfert and Dr. Marianne Schmid Daners, as well as funding from Digital Futures and the Digitalisation platform at KTH, VINNOVA (2022-00849), Stanford's Maternal and Child Health Research Institute, and the American Scandinavian Foundation.

REFERENCES

[1] Dijkema, EJ et al., *Heart*, 103(15):1148-1155, 2017.
[2] Schubert, C. et al., *Sci Rep*, 10, 18894, 2020.
[3] Cnota, J. F. et al., *Med Sci Sports Exerc*, 35, 1503–1510, 2003.
[4] Truccone, N. J. et al., *Circulation*, 56, 79–82, 1977.
[5] Zimmermann, J. et al., *Sci Rep*, 11, 6703, 2021.
[6] Petrou, A. et al, *ASAIO Journal*, 65, 495, 2019.
[7] Perra, E. et al., *Functional Imaging and Modeling of the Heart*, 505–514, 2023.
[8] Cumming, G. R. et al., *Br Heart J*, 32 (3), 1970

SB^{3}C2024
Summer Biomechanics, Bioengineering and Biotransport Conference
June 11-14, Lake Geneva, WI, USA

MICROSTRUCTURAL ALTERATIONS IN THE MURINE THORACIC AORTA: UNVEILING A MECHANISM FOR BIOMECHANICAL REMODELING IN LATE-GESTATION PREGNANCY

Ana I. Vargas (1), Turner Jennings (2), Rouzbeh Amini (1,2), Chiara Bellini (1)

(1) Department of Bioengineering, Northeastern University, Boston, MA, USA
(2) Department of Mechanical and Industrial Engineering, Northeastern University, Boston, MA, USA

INTRODUCTION

During pregnancy, the maternal body undergoes profound hemodynamic transformations impacting the cardiovascular system. Changes to the maternal body may reveal previously hidden pathologies, leading to ∼4% of global pregnancies complicated by cardiovascular disease (CVD) [1, 2]. In the US, cardiovascular complications account for over one-third of pregnancy-related deaths, making CVD the leading cause of maternal mortality [3]. Despite observing significant changes in the maternal body, the mechanisms of tissue remodeling and mechanical adaptation of elastic arteries in response to pregnancy remain largely unknown.

The aorta plays a crucial role in storing elastic energy and enhancing blood flow throughout the cardiac cycle, while simultaneously maintaining the mechanical strength necessary to withstand hemodynamic forces and prevent structural failure [4]. Its layers, composed of essential extracellular matrix (ECM) components (elastic fibers and fibrillar collagen), are regulated by endothelial cells, smooth muscle cells, and fibroblasts [5]. Our macro-scale functional mechanics data have shown— for the first time—that during pregnancy the aortic wall remodels, becoming thicker and wider but simultaneously experiencing material softening [6]. By imaging the aortic wall under biaxial mechanical loading, we further explored this pregnancy-induced remodeling of the aortic wall, and how the ECM components, specifically collagen fibers, re-orient to account for the macro-scale response of the tissue we previously observed [6]. Therefore, the purpose of this project was to quantify the orientation and distribution of collagen fibers of the descending thoracic aorta (DTA) as a function of mechanical loading. We hypothesized that in the pregnant tissue collagen fibers remodel in response to changes in mechanical loading.

METHODS

Sample Preparation – Segments of the DTA were collected from pregnant C57BL6 mice at gestation day 18 $\pm$ 1 (n=4) and female age-matched control mice (10 $\pm$ 1 weeks of age, n=4). Specimens were cleaned, and stained for the cell nuclei. Tissue samples were then cannulated into our custom-made pressurization device and stretched to group-specific in vivo axial stretch.

Multiphoton Microscopy & Image Analysis – A two-photon microscope was used to image collagen, elastin, and the cell nuclei simultaneously, across the thickness of the aortic wall. Three-dimensional images (z-stack) were acquired at different pressure levels, ranging from 0 - 140 mmHg. After obtaining images for the three signals (collagen, elastin, and cell nuclei), each image underwent post-processing, and z-stacks were transformed to flatten the image and facilitate image in-plane fiber distribution analysis.

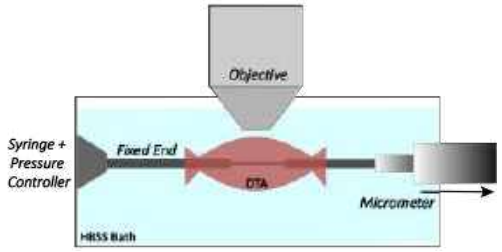

Figure 1: Custom-made pressurization device for ex-vivo multiphoton imaging.

In-plane Collagen Distribution Orientation – Flattened collagen images were post-processed using OrientationJ (ImageJ) to quantify the distribution of the collagen fibers. To model fiber directionality, we assumed our fibers followed a von Mises distribution (Eq. 1) [7]. This distribution function (f) allowed us to quantify the primary orientation angle (μ) and a concentration parameter (κ), of the orientation in circular coordinates (θ).

$$f(\theta \mid \mu, \kappa) = \frac{\exp(\kappa \cos(2\theta - 2\mu))}{\pi I_0(\kappa)} \tag{1}$$

where $I_0(\kappa)$ is a modified Bessel function [8].

Mechanical Behavior Analysis – To get information regarding the mechanical behavior of the aortic tissue and how this compares to the observed structural changes, we analyzed the components of the intrinsic stiffness tensor $\mathscr{C}_{ijkl}$, which was computed using the "small-on-large" theory described by Baek et al. [9] and data collected from passive biaxial mechanical testing [6]:

$$\mathscr{C}ijkl = 2\delta ikF^o_{lA}F^o_{jB}\left.\frac{\partial W}{\partial C_{AB}}\right|_{\mathbf{C}^o} + 2\delta jkF^o_{iA}F^o_{lB}\left.\frac{\partial W}{\partial C_{AB}}\right|_{\mathbf{C}^o} + 4FiA^oF^o_{jB}F^o_{kP}F^o_{lQ}\left.\frac{\partial^2 W}{\partial C_{AB}\partial C_{PQ}}\right|_{\mathbf{C}^o} \quad (2)$$

where $\mathbf{F}^o$ and $\mathbf{C}^o$ represent the deformation gradient tensor and the right Cauchy green tensor at an intermediate loaded condition, respectively. W is a validated strain energy function that models the aortic wall [10]. The ratio of axial to circumferential stiffness ($\mathscr{C}_{zzzz}/\mathscr{C}_{\theta\theta\theta\theta}$) serves as an indicator of the tissue's anisotropy, indicating how its mechanical properties vary in different directions.

RESULTS

The distribution of collagen fiber orientation differed between pregnant and control samples (visualized in Fig. 2). Our Von Mises distribution analysis reveals that pregnant tissue exhibits a less organized collagen structure in contrast to the arrangement observed in the control samples (Fig. 3A), as observed by lower κ values. Both groups share a common trend with κ decreasing, signifying less fiber organization, with higher pressures. The primary orientation of both groups (μ), pregnant and control, suggests that at low pressures, most of the fibers are aligned in the axial direction (Fig. 3B). As pressure increases, the fibers shift more towards the circumferential direction. The pregnant group appears to shift faster towards this direction, reaching values closer to 180 degrees as compared to the control.

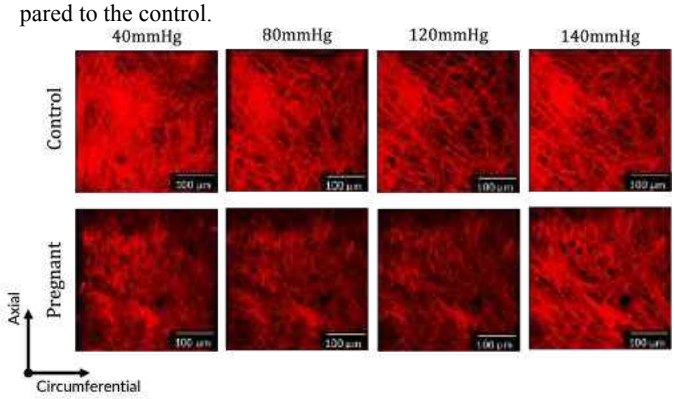

Figure 2: Illustrative projections of 3D images of collagen fibers within the same samples at increasing pressures.

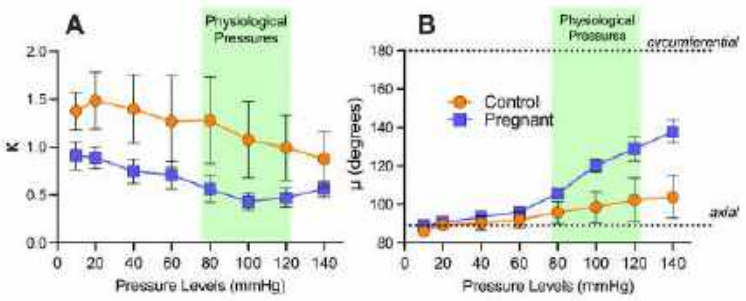

Figure 3: Organization of collagen fibers at in vivo axial stretch. (A) Concentration parameter, κ versus pressure levels. (B) Primary orientation parameter, μ, versus pressure levels. A nonparametric Spearman correlation test indicated a significant p-value for both control (r = -0.90 κ, 1.00 μ) and pregnant (r = -0.83 κ, 1.00 μ) variables.

Our functional mechanics data indicate that, for both groups, axial stiffness surpasses circumferential stiffness (Fig 4). As pressure increases, the increase in circumferential stiffness outpaces the increase in axial stiffness. This phenomenon results in a reduction of our anisotropy ratio ($\mathscr{C}_{zzzz}/\mathscr{C}_{\theta\theta\theta\theta}$), suggesting a shift towards a more isotropic response in the fibers. Notably, in pregnancy, this shift appears to occur more rapidly, with a faster gain in circumferential stiffness and lower anisotropy ratio values reached at equivalent pressure levels compared to the control group. This observation aligns with the faster re-orientation of fibers toward the circumferential direction during pressurization, as illustrated in Fig. 2B.

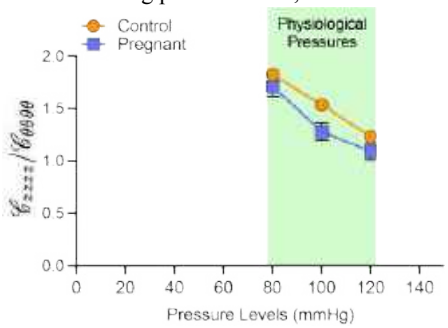

Figure 4: Ratio of circumferential stiffness to axial stiffness versus pressure levels.

DISCUSSION

It is crucial to understand the aortic remodeling process throughout gestation to gain insights into both the immediate and long-term impacts of pregnancy on maternal cardiovascular health. In this study, we present a microstructural assessment of the collagen fibers in the DTA of late-gestation wild-type mice to characterize the remodeling of the tissue at the micro-scale level.

Our functional mechanics data indicate that pregnancy is associated with a more rapid gain in circumferential stiffness under pressurization (Fig. 4), causing a more isotropic mechanical response ($\mathscr{C}_{zzzz}/\mathscr{C}_{\theta\theta\theta\theta} \approx 1$). This dynamic behavior may be attributed to the rapid re-orientation of axially aligned collagen fibers shifting towards the circumferential direction (Fig. 2B). While the shift in mean fiber direction is larger in the pregnant group, it is worth noting that the fibers in are more disorganized than the control group (Fig. 2A).

The changes observed in the microstructure of the tissue may be connected to the macro-scale remodeling we reported in our recent work [6]. Specifically, the pregnant tissue tends to shift in material response towards an isotropic material, which might be connected to the material softening we observed at the macro-scale level. The less uniform organization of collagen fibers in the pregnant group could influence the overall material response, leading to increased distensibility and altered wall stress patterns. These connections indicate that changes at the microstructural level may affect the macro-scale response of the tissue during pregnancy, contributing valuable insights into maternal cardiovascular health. However, to *fully* elucidate how the aortic tissue remodels during pregnancy, a multi-scale computational approach must be employed to relate changes in the micro-environment to macro-scale loading.

Our ongoing research is focused on further analyzing multiphoton microscopy data to include information regarding elastin fiber directionality and lamellae separation, cellular density, and cellular alignment as inputs to our multi-scale computational model.

ACKNOWLEDGEMENTS

Support for this work was provided in part by the National Science Foundation (CAREER 2049088) and the American Heart Association (24PRE1195859). We thank the Institute for Chemical Imaging of Living Systems at Northeastern University for imaging support.

REFERENCES

[1] Duley L. *Semin Perinatol* 33 (3 2009).
[2] Regitz-Zagrosek V et al. *Eur Heart J* 39.34 (2018).
[3] Petersen EE et al. *MMWR-Morbid Mortal W* 68 (18 2019).
[4] Humphrey JD et al. *Am J Physiol-Heart C* 316.1 (2019).
[5] Humphrey JD et al. *Nat Rev Mol Cell Bio* 15.12 (2014).
[6] Vargas AI et al. *Curr Res Physiol* (2023).
[7] Rezakhaniha R et al. *Biomech Model Mechan* 11 (2012).
[8] Gatto R et al. *Stat Methodol* 4.3 (2007).
[9] Baek S et al. *Comput Method Appl M* 196.31-32 (2007).
[10] Farra YM et al. *Am J Physiol-Heart C* 320.6 (2021).

STRAIN, STIFFNESS, AND COMPOSITION EFFECTS ON LUNG FIBROBLASTS AND THEIR IMPLICATIONS IN PULMONARY FIBROSIS

Qi Wang (1, 2), Kristan S. Worthington (1), Edward A. Sander (1)

(1) Roy J. Carver Department of Biomedical Engineering, University of Iowa, Iowa City, IA, USA
(2) Medical Scientist Training Program, Roy J. and Lucille A. Carver College of Medicine, University of Iowa, Iowa City, IA, USA

INTRODUCTION

Pulmonary fibrosis is characterized by abnormal accumulation of fibroblast-secreted extracellular matrix (ECM) in the pulmonary interstitium. This fibroproliferative response appears to proceed through a feedforward loop that is regulated by mechanotransductive and biochemical pathways. Dissecting the relative involvement of each pathway in disease development is difficult because fibrotic lesions are not only stiffer (~2kPa for healthy and ~14 kPa for fibrotic lung tissue) than healthy tissue but they also have altered ECM chemistry, including increased collagen, hyaluronan (HA), and fibronectin.[1,2]

To begin to untangle these factors, we leverage dynamic mechanical loading of photopolymerized hydrogels as a method to mimic mechanical and biochemical signals from three sources: cyclic strain during normal breathing and mechanical ventilation; substrate stiffness; and substrate composition (namely, HA content). This platform provides a means to isolate stiffness, strain magnitude, and biochemical signals as they contribute to expression of genes involved in pulmonary fibrosis. Our long-term goal is to use this platform to help identify the molecular mechanisms involved in initiating lung fibrosis, enabling the identification of potential therapeutic targets.

METHODS

Fabrication of hydrogels: Methacrylated gelatin (*GelMA*), methacrylated hyaluronan (*HAMA*), and non-methacrylated gelatin (*Gel*) were mixed in various concentrations as base materials. Hydrogels were formed via ultraviolet light (0.5W/cm^2) for 90 seconds, with 1%vol Irgacure-2959 as a photoinitiator.

Mechanical testing: Stress-relaxation and compression tests were performed using a Kinexus Ultra+ (Malvern Panalytical) rheometer fitted with an Omnicure S2000 UV light source. Compressive modulus was calculated using the slope of stress-strain curves.

Cyclic Strain: Pre-polymer mixtures were applied to and photopolymerized directly on attachments designed for a force bioreactor (ADMET Inc.), resulting in solid hydrogels attached to the bioreactor. After cell seeding, these hydrogels were then deformed at 0.2 Hz at 5% pre-strain, 25% cyclical strain (Breathing) or 20% pre-strain, 35% cyclical strain (Mechanical Ventilation, MV) conditions.

Cell Culture: Normal human lung fibroblasts (NHLFs) at low passage number (<P7) were cultured in EMEM + 10% FBS. Cells were allowed to attach on hydrogels overnight before mechanical loading.

Gene expression analysis: RNA extraction was performed using TRIzol lysis followed by ethanol precipitation of aqueous phase and Zymo RNA Clean and Concentrator column. cDNA was then synthesized using Superscript VILO cDNA synthesis kit. qPCR for 30 genes related to mechanosensing and fibrogenesis was then performed using Power SYBR green with primer sequences from Primer Bank. Three technical replicates were performed for each condition and expression was normalized to NHLFs of parallel cell seeding on tissue culture plastic.

Statistical analysis: Two-way ANOVA and Tukey's post-hoc analyses were performed using GraphPad Prism. * $p \leq 0.05$, ** $p \leq 0.01$, *** $p \leq 0.001$, **** $p \leq 0.0001$

RESULTS

Compressive moduli were measured after photopolymerization. *Gel* can be added to *GelMA* and *HAMA*, effectively reducing methacrylate group concentration to decrease compressive modulus, thus maintaining similar concentrations of integrin RGD binding sites (**Fig. 1**). The resulting hydrogels with and without *HAMA* had comparable stiffness. However, no proportion of gelatin could be added to *HAMA* mixtures to reduce the compressive modulus to the range of healthy tissue.

Out of the 30 genes investigated with qPCR, expression of MMP1, CTGF, and ROCK1, among others, were significantly impacted by cyclical strain, substrate properties, and their interactive effects (**Fig. 2**). Generally, expression increased substantially with the addition of cyclic strain on *GelMA:Gel* substrates with moderate or fibrotic stiffness.

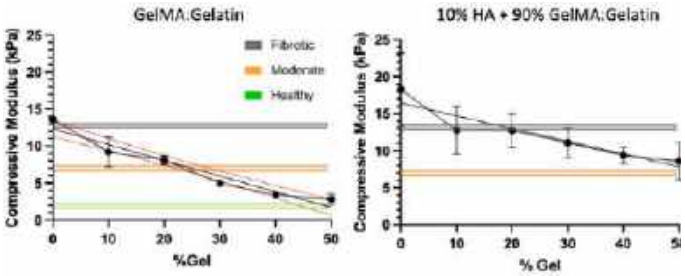

Figure 1. Compressive moduli of hydrogel formulations.

However, the influence of strain was dampened on substrates with healthy stiffness or those containing *HA*. Expression of FN1 was significantly impacted by substrate properties and interactive effects, similar to MMP1 and CTGF, but with more variability when substrates contained *HA*. Surprisingly, strain induced a significant decrease in COL3A1 and DCN expression.

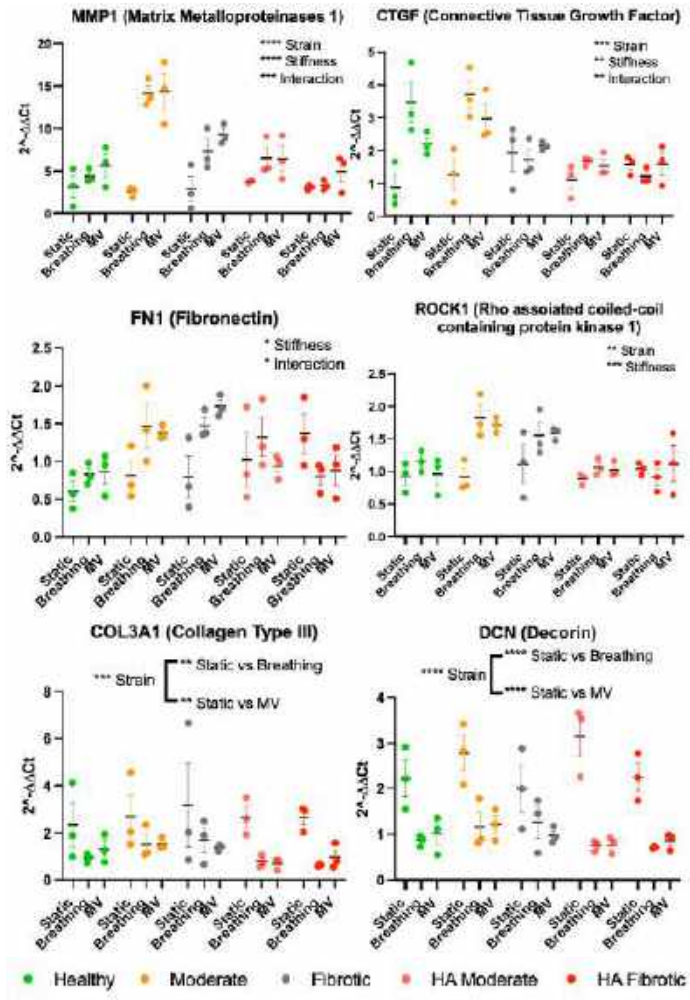

Figure 2: qPCR results of selected genes

DISCUSSION

Various combinations of *GelMA*, *HAMA*, and *Gel* were successfully used to tune the hydrogel compressive modulus within reported ranges of healthy and fibrotic lung tissue. There was a proportional decrease in compressive modulus as the concentration of *Gel* increased. However, the lower limit of compressive modulus for *HAMA* gels is most likely due to the hygroscopic nature and charge interactions associated with HA.

qPCR revealed significant increases in expression of MMP1, CTGF, and ROCK1 due to strain, stiffness, or their interaction. Furthermore, FN1 and several other genes (not shown) had expression patterns similar to MMP1, CTGF, and ROCK1. In general, expression changes in response to strain were only substantial on moderate and fibrotic *GelMA:Gel* hydrogels and not on healthy stiffness, suggesting that the stiffer gel heightened the strain-induced response. However, in several cases, response to strain was dampened when 10% *HAMA* was introduced, even though these hydrogels had comparable stiffness. Overall, these results suggest that the combination of increased stiffness and cyclic strain promote a strong remodeling response, as MMP1, CTGF, FN1 and ROCK1 are elevated in fibrotic pulmonary tissue. Previous studies have shown that CTGF and MMP1 expression increase due to cyclical strain,[3,4] and our results add a new dimension by demonstrating the importance of interactions between dynamic mechanical signals and substrate characteristics. Although additional experiments are needed to further explore the differential responses to strain on *GelMA:Gel* vs. *HAMA* hydrogels, this could be related to cell attachments to HA via CD44. Briefly, more attachments to HA could impact mechanotransduction and alter the effect of integrin binding to RGD.

In contrast to the genes described above, COL3A1 and DCN had decreased expression with cyclical strain. A decrease in COL3A1 expression is unexpected as fibrillar collagens (type I and III) are usually overexpressed in fibrotic disease. However, the ratio of type III to type I is usually lower in stiff scar tissues, which means the decrease observed here could be representative of pro-fibrotic collagen remodeling.[5] DCN regulates ECM assembly and is also an inhibitor of TGF-β1 signaling pathway.[6] The reduction in expression of DCN thus may indicate that strain contributes to fibrosis.

In conclusion, our platform enabled us to use photopolymerizable hydrogels to isolate the effects of dynamic strain, substrate stiffness, and composition on pulmonary fibroblast gene expression. Future work will include characterizing ECM protein production in response to these factors, as gene expression levels are transient and not always indictive of the protein secreted. In the future, we will also leverage the photopolymerizable capabilities of our hydrogel to create finer structures mimicking fibrotic foci to study cell interactions with localized changes in substrates.

ACKNOWLEDGEMENTS

Support for this work was provided by the National Institute of Health (NIH T32 GM007337, NIH T32 HL144461), Roy J. Carver Department of Biomedical Engineering Research Excellence Fund, and Roy J. Carver Department of Biomedical Engineering Carver Graduate Fellowship.

REFERENCES

[1] Herrera, J. Et al. *JCI Insight* **4** (2019)
[2] Booth, A.J. et al. *Am. J. Respir*. CCM. **186** (2012)
[3] Guo, F. et al. *Plos ONE* **6** (2011)
[4] Jacho, D. et. Al. *Sci Rep* **12** (2022)_
[5] Seyer, J.M. et al. *J Clin Invest* **57** (1976)
[6] Zhang, W. Et al. *Oncotarget* **9** (2018)

EFFECTS OF THE LOADING RATE ON THE MECHANICAL BEHAVIOR OF PROXIMAL SUPERFICIAL FEMORAL ARTERY

A. Zolfaghari Sichani (1), M. Jadidi (1)

(1) Department of Biomechanics, University of Nebraska at Omaha, Omaha, NE, USA

INTRODUCTION

Soft tissues, including blood vessels, are known for their rate-dependent mechanical behavior. Previous researchers have studied the dependency of loading rate on various tissues. The study of Grashow, J. S. et al. [1] demonstrated the effects of strain rate on the biaxial mechanical properties of the mitral valve anterior leaflet (MVAL). Fresh porcine MVAL specimens were subjected to a range of strain-controlled biaxial loading protocols with cycle periods of 15, 1, 0.5, 0.1, and 0.05 s. The researchers reported that the stress–strain behavior of the MVAL was independent of strain rate in both directions over the full range of cycle periods studied. Also, Noble C. et al. [2] found no notable rate-dependent response for porcine aortic heart valve biomaterials. In another study, Anssari-Benam, A. et al. [3] used porcine samples and subjected them to biaxial deformation at different stretch rates. Their analysis showed that the samples exhibited a marked rate-dependency in their deformation behavior, typically stiffening with an increased rate. Delgadillo, J. O. V. et al. [4] found that porcine aorta samples showed reduced loading forces up to 20% when the deformation rate was increased from 10 to 200 $\%s^{-1}$.

The results of these studies have been inconsistent, with some finding that the rate of deformation does not significantly affect stress-strain behavior, while others report the opposite. This inconsistency could arise from different tissue types, loading rates, and testing environments. In this study, our goal was to investigate the loading rate dependency on the mechanical behavior of human superficial femoral arteries (SFA), the main artery in the leg. These properties are crucial to understanding their function and viscoelastic behavior.

METHODS

In this preliminary analysis, we tested proximal SFA (pSFA) samples from 5 deceased male donors (age range: 45 to 55, mean age 48±3 years). This stringent criterion has been imposed to mitigate potential age and sex-related effects on arterial mechanical properties [5]. In the future, this study will be continued by testing female arteries and assessing the role of sex. Each artery was dissected from the surrounding tissues, and subsequently, a 13 mm long tube was cut from the pSFA location. The tube was cut open longitudinally using a scissor and a 10×10 mm square specimen was cut and attached to a CellScale biaxial device, equipped with 2.5 N loadcells. The specimen was attached such that the circumferential direction of the artery aligned with the biaxial device's vertical axis, and the artery's longitudinal direction aligned with the biaxial device's horizontal axis (Figure 1).

The tests were performed in 37°C PBS. After performing 10 preconditioning cycles to obtain repeatable stress-stretch response, these specimens were subjected to load-control tests at five different speed rates: 10, 20, 30, 40, and 50 mN/s at circumferential to longitudinal directions force ratios: 1.0:1.0, 1.0:0.5, 1.0:1.0, 0.5:1.0, and 1.0:1.0. Each speed test was executed sequentially from slow to fast. All samples were stretched to 800 mN load in both directions in equibiaxial protocol. This load was selected based on previous studies [5] that have shown at this level, the human pSFA 45-55 years old will show a nonlinear stress-stretch response while not reaching the plastic domain.

Images and stretch and force data were collected at 5 Hz frequency. We further employed image processing to measure the deformation gradient at the center of the specimen, away from the rakes. We also calculated the experimental Cauchy stress tensor and determined its diagonal components in the circumferential and longitudinal directions, i.e, $T_{\theta\theta}$ and T_{zz}.

In order to compare the samples statistically, we determined the stretches corresponding to the maximum stress level in all samples. In the equibiaxial protocol, we noted that the maximum stress level was 70 kPa in both directions. We selected this stress level for our analysis as it was a consistent measure observed between all samples. We further compared the samples at the stress level of 70 kPa using ANOVA and set the significance level at p-value of 0.05. In addition to the tests of

within-subjects effects, we also conducted pairwise comparisons between different groups.

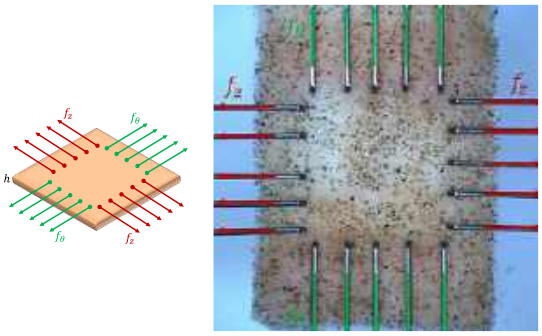

Figure 1. Left: A schematic representation of the planar biaxial test. Right: A view of the experimental setup, showcasing the sample undergoing stretching under applied forces. f_θ and f_z are the applied forces in the circumferential and longitudinal directions of the arterial wall specimen, respectively.

RESULTS

Table 1 provides a detailed overview of the stretch values at 70 kPa equibiaxial protocol for 5 samples. We observed a decrease of approximately 2.5% in the longitudinal direction between the rates of 10 and 50 mN/s for samples 1 and 4. However, we can see an increase of about 1.5% for samples 2 and 3 in the same direction. Similarly, between these rates, there was a decrease of about 2% in the circumferential direction for all samples, with the exception of sample 5.

Table 1. Stretch values of 5 samples at various loading rates, measured at a stress level of 70 kPa.

		Rates (mN/s)					
ID	Age	10	20	30	40	50	Dir.
1	50	1.2619	1.2426	1.2544	1.2246	1.2271	Longitudinal
2	45	1.2484	1.2511	1.2655	1.2636	1.2673	
3	52	1.2536	1.2602	1.2602	1.2620	1.2721	
4	48	1.3270	1.3128	1.3157	1.2979	1.2924	
5	47	1.3900	1.3970	1.4006	1.4008	1.3968	
1	50	1.1202	1.1184	1.1124	1.1174	1.1019	Circumferential
2	45	1.1599	1.1556	1.1420	1.1378	1.1354	
3	52	1.0900	1.0870	1.0768	1.0744	1.0716	
4	48	1.1550	1.1392	1.1283	1.1273	1.1266	
5	47	1.1574	1.1455	1.1469	1.1532	1.1743	

In the statistical analysis of our data, for the circumferential direction, the p-value was 0.057, indicating a trend toward significance. This suggests that the load rate might have an effect on the stretch values in the circumferential direction, although the results did not reach statistical significance at the conventional 0.05 level. For the longitudinal direction, the p-value was 0.690. These results indicate that the load rate does not have a significant effect on the stretch values in the longitudinal direction. The pairwise comparisons revealed significant differences in circumferential stretch values between the groups tested at 10 mN/s and 50 mN/s.

Figure 2 provides a visual representation of the mechanical behavior of a pSFA sample (50-year-old male) under varying loading rates in two directions. The stretch values in the longitudinal direction consistently exceed those in the circumferential direction across all load rates. Moreover, the stretch values vary across different loading rates. This pattern is observed in both the longitudinal and circumferential directions. Furthermore, the difference in stretch values is more noticeable when comparing the rates of 10 mN/s and 50 mN/s. For this sample, we observed a decrease in stretch values from 1.26 to 1.23 in the longitudinal direction, and from 1.12 to 1.10 in the circumferential direction, at the stress level of 70 kPa.

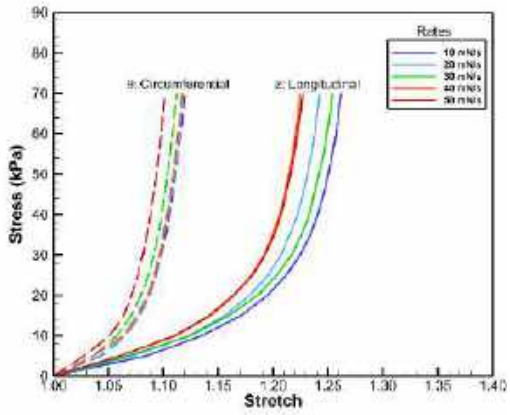

Figure 2. Stress-stretch curves of a 50-year-old sample in both the longitudinal and circumferential directions at different loading rates.

DISCUSSION

Our results indicate a trend toward stiffening of pSFA samples in the circumferential direction with an increase in loading rates, although it did not reach statistical significance. In the longitudinal direction, we showed that the mechanical properties of the samples remain almost unchanged with an increase in loading rates.

While these observations add to the growing body of evidence supporting the rate-dependent mechanical behavior of soft tissues, they should be interpreted within the context of the study's limitations. Firstly, our analysis was preliminary and only included 5 male subjects. To ensure a more robust and meaningful statistical analysis, future studies should aim to include a larger sample size with representation from both sexes. Secondly, our comparison was focused solely on the 70kPa stress level of the equibiaxial protocol. For a more comprehensive understanding, future investigations should compare the loading rates at other stress levels across all protocols.

In conclusion, while our study provides valuable insights into the rate-dependent mechanical behavior of pSFA, further research is needed to fully understand these effects, particularly in different types of tissues and under varying loading conditions.

ACKNOWLEDGEMENTS

This work was partly supported by the Nebraska Tobacco Settlement Biomedical Research Development Fund and National Institute of General Medical Sciences (NIGMS) P20GM152301. The authors would also like to thank Live On Nebraska and donors and their families for their help and support in making this study possible.

REFERENCES

[1] Grashow, J. S. et al., *Ann. Biomed. Eng.* 34: 315–325, 2006.
[2] Noble C. et al., *J. Eng. Med. Biol.* 1: 197–202, 2020.
[3] Anssari-Benam, A. et al., *Acta Biomater.* 88: 120–130, 2019.
[4] Delgadillo, J. O. V. et al., *J. Biomed. Sci. Eng.* 3: 124–137, 2010.
[5] Jadidi, M. et al., *Acta Biomater.* 103: 172–188, 2020.

CREATION OF A MULTI-SCALE MODEL OF SKIN GROWTH TO UNDERSTAND THE EFFECT OF MICROSTRUCTURE AND TISSUE HETEROGENEITIES ON SKIN MECHANOBIOLOGY

O. Moreno Flores (1), Maria Holland (2) A. Buganza Tepole (1,3)

(1) School of Mechanical Engineering, Purdue University, West Lafayette, Indiana, USA
(2) Department of Mechanical and Aerospace Engineering, University of Notre Dame, South Bend, Indiana, USA
(3) Weldon School of Biomedical Engineering, Purdue University, West Lafayette, Indiana, USA

INTRODUCTION

Understanding and correctly simulating the mechanics of skin is crucial for many medical applications, e.g. planning reconstructive surgery or monitoring wound healing. The field of skin biomechanics has often modeled this tissue as a homogeneous material because its response at finite deformations is governed by the dermis due to its collagen content. However, skin consists of two main layers with different mechano-physiology: epidermis at the top and dermis below it. Recently, multi-layer models of skin have been developed to study wrinkling and transport [1]. Still, those models assumed a flat interface between epidermis and dermis when in reality the profile of the interface is sinusoidal, termed *Rete ridges*. We have recently contributed to the modeling of skin mechano-physiology including the effect of this wavy interface [2]. We were interested in the elastic response. However, like all living tissue, a key characteristic of skin is that it grows in response to stretch [3]. This has been used for the reconstructive technique of tissue expansion, in which new skin is grown by over-stretching it via slow inflation of a balloon inserted underneath the skin [3].

The key question we answer here is how is new skin growth able to maintain the Rete ridges [4]. As will be shown later, it is essential to consider two sub-layers within the epidermis: the basal layer, which is the most proliferative, and the rest of the viable epidermis, which is not proliferative and mostly grows from asymmetric cell division in the basal layer pushing cells toward the upper epidermis [5]. Additionally, the existence of different homeostatic pre-strain per layer is needed. Crucially, the skin as a whole remains under tensile pre-stress. We show that different homeostatic stretches for different layers are key to allow buckling of the interface while keeping an overall tensile stress.

METHODS

The 2D multilayered model is made up of three layers which include the epidermis, basal interface, and dermis. Two models, one with a sine wave interface and one with a flat interface are shown in this abstract. The total width and thickness of the model are 0.8002 mm and 1 mm. The interface thickness is h_i =0.0125 mm. The thickness of the dermis is $h_d = 0.9$ mm, whereas the top of the epidermis has a variable thickness $h_e \in [0.1,0.2]$ mm. For the model with the initial sine interface the amplitude is 0.015 mm and the period 0.080 mm, according to physiological values [2]. The three layers are modeled as neo-Hookean with shear moduli μ_e, μ_i, μ_d for epidermis, interface and dermis. The homeostatic pre-stretches are denoted $\lambda_e^{\text{crit}}, \lambda_i^{\text{crit}}, \lambda_d^{\text{crit}}$ and the growth rates k_e^g, k_i^g, k_d^g. To account for the capacity of skin to growth, the total deformation in the x direction, λ, is decomposed into elastic and growth contributions, for each of the layers:

$$\lambda = \lambda_e^e \lambda_e^g = \lambda_i^e \lambda_i^g = \lambda_d^e \lambda_d^g$$

Where the superscript e, g denotes elastic or growth deformation, and the subscript e, i, d denotes epidermis, interface or dermis. The strain energy (and consequently stress) of each layer depends only on the elastic deformation and shear modulus of each layer. The growth deformation obeys the differential equation

$$\dot{\lambda}_*^g = k_*^g(\lambda_*^e - \lambda_*^{\text{crit}})$$

Where $*$ should be substituted for e, i, d for each of the layers.

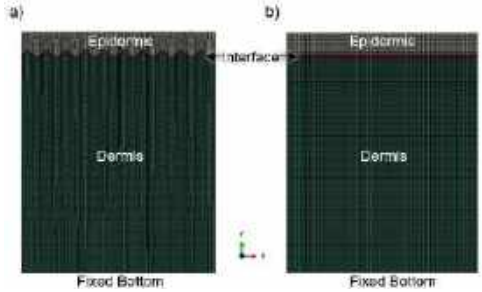

Figure 1: Finite element model with sinusoidal interface (a), and flat interface (b).

RESULTS

Stretching the model with a stress-free sinusoidal interface to twice its original size, in increments similar to what would be done in tissue expansion, triggers growth in all layers such that each layer goes back to its homeostatic pre-stretch. However, the resulting interface, while still sinusoidal, has twice the physiological period. In other words, the interface maintains the initial peaks and valleys, rather than developing new peaks and valleys (Fig 2, left column). The initially flat model, upon initial equilibration to homeostatic value, buckles, leading to a physiological sinusoidal interface. Upon repeated stretching and growth, the different interface points undergo different growth. What was initially the valley grows more compared to what was initially the peak. However, even though growth at the valley is higher, this region is under compression (Fig 3) whereas the initial peaks release some of the compression at each expansion step. As a result, the initial peaks get stretched, leading to valleys separated by flatter interface regions. At some point, however, the growth at the stretched peaks leads to new buckling. What used to be a peak eventually leads to secondary buckling where a valley forms (Fig 2 right column).

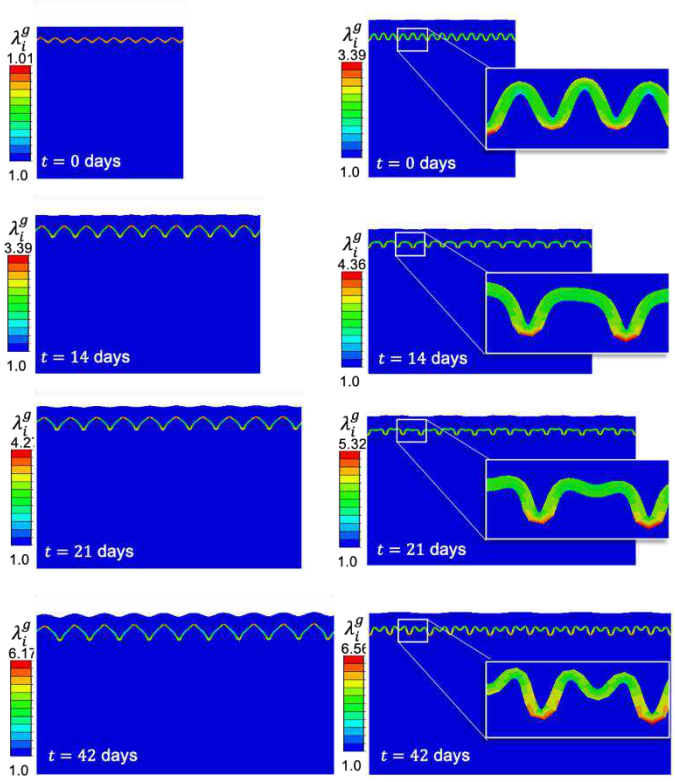

Figure 2: Contour plot of growth at the interface for the model with initial stress-free sinusoidal interface (left) and initially flat interface which by day 0 of tissue expansion already has a sine wave interface due to growth-induced buckling.

Based on work from Colin and Holland [5], who did stability and buckling analysis in bilayer systems, we know that the thickness of the upper layer and contrast of shear modulus between upper and lower layers affects the buckling in bilayer and tri-layer systems. For our case, by changing the epidermis modulus and the homeostatic pre-stretch of the interface we observe the effect on the buckling period and amplitude (fig 4). For softer epidermis (lower shear modulus) is easier to buckle and leads to a higher amplitude and period.

The most important parameter is the homeostatic pre-stretch of the interface, λ_i^{crit}. Note that for the flat interface to buckle, the homeostatic pre-stretch of the interface actually has to be <1 to induce compression and buckling of this middle layer. As λ_i^{crit}>0.8 the buckling disappears and a flat interface remains. As λ_i^{crit}decreased, < 0.8, greater amplitude buckling develops. The period of the sine wave that develops through buckling is also more sensitive to λ_i^{crit}than μ_e, with smaller λ_i^{crit} (greater homeostatic compression) leading to slightly smaller period. However, in our simulations we applied a perturbation to foster the initial buckling, and the perturbation was taken as the physiological period of skin. This perturbation clearly drives the buckling period even as λ_i^{crit}changes. Nevertheless, there is an effect of λ_i^{crit} on the period of the buckling and it is more pronounced than the effect of μ_e.

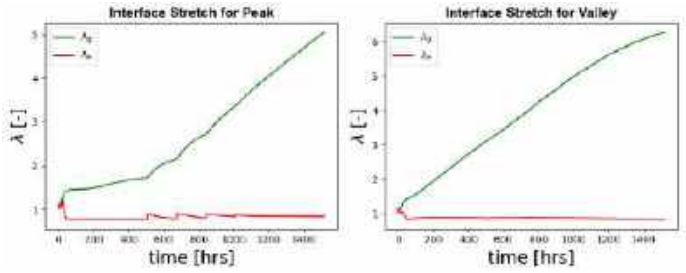

Figure 3: Elastic deformation and growth for the flat interface model at the two locations of interest: peak and valley.

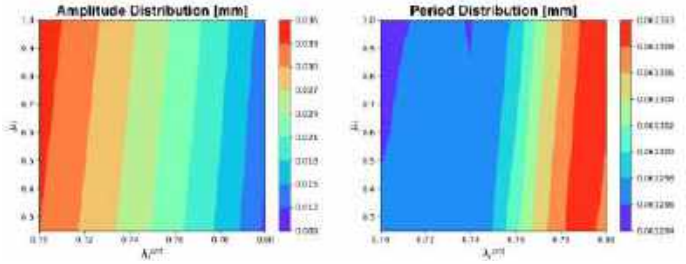

Figure 4: Contour plots of the amplitude and period variation in the flat model with a combined thickness between the epidermis and interface of 0.1 mm.

DISCUSSION

Our analysis shows that considering a stress-free sinusoidal interface does not allow us to recover the subsequent buckling needed to retain physiological Rete ridges during tissue expansion. Instead, an initially flat interface buckles leading to the Rete-ridges, and subsequent buckling during tissue expansion can maintain this physiological feature of skin. The most important parameter is the homeostatic pre-stretch of the interface layer λ_i^{crit}. The pre-stretch needs to be <0.8 to place the layer under enough compression. The compression in the interface layer and the tension in the dermis layer, with a pre-stretch λ_d^{crit}=1.15, allow for buckling of the interface and also physiological pre-tension of skin.

ACKNOWLEDGEMENTS

Supported by NIAMS R01AR074525

REFERENCES

[1] Zhao et al., *J Mech Behav Biomed Mat*, (2020) 105:103694.
[2] Moreno-Flores et al., *Biomech Model Mechanobiol*, (2023)
[3] Han, T. et al, *Acta Biomaterialia* (2022)
[4] Topczeusca et al, *J Tissue Eng Gen Med* (2019), 13(11).
[5] Colin J., Holland M.A, *Int J Solids Struct* (2019)

EFFECT OF BREATHING TECHNIQUE FOR TARGETED LARYNGOPHARYNGEAL DRUG DELIVERY

Shamudra Dey (1), Guilherme J.M. Garcia (1,2)

(1) Joint Department of Biomedical Engineering, Marquette University and Medical College of Wisconsin, Milwaukee, WI, USA
(2) Department of Otolaryngology and Communication Sciences, Medical College of Wisconsin, Milwaukee, WI, USA

INTRODUCTION

Laryngopharyngeal reflux (LPR) affects approximately 20% of the population in the United States and corresponds to 10% of visits to otolaryngology clinics [1-3]. Like gastroesophageal reflux disease (GERD), LPR is caused by retrograde flow of stomach content, but LPR is associated with symptoms at the larynx and pharynx while GERD causes damage to the esophagus. Currently, there is no gold standard medical therapy to treat LPR. Placebo-controlled trials have shown that acid-suppression therapy (i.e., proton pump inhibitor) that is effective against GERD is not effective against LPR [4]. Therefore, there is an unmet need to develop new pharmaceutical products to treat LPR.

Dry Powder Inhalers (DPIs) were originally developed to treat asthma and chronic obstructive pulmonary disease (COPD). The target site for drug delivery for asthma and COPD is the lungs. The Food and Drug Administration (FDA) specifies that aerodynamic particle size distribution (APSD) and inhalation rates are critical quality attributes of DPIs because these attributes have a major impact on the regional drug distribution in the airways [5]. Currently, the optimal APSD and breathing technique for maximizing drug delivery to the laryngopharynx are unknown. The main objective of this research is to study the effect of breathing techniques (fast, normal, and slow inhalation) for optimized laryngopharyngeal drug delivery using a newly proposed DPI to treat LPR.

METHODS

The 3D model was created using Materialise MIMICS software and is based on the MRI of healthy 49-year-old female (**Fig. 1A**). Poly-hexcore meshes of 2.9 million (coarse), 5.6 million (medium) and 9.2 million (fine) cells and 5 prism layers were created in ANSYS Fluent Meshing. **Fig. 1B** shows a poly-hexcore mesh of 5.6 million cells with 5 prism layers. CFD simulations were performed in ANSYS Fluent using the k−ω SST turbulence model. The transient simulations were implemented with a sinusoidal breathing profile (**Fig. 2**):

$$Q(t) = Q_{max} * \sin(2\pi t/T) \quad (1)$$

where, $\bar{Q}$=30 L/min is the time-averaged inhalation rate and T is the breath duration. We studied three inhalation rates, namely fast (T = 2s), normal (T = 4s), and slow (T = 6s) inhalation.

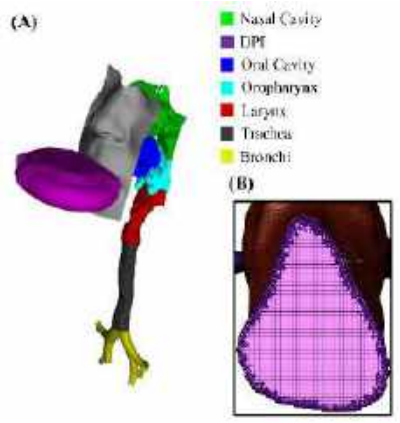

Figure 1: (A) Three-dimensional model of the human respiratory tract. (B) Poly-hexcore mesh with 5.6 million cells and 5 prism layers.

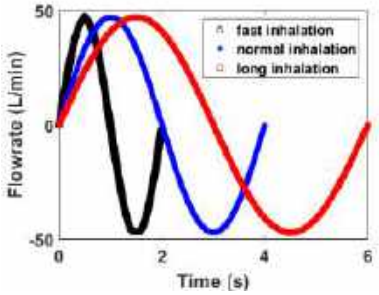

Figure 2: Sinusoidal breathing profiles with fast (T=2s), normal (T=4s) and long (T=6s) inhalation.

To perform discrete phase modeling, 25 log-spaced particle sizes of 1-to-50-micron particles of density $1000\ kgm^{-3}$ were released once the oral inhalation rate reached 15 L/min. The duration of particle release was 0.5 sec, which is the typical emptying time of DPIs based on literature [6]. We assumed a log-normal particle size distribution, where X_{50} = mass median aerodynamic diameter (i.e., half the aerosol mass is in particles smaller than X_{50}) and σ_g = geometric standard deviation (represents the width of the distribution).

RESULTS

The CFD simulations were validated by comparing the CFD-predicted extrathoracic dose (i.e., oral cavity, pharynx, larynx, and trachea) with in vitro experiments by Stahlhofen et al. (1989) [7]. A grid independence study revealed that a mesh with 5.6 million elements provided a nearly mesh independent results for both the air velocity field and particle deposition. **Fig 3** shows both validation of CFD results by comparing them to experimental results and grid independence study of particle deposition.

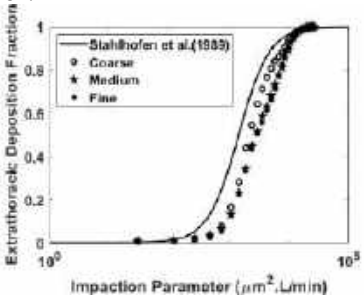

Figure 3: Prediction of Extrathoracic deposition compared to the experimental data of Stahlhofen et al. (1989).

Laryngopharyngeal deposition was predicted to be maximized by an impaction parameter, $IP = d_a^2 Q = 5525$ μm².L/min, where d_a is the particle aerodynamic diameter and Q is the inhalation rate (**Fig. 4**). This suggests that a monodisperse aerosol with d_a = 13.56 μm inhaled with a slow inhalation rate of 30 L/min (corresponding to IP = 5525 μm².L/min) would provide the highest laryngopharyngeal deposition fraction of 0.61 (i.e., 61% of the DPI dose would deposit in the laryngopharynx). However, DPIs are polydisperse. To illustrate the importance of the APSD, we investigated two hypothetical DPIs (DPI-1 & DPI-2) with constant $\sigma_g = 2$ (**Fig. 5**). DPI-1 has an X_{50} = 10 μm, which is hypothesized to be optimal to treat LPR compared to DPI-2, which has X_{50} = 3 μm (representative of current commercial DPIs).

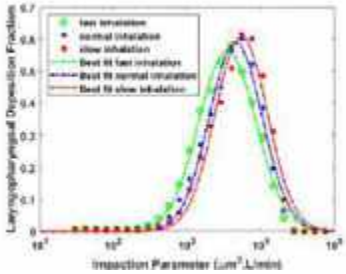

Figure 4: Effect of Breathing techniques on laryngopharyngeal Deposition Fraction for DPI-1 (X_{50} = 10 micron).

Our results suggest that the effect of inhalation rate (breathing technique) is negligible for DPI-1 (30.3 % laryngopharynx DF for normal inhalation and 30.6 % laryngopharynx DF for fast inhalation) (**Fig. 6**). In contrast, the simulations predicted that for DPI-2, a higher laryngopharynx deposition would be achieved with a faster inhalation. However, our simulations predicted that the laryngopharyngeal dose delivered by DPI-1 is significantly higher than the dose delivered by DPI-2 (i.e., 30.6% vs. 9.1% of the total mass for DP1-1 and DPI-2, respectively, for a fast inhalation) (**Fig. 6**).

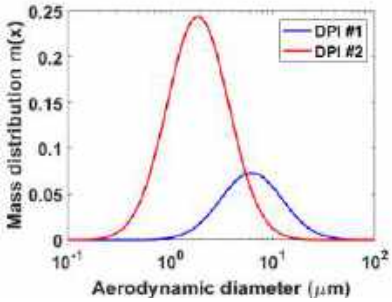

Figure 5: Log-normal particle size distribution of two hypothetical DPIs: DPI-1 (X_{50}= 10 microns and $\sigma_g = 2$) and DPI-2 (X_{50}= 3 microns and $\sigma_g = 2$).

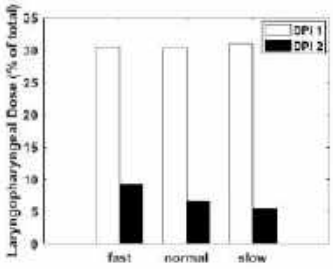

Figure 6: DPI-1 (X_{50} = 10 μm, $\sigma_g = 2$) has significantly higher laryngopharyngeal deposition than DPI-2 (X_{50} = 3 μm, $\sigma_g = 2$).

DISCUSSION

This study investigated the impact of breathing technique (slow vs. fast inhalation) on laryngopharyngeal drug delivery. The study has multiple limitations, including the small sample size (n=1 anatomy). However, this study provides crucial information to design DPIs to treat LPR. For our proposed DPI-1, we observed minimal effect of breathing technique with similar laryngopharyngeal deposition for all three cases. In contrast, for commercially available DPIs ($X_{50} \leq 5$ μm for lung delivery), we observed that faster inhalation led to higher laryngopharynx deposition. However, current DPIs in the market have much smaller laryngopharyngeal deposition compared to our proposed DPI-1. We conclude that DPI-1 (X_{50} = 10 μm) is expected to provide significantly higher laryngopharyngeal deposition compared to DPI-2 (X_{50} = 3 μm).

ACKNOWLEDGEMENTS

The authors would like to acknowledge support provided by the MCW Research Computing Center.

REFERENCES

[1] Altman, KW et al., *Laryngoscope* 115:1145-1153, 2005.
[2] Koufman, JA et al., *Otolar Head Neck Surg*, 34:859-871, 2000.
[3] Reulbach, TR et al., *Otolar Head Neck Surg*, 124:448-450, 2001.
[4] Steward, DL et al., *Otolar Head Neck Surg*, 131:342-350, 2004.
[5] FDA, Metered dose inhaler (MDI) and dry powder inhaler (DPI) products - Quality considerations - Guidance for Industry, 2018.
[6] Longest, PW et al., *Pharm Res*, 29:1670–1688. 2012.
[7] Stahlhofen, W et al., *J Aerosol Medicine*, 2:285-308, 1989.

TAILORED DELIVERY OF A SMALL MOLECULE AGONIST FOR HEDGEHOG SIGNALING ACTIVATION IN TENDON-TO-BONE INTEGRATION

J. Marcelin (1), R. Madi (1), T. Kamalitdinov (1), X. Jiang (1), D-H. Kim (1), R. L. Mauck (1), A. Kuntz (1), N. Dyment (1)

(1) Department of Orthopaedic Surgery, University of Pennsylvania, Philadelphia, PA, USA

INTRODUCTION

Tendon injuries often occur at the tendon-to-bone junction (i.e., enthesis) and frequently result in disorganized scar tissue formation following injury [1]. The Hedgehog (Hh) signaling pathway plays a vital role in regulating fibrocartilage formation at the enthesis during growth [2-4]. In our prior research, we demonstrated that activating the Hh pathway, either genetically or through systemic Hh agonist administration, promoted tendon-to-bone attachment formation post anterior cruciate ligament reconstruction (ACLR) [5]. Therefore, targeting this pathway shows promise in improving tendon-to-bone repair by encouraging zonal enthesis formation.

Recognizing the importance of Hh signaling in the maintenance of various tissues [6], there is an unmet need to develop localized therapies to leverage this pathway to enhance repair outcomes, while minimizing off target effects. Thus, we developed an electrospun scaffold release system with varying concentrations of SAG, a small-molecule Hh agonist, to locally stimulate Hh signaling in the cells that contribute to tendon-to-bone integration during repair. Thus, this study aimed to incorporate SAG into the scaffold, evaluate scaffold properties post-incorporation, establish the *in vitro* release profile and bioactivity of SAG, and investigate the local activation of the Hh pathway by these scaffolds in promoting tunnel integration in a high throughput bilateral transverse tibial tunnel (TTT) surgical model.

METHODS

Scaffold Fabrication: A PCL solution (35 wt%) was prepared in DMF/THF with the Hh agonist (SAG) at different concentrations (0, 0.001, 0.01, 0.1 mg/ml). The solution (2mL) was spun from an 18G needle at 15kV onto a rotating mandrel (8 m/s, 2.5 ml/hr).

SEM: Fibril alignment and fibril diameter were measured using the OrientationJ plugin and the General Image Fiber Tool (GIFT) in FIJI from images acquired on an FEI Quanta 600 ESEM.

SAG Release Study: All animals and procedures were approved by Institutional IACUC. Blank and SAG-infused scaffolds were placed in culture media in tubes on a shaker at 37ºC (**Fig. 1A**) and conditioned media (CM) was collected over 28 days. CM samples from days 2, 8, 16, or 26 were applied to bone marrow stromal cell (bMSC) cultures for 4 days. Gli1 gene expression was assessed by qPCR.

Tunnel Integration Study: TTT surgeries were performed on 24 mice to test the effect of SAG release on Hh activity and tunnel integration. This procedure was utilized as a simpler, higher throughput model than the ACLR model we used previously [1,5]. Graft tail tendons were harvested from mice and a sterile scaffold was added to the graft bundle. A transverse tibial tunnel was drilled in the metaphysis using a 27G needle. The graft with the scaffold was passed through this tunnel and the samples were assessed on day 14 post-surgery.

Mineralized Cryosectioning, qPCR, and Imaging: Limbs were fixed, embedded, sectioned undecalcified with cryofilm. The medullary canal was microdissected from tissue sections for qPCR. Adjacent sections were stained with Alizarin Complexone (AC) to visualize deposited mineral fluorescently on a Zeiss Axio Scan.Z1. AC area was normalized to the area of the tendon graft and scaffold and quantified.

Statistical Analysis: Fiber diameter, scaffold mechanical properties, and *in vivo* qPCR and AP activity were compared via one-way ANOVA ($p<0.05$). Gli1 expression from *in vitro* release was compared via two-way ANOVA with Sidak's post-hoc tests ($p<0.05$).

RESULTS

SAG incorporation affected fiber alignment but not diameter of electrospun PCL scaffolds: We found that SAG incorporation reduced the overall fiber alignment (SD_{blank} = 15.8º, $SD_{0.01}$ = 19.1º, $SD_{0.001}$ = 25.3º, $SD_{0.1}$ = 26.6º) in the scaffold. However, fiber diameters of the SAG scaffolds were not significantly different from the blank scaffold (0.33+/-0.06, 0.32+/-0.07, 0.35+/-0.05, 0.32+/-0.11 μm; mean+/-SD for 0, 0.001, 0.01, and 0.1mg/ml respectively).

Delivery of conditioned media to bMSCs increased Gli1 expression in

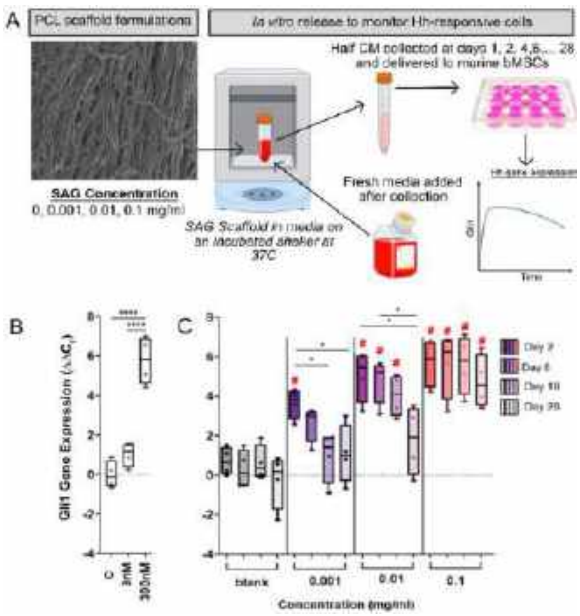

Figure 1: SAG released from scaffolds in dose and time dependent manner. *In vitro* release study design (A). Gli1 ΔΔCq for CM from controls (B) and scaffolds at the four timepoints (C). ****p<0.0001, *p<0.05; # p<0.05 vs. blank.

a dose- and time-dependent manner: As anticipated, we found a significant increase in Gli1 expression with 3nM (2-fold) and 300nM (70-fold) of SAG added directly to the media (p<0.05, **Fig. 1B**) vs control media. CM media from the SAG scaffolds increased Gli1 expression in a dose- and time-dependent manner (p<0.05, **Fig. 1C**). While Gli1 expression did not change over time in the blank scaffolds, it was significantly higher in the SAG scaffolds compared to the blank scaffolds in CM collected on day 2. Interestingly, Gli1 expression remained elevated in the 0.1 mg/ml SAG scaffold for a longer period compared to the other concentrations. The results suggest that the 0.1 mg/ml SAG scaffold released enough SAG to maintain activated Gli1 expression in bMSCs over a 26-day period.

Localized delivery of SAG to the bone tunnels increased Gli1 activity while also promoting mineralized fibrocartilage (MFC) formation in the tendon graft and mineral deposition in the scaffold: To determine the local effect of SAG released from the scaffold on nearby cells in an *in vivo* setting, we microdissected tissue within the medullary canal, including the surgically drilled tunnel (**Fig. 2C**), from cryosections using a needle and performed qPCR. SAG release yielded a dose dependent effect on Gli1 expression, with the 0.1 mg/ml SAG group having ~3-fold higher expression (p=0.009, **Fig. 2D**). To monitor the tunnel integration process, we measured the deposited mineral area in the tendon graft and scaffold (red in **Fig. 3A**). We found that SAG concentration affected AC deposition in a dose-dependent manner, with the 0.1mg/ml group having higher MFC formation in the tendon graft (p=0.044, **Fig. 3C**) and higher mineral deposition in the scaffold region of the 0.01 mg/ml (p=0.048) and 0.1 mg/ml (p=0.047) groups (**Fig. 3D**).

DISCUSSION

Incorporating the Hh signaling agonist, SAG, into electrospun PCL scaffolds enabled controlled release *in vitro* and *in vivo* while maintaining bioactivity. *In vitro*, a dose- and time-dependent release profile revealed sustained Gli1 expression at 0.1 mg/ml, contrasting with reduced levels at other doses over one month. In the *in vivo* TTT model, SAG-treated scaffolds demonstrated a dose-dependent increase in Gli1 expression (**Fig. 2D**) and prompted a dose-dependent augmentation in mineral deposition, notably the 0.1 mg/ml group exhibiting greater MFC formation in the tendon graft and scaffold region (**Fig. 3**). This result is consistent with our previous work using systemic injections of a Hh agonist [5]. The findings support the idea that Hh signaling is a strong regulator of the tendon-to-bone integration process [2-4] and enhance our understanding of Hh pathway dynamics in later stages of zonal attachment formation. Our work suggests that using the Hh pathway for therapy could revolutionize the treatment of tendon and ligament injuries. Delivering agonists within a specific therapeutic window could improve tendon-to-bone repair and recovery times. However, more research is needed to fully understand the Hh pathway and develop new therapies. Therefore**,** future studies will apply the SAG-delivering scaffolds in our more clinically relevant, yet lower throughput, ACLR model to improve the tendon-to-bone integration processes.

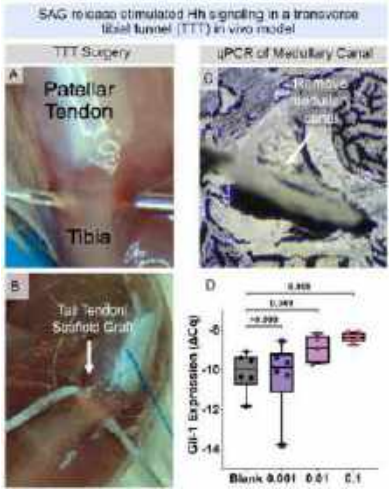

Figure 2: SAG release in a TTT model (A, B) stimulated Gli1 expression from micro-dissected tissues (C, D).

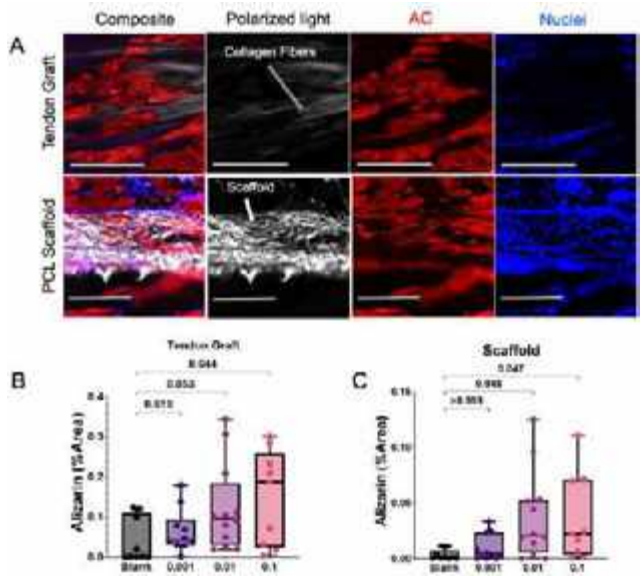

Figure 3: SAG release promoted mineral deposition in the tendon graft (A,B) and PCL scaffold (A,C). Scale = 200μm.

ACKNOWLEDGEMENTS Work supported by NIH R21 R21AR078429, P30AR069619, R01AR076381, F31AR079840 (TK), and T32-AR007132.

REFERENCES [1] Kamalitdinov, T et al., *JOR*, 2020 [2] Lu, H et al., *Annu. Rev. Biomed. Eng*., 2013 [3] Liu, C-F et al, *PLoS One*, 2013 [4] Dyment, N et al., *Dev Biol*, 2015 [5] Kamalitdinov, T et al., bioRxiv, 2022 [6] Ingham, P et al., *Nat Rev Genet.*, 2011.

CELL-EXTRACELLULAR MATRIX FEEDBACK RESULTS IN SPONTANEOUS CELLULAR ORIENTATION AND CONTACT GUIDANCE BEHAVIOR IN 3D DISCRETE FIBER MODELS OF CELL COMPACTION

Adam W.Y. Ley (1), Lauren M. Bersie-Larson (1), Ryan P. Collanton (2), Sabin Adhikari (2), Robert T. Tranquillo (1,2), Kevin D. Dorfman (2), Victor H. Barocas (1)

(1) Biomedical Engineering, University of Minnesota, Minneapolis, MN, USA
(2) Chemical Engineering and Materials Science, University of Minnesota, Minneapolis, MN, USA

INTRODUCTION

Cell-mediated remodeling processes are responsible for tissue organization in developmental biology [1] and tissue reorganization in disease states such as cancer [2]. Thus, a more thorough understanding of how cells interact with and remodel their microenvironment can better inform tissue engineering strategies seeking to mimic or counteract these phenomena. Recent work has investigated how cell-mediated remodeling affects the development of multi-cellular structures, such as angiogenesis [3]. However, a vast majority of the existing body of theoretical work uses a continuum representation of the extracellular matrix (ECM), which does not capture non-affine deformations characteristic of loosely connected fiber networks. While some discrete models of cell-matrix contraction exist [4,5], many simulate the process in 2D or fail to incorporate fiber-fiber interactions, such as entanglement or crosslinking, which result in permanent changes to the ECM structure. This work seeks to address these gaps by using a discrete model of the ECM in a molecular dynamics framework to simulate cell contraction and matrix reorganization. In particular, we explored how feedback between cells and their extracellular matrix can result in spontaneous cellular alignment and directed ECM reorganization. We tested the hypothesis that cell-driven remodeling can induce structural anisotropy in the ECM, in turn leading to preferential cell alignment.

METHODS

ECM Network Generation

Networks were generated to represent a 70x70x70 μm^3 volume of a 4 mg/mL collagen gel. Isotropic ECM networks were generated from periodic 3D Voronoi tessellations on randomly seeded points [6]. Collagen fibrils were modeled as a segmented, bead-spring chains composed of equally spaced beads connected by harmonic bonds (Fig. 1.A-B). To allow for plastic ECM remodeling [7], beads could interact via strong, short-distance Lennard-Jones potentials with a resting length corresponding to a fiber radius of 100 nm (Fig. 1.C).

Cell Model

The cell was modeled as a static ellipsoid at the center of the network. At each time step, the cell was described by its 3 semiaxes and their corresponding unit vectors. During the simulation, the cell volume was kept constant at 1300 μm^3. Pseudopods were generated on a similar ellipsoid 8-times the volume of the cell, modeling pseudopod extension beyond the cell's surface. These pseudopods were bound to the static cell center with a harmonic bond that equilibrated at the cell surface. Pseudopods were able to bind to the ECM via strong Lennard Jones potentials that equilibrated at the radius of the pseudopod, about 7 μm. In this way, ECM beads bound to the pseudopod surface were also retracted towards the cell center during cell contraction.

A model of cell sensing enabled the cell to respond to dynamic changes in the matrix. Prior to pseudopod placement, an ellipsoidal volume of the fiber network centered at the cell and 8-times the cell volume was analyzed. A fiber orientation tensor Ω (Eq. 1) was calculated for fiber segments within this ellipsoid. For each segment,

$$\Omega_{ij} = \frac{1}{l^{f,total}} \sum l^f n_i^f n_j^f \quad (1)$$

the outer product of the normal vector n^f and itself was scaled by the length of the segment l^f. The resulting tensor was then normalized by the total length of fibers within the volume $l^{f,total}$. For isotropic networks, $\Omega_{11}=\Omega_{22}=\Omega_{33}=0.33$. For networks completely aligned in the x-direction, $\Omega_{11}=1$ and $\Omega_{22}=\Omega_{33}=0$. The semiaxes of the cell were updated to match this orientation tensor. Pseudopod locations were randomly generated beyond the surface of the updated morphology, biasing the longer axes to emulate contact guidance behavior [8].

Simulation Procedure

Simulations were conducted using HOOMD [9], a molecular dynamics simulation software (Fig. 1.D). Networks were first allowed to relax before gross network characteristics like density and alignment

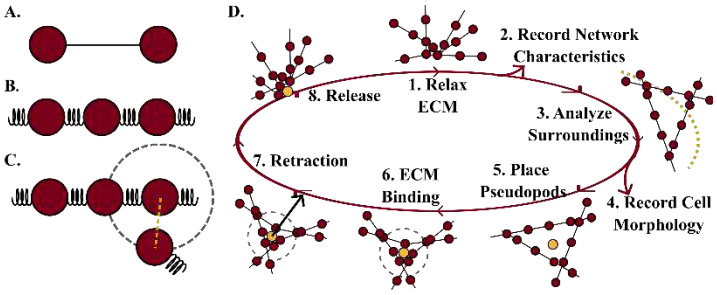

Figure 1: (A, B) Segmented fiber networks were allowed to reorganize (C) and bind neighboring nodes to simulate ECM remodeling during (D) simulations of cell contraction.

were recorded. Spherical cells were then seeded in the center of the network and an orientation tensor was calculated for the network surrounding it. The cell morphology was updated using the orientation tensor, and pseudopods were generated outside the surface of the cell. Pseudopods bonded to the ECM via Lennard Jones potentials before being retracted towards the surface of the cell. Pseudopods were then removed from the simulation, and the network was allowed to relax. This protocol was repeated for each contraction cycle.

Cases Studied

First, a simulated cell contracted within an isotropic network for 40 cycles. After each contraction, spherical subregions of the matrix centered around the cell were analyzed for density, alignment, and strain. This study was a validation of the basic principle and was directly comparable to published experimental work [10].

Next, compaction of 3 different periodic networks was simulated: isotropic, aligned, and narrow. Isotropic gels were created as above. Aligned gels were generated by creating rectangular tessellations that were then morphed into cubes to induce alignment in the x direction with Ω_{xx}=.5. Narrow networks were created by seeding isotropic gels in a unit volume with a 1:3:3 aspect ratio, with the x-direction being the shortest. Since the boundaries are periodic, a narrow domain corresponds to a lattice of cells with smaller spacing in the x direction. Cells were allowed to undergo 6 contractile cycles and cellular Ω_{xx} values were recorded to track cell alignment in the x-direction (Fig.3.A).

RESULTS

Matrix Compaction and Reorganization in Isotropic Networks

Over the course of the simulation, fiber density increased the most in regions close to the cell (Fig. 2.A). Additionally, after many contraction cycles, a plateau in the densification was observed, which is consistent with recent experimental findings [10] (Fig 2. B). In this way, the model suggests that fiber densification varies with both position and time during cell-driven compaction. The shape characteristics of the matrix were recorded. As demonstrated in the insets (Fig. 2.C), repeated contractions resulted in a matrix that was densest around the cell and aligned radially away from the cell center.

Finally, the distribution of fibers' resting strains were recorded at each step. Over the course of the simulation, the proportion of segments in tension (Fig 2.D) and the mean fiber strain increased. Further, the distribution of fiber strains differed from earlier time sequences (P<0.01). These results indicate that not only did the ECM's structure change, but the mechanical properties of the matrix were also changed.

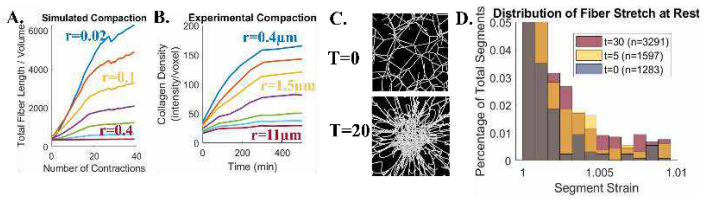

Figure 2: (A) Simulated and (B) experimental [10] densification, (C) matrix reorganization, and (D) resting strain distribution.

Spontaneous Cellular Alignment due to ECM Mechanical Feedback

Cells in isotropic networks did not align in x, whereas cells in aligned networks immediately aligned in the x-direction (Fig. 3.D). Cells in narrow gels started aligning randomly but began aligning in the x-direction with subsequent contractions. By contraction 6, Ω_{xx} for cells in narrow gels differed significantly from that of cells in cubic isotropic gels (P<0.05). In contrast, cells in aligned gels decreased in alignment over the experiment. Despite this, they remained more aligned than cells in the isotropic and narrow gels (P<0.01).

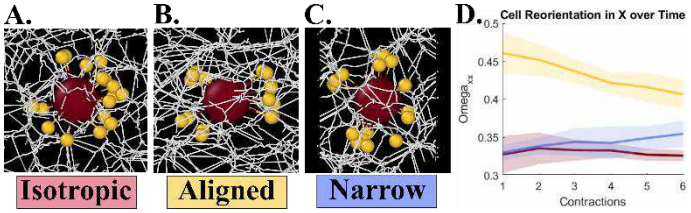

Figure 3: Ω_{xx} indicated that cell orientation remained unaligned in (B) isotropic gels, but aligned in (C) aligned and (D) narrow gels

DISCUSSION

This project sought to create a computational mechanical model of feedback between a contracting cell and its dynamic microenvironment, driving matrix reorganization and cell reorientation. Simulated results of single-cell contraction demonstrate that the model can recapitulate experimental findings like spatiotemporal trends in matrix densification and ECM reorientation. Furthermore, the model incorporates permanent remodeling of the ECM due to cell-mediated fiber rearrangement, as indicated by the distribution of fiber strains at rest. These results appear consistent with findings that cells mechanically remodel their environment, changing ECM density [10] and stiffness [7].

The periodic nature of the simulation presents both an opportunity and a challenge. For one, it enables investigations of cell-ECM-cell interactions, where cells can respond to cues across neighboring unit cells. This was the intention in the narrow simulations, but this phenomenon might also be affecting the other test cases. Thus in order to isolate the effects of one cell, or even two cells, significantly larger unit volume may be needed. Finally, while the model incorporates elements of contact guidance, recent literature suggests that this process is mediated by anisotropic force generation due to structural cues in the network [8,11,12], not just topography. Though this model does not probe for local stiffness anisotropy, the alignment-feedback mechanism coupled with plastic matrix deformation framework allows for more robust investigations into cell-ECM interactions.

ACKNOWLEDGEMENTS

This work was supported by NIH training grant T32-HL139431, NIH grant R21 GM147898.

REFERENCES

[1] Barrasa-Ramos, S et al., *J R Soc Interface* 19(197):20220360, 2022; **[2]** Ahmadzadeh, H et al., *PNAS* 114(9): E1617-E1626, 2017; **[3]** LaBelle, S et al., *PLoS Comp. Bio*. 19(10):e1011553, 2023, **[4]** Hall, M et al., *PNAS*, 113:1403–24048, 2021; **[5]** Feng, J et al., *Soft Matter* 15:4856-4864, 2019; **[6]** Nachtrab, S et al., *Adv Mater*, 23: 2633–2637, 2011; **[7]** Chaudhuir, O et al., *Nature*, 584:535–546, 2020; **[8]** Thrivikraman, G et al., *PNAS*, 118(29):e2024942118, 2021; **[9]** Anderson, J et al., *Com Mat Sci*, 173:109363, 2020; **[10]** Shakiba, D et al., *ACS Nano*, 14(7):7868–7879, 2020; **[11]** Bersie-Larson, L et al., *J R Soc Interface*, 19(190): 20210951, 2022; **[12]** Ray, A et al., *Nat Comm*, 8:14923, 2017.

SB³C2024
Summer Biomechanics, Bioengineering and Biotransport Conference
June 11-14, Lake Geneva, WI, USA

LYMPHO-VASCULARIZED BREAST-SKIN PLATFORM FOR MODELING TUMOR INVASION IN ADVANCED BREAST CANCER

Melika Mehrabi-Dehdezi (1), Marissa Nichole Rylander (1,2,3)

(1) Walker Department of Mechanical Engineering, The University of Texas at Austin, Austin, Texas, USA
(2) Department of Biomedical Engineering, The University of Texas at Austin, Austin, Texas, USA
(3) Oden Institute of Computational Engineering and Sciences, The University of Texas at Austin, Austin, Texas, USA

INTRODUCTION

Inflammatory Breast Cancer (IBC) stands out as a distinct and aggressive form of breast cancer, accounting for 10% of breast cancer deaths despite its relatively rare occurrence. A significant characteristic of IBC is the invasion of cancer cells into the lymphatic and blood vessels near the skin, leading to the formation of tumor emboli and lymphovascular spread[1]. This phenomenon, known as lymphovascular space invasion (LVSI), plays a crucial role in the clinical manifestations of IBC, making traditional skin-sparing and breast-conserving surgeries ineffective choices. The mechanisms underlying LVSI, particularly its progression from breast tissue into the overlying skin within the lymphatics, termed dermal lymphatic invasion (DLI), remain poorly understood and representative models that account for lymphatics, surrounding metastatic sites, and immune cells do not exist to understand this phenomenon. The goal of this research is to create a Breast-Skin platform with functional blood and lymphatic vessels that can be used for elucidation of LVSI and screening therapeutics.

METHODS

We created physiologically representative breast tumor and skin platforms and integrated them into a multi-tissue Breast-Skin platform with functioning blood and lymphatic vessels. To mimic breast tumor tissue, 1 million MDA-IBC3 cells/mL and THP-1 macrophages were cultured in a matrix of 7 mg/mL collagen type 1 which was polymerized around 22-gauge needles to create the vessels. In order to mimic relevant breast tumor properties that affect drug transport, we characterized tumor porosity using SEM. Vessel permeability was measured by injecting 70 kDa dextran into the channels and imaging its fluorescent intensity that crossed the endothelium in a ROI in images taken every 2 minutes over the course of 30 minutes. After 24 hours, the breast tumor platform was exposed to 5 µm PM37 for 24 hours (end of Day 1). PM37 is a phosphoSTAT6 inhibitor that has been shown to prevent M0 macrophage polarization into the M2 phenotype as well as reverse M2 polarization[2]. For the skin platform the dermis layer of the skin platform was created using a layer of 4 mg/mL collagen solution or 50/50 C/KTN hydrogel solution seeded with 0.1 million cells/mL of primary normal human dermal fibroblasts (NHDFs). A blood vessel was created in the dermis similar to the breast tumor platform. The epidermis layer was created by seeding Ker-CT on top of the platform in the upper compartment in proliferation media at a seeding density of $0.4x10^6$ cells/sample. Vessels were perfused with 1×10^7 cells/mL mKate-labeled tumor microvasculature endothelial(TIME) and 1×10^7 cells/mL Human dermal lymphatic endothelial cells (HDLECs) for blood vessels and lymphatics respectively. We also compared different formulations of matrix materials of collagen solution and 50/50 C/KTN hydrogel solution on the barrier function, epidermal thickness, and vessel permeability of the skin platform. We measured vessel permeability similar to the breast tumor platform, barrier function with Transepithelial electrical resistance (TEER), and characterized epidermal thickness with Hemotoxylin and Eosin staining. By integrating these two platforms we developed Breast-Skin platforms for studying LVSI. Breast-Skin platforms were rotated on all 4 sides for 4 minutes each rotation and then this process was repeated so the endothelial cells could attach on all the surfaces of the hollow channel. All Breast-Skin platforms were then placed in 6 well plates with 1.5-2 mL of complete endothelial cell media in each well surrounding the platform and put back on the rocker for 3 days to allow formation of a confluent vessel.

RESULT S

The presence of THP-1 macrophages is inherent in the IBC tumor microenvironment and resulted in a significantly more permeable

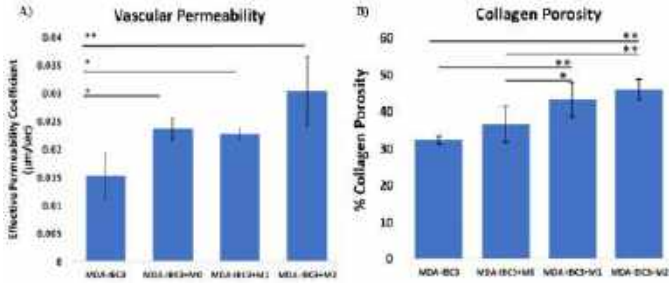

Figure 1: A) Effective permeability of vasculature in breast tumor platform. B) Collagen (ECM) porosity in breast tumor platform.

endothelium compared to platform containing only MDA-IBC3 cells (Fig.1A). We have also shown that incorporating THP-1 macrophages has a significant impact on ECM porosity and vasculature permeability allowing collective tumor cell migration and intravasation. Porosity measurements from SEM processed images revealed the influence of THP-1 macrophages on matrix remodeling. Platforms with the THP-1 M1 or M2 macrophages were significantly more porous than the platforms with THP-1 M0 and the MDA-IBC3 only platforms[3](Fig.1B).

After observing macrophage induced matrix porosity, we perfused the *in vitro* platforms with PM37 to see if we could diminish the increased angiogenic response for therapeutic consideration. Cytokine analyses revealed a transient effect in expression of proangiogenic factors right after treatment, but once PM37 was removed, the expression levels of measured cytokines reverted back to control levels. EGF, bFGF, VEGF-A also decreased following in the MDA-IBC3+M2 platforms on Day 1 right after treatment ended, but these same cytokines were increased in the treatment platforms at the same timepoint in the MDA-IBC3+M1 platform revealing a phenotype dependent response to PM37(Fig.2).

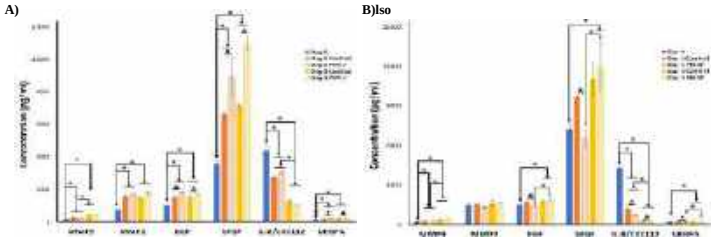

Figure 2: Effect of PM37 on cytokines expression in the A) MDA-IBC3 + M1 *in vitro* platform B) MDA-IBC3 + M2 in vitro platform.

Similarly, we created the first vascularized multi-layer human skin platform (Fig.3) comprised of a collagen dermal layer seeded with normal human dermal fibroblasts (NHDFs, blue, Fig.3A) containing an endothelialized blood vessel with functional endothelial (TIME) cells in red and an epidermal layer above consisting of a unique collagen/keratin blend with keratinocytes that promoted barrier function (green, Fig. 3A). We demonstrated keratinocyte differentiation characteristic of native epidermis with a stratified epidermis (Fig. 3B). TEER measurements showed a significant increase in resistance measured for 50/50 C/KTN hydrogel models compared to collagen hydrogels (Fig. 3C). For permeability measurement, 70 kDa dextran was perfused through the vessel of the vascularized skin platform. Images were taken every 2 minutes to measure the fluorescence intensity over time. The permeability coefficient of the skin layer composed of 100% collagen was significantly higher than that of 50/50 C/KTN hydrogels, indicating a stronger barrier created with the 50/50 C/KTN hydrogel (Fig.3E).

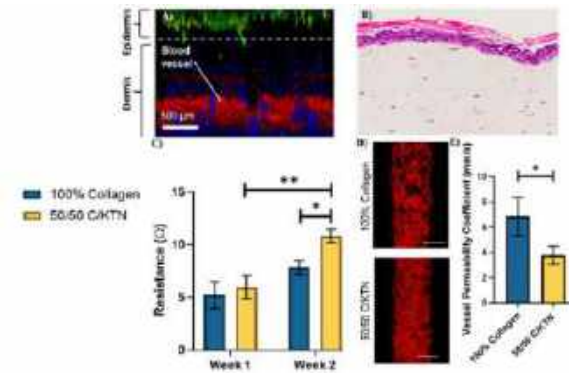

Figure 3: A) Confocal image of longitudinal cross section of multilayer skin platform with endothelial cells (red), fibroblasts(blue) in the dermis, and keratinocytes (green) in the epidermis. B) H&E-stained section of skin platform with stratified epidermis. C) TEER of skin platform at week 1 and 2. D) Confocal images of vessels in 100% collagen and 50/50 C/KTN hydrogel. E) Vessel permeability coefficient in skin platform.

By integrating the breast tumor and skin platforms, we created the first multi-tissue lymphovascularized Breast-Skin platform and generated multiple confluent blood vessels in both the skin and breast tissue, which were subsequently visualized using confocal microscopy (Fig.4). Notably, the channels in the breast tumor tissue appeared brighter than those in the skin, attributed to the increased depth of collagen that the laser had to penetrate to reach the upper layer. As it can be seen in Figure 4B, we also showed IBC cells invading the skin. We also observed the formation of MDA-IBC3 tumor emboli surrounded by newly established vascular vessels and emboli intravasation, a characteristic feature of *in vivo* IBC tumors (Fig. 4C).

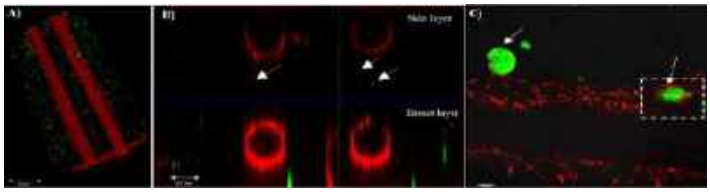

Figure 4: Confocal image of multilayer vascularized Breast-Skin platform. Breast-Skin platform layer seeded with MDA-IBC cells (green) and a vascular endothelium (red) overlaid with skin platform consisting of fibroblasts (unlabeled) around a vascular vessel (red). A) Top view of the Breast-skin platform. B) Cross section of the Breast-Skin platform showing MDA-IBC3 cells in the skin layer (denoted by white arrows). C) Center plane of vascular platform (red) showing tumor emboli (denoted by white arrows) invading vessels.

DISCUSSION

This study demonstrates the creation of the first *in vitro* Breast-Skin platform, with contiguous physiological tissues equipped with functional blood vessels and lymphatics. We have increased the complexity of our existing *in vitro* IBC platform by incorporating macrophages and observed the significance of incorporating different phenotypes of macrophages for studying cancer cells migration. We observed MDA-IBC3 emboli surrounded by these vessels, attempting to intravasate. The observation of vascular endothelium sprouting, and adjacent tumor emboli is solely facilitated by interactions between tumor and endothelial cells, representing the *in vivo* behavior of IBC. Additionally, we utilized the capability of the *in vitro* platforms to study tumor response to therapeutics and revealed a phenotype dependent response. Furthermore, we showed that the presence of KTN in the hydrogel increased barrier function by lowering the permeability of dextran through the developed epidermis and increased the transepithelial electrical resistance. Overall, our platform design enables the evaluation of various functional endpoints, such as intravasation, vessel sprouting, ECM porosity and the presence of stromal emboli. In further studies, we will measure LVSI, DLI, angio/lymphogenesis, vessel permeability, and cytokine expression. This will enable the contribution of metastasis through blood and lymphatic vessels in tumor metastasis.

ACKNOWLEDGEMENTS

This research is supported by IBC network foundation and cell resources were provided by the MD Anderson cancer center.

REFERENCES

1. Woodward, W. A. *et al.* Inflammatory breast cancer. in *Seminars in radiation oncology* vol. 19 256–265 (Elsevier, 2009).
2. Rahal, O. M. *et al.* Blocking Interleukin (IL)4- and IL13-Mediated Phosphorylation of STAT6 (Tyr641) Decreases M2 Polarization of Macrophages and Protects Against Macrophage-Mediated Radioresistance of Inflammatory Breast Cancer. *International journal of radiation oncology, biology, physics*, *100*(4), 1034–1043(2018).
3. Gadde, M., Mehrabi-Dehdezi, M. *et al.* Influence of Macrophages on Vascular Invasion of Inflammatory Breast Cancer Emboli Measured Using an In Vitro Microfluidic Multi-Cellular Platform. *Cancers (Basel).* **15**, 4883 (2023).

ENZYME- AND COMPARTMENT-FREE SINGLE PROTEIN DETECTION BY DIGITAL PLASMONIC NANOBUBBLE

T. Zhang (1), Y. Gao (1), Y. Liu (1), Z. Qin (1,2,3,4)

(1) Department of Mechanical Engineering, University of Texas at Dallas, Richardson, Texas, USA
(2) Department of Bioengineering, University of Texas at Dallas, Richardson, Texas, USA
(3) Center for Advanced Pain Studies, University of Texas at Dallas, Richardson, Texas, USA
(4) Department of Biomedical Engineering, University of Texas at Southwestern Medical Center, Dallas, Texas, USA

INTRODUCTION

Protein biomarkers have found widespread use in disease diagnostics such as for cancer and neurodegenerative disorders. The ability to detect and quantify low abundance protein biomarkers is essential for early diagnosis. Digital enzyme-linked immunosorbent assay (dELISA) opens a new era of ultra-low protein concentration detection (attomolar) compared with conventional approaches such as ELISA, mass spectrometry, and Western blotting.[1] dELISA is built upon two fundamental technologies, namely (1) separating the target protein into a large number of fL-pL compartments (microwells or droplets) with each compartment containing no more than one protein molecule, and (2) enzymatic amplification in each compartment to indicate the presence or absence of single molecules. While this method allows single molecule detection and absolute quantification, dELISA is complex, has high cost, and requires sophisticated instrumentation (e.g. Quanaterix SIMOA). [2, 3] Recently, an on-bead amplification using rolling cycle amplification (RCA) removes the need for microscale compartments.[4] but still requires enzyme amplification. Further simplifying dELISA can lead to wider adoption and clinical use.

In this study, we introduce an enzyme- and compartment-free single protein detection platform named Digital Plasmonic Nanobubble Detection for Protein biomarkers (DIAMOND-P). DIAMOND-P is an immunoassay-based platform that involves antibody-coated silica microbead to capture single protein molecules and gold nanoparticle to label the captured proteins. We then applied short laser pulses to generate nanobubbles around the captured gold nanoparticles (AuNPs), allowing instantaneous amplification and detection due to the strong light scattering.[5] Compared with dELISA, DIAMOND-P provides similar attomolar sensitivity while removing the need for slow enzymatic amplification and the use of physical microscale compartments. Moreover, DIAMOND-P can work well at room temperature with small sample volumes (less than 10 µL). Our new DIAMOND-P is a new method for enzyme- and compartment-free digital protein detection at room temperature and can accelerate its wider use in biomarker discovery and diagnostic testing for many disease applications.

METHODS

Plasmonic nanobubble generation and detection:

The generation of plasmonic nanobubbles was using 532 nm pump laser (Ekspla PL2230). Testing sample flowed through a 200 µm micro-capillary. For nanobubble detection, a continuous Red HeNe laser (633 nm, model R-30989, Newport) was used.

Poisson statistic:

The theoretical prediction by Poisson statistics was calculated by:

$$P(x = k; \lambda) = \frac{e^{-\lambda} \cdot \lambda^k}{k!} \qquad (1)$$

where k and λ are the actual and average number of AuNPs per detection zone (pulse laser excitation volume), respectively.

RESULTS

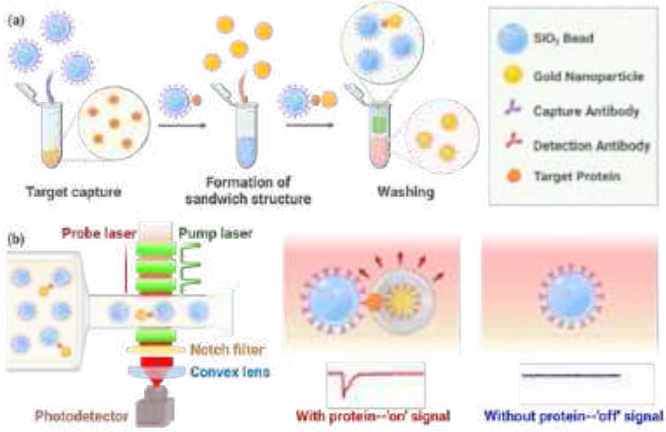

Figure 1: DIAMOND-P assay workflow for protein detection. (a) Bead-based sandwich immunoassay formation. **(b)** Digital counting principle for protein detection.

The detailed schematics for DIAMOND-P, which combines a microbead-based sandwich immunoassay and digital plasmonic nanobubble counting, are illustrated in **Figure 1**. Initially, silica beads coated with specific capture antibodies are introduced to a sample containing target proteins (**Figure 1a**). Gold nanoparticles, modified with detection antibodies, bind to these proteins, forming AuNP-labeled immunocomplexes. A filtration step follows, removing unbound reagents and excess AuNPs, thus isolating the targeted immunocomplexes. **Figure 1b** shows plasmonic nanobubbles (PNBs) generation when gold nanoparticles absorb energy from short laser pulses. These PNBs exhibit strong light scattering, detectable by a second probe laser. This system detects the presence ('on' signal) or absence ('off' signal) of gold nanoparticles that bind to target proteins.

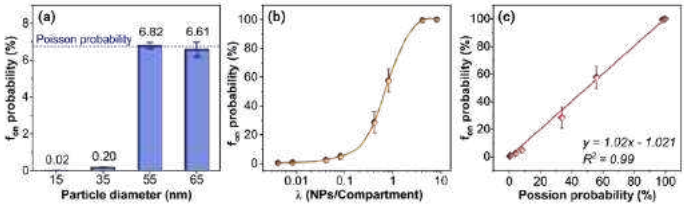

Figure 2: Single Au NPs detection. **(a)** Quantitative analysis of Au NPs of different sizes. **(b)** Quantitative analysis of 65 nm AuNP. **(c)** Linear correlation between experiment and Poisson statistics.

First, we evaluated the ability of the DIAMOND-P to detect single and count AuNP (**Figure 2**). To determine the AuNP size that can be detected by the DIMOND-P platform, we analyzed the probability of nanobubble signals from variously sized AuNP and compared them with the Poisson statistics (**Figure 2a**). The average number of AuNP per detection volume (λ) is 0.07. With 2 J/cm² pulse laser excitation, the result shows that the platform can reliably detect AuNPs larger than 55 nm. We further the ability to count single 65 nm AuNP by varying its concentration (**Figure 2b**). Comparison of the experimental f_{on} and Poisson statistics shows a good linear correlation (**Figure 2c**). These results demonstrate the ability of DIAMOND-P platform in single AuNP detection and quantification.

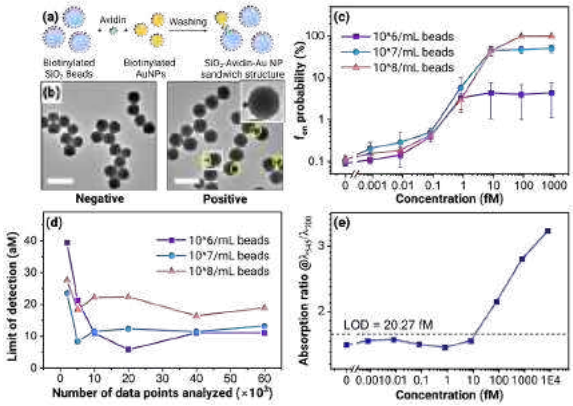

Figure 3: Avidin detection using the DIAMOND-P assay. **(a)** Formation of the SiO_2-Avidin-Au NP sandwich immune structure. **(b)** TEM imaging of post-washing samples with the scale bar of 1 μm, where inset shows the details of single SiO_2-Avidin-Au NP sandwich immune structure. **(c)** Avidin detection calibration curves. **(d)** Data Analysis Impact on Limit of Detection (LOD). **(e)** Colorimetric analog analysis of post-washing samples.

Second, we tested DIMOND-P platform to detect avidin as a model protein (**Figure 3**). We first mixed biotinylated 500 nm SiO_2 beads with avidin for 20 minutes at room temperature, and then incubated with biotinylated AuNPs for 15 minutes. After a filtration washing step to remove unbound reagents and excess AuNPs, we imaged the SiO_2-Avidin-Au NPs complex formation under transmission electron microscopy (TEM). **Figure 3b** shows that AuNPs are captured on SiO_2 beads only in the presence of avidin. **Figure 3c** shows the calibration curves for avidin detection with different SiO_2 bead concentrations (λ = 0.07, 0.7, 7). We further analyzed the limit of detection (LOD) as a function of the number of data points (laser pulses) and the results show that the DIAMOND-P can reach the average detection limit of 12 aM (**Figure 3d**). Compared with the colorimetric analog assay (**Figure 3e**), the LOD of DIAMOND-P is <u>three orders of magnitude lower.</u>

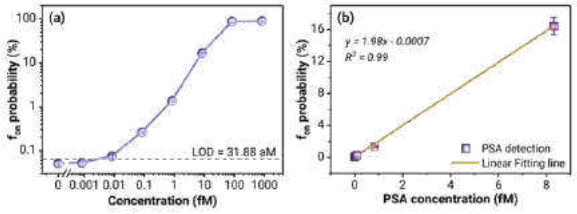

Figure 4: Prostate-Specific Antigen (PSA) detection with the DIAMOND assay. **(a)** Calibration curve for PSA detection. **(b)** Linear correlation analysis of PSA detection.

Lastly, we tested the DIAMOND-P assay's capabilities by detecting prostate-specific antigen (PSA), a crucial biomarker of prostate cancer. First, we established the calibration curve for PSA detection (**Figure 4a**) using SiO_2 beads at a concentration corresponding to λ = 2, where the dashed black line indicates the limit of detection of PSA detection at 31.88 aM. Secondly, we further validated the assay's accuracy through a linear correlation analysis (**Figure 4b**) between the frequency count (f_{on}) obtained experimentally and the PSA concentration. The above results confirm the reliability of the DIAMOND-P assay in quantifying PSA levels, demonstrating its potential in clinical settings.

DISCUSSION

In this study, we introduce a novel enzyme- and compartment-free digital protein detection platform, DIAMOND-P, with attomolar sensitivity. We have demonstrated its capability to count single AuNPs, and detect single protein molecules (avidin, PSA). Future work includes demonstrating the multiplexed detection for a panel of protein biomarkers, which is important in clinical applications for cancer and neurodegenerative diseases. The DIAMOND-P platform has significant potential to simplify the assay complexity of current dELISA platforms and find broader applications in early disease diagnostics.

ACKNOWLEDGEMENTS

Research reported in this abstract was supported by National Institute of Allergy and Infectious Diseases of the National Institutes of Health under award number R01AI151374. The content is solely the responsibility of the authors and does not necessarily represent the official views of the National Institutes of Health.

REFERENCES

[1]. N. Momenbeitollahi et al., Analytical and Bioanalytical Chemistry, 413:5995-6011, 2021.
[2]. D.M. Rissin et al., Nature Biotechnology, 28:595-599, 2010.
[3]. L. Cohen et al., ACS Nano, 14:9491-9501, 2020.
[4]. C. Wu et al., ACS Nano 16:1025-1035, 2022.
[5]. Y. Liu et al., Nature Communications, 13: 1687, 2022.

HUMAN AIRWAY TISSUE BIAXIAL TENSILE MECHANICS

Crystal A. Mariano (1), Mona Eskandari (1,2,3)

(1) Department of Mechanical Engineering, University of California Riverside, Riverside, CA, USA
(2) BREATHE Center, School of Medicine, University of California Riverside, Riverside, CA, USA
(3) Department of Bioengineering, University of California Riverside, Riverside, CA, USA

INTRODUCTION

Respiratory illnesses, a known cause of morbidity and mortality, are a continuously rising concern in the United States linked to cigarette smoking and air pollution [1,2]. Major pulmonary conditions, such as emphysema and asthma impact the structural integrity of airway tissue. While the organ pathways responsible for air delivery to the lungs merits greater research focus, investigations regarding the multidirectional physiological mechanics of human airways remains absent from the literature [3]. Previous studies utilizing equibiaxial tensile tests explore the mechanics of healthy porcine tissues, which may not accurately reflect the variable human tissue mechanics [4], and prior works considering human tissues, solely focus on the trachea while restricted to uniaxial tensile testing [5,6].

In this study, for the first time, we examine the scarce and variable mechanics of healthy human transplant eligible airway tissue. The biaxial tensile mechanics of the human trachea and branching bronchi are quantified, focusing on the non-cartilaginous section allowing extension during breathing. We additionally explore regional heterogeneity and anisotropic features by comparing the understudied primary bronchi regions with the trachea, and by contrasting axial and circumferential material properties. These novel insights can accompany future comparisons of factors such as sex, smoking history, and lung health state, which will be necessary for computational models and early detection of progressive respiratory illnesses.

METHODS

Human airway tissue samples were extracted from three donor lungs (age and sex: 17F, 32F, 48F) within 48 hours after surgical retrieval (IRB exemption approval HS 20-180); these rare specimens were deemed healthy enough to be transplanted but were ultimately rejected and designated for research purposes. 48F had no mentioned history of smoking or pulmonary condition, and while lung transplant eligible, 32F smoked a pack a week and 17F had asthma. The non-cartilaginous smooth muscle section from the airways were carefully dissected from the horseshoe-shaped cartilage tracheal and bronchial segments [7]. Square samples of 5.2x5.2 mm uniform effective testing size were collected from each trachea, left primary bronchus, and right primary bronchus [8]. Specimen collection for each subject was limited to 2-3 samples per region, which resulted in 7-9 samples across each region, and a total of 22 samples tested overall (Figure 1A). Axial and circumferential orientations for each sample were noted upon excision.

Preliminary tests found consistent tearing at 60% strain, and thus, samples were equibiaxally stretched at a rate of 1%/s to a maximum of 50% tensile strain, preceded by 10 preconditioning cycles (CellScale Biomaterials Testing, Waterloo, Canada) [9]. A 10N load cell was used, and specimens were submerged in a temperature controlled 37 ℃ 1X phosphate-buffered saline bath throughout testing [10].

The engineering stress-strain loading curves for each lung region and loading direction were analyzed. The bilinear slopes were calculated based on the initial and ultimate modulus (stiffnesses of the low and high strain regimes, respectively), as in prior studies, with a linear fit of $R^2 > 0.90$ [11]. The initial and ultimate modulus, signifying uncrimping of the microstructural airway fibers, along with the maximum stress value at 50% strain, were compared across regions, loading direction, and subjects. A two-way ANOVA with post-hoc Bonferroni was used to compare regional and directional elasticity characteristics between subjects with defined significance of *$p<0.05$, **$p<0.01$, ***$p<0.001$, and ****$p<0.0001$ [4].

RESULTS

The circumferential and axial stress-strain loading curves were averaged (+/- standard deviation) across each airway region (Figure 1B) or each subject (Figure 1C). For Figure 1B, the axial stresses averaged over all regions appeared greater than circumferential counterparts, more so for increasing strain. The trachea and right primary bronchus stress-strain curves were most comparable and overlapped for the axial

direction. The decreased stiffness at high strains for the left bronchus both axially (134.5 ± 173.3 kPa) and circumferentially (65.2 ± 59.5 kPa) compared to the trachea (334.2 ± 280.4 kPa, 81.0 ± 31.0 kPa) and right bronchus (332.5 ± 367.9 kPa, 100.5 ± 116.6 kPa) was a trend, but statistically insignificant (Figure 1B inset, initial and ultimate moduli).

In Figure 1C, inter-subject comparisons observed 48F showed greater stresses at maximum strains in all regions and directions, except for the circumferential trachea, where 17F had the greatest stresses. Additionally, while 48F and 32F tended to exhibit higher tracheal stresses axially than circumferentially, 17F appeared to show no directional dependence.

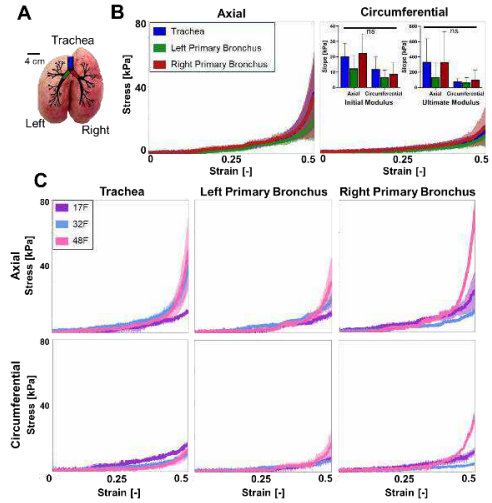

Figure 1: A) Human lung airway regions (trachea, left/right bronchi). The average +/- standard deviation of the stress-strain loading profiles in the circumferential and axial directions B) for each lung region and C) for each human subject.

In Figure 2, the airway smooth muscle stiffness between subjects exhibited shifting and varying regional mechanics. The initial modulus (i.e., low strain regime), showed significantly greater compliance for 48F compared to 17F for the circumferential trachea (4.9 ± 3.8 kPa, 21.2 ± 4.2 kPa, respectively), and greater stiffness (35.0 ± 3.2 kPa) than 32F (11.8 ± 1.1 kPa) for the axial right bronchus. For the ultimate modulus (i.e., high strain regime), the 48F axial right bronchus (872.1 ± 176.5 kPa) was significantly greater across 32F and 17F counterparts (55.3 ± 15.3 kPa, 157.4 ± 137.8 kPa). Maximum stresses in the axial right bronchus for the 48F averaged the greatest across all subjects and regions (73.9 ± 9.6 kPa).

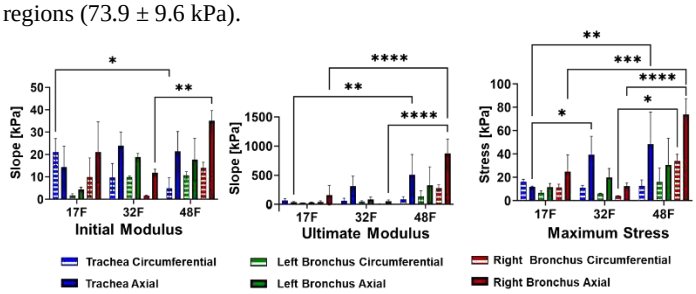

Figure 2: The average +/- standard deviations of the initial and ultimate moduli, and maximum stress of each airway region and orientation.

DISCUSSION

The regional mechanical differences between airway segments observed in our study may be attributable to the micro and macro morphology of human lungs. A recent histological study discovered the majority of tracheal elastic bundles continued distally into the right primary bronchus after initial bifurcation [12], suggesting the shared structural weave of the fiber network. We find our tracheal mechanics values to behave more similar to porcine equibiaxially planar stretched specimens [4] compared to human uniaxial studies, which reported 10x greater stresses at 50% strain [5]; this also indicates that uniaxial versus biaxial mode affects the fiber directional loading response. Furthermore, the trachea and right bronchus share larger airway diameters compared to the left primary bronchus due to the positioning of the heart. These findings substantiate the similar stress-strain curves observed between the trachea and right primary bronchus.

We find human subjects tend to exhibit greater average axial stiffness compared to circumferential direction. This behavior is most prevalent in the high strain regime, likely a result of the structural properties of the airway fiber network, which is predominantly axially oriented [12]. These anisotropic findings concur with prior uniaxial studies on the human trachealis muscle [14,15], as well as tracheal and bronchial porcine airway tissue [9]. However, the tracheal mechanics of one subject (17F) in our study contradicted counterpart trends (32F and 48F) and the established literature. This could be due to its asthmatic nature, since asthma is known for its fibrosis stiffening, which could correlate with the measured stiffer tracheal circumferential behavior [16]; however, the role of age cannot be disregarded given 17F was the youngest subject. Prior studies associate aging with declining lung function, as well as increasing elastic modulus [17,18], and this trend of increasing stiffness with age observed in the oldest subject (48F) is similarly reflected here. The minor smoking history of 32F may also be a factor, since smoking is also known for its stiffening effects [19].

This study's limitations stem from the intrinsic challenges of collecting viable and rare human tissues. The inherent variability of human lung mechanics can be better addressed with additional specimens to adequately substantiate age and conditional effects. Despite these limitations, these novel characterizations of airway mechanics better inform physiologically relevant computational lung models and contribute to our understanding of pulmonary illness.

ACKNOWLEDGEMENTS

This work was supported in part by the National Science Foundation Graduate Research Fellowship under Grant No. DGE – 1840991 to Crystal A. Mariano and the Dassault Systemes U.S. Foundation Grant to Dr. Mona Eskandari.

REFERENCES

[1] Mokdad, A. H. et al., *Jama*, 319(14):1444-1472, 2018 [2] Mariano, CA et al, *Front Physiol*, 11:600492, 2020 [3] Vindin, HJ et al., *Curr Opin Biotechnol*, 74:1-6, 2022 [4] Sattari, S et al, *Acta Biomater*, 155:410-422, 2023 [5] Safshekan, F et al, *Materials*, 9(456):1-13, 2016 [6] Teng, Z et al, *J Biomech*, 45(9):1717-23, 2012 [7] Safshekan, F et al, *J Biomech Eng*, 139(011007):1-9, 2017 [8] Santhi, B et al, *Int J Anat Res*, 5(3.2):4280-83, 2017 [9] Eskandari, M et al, *J Appl Physiol*, 125:878-888, 2018 [10] Noble, PB et al, *J Appl Physiol*, 99(6):2061-66, 2005 [11] Smith, LJ et al. *Ann Biomed Eng*, 36: 214-223, 2008 [12] Kamel, KS et al, *Clin Anat*, 22:689-697, 2009 [13] Mariano, CA et al, *Resp Res*, 24(105), 2023 [14] Trabelsi, O et al, *Med Eng Phys*, 32(1):76-82, 2010 [15] Sarma, P et al, *J Biomed Mater Res A*, 65(1):1-8, 2003 [16] Noble, PB et al, *Pulm Pharmacol Ther*, 29(2):96-107, 2014 [17] Sicard, D et al, *Am J Physiol Cell Mol Physiol*, 314(6):L946-L955, 2018 [18] Wicher, SA et al, *PLos ONE*, 16(7):e0254710, 2021 [19] Langton, AK et al, *J Pathol*, 251:420-428, 2020

CAM MORPHOLOGY AND SEX-BASED DIFFERENCES IN THE PROXIMAL FEMUR ANATOMY OF COLLEGIATE ATHLETES WITHOUT HIP PAIN: A THREE-DIMENSIONAL STATISTICAL SHAPE MODELING ANALYSIS

Bergen Braun (1), Joseph D. Mozingo (2), Penny R. Atkins (2,3), K. Bo Foreman (4), Allan K. Metz (2), Stephen K. Aoki (2), Travis G. Maak (2), Andrew Anderson (1,2,3,4)

(1) Department of Biomedical Engineering, University of Utah, Salt Lake City, Utah, United States
(2) Department of Orthopaedics, University of Utah, Salt Lake City, Utah, United States
(3) Scientific Computing and Imaging Institute, University of Utah, Salt Lake City, Utah, United States
(4) Department of Physical Therapy, University of Utah, Salt Lake City, Utah, United States

INTRODUCTION

Femoroacetabular impingement syndrome (FAIS) is defined as a painful, motion-related disorder of the hip wherein patients present with cam, pincer, or combined cam/pincer morphology [1]. Cam morphology is described as an aspherical femoral head that causes abnormal contact between the femur and pelvis and commonly occurs in young, active individuals [2]. In athletes, FAIS is known to negatively affect athletic performance from pain and associated degenerative changes to the hip [3,4]. Safran et al. reported that 3% of Division I collegiate athletes are diagnosed with FAIS [3]. Additionally, radiographic studies have reported a high prevalence of cam-type morphology in asymptomatic athletes, suggesting these individuals are at an elevated risk of developing FAIS [5-7].

When diagnosing cam-type FAIS, measurements of plain film radiographs, including the alpha angle and head-neck offset distance, are frequently used to identify abnormal hip morphology. However, more recent research has shown that the two-dimensional measurements used in radiographic studies do not accurately characterize cam deformities [8]. Recent research has also demonstrated that the location of the cam lesion differs between males and females, which may limit the ability of plain film X-rays to distinguish deformities between the sexes [9].

Statistical shape modeling (SSM) is a mathematical method used to quantify 3-D geometric variation within a class of surfaces [10]. SSM provides the ability to define mean group shapes, statistically compare the mean shapes of two or more groups, and identify and isolate the location of regions of morphologic differences. In contrast to radiographic measurements, SSM allows for objective analysis of shape and shape variation across the entire shape of interest, enabling the discovery of anatomic features driving the disease process without the need to predefine specific areas of interest on the shape.

The purpose of this study was to use a three-dimensional statistical shape model of the proximal femur to evaluate how the femur shape of asymptomatic collegiate athletes compares to the shape of radiographically screened controls and cam FAIS patients by (1) quantifying shape variation, (2) establishing sex-based shape differences, and (3) comparing shapes between athletes and cam-type FAIS patients.

METHODS

The study population consisted of three cohorts: athletes (28 M, 23 F), controls (30 M, 17 F), and cam FAIS patients (26 M, 0 F). Double echo steady-state magnetic resonance images were prospectively acquired of the hips of Division I collegiate athletes. An existing dataset of computed tomography scans of cam-type FAIS patients and morphologically screened controls was evaluated. The proximal femur was segmented, reconstructed into a three-dimensional surface, and analyzed to generate a correspondence model using the open-source software, ShapeWorks.

Principal component analysis (PCA) was used to consolidate the dimensionality of the model to a set of linearly uncorrelated modes to describe the dominant shape variations among a given particle set. PCA was performed on the correspondence particles for different groups of femur surfaces, which included Group I - athletes, controls, and patients; Group II - athletes and controls; and Group III – males only. Group II was further broken down into partial cohorts, comparing male and female athletes, female athletes and controls, and male athletes and controls.

Modes containing significant variation were identified via parallel analysis. For groups I and III, PCA component scores were compared between cohorts for significant modes using a one-way ANOVA. When a significant effect of the group was found, the Tukey-Kramer method was applied for multiple comparisons. For group II, PCA component scores between cohorts and partial cohorts for a given mode were compared using two-tailed unpaired t-tests. Given that multiple t-tests were performed for each mode, a Holm-Sidak correction was applied.

Type I error rate was set at 0.05 for all statistical testing. For the group with only males, linear discriminant analysis was performed to distill the high-dimensional particle data to a single numeric "shape score". Shape scores between male cohorts were compared via a one-way ANOVA with a type I error rate set at 0.05, followed by the Tukey-Kramer method for multiple comparisons.

RESULTS

When analyzing the full cohort, significant differences were found between athletes and controls (Mode: VIII, adj. p=0.010), athletes and patients (Modes: I, IV, adj. p=0.002, 0.003), and patients and controls (Modes: IV, VIII, p<0.001). When analyzing only athletes and controls, significant differences were found (Mode: VIII, adj. p=0.040), as well as when analyzing only male and female athletes (Modes: I, II, adj. p=0.006, 0.009). When analyzing only males, significant differences were found between athletes and patients (Mode: IV, adj. p=0.020) and patients and controls (Mode: IV, adj. p=0.003)**.** Shape scores, which represent a generalized value of the entire shape, were significantly different between athletes and patients (adj. p=0.003) and patients and controls (adj. p<0.0001), but there was no difference between athletes and controls (adj. p=0.400) (Figure 1)

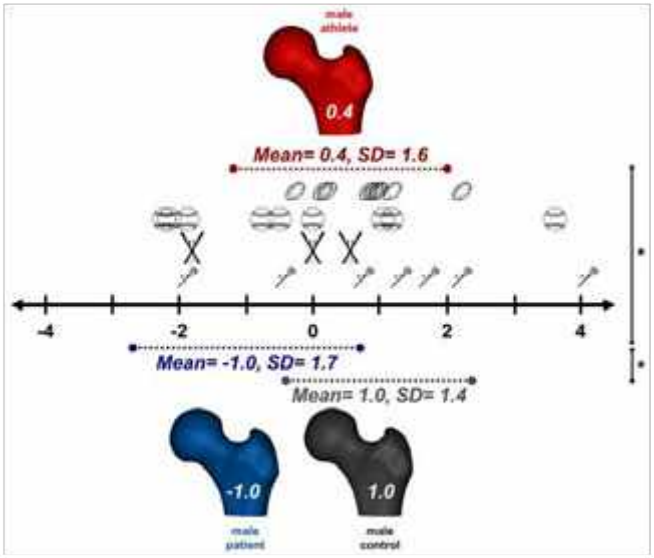

Figure 1. Surface reconstructions representing the mean shape of the male patient (blue), male control (gray), and male athlete (red) proximal femur, as well as sports icons representing each individual athlete's shape score as determined by linear discriminant analysis. Positive shape scores indicate femurs resembling controls, and negative shape scores indicate femurs resembling patients. Horizontal dotted lines represent the standard deviation for each group. Vertical lines indicate a significant difference between athletes and controls and controls and patients.

DISCUSSION

FAIS is a common cause of hip pain and disability in athletes. It is important to recognize that many athletes exhibit cam morphology without symptoms. This study aimed to objectively characterize shape and quantify anatomical variation in proximal femur anatomy of Division I collegiate athletes without hip pain using 3D SSM. A key finding from our analysis is that athletes had proximal femur morphology that more closely resembled that of controls screened for cam morphology.

Previous studies have examined the radiographic prevalence of asymptomatic cam morphology in baseball and football players [5-7]. We found that 66% (6/9) of baseball players had patient-leaning shape scores, which is consistent with the results of a previous study that showed that approximately 70% of baseball players had at least one radiographic sign of cam morphology [7]. However, in our study, the vast majority of football players (90%; 8/9) had a control-leaning shape score, whereas Kapron et al. and Nepple et al. reported that approximately 75% of football players in their studies had at least one radiographic sign of cam morphology [5,6]. The disparities between our study and previous studies examining football players may be due to measurements of plain film X-rays not accurately representing the cam deformity [8], so the deformities seen on radiographs may not be as severe and prevalent as once predicted. Another reason is that we used a higher threshold to define cam morphology (>60°), whereas the aforementioned studies of football players used (>50° or >55°) [5-7]. Still, none of the football players in our study had an alpha angle greater than 55°.

In our study, PCA determined modes I and II (athlete and control group) to exhibit significant differences in shape between male and female athletes. These modes highlighted differences in the shape of the femoral head, concavity of the head-neck junction, and amount of femoral offset. Variability in these regions may point to an increased susceptibility of cam-type FAIS because a decrease in the concavity of the femoral head at the head-neck junction and the femoral offset are a hallmark of cam morphology. SSM enhances our ability to visualize differences in areas of variation that are typically associated with cam morphology.

There is a limitation in this study that warrants consideration. We used an older dataset of patients with FAIS with only four females. Given the small sample, we chose to exclude the female patients from this study. It was previously thought that cam FAIS/morphology was primarily identified in males; however, recent research has shown that cam morphology is just as prevalent in females as it is in males [11]. Future work should include female FAIS patients in the analysis.

In summary, this study used SSM to characterize shape and shape variation in the proximal femur in asymptomatic Division I collegiate athletes. We determined that the athletes in our study had femurs that resemble control femurs, which refutes previously published research. Our results provide further evidence that 2D measurements of the proximal femur are unlikely to provide a complete picture of cam deformities. Utilizing SSM, we can objectively analyze the 3D femur morphology of athletes to identify and better understand morphology that may predispose individuals to FAIS. Future studies should include the pelvis and entire femur as part of the SSM to better understand the role of deformities in the development of FAIS in athletes.

ACKNOWLEDGEMENTS

This work was funded by the PAC12 Student Athlete Health and Well-being Initiative, the National Institutes of Health (F32 AR078019, R01 EB016701, U24-EB029011, P41GM103545), and the LS Peery Discovery Program in Musculoskeletal Restoration.

REFERENCES

[1] Griffin, DR et al. *Br J Sports Med.* 2016;50(19):1169-1176.
[2] Philippon, MJ et al., *Am J Sports Med.* 2013;41(6):1357-1362.
[3] Safran, MR et al., *Orthop J Sports Med.* 2022; 10(4):23259671221084979.
[4] Philippon, M et al., *Knee Surg Sports Traumatol Arthrosc.* 2007;15(7):908-914.
[5] Kapron, AL et al., *J Bone Joint Surg Am.* 2011;93(19):e111(111-110).
[6] Nepple, JJ et al., *Arthroscopy: The Journal of Arthroscopic & Related Surgery.* 2012;28(10):1396-1403.
[7] Uquillas, CA et al., *J Hip Preserv Surg.* 2022;9(3):145-150.
[8] Atkins, PR et al., *Clin Orthop Relat Res.* 2019;477(1):242-253.
[9] Bugeja, JM et al., *J Orthop Res.* 2024; 42; 385-394.
[10] Cates, J et al., *Statistical Shape and Deformation Analysis.* Academic Press; 2017:257-298.
[11] Levy, DM et al., *Front Surg.* 2015;2:61.

TOMOPINNS: COMPUTED TOMOGRAPHY ENRICHED PHYSICS-INFORMED NEURAL NETWORKS FOR PREDICTING HEMODYNAMIC DESCRIPTORS

Sangeeta Yadav (1), Forouzan M Naderi (1), Zayeed Bin Mamun, Amin Pashaei Kalajahi (1), Amirhossein Arzani (2), Roshan M D'Souza (1)

(1) Department of Mechanical Engineering, University of Wisconsin-Milwaukee, Milwaukee, Wisconsin, USA
(2) Mechanical Engineering Department and Scientific Computing and Imaging Institute, University of Utah, Salt Lake City, Utah, USA

0.1 INTRODUCTION

Cardiovascular diseases (CVDs) encompass a wide range of pathological conditions affecting the human vascular system, including ailments such as aneurysms, arterio-venous malformations, vasospasms, atherosclerosis, peripheral artery disease, and more. Much of the adult US population is affected by CVDs. Preventive surgical and endovascular interventions are increasingly considered as therapeutic options to avert catastrophic conditions such as subarachnoid hemorrhages and stroke. However, these interventions carry significant risks [1, 2]. Clinical decisions currently rely on anatomical measures such as size, location, and the morphology of vascular malformations, assessed through anatomical imaging. These anatomical measures are derived from extensive patient population studies and fail to capture the patient-specific state of diseases. Consequently, decisions based on such anatomical measures can result in unnecessary or incorrect interventions, leading to associated costs and patient morbidities [3, 4]. Recent investigations have revealed that hemodynamic forces, arising from the interaction of blood with vascular walls, play a crucial role in the progression of cardiovascular diseases. This occurs through cell-mediated mechanotransduction and near-wall biochemical transport processes. Hemodynamic flow descriptors, such as pressure gradients, wall shear stresses, and oscillatory shear index derived from blood flow velocity, can potentially indicate the onset of acute life-threatening conditions long before they are observable on anatomical scans. Consequently, these descriptors may offer quantitative data for making objective, patient-specific clinical decisions. Central to hemodynamic descriptor-based patient-specific clinical decision-making is the accurate and reliable estimation of time-resolved blood flow velocities. Currently, there are three leading modalities for estimating blood flow velocities: (a) imaging using three dimensional time-resolved phase contrast magnetic resonance imaging (4D-Flow MRI), (b) patient-specific computational fluid dynamics (CFD), and (c) hybrid methods which combine CFD and 4D-Flow MRI through a process of data-assimilation to improve the fidelity of CFD. The accuracy of estimating blood flow velocities using 4D-Flow MRI is limited by its spatio-temporal resolution, noise, and image artifacts. In addition, 4D-Flow MRI is a new imaging protocol that is currently not used in routine clinical settings. The fidelity of estimating blood flow velocities using patient-specific CFD is limited by modeling assumptions, errors in model parameters, geometry, and boundary conditions. While hybrid methods address some of these issues, they inherit the tedious, error prone, and operator dependent data preparation tasks of patient-specific CFD. Additionally, the accuracy is impacted by errors in image registration across multiple spatio-temporal resolutions that is required to co-locate image and computational domains.

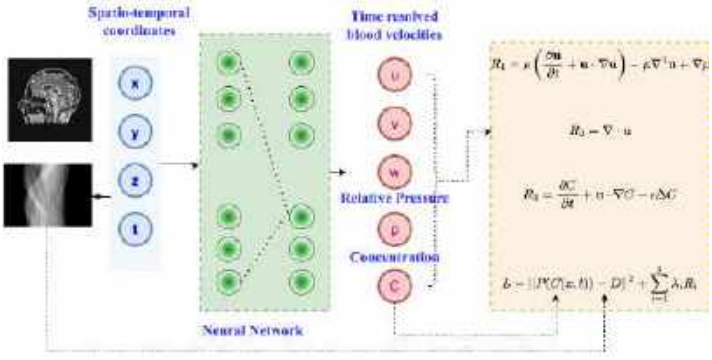

Figure 1: TOMOPinns

0.2 Contributions

We hypothesize that it is possible to estimate time-resolved blood flow velocities and relative pressures from computed tomographic angiography (sCTA) imaging. Nominally, sCTA images are static and highlight vascular structures where contrast is present. By incorporating mass transport and blood flow physics into processing of sCTA sinograms (image precursor X- Ray projection data), we will be able to estimate the underly-

ing spatio-temporally varying blood velocities and relative pressures. We make following contributions through this work:

- Modelled blood flow velocity, contrast concentration, and pressure gradient as functions of spatio-temporal coordinates, demonstrating their learnability from patient-specific CT scan data.
- Developed training data from randomly sampled contrast concentration by applying Radon transform to generate simulated sinograms.
- Demonstrated the efficacy of a CT scans enriched loss function, resulting in better accuracy and faster convergence.

0.3 PROPOSED METHOD

We introduce TOMOPinns, a neural network designed to predict blood flow velocity, contrast concentration, and pressure gradients within a specific region of the human body, utilizing readily available CT scan projections. We considered the transport of a contrast agent with concentration $c(t, x, y, z)$ by the blood flow moving with velocity field $u(t, x, y, z) = [u(t, x, y, z), v(t, x, y, z), w(t, x, y, z)]$, which satisfies the incompressible Navier-Stokes (NS) equations. The contrast agent is advected by the flow and diffused but has no dynamical effect on the fluid motion itself. We sample random spatio-temporal coordinates and concentration values at these points. Additionally, we apply the Radon transform to the concentration data, extracting the ground truth values of sinograms. These sinograms are approximations of synthetic sCTA images. In training the neural network, we align the predicted sinogram with the observed sinogram data, ensuring data fidelity, while simultaneously incorporating object physics through regularization. As illustrated in Fig. 1, we have modeled the spatio-temporal functions for blood flow velocity, relative pressure, and contrast concentration as a deep neural network (DNN).

$$(u, v, w, p, C) = \text{TOMOPinns}_\theta(x, y, z, t) \tag{1}$$

The input to these DNN is the spatio-temporal co-ordinates denoted by $\mathbf{x} = (x, y, z, t)$. Here, $theta$ are the weights of the neural network. We will learn optimal θ^* by backpropagating the loss defined in Eq. 2.The output of the neural network encompasses velocities u, v, w, relative pressure p, and concentration C. Our training process involved aligning the acquired scan data in the projected form and imposing regularization terms that incorporate the physics of fluid flow and contrast transport. Given that the actual scan data is presented as the line integral of the time-varying spatial concentration, we line-integrated the output of the neural network modeling the contrast concentration along the respective beam lines to generate the predicted sinograms. For a given blood density ρ, blood viscosity μ, and contrast diffusivity ϵ, the Navier-Stokes, mass conservation, and advection-diffusion equations, are given as follows:

$$\begin{aligned} R_1 &= \rho\left(\frac{\partial \mathbf{u}}{\partial t} + \mathbf{u}\cdot\nabla\mathbf{u}\right) - \mu\nabla^2\mathbf{u} + \nabla p \\ R_2 &= \nabla\cdot\mathbf{u} \\ R_3 &= \frac{\partial C}{\partial t} + \mathbf{u}\cdot\nabla C - \epsilon\Delta C \\ L &= ||P(C(x,t)) - D||^2 + \sum_{i=1}^{3}\lambda_i R_i \end{aligned} \tag{2}$$

In this equation, $P(C(x,t))$ is the line integral of the predicted concentration, D is the observed sCTA sinogram data, λ_i are tuning parameters, and R_i represents the physics regularization terms, which are partial differential equations (PDEs).

$$\text{RMSE} = \sqrt{\frac{1}{n}\sum_{i=1}^{n}(y_i - \hat{y}_i)^2} \tag{3}$$

RMSE is a measure of the average deviation between observed values y_i and predicted values $\hat{y}_i$.

0.4 RESULTS

To asses the performance of the proposed network TOMOPinns, we have calculated the RMSE error between the predicted and the ground truth values of u, v, w, p, C.

Table 1: RMSE for time steps 1 to 5 (u, v, w)

Time Step	u	v	w
1	9.7×10^{-4}	7.3×10^{-4}	5.9×10^{-4}
2	8.3×10^{-4}	6.2×10^{-4}	5.1×10^{-4}
3	7.1×10^{-4}	5.4×10^{-4}	4.6×10^{-4}
4	1.2×10^{-4}	3.8×10^{-4}	2.7×10^{-4}
5	1.1×10^{-4}	2.5×10^{-4}	2.3×10^{-4}

Table 2: RMSE for time steps 1 to 5 (p, C)

Time Step	p	C
1	5.6×10^{-2}	8.2×10^{-4}
2	5.2×10^{-2}	7.6×10^{-4}
3	4.8×10^{-2}	6.8×10^{-4}
4	4.2×10^{-2}	5.7×10^{-4}
5	3.9×10^{-2}	5.1×10^{-4}

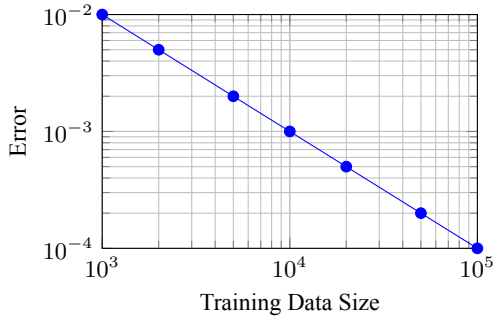

Figure 2: Scaling of TOMOPinns: Error vs Training Data Size

In this section, we discuss the results presented in Tables 1 and 2, which show the RMSE for different variables (u, v, w, p, C) at various time steps (1 to 5). Table 1 presents the RMSE for the velocity components (u, v, w) at each time step. We observe a general trend of decreasing errors as the time steps progress. For example, the error in u decreases from 9.7×10^{-4} at time step 1 to 1.1×10^{-4} at time step 5. Similar trends are observed for v and w. This suggests that the simulation results become more accurate with increasing time steps. Table 2 focuses on the RMSE for pressure (p) and concentration (C) at each time step. The errors in both p and C also exhibit a decreasing trend over the considered time steps. The error in p decreases from 5.6×10^{-4} at time step 1 to 3.9×10^{-4} at time step 5, indicating improved accuracy in pressure prediction. Similarly, the error in C follows a decreasing trend. Overall, the decreasing RMSE across all variables suggest that the simulation model provides more accurate results as the simulation progresses in time. Fig 2, provides insights into the scaling behavior of TOMOPinns concerning the training dataset. As the training data size increases, the error logarithmically decreases, demonstrating the impact of data quantity on the performance of TOMOPinns.

REFERENCES

[1] Brisman JL et al. *New England Journal of Medicine* 355.9 (2006).

[2] Fleetwood IG et al. *The Lancet* 359.9309 (2002).

[3] Williams LN et al. *Neurology: Clinical Practice* 3.2 (2013).

[4] Rajah G et al. *Neurosurgical Focus* 42.6 (2017).

EFFECT OF REAR IMPACT ON THE INSTRUMENTED SPINE: A FINITE ELEMENT STUDY

Balaji Harinathan (1,3), Karthik Devaraj (1), Aditya Vedantam (1,2), Narayan Yoganandan (1,2)

(1) Department of Neurosurgery, Medical College of Wisconsin, Milwaukee, WI, USA
(2) Neurosurgery Research, VA Medical Center, Milwaukee, WI, USA
(3) School of Mechanical Engineering, Vellore Institute of Technology,Chennai, India

INTRODUCTION

Degenerative cervical myelopathy (DCM) is growing in prevalence as evident from recent epidemiological data.[1] The management of DCM often involves spinal cord decompression with instrumentation. Given the rising incidence of spinal instrumentation in the United States, there is an increasing prevalence of persons living with spinal instrumentation and at risk of sustaining minor trauma. Whiplash injuries, commonly resulting from rear impacts, can lead to various issues, including capsular ligament injury, dama ge to the anterior longitudinal ligament and anterior disc fibers, as well as spinal cord trauma. Such injuries often manifest as neck pain, discogenic pain, and myelopathic trauma, typically without associated vertebral body injuries like compression or burst fractures. While numerous studies have examined rear impact scenarios in Post Mortem Human Subjects (PMHS) and through Finite Element Modeling (FEM), they have primarily focused on the spinal column, often overlooking the spinal cord due to its complexity. This study aims to compare the effect of rear impact on spine and spinal cord responses in three different surgical conditions. The results will highlight the risk of spinal cord injury after minor trauma such as rear impact in humans with spinal instrumentation.

METHODS

In this study, A previously validated finite element model of the human head-neck complex was used.[2] This model encompasses the cervical column from C2 to T1, inclusive of vertebral bodies, posterior elements, disks, ligaments, and the spinal cord, along with the denticulate ligaments, pia mater, dura mater, and CSF. Rear impact acceleration was applied to the constrained T1 vertebra at 2.6 m/s.[3] This model also incorporates active Hill-type muscles. Our study further delved into the biomechanical impacts of three distinct cervical surgical interventions under rear impact. These are anterior cervical discectomy and fusion (ACDF), posterior cervical laminectomy and fusion (PCLF), and laminoplasty (LP). In the ACDF, the intervertebral disk was removed and inserted graft between the vertebral bodies C4-C7. For the PCLF procedure, laminectomy was performed at C4-C6, followed by rod and screw insertion from C3-C7. Laminoplasty was performed at the C4-C6 levels. Used von Mises stress for stress metrics and Maximum principal strain for strain metrics. Measured the biomechanical effects on the spinal column and spinal cord due to these surgeries under rear impact conditions at 2.6m/s. Parameters such as spinal cord stress and strain, range of motion, capsular ligament strain, and anterior longitudinal ligament strain were quantitatively evaluated and compared with laminoplasty intervention.

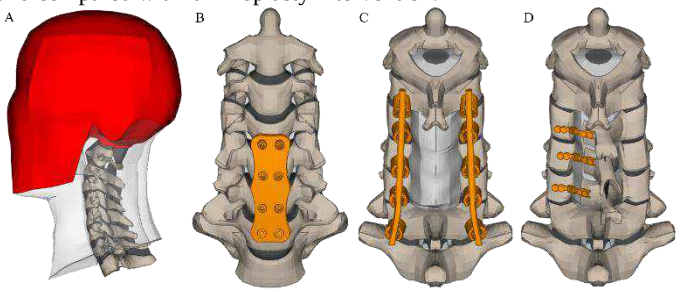

Figure 1: (A) Finite element model of head and neck (B) Anterior cervical discectomy fusion C4-C7 (C) Posterior cervical laminectomy C4-C6 and fusion C3-C7 (D) Laminoplasty C4-C6

RESULTS

In our study, Rear impact was simulated for three different surgical interventions, by applying a linear acceleration corresponding to a change in velocity of 2.6 m/s at T1 vertebrae. Figure 2. demonstrates the variations in neck motion over time due to the impact.

ROM: The mean segmental range of motion at index levels, compared to laminoplasty (LP), decreases to 75% for ACDF and 57.7% for PCLF. LP with its higher ROM, is evidently a motion preservation intervention. At the superior adjacent level, ROM increases by 9% for

ACDF but decreases by 54.7% for PCLF, largely due to PCLF's extended instrumentation at C3-C4. At the inferior adjacent level, ROM decreases by 25.9% for ACDF and increases by 39.2% for PCLF.

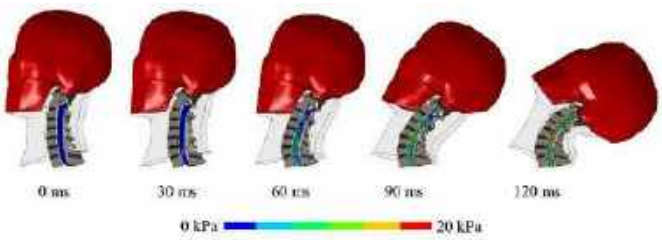

Figure 2: Neck motion and spinal cord stress during the rear impact

Spinal cord stress and strain: In terms of spinal cord stress at index levels, when compared to laminoplasty (LP), ACDF shows a notable increase in spinal cord stress by 105%, whereas PCLF demonstrates a decrease of 60.1%. Notably, ACDF presents higher stress levels despite having a lower range of motion than other surgeries. At the superior adjacent level, stress increases by 65% for ACDF and decreases by 52.6% for PCLF. In contrast, at the inferior adjacent level, stress for ACDF increases by 40.8% while it decreases by 16.2% for PCLF. Regarding spinal cord strain at index levels, compared to LP, ACDF results in a 60% increase in spinal cord strain, whereas PCLF shows a reduction of 31.7%. This trend in ACDF is similar to that observed in stress, where a higher strain is noted despite a lower range of motion relative to other surgical methods. At the superior level, the strain in ACDF increases by 16.3%, and in PCLF, it decreases by 65.6%. Conversely, at the inferior level, ACDF shows an increase in strain by 37.7%, and PCLF also exhibits an increase in strain by 18.1%.

Ligament strain: For the capsular ligament strain at index levels, the strain decreases to 85.7% for ACDF and 27.5% for PCLF compared to LP. Both fusion interventions result in a reduction of strain at the superior level relative to LP. At the inferior level, ACDF shows a reduction in strain to 68.5%, and PCLF decreases further to 22.4%. In the context of the anterior longitudinal ligament (ALL), when comparing PCLF with LP, there is a 13.1% increase in strain for PCLF. In contrast, for ACDF, the ALL is completely severed to facilitate the insertion of the graft from the anterior side. When compared to LP, at the superior level, ACDF shows a slight increase in strain by 0.8%, whereas PCLF shows a more significant increase of 35%. At the inferior level, ACDF exhibits a reduction in strain by 35.8%, whereas PCLF shows a substantial increase of 61.2%.

DISCUSSION

In this study, we conducted simulations on three different cervical surgical interventions: ACDF, PCLF, and LP, Simulated under the rear impact by applying a linear acceleration corresponding to a change in velocity of 2.6 m/s at T1 vertebrae, comparing their biomechanical outcomes with laminoplasty. The FE intact, non-stenotic spine model was validated using range of motion data derived from human cadaver experiments for segments C2–C3 to C7–T1, ensuring the FEM's response under load accurately reflected experimental data.[4] The rationale behind comparing fusion surgical interventions with LP, LP is a motion-preserving procedure compared to ACDF and PCLF, which are fusion surgeries.[5] This comparison allows for an understanding of how fusion surgeries alter spinal biomechanics relative to motion preserving techniques.

For both fusion techniques, ACDF and PCLF, there was a significant reduction in ROM at the index level. In contrast, laminoplasty, as a motion-preserving intervention, showed a higher ROM, as shown in cadaver studies.[5] The ROM at the inferior level was notably higher than at the superior adjacent levels, consistent with previous in vivo and in vitro studies indicating hyperextension in the lower cervical spine during the initial phase of whiplash.[6,7]

The timing of the maximum S-curve, defined as the moment when C2–C3 reaches peak flexion, was observed at 40-45 ms across all surgical interventions, followed by an extension phase.[4]

Regarding spinal cord mechanics, posterior approaches showed lower spinal cord stress and strain compared to the anterior approach after rear impact. This is primarily due to two factors: the ability of posterior approaches to widen the spinal canal and the limited expansion of the spinal canal observed in anterior approaches. During rear impact, which predominantly causes neck extension, a greater portion of the load is transferred to the facet joints. In the case of PCLF, instrumentation in the lateral mass area restricts motion, contributing to its effectiveness in protecting the spinal cord.[8]

In our FE model, muscle activation played a crucial role, as evidenced by a study from Fice et al., which showed a reduction in CL strain from 28% to 13% with active muscles in a 7g rear impact scenario.[9]

Capsular ligaments are particularly critical, given that cervical facet joints are implicated as a primary source of chronic neck pain post-whiplash in 60% of cases. In posterior approaches, notably higher CL strain was observed at inferior adjacent levels, with 163% in PCLF and 133% in LP. findings from Siegmund et al., where maximum principal strain in flexibility tests was significantly lower than in subcatastrophic failures.[10] Posterior approaches demonstrated unfavorable outcomes in CL strain, whereas anterior approaches resulted in only 40% strain.

For the ALL, which is crucial in extension movements, the study by Yoganandan et al. suggests a strain threshold range of 40-45%.[11] In our study, the average ALL strains were below this failure threshold, at under 36%, indicating a lower risk of damage.

In conclusion, this FE study looked at the impact of rear trauma on instrumented spines post-cervical surgeries. Our findings indicate that posterior approaches PCLF and LP exhibit lower spinal stress and strain compared to ACDF, primarily due to the enhanced canal expansion they offer. The study also underscores the importance of muscle activation in reducing capsular ligament strain during rear impacts. Additionally, ALL strains were observed to remain below the failure threshold, suggesting a lower injury risk. These findings offer valuable guidance for clinicians in understanding the biomechanical implications of different cervical surgical techniques, especially in patients who are at risk of sustaining minor trauma post-surgery.

ACKNOWLEDGEMENTS

The study was supported in part by the Zablocki VA Medical Center, Milwaukee, Wisconsin, and the Department of Neurosurgery at the Medical College of Wisconsin. Dr. Narayan Yoganandan is an employee of the VA Medical Center.

REFERENCES

[1] Wu, J.C., et al., Neurosurgical focus, 2013.
[2] Harinathan, B., et al., Spine, 2023.
[3] Stemper, B.D., et al., Annu. Proc. Assoc. Adv. Auto. Med., 2004.
[4] John, J.D., et al., J. Biomech. Eng., 2019.
[5] Hirabayashi, K., et al., Spine, 1988.
[6] Grauer, J.N., et al., Spine, 1997.
[7] Kaneoka, K., et al., Int. Conf. New Frontier Biomech. Eng., 1997.
[8] Eck, J.C., et al., Spine, 2002.
[9] Fice, J. B., et al., Annals of biomedical engineering, 2011.
[10] Siegmund, G. P., et al., Spine, 2001.
[11]Yoganandan, N., et al., J. Biomech. Eng., 2000.

MULTISCALE MODELING OF BLOOD FLOW IN AORTIC ROOT ANEURYSMS

Yurui Chen (1), Hannah Zhai (1), Hiroo Takayama (2), Vijay Vedula (1)

(1) Mechanical Engineering, Columbia University, New York, NY, USA
(2) Department of Surgery, Columbia University Medical Center, New York, NY, USA

INTRODUCTION

The aortic root at the proximal end of the ascending aorta is frequently prone to diseases such as aortic root aneurysm (ARA) and dissection. These life-threatening conditions have high mortality rates, with no effective pharmacological therapies to prevent rupture. [1] Current risk assessment and surgical planning criteria are based on morphological measurements, often estimated on a 2D slice from medical imaging. Further, the same size-based threshold is applied to all ascending thoracic aortic aneurysms (aTAAs), including the proximally located ARA, and the distally located, mid-aortic aTAA, despite clinical evidence suggesting that ARAs are more malignant than aTAAs in imparting major adverse events (MAEs), such as dissection, rupture, or death. [2] Moreover, it is well-known that the biomechanical environment of an aortic root is substantially different from the mid-aortic segment of the ascending aorta. However, the hemodynamic factors contributing to the growth and severity of ARA compared to a mid-aTAA remain less understood.

Here, we present a workflow to perform multiscale blood flow simulations in ARA patients, coupling the 3D model of the aorta with a closed loop, 0D lumped parameter network (LPN)-based model of blood circulation. The 0D model, with parameters tuned to match the patient data, provides physiological boundary conditions, while the 3D model is constructed from CT data using SimVascular. [3] We then present a novel approach to reconstruct a healthy aorta from the dilated state, and compare hemodynamics by performing blood flow simulations using a validated, stabilized finite element method-based flow solver. Finally, we discuss our plan to extend the framework to perform fluid-structure interaction (FSI) simulations and evaluate hemodynamics in different aTAA phenotypes.

METHODS

We employ SimVascular to perform multiscale blood flow simulations in the ascending aorta of ARA patients, including coronary arteries. [3] We identified an ARA patient in the database at Columbia University Medical Center (CUMC) under an IRB-approved protocol (Fig. 1a). The patient was diagnosed as having a root-only aneurysm, with a cusp to sinus diameter measuring 5cm at the aortic root.

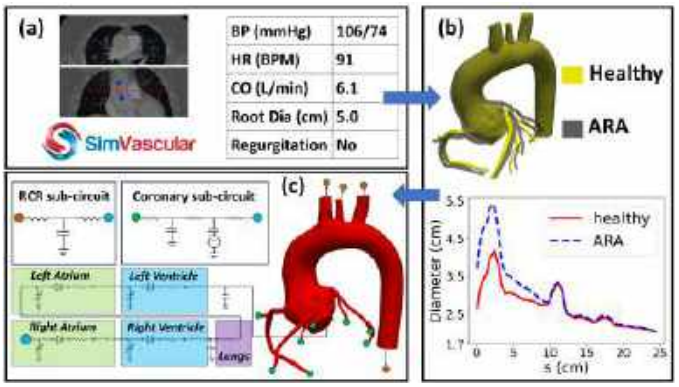

Figure 1: Workflow for patient-specific multiscale blood flow simulations in ARA patients. (a) Model of the ascending aorta constructed using SimVascular; [3] table includes clinical characteristics. (b) (top) Reconstructing a 'healthy' aorta (yellow) from the dilated model (black); (bottom) comparing the centerline diameter between healthy and dilated states. (c) A schematic of the closed-loop 0D/3D model for multiscale blood flow simulations.

We realize that it is pivotal to understand the changes in blood flow and shear forces during aneurysm growth to dissect the hemodynamic factors responsible for disease progression. However, when we measured the growth rate of the ascending aorta in a sample of aTAA patients (N=5) by analyzing their longitudinally acquired CT data for up to 5 years after the initial diagnosis, we found that the aneurysm grew by only a few mm/year. This led to no discernible differences in the dilated ascending aortic morphology, yet these patients were considered clinically at high risk.

Therefore, we developed a novel workflow to reconstruct a 'healthy' pre-dilated aorta from the ARA patient by using morphing techniques (Fig. 1b). The dilated portions of the aortic root and ascending aorta are morphed radially inward toward the vessel centerline, until the dimensions match that of a 'reference' normal subject, appropriately scaled by the BSA (Fig. 1b). This 'reference' subject's dimensions of the ascending aorta are determined from a previously characterized study among 70 normal subjects. [4] At the vessel bifurcations, the diameter scaling factors are smoothly extended through the entire daughter branch from the main parent vessel.

Lastly, any surface irregularities due to morphing are resolved using local smoothing operations in MeshMixer (Autodesk Inc.).

In principle, one could interpolate the healthy and the dilated states of the root aneurysm to create multiple intermediate phases, and assess the hemodynamic changes through a progressing aneurysm. However, in this preliminary analysis, we focus only on the end-states.

We model blood as incompressible and Newtonian, and assume the walls to be rigid. We employ a modular coupling method between the 3D and the 0D domains (Fig. 1c), [5] implemented in the stabilized finite element flow solver, svFSI. [6] A manual tuning is performed to match the LPN model parameters with the clinical data. Because of the proximity of the root with the coronary ostia, we incorporate coronary arteries in our 3D model and add appropriate downstream boundary conditions. [7] Blood flow simulations are performed in healthy and dilated root cases using the bi-partitioned method to solve the Navier-Stokes equations.[8]

RESULTS

Simulated blood flow in the reconstructed healthy aorta is shown in Fig. 2. A volume rendering of the velocity field, colored by its magnitude is shown at peak systole, highlighting the complexity of the flow in the aortic root. Time-dependent flow waveforms are shown at various sections in Fig. 2, including the inlet (A), outlet (RCR, B), left coronary artery (LCA, C), and right coronary artery (RCA, D).

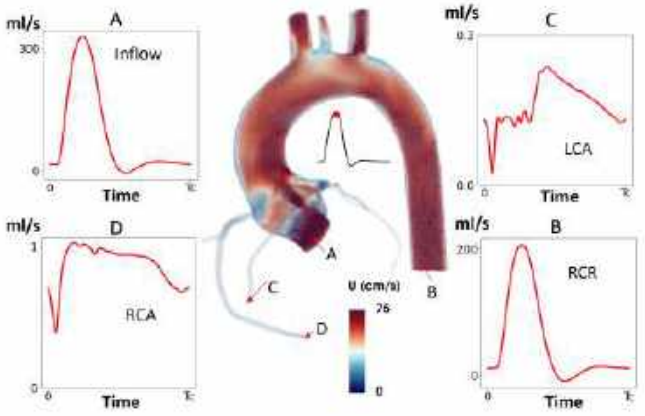

Figure 2: Velocity field at peak systole and time-dependent sectional flow waveforms in the reconstructed healthy aorta.

These simulations were performed using a mesh comprising ∼1.3M linear tetrahedral elements, including boundary layers and locally refined mesh in the coronaries. The simulation takes about 6h for six cardiac cycles on 96 CPU cores.

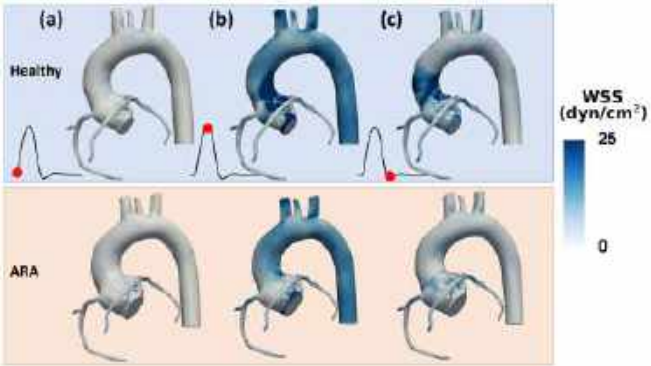

Figure 3: A comparison of spatial variation of wall shear stress (WSS) between healthy (top) and dilated root (ARA, bottom) at (a) onset of systole, (b) peak systole, and (c) end of systole.

Fig. 3 compares the spatial variation of wall shear stress (WSS) between the reconstructed healthy aorta and ARA patient, at three distinct phases of systole, while the time-averaged quantities, including the time-averaged WSS (TAWSS), area-averaged WSS (AWSS), and oscillatory shear index (OSI) are compared in Fig. 4. We note that the WSS and its related indices are generally elevated in the healthy case compared to the dilated root.

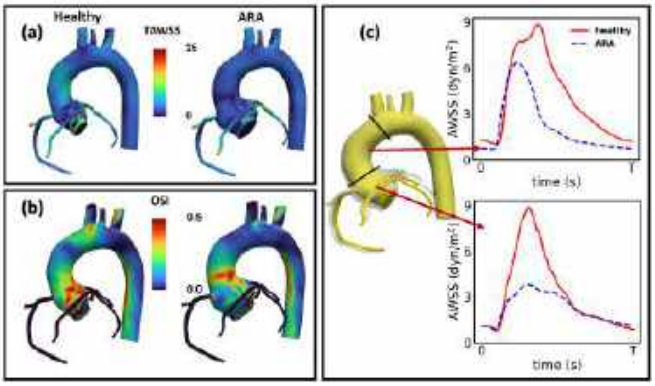

Figure 4: A comparison of WSS-related metrics between healthy and ARA. (a) time-averaged WSS (TAWSS), (b) oscillatory shear index (OSI), and (c) area-averaged WSS (AWSS).

DISCUSSION

Here, we developed a workflow to perform personalized multiscale blood flow simulations in ARA patients. We argued that because the root is already dilated by the time of the first image acquisition, we must reverse engineer a pre-dilated ascending aorta for the patient, with normal dimensions. We demonstrated this approach by radially morphing the dilated segments of the aorta with respect to the vessel centerline. This enables us to evaluate changes in hemodynamics during aneurysm development and dissect factors correlating worsening hemodynamics with changes in morphology, tissue characteristics, and function.

In our preliminary analysis, we showed that WSS is substantially reduced from a healthy state to the dilated aortic root (Fig. 3). Further, we observe a higher level of reduction in the WSS in the aortic root compared to the mid-aortic segments of the ascending aorta (Figs. 3, 4). Likewise, the OSI is markedly high, and uniform across the aortic root sinuses, in the healthy subject compared to the ARA (Fig. 4).

It is important to acknowledge the limitations of this work to plan work ahead. Rigid walls and lack of fluid-structure interaction (FSI) with the aortic valve are two major limitations, and could likely impact the results. For e.g., the asymmetric jet at the inflow (Fig. 2) is likely due to the D-shaped annulus of the ventricular outflow tract during diastole. Including an FSI model of the tissue may, however, lead to a more circular cross-section of the outflow tract, and may not result in the asymmetrically directed jet impingement on the wall of the ascending aorta. We plan to address some of these issues in the near future using our FSI framework.[9] We will also plan to include additional patients to demonstrate statistical significance.

ACKNOWLEDGEMENTS

The authors would like to acknowledge funding received through the Columbia SIRS Blavatnik seed funding program and computing resources through the Columbia SRPC and Ginsburg HPC cluster.

REFERENCES

[1] DeMartino RR et al. *Circ. Cardiovas. Qual Outcomes* 11.8 (2018).
[2] Kalogerakos PD et al. *J. Am Heart Assoc* 10.14 (2021).
[3] Updegrove A et al. *ABME* 45.3 (2017).
[4] Hager A et al. *JTCVS* 123.6 (2002).
[5] Esmaily Moghadam M et al. *JCP* 244 (2013).
[6] Zhu C et al. *JOSS* 7.78 (2022).
[7] Tran JS et al. *Comput. Fluids* 142 (2017).
[8] Esmaily-Moghadam M et al. *CMAME* 286 (2015).
[9] Bäumler K et al. *BMMB* 19.5 (2020).

THREE-DIMENSIONAL SHAPE ANALYSIS OF THE PELVIC FLOOR: IDENTIFYING DEFECTS IN CYSTOCELE DEVELOPMENT

Liam Martin (1), Alireza Hadizadeh (2), Henry Chill (2), Ghazaleh Rostaminia (2), Steven Abramowitch (1)

(1) Department of Bioengineering, Swanson School of Engineering, University of Pittsburgh, Pittsburgh, PA, USA
(2) Department of Urogynecology, University of Chicago, Northshore University HealthSystem, Skokie, IL, USA

INTRODUCTION

Cystocele is the most prevalent presentation of pelvic organ prolapse, wherein the bladder is displaced into the anterior vaginal wall, causing it to extend near or past the vaginal opening. This uncomfortable and debilitating condition significantly impacts the quality of life for affected women. Approximately 10% of women in the United States undergo surgery for this condition during their lifetime, and the rates of recurrence, resulting in two or more surgeries, are as high as 50% [1].

Part of the reason for the high recurrence rates can be attributed to the repair not addressing the root cause of the cystocele. While it is understood that a cystocele results from a loss of support to the vagina and bladder, the specific tissues responsible are still debated. Some argue that it results from a direct loss of levator muscle function, while others believe that it arises from a defect in the connective tissues supporting the vagina. However, the precise location of the defect, whether at Level I (the more apical uterosacral ligament) or Level II (the paravaginal attachments), remains unclear. Certainly, it is possible that a partial or complete loss of function in all these structures is necessary. This information is critical for accurate diagnoses and the selection of the appropriate repair procedure.

Unfortunately, diagnosis is often limited to an external examination where a clinician measures or estimates the position of the vaginal wall relative to the vaginal opening as a patient strains (increases intra-abdominal pressure) via the pelvic organ prolapse quantification (POP-Q) exam. While this enables the clinician to assess the extent of the prolapse and whether the anterior wall, apex, or posterior wall is more or less affected, they are unable to visualize internally to determine the defect responsible for the prolapse. Cystocele is less commonly measured using bony landmarks on dynamic MR imaging. While this method offers a quantitative assessment of internal structures, the specific defect causing bladder descent cannot be easily observed. Therefore, diagnosis is based on the relative motions of the organs. A rigorous understanding of patient anatomy and normal physiological motions, and how those two differ from anatomy and organ motion consistent with different forms of prolapse, should, in theory, enable a specific defect to be inferred from this type of imaging. However, the diagnosis of cystocele via imaging is frequently inconsistent with findings based on the POP-Q, and the latter is better correlated with patient symptoms. Indeed, dynamic imaging provides the potential to improve diagnoses and repair, but our lack of understanding of the functional anatomy of the female pelvis is limiting. A goal of our laboratory's research is to couple dynamic imaging of the female pelvis with biomechanical analyses to enable the extraction of more clinically useful information from imaging.

Building on our previous work that enhanced radiologic diagnostic criteria for cystocele [2], the goal of the current study is to use three-dimensional statistical shape analysis (SSM) to test the hypothesis that specific defects or functional changes in pelvic floor musculature can be identified in patients who are separated based on these criteria.

METHODS

We conducted a retrospective search for patients diagnosed with radiologic cystocele, determined through dynamic MR imaging based on traditional criteria. To be included in the study, the patient data needed to include complete geometry (entire pelvic floor visible within the MRI volume) for static and dynamic (MR defecography) scans, as well as full demographic data in their patient files. To diagnose cystocele based on our enhanced criteria, we assessed how closely the most inferior bladder point approached the genital hiatus during evacuation in the MR defecography series. Based on these criteria, subjects whose bladder descended within 1 cm of the genital hiatus were classified as having a "clinically relevant cystocele," while subjects whose bladder remained higher than 1 cm were not, independent of the diagnosis based on traditional criteria.

The pelvic floor muscles at rest (excluding the bulbocavernosus, perineal membrane, transverse perinei muscles, and anococcygeal ligament) of all the subject scans were segmented using 3D Slicer (v. 5.2, `https://www.slicer.org/`). Our laboratory's SSM workflow reconstructed the 3D geometries, smoothed, aligned, and scaled them based on correspond-

ing points using Deformetrica, and then performed a principal component analysis on those corresponding points [3]. The individual patient scores (i.e., their position on the axes describing the principal components) were then used to compare shape differences between groups independent of rotation, translation, and scale. Principal components that describe more shape variation than random noise (determined through a parallel analysis) were included in our analyses. Statistical analysis was conducted on both the continuous demographic data and the principal component scores of the shapes for each included principal component using an ANOVA followed by a Benjamini-Hochberg correction post-hoc. Categorical variables were assessed using a Mann-Whitney U Test.

RESULTS

Our database search identified 67 subjects diagnosed with cystocele on MR defecography. The average age of the sample was 56 years-old, with a median parity of 2 (range: $(0-7)$). Based on our enhanced criteria, twenty-eight subjects were identified as having clinically relevant cystocele, while the remainder were not. Subjects in this group were significantly older ($p = 0.001$), had more pregnancies ($p = 0.020$), and more deliveries ($p = 0.010$) compared to those with non-clinically relevant cystocele.

Twelve principal components describe more variance in the data than random noise according to the parallel analysis. After correcting for multiple comparisons, only one principal component (PC 1) was found to be statistically different between the two groups ($p = 0.009$, 24.7% of the shape variation). Figure 1 shows the shape differences described by PC 1, where non-clinically and clinically relevant cystocele are represented by the left and right columns, respectively. PC 1 primarily captured variation laterally and in the distal portion of the pelvic floor, i.e., descent of the perineal body. Subjects with clinically relevant cystocele exhibited greater descent of the pelvic floor muscles away from their attachment to the arcus tendineus fascia pelvis (ATFP). At this level, connective tissues link the obturator internus and the levator ani through the ATFP (Figure 2). This change is particularly evident in the sagittal view (second row). Accompanying this descent, there was a noticeable ballooning of the pelvic floor. When viewed from the top/front (first row), the cystocele group on the right side of the figure appeared to have an increased levator bowl volume, a feature commonly associated with prolapse, compared to the shapes on the left. Because these differences exist on the same principal component, one does not exist without the other in this cohort, implying that the link to the ATFP, descent of the perineal body, and levator bowl volume are all correlated.

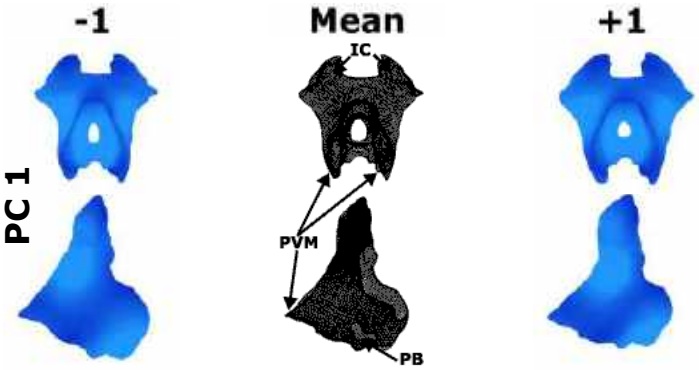

Figure 1: The average shape $\pm$ one standard deviation for pricipal component 1, non-clinically relevant cystocele (left) and clinically relevant cystocele (right). The colormap represents the surface's distance away from the mean (blue = closer, white = further). PVM = pubovisceral muscle, IC = iliococcygeus, and PB = perennial body.

DISCUSSION

Based on enhanced diagnostic criteria, this study identified a specific shape change in the pelvic floor of women associated with the development of cystocele, supporting our hypothesis. It further highlighted the connection of the pelvic floor muscles through the ATFP as a potentially important anatomical defect in these patients. This lends support for theories indicating that a defect within Level II support contributes significantly to the development of cystocele. Moreover, it demonstrates the importance of our enhanced diagnostic criteria in the identification of these patients. While it might be argued that all of these women had a cystocele and we are simply identifying a specific phenotype of cystocele, it should be noted that our previous study demonstrated that the traditional diagnostic criteria often misdiagnosed young, nulliparous, and well-supported women as having a cystocele, suggesting they were not rigorous enough [2].

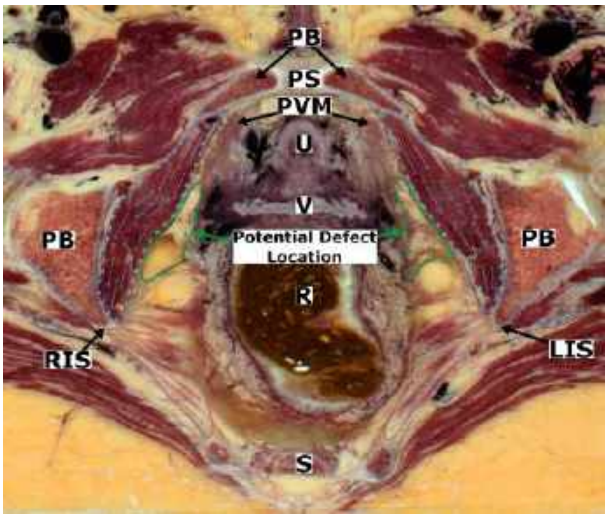

Figure 2: Visualization of the connection of the pelvic floor to the obturator interus muscle, region outlined in green is the area of the potential paravaginal defect leading to cystocele development. Blue, short dashes, obturator internus, red, solid line, iliococcygeus. Estimates of the fiber directions of the muscle in this plane is shown by arrows. PB = pubic bone, PS = pubic symphysis, PVM = pubovisceral muscle, U = urethra, V = vagina, R = rectum and stool, S = sacrum, RIS, LIS = right/left ischial spine.

While this study does not eliminate the possibility of other factors contributing to the development of symptomatic cystocele, it does suggest a potential reason why surgeries that primarily focus on providing support to the vaginal apex are likely to fail in the anterior compartment (i.e., the root cause of the prolapse is not being sufficiently addressed). Our results imply that, to directly treat some forms of cystocele, specifically addressing the defect in Level II support may be necessary, i.e., the area identified in green in Figure 2.

The limitations of this study include its retrospective design and relatively small sample size. Due to the retrospective study design, a POP-Q analysis was not available for all subjects therefore, we chose to replace the assessment in this study with the dynamic MRI-based analog. Our sample of 28 subjects with cystocele is not representative of all types of cystocele and further study is required to include them.

To further understand the functional implications of these findings, our group will aim to perform simulations of defecation using geometries with and without this specific defect.

ACKNOWLEDGEMENTS

NSF 2053851

REFERENCES

[1] Vollebregt A et al. *BJOG* 118.12 (2011). ISSN: 1470-0328, 1471-0528. DOI: 10.1111/j.1471-0528.2011.03082.x.

[2] Martin L et al. *Int Urogynecol J* 34.2 (2023). DOI: 10.1007/s00192-022-05282-7.

[3] Routzong MR et al. en. *Annals of Biomedical Engineering* 51.7 (2023). ISSN: 0090-6964, 1573-9686. DOI: 10.1007/s10439-023-03150-z.

DIRECT QUANTIFICATION OF ERRORS IN BONE POSITIONS AND LIGAMENT TENSIONS USING THE SUPERPOSITION TECHNIQUE WITH A ROBOTIC TESTING SYSTEM

Lesley R. Arant (1), Joshua D. Roth (2, 3)

(1) Department of Biomedical Engineering, University of Wisconsin-Madison, Madison, WI, USA
(2) Department of Orthopedics and Rehabilitation, University of Wisconsin-Madison, Madison, WI, USA
(3) Department of Mechanical Engineering, University of Wisconsin-Madison, Madison, WI, USA

INTRODUCTION

The superposition or sequential sectioning technique is a ubiquitous method to quantify *in situ* ligament tensions using a robotic testing system.[1] This technique has been used for a range of applications including to ascertain healthy ligament mechanics[2,3], and to determine the effects of injury[4,5] and surgical interventions[6,7] on ligament mechanics. In this technique, the same kinematics are prescribed to a joint with a ligament of interest intact and then resected. The tension in that ligament is computed as the vector difference in the joint reaction forces between the ligament-intact and ligament-deficient states.[1]

In superposition testing to date, joint kinematics have been measured and controlled by applying a rigid transformation from the position of the robot end effector to the position of the joint, referred to herein as robot kinematic control. However, compliance in any structure in the testing system except the ligament of interest (e.g., robot, fixtures, bones) can lead to deflection of the robot and/or the robot-mounted bone between the intact and ligament-deficient states. This deflection can, in turn, introduce errors in joint kinematics leading to errors in superposition-computed tensions. To account for system compliance, joint kinematics can also be measured and controlled using the position of an optical motion capture sensor fixed to the robot-mounted bone, referred to herein as motion capture kinematic control. To date, the superposition technique has not been directly validated in cadaveric joints using either kinematic control mode.

Therefore, the ***objectives of this study*** were to quantify the following errors when using robot kinematic control and motion capture kinematic control: (1) the errors in the positions of the robot-mounted bone between the intact and ligament-deficient joint and (2) the errors in superposition-computed tensions. ***Our overall hypothesis*** was that the motion capture kinematic control mode would result in lower errors in the position of the robot-mounted bone that would, in turn, lower the errors in superposition-computed tensions. We used the lateral collateral ligament (LCL) of the knee as a representative ligament in this study.

METHODS

We prepared five cadaveric knees for robotic testing as previously described (**Figure 1a**).[8] To provide a direct, gold-standard measure of LCL tension, we potted the distal end of the proximal fibula of each knee in an aluminum tube and attached it in-series with a single-axis load cell (Futek LSB210, reported nonlinearity = 0.9 N) to the fixed tibial bone tube (**Figure 1b**). Then, we resected the articular surfaces of the tibiofibular joint to free the fibula from the tibia such that the single-axis load cell directly measured LCL tension.

After fixing a motion capture sensor to the femur, we mounted each knee in our robotic testing system (KR300 2700-2, KUKA) controlled using simVITRO's eXactoPOSE® (**Figure 1a**).[9] After defining a functional coordinate system[10], we prescribed kinetic-control varus (15 Nm) and external rotation (5 Nm) ramp load-unload trajectories. These trajectories were prescribed at 0°, 30°, 60°, and 90° flexion in three specimens and at 0° flexion in the two other specimens. Then, we

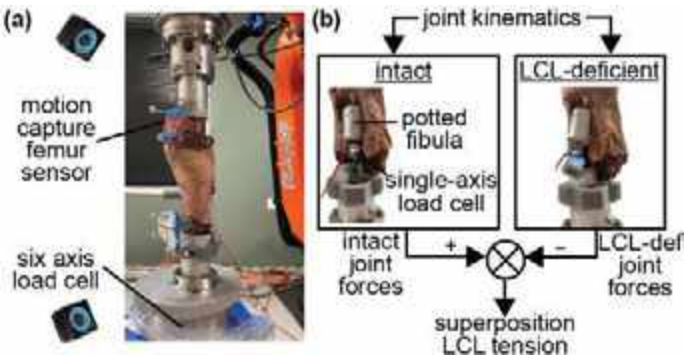

Figure 1: (a) We fixed a motion capture sensor to the femur and mounted each knee in a robotic testing system. (b) We computed superposition tensions using the difference in joint reaction forces between the intact and LCL-deficient states.

prescribed the kinematics measured during these kinetic-control trajectories to the knee using both the robot and motion capture kinematic control modes. We prescribed these kinematics to the intact joint and to the joint with the LCL attachment disconnected (**Figure 1b)**.

We calculated the errors in the motion capture femur sensor position as the magnitude of the difference between the position vectors in the intact and LCL-deficient states for each trajectory and control mode. We used the principle of superposition[1] to compute the *in situ* tension in the LCL for each trajectory and control mode (**Figure 1b**). We calculated the errors between the superposition-computed and load-cell-measured tensions in all specimens. We pooled the errors in the motion capture femur sensor position and superposition tension across specimens and trajectory types (i.e., varus or external rotation) and computed the bias and precision errors.[11] Additionally, we performed paired t-tests (significance level = 0.05) to test the specific null hypotheses that (1) the motion capture femur sensor errors at peak tension are not different between the two control modes and (2) the peak tension errors are not different between the two control modes.

RESULTS

The errors in the motion capture femur sensor position were smaller for the motion capture kinematic control mode than for the robot kinematic control mode ($p < 0.001$) (**Figure 2a**, **Table 1**). For both robot kinematic control and motion capture kinematic control modes, superposition-computed LCL tensions tended to underestimate true LCL tensions. The tension errors were smaller for the motion capture kinematic control mode than for the robot kinematic control mode ($p < 0.001$) (**Figure 2b**, **Table 2**).

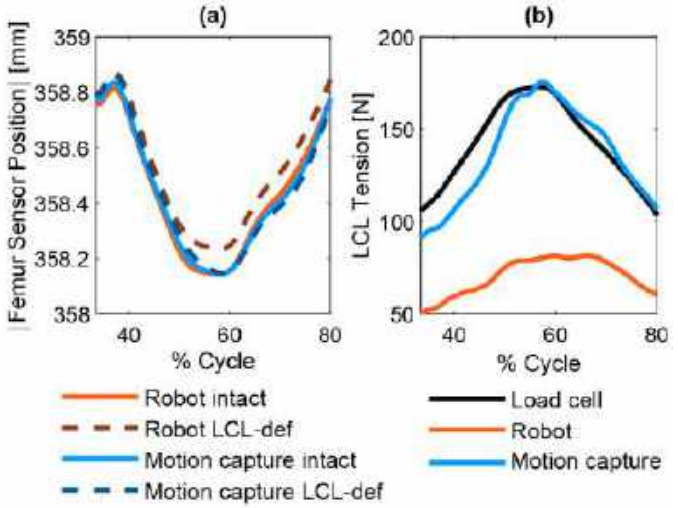

Figure 2: Representative data around peak loading for a varus ramp trajectory at 30° flexion for each control mode depicting (a) the magnitude of the femur motion capture sensor position vectors and (b) the LCL tensions.

Table 1: Errors (bias ± precision) in motion capture femur sensor positions between the LCL-deficient and intact joint states for the robot kinematic control mode and the motion capture (MoCap) kinematic control mode.

	External rotation		Varus	
	Robot	MoCap	Robot	MoCap
Femur sensor error [μm]	117 ± 100	19 ± 15	261 ± 251	41 ± 38
Femur sensor error at peak tension [μm]	178 ± 90	24 ± 21	500 ± 314	47 ± 34

Table 2: Errors (bias ± precision) in LCL tensions between superposition-computed and load cell-measured tensions for the robot kinematic control mode and the motion capture (MoCap) kinematic control mode.

	External rotation		Varus	
	Robot	MoCap	Robot	MoCap
LCL tension error [N]	-17 ± 21	-7 ± 16	-38 ± 35	-3 ± 19
Peak LCL tension error [N]	-35 ± 24	-18 ± 18	-89 ± 24	-10 ± 22

DISCUSSION

Our ***first key finding*** was that the traditional robot kinematic control mode for performing superposition testing can result in large errors in the motion capture femur sensor positions between the intact and ligament-deficient joints (**Table 1**), which violates a key assumption of the principle of superposition.[1] Consequently, we found that the errors in superposition-computed tensions using the robot kinematic control mode were large (**Table 2**). Our ***second key finding*** was that using the motion capture kinematic control mode decreased the errors in the motion capture femur sensor positions (**Table 1**) that in turn lowered the errors in superposition-computed tensions (**Table 2**). Together, ***these key findings support our overall hypothesis*** and indicate that motion capture kinematic control is an attractive alternative to robot kinematic control for determining superposition-computed ligament tensions.

The root cause of the larger errors in superposition-computed tensions using the robot kinematic control mode is deflection of the robot. When a ligament is removed, the loads applied to the robot decrease, resulting in deflection of the robot and robot-mounted bone that can alter joint kinematics (**Figure 2a**). When using robot kinematic control, the robot cannot detect this deflection, and therefore cannot correct for it. In contrast, when using motion capture kinematic control, the motion capture femur sensor measures this deflection, and can correct the prescribed robot motion (**Figure 2a**). We believe that the remaining errors in the superposition-computed tensions for the motion capture kinematic control mode are largely due to noise in our motion capture data. We originally used both the femur and tibia motion capture sensors for control, but found that the motion capture noise outweighed any advantage of accounting for deflection of the tibia. Thus, ongoing work is focused on improving motion capture precision.

Superposition testing has been and will continue to be a valuable experimental approach to quantify ligament tensions. For both control modes, it is necessary to report the errors in superposition-computed tensions to properly interpret the reported ligament tensions, especially because errors will vary with different robotic testing and motion capture systems. Based on our results, we recommend adopting motion capture kinematic control for superposition testing over the traditional robot kinematic control to significantly reduce the errors in superposition-computed ligament tensions.

ACKNOWLEDGEMENTS

We acknowledge the technical support of the simVITRO® team to implement the eXactoPOSE® algorithm.

REFERENCES

[1] Fujie, H et al., *J Biomech Eng*, 117:1-7, 1995. [2] Dalmau-Pastor, M et al., *Am J Sports Med*, 51:2169-2175, 2023. [3] Imhauser, CW et al., *J Biomech*, 64:212-218, 2017. [4] Battaglia, MJ et al., *Am J Sports Med*, 37:305-311, 2009. [5] Debski, RE et al., *JBJS*, 83:1344-1351, 2001. [6] Mae, T et al., *Arthroscopy*, 17:708-716, 2001. [7] Okada, Y et al., *JBJS*, 100:e114, 2018. [8] Arant, LR et al., *ORS*, 2023. [9] Gillespie, CM et al., *SB3C*, 2023. [10] Nagle, TF et al., *J Biomech*, 127:110664, 2021. [11] ASTM E177-13. 2020.

ASSESSING THE EFFECT OF DIMETHYL SULFOXIDE ON THE PROPERTIES OF REGULATORY ENZYME FRUCTOSE 1,6-BISPHOSPHATASE IN GLUCONEOGENESIS CONDITIONS

A. Sabaghan (1), N. Ghousifam (1), M. Rezaeeyazdi (1), C.L.Riley (2), D.Romanovicz (1), M.N. Rylander (1,3), and M. Uden (4)

(1) Department of Mechanical Engineering, The University of Texas at Austin, Austin, TX, United States
(2) Department of Molecular Biosciences, The University of Texas, Austin, TX, United States
(3) Department of Biomedical Engineering, The University of Texas, Austin, TX, United States
(4) Department of Psychology, The University of Texas, Austin, TX, United State

INTRODUCTION

Cryopreservation of organs has an important role in transplantation and enabling flexible scheduling of surgeries. The major challenge to overcome at low temperatures is the water-to-ice phase transition for cells. In addition, freezing can be extremely fatal to living organisms as both intra- and extracellular ice crystal formation can result in chemical changes in the cells which can lead to extreme mechanical strain on cells [1].

The freezing behavior of cells can be altered in the presence of a cryoprotective agent (also called cryoprotectant), which affects the rates of water transport, nucleation, and ice crystal growth [1,2]. Dimethyl sulfoxide (DMSO) is the most commonly used cryoprotectant that penetrates across lipid bilayers of the cell membrane and prevents intracellular ice formation by reducing the water content inside the cell [1, 2]. However, DMSO can cause concentration-dependent cell toxicity by altering the structure of cell proteins and membrane [3]. The most common DMSO concentration to use in organ cryopreservation has been 30% (v/v) [4].

Previous studies suggest that part of the toxic effect of DMSO on cells is caused by exerting damage to enzyme fructose 1,6-bisphosphatase (FBP1) and ultimately disturbing gluconeogenesis [4]. FBP1 is a rate-limiting enzyme responsible for controlling energy metabolism and glucose in cells through catalyzing gluconeogenesis and glycolysis. It is a complex tetramer and a highly regulated enzyme whose activity is modulated synergistically by the inhibitors 5'-adenosine monophosphate (AMP) and fructose 2,6-bisphosphate (FBP) [5]. In the present study, we aimed to identify whether DMSO exposure modulates FBP1 enzyme properties, which would consequently alter the production mechanism of adenosine triphosphate (ATP) affecting the ultimate cell survival rate. In order to do this, purified pig kidney FBP1 was exposed to DMSO followed by performing a series of characterization techniques to determine whether DMSO is capable of modifying enzyme activity and conformation.

METHODS

FBP1 synthesis: *Bacterial growth*: T7 express lys Y competent E. Coli (BioLabs Inc., C3030J) was mixed with pig FBPase plasmid and cultured on LB agar plates. Bacteria was cultured further in autoclaved TB solution containing glycerol and ampicillin while being shaken at 250 rpm and 30 °C. While induced with Isopropyl-beta-D-thiogalactopyramoside (IPTG) to the final concentration of 120 mM.

FBPase purification: Bacteria were washed with cold phosphate buffer saline (PBS, pH 7.4). The bacteria pellet was then resuspended in 50 mM Tris buffer containing 150 mM sodium chloride, 10% (v/v) glycerol protease phosphate (1:1000), basement membrane extract (BME) (1 mM), Lysozyme (0.1 mg/ml), and RNase/DNase (2.5 units/ml) while keeping the pH at 7.4. The cell suspension was placed on ice and shaken for one hour. The cells were lysed by using a transonic T460/H sonicator (John Morris Scientific Pty Ltd.) for 5 minutes, cycling 5 seconds on and 30 seconds off on ice. The cell debris was removed by centrifugation at 15000×g for 30 min at 4°C. The supernatant containing protein extracts was then mixed with beads at 4°C for one hour. FBP1 stock concentration was measured using the Bradford assay with the absorbance at 595 nm.

Enzymatic activity: Malachite Green Phosphate Assay Kit (Sigma-Aldrich, MAK307) was used to assess the activity of purified FBP1. The activity assay was performed in a Tris buffer pH 7.5 made of 50 mM Tris and 5 mM potassium chloride in DI water. Purified FBP1 stock was desalted against the prepared Tris buffer using Zeba™ Spin Desalting Columns (Thermo Scientific, 89882), and then diluted in Tris buffer to a concentration of 200 nM. Samples containing 200 nM FBP1 in Tris buffer, 200 nM FBP1 in 30% DMSO prepared in Tris buffer, 200 nM FBP1 in 2.4 μM coenzyme A (CoA) prepared in Tris buffer, and 200 nM FBP1 in 30% DMSO and 2.4 μM CoA prepared in Tris buffer were incubated with different concentrations of FBP (0-250 μM).
FBP1 was diluted to a final concentration of 200 nM in Tris buffer containing various amounts of DMSO (0, 0.1, 0.2, 0.5, 1.0, 2.0, 5.0, 10,

20, 30, 40, and 50 % (v/v)) and 250 µM FBP. IC50 and Hill slope were then calculated using Graphpad Prism 9. Tris buffer containing 200 nM FBP1 and various amounts of DMSO (0-50 % (v/v)) were used as control samples for this experiment.

Dynamic light scattering (DLS): Zetasizer Nano ZS-MAL1043824 was used to evaluate the size and size distribution of purified FBP1. In order to study the effect of DMSO on the purified FBP1 protein, DMSO was added to the FBP1 solution to a concentration of 30% (v/v) and incubated at 37°C for an hour before DLS analysis.

RESULTS

The first characterization analysis selected for the purified FBP1 in this study was evaluating the activity of this enzyme using Malachite Green Phosphate activity assay. Results shown in Figure 1 revealed that the activity of purified FBP1 changes with concentration of substrate (FBP). These results indicated that the purified FBP1 in this study is highly active and the activity of FBP1 didn't change upon incubation of the enzyme at 37°C for 24 hours. Incubation with CoA for one hour at 37°C didn't affect the activity of FBP1, while incubation with DMSO inhibited the activity of the enzyme significantly, regardless of incubation time. In addition, CoA didn't repair the oxidation stress that was applied to the FBP1 enzyme by DMSO which resulted in reducing the activity of the enzyme significantly. After 24 hours of incubation with CoA at 37°C, the activity of FBP1 was inhibited.

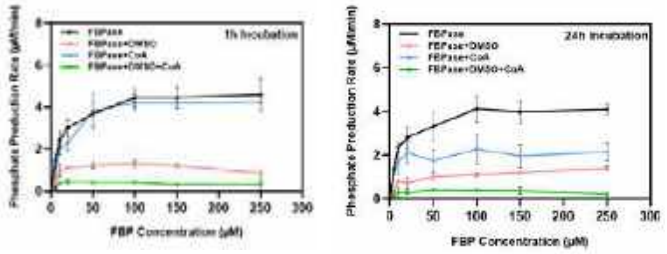

Figure 1. Enzymatic activity of purified FBP1 after incubation with 30% (v/v) DMSO and 2.4 µM CoA for 1 and 24 hours.

In order to assess the inhibition of FBP1 enzyme by DMSO, the IC50 value for FBP1 samples exposed to different concentrations of DMSO was determined using Malachite Green Phosphate activity assay. The IC50 value was calculated to be 2.2 M (20% v/v) with a HillSlope of -2.9 which indicates that at 20% (v/v) DMSO 50% of the FBP1 enzyme's active sites are inhibited.

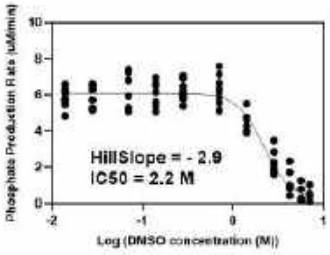

Figure 2. The IC50 value for FBP1 enzyme exposed to different concentrations of DMSO.

Dynamic light scattering (DLS) was used to evaluate the size and size distribution of purified FBP1 enzyme before and after interaction with DMSO. DLS results (Figure 3) showed a homogeneous size distribution of 10 nm for purified FBP1 with minimum aggregation. Upon incubation with DMSO for one hour, a heterogeneous size distribution consisting of two signals were detected for FBP1; one at about 20 nm and the other one at 200 nm which could indicate aggregation of the FBP1 enzyme upon interaction with 30% DMSO.

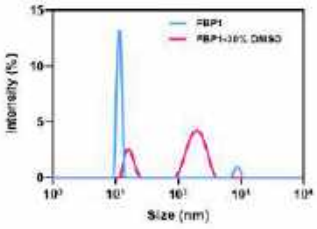

Figure 3. Dynamic light scattering (DLS) analysis of purified FBP1 before and after incubation with 30% DMSO.

DISCUSSION

Understanding the mechanisms of cryoprotectant toxicity could be the means to eliminate toxicity and increase the number of successful organs cryopreserved. Prior research indicates that the detrimental impact of DMSO on cells may arise from its ability to cause damage to FBP1, thereby disrupting gluconeogenesis. It's been shown that high concentrations of DMSO can bind to proteins which can lead to protein unfolding [6]. Furthermore, it's been demonstrated that one of the possible pathways for DMSO cytotoxicity at high concentrations is related to its tendency to aggregate proteins within human cells and pharmaceutical samples [7]. This study aimed to investigate whether exposure to DMSO influences enzyme properties, potentially leading to alterations in ATP production and, consequently, impacting cell survival rates. To this end, the effect of DMSO interactions with FBP1, as the protein responsible for production of ATP and cell survival, was evaluated in this study. The results of DLS measurements (Figure 3) revealed that incubation of FBP1 enzyme with DMSO significantly affects the enzyme's size indicating aggregation of the enzyme which resulted in reduction of its activity and kinetic parameters; these effects worsened over time (1 h vs. 24 h). Furthermore, the enzyme activity, when FBP1 was simultaneously co-incubated with DMSO and CoA, were explored. Coenzyme A is used to protect proteins from irreversible sulfhydryl overoxidation [8]. However, the results in this study (Figure 1) showed no improvement in the activity of FBP1 enzyme upon co-incubation with CoA and DMSO compared to that of DMSO alone. Overal, the data obtained reveals significant changes in FBP1 properties at high concentrations of DMSO, notably a marked inhibition of enzyme activity and consequential alterations in kinetic parameters. These findings provide new insights into DMSO toxicity, suggesting its potential contribution to damage in FBP1 and, consequently, disruptions in glycolysis and gluconeogenesis pathways. The results motivate further investigations to enhance our understanding of the molecular aspects underlying this phenomenon.

ACKNOWLEDGEMENTS

This work was funded by a gift from the Elizabeth Crook & Mark Lewis Foundation.

REFERENCES

[1] Whaley, D et al., *Cell Transplantation*, 30:0963689721999617, 2021.
[2] Elliott, GD et al., *Cryobiology*, 76:74-91, 2017.
[3] Verheijen, M et al., *Scientific Reports* 9(1):4641, 2019.
[4] Baxter, SJ et al., *Biochemical Pharmacology*, 20:1079-1091, 1971.
[5] Topaz, G et al., *Bioscience Reports*, 39(2):BSR20180960, 2019.
[6] Arakawa T et al., *Biophys Chem* 131:62-70, 2007.
[7] Giugliarelli, A et al., *J. Phys. Chem. A,* 120:5065-5070, 2016.
[8] Tsuchiya, Y et al., *Biochem J,* 475:1909-1937, 2018.

PROBING THE RAT URINARY BLADDER DURING ISOTONIC ACTIVE CONTRACTION USING MULTIPHOTON MICROSCOPY

A. Asadbeygi (1), Y. Tobe (1), S.D. Stocker (2), S. Watkins (3,4), P.N. Watton (1,5), C. Hardin (6), N. Yoshimura (7), A.M. Robertson (1,8)

(1) Department of Mechanical Engineering and Materials Science, University of Pittsburgh, Pittsburgh, Pennsylvania, USA
(2) Department of Neurobiology, University of Pittsburgh, Pittsburgh, Pennsylvania, USA
(3) Department of Cell Biology, University of Pittsburgh, Pittsburgh, Pennsylvania, USA
(4) Center for Biologic Imaging, University of Pittsburgh, Pittsburgh, Pennsylvania, USA
(5) Department of Computer Science, University of Sheffield, Sheffield, UK
(6) Division of Food, Nutrition and Exercise Sciences, University of Missouri, Missouri, USA
(7) Department of Urology, University of Pittsburgh, Pittsburgh, Pennsylvania, USA
(8) Department of Bioengineering, University of Pittsburgh, Pittsburgh, Pennsylvania, USA

INTRODUCTION

The structure of urinary bladder, as a collagenous active tissue comprises several layers, each with specific constituents. The innermost layer or urothelium serves as a protective barrier. Below it, the lamina propria (LP) which contains collagen and elastin fibers, providing flexibility. The key layer for bladder contractile function is the muscularis propria or detrusor smooth muscle layer (DSM), primarily consisting of smooth muscle cells (SMCs), crucial for bladder contraction and relaxation. Collagen fibers are present throughout the wall with different conformations in the different wall layers. In the DSM layer, they are integrated with the SMC bundles [1]. Overall, the collagen fibers contribute the structural stiffness and strength to the bladder wall [2].

The urinary bladder's ability to fill and void is a finely tuned physiological process, integral for normal urinary function. Changes to the aforementioned constituents have been associated with lower urinary tract syndromes (LUTS) including both overactivity and incomplete voiding. Specifically, previous studies have shown that the changes to the structural and physiological response of SMCs as well as their interaction with collagen fibers can lead to micturition issues. Moreover, other studies revealed that the structure of the constituents in the LP and DSM layers and the lumen shape (surface topology) have a significant impact on bladder compliance [1]. Such changes can arise from aging [1] or from diseases such as bladder outlet obstruction (BOO) [3,4]. Therefore, it is essential to study the structure of the constituents and the surface topology simultaneously during active contraction in healthy and diseased tissues.

Previous investigations into bladder wall changes during active contraction primarily relied on 2D histological scans of fixed tissues, providing valuable insights but lacking a comprehensive view of 3D topology during active contraction [5]. A prior study explored active contraction in 3D sections of uterine tissue under isometric loading conditions [6]. However, in such conditions, the tissue cannot contract truly due to the fixed boundaries inherent in isometric loading.

The present study focuses on understanding changes in bladder wall topology during active contraction and imaging the layer-wise constituents, specifically collagen and smooth muscle cells (SMCs), in their contracted state. To achieve this objective, we designed a custom biaxial device for isotonic loading of specimens under multiphoton microscope (MPM). Using this system, for the first time, the in vitro active contraction of bladder under isotonic load is imaged under multiphoton microscope, using our custom designed isotonic biaxial apparatus. This work introduces a protocol for imaging live tissue constituents in both active and passive states under isotonic biaxial loading.

METHODS

Biaxial Isotonic Contraction Apparatus: An important design requirement for the experimental system is physical compatibility with the multiphoton microscope (Nikon A1R MP HD, Tokyo, Japan) considering factors such as chamber size and operational limitations of the lens. Furthermore, the tissue must be firmly clamped without tissue damage and maintained viable for the active contraction during long scanning times. The common commercial isotonic systems are not operational under multiphoton microscopes. Inspired by the simple weight-hanging vertical uniaxial systems, here we designed and fabricated a biaxial isotonic apparatus in which the desired force derives from weights that are hung using a triple-pulley mechanism (Figure 1).

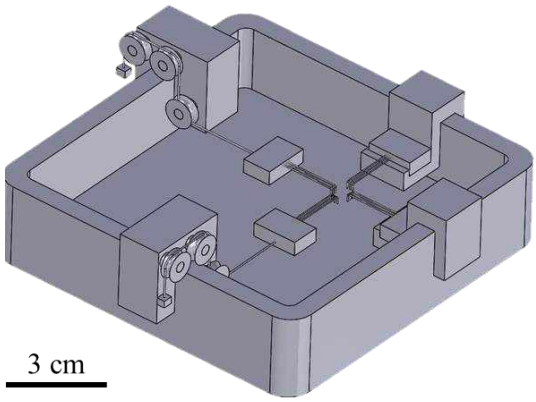

Figure 1. The custom made isotonic apparatus for multiphoton imaging of small tissues. The force is set by hanging weights.

Due to the very small size of the samples (~5mm) and MPM scan area limitations, the previously used commercial rakes [3] could not be used for mounting the bladder samples. Therefore, custom rakes with the appropriate needle diameter and claw length (250 um and 3mm, respectively) were designed with holders fabricated from PLA using 3D printing (an order of magnitude cheaper than the commercial ones). The rake holders were designed to be 90% porous, so they easily float on water within the biaxial tank. The tank with the appropriate size and fixtures was also 3D printed from PLA. Temperature is maintained using a digital temperature controller and a heater located at the base of the tank.

In this study, bladder tissue was obtained from 2 month old male rat bladders which were cut open longitudinally and mounted on the rakes using a custom 3D printed platform with Styrofoam substrate. 1g weights were applied as the isotonic loads. Experiments were performed at 37° C. The tank was filled with KREBS solution [6] aerated with a gas mixture of 95% O_2 and 5% CO_2 to provide physiological environment to ensure cell viability and function.

MPM Scan and Active Contraction of SMCs: The active contraction was induced by addition of KCl to the KREBS solution to achieve 80mM concentration [6]. Two MPM scans were performed before and after contraction, using optimized parameters to make the scan as short as possible (to maintain cell viability). The scanned results were reconstructed and analyzed using IMARIS 10.1.0 (BitPlane AG, Zurich, Switzerland).

Tissue Fixation and staining: The same procedure was performed on another sample. At the end, while the tissue is attached to rakes, the Krebs solution in the tank was replaced with 4% paraformaldehyde in PBS, to fix the tissue in the contracted state under the biaxial loading. The fixed sample was stained with Monoclonal mouse anti-human smooth muscle actin clone 1A4 IgG2a antibody (Dako, Denmark) as the primary antibody and Alexa Fluor 568 goat anti-mouse IgG2a (Invitrogen, USA) for the secondary antibody.

RESULTS

Figure 2a shows a 3D projection of stacks of MPM images from the lumen side of the contracted bladder, while under isotonic loading. The red and green channels correspond to collagen and urothelial cells, respectively. The yellow lines show the location of the in-silico bisection that is visible on the right and bottom of the central square region. Large folds (up to 500 um) form in the upper region which corresponds to the bladder dome (white arrow). These folds are also visible in the vertical bisection (white arrow). These folds are larger in magnitude and wavelength, compared with the trigonal area (bottom, yellow arrow). The smaller amplitude "rugae" in trigonal area are

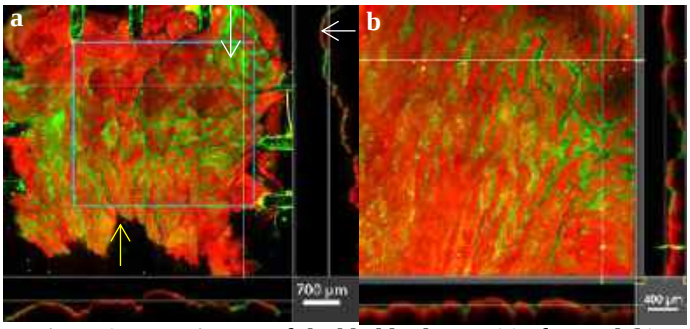

Figure 2. MPM images of the bladder lumen (a) after and (b) before contraction. Large folds can be seen in the contracted tissue, forming convex and concave surfaces on the lumen.

largely oriented longitudinally (vertical in Figure 2), forming a relatively flat surface. The larger folds form convex and concave surfaces after contraction. Although the urothelial cells cover the surface of the lumen, they are folded together in the convex areas, resulting in a higher intensity green signal.

To evaluate changes in surface topology during contraction, a zoomed in area of contracted tissue (blue rectangle in Fig. 2a) is shown in Figure 2b. The surface topology can be seen to change substantially with contraction. In the uncontracted state, the folds uniformly have a smaller amplitude (maximum of 150 µm) than in the contracted state with higher frequency. The orientation of the folds are similar in the contracted and uncontracted states in the trigonal area.

Figure 3 illustrates an orthogonal cross section of bladder with autofluorescent collagen (red), and aSMA stained SMCs (orange) that appear as SMC bundles (blue arrows). The multilayered structure of the bladder wall is seen. It is seen that the SMC bundles have multidirectional orientation. The presence and interaction of collagen fibers between SMC bundles are well illustrated.

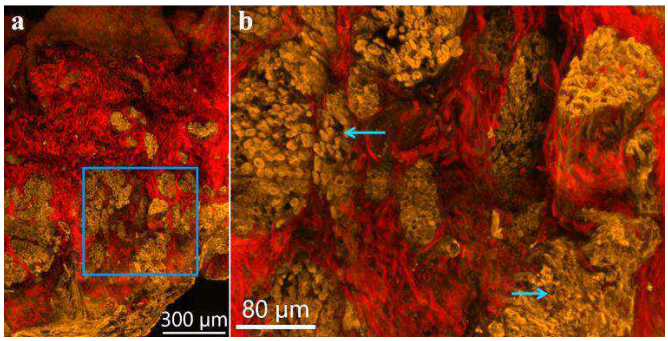

Figure 3. MPM image from a 2D thick-cut section of the contracted bladder, fixed under isotonic loading. Bladder was sectioned orthogonal to the lumen (lumen is up in image). The autofluorescent collagen fibers (red) and SMC bundles (aSMA stained, orange) are illustrated. (a) The whole wall thickness, (b) 4X zoomed in image from blue square in (a).

DISCUSSION

A custom apparatus for biaxial isotonic loading of live tissues is designed and fabricated, that is compatible with multiphoton microscopy. In contrast to the common isometric devices, this isotonic mechanism enables us to image the deformation patterns in active tissues. Using this MPM compatible system, the 3D tissue topology including collagen fibers can be imaged in the same live sample in the uncontracted and contracted state. This is not possible using other imaging modalities like micro-CT or confocal microscopy.

Here we demonstrated the capability of using this system for studying bladder wall constituents and deformation patterns due to active contraction of rat bladder, relevant to the voiding phase. This study identified a spatial heterogeneity even in the qualitative topological features of the contracted bladder. After contraction, the internal layer (LP) buckles in almost all the regions, with larger amplitude in the dome region. These large buckles are three dimensional and are distinct from the small rugae reported in the literature. The heterogenous and multidirectional organization of smooth muscle bundles imaged here in 3D using MPM [7], as the contractile elements of the bladder can justify these heterogenous deformation patterns. Future studies can investigate the observed buckling phenomena, based on the mechanics of multilayer composite sheets.

The proposed methodology enables us to image the deformation patterns and strains in active response of any other live tissues. Of importance, the advanced MPM scanning can image the collagen fibers organization up to single fiber scale (100nm), without any staining. Moreover, following the proposed fixation and staining techniques, the constituents like SMCs can be imaged in their physiological contracted state. This can provide valuable insights for understanding the structure and organization of SMCs in diseased conditions such as BOO bladders, in which hypertrophy and ischemia mechanism results in deficient contractility of SMCs in the voiding function. Although an orthogonal section was stained and imaged in this study, the presented methodology has the potential to image the 3D organization of SMCs throughout the entire bladder in its contracted state. This can be achieved by optically clearing the tissue before staining [7]. Such microstructural information can significantly enhance current computational models, aiding in the development of a high-fidelity digital twin of the bladder, which is the current objective of this research group.

ACKNOWLEDGEMENTS

We acknowledge receiving funds from two NIH grants R01 DK133434-01A1 and R01 1S10OD025041.

REFERENCES

[1] Cheng, F et al., Biomech Model Mechanobiol (2018) 17:403–417.
[2] Ewalt, DH et al., J Urol 148(2 Pt 2):544–9.
[3] Hald T, Horn T, Br J Urol 1(2):59–64 82 Suppl.
[4] Nagatomi, J et al., Ann Biomed Eng 32(10):1409–1419.
[5] Nguyen, NM et al., World J Mens Health. 2021 Jan; 39(1): 131–138.
[6] Huntington, AJ et al., Acta Biomaterialia 129 (2021) 178–187.
[7] Tobe,Y et al., arXiv preprint arXiv:2305.10253.

EXPERIMENTAL VALIDATION OF 3D DYNAMIC MRI USING AN EX-VIVO PORCINE MODEL OF THE BLADDER

J. Rice (1,4), M. Stellon (2,4), W. Bushman (3), A. Roldan-Alzate (1,3,4)

(1) Department of Mechanical Engineering, University of Wisconsin – Madison, Madison, WI, USA
(2) Department of Surgery, University of Wisconsin – Madison, Madison, WI, USA
(3) Department of Urology, University of Wisconsin – Madison, Madison, WI, USA
(4) Department of Radiology, University of Wisconsin – Madison, Madison, WI, USA

INTRODUCTION

Lowery urinary tract symptoms (LUTS) and changes in bladder function occur with age[1-3]. Patients with LUTS are evaluated with multi-channel urodynamics studies to determine bladder flow and pressure during voiding and filling to assess the presence and severity of symptoms[4]. These tests, however, are invasive and do not provide information about anatomy and flow as the bladder changes shape[5]. Recently, noninvasive techniques based on MRI acquisitions of the bladder during voiding and filling have been developed to paint a broader picture of 3D anatomy and function for lower urinary tract assessment[6]. While this technique provides a more comprehensive picture of bladder function, it largely remains unvalidated.

To combat this, highly controlled experimental validation using an in-vitro, synthetic, bladder mimicking phantom has recently been investigated[7]. While this approach has proved useful, one major limitation is the difficulty in reproducing the tissue-specific behavior of the bladder wall during the flow state. The goal of this study was to perform highly controlled experimental flow validation studies for bSSFP and DISCO Flex-based 3D MRI volumes of the bladder in an ex-vivo porcine model. In doing so, we aimed to better replicate the behavior of urothelium during voiding and filling to more accurately assess the validity of these MRI techniques in obtaining volumetric renderings of the bladder.

METHODS

Porcine bladder tissue was obtained from pigs euthanized for unrelated purposes. To prepare the bladders for flow studies, the ureters were dissected from the renal hilum and the urethra was dissected as distally as possible given anatomical restrictions. The ureters, urethra and bladder were removed *en bloc*. After excision, the ureters and urethra were isolated. Two infusion catheters were placed inside each ureter while a drain catheter was placed in the urethra at the level of the bladder neck. These were sutured in place and connected to a programmable syringe pump to simulate bladder voiding and filling. Two 300cc syringes were utilized, filled to 250cc, and facilitated flow. For all filling and voiding events, 300cc of water was injected through the ureters and withdrawn from the urethra, respectively.

Once air was removed from the system, the porcine bladder was placed in a 3.0T clinical MRI scanner (GE Healthcare) and volumetric data was acquired using two different sequences: (1) 3D Differential Subsampling with Cartesian Ordering (DISCO) Flex and (2) 3D Balanced Steady-State Free Procession (bSSFP). Three different flow rates for both filling and voiding events were simulated in our study – 100, 200 and 300cc/min – resulting in 12 total volumetric acquisitions. bSSFP acquisitions were carried out followed by DISCO Flex due to the requirement of gadolinium-based contrast for signal enhancement during DISCO acquisition. Prior to DISCO acquisitions, 5 ml of gadolinium-based contrast (0.1mmol/kg) was hand-injected into a 1L volume of DI water used to fill the syringes in the flow loop. A summary of acquisition parameters for each sequence are shown in **Figure 1**.

During each MRI acquisition, pressure measurements were acquired by placing an MRI-compatible, fiber-optic pressure transducer (OPP-M200, Opsens Inc) 1cm inside the bladder. Pressure measurements were acquired for the entirety of each flow test at 1000Hz. After acquisitions, pressure and MRI-volumetric data were processed using a custom MATLAB script. A semi-automatic segmentation process was used to determine bladder volume change during and compared to the pump control volume. Changes in successive volumes and the acquisition time were utilized to determine time-resolved volumetric flow rate and compared to imposed flow rates.

RESULTS

Figure 2 depicts typical ex-vivo porcine model volumes over time during a voiding and filling event generated at a flow rate of 300cc/min. MRI-derived flow rates agree within 10% when compared to the known flow rates imposed by the syringe pump with average errors of 8.9% for

total volume error and 8.52% for flow rate error. bSSFP MRI acquisitions led to slightly higher errors in total volume change and flow rate when compared to DISCO Flex for both voiding and filling (9.07% and 10.3% / 8.79% and 6.73 %, respectively).

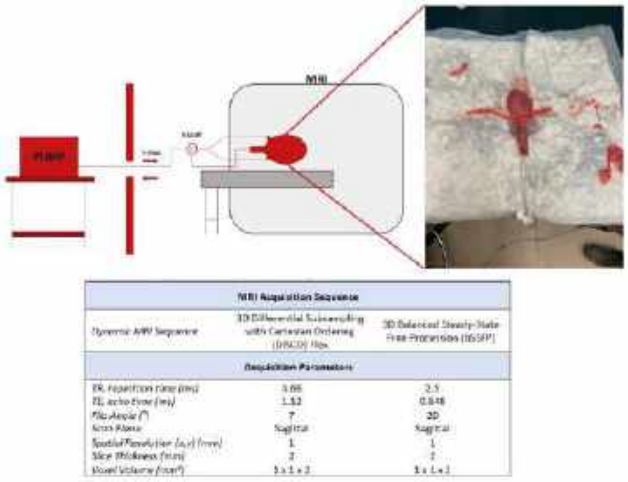

MRI Acquisition Sequence		
Dynamic MRI Sequence	3D Differential Subsampling with Cartesian Ordering (DISCO) Flex	3D Balanced Steady-State Free Precession (bSSFP)
Acquisition Parameters		
TR: Repetition Time (ms)	3.66	2.5
TE: echo time (ms)	1.52	0.848
Flip Angle (°)	7	20
View Plane	Sagittal	Sagittal
Spatial Resolution (x,y) (mm)	1	1
Slice Thickness (mm)	2	2
Voxel Volume (mm³)	1 x 1 x 2	1 x 1 x 2

Figure 1: (Top) Schematic of experimental ex-vivo MRI setup. (Bottom) Summary of DISCO Flex and bSSFP MRI parameters.

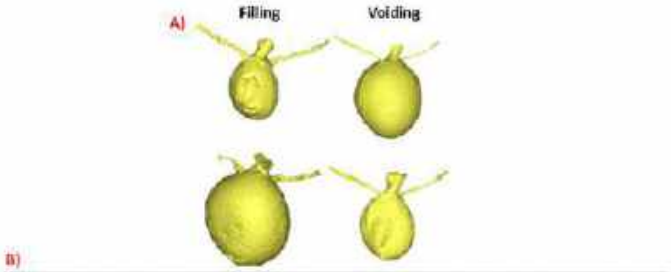

Figure 2: (A) Ex-vivo bladder model renderings obtained from MRI for a 300 cc/min filling and voiding cycle. (B) Total volume change, volumetric flow rate and error analysis for all 12 MRI acquisitions.

Figure 3 Depicts pressure-volume (PV) loops obtained for each voiding and filling test. A pressure drop is observed for all voiding events while pressure increases are seen during filling. The work associated with bladder emptying and filling is computed as the integral of the PV-loop. More work output was associated with decreased flow rates during voiding and filling. The work done during filling was higher on average than during voiding.

DISCUSSION

Bladder volumes during 12 total voiding and filling tests were successfully calculated from 3D MRI data and used to estimate volumetric flow rate. bSSFP MRI acquisitions yielded slightly larger errors in both total volume change and volumetric flow rate when compared to DISCO Flex. This is likely due to eddy current errors that persist in a few volumes acquired during the bSSFP sequence that render volume segmentations difficult.

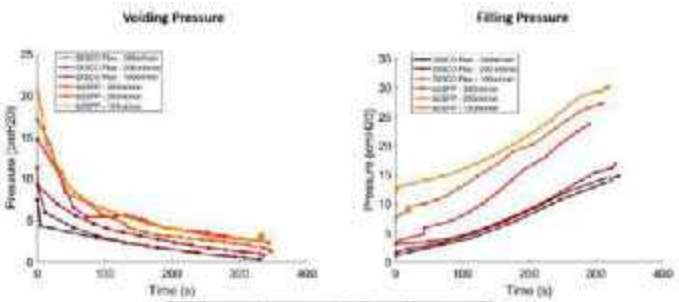

Work (mJ)	100 mL/min	200 mL/min	300 mL/min
DISCO Flex Void	57.65	106.08	116.79
bSSFP Void	163.41	113.58	130.42
DISCO Flex Fill	210.88	253.80	267.89
bSSFP Fill	349.47	535.13	611.53

Figure 3: (Top) Voiding and filling pressure traces during ex-vivo MRI acquisitions. (Bottom) Calculation of work for each voiding and filling test from PV-loops obtained during MRI.

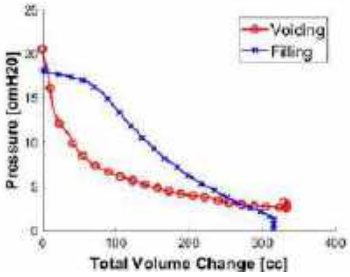

Figure 4: Hysteresis curve generated from the PV loops of the 100 cc/min filling and voiding bSSFP MRI acquisitions.

Both voiding and filling pressure maps were qualitatively similar in profile. Peak pressures in both voiding and filling were higher for lower flow rates. Differences between voiding and filling behavior at the same flow rate are depicted in Figure 4. This represents what can be thought of as a hysteresis curve, displaying the difference in voiding and filling profiles for the same flow rate. This suggests the bladder may deform differently during the emptying compared to filling and more work output is associated with filling events at the same flow rate.

This modeling pipeline represents a novel technique to assess the validity of experimental MRI in the bladder that replicates tissue-specific behavior compared to other modeling methods. Future efforts will focus on analyzing tissue-specific bladder shape changes during experimentation. Visually, it was apparent that the bladder tissue changed during repeated flow tests. We hypothesize that this is a result of the repeated loading and unloading of the tissue outside of the body. Additionally, we would like to better replicate the in-vivo bladder environment in our model (detrusor and abdominal pressures)[8].

ACKNOWLEDGEMENTS

The authors would like to acknowledge support from the NIH (R01 DK126850-01) and GE Healthcare.

REFERENCES

[1] Wei JT, et al. J Urol. 2005; 173:1256-1261
[2] Maserejian NN, et al. Urology. 2013; 82(3):560-564
[3] Bushman W, Urol Clin North Am. 2009; 36(4):403-415
[4] Blaivas J, Urology. 1984; 23(5):421-438
[5] Pewowaruk R, et al. PloS ONE. 2020;15(11)
[6] Gonzalez-Pereira JP, et al. Int Urol Nephrol. 2023
[7] Rice J, et al. Proceedings of the 2022 SB3C Conference
[8] Tentor F, et al. Scientific Reports. 2022; 12;17818.

BLADDER BIOMECHANICS AND SHAPE CHARACTERIZATION: COMPARISON STUDY OF HEALTHY VS BPH USING URO-DYNAMIC MRI

J. Gonzalez-Pereira (1), S. Wells (2), M. Grimes (3), W. Bushman (3), A. Roldan-Alzate (1,2,3,4)

(1) Mechanical Engineering, University of Wisconsin-Madison, Madison, Wisconsin, United States
(2) Department of Radiology, University of Wisconsin-Madison, Madison, Wisconsin, United States
(3) Department of Urology, University of Wisconsin-Madison, Madison, Wisconsin, United States
(4) Biomedical Engineering, University of Wisconsin-Madison, Madison, Wisconsin, United States

INTRODUCTION

Multichannel urodynamic studies (UDS) with or without fluoroscopic imaging and/or urethral pressure profilometry have been the gold standard for assessing the lower urinary tract (LUT) by measuring voiding pressures and urine flow but still provide limited information of LUT anatomy[1]. Pressure-volume analysis is a commonly used technique to analyze cardiac function. This same analysis can be reproduced in the bladder by using UDS-based measurements[6]. Assessment of bladder biomechanics using magnetic resonance imaging (MRI) has been reported in the past[1–3] but lacks detailed analysis of bladder shape as it has only been analyzed using volume-based metrics. Bladder shape during filling has been studied using ultrasound[4]. Similarly, MRI has been used to study bladder shape but not dynamically[5]. The aim of this study is to comprehensively and non-invasively characterize bladder biomechanics in patients with BPH/LUTS and healthy subjects by using pre-existing UDS to analyze bladder energetics, and the recently developed Uro-Dynamic MRI[1] method to analyze anatomy-based biomechanics.

METHODS

Image Acquisition: In this an IRB-approved, HIPAA compliant study. 5 healthy volunteers (37±9 years of age) and 5 subjects diagnosed with BPH (65±6 years of age) were recruited. 15 minutes prior to the MRI scan, 1/3 of a single weight-based dose of gadolinium-based contrast was hand injected for urine enhancement. Subjects were equipped with a condom catheter and instructed to void in the MRI scanner. Urine was collected in a 1L bag attached to the subject's leg. Images were acquired in a 3T MRI scanner (Premier, GE Healthcare, Waukesha, WI) using a high-density flexible array coil (AIR Coil, GE Healthcare) and Uro-dynamic MRI protocol[1].

Bladder Segmentation and Shape Analysis: Images were imported into MIMICS (Materialise, Belgium) where the bladder was segmented and one 3D rendering per time-step was reconstructed within each void (17±4 time-steps). Shape-based metrics, based on the pubic symphysis (PS) and the trigone which are anatomically "static" reference points\, were determined to aid in the characterization of bladder shape throughout the void shown in Fig1A) and Fig1B). Sphericity index, bladder neck angle (BNA) and external BNA (EBNA) were quantified for all subjects throughout the void (Fig1C)[1]. **N** is the distance from the top of the trigone to the PS in black. **LA** is the longest axis long **N** in yellow. **LAN** is the angle between **N** and **LA** in green. **CAS** is the curvature angle in light blue. **DS** is the sagittal curvature length in red. **N**, **LA**, **LAN**, **CAS,** and **DS** are measured in a sagittal plane centered in the PS. **CTB** is the top-bottom distance in blue. **CRL** is the right left distance in purple and **DC** is the coronal curvature distance in red. **CTB**, **CRL**, and **DC** are measured in a coronal plane centered in the PS.

***UDS Analysis*:** A single retrospective UDS was digitized for one of the patients (Healthy 5). Volume measurements were calculated from the constant bladder filling rates and the flow rate for the filling and voiding phases respectively. Detrusor pressure measurements were used for both the filling and the voiding phases. PV curves are shown in Fig2. Work was calculated by integrating over the PV curve of each respective phase.

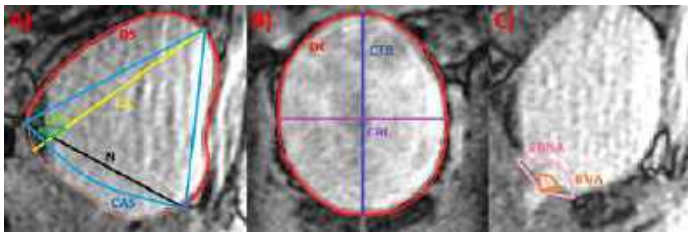

Figure 1: A) Sagittal place displaying the acquired metrics. B) Coronal plane centered in the PS showing acquired metrics. C) Sagittal view showing measurement of BNA and EBNA.

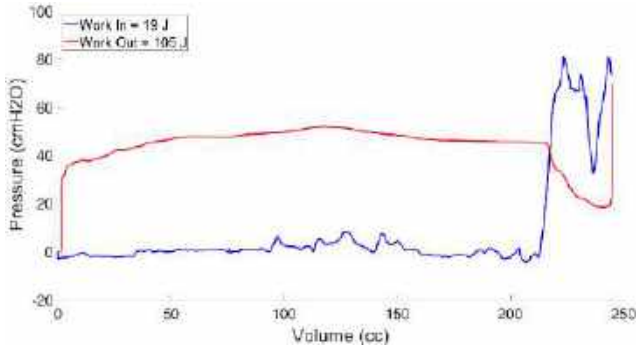

Figure 2: Generated PV curves showing filling (blue) and voiding (red) phases with corresponding work calculations.

RESULTS

Results are summarized in Table 1; Fig.3 contains a complete analysis corresponding to one characteristic subject of each group (highlighted in yellow in Table 1B).

Table 1: A) Maximum and minimum value summary for bladder shape metrics and key metrics highlighted. B) R^2 for all metrics vs flow rate. Characteristic subjects highlighted in yellow.

A)

Bladder Shape Measurements	Healthy		BPH	
	Max	Min	Max	Min
N (cm)	10.9 ± 1.4	4.3 ± 2.1	11.6 ± 1.7	5.1 ± 1
LA (cm)	18.6 ± 3.1	5.8 ± 2.7	15.7 ± 1.8	6.2 ± 2.7
LA/N Angle (°)	157.9 ± 2	83.5 ± 1.8	154.5 ± 19.5	92.8 ± 14.6
CAS (°)	66.5 ± 1.2	36 ± 1.1	64.1 ± 13.2	25 ± 9
DS (cm)	36.8 ± 6.7	10.5 ± 5.2	33.7 ± 4.1	13.2 ± 6.9
Wall Tension Index (LA/N)	2.3 ± 0.4	1 ± 0.3	2.5 ± 0.4	1.1 ± 0.5
Wall Stretch Index (DS/N)	5 ± 1	1.9 ± 0.7	5.4 ± 1.1	1.7 ± 1.2
CTB (cm)	11.9 ± 1.7	3.8 ± 1.9	11.6 ± 1	3.4 ± 2.3
CRL (cm)	10 ± 0.9	3.3 ± 1.5	10.3 ± 0.8	3.7 ± 1.9
DC (cm)	34.7 ± 3.9	11.2 ± 5	35.8 ± 3.2	11.5 ± 6.8
Ellipticity Index	1.3 ± 0.1	0.9 ± 0.1	1.4 ± 0.1	0.8 ± 0.1
Sphericity Index	0.986 ± 0.008	0.856 ± 0.038	0.964 ± 0.006	0.913 ± 0.01
EBNA (°)	178.7 ± 8.1	134.3 ± 6.5	213.2 ± 17.8	135.8 ± 4.4
BNA (°)	144.8 ± 13.9	70.1 ± 12.1	145.4 ± 10	70.9 ± 14.3
Flow Rate (cc/s)	22.4 ± 3.6	0 ± 0	17.5 ± 5.1	0 ± 0.0
Volume (cc)	1056.5 ± 253.4	11.2 ± 152.4	731.6 ± 131.1	104.6 ± 202.8

B)

Subject/ R^2 vs Flow Rate	Sphericity	EBNA	BNA	Wall Tension Index	Wall Stretch Index	Ellipticity
Healthy 1	0.4	0.02	0.25	0.1	0.13	0.18
Healthy 2	0.55	0.68	0.27	0.11	0.43	0.02
Healthy 3	0.5	0.03	0.009	0.12	0.15	0.03
Healthy 4	0.53	0.31	0.01	0.12	0.33	0.3
Healthy 5	0.04	0.25	0.2	0.02	0.01	0.03
BPH 1	0.07	0.002	0.007	0.04	0.06	0.03
BPH 2	0.02	0.08	0.003	0.005	0.002	0.05
BPH 3	0.27	0.59	0.02	0.02	0.06	0.43
BPH 4	0.64	0.15	0.3	0.02	0.27	0.23
BPH 5	0.29	0.68	0.16	0.52	0.3	0.75

DISCUSSION

Healthy volunteers exhibited a larger range of motion across all metrics, lower wall tension and stretch indices. Linear correlation coefficients (R^2) between these metrics and urinary flow rate were found to be higher in the healthy volunteers in most of the cases. Table 1, highlighted in green, shows two BPH subjects without lower urinary tract symptoms (LUTS) that have high correlation values with flow, corresponding to the behavior of healthy subjects. Because of this most of the maximum and minimum metrics are similar but in the case of LAN and CAS, SD values show large disparity in the metrics (highlighted in dark green in Table 1). Thus, Table 1B) was included to show information that might be hidden due to patient-to-patient variability in Table 1A). In Table 1A) the largest differences are highlighted in orange. In addition, measurements taken in the sagittal plane and its derivatives show higher correlation coefficients than metrics taken in the coronal plane. PV curves show higher work measurements during voiding but still exhibit interesting characteristics during the end of filling phase and beginning of voiding phase that could prove to be valuable when coupled with anatomy-based biomechanics.

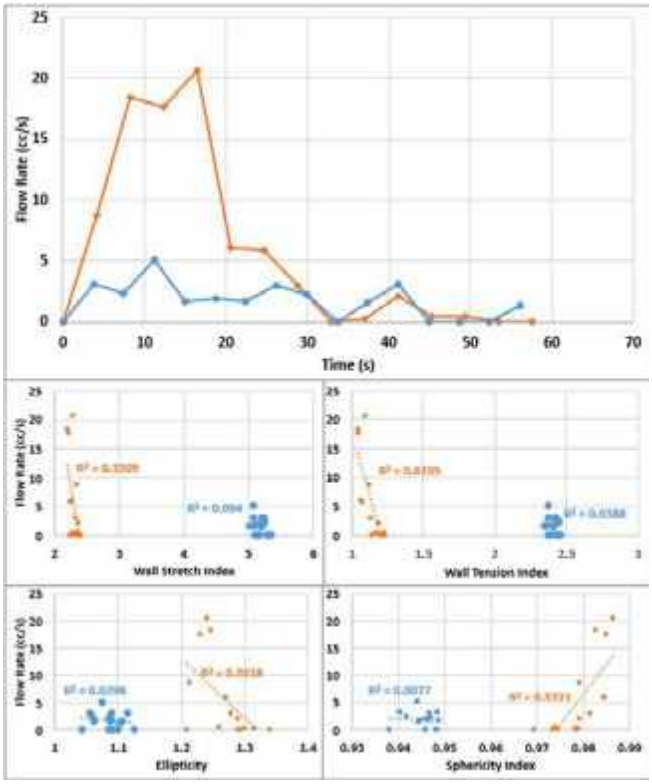

Figure 3: Graph displaying flow rates for Healthy 4 (orange) and BPH 1 (blue). The rest of the graphs show correlation studies with their corresponding correlation coefficients between urine flowrate and calculated bladder shape metrics shown in Table 1.

Uro-Dynamic MRI can capture bladder biomechanics non-invasively both in healthy controls and patients with BPH/LUTS. By adding bladder shape analysis and retrospective UDS, we created a robust framework that could characterize bladder biomechanics and shape and quantify differences between healthy subjects and subjects with LUTS in a more comprehensive way. Limitations include subject orientation during the study, inability to acquire data for more than one void per scanning session and the lack of UDS in healthy volunteers. In addition, to increase the scope of this framework we are currently adding more subjects to both cohorts, performing a comparison between sequences, adding studies in women, and adding different cohorts including overactive bladder (OAB) and neurogenic bladder.

ACKNOWLEDGEMENTS

We would like to acknowledge support from GE Healthcare and support from NIH (R01 DK 126850-01).

REFERENCES

[1] Gonzalez-Pereira, J.P. et al., *Int Urol Nephrol*, 2023.
[2] Anzial, L.E. et al., *Abdominal Radiology*, 46:1670-1676, 2021.
[3] Pewowaruk, R et al., *PloS One*, 15, 2020.
[4] Gray, T et al., *Ultrasound*, 3:167-175, 2019.
[5] Ateşçi Y.Z., et al., *The Scientific World Journal*, 2014.
[6] Rice J, et al. *Proceedings of the 2022 SB3C Conference*, 2022

TOWARDS IMPROVED SURGICAL SEALANTS BY INVESTIGATING HUMAN VISCERAL PLEURA MECHANICS

Gustavo O. Ramirez (1), Mona Eskandari (1,2,3)

(1) Department of Mechanical Engineering, University of California, Riverside, CA, USA
(2) Department of Bioengineering, University of California, Riverside CA, USA
(3) BREATHE Center, School of Medicine University of California, Riverside CA, USA

INTRODUCTION

The visceral pleura is a thin tissue layer that encases, protects, and maintains an airtight seal around the lung. Life altering pulmonary conditions, such as chronic obstructive pulmonary disease (COPD) and various forms of lung cancer, may require invasive surgical removal of bulk lung tissue to alleviate symptoms and improve quality of life for patients [1]. These procedures compromise the airtight seal around the organ and injure the visceral pleura network, which may cause air leaks from the lung into the pleural cavity, one of the most common complications in surgical lung procedures [2]; moreover, prolonged air leaks are linked with longer hospital stays and higher mortality rates [3].

To help mitigate air leaks in lung surgery, surgical adhesives are designed to reseal the lung at the injury site [4]. Sealants available on the market show excellent biocompatibility and various magnitudes of elasticity, but the lack of positive outcomes (air leak prevention and length of stay reduction) suggest they are not yet a sustainable solution [5,6]. An effective sealant is expected to adhere to and stretch with the visceral pleura. It should be biocompatible, elastic, and robust enough to maintain a seal for the cyclic and heterogenous strain environment the lung presents. Sealants with mechanics outside of the native tissue properties are likely to delaminate/fail or, in extreme cases, damage neighboring tissue [7]. To address these requirements, sealants in development are tested often on rat and pig tissue for burst pressure and biocompatibility [4,8,9]. Our recent work explored biaxial rat and pig visceral pleura mechanics; however, how the mechanics of pig and rat visceral pleura tissue compares to human visceral pleura tissue is still unknown.

For the first time, in this present study, we explore the biaxial mechanics of human visceral pleura, further comparing healthy and smoker lungs; abnormal lungs were of interest given the likelihood of contracting pulmonary disease and requiring pulmonary surgery [10]. This study supports the development of future sealant design by providing a baseline for mechanical synchrony with visceral pleura mechanics to ultimately help mitigate air leaks in surgical lung procedures.

METHODS

Human healthy lungs (transplant eligible lungs, N = 3: 63M, 48F, 30M) and smoker (non-transplantable lungs, N = 3: 46F, 57F, 44F) were acquired via a donor network (IRB exemption approval HS 20-180; Donor Network West, San Ramon, California). Healthy lungs had no history of smoking while non-transplantable lungs were from donors with a smoking history greater than 20 pack years. Surgical forceps were used to excise visceral pleura samples from each lung, noting the cranial-caudal and ventral-dorsal orientation for anisotropy considerations, while collecting an equal number of specimens from upper and lower lobes on both medial and costal surfaces to consider regional dependencies. Therefore, 12 samples were collected from each lung, totaling 36 samples for the healthy and 36 samples for the smoker groups. Each sample was cut into a square with a 1x1 cm test area in preparation for biaxial testing. Samples were collected and tested within 72-hours post mortem.

Visceral pleura samples were loaded on a biaxial displacement-controlled tensile tester with a 1.5 N load cell (Cellscale Biomaterials Testing, Waterloo, Canada). Each sample was tested in a heated 1X Phosphate Buffered Saline bath (37°C) to prevent tissue dehydration. Samples were elongated to 40% strain via equiaxial displacement at a rate of 0.2%/s, where the analyzed test and stress relaxation hold for 300 seconds were preceded by two cycles of preconditioning.

The first Piola Kirchoff stress was calculated using the force and the cross-sectional area of each specimen (thickness measured via confocal imaging and thickness gauge [11]). The initial and final moduli were determined using a linear fit to $R^2 > 0.90$ for the low and high strain regimes, as previously described [12]. The strain transition between the initial to final moduli, linked to the uncrimping of the collagen fiber microstructure, was defined as the intersection of their respective linear

fits. Stress relaxation was calculated as the percent difference of the initial and final stress value normalized by the initial stress value during the hold.

As an additional limited evaluation, results were compared to findings from pig and rat visceral pleura tissue [13]. While studies on pig and rat tissues allowed a consistent and reproducible maximum strain at 60%, where the secondary slope of the bilinear J-shaped stress-strain curve would only emerge beyond 40% strain, translating these extended strains to human specimens would cause irreparable tissue damage and therefore, forced a tradeoff in interspecies protocol design.

A two-way ANOVA test was used for statistical comparisons (GraphPad Prism, San Diego, California). Corresponding p-values were used to determine statistical significance between groups with the thresholds defined as *p<0.05, **p<0.001, ***p<0.0001, ****p<0.00001.

RESULTS

Human healthy and smoker visceral pleura was found to exhibit a bilinear stress-strain response, which was not dependent on the specimen orientation (and therefore, isotropic) nor region (and therefore, homogenous). The averaged regional and directional (combined) stress-strain responses for healthy and non-transplantable lung visceral pleura were shown in Figure 1. Similar curves were found for pig and rat lungs, where the metrics of each species were reported in Figure 2. The bilinear curve exhibits a compliant initial modulus followed by a stiffer final modulus, as the tissue approached its strain limits. Both healthy and smoker human groups yielded average initial moduli between 1.3-1.5 kPa, which is similar to pig tissue (1.4 ± 0.6 kPa) but disparate from rat tissue (2.7 ± 1.1 kPa) (Figure 2). Further differences were found in the final moduli, where human groups exhibited a significantly stiffer response compared to other species, despite straining to only 40% compared to pig and rat (extended to 60%): both human healthy and smoker groups demonstrated an average final modulus of 135.8 ± 98.8 and 132.8 ± 74.0 kPa respectively. This is significantly larger than the pig (21.8 ±17.7 kPa) and rat (10.13 ± 4.6 kPa).

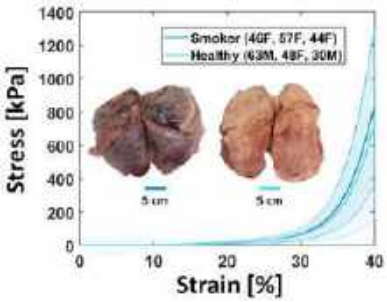

Figure 1: Human healthy and non-transplantable lungs and their average stress strain curves

The difference in strain transition points highlights this alternate extensibility amongst the three species (Figure 2). Human visceral pleura was the least extensible, undergoing the smallest strain transition at 34.2 ± 1.5 and 34.3 ± 1.1 % for healthy and smoker visceral pleura respectively, followed by rat (41.4 ± 4.6 %) and pig (47.8 ± 5.0 %). Finally, the only metric found to significantly differ between healthy and smoker human groups was the stress relaxation was found to be significantly different than smoker counterparts (16.6 ± 3.3 for healthy and 19.0 ± 4.8 % for smoker respectively).

DISCUSSION

This study explores human visceral pleura mechanics for the first time, further comparing elasticity metrics of healthy and smoker lungs. Differences between healthy and smoker lungs were sparce, with percent relaxation being the only metric in which smoker lungs were statistically different from healthy lungs. Each donor had a smoking history greater than 20 pack years but was not diagnosed with pulmonary disease. Lungs with diseases such as COPD, may present mechanical differences when compared to healthy visceral pleura.

We evaluate the potential applicability of quantification metrics between human and common animal models traditionally utilized for sealant testing. We report similar initial stiffness between human lungs and pig lungs. Additionally, we also find significantly larger final modulus and reduced strain transition of human visceral pleura when compared to pig and rat counterparts. This reduced extensibility associated with stiffness is consistent with recent studies reporting the surface strain patterns of inflating human lungs is decreased compared to pig lungs at comparable tidal volumes [14,15]. Despite the variation in surface strain profiles, the pig lung visceral pleura exhibits similar stiffness values when compared to human lungs at lower strains, which indicates it may serve as an effective animal model for investigating the visceral pleura and surgical sealant mechanics (unlike rat tissue).

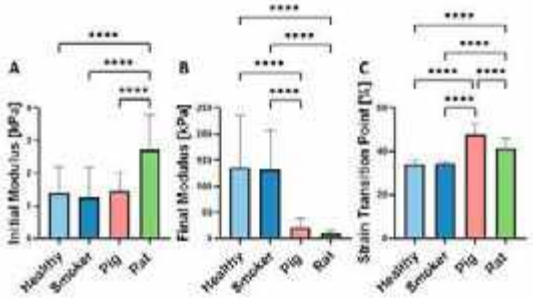

Figure 2: Mechanical metrics of human healthy, human smoker, pig and rat lung visceral pleura: A) Initial Modulus, B) Final Modulus, and C) Strain Transition.

Surgical sealants used in lung surgery have a wide range of elastic moduli ranging from 1 kPa to over 1000 kPa, all with a various range of extensibility, adhesive strength, and burst resistance [4,8,9]. The heterogeneity of the lung surface strains and varying internal pressures, as presented in other studies, present a challenging task for sealants. Modern studies continue to focus on burst pressure and biocompatibility; however, evidence of delamination caused by the asynchronous mechanics of the sealant and the visceral pleura interface merits further investigation [16], and is the subject of future work.

ACKNOWLEDGEMENTS

Supported in part by the Opportunity to Advance Sustainability Innovation and Social Inclusion (OASIS) UCR and State of California Climate Action Through Resilience Program Grant.

REFERENCES

[1] Bronstein, M. E., et al., *Ann Transl Med,* 7(15):361, 2019. [2] Mueller, et al., *J Thorac Dis*, 6(3):271–84, 2014. [3] Yoo, A., et al., *ClinicoEcon Outcomes Res*, (6):373–83, 2017. [4] Annabi, N., et al., *Sci Trans Med*, 9(410), 2017. [5] Fuller, C., *J Cardiothorac Surg*, 8(4):90, 2013. [6] Gologorsky, R. C., et al., *Perm J* 23, 2019. [7] Annabi, N., et al., *Eur J Pharm Biopharm*, 95(Pt A):27–39, 2015. [8] Gasek, N., et al., *Acta Biomater*, 131(9):222–35, 2021. [9] Pedersen, T. B., et al., *Ann Thorac Surg* 94(1):234–40, 2012. [10] Pulmonary Diseases, *CDC (US)*, 2010 [11] Ramirez, G. O., et al., *In Preparation*, 2024 [12] Sattari, S., et al., *Acta Biomater*, 10.047, 2022. [13] Ramirez, G. O., et al., *SB3C*, 2023 [14] Eskandari, M., et al., *D109. ATS Conference*, 2022. [15] Mariano, C. A., et al., *Respir* Res, 23(1):1–13.2022. [16] Yamaoka, M., et al., *Ann Thorac Surg*, 107(6):1656–62.2019.

FEASIBILITY AND POST-PROCEDURAL RISK ANALYSIS OF REDO-TRANSCATHETER AORTIC VALVE REPLACEMENT: A PATIENT-SPECIFIC FLUID-STRUCTURE INTERACTION BASED STUDY

Symon Reza (1), Brandon Kovarovic (1), Danny Bluestein (1)

(1) Biomedical Engineering, Stony Brook University, Stony Brook, NY, USA

INTRODUCTION

Transcatheter aortic valve replacement (TAVR), a minimally invasive procedure, has become the standard procedure for high and intermediate-risk aortic stenosis patients. Recently, TAVR has also been approved for use in low-risk patients. However, prosthetic TAVR leaflets are inherently subjected to degeneration, along with calcification and thrombosis [1]. Recent clinical studies have found evidence of early leaflet thrombosis formation that is associated with an earlier risk of structural valve degeneration. Hence, durability remains one of the major concerns for TAVR technology. This evidence of thrombosis and rapid degeneration of TAVR valves poses a significant risk to the increasing number of young and low-risk TAVR recipients who may neccesitate repeat intervention. Transcatheter aortic valve-in-transcatheter aortic valve (TAV-in-TAV), aka redo-TAVR, is being considered as a potential treatment of choice for transcatheter heart valve (THV) degeneration and has shown success in addressing suboptimal outcomes. While current data is insufficient, redo-TAVR holds promise as a rescue option for TAVR valve degeneration, requiring further research. Recently, an *in-vitro* study has suggested combination dependent hemodynamic performance of redo-TAVR in idealized aortic root [2]. Performance of redo-TAVR may also depend upon factors including the diseased patient-specific anatomy and complex flow domain formed by the native leaflets and two TAVR device prostheses. A comprehensive structural and hemodynamic performance analysis of different redo-TAVR combinations in a patient-specific scenario may provide vital insights into the feasibility of redo-TAVR procedures and help identify the optimal combination.

METHODS

A patient with 23.5mm CT-derived annular diameter was selected for this study. The patient model was reconstructed (Figure 1a) following the procedures described in our previous study [3]. The most widely used self-expandable (SE) Evolute (Medtronic plc, Minneapolis, MN, USA) and balloon-expandable (BE) Sapien (Edwards Lifesciences, Irvine CA) TAVR systems were considered for this study where 26 mm Evolut R and Sapien 26 mm TAVR devices were selected as the first TAVR devices and the most recent versions of Evolut and Sapien TAVR systems (26 mm Evolut Pro and 26 mm Sapien 3 Ultra) were used as the second TAVR devices. TAVR implantation simulations were then performed following our previous studies (Figure 1b) [4] using Abaqus Explicit 2019 (SIMULIA, Dassault Systèmes, Providence, RI). The selected TAVR devices result in four TAV-in-TAV combinations (Figure 1c) including - i) SE-in-BE, ii) BE-in-BE, iii) BE-in-SE, and iv) SE-in-SE. A 2-way coupled fluid structure interaction (FSI) using a body-fitted sub-grid geometry resolution (SGGR) method was then performed following our previous study [5]

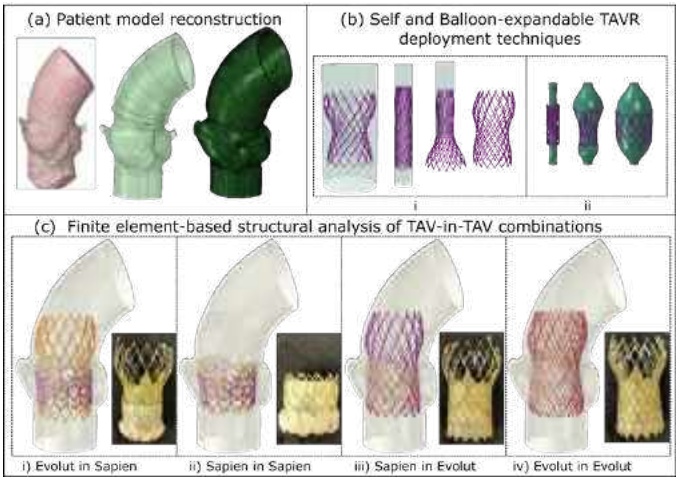

Figure 1: Schematic of the (a) model reconstruction process, (b) implantation process of i) self-expandable, ii) balloon-expandable TAVR devices, (c) four combinations of redo-TAV deployed inside the aortic root of the selected patient model with in-vitro representation [3] of the corresponding redo-TAV combinations.

to analyze the hemodynamic performance of the redo-TAV combinations. FSI simulations were performed coupling the fluid solver, FlowVision 3.12 (Capvidia NV, Leuven, Belgium) and Abaqus

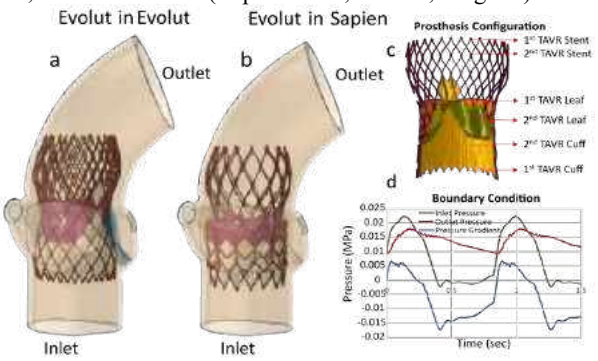

Figure 2: Fluid domain of (a) SE-in-SE and (b) SE-in-BE. (c) Pressure based BC, and redo-TAVR components. A patient with high blood pressure BC was chosen in this study.

Explicit 2019. The thrombogenic risk assessment analysis was performed following our previously developed and validated technique where Lagrangian particles representing platelets are injected into the flow and the stress accumulation (SA) is computed along each particle trajectory. The SA data is then collapsed into a probability density

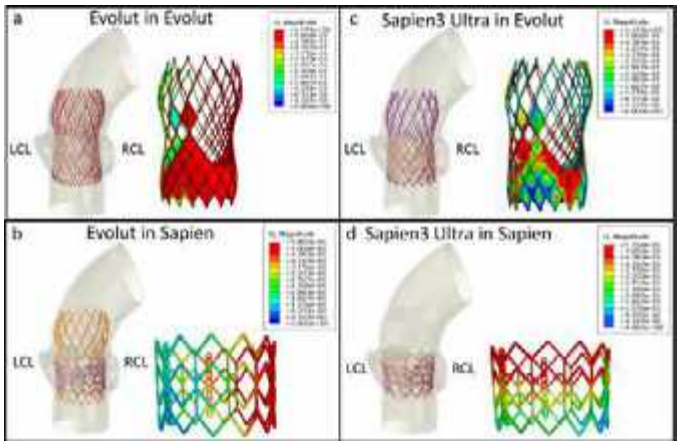

Figure 3: Displacement locations of the damaged THV caused by the second THV.

function (PDF) to compute "thrombogenic footprint" [6] for each TAV-in-TAV combination.

RESULTS

Structural and hemodynamic analyses were performed following redo-TAVR simulations. The SE-in-SE combination demonstrated the highest eccentricity (Figure 2) and the narrowest coronary access (Figure 3). The combinations involving SE devices (BE-in-SE, and SE-

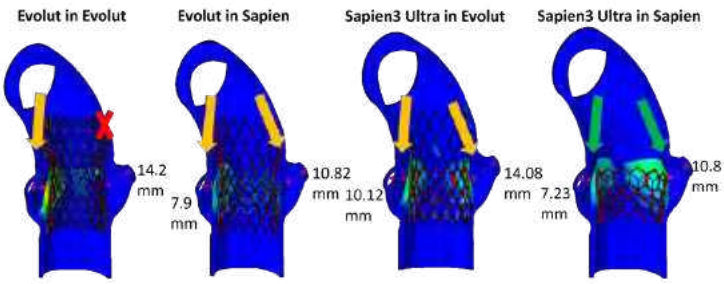

Figure 4: Coronary access impairment analysis.

in-BE) demonstrated limited coronary access (Figure 4). SE-in-BE demonstrated the narrowest opening at the annular plane. BE-in-BE demonstrated superior performance from the structural perspective with the widest coronary access and opening at the annular plane. However, BE-in-SE demonstrated 40% leaflet overhang which may impact the

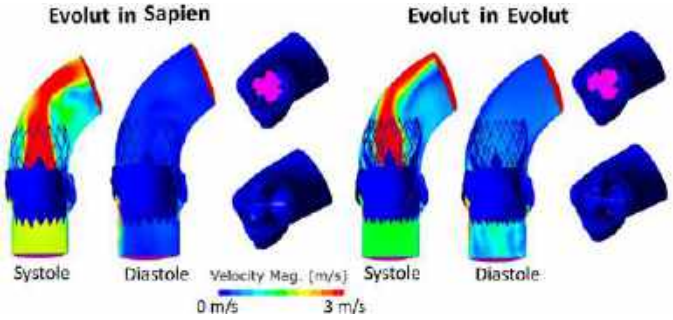

Figure 5: Preliminary FSI results for 2 redo-TAVR combinations.

hemodynamic performance. Initial results from the hemodynamic analysis demonstrated combination-specific performance. SE-in-SE demonstrated higher velocity and paravalvular leakage compared to SE-in-XT. Further investigations are being performed to identify the optimal redo-TAVR device combination with an efficient hemodynamic performance coupled with thrombogenic risk on a patient-specific basis.

DISCUSSION

Successful implantation and optimal hemodynamic performance of redo-TAVR requires careful assessment of specific device characteristics due to the technical and structural differences in TAVR prostheses, including mode of deployment (BE and SE), valve function (intra-annular and supra-annular), and valve design (skirt and stent frame design, and height). Patient-specific features and the interaction between the second THV with the patient anatomy also play a crucial role in the performance of redo-TAVR procedure. Therefore, patient-specific preprocedural planning is critical in minimizing peri-procedural and post-procedural risk. In this study, we addressed the clinical concerns performing a set of computational analyses encompassing finite element based TAVR deployment in patient specific models to FSI based hemodynamic analysis coupled with particle stress accumulation analysis that accounts for blood flow stasis and exposure to high shear. Using these techniques, we analyzed the feasibility and performance of redo-TAVR combinations. The initial results illustrated the pros and cons of different redo-TAVR combinations in a patient model where BE-in-BE, seems to be the optimal combination of redo-TAVR. However, further analysis on the hemodynamic effect of leaflet overhang associated with BE-in-BE is required.

In summary, this study presented a thorough computational protocol to analyze patient-specific structural and hemodynamic performance and assess thrombogenic risk of redo-TAV combinations and generated knowledge addressing current clinical concerns on THV degeneration and its potential solution, redo-TAVR. These techniques can potentially be used to aid the clinicians in lifetime management of aortic stenosis patients through optimal first and second THV selection.

ACKNOWLEDGEMENTS

Funding provided by NIH-NIBIB BRP U01EB026414 (DB)

REFERENCES

[1] Sellers, SL et al. *JACC Cardiovasc Imaging.* 2019.
[2] Hatoum, H et al. *JTCS* 161.2 (2021): 565-576.
[3] Reza, S et al. *Artificial Organs* 46.7 (2022): 1305-1317.
[4] Bianchi, M et al. *BMMB* 18.2 (2019): 435-451.
[5] Ghosh, R et al *BMMB* 19 (2020): 1725-1740.
[6] Chiu, W.C. et al. *Sci Rep* 9, 2946 (2019).

ELEVATED VWF LEVELS DRIVE THROMBUS INSTABILITY

A. Obenaus (1), D. Truong (2), D. Macatangay (1), A. Ke (1), J. Chen (3), J. López (1,3), N. Sniadecki (1)

(1) University of Washington, Seattle, WA, USA
(2) University of Washington, Bothell, WA, USA
(3) Bloodworks Northwest Research Institute, Seattle, WA, USA

INTRODUCTION

After a stroke, dual antiplatelet therapy (DAPT) is prescribed to prevent a recurrence of thrombosis. However, 5-10% of patients receiving DAPT experience a recurrent thrombotic event. Patients with high levels of von Willebrand factor (VWF) in their blood often show resistance to DAPT. VWF is critical for hemostasis for it binds to collagen at a wound site and becomes elongated under flow, thereby enabling platelets to adhere to it through their GPIb receptors. Conversely, elevated levels of VWF are associated with thrombotic risk due to excessive amounts of platelet adhesion.

DAPT targets the activation of platelets via thromboxane and ADP, but it may not fully address platelet activation by VWF-mediated mechanotransduction. Shear flow creates a force on the GPIb receptor when a platelet is bound to VWF. This force unfolds the mechanosensory domain of GPIb and triggers intracellular calcium signaling and activation of integrin $\alpha_{IIb}\beta_3$ in platelets for adhesion.

Here, we present a microfluidic approach for examining the effectiveness of DAPT in the context of elevated VWF levels. Our microfluidic approach induces platelets to adhere, aggregate, and activate due to shear flow. Platelet-rich thrombi that form in the microfluidic device are contractile and generate nanoscale forces to hold together. They are also fragile and can detach under high shear flow. Thus, the goal of this work is to examine thrombosis and embolization in the context of elevated VWF and DAPT.

METHODS

Studies on VWF are challenging to perform *in vivo* because manipulating VWF levels may cause unintended changes to an animal's physiology; additionally, VWF function is shear-dependent, but it is difficult to control shear rates *in vivo*. Thus, a microfluidic approach addresses these problems and provides a platform that requires small volumes of blood and low consumption of costly reagents. The design is an adaptation of our previous design [1], but contains one rigid block and twelve flexible posts for spatial resolution of platelet forces within a thrombus (Fig. 1A-B).

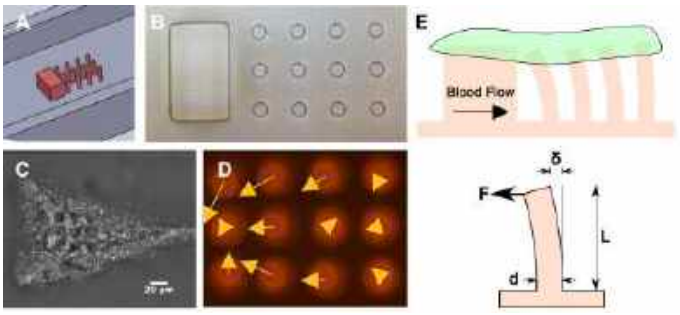

Figure 1: The microfluidic device. (A) Isometric and (B) top views of microfluidic device with one block and twelve posts. (C) Thrombus formed 120 secs after blood entered the channel. Scale bar: 20 µm. (D) High spatial resolution of platelet forces in a thrombus at 120 secs. Yellow arrows are force vectors where $\sum|\boldsymbol{F}| = 478.6\,\boldsymbol{nN}$. (E) Platelets (green) encapsulate the top of the block and post. Post deflection (δ) was measured to calculate platelet forces ($\boldsymbol{F}$) using Hooke's Law ($\boldsymbol{F} = \boldsymbol{k\delta}$), where $\boldsymbol{k} = \boldsymbol{3\pi E d^4/64L^3}$, $\boldsymbol{E}$ is the modulus of elasticity, $\boldsymbol{d}$ is the diameter of the post, and $\boldsymbol{L}$ is the length of the post. [2]

Due to the high shear gradient produced by the rigid block, platelets form a thrombus (Fig. 1C) and generate contractile forces that deflect the posts (Fig. 1D-E). We used the microfluidic device to form platelet-rich thrombi at a wall shear rate of 40,000 s^{-1} for whole blood samples doped with DAPT (0.3 mM acetylsalicylic acid for inhibiting the generation of thromboxane, 10 µM 2-MeSAMP for inhibiting the ADP receptor, $P2Y_{12}$), 50 µg/mL human purified VWF, or both VWF and DAPT. We used quantitative image analysis of brightfield images

to assess platelet aggregation and thrombus stability by the projected area of the thrombi. Additionally, we added FITC-labeled antibodies into whole blood samples to assess platelet activation by granule secretion (P-selectin, 8 µg/mL) and integrin activation (PAC-1, 1 µg/mL). The deflection of the posts was used to assess platelet forces and the drag forces acting on the thrombi.

RESULTS

We find that large thrombi form in all four conditions under the influence of high shear regardless of inhibition with DAPT (Fig. 2A). However, the addition of VWF decreases the stability of the thrombi, leading to frequent detachment events, or emboli (Fig. 2B). Additionally, high VWF levels cause a percentage of thrombi to grow massively large. These emboli are often catastrophic and completely detach from the force sensors (data not shown).

Surprisingly, DAPT did not prevent integrin activation (Fig. 2C) or granule secretion (Fig. 2D), which are both markers of platelet activation. This was unexpected as DAPT is supposed to prevent platelets from activating. However, there are other methods of platelet activation that do not involve soluble agonists, e.g., activation via the GPIb mechanotransduction pathway.

Forces in the opposite direction of flow (contractile force) dominated for the control condition, but drag forces were more dominate when DAPT was added to the sample. This reduction in contractile force with antiplatelet drugs is consistent with what we have observed previously. [1] The drag forces continued to dominate contractile force with the addition of VWF (Fig. 2E). We suspect the dominate drag forces in the high VWF conditions contribute to the instability of the thrombi and frequent detachment events.

DISCUSSION

Our findings suggest that DAPT is not a sufficient suppressant of thrombosis. In a high shear environment, DAPT does not prevent platelet aggregation or activation. When a high VWF concentration is added to the blood, the thrombi become more unstable. Thus, high levels of VWF in a patient can lead to thrombus instability even in the presence of DAPT. These detachment events are consistent with the size of microemboli that are thought to occlude blood flow in the capillaries and arterioles. Furthermore, microemboli are thought to cause damage to areas of the brain and are associated with recurrence of transient ischemic attack and silent strokes.

We hypothesize that the GPIb-mediated platelet activation pathways is able to circumvent any platelet inhibition from soluble agonists. Essentially, platelets bind to VWF via GPIb; VWF also binds to exposed collagen. Under shear flow, the VWF is in tension and pulls on the GPIb receptor, which initiates a mechanotransduction pathway, resulting in platelet activation. Our results suggest this method of platelet activation can overcome other types of inhibition. Additionally, we are curious to explore thrombus formation and instability under lower shear rates. While current stroke treatments may not be effective under certain biological and mechanical conditions, there are not alternatives available. We think it may be more effective to treat thrombosis through other mechanisms, such as VWF self-association, cleavage of VWF into low molecular weight multimers by ADAMTS13, or blocking the GPIb mechanosensory domain. Further investigation is needed to determine the possible effectiveness of these strategies and to identify patients that would benefit from alternate treatments.

This work has three long-term clinical translations: (1) identify better drug targets for individuals with high VWF levels to prevent repeat ischemia and (2) provide additional metrics and diagnostic tests, e.g. protein levels and thrombi behavior under flow, for evaluating how a stroke patient should be treated for more personalized medicine. (3) The microfluidic technology described, could be a point-of-care device to determine a patient's thrombotic risk before ischemia occurs.

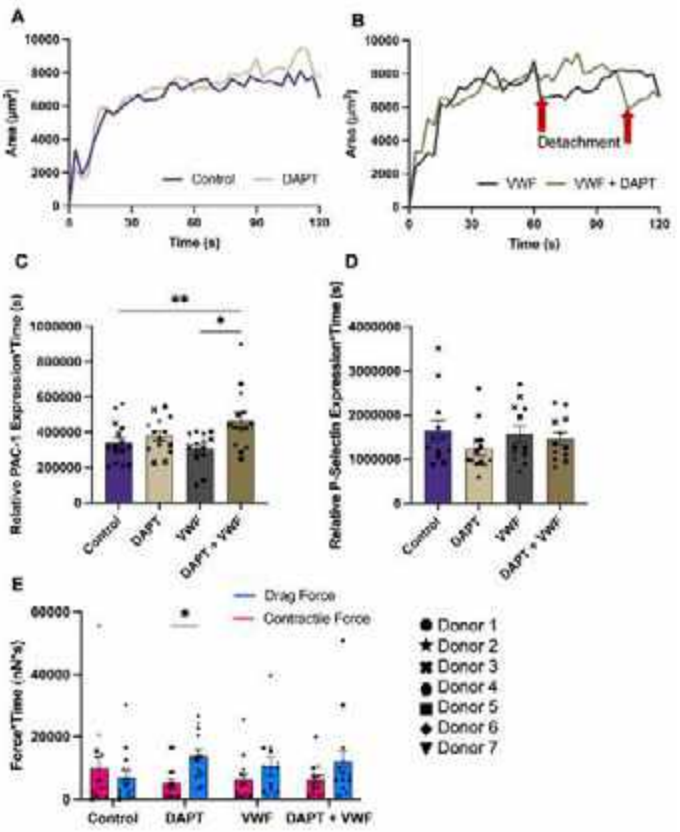

Figure 2: Results of microfluidic experiments. (A) Area vs. time for control and DAPT samples. (B) Area vs. time for VWF and VWF + DAPT samples. Red arrows represent detachment events. (C) Integral of PAC-1 expression vs. time, normalized by area. (D) Integral of P-Selectin expression vs. time, normalized by area. (E) Integral of the positive x-component of force (drag force) and negative x-component of force (contractile force) vs. time. Each symbol represents a unique donor. Statistics were determined using a mixed-effects model with post-hoc analysis (*p < 0.05, **p < 0.01).

ACKNOWLEDGEMENTS

Research reported in this publication was supported by the National Institutes of Health (NIH) under Award Number F31HL156697. The content is solely the responsibility of the authors and does not necessarily represent the official views of the NIH.

REFERENCES

[1] Ting, L. H. *et al.* Contractile forces in platelet aggregates under microfluidic shear gradients reflect platelet inhibition and bleeding risk. *Nat. Commun.* **10**, 1–10 (2019).

[2] Miles, J. *et al.* Storage temperature determines platelet GPVI levels and function in mice and humans. *Blood Adv.* **5**, 3839–3849 (2021

RAMAN MONITORING OF ENGINEERED CARTILAGE DEVELOPMENT ACROSS DIFFERENT HYDROGEL SCAFFOLDS

Dev R. Mehrotra (1), Carolina V. Cordova (1), Erik E. Ersland (2), Thomas P. Schaer (3), Mark W. Grinstaff (1), Brian D. Snyder (4), Mads S. Bergholt (5), Michael B. Albro (1,2)

(1) Biomedical Engineering, Boston University, Boston, MA, USA
(2) Mechanical Engineering, Boston University, Boston, MA, USA
(3) Department of Clinical Studies New Bolton Center, University of Pennsylvania, Kennett Square, PA, USA
(4) Center for Advanced Orthopaedic Studies, Beth Israel Deaconess Medical Center, Boston, MA, USA
(5) Department of Craniofacial Development & Stem Cell Biology, King's College London, London, UK

INTRODUCTION

Osteoarthritis (OA), a debilitating condition affecting millions of individuals, is characterized by the breakdown of hyaline cartilage, a biphasic, poroviscoelastic tissue, enabling smooth, low friction locomotion of joints. Hyaline cartilage is primarily comprised of a negatively charged sulfated glycosaminoglycans (sGAG) matrix interspersed within a type-II collagen (COL) fibril network and interstitial water, providing remarkable rheological and tribological properties necessitated for joint function. OA progression initiates with sGAG loss, followed by COL matrix breakdown and tissue swelling.[1] As such, many emerging treatments aim to recapitulate this dynamic, multi-component structure of native cartilage to restore healthy joint mechanical functionality and biochemical properties.

One particularly promising treatment is cartilage tissue engineering (CTE), whereby isolated chondrogenic cells are typically seeded in a resorbable scaffold material or pelleted. CTE workflow incorporates a brief 2–6-week *in vitro* culture period of the formed tissue construct in a chondrogenic milieu prior to implantation at the patient's OA-afflicted joint site. CTE outcomes often widely vary on an experimental basis determined by cell source, cell density and scaffold material among other factors.[2] A significant impediment in advancement of CTE treatments is the lack of non-destructive techniques capable of longitudinal assessments of evolving neocartilage composition, structure, and material properties both *in vitro* and *in vivo*. Conventional biochemical assays, histopathological assessments and immunohistochemistry used for *in vitro* growth monitoring are destructive, restricting clinical use, while arthroscopic tissue grading systems (Outerbridge, ICRS) and/or MRI (T1rho, T2*) used for *in vivo* assessments only moderately correlate with tissue biochemical distribution and material properties.

Spectroscopy analysis can successfully bridge this gap for repeated, non-destructive, and highly specific quantification of CTE biochemical content and material properties both *in vitro* and *in vivo*. Raman spectroscopy is an inelastic light scattering technique reflecting vibrational modes of different molecular bonds (amides, sulfates, hydroxyls) that comprise the major cartilage ECM constituents: sGAG, COL, H_2O. We have developed a Raman spectroscopic needle probe (**Fig.1A)** and unique spectral analysis platform capable of extracting ECM-specific compositional biomarkers indicative of the material properties of native and TE cartilage[3-5] (**Fig.1B-C**). In this study, we demonstrate the ability of Raman spectroscopy-derived biomarkers in longitudinal monitoring of evolving TE neocartilage composition utilizing a range of different scaffold materials: agarose, collagen, polyethylene glycol (PEG), hyaluronic acid and scaffold-free.

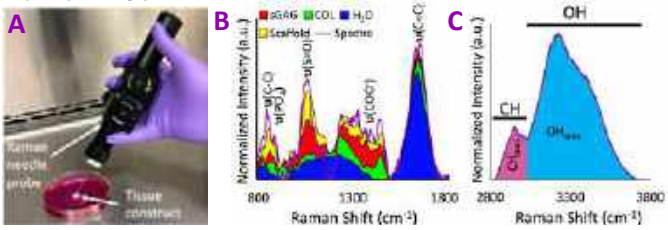

Figure 1: (A) Raman needle probe. (B) Cumulative contribution of ECM constituents and hydrogel scaffold to construct fingerprint spectra. (C) Organic content (CH_{area}) and water (OH_{area}) associated bands within construct highwave spectra.

METHODS

Tissue constructs: Immature bovine chondrocytes were isolated and seeded at a density of 30×10^6 cells/mL in hydrogel scaffolds of agarose (2% w/v; type VII), collagen (3mg/mL; rat tail type-I), or PEG (10% w/v; 4-arm PEG thiol + 4-arm PEG acrylate), or hyaluronan (HA; 2% maleimide-functionalized HA crosslinked with 4-arm PEG thiol) to generate ∅4×2mm cylindrical plugs, or assembled in a scaffold-free pellet (4×10^6 chondrocytes). All constructs were cultured in chondrogenic medium ± TGF-β3 (10ng/mL) for the initial 2 weeks,

except for scaffold-free constructs (cultured -TGF-β3) and PEG constructs (cultured +TGF-β3). Constructs were removed weekly (n=6 per scaffold per TGF-β group) for Raman, mechanical, and biochemical analysis for 56 days for agarose, biweekly for 42 and 56 days for HA and PEG, and weekly for 28 days for other scaffolds. **Raman probe:** A fiber-optic Raman probe (∅10mm; RIP-RPB, OceanOptics) coupled to a NIR diode laser (ex=785nm, 125mW) and a spectrometer (QEPro, OceanOptics). Spectra were collected with the probe focused ~10mm from the construct surface for a 30s exposure. **Spectral analysis:** Construct spectra were divided into fingerprint (800-1800cm^{-1}) **(Fig.1B)** and high-wavenumber regions (2800-3800cm^{-1}) **(Fig.1C)**. The fingerprint region was fit to a multivariate linear regression model:

$$Construct_{spectra} = sGAG_{score} * (sGAG_{REF}) + COL_{score} * (COL_{REF}) + H_2O_{score} * (H_2O_{REF}) + Scaffold_{score} * (Scaffold_{REF}) \quad (1)$$

where $sGAG_{REF}$, COL_{REF}, H_2O_{REF}, and $Scaffold_{REF}$ are reference spectra of purified powder chemicals for each constituent. Biomarker "scores" are regression coefficients reflecting relative contributions of constituents to the composite spectra (**Fig.1B,2A**). In the high-wavenumber region, the area under the OH & CH peaks (OH_{area} & CH_{area}) reflect tissue hydration and organic content deposition (**Fig.1C**)[5]. No $Scaffold_{REF}$ was used for collagen scaffold constructs and a dried cell pellet was used for scaffold-free constructs. **Tissue analysis:** Compressive Young's modulus (E_Y), H_2O content (gravimetric), sGAG content (DMMB) and COL content (OHP) were measured.

RESULTS

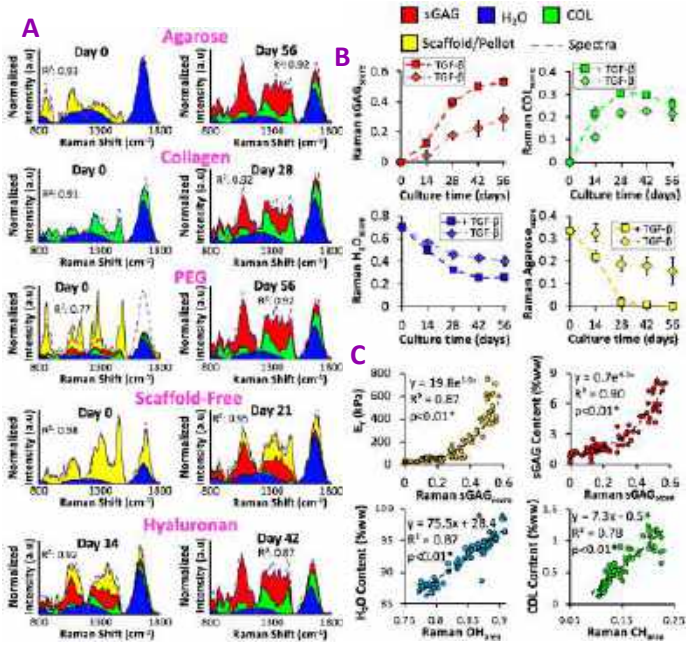

Figure 2: (A) 2D stacked area plots of early/late timepoint constructs depicting contribution of ECM and scaffolds to spectra for each scaffold type, (B) Raman "score" progression, (C) correlation of Raman biomarkers vs E_Y and biochemical content.

Our multivariate regression model reconstructions accounted for 91% ± 4% of the variation in the acquired construct Raman spectra across all scaffolds. For all scaffolds, Raman sGAG and COL biomarker scores increased over time, while H_2O and scaffold scores mostly decreased (H_2O trend not observed for scaffold-free) (**Fig. 2A-B**). Raman $sGAG_{score}$ accounted for 90%, 74%, 76%, 64% and 78% of the variation in sGAG content in agarose, collagen, PEG, scaffold-free and HA, respectively (**Fig.2C & Table 1**). For H_2O content, Raman OH_{area} accounted for 87%, 75%, and 77%, 64% of the variation in agarose, collagen, PEG and HA, respectively, but was not correlated with scaffold-free constructs (p=0.17). For COL content, CH_{area} predicted 78%, 58%, 54%, 54% and 70% of variation for agarose, collagen, PEG, scaffold-free and HA respectively. Raman $sGAG_{score}$ accounted for 87% and 63% of the variation in E_Y for agarose and collagen constructs respectively. Multivariate linear regression combining $sGAG_{score}$ and OH_{area}, improved predictions of the variation in E_Y for collagen scaffold constructs (63% to 77%) and predictions of the variation in sGAG content (64% to 90%) for scaffold-free constructs.

Scaffold	Tissue property	Raman scores					
		Univariate (R^2)				Multivariate (R^2)	
		sGAG	COL	H_2O	OH_{area}	sGAG+OH	sGAG+COL
Agarose	E_Y (kPa)	0.87*	0.33*	0.86*	0.85*	0.86*	0.77*
	sGAG	0.90*	0.47*	0.88*	0.83*	0.87*	0.83*
	H_2O	0.82*	0.55*	0.79*	0.87*	0.87*	0.82*
	COL	0.81*	0.63*	0.76*	0.78*	0.81*	0.82*
Collagen	E_Y (kPa)	0.63*	0.03	0.73*	0.69*	0.77*	0.74*
	sGAG	0.74*	0.03	0.71*	0.58*	0.81*	0.78*
	H_2O	0.53*	0.11	0.77*	0.75*	0.78*	0.76*
	COL	0.19*	0.23*	0.42*	0.58*	0.62*	0.48*
Scaffold-free	sGAG	0.64*	0.04	0.001	0.17	0.90*	0.72*
	H_2O	0.06	0.01	0.22	0.14	0.21	0.07
	COL	0.36*	0.09	0.44*	0.54*	0.54*	0.61*
PEG	sGAG	0.76*	0.19*	0.59*	0.57*	0.78*	0.76*
	H_2O	0.81*	0.30*	0.71*	0.77*	0.82*	0.83*
	COL	0.77*	0.21*	0.56*	0.54*	0.79*	0.79*
Hyaluronan	sGAG	0.78*	0.11	0.48*	0.41*	0.80*	0.79*
	H_2O	0.89*	0.09	0.77*	0.64*	0.89*	0.89*
	COL	0.66*	0.34*	0.62*	0.70*	0.75*	0.79*

Table 1: Correlations for Raman biomarkers versus assay measured biochemical content and material properties. *p<0.05.

DISCUSSION

Extracted ECM-specific Raman biomarkers allowed for successful longitudinal monitoring of newly deposited ECM (sGAG, COL) and distinction between ECM and a range of scaffold materials with unique spectral signatures, including natural carbohydrates (agarose, HA), natural protein (collagen), and synthetic polymer (PEG) or scaffold-free. Combining biomarkers further improved E_Y and sGAG content predictions. The Raman probe adopted in this study is ideal for *in vitro* monitoring of neocartilage owing to its high spectral collection efficiency and long-distance lens offset from the construct surface. A subsequent study (not shown) exhibited similar biomarker progression, with no cell viability or E_Y loss following weekly, aseptic repeated-measure Raman acquisition of live constructs. Previously, we demonstrated a Raman needle probe (∅2mm, **Fig. 1A**) configured for arthroscopic assessments of cartilage can achieve similar accuracy predicting agarose-scaffold CTE neocartilage composition and material properties (R^2=0.72-0.88)[5], demonstrating *in vivo* monitoring capability in preclinical large animal models and clinically in second-look arthroscopy. Ultimately, this study exhibits a Raman analysis platform successful in monitoring evolving neo-cartilage composition germane to its material properties across a wide variety of CTE protocols, providing the field with a non-destructive, quantitative, and highly sensitive technique for longitudinal *in vitro* and *in vivo* assessments, heretofore to be seen for CTE or other OA treatment modalities.

ACKNOWLEDGEMENTS

NIAMS AR081393, NIH T32GM145455, the Arthritis Foundation, MTF Biologics, and the BU MSE Innovation Award.

REFERENCES

[1] Cohen, NP et al., *J Orthop Sports Phys Ther*, 28(4): 203-15, 1998. **[2]** Huang, BJ et al., *Biomat*, 98: 1-22, 2016. **[3]** Kroupa, KR et al., *JOR*, 40: 1338-48, 2021. **[4]** Jensen, M et al., *Optics Lett*, 45(10): 2890-3, 2020. **[5]** Mehrotra, DR et al., ORS Ann Mtg no. 223, 2022.

A MICROMECHANICS BASED MULTISCALE MODEL FOR PLATELET-DRIVEN CLOT CONTRACTION

Chayut Teeraratkul (1), Debanjan Mukherjee (1)

(1) Paul M Rady Department of Mechanical Engineering, University of Colorado Boulder, Boulder, CO, USA

INTRODUCTION

Blood clots undergo a significant extent of volume shrinkage after formation, a phenomenon commonly referred to as clot contraction or retraction. Contraction is driven by activated platelets within the clot, and is related to several key patho-physiological roles. For instance, clot contraction enables forming a tight seal around damaged vascular sites preventing blood loss during hemostasis [1]. Additionally, impaired contraction can be related to embolism risks that underlie severe conditions like acute ischemic stroke [2] and venous thromboembolism. Despite its significance, platelet-driven clot contraction biomechanics remains poorly understood. This is partly due to a lack of existing quantitative approaches that can sufficiently characterize the heterogeneous, multiscale, contraction dynamics originating from microscale contractile activity [3]. Currently, a common methodology to study clot contraction involves taking successive images of whole blood clotting in a cuvette (*in vitro*) [4, 5]. These experiments can be costly to setup [5] and the results are limited to clot contraction kinematics. Micro-scale experimental characterization of platelet contractile forces [6] and fibrin-platelet interactions [1] have been demonstrated; yet extrapolation of these to quantify macroscale contraction behavior is non-trivial. There is presently no viable avenue to obtain information regarding the local state of flow during contraction and the local state of stress inside the clot; both of which are intimately tied to clot structure, clot stability, embolization risks, and resistance to lysis. Furthermore, it remains difficult to accurately recreate the complex human *in vivo* clot-flow interactions in a vessel using *in vitro* experiments. Recent advances in computational modeling can enable viable alternatives to address this gap. In this contribution, we propose an *in silico* modeling approach for clot contraction. This methodology is based on a mesoscopic discrete element clot model coupled with a custom finite element method for fluid flow. We establish here that our technique can robustly capture macroscale contraction behavior, local state of flow, and state of stress in the clot specimen.

METHODS

Discrete element approach for contraction micromechanics: In our methodology, the clot domain is represented by a statistically representative ensemble of discrete particles, with fiber connectors connecting between each particles. Together, these represent a mesoscopic coarse-graining of platelets and fibrin strands which constitute the blood clot. Individual discrete elements interact with each other via inter-element near-field and contact forces, as well as contractile forces along the fiber connectors. The resulting particle dynamics equations are numerically integrated using a Leap Frog scheme.

Platelet-driven contraction force: A time-varying contraction force is applied along the connectors direction which connects the discrete elements. The contraction force model is based on data for single-platelet force which is experimentally obtained from *in vitro* measurements in [6]. This individual platelet-driven contraction force is then coarse-grained into the model as a multiple of the measured force times the platelet-fiber connection density in each discrete elements.

Dynamic coupling with background flow: Each individual mesoscopic discrete element is in turn two-way coupled with the background fluid flow using a custom fictitious domain immersed finite element method. Briefly, a Petrov-Galerkin stabilized finite element algorithm is modified by applying a fluid-particle interaction force at each particle location. This can simultaneously resolve contraction dynamics and associated background flow interactions with the clot.

RESULTS

Proposed method replicates *in vitro* clot contraction kinematics: First, we aim to replicate the 3-phase clot contraction kinematics as observed in [4]. An initial clot filling a cuvette of dimension $7mm \times 12mm \times 1mm$ is reconstructed as a mesoscopic discrete element ensemble, with an average element size of $0.1\ mm$. Each discrete element is connected to its nearest neighbors (*here we chose 4 nearest neighbors*) with a connector. Cuvette walls are treated as impermeable walls, and the top of the clot sample is held fixed, mimicking a surface tension effect noted in the experiments. Resulting *in silico* contraction dynamics is shown in Figure 1 a1-a4. We establish that the resulting clot contraction kinematics (Figure 1.c.) can capture the 3-phase contraction behavior as described in prior works (see Figure 1.b.). We note that an exact quantitative matching

of contraction and contraction rate was not our goal as that would require tuning against exact experiment blood sample data which we did not possess.

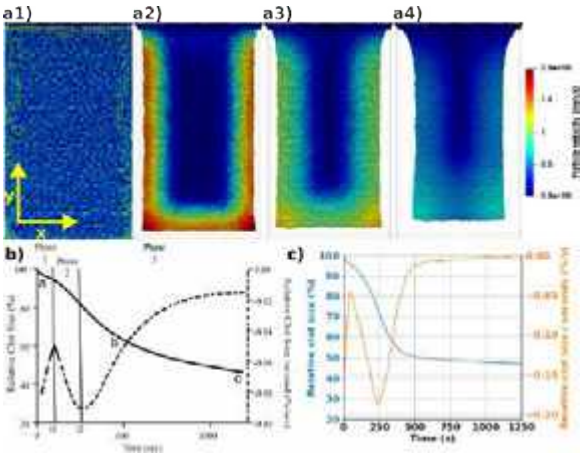

Figure 1: Discrete element simulation of clot contraction in a cuvettes. Panels a1-a4 show the clot at each time point during contraction. The transition from panel a1 to a2 show the lag time in contraction associated with contraction phase 1 in the contraction kinematics shown in panel b). Panel b) show the clot contraction kinematics observed in [4]; panel c) demonstrate the the discrete element representation can capture all 3 phases of the clot contraction kinematics.

Proposed method recovers effective stress during contraction: With the mesoscale representation of the micromechanics of the contraction, we can further post-process the interaction forces across the discrete element ensemble to estimate an effectivs state of internal stress during contraction. The stress is computed using an averaging of the interaction forces across the ensemble as illustrated in Figure 2 (*inset*), where $\underline{\mathbf{l}}^{qp} = \underline{\mathbf{x}}^q - \underline{\mathbf{x}}^p$ is the vector pointing from discrete element p to discrete element q in the ensemble, and the force vector $\underline{\mathbf{f}}^{pq}$ is the pair-wise interaction force between elements p and q; N_v is the total number of particles in the volume V. The resulting stress evolution for the contracting clot represented in Figure 1, is illustrated in Figure 2. We note that the overall state of stress is dilatational, with the shear/deviatoric components approx 4 orders of magnitude lesser (*not shown here for brevity*). Figure 2 presents the normal stress components along x and y (*indicated in Figure 1*), which are compressive stresses that increase as clot contraction progresses, which is intuitively expected.

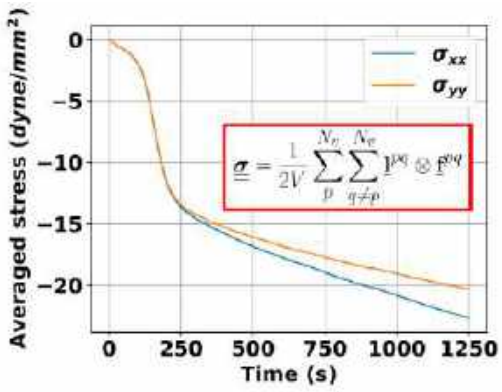

Figure 2: Effective stress state of the discrete element representation of the clot contracting in a cuvette.

Proposed method resolves local flow during contraction dynamics: We present an additional case-study for an idealized 2D hemispherical clot (radius 3 mm) immersed in an initially stagnant background flow, constrained within a channel with impermeable walls (width 6 mm). The fluid density is $\rho = 1.06 g/cu.cm$ and dynamic viscosity is $\mu = 4cP$, matching that of blood. The clot represents a 50% occlusion of the channel. As contraction initiates, the resulting dynamics squeezes out flow from the interstitial space into the clot exterior. Figure 3 shows 4 successive time snapshots of this contraction-mediated expulsion flow. At the initial contraction phase, we get a larger extent of flow expulsion. As contraction progresses, clot porosity rapidly reduces leading to a tightly packed clot, and continuously decreasing extent of fluid expulsion. These demonstrate the high resolution flow information during contraction that our method can quantify; information that is otherwise challenging to obtain *in vitro*.

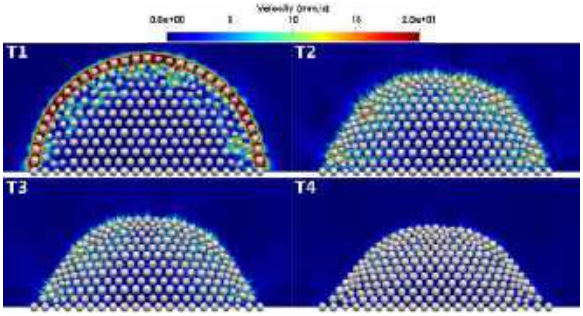

Figure 3: Expulsion flow due to clot contraction across multiple time steps during the simulation. T1 is the early step of the contraction process; T2 show the squeeze flow emanating out of the clot due to contraction; T3 and T4 subsequently correspond to clot approaching equilibrium, resulting in an increasingly tightly compressed clot.

DISCUSSION

Here we have demonstrated a novel *in silico* micromechanics based multiscale model for platelet-based clot contraction. Microscale platelet-level forces are integrated to define the discrete element interactions, and resulting emergent behavior consistently captures the 3-phase clot kinematics as observed experimentally. Owing to the discrete representation of the clot structure, heterogeneities such as spatial porosity evolution within the clot during contraction can be readily obtained (as opposed to continuous media representation of clots). We demonstrate that our proposed method can offer insights into quantities that are otherwise difficult to measure in experiments such as stress in the clot, and squeeze or expulsion of flow during contraction. The results from the case-studies indicate that our *in silico* model can potentially be used to study human blood clot contraction under physiologically realistic flow conditions, an endeavor that is currently not possible experimentally. Additionally, for existing *in vitro* assays or experiments, the proposed *in silico* approach can be used as a virtual twin to rapidly evaluate a range of *what if* scenarios for experiment design, and parameter evaluations. Continued development and refinement of this modeling approach will focus on conducting uncertainty quantification and parameter sensitivity analysis for model parameters, and on systematic contraction biomechanics studies using data-integration from experiments.

ACKNOWLEDGEMENTS

We acknowledge resources from the CU Boulder Research Computing Group, which is supported by NSF (awards ACI-1532235 and ACI-1532236), CU Boulder, and Colorado State University.

REFERENCES

[1] Michael C et al. *Comm Biol* 6.1 (2023).

[2] Tutwiler V et al. *Arterioscl Throm Vas* 37.2 (2017).

[3] Litvinov RI et al. *Res Prac Thromb Haemost* 7.1 (2023).

[4] Tutwiler V et al. *Blood* 127.1 (2016).

[5] Prakhya KS et al. *Res Prac Thromb Haemost* 6.5 (2022).

[6] Myers DR et al. *Nat Mater* 16.2 (2016).

A NEW STRATEGY TO ENHANCE RADIOFREQUENCY ABLATION WITHIN THE LOW ELECTRICAL CONDUCTIVITY REGION OF ATHEROSCLEROTIC PLAQUE: A MATHEMATICAL MODELING

Ruizhe Hou, Hongying Wang, Shiqing Zhao, Aili Zhang

School of Biomedical Engineering, Shanghai Jiao Tong University, Shanghai, China

INTRODUCTION

Radiofrequency (RF) ablation of the atherosclerotic plaque has been proven to lead to a major reduction in local smooth muscle cell content. However, there is a large amount of macrophage foam cells would hinder the delivery of electric current and the conduction of heat generated due to the 'oven effect' caused by the containing lipids with lower electrical and thermal conductivity than normal tissue[1, 2], which brings a great challenge to the ablation of the plaque rich of lipid.

To effectively ablate the lipid core, a new RF heating strategy utilizing the collaborative control of the RF sensitizer-loaded thermo-sensitive nanoparticles and a specialized temperature field was proposed to adjust the ablation shape and depth. The role of sensitizers is to enhance the apparent electrical conductivity of tissue by increasing the concentration of free ions in the extracellular space and the thermo-sensitive nanoparticles would break after being heated to a certain temperature so that sensitizers would be released effectively in the target area, reducing their accumulation and damage to healthy tissue. The specialized temperature field was used to reshape the distribution of the sensitizers based on the temperature dependence of its diffusivity.

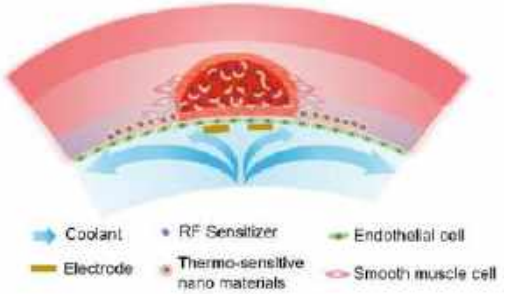

Figure 1: Schematic illustration of the ablation shape controlled by RF sensitizer-loaded thermo-sensitive nanoparticles and the specialized temperature field

METHODS

To evaluate this new strategy, the finite-element method was used and a 2D model that coupled RF propagation, heat transfer, and mass transport of both the nanoparticles and the sensitizers was created with COMSOL Multiphysics 5.4. The model consisted of the blood vessel with intima, media, adventitia, lipid core, and peripheral tissue.

The RF propagation in tissue is:

$$\nabla \cdot (\sigma \nabla V) = 0 \quad (1)$$

The heat-transfer equation was adapted:

$$\rho c_P \frac{\partial T}{\partial t} = \nabla \cdot (k \nabla T) + Q_e \quad (2)$$

where Qe represents the heat generated by RF current and can be expressed as[3]:

$$Q_e = \sigma_{p,i} (\nabla V)^2 \quad (3)$$

It's noted that the apparent electrical conductivity ($\sigma_{p,i}$) of tissue is sensitizer-dependent. A linear relationship was applied to describe the positive correlation between $\sigma_{p,i}$ and the concentration of free sensitizers c_{fd} and it's based on the original electrical conductivity σ_i of different tissues:

$$\sigma_{p,i} = A * c_{fd} + \sigma_i \ (i = vessel, lipid, peripheral\ tissue) \quad (4)$$

in which A is the experimental constant obtained from [4].

The thermo-sensitive nanoparticles are designed to release their contents rapidly upon heating. The extracellular concentration of the released drug c_{fd} and encapsulated drug c_{ed} were modeled as[5]:

$$\frac{\partial c_{fd}}{\partial t} = \nabla \cdot \left(D_{fd} \nabla c_{fd}\right) + c_{ed} K_{rel} \quad (5)$$

$$\frac{\partial c_{ed}}{\partial t} = \nabla \cdot (D_{ed} \nabla c_{ed}) - c_{ed} K_{rel} \quad (6)$$

Here, D_{fd} is the diffusion coefficient of the released drug that is temperature-dependent[6]:

$$D_{fd} = 1.1924 e^{-6} \cdot \exp(-2387/T) \quad (7)$$

K_{rel} refers to the drug release rate calculated from the in-vitro data.

The special temperature field was used to control the release and the diffusion process of the RF sensitizers and nanoparticles, and it was applied as the input boundary condition for the control equations (2) and (3).

RESULTS

As Fig2 a-c shows, when freely diffusing (FD) at body temperature, the pure sensitizers (S) can move to a depth more than just covering the lipid core within 120s. In the case of the RF sensitizer-loaded thermo-sensitive nanoparticles (S-TSNP, Fig2 d-f), after the same time, the released free drug only accumulated near the inner wall of the blood vessel, reaching the lower boundary of the lipid core since the weak release of nanoparticles at 37℃.

When a specialized temperature field (STF) was applied with a couple of electrodes and the coolant on the inner surface of the vessel, the tissue away from the electrodes was cooled while the closer was heated (Fig3 a). Thus, the diffusion of pure sensitizers was more intense in the depth direction in the region between the two electrodes. As for nanoparticles, the concentration of free drug on both sides of the electrode pair was significantly reduced and the distribution range was restricted to the edge and the central area of the electrode pair.

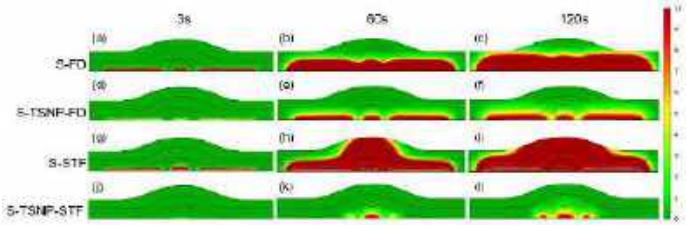

Figure 2: Distribution of free drug with or without a specialized temperature field. Unit: mol/m^3.

Figure 3 shows the temperature distribution of ablation of different cases and the area included in the white lines indicates the ablation margin with a temperature over 60℃.

Compared to the treatment with the specialized temperature field but without the drug (Fig3 a-c), the application of free sensitizer expanded the ablation area greatly in several seconds which penetrated the entire vessel wall by forming a 'deep-pit-like' ablation zone without endothelium protection and extended further in the axial direction of the vessel (Fig3 d-f). However, the use of thermo-sensitive nanoparticles could restrict the destroyed area with the formation of a 'scallop-shaped' ablation zone that covered the lipid core (Fig3 g-i), which had an ablation depth of 0.99mm within the region of media and protection of endothelium of 0.179mm. The lipid ablation ratio (%) could reach up to 70% while none could be ablated in STF and 56.5 times the ablation area in S-STF (Fig4).

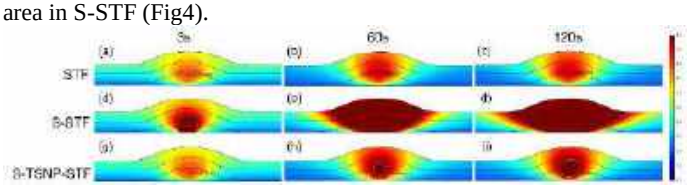

Figure 3: Temperature distribution of ablation processes without drug (a-c), with free drug (d-f), and with nanoparticles (g-i) under a specialized temperature field. Unit: ℃.

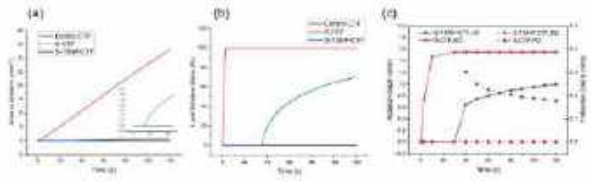

Figure 4: Spatial distribution of free drug with or without a specialized temperature field.

By analyzing the electrical parameters, it was shown that the free sensitizers increased the electrical conductivity and reduced the electric field gradient at the edge of the lipid core significantly, resulting in higher energy conversion efficiency from electromagnetic energy to heat to more area including the lipid core and deeper places in the vessel wall (Fig 5). As for thermo-sensitive nanoparticles, the area of electrical conductivity improvement was limited to the thickened intima and the lipid core (0.11S/m vs 0.04S/m for lipid with and without TSNP, respectively), and the electric field gradient decreased in the core, resulting in more deposition of RF energy in the plaque.

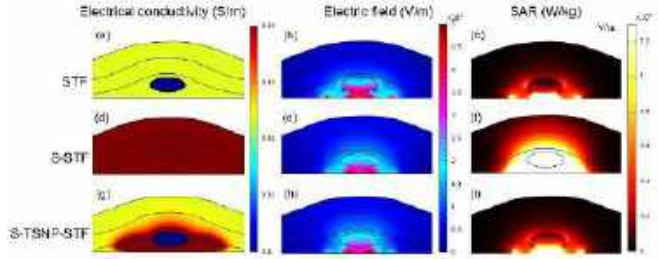

Figure 5: Distribution of electrical conductivity, electric field, and SAR without the drug (a-c), with free drug (d-f), and with nanoparticles (g-i) under a specialized temperature field.

DISCUSSION

With the specialized temperature field, the thermo-sensitive nanoparticles only release RF sensitizers in the center region of the electrodes due to the heat generation of RF current in tissue, and reduce the damage to healthy tissue caused by an ion-overload and a surge of extracellular osmotic pressure due to the excessive ion enrichment on both sides of the electrode pair comparing with the pure free sensitizers' delivery. Simultaneously, the released sensitizers can enhance the electric-to-heat energy conversion efficiency and ablate a major area of the lipid core successfully by increasing the electrical conductivity and decreasing the electric field gradient of the targeted area. Most importantly, effective protection of endothelium and restricted ablation depth and width would not destroy the adventitia and normal part of the vessel due to the controlled drug release and diffusion, which would reduce the risk of restenosis and blood vessel perforation.

Consequently, the new strategy combining a specialized temperature field and the RF sensitizer-loaded thermo-sensitive nanoparticles to enhance the radiofrequency ablation of low electrical conductivity region of atherosclerotic plaque was proved to be feasible mathematically.

In the future, other drugs with abilities like lowering cholesterol levels such as statins could be also loaded in the thermo-sensitive nanoparticles and accumulate to the lipid core directly by this new drug-delivery strategy, resulting in a synergistic effect between RF ablation and chemotherapy.

ACKNOWLEDGEMENTS

National Natural Science Foundation of China under Grants 51890892

REFERENCES

[1] Otsuka, F. *et al.*, *Cardiovasc Diagn Ther,* 6:396-408, 2016.
[2] Liu, Z. *et al.*, *Int J Hyperthermia,* 22:327-342, 2006.
[3] Zhao, S. *et al.*, *IEEE. Trans. Biomed. Eng.*, 66:2663-2670, 2019.
[4] Bennett, D., *Mat Sci Eng C,* 31:494-498, 2011.
[5] Sedaghatkish, A. *et al.*, *Int J Therm Sci,* 158:106540, 2020.
[6] Djelveh, G. *et al.*, *Meat Sci.*, 24:11-20, 1988.

AGED TENDONS HAVE A HIGHER STRAIN THRESHOLD FOR STIMULATION FROM DYNAMIC COMPRESSION THAN YOUNG TENDONS

Samuel J. Mlawer (1), Brianne K. Connizzo (1)

(1) Department of Biomedical Engineering, Boston University, Boston, MA, USA

INTRODUCTION

Rotator cuff tendinopathy affects over 50% of the population above that age of 60 and is characterized by pain and impaired daily performance [1]. The cause of rotator cuff tendinopathy is multifactorial with previous studies reporting that external impingement of rotator cuff tendons is one of major mechanisms that influences disease onset and progression [2]. While we know that both age-related degenerative changes and external compression influence tendon disease, it is often difficult to decouple these effects *in vivo*. We previously developed an *in vitro* murine explant culture model [3] to examine the effects of a single acute compressive injury [4] on tenocyte health, demonstrating a lack of adaptive response in aged tendons. However, it is more physiologically relevant to consider repeated compressive loading. Therefore, the purpose of this experiment was to use our previously developed *in vitro* compressive injury model to explore the response of tendon to continuous dynamic compressive loads and to discover the effect that age has on this response. Like our work with single acute compressive loads, we expected to see a greater adaptive response in the young mice compared to explants harvested from aged mice.

METHODS

Flexor digitorum longus tendon explants were harvested from young (4 months) and aged (22-24 months) male mice. After harvest, tendons were immediately loaded into grips with a 10-mm gage length and placed into custom-built multiaxial loading bioreactor (Fig. 1). All explants were held at 3% static tensile strain throughout the culture period. The acute injury ("AI") group was pre-loaded in compression to ensure contact, compressed to 50% strain over 1 second, and then the compression was released. The 15% and 50% groups received dynamic compressive loading at their respective strain levels 1 Hz for 1 hour, four times a day, with a rest period of 5 hours between each loading cycle. We also had a non-compression ("NC") group that received only the initial static tensile strain. After one week, metabolic activity was measured through a resazurin reduction assay. Tendons were then removed from culture, digested, and assayed for total DNA content (PicoGreen), sGAG content (DMMB), and collagen content (OHP). Synthesis of sGAG and collagen were measured respectively via incorporation of ^{35}S-Sulfate and ^{3}H-Proline radiolabel [3]. All biochemical assays were normalized to explant dry weight. Statistical analyses were performed via two-way ANOVAs with Bonferroni post-hoc corrected t-tests where significance was set at $p<0.05$ (* or solid lines).

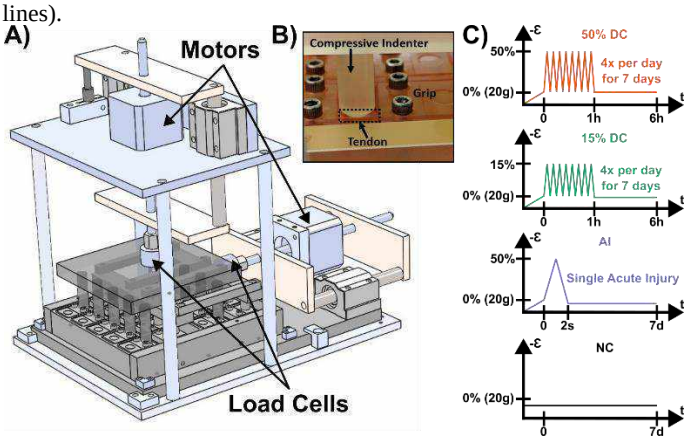

Figure 1. (A) Labelled biaxial loading device with (B) a close-up showing a single well with a tendon being compressively loaded and (C) the compressive loading profiles for each group.

RESULTS

In young explants, metabolic activity in the 15% group was significantly higher than all other groups. Metabolic activity was also lower in the 50% group than the NC group. In aged explants, the 50% group had higher metabolic activity than the NC and AI groups and the

AI group also had decreased metabolic activity compared to the NC group. DNA content was higher in the AI group than the 15% and 50% groups in young animals and higher than the 15% group only in the aged animals.

sGAG content was higher in the AI group compared to other groups in young explants, while there were no differences in groups in aged explants (Figure 2A). In young explants, sGAG synthesis is higher in the 50% and AI group compared to both the NC and 15% group. In aged explants, the 50% group stimulated sGAG synthesis but it was only significantly higher than the NC group (Figure 2B). Both age groups have similar results in collagen content with elevated content in the 50% group compared to other groups. In young groups, collagen synthesis was higher in the AI group than the NC group. In the aged groups, collagen synthesis in the 15% and 50% groups were lower than NC.

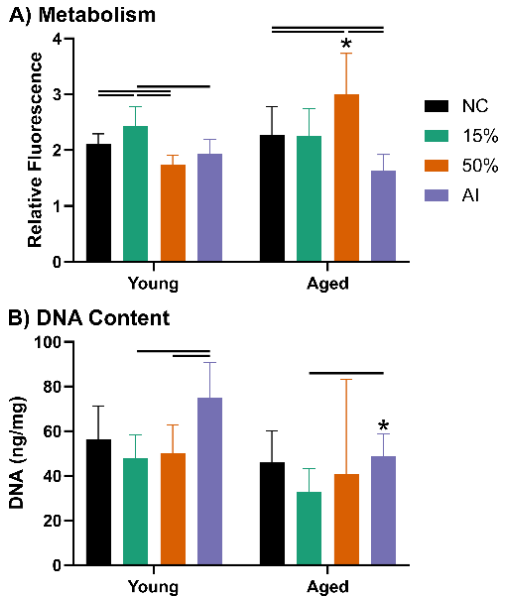

Figure 2. Measurements of (A) metabolic activity and (B) DNA content in the young and aged explants at a variety of strain levels. Data is presented as mean ± 95% confidence interval. Significance between strain levels is denoted with a bar (-) and significance between age groups is denoted with a star (*).

DISCUSSION

Our previous studies on the effects of acute injury on tendon concluded that aged tendons lacked the adaptive response that was found in young tendons [4]. In this study, where we instead look at the effects of dynamic compression, we see differential adaptive responses in both age groups to our two dynamic strain levels. In young mice, we see an increase in metabolic activity due to 15% strain, but in aged mice we only see an increase from 50% strain. This implies that aged mice have a higher strain threshold for stimulation, perhaps due to repeated compressive loads throughout their life cycle muting the adaptive response to smaller loads. This could also be related to insufficient stimulation of glucose metabolism, which appears to be mechanically regulated in tendons, and decreases as mice age [5].

We also found that high compressive strain regardless of timing (AI and 50% DC) stimulated sGAG synthesis in the young groups, while only repeated loading (50% DC) resulted in the same phenomena for aged tendons. Excess sGAGs are often a symptom of tendinopathy, but sGAG accumulation also better regulates fluid flow to help tendon better resist future compressive loads. This suggests that aged tendons may require more sustained loads to stimulate adaptive remodeling. We also saw a reduction of collagen synthesis in both dynamic compression groups, which implies that aged tendon exhibits an inappropriate adaptive response that could leave tendons predisposed to chronic use injuries. In contrast, young tendons exhibit no change in collagen synthesis with dynamic compression.

In summary, we demonstrate age-related differences in the response to dynamic compressive loading leading to aberrant matrix turnover. Aged tendons require higher and more sustained loads than young tendons to adapt, perhaps due to enduring and adapting to repeated compressive loads throughout their longer lifetime. Future studies will aim to use more comprehensive and specific proteomic assays to determine the exact timing and profile of ECM turnover. In addition, we plan to determine the role of sex in the response to compressive injury. We also plan to look at the effects of different loading frequencies and durations to determine how these conditions effect the biological response, and further explore compression versus tension-mediated signaling pathways.

Regardless, our explant system allows us to examine tendon's long-term response to a variety of compressive loading conditions. Our objective is to use this system to identify the main factors involved in tendon degeneration due to compressive damage, and to better understand mechanisms of mechanical adaptation in this complex and multiaxial loading environment. Beyond that, this information could be used to establish rehabilitation strategies or to identify potential signaling pathways relevant to efficient ECM turnover that can be targeted for therapeutics.

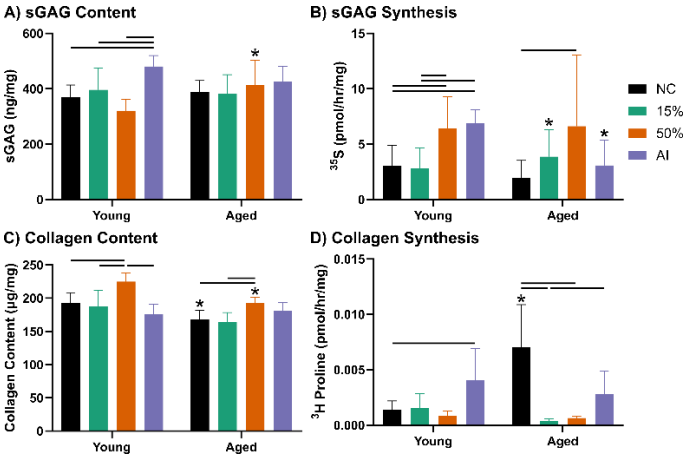

Figure 3. Measurements of (A) sGAG content, (B) sGAG synthesis, (C) collagen content, and (D) collagen synthesis in the young and aged explants at a variety of strain levels. Data is presented as mean ± 95% confidence interval. Significance between strain levels is denoted with a bar (-) and significance between age groups is denoted with a star (*).

ACKNOWLEDGEMENTS

This study was supported by Boston University and NIH/NIA R00-AG063896. Research was supported by the Boston University Micro and Nano Imaging Facility and NIH/NIA S10-OD024993.

REFERENCES

[1] Seitz, A et al., *Clinical Biomechanics*, 26:1-12, 2011. [2] Carpenter, J et al., *The American Journal of Sports Medicine*, 26:801-807, 1998. [3] Connizzo, B et al., *Connective Tissue Research*, 61:48-62, 2019. [4] Mlawer, S et al. *Journal of Orthopedic Research*, online, 2023. [5] Floridi, A et al. *Connective Tissue Research*, 9:95-97, 1981.

SELECTION OF LOADING CONDITIONS FOR RELIABLE VIRTUAL MECHANICAL TESTING OF BONE FRACTURE HEALING IN SHEEP AND HUMANS

Mehran Bahrami (1), Kylie Frew (1), Hannah L. Dailey (1)

(1) Mechanical Engineering & Mechanics, Lehigh University, Bethlehem, PA, USA

INTRODUCTION

In preclinical models of fracture healing, torsional loading is the postmortem mechanical test of choice because it is not sensitive to errors arising from specimen malalignment. Bending and axial loads are arguably more physiologically relevant, but those tests are highly sensitive to alignment due to the natural shape variations in long bones. The irregular curved contours of the diaphysis make repeatable alignment for bending tests difficult to achieve. Curvature along the bone axis also makes achieving pure axial loading without any bending very difficult in experiments. For these reasons, we previously validated our methods for image-based virtual mechanical testing of fracture healing using postmortem physical torsion tests.[1] In a clinical setting, we have also used virtual torsion tests to measure human tibial fracture healing under normal healing conditions.[2] However, the relevance of the torsional test for predicting whole-bone mechanics under physiologic loads is unknown. Accordingly, the purpose of this study was to assess the strength of association between virtual torsion, axial, and bending tests conducted under highly controlled virtual alignment conditions. We developed a methodology for virtually measuring the bending flexural rigidity and axial stiffness of fractured long bones using ovine and human data. The study hypothesis was that virtual axial stiffness (VAS) and flexural rigidity (VFR) are strongly correlated with virtual torsional rigidity (VTR) and capable of detecting differences in healing outcomes ranging from nonunion to fully healed.

METHODS

Two datasets were used in this analysis: ovine tibial osteotomies and human tibial fractures. The study protocols were reviewed and approved by the local ethical committees. The sheep (N = 23) were all stabilized by medial plating, with osteotomy defect sizes from 3-mm to 17-mm with allograft.[2] Postmortem (9 and 12 weeks) micro computed tomography (μCT) scans were down-sampled to 400 μm isotropic resolution. The clinical fractures (N = 29, 7 female, 22 male) were prospectively recruited from a single Level I trauma center and CT scanned at 12 weeks post-op.[2] Clinical scans had an average in-plane resolution of 0.41 mm and average thickness of 1.2 mm. All human patients were treated by intramedullary (IM) nailing.

Scans were processed in Mimics Innovation Suite (v.23, Materialise Inc.) to reconstruct 3D models of the fractures. Regions of cortical bone and callus were thresholded, volumetrically reconstructed, and meshed with quadratic tetrahedral (tet10) elements. All models were carefully aligned to the global coordinate system. Elementwise elastic moduli (E) values were specified using species-specific scaling equations:

$$\text{Human:}\quad E = 0.00704 \times HU \times 1000 \quad [\text{MPa}] \tag{1}$$

$$\text{Ovine:}\quad E = \begin{cases} 10225 \times \left(\frac{\rho_{QCT}}{1000}\right) & \rho_{QCT} > \rho_{cut} \\ 50 & \rho_{QCT} < \rho_{cut} \end{cases} \quad [MPa] \tag{2}$$

$$\rho_{QCT} = 0.38010 \times HU - 7.37444$$

where HU is Hounsfield unit value and ρ_{QCT} is phantom calibration radiodensity.[1]

Finite element (FE) models were exported to ANSYS Workbench Mechanical (R2020, ANSYS Inc., Canonsburg, PA) for virtual mechanical testing. Bending, torsional, and axial loading scenarios were applied to the models (**Figure 1**). Virtual flexural rigidity (VFR) was calculated as follows:

$$VFR = M_b \rho \quad [\text{N.m}^2] \tag{3}$$

where M_b = 31 N-m is the applied bending moment (see **Figure 1c**) and ρ is the bent radius of the curvature of the model. Bending direction was set by defining a local reference coordinate system at the distal end plane. Radius of curvature (ρ) was calculated using a custom MATLAB code that found the line produced by the intersection of the proximal and distal cut surface planes in the deformed model and calculated the distance from this intersection line to the FE model centerline (see **Figure 2**). Virtual torsional rigidity (VTR) was calculated as:

$$VTR = \frac{M_T L}{\phi} \quad [\text{N.m}^2/^\circ] \tag{4}$$

where M_T is the reaction torque calculated in the model, L is the working length of the test segment, and ϕ is the applied 1° angle of twist. Virtual axial stiffness was calculated as:

$$\text{VAS} = \frac{\delta_z}{F_z} \quad \text{[N/mm]} \qquad (5)$$

where δ_Z is the z-deformation of the proximal surface and F_z is the axial load (670N for sheep and 2175N for humans).

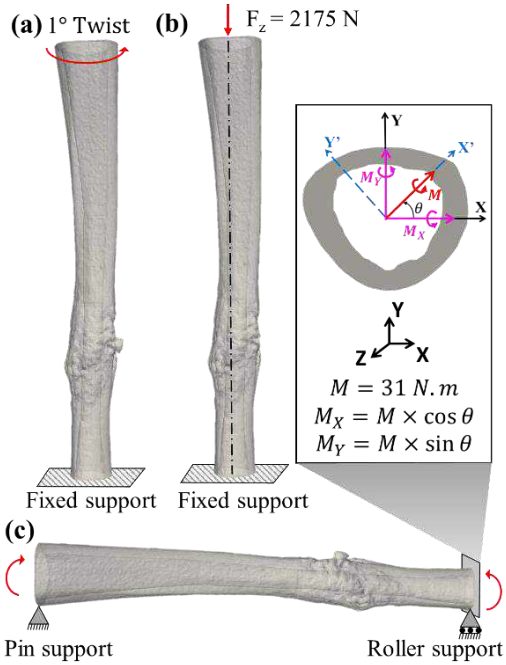

Figure 1: Illustration of different virtual mechanical tests on a representative human tibia: (a) torsion test, (b) axial compression test, and (c) bending test with variable bending direction.

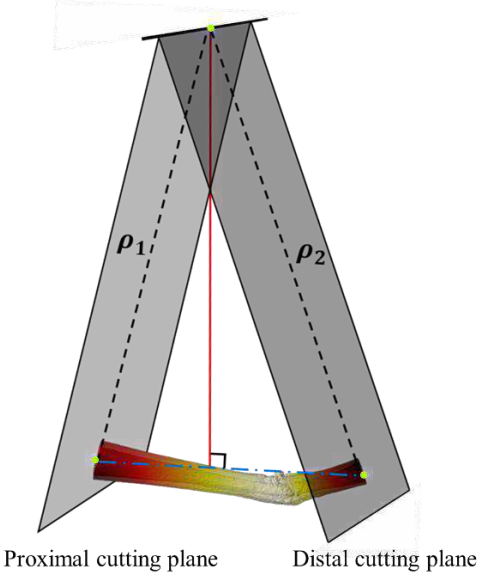

Figure 2: Schematic showing the method for calculating radius of curvature ($\rho = \frac{\rho_1+\rho_2}{2}$) for the bending test.

RESULTS

Correlations between VFR, VTR, and VAS are shown for sheep and human fracture models in **Figure 3.** VFR values are presented for anteroposterior bending only for simplicity (physiologically relevant anterior tension and posterior compression). In both sheep and humans, the bending and torsional rigidities were very strongly and significantly correlated. Axial stiffness was moderately-to-strongly and significantly correlated with torsional rigidity in both species.

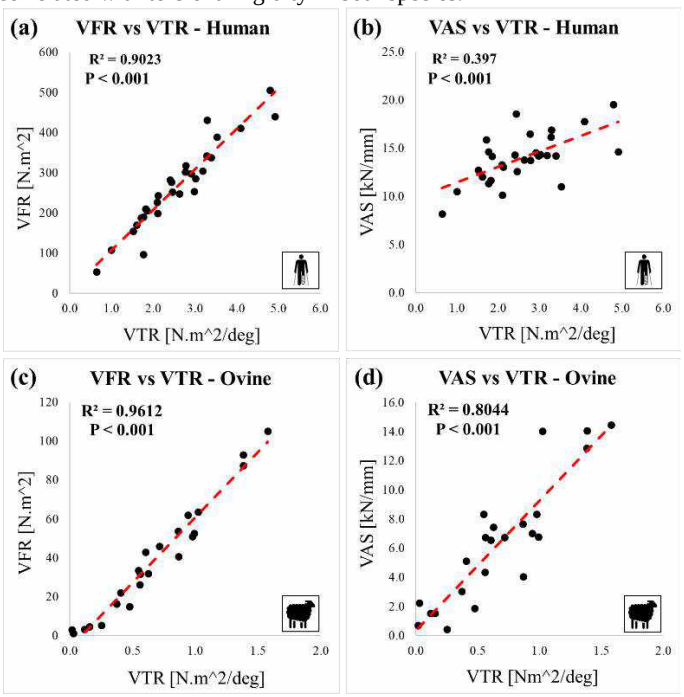

Figure 3: Correlation study between values of (a) VFR and VTR, (b) VAS and VTR for human data, (c) VFR and VTR, (d) VAS and VTR for Ovine data.

DISCUSSION

The results of this study demonstrate that although the torsion is not the predominant physiologic mode of loading, it is the ideal simplified mechanical test because it captures variations in bending rigidity and axial stiffness related to fracture healing without the challenges of direction-dependency. Compared to virtual bending and axial tests, virtual torsion tests are much easier to set up, with very simple post-processing. The virtual torsion test has also been robustly validated to experimental data.[1] In this analysis, there were no obvious outliers, indicating that torsion is a robust surrogate for more complicated physiologic loading states when the goal is to assess whole-bone mechanical integrity ranging from extremely delayed healing to full healed. Stronger correlations between rigidity and stiffness measures in sheep compared to humans were attributed to the regularity of the osteotomy animal model compared to the high variability of fracture patterns in naturally occurring clinical fractures.

ACKNOWLEDGEMENTS

This work was supported by NSF (CMMI-1943287). Simulations were run on Lehigh University's Research Computing infrastructure, partially supported by NSF Award 2019035. The content is solely the responsibility of the authors and does not necessarily represent the official views of NSF.

REFERENCES

[1] Inglis+, *Sci Rep*. 12(1):2492 (2022).
[2] Dailey+, *J Bone Jt Surg*, 13(101-A):1193-1202 (2019).

AUTOMATIC BOUNDARY DETECTION AND MESHING FOR VIRTUAL MECHANICAL TESTING OF TIBIAL FRACTURE HEALING

Alireza Ariyanfar (1), Mehran Bahrami (1), and Hannah L. Dailey (1)

(1) Department of Mechanical Engineering & Mechanics, Lehigh University, Bethlehem, Pennsylvania, US

INTRODUCTION

Bone fracture healing involves the gradual restoration of structural rigidity by formation of a callus. In animal experiments, postmortem mechanical testing is often used to measure bone rigidity as an indicator of healing status. These tests are destructive and can only be completed postmortem. An image-based alternative known as *virtual mechanical testing* has attracted attention to avoid these limitations.

Previously, we established workflows virtually reconstructing bone models from computed tomography (CT) images for subsequent finite element analysis using several commercial software packages [1-2]. However, the learning curve and license fees associated with the software required to replicate this analysis is a barrier to broader use.

The purpose of this work was to replace the commercial software we used previously for segmentation and meshing (Mimics Innovation Suite - v23.0, Materialize, Leuven, Belgium) with open-source codes. We addressed the challenge of boundary detection using an active contour model and explored approaches to elementwise material property assignment to capture bone gradients and manage partial volume effects. Finally, we performed virtual mechanical testing of long bones in ANSYS Workbench Mechanical (R2020, ANSYS, Inc, Canonsburg, PA) and validated the results.

METHODS

Animal Data: Osteotomized tibiae from N = 13 Swiss alpine sheep were excised at 9-12 weeks post-op and µCT scanned at l = 60.7 µm resolution in a previously completed study [1]. Osteotomy gaps ranged from 3-17 mm (normal and delayed healing models).

Algorithm for Boundary Detection: In each scan, two consecutive cross-sectional images differed only slightly in shape. Hence, the boundary (**B**) detected in one slice (**J**) served as a guess for the subsequent slice and was altered using an active contour model [3] (snake, Figure 1). Each point ($\mathbf{p}_j, 0 \le j < M$) on an old boundary ($\mathbf{B}_{i-1}$) was relocated ($\mathbf{q}_j$) to form the new boundary ($\mathbf{B}_i$). A square

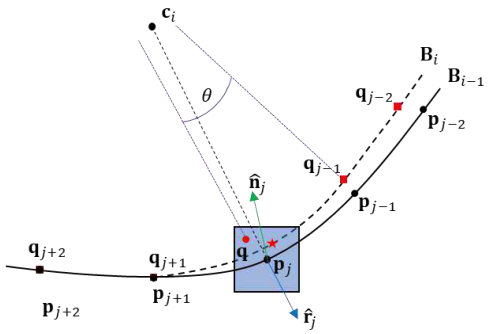

Figure 1. Detecting the outer boundary ($\mathbf{B}_i$) of bone/callus through point-by-point alteration of that ($\mathbf{B}_{i-1}$) in its previous image using an active contour model (snake).

neighborhood (**Q**) was defined as the domain of relocation. The neighborhood (**Q**) was centered at the old point ($\mathbf{p}_j$) unless the evolving new boundary ($\mathbf{B}_i$) became concave at the old point ($\mathbf{p}_j$), in which case the normal vector ($\hat{\mathbf{n}}$) became outward and the neighborhood (**Q**) was shifted along the normal vector ($\hat{\mathbf{n}}$) by a shifting factor (f_s). Every pixel point (**q**) inside the neighborhood (**Q**) underwent an energy (e) evaluation. The old point ($\mathbf{p}_j$) relocated to the pixel position associated with the minimum energy (e_{min}). Energy (e) consisted of normalized terms ($\bar{\boldsymbol{e}}$) with corresponding weights ($\boldsymbol{w}$) for different aspects of the boundary (**B**).

$$e = \boldsymbol{w}^T \bar{\boldsymbol{e}} \tag{1}$$

Angular-distance energy (e_θ) controlled the angular distance (θ) of a point ($\boldsymbol{q}$) with its spatially previous point ($\boldsymbol{q}_{j-1}$) measured with respect to the center of the new boundary ($\mathbf{B}_i$):

$$e_\theta(\boldsymbol{q}) = \left|\frac{2\pi}{M} - \theta\right| \tag{2}$$

Curvature energy (e_κ) contributed boundary smoothness at point ($\boldsymbol{q}$):

$$e_\kappa(\boldsymbol{q}) = \left\| (-1/12)\boldsymbol{q}_{j-2} + (4/3)\boldsymbol{q}_{j-1} + (-5/2)\boldsymbol{q} + (4/3)\boldsymbol{q}_{j+1} + (-1/12)\boldsymbol{q}_{j+2} \right\| \quad (3)$$

Image derivative energy (e_d) created an attraction between edges in the image and the point ($\boldsymbol{q}$):

$$e_d(\boldsymbol{q}) = \|\nabla \mathbf{J}\|(\boldsymbol{q}) \quad (4)$$

Meshing: After boundary detection, meshing was achieved by grouping pixels by a down-sampling factor (f_{ds}) equal to the number of pixels placed along the edge of an 8-node hexahedral element. Low-density pixels were not added to the model if their gray values were less than a threshold (τ). Noise islands were removed. Elementwise material properties were then assigned using our validated dual-zone material model for ovine cortical bone and callus [2].

FE Modeling: Virtual mechanical models were set up in ANSYS by inputting the mesh and material assignment files, fixing the proximal end, and twisting the distal end by 1° to calculate virtual torsional rigidity (VTR) [1].

RESULTS

Preliminary analysis during algorithm development revealed the appropriate values for down-sampling factor (f_{ds}), element formation threshold (τ), and other constants (Table 1).

Table 1. Constant parameters of the model and their calibration

Parameter	Symbol	Value
No. of points on boundary	M	72
Shifting factor	f_s	5
Energy weights	$[w_\theta\ w_\kappa\ w_d]$	[1 0.1 0.2]
Down-sampling factor	f_{ds}	5
Element formation threshold	τ	2750

The snake model successfully captured the outer boundary of images robustly without being affected by artifacts like nutrient artery canal or screw holes, both introducing strong edges (Figure 2).

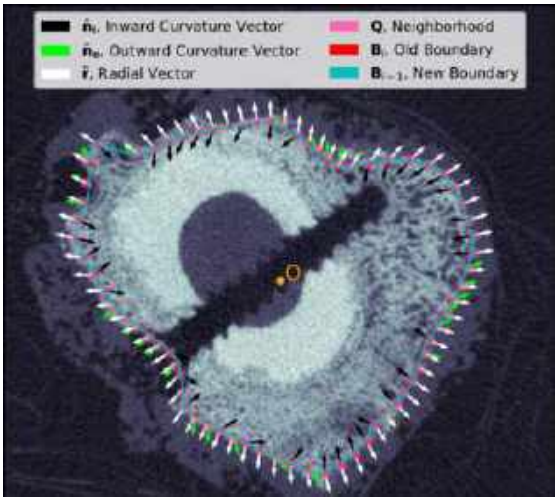

Figure 2. This example slice image shows the cortical cross section with a large callus and a prominent screw hole defect. The snake model identified the boundary by searching for minimal energy over a neighborhood positioned based on the convexity/concavity of the new boundary at that point. The angle between the radial vector and curvature vector determined the direction of curvature.

Figure 3 shows total deformation of an example reconstructed FE model of a fracture bone with callus that was processed and solved in ANSYS in ~10 minutes on a desktop workstation.

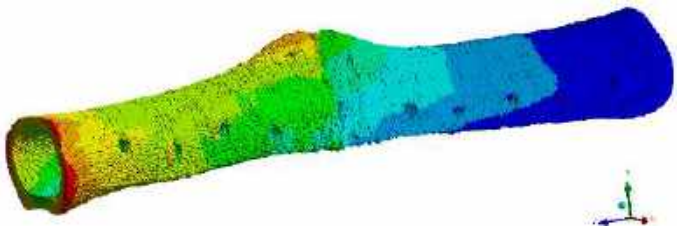

Figure 3. Example FE model created by down-sampling the segmented image and meshing with hexahedral elements. The postmortem biomechanical torsion test was replicated. Contours here illustrate total deformation.

Virtual torsional rigidity (VTR) was very strongly correlated with physical testing torsional rigidity (GJ) (R^2=0.86, p < 0.001), Figure 4. Absolute agreement between VTR and GJ indicated high rest reliability (RMSE = 0.16 Nm^2/° was less than the standard deviation of GJ = 0.41 Nm^2/°).

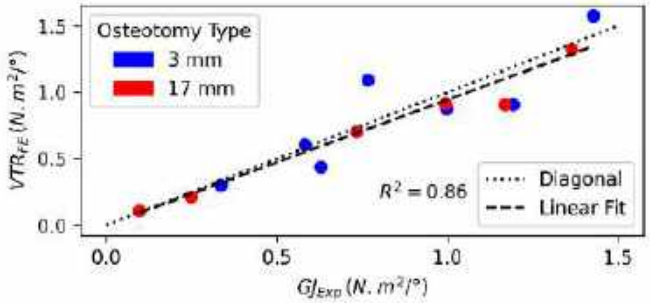

Figure 4. Virtual torsional rigidity (VTR) had very good agreement with torsional rigidity from physical testing (GJ).

DISCUSSION

A novel workflow was presented to eliminate the requirement for commercial software to prepare image-based finite element models for virtual mechanical testing to measure fracture healing in sheep. The similarity of axially consecutive cross-sectional images motivated us to detect boundaries recursively. The complexity of callus shape and image artifacts posed a challenge. The former required a flexible snake which was distracted easily by the latter. This problem was partially addressed by assigning a low value to curvature weight (w_κ) that rendered the snake flexible. To avoid the attraction of the snake to artifacts like nutrient artery canal or screw hole wall, a kick-out mechanism was introduced. When triggered by concavity, it shifted the neighborhood outward and away from the artifact. This strategy avoided attraction to artifacts, but at times deprived the snake from capturing severe concavity of callus and, consequently, took as callus some black background space. These boundary detection defects were subsequently managed at the meshing stage because pixels with such low gray values did not turn into elements because of applying the element formation threshold (τ). Overall, the resulting FE models showed outstanding agreement with benchmark physical tests.

ACKNOWLEDGEMENTS

This work was supported by NSF (CMMI-1943287) and NIH-NIAMS (R21AR081435). The content is solely the responsibility of the authors and does not necessarily represent the official views of NIH or NSF.

REFERENCES

[1] Schwarzenberg P et al., *J Orthop Res*, 39:727-738, 2020
[2] Inglis B et al., *Sci Rep*, 12:2492, 2022
[3] Williams D and Shah M, *CVGIP-Imag. Understan.*, 55:14-26, 1992

DETERMINING HIGH STRAIN RATE PORCINE BRAIN MATERIAL PROPERTIES USING INERTIAL MICROCAVITATION

Elizabeth C. Bremer-Sai (1), Anastasia Tzoumaka (2), Surya S. Kolluri (2), David L. Henann (2), Christian Franck (1)

(1) Department of Mechanical Engineering, University of Wisconsin - Madison, Madison, WI, USA
(2) School of Engineering, Brown University, Providence, RI, USA

INTRODUCTION

1.74 million people will be affected by Traumatic Brain Injury (TBI) in the United States each year [1]. The prevalence of TBI emphasizes the necessity to reliably measure and predict the material behavior of soft tissues in response to a variety of mechanical loading scenarios in order to better be able to predict the occurrence of injury. Computational modelling toward this effort has seen significant growth in recent years and is a powerful tool to garner crucial knowledge of the brain [2,3]. Computational head models are becoming more widely utilized as a tool to simulate varying types of head insults. While these models provide considerable anatomical accuracy, their ability to make accurate stress and strain predictions is limited by knowledge and accuracy of their underlying constitutive properties [2,3]. To this end, considerable effort has been given to the determination of low and quasi-static strain rate behavior, and whilst not in absolute agreement, promising results, methodologies, and reviews are available [2]. High and ultra-high strain rate material behavior, however, has remained elusive, due largely in part of experimental challenges when dealing with soft materials [2-4]. Soft tissues are highly compliant materials, rendering many existing high-rate characterization techniques difficult, if not completely ineffectual, to employ [2,3]. The absence and ambivalence of high-rate properties is a crucial limitation for the predictive capability of computational head models, specifically toward blast, high-velocity impact, and directed energy insults, and thus motivates the acquisition of quantitative constitutive properties for brain tissue at strain rates greater than 10^3 1/s. To address this, we utilize our previously developed ultra-high-rate rheological method, coined 'Inertial Microcavitation Rheology (IMR)'. IMR was designed to address the deficiency of high-rate properties by creating a tool capable of characterizing the behavior of highly compliant, soft materials under high-rate loading conditions (10^3 - 10^8 1/s) [6-8]. Here, we employ IMR to quantify the shear modulus (G) and viscosity (μ) within the context of a finite deformation, isotropic, hyperelastic constitutive model in five regions of interest (ROIs) in fresh and formalin-fixed porcine brain. It is a widely regarded notion that brain tissue is highly heterogeneous, not just between white and gray matter, but inter-regionally as well [2-5]. To address this, five anatomical regions were selected: Cerebellum, Cortex, Corona Radiata, Corpus Callosum, and Thalamus/Basal Ganglia. From this characterization, we aim to create a regional map showcasing the high-rate material properties and their spatial diversity across the porcine brain.

METHODS

The generation of inertial microcavitation events and the theoretical framework that underlies them has been thoroughly documented in the literature [6-8]. Briefly, inertial microcavitation is generated from a pulsed, 532 nm, frequency-doubled, Q-switched Nd:YAG Minilite II laser (Continuum, Milpitas CA) that is expanded and pathed into the rear port of a Ti2 Eclipse microscope (Nikon Instruments Inc., Japan). The laser pulse is then focused on the sample through a dichroic mirror and Nikon S Plan Fluor 40X/0.6 NA ELWD imaging objective (Nikon Instruments Inc., Japan). Finally, the cavitation event is recorded with bright-field microscopy at 2,000,000 fps on a Shimadzu HPV-X2 (Shimadzu Corporation, Kyoto, Japan).

The porcine brain is sectioned coronally into 5 mm thick segments using an aluminum brain matrix (Zivic Instruments, Pittsburgh PA) and cylindrical samples are extracted from each ROI with an 8 mm tissue biopsy punch. Low-melt agarose is used to embed these samples into a syringe modified with a flat-end before slicing into thin discs around ~150-350 μm thick to maximize optical transparency for each sample. These discs are then wedged between two hydrophilically treated cover glass slips and hydrated with Phosphate-buffered Saline (PBS).

RESULTS

After recording the cavitation event, the bubble's radial evolution is extracted and analyzed using a modified finite element based (FE-

IMR) framework adapted to account for the thin sample geometry. Within this framework, the radial cavitation kinematics are fitted to a Neo-Hookean Kelvin Voigt material model to obtain the shear modulus (G) and viscosity (mu) for each case. The initial findings from three cavitation events in fixed (Figure 1A) and fresh (Figure 1B) porcine cortical gray matter yielded shear moduli of 110 kPa and 11 kPa, and viscosities of 0.05 Pa·s and 0.11 Pa·s for fixed and fresh samples, respectively.

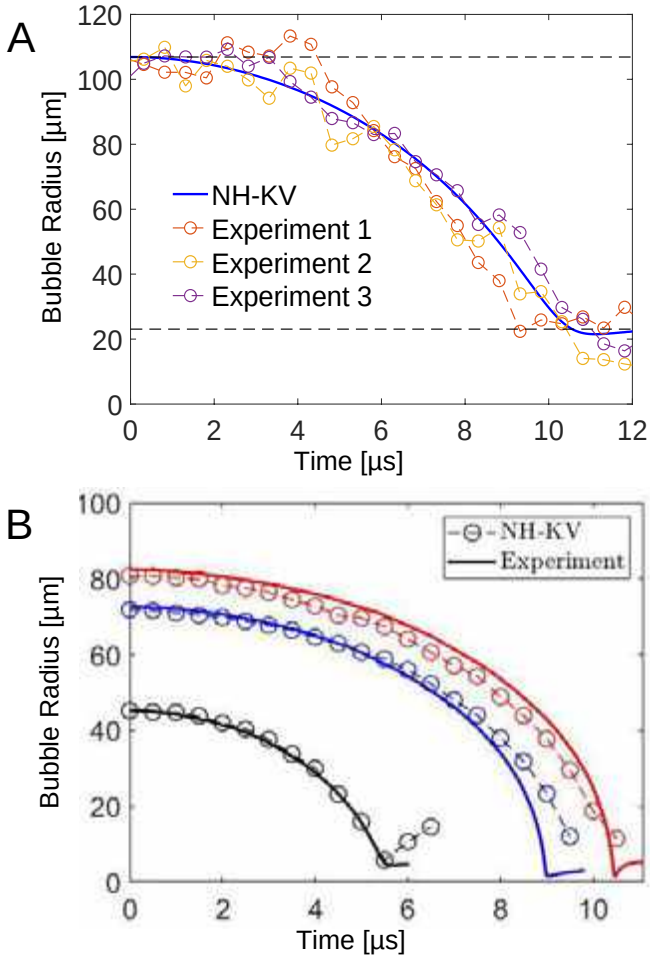

Figure 1: NH-KV model fits for cortical gray matter in (A) fixed and (B) fresh porcine brain.

DISCUSSION

Computational models remain a powerful, promising tool toward understanding the response of the brain to diverse loading conditions. However, their predictive capability is crucially limited by an absence of high-rate constitutive behavior, which stems from a lack of appropriate methods to study soft, highly compliant materials [2-4]. Here, by successfully creating a sample geometry that can be integrated with existing inertial cavitation protocols and by adapting our previously developed IMR framework with finite elements to account for this geometry, constitutive behavior of brain tissue at high rates can be examined, specifically the shear modulus and viscosity.

The deficiency of existing high-rate constitutive data prevents a direct comparison of our initial findings with the literature. However, inferences can be made to gain insight towards understanding if our values are realistic, starting with the fresh tissue findings presented (Figure 1B). At current, the strain rate dependence of brain tissue is unequivocal, specifically showing an increase in stiffness with increasing strain rates [2,9]. A study using MR Elastography considering fresh porcine brain reports a stiffness between 2 and 5 kPa when a range of frequencies between 50 and 300 Hz was investigated [9], making 11 kPa appear reasonable. There are, however, limitations to this inference as constitutive properties of brain tissue varies from region-to-region [2-5]; the preliminary values reported here are specific to cortical gray matter, while the MRE *ex vivo* study was conducted on a cylindrical sample of corpus callosum, a white matter region, with the inclusion of some superior gray matter.

Moving to the initial properties reported for fixed brain tissue (Figure 1A); large differences between the stiffness of fresh and fixed tissue can be expected as a consequence of the fixation procedure. Formalin fixation is done to prevent degradation of the native tissue structure, which is accomplished through the introduction of crosslinks to the tissue. These crosslinks are expected to drastically increase the stiffness response of the tissue, which agrees with our preliminary findings of 110 kPa and 11 kPa in formalin-fixed and fresh brain tissue respectively.

Finally, while isolating the tissue from its native environment inherently limits the ability of *ex vivo* studies to represent the native material behavior, the successful integration of tissues with the FE-IMR framework, overall, holds immense promise towards understanding complex biological systems and their response to mechanical stimuli at high-rates.

ACKNOWLEDGEMENTS

This material is based upon research supported by the U.S. Office of Naval Research under PANTHER award numbers N00014-21-1-2034 and N00014-22-2107 through Dr. Timothy Bentley.

REFERENCES

[1] Faul M, Xu L, Wald MM, et al., “Traumatic brain injury in the United States: national estimates of prevalence and incidence, 2002-2006,” Injury Prevention, 16, A268–A268, 2010.

[2] Meaney DF, Morrison B, Dale Bass C, “The Mechanics of Traumatic Brain Injury: A Review of What We Know and What We Need to Know for Reducing its Societal Burden”, Journal of Biomechanical Engineering, 136 (2), 021008, 2014.

[3] Budday S, Ovaert TC, Holzapfel GA, et al., “Fifty Shades of Brain: A Review on the Mechanical Testing and Modeling of Brain Tissue”, Archives of Computational Methods in Engineering”, 27 (4), 1187-1230, 2020.

[4] Goriely A, Geers MGD, Holzapfel GA, et al., “Mechanics of the brain: perspectives, challenges, and opportunities”, Biomechanics and Modeling in Mechanobiology, 14 (5), 931-965, 2015.

[5] Weickenmeier J, De Rooij R, Budday S, et al., “Brain stiffness increases with myelin content”, Acta Biomaterialia, 42, 265-272, 2016.

[6] Estrada JB, Barajas C, Henann DL, et al., “High strain-rate soft material characterization via inertial cavitation”, Journal of the Mechanics and Physics of Solids, 112, 291-317, 2018.

[7] Yang J, Cramer HC, Franck C, “Extracting non-linear viscoelastic material properties from violently-collapsing cavitation bubbles”, Extreme Mechanics Letters, 39, 100839, 2020.

[8] Yang J, Cramer HC, Bremer EC, et al., “Mechanical characterization of agarose hydrogels and their inherent dynamic instabilities at ballistic to ultra-high strain-rates via inertial microcavitation”, Extreme Mechanics Letters, 51, 101572, 2022.

[9] Guertler CA, Okamoto RJ, Schmidt JL, et al., “Mechanical Properties of Porcine Brain Tissue in Vivo and Ex Vivo Estimated by Mr Elastography”, Journal of Biomechanics, 69, 10-18, 2018.

IN VITRO CLOT TRAPPING EFFICIENCY OF THE FDA GENERIC INFERIOR VENA CAVA FILTER IN THE SUPINE POSITION

I. Goetz (1), R. Frasca (1), G. Campbell (1), T. Barraclough (1), K.I. Aycock (2), B.A. Craven (2), K.B. Manning (1,3)

(1) Department of Biomedical Engineering, The Pennsylvania State University, University Park, PA, United States
(2) Office of Science and Engineering Laboratories, Center for Devices and Radiological Health, United States Food and Drug Administration, Silver Spring, MD, United States
(3) Department of Surgery, Penn State College of Medicine, Hershey, PA, United States

INTRODUCTION

Inferior vena cava (IVC) filters play a crucial role in preventing life-threatening complications associated with venous thromboembolism (VTE), a condition affecting 1 out of 1000 individuals [1]. A common subset of VTE, deep vein thrombosis (DVT), involves the formation of blood clots in the deep veins of the lower extremities, which can potentially dislodge and travel to the lungs causing pulmonary embolism (PE). This potentially deadly event occurs in about one-third of all DVT cases [2]. IVC filters are medical devices designed to mitigate the risk of PE by capturing and preventing emboli from traveling to the pulmonary arteries where they could lodge and obstruct blood flow. Typically implanted using a catheter into the inferior vena cava, these filters act as a mechanical barrier and are particularly used in situations where patients do not respond to anticoagulant therapy or anticoagulants are contraindicated.

While IVC filters can be a valuable tool for PE prevention, questions regarding their effectiveness remain. Variation in design and purpose, whether permanent or retrievable, can be seen between filters, leading to the question of how to properly characterize the effectiveness of IVC filters and their ability to catch emboli originating from the lower extremities.

Using a generic IVC filter designed by the U.S. Food and Drug Administration (FDA) and collaborators at Confluent Medical Technologies for research purposes, the objective of this study is to build upon previous *in vitro* research done in the upright orientation [3] and help validate computational research characterizing the clot trapping efficiency of this filter. Specifically, this study characterizes the capture efficiency of the filter for both spherical and cylindrical clots of various clinically relevant sizes in the supine position under worst-case physiological flow conditions.

METHODS

To perform clot trapping experiments, a rigid, three-dimensional IVC model was fabricated based on averaged dimensions from patient computed tomography (CT) scans [4]. The IVC model is simplified while still maintaining the anatomical features of the iliac veins, infrarenal IVC curvature, and non-circular vessel cross-sections, all of which affect IVC hemodynamics and embolus migration. The FDA generic IVC filter (Figure 1A) was inserted into the model for experimentation. The filter is made of nitinol and has 16 identical struts shaped in a conical fashion. The largest gap between these struts is 5 mm and decreases as the struts join in the center at the top of the filter.

An *in vitro* flow loop (Figure 1B) was used to replicate physiological flow conditions. A Newtonian blood analog solution was created using a mixture of water and glycerin to provide a clot-to-fluid density ratio of approximately 1.05-1.1.

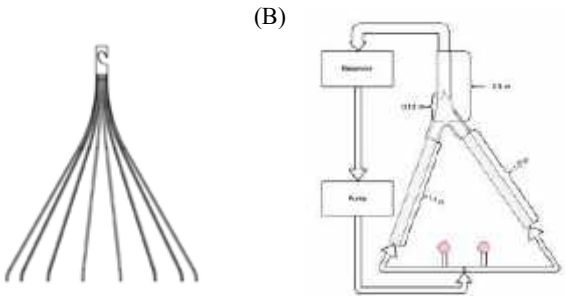

Figure 1: (A) Diagram of *in vitro* experimental flow loop. Red dots indicate injection ports for both iliac veins. (B) FDA generic IVC filter (adapted from [3]).

Physiological exercise conditions were used with an average flow rate of 5.06 liters per minute through the IVC using a centrifugal pump

[5,6]. The flow was split 50/50 between each iliac vein. Clots were introduced into the system upstream of the entrance tubing to the IVC model via a ball valve injection system, with enough tubing to allow for the flow to become fully developed before reaching the model.

Blood clots were formed following a previous experimental protocol [3]. Briefly, clots were created using bovine blood obtained through an approved IACUC protocol. A ratio of 50:50 red blood cells and platelet-rich plasma was used, and the initiation of coagulation was achieved using a 1:50 ratio of the blood solution and 0.5M $CaCl_2$. Clots were allowed to coagulate overnight at 37°C. Spherical clots (n=140) were formed in oversized, custom 3D printed resin molds, accounting for contraction of clots during coagulation. Three sizes were used: 3.26±0.27 mm, 4.81±0.40 mm, and 6.13±0.16 mm diameter. Cylindrical clots (n=90) were formed by injecting the reconstituted blood into Tygon tubing and clamping both ends. Clots of diameters 2.31±0.22 mm, 4.24±0.13 mm, and 4.82±0.14 mm were cut to lengths of 1x, 3x, and 5x the clot diameters. Both clot types were injected into the IVC flow loop, and the iliac vein of origin and trapping outcomes were recorded.

RESULTS

The filter trapping efficiency for spherical clots generally increased with clot diameter. As illustrated in Figure 2, the total clot trapping efficiencies were 35.7%, 85.7%, and 100% for 3.26 mm, 4.82 mm, and 6.13 mm diameter clots, respectively. There were no differences in the trapping efficiencies for clots migrating from the left and right iliac veins.

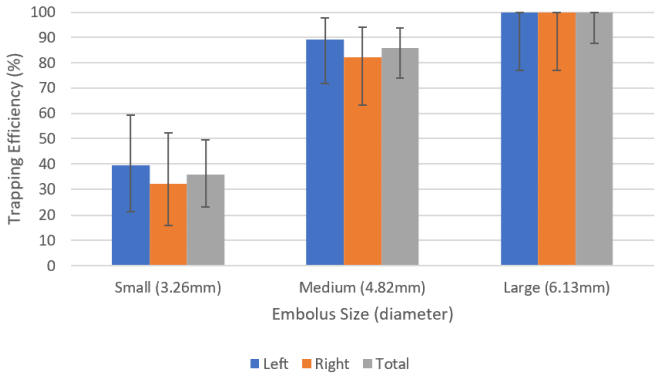

Figure 2: Clot trapping efficiencies for spherical bovine blood clots, categorized by small, medium, or large diameters, corresponding to 3.26 mm, 4.82 mm, and 6.13 mm, respectively. Colors indicate the iliac vein of origin from which clots were injected into the flow loop. Error bars represent Clopper-Pearson 95% binomial confidence intervals.

Figure 3 presents the observed trapping efficiencies of the IVC filter for cylindrical blood clots for various diameters and lengths. Overall, the clot trapping efficiencies increased with both clot diameter and length. The total capture rate for clots of 2.31 mm diameter and 1x diameter was 8.33%. All medium 4.82 mm diameter clots, regardless of length, were caught with 100% efficiency. The remainder of the small and medium diameter clots had capture efficiencies that increase with diameter and length until reaching 100%. The capture efficiency between iliac veins of origin was very similar for all clot sizes.

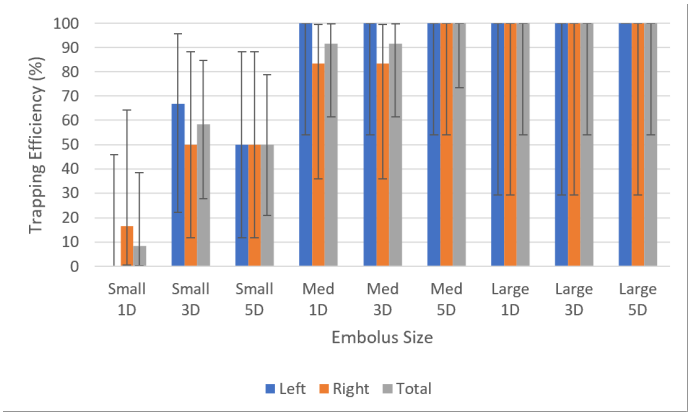

Figure 3: Clot trapping efficiencies for cylindrical bovine blood clots, categorized by diameter and length. Small, medium (Med.), and large, correspond to diameters of 2.31 mm, 4.24 mm, and 4.82 mm, respectively. Clot lengths are 1x (1D), 3x (3D), and 5x (5D) the clot diameters. Colors indicate the iliac vein of origin from which clots were injected into the flow loop. Error bars represent Clopper-Pearson 95% binomial confidence intervals.

DISCUSSION

The objective of this research is to characterize the in vitro clot trapping efficiency of the FDA generic IVC filter in the supine position. A previous study was performed using this experimental setup with the same filter in an upright (i.e., vertical) orientation [3]. As patients spend a significant amount of time during recovery, medical procedures, and sleep in the supine position, understanding the functionality and capture efficiency of filters under these conditions is important. The results of this study help to provide a more comprehensive understanding of the filter trapping efficiency when patients are in this orientation.

There is a clear trend in our results from these experiments showing an increase in trapping efficiency with an increase in clot size for both spherical and cylindrical clots. There is a significant difference in the trapping efficiency of spherical clots with a 6.13 mm diameter and the smaller clots with a diameter of 3.26 mm. The results can be explained by the geometry of the IVC filter. The largest gaps between struts of the IVC filter is 5 mm, thus a clot with a diameter larger than this gap size would be expected to be caught. This trend continues with cylindrical clots for both diameter and length. The cylindrical clots were found to deform as they moved through the flow loop, making them easier to become ensnared in the filter. The larger the clots, the more likely they are to make contact with the struts and, thus, become funneled towards the filter apex where gaps between the struts are smaller.

In this study, we did not find that the iliac vein of origin had a significant effect on the trapping efficiency of the filter in a supine position. These results suggest that with the IVC anatomical model used in this experiment, any subtle differences in flow patterns between the left and right iliac veins do not appreciably affect the filter trapping efficiency.

REFERENCES

[1] Silverstein, M et al., *Arch Intern Med*, 158(6):585-593, 1998
[2] Kearon, C., *Circulation*, 107(23):I-22-I-33, 2003
[3] Riley, J et al., *Cardiovasc Eng Technol*, 12(3):339-352, 2021
[4] Rahbar, E et al., *J Vasc Interv Radiol,* 22(6):835-842, 2011
[5] Cheng, C et al., *Am J Physiol Heart Circ Physiol,* 282(4):H1161-H1167, 2003
[6] Gallagher, M et al., *Cardiovasc Eng Technol,* 9(4):641-653, 2018

PREGNANCY AND AGE DIFFERENTIALLY AFFECT STIFFNESS, COLLAGEN MICRODAMAGE SUSCEPTIBILITY, AND COMPOSITION OF UTEROSACRAL LIGAMENTS

Catalina S. Bastías (1,2), Lea M. Savard (3), Kathleen Connell (4), Kathryn Jacobson (3), Sarah Calve (2,3,5), Virginia L. Ferguson (2,3,5), Callan M. Luetkemeyer (1)

(1) Department of Mechanical Science and Engineering, University of Illinois Urbana-Champaign, IL, USA
(2) Biomedical Engineering Program, University of Colorado Boulder, Boulder, CO, USA
(3) Paul M. Rady Department of Mechanical Engineering, University of Colorado Boulder, Boulder, CO, USA
(4) Department of Obstetrics and Gynecology, University of Colorado Anschutz, Aurora, CO, USA
(5) BioFrontiers Institute, University of Colorado Boulder, Boulder, CO, USA

INTRODUCTION

Pelvic organ prolapse (POP) is characterized by the descent of any of the pelvic floor organs (i.e., bladder, uterus, rectum) from their natural position, and it affects 50% of women in their lifetime [1]. Uterosacral ligament (USL) injury is a major cause of uterine POP, as USLs provide structural support for the uterus by tethering the cervix to the sacrum. Pregnancy, parturition, and age are known risk factors for POP; the former two are believed to increase the likelihood of USL injury by increasing mechanical stress and strain on the USLs [2]. Extracellular matrix (ECM) components like collagens, elastin, glycosaminoglycans (GAGs), and proteoglycans contribute to the mechanical integrity of the USL. Type I collagen is the major load-bearing ECM component of ligaments, and for that reason, collagen damage is likely implicated in USL injury and POP [3]. However, how stiffness, collagen damage mechanics, and composition of the USL change with pregnancy and maturation has not been explored.

In this study, we employed a murine model to investigate the effects of pregnancy and age on USL stiffness, mechanical injury susceptibility, and biochemical composition. We hypothesized that pregnancy-induced ECM remodeling would enable USLs from late-pregnant and recently post-partum mice to be more resilient to strain-induced collagen damage and more compliant than those from nulliparous mice. We further hypothesized that normal ECM changes that occur with maturation beyond adolescence would both increase the stiffness of USLs and lower their resilience to strain-induced damage.

METHODS

Female C57BL/6J mice were euthanized according to the University of Colorado Boulder's Animal Care and Use Committee. Both young adult (YA, 10-15 weeks, n = 5-6) and adult (A, >17-weeks, n = 3-5) murine USLs were collected at three different stages of pregnancy: nulliparous (NP), embryonic gestation day 18.5 (E18.5), and post-partum day 1 (PP1). USLs were isolated, and a suture was tied at the cervical end. One USL was used for mechanical analysis and left attached to the pelvis and a piece of the cervix, which acted as anchors, and tested while freshly harvested. The contralateral USL was flash frozen with liquid N_2 and later analyzed with Raman spectroscopy.

For mechanical testing, samples were stained in a solution of Ghost Dye Red 780 (Tonbo Bioscience), which stained all free amine groups, for 2 hrs at 4°C. For the last 10 min, Sytox Deep Red (ThermoFisher Scientific) was added into the solution. The sample was placed into a custom loading chamber in a 1×PBS bath, and tested with a 100 mN FemtoTools load cell under an upright confocal microscope (Leica STELLARIS 5) [4]. A ~500 µN pre-load defined the reference state.

Collagen hybridizing peptide (CHP) was used to determine regions with significant fibrillar collagen denaturation (damage) [5]. Prior to mechanical testing, the 1×PBS bath was replaced with a 10 µM solution of CHP for 15 min. This process was repeated after each deformation state to record the change in collagen damage. The samples were imaged at 10× before, during, and after deformation. Deformed configurations were determined by actuator displacements of 1000, 1500 and 2000 µm, and allowed a stress-relaxation period of 5 minutes.

Maximum intensity projections from reference and deformed Ghost Dye and Sytox image stacks were used to estimate 2D displacement fields with MATLAB's *imregdemons* function, from which Lagrange strain fields were derived (Fig. 1). A previously developed moving threshold was used to determine pixels with significant collagen damage [6]. Average axial (E_{11}), transverse (E_{22}), and shear (E_{12}) strains were calculated, as well as percent damaged area, for the intermediate region. Linear mixed models (LMM) were used to determine the effect of pregnancy and age on collagen damage vs. average E_{11} and average axial stress vs. E_{11}.

Raman spectroscopy was used to analyze the biochemical composition of the contralateral USLs. Thawed, the samples were placed in a custom well and evaluated using a confocal Raman microscope system (Renishaw inVia, 758 nm red laser). A grid of 100

μm × 150 μm (~3 × 12) spectra along each USL was obtained, and the average signal for the intermediate section of each sample was computed. Principal component analysis (PCA) was used to evaluate the relative composition of each sample using the MATLAB function *pca* and spectra for fibrillar collagen, GAG, and elastin from the literature [7]. Two-way ANOVA was used to determine whether pregnancy and age had significant effects on USL composition. Asterisks indicate significance in Figs. 2-3.

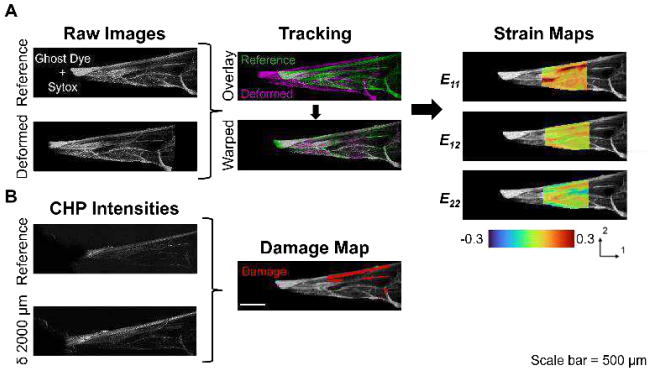

Figure 1: (A) Displacements were tracked with reference and deformed Ghost Dye and Sytox images and differentiated to compute strain fields. (B) Corresponding damage maps from CHP images permitted analysis of injury susceptibility.

RESULTS

Only pregnancy appeared to alter injury susceptibility (Fig. 2A). LMM analysis determined that USLs from NP mice were more susceptible to mechanically-induced collagen damage than those from PP1 ($p<0.05$). However, USLs from E18.5 mice showed no difference in collagen damage vs. strain compared to those from NP mice. Age also did not significantly affect injury susceptibility.

Both pregnancy and age significantly altered USL stiffness (Fig. 2B). Pregnancy was observed to increase USL compliance; USLs from NP mice were stiffer than those from E18 and PP1 mice ($p<0.05$). Conversely, maturation resulted in increased USL stiffness; USLs from A mice were stiffer than USLs from YA mice ($p<0.05$).

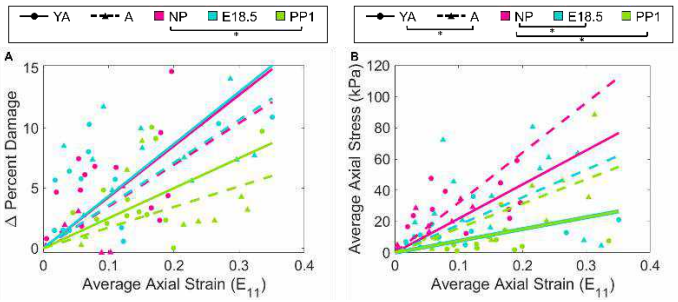

Figure 2: USL injury susceptibility (A) was significantly lower at PP1 compared to NP, while USL stiffness (B) was differentially affected by age and pregnancy.

PCA of Raman spectra determined that 3 Principal Components (PCs) represented 90% of the total variance. PC1 loadings were found to resemble fibrillar collagen spectra, while PC2 and PC3 loadings resembled GAG and elastin spectra, respectively (Fig. 3, right). All PC loadings significantly changed with pregnancy ($p<0.05$), but not with age (Fig. 3, left). Results suggest that the relative amounts of collagens (A) and GAGs (B) increase during pregnancy, while the relative amount of elastin (C) decreases.

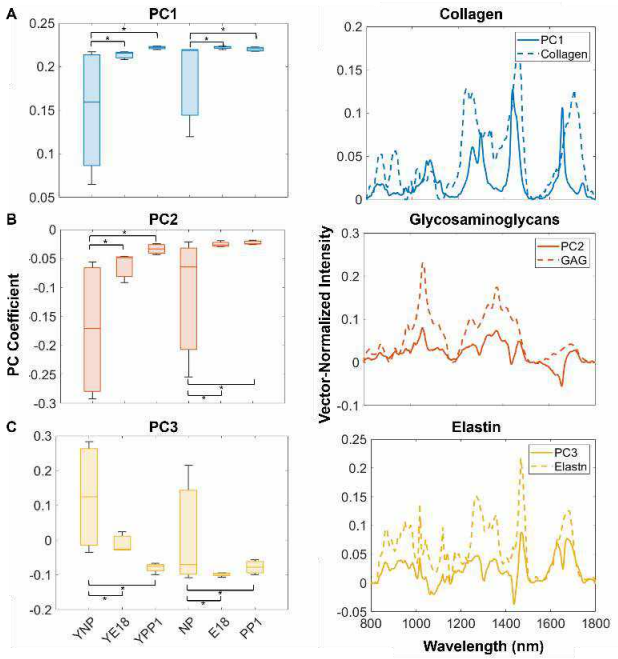

Figure 3: PCA of Raman spectra revealed an effect of pregnancy on USL composition. Comparisons between pure ECM spectra and PC projections for a YA NP sample are shown at right.

DISCUSSION

Our findings indicate that pregnancy causes ECM remodeling in the USL that alters composition, decreases stiffness, and lowers susceptibility to mechanical damage. The relationship between collagen damage and strain was significantly different after parturition, with USLs from PP1 mice sustaining less damage at similar levels of strain than those from NP mice. This suggests that the ECM remodels in late pregnancy to reduce strain-induced injury susceptibility for childbirth. Results from Raman spectroscopy reveal a significant increase in relative fibrillar collagen and GAG content during pregnancy, with a further increase the day following parturition. A similar trend in decreasing relative elastin content was also observed.

Aging and vaginal delivery are key factors in developing POP, and understanding how these factors play a role in the integrity of the USL is important, as our current preventative strategies are limited. This is the first study to investigate the effects of both age and pregnancy on USL mechanics, injury susceptibility, and ECM composition. Limitations in this study include a small sample size, especially for identifying compositional differences. Future work will investigate whether micro-organizational changes also protect the USL from injury.

ACKNOWLEDGEMENTS

This work was supported by CU UROP grant (CB), the NSF GRFP (LS), the University of Colorado Innovative Grant Program, and the Anschutz Boulder Nexus Seed Grant.

REFERENCES

[1] Donaldson K et al., *Ann Biomed Eng*, 49(8):1788-1804, 2021.
[2] Dietz HP et al., *ANZJOG*, 48(6):587-591, 2008.
[3] Zhu YP et al, *Int Urogynecol J*, 32(8):2273-2281, 2021.
[4] Bastias CS el al., *J. Vis. Exp*, 193: e65074, 2023.
[5] Zitnay JL et al., *Nat Comm*, 8(1):1-12, 2017.
[6] Luetkemeyer CM et al., *Acta Biomat*, 168:252-263, 2023.
[7] Bergholt MS et al., *Front Bioeng. Biotechnol*,7:303, 2019.

EXTENSION OF MURRAY'S LAW TO THREE DIMENSIONS WITH MULTIPLE DAUGHTER VESSELS

Seth Street (1), David Dierker (1), Mark Johnson (1), Samer Hoz (2), James Castiglione (3), Charles J. Prestigiacomo (1)

(1) Department of Neurosurgery, University of Cincinnati, Cincinnati, Ohio, United States
(2) Department of Neurological Surgery, University of Pittsburgh, Pittsburgh, Pennsylvania, United States
(3) Department of Neurosurgery, Thomas Jefferson University, Philadelphia, Pennsylvania, United States

INTRODUCTION

The principles governing the natural development of vascular geometry have been the interest of biophysical research for over 100 years[1]. A widely popular theory is that proposed in 1926 by Cecil D. Murray, who applied the principle of minimum work to predict optimal two-dimensional vascular geometry at a bifurcation in terms of both vessel caliber and branching angles[2,3]. Although more recent work has been done to generalize the theory as it applies to vessel caliber[4], we are not aware of any efforts to generalize the theory's predictions of ideal branching angles to three dimensions or to more than two daughter vessels. In this study, we present a generalized form of Murray's Law to predict optimal branching angles for any number of daughter vessels in three dimensions and compare these predictions to angles observed in cerebrovascular computed tomography angiograms.

METHODS

The same assumptions that Murray applied in his original derivation in 1926 were utilized to develop a generalized form[3]. Specifically, Poiseuille flow and a metabolic energy cost proportional to the volume of blood were assumed[3]. Measurements of radii and angles were made on 3D models acquired from computed tomography angiograms of M1-M2 middle cerebral artery (MCA) bifurcations and basilar terminus (BT) "tetrafurcations" (where the posterior cerebral arteries (PCA) and superior cerebellar arteries (SCA) were treated as originating from a common point). Comparisons between the measured and predicted geometries and between MCA and BT adherence with predicted ideality were performed using two-tailed t-tests with a critical value of $\alpha = 0.05$.

RESULTS

It was found that branching geometry is ideal when the following relationship is true for a system with n daughter vessels:

$$\frac{r_0^2+\sum_{j=1}^{n} r_j^2}{\sum_{j=1}^{n}\left(\cos\theta_j r_j^2+\cos\theta_j r_0^2-\sum_{a=1}^{j-1}\cos\theta_{a,j} r_a^2-\sum_{a=j+1}^{n}\cos\theta_{j,a} r_a^2\right)} = BI = 1 \qquad (1)$$

where BI is the Branching Index, r_i is the radius of vessel i ($i = 0$ represents the parent vessel and $i > 0$ represents a daughter vessel), θ_i is the angle between the parent vessel's flow axis extended beyond the branching point and the flow axis of daughter vessel i, and $\theta_{i,k}$ is the angle between the flow axes of daughter vessels i and k ($i < k$). These relations are visualized in Figure 1.

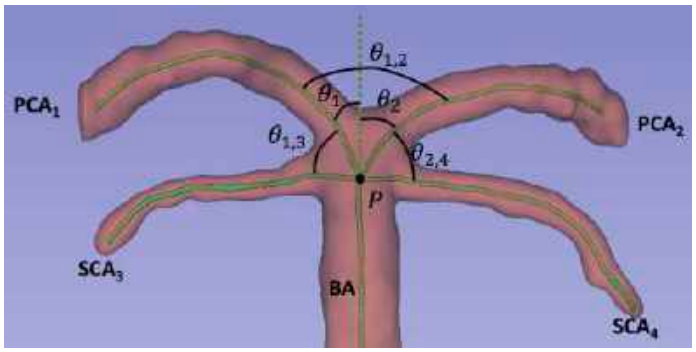

Figure 1A: Example of a 3D model of the basilar tip with illustrated definitions of angles. Some angles have been omitted from the figure for clarity. The model is a coronal view of the basilar tip, with green solid lines representing center flow axes within the visualized arteries. The dotted green line represents extension of the basilar artery flow vector beyond the branching point from which the posterior cerebral and superior cerebellar arteries originate.

BA:	Basilar Artery
PCA:	Posterior Cerebral Artery
SCA:	Superior Cerebellar Artery
P:	Common branching point of PCAs and SCAs from parent BA
θ_1:	Angle between flow vector of PCA_1 and BA
θ_2:	Angle between flow vector of PCA_2 and BA
$\theta_{1,2}$:	Angle between flow vector of PCA_1 and PCA_2
$\theta_{1,3}$:	Angle between flow vector of PCA_1 and SCA_3
$\theta_{2,4}$:	Angle between flow vector of PCA_2 and SCA_4

Figure 1B: Definitions of abbreviations and terms used in Figure 1A.

Using measured values for the radii and angles of 12 BT tetrafurcations, the average value of the equation was found to be $BI_{BT} = 1.20$ ($\sigma = 0.13$), which is significantly larger than the predicted value of $BI = 1$ ($P < 0.001$). For 22 MCA bifurcations, the average value was $BI_{MCA} = 1.09$ ($\sigma = 0.10$), which is also significantly larger than 1 ($P < 0.001$). Comparing BI_{BT} and BI_{MCA} reveals that BI_{BT} was significantly larger than BI_{MCA} ($P = 0.024$).

DISCUSSION

Given that both BI_{BT} and BI_{MCA} were significantly larger than 1, it seems that more than just minimization of work at a branching point determines arterial geometry. However, it should also be noted that both branching points exhibited geometries which produced values for BI close to 1 with small standard deviations. This may indicate that vascular geometry develops in such a way as to minimize energy loss within the confines of other constraints, such as conforming with the gross anatomy of the tissues that the vasculature supplies. This is similar to the theory proposed by Ingebrigtsen et al.[5] Our results also showed that BI_{BT} was significantly greater than BI_{MCA}, which further supports this theory given that the BT participates in the circle of Willis and is thus subject to greater anatomic constraints than is the MCA bifurcation, which is located in the Sylvian fissure[5].

Less ideal branching geometry may manifest as an increased rate of cerebrovascular pathology. For example, it is known that the pathogenesis of intracranial aneurysms is highly influenced by local hemodynamics[6]. Although the rate of formation of intracranial aneurysms is greater at the MCA bifurcation than at the BT, the rate of rupture of existing aneurysms is approximately 4 times greater in the posterior circulation (in which the BT participates) than at the MCA bifurcation[7]. This discrepancy in rupture risk may be attributable to the relative lack of ideality in branching geometry at the BT demonstrated in this study. Future research may further explore this observation by calculating Branching Index values for the most common site of both intracranial aneurysm formation and rupture, the anterior communicating artery[8].

ACKNOWLEDGEMENTS

The authors have no conflicts of interest to disclose.

REFERENCES

[1] Hess, WR, *Pflügers Archiv European Journal of Physiology* 168:439-490, 1917.

[2] Murray, CD, *Proceedings of the National Academy of Sciences of the United States of America*, 12(3):207–214, 1926.

[3] Murray, CD, *The Journal of General Physiology*, 9(6):835-841, 1926.

[4] Stephenson, D et al., *Journal of Applied Physics*, 118(17):174302, 2015.

[5] Ingebrigtsen, T et al., *Journal of Neurosurgery*, 101(1):108-13, 2004.

[6] Staarmann, B et al., *Neurosurgical Focus*, 47(1):E2, 2019.

[7] Rinkel, GJ et al., *Stroke*, 29(1):251-256, 1998.

[8] Chen, J et al., *Frontiers in Neurology*, 11:1020, 2020.

BIOMECHANICAL IMPACT OF NEOCHORDOPLASTY AND LEAFLET RESECTION FOR MITRAL VALVE PROLAPSE REPAIR

Gediminas Gaidulis (1), Muralidhar Padala (2), Lakshmi Dasi (1)

(1) Cardiovascular Fluid Mechanics Laboratory, Georgia Institute of Technology, Atlanta, GA, USA
(2) Nyra Medical Inc., Atlanta, GA, USA

INTRODUCTION

Mitral valve prolapse (MVP) is a valvular heart disease, diagnosed in 2-3% of the general population **[1]**. In MVP patients, one or both mitral valve (MV) leaflets are degenerated, elongated, and override each other during valve closure. Along with leaflet degeneration and elongation, elongation and rupture of the chordae are also seen, contributing to leaflet overriding. In such condition, a gap between the leaflets occurs in systole, causing the backflow of the blood from the left ventricle into the left atrium, and resulting in pulmonary congestion, elevated left atrial pressure and distension, and highly inefficient pumping of the heart leading to heart failure over time **[2]**.

Surgical repair of MVP is the current gold standard of care. The techniques used for MVP repair are generally classified into two categories: (1) non-resective techniques, where the native leaflet tissue is fully preserved, and surgical repair is focused on implanting artificial neochordae into the leaflets and appropriately sizing and tensioning them to restore proper valve closure; and (2) resective techniques, where the native leaflet tissue is cut and reduced in its area, so that the intact chordae are realigned to restore proper valve closure. Both techniques have merit, but post-repair valve biomechanics can differ significantly, and often impact repair durability **[3]**. In addition to these techniques, all repairs are stabilized with an annuloplasty ring, especially when MVP is accompanied by the dilated mitral annulus, usually due to degenerative MV disease **[4]**, to ensure that the valve closure achieved at surgery remains so in the long term **[5]**. The biomechanically optimal approach to repair MVP is often discussed by surgeons, but quantitative studies on this topic are very limited.

In this study, we sought to compare the biomechanical effects of different mitral valve repair strategies to repair the most common form of MVP – posterior leaflet (PL) prolapse. Firstly, the impact of leaflet preserving and leaflet resection approaches on valve biomechanics was assessed. Secondly, the impact of annular stabilizing techniques on both prior MV repair strategies was evaluated.

METHODS

A computational model of the MV was created from transesophageal echocardiography data of a patient. To simulate valve closure, patient-specific motion of the mitral annulus and the papillary muscles was prescribed to the model, and physiological transvalvular pressure gradient was applied to the ventricular surface of the leaflets. MVP was induced by transecting the chordae inserted into the P2 segment of the PL. The annular dilation was mimicked by uniformly displacing annular nodes away from the MV centroid to achieve the annular size inherent to the valve with degenerative MV disease. Dynamic simulation of the MV closure was run in Abaqus and systolic configuration of the valve with P2 prolapse was obtained.

Neochordoplasty was performed by inserting the neochordae into the free edge of the prolapsing leaflet and anchoring them to the papillary muscles. Two repair scenarios were studied, starting with 2 neochordae and then 4 neochordae inserted into the P2 segment. Three annuloplasty ring models of different sizes, i.e., true-sized ring of 36 mm, and two down-sized rings of 34 mm and 32 mm, were created based on the measurements of Carpentier-Edwards Physio I ring. Each ring was positioned near the regions of left and right fibrous trigones, and the mitral annulus was then deformed to the ring configuration (**Fig 1**). The physiological transvalvular pressure gradient was applied to the leaflets and dynamic simulations of the valve closure were run in Abaqus for both neochordoplasty scenarios with each ring size.

Two repair scenarios for leaflet resection were investigated: triangular resection and quadrangular resection. In each scenario, either a triangular or a quadrangular segment of the prolapsing P2 segment was removed. The PL was then reconstructed by approximating the free edges of the resection and applying the tie constraint at the junction site so that there was no relative motion between the resected edges (**Fig 1**). For both leaflet resection scenarios, three annuloplasty rings created previously were used to reshape the mitral annulus in the same manner as described before, and valve closure was simulated in Abaqus.

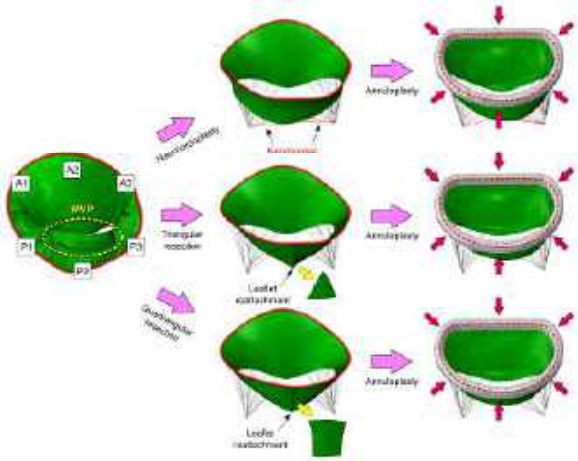

Figure 1: Schematic representation of the study workflow.

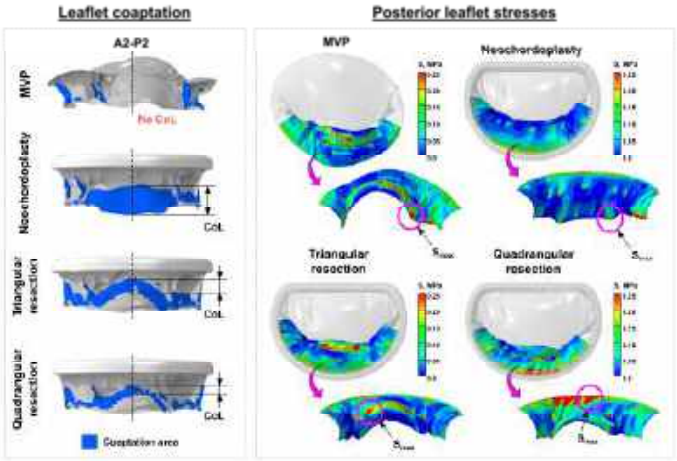

Figure 2: Leaflet coaptation and PL stress distribution before and after neochordoplasty and leaflet resection with true-sized ring.

RESULTS

In pre-repair model, the presence of MVP and annular dilation resulted in the absence of leaflet coaptation at A2-P2, excessive PL mobility, elevated leaflet stresses and chordal tension forces. All investigated MVP repair techniques were able to reduce P2 segment prolapse and restore different levels of leaflet coaptation (**Fig 2**) and clinically acceptable tenting height (< 5 mm). The excessive mobility of the PL seen in the MVP model was also reduced with all repair techniques and annuloplasty ring sizes. With 36 mm and 34 mm rings, stresses on the PL were reduced after neochordoplasty, but increased with both resection techniques (**Fig 2**). Triangular resection reduced PL stresses only with 32 mm ring. Quadrangular resection was not able to reduce stresses on the PL with any ring size. Tension forces in the intact PL marginal chordae were greatly reduced after neochordoplasty. Both leaflet resection techniques reduced chordal forces as well, but the reduction was smaller than after neochordoplasty. The computational results for pre- and post-repair models are presented in **Table 1**.

Table 1: Simulation results for different MVP repair techniques.

	Coaptation length (mm)	Coaptation area (mm^2)	Tenting height (mm)	Tenting area (mm^2)	PL excursion angle (deg)	Peak PL stress (MPa)	Peak PL marginal force (N)
MVP	0	107.9	-	-	89.4	0.75	0.56
	36 mm ring						
2 neochordae	5.86	338.7	3.57	47.5	62	0.47	0.056
4 neochordae	5.9	353.5	3.9	51.9	60.2	0.39	0.038
Triangular	2.78	296.8	1.42	18.9	75.3	0.79	0.3
Quadrangular	1.72	230	2.87	38.2	70.4	2.04	0.35
	34 mm ring						
2 neochordae	6.43	463.8	2.93	37.2	64.5	0.45	0.036
4 neochordae	6.52	483.8	3.19	40.5	63.1	0.31	0.026
Triangular	3.76	449	0.98	12.4	77.2	0.78	0.2
Quadrangular	1.93	349	2.68	34	68.3	1.22	0.27
	32 mm ring						
2 neochordae	7.44	595.9	2.27	26.3	66.5	0.41	0.024
4 neochordae	7.52	630.6	2.42	28.1	65.7	0.28	0.015
Triangular	5.53	593.8	0.59	6.8	78.6	0.57	0.11
Quadrangular	6.07	520.7	2.27	26.3	62.3	0.87	0.094

DISCUSSION

Our MVP model with annular dilation demonstrated the presence of poor leaflet coaptation, excessive PL mobility, elevated stresses on the PL, and increased tension forces in the intact marginal chordae. All repair techniques reduced prolapse and improved contact between the MV leaflets, increasing leaflet coaptation length and area. The better outcomes were observed after neochordoplasty, as clinically adequate coaptation length at A2-P2 (> 5 mm) was achieved with all ring sizes. After leaflet resection, however, annular downsizing with 32 mm ring was required to improve coaptation adequately, as larger rings were not able to ensure clinically acceptable coaptation length. Similarly, better outcomes in leaflet stress reduction were achieved after neochordoplasty as well. Both neochordoplasty scenarios with each ring size reduced peak stresses on the PL, while after leaflet resection stresses on the PL mainly increased. Finally, tension forces in the intact marginal chordae were reduced with both MVP repair techniques, but after leaflet resection peak forces in the marginal chordae were considerably higher than after neochordoplasty.

Between the implantation of 2 and 4 neochordae, the better MVP repair outcomes were achieved with the higher number of neochordae. As 4 neochordae were distributed wider along the free edge of the P2 segment, the larger portion of the leaflet was restricted from the excessive motion, and therefore larger coaptation area and length was observed with each annuloplasty ring size. Similarly, leaflet stresses and chordal forces were lower with the higher number of neochordae, showing that partial force transfer from native chordae to neochordae not only reduces forces in the intact chordae, but also helps to reduce stresses on the leaflets. Downsizing the annulus with a ring reduced leaflet stresses, chordal forces, and increased coaptation even more, thus further improving post-repair valve biomechanics.

In conclusion, our computational results suggest that neochordoplasty for P2 segment prolapse correction is biomechanically optimal and may result in a clinically more durable repair than leaflet resection. However, translational studies will be needed to confirm these findings.

REFERENCES

[1] Delwarde, C et al., *Front Cardiovasc Med*, 10:1077788, 2023.
[2] Apostolidou, E et al., *Glob Cardiol Sci Pract*, 2017:e201703, 2017.
[3] Paulsen, MJ et al., *JTCVS Tech*, 10:244-251, 2021.
[4] Antoine, C et al., *Circ Cardiovasc Imaging*, 11:e005971, 2018.
[5] Abt, BG et al., *JTCVS Open*, 13:106-116, 2023.

INVESTIGATING THE MECHANISMS OF PATELLA OSTECHONDRAL ALLOGRAFT TRANSPLANT FAILURE USING FINITE ELEMENT METHODS

Michael A. Hernández Lamberty (1), John A. Grant (4), Rhima M. Coleman (1,2), Ellen M. Arruda (1,2,3)

(1) Department of Mechanical Engineering, University of Michigan, Ann Arbor, Michigan, USA
(2) Department of Biomedical Engineering, University of Michigan, Ann Arbor, Michigan, USA
(3) Program in Macromolecular Science and Engineering, University of Michigan, Ann Arbor, Michigan, USA
(4) Department of Orthopaedic Surgery, University of Michigan, Ann Arbor, Michigan, USA

INTRODUCTION

Articular cartilage is a connective tissue that is found in diarthrodial joints, where it facilitates locomotion of the joint by providing a low-friction surface. Articular cartilage injuries are present in up to 66% of knees undergoing cartilage diagnostic procedures for knee pain, where 20% of these lesions are observed in the patella [1]. Full cartilage thickness defects have a prevalence of 4.2% to 6.2% in the general population but increase to 36% in athletes [2]. These defects can impair quality of life and, over time, cause the onset of osteoarthritis. Articular cartilage is both avascular and aneural, with limited regenerative capacity, often requiring surgical intervention to repair defects.

Osteochondral allograft (OCA) transplantation is one of the surgical methods for treating cartilage defects of the knee. The main advantage of this procedure being that a single operation can restore the cartilage surface in the defect site. In this procedure, a donor graft of cartilage along with the underlying bone is transplanted into the cartilage defect site of the patient. The underlying bone allows the graft to be press-fit into the defect for stability. OCA transplants have shown positive patient outcome scores and graft survival rates ranging from 79% to 100% at 5 years and up to 78.7% at 10 years [3]. For the patella, however, this procedure is associated with a high level of reoperation and failure, 51.6% and 20.1% respectively [4]. The mechanism of failure of OCA transplants is currently unknown. Matching the thickness and mechanical properties of the transplanted cartilage to the recipient tissue is not part of the graft selection protocol for OCA transplants. Our hypothesis is that geometric and mechanical mismatches in donor and recipient cartilage will cause local stress concentration on the graft boundary that may lead to OCA transplant failure.

METHODS

Finite element (FE) methods were used to vary several geometric and mechanical properties that could influence failure rates. Simplified 2D axisymmetric FE models were created in ABAQUS (SIMULIA) for this project (Fig 1), where the donor cartilage radius from the center of the OCA graft (rotation axis) is 8 mm. In these models a surface pressure of 1 MPa was applied to the patella cartilage surface, while the subchondral bone surface was fixed. Donor/Recipient (D/R) thickness ratio was varied using 9 combinations, 5 combinations having $D/R \geq 1$ and 4 having $D/R < 1$. The cartilage was assumed to be a linear elastic material with Poisson's ratio of $\upsilon = 0.46$ and the Young's Modulus varied between $E = 2.5$ MPa and 7 MPa for of total 11 different combinations where either the donor or recipient cartilage section was fixed at 7 MPa. The models were meshed with quadratic eight-node axisymmetric (CAX8) elements. Four different outcomes were obtained from all the models; these were compressive stress, compressive strain, shear stress and shear strain. The magnitude for these outcomes were plotted 1 mm from the graft boundary and the peak value was obtained. The model with D/R thickness ratio equal to 1 and equal mechanical properties between cartilage sections was considered as the control. The peak value for each outcome for the different variations in D/R thickness ratio and mechanical properties was compared to that of the control model.

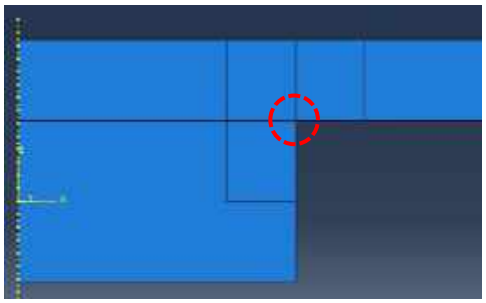

Figure 1: Example of 2D axisymmetric FE models used to vary D/R thickness and mechanical properties. The highlighted section is where local stress concentration occurs.

RESULTS

Based on the number of combinations for the D/R thickness ratio of the cartilage sections and Young's modulus, there were 99 peak value magnitudes for each outcome previously stated. For both stress outcomes, when the mechanical properties were fixed, and the D/R ratio increased in disparity, the magnitude of the stress outcomes increased. A combinatorial effect was present where a high disparity in both D/R ratio and mechanical properties increased stress magnitude. This can be observed in opposite top-right and bottom-left corners of the heatmap on Fig 2(A). The control model had a magnitude of compressive stress of 1 MPa at the graft boundary, while the maximum values occurred when both disparities of D/R ratio were highest. The compressive stress magnitude increased to 6 MPa when D/R is 3.25 and the moduli combination is 2.5/7 (Young's modulus for donor and recipient cartilage is 2.5 MPa and 7 MPa, respectively). The increase in magnitude for the compressive stress of both extrema of the moduli combinations against the control combination can be observed in Fig 3.

The control model had no shear stress present at the graft boundary but when the D/R ratio was increased to 3.25 and the moduli combination is 2.5/7, the shear stress increased to 1.8 MPa. For the strain outcomes, a similar effect was observed where if the mechanical properties are fixed, then increasing the D/R ratio disparity caused an increase in magnitude of the strain in the graft boundary. This increase in magnitude of the strain outcomes was also observed if the D/R thickness ratio was fixed and the moduli of the cartilage sections increased in disparity. Both trends can be observed in the heatmap in Fig 2(B). The control model had a compressive strain of 0.03; however, when both factors increased in disparity the strain increased up to 0.60. While the shear strain control model has a value of 0, once the disparities in both factors were present the value for strain increased up to 0.78 at highest D/R thickness and moduli combination disparity.

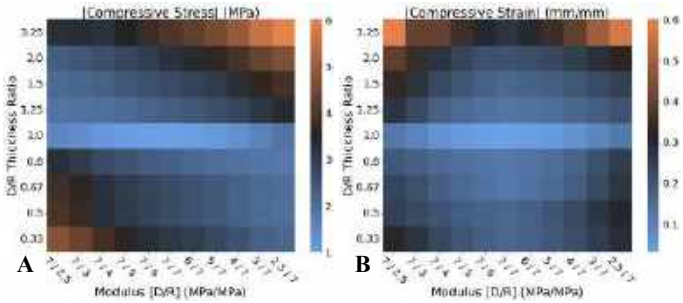

Figure 2: Heat maps for two of the four outcomes for the magnitude of the peak values of (A) compressive stress and (B) compressive strain.

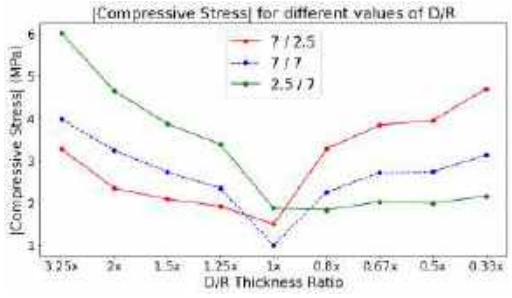

Figure 3: Plots for compressive stress magnitude at different D/R thickness ratios for three D/R moduli combinations.

DISCUSSION

The 2D models used demonstrated increased magnitudes of the stress and strain outcomes when a disparity in D/R thickness ratio and mechanical properties were present. This effect was further exacerbated when a high disparity for both factors was present in the model. Compressive stress values increased sixfold when both factors were mismatched to their maximum. The compressive strain increased from 0.031 to 0.60 at the maximum disparity. According to previous work done [5-6], the observed value of stress and strain could possibly cause apoptosis of the cartilage's chondrocytes. This could lead to the donor and recipient cartilage sections not integrating correctly or the transplant failing altogether.

It is important to also mention the limitations of this study. The articular cartilage was assumed to be a linear elastic material and it is understood that cartilage is an anisotropic material with depth dependent material properties. Utilizing a physiologically accurate material model for the FE models will help further inform on the effect of the mismatched thickness and mechanical properties. This will be addressed by creating a functional gradient of the cartilage through-thickness material properties and using non-linear, anisotropic material models. In addition, simplified 2D axisymmetric models were used to model the patella's cartilage and its loading condition. Due to the axisymmetric models, the load was applied throughout the whole surface of the cartilage. This is not the physiological loading conditions on the patella since its contact with the femur depends on the knee flexion angle and the full surface is never fully engaged. We will address this by utilizing 3D patient-specific FE models which can be accessed through deidentified CT scans of patellae with OCA transplants and varying the surface pressure based on knee flexion angle. Overall, the results from this study support our hypothesis that a greater thickness and mechanical property mismatch between the donor and recipient cartilage create local stress concentration on the graft boundary that exceeds the value that could cause OCA transplant failure.

ACKNOWLEDGEMENTS

The authors would like to thank Dr. Jonathan Estrada, Dr. Ulrich Scheven, Nathaly Villacis, Charlotte Andreasen, and Peter Kuetzing for their feedback on the model and data analysis and the results.

REFERENCES

[1] Åroøen, A et al., *Am. J. Sports Med.*, 32(1):211-215, 2004
[2] Lamplot, J D et al., *Orthop. J. Sports Med.*, 6(3), 2018.
[3] Haber, D B et al., *Int J Sports Phys Ther*, 14(3):487-499, 2019
[4] Chala, J et al., *Am. J. Sports Med.*, 47(12):3009-3018, 2019
[5] Chen, C T et al., *J. Orthop. Res.*, 21(5): 888-898, 2003
[6] Bonnevie, E D et al., *J. Biomech.*, 74:72-78, 2018

CELLULAR MICRO-BIAXIAL STRETCHING FOR CHARACTERIZING STRESS-STRAIN RELATIONS FOR SINGLE CARDIOMYOCYTES EXPOSED TO COMPLEX DEFORMATIONS

Taylor M. Rothermel (1), Anna Grosberg (2), Patrick W. Alford (1)

(1) Biomedical Engineering, University of Minnesota, Minneapolis, MN, USA
(2) Biomedical Engineering, University of California-Irvine, Irvine, CA, USA

INTRODUCTION

Cardiovascular tissues are exposed to constant dynamic mechanical loads *in vivo*. During a normal cardiac cycle, the ventricular myocardium undergoes large multidirectional strains [1], which can be altered by disease, such as post-myocardial infarction [2], or as a result of surgical interventions [3]. Contractile functionality is influenced by these changing strains, thus, there is a need to understand how the heart mechano-adapts to its mechanical environment.

Here we aim to measure and characterize how the force of contraction in single neonatal cardiac myocytes is influenced by biaxial deformation. We previously developed the cellular microbiaxial stretching (CμBS) method to measure single-cell mechanics and characterize the anisotropic mechanical properties of cells exposed to complex loading conditions in vitro [4,5]. We hypothesize that myocyte stress-strain relations are more complex than the typical length-tension relationship used to characterize striated muscle cell contraction. Here, CμBS is used to strain cardiac myocytes micropatterned with in vivo-like geometries to test this hypothesis.

METHODS

Cellular Microbiaxial Stretching. The CμBS device is a custom built, microscope-mounted stretcher consisting of four linear actuators that transfer strains to the cells micropatterned on polyacrylamide (PA) gels on flexible elastomer membranes [5] (Fig 1A). Micropatterned CμBS substrates were prepared as previously described [5] with rectangular features (aspect ratio: 7:1, area: 2400 μm^2) (Fig 1B) for micropatterning cardiac myocytes into an in vivo like geometry. Cardiomyocytes were isolated from pups from timed pregnant Black 6 mice using standard methods [6] and seeded onto the prepared substrates. Four straining protocols were applied to the micropatterned cells such that the cell was extended (tension) or shortened (compression) parallel to its long (axial) or short (transverse) axis (Fig 1C). Strains were applied in 5% increments at 0.5 %/s to a maximum of 30% applied strain for tension or -15% applied strain for compression. At each increment, high temporal resolution (100 frames per second) images of the fluorescent bead layer under the contracting cell were acquired. Myocytes were paced at 1 Hz to induce contraction. Traction force microscopy techniques were used to analyze cell forces using acquired image data.

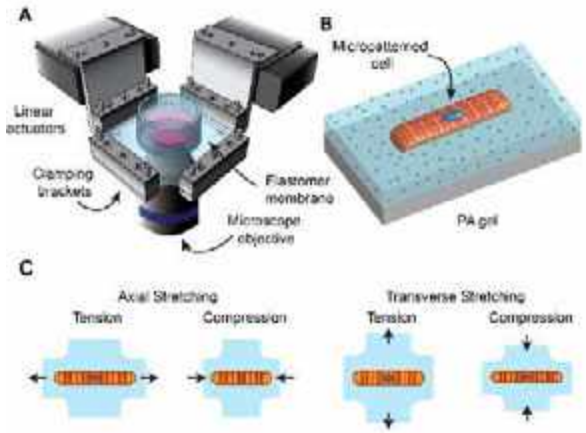

Figure 1: CμBS used to measure strain-dependent forces in single neonatal cardiac myocytes. (A) Schematic of the CμBS device above the microscope objective (B) Schematic of a cardiac myocyte micropatterned in an elongated geometry on a fluorescent bead-doped polyacrylamide gel adhered to an elastomer membrane, (C) Schematics of the stretching protocols applied to myocytes

Strain-dependent contraction model. Two models of strain-dependent contraction were considered: (1) the sarcomere length model in which the force is dependent on the length of the sarcomere as measured from z disc to z disc. This a standard length-tension model [7]. (2) the length-radial spacing model in which the force is dependent

on the length of the sarcomere as well as the radial distance of the actin from the myosin. This is consisten with prior models that suggest that the length-tension relationship is also influenced by acto-myosin lattice spacing. [8]. In both models, the cell was treated as anisotropic and incompressible, undergoing deformation in the principal orientation. The active stress in the cell is a function of the elastic stretch ratio λ^* defined as $\lambda = \lambda^*\lambda_a$, where λ is the observed stretch ratio from CμBS, λ_a is the activation stretch ratio. Active stress is given by

$$\sigma_a = \begin{cases} C_a(\lambda^*)(\lambda^* - 1)(\lambda^*_{crit} - \lambda^*)(1 - R), & \text{for } \lambda^* \le 1 \text{ and } \lambda^* \le \lambda^*_{crit} \\ 0, & \text{for } \lambda^* > 1 \text{ and } \lambda^* > \lambda^*_{crit} \end{cases} \quad (1)$$

where material coefficient C_a is the active cell stiffness. In this model, the active force is zero when the cell is undeformed relative to its zero-stress length, λ^*, or when stretched beyond a maximum value, λ^*_{crit}.

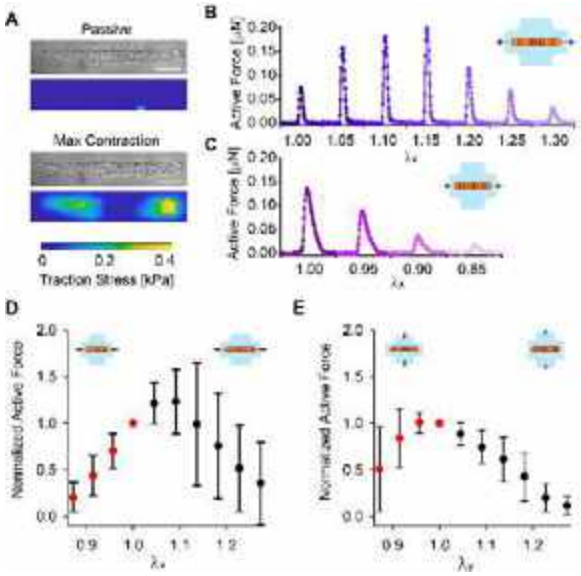

Figure 2: Stretch-mediated contractile force in micropatterned neonatal cardiac myocytes. (A) Bright field images and corresponding traction stress maps for a cardiac myocyte at rest and at maximum contraction (scale bar: 20 μm) (B) Active force for the duration of a single beat in a representative cell paced at 1Hz vs axial stretch ratio, when lengthened. (C) Active force for a representative cell paced at 1Hz vs axial stretch ratio, when shortened (D) Active force - stretch normalized to the unstretched force for cells stretched axially (n=17 stretched, 23 compressed) (E) Active force - stretch data normalized to the unstretched force for cells stretched transversely (n = 15 stretched, 11 compressed). For (D,E) black dots = stretched cells, red dots = shortened cells

In the sarcomere length model, $R = 0$. In the length-radial spacing model, consistent with previous models of lattice spacing and force [8], we assume that contractile force is maximized at an optimal actin-myosin spacing of r_o and that deformation in x alters this spacing as

$$r = r_0\lambda_y\lambda_z\left(\lambda_z^2\cos^2\theta + \lambda_y^2\sin^2\theta\right)^{-1/2} \quad (2)$$

And R is given by

$$R = \frac{1}{\pi/2}\int_0^{\frac{\pi}{2}}\left(C_R\left(1 - \frac{r}{r_0}\right)^2\right)d\theta \quad (3)$$

Where C_R is a scaling parameter to be fit.

RESULTS

Using CμBS, we directly measured the effects of deformation on contractile force generation of micropatterned neonatal cardiac myocytes using traction force microscopy methods to measure the difference in passive and contracted myocytes (Fig 2A) Contraction of two representative cells are shown in Fig 2B,C (Fig 2B shows a cell being stretched axially, Fig 2C shows a cell being shortened axially), demonstrating the high temporal resolution of the force measurements. When all measured myocytes were compiled, a clear trend emerged. When cells were axially extended, the active force initially increased, but then generally decreased for stretch ratios greater than 1.15 (Fig 3D). When the myocytes were axially compressed, the active force decreased as the cells were compressed (Fig 3D). This result is consistent with the length-tension relationship for straited muscle tissue [9]. Surprisingly, a similar trend was observed when the cells were stretched transversely. When the cells were stretched or shortened transversely, the axial force decreased (Fig 3E).

To better understand the force-deformation relationship, we first developed an elasticity-based model that incorporated the sarcomere length-tension relation (Eq (1), $R = 0$). This model showed good agreement with our axial stretching data (Fig 3B), but poor agreement with transverse stretching data (Fig 3C). The radial spacing term (Eqs (1)-(3)) was added to the model to account for the 3D lattice structure of the sarcomere and radial organization of actin thin filaments around myosin thick filaments (Fig 3A). With lattice deformation incorporated, the model better matched all experimental data.

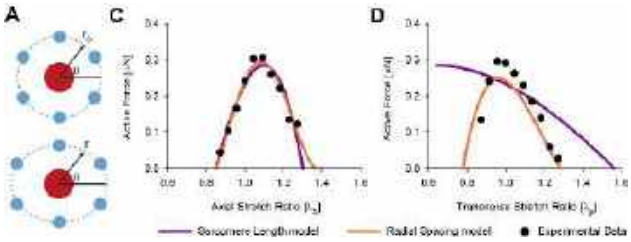

Figure 3: Active-contraction based model considering sarcomere length and lattice spacing recapitulates experimentally observed force trends. (A) Schematic of the rationale behind the radial term for the model, (B,C) Sarcomere length and radial spacing models compared to experimental data for (B) axial stretching, and (C) transverse stretching.

DISCUSSION

The sarcomere cytoskeleton within striated muscle is a three-dimensional lattice of actin and myosin. It has also been theorized that lattice spacing in addition to sarcomere spacing influences the force generation in striated muscle [8]. Because measuring lattice spacing during stretch is complex, teasing out its influence on force is more challenging to accomplish experimentally. Here, we use CμBS to measure single-cell deformation-dependent contraction of cardiomyocyte's and find that standard models that only account for z-line spacing are unable to capture our experimental data. This result suggests that the biaxial nature of cardiac loading should be included in models of cardiac mechanics and mechano-adaptation.

ACKNOWLEDGEMENTS

This study was funded by the National Science Foundation CMMI-2230435 (PWA), CMMI-2230503 (AG)

REFERENCES

1. Voigt, J.U. et al. JACC Cardiovasc. Imaging. 12:1849–1863, 2019.
2. Torres, W.M., et sal. Am. J. Phys. Circ. Phys. 315:H958–H967, 2018.
3. Rösner, A., et al. Echocardiography. 32:1809–1820, 2015.
4. Win, Z., et al. J. Biomech. Eng. 139:1–10, 2017.
5. Rothermel, T.M., et al. Curr. Protoc. 2, 2022.
6. Ehler, E., et al. J. Vis. Exp. 15:1–10, 2013.
7. Taber, L.A., et al. J. Biomech. Eng. 114:427–434, 1992.
8. Williams, C.D., et al. Proc. R. Soc. B Biol. Sci. 280:20130697, 2013.
9. Brady, A.J. Am. Zool. 7:603–610, 1967.

ENHANCING UNDERSTANDING OF DRUG EFFICACY AND CARDIOVASCULAR DIAGNOSTICS THROUGH A COMPUTATIONAL BIOTRANSPORT MODEL

Abhi Roop Reddy. Tokala (1), Dr. Mahsa Dabagh (1)

(1) Biomedical Engineering, College of engineering and applied sciences-University of Wisconsin Milwaukee, Milwaukee, Wisconsin, USA

INTRODUCTION

In the realm of pharmacology and cardiovascular health, accurately predicting the interplay between drug kinetics and body dynamics is pivotal. Existing computational models often fall short in mirroring the intricacies of drug distribution and cardiovascular responses in individuals. This gap underscores the need for a more sophisticated and personalized approach.

Several studies emphasize this point[1], [2], [3]. Siccardi et al., demonstrated in 2016 the effectiveness of physiologically based computational models in optimizing antiretroviral doses, showcasing the potential of such models in predicting pharmacokinetics in complex clinical scenarios[1]. Similarly, Chabiniok et al. emphasized the role of computational modeling in understanding the heart's complex hierarchical structure and function, integrating experimental and clinical data for translational cardiac modeling [2]. Furthermore, [3] proposed a comprehensive public domain resource for cardiovascular researchers, highlighting the need for less computationally intensive model, that can give a general result and later a more personalized and computationally intensive model that would specific result[3].

Our project aims to develop a computational biotransport model that integrates pharmacokinetics, pharmacodynamics, and cardiovascular physiology. This model attempts to enhance the precision of drug behavior predictions and cardiovascular responses, which could make way to personalized digital medicine solutions by providing healthcare professionals with a robust tool for understanding and possibly optimizing treatment efficacy and safety. The evidence from existing research supports the feasibility and necessity of this approach in improving drug safety and efficacy in cardiovascular health[1], [2], [3].

METHODS

Our approach involved developing a MATLAB-based and Simulink-based computational model integrating various biotransport mechanisms. The model employed a physiologically based pharmacokinetic (PBPK) model framework to simulate drug distribution and elimination. The Windkessel model, representing cardiovascular dynamics, was adapted to assess the impact of drug interactions on heart rate and blood pressure. Parameters specific to drugs obtained from publicly available information and patient specific information are incorporated through user input. This integration allowed for the simulation of drug concentration over time and its physiological effects, offering a nuanced view of drug behavior in the cardiovascular system.

Equations:

PBPK model:

$$C(t) = \frac{D}{Vd} e^{-ke*t} \quad (1)$$

$$ke = \frac{ln(2)}{t\left(\frac{1}{2}\right)} \quad (2)$$

$$\frac{dC(t)}{dt} = Q(C_{blood} - C_{tissue}) \quad (3)$$

$$Q = CO \times BF \quad (4)$$

$$Kp = C_{tissue}/C_{plasma} \quad (5)$$

$$clearance = ER_{organ} \times Q_{organ} \quad (6)$$

$$\frac{dP(t)}{dt} = \frac{Q(t) - \frac{P(t)}{R}}{C} \quad (7)$$

$$E(t) = \frac{[A(t)]^n}{[A(t)]^n + EC50^n} E_{max} \quad (8)$$

RESULTS

Results for Sample drug- Amiodarone(Antiarrhythmic):

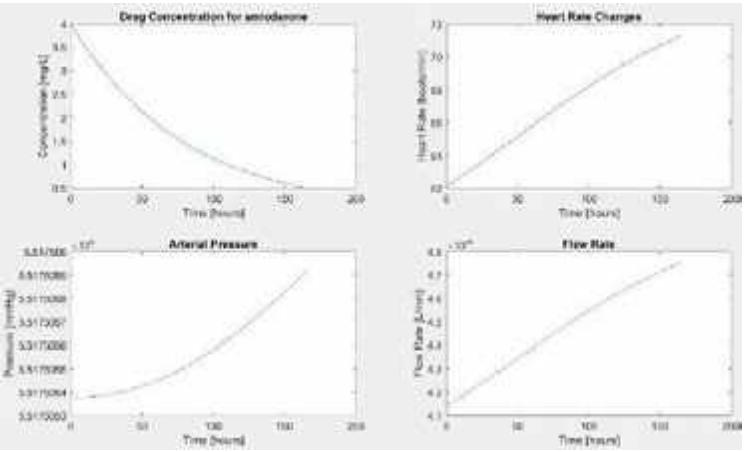

Figure 1: Plots: top left-drug concentration over time in hours, top right-heart rate changes over time in hours, bottom left-arterial pressure over time in hours and bottom right-flow rate over time in hours.

Parameters used:

Drug	Amiodarone
Dose (mg)	300-400 (IV loading dose)
Volume of Distribution (L)	60-140
Drug Half-Life (hours)	40-55
Baseline Heart Rate (beats/min)	75
Maximum Change in Heart Rate (beats/min)	+/- 20
EC50 for Heart Rate Change (mg/L)	2.2

Table 1: Table showing parameters relevant to amiodarone that were input.

DISCUSSION

The model's ability to simulate pharmacokinetics and patient-specific cardiovascular responses under varying conditions align well with current biomedical research trends focusing on personalized medicine. While traditional models often provide a generalized approach, our model's ability to adjust parameters like drug dosage, type, and patient-specific factors allows the model to predict individual responses more accurately, leading to tailored therapeutic strategies.

In a scientific context, while the model provides an advanced simulation of biotransport phenomena, its accuracy is contingent upon the reliability of the input parameters and the model's assumptions. Continued validation with relevant clinical data is essential to refine its predictive capabilities.

With higher computational intensity and numerical complexity, such models have profound implications for digital medical solutions. These models represent a significant step towards personalized healthcare, where treatment plans are optimized based on individual physiological characteristics. This not only enhances the efficacy of therapies but also minimizes the risk of adverse effects like overdosing. In the era of digital health, these models could serve as powerful tools for clinicians and researchers, aiding in drug development, therapeutic planning, and understanding complex biotransport mechanisms.

In conclusion, our findings underscore the potential of computational models in enhancing personalized healthcare, suggesting a future where treatment plans are more accurately tailored to individualized patient needs.

ACKNOWLEDGEMENTS

The model was developed with the guidance of Dr.Mahsa Dabagh, who asked important questions which allowed for the creation of the model. Dr. Mahsa Dabagh has also provided meaningful motivation and enthusiasm toward the project. The model was tested through the use of multiple drugs/drug types by Aaron, Se-jin and Alejandro.

REFERENCES

[1] M. Siccardi, L. Dickinson, and A. Owen, "Validation of Computational Approaches for Antiretroviral Dose Optimization," *Antimicrob. Agents Chemother.*, vol. 60, no. 6, pp. 3838–3839, May 2016, doi: 10.1128/AAC.00094-16.

[2] R. Chabiniok *et al.*, "Multiphysics and multiscale modelling, data–model fusion and integration of organ physiology in the clinic: ventricular cardiac mechanics," *Interface Focus*, vol. 6, no. 2, p. 20150083, Apr. 2016, doi: 10.1098/rsfs.2015.0083.

[3] S. Safaei *et al.*, "Roadmap for cardiovascular circulation model," *J. Physiol.*, vol. 594, no. 23, pp. 6909–6928, Dec. 2016, doi: 10.1113/JP272660.

COMPARATIVE ANALYSIS OF MYOCARDIAL WALL THICKNESS: INSIGHTS FROM MRI-DERIVED MODELS AND BIOMECHANICAL SIMULATIONS ACROSS THE CARDIAC CYCLE

M. Darayi (1), M. Robakowski (1,2), Y. Fan (3), D. Kara (1), O. Potdar (4), C. Nguyen (1), D. Goswami (1)

(1) Cardiovascular Innovation Research Center, Heart, Vascular & Thoracic Institute, Cleveland Clinic, Cleveland, OH, United States
(2) Department of Chemical and Biomedical Engineering, Cleveland State University, Cleveland, OH, United States
(3) Institute for Medical Engineering and Science, Massachusetts Institute of Technology, Cambridge, MA, United States
(4) Department of Physics, Case Western Reserve University, Cleveland, OH, United States

INTRODUCTION

For many years, researchers have been trying to create realistic computational models that accurately represent the mechanical behavior of the heart [1]. However, this is a difficult task involving accounting for the heart's complex dynamics, fiber structure, and material properties. Additionally, modeling efforts are complicated by the need to reproduce the circulatory system and the cyclical function of the heart accurately, which are crucially linked to heart function [2]. Recent technological advancements in individual anatomy reconstruction and computational models have simplified the validation process, facilitating creation of patient-specific models that replicate the characteristics of an individual's heart. These models simulate the cardiac cycle using computational techniques by starting from 3D reconstructions of clinical images and incorporating rule-based fiber orientation for the left ventricle (LV) [3]. They can help identify functional aspects or pathological variations by analyzing patient-specific heart mechanics.

Our goal is to use high resolution (both spatial and temporal) patient-specific magnetic resonance imaging (MRI) data to validate computational models and improve our understanding of left ventricular (LV) mechanics. Traditional cardiac modeling often relies on generalized data (e.g. non-patient specific and static), which may only capture a portion of LV dynamics. In contrast, our approach compares simulation results with patient-specific high temporal resolution MRI data across different cardiac phases. We focus on pressure-volume relationships and variations in LV wall thickness to ensure model accuracy. Analyzing high resolution MRI frames throughout a cardiac cycle can bridge the gap between microscopic and macroscopic changes in response to cardiac dynamics and unlock the potential for more precise patient-specific simulations for diagnosis and treatment [4]. Additionally, this high-resolution capability could enhance machine-learning methods for predicting cardiac mechanics [5].

METHODS

We utilized 4D patient-specific cardiac geometries obtained from MRI scans to perform finite element (FE) simulations of the left ventricle (LV) during the cardiac cycle. To construct a model of the LV, we initially created a 3D representation of the heart's geometry acquired through a high-resolution (1.6 mm × 1.6 mm × 1.6 mm, 30 frames/s) MRI of a patient's (75 year old male with constrictive pericarditis) torso using a 3T MR system (MAGNETOM Cima.X, Siemens Healthineers AG, Erlangen, Germany). We manually segmented the LV using 3D Slicer, an open-source medical image viewing and editing software. We utilized the Cotan smoothing function on Meshmixer [6] with a smoothness setting of 1 and a scale of 4 to improve the 3D LV model while preserving its essential features. The resulting boundary contours were then exported to SolidWorks (Dassault Systemes, MA USA) for geometry reconstruction and subsequently meshed using ABAQUS

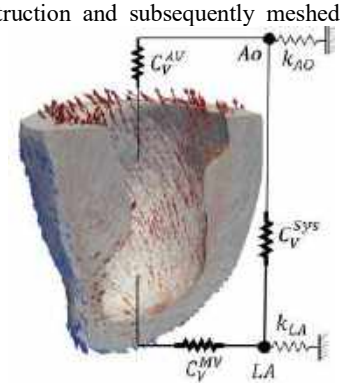

Figure 1. Human LV reconstructed from MRI with a rule-based fiber architecture model and circulatory system.

(Dassault Systemes, Johnston, RI, USA) with 65186 tetrahedron elements (C3D4) having an element edge length of approximately 2.5 mm, resulting in 4–5 layers of elements across the myocardial wall.

To account for the varied fiber distribution within the LV, we generated a layered fiber architecture using a rule-based method (RBM) and the Laplace–Dirichlet Rule-Based (LDRB) algorithm [7], with epicardial–endocardial helix angles ranging from -60° to 60° (Figure 1). The passive behavior of the myocardium was represented as a transversely isotropic hyperelastic model with the Fung strain energy density function [8],

$$\psi(\boldsymbol{E}) = \left(\frac{C_0}{2}\right)\left(e^{Q(\boldsymbol{E})} - 1\right) + \frac{1}{D}\frac{(J^{el})^2 - 1}{2} - ln(J^{el}) \qquad (1)$$

involving parameters such as C_0 (elastic constant), Q as a function of Green-Lagrange strain tensor $\boldsymbol{E}$, D (equal to $\frac{2}{K}$, where K is the bulk modulus), and J^{el} (elastic volume ratio). For details regarding the parameters refer to [3]. A time-dependent active tension or active strain was added to the hyperelastic constitutive model using the ABAQUS Explicit software to simulate active contraction during systole.

This model simulates heart functions by integrating the LV with the pulmonary and systemic circulations (Figure 1). It mimics diastolic filling and systolic ejection using surface-based fluid cavities and exchanges, ensuring accurate physiological pressure and blood flow. Key components include the aorta (Ao), left atrium (LA), aortic (AV), and mitral valves (MV), along with systemic circulation (Sys). The Ao and LA cavities have spring stiffness (k) for compliance, and Cv represents viscous resistance. Valves permit one-way fluid flow. For details refer to [2].

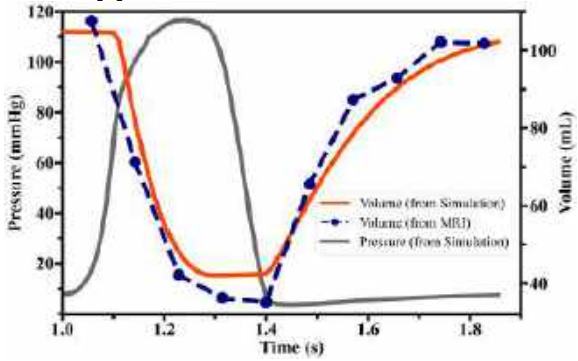

Figure 2. Simulated pressure and volume, and actual volume obtained from MRI

RESULTS

We analyzed myocardial wall thickness by combining data from 10 manually segmented 4D MRI frames with simulated results. First, in Figure 2, we compare LV pressure-volume relationships derived from our FE simulations across various phases of the cardiac cycle with the actual volumes obtained from MRI data at corresponding stages of the left ventricular cycle. Figure 3 shows the variation of the LV wall thickness with time over a cardiac cycle (green line). There is a gradual increase in the median thickness of the LV wall, extending from end-diastole to its peak at end-systole. This aligns with heart physiology, where a decrease in ventricular volume and a simultaneous pressure increase during systole lead to thicker myocardial walls. The initial difference in LV thickness between the simulation and MRI data could be attributed to our simulation methodology. We started the simulations near the end-diastole and then increased the pressure by 8 mmHg to replicate the end-diastolic state.

The wall thickness decreases as the cycle progresses towards end-diastole, indicating ventricular relaxation and volume expansion phases—similarly, the wall thickness increases during systole, followed by a decrease towards diastole. Although the simulation and MRI measurements show a slight (1-2 mm) difference, both datasets demonstrate a consistent pattern. This trend is evidence of the accuracy of our model in representing fiber orientation and active contraction during the systolic phase. The box plots in Figure 3, centered around the median thickness for each frame, highlight the asymmetry in thickness distribution throughout the cardiac cycle. MRI and simulation data show that the minimum values are closer to the median, whereas the maximum values are more distant. For example, during systole, the maximum normalized values reach roughly 1.75 times the median, while the minimum values fall below 0.5 times the median. This difference is slightly more noticeable in diastole, where the maximum values extend to 1.8 times the median. Consistent skewness throughout the cycle offers insights into myocardial wall stress and strain, reflecting how different myocardial regions respond to pressure and volume changes.

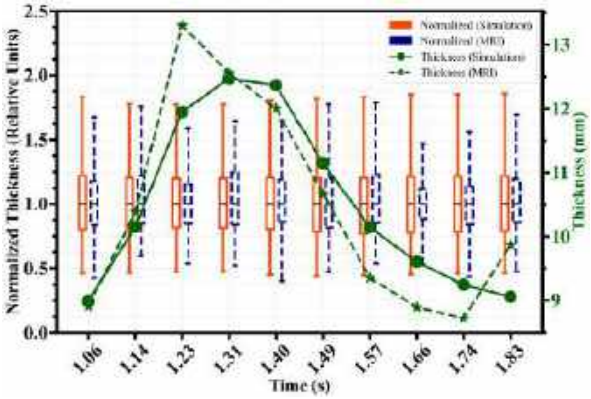

Figure 3. Median myocardial wall thickness and normalized distribution across ten cardiac cycle frames, comparing MRI-derived STL models and simulation data.

The findings mentioned here are crucial for research studies on changes in myocardial thickness. By examining the variability, skewness, and median thickness of the distribution, we can understand the structural dynamics and cardiac function during the cardiac cycle. These results align with physiological principles and provide a basis for advanced modeling in cardiac research.

DISCUSSION

Our study provides a detailed analysis of myocardial wall thickness across the cardiac cycle, offering insights into cardiac mechanics. We observe changes in wall thickness from end-diastole to near-end systole, correlating them with pressure-volume relationships. The pattern of increasing median LV wall thickness during systole, followed by a decrease in diastole, aligns with physiological expectations, highlighting the interplay between ventricular volume, myocardial wall stress, and thickness. These variations indicate differential responses to pressure and volume changes in various myocardial regions, aiding in understanding asymmetric myocardial behavior and potentially detecting cardiac pathologies. Combining simulation and imaging data validates the simulation model, paving the way for enhanced diagnostic and therapeutic strategies in cardiology, bridging theoretical models and clinical imaging, and advancing cardiac research and clinical practice.

REFERENCES

[1] A. Lopez-Perez, et al., *Biomed. Eng. Online*, 14:1-31, 2015.
[2] D. Guan, H. Gao, et al., *Comput. Biol. Med.*, 145:105417, 2022.
[3] Y. Fan et al., *Int. J. Numer. Meth. Biomed. Eng.*, 35:e3213, 2019.
[4] T. Huelnhagen *et al.*, *Sci Rep*, 8:3974, 2018.
[5] Y. Dabiri, et al., *Front. Phys.*, 7:117, 2019.
[6] Autodesk Meshmixer. Autodesk Inc., 2019.
[7] J. D. Bayer, et al., Ann. *Biomed. Eng.*, 40:2243–2254, 2012.
[8] ABAQUS 2018 Documentation. Dassault Systèmes., 2018.

CHARACTERIZATION OF THE MECHANICAL AND COMPOSITIONAL EFFECTS OF MMP-9 EXPOSURE ON NEURON-COLLAGEN CONSTRUCTS: IMPLICATIONS FOR JOINT DEGENERATION

Chang Wang (1), Michelle Meyers (1), Prabesh Ghimire (1), Mistica Lozano Pérez (1), Beth A. Winkelstein (1,2)

(1) Department of Bioengineering, University of Pennsylvania, Philadelphia, PA, USA
(2) Department of Neurosurgery, University of Pennsylvania, Philadelphia, PA, USA

INTRODUCTION

Chronic pain is a major health problem with large costs [1,2]. Although degeneration is a primary source of joint pain and can result from trauma [3,4], its specific pain mechanisms are not well-defined. The spinal capsular ligament encloses the facet joint and is primarily composed of collagen with afferents that can transduce nociceptive signals [5-8]. Ligament injury can alter the extracellular matrix (ECM) and induce collagen reorganization, which also induces pain [9-11]. The matrix metalloproteinases (MMPs) are important regulators of ECM modifications, regulate pathological processes of collagen degradation and can cause pain [12-14]. MMP subtypes increase in injured and/or painful joints [14-16]. While MMP-1 and MMP-2 degrade type I collagen [17,18], MMP-9 regulates collagen organization, and its expression is correlated with MMP-1 in painful joints [19-21].

Although the mechanistic role of MMP-1 in mechanical joint pain has been investigated [21,22], such relationships between MMP-9 and collagen biomechanics are not yet defined. This study utilized an existing in vitro model of the capsular ligament [10,23] to investigate the effects of MMP-9 exposure on the biomechanical response of collagen under its uniaxial stretch to failure. Our neuron-collagen construct (NCC) system that simulates the structure of a capsular ligament was exposed to MMP-9 at a dose comparable to levels in the synovial fluid of human joints diagnosed with rheumatoid arthritis [24]. In addition to defining the macroscale biomechanics at failure, after MMP-9 exposure, effects on collagen were measured using immunohistochemistry and quantitative densitometry.

METHODS

NCCs (n=11) were prepared using 2mg/mL rat tail collagen I and dorsal root ganglia neurons ($3x10^5$ cells/mL) extracted from embryonic day 18 rats [10,23]. Neurons were dissociated, seeded on the collagen gel surface, and cultured at 37˚C in 5% CO_2. On day 3, more collagen (150µL) was added to encapsulate the neurons [10,23]. On day 7, the NCCs were transferred to 1xPBS with 1% Pen-Strep and cut into a strip (21mmX8mm). The remaining parts served as unloaded controls (n=2) for immunolabelling. A grid of nodes was drawn on the surface of the NCCs to define elements for strain analysis (Fig. 1). Before stretch, NCCs were exposed for 15mins to 150µL of either 2µg/ml of MMP-9 (R&D Systems) in PBS (n=5) or PBS as a vehicle (n=6). All NCCs were submerged in a 37˚C PBS bath and mounted in a planar testing machine (TestResources) for uniaxial stretch (Fig. 1). The reference state was established for each NCC when slack in the gel was removed. Each loading arm was moved apart by 6mm at 0.5mm/s until failure. During stretch, force-displacement data were recorded at 500Hz, and a high-speed Phantom-v9.1 camera (Vision Research) tracked the NCC and its grid at 500fps; video and transducer data were synchronized.

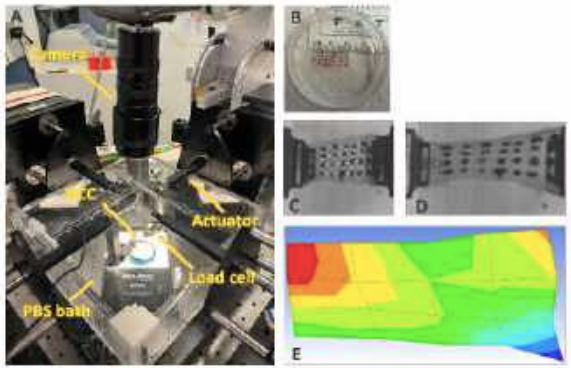

Figure 1. (A) Test set-up. (B) Grid on NCC before mounting in device arms (C) before stretch and (D) at failure. White lines in (C) define elements. (E) Corresponding MPS map at failure.

Force and displacement data were filtered with a 600-point moving average filter in MATLAB. For each NCC, macroscopic mechanical parameters were measured from the force-displacement curves: failure

force, failure displacement, stiffness, toe region, and area under the curve (AUC) of the toe region [10,11]. Failure was defined as the peak of the force-displacement curve; stiffness was calculated as the slope of the linear region of the force-displacement curve from 20-80% of failure (Fig. 2). The toe region was defined as up to 20% of failure (Fig. 2) and the AUC was calculated by the MATLAB trapezoidal numerical integration function. ProAnalyst software (Xcitex) tracked displacements of the marker nodes defining NCC elements during stretch (Fig. 1) [10,11]. LS-DYNA (LSTC) calculated the maximum principal (MPS) and shear strains for each element (Fig. 1) of each NCC; the average across all elements and peak in any NCC of MPS and shear strains were calculated. These mechanical outcomes were compared between MMP-9 and vehicle exposed groups by a Student's t-test.

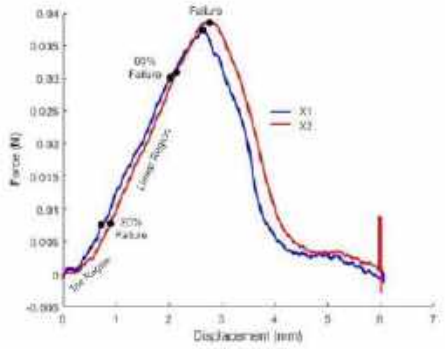

Figure 2. Force-displacement curves for each arm (X1, X2) of NCC exposed to MMP-9 labeling failure, linear region, and toe region.

A subset of NCCs (n=5 MMP-9; n=2 vehicle) was fixed in 4% PFA for 2hrs after loading and then triple-washed by PBS for 10mins each. NCCs were blocked for 2hrs using 0.3% Triton-X and 10% normal goat serum in PBS at room temperature and then incubated with primary antibody mouse anti-collagen antibody (1:200; Abcam) overnight at 4°C to label collagen. The next day they were washed with PBS and incubated for 2hrs in goat anti-mouse AlexaFluor568 antibody (1:500; Invitrogen). Images (n=4-5/NCC) were captured across the grid of nodes using a Leica TCS SP8 confocal microscope at 63X. Quantitative densitometry measured the percent of pixels positive for collagen and averaged across images for each NCC [23]. Averages were determined for both groups of NCCs and compared using a Student's t-test.

RESULTS

Based on the linear region of the force-displacement curves, the MMP-9 group (0.026±0.01 N/mm) is less (p=0.016) stiff than the group exposed only to PBS (0.19±0.14 N/mm). Interestingly, the force at failure is higher (p<0.001) for the MMP-9 group (37.8±4.9mN) than the vehicle group (17.9±7.1mN), while MMP-9 exposure reduces the displacement at failure (2.0±0.5mm) compared to the vehicle group (3.0±1.8mm), but not significantly (p=0.14). The AUC for the toe region is larger (p=0.017) for the vehicle group (0.13±0.12 N·mm) than the MMP-9 (0.002±0.0008 N·mm).

While most NCCs failed with a tear in the gel, 1 of the MMP-9 and 2 of the vehicle NCCs slipped out of a grip. Failure strains increase in NCCs exposed to MMP-9 compared those exposed to vehicle. Both peak MPS (0.89±0.44) and peak shear strain (1.02±0.44) are greater (p<0.006) after MMP-9 exposure than a PBS vehicle exposure (0.30±0.09 MPS; 0.35±0.12 shear strain). When considering average strain responses across elements there are no significant differences between treatment groups for either MPS (0.23±0.07 MMP-9; 0.20±0.06 vehicle) or shear strain (0.28±0.07 MMP-9; 0.25±0.08 vehicle). Consistent with the average strain data, the amount of collagen in NCCs is not different (p=0.25) regardless of whether they are exposed to MMP-9 (49.7±13.1%) or PBS vehicle (42.1±4.3%).

DISCUSSION

The reduced NCC stiffness and AUC for the toe region observed with MMP-9 exposure suggests a weakened state for the NCCs after MMP-9 exposure despite no detectable change in collagen (42-50%) between groups. However, the force at failure nearly doubled after MMP-9 which implies a stronger state. Of note, failure force varies substantively (~39% of mean) for the vehicle group and 2 of the 6 samples slipped out of the grips. It is possible that the increase in failure force that is detected may be due to artefacts of the testing set-up, including the initial positioning and/or mounting in the grips. Since the initial configuration was taken to be the state when the gel had no slack evident, any subjectivity and/or variability across gels could impact the outcomes. In fact, the peak strain data support greater distortion after MMP-9 exposure. Additional studies are needed that better quantify the starting position for both groups and also evaluate additional biomechanical and compositional metrics.

MMPs have a broad range of actions, including MMP-1 affecting the biomechanical and pain responses of ligaments and collagen constructs [21,22]. Although less is known about MMP-9, its active form is related to articular cartilage degradation and pain in human patients and its cleavage effects depend on the timing in vivo [14,25]. This study used human MMP-9 on mouse collagen and exposures of only 15mins for ease of experimental design. Future studies evaluating the temporal effects of the active form of mouse MMP-9 would help elucidate potential mechanisms of degradation, micromechanical responses, and also potential effects on the embedded neurons. Since MMP-9 activates the NR1/NR2B receptor and cleaves IL-1β [26,27], it likely has direct effects on neuronal regulation of pain.

ACKNOWLEDGEMENTS

Funding from the NCCIH (AT010326). Thanks to the University of Pennsylvania's Cell and Developmental Biology Microscopy Core for confocal microscopy assistance and CNS Cell Culture Service Center of the Mahoney Institute of Neuroscience for rat embryos.

REFERENCES

[1] Mills S et al, *Br J Anaesth*, 123: e273-e283, 2019; [2] Phillips CJ, *Expert Rev Pharmacoecon Outcomes Res*, 6(5):591-601, 2006; [3] Gellhorn AC et al, *Nat Rev Rheumatol*, 9:216-24, 2013; [4] O'Leary SA et al, *Annu Rev Biomed Eng*, 20:145-70, 2018; [5] Chen C et al, *J Bone Jt Surg Am*, 88(8):1807-16, 2006; [6] Kallakuri S et.al, *Eur Spine J,* 17(4):556-63, 2008; [7] Yamashita T et al, *Spine J*, 21(5):538-43, 1996; [8] Yahia L & Garzon S, *Ann Anat*, 175(2):185-8, 1993; [9] Quinn K et al, *Stapp Car Crash J*, 51:169-87, 2007; [10] Zhang S et al, *J Biomech Eng*, 138:021013, 2016; [11] Zhang S et al, *J Orthop Res,* 36(2):770-7, 2018; [12] Chan ZC et al, *Neurosci Lett*, 724:134822, 2020; [13] Shapiro SD et al, *Am J Respir Cell Mol Biol*, 20(6):1100-2, 1999; [14] Ita ME et al, *J Orthop Res*, 40(2):338-47, 2022; [15] Cohen MS et al, *J Shoulder Elbow Surg*, 16(4):484-90, 2007; [16] Haller JM et al, *Clin Orthop Relat Res*, 473(10):3280-8, 2015; [17] Visse R & Nagase H, *Circ Res*, 92:827-39, 2003; [18] Ronald TA & James PQ, *J Biol Chem*, 270(11):5872-6, 1995; [19] Chad J & Zorina SG, A*rterioscler Thromb Vasc Biol*, 24:54-60, 2004; [20] LeBert DC et al, *Development*, 142(12):2136-46, 2015; [21] Ita ME & Winkelstein BA, *Front Mech Eng*, 8, 2022; [22] Ita ME et al, *Front Bioeng Bio*, 10:926675, 2022; [23] Singh S & Winkelstein B, *BMMB*, 21:885-98, 2022; [24] Kim KS et al, *Rheumatol Int*, 31:543-7, 2011; [25] Zhen EY et al, *Arthritis Rheum*, 58:2420-31, 2008; [26] Liu WT et al, *J Neurosci*, 30(22):7613-23, 2010; [27] Kawasaki Y et al, *Nat Med*, 14(3):331-6, 2008.

FIBROBLAST-ADIPOCYTE INTERACTIONS ALTER EXTRACELLULAR MATRIX PRODUCTION

Edward A. Sander (1), Mariam El-Hattab (1), Kathryn R. Jacobson (2), James A. Ankrum (1), Sarah Calve (2)

(1) Roy J. Carver Department of Biomedical Engineering, University of Iowa, Iowa City, IA
(2) Paul M. Rady Department of Mechanical Engineering, University of Colorado, Boulder, CO

INTRODUCTION

Fibrosis and scarring remain significant problems that impact quality of life for millions of people [1]. A range of treatment options to reduce scarring have been explored that target a variety of cell types, including myofibroblasts due to their central role in synthesizing extracellular matrix (ECM) proteins during the healing process [2]. Recent work indicates that some adipose tissues also contribute to the wound healing process [3]. In addition, there are reports that fat grafting in reconstructive surgery can improve the appearance of existing scars [4]. Adipose tissues are composed of a continuum of cell types that include adipocyte-derived stem cells (ADSCs), preadipocytes, and adipocytes, each of which can contribute to ECM remodeling. To better understand how adipocyte lineage cells interact with fibroblasts during wound healing, we have begun using engineered *in vitro* systems to characterize how these cells interact with each other to remodel the ECM. We have found that adipocytes secrete factors that convert human dermal fibroblasts into highly contractile, ECM producing myofibroblasts through a TGF-β1-independent mechanism [5], and that preadipocytes have a substantially different adipokine secretion profile from adipocytes [6]. Here, we use our *in vitro* system to investigate how fibroblast-adipocyte lineage cell interactions evolve over time via time-lapse imaging and proteomic analysis of the ECM proteins they produce. Our ultimate goal is to use this information to develop an effective adipose-tissue-based therapeutic strategy for reducing scar tissue.

METHODS

Spheroid Formation: Immortalized human dermal fibroblasts were formed into spheroids containing ~20,000 cells and placed on the surface of ~ 6 mg/mL fibrin gels. Immortalized human ADSCs, were converted into pre-adipocytes and formed into spheroids, as described in [5,6]. A subset of these spheroids were also converted into adipocytes by culturing them for 10 days in differentiation medium (PDM2). Six combinations of spheroid pairs were examined: (1) fibroblast-fibroblast (FF), (2) preadipocyte-preadipocyte (PP), (3) adipocyte-adipocyte (AA), (4) fibroblast-preadipocyte (FP), (5) fibroblast-adipocyte (FA), and (6) preadipocyte-adipocyte (PA). Each spheroid pairing involved carefully positioning them 1 mm apart at the center of the fibrin gel with the aid of a stencil. The gel-spheroid system was then incubated at 37 ºC and 5% CO_2 for 3 hours to allow for cell attachment before low serum DMEM with 0.5% fetal bovine serum (FBS), 1% penicillin/streptomycin and 0.1% amphotericin B was added.

Microscopy: Prior to placement on the fibrin gel, cells were stained with either wheat-germ agglutinin conjugated with Alexa Fluor 647, or CellTracker-Red. Collagen was visualized with CNA35 [7] conjugated with AlexaFluor 488. Time-lapse image sequences were acquired over seven days using a Nikon TI-E2 A1 confocal microscope and an Oko Labs environmental control unit. Tiled 4x4 images were acquired with a 10x lambda Plan Apo objective every 3 hours.

Mass Spectrometry: Liquid chromatography-tandem mass spectrometry (LC-MS/MS) was employed, as described previously [8], to identify differences in the ECM proteins produced by each of the spheroid combinations imaged. To enrich for ECM proteins, the experiments were repeated in the absence of fibrin gels on tissue culture plastic. Raw data files were imported into MaxQuant, peak lists were matched against the Homo Sapiens Uniprot FASTA database, and raw protein intensities were filtered and analyzed in Excel and visualized and statistically analyzed in GraphPad Prism 9. Identified proteins were grouped into categories based on lists derived from the Gene Ontology (GO) Consortium and The Matrisome Project.

RESULTS

Within hours of placement, the spheroids begin to remodel the fibrin gel. Differences in fibrin reorganization, cell migration, and CNA35 labeling were apparent between the different pairings (Fig. 1). In particular, CNA35 labeling appeared more prominently in and

around the adipocyte spheroids (Fig. 1B, G). However, because CNA35 binds multiple collagens, including types I-VI with different binding affinities, it is difficult to correlate fluorescence intensity with the amount of collagen present.

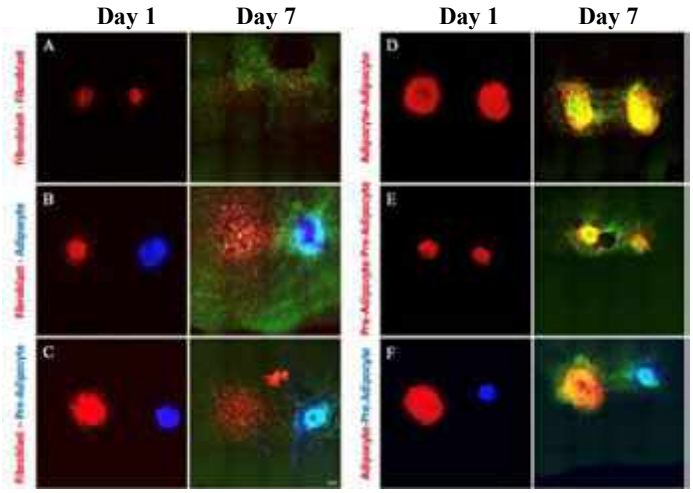

Figure 1: (A-F) Confocal z-projections of spheroid co-cultures on fibrin gels days 1 and 7. Scale bar 100 μm.

Consequently, mass spectrometry was performed to identify and quantify the abundance of collagens and other ECM proteins produced in each spheroid pairing.

For all spheroid pairings, the largest percentage of identified proteins belonged to the *Cytoskeletal* classification, which ranged between 29.3 ± 1.3% (AA) to 47.6 ± 0.8 % (FF), followed by the *Nuclear*, *Cytosolic*, *Matrisome*, and *Membrane* (Fig. 2A).

The distribution of *Matrisome* subcategories differed significantly among the different spheroid pairings (Fig. 2B), with *Collagens* representing the largest subcategory for all cases, except F-F, a behavior consistent for fibroblasts in low serum medium devoid of exogenous growth factors.

The distribution of *Collagens* differed substantially among the groups (Fig. 2C). In total, 9 different collagens (14 total alpha chains) were identified, but in many cases the collagens detected represented less than 1% of all the collagen alpha chains quantified for a given spheroid pairing. In all spheroid combinations, the alpha chains COL4A1, COL4A2, COL12A1, COL14A1, COL18A1 represented 2% or less of the collagens present. The largest percentage of collagen alpha chains identified were associated with type VI and type I collagen. The spheroid combinations of AA, FA, and FF had the most alpha chains associated with type VI collagen, with the sum of the percentage of collagen intensities of COL6A1, COL6A2, COL6A2 being AA – 61.1%, FA – 64.0%, and FF – 73.3%). For FP and PP, the majority of alpha chains were associated with type I collagen (sum of COL1A1 and COL1A2, FP – 76.8%, PP – 75.3%). PA was split between type VI and type I at 44.6% and 46.3%, respectively.

Label free quantification (LFQ) was performed in MaxQuant to facilitate direct comparisons of protein abundance among the six groups. LFQ scales the raw intensities of each sample based on common peptides. The resulting number of matrisome proteins retained for each spheroid pairing was FF - 38, FP - 68, PP - 74, FA - 74, PA - 76, and AA – 97. Of the 38 FF proteins identified, 37 of them were present in all spheroid pairings.

From these data some observations can be made: (1) fibroblasts alone did not deposit basement membrane components. Other than fibulin-2 (FBLN2), basement membrane proteins (e.g., COL4A1, COL4A2, and FBLN1) were only found in parings containing adipocytes or pre-adipocytes. FBLN2 which also associates with elastin in the interstitial matrix, was only present in FF. (2) Proteins affiliated with type I collagen fibrillogenesis were highly abundant in spheroid pairings with adipocytes and preadipocytes. (3) The spheroid pairing that produced the most collagens was FP.

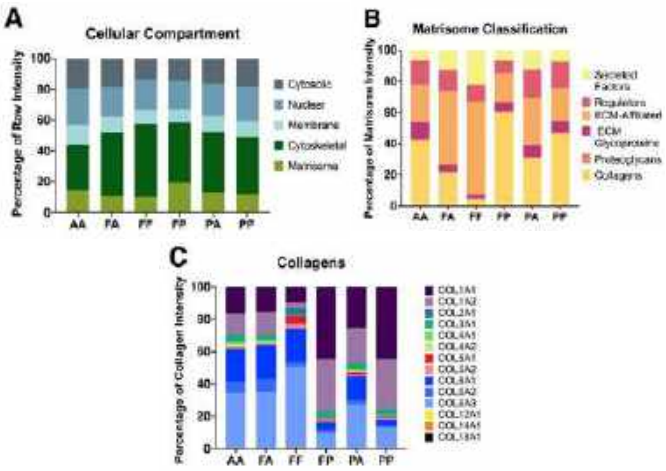

Figure 2: LC-MS/MS distribution of (A) all proteins (B) matrisome proteins (C) collagen alpha chains. AA – adipocyte-adipocyte; FA – fibroblast-adipocyte; FF – fibroblast-fibroblast; FP – fibroblast-preadipocyte; PA – preadipocyte-adipocyte; PP – preadipocyte-preadipocyte.

DISCUSSION

In this study, we used our *in-vitro* fibrin gel system to observe how different combinations of adipocyte lineage cells and dermal fibroblasts remodel fibrin gels. Fibrin gels serve as a simple mimic of a healing wound. Cell spheroids mimic aspects of native tissue function, particularly with respect to adipocyte secretion profiles. Combined the components of our engineered system facilitate manipulation, visualization, and quantification of cell-cell and cell-matrix interactions that coincide with remodeling events, such as those purported to occur with fat grafting. The addition of LC-MS/MS provides an unprecedented view of how these cell types interact to produce ECM proteins. Current efforts are now focused on quantifying how differences in ECM composition relate to mechanical properties. Such data will help us develop adipose-tissue based therapeutic strategies to improve healing and reducing existing scar tissue.

.

ACKNOWLEDGEMENTS

Support for this work was provided by the National Institutes of Health, NIGMS R01GM145626.

REFERENCES

[1] Block, L et al., *Adv Wound Care*, 4, 607-614, 2015.
[2] Hinz, B et al., *Curr Res Transl Med*, 64, 171-177, 2016.
[3] Shook, B et al., *Cell Stem Cell*, 26, 88-0-895, 2020.
[4] Spiekman, M et al., *J Tissue Eng Regen Med*, 11, 3220-235, 2017
[5] El-Hattab, M et al., *Scientific Reports*, 10(1), 10286, 2020.
[6] El-Hattab, M et al., *J. R. Soc. Interface*, 20(202), 2023004, 2023.
[7] Zong, Y. et al., *EMBO J.*, 24, 4224-36, 2005.
[8] Jacobson, KR et al., *J. Proteome Res*., 19, 3955-3967, 2020.

HEMODYNAMIC EVALUATION OF THE SENSITIVITY OF GRAFT MORPHOLOGY ON DIRECT VASCULAR SURGERY FOR MOYAMOYA DISEASE: AN IN VITRO AND IN SILICO STUDY

Cheng Peng (1), Ephraim W. Church (2), Melissa C. Brindise (1)

(1) Department of Mechanical Engineering, Pennsylvania State University, University Park, PA, US
(2) Department of Neurosurgery, Hershey Medical Center, Hershey, PA, US

INTRODUCTION

Moyamoya disease (MMD) is a rare condition marked by reduced brain blood supply due to carotid artery narrowing. This stenosis in the anterior intracranial circulation results in the proliferation of small vessels, resembling a "Puff of Smoke" in angiography [1]. MMD raises the risk of ischemic events and strokes [2]. With no standard drug treatment, direct revascularization surgery is most often used. It involves grafting from extracranial to intracranial to enhance blood supply [3], [4], immediately boosting cerebral perfusion and preventing rebleeding or future strokes [5]. However, significant complications can arise from the direct procedure, including hemorrhage or neural damage leading to neurodegenerative disease onset or cognitive function decline [4], [6]. Hemodynamic abnormalities significantly impact revascularization outcomes. Surgical choices, including donor and recipient vessel selection, graft anastomosis shape, and bypass complex geometry, influence the hemodynamic environment and surgical results. Despite this, few studies have quantitatively assessed the impact of each parameter on bypass hemodynamics. As a result, surgical decisions are often subjective. [7], [8]. In this study, we address this gap by investigating how vessel flow rates and graft vessel attachment angle affect the proportion of back perfusion using both *in vitro* experiments and *in silico* simulations.

METHODS

Three idealized direct bypass surgery models with varying graft angles (30°, 60°, 90°) were manufactured as polydimethylsiloxane (PDMS) blocks (Fig. 1a). An *in vitro* flow loop was designed to simulate the *in vivo* conditions, with a free inlet reverse design (Fig. 1c). The working fluid was water-glycerol-urea mixture with similar viscosity and density as blood [9]. For this study, steady flow was used. Stereo particle image velocimetry (PIV) was used. Particle images were captured in the central plane of the model (Fig. 1b) using a laser (EverGreen, λ=532nm) and two high-speed cameras (ImagePro X,

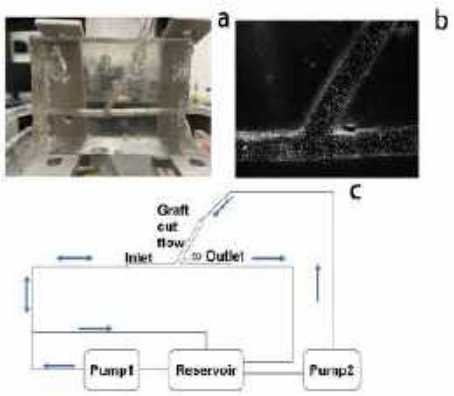

Figure 1. (a) 60º PDMS model, (b) Sample PIV image, (c) Flow loop schematic. Two pumps were used to freely allow inlet backflow.

LaVision). Particle images were processed using Davis 10.0 (LaVision Inc.) using stereo sum of cross-correlation with 150 image pairs.

Computational fluid dynamic (CFD) simulations were performed using Fluent 2023 R2 (ANSYS). Non-Newtonian, incompressible, and laminar flow were assumed. A total of 45 cases are evaluated with inlet flowrates of 0-5 ml/min, graft flowrates of 0-25 ml/min, and 30º, 60º, and 90º angles. Considering the goal of direct revascularization surgery, the best performing scenarios are defined as those which yield the largest backward flowrate in the inlet vessel.

RESULTS

Fig. 2 shows the velocity fields for the 90° and 60° graft angles with inlet/graft flow rates of 5/5 mL/min and 5/20 mL/min. Fig. 2a-d show PIV velocity fields while Fig. 2e and 2f show CFD velocity fields. Comparing Fig. 2a and 2b, the 90º angle yielded only forward perfusion, while the 60º angle resulting in about no perfusion. By increasing the

graft vessel flow rate to 20 mL/min (Fig. 2c and 2d), backflow is observed for both angle cases, with the 60º case still resulting in a larger backflow flowrate. Comparing Fig. 2c and 2d with 2e and 2f, respectively, good agreement between the PIV and CFD velocity fields is observed. Quantitative validation of the CFD is forthcoming. Nonetheless, this validation of our CFD model enables additional test cases to be run using CFD only.

Fig. 3 summarizes the amount of inlet backflow observed across each of the preliminary test cases. The reverse percentage was calculated through the negative(reversed) inlet flow divided by outlet flow. When the inlet flowrate was 0mL/min, no difference in the backflow was observed across graft angle. However, as the graft flowrate increased, the 60° graft angle produced about 5%-20% more back flow than the 90º case with different inlet flow.

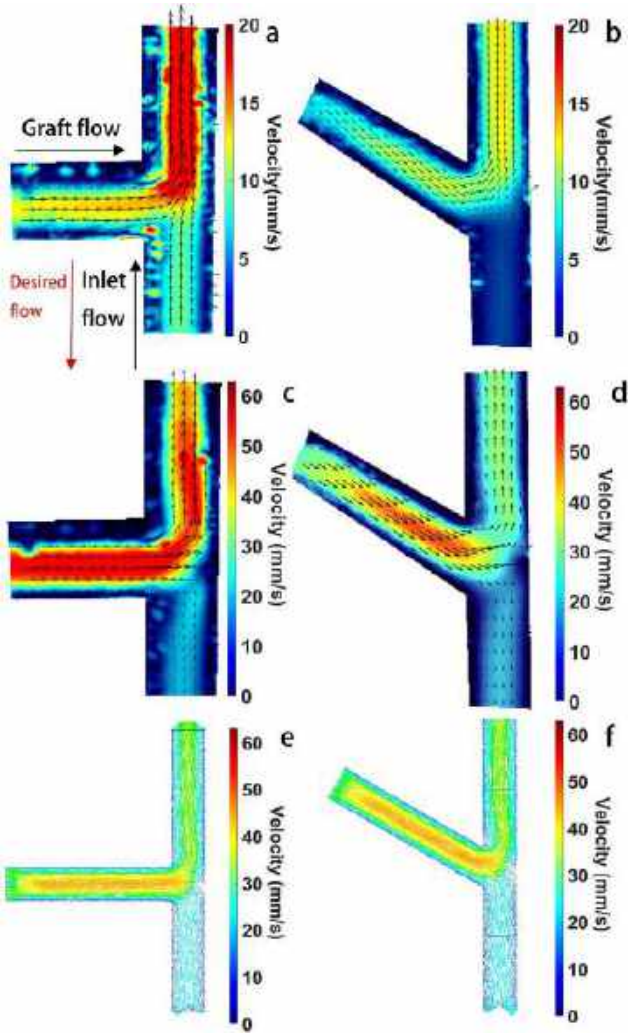

Figure 2. PIV velocity fields for (a) 90°and (b) 60°graft angles with a 5ml/min inlet and 5ml/min graft flowrate. PIV/CFD velocity fields for (c)/(e) 90° and (d)/(f) 60° graft angles with 5ml/min inlet and 20ml/min graft flowrates.

DISCUSSION

This work presents a novel multi-modal investigation aimed at improving the efficacy and outcomes of direct revascularize surgery in MMD. To the best of our knowledge, this is the first such study to evaluate how graft angle affects the bypass hemodynamics. Previous studies have focused on the surgical outcomes and techniques from a statistical point of view.

The main purpose of the surgery is to increase perfusion in the brain regions where the vessels became narrowed. Compared with the 90° cases, the 60° bypass delivered more fluid to the target area, with a higher percentage of reverse flow across the inlet (Fig. 3). Studies [4]–[6] indicate that a high graft flowrate raises complications risk. Therefore, exploring methods to boost backflow without increasing the graft flowrate is crucial. Increased graft angle enhances perfusion without elevating the graft flowrate, potentially improving surgical outcomes. No backflow was observed until the graft (cut) flow was increased to 10ml/min. Currently, extracranial vessels such as carotid artery are most often used; however, the graft vessel flowrate can be adjusted by changing the graft location. This highlights the importance of choosing a proper donor vessel. Because of the natural pressure gradient of the normal inlet, the outlet flowrate was higher than the backflow among all the cases, securing the downstream perfusion. Moreover, Fig. 2 suggests there was no significant increase in the shear stress or high-pressure area, indicating hemolysis or vessel wall damage are not expected for any case.

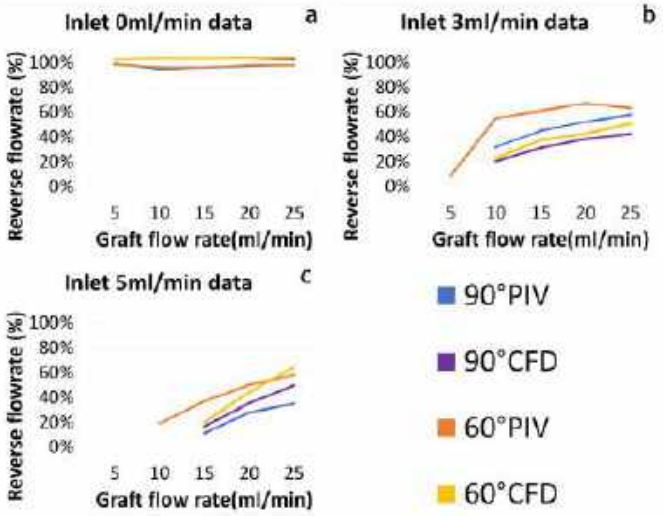

Figure 3. The percentage of reverse flow for (a) 0mL/min (b) 3 mL/min (c) 5ml/min inlet flowrates from PIV experiments & CFD simulations.

Our results emphasize that surgical decisions affecting graft morphology can significantly impact the expected revascularization and thus the surgery outcome. This highlights the importance of our study and need for additional follow up studies aiming to better inform these bypass surgeries. Future studies should focus on using more complex, patient-specific geometries.

ACKNOWLEDGEMENTS

This work is supported by a Penn State College of Medicine Catalyst Award.

REFERENCES

[1] J. A. Berry et al., *Cureus*, 12: e10994, 2020.
[2] M. Ihara et al., *Lancet Neurol*, 21: 747–758, 2022.
[3] T. Chiba et al., *J. Stroke Cerebrovasc. Dis*, 27: 3373–3379, 2018.
[4] Y. Katakura et al., *Acta Neurochir. (Wien)*, 164: 1037–1045, 2022.
[5] J. Mayeku and M. A. Lopez-Gonzalez, *Cureus*, 12: e11332, 2020.
[6] S. Uchida et al., *Cerebrovasc. Dis. Extra*, 11: 145–154, 2021.
[7] X. Zhang et al., *Curr. Neuropharmacol*, 20: 292–308, 2022.
[8] T. Funaki et al., *J. Neurosurg*, 128: 777–784, 2017.
[9] M. C. Brindise et al., *Exp. Fluids*, 59: 173, 2018.

SB³C2024
Summer Biomechanics, Bioengineering and Biotransport Conference
June 11–14, 2024, Lake Geneva, Wisconsin, USA

AORTIC LOCATION AND SEX SPECIFIC ALTERATIONS IN MECHANICS AND WALL REMODELING IN A MOUSE MODEL OF MARFAN SYNDROME

Krashn Kumar Dwivedi (1), Jacob Rother (1), Jessica E. Wagenseil (1)

(1) Department of Mechanical Engineering and Materials Science, Washington University in St. Louis, St. Louis, MO

INTRODUCTION

Marfan syndrome (MFS) is a hereditary disorder associated with life threatening thoracic aortic aneurysms. MFS results from mutations in fibrillin-1 (*FBN1*), one of the extracellular matrix (ECM) glycoproteins necessary for elastic fiber assembly and their ability to maintain aortic elastic recoil [1,2]. Mutations in *FBN1* cause alterations in ECM constituents, such as fragmentation of elastic fibers and disorganization of collagen fibers, which results in deterioration of aortic mechanics and aneurysm formation. Previous work primarily focused on the mechanics and ECM remodeling of the ascending aorta, where the aneurysm typically occurs, however there is evidence that MFS affects the mechanical function of other segments of the aorta even in the absence of aneurysm [3]. The compromised mechanical properties of the aorta, particularly in distal locations, may affect the overall hemodynamics, which may increase the load on the heart and cyclic stress on the proximal aorta. Additionally, the outcomes of MFS in aneurysm formation are sex specific [4], however, MFS is equally prevalent in males and females. The aim of this work is to investigate sex and aortic location specific alterations of aortic mechanic and ECM remodeling in a mouse model of MFS.

This study presents a comparison of geometry, mechanical properties, and ECM remodeling between the ascending (AA), descending (DA), superior (SAA), and inferior (IAB) abdominal aorta for three months old *Fbln1*$^{mgR/mgR}$ (MU) (model of MFS) [1] and littermate wild type (WT) male and female mice. The results of this work can be used to include the effects of aortic location and sex specific alterations in mechanical properties and structural integrity of the aortic wall on hemodynamic simulations that determine wall stresses and may correlate with aneurysm propensity and outcomes.

METHODS

Mouse model. Three month old male and female MU and WT mice were genotyped, sacrificed, and the AA, DA, SAB, IAB were removed. The tissues were stored in phosphate buffered saline solution at 4°C for up to 3 days before mechanical testing. All experimental protocols were approved by the IACUC.

Mechanical testing. Samples were removed from the fridge and brought to room temperature for 30 min. Samples were cannulated on a pressure myograph for biaxial mechanical tests. The inflation-extension tests on each aorta were performed according to the protocol described previously [5]. Experimental data including pressure, outer diameter, and force corresponding to the in vivo stretch were used to determine the mechanical properties of the aorta. After mechanical tests, three rings from each section were cut and imaged. The images were used to measure the unloaded outer diameter and thickness. Compliance was calculated by,

$$Compliance\ (1/mmHg) = \frac{(D_{i+1}-D_i)}{D_i\times(P_{i+1}-P_i)} \quad \text{, (Eqn. 1)}$$

where P_i and D_i are the applied pressure and corresponding outer diameter at *ith* time point.

Multiphoton imaging. After mechanical testing, a subset of samples was fixed in 4% paraformaldehyde. Samples were flash frozen and 10 µm thick cross sections were cut using a cryostat microtome and cover slipped. Samples were imaged using a Leica Sp-8 DIVE multiphoton microscope with a 40x objective. Collagen, elastin, and cell nuclei were excited at 880 nm and imaged using second-harmonic generation (emission: 420-460 nm), autofluorescence (emission: 495-540 nm), and staining with DAPI (390-460 nm), respectively [6]. Quantitative analyses of the images is ongoing.

Statistics. Statistical analysis was done using GraphPad Prism. Data are presented as mean ± standard deviation. Experimental groups were compared using three-way ANOVA and Sidak's multiple comparisons. P-values <0.05 were considered significant.

RESULTS

Geometry. **Figs. 1A, B** shows the unloaded outer (OD) diameter and thickness of different aortic regions for WT and MU, male and female mice. The results show the increased AA diameter in MU mice compared to WT, associated with aneurysm formation. While both male and female MU mice have overall increased diameters, more individual male mice have increased diameters than female mice. For other aortic regions, OD is almost the same for MU and WT mice, indicating no dilation. There are no significant differences between MU and WT mice for the thickness of any aortic region. OD and thickness values depend significantly on sex (S).

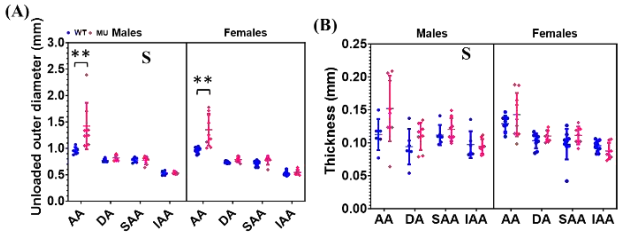

Figure 1: Unloaded outer diameter (A) and thickness (B) of different aortic regions for MU and WT mice. N = 5 – 8/group.

Mechanical testing. Pressure-compliance curves (**Figs. 2A, B**) show a shift of the compliance peak toward lower pressures in MU mice compared to WT, independent of aortic location and sex. At higher pressures, there is reduction in compliance of the aorta which is more significant in MU mice than WT. Based on these observations, we further measured the compliance at low pressure (elastin dominated region) and high pressure (collagen dominated region) (**Figs. 2 B, C**). The significant increase in low pressure compliance in MU aorta (for all sections and in both sexes) indicates possible compromises in elastic fiber integrity. The low pressure compliance increase is greatest in the AA, consistent with dilation of that specific region. The significant decrease in high pressure compliance in MU aorta (for all sections and in both sexes) indicates possible increases in collagen fiber deposition. The AA has the largest decrease in high pressure compliance of all aortic regions, consistent with aneurysm driven wall remodeling in that region. There is a significant interaction between sex (S) and genotype (G) for low and high pressure compliance, indicating sex dependent effects of MFS on aortic mechanics.

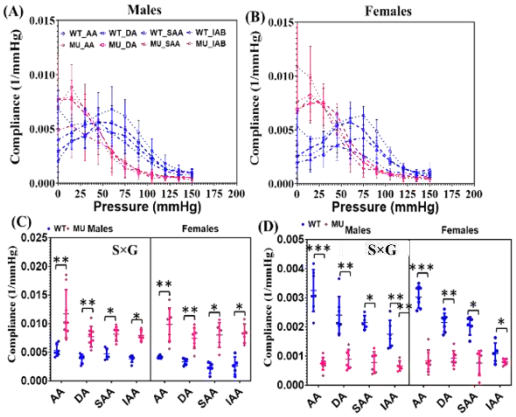

Figure 2: Pressure-compliance curves for WT and MU (A) males and (B) females. Comparison of low pressure (C) and high pressure (D) compliance between MU and WT, male and female mice. N =5-8/group.

Multiphoton imaging. Fig. 3 shows representative multiphoton images of all four aortic regions for WT and MU, male and female mice. In these images, elastic fibers, collagen fibers and cell nuclei are in green, red, and blue/white color, respectively. The images show fragmentation of elastic fibers and deposition of collagen fibers in MU aorta. Quantification of the images is ongoing, however the ECM changes appear to be more apparent in the AA and in male mice.

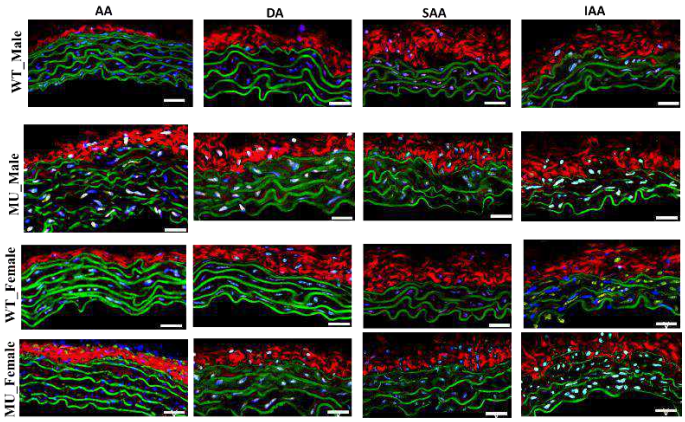

Figure 3: Multiphoton images of AA, DA, SAA and IAA for WT and MU mice. Scale bar = 50 µm.

DISCUSSION

This study investigates sex and aortic location specific differences in a mouse model of MFS. We present data for geometry, mechanics, and wall structure of the AA, DA, SAA, and IAA. The results show that even in the absence of an aneurysm, a mutation in *FBN1* affects the mechanics and ECM remodeling of the aorta throughout the length, and these changes are location and sex specific. The aortic location and sex specific increase in low pressure compliance and decrease in high pressure compliance may be related to location and sex dependent fragmentation of elastic fibers and deposition of collagen fibers, respectively. Qualitatively we observed large fragmentation of elastic fibers and deposition of collagen fibers in MU male AA with aneurysm. The increase in compliance at low pressure may make the aorta susceptible to overdistension in some cases and damage smooth muscle cells within the wall. Further, the decrease in compliance at high (physiologic) pressures for all segments of the aorta can adversely affect cardiovascular hemodynamics. For example, decreased compliance would increase the pulse wave velocity and resulting pulse pressure, leading to an increase in load on the heart and cyclic wall stress on the proximal part of the aorta. Our results indicate that sex specific dilation of AA in MFS may be linked to heterogeneous changes in mechanical properties and structural integrity of the aorta.

ACKNOWLEDGEMENTS

Funding provided by NIH R01 GR0024992

REFERENCES

[1] Dietz, et al., *Nature*, 352:337-339, 1991.
[2] Marque., et al., *Thromb. Vasc. Biol*, 21:1184-1189, 2001.
[3] Jeremy, et al., *Am. J. Cardiol*, 74: 369-373, 1994
[4] Francesc, et al., *Front. Physiol*, 8: 933, 2017
[5] Le, et al., *J R Soc Interface*, 12(104):20141350, 2015
[6] Crandall, et al., *J Biomech*, 145:111360, 2022.

AGE AND SEX SPECIFIC BIOMECHANICS AND EXTRACELLULAR MATRIX REMODELING OF THE ASCENDING AORTA IN A MOUSE MODEL OF MARFAN SYNDROME

Krashn Kumar Dwivedi (1), Jacob Rother (1), Jessica E. Wagenseil (1)

(1) Department of Mechanical Engineering and Materials Science, Washington University in St. Louis, St. Louis, MO

INTRODUCTION

Thoracic aortic aneurysm (TAA) is characterized by progressive diameter dilation due to weakening of the aortic wall. TAA is associated with Marfan Syndrome (MFS), caused by mutations in fibrillin-1 (*FBN1*), an extracellular matrix (ECM) macromolecule [1]. Mutations in *FBN1* causes alterations in ECM constituents such as fragmented elastic fibers and improper deposition of collagen fibers, leading to changes in aortic geometry and compromised mechanical properties that contribute to TAA formation and eventual rupture. Male patients with MFS have a higher risk of TAA development, progression, and rupture than age matched female patients with MFS, however the incidence of MFS is not sex dependent [2]. The mechanisms behind the sex specific outcomes of TAA are not clear.

This study presents longitudinal (1, 2, 3 and 4 months old) data on geometry, mechanics, and ECM remodeling of the ascending thoracic aorta in *Fbln1*$^{mgR/mgR}$ (MU) (model of MFS) [3] and littermate wild type (WT) male and female mice. The results are compared amongst age, sex, and genotype to reveal connections between mechanics and ECM remodeling associated with TAA formation and progression. The outcomes of this work can provide biophysical biomarkers for predicting TAA outcomes and its management in males and females.

METHODS

Mouse model. After genotyping, the MU and WT mice were separated according to sex and further divided into age groups of 1, 2, 3 and 4 months. This age range was chosen according to preliminary survival data, as a very low survival rate of MU male mice was found at 4 months of age. All experimental protocols were approved by the IACUC. Each group and experimental measurement has 5-8 mice.

Ultrasound measurement. The in vivo geometry was measured using a small animal ultrasound imaging system (Visualsonics Vevo 2100). Mice were anesthetized with 2% isoflurane, kept warm, and imaged to obtain collect B- mode and M-mode images of the ascending thoracic aorta (ATA) (**Figure 1A**). Images were postprocessed in Visualsonics software to calculate systolic and diastolic diameters. Both diameters were normalized by the mouse weight and in vivo strain was calculated as the % change in diameter from diastole to systole. After imaging, the mice were sacrificed and the ATA was isolated and stored in phosphate buffered saline at 4° C for mechanical testing and ECM imaging.

Mechanical testing. The ATA was cannulated on a pressure myograph for biaxial mechanical tests. The inflation-extension tests on each ATA were performed according to the protocol described previously [4]. Experimental data including pressure, outer diameter, and force corresponding to the in vivo stretch were used to determine the mechanical properties of the ATA. Compliance was measured by,

$$\text{Compliance } (1/\text{mmHg}) = \frac{(D_{i+1}-D_i)}{D_i\times(P_{i+1}-P_i)} \quad \text{, (Eqn. 1)}$$

where D_i = outer diameter at applied pressure P_i at *ith* time step. Mid-wall circumferential stretch and stress were determined from the recorded data and unloaded dimensions assuming an incompressible cylinder with no shear. The toe modulus (TM) (elastic fiber dominated modulus) and linear modulus (LM) (collagen fiber dominated modulus) were calculated by linear regression of the initial 20-30 and last 20 data points of the circumferential stress-stretch curve, respectively.

Multiphoton imaging and ECM analysis. After mechanical testing, ATAs were fixed in 4% paraformaldehyde, flash frozen, and 10 µm thick cross sections were cut using a cryostat microtome. Samples were imaged using a Leica Sp-8 DIVE multiphoton microscope with a 20x objective to visualize elastin and collagen fibers [5]. To quantify the fragmentation of elastic fibers, the elastin channel was isolated and analyzed in ImageJ (NIH) using the skeletonize function [5].

Statistics. Statistical analysis was done using GraphPad Prism. Data are presented as mean ± standard deviation. Experimental groups were compared using three-way ANOVA and Sidak's multiple comparisons. P-values <0.05 were considered significant.

RESULTS

Mouse model and ultrasound measurement. Survival analyses show 60-80% mortality in male and 30-35% mortality in female MU mice by 4 months old. **Figs. 1B, C** illustrate that the ATA starts dilating in male and female MU mice at 1 month old. With age dilation of the ATA is greater in males than females and ATA size is significantly affected by interactions of genotype (G), age (A), and sex (S). In vivo strain (**Fig. 1D**) significantly decreases in MU mice and with age and there are interactions between age (A) and genotype (G). Multiple comparison analyses indicate larger decreases for in vivo strain in male than female MU mice, compared to their respective WT controls, indicating more significant stiffening of the ATA in male MU mice.

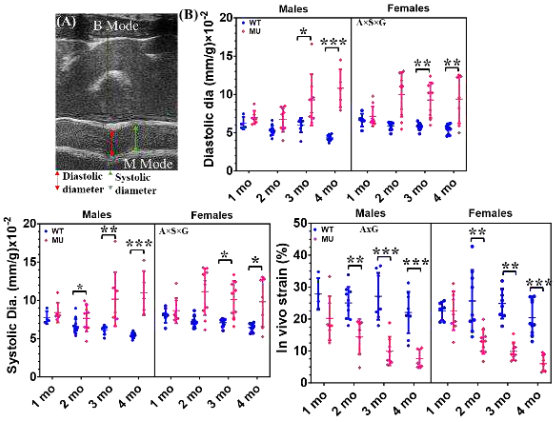

Figure 1: Representative ultrasound B- and M-mode images of the ATA (A). Comparison of diastolic (B) and systolic (C) diameter, and in vivo strain (D).

Mechanical testing. Pressure compliance curves (**Figs. 2A, B**) show that MU ATA is more compliant than WT ATA at low pressures and less compliant at high pressures. This trend is found for male and female mice at all ages. After 1 month old, TM significantly decreases in MU mice and there are significant interactions between age (A) and sex (S) (**Fig. 2C**). After 2 months old, LM significantly increases in MU mice and there are significant interactions between age (A) and genotype (G), and sex (S) and genotype (G) (**Fig. 2D**). There is a larger decrease of TM and a larger increase of LM in MU males than females, compared to WT littermates. These results suggest that male and female mice follow different timelines of alterations in ATA mechanics associated with MFS.

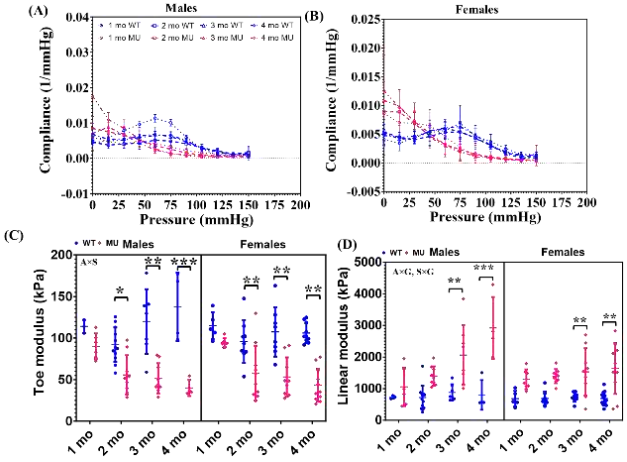

Figure 2: Pressure compliance curve for WT and MU (A) males and (B) females. Comparison of toe modulus (C) and linear modulus (D) of ATA between WT and MU male and female mice.

Multiphoton imaging and ECM analysis. In comparison to WT littermates, the ATA of MU male mice shows fragmentation of elastic fibers, deposition of collagen fibers in the media and adventitia, and loss of cell nuclei (**Figs. 3A, B**). In contrast, in MU female mice, very few fragmented elastic fibers are observed, but there are increased numbers of thin and buckled elastic fibers compared to WT littermates (**Figs. 3C, D**). Elastic fiber fragmentation analyses (**Fig. 3E**) shows a significant reduction in slab size (elastic fiber length) and a significant increase in end points (elastic fiber fragmentation) in the ATA of 3- and 4-month old MU males compared to WT littermates. However, these parameters are almost unchanged between MU and WT female ATA for all age groups. A significant interaction is found between age (A), sex (S), and genotype (G) for the slab size and endpoints.

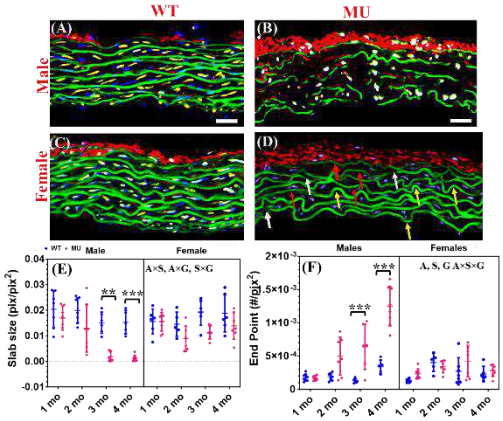

Figure 3: Representative images of 4-month-old WT and MU male and female mice (A-D), red = collagen fibers, green = elastic fibers, blue/white = cells. In panel (D), red, white, and yellow arrows indicate thin, fragmented, and buckled elastic fibers, respectively. Comparison of slab size (E) and end points (F). Scale bar = 50 µm.

DISCUSSION

This study presents longitudinal data of in vivo geometry and strain, ex vivo mechanical properties, and ECM remodeling for the ATA from MU and WT male and female mice. We observed sex and age specific outcomes for ECM remodeling and ATA mechanics. Significant fragmentation of elastic fibers and deposition of collagen fibers in MU male compared to MU female ATA may be the cause of sex-specific alterations in compliance and linear modulus in different pressure regions. The fragmentation of elastic fibers may cause irreversible dilation of the ATA, whereas the increase in collagen fiber deposition may cause plastic deformation during in vivo loading, contributing to TAA formation and eventual rupture in male MU mice. However, in female MU mice, the thin and buckled elastic fibers may be responsible for irreversible dilation of ATA, but at in vivo pressures these elastic fibers become straight and support the load, which may compensate for the reduction in tissue elasticity due to deposition of collagen fibers and protect the ATA from rupture. Overall, our results indicate that age and sex specific ECM remodeling may be a factor accounting for different TAA outcomes between male and female mice.

ACKNOWLEDGEMENTS

Funding provided by NIH R01 HL164800.

REFERENCES

[1] Wagenseil, et al., *Birth Defects Res C Embr Today*, 4:229-40, 2007.
[2] Detaint, et al., *Eur. Heart J*, 31:2223-2229, 2010.
[3] Pereira, et al., *Nat Genet*, 17(2): 218-22, 1997
[4] Le, et al., *J R Soc Interface*, 12(104):20141350, 2015
[5] Crandall, et al., *AJP Heart Circ*, 325:113-124, 2022.

ENHANCING FLUID INFUSION VIA INTRODUCTION AND ENLARGEMENT OF MICROCRACKS IN TUMORS – THEORETICAL SIMULATIONS

Md Jawed Naseem, Ronghui Ma, Liang Zhu

Department of Mechanical Engineering, University of Maryland Baltimore County, Baltimore, Maryland, USA

INTRODUCTION

In chemical ablation of tumors, convection-enhanced delivery (CED) is commonly used to infuse chemicals such as ethanol via a single cannula inserted into tumors. Unfortunately, very high interstitial fluid pressure (IFP) and small porosity in tumors often cause backflow through the needle track. This leads to leakage of the chemicals to surrounding healthy tissue, resulting in collateral damage or severe pain to patients. In recent years, novel devices have been manufactured to incorporate retractable tines. The original design aimed at using the tines for infusion and the retract ability of the tines allows more infusing sites to enlarge the infused tissue volume. Previous experiments using ethanol for liver tumor ablation demonstrated less pain experienced by patients, implying less leakage.[1] None of the previous studies evaluated a CED system with a retractable needle only for generating microcracks in tumors and the resulting change of flow resistance in tumors during direct fluid infusion.

In this study, we perform theoretical simulation to evaluate how introduction of a microcrack in tissue reduces the overall flow resistance in a porous tumor, as well as further decrease in the flow resistance as this microcrack enlarges in a direct infusion process using CED. Both Darcy's law and the poroelasticity theory are used in the simulation to understand the fluid transport in porous tumors with or without microcrack introduction and/or enlargement. We expected that the study would provide quantitative measures to evaluate whether this approach is effective to enhance the fluid transport in dense porous tumors.

METHODS

A tumor, modeled as a sphere (10 mm in radius), undergoes a direct fluid infusion modeled as a prescribed high pressure on a spherical surface in the tumor center (0.64 mm in radius). The backflow through the infusion needle is not included in this study, since our focus is on the role played by an induced microcrack in tumors. In Figure 1a, model 1 represents a porous tumor without any microcrack. An induced microcrack is included in model 2 as a cylindrical column (0.05 mm in radius, 3 mm long). The microcrack initiates on the infusion surface and extended towards the tumor periphery (Figure 1b). Both the microcrack and the remaining tumor region are each modeled as uniform porous media with different porosities and permeabilities. The obtained fluid pressure field of the tissue region is the input needed for the poroelastic simulation to predict tissue deformation during the infusion process. The geometry of the enlargement of the microcrack is exported from the poroelastic simulation of tissue deformation in model 2. The shape and the geometry of the microcrack after enlargement are then re-generated and introduced to the porous tumor. Finally, we construct model 3 in which the microcrack enlargement is included, shown in Figure 1c. Both the microcrack and the remaining tumor region are again modeled as uniform porous media with different porosities and permeabilities. In model 3 (Figure 1c), only Darcy's law is used to simulate the updated pressure and velocity fields with the enlarged microcrack.

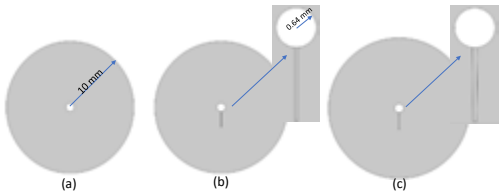

Figure 1. Geometries of the three models

In this study, Darcy's law is used to describe how fluid flows in the porous tumor tissues, which is given by,

$$\nabla \cdot \left(\phi \vec{V}_f\right) = 0, \quad \nabla P_f = -\frac{\mu\phi}{K}\vec{V}_f \qquad (1)$$

where $\vec{V}_f$ is interstitial fluid velocity vector, P_f is interstitial fluid pressure, μ is fluid dynamic viscosity, ϕ is tumor porosity, and K is permeability of the porous tumor medium. Boundary conditions include

a prescribed pressure at the infusion surface (P_0 = 2*10^5 Pa) and zero pressure at the tumor outer surface.[2]

In the porous tumor, the fluid pressure in the interstitial fluid space is not uniform during a direct fluid infusion. The non-uniformity of the fluid pressure would add extra displacements and strains to the tissue. In the poroelasticity theory, the fluid pressure is included in the constitutive equation for tissue deformation as

$$G\nabla^2\vec{u} + (\lambda + G)\nabla(\nabla \cdot \vec{u}) = \nabla \cdot (\phi P_f), \qquad (2)$$

where $\vec{u}$ is the tissue displacement vector, G and λ are Lame constants that can be determined by the Young's modulus E and the Poisson's ratio ν using the follow expressions:

$$\lambda = E\upsilon/((1+\upsilon)(1-2\upsilon)); G = E/(2(1+\upsilon)) \qquad (3)$$

Eq. 2 can be solved once the distribution of the fluid pressure is obtained from Darcy's law. Boundary conditions needed for solving the displacement field are a roller boundary at the infusion surface and zero displacement at the tumor outer surface. The displacement at the interface between the tumor and microcrack is used to generate the enlarged microcrack in model 3.

In each model, the volumetric flow rate is calculated by integrating the normal velocity over the outer surface of the tumor. The flow resistance (R_{flow}) is defined as the pressure difference between the infusion surface and the tumor outer surface divided by the calculated volumetric flow rate, and is given by,

$$R_{flow} = (P_0 - 0) / (\text{volumetric flow rate}) \qquad (4)$$

All the simulations are performed in COMSOL® 6.1 using the sub-surface module. Sensitivities to mesh sizes are checked to ensure that doubling the total number of mesh elements would result in less than 0.1% changes in the simulated results.

RESULTS

The mechanical properties used in the models are listed in Table 1. Note that both the tumor region and the microcrack region are porous media with different properties.

Table 1: Mechanical properties[2]

μ, Pa s	0.001	E_{tumor}, MPa	0.3
K_{tumor}, m^2	5*10^{-16}	E_{crack}, MPa	0.003
K_{crack}, m^2	2.02*10^{-13}	ν_{tumor}	0.4
ϕ_{tumor}	0.2	ν_{crack}	0.4
ϕ_{crack}	0.8	ρ, kg/m^3	1000

Figure 2 illustrates the pressure fields of the three models. Without introduction of a microcrack (Figure 2a), the pressure field is one-dimensional, varying only in the radial direction. The pressure decreases to 50% of P_0 at 0.7 mm away from the infusion surface, and a further decrease to 50% of P_0 occurs at 4.2 mm from the infusion surface. The effect of the introduced microcrack in the tumor is examined in model 2 (Figure 2b). One observes that the maximal pressure again occurs at the tumor central region. Since the permeability of the microcrack domain is much larger than that in the regular tumor region (Table 1), flow through the microcrack is much easier than that through the tumor. Figure 2b shows a very small pressure drop from the infusion surface to the tumor-crack interface, equivalent to an extension of the maximal isobaric contour from the original infusion surface. Therefore, the fluid transport is expedited by the crack due to a shorter distance between the tip of the microcrack to the tumor periphery.

The tissue displacement vector is exported to reconstruct the enlarged microcrack. Overall, the magnitude of the displacement in the lateral direction of the interface varies from 0.025 mm near the infusion surface to 0.0073 mm at the tip of the microcrack, leading to a frustum-shaped crack. The deformation is significant since the original microcrack radius is 0.05 mm. The volume of the frustum is 2.26 times of the original value, due to the fluid infusion-induced tissue deformation. The rapid decrease in the fluid pressure field with the enlarged microcrack is shown in Figure 2c, with a slightly longer push towards the tumor outer surface than that in Figures 2b.

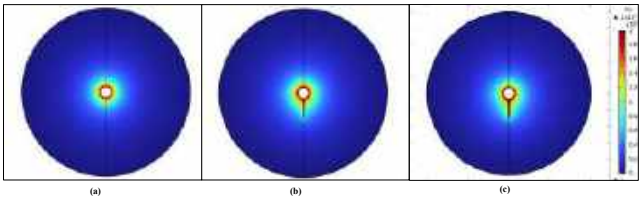

Figure 2. Contours of the fluid pressure field.

The minimal and maximal velocities of the three models are presented in Table 2. Based on the simulation parameters in model 1, the maximal velocity occurring at the infusion surface is 1.66*10^{-4} m/s. The magnitude of the velocity vector decreases in the radial direction, to 6.84*10^{-7} m/s, satisfying fluid mass conservation in the simulation. With the introduction of the microcrack in model 2, the maximal velocity is two orders of magnitude larger than that in model 1. The dispersal of fluid is not uniform in the tissue but concentrated along the microcrack where the fluid is spreading out more intensely than other tumor regions. The minimal velocity at the tumor outer surface increases by 3.9% from 6.84*10^{-7} to 7.11*10^{-7} m/s. Once the microcrack is enlarged in model 3, the maximal velocity is 1.06*10^{-2}, which is at the same order of magnitude of, however, smaller than that in model 2. This result may be explained by the large cross-sectional area due to the lateral enlargement of the microcrack from the original radius of 0.05 mm to 0.085 mm. The minimal velocity in model 3 is 7.29*10^{-7} m/s, the largest in the three models. This implies that model 3 has the largest volumetric flow rate with the enlarged crack among the three models.

Table 2: Velocity and flow resistance in the three models

	model 1	model 2	model 3
V_{max}, m/s	1.66*10^{-4}	1.78*10^{-2}	1.06*10^{-2}
V_{min}, m/s	6.84*10^{-7}	7.11*10^{-7}	7.29*10^{-7}
R_{flow}, Pa.s/m^3	2.33*10^{14}	2.12*10^{14}	2.00*10^{14}

Using Eq. 4, one determines the flow resistance in the tumor. Shown in Table 2, introduction of a microcrack to the spherical tumor decreases the flow resistance from 2.33*10^{14} in model 1 to 2.12*10^{14} Pa.s/m^3 in model 2. With the enlarged microcrack (model 3), the flow resistance is further reduced from that in model 2. Overall, having an enlarged microcrack results in a decrease by 14% from that without microcrack, or 5.7% from that without crack enlargement.

DISCUSSION

The theoretical simulation results have illustrated significantly altered pressure and velocity fields in a porous tumor due to introduction of a microcrack. The non-uniform fluid pressure field enlarges the cylindrical microcrack to a frustum, with a crack volume more than doubled. Due to the large permeability and porosity in the microcrack, flow from the infusion surface to the tumor periphery is much easier than that without microcrack. Overall, the flow resistance with the enlarged microcrack is reduced by 14% from the baseline case. We conclude that introducing a microcrack in porous tumors is an effective way to facilitate fluid flow in porous tumors using CED.

REFERENCES

[1] Kuang, M et al., *Radiology*, 253(2):552-561, 2009.
[2] Su, D. Et al., *Medical and Biological Engineering & Computing*, DOI 10.1007/s11517-011-0819-y, 2011.

INVESTIGATING DYNAMIC LOADING-INDUCED FLUID EFFECTS ON BONE CELLS IN 3D

Kailin Chen (1), Alessandro Maggi (2) Alexander Bolanos-Campos (3), Mistica L. Perez (3), Michael Abrams (4), Julia R. Greer (2), Ottman A. Tertuliano (1)

(1) Mechanical Engineering and Applied Mechanics, University of Pennsylvania, Philadelphia, PA, USA
(2) Division of Engineering and Applied Science, California Institute of Technology, Pasadena, CA, USA
(3) Department of Bioengineering, University of Pennsylvania, Philadelphia, PA, USA
(4) Division of Biology and Biological Engineering, California Institute of Technology, Pasadena, CA, USA

INTRODUCTION

It has been well-established that physical activity has a positive effect on the bone remodeling process. At the macroscopic level, mechanical stimulations such as cyclic stress and strain are found to alter bone mechano-transduction process, where physiological loads convert to mechanical signals sensible to bone cells [1,2]. For example, Javaheri et al. (2020) revealed that bone mechanoadaptation can be restored after applying a threshold primary load by characterizing the load-induced strain using mice tibia bone piece with 3D microCT [3]. In addition, it has been found that compared with static loading, dynamic loading will induce more osteogenic responses [4,5]. While macro-scale mechanical loading on bone matrix has been extensively studied, the intrinsic cellular-level responses under dynamic mechanical loading remain largely unknown. As two main mechanically sensitive bone cells, osteocytes and osteoblasts both contribute positively to bone formation process by translating external mechanical stimuli to biological signals, i.e., mechano-transduction. It has been well defined theoretically and experimentally that the lacuna-canaliculi structure surrounding the osteocyte conveys both matrix force and interstitial fluid shear to osteocyte surface, where the induced fluid shear stress ranges from 0.8 to 3 Pa [6,7]. However, the mechanical environment around osteoblasts and its corresponding effects on cell responses is much less known. Most of the in-vitro experiments have been focusing on impacts of matrix deformation and fluid shear by directly applying stress, strain, or fluid shear to cell surface [8]. Therefore, it is vital to develop a platform which integrates effects of both matrix deformation and fluid shear for characterization of osteoblast mechanical responses.

The current work aims at developing a micro scale three-dimensional cell-matrix system which enables investigating the dynamic effects of matrix deformation and fluid shear stress on mechanical responses of osteoblasts by actin fluorescence intensity after stimulation.

METHODS

In this work, a micro-scale three-dimensional hollow TiO_2 lattice structure is designed as the scaffold with osteoblastic-like (SAOS2) cells seeded on. Four structures with different stiffness are fabricated along a row on a 1 cm by 1cm silicon chip with a 7 mm by 7mm etched down well, where contains the culture media. The cells are seeded on the lattices for 12 days, grow in culture media for 3 days and then be compressed for two consecutive days. Different dynamic loading processes, such as constant strain and constant stress were applied to the four structures with wall thickness ranging from 18 nm to 260 nm, enabling stiffnesses ranging from 0.7 MPa to 35 MPa, shown in Fig. 1. To independently investigate the effect of loading frequency, we choose a structure of E = 5 MPa and performed constant stress experiments on different samples with loading frequency of 0.1 Hz, 1Hz, and 3Hz, which corresponds to standing, slow walking and running. The dynamic compression processes were applied using Nanoindenter with a flat-top diamond tip. The actin responses after stimulation are characterized by fluorescence intensity using confocal microscopy. The fluid field induced by the compression process was estimated using a theoretical squeezing flow model between two parallel plates as shown in Fig. 2.

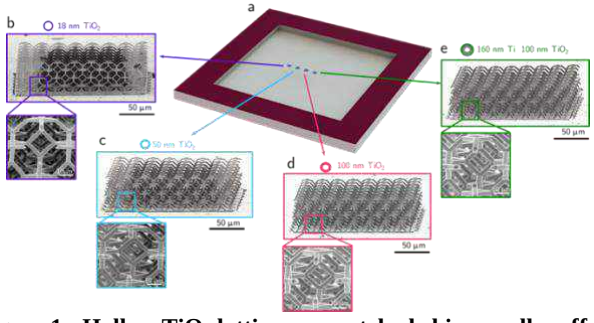

Figure 1: Hollow TiO_2 lattice on an etched chip as cell scaffold.

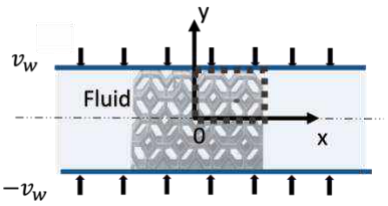

Figure 2: Squeezing flow model between two parallel plates simulates compression-induced fluid field.

GOVERNING EQUATIONS OF THE FLUID FIELD

$$\frac{\partial u}{\partial x}+\frac{\partial v}{\partial y}=0 \quad (1)$$

$$\frac{\partial u}{\partial t}+u\frac{\partial u}{\partial x}+v\frac{\partial u}{\partial y}=-\frac{1}{\rho}\frac{\partial P}{\partial x}+\nu\left(\frac{\partial^2 u}{\partial x^2}+\frac{\partial^2 u}{\partial y^2}\right) \quad (2)$$

$$\frac{\partial v}{\partial t}+u\frac{\partial v}{\partial x}+v\frac{\partial v}{\partial y}=-\frac{1}{\rho}\frac{\partial P}{\partial y}+\nu\left(\frac{\partial^2 v}{\partial x^2}+\frac{\partial^2 v}{\partial y^2}\right) \quad (3)$$

where u is the fluid velocity component along x direction, v is the fluid velocity component along y direction, t is time, ρ is fluid density, ν is fluid kinematic viscosity, P is pressure. The fluid is assumed to be viscous and incompressible. The boundary conditions are

$$y=a(t): u(x,y,t)=0; v(x,y,t)=V_w(t) \quad (4)$$

$$y=0: \frac{\partial u(x,y,t)}{\partial y}=0; v(x,y,t)=0 \quad (5)$$

where $V_w(t)=da/dt$ is the plate velocity.

RESULTS

Dynamic loading at a constant strain amplitude was applied to the four lattices fabricated in Fig. 1. Because of the increasing modulus, the lattices undergo increasing stress at constant strain amplitude. Fig. 3a, shows the actin intensity (normalized to the lowest stiffness sample) increases with increasing stiffness. This trend is quantitatively similar regardless of whether the samples are the uncompressed or compressed (Fig. 3a). A similar trend was observed with constant stress amplitude, suggesting within the investigated range, 3D substrate stiffness controls cytoskeletal organization rather than external stimulation. However, Fig 3b shows that with increasing loading frequency actin intensity increases on a given structure of one stiffness (E = 5 MPa),. The dynamic, frequency dependent cell response suggests the fluid stimulation is more important than the solid deformation in the 3D scaffold. The estimated fluid shear stress field in Fig. 4 which corresponds to the three loading frequencies, increases with faster plate velocity, i.e. loading frequency.

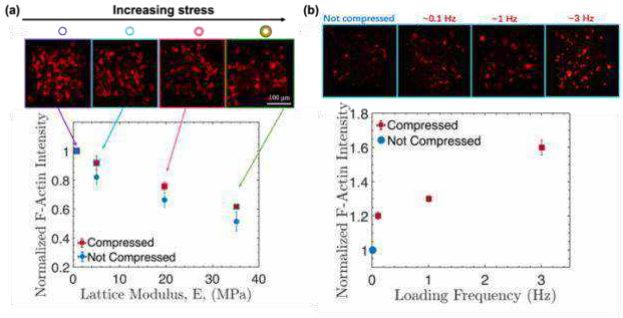

Figure 3: (a) Maximum intensity projection (MIP) images of showing f-actin intensity after constant strain compression on different stiffness structures. (b) MIP results with different loading frequencies on a structure of E = 5 MPa.

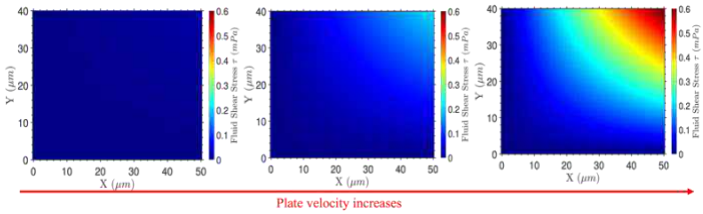

Figure 4: Compression-induced fluid shear stress field increases with faster plate velocity which corresponds to the larger loading frequency.

DISCUSSION

With increasing stress/strain loading, the very similar actin intensity trend before and after loading indicates that in this case the cells are relatively not sensitive to matrix deformation, the fluid shear stress induced by the compression process, which differs more with different frequencies, might be the main stimulator for actin formation of osteoblasts compared with solid deformation of the scaffold. In addition, the magnitude of the fluid shear stress is with the scale of millipascal, which is much smaller than the 0.8-3 Pa range for osteocyte as expected, because of the less constrained mechanical environment around osteoblasts. It is of great interests to dig into the active in-vitro response range of osteoblasts with a 3D bone-like cell-matrix system in the future.

ACKNOWLEDGEMENTS

The project is funded by CEMB of University of Pennsylvania. Technical supports from McKay Orthopaedic Research Laboratory and Singh Center of University of Pennsylvania are greatly acknowledged.

REFERENCES

1. Wolff, J., 1893. Das gesetz der transformation der knochen. DMW-Deutsche Medizinische Wochenschrift, 19(47), pp.1222-1224.
2. Mellon, S.J. and Tanner, K.E., 2012. Bone and its adaptation to mechanical loading: a review. International Materials Reviews, 57(5), pp.235-255.
3. Javaheri, B., Razi, H., Gohin, S., Wylie, S., Chang, Y.M., Salmon, P., Lee, P.D. and Pitsillides, A.A., 2020. Lasting organ-level bone mechanoadaptation is unrelated to local strain. Science Advances, 6(10), p.eaax8301.
4. Lanyon, L.E. and Rubin, C.T., 1984. Static vs dynamic loads as an influence on bone remodelling. Journal of biomechanics, 17(12), pp.897-905.
5. Turner, C.H., Owan, I.C.H.I.R.O. and Takano, Y.U.I.C.H.I., 1995. Mechanotransduction in bone: role of strain rate. American Journal of Physiology-Endocrinology and Metabolism, 269(3), pp.E438-E442.
6. Wittkowske, C., Reilly, G.C., Lacroix, D. and Perrault, C.M., 2016. In vitro bone cell models: impact of fluid shear stress on bone formation. Frontiers in bioengineering and biotechnology, 4, p.87.
7. Weinbaum, S., Cowin, S.C. and Zeng, Y., 1994. A model for the excitation of osteocytes by mechanical loading-induced bone fluid shear stresses. Journal of biomechanics, 27(3), pp.339-360.
8. Liu, P., Tu, J., Wang, W., Li, Z., Li, Y., Yu, X. and Zhang, Z., 2022. Effects of mechanical stress stimulation on function and expression mechanism of osteoblasts. Frontiers in Bioengineering and Biotechnology, 10, p.830722.

THE MECHANICALIZATION OF LOCOMOTOR TRAINING FOR GAIT REHABILITATION DUE TO DAMAGE CAUSED BY PARTIAL SPINAL INJURIES: DEFING PARAMATER OF KNEE JERK REFLEX STIMULATION DEVICE

Hannah Khelfa (1), Mohammed Sbai (2), Sanford Meek (3)

(1) Biomedical Engineering
University of Utah
Salt Lake City, Utah, United States of America

(2) Collage of Health
University of Utah
Salt Lake City, Utah, United States of America

(3) Mechanical Engineering
University of Utah
Salt Lake City, Utah, United States of America

INTRODUCTION

Locomotor training (LT) is a gait rehabilitation treatment method. By placing a patient on a treadmill, and moving their legs in a walking motion, while stimulating the corresponding muscles (through tendon compression), a new pathway for generating movement is formed. Allowing the patient to regain some, if not all, of their legs motor control. Patients who have been rendered immobile due to incomplete spinal cord injuries (SCI), stroke, Cerebral Palsy, and many other neurological conditions have been treated using LT [1]. Despite its success in countries like Germany, Norway, and Switzerland, it is not widely available in America [2,3]. LT is a human-driven rehabilitation method, requiring four physical therapists. The body weight supports used to place the patient above the treadmill holds 30-70% of the patient's body weight [4]. This leaves another 30-70% of the weight for the therapist to overcome to move the patient's legs, taking a considerable amount of physical effort. Resulting in short treatment sessions. The amplitude and duration of the pressure used in LT must be precise; if either the stimuli or coordination are off it may result in an inaccurate stimulation [5]. Limitations of LT can be solved through Mechanicalization. Robots are not subjected to the limitations of human stamina. They are capable of outputting a constant and accurate force, reducing the chances of inaccurate stimulation, leading to higher treatment efficiency. The device itself will contain the LT protocol, decreasing the amount of training and therapists needed. The overall purpose of the lab is to improve LT. The full design will consist of an exoskeleton to physically move the patients' legs, and a tendon stretching device. Currently there are no existing robotic tendon stretching devices. Tendon compression is essential to LT. Thus, the scope of this project was limited to the designing, building, and preliminary testing of a device that will be used to apply pressure to the patellar tendon (PT).

METHODS

The device was designed to mimic the LT treatment protocol. Device specifications included: an output of at least 111N, a compression speed of at least 100ms, a compression mechanism capable of recording force, and a snug fit against the leg. Attachment of the device consisted of a half-circle platform (Fig.1) with straps. Creating a one-size-fits-all design, while providing stability to its platform. The device sits distal to the knee, attaching around the calf, to indent the PT. Preliminary design stages, established that a rack and pinion system is suited for the device's linear compression. A rack and pinion system, using a pinion, 12mm in diameter, requires a motor with at least 404rpm and torque of 17mNm, to generate a force of 111N. In short, the rack and pinion adheres to the design specifications. Attached to the distal end of the rack is the pusher. The pusher portion of the device consists of a pusher head, and a force sensor holder. The pusher head is the part of the device that will physically indent into the skin. The holder allows recording of the impact force.

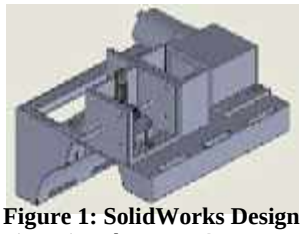

Figure 1: SolidWorks Design

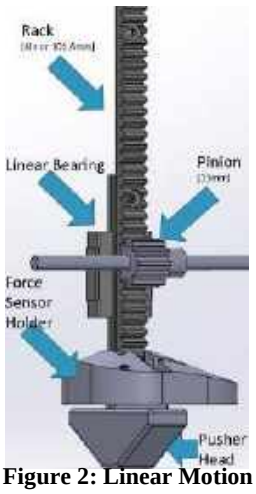

Figure 2: Linear Motion

To control the device's variable parameters and record the outputs, a LabVIEW user interface was developed with an Arduino backend. Variable parameters included the pusher head design, position of device, device input voltage, and holding duration. Output parameters included the impact force

and the recorded action-potential-peak EMG value (AP-EMG). Myolab II (Motion Control, SLC, UT) performed the EMG amplification process. Two electrodes were placed axially on the left leg, at the top and bottom quadrants of the quadricep muscle. Two designs of the pusher head were tested. Design 1 was a simple overall curve. Design 2 was altered to reduce the curved width to a 20mm point. Two device positions were tested. Position 1, the platform is anterior to the leg, hitting in the center of the PT. Position 2 is angled 20 degrees medial (hitting the side of the PT).

Compression of the PT at high levels of stimulation results in the myotatic (knee-jerk) reflex. To confirm the devices effects on the nervous system, EMG of the resulting knee-jerk reflex were recorded. Analyzation of the data was completed using MATLAB. The point of interest is the action potential peak (AP) as it travels up the leg to the spinal cord. A combination of a notch filter and band-stop filter [20-40 Hz] was applied to the EMG. For further analyzation of the data the AP-EMG and max force values were identified. The magnitude of the AP-EMG indicates the magnitude of recruited muscle fibers.

RESULTS

The goal of device testing was to provide its preliminary basis and adherence to the LT treatment protocol. The device's average impact duration (quick hit and retreat) was 50ms. And reached an output of 111N, using a device input voltage of 30volts. EMG experiments were performed as a preliminary check for the device parameters. When comparing the 20mm-curve pointed design to the over-all-curved pusher-head design, it produced significantly higher EMG values (0-2.5volts compared to 0-0.045volts, with a p-value of 0.013). Further testing was conducted using the 20mm-curve pointed design. The device-input-voltage, AP-EMG, and the impact force relationship was examined by testing device input voltages of 12-30volts, in increments of 3. Position 1 produced forces from 2-49N and 62-80N. Position 2 produced forces from 13-80N. Trend lines for both positions displayed a nearly linear increase at lower forces (2-31N and 13-33N), then a steady drop (31-58N and 33-53N), and a subsequent, slight, increase at higher forces (58-80N and 53-80N). Establishing a optimal force range of 18-40N and 22-40N, respectively. Position 1, at lower forces, has higher AP-EMG values than position 2. At higher forces, it has lower AP-EMG values. Position 2 forces have a normal distribution and increase steadily in correlation to the increasing device input voltage. While position 1 has a non-normal distribution, with significantly more forces on the lower range (1-17N). The minimum device input voltage required to elicit an AP, for position 1 and 2 is 14volts and 10volts, respectively. EMG noise approximation is 0.008 volts; values below or equal to 0.008v indicate no AP occurred, consequently no knee-jerk reflex. Further testing was conducted using position 2. In general, the addition of a holding force, post initial impact, with a duration of 100-500ms provided significantly higher EMG values. In regard to producing the highest average AP-EMG value the holding durations are in the order of 0, 200, 400, 500, 100, and 300ms. Forces range 2 to 53N. It is important to note that similar to the original Force-EMG graph, when holding is present there is still an optimal force range. The scaling and shift in its range are holding duration dependent. Holding duration of 1-4s, display a linearly decreasing trend line. Forces ranged 4 to 49N.

DISCUSSION

Preliminary testing confirms that the device adheres to the desired design specifications. As previously mentioned, this is an entirely novel device, lacking an established framework for optimal testing. Thus, our approach involved casting a broad net, encompassing testing of various device parameters on a single subject, to provide basic preliminary data. The goal was not to concretely define the reflex, but rather to serve as a foundation, providing direction for future testing. The 20mm pointed design resulted in higher EMG values due to mechanical and physiological factors. The average width of the patellar tendon is 20mm [6]. A pointed design allows for targeted stimulation of the PT. Due to the shape of the knee, position 1 is hitting a curved surface. If a normal impact force is higher than the friction force, horizontal sliding will occur [7]. This accounts for the alterations seen at higher forces in position 1. Position 2 impacts a relatively flat surface area of the knee. Various studies indicate that an increase in force or holding duration results in an increase in EMG [8]. Our data partially mimics the increasing trend found in current research. At higher forces and holding durations there are noticeable deviations. This is likely due to the force-length relationship of muscles and the inverse myotatic reflex. Striated muscle fibers' have lower force production at higher and lower lengths; the middle ranges correspond to the optimal length which generates max force [9]. Compression of the PT stretches (elongates) the connected quadriceps muscles. At higher forces, the PT is likely stretching the muscle beyond its optimal length (dropping the AP-EMG).

The inverse myotatic reflex acts opposite to the myotatic (knee-jerk) reflex [9]. Continuous force elicits a relaxation reaction of the muscles to prevent injury [10]. The longer the holding duration, the more this reflex comes into play. This is especially prevalent in durations 1-4s, which display a decreasing linear tend line.

Regarding LT, the data analyzed provides conformation that the device is capable of stimulating the muscles proprioception. LT treatment protocol does not elicit the knee-jerk reflex. Instead, low levels of proprioception stimulation, and neuroplasticity, allows the brain to establish a new pathway for lower limb movement [11]. Recording low-stimulation requires complex or invasive techniques. Tendon compression for LT rehabilitation will require additional testing and may differ in outcome. The purpose of this research was to simply confirm the devices capability, not the optimization of the treatment protocol. Thus, high stimulation levels, triggering the reflex, are sufficient. The data not only provided the upper limits for future treatment protocols (<10 or 14volts depending on position), but also helped identified potential relationships of various device parameters. Parameters such as impact force, holding duration, and device input voltage will dramatically affect muscle response. Future testing and quantification of these parameters using this device will not only aid in the optimization of the LT treatment protocol, but also in the general understanding of this reflex. The development of this tendon stimulating device puts us one step closer to an improved LT rehabilitation method.

ACKNOWLEDGEMENTS

H. Khelfa thanks the principal investigator Sanford Meek, and the advising neurologist Mohammed Sbai. Thanks, given to the University of Utah for the UROP grant. Thanks, given to parents of H. Khelfa: Souad Ouahib Khelfa and Abdelfatah Khelfa for their love and support.

REFERENCES

[1] Hesse S., NeuroRehabilitation, 16(3):133-9, 2001.
[2] Mehrholz, J et all., Cochrane review, 2017.
[3] Andrews, S., rollxvans, 2013.
[4]Hesse S., NeuroRehabilitation, 23(1):55-65, 2008.
[5] Harkema, S et al., OUP, 2011.
[6] Shelbourne, K.D. et all., Am J Sports Med 22(6):774-7, 1994.
[7] Iran, S et al., J. Neurophysiol, 81(2):845-857, 1999.
[8] Fitzpatrick, R.D. et al., Physiol. J, 478:363-372, 1994.
[9] Rassier D.E et al., J Appl Physiol, 86(5):1445-57, 1985.
[10] Jelvéus, A., Sciencedirect, 1(6):75-95, 2011.
[11] Winchester, P et al., NCBI, 19(4):313-24, 2005.

MARGINAL CHORDAE FORCE DATA IN A PHYSIOLOGICAL IN VITRO MITRAL VALVE SETUP

Mads V. Ancker, BS (1), Sam E. Stephens, MS (1), Neil B. Ingels, PhD (1), Jonathan F. Wenk, PhD (2), Morten O. Jensen, PhD, DrMed (1)

(1) Department of Biomedical Engineering, University of Arkansas, Fayetteville, AR, USA
(2) Department of Mechanical Engineering, University of Kentucky, Lexington, KY, USA

INTRODUCTION

Optimal mitral function plays a crucial role in the comprehensive cardiovascular performance. The intricacies of the mitral valve (MV), especially the chordae tendineae (CT), exhibit variations among individuals. While prior research has investigated force magnitudes and distributions in the belly and annular chords, limited attention has been given to the marginal chords. In this study, we introduce a technique for quantifying the forces acting on these marginal chords, which are defined as those reaching the anterior or posterior leaflets in the ”rough” / coaptation zone.

METHODS

Weighing, Sizing, and Dissection: Porcine heart, from which MVs were dissected, were obtained from an abattoir. The left ventricular myocardium's papillary muscles (PM) were surgically excised, and the valve separated from the left atrium and ventricle by cutting 5-10mm into the atrial and ventricular myocardium from the annulus. The valve was then trimmed to keep about 10mm of PM tissue beneath fibrous membranes and 5mm of tissue outside the annulus, around the entire circumference.

Annulus Clamp: The dissected MV, trimmed as needed, is secured in a custom 3D-printed annulus clamp [1] (Fig. 1 a+c), which consists of two halves and ensures a physiologically realistic configuration. Each PM is then attached to a stitching ring for connection to the pressurization system, completing the assembly with the fully mounted valve (Fig. 1c).

Vacuum system: The MV, connected to a previously described pressurization system [2], closes via vacuum pressure on the atrial side, creating physiological trans-mitral pressure differences. This inverted setup allows measurement of the ventricular side (CT and PMs), with a small water column above the annulus to maintain moisture. Pressure comes from a pre-charged chamber. A refill system prevents valve leakage, and a clear acrylic front facilitates visual inspection. A standoff with a clear acrylic window allows qualitative measurement of valvular leak rates.

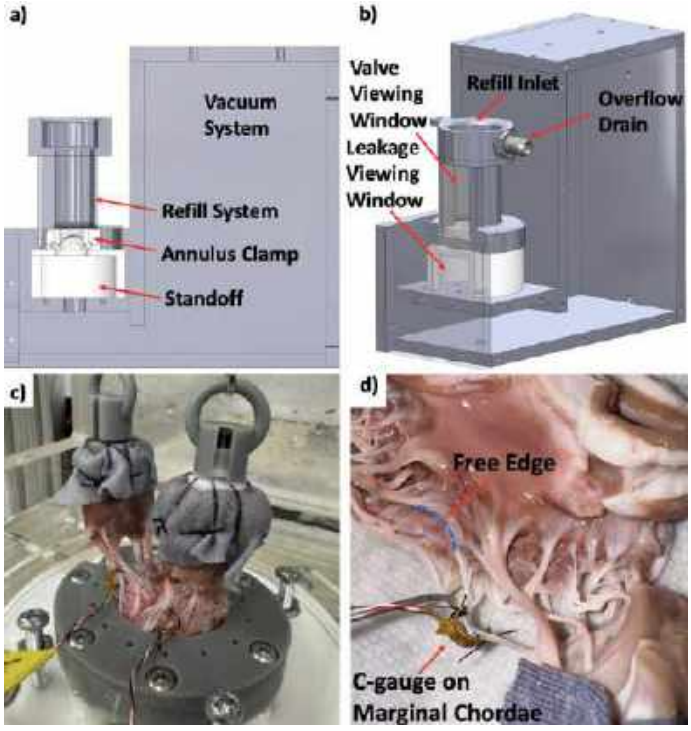

Figure 1: a+b) The vacuum system c) MV in the vacuum closure system without the refill system (for clarity). d) Exemplar image of a C-gauge on a marginal chord. The chord is uncut at time of photograph.

Chordal Force Measurement: Marginal chordae, tendinous structures on MV leaflets, were identified during porcine heart dissection [3], ensuring chords without significant branches and sufficient length for C-gauge mounting. Silk-braided sutures (size 5/0) secured the C-gauge in the frame's perforations at specific length intervals [4]. Careful suturing avoided tension issues that could compromise force measurements. After suturing, chordae were precisely divided between suture points, so that tension was transmitted to the C-gauge in the subsequent vacuum test. Due to documented variability in marginal chordae forces, concurrent measurements with well-established strut chordae force assessments were conducted to validate strain gauge function and placement [2, 5, 6].

RESULTS

Table 1 displays marginal chordal forces measured during the experiments, along with corresponding transvalvular pressure values.

Table 1: Marginal chordal force at transvalvular pressures of 80-110 and 120mmHg (n=5 and 3). Four porcine hearts were utilized, with three hearts having a single C-gauge on a marginal chord, and one heart having two C-gauges on separate marginal chords (data from two more hearts will be presented).

Transvalvular Pressure (mmHg)	Marginal Chordal Force (N) – Mean +/- SD
80	0.0098 +/- 0.0079
90	0.0094 +/- 0.0078
100	0.0106 +/- 0.0086
110	0.0115 +/- 0.0098
120	0.0074 +/- 0.0111

The standard systolic blood pressure, 120 mmHg, is a pivotal value, where the marginal chordal force was measured with a mean value of 0.0074 N, as shown in Table 1. The measurement of strut chordal force was conducted to validate the proper valve function and utilization of C-gauges. Figure 2 illustrates an exemplary dataset derived from measurements on a marginal chordae, a strut chordae, and transvalvular pressure. The observed strut chordal force is recorded as 0.61 N at a transvalvular pressure of 134.6 mmHg, falling within an acceptable range [2, 5, 6].

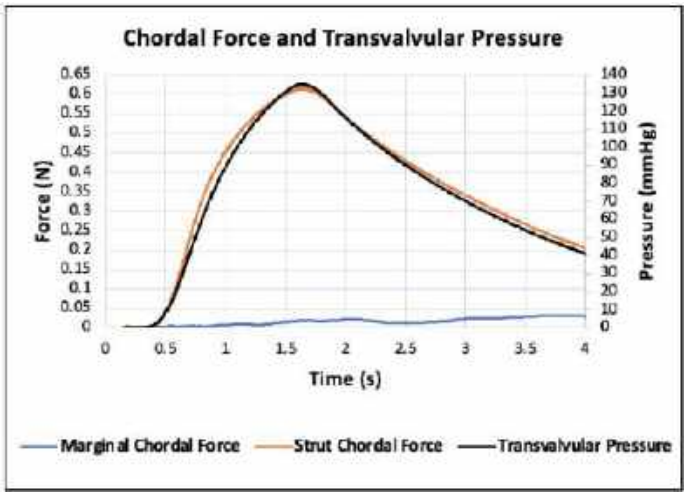

Figure 2: Concurrent force measurements on a marginal chordae, a strut chordae, and the recorded transvalvular pressure.

DISCUSSION

Marginal chord examination shows low forces, aligning with expected contact in the coaptation zones of the self-supporting MV leaflets [7]. Measured forces in marginal chords consistently remain low and show no significant correlation with transvalvular pressure, unlike strut chords. This concept is illustrated in Figure 3.

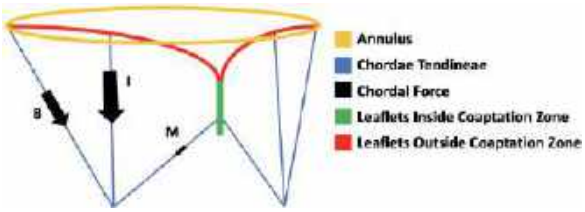

Figure 3: The mitral valve exhibits three chord types: basal (B), intermediate (I), and marginal (M). Force magnitudes in each chord type are represented by arrow size, with intermediate chords (strut chords) showing significantly larger forces than marginal chords.

The inherently low forces in marginal chords are unsurprising due to direct leaflet contact at the insertion point and the convex/concave self-supporting shape of the leaflets [7]. Strut chord forces align with reported ranges in other studies, indicating a valid force measurement setup and proper valve functioning, and that the marginal chordal forces presented in this study are reliable. This implies that strut chord force measurements reflect consistent valve performance based on established scientific benchmarks. Chordal forces and leaflet strain in in vitro models with diverse annulus shapes for both porcine and human valves have been studied previously, indicating higher marginal chordal forces with a flat annulus [8-11]. In this study, the natural shape of the annulus is modeled, which has been shown to enhance valve leaflet self-support [7] and lower strain on the individual valve components [12-13]. Our investigation used a saddle-shaped annulus clamp, aligning more closely with previous results when employing a similar annulus shape [8]. Notably, posterior leaflet marginal chordal forces have been previously found to match those found in the present study, regardless of annulus shape, while anterior leaflet forces were an order of magnitude larger, around 0.2N [9,10]. The annulus, leaflet configuration, and marginal chord spatial arrangement relative to the coaptation zone during valve closure play vital roles in chordal forces under physiological trans-mitral pressures. This underscores the importance of considering anatomical and structural factors, especially varying annulus shapes, in interpreting MV biomechanics.

ACKNOWLEDGEMENTS

This project was supported by NIH Award R15 HL145585-01 and Chawla Heart Technologies, LLC.

REFERENCES

[1] Stephens, S et al., *PLoS One*, 12(8):e0184042, 2017.
[2] Stephens, S et al., *J Cardiovasc Trans Res.*, 15(4):845-854, 2022.
[3] Gunnal, S et al., *Heart Views*, 16(1):1-12, 2015
[4] Nielsen, S et al., *Ann Biomed Eng.*, 32(8):1050-7, 2004.
[5] Jimenez, J et al., *Ann Biomed Eng.*, 33(5):557-66, 2005.
[6] Siefert, A et al., *Cardiovasc Eng Technol.*, 5(1):35-43, 2014.
[7] Ingels, N et al., *Mitral Valve Mechanics*, 2015.
[8] Jimenez, J et al., *J Thorac Cardiovasc Surg.*, 134(6):1562-8, 2007.
[9] Jimenez, J et al., *Ann Biomed Eng.*, 31(10):1171-81, 2003.
[10] Jimenez, J et al., *Ann Biomed Eng.*, 33(5):557-66, 2005.
[11] Jimenez, J et al., *J Heart Valve Dis.* 14(3):295-302, 2005.
[12] Padala, M et al., *Ann Thorac Surg.* 88(5): 1499-504, 2009.
[13] Jensen, M et al., *Circulation* 118(14): 250-5, 2008.

NUMERICAL SIMULATION OF MULTI-FREQUENCY VENTILATION WITHIN THE CENTRAL AIRWAYS OF A PORCINE LUNG

Bing Han (1,2), Emmanuel A. Akor (3), Mingchao Cai (1), David W. Kaczka (2,3,4)

(1) Department of Mathematics, Morgan State University, Baltimore, MD, USA
(2) Department of Anesthesia, University of Iowa, Iowa City, IA, USA
(3) Roy J. Carver Department of Biomedical Engineering, University of Iowa, Iowa City, IA, USA
(4) Department of Radiology, University of Iowa, Iowa City, IA, USA

INTRODUCTION

Patients with acute respiratory failure often require supportive mechanical ventilation to maintain adequate gas exchange. In contrast to conventional mechanical ventilation, oscillatory ventilation relies on low tidal volumes cycled at supraphysiological rates, which produce fundamentally different mechanisms for gas transport and exchange [1]. Multi-frequency ventilation (MFV), a modality that combines desirable features of CMV and oscillatory ventilation, provides more uniform ventilation throughout the lung with asymmetric airway branching and/or heterogeneous mechanical properties. In this study we simulated gas flow in computational porcine lung model, consisting of a central airway tree from the trachea to the fourth generation of airway segments, as well as dynamic peripheral boundary conditions. Simulated flow waveforms at the trachea included CMV cycled at 0.27 Hz, as well as MFV consisting of low-amplitude 3.5 Hz and 7.0 Hz sinusoidal components superimposed on a 0.27 Hz CMV component. Dynamic pressures at various airway segments were predicted based on the interactions of internal flows with downstream elastances and peripheral airway resistances. The resulting internal airflows were simulated and analyzed in both time- and frequency-domains. Our simulations indicate that compared to CMV, MFV results in stronger flow asymmetry at end-inspiration and end-expiration (i.e., "pendelluft"), as well as larger phase differences between the inlet and outlets for pressure and flow. Our data are consistent with the notion that MFV has potential to enhance gas mixing, thus facilitating the efficiency of ventilation in the mammalian lung.

METHODS

A three-dimensional (3D) airway tree was segmented from a thoracic CT image of a healthy porcine subject. The tree was then truncated from the proximal third of the trachea to half of the 4th generation segments. Due to asymmetric branching, the resulting tree consisted of thirteen peripheral outlets. Simulated CMV and MFV airflow waveforms were scaled to yield delivered tidal volumes at the trachea of about 7 mL kg^{-1}. The CMV and MFV waveforms were then imposed in sequence as boundary conditions at the trachea of the CFD model. Dynamic pressure variations at each of the thirteen outlets of the airway tree were induced by the effects of downstream parenchymal tissue elastances, peripheral airway resistances, and gas inertia, which were applied as downstream boundary conditions. All values of downstream airway resistance and gas inertance were estimated by inverse modeling regression [2]. The airway walls were assumed to be rigid, with a no-slip boundary condition. The turbulence was modeled using the Navier-Stokes equations incorporating the k-ω Shear-Stress Transport (SST) model. To address convergence sensitivity challenges in dynamic pressure at the outlets, the equations were solved by employing the Splitting of Operators (PISO) algorithm with a time step size of 0.001 seconds.

RESULTS

In the time-domain, the pressure variations at the thirteen outlets were similar in magnitude and delay, regardless of airway opening waveform. For both CMV and MFV, elastic pressure dominated the outlet pressures by about 7 cmH_2O, with 90^o phase differences observed among the elastic, resistive and inertial pressure components. However, MFV resulted in more turbulent flows and stronger pendelluft at phase shifts between inspiration and expiration, as shown in Figure 1. In the frequency-domain, the pressure and flow magnitudes at the tree outlets were dominated by spectral energy at 0.27 Hz during CMV, but by energy components 0.27 Hz, 3.5 Hz and 7 Hz during MFV. Outlet pressure variations lagged the inlet pressure by only about 1^o at 0.27 Hz

during CMV, but increased to 2.5º during MFV. Phase differences in flow rates between the inlet and outlets ranged from -0.8º to 0.4º for CMV, and from -1.5º to 1.8º during MFV. These results suggest that the slower 0.27 Hz CMV component of the MFV waveform was nonlinearly influenced by the high-frequency oscillations of 3.5 Hz and 7 Hz, thus enhancing inlet-outlet phase differences in low-frequency flow and pressure.

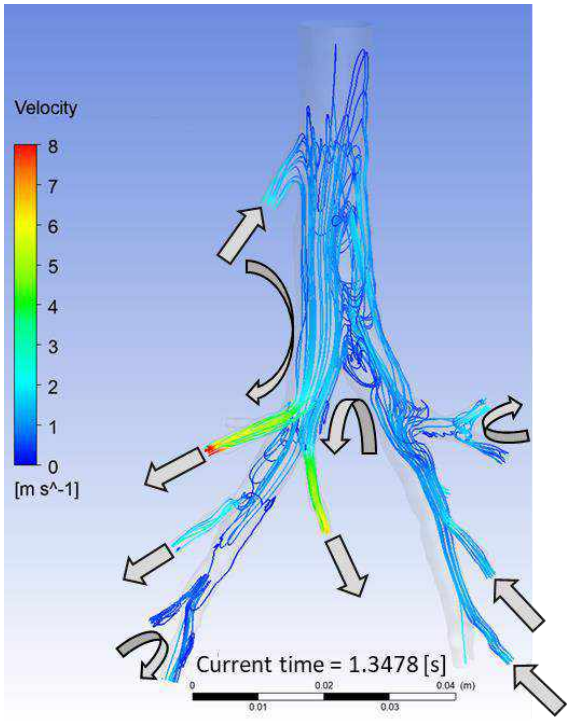

Figure 1: Pendelluft movements across the central airways indicated by streamlines at one of the end-inspirations during MFV (directions of the movements are suggestively marked by grey arrows).

DISCUSSION

In this study, we simulated airflow within a porcine central airway tree during CMV and MFV. The transient 3D Navier-Stokes equations were solved by applying experimentally realistic flow rate boundary condition at the airway inlet and dynamic pressure boundary condition at the outlets. Airflows were simulated and analyzed in both time- and frequency-domains. The high-frequency components of the MFV waveform nonlinearly influence its fundamental low-frequency component, which allow for enhanced pendelluft and gas mixing. Our simulations offer an effective way to reveal flow phenomena for specific airway regions across various ventilation modalities. These results also highlight the importance of applying realistic boundary conditions in such numerical airflow simulations.

ACKNOWLEDGEMENTS

Supported in part by the Office of the Assistant Secretary of Defense for Health Affairs, through the Peer Reviewed Medical Research Program under Award Number W81XWH-21-1-0507 and the Army Research Office Program under Award Number W911NF-23-1-0004. Opinions, interpretations, conclusions, and recommendations are those of the authors and are not necessarily endorsed by the Department of Defense.

CONFLICTS OF INTEREST

DWK is a co-founder and shareholder of OscillaVent, Inc., and is a co-inventor on a patent involving multi-frequency oscillatory ventilation. DWK also receives research support from ZOLL Medical Corporation. The authors maintain that the industry had no role in the design and conduct of the study; the collection, management, analysis, or interpretation of the data; or the preparation, review, or approval of the manuscript.

REFERENCES

[1] Herrmann J, Tawhai MH, Kaczka DW, Parenchymal strain heterogeneity during oscillatory ventilation: why two frequencies are better than one, *J Appl Physiol* (1985), 124(3):653-663, 2018.

[2] Kaczka DW, Barnas GM, Suki B, Lutchen KR, Assessment of time-domain analyses for estimation of low-frequency respiratory mechanical properties and impedance spectra, *Ann Biomed Eng*, 23:135-151, 1995.

VALIDATION OF FEA MODELS FOR DESIGN OF ENGINEERED FOAM FOR SCOLIOTIC BRACES

Robert Rizza (1), Xue-Cheng Liu (2), Vince Anewenter (3)

(1) Department of Mechanical Engineering, Milwaukee School of Engineering, Milwaukee, WI, USA
(2) Department of Orthopedic Surgery, Children's Wisconsin, Medical College of Wisconsin, Milwaukee, WI, USA
(3) Rapid Prototyping Center, Milwaukee School of Engineering, Milwaukee, WI, USA

INTRODUCTION

The Thoracic Lumbar Sacral Orthosis (TLSO) is widely applied for children with idiopathic scoliosis and provides curve correction or stabilization with derotation and lateral bending using a three-point loading mechanics and circumferential compression. Typically, the TLSO is designed in modular form, including anterior and posterior polymer lateral panels (typically made of Polyethylene), padded with foam and secured with Velcro straps. Some new designs incorporate 3D printing for the lateral panels (but not the padding) [1-4]. By exploiting the accuracy and speed of the 3D printing process, some advancements in brace design and manufacturing have been made [2].

Although the literature suggests extensive research and modeling of the hard polymer layer, research into the effect of the foam padding is virtually non-existent. What knowledge exists is rather empirical, poorly quantified and focused on foams used in foot orthotics [5]. Nonetheless, the foam plays a vital role in correcting the deformity and providing cushioning. Its role needs be investigated, quantified, and understood.

For scoliosis braces and orthotics, the typical foam used is Ethylene-Vinyl Acetate (EVA), which is "rubber-like" in terms of softness and flexibility. Typical values of stiffness for these foams are 1500 N/mm for a medium density and 2600 N/mm for firm density.

EVA is closed cell which has the beneficial property of preventing absorption of moisture which often leads to odor, mildew growth and in some cases Dermatitis [6]. However, closed cell foams do not permit air flow. Lack of air flow makes the device more uncomfortable and hotter which reduces compliance with the brace or orthotic.

An Engineered Foam is 3D Printed using newly developed flexible 3D printing materials (PEBA®, BASF® 88A TPU, etc.). The engineered foam geometry is open cell and is characterized by repeated cells of a lattice structure composed of bars called "struts" that connect vertices together to form the cell (Figure 1). The diameter of the strut is a design parameter. By changing the diameter, a foam with a different stiffness may be produced. The geometry which matches the cellular structure of traditional foam is the octagonal geometry.

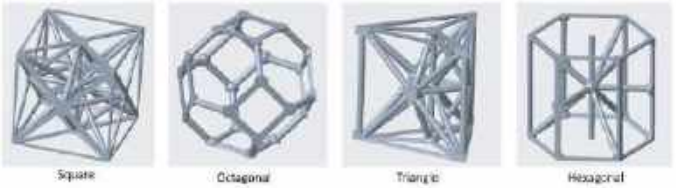

Figure 1: Various lattice geometry cells that may be used for the engineered foam.

Engineered foams may be custom designed to meet the needs of the patient. Already there has been successful implementation of such foams in Riddle 3D printed NFL football and EOS bicycle helmets. However there has been little to no application to orthotics and braces.

Also, it appears that there has been no development of Finite Element (FEA) models for 3D printed engineered foams in Scoliotic braces. The purpose of this study was to create and validate these models.

METHODS

Two recycled brace plaster mold negatives used in the traditional manufacturing of braces and the corresponding braces were acquired from a local facility (Hangar O & P, Milwaukee). The pressure at the plaster wall/foam interface was measured using Tekscan Flexiforce® pressure sensors. Thus the force that should be applied in the FEA was obtained. The average level of force was found to be 156N.

TPU 88A (BASF, Florham Park, NJ) was selected as the printing material. In order to establish the mechanical properties for this

material, a compression test was performed on five 3D printed (SLS) samples. The stress strain curve was obtained for this material and found to be non-linear as expected. The Young's modulus of the material was determined to be 2.869 ksi (19.78 MPa).

For validation, an MTS Alliance RT/50 was used. This frame has a 6 in (15.24 cm) diameter platen. According to ASTM D3574 C, for compression testing of foams the sample must be greater than the platen diameter, so the diameter of the foam was set at 7 in (17.78 cm).

Creo® (PTC, Boston) was implemented to create CAD models of the engineered foam. The models created were round with a 7 in diameter and having the octagonal lattice structure. The size of the cell was varied from 4 to 9 mm and the diameter of the strut was varied from 1 to 2 mm. The number of cells filling the CAD model varied as the cell size varied. The thickness of the foam was set at 7 mm as this value matched the thickness of traditional foam sheets. The optimal design yielding the two target foam stiffness (1500 and 2600 N/mm) was 7 x 7 x 7 mm.

Simulations were carried out using Ansys (Ansys, Canonsburg, PA). Because TPU 88A is non-linear, a multilinear isotropic hardening material model employing true stress and strain was used. Figure 2 shows an edge view of the foam with the applied boundary conditions that generate a mechanical environment comparable to the compression testing. They include a frictionless support over the entire bottom face to simulate the compression plate and a displacement of 0 mm in the direction normal to the faces on the edges of the foam.

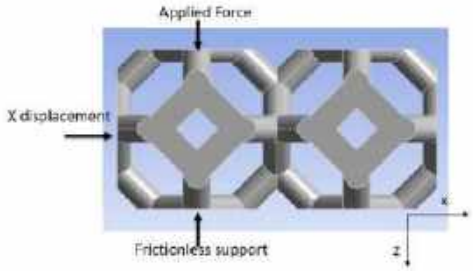

Figure 2: Boundary conditions applied in the FEA model.

The optimal designs were 3D Printed using the SLS method at the MSOE Rapid Prototyping Center using a DTM Sinterstation 2500 plus. Two samples of each stiffness were printed. Figure 3 shows a picture of one of the samples being tested in compression.

Figure 3: Engineered foam undergoing compression testing.

RESULTS

Because stress is not defined in the same way in compression testing as it is in FEA, stiffness was used. The stiffness as predicted by the FEA and as measured from the compression testing is given in Table 1. We see that the values are within experimental and numerical error.

Table 1: Results of the FEA compared to the compression testing.

Foam	Strut diameter (mm)	Stiffness (N/mm)		% difference
		FEA	Testing	
Medium	1.20	1512	1591	5.0
Firm	1.44	2614	2620	0.23

DISCUSSION

As we can see in Table 1, the difference in the prediction of stiffness between the FEA simulations and the compression testing is quite small. This implies that the FEA models are valid and may be used for subsequent simulations involving different values of foam stiffness. As the objective of this study was to generate validated FEA models for the design of Engineered Foam in brace applications, the study goals were achieved.

It was observed that the typical level of force applied to the foam (156N) is actually quite small. And while the behavior of the TPU 88A shows hyperelastic behavior, the deformation under 156N is less than 2% strain. This implies that linear FEA material models may be used. In fact, the optimal design was rerun in Ansys with a linear material model having a Young's Modulus of 2.869 ksi (19.78 MPa) and a Poisson ratio of 0.1 to yield the same stress and strain results as when the multilinear isotropic hardening material model was used. Since a linear model is easier to implement and runs faster, the linear material model is recommended for this application.

ACKNOWLEDGEMENTS

The authors wish to recognize the hard work of Chase Blum and Megan McKee, undergraduate students at the Milwaukee School of Engineering for their hard work in completing the FEA simulations.

REFERENCES

[1] Thometz, J. and Liu, XC. 2021. "Follow-Up of an Elongation Bending Derotation Brace in the Treatment of Infantile Scoliosis," Research into Spinal Deformities 9. XC. Liu, and J. Thometz, eds., IOS Press, Amsterdam, The Netherlands, pp. 174-178.

[2] Thometz, J., Liu, X., Rizza, R. *et al.* 2018. Effect of an Elongation Bending Derotation Brace on the Infantile or Juvenile Scoliosis. Scoliosis and Spinal Disorders. 13, pp. 1- 6 (doi:10.1186/s13013-018-0160-4).

[3] Cobetto, N., et al. 2017. 3D Correction of AIS in Braces Designed using CAD/CAM and FEM: A Randomized Controlled Study. Scoliosis and Spinal Disorders. 12, pp. 12-24 (doi: 10.1186/s13013-017-0128-9).

[4] Pea, R., Dansereau, J., Caouette, C., et al. 2018. Computer-Assisted Design and Finite Element Simulation of Braces for the Treatment of Adolescent Idiopathic Scoliosis Using a Coronal Plane Radiograph and Surface Topography. Clinical Biomechanics. 54, pp. 86-91.

[5] Spirka, T., Erdemir, A., Spaulding, S., et al. 2014. Simple Finite Element Models for use in the Design of Therapeutic Footwear. Journal of Biomechanics. 47(12), pp. 2948-2955.

[6] Pedragosa R., Romaguera C., Mascaro JM, Vidal J., and Jariod J. 1985. Dermatitis Caused by Milwaukee Braces. Med. Cutan Ibero Lat Am.13(3), pp. 205-208.

SYNTHESIS OF CORONARY ARTERIAL NETWORKS FROM MYOCARDIAL BLOOD VOLUME MAPS

Mostafa Mahmoudi (1,2), Amirhossein Arzani (3,4), Kim-Lien Nguyen (1,2)

(1) Departments of Medicine, Radiology, and Bioengineering, David Geffen School of Medicine, University of California, Los Angeles, CA, USA
(2) VA Greater Los Angeles Healthcare System, Los Angeles, CA, USA
(3) Department of Mechanical Engineering, University of Utah, Salt Lake City, UT, USA
(4) Scientific Computing and Imaging Institute, University of Utah, Salt Lake City, UT, USA

INTRODUCTION

Despite recent advances in clinical medical imaging, limitations in spatial resolution prevent depiction of the microvascular arterial network. Adequate myocardial perfusion depends on the intricate balance between the epicardial and microvascular arterial system. Therefore, understanding and accurate mapping this network is required for development of diagnostic and therapeutic strategies in cardiovascular medicine.

Several methodologies for myocardial arterial network generation have been proposed, with each offering unique insights and challenges. Fractal models effectively capture the complex branching nature of vascular networks [1], while optimization methods aim to efficiently represent the vascular system, focusing on critical parameters like tree volume or kinetic energy [2]. Although continuous models using porous media flow simulations complement these methods and broaden our perspectives on myocardial perfusion, they risk oversimplifying structural details [3].

More advanced techniques such as Constraint Constructive Optimization (CCO)-based methods have gained popularity, particularly the adaptive CCO approach, which is tailored to reflect the physiological and anatomical variations of the myocardial arterial network [4]. These methods excel in capturing intricate network topology and accommodating patient-specific physiological variations, which is invaluable for creating personalized models.

The automatic generation of arterial networks in the myocardium, based on myocardial blood volume (MBV) maps [5, 6] may further transform our understanding of the relationship between the coronary circulation and myocardial perfusion. The MBV reflects the autoregulatory adaptation necessary to maintain resting myocardial blood flow over a range of coronary perfusion pressure, whereby additional blood supply requires arteriole vasodilation and capillary recruitment. Despite the advancements in modeling techniques, significant unknowns remain, particularly for generating large physiologically-sound vascular networks that supply blood to various myocardial segments. These unknowns include the precise replication of the myocardial perfusion and their integration into patient-specific arterial network models.

The primary objective of this study is to develop a framework for automatically generating a one-dimensional arterial network in the myocardium, based on MBV maps. This approach aims to bridge the gap between perfusion imaging and vascular modeling to provide a more integrated and accurate representation of the coronary circulation.

METHODS

Myocardium. An ideal left ventricular (LV) myocardial geometry was generated from coronary computed tomography angiograms (CTA) and was segmented according to the American Heart Association (AHA) 17-segment model. Representative MBV maps of the LV were estimated using Kassab's myocardial mass-flow rate relationship [7].

Coronary Tree. The 3D model of left anterior descending (LAD) artery was extracted from the CTA images using Simvascular software package. The centerlines for the LAD were extracted and a 1D model of LAD was reconstructed.

Arterial Network Generation. A modified adaptive, multistage CCO method was developed to generate the vascular network. In brief, locations of virtual terminal nodes were generated randomly, and 15 closest arterial segments were identified. To find the best location for the bifurcation point, physiological and geometrical constraints were incorporated, and an optimization problem was solved where the objective function is the total volume of the arterial tree. The construction of the arterial tree for different myocardial segments continues until the diameter of the terminal segments reaches 150 μm.

Global Optimization of Diameters. An iterative optimization method was developed to correct each arterial segment diameter such that the flow rate supplying each myocardial segment matches the MBV maps with a tolerance of 0.2 %.

Reproducibility and Seed Dependency Analysis. Since the terminal node selection process is based on a random coordinate generator, five arterial networks were generated based on different seeds, and the distributions of arterial segment diameters were compared. Also, the resultant synthetic MBV maps were compared with the prescribed MBV maps.

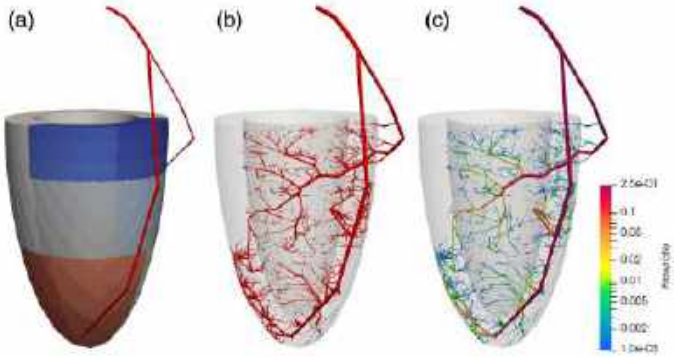

Figure 1: (a) Left ventricular myocardial segments corresponding to the LAD territory and the initial 1D tree; (b) Generated synthetic arterial network consisting of 1500 arterial segments; and (c) Distribution of flow rate (cm^3/s) in the LAD arterial tree.

RESULTS

Shown in Figure 1 is the LAD myocardial territory, along with the corresponding CTA-derived 1D epicardial coronary tree, the generated synthetic arterial network from Seed 1, and the flow distribution. Near uniform flow rate distribution can be seen in the terminal segments.

Figure 2 shows the distribution of terminal segment diameters for five synthetic arterial trees. The terminal segment distributions are similar for all five synthetic networks (coefficient of variation = 0.21). The mean terminal segment diameter for all seeds was 131±28 μm and the average arterial tree volume was 392±13 mm^3.

Figure 3 shows the relationship between the percent flow rate calculated based on myocardial mass [7] and the percent flow rate obtained from the synthetic networks. The trendline indicates minimal discrepancies between the target flow percentages and the flow percentages computed from the synthetic networks (R^2=0.93, and Pearson's r=0.97). The mean error between segment-wise flow percentages was 3.1±2.6%.

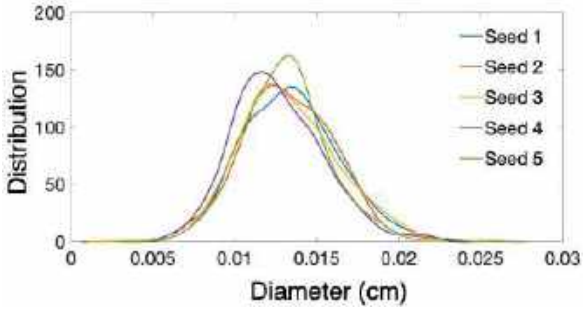

Figure 2: Distribution of terminal segment diameters for five different random seeds.

DISCUSSION

The synthetic arterial trees successfully populated the LAD distribution of the perfused myocardium while meeting all the physiological and anatomical constraints (see Figure 1). The synthetic network conforms to the shape of myocardium while effectively generating larger arteries on the epicardial surface and branching into smaller arterial segments inside the myocardium (Figure 1c). The distribution of the terminal segments for five separate synthetic trees were consistent (coefficient of variation equal to 0.21). To further confirm the reproducibility of our arterial network generation algorithm, we generated synthetic MBV maps for all 5 arterial networks. We compared the absolute difference between the myocardial mass derived MBV maps and the synthetic MBV maps. The median synthetic MBV was within 3% of the myocardial MBV maps. The results (Figures. 2 and 3) support the robustness of our proposed computational framework for simulating the distribution of blood inside the synthetic microvascular tree based on MBV maps. The results imply that our current model can calculate the resistances in the microvascular network accurately.

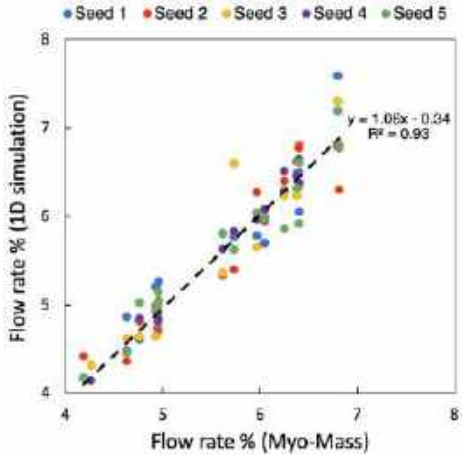

Figure 3: Relationship between flow rate calculated based on the myocardial mass and flow rate obtained from the synthetic arterial network.

The findings of our study have significant implications for epicardial and microvascular ischemic heart disease. The ability of our synthetic arterial networks to accurately replicate the coronary arterial tree and MBV maps underscores its potential to enable further study of the relationships between the epicardial coronaries and microcirculation. The strength of our approach lies in its robustness and reproducibility. However, it is important to consider the limitations of this study. While the synthetic networks showed high fidelity in replicating the physiological and anatomical features, they are based on simplified models and limited physiological data. Work is under way to apply the developed framework to patient-specific MBV maps with patient-specific epicardial coronary arterial tree and myocardial geometry. Despite these limitations, our study represents a significant step forward in filling the gap between perfusion imaging and computational coronary blood flow modeling, providing a more integrated and accurate representation of the coronary arterial network.

ACKNOWLEDGEMENTS

This study is supported in part by grants from the National Institutes of Health (R01HL127153) and from the Veterans Health Administration (I01CX001901).

REFERENCES

[1] Karch, P et al., *J Gen Physiol*, 122:307-322, 2003.
[2] Jaquet, C et al., IEEE Trans Biomed Eng, 66:946-955, 2019.
[3] Guy, A et al., IEEE Trans Biomed Eng, 76:1650-1663, 2020.
[4] Talou, GDM et al., Scientific Reports, 6180, 2021.
[5] Colbert, CM et al., Magn Reson Med, 89(4):1557-1566, 2023.
[6] Colbert, CM et al., J Magn Reson Imaging, 53(6):1699-1709, 2021.
[7] Choy, J and Kassab, G, J Appl Phyiol, 104:1281-1286, 2008.

INSIGHTS INTO CURVED AND INCOMPLETE GLOTTAL CLOSURE PATTERNS: AN EULER-BERNOULLI APPROACH

Mohamed A. Serry (1), Gabriel A. Alzamendi (2), Matías Zañartu (3), Sean D. Peterson (4)

(1) Applied Mathematics, University of Waterloo, Waterloo, Ontario N2L 3G1, Canada
(2) Institute for Research and Development on Bioengineering and Bioinformatics (IBB), CONICET-UNER, Oro Verde, Entre Ríos 3100, Argentina
(3) Department of Electronic Engineering, Universidad Técnica Federico Santa María, Valparaíso, Chile
(4) Mechanical and Mechatronics Engineering, University of Waterloo, Waterloo, Ontario N2L 3G1, Canada

INTRODUCTION

The configuration of the vocal folds (VFs) and the surrounding laryngeal tissue is pivotal in voice production as it affects voice quality and may have consequences on vocal health. Laryngeal configurations are modulated by complex interactions between the laryngeal passive tissues, cartilages, and muscles, which are not fully understood. Incomplete glottal closure is a laryngeal configuration wherein the glottis is not fully obstructed prior to phonation, which can exhibit an array of curved VF patterns (see Figure 1).

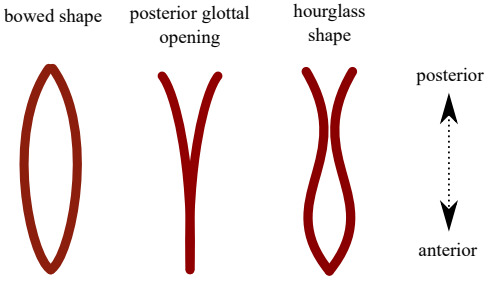

Figure 1: Schematic diagram (superior view) of some incomplete and curved glottal closure patterns that are observed clinically.

The underlying physical mechanisms of curved and incomplete glottal closure patterns are not well understood. However, there exist several experimental and clinical studies in the literature that link certain curved and incomplete glottal closure patterns to particular laryngeal maneuvers [1–4]. Besides, numerical simulations using high-fidelity numerical models [5, 6] qualitatively agree with the aforementioned clinical and experimental studies.

Despite these valuable efforts, there is a lack of comprehensive understanding of the physical mechanisms inducing different glottal patterns. This is due to the difficulty of isolating and controlling the factors underlying posturing mechanics in clinical or experimental setups, and the lack of clear intuitive understanding of the mechanics of posturing when adopting high-fidelity numerical models.

In this work, we present an Euler-Bernoulli composite beam VF model [7] that produces qualitatively similar incomplete glottal closure patterns as those observed in experimental and high-fidelity numerical studies, thus offering insights in to the potential underlying physical mechanisms.

METHODS

We hypothesize that the layered non-homogeneous structure of the VFs underlies, at least in part, the different glottal shapes displayed in Figure 1. As such, we propose an Euler-Bernoulli composite beam model of the VFs (see Figure 2).

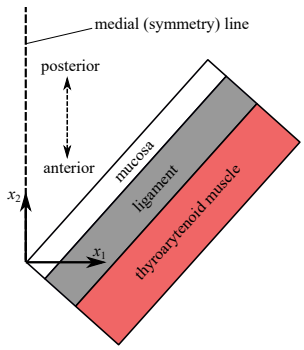

Figure 2: Schematic diagram of the VF composite beam model.

The proposed beam model is integrated with the muscle-controlled posturing model of Titze and Hunter [8] that relies on five normalized muscle activation parameters, a_{ta}, a_{ct}, a_{lca}, a_{ia}, and a_{pca}, which correspond to the thyroarytenoid (TA), cricothyroid (CT), lateral cricoarytenoid (LCA), interarytenoid (IA), and posterior cricoarytenoid (PCA) muscles, respectively. This integration aims at gaining refined physiological insights into how intrinsic laryngeal muscles may influence glottal geometry.

RESULTS

We consider numerical simulations of the proposed model that incorporate laryngeal maneuvers associated with adductory (TA, LCA, and IA) and abductory (PCA) muscles as they have been found to play major roles in inducing curved glottal geometries. Simulation results show that (1) co-activation of the LCA and IA muscles leads to posterior glottal closure with a remaining mid-membranous gap (see Figure 3(top left)); (2) isolated activation of the TA muscle leads to anterior and mid-membranous glottal closure with a remaining posterior opening, while also shortening the folds (see Figure 3(top right)); (3) starting from non-zero coactivation of the LCA and IA muscles, increased TA activation yields a medial bulge, whereas anteriorly the glottal geometry is still convex, resulting in an overall hourglass shape (see Figure 3(bottom left)); and (4) starting from a fully adducted state where all the adductory muscles are co-active, increasing PCA activation leads to posterior opening, while the VFs are sustaining concave shapes similar to those presented when TA is activated solely (see Figure 3(bottom right)). These results are in alignment with previous studies [1, 3, 6].

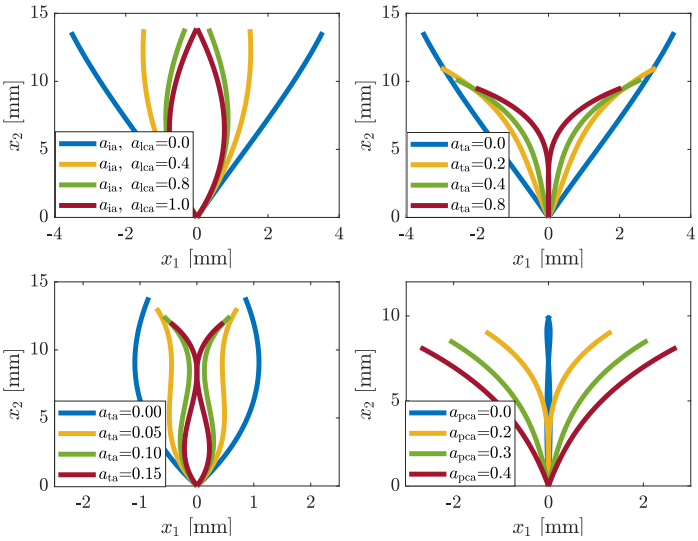

Figure 3: Glottal shapes for (top left) increasing LCA and IA activation levels and other intrinsic muscles being inactive, (top right) increasing TA activation levels and other intrinsic muscles being inactive, (bottom left) increasing TA activation levels and other intrinsic muscle activation levels being at $a_{\text{lca}} = a_{\text{ta}} = 0.6$ and $a_{\text{ct}} = a_{\text{pca}} = 0$, and (bottom right) increasing activation of the PCA muscle with the activation levels of the other muscles being $(a_{\text{lca}}, a_{\text{ia}}, a_{\text{ta}}) = (0.45, 0.45, 0.7)$ and $a_{\text{ct}} = 0$.

DISCUSSION

The predictions from the proposed Euler-Bernoulli beam model highlight potential mechanisms underlying different patterns of incomplete glottal closure observed clinically. In particular, results indicate that bowed VF shapes result, in part, from low or null activation of the TA muscle in combination with co-activation of the LCA and IA muscles. The predominant mechanism in this case is the anterior reactive moments that resists bringing the VFs together during adduction. In addition, the proposed model suggests that posterior glottal opening with combined VF concavity results from high activation of the TA muscle and low or null activation of the LCA and IA muscles. The driving mechanism herein is the internal moments induced by the TA muscle activation. A similar glottal pattern also occurs when all adductory muscles are activated in addition to the activation of the PCA muscle. Finally, our analysis suggests that the hourglass glottal shape may emerge from laryngeal maneuvers that involve, for example, moderate co-activation of all adductory muscles, where both anterior reactive moment and the internal moment due to TA muscle activation are at play and opposing each other.

These implications may help guiding speech therapists to uncover the underlying laryngeal mechanisms associated with some voice disorders. Incomplete glottal closure can be linked to voice disorders that are characterized by excessive, imbalanced, or deficient activity of the intrinsic and extrinsic muscles such as muscle tension dysphonia (MTD) and Parkinson's disease. Our analysis suggests that insufficient activation of the TA muscle may be a potential mechanism underlying bowed VFs in some patients with voice disorders. Furthermore, our analysis posits that patients with abnormal posterior glottal opening and concave VF geometry, either (a) insufficiently activate the LCA and IA muscles, whereas the TA muscle is activated sufficiently (in comparison to normal posturing scenarios), or (2) suffer from excessive activation of all adductory and abductory muscles, where the PCA muscle activation mitigates the effects of the LCA and IA muscles, in agreement with the postulation in Morrison et al. [1] concerning patients with MTD.

ACKNOWLEDGEMENTS

Research reported in this work was supported by the NIDCD of the NIH under Award No. P50DC015446, and ANID BASAL FB0008. The content is solely the responsibility of the authors and does not necessarily represent the official views of the National Institutes of Health.

REFERENCES

[1] Morrison MD et al. *Acta oto-laryngologica* 113.3 (1993).

[2] Choi HS et al. *Annals of Otology, Rhinology & Laryngology* 102.10 (1993).

[3] Chhetri DK et al. *The Laryngoscope* 125.12 (2015).

[4] Chhetri DK et al. *The Journal of the Acoustical Society of America* 131.2 (2012).

[5] Yin J et al. *Journal of biomechanical engineering* 136.11 (2014).

[6] Yin J et al. *The Journal of the Acoustical Society of America* 140.3 (2016).

[7] Serry MA et al. *Journal of the Mechanical Behavior of Biomedical Materials* 147 (2023).

[8] Titze IR et al. *The Journal of the Acoustical Society of America* 121.4 (2007).

A CONTINUUM MODEL MAY ARTEFACTUALLY HOMOGENIZE LOCAL STRAINS WHILE ALSO ARTEFACTUALLY DISRUPTING LONG DISTANCE STRAIN TRANSMISSION

Xuehuan He (1), Mohammad R. Islam (3), Bingrui Wang (1), Ian A. Sigal (1,2)

(1) Department of Ophthalmology, University of Pittsburgh, Pittsburgh, PA, USA
(2) Department of Bioengineering, University of Pittsburgh, Pittsburgh, PA, USA, Department,
(3) Department of Mechanical Engineering, University of Texas Rio Grande Valley, Edinburg TX, USA

INTRODUCTION

Historically, the sclera and other fibrous soft tissues have been modeled within a continuum framework, leading to the development of constitutive material models to describe their properties [1]. Recent advancements of imaging technologies have provided more detailed information of the three-dimensional (3D) organization of tissue fiber architecture, enabling the emergence of discrete approaches that explicitly model the fibrous structures [2]. The fiber bundles within the sclera exhibit complex 3D organization and continuity. To account for this complexity, our group has developed a discrete finite element modeling framework that incorporates long and continuous collagen fiber bundles, utilizing 3D spatial organization data derived from Polarized Light Microscopy (PLM) and considering interactions between fiber bundles [3]. Conventional continuum approaches that utilize constitutive models typically assume affine relationships between individual fibers and macroscopic tissue deformation, without considering fiber-fiber interactions, whereas the fiber model does not enforce this assumption. This raises critical questions about the ability of the continuum model to accurately capture complex fiber deformation behaviors and transmit macroscopic tissue strains through the fibers to the cellular level.

Our goal in this study was to compare a continuum model developed for sclera fiber bundles in the Optic Nerve Head (ONH) region with our previously proposed fiber model [3].

METHODS

Continuum model geometry and boundary conditions. We constructed a continuum model that aimed to mirror the fiber model introduced in [3] in terms of geometries of the sclera, laminar cribrosa and neural tissue, and boundary conditions (Figure 1). The model was subjected to an intraocular pressure (IOP) of 30 mmHg. A radial displacement (RD) of 0.1 mm was applied to the model's periphery to simulate the radial tension of the sclera due to IOP (Figure 1).

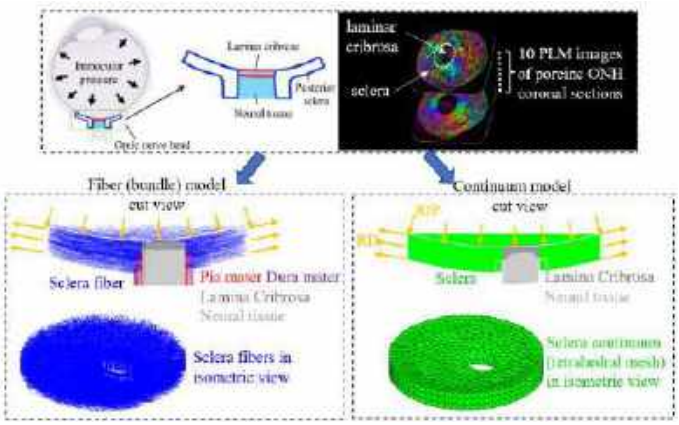

Figure 1: Schematic illustration of the geometry and boundary conditions of the fiber model and continuum model. The same boundary conditions were applied to both models to simulate an inflation experiment. The continuum model was meshed using tetrahedral elements.

Material properties. The lamina cribrosa (LC) and neural tissue (NT) regions were modeled as linear elastic material (ELC = 0.1 MPa, ENT = 0.01 MPa), same as the fiber model. The sclera tissue in the continuum model was characterized using the Holzapfel-Gasser-Ogden (HGO) strain energy function [4]. Element-wise fiber parameters, such as fiber dispersion, fiber volume fraction, and mean fiber direction were determined based on the scleral fiber structure reconstructed in the fiber model based on 10 PLM images of porcine optic nerve head (ONH) coronal sections (Figure 1) and are presented in Figure 2a. Fiber stiffness parameter k_1 and exponential parameter k_2 were inversely identified as $k_1 = 45Mpa$ and $k_2 = 45$ by matching the IOP-induced

peripapillary sclera's (PPS) posterior displacement (Figure 2b) and scleral canal expansion with those derived from ex-vivo inflation experiments documented in the literature [5]. Due to space constraints, we cannot present here the details of the material formulation and fiber mean orientation as well as the scleral canal expansion. These will be shown in the presentation at the conference. The solution was obtained using the FE solver Abaqus/Standard.

Comparison of fiber strains between the continuum and fiber models. We compared the distributions of fiber strains in scleral fiber bundles derived from both the fiber and continuum models. In the fiber model, fiber strain was the axial strain of the fiber element. For the continuum model, fiber strain was determined by mapping the strain tensor in the direction of the fiber element. The standard deviations of fiber strains derived from both models were calculated to quantify the degree of variation in fiber strains for fiber segments within each continuum element and along each entire fiber, respectively.

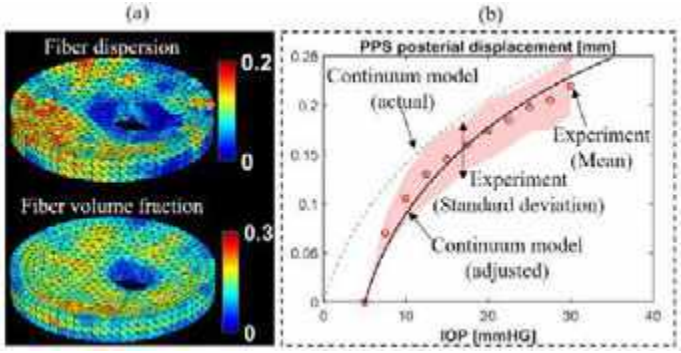

Figure 2: (a) The distributions of calculated element-wise fiber dispersion and volume fraction in the isometric view. Note the fibrous ring surrounding the canal. (b) Plot of the peripapillary sclera's (PPS) average posterior displacement as a function of Intraocular pressure (IOP) as obtained from the continuum model and experiments [5]. The model responses are adjusted by 5 mmHg on the IOP axis for direct comparison with the experimental data. In the experiments, configurations at 5 mmHg were utilized as the reference undeformed state.

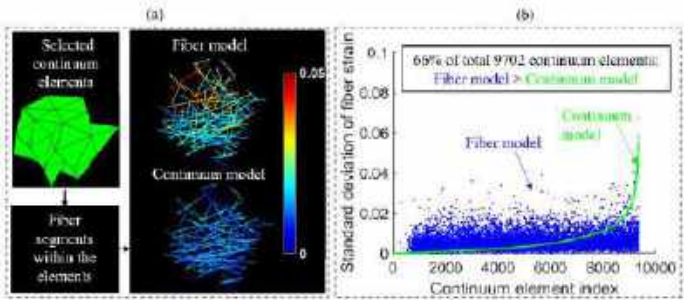

Figure 3: (a) Fiber segments within 10 selected continuum elements are shown colored according to the strains derived from the fiber (top) and continuum (bottom) models. Note how the varied fiber strains in the fiber model are homogenized in the continuum model. (b) Scatterplots of standard deviations of fiber strains derived from two models for fiber segments within each continuum element as a function of the continuum element index for a total of 9702 elements. The indices are sorted based on the standard deviation of fiber strain derived from the continuum model.

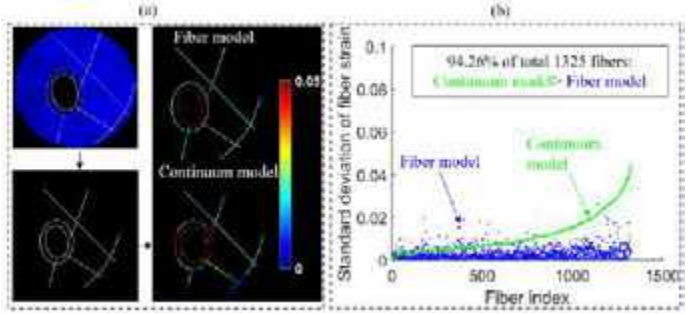

Figure 4: (a) Seven fibers (white) randomly selected from the fiber model are shown here colored according to the strains derived from the fiber (top) and continuum (bottom) models. Note how the smooth strains in the fiber model are disrupted in the continuum model. (b) Standard deviations of fiber strains for fiber segments along each fiber derived from two models, plotted against the fiber index for a total of 1325 scleral fibers. The fibers are indexed based on the standard deviation of fiber strains derived from the continuum model. Notice that the fiber strains derived from the fiber model along each fiber are quite uniform, with 97% of the fibers exhibiting standard deviations less than 0.01.

RESULTS

The degrees of variation in fiber strains derived from the fiber model and the continuum model, for fiber segments within each continuum element and along each whole fiber, are shown in Figure 3 and Figure 4, respectively. Overall, the fiber strains demonstrated a much lower degree of variation in the continuum model than in the fiber model within each continuum element (Figure 3), but the opposite was observed along each fiber (Figure 4).

DISCUSSION

An accurate representation of fiber deformation is essential for models that connect tissue biomechanics to cell mechanobiology. Our overall goal was to investigate whether a developed continuum model can accurately represent the strains of scleral fiber bundles by comparing it with our previously proposed fiber model. Specifically, in this project, we aimed to check if the continuum model could capture the complex local fiber strains and the long-distance strain transmissions. We found that the continuum model tends to homogenize local fiber strains, even after accounting for directions of varied local fiber segments. Additionally, the continuum model disrupts the smooth strain transmission along each fiber. These results suggest that while the continuum model is effective in modeling macroscopic tissue response, it may not faithfully represent the intricate fiber deformation behaviors. Consequently, its ability to link macroscopic tissue responses with cellular and sub-cellular level activities should be carefully evaluated.

ACKNOWLEDGEMENTS

NIH R01-EY023966, P30-EY008098 and T32-EY017271 (Bethesda, MD), the Eye and Ear Foundation (Pittsburgh, PA), and Research to Prevent Blindness (unrestricted grant to UPMC Ophthalmology, and Stein innovation award to Sigal IA)

REFERENCES

[1] Girard, M. J. et al., *J. Biomech*, 131 (5), 2009.
[2] Hadi, M. F. et al., *J. Biomech*,135(2), 2013.
[3] Islam, M. R. et al., *Acta Biomater*, 2023 (In press).
[4] Holzapfel, G. A. *J. Elast*, 61, 1-48, 2000.
[5] Pavlatos, E. et al., *IOVS*, 59(8), 3779-3788, 2018.

IL-1β INCREASES MITOCHONDRIAL TRANSFER FROM MESENCHYMAL STROMAL CELLS TO ANNULUS FIBROSUS CELLS

Ashley B. Cardenas (1), Lawrence J. Bonassar (1,2)

(1) Biomedical Engineering, Cornell University, Ithaca, NY
(2) Mechanical and Aerospace Engineering, Cornell University, Ithaca, NY

INTRODUCTION

Low back pain is the most common musculoskeletal condition worldwide.[1] Although intervertebral disc (IVD) degeneration accounts for over 400 million cases of back pain[2], there are currently no clinically available treatment options that restore the structural or mechanical properties of the native disc. In the last two decades, mesenchymal stromal cells (MSC) have been widely studied for the treatment of degenerative diseases due to their differentiative, immunomodulatory, and trophic properties.[3] Recent clinical trials show that MSCs can improve disc hydration and patient-reported outcomes through direct injections in combination with biomaterial carriers.[4] Despite the promising results, the exact mechanisms employed by MSCs to help promote healing remain unclear.

Previously, MSCs were thought to stimulate regeneration of tissues primarily through differentiation to target cell types.[5] However, only a small fraction of MSCs survive and are retained locally.[6] Therefore, current research is focused on elucidating their paracrine abilities specifically related to growth factors and extracellular vesical (EV) secretion.[6] Within this domain, many groups have demonstrated that MSCs donate mitochondria (MT) through tunneling nanotubes, MT-containing EVs, and cell fusion to injured cells including tenocytes[7], chondrocytes[8], and nucleus pulposus cells (NPCs).[9] Although MT transfer has been shown to prevent inflammation in tenocytes[7] and reduce reactive oxygen species (ROS) and cell apoptosis in NPCs[9], the ability of MSCs to transfer MT to annulus fibrosus cells (AFCs) and its functional consequences for IVD degeneration have not yet been investigated. The goal of this study was to determine (1) whether MSCs donate MT to AFCs and (2) the extent to which the inflammatory mediator, IL-1β, can stimulate MT transfer. We hypothesize that inflammatory stimulation via IL-1β will promote MT transfer from MSCs to AFCs.

METHODS

Cell isolation: Five IVDs were harvested from one neonatal bovine tail and the nucleus pulposus of each IVD was removed using a scalpel. The AF was digested in a 0.3% collagenase solution for 6 hours. Isolated AFCs were expanded in monolayer culture to passage two with Ham's F-12 media supplemented with 10% FBS and 1% AbAm at 37°C and 5% CO_2. MSCs were harvested from neonatal bovine femoral trabecular bone, transduced with a mCherry-Mito lentivirus to allow for mitochondrial visualization, and expanded to passage five.

Coculture: AFCs were plated onto chambered cover slides, allowed to adhere overnight, then cultured in the presence or absence of IL-1β. After 24 hours, AFCs were stained with Vibrant™ CFDA SE. Following AFC staining and washing, MSCs were added using an AFC:MSC ratio of 2:1. During co-culture, 10ng/mL IL-1β was maintained in the IL-1β group. Cells were co-cultured for 24 hours before imaging.

Imaging: Cocultures were imaged using a Zeiss LSM inverted confocal microscope. For each sample, 8-14 imaging fields (resolution: .21-.35 μm/pixel) containing at least one MSC were randomly chosen. All imaging fields contained 10-20 Z-stack slices.

Image analysis: Mitochondrial transfer events were identified by areas of colocalization between the CFDA and mCherry channels. Colocalization was identified using an established ImageJ plugin (Colocalization Image Creator)[10] with custom settings for detecting mitochondrial transfer. The AFC and MSC channels were thresholded using Huang and Isodata automatic thresholds respectively. All colocalized signals above one-pixel unit in area were considered a mitochondrial transfer event and manually counted for each image (Fig. 2). Cell areas were manually calculated using the ImageJ freehand selection tool, while colocalization areas were calculated using automatic particle measurement.

Statistics: Statistical analysis was performed using a one-way ANOVA in Rstudio with a p-value less than 0.05 considered statistically significant (n=8 cocultures per group).

RESULTS

MSCs transfer mitochondria to AFCs in 2D contact co-culture. Confocal microscopy revealed multiple instances of red fluorescent signal within AFCs for both the control and IL-1β groups. These instances of signal overlap appeared as either punctate red signal broadly distributed throughout AFCs (Fig. 1a & 1b), concentrated areas of red signal near AFC membranes (Fig. 1c), or as larger red areas wrapping around and/or blending into AFCs (Fig. 1d). Image analysis confirmed apparent signal colocalization (Fig. 2a-c) through multiple image slices (Fig. 2d), as seen through cell tracing (Fig. 2c) and orthogonal viewing of whole Z-stacks (Fig. 2d).

IL-1β increased the frequency of MT transfer. On average 29% of IL-1β-stimulated AFCS and only 23% of control AFCs exhibited red/green signal colocalization ($p = 0.03$, Fig. 3a). Ratios of colocalization area to cell area indicate the majority of signal colocalization occupied less than 5% of the total cell area for both the IL-1β and control groups.

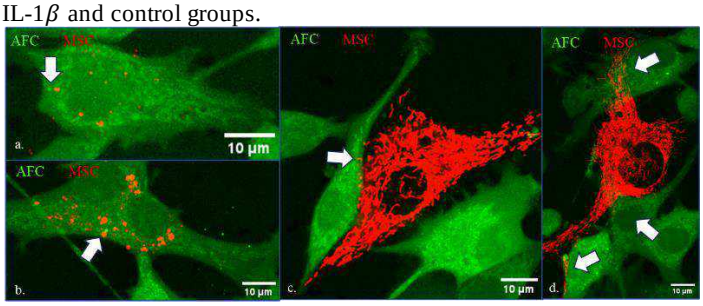

Figure 1: Observed categories of MT transfer. All images are collapsed Z-stacks with arrows pointing to possible transfer events. (a.)(b.) Punctate red signal within AFCs. (c.) Apparent MSC/AFC fusion through cell bodies with concentrated red signals merging with AFCs. (c.) Tunnel nanotubes extending over multiple AFCs.

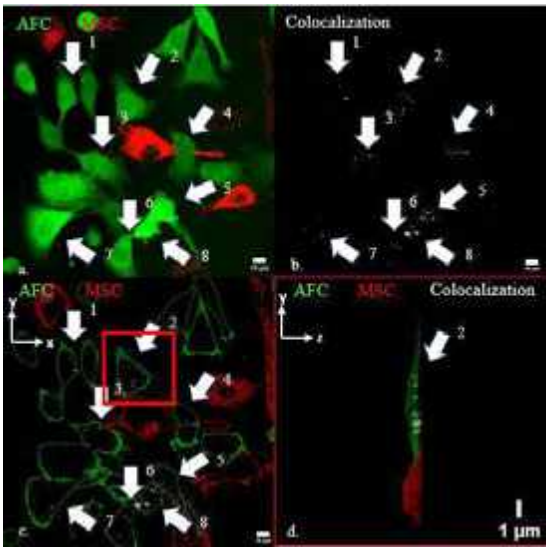

Figure 2: Evidence of MT transfer through signal colocalization. Images a-c are collapsed Z-stacks with arrows pointing to signal colocalization. (a.) Raw composite image. (b.) Processed image containing only specific areas of signal colocalization. (c.) Processed image containing outlined cells and signal colocalization. (d.) Orthogonal view of an AFC with signal colocalization.

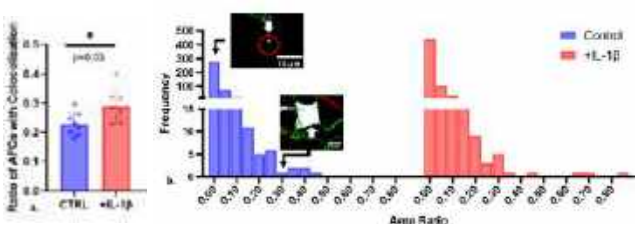

Figure 3: Inflammation stimulates mitochondrial transfer. (a.) IL-1β significantly increases the number of AFCs presenting signal colocalization. (b.) The majority of colocalized signals occupy less than 5% of the total cell area.

DISCUSSION

The goal of this study was to determine the capacity of MSCs to transfer mitochondria to healthy and IL-1β-stimulated AFCs. 24-hour AFC/MSC coculture resulted in multiple instances of red and green signal overlap spanning multiple Z-stack slices, indicating MT transfer events. MT transfer has been shown to occur through cell fusion, tunneling nanotubes, and extracellular vesicle uptake. Herein, there was evidence of cell fusion and tunneling nanotubes (Fig. 1b-c). Although there are no direct signs of MT EVs, AFCs with sparse punctate signal colocalization that are not in direct contact with an MSC (Fig 1a,b) may indicate EV-mediated transfer.[8]

IL-1β stimulation increases the frequency of transfer events between MSCs and AFCs (Fig. 3a). Inflammation is a key characteristic of IVD degeneration and specifically inflammatory cytokines including IL-1β are upregulated in degenerative IVDs.[11,12] IL-1β's effect on transfer may be due to its established ability to cause aberrant intracellular changes in AFCs that include upregulation of matrix-degrading enzymes and ROS.[12] Previous studies show that MSCs are also capable of donating mitochondria to nucleus pulpous cells treated with rotenone.[9] In comparison, we show that a general inflammatory model, rather than specific MT inhibition, of IVD degeneration is sufficient to stimulate MT transfer. To the best of our knowledge, this is the first study to show that MSCs donate MT to healthy and IL-1β stimulated AFCs. Although there were no differences in the area ratio between groups, it is important to note that most transfer events were on the lower end of the histogram, indicating singular or few mitochondrial transfer events per cell (Fig. 3b).

In this study, we show that MSCs donate mitochondria to inflammatory-stressed AFCs. Given that MSC MT transfer has shown great promise in reducing cell stress and promoting cell survival[13], it may prove to be a novel strategy for stimulating the healing of degenerative IVDs. Future areas of investigation should focus on what mechanisms affect transfer and how we may be able to upregulate transfer for improved therapeutic outcomes.

ACKNOWLEDGEMENTS

This work was funded by the NIH 3T32AR078751-03S1 and Cornell SEED grants and made use of the Cornell Biotechnology Resource Center which is supported through the NYSTEM CO29155 and NIH S10OD018516.

REFERENCES

[1]WHO 2023; [2]Ravindra+ GSJ 2018; [3]Merimi+ Cell. Dev. Biol. 2021; [4]Wei+ Transl. Pediatr. 2014; [5]Hwang+ Wiley Interdiscip. Rev. Syst. Biol. Med. 2009; [6]Kumar+ Arch. Bone JT. Surg. 2020; [7]Wei+ Stem. Cell Res. Ther. 2023; [8]Fahey+ Sci. Rep. 2022; [9]Yang+ Oxid. Med. Cell Longev.2022; [10]Lunde+ Sci. Rep. 2020; [11]Wang+ Biomed. Pharmacother. 2020; [12]Yang+ Int. J. Clin. Exp. Med. 2017; [13]Paliwal+ J. Biomed. Sci.

MULTISCALE CARDIAC MODELING OF PRETERM NEONATES

Salla M. Kim (1), Mitchel J. Colebank (1), Filip Jezek (2), Kara N. Goss (3), Pim Oomen (1), Daniel A. Beard (2), Naomi C. Chesler (1)

(1) Edwards Lifesciences Foundation Cardiovascular Innovation and Research Center
University of California, Irvine
Irvine, USA

(2) Molecular and Integrative Physiology
University of Michigan
Ann Arbor, Michigan, USA

(3) Medicine and Pediatrics
University of Texas, Southwestern
Dallas, Texas, USA

INTRODUCTION

Moderate to severe preterm birth (< 32 wks gestation) exposes the newborn to a relatively hyperoxic (i.e., abnormally high oxygen) environment compared to in utero. The resulting oxidative stress can impair the still-developing heart and lung and lifesaving supplemental oxygen increases this effect. Preterm birth affects cardiopulmonary function across multiple spatial and temporal scales; in fact, it is associated with an up to 17-fold increased risk for heart failure through early adulthood [1]. However, the short- and long-term cardiopulmonary effects are still poorly understood. It is commonly thought that increased right ventricle (RV) afterload from the damaged pulmonary vasculature drives RV dysfunction in preterm birth. Clinical and preclinical studies also suggest that direct injury to the RV itself may be a driver of early dysfunction [2]. Thus, the question is how do direct injuries to the myocardium contribute to long-term RV dysfunction under chronically increased afterload in the setting of preterm birth?

The currently accepted animal model for studying preterm birth uses postnatal hyperoxia (Hx) exposure in rodents. Rat lungs continue to develop after birth thus term-born rat pup lungs are at a similar developmental stage as humans in the third trimester. Hx rats at postnatal day 21 (P21) demonstrate RV hypertrophy and increased pulmonary artery pressures compared to the normoxic (Nx) controls [2]. These organ-scale injuries at P21 for the Hx animals correspond with cellular and subcellular mitochondrial injuries [2]. At postnatal day 90 (P90) these measures normalize in the Hx animals, but organ and subcellular abnormalities return by postnatal day 365 (P365). Thus, experimental results show a dynamic time course of increased afterload and mitochondrial RV injury in response to postnatal Hx, but it remains unclear how these independent factors drive long-term RV dysfunction.

Investigating the mechanisms underlying RV dysfunction in response to postnatal Hx is complicated by the multifactorial nature of pathophysiology and the long timescale of disease progression. When based on robust experimental data, in silico modeling can be used to test proposed mechanisms across multiple age points and predict functional growth curves. Biophysics models can readily integrate multiple data modalities and test mechanistic hypotheses related to functional interactions across different spatial and temporal scales. Here we used a multiscale cardiovascular model to investigate potential multiscale injuries due to preterm birth based on rat data.

METHODS

We used our recently published model of the heart [3] using the TriSeg method [4] and myofiber mechanics from [5], integrated within a lumped cardiovascular system model comprising six arterial, venous, and ventricular compartments. The TriSeg method approximates the ventricles as semi-spherical, thick-walled chambers with a shared septal wall, and the cardiovascular model is a 0D closed-loop circuit model invoking linear pressure-flow and pressure-volume relationships.

The myofiber mechanics model based on [5] integrates crossbridge mechanics to simulate active myocardial wall stress σ_{active} (kPa). The crossbridge model includes five states (calcium unbound, calcium bound, loosely attached, strongly attached, post-ratcheted) and the transition rate between states is regulated by mitochondrial metabolite concentrations of cytosolic adenosine triphosphate (ATP), adenosine diphosphate (ADP), and inorganic phosphate (Pi). The calcium activation is based on [6] and mediates the transition from calcium unbound to calcium bound states and includes a force-dependent transition from unbound to bound states. The actives stress is computed from contributions for pre- and post-ratcheted states, such that

$$\sigma_{active}(t) = OV_{thick}(k_{stiff,1}(p_2^1 + p_3^1) + k_{stiff,2}\Delta rp_3^0$$

where OV_{thick} (unitless) is the fraction of thick filament overlap, $k_{stiff,1}$ and $k_{stiff,2}$ are stiffness constants (mmHg/μm), Δr is the crossbridge strain associated with ratcheting deformation, and p_2^1 (μm), p_3^1 (μm), and p_3^0 (unitless) are state variables of the crossbridge model. The passive stress, $\sigma_{passive}$ (kPa), formulation depends on the time-dependent sarcomere length (SL, μm) and the sarcomere rest length (SL_{rest}, μm), such that

$$\sigma_{passive}(SL) = k_{passive}(SL - SL_{rest}) + \sigma_{passive\ collagen}(SL),$$

and includes an exponential relation for collagen recruitment. A flow chart of our multiscale model is shown in **Figure 1**.

We simulated a Nx case and a Hx case. Geometric, pressure, and volume data including end-diastolic and end-systolic pressures and volumes and animal weights from Nx and Hx rats at P21, further described in [2], are averaged and used to estimate parameters e.g. ventricular refence areas and volumes, systemic and pulmonary resistances, and venous and systemic arterial and pulmonary compliances. The Hx animals had increased pulmonary artery elastance, thus we increased pulmonary arterial resistance in the model by a factor of two from the Nx case to achieve higher pulmonary arterial pressures.

Then, to achieve an increase in RV systolic pressure and reasonable end-diastolic volumes we used three strategies to interrogate the role of RV hypertrophy and mitochondrial dysregulation in RV function in Hx rats at P21. 1) Decreasing ATP, ADP, and Pi concentrations for the RV, with Pi having the largest influence. 2) Increasing RV wall volume. 3) Both decreasing the metabolite concentrations and increasing RV wall volume.

Finally, since the described model does not include regulatory mechanisms like the baroreflex, we employed a compensatory volume overload to maintain mean systemic arterial blood pressure as in [4].

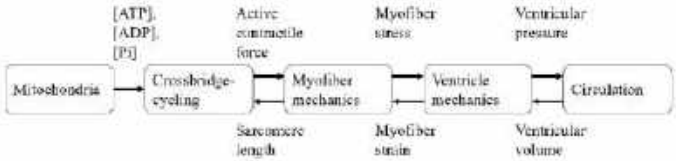

Figure 1. Cardiovascular model schematic.

RESULTS

The top panels of **Figure 2** show the model-predicted pressure volume loops for the group averaged Nx data at P21. For the three strategies used to fit the Hx data, the model-predicted pressure-volume loops are shown in the bottom panels of **Figure 2** and the scaling factors are shown in **Table 1**. Notably all end-systolic and end-diastolic volumes and pressures fall within one standard deviation of the mean values from [4], which were used as inputs to the Nx and Hx models.

Table 1. Scaling factors used to achieve model fits to data.

	[ATP][ADP][Pi]	RV Wall Volume
Strategy 1	0.6	1.0
Strategy 2	1.0	1.6
Strategy 3	0.8	1.3

DISCUSSION

Here we have modeled multiscale right ventricular dysfunction of the preterm heart in silico. The hand-tuned parameters to the average group data provide predictions within one standard deviation of the mean, corresponding to known physiological changes. Namely, the Nx model requires increases in pulmonary elastance and resistance to match Hx data. These changes are consistent with the expected pulmonary damage in preterm-born infants and the findings from Hx rat models of preterm birth. Reducing mitochondrial metabolite concentrations enabled a reasonable model fit to the Hx data, which also corresponds with the dysregulated mitochondrial respiration observed in cells from blood samples of human subjects born preterm [7]. Increasing RV wall volume to simulate hypertrophy, observed clinically [2], also provided a reasonable fit, as did the combination of mitochondrial dysfunction and RV hypertrophy. In the absence of additional experimental data, these results suggest that different injuries and adaptations across scales can explain the impact of Hx and preterm birth on RV function.

The multiscale model adapted from [3] allows investigation of the causes and consequences of preterm birth and their multiscale nature. Since somatic growth is a prominent factor to consider in preterm birth, a lower order model such as ours allows future implementation of somatic growth and remodeling, which is critical for longitudinal modeling efforts.

Limitations of this modeling framework include assumptions and limitations propagated from the TriSeg model and myocyte mechanics model, such as the assumption of spherical ventricular geometry and sarcomere lengths determined from isolated rat trabeculae, respectively. Additionally, we parameterized the model to fit group average values, which obscures features that may be present in individuals.

The work presented here establishes a modeling framework for investigating the multiscale and somatic growth features of RV dysfunction in preterm birth and provides the basis for future subject specific parameterizations at P21 (infant), P90 (adolescent), and P365 (adult).

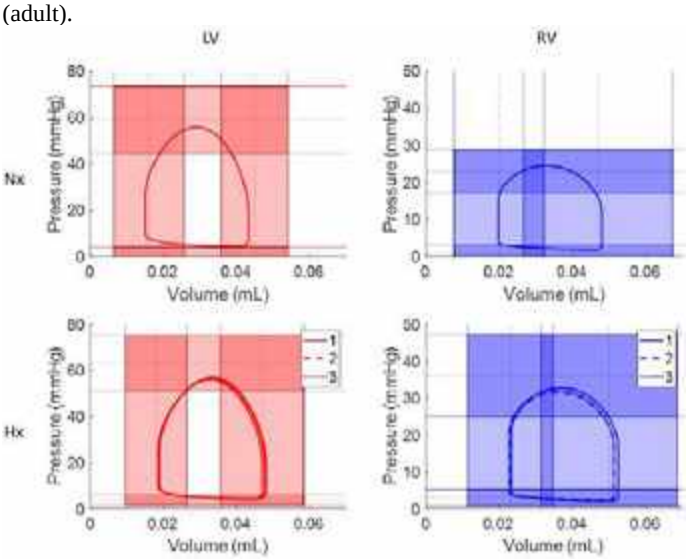

Figure 2. Model-predicted LV (red) and RV (blue) pressure-volume loops for average normoxic (Nx) and hyperoxic (Hx) subjects at P21. Results for Hx strategies 1-3 are indicated in the legend. The dashed lines represent the mean and shaded regions represent ± one standard deviation from the mean.

ACKNOWLEDGEMENTS

Funding from NIH R01 HL154624 and NIH TL1 TR001415 is gratefully acknowledged.

REFERENCES

[1] Carr, H et al., *J Am College of Cardiology*, 69(21):2634-2642, 2017.
[2] Kumari, S et al., *Am J Physiol*, 317(6):H1272 H1281, 2019
[3] Kim, S et al., *J of Physiol*, 14:1231688, 2023.
[4] Lumens, J et al., *Ann Biomed Eng*, 37(11)2234-2255, 2009.
[5] Marzban, B et al., *Physiome*, 2020.
[6] Campbell, KS et al., *Biophys J*, 115(3):543-553, 2018.
[7] Kumari, S et al., *Pediatric Research*, 90(6):1147-1152, 2021.

QUANTIFYING CHANGES IN MORPHOLOGICAL AND BIOCHEMICAL PROPERTIES OF SENESCENT CELLS

A. Singam (1), K. Ramirez (1), D. Kim (2), J. Chen (3), S. Park (1)

(1) Mechanical Engineering, University of Nevada Las Vegas, Las Vegas, NV, USA
(2) Department of Biomedical Engineering, Johns Hopkins University, Baltimore, MD, USA
(3) Nevada Institute of Personalized Medicine, University of Nevada Las Vegas, Las Vegas, NV, USA

INTRODUCTION

Aging is the progressive loss of tissue and organ function over time. Cellular senescence is one of the driving factors for aging and age-related diseases[1]. Senescent cells secrete proinflammatory and matrix-degrading molecules, known as senescence-associated secretory phenotypes (SASPs). Aging can be induced by internal and external stimuli also known as stressors. As of today, only a few biomarkers that can selectively identify aging cells have been established. The aim of this study is to study different stressors that induce senescence and understand the molecular and cellular changes, thereby finding potential biomarkers for aging. SASPs in aging induced cells can be studied by changes in cell morphology and measurement of increased activity of beta-galactosidase (β-gal) in the cells. For example, in 2D culture conditions, senescent cells become larger, more flat, vacuolated and have multiple nuclei[2]. To this end, fluorescence microscopy and novel label free 3D Holotomography will be explored. We aim to study the changes that occur at morphological level and the try find the interconnections between types of stress factors and their functional effect on cells. This study was conducted using two human cell lines, human microglial (HMC3) and embryonic kidney cells (HEK293).

METHODS

Changes in cell morphology and SASP markers like SA-β-gal activity was studied in HMC3 and HEK293 cells with exposure to hydrogen peroxide (H_2O_2) and anti-cancer drugs (Palbociclib and Doxorubicin). Briefly, $1X10^5$ cells per well were seeded in 24 well plate and allowed to attach overnight. Next, they were treated with H_2O_2/Pal/Dox for 1/24/48 h respectively. Post treatment the cells were fixed with paraformaldehyde, stained with phalloidin, DAPI and Senescence green detection kit followed by imaging under fluorescence microscope. Along with the SA-β-gal assay the viability of the cells with the treatment of these stressors was studied *via* MTT (3-(4,5-dimethylthiazol-2-yl)-2,5-diphenyl-2H-tetrazolium bromide) assay.

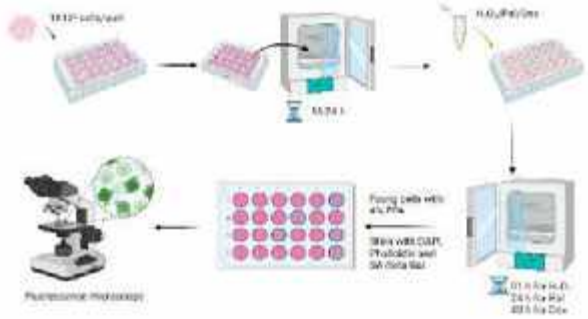

Figure 1: SA-β-gal assay in HMC3 and HEK293 cells.

RESULTS

The SA-β-gal assay confirms aging phenotype in the cells treated with H_2O_2 and anti-cancer drugs (Pal and Dox). From this assay and MTT assay we could establish the concentrations or dosage of the external stress inducers that promote aging in cells. As seen in fig. 2, the MTT assay provided an insight to the threshold concentration of test sample up to which aging can be studied. The conc. below the IC_{50} proved to be inducing aging as confirmed by the SA-β-gal assay. Fig. 3 and 4 depict an increase in green fluorescence intensity with increasing conc. of H_2O_2 and drug (Dox). For instance, the intensity increased around 100 μM for H_2O_2 and 50 nM for Dox. Along with the green intensity other cell morphological parameters like cell shape index, cell size, area, perimeter and nuclear size, area, perimeter were also calculated using imageJ.

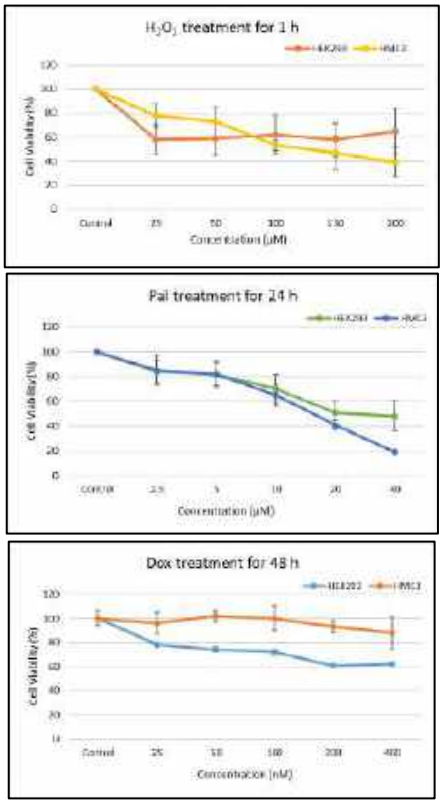

Figure 2: Cell viability performed in HEK293 and HMC3 cells *via* MTT assay.

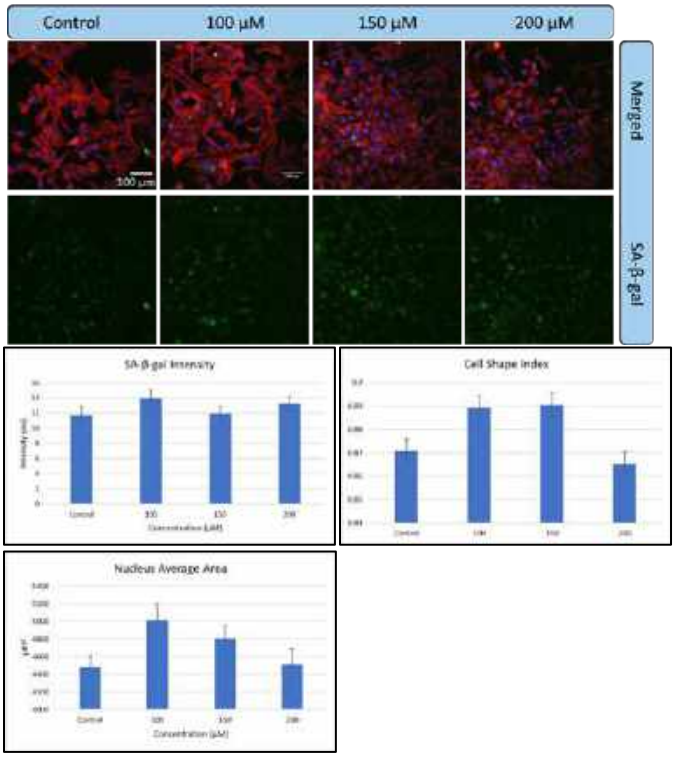

Figure 3: SA-β-gal assay images and quantification data of HMC3 cells treated with varying concentrations of H_2O_2.

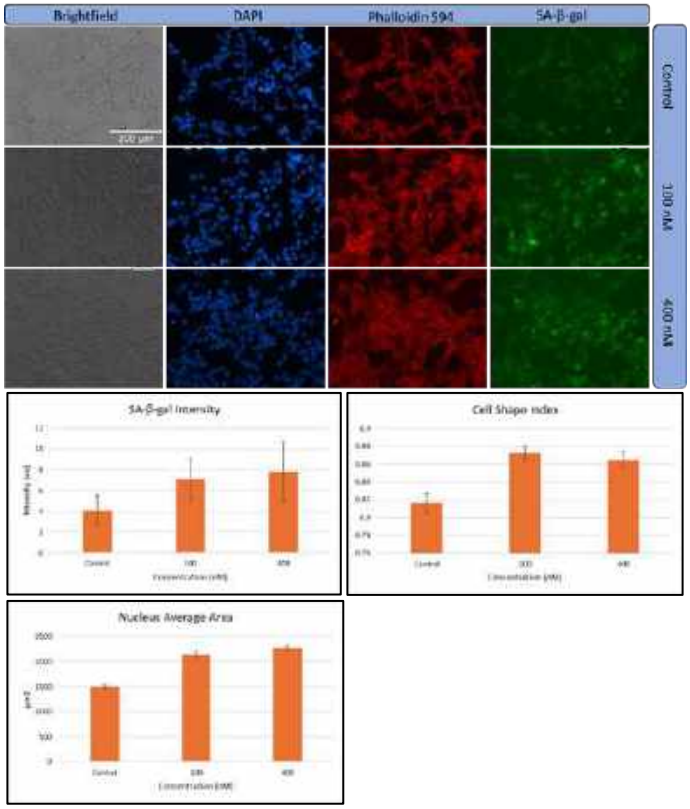

Figure 4: SA-β-gal assay images and quantification data of HEK293 cells treated with varying concentrations of Dox.

DISCUSSION

The cellular and organelle morphology exhibited significant changes following the exposure to H_2O_2, Pal and Dox. The increase in SA-β-gal activity with increasing H_2O_2/drug concentration was observed, suggesting an augmentation of cellular senescence. Changes were also noticed in the actin filament rearrangement with the treatment. In the future, we plan to employ holotomography for the comprehensive 3D quantification of a wide range of functional properties, including morphology, structural, mechanical and biochemical properties.

ACKNOWLEDGEMENTS

This study was supported by the National Institute on Aging (NIA) of the National Institutes of Health (NIH) under award number K25AG070286.

REFERENCES

[1] Childs, B et al., Nat Medicine, Nat Medicine, 21:1424-1435, 2015.

[2] Schmitt, R and Melk, A. *Reg Nephrology*, 231-240, 2022.

THE MATERIAL TUNING OF ANNEALING PVA HYDROGELS FOR THE APPLICATION OF TMJ DISC REPLACEMENT

Hassan Mahmoud (1), Christian M. Puttlitz (1,2,3), Kevin M. Labus (2)

(1) School of Biomedical Engineering, Colorado State University, Fort Collins, Colorado, United States
(2) Department of Mechanical Engineering, Colorado State University, Fort Collins, Colorado, United States
(3) Department of Clinical Sciences, Colorado State University, Fort Collins, Colorado, United States

INTRODUCTION

Temporomandibular joint (TMJ) disorders involving degeneration of the interpositional disc that fail to respond to conservative treatments are often treated with disc resection. However, disc resection fails to reduce pain in 25% of patients, and the procedure does not fully address the underlying causes of the joint degeneration [1]. Subsequently, disc resection can increase stress in the condylar and fossa surfaces, further progressing the degenerative changes [2]. Therefore, there is great clinical interest in an interpositional implant strategy to replace the function of the TMJ disc for patients that require a disc resection. The purpose of this work was to assess Poly(vinyl) alcohol (PVA) as a material for TMJ disc replacement and evaluate the effects of several synthesis parameters on the mechanical properties of annealed PVA hydrogels. Factors that can influence the mechanical properties of PVA hydrogels include annealing, molecular weight (MW), and percent polymer fraction (PPF). The interdependent effects of these synthesis parameters on hydrogel mechanical properties have not been explored thoroughly. Therefore, this study utilized a full factorial design to test the interactive effects of annealing temperature, MW, and PPF.

METHODS

PVA (MW of 89,000-98,000 & 146,000-186,000 99+% hydrolyzed, Sigma Aldrich, St. Louis, Mo) was mixed with deionized water (DI) in an enclosed beaker for a minimum of two hours at 98°C while stirred. Hydrogel sheets of 10% and 20% PPF by weight were synthesized of each of the two molecular weights of PVA. All testing groups prepared underwent 6 freeze-thaw cycles. The hydrogels were dried in an oven at 60°C in between two perforated plates to maintain their flat shape. The hydrogels were then annealed for an hour at a temperature of either 120°C, 135°C, 150°C, or 165°C and rehydrated in DI water, resulting in a total of 16 groups (2 MWs x 2 PPFs x 4 temperatures).

Tensile tests were conducted on n = 5 dog-bone shaped specimens of each hydrogel variant. Cross-sectional area was measured with calipers for stress calculations, and local strain in the center of the specimens was measured via digital image correlation. A 0.05 N preload was applied, and samples were pre-conditioned to 4% strain for 20 cycles. Samples were loaded to failure at a rate of 0.08 s^{-1}. Ultimate tensile stress and elastic modulus were calculated.

Unconfined compression tests were executed on 2 mm diameter biopsy punch samples of the PVA hydrogel sheets. A sample size of n = 5 was used for each group. Samples were mounted on a hydraulic testing system in between two parallel platens. Each of the samples were loaded to 46% compressive strain, at a strain rate of 0.005 s^{-1}. The tangent moduli at stretch values of $\lambda = 1.00$ to $\lambda = 0.96$ and $\lambda = 0.60$ to $\lambda = 0.54$ were determined using localized linear regression. The first stretch range was chosen in order to represent low strain tangent modulus. The second stretch range was chosen in order to represent a physiologically relevant maximum strain based on a finite element model of the human TMJ during clenching [3]. Results were analyzed via two-way ANOVAs with Tukey's *post-hoc* comparisons. ANOVAs compared MW and annealing temperature interactions as well as PPF and annealing temperature interactions.

RESULTS

Across each combination of MW and PPF, the tensile strength and elastic modulus increased with increasing annealing temperature (Figure 1). The 165°C annealed gels exhibited the greatest elastic modulus and strength (Figure 2). The tensile elastic modulus of the 89 kDa group was significantly greater than for the 145 kDa group ($p < 0.001$); however, the 145 kDa group exhibited a significantly greater tensile strength compared to the 89 kDa group ($p < 0.001$) (Figure 2). The 20% PPF group exhibited a significantly greater elastic modulus compared to the 10% group ($p = 0.009$). There were no significant differences in tensile strength between PPFs. There were no significant

interaction effects between synthesis parameters for either the tensile modulus or strength.

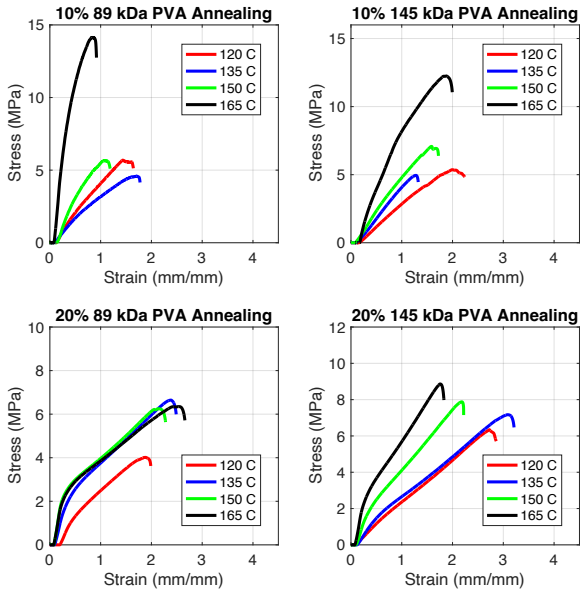

Figure 1: Median tensile stress-strain curves for each group

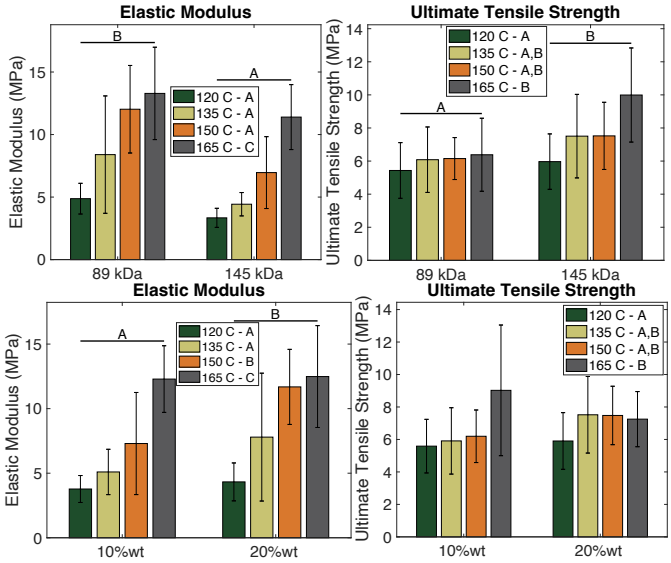

Figure 2: Elastic modulus and ultimate tensile strength results from tensile testing (mean ± standard deviation). Groups that do not share a letter are significantly different.

The results of unconfined compression testing demonstrated no significant differences in low-strain (stretch 1-0.96) tangent moduli between annealing temperatures, but high strain moduli (stretch 0.6-0.56) increased with increasing temperature (Figure 3). The 89 kDa group exhibited a greater low-strain modulus compared to the 145 kDa group ($p < 0.022$). The 20% PPF group exhibited significantly greater low-strain and high-strain moduli compared to the 10% group. There were no significant interaction effects between synthesis parameters for compressive moduli.

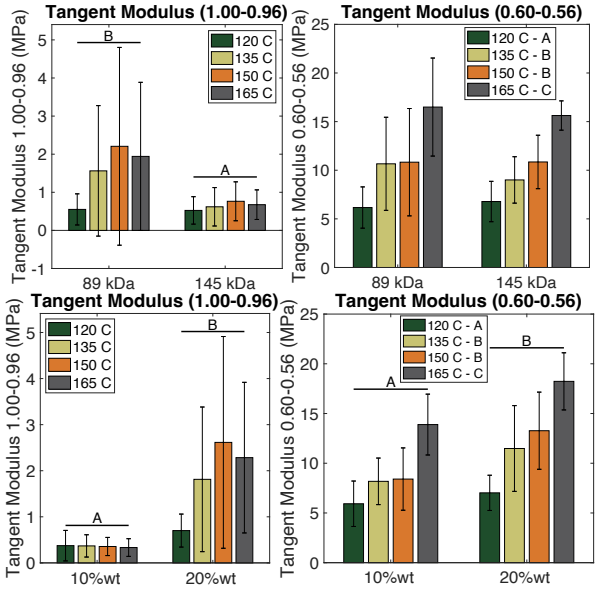

Figure 3: Compressive tangent moduli at λ = 1.00-0.96 and λ = 0.60-0.56 for each hydrogel group (mean ± standard deviation). Groups that do not share a letter are significantly different.

DISCUSSION

Freeze-thaw cycling physically crosslinks PVA hydrogels, and annealing has been shown to further increase crystallinity, which is associated with increased strength and elastic modulus [4]. The mechanical properties can be altered by tuning the MW, PPF, and annealing temperature. No significant interaction effects were seen across the parameters of this study; thus, the main effects of each parameter can be evaluated individually. The results demonstrated that increasing annealing temperature resulted in a significant increase in hydrogel stiffness and strength. The tensile strength of the 145 kDa gels were higher than the 89 kDa gels, but the 89 kDa gels had greater stiffness. The 10% gels exhibited a lower compressive modulus compared to 20% gels, but they had a similar tensile strength. These results indicate that a 145 kDa 10% gel at a 165°C annealing treatment would provide both the compressive softness and high tensile strength most similar to the TMJ disc. Following identical testing methods, the TMJ disc had a mean elastic modulus and strength of 251±75.5 MPa and 26.7±6.49 MPa in the anterior-posterior (primary fiber) direction and an elastic modulus and strength of 21.1±6.12 MPa and 3.31±0.85 MPa respectively, in the transverse direction [5]. In compression, at the stretch ranges of λ = 1.00-0.96 and λ = 0.60-0.56, the average tangent moduli of the TMJ disc were 0.13±0.04 MPa and 3.61±2.75 MPa, respectively [5]. Material properties of the tuned PVA hydrogels were similar to the TMJ disc in compression and in tension in the direction transverse to the fibers but did not match those of the TMJ disc in the fiber direction. These hydrogels may need additional reinforcement to match the fiber-direction properties of the native TMJ disc.

ACKNOWLEDGEMENTS

Funding was provided by NIH (R56DE032760)

REFERENCES

[1] E. Tanaka *et al.*, *J Oral Maxillofac Surg*, 64:1221-4, 2006.
[2] C. K. Hagandora and A. J. Almarza, *J Dent Res*, 91:745-52, 2012.
[3] M. Beek et al., *J Biomech*, 0021-9290, 2000.
[4] C. Ying et al., *Polymer Testing*, 2022.
[5] J. P. Kuiper et al., *Frontier in Physics 10*, 8-11, 2022.

ROLE OF OBESE-LIKE ADIPOCYTES IN THE PATHOPHYSIOLOGY OF ATRIAL FIBRILLATION USING 3D BIOPRINTED MODELS

L. Celebi[1], P. Zorlutuna[1, 2, *]

(1) Bioengineering Graduate Program, University of Notre Dame, Notre Dame, IN 46556

(2) Harper Cancer Research Institute, University of Notre Dame, Notre Dame, IN 46556

INTRODUCTION

According to the World Health Organization, the prevalence of obesity has tripled over the past 40 years and is continuing to increase at an alarming rate (WHO, 2021). Cardiovascular diseases (CVD) were reported to be the primary cause of death associated with a high body mass index and to be responsible for two-thirds of fatalities caused by obesity (GBD, 2017). Epicardial adipose tissue (EAT) is the visceral fat deposit that directly covers the surface of the myocardium without any fascial structure. In case of obesity, EAT expansion causes an infiltration of adipocytes into the myocardium layer and prevents cardiac excitation. This results in irregular beating patterns called arrhythmia. Atrial fibrillation (AF) is reported to be the most prevalent type of arrhythmia affecting more than 60 million people globally (Essien et al., 2021). Obesity was reported to be associated with a 50% increase in the risk of AF development (Chung et al., 2020). Recent imaging techniques were able to assess the EAT thickness, volume, and density to predict the arrhythmogenic risk in obese individuals. These studies showed that increased EAT thickness and infiltration is associated with worse atrial function, higher hospitalization, and mortality rate (Oduah et al., 2023). Laboratory animals such as mice and rats do not have a cardiac fat depot that shares the same circulation with their myocardium (Bale et al., 2018). For this reason, some studies on EAT accumulation and CVDs were conducted on large mammals such as sheep (O'Connell et al., 2015) and pigs (McKenney et al., 2014) which have EAT. However, there remain gaps and limitations since animal models are incapable of simulating the physiology, and progression of EAT infiltration in the human heart. Thus, there is an urgent need for a better understanding of the underlying pathology of EAT infiltration and to develop new therapies to battle obesity.

METHODS

Primary ADSCs were isolated as described previously (Traktuev et al., 2008) and subjected to the adipogenic differentiation using induction media composed of indomethacin, dexamethasone, and IBMX. Then, obese-like induction (OLI) was applied to the experimental group with media supplemented with BSA-Palmitate as reported before (Pieters et al., 2022). To compare the lipid droplet sizes of the experimental and control group, lipid droplets of adipocytes were stained with Nile Red following the manufacturer's protocol and the imaging was performed with a confocal microscope. The insulin sensitivity of both groups was evaluated through immunostaining for phosphorylated-insulin receptor (p-INSR) expression. Finally, a comparison of adiponectin levels in control and obese-like adipocytes was made using a commercially available ELISA kit, following the manufacturer's protocol.

The DiPS 1016 SevA hiPSC line derived from human skin fibroblasts was cultured as reported before (Acun et al., 2019). A previously established protocol was adapted to induce atrial iCM differentiation (Kleinsorge et al., 2020). After differentiation, atrial iCM culture was characterized by MLC2A (atrial cardiomyocyte marker) /MLC2V (ventricular cardiomyocyte marker), Cardiac Troponin T (TnT, cardiac cell marker), and Sarcomeric alpha-actinin (SAA, muscle cell marker) markers. For this, cells were immunostained using the protocol described in the article published by Acun et al. (2019).

To synthesize the photocrosslinkable GelMA hydrogels, previously established protocols were utilized (Nichol et al., 2010) and the degree of methacrylation was quantified with NMR using an adapted protocol (Li et al., 2016). The frequency sweep test was conducted to evaluate the viscoelastic properties of the hydrogels following a reported protocol (Basara et al., 2019).

CELLINK BioX6 Bioprinter and a custom-made G-Code were employed to print the EAT infiltration model. The bioink was prepared using collagen type 1 (6 mg/ml), 20% GelMA and Irgacure2959 photoinitiator solution. Differentiated adipocytes were detached using trypsin-EDTA. After mixing the atrial cardiomyocytes and adipocytes into separate syringes, 22G nozzles were used and quarter cylindrical

constructs with reported dimensions were printed on a sterilized charged glass. Then, the constructs were photocrosslinked using a UV lamp. To characterize the cell types and their locations in the constructs, iCMs were tagged with CellTracker green and adipocytes were tagged with CellTracker orange dyes following the manufacturer's instructions. The tiles images were taken using a fluorescence microscope.

RESULTS

Increase in the intracellular accumulation of lipid droplets was observed after adipogenic induction (Fig.1a). At the end of OLI, the experimental group exhibited larger, and fewer lipid droplets compared to the control group, mimicking caloric overload and, as a result, an obese phenotype (Fig.1b). According to the results, obese-like adipocytes released significantly less adiponectin (Fig.1c) and had lower p-INSR expression compared to the control (Fig.1d).

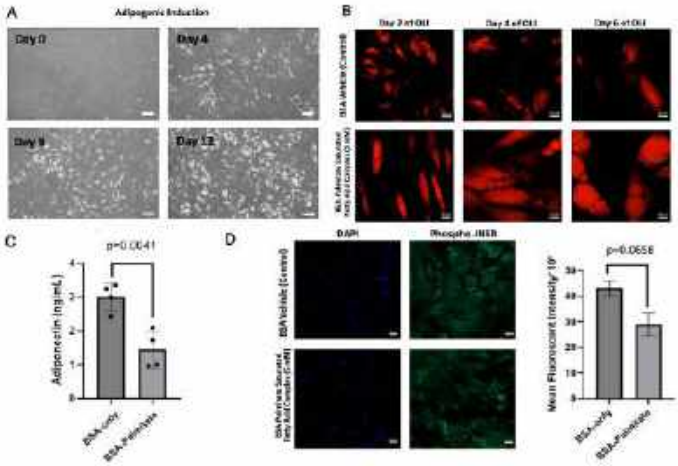

Figure 1: Adipogenic induction of hADSCs and OLI of adipocytes

As reported in the literature, the beating of iCMs was often observed by day 15 of differentiation (Kleinsorge et al., 2020). According to the flow cytometry results, 76% of cardiomyocytes in atrial iCM culture were MLC2A+ (Fig.2b). Results of the immunostaining showed that the culture largely expressed, cardiac Troponin T (TnT, cardiac cell marker), and Sarcomeric alpha-actinin (SAA, muscle cell marker) markers (Fig.2a and Fig.2b). Although atrial and ventricular iCMs were similar in morphology during differentiation, cultures of atrial cardiomyocytes had higher beating frequency than ventricular iCMs.

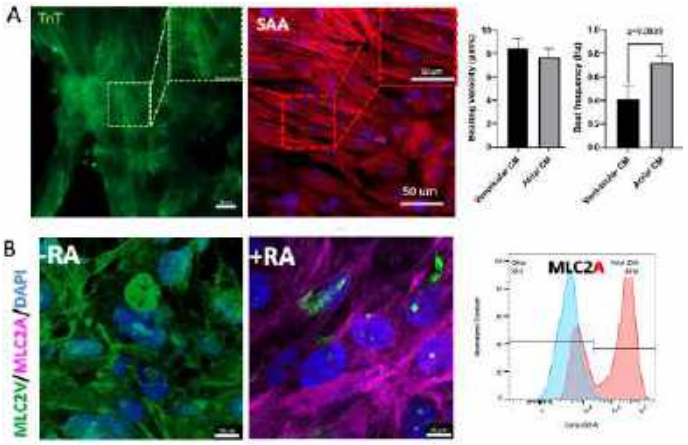

Figure 2: Differentiation of atrial iCMs and characterizations

Lastly, the bioink composed of 10% GelMA 3 mg/mL collagen were characterized in terms of methacrylation degree and viscoelastic properties. The degree of methacrylation of synthesized GelMA hydrogels was determined using NMR as 54%. The bioink had a storage modulus of 2.6 kPa. After bioink characterizations, hydrogels were stained using food coloring and printed using optimized printing parameters (Fig.3b). Then, preliminary printing experiments were conducted and CellTracker tagged cells were localized in the EAT infiltration model (Fig.3d)

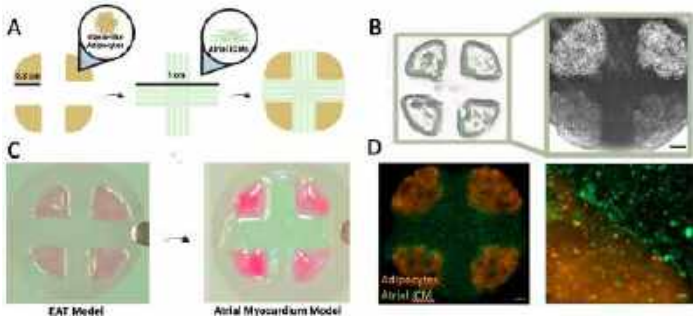

Figure 3: 3D EAT Infiltration model and characterizations

DISCUSSION

Research conducted by The American Obesity Association foresees that half of adults will be affected by obesity by the year 2030. Utilizing human tissues is not feasible and majority of laboratory animals lack EAT. Therefore, engineering an obese heart under laboratory conditions is important to understand underlying pathology and devise new therapies to combat obesity. Here, we observed that the in-vitro obese-like adipocytes are showing important hallmarks of in-vivo obese adipocytes such as the lipid droplet expansion, inhibition of phosphorylation of INSR (p-INSR) and impaired adiponectin release. In a study conducted by Iacobellis et al. (2023), researchers quantified the cytokine levels and analyzed the epicardial adipose tissue thickness measured by echocardiography. They reported that individuals with impaired insulin sensitivity and low adiponectin levels have the highest EAT thickness. This is an indicator that OL adipocytes could be mimicking the cytokine release profile. hiPSC derived atrial cardiomyocytes were reported to have higher beating frequency which was consistent with the literature (Kleinsorge et al., 2020). In flow cytometry results, we showed that the atrial culture was largely expressing MLC2A. Overall, hiPSC-atrial iCMs were showing important characteristics of in-vivo atrial cardiomyocytes.

Type 1 collagen is the most abundant protein in human body and it naturally mimics the ECM (Naomi et al., 2021). However, type 1 collagen alone is not suitable for extrusion bioprinting because of its low viscosity and slow polymerization (Mazzocchi et al., 2018). Multi-component hybrid bioinks are the potential solution for achieving ideal bioprintability with type 1 collagen. The viscosity and printability of type 1 collagen can be enhanced by combining it with semi-synthetic polymers like Gelatin methacryloyl (GelMA) to develop hybrid hydrogels. GelMA is widely used in bioprinting as a bioink due to its printability, tunability, and overall cell activity-enabling properties (Yue et al., 2015). This bioink combination were shown to have suitable viscoelastic properties and ability to be photocrosslinked.

One of the limitations of the study is to struggle of printing adipocytes with high viability and without disturbing the fat droplets. The strength of the study would be that it involves human derived (human iPSC) cells which is important to obtain physiologically relevant results. With this model, we hope to report underlying pathology of EAT infiltration and develop new therapies to battle obesity.

ACKNOWLEDGEMENTS

This work is supported by NIH Award #1 R01 HL141909-01A1 and NSF-CAREER Award # 1651385.

REFERENCES

1. World Health Organization (WHO), 2021, Obesity and overweight.
2. GBD 2015 Obesity Collaborators. *N Engl J Med.* 2017 Jul 6;377(1):13-27.
3. Essien UR et al., *Nat Rev Cardiol*. 2021 Nov;18(11):763-773.
4. Gerdisch, M. et al., *AME Surgical Journal,* 3. doi:10.21037/asj-22-18
5. Chung, M. K et a., *A Scientific Statement From the American Heart Association. Circulation*, 141(16)
6. Oduah MT et al., *Card Fail Rev.* 2023 Apr 15;9:e06.
7. Bale LK et al., *Growth Horm IGF Res.* 2018 Oct-Dec;42-43:1-7.
8. *O'Connell RP* et al., PLoS One. 2015 Aug 14;10(8):e0133052.
9. McKenney et al., *Journal of Cardiothoracic Surgery,* 9(1). doi:10.1186/1749-8090-9-2
10. van Woerden et al., *Circ Heart Fail*. 2022 Mar;15(3):e009238.
11. Traktuev DO et al., *Circ Res.* 2008 Jan 4;102(1):77-85.
12. Pieters VM, et al., *Biofabrication.* 2022 Aug 19;14(4).
13. Kleinsorge M et al., *STAR Protoc.* 2020 Jun 3;1(1):100026.
14. Acun A et al., *Acta Biomater.* 2019 Aug;94:372-391.
15. Basara G et al., *Gels.* 2021 Jun 11;7(2):70.
16. Iacobellis G et al., *Nat Rev Cardiol*. 2022 Sep;19(9):593-606.
17. Mazzocchi et al., *Biofabrication.* 2018 Oct 30;11(1):015003.
18. Yue K et al., *Biomaterials.* 2015 Dec;73:254-71. d

CERVICAL NECK MUSCLE MORPHOLOGY UNDER LOAD-BEARING CONDITIONS AND ITS IMPACT ON SPINAL ALIGNMENT: AN UPRIGHT MAGNETIC RESONANCE IMAGING STUDY

Mahmudur Rahman (1), Ali Warraich (2), Vicky Varghese (3), Aditya Vedantam (1), Narayan Yoganandan (1)

(1) Department of Neurosurgery, Medical College of Wisconsin, Milwaukee, WI, USA
(2) Department of Chemistry, University of Chicago, Chicago, IL, USA
(3) Department of Biomedical Engineering, American International University, Al Jahra, Kuwait

INTRODUCTION

Axial head-neck loading can affect cervical muscle morphology and is linked to increased risk of neck pain and early spinal cord pathologies [1]. The stability of the spinal column relies on the surrounding neck musculature, which maintains functional posture characterized by absence of pain physiologic muscle tone. Changes in muscle morphology can alter the neck's intrinsic biomechanics, influencing load transfer mechanisms and distribution paths [2]. Understanding how altered load distributions through the cervical spine musculature affects the stability of the osteoligamentous cervical column and spinal cord is crucial for assessing the risks and mechanisms underlying neck pain and spinal disorders.

Although previous studies have examined the association between cervical muscle morphology and cervical spine pathology, almost all such studies have used supine Magnetic Resonance Imaging (MRI) to draw conclusions [3]. While clinically most adopted, supine MRI does not yield accurate muscle morphology because the cervical spine muscles are not in a load-bearing condition and the in vivo axial loading on the head is not included in recumbent images.

Our study aims to quantitatively analyze the relationship between cervical neck muscle morphology and spinal column alignment under axial load-bearing conditions by utilizing an upright MRI scanner. Our experimental design simulates load-bearing conditions that are commonly experienced in some occupational settings (head supported mass such as military helmets and mounted devices such as night vision goggles) and recreational activities (virtual reality headsets) more accurately. This approach allows for the examination of musculoskeletal responses in a scenario that mimics real-life stressors on the cervical spine. By analyzing the changes in muscle cross-sectional area and Cobb angle in this controlled setting, the study seeks to examine the relationships between muscle morphology changes and alterations in spinal alignment. Such insights are pivotal in understanding how cervical musculature adapts or responds to external loading and its impact on spinal health, particularly in an asymptomatic population where preemptive insights can be crucial for preventing neck pain and spinal pathologies.

METHODS

Twenty-one healthy volunteers under forty years of age, asymptomatic for neck pain, and no history of cervical injury or abnormalities, were selected for this study. The protocol was approved by the local institutional board and by the United States Department of Defense. All subjects consented for the study. Upright MRIs were used to generate sagittal and axial images of the cervical spine. To simulate load-bearing conditions, participants wore army combat helmet weighing approximately 1.5 kg, which was adjusted for MRI compatibility and individual fit. The participants were given an upright MRI scan before and after four hours of wearing the helmet.

The cross-sectional areas of sternocleidomastoid (SCM) and multifidus (MF) muscles were measured from the C2 to C7 vertebrae at the inferior endplate level using OSIRIX software (Bernex, Switzerland). Although the cross-sectional area for each muscle was measured bilaterally, only the mean of both measurements was used for analysis. Additionally, the Cobb angle of the vertebral body at each level was similarly quantified to assess spinal alignment **(Fig. 1)**.

For statistical analysis, the normal distribution of the data was checked using the Shapiro-Wilk test. For normally distributed data, paired t-tests were used to compare pre- and post-measurements for SCM, MF, and Cobb angle at each spinal level. Wilcoxon signed-rank test was used for non-normally distributed data. Spearman's rank correlation test was applied to assess the correlation between the changes in cross sectional areas of SCM and MF, SCM and Cobb angle, and MF and Cobb angle at each individual spinal cord level. In addition, two observers processed the geometrical measures for intraclass correlation (ICC[3,1]) analysis.

RESULTS

Results of the Shapiro-Wilk test indicated a normal distribution across most spinal levels for both pre and post load-bearing muscle area and Cobb angle measurements, with exceptions noted in the pre-load-bearing cross sectional area of SCM at the C4-C5 level ($p = 0.024$) and the post load-bearing Cobb angle at C2-C3 ($p = 0.058$), suggesting non-normal distributions in these specific cases. Results of the paired t-test or the Wilcoxon signed-rank test (for non-normally distributed data) revealed no statistically significant changes in SCM and MF muscle areas across all spinal levels. Specifically, the Wilcoxon test applied to the SCM C4-C5 region due to its non-normal distribution demonstrated no significant change ($p = 0.838$) **(Fig. 2)**. Similarly, Cobb angle measurements showed no significant variations at any spinal level, including at C2-C3 where a Wilcoxon test was used ($p = 0.441$).

Spearman's rank correlation tests identified a statistically significant and positive correlation between changes in SCM and MF areas at the C7-T1 level ($\rho = 0.679$, $p = 0.0007$). However, no significant correlations were detected between changes in SCM area and Cobb angles, nor between changes in MF area and Cobb angles, across any spinal levels. These results collectively suggest that the load-bearing conditions applied in this study did not lead to significant alterations in muscle areas or spinal curvature from C2-C6 but did have a statistically significant impact at the C7-T1 level.

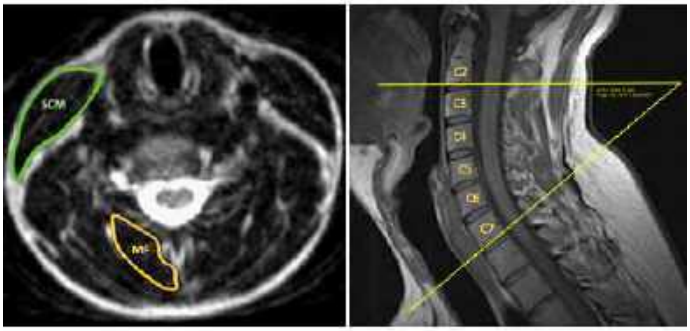

Figure 1: Sternocleidomastoid (SCM) and multifidus (MF) muscles cross-sectional areas at C5 identified in the upright MRI axial scan (left) and the Cobb angle calculated in the sagittal MRI (right).

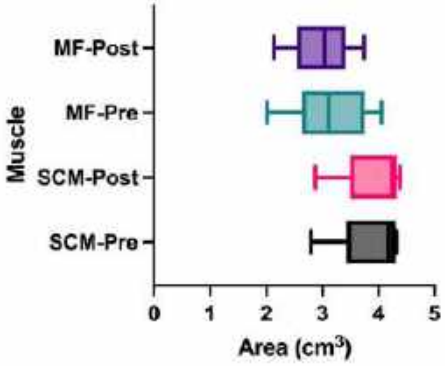

Figure 2: The average cross-sectional area between pre and post MF and SCM muscles are graphed in this figure. The change in cross-sectional are not statistically significant.

DISCUSSION

Upright MRIs were used to study the morphology of two important cervical muscles: the SCM and MF. These muscles were chosen for their significant roles in cervical biomechanics: the SCM for flexion and rotation of the head and neck, and the MF for extension and stabilization of the cervical spine [4]. These upright MRIs were also used to measure the Cobb angle in the vertebral body on a level-by-level basis. The Cobb angle, a standard metric used to assess spinal alignment, is especially relevant in the context of cervical spine health.

This study examined the biomechanical effects of load-bearing headgear on the cervical spine, a topic relevant for occupations requiring protective or heavy headgear. Twenty-one healthy volunteers underwent upright MRI scans before and after axial head loading. The cross-sectional area of SCM and MF muscles, as well as the Cobb angle was measured at each level of the cervical spine. While most of the spinal levels showed no significant changes, our results showed a statistically significant and positive correlation between changes in the SCM and MF muscle areas at the C7-T1 level, suggesting a localized adaptive response to the additional head supported mass in this critical region of the cervical spine.

This relationship between SCM and MF areas at the C7-T1 level underscores the importance of this spinal segment in load-bearing scenarios. The C7-T1 region, positioned at the cervicothoracic junction, is a biomechanically critical region where the cervical spine transitions into the thoracic spine. This junction is known for its unique biomechanical properties, as it marks the transition from the highly mobile cervical region to the relatively rigid thoracic spine [5]. This is also the junction where lordosis of the cervical spine transitions into kyphosis of the thoracic spine.

Furthermore, the SCM and MF muscles at the cervicothoracic junction may respond synergistically to maintain stability and balance in this transitional area under load. These two muscles likely experience altered biomechanical demands when supporting the additional weight of the helmet. This additional load leads to subtle, yet measurable, changes in the muscle areas, especially at segments where mechanical stress is amplified. Musculoskeletal models can be used to determine the change in segmental loads within the osteoligamentous column (disc and facet joints), ligament strains, spinal cord stress-strain profiles, and forces in the selected and other cervical muscles using the data from the present study for a better understanding of the effects of head supported mass.

Further research is necessary to explore these dynamics over a longer duration and in different populations and in different environments (dismounted soldiers, pilots, etc.). Investigating whether these localized changes at the C7-T1 level escalate, stabilize, or reverse over time, and how they correlate with neck pain, fatigue, and function, would provide deeper insights. Additionally, understanding the threshold at which load-bearing begins to significantly impact the osteoligamentous cervical spinal column and spinal cord biomechanics could inform the designers of load-bearing headgear and trainers to develop preventive strategies that mitigate the risk of musculoskeletal disorders in the neck and cervicothoracic region.

ACKNOWLEDGEMENTS

The research was supported by the Office of the Assistant Secretary of Defense for Health Affairs, through the Broad Agency Announcement under Award No. W81XWH-16-1-0010, and by the Department of Veterans Affairs Medical Research. Dr. Yoganandan is an employee of the VA Medical Center. The opinions, interpretations, conclusions, and recommendations are those of the authors and are not necessarily endorsed by the sponsors.

REFERENCES

[1] Nahin, R., *The Journal of Pain*, 18:247–254, 2017.
[2] Suderman, B. et al., *Journal of Biomechanics*, 45:400–404, 2012.
[3] Huang, Z. et al., *World Neurosurgery*, 159:e273–e284, 2022.
[4] Yoganandan, N. et al., *Military Medicine*, 188:385–392, 2023.
[5] Simon, S. et al. *Spine*, 31:44, 2006.

Multiscale Mechanoimmunology: From Molecular Mechanisms to Precision Therapies

Therapeutic immune cells have the potential to treat complex diseases. Some therapies, such as CAR T cells, are effective against blood cancers but are not effective against solid cancers, which comprise about 90% of adult cancers. A key requirement of the role of therapeutic cells in tumor eradication is their ability to migrate to and infiltrate the tumor. To accomplish this, cells navigate various mechanoimmunological factors, such as tissue viscoelasticity. One consequence of viscoelasticity is time-dependent stress relaxation - a decrease in stress in response to applied deformation. However, the mechanisms by which viscoelasticity regulates migration are not fully understood. In addition, limited studies have quantitatively compared the transport of cell therapies in tissue-like environments. My research aims to address these research gaps. To address the potential role of viscoelasticity on 3D cell migration, I developed hydrogels that mimic the stress relaxation behavior of native tissues. I found that enhanced stress relaxation potentiates monocyte migration. Mechanistically, our data support a model whereby WASP-mediated actin polymerization generates physical force at the leading edge of the cell to generate micron-sized channels for cells to migrate through. In a separate project, I integrated macrophage migration data with an unsupervised k-means clustering algorithm to demonstrate that the transport properties of macrophages in tumors depend on macrophage phenotype and morphometric transitions. Together, our studies establish a platform to determine the role of mechanical cues in shaping the immune response and to leverage fundamental mechanisms to enable the rational design of “living drugs.”

SIMULATING THE IMPACT OF TUMOR MECHANICAL FORCES ON GLYMPHATIC NETWORKS IN THE BRAIN PARENCHYMA

S. Siri (1), A. Burchett (1), M. Datta (1)

(1) Departement of Aerospace and Mechanical Engineering, University of Notre Dame, Notre Dame, IN 46556 USA

INTRODUCTION

While meningeal lymphatics have been extensively studied [1], the understanding of brain parenchymal glymphatic networks is limited. Meningeal lymphatics, crucial for brain waste clearance, have received substantial attention. However, the intricate pathways and mechanisms of glymphatic function within the brain, responsible for metabolite clearance, remain unclear. The complexity of brain interstitial fluid dynamics, especially in paravascular spaces, poses a challenge in unraveling glymphatic networks. Further research is essential to comprehend the significance of these networks in maintaining brain health.

Understanding tumor mechanics involves the interplay between fluid and solid components [2, 3]. Tumors, with heterogeneous composition, consist of solid components (tumor cells and extracellular matrix) and fluid components (interstitial fluid and vasculature). Solid constituents contribute to structural integrity and growth, while fluid elements regulate the tumor microenvironment. Brain tumors pose a formidable challenge to glymphatic function, disrupting brain parenchyma integrity. Tumors alter interstitial fluid dynamics, compromising glymphatic flow and solute transport. Tumor-associated factors worsen disruptions, compromising the microenvironment for neural cells.

Understanding brain tumor-glymphatic system dynamics requires integrating experimental findings with computational modeling. Computational models offer a unique vantage point to simulate complex brain microenvironment interactions. Our computational modeling framework aims to elucidate how brain tumors impede glymphatic solute transport, identifying therapeutic targets for proper brain waste clearance. The model analyzes the effects of brain tumors on glymphatic solute transport, providing insights for future therapeutic interventions.

METHODS

The governing equations for FEM structural analysis involve equilibrium equations and constitutive relations. The equilibrium equations represent the balance of forces within the brain parenchyma. They can be expressed as:

$$\nabla . \sigma + f = 0 \quad (1)$$

Where σ is the stress tensor representing internal forces and f is the body force per unit volume. Constitutive relations describe the relationship between stress and strain in the material. For linear elasticity, Hooke's Law is commonly used:

$$\sigma = D . \epsilon \quad (2)$$

Where ϵ is the strain tensor representing deformations, D is the elasticity tensor (material property). Strain-Displacement Relation defines the relationship between strain and displacement. For small deformations:

$$\epsilon = \frac{1}{2}(\nabla u + (\nabla u)^T) \quad (3)$$

Where u is the displacement vector. When these equations are discretized using FEM, the continuous domain of the brain parenchyma is divided into smaller, simpler elements. The displacement field within each element is approximated using shape functions, and the equilibrium and constitutive equations are formulated for each element. Assembled together, these equations generate a system of linear equations that can be solved numerically to determine the displacement and stress distribution within the brain parenchyma under given loading and boundary conditions.

A 2D geometry (Fig. 1A) was created using COMSOL Multiphysics for Finite Element Method (FEM) modeling, including brain astrocytes, extracellular matrix (ECM), capillaries, tumors, and the prevascular space. The FEM model simulated the brain microenvironment, analyzing astrocyte and ECM properties, tumor size, and location's impact on the glymphatic system. Parametric analyses explored variations in astrocyte and ECM properties, assessing their influence on solute transport and fluid dynamics. Three mechanical scenarios (Fig. 1C) were considered to understand the glymphatic system's behavior under different ratios of astrocyte to extracellular space (ECS) contribution. Simulations in MATLAB Simulink and COMSOL Multiphysics comprehensively analyzed the system's response to variations in astrocytic and ECM characteristics, as well as tumor-induced residual stress on the system's geometry.

Lumped parameter models simplify the complex dynamics of the glymphatic system, representing paravascular spaces, astrocytes, and fluid dynamics as discrete compartments. These models, utilizing principles of flow, diffusion, and clearance rates, simulate solute and fluid movement efficiently, enabling analysis of factors affecting glymphatic transport. The astrocyte network model, adapted from Asgari et al. [4], illustrates connectivity between arterial and venous paravascular spaces. Multiple simulations in MATLAB Simulink analyze geometric and physical changes induced by tumors, revealing their impact on glymphatic solute transport and metabolite clearance in the brain parenchyma.

RESULTS

The parametric analysis in Fig. 3B shows the dynamic relationship between mechanical forces, tumor locations, and sizes concerning the glymphatic system and skull proximity. Results indicate an initial stress level of 18 Pa at far tumor distances, gradually increasing as tumors approach the skull, highlighting a clear correlation between stress distribution and distance. The study reveals two key associations: larger tumors correlate with higher stress levels, suggesting potential structural implications, and as tumors get closer to the skull, stress levels surge, particularly near the glymphatic system, emphasizing the vulnerability of this system to external forces near tumor sites.

Figures 1D and 1E illustrate three scenarios with varying displacement and mechanical stress profiles influenced by Astrocytes (Ast.) and the Extracellular Matrix (ECS). In the first scenario, minimal Astrocyte contribution results in the highest displacement profiles, mainly due to ECS (10% compression). The second scenario shows a balanced Astrocyte and ECS contribution, leading to uniform displacement with a predominant concentration in ECS. In the third scenario, increased Astrocyte involvement with lower ECS contribution results in minimal displacements. Interestingly, mechanical stress on Astrocytes peaks when their contribution is lowest and vice versa.

In summary, the growing prominence of astrocytes in the brain corresponds to increased mechanical stress and displacement, driven by heightened pressure from brain tumors. This highlights the intricate relationship between cellular components and physiological responses in pathological conditions like tumors.

Fig. 1F illustrates the variations in venous side flow rate efflux in response to mechanical compression ranging from 0 to 10%. These simulations comprehensively address the impact of mechanical compression on Glymphatic system transport, specifically considering properties related to astrocytes, AQP-4, ECS, gap junctions (GJ), and capillaries. The results highlight a discernible trend wherein a 10% mechanical compression is associated with an approximate 20% reduction in the venous side flow rate, underscoring the significance of mechanical factors in influencing Glymphatic system dynamics.

DISCUSSION

In this study, we investigated how brain tumors induce residual stress affecting the Glymphatic system's structure. We explored the tumor's impact on tissue properties, including alterations in fluid flow dynamics in paravascular spaces. Our analysis focused on mechanical dynamics in brain parenchyma, examining scenarios with varying displacement magnitudes and stress profiles in Astrocytes (Ast.) and the Extracellular Matrix (ECS). These scenarios revealed the intricate interplay between brain tumors and glymphatic system responses under pathological conditions. These findings highlight the importance of a multidimensional approach to assess tumor biomechanical impact on the Glymphatic system. This information is crucial for medical practitioners to anticipate stress concentrations, guiding treatment strategies. The insights contribute to understanding cranial biomechanics, paving the way for personalized medicine and tailored therapeutic approaches for individuals with tumors near the skull.

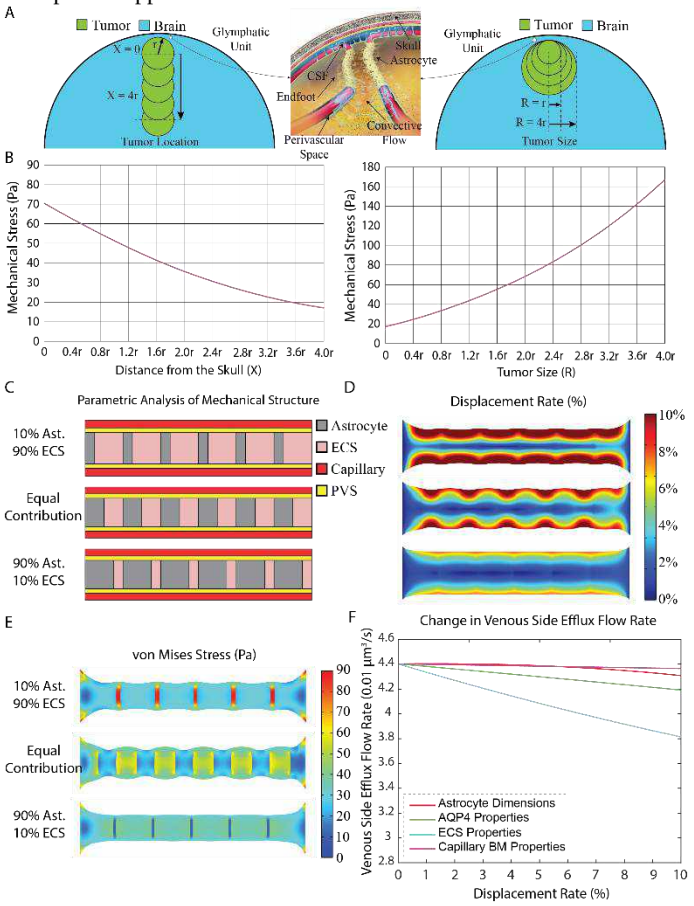

Figure 1: Investigating Brain Tumor Impact on Glymphatic System: (A) 2D brain and tumor model for Finite Element Method (FEM) analysis in COMSOL Multiphysics. (B) Parametric analysis shows stress changes on Glymphatic System at different tumor distances and sizes. X-axis: tumor distances and sizes, Y-axis: mechanical stress. (C) Schematic explores three mechanical scenarios (10% Astrocyte - 90% ECS, Equal Astrocyte-ECS Contribution, 90% Astrocyte - 10% ECS) studying their roles in glymphatic system behavior under brain tumor influence. Simulations cover induced residual stress, altered mechanical properties, tissue deformation, and fluid flow dynamics in paravascular spaces. FEM parametric analyses examine astrocyte and ECM effects on the glymphatic system, demonstrated through (D) Displacement and (E) Mechanical Stress profiles. (F) Exploration of variations in astrocyte, AQP-4, GJ, ECS, and Capillary properties to understand their impact on solute transport and fluid dynamics in brain parenchyma.

ACKNOWLEDGEMENTS

We thank Ms. R'nld Rumbach for her technical support.

This work was supported by the National Cancer Institute (NIH/NCI K22-CA258410 to M.D.).

REFERENCES

[1] S. Da Mesquita, Z. Fu, and J. Kipnis, "The meningeal lymphatic system: a new player in neurophysiology," *Neuron*, vol. 100, no. 2, pp. 375-388, 2018.

[2] H. T. Nia, L. L. Munn, and R. K. Jain, "Physical traits of cancer," *Science*, vol. 370, no. 6516, p. eaaz0868, 2020.

[3] M. Datta *et al.*, "Losartan controls immune checkpoint blocker-induced edema and improves survival in glioblastoma mouse models," *Proceedings of the National Academy of Sciences*, vol. 120, no. 6, p. e2219199120, 2023.

[4] M. Asgari, D. De Zélicourt, and V. Kurtcuoglu, "How astrocyte networks may contribute to cerebral metabolite clearance," *Scientific reports*, vol. 5, no. 1, p. 15024, 2015.

IN-SITU AND IN-VITRO HETEROGENEITY OF PORCINE MENINGES: INSIGHTS FROM 2-PHOTON MICROSCOPY AND CORRELATED MICRO-INDENTATION

S.Mohammad Tabatabaei, Ph.D. (1), Lakiesha N. Williams, Ph.D. (1)

(1) J. Crayton Pruitt Family Department of Biomedical Engineering, University of Florida, Gainesville, Florida, USA

INTRODUCTION

The study of meninges, an essential component in neurobiology, faces significant challenges due to its complex and heterogeneous nature. Traditionally, biomechanical characterization of the dura mater has predominantly relied on in vitro one- and two-axis tensile tests[1], [2]. However, these methods have proven insufficient in capturing the intricate structural and mechanical nuances of this tissue. The inconsistencies and limitations in existing research methodologies have led to a fragmented understanding of the meninges' biomechanical properties. Thus, the complexities of meningeal tissue are not included in computational models of the head or in meningeal grafts for reconstruction.

Our research introduces an innovative approach to address these challenges, hypothesizing that a comprehensive understanding of the meninges requires an integrated analysis that considers its interaction with the underlying brain structures. This study aims to bridge the gap in current biomechanical characterization methods by combining advanced in-situ structural analysis with mechanical testing techniques. By doing so, we seek to capture the meninges' properties in its native state, which is crucial for a more accurate and holistic understanding of native dura and the development of biofidelic grafts.

This approach is grounded in the understanding that the biomechanical properties of the meninges are not only a product of its material composition but are also significantly influenced by its structural relationship with the brain. As such, our methodology is designed to elucidate these complex interactions, providing insights into how the meninges' function is shaped by its dynamic, native environment. This study, therefore, represents a significant departure from conventional biomechanical studies, offering a novel perspective on the intricate biomechanical behavior of the meninges in situ.

METHODS

In this study, we employed a comprehensive methodology to investigate the structural and mechanical properties of meninges in two locations of four anatomical regions (anterior, medial, lateral, and posterior). Meningeal tissue denoted as "sulcus" was examined at the sulcus location of the brain and "gyrus" meningeal tissue was examined at the gyrus locations of the brain. Two-photon confocal microscopy was utilized to capture the Second Harmonic Generation (SHG) signal of the tissue in their respective regions[3]. This advanced imaging technique enabled visualization and quantification of the intricate microstructural features of dura mater in its unstained, native state, thus providing insights into its complex pre-stressed architecture.

For structural evaluation, the 4 anatomical regions were studied using 2 pig brains in both in situ and excised states. This was done to evaluate the differences in the tissue structure across each anatomical location. For each of the four regions, 10 images were captured from four distinct samples on each slide. For in situ samples, the cranial meninges was meticulously fixed with 4% Paraformaldehyde for 24h post-skull removal, ensuring the preservation of its natural state. In contrast, excised, in vitro tested, samples were obtained and then fixed with paraformaldehyde, allowing for a comparison of the impact of the excision process on the tissue's structural integrity while in situ.

In situ mechanical properties were obtained via indentation testing on pre-stressed, non-fixed meningeal tissue [4]. This technique was specifically designed to measure the effective Young's modulus of the meninges in the 4 regions, providing a more comprehensive understanding of its biomechanical behavior. The indentation tests were conducted using the Mach-1 micromechanical tester (Biomomentum, Canada) on pig heads immersed in a PBS bath at room temperature to simulate a physiological environment. In this way, the in-situ conditions were closely replicated. For mechanical properties evaluation, 3 pig brains were tested with 10 indentations at each anatomical location. The indentation depth was less than 1000 μm to ensure consistent and reliable measurements. Additionally, the meningeal samples were

subjected to loading rates of 1 mm/s and 5 mm/s to assess their rate-dependent mechanical behavior. This aspect of the methodology was crucial in understanding how the meninges responds to varying mechanical stresses, which is essential for applications in neurobiology and clinical practice.

RESULTS

The results of this study reveal significant insights into the meninges structural (in situ and in vitro) and mechanical properties (in situ). Structural analysis of the four anatomical regions showed notable differences between in situ and excised meninges (Fig. 1-a, b). The average thickness of in situ meninges was notably thinner, measuring 263.97 ± 55.51 μm, compared to 698.042 ± 178.18 μm for excised meninges. Additionally, compared to the in situ gyrus samples, the thickness of the in situ sulcus samples was observed to be 1.3 times greater, and the thickness of excised sulcus meninges was 1.19 times greater than the excised gyrus meninges (Fig. 1-c). This thickness variance suggests substantial changes in structural integrity resulting from the excision process. Two-photon microscopy revealed that excision altered the well-aligned collagenous structures in in situ samples, leading to an exaggerated waviness in collagen. Anisotropy analysis across regions indicated changes post-excision (Fig. 1-d), hinting at mechanical property variations influenced by the extracellular matrix composition.

Mechanical testing revealed a lower effective Young's modulus for the meninges in situ, at 2.2 Kpa, compared to in vitro results previously reported by our lab [5], which averaged 19.9 MPa. Additionally, these results demonstrated a clear strain-rate dependency. (Fig. 2). Variations in mechanical properties were observed, particularly at lower strain rates, suggesting the influence of structural differences on mechanical response, especially in the gyrus region.

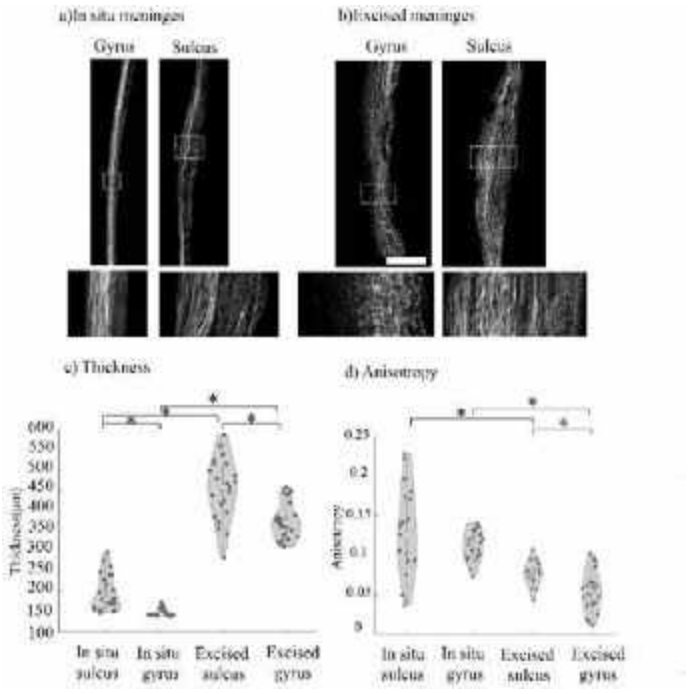

Figure 1**. Comparative SHG imaging of in situ (a) and excised (b) meninges with magnified views and quantification of thickness (c) and anisotropy (d).**

DISCUSSION

The findings from this study offer pivotal insights into the biomechanical complexity of the meninges and cranial meninges overall. The observed thinning in native meninges compared to excised samples underscores the impact of the native microenvironment on the meninges' structural integrity. Additionally, there is significant differences in morphometry of the sulcus and gyrus dura regions, which is important for the meninges role in vivo. This highlights a critical limitation of traditional biomechanical analyses, which often overlook the influence of native tissue states and the role of protection offered in prestressed conditions. The alteration in collagenous structures post-excision and the associated changes in anisotropy emphasize the importance of the meninges' interaction with the brain in maintaining its mechanical properties and providing protection in rotation/translation impact situations.

Moreover, the rate-dependent mechanical behavior observed through indentation illustrates the extent of meningeal viscoelasticity across different regions. The variations in mechanical properties, especially at lower loading rates, point to the significant role of structural differences in influencing the tissue's biomechanical response. These findings suggest that the meninges' function is not solely determined by its material composition but is intricately linked to its structural arrangement and interaction with surrounding brain structures.

This study, therefore, underscores the necessity for integrative biomechanical approaches that consider both structural and mechanical aspects to fully understand the complexities of the meninges.

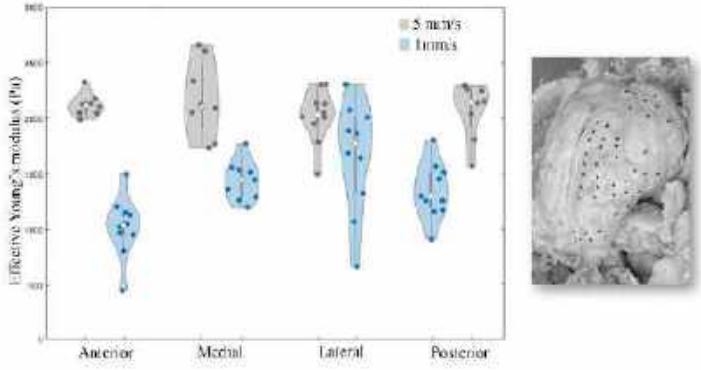

Figure 2. Indentation on porcine meninges; regional effective Young's modulus distribution (left), and sample marking (right)

ACKNOWLEDGEMENTS

The authors would like to thank the University of Florida Animal Care Services for the tissue donation. Research reported was supported by the National Institute of Neurological Disorders and Stroke of the National Institutes of Health under award number R01NS122939.

REFERENCES

[1] Niestrawska, J et al. Acta Biomater, 170: 86–96, 2023.
[2] De Kegel, D et al., J Mech Behav Biomed Mater, 79: 122–134, 2018.
[3] Esquibel, C et al., Front Neurosci,14: 95, 2020.
[4] MacManus, D, et al Acta Biomater, 57: 384–394, 2017.
[5] Sharma,A. et al., Engineered Regeneration: 4-2: 205–213, 2023.

SB^{3}C2024
Summer Biomechanics, Bioengineering and Biotransport Conference
June 11-14, Lake Geneva, WI, USA

SPATIO TEMPORAL MODELING OF BIOMARKER EXPRESSION IN NEURONAL CLUSTERS DURING TRAUMATIC BRAIN INJURY

Debabrata Auddya,Shiva Rudraraju

Department of Mechanical Engineering, University of Wisconsin-Madison, Madison, WI, USA

INTRODUCTION

Traumatic Brain Injury (TBI) is associated with an impact or concussion to the head with the injury being specifically characterized through pathological degradation at various biological length scales. To quantify the sequence of events following TBI, classically, various mechanical modeling techniques have been proposed which establish metrics that demonstrate localised to generic neuronal damage. Broadly, the two categories of degradation encompass physiological deterioration and upregulation of chemical entities such as neurotransmitters which causes initiation of downstream pathophysiological effects. The loss of structural and chemical integrity within neurons and neuron clusters release molecules which serve as critical biological markers crucial to injury diagnosis. Aberration in concentration of essential chemical components in the brain such as neurotransmitters, inflammasomes, cytokines and ionic channels lead to activation of necroptotic pathways which eventually causes neurodegeneration. Recent studies have highlighted the pathological effects caused due to upregulation of these chemical species across the brain. The primary aim of this work is to demonstrate a continuum framework which models the multiphysics of mechano-chemical interactions underlying TBI. Using a coupled PDE (partial differential equation) formulation and FEM (finite element method) discretization, the framework highlights evolution of field variables which spatio-temporally resolves mechanical metrics and chemical species across the neuron cluster domain. Using geometric spatial localisation of specific chemical components, we illustrate dynamics of chemical field evolution across different regions of the neuron microstructure. This enables visualisation of initiation, interaction and progression of field variables, highlighting temporal activation of different components in the downstream necroptotic pathway.

METHODS

The proposed neurodegenerative pathway (Fig.1 (left)) begins with mechanical deformation manifested as increased strain to the brain, which triggers opening of the pannexin channels leading to massive ATP efflux into the extracellular region. Increased ATP causes purinergic receptors to activate, particularly the P2X7R, which causes potassium efflux from the intra- to extracellular milieu. Decrease in ionic concentration of potassium initiates formation of the NLRP3 inflammasome comlex. Simultaneously there is a heightened increase in the demand for oxygen causing oxidative stress and production of reactive oxygen species. This causes the NFκB pathway to trigger, also leading to intracellular formation of the NLRP3 inflammasome complex. This complex is responsible for modulating formation of pro-inflammatory products mainly cytokines such as TNFα and ILs. TNFα causes dysregulation in neuronal signalling by blocking EAAT's on astrocytes thereby reducing glutamate uptake. It also intensifies excitatory transmission by increasing permeability of the glutamate receptors to calcium ions. Increased glutamate concentration in the post synaptic region causes excitotoxicity and is considered as the pivotal step towards necroptosis.

Representation of a reduced pathway (Fig.1 (right)) consisting of quantifiable elements which contribute towards necroptosis. Illustrated in this pathway are ATP, TNF-α [1] and glutamate [2] classified as chemical concentration fields and the P2X7 [3] receptor mathematically as a phase field. This is attributed qualitatively to the opening probability of the channel upon prolonged activation by ATP. The shortened pathway enables formulation of advective-diffusive equations to spatio-temporally resolve the chemical species across the inhomogenous neuronal landscape.

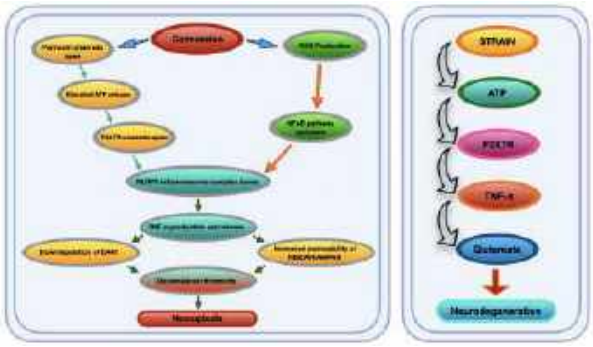

Figure 1: (Left) Proposed Pathway (Right) Modeled Pathway

We consider concentrations of the following chemical species as the primary fields: ATP (c_a), TNF-α (c_t), Glutamate (c_g) and ionic channels represented as a phase field: P2X7 (ϕ_p). The idea behind phase field assumption of ionic channels is the appoximation of gating probability (0-closed, 1-open) due to concentration sensitivity of certain chemical species. The evolution of these chemical species is modeled using the following advection-diffusion equations:

$$\frac{\partial c_a(\mathbf{x},t)}{\partial t} = \nabla \cdot (D_a \nabla c_a) + f(\epsilon), \qquad \mathbf{x} \in \Omega \tag{1}$$

$$\frac{\partial c_t(\mathbf{x},t)}{\partial t} = \nabla \cdot (D_t \nabla c_t) + f(c_a, \phi_p), \qquad \mathbf{x} \in \Omega \tag{2}$$

$$\frac{\partial c_g(\mathbf{x},t)}{\partial t} = \nabla \cdot (D_g \nabla c_g) + f(c_t), \qquad \mathbf{x} \in \Omega \tag{3}$$

$$\phi_p = \Phi(c_a) \tag{4}$$

where the source terms are expressed as $f(\epsilon, c_a, c_t, \dots)$ and Φ represents receptor sensitivity as a function of concentration of ATP. The diffusivity terms are expressed as D_x where the subscript x refers to individual species.

The mechanical response of the underlying viscoelastic framework is modeled using the conservation of linear momentum.

$$\nabla \sigma = 0 \tag{5}$$

A viscoelastic network (Fig.2) consisting of Maxwell elements is used to model the underlying mechanical network as illustrated below:

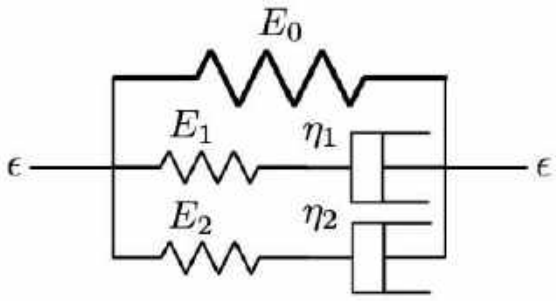

Figure 2: The extracellular matrix and its components is modeled as a viscoelastic network.

The figure below (Fig.3) illustrates the synaptic-microglial region which is further modeled in a FEM framework. This allows compartmentalisation of chemical fields and allows visualisation of diffusive dynamics across the computational domain. The heterogeneity in chemical field concentrations for single neurons and neuron clusters play a pivotal role in demonstrating injury progression driven by mechano-chemical interactions.

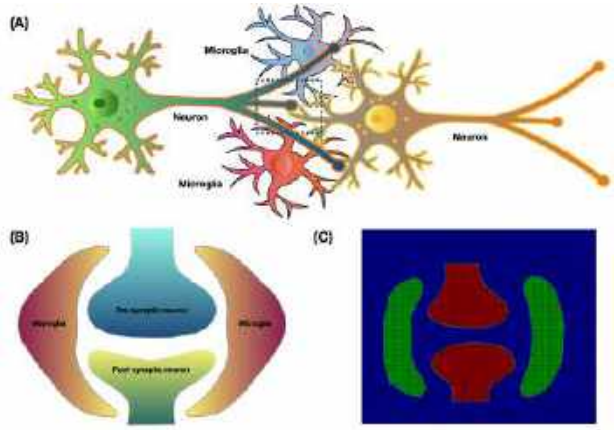

Figure 3: (A) Schematic of neuron synapse and microglial interaction relevant for spatial modeling (B) Specific region under consideration (C) FEM illustration of neuron-microglia assembly

RESULTS

We present some results (Fig.4) from boundary value problems to demonstrate spatio-temporal evolution of biomarkers upon mechanical loading.

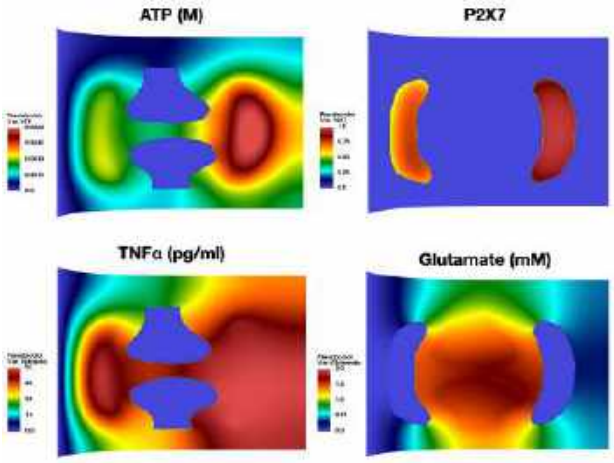

Figure 4: The results are obtained from a tensile loading boundary value problem. The domain is subjected to unaxial tension leading to strain across it. This causes activation of ATP as shown in the first block. At a specific concentration P2X7 receptor opens and the figure highlights those regions. This further triggers the cytokines (TNF-α) to release from the microglial region into the ECM as shown. Finally the cytokine activation causes excess production of glutamate within the synaptic region as illustrated. These simulation results describe a spatio-temporal evolution of biomarkers due to an external mechanical load. The length scale of the domain is in μm and time scale is in ms.

DISCUSSION

We have highlighted a novel mechano-chemical framework which demonstrates mechanical and chemical metrics relevant to traumatic brain injury. The results presented, spatio-temporally resolves these metrics and provides valuable insight and analysis into critical chemical thresholds underlying necroptosis. In a first-of-its-kind representation of mechano-chemical interactions underlying neurons and neuronal clusters we have qualitatively drawn comparison between our results and existing literature and demonstrated injury thresholds. The fidelity of our current modeling approach allows inclusion of additional physics and fields which enables better resolution of injury diagnosis leveraging clinical biomarkers.

ACKNOWLEDGEMENTS

This work was supported by Office of Naval Research (ONR) (Award: N00014-21-1-2918)under the PANTHER program for modeling mTBI.

REFERENCES

[1] You K et al. *Frontiers in Cell and Developmental Biology* 9 (2021).

[2] Olmos G et al. *Mediators of inflammation* 2014 (2014).

[3] Xing S et al. *Frontiers in physiology* 7 (2016).

OVINE FRACTURE HEALING IS ROBUST TO HIGH GAP STRAIN: A VIRTUAL MECHANICAL TESTING AND IMAGE COLOCALIZATION ANALYSIS

Maham Tanveer (1), Hannah L. Dailey (1)

(1) Mechanical Engineering & Mechanics, Lehigh University, Bethlehem, PA, USA

INTRODUCTION

Evidence from large animal and clinical studies have shown that the mechanical conditions at the fracture site controls callus growth. Modern understanding of the role of interfragmentary strain in the mechanoregulation of bone healing has heavily relied on Stephan Perren's "2-10% strain rule" [1]. The rule suggests tolerance limits for fracture gap strains for successful bone healing based on rupture data from bone and cartilage tissue elongation tests. Any strain below 2% (measured as gap closure/original gap length) is suggested to not provide enough stimulation for callus formation, while any strain above 10% suggested to lead to excessive movement, hindering osteogenesis and increasing the risk of nonunion in fracture.

Due to the challenges of measuring strain *in vivo*, finite element analysis (FEA) offers an opportunity to noninvasively characterize the mechanical strain environment during bone healing. In this study, FEA was performed to measure early interfragmentary strain by first determining boundary conditions that represent physiologic loads and then applying those loads to image-based models of early post-operative ovine tibiae. The hypothesis of this study was that early interfragmentary strains higher than 10% do not cause nonunion.

METHODS

Eight representative animal samples were chosen from a library of microCT scans of excised tibiae of Swiss Alpine sheep (average body weight 68 kg, age 2-3 years), which were part of previously completed research studies. Intact and operated limb scans were processed in Mimics (v23.0, Materialize, Leuven, Belgium). Scans were down sampled to an isotropic resolution of 400µm. Operated bones were segmented to isolate old cortical bone from callus. Bone reconstruction was performed by adding mask around the osteotomy in the regions where remodeling had made the cortical bone less dense. Post-operative X-rays and bone structure above the osteotomy were used as a guide to reconstruct bone accurately. No callus was included for these models.

All 3D bone models were aligned axially to the global coordinate system. Right-side contralateral intact bones were mirrored to reduce variability during load optimization (Figure 1). Medullary void spaces were excluded for both operated and contralateral bones.

Figure 1: Preparation of an intact bone model for physiologic load optimization. This example was mirrored and aligned before defining midshaft normal strain probe locations.

Virtual plate installation was performed in Solidworks 2020 (SolidWorks Corps, Waltham, MA). Screw positions were matched to those in the scans and plate placement was referenced to post-op X-rays. A strain visualization region was added to measure strains within and around the fracture gaps (Figure 2) using our established method [2]. Quadratic tetrahedral (tet-10) meshes were created in 3-Matic with a maximum edge length of 1 mm. Material properties were assigned using our validated dual-zone material model to manage partial volumes:

$$E = \begin{cases} E_{sc} & \rho_{QCT} < \rho_{cut} \\ 10225 \times (\rho_{QCT})^{1.0} & \rho_{QCT} \geq \rho_{cut} \end{cases} \quad (1)$$

where E_{sc} = 50MPa and ρ_{cut} = 665 mgHA/cm^3 and ν = 0.3 [3]. A homogeneous material property of E = 0.5 MPa and ν = 0.45 was assigned to the strain visualization region [2].

Figure 2: Workflow showing model creation, meshing, simulation and submodeling (blue zone) to measure interfragmentary strain.

Finite element analysis was performed in ANSYS Workbench Mechanical (R2020, ANSYS, Inc, Canonsburg, PA). Boundary conditions used remote points on proximal and distal faces, with a roller support defined at the proximal remote point and pinned support defined at the distal remote point (Figure 1).

Physiologic-like loading conditions were defined starting with a bodyweight scaled midstance axial load. Variable anteroposterior (AP) and mediolateral (ML) bending moments were applied in superposition to achieve midshaft normal strains comparable to *in vivo* strain gauge data for intact ovine bones [4] (see strain probe locations in Figure 1). A response surface was generated and moments were selected to minimize root mean square error (RMSE) for midshaft normal strains.

Optimized intact tibia loads were applied to the operated tibia models for each animal. A low-load variation of 20% bodyweight (BW) was also applied to represent the loading situation observed with typical loading restriction in the very early post-operative period [5].

To understand the relationship between strain and healing, voxel Hounsfield Units (HU) were sampled from an AP slice view, including voxels within and around the lateral osteotomy gap. HU for each voxel was categorized into hard/soft callus based on our previously validated threshold of 665 mgHA/cc [6]. Voxel data for each sampling region of interest was then mapped to von Mises strain in strain visualization region. Logistic regression was performed with a binarized outcome variable for hard (1) versus soft (0) callus.

RESULTS

The optimized load combination giving the lowest RMSE was an axial load of -1418N, AP bending moment of 20,000 N-mm and ML bending moment of -15,000 N-mm. Strain contours matched the expected physiologic strains for intact sheep tibiae [4] (Figure 3).

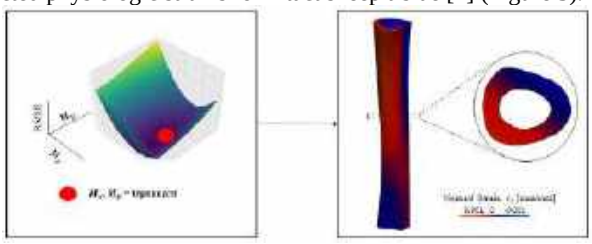

Figure 3: Optimizing the superposition of axial loads and bending moments produced midshaft normal strains with the physiologic isoclines at midstance. Note the slightly medialized anterior tension and lateralized posterior compression state.

At both high and low loading levels, the maximum von Mises strain occurred in/around the fracture gap (Figure 4) and was well above the hypothetical 10% limiting threshold in all eight animals. The peak von Mises strain was 154% ± 28% for full (100%) loading and 36% ± 11% for low (20%) loading. The volume of elements with von Mises strain above 10% was 5.11 ± 3.00 cm^3 for full loading and 0.37 ± 0.19 cm^3 for low loading.

Logistic regression showed hard callus was 2.36 times more likely to form outside the fracture gap compared to inside the gap ($p < 0.05$). Mann-Whitney U test revealed significant differences in von Mises strain between sampling boxes for location "in" versus "around" the fracture gap for both loading cases (20% and 100%) (Figure 5).

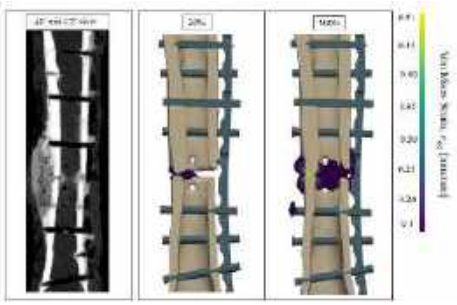

Figure 4: Representative model showing high strains >> 10% under both low (20% BW) and high (100% BW) loads. Von mises strains are illustrated here for simplicity.

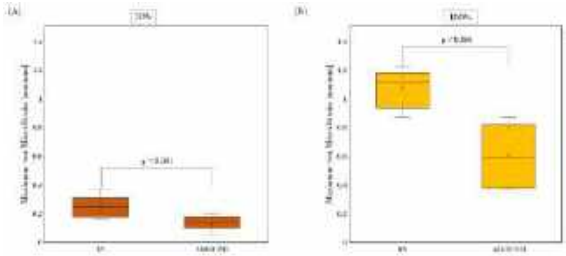

Figure 5: Elements inside the fracture gap had significantly higher strains compared to those around the gap for both partial weightbearing (A) and 100% bodyweight (B).

DISCUSSION

This analysis suggests that fracture gap strains greatly exceed the 2-10% range for physiologically loaded ovine osteotomies, even in the protected low-loading case of 20% BW. Early mineralization was delayed inside the immediate gap zone where von Mises strains were very high, but all animals had successful unions, suggesting that secondary fracture healing is more tolerant to high gap strain values than previously believed. These findings may have a significant implication on the understanding of the effect of strain on bone healing.

ACKNOWLEDGEMENTS

This work was supported by NSF (CMMI-1943287) and NIH-NIAMS (R21AR081435). Simulations were run on Lehigh University's Research Computing infrastructure, partially supported by NSF Award 2019035. The content is solely the responsibility of the authors and does not necessarily represent the official views of NIH or NSF.

REFERENCES

[1] Perren, S.M. et al., *Clin Orthop Relat Res*138:175-196, 1979.
[2] Inacio, J.V. et al., *J Orthop Res*, 41(3):1049-1059, 2023.
[3] Inglis, B et al., *Comp Meth Biomech Biomed Eng*, 26(12):1431-1442, 2023.
[4] Lieberman, D. E et al., *AJPA*, *123*(2):156–171, 2004.
[5] Windolf, M et al., *Medicina*, *58*(7):858, 2022.
[6] Inglis, B. et al., *Sci Rep*, 12(1):2492, 2022.

POSTURAL STABILITY IN HELICOPTER AIRCREW WITH AND WITHOUT NECK AND BACK PAIN: THE MEDICAL COLLEGE OF WISCONSIN MILITARY AIRCREW NECK AND BACK PAIN STUDY

Rachel Cutlan (1), Cory Everts (2,3), Alok Shah (2), Amy Nader (2), Keeley Hamill (2), Narayan Yoganandan (2,4), Lance Frazer (5), Barry S. Shender (6), James B. Sheehy (6), Glenn Paskoff (6), Daniel P. Nicolella (5), Timothy Bentley (7), Brian D. Stemper (1,2,4)

(1) Department of Biomedical Engineering, Marquette University and Medical College of Wisconsin, Milwaukee, WI, USA
(2) Department of Neurosurgery, Medical College of Wisconsin, Milwaukee, WI, USA
(3) 115th Fighter Wing, Wisconsin Air National Guard, Madison, WI, USA
(4) Zablocki Veterans Affairs Medical Center, Milwaukee, WI, USA
(5) Southwest Research Institute, San Antonio, TX, USA
(6) Naval Air Warfare Center Aircraft Divison, Patuxent River, MD, USA
(7) Office of Naval Research, Arlington, VA, USA

INTRODUCTION

Neck and back pain are common in military helicopter aircrew. Over a 12-month period, 67% and 80% of helicopter pilots reported neck and back pain (1,2). Aircrew posture during flight was thought to be a contributing factor for these pain symptoms, along with whole body vibrations and head-borne equipment such as night vision goggles (NVG) (2,3). Flight hours, NVG use, and total NVG flying hours were cited as risk factors for pain (1,4).

Postural control can be affected by neck and back pain. The cervical spinal cord plays an important role in the integration of muscle spindle, vestibular, and visual input, which provide information about the current position of the head (5). Damage and fatigue of sensory tissue in the neck and back may lead to reduced signal accuracy and incorrect center of mass positioning (5,6). Pain can also interfere with these signals, leading to more instability (5,6). This can be observed through increased sway in patients with chronic neck and back pain (7-9).

Deficits in postural control were analyzed in civilians with chronic neck and back pain separately, but the interaction between pain in these two areas has not been extensively explored (7-9). Along with this, postural stability is yet to be reported for the military helicopter population. This study has two goals: understand how neck and back pain in military helicopter aircrew affects measures of postural stability, and how the interaction of neck and back pain may further decrease postural control.

METHODS

Wisconsin Army National Guard (WIARNG) helicopter aircrew signed informed consent forms and completed baseline demographic and flight history surveys, pain assessments, and a postural stability assessment. Pain assessments involved the Neck Disability Index (NDI) and the Oswestry Low Back Disability Index (ODI), both scored 0-50, with the purpose of understanding how neck and back pain affect daily activities. A score of 0-4 is considered “no disability”, and a score of 5-14 is considered “mild disability” (10). Helicopter aircrew were placed into one of four groups based on their NDI and ODI scores: no neck or back pain group (NBPG-; NDI:0-4 and ODI:0-4), neck pain group (NPG; NDI:5-14 and ODI:0-4), back pain group (BPG; NDI:0-4 and ODI:5-14), and neck and back pain group (NBPG+; NDI:5-14 and ODI:5-14).

This study incorporated a published postural stability protocol (7). Each subject stood on a force plate with eyes open and eyes closed for 30 sec. Following these quiet standing trials, participants completed a series of dynamic arm movement trials. In each trial, the subject was instructed to stand still with either eyes open or closed. At a randomized time after this command (10-20 seconds), the subject was instructed to rapidly raise either their left or right arm, then hold it up for 20 seconds. They were then told to relax, and the next trial began. Each combination (eyes open right arm: OR; eyes open left arm: OL; eyes closed right arm: CR; eyes closed left arm: CL) was completed three times in random order.

Three-axis forces and moments were collected at a sampling rate of 1024 Hz during each trial using a force plate. The force plate output data were filtered using a fourth order lowpass Butterworth filter with a cutoff frequency of 10 Hz (9,11). The force and moment data were used to compute center of pressure (COP) sway in the mediolateral (ML) and anteroposterior (AP) directions. The ML sway, AP sway, speed of COP, and sway area were calculated for each trial. The average across the three trials was computed for each subject. Eyes closed metrics were

also normalized against respective eyes open metrics to quantify changes attributed to visual input.

Sway metrics were compared between pain groups. All statistical analyses were conducted in RStudio 2023.03.0. All distributions were determined to be non-normal using a Shapiro-Wilk test. Kruskal Wallis tests determined whether a variable was dependent on pain group. When Kruskal Wallis tests were significant ($p<0.05$), pairwise comparisons between pain groups were completed using Wilcoxon rank sum tests.

RESULTS

Seventeen male WIARNG helicopter aircrew (four crew chiefs and thirteen pilots) completed the postural stability assessment with an average age of 36.4 years (range: 26-47), and 1166 (250-2700) total military flight hours. Sixteen participants were right-handed, with one ambidextrous. Five aircrew members were in the NBPG-, three were in the NPG, and nine were in the NBPG+. No aircrew had back pain without neck pain. There was no difference in age between the pain groups ($p=0.18$).

Sway metrics were compared between pain groups. For CL, AP ($p=0.05$) and ML ($p=0.03$) sway were different between pain groups. NBPG+ had larger AP ($p=0.05$) and ML ($p=0.01$) sway compared to the NBPG-. Change in AP and ML sway from eyes open to eyes closed was not different between pain groups ($p>0.05$).

The speed of the COP was different between pain groups for OR ($p=0.02$), CR ($p=0.04$) and CL ($p=0.05$). The NBPG+ had faster COP speed compared to the NBPG- for all three arm raise combinations ($p<0.05$). Change in COP speed on the non-dominant arm movement from eyes open to eyes closed was also different between pain groups ($p=0.03$) (Figure 1). The NBPG+ had a larger increase in COP speed from eyes open to eyes closed compared to the NBPG- ($p=0.09$) and the NPG ($p=0.13$).

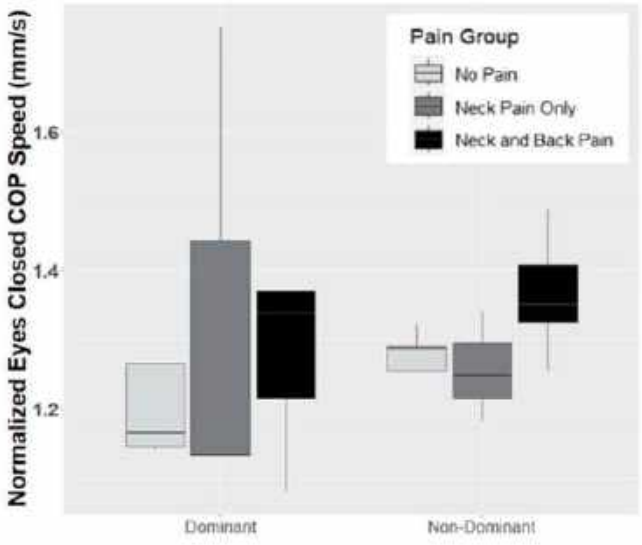

Figure 1: Eyes closed COP speed normalized against eyes open COP speed. Aircrew with neck and back pain exhibited a larger increase in COP speed from eyes open to eyes closed compared to aircrew with neck pain and aircrew with no neck or back pain.

Sway area was different between pain groups for OL ($p=0.01$). The NBPG+ ($p=0.04$) and NPG ($p=0.07$) had larger sway areas than the NBPG-. Change in sway area from eyes open to eyes closed was not different between pain groups ($p>0.05$).

DISCUSSION

This study explored neck and back pain in military helicopter aircrew and related changes in postural stability. This sample of helicopter aircrew with neck and back pain demonstrated decreased postural stability compared to those without neck or back pain. Civilians with chronic neck and back pain also exhibit decreased postural stability compared to healthy civilians (7-9,12). Ruhe et al. reported civilians with chronic neck pain demonstrated increased COP mean velocity and sway area, with a linear relationship between these metrics and the severity of pain score (12). Pain can interfere with proprioceptive information, leading to an incorrect positioning of the center of mass and postural instability (5). Patients with chronic neck or back pain also exhibit delayed muscle response times, which could contribute to the increase in sway (7).

These findings are unique as the postural stability of military helicopter aircrew has not been frequently studied. Studies examining neck position sense were unable to detect any differences between aircrew with and without neck pain (13). While no significant results were found in this study, aircrew with neck pain tended to have increased sway area compared to aircrew members without neck pain ($p<0.2$). These findings are also unique as they explore differences between subjects with neck pain and subjects with both neck and back pain. Previous studies examined neck and back pain separately (7-9,12). The present cohort did not have any aircrew with back pain in the absence of neck pain. This analysis demonstrated individuals with neck and back pain exhibited larger increases in COP speed when vision was removed compared to individuals with only neck pain. This may be due to compounding pain interference from both the neck and back, suggesting that pain management is necessary for this population. Future studies are needed to further explore the relationship between combined neck and back pain on postural stability by utilizing larger sample sizes and a back pain only group.

Decreased postural stability may affect the performance of helicopter aircrew, especially as muscles become fatigued over long duration flights. Deficits in postural stability can be made worse by cervical and low back muscle fatigue (7). Future research may examine how neck and back muscle fatigue from flight affects postural stability for helicopter aircrew with and without pain.

ACKNOWLEDGEMENTS

This research was supported by the Incapacitation Prediction for Readiness in Expeditionary Domains: an Integrated Computation Tool (I-PREDICT) program supported by the Office of Naval Research (ONR) and the Department of Veterans Affairs Medical Research.

REFERENCES

[1] Posch, M et al., *BMC Musculoskelet Disord* 20:1-10 (2019).
[2] Bridger, RS et al., *Aviat Space Environ Med* 73:805-811 (2002).
[3] Thuresson, M, *Thesis* ISBN 91-7140-472-4 (2005).
[4] Harrison, MF et al., *Aviat Space Environ Med* 83:604-608 (2012).
[5] Treleavan, J, *Man Ther* 13:2-11 (2008).
[6] Brumagne, S et al., *Spine,* 25:989-994 (2000).
[7] Hsu, WL et al., *Spine,* 20:530-537 (2020).
[8] Michaelson, P et al., *J Rehabil Med,* 35:229-235 (2003).
[9] Ruhe, M el al., *BMC Musculoskelet Disord* 12:162-169 (2011).
[10] Vernon, H et al., *J Manip Physio Ther* 14:409-415 (1991).
[11] Walsh, M et al., *Perceptual Motor Skills* 128:191-199 (2020).
[12] Ruhe, A et al., *J Back Musculoskelet Rehab* 26:401-409 (2013).
[13] Nagai, T et al., *Aviat Space Environ Med* 85:529-535 (2014).

3D AGE-RELATED BREAST CANCER MODEL WITH AGED AND YOUNG COLLAGEN EXTRACTS FOR DRUG SCREENING

Jun JY. Yang (1), Gokhan GB. Bahcecioglu (2), Aktar AA. Ali (3,5) , Brian BB. Blagg (3,4,5) , Pinar PZ. Zorlutuna (1,2,3,4)

(1) Department of Chemical and Biomolecular Engineering, University of Notre Dame, Notre Dame, Indiana, USA
(2) Department of Aerospace and Mechanical Engineering, University of Notre Dame, Notre Dame, Indiana, USA
(3) Bioengineering Graduate Program, University of Notre Dame, Notre Dame, Indiana, USA
(4) Harper Cancer Research Institute, University of Notre Dame, Notre Dame, Indiana, USA
(5) Department of Chemistry and Biochemistry, University of Notre Dame, Notre Dame, Indiana, USA
(6) Warren Family Research Center for Drug Discovery and Development, University of Notre Dame, Notre Dame, Indiana, USA

INTRODUCTION

Aging is one of the most significant risk factors for breast cancer. The influence of age-related cellular alterations on breast cancer development has been extensively explored in previous studies. Recently, the significance of the aging breast tumor microenvironment has gained growing attention. Despite the significant advances in breast cancer diagnosis and therapies, screenings for novel breast cancer therapies for patients from different age groups are limited by the lack of an aging-related breast cancer model [1]. Extensive literature has demonstrated the changes in mechanical and chemical properties and collagen structure with aging [2]. Age-related alterations [3] in physical properties and glycation of mouse tail tendon collagen have implied the possibility of modeling the aging breast ECM with collagen from mouse tail tendon. Here, we isolated and characterized collagen extracted from young and aged mice tail tendon and constructed a 3D age-related breast cancer model for novel drug screening.

METHODS

Tails and breast tissues of young (2-6 months) and aged (20-23 months) mice were collected. Soluble type I collagen was isolated from the tail tendons for characterization and engineering 3D breast tissue models. Lectin staining was performed to characterize the glycation of collagen in young and aged mouse breast and tail tendon tissue sections. Circular Dichroism was performed to assess the secondary structure and melting point of the isolated collagen I. A solution containing collagen (3 mg/mL) and transglutaminase (100 mg/mL) was prepared to construct 3D breast tissue models. Total collagen assays were performed to assess the degradation of the hydrogel model. Cancerous and normal human mammary epithelial cells were seeded on or in the 3D aged breast models to evaluate migration and invasion, respectively. Tumor spheroids were prepared with the ultra-low attachment method and successfully embedded in the collagen gels to construct the 3D breast cancer model. 3D invasion assessment and drug screening were performed with the automated BioTek BioSpa Live Cell Analysis System and a Biomek i7 Liquid Handler.

RESULTS

Lectin staining confirmed higher level of glycation in collagen fibers in both native breast ECM and tail tendon of aged mice. Degradation studies confirmed the stability of the 3D model within 7-day incubation. Epithelial cells showed significantly increased migration and invasion behavior in/on the 3D aged breast model, in accordance with our findings in the aged breast ECM sections [4]. mRNA qPCR analysis of cancerous and normal epithelial cells and mammary fibroblasts encapsulated in the 3D aged breast tissue models all demonstrated an increased expression in SERPINE1, an established aging marker [5]. These results have indicated the potential of the established 3D age-related breast cancer model for novel drug screening. Tumor spheroids were successfully embedded in the gels to construct 3D age-related breast cancer models. Tumor spheroids embedded in the aging breast cancer models also demonstrated higher 3D invasion ability over the period of 7 days monitor. Tumor spheroids within the aged and young breast cancer models presented different drug responses to selected drug treatments.

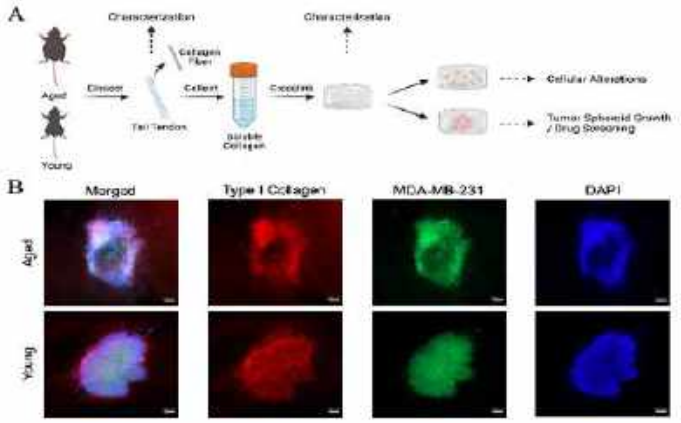

Figure 1: (A) Scheme of the study. (B) Immunostaining of the 3D breast cancer model with the tumor spheroids embedded in extracted type I collagen.

DISCUSSION

In this study, we isolated and characterized soluble collagen I extracted from young and aged mice tail tendon and for the first time in literature utilized the extracted biomaterials to construct a stable 3D age-related breast cancer model for aging-related studies and high-throughput novel drug screening. Our results have indicated the potential of the established 3D age-related breast cancer model for novel drug screening as tumor spheroids within the aged and young breast cancer models presented different drug responses to selected drug treatments.

ACKNOWLEDGEMENTS

This work is supported by The Interdisciplinary Interface Training Program (IITP) Grant, made possible by the Walther Cancer Foundation.

REFERENCES

[1] Bahcecioglu G, Basara G, Ellis BW, Ren X, Zorlutuna P. Breast cancer models: Engineering the tumor microenvironment. *Acta Biomater.* 2020;106:1-21.
[2] Fane M, Weeraratna AT. How the ageing microenvironment influences tumour progression. *Nat Rev Cancer.* 2020;20(2):89-106.
[3] Fong ELS, Harrington DA, Farach-Carson MC, Yu H. Heralding a new paradigm in 3D tumor modeling. *Biomaterials*. 2016;108:197-213.
[4] Bahcecioglu G, Yue X, Howe E, et al. Aged Breast Extracellular Matrix Drives Mammary Epithelial Cells to an Invasive and Cancer-Like Phenotype. *Adv Sci*. 2021;8(22):1-15.
[5] Khan, Sadiya S., et al. A Null Mutation in SERPINE1 Protects against Biological Aging in Humans." *Science Advances*. 2017, 3(11): eaao1617.

DEVELOPMENT OF A NON-INVASIVE IMAGING APPROACH FOR ASSESSING RADIATION-INDUCED CHANGES IN INTESTINAL BARRIER FUNCTION

Austen D Nissen[1], Christopher Hansen[1], Guru P Sharma, PhD[2], Brian L Fish[2], Dana Veley[2], Amit Joshi, PhD[1], Heather A Himburg, PhD[1,2]

1 - Department of Biomedical Engineering, Medical College of Wisconsin, Milwaukee, WI, USA
2 - Department of Radiation Oncology, Medical College of Wisconsin, Milwaukee, WI, USA

INTRODUCTION

Casualties of high-dose radiation exposure will experience dose-dependent toxicity to normal tissue. Exposure to whole-body radiation doses above 5 Gy may result in gastrointestinal (GI) death due to denudation of the intestinal mucosal barrier and subsequent fluid loss, hemorrhage, and/or sepsis[1, 2]. Therefore, in the event of a radiation mass casualty scenario, the development of medical countermeasures (MCM) for the treatment of GI acute radiation syndrome (GI-ARS) is essential.

Our laboratory has recently identified a potent small molecule mitigator of GI-ARS called diminazene aceturate (DIZE)[3, 4]. While DIZE is known to promote activation of the transmembrane enzyme ACE2, the mechanism of action and cellular target in mitigating GI injury is known. Since intestinal barrier function may fail to due intestinal villi denudation and/or loss of endothelial integrity, our long-term goal is to non-invasively discriminate changes in transport across the epithelial and endothelial layers using non-invasive near-infrared (NIR) fluorescent imaging.

Here, we performed a pilot study where we performed (NIR) fluorescent imaging of indocyanine green (ICG) dye in irradiated rats. ICG dye was administered either via oral administration or by intravenous injection. Oral administration of ICG dye will allow visualization of dye transit from the GI compartment across both the epithelial and endothelial barriers before entering into circulation. Conversely, intravenous administration of ICG will enable visualization of dye leakage from the intestinal vasculature.

METHODS

Adult female WAG/RijCmcr rats were exposed to either 13.0 Gy partial body irradiation with minimal bone shielding (n=9) or sham irradiation 0 Gy (n=8) as previously described by Fish et al. 2021[5]. At 3 days post-irradiation ICG imaging was performed.

Each cohort was divided to receive either ICG via tail vein injections or provided ICG mixed in pudding and fed orally before imaging. Following a high dose bolus of ICG (5mg/kg) administration, we performed sequential dynamic imaging with a temporal resolution of 50 ms at time intervals of 30 min, 2 hours post, and 4 hours post-ingestion. Imaging was performed on anesthetized rats with 785 nm or 808 nm diode lasers and NIR-2 emission was captured with 950 nm or 1100 nm long pass filters positioned following the holographic notch rejections filters in the optical path.

RESULTS

We were able to image the transit of the ingested ICG through the intestinal tract over time and use principal component analysis (PCA) to define the region of interest (ROI) for the GI space based on this imaging **(Fig 1)**. Principal component analysis (PCA) along the time dimension was used to convert the imaging data to a k-component vector for each pixel, where k is the number of time frames in the original dataset. The first 8-components were used to identify organ ROIs as shown in **Fig 1**. The fluorescence intensity (I) time course data on ROIs

identified by PCA is then regressed with a double exponential function ($I(t) = A\ e^{-\alpha t} + Be^{-\beta t}$) based on two-compartment pharmacokinetic model[6] for quantitatively comparing the dye wash-in and wash-out rates in the GI space. In our pilot imaging analyses of the irradiated gut, we observed ICG intensity in the GI space is altered by radiation injury with increased dye retention in the GI space.

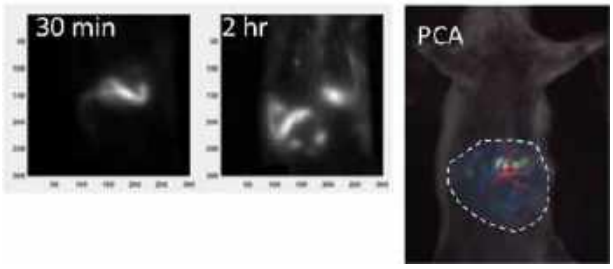

Figure 1: Feasibility study to assess ICG imaging following oral administration. Still images captured from ICG imaging at 30 minutes (left) and 2 hours (middle) post-feeding of ICG in pudding vehicle. PCA analysis of the temporal images was used to define the GI ROI.

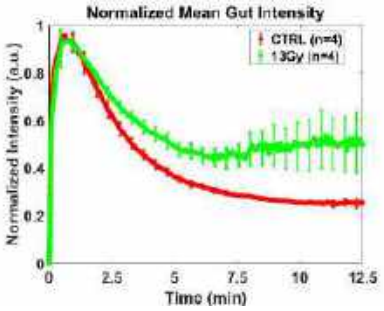

Figure 2: Representative fluorescence time-course data in the GI ROI. Pilot day at day 4 following 13 Gy PBI demonstrates the time course of ICG intensity in the GI space is altered by radiation injury.

DISCUSSION

This pilot experiment aimed to determine the feasibility of non-invasive ICG imaging to characterize radiation-induced changes in intestinal permeability. This work demonstrates the potential of dynamic noninvasive *in vivo* NIR fluorescence imaging for diagnostic motility testing for intestinal disorders or dysfunction and for potential evaluation of therapeutic agents. Future studies will be necessary to evaluate the dysregulation of the intestines post-radiation injury and improvements to imaging techniques.

ACKNOWLEDGEMENTS

Opportunity Funds Management Core of the Centers for Medical Countermeasures against Radiation, NIAID grant number U19AI067773, NIAID U01AI133594, NIAID U01AI38331, Department of Radiation Oncology and Cancer Center, Medical College of Wisconsin

REFERENCES

[1] MacVittie TJ, Farese AM, Bennett A, Gelfond D, Shea-Donohue T, Tudor G, Booth C, McFarland E, Jackson W, 3rd. The acute gastrointestinal subsyndrome of the acute radiation syndrome: a rhesus macaque model. Health Phys. 2012;103(4):411-26. Epub 2012/08/30. doi: 10.1097/HP.0b013e31826525f0. PubMed PMID: 22929470.

[2] MacVittie TJ, Bennett A, Booth C, Garofalo M, Tudor G, Ward A, Shea-Donohue T, Gelfond D, McFarland E, Jackson W, 3rd, Lu W, Farese AM. The prolonged gastrointestinal syndrome in rhesus macaques: the relationship between gastrointestinal, hematopoietic, and delayed multi-organ sequelae following acute, potentially lethal, partial-body irradiation. Health Phys. 2012;103(4):427-53. Epub 2012/08/30. doi: 10.1097/HP.0b013e318266eb4c. PubMed PMID: 22929471; PMCID: PMC4140097.

[3] Sharma GP, Frei A, Fish B, Gasperetti T, Veley D, Szalewski N, Nissen A, Himburg HA. Biological sex differences in renin angiotensin system enzymes ACE and ACE2 regulate normal tissue response to radiation injury. Front Physiol. 2023;14:1191237. Epub 20230519. doi: 10.3389/fphys.2023.1191237. PubMed PMID: 37275232; PMCID: PMC10235526.

[4] Gasperetti T, Sharma GP, Frei AC, Pierce L, Veley D, Szalewski N, Narayanan J, Fish BL, Himburg HA. Mitigation of Multi-Organ Radiation Injury with ACE2 Agonist Diminazene Aceturate. Radiat Res. 2022;198(4):325-35. doi: 10.1667/RADE-22-00055.1. PubMed PMID: 35904437; PMCID: PMC9641750.

[5] Fish BL, MacVittie TJ, Gao F, Narayanan J, Gasperetti T, Scholler D, Sheinin Y, Himburg HA, Hart B, Medhora M. Rat Models of Partial-body Irradiation with Bone Marrow-sparing (Leg-out PBI) Designed for FDA Approval of Countermeasures for Mitigation of Acute and Delayed Injuries by Radiation. Health Phys. 2021 Oct 1;121(4):419-433. doi: 10.1097/HP.0000000000001444. PMID: 34546222; PMCID: PMC8577554.

[6] Gurfinkel M, Thompson AB, Ralston W, Troy TL, Moore AL, Moore TA, Gust JD, Tatman D, Reynolds JS, Muggenburg B, Nikula K, Pandey R, Mayer RH, Hawrysz DJ, Sevick-Muraca EM. Pharmacokinetics of ICG and HPPH-car for the detection of normal and tumor tissue using fluorescence, near-infrared reflectance imaging: a case study. Photochem Photobiol. 2000;72(1):94-102. PubMed PMID: 10911733.

FOSTERING STEM ENGAGEMENT: BUILDING A COLLABORATIVE PARTNERSHIP BETWEEN A RESEARCH UNIVERSITY AND LOCAL HIGH SCHOOL

Ryan M. Castile (1), Jamie Jobe (2), Leanne E. Iannucci (3), Rebecca F. Reals (3), Shawn N. Pavey (1), Jon Fitzgerald (2), Spencer P. Lake (1,3,4)

(1) Department of Mechanical Engineering and Materials Science, Washington University in St. Louis, St. Louis, MO, USA
(2) Pattonville High School, Pattonville R-3 School District, St. Louis, MO, USA
(3) Department of Biomedical Engineering, Saint Louis University, St. Louis, MO, USA
(4) Department of Orthopaedic Surgery, Washington University in St. Louis, St. Louis, MO, USA

INTRODUCTION

Society is increasingly dependent on technology, so it is important to build a workforce that can adapt to rapidly changing advances. To this end, there is a strong need for young minds to engage in science, technology, engineering, and math (STEM) fields [1,2]. In recent years, there has been an increased number of programs and funding opportunities to aid with the development of STEM education. Different opportunities are crucial for fostering and sustaining interest in STEM topics amongst young students [3,4].

When outreach programs bridge multiple educational levels (e.g., high school and university) benefits can be twofold. STEM ideas are introduced to a larger group of younger students, but university-based outreach programs also allow undergraduate and graduate students to have unique opportunities to improve their skills as science communicators. Like many universities, our institution – Washington University in St. Louis (i.e., WashU) – has a population of students who have demonstrated interest in volunteering for outreach programs with middle- and high school-aged students. Here, we (a university research lab at WashU) describe our process of establishing a partnership with a high school in our local community to create several opportunities for high school students to engage in STEM educational activities.

Partnering High School: Pattonville High School (PHS) is part of the fully accredited and nationally recognized Pattonville School District in St. Louis County, Missouri. In the 2013-2014 school year, PHS initiated their involvement in the national Project Lead The Way Biomedical Sciences Program (BSP), a rigorous four-year, four-course sequence in which students learn about medicine, physiology, genetics, microbiology, public health, and forensic science. Because BSP courses focus predominantly on health sciences and biological sciences, the partnership with our lab represents a valuable opportunity to introduce BSP students to bioengineering and related topics.

Main Partnering Washington University Laboratory: The Musculoskeletal Soft Tissue Laboratory (mSTL) is in the Department of Mechanical Engineering & Materials Science at Washington University in St. Louis. The lab investigates the biomechanics of orthopedic soft tissues such as tendons and ligaments to enhance fundamental understanding of healthy tissue properties and elucidate changes that occur in injured or diseased tissues.

Establishing a Connection: While writing a National Science Foundation grant proposal (CMMI 2037125), we discussed potential ideas to engage with our local community. With mSTL's lab manager being an alumnus of PHS, the BSP was brought into focus as a potential group who would benefit from connecting with labs at WashU.

Overall Goal: Here, we aimed to promote and teach STEM concepts to high school students by selecting one local high school (PHS) with whom we could build a strong partnership for outreach/education. This overall goal was pursued with three specific opportunities which were designed to be adaptable as the partnership develops and students' interests change.

METHODS/IMPLEMENTATION

Opportunity 1: Senior Students Visit to WashU Campus: The goal was to host 12th grade BSP students for a half-day field trip to WashU's campus to visit engineering labs and tour engineering facilities.

As an initial focus we decided to engage with senior students who were in their beginning stages of planning their capstone research project. Students received a list of potential labs (all studying biomedical research topics) to visit and created a ranked list based on overall class interest. From this ranked list, three labs were invited to participate in the campus activity. The visit began with a brief welcome/introduction session followed by lab visits and a campus tour. During the lab visits, students learned about current research projects and experienced up-close demonstrations of various experimental techniques utilized by each lab. During the campus tour, student/staff guides focused on showing visiting students the resources available to engineering undergraduates and allowed current engineering students time to answer questions.

During this half-day visit, the PHS seniors completed both pre- and post-visit surveys. Receiving feedback allowed us to gauge interest/knowledge of bioengineering and adjust our plans as needed when planning future visits.

Opportunity 2: Biomedical Research Showcase at PHS: After two years of successful senior visits, we decided to increase engagement with a larger group of BSP students. The goal was to present a showcase of bioengineering research topics to all BSP students (9^{th}-12^{th}) at PHS, increasing the total number of student interactions and allowing more graduate students to strengthen their science communication skills.

We invited a group of research-active graduate students from WashU across a range of biomedical research areas to visit PHS and give 10-minute demonstrations related to their research (Figure 1). PHS students were split into two large groups by grade level, then split again into groups of 4-6 students. Over a 90-minute total period, students rotated to a different demonstration every 10 minutes, learning about a wide variety of bioengineering research topics. Graduate students presented their work on virology, women's health, soft tissue biomechanics, acoustofluidics/microfluidics, optical neuroimaging, and biomedical imaging. At the conclusion of the showcase students were given a survey for feedback on the event.

Figure 1: Graduate students presenting at the research showcase.

Opportunity 3: Collaborative Senior Capstone Project: The final component of the BSP requires senior students to design and execute their own capstone research project. Within our partnership, the goal of Opportunity 3 was to host interested senior students at a WashU lab to conduct basic research for their final capstone project.

To date, one senior student elected to participate and conducted research in the Musculoskeletal Soft Tissue Laboratory. After collecting and analyzing all the data, the student created a final presentation summarizing their work and presented their capstone project at PHS.

RESULTS/EVALUATION

Opportunity 1 Evaluation: Data gathered from pre- and post-visit surveys showed an overall increase in knowledge of biomechanics/biomedical engineering when comparing responses before and after the visit (Fig. 2A). There was also a mid-range level of increased interest in the field after the seniors visited campus (Fig. 2B).

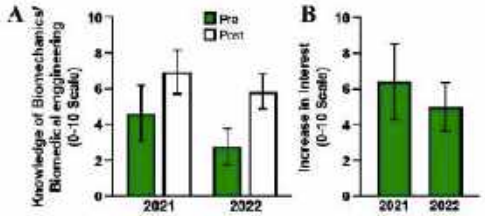

Figure 2: Results of Opportunity 1. (A) Knowledge of bioengineering before and after visit and (B) increase in interest in bioengineering. 0 indicates no knowledge or no increase in interest, 10 indicates total knowledge or max increase in interest. Data shown as mean +/- standard deviation.

Opportunity 2 Evaluation: Post-showcase surveys completed by students (Fig. 3A) show that scores of knowledge prior to the demonstrations were generally lower than scores after the showcase (Fig. 3B). Overall, a majority of the students reported increased interest in biomechanics/biomedical engineering after engaging with the graduate student demonstrations (Fig. 3C).

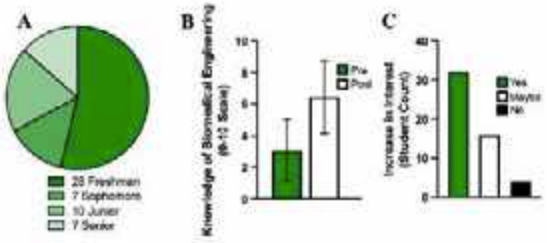

Figure 3: Results from Opportunity 2 showcase. (A) Grade level of students who completed the survey, (B) overall knowledge of biomedical engineering increase from before the showcase to after (0 indicates no knowledge, 10 indicates total knowledge with data shown as mean +/- standard deviation), and (C) number of students demonstrating increase in interest.

Opportunity 3 Evaluation: Although we do not have quantitative data from the student who conducted research in our lab, success of this opportunity can be evaluated based on completion of the student's goals. They successfully built a relationship with their mentor graduate student, planned a project, collected and analyzed data, and completed their final presentation for the BSP.

DISCUSSION

Learning and increased interest in STEM can result from a well-balanced outreach partnership or collaboration. Our goal was to build a mutually beneficial partnership with a local area high school where our university's graduate students could work on becoming better science communicators, while also providing outreach/educational experiences to high school students. We have successfully created three different opportunities that can be repeated each year and built a strong relationship with a high school in our community. To continue increasing interest in bioengineering topics we plan to continue our yearly visit described in Opportunity 1. We also plan to conduct a second annual biomedical research showcase (Opportunity 2) to continue to reach a larger number of students. By connecting with students earlier (freshmen-juniors), we hypothesize that the number of students who complete the four-year BSP will increase, with more students continuing their education within a STEM field. Although only one PHS student has completed a research project through Opportunity 3, additional students have expressed interest; ongoing work involves minimizing logistical challenges to allow more high school students to conduct research in WashU research laboratories. Future work will involve expanding this program to include additional high schools in the local community.

In conclusion, a partnership has been successfully established and grown within the past few years, where we are engaging with over 100 students per year and introducing them to research topics in bioengineering. By sharing these ideas and successes with a larger audience, we aim to provide laboratories at other universities with the tools to build partnerships and outreach opportunities with high schools in their local community.

ACKNOWLEDGEMENTS

National Science Foundation for funding (CMMI 2037125).

REFERENCES

[1] Hinojosa, T et al., April 2016. [2] Tillinghast, RC et al., 2020. [3] VanMeter-Adams, A et al., 2014. [4] Luecke, S et al., 2023.

COMPARISON OF OPENSIM AND ANYBODY MODELING SYSTEM™ PREDICTIONS IN BIOMECHANICAL MODELING OF UPPER EXTREMITIES

Kamal Gautam (1), Mohamed S. Hefzy (1), Abdul A. Mustapha (2), Behrens Kyle (2)

(1) Department of Mechanical, Industrial and Manufacturing Engineering, University of Toledo, Toledo, OH, USA
(2) Department of Orthopaedic Surgery, University of Toledo, Toledo, OH, USA

INTRODUCTION

Understanding the mechanics of upper extremity motions is vital, as these movements are central to numerous normal daily activities. The quality of life of an individual might be significantly affected by impairments in these movements. Consequently, in-depth study of individual muscle forces and joint reaction forces during different upper extremity motions is fundamental. This understanding is essential in sorting out the complexities of neuro-musculoskeletal dysfunctions. In orthopedic and rehabilitation research, computational and modeling software, such as AnyBody Modeling System™ (AMS) and OpenSim, are being more and more used to estimate these forces [1]. These programs, offering diverse modeling environments and musculoskeletal models, are instrumental in biomechanical analysis. It is important to note that OpenSim and AnyBody provide distinct modeling environments and methods for characterizing body parts, Previous studies, notably in gait analysis, have compared the predictions of AMS and OpenSim. These comparisons have highlighted both similarities and differences in kinematics (joint angles) and kinetic (moments, muscle activations and forces) predictions. These results highlight how critical it is to select the right model and parameters to accurately simulate real-world situations in clinical settings [2-4]. It appears that there is a notable gap in research when it comes to the upper extremity; OpenSim provides various user-developed shoulder models while AnyBody lacks a resolute shoulder model. We conclude that there is a lack of direct comparison between OpenSim and AnyBody predictions when it comes to study of upper limb motions.

The purpose of this study is to compare the predictions of muscle forces using this two software during upper extremity motions. This work will primarily focus on simulating static elbow flexion, shoulder flexion, and shoulder abduction maneuvers. It is hypothesized that the muscle forces obtained from AnyBody and OpenSim will show some similarities and differences. This needs to be addressed when using the software to simulate motions involving the upper extremities.

METHODS

A generic model was used in both software that is based on the anthropometry and muscle force-generating characteristics of the 50th percentile adult male. Based on this criteria, Upper Extremity Dynamics Model (UEDM) [5,6] available on OpenSim at SimTk was used. For AnyBody, the Free Posture Full Body Shoulder Rhythm Static model included in the AnyBody Managed Model Repository (AMMR) 2.0.0 was used. In the first step, kinematics for the simulated postures were defined i.e., elbow flexion of 90-degree, shoulder flexion of 80-degree and shoulder abduction of 90 degree.

In OpenSim, the kinematics are defined within the graphical user interface. Forward dynamics simulation was then run for a short duration (1 sec) to generate the motion file, then inverse dynamics and static optimization were run with reserve actuators appended to solve muscle redundancy problem minimizing the sum of the activation levels of the muscles at a discrete time step.

In AMS, customization was made by keeping only the muscles of the right part of the upper extremities, and kinematics were defined on the mannequin.any file under the body model by setting the angular velocities to zero and defining required rotation angles to respective joints. Finally, an initial calibration followed by an inverse dynamics analysis was ran to solve the muscle redundancy problem using a defined polynomial muscle recruitment criterion.

Muscle forces were predicted using OpenSim v4.4 [7,8] and AnyBody v7.1 [9] during the specified upper extremity motions. Predicted muscle forces were then compared with existing literature to evaluate the accuracy of the results and to determine which of the two software is more viable for future research on the upper extremities.

RESULTS

Muscle predictions for the tested conditions using both software are listed in Table 1.

.

Table 1: Predictions of Major Muscle Forces using both software

Motion	Muscle	Forces (Newtons)	
		AnyBody	OpenSim
Elbow Flexion	Brachialis	51	44
	Biceps	20	25
	Brachioradialis	11	9
	Triceps	0	12
	Anconeus	0	3
Shoulder Flexion	Supraspinatus	95	36
	Infraspinatus	94	215
	Deltoid	490	545
	Trapezius	128	N/A
	Serratus	88	N/A
	Triceps	0	422
Shoulder Abduction	Deltoid	508	746
	Trapezius	125	N/A
	Serratus	82	N/A
	Supraspinatus	85	0
	Infraspinatus	132	0
	Subscapularis	510	142
	Triceps	24	571

For elbow flexion, both models predicted the Brachialis as the primary contributor to the muscular activity, with AnyBody and OpenSim predicting 51 N and 44 N, respectively, underscoring its pivotal role in the movement. It is important to note that OpenSim exclusively predicts certain muscle forces in the Triceps and Anconeus during elbow flexion, while AnyBody did not predict any forces in these two muscles.

In shoulder flexion and abduction, high force predictions (highlighted in green in Table 1) for the Deltoid were obtained from both models, illustrating its significance in these movements. Further, AnyBody exclusively provides high force predictions (highlighted in yellow) for the Supraspinatus and Infraspinatus during shoulder abduction contrasting with higher Triceps force predictions from OpenSim (highlighted in yellow) during shoulder flexion and shoulder abduction.

DISCUSSION

In this study muscle forces were predicted using AnyBody and OpenSim during three static postures (elbow flexion, shoulder flexion and shoulder abduction). The major elbow flexor muscles are biceps, brachioradialis, and brachialis [10]. Software predicted relatively large muscle forces for these muscles confirming their role in the static elbow flexion.

While discrepancies were noticed in the triceps, deltoids, rotor cuff, serratus, and trapezius. OpenSim predicts a contractile force for the triceps during elbow flexion indicating that the triceps engages to provide stability and balance to the elbow joint. This likely allows the elbow to be better controlled while the agonist muscles provide the necessary contractile force/load to maintain joint the joint angle against gravity. It was worth noting that the AnyBody did not record this force compared to the OpenSim.

Results from an EMG analysis indicated that the deltoid, pectoralis major, supraspinatus, infraspinatus, serratus anterior, and trapezius were significantly activated during shoulder flexion [11]. Except for the pectolaris major, software predicted forces in these muscles. However, there were differences in the predictions of the muscle contractions during this motion (shoulder flexion) from software. OpenSim does not have the Trapezius and Serratus muscles in their model. Furthermore, OpenSim predicts large muscle forces for the Triceps during both shoulder flexion and shoulder abduction. AnyBody also predicted relatively large muscle forces for all the major shoulder abductors. As indicated above, OpenSim does not have the Trapezius and Serratus muscles in their model which contract during shoulder abduction and predicts high forces for the triceps during this motion, which is not consistent with the literature [12]. Because the Trapezius and Serratus muscles are not included in OpenSim, higher and/or lower forces are predicted in other muscles.

It is hypothesized that the above differences between the software predictions are due to different anthropometric and anatomical definitions (mass and inertia of segments, muscle properties, moment arms) and different scaling procedures between AnyBody (dynamics trial) and OpenSim (static trial). In addition, UEDM of OpenSim does not include several muscles of the upper extremities. This raises concern for its use in simulations related to shoulder motions.

It is important to note that both software couple humeral elevation to scapular rotation which does not accurately predict the muscle forces required to move the scapula and the subsequent upper extremity motions [13]. A more comprehensive model is thus required to be developed that does not couple glenohumeral motions and scapular motions to predict the forces more realistically in all muscles during these motions.

In conclusion, AnyBody appears to be more viable in predicting muscle forces during the simulation of upper extremity motions. This is because OpenSim does not include several muscles in their model.

ACKNOWLEDGEMENT

This work was supported by the department of Mechanical, Industrial and Manufacturing Engineering at the University of Toledo, Ohio.

REFERENCES

[1] Lin, Yi-Chung et al. Journal of Engineering in Medicine, vol. 226, no. 2, 2012
[2] Kim, Y., Jung, Y., J Mech Sci Technol 32, 6037–6044, 2018.
[3] Alexander, Nathalie et al. Gait & Posture, vol. 90, 2021
[4] Trinler, Ursula et al. Journal of Biomechanics, vol. 86, 2019
[5] Saul, K. R. et al. *Comput Methods Biomech Biomed Engin*, vol. 18, no. 13, 2015
[6] McFarland, Daniel C. et al. *Journal of Biomechanical Engineering*, vol. 141, no. 5, 2019
[7] Delp, S. L., et al. IEEE Transactions on Biomedical Engineering 54.11: 1940-50, 2007.
[8] Seth, Ajay, et al. PLOS Computational Biology 14.7, 2018
[9] Damsgaard, Michael, et al Simulation Modelling Practice and Theory 14.8: 1100-11, 2006.
[10] Wilk, Kevin E. et al., W.B. Saunders, pp. 232-58, 2012.
[11] Wattanaprakornkul, Duangjai et al. *Clinical anatomy (New York, N.Y.)* vol. 24(5):619-26, 2011
[12] Escamilla, R.F.. et al. Sports Med 39, 663–685, 2009.
[13] Seth, Ajay et al. Frontiers in neurorobotics vol. 13:90, 2019

FLOW AND TURBULENCE QUANTIFICATION USING 4D FLOW MAGNETIC RESONANCE IMAGING IN A PULSATILE TOTAL ARTIFICIAL HEART

Twan Bakker (1,2), Azad Najar (1,2,3), Thomas Finocchiaro (3), Ina Laura Perkins (3), Jonas Lantz (1,2), Tino Ebbers (1,2)

(1) Unit of Cardiovascular Medicine, Department of Health, Medicine and Caring Sciences (HMV), Linköping University, Linköping, Sweden
(2) Center for Medical Image Science and Visualization (CMIV), Linköping University, Linköping, Sweden
(3) Scandinavian Real Heart AB, Västerås, Sweden

INTRODUCTION

In the development of a mechanical circulatory system a thorough design evaluation before clinical trials is of utmost importance. Various modalities can provide different bits of information about the functionality and performance of the total artificial heart (TAH) and the effect of the mechanical system on the blood constituents and how it contributes to blood damage.

Hemodynamic blood damage has been linked to disturbed or turbulent flow, and one way to quantify the degree of turbulence is through turbulent kinetic energy (TKE). Simulating TKE using computational fluid dynamics (CFD) is challenging in a pulsatile total artificial heart, and therefore we investigated measurements of the flow and TKE using magnetic resonance imaging (MRI). The findings were then used to provide insights for the iterative design process of the mechanical heart prototype.

The goal of this study was to develop a method to measure and analyze flow patterns and TKE in the complex 3D geometry of the mechanical heart through MRI. For this an MRI compatible test rig was created in which physiological representative flow conditions could be simulated.

METHODS

A 4D flow MRI measurement was performed on a legacy prototype, v11.c, of the Realheart pulsatile TAH, fig.1. This prototype functions as a positive displacement pump with an expanding and contracting chamber analogous to the atrium and ventricle. The movement is driven by a motor moving a cylinder connected to flexible membranes in the chambers.

MR-compatibility was achieved by developing a test-rig in which the motor was placed away from the bore of the magnet. Pressures representative of atrium and aortic pressure were regulated in the rig, simulating realistic *in vivo* conditions. The TAH was operated with a heart rate of 105 bpm, providing a cardiac output of 5.0 l·min^{-1}. A prior study on blood damage within the TAH [1] was conducted under the same operating conditions to allow comparison between results.

Flow data of the mechanical heart was acquired with a 4D flow MRI sequence on a 3.0T MR scanner (Philips Ingenia, Philips Medical Systems, Best, the Netherlands), for three encoding directions with an optimized velocity encoding of 70 cm·s^{-1} for turbulence sensitivity. The acquired spatial resolution was 2.2 mm^3 with a Cartesian k-space filling method. A short TR/TE, 5.9/3.6 ms resulted in an effective temporal resolution of 23.7 ms. Applying a parallel imaging factor of 2.5 with SENSE reduced the measurement time to 5:04 minutes. The data was reconstructed to 40 timeframes per cardiac cycle.

Velocity data was analyzed using path line visualization, while volumetric flow rate was computed by integrating the velocity over a cross-sectional area for each phase in the cardiac cycle.

From the magnitude data intravoxel velocity variation was derived as described in Dyverfeldt et al. [2], following eq. 1.

$$\sigma_i^2 = \frac{2}{k_v} \ln\left(\frac{|S_0|}{|S_i|}\right) \quad (1)$$

This metric is a function of the signal ratio of the velocity encoded direction (S_i) and reference signal (S_0), with respect to the applied motion sensitivity (k_v). Voxel wise turbulent kinetic energy (TKE) was then computed by the normal components in three perpendicular directions of the Reynolds shear stress tensor, and the density of the fluid (ρ) following eq 2.

$$TKE = \frac{\rho}{2} \sum_{i=1:3} \sigma_i^2 \ [\text{Pa}] \quad (2)$$

This voxel-wise TKE was then integrated over the volumes of interest (Ω) to calculate the measured integrated TKE in specific locations.

$$\text{integrated } TKE = \int_\Omega TKE \, dV \ [\text{mJ}] \quad (3)$$

RESULTS

The path line visualization of the velocity field (see fig.1) revealed complex flow patterns in the atrium, ventricle, and outflow tract. A recirculation caused by impingement on the wall in both chambers and separation in the bend of the outflow tract was observed and further evaluated. As the bi-leaflet valves contain non-ferromagnetic material, a signal void was present in the near vicinity where flow information could not be quantified.

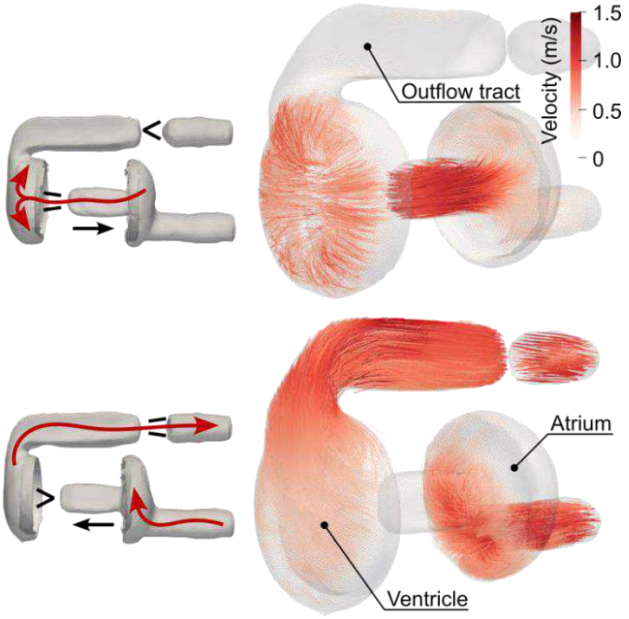

Figure 1: Geometrical changes and valve positions (left), and velocity path lines in diastole (top-right) and systole (bottom-right)

TKE at peak systole and peak diastole are visualized in a maximum intensity projection (MIP), as shown in fig.2. In peak diastole, the MIP reveals increased TKE in the ventricle, which can be explained by the flow passing through the mitral valve and recirculating in this volume. Other regions show low TKE, corresponding to low velocities in these regions. In peak systole, TKE is low in the ventricle, whilst in other regions the levels are elevated. Notable are the atrium with a large region of increased TKE, and outflow tract with the highest peak values that follow along the flow direction.

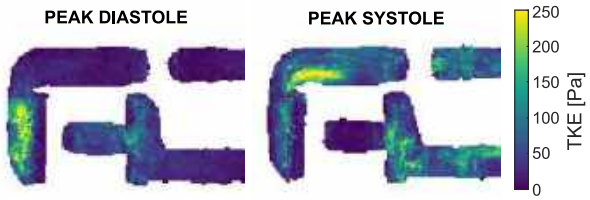

Figure 2: Maximum intensity projection of voxel-wise TKE

Integrated TKE, plotted over time in fig. 3, shows the clear difference between diastole and systole. While peak TKE value was found in the outflow tract, the highest integrated TKE was found in the ventricle, which is a larger volume. In both atrium and outflow tract, the highest values of integrated TKE were found at peak systole albeit with a slight offset. In all three measured locations we see that the measured TKE increased rapidly, during flow deceleration and decreased at a slower rate. The slower decay of TKE afterwards can be related to a conservation of momentum of the fluid which was smoother than the deceleration.

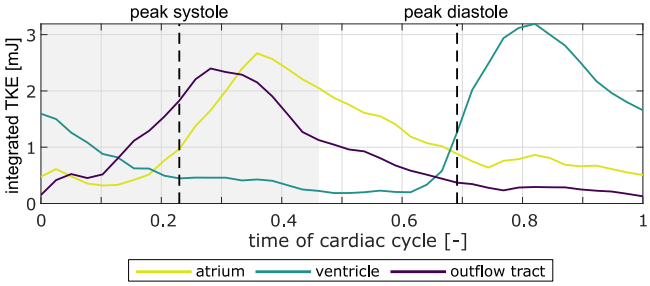

Figure 3: Integrated TKE measures for the atrium, ventricle, and outflow tract in the mechanical heart

DISCUSSION

Evaluation of flow patterns and turbulence is important in the development of a pulsatile TAH. In this study we found flow circulations and revealed turbulence in different cardiac phases that were not reported before. The measured turbulence is slightly higher than measured in a healthy heart, but lower to diseased patients.

Our *in vitro* TKE measurement finds similar values to *in vivo* studies of the human heart. The mean integrated TKE in the atrium of the TAH is equal to the healthy human heart (1.1 vs 1-2 mJ) [2]. In the ventricle and outflow tract where larger recirculation zones are present, slightly higher integrated TKE compared to healthy subjects [3,4] was found. This is however much lower than those found in diseased patients, for instance with pulmonary regurgitation, hypertrophic cardiomyopathy, or aortic stenosis [3,5,6,7].

The velocity field is comparable to a previous CFD study on the same TAH [8]. However, a more in-depth assessment of flow patterns and turbulence was not done in that study. The use of a less resolving turbulence model makes the latter difficult to accurately predict in CFD. The flow rate shows a very similar response and peak value to a previous study on the same TAH under similar operating conditions [9].

The signal void in the MR measurements makes it difficult to evaluate TKE and shear forces in the valves. This might be solved by replacing the valve or part of the valve with non-metallic materials.

Compared to computational fluid dynamics, 4D flow MRI enables the measurement of turbulence with TKE without the need of making modelling simplifications, assuming turbulence models or performing computationally intensive high resolved simulations. The created test-rig in this method required minimal adjustments of the tested prototype and the measurement is fast, compared to other experimental techniques like laser doppler anemometry, allowing for evaluation of fluid dynamics in the TAH in a range of operating conditions in a rapid-prototyping process. In this way, 4D flow MRI measurements, in combination with CFD and blood lab measurements, can enhance the development process of TAH, and reduce the need for donor hearts.

ACKNOWLEDGEMENTS

The authors acknowledge funding from Scandinavian Real Heart AB, and Vinnova/Visual Sweden.

REFERENCES

[1] Perkins et al., *Artificial Organs*, 47:1208-1213, 2023
[2] Dyverfeldt, P. et al., *J. Magn. Reson. Imaging*, 33:582-588, 2011
[3] Fredriksson, A. et al., *J. Magn. Reson. Imaging*, 47:1043-1053, 2018
[4] Chnafa, C. et al., *Ann. Biomed. Eng.*, 44:3346-3358, 2016
[5] Iwata, K. et al., *Magn. Reason. Med. Sci.*, 23:39-48, 2024
[6] Binter, C. et al., *Circ. Cardiovasc. Imaging*, 10:e005486, 2017
[7] Ha, H. et al., *Front. Physiol.*, 9, 2018
[8] Bornoff J. et al., *Sci. Rep.*, 13:5734, 2023
[9] Fresiello et al., *Artificial Organs*, 46:1585-1596, 2022

EFFECT OF TYPE I THYROPLASTY IMPLANT LOCATION AND STIFFNESS ON VOICE PRODUCTION

W. Jiang (1), M. Sangbori (1), L. Oren (2), C. de Luzan (2), E. Gutmark (3), X. Zheng (1), Q. Xue (1)

(1) Department of Mechanical Engineering, Rochester Institute of Technology, Rochester, NY, USA
(2) Department of Otolaryngology-Head and Neck Surgery, University of Cincinnati, Cincinnati, OH, USA
(3) Department of Aerospace Engineering, University of Cincinnati, Cincinnati, OH, USA

INTRODUCTION

Thyroplasty Type I (TT1) is a common procedure for treating unilateral vocal fold paralysis. The procedure involves creating a window in the thyroid cartilage, allowing for the placement of an implant within the paraglottic space. The objective is to improve voice outcomes by narrowing the glottal gap between the paralyzed and healthy folds, thereby reducing leakage and threshold pressure. Traditionally, surgeons manually carve the implant, determining its specifications, including location, stiffness, and shape, through a trial-and-error approach. The impact of these implant characteristics on voice outcome remains an ongoing research topic.

The TT1 implant offers a range of stiffness options, from soft materials like Gore-Tex to harder one like Silastic. Reddy et al. [1] found that, among these materials, Silastic rectangular implant consistently improved voice quality in canine laryngeal experiments. Cameron et al. [2] reported similar observation that stiffer implant enhances acoustics at similar flow rates. Interestingly, Cameron et al. [2] also noted that softer implants excel at low flow rates. Additional studies by Zhang et al. [3], [4] and Smith et al. [5] suggested that a soft implant, with material properties closely resembling real vocal fold, may be preferable for its consistent acoustic outcomes across various conditions. Wu and Zhang [6] pointed out that the impact of implant stiffness also depends on vocal fold stiffness and paraglottic tissue, highlighting the need to consider individual variations. Regarding implant shape, divergent or rectangular implants are more effective [7] [1], but Zhang et al. [3] argued that implant insertion depth and stiffness have a significantly greater impact on acoustic improvement than implant shape.

Regarding insertion location, the implant window is usually made at the vocal fold level and about 5 mm posterolateral to the midline of the thyroid cartilage [3]. Interestingly, clinical observations indicate that medialization in the infraglottal region tends to yield better voice outcome than medialization in the glottal region, although the exact reason remains unknown. In a study by Zhang and Chhetri [8], local medialization using a 2mm-diameter wood stick on excised human larynges showed improved glottal closure and higher-order harmonic excitation in voice when performed at a more inferior location. They hypothesized that inferior medialization contributed to a thicker vocal fold, but the medial surface's shape, including thickness, wasn't quantified, leaving the hypothesis unconfirmed. Zhang et al. [4] provided detailed structural changes before and after implant insertion using magnetic resonance imaging on ex vivo human larynges. They observed increased vertical thickness and significant stretching of the vocal fold tissue in the coronal plane, leading to a decrease in thyroarytenoid (TA) muscle dimension in the medial-lateral direction. However, since phonation experiments were not conducted, the direct relationship between structural changes and the produced sound is unclear.

This study aims to investigate the impact of TT1 implant location and stiffness on vocal fold dynamics and voice outcomes using numerical methods, establishing a direct link among the implant characteristics, vocal fold pre-phonatory conditions, and sound characteristics. Our hypothesis is that, in comparison to glottal-level medialization, infraglottal medialization will create a slightly divergent pre-phonatory shape and a more substantial vertical stiffness gradient, potentially enhancing the produced sound. Through parametric simulations, we will thoroughly explore how implant vertical location and stiffness influence pre-phonatory conditions (shape and stiffness), vocal fold vibration patterns, and sound characteristics.

METHODS

Geometry model. The geometric models of the larynx and implant were created from computed tomography scans of an ex-vivo canine larynx. Both the cartilages and vocal fold were reconstructed. The vocal fold was represented as a two-layer structure consisting of the cover and body layers (Figure 1(a)).

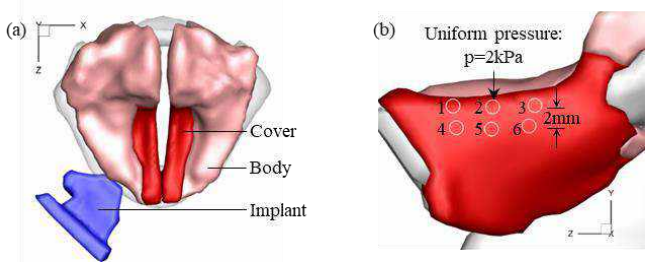

Figure 1. Vocal fold and the implant: (a) Geometric model (b) Indentation locations.

Material property. Fiber reinforced anisotropic material model was employed for both the cover and body layers [9], [10]. To determine material parameters for the body layer, we matched the strain-stress relationship obtained from a canine TA muscle [11]. For the cover layer, material parameters were determined by matching the indentation measurements on the medial surface of a canine vocal fold. Neo-Hookean material model was applied for the cartilages and implant, with implant stiffness provided in Table 1.

Table 1. Implant parameters in parametric simulations.

Parameter	Values
Height	The same and half with the vertical height of the fold.
Location	From superior to inferior side of the vocal fold medial surface.
Stiffness	Four values from 5 to 1400 kPa.

Simulation setup. The simulation comprises two phases. In the initial phase, we conduct a pre-phonatory posturing simulation. Tissue deformation will be modeled using finite element method. The anterior-posterior (AP) insertion location is determined following [3], and the insertion depth is adjusted to ensure appropriate fold adduction. Additional conditions, such as height and vertical location, are outlined in Table 1. Once the implant is inserted, we will assess the shape and stiffness distribution of the medial surface. In the second phase, we will perform a fluid-structure interaction (FSI) simulation to capture vocal fold oscillation, glottal flow waveform, and sound generation [9], [12]. The glottal flow will be modeled by a one-dimensional reduced-order flow model [13].

The stiffness distribution would be obtained through numerical indentation following a prior work [14]. Six indentation locations are denoted in Figure 1(b), distributed along three AP locations. In each AP location, indentation will be performed at the superior and inferior sides of the medial surface. The local stiffness is calculated by $= pR/\Delta x_{max}$, where p = 2kPa is the uniform pressure, R = 0.6mm is the radius of the circular indentation area, Δx_{max} is the displacement at the center of the circle. The stiffness gradient (SG) is calculated by $G = (E_{inf} - E_{sup})/dy$, where E_{inf} and E_{sup} are the stiffness at inferior and superior sides, respectively, dy = 0.2cm is the vertical distance between the two indentation locations.

RESULTS

In the baseline case, we inserted an implant with a height matching the vertical height of the fold at the glottic level. The insertion depth was adjusted so that 80% of the medial surface was adducted to the midline. The implant stiffness is 120 kPa.

Figure 2 illustrates the impact of the implant on the pre-phonatory conditions of the vocal fold at the three AP locations. Figure 2(a) overlays the medial surface profile before (dash) and after (solid) the implant insertion. It shows that the implant effectively adducted the fold toward the midline with only a small leakage in the posterior side. The shape of the medial surface profile does not show a significant difference before and after the implant inserted except that it became slightly more convergent in the posterior side. Vertical thickness is larger in anterior than in posterior side.

Figure 2(b) shows the SG along the three AP locations, measured between the superior and inferior sides of the medial surface as denoted in Figure 2(a). It shows that a stiffness gradient exists before the implant insertion, with the largest value around the mid-coronal location and the smallest value in the anterior side. With the implant inserted, SG increased in all three locations with the largest increase occurred in the anterior side.

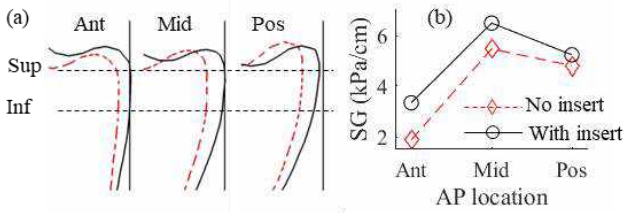

Figure 2. Influence of implant on pre-phonatory status: (a) medial surface profile; (b) stiffness gradient (SG).

DISCUSSION

The preliminary results show that the numerical model is able to simulate the impact of TT1 implant on vocal fold deformation and stiffness distribution before phonation. The simulation results of the baseline case show that when the implant is 120kPa and inserted at the glottis level, it adducted the vocal fold with only small effect on the shape of the medial profile. It increased SG in the whole AP range with the largest increase at the anterior side. In subsequent simulations and analysis, we will change the implant height, vertical location and stiffness as described in Table 1. The effects of these parameters on vocal fold pre-phonatory deformation and stiffness will be investigated. Additionally, FSI simulations will be performed on the obtained pre-phonatory conditions and the relationships among implant characteristics, vocal fold pre-phonatory conditions, vocal fold vibrations and voice acoustics will be studied. We will discuss the results by comparing them with the experimental measurements [8,15,16].

ACKNOWLEDGEMENTS

The research was funded by NIH Grant No. R01DC009435 from the National Institute on Deafness and Other Communication Disorders (NIDCD).

REFERENCES

[1] Reddy, N et al., 10.21437/*Interspeech*.2022-11158, 2022.
[2] Cameron, B.H. et al., *Laryngoscope Investig Otolaryngol*, 5(1): 82-89, 2020.
[3] Zhang, Z. et al., *J Voice*, 29(2):230-235, 2015.
[4] Zhang, Z. et al., *PLoS One* 5(1): e0228464, 2020.
[5] Smith, S.L. et al., *Laryngoscope*, 130(9): 2192–2198, 2020
[6] Wu, L. et al, *J Biomech*, 149: 111483, 2023.
[7] Orestes, M. I. et al., *Laryngoscope*, 124(12): 2791–2796, 2014.
[8] Zhang, Z et al.,*J Acoust Soc Am*, 146(5):EL412–EL417, 2019.
[9] Geng, B. et al.,*J Acoust Soc Am*, 150(2):1176–1187, 2021.
[10] Dhondt, G. The Finite Element Method for Three-Dimensional Thermomechanical Applications. Wiley, 2004.
[11] Hunter, E.J. et al.,*J Appl Physiol*, 103(1):206–219, 2007.
[12] Movahhedi, M. et al.,*JASA-EL*, 1(12):125203, 2021.
[13] Li, Z. et al., *J Biomech Eng*, 142(2), 2020.
[14] Geng, B. et al.,*J Acoust Soc Am*, 141(4): EL351–EL356, 2017.
[15] Maddox, A. et al., *Laryngoscope*, 133(3):621-627, 2023.
[16] Oren, L. et al., *Eur Arch Otorhinolaryngol*, in print, 2024.

A 3D *IN-VITRO* NEURO-VASCULAR HUMAN BRAIN MODEL WITH MENINGEAL LYMPHATICS FOR STUDYING ALZHEIMER'S DISEASE

Xun Wang (1), Seunggyu Kim (1), Maria Proestaki (1), Shun Zhang (1), Georgios Pavlou (1), Se Hoon Choi (3), Rudolph E. Tanzi (3), Roger D. Kamm (1,2)

(1) Department of Biological Engineering, Massachusetts Institute of Technology, Cambridge, MA, USA
(2) Department of Mechanical Engineering, Massachusetts Institute of Technology, Cambridge, MA, USA
(3) Genetics and Aging Research Unit, MassGeneral Institute for Neurodegenerative Disease, Department of Neurology, Massachusetts General Hospital, Harvard Medical School, McCance Center for Brain Health, Boston, MA, USA

INTRODUCTION

As the global population ages, Alzheimer's disease (AD), the prevalent age-related dementia, emerges as a critical challenge for society. With over 6 million individuals in the US living with AD, this number is projected to triple by 2050 [1]. Despite the urgent need for AD treatments, understanding the mechanisms remains elusive, partially due to limited access to human brains, challenges in translating findings from animal studies to clinical applications, and the absence of physiologically relevant *in vitro* models replicating the complexity of the human brain [1-4].

A major challenge in replicating the human brain *in vitro* is the intricate nature of brain vascular structures, particularly the highly selective blood-brain barrier (BBB). Comprising endothelial cells (ECs), astrocytes (ACs), and pericytes (PCs) (Fig. 1), the BBB regulates the entry of molecules into the brain. The complexity extends to meningeal lymphatics, a network of conventional lymphatic vessels situated parallel to the dural venous sinuses and middle meningeal arteries within the mammalian central nervous system (Fig. 1). These lymphatics play crucial roles in clearing toxic molecules, such as amyloid-β (Aβ) peptides, a main component of the senile plaques in AD patients, from the brain parenchyma. Emerging evidence highlights the pivotal role of BBB dysfunction and meningeal lymphatics disruption in AD pathogenesis [2-5]. However, the complex interplay among neurons, the BBB, and meningeal lymphatics during the onset and progression of AD, as well as the role of fluid transport across the BBB, through the brain parenchyma, and exiting via the lymphatic system, remains poorly understood. Although various *in vitro* brain models have been developed to explore vasculature function in AD [2-5], they often fall short in reproducing the complex three-dimensional (3D) structure of the brain or lack a vascularized system for meningeal lymphatics.

To address the need for a physiologically relevant AD model, we introduce a new 3D *in vitro* human brain model self-assembled within microfluidic devices. Integrating human brain ECs, ACs, PCs [4], meningeal lymphatics [7], and human neural progenitor cells (NPC)-derived AD cell culture [8], our model closely mimics the AD brain environment. Notably, it is the first of its kind to incorporate perfusable BBB networks, lymphatic systems, and AD neurons within a unified platform, providing a valuable tool for advancing fundamental understanding of AD pathophysiology and drug screening for AD treatments. Ongoing studies will explore molecular, cellular, and tissue behaviors in AD patients, revealing biomarkers and mechanisms, and accelerating therapeutic development. Moreover, our model's versatility extends beyond AD, benefiting drug discovery in various human brain-like environments.

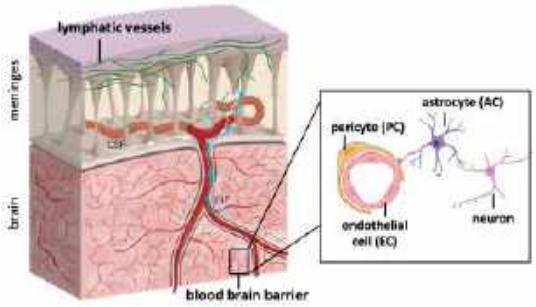

Figure 1. Human brain neurovascular unit with meningeal lymphatics. The blood-brain barrier (BBB), comprising endothelial cells, astrocytes, and pericytes, along with meningeal lymphatics, constitutes the complex entry-exit system within human brain vascular structures. Left schematic adapted from Sweeney *et al.*, 2018 [6].

METHODS

Fabrication of the microfluidic platform. The mold for device fabrication was created using Fusion 360 (Autodesk, Inc.) (Fig. 2a) and subsequently milled on a Delrin block using a micro-CNC milling machine (Bantam Tools). Microfluidic devices based on polydimethylsiloxane (PDMS) were then fabricated following established protocols [4]. The device design includes two 4 mm diameter holes for media channels, two 1.5 mm diameter holes for lymphatic-gel loading, two 2 mm diameter holes for BBB-gel loading, one 2 mm diameter hole for neuron-gel loading, and a top layer with three 4 mm diameter holes for connection to syringes (Fig. 2b). The chamber height is 500 μm.

2D cell culture. Human astrocytes (ScienCell, #1800) and human brain vascular pericytes (ScienCell, #1200) were expanded and cultured in astrocyte media (ScienCell, #1801) and pericyte media (ScienCell, #1201), respectively. GFP expressing human brain microvascular endothelial cells (Angio Proteomie, # cAP-0002GFP) and GFP expressing lymphatic cells were expanded and cultured in VascuLife (LifeLine Technologies, LL-0003) with 10% v/v FBS. Neurons were expanded and cultured using the neural growth media as detailed in [8].

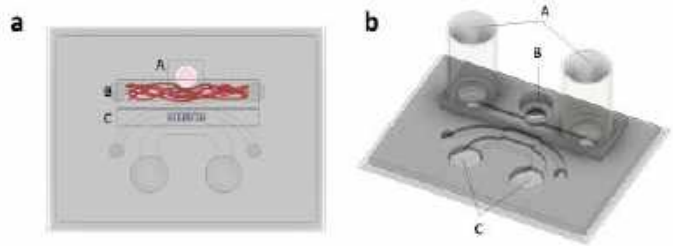

Figure 2. An integrated microfluidic system for modeling the human brain with meningeal lymphatics. a, Schematic showing channels for different cell types. A, neurons; B, self-assembled BBB networks; C, sprouting lymphatic networks. **b,** Schematic showing ports for media addition. A, culture media for the BBB; B, culture media for neurons; C, culture media for lymphatic cells.

3D cell culture in the microfluidic platform. BBB cells were seeded in the central blood vessel culture channel (Fig. 2a, Channel B) in fibrin gel to self-assemble networks. Neurons were seeded in the circular neural culture channel (Fig. 2a, Channel A) in Matrigel (Corning, # 356230). The lymphatic channel (Fig. 2a, Channel C) was filled with fibrin gel for lymphatic cells to sprout and a monolayer of lymphatic cells was deposited onto the side of the lymphatic channel gel. The seeding medium for the BBB (Fig. 2b, Ports A) and lymphatic cells (Fig. 2b, Port C) was made using VascuLife (LifeLine Technologies, LL-0003) with ¼ of the supplemented heparin sulfate and 2% v/v FBS. The seeding medium for neurons (Fig. 2b, Ports B) was the neural differentiation media as detailed in [8].

Imaging. Confocal images were acquired using an Olympus FV1200 confocal laser scanning microscope with 4x and 20x objectives. Images were analyzed using ImageJ.

RESULTS

Perfusable BBB networks and lymphatic sprouts are integrated in one unified flatform. Through meticulous control of media and interstitial flow, self-assembly of BBB cells into networks occurs approximately two days after seeding, with perfusability achieved around the fifth day. Subsequently, lymphatic cells are seeded, and after two days of directed interstitial flow, lymphatic vessels sprout in the designated channel, approaching the BBB networks (Fig. 3a).

Quantification of the perfusable barriers during long-term culture. To quantify the permeability of perfusable barriers, we introduce model large molecules, such as dextran, when the BBB networks become perfusable (Fig. 3b). Monitoring the increase in fluorescence intensity in the surrounding matrix enables quantification of barrier permeability, as detailed in [4]. Our model, designed for extended viability, allows for diverse quantifications over an extended period (Fig. 3c). This longevity feature is pivotal in studying the long-term effects of AD neurons on BBB and lymphatic functions.

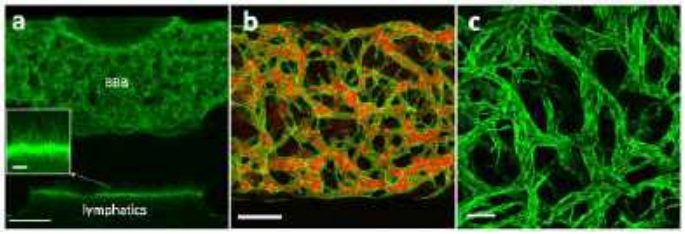

Figure 3. A human brain model with meningeal lymphatics. a, Perfusable BBB networks and sprouting lymphatics are integrated in one device. Green: Top, endothelial cells; bottom, lymphatic cells. Scale bar, 1 mm. Insert, a closer view of the lymphatic sprouts. Scale bar, 200 μm. **b** and **c**, green: endothelial cells. **b**, Dyes are used to visualize and quantify BBB networks. Red, 40k Da dextran. Scale bar, 500 μm. **c**, BBB networks remain perfusable five weeks after seeding. Scale bar, 200 μm.

DISCUSSION

We created a novel microfluidic platform that integrates BBB cells, neurons, and lymphatic cells, which generates physiologically relevant structures to model the human brain. Our model features self-assembled perfusable vascular networks formed by BBB cells and sprouting lymphatic vessels in proximity to BBB networks, mimicking human brain vasculature. The two types of vessels separated by two distinct endothelia, as well as extracellular matrix, allow for the simultaneous measurement of molecular and fluid transport across the vascular and lymphatic endothelia under physiological and pathological conditions. Currently, we are quantifying barrier functions, including molecular and fluid transport. Validation of BBB function involves perfusing large molecules and relevant plasma proteins across the BBB into surrounding matrix, measuring barrier permeability through fluorescence intensity. Lymphatic endothelial permeability will be assessed in the physiologically-relevant basal-to-apical direction by the intensity increase within the lymphatic luminal space after diffusion of molecules in the matrix from the BBB networks. Moreover, the capability to permit the passage of cerebrospinal fluid (CSF) is critical for the correct functioning of the meningeal lymphatics. We will connect the platform to a flow system simulating brain flows. Taken together, this work is the first to incorporate perfusable BBB networks, lymphatic systems, and neurons in one platform, providing a valuable tool for studying human brain pathophysiology. Future integration with *in vivo* studies will enhance understanding of human brain disease mechanisms and expedite therapeutic development.

ACKNOWLEDGEMENTS

This work was supported by the Cure Alzheimer's Fund and the NIH R01 grant (NS121078) to RDK and SHC.

REFERENCES

[1] 2022 Alzheimer's Disease Facts and Figures, Alzheimer's Association. [2] Campisi, M. et al., Biomaterials, 180: 117–29, 2018. [3] Shin, Y. et al., Advanced Science, 6(20): 1900962, 2019. [4] Hajal, C. et al., Nature Protocols, 17(1): 95–128, 2022. [5] Da Mesquita, S. et al., Nature. 560, 185, 2018. [6] Sweeney, M. D. & Zlokovic, B. V. A Nature 560, 172–174, 2018. [7] Serrano, J. C. et al. Advanced Science, 2302903, 2023. [8] Kim, Y. H. et al., Nature Protocols, 10(7): 985–1006, 2015. [9] Offeddu, G. S. et al., Small 15, 1902393, 2019.

CHARACTERISTICS OF RESOLVABLE POLYMERS USED FOR DEVELOPING *IN UTERO* FETAL VALVE REPLACEMENTS

Sanchita S. Bhat (1), Julia Toma (1), Lakshmi Prasad Dasi (1)

(1) Wallace H. Coulter Department of Biomedical Engineering, Georgia Institute of Technology, Atlanta, GA, USA

INTRODUCTION

Congenital heart diseases account for nearly one-third of all congenital defects, and require surgical repair or medical management [1]. Pulmonary atresia with intact ventricular septum (PA/IVS) is one type of extremely rare congenital heart defect that occurs in 1% of total heart defects [2]. In this defect, the pulmonary valve is underdeveloped and atretic leading to hypoplasia of the right side of the heart and limiting flow through the right ventricle and main pulmonary artery. Many of these patients undergo palliation, but are subject to high risks of morbidity and mortality, eventually requiring heart transplantation or a pulmonary valve replacement [3]. Although these replacements are made from biocompatible materials, they can become dysfunctional, requiring further intervention and multiple surgeries.

Fetal cardiac intervention is performed to prevent single ventricle heart disease in pulmonary atresia with intact ventricular septum [4]. Pulmonary valve perforation and balloon valvuloplasty can restore antegrade flow *in utero* and preserve right ventricular size and function. Although mostly successful, recurrent stenosis and atresia *in utero* are common after this procedure. A tissue‒engineered, bioresorbable valve has the potential to prevent this and could grow with the patient postnatally. Understanding the performance characteristics and biomechanics of such a valve could further guide the techniques in developing and testing them. Polymeric materials have been used extensively for their applications in stents. They are ductile and have high tensile strengths, making them excellent candidates for this application [5]. Therefore, this study aims to develop a study polymeric materials to develop a fetal valve replacement and determine characteristics of the materials used, that can aid in anticipating valve performance *in vivo*.

METHODS

Stent Analysis

Three stent designs were developed using SolidWorks (Dassault Systèmes, Vélizy-Villacoublay, France) as shown in **Figure 1** and subject to computational simulations where the prototypes were crimped, balloon expanded (modeled as per commercial NuMed balloons) and deflated using ABAQUS (Dassault Systèmes, Vélizy-Villacoublay, France). Resolvable polymers namely PCL (polycaprolactone) and PLLA (poly-l-lactic acid) were used as stent materials. The simulation pipeline is shown in **Figure 1.** The resultant stress distributions were studied to understand possible areas of failure and deformation due to deployment through stent parameters such as dog boning ratio, foreshortening and recoil. Furthermore, stent width was increased in one of the high stress regions to study the impact of design on stress distributions and overall stent behavior.

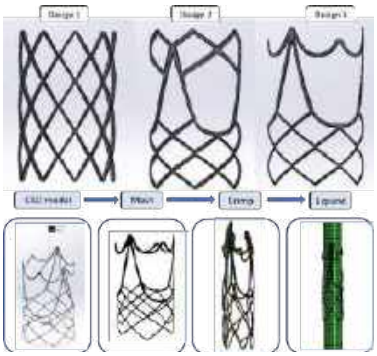

Figure 1: Three candidate designs and simulation pipeline (bottom)

Leaflet Degradation

A stent prototype 5 mm in diameter, 8 mm in height, was manufactured using a laser cutter. PCL (leaflets) were manufactured using solvent casting techniques in chloroform. The leaflets were manufactured with a less dense PCL (0.75% PCL in chloroform) and the commissures and skirt with a high‒density PCL (5% PCL in chloroform), in order to control the degradation and ensure longevity of the valve *in vivo.* Sodium hydroxide (NaOH) is a standard basic agent used for the accelerated degradation of polymers and a 2M NaOH solution was made, which was used in place of the working

fluid in the fetal right heart simulator (FRHS) as shown in **Figure 2**. Setup conditions were tuned as described previously [6]. A camera was placed on the downstream end of the valve, and this camera recorded continuous *en-face* videos of the valve over its degradation period. The degradation experiment was terminated when at least one leaflet failed. N=3 valves were run in this setup and their observations studied.

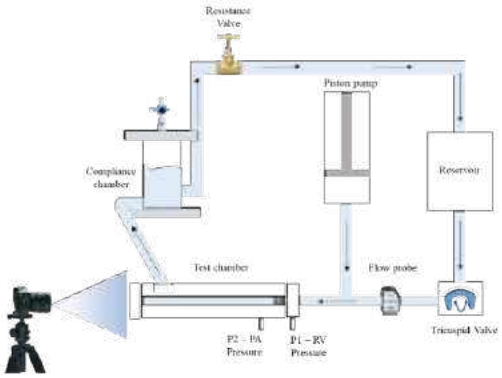

Figure 2: Fetal Right Heart Simulator (FRHS)

RESULTS

Stent Simulations

In the stent simulations, we observed that both polymers overall had good performance characteristics. PLLA had higher recoil and could be a better polymer to use for this application, although it did have higher foreshortening, especially in Design 3. Both materials had good dog boning overall, indicating less potential to stent distortion and good radial expansion (**Table 1**). From the results, Design 2 with PLLA polymer was seen to be the most optimum design and material combination.

Table 1: Deployment characteristics of N=3 designs for PCL and PLLA

Design	Material	Foreshortening (%)	Recoil (%)	Dog boning	
				Side 1	Side 2
1	PCL	12.116	-2.060	0.022	0.032
	PLLA	12.676	-3.270	0.042	0.017
2	PCL	10.186	-0.068	0.001	0.001
	PLLA	-0.621	0.611	-0.013	-0.013
3	PCL	15.738	-4.268	-0.075	0.128
	PLLA	20.039	3.562	0.035	0.002

We were also able to show, that small changes in design parameters such as stent strut width, can cause changes in distribution of stresses and therefore outcome of stent *in vivo.* Figure shows stresses at the stent junction went from 350MPa to 205MPa by only changing the width (**Figure 3**). This indicates that changing design can mitigate risk of stent fracture during deployment.

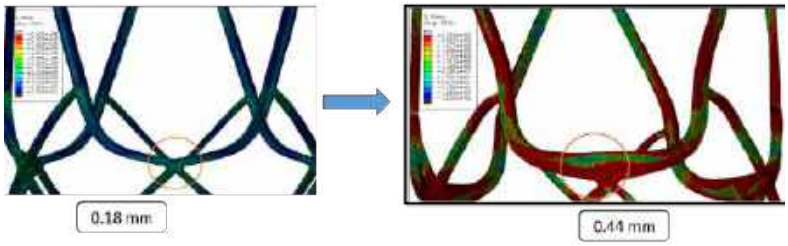

Figure 3: Shown change in peak stresses (MPa) by changing design

Leaflet Degradation

Figure 4 shows the degradation patterns that were recorded and it was observed that the leaflets degraded from the edge and slowly affected coaptation and the overall ability of the valve to maintain steady hemodynamics, up until Stage 6, where multiple tears began to appear on the leaflet free edges and the area adjacent to the commissures. On physical examination, the commissures remained intact even though some of the leaflets catastrophically failed. These results are important and indicate the impact of design on *in vivo* fate of resolvable valve replacements. Due to the unique manufacturing process, we were able to control the degradation and potentially increase the longevity of the valve *in vivo.*

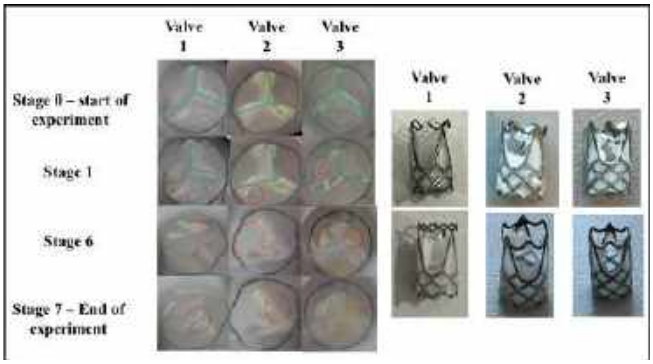

Figure 4: Left - Stages in leaflet degradation (green lines are coaptation lines and red circles show regions of degradation) and right -Valves post-degradation

DISCUSSION

This study improves understanding of fetal sized stent behavior by comparing designs and materials and develops a novel technique that can be optimized and used for sutureless valve assembly. Fetal valve stents are small in size, and therefore extensive biomechanical studies need to be conducted to evaluate their performance. In valve manufacturing, the change in material density can help engineer high importance structures such as the commissures to degrade slower than leaflets.

The development of such a tissue engineered heart valve replacement will eliminate the need for repeat interventions and serve as a permanent solution. Given the few durable options for pediatric patients, this study will improve the feasibility of developing such a device right from the manufacturing to the testing stage. Although these studies need to be supplemented with animal work that will help determine the timeline of valve absorption, by simply looking at biomechanical analyses we can optimize the valve design to ensure that there is no premature failure. This work only studies polymeric materials for stents, however future studies are being done with metal alloys as well which can provide additional advantages and degradation protocols for stents are also underway.

ACKNOWLEDGEMENTS

Members of Cardiovascular Fluid Mechanics Laboratory.

REFERENCES

[1] Farmer, D., et al, Surgical Interv. for Congenital Anomalies, 2015
[2] Gorla, S.R. et.al, StatPearls. 2022
[3] Bautista-Hernandez,V.,et al.,Ann Thorac Surg,2011.91(2)
[4] Devanagondi, R., et al., Pediatr Cardiol, 2017. 38(2): p. 247-254.
[5] Shen et.al, Biomolecules 2022; 12(9): 1245
[6] Bhat S.S., et.al, Ann Biomed Engg, 2023

MEDIAL ILIOFEMORAL LIGAMENT STRAIN AND ORIENTATION FOLLOWING THA IMPLANTATION CORRELATE WITH ITS ABILITY TO CONTRIBUTE TO HIP STABILITY

Clarisse M. Zigan (1), Jennifer Bido (1), Kathleen N. Meyers (1), Jose A. Rodriguez (1), Timothy M. Wright (1), Fernando J. Quevedo Gonzalez (1)

(1) Hospital for Special Surgery, New York, New York, USA

INTRODUCTION

Instability of the hip is the second most common cause for revision of total hip arthroplasty (THA) and third most common cause for early revision [1]. The direct anterior approach (DAA) is considered a solution to lower the risk of instability after THA, but the evidence is inconclusive [2,3]. During a DAA, the medial iliofemoral ligament (mIFL) is often incised to gain access to the capsular compartment [4]. In its native state, this ligament serves as a primary restraint to rotation, yet consensus on capsulectomy extent or the need for capsule repair is lacking [5-7].

Our previous work revealed that the mIFL produced as much as 87% of the total torque resisting anterior dislocation with the hip in full extension, but less than 54% following mIFL transection and subsequent repair. This variability is likely influenced by many factors including the material properties and geometry of the mIFL itself. Material properties are innate to the tissue, but the ligament's geometry can be controlled by the surgeon during THA. For example, during implantation, surgeons can manipulate femoral offset, a variable known to influence strain in the surrounding soft tissues [8,9].

Our objective was to relate the change in ligament strain due to implantation and ligament orientation to mIFL contribution to stability during external rotation. We hypothesized that the contribution to stability and its variability across specimens can be explained by jointly considering these geometric factors. A combination of cadaveric testing and computational modelling was used to relate these variables to the mIFL's contribution to hip stability.

METHODS

Seven cadaveric hips from 10 donors underwent THA through a standard DAA while preserving the mIFL. Pre- and post-operative CT-scans were used to create specimen-specific models to predict the rotation needed to achieve contact between femoral and acetabular components. Specimens were tested on a six-degree-of-freedom robotic manipulator (KR 300 R2500 ultra, Kuka) coupled with a hip-specific control system (simVITRO, Cleveland Clinic Biorobotics Lab) using validated procedures [10]. Testing consisted of externally rotating the femur with the hip in full extension until the target rotation for contact was achieved. Testing was performed with the mIFL intact then cut. The maximum change in rotation-torque curves of the cut condition was used to define the extreme of motion. The torque of the mIFL was isolated by subtracting the cut condition from the intact condition, which included the contribution of the rest of the capsule, then normalized to the intact torque to describe the ligament's contribution to hip stability.

Following robotic testing, mIFL origins on the femur and pelvis were marked with radiopaque beads by a board-certified orthopaedic surgeon (JR) and a fifth-year resident (JB) prior to the 3D scanning of the specimens (HandySCAN 3D, Creaform).

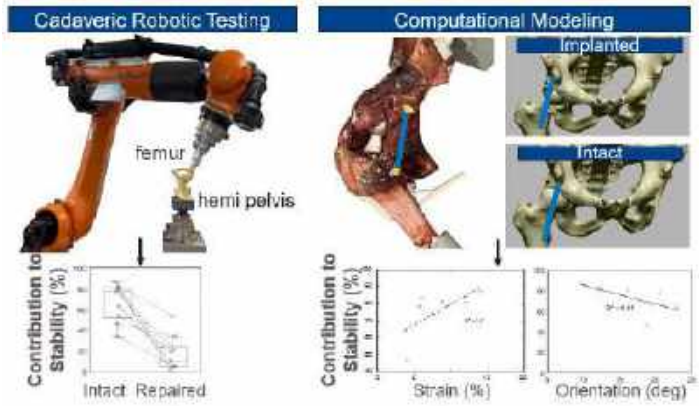

Figure 1: The combination of cadaveric testing and computational modeling was used to describe the influence that mIFL (blue) geometric factors have on its ability to contribute to hip stability.

Scans were aligned to existing specimen computational models and the bead centroids were used to define a vector representing the mIFL (Fig. 1). Ligament vectors were assessed in the intact (pre-implantation) and implanted states.

Implantation strain was calculated as the ratio of the change in ligament length from the intact condition to implanted condition against the intact length. The mIFL orientation relative to the superior-inferior axis of the pelvis was calculated by the dot product of the ligament orientation onto the superior-inferior axis (Eqn. 1) in which a smaller angular deviation was representative of a more vertically oriented vector.

$$Angular\ deviation = \arccos[< \frac{Pelvis_{origin} - Femur_{origin}}{norm(Pelvis_{origin} - Femur_{origin})} > \cdot < S - I\ axis >] \quad (1)$$

For each specimen, implantation strain and angular deviation were compared against the ligament's contribution to stability at the extreme of motion previously measured during cadaveric testing in full extension. Student's t-tests and Pearson's correlations were used for statistical analyses using a significance level of 0.05 (MATLAB vR2023a, MathWorks).

RESULTS

Across all specimens, the mIFL length increased after implantation (p<0.01). We observed a positive relationship between implantation strain and the ligament's resultant contribution to stability during external rotation (R^2= 0.47; Fig. 2).

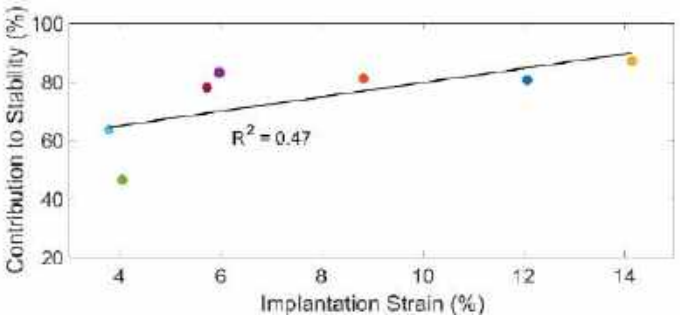

Figure 2: mIFL implantation strain and its contribution to stability demonstrate a positive relationship.

Across all specimens, angular deviations from the superior-inferior axis displayed a negative trend with the ligament's contribution to stability (R^2=0.41; Fig. 3).

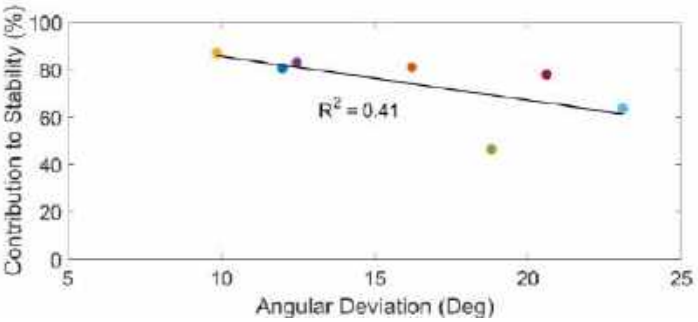

Figure 3: mIFL angular deviation and its contribution to stability demonstrate a negative relationship.

DISCUSSION

Instability following THA remains an unsolved clinical problem. Better understanding how capsular soft tissue relates to joint stability could help identify strategies to minimize instability. To address this question, we combined experimental and computational analyses to investigate the influence of geometric factors of the mIFL (i.e., implantation strain and orientation) on its ability to contribute to hip stability.

Our main finding was that contribution of the mIFL to hip stability tended to be larger for hips that underwent greater ligament stretching after implantation. Ligaments naturally have a slack region during which surrounding muscles can more freely move. A stretched ligament has less slack, therefore is able to resist load more readily, in turn providing stability to the joint. In this way, one of the surgical goals during THA is to achieve sufficient soft tissue tension, and our results corroborate the importance of ligament tension to increase stability. Our results are in line with prior studies that showed direct relationships between soft tissue strains, in particular the quadratus femoris muscle, and the hip torque [8,9].

We also found that the contribution of the mIFL to hip stability tended to be greater in more vertical ligaments following surgery. However, this relationship is confounded by the interdependence between implantation strain and orientation. For example, the specimens with the highest and lowest implantation strains (the yellow and green markers, respectively; Fig. 2) display the reverse relationship between angular deviation and its contribution to stability (Fig. 3). In fact, prior studies of other joints have highlighted the importance of considering orientation alongside material properties when assessing joint mechanics [11,12].

Our study has limitations. First, our sample size was small. According to a post-hoc power calculation, a sample size of at least 10 specimens would be needed to establish a regression between the geometrical variables and the contribution to stability. Second, we assumed the ligament to be linear and did not consider wrapping about the implant or bone. More complex musculoskeletal modeling could help further understand how ligament strains and orientation relate to its contribution to stability.

In conclusion, our results suggest underlying geometric factors (i.e., implantation strain and orientation) play a role in the ligament's ability to contribute to hip stability, thus highlighting the importance of surgical decisions to maximize stability following THA.

ACKNOWLEDGEMENTS

Implants were donated by Exactech, Inc. (Gainesville, FL).

REFERENCES

[1] Rivera, F et al., World J Orthop, 13:388-399, 2022. [2] Driesman, A et al., Arthroplasty, 5:42, 2023. [3] Haynes, J et al., J Arthroplasty, 37:495-500, 2022. [4] Post, Z et al., JAAOS, 22:595-603, 2014. [5] D'Ambrosi, R et al., EFORT Open Rev, 6:545-555, 2021. [6] Ng, K et al., J Bone Jt Surg, 101:2141-2151, 2019. [7] Acuña, A et al., J Orthop, 19:237-243, 2020. [8] Burzynski, S et al., PloS One, 16:e0250397, 2021. [9] McGrory, B J et al., J Bone Jt Surg, 77:865-869, 1995. [10] Goldsmith, M et al., J Biomech, 48:4093-4100, 2015. [11] Kiapour, A et al., Appl Math, 4(5A):91-97, 2014. [12] Farshidfar, S et al., PloS One, 17(1):e0262684, 2022.

SB^{3}C 2024
Summer Biomechanics, Bioengineering and Biotransport Conference
June 11–14, 2023, Lake Geneva, WI, USA

SPATIALLY MAPPING THE TIME-DEPENDENT MATERIAL PROPERTIES OF THE NONHUMAN PRIMATE CERVIX THROUGH GESTATION

Echo Z. Xu[1], Camilo A. Duarte-Cordon[1], Daniella M. Fodera[2], Shuyang Fang[1], Ivan Rosado-Mendez[3,4], Timothy Hall[3], Helen Feltovich[3,5], Kristin M. Myers[1]

[1]Department of Mechanical Engineering, Columbia University, New York, NY, USA
[2]Department of Biomedical Engineering, Columbia University, New York, NY, USA
[3]Department of Medical Physics, University of Wisconsin-Madison, Madison, WI, USA
[4]Department of Radiology, University of Wisconsin-Madison, Madison, WI, USA
[5]Department of Obstetrics & Gynecology, Mount Sinai, New York, NY, USA

INTRODUCTION

In pregnancy, the female reproductive system undergoes substantial growth and remodeling (G&R) to support fetal development and delivery [1]. Notably, the cervix, located at the base of the uterus, connects the uterine cavity and vaginal junctions with the internal os (IO) and external os (EO), respectively (Fig. 1B). In humans, the cervix remains closed throughout pregnancy, serving as a mechanical barrier. Before and during parturition, it undergoes softening and ripening to facilitate fetal passage, exemplifying a physical manifestation of G&R. However, due to ethical concerns with human tissue collection, little is known about the evolution and spatial distribution of cervical tissue properties at mid-gestation timepoints and important anatomical locations. Rhesus macaques, a nonhuman primate (NHP) model with comparable maternal anatomy [2], provides a unique opportunity to study the gestational changes in mechanical behaviors of the cervical tissue at nonpregnant (NP) and three pregnant (PG) timepoints: early 2nd (E2), early 3rd (E3), and late 3rd (L3) trimesters (Fig. 1A). Our previous work examined the mechanical properties of these tissues using single-indent microindentation [3]; this study investigates time-dependent material behaviors of the same tissue groups through nanoindentation (NI) with the addition of the spatial mapping of tissue properties across selected anatomical locations.

METHODS

Per a University of Wisconsin Madison Animal Care and Use Committee protocol, NHP cervical tissue was collected from rhesus macaques following a total hysterectomy for the following groups: NP (n = 3), E2 (n = 3), E3 (n = 3), and L3 (n = 3). Cervical specimens were sliced transversely at IO and EO and dissected into 4 quadrants (Q1–Q4) (Fig. 1C). Following dissection, samples were flash-frozen on dry ice and stored at -80^{o}C until testing. In preparation for NI, cervical tissue was microtomed into 60 µm sections mounted on glass slides and stored in a -80^{o}C freezer. Upon testing, sample slides were glued to Petri dishes and swelled at 4^{o}C in PBS solution at room temperature for 30 mins. Spherical NI (Piuma, Optics11Life, Amsterdam, NL) was utilized to determine the time-dependent material properties of the NHP cervical tissues. Using an indentor with a probe radius of 24 μm and cantilever stiffness of 0.23 N/m, samples were indented to a fixed depth of 3 μm for 15 s, corresponding to a 5% strain, to achieve a load relaxation curve approaching equilibrium (Fig. 1E). The distance between indentation points was fixed at 200 μm. At least 100 indentation measurements were taken for each sample during the full mapping from the cervical canal end to the vaginal wall/ fornix with a fixed width of 1 mm at both ora (Fig. 1C). Load relaxation curves were fit in MATLAB with a combined poroelastic-viscoelastic (PVE) model based on established methods [4-6]. Material parameters of stiffness (E), instantaneous stiffness (E_0), viscoelastic ratio ($\frac{E_\infty}{E_0}$), and intrinsic permeability (k) were determined. Statistical analysis was performed in R using the `lme4` library with significance set at a 95% confidence level. A linear mixed model was implemented to investigate the effects of gestational timepoints (NP, E2, E3, and L3) and anatomical locations (IO and EO) on material properties with the consideration of the dependency due to same-subject sampling. P-value symbols in plots follow a standard GraphPad style $^{*}p \leq 0.05, ^{**}p \leq 0.01, ^{***}p \leq 0.001$.

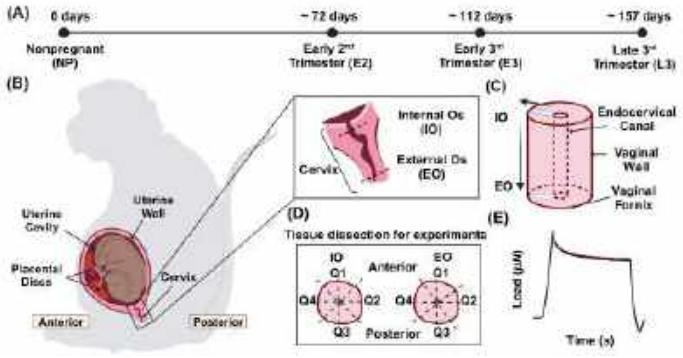

Figure 1: (A) Timeline of NHP pregnancy. (B) Representative illustration of pregnant NHP anatomy in the sagittal plane, including a schematic of the cervix identifying the internal os (IO) and external os (EO). (C) The directions of NI spatial mapping relating to anatomical features. Radial: the cervical canal (connecting the endocervical canal and the vaginal fornix) to the vaginal wall; vertical: IO and EO. (D) Top view of cervical samples dissected for experiments. (E) Representative load relaxation curve (black line) generated from NI testing fit with the PVE model (red line).

RESULTS

Results from Q1–Q4 in both IO and EO across all gestation groups in 1 NHP subject revealed no significant differences in E, E_0, $\frac{E_\infty}{E_0}$, or k; therefore, we tested only Q1 in subsequent samples for feasibility. The complete dataset reveals no significant differences in material parameters measured at this strain level between IO and EO at any timepoint, nor changes across gestation at both locations (Fig. 2). E and E_0 present similar distribution across gestation and anatomical locations, with E_0 consistently greater than E (Fig. 2A & B). $\frac{E_\infty}{E_0}$ ranges from 0.45 to 0.55 across all timepoints and locations, highlighting the viscoelastic nature of the tissue. Permeability shows no trends across all gestation and location groups, with most values around 10^{-16} m^2. We also examined the spatial variation of material properties from the cervical canal to the vaginal wall (Fig. 3) and compared the coefficient of variation (CV), defined as the ratio of the standard deviation to the mean (Fig. 2). No difference in CV values was observed across gestational groups and anatomic regions, suggesting that the cervix exhibits a similar degree of heterogeneity in the radial direction. Among all parameters, $\frac{E_\infty}{E_0}$ displays the lowest level of variation with CV values around 0.18, while k shows the highest level of variation with most CV values above 0.8.

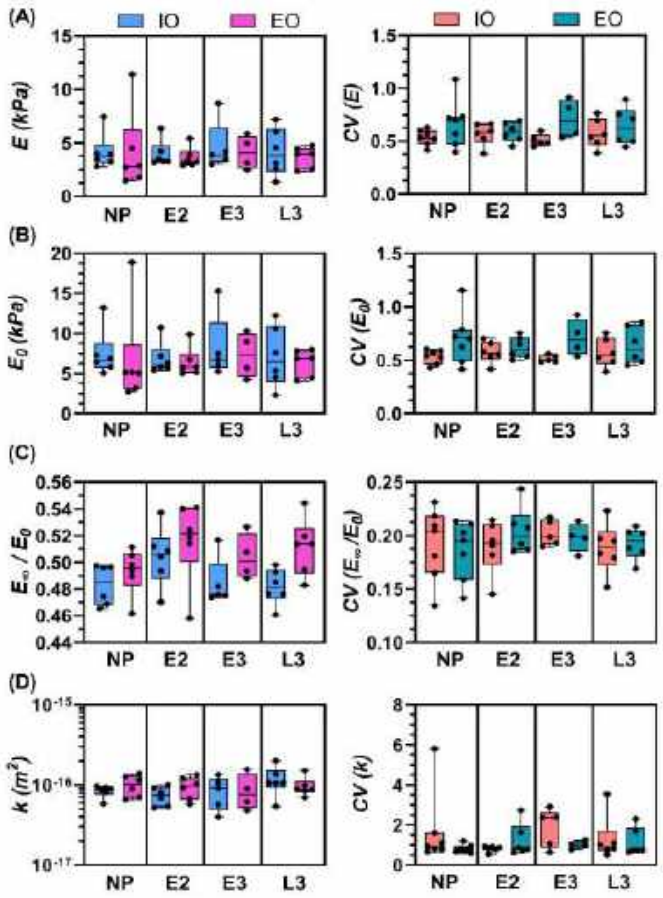

Figure 2: (A) Stiffness, (B) Instantaneous stiffness, (C) Viscoelastic ratio, and (D) Permeability of NP, E2, E3, and L3 NHP cervical tissue at IO and EO. Left: material property. Right: corresponding CV of the material property. Each symbol represents the median value of all indentation points from an individual test.

This unique dataset validates our NI protocol, demonstrating results comparable to established indentation methods. The material properties obtained with NI are compared with PVE results fit with our microindentation (2.5 mm indentor) data from the same NHP subject [3]. Those values are close in scale, especially for elastic properties like E, denoting the validity of NI as a faster, more flexible testing tool compared to microindentation. We also observed a broader distribution in values for time-dependent properties from microindentation, consistent with the findings in studies on indentation size effects [7].

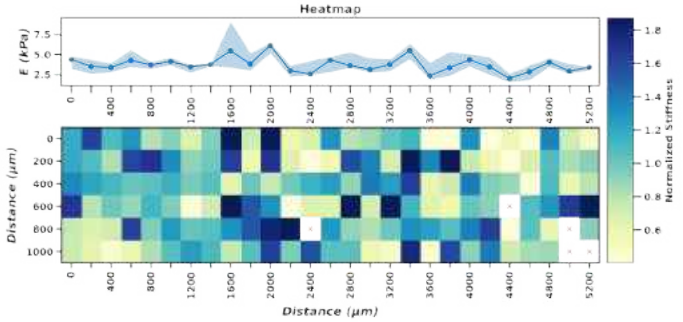

Figure 3: Representative stiffness heatmap of an NI test. Top: the median of stiffness values in each column with the deviation shaded. Bottom: spatial distribution of stiffness from the cervical canal (left) to the vaginal wall (right). Color-plotted values represent stiffness between the 10^{th} and 90^{th} percentiles, normalized to the median. Red crosses indicate failed indentation points.

DISCUSSION

Here, we characterize the time-dependent properties of the NHP cervix at distinct gestational timepoints, addressing a significant knowledge gap in tissue G&R during pregnancy. Specifically, this robust dataset, collected via NI, describes the mechanical properties of the cervix at IO and EO and the spatial variation of those properties from the cervical canal to the vaginal wall. At the length scale of NI, cervical tissue maintains consistent mechanical properties and heterogeneity across gestation and different anatomical locations. This observation agrees with our previous results using microindentation on the same subjects at a small strain regime, although contrary to results from tensile tests with large deformation and another NI study on rat cervix that cervical tissue softens at later stages of pregnancy [3, 9]. During cervical G&R, mature collagen is replaced by newly synthesized collagen to enhance tissue compliance without altering total collagen content in pregnancy [8]. We hypothesize that at the strain level of NI (5%), the collagen fiber network experiencing structural and compositional G&R is not effectively engaged, resulting in similar material property values across gestation. Additionally, the NI study, which observed reduced stiffness in rat cervix during pregnancy, employed the Hertzian contact model. This contrasts with our use of the PVE model, as the Hertzian approach focuses on the linear elastic loading regime, potentially leading to differing results.

We will further our investigation of cervical G&R by examining the gross tissue morphology through histology staining and analyzing the biochemical composition quantitatively.

ACKNOWLEDGEMENTS

The research was supported in part by the Iris Fund, the Eunice Kennedy Shriver National Institute of Child Health Human Development Grant R01HD072077 to TH, IRM, HF, and KM, and the Office of The Director, NIH Award P51OD011106 to the Wisconsin National Primate Research Center, University of Wisconsin-Madison.

REFERENCES

[1] Myers & Elad. *WIREs Syst. Biol. Medicine*. 2017. [2] Clark & Corner. *The Anat. Rec.* 1935. [3] Fang et al. *J. Biomech. Eng.*. In Press. [4] Mattice et al. *J. Mater. Res*. 2006. [5] Hu et al. *Appl. Phys. Lett*. 2010. [6] Islam and Oyen. *Exp. Mech*. 2021. [7] Oyen et al. *J. Mater. Res*. 2011. [8] Nallasamy et al. *Biol. Reprod.*. 2021. [9] Moghaddam et al. *Acta. Biomater.* 2023.

OPTIMAL LATTICE GEOMETRY FOR IMPLEMENTATION IN SCOLIOTIC BRACES

Robert Rizza (1), Xue-Cheng Liu (2), Vince Anewenter (3)

(1) Department of Mechanical Engineering, Milwaukee School of Engineering, Milwaukee, WI, USA
(2) Department of Orthopedic Surgery, Children's Wisconsin, Medical College of Wisconsin, Milwaukee, WI, USA
(3) Rapid Prototyping Center, Milwaukee School of Engineering, Milwaukee, WI, USA

INTRODUCTION

The prevalence of adolescent idiopathic scoliosis (AIS) is estimated from 2% to 3% for children between 10 and 16 years of age [1]. With this disability not only does a larger spinal curve affect posture and cosmetics but it causes pain and pulmonary function and activity of daily life deficits.

For treatment, the Thoracic Lumbar Sacral Orthosis (TLSO) has become widely used. This brace provides 3D treatment of spinal curvature by implementing a three-point loading principle, elongational, flexural and derotational mechanism. The typical design of the TLSO is a modular one with anterior and posterior polymer panels (typically made of Polyethylene), foam padding and secured with Velcro straps. Newer designs incorporate 3D printing for the panels [2-5] that exploit this manufacturing method's accuracy and speed. This has led to some advancements in manufacturing of Scoliotic braces [5].

Patient compliance with the brace is affected by the bulkiness and weight of the polymer shell. Because the polymer acts as a barrier to air flow the device is often uncomfortable and hotter which reduces compliance.

Often, small hole patterns are placed in the hard-shell of the brace to reduce weight. In addition, these holes allow for air flow which helps in preventing absorption of moisture which may lead to odor, mildew growth and in some cases Dermatitis [6].

In [5], the optimal size, shape and separation distance between the holes was obtained. Implementation of the optimal hole pattern led to a brace design which is 10% lighter than the traditional design.

Lattice structures are characterized by repeated cells of interconnected bars called "struts" that connect vertices together to form the cell. The mechanical properties of the cell is controlled by the size and geometry of the cell as well as the diameter of the strut. By properly optimizing these parameters it is possible minimize the weight of a mechanical component while maintaining the structural efficiency.

Several different geometries are possible for the lattice structure. These include: square, octagonal, triangular and hexagonal geometries.

Unlike holes, lattice structures are truly three dimensional and remove more material from the solid volume compare to hole patterns. Furthermore, lattice structures are more structurally efficient than holes as they have lesser stress concentrations.

While lattice structures have been implemented in other areas of mechanical engineering design there has been no development in utilization of these structures for Scoliotic braces. The objective of this study was to obtain the optimal lattice geometry for implementation in the polymer shell of a Scoliotic brace.

METHODS

Comparison of the various lattice geometries was achieved by constructing CAD models of standard tensile specimens using Creo® (PTC, Boston). Each specimen had a different lattice geometry. For each specimen, the strut diameter (1-3 mm) and cell size (4 - 9 mm) were varied to produce multiple designs of the same geometry.

Linear FEA simulations were carried out using Ansys (Ansys, Canonsburg, PA) for each design variation. A parametric approach was undertaken. An axial tensile force was applied ranging from 0 to 1000 N. The boundary conditions applied to the model were such that they mimic axial tensile loading of the specimen (Figure 1). One end of the specimen was fixed while at the other end, the force was applied.

The axial deformation of the specimen was obtained for each load case. From this data, the stiffness of the lattice geometry was calculated.

Material properties for the 3D printing material Duraform PA (3D Systems, Eden Prairie, MN) was used in the FEA. This material is used in the 3D printing of braces, hence its selection [5]. It exhibits linear behavior. The material has a Secant Modulus of 160 MPa and Poisson ratio of 0.40.

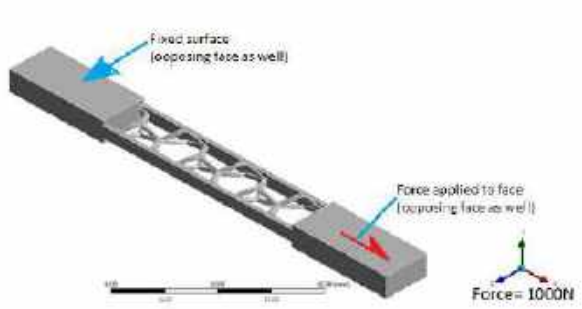

Figure 1: Boundary conditions applied to the model of a lattice specimen with a square lattice geometry.

Each specimen was 3D Printed using the SLS method at the MSOE Rapid Prototyping Center using a DTM Sinterstation 2500 plus. Five samples of each specimen design variation were printed.

For FEA validation, an MTS Alliance RT/50 was used. The specimens were tested in axial tension to fracture using ASTM D638-14 standard. The load-displacement curve was obtained from the test and the stiffness of the lattice geometry was obtained.

Since weight is an important factor in determining the optimal lattice geometry, the stiffness to weight ratio was calculated. The higher the ratio, the greater the capacity of the lattice geometry to carry load at a lower weight.

RESULTS

For the sake of brevity we have listed in Table 1 only the three geometries which give the highest stiffness to weight ratio. We see that the highest ratio was 70.04 N/mm·kg for a square geometry but there is an octagonal design which yields nearly the same value.

Table 1: Lattice geometries with highest strength to weight ratios.

Geometry	Stiffness/Weight (N/mm·kg)
Square	70.04
Octagonal	69.31
Hexagonal	63.52

Table 2 shows the peak load, and maximum extension of the three geometries when loaded to fracture. The square geometry had the highest load capacity to fracture at 295N, whereas the hexagonal geometry had the longest extension at 2.6 mm. Stress and strain are not used as the stress is an average stress in the testing but a localized stress in the FEA and hence not comparable.

Table 2: Peak load and extension to fracture of the three top geometries.

Geometry	Peak Load (N)	Peak Extension (mm)
Square	295	1.7
Octagonal	280	2.25
Hexagonal	247	2.6

In Table 3, we list the stiffness of the top three geometries from Table 1 as obtained from the FEA results and the tensile testing. We see the difference between the FEA results is relatively small. With the largest error being for the hexagonal geometry at 8.32%.

Table 3: Results of the FEA compared to the tensile testing.

Geometry	Stiffness (N/mm)		
	FEA	Testing	% Difference
Square	244.22	232.03	5.25
Octagonal	187.28	196.21	4.55
Hexagonal	245.41	226.56	8.32

DISCUSSION

As we can see in Table 1, the square or octagonal geometries give the highest stiffness to weight ratios. The difference between the two is quite small so either geometry is acceptable as an optimal geometry. The strut diameter for the square geometry is slightly larger at 1.5 mm, while the strut diameter for the octagonal geometry was 1.3 mm. Both values are greater than 1 mm, which is the lower bound for successful printing with SLS. We saw no differences in the quality of the print due to the geometry of the lattice.

In Table 2, the square geometry has the highest load carrying capacity to fracture but the extension is less than the octagonal geometry. Again, there is little difference between the square and octagonal geometries. As the octagonal geometry has a large range of extension, this suggests that the octagonal is more optimal than the square geometry.

Table 3 indicates that the FEA models are valid and may be implemented in the future for continued design of braces with lattice structures.

ACKNOWLEDGEMENTS

The authors wish to recognize the hard work of Sophia Meinshausen, Julian Kay, Rieke Wittorf, Emma Knutson, Florian Kleis and Dennis Niemeyer, undergraduate students at the Milwaukee School of Engineering for their hard work with the FEA simulations and testing.

REFERENCES

[1] Weinstein, S.L. 2019. The Natural History of Adolescent Idiopathic Scoliosis. Journal of Pediatric Orthopaedics. 39, pp. S44-S46.

[2] Thometz, J., Liu, X., Rizza, R. *et al.* 2018. Effect of an Elongation Bending Derotation Brace on the Infantile or Juvenile Scoliosis. Scoliosis and Spinal Disorders. 13, pp. 1- 6 (doi:10.1186/s13013-018-0160-4).

[3] Cobetto, N., et al. 2017. 3D Correction of AIS in Braces Designed using CAD/CAM and FEM: A Randomized Controlled Study. Scoliosis and Spinal Disorders. 12, pp. 12-24 (doi: 10.1186/s13013-017-0128-9).

[4] Pea, R., Dansereau, J., Caouette, C., et al. 2018. Computer-Assisted Design and Finite Element Simulation of Braces for the Treatment of Adolescent Idiopathic Scoliosis Using a Coronal Plane Radiograph and Surface Topography. Clinical Biomechanics. 54, pp. 86-91.

[5] Rizza, R., Liu, X.C., and Anewenter, V. 2022. Effect of Window and Hole-Pattern Cut-Outs on Design Optimization of 3D Printed Braces. Frontiers in Rehabilitation Sciences. Doi: 10.3389/fresc.2022.889905.

[6] Pedragosa R., Romaguera C., Mascaro JM, Vidal J., and Jariod J. 1985. Dermatitis Caused by Milwaukee Braces. Med. Cutan Ibero Lat Am.13(3), pp. 205-208.

NECK STRENGTH AND ENDURANCE AFTER 1-HOUR EXPOSURE TO VERTICAL WHOLE-BODY VIBRATION

Ana I. Lorente, Robert S. Salzar

Center for Applied Biomechanics, University of Virginia, Charlottesville, Virginia, USA

INTRODUCTION

The vibrational environment that military helicopter aircrew experience has been related to neck and back pain. This pain may lead to injuries and incapacitations in the most severe cases. Although the prevalence is higher for the lumbar region [1], neck pain has also been related to rotary-wing missions [2, 3]. However, previous studies trying to understand how whole-body vibration (WBV) in helicopters may influence back muscle physiology have only been focused on the lumbar spine, without including any neck muscle [4].

The fatigue in the cervical spine muscles has been studied in military helicopter aircrew [5], but the literature is lacking any performance assessment right before and right after a flying exposure. This information would provide insight into short-term effects on muscle response, which could be related to neck injuries and incapacitations in a long-term scenario.

Specific training programs for the neck muscles could reduce the pain related to flight missions but would be more effective if the effects on the neck musculature of these flights and their vibrational environment were more well understood.

The goal of this study was to quantify if the strength and endurance of neck muscles are altered due to a 1-hour vibrational exposure that simulates a helicopter flight. Our hypothesis was that muscle performance would decrease after the vibrational load exposure.

METHODS

Fourteen healthy subjects (7 males, 7 females) participated in this study (25.7 ± 2.9 years-old, 1.70 ± 0.08 cm, 68.9 ± 13.6 kg). Volunteer exclusion criteria included neck or spine injuries/surgeries, being prone to motion sickness, and being pregnant. All participants gave their consent following the test protocol approved by the University of Virginia Institutional Review Board for Health Sciences Research (HSR220143) and the U.S. Army Office of Human and Animal Research Oversight (OHARO, W81XWH-18-9-0001).

Three isometric strength exercises were performed: (1) head-neck forward pushing, (2) head-neck backward pushing, and (3) unilateral 100° shoulder abduction [6, 7]. The three exercises were performed while being seated, with the two arms (head-neck exercises) or only one arm (shoulder exercise) positioned across the chest. The subjects were instructed to gradually increase their effort to maximum, having 3 seconds to hold that force, and 3 seconds to release it [7]. This rate was indicated with an audio saying “start”, “maximum”, and “release”. There were 3 repetitions for each exercise with a 2-minute rest between repetitions. After the 3 repetitions, the endurance assessment was performed holding 70% of the highest measured force. Participants held this effort as long as possible, up to 3 minutes.

The strength and endurance were evaluated right before and after being exposed to 1-hour of vertical whole-body vibration at 0.2 g and 4 Hz. During the hour, the participants were seated on a metal seat geometrically representative of a H-60 helicopter seat. Their hands and feet were on the hand controls and pedals of a flight simulator. The back support consisted only of two lateral vertical posts joined by two horizontal wires. This back support allowed the use of motion sensors. The participants were wearing an HGU-56/P helmet during the vibrational load exposure. The size of the helmet (small, medium, large) was always individually selected for each subject.

Paired T-test was used to compare the results before and after WBV ($p < 0.05$).

RESULTS

After 1-hour exposure to a vertical vibrational load simulating helicopter flight, there was no significant change in neck muscle strength (Figure 1). A slight increase in the measured force was even observed in the head-neck backward pushing exercise after the vibrational load exposure (from 127.2 ± 59.5 N to 134.6 ± 61.9 N). The same average value was obtained in both measurements for the head-neck forward pushing (108 N, Table 1).

However, a statistically significant decrease in muscle endurance was detected in the three exercises post-vibrational exposure, with the most notable changes in the head-neck forward pushing and the shoulder abduction, both by 34% (Table 1). The decrease in the head-neck backward pushing exercise was 14%.

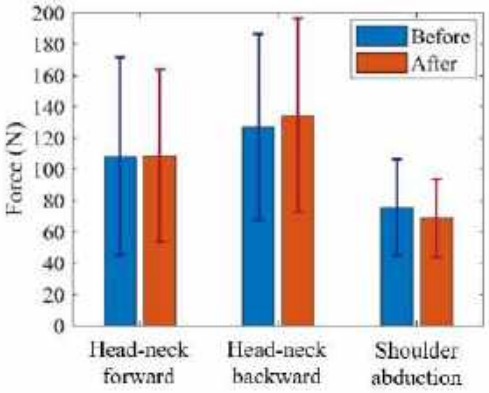

Figure 1: Force before and after the vibrational exposure for the three exercises.

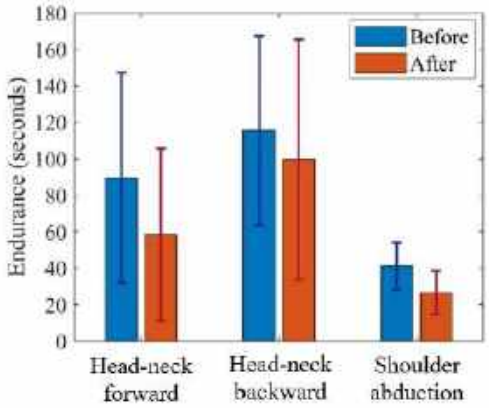

Figure 2: Endurance (seconds holding the effort) before and after the vibrational exposure for the three exercises.

Table 1: Force (Newtons) and endurance (seconds) before and after the vibrational exposure.

	Head-neck forward	Head-neck backward	Shoulder abduction
Force (N)			
Before WBV	108.4 ± 63.3	127.2 ± 59.5	75.6 ± 30.7
Range	27.0 – 244.0	58.0 – 256.9	20.0 – 127.4
After WBV	108.7 ± 55.0	134.6 ± 61.9	68.8 ± 25.1
Range	42.5 – 191.8	66.0 – 285.0	28.0 – 115.0
P-value	0.981	0.260	0.050
Endurance (seconds)			
Before WBV	90 ± 58	116 ± 52	41 ± 13
Range	22 – 180	43 – 180	17 – 58
After WBV	59 ± 48	100 ± 66	27 ± 12
Range	12 – 180	17 – 180	11 – 54
P-value	*0.032*	*0.029*	*< 0.001*

DISCUSSION

The endurance performance decreased after 1-hour of vibrational load exposure while muscle strength remained the same. This result indicates that a focus towards increasing muscle endurance may be relevant to decrease the neck pain seen in military aircrew. Improving endurance instead of strength when working on muscle performance for aircrew members has been previously discussed by Harrison et al. (2009) [5]. Our results support this approach as the maximum force remained equal after the vibrational load exposure.

Opposite to what one might think, lower muscle strength in the neck has not been related to neck pain in aircrew members. A trend showing lower muscle strength in subjects with neck pain was presented with 117 helicopter crew members (29% with neck pain), but the trend had no statistical significance [8]. Two other studies did not find any relationship between neck strength and neck pain: one had 40 pilots and flight engineers (53% with neck pain) [3] and the other had 30 helicopter pilots (50% with neck pain) [2]. However, this last study did find lower strength in the neck extensors in fighter pilots with neck pain, without observing any difference in the neck flexors [2].

Although the WBV exposure of helicopters has been related to back injuries, this may not be the only cause, and the posture held during flights may also contribute [1]. The subjects of the present study were not instructed to hold a specific back posture, but were told to keep their feet on the pedals and to hold the hand controls. The backrest design of the seat did not replicate a real helicopter seat. It only consisted of two horizontal wires at the thoracic and lumbar levels. This modification is unlikely to affect the neck muscle performance. Furthermore, real helicopter pilots often hold a posture with the shoulders leaning forward ("helicopter hunch"), moving the shoulders away from the backrest.

One limitation of the present study is the use of helmets with subjects that are not conditioned to wearing them. The helmets weighed 1.4 kg. The results presented herein may differ if this same protocol is followed by military personnel who are used to wearing helmets.

The vibrational load experienced by the subjects reproduced the vertical load of an actual helicopter in flight, but not the associated motions typical of crew duties. Also, actual flights usually last more than 1 hour and helmets can be heavier than 1.4 kg. This same protocol, along with the strength and endurance exercises, could be applied to personnel before and after real helicopter flights. Actual helicopter flights may also decrease the endurance performance of neck muscles, as it was observed in this 1-hour simulated flight. Understanding how military vibrational environments may affect endurance in the short and long terms would aid in the design of specific training programs with a goal of decreasing neck pain in helicopter aircrew members.

ACKNOWLEDGEMENTS

The authors thank Dr. Timothy Bentley of the Office of Naval Research and Glenn Paskoff of the Naval Air Warfare Center Aircraft Division for their support during the performance of contract W81XWH-18-9-0001.

REFERENCES

[1] Cunningham, LK et al., *Aviat Space Environ Med*, 81:774-778, 2010.
[2] Äng, B et al., *Aviat Space Environ Med*, 76:375-380, 2005.
[3] Harrison, MF et al., *Aviat Space Environ Med*, 82:1125-1130, 2011.
[4] De Oliveira, CG et al., *J Biomech*, 34:1309-1315, 2001.
[5] Harrison, MF et al., *Mil Med*, 174:1183-1189, 2009.
[6] Schüldt, K, *Scand J Rehabil Med*, 19:1-49, 1988.
[7] Al-Qaisi, S, *Procedia Manuf*, 3:4578-4583, 2015.
[8] Van Den Oord, M et al., *Aviat Space Environ Med*, 81:46-51, 2010.

INVESTIGATING THE EFFECT OF CO AND CR SUBSTITUTIONS ON BIOMIMETIC APATITE MATURATION

Kennedy A. Drake (1), Julianna DeSantis-Raymond (2), Stephanie Wong (1), Alix C. Deymier (1),

(1) Biomedical Sciences, University of Connecticut Health Center, Farmington, Connecticut, USA
(2) Biomedical Engineering, University of Connecticut, Storrs, Connecticut, USA

INTRODUCTION

In the late 20th century, metal-on-metal hip implants, primarily made of cobalt and chromium alloys, gained popularity for their durability, especially among younger and more active patients [1,2]. However, the degradation of these implants containing cobalt (Co) and chromium (Cr) has been associated with the release of heavy metal ions and increased risk of bone fracture. Given that the predominant mineral in bone, bioapatite, has a high propensity for cationic substitutions, it is likely that these heavy metals could be up taken by bone mineral during bone formation. This is expected to have significant effects on the crystal mechanics and structure.

The maturation of apatite during and after bone formation involves the transformation of small, disordered crystals of apatite within the collagen matrix into larger crystals with increased carbonate content and crystallinity. This maturation enhances the bone's mineral density and mechanical strength. However, it is unknown how cationic substitutions, such as the inclusion of Co and Cr, affect this maturation process and in turn bone health.

Due to the difficulty in isolating apatite crystals from bone tissues, biomimetic apatite formation, a process replicating natural mineralization processes, becomes a critical tool in understanding mineral behaviors. This approach enables the creation of materials that closely mirror bone mineral composition and structure, facilitating improved integration and functionality in the laboratory.

Here we are exploring two methods for the formation of mature cobalt (Co) and chromium (Cr) substituted apatite's. The Maturation method [3] and the Direct Precipitation method [4] replicate different maturation processes to determine the effects of Co and Cr substitutions.

METHODS

Maturation method for Apatite Formation: Apatites were precipitated by combining phosphate and calcium containing solutions. Solution A was made by dissolving 3.12g calcium nitrate and either 0.53g chromium nitrate or 0.39g of cobalt nitrate in 45mL Milli-Q water. Solution B was formed by dissolving 5.40g sodium bicarbonate and 5.40g ammonium phosphate in 90mL Milli-Q water. The solutions were combined, agitated, and aliquots of apatite were collected after 7, 14, and 21 days of maturation.

Direct Precipitation method for Apatite Formation: Three solutions were prepared. 5.40g sodium bicarbonate in 180mL water was heated to ~70°C in a round bottom flask. Simultaneously, 3.13g calcium nitrate and either 0.39g of cobalt nitrate or 0.53g of chromium nitrate were dissolved in 40mL of water. Additionally, 5.40g of ammonium phosphate was dissolved in 40mL water. These two solutions were placed in burettes and were titrated simultaneously at 1mL/min until exhaustion. pH was maintained at ~9 with 0.5 M sodium hydroxide, and the reaction was digested for 2 hours at pH 9 and 65°C. This process allows for rapid maturation of the crystals.

Filtering and drying: After collection, the powders were filtered, rinsed three times with Milli-Q water, and dried overnight at 60°C. The powders were ground and stored in a closed glass vial.

XRD: Crystals were analyzed via X-ray diffraction using a Bruker D2 Phaser X-ray Diffractometer. Operating at 30kV and 10mA, the mineral powders were analyzed from 20-80° 2θ with a step size of 0.02°, and an acquisition time of 1.5 seconds. The 002 and 310 peaks were fit as pseudo-Voigt peaks in DIFFRACT.EVA software. The crystal d-spacing along the (002) and (310) peaks were determined from the peak locations. The full width half max (FWHM) of the (002) peak was used as an inversely proportional measure of the crystallinity.

Raman: Compositional measures were made using a Witec α300 Raman spectrometer. Ten spectra were acquired for each powder with a 785 nm laser using a 50x objective and an acquisition time of 45x2sec. The 960 cm^{-1} PO_4^{3-} and 1070 cm^{-1} CO_3^{2-} peaks were fit as Lorentzian peaks using Witec Program 5.1. The PO_4^{3-} peak width is inversely proportional to crystal atomic order. Carbonate content was determined from the area ratios of the 1070/960 peaks (CO_3/PO_4). Only cobalt containing apatite's were assessed via Raman due to chromium fluorescence affecting the Raman signal.

RESULTS

Apatite formation: Cobalt and chromium apatites were synthesized using both the maturation method and the direct precipitation method. The maturation method resulted in subtle yet noticeable variations in color, with the most mature apatites at 21-days exhibiting the darkest color for both cobalt and chromium. In contrast, the direct precipitation method yielded a color consistent with the 21-day matured apatites. Both methods produced fine powders.

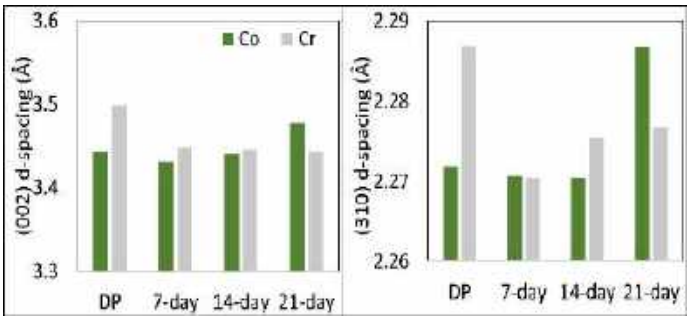

Figure 1: d-spacing of the (left) (002) and (right) (310) peaks for Cr and Co containing apatites.

XRD: The (002) d-spacing decreased with maturation in the chromium apatites while it increased in the cobalt apatites, Fig 1. While the (310) d-spacing also increased with maturation in chromium apatites, it exhibits an initial decrease followed by a sharp rise at 21 days in the cobalt apatites. The width of the (002) and (310) peaks generally decreased with maturation for the Cr apatites, Fig 2. These trends are much less clear for the Co apatites.

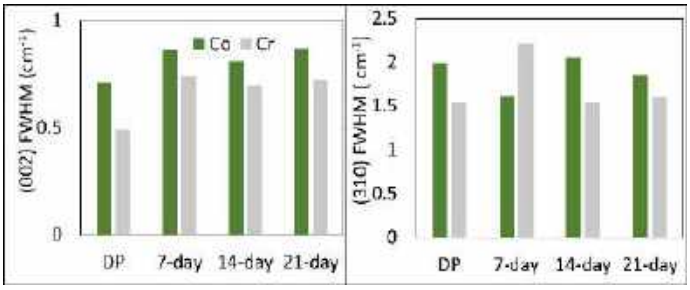

Figure 2: FWHM of the (left) (002) and (right) (310) peaks for Cr and Co containing apatites.

Raman (Co-only): The location of the PO_4^{3-} peak increased in early maturation while the direct precipitation method resulted in peak locations similar to mature apatite (not shown). The width of the PO_4^{3-} peak decreases significantly over time with maturation, while the direct precipitation method consistently yields the smallest width, Fig 3. The carbonate to phosphate ratio (CO_3:PO_4) exhibits an increasing trend over time with the maturation method, with the direct precipitation method having the highest ratio.

DISCUSSION

Traditional biomimetic apatite maturation exhibits a number of key features including increased (002) and (310) d-spacing dimensions, increased crystal size, increased carbonate content and increased crystallinity [5]. The substitution of Co and Cr into the apatite structure could have significant effects on maturation of apatite resulting in compromised bone properties.

Much like traditional maturation, the cobalt containing apatite's exhibit simultaneous expansion of the (002) and (310) d-spacing suggesting that the cobalt does not inhibit lattice modifications associated with maturation. On the contrary, the presence of Cr leads to a decrease in the (002) d-spacing. This points to a modified maturation process possibly resulting from chromium substituting into the apatite as the anion chromate instead of the chromium cation [6]. Interestingly, despite the changes in lattice spacing, there is not an associated change in the mineral crystallinity. Crystallinity is inversely proportional to the FWHM of the (002) peak and thus is expected to decrease with maturation. This decrease is observed in the Cr-apatites but not the Co apatites. Crystallinity can be controlled by either crystal size or ordering of the crystalline core. Changes in the d-spacing could thus be isolated from the crystallinity if the latter is primarily being controlled by changes in crystal size. Interestingly, for the Co apatite's there is a distinct decrease in the width of the PO_4^{3-} peak with increasing maturation suggesting an increase in atomic order. The improved atomic order and changes in d-spacing suggest that Co-apatites may undergo traditional maturation while having limited effects on crystal size. This is further supported by the increase in CO_3^{2-} seen with Co-apatite maturation. Together these results suggest that Co does not significantly affect apatite maturation.

Chromium apatites exhibits the reverse behavior with an unexpected change in d-spacing but the expected increase in crystallinity with maturation This could be indicative of an increase in crystal size with Cr substitutions. Due to Cr fluorescence, it is not possible to comment on the Cr apatite's atomic order or CO_3^{2-} content. To date, the results suggest that Co- has a less impactful effect on the maturation of biomimetic apatites as compared to Cr. Further investigations will include further determinations of crystal atomic order via FTIR, measurement of the crystal size via TEM, compositional investigations with ICP-OES, and finally mechanical testing via synchrotron X-ray diffraction.

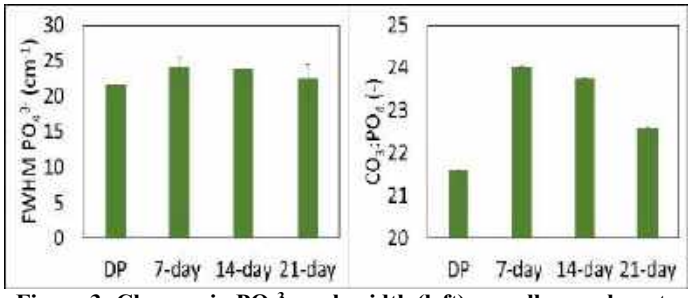

Figure 3: Changes in PO_4^{3-} peak width (left) as well as carbonate content as CO_3:PO_4 (right)ad determined via Raman for Co apatite.

ACKNOWLEDGEMENTS

Funding for KD was provided by the Young Innovative Investigators Program at the University of Connecticut. Additional funding was provided (NSF #2323500).

REFERENCES

[1] Matharu, V. K., & Matharu, G. S. *British Journal of General Practice 67*(665), 544–545, 2017. **[2]** Center for Devices and Radiological Health. U.S. Food and Drug Administration, 2019. **[3]** Vandecandelaère, N., et al. *Journal of Materials Science: Materials in Medicine*, *23*(11), 2593–2606, 2012. **[4]** Yoder, C. H. et al. *Polyhedron*, *127*, 403–409, 2017. **[5]** A. Grunenwald, C. Keyser, A.M. Sautereau, E. Crubézy, B. Ludes, C. Drouet. Journal of Archaeological Science, Volume 49, 2014, Pages 134-141, ISSN 0305-4403, **[6]** Banks, E. and K. L. E. Jaunarajs. Inorganic Chemistry **4**: 78-83, 1965. **[7]** Wong, S et al. Materialia. 29: 101795, 2023.

DEVELOPMENT OF A HIGH-THROUGHPUT DRUG SCREENING PLATFORM VIA PIPETTING GEL DROPLET MICRO-ORGANOIDS MODELS

D. Montes-Pinzon (1), A. Taglione (1), F. Fan (2), L. Chen (1), X. Lu (3, 4), S. Stack (4, 5), D. Hanjaya-Putra (1, 2, 3, 5, 6) H. C. Chang (1, 4)

(1) Chemical and Biomolecular Engineering, University of Notre Dame, Notre Dame, IN 46556
(2) Bioengineering Graduate Program, University of Notre Dame, Notre Dame, IN 46556
(3) Department of Biological Sciences, University of Notre Dame, Notre Dame, IN 46556
(4) Harper Cancer Research Institute, University of Notre Dame, IN 46556
(5) Department of Chemistry and Biochemistry, University of Notre Dame, Notre Dame, IN 46556
(6) Aerospace and Mechanical Engineering, University of Notre Dame, Notre Dame, IN 46556
(7) Center for Stem Cell and Regenerative Medicine, University of Notre Dame, Notre Dame, IN 46556

INTRODUCTION

In vitro disease modeling strategies enable a better understanding of pathophysiological pathways leading to disease progression and improve decision-making for patient treatments [1-4]. In cancer development, disease modeling platforms have been developed to mimic the mechanistic pathways of cancer progression and drug sensitivity. Nonetheless, most of these strategies rely on 2D arrangements, limiting their physiological relevance [5-9]. Cancer organoids have been shown to be reliable platforms for modeling tumor growth and drug screening due to their ability to preserve physiologically relevant aspects of native tumor microenvironments such as cell-cell interactions, proliferation, mechanical stimuli, and tissue development [10]. However, their widespread usage to guide clinical decisions is hindered by time-limited production of organoids and their inherent lack of reproducibility. Hence, a platform for producing a high quantity of reproducible organoids is required to provide better models for cancer progression and drug screening.

METHODS

We have developed a home-made pipette microfluidic device for the high-quantity generation of cancer micro-organoids via cell encapsulation by droplet emulsion for high-throughput drug screening. We synthesized norbornene-modified hyaluronic acid (NorHA) polymers, which serve as extracellular matrix (ECM) mimics, to create a suitable cell-encapsulation platform. The viscosity of the polymer solution was adjusted to enable its extrusion by a home-made elliptical pipette for droplet generation with suspended ovarian (OVCAR 5) and prostate (LNCaP) cancer cells ($4x10^6$ cells/mL) via water-in-oil (W/O) emulsification.

RESULTS

An automated system for pipetting was used to generate microgels and test the effect of pipetting cycles and flow rate on the droplets sizes (**Fig. 1A**). The results showed that by increasing the pipetting cycles the uniformity of the droplets was improved (**Fig. 1B**). Moreover, for the cell encapsulation we observed that upon separation, a large quantity of droplets coalesced releasing cells that remained floating freely, which suggested that the system was unoptimized (**Fig. 1C**). Hence, further experiments were carried out to increase the polymer concentration up to 20 mg/mL, being able to observe a higher microgels separation efficiency (up to 80%), with fewer free-floating cells (**Fig. 1D**). The permeability of the microgels was evaluated using TRITC-Dextran (4400 Da), which revealed that fluorophore internalization after 30 minutes, with accumulation and aggregation seen after ~1 hour (**Fig. 1E**). The mitochondrial activity assessment exhibited an increase in cell count was ~47% (**Fig. 1F**), with the relative proliferation of encapsulated cells being slightly lower than in monolayer culture (**Fig. 1G**). Screening with doxorubicin (DOX) was used to model the sensitivity of the micro-organoids towards therapies administration.

DISCUSSION

Overall, the developed microgels platform showed suitability for the encapsulation of different cancer cell lines and organoids' growth, which would allow the screening of multiple tumor microenvironment conditions. The versatility of the technology allows it to be scaled up with multi-channel and/or robotic systems and integrated with flow cytometry to realize a high-throughput platform for patient-derived micro-organoids generation and drug screening.

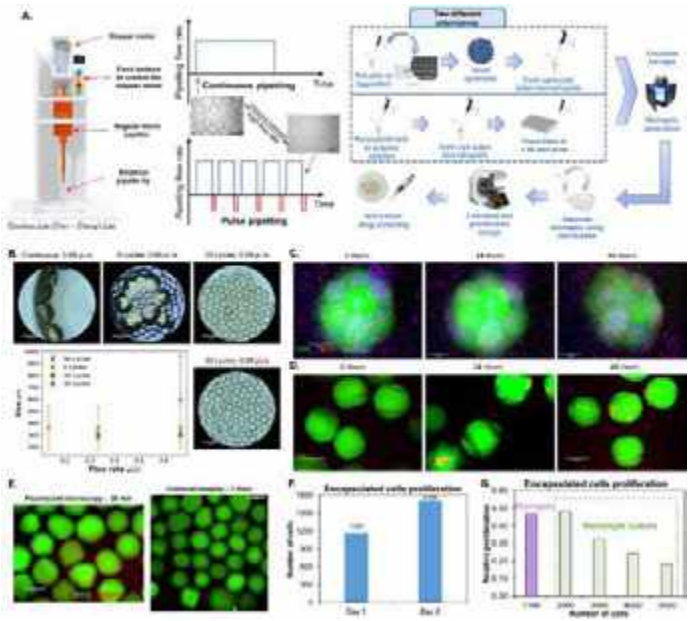

Figure 1. (A) Automated pipetting system including different cycles and alternatives for encapsulating cells and producing micro-organoids. **(B)** Effect of flow rate and number of pipetting cycles on the droplet sizes. **(C)** Unoptimized RFP-OVCAR5 cells encapsulation with a density of $5x10^6$ cells/mL using 15 mg/mL of NorHA. **(D)** Optimized cell encapsulation using RFP-OVCAR5 cells with a density of $4x10^6$ cells/mL and 20 mg/mL of NorHA. FITC was used to label the microgels (green), RFP (red) expressed by OVCAR5 cells, and Hoechst dye (blue) used for staining cells' nucleus. **(E)** TRITC-Dextran (4400 Da) permeability assays. Fluorescent microscopy (30 min) was used to assess the fluorophore internalization, while confocal microscopy (1 hour) was used showed to show the accumulation and aggregation of the fluorophore in the microgels. **(F)** Increase in number of cells over time estimated with the calibration curve. **(G)** Relative cell proliferation comparing encapsulated RFP-OVCAR5 cells with 2D cultures.

ACKNOWLEDGEMENTS

We acknowledge support from the University of Notre Dame through "Advancing Our Vision" Initiative in Stem Cell Research, NSF IUCRC Center for Bioanalytical Metrology Grant (1916601 to D.H.-P. and H.-C.C.), Harper Cancer Research Institute – American Cancer Society Institutional Research Grant (IRG-17-182-04), American Heart Association through Career Development Award (19-CDA-34630012 to D.H.-P.), National Science Foundation (2047903 to D.H.-P.) and from National Institutes of Health (1R35-GM-143055-01 to D.H.-P.).

REFERENCES

[1] R. G. Rowe and G. Q. Daley, "Induced pluripotent stem cells in disease modelling and drug discovery," *Nature Reviews Genetics,* vol. 20, pp. 377-388, 2019.

[2] M. A. Lancaster and M. Huch, "Disease modelling in human organoids," *Disease models & mechanisms,* vol. 12, p. dmm039347, 2019.

[3] Y. Zhao, N. Rafatian, N. T. Feric, B. J. Cox, R. Aschar-Sobbi, E. Y. Wang*, et al.*, "A platform for generation of chamber-specific cardiac tissues and disease modeling," *Cell,* vol. 176, pp. 913-927. e18, 2019.

[4] C. S. Murphy, L. Liaw, and M. R. Reagan, "In vitro tissue-engineered adipose constructs for modeling disease," *BMC biomedical engineering,* vol. 1, pp. 1-19, 2019.

[5] M. X. Doss and A. Sachinidis, "Current challenges of iPSC-based disease modeling and therapeutic implications," *Cells,* vol. 8, p. 403, 2019.

[6] I. S. de Oliveira, G. M. A. Silva, F. A. Cordeiro, E. L. P. Júnior, I. G. Ferreira, F. A. Cerni*, et al.*, "Research models in biomedical sciences: Advantages and limitations," 2020.

[7] H. Savoji, M. H. Mohammadi, N. Rafatian, M. K. Toroghi, E. Y. Wang, Y. Zhao*, et al.*, "Cardiovascular disease models: a game changing paradigm in drug discovery and screening," *Biomaterials,* vol. 198, pp. 3-26, 2019.

[8] K. Duval, H. Grover, L.-H. Han, Y. Mou, A. F. Pegoraro, J. Fredberg*, et al.*, "Modeling physiological events in 2D vs. 3D cell culture," *Physiology,* vol. 32, pp. 266-277, 2017.

[9] A. G. Souza, I. B. B. Silva, E. Campos-Fernandez, L. S. Barcelos, J. B. Souza, K. Marangoni*, et al.*, "Comparative assay of 2D and 3D cell culture models: proliferation, gene expression and anticancer drug response," *Current pharmaceutical design,* vol. 24, pp. 1689-1694, 2018.

[10] J. Drost and H. Clevers, "Organoids in cancer research," *Nature Reviews Cancer,* vol. 18, pp. 407-418, 2018.

COMPARISON BETWEEN VESSEL WALL MODELS TO ESTIMATE HEMODYNAMICS IN CORONARY ARTERY BYPASS GRAFT PATIENTS

Nhien Tran-Nguyen (1), Andrew T Yan (2,3), Stephen Fremes (4,5,6), Laura Jimenez-Juan (2,3,6), Piero Triverio (1,7,8)

(1) Institute of Biomedical Engineering, University of Toronto, Toronto, Ontario, Canada
(2) Department of Medical Imaging, University of Toronto, Toronto, Ontario, Canada
(3) St. Michael's Hospital, Toronto, Ontario, Canada
(4) Department of Surgery, University of Toronto, Toronto, Ontario, Canada
(5) Sunnybrook Health Sciences Centre, Toronto, Ontario, Canada
(6) Sunnybrook Research Institute, Toronto, Ontario, Canada
(7) Department of Electrical and Computer Engineering, University of Toronto, Toronto, Ontario, Canada
(8) Department of Mechanical and Industrial Engineering, University of Toronto, Toronto, Ontario, Canada

INTRODUCTION

Coronary artery bypass graft (CABG) surgery is one well-established intervention for patients with coronary artery disease, which entails the grafting of harvested blood vessels to bypass stenotic regions of the coronary arteries and improve myocardial perfusion. However, graft remodeling and failure through total occlusion can occur, limiting the long-term treatment efficacy. While the precise mechanisms behind graft failure remain unknown, hemodynamic quantities such as wall shear stress (WSS) are thought to potentially play a role [1]. Despite advances in medical imaging technologies, however, non-invasive measurements of coronary artery flows *in vivo* are difficult to obtain due to the imaging resolution required.

Computational fluid dynamics (CFD) is an emerging method in which the Navier-Stokes equations are numerically solved to estimate blood flow and other hemodynamic quantities in human vasculature. These simulations can be made patient-specific by integrating information from medical images and by tuning simulation boundary conditions based on clinical information. Additional assumptions can be introduced to improve the faithfulness of the simulations, such as the inclusion of vessel wall compliance [2]. However, an open question is how vessel wall compliance would affect hemodynamics in coronary artery bypass grafts, which is an important consideration for clinical translation. Given the additional computational time and uncertainty in vessel wall material properties, researchers often must make a pragmatic consideration of whether the additional computational complexity of implementing a compliant wall model provides more accurate and clinically relevant hemodynamic information that cannot be resolved using a rigid wall model alone.

In this study, we compared hemodynamic measures computed from CFD simulations employing different wall models to quantify the impact of compliance on clinically relevant metrics in a cohort of CABG surgery patients. As we observed differences in the hemodynamic metrics computed from rigid and compliant wall models, we also propose a pragmatic approach to rescale rigid wall WSS based on a population average to estimate compliant wall hemodynamics in a cohort of bypass grafts and evaluate when such an approach may be appropriate to reduce computational time and model complexity.

METHODS

The retrospective study population consisted of 10 patients who underwent coronary artery bypass graft (CABG) surgery at the Sunnybrook Health Sciences Centre from November 2017 to August 2018. Imaging and computational fluid dynamics simulations were performed as described in previous studies [3]. Briefly, cardiac CT and 4D flow MRI were obtained from study participants 3-6 weeks after surgery. Cardiac CT images were segmented using SimVascular (Stanford University, Stanford, California) to generate 3D meshes of each patient's aorta, supra-aortic branches, coronary arteries, and implanted bypass grafts, with local element size determined through spatial resolution studies. Three-element Windkessel models were used as outlet boundary conditions at the descending aorta and supra-aortic branches, while lumped parameter models were used to estimate coronary boundary conditions. Parameter values for boundary conditions were iteratively tuned to match patient cuff-measured blood pressure. Flow to the coronary arteries was assumed to be 4% of the total cardiac output [4].

In this study, three different wall models were compared: compliant, rigid, and rescaled. Compliant wall simulations were performed for each patient on the individual left and right coronary territories using the coupled momentum method implemented in SimVascular. The individual coronary territories were simulated separately due to the prohibitively high computational cost of performing compliant simulations of the full model of the aorta and both coronary trees. Inflow boundary conditions at the origins of the left and right coronary trees were obtained from post-processing of the rigid wall CFD.

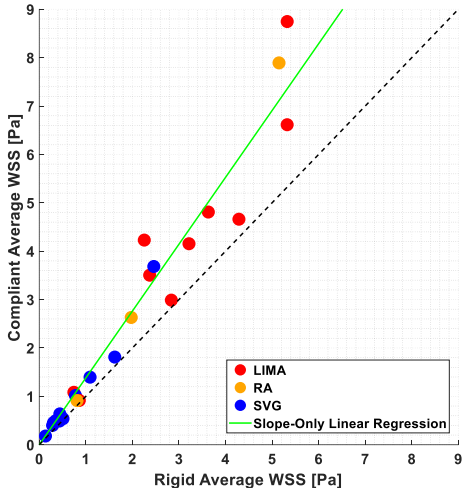

Figure 1: Average WSS from rigid and compliant models.

Rigid wall simulations were also performed for each patient on the full model of the aorta, supra-aortic branches, coronary arteries, and bypass grafts. The inflow boundary condition at the ascending aorta was set to be the pulsatile blood flow rate measured from 4D flow MRI.

Finally, we investigated a linear rescaling approach to reduce some of the discrepancies between rigid and compliant model WSS and to estimate compliant wall hemodynamics using rigid wall simulations alone. To calculate the rescaling factor, the average WSS in each graft was computed for both rigid and compliant wall simulations, and a slope-only linear regression model was applied on data from odd-numbered patients as follows:

$$\tau_c = \beta \tau_r \quad (1),$$

where τ_r is the WSS magnitude from the rigid model, τ_c is the WSS magnitude from the compliant model, and β is the linear regression slope. This rescaling factor was then applied to τ_r in grafts from even-numbered patients. As this rescaling approach requires no additional simulation time, its computational cost is essentially the same as the original rigid wall simulation.

For each wall model, we computed hemodynamic metrics in bypass grafts that may be of clinical interest, including average WSS, the temporal and spatial average of WSS across a vessel over a single cardiac cycle, and abnormal WSS area, the proportion of vessel wall area that is below a clinically relevant threshold (<0.5 Pa and <1 Pa) [5]. Bland-Altman limits of agreement were computed to compare the rigid and rescaled models against the compliant model, providing an estimate of the range of expected discrepancies for each hemodynamic metric.

RESULTS

Figure 1 shows a scatterplot of average WSS in each of the 24 grafts in the study for both the rigid and compliant wall models. In our cohort, although average WSS was correlated between the rigid and compliant models (R^2=0.949), the rigid model tended to underestimate average WSS compared to the compliant model. From a linear regression using only odd-numbered patients, the slope was 1.265. We then applied this slope to τ_r in the rescaled model and compared hemodynamics from even-numbered patients across all 3 models.

Table 1 shows a summary of the hemodynamic metrics computed in each wall model for even-numbered patients, and Table 2 shows the limits of agreement when comparing the rigid and rescaled models to the compliant model. The average WSS and abnormal WSS areas (<0.5 Pa and <1 Pa) in the rescaled model were closer in agreement to the compliant model compared to the rigid model, as seen by the smaller mean differences and the narrower confidence intervals in Table 2.

Table 1: Summary of hemodynamic metrics (mean ± SD).

Graft Type	Wall Model	Average WSS [Pa]	Abnormal WSS Area (<0.5 Pa) [%]	Abnormal WSS Area (<1 Pa) [%]
LIMA (n=5)	Compliant	5.32 ± 1.94	0.4 ± 0.3	1.7. ± 1.4
	Rigid	3.74 ± 1.15	0.8 ± 1.0	3.6 ± 5.9
	Rescaled	4.73 ± 1.46	0.5 ± 0.5	2.3 ± 3.7
RA (n=1)	Compliant	7.89	0.002	0.011
	Rigid	5.15	0.004	0.056
	Rescaled	6.51	0.004	0.004
SVG (n=4)	Compliant	0.89 ± 0.41	29.6 ± 33.6	73.7 ± 22.8
	Rigid	0.69 ± 0.31	44.3 ± 40.5	83.8 ± 14.8
	Rescaled	0.87 ± 0.40	35.8 ± 35.8	72.8 ± 21.7

Table 2: Bias and limits of agreement between wall models.

Hemodynamic Metric	Difference (Rigid – Compliant)		Difference (Rescaled – Compliant)	
	Mean	95% CI	Mean	95% CI
Average WSS [Pa]	-1.13	(-3.48, 1.21)	-0.43	(-2.11, 1.23)
Abnormal WSS Area (<0.5 Pa) [%]	7.5	(-23.9, 38.8)	3.2	(-16.6, 23.1)
Abnormal WSS Area (<1 Pa) [%]	2.5	(-6.6, 11.6)	-0.1	(-4.2, 4.0)

DISCUSSION

Our findings are somewhat in agreement with previous studies that have compared rigid and compliant wall simulations in the coronary arteries, generally concluding that the time-averaged WSS is correlated between the two models [6]. While previous studies showed more agreement between rigid and compliant wall simulations, this discrepancy may be due to differences in anatomy and in study methodology. The present study includes a sample size of 24 bypass grafts from 10 patients, larger than in previous studies. Additionally, the compliant wall simulations in this study were based on the left and right coronary territories alone rather than a full model that includes the aorta and supra-aortic branches due to the high computational cost.

While our findings suggest that rescaling may ameliorate some of the discrepancies in WSS between rigid and compliant models, future work should validate the rescaled model in a prospective and larger patient cohort. Depending on the application, a pragmatic approach of rescaling WSS from rigid wall simulations based on a cohort of patient anatomies may be considered in lieu of performing computationally expensive compliant wall simulations, especially in the absence of patient-specific information on wall material properties.

ACKNOWLEDGEMENTS

This work was supported by the RSNA Scholar Grant #RSCH1716, the Department of Medical Imaging of the University of Toronto, the Jean & Lauri Hiivala Research Fund for Heart Health, the Institute of Biomedical Engineering of the University of Toronto, the Canada Research Chairs program, and the Digital Research Alliance of Canada.

REFERENCES

[1] Shuhaiber, J et al., *J Cardiothorac Surg*, 22(3):387-396, 2002.
[2] Figueroa, C et al., *Comput Methods Appl Mech Eng*, 192(41):5685-5706, 2006.
[3] Tran-Nguyen, N et al., *Ann Biomed Eng*, 50(12):1882-1894, 2022.
[4] Ramachandra, A et al., *J Cardiovasc Transl Res*, 9:279-290, 2016.
[5] Chatzizisis, Y et al., *J Am Coll Cardiol*, 49(25):2379-2393, 2007.
[6] Eslami, P et al., *J Biomech Eng*, 142(2):0245031-02450310, 2019.

A NOVEL MILLIFLUIDIC DUAL-FLOW BIOREACTOR FOR RECAPITULATING SHEAR STRESS *IN VITRO*

Fariha N. Ahmad, Katrina Cao, Jane Grande-Allen

Department of Bioengineering, Rice University, Houston, Texas, United States of America

INTRODUCTION

Gastrointestinal diseases (GDs) involving pathogens such as enteroaggregative E. coli (EAEC) lead to child malnutrition and cognitive impairment in low-resource settings.[1–3] Despite the high morbidity and costs associated with bacterial-associated GDs, it is difficult to elucidate the mechanisms involved in the bacterial infection of small intestinal epithelium (SIE) in vitro. This is in part due to the complex microanatomy governing the physiology of the SIE, which cannot be recapitulated using standard cell culture techniques.[4]

The microenvironment of the SIE is affected by a variety of factors, including apical and basolateral flowstreams. Flow above and below the SIE is responsible for transport. Traditional cell culture techniques do not incorporate flow. While new tools have been developed to better represent these factors, none modelling the effects of flow to create representative models of the SIE remains challenging. Thus, cell culture frameworks more closely resembling the anatomy of the small intestine are necessary to effectively study the mechanisms of bacterial infection.

To address this, we have developed a novel biomimetic cell culture platform better representing the shear stress experienced by the SIE. The dual-flow device (DFD) was designed as a millifluidic apparatus capable of applying apical and basolateral flow. Additionally, the DFD was cheaply produced and easily disassembled by users desiring to harvest cells cultured within the device. The goal of this project is to design, manufacture, and validate biocompatibility of the DFD using Caco-2 cells, a model intestinal cell line. We hypothesized that the DFD could yield leak-proof flow following assembly, autoclaving, and perfusion. We also hypothesized that culturing Caco-2 cells in this device will yield a cell viability of at least 90%. In the future, this platform will enable accurate modeling of human intestinal organoid (HIO) response to bacterial infection.

METHODS

DFD Fabrication. Previously, our lab created a millifluidic perfusion cassette which applied flow apically over cell monolayers cultured in a chamber with an area (0.33 cm^2) similar to a 96-well plate well (0.32 cm^2).[6] When designing the DFD, we adopted the design of this cell culture chamber to create a bioreactor to apply physiological flowstreams over and under cells seeded on a semipermeable membrane (Figure 1). The DFD and casing components were designed using Solidworks. Computational fluid modeling (ANSYS) and Equation 1 were used to ensure that resulting shear stresses were within the physiological range (0.002-0.08 dyn/cm2).[7] A variety of flow rates were used for the experiments described below.

$$\tau = \frac{6 \cdot \mu \cdot Q}{w \cdot h^2} \quad (1)$$

Components were fabricated using the Formlabs Form3B printer and were printed using BiomedClear, a medical-grade resin produced by Formlabs. Gasket-like compressors designed using Solidworks were printed on the Form3B printer using Elastic 80A resin. After completing post-processing wash and UV-cure steps, the DFD bioreactor was assembled using 0.4 micron transparent PETE membrane, vacuum grease, eight 4-40x1/2" screws, and two 25x25 mm cover glasses (Figure 1). The assembled bioreactor was then sterilized by autoclaving for 30 min at 121°C. Silicone tubing (1/16" ID x 1/8" OD) was sterilized separately.

DFD Fabrication Validation. To assess sterility and leakproof flow, DI water colored with red and blue liquid food dye was perfused through the system for 48 hours at 100 µL/hr. DI water was loaded into 5 mL syringes, attached to the silicone tubing with female-Luer hose-barb adaptors. The syringes were compressed using a Harvard Apparatus syringe pump. Following perfusion, the DFDs were visually observed for leaking. Perfused DI water will be analyzed for changes in absorbance—demonstrating mixed, leaking flowstreams—using

spectroscopy. Additionally, DI water was added to tryptic soy agar plates, incubated for 2 days, and observed for bacterial colony growth.

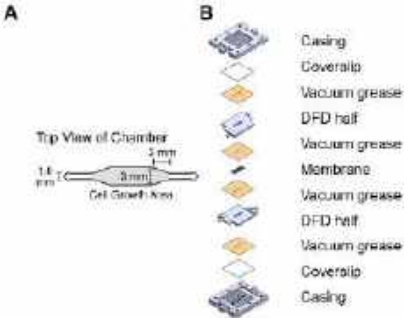

Figure 1: A) DFD cell culture chamber and B) assembly schematic.

Caco-2 Biocompatibility Studies. Following DFD fabrication validation, Caco-2 cells were cultured on the apical side of the membrane in the device for two days to assess the biocompatibility of the DFD. DFDs were coated with collagen-IV (33 mg/mL) diluted in 100 mM acetic acid overnight before seeding cells. Caco-2 cells were cultured for 4 days in media before passaging and seeding at a cell density of $3x10^5$ cells/cm^2. Media included high-glucose DMEM supplemented with 1% (v/v) nonessential amino acids, 10 mM HEPES, 100 U/mL penicillin/100 µg/mL streptomycin, and 10-20% fetal bovine serum. Cells were allowed to adhere to the membrane for one day before media perfusion started. After two days, the DFD was disassembled, and the cell-laden membrane was added to a 6-well plate. Cell viability was evaluated fluorescently using calcein-AM and ethidium homodimer (live-dead), with Hoechst used as a DNA counterstain. Caco-2 monolayer integrity, representing adherence, proliferation, and confluence, will be completed using immunofluorescent staining of the tight junction protein occludin.[8] Caco-2 cells cultured in Transwell inserts will serve as positive controls. All experiments will be conducted in technical triplicates. Data will be summarized using means and standard deviations. Statistical analysis will be performed using a Student's t-test or ANOVA with a post-hoc Tukey's test. Significance will be defined as $p < 0.05$.

RESULTS

Printing and post-processing procedures for the DFD, casing, and compressor components were adapted and optimized from Formlabs materials recommendations. We found that decreasing the size (0.45 mm) and density (0.5) of supports prior to the printing process, and sanding components after UV curing, allowed for the creation of smooth surfaces that enabled replicable assembly of the DFD bioreactor.

We then tested the ability of the DFD to maintain leakproof-flow. Colored DI water was successfully perfused through the DFD, allowing visual confirmation of leakproof-flow (Figure 2). Additionally, Caco-2 media perfused through the DFD and cultured on tryptic soy agar plates showed no sign of bacterial colony growth.

Figure 2: DFD prototype showing leakproof flow.

After culturing Caco-2 cells in the DFD, the cell-laden membranes were transferred to a 6-well plate, necessarily exposing the cells to the vacuum grease on the membrane. Cell viability was analyzed using live-dead staining (Figure 3) and was calculated to be 97% following two days of exposure to vacuum grease. Additionally, the vacuum grease appeared to contain cell growth to the intended cell culture chamber.

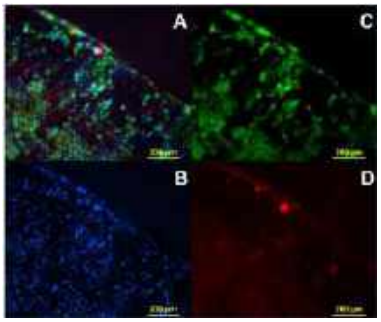

Figure 3: Viability staining of cells cultured in the DFD. A) Overlay of B) Hoechst nuclear, C) live and D) dead staining of Caco-2 cells.

DISCUSSION

We have successfully fabricated the DFD bioreactor and have refined manufacturing techniques to recreate leakproof flow. Preliminary studies have shown that DFD sterilization is successful, with no growth of bacterial colonies or contamination of Caco-2 cultures observed.

Preliminary biocompatibility studies involving Caco-2 cells seeded within the DFD have shown that Caco-2 cells can adhere to and stay viable in the DFD. Caco-2 cells have also shown the ability to survive following perfusion at physiologic shear stress. After subjecting the cells to perfusion, the DFD was disassembled to perform fluorescent staining in a 6-well plate, exposing the Caco-2 cells to vacuum grease for an additional two days. The presence of vacuum grease did not appear to negatively affect the viability of the cells. Additionally, the presence of the vacuum grease, which was used as leakproof sealant, appeared to serve as another control of cell culture area on the membrane. This alleviated any concerns of uncontrolled cell growth in the case of nonvisible leaking. In future studies, Caco-2 cells will be cultured in the DFD for longer time periods, fluorescent staining will be attempted within the assembled DFD, and occludin staining will be completed. Then, HIOs will be cultured in the DFD.

Here we have developed a new biomimetic tool capable of recapitulating the shear stresses of the SIE *in vitro*. Previously developed tools have had significantly smaller cell culture areas, have complicated assemblies, or do not account for apical and basolateral flow.[6,9-10] The DFD resolves these limitations; however, the assembly process can be labor intensive. This is being refined by creating a screwless design, making assembly/disassembly easier. By creating a millifluidic bioreactor with few components, we can create more physiologically-relevant *in vitro* models for studying disease pathology and, in the future, therapeutics.

ACKNOWLEDGEMENTS

This work was supported by the National Institute of Health (NIH U19AI116497). Additionally, the authors would like to thank Dr. Jennifer Connell for her mentorship throughout this project.

REFERENCES

[1] Chan, JSH et al., *J Gastroenterol Hepatol*, 34:124–131, 2019.
[2] Everhart, JE et al., *Gastroenterology*, 136:741-754, 2009.
[3] Kotloff, KL et al., *The Lancet*, 382:209-222, 2013.
[4] Hewes, SA et al., *Tissue Eng Part B Rev*, 26:313-326, 2020.
[5] Malijauskaite, S et al., *Cytokine Growth Factor Rev*, 60:76-88, 2021.
[6] Wilson, RL et al., *Ann Biomed Eng*, 49:1233-1244, 2021.
[7] Carvalho, V et al., *Micromachines*, 12:1149-1163, 2021.
[8] Price, DB et al., *Cell Physiol Biochem*, 33:1758-1777, 2014.
[9] Kim, HJ et al., *Lab Chip*, 12:2165–2174, 2012
[10] Anderson, EJ et al., *BioMed Eng OnLine*, 6:46

DESIGN OF A μ-FLUIDIC CHIP FOR *IN SITU* QUANTIFICATION OF TRAUMATIC BRAIN INJURY BIOMARKER RELEASE

Mauricio Araiza Canizales (1), Alexander McGhee (2), Rafael D. González-Cruz (3,4,5), Diane Hoffman-Kim (3,4,5), Christian Franck (1)

(1) Department of Mechanical Engineering, University of Wisconsin-Madison, Madison, WI, USA
(2) Department of Biomedical Engineering, University of Arizona, Tucson, AZ, USA
(3) Department of Neuroscience, Brown University, Providence, RI, USA
(4) Carney Institute for Brain Science, Brown University, Providence, RI, USA
(5) Institute for Biology, Engineering, and Medicine, Brown University, Providence, RI, USA

INTRODUCTION

Traumatic brain injury (TBI) remains a significant burden to the public health system, affecting approximately 1.7 million Americans every year [1, 2].Current technologies to detect TBI rely primarily on the Glasgow Coma Scale, and neuroimaging, but their limitations in terms of accuracy and cost prevent them from effectively assessing the severity of the injury [3]. Thus, a new area of research focused on detection methods using TBI-specific biomarkers has sprung up over the last years. Two notable TBI-biomarkers, GFAP and UCH-L1, have been granted FDA approval to be used in a blood test to identify intracranial lesions, which are indicative of moderate to severe TBI [4]. This is accomplished thanks to the fact that the brain blood barrier (BBB) is compromised in moderate to severe cases of injuries, which facilitates high concentrations of biomarkers to travel through the bloodstream. However, 75-90% of TBI cases in the U.S. are mild-TBI (mTBI) in which the BBB remains largely intact, severely restricting the flow of biomarkers for detection [3, 5], having spurred significant developments toward ultra low concentration detection methods. Furthermore, the temporal profiles of mTBI biomarkers and their relation with injury severity, strain, and strain rate are not well understood. *In vivo* studies have shown considerable variability in the release profile of biomarkers, such as GFAP, UCH-L1, and IL-6, some of which are detected <6 h to several days post-injury and with concentrations as low as 2 pg/mL [6, 7]. Although *in vivo* studies present a more accurate depiction of mTBI, they lack the needed access for resolving the critical spatiotemporal expression profiles for each biomarker of interest.

To address this gap, we have developed a novel *in vitro* microfluidic platform that enables the controlled injury of cortical spheroids at relevant strain and strain rates. This innovative approach allows for a more precise study of the release of mTBI-relevant biomarkers, providing valuable insights into their spatiotemporal expression profiles.

METHODS

Cortical spheroids were selected as an *in vitro* representation of the brain due to their ability to mimic both physiological and mechanical properties observed *in vivo*, including the presence of diverse neural subtypes, electrical activity, and stiffness [8]. Using established protocols, primary cortical tissues from P0-P1 Sprague-Dawley rat pups were isolated and subsequently placed in 2% agarose μ-molds for self-assembly over a period of 14 days. A novel μ-fluidic platform was developed to induce controlled injury to the living spheroids.

The construction of a three-layer PDMS μ-fluidic chip involved designing three master molds: (1) a spheroid distribution layer, (2) a compression layer, and (3) a pressure layer (Figure 1a). After alignment and assembly, the spheroids were introduced into the distribution layer (Figure 1b) and then selectively transported through μ-channels using a microscope-assisted pick-and-place system (Figure 1c). The compression layer, comprising PDMS pillars, could be elevated through a pressure differential in the third layer, effectively trapping the spheroids (Figure 1d). Continuous

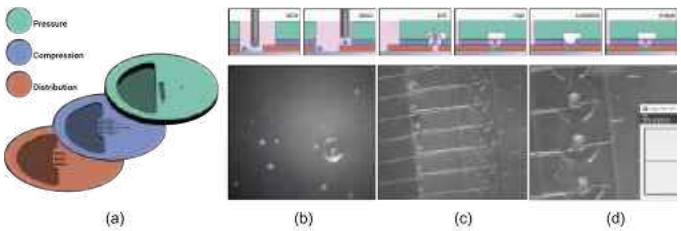

Figure 1: (a) Three-layer chip design. (b) Spheroids being picked and placed into the chip. (c) organoids being placed inside the μ-channels. (d) Trapped spheroids before injury. Microscope images taken with a 4X objective.

media flow through the channels ensured a constant supply of nutrients to the spheroids. To induce compressive injury, the pressure within the third layer was adjusted at a fixed strain and strain rate.

Cell viability assays were deployed at 1 and 24 hours post-injury using Hoechst-33342 for nuclear staining and Ethidium Homodimer-1 to identify deceased cells. These assays were captured using a Nikon confocal microscope. Following imaging, the tissues were fixed and stained for GFAP and β-III tubulin to examine structural changes in astrocytes and microtubules post-injury.

RESULTS

Our innovative μ-fluidic platform, designed for inducing highly controlled and repeatable mechanical injury to cortical spheroids, has demonstrated the ability to simulate mild traumatic brain injury (mTBI). Initial findings for a 25% strain indicate that the custom microscope-assisted pick-and-place system does not impact the viability of the control samples, ensuring a consistent baseline for data collection (Figure 2 left). Furthermore, following the induction of mechanical injury by compressing the cortical spheroids by 25%, an average of 32% of cells exhibited post-injury death, compared to an average of 26% for the control samples (Figure 2 right).

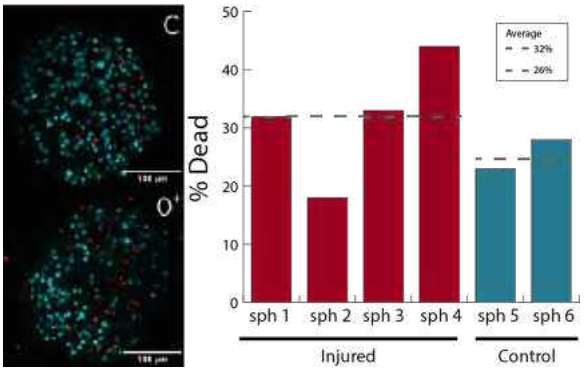

Figure 2: (Left) Control (top) and injured (bottom) spheroids showing cell nuclei in blue and dead cells in red. (Right) Percent dead of spheroids computed as the ratio of dead cells to cell nuclei for 25% strain after 1hr. C: control spheroid. 0^+: injured spheroid after 1 h.

In addition to live/dead assays, this novel platform enables *in situ* immunostaining for various mTBI-specific biomarkers, such as GFAP (Figure 3), under different strain and strain rate conditions. Comparison between the control and injured spheroids showed less astrocyte branching after being injured.

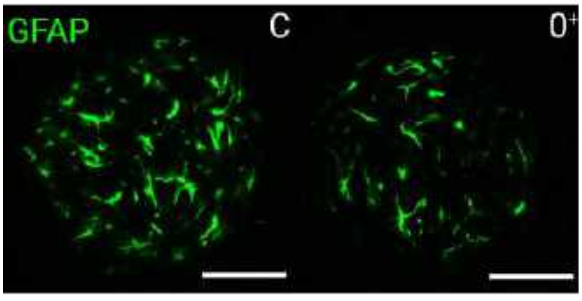

Figure 3: Control (left) and injured (right) spheroids showing less astrocyte branches for 0^+ after being injured by 25% strain. C: control. 0^+: injured spheroid after 1 h. Scale bars for both images are 100 μm.

DISCUSSION

Our novel μ-fluidic chip was capable of successfully injuring cortical spheroids at a strain of 25%. Live/dead results showed that compression caused an increased in percent dead cells, as expected for TBI. It is well known that TBI injuries, specially those of high strain and strain rate, contribute to a decrease in cell viability [9, 10]. Moreover, the same spheroids showed a decrease in astrocyte branches when they were stained for GFAP, which could function as an indicator for TBI. In this study, our μ-fluidic chip has proved effectively at injuring an *in vitro* model of the brain; however, no significant advances have yet been made towards understanding the temporal release profiles of biomarkers. To accomplish this, a kinetic assay using the same platform can be performed by collecting media at the outlet and analyzing the concentrations for GFAP and UCH-L1 for different strain and strain rates.

ACKNOWLEDGEMENTS

This material is based upon research supported by the U. S. Office of Naval Research under PANTHER award numbers N000142112044 and N000142112855 through Dr. Timothy Bentley.

REFERENCES

[1] Wright DW et al. *MMWR Morb Mortal Wkly Rep* 62.27 (2013). ISSN: 0149-2195. URL: https://www.ncbi.nlm.nih.gov/pmc/articles/PMC4604943/.

[2] Fawzi AL et al. *Concussion* 8.2 (2023). ISSN: 2056-3299. DOI: 10.2217/cnc-2023-0005.

[3] Di Pietro V et al. *Front. Neurol.* 9 (2018). ISSN: 1664-2295. DOI: 10.3389/fneur.2018.00429.

[4] Nishimura K et al. *Cureus* (2022). ISSN: 2168-8184. DOI: 10.7759/cureus.23804.

[5] Agoston DV et al. *Brain Injury* 31.9 (2017). ISSN: 0269-9052, 1362-301X. DOI: 10.1080/02699052.2017.1357836.

[6] Reyes J et al. *Neurology* 101.20 (2023). ISSN: 0028-3878, 1526-632X. DOI: 10.1212/WNL.0000000000207881.

[7] Wang KK et al. *Expert Review of Molecular Diagnostics* 18.2 (2018). ISSN: 1473-7159, 1744-8352. DOI: 10.1080/14737159.2018.1428089.

[8] Dingle YTL et al. *Tissue Engineering Part C: Methods* 21.12 (2015). ISSN: 1937-3384, 1937-3392. DOI: 10.1089/ten.tec.2015.0135.

[9] Akamatsu Y et al. *Neurotherapeutics* 17.2 (2020). ISSN: 18787479. DOI: 10.1007/s13311-020-00840-7.

[10] Cullen DK et al. *Crit Rev Biomed Eng* 39.3 (2011). ISSN: 0278-940X. DOI: 10.1615/CritRevBiomedEng.v39.i3.30.

MORPHOLOGICAL AND HEMODYNAMIC CHANGES TO THE RV MICROVASCULAR NETWORK IN RESPONSE TO CHRONIC PRESSURE OVERLOAD

I, Essafri (1); K, Ichimura (2); KR, Stenmark (1); E, Spiekerkoetter (2); VO, Kheyfets (1)

(1) Cardiovascular Pulmonary Research Laboratories, Division of Pulmonary Sciences and Critical Care Medicine, Division of Pediatrics-Critical care, Department of Medicine and Pediatrics, University of Colorado Anschutz Medical Campus, Aurora, CO, USA.
(2) Department of Medicine, Division of Pulmonary, Allergy and Critical Care Medicine, Stanford University, Stanford, CA, USA.

INTRODUCTION

Right ventricular (RV) failure is a common complication of pulmonary hypertension, manifesting in myocardial thickening, fiber re-orientation, and tissue stiffening [1]. Recent studies from our labs have observed morphological changes of the microvascular network as a characteristic response of the RV to pressure overload, yet little is known about the true nature of these changes, their coupling to coronary hemodynamics, and their role in organ-level functional adaptation or maladaptation. The coronary microcirculation consists of an intricate network of vessels that supply the RV myocardium with oxygen and nutrients to sustain proper heart muscle function. Insights into this process not only refines our understanding of RV adaptation to chronic pressure overload but also holds promise for identifying therapeutic targets aimed at preserving coronary microvascular function and, by extension, supporting overall RV health. While previous investigations have suggested an inadequate adaptative growth of the RV microvasculature in RV failure [2], our study aims to shed light on the lesser-known hemodynamic changes caused by changes in microvascular network properties during the remodeling process by analyzing the microvasculature in 3D.

In this work, we hypothesized that chronic pressure overload led to microvascular morphological changes (e.g., changes in radius, length, tortuosity), which would result in changes to local hemodynamics (e.g., wall shear stress, vascular resistance). We also explored whether this microvascular response is consistent across male and female mice. This hypothesis aims to uncover intricate relationships between chronic pressure challenges, microvascular adaptations, and potential differences between male and female subjects in RV microvascular dynamics, contributing to our understanding of RV health.

METHODS

To address the aforementioned hypothesis, we performed deep tissue imaging on RV free-wall tissue harvested from 11 Sham (C57BL/6, 8-10 weeks) and 10 pulmonary arterial banded (PAB) mice (tissue harvested 7-weeks post PAB). With our custom in-house software (MATLAB 2023b), we generated 3D models of the microcirculation from 2D image stacks, as shown in Fig. 1a and b. A volume mesh was created for vessel centerline computation using VMTK software [3]. Vessel segments, defined as centerlines between two junctions, were analyzed for vascular tortuosity, orientation, length, and radius. We computed tortuosity as the segment curve length divided by the line connecting the segment ends.

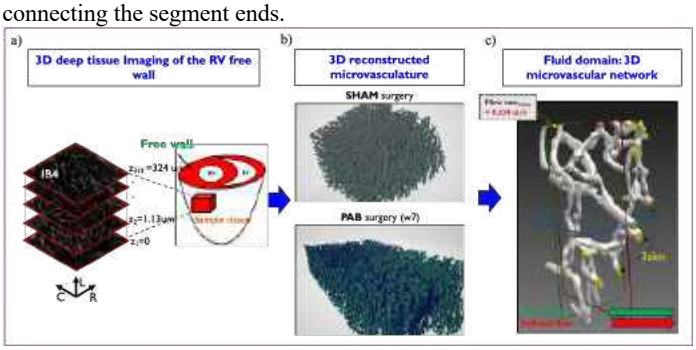

Figure 1: a) deep tissue imaging Procedure: RV free wall to 2D Image stack. b) 3D reconstructed Microvasculature visualization. c) 3D Fluid Domain for Simulations displays the 3D fluid domain with flow rate and differentiation between direct and indirect flow simulations.

Within the entire reconstructed 3D network, we isolated the largest volume for computational fluid dynamics (CFD) simulations using Simvascular (Fig. 1c) [4]. We prescribed for each inlet a constant volumetric flow rate as a parabolic velocity profile and a zero boundary conditions at the outlets. The vessel wall was considered rigid. We maintained uniformity in hemodynamic conditions by applying the same flow rate to both PAB and Sham mice. We deliberately chose this simulation setup to examine how microvascular structural alterations alter hemodynamics yet are aware that our simulations do not mimic the

much for complex in vivo flow parameters. We conducted two sets of simulations: one with direct flow (15 inlet and 15 outlet boundaries) and the other with flipped (a.k.a. "indirect") flow (outlet boundaries inverted) (Fig. 1c). Blood was modeled as a non-Newtonian fluid using Carreau-Yasuda model given by the equation:

$$\eta(\dot{\gamma}) = \eta_0 + (\eta_0 - \eta_\infty)[1 + (\lambda\dot{\gamma})^a]^{(n-1)/a}$$

Where η_∞ is the viscosity at infinite shear rate $\{\eta_\infty = 3.265$ mPa.s$\}$, η_0 is the viscosity at zero shear rate $\{\eta_0 = 14.49$ mPa.s$\}$, λ is the characteristic time $\{\lambda = 01839$ s$\}$ and (a and n) are fitting parameters $\{a = 2.707, n = 0.4136\}$. a, n and λ are empirically determined [5]. After validating mesh independence, we conducted steady-state CFD simulations to assess microvascular resistance, blood velocity and wall shear stress (WSS). Hypothesis testing was done using linear mixed effect modeling to account for repeated measures across two investigated fixed effects: (1) Sham vs. PAB ("condition"); (2) Female vs. Male ("sex"). Significance was set at $p < 0.05$.

RESULTS

Our study reveals significant microvascular adaptations in response to chronic pressure overload, exhibiting sexual dimorphism. The microvascular analysis revealed shorter segments in PAB, with females having the shortest segments (Fig 2a). We also observed a ($p < 0.05$) significant difference in the radius of individual segments between PAB and SHAM, with an increased radius in PAB and females having the largest radius. As illustrated in Fig. 2b, a comparable trend was observed for segment tortuosity, with percentages indicating segments with tortuosity indices ≥0.1, emphasizing distinctions among all microvasculatures. To better understand the impact of RV morphological changes on the local hemodynamic stress, we examined blood flow simulations results. Linear mixed-effects modeling identified a significant spatially averaged WSS (SAWSS) decrease in PAB vs SHAM microcirculations (Fig. 3a), with females exhibiting a lower WSS at baseline and a more pronounced decrease after PAB. Additionally, we identified a statistically significant difference in flow resistance between PAB and SHAM mice, with the lowest microvascular resistance observed in females (Fig. 3b). No significant difference in spatially averaged blood velocity was found between PAB and SHAM or between females and males.

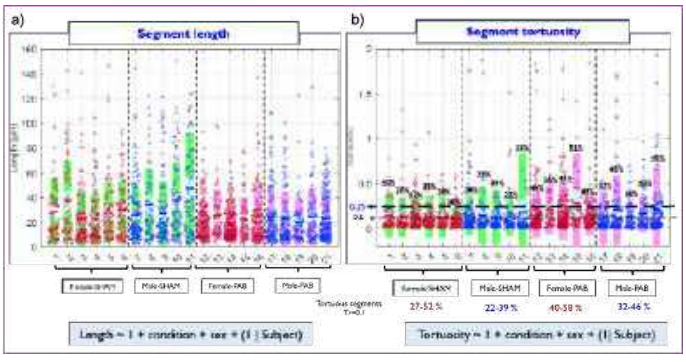

Figure 2: Microvasculature Analysis, featuring a jittered plot displaying a) tortuosity and b) length of the microvascular segments, along with the corresponding statistical models provided below.

DISCUSSION

Putting these findings into context, our study significantly contributes to the understanding of microvascular adaptations to chronic pressure overload, shedding light on sex-specific variations. The observed reduction in SAWSS in PAB mice would suggest a remodeling response that modulates and is possibly coupled to vascular hemodynamic stress. Numerous studies have shown that hemodynamic stress levels outside the normal physiological range can induce endothelial dysfunction and result in morphological and transcriptional changes in endothelial cells [6]. Of particular note is the distinct adaptive response observed in females in terms of microvascular resistance, segment lengths, and radii. Females exhibited a 35% decrease in microvascular resistance, a more modest reduction compared to males' 44.8%. This aligns with our hypothesis that females, potentially benefiting from a more favorable baseline, may necessitate less resistance reduction. In contrast, males, commencing with higher baseline resistances, may require more pronounced structural adaptations to achieve a comparable reduction under chronic pressure overload.

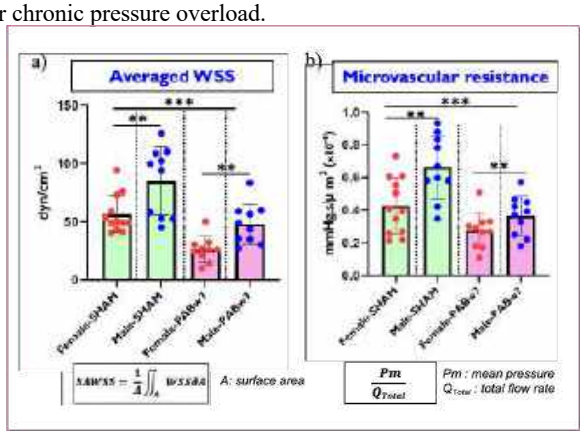

Figure 3: hemodynamic analysis, including a) Spatially Averaged Wall Shear Stress (SAWSS) and b) microvascular resistance, with the corresponding equations provided below. The figures reveal significant differences between PAB and SHAM groups, with sex-specific variations detected and analyzed through a linear mixed-effects model.

Sex-specific variations in remodeling may stem from inherent physiological differences, hormonal influences, or other factors affecting vascular responses to chronic pressure overload [7-10]. The combined microvascular changes, including increased branching, altered segment length and radius, and changes in tortuosity may be viewed as beneficial for maintain blood flow efficiency and minimizing the impact of chronic pressure overload on RV muscle proper function. These adaptations point towards the development of more complex microvascular network. Future work will explore if this increased complexity might lead to improved blood supply to the microvasculature and therefore increased nutrient supply to the surrounding tissue.

In conclusion, our study highlights compelling evidence of sex-specific microvascular adaptations under chronic pressure overload. These changes contribute to maintaining blood supply to RV muscle tissue. Insights from these PAB w7 inspired our ongoing study, which explores additional time points to unravel dynamic microvascular changes.

ACKNOWLEDGEMENTS

This work is supported by the National Institutes of Health under award numbers: NIH R01HL160940 (PI: Kheyfets), R01HL158868-01 (PI: Spiekerkoetter).

REFERENCES

[1] Hill MR. et al. Annals of Biomedical Engineering.2014Dec;42(12):2451-2465.
[2] Graham BB et al. Am J Respir Cell Mol Biol. 2018 Oct;59(4):479-489.
[3] Antiga L. et al. Med. Biol. Eng. Comput. 46, 1097–112.
[4] Updegrove A. et al. Ann Biomed Eng. 2017 Mar;45(3):525-541.
[5] Bernabeu Miguel et al. 2014. J. R. Soc. Interface.112014054320140543.
[6] Ballermann BJ et al. Kidney Int Suppl. 1998 Sep ;67:S100-8.
[7] Wang J. et al. Am J Physiol Heart Circ Physiol. 2010Apr;298(4):H1146-54.
[8] Gonzales RJ. et al. Microcirculation. 2008 Aug ;15(6):473-84.
[9] Witt H. et al. J Mol Med (Berl). 2008 Sep ;86(9):1013-24.
[10] Fliegner D. et al. Am J Physiol Regul Integr Comp Physiol. 2010 Jun;298(6):R1597-606.

DIETARY CHOLESTEROL STIFFENS THE STEATOTIC LIVER

David Li (1,2), Abigail E. Loneker (2,3), Paul A. Janmey (2,3,4,5), Rebecca G. Wells (1,2,3)

(1) Department of Medicine (Gastroenterology and Hepatology), University of Pennsylvania, Philadelphia, PA, USA
(2) NSF Science and Technology Center for Engineering MechanoBiology, University of Pennsylvania, Philadelphia, PA, USA
(3) Department of Bioengineering, University of Pennsylvania, Philadelphia, PA, USA
(4) Institute for Medicine and Engineering, University of Pennsylvania, Philadelphia, PA, USA
(5) Department of Physiology, University of Pennsylvania, Philadelphia, PA, USA

INTRODUCTION

Hepatic steatosis is the pathological accumulation of fat in the liver. It is the hallmark of fatty liver diseases such as metabolic dysfunction-associated steatotic liver disease (MASLD), which can progress to fibrosis and cirrhosis [1]. Intracellular lipid accumulation into lipid droplets (LDs) precedes other pathological changes in MASLD and has been shown to soften liver tissue, hinting at a mechanical role for lipids in the earliest phases of disease [2]. However, it is unknown whether lipid accumulation can also exert a direct stiffening influence, which is critical as stiffening has been found to be the mechanical driver of fibrotic processes [3]. Changes in hepatic lipid composition observed in MASLD may cause changes in the effects of lipid accumulation on liver mechanics. Increases in hepatic abundance of cholesterol and cholesteryl esters (CEs) are associated with disease progression [4], and can have modifying effects such as ordering of LDs and other lipid aggregates [5]. This ordering is known to affect mechanics in other systems such as atherosclerotic plaques [6]. We thus hypothesize that the mechanical contribution of intrahepatic fat may be dependent on changes in intracellular lipid composition and organization.

Here, we investigate how cholesterol affects both the whole organ and microenvironmental mechanics of steatotic liver. Using dietary rat models of liver steatosis and increased dietary cholesterol, we examine whether cholesterol changes steatotic liver mechanics. We find that increased dietary cholesterol stiffens the steatotic liver while increased fat alone does not. We further find that dietary cholesterol induces formation of lipid crystals, which are sufficient to stiffen their microenvironment. These results may help inform the diagnosis and treatment of steatotic liver diseases in their earliest phases.

METHODS

We used a dietary rat model of simple steatosis (high fat, HF), along with a model of steatosis with increased dietary cholesterol (high fat high cholesterol, HFHC) to investigate the effects of cholesterol on the steatotic liver. All experiments were performed at 3, 6, or 9 weeks after the start of the selected diet to examine the course of disease. Lipid content, inflammation, and fibrosis were quantified by staining with BODIPY 493/503, anti-myeloperoxidase, and picrosirius red and subsequent image analysis. Birefringent lipid crystals were visualized using polarized light microscopy.

Ex vivo parallel plate rheometry was performed to measure whole liver mechanics without fluid pressure confounding [7, 8]. Microindentation with modifications to demarcate measured regions for histological analysis was performed as described previously [2]. Briefly, demarcation with DAPI within a parafilm ring after the microindenter probe was fully indented results in a DAPI ring around the probe-indented region. Liver samples were then stained with Oil Red O and visualized by whole mount epifluoresence microscopy, permitting quantification of lipid content within the indented regions by examining the degree of Oil Red O staining in DAPI demarcated regions. Confocal reflectance microscopy was performed on tissue samples to assess for increased reflectance indicative of changes in the ordering of lipid aggregates.

Lipid droplets and crystals were isolated from HFHC livers using a sucrose density gradient and embedded into fibrin gels made with 17 mg/mL bovine plasma fibrinogen, 2 U/mL bovine plasma thrombin, 30 uM $CaCl_2$, and 50mM HEPES. Rheometry was performed on hydrogels as done previously [9] with a plate diameter of 25mm, gap of 1 mm. The shear modulus was measured at a low oscillatory shear strain of 1% at a frequency of 10 $rad \cdot s^{-1}$, changing the axial strain by adjusting the gap between the plates and allowing the samples to relax.

Statistical significance was determined using a Student's t-test for tissue stiffness at zero compression and a two-way ANOVA for gel stiffness, corrected for multiple comparisons using Holm-Sidak and Dunnett, respectively.

RESULTS

We found that livers from HFHC rats were significantly stiffer than those from rats fed either HF or normal diets by shear rheometry (Figure 1), despite fat accumulation being observed in both HF and HFHC. Staining for markers of fibrosis revealed that the stiffening precedes the onset of fibrosis, first detectable at 9 weeks of diet.

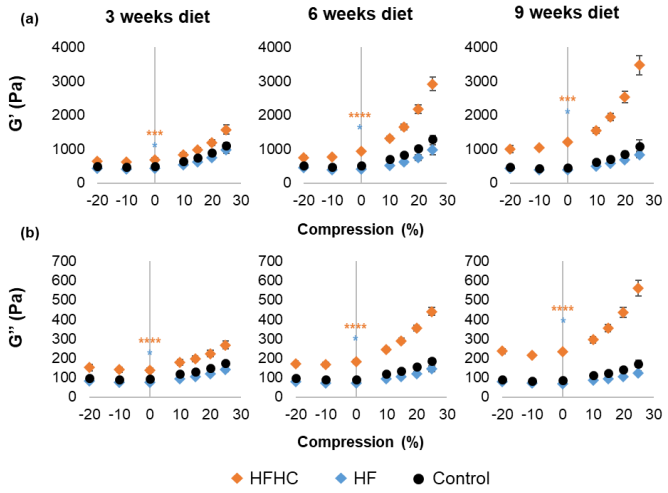

Figure 1: Dietary cholesterol stiffens the steatotic liver.

HFHC steatotic livers were found to contain crystals exhibiting birefringence under polarized light microscopy at room temperature and confocal reflectance microscopy when maintained at 37°C, which were not found in HF steatotic or control livers (Figure 2), suggesting that dietary cholesterol induces crystalline ordering of intracellular lipid droplets. Local stiffness was found to increase with greater local crystal content by demarcated microindentation coupled to microscopy of associated sub-millimeter regions of liver tissue.

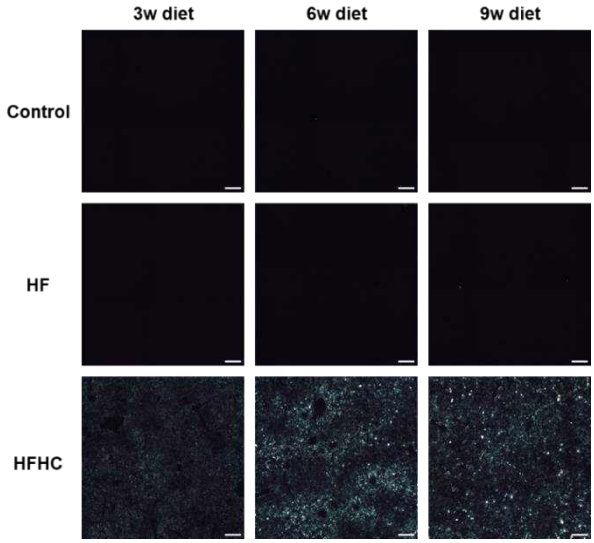

Figure 2: Dietary cholesterol induces formation of birefringent lipid crystals in the steatotic liver.

LDs and birefringent lipid crystals isolated from HFHC livers were found to stiffen fibrin gels in which they were embedded at the concentrations found in the HFHC liver (Figure 3), as opposed to LDs isolated from HF livers which did not affect fibrin mechanics. Together, these results suggest that lipids crystallize within the liver as a result of elevated dietary cholesterol, and that these intrahepatic cholesterol crystals are sufficient to stiffen their microenvironment.

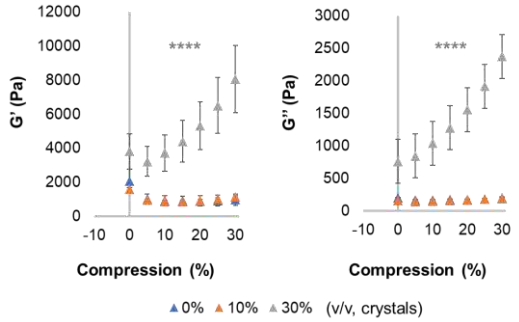

Figure 3: Lipid crystals from HFHC livers stiffen fibrin gels.

DISCUSSION

The finding that a HFHC diet induced liver stiffening while an HF diet alone did not is potentially of great importance in MASLD, in which progression of the disease ranges from fibrosis and cirrhosis to no progression at all [1]. The stiffening caused by the addition of dietary cholesterol could be a key contributor to disease progression, as tissue stiffening is a well-established source of profibrotic stimuli in other models of liver injury [3]. Dietary cholesterol-induced liver stiffening may thus have implications in preventative care and developing therapeutics for MASLD and other fatty liver diseases.

The birefringence observed in fatty livers with added dietary cholesterol suggests increasing order of lipid aggregates in the HFHC liver. Previous *in vitro* work in cell lines has provided evidence that increasing the amount of cholesterol or cholesteryl esters causes intracellular lipid droplets to become more ordered and gain crystalline properties [10]. Free cholesterol has also been observed to form intracellular solid crystals as well [5]. These birefringent crystals may be responsible for the increase in cell and tissue stiffness we observe in HFHC livers. The direct stiffening influence of lipid crystals isolated from HFHC livers on fibrin gels suggest that lipid accumulation may directly stiffen liver tissue, providing a fibrogenic mechanical signal in the earliest stages of steatotic liver diseases.

In conclusion, our results indicate that dietary cholesterol causes stiffening of the fatty liver, and that this stiffening is associated with the ordering of lipid droplets into more crystalline structures within the liver. These findings may open new avenues into novel diagnostics, preventative measures, and therapeutics for diseases of the steatotic liver and of other tissues where crystals may be found.

ACKNOWLEDGEMENTS

This study was supported by NIH grant R01EB017753, the Center for Engineering MechanoBiology under NSF grant CMMI1548571, and an NIH T32 fellowship grant T32DK007066 to DL.

REFERENCES

[1] Angulo, P, *N Engl J Med*, 346:1221-1231, 2002.
[2] Li, D et al., *FASEB Bioadv*, 5:251-261, 2023.
[3] Wells, RG, *Hepatology*, 47:1394-1400, 2008.
[4] Ioannou, GN, *Trends Endocrinol Metab*, 27:84-95, 2016.
[5] Ioannou, GN et al., *J Lipid Res*, 54:1326-1334, 2013.
[6] Loree, HM et al., *Arterioscler Thromb*, 14:230-234, 1994.
[7] Perepelyuk, M et al., *PLoS One*, 11:e0146588, 2016.
[8] Mueller, S, L Sandrin, *Hepat Med*, 2:49-67, 2010.
[9] van Oosten, ASG et al., *Nature*, 573:96-101, 2019.
[10] Mahamid, J et al., *PNAS*, 116:16866-16871, 2019.

THE ROLE OF EARLY LIFE (PSYCHOLOGICAL) STRESS ON CENTRAL ARTERY AGING AND REMODELING

Brooks A. Lane (1), Nazli Gharraee (1), Gabrielle Lohrenz (1) Abigail M. Polter (2), Paul J. Marvar (2), John F. Eberth (1)

(1) Biomedical Engineering Science and Health Systems, Drexel University, Philadelphia, PA, USA
(2) Pharmacology and Physiology, George Washington University, Washington, D.C., USA

INTRODUCTION

Psychological stress is a mental or emotional state triggered by adverse life situations that an individual perceives to challenge or exceed their ability to adapt [1]. These stressors can be as simple as chronic environmental irritations accumulating over time, or exposure to acute but traumatic events. Fortunately, the body has evolved to react to stressors through a complex network of nerves, hormones, and feedback mechanisms that regulate important cardiovascular (CV) functions such as blood pressure/volume, heart rate/contractility, vasomotor tone, and blood distribution [2,3]. While these functions play an essential role in human physiology and survival, they are also well-known drivers of vascular remodeling [4]. It is not surprising therefore that psychological stress has been linked to CV disease [1,5] and may contribute broadly to vascular aging (i.e., stiffening, dysfunction, etc.).

Early life stress (ELS) occurs during a vulnerable developmental period where both the body and the brain are rapidly growing and adapting [6,7]. Stressors may include childhood trauma, neglect, abuse, family instability, loss of a caregiver, or exposure to violence [1,6]. Given the established interplay between the brain and the CV system, ELS could manifest as altered structural and functional vascular aging or remodeling. Indeed, early onset vascular stiffening has been observed in individuals living in adverse environments, experiencing childhood trauma, or when exposed to chronic discrimination [3,5]. Unfortunately, initiating factors can be difficult to isolate and in vivo techniques (i.e., human ultrasound) limit correlation with structural mechanics and histology. Despite the strong clinical evidence, surprisingly very few studies have examined the impact of ELS on vascular histomechanics.

Motivated by the need to better understand and improve the human condition, mice permit control over the nature and timing of stressors while maintaining environmental and genetic consistency. A wide range of models are available to help elucidate the underpinnings of vascular pathologies. Here we report the preliminary biaxial mechanics of the descending and infrarenal aortas from a mouse model of ELS [6].

METHODS

The limited bedding and nesting model of ELS is one of neglect and marked by maternal care that is fragmented and unpredictable [5]. To use this model, mouse litters on a C57BL6 background, were culled to four pups and the dam and pups were transferred to a standard-sized cage on postnatal day 4. Control (CTRL) pups were left undisturbed with the dam in standard housing (corncob bedding and one cotton nestlet) while ELS pups were transferred to a cage with limited nesting material (i.e., aluminum mesh bottom, half standard nestlet) for 7 days and then returned to standard housing. All mouse procedures were reviewed and approved by the George Washington University IACUC.

At 13-16 weeks of age, ELS (n=7) and CTRL (n=4) male and female mice were euthanized and the descending thoracic (DTA) and infrarenal abdominal (IAA) aortas were excised and gently cleaned of loose perivascular tissue. Samples were placed in a protease-inhibitor cocktail at 4°C, transported to Drexel University, and mechanically tested within 48 hours using the biaxial inflation-extension testing described in [6]. Briefly, samples underwent five preconditioning cycles of pressurization and axial extension. Then pressure, axial force, and diameter data were measured in triplicate during inflation from 0 to 160 mmHg (10 mmHg increments) at the estimated *in vivo* axial stretch and ± 10% this value. Stress and stretch ratios were calculated as:

$$\sigma_\theta = \frac{pr_i}{h}, \sigma_z = \frac{f}{\pi(r_o^2 - r_i^2)}, \lambda_\theta = \frac{(r_i + r_o)}{(R_i + R_o)}, \lambda_z = \frac{\ell}{L} \qquad (1\text{-}4)$$

where θ and z are the circumferential and axial directions, R and r the unloaded and deformed inner (i) and outer (o) radii, H and h the undeformed and deformed wall thicknesses, ℓ and L the deformed and undeformed lengths, p the transmural pressure, and f the axial force. The lumen area compliance ($c = \pi \Delta r_i^2 / \Delta P$) was calculated between diastolic and systolic pressures and the physiological modulus, M, the slope of the circumferential stress-strain curve at 100 mmHg.

Statistical analysis was performed using GraphPad Prism. Metrics were compared using a two-way ANOVA with post-hoc Tukey's t-test.

RESULTS

Passive mechanical testing was performed successfully on all samples after which vessels were prepped and stored for histological analysis. Although continuous data was collected throughout experimentation, 12 discrete variables of structural or mechanical assessment were compared with all but three (R_i, Ro, H) measured at 100 mmHg and the *in vivo* axial stretch ratio (see also [7]). ANOVA results (**Fig. 1**) revealed sex (Male vs. Female), stressor (ELS vs. CTRL), and aortic location (DTA vs. IAA) as the sources of variation in the data. Stressor-linked data included axial stress and deformed inner and outer radii, compliance, and axial stress and stretch. Interaction metrics included axial stretch, unloaded inner radius, circumferential stress, compliance, and physiological modulus.

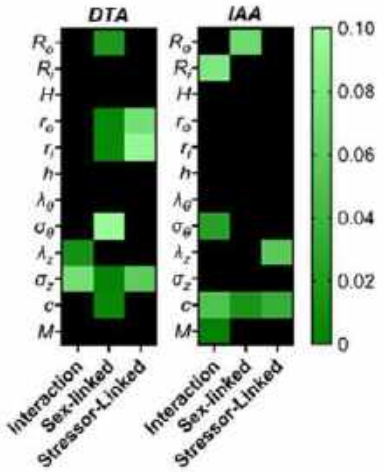

Figure 1: Heatmap results of p-values from two-way ANOVA analysis for identifying sources of variation.

Not surprisingly, sex and anatomical location play important roles in governing the structural and mechanical properties of mice. Therefore, we separated the continuous data in terms of pressure-stretch, force-pressure, and circumferential and axial stress-stretch, by sex and location. Reported here for brevity are the pressure-outer diameter curves of each vessel. DTAs from ELS male (Fig. 2A), and to a lesser extent, female mice, illustrated a rightward shift (dilation) compared to controls. Interestingly, this pattern was not observed in any of the IAAs. In fact, the IAAs of female ELS mice tended to be slightly smaller than controls, albeit not statistically significant. Loaded wall thickness, was unaffected by ELS in any tested segment. Taken together, these geometric results suggest an outward hypertrophic or eutrophic remodeling in the DTAs of ELS mice.

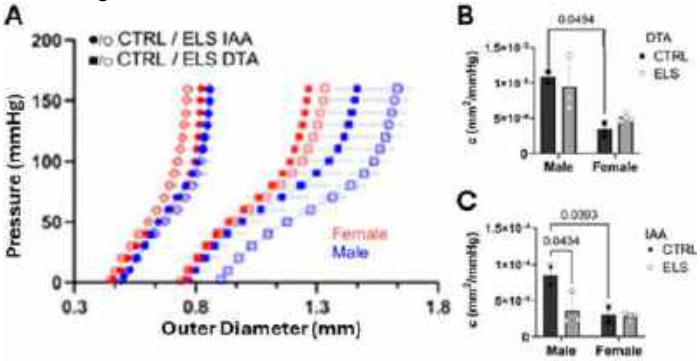

Figure 2: A. Pressure-diameter curves of the DTA and IAAs from CTRL and ELS mice grouped by sex (mean ± SEM). Luminal area compliance of the (B) DTA and (C) IAAs over diastolic-systolic pressures (mean ± STD).

The aortas of all male mice were generally more compliant than their female counterparts (**Fig.2 B, C**). Lumen area compliance depends on the size of the animal and unfortunately, we did not record weight in this preliminary study [8]. Nevertheless, the area compliance was significantly reduced in the IAAs of ELS male mice and may be an indicator of premature vascular aging. (p=0.043).

DISCUSSION

Chronic or early life stress has a long-established role in cardiovascular function and pathology [1,3-6]. Correlating behavioral and structural mechanics is challenging given that many of these changes may be subtle and are often compensatory. *Ex vivo* biaxial micromechanics is more thorough than in vivo ultrasound or isolated ring testing because it captures wall thickness, anisotropy, heterogeneity, and the large strains common to soft biological tissues. To the best of our knowledge, this is the first study linking ELS to biaxial blood vessel mechanics.

Further research is needed to determine if male DTA dilation is compensatory or pathological. Stiffening, on the other hand, is one of many undisputed metrics of vascular aging. To maintain consistency with clinical ultrasound we used lumen area compliance as our comparator. Male mice showed a significant decrease in compliance, supporting the notion of premature vascular aging in ELS [4]. Our data further suggests that ELS outcomes have sex and location dependency and that interactions exist between these variables. Indeed, other researchers have shown sex-dependent neurobiological characteristics, increased sympathetic activation, and changes in blood pressure of male but not female mice using the ELS model [9]. Blood pressure and cardiac output are part of our ongoing study and will later be used to refine our measures of mechanical assessment. It is not surprising, however, that regional differences exist between the DTA and IAA since these have unique functional and pathological characteristics [6]. For the most part, mechanostasis, in terms of mechanical stress-mediated growth and remodeling in DTA and IAAs has been achieved as evidenced by circumferential and axial stress preservation across groups [2]. Despite the common naming convention, mechanical and psychological stresses differ in their nature, origin, and tools used to estimate them. For healthy gene expression, the mechanical stresses on vascular cells must be non-zero but less than a threshold that causes physical damage. The minimum for psychological stress, on the other hand, remains unknown. What is known is that exceeding thresholds of psychological stress leads to the premature onset of cardiovascular disease [1,5].

Gaining insight into the relationship between ELS and aging is crucial to understanding the consequences of stress in brain-vascular function and susceptibility to cardiovascular disease in later years. Such endeavors may contribute to the identification of potential therapeutic interventions. That said, the data reported here is preliminary and care must be taken not to overinterpret our findings based on small sample sizes. Ongoing studies seek to increase numbers and focus on elucidating functional and histopathological variables. Still, the notion that events witnessed during childhood could impact vascular health later in life is profound.

ACKNOWLEDGEMENTS

This project was funded by NIH RO1HL145064 and the Hartwell Foundation.

REFERENCES

[1] Coehn S, et al., *JAMA*, 298(14):1685-1687, 2007
[2] Coote JH, *Exp Physiol*, 92:3-18, 2007
[3] Loria AS, et al. *Acta Physiol (Oxf)*, 210(2):277-87, 2013
[4] Humphrey JD, *Am J Hypertens*, 34(5): 432-441, 2021
[5] Rafiq T, et al., *J Child Adolesc Trauma,* 13(4)505-514, 2020
[6] Gallo M, et al., *Front Neurosci*, 13: 167, 2019
[7] Lane et al., *J Biomech,* 125: 110543, 2021
[8] Prim et al., *PLoS One*, 13(8), e0202123, 2018
[9] Dalmasso C, et al., *JAHA*, 13, e029511, 2024

EVALUATING THE BIOMECHANICAL RESPONSE OF 3D PRINTED SYNTHETIC TISSUE-MIMICKING MATERIALS FOR CARDIOVASCULAR APPLICATIONS

Vivian Tan (1), Daniella Eliathamby (2), Craig Simmons (2), Jennifer Chung (3), M. Owais Khan (1)

(1) Department of Electrical, Computer, and Biomedical Engineering, Toronto Metropolitan University, Toronto, ON, Canada
(2) Institute of Biomaterials & Biomedical Engineering, University of Toronto, Toronto, ON, Canada
(3) Division of Cardiovascular Surgery, University Health Network, Toronto, ON, Canada

INTRODUCTION

Cardiovascular diseases are the leading cause of morbidity and mortality around the world. In recent years, the field of cardiovascular medicine has seen a transformative shift from a population-centric approach towards personalized and patient-centric treatment strategies. One innovative technology is Polyjet 3D printing that offers the potential to use multi-material mixtures and pixel-level control to 3D print patient-specific cardiovascular structures. Traditional printing strategies, such as stereo-lithography (SLA), only permit a single material with high wall thicknesses, and thus, have limited applicability to mimic mechanical heterogeneity of native vascular structures.

One exciting area of research has been to develop photopolymer materials that can potentially mimic the mechanical and structural properties of native vascular and cardiac tissues. Patient-specific anatomies printed with such materials could open up exciting opportunities, such as pre-planning and simulating surgical scenarios, assessing hemodynamics ex-vivo or optimizing medical device deployment. However, despite recent availability of a range of polyjet materials, especially those marketed as vascular tissue replicas, there still remains a paucity of available data that compares their mechanical response to native tissues.

In this study, we have compared the mechanical response of commercially-available polyjet materials, marketed as vascular tissue replicas, from a popular vendor (Stratasys) and silicone-based elastomers typically used in SLA printing against those of native tissues.

METHODS

Polyjet Material Samples. Twelve tissue-mimicking materials were acquired from Stratasys (Eden Prairie, Minnesota) which are used in their PolyJet J850 Digital Anatomy Printer series. In particular, these materials utilize the Structural Heart TissueMatrix, which is advertised as the softest commercially available 3D printing material that behaves like native tissue providing elastic moduli and failure modes similar to native tissues. All samples were re-sized to 14 x 14 mm to facilitate in biaxial testing. The sample thickness was 3 mm.

Silicone Elastomer Samples: Six silicone-based elastomers with a range of elastic moduli were acquired from Gluck Medical (Seoul, Korea), a 3D printing service provider for cardiothoracic surgical simulations. All samples were resized to 14 x 14 mm to facilitate in biaxial testing. The sample thickness was 5 mm.

Biaxial Testing. Equibiaxial mechanical testing of polyjet and silicone elastomer materials was performed using a CellScale BioTester (Waterloo, Canada). The samples were mounted onto tungsten rakes with 5 attachment points each and a 23 N capacity load cell [1]. Four dots were marked in the middle of the sample for strain tracking in post processing (see Figure 1).

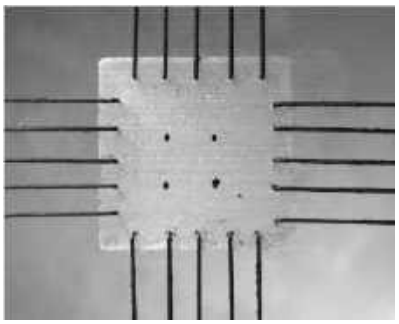

Figure 1. Biaxial testing setup. Four dots mark locations used in strain tracking.

Each test consisted of at least one preconditioning cycle at a strain rate of 0.0088/s followed by one testing cycle, all straining to at least a 5% rake-rake displacement.

Post Processing. The stress-strain curves in the both X and Y directions were obtained for both loading and unloading conditions. The loading curves were linearly fitted to determine the Young's modulus of each material. For each sample, there was a slight deviation in moduli between the two directions ($\mu \pm 15\%$). The direction showing the

higher modulus was used for comparison as this value was more significant when matching to native tissues.

RESULTS

Figure 2 shows the Young's moduli of a subset of polyjet materials and silicone elastomers tested in this study. Note that one of the polyjet material ("valve leaflet – extensively stiff") was not tested due to very high stiffness, which hindered attachment of the biorakes.

As seen in Figure 2, the elastic moduli ranged from 0.5 – 3.4 MPa for polyjet materials and from 0.08 – 0.57 MPa for Gluck Medical's silicone elastomers. Interestingly, the most compliant polyjet material had an elastic modulus that was comparable to the stiffest silicone elastomer (Hardness 20).

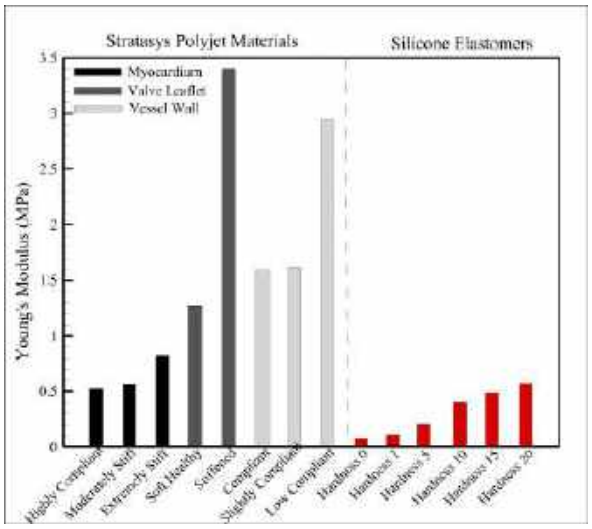

Figure 2: Young's moduli of Stratasys synthetic tissue-mimicking materials and Gluck Medical's silicone-based elastomers.

Figure 3 compares the elastic moduli of the most compliant polyjet material ("Myocardial – Highly Compliant") and silicone elastomers of various stiffnesses against those of native aortic tissues obtained from literature, consisting of mechanical test data performed on three aortic valve and five healthy aortic tissues [2][3]. Note that the elastic moduli of native tissues have been reported for the post-transition, linear elastic region linked with elongation of elastic and collogen fibers. The elastic modulus of the most compliant polyjet material was notably greater than those of native tissues. In contrast, the silicone-based elastomers demonstrated a much wider variation. In particular, the silicone material with "Hardness 5" provided the closest match to the native aortic tissues.

DISCUSSION

We have compared the mechanical properties of polyjet materials used in Stratasys J850 DAP along with Gluck Medical's silicone-based elastomers. Stratasys is the most popular vendor of polyjet technology, offering a range of synthetic tissue-mimicking materials. Stratasys DAP printer has already been used in clinical and surgical applications, such as surgical training [4], and ex-vivo hemodynamic analysis [5] but how well their materials model the biomechanical response of native tissues has not been thoroughly investigated. Verga et al. analyzed the nonlinear viscoelastic properties of Stratasys' synthetic tissues and reported notable deviations between the most compliant material tested

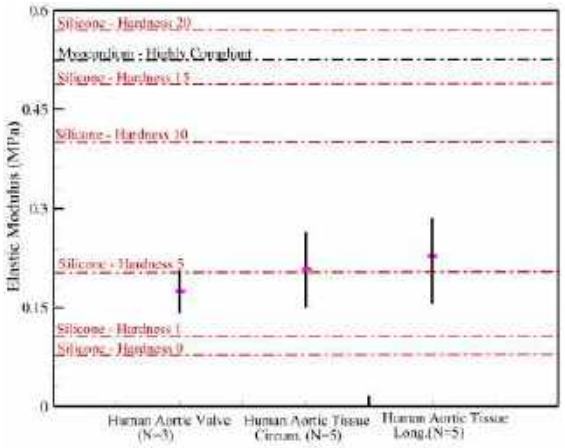

Figure 3: Comparison of elastic moduli of synthetic polyjet (black) and silicone-based materials (red) against healthy aortic valve and aortic wall tissues.

compared to porcine aortic wall specimen [6], consistent with our findings. Our findings also demonstrate that silicone-based elastomers, typically used in SLA printing, have elastic moduli that are much closer to native tissues, and thus, have a distinct advantage in applications such as surgical training. However, SLA has limited capabilities in printing intricate cardiac sub-structures and is limited to a single material.

Our findings have exciting implications for designing patient-centric treatment strategies. In addition to surgical pre-planning, the polyjet materials can be potentially be used to customize grafts in patients, such as to design aortic patches in patients' undergoing Norwood surgeries, or as support materials for tissue-engineered vascular grafts. Future work will focus on hemodynamic characterization of these materials to assess how well these materials can mimic in-vivo blood flow conditions.

ACKNOWLEDGEMENTS

MOK acknowledges support from NSERC Discovery Grant and Banting Research Foundation Discovery Award. VT acknowledges support from Office of the Vice-President, Research, and Innovation at the Toronto Metropolitan University.

REFERENCES

[1] Tang, M. et al., Journal of Mechanical Behavior of Biomedical Materials, 124:104736, 2021.
[2] Hasan, A. et al., Journal of Biomechanics, 47:9, 2014.
[3] Guo, X. et al, Computers in Biology & Medicine, 166: 107561, 2023
[4] Shen, Y et al., Smart Materials in Medicine, 5:36-51, 2023.
[5] Hussein, N et al., Seminars in Thoracic and Cardiovascular Surgery, 32(1): 98-105, 2020.
[6] Verga, AS. Et al., Frontiers in Mechanical Engineering, 8: 862375, 2022.

IN VITRO FLUID MECHANICS AND BLOOD STUDY TO EVALUTE CATHETER-RELATED THROMBOSIS

H. Palahnuk (1), B. Su (1), T. Harbaugh (2), E. Rizk (2), S. Hazard (2,3), J. Bernstein (4), K. B. Manning (1,5)

(1) Department of Biomedical Engineering, Pennsylvania State University, University Park, PA, USA
(2) Department of Neurosurgery, Penn State Hershey Medical Center, Hershey, PA, USA
(3) Department of Anesthesiology, Penn State Hershey Medical Center, Hershey, PA, USA
(4) Division of Pediatric Hematology/Oncology, Penn State Hershey Children's Hospital, Hershey, PA, USA
(5) Department of Surgery, Penn State Hershey Medical Center, Hershey, PA, USA

INTRODUCTION

Central venous catheters (CVCs) provide long term venous access for blood draws, medication administration, and fluid infusions [1]. However, CVCs are associated with complications such as catheter-related thrombosis (CRT). CRT can present as a deep vein thrombosis (DVT), venous thromboembolism, or a clot on/within a CVC. CVC complication rates vary based on study type and patient risk factors, but the incidence of CRT, specifically in the form of upper extremity DVT, is reported between 14-18% [2]. Multiple risk factors are associated with CRT including cancer, endothelial damage during insertion, and a catheter-to-vein ratio (CVR) > 0.45 [1]. Although the CVR is reported to have a significant effect on thrombosis, previous work has not established a standard value for CVR, with clinical centers using a range from 0.33 - 0.45 [3]. The CVR is defined as the outer diameter of a catheter divided by the inner diameter of a patient's vein (**Equation 1**).

$$CVR = \frac{CVC\ Outer\ Diameter}{Vein\ Inner\ Diameter} \quad (1)$$

The CVR variation stems from a lack of understanding of CRT from a fluid mechanics and hematologic perspective [1, 2]. Previous work has shown the effect of CVC insertion on flow and that a CVR of 0.15 compared to 0.33 has a minimal effect on the fluid mechanics *in silico* when there is no flow through the CVC [4]. The purpose of this study is to quantify the CVR's effect on CRT across multiple flow conditions using particle image velocimetry (PIV) and *in vitro* blood studies.

METHODS

Flow Visualization: A custom acrylic model was fabricated (Atlantic Industrial Models, Essex, MA) and consisted of a rigid outer tube to model the superior vena cava (SVC, ID = 1.6 cm) and three acrylic CVCs for CVRs of 0.20, 0.33, and 0.49. The acrylic CVCs were replicas of Teleflex® Arrow dual lumen CVCs with one side hole and a tapered tip design. A steady flow loop was assembled, and a non-Newtonian blood analog fluid seeded with 10 μm glass particles was used (51.47 wt. % sodium iodide, 15.5 wt. % glycerin, 33 wt. % water, 0.03 wt. % Xanthan gum). A high-speed Terra PIV laser (Continuum, San Jose, CA) was coupled with a laser light arm (TSI Inc., Shoreview, MN) to illuminate the centerline plane. Data were collected at five locations downstream of the incoming flow (**Figure 1**). Two hundred image pairs were collected with a high-speed camera at Reynolds number (Re) = 200, 800, and 1300 for each CVR.

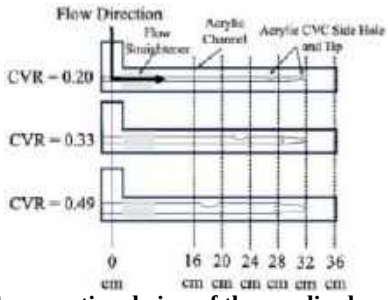

Figure 1. Cross sectional view of the acrylic channels and CVCs for PIV measurements at three CVRs (0.20, 0.33, and 0.49).

Blood Experiments: An *in vitro* flow loop was developed to assess CRT across three CVRs and multiple flow conditions. A 5-French Teleflex® Arrow dual lumen CVC was fixed in the center line of a 3D printed (FormLabs) channel to model a CVC in the SVC; this channel allowed control over CVC location. The inside of the flow loop was soaked in 3% bovine serum albumin (Sigma-Aldrich) prior to experiments. Human blood was collected (Institutional Review Board approved) in 3.2% sodium citrate (J.T. Baker®), reconstituted to 40% hematocrit and 214×10^6 platelets/mL, and recalcified to 20 mM $CaCl_2$

(Sigma-Aldrich). The CVC lumens were filled with 1X phosphate buffered saline and clamped off; blood was then driven through the loop by a peristaltic pump (Cole-Parmer®) for 1 hour at a prescribed Re and CVR (**Table 1**).

Table 1. Flow conditions for blood experiments (n=6).

CVR	Channel Diameter (cm)	Flow Rate (L/min)	Re
0.20	0.80	1.10	800
0.33	0.50	0.14	200
0.33	0.50	0.70	800
0.33	0.50	1.10	1300
0.50	0.34	0.16	200

A fresh CVC was used for each experiment and no flow used through the lumens to match previous work [4]. Any clots formed on the device were analyzed for clot area and location. The CVC was segmented into "Zones" for location data (**Figure 2**). Clot data were analyzed with unpaired two-sample t-tests.

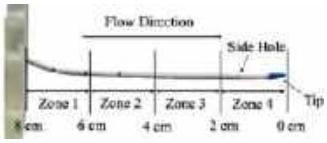

Figure 2. "Zone" segmentation of CVC.

RESULTS

Flow around the acrylic CVCs at Re = 200, 800, and 1300 is shown in **Figure 3**. The flow field is segmented with vertical black lines according to data collection locations (**Figure 1**). There is stagnant flow in the side hole and in the wake distal to the tip in each CVR case, and the effects of each are more pronounced as the CVR increases within each Re.

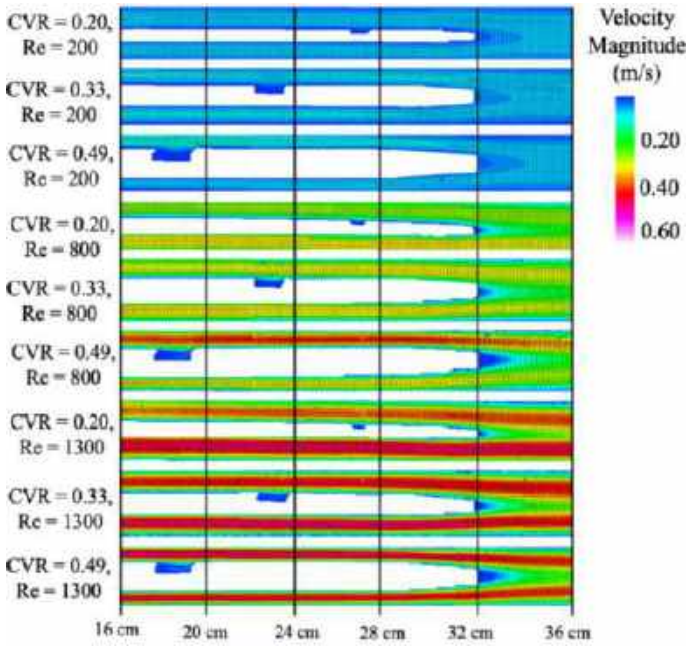

Figure 3. Flow visualization data around acrylic CVCs.

Clot sizes and locations across each CVR and Re in the blood experiments are shown in **Figure 4**. There were significant differences ($p<0.05$) in clot size across multiple cases with different flow conditions and/or CVRs (**Figure 4A**). These results can partly be explained by higher surface velocities for higher Re or CVR conditions (as shown in **Figure 3**), which can promote the washing of platelets and/or adhesive proteins during the experiment and reduce potential thrombus formation compared to lower CVR/Re cases.

Clots formed in Zone 4 were located only at the side hole for the 0.20 CVR case (**Figure 4B**). For all conditions with a CVR higher than 0.20, clots formed at the side hole and the tip, which may be explained by the increased wake size distal to the tip with an increased CVR (**Figure 3**). In both Re = 200 conditions, clots formed in multiple Zones.

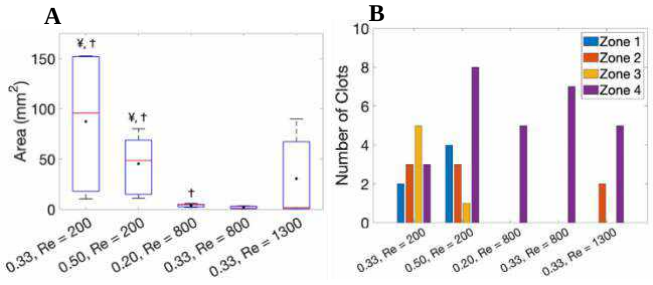

Figure 4. A: Clot area across 5 experimental conditions. ¥ = Significant difference from 0.20, Re = 800; † = Significant difference from 0.33, Re = 800 ($p < 0.05$). B: Clot locations data.

DISCUSSION

CVC insertion will likely obstruct flow in a vessel, increasing hydraulic resistance and potentially slowing the flow around the device. This study shows that with a combined higher CVR and lower flow condition, clot size is larger and formation location is not exclusive to the side hole or tip regions (**Figure 4**). Importantly, the clot size and frequency were higher for both Re = 200 (CVR = 0.33, 0.50) conditions as compared to lower CVR Re = 800 cases. This study, therefore, suggests that if CVC insertion greatly reduces flow in a vessel, an increased CVR may cause increased thrombus size and frequency when compared to a lower CVR case with a higher Re. For the high flow condition (0.33 CVR, Re = 1300), clot formation in Zone 2 and an increased clot size was potentially due to high-shear phenomena, activating platelets and unfurling von Willebrand factor for an increased platelet capture on the CVC.

This study demonstrates that there are multiple aspects to consider regarding CVR on clot formation: the flow condition and CVR both alter thrombus size and location. The tip is currently a location of interest for higher CVR cases: the occurrence of tip clots with an increased CVR can be explained by larger stagnation zones distal to the tip with an increased CVR. Meanwhile, low and high flow conditions can facilitate thrombosis throughout the CVC surface. In total, multiple aspects must be considered for CVC placement, including vein and catheter size, and future work should quantify the impact(s) of CVC insertion on native vessel flow.

ACKNOWLEDGEMENTS

The project described was supported by the National Center for Advancing Translational Sciences, National Institutes of Health, through Grant UL1 TR002014. The content is the responsibility of the authors and does not necessarily represent the official views of the NIH.

REFERENCES

[1] Sridhar, C et al., *Thromb Res*, 187:103-112, 2020.
[2] Faustino, E et al., *J Pediatrics*, 162:387-39, 2013.
[3] Sharp, R et al., *BMJ Open*, 11, 2021.
[4] Su, B et al., *Ann Biomed Eng*, Under Review, 2023.

CAN PATTERN RECOGNITION RECEPTOR AGONISTS MODULATE TENDON HEALING IN VITRO?

S. Winston (1), A. Stoner (1), J. Kurihara (2), L. Chow (2), L. Pezzanite (2), S. Dow (2), K. McGilvray (1)

(1) Department of Mechanical Engineering, Colorado State University, Fort Collins, Colorado, USA
(2) Department of Clinical Sciences, Colorado State University, Fort Collins, Colorado, USA

INTRODUCTION

The more than 250,000 surgeries occurring annually in the United States, rotator cuff (RC) repair surgeries regrettably fail at unacceptably high rates. Failure rates range from 20-94% depending on the size of the tear, as well as age and the weight of the patient [1,2]. It is estimated that these failed surgeries cost the United States healthcare system roughly $3.4B annually [3]. Histological analysis of these failed repairs show that the surgically repaired tendon is not returning to its original tissue composition and is instead scarring [4]. Tendon healing overall, is a largely unknown cascade, however, it is known that the immune response to the injured tendon has a large effect on whether the tendon scars or heals correctly.

This has brought large interest in modulating the immune response to improve the overall clinical success of these repairs. Our novel approach is to functionalize Pattern Recognition Receptor Agonists (PRRA), which are molecules that have been used in cancer research effectively as an immunotherapy approach [5,6]. These agonists activate the innate immune system through the Toll-like and Nod-like receptor pathways. **We hypothesize that PRRAs can be utilized to activate the immune system to increase clinical outcomes of tendon healing. To investigate this, we aim to examine how gene expression changes in tendon when exposed to PRRAs *in vitro*.**

METHODS

Biopsies (10 mm) were taken (N=3) from (N=4) sheep (ovis aries) supraspinatus tendons. Tendon samples were then cut in half and cultured in media with 50 ng/ml concentrations of the selected PRRAs. PRRAs were NLR3 agonist ALOH (Invivogen), TLR3 agonist Poly(I:C) HMW (Invivogen), STING (Invivogen), and TLR9 agonist CpG ODN (Invivogen); generating n = 6 samples for each experimental group. Tendons were cultured overnight then frozen (-80 °C) to prevent RNA degradation. Tendon samples left in media overnight with no agonists served as control samples. RNA was then extracted, purified, and then sent for genomic sequencing (Novogene Inc.). Gene expression data were processed and analyzed using Partek Flow. Gene Ontology of Biological Processes (GOBP) was used to analyze gene enrichment of each agonist group compared against the controls using gene set enrichment analysis (GSEA) to determine the overall effect of the applied agonists.

RESULTS

Two samples from the control and Poly(I:C) groups were removed due to lack of quality RNA. ALOH, CpG, Poly(I:C), and STING treatments had 82, 110, 168, and 153 significantly upregulated genes and 64, 9, 45, and 101 significantly down regulated genes from control samples respectively (Figure 1). Seventeen of these altered gene expressions were shared between all groups versus the control indicating that there are similarities in the response of each agonist. Poly(I:C) and STING shared the most genes differentially expressed with 65 genes.

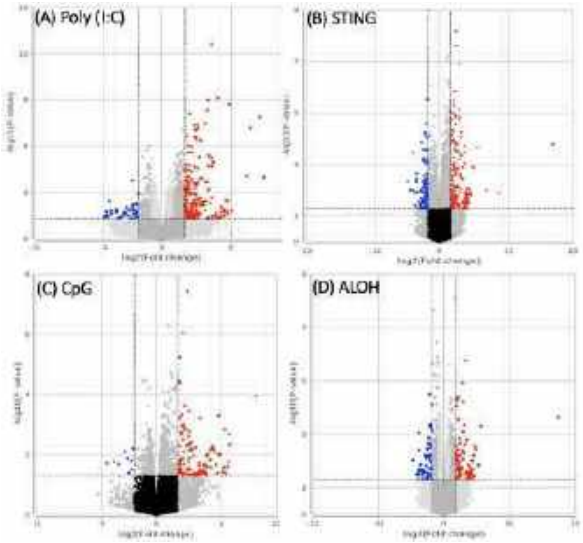

Figure 1: Volcano plots of comparing gene expression of control samples to (A) Poly(I:C), (B) STING, (C) CpG, and (D) ALOH, greater than 2x fold change or p < 0.05 are highlighted.

GOBP analysis of Poly(I:C) revealed upregulation of proinflammatory pathways such as Interferon alpha and gamma (IFNα and IFNγ) responses as well as TNFα signaling (Figure 2). It also upregulated pathways relating to cartilage development such as chondrocyte differentiation and cartilage development and down regulated adipogenesis.

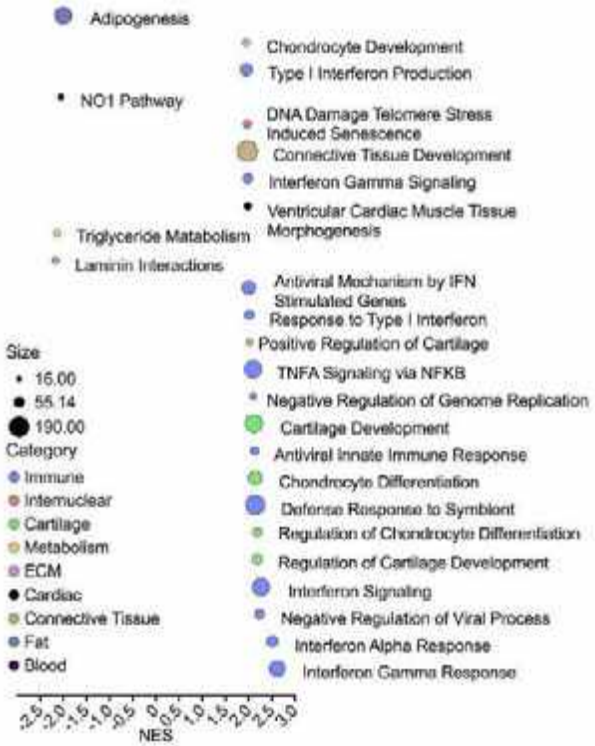

Figure 2: Bubble plot graphing the results of gene set enrichment analysis (GSEA) of Poly(I:C) compared to control. Top 25 results of largest magnitude normalized enrichment scores that had a false discovery rate of < 5%.

DISCUSSION

PRRAs had meaningful effects on genetic changes in the tissues. In the controls TNFα, IFNα, and IFNγ (all proinflammatory cytokines) are known to play an important role in the early stages of wound healing [7], were upregulated. In comparison Poly(I:C), gave a higher proinflammatory response. Poly(I:C) also had a mixed effect on specific tendon healing markers including fatty infiltration and an increase in cartilage formation, which are documented signs of tendon degeneration [8]. Poly(I:C) down regulated adipogenesis and upregulated pathways related to cartilage formation. Taken together these data indicate Poly(I:C) is directly affecting tendon health in a positive way through the limiting of fat production and the increase in immune cytokines that are instrumental in proper wound healing. TLR3 activation through Poly(I:C) has been shown to improve wound healing times in human and mouse skin, but its effects on tendon healing have not been characterized. These preliminary data illustrate that the regulation of extracellular matrix production and immunomodulatory properties of Poly(I:C) have the potential to be a novel tendon therapy.

ACKNOWLEDGEMENTS

We would like to acknowledge Colorado State University's College of Engineering Walter Scott Jr. 'High Impact' Grant mechanism for funding this research. As well as the Colorado State University Lab for Immunotherapy for supporting this work through their mentorship and expertise.

REFERENCES

[1] Cole, B et al., *J of Shoulder and Elbow Surgery,* 16:579-585, 2007.
[2] Galatz, L et al., *J of Bone and Joint Surgery,* 86:219-224, 2004.
[3] Mather, R et al., *J bone and Joint Surgery,* 95:1993-2000, 2013.
[4] Zumstein, M. et al., *Orthopaedics and Traumatology: Surgery and Research,* 103:S1-S10, 2017.
[5] Chakroborty, S., et al., *Frintiers in Immunology*, 14, 2023
[6] Kaczanowska S., et al., J Leukocyte Biology, 93:847-863
[7] Arvind, V. et al., *Frontiers in Bioeng and Biotech,* 9, 2021
[8] Lin, Q. et al., *J Investigative Dermatology,* 132:2085:2092, 2012

A 3D MODEL FOR THE STUDY OF MACROPHAGE-INDUCED SOLID STRESS

Alice Burchett (1), Saeed Siri (1), Meenal Datta (1)

(1) Aerospace and Mechanical Engineering, University of Notre Dame, Notre Dame, IN, USA

INTRODUCTION

Macrophages play a critical role in health and disease, but their response to and generation of mechanical forces is incompletely understood. From atherosclerotic plaques to tuberculosis granulomas to solid tumors, macrophages play an important role not just in immune effector function and orchestration, but also as active constituents of the mechanical microenvironment [1]. This is especially true in cancer, as macrophages accumulate in tumors in large numbers and contribute to tumor growth and disease progression. Macrophage polarization – whether they contribute to an inflammatory or anti-inflammatory immune response – is plastic and can reverse if they are exposed to shear stress, cyclic compression or stretching, or hydrodynamic pressure changes [2]. However, the degree to which macrophages can contribute to mechanical stress in disease, especially compressive stress generated by a growing mass, has not been studied.

This work aims to characterize the solid stress that macrophages generate through proliferation in a confining agarose gel, simulating the mechanics of the tissue microenvironment independent of confounding biological cues. We explore how matrix stiffness, inflammatory and anti-inflammatory cues, drug treatment, and hypoxia affect the generation of compressive solid stress in this novel and high-throughput macrophage spheroid model. Understanding how macrophages generate stress, and how they respond to external cues under chronic compressive stress, will inform strategies to target or reprogram macrophages in the plethora of diseases that involve macrophage accumulation. This platform also has promise for screening macrophage-targeted drugs and is highly tunable to be applicable to a range of diseases.

METHODS

Single-cell suspensions of RAW264.7 murine macrophages were mixed with low-gelling-temperature agarose to create a cell-laden agarose gel. Gels were created with 0.5%, 1%, and 2% to tune the gel stiffness. Small gel pieces were immersed in growth medium and incubated in standard culture conditions.

For polarization of the macrophages, the media was supplemented with IFNγ and LPS to induce an inflammatory M1 phenotype, and IL4 to produce an M2 anti-inflammatory phenotype. Media was supplemented with LPS alone to assess macrophage response to inflammatory stimuli. Dexamethasone and temozolomide were also added to the media as representative treatments given to GBM patients. Hypoxia treatment was achieved using a separate incubator with 1% oxygen.

Brightfield images of the gels were used to quantify differences in size and shape between conditions. We analyzed these images for spheroid area and shape using ImageJ. Gels were stained with calcein-AM and propidium iodide to assess viability. Gels were also fixed in paraformaldehyde and stained with DAPI and CellMask Actin Tracking Stain to assess 3D morphology. These stained gels were imaged with a confocal microscope, and image stacks were then used to create a 3D reconstruction of the spheroid surface.

For computational analyses, the shape of the spheroid was simulated in 2D by creating a line and modeling its expansion into an ellipsoid shape using COMSOL. This models the case where a growing spheroid creates a crack in the agarose gel and grows into an axisymmetric discoid shape. ImageJ was also used to generate 3D files representing the spheroid surface, which will be used for more accurate 3D models that are currently under development.

RESULTS

RAW264.7 cells readily form spheroids when embedded in agarose at a range of concentrations and display excellent long-term viability, with only a small minority of cells staining positive for propidium iodide after 2 weeks (**Fig. 1A**). 3D imaging revealed that most spheroids adopt a flattened discoid shape, rather than a spherical shape (**Fig. 1B**). Because macrophages cannot alter the plant-derived agarose matrix, any

increase in spheroid size must cause displacement of the surrounding gel, generating solid stress. Given an estimate of the spheroid geometry and the mechanical properties of the gel, we generated a simulation of the stress field in the gel surrounding the spheroids (**Fig. 1C**).

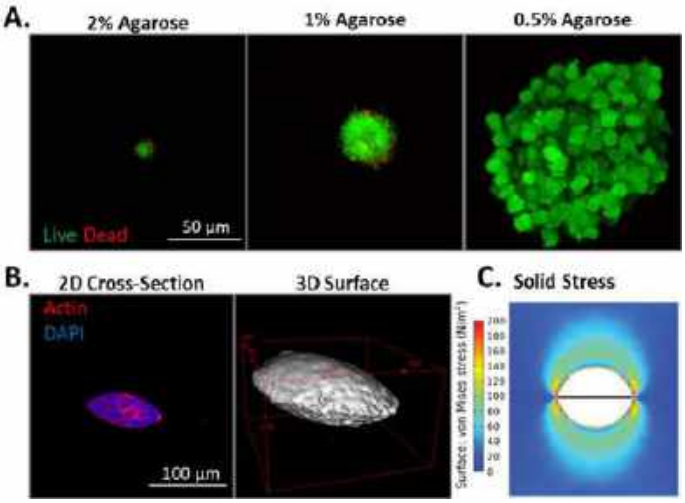

Figure 1: Macrophage spheroids embedded in agarose display sustained viability and generate solid stress. (**A.**) Projections of macrophage spheroids 16 days after seeding show viable cells throughout the spheroid, in three different concentrations of agarose. (**B.**) Most spheroids take on a discoid shape, as illustrated by actin staining of an optical cross-section and the 3D surface reconstruction. (**C.**) This shape is simulated in COMSOL to show the resulting stress field in the surrounding agarose.

As agarose concentration decreases, the average spheroid size increases significantly (**Fig. 2A)**. In 0.5% agarose, spheroids are much less regular in shape than those in 1% and 2%, which is apparent in images and is quantified by perimeter solidity. Treating the agarose-embedded macrophages with 200 ng/ml LPS resulted in significantly increased spheroid size compared to untreated, in all three agarose concentrations. LPS also generally increased ellipticity, a measure of spheroid deviation from a circle. However, treatment with 20 ng/ml IFNγ in addition to 200 ng/mL LPS (M1 treatment) decreased spheroid size (**Fig. 2B**). Treatment with 20 ng/ml of IL-4 (M2 treatment) did not significantly change spheroid size, but did result in a slight increase in solidity, a measure of perimeter regularity. Interestingly, hypoxia, dexamethasone, and temozolomide did not significantly alter spheroid size or shape.

The size and shape comparisons discussed were made based on 2D imaging data. We are currently developing image processing pipelines to analyze 3D data from confocal images for more in-depth morphology comparisons. We are also currently optimizing computational models to obtain quantitative comparisons of the generated solid stress.

These results illustrate the utility of this novel 3D macrophage mechanics culture model. They also highlight an interesting interaction between inflammatory stimuli and the generation of stress, where LPS stimulation increases the ability of macrophages to grow and therefore compress their surroundings. However, the addition of IFNγ is enough to reverse this effect. These results highlight the need for a greater understanding of macrophages and their active contribution to the mechanical microenvironment.

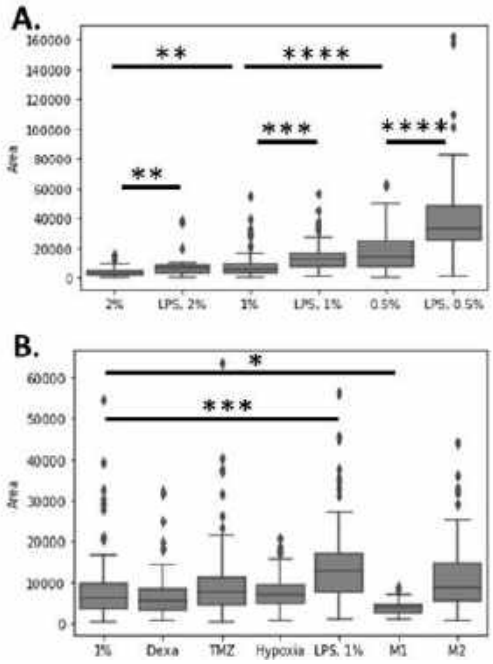

Figure 2: Spheroid area varies with agarose percent and treatment. (**A.**) LPS treatment increases spheroid size compared to untreated at all three agarose concentrations, and reducing the agarose concentration significantly increases spheroid size. (**B.**) Treatment with LPS significantly increases spheroid size, while treatment with LPS plus IFNγ (M1) significantly reduces spheroid size.

DISCUSSION

For the first time, these results show how macrophages respond to various conditions in a 3D confining gel. Interestingly, IFNγ is enough to reverse the effect of LPS on spheroid growth. It is also interesting that relevant doses of temozolomide, dexamethasone, and hypoxia do not significantly impact spheroid stress generation, suggesting that these mechanical processes may occur independently from other biological responses. This work also reveals an interesting 3D growth pattern, as macrophages adopt a flattened discoid shape, rather than a spheroidal shape. This could indicate either a physical process, such as the formation of a planar crack in the gel, or a biological process, such as differential proliferation in different regions of the spheroid. Further work to characterize these spheroids, such as histology, western blot, and PCR is underway to further understand these biological mechanisms, which may have *in vivo* parallels in health and disease.

These constructs have excellent potential for short-term and long-term experiments and are easily tunable to include different cell types or matrix modifications. For example, co-culturing macrophages with cancer cells can easily be implemented, and would elucidate novel mechano-immune interactions in cancer. Overall, this work demonstrates that the agarose-embedded 3D macrophage model is a promising platform to screen different treatments or experimental conditions for their effect on the mechanical activity of macrophages.

ACKNOWLEDGEMENTS

Funding for this work was provided by the NIH, the Indiana CTSI, and the Berthiaume Institute for Precision Health.

REFERENCES

[1] Park M. D. et al., Cell, vol. 185, 34: 4259–4279, 2022.
[2] Adams S. et al., Ann Biomed Eng, 47: 2213–2231, 2019.

COMPUTATIONAL STUDY ON THE HEMODYNAMICS OF BIOPROSTHETIC PULMONARY VALVES IN PATIENTS WITH REPAIRED TETRALOGY OF FALLOT

Kwang-Bem Ko (1), Jung-Hee Seo (2), Ashish Doshi (3), Danielle Gottlieb-Sen (4), Rajat Mittal (2)

(1) Department of Biomedical Engineering, Johns Hopkins University, Baltimore, MD, USA
(2) Department of Mechanical Engineering, Johns Hopkins University, Baltimore, MD, USA
(3) Department of Pediatrics, Johns Hopkins Medicine, Baltimore, MD, USA
(4) Department of Surgery, Johns Hopkins Medicine, Baltimore, MD, USA

INTRODUCTION

Tetralogy of Fallot is a congenital heart disease which results in poorly oxygenated blood flow to the body. A commonly performed intervention is the pulmonary valve replacement surgery; however, patients who undergo these procedures require multiple repeat surgical interventions during their lifetimes. This is attributed to structural valve deterioration [1], a mechanism which is responsible for the mechanical degradation of the valve implant.

Cardiac surgeons are interested in developing strategies to increase the valve implant longevity. One hypothesis is that an optimal valve implant position and orientation exists that results in favorable hemodynamics and valve leaflet dynamics. Additionally, determining optimal orientations has clinical importance, as surgeons are required to constrain multiple degrees of freedom when implanting the valve. Thus, quantifying favorable valve orientations will assist in developing a set of surgical guidelines.

Therefore, the purpose of this study is to develop a novel in-silico pipeline to quantify bioprosthetic pulmonary valve implant geometry, to perform computational fluid dynamics simulations of various pulmonary artery and valve models, and to evaluate the subsequent hemodynamic forces applied to the implanted valve that may impact structural deterioration.

METHODS

To quantify the valve implant orientation, pulmonary artery centerlines along with the valve implant position and orientations were extracted from 3D models. Using these datapoints, an ideal implant plane was constructed from which 2 characteristic valve implant angles α and β were estimated (Figure 1).

In our investigations, we developed both canonical and patient-specific models. The canonical models consisted of idealized pulmonary arteries in which we perturbed the bioprosthetic valves along angles α and β. The patient-specific models were obtained from segmentations of CT and MR angiogram images of 15 patients with repaired tetralogy of Fallot who had undergone pulmonary valve replacements.

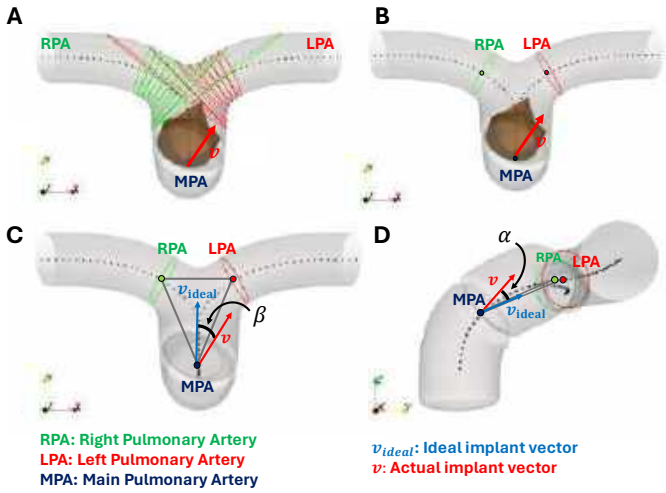

Figure 1: Pipeline to obtain pulmonary valve implant angles α and β. (A) Normal cross-sectional slices of position coordinates. (B) Selection of 3 position coordinates to construct the ideal plane. (C) and (D) Measurement of angles β and α respectively.

We performed computational fluid dynamic simulations of our models using a sharp-interface immersed boundary flow solver which included a reduced-degree-of-freedom fluid-structure interaction (FSI) model of the pulmonary valve. More details of our valve model can be accessed in a previous study [2].

We assessed the flow distributions to the branch pulmonary arteries. Thus, the flow rates were measured at the outlet of the left (LPA) and right (RPA) pulmonary arteries. The flow rates were then integrated and then divided by the common net flow (MPA) applied to the models (Equations 1 and 2).

$$Q_{\mathrm{RPA}} = \int_0^T Q_{\mathrm{RPA}}(t)\,dt \text{ and } Q_{\mathrm{LPA}} = \int_0^T Q_{\mathrm{LPA}}(t) \quad (1)$$

$$\%Q_{\mathrm{RPA}} = \frac{Q_{\mathrm{RPA}}}{Q_{\mathrm{MPA}}} \cdot 100 \text{ and } \%Q_{\mathrm{LPA}} = \frac{Q_{\mathrm{LPA}}}{Q_{\mathrm{MPA}}} \cdot 100 \quad (2)$$

To predict regions of the valve leaflets that had greater potential for structural valve deterioration, we computed the cycle-averaged pressure differentials across the valve leaflets, which is provided as

$$\overline{|\Delta P(X)|} = \frac{1}{T}\int_0^T |\Delta P(X,t)|dt \quad , \quad (3)$$

where X is the triangular element belonging to the valve leaflet surface mesh and $\Delta P(X,t)$ is the local pressure differential forces that the surrounding fluid imposed onto the valve leaflets.

RESULTS

The pressure differential plots of the various valve implant perturbations that were applied to the canonical pulmonary artery model have been provided in Figure 2. Additionally, the flow distributions at the branch arteries have been recorded in Table 1.

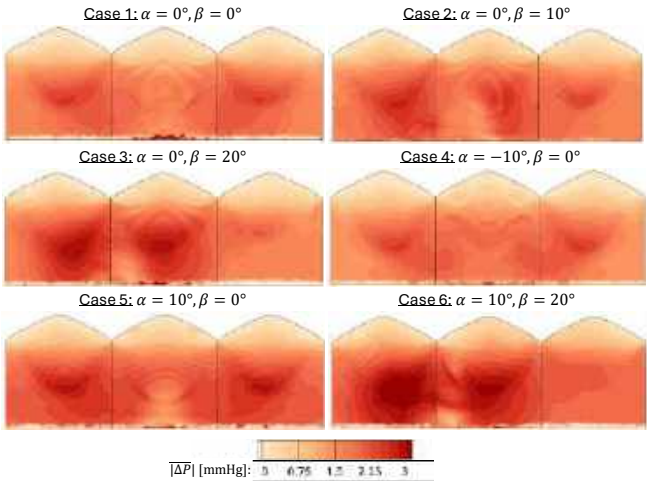

Figure 2: Cycle-averaged pressure differential plots for 6 valve implant orientation cases.

Table 1: Branch Artery Flow Distributions of Various Cases

Case	α [°]	β [°]	$\%Q_{\mathrm{RPA}}$	$\%Q_{\mathrm{LPA}}$	$\lvert\Delta P_{\mathrm{max}}\rvert$ [mmHg]
1	0	0	50.1	49.9	2.55
2	0	10	46.5	53.5	5.22
3	0	20	44.0	56.0	5.14
4	-10	0	50.0	50.0	2.51
5	10	0	50.0	50.0	2.89
6	10	20	46.6	53.4	5.44

A small subset of the patient-specific models has been visualized in Figure 3. In addition, the flow distribution data as well as the maximum leaflet differential pressure have been provided in Table 2.

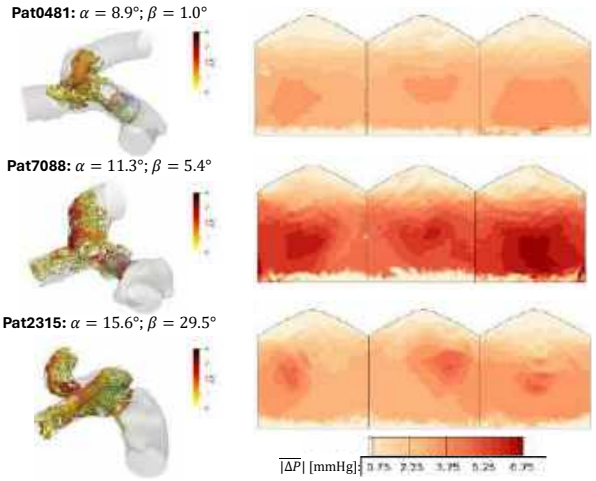

Figure 3: Visualization of 3 models from our 15 patient cases. Iso-surfaces of Q-criterion contoured by the velocity magnitude at peak systole (left). Pressure differential plots of the valve implant (right).

Table 2: Flow Distributions and Maximum Leaflet Pressures of 3 patient-specific models

Patient #	α [°]	β [°]	$\%Q_{\mathrm{RPA}}$	$\%Q_{\mathrm{LPA}}$	$\lvert\Delta P_{\mathrm{max}}\rvert$ [mmHg]
0481	8.9	1.0	52.3	47.7	8.78
7088	11.3	5.4	35.0	65.0	12.1
2315	15.6	29.5	43.4	56.6	9.83

DISCUSSION

Our canonical model simulation results (Figure 2 and Table 1) show that an optimal orientation exists ($\alpha = \beta = 0°$) where there is symmetric flow distribution to the branch arteries as well as the lowest pressure differentials across the valve leaflets. If the valve implant orientation increases along α, a symmetric flow distribution is preserved while the leaflet pressure magnitudes increase. If the valve implant orientation increases along β, then there is increased flow distribution asymmetry as well as asymmetry in the leaflet pressure differentials.

If the patient-specific results are considered (Figure 3 and Table 2), there is additional complexity not observed in the canonical model cases. For instance, although β may indicate flow asymmetry, local vessel geometries such as stenosis and curvature effects also contribute to increasing the observed asymmetries. Thus, valve orientation is not the sole predictor of unfavorable hemodynamics and leaflet dynamics.

Nevertheless, our results indicate that intentional positioning of implanted pulmonary valves could lead to improved hemodynamics for bioprosthetic valve durability. Because pulmonary valve geometries are more controllable than other valve prosthesis, our in-silico pipeline provides a general approach to guide optimal valve position and potentially limit the effects of structural deterioration.

ACKNOWLEDGEMENTS

The authors would like to thank Kate Calligy, Thaniyyah Ahmad, and Camille Shantz for their support during this study.

REFERENCES

[1] Kostyunin, A.E. et al., Journal of American Heart Association, 9(19), 2020

[2] Seo, J.H. et al., International Journal of Heat and Fluid Flow, 86:108740, 2020

CONTROLLING CELLULAR REARRANGEMENTS IN AN EPITHELIAL MONOLAYER THROUGH MICROPATTERNING TECHNIQUES

Molly K. McCord (1,2), Jacob Notbohm (1,2)

(1) (1) Department of Mechanical Engineering, University of Wisconsin - Madison, Madison, Wisconsin, USA
(2) (2) Biophysics Program, University of Wisconsin - Madison, Madison, Wisconsin, USA

INTRODUCTION

Collective cell migration is a complex biological phenomenon that occurs in cancer metastasis, wound healing, and development [1,2,3]. Cells within the collective move together with coordinated motion, and the interplay between directed motion and mechanical interactions occurs on scales of up to ten cells [4]. Since there can be no holes or overlapping cells within the monolayer, shape change must result from rearrangement events, wherein cells slide past their neighbors, hence rearranging their local positioning. The ability for cells to rearrange defines whether a tissue is solid-like or fluid-like, with a solid-like tissue having a finite energy barrier to rearrangements and a fluid-like tissue having no energy barrier to rearrangements [5,6,7] . The notion of two phases—solid and fluid—is a useful framework to investigate collective motion, but most prior studies have observed epithelial cell layers to be fluid-like. It is not yet clear how to distinguish between different fluid-like systems. A major limitation towards this goal is that there is a lack of well-established methods to control rearrangements within the cell layer for subsequent study.

Here, we describe methods to produce well-controlled regions of rearrangements within a cell layer. To this end, we used micropatterning to confine cells in islands having different shapes. Compared to circular cell islands, elongated cell islands had substantially more rearrangements between neighboring cells. Using optical microscopy, traction force microscopy, and monolayer stress microscopy, we computed the cell velocities, tractions, and stresses in both circular and elongated cell islands.

METHODS

Polyacrylamide (PA) gels were fabricated with an elastic modulus of 6 kPa; fluorescent particles were embedded at the surface as described previously [8]. Traditional lithography techniques were used to create a silicon master mold containing elongated islands with dimensions of 300 μm x 1 mm. This master mold was spin coated with PDMS, which was then cured at 60°C overnight and cut into masks. The masks were then adhered to the PA gels. The areas of the gels that were not covered by a mask were functionalized by collagen I using the crosslinker sulfo-SANPAH as described previously [8]. The masks were removed, and the areas free of collagen were passivized with 3% bovine serum albumin to prevent non-specific cell adhesion to the collagen-free regions. Madin-Darby canine kidney (MDCK) type II cells were seeded onto the gels at a concentration of 1.25×10^6 cells/gel and allowed to come to confluence on each collagen island overnight. Cell proliferation was then inhibited with a treatment of 10 μg/mL mitomycin-C. Cell islands and fluorescent particles were imaged on an Eclipse Ti microscope (Nikon, Melville, NY) and an Orca Flash 4.0 digital camera (Hamamatsu, Bridgewater, NJ) every 10 min for 24 hrs at 37°C. Trypsin was added to remove the cells from each gel, allowing for the gel to return to an undeformed state. Following the return to an undeformed state, a reference image of the fluorescent particles was taken.

Fast Iterative Digital Image Correlation (FIDIC) [9] was used to compute cell-induced substrate displacements (with respect to the undeformed reference image) and cell velocities. Fast Fourier traction cytometry [10] with a correction for finite substrate thickness [11,12] was used to compute cell-substrate tractions, which were subsequently used to compute the cell-cell stresses using monolayer stress microscopy [13,14,15]. Here, we focused on the maximum shear stress, which was computed by taking the difference between the first and second principal stresses and dividing by two.

RESULTS

We began by searching for rearrangement events in a circular island of 1 mm (Fig. 1a). Results showed that motion was uncontrolled, with rearrangement events occurring sporadically at different positions and different points in time. This complex behavior makes it hard to study rearrangements in a controlled way. Within the 1 mm island, there appeared to be a seemingly random distribution of shear stresses, which again indicates the randomness present in these large circular islands (Fig. 1b). A zoomed in view of the cell morphology can be seen in Fig. 1c. Note that a majority of the cells were rounded, and shear stress is relatively uniform across the island,

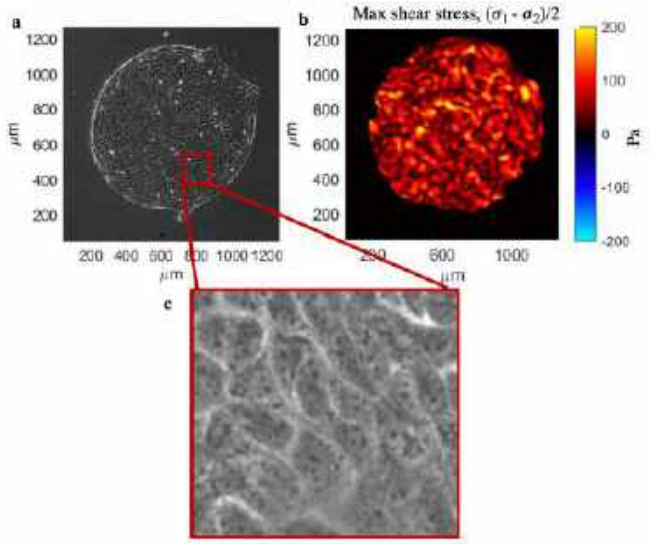

Figure 1: Cell elongation and max shear stress in a 1 mm diameter cell monolayer. (a) Phase contrast image of the cell monolayer. (b) Max shear stress within the cell monolayer. (c) Enlarged view of the phase contrast image in the highlighted region in panel a. Note that the cells are rounded.

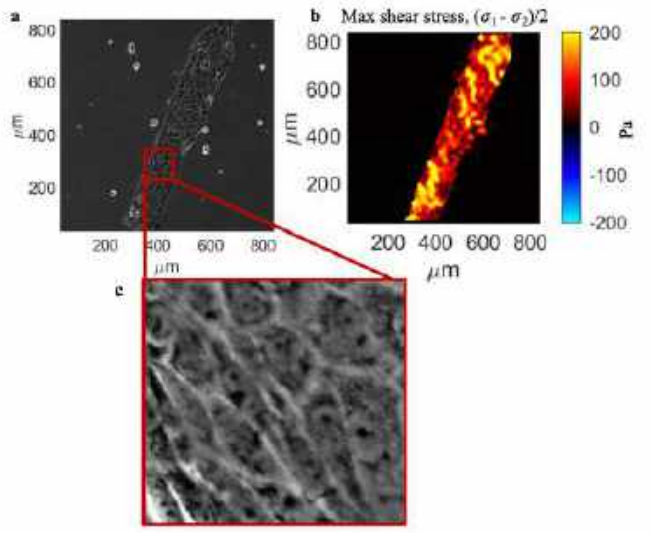

Figure 2: Cell elongation and max shear stress in a micropatterned island. (a) Phase contrast image of the cell monolayer. (b) Max shear stress within the cell monolayer. (c) Enlarged view of the phase contrast image in the highlighted region in panel a. Note that the cells are elongated.

making the dynamics associated with cell elongation and rearrangement challenging to study.

When cells were confined to an ellipsoid island, as seen in Fig. 2a, they had a natural tendency to rotate circularly as a collective. We hypothesized that this would give rise to elongated cells and controlled areas of rearrangement, and in turn, high shear stress relative to an unconfined monolayer [16]. Results showed that the shear stress was not random throughout the island, but rather there were areas of large shear stress with cells undergoing rearrangement events (Fig. 2b.). These areas of large shear stress were organized in space, as they typically occurred at the top and bottom of the elliptical island. Additionally, an enlarged view of the island, seen in Fig. 2c, shows that more than half of the cells elongated with strong alignment between neighboring cells.

DISCUSSION

This study focused on controlling rearrangements within a cell monolayer. To this end, we combined micropatterning techniques with optical microscopy and monolayer stress microscopy. In unconfined 1 mm islands, cells exhibited complex and unpredictable movement. The shear stress fluctuated throughout the island, making it challenging to study the dynamics that are associated with cell elongation and cell-cell interactions during rearrangement events. To address these issues, we patterned cells in elongated islands, in which the cells displayed a natural tendency to migrate collectively around the island. Along with moving rotationally, the cells were elongated, and locations of high shear stresses occurred near the ends of the elongated islands. In future work, we aim to investigate in more detail the stresses associated with rearrangement events within the monolayer.

ACKNOWLEDGEMENTS

This project was funded by National Science Foundation award number CMMI-2205141.

REFERENCES

[1] Spatarelu, C et al., *ACS Biomaterials Science & Engineering* 5 (8):3766-3787, 2019.
[2] Scarpa, E et al., *J Cell Biol*, 212 (2):143–155, 2016.
[3] Martin, P et al., *Development,* 131 (13): 3021–3034, 2004.
[4] Hino, N et al., *Developmental cell,* 53(6):646-60, 2020.
[5] Chiang, M et al., *Europhysics Letters*, 116(2):28009, 2016.
[6] Bi, D et al., *Nature Physics*, 11(12):1074-9, 2015.
[7] Park JA et al., *Nature materials*, 14(10):1040-8, 2015.
[8] Saraswathibhatla A, et al., *Physical Review X,* 23;10(1):011016, 2020.
[9] Bar-Kochba, E et al., *Exp. Mech*. 55:261-274, 2014.
[10] Butler, JP et al., J. Physiol. *Cell Physiol*. 282(3):C595-605, 2002.
[11] Del Alamo, JC et al., *Proc Natl Acad*, 14;104(33):13343-8, 2007.
[12] Trepat, X et al., *Nature Phys,* 5:426–430, 2009.
[13] Tambe, D. T., et al., *Nat. Mater*, 10:469–475, 2011.
[14] Tambe, D. T. et al., *PLoS One*, 8:e55172, 2013.
[15] Saraswathibhatla A, et al., *Scientific Data*, 7(1):197, 2020.
[16] Duclos, G et al. *Nature physics*, 14(7):728-32, 2018.

SPATIAL HETEROGENEITY IN ENGINEERED HEART TISSUE MECHANICS FOLLOWING IN VITRO INFARCTION

Michael J. Potter (1), Samuel J. Coeyman (1), Jonathan G. Heywood (1), William J. Richardson (2)

(1) Department of Bioengineering, Clemson University, Clemson, SC, USA
(2) Department of Chemical Engineering, University of Arkansas, Fayetteville, AR, USA

INTRODUCTION

Remodeling after myocardial infarction requires careful balancing of numerous ensuing phases to achieve an optimal outcome. Within each phase, there are various factors impacting myocardial wall mechanics which can tilt the overall response towards improved or worsened results. Clear relationships between cardiac fibroblasts, environmental stiffness, and dynamic mechanics have been established.[1–5] A better understanding of myocardial mechanics and the resultant cell response during the development and progression of these pathophysiological states is critically needed to enable development of effective therapies and treatment regimens.

We have developed an in vitro engineered heart tissue platform consisting of a fibrin-based hydrogel with embedded cardiofibroblast and cardiomyocyte populations, which are subjected to controlled electrical and mechanical stimulations. In this study, we subjected these engineered-heart tissue constructs to simulated infarctions via cryo-probe injury and evaluated the temporal changes in regional mechanics that developed as a result of the injury and the embedded cell population response.

METHODS

Primary ventricular cardiofibroblasts and cardiomyocytes were isolated directly from neonatal Sprague Dawley rats in accordance with an IACUC approved protocol. Cell-containing fibrin gel solution was pipetted into the wells of the custom-fabricated platform. Wounding was applied via custom manufactured cryo-stamps dipped in liquid nitrogen which ensured a uniform cryo-wound application to each sample. Gels were subjected to cyclical electrical stimulation and a constant mechanical stretch. Stretch was applied via electromagnets acting upon magnetic grips attached to each gel within the platform. Images were acquired during a daily stretching phase consisting of discrete electromagnetic field strength step increases to evaluate stiffness via surface strain mapping. Surface strain mapping analysis was performed via NCORR 2D digital image correlation MATLAB software.[6] Force values resulting from the discrete amperage levels of the electromagnets were previously experimentally generated via spring compression calibration utilizing springs with known material properties.[7]

To assess regional variation in mechanical properties, constructs were segmented into sixteen subregions. Three neighboring subregions were joined to form an analysis region. Three analysis regions were selected corresponding to the infarcted, border, and remote regions of the construct. The stress-strain pairs of each sample were calculated for each analysis region and for the sample as a whole. A regression was performed using the stress-strain pairs to attain the estimated modulus of elasticity value.

For statistical analysis, paired t-tests were performed for all intra-condition comparisons with significance reported at $p < 0.05$. Two-sample t-tests were performed for all inter-condition comparisons with significance reported at $p < 0.05$. The unwounded control treatment group possessed a sample size of $n = 4$ for all calculations. The wounded experimental treatment group possessed a sample size of $n = 6$ for all calculations.

RESULTS

When evaluating the macro-modulus of elasticity, there is a clear trend of stiffening within the unwounded control group that the wounded group does not exhibit. While the maximum modulus values of the wounded group shown in the box plots of Figure 1A do appear to increase day to day starting after wounding on day 1, there is no statistical significance observed between groups. The unwounded control group highlighted in Figure 1B on the other hand exhibited significant levels of stiffening from day 1 to day 3 and 7. When comparing modulus of the control and wounded groups directly at each day, no significant differences are reported. By day 7, the average

modulus of the unwounded group is beginning to separate itself from the wounded constructs.

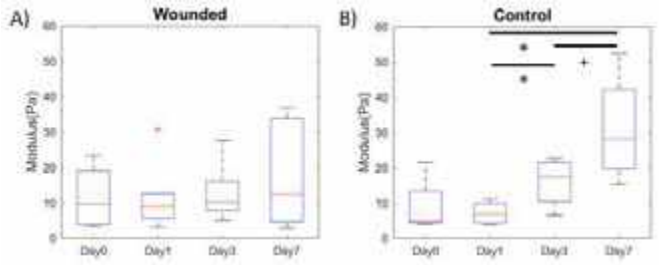

Figure 1: Macro-modulus of wounded and unwounded gels. A) Box plot of wounded whole gel modulus (n = 6). B) Box plots of unwounded control whole gel modulus. (*: p<0.05;+p<0.1 | n = 4).

Regional comparisons of stiffness moduli shown in Figure 2 reveal a mostly uniform unwounded control construct throughout the time course that only exhibits trends towards significance between neighboring regions on day 7. While the wounded group also exhibits an apparent near uniformity of modulus among regions initially, clear differences arise after wounding. By day 1 post-wound, the remote and border regions both exhibit significantly greater stiffness than the wounded region. On day 3, significance persists between the stiffness of the remote and the wounded regions while the disparity between the bordering region and the wound is reduced to near significance. On day 7, the regions of the wounded gel have again reached statistically indistinguishable levels of stiffness.

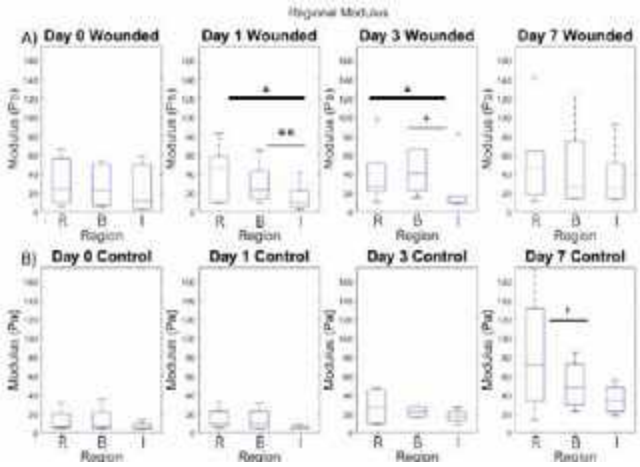

Figure 2: Intra-day comparison of regional moduli across timecourse. Region(R-Remote, B-Border, I-Infarct). A) Wounded gel regional moduli (: p<0.01; *: p<0.05; +: p<0.1 | n = 6). B) Unwounded control gel regional moduli (+: p<0.1 | n = 4).**

Within the unwounded control condition, regions show little variability throughout the time course until day 7 where the remote region appears to be stiffening to a greater value. However, all regions increase in stiffness through day 3 and 7 compared to initial values.

DISCUSSION

The healing infarct is without question a very complicated subject. It is a tumultuous environment with dynamic mechanics, varied geometries, spatial inconsistency, and overall uncertainty. Therefore, simple, effective, and consistent therapeutic strategies evade discovery and enactment. Clarke et al presented a review of literature highlighting that experimental models of myocardial infarction vary wildly in collagen structure, mechanics, and remodeling. The authors concluded that it is difficult to ascertain possible therapeutic efficacy without testing across a range of species, infarct locations, and reperfusion protocols due to the inherent complicated biology and mechanics of the healing infarct that are often counterintuitive and extremely complex.[8] This conclusion was supported by a separate finite element analysis that investigated the effect that infarct location had on traditional functional output measures of cardiac efficiency. It was concluded that tradeoffs exist between therapeutic options of interest and that infarct location likely plays a significant role in what therapeutic route would most appropriately induce recovery in an infarcted myocardium.[9]

These results suggest that again the healing infarct is a very complicated subject matter and that a simpler, more consistent, and more widely applicable methodology of evaluating therapeutic efficacy is desperately needed. These results in part inspired the experimental analysis conducted within our study as a preliminary investigation into the natural progression of a simplified engineered cardiac tissue construct following myocardial injury. As literature findings clearly demonstrate the importance of wall mechanics, investigating the progression of the stress-strain relationship and regional stiffness found within our mechanically active constructs is an important contribution towards the development of an improved understanding of the progression of mechanics within the early infarct. Sample to sample variation within the sample fabrication process can increase the uncertainty in direct value to value comparisons across treatment groups. This variation is believed to be related to the prototype nature of the technology platform. Room for refinement within the protocols exists with some example targets including: thrombin concentration during gelation, final fibrin gel density, cellular density, myocyte to fibroblast ratio, and electrical and mechanical stimulation regimes. When analyzing the gels holistically, the control groups follow a gradual stiffening over the time course while the experimental gels appear to maintain a similar stiffness throughout, only broken up by an increased value range on the ultimate day. These observations seem to suggest that while the wounding did not disrupt the architecture of the underlying gel, wounding is responsible for the disruption of the stiffening process. While evaluating the overall stiffening trends is useful and provides a test bed with parallels to that of the stiffening infarct, gaining insights into the spatial heterogeneity of mechanics from within the infarct to the remote tissue can elucidate the finite and incremental nuance of the recovery process.

ACKNOWLEDGEMENTS

We acknowledge support to complete this research from the National Institutes of Health [GM121342, HL144927].

REFERENCES

[1] Adapala, R. K. et al. *Basic Res Cardiol* **115**, 14 (2020).
[2] Baxter, S. C. et al. *Cell Biochem Biophys* **51**, 33–44 (2008).
[3] MacKenna, D. *Cardiovasc Res* **46**, 257–263 (2000).
[4] Galie, P. A.et al. *Cardiovascular Pathology* **20**, 325–333 (2011).
[5] Huang, X. et al. *Am J Respir Cell Mol Biol* **47**, 340–348 (2012).
[6] Blaber, J. et al. *Exp Mech* **55**, 1105–1122 (2015).
[7] Coeyman, S. J. et al. *J Biomech* **147**, 111458 (2023).
[8] Clarke, S. A. et al. *J Mol. and Cell. Card.* **93. P115-124.** (2016).
[9] Fomovsky, G. M. et al. *J Cardiovasc Transl Res* **4**, 82–91 (2011).

The Role Of Cyclic Convective Fluid Filtration (CCFF) In Atherosclerosis: A Biomechanical Model For Atherogenesis

Bruce R. Simon (1), Paul H. Rigby (2), Paul F. Howard (3), Jonathan P. Vande Geest (4,5)

(1) Aerospace and Mechanical Engineering Department, University of Arizona, Tucson, AZ, USA
(2) RaytheonTechnologies, Tucson, AZ, USA
(3) Midwest Cardiovascular Specialists Indiana University Bloomington, South Bend, IN, USA
(4) Department of Bioengineering, University of Pittsburgh, Pittsburgh, PA, USA
(5) McGowan Institute for Regenerative Medicine, University of Pittsburgh, Pittsburgh, PA, USA

INTRODUCTION

Atherosclerosis is an arterial disease that is the cause of worldwide morbidity and mortality. Atherogenesis occurs in regions of geometric complexity for example in branches, bifurcations, and sharp curvatures where blood flow altered hemodynamic stresses can damage the endothelium. Clinical 'risk factors' for atherosclerosis include high blood pressure, smoking, and elevated levels of LDL in the blood. Atherogenesis has been described as a process of white blood cells (WBCs) entering through damaged endothelium joining with damaged smooth muscle cells (SMCs) to produce plaque. Atherogenesis is related to the vasa vasorum (VV) however its specific role is not yet fully understood [1]. The long-term cyclic pressure response of arteries should produce a cyclic tissue fluid reaction both at the internal and the external surfaces of the artery, however these phenomena, especially in response to vascular damage, has not received significant attention in the literature.

The goal of this abstract is to utilize a computational model to demonstrate that such radial cyclic fluid velocities can and do occur. Furthermore, how these are altered in arteries with varying degrees of endoluminal vascular damage will also be quantified. The relationship between the pore fluid flows and atherogenesis described here is also discussed with the goal of adding to the quantitative biomechanical view of atherogenesis.

METHODS

Poroelasticity is a continuum model for materials composed of a porous elastic solid and a mobile fluid (water/saline) that flows relative to the deforming solid. Consider the solid to be fluid-saturated and described by porosity. The pore fluid pressure is related to interstitial fluid flow by a Darcy law defining hydraulic permeability. PoroHyperElasticity (PHE) includes "large" deformations /strains in a nonlinear hyperelastic porous solid and an incompressible mobile fluid. When quasistatic loading is applied to the poroelastic material, a 'consolidation' response is generated. Application of cyclic internal pressure to a poroelastic cylinder with an impermeable internal surface (hydraulic permeability = 0) would result in moderate cyclic fluid flow at the open external surface. However, if the inner surface is permeable and exposed to prolonged pulsatile pressure, a large convection fluid flow can occur at both the internal and external surfaces, with relative low fluid flow over most of the interior of the cylinder. This condition will be termed here as Cyclic Convective Fluid Filtration (CCFF) and is shown in **Figure 1**. A 'sawtooth' pressure excites CCFF with influx/efflux luminal flow and corresponding efflux/influx outer adventitial flow. This cyclic flow phenomenon is suggested in early works, for example see Wang and Tarbell [1] and Kenyon [2].

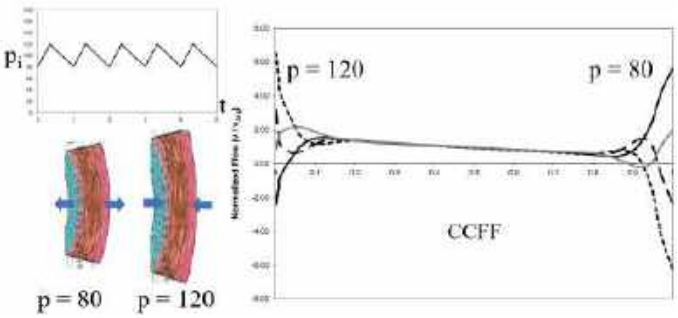

2 a **2 b**

Figure 1: Cyclic convective fluid filtration (CCFF) in a Porohyperelastic artery

Plots of relative pore fluid velocity showing CCFF were generated using ABAQUS to develop finite element models (FEMs) of rabbit carotid arteries. PHE FEMs These FEMs were layered cylinders (finite plane strain) subjected to the 'sawtooth" (120/80 cardiac cycles) pulsatile internal pressure. Carotid arterial geometry and structure were

obtained from excised vessels. The FEMs included endothelium, intima, media, SM, elastic, and collagen fibers. Nonlinear anisotropic hyperelastic materials and a coupled Darcy equation with nonlinear permeability, porosity, and saline tissue fluid were incorporated into the PHE FEM. PHE material properties/parameters were taken from experimental data in the literature.

RESULTS

PHE FEMs were used to consider the effects of variable material and structural parameters. **Figure 2** illustrates the effects of endothelial damage (luminal permeability > 0) on CCFF development. The lower plot in the figure shows response when the endothelium is impermeable, i.e. the 'normal' artery. No tissue fluid flow crosses the endothelium, moderately low convection develops in interior and at the external surface. When permeability is nonzero, the CCFF response occurs immediately and is increased as permeability increases, CCFF becomes markedly larger at interior and exterior surfaces. Similar parametric studies showed only small sensitivity of CCFF to hypertension and increased HR.

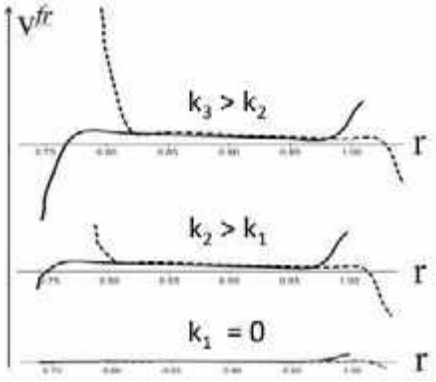

Figure 2: Parametric study on luminal permeability on CCFF

DISCUSSION

The presence of CCFF can provide a unique view of atherogenesis. A 'normal' artery subjected to pulsatile internal pressure will not develop CCFF since the endothelium is impermeable. Oxygen and nutrients are delivered by diffusion from the endothelium to the intima and diffusion from VV located in the externa and adventitia. Damage to the endothelium, if not repaired, will make the endothelium permeable. CCFF, a repeating cyclic convective flow of pore fluid that produces a relatively large influx and efflux occurring at the inner and outer/externa interfaces. CCFF can then be related to the process of atherogenesis in three ways—refer to **Figure 3**. Note that these effects can occur simultaneously but are shown separately for clarity.

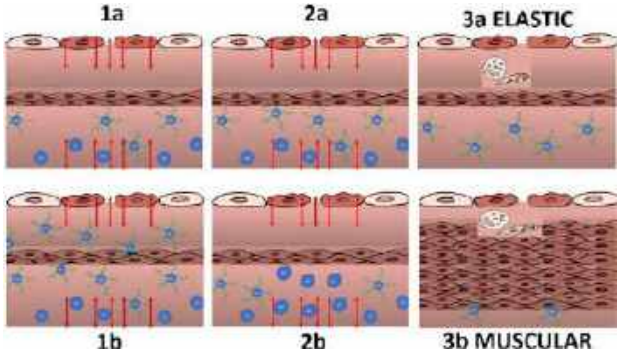

Figure 3. Role of CCFF in atherogenesis

1. The endothelium is 'damaged' and becomes permeable. CCFF can develop and LDL is convected by the influx/eflux into the intima. CCFF will disrupt the normal process of diffusion and the loss of oxygen and nutriments will be compensated by formation of new VV. CCFF also has the potential to draw in more white bloods cells.

2. CCFF at the internal surface will also cause CCFF, i.e. cyclic efflux/influx of tissue fluid, at the externa/adventitia surface. Diffusive transport from the VV would be disrupted by CCFF. This suggests another mechanism by which the VV can be linked to atherogenesis (as described in the literature).

3. In "elastic" arteries, CCFF at internal and external wall surfaces can disrupt delivery of oxygen and nutriments to the SMC layers leading to cell death/detachment and differentiation into foam cells (in addition to foam cells originating from white cells in the blood). In "muscular' arteries, CCFF can impinge directly on the SMCs near the endothelium [1]. PHE FEMs can simulate both cases by developing parametric studies of CCFF over a range of diameter/thickness ratios as well as consideration of CCFF effects ranging from elastic to muscular arteries. Variation of material properties, e.g. elasticity, endothelial permeability (as in **Figure 2**) can also be considered.

Only two relevant poroelastic arterial FEMs were found in the literature, i.e. a biphasic FEM (Johnson and Tarbell, [3]) and a FEM by Koshiba et al [4]. The latter paper used our PHE material model in a combined FSI/FEM of a curved coronary artery with LDL entering from flowing blood. This study considered cyclic pressures but did not report a CCFF pore fluid motion. In this work we have shown here that a PHE model of a carotid artery with injured endothelium, when exposed to a pulsatile pressure, can develop a cyclic interference pattern (CCFF) in tissue fluid flow. This phenomenon has not been extensively explored in the literature. CCFF can be related to atherogenesis by a) developing high cyclic convection at inner and outer surfaces; b) disruption of the normal diffusive transport at the endothelium and VV; promotion of LDL and white blood cells in the media; and c) SMC detachment from the matrix form foam cells. Future research efforts should focus on identifying the relative contributions of the numerous porohyperelastic parameters – including well designed experimental studies to generate and test these novel mechanisms of atherogenesis.

ACKNOWLEDGEMENTS

This research was supported in part by the NIH (1R01HL157017 to JPVG).

.

REFERENCES

[1] Wang DM and Tarbell JM, Modeling interstitial flow in an artery wall allows estimation of wall shear stress on smooth muscle cells, Sep 1995, *Journal of Biomechanical Engineering* 117(3):358-63.

[2] Kenyon DE, A mathematical model of water flux through aortic tissue, February 1979, *Bulletin of Mathematical Biology* 41(1):79-90.

[3] Johnson M and Tarbell JM, A biphasic, anisotropic model of the aortic wall, *Journal of Biomechanical Engineering*, Feb 2001, 123(1): 52-57.

[4] Koshiba N, Ando J, Chen X, Hisada T, Multiphysics simulation of blood flow and LDL transport in a porohyperelastic arterial wall model, *Journal of Biomechanical Engineering*, 2007 Jun;129(3):374-85.

SB^{3}C2024
Summer Biomechanics, Bioengineering and Biotransport Conference
June 11-14, Lake Geneva, WI, USA

BIOPHYSICAL CHARACTERIZATION OF INCREASED PROSTATE CANCER CELL SURVIVAL IN MUSCLE TISSUE

Jonah J Spencer (1,2), Anne E Cress (3), Jacob K Notbohm (1,2)

(1) Department of Mechanical Engineering, University of Wisconsin–Madison, Madison, Wisconsin, United States
(2) Biophysics Program, University of Wisconsin–Madison, Madison, Wisconsin, United States
(3) Department of Cellular and Molecular Medicine, University of Arizona, Tucson, Arizona, United States

INTRODUCTION

Metastasis relies on the ability of cancer cells to invade areas distal to the original growth. While rare, it is possible for cancer cells to invade through muscle tissue to metastasize [1]. The rarity is because contraction and elongation of muscle fibers cause large deformations to the cells, which often leads to cell death [2]. Interestingly, cells that invade through muscle in collective groups survive at a higher rate than individual cells [3]. These observations suggest that the collective behavior of a group of cells may be necessary for inter-muscular survival, yet the precise explanation remains unknown. Using two prostate cancer cell phenotypes, one exhibiting a low survival rate in muscle (DU145) the other a heightened ability to survive in muscle tissue (DUAA), we explored the question of how groups of cells are able to invade through muscle tissue while avoiding cell death.

Within collective groups, cells can exhibit material qualities classified as solid-like (jammed) or fluid-like (unjammed) [4]. In a fluid-like state, cells can slide past their neighbors, whereas for solid-like, they cannot. These material states are affected by cell-cell adhesions and force production which in turn alter cellular migration. Considering that survival in muscle requires cellular collectives to undergo large shape change, we hypothesized that DUAA cell collectives exhibit a more fluid-like state that allows them to easily slide past their neighbors, in turn enabling large collective shape changes during expansion and contraction of the muscle. By contrast, we hypothesized that DU145 cell collectives are more solid-like, meaning that in muscle the individual cells would undergo large shape changes that frequently lead to cell death. Here, quantify cell movement, shape index, and cellular forces in DU145 and DUAA cells to identify if DUAA cell collectives exhibit a more fluid-like state as compared to DU145 cell collectives.

METHODS

Cell Culture. The cells used were DU145 and DUAA cells, as described previously [3], and both of which are human prostate cancer cell lines. Cells were maintained in Modified DMEM No Glutamine, No beta-Mercaptoethanol (eg, Corning Iscove's Modification of DMEM Corning 15-016-CV) with 10% fetal bovine serum (FBS, Corning) and 1% Penicillin-Streptomycin. Cells were passaged every 4-5 days at 70-90% confluency.

Substrate Fabrication. A protocol previously published by our lab [5] was used to fabricate substrates of Young's modulus 5 kPa with flourescent particles for traction force microscopy. A polyacrylamide solution was prepared with 5% weight/volume (w/v) acrylamide (Biorad Laboratories, Hercules, CA), 0.2% w/v bisacrylamide (Biorad), 0.002% (v/v) TEMED (Biorad), 0.006% (w/v) ammonium persulfate (Biorad), and 18 µm of 2.6×10^{12} particles/mL of 0.2 µm red fluorescent (580/605 nm) 2% solids FluoSpheres Amine-Modified Microspheres (Thermo Fisher Scientific, Waltham, MA). A 20 µL droplet was pipetted onto a #1.5 glass bottom dish (Cellvis, Mountain View, CA). A 18 mm circular glass coverslip was placed over the 20 µL droplet forming a thin gel layer. To localize fluorescent beads to the surface of the gel, gels were placed in a centrifuge upside down and centrifuged at 30 rcf for 16 min.

Micro Patterning Cell Islands. Polydimethysiloxane (PDMS) (Sylgard 184, Dow Corning, Midland, MI) was prepared according to manufacturer instructions and poured into petri dishes at a thickness of 500 µm. The PDMS was then cured in a incubator at 60°C overnight. After curing the PDMS was cut into 16 mm circles which were then punched with a 1 mm biopsy punch. Each resulting PDMS mask was then sterilized by 70% ethanol and incubated in 2% Pluronic F-127 (Sigma-Aldrich, St. Louis, MO) to prevent cell adhesion to the PDMS. The masks were then placed on top of the polyacrylamide substrates, where the open 1 mm circles were functionalized with type I rat tail collagen (BD Biosciences, Franklin Lakes, NJ; 0.01 mg/mL, 1–2 mL per 18 mm diameter gel) using the crosslinker sulfo-SANPAH (Pierce Biotechnology, Waltham, MA; 2 mg in 200 mL 0.05 M HEPES). 8×10^5 cells/mL cell solution was prepared and 200 µL of cell solution pipetted onto each PDMS mask. 1–2 hr after seeding, the PDMS masks were removed and the glass bottom dishes were incubated at 37°C and 5% CO_2 for 12–16 hr, allowing for the cell is-

lands to reach the desired confluency. Only fields of view where the cells were confluent were used, fields of view that were over and under confluent were disregarded. This allowed us to make a more direct comparison between the two cell types.

Time-Lapse Imaging. Dishes with desired density were placed in a custom built cage incubator to maintain environmental conditions of 37°C and 5% CO_2. An Eclipse Ti-E microscope (Nikon, Melville, NY) with a 10×0.5 numerical aperture objective (Nikon) and an Orca Flash 4.0 digital camera (Hamamatsu, Bridgewater, NJ) running on Elements Ar software (Nikon) was used to image the cell islands and fluorescent particles in the substrates every 10 min for 24 hr.

Cell Shape. Using Seedwater Segmenter software [6] on phase contrast images of the two cell types resulted in a watershed. The watershed image was then converted into a binary image from which each cell's area (A) and perimeter (p) were calculated. The resulting areas and perimeters were used to compute the shape index q defined as $p/\sqrt{A}$. A larger q represents a more elongated cell; a smaller value indicates a more rounded cell. The smallest possible value of q is 3.543 for a circle.

Cell Movement. Using Fast Iterative Digital Image Correlation (FIDIC) [7], phase-contrast images of the cells were correlated over time to extract cell motion over time using 64×64 pixel subsets at a spacing of 16 pixels. From this data, we computed the average cell speed and a parameter to quantify rearrangements between neighboring cells, D^2_{min}. For each cell D^2_{min} was calculated according to

$$D^2_{\text{min}} = \frac{1}{N}\sum_{j=1}^{N}\left[\Delta\vec{d}_{ij} - E_i\vec{d}_{ij}\right]^2, \quad (1)$$

where N is a chosen number of nearest neighbors to the i^{th} cell ($N = 8$ was used here), $\vec{d}_{ij}$ is the position vector between cell i and neighbor j, $\Delta\vec{d}_{ij}$ is the change in $\vec{d}_{ij}$ between two consecutive time points, and E_i is the strain tensor defining the average motion undergone by cell i and its N neighbors [8]. Lastly, D^2_{min} was normalized to account for differences in average cell speed between the two cell types.

Traction Force Microscopy. Using FIDIC [7], time-lapse images of fluorescent particles were correlated to a stress-free reference image to compute cell-induced substrate displacements. The displacements were computed using 64×64 pixel subsets at a spacing of 16 pixels. Cell-substrate tractions were calculated using Fourier transform traction microscopy [9].

RESULTS

To explore the hypothesis that DUAA cells exhibit a more fluid-like state allowing them to undergo a collective shape change to avoid large single-cell deformations, we began by studying the movement of the two cell types. Using the velocity data obtained from FIDIC [7], we computed the average single-cell velocity and D^2_{min}. Results of the single-cell velocity data showed that DU145 cells had a higher average speed compared to the more invasive DUAA cells (Fig. 1a). The speed has little implication to a fluid-like state, however, as fluid-like behavior is defined by the ability of cells to rearrange positions with their neighbors. Defined above (Eq. 1), D^2_{min} is representative of each cell's ability to rearrange and slide past its neighboring cells. A low value shows the motion of the i^{th} cell is well coordinated with its neighbors indicating less rearrangements, whereas a higher value indicates less coordination and thus more rearrangements which is an indicator of a more fluid-like system. Compared to DU145 cells, DUAA exhibited a higher average D^2_{min} (Fig. 1b), indicating that DUAA cells exhibited more fluid-like behavior than DU145.

Given the movement measurements studied, we then looked into the shape index of the two cell types. Defined above, q is the shape index used to determine the morphology of the cell types. In the plot of mean q (Fig. 1c), the DUAA cells have a higher value, indicating that they are more elongated than the DU145 cells. More elongated cells indicate a more fluid-like cell monolayer, which allows for more cell rearrangements [4], which is also consistent with our hypothesis.

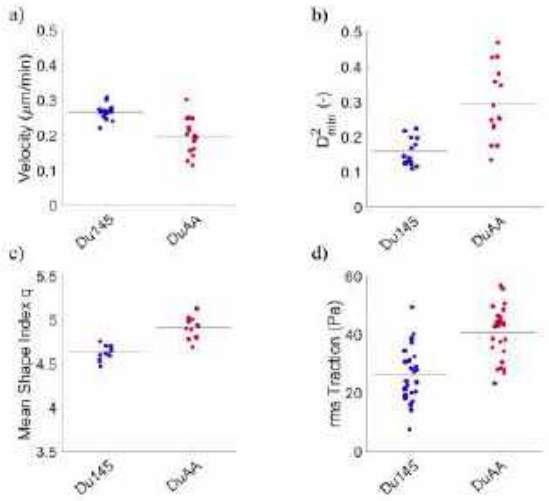

Figure 1: Motion, shape index, and force production plots for the two cell types studied. Each point represents a mean over a field of view, black dashes represent the mean of all fields of view for each given cell type. Data plotted is (a) average cell velocity ($p = 3.75 \times 10^{-4}$), (b) D^2_{min} ($p = 1.90\times10^{-4}$), (c) mean shape index q ($p = 4.74\times10^{-4}$), and (d) root mean square traction ($p = 8.32 \times 10^{-6}$). p values were calculated using rank sum tests.

Lastly we measured the cell-substrate tractions produced by the two cell types, because larger tractions are often the cause of the larger shape index [5], which in turn results in the more fluid-like state. Using Fourier traction force microscopy [9], cell-substrate tractions were computed and averaged for each cell layer by taking the root mean square, which was larger for DUAA compared to control (Fig. 1d). These observations align with our hypothesis of a more fluid-like state.

DISCUSSION

Though the concepts of cell motion, shape index, and force production are well studied [4, 5], our application to the phenomena of cancer cell invasion through muscle provides new insights of how collective cell fluidity may play a role in cancer metastasis. Here, the data point to the conclusion that DUAA cells exhibit a more fluid-like state as compared to DU145. The more fluid behavior would allow these cells rearrange with their neighbors, thereby enabling large changes in the shape in of the collective with minmal shape changes of the individual cells, reducing the likelihood of cell death during invasion through muscle tissue.

ACKNOWLEDGEMENTS

This work was supported by NIH-R35GM151171.

REFERENCES

[1] Surov A et al. *Cancer Imaging* 14.1 (2014).

[2] Sciorati C et al. *Cell Death Differ* 23.6 (2016).

[3] Marr KD et al. *Biophys J* 122.21 (2023).

[4] Bi D et al. *Nat Phys* 11.12 (2015).

[5] Saraswathibhatla A et al. *Phys Rev X* 10.1 (2020).

[6] Mashburn DN et al. *Cytom Part A* 81.5 (2012).

[7] Bar-Kochba E et al. *Exp Mech* 55.1 (2015).

[8] Lee RM et al. *New J Phys* 15.2 (2013).

[9] Butler JP et al. *Am J of Physiol-Cell Ph* 282.3 (2002).

MECHANICAL CHARACTERIZATION OF CALCIFIED CLOT ANALOGS

Jose L. Monclova (1), Daniel J. Walsh (1), Vikas Kannojiya (1), Scott D. Simon (2), Francesco Costanzo (1,3), Keefe B. Manning (1,4)

(1) Department of Biomedical Engineering, The Pennsylvania State University, University Park, Pennsylvania, USA
(2) Department of Neurosurgery, Penn State Hershey Medical Center, Hershey, Pennsylvania, USA
(3) Department of Engineering Science and Mechanics, The Pennsylvania State University, University Park, Pennsylvania, USA
(4) Department of Surgery, Penn State Hershey Medical Center, Hershey, Pennsylvania, USA

INTRODUCTION

Acute ischemic stroke was the fifth leading cause of death in the US in 2022, with nearly a quarter of strokes recurrent within the first two years [1,2]. Due to the high rates of incomplete recanalization in ischemic stroke, researchers have investigated the effect of clot stiffness on endovascular thrombectomy (EVT) outcomes [3]. However, it is unclear whether factors other than hematocrit directly influence EVT. Recent clinical case studies describe calcified cerebral emboli that cause complications in EVT surgeries, yet only present in approximately 3% of cases [4]. Despite the major concern these thrombi pose, little is still known about their mechanical properties, impeding the development of new therapeutics. For this reason, this study focuses on characterizing the rate dependent material properties of aged and calcified clot analogs. In this way, we can study the material properties of these clot analogs to inform future modeling of EVT in AIS to improve surgical outcomes.

METHODS

EA Formation Conditions: To study the effect of calcification on clot mechanical properties, clot analogs were created using human blood, following an approved institutional protocol. Briefly, extracted whole blood was anticoagulated with 0.32% weight sodium citrate. Blood was separated into red blood cells (RBCs), platelet rich plasma (PRP), and platelet poor plasma (PPP) via centrifugation. Blood was reconstituted to 214 x 10^6 platelets per mL, and hematocrit was controlled in clots by addition of 40% volume RBCs. To counter the effects of the anticoagulant, blood was recalcified with 20 mM calcium chloride ($CaCl_2$) and 0.25 NIH Unit/mL thrombin from human plasma (BioPharm, Bluffdale, UT, USA). Clots were then formed in a Chandler loop, which was rotated at 65 rpm for 1 hour at 37°C, and the resultant 4 mm diameter clot was removed from the tubing. Clots were then placed in 0 (cell media), 0.2, and 2 M $CaCl_2$ baths for 1 and 10 days, with control clots tested on day 0.

EA mechanical testing: For compressive testing, clots were sectioned into right cylindrical specimens with a height of 2 mm and mounted on an Instron uniaxial load frame (Instron 68SC, Norwood, MA, USA). Clots were then loaded in compression at 5, 10, and 15% strain per second to 80% strain, with a one-minute relaxation period. Peak stress, percent relaxation, and 10 and 75% tangent stiffnesses were calculated, similar to previous work [3]. For tensile testing, clots were mounted on custom, sandpaper lined grips of a uniaxial load frame. Clots were then loaded, in tension, at 5%, 10%, and 15% strain per second to 80% strain, with a one-minute relaxation period. A fourth tensile test was conducted to measure the fracture stress and strain of the samples, in which the clots were loaded at 10% strain per second until sample failure. Untested clots were embedded in paraffin wax and stained with a Carstairs protocol for histological analysis.

Statistics: Due to variability in coagulation, clot contraction, and variability between donors' blood, multiple sources (n = 6) were collected with replicates (n = 6) tested for each source. Mean values were computed with standard deviation, and a Kruskal-Wallis analysis of variance was applied to compare means. All data analysis was carried out using MATLAB's multiple comparison function.

RESULTS

Average tangent stiffnesses at 75% strain were nearly an order of magnitude higher for the day 1 and day 10, 2 M $CaCl_2$ clots, than for all other conditions, as shown in Figure 1. Low-strain tangent stiffnesses followed a similar trend, with both day 1 and day 10, 2 M calcium clots exhibiting significant increases in stiffnesses. The 2 M calcium clots also showed a significant decrease in compressive percent relaxation, indicating an increase in the viscous behavior of the blood clots. These clots also revealed a significant decrease in mass loss after testing,

suggesting a correlation between extent of calcification and plasma retention.

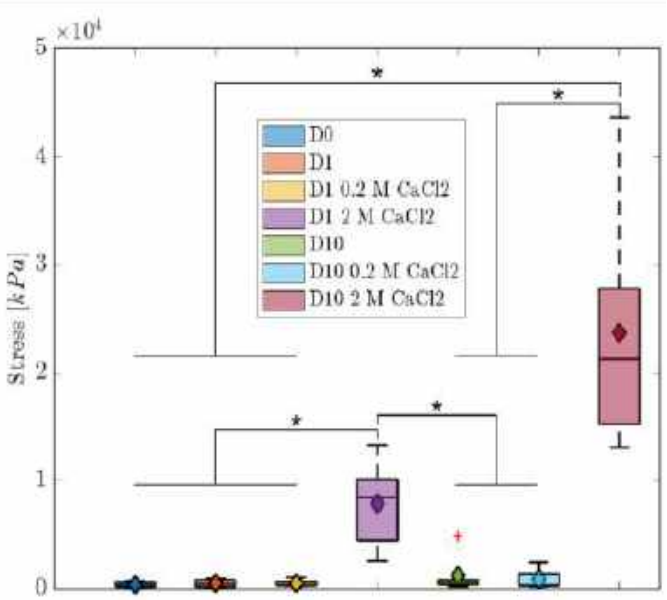

Figure 1: Box plots showing 75% tangent stiffness (at 10% strain per second) for each clot-type in high strain compression tests, with asterisks denoting significant differences (α<0.05), and mean values shown as diamonds.

In tension, the day 10, 2 M $CaCl_2$ clots revealed an order of magnitude increase in stiffness over all other conditions, when loaded to 80% strain at 10% strain per second, as shown in Figure 2. These 2 M $CaCl_2$ clots demonstrated a nonlinear behavior in tension. The 0.2 and 2 M $CaCl_2$ clots also decrease in percent relaxation when compared to the non-calcified counterparts. This suggests that the influence of the viscous element within the clots has decreased with increased calcium content. Despite this, the stiffening effect seen in compression at high strains was not observed in tension. The peak stress at 80% strain was an order of magnitude lower in tension than in compression for all conditions.

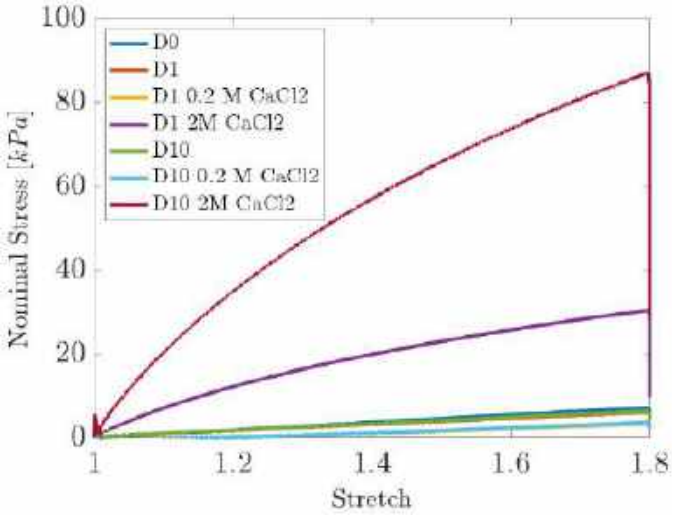

Figure 2: Stress versus stretch tensile curves for each clot type loaded at 10% strain per second to 80% strain.

The Carstairs analysis reveals day 0 and day 1 clots with regions of dense fibrin aggregates along the exterior of the clots. This is a well-known phenomenon of exterior clot sealing with a fibrin dense crust that becomes resistant to thrombolysis. As the clots continue to age, the red blood cell content within the clot (yellow portion) decreases as the red blood cells decay, as shown in Figure 3. This decay seems to be enhanced by the calcification, which seemingly increases the fibrin concentration, but is most likely lysing the red blood cells. Structurally, the red blood cells provide a viscous element to the clot, yet as the clots calcify, their fibrin skeleton becomes predominant.

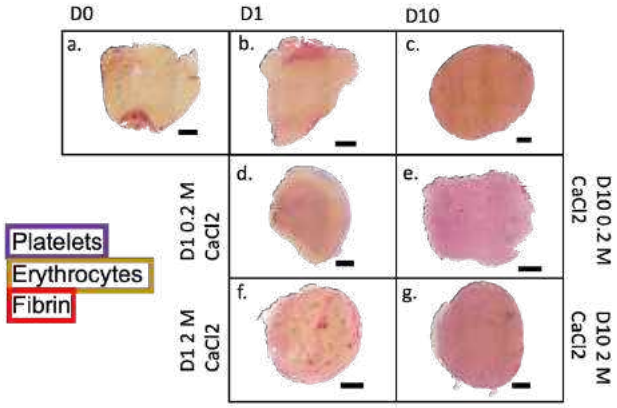

Figure 3: Representative clot images stained with a Carstairs protocol for a. day 0 clots, b. day 1 clots, c. day 10 clots, d. day 1 0.2 M $CaCl_2$ clots, e. day 10 0.2 M $CaCl_2$ clots, f. day 1 2 M $CaCl_2$ clots, and g. day 1 2 M $CaCl_2$ clots. Blue/purple indicates platelets, yellow represents red blood cells, and red represents fibrin.

DISCUSSION

Overall, the calcification process has been shown to significantly increase the tensile and compressive stiffness of blood clots. In compression, both the low and high strain stiffnesses were affected by the clot calcification, suggesting a structural change within the clots. In contrast, a decrease in percent relaxation of the calcified clots in tension corroborates the increase in fibrin density of the calcified clots seen in histology. Histological analysis revealed an overall decrease in the red blood cell content and an increase in the overall fibrin density. This suggests the hypotonicity initiated by the calcium may be altering the load-bearing components of the clot, i.e. the fibrin and red blood cells. The clot analogs have significant stiffening behavior in compression, and a linear-like behavior in tension, with compressive high strain stiffness an order of magnitude greater than in tension. Overall, this suggests that these calcified clots may be prone to *in situ* compressive compaction in the vessel during stent retriever EVT, making them a suitable surrogate for the clot phenotype causing EVT complications.

ACKNOWLEDGEMENTS

This research was supported, in part, by the Penn State Clinical Research Center in the Clinical and Translational Science Institute, the Penn State Huck Institutes' Microscopy Core Facility (RRID: SCR_024457), U.S. NIH grant HL146921, NIH T32GM108563, an Alfred P. Sloan and a Gates Millennium Scholarship.

REFERENCES

[1] J. Ortaliza *et al.*, *PKFF* (2022)
[2] C. W. Tsao *et al.*, *Stroke* (2022)
[3] R. Cahalane *et al.*, *Annals of BME* (2023)
[4] B. Walker *et al.*, *American J. of Neuro. Rad.* (2014)

EFFECTS OF MECHANICAL DYSSYNCHRONY ON MYOCARDIAL CONTRACTILITY

Lei Fan (1), Jenny S. Choy (2), Chenghan Cai (1), Ghassan S. Kassab (2), Lik Chuan Lee (3)

(1) Joint Department of Biomedical Engineering, Marquette University and Medical College of Wisconsin, Milwaukee, Wisconsin, US
(2) California Medical Innovations Institute, San Diego, California, US
(3) Department of Mechanical Engineering, Michigan State University, East Lansing, Michigan, US

INTRODUCTION

Heart failure (HF) is an emerging epidemic affecting approximately 1% to 2% of the adult population. Patients with HF often develop mechanical dyssynchrony (MD) that affects regional cardiac function and coronary blood flow in the septum and left ventricular free wall (LVFW), which are fed by the left anterior descending (LAD) and left circumflex (LCx) arteries, respectively [1,2]. The effects of MD on global left ventricular (LV) functions, i.e., LV pressure and volume, and ejection fraction (EF), have been assessed from experimental/clinical studies. However, it remains unclear how MD affects regional contractile function and coronary perfusion in the LV as it is difficult to measure these quantities directly in experiments. The lack of this knowledge is an impediment to improving the current 30% non-responder rate of cardiac resynchronization therapy (CRT), which is frequently used to treat HF patients. Here we seek to address this issue by developing an inverse finite element (FE) modeling framework based on animal-specific 3D echocardiographic (ECHO) images and hemodynamics measurements acquired from a swine MD model to understand the impact of MD on regional contractile function and coronary blood flow distribution in the LV.

METHODS

Animal Experiments and Postprocessing: All animal experiments were performed in accordance with national and local ethical guidelines regarding the use of animals in research. Yorkshire domestic, female swine (n = 9), with body weight of 58.9±3.4 kg, were used in this study. All measurements were acquired under healthy and MD conditions by right atrium pacing (RAP) and right ventricular pacing (RVP), respectively, at heart rates of 100 bpm and 140 bpm (randomly chosen). The heart was paced individually from the RA or RV (apex) at 100 bpm and 140 bpm using temporary pacing electrode catheters (Bard Medical, Covington, GA) connected to an external pacemaker (Pace 203H, Oscor, Palm Harbor, FL, USA). In each condition, 3D ECHO images were acquired with the animals placed in the supine position while simultaneously recording LV end-diastolic volume (EDV), LV end-systolic volume (ESV), stroke volume, EF. Left ventricular pressure and volume were measured using a 5F pressure-volume catheter (Ventri-Cath 507, Millar, Inc., Houston, TX), connected to an MPVS Ultra PV loop system (Millar, Inc., Houston, TX). Pressure and volume waveforms were recorded using a data acquisition system (LabChart Pro, ADInstruments, Colorado Springs, CO). Then the chest was opened through a midline sternotomy and an incision was made in the pericardial sac with the creation of a sling to support the heart. The LAD and LCx arteries were carefully dissected free from their surrounding tissue in their proximal regions and a 3 mm flow probe connected to a flow meter (Transonic, Ithaca, NY) was placed around the coronary arteries to measure the coronary flow rate under regulated condition in the LAD and LCx simultaneously. The passive coronary flow rate was then measured in the fully dilated vessels after the injection of adenosine.

The 3D ECHO images were postprocessed using TomTec Arena (2014-2020) Imaging Systems GmbH (Philips Healthcare, Andover, MA) to calculate systolic dyssynchrony index (SDI) to represent the degree of MD, reconstruct 3D LV geometry corresponding to the ES time point based on segmented endocardial and epicardial surfaces, and derive the regional longitudinal and circumferential strain waveforms in each AHA segment. Left ventricular end-diastolic pressure (EDP) and end-systolic pressure (ESP), $dP/dt_{(max)}$, $dP/dt_{(min)}$, LVEDV, LVESV, and coronary flow rate waveforms were determined and averaged over a minimum of 10 cardiac cycles using LabChart Pro.

Computational Model: An inverse finite FE modeling framework was developed based on the reconstructed LV geometry as well as measurements of the LV pressure-volume (PV) loops, regional longitudinal and circumferential strains to estimate the regional contractile function under the 2 pacing conditions (**Fig. 1A1**). Specifically, parameters associated with the passive myocardium were

first adjusted until the values of LVEDP and LVEDV match the measurements after loading the LV from an unloaded configuration. Thereafter, the local time-dependent active stress parameter in the active constitutive model, which reflects the local myocardial contractility, is estimated by minimizing the mismatch between simulated and measured LV PV loops and regional strains. This is accomplished by solving a PDE-constrained optimization problem as in our previous work [3,4]. Global and regional load-independent contractility was optimized until the model predicted LV PV loops and regional strains match the measurements. All computational frameworks are implemented using the freely available open-source libraries FEniCS and dolfin-adjoint.

RESULTS

The experimental measurements show that RVP produces MD as well as changes in the LV function and coronary flow in the LAD and LCx. Specially, the SDI with RAP was 8.6±1.2% at 100 bpm (p<0.05) and 8.9±2.0% at 140 bpm (p<0.05), whereas SDI with RVP was 14±4.8% at 100 bpm (p<0.05) and 19.4±6.9% at 140 bpm (p<0.01). These results indicate that the degree of MD increases with RVP, and the increase is more significant at higher heart rates. **Fig. 1B** shows the changes in LVEDP and LVESP between RAP and RVP. LVEDP was significantly decreased with RVP (-4.4±1.0 mmHg at 100 bpm, p<0.01, and -6.5±1.5 mmHg at 140 bpm, p<0.01). Similarly, LVESP was also significantly decreased with RVP (-25.6±4.0 mmHg at 100 bpm, p<0.001, and -35.7±5.4 mmHg at 140 bpm, p<0.001). **Fig. 1C** shows the effects of MD on LVEDV and LVESV. LVEDV was significantly decreased with RVP (-14.7±1.8 mL at 100 bpm, p<0.001, and -11.3±3.3 mL at 140 bpm, p<0.05). Similarly, LVESV was significantly decreased with RVP at 100 bpm (-4.6±1.4 mL, p<0.05). At 140 bpm, ΔLVESV was -4.2±2.4 mL but did not reach significance. **Fig. 1D** and **E** show the changes in both regulated and passive mean LAD and LCx flow rates between RAP and RVP. Regulated and passive mean flow rates in the LAD artery (**Fig. 1D**) was significantly decreased with RVP (-7.6±2.3 mL/min, p<0.01 and -33.2±8.9 mL/min, p<0.05 at 100 bpm, respectively, whereas at 140bpm, the change in regulated flow was -5.7±0.8 mL/min, p<0.001, and in passive flow -54.0±7.4 mL/min, p<0.01). On the other hand, regulated flow in the LCX artery (**Fig. 1E**) almost did not change (-0.2±1.3 mL/min at 100 bpm and -3.6±2.6 mL/min at 140 bpm). Passive flow rate, however, was significantly decreased with RVP (-17.5±7.8 mL/min at 100 bpm, p<0.05 and -31.1±8.0 mL/min at 140 bpm, p<0.01). In addition, the inverse FE model predicts the effects of MD on myocardial contractility of the LV. The error between experimental measurements and model predictions of the LV PV loops is less than 5% in each case. The model predicted that global LV contractility is reduced from RA to RV pacing by 70±51, p<0.002 mmHg at 100 bpm and 100±86, p<0.02 mmHg at 140 bpm, respectively. As shown in the AHA segment, the estimated regional contractility in septum is reduced by 16±163 mmHg, p=0.77 at 100 bpm and 93±91 mmHg, p<0.1 at 140 bpm with RVP (compared to RAP) (**Fig. 1F)**. The estimated regional contractility in LVFW is reduced by 120±187 mmHg, p<0.05 at 100 bpm and 46±102 mmHg, p=0.24 at 140 bpm with RVP (compared to RAP) (**Fig. 1F)**.

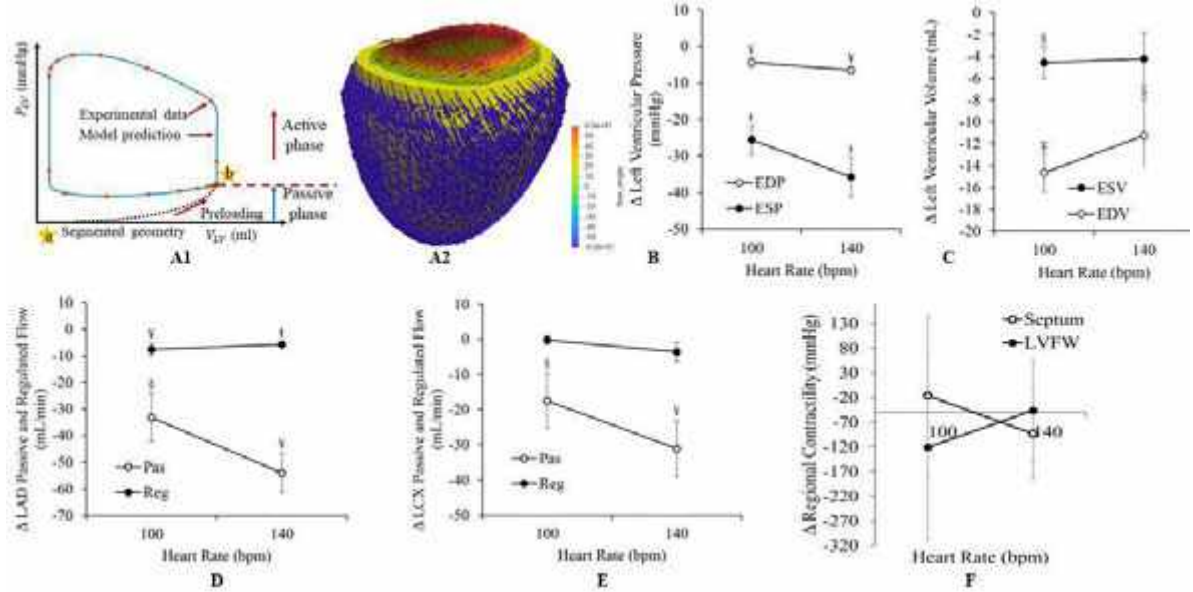

Fig. 1: A1. Schematic of inverse finite element modeling for model parameter estimation process; **A2**. animal-specific LV geometry with fiber distribution; Effects of MD on **B.** LV EDP and ESP; **C.** EDV and ESV; passive and regulated coronary blood flow in the **D.** LAD and **E.** LCx, **F.** LV regional contractility.

DISCUSSION

In this study, we have systematically investigated the acute effects of MD on LV hemodynamics, regional contractile function and coronary perfusion based on a clinically-relevant swine model. We show that MD not only negatively affects the LV function and hemodynamics, but also reduces LAD coronary blood flow under both passive and regulated conditions, LCx coronary flow under passive condition. In addition, inverse FE modeling using the measurements show that the estimated global LV contractility is also reduced in MD. The adverse effects of MD on LV contractility and regional coronary hemodynamics may be interrelated based on the "perfusion-contraction matching". Identification of these interrelated factors may have clinical implications in the identification of treatment of MD (i.e., CRT [4]) and improvement in treatment strategies.

ACKNOWLEDGEMENTS

This work was supported by NIH R01HL134841 and R01 HL160997.

REFERENCES

[1] Fan, L et al., *Am. J. Physiol. – Hear. Circ. Physiol*. 320, H1037-H1054, 2021.

[2] Fan, L et al., *Front. Physiol.* 11, 915 (2020).

[3] Finsberg, H et al., *Am. J. Physiol. – Hear. Circ. Physiol.* 317, H1363-H1375, 2019.

[4] Fan, L et al., *Comput. Biol. Med.* 105050, 2021.

IN VITRO REGIONALIZATION OF EARLY MIDBRAIN AND HINDBRAIN TISSUES DERIVED FROM MICROPATTERNED HUMAN PLURIPOTENT STEM CELLS

T. Xie (1), H. Jiang (1), L. Brown (2), C. Pak (3), Y. Sun (1,2)

(1) Department of Mechanical and Industrial Engineering, University of Massachusetts Amherst, Amherst, MA, USA
(2) Department of Biomedical Engineering, University of Massachusetts Amherst, Amherst, MA, USA
(3) Department of Biochemistry and Molecular Biology, University of Massachusetts Amherst, Amherst, MA, USA

INTRODUCTION

The central nervous system is developed from anteroposteriorly patterned neural tube consisting of forebrain, midbrain, hindbrain, and spinal cord. Recently, engineered development models and organoids based on human pluripotent stem cells (hPSCs) have provided opportunities for investigating how the neural tube is developed and patterned in vitro [1-2]. However, none of existing systems consist of regionalized midbrain and hindbrain simultaneously.

The midbrain-hindbrain boundary is an evolutionarily conserved structure that forms at the junction of the anterior OTX2+ midbrain region and the posterior GBX2+ hindbrain region, followed by constriction morphogenesis that separates the adjacent mesencephalon and rostral metencephalon into distinct compartments. Such compartmentalization is essential for proper cell differentiation in later stage development. While developmental biology studies using model systems have established the important roles of key morphogens such as FGF8 in the midbrain-hindbrain patterning [3], it remains unclear if other mechanisms exist in human brain development. Building regionalized midbrain and hindbrain tissues in vitro have not been achieved yet.

In this work, we have developed a self-organized in vitro model for AP neural patterning using micropatterned hPSCs by regulating RA, BMP, SHH, and WNT signals. We found that the reaction-diffusion of BMP/Noggin played a role in AP regionalization of OTX2+FOXA1+ midbrain and HOXB4+ hindbrain tissues. We further demonstrated that the model could predict the effects of different teratogens on the midbrain and hindbrain development. In the future, our platform can be used to investigate the mechanisms of human AP neural regionalization and border formation in neural development at the molecular level.

METHODS

Cell culture: SOX10 :: EGFP bacterial artificial chromosome hES cell reporter line (H9) and human induced pluripotent stem (hiPS) cell line (male; generated from human primary T-cells using episomal reprogramming method) were cultured in Essential 8 growth medium on hES cell-qualified Geltrex. ***Microcontact printing:*** Soft lithography was used to generate micropatterned polydimethylsiloxane (PDMS) stamps from negative SU8 molds that were fabricated using photolithography. These PDMS stamps were used to generate micropatterned cell colonies using microcontact printing, as described previously [4]. ***Image acquisition and analysis:*** Confocal images were collected with NIS-Elements AR software using Nikon A1 Resonant scanning confocal inverted microscope. ***Drug-screening assay:*** Valproic acid (Cat. No. P4543, Sigma-Aldrich) and penicillin G (Cat. No. 13752-1G-F, Sigma-Aldrich) were dissolved in Milli-Q water. Isotretinoin (Cat. No. 21648, Cayman Chemical) was dissolved in DMSO. ***Quantification and statistical analysis***: Data are represented as mean ± s.e.m. All the micropatterning experiments were repeated at least three times independently (biological replicates), with at least two technical replicates within each replicate. Statistical analysis was performed using two-sided unpaired Student's t-test.

RESULTS

We first discovered that by activating RA, Shh, BMP4, and Wnt signals while inhibiting TGF-β signal, geometrically confined hPSCs were differentiated into two distinctly separated domains, i.e., Otx2+ forebrain/midbrain region (center) and HoxB4+ hindbrain region (boundary) on day 6 (Fig. 1a). FOXA1 and FOXG1 (not shown) staining confirmed midbrain fate in the central region, and TTR staining excluded choroid plexus fate. Strikingly, the patterned cells underwent drastic morphological changes and the boundary HoxB4+ cells collectively migrated to the center of the pattern, forming a ring structure (Fig. 1b). Confocal microscopy showed that Otx2+ cells remained at the bottom, forming a sharp boundary with HoxB4+ cells. Compared to randomly distributed cells on unconfined controls, our

data suggest geometrical confinement is sufficient to induce the regionalization of cells with midbrain and hindbrain fate.

To understand the mechanisms of this cell fate separation, we first tested whether differential cell proliferation might lead to boundary cell folding. We stained phospho-histone H3 (pHH3) and found that the peak of pHH3 intensity did not match with the OTX2/HOXB4 boundary (data not shown). In addition, treating cells with aphidicolin did not alter the folding process, further supporting differential growth does not contribute to this separation process. Next, we investigated whether higher mechanical stress in the boundary cells would control the anteroposterior cell fates patterning (Fig. 2a). We found that treating cells with Blebbistatin or Y27632, two small molecules widely used to inhibit cellular actomyosin contractility, did not change the Otx2 and HoxB4 patterns. We found that lowering RA concentration to 0.1 μM led to weaker HOXB4 signals without changing the relative localization of OTX2 and HOXB4 expressions (Fig. 2b). Similarly, lowering CHIR concentration to 30 nM or increasing it to 600 nM did not significantly change the midbrain/hindbrain patterning. Notably, the cells induced with high CHIR concentration (600 nM) on day 6 displayed similar patterns that were observed in cells induced with intermediate CHIR (60 nM) on day 7 (Fig. 2b), which can be explained by the effects of WNT activation on cell proliferation. However, when cells were induced with a high concentration of BMP4 (10 ng/ml), the area covered by OTX2+ cells became significantly smaller and the peak of HOXB4 signals shifted dramatically inwardly to the center of the micropattern (Fig. 2b). Reducing BMP4 concentration to 1 ng/ml led to the expansion of the OTX2+ zones. Together, our data suggest that RA and WNT are permissive signals that are required for the caudalization, while the BMP4 signal instructs the midbrain/hindbrain patterning.

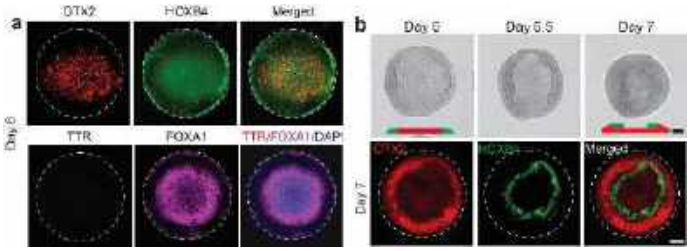

Figure 1: (a) Staining showing midbrain markers OTX2/FOXA1, choroid plexus marker TTR, and hindbrain marker HOXB4 at Day 6; (b) Images/illustrations showing moving of the hindbrain region (green) to the top of the pattern at day 7. Scale bar, 100 μm.

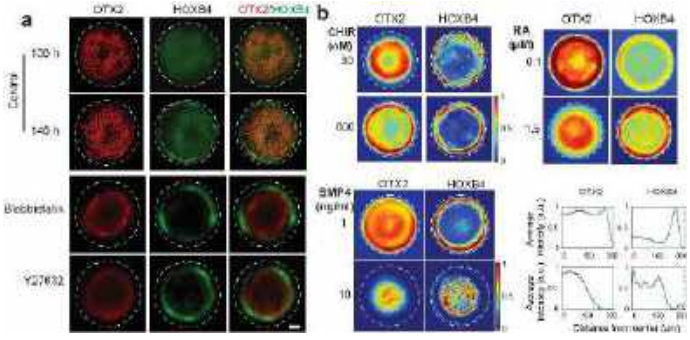

Figure 2: (a) Inhibiting contractility using blebbistatin and Y27632 did not change cell fate patterning. (b) Colorimetric maps and intensity plots showing average intensities of OTX2 and HOXB4 at different CHIR, RA and BMP4 concentrations.

We further demonstrated that our model can be used as a drug screening platform. We tested two known teratogens, VPA [5] and isotretinoin [6], which cause neural tube defects when women was exposed during pregnancy. We found that both VPA and isotretinoin disrupted midbrain-hindbrain boundary formation in our system, with distinct phenotypes, compared to a nonteratogenic drug penicillin G (Fig. 3). VPA treatment led to reduced expression of both OTX2 and HOXB4, while isotretinoin treatment led to randomly distributed OTX2+ and HOXB4+ cells. These findings are consistent with clinical reports that VPA causes smaller midbrain size and an increase in the midline gap of the hindbrain, while isotretinoin was linked to disproportionately long midbrain and dysplasia of the quadrigeminal plate and vermis.

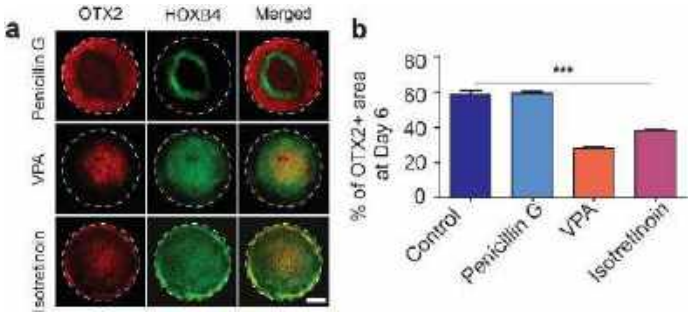

Figure 3: Effects of drugs on cell patterning. Scale bar, 100 μm

DISCUSSION

In this work, we have developed an in vitro model for AP patterned midbrain/hindbrain tissues using hPSCs. Contrary to the traditional view that morphogen gradient of FGF8 is the driving factor for the midbrain-hindbrain boundary formation, here we found that BMP/Noggin reaction-diffusion, rather than differential growth or contractility, played the dominant role in anteroposterior regionalization. Further, our model can be used to quantitatively study the effects of common medications on human early midbrain and hindbrain development. It is notable that our in vitro midbrain/hindbrain model so far can mimic only the early-stage development of the human brain since the total duration of organized cell culture is limited due to the geometrical confinement. Despite these limitations, our model is complementary to current animal models and traditional 2D cell culture systems and provides an excellent experimental platform to investigate the mechanism of human brain development and patterning.

ACKNOWLEDGEMENTS

This work is partially supported by the National Science Foundation grant (CMMI 1846866), National Institute of Diabetes and Digestive and Kidney Diseases (R01DK129990), and National Institute of Mental Health (R21MH130843).

REFERENCES

[1] Xue, X et al., *Nat. Mater.*, 17:633-641, 2018.
[2] Rifes, P et al., *Nat. Biotechnol.* 38: 1265-1273, 2020.
[3] Harada, H et al., *Dev Growth Differ* 58: 437-445, 2016.
[4] Xie, T et al., *Matter*, 2: 1621-1638, 2020
[5] Muhsen, M et al., *Epilepsia* 62: 1689-1700, 2021.
[6] Merlini, L. et al., *J. Child Neurol.* 29: 538-544, 2014.

PROPYLPARABEN EXPOSURE ALTERS UTERINE MICROSTRUCTURE AND INDENTATION MODULUS

Mahmuda R. Arshee (1), Indrani C. Bagchi (2,3,4), Ayelet Ziv-Gal (4), A. J. Wagoner Johnson (1,2,3,5)

(1) Mechanical Science & Engineering, Grainger College of Engineering, University of Illinois at Urbana-Champaign, Urbana, IL, USA
(2) Carl R. Woese Institute for Genomic Biology, University of Illinois at Urbana-Champaign, Urbana, IL, USA
(3) Biomedical & Translational Sciences, Carle Illinois College of Medicine, University of Illinois at Urbana-Champaign, Urbana, IL, USA
(4) Comparative Biosciences, College of Veterinary Medicine, University of Illinois at Urbana-Champaign, Urbana, IL, USA
(5) Beckman Institute for Advanced Science & Technology, University of Illinois at Urbana-Champaign, Urbana, IL, USA

INTRODUCTION

Research on the impact of environmental factors on reproductive health is gaining increasing attention. Parabens, ubiquitous preservatives incorporated in consumer products like cosmetics, food, and pharmaceuticals are one such factor. Prior studies indicated that exposure to paraben is associated with decreased fertility [1] and adverse birth outcomes, like lower birth weight [2]. Yet, while some research suggests that parabens are endocrine disruptors with limited estrogenic effect, there is a notable gap in knowledge of how paraben exposure can influence uterine function.

This study aims to investigate the effects of propylparaben (one of the most prevalently used parabens) on the mechanical properties of the uterus through indentation and the collagen microstructure using quantitative Second Harmonic Generation (qSHG) imaging in a mouse model. By addressing these research questions, we seek to determine the consequences of propylparaben exposure on uterine structure as a potential reason for paraben effects on fertility and pregnancy outcomes.

METHODS

Animal model: Female CD-1 mice aged 3 months were randomly divided into four groups and received daily oral doses of a vehicle control (corn oil) or propylparaben (PP) at doses of 2, 20, and 200 µg/kg/day. Dose selection was guided by women's urinary PP levels in NHANES 2015-2016 database and thus are human relevant. After 6 months of dosing, mice were euthanized during the diestrus stage of the estrous cycle and uterine horns were collected and frozen until use.

SHG microscopy: Uterine horns were thawed, and transverse sections were cut into 2 mm lengths, embedded in an optimal cutting temperature compound, and cryo-sectioned (-20 ◦C) in preparation for both nanoindentation and qSHG imaging. qSHG imaging, which preferentially shows collagen, was performed both in the forward and backward directions using a confocal microscope (Zeiss LSM 710) with a 70-fs laser (MaiTai DeepSee) centered at 780 nm illuminating the sample. A 20x objective was used to image the entire cross section and a 40x water immersion objective for high magnification, volumetric images (212*212*20 µm) from which sub-images (50*50*20 µm, n=6 images/mouse, 2 mice/group) were used for the following quantitative analyses: spherical variance, SV, assesses the degree of collagen fiber organization in 3D (0- aligned, 0.5- disorganized); out-of-plane angle, φ, indicates orientation relative to the imaging plane (0- in-plane, 90- out-of-plane) [3]; and forward to backward ratio, F/B, is the ratio of the forward and backward signal intensity. An increasing F/B indicates collagen that is more disorganized and/or more out-of-plane fibrils and/or larger fibrils [4]. Because of space limitations, data shown are from the indentation-qSHG co-registered data and we reference the data from the two mice per group that were imaged separately.

Nanoindentation (NI): Similar to our work in [3], a Piuma nanoindenter (Optics11, Amsterdam, Netherlands) indented the tissue submerged in PBS at 50 µm increments along a medial-lateral line using a spherical probe of 99 µm radius and 0.5 N/m stiffness. We evaluated the indentation modulus, E*, as a measure of local stiffness using the Hertz model. The Piuma camera captured images allowing the data to be co-registered with the SHG data. For the correlation between local E* and F/B, SV and φ, the sample size was n=8 measurements/mouse and one mouse from each treatment group.

Statistical analysis: A two-way ANOVA with post-hoc Tukey test compared between treatment groups and regions, with significance level set at $p<0.05$. Due to space constraints, box plots indicating significant differences are not shown, but are reported. Pearson's correlation coefficient assessed the linear correlation between E* and SHG parameters.

RESULTS

SHG images (Fig. 1) show the collagen microstructure with overlaid forward and backward signals, with the longitudinal

myometrium (LM) and circumferential myometrium (CM) indicated. The endometrium (E) is shown for reference, but was not analyzed. qSHG data from uterine cross sections co-registered with the indentation data (Fig. 2) indicated a significant increase in E* with increasing exposure.

Fig. 3 shows co-registered indentation and qSHG data. While φ for CM and LM were significantly different within a treatment, the F/B change across regions was not significant (Fig. 3a). In contrast, F/B for all pairs of treatments were significantly different except for the two highest doses. Together, these data suggest that the changes in F/B do not strongly depend on orientation here. SV was only significantly different between the 0 and 20 and 0 and 200 (not shown), indicating similarly that SV does not have a strong influence on F/B.

We observed significant increases in E* with treatment in both regions for all treatment pairs except for 0 vs 20 µg/kg/day=. While higher E* is expected with higher φ based on previous work [3] the difference in E* is much smaller with changes in angle compared to treatment (Fig. 3b). SV does not appear to have a strong influence on E* (Fig. 3c). Interestingly, there is a strong and significant correlation between E* and F/B, with all treatments and regions falling on a single line (Fig. 3d). This contrasts with Fig. 3a-c, in which distinct data clusters are evident. We hypothesize that the increased F/B in the exposed uteri is related to fibril thickening, which is supported by the observed increase in E* with treatment.

There were a number of strong and significant correlations in Fig. 3, which are not indicated here due to space.

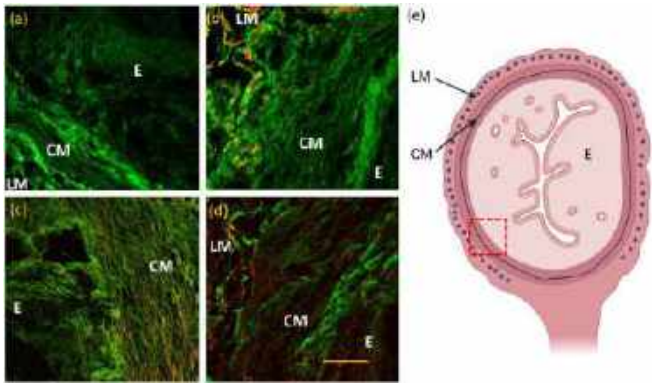

Figure 1: 40X images from mice uteri. (a) control and PP doses (b) 2, (c) 20, and (d) 200 µg/kg/day. Orange indicates overlapping backward (green) and forward (red) signals. Scale bar: 50 µm. (e) schematic transverse cross-section of uterus for reference (Created with BioRender), CM and LM- circumferential and longitudinal myometrium, E- endometrium.

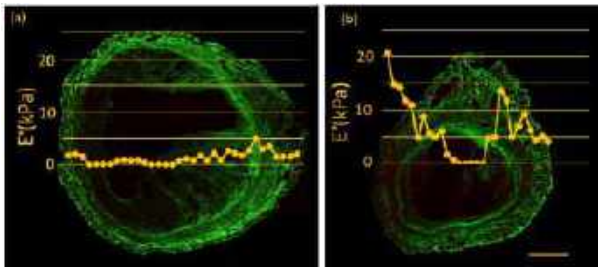

Figure 2: Indentation modulus overlaid on SHG images for (a) control and (b) 200 µg/kg/day PP dose. The line of indentation coincides with the X axis where Y=0. Scale bar: 500 µm.

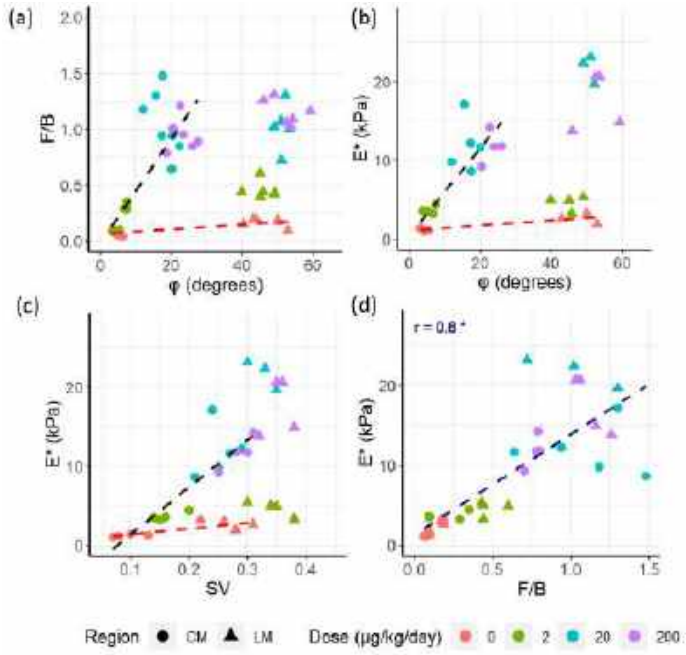

Figure 3: The variation of (a) F/B with φ, and E* with (b) φ, (c) SV, and (d) F/B, for regions CM and LM and with dose. E* and F/B have a strong and significant correlation. There were other strong and significant correlations not shown for brevity.

DISCUSSION

This study investigated the effects of PP exposure on the murine uterus, revealing both microstructural alterations and micromechanical changes by integrating quantitative parameters from SHG imaging and nanoindentation. Our analysis revealed disorganization in the collagen microstructure, accompanied by a stiffer indentation response in the treated groups. We found that not only do the fibrils become more disorganized and more out-of-plane due to the treatment, but there is also indication of fibril thickening, indicating potential fibrosis.

While the primary focus here is understanding the impact of PP exposure on the murine uterus, these discoveries also offer a way to identify fibrosis in other collagenous tissues. Our focus primarily centered on collagen alterations as a response to PP exposure. However, the other components of uterus, such as elastin, muscle, and extracellular matrix proteins, may also have contributed to changes in tissue stiffness. Ongoing studies further examine additional implications of PP exposure on female reproductive health, including pregnancy outcomes in the dams and offspring.

ACKNOWLEDGEMENTS

Research was carried out at Carl R. Woese Institute for Genomic Biology and the Materials Research Laboratory, University of Illinois at Urbana-Champaign. AZV acknowledges NIH for 1R03ES032887-01A1.

REFERENCES

[1] A. Karwacka et al., *Human Fertility*, vol. 22, no. 1, pp. 2–25, 2019
[2] L. A. Geer et al., *Journal of Hazardous Materials*, vol. 323, pp. 177–183, 2017
[3] A. Ostadi Moghaddam *et al.*, *Acta Biomaterialia*, vol. 158, pp. 347–357, 2023
[4] M. Sivaguru *et al.*, *Opt. Express*, vol. 18, no. 24, p. 24983, 2010

BALANCING COMPETING EFFECTS OF EPITHELIAL TISSUE GROWTH AND CYTOSKELETAL REGULATION DURING ORGANOGENESIS

N. Kumar (1, #), J. R. Ambriz (2, 3, #), K. Tsai (2, 3, #), M. S. Mim (1), M. Flores-Flores (1), W. Chen (2,3), M. Alber (2, 3, *), J. J. Zartman (1, 4, *)

(1) Department of Chemical and Biomolecular Engineering, University of Notre Dame, Notre Dame, Indiana, United States of America
(2) Department of Mathematics, University of California, Riverside, California, United States of America
(3) Interdisciplinary Center for Quantitative Modeling in Biology, University of California, Riverside, United States of America,
(4) Department of Biological Sciences, University of Notre Dame, Notre Dame, Indiana, United States of America
(#) These authors contributed equally to this work.
(*) Authors for correspondence: malber@ucr.edu (MA), jzartman@nd.edu (JJZ)

INTRODUCTION

How a developing organ robustly coordinates the cellular mechanics and growth to reach a final size and shape remains poorly understood. Through iterations between experiments and new model simulations that include a mechanistic description of interkinetic nuclear migration, we show that the local curvature, height, and nuclear positioning of cells in the *Drosophila* wing imaginal disc, a model epithelial organ used as a test case, are defined by the concurrent patterning of actomyosin contractility, cell-ECM adhesion, ECM stiffness, and interfacial membrane tension. We show that increasing cell proliferation via different growth-promoting pathways results in two distinct phenotypes. Triggering proliferation through insulin signaling increases basal curvature, but an increase in growth through Bone morphogenetic protein (BMP)/Decapentaplegic (Dpp) signaling and Myc causes tissue flattening. These distinct phenotypic outcomes arise from differences in how each growth pathway regulates the cellular cytoskeleton, including contractility and cell-ECM adhesion. The coupled regulation of proliferation and cytoskeletal regulators is a general strategy to meet the multiple context-dependent criteria defining tissue morphogenesis.

METHODS

We utilized the GAL4-UAS system for tissue-specific gene expression in an accessible and powerful genetic system for studying organ growth control mechanisms, the *Drosophila* wing disc. In parallel, a multi-scale Subcellular Element (SCE) modeling approach was employed to simulate cell mechanics and division dynamics. This involved computational simulations validated against experimental data to predict the impact of various mechanical factors on tissue morphology.

The general SCE modeling approach[1–3] was used as the basis for the model presented here. Our novel SCE-type multi-scale model in detail represents cell deformation and proliferation and integrates mechanical properties, including cell membrane elasticity, cell pressure, polarized actomyosin contractility with nuclear movement, and cell-cell and cell-ECM adhesivity. Another key advantage of this novel SCE modeling approach is that most of the cell mechanical properties considered can be directly or indirectly calibrated based on experimental data[1,4]. This computational modeling framework is used to simulate a two-dimensional (2D) cross-sectional profile of the *Drosophila* wing imaginal disc along the anterior-posterior axis adjacent to the DV compartment boundary. Using a detailed 2D model allows for simulating large numbers of cells with high resolution and with particular attention to mechanical cell properties and small changes in tissue structure and shape. Given that the cross-section is composed of boundary cells, squamous cells, and columnar cells, the model includes a separate description for each cell type. Important distinctions from our previous model[3] are detailed representations of cell division and actomyosin contractility in different parts of a cell. The model includes membrane nodes, nucleus nodes, and ECM nodes. Energy potentials are used to describe interactions between different nodes, as in Nematbakhsh and Levis et al.[3].

RESULTS

In this study, we iterated between quantitative analysis of wing disc morphogenesis unders specific genetic perturbations and computational simulations of wing disc growth, which provides a mechanism for hypothesis generation.

Our results demonstrated that the ratio of apical to basal contractility, ECM stiffness, and cell-ECM adhesion are key determinants of basal curvature. We categorized growth regulators into

two classes based on their impact on tissue curvature: one class increased basal curvature, while the other led to tissue flattening with growth. The simulations confirmed that these outcomes are tied to their differential regulation of the cytoskeleton.

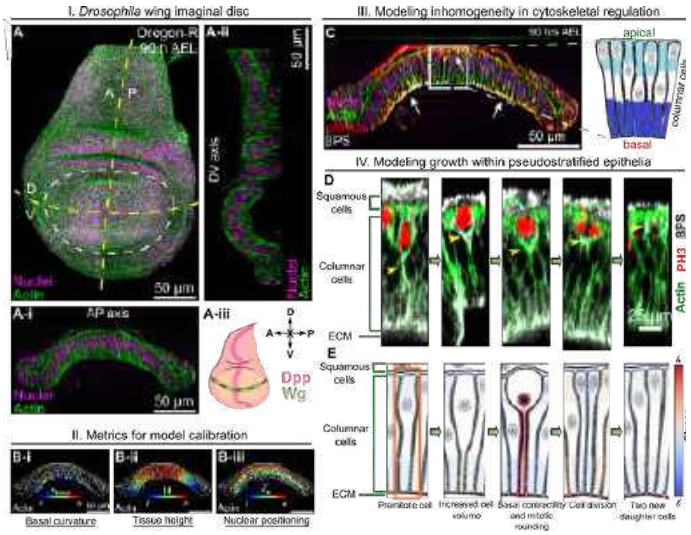

Figure 1: Multi-scale SCE model simulation of proliferation in a pseudostratified epithelium predicts proliferation dynamics and cytoskeletal regulation.

DISCUSSION

The morphogenetic processes observed in the *Drosophila* wing disc are similar to those in other developmental systems, such as the formation of the mammalian optic cup, suggesting a commonality in the underlying mechanisms across species. Our findings underscore the importance of a balanced regulation between proliferation and cytoskeletal dynamics in shaping organs. The study's insights broaden our understanding of developmental biology and provide a foundation for future explorations into organogenesis. Overall, the principal findings identified in our work can be generalized and incorporated into our understanding of development across multiple organ systems in animals due to the underlying biochemical and biomechanical similarities that drive morphogenesis[7,8].

ACKNOWLEDGEMENTS

This work was supported by the National Science Foundation grant NSF2029814 to all co-authors and by a pilot grant from the Northwestern University NSF-Simons Center for Quantitative Biology to JZ. The Zartman group was also supported in part by NSF DBI-2120200 and NIH Grant R35GM124935. The authors would also like to thank members of the Zartman lab for helpful discussions. Model simulations were run on UC Riverside HPCC.

REFERENCES

1. Nematbakhsh A, Sun W, Brodskiy PA, Amiri A, Narciso C, Xu Z, Zartman JJ, Alber M. Multi-scale computational study of the mechanical regulation of cell mitotic rounding in epithelia. Asthagiri AR, editor. PLoS Comput Biol. 2017 May 22;13(5):e1005533.

2. Sweet CR, Chatterjee S, Xu Z, Bisordi K, Rosen ED, Alber M. Modelling platelet–blood flow interaction using the subcellular element Langevin method. Journal of The Royal Society Interface. Royal Society; 2011 Dec 7;8(65):1760–1771.

3. Nematbakhsh A, Levis M, Kumar N, Chen W, Zartman JJ, Alber M. Epithelial organ shape is generated by patterned actomyosin contractility and maintained by the extracellular matrix. PLoS Comput Biol. 2020 Aug;16(8):e1008105.

4. Sandersius SA, Chuai M, Weijer CJ, Newman TJ. Correlating Cell Behavior with Tissue Topology in Embryonic Epithelia. PLOS ONE. Public Library of Science; 2011 Apr 29;6(4):e18081.

5. Eiraku M, Takata N, Ishibashi H, Kawada M, Sakakura E, Okuda S, Sekiguchi K, Adachi T, Sasai Y. Self-organizing optic-cup morphogenesis in three-dimensional culture. Nature. Nature Publishing Group; 2011 Apr;472(7341):51–56.

6. Chauhan BK, Lou M, Zheng Y, Lang RA. Balanced Rac1 and RhoA activities regulate cell shape and drive invagination morphogenesis in epithelia. Proceedings of the National Academy of Sciences. Proceedings of the National Academy of Sciences; 2011 Nov 8;108(45):18289–18294.

7. Zartman JJ, Shvartsman SY. Unit operations of tissue development: epithelial folding. Annu Rev Chem Biomol Eng. 2010;1:231–246. PMCID: PMC6049827

8. Aydin O, Passaro AP, Raman R, Spellicy SE, Weinberg RP, Kamm RD, Sample M, Truskey GA, Zartman J, Dar RD, Palacios S, Wang J, Tordoff J, Montserrat N, Bashir R, Saif MTA, Weiss R. Principles for the design of multicellular engineered living systems. APL Bioengineering. 2022 Mar 2;6(1):010903.

THE COMPOUND STIMULATION OF MATRIX STIFFNESS AND COLLAGEN CONCENTRATION ON TUMOR ORGANOID MIGRATION

Bo-Jiang Lin (1), Hiromichi Fujie (1,2), Masashi Yamazaki (1,2), Koji Takahashi (1), Naoya Sakamoto (1,2)

(1) Department of Mechanical Systems Engineering, Tokyo Metropolitan University, Hachioji, Tokyo, Japan
(2) Research Center for Medicine-Engineering Collaboration, Tokyo Metropolitan University, Hachioji, Tokyo, Japan

INTRODUCTION

Metastasis is the malignant progression in which the cancer cells collectively migrate away from the primary tumor and localize to the distal secondary organ with invasion and proliferation [1]. The multicellular organoid/spheroid model has been developed for pathophysiology-mimicking metastasis [2]. The metastatic preference for secondary organs is specific to the cancer type [3]. The mechanical properties among these organs differ from 1~2 kPa to 25~40 kPa in Young's modulus [4]. From the mechanobiological perspective, previous studies have shown that tumor cells preferentially migrate toward the stiff matrix by sensing the surrounding 10-20 μm matrix in depth [5,6]. Many of these studies used artificial matrices, including polyacrylamide gels with different stiffness. On the other hand, a latest study attempted to adjust the stiffness of natural ingredients, such as collagen, through compression [7]. The usage of natural ingredients is thought to lead to more pathophysiological behaviors of cancer cells because the cells may change the stiffness and geometry of the matrix in the process of metastasis [8]. However, besides matrix stiffness, the organization of collagen fibers can also promote directional migration [9]. How the mutual interaction of stiffness and fiber organization guides the directional migration remains unclear.

We hypothesize that mixed effects of collagen stiffness, fiber density, and cell-cell interaction modulate the migration preference of tumor spheroids. In this study, we examined the influence of the matrix stiffness and fiber density, which were managed separately, on tumor spheroid migration.

METHODS

A549 adenocarcinoma cells (JCRB0076, Nibiohn), originated from a lung cancer patient, were cultured in T25 flasks with E-MEM (Fujifilm) with 10% FBS (Gibco) under 37℃ in an incubator with 5% CO_2. As the establishment of the spheroid, A549 cells were resuspended by 5 min incubation with 0.05% trypsin and seeded on a low-attachment 96-wells plate (Thermo Fisher) at 1000 cells/well. The plate was centrifuged at 1800 rpm for 20 min for cell precipitation. A549 cells aggregated into the spheroid for 4 days. The diameter of A549 spheroids was analyzed by microscopy (Olympus).

The collagen construct was prepared with 5 mg/ml type I collagen (Koken), reconstruction buffer, and 10xMEMα at the mixed ratio of 8:1:1 in a stretch chamber (Strex) for more than 1 day. The collagen construct was covered with a filter and a silicone membrane and then compressed by centrifugation at 3430 rpm for 20 min [10]. Finally, the A549 spheroids were transferred and cultured on the collagen construct for 4 days. The stiffness of the collagen construct was measured by atomic force microscopy indentation test.

To evaluate the effect of only the fiber density, we also prepared the collagen film which was the thin-collagen gel substrates at different densities and whose thickness was less than 10 μm, on a cover glass. The collagen solution was prepared with 5 mg/ml type I collagen (Koken), reconstruction buffer, and 10xMEMα at the mixed ratio of 8:1:1 or 2:4:4, referred to as 80% or 20%, and smeared on the cover glass with a silicone scraper. The surface image of the collagen was scanned by scanning electron microscopy (KEYENCE). Fiji ImageJ was used for calculating the area fraction of fibers, indicating the fiber density, over the whole image.

After culturing spheroids on the collagen substrate for 4 days, the phase-contrast images of A549 spheroids were captured daily with a microscope. The spreading diameter of the spheroid was analyzed with Fiji ImageJ.

Statistical analyses (ANOVA with Tukey HSD) were performed using R ($\alpha = 0.05$, GNU). Results were presented as the average ± standard errors of the mean.

RESULTS

The compressed collagen construct shared a similar topology with the 80% collagen film but exhibited a different surface structure from

the uncompressed collagen construct and 20% collagen film. The uncompressed collagen construct had a loose fibrous surface though it contained clusters of nodules. The 20% collagen film was the sparse fibrous surface.

The centrifugation stiffened the collagen matrix from 2.9 ± 0.5 kPa to 17.2 ± 2.3 kPa (Figure 1B). Meanwhile, the centrifugation condensed the collagen fiber from 33.9 ± 2.4% to 56.8 ± 3.6% (Figure 1C).

There was no difference in height between 80% and 20% collagen film (data not shown); however, the collagen density of 80% collagen film was higher than the 20% collagen film, which was 56.8 ± 2.6% and 13.8 ± 1.7% separately (Figure 1C). The fiber density of 80% collagen film was analogous to the compressed collagen construct, but more condensed than the uncompressed collagen construct. For 20% collagen film, the fiber density was lower than that of the compressed collagen construct and higher than the uncompressed collagen matrix.

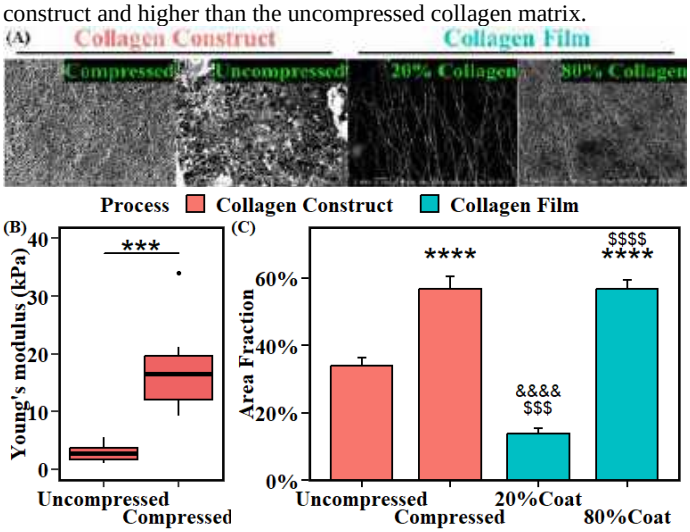

Figure 1: Collagen matrix properties. (A) SEM images, (B) Young's modulus, and (C) Fiber density (N = 5 ~ 10). (**, P < 0.0001 within-process; &&&&, P < 0.0001 vs Compressed; $$$, P < 0.001, $$$$, P < 0.0001 vs Uncompressed)**

A549 spheroids grew into a compact spheroid with a mean diameter of 317.6 ± 4.4 μm in 4 days of spheroid preparation. After being transferred to the collagen matrices, A549 spheroids expanded under the culture of 4 days (Figure 2). On the fourth day, the boundary of A549 spheroids remained sharp on the 80% collagen film and compressed collagen construct, but these became blurred on the 20% collagen film and uncompressed collagen construct.

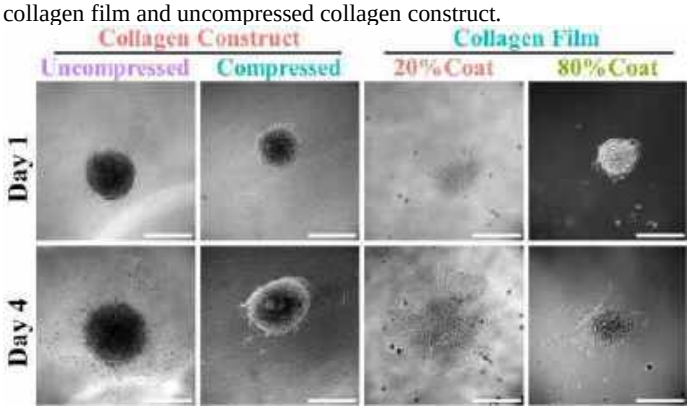

Figure 2: Phase-contrast Spheroid Image (scale = 400 μm)

Quantitatively, the A549 spheroids on the uncompressed collagen construct (D4 = 993.5 ± 59.3 μm) expanded considerably than those on the compressed collagen construct (D4 = 815.3 ± 41.0 μm); however, the spheroids on the 80% collagen film (D4 = 888.1 ± 29.0 μm) expand sedately than those on the 20% collagen film (D4 = 573.9 ± 20.0 μm) (Figure 3).

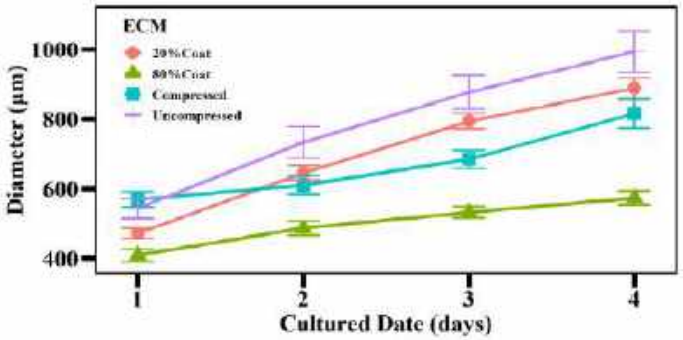

Figure 3: Time-Course of Spheroid Expansion (N = 6 ~ 24)

DISCUSSION

The A549 spheroid expanded more slowly on the compressed collagen construct, which was condensed and stiff collagen matrix condition, than on the loose and soft uncompressed collagen. On the collagen film, assuming the comparable apparent stiffness, the A549 spheroid grew more sedately on the condensed fibrous collagen film (80%) than on the loosened 20% collagen film. Besides that, there was no difference in the fiber density between the compressed construct and the 80% collagen film. The A549 spheroid showed the lowest expansion on the compressed collagen construct. In total, our results suggest that the matrix stiffness and fibrous density contribute to tumor expansion simultaneously and provide mechanobiological insight into tumor metastasis. Tumor invasion requires the disruption of the extracellular matrix (ECM), remodeling the structure, and modulating the stiffness of the ECM [8,11,12]. It implies that the matrix stiffness might be a robust influencer on tumor metastasis compared to collagen fiber density.

The current results did not investigate the cellular interaction with matrix stiffness and fibrous density separately. Further investigation will examine the cellular mechanism of matrix stiffness and fibrous density on tumor migration individually.

ACKNOWLEDGEMENTS

This work has been supported by Grant-in-Aid for Scientific Research (KAKENHI) (18H03521, 18K19934, 22K19898), Tokyo Metropolitan Government Advanced Research (R2-2) and Tokyo Metropolitan University Emergent Future Society Research Project.

REFERENCES

[1] Ha, N-H et al., *Cancer Targeted Drug Delivery*, 9781461478768:435–458, 2013
[2] Grimm, D et al., *Int J Mol Sci*, 23:3073, 2022
[3] Nicolson, GL, *Biochimiea et Biophysica Acta*, 948:175–224, 1988
[4] Barney, LE et al., *Curr Opin Chem Eng*, 11:85–93, 2016
[5] DuChez, BJ et al., *Biophys J*, 116:670–683, 2019
[6] Buxboim, A et al., *Journal of Physics: Condensed Matter*, 22:194116, 2010
[7] Hadjipanayi, E et al., *Cell Motil Cytoskeleton*, 66:121–128, 2009
[8] Wisdom, KM et al., *Nat Commun*, 9:4144, 2018
[9] Oudin, MJ et al., *Cold Spring Harb Symp Quant Biol*, 81:189–205, 2016
[10] Ye, X et al., *Biosurf Biotribol*, 9:78–83, 2023
[11] Deryugina, EI et al., *Cancer Metastasis Rev*, 25:9–34, 2006
[12] Park, JH et al., *Bioact Mater*, 20:381–403, 2023

A BIOREACTOR PLATFORM DESIGNED TO ESTIMATE CELL GENERATED STRESSES WITHIN UNIAXIALLY CONSTRAINED TISSUE EQUIVALENTS

Andrew V. Glick (1), Daniel Paukner (2), Christian J. Cyron (2), Jacopo Ferruzzi (1,3)

(1) Department of Bioengineering, University of Texas at Dallas, Richardson, TX, USA
(2) Institute for Continuum and Material Mechanics, Hamburg University of Technology, Hamburg, Germany
(3) Department of Biomedical Engineering, University of Texas Southwestern Medical Center, Dallas, TX, USA

INTRODUCTION

Tissue homeostasis is an essential requirement for multicellular life and requires control over cell proliferation, differentiation, paracrine signaling, and physical interactions with other cells and with the surrounding extracellular matrix (ECM). Among the many physiological variables that are under homeostatic control, the physical properties of most cells, tissues, and organs are optimized to operate under a preferred state of mechanical tension [1]. Much of what is known about mechanical homeostasis of tissues under tension, or "tensional homeostasis", is based on experiments on tissue equivalents, that is fibroblast-populated collagen gels [2]. Tissue equivalents cultured in presence of a physical constraint at their boundary develop tensile forces under static conditions [3], which has led to postulate the existence of a homeostatic tensile force [4]. However, it is conceivable that the homeostatic target is a material quantity, such as stress.

To gain a mechanistic understanding of how tensional homeostasis is developed and maintained in healthy soft tissues, and subsequently disrupted by disease processes, there is a need for improved tissue engineering platforms, also known as bioreactors. Recent studies have presented bioreactors capable of culturing fibroblasts in 3D collagen matrices under both uniaxial and biaxial tension [5-6]. However, current bioreactors have limited imaging capabilities, with the acquisition of structural information occurring only at discrete time points (due to the lack of sterility while imaging). To address these limitations, we have developed the first miniaturized computer-controlled biaxial bioreactor fully integrated with a confocal microscope. The bioreactor design was inspired by Eichinger et al. [6] and built with the following objectives: (1) to allow bioreactor functionality outside of a cell culture incubator; (2) to miniaturize the biomechanical testing apparatus; and (3) to enable continuous confocal imaging functionality. Here, we present the bioreactor design and showcase its ability to dynamically measure homeostatic force evolution, structural remodeling of collagen, and cross-sectional area to estimate stresses in uniaxial tissue equivalents.

METHODS

The bioreactor is designed to fit the stage of a Nikon AX confocal microscope (Nikon, Tokyo, Japan). An aluminum base plate is equipped with compact linear actuators (Physik Instrumente, Auburn, MA) [7] and force transducers (Aurora Scientific, Aurora, Canada) to enable both dynamic stretching and continuous force recording. The core of the bioreactor is a circular chamber 3D printed using an autoclavable resin (Formlabs, Somerville, MA) which houses a disposable 100 mm dish (MatTek, Ashland, MA). A constant temperature of 37°C is achieved by combining a plate heater within a heated microscope enclosure, while an external humidifier (Tokai-Hit, Fujinomiya, Japan) supplies 5% CO_2 to the chamber, thus enabling long-term culture. Figure 1a shows the device mounted on a microscope in a uniaxial configuration.

NIH/3T3 fibroblasts (ATCC, Manassas, VA) were serum-starved for 24 hours to minimize proliferation [6] and dispersed in a collagen solution, which was polymerized using established protocols [8]. A dogbone-shaped PDMS mold was used to form cell-laden collagen gels anchored to sterile porous inserts [6]. After one hour of polymerization, the gels were floated using a standard media formulation [6], resulting in uniaxially constrained tissue equivalents. Dynamic force acquisition with simultaneous confocal imaging was carried out every 20 minutes for 24 hours (Figure 1b). Both brightfield and reflection images were acquired using a 10× lens as 1×16 tiled, 2650 μm stacks with a 50 μm step, using an excitation wavelength of 488nm. To estimate the sample cross-sectional area, a calibration experiment was conducted to compare multiphoton and confocal areas in the central region of the sample. Briefly, a set of uniaxial samples was imaged at discrete time points using both confocal and multiphoton microscopy (for increased penetration depth). Cell-endogenous NADH was excited at 740 nm and two-photon excitation fluorescence (TPEF) was collected through a bandpass filter (460-500 nm). The collagen matrix was imaged by exciting samples at 1060 nm and collecting second harmonic generation (SHG) signals through a bandpass filter (520-560 nm).

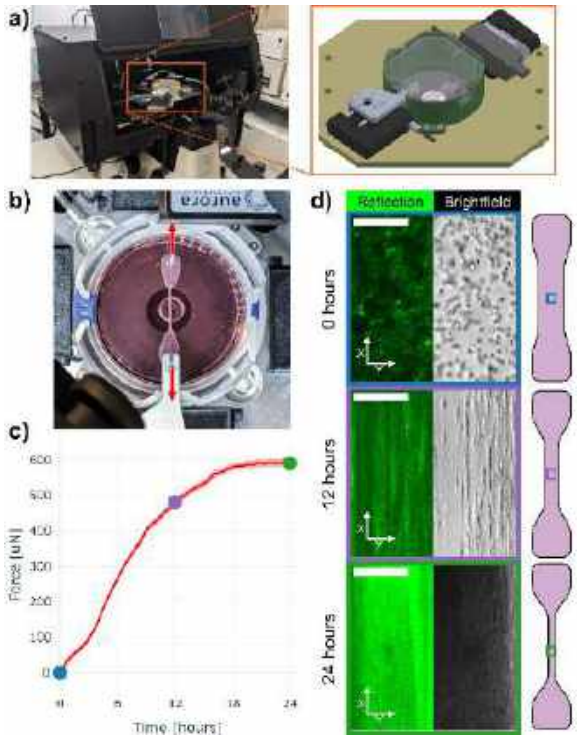

Figure 1: (a) Bioreactor mounted on a confocal microscope and magnified Solidworks assembly. (b) Top view of a uniaxially constrained tissue analog after 24 hours of culture (red arrows indicate contractile forces). (c) Time course of force development by a 0.8 mg/mL collagen gel loaded with 10^6 cells/mL. (d) Confocal images reveal underlying structural changes in both collagen (reflection, green) and cells (brightfield, grey). Scale bars indicate 200 µm while cartoons indicate the approximate imaging location.

RESULTS

Our bioreactor allows long-term NIH/3T3 fibroblast culture, with high cell viability and limited loss of media due to evaporation. Figure 1c displays the tensile forces generated by fibroblasts over 24 hours and shows that our results are comparable to previous reports, both in terms of magnitude and time course [6]. More importantly, confocal imaging captures the structural evolution of the tissue analog over time. Starting from an isotropic collagen matrix populated by circular cells at 0 hours, the construct develops into a highly anisotropic collagen network populated by aligned cells at 12 hours, and ultimately into a high-density tissue when the force steady state is achieved at 24 hours (Figure 1d). As the tissue analog compacts laterally it becomes progressively denser, thereby making optical penetration increasingly difficult. For this reason, we used multiphoton imaging to capture the entire cross-section of the gels (Figure 2a). SHG imaging shows that the bottom surface contracts more than the top surface, which leads to tissue folding. On the other hand, TPEF imaging shows that fibroblasts are evenly distributed at 0 hours, while at later time points occupy only a portion of the gel's cross-section and arrange into a semicircle. Indeed, collagen densification and alignment occur only where cells reside, suggesting that stress is developed only in cell-populated areas. We observe similar geometrical changes using confocal imaging and find that the cell-populated area can be quantified by approximating the top surface using a circular arc (Figure 2a-b). By employing such approximation, we can combine force and effective cross-sectional area measurements at each time point. Our initial stress estimations indicate that NIH/3T3 fibroblasts generate a stress of ~1 kPa at 24 hours (Figure 2c).

DISCUSSION

Stromal fibroblasts remodel their extracellular environment using various mechanisms, including the generation of contractile forces. Here, we propose a new bioreactor design informed by previous approaches [3-6] that combines biomechanical, microstructural, and geometrical measurements. This work focused on the bioreactor design, and on combining force and geometrical data on fixed uniaxial specimens. In the future we plan to conduct studies on both uniaxial and biaxial specimens and to apply external deformations. Our work is limited by the manual estimation of areas, but we plan to automate the cross-section approximation by using a cubic Hermite spline to extrapolate the top surface of the tissue analogs. We conclude that our bioreactor design represents a promising tissue engineering platform to explore tensional homeostasis in both healthy and diseased soft tissues.

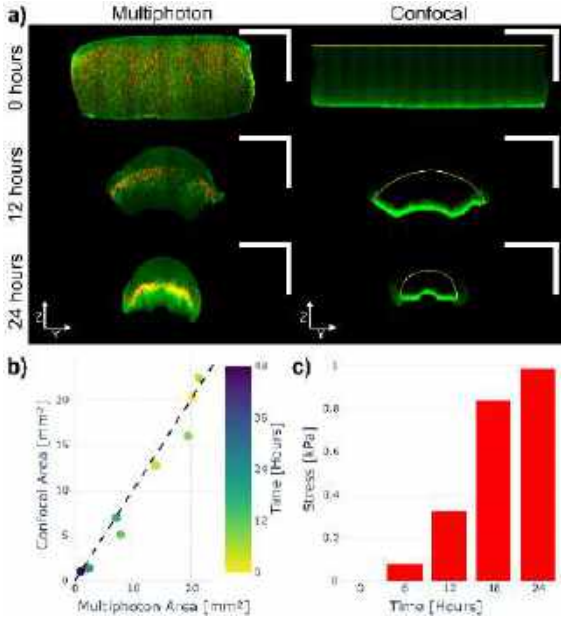

Figure 2: (a) Resliced image stacks show cross-sections of tissue analogs captured using multiphoton (left) and confocal (right) microscopy. Multiphoton images display TPEF signal from cells in red and SHG signal from collagen in green, while confocal images display reflection signal from collagen in green. Scale bars indicate 2000 µm in both directions. To capture the effective area from reflection images, we added a circular arc approximation of the top surface (yellow line). (b) Comparison between cross-sectional areas estimated using the two imaging approaches confirms that confocal areas can be used to calculate stresses as shown in (c).

ACKNOWLEDGEMENTS

We acknowledge Professor Jay D. Humphrey (Yale University) and Professor Patrick W. Alford (University of Minnesota) for fruitful conversations on bioreactor design. This project was partially funded by The University of Texas at Dallas Jonsson School Research Initiative.

REFERENCES

[1] Humphrey J.D. et al., *Nat Rev Mol Cell Biol*, 15: 802-812, 2014.
[2] Stamenović D. and Smith M.L., *Soft Matter*, 16: 6946–6963, 2020.
[3] Delvoye P. et al., *J Invest Dermatol*, 97: 898-920, 1991.
[4] Brown R.A. et al., *J Cell Physiol*, 175: 323-332, 1998.
[5] Bai Y. et al., *Ann Biomed Eng*, 42: 1791-1805, 2014.
[6] Eichinger J.F. et al., *J Biomech Eng*, 142: 071011, 2020.
[7] Win Z. et al., *J Biomech Eng*, 139: 071006, 2017.
[8] Ferruzzi J. et al., *Sci Rep*, 9: 1-16, 2019.

QUANTITATIVE ANALYSIS OF THE COMPRESSIVE FORCE APPLIED TO THE ACL TIBIAL ENTHESIS

D. Ishii (1), S. Sato (1), H. Fujie (1)

(1) Graduate School of Systems Design, Tokyo Metropolitan University, Hachioji, Tokyo, Japan

INTRODUCTION

Ligament, tendon, and their attachments (enthesis) have been studied to improve the prevention and treatment of ligament injury and tendon enthesopathy. Anatomical and histological studies have revealed that ligaments and tendons often wrap around bony pulleys and attach to bone via fibrocartilage [1,2]. These studies also suggest that not only tensile but also compressive forces are applied to the enthesis. However, a detailed analysis of the forces acting on the entheses during joint loadings has not been conducted. In this study, focusing on the anterior cruciate ligament (ACL) tibial enthesis in the knee joint, the forces applied to the enthesis due to a joint loading were analyzed.

METHODS

Immature porcine knee joints (n=5) were used. After each knee joint was fixed to the 6-DOF robotic system (FRS-2015, Technology Services) [3], an anterior tibial loading test of 200 N was performed in full extension (approximately 30-40° of flexion) and 60° of flexion. Sagittal sections were performed for the ACL in parallel to the fiber direction with a special care not to damage ligament fibers [4]. The medial part of the sectioned ACL was removed so that the cross section of the ACL enthesis can be observed (Figure 1a,b). Note that the anteromedial (AM) bundle and the intermediate / posterolateral (I/P) bundle were clearly partitioned by the lateral meniscus attachment, as indicated by Tantisricharoenku et al [5]. The deformation behavior of the ACL tibial enthesis was observed by a digital microscope (3R-MSBTVTY, 3R Solution) while the 3D motion recorded in the anterior tibial loading test was reproduced [4]. In the obtained images, the fiber orientation angles of the AM and I/P bundles to the ACL attachment were analyzed using Image J (NIH) (Figure 1c). In addition, a histological examination was performed for the same cross sections to determine the fibrocartilage distribution.

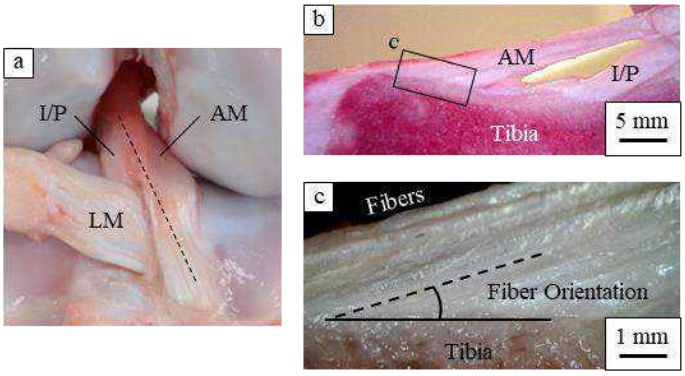

Figure 1: Procedures for sagittal section preparation. (a) The ACL tibial attachment of porcine knee joint. The AM and I/P bundles were divided by lateral meniscus (LM). The sagittal section was made parallel to the fiber direction (dotted line). (b) ACL enthesis observed by digital microscope. (c) The fiber orientation angle of each bundle relative to the attachment was analyzed from this image.

Next, an anterior tibial loading test up to 200 N was performed on other porcine knee joints (n=5) in full extension and 60° of flexion using the robotic system. The resultant force applied to the tibia during the test was determined from the outputs of the 6 DOF load transducer of the robotic system [6], while the attachment positions of the AM and I/P bundles to the ACL tibial attachment plane was analyzed [7].

Using the average of the fiber orientation, attachment position of the bundles, and resultant force, the magnitude and direction of the bundle (tensile) and compressive force applied from the AM and I/P bundles to the ACL tibial enthesis were calculated by subtracting the bundle force from the resultant force (Figure 2). For the calculation, we

assumed that the magnitude of the bundle force was equal to that of the resultant force with no friction between bundle fibers and between fibers and bone. We also assumed that the bundle force was applied to the attachment position in parallel to the fiber orientation.

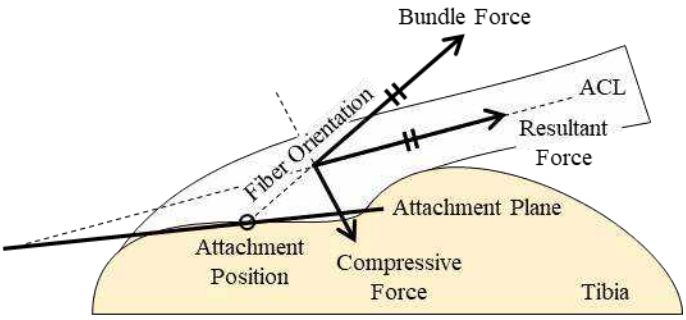

Figure 2: Schematic drawings of bundle (tensile) and compressive force analysis. Bundle and compressive forces were analyzed from the fiber orientation, attachment position of each fiber bundles to the ACL attachment plane, and resultant force under several assumptions.

RESULTS

Histological examination indicated that the cartilage matrix was more clearly observed in the I/P bundle enthesis than in the AM bundle enthesis and on the surface of bony pulley (Figure 3).

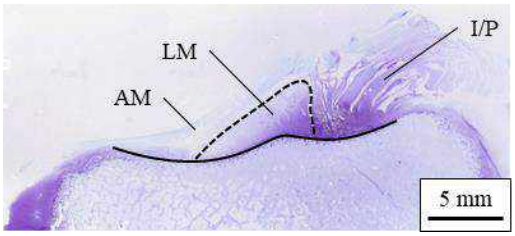

Figure 3: ACL tibial enthesis. Fibrocartilage areas (blue staining area) were clearly observed in the I/P enthesis by toluidine blue staining.

In the ACL tibial enthesis, not only tensile forces of 68-117 N but also compressive forces of 14-51 N were applied from the AM and I/P bundles under an anterior tibial force of 200 N. The compressive forces acted within I/P bundle enthesis or around the bony pulley (Figure 4).

DISCUSSION

Previous studies have suggested that compressive forces are applied to the ligament/tendon attachments during joint motion [1,2,8]. They have also suggested that these compressive forces are related to remodeling of fibrocartilaginous entheses and tendon enthesopathy. Although these are important findings, the compressive forces have not been identified, and thus have remained a matter of speculation. In the present study, the tensile and compressive forces acting on the ACL tibial attachments were quantified using an original method, and it was clarified that the compressive force applying around the ACL tibial enthesis was up to 45 % of the anterior tibial force. In addition, the compressive forces were found to act within I/P bundle enthesis or around the bony pulley.

The ACL peak force of human during gait occurs at about 15° of flexion, not at full extension [9], and the flexion angle of porcine knee joint during gait varies between 43-48° and 85-92° [10]. Therefore, the

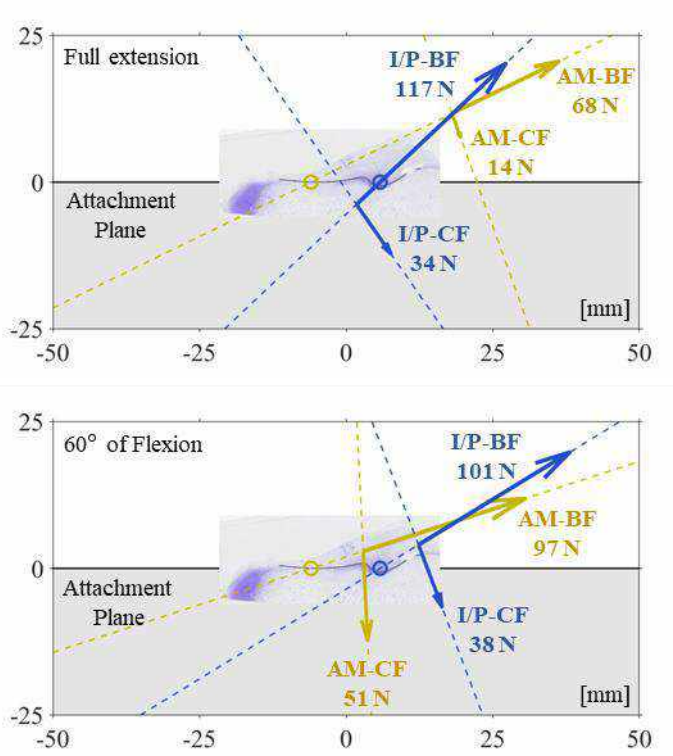

Figure 4: Bundle force (BF) and compressive force (CF) vectors applied to the ACL tibial attachment plane at full extension and 60° flexion in response to 200 N of anterior tibial load. Note that the attachment positions of the AM and I/P bundles are indicated by the yellow and blue circles, respectively. In addition, the histological image with toluidine blue stain is superimposed.

ACL force of pig is expected to be maximum at about 60° of flexion during walking. In the present analysis, the compressive force was greater at 60° flexion than at full extension, and also it was greater within the I/P enthesis than within AM enthesis and posteriorly out of the I/P enthesis (Figure 4). Furthermore, histological examination showed that fibrocartilage was more clearly observed in the I/P enthesis than in other areas (Figure 3). Therefore, it is suggested that fibrocartilage contributes to the compressive forces applied in the ACL tibial enthesis during knee joint motion.

ACKNOWLEDGEMENTS

This work was supported by the Sasakawa Scientific Research Grant from The Japan Science Society and Tokyo Metropolitan Government Advanced Research Grant (#R2-2).

REFERENCES

[1] Benjamin M, Ralphs JR, J Anat, 193: 481-494, 1998.
[2] Shaw HM, Benjamin M, SJMSS, 17(4): 303-315, 2007.
[3] Kimura K, Fujie H, Transactions of the JSME, 81(826): 1-12, 2015.
[4] Sato S, et al., Biotribology Fukuoka 2023, G28, 2023.
[5] Tantisricharoenkul G, et al., KSSTA, 22: 961-971, 2014.
[6] Fujie H, et al., J. Biomech Eng, 117(1): 1-7, 1995.
[7] Ishii D, et al., SB3C2023, P102, 2023.
[8] Cook JL, Purdam C, BJSM, 46(3): 163-168, 2012.
[9] Shelburne KB, et al., J Biomech, 37(6): 797-805, 2004.
[10] Stavrakakis S, et al., Animal, 8(2): 338-346, 2014.

A MECHANISTIC IN VIVO STUDY ON THE RELATIONSHIP BETWEEN THE PATHOPHYSIOLOGY OF THE ASCENDING AORTA AND THE COHERENCE OF LARGE SCALE BLOOD FLOW

Karol Calò (1), Andrea Guala (2), Valentina Mazzi (1), Maurizio Lodi Rizzini (1), Lydia Dux-Santoy (2), Jose Rodriguez-Palomares (2), Stefania Scarsoglio (1), Luca Ridolfi (3), Diego Gallo (1), Umberto Morbiducci (1)

(1) PoliTo^{BIO}Med Lab, Department of Mechanical and Aerospace Engineering, Politecnico di Torino, Turin, Italy
(2) Vall d'Hebron Institut de recerca, Barcelona, Spain
(3) PoliTo^{BIO}Med Lab, Department of Environment, Land and Infrastructure Engineering, Politecnico di Torino, Turin, Italy

INTRODUCTION

Aortic diseases, including those involving the ascending aorta (AAo), account for significant cardiovascular morbidity and mortality worldwide. Congenital bicuspid aortic valve (BAV) is one of the most common pathological conditions among these, along with AAo dilation and aortic stenosis, which are both often BAV-related. Due to the recognized crucial role played by hemodynamics in the pathophysiology of the aorta, several efforts have been done in the study of aortic flows. However, there is still work to be done to improve risk stratification of aortic diseases, promoting the clinical translation and refining clinical decision making. In this context, the present study adopts a network approach to investigate the impact of the BAV pathological condition on the physiological AAo flow coherence, following a recent study on large-scale coherent motion in the healthy aorta [1]. In detail, in vivo 4D flow MRI data were used to quantify flow coherence in terms of correlation between the blood flow rate waveform at the AAo inlet and the axial velocity waveforms obtained at each voxel in the acquired AAo region of interest. Then, the anatomical persistence length of such correlation was computed through an *ad-hoc* complex network-based approach, and its association with the main AAo canonical hemodynamic and anatomic features was explored.

METHODS

The study population include 64 subjects presenting with a tricuspid aortic valve (TAV) and 43 BAV patients matched in terms of age, sex, body surface area and blood pressure. Both TAV and BAV populations include patients affected by AAo dilation and mild-to-severe aortic valve stenosis. Details on 4D flow MRI acquisition protocol and data processing are reported elsewhere [2]. The study was approved by the ethics committee of the Vall d'Hebron Hospital and written informed consent was obtained from all participants. 3D anatomic models of the aortas were reconstructed from 4D flow MRI-derived angiography. Anatomical landmarks of the sinotubular junction (STJ) and the brachiocephalic artery bifurcation, identified from co-registered 2D cine images, were used to define the AAo region of interest. A network-based approach was adopted to quantify the coherence of large-scale AAo fluid structures in terms of similarity to the subject-specific inlet blood flow rate waveform, here considered as driving waveform of the aortic flow [1]. Briefly, from the phase-contrast velocity data, the blood flow rate $Q(t)$ waveform was computed at the STJ cross-section and the (through-plane) axial velocity component $V_{ax}(t)$ waveform in each voxel of the AAo fluid domain was obtained as proposed in [5]. Then, for each subject, a *"one-to-all"* network (**Fig. 1**) was built, consisting of: (1) one reference node represented by $Q(t)$, located at the STJ section's center of mass; (2) the N nodes represented by the waveforms $V_{ax,i}(t)$ at each voxel (i, for i=1,..,N) belonging to the AAo region of interest.

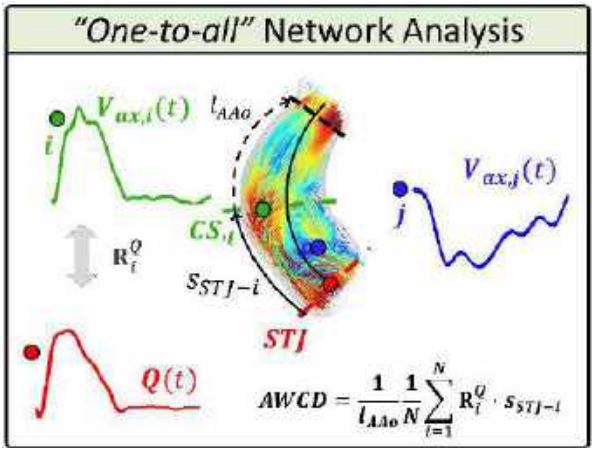

Figure 1: Network-based characterization of AAo flow coherence.

The link between the STJ node and the i-th node was weighted by the Pearson correlation coefficient R_i^Q between $Q(t)$ and $V_{ax,i}(t)$ waveforms, thus measuring the dynamic similarity of the voxel-based $V_{ax}(t)$ waveform with the driving aortic flow rate. Finally, the anatomical length of persistence of the $Q(t)$-$V_{ax}(t)$ correlation was quantified using the network-based metric *Average Weighted Curvilinear Distance* (*AWCD*) defined as [1]:

$$AWCD = \frac{1}{l_{AAo}} \frac{1}{N} \sum_{i=1}^{N} R_i^Q \cdot s_{STJ-i}, \qquad (1)$$

where l_{AAo} is the curvilinear length of the AAo centerline, and s_{STJ-i} is the curvilinear distance between the cross-sections containing the nodes where waveforms $Q(t)$ and $V_{ax,i}(t)$ are defined (**Fig. 1**). To assess the main factors determining the persistence length of the $Q(t)$-$V_{ax}(t)$ correlation, statistical associations of *AWCD* with canonical hemodynamic descriptors quantifying, e.g., $Q(t)$ average value and dynamics, flow eccentricity and blood kinetic energy, and anatomic attributes based on AAo size, curvature, torsion, and aortic arch shape were investigated.

RESULTS

The median and interquartile range of R_i^Q correlation coefficients and *AWCD* are 0.53(0.19-0.75) and 0.24(0.18-0.32) respectively, for the entire population under study. The effect of aortic valve phenotype on AAo flow coherence is presented in **Fig. 2**, where the volume maps of R_i^Q values above the median ($\tilde{R}_i^Q$=0.53) and the *AWCD* values in the AAo are displayed for two explanatory cases. In detail, the healthy TAV subject presenting with the maximum *AWCD*, and the BAV patient, with neither aortic dilation nor stenosis, characterized by the minimum *AWCD* value, are presented here. In the healthy aorta, strong correlations between $V_{ax}(t)$ and $Q(t)$ are uniformly distributed along the entire AAo volume, and the anatomical length of persistence of large-scale flow coherence can reach the 43% of the AAo length (**Fig. 2a**). In a BAV phenotype, *AWCD* is significantly lower compared to TAV (p<0.01), with values down to 15% of the AAo length (**Fig. 2b**).

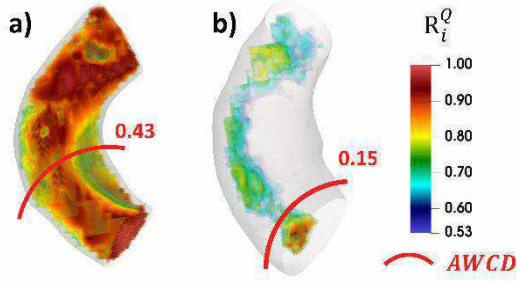

Figure 2: R_i^Q maps and *AWCD* for two explanatory cases.

The analysis revealed that *AWCD* decreases with age (p < 0.001) in the entire population under study (ALL), as well as considering the TAV and BAV subpopulations separately. The scatter plots of the most relevant associations (adjusted with age) of *AWCD* with the canonical hemodynamic and anatomic features are presented in **Fig. 3**. It emerged that *AWCD* is positively correlated with the average flow rate $\bar{Q}$ when considering the entire population and, more strongly, in TAV subjects (R=0.57, p<0.001). In BAV subjects, on the contrary, no association emerged for *AWCD* with $\bar{Q}$, while *AWCD* resulted positively correlated with the peak kinetic energy $\overline{KE}_{peak}$ in AAo (R=0.43, p<0.01). Furthermore, a significant negative correlation emerged between *AWCD* and the flow jet angle *FJA* (a measure of flow eccentricity) [6] in BAV patients (R=-0.54, p<0.001), but not in the TAV group. The aortic anatomic attribute D_{ratio}, defined as the ratio between AAo maximum diameter and the aortic root maximum diameter, presented a significant negative correlation with *AWCD* in both BAV and TAV subjects, with correlation stronger in the former group (**Fig. 3**).

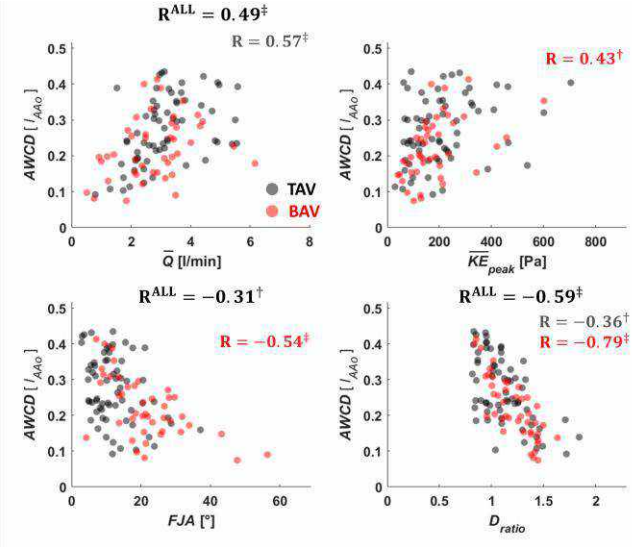

Figure 3: Explanatory scatter plots of *AWCD* with aortic hemodynamic and geometric quantities.
***p<0.05; †p<0.01; ‡p<0.001**

DISCUSSION

A network approach is here adopted to synthesize the 4D complexity of aortic hemodynamics using the concept of large-scale flow coherence, quantified in terms of similarity of the forward flow with the driving aortic flow rate. The main findings suggest that: (1) a BAV phenotype strongly reduces the persistence length of AAo flow coherence, as measured by *AWCD*; (2) the inertial effect of the average aortic flow rate $\bar{Q}$ sustains the transport of coherent fluid structures to the distal AAo, confirming previous observations in healthy subjects [1], and that such effect is cancelled by the presence of BAV phenotype; (3) the aortic dilation, quantified in terms of D_{ratio}, may act as an impediment to the transport of flow coherence regardless of valve phenotype, suggesting that an increasing AAo dilation could progressively compromise the physiological spatiotemporal coherence of large-scale forward flow [3,7]. In conclusion, the present findings contribute to broaden the current mechanistic understanding of the coherence transport of large-scale blood flow in aortic pathophysiology. Future studies may adopt this network approach to evaluate the impact of aortic dilation and/or stenosis on AAo flow coherence.

ACKNOWLEDGEMENTS

KC, VM, MLR, DG and UM have been supported by MIUR FISR—FISR2019_03221 CECOMES. AG has received funding from "la Caixa" Foundation (LCF/BQ/PR22/11920008).

REFERENCES

[1] Calò, K et al., *IEEE Trans Biomed Eng*, 70:1095-1104, 2023.
[2] Dux-Santoy, L et al., *Eur Heart J Cardiovasc Imaging*,34:1-11, 2019.
[3] Calò, K et al., *Ann Biomed Eng*, 49:2441-2453, 2021.
[5] Morbiducci, U et al., *J Biomech*, 48:899-906, 2015.
[6] Sigovan, M et al, *J Magn Reson Imaging*, 34:1226-30,2011.
[7] De Nisco, G et al., *Med Eng Phys*, 82:119-129, 2020.

DEVELOPMENT AND IN-VITRO VALIDATION OF A SIMPLE 1D MECHANICAL MODEL FOR PEDIATRIC VASCULAR PATCH PLANNING

Shannen B. Kizilski (1,2), Dominic P. Recco (1,2), Jocelyn M. Davee (3), Patrick D. Earley (1), Nicholas E. Kneier (1), Lauren E. Marshall (1), Peter E. Hammer (1,2), David M. Hoganson (1,2)

(1) Department of Cardiac Surgery, Boston Children's Hospital, Boston, MA, USA
(2) Harvard Medical School, Harvard College, Cambridge, MA, USA
(3) Department of Cardiology, Boston Children's Hospital, Boston, MA, USA

INTRODUCTION

Patch augmentation of hypoplastic or stenosed vessels is a staple of congenital cardiovascular surgery. Reconstruction of critical anatomic features such as the aortic arch and the pulmonary arteries (PAs) during the newborn and infant periods can have significant impact on long-term outcomes and survival. Reintervention rates due to residual obstruction and/or restenosis are as high as 18% for arch reconstruction [1] and 60% for branch PA plasty [2]. Presently, patches are shaped intraoperatively with reference to the unpressurized native vessel dimensions, which limits the ability to achieve precise reconstructed geometry under physiologic loads.

Our group aimed to develop a preoperative planning workflow that generates patient-specific patch designs via 1D mechanical model, accounting for properties of the vessel and patch materials as well as material uptake at the suture line. Considering these factors through prospective patch design will reduce the burden of intraoperative patch reshaping and enable the surgeon to achieve targeted geometry under postoperative physiologic loads, thereby reducing the need for reintervention and improving patient outcomes. We have conducted preliminary validation with a silicone model of branch PA stenosis.

METHODS

Silicone Model Creation: A physiologically compliant silicone model of an infant branch PA was created with 4.5mm nominal diameter and a central stenosed region of 2mm at zero pressure under 30% prestretch [3], reaching 5.8mm nominal diameter (30% distension) and 2.5mm stenosis at a mean PA pressure of 30mmHg. Molds were fabricated with an SLA printer at 25µm layer height (Form 3, FormLabs, Somerville, MA). Tubes were molded from EcoFlex 00-20 silicone (Smooth-On, Macungie, PA) to achieve high distensibility with a uniform wall thickness of 2mm suitable for suture retention.

Patch Design via 1D Mechanical Model: Molded tubes were prestretched and mounted into an apparatus for CT imaging at 0 and 30mmHg pressure (Fig. 1a). The 30mmHg state represents physiologic loading, while zero pressure reflects the vessel after it has been clamped and depressurized during surgical repair. In the clinical patch-planning setting, only preoperative pressurized measurements of the vessel would be available, so these are used as inputs to the 1D model. Scans taken at 30mmHg were loaded into SimVascular [4] for automatic batch segmentation (Fig. 1b), and the resulting contour groups were imported into MATLAB (MathWorks, Natick, MA) to extract preoperative diameter at fixed increments along the vessel axial length.

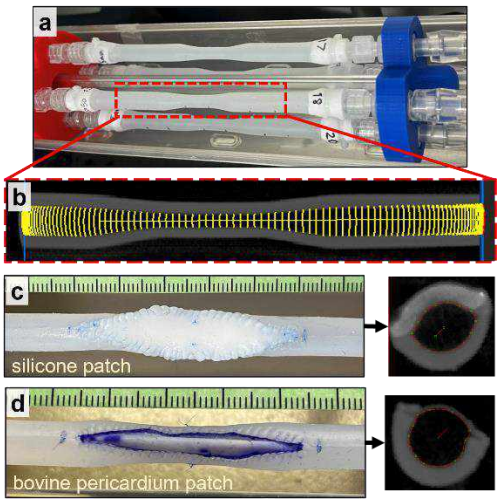

Figure 1: (a) Stenosed branch PA silicone models mounted for pneumatic pressurization during CT scan. (b) Example segmentation from imaging. (c) Silicone and (d) bovine pericardium patches sutured into silicone PA models, with example pressurized CT cross-sectional images on the right.

Using the known pressure (30mmHg), measured diameter, axial prestretch (30%), and unloaded wall thickness (2mm), the circumferential stress was calculated with Law of Laplace, and circumferential stretch was estimated for each cross section of the tube using biaxial data for the silicone material. This stretch estimate was used to calculate the circumference of native tissue at zero pressure. Since the native tissue will be opened to a new, larger diameter following repair, its hoop stress will be higher than preoperatively, meaning that it will stretch to a larger circumference under the same pressure load. To account for this effect, the circumference of native tissue available in the stenosed region opened up to the target diameter (set equal to the proximal non-stenosed diameter) under 30mmHg pressure was estimated following the same procedure. The difference between the target circumference and the extent of native tissue defines the required patch width under load. Using material properties for the patch, the same scaling procedure was performed to determine the unloaded patch size. Finally, a uniform offset was added to the unloaded patch to account for material loss from the suturing process. This suture offset was tuned through measurement of suture uptake between samples of the tube and patch materials.

In this study, two patch materials were tested: 1) a 2mm-thick silicone sheet (with 2% Barium for contrast), representing a pulmonary homograft patch (Fig.1c), and 2) 0.3mm-thick bovine pericardium (BP) (Fig. 1d). For each patch material, one set of tests was initially conducted with tubes reconstructed to target zero pressure dimensions by using the 0mmHg scans as input, isolating the geometric and suture uptake pieces of the procedure. A second set of tubes was then reconstructed to target dimensions at 30mmHg to incorporate the scaling component.

Patch Placement & Measurements: Patch designs were laser projected onto the patch surface and traced [5]. Patches were sutured into tubes with 7-0 Prolene, and the suture line was made airtight with a thin layer of silicone adhesive. Postoperative CT scans were acquired under zero pressure and 30mmHg to assess accuracy of reconstruction. Perimeter of the patched region was averaged over a 20mm axial length and compared to the targeted dimensions. Measurements are reported as mean ± standard deviation across multiple samples.

RESULTS

Four different patch designs were generated with the 1D model for the two targeted loading states (0 and 30mmHg) and two patch materials: silicone and BP. All patches included a 1mm suture bite offset, though BP patches were axially trimmed by 0.5mm due to smaller measured suture-line material uptake in the axial direction versus circumferentially. Compared to the 14.1mm perimeter target, models reconstructed to a zero-pressure target achieved 13.5±0.2mm with silicone patches (n=3) and 14.2±1.1mm with BP (n=7) (Fig. 2a).

Under 30mmHg pressure, circumference of the stenosis was predicted to increase by 1mm when opened to the pressurized target diameter. Patches designed for 30mmHg were both longer and wider than zero-pressure patches for both materials (Fig. 2c). The BP patch was the same length as the silicone patch but 0.2mm wider given its higher stiffness. Compared to the 18.4mm perimeter target, models reconstructed to a 30mmHg pressure target achieved 17.6±0.4mm with silicone patches (n=3) and 19.3±0.4mm with BP (n=6) (Fig. 2b). All silicone-patched samples were within 6% of the targeted dimensions, while BP-patched samples had up to 10% error (Fig. 2d).

DISCUSSION

This study demonstrated the utility of a 1D mechanical model to design vascular patches that achieve vessel dimensions within 2mm maximum of the targeted perimeter. Tissue distensibility, vessel prestretch, and suture uptake are essential factors that must be considered to correctly size the patch for physiologic loading. Patches planned for different pressure levels were completely different sizes in the unloaded state, while using different patch materials had a more modest impact. Suture uptake is a function of bite depth from the tissue edge but also depends on which two materials are being joined (and their thicknesses). In infant-sized anatomy, this factor can have a significant impact on the reconstructed geometry and will require further dedicated studies.

We envision a patch-planning workflow in which patient-specific preoperative imaging is segmented and fed into this model, along with targeted postoperative dimensions based on normative population data. The vessel and patch will be assigned average material properties from our library of biaxial data, and a material-specific, surgeon-specific suture offset will be applied to the unloaded patch design. The design will be laser-projected in the OR for use by the surgeon as a patch template. Prior to implementation, we will rigorously test the model with more complex geometry and additional biologic materials.

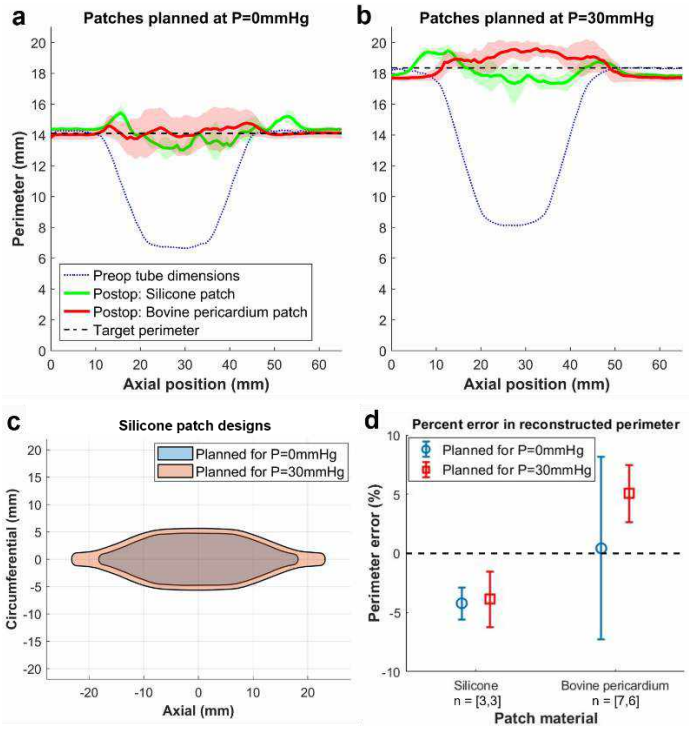

Figure 2: Perimeter measurements for PA model reconstructed with patches designed at either (a) 0 or (b) 30mmHg pressure. Shaded regions show standard deviation across samples. (c) Comparison between unloaded silicone patches designed for 0 vs. 30mmHg pressure state in the same PA model. (d) Error between achieved vs. targeted perimeters for each patch type.

ACKNOWLEDGEMENTS

The authors acknowledge the Small Animal Imaging Laboratory at Boston Children's Hospital for use of their facility.

REFERENCES

[1] Hill, K. D., *et al.*, *Circulation*, 128(9):954–961, 2013.
[2] Vida, V. L., *et al.*, *J. Card. Surg.*, 28(4):439–445, 2013.
[3] D'Souza, G. A., et al., *Prog. Pediatr. Cardiol.*, 47:49–57, 2017.
[4] Lan, H., et al., *J. Biomech. Eng.*, 140(2), 2018.
[5] Saunders, T., et al., *Interdiscip. Cardiovasc. Thorac. Surg.*, 37(2):ivad129, 2023.

SB³C2024
Summer Biomechanics, Bioengineering and Biotransport Conference
June 11-14, Lake Geneva, WI, USA

INTERACTION WITH ENDOTHELIAL CELLS INDUCES VASCULAR SMOOTH MUSCLE CELL ORIENTATION UNDER WALL SHEAR STRESS CONDITION

K. Sawasaki (1), M. Nakamura (2), N. Kimura (3), K. Kawahito (4), M. Yamazaki (1), H. Fujie (1,5), and N. Sakamoto (1,5)

(1) Department of Mechanical Systems Engineering, Tokyo Metropolitan University, Hachioji, Tokyo, Japan
(2) Department of Electrical and Mechanical Engineering, Nagoya Institute of Technology, Nagoya, Aichi, Japan
(3) Department of Cardiovascular Surgery, Saitama Medical Center, Jichi Medical University, Omiya, Saitama, Japan
(4) Department of Cardiovascular Surgery, Jichi Medical University, Shimotsuke, Tochigi, Japan
(5) Research Center for Medicine-Engineering Collaboration, Tokyo Metropolitan University, Hachioji, Tokyo, Japan

INTRODUCTION

Circumferential alignment of vascular smooth muscle cells (SMCs) in the medial wall of arteries plays a crucial role in vasodilatation and vasoconstriction [1]. Biochemical and biomechanical interactions between vascular endothelial cells (ECs) and SMCs are essential for the formation and maturation of the structure of the arterial wall including the SMC alignment in a development process [2]. Even in matured arteries, these structure and alignment are maintained by quiescent SMCs; however, proliferated and migrated SMCs and their disordered alignment are frequently found in cardiovascular diseases [3,4]. ECs respond to hemodynamic stimuli, including wall shear stress (WSS), thereby changing their functions and bidirectionally communicating with SMC to contribute to vascular physiology and pathology such as angiogenesis, vascular remodeling, and vascular tonus [5,6]. Although interactions between EC and SMC could contribute to the regulation of the SMC alignment, the detailed mechanism is poorly understood.

Here we investigated the effect of EC-SMC interactions under hemodynamic conditions on the morphology of SMCs using the EC-SMC coculture model previously established with a centrifugally compressed cell–collagen combined construct (C6)[7,8].

METHODS

Primary Human Aortic SMCs and Human Aortic ECs were purchased from Lonza (USA). A type I collagen gel in which 450,000 cells of SMCs were embedded was compressed by 1,000 *g* centrifugal force for 10 min with a plate centrifuge (Fig. 1). The compressed collagen gel construct (C6) [7,8] was cultured for 6-7 days in Medium 199 (Thermo Fisher Scientific, USA) supplemented with 20% fetal bovine serum (Nichirei Biosciences Inc., Japan) and 10 ng/mL basic fibroblast growth factor (FUJIFILM Wako, Japan), and then ECs were seeded on the C6 and cocultured 1-2 more days. A SMC model, constructed without ECs, was also prepared for comparison.

The SMC and coculture models were exposed to 2 Pa WSS, which is a representative value of physiological conditions in large arteries, with a parallel-plate flow chamber. After the WSS exposure for 24 h, αSMA as a SMC marker, CD31 as an EC marker, and cell nuclei in the models were fluorescently stained for morphological analysis. The fluorescent images were acquired with a laser-scanning confocal microscope (Olympus, Japan). The orientation angle of cell nuclei against the direction of the flow was calculated on ImageJ software (National Institute of Health, USA).

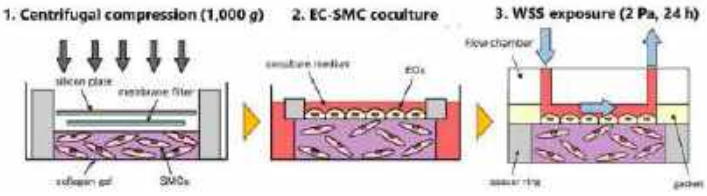

Fig. 1: Schematic diagram of the construction method of the EC-SMC coculture model with C6.

RESULTS

Figure 2 shows representative fluorescent images and the relative frequency of the nuclear orientation angle of ECs and SMCs after the WSS exposure. Morphological analysis of SMCs was performed in 3 different layers: the upper layer near the surface, the middle layer, and the lower layer around the bottom of C6. In the SMC models, only SMCs in the upper layer, which can directly contact with the flow, but

not in the middle layer, tended to align with the direction of the flow. SMCs in the lower layer also did not show orientation in any specific direction (data not shown). In contrast, in the coculture model, SMCs in C6 were found to orientate perpendicularly to the direction of the flow even though the SMCs were below the EC monolayer and not directly exposed to the flow. ECs on the surface of the C6 aligned with the flow.

We subsequently sought to confirm whether WSS-related signaling mediated by ECs causes this SMC orientation or not. The coculture model was treated and exposed to WSS for 24 h with 20 μM DAPT, an inhibitor of Notch signaling, which is known to contribute to sensing and responding to WSS, as well as interaction with neighboring cells [9]. As a result, ECs on the surface of the C6 did not align with the flow by the DAPT treatment (Fig. 2). The perpendicular orientation of SMCs was slightly reduced in the upper layer and suppressed in the middle and lower layers.

DISCUSSION

The alignment of SMCs with the flow was only observed in the upper layer of SMC models. These SMCs are thought to be directly exposed to the WSS, and this result is consistent with a previous report [10]. In contrast, the SMCs in the coculture models orientated perpendicular to the direction of the flow regardless of layers. Since the SMCs in the coculture models were not directly exposed to the flow, our results indicate that SMCs indirectly sense the flow environment, including the direction of WSS, through communications with ECs.

Since bioactive factors mediating EC-SMC communications are generally considered not to transmit the direction of mechanical stimuli, the other unclarified mechanisms may cause the perpendicular orientation of SMCs. We showed the inhibition of mechanical sensitivity of ECs and EC-SMC interactions by the DAPT treatment reduced the perpendicular orientation of SMCs in the coculture model. Therefore, our results imply that responses of ECs to WSS via Notch signaling are involved in the perpendicular orientation of SMCs. On the one hand, it has been reported that the expression and activity of Notch receptors are involved in the responses of SMCs to mechanical stimuli [11]. Since the DAPT treatment in the present study could inhibit the mechanical sensitivity relating to Notch signaling of not only ECs also SMCs, the transmission of mechanical environment information between SMCs was thought to be inhibited. SMC-SMC interactions via Notch signaling may also contribute to the perpendicular orientation of SMCs.

Our future work will be required to identify the role of WSS-related Notch signaling in the regulation of the circumferential alignment of SMCs. Clarifying the underlying mechanisms will contribute to a better understanding of not only vascular physiology but also the pathogenesis of vascular diseases accompanied by abnormal morphological features of SMCs.

ACKNOWLEDGEMENTS

This study is supported in part by Grants-in-Aid for Scientific Research from the MEXT of Japan (Nos. 18K19934 and 22K19898), a Tokyo Metropolitan Government Advanced Research Grant (R2-2), the TMU Research Project for Emergent Future Society, and JST SPRING (No. JPMJSP2156).

REFERENCES

[1] Greif et al., *Dev Cell.*, 23(3): 482-93, 2012
[2] Scheppke et al., *Blood.*, 119(9): 2149-58, 2012
[3] Frid et al., *Arterioscler Thromb Vasc Biol.*, 17(7): 1203-9, 1997
[4] Moulton et al., *JCI Insight.*, 3(4): e97228, 2018
[5] Chistiakov et al., *Acta Physiol (Oxf).*, 219(2): 382-408, 2017
[6] Méndez-Barbero et al., *Int J Mol Sci.*, 22(14): 7284, 2021
[7] Hiroshima et al. *Ann Biomed Eng.*, 50(8): 951-63, 2022
[8] Ye et al., *Biosurface and Biotribology*, 9(3): 78-83, 2023
[9] Mack et al., *Nat Commun.*, 8(1): 1620, 2017
[10] Rice et al., *Biotechnol Appl Biochem.*, 55(2): 85-90, 2010
[11] Zhu et al., *Am J Physiol Heart Circ Physiol.*, 300(5): H1770-80, 2010

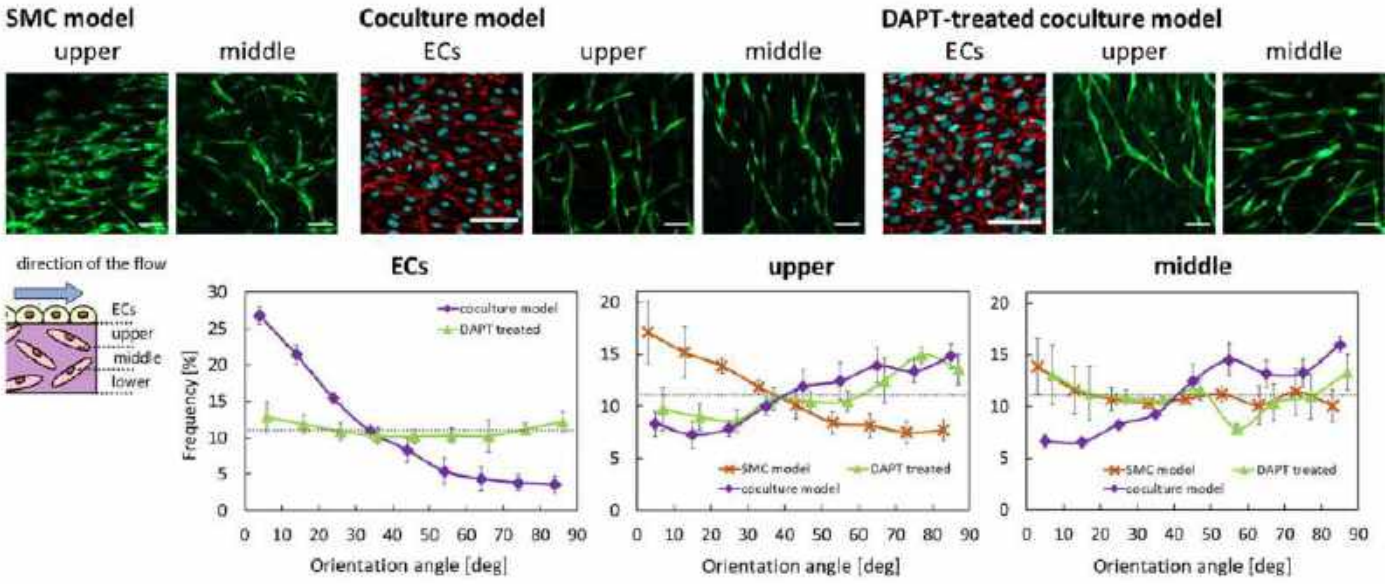

Fig. 2 Upper: Fluorescent images for αSMA (green) and nuclei (blue) of SMCs and PECAM-1 (red) of ECs in the SMC model, coculture model, and DAPT-treated coculture model after the 24 h WSS exposure. Scale bars = 100 μm. Lower: Relative frequency of the orientation angle of ECs and SMCs after the WSS exposure. The gray dotted line shows a random distribution. The values are expressed as a percentage of the total cell number for each experiment and are presented as mean ± SEM; N =4.

A FINITE ELEMENT MODEL FOR SIMULATING CLOSED-HEAD IMPACT INJURY IN A MOUSE MODEL: IMPLICATIONS FOR TAU PATHOLOGY IN TRAUMATIC BRAIN INJURY

R. Chi (1,2), P.W Alford (2)

(1) Mechanical Engineering, University of Minnesota Twin Cities, Minneapolis, Minnesota, United States
(2) Biomedical Engineering, University of Minnesota Twin Cities, Minneapolis, Minnesota, United States

INTRODUCTION

Traumatic brain injury (TBI) is a significant public health concern, with more than 25 million new cases of TBI per year globally [1]. The primary causes of TBI are falls, pedestrian road injuries, motor vehicle injuries, military mission injuries, and contact sports injuries. Single and multiple impacts can cause varying degrees of brain injury. In prior studies, we found that high strain rate deformation of neurons can lead to tau mislocalization [2]. Tau mislocalization can cause further hyperphosphorylation which leads to formation of neurofibrillary tangles (NFTs) that characterize chronic traumatic encephalopathy. In the human brain, NFTs tend to accumulate in sulcal depths, which modeling suggests experience the highest stresses during head injury [2]. Mouse brains do not have sulci, but the geometrically similar corpus callosum has been found to have the most tau-associated pathology in closed-head impact experiments performed in mice [3]. However, the mechanical relationships between axonal injuries and traumatic brain injury in these regions are not well understood.

We hypothesize that the temporal stresses generated by impact are highly correlated to the tau-mediated axonal injury of specific regions such as the corpus callosum of the mouse brain. Here, we present a viscoelastic model of mouse brain injury to test this hypothesis.

METHODS

3D geometry model. The brain and skull geometry were generated using data from the Allen Brain Atlas (Fig 1). The 3D brain slice used in this project was built based on the AP0 section of the P56 Mouse Model in the Atlas database [4]. This is the same section that was studied in the experimental studies that we are comparing our model against [3]. The primary region of injury in the experimental model is highlighted in the red circle in Figure 1. And two spots we monitored are highlighted in the red dot (α & β) in Figure 1. The geometry was constrained on two sides of the skull, which simulates the head-fixation device in the prior studies [3] [7].

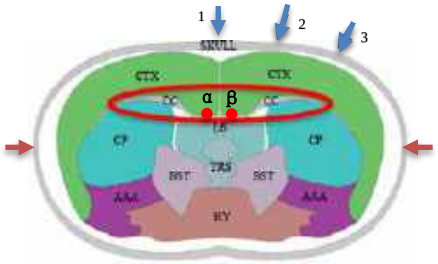

Figure 1: Brain and Skull 3D geometry map. Three impact locations are noted on the map. (Position 1: 0 degrees, middle of the skull; Position 2: 30 degrees off the midline, Position 3: 45 degrees off the midline.) Spots of interest α & β were monitored. CTX: Cerebral Cortex area; CC: Corpus Callosum area; CP: Caudoputamen area; LS: Lateral Septal Nucleus area; TRS: Triangular nucleus of septum area; BST: Bed nuclei of stria terminalis area; HY: Hypothalamus area; AAA: Anterior amygdalar area

Brain and skull material properties. Some material properties used for brain and skull geometry in this study were derived from previous literature [5]. Different methods and research interests affect the material properties of the brain tissues. Therefore, we assumed some properties, and the brain tissues were defined as viscoelastic material. The skull was defined as linear isotropic elastic material [6] (Table 1).

Skull		**Brain**	
Elastic Modulus	$1.8 * 10^7\ kpa$	**Elastic Modulus**	$3.735 * 10^6\ kpa$
Poisson's ratio	0.3	**Poisson's ratio**	0.3229
Mass density	$1920\ kg/m^3$	**Mass density**	$1020\ kg/m^3$
Shear Modulus	$4.2 * 10^4\ kpa$	**Shear Modulus**	$1.41 * 10^6 kpa$
Tensile Strength	$1.65 * 10^4\ kpa$	**Time Value (Bulk & Shear Relaxation Modulus 1)**	10000000
Yield Strength	$1.65 * 10^4\ kpa$	**Bulk & Shear Relaxation Modulus 1**	1

Table 1: Brain and Skull material properties.

Brain stress was taken as

$$\hat{\sigma}(t) = \int_0^t 2G(t-\tau)\frac{\partial \hat{e}}{\partial x}\partial\tau + \hat{I}\int_0^t K(t-\tau)\frac{\partial \emptyset}{\partial x}\partial\tau \quad (1)$$

where G and K are shear and bulk relaxation functions. G_0 and K_0 are initial shear and bulk modulus, and $\hat{e}$ and $\emptyset$ are the deviatoric and volumetric strain. The relaxation functions were taken as.

$$G(t) = G_0[1 - \sum_{i=1}^{N_G} g_i(i - e^{-\frac{t}{\tau_i^G}})] \quad (2)$$

$$K(t) = K_0[1 - \sum_{i=1}^{N_K} k_i(i - e^{-\frac{t}{\tau_i^K}})] \quad (3)$$

where g_i and k_i are shear and bulk relaxation modulus. Time values are presented as τ_i^g and τ_i^k.

Solution. Using SolidWorks, a single impact was modeled as a curved force applied to the skull at 3 locations, middle of the skull, 30 degrees off from the midline, and 45 degrees off from the midline of the skull (see Fig 1). The total duration of the solution is 1 second, and it reaches the peak force at 0.5s.

During the simulation, FFEPlus is the solver used in this study. SolidWorks chose it automatically based on the situation. FFEPlus is the best solver using iterative method since this model has more than 200000 degrees of freedom and more than 40000 elements [6].

Finally, the spatial-temporal stresses were qualitatively compared to the injuries reported in the prior studies [7] to verify the results from this simulation study.

RESULTS

Following impact, stresses vary spatiotemporally throughout the brain tissue (Fig 2). Notably, the stress is elevated in the corpus collosum region where injury has been previously observed experimental (Fig 2B, D, F, H). The stress generated at the corpus callosum reaches the first peak value at 0.26 seconds where the 80 N force was applied at position 1 (Fig. 3(E)). The aligned area of the corpus callosum also has elevated stress following the impact. Other high-stress regions are located at the interface between different regions (Fig. 2).

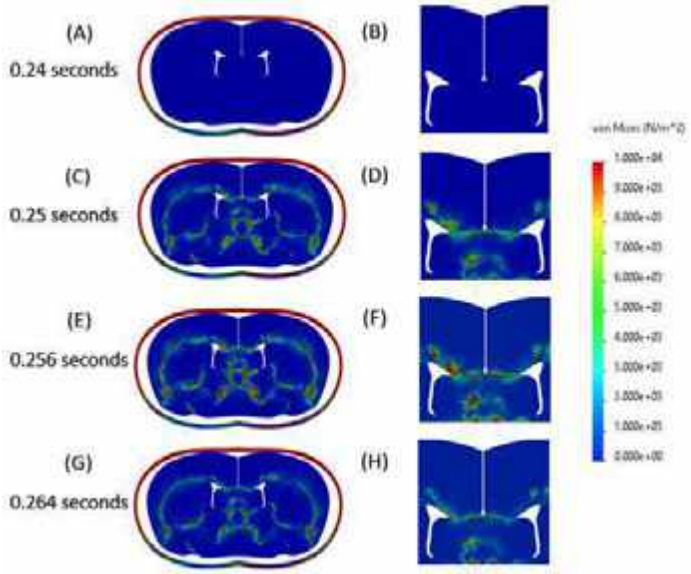

Figure 2: Brain stress heat map at different time steps exposed to 80 N impact at top middle of the skull and the zoomed-in map focusing on corpus callosum region (A)&(B) 0.24s (C)&(D) 0.25s (E)&(F) 0.256s (G)&(F) 0.264s.

Temporal stresses and overall magnitude of stress are influenced by impact location and magnitude. Figure 3 shows the temporal stress in the corpus callosum from t=0.2s to t=0.35s at spots of interest, following single impact at two locations. The stresses generated at spot β during the first contact shown in Fig 3 (B), are more stable and larger than the stresses under position 2 impact in Fig 3(A). Fig 3(C) is comparing the peak stresses at spot β between impact position 1 and impact position 2. Ratio of the stresses elevated at spot α to spot β which follow the impact at position 2 is shown in Fig 4 (D).

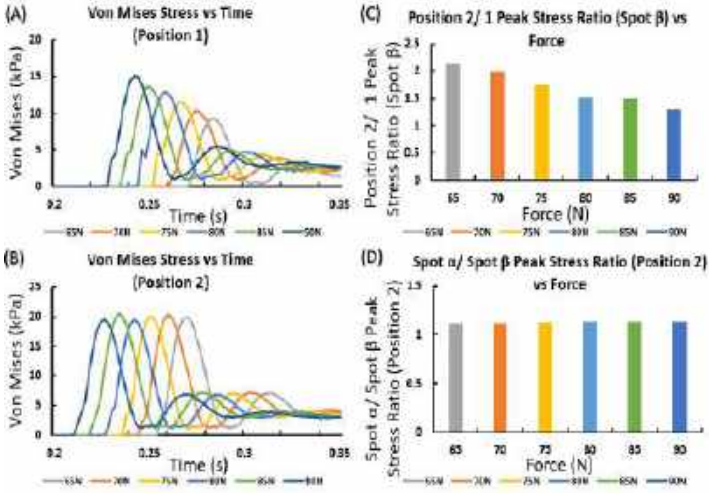

Figure 3: (A) Von Mises Stress vs Time (Impact Position 1, Spot β). (B) Von Mises Stress vs Time (Impact Position 2, Spot β). (C) Ratio of Peak Stress under Impact Position 1 to Position 2 (Spot β) vs Force. (D) Ratio of Peak Stress at Spot α to Spot β (Impact Position 2) vs Force.

DISCUSSION

In this study, we used a viscoelastic model finite element model to study the predicted stresses in a mouse brain during closed-head impact. Consistent with experimentally identified locations of post-injury pathology [3] [7], the model predicts significant elevated stress in the corpus callosum following a single impact on the surface of the skull. Notably, there are some other predicted regions of high stress (Fig 2) which were not studied in the prior experiments.

Limitations: The viscoelastic properties of some brain regions are not known which are based on assumptions. Ongoing parameter studies aim to test the relevance of these assumptions to the overall findings.

Overall. This study suggests that tissue stresses during injury correlate with tau-associated pathology in TBI. Taken together with prior research showing that stresses are elevated in the sulcal depths of human brain, these results are consistent with our hypothesis that the axonal injury following TBI is highly correlated with the high stress.

ACKNOWLEDGEMENTS

This work was funded through the Henry Jackson Foundation in partnership with the Uniformed Services University of Health Sciences (PI Regina Armstrong)

REFERENCES

[1] Guan, B et al., (2023). BMJ open, 13 (10). [2] Braun, N. J et al., (2020). Proc Natl Acad Sci U S A, 117(46). [3] Christina, M et al., (2019). Exp Neurol, 321. [4] Allen Institute for Brain Science, (https://atlas.brain-map.org). [5] Budday, S et al., (2017), J Mech Behav Biomed Mater, 74. [6] Brown, A. D et al., (2021), J Mech Behav Biomed Mater, 116,104343 [7] SolidWorks Help, (https://help.solidworks.com). [8] Yu, F et al., (2023). Acta neuropathologica, 146(4), 585–610.

3D ASSESSMENT OF RAT KNEE JOINT ANATOMY USING HIGH FIELD MRI

Olivia L. Dyer (1), Mackenzie N. Conner (1), Stephanie G. Cone (1)

(1) Biomedical Engineering, University of Delaware, Newark, Delaware, USA

INTRODUCTION

Across species, the knee joint retains a complex arrangement of bones and soft tissues, including ligaments, menisci and cartilage [1]. Identification of healthy knee morphology is important to characterize changes in morphology due to injury and disease. Previously, studies have quantified morphological properties of the bones and completed histological analysis of the ligaments in rat knees [2]. Deepening our understanding of rat knee morphology is valuable because rats are a commonly used preclinical model in orthopaedic research [3]. In this study, a high field 9.4T magnetic resonance imaging (MRI) scanner was used to develop high quality 3D models and quantify rat knee anatomy. The objective of this research was to expand on current knowledge of rat knee morphology, specifically in terms of the 3D anatomical properties of ligaments and menisci. This technique and baseline data will support future work exploring how morphology changes in injury models as well as in growth studies.

METHODS

Knee joints were collected post-mortem from Long Evans rats (n = 8). The knees were stored at -20°C and then thawed to room temperature and imaged in full extension in a 9.4T Bruker Biospec 94/20 AV Neo MRI machine with a T1 FLASH 3D scan sequence (flip angle: 10 degrees , TR: 38.0ms, TE: 4.42ms, acquisition time: 5.004ms, FOV: 16mm x 16mm x 16mm, voxel size: 0.1x0.1x0.1mm, no gap) using a 15mm volumetric coil.

Images were imported into commercial software (Simpleware, Synopsys) for analysis and 3D models of the four ligaments (ACL, PCL, MCL, LCL) and the medial and lateral meniscus were generated [4]. Each model was smoothed using a Gaussian filter before being exported as .stl files and imported into MATLAB (Figure 1). The volumes of the medial and lateral meniscus segmentations were recorded. Width and height measurements of the menisci were recorded at the anterior horn, two central locations, and the posterior horn on both the medial and lateral meniscus [5]. Using a custom MATLAB code, each tissue was converted into point clouds and for each 0.1mm slice along the tissue the cross-sectional area (CSA) was calculated. The middle 50% of the CSA slices along the tissue were averaged together to determine the CSA of the tissue [4].

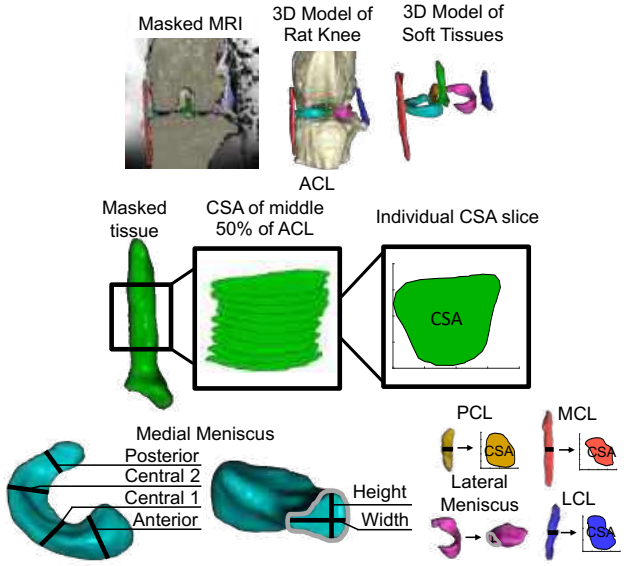

Figure 1: 3D models of the ligaments and menisci of rat knees were generated from MRI scans. CSAs were recorded for each ligament, while height, width and volume of the medial and lateral menisci were recorded at four locations.

Statistical analyses were performed using a custom MATLAB code and included a one-way ANOVA to compare average CSA of the

four ligaments (alpha = 0.05). Meniscus volume was compared using a paired nonparametric t-test. Two -way ANOVAs were used to compare the width and height of the meniscus between locations and between the medial and lateral meniscus (alpha = 0.05).

RESULTS

There was a significant main effect of ligament in CSA measurement ($p = 0.024$). The PCL had a significantly greater CSA compared to the ACL and LCL, with an average CSA of 0.48 ± 0.14mm^2 ($p = 0.015$ and $p = 0.002$, Table 1). Additionally, the MCL had the widest range in variance with CSAs ranging from 0.09mm^2 to 0.80mm^2, while the ACL had the least variability of the four ligaments with CSAs ranging from 0.21mm^2 to 0.45mm^2 (Figure 2).

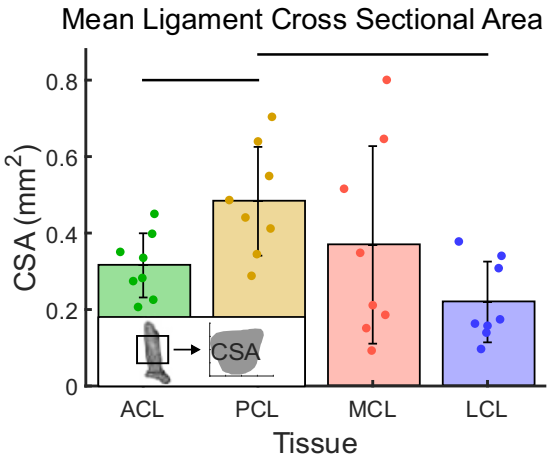

Figure 2: CSA measurements for each of the four ligaments (ACL, PCL, MCL, LCL). Points represent individual tissues, bars and error bars represent mean and standard deviation, image describes the CSA measurement. Bars represent significant differences between tissues.

The average volume of the medial meniscus and lateral meniscus was 2.83mm^3 ± 0.53mm^3 and 3.17mm^3 ± 0.70mm^3, respectively, with no significant difference between sides ($p = 0.46$).

The anterior horn of the medial meniscus had a slightly larger average width of 1.07mm ± 0.11mm, compared to the other three locations along the medial meniscus (Table 1). There was a significant main effect of anatomical location for the heights and widths of the medial and lateral menisci ($p < 0.001$, Figure 3). The height of the medial and lateral meniscus was significantly different at the anterior horn ($p = 0.003$, Figure 3). There was no main effect of the medial and lateral menisci in the widths and heights ($p = 0.18$ and $p = 0.55$).

Table 1: CSA of the four ligaments of the knee (ACL, PCL, MCL, LCL) and the widths and heights of the medial and lateral menisci measured at four locations around the meniscus.

Ligament Geometry (mm^2)				
	ACL	**PCL**	**MCL**	**LCL**
CSA	0.32 ± 0.08	0.48 ± 0.14	0.37 ± 0.26	0.22 ± 0.11
Meniscus Geometry (mm)				
	Anterior	**Central 1**	**Central 2**	**Posterior**
MM width	1.07 ± 0.11	0.60 ± 0.09	0.56 ± 0.08	0.58 ± 0.16
LM width	0.80 ± 0.12	0.78 ± 0.19	0.71 ± 0.16	0.75 ± 0.19
MM height	0.94 ± 0.15	0.83 ± 0.13	0.82 ± 0.09	0.79 ± 0.18
LM height	1.03 ± 0.16	0.79 ± 0.18	0.76 ± 0.18	0.90 ± 0.11

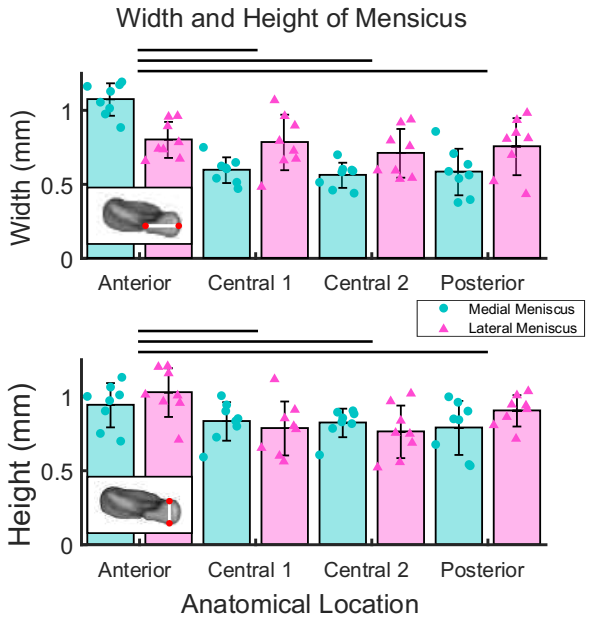

Figure 3: Width and height of the medial and lateral meniscus recorded at four anatomical locations. Points represent individual tissues, bars and error bars represent mean and standard deviation, images describe the measurements. Bars represent significant differences in width and height at anatomical locations.

DISCUSSION

In this study we were able to identify and quantify 3D rat knee tissue morphometry using high field MRI. The PCL had the largest CSA and was significantly different from the ACL and LCL CSA. The heights and widths of the menisci were significantly different at each anatomical location indicating greater tissue size in the anterior aspect of the rat menisci. There were no significant differences in meniscus volume between medial and lateral menisci. The use of high field MRI with a FLASH 3D sequence enabled these findings, as imaging with sub-micron isotropic voxels was necessary for resolving tissue features of this small scale. We found that rat knee morphology retains similar anatomical features to that of human knees and other preclinical models [2,3]. This work followed techniques described in established studies used to characterize knee morphology in large animal models applied to a commonly used preclinical small animal model - rats [4]. Limitations of this work include a relatively small sample size and future work will include increasing sample size, expanding this approach to other small animal models, and comparing healthy knees to injured knees. This study was the first of its kind to establish a methodology to quantify 3D rat knee soft tissue morphometry using high field MRI, enabling future work to explore how knee anatomy changes throughout growth and assess structural effects due to musculoskeletal disorders, such as osteoarthritis.

ACKNOWLEDGEMENTS

This research was supported by the NIH (P20GM103446, P20GM139760).

REFERENCES

[1] Proffen, B. Et al, *Knee*., 19(4): 493–499 (2012)
[2] Song, Z. et al, *J. sports med. ther.*, 2573-1726 (2023)
[3] Little, D. et al, *J Orthop Res*., 41: 2133-2162 (2023)
[4] Cone, S. et al, *PLoS One*, 4(10): e0219637 (2019)
[5] Wirth, W. et al, *Magn. Reson. Med.*, 63:1162–1171 (2010)

SB³C2024
Summer Biomechanics, Bioengineering and Biotransport Conference
June 11-14, Lake Geneva, WI, USA

STUDENTS' PERCEPTIONS ON USING GENERATIVE ARTIFICIAL INTELLIGENCE (GAI) IN ENGINEERING COURSES

Victor K. Lai

Department of Chemical Engineering, University of Minnesota Duluth, Duluth, MN, USA

INTRODUCTION

The introduction of generative artificial intelligence (GAI) tools, notably ChatGPT which became publicly available in November 2022, marks an exciting frontier accompanied by numerous uncertainties in higher education. GAI tools such as ChatGPT have the capability to compose entire essays from a single prompt, eliciting concerns among educators particularly in subjects heavily reliant on writing in their curriculum. In STEM fields, however, ChatGPT is yet unable to accurately perform mathematical operations, although the paid version (ChatGPT 4.0) addresses this limitation through a collaboration with Wolfram Alpha. Aside from the issues of academic integrity, accuracy, and reliability, arguments against the integration of GAI in classrooms include the potential decline in critical thinking and writing skills [1] and perpetuating bias in how content is presented [2].

Despite concerns that GAI will replace jobs, a working paper by the International Labour Organisation (ILO) suggests that GAI may *augment* rather than destroy jobs [3]. Anecdotally, an increasing number of students at the University of Minnesota – Duluth (UMD) returning from internships or co-ops reported tasks involving the use of GAI in their work or contributing to the development of GAI tools for their respective companies. Moreover, the surge in job openings related to GAI highlights the growing significance of these skills in various industries [4]. Consequently, it becomes crucial for higher education instructors to guide students in the ethical use of GAI tools to ensure their relevance upon graduation.

This study delves into students' perspectives on using ChatGPT in two courses at the UMD: ChE 3111 - Fluid Mechanics, a junior-level course which primarily focuses on well-defined engineering problems typically with a single correct numeric answer, and ChE 4502 - Chemical Engineering Design II, the capstone design project course for seniors, characterized by open-ended projects with a substantial report-writing component. This study holds an exemption status approved by the University of Minnesota Institutional Review Board (IRB).

METHODS

At the beginning of the semester, students in both courses were tasked with filling out a pre-course survey to gauge their familiarity with GAI tools such as ChatGPT. The survey aimed to gather insights on how students had previously utilized GAI tools to support their learning, if applicable, and to understand their general perceptions of using such tools in higher education.

For ChE 3111: Fluid Mechanics (n = 24), students were explicitly informed that they had the option to use GAI tools for assignments, provided they declared it through a Google form detailing how GAI was utilized. Additionally, a brief in-class exercise was conducted, where all students attempted to use ChatGPT to solve an engineering problem (calculate a Reynolds number).

In ChE 4502: Chemical Engineering Design II (n = 17), students engaged in a short exercise introducing various ways of employing ChatGPT to aid in report writing. They were assigned the task of conceptualizing a paragraph on GAI by (1) jotting down 3 – 4 key points about GAI, and (2) independently composing the paragraph using those key points. Subsequently, in the following class, students explored the use of ChatGPT in writing through three approaches: (1) prompting ChatGPT to generate a paragraph on GAI and comparing it with their original writing, (2) prompting ChatGPT to edit their written paragraph, and (3) instructing ChatGPT to compose a paragraph using the provided 3 – 4 key points in the prompt. In each scenario, students were tasked with critically evaluating ChatGPT's output and determining whether and how they would edit or use the output.

Towards the end of the semester, students in both courses were invited to complete a post-course survey on how frequently they had used GAI tools for the course (and in what manner, if applicable), as well as their overall perceptions of using such tools. Regrettably, due to the absence of dedicated class time after the final presentations for ChE 4502 to administer the survey, only 3 out of 17 students responded to email requests to complete the post-course survey.

RESULTS

Pre-course survey responses indicated all students in both courses were familiar with GAI tools like ChatGPT, with over half primarily for personal enjoyment rather than coursework. Noteworthy instances of self-reported GAI use involve creating study guides, troubleshooting code, and writing resumes and cover letters (data not shown).

In general, students in both courses express a belief that GAI tools should have a more prominent role in education to some degree. Surprisingly, post-course surveys reveal a decline in these percentages, with more students adopting a neutral stance than a positive one (Figure 1). Regarding the ethical aspect of using AI tools for assignments, most students were either neutral or slightly in agreement, with minimal changes in sentiment from pre-course to post-course surveys (Figure 2).

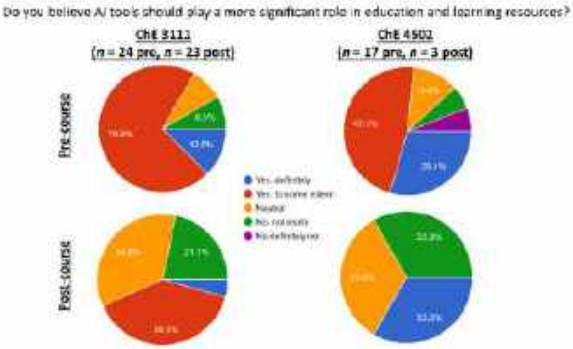

Figure 1: Pre- and post-course survey responses on whether AI tools should play a larger role in education.

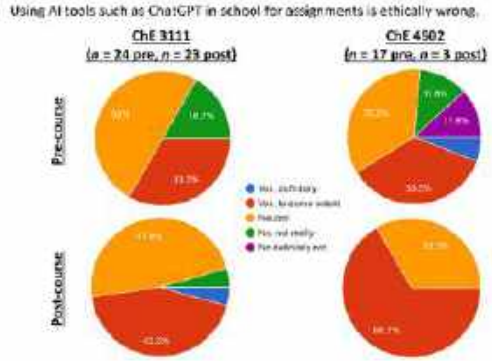

Figure 2: Survey responses on whether using AI tools for assignments is ethically wrong shows little change in sentiment pre- and post-course.

Post-course surveys (Figure 3) indicate infrequent or nonexistent use of GAI tools in both courses, despite students reporting more frequent utilization in other courses. When questioned about the areas in which they employed AI tools in ChE 3111, common responses included information gathering (44%), generating narrative text (26%), developing ideas or outlines for papers (26%), and tackling more complex problems (26%). Despite students' ethical concerns of GAI use in assignments, a majority of students expressed that they would continue to use these tools in future courses if allowed.

Encouragingly, when asked to write any concerns they have with GAI tools, several students demonstrated an awareness of the potential dangers of over-reliance, emphasizing the need to build fundamental skills and creative thinking first (data not shown). At the same time, students felt an urgent need to learn about GAI, with one student saying "that AI learning will be largely implemented across the entire cooperate world within a few short years. I do not want to be lacking of knowledge in this subject when that time comes."

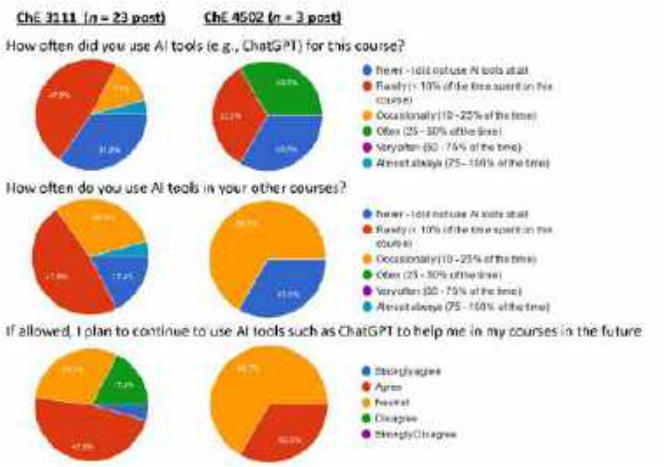

Figure 3: Few students used GAI tools throughout these courses, with slightly higher use in other courses.

DISCUSSION

Overall, few students in these courses utilized GAI tools with their assignments even though they were allowed to. For ChE 3111, this lack of use of could likely be due to students realizing early on during the in-class exercise involving the calculation of Reynolds number that ChatGPT struggled with accurate mathematical calculations. However, they appreciated the tool's ability to provide explanations of the steps involved which were largely correct, and critically evaluated the output to determine where/how ChatGPT was wrong. Consequently, only two students declared using GAI tools for their assignments for the semester, with both instances occurring within the first month. The inability of ChatGPT to perform mathematical functions and solve engineering problems could explain why sentiment towards GAI use in education dropped between pre- and post-course surveys.

For ChE 4502, the lack of responses for the post-course survey rendered the data difficult to interpret. However, I know from meetings with design groups to discuss their reports that ChatGPT was used by several students in report writing. In some instances, I *encouraged* students to use ChatGPT to help edit their drafts. While ChatGPT aided students in report writing, guidance was required for some students in ensuring that the *tone* was suitable for a technical engineering report.

Overall, GAI will likely become a ubiquitous and important tool for many industries in the future. As such, the responsibility lies with educators to train students in the ethical use of such tools, recognizing their limitations and emphasizing the importance of building fundamental skills alongside technological assistance. As one student aptly writes: "I believe it is somewhat synonymous with Simulation Software. It's critically important to understand the underlying functions so that we can discern between accurate and inaccurate outputs. Engineers need to be able to read and write technical information before they rely on something else to do so." From this standpoint, our role in teaching fundamental technical skills and critical thinking remain unchanged, even though the media and tools to do so continue to evolve.

ACKNOWLEDGEMENTS

ChatGPT 3.5 was used to edit this abstract for clarity.

REFERENCES

[1] E. Kasneci et al., *Learn. Individ. Differ.*, vol 103, p.102274, 2023.
[2] N. Gillani et al., *Educ. Technol. Soc.*, vol. 26, no. 1, pp. 99, 2023.
[3] J. Berg et al., Geneva: ILO, 2023.
[4] D. Acemoglu et al., *J. Labor Econ.*, 40:S1, pp. S293–S340, 2022

LONGITUDINAL CHANGES IN MECHANICAL PROPERTIES OF AORTA FROM ANGIOTENSIN-II INFUSED MICE OBTAINED BY AN INVERSE FINITE ELEMENT METHOD

Hadi Wiputra (1), Sydney Q. Clark (2), Craig J. Goergen (2), Victor H. Barocas (1), Matthew R. Bersi (3)

(1) Department of Biomedical Engineering, University of Minnesota, Minneapolis, Minnesota, USA
(2) Weldon School of Biomedical Engineering, Purdue University, West Lafayette, Indiana, USA
(3) Mechanical Engineering & Materials Science, Washington University, St. Louis, Missouri, USA

INTRODUCTION

Aortic aneurysms affect 17,000 Americans annually and have a 90% mortality rate when the aneurysm ruptures [1]. Mice infused with Angiotensin-II (AngII), are often used as surrogate models of aortic aneurysm development [2-4]. Following infusion of AngII, elevated blood pressure causes the aortic walls to remodel to be thicker and dilated [2]. Given the large variation in the ruptured aorta's mechanical properties [5] and the large extent of remodeling that aortic aneurysm undergoes [6], analyzing the growth and remodeling of aortic aneurysm in a subject-specific application is important.

To achieve mouse-specific characterization of the growth and remodeling process, we require a non-invasive means to track changes in aneurysm's material properties over time. In this study, we used inverse modeling of high frequency ultrasound images to track the changes in material property of aorta over time. We infused wild-type mice with AngII for 28 days, a period during which the aorta was expected to grow and remodel [3,4]. Changes in material properties from 0 to 28 days of AngII infusion were tracked via inverse finite element (FE) methods based on non-invasive image data. After 28 days, the aortas were harvested and tested in a biaxial stretch-inflation test [7] to assess accuracy of the inverse FE method used.

METHODS

Ultrasound images were obtained from ten 16-week-old C57Bl/6J mice, including three saline-infused controls and seven (two have incomplete dataset) infused with 1000ng/kg/min AngII for 4 weeks. 4D ultrasound images of the thoracic aorta were obtained at day 0 and 28 of infusion, with a high frequency ultrasound system (25-55 MHz, Vevo3100, FUJIFILM VisualSonics), resulting in image of approximately 0.03x0.03x0.1mm resolution and 40 timepoints per cardiac cycle. The ascending and proximal descending thoracic aorta were segmented, and deformations were tracked over the cardiac cycle with B-spline Fourier image registration [8]. Inverse FE analysis was performed on the images, where an initial set of material properties was tested and updated repeatedly until the FE-model-calculated changes in vessel geometry matched those obtained from ultrasound. A four-fiber-family material model [3] was used:

$$W = \frac{c}{2}(I_1 - 3) + \sum_{a=1}^{4} \frac{c_1^{(a)}}{4c_2^{(a)}} \left\{ e^{c_2^{(a)}(IV_c - 1)^2} - 1 \right\} \quad (1)$$

where W is the strain energy density and c describes a neo-Hookean matrix stiffness with four embedded fiber families (i.e. a=1..4). c_1(a) and c_2(a) represent the linear and exponential stiffnesses of the four fibers. I_1 is the first invariant, and IV_c is the direction-dependent stretch invariant in the fiber direction. The four families are aligned axially (z), circumferentially (θ), and diagonally (diag) along the aorta. In this study, we assumed that the exponential properties of the fibers (c_2(a)) were constant, obtained from the averages of the two incomplete mouse datasets.

The finite element model used, and the appropriate boundary conditions are illustrated in Fig 1a below. The outer wall was given a Robin boundary to model the surrounding tissue's stiffness; the deformation of the inlet, outlet, and three head branches were prescribed from the tracked ultrasound images. The pressure exerted on the geometry is based on a lumped parameter model of blood flow, with a resistor-capacitor-resistor (RCR) circuit attached to the branched ends of the aorta. The flow models were calibrated to Pulsed Wave Doppler ultrasound and tail-cuff-measured blood pressures.

The unloaded configuration was approximated by progressively shrinking and expanding the aortic mesh geometry until the diameter of the aorta at physiological pressure matched that in the ultrasound image. Biaxial tests were modeled in silico, and the axial pre-stretch was taken as the axial stretch that produces a plateau in the pressure-force curve [5]. Inverse FE analysis results on day 28 and the unloaded geometry configuration were validated against findings from *ex vivo* biaxial testing [7].

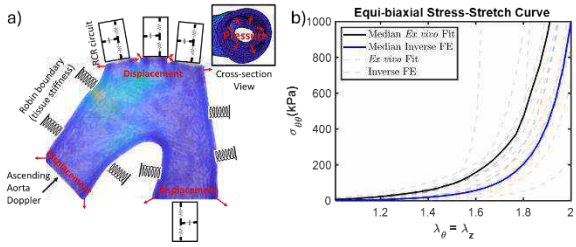

Figure 1a: Boundary condition for the inverse finite element (FE) model. b) Equi-biaxial stress-strain curve comparing the inverse FE model to *ex vivo* biaxial test after 28 days of AngII infusion.

RESULTS

A comparison of the equibiaxial stress-strain relationships obtained from inverse FE modeling and from *ex vivo* biaxial testing is shown in Fig 1b, with an average r^2 between inverse FE and *ex vivo* testing is 0.86±0.23 (mean±sd) at day 28 of infusion. Material stiffness was generally underestimated by the inverse-FE method compared to *ex vivo* stretch-inflation tests, which can be attributed to a smaller unloaded diameter and length estimated by the inverse FE. The smaller initial length and diameter resulted in the obtained material properties being more compliant than that tested *ex vivo*. The difference between inverse FE and ultrasound tracked radius, normalized by ratio of the difference in diastolic to systolic radius, was 13.9 ± 3.9%.

Material properties from AngII infused and control mice are compared in Fig 2. Many measures did not show a significant trend (by a paired 1-tailed t-test), owing to the large variation in the AngII response of mice aorta and uncertainty from the inverse FE method. However, there is a trend towards reduction in axial stiffnesses of AngII mice at 28 days of infusion that was not observed in controls (p=0.097; Fig 2a,b). This trend did not, however, manifest in significant changes in the axial and circumferential tangential stiffness during systole (p=0.16, 0.22; Fig 2c,d), as the less stiff axial fibers were supported by stiffening of diagonal fibers (p=0.84; Fig 2a,b). We also observed a slight, but not statistically significant decrease in systolic axial and circumferential stretches (p= 0.16, 0.21; Fig 2e,f).

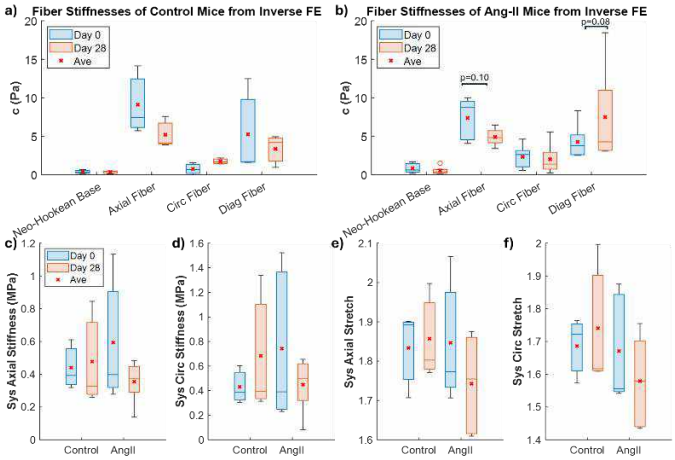

Figure 2: Fiber stiffnesses from the four-fiber family model, obtained from inverse FE model, for a) control mice and b) AngII infused mice. Furthermore, systolic material properties were compared: axial and circumferential stiffness (c,d); axial and circumferential stretch (e,f). P-values were obtained from paired 1-tailed t-test and only p-values below 0.1 are shown.

DISCUSSION

The inverse FE method showed acceptable agreement with *ex vivo* mechanical characterization (Fig. 1b). In addition, certain observations from the AngII-infused mice were consistent with prior studies. Specifically, we saw a decrease in axial fiber stiffness and no change along the circumferential direction between day 0 and day 28 of AngII infusion (Fig. 2b). This is consistent with previous study that compared *ex vivo* mechanical properties of AngII infused mice with the same dosage and dosing period [3]. Furthermore, under increased pressure, the aorta responds by reducing its axial stretch [9, 10], and a similar trend was observed in our study, although not statistically significant. Therefore, the pattern we observed in our study is consistent with previous reports.

Despite the promising results, our study pointed to limitations in the inverse FE approach. The method brings considerable uncertainty in estimation of the material properties, which hindered detection of trends. The amount of information provided from the image is also limited. Unlike the large amount of deformation space that can be explored in *ex vivo* biaxial testing, inverse FE relies only on information from the deformation between diastole to systole, which is often small (diastole-systole radius dilation by 1.06x) and does not allow for controlled axial stretching. These issues highlight the need for validation of inverse FE against ground truth *ex vivo* testing, which can be rare in the literature [11] and is an important part of this study.

Additionally, there is large variation in the effect of AngII on the aorta [3, 12]. The aorta expresses fewer angiotensin receptors compared to smaller vessels, limiting the direct vasoactive effect of AngII on aorta [3]. The effect of AngII on the aorta is primarily indirect, via a systemic effect from changes in peripheral vessels and inflammation [3]. The combination of methodological uncertainty and large variability of the AngII response made it difficult to obtain statistically significant observations. This difficulty is not necessarily problematic in the current study, which aimed primarily at method development, but it draws attention to a potential challenge when using image-based inverse methods of this sort.

The non-invasive nature of this method will be valuable to study the development and evolution of aortic aneurysm in a subject-specific manner. Depending on conditions, aortic aneurysms can develop into similar geometries but with vastly different material properties [13]. Inverse FE models, such as the one employed herein, can be valuable in distinguishing among aneurysms with similar appearance provided one can manage the potential error in the material property estimates.

ACKNOWLEDGEMENTS

This work was supported by: U01-HL139471, R01 HL164800, AHA Postdoctoral Fellowship (HW), AHA Career Development Award (MRB), the Indiana University School of Medicine (SQC), and computational resources of the Minnesota Supercomputing Institute.

REFERENCES

[1] Melo, G.E.R. et al., *Semin Thorac Cardiovasc Surg*, 34(1):1-16, 2022. [2] Gadanec, L.K., et. al, *Mol. Cell. Biochem*,1-10 ,2023. [3] Bersi, M.R., et al., *Hypertension*, 67(6): 890-896, 2016. [4] Bersi, M.R., et al., *Int J Adv Eng Sci Appl Math*. 4(4): 228–240, 2013. [5] Luo, Y., et al, *Acta Biomaterialia*, 42:286-295, 2016 [5] Weizsäcker, H.W., et al., *J. Biomech.*, 16(9): 703-715, 1983. [6] Bojan, I.B., et al., *Diagnostics*, 13(2), 253, 2023. [7] Hiratzka F. L, et al., *Circ.*, 121(13): e266-369, 2010. [8] Wiputra, H., et al., *Sci. Rep.*, 10(1):18510, 2020. [9] Eberth, J.F., et al., *J Biomech.*, 44:2532–2537, 2011.[10] Maiellaro-Rafferty K., et. al, *Am J Physiol Heart Circ Physiol*, 301(2): H355-36, 2011. [11] Wang L., et al., *J. Funct. Biomater.*, 13: 147, 2022. [12] Zhou, Y., et al., *Am J Physiol Heart Circ Physiol*, 285(6): 2797-2803, 2003. [13] Mahutga, R.R. & Barocas, V.H., *J. Biomech.*, 142(11):111007, 2020.

PRE-SURGICAL ASSESSMENTS OF CSF FLOW AND BRAIN MOTION ARE INDICATIVE OF IMPROVED CEREBRAL DYNAMICS FOLLOWING SURGERY IN CHIARI MALFORMATION I

G McIlvain (1), S Mohsenian (2), MM Al Samman (2), B Williams (1), DL Barrow (3), F Loth (1), JN Oshinski (1)

1. Department of Radiology & Imaging Sciences, Emory University, Atlanta, GA, USA
2. Mechanical and Industrial Engineering, Northeastern University, Boston, MA, USA
3. Department of Neurosurgery, Emory University, Atlanta, GA, USA

INTRODUCTION

Chiari Malformation I (CM-I) is a condition characterized by cerebellar tonsil herniation of >5mm through the foramen magnum. CM-I causes a reduction of cerebrospinal fluid (CSF) flow [1] and an increase in cardiac-induced brain tissue motion [2], and is associated with headaches, paresthesia, dysphagia, and sleep apnea [3,4].

In symptomatic cases, posterior fossa decompression (PFD) surgery is often performed, which involves removing bone to enlarge the foramen magnum and cervicomedullary junction to establish normal CSF flow [5] (Figure 1). Successful PFDs improves symptoms in ~70-80% of patients [6]. However, the surgery involves risk, and identifying which candidates will benefit from surgery is important.

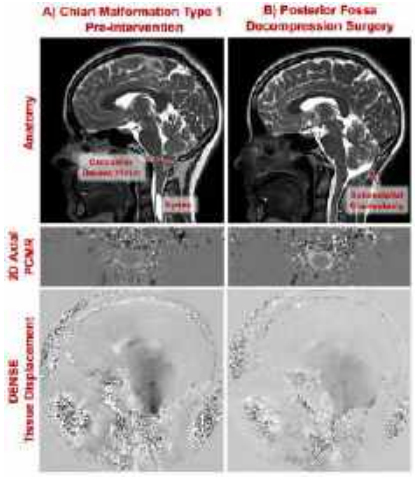

Figure 1: Anatomical images, PCMR images showing CSF flow, and DENSE showing brain motion for A) a symptomatic CM-I patient with syringomyelia and, B) The same individual after posterior fossa decompression surgery, CSF flow is free flowing on both the anterior and posterior of the foramen magnum and syrinx has resolved.

The degree of tonsillar herniation does not correlate with symptom severity or with surgical outcomes [7,8]. Therefore, we seek to use advanced neuroimaging methods to quantify how PFD affects cerebral dynamics. *We hypothesize that CSF flow and brain motion are better metrics to elucidate which patients will have the greatest likelihood of cerebral dynamic improvements from surgery.*

METHODS

We imaged 89 patients (18-71yrs, mean=37.2yrs; M/F=18/71) with a clinical diagnosis of CM-I on a Siemens 3T PrismaFit. Of these patients, 49% (N=44 patients) underwent PFD and participated in a three-month follow-up MRI.

To measure CSF flow, we collected a retrospectively gated, 2D-axial PCMR scan at 1.2x1.2x5mm resolution, VENC=5cm/s, with 25 images per cardiac cycle. CSF was manually segmented, and pixel-wise velocity was integrated to determine flow at each time-point. Stroke volume was defined as the average of the absolute value of the cranial and caudal flow.

To measure brain pulsatile motion, we used displacement-encoding with simulated echoes (DENSE). Images were acquired in the sagittal plane at the midline using a two-dimensional spiral cine sequence with peripherally pulse unit-gating. 13–29 frames were acquired over the cardiac cycle depending on heart rate. Image resolution was 0.9x0.9x8.0mm [9]. Displacement was calculated pixel-wise over the cardiac cycle from the phase images. To measure tonsillar descent, we collected a sagittal T_2-weighted image.

Data was analyzed using both unpaired t-tests, with the pre-surgical group including all patients, and pairwise t-test with just patients who underwent surgery. Pearson correlations were used for continuous variables. $P<0.05$ was considered significant.

RESULTS

CSF stroke volume was 0.86±0.58ml in CM-I patients. CSF stroke volume after PFD surgery was 1.14±0.43ml ($p=0.036$; Figure 2). Pairwise (pre/post-surgery) we saw a 40.5% increase to CSF stroke volume ($p=0.011$).

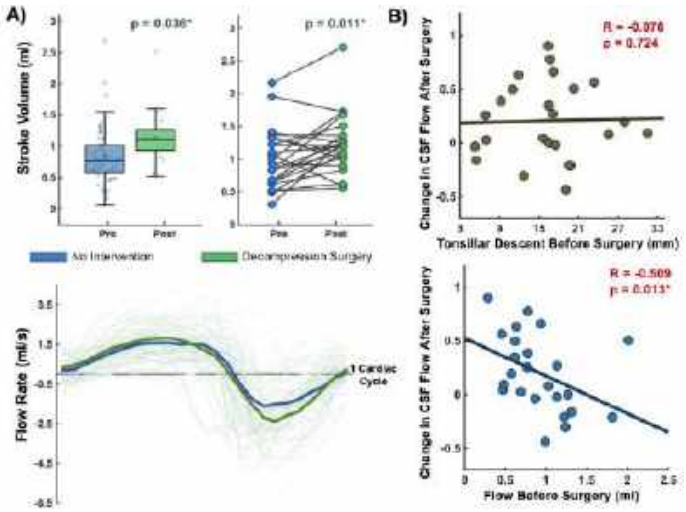

Figure 2: A) CSF stroke volume increases after PFD surgery. B) Change in CSF flow compared to tonsillar descent and presurgical CSF flow respectively. Improvements to CSF is better predicted by presurgical CSF flow, than by tonsillar descent.

Notably, we found that CSF flow increases seen after surgery had *no relationship* to tonsillar descent (R = -0.078, p =0.724), but *did relate* to amount of pre-surgical flow (R = -0.509, p=0.013; Figure 3). *Showing that only subjects with low initial flow had a significant post-surgical increase in flow, regardless of severity of tonsillar descent.*

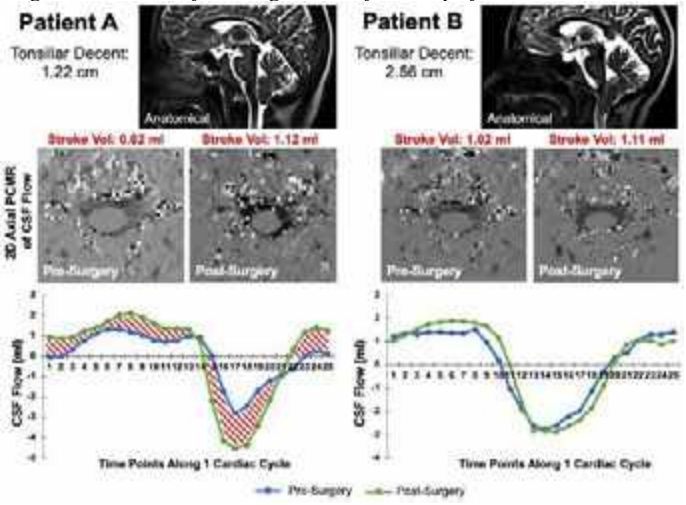

Figure 3: Representative CM-I patients showing presurgical CSF flow better predicts surgical CSF improvements than tonsillar decent. Shaded area represents gain in stroke volume. Patient A has less tonsillar decent but worse initial flow, so benefits more in CSF flow from surgery.

We also found that pulsatile motion decreases significantly after surgery, with brainstem motion decreasing 17.3% (p=0.007) and cerebellum motion decreasing 45.2% with surgery (p<0.001). We again found that improvements were better predicted by the amount of pre-surgical motion (Brainstem: R = -0.638, p<0.001; Cerebellum: R = -0.878, p<0.001) than by tonsillar descent (Brainstem: R = -0.312, p=0.093; Cerebellum: R = -0.620, p<0.001). *This implies that subjects with high initial brain motion had a significant post-surgical decrease in motion, regardless of severity of tonsillar descent.*

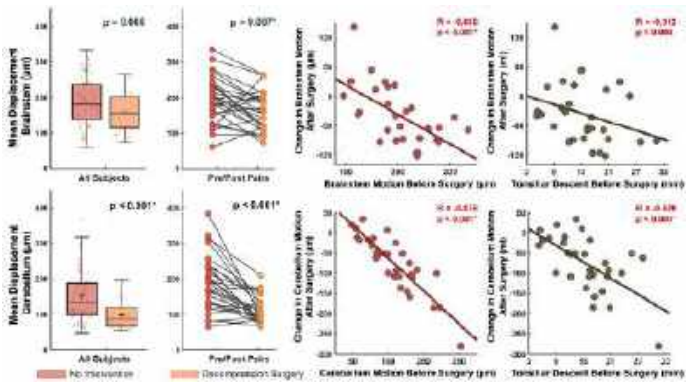

Figure 4: Cardiac related motion in the brainstem (top) and cerebellum (bottom) decreases significantly in both regions after PFD surgery. The amount of change in brain motion is better predicted by presurgical brain motion, than by tonsillar descent.

DISCUSSION

The Monroe-Kellie Doctrine dictates that to maintain normal intracranial pressure, the cranial cavity must maintain consistent volume, and therefore when the arterial pulse leads to systolic expansion of brain tissue, CSF is passively pushed out of the skull [10]. However, in CM-I, the passive flow of CSF is obstructed, and to compensate, the brainstem and cerebellum must displace more to maintain cerebral homeostasis [11]. These changes to cerebral dynamics are presumed to cause clinical symptoms [12]. *With the creation of adequate space for CSF flow through PFD surgery, CSF flow increases and brain motion decreases towards normal*.

While amount of tonsillar decent is the standard imaging marker, it has proven to be a poor measure of CM-I severity, as other factors like foramen magnum size and crowding also affect cerebral dynamics. Here we instead directly measured cerebral dynamics. We showed that only the patients who had severely impacted CSF flow and brain motion realized improved cerebral dynamic after surgery, regardless of tonsillar descent. While CSF flow is frequently assessed in PFD, it is commonly with PCMR acquired in a sagittal plane which is inadequate to characterize flow. Often qualitative assessments of geometric images are used to assess crowding and then infer the CSF flow dynamics for a given subject which may not be reliable. Brain motion has only recently been measured in CM-I, and therefore work in this area is limited [2,13]. Here, we showed cerebral dynamics in CM-I are important indicators of potential benefits from PFD surgery. Further research is needed to determine how cerebral dynamics affect clinical outcome measures.

ACKNOWLEDGEMENTS

Conquer Chiari Foundation, T32 HL007745

REFERENCES

[1] Ramón C, et al. *Curr Pain Headache Rep*. 15:157-163. 2011.
[2] Eppelheimer MS, et al. *Radiology*. 301:187-194. 2021.
[3] Langridge B, et al. *World Neurosurg*. 104:213-219. 2017.
[4] Chavez A, et al. *J Clin Neurosci*. 21:2201-2206. 2014.
[5] Tubbs RS, et al. *Neurosurgery*. 48:1050-1055. 2001.
[6] de Oliveira Sousa U, et al. *Neurosurg Rev*. 41:311-321. 2018.
[7] Bejjani GK. *Neurosurg Focus*.;11:1-8. 2001.
[8] Ventureyra ECG, et al. *Child's Nerv Syst.* 19:109-113. 2003.
[9] Pahlavian, SHs et al., *J Biomech Eng*. 140:081010, 2018.
[10] Zhong, X et al., *Med Phys*. 36:3413-3419, 2009.
[11] Wilson, MH., *J Cereb Blood Flow Metab*. 36:1338-1350, 2016.
[12] Ciaramitaro, P et al., *Child's Nerv Syst*. 35:1673-1679, 2019.
[13] Leung, V et al., *J Neurosurg Spine*. 24:546-555, 2016.

FLOW DYNAMIC FACTORS CORRELATED WITH DEVICE-RELATED THROMBOSIS AFTER LEFT ATRIAL APPENDAGE OCCLUSION

B. Vogl (1), A., Sularz (2), A. Bavo (3), M. De Beule (3), J. Nielsen-Kudsk (4), O. De Backer (5), M. Alkhouli (2), H. Hatoum (1)

(1) Biomedical Engineering, Michigan Technological University, Houghton, MI, USA
(2) Cardiovascular Medicine, Mayo Clinic, Rochester, Minnesota, USA
(3) FEops, Gent, Belgium
(4) Department of Cardiology, Aarhus University Hospital, Aarhus, Denmark
(5) Department of Cardiology, Copenhagen University Hospital, Copenhagen, Denmark

INTRODUCTION

Atrial fibrillation (AF) is the most common arrythmia that can cause cardioembolic events. Stroke prevention is the main concern in the management of AF. Blood stasis in the atrium is associated with thrombus development and often occurs in the left atrial appendage (LAA). While anticoagulants are effective in mitigating strokes, bleeding risk, noncompliance, and other side effects make them unused in more than 50% of eligible patients. Instead, another method for reducing LAA related cardioembolic stroke, is left atrial appendage occlusion (LAAO) using an occlusion device such as the WATCHMAN™ (Boston Scientific Corporation, St. Paul, Minnesota). Although these devices have shown improved long-term outcomes, studies have also shown that about 4% of patients develop device related thrombosis (DRT)[1]. The factors leading to DRT are still unclear despite several clinical studies investigating potential predictors.

The aim of this study is to evaluate the hemodynamic profiles of the left atrium (LA) in patients who have received a WATCHMAN™ device, and to identify potential predictors for DRT. We hypothesize that DRT is more likely to occur in patients with blood stasis and complex flow patterns at and around the WATCHMAN™ device. We propose a combined finite element analysis (FEA) and computational fluid dynamics (CFD) approach to investigate this hypothesis.

METHODS

Echocardiographic (ECHO) and computed tomography (CT) images were taken before and after device deployment and were provided by Mayo Clinic, Aarhus, and Copenhagen University hospitals under an IRB approved protocol. A total of 38 patients were selected for this study.

The CT images were imported into Mimics Research 23.0 (Materialise, Belgium) for processing and segmented to create a patient-specific 3D digital model of the left atrium (LA). Finite-element simulations were performed by FEops NV (Gent, Belgium) to deploy an LAAO device into each model in a position that matched the post-procedural CT positioning for each patient. The output of the finite-element simulations was retained and used as input for the computational fluid dynamic (CFD) simulations. The mitral valve (MV) was segmented as a saddle shaped opening and the PVs were cut at the ostium. The models were imported into Ansys Workbench 2020 R1 (Canonsburg, PA). Extensions were made at the inlets (n=4) and outlet equal to 10x the diameter of each PV and the MV to overcome entrance effects and to ensure an appropriate velocity profile. The models were meshed with an element size 0.8mm based on the results of a mesh sensitivity study. Transient CFD simulations were completed using Ansys Fluent (Canonsburg, PA). A laminar flow model (Re < 2000) was used. Each PV was set as a pressure inlet with 0 pressure. The MV was set as a velocity waveform outlet with a unique patient-specific profile for each model. A total of 3 cardiac cycles were simulated for each patient and only the last cycle was used for analysis. The workflow used is shown in **Figure 1**. The parameters of interest were time averaged wall shear stress (TAWSS; **EQ1**), oscillatory shear index (OSI; **EQ2**), and endothelial cell activation potential (ECAP; **EQ3**)[2], with T being the cardiac cycle duration.

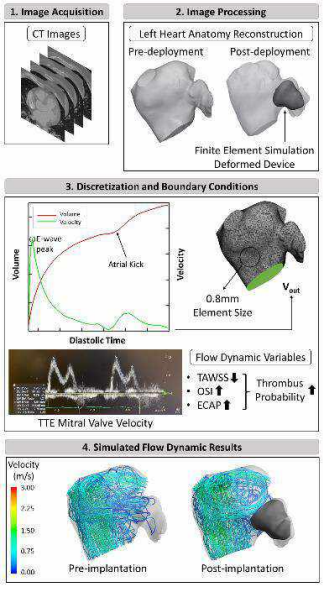

Figure 1. Workflow adopted for this study.

$$TAWSS = \frac{1}{T}\int_0^T |\overline{WSS}|\, dt \qquad \textbf{(EQ1)}$$

$$OSI = 0.5\left(1 - \frac{\left|\int_0^T \overline{WSS}\, dt\right|}{\int_0^T \overline{WSS}\, dt}\right) \qquad \textbf{(EQ2)}$$

$$RRT = \frac{1}{(1-2*OSI)*TAWSS} \qquad \textbf{(EQ3)}$$

RESULTS

Given the cohort size, only a sample of the patients are shown in contour images of **Figure 2**. The TAWSS contour plots are shown in **Figure 2A**. To quantify the differences between patient populations, **Figure 2A** shows a global account of the TAWSS values as a Box and Whisker plot. The mean TAWSS was found to be 1.76±1.24 Pa for the DRT cohort and 2.90±2.70 Pa for the control cohort with p <0.0001.

The OSI contour plots are shown in **Figure 2B**. To quantify the differences between patient populations, **Figure 2B** shows a global account of the OSI values as a Box and Whisker plot. The mean OSI was found to be 0.19±0.11 for the DRT cohort and 0.17±0.11 for the control cohort with p <0.0001.

The ECAP contour plots are shown in **Figure 2C**. To quantify the differences between patient populations, **Figure 2C** shows a global account of the ECAP values as a Box and Whisker plot. The mean ECAP was found to be 0.23±0.58 Pa-1 for the DRT cohort and 0.17±0.30 Pa^{-1} for the control cohort with p <0.0001.

The boundaries of the thrombi found in each DRT patient's post-CT scan are overlayed for each flow dynamic parameter (**Figure 2)**. The thrombi were mainly observed in regions of low WSS, high OSI, and high ECAP. The total mean volume of the thrombi was 1.44±2.01mL.

DISCUSSION

Endothelial cell dysfunction is a known predictor of thrombus formation. Numerous studies have explored WSS as a possible factor in endothelial dysfunction, [3] particularly noting the association of low WSS levels with thrombogenesis[5]. In line with these previous findings, our study shows that DRT patients had a lower TAWSS compared to controls. A low TAWSS indicates a region of blood stasis, which can induce thrombosis due to the accumulation of procoagulant components [4]. Furthermore, our study documented that DRT was mainly located within or close by regions with low levels of TAWSS. These lower TAWSS values may be related to device deployment. Zhong et al.[6] have shown that a deep device deployment depth resulted in lower TAWSS whereas a device deployed at the LAA ostium was higher. Clinical studies have also shown a higher incidence of DRT with deeper device deployments (34,35). When the device is deployed deep into the LAA, a shallow 'valley' is created above the device that serves as a nidus for blood stagnation and thrombus formation.

Another important flow dynamic parameter investigated was OSI. Oscillatory flow can promote an inflammatory state which can result in endothelial cell dysfunction, a potential nidus for thrombus formation [5]. The presence of an LAAO device may influence the flow patterns within the atrium, potentially resulting in increased oscillatory shear. In the case of a deeper device deployment, a recirculation region develops on top of the device increasing the oscillatory shear around the device. In this study, the DRT cohort was observed to have higher OSI than the controls. In addition, there was a correlation between the location of the thrombus identified from in-vivo imaging and regions of high OSI. Although not seen in this study, residual (micro) peri-device leaks may also influence OSI.

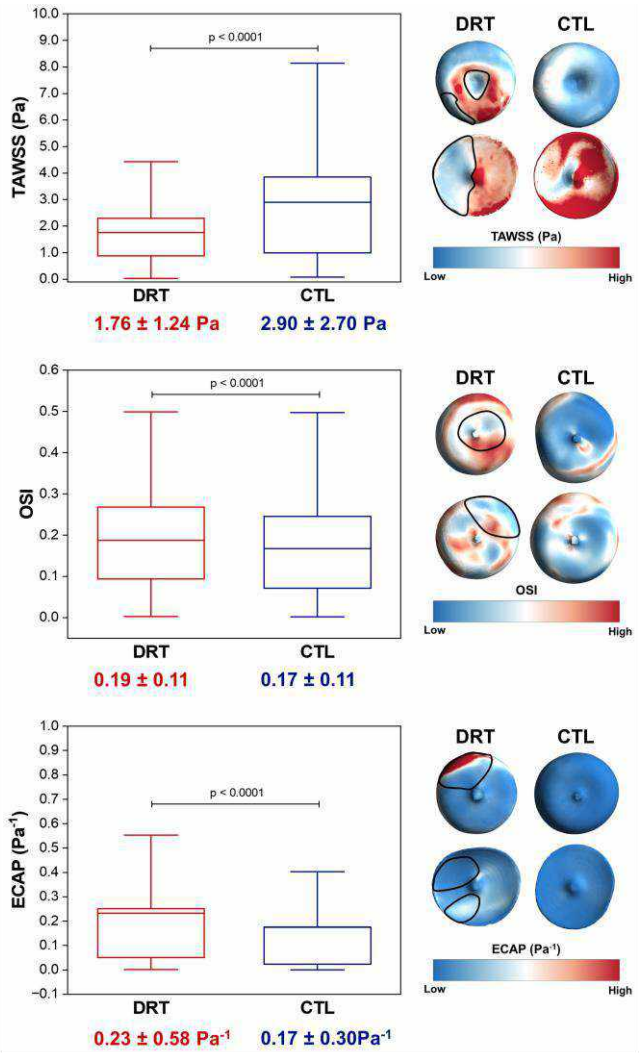

Figure 2. Global account of TAWSS (A), OSI (B), and ECAP (C) for the DRT and control (CTL) populations. Contours of each parameter for the top surface of the device are displayed to the right of each box plot. Thrombus locations from in-vivo imaging are shown by the black line for each DRT patient displayed.

ECAP has been shown in various studies to confer areas of susceptibility at the vessel walls [6]. ECAP is defined as the ratio of OSI and TAWSS, where a high value indicates a high OSI and a low TAWSS, both of which have been shown to be related to thrombogenesis. Endothelial cells naturally provide an antithrombotic surface [7], but when activated, this property is negated, which can result in thrombus formation [7]. In this study, we observed an elevated ECAP for the DRT cohort compared to the controls further confirming the potential role of CFD parameters in predicting DRT.

REFERENCES

[1] Lempereur, M et al., *CCI*, 90(5):E111-E12, 2017
[2] Achille, P et al., *Proc. Math. Phys. Eng*, 470(2172):20140163, 2014
[3] Chiu, J et al., *Physiological Reviews*, 91(1):327-387, 2011
[4] Mackman, N et al., *JCI*, 122(7):2331-2336, 2012
[5] Hathcock, J et al. *ATVB*, 26(8):1729-37, 2006
[6] Zhong, Z et al., *Clinical Research in Cardio.*, 1-14, 2023
[7] Y, J et al., *BMC Cardio. Disorders*, 15(1):1-11, 2015

EVALUATION OF FLOW DYNAMICS IN THE LEFT ATRIUM AFTER HYBRID ABLATION FOR ATRIAL FIBRILLATION

B. Vogl (1), G. Hoeppner (1), H. Labonte (1), E. Vitale (1), A. Sularz (2), A. Chavez-Ponce (2), A. Killu (2), M. Alkhouli (2), and H. Hatoum (1)

(1) Biomedical Engineering, Michigan Technological University, Houghton, MI, USA
(2) Cardiovascular Medicine, Mayo Clinic, Rochester, MN, USA

INTRODUCTION

Atrial fibrillation (AF) is the most common arrhythmia in the world and is associated with adverse cardioembolic events. As a result of the irregular beating of the heart caused by AF, blood stasis is often reported in the left atrium (LA), and in particular the left atrial appendage (LAA). This stasis promotes thrombogenesis and therefore, stroke management is the main concern in these patients. Antiarrhythmic and anticoagulant medications can be used to reduce the risk of stroke; however, their side effects make them unusable in many patients[1]. A possible alternative is the use of radiofrequency (RF) ablation to restore the heart to a normal rhythm. This procedure can be performed invasively (surgical ablation), noninvasively (catheter ablation), or a combination of both (hybrid ablation). In addition, the LAA can also be closed during a surgical ablation, preventing blood flow into it. Compared to the use of only surgical or catheter ablation, hybrid ablation has been shown to have positive outcomes for restoring rhythm with less recurrence of AF and the need for repeat ablations [2]. Although there has been clinical success of a hybrid ablation approach, it remains unclear whether this procedure in combination with LAA closure (LAAC), influences the flow dynamics of the LA. Changes in the flow could potentially cause complications if left unaddressed. We have previously shown that the use of catheter ablation influences the LA geometry and flow dynamics in the LA by changing the velocities and vortex formations [3].

The aim of this study is to evaluate the flow dynamics in the LA after a hybrid ablation procedure with closure of the LAA. We hypothesize that combination of the ablation and closure procedure will have a profound effect on the overall flow dynamics and LA geometry.

METHODS

The hybrid ablation procedure consisted of surgical epicardial RF ablation of the left atrial posterior wall and closure of the LAA, and catheter RF ablation of the pulmonary veins (PV). Echocardiographic (ECHO) and computed tomography (CT) images were taken before and after each procedure and were provided by Mayo Clinic under an IRB approved protocol. A total of 10 patients (thus 30 CT scans), matched by age and sex, were selected for this study. Geometric measurements of the LA and PVs were recorded for each as well.

The workflow used is shown in **Figure 1**. The CT images were imported into Mimics Research 23.0 (Materialise, Belgium) for processing and segmented to create a patient-specific 3D digital model of the LA. The mitral valve (MV) was segmented as a saddle shaped opening and the PVs were cut at the ostium. The models were imported into Ansys Workbench 2020 R1 (Canonsburg, PA). Extensions were made at the inlets (n=4) and outlet equal to 10x the diameter of each PV and the MV to overcome entrance effects and to ensure an appropriate velocity profile. The models were meshed with an element size 1.0 mm based on the results of a mesh sensitivity study. Transient computational fluid dynamic simulations were completed using Ansys Fluent (Canonsburg, PA). A laminar flow

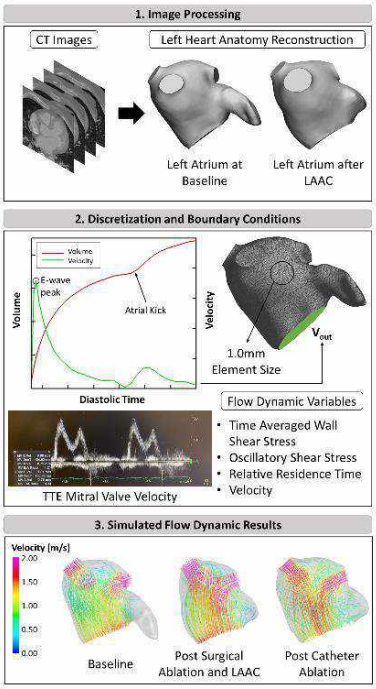

Figure 1. Adopted image processing and CFD workflow.

model (Re < 2000) was used. Each PV was set as a pressure inlet with 0 pressure. The MV was set as a velocity waveform outlet with a patient-specific profile that matched the rhythm (sinus, AF, or atrial flutter) at each procedure from ECHO. A total of 3 cardiac cycles were simulated for each patient and only the last cycle was used for analysis. The parameters of interest were time averaged wall shear stress (TAWSS; **EQ1**), oscillatory shear index (OSI; **EQ2**), relative residence time (RRT; **EQ3**), and velocity in the atrium with T being the cardiac cycle duration.

$$TAWSS = \frac{1}{T}\int_0^T |\overline{WSS}|\, dt \qquad \text{(EQ1)}$$

$$OSI = 0.5\left(1 - \frac{\left|\int_0^T \overline{WSS}\, dt\right|}{\int_0^T \overline{WSS}\, dt}\right) \qquad \text{(EQ2)}$$

$$RRT = \frac{1}{(1-2*OSI)*TAWSS} \qquad \text{(EQ3)}$$

RESULTS

Because of space limitations, we are showing the results of one patient representative of the whole dataset. The average velocity increased from baseline to post catheter ablation (**Figure 2**). Initially, E-wave velocity was 0.39 ± 0.24 m/s at baseline, 0.51 ± 0.28 m/s after the surgical ablation and LAAC, and 0.81 ± 0.52 m/s after catheter ablation. A more centralized flow that increased in magnitude at the E-wave peak was shown after each procedure. Velocities were low and near zero in the LAA at baseline and after LAAC.

The average TAWSS increased with each ablation procedure (**Figure 3**). Initially, TAWSS was 1.69 ± 1.63 Pa at baseline, 1.87 ± 0.73 Pa after the surgical ablation and LAAC, and 3.19 ± 1.20 Pa after catheter ablation. The increase in TAWSS was mostly observed to occur on the posterior portion of the LA. In addition, after catheter ablation, there is a drastic increase in TAWSS at the PVs. Despite the closure of the LAA, the portion of the appendage that remained had lower TAWSS values that were comparable to those at baseline.

There was a negligible change in OSI after each procedure (**Figure 3**). OSI was 0.16 ± 0.09 at baseline, 0.16 ± 0.11 after the surgical ablation and LAAC, and 0.15 ± 0.10 after catheter ablation. The concentration of OSI appeared to increase on the anterior side with each procedure.

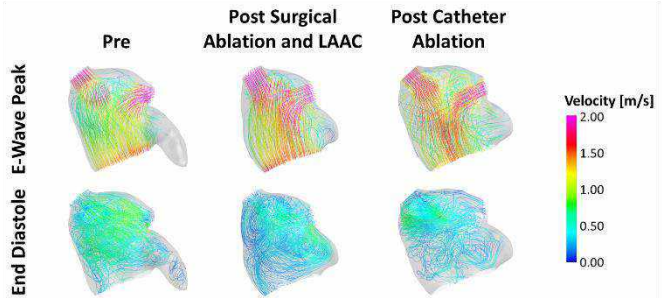

Figure 2. Atrial velocities at the E-wave peak and end diastole after each procedure.

The average RRT drastically decreased after each procedure (**Figure 3**). RRT was 2.93 ± 8.76 Pa^{-1} at baseline, 1.19 ± 1.46 Pa^{-1} after the surgical ablation and LAAC, and 0.66 ± 0.93 Pa^{-1} after catheter ablation. The region with the highest RRT at baseline was at the LAA. After catheter ablation, there was a decrease in RRT at the PVs.

A decrease in overall surface area and volume was seen after each procedure independent of the decrease in volume from the LAAC. The PVs ostia areas decreased from baseline to post catheter ablation.

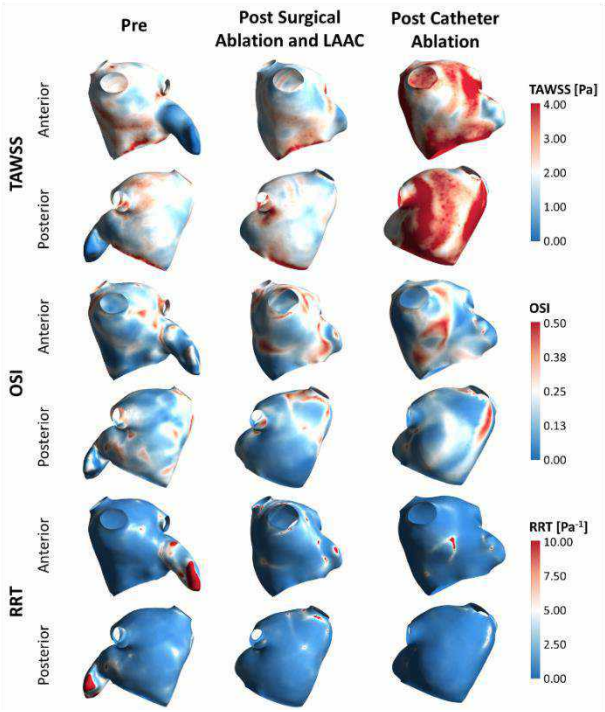

Figure 3. Flow dynamic parameters on the anterior and posterior surfaces at baseline and after each procedure.

DISCUSSION

In this study, several parameters were investigated using CFD to elucidate the effect of hybrid ablation of LA flow dynamics. We observed lower TAWSS in the LAA at baseline, reaffirming the appendage as an ideal location for flow stagnation. After LAAC the remaining portion of the LAA still has a lower TAWSS compared to the rest of the LA. Depending on the size of the remaining LAA, thrombogenesis in this region may still be a concern. Interestingly, a majority of TAWSS increase was observed on the posterior side and near the PVs, the locations where the ablations were performed. A decrease in LA volume has been reported after RF ablation [4], which could result in increased velocities and thus WSS. We also observed this in our study.

Oscillatory shear has been associated with inflammation which can assist the thrombotic process [5]. The average OSI in this study was low however, there was an increasing concentration of high OSI after each ablation procedure. This may indicate potential problem regions within the LA for a higher probability of thrombogenesis after ablation.

The LAA was identified as the region with the highest RRT at baseline, indicating little to no blood flow. The absence of the A-wave results in lower average velocities during diastole. When the heart is restored to normal rhythm after an ablation procedure, there is now an increase in average velocities. As a result, blood is guided out of the LA quicker, ultimately reducing the likelihood of high RRT. This study is a proof of concept to the unique flow features that occur after ablation procedures. More follow-up is needed to connect the findings to actual clinical outcomes.

REFERENCES

[1] Holmes, D et al., *Mayo Clinic Proceedings*, 94(5):864-874, 2019
[2] Kress, D et al., *Clinical Electrophysiology*, 3(4):341-349, 2017
[3] Vogl, B et al., *JICE*, 65(1):83-96, 2022
[4] Lemola, K et al., *Heart Rhythm*, 1(5) 576-581, 2004
[5] Hathcock, J et al. ATVB, 26(8):1729-37, 2006

MECHANICAL HETEROGENEITY IN HUMAN CEREBRAL ANEURYSMS: EXPLORING THE ROLE OF TISSUE MICROSTRUCTURE AND INFLAMMATION

Sergio A. Pineda-Castillo, PhD. (1), Elizabeth D. Shih, Ph.D. (1), Andrew W. Grande, MD. (2), Patrick W. Alford, Ph.D. (1)

(1) Department of Biomedical Engineering, University of Minnesota, Minneapolis, Minnesota, USA
(2) Department of Neurosurgery, University of Minnesota, Minneapolis, Minnesota, USA

INTRODUCTION

Ruptured cerebral aneurysms (CAs) are the cause for subarachnoid hemorrhage (SAH) in 7.9 (95% CI: 6.9-9.0) per every 100,000 persons yearly [1]. Considering the great mortality and morbidity associated with SAH, understanding the mechanisms that lead to aneurysm rupture is crucial. Over the years, numerous studies have been conducted to understand risk factors associated with aneurysm rupture, including demographics, CA geometry, and ethnicity [1,2]. However, the role of tissue microstructure and inflammation in CA rupture mechanisms remains unsolved, despite recent efforts [3,4]. In our group, we have previously demonstrated that CAs have heterogenous mechanical properties, which may contribute to aneurysm rupture [5]. Currently, we aim to develop methods to explore the role of *transmural* tissue heterogeneity and macrophage infiltration in the mechanical heterogeneity of CAs. Here, we present characterizations of three different unruptured CAs using biaxial testing, histological orientation analysis, and confocal microscopy, respectively. We found that CAs exhibit the presence of clusters of high cellular organization, which are surrounded by areas of lower organization. We also observed the presence of M1/M2 macrophages in an area of low fibrous organization. We hypothesize that CA mechanical heterogeneity is correlated with the presence of these clusters of high cellular organization and M1/M2 macrophages. Further exploration will shed light on this theory and will potentially elucidate mechanisms of CA rupture and formation.

METHODS

CA Tissue Dissection: Three CA tissues were obtained from a cadaver circle of Willis (n=1, tissue #1) and after surgical clipping in living patients (n=2, tissues #2-3). All patients were female. Tissues #2-3 were fixed in 4% paraformaldehyde for 24h prior to imaging.

Biaxial Testing & Generalized Anisotropic Inverse Mechanics (GAIM): Biaxial testing of tissue #1 was performed in a commercial biaxial tester. Forces were measured using 4 load cells on independent arms during 15 unique loading protocols. Boundary stresses were correlated with strain tracking of the tissue to perform GAIM analysis to characterize mechanical heterogeneity, as described previously [5].

Histology and Orientation Analysis: Histology was performed at the UMN Histology core using standard procedures for hematoxylin and eosin staining of tissue #2. Planar (transmural) sections of 10μm in thickness were used for staining. Cellular orientation analysis was performed using the OrientationJ plugin for Fiji ImageJ. Orientation analysis yielded two measurements: local fiber/cell orientation, and coherence, which is a measure of the local anisotropy. Orientation was obtained for regions of the tissue where coherence>0.55, which indicates a relatively high level of cellular/fibrous alignment. Orientation data was divided in three angular groups for visualization purposes: (i) blue: 0-59º; (ii) red: 60-119º, and (iii) green: 120-180º.

Confocal Microscopy: Tissue #3 was optically cleared using a protocol for SmartBatch+ electrophoretic clearing system. After clearing, tissues were immunostained for CD68 and CD206, which are markers for identification of all macrophages, and M2 macrophages, respectively. Tissue microstructure was imaged using autofluorescence at 488nm. Imaging was performed in a Nikon A1Rsi HD Confocal SIM Super Resolution microscope. Images were denoised and background was subtracted. Images presented here are Z projections of maximum intensity of the obtained multiplanar z-stack.

RESULTS

Biaxial testing of tissue #1 and subsequent GAIM analysis demonstrated mechanical heterogeneity in the tissue. Figure 1 represents a heatmap of the Kelvin moduli, demonstrating neighboring regions of heterogenous stiffness. For example, the top right edge of the tissue demonstrates Kelvin moduli close to 10MPa (in red), while the opposite end of the tissue exhibits magnitudes of ~7MPa. Simultaneously, the area in the center of the tissue is softer (~3MPa). Also, the preferred alignment of these regions demonstrate that the center of the tissue is isotropic while the edges are anisotropic.

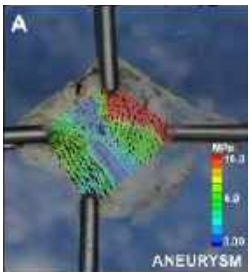

Figure 1: Photograph of tissue #1 mounted on the biaxial testing system. Overlaid heatmap represents the Kelvin moduli (MPa) and the preferred local orientation obtained with GAIM.

Inspired by the mechanical heterogeneity of tissue #1, demonstrated with GAIM, we explored the transmural tissue microstructure using histology. By performing an orientation analysis, we observed the presence of regions with high coherence. These anisotropic clusters were observed at different depths of the vascular wall and appear to shift in position radially (Figure 2).

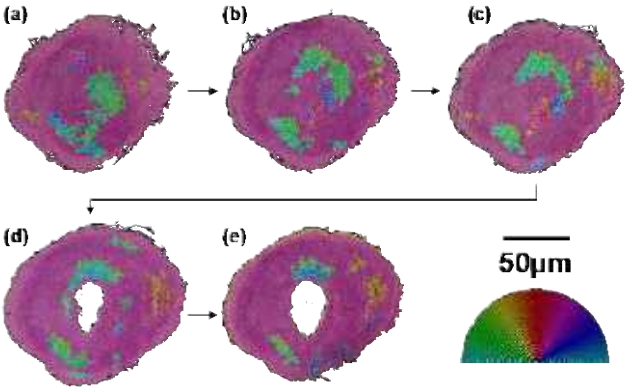

Figure 2: Selected transmural histological sections of tissue #2. Depth from top to bottom of the dome: (a) 0µm, (b) 30µm, (c) 40µm, (d) 60µm, (e) 80µm. Colored regions are clusters of high coherence, and the colors represent preferred local orientation.

By segmenting the regions of coherence>0.55, we observed that anisotropic clusters are surrounded by areas of low cellular organization and no preferred orientation (Figure 3). Further, some neighboring clusters exhibit orthogonal relationships and are separated by areas of low coherence (Figure 3, white ovals).

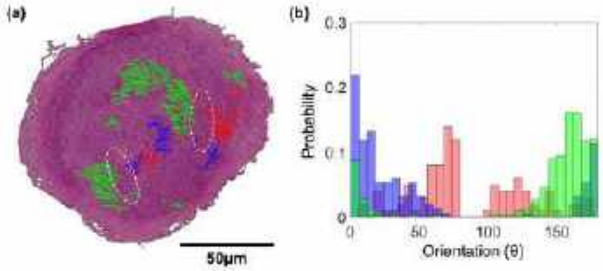

Figure 3: (a) Overlay of preferred direction vectors in high coherence regions of a histological section of tissue #3 (Fig. 2b). Colors of the vectors represent the binned preferred orientation. (b) Histogram of the orientation of the three angular groups.

To explore the potential role of inflammation in the remodeling of the low coherence regions of tissue #2, we immunostained tissue #3 for CD68 and CD206 to explore the presence of M1/M2 macrophages using confocal microscopy. The imaging demonstrated the presence of both M1 ($CD68^{+}CD206^{-}$) and M2 ($CD68^{+}CD206^{+}$) macrophages in a region of low fibrous organization (Figure 4).

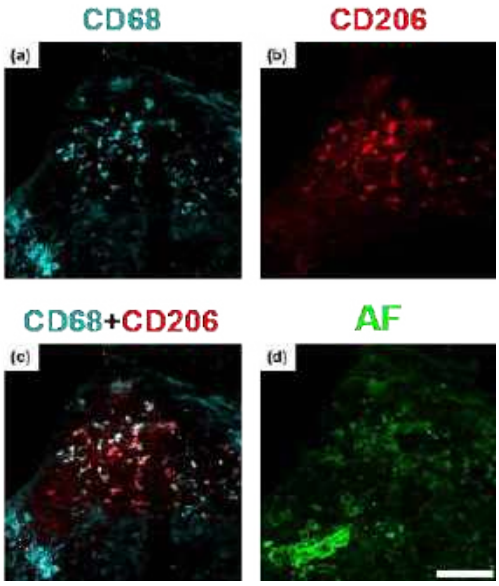

Figure 4: Z projection of the multiplanar stacks obtained for tissue #3. (a) CD68 (all macrophages). (b) CD206. (c) CD68+CD206 (M2 macrophages: CD68+CD206+). (d) Autofluorescence (AF) of the tissue, demonstrating low fibrous organization. Scale bar: 100µm.

DISCUSSION

In this study, we performed exploratory assessments of three different human CA tissues. Through GAIM analysis, we observed mechanical heterogeneity in tissue #1. Histological analysis demonstrated the transmural microstructural heterogeneity of tissue #2. Immunostaining of tissue #3 demonstrated the presence of M1/M2 macrophages in a region of low fibrous organization. These findings agree with the observations made of Robertson et al. [3], who demonstrated great variability in the tissue microstructure of surgically dissected human CA tissues using confocal microscopy. However, Robertson's images are limited to relatively small regions of the tissue (~300x300µm area). Our approach to microstructural characterization using planar histological sections allows for the characterization of the *complete* transmural microstructure. In addition, the presence of M1/M2 has been demonstrated (and their ratios extensively debated) [6-8], but their relationship to the *local* tissue microstructure has not been explored. The findings of this study inspire further *whole tissue* characterization of CAs to understand the relationship of inflammation and microstructural and mechanical heterogeneity. The clusters of high anisotropy observed in this study might explain the great mechanical heterogeneity of CAs. We aim to perform GAIM analysis, light sheet microscopy/immunostaining and orientation analysis in the coming months for at least n = 5 human CAs.

ACKNOWLEDGEMENTS

This work was supported by the National Institutes of Health (NIH-R01NS126762). We would like to acknowledge the University Imaging Centers of the University of Minnesota – Twin Cities.

REFERENCES

[1] Etminan N. et al., *JAMA Neurology*, 76:588-597, 2019.
[2] Morel S. et al., *Neurosurg Rev*, 45:1233-1253, 2022.
[3] Robertson, A. et al., *Ann Biomed Eng*, 43:1502-1515, 2015.
[4] Frösen, J. et al., *Neurosurg Focus,* 47:E21, 2019.
[5] Shih, E. et al., *J Vasc Res*, 59:34-42, 2021.
[6] Hasan, D. et al., *J Neuroinfl,* 9:222.
[7] Stratilová, et al., *Acta Neurochirug*, 165:177-186, 2023.
[8] Koseki, H. et al., *Transl Stroke Res*, 11:80-92

DIFFERENCES IN FLOW DYNAMICS BETWEEN CORONARY ARTERY ANEURYSMS AND ECTASIA

B. Vogl (1), E. Vitale (1), S. Lee (2), J. Kovalchin (3), H. Hatoum (1)

(1) Biomedical Engineering, Michigan Technological University, Houghton, MI, USA
(2) Department of Pediatrics, Lurie Children's Hospital of Chicago, Chicago, IL, USA
(3) Department of Pediatrics, Nationwide Children's Hospital, Columbus, OH, USA

INTRODUCTION

Kawasaki disease (KD) is a rare heart condition often seen in children under the age of 5 that can cause vasculitis (inflammation of the blood vessels). Without early intervention, these children are at risk of developing coronary artery aneurysms (CAA), coronary artery ectasia (CAE), or both. The coronary arteries (CA) are typically monitored after a positive diagnosis to monitor these dilations. Excessive dilation of the CAs is rare but the development of giant CAAs is possible. Patients with dilations, whether it be CAA, CAE, or both, are at a higher risk for myocardial infarction, atherosclerosis, and thrombogenesis[1].

The geometry of CA dilation can induce flow separation and recirculation which increases the risk of blood stagnation and thrombogenesis, atherosclerosis, and sluggish flow. Furthermore, thrombosis occurrence has been associated with CA shape and size, though only CAAs have been assessed [2]. Currently, there is little known about the incidence of CAE-related thrombogenesis from a flow dynamics standpoint and whether clinical outcomes are worsened. Because the geometry dictates the flow patterns, differences should be seen between CAA and CAE. Therefore, this study aims to compare the flow dynamics between these two dilation types (CAA and CAE) and to correlate their differences with clinical outcomes.

METHODS

CT images of 20 CAA, CAE, or both were transferred to Michigan Technological University by Nationwide Childrens Hospital under an approved IRB protocol. The CT images were imported in Mimics Research 23.0 (Materialise, Beligium) for processing. A mask (using a threshold that isolates blood from soft tissue) was applied to the CT images and segmentation was performed to create a patient-specific 3D digital model of the CAs. Each model was trimmed at the coronary ostium and downstream of the aneurysm or ectasia. Geometric measurements of the coronaries were recorded for each patient. The models were imported into Ansys Workbench 2020 R1 (Canonsburg, PA). Extensions were made at the inlet and outlet equal to 10x the diameter of each. These extensions help to overcome entrance effects and to ensure an appropriate velocity profile. The models were meshed with an element size 0.3 mm based on the results of a mesh sensitivity study. Transient computational fluid dynamic simulations were completed using Ansys Fluent (Canonsburg, PA). Each simulation used a laminar flow model (Re < 2000) and an incompressible Newtonian fluid with a density (ρ) of 1060kg/m^3 and a dynamic viscosity (μ) of 3.5cP. Patient-specific boundary conditions from literature were applied to the velocity inlet and pressure outlet. A total of 3 cardiac cycles were simulated for each patient but only the last cycle was used for analysis. An example of the workflow used is shown in **Figure 1**. The parameters of interest were time averaged wall shear stress (TAWSS; **EQ1**), oscillatory shear index (OSI; **EQ2**), relative residence time (RRT; **EQ3**), and velocity.

$$TAWSS = \frac{1}{T}\int_0^T |\overline{WSS}|\, dt \qquad \textbf{(EQ1)}$$

$$OSI = 0.5\left(1 - \frac{\left|\int_0^T \overline{WSS}\, dt\right|}{\int_0^T \overline{WSS}\, dt}\right) \qquad \textbf{\textit{(EQ2)}}$$

$$RRT = \frac{1}{(1-2*OSI)*TAWSS} \qquad \textbf{\textit{(EQ3)}}$$

A percentage of area that exceeded a specified threshold (0.4Pa for TAWSS, 0.2 for OSI and 4.17 Pa^{-1} for RRT)[3] for each parameter was also calculated.

RESULTS

The figures presented herein only show a sample from the patient population, but all values listed are the mean ± standard deviation of the

entire population. The geometric measurements for the population are shown in **Table 1**.

Table 1. Geometric measurements of each CA classification. Neck denotes the entry segment to the dilation.

Classification	Diameter neck (mm)	Diameter max (mm)	Length (mm)
CAA	4.51 ± 2.87	10.56 ± 6.61	15.36 ± 10.63
CAE	3.11 ± 0.61	5.68 ± 1.84	15.22 ± 8.4
CAA and CAE	3.35 ± 2.02	6.97 ± 1.62	10.19 ± 6.42

Lower velocities and circulation were observed in regions where a CAA or CAE was present; this was amplified in the patients with larger dilations (**Figure 2**). As the flow passed the CAA and CAE, some patients saw a drastic increase in velocity in the distal direction.

TAWSS was lower in the regions of CAA and CAE compared to the rest of the CA (**Figure 3**). The average TAWSS was 2.33 ± 3.97 Pa for a CAA, 6.58 ± 6.18 Pa for CAE, and 1.31 ± 2.19 Pa for a combined CAA and CAE. Larger dilations were observed to have lower TAWSS regardless of the type (CAA or CAE). The percentage of area with TAWSS<0.4 Pa was 32.98 ± 19.77 %, 52.22 ± 66.35%, and 48.32 ± 23.5% for CAE, CAA, and both, respectively.

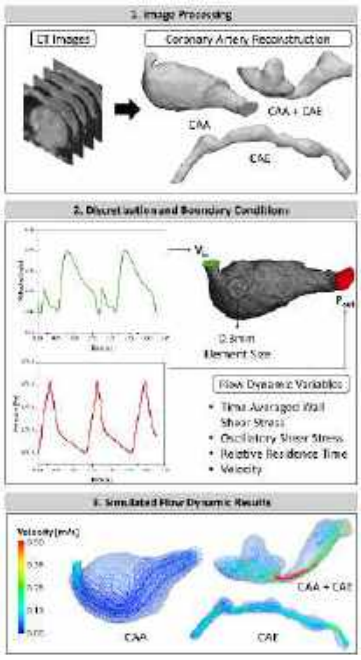

Figure 1. Adopted image processing and CFD workflow.

We observed a higher OSI in the distal portions of the CAA and CAE (**Figure 3**). In addition, OSI was higher in the larger dilations. OSI was low for the regions of the CA that did not have a CAA or CAE. The average OSI was 0.044 ± 0.068 for a CAA, 0.025 ± 0.051 for CAE, and 0.026 ± 0.055 for a combined CAA and CAE. The percentage of area with OSI>0.2 was 3.17 ± 2.95 %, 10.49 ± 11%, and 2.58 ± 2.1% for CAE, CAA, and both, respectively.

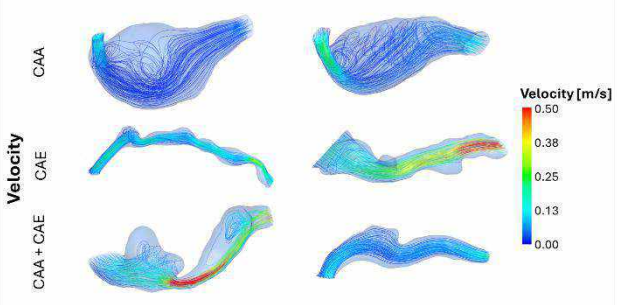

Figure 2. Velocity streamlines for CAs with CAA, CAE, and CAE+CAA.

RRT was higher in the regions of CAA and CAE (**Figure 3**). The average RRT was 6.37 ± 17.95 Pa^{-1} for a CAA, 27.86 ± 52.25 Pa^{-1} for CAE, and 6.55 ± 13.85 Pa^{-1} for a combined CAA and CAE. The larger the dilation, the higher the RRT. The percentage of area with RRT>4.17 Pa^{-1} was 37.3 ± 39.5 %, 50.77 ± 66.36 %, and 32.34 ± 15.68% for CAE, CAA, and both, respectively.

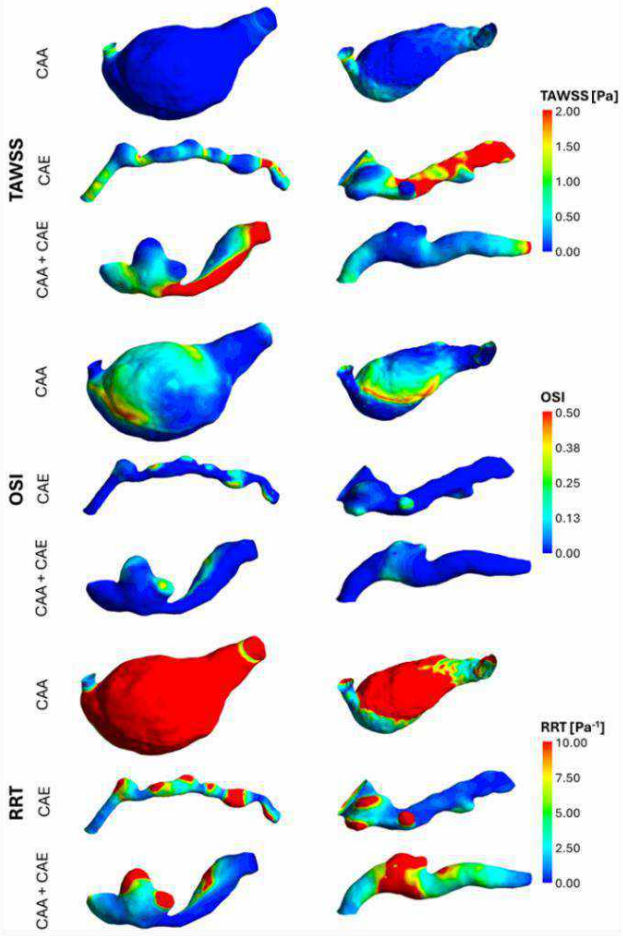

Figure 3. TAWSS, OSI, and RRT for CAs with CAA, CAE, and CAA+CAE.

DISCUSSION

This study assessed the differences in flow dynamics between CAA and CAE. We observed flow separation and recirculation in both types; however, recirculation zones were larger in the CAA cases. The larger volume of the CAAs allows for more of the separated flow to enter the dilation causing more recirculation. Elevated RRT indicates regions where flow stasis may occur. Low TAWSS and high OSI, potential indicators of blood stasis, have been associated with thrombogenesis [4]. We observed that TAWSS was lowest in the models with combined CAA and CAE, but OSI was highest for the CAA only models. OSI is a measure of the unidirectionality of WSS. Due to the "rounder" shape of CAA, more recirculation is seen in addition to lower shear stresses and lack of unidirectionality. Based on the results presented herein, KD patients with CAA are at a higher risk of developing thrombosis, which agrees with clinical findings[5].

REFERENCES

[1] McCrindle, B et al., *Circ.*, 6135(17):e927-e999, 2017
[2] Asadbeygi, A et al., *CMPB*, 224:107007, 2022
[3] Chiastra, C et al., *J Biomech*, *58*:79-88, 2017
[4] Hathcock, J et al., *ATVB*, 26(8):1729-1737, 2006
[5] Luo, Y et al., *Angiology*, *68*(9):823-830, 2017

3D PRINTING PATIENT-SPECIFIC LEFT-HEART MODELS FOR SURGICAL PLANNING

Jakari C.L. Harris (1), Scott J. Hollister (2), Lakshmi P. Dasi (3)

(1) Wallace H. Coulter Department of Biomedical Engineering, Georgia Institute of Technology | Emory University, Atlanta, Georgia, USA
(2) Wallace H. Coulter Department of Biomedical Engineering, Georgia Institute of Technology | Emory University, Atlanta, Georgia, USA
(3) Wallace H. Coulter Department of Biomedical Engineering, Georgia Institute of Technology | Emory University, Atlanta, Georgia, USA

INTRODUCTION

Medical Errors in the healthcare field are unintentional acts or ones that fail "achieve its intended outcome" [1]. This can be due to several reasons, including "the failure of a planned action to be completed as intended, the use of the wrong plan to achieve an aim, or a deviation from the process of care that may or may not cause harm to the patient." Although medical errors are severely underreported, Makary and Daniel report that the mean rate of medical errors-related deaths from 1999 to 2013 was 251,454 per year. They received reports and information from a number of sources, including the US Department of Health and Human Services, Institute of Medicine, and Agency for Healthcare Quality and Research Patient Safety Indicators. At the time of the 2016 report, medial errors ranked third in leading causes of death in the United States. The reasons why medical errors occur have a common thread in the plan or procedure that is intended to be carried out. Terrentine et al. believe that inability to correctly recognize and interpret imaging information can contribute to errors in diagnosis [2]. Imaging modalities, such as computed tomography (CT) and magnetic resonance imaging (MRI), are limited in the ability to accurately represent organ 3D structures and lack kinesthetic feedback. With imaging modalities being the gold standard for surgical planning and preoperative information, there needs to be a better tool that can fill these gaps.

Cardiovascular disease (CVD) is currently and has been the leading cause of death worldwide for decades. The heart is a complex organ, and no doubt contributes substantially to medical error-related deaths. There needs to be a better diagnostic tool for heart disease and to help make a dent in this looming statistic. Heart failure can be classified into either left-sided heart failure (LSHF) or right-sided heart failure (RSHF). LSHF is more common out of the two and can often lead to RSHF [3]. Due to the complex nature of the heart and the fact that LSHF is more prominent, we will be modeling the left side of the heart solely.

3D modelling and segmentation is the process of converting a 2D image, usually in the form of CT, into a 3D virtual representation [4]. For our model, we will be isolating the following regions of interest (ROI) during segmentation: left ventricle (LV), left atrium (LA), aortic valve (AV), mitral valve (MV), aorta (AO). Segmentation allows for 3D models to be patient-specific and can be exported to a 3D printer after being saved as a stereolithography (STL) file. Additive manufacturing, otherwise known as 3D printing, is the process of creating a 3D object layer-by-layer. There are numerous types of 3D printers, but we will be using a polyjet printer for this model. Polyjet printers can mix different resins to create combinations that exhibit various colors and material properties. This feature will allow us to fine-tune the material properties of each ROI for the left-heart model. Researchers have created various heart models over the years, but they all lack one thing. Most groups have not investigated native heart tissue mechanics and matched that to their heart model materials. Another unexplored area is the lack of validation for these models, specifically an ex-vivo benchtop model to test the functionality of their models.

The objective of this project is to 3D print a patient-specific left-heart model that closely resembles the geometry, material properties, and overall functionality of the patient's native heart. We hypothesize that matching the geometry and materials will be essential to validate the model functionality to patient data.

METHODS

To carry out this objective, the first step was to match native heart tissue mechanical properties to constitutive models. A literature search was conducted where researchers performed planar biaxial testing on human left-heart tissue specimens. The regions of interest were the myocardium, mitral valve, aortic valve, and aorta. After gathering mechanical property data on each ROI, further data analysis was done to fit the raw experimental data to constitutive models (Holmes-Mow (HM), Mooney-Rivlin (MR), Anisotropic Neo-Hookean (ANH),

Holmes-Mow with Fiber (HMF)). Eventually, a comparative analysis was done to conclude which model best fit the native heart tissue data.

Holmes-Mow (HM) Biaxial Test Strain Energy Function

$$\psi = \frac{1}{2}\frac{c_1}{c_2}\left[e^{c_2(\tilde{I}_1-3)}-1\right]+U(J) \Rightarrow \frac{1}{2}\frac{c_1}{c_2}\left[e^{c_2(\tilde{C}_{11}+\tilde{C}_{22}+\tilde{C}_{33}-3-3)}-1\right]+U(J) \quad (1)$$

Table 1: R^2 values of Constitutive Models Fit to Regions of Interest.

RESULTS

Region of Interest (ROI)	Constitutive Model	R^2 Value
Left Ventricle (LV)	HM	0.77702
	MR	0.79125
	ANH	0.65725
	HMF	0.99606
Left Ventricle Free Wall (LVFW)	HM	0.74899
	MR	0.74899
	ANH	0.72305
	HMF	0.99
Septum	HM	0.65992
	MR	0.64724
	ANH	0.9788
	HMF	0.99277
Ascending Aorta (AA)	HM	0.8871
	MR	0.7532
	ANH	-0.2646
	HMF	0.97064
Sinotubular Junction (SJ)	HM	0.9804
	MR	0.90557
	ANH	0.752
	HMF	0.978
Sinus of Valsalva (SOV)	HM	0.8095
	MR	0.58912
	ANH	0.4949
	HMF	0.9952
Left Coronary Leaflet (LCL)	HM	0.99254
	MR	0.71756
	ANH	0.55592
	HMF	0.20718
Right Coronary Leaflet (RCL)	HM	0.97153
	MR	0.63303
	ANH	-25.0569
	HMF	0.9285
Non-coronary Leaflet (NCL)	HM	0.98163
	MR	0.69421
	ANH	0.60012
	HMF	0.30907
Anterior Mitral Leaflet (AML)	HM	0.9951
	MR	0.63375
	ANH	0.57977
	HMF	0.8678
Posterior Mitral Leaflet (PML)	HM	0.99939
	MR	0.6816
	ANH	-5.7453
	HMF	0.62967

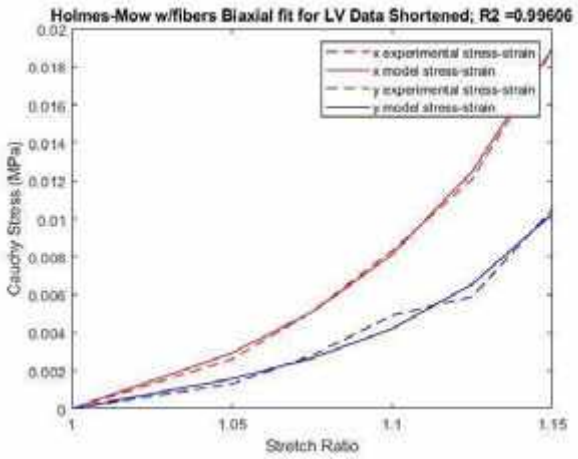

Figure 1: Left Ventricle Data Fit to Holmes-Mow w/fiber Model.

DISCUSSION

All of the ROIs fit best to either the HM or HMF models. The ROIs that are more fibrous and have a more dynamic motion with twisting, contracting, and expanding fit best to the model with fibers incorporated into it. This reflects the known anisotropy of tissue like the left ventricle. This study has fit the most diverse set of constitutive models to human heart tissue. A limitation of this work includes the shortage of mechanical testing data of human heart tissue currently in literature. The studies also could have separated the samples based on demographics. In the future, we will match these tissue mechanical properties to 3D printer material properties and print patient-specific left-heart models with the appropriate materials for each ROI.

ACKNOWLEDGEMENTS

This material is based upon work supported by the National Science Foundation Graduate Research Fellowship under Grant No. DGE-2039655.

REFERENCES

[1] Makary, M. A., & Daniel, M. (2016). Medical error—the third leading cause of death in the US. *Bmj*, *353*.

[2] Turrentine, F. E., Schenk, W. G., McMurry, T. L., Tache-Leon, C. A., & Jones, R. S. (2020). Surgical errors and the relationships of disease, risks, and adverse events. *The American Journal of Surgery*, *220*(6), 1572-1578.

[3] InformedHealth.org. Cologne, Germany: Institute for Quality and Efficiency in Heath Care (IQWiG); 2006-. Types of heart failure. 2018. Available from https://www.ncbi.nlm.nih.gov/books/NBK481485

[4] Vukicevic, M., Mosadegh, B., Min, J. K., & Little, S. H. (2017). Cardiac 3D printing and its future directions. *JACC: Cardiovascular Imaging*, *10*(2), 171-184.

[5] Sommer, G., Schriefl, A. J., Andrä, M., Sacherer, M., Viertler, C., Wolinski, H., & Holzapfel, G. A. (2015). Biomechanical properties and microstructure of human ventricular myocardium. *Acta biomaterialia*, *24*, 172-192.

[6] Pham, T., Sulejmani, F., Shin, E., Wang, D., & Sun, W. (2017). Quantification and comparison of the mechanical properties of four human cardiac valves. *Acta biomaterialia*, *54*, 345-355.

[7] Xuan, Y., Wisneski, A. D., Wang, Z., Lum, M., Kumar, S., Pallone, J., ... & Ge, L. (2021). Regional biomechanical and failure properties of healthy human ascending aorta and root. *Journal of the Mechanical Behavior of Biomedical Materials*, *123*, 104705.

ANALYSIS OF ENERGY AND PRESSURE IN THE SINUS UNDER DIFFERENT BLOOD PRESSURES AFTER AORTIC VALVE REPLACEMENT

B. Vogl (1), A. Sularz (2), S. Lilly (3), V. Thourani (4), B. Lindman (5), M. Alkhouli (2), H. Hatoum (1)

(1) Biomedical Engineering, Michigan Technological University, Houghton, Michigan, USA
(2) Cardiovascular Medicine, Mayo Clinic, Rochester, Minnesota, USA
(3) Cardiovascular Medicine, The Ohio State University, Columbus, Ohio, USA
(4) Cardiovascular Surgery, Marcus Valve Center, Piedmont Heart Institute, Atlanta, Georgia, USA
(5) Structural Heart and Valve Center, Division of Cardiovascular Medicine, Vanderbilt University Medical Center, Nashville, Tennessee, USA

INTRODUCTION

Aortic stenosis is one of the most common forms of aortic disease and it necessitates aortic valve replacement in most cases. Surgical and transcatheter aortic valve replacement (SAVR and TAVR, respectively) are the only effective therapy to address aortic stenosis.

Immediately after SAVR and TAVR, patients experience elevated blood pressures (BP) due to the abrupt correction of the flow obstruction (afterload) resulting from stenosis. Lindman et al. have shown that patients with more elevated blood pressures had better outcomes and improved survival rates [1]. They also showed that BPs, as recommended by the current guidelines, in patients with aortic valve replacement, were associated with increased all-cause and cardiovascular mortality [1]. We have shown that epicardial coronary flow drops below the threshold for myocardial ischemia at lower BPs[2]. There is currently no specific guidance for blood pressure regulation after aortic valve replacement and these counter-intuitive findings necessitate more controlled systematic studies to understand the complex ventriculo-aortic-arterial interactions and the flow dynamic environment.

The aim of this study is to investigate the effect of changing systolic and diastolic blood pressures (SBP and DBP, respectively) on epicardial coronary flow, sinus pressure, and energy after TAVR and SAVR.

METHODS

A 26mm SAPIEN 3 transcatheter aortic valve and a 25 mm Magna Ease surgical aortic valve were deployed in an aortic root chamber inside a pulse duplicating left heart flow loop simulator flow. The flow loop consisted of a fluid reservoir to store a blood analog (water-glycerin, 60-40% in volume), a mechanical mitral valve separating the fluid reservoir and pump, a bladder pump controlled by an in-house LabView program, an idealized aortic model, a compliance chamber to simulate arterial distensibility, a gate valve to control the aortic flow, a pinch valve to control the total coronary flow, and ultrasound clamp-on flow rate sensors to measure the flows before the valve and in the total coronary branch. Out of the aortic chamber sinus, we extended a connection that represented the total coronary branch. The total coronary flow was calculated to be 4-5% of the cardiac output that was selected to be 5 L/min, leading to an average coronary flow range between 200 – 250 mL/min. The average coronary flow was calibrated within these physiological limits at 120/60 mmHg, by controlling the resistance of the coronary circuit once the experiment started. Once the baseline physiological coronary conditions were met, the coronary circuit parameters were fixed as the systemic blood pressures were varied. The heart rate selected was 60 bpm and the blood pressure ranges were selected to span a wide interval of SBP (100, 120, and 160mmHg) and DBP (40, 60 and 90mmHg). Millar catheters were used to measure the pressures at the ventricular and aortic sides. Fifty consecutive cardiac cycles of pressure and flow rate data were recorded at a sampling rate of 100 Hz.

Sinus and coronary flow were assessed using particle image velocimetry (PIV). The region of interest captured parts of the sinus, coronary artery, and flow downstream of the valve. These regions were illuminated by a laser sheet created from a solid-state laser. High-speed images of the fluoresced particles displacement and movement within the areas of interest were recorded. The time-resolved PIV images were acquired at a temporal resolution of 4000 Hz. Velocity vectors were calculated in DaVis using advanced PIV cross-correlation approaches. Post processing was performed using adaptive median filtering in DaVis.

The Laplacian of the pressure ($\nabla^2 P$) through the Poisson equation for pressure was computed as follows:

$$\frac{-1}{\rho}\left(\frac{\partial^2 P}{\partial x^2}+\frac{\partial^2 P}{\partial y^2}\right)=\left(\frac{\partial V_x}{\partial x}\right)^2+2\frac{dV_x}{dy}\frac{\partial V_y}{\partial x}+\left(\frac{\partial V_y}{\partial y}\right)^2 \qquad (\boldsymbol{EQ1})$$

Where ρ is the density in Kg/m^3, P is the pressure in Pa, and V_x and V_y are the x and y components of the velocity vector in m/s. The x and y directions are axial and lateral respectively. The Laplacian of the pressure is the divergence of the gradient of the pressure field, and its physical significance is in its ability to help identify the changes in the pressure field [13]. Through $\nabla^2 P$, we can identify how different the field value is from the surrounding sinus regions. The energy dissipation rate (EDR) was computed as follows[3]:

$$EDR = \mu \left[\left(\frac{\partial V_x}{\partial x}\right)^2 + \left(\frac{\partial V_y}{\partial y}\right)^2 + 0.5\left(\left(\frac{\partial V_x}{\partial y}\right) + \left(\frac{\partial V_y}{\partial x}\right)\right)^2 \right] \qquad (\boldsymbol{EQ2})$$

Where μ is the viscosity with a value of 3.5cP.

RESULTS

Elevated SBP and DBP led to higher coronary flow. However, the waveforms were different in that at higher SBP the peaks were larger whereas at a higher DBP, the coronary waveforms' rise, and decay portions were less steep (160/60 compared with 120/90 mmHg). As SBP increased, the slope of the coronary flow waveform increased more sharply during systole and achieved a higher peak during diastole. This applied to all the valve and heart rate cases. As DBP increased, the peaks during diastole were almost unchanged between 120/40, 120/60 and 120/90 mmHg, however, the rise of the coronary flow waveform was steeper as DBP increased.

With changing aortic BP, it is important to assess the changes in the sinus pressure. **Figure 1** shows the contour plots of the Laplacian of pressure in the sinus. The area of $\nabla^2 P$ increased with an increase in SBP for both valves. The coronary ostium was one of the main locations in the sinus where $\nabla^2 P$ was most pronounced, and more negative than the surrounding. As DBP increased, $\nabla^2 P$ areas also increased, especially at the coronary ostium with a more negative $\nabla^2 P$.

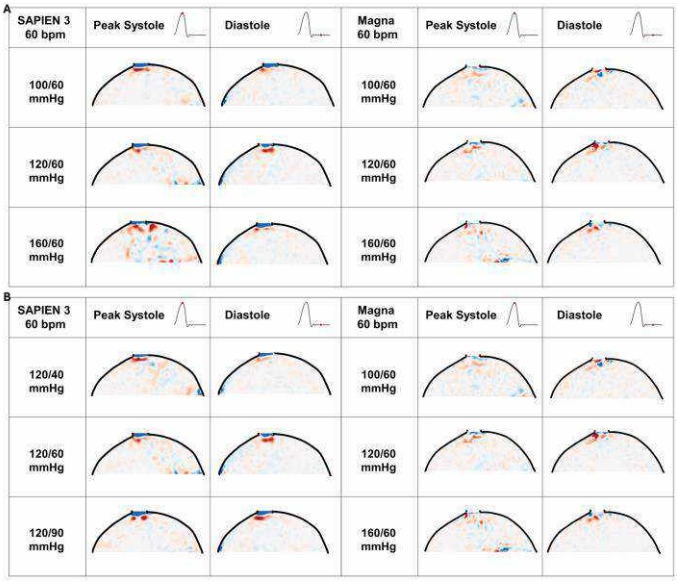

Figure 1. Contour plots of the Laplacian of pressure in the sinus for both valves with an increasing SBP (Top Table, A) and an increasing DBP (Bottom Table, B).

EDR results are shown in **Figure 2**. The total energy (EDR area under the curve) increased from 12.74 ± 0.41 J/m^3 to 17.45 ± 1.39 J/m^3 with an increasing SBP and decreased from 12.05 ± 1.42 J/m^3 to 5.63 ± 9.74 J/m^3 with an increasing DBP for the SAPIEN 3. The MAGNA did not follow the same trend as the SAPIEN 3, instead the total energy increased and decreased with the changing SBPs and DBPs.

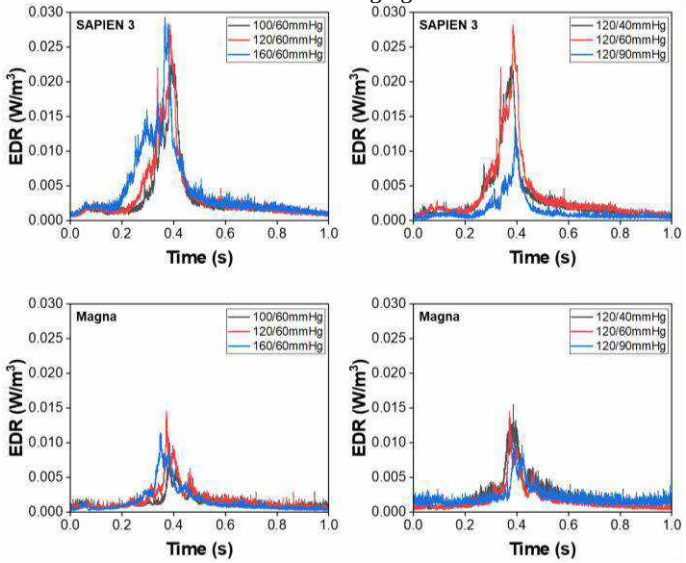

Figure 2. EDR for both valves with an increasing SBP (column 1) and DBP (column 2).

DISCUSSION

The results obtained in this study showed that the rise and decay of the coronary flow waveforms were different as DBP changed. A decrease in DBP led to sharper rise and decay of the waveform, with significantly lower mean flow. These results can be explained through the role of DBP in coronary perfusion. Generally, low DBP has been associated with myocardial ischemia [4] and is a key factor in coronary perfusion pressure. At the coronary ostia in all the cases, a more negative $\nabla^2 P$ was observed at the ostium. This indicates a lower pressure compared with the surrounding regions. As previously mentioned, evaluating $\nabla^2 P$ in the sinus provides information on how different the field value (pressure) is with respect to the surrounding. Therefore, from the results, it seems that as SBP and DBP increase, the flow is encouraged to enter the coronary from the sinus, evident from the much lower pressure at the ostium. An increase in SBP led to a significant upward shift in the coronary flow curve, with a clear increase in mean coronary flow. Also, the rise and decay of the waveforms were almost parallel. Within the aortic BP waveform, SBP occurs due to the stretch that large arteries undergo to accommodate the systolic ejection volume. As SBP increases, the metabolic demands of the myocardium increase, leading to a potential increase in the coronary flow [5]. We have previously shown an increase in sinus velocity with an increase in SBP with a SAPIEN 3[6], which would also correspond to an increase in the kinetic energy. This was reflected in the current study by an increase in the total energy with an increase in SBP. In addition, the increase in SBP is met with an increase in EDR. A possible culprit for this energy dissipation may be the stent frame of the SAPIEN, since this pattern was not observed in the Magna.

REFERENCES

[1] Lindman, B et al., *Cardiovascular Img.*, 10(7):e006308, 2017
[2] Vogl, B et al., *Struct. Heart*, 100230, 2023
[3] Okafor, I et al., *J Biomech.*, 137(10):121007, 2015
[4] Khan, N et al., *Hypertension*, 71(5):840-847, 2018
[5] Rabkin, S et al., *Current Cardio. Rev.*, 13(1):75-83, 2017
[6] Vogl, B et al., *Annals of Biomed. Eng.*, 1-10, 2023

HIGHER PERCENT LOAD THROUGH THE INTACT MENISCUS RESULTS IN HIGHER REDUCTION IN MENISCAL LOADING AFTER PARTIAL MENISCECTOMY AT HEEL STRIKE IN SIMULATED GAIT

Kalle L. Chastain (1), Sean C. Letendre (1), Heath P. Gould (2), Ian D. Hutchinson (2), Joshua I. Wright-Chisem (2), Arden Wach (1), Anil S. Ranawat (2), Scott A. Rodeo (2), Suzanne A. Maher (1,2)

(1) Biomechanics, Hospital for Special Surgery, New York, New York, USA
(2) Sports Medicine, Hospital for Special Surgery, New York, New York, USA

INTRODUCTION

Partial meniscectomy (PM) is a commonly performed orthopaedic procedure with over 700,000 cases annually in the United States.[1] However, the mid to long term clinical results are variable, with a subset of patients manifesting silent and relatively rapid knee joint degeneration.[2] Variability in force redistribution across the articular surface after PM may explain this heterogeneous response. We previously observed that the distribution of forces across articular surfaces in uninjured intact human knees is highly variable, with some knees distributing a high proportion of compartmental force through the meniscus during simulated gait – so called 'meniscal dominant loaders', while others largely bypass the meniscus to predominantly load the cartilage-to-cartilage contact zone, so called 'cartilage-cartilage dominant loaders'.[3] The objective of this study was to quantify the effects of PM on joint biomechanics and contact force redistribution across the tibial plateau of human knees during simulated gait. Our hypothesis was knees with higher percent meniscal loading would have a greater decrease in percent meniscal loading after PM throughout the gait cycle.

METHODS

Nine human cadaveric knees with no clinical history of osteoarthritis were denuded of skin, subcutaneous fat, muscle, and patella while maintaining the cruciate ligaments, collateral ligaments, and joint capsule. The femur and tibia were transected ~10 cm above and below the joint line, respectively. With the use of fluoroscopy, a 2.5 mm Kirschner wire was inserted along the femoral epicondylar axis. The femur was then suspended via K-wire, aligned to the rotation of the simulator, and the tibia was centered in the base of the simulator and cemented in place such that the plateau was parallel to the ground in full extension. The knees were mounted on a multi-axis testing apparatus [VIVO, AMTI] programmed to apply dynamic forces that mimic level walking (from ISO standard #14243), **Fig. 1A**. Simulated gait consisted of 12 cycles of multidirectional and dynamic standard gait input waveforms applied at 0.2 Hz and normalized to specimen-specific bodyweight. An electronic pressure sensor [Model 4011, Tekscan] was equilibrated, calibrated, and inserted into each knee underneath the meniscus and attached to the posterior capsule and ACL via suture and used to record joint contact forces.[4]

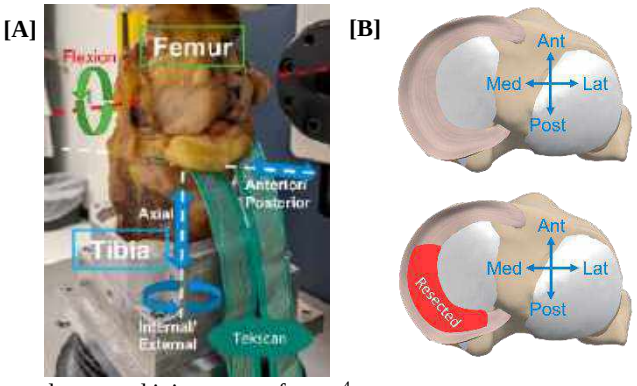

Figure 1: A) Simulator setup with a representative knee and Tekscan sensor attached, B) representation of testing conditions, with the intact condition in the top image and PM in the lower image.

Knees were tested in the following conditions: (1) native meniscus – 'intact', (2) PM, where 75% of the meniscus was removed from the posterior and central region of the medial compartment, **Fig. 1B**. A custom MATLAB program [Mathworks Inc] was used to determine peak contact stress, contact area, and to delineate the meniscal footprint from the cartilage-to-cartilage contact region. The percent of compartment force through the meniscus (percent meniscal loading) throughout the stance phase of simulated gait was calculated by

Equation (1) where ΣF_M is the sum of the force in the meniscal footprint and ΣF_C is the sum of the force in the cartilage-to-cartilage contact region. The difference between the intact state and PM condition was calculated for each metric and each knee. The averages and 95% confidence intervals (CI) were then computed. Significant differences were identified when the 95% CI $\neq$ 0. Correlations between intact percent meniscal loading vs change in percent meniscal loading after PM were explored using linear regression.

$$Percent\ meniscal\ loading = \Sigma F_M/(\Sigma F_M + \Sigma F_C) \quad (1)$$

RESULTS

PM resulted in a significant increase in peak contact stress of 1.5 ± 0.2 MPa in all but the very early stance phase of simulated gait, **Fig. 2**. PM resulted in a significant decrease in contact area of 219 ± 63 mm^2 over the entirety of simulated gait, **Fig. 3**. PM resulted in a significant decrease in percent meniscal loading of 32 ± 19% over the majority of simulated gait, **Fig. 4**. An inverse, proportional relationship was found between percent force through the native meniscal footprint and the change in percent meniscal loading following PM at heel strike, **Fig. 5,** where knees with higher loads through the meniscus in the intact condition had a larger reduction following PM. No other relationship was found throughout simulated gait.

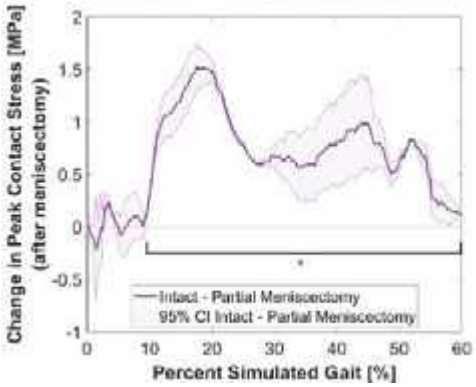

Figure 2: Average and 95% confidence interval of the change in peak contact stress following PM throughout the stance phase of simulated gait. Bracket represents significant difference.

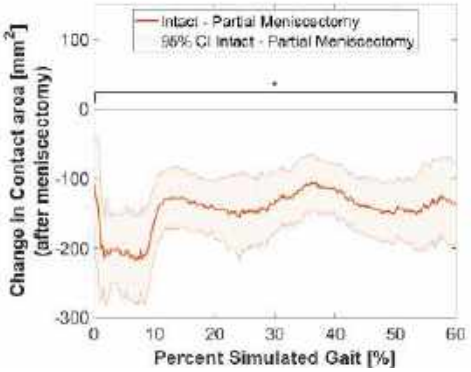

Figure 3: Average and 95% confidence interval of the change in contact area following PM throughout the stance phase of simulated gait. Bracket represents significant difference.

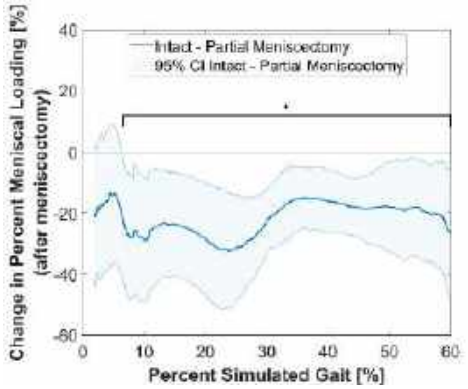

Figure 4: Average and 95% confidence interval of the change in percent meniscal loading following PM throughout the stance phase of simulated gait. Bracket represents significant difference.

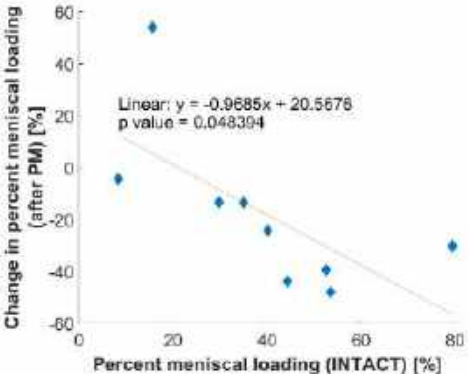

Figure 5: Correlation of intact percent meniscal loading to change in percent meniscal loading after PM with linear regression. Data is shown at 4% simulated gait (heel strike). The higher the initial percent loading, the higher the reduction after PM.

DISCUSSION

Using a multi-directional testing apparatus, we quantified the effects of PM on the redistribution of knee joint contact forces. All knees experienced a significant increase in peak contact stress and a significant decrease in contact area through most of simulated stance phase, with the magnitude of change similar to that reported in static and quasi-static tests[5,6]. All knees experienced a significant decrease in percent meniscal force following PM throughout most of stance phase of gait, with the exception of heel strike. During heel strike, we found that knees with higher loads through the meniscus in the intact condition had a larger reduction following PM. No other relationship was found throughout simulated gait; leading us to reject our hypothesis. Given the increased shear forces and rapid decrease in contact velocity during heel strike, the biomechanical relevance of the variability in this phase of the gait cycle warrants further investigation.

ACKNOWLEDGEMENTS

We thank the following sources of support: The National Institutes of Health (AR075523), the Russell Warren Chair for Tissue Engineering and the HSS Surgeon-in-Chief Fund.

REFERENCES

[1] Hall MJ, et al., *Natl health Stat Report*, (102):1-15, 2017. [2] Souza R., et al., *Knee Surgery, Sports Traumatology, Arthoscopy*, 23:188-97, 2015. [3] Guo, et al., *J Biomechanics*, 48(8):1444-53, 2015. [4] Brial C, et al., *Am J Sports Med.*, 47(10):2437-2443, 2019. [5] Bedi, et al., *JBJS*, 92(6):1398-408, 2010. [6] Bae, et al., *Medical & biological engineering & computing*, 50:55-60, 2012

CORONARY HEIGHT AND PEAK SYSTOLIC VELOCITY AS MAIN PREDICTORS OF POST-TAVR THROMBOSIS

F. Esmailie (1)*, A. Venkatesh (2)*, H. Hatoum (3), H. Chen (4), B. Yeats (2), B. J. Lee (2), Ph. Ruile (5), F. J. Neumann (5), L. P. Dasi (2)

(1) Department of Biomedical Engineering, University of North Texas, Denton, TX, USA
(2) Wallace H. Coulter Department of Biomedical Engineering, Georgia Institute of Technology Emory University, Atlanta, GA, USA
(3) Michigan Technological University, Houghton, Michigan, USA
(4) University of Nevada, Las Vegas, Nevada, USA
(5) Department of Cardiology and Angiology, Medical Center - University of Freiburg, Germany and Faculty of Medicine, University of Freiburg, Germany
* co-First authors

INTRODUCTION

Aortic valve dysfunction led to the death of more than 140,000 people in the U.S. in 2020 [1,2]. Valve dysfunction can be caused by a buildup of calcium and restricting the aortic valve opening leads to reduced blood flow and elevated blood pressure [3]. To treat valve dysfunction, one minimally invasive FDA-approved method is a transcatheter aortic valve (TAV) replacement (TAVR). Despite the overall success of TAVR, blood clot formation (thrombosis) on the TAV remains a relevant adverse event [4,5], which occurs in up to 15 % of patients after TAVR [6]. Leaflet thrombosis can be detected on Computed Tomography (CT) images as hypoattenuating leaflet thickening (HALT) with varying severities based on additional thickening of the leaflet [7]. Thrombosis may lead to early valve deterioration and life-threatening conditions such as reduced leaflet motion [8], elevated transvalvular blood pressure [8], and increased risk of stroke [9,10]. To prevent thrombus formation on prosthetic heart valves, physicians prescribe an anticoagulant regimen [11]. However, anticoagulation therapy increases the risk of excessive bleeding without preventing thrombosis in all cases [12], leading to lower patient quality of life. It is imperative to predict the post-TAVR thrombus formation risk to avoid unnecessary anticoagulant therapy or alter procedural plans to optimize outcomes.

In our prior work, we hypothesized that two main energy sources drive blood out of the neo-sinus area, including the movement of prosthetic leaflets and the backflow [13,14] . We then developed a dimensionless parameter called normalized circulation (NC) and showed that NC was correlated with the risk of post-TAVR thrombosis in six patients. We developed a semi-automatic algorithm to extract anatomical and hemodynamic parameters from pre- and post-TAVR Computed Tomography (CT) images. Then we calculated the normalized circulation for 45 patients and correlated it with the risk of post-TAVR HALT [14].

In this work, we employed various anatomic and hemodynamic parameters as input features in multiple classification Machine Learning (ML) algorithms. The goal was to identify the most relevant anatomical and hemodynamic parameters that could be associated with the risk of post-TAVR leaflet thrombosis.

METHODS

For a dataset consisting of 40 patients (20 HALT$^+$, 20 HALT$^-$), we manually reconstructed the pre-TAVR patient-specific model of the aortic wall, diseased aortic valve, and calcium nodules from pre-TAVR CT images. Then, we applied our reduced order model (ROM) [15] to virtually deploy the TAV and extract the final position of TAV stent and prosthetic leaflets. We used a semi-automated algorithm to extract anatomical parameters such as left coronary height (H_{LC}), right coronary height (H_{RC}), sinotubular junction height (H_{STJ}), peak systolic velocity (V_{max}), ejection volume ($v_{ejection}$), and ejection time ($T_{ejection}$) from pre-TAVR CT images. We used the post-TAVR results from our ROM model to extract stent outflow area (A_{so}), stent deformation index ($I_{deformation}$), and neosinus top area (A_{NS}) (see Fig. 1 (a)). We used several classification ML algorithms to correlate the anatomical and hemodynamic parameters with the risk of post-TAVR thrombosis.

We used a MATLAB code to randomly separate 30% of HALT$^+$ cases (6 patients) and 30% of HALT$^-$ patients (6 patients) for testing the ML algorithms. The rest of the dataset (60% of the cases - 28 patients, 14 HALT$^+$, 14 HALT$^-$) was used for training the ML algorithms. We applied all available classification algorithms in MATLAB, including Support Vector Machines (SVM) and K-Nearest Neighbors (KNN), for each combination of parameters (called features in the context of ML) with a 5-fold validation. We used a combination of features that did not overlap; for example, when the peak systolic velocity was applied as a feature, the ejection volume and ejection time were eliminated from the possible combination of features to avoid overfitting.

RESULTS

The best combination of features was A_{NS}, H_{RC}, $T_{ejection}$, $I_{Deformation}$, and H_{LC} (see Fig. 1 (b)), with 88.9% test accuracy and area under receiver operating characteristic (ROC) curve (AUC) of 1 using a weighted KNN algorithm. An ANOVA analysis was conducted at the same time to rank the impact of these features, and A_{NS}, H_{RC}, $T_{ejection}$ were the top three features. Another promising trained algorithm was a Medium Gaussian SVM algorithm with V_{max}, H_{RC}, and H_{LC} as features. This algorithm had 75% accuracy in the test with an AUC of 0.72 (see Fig 1 (c)).

DISCUSSION

The main challenge in evaluating the post-TAVR thrombosis risk using anatomic and hemodynamic parameters is extracting these data from raw CT images. Using our semi-automated algorithm combined with the ROM TAV deployment model, the key anatomic and hemodynamic parameters are extracted in less than two hours. Then, these parameters are correlated with the risk of thrombosis using classification ML algorithms. The combination of ROM finite element TAV deployment model, the semi-automated algorithm, and classification ML algorithms provides physicians with a powerful tool to predict the risk of post-TAVR thrombosis using pre-TAVR CT images.

The peak systolic velocity and the heights of the right and left coronaries are the most important features in the present dataset. However, this conclusion is subject to change in a different set of patient data. We are aware of the limitation of this work with the small size of our dataset for training ML algorithms. The ML algorithm should be trained with a larger dataset before we can certainly distinguish the best combination of features and correlate them with post-TAVR thrombus formation risk. We are continuously collaborating with physicians to collect and process a larger cohort of patient data to identify the post-TAVR thrombus formation risk factors.

REFERENCES

1. Tsao, C. W. *et al*. *Circulation* **145**, e153–e639 (2022).
2. Aluru, J. S *et al*. *Medical Sciences* **10**, 32 (2022).
3. Pujari, S. H. *et al*. *Aortic Stenosis*. (2023).
4. Dangas, G. *et al. Structural Heart* **4**, 382–388 (2020).
5. Makkar, R. R. *et al. J Am Coll Cardiol* **75**, 3003–3015 (2020).
6. Ranasinghe, M. *et al*. *J Clin Med* **8**, 280 (2019).
7. Makkar, R. R. *et al.* Possible Subclinical Leaflet Thrombosis in Bioprosthetic Aortic Valves. *New England Journal of Medicine* **373**, 2015–2024 (2015).
8. Blanke, P. *et al. J Am Coll Cardiol* **75**, 2430–2442 (2020).
9. Chakravarty, T. *et al. The Lancet* **389**, 2383–2392 (2017).
10. Hafiz, A. M. *et al. Structural Heart* **1**, 256–264 (2017).
11. Sibilitz, K. L. *et al*. *Ann Cardiothorac Surg* **9**, 505–507 (2020).
12. Granger, C. *et al*. *J Clin Med* **11**, 2190 (2022).
13. Hatoum, H. *et al. Cardiovasc Eng Technol* **12**, 576–588 (2021).
14. Venkatesh, A. *et al. J Am Coll Cardiol* **82**, B243 (2023).
15. Shah, I. *et al. Ann Biomed Eng* (2023) doi:10.1007/s10439-023-03360-5.

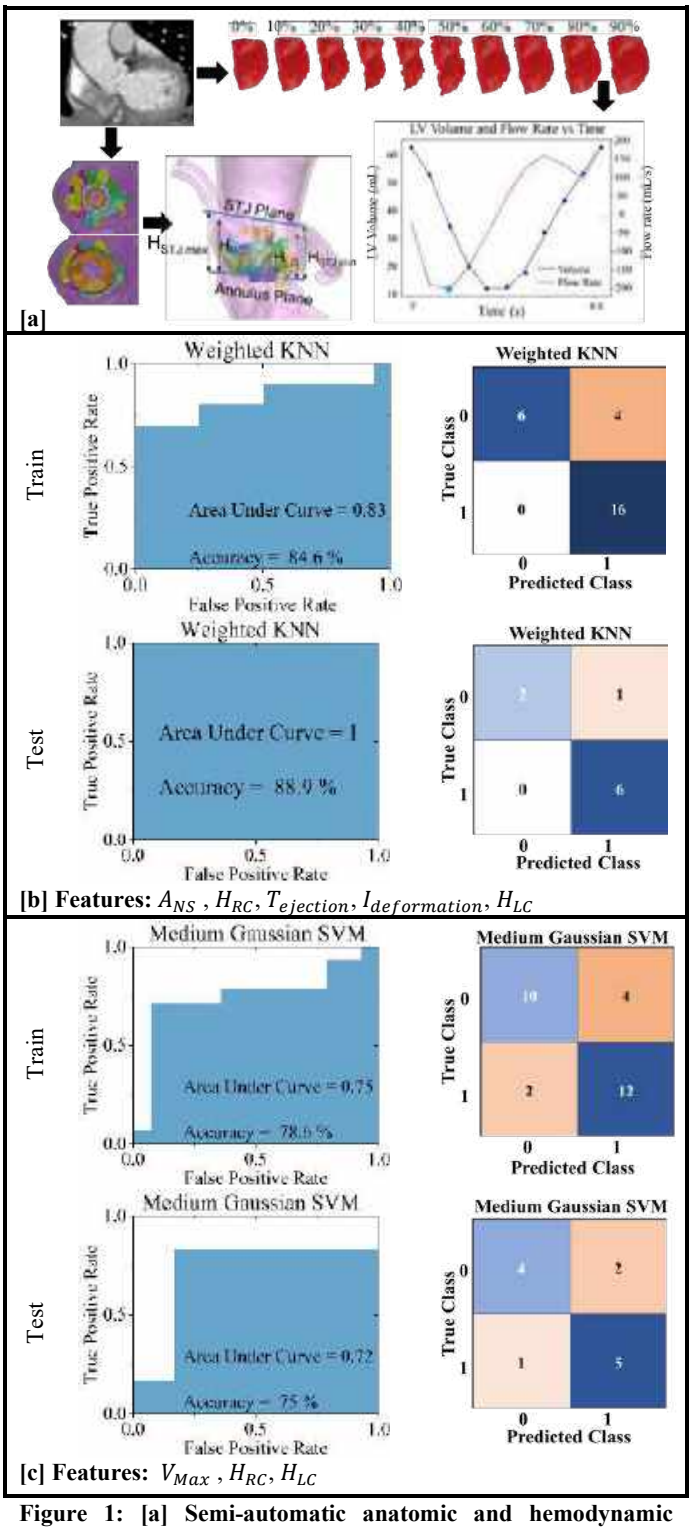

Figure 1: [a] Semi-automatic anatomic and hemodynamic measurements, [b] ML prediction of post-TAVR thrombosis risk using four anatomic and one hemodynamic features, [c] and ML prediction post-TAVR thrombosis risk using two anatomic and one hemodynamic features.

Y-SHAPED CUTTING OF SOFT SOLIDS: POTENTIAL FOR SOFT BIOLOGICAL MATERIAL CHARACTERIZATION

S. Zhan (1), A.J. Wagoner Johnson (1,2,3,4), S.B. Hutchens (1,3)

(1) Mechanical Science and Engineering, University of Illinois at Urbana-Champaign, Urbana, IL 61801, USA
(2) Biomedical and Translational Sciences, Carle Illinois College of Medicine, University of Illinois at Urbana-Champaign, Urbana, IL 61801, USA
(3) Carl R. Woese Institute for Genomic Biology, University of Illinois at Urbana-Champaign, Urbana, IL 61801, USA
(4) Beckman Institute, University of Illinois at Urbana-Champaign, Urbana, IL 61801, USA

INTRODUCTION

Y-shaped cutting offers a unique combination of cutting and tearing-induced crack-tip loads to understand the threshold fracture-relevant length scale and failure energy of a soft material. Proposed by Lake & Yeoh in 1978 [1], this geometry-independent cutting method offers several advantages over typical tearing or cutting tests, and therefore provides a way to explore the fracture of biological materials. First, blade-induced failure concentrates the zones governing new surface creation [2] relative to tearing geometries [3], resulting in a reduced influence of sample size. A very small sample, therefore, may be possible to characterize via Y-shaped cutting while avoiding interactions between the failure-governing zone and the sample boundary. Second, because of the concentrated failure zone and smaller stretch, Y-shaped cutting facilitates high magnification, *in situ* observation of this critical microstructurally-governed region under a microscope, aiding in the failure mechanism identification including microstructural rearrangement [4] or bond breakage outside of the new surface [5]. Third, by performing tests at a constant propagation rate, fracture initiation effects encountered in many 'tearing' tests are avoided. Finally, despite the introduction of the blade in Y-shaped cutting, the friction between the blade and the sample is frequently limited and even negligible [6], providing a more direct measurement of the intrinsic material response.

Despite these advantages, this technique is not widely used on many materials, including biological and composite materials. Among a few groups applying this technique, most of them primarily compared failure responses between elastomeric solids, instead of exploring the relationship between tearing and cutting. This is likely due to the slightly unusual test geometry, unfamiliarity with Y-shaped cutting conditions and implications, as well as a lack of standards for using this cutting approach.

A primary purpose of this study, therefore, is to provide researchers with a detailed roadmap of the strengths and limitations of Y-shaped cutting as well as a practical guide to designing, performing, and interpreting the results of this class of failure tests. We establish a pseudo-standard for Y-shaped cutting using silicone (Sylgard 184, Dow Corning) as the standard material, hoping this highly tunable cutting method will offer insights into other classes of materials in the future.

METHODS

***In situ* Microscope Y-shaped Cutting Setup** Figure 1 illustrates the Y-shaped cutting method. The method gets its name from an initially rectangular sample transformed into a Y-shape by pulling on the two thin legs B with constant preload f_{pre} at a fixed angle θ from the sample's midline. A pulley system provides force redirection from θ (achieved by the angle adjust system) to vertical (gravity). The blade is mounted on a load cell, which is attached to a vertical adjust system (Figure 1), and aligned with the sample midline. To maintain a constant angle and preload, the intersection of the sample and blade (i.e., the crack tip) is fixed above the microscope objective lens while the sample translates horizontally in the Y direction. A constant XY sample plane is maintained throughout the test by aligning the tension line and the pulley arms in this plane. To precisely position the force sensor, the angle adjust system, and the pulley system, we use a commercial 3-way micro-adjustment stage. We also use a separate blade positioning adjustment and the microscope stage (XY plane) to precisely position the cut within the objective's field of view. Visualization of the full-field deformation and microstructure during cutting could provide insights into failure for a variety of complex materials including composites and tissues.

Cutting Strain Energy Release Rate G_{cut} Calculation The energy release rate due to cutting G_{cut} is derived via the same approach used by Rivlin and Thomas [1, 6, 7], *i.e.,* the differential energy change between work done on the system and strain energy released due to crack growth per unit of crack area produced (Figure 2 (a)). This is expressed as

$$G_{cut} = dU_{work}/dA - dU_{strain}/dA \quad (1)$$

Force, displacement, and time data are collected, though only the force data f_{cut} are needed to calculate G_{cut} using the equation derived by Lake & Yeoh [1], including tearing (T) and cutting (C) terms.

$$G_{cut} = \underbrace{\frac{2f_{pre}\bar{\lambda}}{t}(1-\cos\theta)}_{} + \underbrace{\frac{f_{cut}\bar{\lambda}}{t}}_{} \quad (2)$$

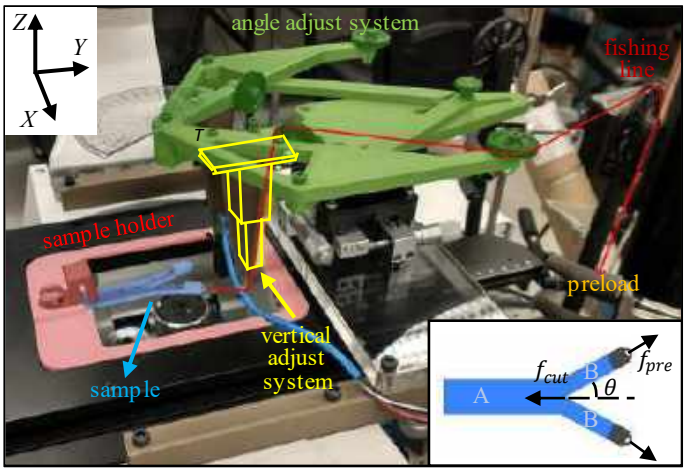

Figure 1: A photograph of the *in situ* Y-shaped cutting device with false-color added to indicate key design features. Inset: Sample with single leg 'A' from which two equal legs 'B' are cut to create a 'Y' shape with leg angle θ.

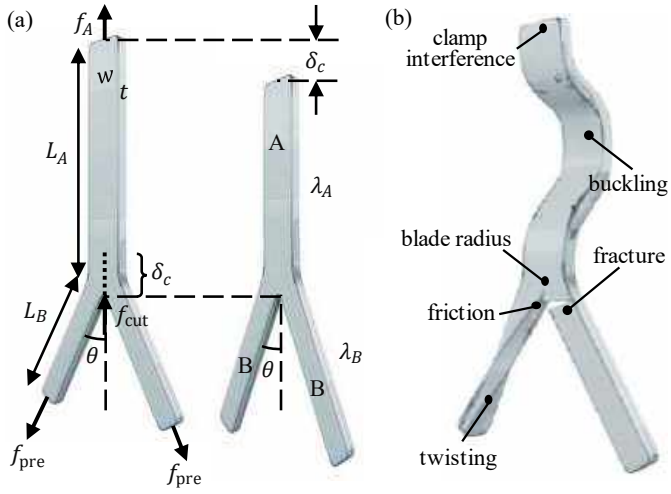

Figure 2: (a) A precut separates a rectangular sample (width w, thickness t) into two parts, body A (length L_A) and legs B length L_B). Preload f_{pre} separates two legs B at a fixed angle θ from the midline and induces prestretch on both body A (λ_A) and legs B (λ_B). During cutting, the blade cuts the sample in the midline with a cutting force f_{cut}. Strain energy release rate derives from the external work done by f_{pre} and clamp reaction force f_A and the stored strain energy within the sample as it translates an incremental crack extension distance δ_c. (b) Typical limitations and challenges when performing Y-shaped cutting tests

RESULTS

Typical Cutting Responses The typical cutting response contains four regimes: 1) loading, 2) cut initiation, 3) cutting, and 4) unloading (Figure 3, left). The blade indents the sample until the cut initiation occurs. Once the crack begins to propagate, the force drops to a relatively constant value during constant rate cutting.

A Pseudo-standard for Y-shaped Cutting By adjusting the tearing contribution via changes in either or both f_{pre}/Ewt and θ, using different sample geometries, we gather the cutting response over a wide range of experimental conditions. Separating the failure energy contributions into C and T produces the dual-regime curve in Figure 3, right. Similar to the behavior reported by Lake & Yeoh [1], as T reduces, Sylgard 184 enters a 'pure cutting' regime for which decreases in applied T are proportionally compensated for by one-to-one increases in C. In this region, C versus T has a slope of -1.

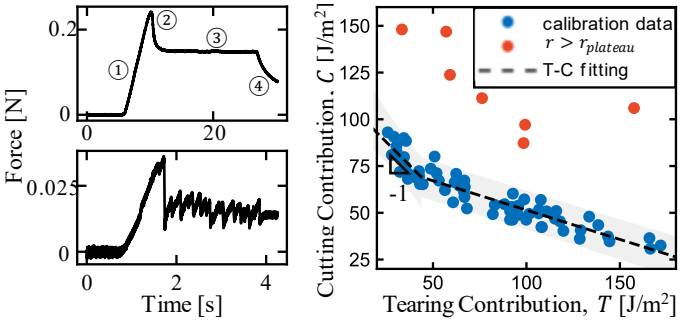

Figure 3: Left: Typical cutting response for PDMS (upper, no slip response) and bovine liver membrane (lower, stick-slip response). Right: A calibration 'standard' C-T curve for Sylgard 184 10:1, with test data (blue dots) and over-estimated data (red dots). The black dashed line is a piece-wise linear fit to the data. The gray shading corresponds to 95% prediction intervals.

DISCUSSION

The pseudo-standard C-T curve can be used to verify the accuracy and reliability of any other setup, and therefore provides a foundation for measuring other materials. Interestingly, our preliminary test on the bovine liver membrane presents a 'stick-slip' constant rate cutting (Figure 3, lower left). We suspect that it is related to the interwoven fibrous microstructure of the membrane. However, practical considerations can also limit Y-shaped cutting's applicability. Typical challenges (Figure 2 (b)) include preload limits (buckling, fracture), angle θ limits (friction, twisting), and over-estimated of G_{cut} (clamp interference, blade radius effect). The solution is to tune the variables carefully, *i.e.*, tearing contribution, blade radius, and sample geometry.

ACKNOWLEDGEMENTS

This report is based upon work originally supported by the National Science Foundation under grant no. 1562766. It was supported in part by National Science Foundation grant no. 2219787. The authors thank M. Guerena, J. Peng, M. Schmid, and C. Walsh for their assistance in streamlining the microscope-based cutting setup.

REFERENCES

[1] Lake, GJ et al., *Int J Fract*, 14:509-526, 1978.
[2] Long, R et al., *Annu. Rev. Condens. Matter Phys.*, 12:71-94, 2021.
[3] Zhang, B et al., *Soft Matter*, 17(28):6728-6741, 2021.
[4] Bircher, K et al., *Nat Commun*, 10:792, 2019.
[5] Slootman, J et al., *Phys. Rev. X*, 10:041045, 2020.
[6] Zhang, B et al., *Exp. Mech.*, 4:517-529, 2019.
[7] Rivlin, RS et al., *J. Polym. Sci.*, 10(3):291-318, 1953.

SMOOTH MUSCLE CELL MECHANOADAPTATION IS CHRONICALLY DISRUPTED BY HIGH-VELOCITY STRETCHING

Samuel F. Boland (1) & Patrick W. Alford (1)

(1) Department of Biomedical Engineering, University of Minnesota, Minneapolis, MN, USA

INTRODUCTION

Vascular smooth muscle cells (VSMCs) encircle blood vessels and modulate blood flow through active contraction in response to chemical and mechanical cues. In the vasculature, VSMCs are exposed to deformation rates ranging from 1% per year in aneurysm growth[1] to 1000% per second during traumatic brain injury (TBI).[2] VSMC function and gene expression in response to deformation has been extensively characterized at physiological strain rates,[3–6] but our understanding of how VSMCs respond to trauma-like loading is incomplete. Here, we utilized high-velocity cellular microbiaxial stretching (CμBS) to distinguish VSMC mechanical behavior after deformation at increasing strain rates. Our hypothesis was that VSMCs would behave as viscoelastic solids and stress would increase with strain rate, but in fact we found that VSMCs generated lower stress following high strain rate stretch. Further, we uncovered that VSMCs cannot recover basal stress after trauma-like loading, suggesting chronic mechanical dysfunction.

METHODS

Substrate Fabrication and Cell Culture. Human umbilical artery VSMCs were micropatterned with aspect ratio 1:4 (AR4) on a fluorescent-bead-doped polyacrylamide (PA) gel with a Young's Modulus of 13.5 kPa as previously described.[3,7] VSMCs were cultured using a standard protocol to induce a physiological phenotype.[3,8]

High-Velocity Cellular Microbiaxial Stretching (CμBS). CμBS experiments were performed using a custom-built microscope-mounted device (Fig. 1A) to perform traction force microscopy experiments using PA gels on deformable membranes. VSMCs were stretched to an engineering strain of 0.15 at strain rates of 0.001, 0.01, 0.1, or 10 s^{-1}, with the 10 s^{-1} strain rate most representative of trauma-like loading.[2] The experiment was performed over 5 minutes for each strain rate and recovery period. For example, for stretching performed at a rate of 0.001 s^{-1}, stretching takes 2 minutes (stretching phase) and cells are held static (relaxation phase) at 0.15 strain for 3 minutes (Fig. 2A). While held static, cells were imaged at 40X magnification once under bright field microscopy, and then the underlying fluorescent bead layer at the cell-gel interface (Fig. 1B,D) was imaged with a TRITC filter once per second in a time lapse. Cells were then returned to 0 strain (return phase) and imaged over the same time interval while static (recovery phase). Three cycles of stretching were performed on each cell. Cells were then lysed with sodium dodecylsulfate and the gel bead layer fluorescence was captured again at the location of each cell at 0 and 0.15 strain.

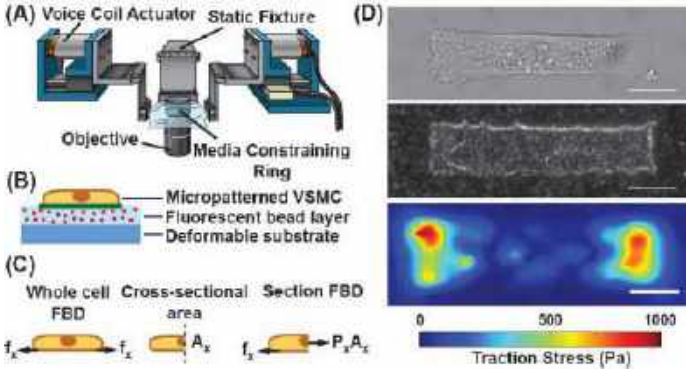

Figure 1: (A) High-velocity CμBS apparatus. (B) AR4 VSMC micropatterned on PA gel. (C) P_x calculation from VSMC free body diagram. Adapted from Rothermel et al.[5] (D) Bright field (top), bead layer (middle), and traction stress map (bottom) for a representative VSMC. Scale bar = 25 μm.

Traction forces at each timepoint were calculated using previously described methods.[3,9] The axial first Piola-Kirchoff stress, represented by $P_x = f_x/A_x$, where f_x is the total traction force in the x-direction and A_x is the undeformed cell cross-sectional area, was calculated at the mid-plane of the cell (Fig. 1C). When comparing data across different treatments, P_x was normalized by dividing the stress at any timepoint by the cell's basal stress. In experiments presented in Fig. 2, all 3 cycles of

stretching were performed at the same strain rate. Peak stress is defined as the stress measured immediately after the stretching phase has completed, and plateau stress is defined as the stress at the end of the relaxation phase (i.e., $t = 5$ min). In the experiments presented in Fig. 3, the first and third stretching cycles were performed at 0.001 s^{-1} and the second at 0.1 or 10 s^{-1}. Peak ratio is defined as the peak stress during cycle 3 divided by the peak stress during cycle 1, and the plateau ratio is defined as the plateau stress during cycle 3 divided by the plateau stress during cycle 1. All statistical comparisons were performed with a student's t-test with a p value < 0.05 considered significant.

RESULTS

Cells were strained according to Fig. 2A. Due to basal tone, cells begin at a non-zero stress. Immediately after stretch, stress reaches a peak, which then decays toward a plateau at $t = 5$ min. After returning to 0 strain, stress reaches a minimum, then recovers back towards the basal stress. During the relaxation phase, P_x vs time curves shift downward with increasing strain rate (Fig. 2B). Notably, for the 10 s^{-1} case, stress after stretching to 0.15 strain remains below the basal stress, suggesting that beyond a certain strain rate threshold, cells soften with deformation. Both the average peak and average plateau stress show statistically significant reductions as strain rate is increased (Fig. 2C,D).

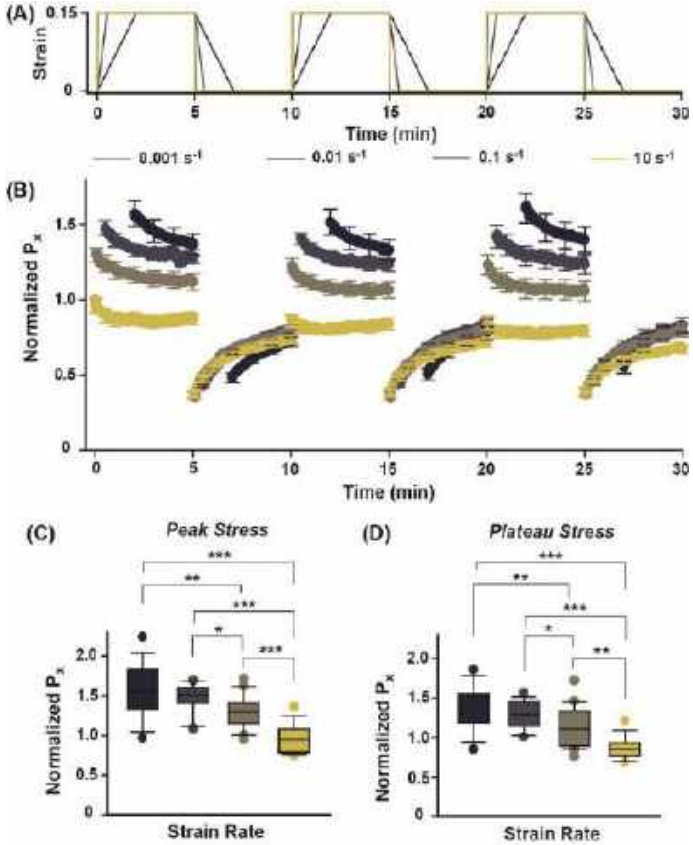

Figure 2. (A) Stretching protocol for four strain rates. (B) Average normalized axial stress (P_x) for cells strained at 0.001, 0.01, 0.1, or 10 s^{-1}. n = 16, 14, 20, 15, respectively. Error bars represent s.e.m. (C) Comparison of average peak stress. (D) Comparison of average plateau stress. Boxes span interquartile range with median marked in black. * p<0.05, ** p<0.01, *** p<0.001.

To investigate whether cells could recover from stretching at high strain rates, cells were stretched in an alternating pattern, with the first and third stretching cycles performed at 0.001 s^{-1} and the second cycle at 0.1 or 10 s^{-1} (Fig. 3A). The ratio of the peak and plateau stress during the third cycle and the first cycle was compared for each cell to determine if cells could recover stress after high strain rate stretch. Both the peak stress and plateau stress ratios showed statistically significant reductions when cells were stretched at 10 s^{-1} during the alternating pattern compared to a second stretch at 0.001 or 0.1 s^{-1} (Fig. 3B,C).

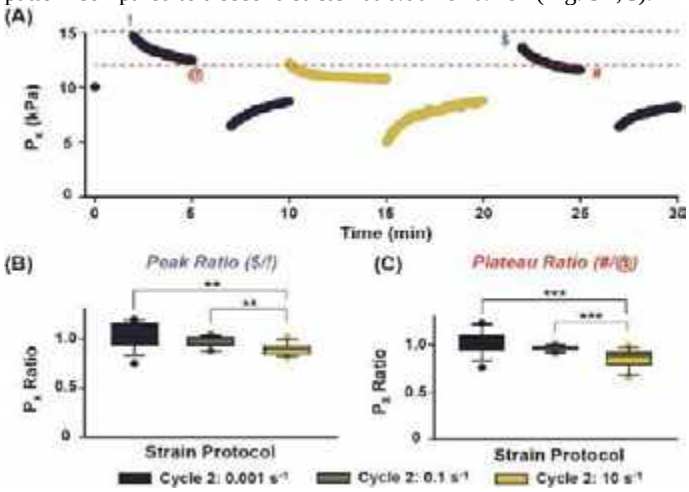

Figure 3. (A) P_x vs time plot for a representative cell stretched in alternating pattern (0.001-10-0.001 s^{-1}). Dashed line marks the peak (blue) and plateau stress (red) of stretch 1. (B) Average ratio of peak stress during third cycle and peak stress during first cycle for cells stretched at 0.001, 0.1, or 10 s^{-1} for second cycle. n = 16, 11, 12, respectively. (C) Average ratio of plateau stress during third cycle and plateau stress during first cycle for cells stretched at increasing rates during second cycle. Symbols in parentheses correspond to points marked in A. Boxes span interquartile range with median marked in black. ** p<0.01, *** p<0.001.

DISCUSSION

In this study, we demonstrated that stress produced by VSMCs stretched to 0.15 strain decreases as the rate of stretching increases. This finding directly contradicts the assumption that cells behave as viscoelastic solids. Our work aligns well with the findings of Trepat et al.,[10] who used magnetic bead twisting cytometry to observe that SMCs soften after a rapid, transient stretch. Importantly, we also found evidence that there is a threshold of strain rate beyond which a cell cannot recover. This is demonstrated by the drop below basal stress in cells stretched at 10 s^{-1} (Fig. 2B), and the inability of cells to recover stress after a 0.001 s^{-1} stretch when stretched at 10 s^{-1} immediately before (Fig. 3B,C). Because 10 s^{-1} stretches commonly occur during TBI, this finding of irreversible contractile dysfunction could help explain vessel remodeling and vasospasm following TBI.[11]

ACKNOWLEDGEMENTS

This work was supported by the NSF (CMMI-1935834) and an NIH Traineeship through the UMN Cardiovascular Engineering Training Program (T32-HL139431). Portions of this work were conducted in the Minnesota Nano Center, which is supported by the NSF through the National Nanotechnology Coordination Infrastructure (NNCI) under Award Number ECCS-2025124.

REFERENCES

[1] Marwick, *J Am Coll Cardiol* 2006. [2] Miller et al., *Front Neurol*, 2021. [3] Win et al., *J. Biomech Eng*, 2017. [4] Win et al., *Biophys J*, 2018. [5] Rothermel et al., *J Biomech Eng*, 2021. [6] Rensen et al., *Netherlands Heart Journal*, 2007. [7] Rothermel et al., *Curr Protoc*, 2022. [8] Han et al., *Am J Physiol – Cell Physiol*, 2006. [9] Butler et al., *Am J Physiol – Cell Physiol*, 2002. [10] Trepat et al., *Nature*, 2007. [11] Hald & Alford, *Transl Stroke Res*, 2014.

LOW-ENERGY IMPACT INDUCED DAMAGE IN CARTILAGE: A MULTISCALE MODELING STUDY USING FE2M

Kosar Safari (1), Ashkan Almasi (1), Phoebe Szarek (2), David M. Pierce (1,2)

(1) School of Mechanical, Aerospace, and Manufacturing Engineering, University of Connecticut, Storrs, CT, USA
(2) Department of Biomedical Engineering, University of Connecticut, Storrs, CT, USA

INTRODUCTION

Osteoarthritis (OA) remains a prevalent and incapacitating ailment with the degeneration of cartilage as a hallmark feature. The underlying causes and anticipated progression of OA remain unknown.

While microcracks in bone have been characterized extensively [1], and sub-millimeter-scale surface fissures are well known for early to advanced osteoarthritis (OA) [2], we recently demonstrated that low-energy impact usually considered non-injurious can in fact cause micrometer-scale cracks in the collagen network of human cartilage [3,4]. Pre-clinical OA may originate with microcracks in the network of collagen, and propagation of these microcracks within the extracellular matrix (ECM) may initiate a cascade of degeneration towards OA . However, the mechanisms of initiation and propagation of microcracks under mechanical loads to cartilage during normal daily activities remains unknown.

We aim to elucidate mechanical damage to collagen and collagen networks in cartilage by leveraging our experimental results and multiscale computational modeling. We simulated, using our custom FE2M modeling framework implemented in FEBio [5], unconfined compression of cartilage explants. We employed Statistically Equivalent Representative Volume Elements (SERVEs) [6] within the superficial zone, while we used standard FE the remaining cartilage volume (middle and deep zones) [7]. We validated the global results of our FE2M simulations by comparing predictions with those recently measured experimentally by us [3]. To better understand our predictions we performed: (1) sensitivity analysis on the modeling framework to quantify prediction sensitivity to input material parameters, and (2) tested stretch and stress within individual collagen fibers as predictors of collagen failure.

METHODS

Experimental Evidence. In previous experiments we examined 76 cylindrical osteochondral plugs (diameter = 3 mm and average thickness = 1.318 mm) [3]. We divided specimens into two low-energy impact groups: low impact (LI) = 1.5-2.5 mJ/mm^3 and high impact (HI): 2.5-4.0 mJ/mm^3). The impact velocity was $V_{\text{imp}} = 0.5$ m/s, the drop height (h) was $(V_{\text{imp}})^2/2g$, and the energy impact (E_{imp}) was mgh/V based on our experimental data, with V the volume of the specimen and g the acceleration constant. We determined the force for impact loading (F) using $F = 2E_{\text{imp}}(V/(V_{\text{imp}})^2)g$. In another study we established the minimum impact energy capable of inducing microcracks in cartilage [4]. From these data we had a third data set corresponding to a maximum impact (MI).

We also independently established the median failure stress for collagen fibers as 41.0 kPa, the maximum failure stress as 47.3 kPa, and the minimum failure stress at 35.8 kPa, along with a median failure stretch as 2.4 [6].

FE2M Modeling Framework. We recently established a 3-D multiscale framework in FEBio which we called FE2M, integrating mixture theory and finite elements for solving two-scale, nonlinear, coupled, and time-dependent boundary value problems (BVPs) in poro-hyperelastic, fluid-saturated porous media [5]. To solve the governing macroscopic partial differential equations we employ the finite element method twice. Initial macroscopic quantities, obtained from an intermediate solution of the macroscopic FE model, serve as boundary conditions on the microscopic Representative Volume Elements (RVEs or SERVEs). These include the deformation gradient $\overline{\mathbf{F}}_{\text{S}}$ and the gradient of pressure times the fluid volume fraction $\nabla(\overline{n^{\text{F}}p})$. After solving the microscopic FE model with these BCs, we evaluate the macroscopic material tangent $\overline{\mathbf{A}}$ and measures $\overline{\mathbf{P}}$, $\overline{(\mathbf{E}_S)'_{\text{S}} \cdot \mathbf{C}_S J_{\text{S}}}$, $\overline{n^{\text{F}}\mathbf{w}_{\text{FS}}}$ at each Gauss integration point through volume averaging of the underlying RVE. We use homogenization of any microscale quantity $\bullet$ over an RVE or a representative surface element to calculate its macroscopic counterpart $\bar{\bullet}$ using 1, where $V_{0\text{S}}$ and $A_{0\text{S}}$ are reference volumes and areas, respectively,

$$\langle\bar{\bullet}\rangle = \frac{1}{V_{0\text{S}}}\int_{\mathcal{B}_{0\text{S}}} \bullet \mathrm{d}V_{0\text{S}}, \quad \lfloor\bar{\bullet}\rfloor = \frac{1}{A_{0\text{S}}}\int_{\mathcal{B}_{0\text{S}}} \bullet \mathrm{d}A_{0\text{S}}. \tag{1}$$

Statistically Equivalent Representative Volume Elements. Leveraging information on the orientation, diameter, and volume fraction of type II collagen fibers within the superfacial zone [8], we generated SERVEs, and used them in the superficial zone of cartilage within our FE2M framework. We included discrete fibers as nonlinear springs, and modeled the

interfibrillar space using a biphasic, neo-Hookean model. We used a two-parameter power law function of stretch to model networked fiber of type II collagen as [6],

$$\Psi = c_1(\sqrt{I_4} - 1)^{c_3},\ \sigma = \lambda c_1 c_3(\lambda - 1)^{(c_3 - 1)}, \quad (2)$$

where c_1 [MPa] and c_3 [−] are model parameters, I_4 is the fourth pseudo-invariant, and λ is the fiber stretch.

Boundary Value Problem. We modeled a 3-D 2° wedge of the cylindrical plug of cartilage with a diameter of 1.5 mm and a thickness of 1.318 mm. In Fig. 1(a) we show a schematic of the model with boundary conditions. We fixed the central node in the *x*-, *y*-, and *z*-directions, and the bottom surface of the model was fixed in the *z*-direction.

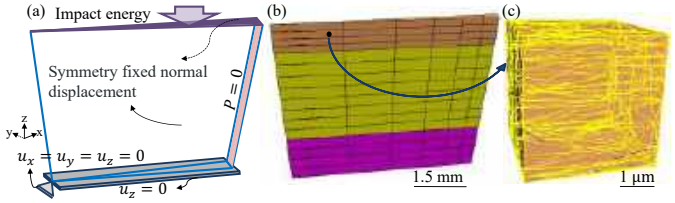

Figure 1: Boundary value problem for cartilage impact and corresponding FE models: (a) schematic of 2° cartilage wedge; (b) mesh of macroscopic structure; (c) SERVE with statistically equivalent orientation, dispersion, and volume fraction of collagen fibers.

We set the fluid pressure to zero on the radial surface, while all other surfaces had flux equals zero. To model impact, we applied a force to a rigid plate placed on top of the cartilage, establishing a contact between the top surface of the cartilage and the plate. Subsequently, we applied forces of 0.08 N, 0.16 N, and 0.20 N with a linear ramp from zero to 1 ms for LI, HI, and MI, respectively. In Fig. 1(b) we show the corresponding mesh used in the two-scale model, while in Fig. 1(c) we illustrate a representative SERVE with statistically equivalent orientation, dispersion, and volume fraction of collagen fibers.

Predictions of Collagen Failure and Microcracking. We concentrate on microcrack density (experimental) and the ratio of failed fibers (computational) as a key parameters for comparison between our experiment and simulation results. Microcrack density is the number of microcracks per unit area #/mm^2 measured in experiments. In our numerical model, we introduced the ratio of failed fibers (number of failed fibers/total number of fibers) to quantify the proportion of failed fibers to the total number of fibers. We established a custom algorithm to identify failed fibers – we compare the stress and stretch of calculated for each fiber to the critical values and then calculates the ratio of failed fibers.

Sensitivity Analyses. We conducted sensitivity analyses on the parameters of the constitutive model for collagen fibers to assess the influence on both macroscopic and microscopic results. To this end we implemented a Monte Carlo sampling method for the random selection of c_1 within the range $[3.82 - 7.82]$ MPa and c_3 within the range $[3.568 - 4.072]$.

RESULTS

In Fig. 2 we show results for the macroscopic structure of cartilage and representative element 76 under HI loading conditions.

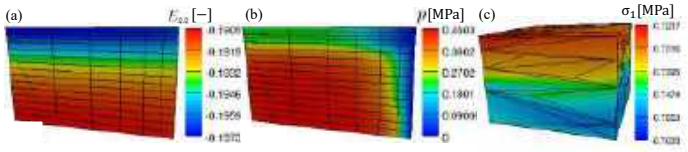

Figure 2: Macroscale and Microscale results for high impact energy: (a) $z-$strain; (b) fluid pressure; (c) first principal stress for representative element 76.

In Fig. 2(a) we show the strain within the cartilage specimen at peak load the *Z*-direction, and in Fig. 2(b) the interstitial fluid pressure. In Fig. 2(c) we show the first principle stress for element 76, which is in the center of the superficial zone.

Utilizing our SERVEs in the superficial zone, we determined the stretch and corresponding stress for each fiber during the impact events. In Fig. 3 the first row shows histograms of the distributions of fiber stretch under LI, HI, and MI, while in the second row we show corresponding histograms of the distributions of fiber stress for the same three tests.

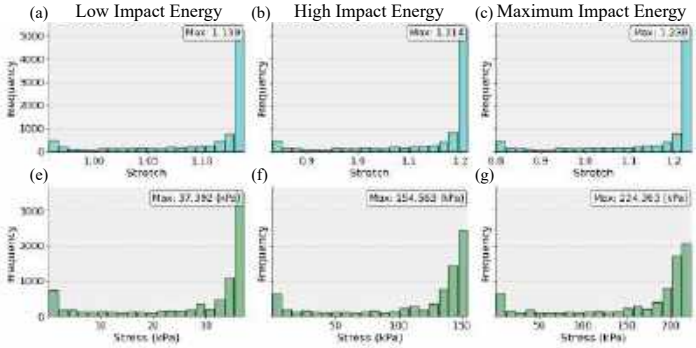

Figure 3: Distributions of stretch and stress for LI, HI, and MI.

Using stress as a predictor of fiber failure, we calculated the ratio of failed fibers as 34.8%, 73.0% and 75.3%, for for LI, HI, and MI respectively. The corresponding experimental values for microcrack density were 2.34 for LI and 3.25 for HI, indicating that microcracks did appear in these impact conditions. Stretch was not a predictor of fiber failure.

In Fig. 4 we show the convergence of the global model with respect to the parameters used to model the stretch-stress response of the collagen fibers (2).

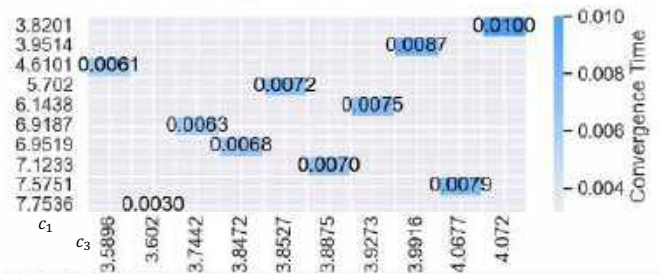

Figure 4: Model sensitivity to constitutive model parameters.

We note that there are combinations of c_1 and c_3 for which the global model will not converge while ramping to the maximum impact load. Additionally, the mechanical response of the global model varies with variations in parameters of the constitutive model for collagen fibers.

DISCUSSION

We present macroscopic and microscopic results for three different impact loadings of cartilage. Our results provide preliminary insights into the mechanical and failure behaviors of type II collagen. Utilizing our SERVEs, we conclude that stress may be a predictor of fiber failure, but stretch is likely not. Sensitivity analyses on constitutive model parameters for collagen reveal their significant impact on the mechanical response of cartilage.

ACKNOWLEDGEMENTS

NSF CAREER 1653358, UConn GTA Fellowship.

REFERENCES

[1] Martin, R, *Bone*, 30:8-13, 2002. [2] Repo, RU et al., *J Bone Joint Surg Am*, 59(8):1068-1076, 1977. [3] Santos, S et al., *Osteoarthritis Cartilage*, 27:1392–1402, 2019. [4] Kaleem, B et al., *Osteoarthritis Cartilage*, 25:544–553, 2017. [5] Almasi, A et al., *submitted for review*. [6] Szarek, P, *The Micro-Mechanics of Collagen Networks within Articular Cartilage*, PhD Thesis, University of Connecticut, 2023. [7] Pierce, DM et al., *Biomech Model Mechanobiol*, 15:229–244, 2016. [8] Szarek, P et al., *Osteoarthritis Cartilage Open*, 2:100086, 2020.

THE IMPACTS OF ESTROGEN AND PROGESTRONE ON EXTRACELLULAR MATRIX REMODELING IN FEMALE MICE ARE STRAIN-DEPENDENT

Allison M. Sander (1), Brianne K. Connizzo (1)

(1) Biomedical Engineering, Boston University, Boston, Massachusetts, USA

INTRODUCTION

Remodeling of the extracellular matrix (ECM) is required for the proper healing, strengthening, and maintenance of tendon. Thus, it is important to investigate the factors which regulate this delicate balance between synthesis and breakdown. There are well documented sex differences in connective tissue injury rates [1][2] and healing outcomes [2][3]. Furthermore, it has been shown that estrogen impedes the increase in protein synthesis rates typically seen in response to exercise [4][5]. However, the individual factors of sex, hormones, and mechanical strain have not been decoupled. In previous work with stress deprived tendon explant cultures, we found that ECM remodeling is dependent on sex hormone signaling when estrogen or progesterone are introduced into the culture media. This work suggested that within the context of stress deprivation, sex hormones were beneficial for female tendons, returning values closer to baseline properties, but detrimental to male tendons, resulting in aberrant matrix turnover [6]. Interestingly, we found that all hormone conditions led to increased breakdown activity in the tendon [6], which had not yet been shown. The objective of this study is to examine the impact of sex hormone induction under different strain conditions to explore the interaction between mechanical strain and hormonal stimulation in female tissues. Based on what is known about estrogen's impact on the response to exercise [4][5], we hypothesized that hormones would have strain-dependent effects on the tendon. We expected breakdown activity to increase in the presence of hormones in all conditions given our previous work.

METHODS

Flexor digitorum longus (FDL) tendons were harvested from young adult (4 month) female C57BL/6J mice. The explants were cultured in either no hormone (89% DMEM +10% FBS + 1% PSA, 'NH'), estrogen-supplemented (1nM 17β-estradiol, 'Est'), progesterone-supplemented (1nM progesterone, 'Pro') or dual hormone (1nM 17β-estradiol + 1nM progesterone, 'Est & Pro') medium. Half of the tendons were cultured in stress deprivation for 7 days and the other half were cultured under 3% static strain in our novel bioreactor system for 12 days. For the static strain condition, tendons were gripped leaving a 10mm gauge distance and tensioned until taught (load reading of 20g). Then, a displacement of 300μm was added to induce a strain of 3% of the tendons. The tendons under static strain were double loaded such that two tendons were present in each media well (Fig. 1).

On the last day of culture, 35S-sulfate and 3H-proline were added for 24 hours to measure the synthesis of sulfated glycosaminoglycans (sGAG) and total protein, respectively. Explant metabolism was measured by a resazurin reduction assay and normalized to day 0 readings from explants of the same sex and hormone treatment. Wet and dry weights were then taken for each explant before digesting with Proteinase K overnight. The sample digests were then assessed for cellularity (PicoGreen assay), GAG content (DMMB assay), and total collagen (OHP assay). Protein synthesis, sGAG synthesis, cellularity, collagen content, and GAG content were normalized to dry weights. Medium was collected on the sixth day of culture for the stress-deprived explants and on the eighth day of culture for the static strain explants to measure matrix degradation using the SensoLyte® 520 Generic MMP Activity Kit. Statistical evaluation was performed through one-way

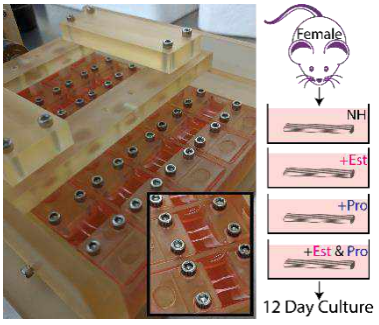

Figure 1: Static tensioning device and study schematic

ANOVAs within each strain condition with post-hoc t-tests where appropriate. Significance is reported at $p<0.05$.

RESULTS

Data from stress deprived cultures is reproduced here for comparison [6]. The effect of estrogen was strain-dependent (Fig. 2A-G). In stress-deprived cultures, estrogen supplementation increased both protein synthesis and breakdown significantly, and also shifted ECM content to decrease collagen and increase GAGs. Estrogen had an opposite effect in static strain conditions, increasing collagen content and decreasing protein synthesis and metabolic activity. Interestingly there was no effect on GAGs or GAG synthesis in static strain conditions and increases in MMP activity were not significant.

Progesterone also had strain-dependent impacts on explant health and ECM synthesis (Fig. 2A-D). Addition of progesterone under stress deprived conditions led to increased protein synthesis and breakdown. Under static strain conditions, metabolic activity and protein synthesis were significantly reduced, and DNA content was increased. Across strain conditions progesterone alone had no impact on sGAG content or synthesis (Fig. 2C, E) and consistently led to an increase in MMP activity and a decrease in collagen content (Fig. 2F-G).

There were some strain-dependent results in the dual hormone condition (Fig. 2B, F), but the impacts remained largely consistent across strain conditions. It is notable that in both strain conditions, only the dual hormone group led to a significant decrease in tendon metabolism and sGAG synthesis (Fig. 2A, C) and returned protein synthesis levels to that of the NH condition (Fig. 2D). In the static strain condition, only progesterone and dual hormone treatments led to increases in MMP activity (Fig. 2G).

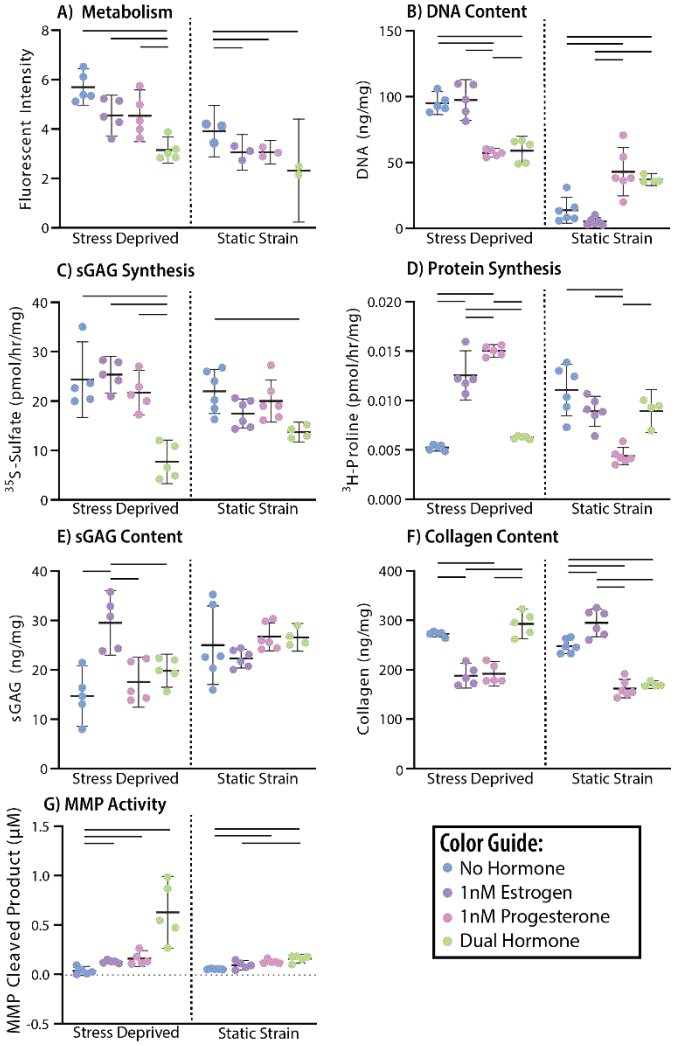

Figure 2: Stress-deprived and 3% static strain culture of female tendons with no hormone, 1nM estrogen, 1nM progesterone, or dual hormone addition. Explant health (A-B), ECM synthesis (C-D), ECM content (E-F) and ECM breakdown (G) were assessed.

DISCUSSION

In agreement with our hypothesis, estrogen and progesterone alone have strain-dependent effects on the biosynthetic parameters we assessed in female tendon tissue. The increase in collagen content with strain and estrogen found in this study is consistent with the current literature based on data from human subjects [7]. Our data validates these findings, as we could remove circulating systemic variables present in *in vivo* studies, but is limited as it does not examine dynamic strain states. The lack of a decrease in protein synthesis may be due to this, as the static strain does not fully represent exercise.

Progesterone has not been studied yet as an independent variable. What is known about progesterone is in the context of the impacts of estrogen and progesterone together in the menstrual cycle [8], where there are apparent differences in musculoskeletal connective tissue injuries based on the phase of the cycle [9]. Interestingly, dual hormone effects in our study appeared to be more influenced by progesterone than estrogen. This could indicate that progesterone may have the dominant effect during cycling, and the balance of tendon remodeling may be altered by the rapid fluctuation of estrogen and progesterone during the menstrual cycle in young females. In stages with higher levels of progesterone (post-ovulatory in humans), our results suggest there would be increased breakdown activity and lower collagen content compared to high estrogen phases (pre-ovulatory). This could result in a more flexible tendon. However, our current study is limited by the constant administration of both hormones at the same concentration, so the focus of future work is to simulate hormone cycling *in vitro* to gain a better understanding of the stage-dependent effects on tendon.

The increased MMP activity with hormones across both strain states is an exciting result, as the breakdown side of ECM remodeling has not been extensively studied. This contributes to the theory that sex hormones increase overall turnover of the matrix, not just synthesis. To further examine this result, we are examining expression of specific ECM molecules and breakdown proteins in the same culture conditions. Our findings lay the groundwork for future work into the impacts of cycling and hormones on tendon healing and repair, as well as the creation of physiologic *in vitro* models to study female tendon biology.

ACKNOWLEDGEMENTS

This work was supported by funding from the NIH MIRA: R35-GM151127 and the Wu Tsai Human Performance Alliance.

REFERENCES

[1] Vosseller, JT et al., *Foot Ankle Int,* 34(1):49-53, 2013. [2] Grävare Silbernagel, K et al., *Orthop J Sports Med*, 3(6):2325967115586768, 2015. [3] Larsson, E et al., *BMC Musculoskelet Disord*, 23:913, 2022. [4] Hansen, M & Kjaer, M, *Exerc Sport Sci Rev*, 42(4):183, 2014. [5] Miller, BF et al., *J Appl Physiol Bethesda Md 1985,* 102(2):541-546, 2007. [6] Sander, AM & Connizzo, BK, *Trans ORS*, 2024. [7] Hansen, M et al, *J Appl Physiol*, 106(4):1385-1393, 2009. [8] Hansen, M, *Proc Nutr Soc*, 77(1):32-41, 2018. [9] Wojtys, EM, *Am J Sports Med*, 30(2):182-188, 2002.

POST-TRANSCATHETER EDGE-TO-EDGE REPAIR PRESSURE GRADIENT PREDICTION AFTER MITRACLIP IN FUNCTIONAL MITRAL REGURGITATION PATIENTS

Shelley C. Gooden (1), Mani A. Vannan (2), Konstantinos D. Boudoulas (3), Vinod H. Thourani (2), Pradeep K. Yadav (2), Lakshmi P. Dasi (1)

(1) Department of Biomedical Engineering, Georgia Institute of Technology, Atlanta, Georgia, US
(2) Marcus Valve Center, Piedmont Heart Institute, Atlanta, Georgia, US
(3) Division of Cardiovascular Medicine, Wexner Medical Center, Columbus, Ohio, US

INTRODUCTION

Mitral regurgitation (MR) is present in about 1.7% of the general population, rising to 9.3% in those age 75 and older [1] and occurs when the two leaflets of the mitral valve (MV) do not close properly during systole. In the case of functional MR (FMR), this is due to structural changes in surrounding anatomy that impact valve competence. For treatment of symptomatic moderate-to-severe or severe MR in patients deemed high-risk for surgical treatment, Abbott's MitraClip transcatheter edge-to-edge repair device may be used. Focusing on FMR, MitraClip is the only FDA approved transcatheter device and one of two CE marked. The device clips the two leaflets together, creating a double orifice and reducing regurgitation.

Analyzing MV pressure gradient (MVG), defined as the mean MVG by simplified Bernoulli through diastole measured by CW doppler, during the MitraClip procedure is important. Leaving patients with gradients of 5 mmHg or more is undesirable and can lead to iatrogenic mitral stenosis, worsening patient prognosis [2-3]. The impact of MitraClip on MVG is important in assessing patient candidacy and may aid in procedural planning. However, post-MitraClip MVG is not straightforward, and there is a lack of quantitative algorithms that do not require full, expansive, time-intensive, patient-specific simulations.

The objective of this study is to develop a framework for post-MitraClip MVG prediction immediately after MitraClip deployment for FMR patients based on routine pre-MitraClip transesophageal echocardiogram (TEE).

METHODS

Fourteen patients with cardiomyopathy and moderate-to-severe or severe FMR on maximally tolerated medical therapy underwent MitraClip implantation with central device placement. Pre- and post-MitraClip TEEs were performed on all patients, and data was acquired under IRB approved protocol.

From the pre-MitraClip 3D TEE scan, a representative model of each MV was generated. A parameterization method was developed and applied to simplify each MV geometry based on annular commissural and septolateral dimensions and leaflet lengths, and the simplified pre-MitraClip geometries were generated. An example of the pre-MitraClip geometry is shown in **Figure 1A.**

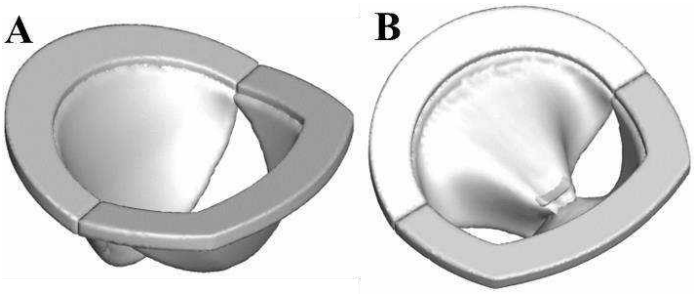

Figure 1: Pre-MitraClip Simplified Mitral Geometry (A) and Post-MitraClip Simulation Geometry (B)

An in-house reduced-order model MitraClip simulation was implemented based on the number of MitraClips implanted in the patient. Because the information of MitraClip size was unavailable, MitraClip NT was assumed based on clinician judgement. The total post-MitraClip MV area (MVA), defined by the leaflet tips, was then measured. An example of the post-MitraClip geometry is shown in **Figure 1B**.

Post-MitraClip MVG for the simulated geometries were calculated. First, the mean diastolic pre-MitraClip mitral volumetric flowrate was calculated for each patient using pre-MitraClip MVA and MVG by manipulation of the simplified Bernoulli's equation, shown in Equation 1.

$$Q_{mean} = MVA_{in\ vivo}\sqrt{\frac{MVG_{in\ vivo}}{4}} \quad (1)$$

In the same manner, this flowrate was then applied to calculate the MVG based on the simulated MVA, as shown in Equation 2.

$$MVG_{simulated} = 4\left[\frac{Q_{mean}}{MVA_{simulated}}\right]^2 \quad (2)$$

Four patients were used to develop a post-MitraClip MVG predictive model to map between the simulated and *in vivo* MVG measures; this equation yields the final predicted MVG. The equation was then assessed on the remaining ten patients. Performance of the predictive model was assessed using a Bland-Altman plot. Acceptance criterion was set to assess the ability of the model to yield a predicted MVG within 1 mmHg of the *in vivo* MVG.

RESULTS

A comparison of the simulation model and patient TEE for pre- and post-MitraClip geometries is shown in **Figure 2**.

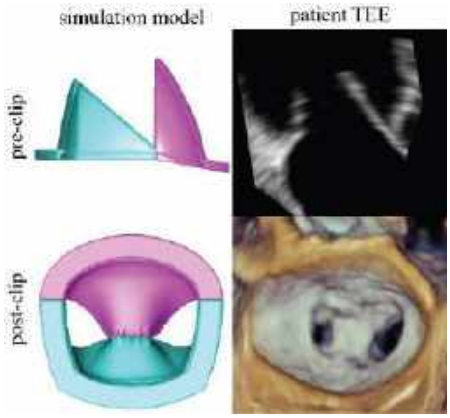

Figure 2: Simulation Model vs Patient TEE

The *in vivo* vs simulated post-MitraClip MVG forming the predictive model is shown in **Figure 3.**

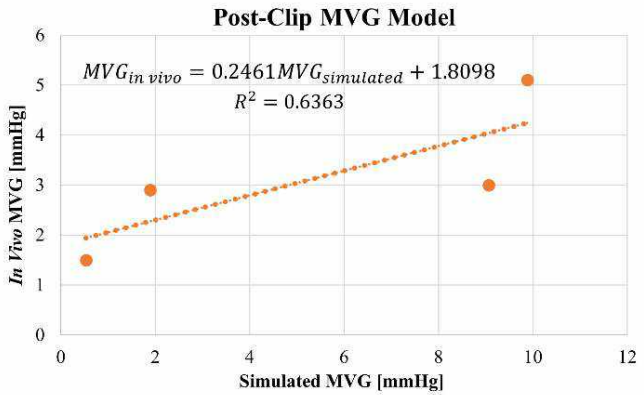

Figure 3: *In Vivo* vs Simulated Post-MitraClip MVG

An equation relating the two measures is formed, shown in Equation 3, with an R-squared of 0.64.

$$MVG_{in\ vivo} = 0.2461MVG_{simulated} + 1.8098 \quad (3)$$

The predictive model was assessed in the Bland-Altman plot shown in **Figure 4**.

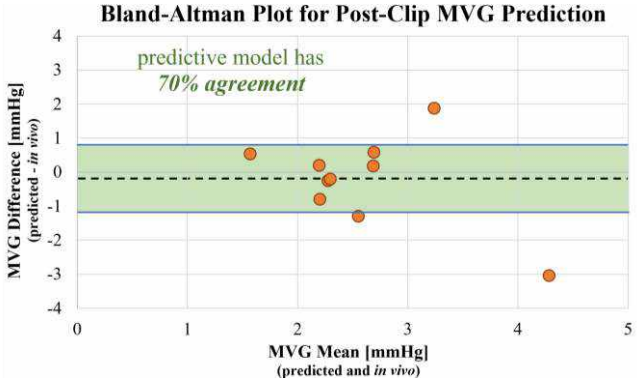

Figure 4: Predictive Model Assessment

The mean difference between the predicted and *in vivo* MVG was -0.22 mmHg, and the predictive model showed 70% agreement across the ten patients assessed.

DISCUSSION

By visual inspection, the MV simplification and simulation yielded geometries representative of patient anatomy (**Figure 3)**.

The predictive model formed had an R-squared of 0.64, indicating the model had a decent correlation between the *in vivo* and simulated post-MitraClip MVG.

Based on the Bland-Altman plot (**Figure 4**), the mean difference between the predicted and *in vivo* MVG was -0.22 mmHg. This shows the predicted MVG was overall slightly lower than *in vivo* MVG. With acceptance criterion of 1 mmHg, the predictive model showed 70% agreement across the ten patients assessed, which shows decent predictive power given the small number of patients used.

This study shows that the MV geometry can be simplified for analysis, and simplified simulations can faithfully capture *in vivo* post-MitraClip geometry and MVG, avoiding expansive simulations commonly performed.

The main limitation of the methodology in this study is the use of a parameterized MV model simulated only for diastole. Incorporation of the full MV apparatus through systole may yield increased predictive efficacy. Only pre-MitraClip MVG was used to assume a mean diastolic flow rate, where effects on post-MitraClip hemodynamics were not accounted for. Another limitation was the assumption of MitraClip NT because implanted device size was not available.

Future work aims to address these shortcomings, in addition to expanding the number of patients assessed and assessing patients with non-central MitraClip placement.

Results from this study lay the basis for the first knowns simplified predictive framework for post-MitraClip MVG. Expanding this model can provide an easy-to-use and important clinical tool for patient candidacy assessment and procedural planning for MitraClip implantation to prevent suboptimal MVG outcomes.

ACKNOWLEDGEMENTS

This research was supported by National Institute of Health (NIH) under Award Number R01HL119824.

REFERENCES

[1] Benjamin, E.J. et al., *Circulation*, 137:e67-e492, 2018.
[2] Itabashi, Y et al., *J Cardiol*, 71:336-345, 2018.
[3] Nishimura, R et al., *J Am Cardiol*, 63:e57-e185, 2014.

DETECTING CARDIAC STATES WITH PHOTOPLETHYSMOGRAPHY WEARABLES: IMPLICATIONS FOR OUT-OF-HOSPITAL CARDIAC ARREST DETECTION

M. Khalili (1), S. Lingawi (2), J. Hutton (1), B. Shadgan (2), J. Christenson (1), B. Grunau (1), C. Kuo (2)

(1) Department of Emergency Medicine, University of British Columbia, Vancouver, BC, Canada
(2) School of Biomedical Engineering, University of British Columbia, Vancouver, BC, Canada

INTRODUCTION

Out-of-hospital cardiac arrest (OHCA) is the unexpected cessation of cardiac mechanical activity and blood circulation that occurs outside of the hospital setting (1). In 2010, there were an estimated 4.4 million OHCA events worldwide (2). In 2020, there were approximately 300,000 reported cases of emergency medical system (EMS)-treated OHCAs in the United States, a significant 33% increase compared to 2015 (3). In Canada, OHCA incidents were estimated at 38,000 cases in 2020 (4), a 16% increase compared to 2017 (5). For unwitnessed OHCAs, only 2-4.1% survive to hospital discharge (6). According to the 2022 US Cardiac Arrest Registry to Enhance Survival report, survival rates in EMS-treated cases were 3 times higher for witnessed vs. unwitnessed events (3). Given that approximately 50% of EMS-treated OHCAs are unwitnessed (3), the main barrier in improving OHCA outcomes is the timely recognition of the event.

Wearable biosensor devices with continuous cardiac monitoring capabilities may serve as witnesses in an otherwise unwitnessed event where no bystanders are present (7). The loss of cardiac function leads to immediate physiological changes, such as cessation of pulsatile blood flow, and drop in oxygenated hemoglobin. One of the most commonly used sensors in consumer wearable devices for continuous cardiac monitoring is photoplethysmogram (PPG) (8). PPG is an optical sensor, capable of monitoring cardiac pulsation. In this study, we hypothesized that PPG waveforms contain relevant information to distinguish between normal cardiac states, occurrence of cardiac arrest (i.e., absence of a pulsatile blood flow), and non-physiologic data (i.e., off-body recordings). Specifically, we investigated the impact of various PPG characteristics, including time- and frequency-domain features, on the performance of cardiac state detection classification models.

METHODS

Our wearable device consisted of 4 Maxim Integrated™ PPGs for synchronized measurements. With this device, we obtained physiologic data on different anatomical locations during normal blood circulation (i.e., cardiac) and interrupted blood flow (i.e., occlusion, representing a cardiac arrest state) as well as non-physiologic (i.e., off-body) measurements. All PPG recordings were split into 10s non-overlapping segments, and filtered (4th-order zero-lag Butterworth filters: 8Hz low-pass cut-off frequency; 0.5-5Hz band-pass cut-off frequency). Time-domain features were extracted from PPG recordings (number of features, n=10). The Welch power spectral density (PSD) analysis was performed to calculate the power distribution of PPG recordings across different frequencies (PSD feature set, n=11). Selected frequency-domain features, such as the total power, frequency center, and spectral spread of PPG signals were extracted from PSD calculations (Frequency feature set, n=5). To diversify feature representations, three additional feature set combinations were created: Time and PSD features (timepsd; n=21), Time and Frequency features (timefreq; n=15), and Time, Frequency, and PSD features (timefreqpsd; n=26). Random forest classification models were trained for each anatomical location to detect between the three possible states of *Normal Cardiac* (NC), *Occlusion* (OCC), and *Off-Body* (OB). Classification pipelines included: 1) feature standardization (subtracting the mean and normalizing to one standard deviation); 2) sequential forward feature selection algorithm; 3) random forest model training with 10-fold cross-validation and hyperparameter tuning using 70% of randomly selected PPG measurements; and, 4) model evaluation using 30% hold-out test dataset.

RESULTS

This study was approved by the Behavioural Research Ethics Board of the University of British Columbia [H22-01587]. Thirty-one healthy volunteers (14 female, 19-58 years old) with no known ongoing cardiac conditions were recruited and provided written informed consent to participate in this study. For each sensor placement (including the fingertip, finger base, and wrist), we compared classification performances when using different feature sets (Figure 1-

left). For all sensor placements, the classification performance of models using both time- and frequency-domain features (i.e., timefreq, timepsd, timefreqpsd) were higher than the models trained on either time- or frequency-domain features (i.e., time, freq, psd). While certain time- or frequency-domain PPG characteristics exhibited similar distributions across cardiac and/or non-cardiac states (e.g., PPG mean of normal cardiac and occlusion measurements), significant differences were observed for all states when considering the combination of time- and frequency-domain features (Figure 2-left). For instance, both the PPG Mean and 1.17 Hz component of the PPG PSD (equivalent to ~70 BPM heart rate) were common features among all sensor placements.

Higher classification performances (macro average F1-Score) were observed on the finger (fingertip: 0.966, finger base: 0.946) compared to the wrist (0.841). Normalized confusion matrices (Figure 1-right) were used to evaluate class-based classification and misclassifications on the hold-out test set. Across all anatomical sites, NC and OB had higher Sensitivity (i.e., lower number of false positives) compared to OCC. Specifically, OCC detection had the lowest performance on the wrist, with over 50% false-negative predictions. Conversely, OCC had higher Specificity compared to NC and OB, indicating low false-positive OCC predictions.

Sample PPG waveforms for normal cardiac and occlusion measurements taken at the fingertip, finger base, and wrist were examined (Figure 2-right). Normal cardiac measurements at the fingertip and finger base had a distinct pulsatile component (PPG AC), differentiating them from pulseless occlusion measurements on those sites. However, normal cardiac measurements on the wrist exhibited a weaker pulsatile component, potentially making it more challenging to distinguish them from pulseless Occlusion measurements.

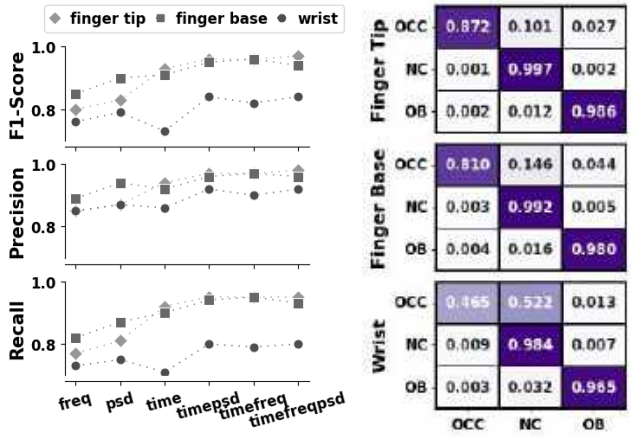

Figure 1. Classification performances across different feature sets and anatomical locations (left). Normalized confusion matrices for each anatomical location (right). NC: Normal Cardiac; OCC: Occlusion; OB: Off-Body.

DISCUSSION

In this study, we developed and tested a PPG wearable device with the capability to detect healthy cardiac, pulseless cardiac, and non-cardiac conditions using machine learning. Classifiers trained and evaluated on PPG recordings on the finger had better performance compared to those using wrist PPG data. While finger clip-type PPG devices are frequently used in clinical settings, obtaining PPG data from the fingertip would not be feasible for everyday use. Our findings suggest that the second-best location to achieve high-classification performance is the finger base. In recent years, wearables adopting a ring form factor with embedded PPG sensors have become available in the market (e.g., Oura ring). While these wearables currently do not have OHCA detection capabilities, our study suggests that they may offer the most suitable form factor for optimal OHCA detection applications. Given the classification performance was significantly lower when using PPG recordings on the wrist, and considering the widespread popularity of wristband wearables in nonclinical settings, it is imperative to employ strategies to enhance classification accuracy in this location. Possible approaches may include training classification models using recordings from multiple PPGs.

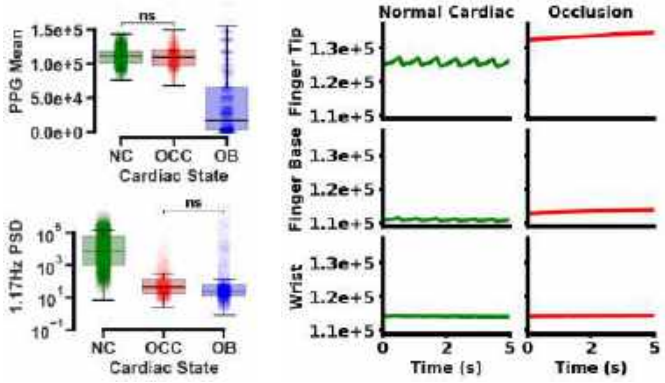

Figure 2. Distribution of sample time- and frequency-domain PPG features across different cardiac and non-cardiac states (left). Sample PPG waveforms on different anatomical locations for cardiac and occlusion states (right). NC: Normal Cardiac; OCC: Occlusion; OB: Off-Body.

ACKNOWLEDGEMENTS

This study was funded by MITACS and Michael Smith Health Research BC, Canada. The authors declare no conflicts of interest.

REFERENCES

1. McNally B, Robb R, Mehta M, Vellano K, Valderrama AL, Yoon PW, et al. Out-of-hospital cardiac arrest surveillance --- Cardiac Arrest Registry to Enhance Survival (CARES), United States, October 1, 2005--December 31, 2010. Morbidity and mortality weekly report Surveillance summaries. 2011;60(8):1–19.
2. Berdowski J, Berg RA, Tijssen JGP, Koster RW. Global incidences of out-of-hospital cardiac arrest and survival rates: Systematic review of 67 prospective studies. Resuscitation. 2010;81(11):1479–87.
3. Cardiac Arrest Registry to Enhance Survival. https://mycares.net/
4. Grunau BE, et al. Comparing the prognosis of those with initial shockable and non-shockable rhythms with increasing durations of CPR: Informing minimum durations of resuscitation. Resuscitation. 2016;101:50–6
5. Heidet M, Grunau B, Vaillancourt C, Baert V. Trends in out-of-hospital cardiac arrest across the world: Additional data from the CanROC and RéAC national registries. Resuscitation [Internet]. 2023;1;187.
6. Hutton J, Puyat JH, Asamoah-Boaheng M, Sobolev B, Lingawi S, Khalili M, et al. The effect of recognition on survival after out-of-hospital cardiac arrest and implications for biosensor technologies. Resuscitation. 2023;190:109906.
7. Hutton J, Lingawi S, Puyat JH, Kuo C, Shadgan B, Christenson J, et al. Sensor technologies to detect out-of-hospital cardiac arrest: A systematic review of diagnostic test performance. Resuscitation Plus. 2022;11:100277.
8. Lee Y, Shin H, Choi HJ, Kim C. Can pulse check by the photoplethysmography sensor on a smart watch replace carotid artery palpation during cardiopulmonary resuscitation in cardiac arrest patients? A prospective observational diagnostic accuracy study. BMJ Open. 2019;9(2):1–5.
9. Charlton PH, Kyriacou PA, Mant J, Marozas V, Chowienczyk P, Alastruey J. Wearable Photoplethysmography for Cardiovascular Monitoring. Proceedings of the IEEE. 2022;110(3):355–81.
10. Castaneda D, Esparza A, Ghamari M, Soltanpur C, Nazeran H. A review on wearable photoplethysmography sensors and their potential future applications in health care. Int J Biosens Bioelectron. 2018;4(4):195–202.

THE EFFECT OF CAM MORPHOLOGY OF THE HIP ON SACROILIAC MOTION DURING FUNCTIONAL HIP BIOMECHANICS

Alexander W. Hooke (1), Mason E. Uvodich (2), Joshua T. Bland (1), Allison M. Tanner (1), Zachary V. Braig (2), Micah J. Nieboer (2), Evan M. Dugdale (2), William W. Cross (2), Chunfeng Zhao (1,2), Aaron J. Krych (2), Mario Hevesi (2)

(1) Biomechanics Core, Mayo Clinic, Rochester, Minnesota, U.S.A.
(2) Department of Orthopedic Surgery, Mayo Clinic, Rochester, Minnesota, U.S.A.

INTRODUCTION

Cam morphology of the proximal femur changes the biomechanics of the hip joint and is commonly linked to femoroacetabular impingement syndrome (FAI).[1] This change in the loading pattern has been shown to affect movement at the pubic symphysis and correction of cam morphology can reduce force at the chondrolabral junction.[2,3] However, this line of research has not been extended to the relationship between FAI, cam morphology, and sacroiliac (SI) joint dysfunction. Quantitative biomechanics data of any kind is particularly lacking in this area with only observational data linking poor hip range of motion with low-back pain.[4] Additionally, the prevalence of radiographic SI joint abnormalities in patients with FAI may be as high as 1 in 4 patients.[5]

The purpose of this study was to quantify the relationship between FAI due to cam morphology of the proximal femoral head and SI joint kinematics using a cadaveric model. Our hypothesis is that hips with cam-type FAI will result in significantly different ipsilateral SI joint kinematics versus those of a hip in a native.

METHODS

5 hips from 3 cadaveric human pelves (85±9.2yrs) were approved for testing by the institution's biospecimens review panel. Specimens were screened to be free from arthritis, hip dysplasia, and evidence of prior surgery.

Optical Metrology

To prepare for measurement of SI joint kinematics, an array of 5–8 fiducial tracking landmarks, made of 3mm diameter acrylic rods, were rigidly fixed to the right and left ilia, and sacrum. Specimens then underwent a computed tomography (CT) scan. The right and left ilia and sacrum were then segmented into separate 3D mesh files with the fiducial landmarks included in each mesh (Figure 1). Tracking markers were fixed on the exposed tip of each landmark.

During testing, two, 12-megapixel cameras equipped with Titanar 24mm lenses (Aramis SRX, Trilion Quality Systems, King of Prussia, PA) were positioned such that each camera could see all tracking markers, tracking the markers in 3D space with a resolution of 0.01mm. The marker arrays of the right and left ilia and sacrum enabled each bone to be tracked as a rigid body in 3D space using the Aramis software (Aramis Pro 2018, Trilion Quality Systems, King of Prussia, PA). The 3D meshes attained were then aligned to the tracking markers by matching the tips of the landmark posts in the meshes with the tracking markers, enabling the right and left ilia and sacrum's 3D meshes to be tracked in 3D space as rigid bodies with a resolution of 0.04mm and relative motion between the 3 bones to be quantified. Anatomic coordinate systems, joint kinematics and kinetics of the pelvis and femur were defined according to the recommendations of the International Society of Biomechanics.

Figure 1: 3D CT reconstruction of pelvis demonstrating fiducial markers. Ovals indicate groups of fiducial markers used to track the 2 ilia and sacrum.

Robotic Testing

To prepare for robotic testing, skin and subcutaneous tissues were removed from the distal end of each exposed femur which were then potted in a urethane resin (Smooth-On 300D). The sacrum was augmented to withstand repeated testing with polymethylmethacrylate avoiding the SI articulation and ligamentous attachments. The pelvis was then secured via the sacrum to a rigid plate using a custom fixture such that the sacrum alone was rigidly fixed, allowing the SI joint and pelvic ilia to remain free. Prepared specimens were mounted to a 6 degree-of-freedom robotic system (KUKA, Augsburg, Germany) with one distal femur mounted to the robot's manipulator equipped with a 6-axis load cell and the sacrum to a floor-mounted platform (Figure 2). The robot was controlled using simVITRO software (Cleveland Clinic, Cleveland, OH, USA).

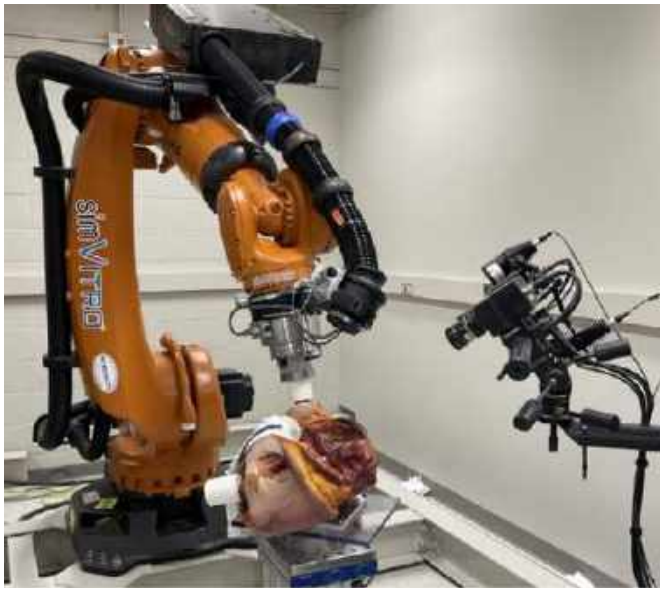

Figure 2: Experimental set-up showing sacrum fixed to pedestal and right femur fixed to robotic arm with optical metrology cameras viewing.

Hips were tested with a starting position of 90° of flexion and neutral adduction and axial rotation. Hips were then internally rotated at a rate of 1°/sec until an internal rotation torque of 18Nm was reached, at which point the joint was returned to its original position. While internally rotating the hip joint, the robot maintained the 90° flexion and abduction angles and allowed joint translation such that 0N of translational forces were maintained at the joint. During each test, the optical metrology and robotic systems were synchronized with the SI kinematics and hip joint kinetics recorded at 8Hz and 100Hz, respectively.

Hip Joint Conditions

Each hip was tested in a native and a simulated cam state. Native hips underwent an anterior longitudinal capsulotomy and subsequent repair prior to testing. The simulated cam state was created with a 3D-printed simulated cam that was designed to contour along the femoral head and neck and placed at the 2 o'clock position at the femoral head-neck junction.

Data Analysis

3D translations and rotations about the SI joint were compared at 6, 12, and 18Nm of hip internal rotation. A within-specimen analysis was performed using a repeated measures ANOVA comparing the effect of the cam with the native state at each of the 3 torque levels and at each of the 6 degrees of freedom.

RESULTS

Amongst all degrees of freedom and both hip joint conditions, motion at the ipsilateral SI joint increased with hip internal rotation torque. Regarding the effect of simulated cam FAI on ipsilateral SI joint kinematics, results are shown in Table 1. The presence of FAI resulted in an anterior, superior, and lateral translation of the ilia relative to the sacrum that increased with hip torque. Rotationally, the presence of the cam resulted in iliac abduction, internal rotation, and extension relative to the sacrum versus the native hip with statistically significant differences present at 12Nm and 18Nm in internal rotation and extension.

DISCUSSION

Limitations of this study include the age of the cadavers, and the simulated cam state as the simulated cam does not perfectly replicate normal joint mechanics. We did not evaluate the native hip head-neck offset nor control for the version of the proximal femur, which may reasonably alter the magnitude of difference between the native and cam states. The precision of our experimental instrumentation allowed us to detect very small movements about the SI joint, and the clinical conclusions of such small movements may be limited. Lastly, our study may have been underpowered to detect differences in some of the outcome variables.

In conclusion, the presence of simulated cam morphology causes identifiable changes in motion at the SI joint relative to a native state. These findings provide a quantitative biomechanical explanation for concomitant SI joint dysfunction in patients with femoroacetabular impingement syndrome. Additionally, this study outlines a method to quantify SI joint behavior resulting from changes in hip biomechanics, enabling further studies on this relationship to be performed.

ACKNOWLEDGEMENTS

Supported by the Mayo Clinic Orthopaedic Research Review Committee and Biomechanics Core.

REFERENCES

[1] Atkins PR, et al. *J Orthop Res*. Apr 2020;38(4):823-833.
[2] Ng KCG et al. *Am J Sports Med*. 2019;47(2):420-430.
[3] Birmingham PM, et al. *Am J Sports Med*. May 2012;40(5):1113-8.
[4] Murray E, et al. *Physical Therapy in Sport*. 2009/11/01/ 2009;10(4):131-135.
[5] Krishnamoorthy VP, et al. *Arthroscopy*. Sep 2019;35(9):2598-2605.e1.

	Translation (mm)						Rotation (°)					
	Anterior		Superior		Lateral		Abduction		Internal Rotation		Flexion	
	mean	*SD*	mean	*SD*	mean	*SD*	mean	*SD*	mean	*SD*	mean	*SD*
6Nm	-0.10	*0.09*	-0.13	*0.16*	-0.18	*0.11*	0.02	*0.03*	0.01	*0.01*	-0.04	*0.02*
12Nm	-0.29	*0.23*	-0.31	*0.34*	-0.31	*0.20*	0.03	*0.04*	0.06*	*0.02*	-0.08**	*0.03*
18Nm	-0.58	*0.44*	-0.62	*0.64*	-0.53	*0.32*	0.03	*0.07*	0.09**	*0.04*	-0.10**	*0.06*

Table 1: Normalized difference in SI joint kinematics between native and simulated cam hips. Direction label defines the positive direction. * indicates significant difference at $p<0.05$. ** indicates significant difference at $p<0.10$.

SB³C2024
Summer Biomechanics, Bioengineering and Biotransport Conference
June 11-14, Lake Geneva, WI, USA

A RANDOM FOREST CLASSIFICATION METHOD TO ESTIMATE RUPTURE RISK OF ABDOMINAL AORTIC ANEURYSMS BASED ON BIOMECHANICAL AND GEOMETRIC SURROGATES

Juan C. Restrepo (1), Merjulah Roby (1), Pratik Mitra (1), Satish C. Muluk (2), Mark K. Eskandari (3), Ender A. Finol (1)

(1) Department of Mechanical Engineering, University of Texas at San Antonio, San Antonio, TX
(2) Department of Cardiothoracic Surgery, Allegheny Health Network, Pittsburgh, PA
(3) Division of Vascular Surgery, Northwestern University School of Medicine, Chicago, IL

INTRODUCTION

An abdominal aortic aneurysm (AAA) is a non-homogeneous dilatation of the aortic wall that delves into a progressive weakening, which can lead to its rupture, an event that carries an overall mortality rate of 80%. The U.S. clinical standard to assess the need for AAA repair is a maximum transverse diameter of 5.5 cm for male patients and 5.0 cm to 5.4 cm for females [1]. However, biomechanical markers such as Rupture Potential Index (RPI) have been postulated to be better predictors of rupture risk compared to size alone. To estimate accurately patient-specific RPI, an AAA's wall stress and wall strength are required, for which knowledge of the patient-specific intraluminal blood pressure, wall and intraluminal thrombus (ILT) material properties, is needed at the time of clinical imaging. In addition, wall strength requires knowing the patient-specific familial history of AAA, sex, local diameter, and local ILT thickness. Conversely, geometric measures other than maximum diameter have also been implicated in rupture risk assessment [2, 3]. These were applied with decision tree-based methods to estimate AAA rupture risk [4].

The present work explores the use of a Random Forest (RF) model for classifying AAAs according to their rupture risk. This approach is based on rupture risk assessment performed through biomechanical and geometrical analyses, which can be utilized to assist physicians in assessing the rupture potential of AAAs. We hypothesized that our model achieves a minimum accuracy of 80% in classifying RPI into three categories: low risk, medium risk, and high risk for training, validation, and testing datasets.

METHODS

We retrospectively acquired images from 73 computed tomography angiography (CTA) exams obtained from a preexisting database at Allegheny General Hospital (Pittsburgh, PA) and Northwestern Memorial Hospital (Chicago, IL), following Institutional Review Board (IRB) approval at both clinical centers. The CTA images were manually segmented by previously trained users from the renal arteries to the aorto-iliac bifurcation using a custom in-house MATLAB®-based (MathWorks Inc., Natick, MA) script [5]. The segmentation yielded binary masks containing three contours of interest (lumen, inner wall, and outer wall), which were then used for volume meshing performed by a mesh generation script for AAAs suitable for finite element analysis (FEA) [6]. Consequently, triangular surface meshes of the outer wall surface for each AAA model were generated ranging from 30,500 to 161,700 elements, with a mean of 77,000 elements. The AAA wall thickness was estimated from the segmented images on a spatially distributed basis and applied to each node of the surface mesh. A nonlinear elastic membrane analysis (NEMA) method was used to compute the first principal normal and shear stresses at the wall [7] without the need to specify material properties as an alternative for the commonly used FEA. The proximal and distal ends of the models were fixed, and an intraluminal pressure of 93.33 mmHg was applied. The wall strength was calculated (in N/cm^2) using Eq. (1) proposed by Vande Geest et al. [8],

$$Wall\ Strength = 72.9 - 33.5 * \left(\sqrt{ILT} - 0.79\right) - 12.3 * (NORD - 2.31) - 24 * HIST + 15 * SEX \quad (1)$$

where ILT is the ILT thickness (in cm) and NORD is the normalized local diameter (dimensionless) at each node of the surface mesh, HIST is the familial history of AAA (+0.5 for positive familial history; -0.5 otherwise), and SEX is the sex of the patient (+0.5 for male; -0.5 for female). The maximum and 99th percentile RPI (99th RPI) of the AAAs were calculated using the nodal based RPI calculation, which is defined as the ratio of the first principal normal stress and the wall strength.

A geometric characterization was performed with the sac of all AAA models to calculate 52 geometric indices using previously developed in-house MATLAB® scripts [2], which are described in detail and available elsewhere [4-6]. Finally, three categories were

generated based on the 99th RPI and maximum diameter: low risk for AAAs smaller than 5.5 cm and a 99th RPI < 0.5, high risk for AAAs greater than 5.5 cm and a 99th RPI > 0.5, and medium risk otherwise. Our dataset is composed of 39 low risk, 28 medium risk, and 6 high risk AAAs, as shown graphically in Fig. 1.

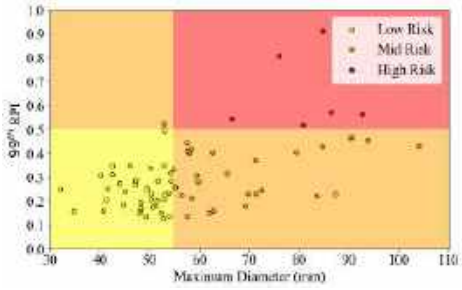

Figure 1. Risk boundaries showing low, medium, and high risk AAAs according to their 99th RPI and maximum diameter values.

Four RF models were compared, each with n estimators, maximum depth, and random state parameters fixed at 5, 5, and 2, respectively. Model 1 was trained using three principal components derived from principal component analysis (PCA) applied to the entire dataset. Model 2 was trained on the entire dataset without any preprocessing. Model 3 was trained using features extracted through Pearson's correlation coefficients to eliminate redundant features. Lastly, Model 4 was trained on a dataset reduced to two principal components, which were obtained by performing PCA on the dataset used for Model 3. The dataset was split into training, validation, and testing datasets in ratios of 60%, 20% and 20%, respectively.

RESULTS

Dimensionality reduction was performed for Models 1 and 4 using Principal Component Analysis (PCA). For Model 1, the feature dimensionality was reduced from 53 to 3, while for Model 4, it was reduced from 9 to 2. The number of principal components was determined by investigating the explained variance ratio for each component in both models. In Model 1, the first principal component accounts for 89.6% of the dataset's variance, the second for 4.3%, the third for 3.3%, and the rest account for less than 2%, as shown in Fig. 2a. For Model 4, the first principal component covers 67.1% and the second 31.5%, with the remaining components accounting for less than 1% of the variance, as illustrated in Fig. 2b.

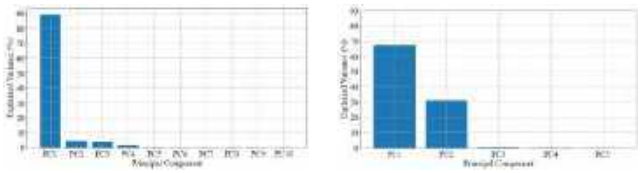

(a) (b)

Figure 2. Principal components and their explained variances for (a) Model 1 and (b) Model 4.

Table 1 shows the accuracies for each subsample of the dataset according to the classification model. Models 2 and 3 overfit the training dataset, as evidenced by their perfect performance in training and significant drops in validation and testing accuracies. Model 4 does not overfit (compared to 2 and 3) but struggles with generalization, as indicated by its lower validation and testing accuracies compared to its training accuracy. The principal component of Model 4 covers marginally more variance than Model 1, albeit worse in performance.

Table 1. Accuracies of each classification model.

Accuracy	Model 1	Model 2	Model 3	Model 4
Training	91.30%	100%	100%	95.65%
Validation	83.33%	66.66%	43.75%	50%
Testing	93.33%	73.33%	60%	73.33%

DISCUSSION

Model 3 improves after performing PCA on the extracted feature space. However, accuracy is significantly higher for Model 1, where no feature extraction was performed. Our previous research on the association between geometric indices and RPI has shown that for most indices there is a moderate association [9]. Therefore, a dimensionality reduction technique such as PCA substantially solves the problem of not having strong dependence and correlation on AAA geometric surrogates. Performing PCA generates a linear combination of input features, which may not be physically meaningful but can be used to improve the accuracy and realism of a model, as demonstrated in Model 1 compared to Model 2. It is observed that by eliminating redundant features, the model's accuracy decreases on validation and testing datasets, and it tends to overfit on training information, as seen in Model 3. For Model 4, accuracy is slightly improved by performing PCA. However, feature selection is used when features have disjointed meanings, unlike PCA, which preserves information associated with the dataset and maintains its meaning. In this application, 52 input features, which are geometric indices, show correlation and dependency on the sample space.

Model 1 satisfies the proposed hypothesis, while Models 2-4 do not. The accuracy of a model can be biased by the sample size, which is a limitation of this study. A well-distributed dataset with an equal number of AAAs for each category, as well as a large sample size, will be required for deeper and more precise tuning of the model. Limitations related to biomechanical analysis are related to the NEMA force-based analysis, which neglects bending stresses and stress gradients through the aortic wall, thus yielding lower stresses compared to the widely used FEA. However, it overcomes the requirement of tissue characterization, which is impossible to perform on a non-invasive, patient-specific basis, for instance, in surveillance programs.

The methods of this study can be integrated into an automatic pipeline for assessing AAA rupture risk. This could be accomplished by leveraging deep learning-based segmentation algorithms to expedite the timing of rupture risk assessments. The goal would be to generate a fully automated pipeline for hospitals, particularly benefiting clinicians who lack the specific biomechanical and data science expertise required for these approaches.

ACKNOWLEDGEMENTS

This work was supported in part by the National Institutes of Health award R01HL159300.

REFERENCES

[1] Chaikof, E.L., et al., *J Vasc Surg*., 67(1):2-77, 2018.
[2] Shum, J et al., *A Biomed*., 39(1):277-86, 2010.
[3] Raut, SS et al., *A Biomed*., 41(7):1459-1477, 2013,
[4] Parikh, et al., *A Biomed*., 46(12):2135-2147, 2018.
[5] Shum, J et al., *M Physics*, 37:638-648, 2010.
[6] Raut, SS et al., *J Biomech.*, 48(10), 53:1972-1981, 2015.
[7] Thirugnanasambandam, M et al., *PhD Thesis*, UTSA, 2018.
[8] Vande Geest, JP et al., *Ann. N.Y. Acad. Sc*., 1085:11-21, 2006.
[9] Restrepo-Perez, JC et al., *SB3C Proc.*, SB³C2023-394, 2023.

CHRONIC OFF-TARGET CARDIOTOXICITY OF DOXORUBICIN IS MEDIATED BY PATHOLOGICAL CHANGES IN PARACRINE SIGNALING AND MIRNA PREVALENCE

G. Ronan (1,2), F. Ketchum (1,2), N. Kowalczyk (2), N. Behnam (3), L. Çelebi (1,2) P. Zorlutuna (1,2,3,4)

(1) Bioengineering Graduate Program, University of Notre Dame, Notre Dame, IN, USA
(2) Aerospace and Mechanical Engineering Department, University of Notre Dame, Notre Dame, IN, USA
(3) Chemical and Biomolecular Engineering Department, University of Notre Dame, Notre Dame, IN, USA
(4) Harper Cancer Research Institute, University of Notre Dame, Notre Dame, IN, USA

INTRODUCTION

Doxorubicin (DOX), an anthracycline, is a powerful chemotherapeutic agent that has historically been used to treat cancers including breast, bladder, lungs, stomach, ovarian, thyroid, soft tissue sarcoma, multiple myeloma, lymphoma, and leukemia. Breast cancer in particular is the most common form of cancer in the United States and globally, affecting 1 in 8 women and comprising nearly 30% of yearly cancer diagnoses. While DOX and its nearly 2000 analogues have shown high success rates in mitigating or otherwise destroying breast cancer, anthracyclines have since demonstrated a high propensity for off-target toxicity. Among the most severe off target effects is off-target cardiotoxicity, with over 10% of women receiving DOX treatment developing acute cardiotoxicity immediately following treatment and approximately 2% of women developing severe cardiotoxicity up to 10 years post-treatment [1]. The mechanisms of this cardiotoxicity have remained elusive, more so in light of established system clearance of DOX within 48 h, and is the subject of intense debate in literature. We suggest that initial DOX exposure pathologically alters paracrine signaling behaviors of some myocardial cells in such a way that propagates DOX-induced cardiac dysfunction and over time results in the onset of cardiotoxic effects.

Local paracrine signaling has been a rising area of study, in part driven by enhanced capabilities to assess small extracellular vesicles (sEVs), commonly extracellular vesicles with diameters of less than 200 μm, as necessary agents of tissue homeostasis and analyze the composition and cargo of these vehicles. Exosomes, a particular subcategory of sEVs with known characteristic surface proteins, and exosome-like sEVs have been widely investigated as targeted agents for delivery of proteins, nucleic acids, and other biosignaling agents. These agents, when transported via sEV, have been shown to be active in angiogenesis, mitochondrial maintenance, immunomodulation, epithelial to mesenchymal transition, and other relevant processes, and have recently been suggested as active contributors to DOX-induced cardiotoxicity [2]. Currently in literature, individual exosomal miRNAs have been investigated as being decisive in this process, but no single miRNA dysfunction has been able to completely recapitulate a similar level of cardiotoxic effects. We suggest that, instead of individual miRNAs, exposure of the cardiac tissue to DOX causes a major shift in the total paracrine miRNA profile. This pathological shift drives further propagation of cardiac dysfunction, exacerbating damage over time. Furthermore, we suggest that the specific features of DOX-cardiotoxicity are mediated by a combination of key miRNAs rather than any single miRNA alone.

METHODS

We first benchmark in 2D culture what the effects of DOX cardiotoxicity are, as this term is poorly defined in literature [---]. We then demonstrate that these effects can be recapitulated in the absence of DOX via treatment of cells in 2D with sEVs in DOX-free media. In both cases, stem cell derived cardiomyocytes (iCMs), cardiac fibroblasts (iCFs), and endothelial cells (iECs) were treated with the treatment (10 nM DOX or 25 μg/mL sEVs) or a PBS blank for 48 h. The beating behaviors of iCMs were assessed by video analysis using in-house software to determine beating strength and rate, as well as by Ca^{2+} staining to obtain a ECG analogue for arrhythmia analysis. Arrythmia analysis was conducted in both time and frequency domains, with supporting sine wave decomposition. The activation and transdifferentiation of iCFs was assessed via immunostaining for α-SMA and cleaved caspace-3. Cell counting and population assessment was performed via ImageJ. Metabolic activity of cells was measured via AlamarBlue, and ROS production was measured via colormetric ROS assay.

3D models were constructed using a combination of gelatin methacrylol (GelMA) and collagen and we seeded with a combination of iCMs and iCFs. Gels were stable and began tissue-like beating within 7 days of seeding. iCMs were kept constant throughout all trials, and

iCFs were treated with a PBS blank or 10 nM DOX for 48 h before seeding. Beating analysis and Ca^{2+} analysis were performed on the 3D models as on the 2D to assess overall beating behavior.

sEVs were isolated from conditioned media via typical exosome ultracentrifugation protocol. Isolated sEVs were assessed via nanoparticle tracking analysis (NTA) and the absence of DOX inside sEVs was verified by UV-Vis spectrophotometry. Surface protein ratios of the sEV population from normal and DOX-treated cell conditioned were assessed via western blot. The contents of sEVs was isolated using a exosomal miRNA isolation kit and purified. miRNA profiling was performed using the Nanostring system to obtain a whole human miRNA profile. Potential target miRNAs were selected via unsupervised analysis of the profile and pathway analysis was performed using the MetaCore pathway analysis software.

RESULTS

Beating analysis of iCMs in 2D culture revealed that treatment with DOX significantly decreased beating velocity ($p < 0.01$, Figure 1A), but not beating rate (Figure 1B). Treatment with sEVs showed an even greater decrease in both beating velocity ($p < 0.001$, Figure 1A) and rate (Figure 1B), though beating rate decrease remained non-significant. ROS production was also increased in DOX-treated iCMs compared to the control ($p < 0.05$), which was recapitulated by sEV treatment ($p < 0.05$). Treatment of iCFs revealed that DOX significantly increased α-SMA expression relative to the control ($p < 0.005$) which was only partially recapitulated by sEV treatment ($p < 0.01$) (Figure 1D). Ca^{2+} analysis of 2D iCM cultures revealed the both DOX and sEV treatment substantially disrupted regular beating patterns despite non-significantly affecting beating rate (Figure 1E). Similar effects were observed in the 3D model comparing control and pre-treated cells.

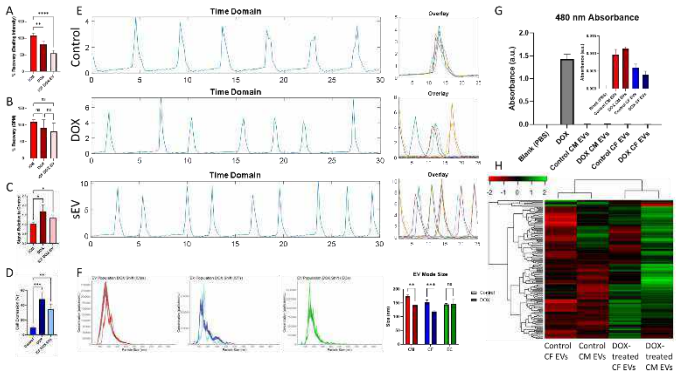

Figure 1: Analysis of iCMs provided beating velocity (A), beating rate (B), and ROS production (C) for control (red), DOX (dark), and sEV (light) treatments. Staining of iCFs for α-SMA expression (D) for control (blue), DOX (dark), and sEV (light) treatments. Ca^{2+} staining of iCMs provided beating signals (E) for the control and treatment conditions, with signals overlaid by average period. NTA of sEVs for control (light) or DOX (dark) size distribution and quantification of mode shift (F). UV-Vis spectrophotometry results to assess the presence or absence of DOX in isolated sEVs (G). Heatmap for unsupervised selected targets from the Nanostring miRNA profiling (H). * $p < 0.05$

Analysis of the sEVs via NTA revealed a significant decrease in the mode size of sEVs of iCMs ($p < 0.01$) and iCFs ($p < 0.005$) in cells treated with DOX for 48 h, but not in iECs. Western blot also showed significantly increased CD63 expression in iCM sEVs ($p < 0.001$) and iCF sEVs ($p < 0.05$), and significantly increased TSG101 expression in iCM sEVs ($p < 0.005$) when comparing DOX-treated cells to negative controls. UV-Vis spectrophotometry revealed that the isolated sEVs did not contain DOX (Figure 1G).

Nanostring analysis revealed a substantial shift in sEV miRNA populations between control and DOX-treated cells (Figure 1H). MetaCore pathway analysis of these miRNAs further implicated 14 miRNA targets as directly contributing to DOX-induced cardiotoxicity, and identified several more miRNAs of interest. MetaCore also revealed sEV miRNA activity in pathways associated with desirable DOX functioning.

DISCUSSION

In 2D culture we were able to first demonstrate results consistent with clinically observed symptoms of DOX cardiotoxicity. In particular, decrease in beating strength and substantial dysregulation of beating behavior without significantly affecting the heart rate overall are common symptoms of DOX cardiotoxicity. We also demonstrated that DOX significantly affects the phenotype of CFs, the cells in the heart primarily responsible for managing the microenvironment and paracrine homeostasis. Furthermore, we showed that these effects were not DOX-dependent, and could be propagated in the absence of DOX via paracrine signaling from cells that had been previously exposed to DOX treatment. This indicates that direct DOX exposure is not vital for the overall onset of cardiotoxicity symptoms, and provides some insight into how symptoms may present in long-term patients (up to 10 years post-treatment).

We also showed that these effects are driven, at least in part, by substantive changes to the sEV profile of cells affected by DOX. DOX-treated cells showed smaller overall sEV profiles, a shift which we have previously shown to be associated with aging and risk of cardiovascular disease. This is corroborated with the increased observable expression of CD63 and TSG101, which we have also previously shown to be correlated with the reperfusion/oxidative stress phase in myocardial infarction. Furthermore, these changes are not driven by the transport of DOX in sEVs, as the isolated sEVs do not contain DOX, but are instead driven by changes in the paracrine miRNA profiles of these cells. In the treatment of cancer this shift is likely advantageous, as we see via pathway analysis that miRNAs can provide a supporting role in the intended function of chemotherapy on a local level. In the heart, however, we also see that DOX treatment stimulates increased expression of miRNAs which inhibit vital pathways of cardiac homeostasis. In particular, 14 miRNAs acting synergistically across 4 pathways, the disruption of which are known to be causal for arrhythmias and heart failure, are likely a major driving force in the propagation and onset of DOX-induced cardiotoxicity. Further study of these target miRNAs, as well as other DOX-induced changes in paracrine signaling, will help elucidate the cause of long-term DOX-cardiotoxicity and aid in the development of preventative measures.

ACKNOWLEDGEMENTS

NIH Award # 1 R01 HL141909-01A1
NIH Award # 1 R01 CA275423-01A1

REFERENCES

[1] Chatterjee, K., Zhang, J., Honbo, N. & Karliner, J. S. Doxorubicin Cardiomyopathy. *Cardiology* 115, 155 (2010).

[2] Tian, C. et al. Potential of exosomes as diagnostic biomarkers and therapeutic carriers for doxorubicin-induced cardiotoxicity. *Int J Biol Sci* 17, 1328 (2021).

[3] Rhea, I. B. & Oliveira, G. H. Cardiotoxicity of Novel Targeted Chemotherapeutic Agents. *Curr Treat Options Cardiovasc Med* 20, 1–10 (2018).

SB^{3}C 2024
Summer Biomechanics, Bioengineering and Biotransport Conference
June 11–14, 2024, Lake Geneva, WI, USA

PHOTOSENSITIZER-MEDIATED LOW-LEVEL LIGHT EXPOSURE ALTERS THE STIFFNESS OF NONPREGNANT AND PREGNANT HUMAN CERVIX TISSUE

Daniella M. Fodera[1], Jiashuai Fan [2], Aidan M. Therien[3], Serena R. Russell[2], Christine P. Hendon[3], Joy Vink[4], Kristin M. Myers[2]

[1]Department of Biomedical Engineering, Columbia University, New York, NY, USA
[2]Department of Mechanical Engineering, Columbia University, New York, NY, USA
[3]Department of Electrical Engineering, Columbia University, New York, NY, USA
[4]Department of Obstetrics, Gynecology, and Women's Health, University of Hawaii, Honolulu, HI, USA

INTRODUCTION

Mechanical softening and dilation of the cervix are necessary for the safe passage of the fetus during labor and rely on a timely process of cervical remodeling [1–2]. Premature cervical remodeling is the final common pathway for many etiologies of preterm birth, occurring in 10% of all pregnancies, and is associated with high rates of perinatal morbidity and mortality [3–4]. Current therapeutic interventions to delay cervical remodeling are extremely limited, and a critical need exists for developing novel, noninvasive solutions [3–4].

Photobiomodulation (PBM) has recently emerged as a technique that utilizes low-level light exposure to alter cell and tissue functionality [5]. Previous work has shown the ability of light on the visible to near-infrared spectrum (400–1100 nm) to promote wound healing, reduce inflammation, and alter the mechanical properties of collagenous soft tissues [6–10]. Notably, ultraviolet (UV) light (100–400 nm), in combination with the photosensitizer riboflavin (Rb), already exists as an FDA-approved method to stiffen the human cornea in cases of keratoconus [6]. Similarly, blue light (450–495 nm), when coupled with Rb, has been shown to increase the stiffness of connective tissues by 1.8–3.5 fold *ex vivo* and is an attractive alternative to UV light due to its decreased cytotoxic effects [7–8]. Collagen cross-linking is well understood to be the primary mechanism of photosensitizer-mediated stiffening in cases of UV and blue light [6–7]. Additionally, red/infared (IR) light (>600 nm) alone has been shown to accelerate collagen deposition and increase the tensile strength of skin tissue by 100–300% [9–10].

It has yet to be investigated whether similar effects of light exposure can be successfully applied to the human cervix as a possible therapy for obstetric disorders. Building off the literature's established methodology, this study seeks to evaluate the effect of low-level light exposure on the stiffness of the human cervix in nonpregnant (NP) and pregnant (PG) states *ex vivo*.

METHODS

In accordance with IRB approval at Columbia University Irving Medical Center, human cervical tissue was collected from NP (N = 5) and third-trimester PG (N = 3) women undergoing total hysterectomies and stored at -80°C. Thawed cervical tissue was dissected in the radial direction into 3-mm-thick specimens and microtomed prior to testing (Fig. 1). Using a customized LED light array, two samples from each patient were exposed to UV (390 nm), blue (450 nm), or red (680 nm) light +/- 1% Rb solution (Table 1, Fig. 1). For each imaging session, one control (No light - Rb) sample was tested per patient. A second control condition (No light + Rb) was not included in this study since preliminary data suggested that Rb alone did not alter tissue stiffness.

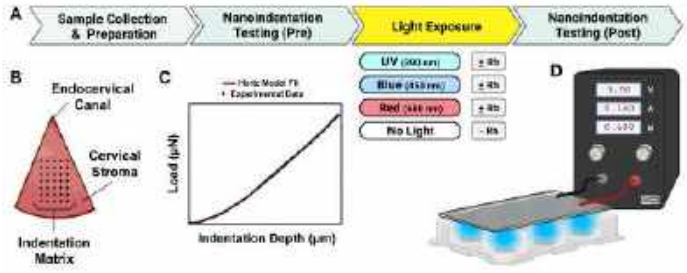

Figure 1: Experimental Methodology: (A) Experimental workflow. (B) Schematic of a cervix tissue specimen marked with a grid of indentation points. (C) Representative load-indentation data fitted with the Hertzian contact model. (D) Schematic of customized light array set-up.

Spherical nanoindentation (Piuma, Optics11Life, Amsterdam, NL) was employed to determine tissue stiffness in this study. Each sample was mechanically tested before and after light treatment to assess relative stiffness changes on an individual basis. Using a 50 μm probe radius (R) and indentation depth (δ) of 4 μm, thirty-five discrete indentation points, spaced 500 μm apart, were measured for each sample with a load-unload protocol (Fig. 1). Tissue stiffness (E_r) in the linear elastic regime was determined by fitting the data with the Hertzian contact model in MATLAB.

Statistical analysis of the nanoindentation data was performed in GraphPad Prism 9.4.0. Normality of the data was first assessed with Q-Q plots. Since the data did not exhibit a Gaussian distribution, a logarithmic transformation was applied to the data prior to statistical analysis. To assess individual sample differences in stiffness before (E_{pre}) and after (E_{post}) light

exposure, a two-tailed t-test was performed on all indentation points ($p < 0.05$). Mean stiffnesses for each sample were calculated and linearly transformed back. Mean relative stiffness change ($\bar{E}_{post}/\bar{E}_{pre}$) was then calculated for each sample. Overall differences across light exposure conditions were assessed with an ordinary one-way ANOVA followed by Šídák multiple comparison tests.

Table 1: Summary of light exposure parameters.

Light Condition	Power (mW/cm^2)	Current (mA)	Time (min)
UV (*385 nm*)	2.26	160	50
Blue (*450 nm*)	2.475	133	45.5
Red (*680 nm*)	1.28	130	88

RESULTS

Prior to light exposure, the baseline stiffness of NP and PG cervical tissue was determined to be 2.258 ± 2.03 kPa and 0.814 ± 0.3 kPa, respectively. In the presence of Rb, UV and blue light stiffened both NP and PG cervical tissue by 2–3 fold on average and were statistically different than their respective no-light controls (Fig. 2). On an individual sample basis, UV + Rb stiffened 8/10 NP and 6/6 PG samples, while Blue + Rb stiffened 6/10 NP and 6/6 PG samples. In the absence of Rb, on average, UV and blue wavelengths had no statistically significant effect on tissue stiffness for NP and PG samples relative to no-light controls (Fig. 2). However, on an individual sample basis, UV - Rb softened 6/10 NP and 1/6 PG samples, while Blue - Rb only softened 1/10 NP and 1/6 PG samples. Interestingly, red light exposure with and without Rb had no consistent effect on tissue stiffness compared to no-light controls (Fig. 2). Yet, individually, Red + Rb only stiffened 1/10 NP and 1/6 PG tissues, while Red - Rb softened 3/10 NP and 1/6 PG samples. As expected, no change in stiffness was observed on average for the no-light control condition, although individual samples exhibited both increases and decreases in stiffness. Given the large degree of both intra- and inter-sample heterogeneity in stiffness for all pre-tested cervix tissues, the effect of light exposure was not statistically significant on unnormalized stiffness values.

DISCUSSION

This study demonstrates, for the first time, the capacity of low-level light therapy to alter the mechanical properties of the NP and PG human cervix *ex vivo*. Specifically, both UV and blue light exposure in the presence of the photosensitizer Rb have a stiffening effect on NP and PG cervix tissue. Relative stiffness changes observed in this study are on par with similar experiments conducted on collagenous soft tissues in the literature [7-10]. Contrary to our expected results, red light treatment had no consistent effect on tissue stiffness with and without Rb.

In line with the existing literature, we posit that the primary mechanism of tissue stiffening by UV and blue light in the cervix is achieved through direct alterations of the extracellular matrix (ECM) components, specifically collagen cross-linking mediated by an oxidative deamination reaction [6–7]. We plan to quantify the amount of collagen cross-linking in our cervical specimens in follow-up experiments with standard biochemical assays. In contrast, given the absence of any mechanical change in tissues

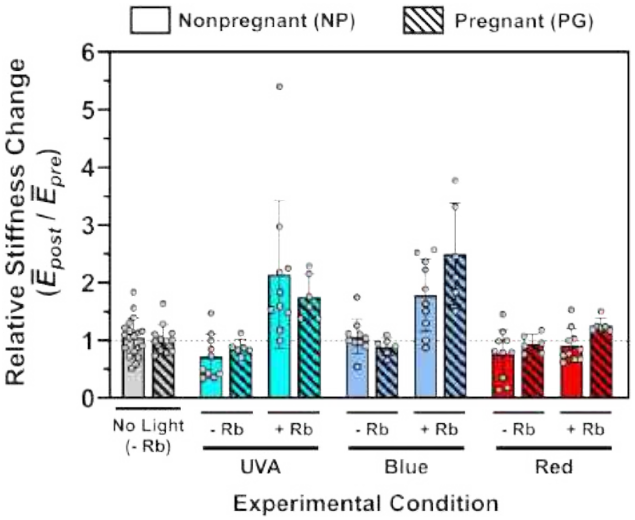

Figure 2: Summary of relative stiffness changes to UV, blue, and red light exposure.

exposed to red light, we hypothesize that an active cellular component is required as an intermediary to generate the stiffening effects reported in the literature and induce ECM remodeling [9–10]. Notably, the cervical tissues utilized in this study underwent multiple freeze-thaw cycles prior to testing and are not believed to contain any viable cellular components. This may explain the lack of any observed mechanical change to red light exposure. Future studies will investigate the contractile and stiffness response of fresh *ex vivo* cervical tissues exposed to UV, blue, and red light in order to disentangle whether the primary mechanism of change is cell- or ECM-mediated.

It is presently unknown whether the stiffening effect measured on the micrometer length scale in this study results in an overall increase in tissue strength under larger deformation. Further, we seek to determine whether light exposure alters the inherent ductility of cervix tissue and results in a material that is more brittle. Follow-up experiments will mechanically test samples in this study under tension with a load-to-break protocol. Lastly, an open question remains as to whether this stiffening effect observed for cervix tissue is maintained over a period of time and is substantial enough to prevent the adverse outcomes associated with spontaneous preterm birth. Additional *in vivo* and *ex vivo* studies are needed to determine if photobiomodulation will be an effective tool to delay human cervical remodeling in pregnancy.

ACKNOWLEDGMENTS

Research was supported in part by the Iris Fund and Eunice Kennedy Shriver National Institute of Child Health & Human Development Grant (1R21HD106061-01). The content is solely the responsibility of the authors and does not necessarily represent the official views of the National Institutes of Health.

REFERENCES

[1] Timmons et al. *Trends Endocrinol Metab*. 2010. [2] House et al. *Semin Perin*. 2009. [3] ACOG Practice Bulletin, No. 234. *Obstet Gynecol*. 2021. [4] CDC/National Center for Health Statistics. 2022. [5] Dompe et al. *J Clin Med*. 2020. [6] Belin et al. *Cornea*. 2018. [7] Schuldt et al. *Acta Ophthalmol*. 2015. [8] Kang et al. *Materials (Basel)*. 2021. [9] Stadler et al. *Lasers Surg Med*. 2001. [10] Solmaz et al. *Lasers Med Sci*. 2017.

EFFECT OF COLLAGEN ACCUMULATION ON RIGHT VENTRICULAR PASSIVE VISCOELASTICITY WITH PULMONARY HYPERTENSION DEVELOPMENT

Yuecheng, Wang (1) Kristen E. LeBar (2), Zhijie Wang (1,2)

(1) School of Biomedical Engineering, Colorado State University, Fort Collins, CO, USA
(2) Department of Mechanical Engineering, Colorado State University, Fort Collins, CO, USA

INTRODUCTION

Heart failure, often precipitated by increased right ventricular (RV) afterload in conditions like pulmonary hypertension (PH), is critically influenced by the RV free wall's (RVFW) viscoelastic properties. These properties, defined by the interaction between elasticity and viscosity, are largely determined by the myocardial extracellular matrix (ECM), specifically collagen content [1,2]. While prior ventricular hyperelastic research has delineated the role of collagen in myocardial elasticity [5,6,7], its impact on viscoelasticity, particularly under biaxial stress, is not well established.

It is accepted that the low-strain elasticity of RV is dominated by myofibers whereas the high-strain elasticity is dominated by collagen fibers [5,6,7]. Moreover, our own research on ovine ventricles has shown positive correlations between high-strain elastic modulus and functional decline of the RV [1]. The accumulation of collagen, particularly type III collagen, is identified in PH ovine RVs, and it is negatively correlated with stroke volume and positively correlated with RV hypertrophy indices [4]. Therefore, collagen deposition during PH progression contributes to the RV mechanical changes and may play a role in regulating RV performance. While the role of collagen in cardiac tissue biomechanics has been extensively investigated, its impact on ventricular viscoelasticity remains largely unknown. To our knowledge, the only study investigating the role of collagen in RV viscoelasticity is performed in papillary muscles, where one dimensional passive viscoelasticity was characterized before and after serine protease (plasmin) treatment to degrade collagen [5]. In both healthy and PH groups, collagen degradation led to decreased elasticity and viscosity in cat papillary muscles. However, the viscoelasticity characterization is simplified, and the anisotropic (biaxial) viscoelasticity is not quantified.

In this study, we sought to determine the role of collagen fibers in the passive, biaxial viscoelasticity of the RVFW with PH development. PH was induced in adult rats and biaxial stress relaxation tests were performed on the RV tissues with and without collagenase treatment. Viscoelastic changes after collagen degradation indicated significant decreases in relaxation modulus and stored and dissipated energies, as well as trends of decreased relaxation rate. These findings reveal a novel role of collagen in the viscoelastic properties of the hypertrophied RV.

METHODS

All procedures were approved by Colorado State University IACUC. Adult male Sprague-Dawley rats, aged 9-12 weeks, received a single intraperitoneal injection of monocrotaline (MCT) at a dose of 60 mg/kg to induce PH. The rats were then housed under standard laboratory conditions for 3 weeks post-injection. Following euthanasia, the RVFW was rapidly excised and immersed in a cardioplegic solution containing 30mM 2,3-butanedione monoxime (BDM) maintained at physiological temperature (37°C) for a minimum of 30 minutes. This step ensured the cessation of myocardial contractions. The longitudinal (L) axis of the tissue samples was aligned from apex to base.

Equibiaxial mechanical tests were performed to quantify passive viscoelastic properties of the RVFW. The tissue was preloaded to 0.025N, followed by 15 cycles of equibiaxial preconditioning to stabilize tissue mechanical behavior. Samples were subjected to equibiaxial stretch to 20% strain at physiological stretch rates of 5Hz and 8Hz, simulating resting and acute stress heart rates, respectively. Following baseline mechanical characterization, the tissues were treated with collagenase (6 mg/mL, Sigma-Aldrich) at 37°C for 1 hour to enzymatically degrade the collagen fibers. Subsequent mechanical testing was performed under the same conditions as the baseline measurements. A rest period of 10 times that of the testing period were applied after each test to ensure complete recovery of the tissue.

The Second Piola-Kirchhoff (2nd PK) (S) stress was calculated using the following equation:

$$S = \frac{F}{A_0 \lambda}$$

Where F represents the force, A_0 is the initial cross-sectional area, and λ is the stretch ratio, which was maintained at 1.2 during the relaxation. Next, the relaxation modulus, stored energy (W_S) and dissipated energy (W_d), were computed at 100 seconds post-peak stress to quantify the elasticity and viscosity of the RV myocardium. The V/E ratio was derived as W_d/W_S. The relaxation rate was derived as the slope of the linear fitting to the logarithmic plots of the stress relaxation curve using least square analysis. These methods have been established [2,3]. Paired student t-test was used to compare before and after collagenase treatment. Data is shown as mean ± SD**.** A p-value of less than 0.05 was considered statistically significant.

RESULTS

Collagen Degradation Diminishes Hypertrophied RV Viscosity and Elasticity

The biaxial mechanical testing post-collagenase treatment revealed a pronounced decline in the mechanical strength of the right ventricular (RV) myocardium. Figure 1 illustrates a significant drop of approximately 50% in peak stress at both 5Hz and 8Hz testing frequencies. Correspondingly, W_d and W_S, indicators of viscous and elastic properties respectively, showed substantial decreases (Table 1). Similar changes were observed at the acute stress condition (8Hz) (Table 1) and in the circumferential direction (data not shown). Finally, the relaxation modulus reduced significantly under both testing conditions, with a larger degree of decrease at 8Hz (Table 1).

Stress Relaxation Rate Tends to Decrease and V/E Ratio Remains Constant after Collagen Degradation

The relaxation rate, a measure of the kinetic decay in stress, showed a strong trend of decrease (p=0.1 for n=2 samples) after collagen degradation, although the change did not reach significant values (Table 1). This implies that the rate at which stress dissipates within the RV myocardium is reduced. Meanwhile, we observed no significant changes in the V/E ratio, suggesting similar degrees of reduction in viscosity and elasticity after degradation of collagen.

DISCUSSION

Collagen deposition is a hallmark of RV failure secondary to PH development and contributes to myocardial stiffening. But how it impacts the RV viscoelasticity is unknown. This study originally investigated the impact of collagen on RVFW passive viscoelasticity with PH development. We observed marked reductions in RVFW viscosity and elasticity as well as other viscoelastic changes after collagen degradation. These changes demonstrate a significant role of collagen in the hypertrophied RVFW viscoelastic properties.

The reductions in elasticity and viscosity after collagen degradation were observed in the longitudinal direction (apex-to-base) of the RV (Table 1). We observed marked reductions in W_d and W_S in the circumferential direction as well, and the degree of reduction was more pronounced than the longitudinal direction (data not shown). But more samples are needed to confirm the observation. These changes not only indicate a significant contribution of collagen to RVFW viscoelasticity, but also suggest an anisotropic effect of collagen in different directions.

Moreover, we saw a strong trend of decrease in relaxation rate after collagen removal, which indicates an altered viscous behavior of the tissue. The removal of collagen will make the myofibers to be dominant in the mechanical behavior of the tissue, even at large strains. Thus, this change may reflect the intrinsic viscous behavior of myofibers.

Finally, we did not observe marked changes in the V/E ratio, although the values showed a mild tendency to increase after collagen degradation. The V/E ratio is a parameter that evaluates the relative strength of viscosity and elasticity in a material. A V/E ratio >1 indicates that the viscous behavior overweighs the elastic behavior, and vice versa. Myofibers as muscle cells may exhibit a larger V/E ratio than fibrous collagen protein network due to the presence of cytoplasmic fluid. The further investigation of this parameter may provide a complete view of the combined effects of viscosity and elasticity on cellular or organ functions.

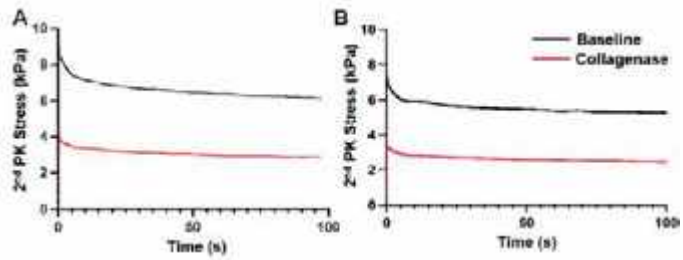

Figure 1. Raw stress-relaxation curves obtained at 5 Hz (A) and 8 Hz (B) before (Baseline) and after collagenase treatment (Collagenase) in the L direction.

Table 1. Changes in diseased RV viscoelasticity with collagen degradation measured by various viscoelastic parameters at 5Hz and 8Hz. Data shown was obtained in the L direction.

	Baseline	Collagenase Treatment	P-Value
At 5 Hz (resting condition)			
W_d (kPa)	**222.3±73.2**	**135.5±14.4**	**0.01**
W_S (kPa)	**471.5±234.3**	**220.4±112.5**	**0.04**
Relaxation Rate	**0.32±0.09**	**0.17±0.021**	**0.1**
Relaxation Modulus (kPa)	**31.0±17.1**	**15.77±6.37**	**0.006**
V/E Ratio	**0.49±0.10**	**0.68±0.36**	**0.28**
At 8 Hz (acute stress condition)			
W_d (kPa)	**187.6±5.3**	**97.7±15.1**	**0.01**
W_S (kPa)	**417.7±193.1**	**194.6±80.3**	**0.04**
Relaxation Rate	**0.24±0.01**	**0.10±0.06**	**0.1**
Relaxation Modulus (kPa)	**27.3±11.6**	**11.8±7.4**	**0.006**
V/E Ratio	**0.50±0.22**	**0.56±0.31**	**0.28**

REFERENCES

[1] Liu, W et al., *J. Integ. Cardio*, 2020.
[2] Liu, W et al., J. Biomech. Eng., 2021.
[3] Liu, W. et al., Front. Bioeng. Biotechnol., 2023.
[4] Nguyen-Truong, M. et al., AMEM, 2020.
[5] Stroud JD, et al. Physiol Heart Circ Physiol. 2002.
[6] Avazmohammadi, et al. Biomech Model Mechanobiol. 2017
[7] Avazmohammadi, et al. Ann Biomed Eng., 2019

COMPARATIVE LIQUID FLOW ANALYSIS IN BATTERY-POWERED SUCTION DEVICES FOR ADVANCED AIRWAY MANAGEMENT

Maria J. Londono (1), Saketh R. Peri (1,3), Zach Fallon (2), David DiRocco (2), David Restrepo (2), Robert A. De Lorenzo (1,2,3), R. Lyle Hood (1,2,3)

(1) Biomedical Engineering, The University of Texas at San Antonio, San Antonio, Texas, USA
(2) Mechanical Engineering, The University of Texas at San Antonio, San Antonio, Texas, USA
(3) Department of Emergency Medicine, The University of Texas Health Science Center at San Antonio, San Antonio, Texas, USA

INTRODUCTION

Airway compromise is the second most common cause of preventable death on the battlefield, accounting for over 10% of total casualties [1]. Portable suction devices are essential in a combat medic's airway management kit. These devices clear the airway by removing blood, vomit, teeth fragments, mud, and other life-threatening obstructions. Designated as a top priority by the Committee on Tactical Combat Casualty Care (CoTCCC), airway control is paramount [2]. Furthermore, suction devices serve additional roles such as tracheal suction for intubated patients, stomach suctioning for patients with nasogastric or orogastric tubes, and addressing fluid accumulation in the chest's pleural cavities [3]. Despite their life-saving capabilities, a significant number of combat medics and civilian first responders opt not to carry these devices due to issues such as excessive weight (in the case of battery-powered devices) and/or insufficient suction (for manually powered ones).

This research assessed the liquid flowrates of three suction devices: the novel Suction Combat Ready Advanced Multifunctional Machine (SCRAMM) and two commercially available devices, Zoll 330 Multifunction Aspirator, and Impact (now Zoll) Ultra-lite 326 / 326M Suction Unit, chosen for their similarity and their higher frequency of use in the US Military Forces.

The goal was to characterize liquid flowrates per the ISO10079-1 standard, anticipating benefits for military end users through SCRAMM's unique modifications. SCRAMM offers high performance with reduced weight.

METHODS

A series of surveys and interviews were conducted by the team through the NSF I-CORPS program to establish priorities in portable suction characteristics relevant to prehospital care. Interviews were conducted (102 in total) with AF end users including paramedics, emergency medical technicians, supply chain personnel, manufacturing representatives, U.S. Food and Drug Administration (FDA) consultants, emergency medicine doctors, US Special Forces, combat medics, and police officers in Texas and the Washington D.C. area [4].

Based on this information, product specifications were defined, and SCRAMM was designed to meet these requirements (due to intellectual property and patent process, some detailed information about SCRAMM was withheld). Liquid Flowrate characterization tests were conducted for the three devices.

To test liquid evacuation flowrates, three solutions were prepared: water, a blood phantom mix (276ml of glycerol + 1224ml of distilled water), and a vomit simulant mix (10g of xanthan gum + 1000ml of distilled water + 100g of glass beads) following ISO 10079-1 standard. The test setups for the three liquids were identical.

A 1L liquid-filled reservoir was placed on a load cell (model LC62SP-6KG, Omega) to track the mass of evacuated fluid during suction. A MATLAB timer was activated when suction started. Simultaneously, a pressure transducer measured vacuum pressure at the suction tube tip. All devices were operated at peak settings for 30 seconds. After the elapsed time, the suction tube was removed, and the experiment reset. Measurements included

time elapsed, initial/final reservoir weight, max. vacuum pressure, liquid volume evacuated, and liquid flowrate.

Each device underwent four tests for each liquid, totaling 36 individual tests. Figure 1 illustrates the experimental setup for liquid flowrate characterization.

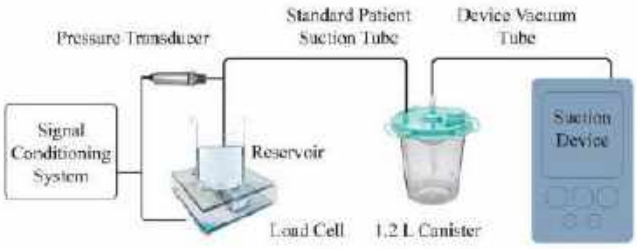

Figure 1: Liquid flowrate test setup

RESULTS

The weight, overall dimensions, and volume of the three devices are shown in Table 1. SCRAMM exhibited a product weight reduction of 29.9% in comparison to its market competitors.

Table 1: Physical properties of the three studied devices

Device	Weight (kg)	Overall Dimensions (cm)	Volume (cm^3)
SCRAMM	3.4	31.5 x 20.5 x 12.5	8071.9
Zoll 330	4.8	31.0 x 23.0 x 11.5	8199.5
Impact 326M	4.9	31.5 x 25.0 x 13.0	10237.5

Liquid flowrates for the three devices across water, blood analog, and vomit simulant with the mean values $\pm$ standard deviation (σ) are illustrated in Figure 2. Specifically, the liquid flowrates for SCRAMM ranged from 4.13 to 1.49 L/min, for Zoll 330 from 6.49 to 2.93 L/min, and for Impact 326M from 6.42 to 2.93 L/min. All devices exceed the ISO 10079-1 standard of 1.2 L/min and the internal specification inferred from AF users of 1 L/min.

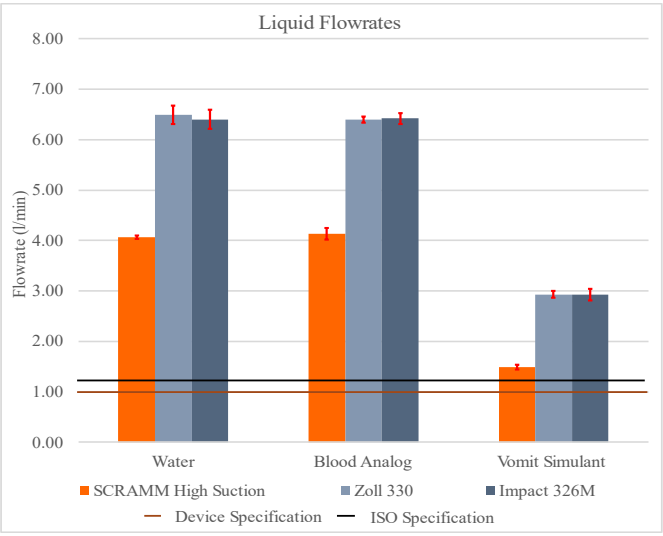

Figure 2: Liquid flowrate results

DISCUSSION

The smaller and lighter SCRAMM unit showed mostly lower flowrate compared to Zoll 330 and Impact 326M, yet still meets the ISO and end-user requirements for oropharyngeal suction. The higher flowrate of the two commercially available devices may be excessive as it is inefficient. Considering the challenges faced by battlefield medics and first responders, who frequently emphasize portability and maneuverability in tough settings, the weight reduction achieved by SCRAMM is especially noteworthy. This reduction fits in with the critical demand for lightweight medical equipment in the field in addition to improving the device's use.

In conclusion, the characterization of liquid flowrates for Impact 326M, Zoll 330, and SCRAMM suction devices highlights improved efficiency of SCRAMM with respect to weight. As future work, further testing will be conducted focusing on characterizing air flowrate, obstruction frequency and noise level during suction for all three devices. Lastly, additional to characterization, end user testing in real and/or simulated environment will be conducted to validate requirements, usability, and standards.

ACKNOWLEDGEMENTS

This work was primarily supported by the AFWERX Direct to Phase II SBIR contract number FA864922P0928.

Research was supported by EmergenceMed, LLC, San Antonio, TX, a university startup, and RAD and RLH are principals in the company.

REFERENCES

[1] Lairet, J. R. et al. Prehospital interventions performed in a combat zone: a prospective multicenter study of 1,003 combat wounded. Journal of Trauma and Acute Care Surgery 73, S38-S42, 2012

[2] jsomonline.org. Journal of Special Operations Medicine, 2017

[3] De Lorenzo, R. A. et al. Summary of Findings and Recommendations for Suction Devices for Management of Prehospital Combat Casualty Care Injuries. Texas University Medical School at San Antonio: San Antonio, TX, USA, 2017

[4] De Lorenzo, R. A. et al. Summary of Findings and Recommendations for Suction Devices for Management of Prehospital Combat Casualty Care Injuries. Defense Technical Information Center (DTIC), 2017

ASSESSMENT OF CLOT ADHESION STRENGTH ON ENDOTHELIAL CELLS AND BIOCOMPATIBLE MATERIALS

Vikas Kannojiya (1), Sara E. Almasy (1), Ian Goetz (1), Jose L. Monclova (1), Francesco Costanzo (2), Keefe B. Manning (1,3)

(1) Department of Biomedical Engineering, The Pennsylvania State University, University Park, Pennsylvania, USA
(2) Department of Engineering Science and Mechanics, The Pennsylvania State University, University Park, Pennsylvania, USA
(3) Department of Surgery, Penn State Hershey Medical Center, Hershey, Pennsylvania, USA

INTRODUCTION

Arterial embolism is a critical global complication that may result in disability and death [1] and occurs when a blood clot becomes lodged in the narrow arterial network. A locally formed clot in an artery or on blood-contacting medical devices may dislodge and travel through the vascular tree, blocking narrower blood vessels. This obstruction can lead to further complications such as myocardial infarctions and stroke [2]. Embolization may depend on the adhesion strength of the clots on the underlying surface. Therefore, this study aims to characterize the adhesion strength of blood clots on endothelial cells and common biocompatible materials using experimental and numerical techniques.

METHODS

Endothelial cells (representing the innermost layer of an artery) and commonly used materials in blood contacting medical devices like Nitinol and Titanium were considered in this study. Human aortic endothelial cells (Millipore Sigma) were passaged on glass slides and grown to confluency (in approximately 3 to 4 days). Material samples of Nitinol and Titanium were cut into 25 mm^2 pieces and cleaned with ethanol to remove any residue.

Clots were created using human blood, following a collection protocol approved by Penn State's institutional review board. Blood was anticoagulated with 0.32% weight sodium citrate. The extracted blood was separated into red blood cells, platelet-rich plasma (PRP), and platelet-poor plasma (PPP) via centrifugation and reconstituted to 214 x 10^6 platelets per mL. Hematocrit was controlled in clots by adding 40% volume of red blood cells to form clots. To counter the effects of the anticoagulant, blood was recalcified with 20 mM calcium chloride ($CaCl_2$) and 0.25 NIH Unit/mL thrombin from human plasma (BioPharm, Bluffdale, UT, USA) to initiate blood coagulation. Recalcified blood (1 mL) was pipetted into cylindrical molds (14 mm diameter), which were placed on the samples. The clots were incubated at 37°C for 1 hour on the endothelial cell layer. Clots were incubated for 30 minutes, 1 hour, and 3 hours on Titanium and Nitinol to evaluate the temporal characteristics of clot adhesion.

Once the clots formed, the samples were removed from molds and attached to the bottom plate of a custom rig on a uniaxial load frame (Instron, Norwood, MA, USA) with a 50 N load cell. A suction pressure of 200 mmHg was applied at the top of the clot to grip the surface. Once the suction was applied, the specimen was loaded at a rate of 10% strain per second (based on sample height) until complete detachment from the sample, where peak stress and strain were recorded. Due to variability in coagulation and clot contraction, Multiple datasets (n = 6) were collected with six replicates (n = 6) from each test.

For the numerical simulation, a Kelvin-Voigt viscoelastic model was applied to the interior of the clot. The clot was assumed to be a circular cylinder of 10 mm in height and 14 mm in diameter, with a mass density of 1080 kg/m^3 [3]. A cohesive zone model, following an Oldroyd-B fluid like behavior, was imposed at the clot-material interface to describe the adhesion [4,5]. A displacement boundary condition is applied at the top surface of the clot using COMSOL Multiphysics (Stockholm, SWE).

RESULTS

The clot adhesion strength was quantified by measuring the stress required to detach the clot from the material surface. Figure 1 shows the distribution of detachment (peak) stress for clots adhered on endothelial cells, Titanium, and Nitinol surfaces. The data showed that incubation time influences the adhesion strength of the clots, and higher adhesion was noticed at longer incubation times for metallic surfaces. A positive correlation between time and detachment stress was observed on the Nitinol surface. On the other hand, a distinct clot adhesive behavior was noticed on the Titanium surface. Statistically, no significant difference was observed in detachment stress data for clots incubated for 30

minutes and 1 hour on the Titanium surface. However, a subsequent significant rise ($p < 0.001$) was observed with further prolonged incubation (3 hours) of the clots. Manivasagam and Popat [6] also reported a similar observation for clotting on non-treated Titanium surfaces. They reported no significant difference in whole blood clotting on the Titanium surface by measuring the plasma-free hemoglobin at 30 minutes and 45 minutes.

At 1 hour of incubation, comparable detachment stress was noticed on Titanium and endothelial cell surface (0.46 ± 0.06 kPa and 0.47 ± 0.20 kPa, respectively). Overall, the strongest adhesion of blood clots was noticed on the Titanium surface with a mean detachment stress of 1.06 ± 0.20 kPa at 3 hours of incubation, which was approximately 42% higher than clots on the Nitinol surface.

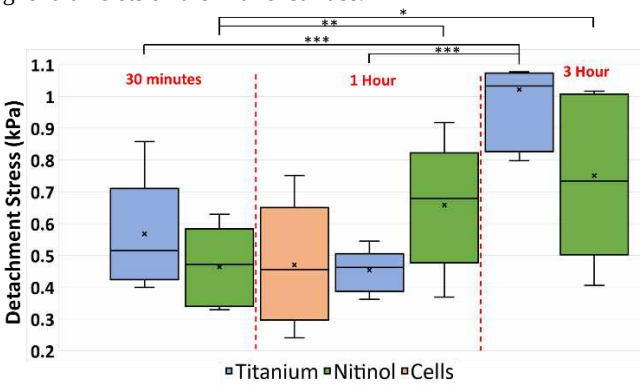

Figure 1: Data showing the distribution of detachment stress for clots attached to different surfaces. Statistical difference is measured in terms of p-value; a lower p-value signifies higher significance. The level of significance difference is represented by an asterisk (*) on the plot, where $p < 0.05$ = *, $p < 0.01$ = ** and $p < 0.001$ = ***.

To characterize clot deformation during detachment, moduli were calculated for clots formed on different surfaces (Figure 2). From the data, it was observed that shorter incubation periods result in lower modulus values. Here, a low modulus value signifies higher axial stretch in the clot. At the same incubation period, clots on endothelial cells undergo higher axial deformation during detachment than those on other materials. Notably, clots on the Titanium surface had higher moduli, were comparatively stable, and exhibited greater stiffness than clots formed on other materials.

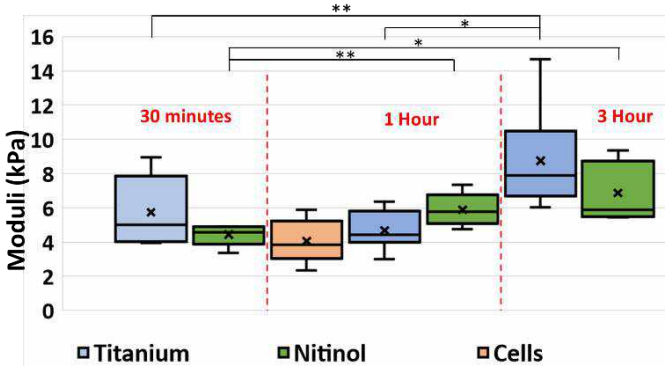

Figure 2: Data showing the distribution of blood clot moduli on Titanium, Nitinol, and endothelial cell layer.

Figure 3 compares the detachment pattern observed in the experimental setup with the viscoelastic simulation framework. From the experimental detachment pattern of clot (Figure 3(a)), it can be observed that the detachment was initiated from the bottom corners and then radiated inward. Further, a non-homogeneous attachment of clots on the surface was observed, leading to irregular detachment (a small clot fragment exhibits prolonged adherence to the substrate compared to the predominant clot mass). Similar detachment initiation is also seen in the displacement contour (in axial-direction) from the simulation prediction (Figure 3(b)).

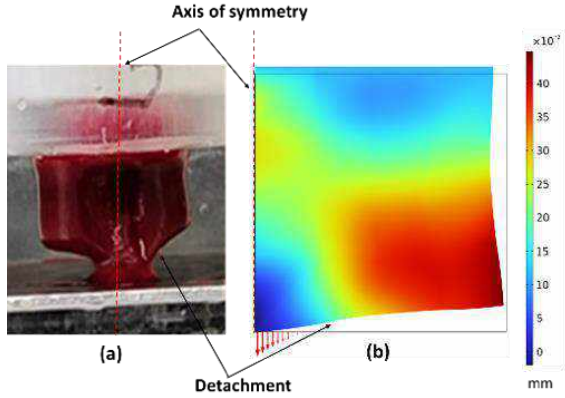

Figure 3: A comparison of clot detachment pattern observed in (a) experimental setup with a (b) Kelvin-Voigt viscoelastic simulation. The axisymmetric center view of a clot detachment simulation with a cohesive zone boundary was taken at t = 0.15 s.

DISCUSSION

The adhesion stress of whole blood clots on different surfaces was quantified. The data showed that clots on the Titanium surface adhered more strongly than other surfaces over time. The characterization of clot deformation in terms of moduli revealed the dynamic nature of its mechanical properties. Clots incubated for a shorter duration showed lower moduli and higher axial strain. In particular, clots on endothelial cells had the lowest moduli than other surfaces. The detachment analysis revealed a non-homogenous clot attachment at the surface, resulting in irregular detachment.

In numerical simulations, the adhesion between the clot and the surface was considered by implementing a cohesive-zone model, exhibiting an Oldroyd-B fluid-like behavior at the interface. The simulations predicted similar detachment patterns as observed in the experiments. Notably, the present simulation framework does not consider the characterization of cohesive zone in relation to material properties. As a future aspect of this work, the cohesive zone model will be tuned with the surface-specific properties. Moreover, in the forthcoming investigations, the temporal behavior of clot adhesion on the endothelial cell layer will also be investigated.

ACKNOWLEDGEMENTS

This research was supported, in part, by the Penn State Clinical Research Center in the Clinical and Translational Science Institute, U.S. NIH Grant HL146921, NSF CMMI-2017805, NIH T32GM108563, an Alfred P. Sloan and a Gates Millennium Scholarship.

REFERENCES

[1] Lyaker MR *et al.*, *Int J Crit Illn Inj Sci*, 3(1):77-87, 2013.
[2] Cho SM *et al.*, *ASAIO J*, 65(8):775-780, 2019.
[3] van Kempen T *et al.*, *Biomech Model Mechanobiol* 15 (2), 279-291, 2016.
[4] Good B *et al.*, *Biomech Model Mechanobiology*, 19(2), 761-778, 2020.
[5] Patki P et al., *Int J Numer Method Biomed Eng.*, 39(2), e3667, 2023.
[6] Manivasagam VK and Popat KC. *ACS Omega*, 5(14): 8108-8120, 2020.

COMPUTATIONAL CONSTRUCTION AND OPTIMIZATION OF A NOVEL TRI-TUBE HEART VALVE DESIGN

J. Li (1), Y. Yu (2), R.T. Tranquillo (2,3)

(1) Department of Mechanical Engineering, (2) Department of Biomedical Engineering, (3) Department of Chemical Engineering & Materials Science, University of Minnesota Twin Cities, Minneapolis, Minnesota, United States

INTRODUCTION

Tissue-engineered heart valve (TEHV) is a promising strategy to treat cardiovascular diseases by replacing the unfunctional heart valve with a bioprosthetic heart valve made of biological tissues. Our group has developed a novel pediatric tri-tube pulmonary valve that demonstrated growth capability in lambs [1]. Figure 1(a) illustrates the experimental construction of the tri-leaflet valve: three identical tubes were engineered and sutured together to form a closed valve, where tube materials are biologically engineered matrix grown in vitro from donor fibroblasts. However, the optimal design of the valve remains unclear.

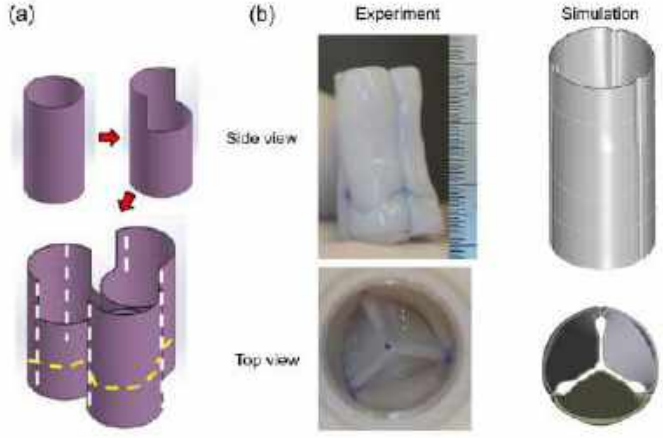

Figure 1: Heart valve conduit consists of three tubes. (a) The schematic of tri-tube constructions [1]. (b) Side and top view of a tri-tube tissue-engineered valve constructed in vitro and in silico.

An ideal design requires proper valve functionality, biocompatibility, and hemocompatibility during the cardiac cycle, which is closely related to the geometric design of the valve [2,3]. To facilitate optimization of the tri-tube valve geometry, we present a robust finite element-based study for in silico construction of the TEHV in Figure 1(a). We aim to identify an optimal design of the tri-tube valve based on the performance in a simulated closure under applied back pressure and gain an understanding of the hemodynamics for the optimal design during a cardiac cycle.

METHODS

In this study, we utilized finite element method (FEM) and optimization techniques to screen multiple valve designs. All simulations and optimization analysis were conducted with ANSYS commercial software.

To construct the valve, we applied an anisotropic hyperelastic material model (AHYPER strain energy law) to account for the highly circumferential alignment of fibers in the tubes and resulting leaflets, mimicking native leaflets [4]. The final geometry of the valve was determined by two design variables of the tube in Figure 2(a): leaflet height H and tube inner diameter D.

Following the experimental procedure in Figure 1(a), each valve was constructed by a two-step construction method using FEM shown in Figure 2(b): three identical engineered tubes were first flattened and then rolled up to form a closed ring. The cut side of each tube was facing inward and fixed to close the tube to form leaflets, mimicking the yellow suture line in Figure 1(a).

The performance of the designed valve was evaluated through a valve closure simulation. A back pressure (Figure 2(c)) ramping up to 1000 Pa (similar to peak pulmonary valve pressure gradient) within 1s was applied on the leaflets and valve wall distal to the leaflets [5]. The goal of the optimization was to identify the design points in the

parameter space of H and D that maximize coaptation area, minimize leaflet pinwheel index, and minimize peak stress, with equal importance placed on each objective.

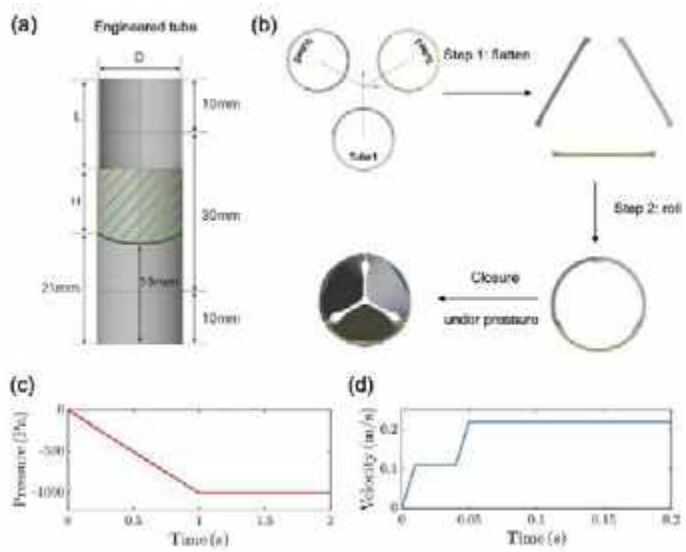

Figure 2: (a) Geometry of an engineered tube used for valve construction. (b) Two-step construction (top view) followed by a valve closure simulation under back pressure. (c) Pressure profile for the closure. (d) Velocity waveform for FSI simulation.

Finally, two-way coupled flow-structure interaction (FSI) simulations were performed for selected optimal designs to examine the hemodynamics. Figure 2(d) shows the velocity waveform for the inlet and the outlet pressure was set to zero. The blood rheology was assumed to be Newtonian. The FSI simulation was done by ANSYS System Coupling with Mechanical and Fluent modules.

RESULTS

Figure 3 presents two design points during the valve closure simulation for comparison. Case 2 indicates a better closure of the valve with a larger coaptation area, while leaflets in Case 1 merely contact that leads to a gap at the center. Case 2 also owns a smaller maximum equivalent stress. Both cases indicate that the peak stress occurred at the commissures.

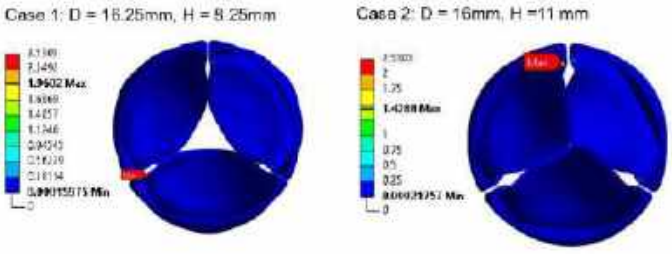

Figure 3: Maximum equivalent stress of two design points during valve closure simulation at t = 1.

Case 2 was further selected to examine the hemodynamics in a steady flow FSI simulation, with the evolution of velocity contour shown in Figure 4. With increasing inlet velocity, leaflets showed evident deformation and were pushed toward wall by the flow. Flow circulations were observed behind the leaflets. The complex fluid-structure interactions and elastic constitutive model also lead to oscillation of leaflets after inlet flow plateaued at t = 0.05s.

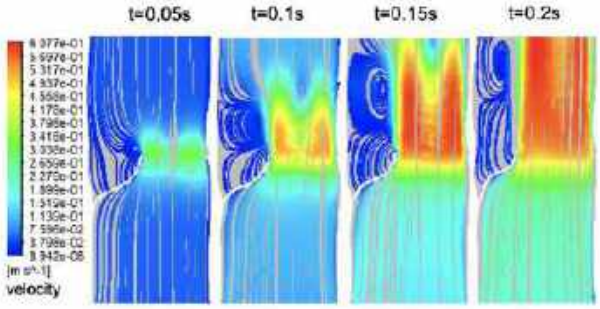

Figure 4: Evolution of velocity contour profile from a selected design point (Case 2 in Figure 3). Snapshots indicate a half slice of the valve, and the white line is a slice of one leaflet.

DISCUSSION

The geometrical design, namely the tube diameter D and the leaflet height H, strongly influences the performance of the tri-tube heart valve during closure simulation. As seen in Figure 3, for two valves with similar tube diameter, the case with larger leaflet height thereby larger leaflet area demonstrated better coaptation under back pressure. This implies a more functional valve that can reduce regurgitation during diastole in a cardiac cycle. Furthermore, lower peak stress in Case 2 is favored because a higher peak stress can lead to tissue failure and valve dysfunction. The following steady flow FSI results also provide more insights into leaflet deformation and hemodynamics, where recirculation behind the leaflet ("washout") is likely important to minimize clotting.

The current study demonstrated an efficient route for the geometrical optimization of a novel tri-tube valve. The in-silico construction and closure simulation largely reduce design variable space and save computation costs to obtain optimal designs for subsequent FSI simulations. Admittedly, important quantities like regurgitation volume cannot be captured in a steady flow simulation. More comprehensive investigation of the full cardiac cycle with pulsatile inlet waveform will be necessary for further optimization of this novel tri-tube valve.

ACKNOWLEDGEMENTS

This project is supported by National Institute of Health (NIH) grant NIH R01 HL107572.

REFERENCES

[1] Syedain, Z et al., *Sci. Transl. Med.*, 13, eabb7225, 2021.
[2] Li, N et al., *Interact. Cardiovasc. Thorac Surg.*, 26:768-776, 2018.
[3] Manji, R et al., *Xenotransplantation.*, 21:1-10, 2014.
[4] Syedain, Z et al., *Ann Biomed Eng.*, 41:2645-54, 2013.
[5] Gerges, C et al., *Chest*, 143:758-766, 2013.

COMPUTATIONAL INSIGHTS ON THE CORRELATION OF MYOFIBER CONTRACTILITY WITH THE DEVELOPED PRESSURE-PRELOAD DYNAMICS IN EX-VIVO BEATING HEARTS

Vahid Ziaei-Rad (1), Lei Fan (2), Jason Bazil (3), Lik Chuan Lee (1)
(1,2,3)

(1) Department of Mechanical Engineering, Michigan State University, East Lansing, Michigan, US
(2) Joint Department of Biomedical Engineering, Marquette University and Medical College of Wisconsin, Milwaukee, Wisconsin, US
(3) Department of Physiology, Michigan State University, East Lansing, Michigan, US

INTRODUCTION

The cardiac developed pressure, governed by the Frank-Starling mechanism, responds to changes in end-diastolic volume (i.e., preload). The pressure increases with increasing preload but reduces when the preload becomes excessive. This phenomenon is reflected at the myocardial level by an increase in twitch force following muscle stretch. At the cellular level, it involves the modulation of the cardiac contractile apparatus's responsiveness to calcium, a key aspect of the Frank-Starling property. Despite extensive studies, the precise correlation from cellular-level to organ-level observations remains unclear, with various theories still unconfirmed.

In this study, we tackle the challenges of experimental research by developing a computational model, inspired by isolated rat heart Langendorff experiments, to explore the underlying mechanisms. Recognizing the gap between organ-level and cellular-level measurements, we employ a finite element (FE) model to bridge these scales. Specifically, we simulate isovolumic heart contractions using a left ventricle (LV) FE model, with material parameters carefully calibrated with measurements from *ex-vivo* Langendorff experiments on rat hearts. The fitting method is performed such that the simulated waveforms closely match the measurements across various preloads. Subsequently, we utilize the model's measurements to determine sarcomere lengths corresponding to each preload, and compare them with existing experimental measurements.

METHODS

Based on the measurements of length, basal inner and outer diameters, and wall thickness of the LV, we constructed a prolate ellipsoid geometry to represent the LV. An LV FE model with myofiber distribution, varying transmurally from -60° at the epicardium to 60° at the endcardium, was developed to simulate the *ex-vivo* beating heart under isovolumic contraction. Following our previous work, e.g. [1], the LV pressures-volumes relationship is obtained by minimizing a functional with components associated with the myocardial tissue strain energy density and the enforcement of constraints on 1) myocardial tissue incompressibility, 2) zero-mean rigid body translation and rotation, and 3) cavity volume. The LV FE model is implemented in FEniCS, a popular open-source computing platform.

Constitutive law of the left ventricular

An active stress formulation was used to describe the mechanical behavior of the LV in the cardiac cycle. In this formulation, the stress tensor $\mathbf{P}$ can be decomposed additively into a passive component $\mathbf{P}_p$ and an active component $\mathbf{P}_a$ (i.e., $\mathbf{P} = \mathbf{P}_p + \mathbf{P}_a$).

The passive stress tensor is defined by $\mathbf{P}_p = \frac{dW}{d\mathbf{F}}$, where $\mathbf{F}$ is the deformation gradient tensor and W is a strain energy function of a Fung-type transversely-isotropic hyperelastic material given by $W = \frac{1}{2}C(e^Q - 1)$ where

$$\begin{aligned} Q =& b_{ff}{E_{ff}}^2 + b_{xx}\left({E_{ss}}^2 + {E_{nn}}^2 + {E_{sn}}^2 + {E_{ns}}^2\right) \\ &+ b_{fx}\left({E_{fn}}^2 + {E_{nf}}^2 + {E_{fs}}^2 + {E_{sf}}^2\right) \end{aligned} \tag{1}$$

where E_{ij} with $(i, j) \in (f, s, n)$ are components of the Green-Lagrange strain tensor $\mathbf{E}$ with f, s, n denoting the myocardial fiber, sheet, and sheet normal directions, respectively. Moreover, material parameters of the passive constitutive model are denoted by $C, Q \propto (b_{ff}, b_{xx}, b_{fx})$.

The active stress $\mathbf{P}_a$ was calculated along the local fiber direction using the active constitutive relationship, where $\mathbf{P}_a \propto T_{max}$, the myocardial contractility.

Results

Isovolumic contraction with different preload corresponding to the experiments is simulated by prescribing a constant LV volume in the model over one cardiac cycle. To calibrate the simulation with experimental data

and subsequently estimate sarcomere length, the following steps are undertaken:

- The measured LV EDPVR (end-diastolic pressure volume relationship) was fitted in the computational model with varying preloads, see Figure 1. Passive parameters C, Q were concurrently calibrated so the model predicted exponential end-diastolic pressure (EDP) matches the measured EDP points using the non-linear least squares fitting technique ($\sum_{\text{preload}} \|EDP_{\text{sim}} - EDP_{\text{exp}}\| < \epsilon$).

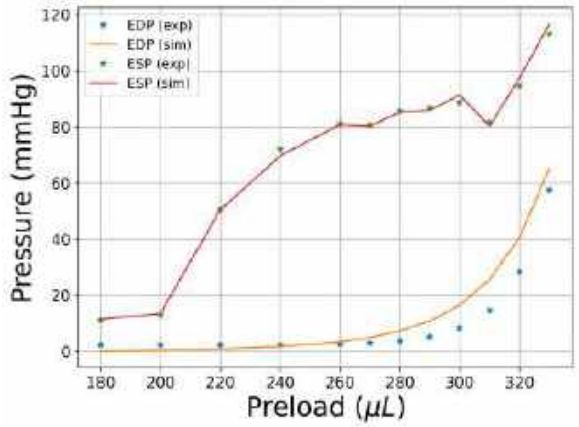

Figure 1: EDP/ESP measurements are indicated by blue/green stars for experimental data (exp) and the orange/red curve for simulations (sim). The passive load shows an exponential behavior, while the ESP is individually tailored to correspond with each preload. The results are depicted from a single rat.

- Unlike passsive parameters, the LV contractility T_{max} was adjusted separately for each preload so that the model predicted LV ESP end-systolic pressure (ESP) agrees with the measured ESP points ($\|ESP_{\text{sim}} - ESP_{\text{exp}}\| < \epsilon$). Consequently, the model predicted LV pressure matches the experimental measurements at different preloads, while T_{max} is varying for each preload. see Figure 1

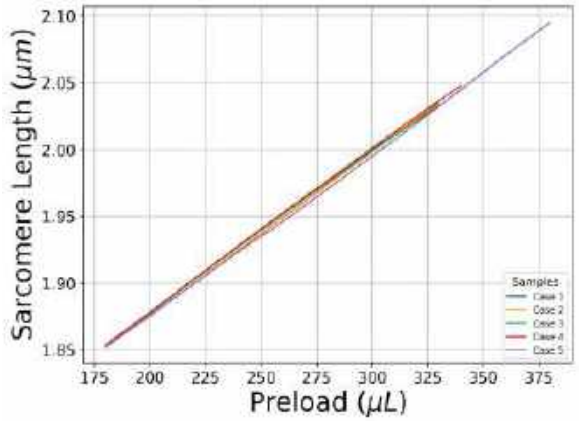

Figure 2: The graph illustrates the relationship between preload and model predicted sarcomere length for five rats.

- After fitting, sarcomere length of the myofiber was computed at different preloads, see Figure 2. The sarcomere length was computed from the fiber strain E_{ff} by the relation $\ell = \ell_0\sqrt{2E_{ff}+1}$ where the sarcomere length in the unloaded reference configuration is prescribed to be 1.85 μm based on previous studies. We note that the mean value of the fiber strain is used to determine the sarcomere length.

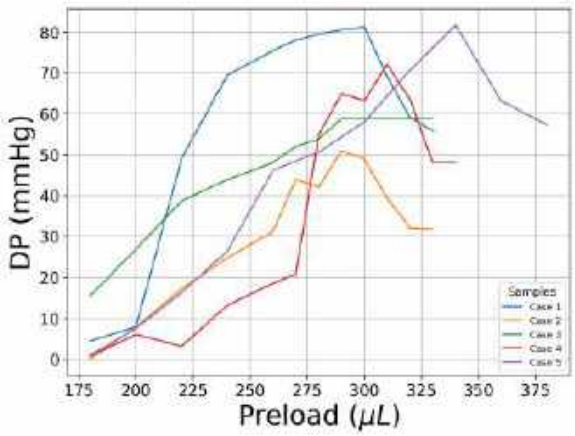

Figure 3: The graph displays developed pressure (DP) as a function of preload for experimental measurements collected from five rats. A non-monotonic trend with peaks occurring at slightly varied locations is observed. Each colored line represents a unique rat case.

DISCUSSION

The overall finding of this study is that the non-monotonic behavior of the developed pressure (DP) with preload is correlated with myocardial contractility, and the transition sarcomere length at which myocardial contractility peaks and starts to reduce is 2.03 μm. This study overcome the challenges associated with measuring the sarcomere length and local active tension in a beating heart. Another study measured that the sarcomere length at the time of peak force is 2.03 from myocardial muscle of rats, which is consistent with our model prediction (mean value of 2.03 μm) [2].

Myocardial contractility (indexed by the active tension) is estimated by fitting the LV FE model prediction with the measured LV pressure waveforms acquired from the hearts at different preloads. We demonstrate that it follows the same behavior as the DP with preload, see Figure 3. The contractility increases first and then start to decrease after the critical balloon volume is reached. This behavior is also similar to the sarcomere-length vs. tension behavior found in isolated myocytes taken from the epicardial muscle of rats [3]. With an increase in sarcomere length from 1.8 μm to 2.2 μm, the active tension increases from 0 to 40 kPa (300 mmHg) at sarcomere length of 2.0 μm and then reduces to 0 μm. Similarly, the model predicted that myocardial contractility increases from a mean value of 20 mmHg at a sarcomere length of 1.85 μm (over 5 rats) to a peak mean value of 150 mmHg at a sarcomere length of 2.03 μm before reducing.

ACKNOWLEDGEMENTS

This work was supported by the National Institute of Health (R01 HL134841 and R01 HL163977).

REFERENCES

[1] Fan L et al. *Comput. Biol. Med.* 141 (2022). DOI: 10.1016/j.compbiomed.2021.105050.

[2] Guccione JM et al. *J. Biomech.* 30(2) (1997). DOI: 10.1016/s0021-9290(96)00122-4.

[3] Weiwad WK et al. *J. Mol. Cell. Cardiol.* 32(2) (2000). DOI: 10.1006/jmcc.1999.1069.

MICROMECHANICS AND MECHANORESPONSIVITY OF THE DEVELOPING PORCINE MENISCUS

Meghan E. Kupratis (1), Yuqi Zhang (1), Jiaqi Xiang (2), Bryan Kwok (2), Elisabeth A. Lemmon (1), Karen L. Xu (1), Nathaniel A. Dyment (1), Lin Han (2), Eiki Koyama (3), Robert L. Mauck (1)

(1) McKay Orthopaedic Research Laboratory, University of Pennsylvania, Philadelphia, PA, USA
(2) School of Biomedical Engineering, Science and Health Systems, Drexel University, Philadelphia, PA, USA
(3) Department of Surgery, The Children's Hospital of Philadelphia, Philadelphia, PA, USA

INTRODUCTION

The meniscus is critical for knee joint stability and load distribution. Unfortunately, its limited endogenous cell-mediated repair capacity means that meniscus injuries often fail to heal in adults [1]. Given the superior repair capacity of juvenile meniscus tissues, understanding their initial formation and specialization mechanisms during embryonic development may provide insights that could be harnessed for tissue regeneration in the adult. Our group previously examined the embryonic formation and postnatal maturation of the murine meniscus, revealing that its region-specific matrix composition and cellular phenotypes are established prenatally [2-3]. Furthermore, we showed that mechanical forces that arise from muscle loading and cellular contraction are essential for meniscus formation and specialization [4], while reduced postnatal weightbearing has little effect on meniscus morphology and micromechanics [5]. While these studies provide critical insight to the mechanoregulation of meniscus morphogenesis, translatability of the murine model is limited by its small size and mechanical and morphological distinctions relative to humans. To overcome these limitations, the goal of the present study was to establish a more translationally relevant model of meniscus development using the Yorkshire pig. Here, we established the timeline for key events in knee joint formation in early gestation (28-45 days after fertilization, E28-45) and evaluated matrix micromechanics and emergent mechanoresponsivity of meniscus cells in pigs from early gestation (E45), mid-gestation (E84), and newborn (P1) stages.

METHODS

Timed pregnancies and embryo collection. Adult female Yorkshire pigs were artificially inseminated at the National Swine Research Center (NSRRC, Columbia, MO). Pregnancy was confirmed via ultrasound, and sows were euthanized on embryonic day 45 or 84, or on postnatal day 1. Micromechanics. Freshly dissected left knee joints were embedded in OCT and cryo-sectioned into 10µm coronal sections. AFM nanoindentation was performed in 1X PBS using polystyrene microspherical tips (Ø25µm, k~0.6N/m) at ≥10 different locations within the inner and outer meniscus per specimen. The effective indentation modulus (E_{ind}) was calculated from the finite thickness-corrected Hertz model [3]. Histology. Left hindlimbs were fixed in 4% paraformaldehyde, embedded in paraffin, and sectioned to 5µm (sagittal and coronal orientations). Cellularity and proteoglycan distribution were assessed from Safranin O/Fast Green staining. Cell isolation. Menisci from the right hindlimbs were identified and isolated under a dissecting microscope. At E84 and P0, menisci were segmented into inner and outer regions. All tissues were minced into ~1mm^3 pieces and cultured in basal medium (DMEM, 10% FBS, 1% anti-anti) to allow for cell egress from the tissue fragments. Mechanoresponse assay. Isolated cells were cultured on fibronectin-coated polyacrylamide (PA) hydrogels (5 or 55kPa) or glass for one day in basal medium. Cells were fixed and stained for YAP (AF-488), actin (phalloidin AF-555), and nuclei (Hoechst 33342, excitation 350nm). Imaging. Confocal z-stack images were obtained at 10X magnification and processed in Cell Profiler to quantify cell area and YAP localization. Statistical analyses: Differences between groups were assessed via two-way ANOVA, with significance level at multiple comparison-corrected α=0.05.

RESULTS

Histological assessments of hindlimb development across early gestation timepoints (E28-42) were used to establish the timing of knee joint formation in the Yorkshire pig. Skeletal rudiments were apparent at E28, as indicated by cartilaginous condensations at the prospective femur and tibia locations (**Fig. 1a**).

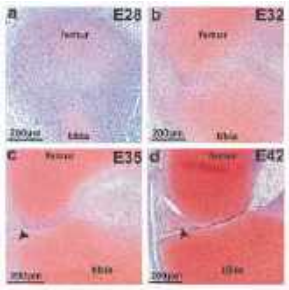

Fig. 1: Knee joint formation during early embryonic development in the pig.

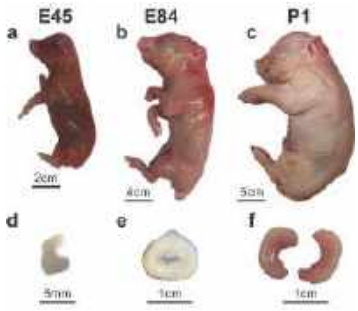

Fig. 2: Gross anatomy (a-c) and isolated menisci (d-f) from embryonic and newborn pigs.

The future joint line was established by E32 (**Fig. 1b**), and primitive menisci were visible, but not yet separated from the adjacent cartilaginous structures at E35 (**Fig. 1c**, arrowhead). The menisci were fully formed and separated from the articular cartilage at E42 (**Fig. 1d**, arrowhead). Subsequent tissue and cellular analyses were performed from E45 onwards, at which point the menisci were readily isolated (**Fig. 2**). Safranin O/fast green staining of menisci from these later timepoints showed that regional matrix specification, namely, proteoglycan enrichment within the inner meniscus, was evident in these tissues (**Fig. 3**).

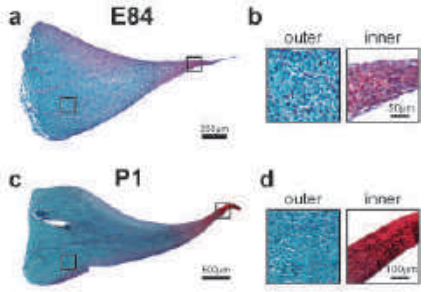

Fig. 3: Regional specification is apparent in the developing pig menisci.

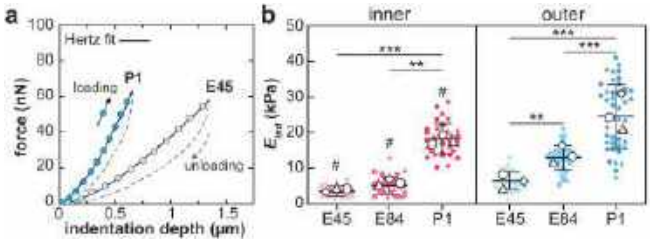

Fig. 4: a) Representative indentation force vs. depth curves for early embryonic and newborn outer meniscus. b) Nanoindentation moduli (E_{ind}) of inner (left) and outer (right) meniscus increase throughout gestation (p<0.001, ***p<0.0001), and E_{ind} of the inner region was less than that of the outer region (#p<0.05). For each animal (n=3), ≥10 indentation locations were tested in each region. White points represent the average E_{ind} from one animal, and colored points of the same shape correspond to multiple indentations from the same animal.**

AFM nanoindentation revealed rapid stiffening of the meniscus primitive matrix throughout gestation (**Fig. 4**) The microscale modulus of the outer zone was significantly greater than the inner zone at all three timepoints (#p<0.03). In the inner meniscus, E_{ind} increased from 3.5±1.4 kPa (mean±SD) at E42 to 18.2±4.3 kPa at P1, while E_{ind} of the outer meniscus increased from 6.5±2.5 kPa to 26.1±8.0 kPa. Together with our histological observations, these data indicate that the inner and outer meniscus develop distinct compositional and mechanical microenvironments early in prenatal development that undergo continued specialization through the end of gestation, and these changes appear to initiate earlier in the outer zone.

Meniscus progenitor cells migrated from isolated meniscus segments onto tissue culture polystyrene over 5-7 days (**Fig. 5**). These cells were allowed to proliferate for an additional 7-10 days, then were passaged and seeded onto PA hydrogels or glass slides. Meniscus progenitors isolated at all three gestational timepoints exhibited increased mechanoactivation (*i.e.,* greater cell area and increased YAP nuclear localization) with increasing substrate stiffness (**Fig. 5**). Interestingly, P1 outer zone cells exhibited higher YAP nuclear localization than P1 inner zone or E42 cells, even on soft substrates.

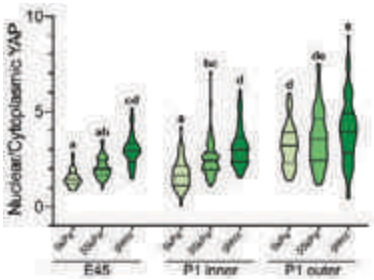

Fig. 5: YAP nuclear:cytoplasmic ratio on substrates of different stiffnesses. Groups not sharing a common letter are significantly different (p<0.05).

DISCUSSION

In the present work, we begin to establish a detailed, multiscale timeline of the coordinated morphological and mechanobiological changes that govern knee joint development in a translationally relevant porcine model. Consistent with prior investigations in the mouse [4-6], we show that meniscus formation and knee joint cavitation proceed rapidly following skeletal rudiment condensation and establishment of the interzone at the prospective joint line. Histological and micromechanical assessments revealed that microenvironmental distinctions between the proteoglycan-rich inner meniscus and type I collagen-rich outer meniscus are apparent as early as E45 in the pig. At this point, embryos and hindlimbs are sufficiently large to allow meniscal tissue isolation with the aid of a dissection microscope. The differing regional matrix composition and micromechanics at this timepoint suggests resident cell identity and matrix synthesis are determined early in embryonic development. Furthermore, cells from E45 exhibited a characteristic mechanosensitive response (*e.g.,* increased cell spreading as a function of substrate stiffness, indicating that resident meniscal cells are able to sense and respond to their mechanical microenvironment as soon as cavitation is complete. Interestingly, P1 outer zone cells showed a distinct mechanoresponse from P1 inner zone and E45 cells, wherein nuclear YAP localization was greater on all substrate stiffnesses, suggesting exposure to a stiffer microenvironment *in vivo* may enhance mechanosensitivity.

Future work will continue probing the phenotypic and mechanosensitive attributes of the developing meniscus, for example, by examining the heterogeneity of these cells and the matrix they synthesize via single cell RNAseq and immunohistochemistry, to establish the spatiotemporal characteristics of meniscus specialization throughout development. By uncovering the mechanisms by which emergent meniscus cells respond to biophysical cues to establish a mature, functional meniscus in the pig, we aim to shed light on mechanobiologic mechanisms that could be harnessed for injury repair and regeneration in adult fibrous tissues.

ACKNOWLEDGEMENTS

This work was supported by the NIH (R01AR075418, P30AR069619) and NSF (CMMI-2047073).

REFERENCES

[1] Makris, E. *et al., Biomaterials,* 32: 7411-7431, 2011.
[2] Tsinman, T. *et al., FASEB J,* 35: e21779, 2021.
[3] Kwok, B. *et al., Acta Biomater.,* 168: 235-251, 2023.
[4] Tsinman, T. *et al., J Orthop Res,* 41(10): 2305-2314, 2023.
[5] Fogarty, N. *et al., J Orthop Res,* 2023.
[6] Kim, M. *et al., Biol Open,*11:bio059381, 2022.

THE INFLUENCE OF ECHOCARDIOGRAPHIC AND COMPUTED TOMOGRAPHY PHASES ON THE RESULTING FLOW DYNAMICS IN THE LEFT ATRIUM

A. Bshennaty (1), B. Vogl (1), A. Sularz (2), M. Alkhouli (2), and H. Hatoum (1,3)

(1) Department of Biomedical Engineering, Michigan Technological University, Houghton, MI, USA
(2) Department of Cardiovascular Medicine, Mayo Clinic, Rochester, MN, USA
(3) Health Research Institute, Center of Biocomputing and Digital Health and Institute of Computing and Cybernetics, Michigan Technological University, Houghton, MI, USA

INTRODUCTION

Experimental modeling and computational simulation have been critical in better understanding cardiovascular diseases and conditions. These tools helped with greatly improving different clinical aspects of cardiovascular health, including the diagnosis, pathogenesis, and treatment of cardiovascular diseases [1, 2, 3, 4, 5, 6, 7]. To truly leverage the power of computational fluid dynamics (CFD), patient specific simulations can lead the way towards cardiac treatment that is tailored to the physiological characteristics of each patient [8]. Patient-specific geometry can be obtained from computed tomography (CT) or Magnetic Resonance (MR) images, and the boundary conditions (BC) for the simulations can be acquired through echocardiography (ECHO) or 4D MR images [9, 10, 11, 12]. However, a reliable classification and better risk stratification require an accurate representation of the hemodynamic conditions. Therefore, as the heart is a dynamic organ, the phase of the cardiac cycle that is chosen for the extraction of geometry and BCs used will dictate a significant part of the flow [13]. Moreover, another issue that is often faced for this kind of study is the incompleteness or lack of patient data. For example, the availability of single-phase CT data instead of multi-phase CT would force the choice of the geometry. The objective of this study is to investigate the impact that the choice of geometry extracted from the CT and the choice of BCs have on the hemodynamics of the left atrium (LA).

METHODS

Multi-phase CT, ECHO, and invasive pressure data from the LA of a patient received from Mayo Clinic under an Institutional Review Boards (IRB) and a data usage agreement (DUA) protocol, were used to perform this study. From the ECHO data, velocity profiles at the mitral valve (MV) and the four pulmonary veins (PV) were extracted. From the CT images, the geometry of the LA was extracted at the E-wave and at the end of diastole. The segmentation and editing of the geometry were done using Mimics Research and 3-matic (Materialise, Belgium). To determine the E-wave and end-diastolic phases, all phases of the CT data were segmented, and the volume of the left ventricle for every phase was recorded to select the E-wave and the end diastole phases as shown in **Fig.1**.

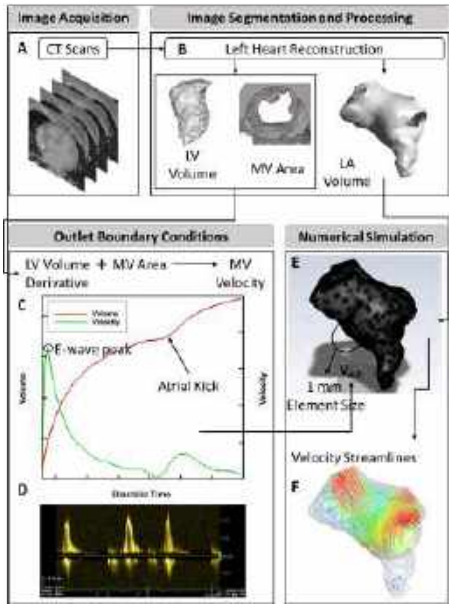

Fig 1. Methodology Pipeline

Each of the two 3D digital models were imported into Ansys Workbench 2020. Then, an extension that is 10 times the diameter of the vessel was added to each PV ostium and to the MV to overcome any entrance effects [14]. A polyhedral mesh of 1 mm element size was

applied to both models, in accordance with the mesh independence study conducted in a previous work [4]. The blood flow was considered to be laminar (Reynolds number < 2000). Each model was simulated with 3 different sets of boundary conditions (BCs):
- BC 1: The velocity profile at the MV was used as the outlet BC while the pressure at the PVs was sent to be constant at 0 Pa [4, 15].
- BC 2: The velocity profiles for the PVs were used as inlet BCs and the mean pressure at the MV was set as outlet BC.
- BC 3: The velocity profiles for the PVs were used as the inlet BC, and 0 pressure was imposed at the MV.

All the simulations were run for 3 cardiac cycles, and all results were extracted from the third cycle [14, 15]. The resulting data from these simulations were LA velocities and the Wall Shear Stress values along its wall. Also, the Time Averaged Wall Shear Stress (TAWSS), Oscillatory Shear Index (OSI), and Relative Resident Time (RRT) were computed [16]. Low TAWSS, high OSI and high RRT Values are associated with the formation of thrombus [17].

RESULTS

EFFECT OF BCs: The velocity at the E-wave and at the end-diastolic phase of the cardiac cycle were extracted and compared as shown in the probability density function (PDF) distribution in **Fig.2**. BC 1 seems to have higher E-wave velocities than BC 2 and BC 3 for both geometries. There does not seem to be any notable differences between BC 2 and BC 3.

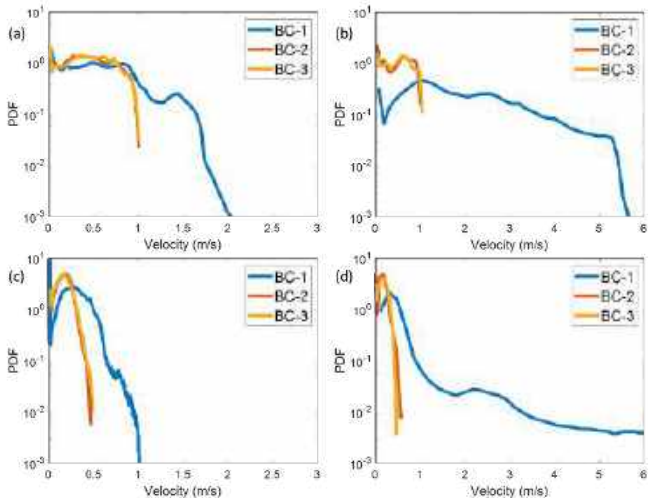

Fig 2. PDF (a) at E-Wave with E-Wave Geometry, (b) at E-Wave with End-Diastole Geometry, (c) at End-Diastole with E-Wave Geometry, and (d) at End-Diastole with End-Diastole Geometry.

The TAWSS contours are presented in **Fig.3** and **Fig.4** for E-wave and end-diastole, respectively. For the E-wave geometry, higher TAWSS were observed for BC 1 compared with BC 2 and BC 3, which appear similar. This was also observed, more prominently, for the end-diastolic geometry. OSI was also extracted and compared. For both geometries, slight differences were shown between the three BCs with an average value that seemed to be close across the BCs. The RRT also seemed to show some differences between the three BCs, especially between BC 1 and the other two. For E-wave geometry, the average value of RRT for BC 1 was slightly lower than those for BC 2 and BC 3. This trend was present more significantly for the end-diastolic geometry.

EFFECT OF GEOMETRY: From **Fig.2**, we notice that the velocity magnitudes, at both phases, seem higher for the end-diastolic geometry than the E-wave geometry when simulated with BC 1.

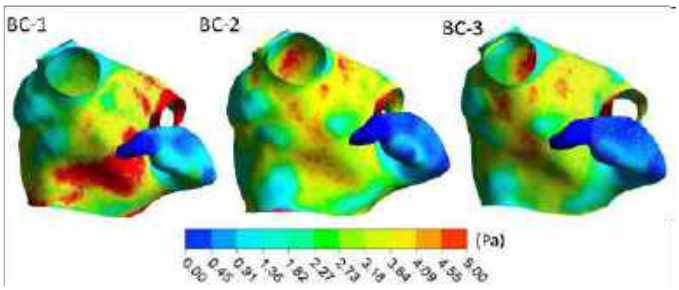

Fig 3. TAWSS Contours with E-Wave Geometry

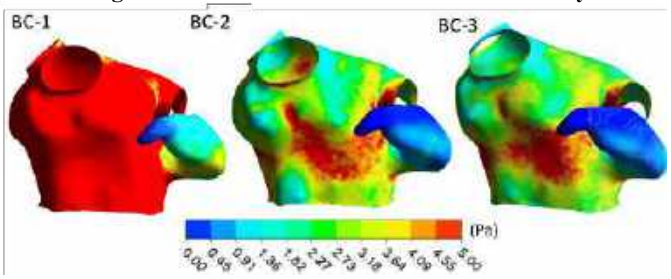

Fig 4. TAWSS Contours with End-Diastole Geometry

However, no notable difference is observed between the two geometries when simulated with BC 2 and BC 3. The velocity and TAWSS distribution for the end-diastolic geometry seemed to have larger values than that for the E-wave geometry when simulated with BC 1. That is still true when simulated with BC 2 and BC 3, but to a much lesser extent. There were some differences in the OSI between E-wave and end-diastolic geometry under all the simulated BCs despite having the average OSI close for both geometries under the 3 different BCs. The RRT indicated a prominent decrease in RRT values for the end-diastolic geometry compared to the E-wave geometry when simulated with BC 1. This is further confirmed as the average RRT value for the end-diastolic geometry was less than that for the E-wave geometry under BC 1. The decrease in RRT was less pronounced with BC 2 and BC 3.

DISCUSSION

The results of this study show how utilizing different types of BCs and geometries can impact the outcomes of patient-specific simulations. Segmentation of the LA at end-diastole led to the occurrence of higher velocities, higher TAWSS, and lower RRT values as compared to the segmentation at the E-Wave. The discrepancy in the results for different BCs highlights the difficulty in obtaining numerical thresholds for parameters and indices when attempting to classify patients for risks of cardiovascular diseases. This highlights the importance of consistency in choosing the appropriate cardiac phase and BCs in future studies.

REFERENCES

1. Hatoum H et al., *JACC:CI*, 2019; 2. Lin T et al., *ABME*, 2006. 3. Wang JS et al., *Experiments in Fluids*, 2017;4. Vogl B et al., *JICE*, 2022; 5. Asadbeygi A et al., *JCTR*, 2023; 6. Cilla M et al., *BMM*, 2012; 7. Kural M et al., *JBM*, 2012; 8. Sadiq S et al., *PTRSA: MPES*, 2008; 9. Capelli C et al., *Interface Focus*, 2018; 10. Farag M et al., *MDCJ*, 2014; 11.Zeng D et al., *JBE*, 2008; 12. García-Villalba M et al., *Frontiers in Physiology*, 2021; 13. Armour C et al., *BMM*, 2021; 14. Trusty P et al., *JBM*, 2020; 15. Bosi GM et al., *FCE*, 2018; 16. Asadbeygi A et al., *CMPB*, 2022; 17. Fiala M et al., *Europace*, 2014.

STRAIN-BASED CELLULAR INJURY THRESHOLDS IN A 3D IN VITRO MODEL OF TRAUMATIC BRAIN INJURY

J. Park (1), A. Daul (1), J. Zhang (1), C. Franck (1)

(1) Mechanical Engineering, University of Wisconsin-Madison, Madison, WI, USA

INTRODUCTION

Traumatic brain injury (TBI) affects over 55 million people worldwide, with both immediate and long-term disabilities as a result. However, the exact mechanism of injury remains unclear [1]. Moderate to severe blunt impact injuries can cause immediate hemorrhaging or contusion, which can be diagnosed using imaging modalities such as MRI. But what about damage that occurs over time? Secondary injury is characterized by cell death that occurs via cellular signaling pathways over a delayed time span after injury. These are more insidious, as a cell does not need to physically rupture to undergo apoptosis. Consequently, diagnosis and prediction of secondary injury after a TBI has remained extremely challenging. Thus, current patient-level evaluation strategies continue to rely on symptom-based reporting, which is highly variable between patients and difficult to standardize [2]. Having a cellular injury threshold, defined as the average strain at which a cell will die, would allow for significant advances in diagnostic and preventive measures for TBI. Here, we present a methodology for determining a cellular injury threshold curve in rat cortical neural cells as a function of sex, cell phenotype, strain magnitude and strain rate.

METHODS

Cortical cells from postnatal day P0-P1 Sprague-Dawley rat pups are dissected and seeded in 3D dog-bone shaped scaffolds made from type-I rat tail collagen. After 7 days in vitro (7 DIV), cells are stained with Calcein AM, a live cell indicator and imaged using multiphoton microscopy with a 20x water immersion objective. Following imaging, samples are stretched in uniaxial tension using a custom on-scope device that utilizes two linear actuators to deliver a controlled impact at programmed strain magnitudes and strain rates (Figure 1). Cells are then returned to the incubator. 24 hours after impact, cells are re-stained with Calcein AM, as well as stained with Hoechst and Ethidium Homodimer-1 (EthD-1), a nuclear stain to streamline analysis, and a dead-cell indicator, respectively, and imaged at the same location as the pre-impact image as shown in the purple box in Figure 2.

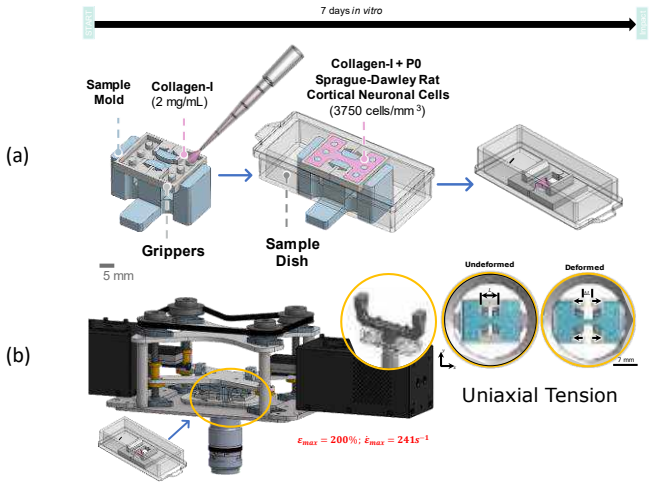

Figure 1:
(a) Dogbone-Shaped, Collagen-I Cell Culture System
(b) On-Scope Impact Device for Controlled Uniaxial Tension

Concurrently, more samples are stained with Calcein AM and imaged following the protocols of a negative control sample. Immediately after imaging, samples are then fixed with 4% paraformaldehyde and sucrose, immunostained for cell phenotype, and imaged at the same location as the live image as shown in the blue box in Figure 2. Both the live image and the immunostained image are then fed into an unsupervised machine learning algorithm to identify cells based on morphology alone.

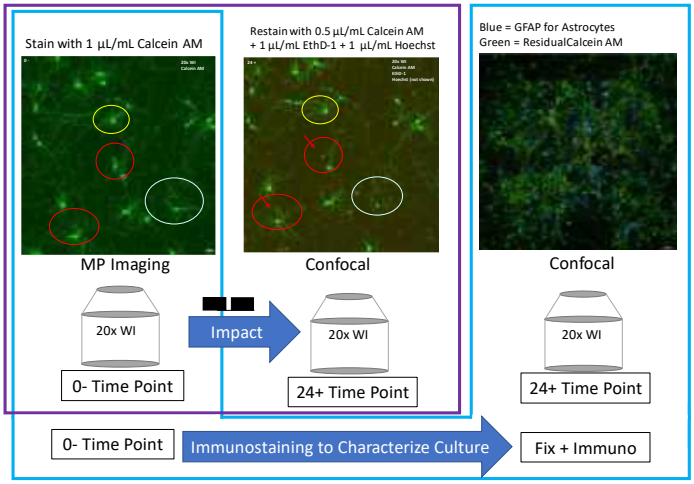

Figure 2: Image Acquisition Workflow

Analysis of acquired images is done following established protocols and processing codes [4]. Images are preprocessed to filter noise, apply gamma correction, and threshold the background to allow for semi-automatic tracing of neurons using a rayburst algorithm based on local image intensity distribution. Traced neurons are then converted to a tree structure in MATLAB. The far field strain, which is well characterized using previously established methods [4,5], is then transformed and mapped onto the local cell structures, represented as the trees in MATLAB. This is done by rotating the far-field strain tensor via a rotation matrix defined by an orthonormal discrete Frenet frame. The average strain experienced by the cell is then associated with whether the cell live or die after impact and is used as a point on the critical injury threshold curve.

RESULTS

We develop a replicable and consistent methodology for applying controlled, measurable uniaxial tension to 3D collagen gels with embedded cortical cells. Furthermore, minor adaptations to a previously established protocol of analysis enable the identification and parsing of strains on individual cells within the scaffold while maintaining a physiologically relevant culture density. The stained live cell image is traced in NeuronStudio, yielding a traced network of cells, output in the form of a SWC file. The SWC file is then used as an input to a machine-learning based algorithm G-Cut, which segments cells, assigning branches to individual cells. These individually tagged cells are then run through the strain-mapping MATLAB code to output a single cell with mapped strains along the branches, mean shear, mean compressive and mean tensile strains across the cell, and branch orientation data (Figure 3).

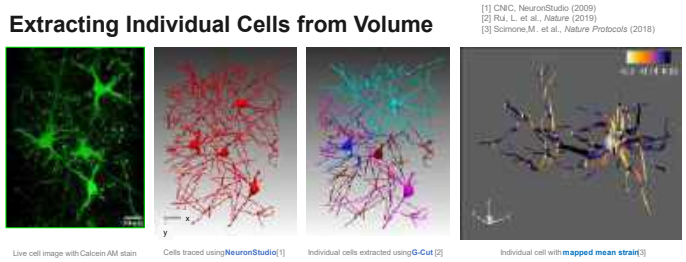

Figure 3: Extracting Individual Cells from Image Volumes using Cell Tracing and Segmentation Software

Preliminary results indicate that cells characterized by having long projections along the x or y orientations exhibited cell death after 24 hours. Conversely, cells with shorter projections did not demonstrate cell death despite experiencing comparable strain magnitudes in both tension and compression. These observations pertain to impacts that occurred at 50 strains/second with a far-field strain magnitude of 30%. Average tension and compression were decoupled as the average tensile values were significantly attenuated by negative values from compression. Furthermore, we develop a methodology for identification of cell phenotypes using a machine learning algorithm that is trained on our datasets (Figure 4).

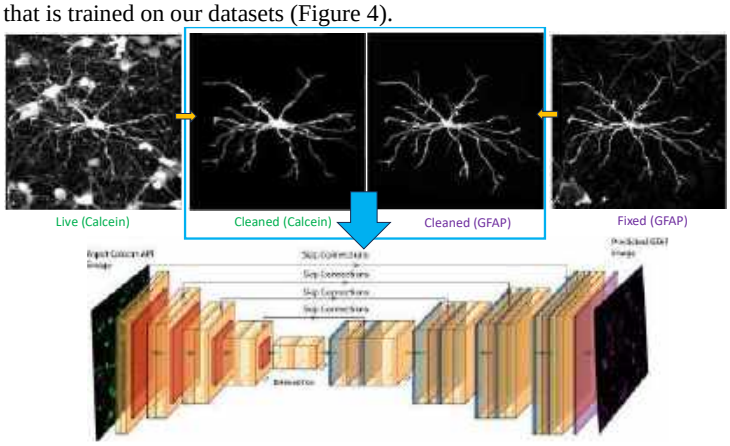

Figure 4: Training Machine Learning to Identify Cell Phenotypes

DISCUSSION

Preliminary results suggest that cell morphology significantly influences cell survival in response to impacts at comparable strain rates and magnitudes, particularly at the cellular level. Comprehensive analysis of factors such as cell phenotype, cell projection length and direction, and other physiological factors are necessary to build a robust and accurate strain injury curve. Next steps include application of our developed methodologies to collect data towards building a secondary injury curve and determining critical injury threshold.

The creation of a secondary injury curve, in combination with existing FE models of the brain and analyses of impact mechanics, will provide enormous potential for development of new predictive injury metrics, diagnostic criteria, and design of protective equipment to prevent not just primary injury but also secondary injury and the enduring consequences associated with it.

ACKNOWLEDGEMENTS

This research is supported by the U. S. Office of Naval Research under PANTHER award numbers N000142112044, N000142112855, and N000142212828 through Dr. Timothy Bentley.

REFERENCES

[1] GBD 2016 Traumatic Brain Injury and Spinal Cord Injury Collaborators, *Lancet Neurol*, Jan;18(1):56-87, 2018
Doi: 10.1016/S1474-4422(18)30415-0.
[2] Strathmann, F et al., *Clinical Biochemistry*, 47: 876-888, 2014.
Doi: https://doi.org/10.1016/j.clinbiochem.2014.01.028.
[3] Summey, L et al, *Experimental Mechanics*, 63: 1445-1460, 2023.
[4] Scimone, et al., *Nature Protocols*, 13: 3042-3064, 2018.
[5] Bar-Kochba, E et al., *Scientific Reports*, 6: 30550, 2016.

SEX DIFFERENCES IN PLACENTA VILLOUS STRUCTURE IN LOW- AND HIGH-RISK PREGNANCIES

Adrienne K. Scott (1), Patrick Yang (1), Abigail Arter (2), Caroline Fosher (2), Ulugbek S. Kamilov (3,4), Anthony O. Odibo (2), Michelle L. Oyen (1,2)

(1) Biomedical Engineering Department, Washington University in St. Louis, St. Louis, MO, USA
(2) Obstetrics and Gynecology Department, Washington University in St. Louis, St. Louis, MO, USA
(3) Computer Science & Engineering Department, Washington University in St. Louis, St. Louis, MO, USA
(4) Electrical & Systems Engineering Department, Washington University in St. Louis, St. Louis, MO, USA

INTRODUCTION

Fetal Growth Restriction (FGR) affects 5–10% of all pregnancies and is the leading cause of perinatal mortality [1]. FGR is most often defined as an estimated fetal weight of less than the 10th percentile for a given gestational age and occurs when the placenta is insufficient to sustain the oxygen and nutrient needs of the growing fetus. Efficient exchange of nutrients and oxygen occurs through the vasculature of the placenta, particularly in the microvasculature of the villous tissue, where the vascular membranes have a high surface area and are the thinnest [2]. Since the placenta is fetal tissue, placental efficiency can depend on fetal sex [3]. Although literature reports alterations in villous structure with FGR [4], how the villous structure changes with fetal sex remains largely underexplored. Furthermore, male fetuses are 20% more likely to experience worse outcomes in complicated pregnancies than female fetuses, demonstrating the impact of fetal sex [3]. To understand how fetal outcomes vary based on sex, literature focuses on changes in gene, steroid, and protein expression in the placenta, but whether these alterations lead to structural and functional changes is unknown [3]. Understanding sex-based differences in the placenta villous tissue may elucidate reasons for sex differences in fetal outcomes. Therefore, the objective of this study was to determine the extent fetal sex influences the multiscale changes in the villous structure of the placenta.

METHODS

Ultrasound Imaging and Placenta Collection: Patients were recruited and imaged with Doppler ultrasound under an IRB approved protocol. All patients were imaged at two gestation time points between 28-32 weeks (second trimester) and 34-38 weeks (third trimester) of gestation (Fig. 1A). The pulsatility index (PI) of blood flow in the intervillous space was measured with Doppler ultrasound. Placenta villous biopsies from a total of 12 patients were collected for analysis. Out of the 12 patients, six patients were diagnosed with FGR and six patients were considered low-risk controls. Within each case and control group, three pregnancies had a male fetal sex and three pregnancies had a female fetal sex. **Optical Clearing & Imaging:** Placenta villous biopsies collected from each patient were optically cleared with Visikol Histo-1 [5]. Using optical coherence tomography (OCT), a minimum of eight 3-dimensional images of each placenta biopsy were acquired (cubes 2 mm on a side). **3D Villi Structure Analysis:** OCT images were segmented and volume reconstructed to calculate the volume fraction, surface area, and the number of branches per cubic millimeter using a custom MATLAB code. **Statistics:** A linear mixed effect model with a type II sum of squares ANOVA was used and p-values were adjusted for multiple comparisons using the Tukey method.

RESULTS

Comparison of PI values of the intervillous blood flow in placentas from FGR and low-risk control pregnancies were not significantly different in the second or third trimester. However, when plotting the measured PI values versus the gestational age at the time of imaging, we found that the PI of the intervillous space decreased throughout gestation, but there was no decreasing trend with FGR patients (Fig. 1B). By performing a linear regression analysis, we found that the slope of the best-fit

line for the control patients was negative and was significantly different than zero ($p = 0.004$, $R^2 = 0.573$). The best-fit line for the FGR patient data did not have a slope significantly different than zero and had an R^2 value of 0.007. When comparing the PI measurements in pregnancies with male fetal sex compared to female fetal sex, no significant differences were observed.

Using OCT, the 3D architecture of the villous tissue was imaged to determine the extent villous structural changes were influenced by fetal sex (Fig. 2). The surface area increased significantly in FGR pregnancies compared to controls for both female and male fetuses. The villous tissue surface area of FGR placentas from female fetuses was not significantly different from control placentas from male fetuses (Fig. 2D). While the volume fraction of the villous tissue in placentas from male fetuses increased with FGR, the volume fraction did not significantly increase in placentas from female fetuses (Fig. 2E). The quantified number of branches per cubic millimeter did not significantly increase with FGR compared to male and female controls respectively. However, the number of branches in FGR placentas of male fetuses is greater than the number of branches in control pregnancies of female fetuses (Fig. 2F).

DISCUSSION

Our results demonstrate microscopic changes in the villous tissue of placentas from female versus male fetuses suggesting there may be sex differences resulting in altered oxygen and nutrient transport. However, we did not observe sex differences with macroscopic blood flow measurements in the intervillous space, suggesting these ultrasound measurements may not be sensitive enough to detect microvascular changes. Although the literature suggests that surface area decreases with FGR [4],

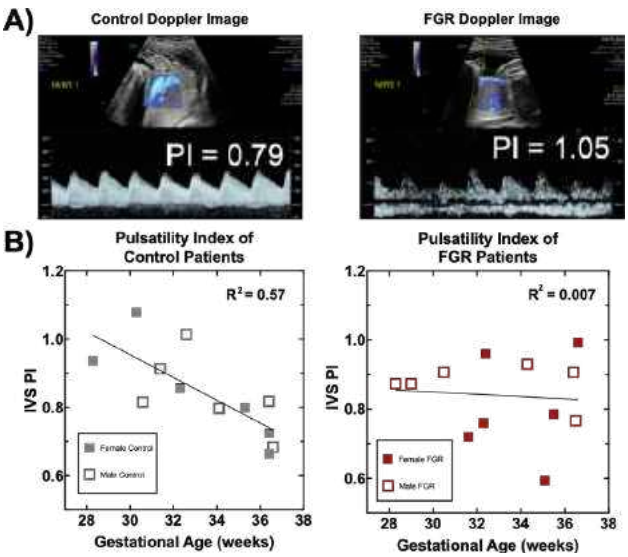

Figure 1: The pulsatility index (PI) of the intervillous (IVS) blood flow decreased throughout gestation for low-risk pregnancies, but not with fetal growth restriction (FGR) pregnancies. A) The PI in the intervillous space of control patients and patients with FGR was measured with Doppler Ultrasound. B) Linear regression analysis demonstrated that the IVS PI decreased throughout gestation only for control patients, but not for FGR patients.

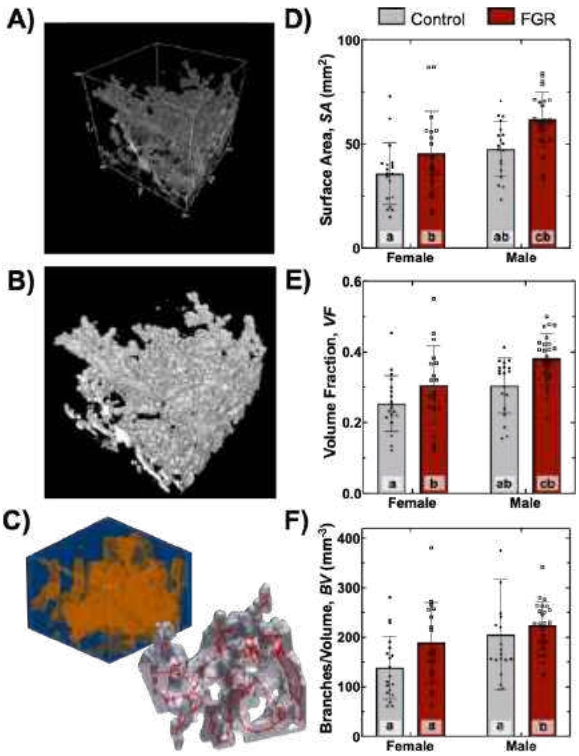

Figure 2: Microscopic changes in surface area, volume fraction, and number of branches per cubic millimeter differed with fetal sex. A) Placenta villous biopsies were imaged with optical coherence tomography (OCT) and B) 3D reconstructed to C) quantify the surface area, volume fraction, and number of branches. D) Fetal sex influenced changes in surface area, E) volume fraction, and F) branching in placentas of patients with and without FGR. ±standard deviation, different letters indicate statistical significance ($p<0.05$)

these results may be contradictory to expectations because our analysis was completed from 3D structures rather than more routinely used 2D histology slides. Interestingly, with surface area and volume fraction, the response was greater in placentas with male fetuses. This observation may help explain why fetal outcomes are typically worse for male fetuses with pregnancy complications. Future work will develop computational models of oxygen transport in the villous structures to understand how sex-dependent changes in villous structure lead to changes in placenta function. Overall, understanding how fetal outcomes are influenced by sex differences will help to better predict and prevent pregnancy complications.

ACKNOWLEDGEMENTS

Work on this project is supported by Wellcome Leap as part of the In Utero Program and the NIH T32 Postdoctoral Training Grant in Regenerative Medicine (T32EB028092).

REFERENCES

[1] Nardozza, L.M.+ *Arch. Gynecol. Obstet.* 295:1061-1077, 2017. [2] Plitman Mayo, R.+ *J. Biomech.* 49:3780-3787, 2019. [3] Clifton, V.L., *Placenta*, 31:S33-S39, 2010. [4] Tun W.M. +, Scientific Reports, 9:9876, 2019. [5] Sargent J.A., Biotechniques, 66:79-84, 2019.

THE IMPORTANCE OF THE LEFT ATRIAL APPENDAGE ON THE FLOW IN THE ATRIUM

A. Bshennaty (1), B. Vogl (1), A. Bavo (2), A. Sularz (3), A. Kramer (4), J. Nielsen-Kudsk (4), Y. Jia (5), O. De Backer (5), M. De Beule (2), M. Alkhouli (3), and H. Hatoum (1,6)

(1) Department of Biomedical Engineering, Michigan Technological University, Houghton, MI, USA
(2) FEops, Gent, Belgium
(3) Department of Cardiovascular Medicine, Mayo Clinic, Rochester, MN, USA
(4) Department of Cardiology, Aarhus University Hospital, Aarhus, Denmark
(5) Department of Cardiology, Copenhagen University Hospital, Copenhagen, Denmark
(6) Health Research Institute, Center of Biocomputing and Digital Health and Institute of Computing and Cybersystems, Michigan Technological University, Houghton, MI, USA

INTRODUCTION

The Left Atrial (LA) Appendage (LAA) is a projection from the left atrium that is believed to be a location for the development of thrombus in patients with atrial fibrillation (AF) [1, 2]. Due to having more distensibility than the main body of the left atrium, it is believed that the LAA acts as a decompression chamber to alleviate pressure buildup in the left atrium and handle an overload of blood volume [3]. The embolism of thrombi from the LAA can lead to an ischemic stroke if the thrombus is carried into the cerebral arteries. Since the role of the LAA is not well-established, the solution for avoiding thromboembolism in AF patients has been the exclusion or occlusion of the LAA [3]. However, possible complications can arise after an LAA exclusion procedure, which include procedure-related stroke, device embolization, and device-related thrombus (DRT) after LAA occlusion (LAAO). This may cast doubt on the effectiveness of excluding the LAA as a therapeutic measure. This study aims to assess the role of the LAA on the flow in the LA. To this end, we used patients who underwent an LAAO procedure and compared the flow dynamics in the LA before and after LAAO to isolate any potential role of the LAA.

METHODS

In this study, we obtained clinical data for 6 patients who underwent an LAAO procedure with Watchman or Amulet devices from Mayo Clinic, Copenhagen University Medical Center, and the Aarhus University Hospital. The obtained data included computed tomography (CT) images and doppler echocardiography data both before and after the LAAO procedure. The segmentation of the left atria was performed using Mimics Research 24.0 and 3-Matic 16.0 (Materialise, Belgium) from the CT images of the 6 patients pre- LAAO to generate 3D digital models. The geometry was extracted at the E-wave while conserving the saddle shape of the mitral valve by using a spline function in Mimics, as previously done by Vogl et al [4]. Finite element simulations were performed by FEops (Ghent, Belgium) to deploy an LAAO device into the LA model that would match the clinical deployment seen in the CT images. This allowed for mimicking the geometry of the LA post-deployment, resulting in 6 post-LAAO 3D digital models. The CFD simulations for each of the 6 patients, pre- and post- LAAO, were conducted in Ansys Workbench 2020. The 3D digital models were imported, and extensions were added at the boundaries of the LA to ensure that the flow was fully developed and to overcome any entrance effects. The boundary conditions (BC) were adopted from echocardiographic data including

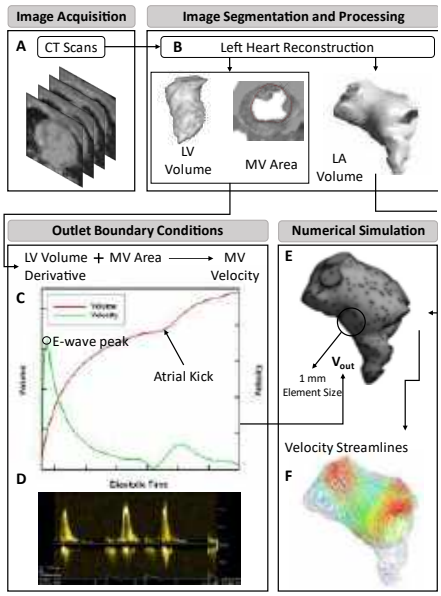

Fig 1. Methodology Workflow

the velocity at the mitral valve for each patient. An element size of 1 mm was chosen for the polyhedral mesh adopted in these simulations based on a previously done mesh independence study [4]. Transient simulations were performed for 3 cardiac cycles each, and the data from the last cycle was used in our analysis [5, 6]. **Fig.1** presents the discussed workflow. From the CFD simulations, we obtained the velocity distribution in the left atrium and the Wall Shear Stress (WSS) distribution along the atrium wall. Using the WSS data, the Time Averaged Wall Shear Stress (TAWSS; EQ1), Oscillatory Shear Index (OSI; EQ2), and Relative Residence Time (RRT; EQ3) were calculated using the below equations:

$$TAWSS = \int_0^T |WSS| \, dt \quad \text{(EQ1)}$$

$$OSI = \frac{1}{2}\left(1 - \frac{\left|\int_0^T WSS \, dt\right|}{TAWSS}\right) \quad \text{(EQ2)}$$

$$RRT = \frac{1}{(1-2 \times OSI) \times TAWSS} \quad \text{(EQ3)}$$

RESULTS

The obtained streamlines and contours for two of the patients are shown in **Fig.2** and **Fig.3**. Velocity streamlines were generated at the E-Wave for both pre- and post- LAAO. This showed a slight decrease in velocity for patient 1, but no appreciable change in patient 2. To better quantify the results, the velocity values were exported and the velocity frequency for each model was plotted. Velocity magnitudes pre- and post- LAAO were close for patient 2, but patient 1 exhibited a difference of 0.6 m/s at low frequencies, where the elevated velocities were more frequent post-LAAO, as well as a different distribution of maximum velocity (**Fig.4**). The TAWSS and OSI contours showed a consistency in the distribution of TAWSS between pre- and post-LAAO. The average value of TAWSS across the LA and across all 6 patients decreased from 2.54 ± 2.61 to 1.36 ± 1.03 post-LAAO ($p < 0.05$). The average value of OSI across the LA and across all 6 patients increased slightly between pre- and post-LAAO (0.16 ± 0.11 and 0.18 ± 0.10, respectively, $p < 0.05$). The RRT contours show a more widespread distribution of elevated RRT post-LAAO. The average value of RRT across the LA and across all patients has increased from 1.57 ± 1.74 to 1.99 ± 1.77 post- LAAO ($p < 0.05$). The two patients also exhibited an elevated pressure post-LAAO.

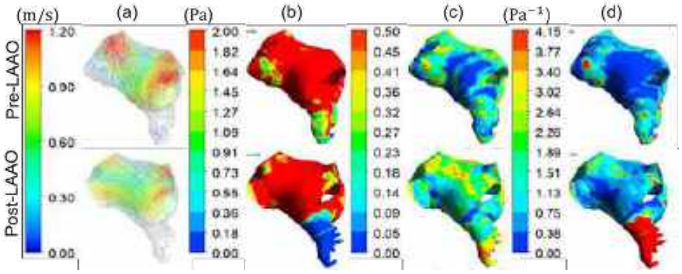

Fig 2. Patient 1 (a) E-Wave Velocity Streamlines, (b) TAWSS, (c) OSI, and (d) RRT Contours

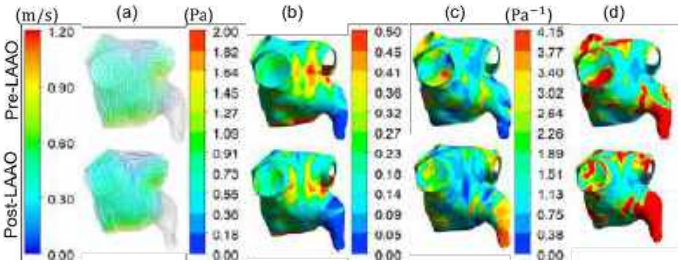

Fig 3. Patient 2 (a) E-Wave Velocity Streamlines, (b) TAWSS, (c) OSI, and (d) RRT Contours

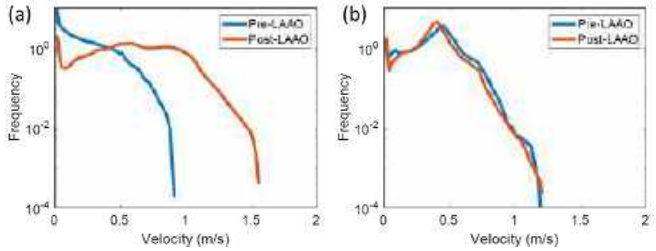

Fig 4. Velocity Frequency at E-Wave for patients (a) 1 and (b) 2

DISCUSSION

Generally, a decrease in TAWSS was observed post-LAAO. This means that despite occluding the LAA, which is clearly a site of low TAWSS pre-LAAO, the average value of TAWSS decreased in the main body of the atrium. This is perhaps due to an elevated pressure inside the body of the LA due to the loss of its distensible decompression chamber. Previous studies showed that an increase in pressure can lead to an increased intima-media thickness (IMT), which in turn is associated with low WSS, so perhaps a similar mechanism is occurring in the LA [7]. The shear stress imposed by the blood flow on Endothelial cells promotes certain intracellular biochemical signals [7]. It was shown that low TAWSS promotes the expression of vasoconstrictor endothelin-1 (ET-1), which in turn activates the expression of adhesion molecules that initiate thrombus formation [9]. The average decrease in TAWSS pre- and post- LAAO explains the increase in RRT despite a relatively consistent OSI average. The results of this study show that the exclusion/occlusion of the LAA may have adverse effects on the hemodynamics of the LA in the long run, possibly enhancing risks of thrombogenesis (including DRT) and consequently thromboembolic events. More patient data is needed to confirm these findings and long-term follow-ups are needed to have a comprehensive understanding of the LAA removal effects.

REFERENCES

[1] Welch W et al., *London, UK: MacMillan and Co*, 1909.
[2] Blackshear J et al., *ATS*, 61(2):755-9, 1996.
[3] Al-Saady N et al., *Heart*, 82(5):547, 1999.
[4] Vogl B et al., *JICE*, 65(1):83-96, 2022.
[5] Trusty P et al., *Journal of Biomechanics*, 109:109917, 2020.
[6] Bosi G et al., *FCE*, 5:34, 2018.
[7] August A et al., *JPHCP*, 293(2):H1031-7, 2007.
[8] Collins C et al., *Experimental Gerontology*, 46(2-3):185-8, 2011.
[9] Grover-Páez F et al., *DRCP*, 84(1):1-10, 2009.

A BIOMECHANICAL EVALUATION OF TWO INTERNAL FIXATION METHODS WITH DIFFERENT SCREW DIRECTIONS FOR CAPITELLUM FRACTURES

Hui Zhang, Justin E. Hellwinkel, Kiran J. Agarwal-Harding, Thomas R. Gardner, Susanne M. Roberts

Department of Orthopedic Surgery, Columbia University, New York, New York, USA

INTRODUCTION

The capitellum of the humerus articulates with the radius of the forearm, playing an important role in the forearm's pronation and supination. Fractures of the capitellum are commonly treated with internal fixation, which uses headless compression screws to restore the elbow's native anatomy and stability. Nevertheless, fixation of distal humerus factures remains a clinical challenge when the fracture does not heal anatomically, which can cause serious issues such as long-term pain and disability. The failure is dependent on many factors, including bone density, angle of the fracture plane, screw orientation and trajectory, etc. So far, very few studies have studied the effect of screw orientation on failure fixation.

In this study, we used two internal repair methods with different screw orientations, parallel and non-parallel, and compared their fixation stability. Computerized tomography (CT) scans of fracture patients were used to define the fracture plane.

The objectives were three-fold: 1) to characterize capitellum fractures from patients' CT data; 2) to define two screw orientations from the literature and retrospective case review; 3) to evaluate and compare the stability of the two screw orientations through mechanical testing. Specifically, the average characteristics of capitellum fracture obtained from CT were used to simulate the fractures on biomimetic sawbones first, and then two internal repairs were performed, and lastly cyclic compression was used to evaluate the fixation results. We hypothesized that the non-parallel screw orientation would provide better fixation stability than the parallel orientation in terms of higher ending peak force and larger number of loading cycles.

METHODS

To characterize the fracture, CT images of 11 female patients were used (age 51.8±24.2 years; BMI 27.3±11.7 kg/m^2) with IRB approval. Each humerus with its capitellum fragment was 3-D reconstructed (Figure 1A), and a plane was best-fitted to the fracture edge. To minimize measurement error attributed to misalignment between anatomical planes of the elbow to the corresponding CT planes, a set of local anatomical planes (sagittal, coronal, and transverse) for the humerus were constructed (Figure 1B). The orientation of the fracture plane was quantified by the distance between the most lateral point on the lateral epicondyle and the best-fitting plane (defined by point-to-plane distance), and by three plane-to-plane angles. The average for the 11 patients of the point-to-plane distance and the plane-to-plane angles defined the cutting plane to simulate the capitellum fracture (Figure 1C).

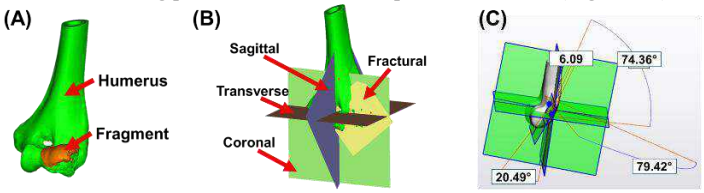

Figure 1: Illustration of (A) reconstructed humerus and fragment from a patient, (B) local anatomical planes (sagittal, coronal, and transverse) and fractural plane, (C) simulated fracture plane on the 3D-scanned biomimetic humerus with plane-to-plane angles of 79.4° (fracture-sagittal), 74.4° (fracture-transverse), 20.6° (fracture-coronal), and 6.1 mm (location).

Capitellar fracture was simulated on 21 biomimetic humeri (Model #3404, Sawbones, Vashon, WA, USA), using a custom-designed, 3D-printed jig. Both methods inserted the screws from the lateral ridge of the capitellum. The paralleled screw orientation was defined as 30˚ off the anteroposterior direction to simulate the clinical setting and to assure the entire screw body embedded in the humerus, whereas the non-parallel method inserted the two screws angled towards the olecranon fossa in diverging directions (Figure 2A). The surgeon secured the jig onto the humerus with K-wires (Figure 2B), and used the slots designed

in the jig to create the fracture plane between the humerus and capitellum with a sagittal saw (blade thickness: 0.38 mm). Afterwards, the surgeon chose randomly between the two sets of screw trajectories in the jig to insert K-wires for directional guidance. The surgeon pre-drilled and inserted the cannulated screws into the sawbones to reattach the capitellum fragment to the humerus. The parallel method was used to repair 10 biomimetic humeri, and non-parallel method was used to repair 11 humeri.

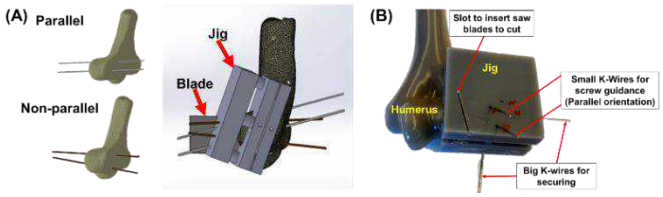

Figure 2: (A) Illustration of the screw orientation of the two repair methods (left) and of the cutting jig mounted on the biomimetic humerus ready for fracture simulation (right). (B) Photograph of a biomimetic humerus with the jig mounted on and with K-wire inserted for parallel-orientation repair.

For mechanical testing, each humerus was cut and potted in a square aluminum cylinder using expansion cement, then mounted in the testing platform (Figure 3), with the angle between the humerus axis and the loading direction of 20 degrees (20-degree flexion, at which maximum load was transmitted through the capitellum [1]). Sinusoidal loads were applied to the fragment, starting with a base of 10 N and peak of 75 N. The amplitude of the load was increased by 75 N every 10,000 cycles until reaching 600 N (total 80,000 cycles) or until clinical failure (defined as the subsidence of the fragment reached 2 mm), whichever came first.

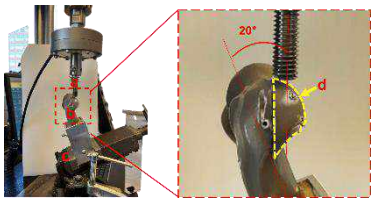

Figure 3: Photograph (left) of testing setup with a closer view (right) of the loading tip and the repaired fragment. (a) Actuator. (b) Potted specimen. (c) Base clamp. (d) Capitellum fragment.

For statistical analysis, maximum applied load, number of cycles, and amount of applied work required to reach clinical failure were analyzed using a Student's t-test to determine if differences existed between the two repair methods. The level of significance was set at $p \leq 0.05$.

RESULTS

The angle between the fracture and sagittal planes, between the fracture and coronal planes, and between the fracture and transverse planes was 79.4±9.0, 20.6±12.2, 74.4±10.8 degrees, respectively (Figure 1C). The distance between the most lateral point on the lateral epicondyle and the fractural plane was 6.1±2.4 mm.

The maximum peak force in the sinusoidal loading until clinical failure for the parallel method was 450.0±106.1 N and 375.0±94.9 N ($p<0.05$) for the non-parallel method. Similarly, the number of cycles reaching clinical failure for was 53,801±16,654 cycles, which was greater than 42,346±14,141 cycles for the parallel method ($p<0.05$). The amount of work applied to the fragment for the parallel method was 330.0±246.5 N·m, and the work for the non-parallel was 287.5±240.3 N·m. There was no significant difference in the amount of work between the two methods ($p = 0.267$).

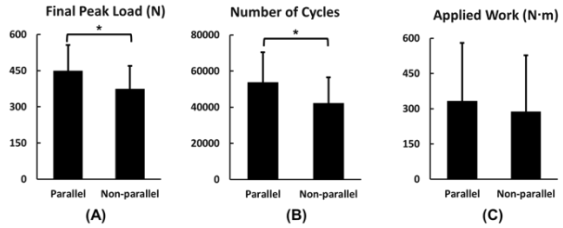

Figure 4: (A) Maximum peak force in sinusoidal loading until clinical failure for each method. (B) Number of cycles. (C) The amount of work applied to the fragment. *p<0.05

DISCUSSION

In this study, we used data from actual patients to simulate the capitellum fracture in biomimetic humeri that were subsequently repaired by one of two internal fixation methods. We found that the method with parallel screw orientation demonstrated better stability than that with non-parallel orientation, in terms of higher final peak force of cyclic loading and larger number of cycle numbers.

The result is opposite to our expectation. Initially, we believed the non-parallel method might be more robust, by embedding the screws using the strongest portion of the humerus i.e. olecranon fossa. The better performance of the parallel method may be explained because the screws, due to their parallel orientation, share the applied load from the actuator. This is in contrast to the screws with non-parallel orientation which resist the load unevenly, with the more superior screw initially absorbing the brunt of the load and exhibiting initial failure, with the load then shifting to the inferior screw.

Compared to a previous study [2], our samples underwent higher force levels (375.0±94.9 N for our Method 2 vs 151.9±52.5 N for their best group) and similar load cycles (42,346±14,141 cycles vs 43,944±21,652 cycles). The high force level may be attributable to the apparently stronger biomimetic humeri used as compared to the cadaveric humeri (from old donors used in [2]). The similar number of load cycle numbers for different humeri maybe be attributable to the application of different clinical failure criteria: subsidence of 2 mm by for this study and 3 mm by their study.

The study has some limitations. First, the sample size of the patients used to generate a representative pattern for capitellar fractures was small. Second, our study is most applicable for younger patients with health bone who are prone to this injury, but the results may be different for the elderly population with decreasing bone density. One advantage of this study is the use of a carefully defined and repeatable fracture plane based on actual patients. Another strength of the study is the use of biomimetic humeri instead of cadaveric humeri to minimize variability due to age, sex, density and geometry.

Therefore, the use of a parallel screw orientation provides a more mechanically robust method of fixation for shear fractures of the capitellum compared to a diverging orientation with purchase in the olecranon fossa. The ability of the capitellum to withstand axial load after internal fixation is paramount to a successful outcome and optimization of fixation constructs may allow earlier range of motion and weight bearing for these patients.

ACKNOWLEDGEMENTS

The study was funded in part by the Orthopaedic Scientific Research Foundation (OSRF 21_006). We also acknowledge Stryker for donating the screws for the project

REFERENCES

[1] Elkowitz, SJ et al., *J Orthop Trauma*, 16.7:503-506, 2002.
[2] Wagner FC et al., *J Shoulder Elb Surg*, 29.9:1912-1919, 2020.

ESTIMATION OF FLOW RATES FROM CLINICAL PRESSURE MEASUREMENTS FOR INDIVIDUALIZED CFD OF CEREBRAL VENOUS STENOTIC DISEASE

Gurnish Sidora (1), Anna Haley (2), Nicole M. Cancelliere (3), Vitor M. Pereira (1,3), David A. Steinman (1,2)

(1) Institute of Biomedical Engineering, University of Toronto, Toronto, ON, Canada
(2) Department of Mechanical & Industrial Engineering, University of Toronto, ON, Canada
(3) Department of Neurosurgery, St. Michael's Hospital, Toronto, ON, Canada

INTRODUCTION

There is increasing interest from clinicians to understand cerebral veins hemodynamically, e.g., transverse sinus (TS) stenosis can cause debilitating symptoms of pulsatile tinnitus (PT) and idiopathic intracranial hypertension (IIH) [1]. Computational fluid dynamics (CFD) can provide insight into the underlying flow instabilities [2]; however, it is not without its challenges [3]. Current clinical workflows for assessing these patients relies solely on computed tomography venograms (CTV) and intra-arterial angiography, which provide anatomical information, and invasive pressure-measurements, which provide some functional information, but leaving CFD engineers without patient-specific flowrates. Unlike cerebral arteries, for which vessel diameters adapt to flow rates in a way that can be used to estimate the latter from the former, low-pressure cerebral venous drainage networks can vary markedly from patient-to-patient, and there is no apparent relationship between vein diameter and flow rate [4].

The primary objective of this study was to develop and employ a simplified Bernoulli method for back-calculating an individual's flow rate from available routine clinical angiography and manometry, and use this to determine the impact of using generic flow rates for venous CFD. A secondary objective was to use CFD to determine how well the Bernoulli-estimated pressure drops agreed with those from the full Navier-Stokes equations.

METHODS

Patient selection: This study included 10 patients with unilateral PT attributed to a moderate to severe ipsilateral TS stenosis, who had undergone endovascular stenting at Toronto's St. Michael's Hospital. Institutional review board approval was obtained for access to the anonymized and de-identified medical records and images. Cases were selected to span a wide range of focal pressure drops obtained during the procedure (see **Table 1**).

Lumen segmentation: CTV datasets were segmented semi-automatically using the seed-driven, gradient-based segmentation algorithm in ITK-SNAP. Intra-arterial angiographic images were used to further guide removal of small cortical veins and smoothing of the surface using MeshMixer. The Vascular Modelling ToolKit was used to remesh and improve the quality of the surface triangulations for subsequent CFD volume meshing.

Flow rate estimation: We simplified Bernoulli's equation along a streamline by assuming centerline stenotic pressure drops are driven primarily by inertial effects, and stenotic velocities are high enough for upstream velocities to be neglected. Exploiting conservation of mass, the following simple formula was derived for cycle-average flow rate:

$$Q = \frac{K}{A_s}\sqrt{\frac{2\Delta p}{\rho}} \quad (1)$$

where Δp is the clinically-measured cycle-average stenotic pressure drop; A_s is the minimum stenosis cross-section area, derived from the CTV segmentation; and ρ is the blood density, assumed to be 1057 kg/m^3. The constant K reflects the assumed velocity profile shape, and can range theoretically from 1 (turbulent/plug) to 2 (laminar/parabolic). Considering that venous Reynolds numbers are O(10^2), we assumed K=1.5 (i.e., halfway between those extremes), which was done prior to performing any CFD calculations so as not be biased by them.

Computational fluid dynamics: The segmented lumens were clipped at the superior sagittal sinus (SSS) inlet proximal to the torcula, and at the internal jugular vein outlets. Fully developed pulsatile flow was imposed at the SSS (and straight sinus, if present, using an 80:20 flow split [5]) by scaling a representative venous waveform [2] by Q. Simulations were performed using a high-fidelity CFD solver and meshing strategy detailed in [6]. Meshes averaged ~4 million tetrahedral and boundary layer elements, with an average ~12,000 time-steps per cardiac cycle to satisfy CFL conditions. Each case was simulated using both the individual Q calculated from Eq. 1. and a generic flowrate of Q=335 mL/min corresponding to average flow in left/right TS [2].

CFD pressure drops were calculated from planes placed at the inlet and stenosis (I-S) to align with the Bernoulli assumptions, as well as from planes proximal and distal to the stenosis (P-D) to reflect the clinical measurement locations. Pressure values were obtained from the point of maximum velocity on the respective planes. Spectral power index (SPI) was calculated from the CFD wall shear stress data, to visualize areas experiencing flow instabilities above 25 Hz [7].

Table 1: Clinical and CFD-derived quantities for the N-10 cases (flow rates in mL/min, pressure drops in mmHg)

Case	Area Stenosis	Clinical Δp	Individual Q	Individual Δp *I-S*	Individual Δp *P-D*	Generic Δp *I-S*	Generic Δp *P-D*
A	83%	3	224	2.75	2.67	5.66	5.39
B	68%	5	491	4.44	3.84	2.26	2.01
C	88%	19	301	18.7	15.9	25.2	23.0
D*	94% 85%	6	320	5.88 6.07	4.72	4.69 6.37	4.75
E	89%	8	209	7.16	6.09	16.6	14.4
F	46%	3	479	3.05	1.81	1.72	1.03
G	80%	4	312	3.63	3.18	4.37	3.48
H	72%	5	270	4.99	4.16	7.42	6.88
I	84%	9	324	9.50	8.14	10.0	8.59
J	80%	11	280	11.7	9.87	17.4	14.1

**For fenestrated case, area stenosis and Δp (I-S) are shown for each channel.*

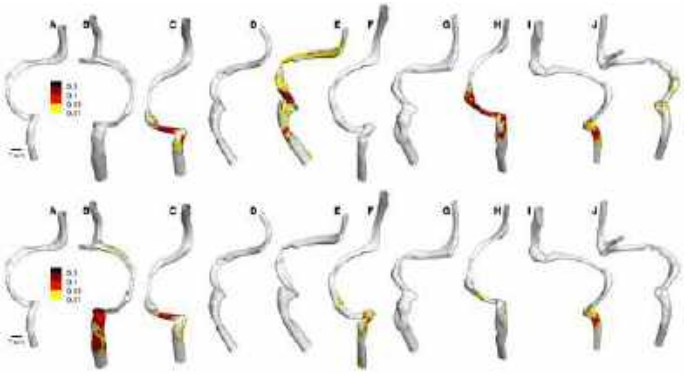

Figure 1: SPI maps of flow instabilities for the N=10 cases, using generic (top) and individual (bottom) flow rates for high-fidelity CFD. Flow direction is top to bottom.

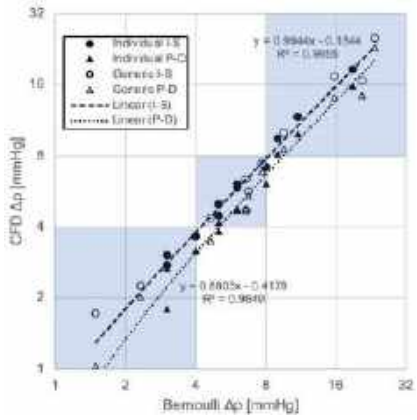

Figure 2: Bernoulli-estimated vs. CFD pressure drops from inlet to stenosis (I-S) and proximal to distal (P-D) to stenosis. Note the log scale of the axes. High sensitivity and specificity are evident from all data points falling within (shaded) clinical categories of low (<4), moderate (4-8), and high (>8) mmHg pressure drop.

RESULTS

Table 1 demonstrates the range of stenosis severities and pressure drops for our cohort, also making it clear that there is no obvious relationship between the two, and hence emphasizing the confounding role of flow rate. Bernoulli-derived Q differed significantly from the generic flow assumption of Q=335 mL/min, with differences of up to 47%. CFD-derived pressures also differed significantly for individual vs. generic simulations, by up to 97%. SPI maps shown in **Figure 1** further demonstrate that the intensity and extent of flow instabilities was not well predicted by the generic flow rates, with apparent differences in all cases expect A, D, G and I.

Table 1 also shows that the pressure drops predicted by CFD using the Bernoulli-derived individual flow rates were remarkably similar to the clinical pressure drops from which the individual flow rates were derived. This is more clearly shown in **Figure 2**, where Bernoulli pressure drops were in near perfect agreement with CFD (I-S) predictions. Regression using the proximal-distal (P-D) data suggests an average pressure recovery (not captured by Bernoulli) of 12%, but with minimal impact on clinical categorization.

DISCUSSION

Our results suggest that individual flowrates have a non-negligible effect on patient specific CFD modelling of venous stenotic flow disturbances. While we have not yet validated the predicted flow rates, we note that they all fall within recently-reported normative values [5]. The near-perfect agreement between CFD and Bernoulli I-S pressure drops confirms our assumption that inertial effects dominate. Minor differences between CFD I-S and P-D pressure drops confirm there is minimal pressure recovery distal to the stenosis. We also note that our Bernoulli formula predicted a 70:30 flow split for fenestrated case D, which was in excellent agreement with the 69:31 actual flow split from CFD. That our educated guess of K=1.5 was reasonable is evidenced by actual values of K=1.42±0.07 from CFD data at the stenosis planes.

An important and exciting corollary of our study is that, given minimum cross-section area and flowrates from, say, MRI, one could readily estimate pressure-drops, providing valuable information to clinicians looking to assess them *non-invasively*. A recent attempt to do so relied on complex post-processing of 4D flow MRI data [8], and while shown to be accurate against invasive manometry, even the editorial introducing this study conceded that the imaging and processing are still too cumbersome from routine clinic use [9].

Our approach is inherently limited to cases with at least mild focal stenoses, or tandem stenoses with limited pressure recovery (e.g., Case J), so is not intended to completely replace cerebral venous manometry. Rather, we believe it shows promise as a *clinically effective* solution for retrospectively estimating (unknown) flow rates *and* prospectively estimating pressure drops in patients with clinically suspect stenoses.

ACKNOWLEDGEMENTS

DAS: Natural Sciences and Engineering Research Council of Canada Discovery Grant. GS: Ontario Graduate Scholarship.

REFERENCES

[1] Narsinh KH et al, *JAMA Otolaryngol Head Neck Surg* 148, 2022
[2] Pereira VM et al, *J Neurointervent Surg* 13, 2021.
[3] Steinman DA et al, *J Neurointervent Surg* 15, 2023.
[4] Riggeal BD et al, *Neurology* 80, 2013.
[5] Roberts GS et al, *Radiology,*307(3), 2023.
[6] Haley AL et al, *J Biomech. Eng* 145:7, 2023.
[7] Khan MO et al*., J Biomech* 52, 2017
[8] Zhang Y et al, *Eur Radiol* 33, 2023.
[9] Battal B and Zamora C, *Eur Radiol* 33, 2023.

NON-NEWTONIAN EFFECTS ON SINUS FLOW AFTER AORTIC VALVE REPLACEMENT

A. Bshennaty (1), B. Vogl (1), Z. Zhang (1), A. Sularz (2), B. Lee (1), M. Alkhouli (2) and H. Hatoum (1,3)

(1) Department of Biomedical Engineering, Michigan Technological University, Houghton, MI, USA
(2) Department of Cardiovascular Medicine, Mayo Clinic, Rochester, MN, USA
(3) Health Research Institute, Center of Biocomputing and Digital Health and Institute of Computing and Cybersystems, Michigan Technological University, Houghton, MI, USA

INTRODUCTION

Aortic Stenosis (AS) is a major complication that affects 5 to 10% of older adults and carries significant health risks [1]. Surgical aortic valve replacement (SAVR) and minimally invasive transcatheter aortic valve replacement (TAVR) are the standard treatments for patients with severe AS [2]. However, both procedures are associated with adverse outcomes such as thrombosis and calcification that can lead to degradation and increase the risk of stroke in case of thrombus embolization [3].

The relationship between hemostasis and thrombus formation has long been established [4]. In-vitro experimental work has been an asset for better understanding blood stasis in the aortic sinus in correlation with thrombosis and calcification [5]. Most of the experimental work often uses saline or water and glycerin mixtures as blood analogs, which fail to capture the non-Newtonian viscoelastic properties of blood. This non-Newtonian behavior is especially important in small vessels and cavities such as the sinus, where blood is subjected to lower shear rates due to recirculation and flow reversal.

This study aims to experimentally investigate the impact of the non-Newtonian properties of blood on flow stasis in the sinus.

METHODS

Two mixtures were considered for the non-Newtonian blood analog, one containing water and xanthan gum (a natural polysaccharide) and another containing water, glycerin, and xanthan gum. The first solution was prepared by adding 0.0375% by weight of xanthan gum to distilled water [6]. The second solution was prepared by adding 37.6% by weight glycerin and 200 ppm xanthan gum to distilled water [7]. The 2 samples were analyzed using a Discovery Hybrid Rheometer (TA Instruments, New Castle, DE, USA) and measurements were recorded for shear rate values between 0 and 300 s^{-1}. Each test for each sample was repeated 3 times. The resulting shear stress and viscosity values were averaged and plotted against the shear rate for all samples. The data was compared with rheological data of whole blood from previous studies by Cherry et al. and Brooks et al. [8, 9].

To test the flow dynamics in the sinus after AVR, we deployed 2 valves (a 25mm Edwards surgical Magna and a 23mm transcatheter Edwards SAPIEN 3 Ultra) in a left heart simulator. Our flow loop is comprised of a reservoir with a valve, representing the left atrium and mitral valve, a bladder pump, representing the left ventricle, and an acrylic chamber, representing the aortic root, in which the bioprosthetic valves were deployed. A LabVIEW code controls a compressed air line which contracts and expands the pump. A compliance chamber and a gate valve were added to emulate arterial compliance and control the flow rate, respectively. The temperature of the solution was set and maintained at 37°C. The cardiac output was 5 L/min under a pressure of 120/80 mmHg. Rhodamine B particles were seeded to perform particle image velocimetry (PIV). A Single Cavity Diode Pumped Solid State, High Repetition Rate Laser (Photonic Industries, NY, USA) was used to illuminate the particles in a plane along the center of the sinus. A high-speed CMOS camera (Photron, Inc) captured time-resolved and phase-locked images of the flow in the sinus at the rate of 4000 frames per second. The images were then run through a multi-pass cross-correlation PIV algorithm to compute the displacement of the particles and their velocities. By post-processing the data, the vorticities and shear stresses were computed.

RESULTS

It was found that the rheology of the non-Newtonian solution comprised of water, glycerin, and xanthan gum was most consistent with that of whole blood (**Fig.1**) compared with different references in literature [8, 9], and this solution was prepared for the PIV experiment.

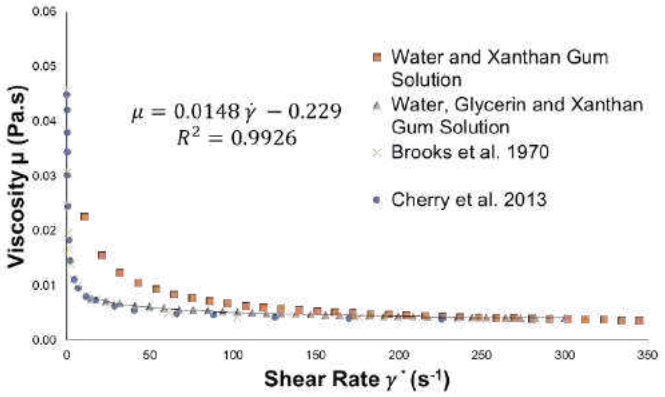

Fig 1. Viscosity vs. Shear Rate plots of the different solutions and comparisons with whole blood from different references [8, 9].

Fig.2 and **Fig.3** show the different phases of the cardiac cycle, namely at peak systole, deceleration, and diastole. For the experiments run using

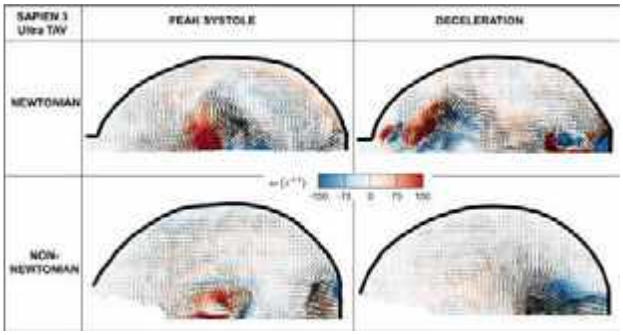

Fig 2. Peak Systole and Deceleration Frames for the SAPIEN 3 Ultra Experiments with Vorticity Contours

the SAPIEN 3 Ultra, there were significant differences in the sinus flow at each of the selected frames. At peak systole, the Newtonian solution exhibited a counterclockwise (CCW) vortex with velocities in the sinus that are higher than those exhibited by the non-Newtonian solution. At

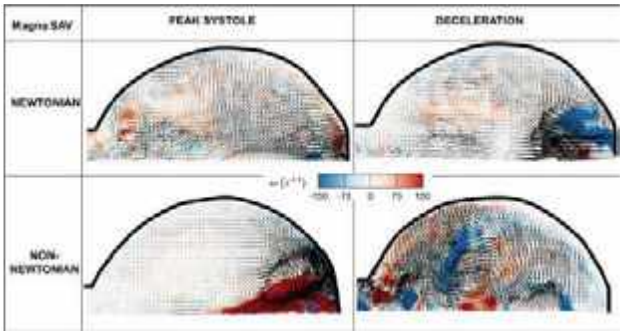

Fig 3. Peak Systole and Deceleration Frames for the Magna Experiments with Vorticity Contours

Deceleration, the interaction of the CCW flow with the returning flow led to high vorticity in the sinus for the Newtonian solution compared to the reverse flow with lower vorticity that was observed for the non-Newtonian solution. Differences in the flow at each frame were also observed for the experiments using the Magna 25mm valve. At peak systole, the non-Newtonian solution led to more elevated vorticity compared with the Newtonian solution. In addition, the location of the CCW vortex was different. At Deceleration, the Newtonian solution had one clockwise vortex by the end of the sinus while the non-Newtonian solution had several vortices. In order to better quantify the results, the

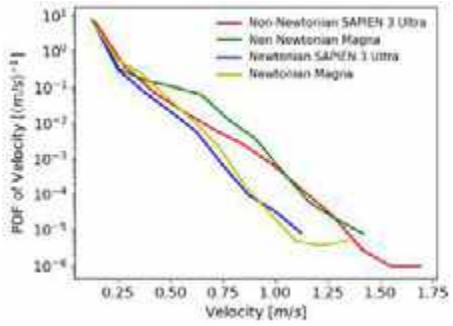

Fig 4. PDF of sinus velocities with the different solutions.

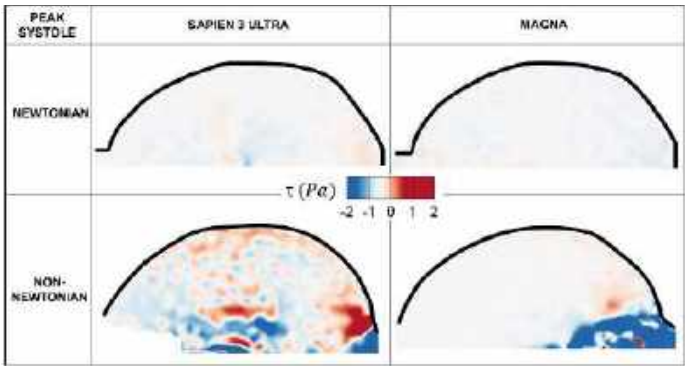

Fig 5. Shear Stress Contours at Peak Systole

probability density function (PDF) of the velocity was plotted in **Fig.4**, showing that higher velocities were more frequent for the non-Newtonian cases than for the Newtonian cases. The contours of the shear stress (**Fig.5**) showed that the shear stress for the non-Newtonian cases was much higher than those for the Newtonian cases.

DISCUSSION

The results of this study have shown considerable differences in the flow dynamics in the sinus between the Newtonian and non-Newtonian solutions. As expected, since the sinus is a region characterized with flow recirculation and in some areas and time points stagnation, the non-Newtonian properties of the fluid at low shear rates should be accounted for in experimental modeling in order to accurately mimic the hemodynamics of the aortic sinus, especially when relevance to potential clinical outcomes is needed. However, it seems that some aspects of flow behavior are impacted more than others. It was found that despite minor differences in the velocity distributions between the Newtonian and non-Newtonian regimes, there are significant differences in the distribution of shear stress. This correlates with the fact that the non-Newtonian solution is expected to exhibit a higher viscosity at low shear rates, which leads to an elevated shear stress. The underestimation of shear stress when using a Newtonian solution should be taken into account when attempting to conduct in-vitro experiments.

REFERENCES

1. Lindman B et al., *Circulation*, 143(15):1455-7, 2021; 2. Spadaccio C et al., *F1000Research*, 8, 2019; 3. De Marchena E et al., *JACC CI*, 8(5):728- 39, 2015; 4. Mikell F et al., *Circulation*, 66(4):755-63, 1982; 5. Hatoum H et al., *JTCS*, 157(2):540-9, 2019; 6. Mann D et al., *Biorheology*, 27(5):711-33, 1990; 7. Moravia A et al., *Journal of Biomechanics*, 2022; 8. Cherry et al., *Physics of Fluids*, 25(7), 2013; 9. Brooks et al., *Journal of Applied Physiology*, 28(2):172-7, 1970.

DEVELOPING AN EXPERIMENTALLY INFORMED STRUCTURALLY REPRESENTATIVE HUMAN LUNG MODEL

A. Badrou (1), C. A. Mariano (1), G. O. Ramirez (1), M. Shankel (1), T. M. Nelson (1), M. Eskandari (1,2,3)

(1) Department of Mechanical Engineering, University of California Riverside, Riverside, CA, USA
(2) BREATHE Center, School of Medicine, University of California Riverside, Riverside, CA, USA
(3) Department of Bioengineering, University of California Riverside, Riverside, CA, USA

INTRODUCTION

Respiratory diseases are a leading cause of morbidity and mortality in the world, resulting in significant healthcare expenditures, as evidenced by the COVID-19 crisis [1]. Research on pulmonary health indicates that the mechanical properties of the lungs undergo alterations in diseased states [2]. However, understanding of basic lung mechanics is highly limited compared to that of other organs (e.g. bone, heart, etc.), highlighting the need for research advancements to ultimately better understand how diseases may affect respiratory system function.

Numerical simulations are an effective tool for exploring lung diseases and developing innovative therapies [3]. However, prior attempts to construct structural lung models either lacked experimental validation or were based on overly restrictive assumptions, and limited to primarily quantifying airflow dynamics within a rigid structure [4,5]. A recent study established the first inverse finite element model (FEM) of an inflating porcine lung specimen using experimental Digital Image Correlation (DIC) for measure deformations [6]. Nevertheless, this study exclusively concentrates on a 3D reduced-order surface of a pig lung and does not represent the entire organ volume (i.e. airways, parenchyma, pleura).

This present study builds upon the previously developed FEM pipeline [6] while proposing the first 3D solid generalized human lung breathing model as informed by global pressure-volume (PV) loads and resulting local tissue deformations. The experimental real-time and continuous expansion dynamics of the lung's pressures, volumes, and local strains—recorded via our custom PV ventilation apparatus system coupled with DIC measurements [7]—are utilized to introduce a novel inverse FEM optimization scheme, robustly calibrated with patient-specific data.

METHODS

Finite Element Model of the Structural Breathing Human Lungs: A commercially available volumetric lung geometry (Zygote Media Group, Inc., USA) was employed. The centerlines of the airways were extracted using 3D Slicer (The Slicer Community). The parenchyma was meshed in Abaqus (Dassault Systemes, France) using 331,996 tetrahedral elements, enveloped by the pleura composed of 50,719 membrane elements with a 0.2 mm section thickness [8]. The airways were modeled using 1,266 beams. The parenchyma was modeled with a generic elastomeric foam material law [9], where the strain density energy function U_{Foam} is as follows:

$$U_{Foam} = \frac{2\mu}{\alpha^2}\left[\lambda_1^{\alpha} + \lambda_2^{\alpha} + \lambda_3^{\alpha} - 3 + \frac{1}{\beta}\left(J_{el}^{-\alpha\beta} - 1\right)\right] \quad (1)$$

where μ is the shear modulus, α a coefficient, λ_i are the principal stretches, J_{el} is the elastic volume ratio, and β is linked to the Poisson's ratio ν such that $\beta = \frac{\nu}{1-2\nu}$.

The hyperfoam law was coupled with permeability p in a poroelastic formulation to represent air diffusion in the lungs [9]. As each lobe may respond differently to airflow [10], permeabilities were individually assigned to each lobe, resulting in five parameters. Pressure was directly applied to the nodes of the parenchyma near the ends of the airways. A Neo-Hookean material law was used to model the airways defined by the strain energy potential U_{NH} such that:

$$U_{NH} = C_{10}(I_1 - 3) + \frac{1}{D}(J_{el} - 1)^2 \quad (2)$$

where C_{10} and D are material parameters and I_1 is the first deviatoric strain invariant.

The pleura was modeled using biaxial experiments from human samples [11] and fitted with a polynomial hyperelastic law through the Abaqus' evaluation tool [9]. The airways were embedded in the parenchyma, and the trachea was constrained. A rigid plate was positioned behind the lungs, and contact was modeled between the lung and the plate, as well as on the surface of the lungs itself for lobar sliding. These iteratively selected and improved modeling approaches enabled the simulations to reflect experimental observations through the PV coupled DIC ventilation system [7].

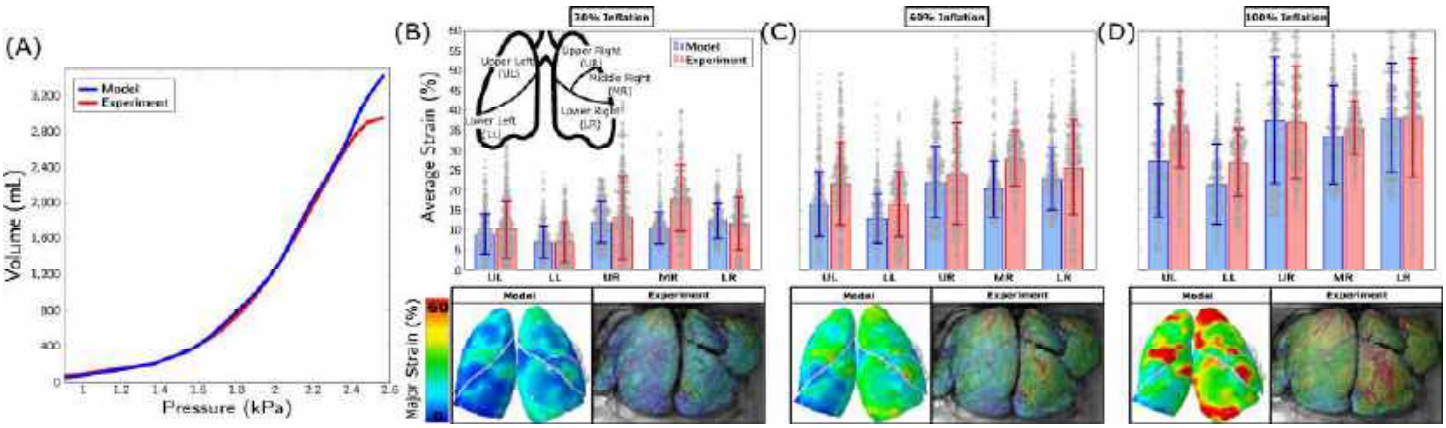

Figure 1: Results obtained after calibrating the model to subject-specific experiments: (A) PV curve during the inflation stage; (B,C,D) show the experimental data versus calibrated model average major strains (± standard deviation) and regional distribution for each lung lobe at 30%, 60%, and 100% of inflation, respectively.

Inverse Finite Element Analysis for Model Calibration: A human lung from a 32-year-old female research-designated donor was tested 48 hours after confirmed brain-stem death (IRB approved exemption, HS 20-180). The lung was placed in a tank and inflated via a volume-control ventilation system at a physiological rate of 15 breaths per minute, where the recorded pressure was used as a model input. Nine material properties (μ and α for the parenchyma, p for each lobe, C_{10} and D for the airways) were calibrated via inverse finite element analysis informed by the experimental global PV and local strains from the DIC [7].

MATLAB's *lsqnonlin* function (MathWorks, USA) minimized the difference between: (i) the model and experimental pressures and volumes at every 0.1 second during inflation resulting in 20 stages to ensure that the PV ventilation curve was adequately represented, and (ii) the average and standard deviation of the major strains calculated for each of the five lobes of the lungs at 30%, 60%, and 100% of total inflation resulting in 15 points of comparison.

RESULTS

The optimization process yielded the material properties listed in Table 1 with 2% and 14% errors for the global PV and local lobe strain, respectively (46hrs on 30 CPUs). The resulting model PV curve accurately represented the shape of experimental inflation trajectory (Figure 1A), especially in capturing the first inflection point commonly observed in expanding human lungs [12]. Similar model average major strain regional distributions and trend values were observed when compared to the three experimental inflation data stages (Figure 1B-D).

Table 1: Initial and calibrated parameters following optimization.

Parameters	Initial Values	Calibrated parameters
μ (kPa)	8.0	4.9
α	1.0	0.8
$p_{UL,LL,UR,MR,LR}$ (10^{-3})(mm s^{-1})	[10;10;10;10;10]	[2.8;2.0;5.0;7.5;4.6]
C_{10} (kPa)	1.0	25
D (MPa^{-1})	1.0	67

DISCUSSION

In this study, we successfully divulge the first 3D structural lung model directly informed by continuous pressures, volumes, and strains experimentally derived from the ventilation of a human lung. While direct one-to-one model-to-experiment comparison is limited, the determined shear modulus for the modeled parenchyma is within the same order of magnitude as results from a previous experimental study that utilized uniaxial tensile tests (when converting the reported elastic modulus with a defined Poisson's ratio of 0.4 to obtain an experimental shear value [13]).

While these preliminary results are promising and highlight the potential of simulating the breathing lung, the model has notable limitations: while it can accurately reproduce the initial PV curve and average strains, the model faces challenges in replicating identical strain patterns, primarily attributed to the strong dependence on areas of pressure distribution and lobe morphology (i.e. initial inflation stages are well represented but then diverge at maximum inflation). Moreover, our model does not yet capture the established anisotropy and viscoelasticity features of the lung [14]. Incorporating these characteristics may enhance our model, particularly when accounting for known heterogeneity in strain patterns [7], and may help to achieve an improved PV match at peak inflation. Nevertheless, the presented results serve as a proof-of-concept for a widely applicable pipeline, intended to be repeated for multiple lungs to create a robust generalized lung model capable of predicting human breathing. Such a model holds the potential to significantly advance the field of pulmonary medicine by deepening our understanding of lung physiology and guiding future research inquiries on both healthy and diseased lung biomechanics.

ACKNOWLEDGEMENTS

Supported in part by a Dassault Systemes U.S. Foundation Grant, the Opportunity to Advance Sustainability Innovation and Social Inclusion (OASIS) UCR and State of California Climate Action Through Resilience Program, the Eugene Cota Robles Fellowship, and the National Science Foundation Graduate Research Fellowship.

REFERENCES

[1] Kaye, A D et al., *Best Pract Res Clin Anaesthesiol*, 35:296-305, 2021 [2] Nelson, T M et al, *Sci Rep*, 13:4564, 2023 [3] Morlion, B et al., *IEEE Trans Biomed Eng*, 52:1180-1187, 2005 [4] Walters, D K et al, *J Biomech Eng*, 133:3-11, 2011 [5] Noferest, S et al, *Math Comput Model Dyn Syst*, 24:87-101, 2018 [6] Maghsoudi-Ganjeh, M et al, *Front Bioeng Biotechnol*, 9, 2021 [7] Sattari, S., et al., *Am. J. Respir. Crit. Care Med.*, 207:577-586, 2023 [8] Dietrich, C., et al., *Ultrasound Med Biol*, 41:351-365, 2015 [9] ABAQUS/Standard User's Manual, v6.9, USA, 2009 [10] Yamada, Y et al, *Respiration*, 99:598-605, 2020 [11] Sattari, S et al, *Acta Biomater*, 155:410-422, 2018 [12] Harris, R S, *Respir Care*, 50:78-98, 2005 [13] Polio, S R et al, *PLoS One*, 13:e0204765, 2018 [14] Eskandari, M et al, *J Appl Physiol*, 125:878-888, 2018

COMPUTATIONAL MODELING OF THE AORTA IN A MOUSE MODEL OF MARFAN SYNDROME TO DETERMINE TEMPORAL CHANGES IN GEOMETRIC BIOMARKERS AND WALL SHEAR STRESS

Yufan Wu (1), Krashn K. Dwivedi (1), Jessica E. Wagenseil (1)

(1) Mechanical Engineering and Materials Science, Washington University in St. Louis, St. Louis, MO, USA

INTRODUCTION

Thoracic aortic aneurysms (TAAs) are characterized by dilation of the aorta, which can dissect or rupture, leading to sudden cardiac death. About 20% of TAAs are associated with mutations in genes associated with elastic fiber assembly, smooth muscle cell contraction, or TGF-β signaling. Mutations in fibrillin-1, an elastic fiber assembly protein, cause Marfan Syndrome (MFS) where TAA is the main cardiovascular complication. In genetically associated TAAs, including MFS, there is evidence that aortic tortuosity correlates with aortic dilation and aneurysm outcomes[1].

Both aortic diameter and tortuosity are geometric parameters that will affect hemodynamic stresses on the aortic wall, which may contribute to aneurysm outcomes. To investigate the effects of diameter and tortuosity on aortic hemodynamics, we built computational models using SimVascular[2] and performed 0D Reduced Order Model (ROM) simulations on wild-type (WT) and fibrillin-1 hypomorphic (*mgR/mgR*)[3] mouse aortas, which are a model of MFS. We present the aortic models along with their tortuosity and maximum radius at different ages during aneurysm progression and for male and female mice. We also obtained the wall shear stress along the aortic length. Future work will extend the models to 3D and determine a range of hemodynamic stresses on the aortic wall over time that may contribute to aneurysm outcomes.

METHODS

Mouse model. Male and female WT and *mgR/mgR* mice were used. Models were created from imaging data on 1 mouse/group that were imaged at 1, 2, 3, and 4 months old. Imaging and modeling for additional mice are ongoing. All studies were approved by the IACUC.

Imaging. Each mouse was anesthetized with 2% isoflurane for magnetic resonance imaging (MRI) on an Agilent 4.7T machine.

Modeling. Images from MRI were loaded into SimVascular. For each image, the path of the aorta was first extracted by connecting points at the center of the aorta. Segmentations were created by outlining the cross-section at each point. Models that represent the shape of the aorta were created by connecting each segmented ring on the software. A similar process was performed on the major branches of the right and left common carotid arteries, the left subclavian artery, and the iliac arteries.

Radius and tortuosity. Centerlines of the aortae were extracted by SimVascular, which contains information about the coordinates of each point and the radius of each segment. Maximum radius was found using MATLAB. Tortuosity (k) was calculated as the ratio of actual length to geometric length,

$$k = \frac{l_{actual}}{l_{geometric}} \quad . \tag{1}$$

0D ROM Simulation. Models with the aorta and the major branches were used to perform 0D ROM Simulation. The 0D ROM simulation iteratively solves the differential equation[4],

$$E(y,t)\dot{y} + F(y,t) + c(y,t) = 0 \ , \tag{2}$$

where E, F, and c are matrices of pressure and flow to be simulated. A resistance-capacitance-resistance (R, C, R) network at the outlets, which quantifies the resistance encountered by blood at the outlet, was chosen as the boundary condition. These values were optimized using MATLAB, with the resistance, capacitance, and inductance (R, C, L) of the aorta as its input. Unlike R, C, R, the values of R, C, L indicate the resistance to blood flow by the vessel itself[3],

$$R = \frac{8\mu L}{\pi R^4}, C = \frac{3L\pi R^3}{2Eh}, L = \frac{\rho L}{\pi R^2} \quad , \tag{3}$$

where μ is the dynamic viscosity of the blood, ρ is the density of the blood, L is the length of the aorta, R is the radius of the aorta, E is the in vivo Young's Modulus of the aorta, and h is the thickness of the aorta.

Wall shear stress. Blood flow in the mouse aorta has a Reynold's number ~ 200 and is considered laminar[5]. Thus, the wall shear stress (WSS) can be derived from the Darcy-Weisbach equation,

$$\tau = \frac{32\,\mu Q}{\pi D^3} \quad , \tag{4}$$

where τ is the wall shear stress, Q is the volumetric blood flow, and D is the aorta diameter.

RESULTS

At 1 month of age, increased diameter of the ascending thoracic aorta and mild tortuosity along the aortic length are visible in *mgR/mgR* mice. An aneurysm (>50% diameter dilation) and more severe tortuosity are apparent in *mgR/mgR* mice around 2 months of age. The aneurysm continues to grow and tortuosity increases with age in *mgR/mgR* mice (Fig. 1).

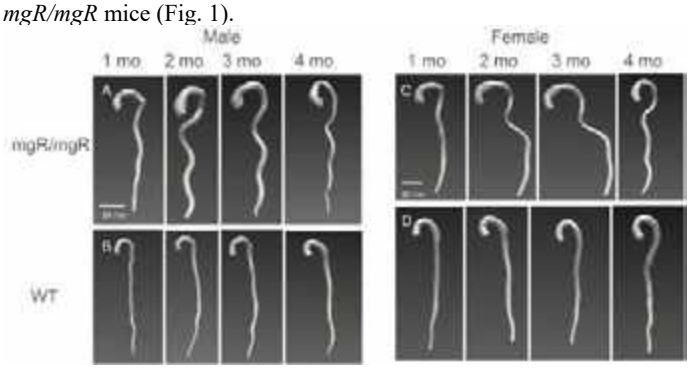

Figure 1: Representative SimVascular models of individual *mgR/mgR* (A, C) and WT (B, D) male (A, B) and female (C, D) mouse aortae at each timepoint (1 – 4 months).

Maximum radius and tortuosity are positively correlated for all mice (Fig. 2A). Maximum radius and tortuosity are lower in WT than *mgR/mgR* aortae and increase with age in both genotypes (Figs. 2B, C).

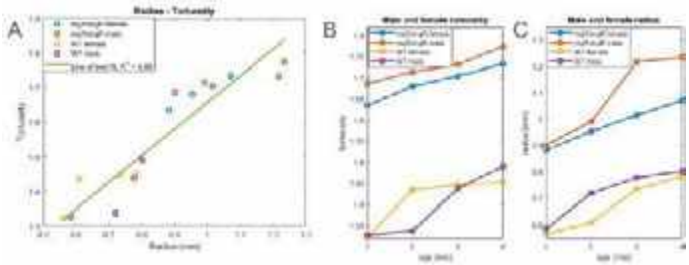

Figure 2: Radius and tortuosity of male and female *mgR/mgR* and WT and mice ages 1-4 months. N = 1 for each sex/genotype.

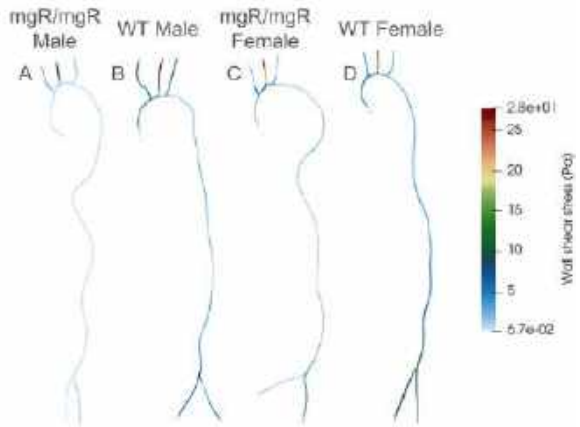

Figure 3: WSS distribution in *mgR/mgR* (A, C) and WT (B, D) male (A, B) and female (C, D) mouse aortae at 4 months old.

From the 0D ROM simulations, lower WSS was observed throughout the aortic length in *mgR/mgR* models than in WT models, as denoted by the lighter blue color on these samples. WSS increased and had a larger variation in WT models around the iliac arteries at the base of the aorta (Fig. 3).

DISCUSSION

Consistent with previous studies, maximum radius and tortuosity increase with age and are larger for *mgR/mgR* mice than WT mice[6]. However, they are simple measurements that indicate only the geometry change during growth and remodeling, and other parameters and computational models are needed to determine how they affect hemodynamic wall stresses in an aneurysmal aorta.

An increase in tortuosity alters the distal pressure and reduces the blood flow[7]. Since WSS and flow are positively related, denoted by Eq. 4, WSS will decrease in more tortuous aortae, which is consistent with our results. Previous studies have indicated that WSS has the potential to be a biomarker for aneurysm outcomes[7]. In our models, the wall shear stress is lower for large aneurysms. Some studies found that lower WSS is related to wall weakening and radius dilation[8, 9], whereas another study found higher WSS to be associated with elastin degeneration and extracellular matrix dysregulation[10].

Although the flow from the 0D simulation can be used to calculate WSS from Eq. 4, the capabilities of 0D simulation are limited, as there are multiple measurements of WSS – time-averaged wall shear stress (TAWSS) and oscillatory wall shear stress (OSI) – that have the potential to be biomarkers for aortic aneurysm outcomes[11]. Therefore, our study presents a preliminary understanding of WSS distribution along the aortic length with and without aneurysms. Additional age and sex dependent simulations on more mice are in progress to examine the temporal development of the disease. Fluid-solid interaction (FSI) simulation will be performed once all data is collected, which will provide a suite of information on biomechanical biomarkers, such as TAWSS and OSI that may be predictive of the growth and eventual rupture of aortic aneurysms.

ACKNOWLEDGEMENTS

Funding provided by NIH R01 HL164800.

REFERENCES

[1] Morris, SA, Curr Opin Cardiol, 30(6):587-93, 2015.
[2] Updegrove, A et al., Ann Biomed Eng, 45(3):525-541, 2017.
[3] Pereira, L et al., Proc Natl Acad Sci U S A, 96(7):3819-23, 1999.
[4] Pfaller, MR et al., Int J Numer Method Biomed, 38 (10):e3639, 2022.
[5] Huo, Y et al., Ann Biomed Eng, 36(5):685-699, 2008.
[6] Takeda, Net al., Int Heart J, 57(3):271-7, 2016
[7] Zegers, ES et al., Neth Heart J, 15(5):191-5, 2007.
[8] Bürk, J et al., Journal of Cardiovascular Magnetic Resonance, 14 (1): 84-84, 2012.
[9] Condemi, F et al., Ann Biomed Eng, 45 (12):2921-2932, 2017.
[10] David, G et al., Journal of the American College of Cardiology, 66 (8): 892-900, 2015.
[11] Bazzi, MS et al., Cardiovasc Eng Technol, 13(4):558-572, 2022.

GEOMETRY AND PHYSICS-INFORMED NEURAL NETWORK MODELING OF FLOWS INSIDE Y-SHAPED BIFURCATED DUCTS

Abdullahi O. Olapojoye (1), Fatemeh Hassanipour(1)

(1) Department of Mechanical Engineering, University of Texas at Dallas, Richardson, TX, USA

INTRODUCTION

Modeling fluid flow in biological structures has significantly benefited from advancements in computational mechanics. Computational tools like Computational Fluid Dynamics (CFD), Fluid-Structure Interactions (FSI), and Finite Element Analysis (FEA) have successfully simulated flows in various biological structures. However, certain challenges arise in solving flows with complex geometries, dynamic boundary conditions, and the high cost of mesh generation and time complexity when applying computational tools to new systems.

To address these limitations, there has been a growing shift toward the application of Deep Learning (DL) solutions. Deep Neural Networks (DNN) excel in generalization by learning to approximate hidden manifolds of input data, allowing interpolation for new inputs. DNN's exceptional approximation capability is crucial for modeling complex spatiotemporal systems [1]. Despite its power, obtaining sufficient training data for DNN in physical problems remains a challenge.

In response to this challenge, Raissi et al. introduced a Physics-Informed Neural Network (PINN) framework [2, 3]. This framework incorporates the governing partial differential equations (PDEs) of fluid flow to constrain the DNN model, enabling consistent predictions even with limited or scarce data. PINN has demonstrated the ability to solve and identify PDEs and has been successfully applied to model various physical systems. For instance, Kissas et al. utilized PINN to model 1D blood flow in cardiovascular vessels using MRI data [4]. Numerous improvements and variations of PINN methods have also been proposed [5–10].

In this study, we propose a Geometry-Informed PINN(G-PINN) method capable of making accurate predictions with or without sparse data. The key advantages of our method include its applicability to complex geometries, such as bifurcated ducts within lung capillaries, the breast ductal system, the ureter, and the aorta; the ability to make predictions without extensive training data; and its suitability for systems with dynamic boundary conditions. We leverage the equations governing flows in conduits, knowledge of flow geometry, and sparse data to predict flows in daughter ducts of a 2D Y-shaped bifurcated structure.

METHODS

We harnessed the capabilities of PINN and modified its framework to deduce solutions at various locations within the computational domain by solving non-linear PDEs that governs fluid flow. A neural network is formulated to encapsulate the solutions of the PDEs within the specified domains. The training process involves instructing the neural network to forecast flows within the system while adhering to physical laws. This is achieved by minimizing the residuals of the PDEs. Details are shown (Figure 1).

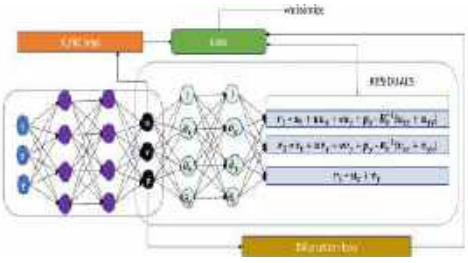

Figure 1: G-PINN architecture for flows through Y-shaped bifurcated structures

Given the nature of the problem we are addressing, which involves splitting geometries (Figure 2), it is imperative to ensure the conservation of mass and momentum at bifurcations. Special attention is devoted to deriving appropriate boundary conditions for the parent and daughter ducts based on the principles of mass and momentum conservation and encoding it as a loss function in the training of our model.

For a simple Y-shaped bifurcated structure containing ducts 1, 2 and 3, the equation for mass conservation at the bifurcation point can be written as:

$$\begin{aligned} U &= (u^2 + v^2)^{1/2} \\ A_1 U_1 &= A_2 U_2 + A_3 U_3 \end{aligned} \tag{1}$$

Where U_1, U_2 and U_3 are the velocity magnitudes in the parent(point 1) and two daughter ducts (point 2 and 3) respectively. A_1, A_2 and A_3 are the cross-sectional areas at points 1, 2 and 3 respectively.

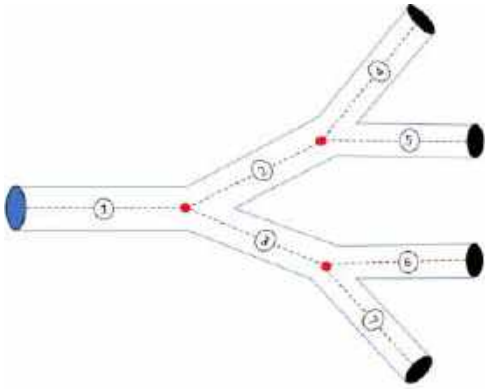

Figure 2: Sample geometry of a 7-ducts Y-shaped bifurcated structure

In the absence of external forces and assuming incompressible flow, the momentum equation can be simplified to:

$$p_1 + \frac{1}{2}\rho(U_1)^2 = p_2 + \frac{1}{2}\rho(U_2)^2 + p_3 + \frac{1}{2}\rho(U_3)^2 \tag{2}$$

Our objective is to integrate these equations as constraints during the training of our model. The model is designed to learn and approximate solutions to these equations throughout the entire computational domain. Through this training process, the model gains the ability to effectively capture and represent the underlying physics described by these equations, enabling it to provide accurate solutions within the given context.

RESULTS

Our model underwent testing in transient flows through Y-shaped structures with one and three bifurcations. The ensuing results are detailed below. It is crucial to emphasize that pressure data was intentionally excluded during the training phase of the model. A periodic velocity is prescribed at the inlet of the parent duct in the geometry, and a no-slip boundary condition is enforced on the walls. At the outlet boundary, a zero-pressure condition is specified. The fluid's density and dynamic viscosity are set to 1028 kg/m³ and 0.02678 kg/(m·s), respectively. The velocity at the inlet is defined as:

$$\begin{aligned} u(t,0,y) &= 0.5Sin^2(2\pi t) \\ v(t,0,y) &= 0. \end{aligned} \tag{3}$$

G-PINN's ability to model flows inside complex structures is accurately described by the snapshots of the evolving flow over time for a simple bifurcated structure having three ducts (Figure 3).

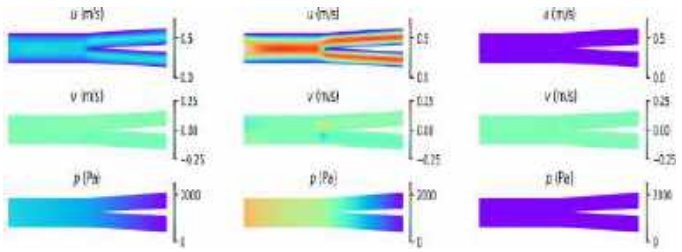

Figure 3: Pressure and velocity predictions snapshots at t = 0s(left), t = 0.25s(center) and t = 0.5s(right).

Advancing our research, we extend the testing of our G-PINN method to a more intricate structure having seven ducts with three bifurcations. The predictions of the G-PINN align closely with the reference solutions, rendering the display of all the reference contours unnecessary. However, we conducted a comparison of the pressure time histories obtained at the midpoints of the parent and daughter ducts with the reference solution from ANSYS Fluent. The pressure time histories for points 4-7 in the distal ducts are illustrated (Figure 4).

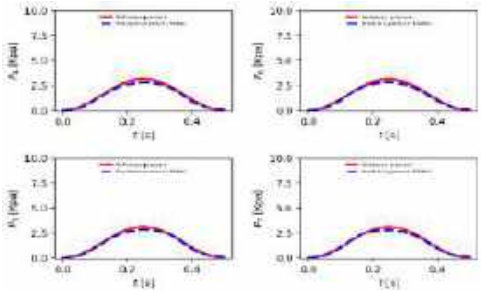

Figure 4: Pressure-time histories for Y-shaped bifurcated ducts with three bifurcation points. Pressure fields at points 4-7.

It is evident that the proposed G-PINN accurately reconstructs the velocity and pressure fields in transient flow through complex geometries such as a Y-shaped bifurcated structure.

DISCUSSION

We introduce a physics-informed and geometry-aware approach for modeling flows in Y-shaped bifurcated structures. The strengths of our proposed scheme include the implementation of peristaltic flow conditions, and the capability to model flows inside intricate structures like a Y-shaped bifurcated duct with limited data. A comparison of predictions with a reference solution demonstrates the high accuracy of the scheme, making it suitable for reconstructing flow fields in complex structures.

It is important to note that the application in this paper is confined to Y-shaped bifurcated structures with symmetrical daughter ducts and constant areas. However, the approach is adaptable for modeling flows through non-symmetric Y-shaped bifurcated structures with varying dimensions. Our future endeavors involve extending this approach to model flows in more intricate bifurcated structures. Additionally, the modeling of the elasticity and versatility of the ducts is left for future work.

ACKNOWLEDGEMENTS

This work was supported by the National Science Foundation under grant number 2121075.

REFERENCES

[1] Rao C et al. *Theoretical and Applied Mechanics Letters* 10.3 (2020).

[2] Raissi M et al. *Science* 367.6481 (2020).

[3] Raissi M et al. *Journal of Computational Physics* 378 (2019).

[4] Kissas G et al. *Computer Methods in Applied Mechanics and Engineering* 358 (2020). ISSN: 0045-7825. DOI: `https://doi.org/10.1016/j.cma.2019.112623`.

[5] Shukla K et al. *Journal of Computational Physics* 447 (2021).

[6] Jagtap AD et al. *Computer Methods in Applied Mechanics and Engineering* 365 (2020).

[7] Lin S et al. *Journal of Computational Physics* 457 (2022).

[8] Hu C et al. *International Journal of Heat and Mass Transfer* 216 (2023). ISSN: 0017-9310. DOI: `https://doi.org/10.1016/j.ijheatmasstransfer.2023.124546`.

[9] Kharazmi E et al. *Computer Methods in Applied Mechanics and Engineering* 374 (2021).

[10] Pang G et al. *SIAM Journal on Scientific Computing* 41.4 (2019). URL: `https://doi.org/10.1137/18M1229845`.

BONE FORMATION DEPENDANCE ON MICROSPHERE SIZE IN 3D PRINTED PLGA MICROSPHERE SCAFFOLDS

Roland M. Klar, James C. Cox, Naren Raja, Stefan Lohfeld

Oral and Craniofacial Sciences, School of Dentistry, University of Missouri-Kansas City, MO, USA

INTRODUCTION

Polymeric biodegradable microspheres are readily utilized to support tissue healing by targeted drug delivery and have been suggested for use as tissue engineering scaffolds [1]. 3D printed microsphere scaffolds enable precision health therapies by delivering biomolecules in an optimized spatiotemporal manner to maximize therapeutic effectiveness at the tissue damage site while also providing microporosity and stiffness for improved tissue regeneration in load bearing locations. 3D printed scaffolds consisting only of microspheres allow for multiple 3D gradients and optimized architectures that includes micro- and macroporosity [2]. To an extreme, microspheres with different payloads, made from different materials, and in different sizes can be included in a single scaffold to provide locally an optimal environment for the desired tissue formation. Compared to mold-based microsphere scaffold fabrication, 3D printing allows to design architectures that promote tissue formation and optimized load transfer. Furthermore, in contrast to heat- or solvent-based production methods, 3D printing via extrusion process enables the inclusion of biomolecules or cells that would not withstand the harsh conditions of, e.g., powder bed fabrication utilizing lasers or solvents for material fusion.

The size of the microspheres influences the microporosity of the printed structure by changing the gap size between the spheres, and the surface roughness of the scaffold. Surface roughness has shown to have an effect on bone induction in the scaffold [3].

The objective of this study was thus to determine the effectiveness of 3D printed poly(lactic-co-glycolic acid) (PLGA) microsphere scaffolds, varying in microsphere sizes, on bone induction.

METHODS

A microsphere-based ink was prepared from mixing PLGA microspheres with 3% carboxymethyl cellulose (CMC). Scaffolds of 5 mm diameter and approximately 2 mm height were printed from 50, 100, 200, and 300 µm PLGA microspheres with a 0°/90° layer pattern with 0.97 mm layer height, 1 mm strut width, and 1.7 mm strut distance. The scaffolds were left to dry, causing the CMC to shrink to a neglectable volume. The dried scaffolds were sintered in dichloromethane solvent vapor for stability. After UV light sterilization the scaffolds were implanted into critical size calvarial defects in a murine model (TOPGAL mouse). Scaffolds that were extrusion printed from PLGA with the same design parameters were implanted as controls without microporosity. During and after a 60-day implantation period, quality and quantity of de novo bone formation was assessed via µCT and histomorphometry analysis.

RESULTS

Histology and µCT images showed that the PLGA scaffolds had been resorbed by the surrounding epicranial muscle tissue after 60 days. New epithelial/connective tissue formation and abundant new capillary formation was observed and rudimentary naturally occurring bone formation near the periphery of the calvarial defect was detected. Beyond that, the control and the 50 µm microsphere scaffolds were lacking new osteogenesis. In

contrast, more significant bone formation by induction was detected within the defect region when 100, 200, and particularly 300 µm microsphere scaffolds were implanted. On average, the new bone accumulated to approximately 3%, 4%, and 8-10% of the defect area for the 100, 200, and 300 µm microsphere scaffolds, respectively. Figure 1 shows µCT scans of the defect areas after completion of the *in vivo* study. The defect on the left was filled with a 50 µm microsphere scaffold, while the defect on the right was treated with a 200 µm microsphere scaffold. The white circles mark the original defect size (5 mm), which corresponds to the remaining defect diameter on the left, apart from minor bone formation, while bone ingrowth into this circled area is clearly visible on the right.

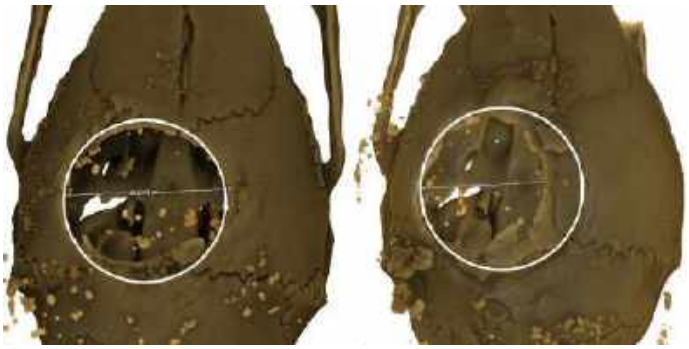

Figure 1: µCT scans of calvarial defect areas in a murine model after 60 days implantation. Defects were treated with scaffolds of microsphere size 50 µm (left) and 200 µm (right). The white circles mark the originally created defects with 5 mm diameter.

DISCUSSION

Our results show that PLGA microsphere-based scaffolds support new bone formation better than scaffolds made from extruded PLGA which do not feature microporosity. Larger microspheres lead to larger micropores and higher surface roughness, which appears to be beneficial for the bone formation. Along with other parameters, a defined macroporosity in a scaffold can better facilitate the formation of the desired tissue [4]. In addition, microporous scaffolds allow for better nutrient flow and removal of metabolic waste and have shown to support vascularization [5]. While the amount of new bone formation in this trial is still limited and the degradation of the PLGA too quick to support bone induction past the 60 days, the results are valuable for understanding the effect of microsphere size in the scaffolds. As the microsphere size influences the printing parameters, the present results help in the optimization of printing microsphere scaffolds targeted at specific tissues. Based on these findings we will develop 3D printed microsphere-based scaffolds with macro- and microarchitectures targeting different tissue types. 3D printing with microspheres allows us to produce multiple 3D gradients in scaffolds with high spatiotemporal control over the release of biomolecules encapsulated in those microspheres, potentially leading to superior tissue regeneration. Scaffolds with 3D gradients are particularly beneficial for tissue interface regions, such as osteochondral defects, where two regenerated tissues need to blend in with their neighboring native tissues.

REFERENCES

[1] V. Gupta, Y. Khan, C.J. Berkland, C.T. Laurencin, M.S. Detamore, Microsphere-Based Scaffolds in Regenerative Engineering, Annu Rev Biomed Eng 19(1) (2017) 135-161. https://doi.org/10.1146/annurev-bioeng-071516-044712

[2] R.M. Klar, J.C. Cox, N. Raja, S. Lohfeld, The 3D-McMap guidelines: 3-dimensional multicomposite microsphere adaptive printing, Biomimetics (revised version under review) (2023).

[3] F.E. Weber, Reconsidering Osteoconduction in the Era of Additive Manufacturing, Tissue Eng Part B Rev 25(5) (2019) 375-386. https://doi.org/10.1089/ten.TEB.2019.0047

[4] A. Cheng, A. Humayun, D.J. Cohen, B.D. Boyan, Z. Schwartz, Additively manufactured 3D porous Ti-6Al-4V constructs mimic trabecular bone structure and regulate osteoblast proliferation, differentiation and local factor production in a porosity and surface roughness dependent manner, Biofabrication 6(4) (2014) 045007. https://doi.org/10.1088/1758-5082/6/4/045007

[5] K. Zhang, Y. Fan, N. Dunne, X. Li, Effect of microporosity on scaffolds for bone tissue engineering, Regenerative Biomaterials 5(2) (2018) 115-124. https://doi.org/10.1093/rb/rby001

MEASURING LIMB LOADS USING A NOVEL PROSTHETIC PYLON FORCE SENSOR

Hanna A. Armstrong (1), Kaleb Burch (2), Amit Chaudhari (2), Sagar Doshi (1), Erik Thostenson (2), Jill Higginson (1,2)

(1) Biomedical Engineering Department, University of Delaware, Newark, DE, USA
(2) Mechanical Engineering Department, University of Delaware, Newark, DE, USA

INTRODUCTION

An estimated 1.4 million Americans are currently living with lower extremity amputations [1]. Despite the high rates of prosthesis usage, a significant majority of amputees express dissatisfaction and experience pain while using conventional prosthetic devices [2]. Given the considerable variability in outcomes following amputation, there is a pressing need to develop interventions that can enhance functional performance for prosthesis users.

The primary goal for patients affected by lower limb amputation is to regain walking capabilities. The conventional rehabilitation process involves patients transitioning from strength to gait training with emphasis on weight bearing and coordination. Through each phase of rehabilitation, patients are instructed to bear a specific amount of weight to mitigate the risk of fatigue and discomfort with phase progression being dependent on gait analysis. Despite advancements made on quantitative biomechanical analysis tools, clinicians continue to use qualitative assessments in part due to high-cost equipment, complex protocols, diverse training, and varying biomechanics experience and knowledge [3]. With minimal to no knowledge of key biomechanical metrics such as ground reaction forces (GRF) available to the user or clinician, it is difficult to gauge daily function.

This critical gap in post-amputation rehabilitation highlights the urgent need for a force-sensing system tailored to prosthetic users that is accurate, cost-effective, and adaptable for non-clinical settings. Looking to fill this gap, we developed a new pressure sensor system (PSS) composed of a nonwoven aramid fabric with fibers coated in nanotube-based composite thin film [4]. Taking a unique approach, two polylactic acid plates were used to secure the sensor at the top of the prosthetic pylon and the base of the residual limb socket (Figure 1) to collect force data during activities of daily living. In this study, we look to validate the PSS's capacity to measure GRF during slow and fast loading cycles found in sit-to-stand (STS) and walking (NW) trials.

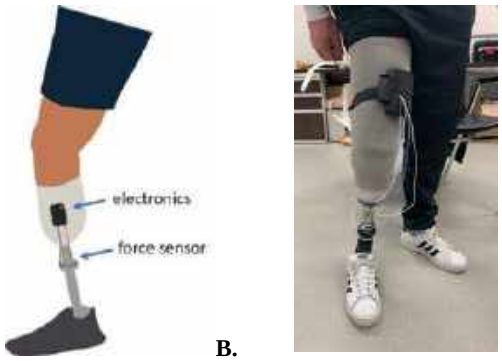

A. **B.**

Figure 1. (A) Illustration and (B) photograph of PSS placed within a pylon. Electronics includes Arduino nano, battery, and circuit board. Data is collected via blue tooth transmission.

METHODS

A single participant with lower limb amputation performed walking and sit-to-stand trials on a force plate (FP) instrumented treadmill (Bertec Corp, Worthington, OH, USA) with the sensor placed in their pylon. During each trial, the force plates recorded GRF (N, 2000 Hz) and the pressure sensor system recorded resistance (ohms, meaning frequency of 14.5 Hz). One 60-second walking trial was conducted at 'normal' self-selected speed and 5 sit-to-stand cycles were conducted.

Due to the piezoresistive effect employed by the PSS, the resistance measurements have an indirect relationship with force and are not normalized to zero [5]. To account for this, each data point in a PSS data set follows Equation 1: one is divided by the individual data point and is subtracted by one divided by the averaged maximum value of that data set, so the overall minimum is zero.

$$\frac{1}{data\ point} - \frac{1}{mean\ (\max values)} = Normalized\ data\ point \quad (1)$$

To prepare for resistance–force alignment and calibration, the peak forces and loading curves are pulled from the PSS and FP data. To identify the loading curves, the data found between local minimum and maximum values for each loading-off-loading cycle are pulled from PSS and FP data sets. For the selected curves, the IPS and FP timestamps(s) are normalized to a minimum value of zero and rounded to the fourth decimal point. The arrays are then overlaid and the points that have matching time stamps are pulled to create the loading curve used for analysis, given the difference in sampling frequency the number of points in a loading curve array varies. To create the calibration factor, 12 loading curves pulled from the walking cycle were used. This factor was applied to the remaining NW and STS PSS data sets to convert the measurements from resistance (ohms) to force (N).

Peak force measurements were compared between PSS and FP using a paired *t*-test and the loading curves with an R^2 Correlation (NW: n=12, STS n=3).

RESULTS

The peak force values measured by the PSS and FP were not significantly different as shown by the Mann Whitney results for NW (Fig 2A, PSS = 883±49.6 N, FP = 886±26.1 N), indicating a 0.3% measurement difference in peak loads. However significant differences were observed for STS (Fig 2B, PSS = 542±10.1 N, FP = 565±7.9 N), indicating a 4% measurement difference for peak force during STS.

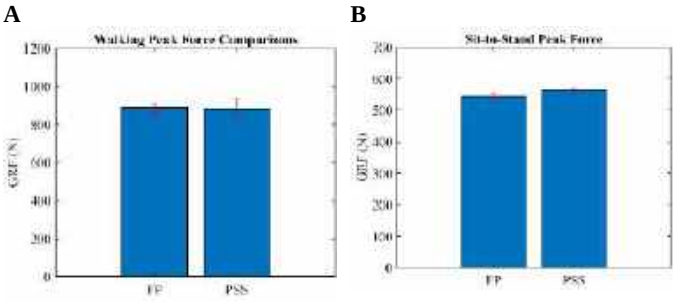

Figure 2: (A) walking (n=12, p = 0.497), (B) Sit-to-Stand (n=3, p = 0.016); note the different axis limits.

The NW loading curves have a moderate correlation of R^2 = 0.494 from no load to peak load between the PSS and FP (Figure 3). However, for STS, there was a high correlation of R^2 = 0.667 (Figure 4).

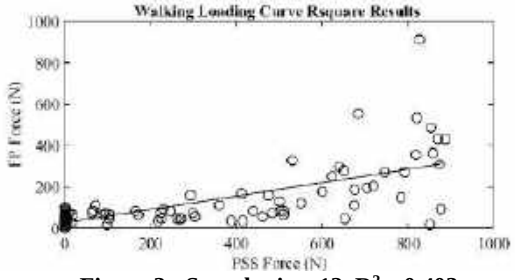

Figure 3: Sample size: 12, R^2 = 0.403

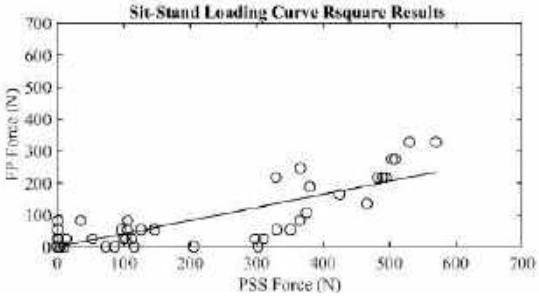

Figure 4: Sample Size: 3, R^2 = 0.667

DISCUSSION

The findings of this study suggest the potential of the newly developed pressure sensor system (PSS) to accurately measure ground reaction force (GRF) during both normal walking and sit-to-stand in an individual with lower-limb amputation.

The study aligns with existing knowledge by emphasizing the importance of quantitative force measurement for prosthetic users, particularly in non-clinical settings. The PSS addresses a critical gap in post-amputation rehabilitation by offering real-time feedback to users outside clinical environments. Comparison to force plate of peak forces for both walking (NW) and sit-to-stand (STS) trials indicate excellent readings by the device with less than a 5% measurement difference between systems. The loading curve correlation between the systems exhibit mixed results with better correlation during the slow STS movement. This may be related to the posture of the limb which is nearly vertical and therefore aligned with the vertical GRF during STS but is more dynamic during normal walking.

The study's strengths lie in the successful validation of the PSS, highlighting its effectiveness in measuring peak force during walking and sit-to-stand. The agreement with force plates adds credibility to the PSS's ability and highlights its potential for broader applications. However, it's essential to acknowledge current limitations, such as the small sample size represented by a single participant out of the anticipated twenty, and the PSS low sampling frequency. The ongoing study will address this limitation, and potentially enhance the generalizability of the findings.

The implications of this study extend to both prosthetic users and healthcare professionals. The PSS has an adaptable design for non-clinical settings, which fills a crucial gap in post-amputation support. Prosthetic users may benefit from real-time feedback on limb loads, improving their ability to manage weight-bearing and enhance functional performance. The successful validation of the PSS opens avenues for future research and development to explore the long-term usability and comfort of the PSS, as well as its integration into different types of prosthetic devices.

In conclusion, this study not only confirms the capacity of the pressure sensor system in measuring pylon load for prosthetic users during daily activities but also lays the foundation for future advancements in sensor technology within the field. The PSS has the potential to revolutionize post-amputation rehabilitation, offering a practical and effective solution for managing limb loads and enhancing the functional performance of prosthetic devices.

ACKNOWLEDGEMENTS

Margaret Neumann Foundation
Independence Prosthetics-Orthotics, Inc
Delaware Limb Loss Clinic

REFERENCES

[1] Dittman JM et al., *Military medicine*, 185:11-12, 2020.
[2] Baars EC et al., *Medicine*, 97:39, 2018.
[3] Hulleck AA et al., *Frontiers in medical technology*, 4:901331, 2022.
[4] Doshi MD et al., *Journal of Materials Chemistry C*, 10:005132, 2021.
[5] Burch, K et al., *Wearable Technologies*, 4:E8, 2023.

A NUMERICAL STUDY ON THE EFFECT OF CORTICAL DIFFUSIVITY ON BRAIN TISSUE GYRIFICATION

Karan Taneja (1), Maria Holland (1)

(1) Department of Aerospace and Mechanical Engineering, University of Notre Dame, South Bend, Indiana, USA

INTRODUCTION

Brain gyrification is a complex phenomenon that is coupled through biology, chemistry and their combined effect on the mechanics of the tissue. Previously, cortical folding has been shown to be affected by variation in cerebrospinal fluid pressure [1], neuronal cell proliferation and migration [2], among other factors. In neurodevelopment, neuronal cells migrate from the inner regions towards the pial surface before spreading out and accumulating [2], indicating spatial variation in their diffusivity throughout the tissue. It has also been observed using Diffusion Tensor Imaging (DTI) of the human fetus during the gestation period that the Mean Diffusivity (MD) of the tissue matter decreases with age, besides showing spatial variation [3, 4].

Previously, Wang et al. [2] incorporated neuronal proliferation of different generations of neurons into a coupled numerical bio-mechanical model of cortical folding by assuming a constant isotropic diffusivity for the young, intermediate and older generations of neurons. This preliminary work investigates the effects of spatial and temporal variation of neuronal migration diffusivity on brain gyrification patterns. As in [2], cortical folding of a 2D Neo-Hookean brain tissue is modelled by coupling neuronal growth and proliferation of three successive generations of neurons, via a user-defined material subroutine in Abaqus [5]. Besides temporal variation, spatial variations in diffusivity are also incorporated and the neuronal cell proliferation and brain gyrification patterns are compared. The simulations indicate that spatio-temporal variations in diffusivity lead to sharper gyrification patterns, indicating the physiological relevance of this phenomena in cortical folding.

METHODS

The kinematics of the biomechanical coupling is defined by splitting the total deformation gradient into the irreversible growth part $\mathbf{F}^{\mathrm{g}}(c)$, defined as a function of the total neuronal cell density c, and, the reversible elastic part $\mathbf{F}^{\mathrm{e}}$ using multiplicative decomposition,

$$\mathbf{F} = \mathbf{F}^{\mathrm{e}}\mathbf{F}^{\mathrm{g}}(c). \tag{1}$$

In this work, three generations (or cohorts) of neurons are considered, such that the total cell density is calculated as,

$$c = \sum_{i=1}^{3} c_i. \tag{2}$$

Further, an advection-diffusion process is used to model the density and migration of the individual neuronal cell cohorts across the brain tissue. The balance of cell density $c_i(\mathbf{x}, t)$, (i.e., the number of cells of the i^{th} cohort per unit current volume) is modelled in the current configuration as

$$\dot{c}_i + c_i \frac{\dot{J}}{J} = f_i^c + \mathrm{div}\mathbf{q}_i, \tag{3}$$

where $J = \det(\mathbf{F})$ is the volume change, f_i^c is the spatial cell source term, and $\mathbf{q}_i$ is the spatial cell density flux term. The term $\mathbf{q}_i$ is written as

$$\mathbf{q}_i = -c_i \hat{H}(c_i - c_0; \alpha_c)\mathbf{v}_i(\mathbf{x}) + \mathbf{D}_i \cdot \mathrm{grad}\, c_i \tag{4}$$

where $\hat{H}(c_i - c_0; \alpha_c)$ is a parameterised heaviside function where c_0 and α_c are the threshold and smoothing parameters, $\mathbf{v}_i(\mathbf{x})$ is the neuronal migration velocity field, and $\mathbf{D}_i$ is the diffusivity tensor.

We assume the standard Fick's first law where cell density flux depends linearly on the cell density gradient. Due to developments in the cortex with gestation age [3, 4] that could potentially affect the neuronal migration, we assume two different forms of the diffusivity $\mathbf{D}_i$ to model the spatio-temporal variation.

Case 1: Constant Spatial Diffusivity

We begin with the assumption that the diffusivity is constant spatially in all directions,

$$\mathbf{D}_i = D_i \mathbf{1}, \tag{5}$$

but for temporal variation each successive cohort has a lower D_i, i.e., $D_1 > D_2 > D_3$. This is based on observations that the MD decreases with gestation age [3, 4], which can potentially affect the neuronal migration and therefore, the brain tissue gyrification.

Case 2: Radially varying Spatial Diffusivity

In this case, the diffusivity coefficient in Equation 5 is considered to vary as an inverse heaviside function of the radial distance,

$$D_i\left(r;\gamma_i,\delta_{r_i}\right)=\gamma_i\left(1.5-0.95\hat{H}\left(-\left(r-\delta_{r_i};\alpha\right)\right)\right) \tag{6}$$

and for temporal variation each successive cohort has a lower γ_i, i.e., $\gamma_1 > \gamma_2 > \gamma_3$, with a similar justification as in Case 1. The threshold value δ_{r_i} for each cohort (calibrated according to Wang et al. [2]), is the position that the diffusivity becomes non-zero, with α being the smoothening parameter and r being the current radial distance from the origin. The parameters from the two cases are mentioned in Table 1, within the physiological range mentioned in Wang et al. [2].

The brain tissue is modelled as a Neo-Hookean material, along with the growth model used in Wang et al. [2]. In this work, a 2D plane-strain half-circle model is considered, with symmetry displacement boundary conditions and zero cell density flux at the boundaries.

Table 1: Parameters used in the two cases.

Case	Parameter	Value
all	R_0	239 µm
	t_{mid}	10 d
	t_{end}	20 d
1	D_1	35×10^3 µm^{2}d^{-1}
	D_2	32×10^3 µm^{2}d^{-1}
	D_3	30×10^3 µm^{2}d^{-1}
2	γ_1	35×10^3 µm^{2}d^{-1}
	γ_2	32×10^3 µm^{2}d^{-1}
	γ_3	30×10^3 µm^{2}d^{-1}
	δ_{r_1}	$0.85R_0$
	δ_{r_2}	$0.90R_0$
	δ_{r_3}	R_0
	α	1.0

RESULTS

Both cases are simulated for a gestation time period (t_{end}) of 20 days (Figure 1), with the 2D half circle having an initial radius of R_0. It is clear that in Case 2, sharper gyrification is observed with larger cell density at the outer layers. The cell density in Case 1 also shows smoother transitions from lower to higher total cell density magnitudes, with lower maximum densities. On the other hand, Case 2 shows sharper transitions of the total cell density magnitude, with large clusters observed near the gyri-like protrusion. A potential explanation for this phenomena is the mechanical interaction of the more pronounced cell clusters with the brain tissue in Case 2 leading to the sharper gyrification as compared to Case 1.

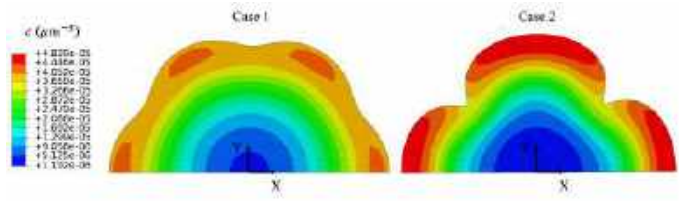

Figure 1: Tissue morphology and cell density in simulations of both homogeneous (left) and spatiotemporally varying (right) diffusivity.

During growth, the outer contours of the brain expand before buckling (Figure 2A). The evolution towards stronger gyrification in Case 2 can be observed with gyri developing in the middle of the simulation whereas the tissue contour remains relatively smooth in Case 1. When looking at the cell densities of the older (c_1), intermediate (c_2) and younger (c_3) neuronal cohorts separately (Figure 2B), Case 2 clearly shows a pronounced clustering behaviour, especially in the youngest neurons.

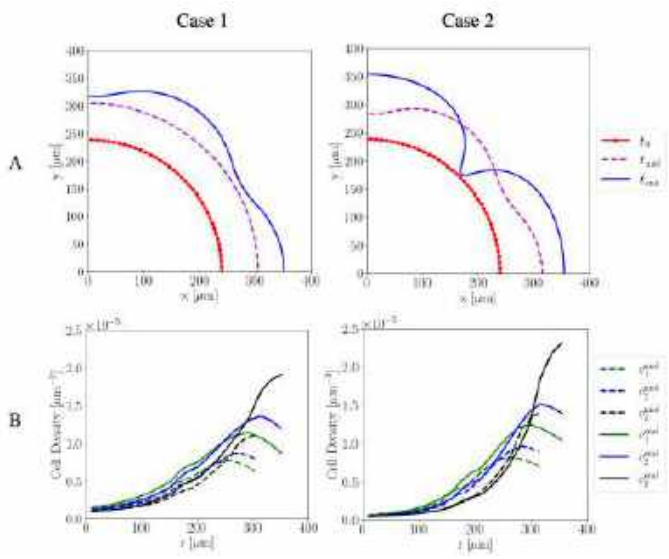

Figure 2: Evolution of tissue morphology and cell density over time for both cases. A: Brain tissue contour at the initial, middle (t_{mid}) and end (t_{end}) of the simulation. B: Radial cell density profiles, calculated along a gyrus, for each of the three cohorts at the middle and end of the simulations.

DISCUSSION

This works numerically investigates whether spatio-temporal variations in neuron migration diffusivity affect brain gyrification. This hypothesis is based on the experimental observations that migrating neurons spread out more as they get closer towards the pial surface, implying a non-linear diffusivity with a higher magnitude closer to the surface [2]. Temporal variation in brain tissue diffusivity has also been observed using DTI [3, 4]. Our results show that including these variations in simulating the coupled biomechanical model leads to distinct gyrification patterns and sharper neuronal cell cluster formations in the tissue. While this indicates a potential correlation between cortical folding and cortical tissue properties such as diffusivity, more rigorous numerical and experimental studies are needed to establish if diffusivity itself is affected by the geometry of the tissue and/or vice-versa. For example, does diffusivity vary more in the gyri than the sulci, indicating a dependence on the tissue deformation? More interestingly, does this variation in diffusivity lead the neurons to stop migrating towards the surface and instead, spread out along the tissue? Investigating these issues will be the focus of our future work.

ACKNOWLEDGEMENTS

This work was supported by the National Institutes of Health (R01NS135852). We also thank Dr. Shuolun Wang for their guidance.

REFERENCES

[1] Jafarabadi F et al. *J. Appl. Mech.* 90.7 (2023). DOI: 10.1115/1.4057020.

[2] Wang S et al. *PLoS Comput. Biol.* 18.6 (2022). DOI: 10.1371/journal.pcbi.1010190.

[3] Machado-Rivas F et al. *Hum. Brain Mapp.* 42.17 (2021). DOI: 10.1002/hbm.25653.

[4] Wilson S et al. *bioRxiv* (2023). DOI: 10.1101/2023.10.16.562524.

[5] Smith M. English. United States: Dassault Systèmes Simulia Corp, 2009.

RADIOFREQUENCY ABLATION FACILITATED BY MICROCHANNEL JETTING

Bo Cao, Hongying Wang, Ruizhe Hou, Shiqing Zhao, and Aili Zhang

Department of Biomedical Engineering
Shanghai Jiao Tong University
Shanghai, China

INTRODUCTION

The radiofrequency (RF) balloon, capable of utilizing its surface microelectrodes to form uniform and regular ablation areas circumferentially, has been widely used for the ablation of transluminal lesions [1]. Cooling media in balloon has been used to reduce the risk of local high temperature, achieving protection of the inner layers of lumen [2]. However, when the lesion area is distant from the lumen surface or forms a certain angle with the lumen, the high temperatures generated by the RF balloon can cause severe irreversible damage to non-target areas [3].

To realize adjustable RF lesions, a RF balloon with tunable jet flow from the microchannel in the balloon catheter is proposed. This design will greatly enhance surface cooling in the region close to the RF electrode, so that the volumetric heating source of the RF heating can be effectively regulated, and thus lesion shape. A model coupling the low temperature jet flow, the RF electrical current and heat transfer in the tissue is then developed. This research examines the impact of various parameters, including jet flow velocity, temperature, and direction, on the morphology of the lesion area. By adjusting the conditions of the cooling medium, it is found RF ablation penetration depth can be increased four times greater than that reported by Wang et al. [4], while offering more versatile lesion shapes across the circumferential and axial dimensions of vascular tissues.

METHODS

The designed dual-layer RF balloon catheter is shown in Figure 1. RF microelectrodes on the surface of the balloon are closely attached to the tissue, while the microchannel on the surface of the inner catheter fosters the low-temperature jet flow toward the inner surface of the balloon. The flow rate and temperature of the inflow are controlled at the inlets and outlets of the dual-layer catheter, and thereby the jet flow condition. The proposed model is built in COMSOL Multiphysics software ((COMSOL, Inc., Burlington, MA, USA)). As shown in Figure 1, a microchannel with a diameter of 0.5 mm is simulated in the model, and it is directed to the middle point of an electrode pair. To simplify computations and enhance the convergence of the model, the space of the balloon's thin wall is neglected, and its heat transfer impact is considered by a thermal thickness approximation.

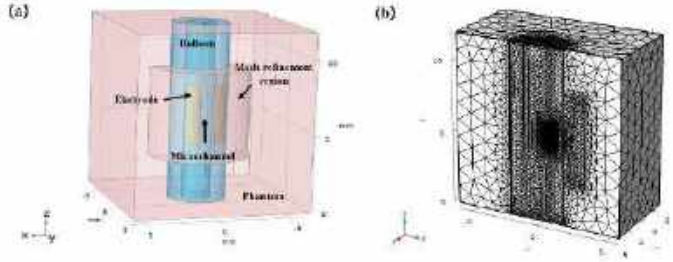

Figure 1: Three-dimensional model of the RFA device.

For fluid dynamics within the conduit, the Reynolds number is around 600-700 which is much smaller than 2100. Hence, a laminar flow model is used. The control equations are:

$$\rho_f \frac{\partial u}{\partial t} + \rho_f (u \cdot \nabla) u = -\nabla \cdot P + \mu_f \nabla^2 V \quad (1)$$

$$\rho_f \nabla \cdot (u) = 0 \quad (2)$$

$$\rho_f C_p \frac{\partial T}{\partial t} + \rho_f C_p u \cdot \nabla T = \nabla \cdot \left(k_f \nabla T\right) \quad (3)$$

Regarding the radiofrequency electric field, under lower RF frequencies (460 kHz), Maxwell's equations can be approximated by the quasi-static field approach.

$$\nabla \cdot [\sigma_a \nabla U] = 0 \quad (4)$$

$$Q_{RF} = \sigma_a |-\nabla U|^2 \quad (5)$$

Finally, the bioheat transfer equation is utilized to integrate the heat transfer effects of the electric and flow fields, focusing on the heating of the target tissue.

$$\rho_a C_p \frac{\partial T}{\partial t} = \nabla \cdot (k_a \nabla \mathrm{T}) + \sigma_a (\nabla U)^2 \quad (6)$$

At the contact boundary between the cooling medium and the balloon, which serves as a fluid-solid coupling interface, a perfect contact condition and no-slip boundary condition are used.

$$k_f \frac{\partial T_f}{\partial \boldsymbol{n}} = k_a \frac{\partial T_a}{\partial \boldsymbol{n}}, r = 2mm \quad (7)$$

$$v = 0, r = 1mm/2mm \quad (8)$$

Table 1: Material properties of the RFA device.

Parameter	Artery	Electrode	Ballon	Fluid(Water)
Electrical conductivity σ (S/m)	0.33+0.0035*（T-20℃）[5]	0	5.76*10^7	5.5X10^-6
Thermal conductivity k (W/m·K^{-1})	0.60+0.0014*(T-0℃)[6]	0.25	386.47	0.63
Density ρ (kg/m^3)	998.2	1300	8935.4	999.8
Specific heat C_p (J/kg·K^{-1})	4183	110	383.9	4202
coefficient of viscosity μ(Pa·s)	/	/	/	0.01779/（1+0.03368T+0.0002210T^2）

RESULTS

To evaluate the effectiveness of jet flow, the ablation results of the RF balloon group (CT Group), the natural convection group (CF Group), and the jet flow group (JF Group) are shown in Fig.2. A 30-second RFA with 27V voltage was simulated. A velocity of 50mm/s and cooling temperature of 5°C is used at the inlet of cooling medium. It is found where there no cooling medium for same RF parameter, the CT Group (Fig. 2a) produces a larger ablation area (60°C isothermal surface，a critical temperature for cell killing [7]) with rapid temperature rise and significant distal expansion. Both the CF Group (Fig. 2b) and the JF Group (Fig. 2c) effectively shaped the ablation area. The JF Group achieved an ablation area further from the electrode, with the region close to the electrode clearly spared from being heated. The ablation area of the JF group is flatter and limited within the lumen (indicated by the pink circle), whereas the CF group penetrates.

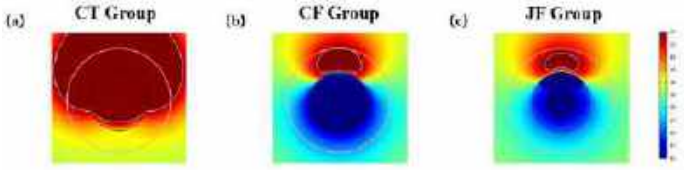

Figure 2: The ablation effect of CT, CF and JF group.

The temperature distribution near the surface of the balloon is shown in Fig.3. The vertical axis of the data graph represents the temperature values near the surface of the balloon, as indicated by the red dashed line in Fig. 3a, while the horizontal axis is the angle formed between the line connecting the points on the dashed line to the center of the circle and the positive X-direction. Temperatures below 60°C are considered safe, as shown by the green rectangular area in Figure 3b. Evidently, lack of a cooling medium, the ablation area of the CT group rapidly exceeded this safe threshold, accounting for approximately 42.6%. In the core ablation area, between two electrodes (from 75.68° to 104.32°), the CF group effectively achieved temperature control. However, the uniform coolant caused a rapid decrease in temperature in the non-ablated areas, dropping as low as 11.1°C and posing a risk of low-temperature damage to the inner layers. The cooling efficiency of the JF group is primarily concentrated in the targeted ablation area, with temperatures in the non-target areas within safe temperatures.

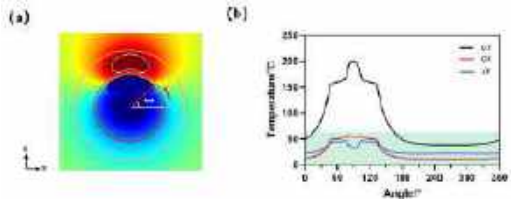

Figure 3: Temperature field distribution around the RF balloon.

When the jet flow was aligned at different angles from the positive X-direction, the morphology of ablation can be adjusted flexibly.
When the jet is directly aligned with the ablation center (angle=90°), it exhibits the highest convective heat transfer intensity, capable of forming a flat and symmetrical ablation area distant from the lumen wall. When the jet is directly facing the position of a single electrode (angle=60°~75°), the ablation area at that position is reduced, resulting in an asymmetrical ablation shape, which better conforms to clinical lesions. The JF Group's ablation morphology was more diverse and flexible, capable of adapting to most RFA scenarios.

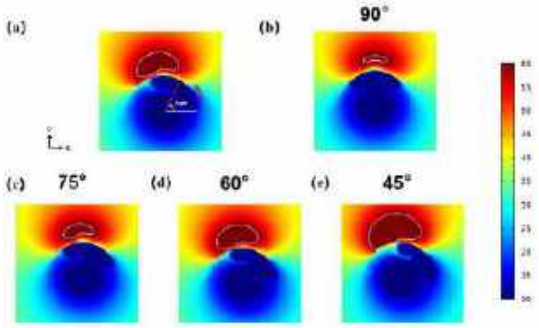

Figure 4: Effect of jet Angle on ablation morphology.

DISCUSSION

This study indicates that the RF balloon with tunable jet flow can achieve localized intense cooling, thereby facilitating high-depth (~0.65mm) transluminal radiofrequency ablation while effectively reducing the risk of low-temperature damage in non-ablated areas. When increasing the flow rate and decreasing the temperature of the cooling medium, the penetration depth can further be enhanced. By adjusting the direction of the jet flow in the inner tube, the morphology of the ablation can be flexibly modified, offering greater adaptability.

This multi-physics coupled simulation results lay the theoretical foundation for the adjustability of RFA morphology by microchannel jetting. In subsequent research, an optimized Shear Stress Transport (SST) model and a porous medium model will be applied to more accurately reflect the heat transfer effects in biological tissues. The efficacy of this design will also be further validated through ex vivo vascular tissue experiments and in vivo animal studies.

ACKNOWLEDGEMENTS

This work was supported by the National Science Foundation of China under Grants 51890892.

REFERENCES

[1] Schilling, Richard et al.,Europace, 23(6):851-860,2021.
[2] Zhao, S. et al., *IEEE TBME*, 66(9):2663-2670, 2019.
[3] Ku, Leizhi. et al., *Eur Heart J*, 44 (7):628,2023.
[4] Wang, H. et al., *Bioengineering (Basel)*, 10(2):162, 2023.
[5] Chen, Roland K et al., *IEEE TBME*, 61(1):182-188, 2014.
[6] Zhao, S. et al., *Biomed Eng Online*, 19(1):44, 2020.
[7] Chu, K.F. et al., *Nat Rev Cancer*, 14(3):199-208, 2014.

DOES TISSUE COMPOSITION ALTER STRAIN-BASED OR STRESS-BASED SUSCEPTIBILITY TO INJURY?

Callan M. Luetkemeyer (1), Catalina S. Bastias (1), Corey P. Neu (2,3), Sarah Calve (2,3)

(1) Department of Mechanical Science and Engineering, University of Illinois Urbana-Champaign, Urbana, IL, USA
(2) Paul M. Rady Department of Mechanical Engineering, University of Colorado Boulder, Boulder, CO, USA
(3) Biomedical Engineering Program, University of Colorado Boulder, Boulder, CO, USA

INTRODUCTION

Soft tissue injuries, such as ligament and tendon tears, are debilitative, costly, and often necessitate surgeries with suboptimal results. Injury prevention strategies, however, remain elusive due to a lack of understanding of the factors that influence injury risk. For example, in populations with increased injury prevalence, is anatomy (geometry) to blame, or the tissue (material) itself?

Injuries result from a critical accumulation of mechanical damage to the extracellular matrix (ECM) [1]. Fibrillar collagens, in particular, impart most of the tensile strength of soft tissues, and are known to exhibit microdamage at multiple length scales (including molecular denaturation) following subcritical mechanical loading [1-2]. However, the effect of ECM composition on susceptibility to mechanical microdamage is not understood. To address this gap, we recently developed a full-field material characterization method for defining *tissue injury criteria*: multimodal strain thresholds for soft tissues [3].

Here, our objectives were to determine whether compositional changes due to (1) a mutation in the *Col1a2* gene (a model of osteogenesis imperfecta) [4], (2) a *Fbn1* "tight skin" mutation (*Tsk*, a model of fibrosis) [5], (3) sex, and (4) treadmill exercise (known to stimulate ECM remodeling [6]) affect stress- or strain-based injury susceptibility of the murine medial collateral ligament (MCL).

METHODS

To investigate the effect of the *Col1a2* mutation, MCLs from 12 week old male wild-type *Col1a2*$^{+/+}$ (WT, n=3), heterozygous *Col1a2*$^{+/-}$ (HET, n=3), and mutant *Col1a2*$^{-/-}$ (MUT, n=3) mice from the same colony were compared. To investigate the effects of the *Tsk* mutation and sex, MCLs from 10 week old female *Tsk* (TSK♀, n=3), female wild-type (WT♀, n=3), and male wild-type (WT♂, n=3) mice from the same colony were examined. Finally, the effect of exercise was investigated by comparing MCLs from 19 week old cage control (CON, n=3) female wild-type mice (Jackson Laboratory) to those from mice run on a treadmill (Stoelting Co.) with either no incline (EX0, n=4) or at a 15 degree incline (EX15, n=4) for 30 minutes/day, 5 days/week, for 10 weeks. All mice were euthanized with protocols approved by the CU Boulder IACUC.

Following harvest, MCLs were isolated and mechanically tested using our previously developed method [3]. Briefly, tibia-MCL-femur specimens were stained with Ghost Dye (Tonbo Biosciences) and NucBlue (ThermoFisher) for 3 hours to provide a fluorescent trackable pattern. MCL samples were stretched in a 1× PBS bath under a confocal microscope (Leica) with a custom testing device that employed a 10 N load cell (Futek) and custom bone grips. MCLs were stained for collagen denaturation prior to testing and after each applied deformation by replacing the PBS bath with a 5μM solution of collagen hybridizing peptide (CHP) for 15 minutes. Confocal images were taken at 10× in each reference and deformed state. Samples were stretched to applied displacements of 500, 750, and 1000 μm.

Displacement fields were estimated using Ghost Dye and NucBlue images of reference and deformed states, and differentiated to calculate Lagrange strain fields. Binary damage maps were estimated with a moving threshold that accounted for stain time. In-plane strain components and damage data were compiled for every pixel in the sample across all stretch states and all samples within an experimental group. Logistic regression was used to determine strain-based injury criteria: the boundary where the probability that significant collagen damage was sustained, P(damage), as a function of in-plane strains, was equal to the probability that it was not.

Group differences in apparent tangent modulus and stress-based susceptibility to collagen microdamage were assessed with linear mixed models (LMM). For these analyses, average axial stress (global force over cross-sectional area) was computed for each sample and compared to average axial strain (from strain fields) or the percent of pixels with significant collagen damage, respectively. For all analyses, statistical significance was defined as $p<0.05$.

RESULTS

The *Col1a2* mutation lowered stress-based (but not strain-based) injury susceptibility, the *Tsk* mutation lowered strain-based (but not stress-based) susceptibility, sex had no effect on either, and exercise altered both. For all figures, bars with asterisks indicate statistical significance ($p<0.05$) and data from different biological replicates are plotted with different shaped markers.

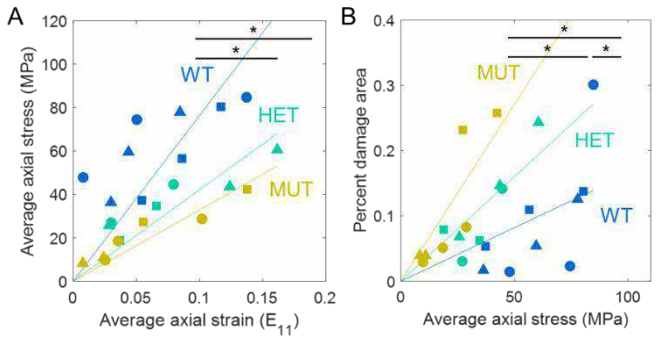

Figure 1: The Col1a2 mutation decreased stiffness (A), increasing stress-based (but not strain-based) injury susceptibility (B).

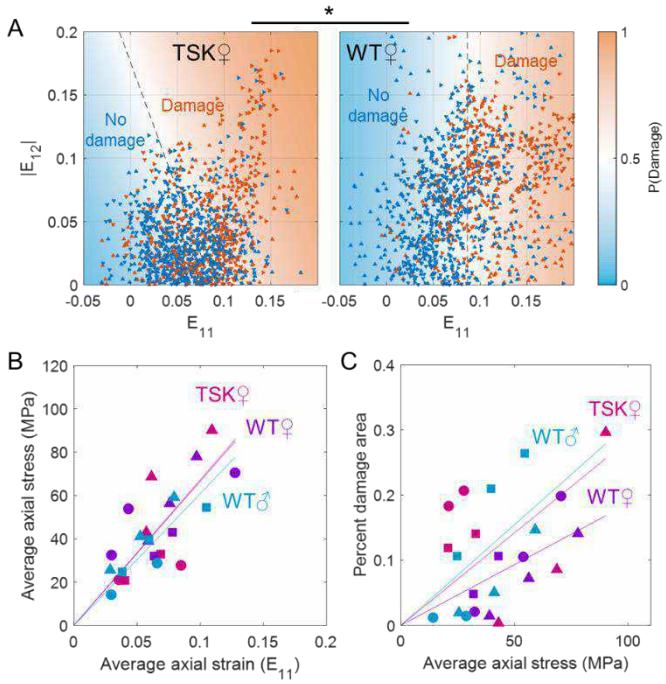

Figure 2: MCLs from Tsk mice were significantly more susceptible to strain-based injury, particularly with respect to shear (A), but showed no difference in stiffness (B) or stress-based injury susceptibility (C) compared to those from WT mice.

MCLs from Col1a2 HET and MUT mice were significantly less stiff than those from WT mice (Fig. 1A). This difference created significant differences in stress-based measures of injury susceptibility across all groups, with MCLs from MUT mice appearing weakest (Fig. 1B). In contrast, MCLs from TSK mice exhibited significantly greater strain-based injury susceptibility than those from WT mice (Fig. 2A), particularly from shear strain (E_{12}). No differences were observed in any measures between MCLs from male and female WT mice (Fig. 2B-C). MCLs from EX0 and EX15 mice exhibited significant differences in all measures compared to those from CON mice (Fig. 3A-C).

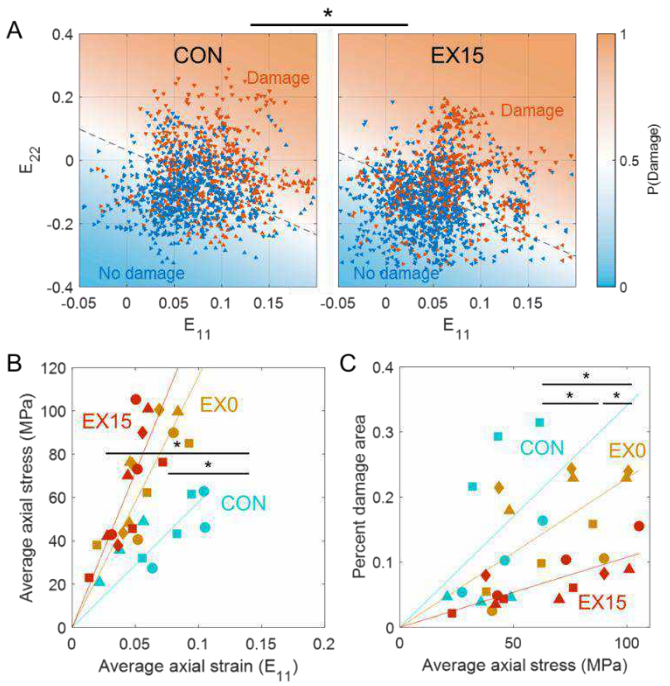

Figure 3: Treadmill exercise slightly increased strain-based injury susceptibility of MCLs (A), but significantly increased stiffness (B) and lowered stress-based injury susceptibility (C).

DISCUSSION

In general, when the axial stress-strain relationship was altered (e.g., Col1a2 mutation and treadmill exercise), stiffer MCLs appeared more robust to stress-based collagen damage, with little or no change in strain-based injury susceptibility. In the case of the Col1a2 mutation, MCLs were less stiff and weaker, but not more brittle. Exercise-induced remodeling, on the other hand, appeared to sacrifice a small loss in ductility in favor of far stiffer and stronger MCLs. In contrast, the Tsk mutation did not affect stiffness or strength, but did result in more brittle ligaments, particularly with respect to shear strain. Raman spectroscopy did not reveal any differences in tissue composition (data not shown), but higher fidelity assessments are currently underway using mass spectrometry to determine the changes in ECM composition that may be responsible for the observed alterations in material properties. This first-of-its-kind study, although limited in terms of sample size, will provide insight into the role of tissue composition in microdamage accumulation and injury of soft tissues. The results will also be important for developing accurate computational models of soft tissue injury and, long-term, have the potential to guide the development of patient-specific injury prevention strategies.

ACKNOWLEDGEMENTS

This work was supported by the Schmidt Science Fellows Program, in partnership with the Rhodes Trust (CML), NIH DP2 AT009833 (SC) and R01 AR063712 (CPN).

REFERENCES

[1] Spiesz, EM et al. *J Orthop Res*, 33.6: 889-897, 2015.
[2] Zitnay, JL et al. *Nat Commun*, 8.1: 14913, 2017.
[3] Luetkemeyer, CM et al., *Acta Biomat*, 168: 252-263, 2023.
[4] Chipman, SD et al. *PNAS*, 90.5: 1701-1705, 1993.
[5] Kielty, CM et al. *JCB*, 140.5: 1159-1166, 1998.
[6] Kjær, M et al. *J Anat*, 208.4: 445-450, 2006.

SB³C2024
Summer Biomechanics, Bioengineering and Biotransport Conference
June 11-14, Lake Geneva, WI, USA

SYNTHESIZING MULTI-BRANCH AORTIC VESSELS USING DIFFUSION MODEL

P. Du (1,2), X. Zhu (3), J. Wang (1,2)

(1) Department of Aerospace and Mechanical engineering, University of Notre Dame, Notre Dame, IN, United States
(2) Lucy Family Institute for Data & Society, University of Notre Dame, Notre Dame, IN, United States
(3) Applied and Computational Mathematics and Statistics, University of Notre Dame, Notre Dame, IN, United States

INTRODUCTION

Cardiovascular disease (CVD) remains a significant global health concern [1]. Image-based computational fluid dynamics (CFD) has proven to be an essential tool for diagnosis and treatment planning, providing comprehensive non-invasive hemodynamic flow information [2]. However, conventional image-based CFD methods require substantial computational resources and time making them impractical for many-query simulations involving uncertainty quantification, parameter estimation, and design optimization [3-5].

With the ever-growing computational capabilities and advancements in artificial intelligence, a significant amount of endeavors have been dedicated to developing deep neural networks (DNNs) as CFD surrogates to promote the efficiency and reduce computational cost [6-9]. Regrettably, most of these models are trained in a data-driven manner, requiring datasets comprising hundreds or thousands of samples. However, obtaining such a large dataset is often impractical due to the scarcity of patient samples and the high costs associated with medical image scans. To the best of the author's knowledge, there is presently no sufficiently large patient-specific geometry dataset available for the direct training of a DNN-based CFD surrogate model. Consequently, the synthesis of cardiovascular geometries becomes indispensable for successfully model training.

The relevant research endeavors on the synthesis of cardiovascular geometries trace back to a decade ago, even predating the emergence of DNN-based CFD surrogate models. These studies often involve computing several macroscopic geometry statistics, referred to as biomarkers, tailored to represent specific organs of interest (e.g., heart chambers, vessels) in a patient. Subsequently, a regression algorithm is developed to link these biomarkers to the outcomes of diagnostic activities, such as aneurysm prognosis [10,11], risk assessment [12,13], treatment planning [14,15], and the design of surgical implant devices [16,17], etc. Despite the success of these tasks, they struggle to capture intricate geometric details due to the reliance on macroscopic biomarkers. Recent explorations have addressed this limitation by incorporating microscopic geometric features, such as vessel skeleton/centerline and surface features, a concept commonly referred to as Statistical Shape Model (SSM). Principal Component Analysis (PCA) is frequently applied to the feature matrix in SSM to reduce dimensionality. This further unlocks the capability to geometry synthesis since random sampling of the PCA coefficients can immediately generate new feature vectors that reconstructs to a complete geometry. This paradigm can be divided into two categories based on the geometric features: Centerline points with local polar coordinates [18-21] and surface point coordinates [22-27]. In the former approach, the geometry (i.e., vessel) is often parameterized using a vessel coordinate system, and a corresponding surface reconstruction function is created to reconstruct a synthesized vessel "skeleton" into a complete surface. On the other hand, the latter approach requires point correspondence built beforehand to equalize the length of each feature vector, a necessary premise for PCA. This typically involves a non-rigid registration task where a deformation algorithm is adopted.

Despite the rich literature, these two approaches have several limitations. The centerline-based approach oversimplifies surface geometries, fails to capture surface details especially on vessel junctions, leading to inaccurate CFD simulation results. Whereas the surface-based approach necessitates point correspondence construction which is cumbersome and inevitably produce error due to discrepancy between deformed surface and target surface. Additionally, it uses a linear encoder like PCA for new sample generation, which may produce unphysical samples outside the underlying probability space. While probabilistic generative models can address this issue, exploration in this direction is still rare. Only Romero et al. [26] and Ostenforf [27] have used generative adversarial models (GANs) on a single branch aorta and an aorta with dissection, respectively. To fill this gap, we propose a novel geometry synthesis algorithm based on a diffusion model that generates an aorta with supra-aorta branches.

METHODS

Prior research on applying diffusion models to 3D shapes has predominantly concentrated on casual objects [28-30]. Inspired by [28], we have developed, for the first time, a shape synthesis framework that employs a diffusion mechanism in a multi-branch geometry context. Our approach involves an initial preprocessing step where we generate uniform point clouds directly on the shape's surface, eliminating the need for point correspondence. Subsequently, we utilize a Point-Voxel CNN [32] to parameterize the denoising process, defined by (x, t), and it is trained using a specifically formulated loss function:

$$\min_{x_t,\epsilon\in N(0,I)} ||\epsilon - \epsilon_\theta(x_t, t)|| \quad (1)$$

where $x_t = \sqrt{\bar{\alpha}_t}x_0 + \sqrt{1-\bar{\alpha}_t}\epsilon$ is the disrupted sample at time t. After the model is trained, we can start from a random white noise and iteratively obtain denoised samples using the following equation:

$$x_{t-1} = \frac{1}{\sqrt{\bar{\alpha}_t}}(x_t - \frac{1-\alpha_t}{\sqrt{1-\bar{\alpha}_t}}\epsilon_\theta(x_t, t)) + \sqrt{\beta_t}z,\ z \sim N(0, I) \quad (2)$$

Figure 1 illustrates the complete pipeline of the proposed model.

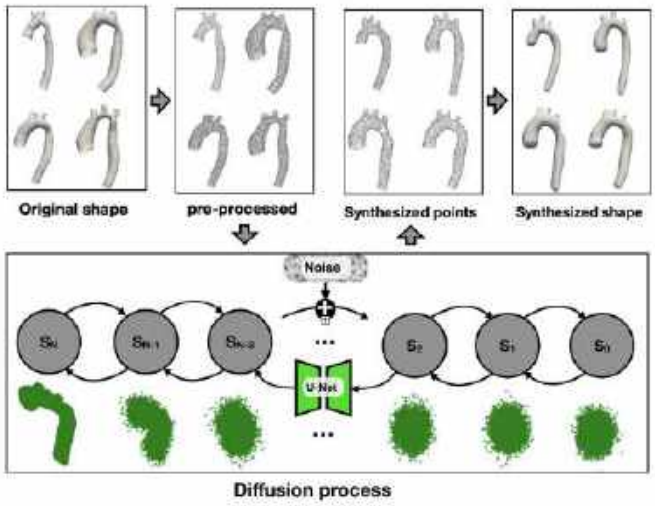

Figure 1: schematic of the proposed model.

RESULTS

To demonstrate the effectiveness of our model. We synthesized 1000 new multi-branch aorta geometries from a dataset in [19]. The original shapes and the synthesized shapes are displayed in Figure 3.

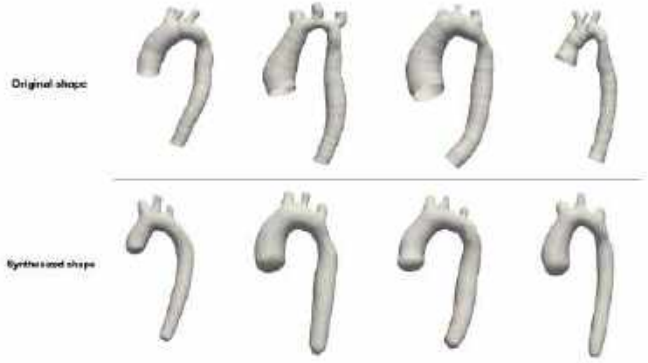

Figure 2: Synthesized aorta shapes

DISCUSSION

From Figure 2, it can be observed that the proposed model generates new multi-branch aorta geometries that differ from the training samples in the dataset, while preserving the geometric characteristics of the original shapes. This demonstrates the strong performance of the proposed model. Future biomarkers will be computed on these newly generated geometries to further verify their validity.

ACKNOWLEDGEMENTS

The authors would like to acknowledge the funds from National Science Foundation under award numbers OAC-2047127, and ND Lucy Family Institute for Data Science and Society Research Accelerate Funding in supporting this study.

REFERENCES

[1] Şahin, B. et al., Health & Social Care in the Community 30.1 (2022): 73-80.
[2] Steinman, D. A. et al., Annals of biomedical engineering 30 (2002): 483-497.
[3] Sankaran, A. et al., Journal for Biomedical Engineering (2011): 031001.
[4] Sankaran, A. et al., Physics of fluids 22.12 (2010).
[5] Tran, J. S., et al., Computers & fluids 142 (2017): 128-138.
[6] Liang, L. et al., Journal of The Royal Society Interface 15.138: 20170844, 2018.
[7] P, Du. et al., Physics of Fluids, 34.8, 2022.
[8] Balu, A. et al., Scientific reports 9.1: 18560, 2019.
[9] Kissad, G. et al., Computer Methods in Applied Mechanics and Engineering,358: 112623, 2020.
[10] De Nisco, G. et al., Medical Engineering & Physics 82 (2020): 119-129.
[11] Wagenseil, J. E. Current opinion in biomedical engineering 5 (2018): 50-57.
[12] Pasta, S., et al. European Journal of Vascular and Endovascular Surgery 54.2 (2017): 254-263.
[13] Poullis, M. P., et al., European journal of cardio-thoracic surgery 33.6 (2008): 995-1001.
[14] Erbel, Raimund, et al., Kardiologia Polska (Polish Heart Journal) 72.12 (2014): 1169-1252.
[15] Petit, C. S. et al., Advances in biomechanics and tissue regeneration (2019): 95-114.
[16] Lortz, J. et al., Journal of Thoracic Disease 10.6 (2018): 3482.
[17] Agnese, V. et al., Journal of Molecular and Cellular Cardiology 135 (2019): 31-39.
[18] Hermida, U., et al. Journal of cardiovascular translational research 16.3 (2023): 738-747.
[19] Thamsen, B., et al. IEEE Transactions on Medical Imaging 40.5 (2021): 1438-1449.
[20]Bridio, S. et al., Applied Sciences 13.18 (2023): 10074.
[21]Romero, P. et al. arXiv preprint arXiv:2311.00888 (2023).
[22]Bruse, J. L. et al., IEEE Transactions on Biomedical Engineering 64.10 (2017): 2373-2383.
[23]Scarpolini, M., Frontiers in Physiology 14 (2023).
[24]Goubergrits, L. et al., Frontiers in Cardiovascular Medicine 9 (2022): 901902.
[25]Saitta, S. et al., Computer Methods and Programs in Biomedicine 233 (2023): 107468.
[26]Romero, P. et al., Frontiers in Physiology (2021): 1375.
[27]Ostendorf, K. Diss. Stanford University, 2023.
[28] Zhou L. et al., Proceedings of the IEEE/CVF International Conference on Computer Vision. 2021.
[29] Lou, S., et al., Proceedings of the IEEE/CVF Conference on Computer Vision and Pattern Recognition(CVPR), 2021.
[30] Vahdat, A., et al., Advances in Neural Information Processing Systems 35 (NeurIPS 2022)
[31] Liu, Z., et al., Advances in Neural Information Processing Systems 32 (NeurIPS 2019)

MULTISCALE CORRELATIONS BETWEEN, JOINT AND TISSUE BIOMECHANICS AND MORPHOLOGY IN OVINE STIFLES

Aritra Chatterjee [1,2], Zachary R. Davis [1], Timothy Lescun [3], Deva D. Chan [1,4]

(1) Weldon School of Biomedical Engineering, Purdue University, West Lafayette, IN, USA
(2) Birla Institute of Technology & Science Pilani, Hyderabad, Telangana, India
(3) Department of Veterinary Clinical Sciences, Purdue University, West Lafayette, IN, USA
(4) School of Mechanical Engineering, Purdue University, West Lafayette, IN, USA

INTRODUCTION

The anatomic structures within the knee – including the tendons, ligaments, meniscus, and articular cartilage – contribute significantly to the movement and stability of the joint (1). Sheep (ovine) are important in preclinical and comparative medicine because their stifles (equivalent to human knees) have a length and load scale that is closest, of commonly used large animal models, to those of the human knee. Multiscale biomechanical studies of the knee joint are therefore critical to designing studies relevant to orthopedic research and late-stage preclinical studies (2). Current computational models, which aim to simulate the joint responses as an ensemble of the component tissues, face certain restrictions in incorporating the tissue geometry and their nonlinear elastic properties. Studies often sample the model inputs from different studies, comprising of different animal models and individuals. This strategy may reduce model reliability due to variability in sampling, specimen size and condition, and variation in measurement techniques (2). To our knowledge, there are yet no studies that adopt a multiscale approach to evaluate the knee biomechanics by determining the individual structural and functional properties of the underlying soft tissues and laxity properties of the same joint in ovine models.

Towards a deeper understanding of such problems, we investigated the relationships between whole joint and individual tissue properties using a combination of mechanical testing and imaging techniques. Specifically, we compared the results from joint laxity measurements and imaging-based joint size parameters to individual tissue mechanical properties collected from the ligaments (ACL, PCL, MCL, LCL), the patellar tendon, menisci, and cartilage. We combined mechanical testing at two length scales and anatomical and quantitative magnetic resonance imaging (MRI) to investigate whether there are any significant correlations between the whole joint mechanics, morphology, and individual tissue properties.

METHODS

Ovine stifles were obtained after humane euthanasia of sheep used for teaching purposes under institutional approval. The collected stifles were cleaned, wrapped in PBS-soaked gauze to maintain hydration, and stored in sealed plastic storage bags at -20°C until testing. Frozen ovine stifles were thawed at 4°C over a period of 24-36 hours before mechanical testing and MRI. Joint laxity testing was performed on ovine stifles using a 10-kN capacity load frame (MTS Systems). Each stifle was preconditioned for twenty cycles, following which they were loaded cyclically to ±1.5-mm sinusoidal displacements for 10 cycles at 0.2mm/s (Figure 1a). The difference between the peak forces at the endpoints of the cyclic displacement input was calculated as a measure of joint laxity force. Stifles were imaged using a Bruker Biospec 70/30 7T MRI (Billerica, MA) in an 86-mm transmit-receive volume coil. Anatomic 3D T_1-weighted FLASH was used to quantify tissue geometry, and a 2D multi-slice, multi-gradient echo sequence was used to determine the T_2* relaxation time within all tissues of interests. T_2* relaxation times were shown to correlate with soft tissue degeneration (4). The femur was manually segmented in Slicer (v5.2.2) to determine the epicondylar distance as a metric of joint size and compared to the force measurements from laxity testing (Figure 1b). MATLAB (v2022b) was used to fit a monoexponential equation (Eqn. 1) of image signal intensity (S) from multi-gradient echo images with multiple echo times (TEs) to estimate maximum signal intensity (S_0) and T_{2*}.

$$S = S_0 e^{-\frac{TE}{T_{2*}}} \quad (1)$$

To quantify tissue-specific biomechanical behavior, specimens were dissected in standardized geometries from the ACL, PCL, MCL, LCL, patellar tendon, menisci, and articular cartilage from the femoral condyles. Stress relaxation tests were performed on these tissues at 5 and 10% strain, with testing under tension for the tendon and ligaments and under compression for the menisci and cartilage. A 3-parameter nonlinear Prony series model (5) was used to quantify the viscoelastic properties of the tissue from the experimental data. The parameters measured from the model fits to data were used to estimate the instantaneous modulus (E_{inst}) and relaxation modulus (E_o) for each

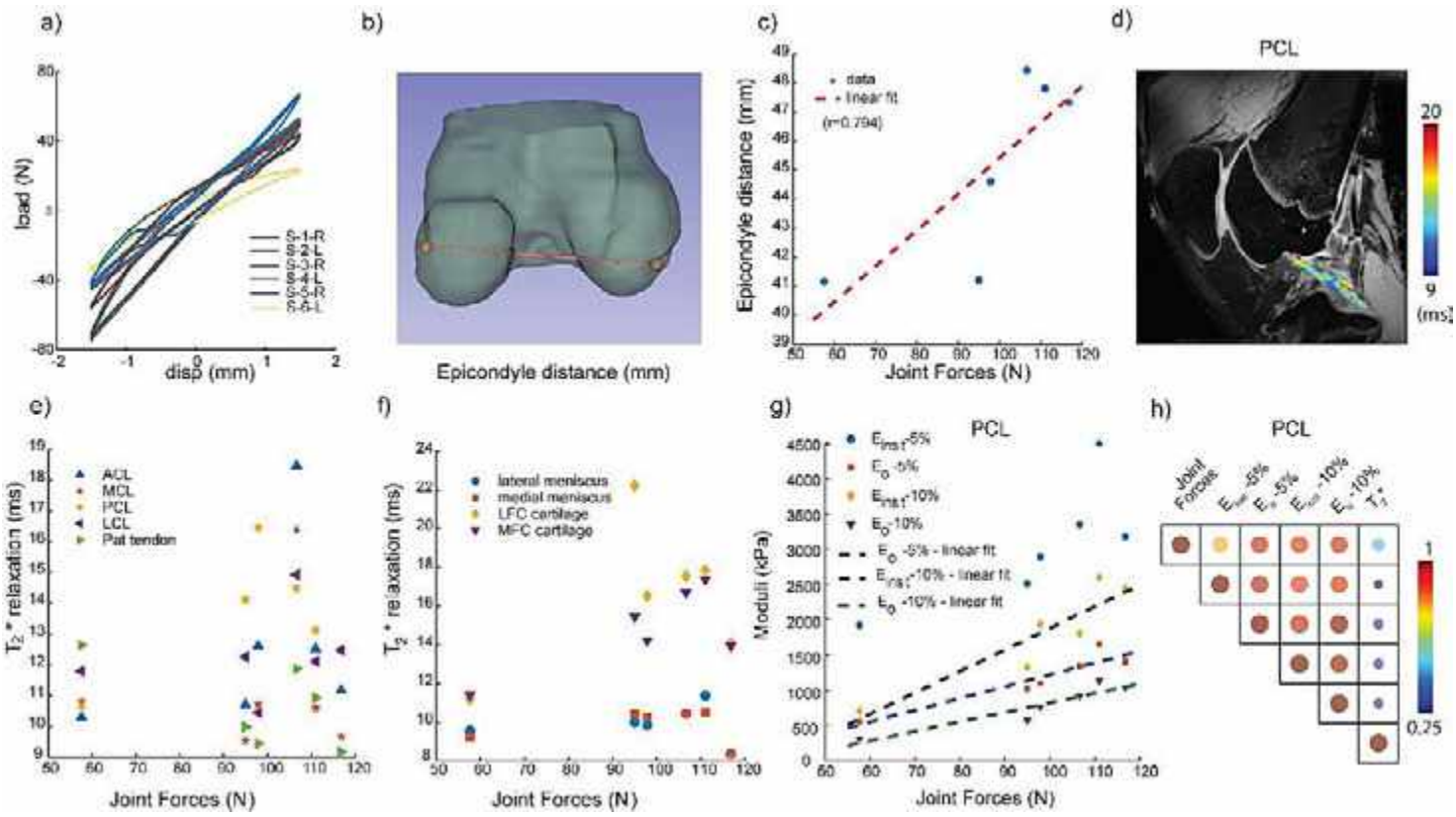

Figure 1: (a) Cyclic load (N) and displacement (mm) profiles over time obtained from joint laxity test. (b) Epicondyle-to-epicondyle distance measured from the segmented femur geometry. (c) Correlations between joint laxity forces and epicondylar distance. (d) Representative T2* relaxation map of ovine PCL (e) & (f) Mean T2* relaxation values (ms) for tissues tested in tension and compression, respectively, plotted against joint forces (g) Variation in PCL viscoelastic moduli (kPa) at 5 and 10% strain plotted against joint forces (N) (h) Pearson's linear correlation (r) between joint forces (N), instantaneous and relaxation tissue moduli (kPa), and mean T2* relaxation times (ms) for PCL.

tissue. These viscoelastic moduli were then compared with joint laxity and MRI-based measurements.

RESULTS

Our results highlight some significant correlations between the whole joint mechanics, joint size metric, and individual tissue properties. We observe a strong positive correlation (r = 0.794) between the joint forces measured from the laxity experiments and the joint morphometric, with the range of measured forces being higher for the stifles having larger femoral epicondylar distance (Figure 1c). From qMRI, we measured the spatial distribution of T_2* relaxation times for each tissue (Figure 1d). Next, we used these measurements to evaluate the variation of the T_2* values against the measured joint forces from laxity tests for tissues tested in tension (Figure 1e) and compression (Figure 1f). Except in articular cartilage from the medial and lateral femoral condyles, we did not observe a significant correlation between the T_2* relaxation and tissue moduli,. Next, we compared tissue-level instantaneous and relaxation moduli and to joint laxity forces for all tested specimens. We noted strong positive correlations (r > 0.8) with the whole-joint forces within the PCL (Figure 1g) and the other ligaments (not shown due to space limitations), as well as the patellar tendon forces. However, no significant correlations or trends were observed between tissue moduli and the corresponding T2* relaxation values in the PCL (Figure 1h) nor other ligaments and tendon. No significant correlations were observed between joint laxity forces and either meniscus or cartilage.

DISCUSSION

In this study, we provide joint laxity forces and tissue viscoelastic parameters for individual tissues from the same joints. Our results show correlations between some of the tested parameters that can provide useful insights into the joint mechanics and facilitate data interpretation for clinical evaluation. Specifically, we observed that the forces measured during whole joint testing correlated directly with the size of the femur bone of the stifles, measured using the inter-epicondylar distance. We also found that the viscoelastic properties of the tendons and ligaments correlated positively with joint laxity forces. These results can provide useful insights into the differential role of individual tissue properties that can be used to design sample specific computational models to assess the knee joint properties as an ensemble of the underlying soft structures for development of better diagnostic techniques and clinical assessment.

ACKNOWLEDGEMENTS

This work was funded in part by the Department of Defense (ARO W911NF2110372). The authors would also like to thank Ms. Shreya Sinha for helping with sample preparation for the joint-laxity tests.

REFERENCES

[1] Adouni, M et al., *Int J Numer Method Biomed Eng,* 37(1), 2021.
[2] Music, E et al., *Osteoarthritis Cartilage*, 26(6):730-740, 2018.
[3] Cheung, E et al., *Curr Rev Musculoskelet Med*, 13(1):115-122, 2020.
[4] Lee, D et al., *BMC Musculoskelet Discord.*, 22(1):424.
[5] Bonifasi-Lista, C et al., *J Orthop Res* .;23(1):67-76, 2005.

IN VIVO LUMBAR INTERVERTEBRAL DISC STRAIN IN FLEXION, EXTENSION, AND DIURNAL MOTIONS: VARIATION WITH AGE IN HEALTHY ADULTS

John M. Peloquin (1), Harrah R. Newman (1), Edward J. Vresilovic (1), Dawn M. Elliott (1)

(1) Biomedical Engineering, University of Delaware, Newark, DE, USA

INTRODUCTION

Intervertebral disc (IVD) degeneration is an important contributor, among other factors, to low back pain and associated disability. IVD degeneration is also a normal part of aging. Spine MRI typically reveals numerous instances of *structural* IVD degeneration, with significant ambiguity regarding which are clinically relevant or may become so. There is a need for methods to better distinguish between pathology and normal aging. Deterioration of mechanical function, i.e., *mechanical* degeneration, is more difficult to measure *in vivo* but its measurement may nevertheless provide significant benefit [1,2]. We previously developed an image registration method to measure IVD strain from MRI [3–5], with successful application to age 20–30 y adults [6]. As the next step towards clinical application, the objective of this study was to measure IVD strain in asymptomatic adults of all ages (1) to provide a realistic measure of normal variation with age and (2) to identify factors that influence IVD strain and thus would support a subject-specific definition of "normal" IVD mechanics.

METHODS

Lumbar (L1–S1) spine MRI was acquired from 84 healthy human subjects without a history of low back pain, under IRB approval, with 7 males & 7 females per decade from 20 y to 70+ y. To assess mechanical degeneration, 3D T1w MRIs were acquired in supine, flexed, and extended positions ~ 8:00 AM, with another supine MRI acquired late in the same day ~ 7:00 PM. IVD strain was measured for these perturbations (flexion, extension, diurnal; Fig 1), with the AM supine image as the reference state, using our established image registration-based method [3–6] (Fig 2), which produces a diffeomorphic displacement field between each reference and deformed image pair. Axial strain (endplate-to-endplate) was averaged within disc regions (Fig 2B,C). To assess structural degeneration, T2w TSE images were acquired for Pfirrmann degeneration grading and T2 CPMG images were acquired to measure nucleus pulposus (NP) T2. A custom U-Net neural network was used to segment each IVD, with manual corrections when needed. The segmentations were used to measure disc height and anterior–posterior (A–P) width and to verify the image registration strain measurement.

Relationships between IVD strain and disc structural factors were analyzed for each perturbation using a linear mixed model (LMM). Subject was a random effect; all other factors were fixed effects. Continuous factors were centered at their mean. For categorical factors, L3–L4, Pfirrmann grade 2 (which had the best coverage across age), and female sex were used as the reference levels. Grade 5 IVDs (34 out of 420 IVDs) were excluded, being fully collapsed. The expected strain for a given subject is the model's intercept plus each factor's fixed effect × its deviation from the reference level.

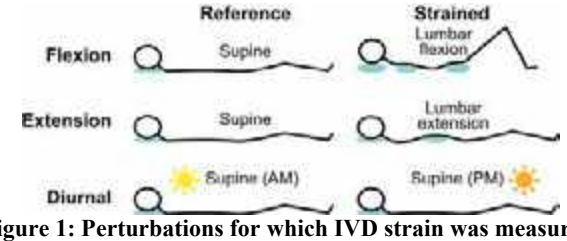

Figure 1: Perturbations for which IVD strain was measured. Flexion and extension were induced with pillows (cyan ellipses).

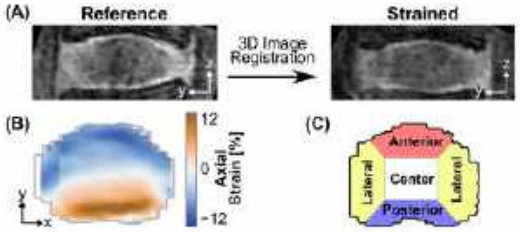

Figure 2: (A) Example reference & strained 3D T1w MRIs (flexion, mid-sagittal slice). (B) Axial slice of resulting axial strain field. (C) Strain field regions used for analysis.

RESULTS

Flexion produced region-dependent strain, with −2.2 ± 0.7 % in the anterior and 3.0 ± 0.7 % in the posterior (Fig 3, Intercept). Because greater flexion causes opposite strains in the anterior and posterior regions, all factors were analyzed as interactions with region (Fig 3). Strain depended on disc level ($p = 0.03$, factor dropout), with lower levels tending to have greater center and lateral compression. Posterior strain differed by −0.5 ± 0.2 % per +10 y of age, 0.22 ± 0.09 % per +1 mm A–P width, and −0.22 ± 0.10 % per +10 lb of body weight. All fixed effects accounted for 30% of the total flexion strain variance.

Extension also produced region-dependent strain, with 3.3 ± 0.6 % in the anterior and −1.3 ± 0.6 % in the posterior (Fig 4, Intercept). Anterior and posterior strain magnitude was greater in the upper levels ($p < 0.001$, dropout). Posterior strain differed by 0.4 ± 0.2 % per +10 y age. Each +1 mm of A–P width was associated with +0.18 ± 0.07 % anterior strain, and each +1 mm disc height with −0.35 ± 0.15 % center strain, with similar trends in the other regions. Pfirrmann grade 4 was associated with +1.7 ± 0.7 % anterior strain, with Pfirrmann grade having a significant overall effect ($p = 0.04$, dropout). The center and posterior regions had lesser strain with greater body height and greater strain with greater body weight, with similar trends for lateral strain. All fixed effects accounted for 45% of the total extension strain variance.

Mean diurnal strain was −4.6 ± 0.6 % in the disc center (Fig 5, Intercept), with the anterior region having 0.9 ± 0.2 % greater strain (less compression) (Fig 5, Region → Anterior). Each +10 y of age was associated with 0.48 ± 0.16 % less compression, each +10 ms NP T2 with 0.14 ± 0.07 % more compression, and each +1 mm A–P width with 0.14 ± 0.05 % more compression. Lower lumbar levels may have had less compression ($p = 0.06$, dropout). All fixed effects accounted for only 8% of the total diurnal strain variance.

DISCUSSION

Disc strain differed with age in all three perturbations despite controlling for structural disc degeneration. The effect of age was consistently opposite the population average strain (intercept); i.e., there was less deformation with age. In contrast, degeneration measures (Pfirrmann ↑ or NP T2 ↓), when they had a significant effect, magnified strain. Thus, disc degeneration as observed by MRI could be interpreted as compensating for latent (unobserved) age-related factors. The effects of disc level and region were consistent with prior observations in age 20–30 y subjects [6,7]. Here, likely due to sampling a broad age range, we additionally found lesser NP T2 (indicating less water and glycosaminoglycan) to be associated with less diurnal compression.

For the purposes of detecting aberrant mechanical function and hence pathology, extension may be especially useful because its LMM accounted for the greatest share of variance; it provides the most stable "normal" baseline. However, the majority of the explained variance was from disc level, possibly due to consistent imposition of extension rather than physiology, so flexion is also a strong candidate. From a basic science perspective, diurnal strain is interesting because its high proportion of unexplained variance suggests influence from unobserved properties (e.g., tissue permeability) uncorrelated with any of the LMM factors. Diurnal strain thus likely provides unique information. Regardless, multivariate modeling is important to isolate each factor's marginal effects, since factors such as age, NP T2, and Pfirrman grade were strongly correlated with each other ($R^2 \sim 0.5$). Ultimately, application to subjects with low back pain will be necessary to establish the method's sensitivity to pathology, and this process is ongoing. As this dataset includes both tension–compression data from flexion & extension and slow (fluid flow related) diurnal deformations from the same IVDs, with an *in vivo* reference state, it is also extremely valuable for the development and validation of spine mechanics models.

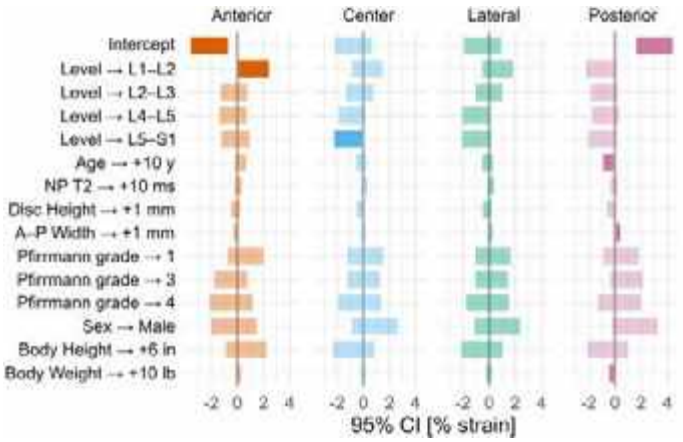

Figure 3: Flexion effect estimates. Dark bars: effect ≠ 0, $p < 0.05$

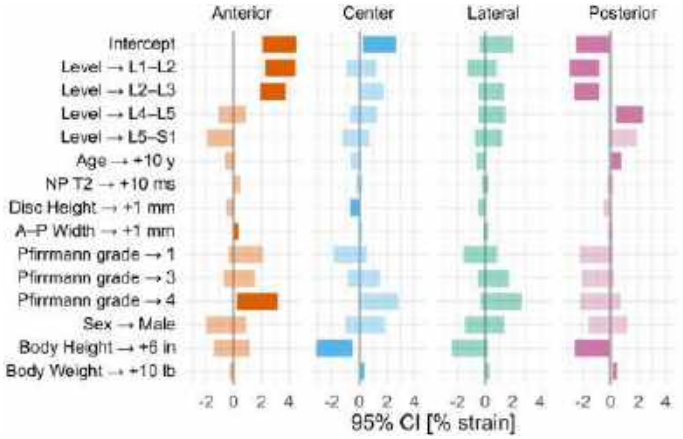

Figure 4: Extension effect estimates. Dark bars: effect ≠ 0, $p < 0.05$

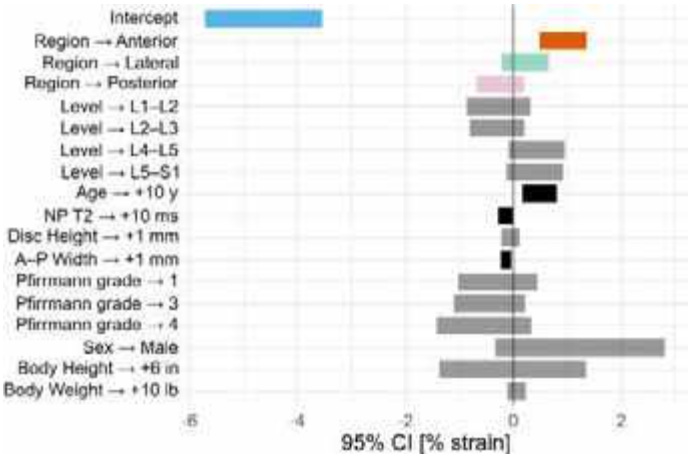

Figure 5: Diurnal effect estimates. Dark bars: effect ≠ 0, $p < 0.05$

ACKNOWLEDGEMENTS

NIH R01AR050052, P20GM139760, R01AR054620, F31AR081687.

REFERENCES

[1] Viggiani, D et al., *Clin Biomech*, 49:85–90, 2017.
[2] Breen, A et al., *Eur Spine J*, 27:2831–9, 2018.
[3] Claeson, A et al., *J Biomech Eng*, 141:111001, 2019
[4] Showalter, B et al., *JOR*, 34:1264–73, 2016.
[5] Yoder, J et al., *J Biomech Eng*, 136:111008, 2014.
[6] Meadows, K et al., *JOR Spine*, 6:e1243, 2023.
[7] Martin, J et al., *JOR Spine*, 5:e1199, 2022.

REAL-TIME SEGMENTATION, VIRTUAL IMAGE MODIFICATION, SURGICAL INTERVENTION MODELING AND 3D PRINTING (REVISIT-3D): A TREATMENT PLANNING WORKFLOW FOR CONGENITAL HEART DISEASE

R. Patrick McCarthy (1), Kasey J. Chaszczewski (2,3), John F. LaDisa (1,2,3,4)

(1) Biomedical Engineering, Marquette University and the Medical College of Wisconsin, Milwaukee, WI, USA
(2) Pediatric Cardiology, Medical College of Wisconsin, Milwaukee, WI, USA
(3) Herma Heart Institute, Children's Wisconsin, Milwaukee, WI, USA
(4) Cardiovascular Medicine, Medical College of Wisconsin, Milwaukee, Wisconsin, USA

INTRODUCTION

Successful surgical treatment of congenital heart disease (CHD) requires intricate understanding of the spatial 3D relationship between complex cardiac structures. While these spatial relationships exist in 3D, preoperative planning has traditionally relied upon imaging modalities viewed in 2D[1]. Translating these 2D views to 3D poses the risk of misunderstanding or underappreciating important intracardiac relationships[2]. As a result, 3D reconstruction, modeling and printing have evolved to improve the understanding of spatial relationships between complex structures, even facilitating virtual treatment planning with current computational tools[3]. The objective of the current work is to use such computational tools through real-time collaboration with clinicians to further advance 3D visualization, better understand intracardiac relationships, and develop an associated surgical plan for patients with complex CHD. We refer to the process as **RE**al-time segmentation, **V**irtual **I**mage modification, **S**urgical **I**n**T**ervention modeling and **3D** printing (**REVISIT-3D**). REVISIT-3D has the goal of improving preoperative understanding of spatial anatomic associations, expanding discussions of surgical options, and improving acute outcomes post-operatively.

METHODS

The workflow for creating visualization products (e.g. virtual and printed 3D structures) from patient data is a multi-step process (Fig 1). De-identified volumetric patient datasets (CT/MRI/3D echo) acquired during routine clinical scans are transferred to biomedical engineering team members following identification of possible visualization products and outcomes/impact measures when possible. The data is then segmented using a combination of modeling and data-processing software, namely 3D Slicer (slicer.org)[4], Blender (www.blender.org), and ITK-SNAP (www.itksnap.org), to isolate cardiac structures of interest. The segments are converted to virtual models and assembled in ParaView (www.paraview.org) for clinical feedback and revision as needed. If necessary, the models are refined, smoothed, or decimated using Blender to emphasize detailed structures or reduce file size based on the clinician-indicated visualization product to be created. If the structures are to be 3D printed, they are then combined in preparation for that process. Baffles and conduits are also created as necessary using specialized modules and extensions in 3D Slicer[5], and then virtually implanted/combined in SolidWorks (www.solidworks.com) while consulting with clinicians. Combining anatomical structures and implementing the conduit/baffle is an iterative process depending on the number and complexity of structures. Structural quantities of interest (e.g. volumes, areas, or distances) are then quantified using SolidWorks, ParaView, or Blender. Dissemination is then performed via one of these software packages.

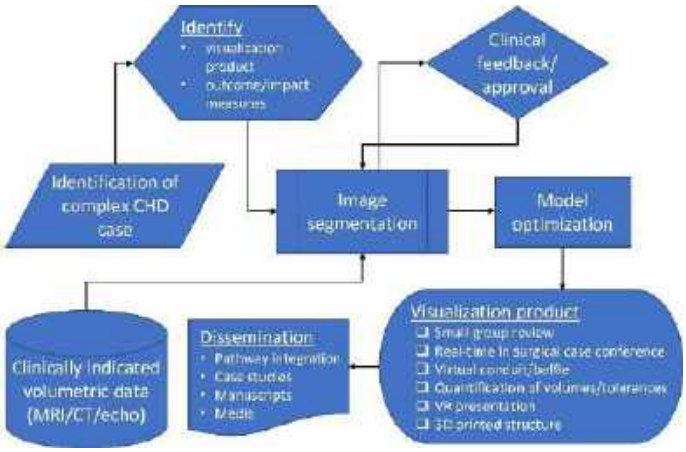

Figure 1: REVISIT-3D workflow showing the steps associated with real-time visualization and collaboration between clinicians and biomedical engineers.

RESULTS

The REVISIT-3D workflow has been applied to three cases with varying forms of CHD since March of 2023, which are further described below.

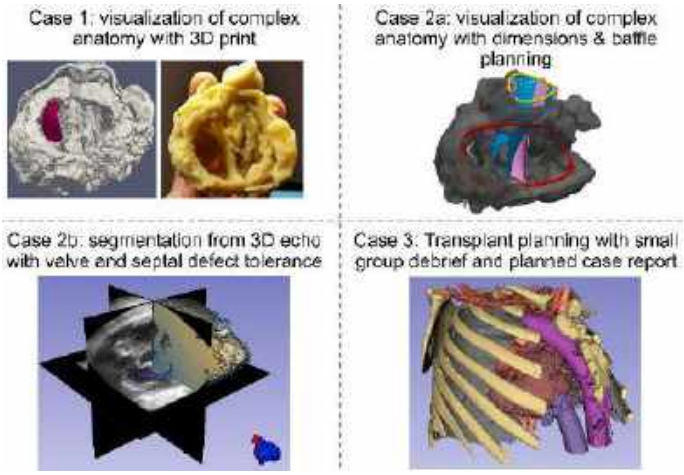

Figure 2: Summary of REVISIT-3D cases to date

Case 1. CT derived model – Virtual reality (VR) analysis and 3D printing provided better clarity of the relationship of a ventricular septal defect to the right ventricular outflow tract. This model served as the testing ground and blueprint for the workflow and provided opportunities to refine and improve each step. The main goal of this case was to create a 3D printed model to better define the ventricular septum and proposed outflow pathways as part of preoperative surgical planning. After the model had been 3D printed, a virtual baffle was implanted into the left ventricle model (Fig 2, in red) to explore the feasibility of the baffle-creation process for potential future use. REVISIT-3D products informed the proposed surgical plan for this patient.

Case 2. MRI derived model – Modeling was conducted to visualize and quantify the relationship of the ventricular septal defect in relation to the left ventricular outflow tract (Case 2a). Visualization products included proposed baffle patches for complex biventricular repair. Three baffle designs were constructed: an ideal (i.e. unrealistic) patch, a best-case patch, and a realistic patch. The quality of each baffle was evaluated based on the minimum distance between baffle and septum (Fig 3). Modeling suggested that the left ventricle-aorta baffle pathway precluded complex biventricular repair and the patient has undergone completion of single ventricle palliation. This case also used 3D echocardiography generated models of the atrioventricular valve to initiate strategies for combining CT/MRI and 3D echocardiography generated models in a single virtual space (Case 2a).

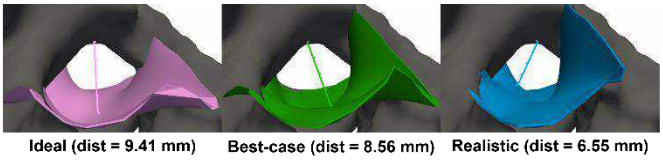

Figure 3: Proposed baffle designs and dimensions for Case2b.

Case 3. CT derived model – The process is being applied for a patient with complex venous anatomy undergoing evaluation for cardiac transplantation. This case required a virtual model only and was used to visualize complex cardiac structures for preoperative planning (Fig 4). The models consisted primarily of the heart, aorta, carotid arteries, pulmonary arteries, and diaphragm. Modeling and planning for optimal transplant strategies is ongoing and planned for conference presentation.

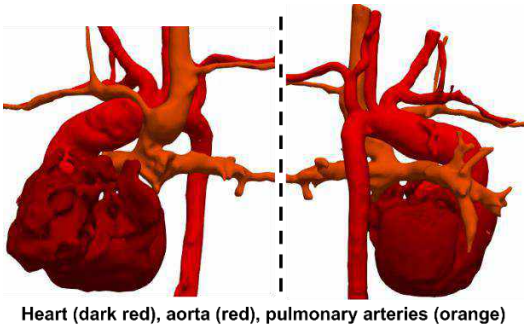

Figure 4: Case 3 virtual model for transplant operative planning: anterior (left), and posterior (right).

DISCUSSION

The REVISIT-3D process has been successfully applied for 3 cases from patents with CHD to create virtual and 3D printed models. Each case demonstrates a specific capability of the process – Case 1 demonstrates the ability to print 3D models from the models created virtually; Case 2 illustrates the value of virtual baffle creation process and comparison of different dimensions with baffle adaptation; Case 3 demonstrates the scalability of the process to larger, more intricate structures. The models have aided clinicians in preoperative planning, providing perspective and tools that have otherwise not been used at our institution to this degree.

Future work to be presented aims to project virtual baffle models as flat representations, which cardiothoracic surgeons can then use as a stencil during surgery[5]. Additional future work involves measuring outcomes of success in response to the implemented processes. For example, we plan to generate anticipated postoperative ventricular volumes based on proposed surgical patch creation and disseminate such data to inform future surgical planning. Moreover, in a subset of patients with double outlet right ventricle undergoing biventricular repair, we plan to compare the proposed/modeled surgical intervention to native postoperative imaging. Differences will be used to better inform future modeling and account for physiologic details arising from observed versus potential ventricular volumes[6].

The work presented here demonstrates the value and potential of the REVISIT-3D process in using computational tools for virtual treatment planning. Future work involves refining and optimizing these tools and measuring outcomes of success in response to the implemented processes.

ACKNOWLEDGEMENTS

This work is partially supported by the Project Bubaloo Reseasrch Grant Program.

REFERENCES

[1] Jacobs S et al., *Interact Cardiovasc Thoracic Surg* 7.1:6-9, 2008.
[2] Schmauss D et al., *Ann Thoracic Surg*. 93.2:e31-3, 2012.
[3] Valverde I et al. *Eur J Cardiothorac Surg*. 52.6:1139-48, 2017.
[4] Fedorov, A et al., *Mag. Resonance Imaging* 30.9:1323-1341, 2012.
[5] Vigil, C, et al., *Ann. of Thoracic Surg.* 111.6:2078-2083, 2021.
[6] Phoon C, and Silverman, N, *J Am Col Cardiol* 30.6:1547-53, 1997.

FINITE ELEMENT MODELING OF BEHIND ARMOR BLUNT TRAUMA FROM INDENTOR IMPACTS TO THE LUNG AND LIVER

Karthik Banurekha Devaraj (1,2), Balaji Harinathan (1,2), Alok Shah (2), Jared Koser (2)
Karthik Somasundaram (3), Brian Stemper (3), Narayan Yoganandan (2)

(1) School of Mechanical Engineering, Vellore Institute of Technology, Chennai, India
(2) Department of Neurosurgery, Medical College of Wisconsin, Milwaukee, WI, USA
(3) Department of Biomedical Engineering, Medical College of Wisconsin, Milwaukee, WI USA

INTRODUCTION

Behind armor blunt trauma is a topic of importance to the military and law enforcement. The current standard of 44 millimeters of penetration in Roma Plastilina No.1 clay was developed from live animal experiments [1,2]. The original research aimed at human safety and soft body armor development. The same criterion continues to be used for both soft and hard body armor. When an actual round, such as bullet or projectile, impacts the armor-covered human thorax and abdomen, deformation from the backface of the armor transmits the external mechanical energy. Additionally, shock waves from the armor can be transmitted to the human torso. Backface deformations of the body armor are attributed to be the principal cause of injury to the soldier and/or law enforcement personnel.

It is well known that the human body is heterogeneous, exhibiting complex geometry and widely varying structural and material properties, in addition to variations in the functions of different components of the biological system. With reference to the thorax and abdomen regions of the human torso, bone and cartilaginous components of the rib cage are considered as skeletal structures, while the internal contents of the thorax and abdomen are considered as soft tissue structures. The lung is an aerated organ, and the liver is a solid organ; both have different but coupled physiological functions in the human body. The consequences of injuries to skeletal and soft tissue structural systems are generally different. For example, a simple non-displaced uni-cortical rib fracture heals quickly, does not impair normal breathing, and is considered a minor injury. Such injuries will not considerably affect the soldier or law enforcement personnel from normal activities. In contrast, severe lung injuries or bleeding from liver lacerations may require immediate attention and can impact the readiness of soldier or law enforcement personnel. It is important to develop injury criteria to advance human safety, develop less weight body armor, and simultaneously protect different thoraco-abdominal regions and skeletal structures that have varying tolerances. Tests with biological models (live animals) are needed to develop tolerance limits or injury criteria. Since biological tests consume resources, computational models are necessary to assist in the design of experiments. The objective of this study is to parametrically analyze the responses from indentor impact-delivering systems for behind armor blunt trauma to the lung and liver organs.

METHODS

Two indentors, replicating the backface deformation profile of hard body armor from actual round impacts to postmortem human surrogates, were used as load-delivering devices to the thoraco-abdominal region of the mid-size male Global Human Body Models Consortium (M50 - v5.1.1) computational model [3,4,7]. The mass of the two indentors were: 150 g, termed as low mass, and 230 g, termed as high mass. They impacted the left lung and liver regions. Initial velocities of 30 m/s, termed as low velocity, and 60 m/s, termed as high velocity, were used. Totally 8 different parametric cases were simulated. Automatic surface-to-surface contact was defined between the human body model and indentors. Maximum rib strains, strain profiles, and strain energy densities in the liver and lung for the respective simulations were outputted for each parametric case. A strain energy density (SED) threshold of 10.8 $\mu J/mm^3$ in the liver was used to estimate the potential for injury. All simulations were completed using LS-Dyna. An analysis was conducted to investigate the role of indentor mass, velocity, momentum, and kinetic energy on the intrinsic responses of the lung and liver to behind armor blunt trauma, using the above parameters.

RESULTS

The kinematics of the impacts were such that the indentor compressed the respective thoracoabdominal organs via local rib cage deformations. Rib strains were the greatest around the region of the impacting surface of the indentor. Figures 1 and 2 show the strain profiles on the ribs from the lung and liver impacts in the extreme cases: low mass and low velocity, and high mass and high velocity cases. For the liver impact simulations, at the low velocity, the SED in the liver was 1.4 $\mu J/mm^3$

for the lower mass indentor and 4.2 μJ/mm³ for the higher mass indentor. At the high velocity, the SED were 9.8 μJ/mm³ to 23.6 μJ/mm³. The SED had a linear relationship with energy (R^2=0.98). For the lung impact simulations, at the low velocity, the SED in the lung was 0.7 μJ/mm³ for the lower mass indentor and 1.5 μJ/mm³ for the higher mass indentor. At the high velocity, the SED were 4.4 μJ/mm³ and 8.6 μJ/mm³. The relationship between SED and energy was linear (R^2=0.96). As expected, greater energy increased SED in both organs, and this observation is discussed in the next section.

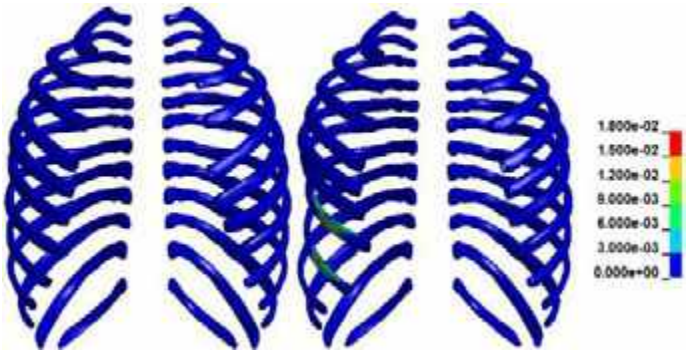

Figure 1: Rib strain patterns for lung (left) and liver (right) impacts for the low mass, low velocity simulations.

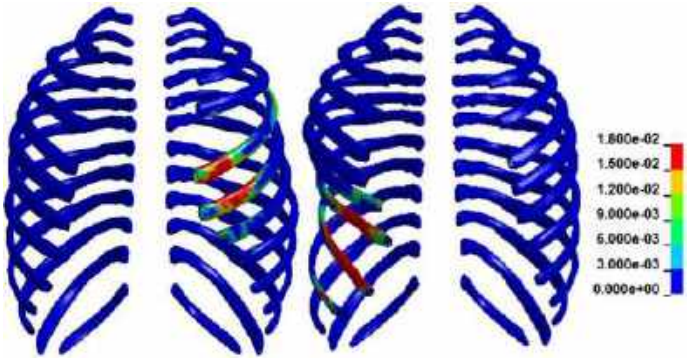

Figure 2: Rib strain patterns for lung (left) and liver (right) impacts for the high mass, high velocity simulations.

DISCUSSION

The objective of the study was to determine the responses of human thorax and abdomen to impacts simulating behind armor blunt trauma. The human body model used in the study has been previously validated using human cadaveric impact tests [4]. Typically, modeling studies use corridors from human cadaver experiments and compare the model-predicted responses via subjective and objective methods. Subjective methods are focused on the predicted response lying within mean plus minus one standard deviation experimental corridors. In contrast, objective methods use correlation analysis that computes the CORA metric between the model-predicted and experimental time history data. The presently used human body model was found to meet both methods of validation in selected test conditions of frontal and side impacts, although they were focused on automotive applications. From this perspective, it would be important to assess the biofidelity of this model to impacts with human cadavers that focus on behind blunt trauma and with the indentors and thoraco-abdominal organs considered in the present study.

The present data may be used to predict injuries to the organs. For the liver, using results from a variety of human cadaver tests conducted by various researchers, a recent study developed injury risk curves using the international standards organization recommendations [5]. At the Abbreviated Injury scale of AIS2+ level, the mid-injury (LD_{50}) cut off for liver injury was estimated at 10.8 μJ/mm^3 [5, 6]. Applying this criterion for the present series of simulations indicated potential for liver injuries at this severity for the high velocity and high mass indentor. This corresponded to the kinetic energy of 414 J. The strain energy density of 9.8 μJ/mm^3 for the low mass indentor at high velocity, corresponding to 270 J, was close to the threshold. A preliminary estimated criterion is that a kinetic energy of 275 J represents the LD_{50} risk for liver trauma under the tested conditions. This may assist the experimentalist in the design of actual experiments/tests.

At a constant velocity, an increase of approximately 1.5 times in the indentor mass increased the strain energy density by 2.7 times for the liver impact cases. For the lung impact cases, the increase was twice, suggesting the differing role of the energy parameter compared to the velocity variable. The inconsistent increases in the strain energy density between the two organs emphasize the role of the type of organ and its placement within the thoraco-abdominal cavity in the human torso and the applied kinetic energy metric. From this perspective, the present parametric study has shown that the responses depend on the region of impact to the thoraco-abdominal complex in behind armor blunt trauma.

While injury risks were estimated for the liver, similar analysis was not possible using the strain energy density metric for the lungs because of lack of data. A similar case was made in a previous study for the spleen organ [5]. Another limitation of this study is that one shape of the indentor was used. The shape was developed based on earlier studies with hard body armor on human cadaver surrogate [2]. The effects of shape variations of the profile of backface deformation were not parametrized in this study. Additional studies are needed to develop tolerances to these organs and conduct parametric analysis to better characterize indentors (mass and geometry). Other injury candidate metrics such as the viscous criterion need further analysis. These topics are being pursued by the authors of this study.

ACKNOWLEDGEMENTS:

The study was supported in part by the Zablocki VA Medical Center, and the Department of Neurosurgery, Medical College of Wisconsin, Milwaukee, WI. Dr. Narayan Yoganandan and Brian Stemper are employees of the VA Medical Center.

REFERENCES

[1] Prather RN, et al., *DTIC*, 1977.
[2] Yoganandan N, et al., *Military Medicine*, 2024.
[3] Bass C, et al., *Int J. of Occupational Safety and Ergonomics*, 2006.
[4] Vavelle NA, et al., *ABME*, 2015.
[5] Beillas P, et al., *IRCOBI*, 2018.
[6] Abbreviated Injury Scale, *AAAM*, 2015.
[7] GHBMC M50 Documentation Users' Manual.

ASSESSMENT OF DNA MOTILITY WITHIN LOCAL NUCLEAR AREA THROUGH TELOMERE MOTION ANALYSIS

M. Yamazaki (1,2), B. Andosiro (3), H. Miyoshi (1,2), S. Ii(1,2), N. Sakamoto(1,2)

(1) Faculty of Systems Design, Tokyo Metropolitan University, Hachioji-shi, Tokyo, Japan
(2) Research Center for Medicine-Engineering Collaboration, Tokyo Metropolitan University, Hachioji, Tokyo, Japan
(3) Graduate school of Systems Design, Tokyo Metropolitan University, Hachioji-shi, Tokyo, Japan

INTRODUCTION

Emerging evidence has revealed fluctuations in DNA motility within the cell nucleus, associated with various gene expression activities such as transcription [1]. Recent reports highlight the influence of the nuclear lamina on DNA motility [2]. Lamin A/C, recognized as a primary component of the nuclear lamina, undergoes changes in both expression levels and nuclear localization in response to the extracellular mechanical environment [3]. This evidence suggests that the regulation of DNA motility by Lamin A/C plays a pivotal role in orchestrating diverse changes in gene expression in response to the extracellular mechanical environment. However, conventional investigations have analyzed DNA motility within the nucleus without considering the spatial dependence. Lamin A/C is proposed to form a finely meshed structure at the nuclear membrane and a coarsely meshed structure in the nuclear interior [2], suggesting potential localized effects on the motility of internal nuclear DNA. In this study, we examined the influence of suppressing Lamin A/C expression on the motility of telomeres localized in nuclear specific regions. Additionally, we investigated the effects of substrate elasticity known to influence Lamin A/C expression on the motility of telomeres.

METHODS

Cell culture

To study the motility of telomeres, we used the mouse teratoma-derived cell line (ATDC5). ATDC5 were maintained in DMEM/F12 medium supplemented with 5% fetal bovine serum and 1% penicillin and streptomycin antibiotics. The cells were cultured on a glass-bottom dish at a density of 10,000 cells/cm^2. After 24 hours, the medium was replaced with Opti-MEM medium containing 10 nM siRNA and Darmafect1. As a control, non-targeting siRNA was transfected instead of the specific siRNA. Following siRNA transfection, the cells were further transfected with the YFP-hTRF1 plasmid using Lipofectamine 2000. For imaging experiments, the cells were cultured for an additional 24 hours after YFP-hTRF1 transfection.

To evaluate the effect of substrate stiffness for DNA motility, ATDC5 were cultured on polyacrylamide gels with elastic modulus of 3.5, 50 and 90 kPa. After 24 hours, YFP-hTRF1 plasmid was transfected following the same method as above.

Particle-tacking for hTRF1-YFP

ATDC5 were incubated at 37°C with a 5% CO_2 level and imaged using an Olympus IX-73 fluorescence microscope with a UPLSAPO 100 x objective, numerical aperture=1.40. The motility of YFP-hTRF1 were recorded at 30 frames per second (30 fps) for 30 seconds by a CCD camera. Intensity-weighted centroids of the hTRF1 were extracted from the time-lapse image of the YFP-hTRF1 with a resolution of 0.058 μm/pixel. The time-averaged mean square displacements (TMSDs) and the anomalous diffusion exponent, defined in Equations (1) and (2), were calculated with τ designating a time lag along the trajectory:

$$< \Delta r^2(\tau) >= \frac{1}{T-\tau}\int_0^{T-\tau}(r(t_0+\tau)-r(t_0))^2 dt_0 \quad (1)$$

$$\alpha(\omega) = \frac{d\ln<\Delta r^2(\tau)>}{d\ln\tau}\Big|_{\tau=\frac{1}{\omega}} \quad (2)$$

where $r(t)$ is the position of YFP-hTRF1 at elapsed time t, and T is the observation time. ω is the reciprocal of t. From the initial image of YFP-hTRF1, bright spots localized within a range of 1 μm from the nuclear membrane were defined as hTRF1 in the nuclear periphery (Periphery), while the bright spots localized in regions further inside than this boundary were defined as hTRF1 in the inner region (Inner).

Immunofluorescence image acquisition

ATDC5 were fixed with 4% paraformaldehyde and immersed in0.5% Triton X-100 in PBS(-) for 5 minutes at room temperature. Samples were blocked in a 0.2% gelatin solution for 60 minutes. And

then, immersed in a 0.2% gelatin solution with a primary antibody against Lamin A/C (1:400) overnight at 4°C, followed by immersion in a 0.2% gelatin solution with a secondary antibody anti-rabbit Alexa-564 (1:1000) for 60 minutes at room temperature. DNA was stained with Hoechst 33258. Finally, samples were imaged by confocal microscopy (FV-3000) with a UPLSAPO 100 x objective.

RESULTS

First, to investigate the contribution of Lamin A/C on DNA motility within local area of nucleus, the motility of telomeres was analyzed in the nucleus of cells which were suppressed expression of Lamin A/C. Fluorescent images of DNA, Lamin A/C and YFP-hTRF1 are shown in Fig.1. The uniform distribution of hTRF1 within the nucleus was confirmed. ATDC5 suppressed Lamin A/C expression (siLamin) exhibited a decrease in Lamin A/C fluorescence intensity compared to the control cells. Quantitative analysis revealed that over 90% of cells showed a decrease in Lamin intensity (data not shown). Additionally, DNA aggregation was increased at interior of the nucleus in Lamin A/C KD cells as opposed to the control cells.

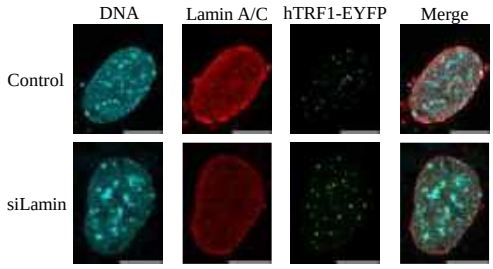

Figure 1: Fluorescence images of DNA, Lamin A/C, and hTRF1-EYFP in Control or siLamin cells. (Cyan: Nucleus, Red: Lamin A/C, Green: hTRF1-EYFP, Bars = 10 µm).

Figure 2 presents representative tracking analysis results of YFP-hTRF1. Individual trajectories of YFP-hTRF1 at both interior and peripheral areas of nucleus were extracted (Fig.2(a-c)). As the anomalous diffusion exponent approaches 1, it indicates random diffusion, while for $\alpha < 1$, slow diffusion is caused by constraints from nuclear structures. The anomalous diffusion exponent α at ω=1[1/s] significantly increased in both nuclear interior and periphery of siLamin cells compared to the Control cells (Fig. 2(d)). From these results, it is suggested that Lamin A/C contributes to DNA confinement in both the nuclear interior and the nuclear periphery areas.

Next, we investigated the effect of substrate stiffness on motility of telomeres within nuclear interior and peripheral areas. As results, anomalous diffusion exponent of the hTRF1 at the nuclear periphery tended to decrease with an increase in substrate elastic modulus. For hTRF1 localized in the nuclear interior, a statistically significant decrease was observed in correlation with an increase in substrate elasticity (Fig.2(e)). These findings suggest that substrate elasticity contributes to the confinement state of DNA in both the nuclear interior and peripheral areas.

DISCUSSION

In this study, we revealed that suppression of Lamin A/C expression affected telomere motility in the entire cell nucleus, and that substrate elastic modulus affected telomere motility in the inner region of the cell nucleus.

The suppression of Lamin A/C expression led to increase in the motility of telomeres in both the nuclear interior and periphery. Lamin A/C is known to possess some chromatin-binding receptors [4]. Also, a previous study indicated that the confinement state of DNA across the

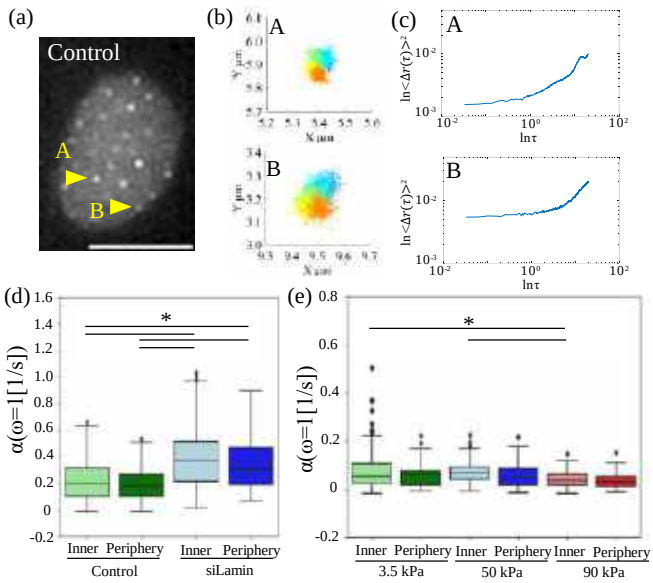

Figure 2: (a) The fluorescent image of typical nucleus of Control cells expressing hTRF1-EYFP marking telomeres (Bar=10µm). (b) Representative two-dimensional trajectories of YFP-hTRF1 (A and B of (a)). (c) Mean square displacement (MSD) of (b). Box plot of the anomalous diffusion exponent α(ω=1[1/s]) in interior and perinuclear area of (d) control and siLamin cells and (e) the cells cultured on substrate with different elastic modulus. (*P<0.05 Bonferroni correction)

entire nuclear area was affected by change in the mesh structure of Lamin A/C [2]. The reduction of Lamin A/C expression might contribute to the disruption of DNA confinement, leading to increase in the anomalous diffusion exponent. Also, changes in substrate elastic modulus caused alternation in motility of telomeres in the nuclear interior region. Previous studies have reported the increase in elastic modulus of culture substrate promotes Lamin A/C expression [5]. DNA might be more restricted in the cells cultured on stiff substrate compared to the cells cultured on soft substrate. On the other hand, the change in DNA motility was larger in the interior area than in each peripheral area of nucleus. This result suggests that changes in substrate elasticity induced localized alterations in nuclear structure.

Although Lamin A/C localized intensively at the nuclear periphery (Fig. 1), no region-dependent differences were observed in motility of telomeres. It was speculated that there are factors other than the local Lamin A/C concentration within the nucleus that control DNA motility. It is also possible that are uniformly secured within the nucleus by the Lamin A/C structure, such as the cell nucleus volume [6], may directly affect the DNA motility. In future study, it is necessary to identify the factor that affect DNA motility directly.

ACKNOWLEDGEMENTS

This work was supported by JSPS KAKENHI (Grant number JP23K19221).

REFERENCES

[1] Nagashima, R et al., *J Cell Biol.*, 218(5):1511-1530, 2019.
[2] Bronshtein, I et al., *Nat Commun*, 6:8044, 2015.
[3] Buxboim, A et al., *Mol Biol Cell*, 28:3333-3348, 2017.
[4] Briand, N et al., *Genome Biol*, 21:85, 2020.
[5] Swift, J et al., *Science*, 341:6149 2013.
[6] Wallace, M et al., *Mol Biol Cell*, 34, 2023.

PERFUSION OPTIMIZATION IN ENGINEERED MICROVESSEL NETWORK DESIGN

Elbert E. Heng (1,2), Lazaros Papamanolis (2,3), Alyssa Garrison (1,2), Daniel Alnasir (1,2), Weiguang Yang (2,3), Zachary A. Sexton (2,3), Aravind Krishnan (1,2), Alison Marsden (2,3), John W. MacArthur (1,2)

(1) Department of Cardiothoracic Surgery, Stanford University School of Medicine, Stanford, CA 94305, USA.
(2) Stanford Cardiovascular Institute, Stanford University School of Medicine, Stanford, CA 94305, USA.
(3) Department of Bioengineering, Stanford University, Stanford, CA 94035, USA.

INTRODUCTION

Tissue engineering of pre-organized artificial vascular networks has been demonstrated to produce regenerative scaffolds capable of restoring microvascular circulation in small animal models of ischemic cardiovascular disease [1]. Uniform perfusion of tissues both during ex vivo cell culture and therapeutic application in vivo is critical to deliver oxygen and nutrients at scale. In particular, vascular regions of slow flow velocities and excess or insufficient endothelial shear stress present challenges in scaffold fabrication and sustaining endothelial function at a large organ scale [2]. While biologically occurring vascular trees are optimized for uniform perfusion under Murray's law of bifurcating diameter ratios [3], optimizing the design of artificial vascular networks in non-tree structures is not yet well described. In the present research, we aim to develop a systematic method utilizing reduced order fluid flow modeling to assess and optimize perfusion uniformity in translationally applicable microvascular network designs.

METHODS

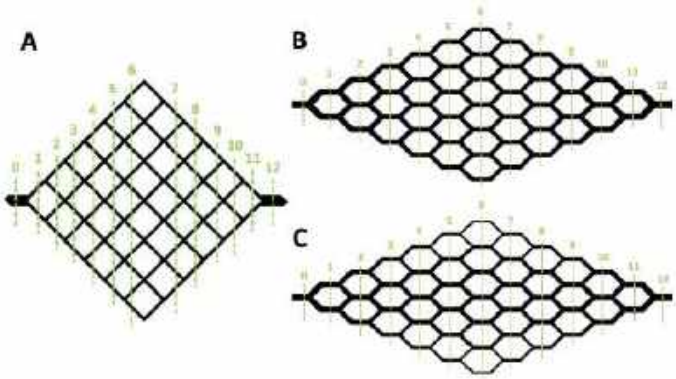

Figure 1: Microvascular network designs with labeled vessel generations. A) 6x6 vascular grid with 100 µm channels B) Vascular lattice with even diameter tapering, and C) Vascular lattice with gradient diameter tapering

Microvascular Network Design: Starting from a root diameter of 400 µm, symmetric vascular networks comprising ~12 generations of vessels were designed (Figure 1). Based on the prevalence of use in tissue engineering applications, a vascular grid pattern was selected as the baseline configuration with constant diameters of 100 µm. Diameters in tapered lattices, hypothesized to improve perfusion uniformity, were either arbitrarily decreased by 50 µm with each generation, or were calculated in accordance with Murray's Law:

$$\sum_{\text{in}} r^3 = \sum_{\text{out}} r^3 \tag{1}$$

where r is the vessel radius. Even taper diameters were calculated with the sum of radii cubed at each generation divided evenly by the number of stems in successive generations. Gradient taper diameters were calculated with the sum of radii cubed divided evenly into daughter branches at each node. Calculated and assigned diameters for the first six vessel generations of respective network designs are shown in Table 1.

Table 1: Diameters by generation in designed vascular networks. Murray's Law calculations for vessel ratios were applied at the generation level (even taper) and the node level (gradient taper).

		Diameter (µm)								
Generation	Stems	Arbitrary Taper	Even Taper	Gradient Taper						
0	1	400	400	400						
1	2	350	317	317	317					
2	3	300	277	252	317	252				
3	4	250	252	200	288	288	200			
4	5	200	234	159	252	288	252	159		
5	6	150	220	126	215	271	271	215	126	
6	7	100	209	100	182	247	271	247	182	100

Perfusion Uniformity Assessment: Blood flow was simulated using the 0D approximation of the Navier-Stokes equations, assuming an inlet flow rate of 115 µl/min and an outlet pressure of 2.14 mBar. Flow rate (Q) simulation results were postprocessed to obtain the mean velocity (v) and wall shear stress (WSS) for each vessel:

$$v = \frac{Q}{\pi r^2} \tag{2}$$

$$\text{WSS} = \frac{4\mu Q}{\pi r^3} \tag{3}$$

where $\mu = 4\,\text{mPa}\cdot\text{s}$ is the blood viscosity. The coefficient of variance ($\text{CV} = \frac{\text{std}}{\text{mean}}$) of mean velocity and WSS was calculated for each vascular network design over all vessels.

RESULTS

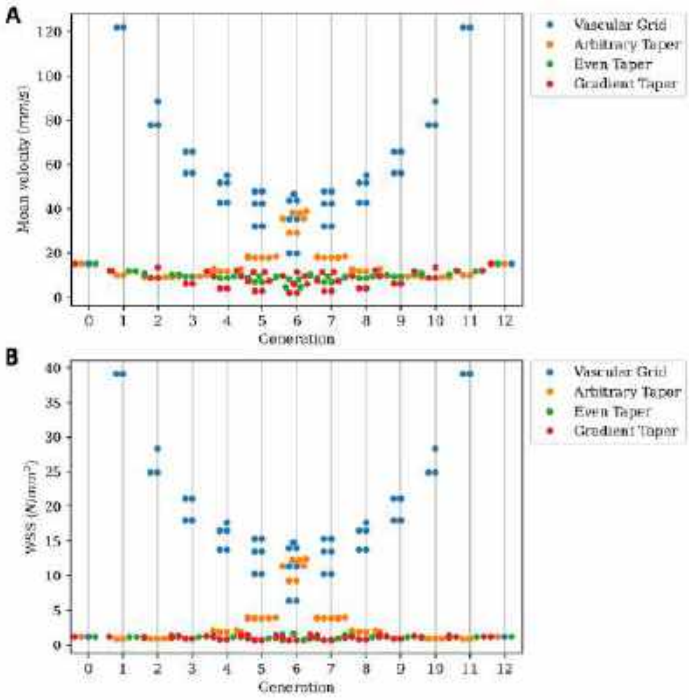

Figure 2: Comparative distributions of A) Flow velocity and B) Wall shear stress across successive vessel generations in distinct vascular network designs

Figure 2 displays the comparative distributions of flow velocity and wall shear stress through designed vascular networks in reduced order blood flow simulation. Simple microvascular grid geometry demonstrated a high variation in flow velocity and shear stress with each successive generation. Tapering vessel diameters in latticed network geometries improved perfusion uniformity, however arbitrary diameter tapering had higher perfusion deviations as compared with diameter tapering determined by Murray's Law correlated ratios. Table 2 displays calculated coefficients of variance for respective vascular network designs, with even diameter tapering demonstrating the most uniform perfusion among simulated networks.

Table 2: Coefficients of variance for flow velocity and wall shear stress across vascular network designs

	Coefficient of variance (std/mean)			
	Vascular Grid	Arbitrary Taper	Even Taper	Gradient Taper
Mean velocity	0.71	0.53	0.20	0.42
Wall Shear Stress	0.72	1.00	0.13	0.20

DISCUSSION

Optimizing microvascular network design can greatly improve perfusion uniformity in engineered microvessel scaffolds. Here we present preliminary results from in-silico analysis of wall shear stress and flow velocity distributions in four microvascular arrangements. Our findings indicate that simple grid geometries, which are prevalently used in current tissue engineering platforms, exhibit suboptimal perfusion distribution that may limit their feasibility of application at scale. Tapering of vessel diameters in correlation with Murray's Law greatly enhances perfusion uniformity in vascular networks. In contrast to prior understanding of Murray's Law in biologic vascular trees, perfusion uniformity in artificial vascular lattices is optimized when the sum of radii cubed is distributed evenly across each network generation as a whole, rather than through each bifurcation point. In future work, we will perform in vitro verification of blood flow modeling within tissue engineered vascular constructs, and explore vascular network optimizations in more complex 3D anatomic space.

ACKNOWLEDGEMENTS

This work has been supported by the National Institutes of Health (R38HL14361504 to Heng EE; R01HL159954-01 to Marsden A).

REFERENCES

[1] Mirabella, T, MacArthur, J, *et al. Nat Biomed Eng:* 1, 0083 (2017).
[2] Strobel, HA, Moss, SM, *et al. Mamm Genome:* 33, 437–450 (2022).
[3] Murray, CD. *Proc. Natl. Acad. Sci:* 12**,** 207–214 (1926)

THE IMPORTANCE OF THE MENISCUS INNER SEGMENT ON THE MECHANICAL FUNCTION OF THE MENISCUS

Satoshi Yamakawa(1), Toshitaka Tsunematsu(2), Issei Ogasawara(1, 3), Tomoki Ohori(2), Akira Tsujii(1), Shoji Konda(1, 3), Seira Sato(4), Takashi Kanamoto(3), Ken Nakata(3)

Osaka University Graduate School of Medicine, Osaka, Japan
(1) Department of Sports Medical Biomechanics
(2) Department of Orthopaedic Surgery
(3) Department of Health and Sport Sciences
(4) Department of Sports Medical Science

INTRODUCTION

The hoop stress is generated in the meniscus under the femoral compression load [1]. We reported that the loss of the inner segment of the meniscus broke the mechanical balance of the meniscus and led to the deformation and extrusion of the meniscus using the material testing apparatus [2]. However, the effect of the inner segment of the meniscus function under knee loading is still unclear. Therefore, the present study aimed to investigate the mechanical function of the inner segment of the meniscus for the knee kinematics and resultant force under knee loading using the robotic testing system.

METHODS

Porcine knee joints (n=5) were used for the test, and the soft tissue around the knee was dissected down except for ligaments, meniscus, and capsule. Before the test, the osteotomy was performed to apply the clinical procedure with a direct view, and it was fixed by metal screws during the test. The varus-valgus (VV) torque was applied to the knees up to 10 Nm at maximum extension using a 6-DOF robotic testing system (FRS2010, Technology Service). During the test, the VV DOF was translated under displacement control at a rate of 0.5 deg/s, and flexion-extension and internal-external DOFs fixed at 30 deg and the neutral position, respectively. All DOFs except those 3 DOFs were set under force control with prescribed force/torque at zero. After the test for intact meniscus, the radial tear with 80% length of the mid-substance width was created from the inner edge at the mid-point of the medial meniscus (MM), and the test was repeated (Figure 1). Finally, the MM had been removed a total of 10 mm anterior-posterior length based on the radial tear and it was defined as partial meniscectomy in the present study, and then the test was repeated. During the test, the knee motion was recorded. After the test for 3 conditions, the recorded knee motion during the test was reproduced to the MM meniscectomized knee, and the resultant force of the meniscus in each condition was calculated based on the principle of the superposition [3, 4].

To measure the deformation and translation of the meniscus during the VV test, a 3-D motion capture system (Prime17W, OptiTrack) was applied to 1 specimen of the test. The total 5 markers for the measurement were placed on the meniscus outer surface at the meniscus-ligament junction of the anterior and posterior horns, the mid-substance, and the mid-point of those 3 points. After the measurement, all soft tissues around the tibia were removed, and the most medial and lateral points of the tibial plateau and the most anterior and posterior points on the line of the tibial eminence were captured by the system. Then, the cross point of the medial-lateral line and anterior-posterior line was determined and defined as the origin of the marker motion. The medial-lateral motion, anterior-posterior motion, and total travel during the test of each marker were determined.

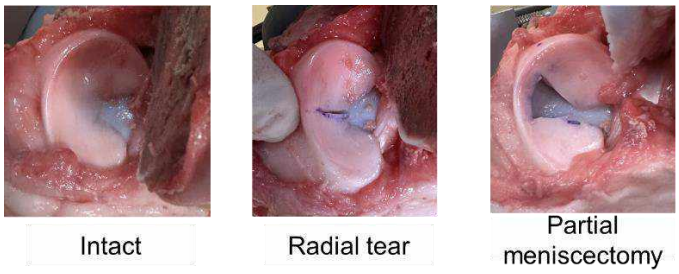

Figure 1 Gross appearance of the medial meniscus in intact, radial tear, and partial meniscectomy conditions

RESULTS

The range of motion (ROM) of the VV was 16.5±5.6 deg in the intact group (Figure 2). In the radial tear group, the ROM was slightly increased, 17.6±5.7 deg, and the partial meniscectomy group showed a significant increase compared to the intact group, 18.7±6.2 deg. The resultant force of the intact meniscus was 123.5±13.5 N (Figure 3). In

the radial tear group, the resultant force was decreased with no significant difference compared to the intact group, 98.2±30.9 N. In the partial meniscectomy group, the resultant force was significantly decreased compared to the intact group, 79.8±28.6 N.

In the meniscus motion, the intact meniscus showed about 1 mm translation in all markers (Figure 4). The radial tear applied and partial meniscectomy performed meniscus showed a similar motion in 3 markers at the anterior horn marker to the mid-substance marker while 0.2-0.5 mm larger translation occurred posterior side markers compared to the intact meniscus.

DISCUSSION

In the present study, the VV ROM and resultant force of the meniscus were determined, and the meniscus motion was measured as a trial. As a result, the radial tear to the inner segment of the mid-substance of the meniscus slightly affected the meniscus function under knee loading, while the loss of the inner segment (partial meniscectomy) was affected significantly.

Our previous report indicated that the inner segment loss leads to V-shape meniscus deformation under compression force to the inner part of the mid-substance using a small sphere indenter, and it results in the extrusion of the mid-substance of the meniscus [2]. In the present study, the inner segment loss led to a decrement in the knee stability and the resultant force of the meniscus, and it was significant compared to the radial tear. In other words, the meniscus function was significantly affected by the partial meniscectomy. In that situation, it is thought that the meniscus extrusion has occurred with V-shape deformation of the meniscus the same as the previous report and it caused the decrement of the meniscus function. However, the meniscus motion indicated an increase of translation at the posterior region of the meniscus compared to the intact while the anterior region did not show the increase. Those data suggested that the meniscus deforms complicated under knee loading differ from the simple V-shape deformation. In the present study, the varus torque applied to the knee and the resultant force was calculated. Although the femur may simply compress the meniscus during the varus torque application, the meniscus motion might be affected by the femur morphology. The femur morphology is generally described as a sphere while it has a complex curved shape in fact. In addition, the femur position is also effective on the location of the center of compression. It is thought that those factors affected the meniscus motion and the motion was complicated. In the present study, internal-external rotation was fixed at the neutral position, and it may also affect the meniscus motion. In future works, the meniscus motion under various knee loading and the relationship between the loss of the inner segment and the motion should be determined.

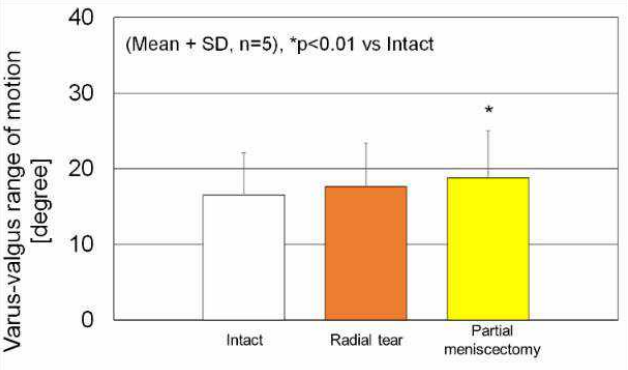

Figure 2 Varus-valgus range of motion in response to 10 Nm of VV torque at 30 degrees of flexion

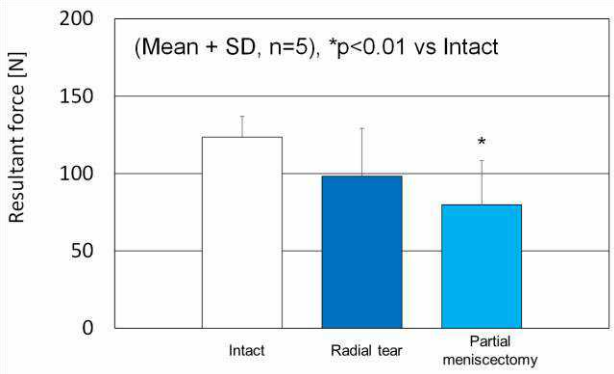

Figure 3 Resultant force of the intact meniscus, radial tear, and partial meniscectomy performed meniscus in response to 10 Nm of varus torque at 30 degrees of flexion

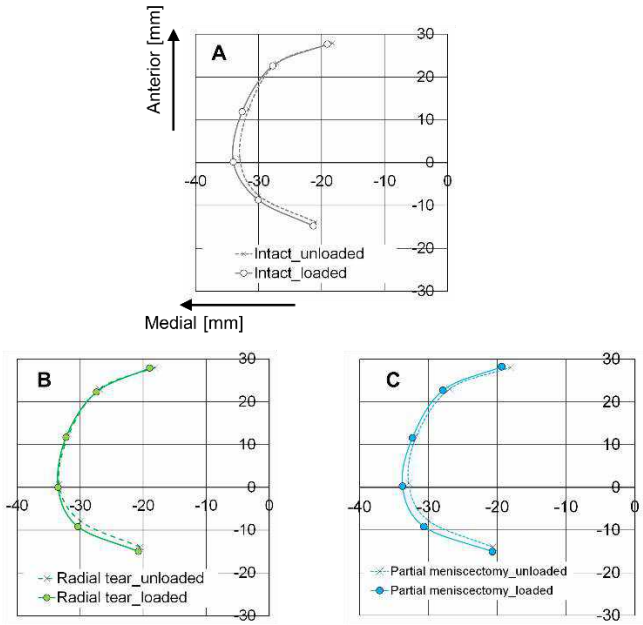

Figure 4 Intact meniscus (A), radial tear (B), and partial meniscectomy (C) performed meniscus motion in response to 10 Nm of varus torque at 30 degrees of flexion

ACKNOWLEDGEMENTS

This work was supported by a grant from the Japan Society for the Promotion of Science, JSPS KAKENHI 21K18054.

REFERENCES

[1] Sharma L, et al, Arthritis Rheum, 58(6): 1716-26, 2008.
[2] Yamakawa S, at el, SB3C, 2023
[3] Fujie H, et al, J Biomech Eng, 115(3):211-217, 1993
[4] Fujie H, et al, J Biomech, 29(12):1577-1585, 1996

THE STIFFNESS OF FALSE LUMEN WALL INCREASED IN CHRONIC TYPE B AORTIC DISSECTION VS. NORMAL TISSUE BASED ON THE UNIFIED-FIBER-DISTRIBUTION (UFD) MODEL

H. Dong (1,2), M. Liu (2,3), H. Cebull (4), M. Piccinelli (4), J. Oshinski (4), J. Elefteriades (5), R. Gleason (1,2), B. Leshnower (1)

(1) Division of Cardiothoracic Surgery, Department of Surgery, Emory University, Atlanta, GA;
(2) School of Mechanical Engineering, Georgia Institute of Technology, Atlanta, GA;
(3) Department of Mechanical Engineering, Texas Tech University, Lubbock, TA;
(4) Department of Radiology and Imaging Science, Emory University School of Medicine, Atlanta, GA
(5) Aortic Institute at Yale-New Haven Hospital, Yale University School of Medicine, New Haven, CT

INTRODUCTION

Aortic dissection is a serious, potentially life-threatening condition [1] which occurs when a tear develops in the inner lining (intimal layer) of the aorta, causing the layers of the aortic wall to separate (dissect) and creating "true" and "false" lumens. Aortic dissections can be divided into two groups [2], depending the physiological location: 1) Type A aortic dissection (TAAD) when the dissection includes the ascending aorta; and 2) Type B aortic dissection (TBAD) when the dissection only involves the descending aorta. TBAD can be further classified into complicated and uncomplicated types based upon the presence of organ malperfusion and/or aortic rupture. TAAD and complicated TBAD are usually treated with surgical or endovascular intervention immediately after their diagnosis. The Uncomplicated TBAD can be managed conservatively with optimal medical therapy (OMT). In the chronic phase of TBAD (CTBAD), the outer false lumen wall (FLW), despite its partial thickness, plays a key role in preventing rupture of CTBAD. It is important to understand the mechanical properties of the FLW in the chronic phase for estimating the stress and clinical risk of CTBAD. In this work, we investigated the stiffness of CTBAD-FLW vs. normal tissues and acute TAAD-FLW, based on biaxial tension testing and the unified-fiber-distribution (UFD) model [3, 4].

METHODS

Patient data: We retrospectively collected false lumen wall (FLW) tissue samples from 9 patients with chronic Type B Aortic Dissection (CTBAD) and 5 patients with acute Type A Aortic Dissection (ATAAD), who underwent open aortic replacement at Emory University Hospital, Atlanta, Georgia. We simulated the FLW (Control-FLW) by stripping partial media and adventitia from descending aortic tissue obtained from 6 heart transplant donors.

Biaxial tension testing: Planar biaxial tension testing (Fig. 1a) in the circumferential (Circ) and axial directions was performed on each of the FLW samples from the three groups, based on the well-established methods [5]. Briefly, a square section of the FLW (Fig. 1a) was delimited by 16 suture hooks, 4 per side. Four graphite markers delineating a 2 by 2 mm square region were fixed with cyanoacrylate adhesive in the center of the testing region for strain tracking. The sample was mounted onto a testing machine in a trampoline-like fashion, and submerged in a 0.9% saline solution maintained at 37 °C for the duration of the test. A stress-controlled testing protocol was applied, with the ratio of the normal stress components $P_{11}:P_{22}$ predefined and with the shear terms $P_{12} = P_{21} = 0$. Samples were subjected to a minimum of 30 equibiaxial preconditioning cycles. Stress strain curves were obtained for the 5 testing protocols (Figs. 1b), with $P_{11}:P_{22} = 1:1, 0.75:1, 0.5:1, 1:0.75, 1:0.5$.

Constitutive Model: We applied our recently developed unified-fiber-distribution (UFD) model [3, 4] to characterize the mechanical behavior of the arteries, assuming that the tissues are incompressible [6, 7]. The strain energy function of the unified-fiber-distribution (UFD) model can be expressed as $\overline{\Psi} = \frac{1}{2}c(\bar{I}_1 - 3) + \frac{k_1}{2k_2}[\exp\{k_2[\zeta^2(\bar{I}_{4\theta} - 1)^2 + (1-\zeta)^2(\bar{I}_{4z} - 1)^2]\} - 1]$, where c, k_1, k_2 and ζ are four material parameters, representing the matrix stiffness, fiber initial stiffness, arterial stiffening factor, and circumferential fiber component, respectively. $\bar{I}_1$ is the 1st invariant of right Cauchy–Green tensor $\bar{\mathbf{C}}$, $\bar{I}_{4\theta} = (\mathbf{a}_{0\theta} \otimes \mathbf{a}_{0\theta}) : \bar{\mathbf{C}}$, and $\bar{I}_{4z} = (\mathbf{a}_{0z} \otimes \mathbf{a}_{0z}) : \bar{\mathbf{C}}$, where $\{\mathbf{a}_{0\theta}, \mathbf{a}_{0z}\}$ are the unit vectors in the circumferential and axial direction, respectively. The UFD model considers the fibers as a unified distribution, rather than separating the fiber distribution into two/several fiber families. The consideration of a unified distribution for the fibers in the UFD model may be more physically consistent with the real fiber distribution of arterial tissues than existing fiber-family-based models.

Histology: A histologic analysis of the tissue microstructure was performed on the collagen and elastin fibers using second harmonic generation (SHG) imaging. A total of 15 FLW samples were imaged

(n=5 for each group) using a Zeiss 710 NLO inverted confocal microscope (Carl Zeiss Microscopy, LLC, Thornwood, NY, USA). The laser was set to 800 nm and emission was filtered from 380 to 430 nm for collagen fibers and from 500 to 550 nm for elastin fibers [8, 9]. Quantification of the composition of Quantification of the composition of collagen and elastin fibers was performed by calculating the fibers' volume fraction from the Z-Stack scans.

RESULTS

The UFD model obtained good fitting accuracy (Fig. 1b) of the experiments. For the stress-strain derived constitutive parameters (Fig. 1c-f), the stiffening factor (k_2) of CTBAD-FLW was significantly larger than that of Control -FLW and Acute-A-FLW (Fig. 1c). The average fiber component in the circumferential direction (ζ) also significantly increased in the CTBAD-FLW tissue in comparison with those Control -FLW and Acute-A-FLW (Fig. 1d). Though the mean value of the fiber initial stiffness (k_1) of CTBAD-FLW was larger (Fig. 1e), no statistical difference was found in the three groups. The matrix stiffness (parameter c) of the Acute-A-FLW was significantly smaller than that of the Control–FLW (Fig. 1f).

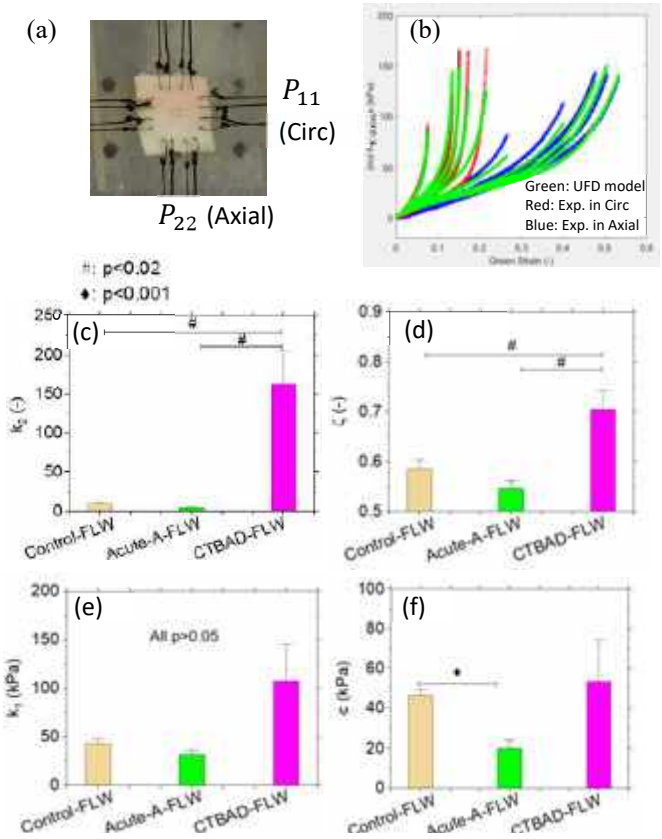

Fig. 1. (a) Biaxial tension testing; (b) Comparison of the fitting results and experimental data; (c-f) Mean and standard error of fitted UFD constitutive parameters.

The histology demonstrated a higher concentration of organized collagen in CTBAD-FLW compared to C-FLW and Acute-A-FLW, and a lower concentration of elastin (Fig. 2a). Quantification of the collagen/elastin profile in the tissue demonstrated a significant increase in the volume fraction of collagen fibers and a significant decrease in the volume fraction of elastin fibers when comparing CTBAD-FLW versus Acute-A-FLW & control-FLW (Fig. 2b). The volume fraction of collagen fiber is larger than that of elastic fibers within CTBAD-FLW, but smaller than that of elastin fibers within Acute-A-FLW & control-FLW (Fig. 2b). The larger volume fraction of collagen and less elastin in CTBAD-FLW explain well the increasing stiffness of CTBAD-FLW vs. Acute-A-FLW & control-FLW.

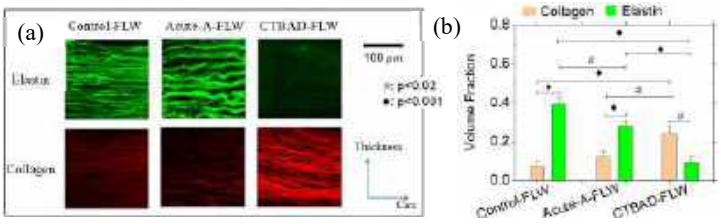

Fig. 3. Microstructure (a) and volume fraction (b) of collagen and elastin fibers.

DISCUSSION

Dissection of the aortic wall results in the outer false lumen wall (FLW) remaining only partial thickness in comparison with the whole wall, which may induce higher wall stress in FLW at the same blood pressure. The change in the composition of FLW extracellular matrix (more collagen and less elastin fibers) may be a protective adaption to the higher wall stress for preventing aortic rupture, which also explains the importance of the adventitia in the surgical repair of aortic dissection (for holding sutures securely).

It has been shown that increasing stiffness of aortic wall can exert an adverse effect on the whole cardiovascular system. For instance, aortic stiffening may result in abnormal ventricular-arterial interactions that promote adverse left ventricular remodeling, dysfunction, and cardiac failure [10]. Stiffening may also induce systolic hypertension and excessive penetration of pulsatile energy into the microvasculature of target organs [11]. It may be worth investigating the effect of the CTBAD-FLW stiffening on the cardiovascular system in future work.

ACKNOWLEDGEMENTS

This study is supported by NIH R01HL155537.

REFERENCES

[1] X. Lou, E.P. Chen, Y.M. Duwayri, R.K. Veeraswamy, W.D. Jordan Jr, C.A. Zehner, B.G. Leshnower, The Annals of Thoracic Surgery 105(1) (2018) 31-38.

[2] C.A. Nienaber, R.E. Clough, N. Sakalihasan, T. Suzuki, R. Gibbs, F. Mussa, M.P. Jenkins, M.M. Thompson, A. Evangelista, J.S. Yeh, Nature reviews Disease primers 2(1) (2016) 1-18.

[3] H. Dong, M. Liu, J. Woodall, B.G. Leshnower, R.L. Gleason Jr, Annals of Biomedical Engineering (2023) 1-12.

[4] H. Dong, W. Sun, Journal of the Mechanics and Physics of Solids 151 (2021) 104377.

[5] M.S. Sacks, W. Sun, Annu Rev Biomed Eng 5 (2003) 251-84.

[6] T.C. Gasser, R.W. Ogden, G.A. Holzapfel, Journal of the royal society interface 3(6) (2006) 15-35.

[7] G.A. Holzapfel, T.C. Gasser, R.W. Ogden, Journal of Elasticity the Physical Science of Solids 61(1-3) (2000) 1-48.

[8] P.S. Gade, A.M. Robertson, C.Y. Chuang, Current protocols in cytometry 87(1) (2019) e51.

[9] F. Sulejmani, A. Caballero, C. Martin, T. Pham, W. Sun, Journal of the mechanical behavior of biomedical materials 97 (2019) 159-170.

[10] T. Weber, J.A. Chirinos, European heart journal 39(43) (2018) 3847-3854.

[11] J.A. Chirinos, P. Segers, T. Hughes, R. Townsend, Journal of the American College of Cardiology 74(9) (2019) 1237-1263.

THE EFFECT OF HYALURONIC ACID AND PROTEOGLYCAN ON THE CENTRIFUGALLY COMPRESSED CELL-COLLAGEN COMBINED CONSTRUCT (C^6)

K. Moribe (1), X. Ye (1), M. Yamazaki (1), H. Fujie (1)

(1) Graduate School of Systems Design, Tokyo Metropolitan University, Hachioji, Tokyo, Japan

INTRODUCTION

Osteoarthritis (OA) is a common disease that dramatically deteriorates quality of life. Self-healing of articular cartilage is difficult due to its poor blood circulation. Therefore, much attention has been paid to approaches that use tissue-engineered materials containing mesenchymal stem cells (MSCs) [1]. Traditional biomaterials for cartilage repair often used scaffolds. Although it is possible to create relatively large constructs cell distribution is uneven and cell density is low in the traditional scaffold-type biomaterials.

We developed a novel cell-scaffold-combined biomaterial, a centrifugally compressed cell-collagen combined construct (C^6), through the application of centrifuged compression to a MSCs-atelocollagen combined construct. Even distribution and high density of MSCs were observed in C^6 [2]. To improve the mechanical property and chondrogenic ability of C^6, it is necessary to promote chondrogenic differentiation of MSCs within C^6. In the present study, the effects of hyaluronic acid (HA) and proteoglycan (PG) on the chondrogenic matrix production and mechanical property of C^6 were determined.

METHODS

Human bone marrow-derived MSCs (PT2501, Lonza, Japan) were subcultured eight times in a culture medium consisting of Dulbecco's Modified Eagle Medium (DMEM), 10% fetal bovine serum (FBS), 1% penicillin-streptomycin (P/S). Subcultured 7.5×10^5 MSCs were mixed with a neutral collagen solution consisting of porcine dermis-derived type I atelocollagen solution or porcine cartilage-derived type II atelocollagen solution (175 µL at a density of 3.72 mg/mL or 4.49 mg/mL), 50 µL of 5-fold DMEM, and 25 µL of collagen gel reconstitution buffer solution. This solution was placed in an incubator with 5% CO_2 at 37 °C, allowed to self-assemble into a gel-state solution with higher ordered three-dimensional structures over 1 day, and centrifuged at 3500 rpm for 10 min (Figure 1).

In the preparation process of C^6, either HA sodium salt (089-10343, Fujifilm, Japan) or salmon nasal cartilage PG (HQPG-AO121-001, Cosmobio, Japan) was dissolved in 5-fold DMEM. The weight ratio of HA or PG to collagen was 20% to roughly simulate physiological concentration. C^6 samples at 28 days of culture were histochemically processed according to a standard method. A microtome was used to slice the samples and histological examination was performed for the sliced specimens using toluidine blue stains.

C^6 samples at 14 days of culture were fixed on a glass bottom dish with adhesive. Indentation test was performed for randomly selected 5 points on the specimens using an atomic force microscope (AFM) (Nano Wizard 3, JPK Instrument, Germany) to determine the tangent modulus of C^6 under the condition of the indentation depth of 2.0 µm, indentation force of 4.0 nN and extend velocity of 15.0 µm/s. The tangent modulus was determined through a curve fit using a database of Sneddon model [3].

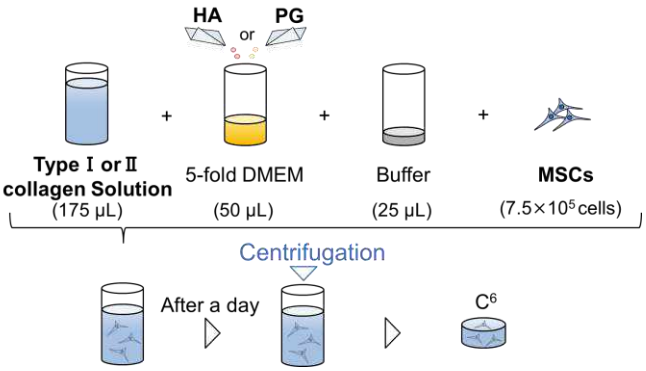

Figure 1: Preparation of the C^6 from the type I or II atelocollagen and MSCs.

RESULTS

Macroscopic observations of C^6 at 14 days and 28 days of culture are shown in Figure 2. It was confirmed that all the samples were contracted as the culture period passed. In particular, the contraction of C^6 mixed with HA was remarkable.

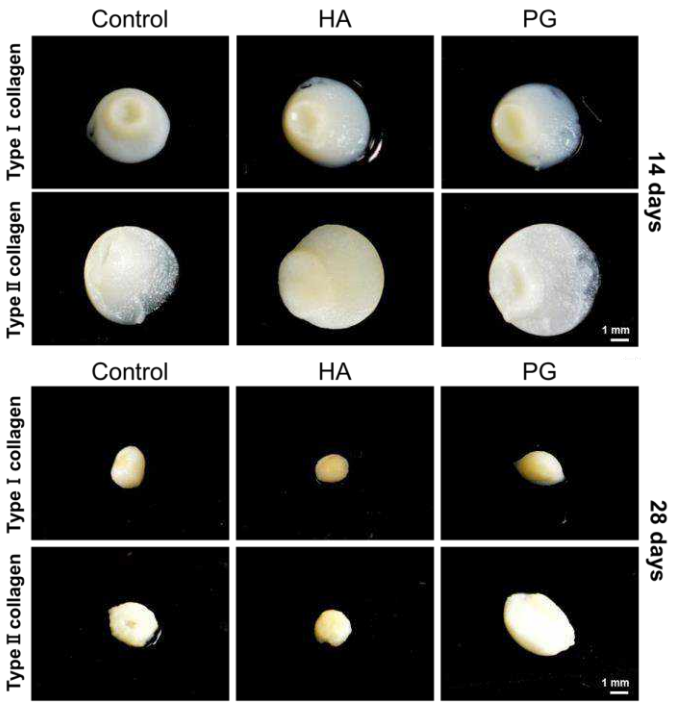

Figure 2: Macroscopic observation of the C^6 after 14 days (upper pictures) and 28 days (lower) of culture (scale bar = 1 mm).

The results of histological examination are shown in Figure 3. Bluish-purple stained areas that indicate chondrogenic matrix production were confirmed under all conditions, with the largest clearly stained area observed in C^6 mixed with HA.

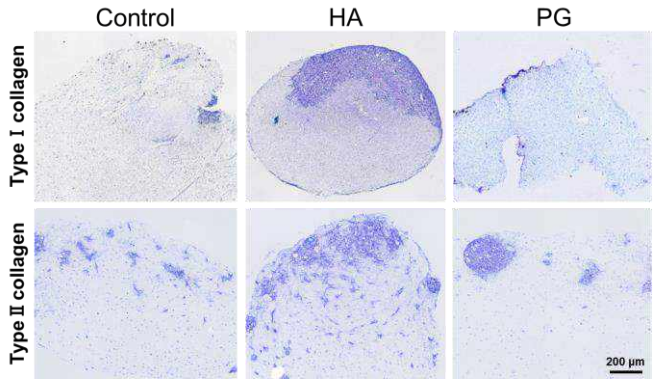

Figure 3: Histological observation with toluidine blue stains of the C^6 after 28 days of culture (scale bar = 200 μm).

The elastic modulus of C^6 at 14 days of culture is shown in Figure 4. The modulus was higher in HA group than in control and PG groups, with the significant increase observed in type I collagen based C^6 in HA group.

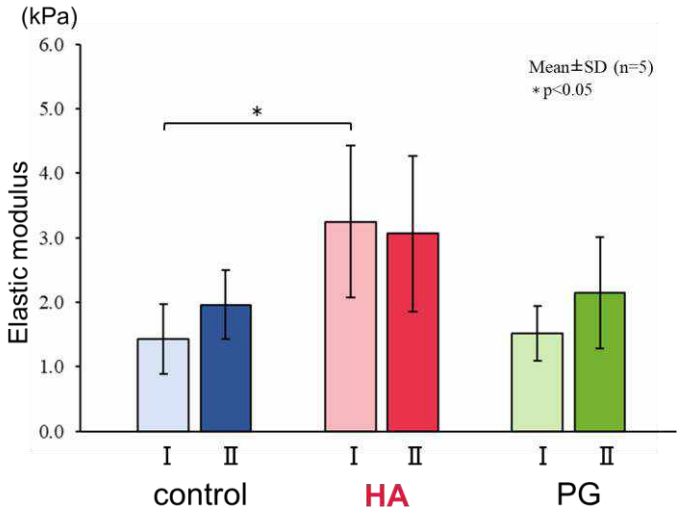

Figure 4: Elastic modulus of the C^6 in control, HA and PG groups.

DISCUSSION

The present study confirmed that the addition of HA improved the chondrogenic matrix production in C^6, with the significantly higher modulus observed in type I collagen based C^6. The present study also confirmed that such effects were not observed for PG. Matsiko et al found that HA interacts with the CD44 receptors on MSCs and contributes to cell migration and chondrogenic differentiation [4]. Such a receptor for PG cannot be found on MSCs. In addition, Ye et al found that the gene expression of SPY-box transcription factor 9 (Sox9), known as a gene relating to chondrogenic differentiation, was significantly higher in type I collagen based C^6 cells than in TEC cells [5]. Their findings imply a molecular level pathway that might happen in HA-containing C^6 in the present study. The present results are consistent with those reported in other biological and biomechanical studies. For example, Davidenko found that HA improved the mechanical property of a freeze dry-processed collagen-containing scaffold [6]. In addition, Uesato et al found that the addition of PG promoted neither chondrogenic differentiation nor resultant chondrogenesis of MSCs in a pellet culture experiment [7]. The present study also confirmed that HA improved chondrogenic matrix production in the type II collagen containing C^6, although modulus increase was not significant. The result is related to our previous finding that Sox9 is upregulated in HA-containing type II collagen based C^6 [8]. In summary, it is suggested that the addition of HA improves the chondrogenic differentiation and matrix production in both the type I collagen based C^6 and type II collagen based C^6.

REFERENCES

[1] Tuan, RS et al., *Arthritis Res Ther*, 5(1): 32-45, 2002.
[2] Ye, X et al., *Japanese Journal of Clinical Biomechanics*, 44: 261-267, 2023.
[3] Ian, NS., *International Journal of Engineering Science*, 3(1): 47-57, 1965
[4] Matsiko, A et al., Journal of the Mechanical Behavior of Biomedical Materials, 11: 41-52, 2012.
[5] Ye, X et al., Biosurface and Biotribology, 9(3): 78-83, 2023.
[6] Davidenko, N et al., Acta Biomaterialia, 6(10): 3957-3968, 2010.
[7] Uesato, R et al., *Hirosaki Med J*, 59: 98-103, 2008.
[8] Ye PhD thesis, 2023

SB^{3}C2024
Summer Biomechanics, Bioengineering and Biotransport Conference
June 11-14, Lake Geneva, WI, USA

INFLUENCE OF IN-VITRO TISSUE CULTURING CONDITIONS ON THE PROPERTIES OF TISSUE-ENGINEERED HEART VALVES - A COMPUTATIONAL ANALYSIS

Elmer Middendorp (1,2), Justina Ghebryal (1,2), Valery L. Visser (3), Polina Zaytseva (3), Sarah E. Motta (3), Simon P. Hoerstrup (3,4), Maximilian Y. Emmert (3,4,5), Frank P.T. Baaijens (1,2), Sandra Loerakker (1,2)

(1) Department of Biomedical Engineering, Eindhoven University of Technology, The Netherlands.
(2) Institute for Complex Molecular Systems, Eindhoven University of Technology, The Netherlands.
(3) Institute for Regenerative Medicine (IREM), University of Zurich, Switzerland.
(4) Wyss Translational Center Zurich, University of Zurich and ETH Zurich, Switzerland.
(5) Department of Cardiothoracic and Vascular Surgery, German Heart Center Berlin, Germany.

INTRODUCTION

Heart valve tissue engineering (TE) has emerged as a promising approach to address the limitations of current heart valve replacement methods, using the body's regenerative capabilities to create living, functional tissues. A significant challenge identified in experimental and preclinical studies is the spatial heterogeneity in scaffold degradation and tissue growth, which leads to uncertainty with respect to the long-term viability and functionality of TE heart valves (TEHVs) [1]. However, the causes and consequences of this heterogeneity on the development of a viable and functional living heart valve replacement are still unclear.

Mechanical cues are well-known regulators of the growth and remodeling (G&R) process within living tissues [2]. Currently, there is a plethora of TE approaches, using a wide range of different mechanical stimuli during the in-vitro tissue culturing phase. Given the large variability across these tissue culture protocols, there is a need to assess the effect of different mechanical stimulation protocols within the culture method on the pre-implant tissue geometry and its retention after implantation, as it has been shown that valve geometry has an important effect on the long-term in-vivo remodeling and thereby valve functionality [3].

The aim of this study was to develop an experimentally-informed computational model to (1) analyze the influence of varying in-vitro tissue culturing conditions on the obtained pre-implant geometry and tissue properties of TEHVs, and (2) investigate how the pre-implant properties subsequently affect shape retention and heart valve functionality post-implantation.

METHODS

In this study, we developed a homogenized constrained mixture model (HCMM) based on the work of Cyron et al. [4], integrated with a finite element model of TEHVs, to simulate the G&R response. As an input for our computational model, we used experimental data of tube-shaped TE matrices (TEM) that were cultured for 6 weeks statically in-vitro, and then manufactured into a TEHV geometry [5]. We used this model to predict tissue G&R as a function of varying in-vitro conditions. In the experimental study, the TEM constructs were created by seeding cells using fibrin as a carrier onto a polymeric, electrospun scaffold. Over time, these two constituents were degraded and new extracellular matrix (ECM) components (glycosaminoglycans (GAGs) and collagen) were deposited (Fig. 1).

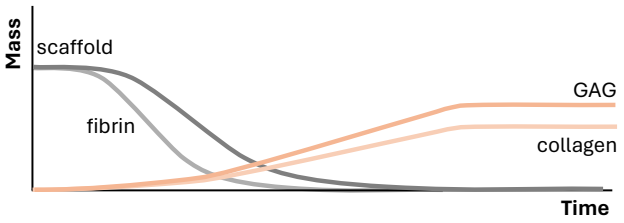

Figure 1: Mass changes during the TE process: degradation of scaffold and fibrin, and production of collagen and GAGs.

Governing equations To describe tissue G&R, a deformation field was determined that satisfies the balance of momentum (Eq. 1), where the total Cauchy stress ($\boldsymbol{\sigma}$) of the tissue is defined as the apparent mass-density (ρ_R^i) weighted constituent stresses ($\boldsymbol{\sigma}^i$).

$$\vec{\nabla} \cdot \Big(\sum_i^n \rho_r^i \boldsymbol{\sigma}^i \Big) = \vec{0}. \tag{1}$$

The apparent mass densities can change as a consequence of the production and removal of each load-bearing constituent (i): collagen, GAGs, fibrin, and the scaffold. For collagen and GAGs we adopted stress-mediated descriptions for mass change given by:

$$\dot{\rho}_R^i(\tau) = M_{\text{dep}}^i \left(1 + k_\sigma^i \Delta\sigma(\tau)\right) - \frac{\rho_R^i}{T^i}, \tag{2}$$

where M_{dep}^i is a basal value of production, $\Delta\sigma(\tau)$ the stress deviation from the original homeostatic target at G&R time τ, k_σ^i a gain-type parameter controlling the sensitivity to the stress-mediated growth response, and T^i the lifetime governing mass removal. Model parameters were assigned from fitting our model to the experimental data [5].

To capture the mechanical behavior of the polymeric scaffold, a Neo-Hookean strain energy density function was adopted. Scaffold degradation was modeled by scaling the scaffold stiffness and scaffold mass using a normalized sigmoid decay function, where k^s and ξ^s describe the offset and speed of degradation, respectively:

$$Q^s(\tau) = \frac{1 + \exp(-k^s \xi^s)}{1 + \exp(k^s(\tau - \xi^s))}. \quad (3)$$

We further assumed a constant tissue density, implying that changes in the total tissue mass were accompanied by equivalent changes in tissue volume. In addition, we applied a constituent-specific kinematic split of the deformation gradient tensor $\mathbf{F}$ to determine the elastic deformation ($\mathbf{F}_e^i$) and stress-free state ($\mathbf{F}_r^i$) of each constituent [4]:

$$\mathbf{F} = \mathbf{F}_e^i \cdot \mathbf{F}_r^i. \quad (4)$$

The turnover-mediated evolution of this stress-free state could then be determined through equation 5, and depends on the difference between the deposition stress and current stress ($\mathbf{S}_{dep}^i$ and $\mathbf{S}^i$) in the constituent, its stiffness ($\frac{\partial \mathbf{S}^i}{\partial \mathbf{C}_e^i}$), and its current elastic deformation ($\mathbf{C}_e^i$):

$$\left[\frac{\dot{\rho}_R^i}{\rho_R^i} + \frac{1}{T^i}\right][\mathbf{S}^i - \mathbf{S}_{dep}^i] = \left[2\frac{\partial \mathbf{S}^i}{\partial \mathbf{C}_e^i} : (\mathbf{C}_e^i \cdot \dot{\mathbf{F}}_r^i \cdot \mathbf{F}_r^{i,-1})\right]_{\mathbf{F}=const}. \quad (5)$$

Simulation plan We first analyzed the tube-shaped geometry, mimicking the TEM constructs in the experiments. Controllable parameters within the in-vitro culture method were varied, particularly focusing on mechanical cues (e.g. the initial load-free tissue formation period, the pressure-driven in-vitro load, and the total in-vitro culturing time). Additionally, in-vivo loading conditions were applied to replicate pulmonary and arterial pressures (Fig. 2). Geometrical parameters were computed after the total in-vitro culture time and after in-vivo implantation. Subsequently, we simulated the impact of the same variations in the in-vitro and in-vivo conditions on the G&R of TEHVs.

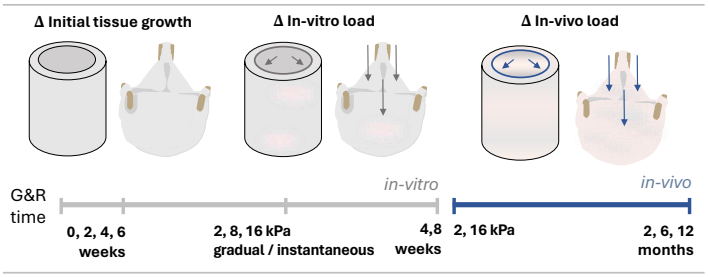

Figure 2: Schematic overview of the simulated in-vitro and in-vivo conditions.

RESULTS

Our simulations reveal that the radius of the tube-shaped constructs is more affected by variations in the initial load-free tissue growth period than by the applied in-vitro pressure, at least for high pressure levels (Fig. 3). Additionally, our results indicate that longer tissue growth periods before in-vitro load application will lead to a lower graft radius.

For TEHVs, our model predicted that the in-vivo geometry is more affected by variations in the applied in-vitro load than by the initial load-free tissue growth time (Fig. 4). A low in-vitro pressure induces leaflet retraction, leading to a valvular insufficiency in-vivo. In contrast, higher in-vitro pressures induce dilation of the leaflets and lead to a decrease in regurgitant orifice area and more sagged, curved valves. Furthermore, the variation in thickness within the valves is much larger than the differences in thickness between the valves for the different in-vitro conditions. Still, the valves with the largest amount of dilation (0w-8kPa and 0w-16kPa) are thinner than the others. All valves show the highest thickness near the commissures due to the high mechanical loads in these regions.

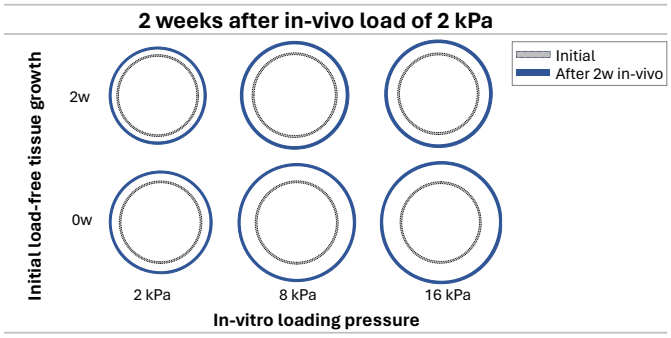

Figure 3: Final cross-section of tube-shaped constructs.

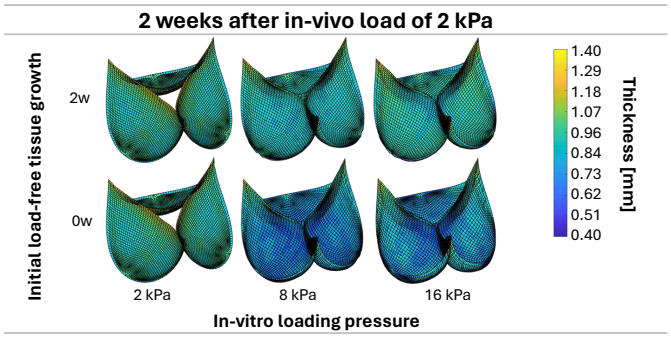

Figure 4: TEHV thickness after 2 weeks of in-vivo implantation.

DISCUSSION

In the present study, we developed a computational model to analyze the degradation of scaffold material and production of ECM constituents in the context of heart valve tissue engineering. We specifically investigated the influence of varying in-vitro culture conditions on the pre-implantation tissue geometry, and the subsequent effects on in-vivo G&R and functionality. We first analyzed the G&R response in tubular-shaped constructs and subsequently simulated the G&R of TEHVs.

Our results showed that higher in-vitro pressures as well as earlier pressure application may lead to tissue dilatation. For the TEHVs, an increase in in-vitro pressure magnitude prevents the valve from regurgitation, and a longer initial load-free tissue growth time limits excessive dilation and thinning of TEHVs. To gain a more comprehensive analysis of the influence of controllable parameters during the in-vitro tissue culture on the G&R response, a broader range of in-vitro loading methods will be investigated in the future, including displacement-driven loading [6], and applying the in-vitro load in an instantaneous manner.

In summary, our model provides a step forward in establishing model-predicted, rational designs for heart valve tissue engineering, which is critical for enabling the successful long-term adaptation and functionality of living valve replacements.

ACKNOWLEDGEMENTS

This project has received funding from the European Research Council (ERC) under the European Union's Horizon 2020 research and innovation program (grant agreement no. 802967 and 852814) and the Dutch Research Council (NWO), project no. 19670 of the NWO Talent Program VIDI.

REFERENCES

[1] Kluin J et al. *Biomaterials* 125 (2017).
[2] Humphrey J. *Cell biochemistry and biophysics* 50 (2008).
[3] Emmert MY et al. *Science translational medicine* 10.440 (2018).
[4] Cyron C et al. *Biomechanics and modeling in mechanobiology* 15 (2016).
[5] Poulis N et al. *Acta Biomaterialia* 158 (2023).
[6] Syedain ZH et al. *Biomaterials* 32.3 (2011).

SPATIOTEMPORAL ANALYSIS FOR HYPERTROPHIC CHONDROCYTE DIFFERENTIATION IN SPHEROID CULTURE

J. Kim (1), K. Tomida (1), E. Maeda (1), T. Adachi (2), T. Matsumoto (1)

(1) Department of Mechanical Systems Engineering, Nagoya University, Nagoya, Japan
(2) Institute for Life and Medical Sciences, Kyoto University, Kyoto, Japan

INTRODUCTION

A valuable *in vitro* method for simulating the development process of biological tissue, 3D cell culture is expected to provide shapes and functions akin to those of living tissue. In previous study [1], we represented that the 3D scaffold-free culture of mesenchymal stem cells highly up-regulated the gene expression levels of hypertrophic chondrocyte differentiation within 7 days in the absence of chemical differentiation supplements, compared to a conventional 2D monolayer model. Recently, we also fabricated a cartilage spheroid model reconstructed by pre-chondrocyte cells to examine the effect of spheroid culture in the chondrocyte differentiation [2]. In this study, we aimed to induce hypertrophic chondrocyte differentiation of mouse chondrocyte precursor cells in spheroid culture and carry out 3D imaging analysis using a confocal laser scan microscopy (CLSM). Furthermore, we quantitatively analyze the 3D morphological features and the distribution of nuclei as well as chromatin condensations inside the spheroids.

METHODS

In this study, we subcultured 2,500 cells of mouse chondrocyte precursor ATDC5 cells in each well of U-bottom ultra-low culture plate (ThermoFisher, USA) to fabricate the cartilage spheroids based on the previous study [2]. The spheroids were incubated for 2, 7, or 14 days with DMEM/F12 medium (Gibco, USA) without chondrogenesis differentiation supplements. We then collected for real-time PCR and cryosectioning to stain with anti-collagen X antibody (Abcam, USA), Hoechst 33342 (Invitrogen, USA), and Alexa Fluor 546 Phalloidin (Invitrogen, USA). The staining images with Hoechst 33342 were also observed using a CLSM (ZEISS LSM880 with AiryScan, Germany) and further analyzed with Imaris (Bitplane, Australia) for 3D image analysis to quantify the nuclear morphology.

RESULTS

Corresponding to the previous study [2], the long term-culture up to day 14 provoked the increase in the size of the spheroid. As a result of real-time PCR in Fig. 1, the14-day spheroid culture up-regulated the gene expression levels of the chondrocyte differentiation markers such as *Acan* and *Col2*. As shown in Fig. 2, immunostaining results represented that the COL10 expression was locally detected around the surface of the 2-day-old spheroid, whereas the COL10 expression was entirely detected in the 14-day-old spheroid. The results altogether indicated that the 14-day spheroid culture induced the hypertrophic chondrocyte differentiation of ATDC5 cells.

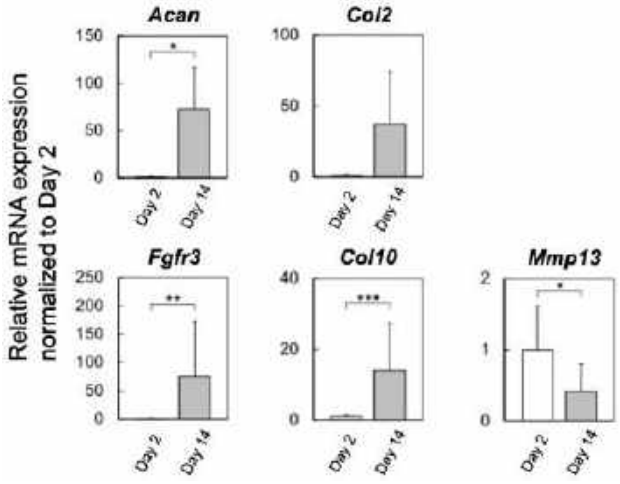

Figure 1: Real-time PCR results to examine chondrocyte differentiation marker (*Acan* and *Col2*) and hypertrophic chondrocyte differentiation marker (*Fgfr3*, *Col10*, and *Mmp13*) of spheroids subcultured for 2 days and 14 days.

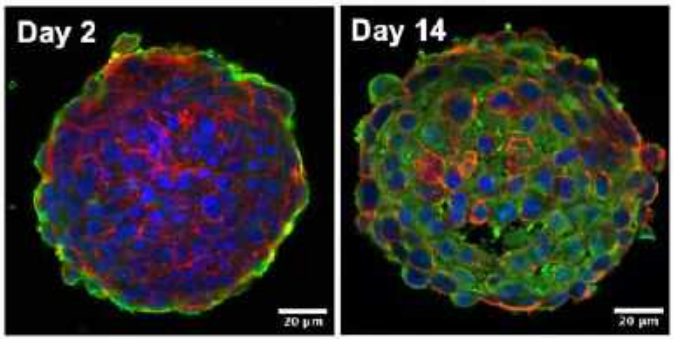

Figure 2: Immunostaining images of COL10 (green), nuclei (blue), and actin filaments (red) in 2-day and 14-day spheroids.

To quantify the nuclear morphology in the spheroid, we then conducted the 3D image analysis using Imaris for segmentation of the nuclei in the spheroid stained by Hoechst 33342. As represented in Fig. 3, each of the nuclei in the 14-day spheroid were hypertrophied than 2-day spheroids.

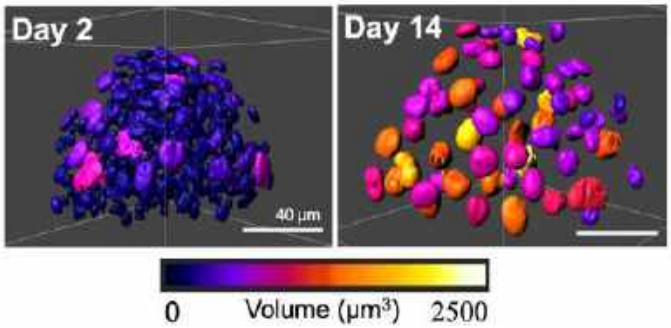

Figure 3: 3D image analysis using Imaris for nuclei in 2-day and 14-day spheroids reconstructed by mouse chondrocyte precursor ATDC5 cells.

As represented in Figs. 4(A) and (B), the chromatin condensations in the nuclei were segmented using 3D image analysis techniques in Imaris. We found out that the number of chromatin condensations in each cell nucleus was greater at day 7 than day 2. However, the total volume of chromatin condensations in each cell nucleus became significantly greater at the day 7 and 14 than day 2. Furthermore, we revealed that the ratio of the chromatin condensation volume in each nucleus was significantly decreased at day 7 and 14 compared to day 2 as shown in Fig. 3(C).

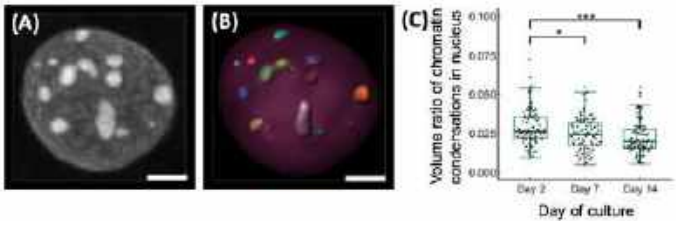

Figure 4: (A) Chromatin condensation in nucleus in the ATDC5 spheroid. (B) 3D image analysis using Imaris for chromatin condensations. (C) Quantification data for volume ratio of chromatin condensation in the nuclei of 2-day, 7-day, and 14-day spheroid.

DISCUSSION

The morphological examination of nuclei and chromatin condensations within a spheroid made from mouse chondrocyte precursor cells was presented in this work. We were able to observe nuclei and chromatin condensations inside the spheroid using CLSM, which also helped us to map out their spatial distribution. Moreover, we used the 3D image analysis method with Imaris to disclose the temporal changes and spatial patterns of the nuclear morphology and chromatin condensations. The current work raised the prospect of integrating biochemical assays with 3D image analysis studies to learn more about the physiology of hypertrophic chondrocyte differentiation.

Our spheroid model exhibited cellular and nuclear hypertrophy as well as the up-regulation of the early hypertrophic chondrocyte differentiation marker genes (*Fgfr3* and *Col10*). In addition, the spheroid demonstrated the expression of COL10, a characteristic of hypertrophic chondrocytes. These findings imply that early hypertrophic chondrocyte development, including morphological changes like those of hypertrophic chondrocyte differentiation *in vivo*, was induced by the spheroid culture of ATDC5 cells. The day 2 spheroid's surface, where relatively large nuclei were located, was where COL10 was expressed. Additionally, on days 7 and 14, when hypertrophied nuclei were present throughout the spheroids, COL10 was found throughout the spheroids. This relationship between nuclear volume and COL10 synthesis is corroborated by the histological characteristic seen in the hypertrophic zone of the epiphyseal plate *in vivo*.

Over the course of 14 days of culture, changes were observed in the amount of heterochromatin, as demonstrated by the quantification of chromatin aggregation volume in individual cell nuclei. Whereas structural study of chromatin condensation in the cell nuclei has been restricted to 2D cultivated cells, our approach is capable of analyzing images of individual chromatin condensations in 3D spheroid model. The ratio of the total chromatin condensation volume to the entire cell nucleus decreased in 7- and 14-day spheroids in comparison to 2-day spheroids. This could imply that as the cell nucleus grew during the spheroid culture, the condensation status of chromatin altered. One explanation is that chromatin condensations may have been in a more relaxed overall state.

In conclusion, we carried out the biomechanical study with an emphasis on morphological and functional alterations for the cartilage spheroid, as well as temporally-varying changes in gene and protein expressions. Thus, we verified that the spheroid culture could induce hypertrophic chondrocyte differentiation, which is a prerequisite for endochondral ossification, even in the absence of chemical differentiation media. We believe our biomechanical analysis will be applicable for other 3D culture model such as organoids.

ACKNOWLEDGEMENTS

This work was supported by the Japan Society for the Promotion of Science (JSPS) KAKENHI (23K17193, 21H04533, and 20K20181), the Foundation of Public Interest of Tatematsu, Nakatani Foundation for Advancement of Measuring Technologies in Biomedical Engineering, and the Japan Science and Technology Agency - Core Research for Evolutionary Science and Technology (JST-CREST) (JPMJCR22L5).

REFERENCES

[1] Kim, J et al. *Sci Rep* 11:13204, 2021.
[2] Kim, J et al. *Biotechnol Bioeng* 119(11):3311-3318, 2022.

PATIENT-SPECIFIC FLUID-STRUCTURE INTERACTION SIMULATIONS OF YOUNG BICUSPID AORTIC VALVE PATIENTS

Hail B. Kazik (1), Harkamaljot S. Kandail (2), Joy Lincoln (3,4), John F. LaDisa, Jr. (1, 3, 4).

(1) Biomedical Engineering, Marquette University & Medical College of Wisconsin, Milwaukee, WI, USA
(2) Medtronic Neurovascular, Irvine, CA, USA
(3) Pediatrics, Section of Pediatric Cardiology, Medical College of Wisconsin, Milwaukee, WI, USA
(4) Herma Heart Institute, Children's Wisconsin, Milwaukee, WI, USA

INTRODUCTION

Bicuspid aortic valve (BAV) is the most common congenital cardiovascular defect and is characterized by formation of two, rather than three, leaflets.[1] Approximately 50% of BAV patients prematurely develop calcification and aortic stenosis (AS) by the age of 35, which is more prominent with fusion of the right and noncoronary (R/NC) leaflets.[2] This holds true for a cohort of 117 patients with R/NC BAV at the Herma Heart Institute (HHI) where 60% developed AS by age 20. Importantly, not all R/NC BAV patients develop AS since some maintain a normal peak aortic gradient into early adulthood (Fig 1).

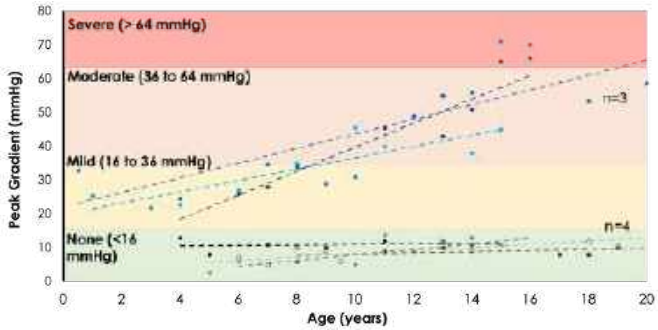

Figure 1. The evolution of peak aortic valve gradients from R/NC BAV patients at our center

The mechanisms underlying premature AS induced by calcification in BAV patients are unknown, but it has been suggested that mechanical stimuli play a role. This is supported by previous computational modeling of adult BAV showing regional differences in mechanical stimuli on BAV leaflets compared to tricuspid aortic valve (TAV) controls.[3] However, studies to date have focused on adult BAV after the onset of calcification and relied on simplified geometry, boundary conditions, and material properties in their models. Our objective is to characterize the mechanical stimuli more accurately in BAV by using patient-specific geometry and boundary conditions, as well as including material properties from biaxial testing of BAV leaflets for the first time. By identifying the BAV-specific regional differences in mechanical stimuli in young patients prior to the onset of calcification and correlating them with known patterns of calcification and downstream gene expression, we can better understand how BAV-induced mechanical stimuli plays a role in premature calcification and AS in R/NC BAV patients.

METHODS

Cardiac MRI data of a 23-year-old patient with R/NC BAV and aged-matched TAV control were obtained following IRB approval. Aortic and coronary artery morphology were extracted using SimVascular (simvascular.github.io). Leaflet geometry was constructed in OnShape (onshape.com) using reported dimensional relationships made patient-specific by scaling to sinus geometry (Fig 2).[4]

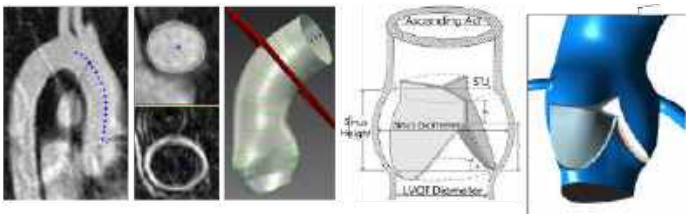

Figure 2. Patient-specific geometry reconstruction.

Physiologic boundary conditions (BCs) were implemented including measured pressure at the aortic inlet, a lumped-parameter model of downstream physiology at the aortic outlet, and flow imposed at coronary artery outlets (Fig 3).

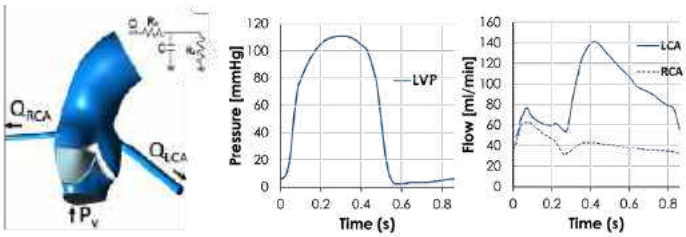

Figure 3. Patient-specific BCs for FSI simulations.

Biaxial testing was performed on aortic valve leaflets obtained from local donors after IRB approval (42-year-old normal control, 79-year-old with BAV). Briefly, samples (~6x6mm) were biaxially stretched at 37° to peak physiological strain in the circumferential (11%) and radial directions (13%) using a BioTester (CellScale) system with a 1.5N load cell using a previously described protocol (Fig 4).[5] Constitutive parameters of the Gasser-Ogden-Holzapfel model for hyperelastic anisotropic material properties were obtained using Hyperfit.[6]

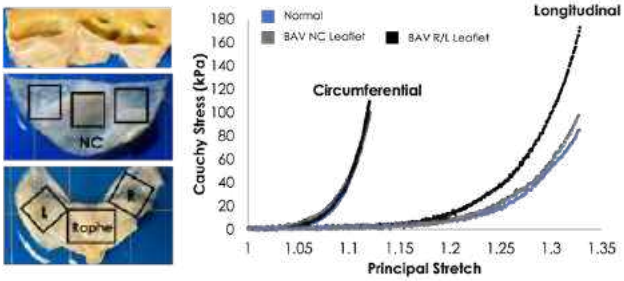

Figure 4: Biaxial testing of normal and BAV patient valve tissue.

Fluid-Structure Interaction (FSI) simulations were performed by coupling FlowVision (Capvidia) with Abaqus/Explicit (Dassault Systems). Wall shear stress (WSS) and von Mises Stress were quantified using Abaqus and ParaView and evaluated for statistical significance using One-Way ANOVA.

RESULTS

FSI studies of the young adult R/NC BAV patient revealed higher WSS magnitude in the coaptation region of the ventricularis surface versus the age-matched TAV control. This is more prominent on the nonfused BAV leaflet compared to the fused leaflet (Fig 5).

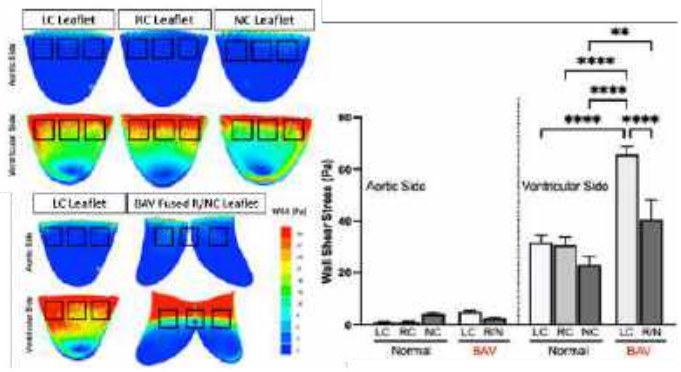

Figure 5. WSS contours & quantification showing higher magnitude in the coaptation region of the ventricularis that is more prominent on the nonfused BAV leaflet.

The magnitude of von Mises stress was higher for BAV leaflets, particularly in the belly/coaptation regions. This is more pronounced in the fused leaflet, primarily near the fusion site (raphe; Fig 6).

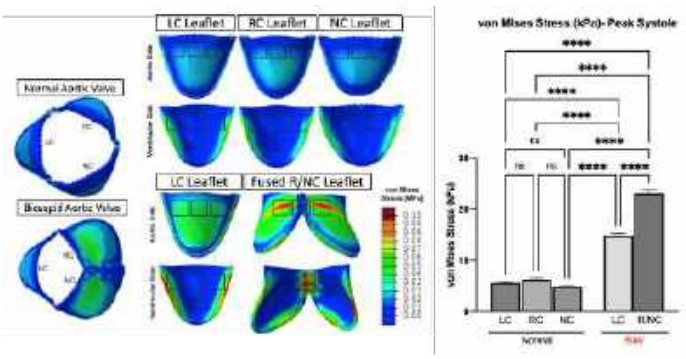

Figure 6. von Mises Stress contours & quantification showing higher magnitude in BAV, mainly at the R/NC fusion site

DISCUSSION

Our FSI studies of a young adult R/NC BAV case revealed pronounced alterations in mechanical stimuli regionalized to the raphe, attachment, and coaptation regions when compared to an age-matched TAV control. Interestingly, previous studies have shown that calcium deposition on aortic valve leaflets typically occurs in those regions.[7] Given that these regionalized changes in mechanical stress are present already at a young age (23-year-old) and localized to regions prone to calcium deposition suggests that BAV-specific mechanical stimuli could be a potential pathogenic contributor. It is believed that these initial findings to be further presented are more accurate since they involve the first ever simulations from biaxial testing of BAV leaflets from patients. Thus we can more accurately characterize BAV-specific mechanical stimuli that may drive the development of premature calcification in BAV. Evaluating the downstream molecular mechanisms in patients remains challenging due to the availability of tissue samples throughout the disease process. To address this we are conducting FSI simulations in a murine model of BAV at equivalent human-to-murine age groups to mimic human progression of premature calcification in BAV.[8] To date we have shown that increased peak aortic gradient driving alterations in WSS precede the increased expression of calcification markers such as *Spp1*, particularly in the attachment and coaptation regions where calcium deposition commonly occurs.[9] This further substantiates our hypothesis that mechanical stimuli could be driving premature calcification in BAV. Future work will translate our findings in the mouse model to our BAV patient cohort to identify predictive indicators for calcification risk and targets for novel molecular therapies.

ACKNOWLEDGEMENTS

This work was supported by NIH/NHLBI R01HL132801 and R01HL127033 (JL), 1R01HL142955 (JFL), Advancing a Healthier Wisconsin 9520519 (JL), an HHI Innovation Award (JL), Children's Research Institute Pilot Award (JL), Project Bubaloo Research Grant (JL). A special thanks to Drs. Benjamin Goot for imaging support, and Harkamaljot Kandail for FSI simulations support.

REFERENCES

[1] Menon V, Lincoln J, Frontiers in Cardiovascular Medicine, 5, 2018.
[2] Tzemos N, JAMA, 300(11), 2008.
[3] Kazik et al., Front. Cardiovasc. Med., 8, 2021
[4] Thubrikar MJ, The Aortic Valve, 1st ed., 1990.
[5] Van Geemen, D., et. al (2016). *PLoS ONE*, *11*(2).
[6] Gasser et al., Royal Society Interface, 3(6):15–35, 2006
[7] Thubrikar et al., Am J Cardiol, 58:304-308, 1986
[8] Fulmer D, et al., Circulation, 140(16):1331–1341, 2019.
[9] Mazur, P et al., Circulation, 81(7);1043-1050, 2017

MODELING HEAT SINK EFFECTS OF CEREBROSPINAL FLUID (CSF) DURING THERMAL THERAPIES FOR TREATMENT OF GLIOBLASTOMA (GBM)

Yash S. Lad (1), Omar Abdulqader (1), Shreeniket M. Pawar (1), Anilchandra Attaluri (1)

(1) Department of Mechanical Engineering, School of Science, Engineering, and Technology, The Pennsylvania State University Harrisburg, Harrisburg, PA 17057, USA

INTRODUCTION

GBM is considered as the most lethal brain tumor, which has a high recurrence rate. The main reason for local recurrence is inefficiency of thermal therapies in treatment of 100% tumor margins due to the heterogeneity of tumor. Treatment of GBM requires predefined temperature constraints, based on the thermal therapies, to be maintained within the tumor for a specified time to kill the cancerous cells. However, it is difficult to achieve clinically acceptable temperature distribution due to blood perfusion and presence of CSF [1]. Most of the GBM tumors are in close proximity to the CSF, which carry away most of the heat supplied to the tumor during these therapies. Understanding the heat transfer characteristics and the amount of heat that can be transferred to the fluidic structures is crucial for optimizing thermal therapies and ensuring their effectiveness in targeting brain tumors. The impact of heat sinks produced by the CSF, ventricles, posterior cerebral artery, and suprasellar and ambient cisterns on the local temperature during LITT has been identified in the literature [2] but has not been studied. Computational fluid dynamics (CFD) combined with conjugate heat transfer (CHT) modeling provides a powerful tool to investigate the dynamics of fluid flow and the associated heat transfer processes within the brain.

This study explores the convective heat transfer between the CSF and tumor during thermal therapies to identify the untreated tumor margins.

METHODS

The human head anatomy was modeled as spherical domains representing skull, CSF general, brain, tumor, and heat source. The CSF ventricles were modeled as rectangular fluid channels with velocity inlet and pressure outlet. The CSF was modeled as a fluid with laminar flow based on the calculation of Reynolds number. Boussinesq approximation to the Navier-Stokes equation was used to account for buoyancy driven flows. Four different cases for the tumor location with respect to CSF general and ventricles were studied. A volumetric heat source with pulsed heating was modeled. Thermal damage-dependent blood perfusion was added as a volumetric heat source in the tumor. Variation of temperature penetration depth into the CSF ventricles were studied for different gravity directions, assuming the patient positioning during the treatment.

Figure 1 shows a representation of the system of interest with simplified geometry. The dimensions of the different components of the human head are approximated from the segmented de-identified patient dataset. The CFD simulations utilize the Navier-Stokes equations, coupled with the energy equation, to capture the fluid flow and heat transfer phenomena.

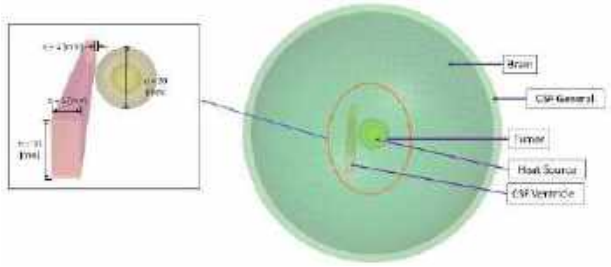

Figure 1: Simplified geometry considering brain, tumor, and CSF ventricles, for model preparation in the CFD software.

Moreover, the Boussinesq approximation to the Navier–Stokes equation, as shown in equation (1), is used to account for buoyancy-driven flow. The temperature change in the fluid region due to the convective heat transfer is given by equation (2). Thermal damage-dependent blood perfusion equation (3), adopted from Pennes' Bioheat equation [3], is applied to the tumor in the form of volumetric heat source. Finally, the convective heat transfer coefficient is calculated from equation (4).

$$\rho\frac{\partial\vec{v}}{\partial t}+\rho\nabla\cdot(\vec{u}\vec{u})=\mu\nabla^2 u-\nabla p+\rho k\vec{g} \quad (1)$$

$$\rho C_p \frac{\partial T}{\partial t} - \nabla(k\nabla T) = -\rho C_p(\vec{u}.\nabla T) \quad (2)$$

$$Q_{Perf} = \rho_b C_{p,b} \omega_{b,tumor}(T_b - T) \quad (3)$$

$$h = \frac{q}{A(T_b - T)} \quad (4)$$

where, ρ is the fluid density [kg/m^3], u is the fluid velocity [m/s], k is the thermal conductivity [W/(m.K)], p is the fluid pressure [Pa], T is the absolute temperature [K], ρ_b is the blood density [kg/m^3], $C_{p,b}$ is specific heat capacity of blood [J/kg.K], ω_b is the blood perfusion rate [1/s], T_b is the blood temperature [K] and g is the gravitational acceleration [m/s^2]. The values of these properties are listed in Table 1.

Table 1: Thermal properties for different domains of the human head anatomy [1,4].

Part	C_p [J/(kg.K)]	ρ [kg/m^3]	k [W/(m.K)]	μ [Pa.s]	u [m/s]
Brain (grey & white matter)	3630	1046	0.51	-	-
Tumor	3700	1056	0.57	-	-
CSF	4096	1007	0.62	7.84×10^{-4}	0.01
Heat Source	750	2200	1.38	-	-
Blood	3617	1050	0.52	3.65×10^{-4}	0.1

RESULTS

Figure 2 shows the simulation results for a tumor located close to the left CSF ventricle. The surface temperature contour in Figure 2b shows the untreated surface with a temperature drop of 2.6 [°C] from the maximum surface temperature of 42.2 [°C]. The temperature contour for the CSF ventricle in figure 2d shows that the CSF ventricle carries away 1.4 [°C] temperature, acting as a heat sink. From the heat transfer report, the convective heat transfer rate for the CSF ventricle was calculated to be 9.32 ×10^{-2} [W]. Therefore, from equation (4), the convective heat-transfer coefficient can be estimated as 7.18 [W/(m^2.K)].

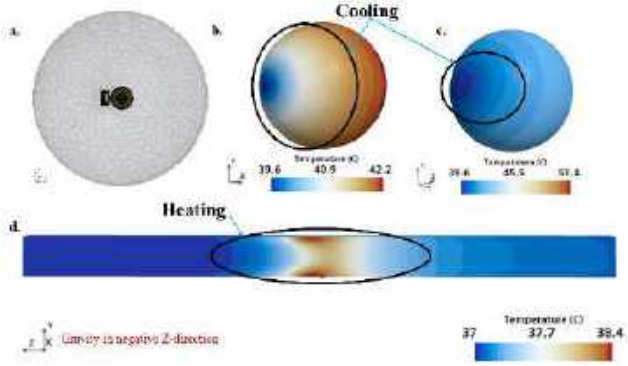

Figure 2: Results for tumor location close to the left CSF ventricle. a. Mesh plot showing the location of the tumor with respect to the CSF. b. Tumor surface temperature shows a 2.6 [°C] drop in temperature closer to the ventricle. c. Tumor domain temperature shows an overall drop of 11.8 [°C] from core to the surface of the tumor. d. CSF ventricle temperature shows a 1.4 [°C] rise in temperature.

To identify the temperature penetration into the CSF ventricle, a line probe was plotted across the width of the ventricle, right at the center of the length exposed to the tumor as shown in Figure 3a. The probe plot (Figure 3b) shows a penetration depth of approximately 1.3 [mm] into the ventricle.

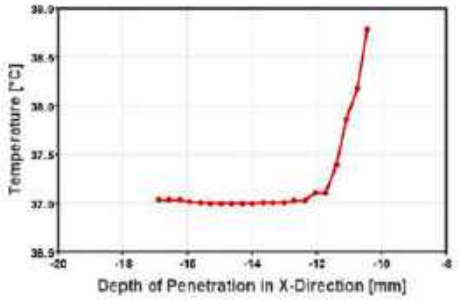

Figure 3: Temperature plot showing the penetration depth of approximately 1.3 [mm] in X-direction.

DISCUSSION

This study demonstrates a substantial heat sink effect of cerebrospinal fluid (CSF) during thermal therapies when the tumor is located in close proximity to the CSF ventricles or CSF general. Hence, accounting for these heat-sink effects of the CSF during thermal therapies is necessary to obtain maximum lesion coverage and avoid tumor recurrence. During the conference presentation, the heat sink effects for different tumor locations will be presented, and the convective heat transfer coefficient will be compared. In addition, the maximum distance between the tumor and CSF, up to which the heat sink effects should be modeled, will be demonstrated, with comparison.

ACKNOWLEDGEMENTS

Funding for this project was provided by the National Cancer Institute of the National Institutes of Health under Award Number R01 CA247290. R.I. and A.A. received additional funding from the National Cancer Institute of the National Institutes of Health under Award Number R01 CA257557. The content is solely the responsibility of the authors and does not necessarily represent the official views of Johns Hopkins University, Pennsylvania State University - Harrisburg, or the National Institutes of Health. We also acknowledge Siemens for providing the computational tool Simcenter STAR-CCM+© for conducting this study.

REFERENCES

[1] Schooneveldt, G.; Trefná, H.D.; Persson, M.; de Reijke, T.M.; Blomgren, K.; Kok, H.P.; Crezee, H. Hyperthermia Treatment Planning Including Convective Flow in Cerebrospinal Fluid for Brain Tumour Hyperthermia Treatment using a Novel Dedicated Paediatric Brain Applicator. Cancers 2019, 11, 1183.

[2] Pruitt, R., Gamble, A., Black, K., Schulder, M., & Mehta, A. D. (2017). Complication avoidance in laser interstitial thermal therapy: lessons learned. Journal of neurosurgery, 126(4), 1238-1245.

[3] Pennes, H. H. (1948). Analysis of tissue and arterial blood temperatures in the resting human forearm. Journal of applied physiology, 1(2), 93-122.

[4] ITIS Foundation. Tissue Properties. Available online: https://itis.swiss/virtual-population/tissue-properties/database/database-summary/ (accessed on 12/27/2023).

PROPORTIONAL INTEGRAL DERIVATIVE (PID) CONTROLLER APPLIED TO MAGNETIC NANOPARTICLE HYPERTHERMIA THERAPY (MNHT)

Nageshwar Arepally (1), Yash S. Lad (1), Shreeniket M. Pawar (1), Ma'Moun Abu-Ayyad (1), Anilchandra Attaluri (1)

(1) Department of Mechanical Engineering, School of Science, Engineering, and Technology, The Pennsylvania State University Harrisburg, Harrisburg, PA 17057, USA

INTRODUCTION

Magnetic nanoparticle hyperthermia (MNPH) therapy is generally used for treatment of tumors in combination with chemotherapy and radiation therapy [1]. In MNPH treatment, heat is generated by the application of alternating magnetic field (AMF) to the magnetic nanoparticles (MNP). Current MNPH treatments are based on the application of pulsed AMF to control the heat within hyperthermia temperatures. However, the major drawback of this method is that there is no feedback control system to prevent the risk of off-target thermal dose deposition and the treatment is entirely based on operator skill and experience [2,3]. In this study we plan to implement thermal damage feedback based PID control system to maintain the tumor temperature within hyperthermia limits, preventing off-target thermal damage. The subcutaneous tumor embedded in muscle is considered as the domain for the study. Uniform distribution of MNP is assumed inside the tumor. Bioheat transfer simulations in combination with the PID controller are carried out for the simplified model. Simulation results show that the PID controller successfully maintains the temperature at the tumor boundary at 43 [°C] with minimal overshoot in the range of 3-5 [%]. The controller output is set to zero once the thermal damage at the tumor boundary reaches the setpoint.

METHODS

A simple geometry assuming spherical tumor and cuboidal muscle, as shown in Figure 1 is modelled for this study. The heat source, i.e., MNP distribution is assumed to be spherical and uniform. The model is built in commercial finite element analyis (FEA) software (COMSOL Multiphysics©) to perform the bioheat transfer simulations. Initially, the muscle, tumor and heat source are assumed to be at 37 [°C]. The convective heat flux of 3.7 [W/(m^{2}K)] is imposed on the part of tumor exposed to surroundings.

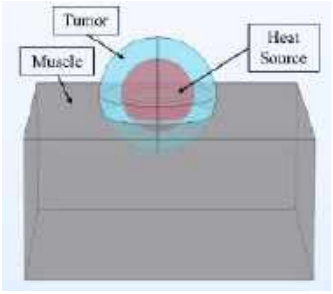

Figure 1: Geometry representing the tumor and heat source as spherical domains embedded in a cuboidal muscle domain.

Pennes' bioheat transfer equation is used to solve heat transfer problem as given in equation 1. Thermal damage dependent blood perfusion was modelled for tumor using equations 2, 3 and 4 [1,4].

$$\rho_i\, C_{p,i}\, \frac{\partial T}{\partial t} - \nabla(k_i \nabla T) = Q_{Perfusion} + Q_{Heatsource} + Q_{met} \quad (1)$$

$$Q_{Perfusion} = \rho_b\, C_{p,b}\, \omega(T)(T_b - T) \quad (2)$$

$$DS = 1 - \exp\left(-A \int_0^t e^{-\frac{E_a}{RT(\tau)}}\right) d\tau \quad (3)$$

$$\omega(T) = \begin{cases} \omega_{b,i}(30DS + 1), (DS \le 0.02) \\ \omega_{b,i}(-13DS + 1.86), (0.02 < DS \le 0.08) \\ \omega_{b,i}(-0.79DS + 0.884), (0.08 < DS \le 0.97) \\ \omega_{b,i}(-3.87DS + 3.87), (0.97 < DS \le 1 \end{cases} \quad (4)$$

where, ρ is the fluid density [kg/m^3], k is the thermal conductivity [W/(m.K)], T is the absolute temperature [K], ρ_b is the blood density [kg/m^3], $C_{p,b}$ is specific heat capacity of blood [J/kg.K], ω_b is the blood perfusion rate [1/s] and T_b is the blood

temperature [K]. The values of these properties are listed in Table 1.

Table 1: Thermal properties for different domains of the human head anatomy [1,4].

Part	C_p [J /(kg. K)]	ρ [kg/ m^3]	k [W /(m. K)]	Q_{met} [W /m^3]
Muscle	3421	1090	0.003	6374.5
Tumor	3760	1045	0.51	31873

Temperature measuring probes were placed at the boundary of the tumor to provide feedback to the PID controller. Cumulative equivalent minutes at 43 [°C] (CEM43) is modelled, as shown in equation (5), and used as a thermal damage feedback for the PID controller. The developed FEA model was exported to MATLAB Simulink® using COMSOL Livelink for Simulink©.

$$\mathrm{CEM43} = \int_{t=0}^{t=final} B^{\frac{43[°C]-T(x,y,t)[°C]}{1[°C]}}, B\begin{cases} 0.5\,, T > 43\ [°C] \\ 0.25,\ T \le 43\ [°C] \end{cases} \quad (5)$$

PID controller was designed in MATLAB Simulink®. Constraints were imposed for temperature at the centre of the tumor to be maintained below 60 [°C] and boundary of the tumor below 43 [°C]. Fuzzy logic control was applied to ensure that once the thermal damage measuring probe at the tumor's boundary registered a CEM43T10 value, the power input was switched off.

RESULTS

Figure 2 shows the simulation results for temperature control using PID. The controller successfully maintains the temperature at the centre of the tumor below 60 [°C]. There is a small overshoot in temperature of about 4 [%] at boundary of the tumor. However, this overshoot is seen only for a small duration. From the figure it is evident that the controller is able to maintain the temperature at boundary of the tumor below 43 [°C] for rest of the treatment time.

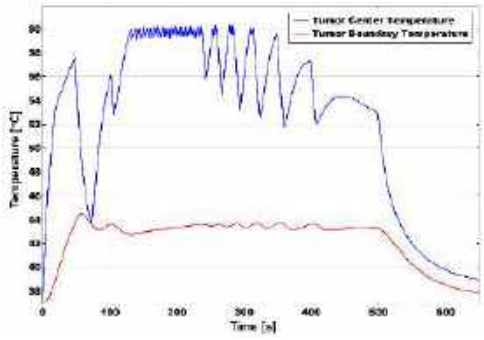

Figure 2: Simulation results for temperature control using PID. The controller successfully maintains tumor centre temperature below 60 [°C] and the boundary below 43 [°C].

Figure 3 shows the CEM43 thermal damage at the tumor boundary. The controller output is zero once the CEM43 reaches value of 10 due to this reason the temperature drop at approximately 600 seconds can be seen in figure 2.

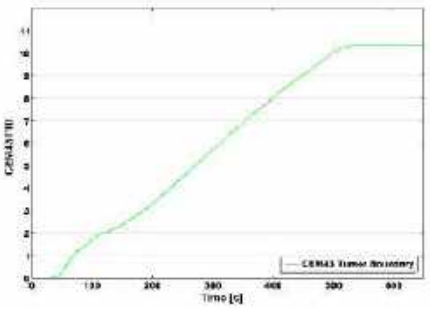

Figure 3: CEM43T10 results using the PID controller the controller output successfully turns off once the target thermal dose of CEM43T10 is reached.

DISCUSSION

This study demonstrates the PID controller design cascaded with fuzzy logic control for MNPH treatments. PID controller is preferred over the conventional pulsed heating as the feedback enhances the control and reduces the dependency on operator skills. In this study PID is designed and implemented to control tumor boundary temperature and stop the heating when the thermal damage reaches the setpoint. However, there is slight overshoot from the setpoint for the tumor boundary temperature. This overshoot might be a concern based on tumor location. This limits the possibility of the controller to be translated into clinical settings. To overcome this limitation, fine tuning of the controller needs to be done based on specific tumor positioning cases.

REFERENCES

1. Attaluri, A., Kandala, S. K., Wabler, M., Zhou, H., Cornejo, C., Armour, M., ... & Ivkov, R. (2015). Magnetic nanoparticle hyperthermia enhances radiation therapy: A study in mouse models of human prostate cancer. International Journal of Hyperthermia, 31(4), 359-374.
2. Kandala, S. K., Liapi, E., Whitcomb, L. L., Attaluri, A., & Ivkov, R. (2018). Temperature-controlled power modulation compensates for heterogeneous nanoparticle distributions: a computational optimization analysis for magnetic hyperthermia. International Journal of Hyperthermia.
3. Sharma, A., Jangam, A. A., Yung Shen, J. L., Ahmad, A., Arepally, N., Carlton, H., ... & Attaluri, A. (2023). Design of a temperature-feedback controlled automated magnetic hyperthermia therapy device. Frontiers in thermal engineering, 3, 1131262.
4. Pennes, H. H. (1948). Analysis of tissue and arterial blood temperatures in the resting human forearm. Journal of applied physiology, 1(2), 93-122.

MECHANICAL CHARACTERIZATION OF HUMAN MESENCHYMAL STEM CELL-DERIVED OSTEOCYTIC SPHEROIDS BY UNIAXIAL COMPRESSION TESTING

T. Inagaki, J. Kim, E. Maeda, T. Matsumoto

Department of Mechanical Systems Engineering, Graduate School of Engineering,
Nagoya University, Nagoya, Aichi, Japan

INTRODUCTION

In recent years, three-dimensional (3D) cultures have gained attention as new cell culture models to mimic *in vivo* environments beyond a conventional two-dimensional (2D) culture model. We have fabricated spheroids with a diameter of about 100 µm derived from human mesenchymal stem cells in a medium containing osteogenic supplements. We found that the spheroid significantly up-regulated osteocyte differentiation markers after two days compared to 2D cultures (1). Additionally, it is known that mineralization of the tissue occurs in the spheroid after the long-term culture (2). In order to evaluate the bone-likeness of the mineralized spheroids quantitatively as the mechanical properties, we previously developed a uniaxial compression testing device by a glass plate to measure the stiffness of the spheroid (3). In this study, we further evaluated the viscoelastic behavior of the spheroids for 2-day and 35-day culture after compression release.

METHODS

Human mesenchymal stem cells (Riken BRC, Japan) were cultured in an incubator maintained at 37°C and 5% CO_2. The basal medium consisted of DMEM (Dulbecco's modified Eagle medium, Gibco, USA) supplemented with 10% immobilized bovine fetal serum (Gibco, USA) and 1% penicillin-streptomycin (Nacalai Tesque, Japan). Cells were passaged every 3-4 days. The experiment was performed by cells with less than 10 passage number.

Human mesenchymal stem cell-derived spheroids were fabricated using the method described in a previous study (4). Cell suspension (2,500 cells/spheroid) was placed in an each well of an ultra-low attachment culture plate (ThermoFisher, USA) and cultured for 2 days to form the spheroids. In this study, spheroids were subcultured for 2 days and 35 days after being placed in the well plate were used for observation of viscoelastic behavior. For spheroid culture, osteogenic differentiation was induced by adding chemical osteogenic supplements. The osteogenic supplements consisted of a mixed solution of 10 mM β-glycerophosphate (Sigma, USA), 50 µM ascorbic acid (Wako, Japan), 100 nM dexamethasone (Nacalai Tesque, Japan) in DMEM + GlutaMAXTM-I (Gibco, USA).

The uniaxial compression testing system is shown in Figure 1. A borosilicate glass thin plate (D263 Teco, Schott, Germany) with 100 mm in length, 1.0 mm in width, and 0.14 mm in thickness was bent by heating with a gas lighter in the middle as shown in Figure 1 (A) and attached to a three-axis micromanipulator (MHW-3, Narishige, Japan). The spheroid was transferred to a square culture dish (CS-TECH, Japan) and placed on the stage of an inverted microscope (IX73, Olympus, Japan). The micromanipulator was operated to press the glass thin plate against the spheroid on the wall of the square dish. Further experiment was performed at room temperature within 1 hour after the spheroids in the incubator were transferred to the square dish.

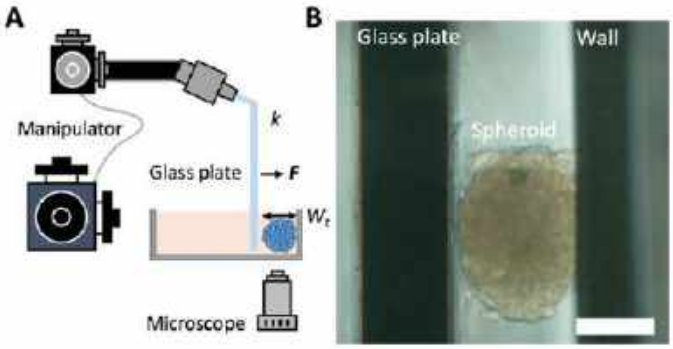

Figure 1: Schematic diagram of a uniaxial compression system using a glass plate controlled by a 3D manipulator (A) and representative images of spheroids derived by human mesenchymal stem cells under compression (B). A white bar indicates 100 µm.

The viscoelastic behavior of the spheroid was investigated using the test system as described in Figure 2. The experiment's outline is as follows: initially, the spheroid was compressed by 50% for 30 seconds (Phase I). Then, the spheroid was kept compressed under the glass plate for either 1 minute or 15 minutes (Phase II) to observe the creep phenomenon of the spheroid. Finally, the glass plate was released from the spheroid, and the recovery of the spheroid strain was observed for 5 minutes (Phase III). The slowness of the strain recovery behavior was determined by approximating the time change of the spheroid width W_t under each condition with an exponential function in equation (1) and calculating the time constant τ.

$$f(t) = a + b\exp^{(-t/\tau)} \quad (1)$$

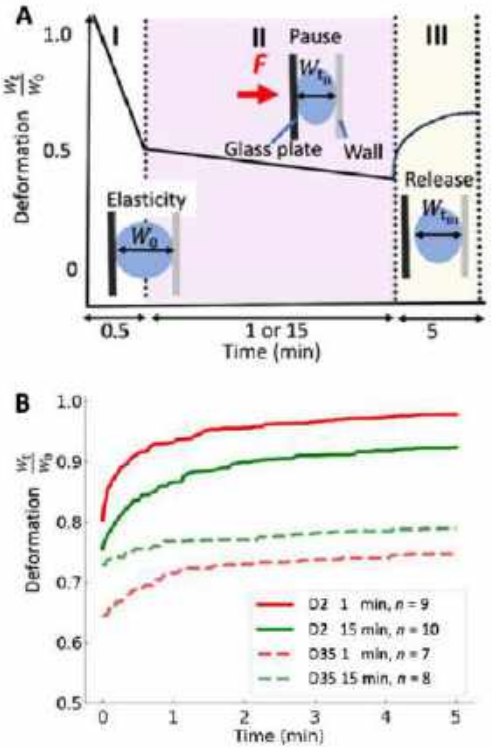

Figure 2: Schema (A) and typical results (B) of creep deformation experiment for 2-day and 35-day spheroids using a glass plate compression system. First, the spheroid was compressed up to 50% strain in 30 s (I), then kept compressed in 1 or 15 minutes (II), and finally released by moving the glass plate apart from the wall (III). Changes in the ratio of the width in the direction of compression of the 2-day and 35-day spheroid 1 min and 15 min after releasing in phase III.

RESULTS

Figure 2(B) shows the strain recovery of human mesenchymal stem cell-derived spheroids for 5 minutes after 50% compression, cultured for both 2 days and 35 days. The ratio of the spheroid width immediately after compression release (W_0) to the spheroid width at the end of observation period III (W_t) was 1.01 ± 0.07 (mean ± SD, N = 3 (number of independent experiments), n = 9 (number of samples)) for spheroids cultured for 2 days with 1 minute of compression (red), indicating recovery to the width before compression. However, for spheroids compressed for 15 minutes (green), the ratio was 0.93 ± 0.07 (N = 3, n = 10), showing a tendency not to return to the original size. On the other hand, for spheroids cultured for 35 days, the ratio was 0.78 ± 0.08 (N = 3, n = 7) for 1 minute of compression (red dashed) and 0.82 ± 0.14 (N = 3, n = 8) for 15 minutes of compression (green dashed), neither of which recovered to the original size.

Additionally, by approximating the time change of the average strain width for each condition of the spheroids with an exponential function, the time constant τ after compression recovery was calculated to be 0.83 and 1.02 for 1 and 15 minutes of compression, respectively, for spheroids cultured for 2 days. For spheroids cultured for 35 days, the time constants were 0.87 for 1 minute and 1.60 for 15 minutes of compression.

DISCUSSION

We established a uniaxial compression test system using a glass plate controlled by a three-axis micromanipulator, and observed the viscous behavior of human mesenchymal stem cell-derived spheroids during compression. Short-term 2-day spheroids underwent plastic deformation by 50% compression, remaining shrunk to approximately 90% of their original size. In other words, they do not return to their original size when compressed for more than 1 minute under compressive strain conditions. Kinoshita's study reported that reconstructing the cytoskeleton actin and the cell adhesion molecule cadherin occurs when African clawed frog embryos are compressed 50% for 5 minutes (5). It is possible that the cytoskeleton and cell adhesion in spheroids cultured for 2 days were thought to be reconstructed while being compressed for more than 1 minute, preventing them from returning to their original shape. Additionally, from the time constant of the width recovery change of the spheroids, it was found that the recovery time for 2-day and 35-day cultures was slower for 15 minutes of compression than for 1 minute. This result might indicate that longer durations of compression contribute to a more noticeable restructuring of the cytoskeleton. Furthermore, spheroids cultured for 35 days underwent greater plastic deformation, remaining shrunk to approximately 70% of their original size, even with 1 minute of short-term compression. The spheroids incubated for 35-day culture are known to induce mineralization from the center of the spheroid (2), implying that the mineralization within the spheroid affected its viscoelastic behavior.

In this study, we utilized a uniaxial compression test system with a glass plate controlled by a three-axis micromanipulator to observe the viscous behavior of human mesenchymal stem cell spheroids. By compressing 2-day and 35-day spheroids and observing the time change of deformation in the compression direction, we evaluated the viscoelastic behavior of the spheroids. The differences in the strain recovery behavior of the spheroids due to culture period and compression time are thought to be influenced by the cytoskeleton, cell adhesion, and extracellular matrix in the spheroids, but their direct involvement is still unclear. To confirm the involvement of the cytoskeleton in the viscoelastic behavior of the spheroids, inhibitor experiments will be required in the future.

ACKNOWLEDGEMENTS

This research was conducted with the aid of KAKENHI (23K17193, 21H04533, 20K20181) and the support of the Tatematsu Foundation.

REFERENCES

[1] Kim J, Adachi T., *Sci Rep*, 11(1), 13204, 2021.
[2] Sasaki J et al., *Integr Biol*, 4(10), 1207–14, 2012.
[3] Inagaki T et al., *Proc JSME Frontiers in Bioeng Conf*, 1E16, 2022.
[4] Kim J et al., *J Biomech Sci Eng*, 15(3), 20–00227–20–00227, 2020.
[5] Kinoshita N et al., *Cell Rep*, 30(11), 3875-3888, 2020.

MICRO-CHANNELS MAINTAIN ENDOTHELIAL CELL ADHESION UNDER PHYSIOLOGIC WALL SHEAR STRESS

Alexander T. Armstrong (1), Robert P. McCarthy (1), Alexander Raskin (2), John F. LaDisa Jr. (1,2,3), Brandon J. Tefft (1)

(1) Department of Biomedical Engineering, Marquette University and the Medical College of Wisconsin, Milwaukee, Wisconsin, USA
(2) Department of Pediatrics Section of Cardiology, Herma Heart Institute, Children's Wisconsin and the Medical College of Wisconsin, Milwaukee, Wisconsin, USA
(3) Departments of Physiology and Medicine Division of Cardiovascular Medicine, Medical College of Wisconsin, Milwaukee, Wisconsin, USA

INTRODUCTION

A common sequela of cardiovascular disease is partial or total occlusion of blood vessels. In these cases, vascular grafts are often needed to restore tissue perfusion. Arterial bypass surgery using autologous vascular grafts (AVG) remains the gold standard for long term revascularization due to their lower risk of complications, including thrombosis. AVGs are often not a suitable option due to patient co-morbidities and previous vascular harvest. In such patients, synthetic vascular grafts (SVG) are used. The use of small diameter (<6mm) SVGs is complicated by a higher risk of thrombosis and stenosis compared to AVGs (1). This necessitates the use of anti-platelet agents but still often leads to a loss of patency requiring reintervention

Loss of patency due to platelet adhesion and thrombosis occurs as a result of failure to establish an endothelial cell (EC) monolayer to reduce interaction with the synthetic material (2). The physiologic wall shear stress (WSS) conditions experienced by small diameter SVGs usually prevents ECs from forming a monolayer post-implantation. Even in cases where ECs are seeded onto the grafts before implantation, physiologic WSS often leads to EC detachment (2). Collectively these prior findings suggest, reducing WSS within a pre-seeded SVG has the potential to improve EC retention. Micro-patterned channels provide a potential method of achieving this desired reduction in WSS. The objective of this study is to develop and test a method of maintaining EC adhesion under physiologic WSS using a micro-patterned channel surface imprinted onto a vascular graft material. We hypothesize that seeded ECs located within channels will be protected from WSS and consequently exhibit superior retention compared to ECs directly exposed to physiologic WSS.

METHODS

Computational fluid dynamics (CFD) simulations were conducted using flow domain geometry based on the dimensions of a Glycotech circular parallel plate flow chamber. Boundary conditions were imposed to establish WSS at physiologic levels (15 dyn/cm^2), with repeating small channels designed to reduce WSS to <1 dyn/cm^2. The distance between channels and channel depth were adjusted to balance favorable velocity patterns with the manufacturing capabilities described below.

Electrospinning was used to create a thin flat sheet (~0.3mm) of Biospan 2F fluorinated polyurethane (PU) adhered to a glass microscope slide. This technique was used to produce a consistent microporous structure conducive to EC adherence. A 3D printed stamp was fabricated to produce micro-channels based on CFD results. A 3D printed frame was paired with the stamp to provide a consistent stamping method and depth across experiments. Scanning electron microscope (SEM) images of both the stamp and the stamped substrates were obtained to confirm the desired stamp geometry and micro-channels had been produced. A set of channels was produced with the stamp on a sterile electrospun PU substrate in preparation for cell seeding. Human umbilical vein endothelial cells (HUVECs) were then used to seed the substrates. A droplet of 400 μL of 250,000 cells/mL cell suspension was applied to the stamped region of the substrate to provide a consistent layer of cells and allowed to incubate for 48 hr to achieve attachment.

A Glycotech circular parallel plate flow chamber and programmable syringe pump were used to apply physiologic WSS (15 dyn/cm^2) to the seeded substrates for 30 min. Cell seeded substrates not exposed to WSS served as a control. After exposure to WSS, ECs on both samples were fixed and permeabilized. Fluorescence staining was preformed using NucBlue (Hoechst) and Actin Red-555 (F-Actin) to determine localization and number of ECs under fluorescence microscopy. Cell quantification was performed on Hoechst stained nuclei in ImageJ. Three channels and the unstamped surfaces directly adjacent were selected at equivalent points for each group and cell density was recorded. Channel and surface pairs were quantified for each third of the flow domain for a total of three pairs in the upstream, middle, and downstream thirds.

RESULTS

Figure 1 shows the most recent CFD simulation with distributions of WSS. WSS is reduced to <1 dyn/cm^2 within the channels compared to 15 dyn/cm^2 atop the surface between the channels (Fig 1).

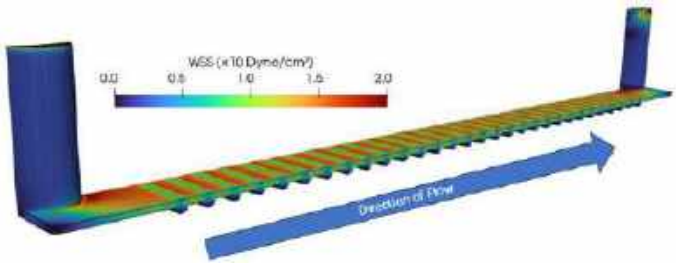

Figure 1: Wall Shear Stress (WSS) contour plot of the parallel plate chamber with stamped surface.

SEM imaging confirmed the fidelity of the stamp and stamped substrate (Fig 2). Side profile imaging of the stamp (Fig 2, left) shows a consistent stamp geometry. The top down image of a stamped substrate (Fig 2, right) displays channels of consistent width, though some channels do not extend to the full width of the flow domain.

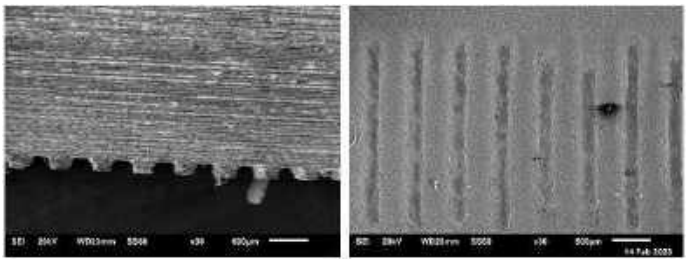

Figure 2: SEM imaging side profile of 3D printed stamp (Left), and the imprint it produces in PU (Right).

When seeded on a stamped PU substrate HUVECs not exposed to WSS are able to adhere evenly across the surface of the stamped region (Fig 3, left). Upon exposure to physiologic WSS, most cells were seen to detach from the substrate when compared to the static control (Fig 3, right). The majority of cells that remained following the application of physiologic WSS were observed within the channels.

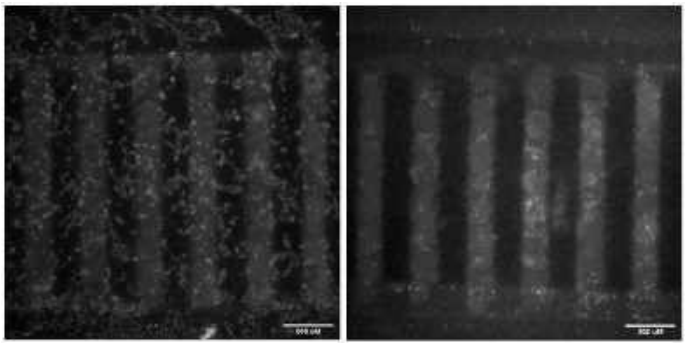

Figure 3: Cells seeded on stamped PU stained with Hoechst, without WSS (left) and after exposure to physiologic WSS of 15 dyn/cm^2 (right).

Quantification shows a significant reduction ($p<0.01$) of cell density both within the channels (channel) and between the channels (surface) of the group exposed to WSS (WSS+) compared to a static control not exposed to WSS (WSS-) (Fig 4, left). Comparing overall cell density between WSS+ within channels and between channels, there is a significant increase ($p<0.05$) in cell retention within the channels (Fig 4, left). Across the flow domain in the same group, there is a trend of increased cell retention within the channels as well, but only differences from the downstream region reached significance ($p<0.05$) (Fig 4, right). The results shown are derived from a single biological replicate of WSS+ and WSS- conditions with significance based on sampling of separate individual channels.

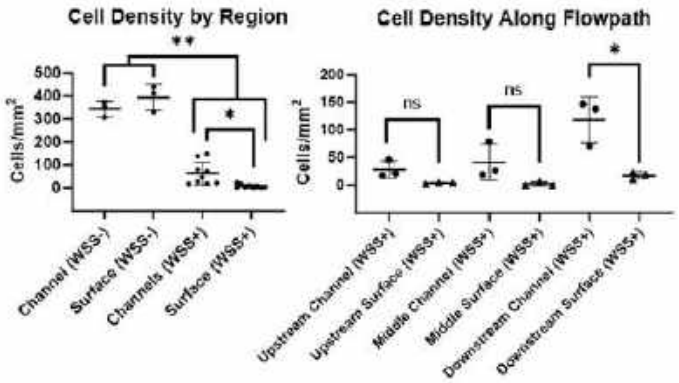

Figure 4: Cell density within channels (channel) and between channels (surface) compared for groups exposed to 15 dyn/cm^2 WSS (WSS+) and static control (WSS-) (left). Cell density within channels (channel) and between channels (surface) across the flow domain subjected to physiologic WSW of 15 dyn/cm^2 (right).

DISCUSSION

Iterative CFD simulation results indicate it is possible to reduce WSS well below physiologic levels within appropriately designed micro-channels. The preservation of some cells within the channels while almost no cells remain outside the channels following exposure to WSS is promising. While EC density is visibly reduced within the channels of the sample exposed to WSS when compared to static control, this finding was dependent upon location in the flow domain. EC retention appeared to vary longitudinally, being lower towards the upstream region compared to the downstream region (Fig 4, right). This suggests inconsistency in WSS across the flow domain and that WSS may not be reduced to the extent predicted by CFD simulations.

Future work will acquire laser scanning microscope images to determine topological variability in the stamped substrate and help improve uniformity during substrate creation. This will allow for confirmatory studies of EC retention within micro-channels. The presented approach will also be adapted to create tubular electrospun constructs for applications in vascular reconstruction.

ACKNOWLEDGEMENTS

This work is supported by the BME Product Development Award and NIH/OD S10OD032136. A special thanks to Bonnie Freudinger and the MCW Engineering Core for 3D printing and design services, and Adam Telega for contributions to stamp design and technique.

REFERENCES

[1] Obiweluozor, FO et al. *Cardiovasc Eng Technol.* 2020; 11(5):495-521.

[2] Wolfe, JT et al. *Tissue Eng Part B Rev.* 2022;28(5):1067-1092.

SB³C2024
Summer Biomechanics, Bioengineering and Biotransport Conference
June 11-14, Lake Geneva, WI, USA

IMPACT OF LUBRICANT PROPERTIES ON THE SYNERGISTIC LUBRICATION OF ARTICULAR CARTILAGE

Emily P. Lambeth (1), Brooklyn Tyndall (2), Sean Farrington (3), David L. Burris (4), Norman J. Wagner (3), Christopher Price (1)

(1) Department of Biomedical Engineering, University of Delaware, Newark, DE, USA
(2) Department of Kinesiology and Applied Physiology, University of Delaware, Newark, DE, USA
(3) Department of Chemical and Biomolecular Engineering, University of Delaware, Newark, DE, USA
(4) Department of Mechanical Engineering, University of Delaware, Newark, DE, USA

INTRODUCTION

Articular cartilage is a phenomenal lubricating material, facilitating remarkably low *in vivo* friction coefficients ($\mu \leq 0.005$).[1] Only recently have *ex vivo* studies recapitulated cartilage's unmatched *in vivo* lubricity on the benchtop, via re-deployment of the convergent stationary contact area (cSCA) testing configuration.[2,3] In the cSCA, and in the presence of PBS, physiologically-consistent sliding speeds promote the hydrodynamically-mediated recovery and maintenance of high fluid load support (FLS) and low friction values ($\mu \sim 0.03$) via 'tribological rehydration'.[2] Intriguingly, when synovial fluid (SF) was introduced into high-speed cSCA studies, stable, truly biofidelic equilibrium friction coefficients ($\mu < 0.004$) were recorded on the benchtop for the first time.[3] We've termed this frictional benefit, due to the presence of SF and hydrodynamically-generated behaviors within the cSCA cartilage contact, 'synergistic lubrication'.[4]

SF is composed of numerous macromolecules thought to influence cartilage lubrication, via mechanisms ranging from viscous to boundary effects.[5-10] One putative lubricant molecule is hyaluronic acid (HA), a non-sulfated, high molecular weight (MW) glycosaminoglycan.[5] When HA is introduced into high-speed cSCA studies, its presence alone is sufficient to replicate synergistic lubrication—like that of SF-lubricated cSCA contacts.[4] This synergistic lubrication could be mediated by either HA-specific articular cartilage/surface molecule interactions (e.g., boundary lubrication) or via more generalizable rheological behaviors (e.g., due to lubricant viscosity).[5-10] Delineating aspects of lubricant properties that influence synergistic lubrication behaviors—and the replication of truly biofidelic lubricity—will undoubtably be key to defining how cartilage achieves its unmatched tribomechanical function and resiliency.

The present study investigated whether non-natural macromolecular polymeric lubricants having similar viscosity profiles as HA-based solutions promote synergistic lubrication outcomes in the cSCA (indicating a relationship to lubricant rheological behaviors), or if the replication of truly biofidelic frictional behaviors are unique to HA-containing solutions (indicating a macromolecule-specific interaction).

METHODS

cSCA explants were extracted from the femoral condyles of skeletally mature bovine stifles.[2-4] Φ19mm osteochondral explants were rinsed and stored in 1X PBS supplemented with L-sucrose (to approximate SF's 400mOsm osmolarity) and protease inhibitors.[2-4,11]

The bathing lubricants utilized were polyethylene oxide (PEO) based. PEO powders at 8, 400, 1000, and 4000kDa were dissolved in PBS at 3mg/mL to study PEO molecular weight (MW) effects. 400 and 4000kDa PEO were dissolved in PBS across a range of 0.1-5mg/mL to study PEO concentration effects.

Tribological testing was performed using a custom reciprocating tribometer.[2] All explants, regardless of study group, first underwent preconditioning, consisting of static compression (9N) against a glass counterface for 30 min, load reduction to 5N (~0.25MPa) for 15 min, then 'slide-in' conditioning at 10, 80, and 10mm/s for 15 min each (under 5N).[4]

In study 1, after preconditioning, "speed sweep" sliding tests (1-80mm/s) were conducted (at 5N) for increasing PEO MW. In studies 2 and 3, sliding tests (80mm/s) were conducted (at 5N) for increasing PEO concentrations of 400 or 4000kDa PEO. For all tests, sliding conditions (*e.g.*, sliding speed or bathing solution) were only changed upon reaching deformation and friction equilibria (*i.e.*, rates of change <1um/min & $<0.01\mu$/min or $<0.001\mu$/min [for $\mu > 0.1$ & <0.1, respectively]).[4]

Equilibrium compressions and kinetic friction coefficients were recorded using LABVIEW across all cycles for each sliding speed and bathing lubricant combination for analysis in MATLAB.

Rheological testing of bathing lubricants was performed on a TA Instruments ARES-G2 rheometer using a parallel-plate testing configuration, forward and backward shear rate sweeps were performed

between 1-100,000s^{-1}.[3] Gap error correction (due to the use of small gap sizes) was performed to calculate each lubricant's 'true viscosity'.[3,12]

RESULTS

PEO exhibited shear rate-dependent rheologic behaviors, with the highest viscosities occurring at the slowest shear rates tested. These rheologic behaviors were like those observed for similar concentrations of high MW HA.[3] PBS, on the other hand, a Newtonian fluid, did not demonstrate shear-rate dependent behaviors.[3] Intriguingly, even at the highest shear rates tested (100,000s^{-1}), the viscosity of 4MDa PEO, like HA, was ~4-fold greater than that of PBS. (**Table 1**)

Table 1: Measured viscosity of 4MDa PEO compared to published values for PBS and 1.4MDa HA[3] (All viscosities reported in mPa·s).

	100s^{-1}	100,000s^{-1}
PBS	0.65	--
1.4MDa HA	13.51	4.36
4MDa PEO	7.12 ± 1.48	2.58 ± 0.01

As expected for the cSCA configuration, the lowest observed equilibrium friction (μ_{Eq}) values for all tested lubricants were always observed at 80mm/s, while maximum μ_{Eq} values occurred at sliding speeds ≤10mm/s (**Fig 1**). μ_{Eq} decreased with increasing PEO molecular weight in a sliding speed-dependent manner (**Fig 1**). At 80mm/s, μ_{Eq} were decreased by up to 4-fold at 4000kDa PEO (as compared to PBS); PEO MW ≥1000kDa supported synergistic lubrication, as demonstrated by the achievement of biofidelic friction coefficients (**Fig 1A**). At 1 and 10mm/s (the max μ_{Eq} speeds), friction coefficients decreased with increasing PEO MW, but the maximal reductions were only ~1.7 & ~3.6-fold for 4000kDa PEO (**Fig 1B,C**).

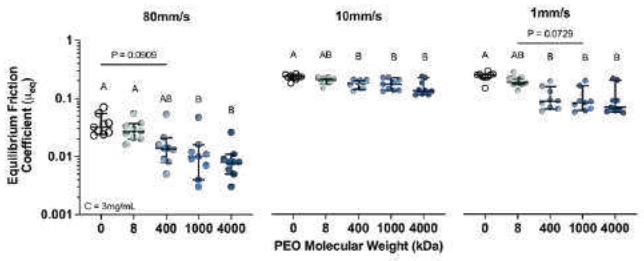

Figure 1: Equilibrium friction coefficients (μ_{Eq}) of bovine cSCA contacts lubricated with PEO solutions (3mg/mL) of increasing molecular weight at sliding speeds of (A) 80, (B) 10, and (C) 1mm/s. Significant differences among groups indicated by dissimilar letters (p<0.05, Friedman's Test).

Changing PEO concentration in our cSCA tests resulted in outcomes consistent with those seen in the variable MW studies. For tests conducted at 80mm/s using an intermediate MW PEO (400kDa), increasing PEO concentration resulted in a maximal ~4.5-fold reduction in friction coefficients (5mg/mL relative to PBS) (**Fig 2**).

DISCUSSION

As this work again demonstrates, the cSCA configuration, through its ability to control interfacial hydrodynamic phenomena in a controllable and sliding speed-dependent manner, represents a valuable tool for exploring cartilage's biofidelic tribomechanical behaviors on the benchtop.[2,3] Furthermore, it has emerged as key platform for exploring lubricant-mediated tribomechanical behaviors across a range of lubrication regimes (spanning 'non-physiological' boundary regimes [μ_{Eq}>0.1] to biofidelic hydrodynamic/synergistic regimes [μ_{Eq}<0.008]).[4]

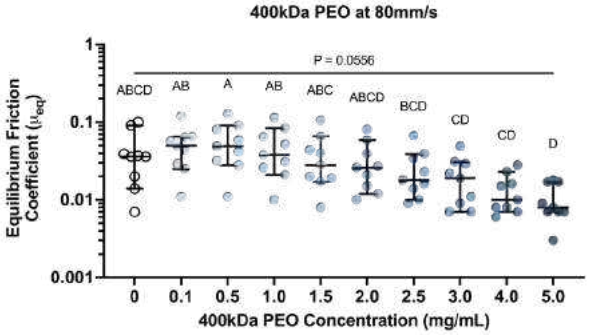

Figure 2: Equilibrium friction coefficients (μ_{Eq}) of cSCA contacts lubricated with increasing concentrations of 400kDa PEO solutions at 80mm/s sliding speed. Significant differences among groups indicated by dissimilar letters (p<0.05, Friedman's Test).

Here, we show that PEO, a synthetic polyether macromolecule derived by the petroleum industry, has qualitatively similar MW- and shear rate-dependent viscosity characteristics as HA.[13,14] However, because it is an exogeneous compound, it should have no biologically informed interactions with cartilage or other lubricating constituents.[10] Nevertheless, PEO demonstrated remarkable synergistic lubricating capabilities, similar to both SF and HA-lubricated cSCA contacts.[4]

Interestingly, in the absence of sliding speed driven interfacial hydrodynamics (*i.e.,* at 10 and 1mm/s), PEO appears to behave similarly to SF and HA as a modest, MW-dependent boundary lubricant.[4] As sliding speeds and hydrodynamically mediated interfacial phenomena increase, the effect of PEO on μ_{Eq} improved dramatically, in a concentration and MW-dependent manner, as with SF and HA-lubricated cSCA contacts. Indeed, at 80mm/s, the fastest sliding speed tested, high concentration (≥4mg/mL), high MW (≥1000kDa) PEO reduced cSCA μ_{Eq} to *in vivo*-like values (μ_{Eq} ~0.008) demonstrating that a synthetic, non-natural polymeric macromolecule (PEO) can function similarly to native SF/HA with regards to synergistic lubrication.[4]

Because lubricant viscosity increases with PEO concentration and MW—like HA—our results suggest an obvious influence of generalizable lubricant rheological behaviors on the biofidelic tribomechanics of articular cartilage.[3,4,14] Complete rheologic characterization of our cSCA lubricants (including SF, HA, and PEO) is being undertaken to permit direct exploration of the effect of lubricant viscosity on articular cartilage function.

Overall, this study once again highlights how sliding driven hydrodynamics and lubricant presence promote a lubrication synergy that generates biofidelic, near frictionless articulation conditions on the benchtop—and presumably *in vivo*. More importantly, this work suggests that synergistic lubrication is not SF-constituent specific, but likely mediated by any large polymeric macromolecule having similar rheological behaviors to SF. Further work will seek to extend these findings to other biologic (e.g., dextran, mucin, cellulose, glycerol) and synthetic (e.g., poly(lactic acid), poly(vinyl alcohol)) 'lubricants'.[15,16] Such insights will continue to advance our understanding cartilage lubrication and how this tissue functions in both health and disease.

REFERENCES

[1] Linn, *J Biomech*, 1968; [2] Moore, *OA&C*, 2017; [3] Farnham, *Trib Let*, 2021; [4] Lambeth, *SB3C Ann Meet*, 2023; [5] Fam, *Biorheol*, 2007; [6] Bonnevie, *J Biomech Eng*, 2020; [7] Krause, *Biomacromol*, 2001; [8] Miyazaki, *J Appl Polym Sci*, 1998; [9] Ogsten, *J Physiol*, 1953; [10] Bonnevie, *PLoS One*, 2015; [11] Baimgarten, *J Bo Join Surg*, 1985; [12] Pipe, *Rheolog Acta*, 2008; [13] Bailey, *Ullman's Encyc Ind Chem*, 2000; [14] Ebagninin, *J Colloid Interf Sci*, 2009; [15] Borzacchiello, *Tiss Eng Nov Deliv Syst*, 2003; [16] Uman, *J App Polym Sci*, 2019.

EFFECT OF PATIENT-SPECIFIC ASCENDING AORTIC CURVATURE ON FLOW IN THE VICNITY OF TAVR

Jae Hyun Kim (1), Vahid Sadri (1), Huang Chen (1), Sanchita Bhat (1), Keshav Kohli (1), Raj Makkar (2), Vasilis C. Babaliaros (3), Rahul P. Sharma (4), Ajit P. Yoganathan (1)

(1) Wallace H. Coulter Department of Biomedical Engineering, Georgia Institute of Technology, Atlanta, GA, USA
(2) Cedars-Sinai Medical Center, Smidt Heart Institute, Los Angeles, CA, USA
(3) Structural Heart and Valve Center, Emory University Hospital, Atlanta, GA, USA
(4) Division of Cardiovascular Medicine, Stanford University, Stanford, CA, USA

INTRODUCTION

Aortic Stenosis (AS) is a prevalent form of valvular heart disease, characterized by hemodynamically significant narrowing of the aortic valve [1]. Recently, transcatheter aortic valve replacement (TAVR) has emerged as a minimally invasive, prominent treatment for both low-risk and high-risk AS patients [2]. Despite the significant improvements in the design over the past decades, procedural complications, particularly subclinical leaflet thrombosis (SLT), remain a clinical concern due to its potential impacts on valve performance and subsequent cardiovascular complications [3]. Virchow's triad associates thrombosis formation with three contributing factors: fluid flow, foreign materials, and biochemistry. Notably, flow patterns in the neo-sinus, a region defined by the native leaflets and transcatheter aortic valve (TAV) leaflets, have been shown to significantly correlate with the post-TAVR thrombosis volume [4]. Thus, various studies have investigated potential factors that may influence such flow patterns, including leaflet mobility, device design, and deployment methods [5-7], as well as patient anatomy [8].

Patient specific anatomy and the displaced native aortic leaflet geometry may critically influence the fluid dynamics in the vicinity of TAV. However, to date, no physiological *in-vitro* studies have been performed to spotlight the link between patient specific ascending aortic geometry and its influence on the flow in the downstream of TAV, as well as native sinus and the neo-sinus. Therefore, this study aims to assess the effects of the patient-specific aortic curvature on the thrombogenic potential by establishing quantitative correlations between the varying patient-specific aortic curvatures with the flow downstream of TAV, neo-sinus, and aortic sinus, using *in vitro* particle image velocimetry (PIV).

METHODS

Patient Specific Models and In-Vitro Circulatory Loop

All patient data was received from Cedars-Sinai Medical Center and was a part of RESOLVE registry through a limited data sharing agreement (Institutional Review Board #H17256). From 111 available datasets, 6 patients were selected for *in vitro* PIV analysis. The post-TAVR CT datasets of the six selected patients were first analyzed using Mimics (Version 24.0, Materialize Mimics) to quantify the ascending aortic curvature and then segmented in ITK-SNAP and 3D printed with a transparent rigid SLA epoxy resin material to ensure clear visual access. The appropriate 26mm SAPIEN 3 valve (Edwards Life sciences, Irvine, CA, USA) with Parafilm (Sigma-Aldrich, St Louis, Mo) attached to mimic the native leaflet was deployed into each model. The patient models were then placed in a validated pulsatile left heart simulator [9], which was tuned to patient specific cardiac output (CO) with frequency of 70beats/min and aortic pressure of 120/80 mmHg (**Figure 1).** The coronary flow was assumed to be 5% of the CO with 80/20 split between the left and right coronary arteries [10]. The working fluid was 3.5 cSt water-glycerin solution to mimic viscosity of blood.

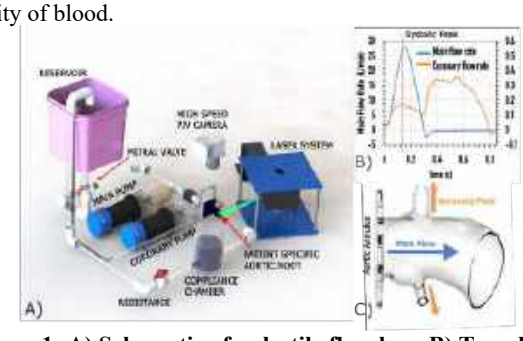

Figure 1: A) Schematic of pulsatile flow loop B) Tuned flow waveforms C) Flow directions through patient-specific models

PIV Setup

The laser planes coincided with the center of each cusp and the center of valve to image each cusp and main jet, respectively (**Figure 2)**. 2D Highspeed Camera was placed orthogonal to the laser plane to

capture the flow through the center of the cusp with frequency of 500Hz for 18 cycles, and the main jet with frequency of 1500Hz for 2 cycles. The flow was seeded with fluorescent PMMA-Rhodamine B particles with diameters ranging from 1 to 20 μm.

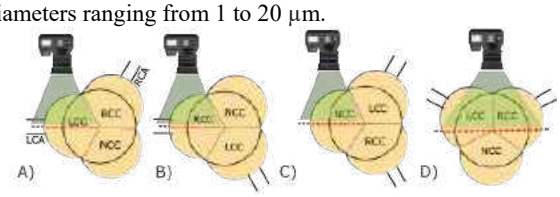

Figure 2: 2D Schematic of Laser Planes to capture A) LCC B) RCC C) NCC D) Main Jet

Hemodynamics Assessment

Acquired PIV images were processed using Davis 8.0 (LaVision GmBH) to acquire instantaneous velocity streamlines and averaged by cardiac cycle using in-house MATLAB code (MATLAB R2021a, MathWorks). To quantify the amount of retrograde backflow from the main jet into the sinus and the neo-sinus, time resolved vector fields were used to calculate vorticity and circulation.

$$\omega_z = -\left(\frac{dV_x}{dy} - \frac{dV_y}{dx}\right) ; \Gamma = \iint \omega \cdot dS_{ROI} \quad (1)$$

Normalized velocity, a comparable dimensionless quantity that accounts for varying patient-specific CO and size of inlet, was calculated, and temporally averaged over the entire cardiac cycle.

$$v_{Normalized} = \frac{v}{CO_{Patient}} * S_{inlet} \quad (2)$$

A Lagrangian particle tracking simulation was used to computationally seed the particles, obtain path lines, and compute neo-sinus and sinus washout times.

Results

The flow downstream of TAV was characterized by recirculation when the central jet hit the proximal ascending aorta due to curvature. The ascending aorta curved towards the left, coupled with the left coronary flow, resulted in the vortices forming in the vicinity of LCC (**Figure 3**). The circulation near LCC in patient 6 (most curved, 0.3248 cm^{-1}) reported 0.018 m^2/s, while patient 4 (least curved, 0.1446 cm^{-1}) reported 0.006 m^2/s.

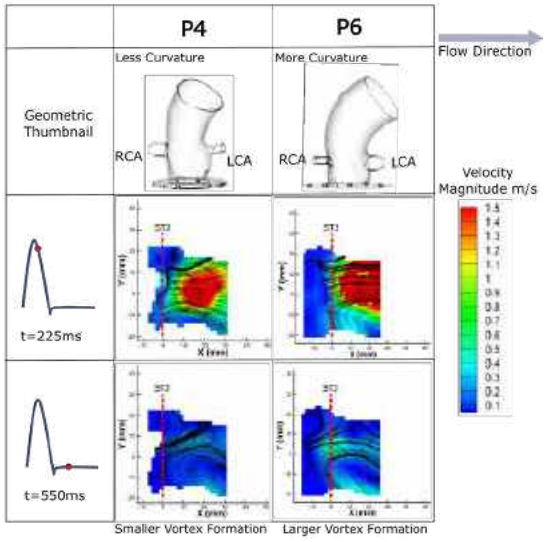

Figure 3: Flow characteristics downstream of TAV between patient with most curved and least curved ascending aorta

The ascending aortic curvature showed significant positive correlation to the circulation proximal to LCC (Rho = 0.771, p = 0.036). Normalized average velocity and washout time in the LCC was overall higher in the patients with higher curvature, while that in RCC was overall higher in the patients with lower curvature. Washout time demonstrated significant negative correlation to circulation (**Figure 4**).

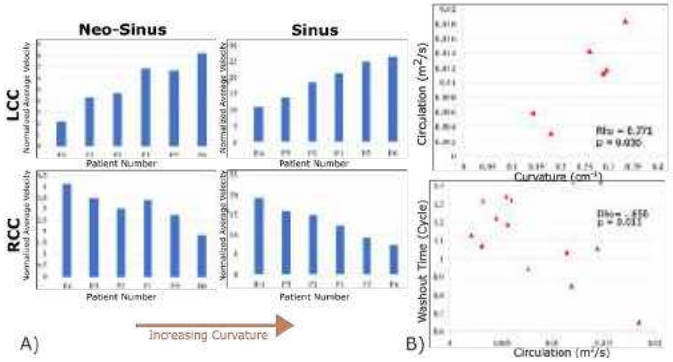

Figure 4: A) Normalized average velocity across patients B) Correlations between circulation, curvature, and washout time

DISCUSSION

The study provides a mechanistic investigation *in vitro* to explore the impact of varying patient-specific aortic curvatures on thrombogenic potentials. The varying curvatures contributed to the development of recirculation zones in the main jet, unique in both relative location and vortex strength. These vortical flow structures in turn influenced the flow velocities in the native sinus and the neo-sinus. In patients with higher curvature, a stronger vortical flow near LCC was observed. This resulted in greater velocities and lower washout time in the sinus and neo-sinus of LCC for patients with higher aortic curvature. These correlations together provide a picture of potential mechanism behind the influence of ascending aorta geometry on the thrombogenic potentials in TAV. As the main jet impinges on the wall of the ascending aorta, the curvature induces a distinct, unique recirculation zone that facilitates the flow back into the proximal cusp, thus influencing the flow velocity and washout time.

The study's results offer clinical considerations for manipulating TAV deployment and directing the main jet in the ascending aorta. This information can help clinicians in pre-TAVR planning to develop optimal deployment strategies and select appropriate valve type based on the frame and impact of jet configuration. Although thrombosis is a multi-factorial phenomenon, the study successfully spotlights a new patient-specific parameter to be considered.

ACKNOWLEDGEMENTS

The authors would like to thank the members and alumni of Cardiovascular Fluid Mechanics Laboratory (CFML) of Georgia Tech for their valuable feedback and support.

REFERENCES

[1] Carabello, B et al, *Lancet*, 373:956-966, 2019.
[2] Thourani, V et al, *The Lancet,* 387(10034), 2016.
[3] Makkar, R et al, *N. Engl. J. Med,* 373:2015-2024, 2015.
[4] Trusty, P et al, *JACC Cardiovasc Interv.,* 12(13):1288-1290, 2019.
[5] Hatoum, H et al, *ABME,* 45(2): 310-331, 2017.
[6] Pott, D et al, *Artificial Organs,* 45(1): 68-78, 2021.
[7] Ncho, B et al, *Journal of Medical Devices ASME,* 16(2), 2022.
[8] Singh-Gryzbon, S et al, *ABME,* 48(10): 2400-2411, 2020.
[9] Mudakauwa-David, I et al, *ABME,* 48(1): 169-190, 2020.
[10] Sakamoto, S et al, *Am. J. Cardiol.,* 111(10): 1420-1424, 2013.

SB^{3}C2024
Summer Biomechanics, Bioengineering and Biotransport Conference
June 11-14, Lake Geneva, WI, USA

QUANTIFYING ENZYMATIC SMALL EXTRACELLULAR VESICLES (SEVS) FOR CANCER COMPANION DIAGNOSTICS USING MAGNETIC NANOPOROUS MEMBRANE (MNM)-BASED ACTIVITY ASSAY

Tiger H. Shi (1), Chenguang Zhang (1), Youwen Zhang (1), Xuemin Lu (2), Gaeun Kim (1), Sonu Kumar (1), Ceming Wang (3), Nan Su (3), Yichun Wang (1), Xin Lu (2), Satyajyoti Senapati (1), Hsueh-Chia Chang (1,3) (1,2,3)

(1) Department of Chemical and Biomolecular Engineering, University of Notre Dame, Indiana, USA
(2) Department of Biological Sciences, University of Notre Dame, Indiana, USA
(3) Aopia Biosciences, Inc., Pleasanton, California, USA

INTRODUCTION

Cancer metastasis is the leading cause of death for cancer patients and metastatic potential is a major consideration during therapy. [1] Active surface proteins like membrane-type matrix metalloproteinases (MT-MMPs) and a-disintegrin and metalloproteinases (ADAMs) have been identified to be highly expressed in cancers. [2] Current bulk plasma activity assays for these enzymes offer little metastatic information and are prone to interfering agents found in plasma. [3, 4] In this study, we overcome these limitations with a Magnetic Nanoporous Membrane (MNM) diagnostic technology which uses superparamagnetic beads to rapidly isolate and enrich specific tumor cell-originated small extracellular vesicles (sEVs). [5, 6] These sEVs inherit their parent cell membrane enzymes and displays them on their lipid bilayer surface. [7] We explore the localization of active ADAM10 in blood plasma and establish that ADAM10$^+$ sEVs serves as an indicator of cancer metastasis. In a pilot clinical study, we demonstrate the potential of ADAM10$^+$ sEVs as a metastatic staging biomarker.

METHODS

ADAM10 activity assay. To quantify ADAM10 activity, a specific peptide sequence was adapted from prior work to serve as the digestible backbone of a molecular beacon. [8] The sequence consists of a DABCYL quencher, the ADAM10-specific peptide sequence, and a 5-FAM fluorophore. The intact beacon does not emit fluorescent signal due to the proximity of the quencher to the fluorophore until the peptide sequence is digested by either free-floating or membrane-bound ADAM10.

Magnetic nanoporous membrane (MNM)-based well-plate platform. Using 3D printing techniques, we developed a sensitive, rapid, multiplexed activity-assay platform and protocol for the quantification of ADAM10 on sEVs using a standard lab plate readers. Multiple wells are concurrently processed for scaleable multiplexing. We can ensure the same 99% capture yield by maintaining the same flux noted in our prior paper. [6] The controlled buffer exchange step allows for the washing and removal of interfering agents. [3, 6] The use of antibody immunocapture allows for the isolation of specific EV subsets of interest characterized by various surface markers. The focus on assaying the enzymatic activity of EV-surface proteins specifically represents of active-form of enzyme, which is the more relevant form in biology.

RESULTS

ADAM10 activity enhancement on sEV carriers. As shown in Figure 1a, approximately all the ADAM10 identified in the CCM is located on the sEV population. This can be seen in that the $10\times$ concentrated CCM ADAM10 concentration approximates the $1\times$ Unlysed sEV ADAM10 concentration and the lack of any ADAM10 found in the ANM FT sample even after enrichment. When the lipid bilayer membrane is disrupted by the surfactant, more ADAM10 is detected by the ELISA affinity assay. Looking at Figure 1b, we find that despite the release of more ADAM10 in the Lysed sEV sample the ADAM10 signal distinctly dropped by four-fold. No ADAM10 signal was detected in the ANM FT sample. These findings demonstrate that all significant ADAM10 activity is localized to the surface of sEVs and lysis of the sEV membrane structure greatly diminishes the activity of the sample's ADAM10 enzymes. Our bulk assays hence indicate that the most sensitive quantification of active ADAM10 is with the sEV activity assay.

Staging metastatic potential in prostate cancer cell cultures with sEV normalized ADAM10 activity assay. Four prostate cancer cell lines with varying metastatic potentials were prepared. In decreasing metastatic potential, these cell lines are PC3, DU145, 22Rv1, and LNCaP. In Fig-

ure 1c, we note that ADAM10 activity signal growth has no correlation to the metastatic potential of the cell lines in either the bulk CCM or the UC-isolated sEVs. Normalizing the ADAM10 activity signal growth to a per-sEV basis, we find that there is a significant difference between the different cell lines correlating to metastatic potential (Fig. 1d). Additionally, we find that the signal growth per sEV isolated from the bulk CCM nearly recapitulates that of the UC-isolated sEVs, meaning nearly all the active ADAM10 in CCM is due to those on sEV surface.

Preliminary pilot study with patients and controls of metastatic colorectal cancer (mCRC) for staging of metastasis using ADAM10-sEV activity. A blinded preliminary clinical metastatic staging experiment using isolated sEVs from the blood of healthy, pre-metastatic, and metastatic colorectal cancer patients. Significant separation is achieved in a 30-minute assay even with small patient pool. Despite the enhanced sensitivity and stage-specificity of bulk sEV ADAM10 activity assay for cancer cell culture media, its sensitivity is insufficient for patient plasma samples. We overcome this issue with another sensitivity enhancement technique – sEV enrichment by MNM.

Benchmarking MNM well-plate platform and activity sensing strategy. Using well-sets lined with MNM at their base, sEVs can be isolated from the sample via magnetic immunocapture with superparamagnetic nanobeads. The overall assay protocol (Figure 2a-d) consists of a 30-60 minute incubation, 60 minute magnetic trapping and buffer exchange, and 30-60 minute read-out. This totals to an assay lasting 2-3 hours. With this MNM well-plate platform, a minimum improvement of sensitivity of 0.5-1 decade in the detection of ADAM10$^+$ sEVs is achieved (Fig 2e-f).

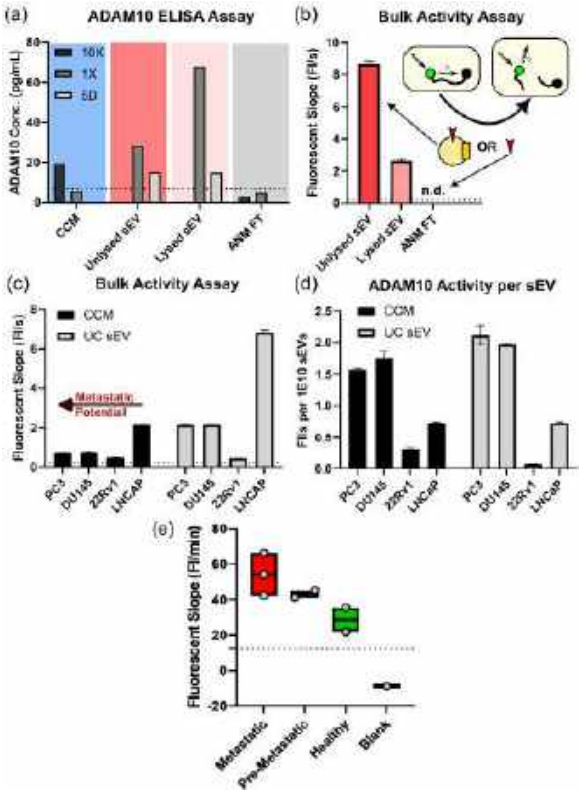

Figure 1: (a-b) Delipidation experiments on ADAM10$^+$ sEVs derived from healthy human dermal cell culture. a Total ADAM10 ELISA experiment for each preparation. b Bulk ADAM10 activity assay of sEV samples and ANM FT. (c-d) Normalization of ADAM10 activity signal to total sEV concentration in prostate cancer cell lines. c Bulk ADAM10 activity assay of raw CCM and sEV samples. d ADAM10 activity signal growth normalized to 10^{10} sEVs. e Preliminary pilot study for metastatic staging of mCRC using ADAM10-sEV activity.

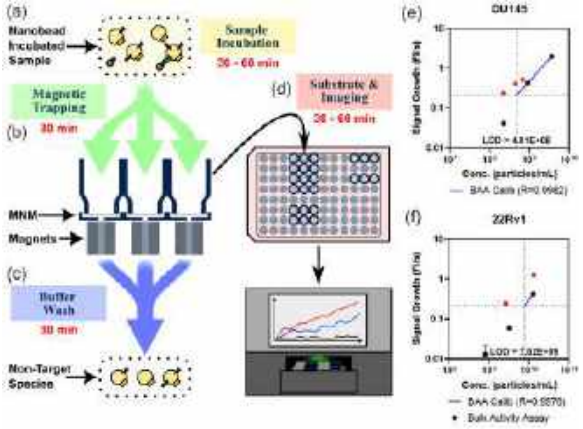

Figure 2: Schematic and Workflow showing assay steps of the MNM well-plate platform. a The sample is incubated with the antibody-functionalized nanobeads and lipophilic dye. b The cocktail is applied to the MNM well-chip and c washed with 1X PBS. d Well-chips are placed in a magnetized 96-well plate. The fluorescent molecular beacon is added and imaging is performed. Preliminary benchmarking of limits of detection for the MNM platform versus the bulk assay with e DU145 and f 22Rv1 sEVs.

DISCUSSION

In this work, we establish the localization of greatest ADAM10 activity from cancer cells to the surface of sEVs. ADAM10$^+$ sEV activity normalized to sEV concentration is indicative of metastatic potential in prostate cancer cell lines. Furthermore, ADAM10$^+$ sEV activity produces significant separation as a general metastatic staging biomarker in mCRC patients. The findings recapitulate existing understandings of ADAM10 in cancer metastasis and focuses the field towards the sEV-bound forms.

Additionally, current work on the MNM well-plate platform is ongoing with significant promise in improving sensitivity down to as low as 1×10^6 sEV/mL. Our group is working on selective pin-down of cancer-specific EGFR$^+$ sEVs in a larger clinical cohort of mCRC patients.

ACKNOWLEDGEMENTS

This work was supported by funds from the NIH and the DOE GAANN MERITS program. We would like to acknowledge the core facilities at the University of Notre Dame – NanoSight NS300 at HCRI, Magellan FESEM at NDIIF, and Density Gradient Ultracentrifugation at NDBIC.

REFERENCES

[1] Seyfried TN et al. *Crit. Rev. Oncog.* 18.1-2 (2013). DOI: https://doi.org/10.1615/critrevoncog.v18.i1-2.40.

[2] Ma B et al. *Front. Genet.* 14.1105900 (2023). DOI: https://doi.org/10.3389/fgene.2023.1105900.

[3] Kumar S et al. *Nat. Commun.* 14.557 (2023). DOI: https://doi.org/10.1038/s41467-023-36258-w.

[4] Fang H et al. *Chem. Sci.* 12 (2021). DOI: https://doi.org/10.1039/D1SC01359A.

[5] Chen S et al. *PLoS ONE* 15.2 (2020). DOI: https://doi.org/10.1371/journal.pone.0229610.

[6] Zhang C et al. *Commun. Biol.* 5.1358 (2022). DOI: https://doi.org/10.1038/s42003-022-04321-9.

[7] Ramirez-Garrastacho M et al. *Br. J. Cancer* 126.3 (2022). DOI: https://doi.org/10.1038/s41416-021-01610-8.

[8] Chen X et al. *Nanoscale* 13 (2021). DOI: https://doi.org/10.1039/D1NR04085E.

IMAGE-BASED 3D RECONSTRUCTION ANALYSIS OF REGIONAL THROMBOSIS AFTER TRANSCATHETER AORTIC VALVE REPLACEMENT

K. Berland (1), B. Yeats (1), T. Becker (2), M. Moscarelli (3), K. Fattouch (3), L. Dasi (1)

(1) Biomedical Engineering, Georgia Institute of Technology and Emory University, Atlanta, GA, USA
(2) Biomedical Sciences, Ohio State University, Columbus, OH, USA
(3) Cardiovascular Surgery, Maria Eleonora Hospital - GVM Care&Research, Palermo, Italy

INTRODUCTION

Transcatheter aortic valve replacement (TAVR) is a minimally invasive procedure that offers high risk patients with aortic valve disease an alternative to open heart surgery. However, thrombus (blood clots) forms on these bioprosthetic valves in 10-20% of patients, which can limit leaflet mobility, accelerate valve deterioration, and increase stroke risk [1]. Hypoattenuated leaflet thickening (HALT), an indicator for subclinical leaflet thrombosis (SLT) detected by cardiac computed tomography (CT), has been correlated with several bioprosthetic valve and native aortic root geometry characteristics including neo-sinus and sinus of Valsalva (SoV; native sinuses) volumes, commissural misalignment, stent deformation, and local hemodynamics [2]. HALT severity is currently evaluated using CT, but this method is limited and subjective because it cannot quantify thrombus volume [3,4]. Thrombus also forms in other regions of the aortic root besides the bioprosthetic valve leaflets, which can be difficult to identify in CT and has yet to be quantified and correlated with factors associated with HALT. The goal of this study was to use image-based 3D reconstructions of patient-specific anatomy to visualize and quantify thrombus in all regions of the aortic root and bioprosthetic valve.

METHODS

Pre-TAVR and post-TAVR CT data (n = 4) were collected from Maria Eleonora Hospital [GVM Care&Research, Palermo, Italy]. Using Materialise Innovation Suite 25.0 [Lueven, Belgium], each patient's aortic root, native aortic leaflets, calcium, Evolut R valve, and thrombus were segmented in the post-TAVR CT. The pre-TAVR CT was used as a guide to accurately segment the sinus volume as the contrast between the thrombus and the aortic root wall was typically low. Similarly, the commissures and annular plane were used to guide the native leaflet length and shape as they were pinned against the device stent in the post CT. Calcium was segmented with a patient specific threshold. A previously developed registration technique was used to register a clean CAD model of the stent to the patient specific device stent to avoid blooming and other artifacts [5]. A soft tissue pixel threshold was used to capture any thrombus volume in the neo-sinuses, native sinuses, Evolut R leaflets, and subvalvular region (Figure 1).

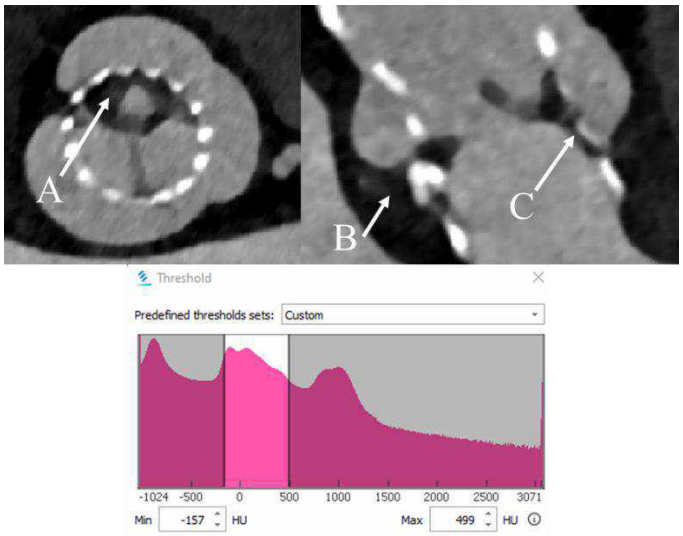

Figure 1: Identification of thrombus in neo-sinus region (A), native sinus region (B), and subvalvular region (C) using a soft tissue pixel threshold.

The registered Evolut R skirt was wrapped to achieve a final thickness of 1mm. The segmented aortic root, stent, native leaflets, calcium, Evolut R leaflets, and registered Evolut R skirt were subtracted from the thrombus segmentation. The remaining thrombus segmentation was trimmed to separate and quantify thrombus volume

located in different regions of the aortic root and valve. Commissural misalignment was measured based on methods previously described [6]. Thrombus volumes, commissural misalignment, and valve depth were then compared across regions and different patients. The final segmentation provided a complete reconstruction of the patient's aortic anatomy and thrombus.

RESULTS

Segmentations (Figure 2) and thrombus volumes with deployment configurations are presented (Table 1). The neo-sinus of the non-coronary cusp had the greatest neo-sinus thrombus volume (SLT) in 3 out of 4 patients. The native non-coronary sinus had the greatest thrombus volume across all patients. The patient with the lowest average SLT volume (Patient 1; 56mm^3) had the lowest average native sinus thrombus volume (133mm^3). Similarly, the patient with the highest average SLT volume (Patient 4; 251mm^3) had the highest average native sinus thrombus volume (592mm^3). Patient 3, who also had high average SLT and native sinus thrombus volumes, had the greatest subvalvular thrombus volume (878mm^3). No trends were observed regarding commissural misalignment and valve depth.

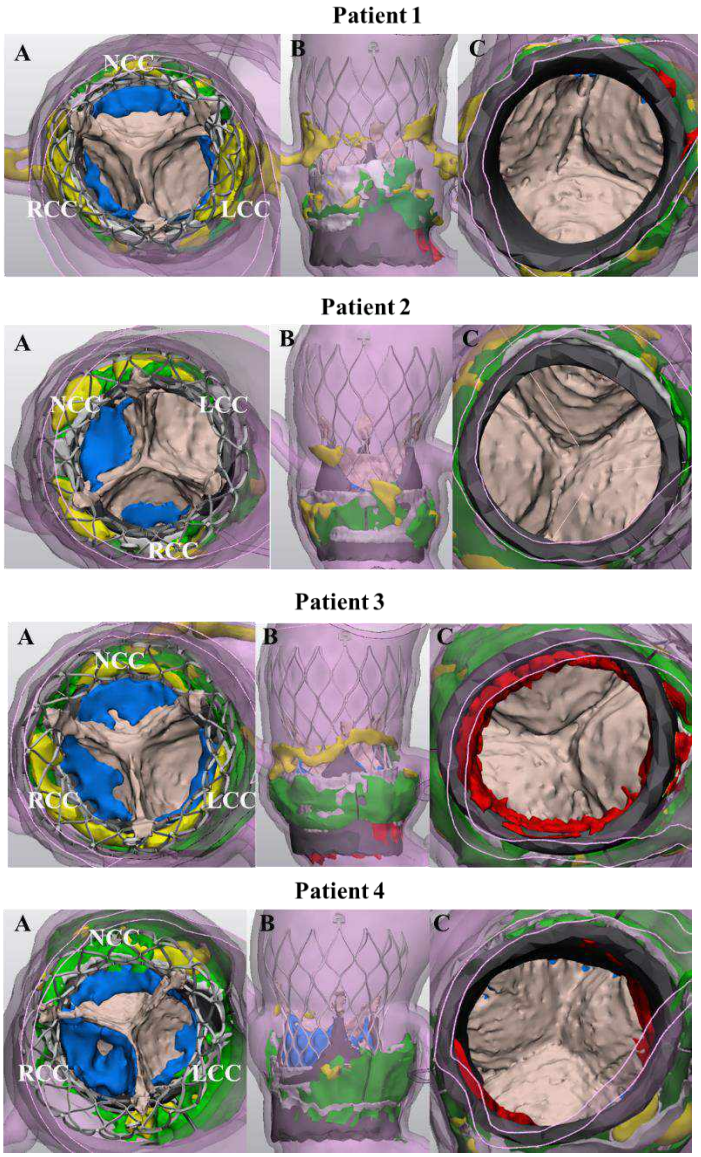

Figure 2: Patient-specific 3D reconstructions of aortic root (pink), Evolut R stent (silver) and skirt (dark grey), native aortic leaflets (white), calcium (yellow) and regional thrombus. A.) SLT (blue) on non-coronary cusp (NCC, brown), right-coronary cusp (RCC, brown), and left-coronary cusp (LCC, brown) in neo-sinus region. B.) Thrombus (green) in native sinus region. C.) Thrombus (red) in subvalvular region.

Table 1: Regional thrombus volumes (mm^3), commissural misalignment (°), and valve depth (mm) for each patient.

Patient #	HALT severity	Neo-Sinus Thrombus Volume (mm^3)			Native Sinus Thrombus Volume (mm^3)			Subvalvular Thrombus Volume (mm^3)
		Non-coronary	Right-coronary	Left-coronary	Non-coronary	Right-coronary	Left-coronary	
1	Mild	93	38	38	177	71	92	15
2	Moderate	139	30	0	411	95	126	0
3	Severe	180	133	87	468	356	446	878
4	Severe	153	502	97	943	256	576	86

Patient #	Left-Right Commissural Misalignment (degrees)	Right-Non Commissural Misalignment (degrees)	Non-Left Commissural Misalignment (degrees)	Valve Depth (mm)
1	0.1	6.3	2.5	-7
2	70.7	38.5	51.4	-3.2
3	0.6	21.7	2.2	-5
4	20.77	2.78	29.86	-4.5

DISCUSSION

Overall, these 3D reconstructions offer a better visualization of the patient-specific anatomy and regional thrombus formation and enable quantification of thrombus in the neo-sinus (SLT), native sinus, and subvalvular regions. The non-coronary cusp of the neo-sinus and native sinus regions were observed to have higher thrombus volumes than other sinuses potentially due to the reduced flow in these regions. Lower velocities in the neo-sinus region have been correlated to increased risk of thrombus formation [7]. Geometric and hemodynamic parameters can be used to develop an equation for normalized circulation that can be correlated to thrombus volume in the Evolut R, similar to previous research with the Sapien 3 valve [7]. Such analysis will be done with the rest of the patient dataset (N=25 total) to support these initial findings. Future studies could include tracking changes in thrombus volume following anti-coagulant treatments and performing cardiovascular fluid dynamic simulations to evaluate patient-specific geometries that influence thrombosis.

REFERENCES

[1] Garcia, S et al., *Circulation: Cardiovascular Interventions*, 15, 2022.
[2] Fukui, M et al., *Circulation*, 146:480–493, 2022.
[3] Jilaihawi, H et al., *JACC: Cardiovascular Imaging*, 10:461-470, 2017.
[4] Makkar R et al., *JACC*, 75:3003-3015, 2020.
[5] Chen H et al., *Annals of Biomedical Engineering*, 50:805-815, 2022.
[6] Tang G et al., *JACC: Cardiovascular Interventions*, 15:1497-1518, 2022.
[7] Hatoum H et al., *Cardiovasc Eng Technol*., 12:576-588, 2021.

A MULTIPHASIC MODEL FOR DETERMINATION OF MOUSE ASCENDING THORACIC AORTA MASS TRANSPORT PROPERTIES WITH AND WITHOUT ANEURYSMS

Keshav A. Kailash (1), Jessica E. Wagenseil (2)

(1) Biomedical Engineering, Washington University, St. Louis, MO, USA
(2) Mechanical Engineering and Materials Science, Washington University, St. Louis, MO, USA

INTRODUCTION

Thoracic aortic aneurysms (TAAs), defined as a 50% increase in aortic diameter, are a significant public health concern. The current clinical treatment is continuous monitoring of the aneurysm size and growth rate with an eventual recommendation for surgical intervention. In this study, we used a clinically identified missense mutation in fibulin-4 (*Fbln4*$^{E57K/E57K}$) that causes TAA in mice. These mice have elastic fiber fragmentation, a pathobiological hallmark of TAA, and have 50% aneurysm penetrance. After breeding these mice with *Lox*$^{+/-}$ mice, we observed 100% aneurysm penetrance and formed four experimental groups: *Fbln4*$^{+/+}$;*Lox*$^{+/+}$ (WT), *Fbln4*$^{E57K/E57K}$;*Lox*$^{+/+}$ without an aneurysm (MU-NA), *Fbln4*$^{E57K/E57K}$;*Lox*$^{+/+}$ with aneurysm (MU-A), and *Fbln4*$^{E57K/E57K}$;*Lox*$^{+/-}$ (MU-XA) [1].

Elastic fibers in the aortic wall are organized in layers alternating with smooth muscle cells (SMCs). They provide reversible elasticity and are thought to provide physical isolation to the SMCs [2]. Fragmentation of elastic fibers affects aortic mechanical behavior and transmural transport across the aortic wall, exposing the SMCs to altered fluid and solute flux. While endothelial cells (ECs) lining the lumen play the major role in regulating transmural transport, EC dysfunction and impaired barrier ability are common in TAA. We previously showed experimental differences in transmural transport in mouse models of TAA that depend on aneurysm severity, but are not directly correlated with elastic fiber fragmentation, indicating a complex role of elastic fiber organization and extracellular matrix remodeling in regulating transmural transport [1].

We previously developed a multiphasic continuum model of the carotid artery and determined differences in the effective diffusivity resulting from genetic or chemical injury to the artery [3]. Here we utilized FEBio to develop biphasic and multiphasic models of a denuded (ECs removed) ascending thoracic aorta (ATA) using measured geometries and mass transport data for our four mouse models with varying aneurysm severity [1, 4]. The objective is to provide further insight into the contributing factors regulating transmural transport in the aneurysmal aortic wall.

METHODS

Animals. 3-4 month old male and female WT, MU-NA, MU-A, and MU-XA mice were used. All animal procedures were approved by the IACUC. Experimentally derived geometry for each group and literature based elastic moduli were used in the models (Table 1) [1, 5]. Note that the outer radius is indicative of aneurysm severity (aortic dilation).

Table 1: ATA geometry and moduli for each mouse model.

Mouse Model Name	Length (mm)	Outer Radius (R_o) (mm)	Thickness (t) (mm)	Elastic Modulus (kPa)
WT	1.61	0.420	0.064	400
MU-NA	3.16	0.464	0.110	800
MU-A	3.74	0.760	0.118	800
MU-XA	4.26	0.760	0.118	1200

Biphasic Modeling. A biphasic model of the aortic wall as a porous-fluid-saturated mixture was constructed in FEBio. The aortic wall was modelled as a cylinder with the geometry in Table 1 for each group. The model was meshed using eight-node hexahedral elements refined radially closer to the inner radius. The aortic wall was given a strain dependent Holmes-Mow hydraulic permeability,

$$k(J) = k_0 \left(\frac{J-\varphi_0}{1-\varphi_0}\right)^{\alpha} e^{\frac{1}{2}M(J^2-1)} \quad , \qquad (1)$$

where k_0 is the isotropic hydraulic permeability, M is an exponential strain-dependent coefficient, α is the power-law exponent, and φ_0 is the solid volume fraction of the porous solid matrix. The aortic wall was considered a Neo-Hookean solid with a Poisson's ratio (ν) set to 0.49 to model an incompressible material and an elastic modulus (E) that depends on the mouse model (Table 1). The solid volume fraction (φ_0) was varied to characterize effects on fluid flux. M and α did not have significant effects on model results in preliminary testing and were both

set to unity. The test bath was also modelled as a biphasic material. φ_0 was set to 0, E was set to the minimum value of 0.01 kPa, and ν was set to 0.49 to model an incompressible fluid. k_0 in the bath was set 1000 x higher than k_0 of the aortic wall. The volume of the bath was 7 mL to match experimental conditions.

Zero-displacement boundary conditions in the radial, circumferential, and axial directions were fixed at the ends of the cylinder to match experimental conditions. A zero fluid pressure boundary condition was set in the bath. The total mixture stress (σ) is affected by both the fluid pressure (p) and the stress from the solid matrix strain (σ^e),

$$\sigma = -p\boldsymbol{I} + \sigma^e \quad , \quad (2)$$

The fluid pressure (p) is defined by,

$$p = \tilde{p} + R\theta\phi c \quad , \quad (3)$$

where $\tilde{p}$ is the effective fluid pressure, R is the gas constant, θ is the temperature, ϕ is the osmotic coefficient, and c is the concentration of the solute. In the biphasic case, there is no solute, so the effective and actual fluid pressure are equivalent, and we prescribed an effective fluid pressure of 13.33 kPa in the lumen to match experimental conditions. We prescribed a σ of -13.33 kPa at the aortic inner wall and 0 kPa at the inner wall of the bath fully interfaced with the aorta.

Multiphasic Modeling. A multiphasic model was created using the same procedures and material properties described in the biphasic section. A prescribed concentration of 5 mg/mL 4 kDA FITC Dextran was added to the lumen of the aorta, as in the experiment. The free diffusivity of the solute was calculated using the Stokes-Einstein equation. Using Eqn. 3, we prescribed an effective fluid pressure ($\tilde{p}$) of 10.11 kPa. In the bath, D_0 was set to be 10,000x higher to maintain well mixed conditions in the bath and D_{eff} was set equal to D_0. Effective solubility ($\tilde{\kappa}$), hydraulic permeability (k_0), elastic modulus (E), and solid volume fraction (φ_0) were varied to understand their effects on fluid (J_v) and solute flux (J_s) in each group.

Fitting Transport Material Properties The aortic transmural transport data for the four mouse models have been previously published [1]. Using the constrained Levenberg–Marquardt optimization algorithm in FEBio, we optimized material properties using average J_v and average Dextran concentration versus time ($\Delta C/\Delta t$) data to determine permeability (k_0) and effective diffusivity (D_{eff}) for each group.

RESULTS

A parametric sweep of the model parameters (Fig. 1) reveals that the largest contributing factor to fluid flux is hydraulic permeability (k_0). Our parametric sweep shows that solute flux is also regulated by solid volume fraction (φ_0), hydraulic permeability (k_0), effective diffusivity (D_{eff}) and effective solubility ($\tilde{\kappa}$). Changes to elastic moduli (E) are well characterized in TAA, and we modulated E based on pressure-diameter curves (data not shown) recorded for this mouse model (Table 1) [5]. Our parametric sweep showed that elastic modulus (E) did not affect J_v and had a minor effect on J_s.

After fitting k_0 using J_v from the solute absent experimental data, we found a trending decrease in hydraulic permeability with more severe aneurysm phenotype (Fig. 2A). Using $\varphi_0 = 0.6$, $\tilde{\kappa} = 1$, and model specific k_0 and E, we fitted effective diffusivity (D_{eff}) to the experimental concentration data for each mouse model (Figs. 2B, C) [1]. The effective diffusivity increased in the MU-NA group only, compared to all others.

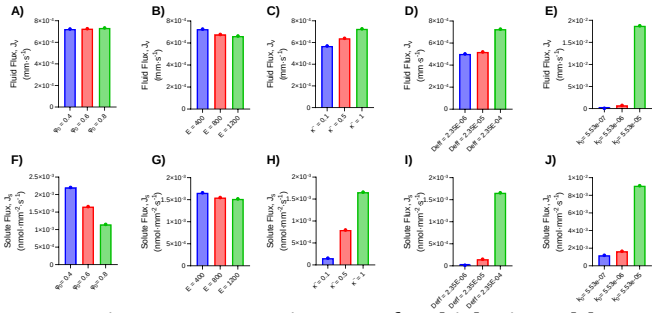

Figure 1. Parametric sweep of multiphasic model illustrating key variables that regulate fluid and solute flux.

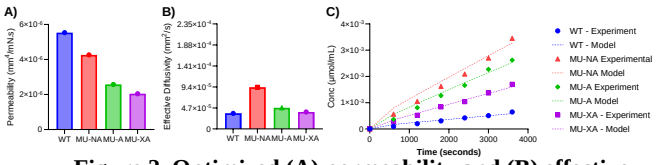

Figure 2. Optimized (A) permeability and (B) effective diffusivity from experimental calculations and (C) model fit to experimental values.

DISCUSSION

We used geometry and elastic moduli specific to each mouse model with varying aneurysm severity in biphasic and multiphasic models to determine mass transport material properties from previous experimental data. Our biphasic results for hydraulic permeability indicate that geometry and elastic modulus alone cannot account for measured changes in fluid flux and that hydraulic permeability varies with aneurysm severity.

Our effective diffusivity results from the multiphasic model illustrate a complex behavior. The MU-NA group has a higher effective diffusivity than the aneurysm groups (MU-A and MU-XA). The higher effective diffusivity could allow for increased transport of cytokines or biologic factors that may be protective or pathological. At early stages of aneurysm formation, when there is elastic fiber fragmentation, but limited dilation, the increased transmural transport may allow cytokine deposition that contributes to protective remodeling of the wall or exacerbates the disease and facilitates aneurysm formation. Future work characterizing transmural transport and wall remodeling over the time course of aneurysm formation will be necessary.

The experimental data used for fitting the hydraulic permeability had a large variability, but we are only using average values from the solute-free experiment [1]. Our model was limited by assuming mass transport properties were isotropic throughout the aorta. Future work is needed to characterize local transport properties. Future work will also investigate whether additional changes to the multiphasic model (i.e solid volume fraction and effective solubility, Fig. 1A, 1E) may be contributing factors to the solute flux in each mouse model. Overall, the model helps to understand contributing factors to changes in mass transport in TAA that may play a role in disease progression or be used for disease treatment.

ACKNOWLEDGEMENTS

Partially funded by NIH R01s HL164800 and HL133662.

REFERENCES

[1] Crandall, C et al., *Am J Physiol Heart Circ Physiol*, 325: 113-124. 2023.

[2] Yanagisawa H. and Wagenseil J, *Matrix Biol*, 85-86:160-172, 2020.

[3] Guang, Y et al., *Archive of Applied Mechanics*, 92:447-459, 2022.

[4] Ateshian, G et al., *J Biomech Eng*, 135(11), 2013.

[5] Wagenseil J and Mecham R, *Physiol Rev*, 89:957-989, 2009.

HEAT SINK EFFECTS OF LARGE BLOOD VESSEL DURING THERMAL THERAPIES

Shreeniket M. Pawar (1), Naveen Kondreddy, (1), Yash S. Lad (1), Anilchandra Attaluri (1)

(1) Department of Mechanical Engineering, School of Science, Engineering, and Technology, The Pennsylvania State University Harrisburg, Harrisburg, PA 17057, USA

INTRODUCTION

Adequate thermal dose control during thermal therapies requires reliable 3D temperature information. Thermally significant blood vessels create a cooling effect. The objective of this study was 3D analysis of cooling effects of large blood vessel (> 6 mm) using conjugate heat transfer simulations to develop empirical relationships and guidelines for thermal therapies. The influence of heat source on vessel distance as well as vascular flow rate on thermal dose is studied. Currently, the convective heat transfer to blood is modelled by convectively enhanced thermal conductivity [1]. Liu et. al., Huang et.al. and Chato shows that the temperature at tumor boundaries is less than the predicted temperature [2-4]. However, there are no models that solve conjugate heat transfer between large blood vessel and the tissue using Navier-Stokes and Pennes bioheat transfer equation [5]. Results of this study show that when the tumor is beyond 11 [mm] with respect to the blood vessel, the heat sink effects are negligible. Additionally, difference between highest and lowest temperature when the blood vessel is at 2 [mm] from the tumor is 2.1 [°C].

METHODS

A simple geometry as shown in Figure1 was considered to evaluate the heat carried away by the blood. The blood vessel was assumed to be a cylindrical volume, and the tumor was a sphere that was embedded in cuboidal tissue.

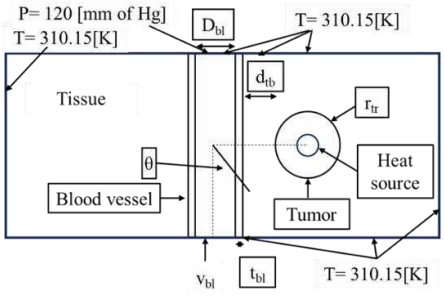

Figure 1: Geometry representing the boundary condition and the inlet and outlet specification for the fluid and solid for the model.

Fluid is assumed Newtonian fluid with an incompressible laminar flow based on Reynolds number calculation. The initial temperature of tissue and fluid is assumed to be 37 [°C]. Secondary flows are neglected as Richardson's number is much less than unity. Governing equations utilized for solving the problem are given in equation (1-3). Equations were solved in commercial finite volume methods (FVM) software (Simcenter STAR-CCM+).

$$\frac{\partial \rho}{\partial t} + \nabla \cdot (\rho \vec{V}) = 0 \quad (1)$$

$$\rho \frac{D\vec{V}}{Dt} = \nabla p + \rho \vec{g} + \mu \nabla^2 \vec{V} \quad (2)$$

$$\rho C_p \frac{\partial T}{\partial t} - \nabla(k \nabla T) = Q_{Perfusion} + Q_{Heatsource} + Q_{met} \quad (3)$$

where ρ is the fluid density [kg/m^3], V is the fluid velocity [m/s], k is the thermal conductivity [W/(m.K)], p is the fluid pressure [Pa], T is the absolute temperature [K], ρ is the blood density [kg/m^3], C_p is specific heat capacity of blood [J/kg.K], ω_b is the blood perfusion rate [1/s] and g is the gravitational acceleration [m/s^2].

Thermal damage-dependent perfusion term was added for the tumor (4) with field function which was evaluated from degree of vascular stasis (5), (6).

$$Q_{Perfusion} = \rho_b C_{p,b} \ \omega(T)(T_b - T) \quad (4)$$

$$DS = 1 - exp\left(-A \int_0^t e^{-\frac{E_a}{RT(\tau)}}\right) d\tau \quad (5)$$

$$\omega(T) = \begin{cases} \omega_{b,i}(30DS + 1), (DS \leq 0.02) \\ \omega_{b,i}(-13DS + 1.86), (0.02 < DS \leq 0.08) \\ \omega_{b,i}(-0.79DS + 0.884), (0.08 < DS \leq 0.97) \\ \omega_{b,i}(-3.87DS + 3.87), (0.97 < DS \leq 1 \end{cases} \quad (6)$$

The values of these properties are listed in Table 1.

Part	ρ [kg/m^3]	C_p [J/kg*K]	k [W/m*K]	μ [Pa*s]
Blood	1050	3617	0.52	$3.65*10^{-4}$
Tumor	1046	3630	0.51	-
Tissue	1056	3700	0.57	-
Heat Source	1046	3630	0.51	-

An implicit solver with a SIMPLE algorithm was utilized. The heat carried away by the blood was accounted for as the convective heat

transfer coefficient (HTC). Mesh independence was achieved for the HTC. Initially, the tumor was 2 [mm] from the blood vessel. The distance between the tumor and the blood vessel was increased to observe the effect of this distance on the HTC. The blood velocity was varied between 0.1-0.2 [m/s] to evaluate dependence of blood velocity on the HTC.

RESULTS

Simulation results predicted HTC of 4.37 [W/m^{2}K] on the blood domain carrying away 2.1 [ºC] from the tumor boundary. The solution was verified from the empirical relationship from Consiliegri et. al. [6], and results of this study are within 5 [%] of the solution predicted by the simulation.

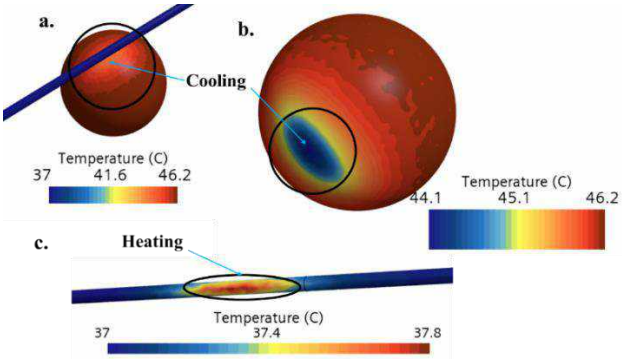

Figure 2: Figure depicting the temperature distribution at tumor and blood surface a. Blood vessel takes away the heat to cool the tumor. b. Cooling of approximately 2.1 [°C] on the tumor is evident due to the presence of blood vessel. c. Heat sink effects observed on the blood vessel by temperature rise of 0.8 [°C].

As the distance between the tumor and blood vessel was increased, the temperature difference was reduced, and at 11 [mm] the HTC was 1.21 [W/m^{2}K] which is negligible as shown in figure 3. Hence, the maximum distance to model HTC can be considered as 11 [mm].

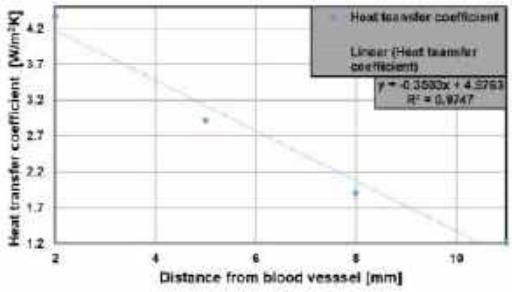

Figure 3: Heat transfer co-efficient as a function of distance from the blood vessel depicting the decrease as the distance is increased from the tumor.

Velocity depicted that as the higher the velocity higher the HTC for the blood which agrees with the HTC predicted by the Consiliegri et. al. [6]. The velocity was limited to 0.2 [m/s] in accordance with the human blood velocity.

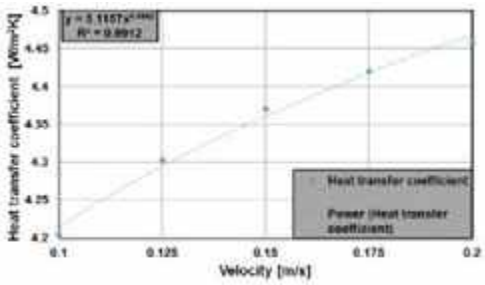

Figure 4: Heat transfer co-efficient as a function of velocity depicting the increased HTC as the velocity if blood is increased.

DISCUSSION

As distance of blood vessel is greater than 11 [mm] from the tumor the heat sink effects can be neglected. Additionally, the maximum velocity of fluid is considered for the equation giving the maximum HTC. The limitation of the study is that the geometry of tumor and fluid domain are kept constant. Further, a study can be set up to vary these parameters. All the dependent variables for the HTC can be evaluated from the study. Additionally, the identified parameters can be made dimensionless by normalizing against the respective parameter which would be the characteristic parameter in the equation. A relationship can be developed for the HTC as a function of characteristic parameters.

ACKNOWLEDGEMENTS

REFERENCES

1. Schooneveldt, G., Dobšícek Trefná, H., Persson, M., de Reijke, T. M., Blomgren, K., Kok, H. P., & Crezee, H. (2019). Hyperthermia treatment planning including convective flow in cerebrospinal fluid for brain tumour hyperthermia treatment using a novel dedicated paediatric brain applicator. Cancers, 11(8), 1183.
2. Liu, K. C., & Chen, T. M. (2018). Analysis of the thermal response and requirement for power dissipation in magnetic hyperthermia with the effect of blood temperature. International Journal of Heat and Mass Transfer, 126, 1048-1056.
3. Huang, H. W., & Horng, T. L. (2015). Bioheat transfer and thermal heating for tumor treatment. In Heat transfer and fluid flow in biological processes (pp. 1-42). Academic Press.
4. Chato, J. C. (1980). Heat transfer to blood vessels.
5. Pennes, H. H. (1948). Analysis of tissue and arterial blood temperatures in the resting human forearm. Journal of applied physiology, 1(2), 93-122.
6. Consiglieri, L., dos Santos, I., & Haemmerich, D. (2003). Theoretical analysis of the heat convection coefficient in large vessels and the significance for thermal ablative therapies. Physics in Medicine & Biology, 48(24), 4125.

DEVELOPMENT AND VALIDATION OF A VEHICLE FRONT PROFILE FINITE ELEMENT MODEL TO EVALUATE PEDESTRIAN IMPACTS

James T. Wolf (1), Karthik Somasundaram (1), Frank A. Pintar (1)

(1) Joint Department of Biomedical Engineering, Maquette University and Medical College of Wisconsin, Milwaukee, WI, USA

INTRODUCTION

In 2021, there were nearly 7500 pedestrians killed in traffic crashes in the U.S., the highest since 1981 [1][2]. Since the year 2000, Europe and Japan have adopted pedestrian crash protection programs for vehicles and have seen a decline in pedestrian fatalities; the U.S. has not yet adopted pedestrian crash protection and has seen an increase in pedestrian fatalities in that same time period [2].

The National Highway Traffic Safety Administration (NHTSA) Fatality Analysis Reporting System (FARS) [2] reported that passenger cars and light trucks were involved in 88% (36,076) of cases where a pedestrian was killed by a single front vehicle crash from the years 2011-2020. From 2015-2021 the number of light trucks registered, and their miles driven steadily increased, while the same criteria for passenger cars decreased [3]. The increased number of trucks on the road in the U.S. may correlate to the increase of pedestrian fatalities.

European New Car Assessment Programme (Euro NCAP) outlines a detailed procedure for evaluations of new vehicles for pedestrian safety through headform, upper legform, and lower legform tests. Euro NCAP also uses generic finite element (FE) vehicle models, representative of different vehicle classes, for safety ratings and analysis of pedestrian kinematics [4][5][6].

While these models are useful, they are not always applicable to the U.S., because they represent the European fleet and do not account for variability in stiffness across the hood and bumper. There are no publicly available FE models representative of a U.S. pickup truck/large SUV that are validated from pedestrian injury data. This study aimed to develop a vehicle front profile FE model, representative of a large U.S. vehicle, and validate the model from pedestrian component test data.

METHODS

Experiment

Raw data from pedestrian headform, upper legform, and lower legform experimental tests on a 2015 Ford F-150 and 2016 Chevrolet Tahoe was acquired from NHTSA's research testing database [7]. A total of thirteen headform, eight upper legform, and six lower legform impacts were analyzed to develop experimental 'target' corridors. Acceleration time corridors were developed for the headform and lower legform tests. Force time corridors were developed for the upper legform tests. All corridors consisted of an average with upper and lower bounds of ± 1 standard deviation. Headform corridors were grouped into categories of "middle", and "front and rear" based upon acceleration data as well as impact locations on the hoods of both test vehicles (**Figure 1**). Lower legform corridors were calculated for the F150 and Tahoe, respectively. One upper legform corridor was calculated for all impacts.

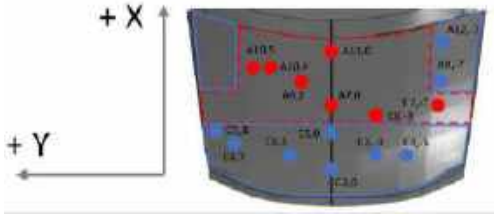

Figure 1: Headform impact locations with an adult ("A") and child ("C") headform. The numbers represent the x- and y-coordinates (x,y) of the impact. Red dots represent "middle" hood impacts, and blue dots represent "front and rear" hood impacts.

FE Model

To capture vehicle geometry, a 3D lidar scan was performed on a high selling U.S. truck. A shell model was created from the scan in Hypermesh (Altair, Troy, MI) and extruded to 10 mm quadrilateral solid elements in Ansa (Beta CAE Systems, Farmington Hills, IL. Material cards and parts were modeled according to Klug et al [6].

Headform, upper legform, and lower legform FE simulations were performed on the vehicle model according to Euro NCAP procedures.

Impact points were the same as those used on the F150 and Tahoe from Suntay et al [8]. LS-Dyna pedestrian child headform, adult headform, upper legform, and lower legform models were used. All simulations were completed using LS-Dyna single precision MPP version R8.0.0 and 64 cores on a cluster. Baseline simulations were run with the model having the same parameters as the Euro NCAP SUV model outlined in Klug et al [7]. Model parameters of stiffness, damping coefficient, and element thickness were optimized to match the calculated experimental corridors. Acceleration (G's) was plotted for the headform and lower legform models. Force (kN) was plotted for the upper legform models.

RESULTS

Baseline parameters of interface thickness, interface stiffness, foam stiffness, and foam damping coefficient were optimized for increased correlation to the experimental corridors for the "middle" hood (**Table 1**), "front and rear" hood (**Table 1**), and bumper (**Table 2**).

For the headform tests, the "middle" and "front and rear" corridors had average peak accelerations of 94.3 g and 140.4 g, respectively. The optimized model had average peak accelerations of 106.9 g and 154.8 g for the "middle" and "front and rear" hood, respectively (**Figure 2**).

Lower legform corridors had average acceleration peaks of 270 g and 367 g for the F150 and Tahoe, respectively. The lower legform exhibited a much stiffer response on the F150, as it reached its peak acceleration in less than 2 ms compared to 4 ms on the Tahoe. The optimized model had an average peak acceleration of 372 g (**Figure 3).**

Upper legform corridors had average peak lower and upper load cell forces of 4.2 kN and 1.0 kN, respectively. The optimized model had average lower and upper load cell forces of 4.7 kN and 2.1 kN, respectively (**Figure 4).** The greater lower load cell force is due to the lower part of the impactor contacting the stiff surface of the bumper. The same bumper properties were used in the upper legform simulations to achieve optimized results.

Table 1: Baseline and optimized hood model properties.

	Middle Hood		*Front and Rear Hood*	
Parameter	**Baseline**	**Optimized**	**Baseline**	**Optimized**
Interface Thickness (mm)	1.3	1.3	1.3	0.8
Foam Damping Coefficient	0	0.14	0	1.0

Table 2: Baseline and optimized bumper model properties.

Parameter	Baseline	Optimized
Interface thickness (mm)	1.86	6.0
Interface stiffness (GPa)	2.5	10
Foam Stiffness (GPa)	6.4E-5	6.5
Foam damping coefficient	0	0.2

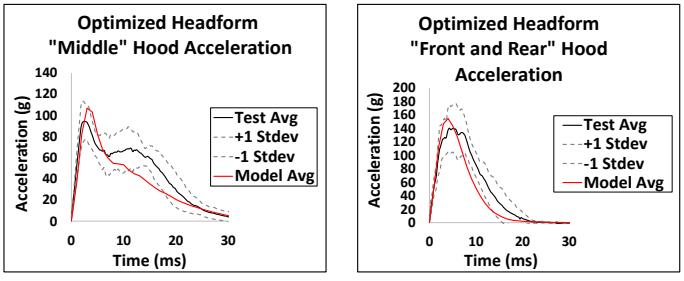

Figure 2: Optimized average headform to hood model acceleration output for "middle" hood corridor (left) and "front and rear" hood corridor (right).

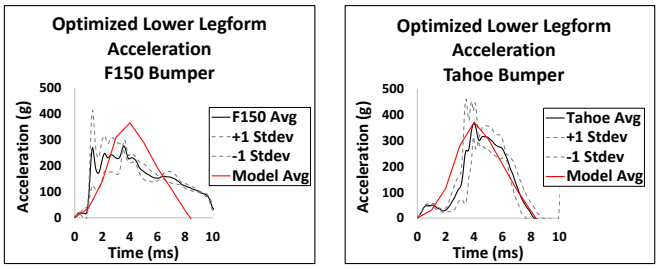

Figure 3: Optimized average lower legform to bumper model acceleration output for F150 (left) and Tahoe (right).

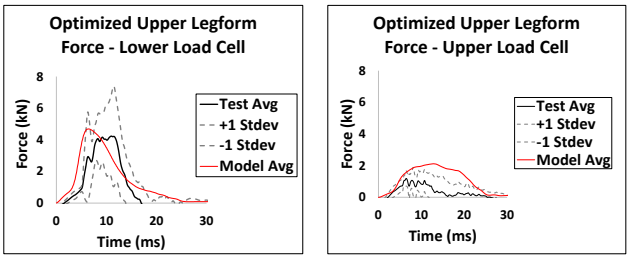

Figure 3: Optimized upper legform to bumper model force output. Lower load cell force (left) and upper load cell force (right).

DISCUSSION

The "front and rear" hood had greater experimental acceleration than the "middle" hood due to rigid under hood parts, such as hinges, that result in a stiffer response [9]. The greater damping coefficient in the optimized "front and rear" hood model allowed for a slower deformation resulting in greater acceleration and a slower time to peak acceleration than the "middle" hood.

The stiff lower legform response on the F150 experiment is likely due to the protruding bumper and its pronounced curvature. The Tahoe bumper has a smoother and flatter surface than the F150. Baseline results from the lower legform model showed small accelerations compared to the corridor since the baseline properties are modeled with low stiffness to represent European bumpers. European vehicles must have compliant, energy absorbing, bumpers to reduce leg injury risk to pedestrians [10]. Increasing the thickness of the interface layer as well as the stiffness and damping of the foam allowed for a more rigid response and increased acceleration, thus better resembling a U.S. vehicle bumper. A larger experiment sample size would improve model validation. Future studies will be performed using Pedestrian Human body models with the FE vehicle to analyze pedestrian kinematics.

ACKNOWLEDGEMENTS

The computational resources provided by MCW Research Computing Center are gratefully acknowledged. This work was also supported in part by the Department of Veterans Affairs research service.

REFERENCES

[1] NHTSA "2021 Data - Pedestrians," 2023.
[2] NHTSA,"Request for Comment: www.federalregister.gov
[3] "NHTSA file downloads."
[4] "Euro NCAP PEDESTRIAN TESTING PROTOCOL," 2018.
[5] Klug et al., "Pedestrian Human Model Certification," 2019
[6] Klug et al., IRCOBI, 2017.
[7] "NHTSA Research Testing Database." https://www.nhtsa.gov
[8] Suntay et al., 2019: www.ntis.gov.
[9] Kerkeling et al., 2005
[10] Suntay et al., 2020: www.ntis.gov.

SUPER-RESOLVING AND DENOISING 4D FLOW MRI OF CSF USING A PHYSICS-GUIDED TEMPORALLY COHERENT NEURAL NETWORK

Neal M. Patel (1), Sriram Baireddy (2), A. J. Schwichtenberg(3), Edward J. Delp (1,2,4), Vitaliy L. Rayz (1,5)

(1) Biomedical Engineering, Purdue University, West Lafayette, IN, USA
(2) Electrical and Computer Engineering, Purdue University, West Lafayette, IN, USA
(3) Health and Human Sciences, Purdue University, West Lafayette, IN, USA
(4) Psychological Sciences, Purdue University, West Lafayette, IN, USA
(5) Mechanical Engineering, Purdue University, West Lafayette, IN, USA

INTRODUCTION

Impaired flow of cerebrospinal fluid (CSF) has been associated with cerebroventricular disorders such as idiopathic normal pressure hydrocephalus (iNPH). Computational fluid dynamics (CFD) models have advanced our understanding of these disorders and indicated flow metrics associated with disease initiation and progression. However, CFD relies on modeling assumptions, such as flow boundary conditions [1]. Alternatively, the flow can be measured *in vivo*, with time-resolved, 3-directional phase contrast MRI (4D flow MRI). While originally 4D flow MRI has been used in cardiovascular flow measurements, recent studies have extended its application to the flow of CSF. Yamada et al. showed that patients with iNPH have higher oscillatory shear stress compared to healthy individuals [2]. However, 4D flow MRI requires balancing acquisition time, spatiotemporal resolution, and velocity-to-noise ratio. 4D flow MRI imaging of CSF flow is particularly challenging due to low velocities and long relaxation times. The limited spatial resolution and noise lead to measurement errors which are further propagated through calculations of velocity gradient-based metrics, such as shear stress and vorticity.

To address these limitations of 4D flow MRI, several neural network methods have been recently proposed, particularly focusing on improving cardiovascular flow quantification [3, 4]. However, most of these deep learning-based methods did not incorporate constraints to ensure consistency with flow physics and did not account for the evolution of the flow over the cardiac cycle. Here, we extend the deep learning approach by examining the use of a long-short term memory (LSTM) network architecture and a loss function incorporating the residual of the vorticity transport equation to denoise and super-resolve 4D flow MRI in a physically consistent and temporally coherent manner.

METHODS

We present TransVort, a neural network to super-resolve and denoise 4D flow MRI by leveraging mass conservation and vorticity transport equations. We extend on our previously developed network which used flow divergence regularization to improve velocity data in the near-wall voxels. Our networks are based on a densely connected super-resolution network (DCSRN) architecture as shown in Figure 1 [5]. Here, we integrate convolutional long-short term layers into this network.

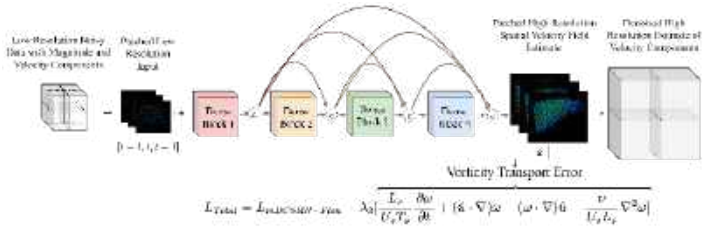

Figure 1: Simplified mDCSRN network architecture trained using a loss function including the residual of the vorticity transport equation

While network training would ideally use paired high- and low-resolution 4D flow MRI datasets, acquiring such data is not practical. Therefore, we train the network using synthetic 4D flow MRI derived from CFD simulations in ten geometries of the third and fourth cerebral ventricles in healthy individuals and in individuals with Alzheimer's disease. The flow domain is subdivided into patches to reduce the dependence on the subject-specific anatomy and focus on intermediate flow scales assumed to be common across the subjects. Three consecutive timeframes of patches are used for the training. For each geometry, CFD is run with four inflow boundary conditions. These 40 simulations of high-resolution flow fields are spatiotemporally

downsampled and converted to synthetic 4D flow MRI cases by manipulating the *venc*, noise, and saturation ratios.

During network training, we examine the use of a loss function which combines our previous divergence regularization term with the residual of the vorticity transport equation. Here, we can express the divergence regularization over a flow region ($\mathcal{F}$) as

$$\mathcal{L}_{div} = \frac{1}{TNI}\sum_{t=0}^{T}\sum_{n=0}^{N}\sum_{i=0}^{I}\left|\nabla\cdot\hat{\boldsymbol{u}}_{i,t}^{(n)}\right| \quad if\ i\in\mathcal{F} \tag{1}$$

where T = 3 is the number of timeframes input into the network, N is the number of patches within a given batch, I is the number of voxels within a given patch, and $\hat{\boldsymbol{u}}$ is the predicted velocity field. We can express the nondimensionalized vorticity transport residual as

$$\mathcal{L}_{VT} = \sum_{n=0}^{N}\sum_{i=0}^{I}\frac{L}{U^{(n)}\Delta}\frac{\partial\hat{\boldsymbol{\omega}}_i^{(n)}}{\partial t} + \left(\hat{\boldsymbol{u}}_i^{(n)}\cdot\nabla\right)\hat{\boldsymbol{\omega}}_i^{(n)} - \left(\hat{\boldsymbol{\omega}}_i^{(n)}\cdot\nabla\right)\hat{\boldsymbol{u}}_i^{(n)} - \frac{\nu}{U^{(n)}L}\nabla^2\hat{\boldsymbol{\omega}}_i^{(n)} \tag{2}$$

Where $\hat{\boldsymbol{\omega}}$ is the vorticity computed from the estimated high-resolution patch normalized velocity fields, L is the high-resolution voxel size, Δ is the temporal resolution, U is the highest component velocity in each patch and ν is the kinematic viscosity.

The network was trained for 100 epochs using the divergence-based loss function. Once pretrained, the LSTM portion of the network was fine-tuned using the full loss function including the residual of the vorticity transport equation. The network was trained using NVIDIA Quadro RTX 6000 graphics processing units.

Once trained, we apply this network to an *in vivo* case of the cerebral ventricles. The cerebral ventricles were imaged structurally using T2 SPACE (1x1x1 mm, TR/TE/flip-angle = 700 ms/11 ms/120°) and functionally using single-*venc* of 10 cm/s (1x1x1 mm, TR/TE/flip-angle = 7.90 ms/5.283 ms/8°).

RESULTS

The results indicate that TransVort outperforms temporally independent methods when assessed on the synthetic 4D flow dataset of CSF flow through the third and fourth ventricles. In comparison to linear interpolation, TransVort outperformed the temporally independent method reducing the error in both core flow voxels (17.9% vs 10.9%) and in edge (near-wall) voxels (39.7% vs 34.5%).

Once the network performance was assessed using CFD data as the ground truth, we applied the network on CSF flow within the 4th ventricle as shown in Figure 2. The raw 4D flow MRI at 1 mm isotropic voxel resolution for four frames are shown on the top and the corresponding 0.5 mm isotropic voxel resolution reconstructions using the TransVort network are shown on the bottom of Figure 2.

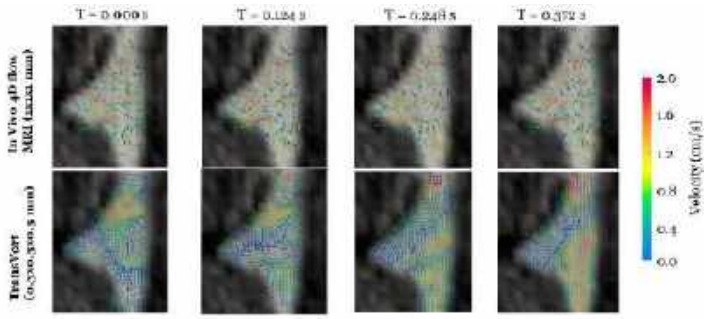

Figure 2: Application of TransVort to CSF flow in the 4th ventricles shows the superior movement of a vortex as well as alignment of near wall velocities.

From the TransVort reconstruction, we see the formation of a vortex in the 4th ventricle around a time of 0.124 s. As the cardiac cycle moves towards diastole, we see that the vortex moves superiorly and dissipates as it approaches the cerebral aqueduct. However, the presence of these structures are difficult to perceive in the raw 4D flow MRI data.

DISCUSSION

In this work, we developed TransVort, a temporally coherent and physics guided neural network that is trained using a loss function that incorporates both divergence regularization and the residual of the vorticity transport equation. The results show that vorticity-based approach enables a better reconstruction of the velocity field in both core and edge voxels. The method was applied to CSF flow in the 4th cerebral ventricle. Improving MRI-based flow quantification in the cerebral ventricles will aid investigation of cerebroventricular diseases such as iNPH.

ACKNOWLEDGEMENTS

We acknowledge the Purdue Institute of Integrative Neuroscience, Grand Challenges in Neuroscience Grant (PI: Schwichtenberg).

REFERENCES

[1] D. A. Steinman and V. M. Pereira, "How patient specific are patient-specific computational models of cerebral aneurysms? An overview of sources of error and variability," *Neurosurg Focus,* vol. 47, no. 1, p. E14, Jul 1 2019, doi: 10.3171/2019.4.FOCUS19123.

[2] S. Yamada *et al.*, "Quantification of Oscillatory Shear Stress from Reciprocating CSF Motion on 4D Flow Imaging," *AJNR Am J Neuroradiol,* vol. 42, no. 3, pp. 479-486, Mar 2021, doi: 10.3174/ajnr.A6941.

[3] D. R. Rutkowski, A. Roldan-Alzate, and K. M. Johnson, "Enhancement of cerebrovascular 4D flow MRI velocity fields using machine learning and computational fluid dynamics simulation data," *Sci Rep,* vol. 11, no. 1, p. 10240, May 13 2021, doi: 10.1038/s41598-021-89636-z.

[4] E. Ferdian *et al.*, "4DFlowNet: Super-Resolution 4D Flow MRI Using Deep Learning and Computational Fluid Dynamics," *Frontiers in Physics,* vol. 8, 2020, doi: 10.3389/fphy.2020.00138.

[5] Y. Chen, A. G. Christodoulou, Z. Zhou, F. Shi, Y. Xie, and D. Li, "MRI Super-Resolution with GAN and 3D Multi-Level DenseNet: Smaller, Faster, and Better," 2020, doi: https://doi.org/10.48550/arXiv.2003.01217.

THE PROTECTIVE EFFECT OF SYNOVIAL FLUID AGAINST CARTILAGE FATIGUE WEAR IS CONCENTRATION DEPENDENT

C.V. Sise (1), Courtney A. Petersen (2), Anna K. Ashford (1), Sinisa Vukelic (2), Clark T. Hung (1), Gerard A. Ateshian (1,2)

(1) Biomedical Engineering Department, Columbia University, New York City, New York, USA
(2) Mechanical Engineering Department, Columbia University, New York City, New York, USA

INTRODUCTION

Osteoarthritis (OA) is a disease of the joint, characterized by the degeneration of articular cartilage from acute or long-term wear. The mechanism of wear that propagates the advancement of OA is not yet understood. It has been established that the primary cause of damage in immature bovine cartilage is fatigue wear through delamination of the superficial zone (SZ) from the middle zone (MZ) [1, 2]. Our recent study expanded upon this result, and determined the cause of the fatigue wear was reciprocating compressive forces and not frictional forces [3]. This finding challenges an implicit assumption that friction coefficient is related to wear severity and progression, but is comprehensively supported by other studies on cartilage wear and friction [4, 5].

Synovial fluid (SF), the fluid that fills the joint space, has recently been shown to decrease the rate of fatigue in immature bovine cartilage [3,6]. In a study designed with a migrating contact area (MCA) configuration (identical to the MCA set-up described in [3]), cartilage samples immersed in PBS damaged at much higher incidence than samples immersed in SF after 24 hours of reciprocating sliding [6]. Paired with the results of [3], which demonstrate that cyclical compressive stresses, but not frictional stresses, cause delamination damage, SF has a beneficial role in wear reduction that is independent of its role as a secondary source of boundary lubrication [7, 8].

On a molecular level, the major constituents of SF, lubricin and hyaluronic acid (HA), have been linked to wear reduction [9]. It has been shown that PRG4 knockout of lubricin results in increased total joint wear in the mouse model [10]. Other studies have found lower levels of lubricin in SF with symptomatic OA, and thus reduced concentration of the molecule may be linked to wear propagation [11]. However, many of these studies link the beneficial effect of lubricin with reduction of the friction coefficient, despite the abundance of evidence that frictional forces do not induce cartilage wear [2-4, 12].

The purpose of this study was to better understand the mechanism by which SF reduces cartilage fatigue wear. To examine this aim, we investigated the effect of SF concentration on the rate of fatigue wear in immature bovine cartilage when subjected to reciprocating compressive stresses in a MCA configuration. This study complements our recent report of wear measurements in pure PBS and pure SF baths [6].

METHODS

Sample Preparation: Full thickness cartilage strips were harvested from the tibial plateaus of ten immature bovine calf knees (five left, five right, 2-3 months old) and microtomed to a thickness of 1.41 ± 0.07 mm. Samples were cut to 10×30 mm rectangular strips, and lightly glued to a ∅ 60 mm petri dish. Prior to testing, samples were kept hydrated in PBS supplemented with inhibitors (0.04% isothiazolone-based biocide and 0.1% protease inhibitor). Three 100 mL batches of mature bovine SF were obtained from a local abattoir, aliquoted into 50 mL tubes, and centrifuged (3000 g, 20 min) to remove excess particulate. The SF was supplemented with the same inhibitors as the PBS. To create a 50% and 25% SF/PBS dilution, 25 mL and 37.5 mL of PBS were added to 25 mL and 12.5 mL of SF, respectively.

Friction Testing: Samples were mounted on two identical custom friction testing devices as described previously [13]. Samples were brought into contact with a hemispherical glass lens (∅25 mm) under a compressive load of 4.45 N and subjected to reciprocating sliding at 1 mm/s. After 24 hours of sliding (~5,400 cycles), samples were taken off the tester and visually assessed for delamination damage. If damage was observed, the test was stopped; if no damaged was observed, the sample was put back on the friction tester and the test was continued to 72 hours (~16,200 cycles). Test groups included 50% SF/PBS (n=8), and 25% SF/PBS (n=8). Throughout testing, samples were hydrated with 15 mL diluted bath solution that was refreshed every 24 hours if applicable.

Sample Assessment: Pressure sensitive Fuji film was used to measure the contact area between the glass platen and the sample prior to testing to ensure consistent contact pressure p_{avg} among test groups. Samples were scanned using a laser scanner to produce a dense point cloud

(50,000 points/cm^2) before and after testing. A custom MATLAB code was used to quantify the root-mean-square roughness (R_q) of sample articular surface. Photographs were taken of the sample, and polarized light microscopy (PLM) was conducted on all samples to analyze subsurface response. One way analysis of variance (ANOVA) tests were conducted to compare R_q (before and after testing), before contact pressures (p_{avg}), and averaged friction coefficient μ_{avg}. Repeated measures ANOVA tests were conducted for R_q for both test groups.

RESULTS

Prior to testing, neither p_{avg} nor R_q was found to be statistically different between the two bath conditions (p_{avg}=0.65 MPa, p=0.57; R_q= 0.52, p=0.59). Similarly, μ_{avg} was not different between the 50% SF/PBS and the 25% SF/PBS groups (p=0.80) (Figure 1).

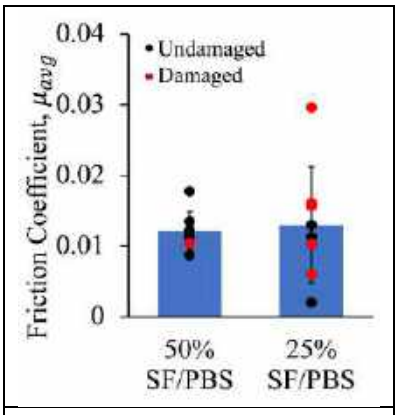

Figure 1: μ_{avg} over all cycles. Markers indicate individual samples. Color indicates damage.

In the 50% SF/PBS group, none of the samples damaged after 24 hours of testing, and all eight samples were subsequently allowed to run for 72 hours (16,200 cycles). In total, two out of eight samples damaged after 72 hours. Surface roughness was not found to be statistically different before and after testing (p=0.43) (Figure 2). In the 25% SF/PBS group, three of the samples damaged after 24 hours of testing, and the test was thus terminated. The other five samples were allowed to run for 72 hours (16,200 cycles), at which time two of five remaining samples damaged. Surface roughness was found to be statistically different before and after testing (p=0.02) (Figure 2). When comparing test groups, the surface roughness after testing was statistically lower in the 50% SF/PBS than the 25% SF/PBS groups (p=0.045) (Figure 3). PLM analysis supported the surface delamination results observed, and indicated no additional subsurface (occult) damage.

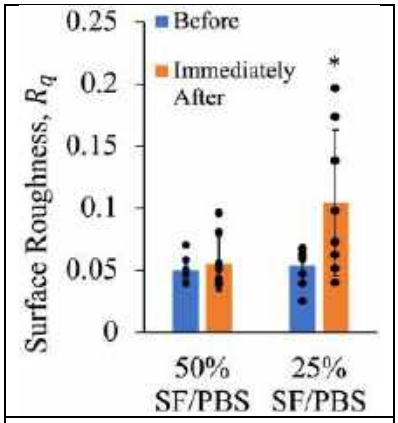

Figure 2: R_q for before and after testing. Markers indicate individual samples. $*$ indicates statistically different before and after testing (p=0.02)

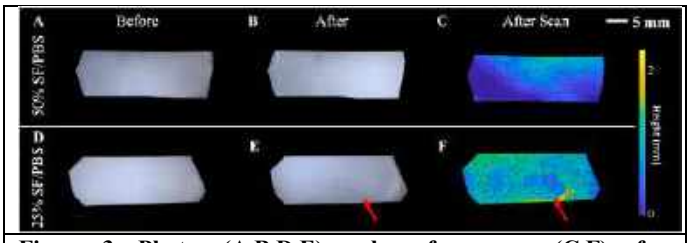

Figure 3: Photos (A,B,D,E) and surface scans (C,F) of a representative 50% SF/PBS (A-C) and 25% SF/PBS diluted samples (D-F). Delamination damage is indicated with red arrows in the 25% SF/PBS sample after photo (E) and scan (F)

DISCUSSION

This study complements our recent report showing that pure SF protects against cartilage wear when compared to pure PBS [6]. Here, results indicated that SF concentration has an effect on fatigue rate in immature bovine articular cartilage. The 50% SF/PBS group had no samples damage after 24 hours and only one sample damage out of eight after 72 hours of sliding. This outcome was very similar to that reported for pure SF [6], which had two samples damage after 72 hours. In contrast, the 25% SF/PBS had a much greater incidence of damage, with three samples delaminated after 24 hours and an additional two after 72 hours. Thus, it can be concluded that a decrease in concentration of SF results in a decrease in SF's protective effect against fatigue wear.

The average friction coefficient for the two bath conditions was not statistically different despite the increased incidence of wear in the 25% SF/PBS group. When compared to previous results with an identical experimental setup [6], the friction coefficient is similar to that of pure SF ($\mu_{avg} \approx 0.012$). This finding is expected as it has previously been shown that SF's effect on friction coefficient is secondary to the effect of interstitial fluid load support on friction coefficient, and thus a dilution should not affect the average coefficient significantly [5, 7]. Despite this statistical similarity in μ_{avg}, the 25% SF/PBS group clearly exhibited a higher degree of damage than the 50% SF/PBS group. This result, paired with the studies cited above [3-5], establish that frictional forces are not responsible for cartilage wear and the friction coefficient is not reflective of damage severity in immature bovine cartilage.

These results are consistent with the hypothesis that molecular constituents of SF (lubricin and HA) are responsible for wear reduction. The samples during testing were immersed in 15 mL of test bath solution, which exceeds the *in situ* value for immature bovine knees (~3 mL). The 50% SF/PBS exhibiting similar damage incidence to pure SF could be attributed to the bath solution (and thus lubricin and HA) being in excess, whereas the 25% SF/PBS was diluted below a critical threshold of available constituents for wear reduction. It has been suggested that lubricin binds to type II collagen in cartilage and sterically charges the extracellular matrix. The repulsive state caused by lubricin coating could correspondingly improve the wear properties of the cartilage during reciprocal sliding [14]. Improved understanding of the beneficial effect of SF could be achieved in future studies, through an examination of evolving lubricin and HA ultrastructure and concentration with reciprocal sliding.

ACKNOWLEDGEMENTS

Prof. X. Edward Guo (Columbia University) for use of microscope. National Institutes of Health (R01 AR073289).

REFERENCES

[1] Oungoulian, S.R., et al., *J Biomech*,. 48(10):1957-64, 2015. [2] Durney, K.M., et al., *J Biomech,* **107**:109852, 2020. [3] Petersen, C.A., et al., *Osteoarthr. Cartil.*, 2023. [4] Caligaris, M., et al.,. *Osteoarthr. Cartil.*, **17**(10):1327-32, 2009. [5] Caligaris, M. et al., *Osteoarthr. Cartil.*, **16**(10):1220-7. 2008. [6] Sise, C.V., et al., *ORS.* Long Beach, CA., 2024: [7] Ateshian, G.A., *J Biomech,* 42(9):1163-76, 2009. [8] Basalo, I.M., et al., *J Biomech Eng*, 126(6):779-86, 2004. [9] Jay, G.D., et al., *Arthritis Rheum*,. 62(8):2382-91, 2010. [10] Waller, K.A., et al. *PNAS*, 110(15):5852-5857, 2013. [11] Szychlinska M.A. et al., *Ann Phys Rehabil Med,* 59(3):149–156, 2016. [12] Charnley, J., *Ann Rheum Dis*, 19:10-9, 1960. [13] Gangi, L.R., et al.,. *J Vis Exp*, 184, 2022. [14] Chang, D.P., et al., *J Biomech*, 47(3):659-66, 2014.

PATIENT-SPECIFIC MODELING OF HEMODYNAMICS DURING SPLENIC ARTERY EMBOLIZATION

Younes Tatari (1,2), Tyler Andrew Smith (3), Jingjie Hu (4), Amirhossein Arzani (1,2)

(1) Department of Mechanical Engineering, University of Utah, Salt Lake City, UT.
(2) Scientific Computing and Imaging Institute, University of Utah, Salt Lake City, UT.
(3) Department of Radiology, University of Utah, Salt Lake City, UT.
(4) Department of Mechanical and Aerospace Engineering, North Carolina State University, Raleigh, NC.

INTRODUCTION

The spleen, an important organ in the human body, plays a key role in immune defense mechanisms, notably in antibody production and the phagocytosis of aging red blood cells. In addition to these functions, the spleen is the most injured organ in instances of blunt abdominal trauma [1]. This high incidence of injury has led to significant advancements in medical procedures aimed at preserving the spleen. Traditionally, splenectomy, the surgical removal of the spleen, was the standard response to such injuries. However, given the spleen's important roles, current medical practice often seeks to avoid splenectomy. The preferred alternative has become endovascular splenic artery embolization, a less invasive procedure that allows for spleen preservation.

Endovascular embolization, however, is a complex procedure that demands a comprehensive understanding of the blood flow environment within the splenic artery. Direct experimental investigation of these blood flow patterns in patients is not an easy task due to the small vessel sizes, vessel tortuosity, and the presence of collaterals. Patient-specific computational fluid dynamics (CFD) simulations are an attractive alternative and enable a detailed assessment. These simulations provide a non-invasive strategy towards understanding the blood flow dynamics, facilitating the planning and execution of precise embolization procedures in a personalized fashion. Nevertheless, the assessment of hemodynamics in the visceral arteries that provide blood to the spleen has been relatively understudied [2]. Particularly, the role of blood flow during the splenic artery embolization procedure is not investigated.

There are two primary methods for splenic artery embolization: proximal embolization, which typically involves the use of coils to block the blood flow at the upstream segment of the artery, and distal embolization, where as an alternative to coiling particles can be released to block the artery closer to the spleen. Each method has its specific indications and applications, depending on the nature and location of the splenic injury. In the case of proximal coil embolization, clinicians are interested in alterations in pressure fields as well as the risk of coil migration. In distal embolization with particles, one is interested in the trajectory of the emboli, particularly in the elderly with tortuous arteries where it is difficult to navigate the catheter close to the target. Our goal in this study is to understand the role of hemodynamics during each procedure and ultimately guide the procedure.

METHODS

In this study, we utilized computed tomography (CT) to construct three models in the open-source SimVascular software and conduct CFD simulations. These simulations were specifically designed to explore the effects of collateral vessels and the placement of coils on the outcomes of embolization procedures. The first model deliberately omits the presence of collateral vessels, providing a baseline to assess their impact on the embolization process. This comparative approach helps in understanding the significance of collateral flow in such procedures. The second model includes all three collateral vessels, making it a more comprehensive representation to better understand the role of collaterals during baseline. The third model introduces a coil as well as the collaterals to examine the hemodynamic consequences of proximal embolization. This inclusion is vital for assessing how coils interact with blood flow and influence the success of the embolization. To simulate pulsatile blood flow, we employed the finite element solver SimVascular. To enhance the accuracy of our simulations, we meticulously selected boundary conditions that closely align with clinical data, ensuring a more realistic representation of blood flow distribution [3,4]. Specifically, 1D blood flow models and steady 3D simulations were used to tune the resistance boundary conditions at the outlets. Consistency in our approach was maintained by applying the same simulation parameters across all three models. Pulsatile flow simulations were conducted and data from the fourth cardiac cycle were used in this study. An overview of the patient-specific model is shown

in Fig. 1. The velocity results from the CFD simulations were used for Lagrangian particle tracking to model distal embolization. Specifically, the Maxey-Riley equation was solved for inertial spherical particles using FlowVC, an in-house code.

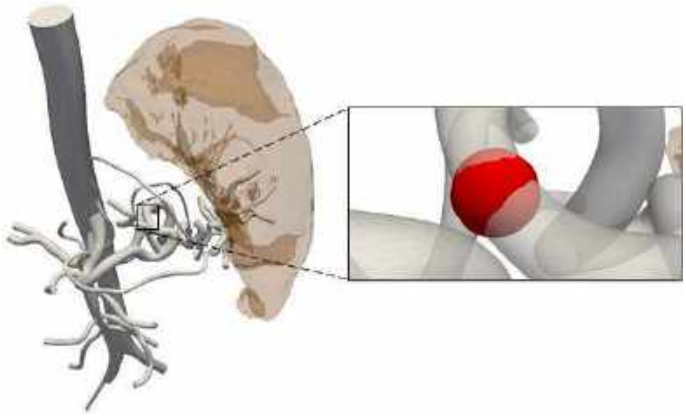

Figure 1: The model with collaterals is shown. On the right side the place of coil for the third case is highlighted. The enlarged spleen is shown in brown color.

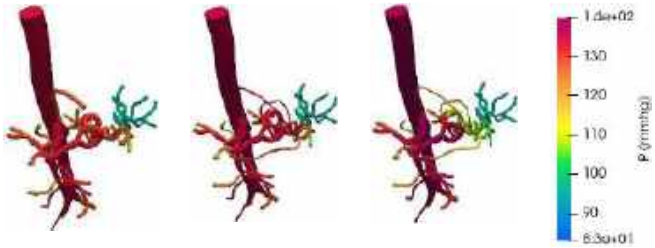

Case 1 Case 2 Case 3

Figure 2: Pressure contour for three models. In the third case which considers the coil there is a higher-pressure difference between the upstream and downstream

RESULTS

Figure 2 shows the pressure distribution results. A closer inspection of the results revealed that the presence of collateral vessels does not significantly alter the pressure distribution when a coil is not in place. This is attributed to their relatively smaller diameter, ranging between 1 and 1.5 mm. However, the hemodynamic environment changes considerably upon the introduction of a coil. In this scenario, collaterals become crucial in maintaining blood supply to the spleen. The application of a coil leads to a substantial increase in maximum velocity within the collaterals up to an order of magnitude (results not shown). Interestingly, the collateral that exhibited relatively lower flow rates in the second case scenario demonstrates an equal flow rate relative to the other two collaterals when a coil is used. Moreover, the introduction of a coil also results in a pronounced increase in the pressure gradient across the celiac trunk, both upstream and downstream. Also, there is a high-pressure difference on the two sides of the coil as expected. These observations underscore the significant impact that coil placement has on the hemodynamic environment within the splenic artery system.

In Fig. 2., It is observed that the collaterals do not significantly impact the pressure distribution, a finding that can be attributed to the application of identical boundary conditions across the models. In contrast, introducing a coil in the splenic artery (as shown in case 3) markedly decreases the overall blood flow rate to the spleen but cannot completely eliminate flow due to collaterals. This reduction in flow is accompanied by a substantial drop in pressure within the splenic artery. Our data demonstrates how the insertion of a coil alters the hemodynamic profile, significantly reducing blood flow (not shown here) and pressure (Fig. 2), important metrics in the embolization procedures.

In the distal embolization case, the percentage of the emboli delivered to the targeted area depends on the place where particles are released. While in certain cases the catheter can be navigated close to the target, in the example here due to the arteries' high curvature, it is difficult for interventional radiologists to navigate very close to the target. Therefore, understanding the particle path and behavior is crucial to determining the amount and size of the particles needed. Figure 3 illustrates a potential release point for these particles. In this figure, the initial particle release location as well as the position of the particles after 0.3 seconds is shown. It is important to note that the particles are represented much larger than their actual size in these images for visualization purposes. Currently, we are in the process of quantifying the optimal release strategy for maximizing the success of particle transport to the spleen.

Figure 3: a) Particle release location and b) their trajectories.

DISCUSSION

We presented one of the early CFD studies on hemodynamics during proximal and distal splenic artery embolization. Our study revealed critical insights into the hemodynamics of splenic artery embolization, emphasizing the influence of collateral vessels and coil placement. Our findings show that collateral vessels have minimal impact on pressure distribution when no coil is used and the introduction of a coil reduces blood flow and pressure in the splenic artery but cannot completely eliminate blood flow to the splenic artery, highlighting the importance of the need for further optimized proximal embolization procedures in future work. This study, while informative, is limited by its reliance on computer models, which may not fully capture the complexities of in-vivo conditions. Future research should aim to validate these simulation results with actual clinical data and further explore the long-term implications of coil embolization on splenic function and collateral vessel adaptation. In summary, our study highlights the potential of using CFD simulations as a predictive tool in planning and executing embolization procedures, and potential for improving their safety and efficacy.

ACKNOWLEDGEMENTS

This study was funded by the NIH R21AG083692 grant.

REFERENCES

[1] K.B. Quencer and T.A. Smith., Journal of Cardiovascular and Interventional Radiology, 2 (2019)

[2] F. Gao et al., Comput. Methods Programs Biomed, 221, 2022

[3] M.J.K. Blomley. et al., J Academic Radiology, 4:13-20, 1997

[4] A.S. Les et al., Annals of Biomedical Engineering, 38:1288-1313, 2010

DEVELOPMENT OF COARCTATION OF THE AORTA SOFTWARE TO COMBAT HYPERTENSION

Shahd S. Sawalhi (1), Arash Ghorbannia (1,2,3) Andrew D. Spearman (2), Robert F. Cooper (1), John F. LaDisa, Jr. (1,2,4),

(1) Joint Department of Biomedical Engineering, Marquette University and the Medical College of Wisconsin, Milwaukee, Wisconsin, USA
(2) Department of Pediatrics - Section of Cardiology, Herma Heart Institute, Children's Wisconsin and the Medical College of Wisconsin, Milwaukee, Wisconsin, USA
(3) Department of Biomedical Engineering, Duke University, Durham, North Carolina, USA
(4) Departments of Physiology and Medicine - Division of Cardiovascular Medicine, Medical College of Wisconsin, Milwaukee, Wisconsin, USA

INTRODUCTION

Coarctation of the aorta (CoA) is a congenital cardiovascular defect characterized by narrowing of the proximal descending thoracic aorta and is often associated with long-term hypertension (HTN) even after treatment. The current >20 mmHg peak-to-peak blood pressure gradient (BPGpp) threshold for intervention[1] does not prevent HTN[2]. Thus new guidelines are required to prevent recurrent HTN.

Current methods used to estimate BPGpp in CoA patients have several limitations that can limit application of new treatment guidelines. For example, BPGpp estimation via BP cuffs placed on the arms and leg is difficult in patients clinically due to children who may be upset, crying or scared during measurement, and/or inappropriately sized cuffs[3,4,5]. Moreover, CoA patients frequently have anomalies in their arterial anatomy that limit accurate determination of BPGpp via BP cuffs[6,7]. Doppler ultrasound offers a common non-invasive alternative, but is well-known to over-estimate gradients[8,9].

Despite its limitations, the simplified Bernoulli equation (SBE) is widely implemented due to its ease of use and availability[10]. To rectify this limitation, our team is working to improve the sensitivity and specificity of echocardiogram (echo)-based indices while allowing clinicians to continue using their current workflow and leverage their familiarity with this imaging modality. Therefore, to more accurately estimate BPGpp, avoid unnecessary invasive testing, and intervene before HTN precursors develop, we recently derived and published a new method called the continuous flow pressure gradient (CFPG). The CFPG uses the diastolic phase of conventional echo tracings and has excellent agreement with catheterization[11]. We are optimistic that using CFPG to assess stenosis severity and refine current treatment thresholds will ultimately lead to improved outcomes in CoA patients following intervention. Our objective is to incorporate the CFPG into a user-friendly website and application that can rapidly provide clinicians with a value that better represents the catheter-based (i.e. true) severity of a BPG in clinical and pre-clinical subjects.

METHODS

The process of calculating the CFPG threshold is echo-friendly (**Figure 1**), meaning that all inputs can be quantified using an echo image with Doppler spectrum. The CFPG calculation is as follow:

$$\mathrm{CFPG} = 4\frac{dPHT}{ln(2)}\left(1 - exp\left(-\frac{ln(2)}{dPHT}\right)\right)(1 - DVI)^2 {V_d}^2 \quad (1)$$

Where *DVI*, *dPHT*, and V_d are Doppler velocity index ($DVI = V_p/V_{pk}$)[9], normalized diastolic pressure half-time (time to the half diastolic pressure/diastolic period)[12], and early diastolic velocity, respectively. V_p and V_{pk} used for DVI are the peak velocities proximal to, and within the CoA region, respectively. Including *dPHT* captures the unique representation of diastolic indices based on severity of the CoA.

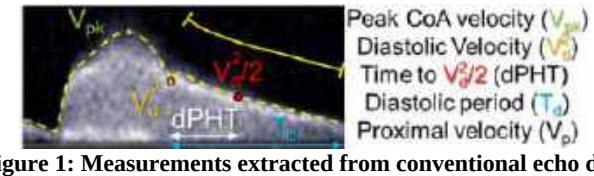

Figure 1: Measurements extracted from conventional echo data for use in the CFPG equation.

The CFPG has been integrated within a newly developed website and IOS application, we refer to as CoACH - Coarctation of the Aorta software to Combat Hypertension. CoACH aims to rapidly provide clinicians with a value that better represents the gold-standard catheter-based severity of a BPGpp in vivo. The developed software obtains values needed to calculate the CFPG in two ways (**Figure 2**): a simple direct entry method, and an Image extraction method. Obtaining values using the direct entry method can be done by hovering the mouse over the tracing on most clinical echo workstations. The values can then be input directly into dedicated fields in CoACH. Values for the image extraction method are obtained from images with a Doppler spectrum

that are uploaded and processed using multiple image processing techniques in Python to obtain the values needed for the CFPG calculation. Image segmentation and color thresholding are used to isolate the EKG signal from the Doppler signal in the images provided. Signal smoothing and peak detection are performed to capture specific values needed for the CFPG equation. Optical character recognition is used to extract data like (e.g. heart rate) from images.

Figure 2: Current welcome page of the CoACH Website (left), IOS launch page (middle), and software algorithm (right).

CoACH uses all available data to date relating the CFPG to catheterization and/or arm leg pressure data in the setting of CoA. Hence, the software is designed to impart meaning from the CFPG value that is calculated to provide clinicians with interpretation relative to the existing treatment thresholds and BPGpp values (**Figure 3**). This software aims to validate the proposed CFPG assessment and any future BPGpp threshold that is recommended for treatment in patients.

CoA Gradient [mmHg]	CoA Patient CFPG cutoff Discrete	Complex
10	0.81	0.73
15	1.46	1.28
20**	**2.52**	**2.14**
25	4.20	3.45
30	6.90	5.49
35	11.22	8.63
40	18.14	13.47

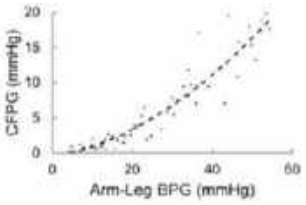

Figure 3: CFPG for a range of clinical CoA gradients (left; ** =current guideline). An example of CFPG to arm-leg cuff BPG in complex CoA patients is shown on the right. This information is incorporated into CoACH to impart meeting from the CFPG value that is calculated, and provide clinicians with interpretation relative to existing treatment thresholds and BPGpp values.

RESULTS

The CoACH software was developed for use on any desired device. The software guides users through the data input process efficiently. After users create their account credentials, they can make a choice between proceeding with clinical or pre-clinical data input. This selection streamlines the subsequent steps tailored to their specific needs. The user then gets the option to choose between the Direct Entry or Image Processing Methods. In the Direct Entry Method, users manually input all required values for the CFPG calculation, with a clear interface illustrated in **Figure 4**. The Image Processing Method prompts users to upload two echo images with Doppler tracings of the subject as shown in Figure 4. Once users complete the input process through either method, they gain access to the database module, which displays a list of all processed subjects, their data and CFPG and interpretation.

Figure 4: Direct Entry method wireframe of the CoACH website (left) and the image processing method wireframe (right).

DISCUSSION

The CFPG formula for assessing CoA severity marks a significant shift from conventional BPGpp guidelines. The current software addresses limitations associated with current approaches, while aiming to foster the eventual rollout and adoption of new treatment guidance, by integrating the CFPG within the CoACH application. The result is expected to be a more accurate, non-invasive, and echo-friendly alternative for assessing BPGpp severity. This advancement is crucial in meeting the demand for precise diagnostic tools in CoA management.

The strengths of CoACH lie in its dual-method CFPG calculation—Direct Entry and Image Extraction—enhancing its versatility across diverse clinical settings. Facilitating assessment of alternative treatment thresholds is a notable advantage, enabling a more nuanced approach to patient care. Also, the image processing method helps limit user variability when determining the values needed from the echo image. Moreover, the use of familiar echo data streamlines the likelihood of adoption to this more accurate and non-invasive diagnostic method. However, the reliance on image processing techniques for the image extraction method may pose challenges in standardization of image masking and segmentation thresholds based on each clinic and their echo image contrast standards, requiring further refinement.

In conclusion, the CoACH software with its included CFPG integration serves as a catalyst to reassess the current BPGpp threshold for CoA. The implementation addresses existing limitations in CoA assessment and lays the groundwork for refining treatment guidelines. This transition holds immense potential in preventing recurrent hypertension in CoA following intervention and enhancing patient care.

ACKNOWLEDGEMENTS

This work was supported by NIH/NHLBI 1R01HL142955. We thank Megan Schoessling and Jessica Stelter for technical assistance.

REFERENCES

[1] Wisotzkey BL, et al., *Cardiol Young*, 25:1348-57, 2015.
[2] Ghorbannia A, et al., *Biomedicines*, 11:1817, 2023.
[3] Alvarez J, et al., *An Pediatr (Engl Ed)*, 96:536 e1-536 e7, 2022.
[4] Palatini P, et al., *J Clin Hypertens*, 20:1100-1103, 2018.
[5] Bird C, et al., *BMJ*, 336:1321, 2008.
[6] Hoffman JI., *Cardiovasc J Afr*, 29:252-255, 2018.
[7] Agasthi P, et al., *World J Cardiol*, 12:167-191, 2020.
[8] Yoganathan AP, et al., *J Am Coll Cardiol*, 12:1344-53, 1988.
[9] Keshavarz-Motamed Z, et al., *J Biomech*, 45:1239-45, 2012.
[10] Feltes TF, et al., *Circulation*, 123:2607-52, 2011.
[11] Ghorbannia A, et al., *J Am Soc Echocardiogr*, 35:1311-1321, 2022.
[12] Hajsadeghi S, et al., *Cardiovasc J Afr*, 23:483-490, 2012.

PLAQUE LENGTH AND STENOSIS INFLUENCE INSTANTANEOUS WAVE-FREE RATIO AND WALL SHEAR STRESS

Arnav Garcha (1), Noelia Grande Gutiérrez (1)

(1) Department of Mechanical Engineering, Carnegie Mellon University, Pittsburgh, PA, USA

INTRODUCTION

Choosing between revascularization and non-surgical therapies to treat coronary non-culprit lesions (NCLs) and mitigate major adverse cardiac events (MACE) is a known clinical challenge [1]. Clinical decisions are typically based on data from angiography or invasive measurements, such as fractional flow reserve (FFR). Revascularization may be considered if an NCL is angiographically significant, i.e., stenosis exceeds 70% or is between 50–69% with FFR ≤ 0.8 [2]. However, other topological features of lesions, such as length, are not commonly used to assess MACE risk and guide clinical treatment.

Several clinical studies suggest that plaque length, high wall shear stress (WSS), and low WSS have prognostic value for MACE [3]–[8]. A recent study analyzing NCL reported that plaques causing MACE were longer compared to quiescent lesions [3]. Instantaneous wave-free ratio (iFR), an alternative to FFR without pharmacological vasodilation [6], falls below the hemodynamic significance threshold (<0.89) for long diffuse plaques [9]. High WSS has been considered to improve MACE prediction by identifying lesions at risk of rupture [7], [10]. Also, recent research suggests low WSS areas independently predict regions of plaque growth [8]. Despite these observational findings, there is little insight into how lesion topology, apart from stenosis, influences these hemodynamic metrics that can support MACE risk stratification.

Computational fluid dynamics (CFD) aids in understanding how lesion topology alters local hemodynamics [11]–[13]. At a constant lesion length, increased stenosis reduces FFR [13]. Without controlling for stenosis, longer lesions correlate with lower FFR in patient-specific anatomies [12]. However, no work has assessed the combined effect of both stenosis and length on iFR, low WSS, and high WSS.

We hypothesize that lesion length, in addition to stenosis, can enhance risk stratification for MACE and inform clinical decision-making regarding revascularization. Using CFD, we conducted a sensitivity analysis of hemodynamic metrics to changes in plaque topology in the left coronary arteries (LCA).

METHODS

Computational experiment design: We used a previously developed computational pipeline [14] to automatically create 3D LCA models, meshes, and simulation files with the SimVascular [15] Python API (Figure 1a). We generated 24 synthetic plaque topologies through a combination of six stenoses (10-60% diameter reduction) and four lengths (0.9-2.5 cm) on a baseline LCA model. Geometric features of the LCA model, including branch diameters, bifurcation angles, and arterial segment lengths, were set to match population averages from published angiographic data [16]. We introduced plaque in the proximal left anterior descending (LAD) artery (Figure 1b). Plaque geometric parameters were obtained from the PREDICTION [8] and PROSPECT [17] clinical trials. The average reported plaque length was 1.7 cm [18], and the average stenosis was near 30%. The starting location of plaques was the same in all models, and all plaques surfaces were smooth.

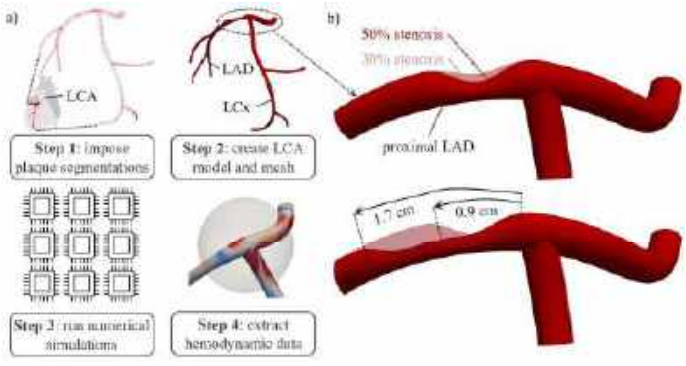

Figure 1: (a) computational pipeline used to build synthetic LCA geometries with varying plaque topologies. (b) Variations in plaque included changes in stenosis and length.

Numerical approach: We used the SimVascular finite element solver to solve the incompressible Navier-Stokes equations that govern blood flow. We employed a tetrahedral mesh with a boundary layer averaging 3 million elements. Mesh parameters were based on a convergence study. The time step was set to 0.001 s. We ran transient CFD simulations for four cardiac cycles to reach a converged solution and used data from the last cycle for the hemodynamic analysis.

Boundary conditions and assumptions: At the inlet, we prescribed a parabolic flow waveform at 70 bpm. Model outlets were coupled to a 0D lumped-parameter model (LPN) to achieve physiological pressures [19]. We manually tuned the LPN to obtain a 120-80 mmHg pressure waveform. Walls were assumed rigid, and zero velocity, no-slip conditions were applied [20]. The flow was assumed laminar as Re $<$ 500. We modeled blood as a Newtonian fluid (dynamic viscosity = 0.04 dynes/cm^2, density = 1.06 g/cm^3), given an average shear rate $>$ 100/s.

Hemodynamic metrics and data analysis: An automatic pipeline was used to analyze hemodynamic simulation results. We computed time averaged WSS (TAWSS), areas of low TAWSS (ALWSS), areas of high TAWSS (AHWSS), and mean velocities at each arterial segment. Low (< 0.5 Pa) and high (> 7 Pa) TAWSS thresholds were defined based on published data for plaque growth and rupture risk, respectively [21]. Since the location of low shear areas varied across models, we measured the percent difference in ALWSS throughout the entire LAD with respect to the mildest plaque geometry (10% stenosis, 0.9 cm). To quantify high shear, we normalized AHWSS to the surface area of the arterial segment with plaque. We measured iFR as the ratio of pressure directly distal to the plaque (P_d) and inlet pressure (P_a) during mid-diastole [22]. Previous studies have reported that the diagnostic potential of iFR is similar to that of FFR [6]. We performed partial correlation coefficient analyses to assess linear correlations between plaque topology and hemodynamic metrics. We used the Mann-Whitney U test to determine if populations were statistically different.

RESULTS

From our simulation results, we obtained iFR < 0.89 for plaques with 60% stenosis across all lengths (Figure 2a). Stenosis strongly correlated with lower iFR (R=-0.82, p=<0.001), while length weakly correlated with iFR (R=-0.38, p=0.078). Normalized AHWSS strongly correlated with both stenosis (R=0.89, p<0.001) and length (R=0.66, p=<0.001) (Figure 2b). Stenosis moderately correlated with ALWSS in the LAD (R=0.59, p=0.0033), while plaque length correlation was weak (R=0.33, p=0.12) (Figure 2c). The spatial distribution of ALWSS varied based on stenosis. ALWSS shifted further downstream of the plaque when stenosis $\geq$ 50% (Figure 2d). ALWSS was larger in models with stenosis $>$ 30% (n=12) than with stenosis $\leq$ 30% (n=12) (p<0.001).

DISCUSSION

Although plaque length weakly correlated with iFR, we observed that iFR substantially decreases with diffuse plaques when stenosis $\geq$ 50%. This may be related to greater AHWSS in these models, which contributes to higher frictional pressure losses. Furthermore, increased AHWSS may suggest that these plaques are at higher risk of rupture. iFR reduction over plaque length was not as pronounced when stenosis $\leq$ 40%. These results encourage the consideration of both plaque length and stenosis when angiographically evaluating lesions. Also, our findings align with a prior observational study in which diffuse plaques accounted for a higher proportion of lesions with iFR $\leq$ 0.89 [9].

For plaques with stenosis $>$ 30%, increased ALWSS may suggest a higher likelihood of *de novo* plaque growth. The ALWSS location greatly varied between the higher stenosed topologies. As such, the location of ALWSS and *de novo* plaque may not occur immediately distal to the NCL of interest, but rather further downstream.

There are some limitations in our work. We did not measure FFR (requiring hyperemia) sensitivity to plaque topology. Given the discordance of iFR and FFR near their thresholds [23], we will evaluate the differences in their hemodynamic sensitivity in future work.

In conclusion, both plaque length and stenosis correlate with iFR and AHWSS, suggesting that length is influential to these metrics and can relate to adverse hemodynamics. ALWSS was significantly larger in topologies with $>$ 30% stenosis and may indicate lesions more prone to distal plaque growth.

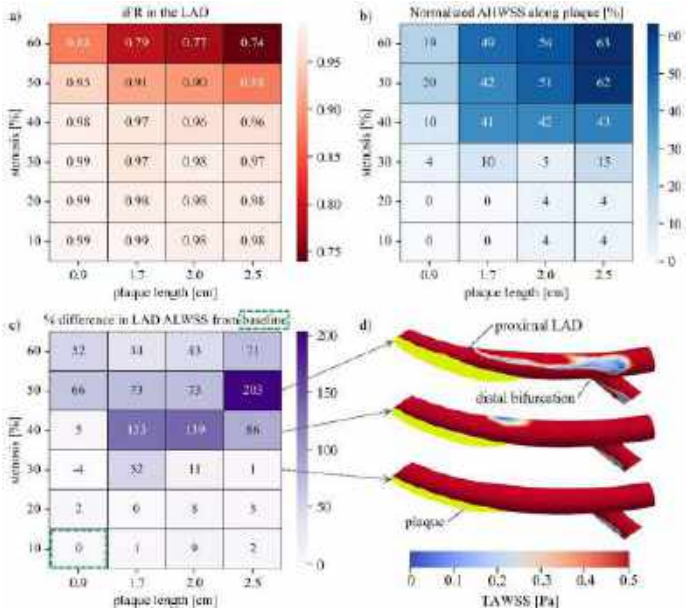

Figure 2: Variations in hemodynamic metrics to stenosis and plaque length, including (a) iFR, (b) plaque-wise AHWSS, (c) percent change ALWSS in the LAD, and (d) TAWSS contours.

ACKNOWLEDGEMENTS

We acknowledge Carnegie Mellon University, Mechanical Engineering, research start-up fund for support.

REFERENCES

[1] Wood *et al.*, *Circulation: Cardio Interv*, 10: e005215, 2017.
[2] Mehta *et al.*, *NEJM*, 381: 1411–1421, 2019.
[3] Safi *et al.*, *Int J Cardiovasc Imaging*, 36: 993–1002, 2020.
[4] Zhu *et al.*, *BJR*, 96: 20220971, 2023.
[5] Gao *et al.*, *Frontiers in Cardiovascular Medicine*, 9: 2022.
[6] Götberg *et al.*, *NEJM*,, 376: 1813–1823, 2017.
[7] Kumar *et al.*, *JACC*, 72: 1926–1935, 2018.
[8] Stone *et al.*, *Circulation*, 126: 172–181, 2012.
[9] Warisawa *et al.*, *Circulation: Cardio Interv*, 12: e007494, 2019.
[10] Eshtehardi *et al.*, *Int J Cardiovasc Imag*, 33: 1089–1099, 2017.
[11] Chiastra *et al.*, *BioMedical Engineering OnLine*, 15: 91, 2016.
[12] Tajeddini *et al.*, *Int J for Numer M in Bio Eng*, 36: e3382, 2020.
[13] Zhang *et al.*, *BioMed Research Int*, 2014: e514729, 2014.
[14] Garcha, A et al, *Bulletin of the American Physical Society*, 2023.
[15] Updegrove *et al.*, *Ann Biomed Eng*, 45: 525–541, 2017.
[16] Medrano-Gracia *et al.*, *EuroIntervention*, 12: 845–854, 2016.
[17] Stone *et al.*, *NEJM*,, 364: 226–235, 2011.
[18] Antoniadis *et al.*, *JACC: Cardio Imag*, 9: 1007–1009, 2016.
[19] Kim *et al.*, *Ann Biomed Eng*, 38: 3195–3209, 2010.
[20] Fogell *et al.*, *Ann Biomed Eng*, 51: 1950–1964, 2023.
[21] Malek *et al.*, *JAMA*, 282: 2035–2042, 1999.
[22] Sen *et al.*, *JACC*, 59: 1392–1402, 2012.
[23] Kovarnik *et al.*, *JAHA*, 11: e021490, 2022.

IOP-INDUCED LAMINA CRIBROSA ASTROCYTE DEFORMATIONS MEASURED DIRECTLY FROM THE ASTROCYTES ARE LARGER THAN THOSE ESTIMATED FROM THE DEFORMATIONS OF THE COLLAGEN BEAMS

Bingrui Wang (1), Susannah Waxman (1), Sofia A. Lusvardi (2), Hannah Schilpp (1), Ashley Linton (1), Yuankai Lu (1), Ian A. Sigal (1,2)

(1) Department of Ophthalmology, University of Pittsburgh, Pittsburgh PA, United States
(2) Department of Bioengineering, University of Pittsburgh, Pittsburgh PA, United States

INTRODUCTION

Glaucoma, a leading cause of irreversible blindness globally, is characterized by progressive retinal ganglion cell death and optic nerve degeneration [1]. Degeneration starts within the lamina cribrosa (LC) in the back of the eye (**Figure 1**) [1]. Although elevated intraocular pressure (IOP) is the main risk factor for glaucoma, the mechanisms leading to the neural tissue damage are not well understood. One of the leading theories postulates that elevated IOP causes distortion of the LC astrocytes, which triggers structural and functional changes that contribute to the neural tissue degeneration [2]. Assessing this theory requires characterizing the IOP-induced distortions of the LC astrocytes. Doing this, however, has proven elusive. Some studies have managed to do this in mouse models taking advantage of their small size [3]. While interesting, the mouse LC lacks some of the main features of the primate LC, such as collagenous beams that likely affect how LC astrocytes respond to IOP. Other studies have instead used imaging techniques that reveal the collagenous LC beams, such as optical coherence tomography (OCT) or second harmonic imaging (SHG), and used the effects of IOP on these beams to estimate distortions on astrocytes [4, 5]. While exciting because this allows in vivo and in situ evaluation of the collagenous primate LC, this approach requires major assumptions about the properties and location of the LC astrocytes. It remains unclear whether the approach accurately represents the effects of IOP on the astrocytes themselves.

Our goal was to measure the IOP-induced LC astrocyte deformation directly from images of the astrocytes and compare these with the deformations estimated from images of the LC collagen beams.

METHODS

Six sheep eyes were obtained within 4 hours of death and the LC was exposed coronally. Individual LC astrocytes were stochastically labeled in situ with DiOlistic labeling [6]. LC collagen and labeled astrocytes were imaged with SHG and multiphoton microscopy, respectively, at low (5mmHg) and high (40mmHg) IOPs.

We measured two astrocyte deformations: 1) indirect, based on the images of collagen, and 2) direct, based on the images of astrocyte. For both methods an image morphing technique [7] was used to determine the displacement fields from low to high IOPs. For each astrocyte, for each of the displacement fields we calculated three measures of deformation: stretch (maximum principal strain), compression (minimum principal strain) and shear (maximum shear strain).

Ten LC astrocytes were analyzed. A linear regression model was then fit to use as a calibration between both measurement approaches.

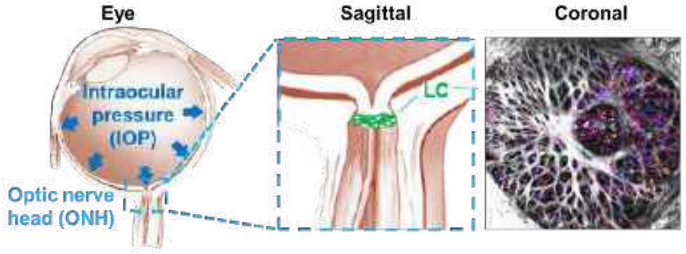

Figure 1. Diagrams of the eye showing the location of the lamina cribrosa (LC), within the optic nerve head in the posterior pole. Image of a coronal section after DiOlistic labeling shows the collagen beams in greyscale and astrocytes in colors.

RESULTS

As IOP was increased from 5 mmHg to 40 mmHg, both collagen and astrocytes deformed (**Figure 2**).

Strain distributions of an example astrocyte calculated directly or indirectly are shown in **Figure 3**. The astrocyte deformation determined directly was greater and more irregular than that obtained indirectly, across all three types of strains. The largest strains were often in the astrocyte branches.

Across the three strains, directly determined astrocyte strains were positively related to indirectly measured strains (**Figure 4**). However, indirect estimates consistently underestimated LC astrocyte strains.

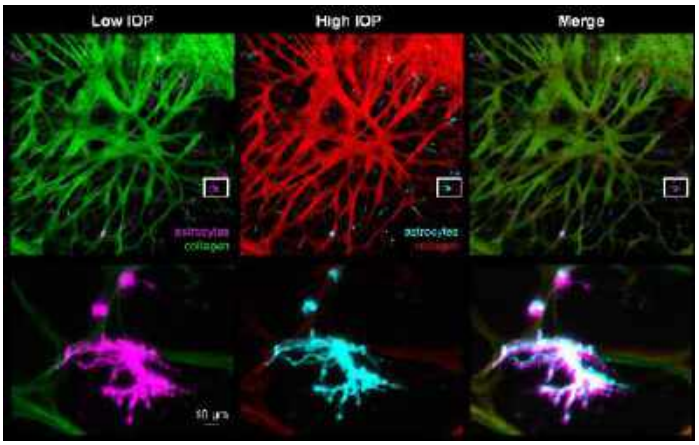

Figure 2. Example LC collagen and astrocytes in situ. Wide views (top) and close-up to an individual LC astrocyte (bottom).

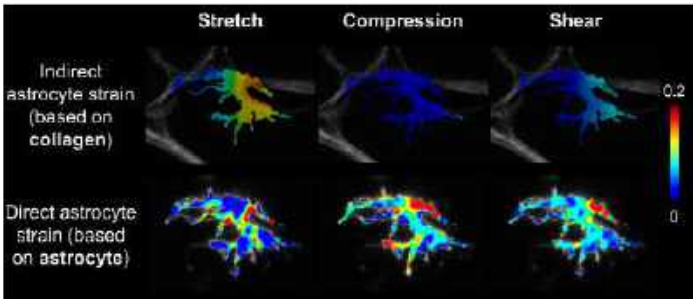

Figure 3. Contour-level plots of IOP-induced strains measured directly (bottom) or estimated indirectly (top). Direct measurement revealed larger and more irregular than indirect estimates.

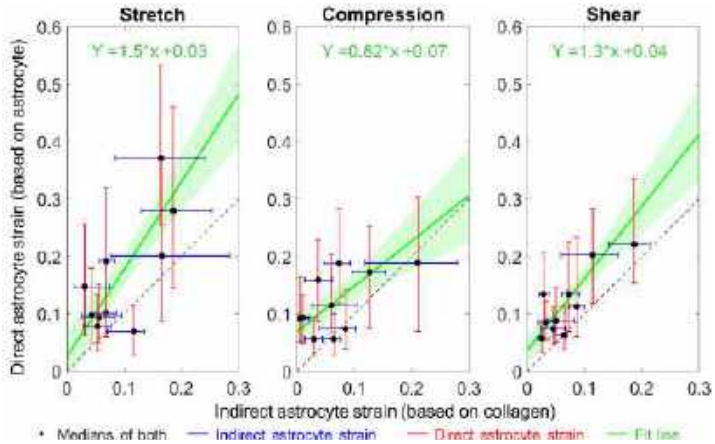

Figure 4. Calibration plots of strain distribution of 10 astrocytes calculated from the collagen and astrocyte images. A black dot is placed at the median values. The blue and red lines indicate the ranges from 25 to 75 percentile of each strain. The green lines show the correlation between the directly and indirectly determined astrocyte strains, with the shaded areas showing the 95% confidence bounds. The grey dashed line is a 1:1 reference. Note how most of the cases are above this line, indicating the overpredicted strains.

DISCUSSION

Our goal was to measure in situ IOP-induced LC astrocyte deformations directly from the astrocytes and compare them with those estimated from the surrounding LC collagen. We point out three main findings arising from this work:

1. It is possible to measure in situ the IOP-induced LC astrocyte and collagen deformations quasi-simultaneously. The techniques we deployed, including DiOlistic labeling allowed visualizing and quantifying LC astrocyte and collagen deformations in the context of their tissue environment. This enables new opportunities to better understand the interplay between mechanical and biological factors involved in glaucomatous neurodegeneration.

2. Elevated IOP induces substantial, large, and highly heterogeneous LC astrocyte deformations. These large deformations may increase the sensitivities of the astrocyte and send messages to the surrounding neural tissue. The heterogenous strain distribution suggested different stiffness within astrocytes. Each astrocyte has a distinct structure, generally comprising the body and the branches. The astrocyte body includes the nucleus and is likely to be stiffer. The astrocyte branches, with thin, long, and wavy structures, are potentially to be softer and more flexible [8]. Astrocytes may potentially also vary in sensitivity to deformation, and thus it remains important to continue to characterize both their mechanical and biological responses.

3. Estimates from LC collagen underestimate LC astrocyte deformations. Across the three types of strains, the median and percentile values (25th and 75th) of indirect measurements were generally lower than direct measurements, indicating that the astrocyte strains are underestimated when indirectly measured from collagen. A potential explanation is the structural role of collagen in supporting the LC neural tissues like astrocyte and axons. However, astrocytes are smaller and softer, they may have more flexibility to move, especially within the pore area. This could have major implications for studies of LC tissue deformation made using OCT [9], where the signal seems to come primarily from LC beam scattering. We are not aware of techniques allowing in vivo visualization of LC astrocytes in the collagenous LC.

In summary, we measured in situ IOP-induced LC astrocyte deformations directly and indirectly. We found substantial IOP-induced deformations that were underestimated when measured indirectly. Results from this study are essential to understanding the mechanisms of the IOP-induced and astrocyte-mediated retinal ganglion cell axon damage in glaucoma.

ACKNOWLEDGEMENTS

NIH R01-EY023966, R01-EY031708, P30-EY008098 and T32-EY017271 (Bethesda, MD), the Eye and Ear Foundation (Pittsburgh, PA), Research to Prevent Blindness (unrestricted grant to UPMC ophthalmology, and Stein innovation award to Sigal IA), CIHR PJT-178008, and BrightFocus Foundation.

REFERENCES

[1] Quigley HA et al. *Arch. Ophthalmol.* 99(4):635-649, 1981.
[2] Hernandez MR, et al. *Prog Brain Res.* 173:353–373, 2008
[3] Sun, D, et al. *J. Comp. Neurol.* 516 (1): 1–19,2009.
[4] Sigal IA, et al. *IOVS.* 55(1), 1-15, 2014.
[5] Midgett, D. E., et al. *Acta Biomater.* 96, 385-399, 2019.
[6] Waxman, S., et al, *Exp. Eye Res.* 230:109458, 2023.
[7] Liao, J., et al. *ACM Trans. Graph.* 33(5), 1-12, 2014.
[8] Lu, Y. B., et al. *PNAS.* 103(47), 17759-17764, 2006.
[9] Wei, J., et al. *Transl Vis Sci Technol.* 11(12), 1-1, 2022.

HEMODYNAMIC ASSESSMENT OF CORONARY ATHEROSCLEROTIC LESIONS IN ELDERLY PATIENTS WITH MYOCARDIAL INFARCTION: A LONGITUDINAL STUDY

Diego Gallo (1), Maurizio Lodi Rizzini (1), Alessandro Candreva (1, 2), Jean Paul Aben (3), Claudio Chiastra (1), Barbara Stähli (2), Simone Biscaglia (4), Gianluca Campo (4), Umberto Morbiducci (1)

(1) PolitoBIOMed Lab, Department of Mechanical and Aerospace Engineering, Politecnico di Torino, Turin, Italy
(2) Department of Cardiology, University Hospital Zurich, Zurich, Switzerland
(3) Pie Medical Imaging BV, Maastricht, the Netherlands
(4) Department of Medical Science, University of Ferrara, Ferrara, Italy

INTRODUCTION

The current assessment of coronary atherosclerosis is limited in its ability to identify risk of future adverse cardiovascular events and guide clinical management. This is particularly critical in older patients (≥75 years of age) experiencing myocardial infarction (MI) and multi-vessel coronary artery disease (MVD), as both age and presence of MVD are major drivers of adverse cardiovascular events [1]. Moreover, 75% of older MI patients show MVD at coronary angiography [1]. The recent Functional Assessment in Elderly MI Patients with Multivessel Disease (FIRE) clinical trial [2] has shown the benefits of a physiology-guided management of older MI patients with MVD. Such management pursued complete coronary artery revascularization by treating with percutaneous coronary intervention not only the lesion culprit of MI, but also all functionally significant non-culprit lesions. The benefits consisted in a reduction of mortality and risk of adverse events at 1 year [2], despite previous studies suggested an association of procedural and periprocedural complications with both age and number of treated vessels [1]. In line with the currently emerging evidence supporting the assessment of coronary physiology in older MI patients with MVD, we hypothesize that the incorporation of advanced hemodynamic and anatomical analysis into such assessment may help identify patients at higher risk of complications. In detail, wall shear stress (WSS) profiles obtained from angiography-derived computational fluid dynamics (CFD) simulations and anatomical lesion parameters obtained from 3D quantitative coronary angiography (3D QCA) were calculated in a large patient cohort to predict major adverse events at 1 year and prove the clinical utility of computational hemodynamic modelling.

METHODS

Study participants. 327 patients from the FIRE trial [2] were included (Table 1). Patients with age ≥ 75 years had MI in a clearly identifiable culprit lesion and at least 1 lesion in a non-culprit coronary artery different from the culprit one. The study protocol was approved by local ethics committee and patients provided informed consent.

Quantitative coronary angiography (QCA). Non-culprit vessel geometries were reconstructed based on 3D QCA using two end-diastolic frames at least 30° apart (CAAS Workstation WSS software, Pie Medical Imaging, the Netherlands). The lesion was defined as the coronary segment including the minimum lumen area, delimited proximally and distally by the intersection of the QCA vessel diameter function line with the interpolated reference line (Fig. 1) [3]. The lesion was characterized in terms of percentage area stenosis (%AS) and lesion length, namely the curvilinear distance between the proximal and distal boundary of the lesion segment (Fig. 1). When a patient presented with multiple non-culprit lesions, the one with the highest %AS (i.e., the most severe one) was considered.

Computational hemodynamics. CFD simulations were carried out on the reconstructed 3D vessel geometries using a finite element-based code (CAAS Workstation WSS software, Pie Medical Imaging). In addition to the time-average WSS (TAWSS) magnitude, the variability of the contraction/expansion action exerted by WSS on the endothelium along the cardiac cycle was quantified in terms of topological shear variation index (TSVI) [3,4]:

$$\mathrm{TSVI} = \left\{ \frac{1}{\mathrm{T}} \int_0^{\mathrm{T}} [\mathrm{DIV_w} - \overline{\mathrm{DIV_w}}]^2 \mathrm{dt} \right\}^{1/2} \quad (1)$$

where $\mathrm{DIV_w}$ is the divergence of the normalized WSS vector field [3] and T is the duration of the cardiac cycle. On each vessel geometry, TAWSS and TSVI values were averaged over the lesion.

Outcomes and statistical analysis. Outcome events were death, MI, stroke, or ischemia-driven coronary revascularization occurring within 1 year after the baseline MI. These outcomes were combined to define the primary outcome. Further outcomes at 1 year were contrast-associated acute kidney injury, cerebrovascular accident, and bleeding. Cox proportional-hazard univariate models were fitted to estimate

hazard ratios (HR) for "conventional" risk factors (i.e., clinical and patient variables), %AS, lesion length, TAWSS or TSVI with respect to the outcomes. A p-value < 0.05 was considered significant. Variables found to be significant at the univariate analysis entered in multivariate models to identify independent predictors. The concordance index (C-index) was used to assess the predictive capacity of each model through its interpretation as the weighted average of the area under time-dependent receiver operating characteristic curves.

Table 1: Patient, lesion and outcome characteristics.

	(N=327)
Median age (interquartile range) – years	80 (77-84)
Female sex – no. (%)	130 (39.8%)
Patients with ≥2 non-culprit lesions – no. (%)	96 (29.3%)
Left anterior descending artery – no. (%)	122 (37.3%)
Left circumflex artery – no. (%)	105 (32.1%)
Right coronary artery – no. (%)	100 (30.6%)
%AS (mean±standard deviation) – %	57.1±12.2
Median lesion length (interquartile range) – mm	12.2 (8.8-18.2)
Median TAWSS (interquartile range) – Pa	2.9 (2.0-4.2)
Median TSVI (interquartile range) – m^{-1}	58.7 (31.5-98.0)
Primary outcome event – no. (%)	56 (17.1%)
All-cause death – no. (%)	35 (10.7%)
MI – no. (%)	17 (5.2%)
Ischemia-driven revascularization – no. (%)	16 (4.9%)
Bleeding – no. (%)	17 (5.2%)

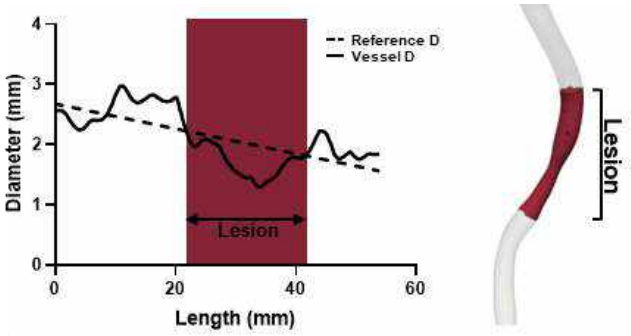

Figure 1: Anatomical definition of the lesion segment.

RESULTS

At the univariate analysis, a higher %AS was associated with a higher risk of the primary outcome (HR 1.02, p=0.041). Longer lesions were associated with a higher risk of all-cause death within 1 year (HR 1.04, p=0.045). TAWSS was not associated with any of the outcomes. Higher lesion TSVI was associated with a higher risk of (i) MI within 1 year (HR 1.01, p=0.012), (ii) ischemia-driven coronary revascularization (HR 1.01, p=0.018), (iii) bleeding (HR 1.01, p=0.012). The addition of anatomic variables (%AS or lesion length) or TSVI to multivariate models based on conventional risk factors led to improvements in the C-index for all predictions (Fig. 2).

DISCUSSION

Lesion severity, length and TSVI represent independent predictors of clinical outcomes within 1 year in elderly patients with MI and MVD, as their predictive ability was maintained in multivariate models with conventional risk factors. The present findings are consistent with the previously reported ability of TSVI in predicting lesion progression over time on swine models [4] and in identifying mild coronary lesions culprit of MI at 5-years follow-up in 80 patients [3]. Despite the shorter follow-up time of 1 year of the present study, the high-risk patient cohort ensured a higher frequency of adverse events compared to previous trials [2]. Notably, no significant predictive ability was found for TAWSS, suggesting that at this advanced stage of coronary disease, the distinct hemodynamic features captured by TAWSS and TSVI may not necessarily concur in determining the risk of complications. The hemodynamic mechanisms contributing to defining that risk are yet to be fully understood. Although the high-risk patient cohort considered here had a high incidence of coexisting illnesses [2], no confounding factors emerged in the analysis.

This study represents the largest investigation to date on the associations between WSS-based haemodynamic quantities and clinical outcomes, an essential step towards proving the clinical utility of computer-based hemodynamic modelling. The present findings may prove helpful to improve the management and the prognosis of patients aged 75 years or older with MI and MVD as it may help identify patients at higher risk of complications, and thus in need of more intensive medical or interventional therapy and close follow-up. Despite the study design is retrospective in nature and based on the ongoing FIRE trial, it offers the advantage of focusing on a patient cohort of relevant clinical interest, paving the way for prospective studies or clinical trials comparing the current best practice with an approach that includes computational hemodynamic modelling.

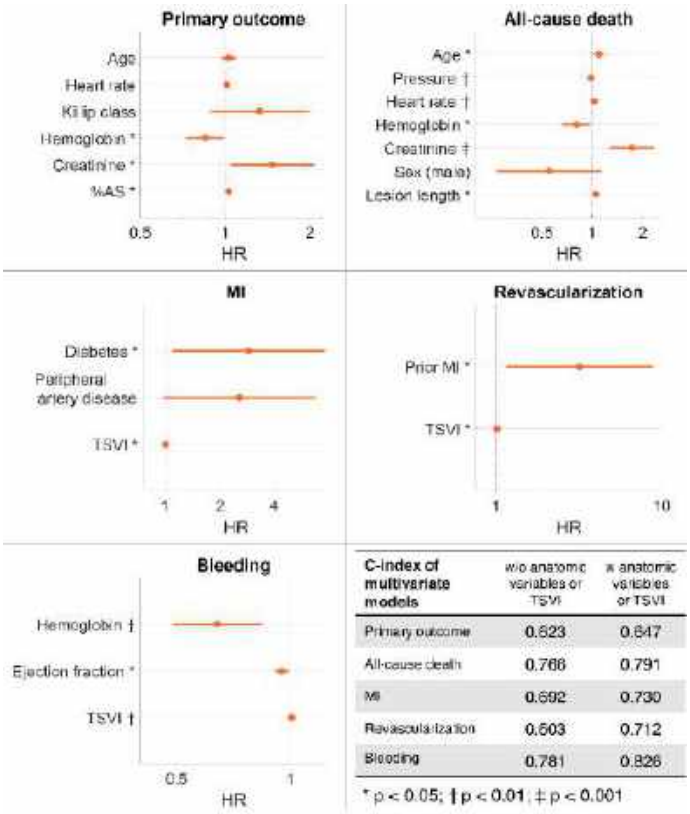

Figure 2: Multivariate analysis with patient and clinical characteristics, and anatomic variables or TSVI.

REFERENCES

[1] Biscaglia, S et al., *Am Heart J*, 229:100-109, 2020.
[2] Biscaglia, S et al., *N Engl J Med*, 389:889-98, 2023.
[3] Candreva, A et al., *Atherosclerosis*, 342:28-35, 2022.
[4] Mazzi, V et al., *Ann Biomed Eng*, 49(9):2606-2621, 2021.

SB3C2024
Summer Biomechanics, Bioengineering and Biotransport Conference
June 11-14, Lake Geneva, WI, USA

MODELLING VASCULARIZATION IN THE HEALING CALLUS AFTER FRACTURE

Joseph P. Soldenwagner, Mahsa Dabagh, Priyatha Premnath
Biomedical Engineering, University of Wisconsin Milwaukee, Milwaukee, Wisconsin, United States

INTRODUCTION

Healing of a fracture begins with an inflammatory response that isolates the damaged tissue by generating a hematoma. Then by intramembranous and endochondral ossification new bone is formed. Depending on the local mechanical microenvironment, progenitor cells differentiate into chondrocytes or osteoblasts. Along the periosteal and endosteal surfaces progenitor cells undergo direct bone formation or intramembranous ossification, and where there is motion in the fracture gap the progenitor cells differentiate into chondrocytes and undergo endochondral ossification [1]. During healing, these chondrocytes mature to hypertrophy and produce vascular endothelial growth factor (VEGF) inducing angiogenesis [2]. This causes vascular invasion of the cartilage callus leading to mineralization of the cartilage matrix and formation of trabecular bone. Trabecular bone then turns into cortical bone through the actions of osteoblasts and osteoclasts.

Vascularization is the formation of blood vessels within tissues and is one of the most important factors in promoting bone healing at the fracture site [3]. Angiogenesis, a crucial component, is the process of new blood vessels forming from existing ones. This response is initiated from the damaged tissue caused by the fracture. Blood vessels transport oxygen, blood, and other essential nutrients to bone cells, vital for regeneration. Vasculature is vital for the success of bone healing, as it removes waste products, promotes cell migration, supports angiogenesis, and contributes to the complex processes in bone repair [4].

The objective of this research is to investigate the relationship between vascularization and the chondrocyte-to-osteoblast transdifferentiation pathway. We will generate a model of a tibial fracture callus including bone, callus and blood vessels. Next, we will employ COMSOL to produce a finite element model to assess how various biological and mechanical elements, and vasculature invasion affect the healing of bone.

METHODS

Bilateral tibial fractures were performed on 26 mice, and 3 without for control, all weighing an average of 26 grams. The mice were properly cared for following institutional IACUC guidelines, and sacrificed at 1 week, 2 weeks, 3 weeks, and 4 weeks. The fractured tibias were harvested and imaged using microCT (Xradia, Zeiss) at a resolution of 6um. Bone, callus and vasculature geometries were segmented using MIMICS. Three-dimensional geometry of bone, callus and vasculature were built in MIMICS and exported as .stl files (Figure 1). The geometries were then smoothed in Mesh mixer. After the 3D model was generated of the fracture callus, it was imported into COMSOL to analyze the various mechanical properties of the fracture callus after 4 weeks of healing. The parameters set in COMSOL were elastic modulus (0.1 MPa), stiffness (13.95 N/mm) and Poisson ratio (0.45). These values were based off literature from [5].

RESULTS

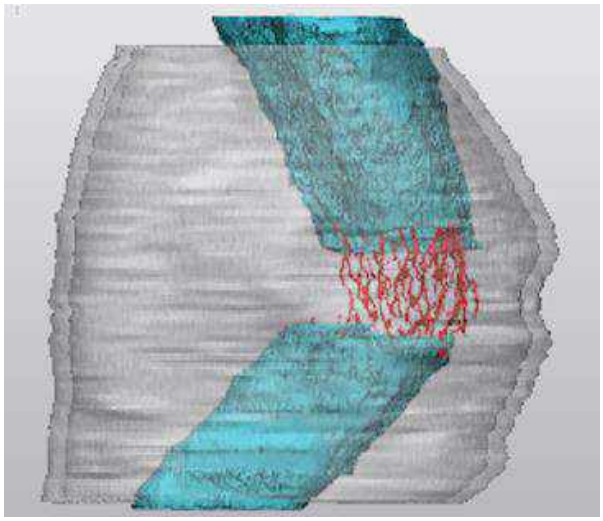

Figure 1: 3-matic model of fracture callus, bone, and vasculature

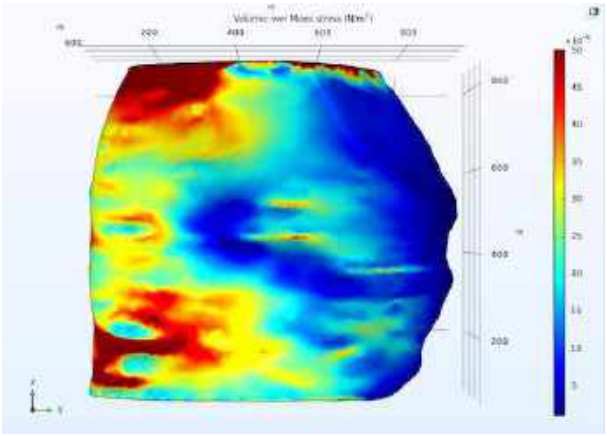

Figure 2: Von Mises stress distribution over the fracture callus

Figure 1 shows a 3D geometry of the fracture containing the vasculature, bone, and callus. The callus is the outer clear gray bubble around the bone, which is blue. The vasculature is in is between where the bone is separated. Figure 2 shows the distribution of Von Mises stresses over the callus surface. Here, we modeled the callus as one homogenous media and presence of bone and vasculature are not included in this model. However, Figure 2 demonstrates that the anatomical geometry of callus leads to significantly different stress values within the callus width and its height.

DISCUSSION

This study is investigating the relationship between vascularization and the chondrocyte-to-osteoblast transdifferentiation pathway in 3D model of a tibial fracture callus. Our results of Von Mises stresses within the callus (Figure 2) show what areas of the callus are under the most stress. We observed high gradients of stresses within the callus width at its central region. Furthermore, the left side (posterior) of the callus is experiencing higher stresses whereas the right side (anterior) is showing lower stresses. A comparison between Figure 1 and 2 demonstrates that the location of bone may impact the stress distribution. This study is the first step in understanding how the stress magnitude correlates with vascularization in the fractured callus. With further research the goal is to include the bone and vasculature in the computational model and observe and compare how they relate to the areas of the callus that are under more stress. Understanding how fractures heal is crucial for developing more effective clinical treatments. This understanding can lead to the creation of therapies that speed up the healing process, which is essential for minimizing patient recovery time, enhancing quality of life, and reducing complications linked to prolonged immobility. Research on fracture healing also plays a key role in advancing our knowledge of bone regeneration, especially in cases involving large bone defects or non-union fractures where traditional healing methods may fall short. Recognizing the factors influencing fracture healing aids in the identification and management of potential complications. Fracture healing research significantly contributes to better patient outcomes, shorter recovery periods, advancements in medical interventions, and overall improvement in the comfort of individuals recovering from fractures [6].

REFERENCES

[1] Diane P. Hu, PubMed 144, 221-234, 2017
[2] Joe Kodama, ScienceDirect 17, 2022
[3] Miller G. J, PubMed 14, 1239-1253, 2015
[4]Zhilun Zhou, Frontiers in Bioengineering and Biotechnology, 2022.
[5] Jared A. Weis, National Library of Medicine, 2009.
[6] Steve Stegen, ScienceDirect 70, 19-27, 2015

SB³C2024
Summer Biomechanics, Bioengineering and Biotransport Conference
June 11-14, Lake Geneva, WI, USA

NEOCARTILAGE CELLULAR MORPHOLOGY AND STRAIN PROFILES ARE IMPROVED BY PHYSIOLOGIC TGF-β DOSES

Yifan Peng (1), Tianbai Wang (2), Sedat Dogru (3), Celina C. Maldonado (1), Michael Albro (1,2,3)

(1) Department of Biomedical Engineering, Boston University, Boston, MA, USA
(2) Materials Science and Engineering, Boston University, Boston, MA USA
(3) Mechanical Engineering, Boston University, Boston, MA USA

INTRODUCTION

Cartilage tissue engineering is a promising osteoarthritis (OA) treatment strategy whereby cell-seeded scaffolds are cultivated to generate neocartilage repair tissues. The long-term survival of neocartilage is dependent on its ability to recapitulate the complex spatial distribution of the composition, structure, and material properties of native hyaline cartilage, which are requisite for load-supporting functionality. This includes both a stiff extracellular matrix (ECM), comprised of dense glycosaminoglycans (GAG) enmeshed within a fibrous type-II collagen (Col-II) network, and a sparse arrangement of chondrocytes isolated within a soft annular type-VI collagen pericellular matrix (PCM). This configuration modulates the transmission of physiologic loads to cells, allowing for the optimal chondrocyte biosynthetic responses needed to maintain cartilage homeostasis.

Transforming growth factor beta (TGF-β) has emerged as one of the most prominent mediators of cartilage regeneration due to its capability to enhance chondrogenesis and accelerate ECM biosynthesis. Conventionally, TGF-β is administered to construct-embedded cells at highly supraphysiologic doses (10-100 ng/mL of active form), representing activity levels that are 10-1,000-fold higher than those present during native cartilage development. Recently, our group has advanced the novel hypothesis that the recapitulation of physiologic TGF-β doses (0.1-1ng/mL), akin to those presented to cells during native cartilage development[2], can yield improved cartilage regenerative outcomes. Our recent work has illustrated the ability of physiologic TGF-β dose administration to yield native-matched neocartilage mechanical properties and GAG content while producing a tissue quality more characteristic of hyaline cartilage, including notably 1) a reduction in the deposition of fibrocartilage-associated Col-I and 2) a reduction in the degree of clustering of chondrocytes induced by cell hyperplasia. The clustered morphology in response to supraphysiologic TGF-β is a striking, potentially detrimental outcome, given its reminiscence to the clustered chondrocyte morphology observed in OA, cartilage. In consideration of the importance of tissue composition and structure on chondrocyte biosynthesis, the native-like isolated cell morphology achieved by physiologic TGF-β may improve the long-term health of neocartilage post-implantation.

In this study, we aim to better understand the physiologic implications of cell morphology outcomes derived from TGF-β dosing on long-term neocartilage tissue function. Here, we performed computational analyses and experimental measures of chondrocyte strain profiles in response to physiologic loading for neocartilage cultivated with physiologic (0.3 ng/mL) or conventional supraphysiologic (10 ng/mL) TGF-β dosing. Further, in order to better understand the implications of cell morphology on tissue structure, we examined the effect of physiologic and supraphysiologic TGF-β dosing on the spatial distribution of the PCM.

METHODS

Tissue Constructs: Primary immature bovine articular chondrocytes were seeded in 2% w/v type VII agarose at 30×10^6 cells/mL and cultured in chondrogenic media supplemented with active TGF-β3 at a physiologic (0.3ng/mL) or supraphysiologic dose (10ng/mL) for the initial two weeks or maintained free of TGF-β (0ng/mL). **Mechanical Assessment**: After 56 days of culture, E_Y of constructs (n=5 per group) was measured in response to 10% unconfined compression. **Cell Morphology**: After 56 days of culture, live constructs (n=4 per group) were diametrically halved and cross-sections were stained with calcein AM and imaged under a confocal microscope. Cellular regions were identified by adaptive Gaussian thresholding and active contouring[5,6], and the fraction of cells in a clustered morphology (cell cluster area fraction [CAF]) versus isolated was determined based on the area and circularity of cell regions[7] using lab-developed code in MATLAB (MathWorks). **PCM Staining**: Constructs (n=5 per group) were fixed after 56 days of culture, paraffin sectioned, and stained for Col-VI (Invitrogen) to detect the PCM. **FEA Cell Strains**: An FEA model was implemented in MATLAB (MathWorks) to predict stress and strain of cells in native cartilage and TGF-β exposed constructs (0.3 or 10 ng/mL TGF-β) in response to applied physiologic loading (applied

compressive static stress=20 kPa). Confocal-derived cell morphology images were binarized and used in the model. Triangular mesh elements (maximum element size: 1 pixel^2; minimum element size: 0.2 pixel^2; number of elements: 825,000) and a linear elastic constitutive relation for cells and ECM was employed. Cellular region mechanical properties were prescribed from prior work (E_Y =1 kPa[8]; ν =0.4[9]). ECM region properties were prescribed from previously measured bulk tissue stiffness (E_Y; 0.3 ng/mL: 630 kPa; 10 ng/mL: 550 kPa; native cartilage: 590 kPa) and prior work (ν=0.2[10]). **Experimental Cell Strains**: At day 56, constructs were diametrically halved, calcein AM stained, and confocal imaged before and after the application of a 40% platen-to-platen axial compressive strain using a custom-made apparatus. The engineering strain ($L-L_0/L_0$) was computed for cellular regions within groups consisting of isolated cells (constructs treated with 0.3 ng/mL), small clusters (constructs treated with 10 ng/mL), and large clusters (constructs treated with 10 ng/mL) (n=3 per group) via ImageJ.

RESULTS

Neocartilage E_Y was enhanced to a similar degree by 0.3ng/mL (629±58kPa) and 10ng/mL (550±75kPa) doses, relative 0ng/mL (179±65kPa). Cell clustering was significantly enhanced by 10ng/mL exposure (CAF=0.79±0.05), relative to 0ng/mL (CAF=0.10±0.01) (Fig. 1A; $p<0.0001$). In contrast, 0.3 ng/mL significantly mitigated cell clustering (CAF=0.18±0.03; $p<0.03$) at a level only marginally above 0ng/mL levels (Fig. 1B). Col-VI staining illustrated a highly organized annular PCM around isolated chondrocytes, akin to native morphology, while 10ng/mL induced a far less organized PCM around clusters (Fig. 1C). Minimum principal strains for ECM and cellular regions were predicted in response to 20 kPa axial compression (Fig. 2A). Models demonstrated that the clustered cellular regions derived from 10 ng/mL exposure exhibited an elevated and more disperse strain distribution (ε=0.33±0.11) relative to more isolated cellular regions derived from 0.3ng/mL (ε=0.21±0.06) or cells in native cartilage (ε=0.21±0.05) (Fig. 2B). Experimental measures of cell strains exhibited similar trends where cell region strains were elevated in large clusters (ε=0.23±0.02), relative to isolated cells (ε=0.07±0.02; Fig. 2D&E; $p<0.002$).

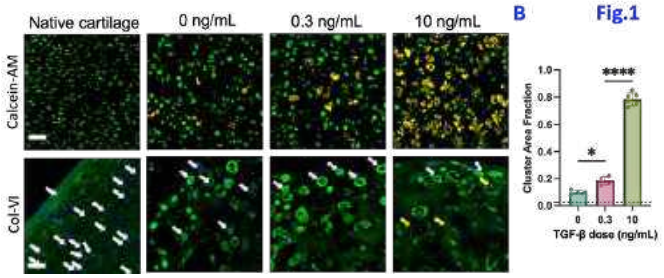

Fig. 1: (A) Representative confocal images showing isolated (green) and clustered (yellow) cell regions in day 56 constructs from physiologic (0.3ng/mL) and supraphysiologic (10ng/mL) TGF-β supplementation doses. Scale bar: 100 µm. (B) Cell cluster area fraction (CAF) of constructs. Dashed line: CAF of native cartilage (<0.01). *p<0.03, ****p<0.001. (C) Representative images showing nuclei (blue) and Col-VI of PCM (green). White arrow: isolated cells and PCM. Yellow arrow: clustered cells and PCM.

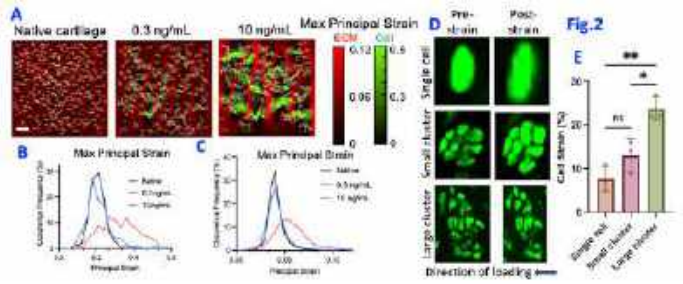

Fig. 2: (A) FEA model derived color maps of minimum principal strain in cells (green) and ECM (red) regions. (B, C) Frequency plots of minimum principal strain in (B) cellular and (C) ECM regions. Scale bar: 100 mm. (D) Representative confocal images of cellular region of different cell morphology pre- and post- 40% compressive strain. Single cells: constructs treated with 0.3 ng/mL TGF-β. Small and large clusters are from constructs treated with 10 ng/mL TGF-β; (E) Cell strain of different cellular regions: ns p>0.12, * p<0.03, **p<0.002.

DISCUSSION

The formation of dense chondrocyte clusters in response to supraphysiologic TGF-β is a striking outcome when considering their similarity to the morphology of pathologic chondrocyte clusters classically observed in OA[11]. Clusters likely result from TGF-β-induced cell hyperplasia while in the confines of an agarose scaffold that restricts cell expansion. FEA analysis and experimental measures together illustrate an important consequence of this aberrant morphology, whereby clusters exhibit elevated and highly heterogeneous strain profiles in response to physiologic tissue loading. Given the high sensitivity of chondrocytes to strain magnitude, it is reasonable to surmise that clustered cells may lose their ability to respond in unison to physiologic mechanical stimuli. Cell clusters are additionally accompanied by an aberrant PCM morphology that may further exacerbate mechanobiological dysregulation. In future work, we aim to better elucidate potential consequences of these PCM abnormalities by performing investigations into calcium signaling[12] and growth factor release[13] in response to mechanical loading. In contrast, cartilage regeneration in the presence of physiologic TGF-β dosing promotes neocartilage with native-matched mechanical properties while maintaining a healthy, more isolated cell morphology. As such, these cells may retain the ability to provide a harmonious response to loading, thus better recapitulating the mechanobiological behavior needed to maintain long-term tissue health. In the future, we aim to perform investigations into long-term functional consequences of aberrant cell morphology in neocartilage and examine potential benefits of physiologic TGF-β administration in improving the long-term tissue health.

ACKNOWLEDGEMENTS

This work was supported by NIAMS AR078299, NIH S10OD024993, and the Boston University Dean's catalyst award.

REFERENCES

[1] Guilak, F et al., *Matrix Biol*; 71-72: 40–50, 2018. [2] Albro, MB et al., *J Biomechanics*; 46(8), 2023. [3] Madry, H et al., *Tissue Eng Part B Rev*; 20, 2013. [4] Wang, T et al., *SB3C*; Abstract no.214, 2023. [5] Kumar, BK et al., *Signal Image Video P*; 7, 2013. [6] Chan, TF et al., *IEEE Trans Image Process*; 10:266-77, 2001. [7] Schmitt, O et al., *Comput Vis Image Underst*; 113, 2009. [8] Guilak, F et al., *Osteoarthritis Cartilage*; 7: 59-70, 1999. [9] Trickey, WR et al., *J Biomech*; 39:78-87, 2006. [10] Jurvelin, JS et al., J Biomech; 30: 235-41, 1997. [11] Lotz, MK et al., *Arthritis Rheum*; 62(8):2206-18, 2010 [12] O'conor, CJ et al., *PNAS*; 111(4):1316-1321, 2014. [13] Ng, KW et al, Cell Mol Bioeng; 2(3): 386-394, 2009

INVESTIGATING THE ROLE OF WALL STRESS IN AORTIC GROWTH OF ACUTE UNCOMPLICATED TYPE B AORTIC DISSECTION USING FLUID-STRUCTURE INTERACTION ANALYSIS

Minliang Liu (1), Yuxuan Wu (3), Adam Mazlout (2), Yuhang Du (1), Rishika Agarwal (2), Hannah L. Cebull (4), Marina Piccinelli (4), John A. Elefteriades (5), Rudolph L. Gleason Jr (2,3), Bradley G. Leshnower (6)

(1) Department of Mechanical Engineering, Texas Tech University, Lubbock, TX, USA
(2) Department of Biomedical Engineering, Georgia Institute of Technology and Emory University, Atlanta, GA, USA
(3) School of Mechanical Engineering, Georgia Institute of Technology, Atlanta, GA, USA
(4) Department of Radiology & Imaging Science, Emory University, Atlanta, GA, USA
(5) Aortic Institute at Yale-New Haven Hospital, Yale University School of Medicine, New Haven, CT, USA
(6) Department of Surgery, Emory University School of Medicine, Atlanta, GA, USA

INTRODUCTION

Type B Aortic Dissection (TBAD) is a lethal disease with an incidence of 4 per 100,000 patients per year[1]. TBAD occurs when a tear develops in the inner lining (intimal layer) of the aorta, causing the layers of the aortic wall to separate (dissect) creating "true" and "false" lumens. In the acute setting, patients with TBAD are categorized as either "uncomplicated" or "complicated" based on the presence of organ malperfusion or aortic rupture. Complicated TBADs have a high in-hospital mortality rate and require emergent thoracic endovascular aortic repair (TEVAR). Uncomplicated TBADs have been traditionally managed with optimal medical therapy (OMT) consisting of an aggressive anti-hypertensive regimen and surveillance imaging. OMT results in low-in-hospital mortality rates; however, OMT produces dismal long-term survival rates of 48-66% and overall intervention-free survival rates of < 50% secondary to aortic aneurysm formation and rupture[2]. Aortic expansion is the most important factor that determines the long-term survival of TBAD patients. For about 73.3% TBADs[3], OMT results in aortic expansion and aneurysm formation at five years.

The complex interplay between hemodynamics and tissue biomechanics alters the aortic wall growth and remodeling. The ability to predict aortic growth would help identify patients at risk of aneurysm formation and would benefit from early intervention (e.g., TEVAR) versus those who would have a stable aortic diameter and can be sufficiently treated with OMT. In this study, we analyzed 6 uncomplicated TBAD patients and obtained the initial CT scans of the acute phase taken during their first diagnosis and additional follow-up CT scans. We developed a computationally efficient one-way fluid-structure interaction (FSI) framework to compute wall stress distributions of patient-specific TBAD geometries. Using FSI, we computed structural wall stress distributions of acute uncomplicated TBADs based on the initial baseline CT scan. We investigated whether the wall stress field of the initial CT scan is associated with the distribution of the local aortic growth rate.

METHODS

We retrospectively collected contrast CT images, transthoracic echocardiographic data, and demographics of 3 male and 3 female patients who were initially treated with OMT. Three-dimensional patient-specific geometries of the dissected thoracoabdominal aorta (including arteries that branch from the aorta), dissection flap, and intraluminal thrombosis were segmented from the initial baseline CT scans. The segmentations were then used to construct fluid domain and solid domain meshes for FEA and CFD simulations. The aortic wall and dissection flap were primarily meshed using 3D hexahedral elements, with preserved nodal connectivity between the aortic wall, flap, and thrombus.

Conventional two-way, fully-coupled fluid-structure interaction (FSI) simulation, which couples fluid and solid mechanics solvers, is extremely computationally expensive (e.g., 2 weeks[4]); therefore, two-way FSI analysis usually limits to only ~1 patient in the literature and could be prohibitively time-consuming to be adopted here. Hence, we developed a simplified, one-way FSI workflow, which is significantly less computationally expensive (< 1 hour). As shown in Figure 1, the

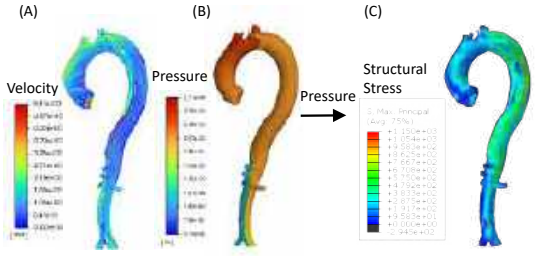

Figure 1: One-way FSI analysis workflow: (A) streamline color-coded with velocity; (B)pressure contour; (C) wall stress field.

one-way FSI analyses were performed using the initial CT scan of each patient with the following steps: (1) patient-specific computational fluid

dynamics (CFD) simulation was performed using velocity inlet flow condition obtained from echocardiography data. Windkessel models with parameters calculated using Murray's law were applied at each pressure outlet to match the blood pressure measurement obtained during the initial hospital admission; (2) the nonuniform pressure distribution of the true and false lumen were extracted from CFD and mapped to the inner aortic wall in the FEA model using an in-house interpolation code; (3) subsequently, stress distributions in the true and false lumen wall, and dissection flap were obtained from structural finite element analysis (FEA) using the CFD-computed pressure distribution as loading condition.

Additionally, distributions of aortic growth rate were quantified using the initial and the most recent follow-up CT scans (range 8-91 months). As can be visualized in Figure 2, the initial TBAD geometry was deformed to match the surface of the follow-up geometry; therefore, the logarithmic strain field can be computed which quantifies the growth in the circumferential direction. The local aortic growth rate was obtained by dividing the strain by the time interval between the initial and follow-up scans. Subsequently, linear regression analysis was performed to investigate the relationship between wall stress and growth rate for each patient.

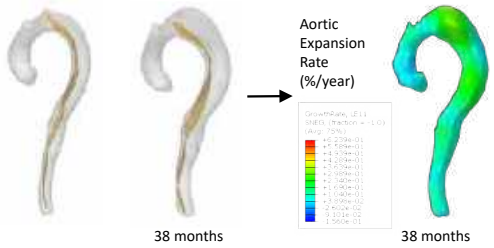

Figure 2: Initial (A) and follow-up TBAD geometries (B) are used to compute the heatmap of local aortic growth rate

RESULTS

FSI simulations indicated a slightly elevated false lumen pressure (137 mmHg) compared to the true lumen (129 mmHg), p=0.59. Structural stress fields computed based on the initial CT scan were compared to the heatmap of the aortic growth rate. 4 representative cases are shown in Figure 3. For all 6 patients, a direct relationship was observed between stress and growth rate: aortic segments experiencing high wall stress exhibited rapid aortic growth. The correlations between stress and growth rate were most evident in P1 and P4.

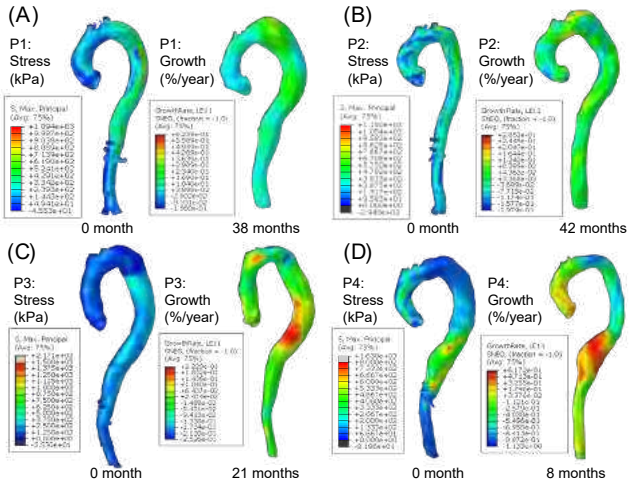

Figure 3: Wall stress distributions and contours of aortic growth rate in 4 representative patients. (A) to (D): P1 to P4.

To quantify their underlying spatial correlation, the wall stress contour and growth rate heatmap were registered to generate scatter data plots. To ensure one-to-one correspondence of the stress and growth data, the stress and growth rate distributions were transformed onto a common mesh template using a non-rigid registration algorithm[5]. Subsequently, the mesh template was divided into 34 equally spaced regions; therefore, the averaged stress and growth rate of each region can be plotted to quantify the spatial correlation. Linear regression analyses were performed which revealed positive slopes between wall stress distributions and growth rate heatmaps for all 6 patients. The positive slopes confirmed the observation that the high-stress region was correlated with a faster aortic growth rate. Figure 4 summarizes the positive correlation between wall stress and growth rate for the 4 representative patients.

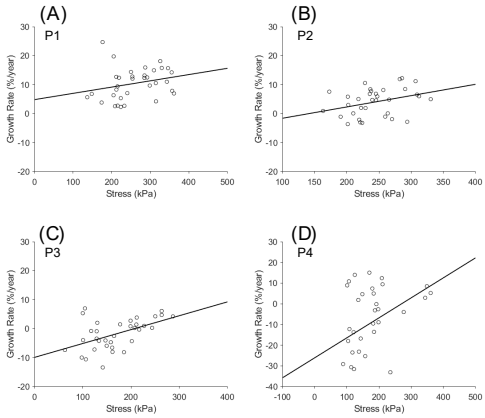

Figure 4: Linear regression analysis demonstrates a positive correlation between wall stress and aortic growth rate in the 4 representative patients. (A) to (D): P1 to P4.

DISCUSSION

In this study, we investigated the association between the wall stress field obtained from the initial CT scan and the distribution of aortic growth rate in uncomplicated TBAD using one-way FSI simulations. Our results indicated that TBAD growth is governed by biomechanical factors. It was found that high wall stress regions were positively associated with high growth rates, which suggests wall stress may be used as a potential predictor for aortic growth rate. By further incorporating growth and remodeling theories into the modeling framework, it is anticipated that the rate and location of aortic growth in acute uncomplicated TBAD may be predicted using information available in the initial baseline CT images.

One-way FSI has been shown to yield accurate true and false pressures compared to two-way FSI in a recent validation study[6].

We are incorporating additional patients into the present FSI study. With more patient data, a threshold stress value may be established to identify patients at risk of fast aortic expansion. Additional biomechanical markers may be identified to predict the risk of aneurysmal formation and the need for early endovascular intervention in acute uncomplicated TBAD.

ACKNOWLEDGEMENTS

This study is supported in part by the National Institutes of Health (R01HL155537).

REFERENCES

[1] Criado et al., *Texas Heart Institute Journal*, 2011.
[2] Leshnower et al., *Annals of Thoracic Surgery*, 2017
[3] Peterss et al., *Journal of the American College of Cardiology*, 2016
[4] Caballero et al., *Journal of the Royal Society Interface*, 2019.
[5] Bone et al., *International Journal of Computer Vision*, 2020.
[6] Zhu et al., *Frontiers in Physiology*, 2022.

COMPRESSION STABILITY OF THREE FIXATION MODES FOR INTRAOPERATIVE FEMORAL CONDYLE FRACTURES DURING KNEE REPLACEMENT

Timothy R. Eastep (1), Brady Killham (1), Yi Hong (1), Cheng-Jen Chuong (1), Dane Wukich (3), Jun Liao* (1), Senthil N. Sambandam* (2)

(1) Department of Bioengineering, University of Texas at Arlington, Arlington, TX, USA
(2) Department of Orthopedic Surgery, Dallas VA Medical Center, Dallas, TX, USA
(3) Department of Orthopedic Surgery, University of Texas Southwestern Medical Center, Dallas, USA

INTRODUCTION

Total knee arthroplasty (TKA) is one of the most performed surgeries to reduce the pain and disability associated with end stage knee osteoarthritis. In total knee replacement surgery, the incidence of intraoperative periprosthetic fracture varies between 0.3% to 4% depending on the patient's risk factors and implants used [1]. Among the fracture types, medial femoral condyle intraoperative fracture is the most common and requires fixation of the fracture [2]. A stable intraoperative fracture fixation is desirable to allow minimal modification to standard total knee replacement protocol. There are various fixation options, but the three commonly used techniques are: (1) Reduce the fracture, fix with screws, and use standard femoral component; (2) reduce the fracture, fix it with plates and screws, and then implant standard component; (3) reduce the fracture and fix it with screws and use a femoral component with a stem attached to the component. The choice of fixation is often determined by surgeon preference with no specific clinical or biomechanical data to support the selection. In this study, we performed incremental cyclic compression testing to assess the mechanical stability of three fixation options.

METHODS

Denuded human right femurs were obtained from Science Care (Phoenix, AZ). Those cadaver femurs are from a similar age range (Male, 65 to 75), with similar size, fresh and no abnormality, and no treatment. Standard knee implants, stem knee implants, bone screws, and locking plates were obtained from Stryker (Addison, TX). With the right femur bones procured and the knee prostheses ready, medial femoral condyle fractures had been created before implantation of the femoral prosthetic component. The fracture had been fixed with three different fixation options, i.e., (1) standard implants with screws alone, (2) Standard implants with locking plate-screws, and (3) Stemmed implants with screws. Instron Machine (Model: 5965) was used for this study. With its TestProfiler software, Instron Machine can apply cyclic loading and unloading, step-by-step loading patterns to mimic the functional use of orthopedic devices. Incremental cyclic compressive loading-unloading protocol up to 1.5 kN (337 lbs) was then programmed to assess the fixation stability and its resistance to cyclic compressive loading.

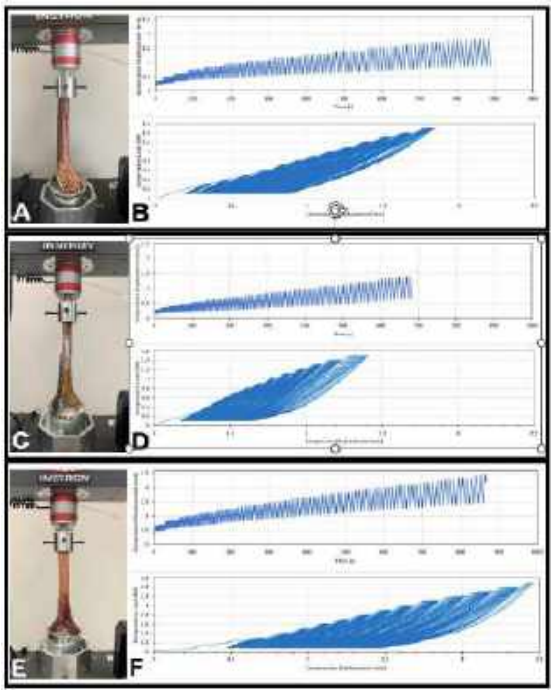

Figure 1: Experimental setup and incremental cyclic compression behavior: (A) & (B) Standard implants with screws alone, (C) &

(D) Standard implants with locking plate-screws, (E) & (F) Stemmed implants with screws.

RESULTS

The mechanical results demonstrated different performances of three fixation options. (1) The locking plate-screws fixation demonstrated the best stability and resistance to cyclic compressive loading. (2) The bone screw-only fixation was able to achieve stability and resistance to cyclic compressive loading similar to the locking plate-screws fixation, only showing slightly lower stability and resistance. (3) The stemmed implants with screws showed the worst stability and resistance to cyclic compressive loading among three fixation options.

DISCUSSION

These important observations point out, under the cyclic axial compressive loading (the dominant, physiologically-relevant loading pattern), the stemmed implants have the worst stability and compressive resistance, the locking plate-screw fixation has the best stability and compressive resistance, and the bone screw only fixation achieves a stability and compressive resistance only slighter lower than the locking plate-screws fixation and might be the most cost-effective fixation option. Furthermore, our observation indicates that the routine use of stemmed implants might not be needed since (i) it is not a stable fixation; (ii) it has disadvantages such as increased bone loss, longer operative time, and higher cost.

ACKNOWLEDGEMENTS

Department of Veterans Affairs NTX Investigator Grant: NIP549

REFERENCES

[1] Lombardi AV, et al., *J Arthroplasty*, 10:643-650, 1995.
[2] Bennett CG, et al., *Arthroplasty Today*. 3(4):253-256, 2017.

AN OPTOGENETIC PLATFORM FOR CONTROLLED RELEASE OF NUCLEOCYTOPLASMIC SHUTTLING PROTEINS

Erin E. Berlew (1,2), Paula Camacho Sierra (1), Joel D. Boerckel (1,2)

(1) Department of Orthopaedic Surgery, University of Pennsylvania, Philadelphia, PA 19104, USA
Department of Bioengineering, University of Pennsylvania, Philadelphia, PA 19104, USA

INTRODUCTION

Dynamic localization of proteins is critical in cell- and mechano-biology, particularly for proteins that shuttle between cellular compartments such as the cytosol and nucleus [1]. Traditional overexpression systems fail to provide a baseline "time zero" for studying shuttling dynamics, limiting readouts to absolute levels of localization at equilibrium without access to nuclear import and export rates. To address this gap, we developed an inducible release system specifically tailored for shuttling proteins.

Existing systems for inducible release are not optimized for mammalian cells [2], are designed for constitutive nuclear localization [3], or anchor the protein of interest to endomembrane organelles, potentially distorting natural nuclear entry dynamics [4]. In this study, we report a protein release system for mammalian cells that anchors proteins of interest (POIs) to the plasma membrane, effectively sequestering them from nuclear importers and other cytosolic factors. Optogenetic recruitment of a protease liberates the POI into the cytosol, enabling real-time tracking of shuttling dynamics. This work presents a new tool for spatiotemporal dissection of shuttling protein dynamics in living cells, including the dynamics of mechanotransduction.

METHODS

In our **two-component system**, blue light recruits a protease to the membrane, where it cleaves and releases a tethered protein of interest (POI) into the cytosol. The first **(protease) component** enables protease-mediated POI release. For our protease, we selected a tobacco etch virus protease (TEV) [2], which is small in size and efficiently cleaves target proteins at a conserved 7-amino acid motif. For optogenetic control, we fused TEV, with mScarlet visualization tag, to the light-sensitive protein, BcLOV4, which binds the plasma membrane via electrostatic interaction in response to blue light [5].

The second **(membrane) component** tethers the protein of interest (POI) to the membrane via a peptide containing the TEV-target motif. To prevent off-target proteolytic cleavage prior to TEV activation, we further added a light-sensitive AsLOV2 domain that protects this cut site in the dark state. Activation with blue light TEV cut site and recruits optogenetic TEV to the membrane for POI cleavage and release.

Protease component fusions were Gibson cloned into the pcDNA3.1 backbone. The membrane component was ordered as a custom synthesis from Twist Biosciences in the pTwist backbone under a CMV promoter. Protease and membrane components were co-expressed in HEK293T cells, at a 4:1 ratio, via transient transfection with lipofectamine. Cells were imaged over a 10-minute time course, with red, green, and blue fluorescence channels imaged every 30 seconds. We imaged N = 15 cells per condition per replicate over three biologically independent replicates. Nuclei and cytosolic regions were manually segmented in Fiji, and fluorescence intensity measurements were calculated using a custom Python script.

RESULTS

System design

We engineered our system to enable three-color imaging for near-simultaneous monitoring of the opto-TEV protease component (visualized in red), the membrane anchor component (blue), and the target POI (green) slated for release (Figure 1). For the protease component, we used BcLOV4, which uniquely enables TEV recruitment to the membrane without an additional engineered protein-protein interaction (as with common heterodimerization systems).

For the anchor portion of the membrane component, we used a modified LCK protein, which docks in the membrane via lipid modification. We had first tried Cdh4, which is commonly used in yeast systems, but this exhibited general localization to endomembrane organelles. In contrast, the modified LCK localized specifically to the plasma membrane. To prevent off-target cleavage of the POI from the membrane anchor component, we added an AsLOV2-TEV cut site fusion protein, separated from LCK by a blue fluorescent protein

(BFP2) visualization tag. AsLOV2 protects the TEV cut site from non-specific cleavage, but undergoes a conformational change in response to blue light that exposes the cut site for cleavage by light-recruited TEV protease. For the POI, we here used fluorescent reporter mNeonGreen, fused to a standard nuclear localization signal (biNLS9) [6].

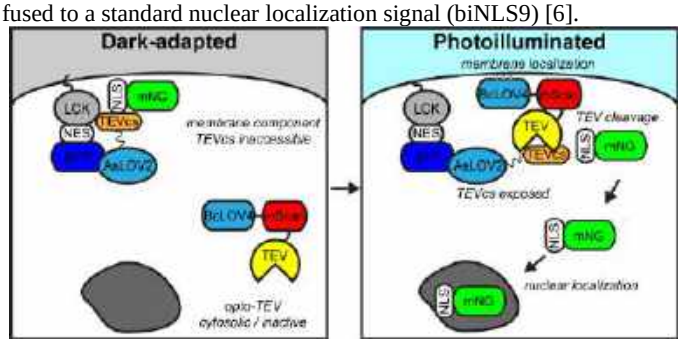

Figure 1: The opto-TEV protease system.

System characterization

We first expressed the membrane component in isolation and quantified its fluorescence within the membrane, cytosol, and nuclear regions, in both blue and green fluorescence channels. We observed a pronounced preferential localization at the membrane in both channels, affirming the specificity of membrane anchoring. After addition of AsLOV2, fluorescence intensities exhibited high correlation across regions, indicating negligible spontaneous cleavage by endogenous cellular proteases.

We identified BcLOV4-mScarlet-uTEV as the protein order permutation with the highest protease activity. We refer to this novel construct as "opto-TEV". We co-expressed the membrane component with either opto-TEV or BcLOV4-mScarlet as a negative control and measured foldchange in nuclear and cytosolic fluorescence of mNeonGreen over the 10-minute optogenetic stimulation time course (Figure 2a-b). Light stimulation had no effect on cytosolic fluorescence in any group, but significantly increase both nuclear fluorescence and nuclear-to-cytosolic ratio in cells that received opto-TEV, indicating proteolytic cleavage of NLS-mNeonGreen by opto-TEV.

To assess the leakiness and off-target cleavage of opto-TEV in the pre-illumination state, we compared mNeonGreen intensities by region at time zero (Figure 2c). We observed no significant differences in the nuclear or cytosolic regions between conditions. We did observe a higher nuclear-to-cytosolic ratio for opto-TEV compared with BcLOV4 control, indicating modest leakiness, but cleavage in the dark state was lower lower than after light activation. Future iterations of the system will minimize the likelihood of productive interactions between the membrane and protease components prior to blue light stimulation, to enhance specificity and efficiency.

DISCUSSION

Here we report a novel system for rapid, inducible release of nuclear and cytosolic proteins from the plasma membrane in mammalian cells via blue light stimulation. This approach enables the direct observation of protein shuttling dynamics from the time of protein release into the cytosol, providing clear advantages in temporal resolution over traditional methods. Importantly, while our proof-of-concept experiments utilized a nuclear localization signal (NLS) fused to a visualization tag as protein of interest (POI), this system is versatile and can be adapted for use with a wide range of POIs, including those without an exogenous NLS, including cytosolic proteins, translocating transcription factors, and proteins containing targeting sequences for other cellular organelles.

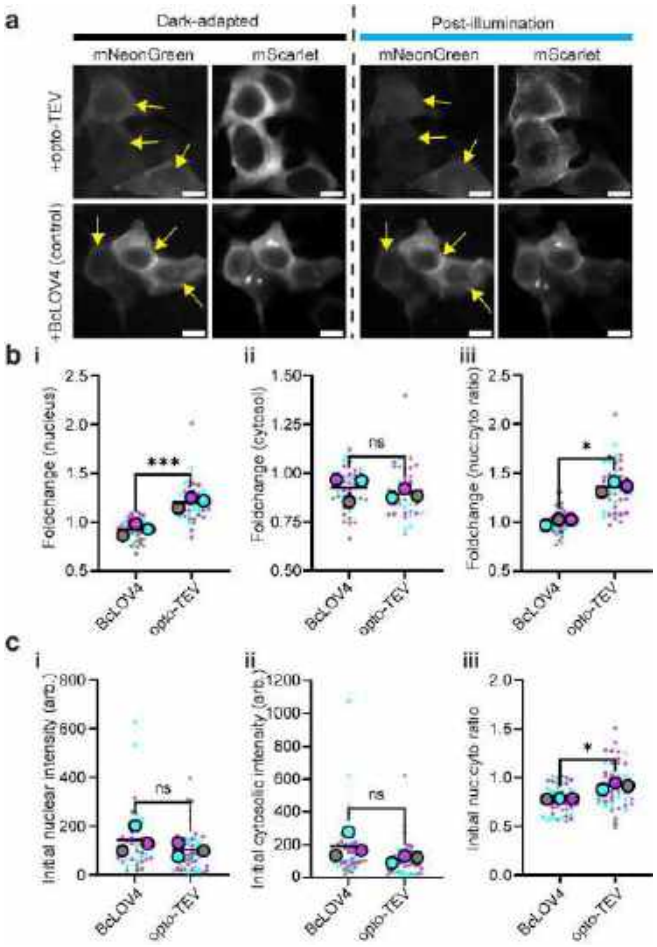

Figure 2: Characterization of the opto-TEV system. (a) opto-TEV and BcLOV4 control co-expressed with the membrane component. Scale = 10 µm. (b) Foldchange in mNeonGreen in by region over a 10-minute stimulation time course. (c) Initial mNeonGreen intensities prior to photoillumination for nuclear (i), cytosolic (ii), and nuclear:cytosolic ratio (iii). (*) = $p < 0.05$, (***) = $p < 0.001$, ns = not significant by T-test.

While dark-state leakiness was low, our future efforts will refine this system to further minimize leakage, enhancing the specificity and efficiency of TEV cleavage. One particularly exciting application of this system, on which we are currently working, is in the study of nuclear import of mechanosensitive proteins, such as the Yes-associated protein (YAP) transcriptional co-activator. Without relying on the fusion of an artificial NLS, we anticipate these applications will provide new insights into YAP transport dynamics and mechanotransduction.

ACKNOWLEDGEMENTS

This work was funded by the NIH (R01 GM143400).

REFERENCES

[1] Fu, X et al., *Int J Mol Sci*, 19:1445, 2018. [2] Sanchez, M et al., *Nat Methods*, 17:167-174, 2019. [3] Di Ventura, B et al., *Curr Opin Chem Biol*, 34:62-71, 2016. [4] Dowbaj, A M, et al., *J Cell Sci*, 134, 3031. [5] Berlew, E E, et al., *ACS Synth Biol*, 11:515-521, 2022. [6] Niopek, D, et al., *Nat Commun*, 5, 2014

A PRE-CHONDROGENIC STEM CELL NICHE FACILITATING ARTICULAR CARTILAGE FORMATION VIA IMPROVING CHONDROGENIC PHENOTYPE VIA CHANGING STIFFNESS AND CELL SEEDING DENSITY

Y. Yang (1), R. Yang (1), K. Downey (1), S. E. Oh (1), E. Noel (2), C. X. Deng (1), R. M. Coleman (1,3)

(1) Department of Biomedical Engineering, University of Michigan, Ann Arbor, Michigan, USA
(2) Department of Biomedical Engineering, Florida International University, Miami, Florida, USA
(3) Department of Mechanical Engineering, University of Michigan, Ann Arbor, Michigan, USA

INTRODUCTION

Articular cartilage, crucial for smooth joint movement, faces challenges like chondrocyte apoptosis, extracellular matrix (ECM) degradation, and reduced matrix synthesis, progressing to post-traumatic osteoarthritis (PTOA). PTOA accounts for 12.4% of all osteoarthritis cases, affecting over 32.5 million US adults with healthcare costs exceeding $100 billion [1]. Effective cartilage regeneration is crucial. Autologous chondrocyte implantation is a widely explored approach, but challenges like chondrocyte dedifferentiation and slow ECM synthesis exist [2]. To address these challenges, our study focuses on manipulating the 'tissue engineering triad' components: cells, scaffolds, and biofactors. However, the intricate interactions between these components create a gap in understanding how exogenous cues influence regeneration-specific genomic pathways during cartilage repair.

Our study concentrates on two external cues—scaffold stiffness and cell seeding density. Altering scaffold stiffness reveals that softer scaffolds favor chondrogenesis [3]. Greater cell seeding density tends to favor chondrogenesis, but nutrient permeation limits maximal density [4]. Our objective is to study the impact of material stiffness and seeding density on chondrocyte redifferentiation using a reproducible 3D scaffold culture system, the pre-chondrogenic stem cell niche (PCN). This research enhances our understanding of how exogenous cues influence genomic pathways, offering insights into effective strategies for cartilage regeneration.

METHODS

PCN Culture Human articular chondrocytes (HACs) (male donor, aged 19 years) were mixed with a hydrogel precursor composed of 5 or 10%w/v polyethylene glycol (PEG), 0.02%w/v methacrylated type I collagen and 0.1%w/v thiolated hyaluronic acid, and 0.3%w/v photoinitiator. After a 30-minute incubation for Michael-type additions, 70 µl samples were crosslinked under UV light (365 nm wavelength, 28 mW/cm^2) for 60 seconds to form hydrogels. Final cell seeding densities were 10, 20, and 40 × 10^6 (M) cells/ml in 5/10%PEG gels.

Live/dead Staining Cell viability on days (D) 0, 14 and 28 was assessed using ImageJ, with $n \geq 6$ stacks acquired through confocal microscopy.

qPCR Expression of ACAN, COL2A1, MMP13, COL10A1 and COL1A1 genes was assessed on D0, 7, 14/15 and 28/29.

sGAG Quantification Sulfated glycosaminoglycan (sGAG) accumulation normalized to DNA content was quantified on D14/15 and 28/29 using the dimethymethylene blue and PicoGreen assays [5].

Immunofluorescence D14 and D28 samples underwent antigen retrieval and blocking prior to primary antibodies incubation for COL2A1, ACAN, COL10A1, RUNX2, or MMP13, followed by Goat anti-Rabbit Alexa Fluor™ Plus 488 secondary antibody and DAPI counterstaining. Protein production normalized to DAPI content was quantified using ImageJ, with $n \geq 9$ stacks acquired through confocal microscopy.

Mechanical Testing The tensile modulus of hydrogels was tested using contactless ultrasound technology, Resonant Acoustic Rheometry [6].

Statistical Analysis Two-way ANOVA or mixed models with post-hoc Tukey's multiple comparison test were employed.

RESULTS

Preservation of Chondrogenic Phenotype by PCN The average cell viability on D0, 14 and 28 was ~80%, indicating robust cell survival post-crosslinking for long-term studies (Fig. 1A). This is supported by sustained high-level expression of chondrogenic genes (Fig. 1B) and elevated sGAG accumulation (Fig. 1C).

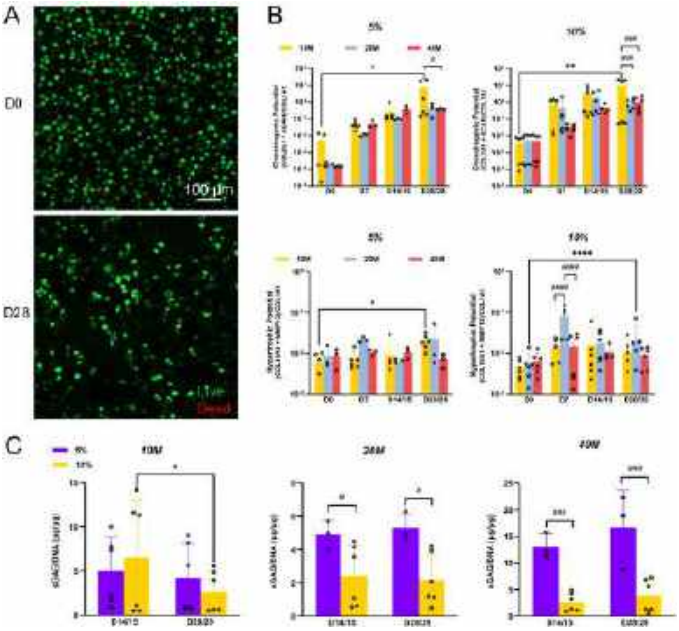

Figure 1: (A) Fluorescent viability images of cells in the PCN. (B) Gene expression ($2^{-\Delta Ct}$ of normalized markers) of cells in 5/10% PEG PCN with varying cell seeding density, showing maintained articular cartilage genotype ('Chondrogenic Potential') and impact on premature cell maturation ('Hypertrophic Potential'). (C) sGAG normalized to DNA of cells with 10/20/40M cells/ml influenced by PCN stiffness.

Promotion of Cartilage Matrix Production by PCN Stiffness In contrast to 10%PEG PCN, the softer 5%PEG facilitated increased sGAG production (Fig. 1C), and elevated expression of ACAN and COL2 (Figs. 2A&B). Moreover, the 5%PEG PCN maintained a stable environment for enhanced matrix production, while the stiffness of the 10%PEG PCN increased faster over time, especially with higher cell seeding density (Figs. 2C).

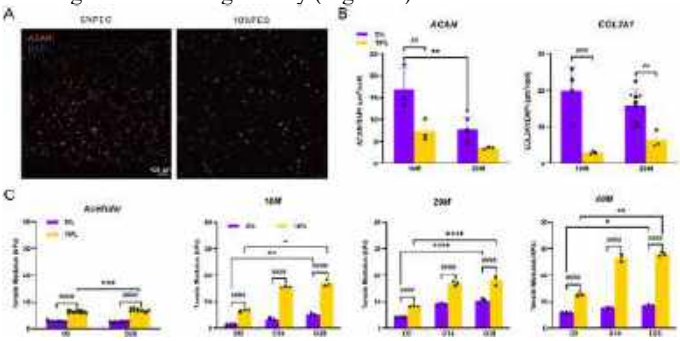

Figure 2: (A) Fluorescent images of ACAN in 5/10%PEG PCN. (B) Quantification of normalized ACAN and COL2 by HACs with 10/20M cells/ml. (C) Tensile modulus of acellular PCN and PCN with 10/20/40M cells/ml.

Promotion of Chondrogenic Phenotype by Lower Cell Density in PCN Compared to 20/40M cells/ml, the PCN with lower seeding density (10M) promoted higher chondrogenic gene expression and lower hypertrophic gene expression (Fig. 1B). Lower density also facilitated increased matrix production of ACAN and COL2 (Fig. 2B). Furthermore, the 10M cells/ml PCN maintained a stable environment for enhanced matrix production, while the PCN with higher cell density increased stiffness more rapidly over time (Figs. 2C).

DISCUSSION

The study showcases the PCN's efficacy in maintaining high cell viability, preserving chondrogenic genes, and promoting sGAG accumulation. The softer PCN (5%PEG) enhances cartilage matrix production, and lower cell seeding density (10M cells/ml) favors chondrogenic gene expression and matrix production, maintaining a more favorable stiffness. This aligns with prior research, indicating increased production of COL2 and proteoglycan in a softer environment, despite minimal influence on chondrogenic gene expression [3]. Low stiffness can reduce cell adhesion and spreading, facilitating the formation of cell aggregates. Our findings diverge from previous studies suggesting higher cell seeding density for matrix production, providing a nuanced explanation linked to the stiffness variation [4]. Future studies will explore hydrogel formulations with lower stiffness and refine cell retrieval methods for deeper insights into HAC redifferentiation. This study underscores the potential of the PCN in advancing cartilage repair methods and contributes to the broader understanding of factors influencing cartilage regeneration.

ACKNOWLEDGEMENTS

Supported by the NSF RECODE # 2225568.

REFERENCES

[1] Cross, M et al., *Ann Rheum Dis*, 73:1323-1330, 2014.
[2] Kiani, C et al., *Cell Res*, 12:19-32, 2002.
[3] Kwon, H et al., *J Mech Behav Biomed Mater*, 17: 337-346, 2013.
[4] Sun, A et al., *Acta Biomater*, 58: 302-311, 2017.
[5] Carrion, B et al., *Adv Healthc Mater*, 5: 1192-1202, 2016.
[6] Hobson, E et al., *Biomaterials*, 269, 2021.

STRUCTURAL AND MECHANICAL ANALYSIS OF TREATED AND UNTREATED AORTIC COARCTATION

Matt A. Culver (1), Michael A. Stellon (2), Leah Gober (2), Luke Lamers (5), Alejandro Roldán-Alzate (3,4) and Colleen M. Witzenburg (1)

(1) Biomedical Engineering, University Wisconsin-Madison, Madison, WI, United States
(2) Department of Surgery, University Wisconsin-Madison, Madison, WI, United States
(3) Radiology, University Wisconsin-Madison, Madison, WI, United States
(4) Mechanical Engineering, University Wisconsin-Madison, Madison, WI, United States
(5) Pediatrics, Division of Cardiology, University Wisconsin-Madison, Madison, WI, United States

INTRODUCTION

Aortic coarctation (COA) is a congenital heart disease (CHD) characterized by a narrowing of the aorta, that typically presents distal to the left subclavian artery. Each year, 1 in every 1,800 babies are born with COA in the United States making it one of the most common CHDs[1]. Symptomatic patients typically present at birth and are preferably treated within the first few years of life[2]. Current surgical or catheter-based interventions can restore flow and reduce the blood pressure gradient across the COA to normal levels. However, *successful technical* intervention does not ensure long-term health as one-third of treated COA patients still develop hypertension (HTN) by adolescence[3]. The underlying cause of increased long-term risk for HTN in treated patients is not fully understood. While various factors have been discussed, irreversible vascular remodeling[4] has become a leading hypothesis. Previous animal studies support this proposed mechanism as reduced elastin content in the proximal aorta persisted following COA correction[5,6].

Our team created the first large animal model of COA in which stenosis was induced and corrected at time-points comparable to humans. The objective of this study was to evaluate aortic remodeling near the site of coarctation via quantitative histologic analysis and mechanical testing. We hypothesized that COA, both with and without treatment, would result in stiffer aortas with reduced and fragmented elastin.

METHODS

Animal Model. In this study, pigs were followed from 2-weeks (~4-5kg) to 20-weeks of age (~60kg). In 12 animals, COA was surgically created at approximately 2-weeks of age with 4 additional animals undergoing sham surgery. Each pig underwent cardiac catheterization at 6, 12, and 20-weeks with necropsy at 20-weeks. At 6-weeks a stent was placed at the COA site to relieve the stenosis in the treatment group (n=6). The stent was subsequently dilated at 12- and 20-weeks to match the diameter of the growing aorta. Within 3h of necropsy, the entirety of the aorta was collected, placed in a 1% phosphate buffered saline solution, and frozen at -80°C. Animal experiments were reviewed and approved by the University of Wisconsin Institutional Animal Care and Use Committee.

Histology. Histologic analysis was performed on regions of the aorta directly proximal and distal to the COA site. At necropsy, these cross-sections were fixed in 10% formalin for ~24 hours, rinsed, placed in 70% ethanol, and submitted to UW-Madison's Experimental Animal Pathology Lab. Samples were stained with Masson's trichrome (MTC) or Verhoeff–Van Gieson (VVG) to visualize collagen and elastin, respectively. A custom MATLAB code developed by Bersi et al[7] estimated the collagen and elastin area fractions via colorimetric analysis (Figure 1). Statistical analysis was performed with one-way ANOVAs with Tukey's multiple comparisons tests.

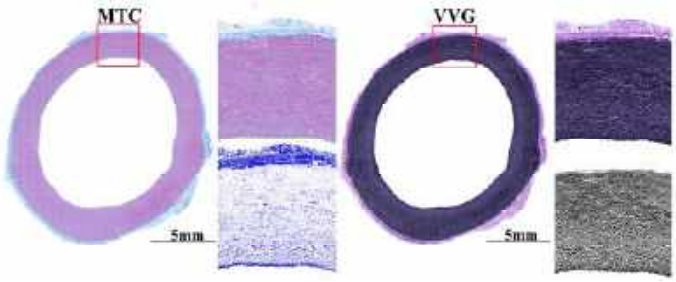

Figure 1: Masson's trichrome (MTC) and Verhoeff–Van Gieson (VVG) with automated visualization of collagen and elastin, respectively, for representative aortic cross sections.

Mechanical Testing. Aortic tissue directly distal to the COA site from all three groups was mechanically tested in both the axial and circumferential directions[4]. Briefly, once thawed, a longitudinal cut was

made and the tissue was divided into 5x20 mm samples, aligned in both directions. Uniaxial, peel, and shear lap tests were performed to failure to characterize the mechanical behavior. Uniaxial tests captured the tensile response along the axial and circumferential axes, peel tests captured the tensile response in the radial axis, while shear lap tests captured the response to shear along the medial lamella. Each test was performed at 3mm/min. Tests in which samples slipped or failed at the clamps were not included in the analysis.

For the uniaxial and shear lap samples, the first Piola-Kirchhoff stress at failure was calculated by dividing the grip force at ultimate failure by the undeformed cross-sectional area of interest. For peel samples, the average peel tension was calculated by dividing the average grip force during peeling, excluding initial extension, by the undeformed sample width.

RESULTS

Mechanical Testing. Uniaxial failure stresses for the sham (3 pigs), COA (1 pig), and treated groups (1 pig) were all higher in the circumferential direction (1902 ± 365, n = 11 samples; 1971 ± 638, n = 3 samples; 1498 ± 296, n = 5 samples), than the axial direction (414 ± 32, n = 4 samples; 898 ± 190, n = 3 samples; 401, n = 1 sample). Failure stresses for the shear lap tests demonstrated a similar trend with the sham, COA, and treated groups, exhibiting higher average stresses in the circumferential direction (274 ± 176, n = 4; 260 ± 178, n = 2; 127 ± 34, n = 4) when compared to the axial direction (133 ± 41, n = 4; 117 ± 53, n = 2; 97 ± 51, n = 3). The sham group displayed a higher peel tension in the circumferential direction (47 ± 15, n = 6) than the axial direction (33 ± 16, n = 4), while the COA and treated groups had a higher peel tension in the axial direction (44 ± 7, n = 2; 40 ± 17, n = 4) than the circumferential direction (29 ± 1, n = 2; 28 ± 17, n = 4).

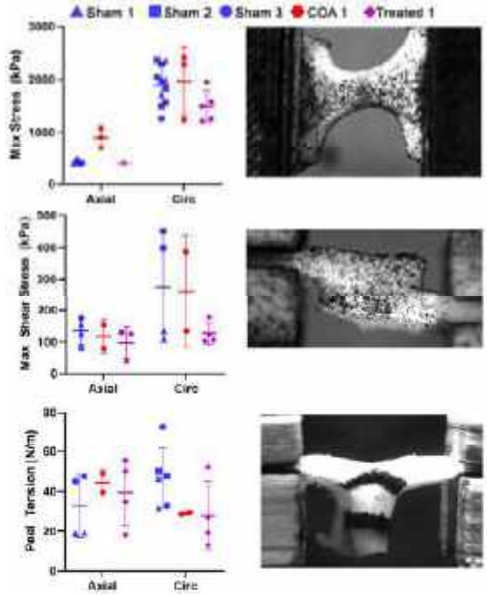

Figure 2. Uniaxial failure stress (left, top), shear lap failure stress (left, middle), and average failure peel tension (left, bottom). Representative images of each test (right).

Histology. The collagen and elastin area fractions were calculated for cross-sections located in the descending aorta both proximal and distal to the COA site from sham (2 pigs), COA (4 pigs), and treated (5 pigs) groups. Note that for this analysis each symbol in Figure 3 represents a cross-section from a different pig. There were no significant differences between the three groups when comparing collagen area fraction for either the proximal or distal descending aorta (Figure 3 top). However, the elastin area fraction proximal to the COA site in the treated group was significantly greater than the sham and COA groups. Distal to the COA site, elastin area fraction was significantly greater in the treated group than the sham and COA groups. It was also significantly greater in the COA group in comparison to the sham group.

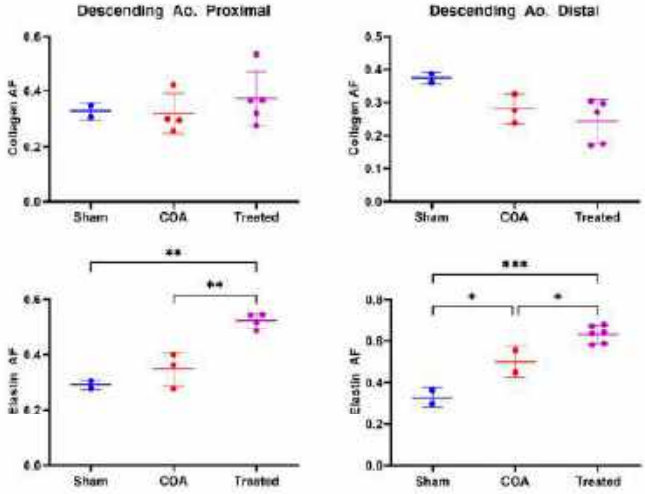

Figure 3: Colorimetric analysis results for the collagen (top) and elastin (bottom) area fractions proximal (left) and distal (right) to the COA site * p < 0.05, ** p < 5e-3, *** p < 5e-4

DISCUSSION

In this study, we quantified the structural and mechanical remodeling of the aorta using a novel pig model of COA. While we have not yet mechanically tested a sufficient number of samples for statistical analysis, initial results suggest that the treated group was slightly weaker, particularly in the circumferential direction, when compared to sham and COA groups. Surprisingly, the histologic analysis yielded the opposite of the expected outcome. We hypothesized that the treated and COA groups would have less elastin than the sham animals, however, elastin content was actually higher in these groups. One potential explanation for this finding is the COA was created early enough in development that the pigs could produce new elastin. Additionally, the placement of the stent may serve as a stimulus for elastin production. The possibility of elastin synthesis in response to COA was supported by the growth of elastin rich collateral vessels in both COA and treated animals near the COA site. This outcome, which is not present in other animal models[5,6] of COA, is further support for this pig model as collaterals are common in humans with COA[8]. To our knowledge, this is the first study to characterize the structural and mechanical changes of COA in an animal model that captures neonatal growth and development.

ACKNOWLEDGEMENTS

This study was funded by an award from the NIH-NCATS/UW Institute for Clinical and Translational Research.

REFERENCES

[1] Mai, CT et al., *BDR*., 111(18):1420-1435, 2019. [2] Dijkema, EJ et al., *Heart*, 103:1148-1155, 2017. [3] O'Sullivan, JJ et al., *Heart*, 88: 163–166, 2002. [4] Witzenburg, C et al., *J Biomechanical Eng.,* 2017. [5] Menon, A et al., *Am J Physiol. Heart Circ Physiol.*, 303(11):H1304-H1318, 2012. [6] Menon, A et al., *J of Pharm. and Tox. Methods*, 65:18-28, 2012 [7] Bersi, M et al., *HTN*, 67:890–896, 2016. [8] Cardoso, G et al., *J Card Surg,* 29:512–8, 2014.

MICROSTRUCTURAL ABNORMALITIES IN HUMAN HYPERTROPHIC SEPTAL TISSUES

Duc Khang Chung (1), Milad Almasian (2), Houjia Chen (1), Katherine M. Copeland (1), Kytai T. Nguyen (1), Matthias Peltz (3), Pietro Bajona (3), Yi Hong (1), Yichen Ding (2), Jun Liao (1)

(1) Department of Bioengineering, University of Texas at Arlington, Arlington, TX, USA
(2) Department of Bioengineering, University of Texas at Dallas, Richardson, TX, USA
(3) Department of Cardiovascular and Thoracic Surgery, University of Texas Southwestern Medical Center, Dallas, TX, USA

INTRODUCTION

Hypertrophic cardiomyopathy (HCM) is often caused by genetic mutations, resulting in abnormal thickening of ventricular muscle, particularly the septum, and causing left ventricular outflow tract (LVOT) obstruction. Hypertrophic cardiomyopathy can be microscopically assessed and diagnosed by enlarged cell size of the hypertrophic cardiomyocytes, disarray of those cells, and a dense abnormal fibrotic microenvironment [1]. The thickening of the ventricular wall and septum can cause poor cardiac outcomes, which consequently lead to heart failure and mortality [2]. The extent of cell hypertrophy and fibrosis can directly impact the mechanical behavior of septal tissues. Determining the microstructural abnormalities is hence essential to better understand the biomechanical properties of the hypertrophic septal tissues. In this study, we assessed the microstructural abnormalities of human hypertrophic septal tissues using histological images and light sheet images, with the goal of revealing the underlying structural causes of the poor mechanical performance of HCM tissues.

METHODS

Hypertrophic septal tissues were obtained as surgical waste following septal myectomy surgery performed by Dr. Pietro Bajona (IRB AHN #2020-240). Patients include both males and females and range in age from 19 years to 71 years. Healthy human septal tissues were obtained from a tissue bank under the same IRB protocol. For histology, all samples were fixed in 10% neutral buffered formalin for 24 hours and were processed through a standard histological preparation protocol, including alcohol-dehydration and paraffin-embedment. 5 μm sections were cut, and a standard Masson's trichrome staining protocol was performed. Masson's trichrome protocol stains heart muscle red and collagen blue. Histological images were taken under a bright light field using a Nikon Eclipse Ti Series Microscope (Nikon). For light sheet imaging, the iDISCO method employs a three-step process comprising dehydration, dilapidation, and refractive index matching. The method involves the complete removal of lipids and dehydration of the tissue, which largely minimizes light scattering. The organic solvent solution is then used to replace the dehydrated and delipidated tissue with refractive index matching. The light sheet is created with a cylindrical lens, and ETL moves the focal region of the Gaussian beam which is synchronized with the active sensor on the camera. The auto-fluorescence emitting from the heart is captured by the detection objective lens and sCMOS camera. A customized LabVIEW control algorithm is used to synchronize the propagation of the laser, the stage movement, the sCMOS camera rolling shutter, and the electrically tunable lens (ETL). During the image acquisition process, the inherent trigger and rolling shutter on the sCMOS are employed to capture sequential uniform 2D images, while the stage continuously translates the tissue across the light sheet at a constant velocity that is determined by the step size and exposure time.

RESULTS

Masson's trichrome staining revealed that the HCM septal tissues had hypertrophic cardiomyocytes that were significantly larger and disarrayed when compared with the healthy cardiomyocytes (**Figure 1-A,B**). We further showed that the light sheet imaging was able to capture the microstructural differences in muscle fiber orientations and alignment. As shown by light sheet images, the healthy septum showed normal morphology with highly-aligned heart muscle fibers and evenly distributed small interfibrillar space (Figure **1-C**), while the human hypertrophic septal tissues showed disarrayed muscle fiber configurations, with wider interfibrillar space that was unevenly distributed (Figure **1-D**).

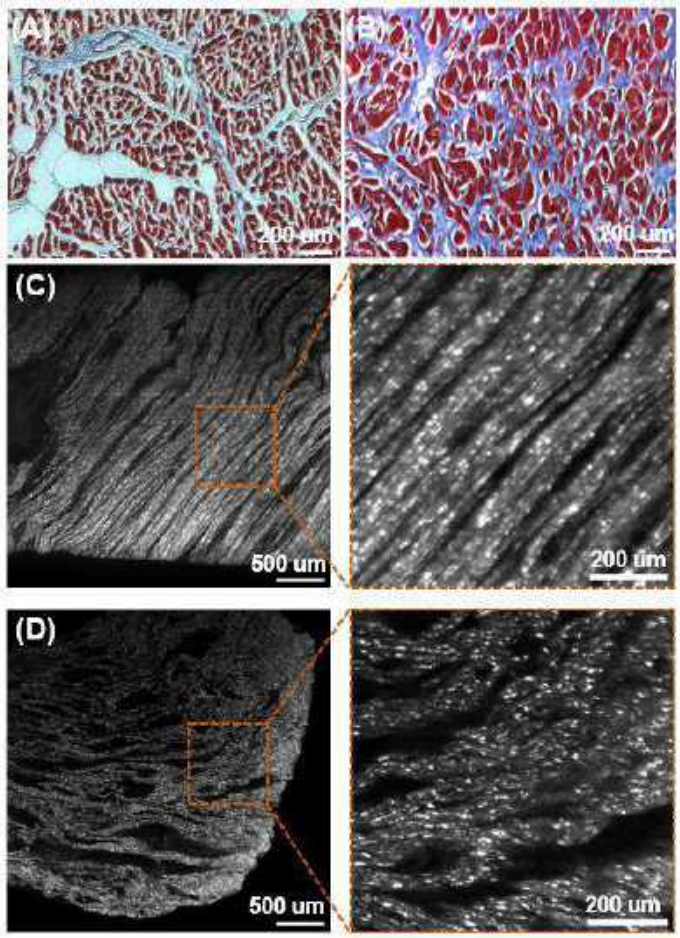

Figure 1: Masson's trichrome images of the healthy (A) and HCM (B) human septal tissues. Light sheet imaging of the healthy (C) and HCM (C) human septal tissues.

DISCUSSION

More detailed quantitative imaging analysis efforts are currently ongoing. In our mechanical study [3], we reported that human hypertrophic septal tissues had larger stress relaxation and larger creep and were stiffer at the initial phase of tissue loading, less nonlinear, less stiff in the linear region, and much weaker in mechanical strength. Both our histological images and light sheet images showed that the hypertrophic septal tissues had a higher degree of disarrayed, enlarged heart muscles and disorganized, higher amount of fibrotic collagen fibers in comparison to the healthy septum. The poorly-organized pathological compositions in the hypertrophic septum resulted in the loss of the benefits of native tissue design. For instance, the higher amount of fibrotic collagen could cause HCM tissues to be stiffer at the initial phase of mechanical loading; however, the pathologically-deposited fibrotic collagen and the disarrayed hypertrophic cardiomyocytes led to a less stiff behavior in the linear region and a much lower mechanical strength of the HCM tissues when compared to the healthy septal tissues [3]. That is to say, the inferior mechanical behavior of the HCM septal tissues can be attributed to microstructural abnormalities.

ACKNOWLEDGEMENTS

NIH R15HL159599, R01HL157050

REFERENCES

[1] A. Varnava, et al., Heart (2000) 84(5): 476-482.
[2] R. Hinojar, et al., International journal of cardiology (2017) 249: 467-472.
[3] K. Copland, et al., SB3C Conference (2023).

GENERATIVE MODELING OF CONGENITAL HEART DEFECT ANATOMIES FOR SURROGATE CARDIAC FLOW SIMULATIONS

Fanwei Kong (1), Alison L. Marsden (1, 2, 3)

(1) Department of Pediatrics, Stanford University, Stanford, CA, USA
(2) Department of Bioengineering, Stanford University, Stanford, CA, USA
(3) Department of Mechanical Engineering, Stanford University, Stanford, CA, USA

INTRODUCTION

Congenital heart defects (CHDs) are the most common birth defects and are characterized by abnormal cardiac anatomies that can dramatically impact cardiac functional outcomes. CHD patients often have unique but complex cardiac malformations and anatomical arrangements that warrant patient-specific treatment planning and surgical interventions. Personalized computer models of the heart derived from patient image data can simulate various aspects of cardiac function. They can thus model complex clinical scenarios in CHD patients and have demonstrated the potential to facilitate personalized treatment planning and decision-making [1]. However, creating digital twin models of patients' hearts and tuning computational model parameters to match clinical measurements requires prohibitive time and computational efforts for practical clinical uses.

Deep learning (DL) methods have demonstrated potential in developing surrogate computational fluid dynamics (CFD) models to enable rapid hemodynamic prediction within patient-specific aorta geometries [2]. Such methods train neural networks on a large dataset containing various physiological aorta anatomies and the corresponding CFD solutions to approximate the mapping between the input geometric space and the flow field solution space. However, CHDs, particularly the more complex types (e.g. double outlet right ventricle and hypoplastic left heart syndrome), are rare conditions. This rarity makes it extremely challenging to acquire sufficiently large patient cohorts and develop DL-based surrogate methods. Furthermore, CHDs encompass a broad spectrum of rare topological variations among different defect types, making it practically impossible to assemble a comprehensive training cohort from clinical imaging data alone.

We thus designed a generative model to tackle the complex task of representing whole-heart cardiac anatomies for a wide range of CHD types [3]. We now apply this model to generate synthetic time-series cardiac anatomies, which we use to perform one-way coupled deforming domain CFD simulations to capture changes in the flow patterns and pressure fields within the left and right ventricles in response to variations in cardiac anatomies and structural abnormalities.

METHODS

Our approach, as presented in Figure 1, enables type-controlled generative modeling of cardiac anatomies, allowing us to create synthetic cardiac anatomies tailored to specific CHD types and conditions. We represent the CHD type-specific heart anatomies and the corresponding abnormalities implicitly using a smooth signed distance function (SDF) learned by Lipschitz-regularized neural networks. This function takes in a CHD diagnosis vector as input and outputs a signed distance field to capture the corresponding unique topologies of complex cardiac anatomies. We learn diffeomorphic deformations using neural ordinary differential equations [4] to morph the anatomies to capture shape-specific anatomical variations in patient cardiac models while preserving the CHD structural anomalies.

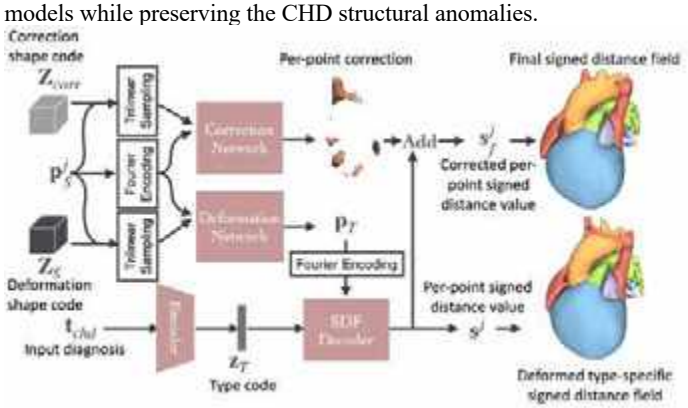

Figure 1: Overview of our generative DL method to generate various types of CHD anatomies.

We used a deformation shape code and a correction shape code to encode the anatomical variations among patients besides the type-

specific abnormalities modeled by the SDF. Leveraging a training dataset containing 67 ground truth anatomies of various CHD types and the corresponding diagnosis information, we learn the posterior probability distribution of the shape codes that best represent the training anatomies. Assuming a Gaussian prior, we can sample a shape code from the prior distribution to construct realistic cardiac anatomies for a specific CHD type beyond those included in the training dataset. Additionally, by interpolating between different CHD-type codes while fixing the shape code, our method can generate meaningful intermediate anatomical representations that are developmentally reasonable and reflect varying degrees of disease severity and anatomy (Figure 2). Further details of this method can be found in [3].

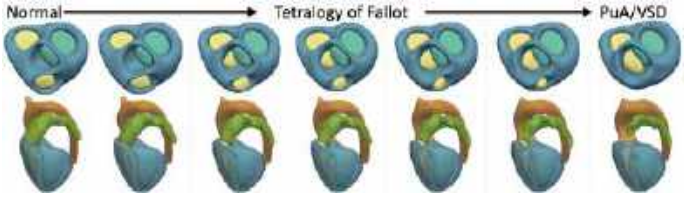

Figure 2: Interpolated cardiac anatomies between normal, Tetralogy of Fallot (ToF) and pulmonary atresia (PuA).

We applied realistic motion obtained from a set of time-series image data (n=10) to the generated CHD cardiac anatomies. Namely, for each time-series image data, we optimize a set of shape codes $\{Z_{time}\}_0^T$ to additionally model the shape changes due to cardiac motion. We then randomly select a set of time-series shape codes and apply them to morph a template mesh derived from the learned CHD type-specific anatomies to generate time-series meshes suitable for CFD simulations. To optimize $\{Z_{time}\}_0^T$, we first freeze the trained network and optimize shape code Z_s to morph the type-specific anatomy to match the patient-specific anatomy obtained from the first time point of the time-series image data. We then freeze both Z_s and the network and optimize Z_{time} to match the deformed type-specific anatomy to the patient anatomy at all other time points. We create template meshes containing the ventricles and the aorta and pulmonary outflow tracks from the CHD type-specific anatomies using SimVascular Python API.

We created volume meshes at the start of systole and simulated the ejection phase of the ventricles. Cubic spline interpolation was applied to obtain 500 interpolated meshes to impose the movement on the volume mesh. We applied the ArbitraryLagrangian-Eulerian (ALE) formulation of the incompressible Navier-Stokes equations with a stabilized FE finite-element Galerkin method implemented in the open-source software package svFSI [5] to simulate the intraventricular flow and account for the moving boundary. Pressure boundary conditions of 100 and 20 mmHg were assumed at the aorta and pulmonary outlets, respectively, for all anatomies.

RESULTS

Our method can generate time-series CHD anatomies meshes for CFD simulations, and the generated cardiac meshes include anatomical abnormalities for specific CHD types. For example, as demonstrated in Figure 3, the generative cardiac mesh for a ToF case presents the overriding aorta, a big ventricular septal defect (VSD, a hole between two ventricles), and pulmonary outflow tract stenosis (PS). To demonstrate the capability of our method in generating synthetic CHD cardiac anatomies and the corresponding flow and pressure field data, we conducted CFD simulations of cardiac ejection for a range of synthetic geometries with increasing severity of the above defects. As shown in Figure 4, the simulated pressure field revealed the increasing trend of right ventricle pressure overload, the flow shunting between the two ventricles through the VSD, and flow acceleration through the narrowed pulmonary outflow tract.

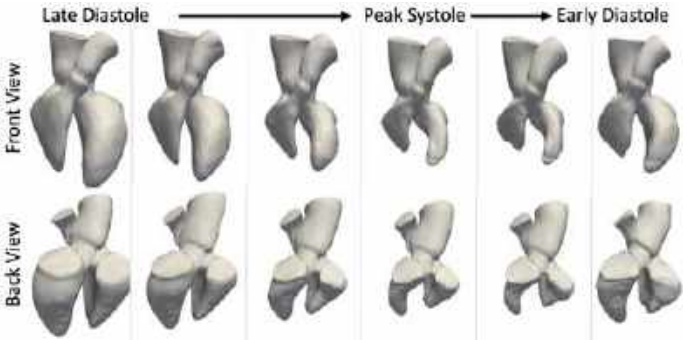

Figure 3: Example time-series meshes of a ToF anatomy.

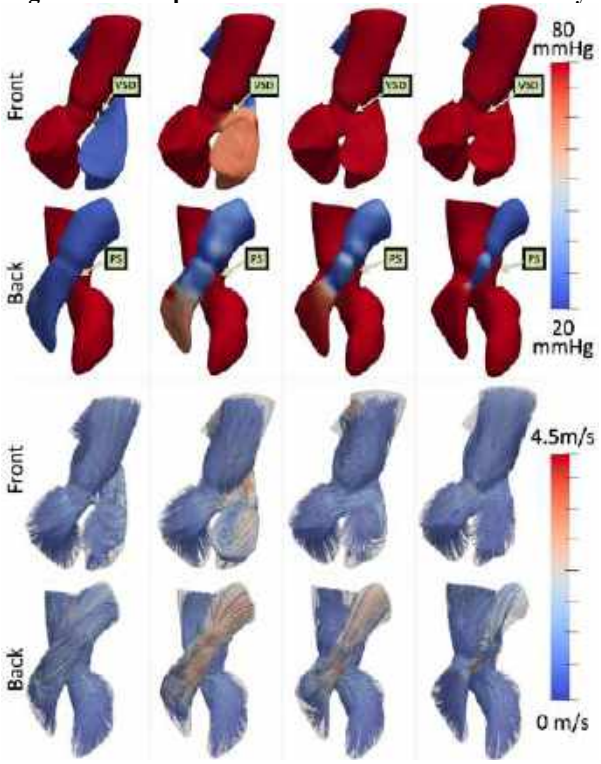

Figure 4: Simulated pressure field and velocity streamlines for CHD anatomies with increasing severity of VSD and PS.

DISCUSSION

DL-based surrogate models can enable rapid flow and pressure field estimation within patient-specific cardiovascular anatomies. However, developing such a model requires a large training dataset, which is challenging to obtain for rare diseases such as CHD. We tackle that challenge with a generative modeling approach to generate synthetic times-series cardiac anatomies that can be used to generate synthetic pressure and flow field data to support DL applications. Future work will include assigning more realistic boundary conditions based on closed-loop lumped parameter models and training neural network models to approximate cardiac flow within CHD anatomies to enable efficient cardiac digital twinning.

ACKNOWLEDGEMENTS

NSF 1663671, NIH R01EB029362, and NIH R01LM013120.

REFERENCES

[1] Marsden AL & Feinstein JA, Curr Opin Pediatr,27(5):587-96, 2015.
[2] Du P & Zhu X & Wang JX, Physics of Fluids, 34 (8): 081906, 2022
[3] Kong F et al., arXiv, 2311.00332, 2023
[4] Chen TQ et al., Neural Information Processing Systems, 2018
[5] Chi Z et al., Journal of Open Source Software, 7(78), 4118, 2022

LOCALIZED GROWTH RATE ANALYSIS ON A GLOBAL ENSEMBLE AVERAGING OF ABDOMINAL AORTIC ANEURYSM GROWTH

Pratik Mitra (1), Juan C. Restrepo (1), Merjulah Roby (1), Satish C. Muluk (2), Mark K. Eskandari (3), Seungik Baek (4), Ender A. Finol (1)

(1) Department of Mechanical Engineering, University of Texas at San Antonio, San Antonio, TX
(2) Department of Cardiothoracic Surgery, Allegheny Health Network, Pittsburgh, PA
(3) Division of Vascular Surgery, Northwestern University School of Medicine, Chicago, IL
(4) Department of Mechanical Engineering, Michigan State University, East Lansing, MI

INTRODUCTION

An abdominal aortic aneurysm (AAA) is a socially relevant vascular disease with an unpredictable growth rate an 80% overall mortality rate. It forms as a confined enlargement of the aorta (≥ 3 cm in diameter) that mainly develops between the renal arteries and aorto-iliac bifurcation. The maximum diameter of an AAA is measured as part of the clinical management process using an ultrasound or computed tomography (CT) exam while under surveillance. In the United States, a maximum diameter of 5.5 cm for men and 5.0–5.4 cm for women with a growth rate of 1 cm/year are the accepted thresholds for surgical/endovascular repair [1]. However, AAA growth patterns during the surveillance period are not fully understood due to insufficient or infrequent imaging. To overcome the shortcomings of the conventional diameter-based growth assessment, Ristl *et al.* [2] investigated volume, while Akkoyun *et al.* [3] evaluated various geometric measures as surrogates for growth rates. Hirose and colleagues [4] proposed that AAA growth follows an exponential behavior over time. Nonetheless, Siika and co-authors [5] claim that AAA growth is linear when measured with diameter and volume. To address this discrepancy, we performed a growth rate analysis with AAA patients under surveillance while using twelve geometric measures as surrogates for growth prediction.

METHODS

Contrast-enhanced CT exams for 40 AAA patients under surveillance (10 females, 30 males) were retrospectively acquired from Northwestern Memorial Hospital (Chicago, IL), Allegheny General Hospital (Pittsburgh, PA), and Seoul National University Hospital (Seoul, Korea), in accordance with established Institutional Review Board guidelines at each clinical center. The follow-ups for each patient ranged from three to seven during the surveillance period. Collectively, 140 CT exams were acquired and used for this study. Binary masks were created using AAAVasc [6] (an in-house MATLAB®-based semi-automated segmentation script) after image segmentation. Volume meshes were generated for each AAA at each imaging follow-up using AAAMesh [7] (another in-house MATLAB®-based script used for volume meshing), which consist of 30,000-90,000 quadratic hexahedral elements.

Growth rates

The exponential expression presented in [3] was used to calculate AAA growth rate according to Eqs. (1) and (2),

$$g = (e^{12r} - 1) \times 100 \quad (1)$$

$$r = \frac{1}{t} \ln \frac{X^{followup}}{X_{baseline}} \quad (2)$$

where *X(.)* is the geometric measure, *t* is the time interval between consecutive scans in months, *r* is the logarithmic growth factor, and *g(.)* is the growth rate of the measure. The Spearman's correlation coefficient was used to quantify the strength of the correlation analysis with growth rate, where a coefficient in the range of 1.00–0.90, 0.90–0.75, 0.75–0.50, 0.50–0.25, and 0.25–0.0, corresponds to a very high, high, moderate, weak, and no correlation, respectively [3].

AAA growth model and growth prediction

The best fit between linear and nonlinear growth models was explored and forecasted using Eqs. (3) and (4),

Linear Growth Model: $Y = \alpha + \beta t$ (3)

Nonlinear Growth Model: $Y = \alpha \times e^{\beta t}$ (4)

where *Y* is the prediction, α is the mean value of the measure (see Table 1), and β is the mean value of growth rate using a first-order time derivative.

Table 1. Geometric measures used to predict growth rate.

V	Vessel volume (cm^3)
V_{ILT}	Volume of intraluminal thrombus (ILT) contained within the AAA sac (cm^3)

D_{max}	Maximum transverse diameter of the AAA sac (cm)
DDr	Maximum diameter to neck diameter ratio
S	Vessel surface area (cm^2)
T	Tortuosity
γ	Ratio of AAA ILT volume to vessel volume
H	Height of AAA (cm)
H_{sac}	Height of AAA sac (cm)
L	Centerline length of AAA (cm)
L_{sac}	Centerline length of AAA sac (cm)
DHr	Diameter-Height ratio

RESULTS

Figure 1 shows the exponential growth rate correlations for the 12 geometric measures using Eqs. (1) and (2). Similar measures were used in [6] to investigate nonlinear growth rates. Very high correlations were observed for V vs. S (r = 0.99), V vs. D_{max} (r = 0.91) and γ vs. V_{ILT} (r = 0.91) for the nonlinear growth model. However, Starck et al. [8] found that S does not correlate with growth rate. In addition, γ is a secondary variable dependent on V. Therefore, we considered only V vs. D_{max} for further growth forecasting.

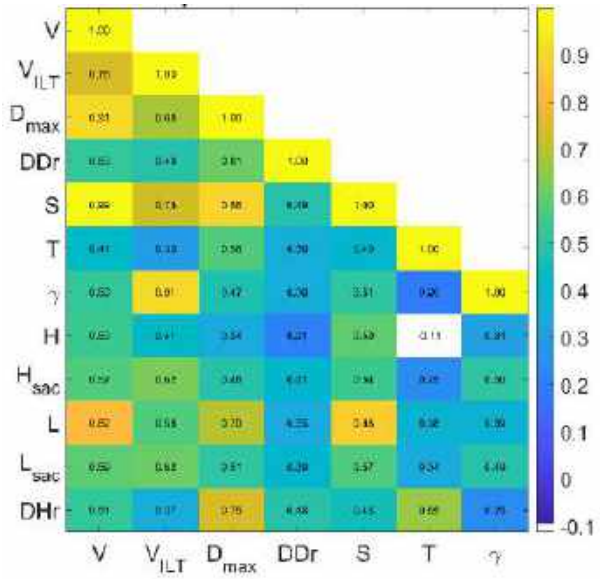

Figure 1. Spearman's correlation coefficients of geometric measures using an exponential growth rate.

Figure 2 illustrates the V vs. D_{max} relationship of the 40 AAA patients over time with a mean (μ) distribution and two standard deviations ($\pm 2\sigma$). The AAA data shows good agreement with the nonlinear growth model, Eq. (4), with almost all within one standard deviation of the mean with a few exceptions. Outliers are observed for 9 patients in the follow-up range of 4 to 6 cm for D_{max}, which is not consistent with other AAA growth models. The follow-up range in volume for these patients is approximately 25 to 75 cm^3. Hence, we investigated the growth of these 9 AAA patients (Group I) in isolation and compared them to the growth of 21 other AAA patients (Group II) that were also within the range of 4 to 6 cm for D_{max} but within one standard deviation of the mean.

Linear and nonlinear growth models were applied to Groups I and II separately using Eqs. (3) and (4), as shown in Table 2. Group II patients, which have a D_{max} between 4 to 6 cm, show R^2 values of 0.708 and 0.699 for the linear and nonlinear growth models, respectively, and with *RMSE* values of 29.72 and 30.17, respectively. Similarly, for Group I, which was outside the two standard deviations of the mean, the linear growth model explains 62.8% of the variance in the growth, with an *RMSE* value of 21.25. Conversely, the nonlinear growth prediction shows that it explains 63.5% of the variance with an *RMSE* value of 21.04.

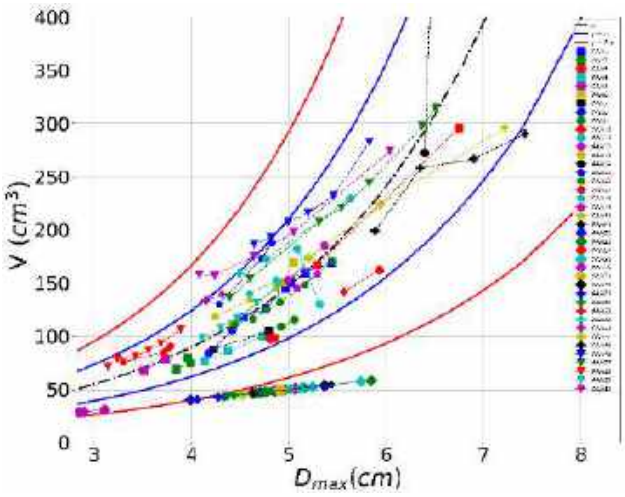

Figure 2. Maximum diameter vs. volume with nonlinear growth model within two standard deviations.

Table 2. Coefficients of determination for Groups I and II according to the predicted growth models.

Growth Model	R^2	
	Group I (n = 9)	Group II (n = 21)
Linear	0.628	0.708
Nonlinear	0.635	0.699

DISCUSSION

An ensemble averaging with curve fitting can define a certain curve that behaves exponentially [4, 9] or linearly [5]. However, the present work indicates that analyzing growth rates locally is necessary for accurate growth prediction. From Fig 2, we observed that Group I patients do not follow the exponential growth rate within two standard deviations of the mean. A separate analysis was performed leading to Group I exhibiting a nonlinear growth while Group II exhibited a linear growth. From these observations, we infer that AAAs with mean volumes of 50 cm^3 during the surveillance experience nonlinear (exponential) growth compared to AAAs with mean volumes of 75 cm^3 or greater, which experience linear growth for the clinically relevant range of maximum diameters of 4 to 6 cm.

ACKNOWLEDGEMENTS

This study was supported in part by NIH award R01HL159300.

REFERENCES

[1] Chaikof, E.L., et al., *J of Vascular Surgery*, 67(1), 2-77, 2018.
[2] Ristl, R., et al., *Int. J of Surgery*, 109(8), 2249-2257,2003
[3] Akkoyun, E., et al., *Comp and Prog in Biomech*, 208, 106256, 2021.
[4] Hirose, Y., et al., *Angiology,* 46(5), 413–419, 1995.
[5] Siika, A., et al., *Scientific Reports,* 13(1), 9283, 2023.
[6] Shum, J. et al., *Medical Physics*, 37(2), 638-648, 2010.
[7] Raut, S.S., et al., *J Biomech*, 48(10), 1972-1981, 2015.
[8] Starck, J., et al., *International Angiology,* 42(1), 65-72, 2023.
[9] Akkoyun, E., et al., *Comp in Biomed,* 117, 06256, 2020.

PROTOTYPING OF A MICROFLUIDIC MECHANOCHEMICAL GRADIENT CHIP BY 3D PRINTED MOLDING FOR IN VITRO DRUG TESTING

M. Fathi (1), A. Mehrasa (1), A. Ozcelikkale (1,2)

(1) Biomedical Engineering Department, Middle East Technical University, Ankara, Türkiye
(2) Mechanical Engineering Department, Middle East Technical University, Ankara, Türkiye

INTRODUCTION

Cancer remains to be one of the leading causes of disease-related deaths. To improve cancer treatment, it is critical to identify effective and safe drugs in the early stages of the in vitro drug screening process. However, drug tests relying on 2D/3D static cell culture is inadequate in reaching this goal since physical features of the tissue microenvironment are not incorporated in the assay. In particular, various cell biological functions including drug resistance are modulated by the mechanical environment [1,2]. While the last decade has witnessed development of microfluidic tissue and organ chips as in vitro models with improved physiological relevance [3], examples of such systems that allow systematic and controlled variation of multiple mechanobiological factors e.g. substrate stiffness and fluid shear stress, together with biochemical/drug concentration in multiplexed settings are rare [4,5]. Moreover, prototyping of microfluidic systems typically relies on photolithography that is costly and time consuming, precluding exploration of novel designs to address the drug testing problem.

To address this challenge, this study aims to develop an in vitro multiplexed *mechanochemical gradient chip* (MCGC) in which cell response can be systematically investigated under the influence of controlled gradients of flow-induced shear stress and drug concentration while cells are cultured on surfaces that can be tuned to different levels of uniform physiological stiffness (**Figure 1**). Towards this goal, prototyping of variable-height flow channels as novel design features for shear stress variation is explored in accordance with the capabilities of our recently developed 3D printing-based replica molding micromanufacturing workflow [6]. The current study includes computational design of the microfluidic chip, prototyping of its key features using stereolithography (SLA) as well as cell culture and drug testing on an early device prototype with a focus on mammary carcinoma cells, MCF-7, and chemotherapy drug doxorubicin.

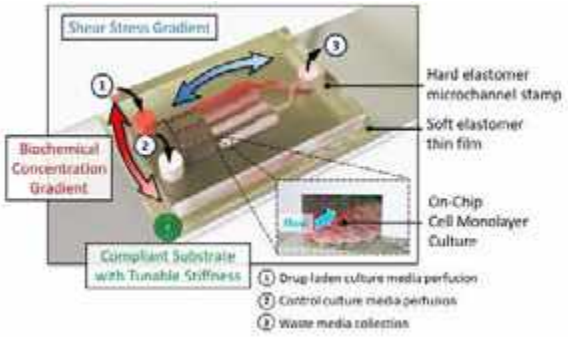

Figure 1: Conceptual design of the mechanochemical gradient chip (MCGC).

METHODS

Computational Modeling: The numerical simulations of fluid flow and species transport were conducted using Comsol Multiphysics under the assumptions of steady-state, laminar flow, and dilute species. Volumetric flow rate and normalized concentration were specified at the inlets and pressure / outflow boundary conditions were specified at the outlets as shown in **Figure 2**.

Device Fabrication: Parametric CAD models of device molds were prepared by a Python program using CadQuery library. Modls were manufactured by Anycubic Photon Mono 4K desktop LCD-SLA 3D printer using 9:1 w/w blend of clear and high-temperature (TR300) resins to prevent mold damage during PDMS baking. Molds were thoroughly washed and cleaned by ultrasonication. PDMS channel stamps were manufactured using Dowsil Slygard 184 using a polymer base to curing agent mixing ratio of 10:1 w/w. The PDMS stamps were bonded on different substrates using air corona treatment. Thin film substrates were produced by spincoating PDMS dielectric gel (Dowsil Slygard 527) on microscopy slides at 750 RPM for 15 seconds. All substrates were cured at 100°C for 210 minutes.

Imaging and Mechanical Characterization: Brightfield and fluoresence imaging of devices and substrates were performed on Nikon Eclipse Ti2 inverted microscope. Elastic moduli of substrates were estimated by measurement of indentation by stainless-steel spheres with diameters ranging between 0.8-4mm under the microscope and use of Hertzian contact theory.

Cell Culture and Drug Testing: Red fluorescent protein (RFP) tagged MCF-7 cells were seeded in channels coated with collagen type I at a concentration of 1 million cell/ml. After 24 hours chips were treated with 10 µM doxorubicin for 2 days. Images were acquired on Days 0 and 3 (0-72 hours) and analyzed by ImageJ.

RESULTS

The conceptual design of the MCGC is provided in **Figure 1**. The device features (i) a tree-like concentration gradient generator for concentration variation within the device, (ii) a culture chamber with single or multiple constant-width variable-height microchannels for shear stress variation within the device, and (iii) a compliant elastomer thin film for culture substrate stiffness variation across devices.

Whether the design leads to the desired functionalities is investigated by numerical modeling of fluid flow and species transport on chip (**Figure 2**). It is found that a well-defined nonlinear concentration gradient can be realized by asymmetric perfusion (1 drug, 2 drug-free media inlets). The nonlinear concentration gradient enables a wide-range drug concentration (20-fold in 6 discrete levels in addition to drug-free control). Similarly, a 10-fold variation of wall shear stress within physiological range is predicted across the bottom surface of the variable-height (step-wise) culture channel. Overall, the model predictions indicate that simultaneous variation of drug concentration and shear stress in orthogonal directions can be realized on MCGC.

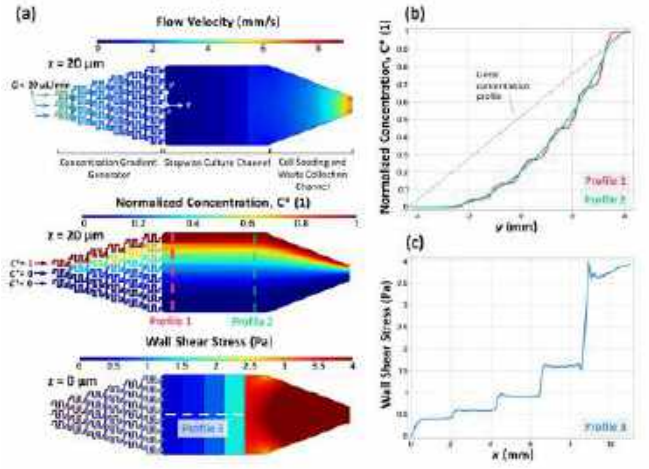

Figure 2: Numerical modeling of fluid flow and species transport. (a) Flow velocity, concentration, shear stress contours. (b) Concentration and (c) wall shear stress across indicated profiles.

Next, major design features of MCGC were fabricated and characterized (**Figure 3**). We recently developed an optimized SLA-based workflow where a CAD model of master molds are prepared by accounting for resolution limits of SLA, printed with temperature resistant resin and thoroughly cleaned by sonication to enable proper curing of PDMS stamps in the mold [6]. With this technique, variable-height microchannels with 5-fold height variation could be produced as intended. For cell culture studies, an initial prototype of the device was produced by assembling a PDMS stamp featuring a single straight microchannel (Slygard 184) with a elastomer thin film (Slygard 527, 61 ± 3 µm thick). The elastic modulus of the film was measured as 1.4 ± 0.3 kPa, in agreement with physiological stiffness [7].

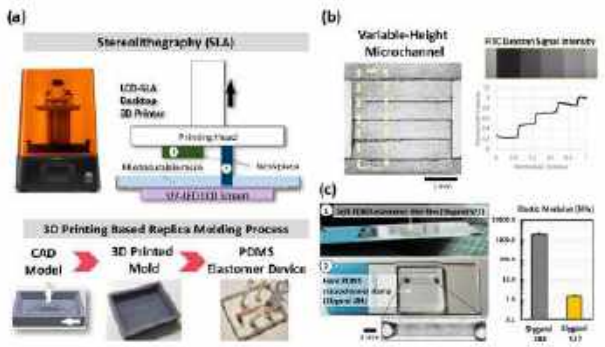

Figure 3: Fabrication characterization of device design features.

Culture of RFP-MCF7 on prototypes where 10 µM doxorubicin was introduced to the channel on day 1 and retained for the next 48 hours indicate that proliferation decreased approximately 2.5-fold in the presence of the drug compared to drug-free control (**Figure 4**).

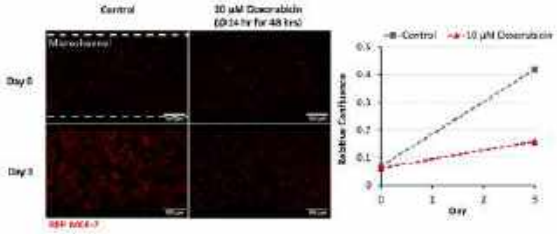

Figure 4: On-chip cell culture and drug treatment on prototype. Proliferation of MCF-7 in microchannel under doxorubicin treatment and untreated control conditions.

DISCUSSION

A microfluidic cell culture platform featuring mechanochemical gradients and physiological substrate stiffness was designed. Novel design features were fabricated and characterized. Cell culture and drug testing on a simplified prototype were illustrated. These early findings provide promising grounds for high-fidelity in vitro models that intersect mechanobiology and drug testing.

ACKNOWLEDGEMENTS

This work was partially supported by grants from TÜBİTAK (118C200) and METU (AGEP-302-2023-11236).

REFERENCES

[1] Ebata, T., Mitsui, Y., Sugimoto, W., Maeda, M., Araki, K., Machiyama, H., Harada, I., Sawada, Y., Fujita, H., Hirata, H., and Kawauchi, K., 2017, BioMed Research International, **2017**, pp. 1–10.

[2] Caymen Novak, Eric N. Horst, Charles Taylor, Catherine Z. Liu, and Geeta Mehta, 2019, Biotechnology and Bioengineering.

[3] Sontheimer-Phelps, A., Hassell, B. A., and Ingber, D. E., 2019, Nature Reviews Cancer, **19**(2), p. 65.

[4] Feng, S., Mao, S., Zhang, Q., Li, W., and Lin, J.-M., 2019, ACS Sensors, **4**(2).

[5] Bryan D. James, Nicolas Montoya, and Josephine B. Allen, 2020, Acs Biomaterials Science &Amp; Engineering.

[6] Fathi, M., Dedekargınoğlu, B., Akalın, A. A., and Ozcelikkale, A., 2023, *2nd MPS World Summit ALTEX Proceedings*, Poster Presentation, Berlin, Germany, p. 235.

[7] Palchesko, R. N., Zhang, L., Sun, Y., and Feinberg, A. W., 2012, PLOS ONE, **7**(12), p. e51499.

[8] Ozcelikkale, A. et al., 2017, Journal of Controlled Release, **266**(Supplement C), pp. 129–139.

FINITE ELEMENT SIMULATIONS OF HEART VALVE FUNCTION WITH SHAPE ENFORCEMENT IN FEBIO

Devin W. Laurence (1,2), Patricia M. Sabin (1), Steve A. Maas (3,4), Jeffrey A. Weiss (3,4), Matthew A. Jolley (1,2)

(1) Department of Anesthesiology and Critical Care Medicine, Children's Hospital of Philadelphia, Philadelphia, PA, USA
(2) Division of Pediatric Cardiology, Children's Hospital of Philadelphia, Philadelphia, PA, USA
(3) Department of Biomedical Engineering, University of Utah, Salt Lake City, UT, USA
(4) Scientific Computing Institute, University of Utah, Salt Lake City, UT, USA

INTRODUCTION

Finite element (FE) simulations are an emerging approach to predict *in vivo* heart valve function. Over the past two decades, several research groups developed in-house solvers, leveraged commercial software packages, or contributed to open-source frameworks with the goal of predicting *in vivo* valve function [1-3]. To this end, we established an *open-source pipeline* to create image-derived FE simulations of heart valve function [3]. We demonstrated that this pipeline provides meaningful comparisons of heart valve function independent of leaflet material properties [4]; however, we have not yet demonstrated acquisition of leaflet deformation from 3D images.

Rego *et al*. [5] developed a sub-routine to constrain FE simulations of heart valve function to medial approximations of the leaflet surface from cardiac images. The authors showed that this method provided accurate predictions of leaflet strains when compared to *in vitro* marker-derived strains. This paradigm has significant translational potential for the assessment of image-derived leaflet strains *in vivo* [6-7].

The objective of this work is to establish an open-source FE shape enforcement method in FEBio, leveraging the sliding-elastic interface and using the augmented Lagrangian method for constraint enforcement. Our central goal is to build upon existing efforts to provide a clinically accessible, generalized workflow for obtaining *in vivo* strains. We used two synthetic mitral valve (MV) test cases to evaluate the efficacy of the method. It is then applied in a proof-of-concept prediction of *in vivo* leaflet strains from 3D echocardiographic images of a child with congenital heart disease (CHD).

METHODS

Finite Element Simulations.

FE Mesh and Material Behaviors. The heart valve leaflets were discretized with linear quadrilateral shell elements and constitutive behavior was represented by the Lee-Sacks model [1] (**Fig. 1**). To obtain the target configuration for the synthetic test cases, the chordae tendineae were represented by tension-only linear springs (emulating [8]) connecting the papillary muscle nodes to the leaflets. The target mid-systolic leaflet surface was represented by a fixed rigid body with shell elements.

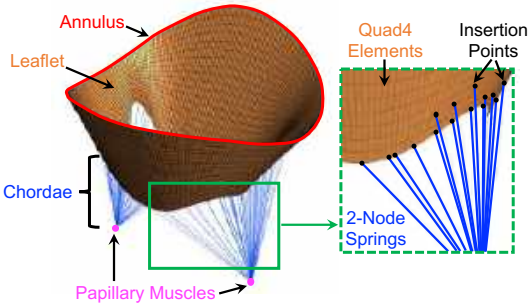

Figure 1: Mitral Valve Simulation in FEBio. The stereotypical MV is modeled using a combination of shell and spring elements.

Boundary and Loading Conditions. Heart valve closure and shape enforcement were simulated in two successive dynamic analysis steps. In the 1st step, a linearly ramped 100 mmHg pressure was applied to the ventricular leaflet surface over 0.05 s and maintained for an additional 0.05 s to achieve steady state. In the 2nd step, the sliding-elastic interface between the simulated and the target leaflet surfaces was enabled.

Chordae Emulating Force. The chordae tendineae were approximated during shape enforcement by a chordae-emulating force (CEF) to improve convergence. The force was applied to the leaflet free edge nodes normal to the annulus plane, and linearly ramped like the applied ventricular pressure. We varied the constitutive model parameters and CEF to determine the optimal CEF that minimizes discrepancies between the shape enforcement results and the known (synthetic) test case. Comparisons were made using the Kolmogorov-Smirnov test.

Sliding-Elastic Interface. The sliding-elastic interface in FEBio seeks

to enforce contact between two surfaces by minimizing the surface-surface gap function [9]. We used a two-step process in which the gap function was: (1) linearly penalized to gradually reduce the surface-surface distance and (2) minimized by approximating the Lagrangian multipliers using the augmented Lagrangian approach.

Simulation Test Cases. We established three test case geometries.

Test Case 1: Simplified Mitral Valve Contact. The first synthetic test case considered contact between the center of two mitral valve leaflets. The target (mid-systolic) surface was achieved by prescribing a ventricular pressure of 13.3 kPa (100 mmHg), and shape enforcement was performed considering one-half pressure (6.66 kPa).

Test Case 2: Stereotypical Mitral Valve. The second synthetic test case considered a stereotypical mitral valve geometry. Like Test Case 1, the target synthetic surface was obtained using a pressure of 13.3 kPa, whereas the shape enforcement considered one-half pressure (6.66 kPa).

Test Case 3: In Vivo Proof-of-Concept. The shape enforcement technique was used to predict *in vivo* leaflet strains for a pediatric patient with CAVC. Unlike the two synthetic cases: (1) the target mid-systolic leaflet surface was obtained from the patient's cardiac images [3], (2) the annulus followed the *in vivo* dynamic motion, and (3) the shape enforcement considered 13.3 kPa approximate ventricular pressure. This was done in accordance with a protocol approved by the Institutional Review Board at the Children's Hospital of Philadelphia.

RESULTS

Tissue Stretch-Dependent Chordae Emulating Force. We found that the optimal CEF depends on the peak stretch of the constitutive model (**Fig. 2**). The relationship for c_0 is independent from that of c_1 and c_2.

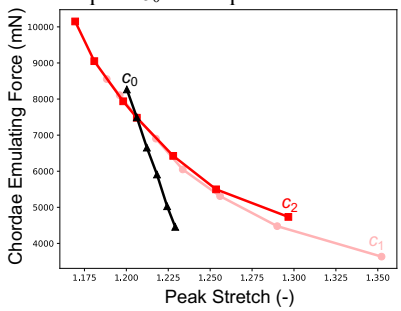

Figure 2: CEF Optimization. The optimal chordae emulating force is related to the tissue stretch, and independently relies on the c_0 term.

Shape Enforcement Accurately Predicts Leaflet Strains. We found that shape enforcement provided good predictions of the synthetic results (**Fig. 3**). The error was larger for the complete MV in the anterior leaflet (~0.1 vs. ~0.03), suggesting there is room for improvement.

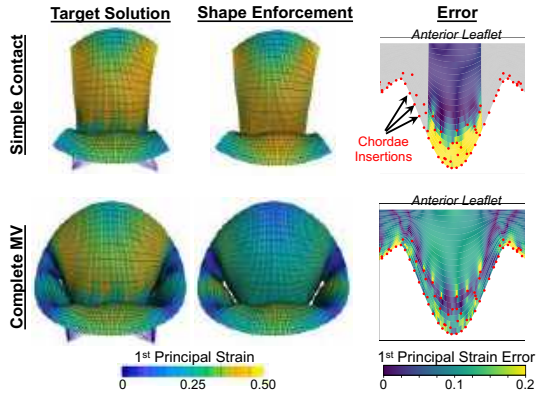

Figure 3: Synthetic Test Cases. Shape enforcement provided excellent agreement with the synthetic test cases.

Patient-Specific Leaflet Strains for Pediatric Patient with CHD. The FE Simulation with shape enforcement for the *in vivo* proof-of-is shown in **Figure 4**. Interestingly, the in-plane principal strains show the valve experiences a combination of tension and compression *in vivo*.

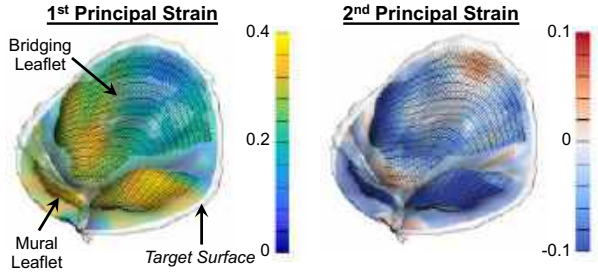

Figure 4: Patient-Specific Shape Enforcement. The simulation provided good visual agreement with the target surface. This patient-specific valve experiences in-plane tension and compression *in vivo*.

DISCUSSION

In this investigation, we evaluated the FEBio sliding-elastic interface for shape enforcement of heart valve simulations fit to mid-systolic leaflet surfaces. The shape enforcement simulations were simplified by replacing the chordae tendineae with a "chordae-emulating force" applied to the free edge of the leaflets [5]. We found that the optimal CEF depends on the tissue extensibility, and the modulus of the Neo-Hookean term (c_0). Next, we showed that our proposed method reproduces the valve leaflet strains for two synthetic test cases. This approach was insensitive to the choice of applied pressure and noise in the target surface (not shown here for brevity). However, we did note the anterior leaflet strain predictions were worse for the complete MV geometry. Finally, we extended the method to predict *in vivo* leaflet strains for a pediatric patient with a complex CHD. This work cumulatively provides a new open-source means for predicting *in vivo* heart valve strains with FE simulations.

There are several limitations and extensions of this work. First, although shape enforcement has been previously validated [5], it would be prudent to perform a similar assessment of our new shape enforcement method. Our forthcoming work will provide the experimental data to accomplish this, and we have currently opted to use synthetic computational data for this purpose. Second, we have only showcased one *in vivo* proof-of-concept. Expanding this effort to consider more patients and different CHD is an ongoing effort in our research group. Third, the CEF must be optimized to minimize its impact on the predicted strains. Future efforts may enhance the method to include additional anatomical constrains (e.g., free edge) between the surfaces. Finally, we only predict the mid-systolic leaflet strains. In the future, we will consider adding multiple time points throughout the cardiac cycle to create true "dynamic" simulations, and improve predictions of complex behaviors (e.g., commissure folding).

ACKNOWLEDGMENTS

Supported by the Additional Ventures Single Ventricle Research Fund, the Cora Topolewski Pediatric Valve Center at CHOP, the Topolewski Endowed Chair, NIH 1R01HL153166, 2R01GM083925 (SAM, JAW), and T32 HL007915 (DWL).

REFERENCES

[1] Lee, C.-H. *et al*., *JB*, 47(9):2055-2063, 2014. [2] Laurence, D.W. *et al*., *IJNMBE*, 36(7):e3346, 202020. [3] Wu, W. *et al*., *JBME*, 144(10):101012, 2022. [4] Wu, W. *et al*., *JMBBM*, 142:105858, 2023. [5] Rego B.V. *et al*., *IJNMBE*, 34(12):e3142, 2018. [6] Simonian, N.T. *et al*., *CET*, 14(5):677-693, 2023. [7] Narang, H. *et al*., *ABME*, 49:3711-3723, 2021. [8] Ross, C.J. *et al*., *ABME*, 48:1463-1474, 2020. [9] Ateshian, G.A. *et al*., *JBME*, 132(6):061006, 2010.

CORRELATION OF PAIN SYMPTOMS IN MILITARY FIGHTER PILOTS WITH SPINAL MORPHOLOGY OBTAINED USING SUPINE AND UPRIGHT MRI SCANS

Rachel Cutlan (1), Vaibhav Porwal (2), Riley McCarty (2), Cory Everts (2,3), Alok Shah (2), Amy Nader (2), Keeley Hamill (2), Narayan Yoganandan (2,4), Keri Hainsworth (5), L. Tugan Muftuler (2), Timothy Meier (2), Hershel Raff (6), Peter Le (7), Chris Dooley (7), Benjamin Gerds (3), Brian D. Stemper (1,2,4)

(1) Department of Biomedical Engineering, Marquette University and Medical College of Wisconsin, Milwaukee, WI, USA
(2) Department of Neurosurgery, Medical College of Wisconsin, Milwaukee, WI, USA
(3) 115th Fighter Wing, Wisconsin Air National Guard
(4) Zablocki Veterans Affairs Medical Center, Milwaukee, WI, USA
(5) Department of Anesthesiology, Medical College of Wisconsin, Milwaukee, WI, USA
(6) Department of Medicine, Surgery, Physiology, and the Cardiovascular Center, Medical College of Wisconsin, Milwaukee, WI, USA
(7) Air Force Research Laboratory, Dayton, OH, USA

INTRODUCTION

Neck and back pain are commonly reported ailments for fighter pilots around the world, with up to 97% of fighter pilots reporting neck pain (1). This pain is often exacerbated by essential neck rotations during flight, such as "checking six," that places the pilot in an awkward and vulnerable position while experiencing high G_z forces on the neck and back (1).

Exposure to high G_z forces may contribute to early functional changes in the spine. Fighter pilots exhibit decreased cervical spine range of motion (CROM) compared to civilians, and older pilots exhibit decreased CROM compared to younger pilots (2,3). Fighter pilots also exhibit signs of increased spinal degeneration compared to civilians (4). Petran-Mallmin demonstrated that even asymptomatic fighter pilots exhibit more osteophytes, disc protrusions, spinal cord compressions, and foraminal stenosis compared to age matched controls (5).

The etiology of neck and back pain experienced by fighter pilots has not been clearly defined. This study aims to determine the etiology of this pain by exploring both chronic and acute pain utilizing pain assessments and MRI scans.

METHODS

Wisconsin Air National Guard (WIANG) fighter pilots completed baseline demographic and flight history surveys, pain assessments, cervical spine supine MRIs, and upright cervical and lumbar spine MRIs. Pilots completed the Pain-DETECT pain assessment at baseline to quantify the nature of their pain. The most common descriptions chosen for the course of pain were "persistent pain with slight fluctuations" and "persistent pain with pain attacks". These two responses were used to place pilots into either a constant pain group or a group that had pain flare ups likely associated with activity.

The Pfirrmann grading scale was used to grade cervical and lumbar intervertebral discs for degeneration (6). Ratings and measurements were completed on mid-sagittal T2-weighted images.

Normalized disc height was quantified for C2-3 to C7-T1 and T12-L1 to L5-S1. The anterior, middle, and posterior disc and vertebral body heights were measured, averaged for the three measurements, and average disc height was divided by average inferior vertebral body height for normalization. Lumbar and cervical posterior disc bulge was measured using a previously described methodology (7).

All statistical analyses were conducted in RStudio 2023.03.0. Non-parametric statistics were utilized when a Shapiro-Wilk normality test revealed a non-normal distribution. Kruskal-Wallis rank sum tests were used to test for differences between supine and upright cervical MRI measurements and differences between the pain type groups. Wilcoxon signed rank tests were used to determine significant pairwise differences. A significance level of $p<0.05$ was used for all tests.

RESULTS

Sixteen WIANG fighter pilots participated in this study with an average age of 39.3 (range: 28-49) years and an average of 2,312 (500-3,500) military flight hours.

Sixteen pilots participated in supine MRI scans and fifteen pilots participated in upright MRI scans. Ninety-six cervical discs (levels C2-3 to C7-T1) and 84 lumbar discs (levels T12-L1 to L5-S1) were analyzed. The total of disc grades for each pilot was not correlated with age (cervical: $p=0.59$, lumbar: $p=0.34$). One pilot had a grade IV disc at C2-3 and seven pilots had a grade IV discs at L5-S1. The most common location of degenerated discs (grade II and above) was C2-3, C3-4 and L5-S1. Fifty-five percent and 67% of cervical and lumbar spine discs were classified as healthy (Pfirrmann grade I) respectively.

The intrarater reliability of disc height measurements was 0.878, using Pearson's correlation coefficient.

Normalized disc height was related to cervical spinal level ($p<0.001$). Normalized C7-T1 disc height was smaller than all other cervical discs ($p<0.001$). The Cobb angle and posterior disc height were dependent on the type of MRI. Cervical Cobb angle was greater for subjects during the upright scan compared to the supine scan ($p=0.05$). Measured posterior disc height was greater in the supine scans at C2-3 ($p=0.007$), C3-4 ($p=0.05$) and C4-5 ($p=0.02$) compared to measured posterior disc height in the upright scans. Disc bulge was different between cervical spinal levels for both supine ($p<0.001$) and upright ($p=0.03$) MRI scans. The largest disc bulge tended to occur between C4-5 and C6-7. There were no differences in disc bulge measurements between the supine and upright scans ($p=0.43$).

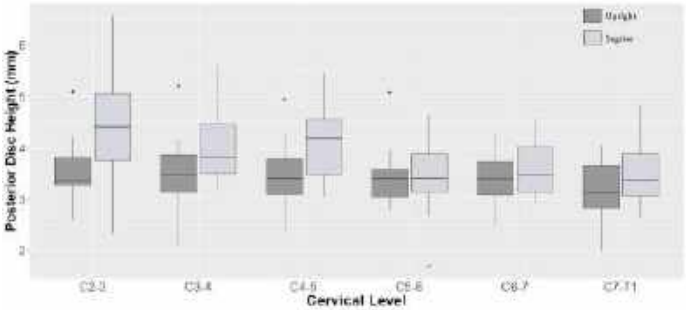

Figure 1: Posterior intervertebral disc heights for the cervical spine for upright and supine scans.

There was no difference in age ($p=0.45$) or total military flight hours ($p=0.51$) between the two pain groups.

There were no differences in normalized disc height across the cervical spine in the supine or upright scans between the pain flare up group and the constant pain group. There was a trend toward decreased disc height at C2-3 (supine: $p=0.18$) and C3-4 (supine: $p=0.22$; upright: $p=0.15$) for the pain flare up group compared to the constant pain group. The pain flare up group displayed a trend toward increased average cervical Pfirrmann grade (median: 1.75; range: 1.5-2.2) compared to the constant pain group (median: 1.42; range: 1-1.83) ($p=0.09$).

Normalized disc height was related to lumbar spinal level ($p<0.001$). Normalized disc height increased from T12-L1 to L3-4, then remained steady until L5-S1, where height decreased ($p's<0.1$). The pain flare up group demonstrated decreased normalized disc height at T12-L1 compared to the constant pain group ($p=0.02$). The constant pain group displayed a trend toward an increased average lumbar Pfirrmann grade (median: 1.83; range: 1-2.17) compared to the pain flare up group (median: 1.25; range: 1-1.83) ($p=0.13$).

Lumbar spine disc bulge size was related to lumbar spinal level ($p=0.02$). The disc bulge size was greater for caudal lumbar discs. The constant pain group had increased disc bulge size at the L5-S1 disc compared to the pain flare up group ($p=0.02$).

DISCUSSION

This study explored cervical and lumbar spine degenerative intervertebral disc changes experienced by fighter pilots and compared those changes between two pain groups: constant pain and pain flare ups. Our sample of fighter pilots exhibited disc degeneration in the upper cervical spine (C2-3 and C3-4). Cervical disc degeneration in fighter pilots has previously been reported to occur at C5-6 (4,8). Our sample of fighter pilots exhibited degeneration at a higher level in the cervical spine compared to previous studies; this may be related to the extreme head positions and rotations necessary during flight.

Our sample of fighter pilots also exhibited the most extreme disc degeneration in the lower lumbar spine, specifically L5-S1. This finding is confirmed by other studies investigating spinal changes in fighter pilots (8,9). Fifty percent (7/14) of the L5-S1 discs examined were given a Pfirrmann grade IV. This high prevalence of severe degeneration is not found in the civilian population at any age. Civilians aged 61-70 have the highest reported prevalence of grade IV degeneration at L5-S1 at around 20% (10). Fighter pilots enrolled in this study demonstrated increased and more severe degeneration in the lower lumbar spine compared to civilians at a much older age.

Differences were also observed in comparing supine and upright measurements. Upright MRI places subjects in a position where the cervical spine bears the weight of the head and the lumbar spine bears the weight of the body. This led to increased cervical lordosis. Accordingly, posterior disc height was also decreased, and disc bulge increased in the upper cervical spine for upright MRI scans. These types of findings may help to explain differing pain symptoms and severity in fighter pilots compared to the civilian population.

To our knowledge, this is the first study to explore structural etiology for differing pain presentations in fighter pilots. These preliminary findings demonstrated that the pain flare up group may have increased upper cervical spine degenerative changes. Three of the four pilots in the pain flare up group had the lowest upper cervical spine disc heights. The lack of statistical significance between the two pain groups is most likely due to the small sample size. Most fighter pilot MRI studies have focused on comparing fighter pilot scans to age-matched control subjects and have not focused on differences related to pain characteristics. Rintala et al. compared cervical and lumbar MRI findings to pain complaints and found no significant associations; this study focused on a much younger sample of pilots (11). Our sample encompassed pilots of various ages, allowing the unique opportunity to more thoroughly explore pain related to functional changes.

Our study will follow the same sample of fighter pilots over the next three years. Previous studies reported that cervical spine degeneration occurred at an increased pace in fighter pilots compared to controls (12). Our study will compare MRI scans at timepoints twice a year for three years to track the accelerated degenerative changes related to high G_z exposure in both the cervical and lumbar spine.

ACKNOWLEDGEMENTS

This research was supported by Air Force Research Laboratory contract FA8650-22-C-6461 and the Department of Veterans Affairs Medical Research. The views expressed are those of the authors and do not reflect the official views of the United States Air Force, nor the Department of Defense. Mention of trade names, commercial products, or organizations do not imply endorsement by the U.S. Government.

REFERENCES

[1] Lange B, *Aviat Space Environ Med,* 82(5):559-63, 2011.
[2] Alricsson M, *Aviat Space Environ Med,* 72(4):336-42, 2001.
[3] Espejo-Antúnez L, *Diagnostics,* 12(2):233, 2022.
[4] Hamalainen O, *Aviat Space Environ Med,* 64(8):692-6, 1993.
[5] Petren-Mallmin M, *Aviat Space Environ Med,* 72(5):443-6, 2001.
[6] Pfirrmann, CWA, *Spine,* 26(17):1873-8, 2001.
[7] Cooley J, *J Manipulative Physiol Ther,* 24(5):317-26, 2001.
[8] Sovelius R, *Aviat Space Environ Med,* 79(7):685-8, 2008.
[9] Landau, DA, *Aviat Space Environ Med,* 77(11):1158-61, 2006.
[10] Oh CH, *Korean J Spine,* 14(4):148-54, 2017.
[11] Rintala H, *Biomedical Human Kinetics,* 9(1):133-9, 2017.
[12] Keskimolo T, *BMG Mil Health,* 169(4):291-6, 2023.

BIOMECHANICAL VARIABILITY IN COMPOSITE LUMBAR SPINE SURROGATES DURING MULTI-LABORATORY COLLABORATIVE TESTING

Emma C. Coltoff[1], Jeremy G. Loss[2], Siril T. Dukkipati[3], Jenna M. Wahbeh[4], Kalle L Chastain[5], Matthew H. Pelletier, PhD[6], Tian Wang, PhD[6], Philip J. Brown[1], Mark Driscoll[3], Sophia Sangiorgio[4], Edward Ebramzadeh[4], Kathleen Meyers[5], William R. Walsh[6], G. Bryan Cornwall[6,7], Brian Kelly[8], Robb W. Colbrunn[2]

[1]Department of Biomedical Engineering, Wake Forest School of Medicine, Winston-Salem, North Carolina, USA
[2]Lerner Research Institute, Cleveland Clinic, Cleveland, Ohio, USA
[3]Department of Mechanical Engineering, McGill University, Montreal, Quebec, Canada
[4]JVL Orthopaedic Research Center, University of California – Los Angeles, Los Angeles, California, USA
[5]Hospital for Special Surgery, New York City, New York, USA
[6]Surgical and Orthopaedic Research Laboratories, University of New South Wales, Sydney, New South Wales, Australia
[7]University of San Diego, San Diego, California, USA
[8]Barrow Neurological Institute, Phoenix, Arizona, USA

INTRODUCTION

Standardizing spine biomechanical testing is challenging due to a wide array of factors – from testing and measurement equipment variability to specifics of test protocol and specimen handling. In this study, seven international laboratories aimed to characterize the magnitude of variability in biomechanical testing outcomes when each laboratory used their "standard" equipment, experimental procedures, testing protocols, data collection, analysis tools, and data management systems. The objective of this study was to quantify outcome variation during standard practices to identify areas of potential standardization.

METHODS

A total of nine Sawbones synthetic lumbar spinal surrogates were obtained by the labs participating in this study. The group of nine were split into sub-groups of five and four spines, which travelled in opposing order through the seven participating labs. Each lab conducted pure moment testing on the surrogates in Flexion-Extension (FE), Lateral Bending (LB), and Axial Rotation (AR) following whatever protocol was deemed "standard" for the lab. The "standard" approach resulted in a mixture of trapezoidal and sinusoidal loading schemes, testing rigs, bending measurement methods, and fixturing choices, summarized in Table 1. Each lab reported the joint translations and rotations for the overall specimen in a joint coordinate system (JCS). The consortium met monthly to discuss findings as each group completed testing on the set of five spines. R was used to perform a linear mixed effects analysis on the effects of test rig, loading approach, and resetting on the resulting bending measures for each loading direction.

Table 1: Summary of equipment and testing choices for each lab. Quantity of each choice denoted by bolded number.

Summary Equipment Table					
Test Rigs	Testing Approach	Specimen Removal	Software	Load Cell	Measurement Method
Robotic Arm **4** -KUKA (3) -Denso (1)	*Primary:* Trapezoidal, *Secondary:* Sinusoidal **2**	No specimen removal/resetting during testing **5**	simVITRO **4**	ATI **4**	NDI **4**
Universal Testing Systems (UTS) **2** -Instron (1) -MTS 1)	*Primary:* Sinusoidal, *Secondary:* Trapezoidal **3**	Specimen removal/resetting during testing **2**	NDI **1**	AMTI **1**	Motion Analysis Corp **2**
Custom Gantry Robot **1**	Sinusoidal Only **2**		Omron **1**	JR3 **1**	From Testing Rig **1**
			Instron **1**	Instron **1**	

RESULTS

The data in this study is only reported for the group of five spines. All labs reported, at a minimum, the rotation angles (in degrees) in FE, LB, and AR for the JCS kinematics of each of the L2-L5 lumbar spinal surrogates. This resulted in average

rotation values in the six primary testing directions as follows: flexion (14.8±2.7°), extension (9.9±1.7°), left lateral bending (11.2±1.6°), right lateral bending (11.8±1.6°), left axial rotation (4.5±1.0°), and right axial rotation (3.8±0.8°). However, reporting these average values alone does not properly capture the variability in bending measures that the surrogates experienced throughout the testing sequence. The following significant effects were identified:

- Test rig had a significant effect on flexion (p = 0.005), raising it 1°±0.26° when using a UTS system over other choices (Figure 1).

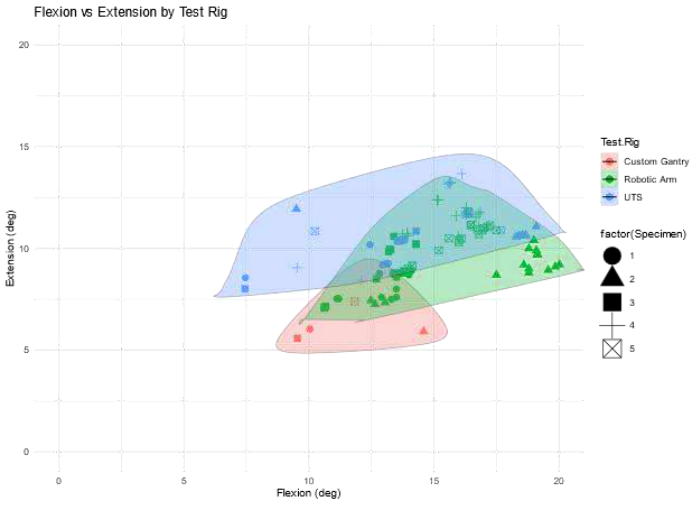

Figure 1: Flexion/Extension data compared against Test Rig.

- Loading approach alone had a significant effect on right axial rotation (p = 0.03), raising it 0.4°±0.17° (Figure 2).

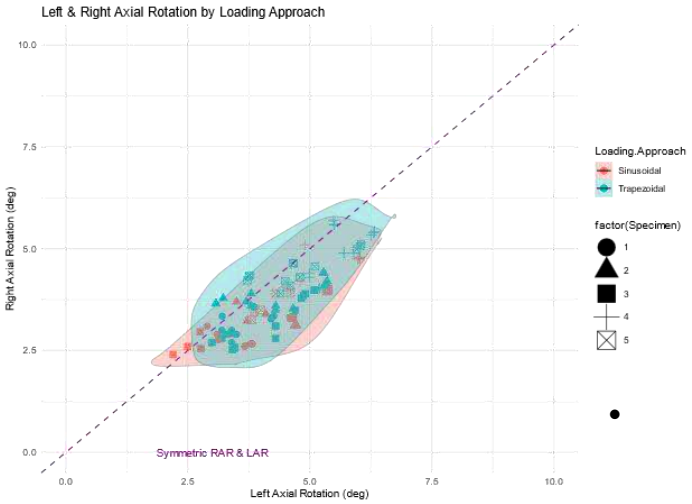

Figure 2: Axial Rotation data compared against Loading Approach.

- Test rig combined with loading approach significantly effected flexion and extension (p = 0.005 and 0.001, respectively).
- Test rig combined with resetting had a significant effect on flexion and extension (p = 0.003 and 0.002, respectively), decreasing flexion but increasing extension by 1.1°±0.3°.

DISCUSSION

This dataset can be used to establish best practices with respect to equipment, procedures, loading protocols, and data analysis. Differences in measured range of motion in each of the testing directions may only be partially accounted for by variability in the specimens themselves. A mixture of testing equipment was used by the participating labs, which may account for differences in both measurement and reporting. Additionally, differences in loading profiles (trapezoidal vs sinusoidal), as well as choices made regarding which trials of testing are representative of true specimen bending, may also impact reported measures.

The group of four spines will also be analyzed for variance in biomechanical behavior and facilitate removal of time as a variable in assessment for the full group of nine specimens due to their alternate path through the participating labs than the group of five spines.

Future work will be conducted to characterize the effects of these factors to identify potential best practices for future spine biomechanical research. Inter-laboratory studies are a crucial part of the standardization of any test protocol and for the wider dissemination of best practices. The labs in this group are representative of global biomechanics labs and will be able to help make recommendations regarding how equipment and protocol execution may impact data accuracy for future spine biomechanics testing.

ACKNOWLEDGEMENTS

The authors would like to acknowledge Sawbones for funding and support of the transportation of the spine surrogates between the participating labs.

IN SITU ROBOTIC MECHANICAL TESTING OF RAT TIBIOFEMORAL JOINTS

Olivia L. Dyer (1), Stephanie G Cone (1)

(1) Biomedical Engineering, University of Delaware, Newark, DE, USA

INTRODUCTION

Small animal models are frequently employed in orthopaedic research including studies of the tibiofemoral (knee) joint. While there have been many innovations in imaging, biological, and behavioral analyses of rat and mouse models [1], there have been relatively few innovations in the biomechanical testing of small animal joints in recent years. Improved biomechanical analysis techniques are of great importance for the direct translation of findings in preclinical studies to biomedical research in human medicine due to the prioritization of functional outcomes in orthopaedic clinical decision making [2]. The current standard for biomechanical testing in rodent joints involve uniaxial manipulation, isolating the load-deformation relationships in a single plane of motion. However, joint function – for example in the knee – cannot be simplified to a single plane. In healthy motion, and even more so in injured cases, joint alignment varies through a series of rotations and translation in all six degrees of freedom to optimize tissue loading and joint stability. To account for these complex motions in biomechanical assessments, the objective of this study was to establish a multi-axial robotic testing system for small animal joint testing, and to apply the system to an orthopaedic topic of great interest: anterior cruciate ligament (ACL) rupture. We hypothesized that ACL rupture would result in destabilization of the rat knee joint in multiple degrees of freedom as revealed through clinically relevant testing strategies.

METHODS

Tibiofemoral joints were collected post-mortem from mature Long Evans rats (n=6) and stored fresh-frozen wrapped in saline-soaked gauze prior to testing. To prepare the joints for robotic testing, all soft tissue was dissected away above and below the joint capsule, and the femur and tibia were bisected in the center of the diaphysis. The bones were then set in custom printed clamps using dental cement. Specimens were kept hydrated with saline throughout all preparation and testing stages.

Robotic testing was performed using a tabletop 6-degree-of-freedom universal force sensing robotic testing system consisting of a Meca500 robotic arm (Mecademic, Montreal, Canada), a multiaxial load cell (ATI Nano25 IP65), and commercially available software (simVITRO, Cleveland Clinic) (Figure 1). Robotic testing followed a similar workflow to previously published studies in large animal models [3].

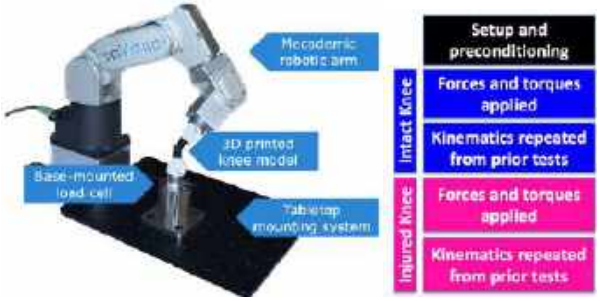

Figure 1: Robotic testing system and testing flowchart.

Briefly, intact joints were affixed proximally to the robotic arm and distally to the load cell and an approximate joint coordinate system was established using digitization of anatomic landmarks based on the Pennock adaptation of the Grood & Suntay convention [4]. The joint was manipulated through passive flexion-extension (20°-60°) and varus-valgus paths (± 0.05 Nm varus torque, @ 40° flexion). For both loading paths, internal rotation was set to 0°, compression loads to 1 N and all other loads minimized. An algorithm was applied to establish functional coordinate systems, redefining the tibia and femur origins and the femur flexion axis [5]. This functional coordinate system was used throughout the remainder of testing to implement the following clinically relevant exams: anterior-posterior (AP) drawer testing at 20°, 40°, and 60° of flexion and varus-valgus (VV) torque testing at 40° of

flexion. Joint flexion angles were limited to a functional working range for the rat knee anatomy, and peak applied forces were set at 2.5N of anterior and posterior force and 0.025N*m of varus and valgus torque due to the size of the joints. This set of AP and VV exams were performed on the intact joint in hybrid control, such that all DOF were controlled with kinetics, except flexion and internal rotation, which were controlled with kinematics. 6DOF kinetics and kinematics were recorded and the resulting kinematics established "intact testing paths". The intact rat knees underwent the "intact testing paths" in kinematic control. Next, the ACL was transected and the AP and VV exams were performed under hybrid control in the injured state. The injured state kinematics were recorded, establishing "injured testing paths". The injured rat knees underwent the "injured testing paths" in kinematic control. Finally, serial dissection was performed with the collateral ligaments, menisci, and posterior cruciate ligament, where the rat knee underwent "intact testing paths" and "injured testing paths" in kinematic control after each sequential dissection. The principle of superposition was used to determine the functional contributions of each tissue under AP forces and VV torques.

Statistical analysis included repeated measures ANOVA testing of joint kinematics and tissue function between injury states (alpha = 0.05).

RESULTS

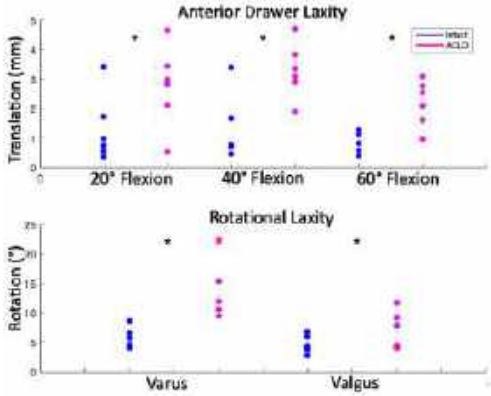

Figure 2: Anterior and rotational laxity increased in all specimens (points) with ACL injury, * represents p<0.05 between states.

Application of anterior-posterior loads (2.5N) and varus-valgus moments (0.025N*m) resulted in mean anterior tibial translations of 1.2 mm and 10.4° of varus-valgus rotation at 40° of flexion (Figure 2, all states summarized in Table 1). Increasing knee flexion during anterior drawer testing resulted in significant decreases in anterior tibial translation within specimens ($p<0.05$ across cases) and decreasing variability between joints. The ACL was the primary soft tissue restraint to anterior tibial drawer across flexion angles (percent load carriage across flexion angles: 51% @ 20°, 94% @ 40°, 97% @ 60°) and contributed significantly to resisting varus-valgus torques.

Table 1: Anterior, varus, and valgus laxity measures (mean ± std).

Anterior translation laxity (mm)			
Flexion angle	20°	40°	60°
Intact	1.30±1.13	1.29±1.10	0.76±0.37
ACL-injured	2.77±1.37	3.31±0.93	2.19±0.79
Rotational laxity at 40° flexion			
	Varus	Valgus	
Intact	5.64°±1.74°	4.71°±1.48°	
ACL-injured	15.34°±5.77°	7.58°±2.94°	

ACL injury resulted in a significant increase in joint laxity across all tests, with 2- to 3-fold increases in anterior tibial translation, 3-fold increases in varus rotation, and 2-fold increases in valgus rotation (Figure 3, Table 1). Following ACL rupture, anterior drawer forces were restrained by the MCL and menisci, varus torques by the medial meniscus and the LCL, and valgus torques by the lateral meniscus and the MCL. Valgus rotations were least affected by ACL rupture.

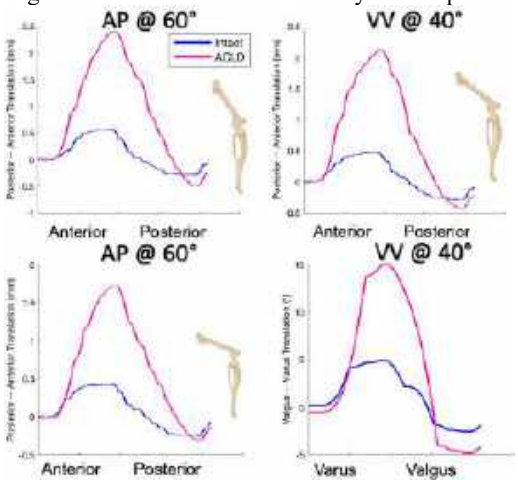

Figure 3: Intact and injured kinematics from a rat knee joint.

DISCUSSION

Multi-axial robotic testing revealed two- to three-fold increases in joint laxity in the rat knee following ACL rupture with both anterior-posterior and varus-valgus challenges. The ACL is the primary passive restraint against anterior tibial drawer across flexion angles, and with the menisci and collateral ligaments the ACL resists varus and valgus torques. This study is the first of its kind, describing multi-axial knee joint mechanics in a rodent model. This innovation is a bridge for functional assessments of orthopaedic studies in common preclinical animal models. The outcomes of this study agree with prior expectations of rat knee function, confirming that the ACL is a pivotal stabilizing tissue in the rat. With the multi-axial hybrid controls demonstrated in this work, more complex testing with rotational controls and dynamic testing modalities are available in the translational biomechanics field. This study was limited in scope due to the availability of specimens, however future work will aim to assess sex- and age-dependent differences in baseline rat knee joint function. Additionally, future studies will address the functional effects of common injury models in rats and mice such as destabilizations of the medial meniscus (DMM).

In summary, this work is the first presentation of multi-axial robotic joint testing in a small animal (rat) model, establishing a new standard of testing for joint laxity in both healthy and injured specimens. This line of study provides value in the translational research field, better informing conclusions from preclinical studies in rodent models and enabling robust assessments of the functional impacts of standard experimental approaches in rodents in future studies.

ACKNOWLEDGEMENTS

This project was supported by the Delaware Center for Musculoskeletal Research (NIH P20GM139760). We additionally thank Tara Nagle for her contributions to this work.

REFERENCES

[1] Little, D et al., *J Orthop Res,* 2023. [2] Woo, SLY et al., *J Orthop Res*, 2006. [3] Cone, S et al., *Clin Orthop Rel Res,* 2019. [4] Pennock, G et al., *J Biomech*, 1999. [5] Nagle, T et al., *J Biomech*, 2021.

MEDICAL IMAGING BASED PATIENT-SPECIFIC BLOOD FLOW MODELLING OF CEREBROVASCULATURE

Amar. Shrivastava (1), Ashish. Suri (2), Sitikantha. Roy (3)

(1) Department of Applied Mechanics, Indian Institute of Technology Delhi, New Delhi - 110016, Delhi, India
(2) Department of Neurosurgery, All India Institute of Medical Sciences, New Delhi - 110029, Delhi, India
(3) Department of Applied Mechanics, Indian Institute of Technology Delhi, New Delhi - 110016, Delhi, India

INTRODUCTION

Cerebrovascular diseases refer to conditions that affect the blood vessels in the brain, leading to a decrease in oxygen and nutrient supply. These diseases include ischemic strokes, hemorrhagic strokes, and transient ischemic attacks (TIAs). Stroke is the leading cause of long-term disability and the third most common underlying cause of death in the United States. Moyamoya is a type of cerebrovascular disease that describes an unusual angiographic image revealing blood vessels located at the base of the brain, collaterals formation, and blockage of the internal carotid artery as shown in **Figure 1**. The term "Moyamoya" is of Japanese origin, meaning something hazy, like a puff of cigarette smoke floating in the air [1]. The primary goal of this study is to perform steady-state and pulsatile bio-fluid dynamic simulations of magnetic angiography Moyamoya patient-specific geometries to predict stroke and TIAs [2].

METHODS

The computational modelling of cerebrovascular disease and stroke is based on two equations: the Continuity equation (1) and the Navier-Stokes equation (2). To model blood, the Carreau-Yasuda model is utilized, which considers it as a non-Newtonian fluid. To find out the bio-mechanical parameters, overall computational framework has been designed as depicted in **Figure 2** and patient details have been shown in **Table 1**.

Equations

$$\nabla . v = 0 \quad (1)$$

$$\rho(v.\nabla v) = -\nabla p + \mu\nabla^2 v + f \quad (2)$$

RESULTS

The biomechanical simulation performed *in silico* demonstrated that the Superficial Temporal Artery-Middle Cerebral Artery bypass surgery has enhanced the wall shear stress (WSS) of the artery as shown in **Figure 3**. The distal branches of MCA now have lower total pressure, and the bypass exhibits higher total pressure, which facilitates the blood flow into these veins. The regions with low WSS are more vulnerable to developing atherosclerosis, which can cause ischemic stroke and transient ischemic attack (TIA).

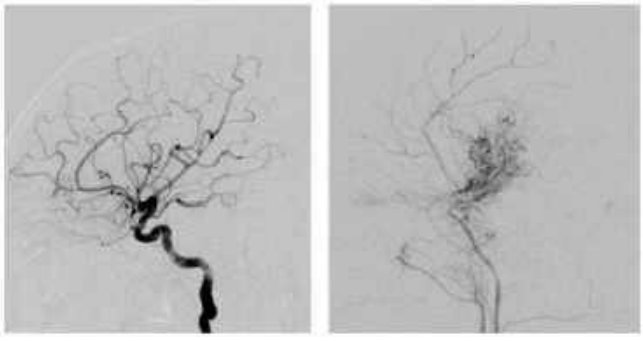

Figure 1: Image on the left showing normal vasculature of a healthy adult and on right hand side of Moyamoya disease patient.

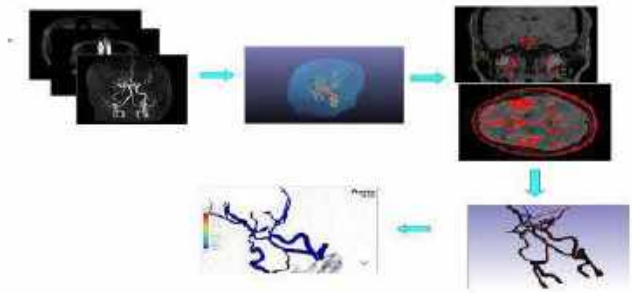

Figure 2: Medical imaging based computational workflow for patient-specific biomechanical analysis.

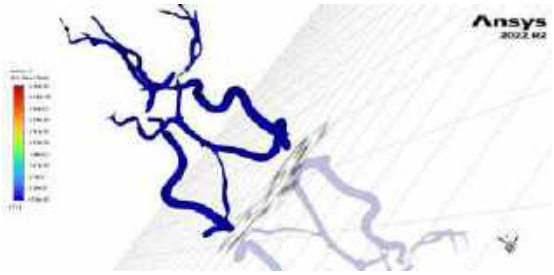

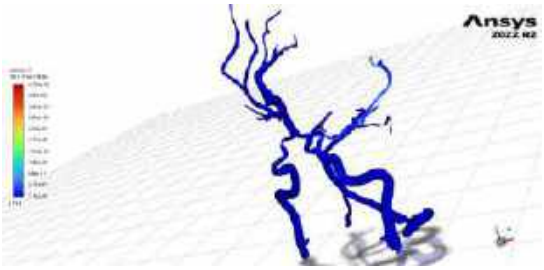

Figure 3: Pre- and post- operative changes in Wall Shear Stress (WSS) in the computational cerebrovascular domain.

Table 1: Radiological details of patient, fluid dynamics modelling and boundary conditions.

Subject No.	Imaging modality	Mathematical Modelling	Inlet B.C.	Outlet B.C.	Wall B.C.
1	MRA	Non-Newtonian model	Velocity B.C.	Pressure	Rigid

DISCUSSION

Hemodynamic flow patterns may lead to thrombus formation, increasing the risk of acute ischemic stroke. Artery walls exposed to low WSS are prone to atherosclerosis, which is the deposition of fatty material on their inner walls along with platelet aggregation. Conversely, high WSS induces platelet activation. The current limitation of our study is we have taken artery wall as rigid and have small sample size.

ACKNOWLEDGEMENTS

The findings of this investigation are a outcome of a research endeavor that received financial support from an extramural grant issued by the Department of Health Research (DHR), which is a subdivision of the Ministry of Health and Family Welfare under the Government of India (DHR-ICMR/GIA/18/18/2020).

REFERENCES

[1] Suzuki, J et al., *Stroke*, 14(1):104–109, 1983.
[2] Scott, R.M. et al., *New England Journal of Medicine*, 360(12), 1226–1237, 2009

ACCELERATED STENT DEPLOYMENT SIMULATIONS VIA MODEL ORDER REDUCTION FOR PREDICTIVE MODELING OF TRANSCATHETER AORTIC VALVE REPLACEMENT

I. Shah (1,4), S. K. Sivakumar (1), F. Ballarin (2), V. Thourani (3), A. Veneziani (4), L. Dasi (1)

(1) Department of Biomedical Engineering, Georgia Institute of Technology, Atlanta, GA, USA
(2) Department of Mathematics and Physics, Università Cattolica del Sacro Cuore, Brescia, Brescia, IT
(3) Piedmont Heart Institute, Atlanta, GA, USA
(4) Department of Mathematics, Department of Computer Science, Emory University, Atlanta, GA, USA

INTRODUCTION

Structural analysis of transcatheter heart valves (THV) via computational modeling has become popular for better understanding the mechanistic interactions between the prosthetic heart valve and the native aortic anatomy. These computational models of transcatheter aortic valve replacement (TAVR) procedures are composed of multiple stages, where each is modeled using commercial full order model (FOM) solvers. The deformations in response to the applied loads from the valve may cause several adverse complications such as coronary obstruction and paravalvular leakage [1]. Predictive biomechanical models play a pivotal role in helping mitigate the risk of such complications, as they can provide interactive visualizations of the post-TAVR configuration and several simulation-derived clinical metrics to quantitively assess the potential risks [2].

Such analyses become extremely computationally expensive, however, largely due to the mechanical complexities of the aortic valve and the multiphysical nature of the deployment process. In addition, the transient nature of the deployment simulations combined with the highly nonlinear mechanics that govern the THV stent results in computing costs that can range from 12 to 15 hours for an individual deployment simulation. Parametrically evaluating different factors (valve type, deployment depth, balloon-filling volume, etc.) may become a trial-and-error based approach for optimizing the TAVR treatment, causing the entire planning process to potentially take several days to complete for an individual patient.

To this end, reduced order models (ROMs) are a common data-driven paradigm used to simplify complex FOMs to their dominant components. Classical projection-based ROMs are divided into a two-phased approach, the *offline* and *online* phases. In the offline phase, computationally expensive FOM simulations are offloaded to form a *snapshot* library of solution, where each entry represents the solution for different parameters. The snapshot library is immediately recycled in the online phase for a new parameter of interest, with drastically reduced computational costs. We have recently developed a ROM framework based on the Proper Orthogonal Decomposition (POD)-Galerkin approach for real-time structural deformation simulations of the Medtronic Evolut R valve, where radial deformations of the Evolut stent frame are able to be simulated in a matter of seconds [3].

The primary objective of this study is to advance the previously developed POD-based ROM for capturing the full TAVR deployment process and performing real-time, idealized deployment simulations of the Evolut R valve in response to applied radial deformations. This includes incorporating appropriate hyper-reduction techniques for further accelerating nonlinear constitutive models in transient regimes, as well as developing a paradigm based on separate ROM libraries to realistically capture the deployment of the crimped valve stent frame. The goal is to use such an ROM framework to significantly reduce the computing costs of performing these idealized deployment simulations.

METHODS

As an initial attempt to capture the transient deployment process of the crimped valve, separate ROM libraries are constructed for the deformation of the top and bottom halves of the stent frame. In the offline phase of each ROM, a total of 105 traditional finite element (FE) simulations are performed with parameterized applied loads enforced to construct the snapshot libraries. For each FE simulation, a hyperelastic material model in the form of a generalized Neo-Hookean strain-energy density function is prescribed, which serves as an initial approximation of the self-expandable nature of the Evolut stent frame. The stent frame is modeled with a Young's modulus of 50 GPa and Poisson's ratio of 0.33, and in the case of the transient simulations, a semi-implicit approach is utilized ($dt = 0.01\ s, T = 0.3\ s$).

For the first ROM library, zero displacement boundary conditions ($u = 0$) are prescribed at all nodes along the top half of the stent frame. So called "force-pair" conditions are also implemented as seen in Fig. 1, where the normal stress is prescribed at a set of 15 points along the bottom half of the stent frame, i.e. $\sigma \cdot n(P_i) = d_i$ for $i = 1,2, \dots,15$. All

possible pairs among the 15 points are obtained, and the vector d_i is defined such that it is oriented along the line connecting two end points of each pair. These boundary conditions are similar but inverted in the second ROM library, where the fixed conditions are prescribed along the bottom half of the stent frame and the force-pair conditions are prescribed at 15 nodes selected from the top half of the frame. The outline for the prescribed conditions in both ROM libraries are summarized in Fig. 2.

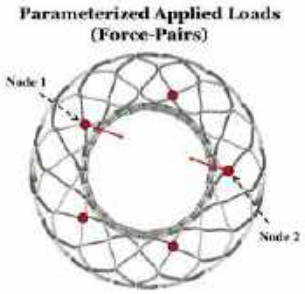

Figure 1. Prescribed force-pair loads for ROM.

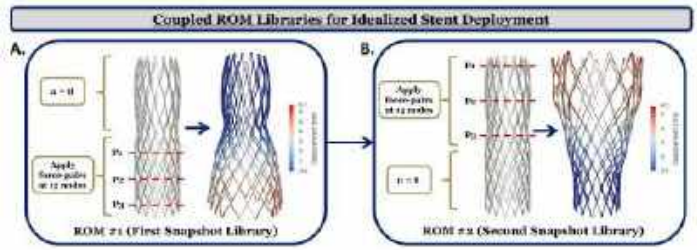

Figure 2. Construction of ROMs for capturing valve deployment.

In the online stage of the ROM frameworks, a filtering step is first performed via the Singular Value Decomposition (SVD) approach to identify the most high-energy principal components of the generated snapshot libraries. A small number of eigenvectors associated with the largest singular values are used to project the elasticity problem to a lower dimensional subspace via the POD approach. When substituted into the traditional linear systems of equations that are obtained from the FE discretization, the reduced order problem reads as follows.

$$W^T A W = W^T b \quad (1)$$

The Galerkin POD approach is naturally stated for linear problems. However, in the case of nonlinear problems such as hyperelasticity, more advanced approximation techniques are required and in this study we employ the Discrete Empirical Interpolation Method (DEIM) for each ROM framework [4]. The DEIM approach allows for an efficient reduction of the nonlinear terms that arise in the governing problem by essentially performing a secondary SVD evaluation on a separate snapshot library that only evaluates the nonlinear terms. More precisely, if we label the matrix N as the secondary snapshot matrix of the nonlinear evaluations (with up to m entries), then the secondary SVD evaluation resembles the following.

$$N = \Xi \Sigma_N V_N \quad (2)$$

The matrix Ξ here consists of the POD modes associated with the nonlinear terms, and from this matrix, a low dimensional basis is formed (Ξ_p) as in the POD approach. Using the entries of the matrix Ξ_p, a series of interpolation indices that form a separate matrix known as the interpolation matrix (P^T) are calculated by computing the residual against Ξ. This interpolation matrix captures the relationship between the selected indices and the original nonlinear snapshot data. Finally, the reduced order system is constructed which reads as follows, where the projection of the nonlinear terms is indicated on the right-hand side.

$$N \sim \Xi_p \left(P^T \Xi_p\right)^{-1} P^T N \quad (3)$$

The two ROM libraries are then coupled together in a sequential manner to capture the deployment. In the online phase of the first library, the bottom half of the stent frame is deformed in a time-dependent manner to mimic the initial release of the crimped stent from the catheter. The online stage of the second library is then used to deform the remaining top half of the stent frame, mimicking the release of the remaining part of the stent as the catheter is pulled back. Using this pipeline, idealized stent deployment simulations were performed in a patient-specific aortic root model. The entirety of the ROM frameworks are implemented in *RBniCS*, an open-source model reduction library which automates all of the above steps (offline stage FE simulations, POD-DEIM model reduction, and online stage).

RESULTS

The von Mises stress distribution along the stent frame as the valve is deployed is shown in Fig. 3. The solutions obtained via the ROM were in strong agreement with full order model (FOM) simulations performed in the FE library *FEniCS*, highlighting the accuracy of the approach. Computational costs of simulating the idealized deployment process using the ROM were significantly reduced as well, requiring only 40-50 seconds to fully simulate depending on the magnitude of the applied loads prescribed in the online stages. Comparing these costs to a previously validated FE-based TAVR deployment simulations performed using commercial FE solvers, which require up to 12-15 hours to complete, the ROM was successfully able to reduce the computing costs with speed-up factors ranging from 92.8% to 99.7%.

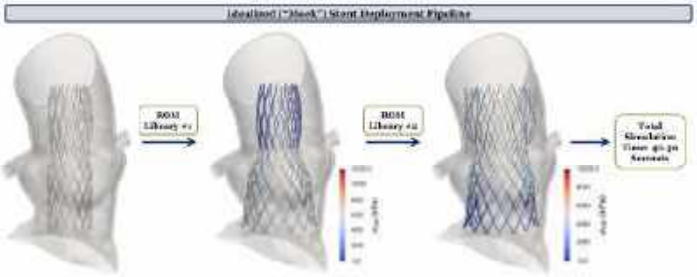

Figure 3. Visualization of the idealized deployment pipeline.

DISCUSSION

In this study we introduce and advance a previously developed ROM framework using a projection-based, POD-DEIM algorithm for performing near real-time idealized stent deployment simulations of the Evolut R valve stent frame. The framework significantly reduced the computational cost of performing the idealized deployment simulations as compared to a previously validated FE-based simulation pipeline, while also providing accurate results as compared to FOM simulations with similarly applied loads. The inclusion of the DEIM algorithm showed especially promising results in the presence of the nonlinear mechanics prescribed here, as especially large reductions in computing costs were seen with the combination of the POD-DEIM approach. A major limitation of the study is the lack of a true superelastic material model that accurately captures the properties of the stent frame. In addition, the framework currently is unable to handle the contact problem as the stent frame collides with the surrounding aortic anatomy. Further refinements are underway to implement both an idealized superelastic constitutive model, as well as a collision detection and response algorithm to simulate the contact of the stent frame with the native leaflets and aortic root. Such a comprehensive framework will provide clinicians with mechanistic insight at a patient-specific level in a real-time fashion via several potential simulation-derived clinical metrics to help mitigate post-TAVR complications.

ACKNOWLEDGEMENTS

Research was supported by the NSF Project 2012286 (A.V.).

REFERENCES

[1] Kodali, S. K. et. al., *N Engl J Med*, 366(18):1685-95, 2012.
[2] Heitkemper, M. et. al., *J Thorac Cardio Surg*, 159(3):829-38, 2020.
[3] Shah, I. et. al., *Ann Biomed Eng*, doi:10.1007/s10439-023-03360-5.
[4] Chaturantabut, S., *SIAM Scient Comp*, doi.org/10.1137/090766498.

ASSESSING THE IMPACT OF HYALURONIC ACID ON THE RHEOLOGICAL PROPERTIES OF COLLAGEN HYDROGELS

Nicholas T. Gigliotti (1), Vivian H Su (1), Mitra L. Taheri (1)

(1) Department of Materials Science and Engineering, Johns Hopkins University, Baltimore, Maryland, USA

INTRODUCTION

Each year, roughly 1 in 10 pregnancies result in preterm birth (PTB), increasing the risk of negative health outcomes for both mother and child.[1] Although PTB is prevalent, little is known about how or why it occurs. The cervix has emerged as a key research target for PTB due to its role as the barrier between the fetus and the birth canal. Throughout pregnancy, the cervix undergoes significant changes to its mechanical properties, allowing for the passage of the fetus into the birth canal during labor, a process which occurs prematurely in the case of PTB.[2] Uncovering the mechanisms driving cervical remodeling is paramount to understanding why PTB occurs and how to predict and prevent it.

Within the cervix, network-forming fibrillar collagen is primarily responsible for the structure and properties of the tissue. However, basic fiber mechanics alone do not explain the changes in tissue properties that are observed in the cervix, suggesting that the chemical environment of the extracellular matrix (ECM) also contributes to the observed mechanical changes.[2] Hyaluronic acid (HA), a non-sulfated glycosaminoglycan in the cervical ECM, has been well studied throughout pregnancy.[3] In the early stages of pregnancy, HA is mostly present in its low molecular weight form. As pregnancy progresses, the overall concentration of HA increases, as does the chain length of the polymer.[2] Hyaluronic acid contains negatively charged carboxylate groups that bind to water, meaning that the increase in molecular weight and concentration allows for an increase in bound water content within the tissue.[3] It is hypothesized that these changes impact collagen fibrillogenesis and the mechanical properties of the whole tissue. Previous studies have been conducted examining the impact of HA concentration on collagen hydrogel mechanics[4] and on how adding HA to collagen scaffolds impacts cellular viability.[5,6] However, little investigation has been done on how HA impacts the structure of self-assembled collagen and the resulting structure-property relationships in a controlled environment. In this study, collagen hydrogels were chosen to isolate the collagen from the rest of the ECM and provide a tunable platform with complete control over synthesis parameters.[7,8] Hydrogels were prepared with varying biologically relevant molecular weights and concentrations of HA to study the impact of HA on collagen fibrillogenesis and network formation.

METHODS

Hydrogels were prepared by combining 3mg/mL type I collagen and 10X PBS with solutions of 20kDa or 200kDa HA in water to final concentrations of 1X PBS, 1.5mg/mL collagen, and either 1 or 10 nmol HA per mg of collagen. Solutions were pH adjusted with 1N NaOH and placed in an incubator at 37 C for 24 hours for gel formation and equilibration.

Rheology was performed with a frequency sweep at 1% strain from 0.01 to 100 rad/s. Resulting storage moduli, loss moduli, and loss factor (tan(δ)) were examined to determine gel stiffness, degree of cross-linking, and whether the plastic or elastic response was dominant.

Imaging of individual collagen fibers was performed using an environmental SEM at 15keV with a chamber pressure of 70 Pa. Individual fiber diameters were measured by taking 3

randomly spaced measurements per fiber at 90° to the fiber edge using imageJ.

RESULTS

Rheology measurements indicated an increase in storage modulus for low molecular weight (MW) HA samples from the pure collagen gels. High MW HA showed significant decreases in storage modulus as concentration of high MW HA increased. The loss moduli for each of the samples were similar at low frequencies. At higher frequencies, each of the HA containing species showed a decrease in loss modulus, although these results were not statistically significant. Loss factor (or tan(delta)) indicated that the degree of cross-linking increased for samples containing low MW HA compared to pure collagen gels, while the degree of cross-linking significantly decreased with increasing concentration for high MW HA samples.

ESEM imaging suggested no change in fiber diameter between pure collagen and low MW HA samples. The low concentration, high molecular weight sample, however, showed a slight increase in average fiber size, although the results were not statistically significant. No images showing collagen fibers were able to be acquired for the high concentration, high MW sample due to increased water content.

DISCUSSION

The addition of HA to collagen gels has a significant impact on the rheological properties of the collagen network. The large decrease in storage modulus and dominant plastic behavior of the high MW HA samples compared to both pure collagen and low MW samples shows that the larger molecule size is the driving factor in how HA affects tissue properties. Specifically, the decrease in relative degree of cross-linking indicated by tan(delta)>1 demonstrates that high MW HA impedes collagen network formation, whereas low MW HA does not, but rather occupies space within the lattice and assists in stiffening the matrix. Furthermore, imaging of individual fibers suggests that the low molecular weight HA does not impact fiber swelling and may be too small to create noticeable changes in the interfibrillar spacing of collagen. However, the slight increase in size observed in the higher MW sample may indicate that the HA is adhering to the collagen fibrils, resulting in an increase of interfibrillar spacing and a larger fiber diameter. One of the primary mechanisms for deformation of collagen is bundled fibrils sliding past each other within a fiber, so increased interfibrillar spacing may have a large impact on collagen extensibility and tissue properties via this mechanism.

The results of this study agree with previously proposed molecular crowding mechanisms for the opposing impacts of low and high MW HA with collagen.[2,9,10] We were able to demonstrate these competing mechanisms through our hydrogel model at biologically relevant concentrations found in the cervix during pregnancy. Additionally, we were able to gain some limited insight into whether HA is adhering to collagen fibrils within the fibers, causing the fibers to swell. When coupled with the proposed sliding mechanism for collagen deformation, HA could be a significant contributor to the mechanical and structural remodeling of the cervix, although further studies are required to address the limitations of this study.

Future studies will be aimed at increasing the range of molecular weights examined. Although the difference between low and high MWs in this study is an order of magnitude, HA may be present in molecules as large as 2000 kDa, so further investigation into the impact of such high molecular weights should be pursued. Additionally, environmental SEM proved to be a challenging imaging mode as we were unable to identify collagen fibers in one of the samples, likely due to the increased water content from the high MW HA. Alternative imaging modes, such as AFM, may be useful to quantify fibers in their native environment and hydration state, eliminating unwanted changes in hydration and swelling caused by sample processing or imaging under vacuum conditions. Cryo-TEM may also be used to measure interfibrillar distance as a function of HA MW.

ACKNOWLEDGEMENTS

The authors would like to acknowledge funding in part from the Johns Hopkins University Whiting School of Engineering and from the March of Dimes Prematurity Research Center at the University of Pennsylvania, under contract 22-FY17-890.

REFERENCES

[1] Martin, JA et al., *NCHS Data Brief*, 477, 2023.
[2] Mahendroo, M., *Matrix Biology*, 78-79: 24-31, 2019.
[3] Dovedytis, M et al., *Engineered Regeneration*, 1:102-113, 2020.
[4]Vulpe, R et al., *Mater Sci Eng C Mater Biol Appl*, 1(69):388-397, 2016.
[5] Veettil, SRU et al., *Acta Biomateriala*, 130:183-198, 2021.
[6] Muran, AC et al., *Journal of Cartilage & Joint Preservation*, 3(2), 2023.
[7]Antoine, EE et al., *Tissue Eng Part B Rev*, 20(6): 683-696, 2014.
[8] Xu, Q et al., *Materials Science and Engineering: R: Reports*, 146, 2021
[9] Akgul, Y et al., *J Clin Invest.*, 124(12): 5481-5489, 2014.
[10] Saeidi, N et al., *Biomaterials*, 33(30):7366-7374, 2012.

.

STUDY OF THE STRUCTURES THAT LIMIT COMBINED ABNORMAL HYPEREXTENSION AND ABNORMAL VARUS OF THE KNEE

Rebekah M. Deardurff (1,2,3), Edward S. Grood (1,2), Frank R. Noyes (2,3,4)

(1) Department of Biomedical Engineering, College of Engineering and Applied Science, University of Cincinnati, Cincinnati, Ohio, USA
(2) Cincinnati SportsMedicine Research and Education Foundation, Cincinnati, Ohio, USA
(3) Cincinnati Sports Medicine and Orthopedic Research, The Jewish Hospital, Mercy Health, Cincinnati, Ohio, USA
(4) Noyes Knee Institute, Cincinnati, Ohio, USA

INTRODUCTION

Knee hyperextension (genu recurvatum) is a common injury amongst the general population and can result from injury, physiological laxity, or other knee disorders[1,2,3,4]. Hyperextension is classified as normal up to 5° past full extension, and abnormal beyond that[5]. There are few biomechanical studies on hyperextension from which to draw conclusions about the structures responsible for it. Morgan et al attributed the oblique popliteal ligament (OPL) as a crucial hyperextension restraint, carrying 36-41% of load[6]. However, a study by Noyes et al concluded that there is no singular primary structure responsible for preventing knee hyperextension[7].

Varus is a deformity in which an anatomical part is angled toward the midline of the body to an abnormal degree[8]. In a radiographic study conducted by Moreland et al, a knee has a normal varus from 1.1° to 1.5° varus; therefore, abnormal varus can be classified as more than 1.5° varus[9]. Studies from LaPrade and Gollehon explore varus-valgus rotation in flexion and conclude that there are some structures more impactful than others; however, no singular structure is responsible for limiting varus rotation[10,11].

Varus recurvatum has no clear definition in literature but is described as abnormal varus with abnormal hyperextension[5]. The purpose of this study is to investigate and identify what soft tissue structures, if any, are primarily responsible for limiting varus recurvatum. Additional purposes are to see if a varus recurvatum injury can be present with an intact anterior cruciate ligament (ACL) and if either the popliteus tendon (POP) or lateral collateral ligament (LCL) is more effective in varus recurvatum (VR) prevention than the other.

METHODS

In this study, 8 cadaveric knee specimens (mean age, 39.5 years; range 24-49 years) were mounted onto a 6 degrees of freedom (DOF) robotic system designed with the joint coordinate system described by Grood and Suntay[12] that uses a 6-component force-torque transducer (Delta model; ATI Industrial Automation). A 7 Nm varus moment was applied while the specimens were extended from terminal hyperextension using a 25 Nm hyperextension load up to 90°. All other motions were unconstrained to maintain no load unlike the previous study by Noyes[7], which constrained the motions to the positions consistent in the intact knee. The specimens' tissues were dissected in four different cutting sequences (Fig 1). By alternating the cuts of the POP and LCL, the effect of individual and combination cutting can be analyzed. The role of the posterior capsule was investigated by cutting the structures before or after the LCL, POP, and ACL.

Figure 1: All cutting sequences for this study.

The knee joints were prepared and aligned as described in Noyes et al[7]. Additionally, the specimens were cycled through limit tests for each DOF from -5 degrees to 90 degrees flexion. Anteroposterior limits were measured at ±135 N, ab-adduction limits were measured at ±7 Nm, and external-internal limits were measured at ±5 Nm.

All statistical and graphical results were produced with Excel (Microsoft) after importing the data from the robot. Data were analyzed using descriptive statistics for cutting groups and POP/LCL involvement.

RESULTS

The average hyperextension at the peak extension moment in the intact knee ranged from 6.3° to 20.4°, with an average of 11.8° ± 4.7°. Furthermore, an average varus of 3.8° ± 2.4° was found after all cuts were made. In the intact knee, the average was 0.1° ± 1.1° valgus for all specimens at the peak extension moment of 25 Nm.

The preliminary results from this study indicate that varus recurvatum can be present without an ACL injury (Figs 2-5). This agrees with a previously published study by McDonald et al[13] which concluded that the effect of creating an isolated ACL injury did not create a lateral joint opening large enough to be classified as abnormal varus. Each graph below shows the individual cuts for each cutting order (legend) with a black horizontal line that represents where the average varus is for a normal knee. The graphical results demonstrate that for 75% of the specimens, varus recurvatum is present for cuts prior to the ACL which is consistent with McDonald's findings.

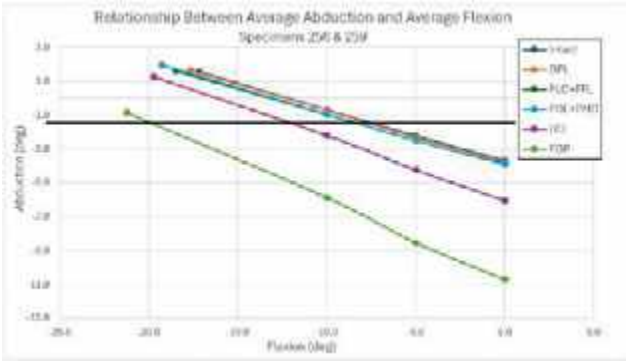

Figure 2:Abduction vs Flexion Averages for Specimens 256 & 259.

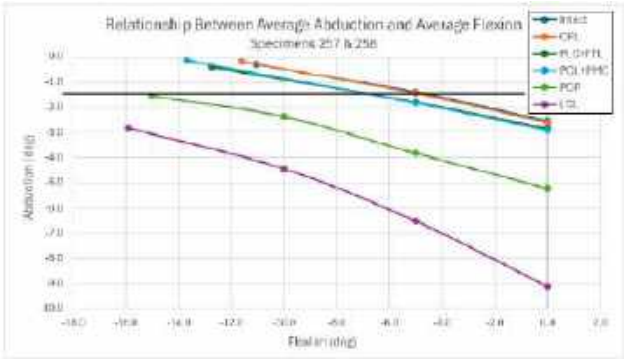

Figure 3:Abduction vs Flexion Averages for Specimens 257 & 258.

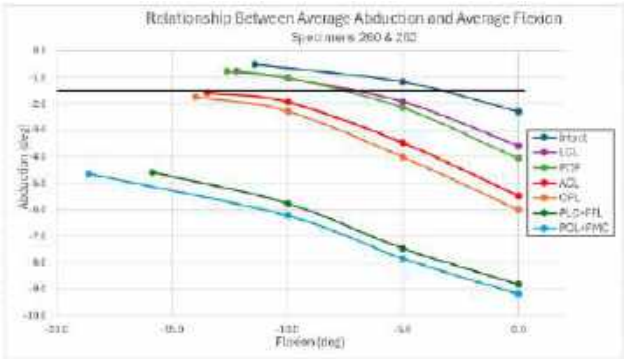

Figure 4:Abduction vs Flexion Averages for Specimens 260 & 262.

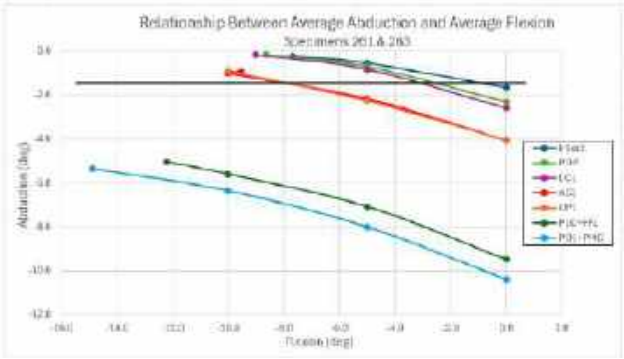

Figure 5:Abduction vs Flexion Averages for Specimens 261 & 263.

DISCUSSION

The preliminary results of this study are consistent with the hypothesis that varus recurvatum can be present in an injured knee with an intact ACL. Moreover, the LCL and POP have individual effects on VR and the magnitude of the effect depends on the order in which they are sectioned. This study can also be used to clearly define varus recurvatum which has not been consistent in the literature and may help clinicians identify such injuries in a patient.

Furthermore, these preliminary findings illustrate that an ACL injury is not required for a person to have a varus recurvatum. Natural hyperextension and varus could be exacerbated by an LCL and/or POP injury without injuring the ACL or posterior capsule. The preliminary findings also suggest that the major restraints for varus recurvatum are likely the popliteus tendon and lateral collateral ligament.

The major limitation of this preliminary study is that it only has an n=2 for each cutting sequence. Ideally, there would be at least 4 specimens per group to do a power analysis and subsequent testing. Subsequent testing will provide more conclusive data on the structures that restrain hyperextension and varus recurvatum.

ACKNOWLEDGEMENTS

The authors would like to thank the Noyes Knee Institute and Cincinnati SportsMedicine Research Education and Foundation for their continued financial and research support.

REFERENCES

[1] Farmer, KW et al., *Clin J Sport Med*, 13:53-56, 2003.
[2] Fornalski, S et al., *Am J Sports Med*, 36(1):80-84, 2003.
[3] Moorman, CT et al., *J Knee Surg*, 18(02):137-145, 2005.
[4] Wu, XD et al., *Sci Rep*, 7:42698, 2017.
[5] Noyes, FR et al., *Noyes' Knee Disorders*, 2017.
[6] Morgan, PM et al., *Am J Sports Med*, 38(3):550-557, 2010.
[7] Noyes, FR et al., *Am J Sports Med*, 51(5):1146-1154, 2023.
[8] *Merriam Webster*, https://www.merriam-webster.com/dictionary/varus, 2024.
[9] Moreland, JR et al., *J bone and joint surgery*, 69(5):745-749, 1987.
[10] Gollehon, DL et al., *J bone and joint surgery*, 69(2):233-242, 1987.
[11] LaPrade, RF et al., *Am J Sports Med*, 32(6):1405-1414, 2004.
[12] Grood, ES et al., *J Biomech Eng*, 70(1):88-97, 1988.
[13] McDonald, LS et al., *The Knee*, 23:1064-1068, 2016.

THE IMPACT OF RIGHT VENTRICULAR FIBER RE-ORIENTATION ON LEFT VENTRICULAR CONTRACTION: A NUMERICAL STUDY

M. Zhang (1), K. Ichimura (2); KR. Stenmark (1); E. Spiekerkoetter (2); VO. Kheyfets (1)

(1) Cardiovascular Pulmonary Research Laboratories, Division of Pulmonary Sciences and Critical Care Medicine, Division of Pediatrics-Critical care, Department of Medicine and Pediatrics, University of Colorado Anschutz Medical Campus, Aurora, CO, USA.
(2) Department of Medicine, Division of Pulmonary, Allergy and Critical Care Medicine, Stanford University, Stanford, CA, USA.

INTRODUCTION

Pulmonary hypertension (PH) results in right ventricular (RV) pressure overload and eventual failure. While most ongoing research has been focused on characterizing the RV's morphological, biomechanical, and metabolic changes, few studies have considered how these changes impact left ventricular (LV) function and contractile mechanics. However, decreased LV torsion and torsion-rate during systole has been reported in children with PH [1,7]. A decline in both LV and RV ejection fraction (EF) in pulmonary artery banding (PAB) mice has also been reported [2]. The underlying mechanism for this observation is unclear. The objective of this study is to develop a computational model of the biventricular heart to study physiological LV contractile mechanics in response to RV remodeling (e.g., fiber re-orientation). The ultimate objective is to enhance our understanding of how various factors of RV remodeling contribute to the observed biomechanical and transcriptional changes in LV contractile mechanics in children and pre-clinical models of PH.

METHODS

A biventricular finite element computational model was developed to study how well-established mechanisms of RV remodeling to pressure overload (e.g., fiber re-orientation) impact LV and RV function, and LV contractile mechanics. The model was reconstructed from short axis cine stack magnetic resonance imaging (MRI) of a healthy 10-year-old male pediatric subject at end systole using ScanIP (Simpleware).

Fiber orientation and remodeling

Since the purpose of the model was to investigate how the LV responded to RV myofiber re-orientation, a well-known phenomenon in RV remodeling [3], we explored 3 RV fiber orientation scenarios (LV fiber orientation was not changed). Baseline endocardium and epicardium fiber assignment for this study is depicted in Fig. 1. Fiber orientation in F1 corresponds to a healthy rat heart, which in response to pressure overload- gradually progresses to F2, and ultimately to F3 [3]. Within the finite element model, fiber orientation was incorporated by solving $-\nabla \cdot (\nabla\theta) = 0.025$ where θ is the fiber angle and Fig. 1 shows epicardial/endocardial boundary conditions [4,5]. To address the specific study questions, only fibers within the RV change orientation from F1 to F3 (see Fig. 1) while LV fiber orientation remains constant.

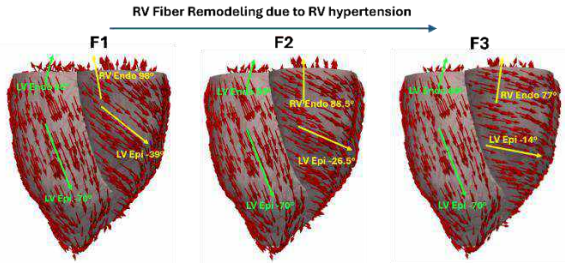

Figure 1 Fiber Assignment

Constitutive model

In this study, we characterized the passive and active properties of myocardial tissue by a transversely isotropic hyperplastic constitutive model [6,8] that incorporates an additive active stress decomposition aligned with the fiber (Eq. (1))

$$\sigma = \sigma^p + \sigma^a \quad (1)$$

The passive stress response (σ^{p}) is governed by a transversely isotropic Fung-type strain energy function (Ψ), with a decomposition into deviatoric (Ψ^{dev}) and volumetric (Ψ^{vol}) components to enforce the constraint of incompressibility.

$$\Psi = \Psi^{dev} + \Psi^{vol} \quad (2)$$

The active contraction stress (σ^{a}) is generated along the fiber direction e_1 by adjusting active fiber stress (T_a):

$$\boldsymbol{\sigma^a} = \boldsymbol{T_a e_1} \otimes \boldsymbol{e_1} \quad (3)$$

All the material parameters were determined and calibrated based on published experimental data but are omitted due to space constraints.

RESULTS

Changes of RV and LV shape during ejection

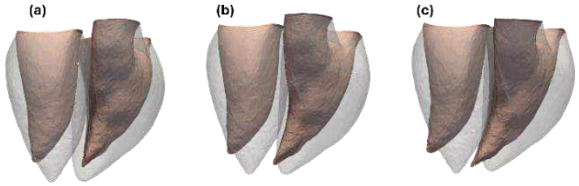

Figure 2 LV and RV structural changes during ejection

For normal fiber orientation, the RV and LV undergo pronounced radial and circumferential contraction, and subtle longitudinal contraction, during ejection (see Fig. 2a). After RV fiber re-orientation (see Fig 2b, c), the RV contract radially without any visible evidence of longitudinal shortening. Changes in the circumferential direction are discussed below.

Changes in RV and LV systolic function, contractile mechanics, and stroke work

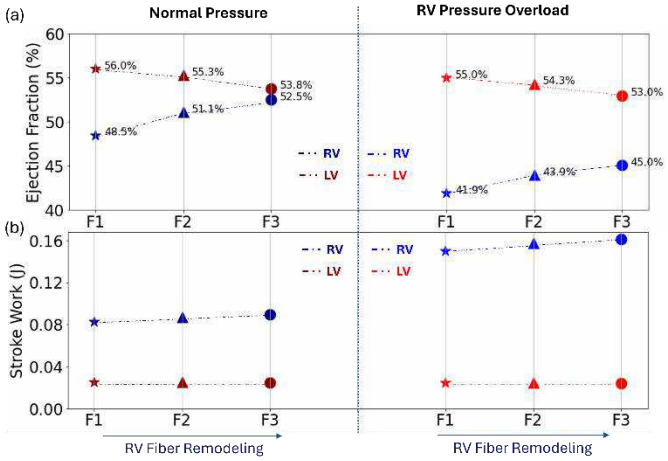

Figure 3 RV and LV systolic function and stroke work

Fig. 3 presents the impact of RV fiber re-orientation on RV and LV systolic function. The figure encompasses six simulation outcomes, wherein three distinct fiber orientation models (F1, F2, F3) are simulated under both normal and hypertensive RV pressure conditions. The hypertensive pressure is considered as a 2-fold increase in RV peak systolic pressure relative to the normal simulation. Fig. 3(a,b) illustrate the alterations in EF and stroke work respectively.

This data shows that, as the remodeling of fiber orientation changes from F1 state to F3 state, the EF of the RV increases by 8.2% while the LV slightly decreases (around 3.9%). Similar trends were observed for the case with hypertensive RV pressure. The simulations show that, under F1 fiber orientation, hypertensive pressure leads to significant RV EF decline compared with normal pressure. Shifting the fiber orientation to F3 is expected to enhance RV function, albeit with a slight decline in LV function. Fig. 3 (b) illustrates that under RV pressure overload, the RV must do substantially more work, but the LV responds with a small decrease in stroke work. This finding aligns with experimental mouse data presented in [2].

Fig. 4 reveals simulation results from a numerical experiment intended to explore how RV fiber re-orientation impacts LV apex rotation rate. Here we see that RV fiber re-orientation and RV pressure overload both have pronounced effects on decreasing LV apex rotation rate. The results agree with our previous [experimental] observation that LV apex rotation rate decreased in mice after PAB [2] and children with PAH [7].

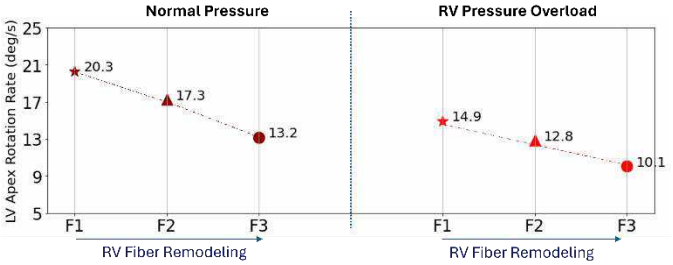

Figure 4 LV apex rotation vs RV fiber re-orientation

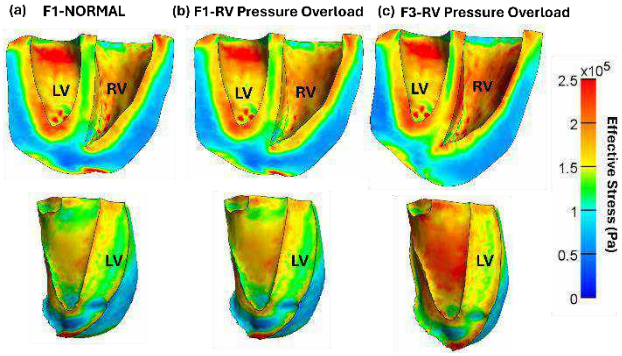

Figure 5 Stress Distribution

Fig. 5 shows the effective stress distribution within the LV (septum and free-wall) and the RV free-wall at end-systole. Under normal circumstances *in vivo*, RV fiber re-orientation would be accompanied by an increase in RV myofiber contractility. Therefore, in this numerical study, we only simulated fiber re-orientation without an increase in contractility to isolate the impact of that remodeling response. Here we see that, without an increase in RV contractility, pressure overload has a minor impact on LV, septal, or RV free wall stress although it understandably reduces RV end-systolic cavity volume. However, after RV fiber re-orientation, septal stress is notably increased (see Fig. 5c).

DISCUSSION

This study was triggered by our previous findings that LV torsion rate is decreased in rodents and children with chronic RV pressure overload [2,7]. In rodents, this decrease in LV torsion rate was accompanied by LV transcriptomic changes and a decrease in LV systolic function [2]. This study found that RV fiber re-orientation, which has been documented in multiple rodent studies [8], is enough to be a mechanistic cause for these clinical and pre-clinical findings in the LV. In conclusion, this study shows how RV structural remodeling impacts LV contractile mechanics and function. Ongoing studies are aimed at identifying how this phenomenon also influences LV-to-RV mechanical energy transfer.

ACKNOWLEDGEMENTS

This work was supported by: NIH R01HL152250.

REFERENCES

[1] Dufva, M. J. et al., *JCMR*, 2016; [2] Kheyfets V. O. et al., *Physiol. Rep.*, 2020; [3] Mendiola E. A.et al., *Circ. Heart Fail.*, 2023; [4] Kheyfets V. O. et al., *J. Biomech. Eng.*, 2019; [5] Wong J. et al., *CMBBE*, 2014; [6] Land S. et al., *Proc. Math. Phys. Eng. Sci.*, 2015; [7] Dufva M. J. et al., *Pulm. Circ.*, 2018; [8] Mendiol, E. A. et al., *Circ. Heart Fail.*, 2023

EFFICIENT SHAPE OPTIMIZATION OF THE TOTAL CAVOPULMONARY CONNECTION VIA HYPER-REDUCED ORDER MODELS AND FREE FORM DEFORMATION

I. Shah (1,3), F. Ballarin (2), L. Dasi (1), A. Veneziani (3)

(1) Department of Biomedical Engineering, Georgia Institute of Technology, Atlanta, GA, USA
(2) Department of Mathematics and Physics, Università Cattolica del Sacro Cuore, Brescia, Brescia, IT
(3) Department of Mathematics, Department of Computer Science, Emory University, Atlanta, GA, USA

INTRODUCTION

Fontan surgical planning via computational fluid dynamics (CFD) is a well-established technique for pre-operatively characterizing the hemodynamics of the total cavopulmonary connection (TCPC) [1]. The pipeline involves modeling the baseline anatomy of the patient, from which the effects of individual variables on the flow dynamics of the potential surgical option are assessed. These variables are evaluated in a parametric setting and include the caval offset (offset between the superior and inferior vena cavae (SVC, IVC)), the design of the Fontan circuit, and the type of baffle utilized [2]. Two of the most critical endpoints of clinical interest are the hepatic flow distribution (HFD) and power loss (PL). HFD is defined as the amount of hepatic flow carried from the liver via the IVC to the left or right pulmonary arteries (LPA, RPA), while PL is the total energy loss that occurs within the TCPC.

This pipeline essentially represents a shape optimization problem, where different anatomical connections between the IVC and LPA/RPA result in unique hemodynamics. The HFD and PL metrics are used to identify the optimal morphology, where the aim is to provide a balanced HFD split and minimize the PL in the constructed anatomy. Although this surgical planning pipeline is effective in optimizing the TCPC, the computational costs of simulating physiologically accurate conditions becomes extremely expensive. This is especially true for repetitive testing of various TCPC options in a trial-and-error fashion, which may take several weeks or months to complete for a single patient.

To this end, we have recently developed a *reduced order modeling* (ROM) framework using the Proper Orthogonal Decomposition (POD) approach coupled with trust-region optimization methods for real-time shape optimization of idealized TCPC geometries. Projection-based ROMs are traditionally divided into two stages, the *offline* stage, where the computationally expensive simulations are offloaded, and the *online* stage, where the generated *snapshots* are recycled for a rapid, reduced order solution. The POD-ROM framework has shown promising results for real-time shape optimization using a point-based parameterization of the geometry, where the optimal morphology for a desired HFD value or minimization of the PL can be determined in under 15 minutes.

The primary objective of this study is twofold. First, we aim to develop a paradigm for parametric geometrical transformations of idealized TCPC geometries using the free form deformation (FFD) technique. The FFD approach will be coupled with the previously developed POD-ROM framework, allowing for a wide range of smooth, physiologically relevant transformations of the TCPC geometry which aims to be more robust than a point-based boundary variation method. Second, we aim to implement hyper-reduction techniques to the framework in the form of the discrete empirical interpolation method (DEIM), which will allow for greater computational savings in the presence of the highly nonlinear Navier-Stokes equations (NSE) and in turn allow for real-time identification of the optimal TCPC morphology.

METHODS

An initial reference geometry of an idealized 2D TCPC is generated as seen in Fig. 1 and the FFD technique is implemented to perform the parametric shape transformations. FFD is an approach based on tensor products of splines that allows for the deformation of a volume based on a control lattice which encapsulates the mesh of interest. The method allows for smooth deformations of the mesh volume, which is critical for obtaining physiologically relevant configurations of the TCPC (varying caval offsets, flaring or angled

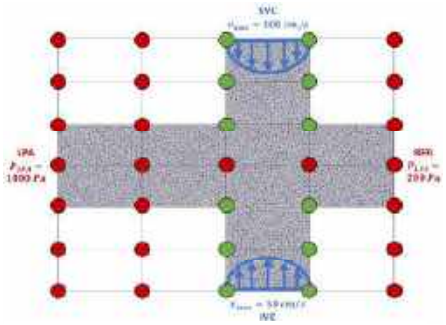

Figure 1. Idealized TCPC geometry with control points overlayed.

connections, etc.). A grid of control points is layered onto the reference mesh (Fig. 1), where only certain control points associated with the IVC and SVC are activated (in green). This allows for varying deformations of the IVC and SVC with respect to the LPA and RPA, serving as a preliminary attempt to capture the variability in which the TCPC can be constructed. Parabolic velocity profiles are prescribed at the inlets, and pressure conditions are employed at the LPA/RPA for each of the geometries (Fig. 1). In the offline stage, a total of 100 finite element based CFD simulations are performed using the parameterized models, where the displacement of the activated control points is varied within a given range to ensure the generation of realistic geometries.

In the online stage of the ROM, a filtering step is first performed via the *Singular Value Decomposition* (SVD) technique. Using a small number of eigenvectors that are associated with the largest singular values of the generated snapshots, the governing problem is projected to a lower dimensional subspace using the POD approach. When substituted into the traditional linear system of equations that results from the discretization of the NSE via the finite element method, the reduced order problem reads as follows.

$$W^T A W = W^T b \quad (1)$$

However, in the case of nonlinear problems such as the NSE, specific approximation techniques are required to rapidly solve the nonlinear terms. Here, we resort to the DEIM approach, which allows for efficient reduction of the nonlinear terms arising in the governing problem, which the traditional POD approach is unable to reduce effectively since it would not be possible to precompute $W^T A W$ once and for all, as the matrix A itself depends on the solution at the previous nonlinear iteration [3]. The DEIM algorithm consists of performing a secondary SVD evaluation on a separate snapshot library that evaluates only the nonlinear terms of the governing problem. The goal is to isolate the nonlinear terms and their evaluations via the secondary snapshots and find its separate low dimensional representation and projection.

The POD-DEIM ROM framework is implemented using the open-source model reduction library *RBniCS*. The FFD approach is implemented within an in-house code which is coupled directly to the ROM framework, allowing for the shape parameterization of the TCPC. In the online phase, new parameters different from those used to generate the snapshot library were applied, and the reduced order solution was compared against the full order model (FOM) solution.

RESULTS

The ROM solution for the parameterized TCPC geometry in the online phase is shown in Fig. 1, with the velocity streamlines displayed. The FFD approach was able to parametrically deform the TCPC geometry in a smooth manner during the offline and online phases, where the IVC (A) and SVC (B) connections to the LPA/RPA was uniquely deformed to achieve various junctions with respect to the connection angle and flaring. In addition, the ROM solutions were in strong agreement with the FOM CFD solution with regards to resultant velocity and pressure contours.

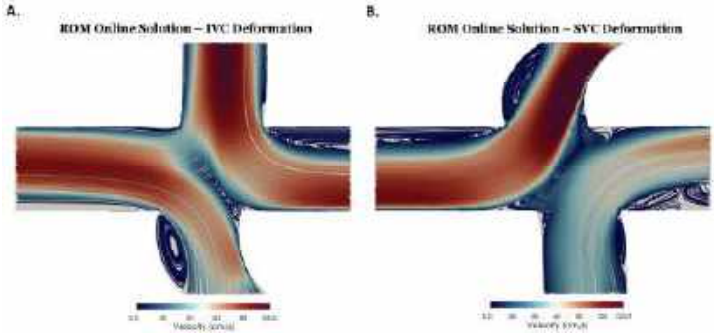

Figure 2. ROM solutions with FFD-based deformations of TCPC.

In terms of computational costs, the POD-ROM was able to reduce the costs of the online simulation to approximately 50.48 seconds, down from an average of 153.46 seconds for the FOM simulation. Even greater speed-ups were seen with the use of the POD-DEIM algorithm, with the online phase solution requiring only an average of 7.94 seconds to simulate, a 94.83% decrease in computing costs (Table 1).

Table 1. Computational details for ROM simulations.

Simulation Type	# of Snapshots	# of FE DOFs	# of ROM DOFs	Wall Clock Time (s)		Speed Up Percentage
				FE	ROM (Online)	
POD	100	25841	u - 99, p - 97	153.46	50.48	67.1%
POD-DEIM	100	25841	u - 99, p - 97	153.46	7.94	94.8%

DISCUSSION

This study introduces a POD-DEIM ROM framework that utilizes a FFD shape parameterization of idealized TCPC geometries. The framework resulted in real-time online stage simulations that were in strong agreement with FOM CFD simulations. The FFD shape parameterization also resulted in robust geometrical transformations of the TCPC as compared to traditional point-based boundary variation approaches explored previously. This is especially critical for capturing variables that are parametrically evaluated in Fontan surgical planning, such as the offset between the IVC and SVC or the angle at which the IVC connects to the LPA/RPA. More importantly, FFD is critical for parameterizing 3D geometries, as boundary variation methods are unable to efficiently evaluate these variables parametrically in a 3D setting. To this end, we have begun adapting this ROM to idealized 3D TCPC geometries as well, with preliminary results shown in Fig. 3.

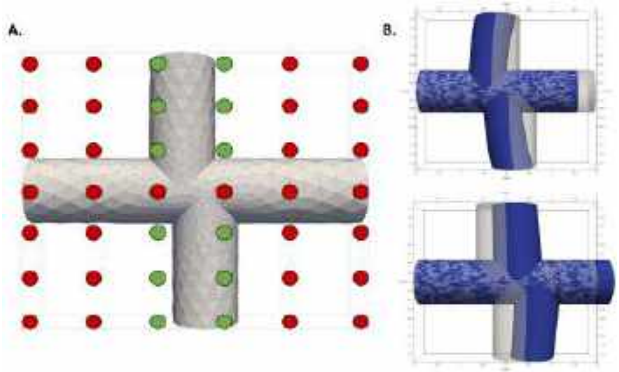

Figure 3. Idealized 3D TCPC with control points overlayed (A). FFD-based parameterization of the geometry (B).

A major limitation of this study is the stability of the applied boundary conditions as the TCPC geometry is parameterized during both phases of the ROM, as evidenced by the presence of potentially unrealistic flow separation zones near the inlets. This may occur due to large displacement ranges of the control points, as well as the stability of the DEIM approach. To overcome these limitations, we will explore adaptive inflow conditions that fit more closely with the deformed TCPC geometries, as well as additional hyper-reduction approaches in the form of regression based or domain decomposition methods.

In conclusion, the presented POD-DEIM ROM framework with an FFD-based parameterization of the geometry resulted in significantly reduced computational costs of simulating flow dynamics within idealized TCPC morphologies. Further refinements are underway to implement the FFD-based shape optimization problem, as well as translate the framework to patient-specific TCPC anatomies.

ACKNOWLEDGEMENTS

Research was supported by the NSF Project 2012286 (A.V.).

REFERENCES

[1] de Zélicourt, D. et. al., *Prog Pediatr Cardiol*, 30(1):31-44, 2010.
[2] Haggarty, C. et. al., *J Thorac Cardiovas Surg*, 148(4):1481-9, 2013.
[3] Chaturantabut, S., *SIAM Scient Comp*, doi.org/10.1137/090766498.

THE EFFECT OF TISSUE ENGINEERED HEART VALVE DESIGN ON REMODELING: OPTIMIZING VALVE FUNCTIONALITY AND COLLAGEN ORGANIZATION

Valery L. Visser (1), Sarah E. Motta (1), Simon P. Hoerstrup (1,2), Frank P. T. Baaijens (3,4), Sandra Loerakker (3,4), Maximilian Y. Emmert (1,2,5,6)

(1) Institute for Regenerative Medicine, University of Zürich, Switzerland
(2) Wyss Translational Center Zürich, University of Zürich and ETH, Zürich, Switzerland
(3) Department of Biomedical Engineering, Eindhoven University of Technology, The Netherlands
(4) Institute for Complex Molecular Systems, Eindhoven University of Technology, The Netherlands
(5) Department of Cardiothoracic and Vascular Surgery, German Heart Center Berlin, Germany
(6) Department of Cardiovascular Surgery, Charité Universitätsmedizin Berlin, Germany

INTRODUCTION

The remodeling abilities of tissue engineered heart valves (TEHVs) make them promising substitutes for current mechanical or bioprosthetic valves. Upon implantation, host cells enter the TEHV scaffold and initiate a remodeling response to finally integrate a native-like heart valve. The mechanical stimuli emerging from the hemodynamic environment affect this cell-mediated remodeling response [1].

Computational finite element models can be employed to evaluate the mechanical stimuli on TEHV and the subsequent leaflet deformation depending on their geometry. With this, a variety of novel leaflet designs could be generated, all achieving significantly different mechanical stimuli [1-2]. A proof-of-concept in-vivo study showed that computationally-designed TEHVs develop significantly less leaflet retraction than the previous designs, and obtain a circumferential collagen fiber orientation that approached the native-like ones [3]. However, a proper understanding of the specific design attributes that facilitate either effective valve closure, optimal collagen orientation, or a combination of both remain unknown.

This study aims to employ a systematic approach to explore the effect of design features on the remodeling in TEHVs. Furthermore, an evaluation will be conducted to determine the feasibility of concurrently optimizing collagen alignment and retraction. This will be followed by design guidelines, which allow rational and efficient development of next-generation TEHVs.

METHODS

A previously developed bio-inspired remodeling model was used in order to capture the mechano-mediated cellular remodeling [3]. In short, tissue is modeled as a continuum of cells (primarily their actin stress fibers), collagen fibers, and extracellular matrix (ECM). The fibrous materials were described using 30 fiber directions with orientations spanning in the plane between a circumferential and a radially oriented unit vector.

Cellular remodeling was described by (de)polymerization of actin monomers, with decreased polymerization in direction of high stretch, effectively reorienting cells away from directions with high stretch. Collagen fibers were crimped by cells, with a target stress similar to cellular stress fiber stress. Collagen was isotropically deposited initially, and a strain-dependent collagen degradation law was incorporated.

Valve designs with variations in belly curvature and attachment edge curvatures (Figure 1a) were developed, based on a slightly adapted parametrized design [4]. For each curvature, three variations were adopted, resulting in 3*3 design variations (Figure 1b-c). Half of a leaflet was simulated, with a symmetry boundary condition through the belly profile, fixation of the attachment edge and the application of a diastolic pressure of 2 kPa representative of pulmonary pressure conditions.

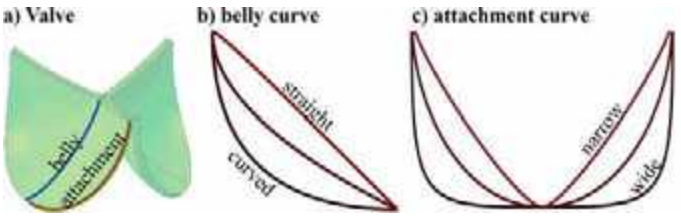

Figure 1 a) Tri leaflet valve geometry. Variations in b) belly and c) attachment curvature.

Valve performance was assessed by the opened area of the valve during diastole (regurgitant orifice area ROA), and a fiber orientation parameter S:

$$S = \int \phi_f(\gamma) \cos(2\gamma)\, d\gamma\,, \qquad (1)$$

with γ the fiber orientation angle with respect to circumferential direction, and ϕ_f the collagen fiber volume fraction.

RESULTS

Deformation of a representative TEHV design before remodeling resulted in marginally positive or negative radial strains and proper valve closure, as shown for two representative design variations (Figure 2a;c). Subsequent remodeling, however, resulted in changes in TEHV appearance and performance, where significant retraction is evident after remodeling under pulmonary conditions (Figure 2b;d), resulting in a loss of the valve's ability to close properly. Importantly, design variation B showed reduced retraction in comparison to variation A.

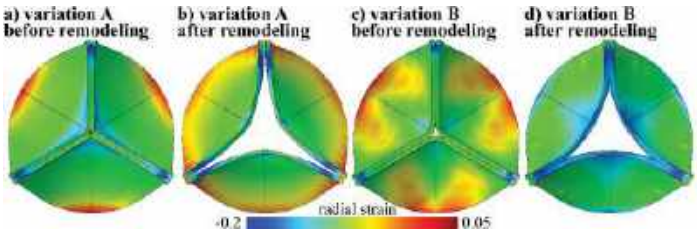

Figure 2 Radial strain in a) design variation A before remodeling and b) after remodeling, c) design variation B before and d) after remodeling.

Additionally, remodeling of these representative TEHV designs induced reorientation of collagen fibers towards a mildly anisotropic (S=0.06 & S=0.12) fiber distribution with the circumferential direction as main fiber angle (Figure 3a). As variation B had higher radial strain, collagen in that direction was less degraded, inducing a lower circumferential anisotropy. Cellular stress fibers also oriented towards the circumferential direction and showed a higher degree of variation in fiber alignment (S=0.14 & S=0.30) (Figure 3b). The pronounced anisotropic alignment observed in design variation A resulted from substantial radial compaction of the TEHV, causing the reorientation of cellular stress fibers which tend to avoid this compaction. Consequently, these fibers aligned more in the circumferential direction. In contrast, the reduced retraction observed in variation B led to a less pronounced anisotropy.

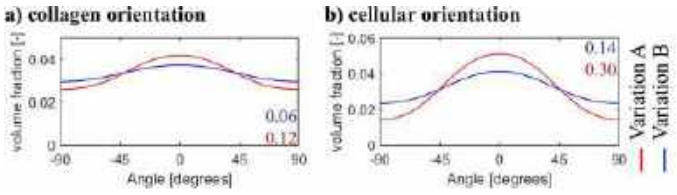

Figure 3 Example of a) collagen and b) cell orientation analysis after remodeling under pulmonary pressure conditions.

Retraction differed significantly for each design variation (Figure 4a), with higher retraction in designs with narrow attachment edges or straight belly curvatures. Collagen and cell alignment for all designs were positive, indicating mild circumferential anisotropic alignment. Generally, the average orientation parameter of cells (0.25) was significantly higher than average alignment of collagen (0.09). A design-dependent effect on collagen and cellular alignment was evident as well, were both had a more anisotropic circumferential alignment with more narrow attachment edges and straight belly curvatures.

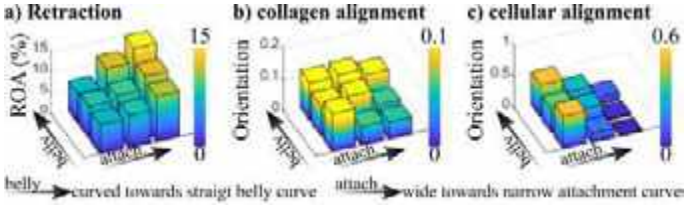

Figure 4 a) retraction, b) collagenous orientation and c) cellular orientation of design variations after remodeling

The predictions of decreased retraction and mild collagen alignment in curved bellied geometries is in line with previous *in-silico* predictions and *in-vivo* results [3]. The findings in the current study have the potential to refine the aforementioned predictions, suggesting that additional improvements might be achieved through optimization of the valvular attachment edge.

DISCUSSION

This study aimed to systematically assess the effect of design features on TEHV remodeling on a functional and tissue level. This was accomplished through the utilization of *in-silico* models that predict mechano-mediated tissue remodeling following *in-vivo* implantation.

The results indicate that in order to prevent retraction, designs with curved bellies and wider attachment edges should be utilized. However, in order to achieve native-like circumferentially anisotropic cell and collagen alignment, straight belly profiles and narrow attachment edges are more efficient. This suggests that design features that decrease leaflet retraction, generate more isotropic collagen and cell alignment. Therefore, during the development of next-generation designs it is essential to ascertain whether it is more critical to prevent TEHV leaflet retraction or induce proper fiber alignment. Thereafter, the design features as suggested here may be utilized in order to optimize the TEHV design.

Even though the current results do not show a decline of TEHV functionality with low circumferential cell and collagen anisotropy, it is possible that over the long-term, these properties could potentially impact valve remodeling and function. Therefore, future (*in-vivo* and *in-silico*) studies could focus on the chronic effect of non-native like fiber alignment on TEHV remodeling.

To conclude, these results increased our understanding of the effect of design features on TEHV remodeling in a systematical manner. This provides practical tools for the development of next-generation designs, thereby enhancing the clinical potential of TEHVs.

ACKNOWLEDGEMENTS

This project is funded by the European Research Council (ERC) under the European Union's Horizon 2020 research and innovation programme, grant agreement no. 852814 (TAVI4Life).

REFERENCES

[1] S. Loerakker et al. *Journal of the Mechanical Behavior of Biomedical Materials.* 58 (2016)

[2] B. Sanders et al. *Annals of Biomedical Engineering* 44 (2013)

[3] M. Y. Emmert et al. *Science Translational Medicine* 10 (2018)

[4] U. Gulbulak et al. *J. of the Mech. Beh. Of Biom. Materials.* 112 (2020)

MULTIPHYSICS SIMULATION OF FLOW AND OXYGEN TRANSPORT IN A POROELASTIC VOCAL FOLD MODEL

Isabella McCollum (1), Manoela Neves (1), Rana Zakerzadeh (1)

(1) Department of Biomedical Engineering, School of Science and Engineering, Duquesne University, Pittsburgh, PA, USA

INTRODUCTION

Vocals folds (VFs) are two bands of smooth muscle tissue found in the larynx. During voice production, pressurized air from the lungs passes through the larynx causing the folds to self-oscillate, resulting in phonation. Phonation results from the biomechanical fluid-structure interactions (FSI) between the glottal airflow and the poroelastic tissue of the VFs. Computational modeling of this FSI provides a prediction of VF dynamics and glottal flow which can lead to an improved understanding of these interactions. When modeling the VFs, the tissue is commonly assumed to be an elastic model, however, the folds behave more closely as a poroelastic tissue, with an 80% fluid volume fraction [1]. Thus, modeling of the fluid-porous structure interactions is a more realistic model that can better help us understand VF behavior and lead to treatment or prevention of voice-related disorders such as vocal fatigue or dehydration. In our previous research, a poroelastic model was developed to study the liquid dynamics within the VF tissue [2]. In this study, we aim to combine the FSI-porous VF model with a mass transport model to investigate the association of interstitial flow with oxygen transport within the VF. Previous experimental observations report contradictory relationships regarding the effects of phonation on the flow within the tissue and the associated oxygen partial pressure [3]. It has been hypothesized that physiological relationships may influence VF oxygenation, which corresponds with dysfunctions such as hypoxia and localized lesions. This study aims to analyze the role of porous media in modeling the flow and oxygen transport in the context of human phonation modeling. We develop a multiphysics coupled mass transport-FSI computational framework able to numerically simulate the complex flow fields, mechanical stresses, and oxygen delivery.

METHODS

A three-dimensional geometrical model of the VF and larynx domain was created using Autodesk Fusion 360 software. The model was implemented into the commercial modeling ANSYS Workbench software to perform computational analysis. A transient airflow coupled to the porous vocal fold dynamics was simulated. The airflow and interstitial flow dynamics were defined using ANSYS CFX software, and the VF tissue mechanics were modeled in ANSYS Mechanical.

The unsteady incompressible Navier-stokes equation was used to model the glottal airflow. The VF was modeled as homogeneous and isotropic, and its deformation was modeled using the momentum equation for a balance of total forces. Mass and momentum balance equations for the porous media were modeled via the Brinkman equation for the flow inside the VFs combing viscous terms from Stokes with friction terms from Darcy's equation was used to model the interporous flow. Lastly, the advection-diffusion reaction equation was used to model the convective oxygen transport with the consumption of oxygen in smooth muscle cells.

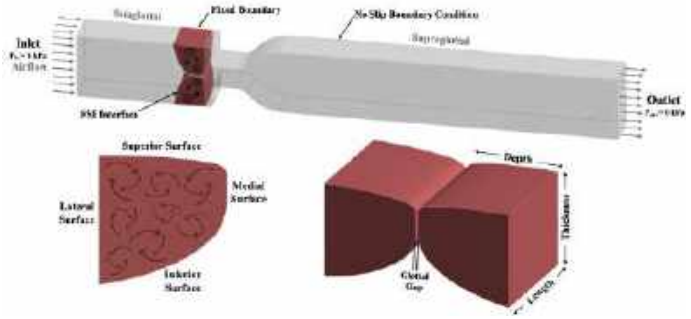

Figure 1: 3D laryngeal model and boundary conditions.

A static inlet pressure of 1 kPa was defined at the subglottal region while the pressure at the outlet of the supraglottal region was fixed at 0 kPa with a zero normal velocity gradient condition applied across the domain. The 3D model and prescribed boundary conditions are shown in **Figure 1**. The surfaces of the VF in contact with the fluid domain are free to move with no-penetration conditions. The lateral surfaces of the

VFs in contact with the outside are treated with opening conditions for fluid to circulate within the folds. All other exterior surfaces of the domains are treated with no-slip and no-penetration conditions. The FSI occurs on the superior, medial, and inferior surfaces of the VF. The material properties of the VFs and airflow used in numerical simulations were derived from our previous study [2]. The permeability constant of the VFs was varied, and the coupled system was solved for each case to provide a prediction of the interstitial fluid flow and oxygen concentration within the VF tissue.

The CFX and Mechanical components were joined along the FSI boundary using the ANSYS Workbench platform System Coupling module, which solves the fluid and solid domains separately to obtain pressure loads from the airflow in CFX that are applied to the VFs on the fluid-solid interface, solving for tissue dynamics in Mechanical. This process of the System Coupling algorithm in ANSYS is illustrated in **Figure 2**. The FSI loads from solving the coupled glottal fluid flow and VF deformation system are exported from the CFX component in the form of the pressure gradient. This data is then imported into the second CFX component containing the permeable VF mass transport model to capture the fluid circulation and the oxygen concentration within the porous tissue.

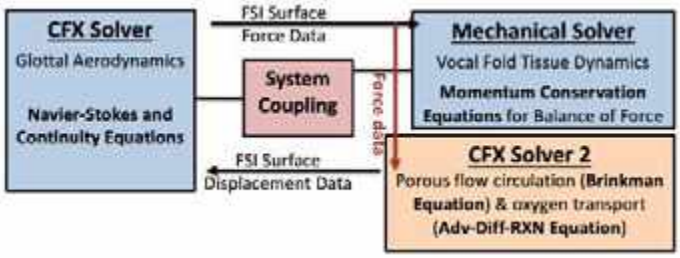

Figure 2: FPSI-mass transport algorithm in ANSYS Workbench.

RESULTS

The results for glottal aerodynamics, specifically the velocity contours at five different timesteps, are shown in **Figure 3**. We can see the velocity reaches the highest magnitude at the glottis region between the folds. We can also see that the airflow recirculates past the glottis region, entering the subglottal region. As time goes on, we can see the airflow increases and dissipates once it reaches the subglottal region.

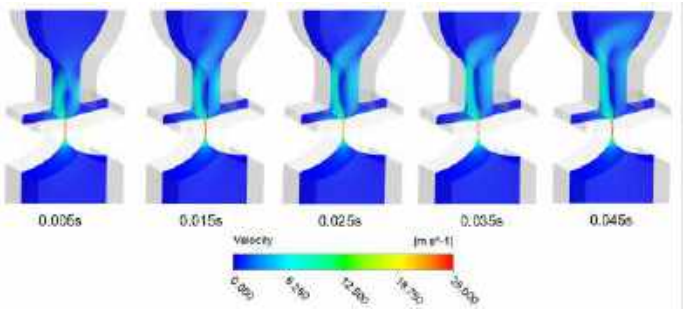

Figure 3: Glottal airflow velocity contours at five timesteps during one phonation cycle.

Next, we look at the results for the VF tissue displacement in one phonation cycle at five different timesteps displayed on the mid-coronal plane as shown in **Figure 4**. The undeformed positions are represented by solid black lines. The T_3 timestep corresponds to the fully open position of the glottis, deforming in the superior direction. The displacement contours are obtained from opening to fully open, then returning to the closed position to complete one phonation cycle. We can see as air flows between the folds, a rhythmic vibration occurs causing the folds to self-oscillate.

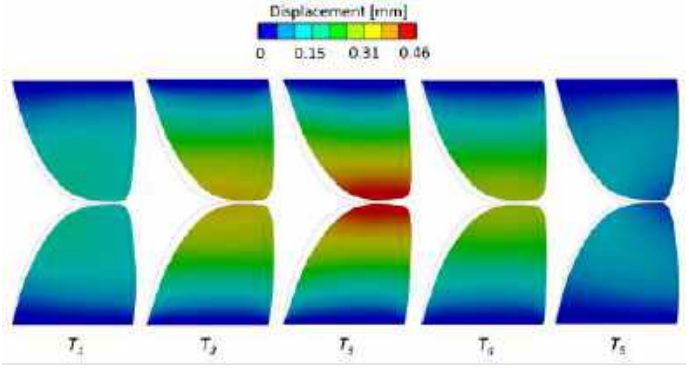

Figure 4: VF displacement pattern profiles at five-time instants during one phonation cycle.

The streamlines of fluid flow through the porous VF and oxygen concentration contours are shown in **Figure 5** for three cases with varying permeability. As the permeability increases, the interstitial velocity increases, thus there is a greater circulation of fluid within the tissue. Likewise, we can see that the amount of oxygenation occurring in the tissue greatly increases with an increase in permeability.

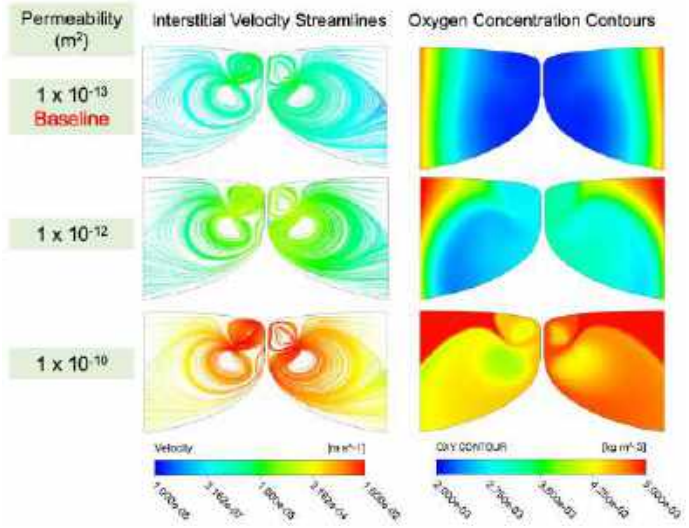

Figure 5: Interstitial velocity streamlines and oxygen concentration contours for cases with varying permeability.

DISCUSSION

An FPSI framework combined with a mass transport model of the VF and larynx domain was developed to investigate the interstitial fluid dynamics and oxygen transport within the VF tissue. Our results in **Figures 3-4** are consistent with previous studies, validating our fluid-structure interaction methodology framework. In **Figure 5**, we observed that the VF permeability was directly related to both the oxygenation of the tissue and filtration velocity. Thus, tissue perfusion is a key characteristic of biotransport in phonation models. Results highlight the association of poroelasticity with oxygen flow, as well as the interplay between permeability and interstitial liquid velocity within the permeable VF structure.

ACKNOWLEDGEMENTS

This study is supported by CBET 2138225 from the NSF.

REFERENCES

[1] Noordzij, J.P., et al. Otolary Clinics of Nor Amer, 39(1): 1-10, 2006.
[2] McCollum, I., et al. Phys of Fluids, 35(12): 2023.
[3] Arnstein, D. P., et al. Ann Otol Rhinol Laryngol 98 (10), 1989.

TEMPORAL VARIABILITY IN COMPOSITE LUMBAR SPINE SURROGATES DURING MULTI-LABORATORY COLLABORATIVE TESTING

Emma C. Coltoff[1], Jeremy G. Loss[2], Siril T. Dukkipati[3], Jenna M. Wahbeh[4], Kalle L Chastain[5], Matthew H. Pelletier, PhD[6], Tian Wang, PhD[6], Philip J. Brown[1], Mark Driscoll[3], Sophia Sangiorgio[4], Edward Ebramzadeh[4], Kathleen Meyers[5], William R. Walsh[6], G. Bryan Cornwall[6,7], Brian Kelly[8], Robb W. Colbrunn[2]

[1]Department of Biomedical Engineering, Wake Forest School of Medicine, Winston-Salem, North Carolina, USA
[2]Lerner Research Institute, Cleveland Clinic, Cleveland, Ohio, USA
[3]Department of Mechanical Engineering, McGill University, Montreal, Quebec, Canada
[4]JVL Orthopaedic Research Center, University of California – Los Angeles, Los Angeles, California, USA
[5]Hospital for Special Surgery, New York City, New York, USA
[6]Surgical and Orthopaedic Research Laboratories, University of New South Wales, Sydney, New South Wales, Australia
[7]University of San Diego, San Diego, California, USA
[8]Barrow Neurological Institute, Phoenix, Arizona, USA

INTRODUCTION

Biomechanical testing of the spine has evolved greatly over the past several decades with the development of new testing techniques, improved testing fixtures and software, novel methods of in vivo measurement, and determination of crucial anatomical structure-function relationships. However, despite previous efforts to capture best practices in spinal biomechanical testing [1], no consensus has been drawn. Artificial composite spine surrogates have been used to counteract some of the challenges with using cadaveric specimens for biomechanical testing standardization and comparison across labs such as degradation over time, inter-specimen variability, storage requirements, and transportation regulations [2]. However, while these composite spines have been used for hundreds of orthopaedic studies, large scale evaluation of these surrogates' performance for use in spine biomechanical testing standardization has not been conducted. The objective of this study was to characterize changes seen in composite surrogates over a long-term, multi-laboratory study to illuminate time-based, repeated testing specimen variation and inform future surrogate development.

METHODS

Seven established biomechanical testing laboratories conducted the testing reported in this study over a total time of 26 months. Five Sawbones synthetic lumbar spinal surrogates were passed through the seven participating labs (Figure 1). Each lab conducted pure moment testing on each of the surrogates in Flexion-Extension (FE), Lateral Bending (LB), and Axial Rotation (AR) through trapezoidal and/or sinusoidal loading schemes (Figure 2).

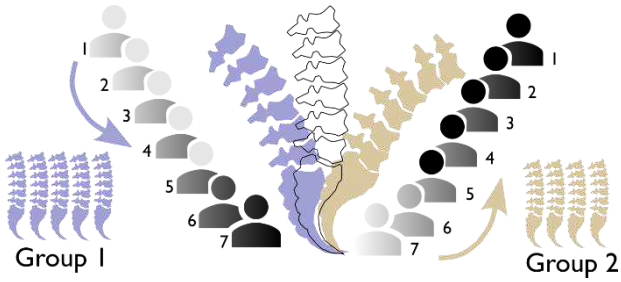

Figure 1: Path of surrogate spines through participating labs.

All labs reported, at a minimum, the bending angles (in degrees) in FE, LB, and AR for the overall joint coordinate system (JCS) kinematics of each of the L2-L5 lumbar spinal surrogates. Most labs were able to report Anterior, Lateral, and Superior translations as well as individual functional spinal unit behavior for the L2-L3, L3-L4, and L4-L5 vertebral pairings. This report is centered on the behavior of the JCS kinematics and specifically the overall L2-L5 spine rotation in the primary direction of loading. The consortium met monthly to discuss findings as each group completed testing on the set of five spines, and to troubleshoot any issues or confusion that arose in testing.

RESULTS

This study resulted in ranges of reported rotation values in the six primary testing directions – flexion (7.4° to 19.8°), extension (5.6° to 13.3°), left LB (4.3° to 15.4°), right LB (7.2° to 16.6°), left AR (2.7° to 6.3°), and right AR (2.6° to 5.6°). The average rotation angle in the primary direction of the loading experienced non-significant increases

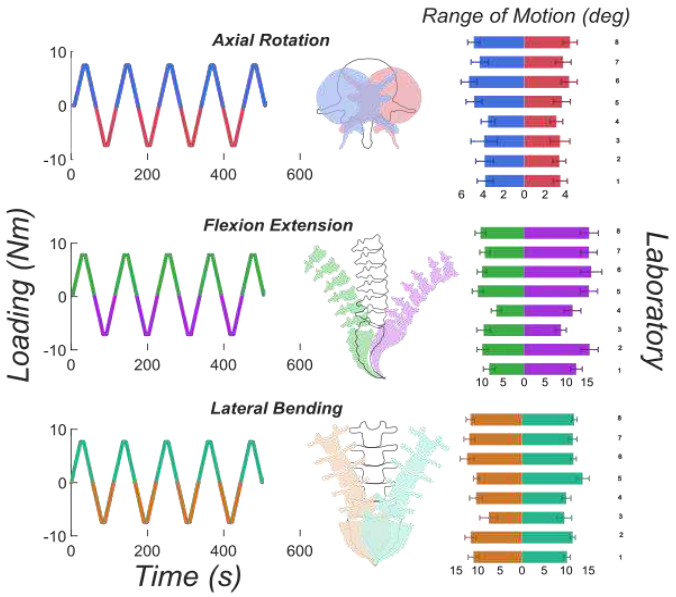

Figure 2: Loading profiles and corresponding data spread by lab.

ranging from 0.9° (right AR) to 3.1° (flexion) between the first and last test (same lab) for all testing directions. Despite an increase in average rotation angle across all testing directions, the standard deviations for each testing direction mostly decreased over time (0.7° to 0.6° for AR, 1.5° to 2.2° for Flexion, 1.4° to 1.3° for Extension, 1.0° to 0.8° for LB). These data are shown in Figure 3.

Figure 3: Surrogate rotation spreads across lab. Note that Lab 1 and 8 were the same lab at the start and end of the testing path.

DISCUSSION

Some of the Sawbones surrogate spines experienced significant visible deterioration shown in Figure 4. However, despite this degradation, the surrogates did not experience significant time-based changes to their range of motion measures in any of the tests reported. Asymmetries in left and right bending (LB, AR) were visible. The highest variation between labs occurred in FE testing while the lowest variation occurred in AR. This both reflects the expected normal variation in these ranges of motion and is consistent with prior testing on these surrogate types [2]. Inter-laboratory variation was larger than temporal variation. Future studies are required to investigate variations in reported rotation angles due to differences in test methods, equipment, etc. Inter-laboratory studies are a crucial part of the standardization of any test protocol and for the wider dissemination of best practices. This is the largest inter-laboratory study conducted on widely used synthetic spinal surrogates, to the knowledge of the authors. These results indicate that additional factors outside of specimen variability play a role in the measured range of motion across laboratories. This study is part of a greater effort to not only provide best practices for spinal biomechanics testing, but also how to manage specimen degradation over time and how to manage a comprehensive spine biomechanics dataset.

Figure 4: Spine surrogate degradation during testing

ACKNOWLEDGEMENTS

The authors would like to acknowledge Sawbones for their funding support of the transportation of the spine surrogates between the participating labs.

REFERENCES

[1] D. J. Wheeler et al., J. Biomech., vol. 44, no. 13, pp. 2383–2387, Sep. 2011

[2] R. Zdero, P. Brzozowski, and E. H. Schemitsch, Med. Eng. Phys., vol. 118, p. 104017, Aug. 2023

Reverse-engineering cancer mechanics: Piezo regulates epithelial topology and promotes precision in organ size control

(1) Nilay Kumar*, (1) Mayesha Sahir Mim*, (1) Megan Levis, (1) Maria Unger, (1) Gabriel Miranda, (1) Trent Robinett, (1) Jeremiah Zartman

(1) Chemical and Biomolecular Engineering, University of Notre Dame, Notre Dame, IN, USA
* Equal contributions

INTRODUCTION

Mechanosensitive Piezo channels have been implicated in the progression of multiple types of cancer[1,2]. Piezo, a mechanosensitive calcium channel, promotes cell division by activating ERK signaling or can activate Rho signaling to mediate cell extrusion and cell death[3,4]. However, the systems-level functions of Piezo in organogenesis and tissue homeostasis remain poorly understood. To reverse-engineer how Piezo impacts cellular processes in multicellular systems, we focus on a highly accessible model system of organ size control, the *Drosophila* wing imaginal disc. Here, we demonstrate that Piezo controls epithelial cell topology to ensure precise organ growth by integrating methods, including live imaging experiments coupled with pharmacological and genetic perturbations and computational modeling. Our findings demonstrate that Piezo promotes robustness in regulating epithelial topology and is necessary for maintaining precise organ size control. These insights into the multiscale roles of Piezo lay the foundation for identifying new therapeutic strategies crucial for cancer engineering[5].

METHODS

We used the GAL4-UAS system to express RNAi to knockdown (KD) Piezo or overexpress Piezo in the *Drosophila* wing imaginal disc. We also characterized the complete knockout (KO) of Piezo. A hybrid polyethylene terephthalate laminate (PETL) microfluidic device[6] was used in combination with confocal microscopy to ensure extended periods of stable ex vivo imaging and allow the addition of a constant flow of media. Immunohistochemistry was utilized for systematic characterization of cell processes and tissue structure was pursued through immunohistochemistry. Additional analysis included laser ablation and computational modeling.

RESULTS

Our results show that knockout or knockdown of *Piezo* led to bilateral asymmetry in wing phenotypes and increased the variability of organ size, indicating Piezo provides feedback control on organ size regulation (**Fig. 1**). While pharmacological activation of Piezo stimulated an increase in the frequency of spikes in cytosolic Ca^{2+}, we discovered that *Piezo* overexpression counterintuitively reduces Ca^{2+} signaling dynamics. Piezo overexpression also increases the hexagonality of cellular topology. In contrast, Piezo knockdown inhibited proliferation and decreased global apoptosis, resulting in an overall increase in epithelial overcrowding. To further characterize how Piezo regulates cell topology, we formulated computational simulations to investigate how expression levels of Piezo protein regulate cell proliferation and apoptosis through modulation of the cut-off tension required for Piezo channel activation. Quantitative experimental analysis validated computational simulation predictions of how perturbations to *Piezo* impacted epithelial topology.

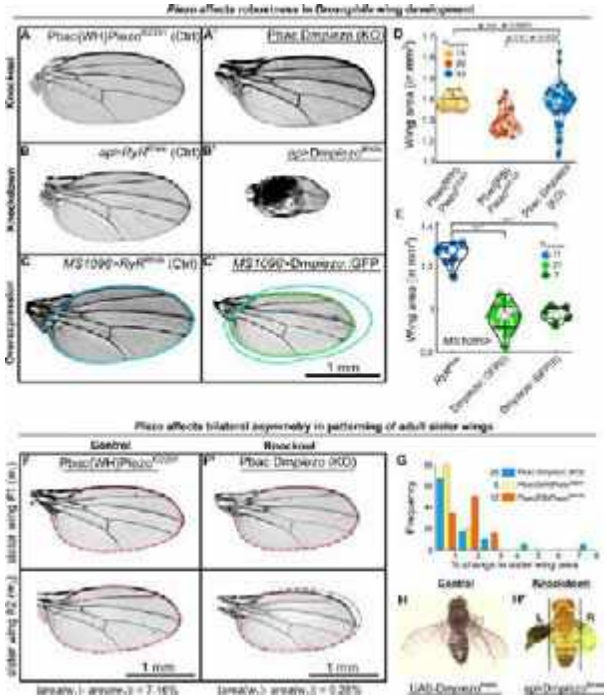

Figure 1: Divergent and spatial effects of Piezo expression in regulating size precision in bilateral organs. Piezo determines size precision in bilateral organs. (A-A') Drosophila wings from a Piezo knockout line do not exhibit significant changes in average wing size compared to the control line used to generate the knockout line. (B-B') Wing phenotypes from RNAi-mediated knockdown of Piezo and a previously characterized cross against RyR^{RNAi}. (C-C') Overexpression of Piezo in the wing disc results in smaller wings than control discs targeting a non-expressed gene with no observed phenotype. (D) Piezo knockout wings exhibit significant heterogeneity in wing size compared to the original Piggybac lines used to generate the knockout. Beeswarm plot showing the distribution of wing area for different perturbations to Piezo. KO represents the Piezo knockout line. The p-value comparing means and variances of populations are indicated. (E) Beeswarm plot showing the quantified distribution of wing area for overexpression of Piezo. Superscripts I and II against the Piezo label indicate two different overexpression lines (detailed in the methods section). (F-F') Sister wings of the control and Piezo knockout lines demonstrate significant variation between bilateral organs. Yellow lines outline the contour of a sister wing. The same contour is depicted as a dashed red line for the other sister wing. (G) The bar graph shows the distribution of differences in the area between the Piezo knockout and knockdown

lines' sister wings. (H) Adult $^{UAS\text{-}PiezoRNAi}$ fly. (H') Adult *ap>Piezo*^{RNAi} fly showing significant patterning and symmetry defects between each wing.

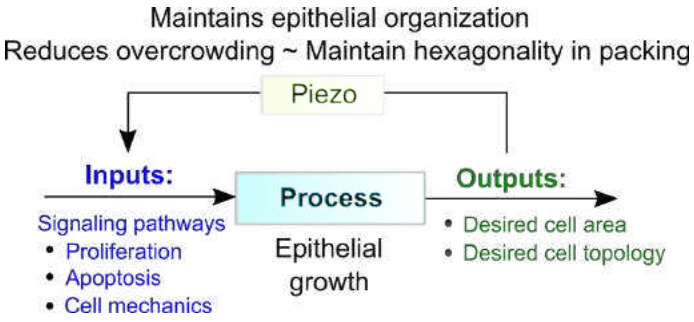

Figure 2: Piezo is a critical component in feedback control to ensure regular epithelial topology and precision in organ size control.

DISCUSSION

This work demonstrates how Piezo channels influence organ size and the structure of epithelia (**Fig. 2**). We posit that Piezo channels act as feedback controllers to regulate cellular topology and epithelial packing through control of downstream processes such as proliferation, apoptosis, and cytoskeletal regulation. Thus, targeting the strength of feedback through Piezo may be an attractive modality for pursuing optogenetics[7] and cancer therapeutics.

ACKNOWLEDGEMENTS

Thanks to Dr. Sara Cole from Notre Dame Integrated Imaging Facility for helping with imaging. The work was supported by NIH 1R35GM124935-01, NSF CBET-2225601, and EMBRIO Institute, NSF DBI contract #2120200.

REFERENCES

1. Luo M, Cai G, Ho KKY, Wen K, Tong Z, Deng L, Liu AP. Compression enhances invasive phenotype and matrix degradation of breast cancer cells via Piezo1 activation. BMC Molecular and Cell Biology. 2022 Jan 3;23(1):1.

2. Yu JL, Liao HY. Piezo-type mechanosensitive ion channel component 1 (Piezo1) in human cancer. Biomedicine & Pharmacotherapy. 2021 Aug 1;140:111692.

3. Gudipaty SA, Lindblom J, Loftus PD, Redd MJ, Edes K, Davey CF, Krishnegowda V, Rosenblatt J. Mechanical stretch triggers rapid epithelial cell division through Piezo1. Nature. 2017 Mar 2;543(7643):118–121. PMCID: PMC5334365

4. Eisenhoffer GT, Loftus PD, Yoshigi M, Otsuna H, Chien CB, Morcos PA, Rosenblatt J. Crowding induces live cell extrusion to maintain homeostatic cell numbers in epithelia. Nature. 2012 Apr 15;484(7395):546–549. PMCID: PMC4593481

5. Kumar N, Mim MS, Levis M, Unger M, Miranda G, Robinett T, Zartman JJ. Piezo regulates epithelial topology and promotes precision in organ size control. bioRxiv. Cold Spring Harbor Laboratory; 2023;2023–08.

6. Levis M, Kumar N, Apakian E, Moreno C, Hernandez U, Olivares A, Ontiveros F, Zartman JJ. Microfluidics on the fly: Inexpensive rapid fabrication of thermally laminated microfluidic devices for live imaging and multimodal perturbations of multicellular systems. Biomicrofluidics. 2019 Mar;13(2):024111. PMCID: PMC6486393

7. Mim MS, Knight C, Zartman JJ. Quantitative insights in tissue growth and morphogenesis with optogenetics. Phys Biol. 2023 Sep 28;20(6):061001. PMCID: PMC10594237

ALTERATIONS IN MICROGLIA MORPHOLOGY AND VIABILITY FOLLOWING IN VITRO TRAUMATIC BRAIN INJURY

E. Blick (1), C. Franck (2), A. Hai (1)

(1) Department of Biomedical Engineering, University of Wisconsin - Madison, Madison, WI, United States
(2) Department of Mechanical Engineering, University of Wisconsin - Madison, Madison, WI, United States

INTRODUCTION

Chronic neuroinflammation following Traumatic Brain Injury (TBI) remains an understudied link between a primary injury and neurodegenerative disease, with post-mortem analysis of TBI patients demonstrating a brain-wide immune response up to 18 years after injury [1]. Microglia, the resident immune cells of the brain, are crucial in this process as their prolonged activation is associated with driving secondary injury, cognitive decline, and cell death. Microglia are sensitive to their microenvironment and undergo functional and morphological transitions in response to inflammatory signals, adopting either anti- or proinflammatory roles [1].

Most research on microglia activation relies on using lipopolysaccharide (LPS), a bacterial membrane component that targets microglia-specific receptors, but the research investigating the response of microglia to mechanical impacts is lacking [2]. Furthermore, most TBI studies are conducted *in vivo* and, although biologically complex, they preclude reliable application of strain with the accuracy required to determine a correlation between impact and inflammatory response at a single cell level.

Stretch-based TBI models are commonly used to reproduce mechanical insults linked to the pathological development of diffuse axonal injury [3]. Several previous studies have begun to characterize the response to microglia, but results are inconsistent across studies and lack the evaluation of a range of strain and strain rates [4],[5]. Two studies assessing microglial response to 20% strain at a singular rate observed alterations in microglia migration, cytokine expression, and morphology [4],[5]. In order to further characterize the mechanosensitive properties of microglia, a range of TBI-relevant strain and strain rate parameters must be evaluated. In this study, we utilize a novel and highly precise in vitro model of TBI to evaluate alterations in microglia viability and morphology in response to controlled mechanical stress.

METHODS

Polydimethylsiloxane (PDMS) is used as a substrate for cell seeding due to its nearly linear elastic nature and optical transparency. The PDMS is prepared with a 10:1 mixture of Sylgard 184. The mixture is added to dog bone – shaped molds fabricated on an SU-8 wafer. The dog bone shape enables the use of high strains without disrupting the gripping points and results in the center area hosting the cells to experience a uniform strain field. The PDMS is cured at 80 ℃ for 20 minutes, removed, and adhered with additional PDMS between two 3D printed grippers that were printed with Biomed Clear, a biocompatible resin. Samples are then moved to a culture dish and coated with a 40 µL drop of Poly-D-Lysine for 2 hours (Fig 1.A).

Mixed glial cultures are obtained from P0/P1 Sprague Dawley rat cortices. Cells were suspended in 1 mL of media containing DMEM, 10% FBS, and 1% Pen Strep at a concentration of 5,000,000 cells/mL and added to a T25 flask. The media was refreshed every 2 days for 14 days when flasks were near confluency. Microglia were isolated on DIV 14 using mild trypsinization. Flasks were incubated for approximately 15 minutes in a 1:4 solution of .25% trypsin-EDTA to DMEM/F12 after which the top layer of cells, mainly astrocytes, detached and the media was discarded [6]. Microglia were recovered by a brief 3-minute trypsinization with .25% trypsin-EDTA. The media was collected and centrifuged at 1000 rpm for 10 minutes. The cell pellet was resuspended in 300 µL of media and counted. Microglia were seeded onto the center of the PDMS dog bones at 125,000 cells/mL in a 38 µL drop. Samples were incubated and allowed to adhere for 1 hour, then 3 mL of additional media was added to submerge the dog bone and grippers and cultures were left to settle overnight (Fig 1.B).

The stretch injury was conducted using a micro-tensile impact device built in-house [7]. The customized device consists of two linear actuator motors and 3D-printed “fingers” to contact the sample grippers on either side. The device is placed on the stage of an inverted fluorescent microscope and enables live cell imaging before, during and

after stretch. Samples are stained with Calcein-AM, a live cell indicator, and placed into the device. The device "fingers" are lowered to contact the grippers and aligned. A 10X image is collected as a reference prior to stretch. Applied strain and strain rates are programmed into a macro interfacing with the device and then a brief, symmetric displacement is applied to the sample. For this study, 30% strain at strain rates of 1 s^{-1} and 50 s^{-1} were evaluated. Immediately after stretch the device releases from the sample and the dog bone recovers (Fig 1.C). Samples are then placed back in the incubator for 24 hours prior to subsequential analysis.

At 24 hours post-impact, cultures are restained with Calcien-AM and Ethidium Homodimer-1, a dead cell indicator, and another 10X image is acquired. Samples are then fixed with 4% paraformaldehyde and permeabilized with .5% Triton-X. Cells are stained with Iba-1 to mark microglia and DAPI to assess morphology and sample purity. Stained samples are imaged at 20X magnification. CellProfiler is used to count live and dead cells to calculate percent viability, cell area, perimeter, and form factor.

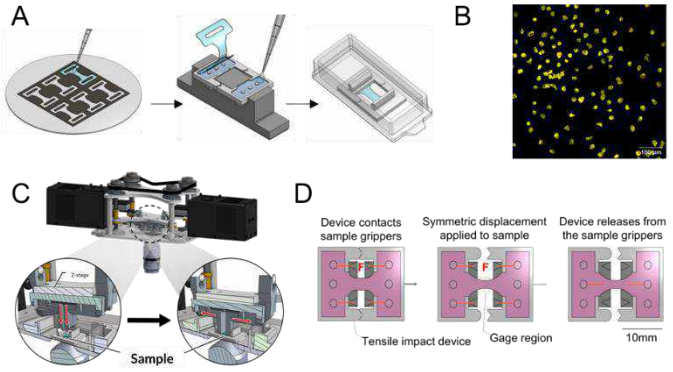

Figure 1: Overview of substrate fabrication and stretch injury system. (A) PDMS substrate fabrication workflow (B) Sample stained with Iba-1 (C) Tension device (D) Schematic of substrate stretch

RESULTS

Preliminary results suggest a rate-dependent reduction in microglia viability 24 hours after stretch. Cultures stained with Calcein-AM and Ethidium Homodimer-1 24 hours after impact are shown. A sham sample is included to account for any cell death related to imaging or placement into the device (Fig.2A). The viability in the sham condition was approximately 78 %. For impact conditions, the sample that underwent a stretch at 30 % strain at 1 s^{-1} demonstrated a comparable viability to the sham sample at around 70 % (Fig.2B). Interestingly, a sample stretched at the same strain of 30 % but at a strain rate of 50 s^{-1} had a large decrease in viability to about 48 % (Fig.2C). Overall, these preliminary findings point to strain rate as a factor to consider when characterizing mechanosensitive of microglia.

DISCUSSION

The presented study begins to address the mechanosensitive response of microglia following TBI-relevant mechanical stimuli using an in vitro model and a micro-tensile impact device. Previous studies have contributed to the understanding of microglial response at singular strain and low strain rate levels. This investigation therefore focuses on the comparison of viability under different impact conditions, particularly the significance of strain rate. The preliminary findings suggest a rate-dependent response in microglia viability, with a reduction in viable cells at a higher strain rate of 50 s^{-1} versus 1 s^{-1} 24 hours after impact. These findings highlight the

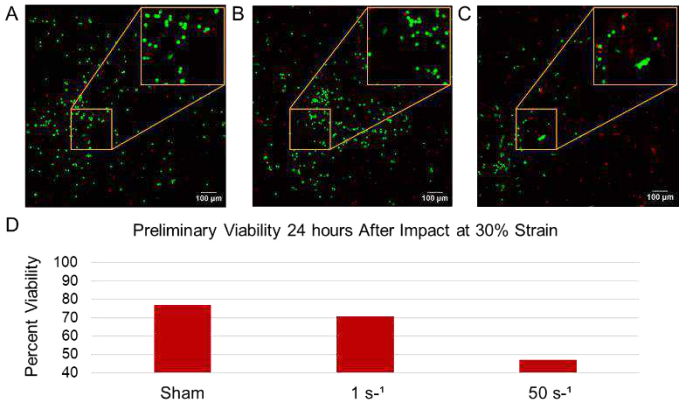

Figure 2: Preliminary Viability Results. Cultures stained 24 hours after impact with Calcein-AM (green) and Etihidum Homodimer-1 (red). (A) Sham (B) 30% strain at 1 s^{-1} (C) 30% strain at 50 s^{-1}

importance of considering strain rate when predicting neuroinflammation.

In order to draw further conclusions about the dose-dependent response of microglia to a range of strain and strain rates, more parameters need to be tested. Additionally, microglia are highly dynamic and collaborative cells and crosstalk with other neural cells must be considered. Therefore, more complex in vitro models containing multiple cell types should be characterized in the future to determine how microglia mechanosensitivity is altered in the presence of neurons and astrocytes. In conclusion, this study introduced a novel in vitro model for applying reproducible mechanical stress to microglia. The results provide preliminary evidence pointing towards the importance of strain rate on microglia viability, contributing to the broader understanding of TBI-related neuroinflammation.

.

ACKNOWLEDGEMENTS

This material is based upon research supported by the U.S. Office of Naval Research under PANTHER award numbers N000142112044 and N00142112855. Additional thanks the Biotechnology Training Program at UW Madison for their support.

REFERENCES

[1] Johnson VE, Stewart JE, Begbie FD, Trojanowski JQ, Smith DH, Stewart W. Inflammation and white matter degeneration persist for years after a single traumatic brain injury. Brain. 2013 Jan;136(Pt 1):28.
[2] Lively S, Schlichter LC. Microglia Responses to Pro-inflammatory Stimuli (LPS, IFNγ+TNFα) and Reprogramming by Resolving Cytokines (IL-4, IL-10). Front Cell Neurosci. 2018 Jul 24;12:215.
[3] Hanna E., Pfister B. Advancedments in in vitro models of traumatic brain injury, Current Opinion in Biomedical Engineering, 25, 100430.
[4] Shaughness, M., Byrnes, K. Assessment of the Effects of Stretch-Injury on Primary Rat Microglia. Mol Neurobiol 58, 3545–3560 (2021).
[5] Procès A, Alpizar YA, Halliez S, Brône B, Saudou F, Ris L, Gabriele S. Stretch-injury promotes microglia activation with enhanced phagocytic and synaptic stripping activities. Biomaterials. 2023 Dec 15;305:122426.
[6] Saura J, Tusell JM, Serratosa J. High-yield isolation of murine microglia by mild trypsinization. Glia. 2003 Dec;44(3):183-9.
[7] Summey, L., Zhang, J., Landauer, A. et al. Open Source, In-Situ, Intermediate Strain-Rate Tensile Impact Device for Soft Materials and Cell Culture Systems. Exp Mech 63, 1445–1460 (2023).

DEVELOPMENT OF HORMONALLY RESPONSIVE TUNABLE HYDROGEL

Vivian H. Su (1), Nicholas T. Gigliotti (1), Juan Diego Carrizo (2), Mitra L. Taheri (1)

(1) Materials Science and Engineering, Johns Hopkins University, Baltimore, MD, USA
(2) Bioengineering, University of Pennsylvania, Philadelphia, PA, USA

INTRODUCTION

In the United States, one in ten children is born prematurely. Preterm birth (PTB) has been reported to have lifelong effects, such as neurological disorders, feeding difficulties, and vision problems [1]. Makena, a drug previously approved to reduce the risk of PTB, was withdrawn from the market by the FDA in April 2023 [2]. Makena and its generics were determined to be ineffective and there remains an absence of FDA-approved therapeutics addressing PTB. This gap emphasizes the critical need to understand the biological mechanisms of cervical remodeling during pregnancy.

Cervical remodeling is a widely studied phenomenon as it plays a significant role in its structural integrity. There is a lack of comprehensive understanding due to its dynamic and multifactorial nature. In this study, we aim to address this knowledge gap by focusing on the role of progesterone, a hormone that has been shown to play a dominant role in cervical softening. Motivations include evidence of spontaneous birth upon mifepristone-induced progesterone receptor blockage and the impact of progesterone on collagen synthesis in human cervical fibroblast 3D culture [3-5].

Due to ethical and safety considerations, we propose developing a hydrogel system to conduct these studies. Light-based bioprinting was utilized to develop a tunable *in vitro* hydrogel system to mimic the mechanical properties of the human cervix. The development of the hydrogel incorporated gelatin methacryloyl (GelMA), which is gelatin modified with methacryloyl groups in methacrylic anhydride. Previous studies have shown GelMA to have excellent thermostability and cell attachment and proliferation motifs, indicating its promising potential as a bioink with high tunability of mechanical factors [6]. Upon UV-light exposure, GelMA has the ability to polymerize to a desired stiffness.

We hypothesize that a tunable 3D culture system made with GelMA seeded with human cervical fibroblasts will exhibit softening from progesterone exposure. This study aims to elucidate how dynamic mechanical and biological changes during pregnancy drive cell-specific events that modulate cervical remodeling. By addressing this research gap, our work seeks to contribute to the development of effective treatments for PTB.

METHODS

A preliminary study of the photopolymerization and cytocompatibility of the constructed hydrogel system gelatin methacrylate (GelMA) with 0.25% lithium phenyl-2,4,6-trimethylbenzolphosphinate (LAP) photoinitiator was assessed. The prepared bioink was extruded through a 25G nozzle and crosslinked at 405nm to reach mechanical values comparable to previous studies by adjusting the light intensity and duration. The compressive modulus was measured by compression testing with a 5N load cell. The surface topography of the hydrogel was imaged by environmental SEM at 70Pa, which was then used to quantify pore diameters using ImageJ. The degree of hydration was measured using the weights of the dried and wet samples. Human uterine fibroblasts were seeded in the hydrogel and analyzed for cell viability on Day 0, 4, and 7 using a Live/Dead cell assay.

RESULTS

The stiffness of the constructed hydrogel was within 5-15kPa, which reflects the stiffness of the human cervix. It was also observed that the increase of light intensity was directly proportional to the compressive modulus. Pore diameters were greater than 5μm; the duration of the light exposure was inversely proportional to the pore size. The swelling ratio was observed to increase as light intensity decreased. Cells maintained viability throughout the timepoints.

DISCUSSION

In this study, we engineered a hydrogel system using GelMA and achieved stiffness values comparable to those found in literature. The pore sizes were greater than the average cell diameter, which indicates facile transport of cells and nutrients within the network. The observed relations between the light exposure dose and stiffness and pore size values demonstrated the tunability of the hydrogel. With the control of the photoinitiation and production of free radicals, we adjusted the hydrogel's mechanical properties. The hydrogel system was also shown to have cytocompatibility throughout the 7 days from myometrial fibroblasts.

The results of this preliminary study demonstrate the promising potential of utilizing a GelMA-based hydrogel to conduct a progesterone study. Next steps include culturing the GelMA hydrogel construct in progesterone-supplemented media and analyzing for changes within the mechanical properties (stiffness, pore diameter, swelling ratio). An analysis of the collagen concentration and crosslinking would be compared with the current understanding of the native tissue during the remodeling process. To further determine the validity of this engineered hormonally responsive platform, an RNA-seq would be performed similar to the study done by House, et al (2018) [5].

ACKNOWLEDGEMENTS

We would like to acknowledge the Johns Hopkins University's Whiting School of Engineering and the March of Dimes for funding support.

REFERENCES

[1] Centers for Disease Control and Prevention. Preterm Birth, Oct 2023
[2] U.S. Food and Drug Administration. FDA Commissioner and Chief Scientist Announce Decision to Withdraw Approval of Makena, April 2023
[3] Rigterink, E et al., *Women and Health,* 2:235-250, 2013
[4] Tripathy, S et al., *J Steroid Biochem Mol Biol*,
[5] House, M et al., *Tissue Engineering: Part A*, 24:1765-1774, 2018
[6] Sun, M et al., *Polymers (Basel)*, 10(11): 1290, 2018

LAMINA CRIBROSA VASCULAR NETWORK ANALYSIS: ASSOCIATIONS BETWEEN STRUCTURAL AND FUNCTIONAL PARAMETERS

Yuankai Lu (1), Hua Yi (3), Ruhani Gill (2), Andrew Theophanous (2), Shaharoz Tahir (2), Po-Yi Lee (1), Ian A. Sigal (1,2)

(1) Department of Ophthalmology, University of Pittsburgh, Pittsburgh, PA, USA
(2) Department of Bioengineering, University of Pittsburgh, Pittsburgh, PA, USA
(3) Department of Biomedical Engineering, University of Mississippi, Oxford, MISS, USA

INTRODUCTION

Glaucoma is characterized by progressive degeneration of retinal ganglion cells and their axons [1]. The axon damage is known to start within the lamina cribrosa (LC) region in the back of the eye. Although the mechanisms leading to axon damage remain not fully understood, a leading hypothesis is that insufficient supply of blood or oxygen within the LC would contribute to this process. Currently, it is challenging to experimentally measure in-vivo LC hemodynamics or oxygenation, which are crucial to understanding glaucoma development. Therefore, assessing the structural properties of the LC vasculature, whether in-vivo or ex-vivo, could potentially serve as a predictor for these essential functional parameters.

Our goal was to characterize the vasculature of the monkey LC through several geometrical and functional parameters, including both hemodynamics and oxygenation, and to identify potential correlations between the parameters.

METHODS

Vascular network: We reconstructed detailed 3D models of the LC vascular networks of four healthy monkey eyes using histological techniques, as described before [2]. Each vessel segment was defined as the path between two adjacent branch vertices (or boundary vertex). We calculated four geometric parameters for each vessel: length, tortuosity, inclination, and polar orientation. The detailed definitions of these parameters are shown in figure 1.

Hemodynamics and oxygenation: For each of the four vessel networks we used numerical methods to simulate the hemodynamics and oxygenation using the methods reported elsewhere [3]. Briefly, blood pressure boundary conditions were applied to simulate the physiological blood supply for the LC: Blood inflow from the circle of Zinn-Haller in the periphery, drainage through the central retinal vein, and interactions with the anterior and posterior LC regions. Blood flow was considered as incompressible laminar flow, described by the Poiseuille equation. Oxygen transport in the tissue was described by the diffusion-consumption equation. Three parameters of each vessel were quantified: blood flow, blood pressure, and oxygenation in surrounding tissues.

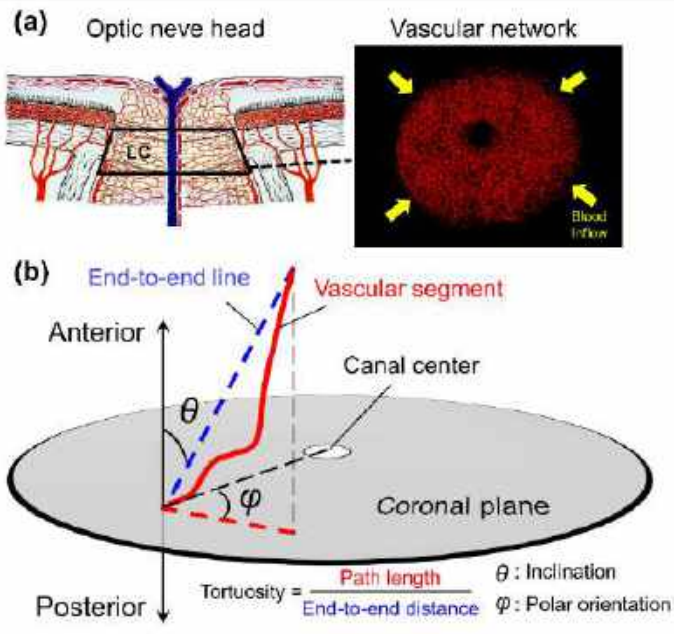

Figure 1: (a) Diagram of the lamina cribrosa (LC) vascular network (left) and example vascular network model. Blood inflow was from the periphery representing the circle of Zinn-Haller (yellow arrows) [4]. (b) Diagram illustrating the definition of the four geometric parameters of a vascular segment [2]: length, tortuosity, inclination, and polar orientation.

Statistical analysis: Using linear mixed effect models we evaluated the correlations between the four geometric parameters (length, tortuosity, inclination, and polar orientation), hemodynamics parameters (blood flow, blood pressure), and oxygenation parameters (oxygenation).

RESULTS

Illustrations of the distribution of all the parameters of one LC vascular network are shown in Figure 2. We did not discern any clear spatial patterns in the geometric parameters. Polar orientations followed a nearly uniform distribution, indicating no preferential polar angle of the capillaries. The hemodynamic and oxygenation parameters exhibited a radial-like spatial distribution. The peripheral region had a higher flow rate, blood pressure, and oxygenation. The central region had a lower flow rate, blood pressure, and oxygenation.

Scatterplots and correlation between the geometric parameters and hemodynamic/oxygenation parameters are shown in Figure 3. All associations shown were significant, although the correlation coefficients were weak ($r < 0.2$). Among the geometric parameters, the length and the tortuosity had weak negative correlations to flows and oxygenation, whereas both orientations were not correlated with flows and oxygenation.

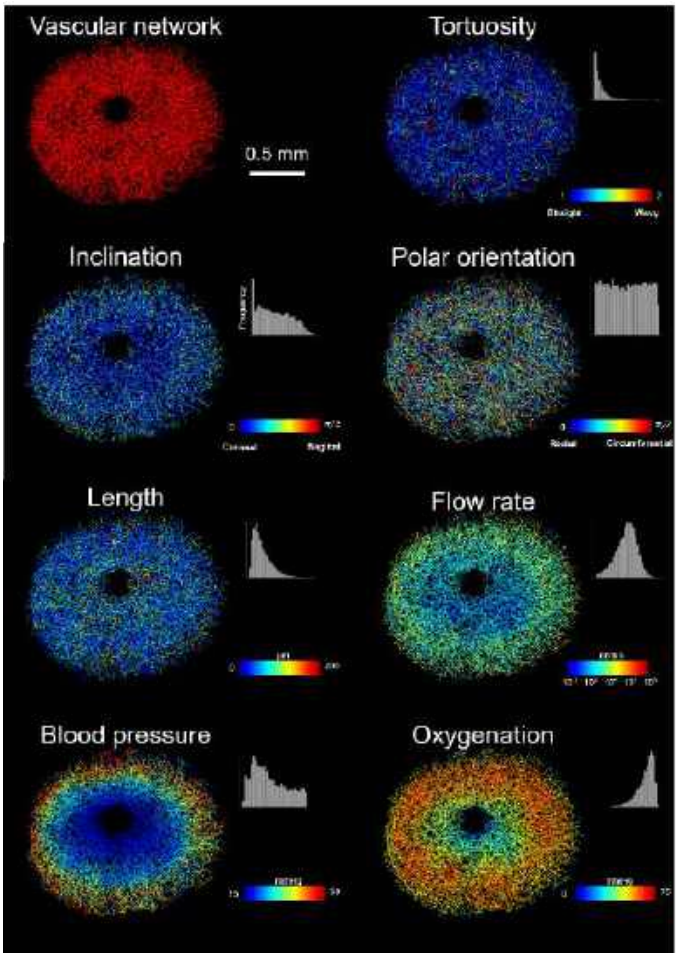

Figure 2: The distributions of the geometric parameters (length, tortuosity, inclination, and polar orientation), hemodynamics parameters (blood flow, blood pressure), and oxygenation parameters (oxygenation) of one healthy monkey LC. All four LCs showed similar features.

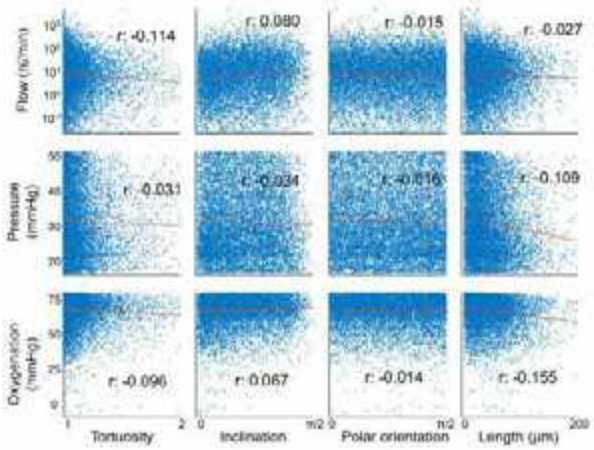

Figure 3: Scatterplots of the geometric parameters (columns) and the hemodynamic/oxygenation parameters (rows) for one eye. Each dot represents a vessel segment, "r" represents the correlation coefficient. The strongest negative correlation was -0.155 between segment length and oxygenation. Correlations between the two orientations and the hemodynamic and oxygenation parameters were quite weak (r<0.1).

DISCUSSION

We leveraged 3D eye-specific numerical models to characterize the geometry, blood supply and oxygenation of the LC vascular network. Specifically, we investigated the distributions and correlations of the geometric, hemodynamics, and oxygenation parameters. Two main findings arise from the work: The geometric parameters did not show any clear spatial patterns, while the hemodynamics/oxygenation parameters exhibited a radial-like spatial distribution. There were some weak associations between structural and functional parameters.

The spatial distribution of geometric parameters suggested a highly random and evenly distributed LC vasculature. The small spatial variations across the LC vasculature may contribute to a smooth blood/oxygen irrigation for the LC region. The radial patterns in hemodynamics/oxygenation parameters can be explained from the LC blood supply, which flows from the periphery to the center.

One may expect that the general radial LC blood supply may lead to correlations between the structural and functional parameters, e.g., radial vessels having higher flow rates and oxygenation. However, our findings indicated only weak associations between those parameters. The weak associations suggest that the geometric parameters are not sufficient to predict the blood or oxygen supply.

In summary, we used 3D eye-specific models to analyze the morphology, hemodynamics, and oxygenation for LC vasculature. Results from this study help us understand the association between the structure and function of LC. It can potentially lead to new biomarkers for LC hemodynamics/oxygenation, which contribute to the glaucoma diagnosis and management.

ACKNOWLEDGEMENTS

National Institutes of Health R01-EY023966, R01-EY031708, R01-HD083383, P30-EY008098 and T32-EY017271 (Bethesda, MD), the Eye and Ear Foundation (Pittsburgh, PA), Research to Prevent Blindness (unrestricted grant to UPMC ophthalmology, and Stein innovation award to Sigal IA) and BrightFocus Foundation.

REFERENCES

[1] Quigley, H et al., *Glaucoma Lancet*, 1367-1377, 2011.
[2] Lee, P. Y. et al., J. Biomech. Eng., 144.6: 061006, 2022
[3] Lu, Y et al., PloS one, 16.2, e0247641, 2021
[4] Hayreh, S. S. Prog. Retin. Eye Res., 20(5), 595-624.

DISTINCT MOLECULAR AND STRUCTURAL TRAITS OF PERMANENT VERSUS TRANSIENT CARTILAGE IN EARLY DEVELOPMENT

J. Xiang (1), B. Kwok (1), M. Fan (1), M. E. Kupratis (2), S. Tufa (3), D. R. Keene (3), R. L. Mauck (2), N. A. Dyment (2), E. Koyama (4), L. Han (1)

(1) School of Biomedical Engineering, Science and Health Systems, Drexel University, Philadelphia, PA, United States
(2) McKay Orthopaedic Research Laboratory, University of Pennsylvania, Philadelphia, PA, United States
(3) Micro-Imaging Center, Shriners Hospital for Children, Portland, OR, United States
(4) Translational Research Program in Pediatric Orthopaedics, The Children's Hospital of Philadelphia, Philadelphia, PA, United States

INTRODUCTION

Hyaline cartilage is a family of cartilaginous tissues whose extracellular matrix (ECM) is characterized by a porous collagen II fibril network entrapping densely packed proteoglycan [1]. In vivo, early skeletal development starts with the formation of transient hyaline cartilage at the epiphysis (Fig. 1a), providing the template that remodels into bone [2]. Unlike epiphyseal cartilage, articular cartilage is not replaced by bone, but retains its hyaline traits throughout lifespan, which endows the joint with its load transmission and energy dissipation functions [3]. These two hyaline cartilages thus follow distinct developmental trajectories and have different functions in vivo. However, due to similarities in their composition, there have been few attempts to delineate differences in their matrix structure-function relationships or assembly/remodeling paths. This study aims to distinguish the molecular, structural and mechanical traits of these two cartilages in small (murine) and large (porcine) animal models during the initial phase of matrix formation.

METHODS

Knee joints were harvested from wild-type (WT) C57BL/6J mice at embryo day 15.5 (E15.5) and postnatal day 0 (P0), and from Yorkshire pigs at E42 and P0. RNAscope in situ hybridization was applied to visualize the spatial expression profiles of *Col2a1* and *Acan* genes on P0 murine joint sections. Safranin-O/Fast Green histology staining was applied to evaluate joint morphology and sulfated glycosaminoglycans (sGAGs) distribution in sagittal and coronal paraffin sections of murine and porcine joints, respectively. Immunofluorescence (IF) staining was performed to assess the protein distributions of collagen VI, perlecan and collagen V. Transmission electron microscopy (TEM) was applied to quantify collagen fibril nanostructure in P0 murine joints. Atomic force microscopy (AFM)-nanoindentation was applied to 10 μm-thick, unfixed cryo-sections to quantify the tissue modulus, following our established methods [4]. Two-sample student's *t*-test was applied to detect differences in fibril diameter and modulus at $\alpha = 0.05$.

RESULTS

In murine joints, we found active expression of *Col2a1* and *Acan* in both articular and epiphyseal cartilage at P0, but with much higher expression in epiphyseal chondrocytes (Fig. 1b). Safranin-O/Fast Green histology also showed stronger sGAGs staining in epiphyseal cartilage at E15.5 and P0 (Fig. 1c). In addition, these two tissues showed differential distributions of key matrix molecules. Collagen VI, the biomarker of pericellular matrix (PCM) [5], was present in articular cartilage, but absent in epiphyseal cartilage. However, perlecan, the other PCM biomarker [6], was present throughout both tissues (Fig. 1d). Surprisingly, we found that collagen V, the initiator of collagen I fibrillogenesis [7], was localized in developing articular cartilage, and absent in epiphyseal cartilage (Fig. 1e). TEM imaging detected thicker collagen fibrils in articular cartilage than epiphyseal cartilage at P0 (arrowheads, Fig. 1f). Meanwhile, epiphyseal cartilage showed moderately higher modulus than articular cartilage at E15.5. By P0, however, these two tissues showed a similar modulus (Fig. 1g).

In E42 and P0 porcine knee joints, we found similarly higher staining of sGAGs in epiphyseal than articular cartilage (Fig. 2a). Also, collagens VI and V were localized in articular cartilage, while perlecan was present in both tissues (Fig. 2b,c). In P0 porcine joints, articular cartilage already developed distinct collagen VI-exclusive PCM domains (Fig. 2b), illustrating differences in the development of porcine versus murine joints. Indeed, in porcine joints, epiphyseal cartilage had similar modulus as articular cartilage at E42 but showed higher modulus at P0 (Fig. 2d), a trend different from that of murine joints.

DISCUSSION

This study highlights that transient (epiphyseal) and permanent (articular) cartilage develop distinct molecular and structural traits upon their initial establishment (~ E15.5 in mice [8]) in both small and large

animals, despite both being characterized by high collagen II and aggrecan contents. For example, the presence of collagen VI in articular cartilage, but not epiphyseal cartilage (Figs. 1d, 2b), suggests differences in their initial cellular microniche, which could contribute to their different cellular mechanosensitive signaling. The high concentration of perlecan in epiphyseal cartilage (Figs. 1d, 2b) could be associated with its potential role in endochondral ossification through FGF signaling [9]. Furthermore, the unexpected presence of collagen V in articular cartilage (Figs. 1e, 2c) suggests that collagen V may participate in the initial templating of permanent cartilage matrix, a role beyond the canonical understanding of collagen II/IX/XI fibrils in hyaline cartilage [1]. Indeed, the different fibril assembly routes of these two tissues are supported by the much thicker collagen fibrils found in articular cartilage (Fig. 1f). As a result, despite the higher sGAGs in epiphyseal cartilage, we found similar modulus in these two tissues at P0 mice (Fig. 1g). Together, our results provide a new knowledge basis for improving cartilage repair. One key roadblock in cartilage regeneration is the adverse effect of aberrant ossification [10], and heterotopic ossification in vivo is initiated with a proteoglycan-rich cartilaginous template [11]. Understanding the initial traits that differentiate permanent versus transient cartilage will provide a path to address these key challenges in musculoskeletal pathology.

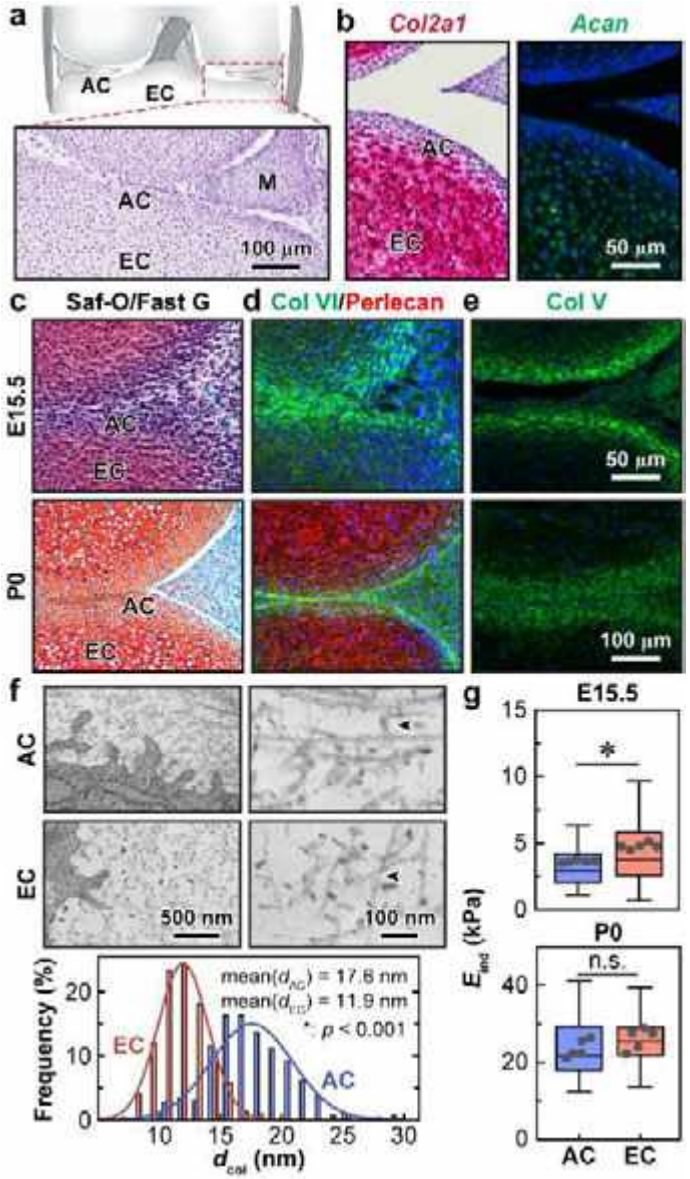

Fig. 1: Distinct molecular composition, nanostructure and mechanical properties of articular cartilage (AC) and epiphyseal cartilage (EC) in developing murine joints. a) Schematic illustration showing the regions of interest of AC and EC in murine knee joints. b) RNAscope images of *Col2a1* and *Acan* spatial gene expression at P0. c) Safranin-O/Fast Green histology, immunofluorescence (IF) images of d) collagen VI/perlecan and e) collagen V of murine knee joints at E15.5 and P0. f) Representative TEM images of AC versus EC, and corresponding histogram of fibril diameter distribution (> 280 fibrils). g) Box-and-whisker plot of AC and EC micromodulus, E_{ind} (≥ 75 locations from n = 5 animals for each age).

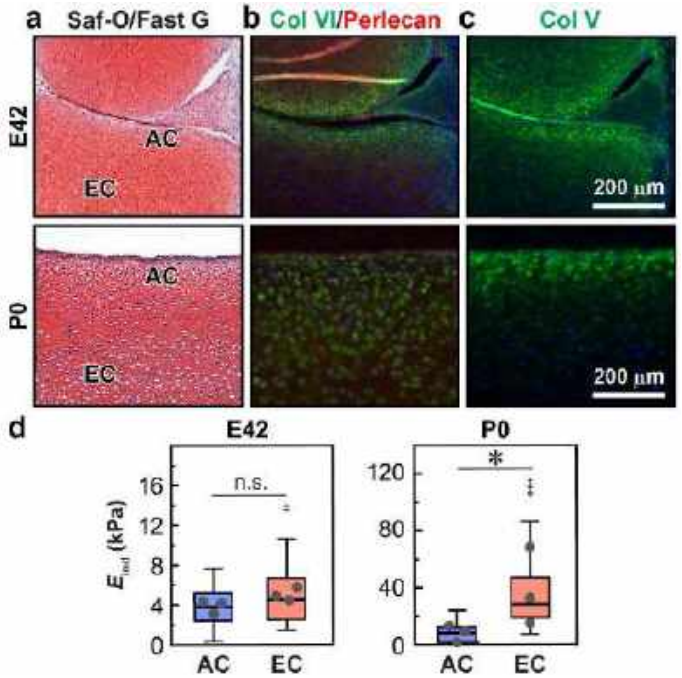

Fig. 2: Distinct molecular composition and mechanical properties of articular cartilage (AC) and epiphyseal cartilage (EC) in developing porcine joints. a) Safranin-O/Fast Green histology, IF images of b) collagen VI/perlecan and c) collagen V staining of porcine knee joints at E42 and P0. d) Box-and-whisker plot of porcine AC and EC micromodulus, E_{ind} (≥ 60 locations from n = 3 animals for each age).

ACKNOWLEDGEMENTS

This work was supported by NIH R01AR075418, NSF CMMI-2047073 and UPenn PCMD NIH P30AR069619.

REFERENCES

[1] Han, L., et al., *Annu Rev Mater Res*, 41: p. 133–168, 2011.
[2] Xie, M., et al., *Bone*, 142: p. 115701, 2021.
[3] Maroudas, A., In *Adult Articular Cartilage*, p. 215-290, 1979.
[4] Kwok, B., et al., *Acta Biomater*, 168: p. 235–251, 2023.
[5] Poole, C.A., et al., *J Cell Sci*, 90: p. 635–643, 1988.
[6] SundarRaj, N., et al., *J Cell Sci*, 108: p. 2663–2672, 1995.
[7] Sun, M., et al., *J Cell Sci*, 124: p. 4096–4105, 2011.
[8] Kim, M., et al., *Biol Open*, 11: p. bio059381, 2022.
[9] Vincent, T. L., et al., *Osteoarthr Cartil*, 15: p. 752–763, 2007.
[10] Staines, K. A. et al., *J Endocrinol*, 219: p. R1–R12, 2013.
[11] Medici, D., et al., *J Bone Miner Res*, 27: p. 1619–1622, 2012.

SB³C2024
Summer Biomechanics, Bioengineering and Biotransport Conference
June 11-14, Lake Geneva, WI, USA

THE BALANCE OF VON WILLEBRAND FACTOR AND PLATELET ACTIVATION IN CAUSING BLEEDING IN AN AORTIC STENOSIS

Alice Liu (1), Katrina Ashworth (2), Nina Lasky (2), Yi Qiao (2), Kimsey Platten (2), Jorge Di Paola (2), David Bark (1,2)

(1) Department of Biomedical Engineering, Washington University in St. Louis, St. Louis, MO, USA
(2) Department of Pediatrics Division of Hematology and Oncology, Washington University School of Medicine, St. Louis, MO, USA

INTRODUCTION

An aortic stenosis (AS) occurs when the aortic valve does not fully open, thereby creating a stenosis or restriction to the flow. Severe AS leads to bleeding, initially known as Heyde's syndrome. It was discovered that this may be due to the loss of high molecular weight multimers (HMWM)s of the very large mechanosensitive plasma protein, von Willebrand factor (VWF). This loss is known as acquired von Willebrand syndrome (AVWS). VWF otherwise exists in plasma in a wide range of sizes due to natural cleavage by it's metalloproteinase, ADAMTS13. It plays a crucial role in hemostasis, more commonly known as blood clotting, with the largest multimers providing the greatest hemostatic ability. It does so by tethering platelets to collagen and to each other in regions of high shear flow typical of the arterial side of circulation and in most cases of vessel puncture.

VWF generally circulates in a globular form, but can extend when sufficient fluid drag forces are applied. Extension increases the tension along the multimer. If this tension exceeds approximately 20 pN of force at a given region, it will expose key domains for both platelet binding and for ADAMTS13 cleavage [1–3]. It's thought that the high shear associated with an AS is the cause for AVWS due to exposure of the ADAMTS13 cleavage site, as supported by the increasing loss of high molecular weight multimers with increasing AS severity [4]. However, the amount of cleavage seen from high shear is modest and does not account for the substantial loss of HMWMs seen in AS patients [2]. Furthermore, the shear required to cause a tension of 20 pN may be excessively high [1, 5]. Lastly, high shear also leads to shear-induced platelet activation and aggregation (SIPA) and it's not clear whether this occurs in AS.

Recently, our group discovered unprecedented VWF cleavage when exposing it to turbulent flow [6]. However, our studies also involved very high shear stress and we did not study the impact on platelet activation. In this current work, we probe the flow found in AS and evaluate the effects on both VWF and SIPA, combining *in vivo* an *ex vivo* work to better understand bleeding in AS. Results also translate to other cases of non-physiological shear, like in the case of ventricular assist devices.

METHODS

***In Vivo* Transthoracic Aortic Constriction** We create a transthoracic aortic constriction (TAC) in the mouse aorta to recapitulate characteristics of AS in humans, noting that the scale is much smaller. This is done by tying off a needle of set gauge along the aortic arch, and removing to the needle to create a controlled reduction in aortic diameter. We also use VWF-/- and ADAMTS13-/- genetic lines. We quantify flow through computational fluid dynamics (CFD) with computed tomography images, matched with Doppler ultrasound. ***Ex Vivo* Experiments** We recreate flow characteristics of the TAC model using a benchtop vortexer, combined with a 96 well plate, with flow characterized through both CFD and particle imaging velocimetry (PIV). Platelet poor plasma and platelet rich plasma is obtained from centrifugation steps of citrated human blood. **Measurements** We quantify VWF size through multimer gels and function by quantifying binding capacity. We also quantify platelet activation through flow cytometry and through microfluidic collagen-binding assays. Lastly, we quantify overall bleeding in mice through a tail bleeding assay, where the tail is cut.

RESULTS

***In Vivo* Mouse Model** The bleeding time for cut tails in mice increases with increasing stenosis severity, 7 days post-procedure. Excessive bleeding times are found for VWF-/- mice, extending to our maximum time point of 10 minutes, demonstrating the importance of VWF in hemostasis, Fig. 1. Compartively, ADAMTS13-/- mice have no cleavage from ADAMTS13 and we find that bleeding times are the shortest for these mice. HMWMs are reduced with increasing stenosis severity, as early as 24 hours after the TAC procedure, and remain reduced for our maximum time point of 7 days, Fig. 2a. HMWMs are at a normal level for ADAMTS13-/- mice. The percent of platelets activating, based on integrin activation and granule release, increase with increasing stenosis severity at 24 hours post-procedure, whereas the amount of activation significantly decreases at 7 days, Fig. 2b.

VWF-/- mice exhibit no platelet activation, whereas ADAMTS13-/- continue to have high levels of platelet activaiton at 7 days. Lastly, we determined the shear rates and turbulent kinetic energy through CFD so that they can be matched in *ex vivo* experiments.

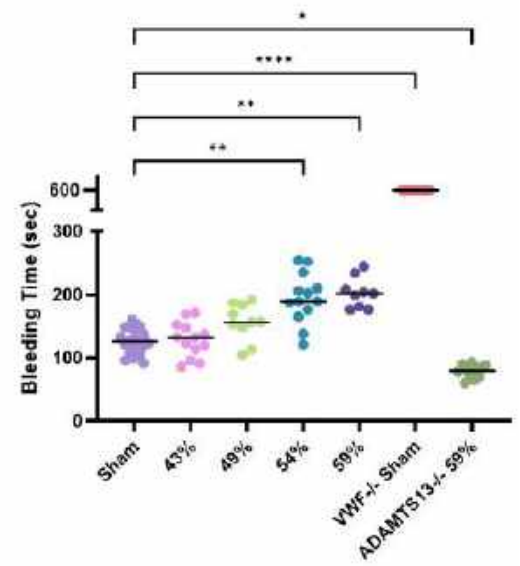

Figure 1: Bleeding time from tail cuts in VWF-/-, ADAMTS13-/-, and littermate wildtype mice at 7 days after a TAC procedure. Percentages in the abscissa pertain to the % reduction in aorta diameter. * P<0.05, ** P<0.01, **** P<0.0001

***Ex Vivo* Vortexer** We use four different speeds on the vortexer, 34, 112, 150, and 230 rad/s to cover a range of shear rates. Furthermore, flow becomes transitional at 150 rad/s and turbulent at 230 rad/s. Thrombus growth in a collagen-coated microfluidic device decreases with increasing rotational speeds. HMWMs decrease for increasing vortexing speed, with a sudden decrease at 150 rad/s. Similarly, VWF function decreases with a dramatic loss in function at 150 rad/s. The percent of platelets activating in this system increase with increasing speeds. Various inhibitors were used and the inhibitor with the greatest effect blocks platelet binding to VWF, where almost no platelet activation is seen. Finally, to determine the relative role of turbulence, we increase the viscosity of our sample by adding dextran, thereby lowering the Reynolds number to convert turbulent flow to laminar flow, while simultaneously increasing shear stress. In these experiments, the amount of VWF cleavage is significantly reduced and the amount of platelet activation is reduced.

DISCUSSION

We demonstrate that an AS leads to VWF cleavage through ADAMTS13, leading to AVWS that becomes more severe with increasing stenosis severity, in agreeement with what has been found in humans [4]. However, we also show that this is greatly enhanced if the AS leads to turbulence, as supported by our earlier work [6]. For the first time, to our knowledge, we show that SIPA in this system can occur when HMWM VWF is present, but that is greatly reduced as plasma VWF size distribution decreases due to cleavage. These results demonstrate a fine balance between VWF size and platelet activation that can tend toward bleeding when VWF size is reduced, or thrombosis, when HMWMs remain in the plasma.

In other cases of nonphysiological flow, like ventricular assist devices, AVWS is prevalent, occuring in almost all patients receiving these devices. However, these patients are not just at risk for bleeding, they are also at risk for thrombosis (or blood clotting that can block blood flow). We believe this can be due to high levels of SIPA where perhaps VWF size remains sufficient to induce SIPA or perhaps the shear stress is so high that it can also lead to VWF extension and 'activation' despite the lack of HMWMs. We also acknowledge that the cause of thrombosis in these patients may also relate to blood-material interactions, as opposed to being purely flow-induced.

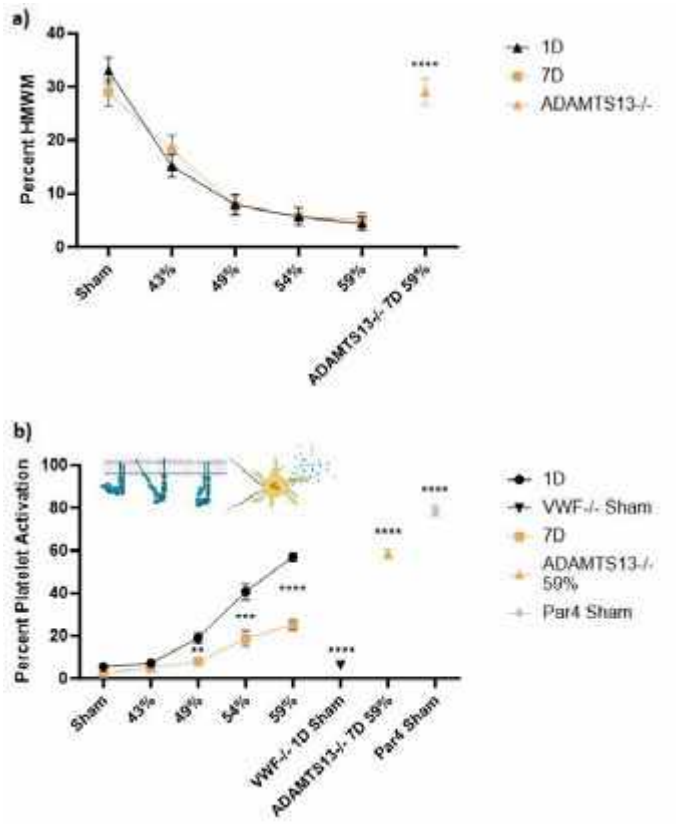

Figure 2: a) Percent HMWM remaining, as measured by densitometry of multimer gels. b) Percent of platelets activating. Percentages in the abscissa pertain to the % reduction in aorta diameter. ** P<0.01, *** P<0.001, **** P<0.0001

ACKNOWLEDGEMENTS

We acknowledge funding support from National Institutes of Health, National Heart, Lung, and Blood Institute (R01HL164424), National Institute of Biomedical Imaging and Bioengineering (R21EB034579), the National Science Foundation (2104093), and the American Heart Association (18CDA34110134).

REFERENCES

[1] Fu H et al. *Nature communications* 8.1 (2017).

[2] Sadler J. *Journal of thrombosis and haemostasis* 3.8 (2005).

[3] Springer TA. *Blood, The Journal of the American Society of Hematology* 124.9 (2014).

[4] Vincentelli A et al. *New England Journal of Medicine* 349.4 (2003).

[5] Sharifi A et al. *Fluids* 6.2 (2021).

[6] Bortot M et al. *Arteriosclerosis, thrombosis, and vascular biology* 39.9 (2019).

ESTROGEN RECEPTOR EXPRESSION IS GREATER THAN PROGESTERONE RECEPTOR EXPRESSION IN THE PORCINE ANTERIOR CRUCIATE LIGAMENT AND VARIES ACROSS AGE AND ANIMAL

Jacob D. Thompson (1), Matthew B. Fisher (1,2)

(1) Joint Department of Biomedical Engineering, North Carolina State University and University of North Carolina at Chapel Hill, Raleigh, NC, USA
(2) Department of Orthopaedics, University of North Carolina at Chapel Hill, Chapel Hill, NC, USA

INTRODUCTION

Pediatric anterior cruciate ligament (ACL) injuries and subsequent reconstruction surgeries have been rising over the past 20 years. [1,2]. Furthermore, adolescent female athletes are 3 to 4 times more likely to tear their ACL in specific sports [3-5]. As a result of these sex-specific differences in injury rates, female sex hormones have received considerable attention, with several groups drawing associations between ACL injuries, menstrual cycle phases, and corresponding serum sex hormones [6,7]. Furthermore, sex-specific structural differences have been identified in the porcine ACL, with the posterolateral (PL) bundle size plateauing in adolescent female animals near the onset of puberty, while the male PL bundle continues to increase in size [8]. Likewise in humans, the cross-sectional area of the ACL increases more rapidly in males than in females following puberty [9]. However, there is no clear mechanism for these structural changes. Previous work has identified sex hormone receptors within cells throughout the adult ACLs [10]. Additionally, after monolayer culture of adult ACL fibroblasts, only ~5% of the cell population express these receptors [11]. There is currently no understanding of changing hormone receptor expression in the ACL throughout growth, specifically in pre- vs. post-puberty. The objective of this work was to determine native levels of female sex hormone receptors in juvenile and adolescent ACL bundles and determine if hormone receptor expression is retained in-vitro.

METHODS

Twelve female pig hindlimbs were collected at pre-puberty (8 weeks) or post-puberty (>8 months) ages (n=6 animals/age). Animals were sourced from various research projects performed at NC State. The ACL was dissected into the anteromedial (AM) and PL bundles. The bundles were snap frozen in liquid nitrogen and cryosectioned at 10 um section thickness. Prior to immunostaining, sections were washed and warmed to room temperature in 1X PBS for 10 minutes. Sections were then permeabilized for 15 minutes with 0.1% Triton-X in 1X PBS and blocked in a solution of commercial IHC/ICC blocking buffer (45%), 0.1% Triton-X in 1X PBS (45%), and donkey serum (5%) for 1 hour. After blocking, primary antibodies were added for estrogen receptor-alpha (1:400, ERα) and progesterone receptor-beta (1:200, PRβ) in the blocking solution at 4°C overnight. Corresponding rabbit IgG isotypes, no-primary controls, and positive uterine tissue were used to determine the non-specific binding antibodies and to verify positive staining. Slides were washed with 0.1% Tween-20 in 1X PBS, and anti-rabbit secondary antibodies were added for 2 hours at room temperature in the dark. The slides were washed again with 0.1% Tween-20 in 1X PBS mounted with Prolong Gold with DAPI. All images were acquired with a cellSens Olympus LS fluorescent microscope.

ACL fibroblasts were isolated from the AM and PL bundles of the ACL to assess hormone receptor density during monolayer culture. Synovium was aseptically removed from the AM and PL bundles, and cleaned bundles were placed in sterile PBS. The sections were diced and placed in a 2 mg/mL solution of collagenase type I in complete media (10% fetal bovine serum, 1% penicillin/streptomycin/fungizone in DMEM). Tissues were incubated for 6-8 hrs at 37°C. Following incubation, cells were isolated and plated as passage 0, and cultured in complete media at 37°C and 5% CO_2. Tissue explants were also plated to allow cell migration from the tissue. Once the cells reached confluency, they were fixed with 4% paraformaldehyde and washed with PBS. They were then stained for ERα and PRβ.

Immunostaining results were quantified by thresholding images set by the isotype and no primary controls in ImageJ. The area of the signal was then recorded for DAPI and the secondary antibodies. The expression index reported was the area of the signal for ERα and PRβ divided by the DAPI area. Two-way ANOVAs were used to determine overall effects of age and bundle on hormone receptor expression and Hold-Sidak post-hoc tests were used for multiple comparisons. Statistical analyses were performed at a set alpha value of 0.05.

RESULTS

Age had a significant effect on ERα expression (p=0.005), with a 6-fold higher ERα expression in the pre-pubescent group on average (Figure 1). Across bundle, there was only a 1.5-fold higher ERα expression in the AM bundle compared to the PL bundle on average, which was not statistically significant (p=0.27). In the PL bundle, the post-pubescent animals had a 79% lower expression than in the pre-pubescent animals on average, but this was not statistically significant (p=0.09, Figure 1A). For PRβ expression, there was a statistically significantly higher expression in the PL bundle for the pre-pubescent group compared to the AM bundle (p=0.008, Figure 1B). Additionally, there was statistically significantly higher expression of PRβ in the pre-pubescent PL bundle than in the post-pubescent PL bundle (p=0.01). Pooling pre- and post-pubescent animals, ERα expression was significantly higher in both bundles than PRβ expression (AM bundle: p=0.003, PL bundle: p=0.03; Figure 1C).

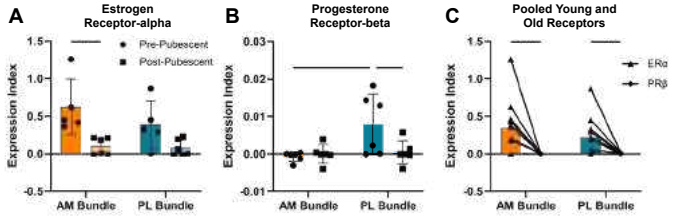

Figure 1: ERα expression decreases after puberty and is significantly higher than PRβ expression. (A) ERα expression (ERα/DAPI) and (B) PRβ expression (PRβ/DAPI) by age group and ACL bundle. (C) Receptor data pooled from pre- and post-pubescent animals. Bars indicate p<0.05.

While there were statistically significant differences across age for ERα, a binary ERα expression was observed across animals in the post-pubescent group (Figure 2). Three of the six animals positively stained for ERα with a similar expression index of 0.20 in the AM bundle, and the other three animals had zero expression (Figure 2). This differs from the pre-pubescent AM bundle group where all animals had some baseline expression of ERα (images not shown). In the post-pubescent group, Pigs 1, 2, and 3 were also known to be 2-3 days before ovulation (based on research studies involving reproductive status).

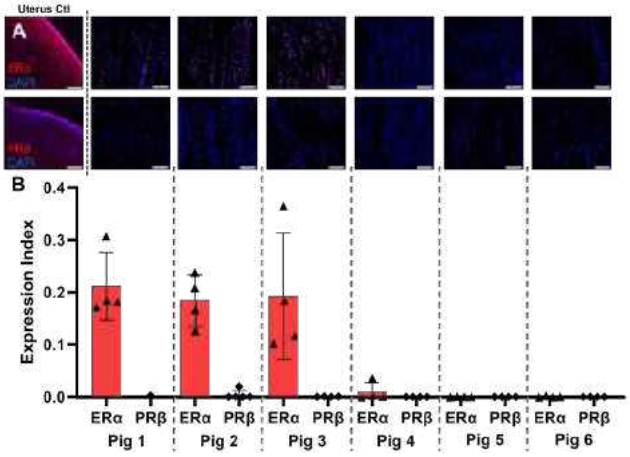

Figure 2: ERα expression dichotomy in post-pubescent animals. (A) Representative images of ERα and PRβ expression in the ACL (AM bundle) by animal, with positive control. (B) Quantification of ERα and PRβ expression by animal. Each point represents one image. Scale bars are 100µm.

To further study the hormone receptor density in-vitro, cells were isolated from the AM and PL bundle of post-pubescent Pig 3 via digestion and explants and stained for hormone receptors. After the initial plating of cells (P0), there was no ERα expression for either Pig 3 AM or PL fibroblasts despite the strong staining in the tissue (Figure 3). This loss was sustained throughout passage 1 and 3.

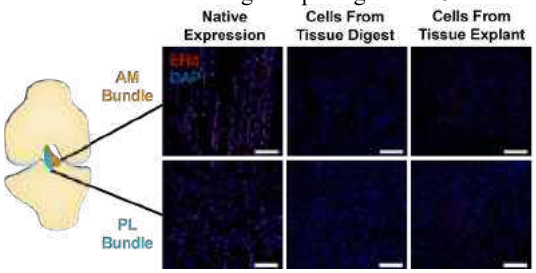

Figure 3: ERα disappears rapidly after AM and PL bundle fibroblast isolation and several days of monolayer culture. Cells were isolated from the same animal. Scale bars are 100µm.

DISCUSSION

There was strong effect of age on ERα expression in the ACL, with higher expression in the pre-pubescent porcine ACL than in the post-pubescent group. Furthermore, there was an interesting binary expression of either strong or no ERα staining in post-pubescent animals. There was relatively little PRβ expression in any of the animals (all groups were not significantly different from 0 (p>0.05; secondary statistical analysis, data not shown). When isolating ACL fibroblasts for subsequent cellular studies from one of the animals with strong ERα staining, the ERα expression was lost rapidly in monolayer culture.

The presence of hormone receptors in healthy pre-pubescent porcine ACLs indicates that there may a be direct hormonal impact on ACL growth and development prior to sexual maturity, an idea that is supported by circulating low levels of estradiol in prepubescent humans [12]. Additionally, the presence of ERα in both ACL bundles may not support the role of estradiol on differences in bundle size during adolescence. The minor staining of PRβ also may indicate a lesser effect of progesterone on the ACL. However, a larger sample size is needed to support these findings, and longitudinal studies across the reproductive cycle may elucidate fluctuations in receptor expression. Finally, the loss of hormone receptors after monolayer culturing regardless of technique indicates early phenotypic drift in ACL fibroblasts from skeletally immature animals in in-vitro culture, which confirms other studies tracking loss of phenotype in primary cell culturing [13]. Overall, the change in receptor density across age and potentially estrus cycle phase reinforces the idea that the ACL is responsive to sex hormones during growth. Future work will identify how sex hormones impact extracellular organization and tissue mechanics.

ACKNOWLEDGEMENTS

We would like to thank Laboratory Animal Resources (NC State). Funding provided by NSF (DGE-1746939) and NIH (R01 AR071985).

REFERENCES

[1] Werner, B et al., *J Pediatr Orthop*, 36(5):447-452, 2016; [2] Dodwell, E et al., *Am J Sports Med*, 42(3):675-680; [3] Bram, J et al., *Am J Sports Med*, 49(7):1962-1972, 2021; [4] Joseph, A et al., *J Athl Train*, 48(6):810-817, 2013; [5] Stanley, L et al., *Am J Sports Med*, 44(6):1565-1572, 2016; [6] Park, S et al., *Am J Sports Med*, 37(3):588-598, 2009; [7] Beynnon, B et al., *Am J Sports Med*, 34(5):757-764, 2006; [8] Howe, D et al., *J Orthop Res*, 40(8):1853-1864, 2022; [9] Hosseinzadeh, S et al., *J Orthop Res,* 39(4):841-849, 2020; [10] Liu, S et al., *J Orthp Res*, 14(4):526-533, 1996; [11] Faryniarz, D et al., *In Vitro Cell Dev Bio Anim,* 42(7):176-181, 2006; [12] Janfaza, M et al., *J Pediatr Endocrinol Metab,* 19(7):901-909, 2006; [13] van Vijven, M et al., *J of Orthop Res*, 39(7):1561-1571, 2021.

SB³C2024
Summer Biomechanics, Bioengineering and Biotransport Conference
June 11-14, Lake Geneva, WI, USA

MICROSCALE SHEAR WAVE TENSIOMETRY TRACKS AXIAL STRESS IN TENDON FASCICLES

Shreya R. Kotha (1), Samantha M. Kahr (1), Jonathon L. Blank (2), Alex J. Reiter (3), Darryl G. Thelen (1,4)

(1) Department of Biomedical Engineering, University of Wisconsin-Madison, Madison, WI, USA
(2) McKay Orthopaedic Research Laboratory, University of Pennsylvania, Philadelphia, PA, USA
(3) Department of Biomedical Engineering, St. Louis University, St. Louis, MO, USA
(4) Department of Mechanical Engineering, University of Wisconsin-Madison, Madison, WI, USA

INTRODUCTION

Shear wave tensiometry is a noninvasive method to gauge axial stress in tendons based on wave propagation. Tensiometry is premised on a tensioned Timoshenko beam model [1], which predicts that shear wave speed will varies in proportion to the square root of axial stress in structures with a low tangential shear modulus. It was previously shown that the tensioned beam model applies to whole tendons subjected to axial loading [1]. However, it is unknown whether this model and measurement system holds across microstructural scales of tendinous tissue, such as in tendon fascicles.

The objective of this study was to investigate microscale shear wave propagation in isolated tendon fascicles. We hypothesized that a tensioned beam model would describe the shear wave speed-stress relationship across fascicles after accounting for differences in morphology. The results of this study can inform tensiometry measurements in whole tendons, while providing an experimental platform for probing how fatigue loading and damage can affect wave propagation in individual fascicles.

METHODS

Specimen Preparation: Tails from two 9-month-old rat tails (F334xBN), were dissected, stored at -20°C, and then thawed before testing. Individual fascicles (n = 6) were extracted from the proximal end of the tail and then immediately tested. Fascicles were immersed in a 1X PBS bath and secured on either end to waveform grips of a custom benchtop loading device (Aerotech PRO165LM, Fig. 1a). One grip was attached to a 10-lb miniature submersible load cell (Futek LSB210) to monitor axial loading. Fascicles were preloaded to 0.1 N. The gauge length of each fascicle in the grips was measured using a vernier caliper.

Wave Speed Measurement: Shear waves were induced using impulsive lateral taps (50 Hz, 0.3 ms pulse) at a fascicle cross-section located 5 mm from a grip. Wave propagation was measured using two laser Doppler vibrometers (Polytec PDV 100) centered on the fascicle at 20 and 50 mm from the tap (Fig. 1a). Wave travel time between vibrometer points was computed using cross-correlation of vibrometer signals within a Kalman filtering routine [2]. Wave speeds, in meters per second, were computed using the known distance between laser vibrometer points (30 mm).

Mechanical Testing: Fascicles underwent 10 cycles (1 Hz) of preconditioning between 0 and 5% strain. Following a 300s rest interval, the fascicles were then harmonically stretched to 5% strain at 0.1, 0.2, and 0.4 Hz. Two 10-second trials at each frequency were performed, with a 60-second rest interval between trials. Laser vibrometer, load cell, and stage displacement were synchronously recorded at 100,000 Hz using an 8-channel AD board (NI USB-6251).

Cross-sectional Area: Fascicle profiles and cross-sectional areas were measured at 3 cross-sections by rotating each fascicle within a laser micrometer (Keyence LS-7010) [3]. Fascicles were kept hydrated throughout the measurement using miniature ultrasonic humidifiers. The maximum cross-sectional area for each fascicle was used to compute axial stress (σ) from the measured force.

Analysis: A tensioned Timoshenko beam model predicts that the shear wave speed, c, is dependent on the tangential shear modulus (μ) of the tissue, the axial stress (σ), a shear correction factor (k'), and the effective density (ρ) of the tissue (Eq. 1):

$$c = \sqrt{\frac{k'\mu + \sigma}{\rho}} \quad (1)$$

We used nonlinear least squares fitting to estimate fascicle shear modulus (μ, *assuming* $k' \cong 1$) and effective density (ρ) given measurements of wave speed and stress. Goodness of fit was assessed by the coefficient of variation R^2, which represents the proportion of the variance in wave speed explained by a tensioned beam model.

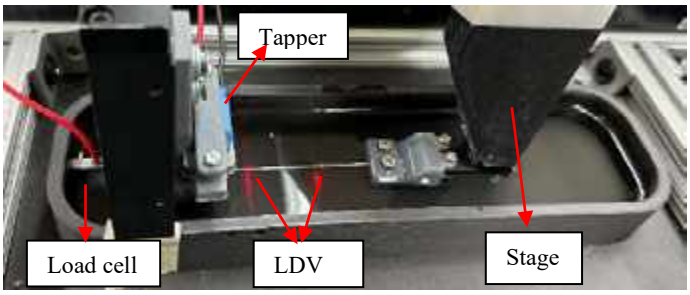

Figure 1: (a) Shear waves were induced by an electrodynamic tapper and tracked via laser Doppler vibrometers while a linear stage cyclically stretched the fascicle.

RESULTS

Fascicles exhibited characteristic strain-stiffening behavior and hysteresis in response to cyclic stretch (Fig. 2a). The lack of hysteresis in the wave speed-stress relationship (Fig. 2b) supports the premise that wave speed depends directly on the applied stress. Wave speeds were well described by a tensioned beam model (average R^2=0.99).

At the 0.4 Hz loading rate, estimates of effective density were 2182±537 (mean±1sd) kg/m^3, while shear modulus averaged 0.66±0.78 MPa. These parameters did not vary substantially across the loading rates considered.

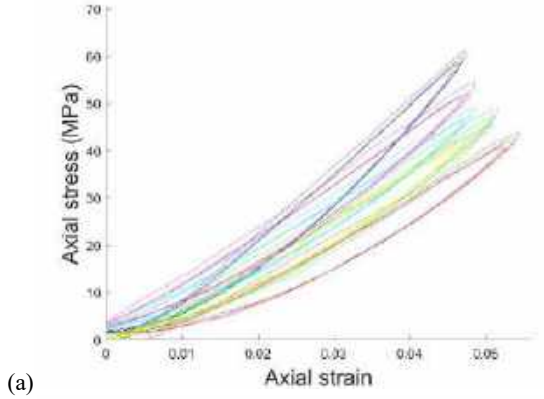

(a)

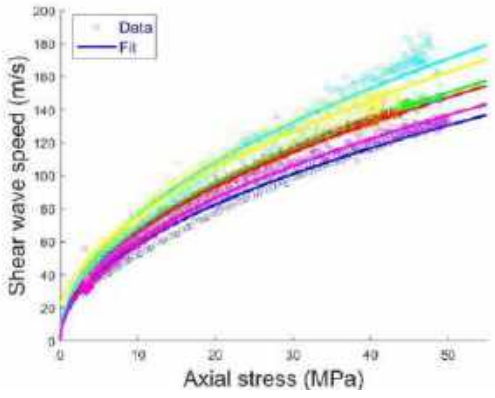

(b)

Figure 2: (a) Fascicles exhibited strain stiffening behavior and hysteresis with cyclic loading. (b) Shear wave speeds increased with the square root of axial stress, as predicted by a tensioned beam model, during both loading and unloading phases. Each color represents a different fascicle tested at a 0.4 Hz cyclic loading rate.

DISCUSSION

This study investigated the wave speed-stress relationship in tendon fascicles. Our results show that fascicle wave speeds depend directly on stress during axial stretch, with the general relationship well described by a tensioned beam model. To our knowledge, this is the first application of shear wave propagation for measuring tissue mechanics at the microscale. To date, shear wave tensiometry and ultrasound elastography studies in tendons have generally focused on measuring shear waves in an entire tendon unit [4]. By studying smaller constituents of tendons, such as fascicles, microscale tensiometry may enable noninvasive investigations of soft tissue structure-function relationships following repetitive loading, microstructural damage, or disease. Such focused study could better inform the use and interpretation of *in vivo* shear wave speed measurements in tendon.

Wave speed varied with the square root of axial stress, as predicted by a tensioned beam model. Estimates of effective density were substantially higher than the tissue itself (1060 kg/m^3), which likely reflects the added inertia effects due to the fascicle vibrating in a water bath. It has been estimated that the added mass effect of the bath can substantially increase the effective density [5], which is consistent with our observations.

Our estimate of fascicle shear modulus μ were <1 MPa, but did exhibit considerable variability across specimens. The inherent shear modulus is the determinant of the unloaded wave speed, which was estimated to be <20 m/s. Unloaded *in vivo* tendon wave speeds are in a similar range, averaging ~15 m/s in the human Achilles tendon [6]. Unfortunately, we were unable to directly assess wave speed in unloaded fascicles, due to lack of laser alignment on the fascicle in a slack condition.

We note that our model fitting approach assumed a constant shear modulus throughout the loading regime. Prior experimental studies would suggest that shear modulus may increase with loading due to strain-stiffening behavior [7]. It is challenging to empirically delineate the increase in wave speed due to axial stress and shear modulus stiffening.

In summary, this study introduces microscale tensiometry, which can be used to noninvasively characterize loading in tendinous substructures. Future studies will ascertain how wave speeds vary across hierarchical scales of a tendon, and will also investigate how fatigue-related damage in fascicles may be evident in wave speed metrics.

ACKNOWLEDGEMENTS

NSF GRFP DGE-177503, DOD CDMRP (129866603)

REFERENCES

[1] Martin JA et al., *Nat. Commun*., 9:2–10, 2018.
[2] Schmitz DG et al., *Sensors*, 22:2283– 2298, 2022.
[3] Zitnay JL et al., *Science Adv*., 6, 2020.
[4] Blank JL et al., *Ann. Biomed. Eng*., 50:751-768, 2022.
[5] Martin JA et al., *J. Biomech*., 90:9-15, 2019.
[6] Keuler EM et al., *Sci. Rep.,* 9:13419, 2019.
[7] Blank JL et al., *J. Mech. Behav. Biomed. Mater.,* 125, 2022.

SPATIOTEMPORAL VARIATIONS IN BLOOD VELOCITY AND HEMATOCRIT IN A MICROFLUIDIC CAPILLARY NETWORK

Solomon Oshabaheebwa (1), Christopher A. Delianides (2), Michael A. Suster (2), Pedram Mohseni (1,2), Umut A. Gurkan (1,3)

(1) Department of Biomedical Engineering, Case Western Reserve University, Cleveland, OH, USA
(2) Department of Electrical, Computer, and Systems Engineering, Case Western Reserve University, Cleveland, OH, USA
(3) Department of Mechanical and Aerospace Engineering, Case Western Reserve University, Cleveland, OH, USA

INTRODUCTION

Current blood rheology technologies investigate the flow of red blood cells (RBCs) mostly through large-diameter vessels. However, *in vivo*, RBCs flow through a wide range of vessel diameters from 3 cm in the aorta down to 3 μm in the smallest capillaries. Rheology in the capillaries is especially unique due to their intricate topology involving a high degree of winding, bifurcation, and merging. Devices that mimic these complex flow conditions are needed to identify subtle pathological alterations in blood rheology that manifest in the capillaries.

Microfluidics offers the potential to investigate rheology in physiologically relevant geometries. To maximize the utility of such devices, computational modeling can be used to predict flow dynamics and optimize design parameters. Here, we detail a simple computational model designed to reflect spatiotemporal variations in RBC velocity and distribution in a microfluidic capillary network. The modelled microfluidic device was previously used to assess RBC deformability based on the tendency of stiff RBCs to occlude narrow openings [1]. However, abnormal RBCs may pass through narrow capillaries and still alter rheology, leading to chronic pathology. Studying RBC velocity and distribution profiles may reveal rheologic disturbances missed by occlusion measures and other bulk flow rheology assays.

METHODS

The microfluidic device model was developed in COMSOL Multiphysics 6.0 and comprised a 155 μm × 350 μm rectangular channel containing 20 μm × 10 μm micropillars arranged to create 4-μm inter-pillar openings with 20-μm separation between rows (Fig. 1). 12-μm-wide side passages were incorporated to mimic arterio-venous anastomoses. The channel height was set to 12 μm. A no-slip condition was assumed on all walls. For each simulation, blood was perfused at a constant inlet pressure of 5 mbar, with the outlet maintained at atmospheric pressure. Blood was modelled as a non-Newtonian fluid governed by the Carreau-Yasuda model as previously published [2].

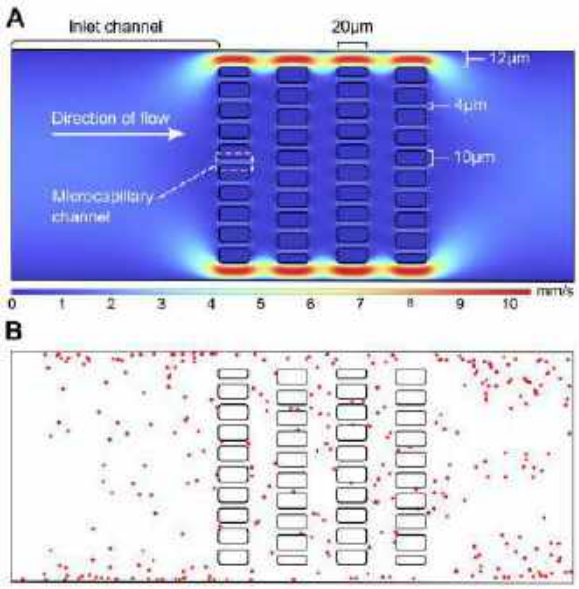

Figure 1: Velocity and RBC distribution profiles in the microfluidic device. (A) Model-predicted high velocity and stagnation regions based on channel geometry. (B) Distribution profile shows a higher density of RBCs in low-velocity regions. RBC size was reduced for this image to aid in visualization.

A particle tracing module within COMSOL was used to predict the distribution of RBCs in the device. The RBCs were modelled as particles of 8-μm diameter with a density of 1,060 kg/m^3. Particles were released at the inlet with a random starting distribution and zero initial velocity. They were subsequently transported by the viscous drag force due to bulk flow (1).

$$F = \frac{18\,\mu}{\rho d^2} m(u - v)\,, \qquad (1)$$

where F is the drag force, μ is viscosity of the bulk fluid, ρ, d, and m are the particle density, diameter, and mass, respectively, u is the fluid velocity at the particle's position, and v is the velocity of the particle.

Particles were left to flow for 500 msec to reach quasi-steady state, after which data was collected at 25 msec intervals over 1 sec. As shown in (2), the hematocrit was measured as the ratio of the total volume of RBCs in a channel to the total channel volume (2).

$$H = \frac{N\,V_c}{l \cdot w \cdot h} \times 100\%, \qquad (2)$$

where H is hematocrit, V_c is the volume of one RBC (set to 90 fL), N is the number of RBCs in the channel, and l, w, and h are the channel length, width, and height, respectively. Results are reported as mean ± standard deviation (SD).

RESULTS

Figure 1A displays the bulk flow velocity distribution profile, reflecting the spatial variation in velocity resulting from channel geometry. Velocity was highest in the side passages given their increased width (12 μm) relative to the capillary openings (4 μm). Anatomically, anastomoses are known to dilate or constrict to regulate the velocity and volume of blood flowing through a capillary network. RBC distribution was spatially non-uniform, with RBCs accumulating in low-velocity regions near channel edges and inter-pillar spaces (Fig. 1B). These variations in distribution profiles point to non-uniformity in rheological properties within the channel since the rheology of blood is known to be significantly modulated by hematocrit.

We analyzed the velocity of individual RBCs in both the inlet channel and the capillary network. The mean velocity of RBCs was lower in the microcapillary network (0.39 ± 0.05 mm/s) than in the inlet channel (0.83 ± 0.26 mm/s) due to interactions with micropillar walls. Additionally, the shape of the velocity distribution differed between the two regions, with inlet channel velocities skewed to the right and microcapillary channel velocities skewed to the left (Fig. 2).

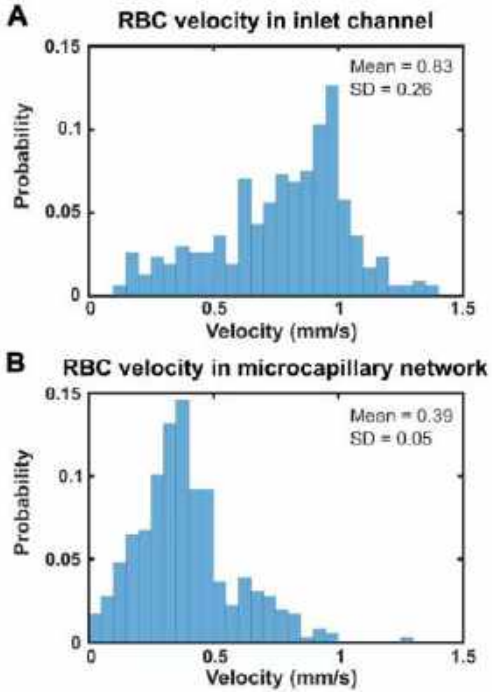

Figure 2: Velocity distribution of RBCs in (A) the inlet channel and (B) the microcapillary network.

The hematocrit within the inlet channel and a 4 μm-wide microcapillary channel (Fig 1A) was sampled every 25 msec over a simulation period of 1 sec. The hematocrit within the inlet channel was 6.5% ± 0.6%, compared to 10.1% ± 10.6% within the microcapillary channel. Importantly, hematocrit within the microcapillary channel showed far higher variability over time, with values ranging from 0% to 38% (Fig. 3).

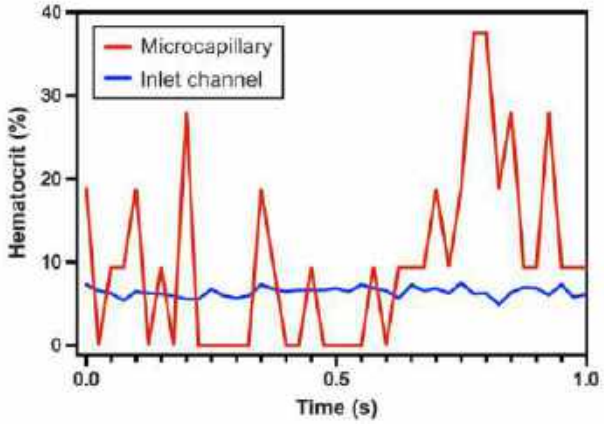

Figure 3: Temporal variation in hematocrit in the inlet channel and a 4 μm-wide microcapillary channel.

DISCUSSION

The models detailed above demonstrate the spatiotemporal variation in RBC velocity and distribution resulting from intricate microcapillary geometry. However, only particles with uniform physical properties were utilized, and cellular deformation was ignored. RBCs, especially in disease, often have heterogenous physical properties and deformability that may alter their rheology. The extension of this work to include variations in RBC physical properties may provide a new method to differentiate RBC subpopulations based on their transit times or spatial distributions. Additionally, localized hematocrit spikes in small capillaries can greatly increase blood viscosity and flow resistance, altering cellular interactions and rheology in ways unobserved in larger vessels. This has important implications for monitoring conditions such as sickle cell trait in which a small population of abnormal RBCs can cause chronic organ damage [3] and yet are undetectable by conventional techniques such as bulk ektacytometry [4]. Microfluidic models such as the one presented here can support the development of novel devices to address present limitations in rheologic monitoring leading to improved patient care. We are currently conducting experimental studies to validate the results obtained from these models and to characterize the velocity and distribution profiles of healthy and diseased RBCs.

ACKNOWLEDGEMENTS

This work is supported the National Heart, Lung, and Blood Institute (R56HL165946), National Institutes of Health Office of the Director (U01AI176469), and National Heart, Lung, and Blood Institute Small Business Innovation Research Program (R42HL162214). We acknowledge Natnael A. Anjulo for his expert guidance with COMSOL.

REFERENCES

[1] Man, Y, et al., Lab on a Chip, 20(12):2086-99, 2020.
[2] Weddell, J.C, et al., PloS one, 10(4):e0124575, 2015
[3] Xu, J.Z., Haematologica, 104(6):1106, 2019.
[4] Franck, P, et al., Eur. J. Haematol., 108(5):413-22, 2022.

SB³C2024
Summer Biomechanics, Bioengineering and Biotransport Conference
June 11-14, Lake Geneva, WI, USA

MECHANICAL COVARIANCE NETWORKS OF THE CORTEX REGIONS AS IDENTIFIED BY MAGNETIC RESONANCE ELASTOGRAPHY

Kyra E. Twohy (1), Alexa M. Diano (2), Olivia M. Bailey (2), Mary K. Kramer (2), Curtis L. Johnson (1,2)

(1) Department of Mechanical Engineering, University of Delaware, Newark, DE, USA
(2) Department of Biomedical Engineering, University of Delaware, Newark, DE, USA

INTRODUCTION

Neural connections allow for signals to pass between physically disparate regions of the brain to create behaviors, movement, and memories. Because signal transfer requires a physical connection, they also makeup part of the structure of the brain [1]. In the cortex, particular interest is placed in categorizing which disparate regions are used together during specific tasks as functional networks, which are often characterized through functional MRI (fMRI) [1]. In a physical sense, functionally correlated regions require increased connections of neurons to seamlessly coordinate actions, something that can be quantitatively assessed through diffusion MRI [1].

Additional imaging studies have been done to investigate how the structural integrity of cortex regions, measured via regional morphometry, compare across established functional networks and how this impacts network health [2,3]. Original studies in structural covariance and graph theory showed that similarities in the cortex shape were found both in neighboring regions and more distant ones [4]. This "structural covariance network" showed small world properties and short mean distance between neighboring regions. More recent applications of this work compared the network structures between patient populations and cognitively normal controls, identifying variations in the structure that could contribute to cognitive differences [3]. However, volumetric studies fail to capture the microstructural nuances that more sensitively reflect tissue integrity. Magnetic resonance elastography (MRE) measures are sensitive to changes in the microstructure and have been shown to vary across the regions of the cortex [5]. Previous MRE research has not looked at covariance because property recovery was limited to larger regions that would not provide enough complexity to study the area as a network.

The goal of this study was to identify "mechanical covariance networks" through MRE measure of shear stiffness for the first time utilizing improved cortical property recovery techniques. We hypothesize that shear stiffness will vary together across cortical regions, establishing a network. We also hypothesize that highly connected cortical regions of the network will overlap with already established functional hubs.

METHODS

This study comprised of 61 subjects (37.7 ± 20.5 years, 28M/33F) with ages ranging from 14 to 80. Each participant underwent an MRI scan consisting of both MRE and standard structural scans on a Siemens 3T scanner. For the MRE portion of the protocol, a custom high-resolution 3D multiband, multishot spiral sequence (resolution: 1.5 mm^3 isotropic) was used with 50Hz vibrations delivered to the posterior of the head to induce shear displacements. A T_1-weighted MPRAGE (resolution: 0.9 mm^3 isotropic) was also acquired and used to segment all 60 unilateral cortex regions in Freesurfer. Displacement data collected from the MRE scan was converted to shear stiffness using a nonlinear inversion algorithm (NLI) [6]. To reliably capture the mechanical properties in the small cortex regions, soft prior regularization and reduced spatial filtering were added to NLI following procedures documented in Hiscox et al. [6]. These techniques work to eliminate the influence of surrounding tissue on the property estimates by minimizing divergence of the properties within the anatomical regions as defined by the Freesurfer segmentations and decreasing filtering over the thin structure. Complex shear modulus (G) is calculated using the storage (G') and loss (G'') moduli. From complex shear modulus, shear stiffness (μ) can be calculated using Equation 1.

$$\mu = 2\,|G|^2/(G' + |G|) \quad (1)$$

For each subject, the shear stiffness for all 60 cortical regions was calculated. Correlation matrices were created to show how the properties of regions varied together by running partial correlations for shear stiffness between each region, controlling for age and sex. Nonsignificant correlations ($p>0.05$) were set to 0, as well as the correlations between a region and itself to integrate into the Brain Connectivity Toolbox in MATLAB [7]. This toolbox was used to generate the network backbone based on a minimum-spanning-tree

based algorithm (Figure 1). BrainNet Viewer in MATLAB was used to visualize the network backbone anatomically [8].

RESULTS

Examination of cortical stiffness showed regions that strongly varied together across individuals. The covariance matrix for shear stiffness and the simplified backbone matrix are shown in Figure 1. The backbone matrix highlights the dominant connections of the original matrix. Pairs of regions appear down the diagonal of this matrix, indicating strong connections between the bilateral pairs of a given cortical region thus connecting the two hemispheres. This backbone matrix also highlights regional modules of the network, i.e. the upper left corner of the backbone matrix shows connections between frontal lobe regions. Most of these connections are within a given hemisphere. The same pattern is also seen in the bottom right corner with the parietal and occipital cortical regions. Hub nodes that connect the lobe modules can be seen in the upper right and bottom left corners.

This information can also be seen anatomically in Figure 2. Here the pairing of the left and right regions can be seen on the coronal and transverse views with the connections that are horizontal. The regional modules are visible with more connections spanning within the lobe than between lobes. The between lobe connections rely on the hub regions, indicated with the larger size, particularly the precentral region, which had the highest number of connections at 6.

DISCUSSION

This study presents preliminary findings from an examination of mechanical covariance networks in the brain from MRE measures. 60 subregions of the cortex were used as nodes of the generative network. High covariance across the cortex was seen when using shear stiffness. Centrally located regions including multiple regions in the temporal lobe and the precentral cortex were the hub nodes of the network connecting to multiple regions and connecting the larger modules to each other.

Another hallmark of our findings was the reliance of paired right and left regions of the cortex, creating connections that spanned the hemispheres. This occurred for midline regions, like the precentral cortex, as well as more lateral regions like the superior temporal cortex. This analysis also created two distinct modules that aligned on lobe boundaries. One module was composed of frontal regions, while the second module was composed of the parietal and occipital regions combined.

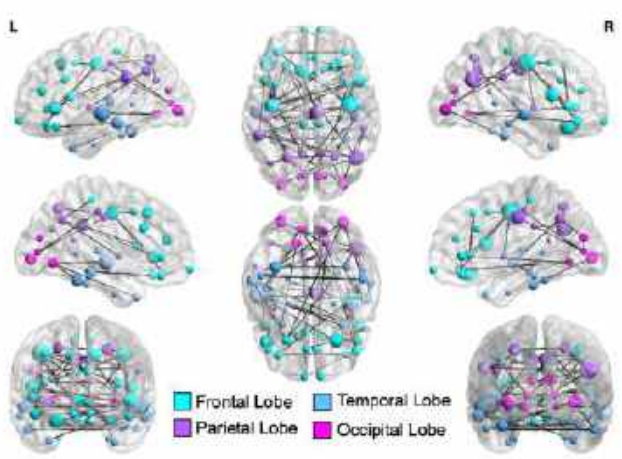

Figure 2: Anatomical visualizations of the network backbone, where each region is represented as a node and the color indicates the lobe. Larger nodes show an increased number of connections.

Structural covariance and graph theory are promising tools to use with MRE in future studies, especially in the identification of structural differences between cognitively normal and patient populations. In this application, graph theory will benefit from the increased sensitivity to structural changes that MRE provides to create tools for understanding the structure of the brain.

ACKNOWLEDGEMENTS

This work was supported by the NIH grant U01-NS112120.

REFERENCES

[1] Park, HJ et al. Science, 342:80, 2013.
[2] Evans, AC. Neuroimage, 80: 489-504, 2013.
[3] Gupta, CN et al. Brain Struct. Funct., 224:3031-3044, 2019
[4] He, Y et al., Cerebral Cortex, 17:2407-2419, 2007.
[5] Hiscox, LV et al., Neuroimage, 232:117889, 2021.
[6] Hiscox, LV et al., Phys. Med. Biol., 67: 095002, 2022.
[7] Rubenov, M and Sporns, O. Neuroimage, 52:1059-1069, 2010.
[8] Xia, M, et al. PLoS ONE, 8:e68910, 2013.

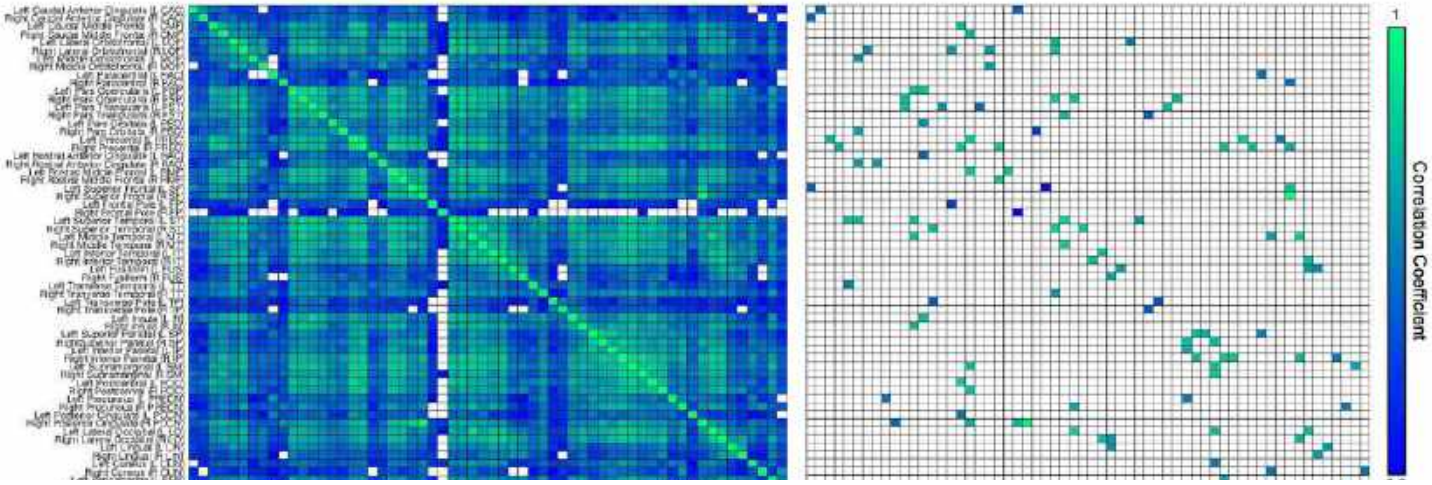

Figure 1: (Left) The raw connectivity matrix showing partial correlations between stiffness of all cortical regions, with lighter green colors indicating a stronger connection. (Right) The simplified backbone matrix highlights the primary connections of the network.

FLEXIBLE CARBON NANOTUBES (CNT)–POLYDIMETHYLSILOXANE (PDMS) FORCE SENSORS FOR THE RATE–DEPENDENT CHARACTERIZATION OF COMPLIANT BIOMATERIALS

S. Candan (1, 2), V. Barton (1), J. Andrews (1, 3), J. Notbohm (1, 2), C. Franck (1, 2)

(1) Mechanical Engineering, University of Wisconsin-Madison, Madison, WI, USA
(2) Biomedical Engineering, University of Wisconsin-Madison, Madison, WI, USA
(3) Electrical and Computer Engineering, University of Wisconsin-Madison, Madison, WI, USA

INTRODUCTION

Accurate measurements of forces in highly compliant and rate-dependent biomaterials including hydrogels remain challenging. First, most hydrogels are extremely soft (Young's Modulus E~1-100 kPa) such that for most sample geometries force sensors need to be able to measure 10s to 100s of μNs. Second, hydrogels often require complete hydration, which challenges existing miniature force sensing modalities due to the operation within a liquid environment. Third, for microstructurally complex hydrogels, mechanical characterization often requires in situ imaging of the microstructure. Therefore, sensors with customizable form factors are optimal for integrating optical imaging or microscope setups. Finally, hydrogels are rate-dependent materials and often demonstrate distinct mechanical characteristics such as elevated stiffness and hysteresis with increasing strain rates. Unfortunately, high-rate (1-100 s^{-1}) constitutive tensile data and experimental methods for determining those have remained scarce in the literature. This hinders the development of accurate constitutive models for soft biomaterials under impact like loading conditions. Thus, in addition to providing micronewton force resolution, the force sensor should also feature a high temporal response in the order of 0.1-1 ms to accurately resolve forces at strain rates of 1-100 s^{-1}. Several past studies have explored methods for measuring forces in soft hydrogels. One notable approach involves a micro electromechanical system (MEMS) [1] offering sensitivity of 5-50 μN. However, this method is incompatible with in situ aqueous sample testing, requiring an interlink between the sensor and the sample which induces unwanted moments on the hydrogel. In another application specific for cell cultures, forces were being measured by monitoring the deflection of PDMS beams attached to the cell culture [2]. This method could be extended to hydrogel testing, but for samples larger than ~500 μm, simultaneous optical tracking of PDMS beam deflections and microstructural imaging of the sample becomes intractable, necessitating a more complex, multi-camera setup. To address the above-mentioned challenges within a single force sensor, we designed soft piezoelectric force sensors composed of Polydimethylsiloxane (PDMS) and carbon nanotubes (CNTs). In this composite material, the CNTs are dispersed within the PDMS matrix and form a percolation network [3] permitting electrical conduction and produce resistivity changes proportional to the applied material strain. PDMS-CNT composites can be injection molded, water sealed, and made flexible. They demonstrate high temporal response rate, capable of following cyclic deformation at 1 Hz, across a broad range of strains [4]. Thus, these materials hold significant potential for deployment in various scenarios, particularly for accurately measuring forces in soft hydrogels, biomaterials, and tissues at high strain rates.

METHODS

Due to lack of tensile constitutive data, we aim to characterize hydrogels under uniaxial tension by using PDMS-CNT force sensors. We use a previously custom built tensile test setup that is compatible with in-situ imaging of the microstructure [5]. Dogbone shaped hydrogel and PDMS-CNT samples are connected in series, ensuring that the force applied to the hydrogel is equal to the force being transmitted to the PDMS-CNT. During loading, we monitor the electrical resistance changes in the PDMS-CNT, using a source measurement unit (SMU, Keysight B2902A) which has a baseline signal-to-noise ratio of 40 dB. To correlate change of resistance with the applied force, we use a separate calibration setup where the PDMS-CNT is linked with a dog bone shaped PDMS sample of known material properties in series. We employ the PDMS itself as a tool to calibrate our sensors. Because there is a lack of commercially available force sensors capable of detecting low force magnitudes in the range ~100-1000 μN, at varying strain rates (0.1–100 s^{-1}) with low latency and featuring low form factors. The force is calculated by measuring the PDMS strain via digital image correlation (DIC). We use the known material and geometric properties of the PDMS sample to convert the obtained strain information into stress and force. Once validated, we integrate our force sensor into our

Figure 1 – Steps for PDMS-CNT manufacturing, sensor calibration, and Collagen–I test protocol.

existing tension test platform to simultaneously collect microstructural images of the deforming collagen gel. PDMS-CNT composites are prepared according to a protocol presented in literature [3]. We use mixture of Sylgard 527, 70% by weight, and Sylgard 184, 30% by weight, mixture for both CNT matrix and calibration sample. CNT weight percentage is chosen to be 2% to optimize the baseline resistance for achieving a high signal-to-noise ratio. PDMS-CNT sensors are covered with a PDMS layer to generate a waterproof seal. Further manufacturing and sample details are summarized in Figure 1.

RESULTS

Before calibrating the PDMS-CNT force sensor and using it to measure stresses developed in collagen-I gels, we measured just the PDMS-CNT strain-resistance response under deformation. These initial tests mimic the eventual collagen-I testing conditions which consist of uniaxial tension load-unload cycles at different strain rates up to 50% maximum strain. It is important to note that our current loading profile enforces displacement control upon loading and force control under unloading (future experiments will also enforce displacement control during the unloading phase). Separate experiments have shown collagen gels to reach a peak stress of up to ~3 kPa at 50% strain, and PDMS-CNT samples have Young's Modulus E~0.3 MPa under quasi-static loading. As the PDMS-CNT sensors are stiffer, the sensors will undergo less strain than the collagen-I gel, estimated to be around ~10%. To mimic this condition, PDMS-CNT sensors are individually tested up to 12.5% maximum tensile strain. To examine our sensors temporal response, we repeated the tests at different strain rates of 0.125, 1.25, and 12.5 s^{-1} as seen in Figure 2 (a-c). At all rates, the sensor provides excellent temporal response during the loading (displacement control) phase with almost no delay. However, we observe significant latency during the unloading phase (force control) such that the resistance does not come back to its starting value within the timescale of loading. This is a well appreciated phenomenon for carbon-silicone composite strain sensors under creep [6]. These observations should be considered while fitting resistance-force calibration curves to the data before hydrogel testing, or strictly enforce displacement control during the loading and unloading phase. To estimate the smallest force PDMS-CNT sensors can detect, we manufactured a PDMS-CNT strip with 1 mm^2 area and applied quasi-static 0.25% strain to the sensors. Resistance change was measured around 1 Ohm with ~500 Ohm base resistance. Omitting the viscoelastic effects, and observing that E~0.3 MPa, estimated force is 350 μN. These preliminary experiments provide an idea about expected force-resistance calibration curves at varying strain rates.

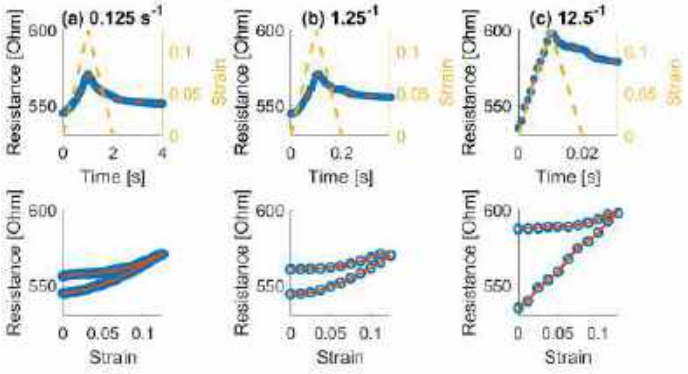

Figure 2 – Load-Unload cycles at (a) 0.125 s^{-1}, (b) 1.25 s^{-1}, and (c) 12.5 s^{-1} rates

DISCUSSION

This study presents the development of a flexible force sensor that features both excellent sensitivity and temporal response albeit showing high latency during the unloading phase when creeping. We show the sensor's potential for measuring small forces even for large strain rates up to 12.5 s^{-1}, while its flexibility, and low footprint allows for simultaneous in-situ imaging of millimeter-sized soft and fully submersed hydrogels. That is, the sensor can record the full stress-strain response of highly compliant collagen I hydrogel over the full finite deformation range (up to 50% strain) and decades of strain rate to provide a more accurate constitutive characterization of these hydrogels and tissues. We will explore these sensors to even higher strain rates (up to 100 s^{-1}) to characterize the complete, finite-deformation, rate-dependent response while also resolving microstructural changes that occur during the loading and unloading process with micron to submicron resolution. Additionally, we will use the sensor for constitutive characterization of other biopolymer gels used for in vitro models, ex vivo tissues, and in vivo tissues which will enlighten the gap of higher rates and concurrent microstructure evolution.

ACKNOWLEDGEMENTS

This material is based upon research supported by the U. S. Office of Naval Research under PANTHER award numbers N000142112044 and N000142112855 through Dr. Timothy Bentley.

REFERENCES

[1] J. M. Jimenez *et al.*, *Acta Biomater.*, vol. 162, pp. 292–303, 2023.
[2] B. Emon *et al.*, *Sci. Adv.*, vol. 7, no. 15, p. eabf2629, 2021.
[3] J. H. Kim *et al.*, *Sci. Rep.*, vol. 8, no. 1, p. 1375, 2018.
[4] M. O. Tas *et al.*, *ACS Appl. Mater. Interfaces*, vol. 11, no. 43, pp. 39560–39573, 2019.
[5] L. Summey *et al.*, Exp Mech 63, 1445-1460, 2023.
[6] H. Yang *et al.*, *Compos. Sci. Technol.*, vol. 167, pp. 371–378, 2018.

NOVEL COMPUTATIONAL MODEL FOR PLANNING PATENT DUCTUS ARTERIOSUS STENTING PROCEDURE

Luis René Mata (1), Srujana Joshi (1), Shweta Karnik (1), Leon Cheng (1), Andrew Marini (1), Shobana Santhanam (1), Rahav Kothuri (1), Charles Federico (1), Suhaas Bonkur (1), Lakshmi P. Dasi (1), Holly D. Bauser-Heaton (1,2)

(1) The Wallace Coulter Department of Biomedical engineering, Georgia Institute of technology and Emory University, Atlanta, Georgia, USA
(2) Children's Healthcare of Atlanta, Atlanta, Georgia, USA

INTRODUCTION

Ductal-dependent cyanotic congenital heart disease is a condition where circulatory equilibrium relies on a patent ductus arteriosus (PDA), a fetal connection from the aorta and pulmonary artery. While this conduit normally closes after birth, its patency is crucial for proper pulmonary blood flow supply in affected patients. Palliative interventions, such as PDA stenting, are employed to maintain continuous pulmonary blood flow ensuring the patient gain weight and stability until definitive surgical repair can be performed[1,2]. Although stenting has shown advantages over its surgical alternative, the Blalock-Taussig-Thomas shunt (BTTS), including reduced operative risks and hospital length of stay, it comes with an increased rate of reinterventions and procedure-related complications[1].

The challenges arise from the complex and tortuous anatomy of the PDA, making successful stent deployment dependent on medical expertise[2]. A critical consideration in procedural planning is the selection of the most appropriate stent length and diameter to ensure complete PDA coverage[1]. Failure to do so could result in incomplete stenting, hindering pulmonary blood flow and pulmonary artery growth, as uncovered segments may undergo natural obliterative processes, leading to constriction.

We hypothesize that enhancing preprocedural planning, leading to the optimal selection of stenting parameters, can mitigate the risk of partial stent coverage. To achieve this, we propose the development of a patient-specific computational framework based on finite element analysis (FEA). This pipeline aims to study the mechanical interactions of medical devices involved in the procedure (angioplasty balloon, stent, and guidewire) with the patient's PDA anatomy. The model could serve as a valuable tool for interventional cardiology teams, aiding in the selection of stenting parameters, predicting the extent of PDA stenting coverage, and providing insights into the patient's candidacy for this procedure.

METHODS

We established a computational simulation FEA-based pipeline for the stenting of PDA with relatively straight anatomies, categorized as Qureshi's type I PDA[1,2]. The methodology involves the following key steps:

1. **DA Segmentation**: Utilizing Mimics software, we segmented the region of interest, including the Ductus arteriosus and adjacent sections of the aorta and pulmonary arteries. Meshing and refinement processes were then carried out using 3-Matic software.
2. **CAD Modeling and Meshing**: We created CAD models for the stent, guidewire, and angioplasty balloon in Solidworks, incorporating data from MicroCT scans obtained through the MicroCT50 equipment (Scanco medical). Following this, hexahedral meshing in Hypermesh was performed, setting the stage for subsequent FEA simulations executed in Abaqus.
3. **Balloon Compression and Stent Crimping**: We simulated radial compression on the stent and angioplasty balloon to obtain the pre-deployment configurations.
4. **Guidewire Modeling**: Using wire elements and displacement boundary conditions, we modeled the PDA straightening in the pre-stenting phase by simulating the advancement of the guidewire through the PDA.
5. **Stent Deployment Simulation**: We conducted simulations involving the angioplasty balloon inflation-deflation processes, incorporating fluid cavity and exchange interactions. We captured the dynamic aspects of stent deployment through amplitude changes. Default configurations of the stent and PDA anatomy were utilized to study their interaction.

Figure 1 is a diagram of the steps involved in our methodology.

RESULTS

In our study, we applied our FEA-based framework to simulate the stenting of a PDA in a patient with a moderately straight anatomy

(Qureshi's type I) who underwent the stenting procedure at the Children's Healthcare of Atlanta (CHOA). The segmentation of the PDA and adjacent vascular structures was performed using pre-procedural CT scans. Centerline analysis revealed a PDA dimension of 13.95 mm, a minimal diameter of 3.65 mm (located at the aortic origin), and a maximal diameter of 4.10 mm on the pulmonary side. Considering the recommended aortic protrusion of ~2 mm and a pulmonary protrusion of 2-4 mm, a Promus Premier stent (Boston Scientific) of dimensions 4x20 was employed for the simulations. In the pre-stenting simulation, which included guidewire modeling, we observed a straightening of the PDA primarily on the left pulmonary end, a preferred location for stenting due to a more straightforward path and the avoidance of excessive stent deformation, given the presence of an elbow configuration. Given the vertical PDA configuration, we positioned the guidewire to simulate carotid vascular access and aligned with the longitudinal axis of the PDA (Figure 2a).

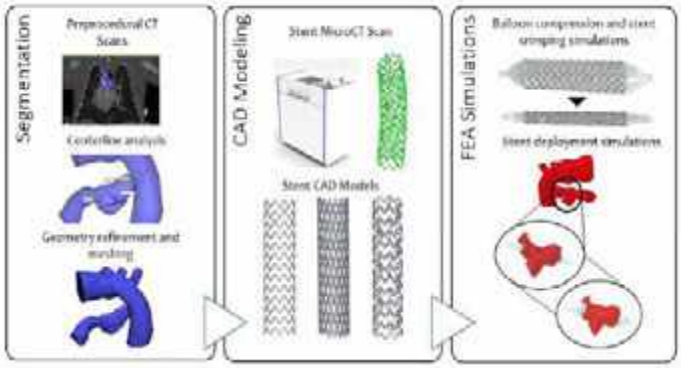

Figure 1: Methodology of FEA-based simulation pipeline for PDA stenting procedure.

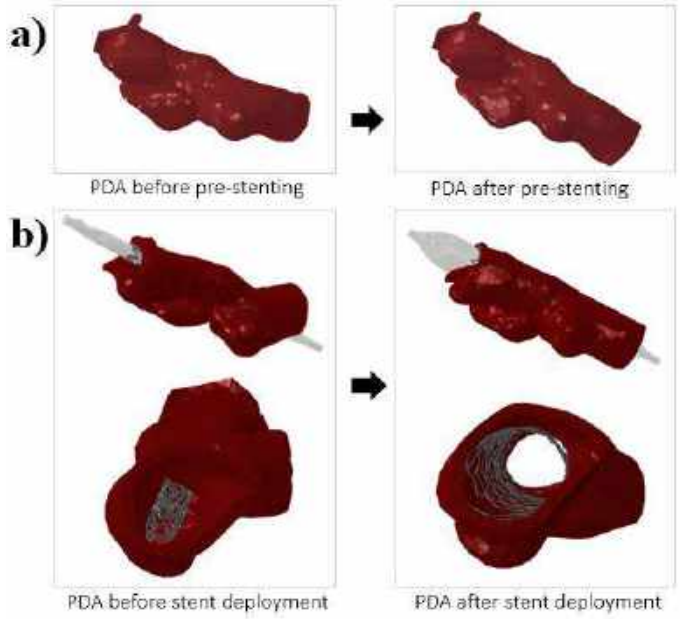

Figure 2: a) Results of pre-stenting simulation before and after positioning of the guidewire. b) Stent deployment simulation results showing the pre and post deployment configurations of the stent, angioplasty balloon and stent. The angioplasty balloon was removed in the pictures at the bottom for improved visualization of the stented PDA.

Concerning the stent deployment simulation, minimal stent recoil was noted at the end of the inflation step where we incorporated a slight deflation equivalent to 5% of the balloon volume. The stent conformed to the tortuous PDA geometry, exhibiting flare at the fixation on the aortic side where the minimal diameter is present. On the pronounced curves in the PDA, located immediately after the aortic origin, we observed significant straightening of the stent rings. In general, there was a distinctive straightening of the PDA morphology caused by the inherent rigidity and tubular configuration of the stent. Also, tissue bulges after the original connection of the PDA with the left pulmonary artery were formed; however, no stenosis was formed (Figure 2b).

Analysis of Von Mises stress distribution showed accentuated stress on the stent fixation at the aortic side due to the tight tolerance between the stent and PDA on the minimal diameter section. Additionally, stress concentration within the stent was predominantly present on the straight sections of the struts (Figure 3).

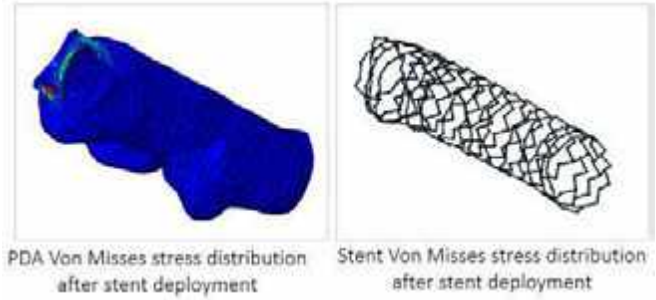

Figure 3: Von Misses stress distribution on the PDA and stent after stent deployment.

DISCUSSION

The simulation results present several noteworthy observations with implications for the stenting procedure in patients with moderately straight PDA anatomies (Qureshi's type I)[1,2]. The stent model in our simulations exhibits multiple deformation zones, including flares and strut straightening, which raises concerns about potential stress concentration. This could pose risks such as vascular spasm and in-stent restenosis over the long term. It is crucial to acknowledge the role of aortic and pulmonary protrusions in ensuring complete stenting coverage and proper fixation points, even though it comes with the drawback of increased stress concentration. Moreover, the simulations enable us to evaluate the potential extent of stenosis caused by tissue bulges, which holds clinical relevance for anticipating the need for reinterventions. In such cases, additional stents may need to be telescopically implanted to improve pulmonary blood flow.

Looking ahead, our future work will involve applying this simulation pipeline to a broader range of patient-specific geometries. We plan to introduce additional steps to model stent deployment in more complex PDA geometries, such as Qureshi's types II and III[1,2], accompanied by a rigorous validation process to enhance the accuracy and reliability of our simulations.

ACKNOWLEDGMENTS

Heart Research and Outcomes Center (HeRO) grant.

REFERENCES

[1] Bauser-Heaton, H., Price, K., Weber, R., El-Said, H. *Journal of the Society for Cardiovascular Angiography & Interventions* **Volume 2,** Issue 4, 2023.

[2] May, L. A.; Masand, P. M.; Qureshi, A. M.; Jadhav, S. P. The ductus arteriosus: a review of embryology to intervention. *Pediatric Radiology* 2023 Mar;53(3).

IMPACT OF PARTICLE SEEDING ON THE RHEOLOGICAL CHARACTERISTICS OF BLOOD ANALOG FLUID USED IN LASER DOPPLER VELOCIMETRY

Shreyash M. Manegaonkar (1), Israel Ajiboye (1), Gavin A. D'Souza (2), Rupak K. Banerjee (3)

(1) Department of Mechanical and Materials Engineering, University of Cincinnati, Cincinnati, Oh, USA
(2) Office of Science and Engineering Laboratories, US Food and Drug Administration, Silver Spring, MD 20993, USA
(3) Department of Biomedical Engineering, University of Cincinnati, Cincinnati, Ohio, USA

INTRODUCTION

Conducting *in vitro* experiments with real blood presents various challenges including coagulation complexities, storage, and procedural handling concerns. To overcome these challenges, blood analog fluid (BAF), typically comprised of water, glycerin, and Xanthan gum, is often used to characterize the hemodynamic performance of blood-contacting medical devices and novel diagnostic indices. The BAF composition enables a close approximation of the shear-thinning behavior of real blood [1]. Occasionally, the BAF composition also includes microsphere particles to facilitate flow visualization studies using Laser Doppler Velocimetry (LDV). Flow visualization studies are important to characterize the flow field within the cardiovascular system and in medical devices (such as blood pumps, valves, grafts), and thereby evaluate adverse flow regions that pose hemolytic and thrombotic risks. Additionally, flow visualization is also used to validate computational models.

Blood viscosity is influenced by multiple factors, such as blood composition (e.g., hematocrit level), temperature, shear rate, vessel diameter leading to Fähraeus-Lindqvist effect, cell aggregation, shape, deformation, orientation, and plasma viscosity [2]. Thus, it is hypothesized that the addition of particles in the form of polymer microspheres in BAF solution affects the rheological properties of the fluid.

Therefore, this research aims to characterize the effect of polymer microspheres on BAF viscosity, and thereby facilitate *in vitro* flow visualization using LDV under relevant physiologic conditions observed *in vivo*. The outcomes of this work are expected to enhance the clinical relevance of *in vitro* hemodynamic evaluations of medical devices and diagnostic indices.

METHODS

Formulation of BAF. In the current composition of BAF, glycerin controls the viscosity at infinite shear rates, whereas Xanthan gum is introduced to modulate the non-Newtonian behavior, particularly at low shear rates [3]. An optimal ratio of glycerin, water, and Xanthan gum must be achieved in order to create a BAF that accurately mimics the rheological characteristics of actual blood [4, 5].

Incorporation of Microspheres in BAF. Microspheres induced in BAF have an important role, particularly in generating the scattering signal essential for LDV measurements. The selection of the type and size of microspheres significantly influences the precision of LDV measurements. In the current study, solid polymer microspheres with a diameter of 8 $\boldsymbol{\mu}$m were utilized.

Three different test fluids comprising of 16 ml BAF solution with the following varying concentrations of polymer microspheres were created: 1% (weight/volume; w/v) and 2% w/v represent test samples, whereas 0% w/v represents a control sample. Three experiments (n = 3) were performed for each test fluid. Each experiment was carried according to an identical approach. For each test fluid, the recorded viscosities from the three measurements were averaged. This methodology of three experiments and a subsequent averaging, provides robust and reliable viscosity data for comparisons of variable microsphere seeding compositions.

To measure the viscosity of BAF with and without polymer microspheres, a concentric cylinder viscometer (Brookfield Engineering Laboratories Inc.) was used. The recorded viscosity data was then fitted to the Carreau model using the equation [1] below:

$$\mu = \mu_\infty + (\mu_0 - \mu_\infty) \times (1 + (\lambda\dot{\gamma})^2)^{\frac{n-1}{2}} \quad (1)$$

where λ = time constant, n = power law index, μ_0 = zero shear viscosity (cP), μ_∞ = infinite shear viscosity (cP), and $\dot{\gamma}$ = shear rate (1/s).

RESULTS

Figure 1 presents a visual comparison of viscosities among BAF with different polymer microsphere concentrations of 0%, 1%, and 2%. Table 1 outlines the Carreau model coefficients for BAFs with and without polymer microspheres. The subsequent section demonstrates differences in viscosity profiles between real blood (solid line) [6] and the various BAF compositions.

BAF for 0% microspheres (base line), comprising 80% (volume/volume; v/v) distilled water, 20% (v/v) glycerol and 0.027% (w/v) Xanthan gum, had a viscosity profile that is similar to real blood over shear rates ranging from 1 s^{-1} to 100 s^{-1}. The Carreau model coefficients for BAF with 0% microspheres were obtained as λ = 3.1, n = 0.4, μ_0 = 42.3 cP, μ_∞ = 5.4 cP. These values were found comparable with the Carreau model coefficients of blood [6].

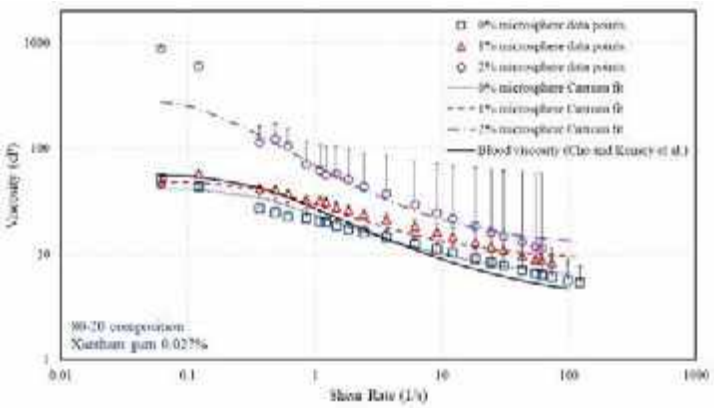

Figure 1: BAF viscosity with a) 0%, b) 1%, and c) 2% (w/v) polymer microsphere in 80/20 composition.

	μ_∞	μ_0	λ	n
0% microspheres	5.4	42.3	3.1	0.4
1% microspheres	8.5	49	2.5	0.35
2% microspheres	12	300	7.5	0.21

Table 1: Carreau coefficients comparison between a) 0%, b) 1%, and c) 2% (w/v) polymer microsphere in BAF 80/20 composition.

For the 1% microspheres, an absolute increase of 3.1 cP in μ_∞ and a 6.7 cP increase in μ_0 (Figure 3) were observed in comparison to the baseline (0% microspheres) values of BAF. The Carreau model coefficients for BAF, incorporating 1% microspheres, were determined as λ = 2.5, n = 0.35, μ_0 = 49 cP, and μ_∞ = 8.5 cP (Figure 1 and Table 1).

Similarly, with 2% microspheres, there was an increase in the absolute value of μ_∞ by 6.6 cP and a 264.3 cP increase in μ_0 (Figure 3) in comparison to the baseline (0% microspheres) BAF values. The Carreau model coefficients for BAF with 2% microspheres were reported as λ = 7.5, n = 0.21, μ_0 = 300 cP, and μ_∞ = 12 cP (Figure 1 and Table 1).

DISCUSSION

BAF plays an important role in many flow visualization experiments, enabling controlled velocity measurements for testing cardiovascular devices such as blood pumps, valves, stents, grafts etc. As observed in Figure 1, a relatively small % of microsphere seeding significantly influences BAF viscosity. Sensitivity of microsphere-seeding concentration in BAF suggests improved optimization is required for accurate mimicking of physiological conditions during LDV measurements.

In conclusion, incorporation of polymer microspheres results in significant changes in non-Newtonian viscosity, both μ_0 and μ_∞, of BAF in relation to viscosity of human blood. Therefore, accounting for the effects of microspheres is essential for better quantification of hemodynamics in medical devices during LDV experiments.

A

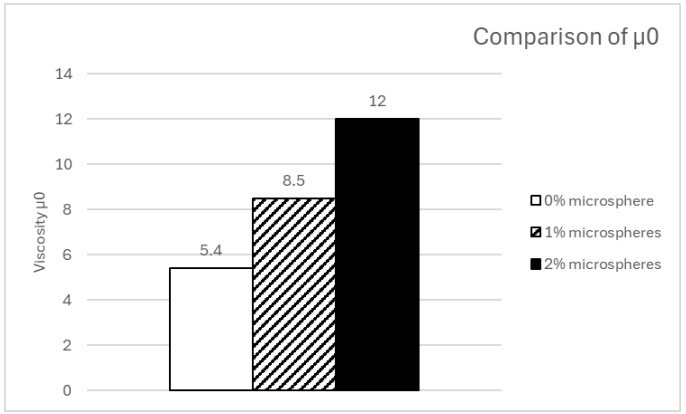

B

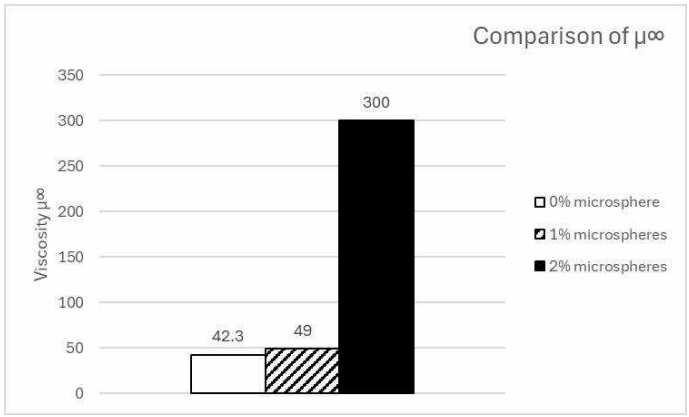

Figure 3: Comparison of BAF viscosity with varying polymer microsphere concentrations a) μ_0, and b) μ_∞.

REFERENCES

[1] Brookshier, K. K. et al., Biorheology, 28(6), pp. 569-587.
[2] Sousa, P. C. et al., Biomicrofluidics, 5(1).
[3] Banerjee, R. K. et al., Biomed Eng Online, 7, p. 24.
[4] Anastasiou, A. D. et al., Med Eng Phys, 34(2), pp. 211-218.
[5] D'Souza, G. A. et al., J Biomech Eng, 136(2), p. 021026.
[6] Cho, Y. I. et al., Biorheology, 28(3-4), pp. 241-262.

SELECTIVE BUNDLE ACL RECONSTRUCTION DOES NOT INITIALLY RESTORE THE NORMAL ACL FORCE DISTRIBUTION IN AN ADOLESCENT PORCINE MODEL: IMPLICATIONS FOR TREATMENT OF PARTIAL ACL INJURIES

Yukun Zhang (1), Kaan Gurbuz (2), Jeffrey T. Spang (3), Matthew B. Fisher (1,3)

(1) Joint Department of Biomedical Engineering, North Carolina State University and University of North Carolina at Chapel Hill, Raleigh, NC, USA
(2) Kayseri State Education & Research Hospital, Kayseri, Turkey
(3) Department of Orthopaedics, University of North Carolina at Chapel Hill, Chapel Hill, NC, USA

INTRODUCTION

There has been an increase in the occurrence of anterior cruciate ligament (ACL) injuries among children and adolescents, with approximately 25% of these being partial tears [1]. Partial injury typically happens to either the anteromedial (AM) or posterolateral (PL) bundles of the ACL, which share in providing overall ACL function. When only one bundle is disrupted, reconstruction surgery may be performed on the injured bundle while preserving the healthy bundle [2]. Clinical studies have shown that selective bundle ACL reconstruction preserves the intact ACL fibers and enhances vascularization of the graft, as well as significantly reduces the differential joint laxity relative to the healthy side at 1-3 years follow-up [3,4,9], with similar values after AM or PL bundle reconstruction [5,6]. Yet, there is a lack of research comparing the relative forces within the graft and remaining intact bundle, which may impact re-injury risk and long-term degenerative outcomes. In the porcine model, the ACL bundles undergo changes in size and function throughout skeletal growth [7], thus age-specific bundle function should be controlled for in experimental studies, which is difficult in clinical studies. Therefore, the objective of this study was to evaluate the initial joint stability and bundle function following selective AM and PL bundle ACL reconstruction within an adolescent porcine model.

METHODS

A total of 8 pairs of deep digital flexor tendons and 8 pairs of normal hindlimbs were collected from adolescent (6 months old) pigs from separate studies. The specimens were divided into two groups for AM bundle reconstruction (n=8) and PL bundle reconstruction (n=8). A 6-degree-of-freedom robotic testing system with a universal force-moment sensor was used to test joint function (Kuka, simVITRO) (Figure 1A). The intact joint was separately subjected to a 100 N anterior-posterior (AP) load, a 150 N compression, and a 5 N·m varus-valgus (VV) torque at 60° of flexion. Kinematics were recorded, then repeated while recording forces for the intact joint and after capsule removal. The same loading conditions were then applied after AM bundle transection (AMT) or PL bundle transection (PLT) while recording the kinematics, which was then repeated with forces/moments recorded. Selective bundle reconstruction was then performed for AM and PL groups: 1) AM bundle reconstruction (AMR) while preserving the remaining intact PL bundle; 2) PL bundle reconstruction (PLR) while preserving the remaining intact AM bundle. Deep digital flexor tendon grafts were used for both AMR and PLR. A complete transphyseal technique was performed with tunnels drilled through the footprints of the transected bundle. Femoral fixation was achieved with a #2 FiberWire (Arthrex) and an ABS button (Arthrex), followed by 5 cycles of passive flexion-extension preconditioning at 22 N of tension. Tibial fixation was then accomplished by a staple (Arthrex) with 100 N pretension applied to the graft at maximum posterior translation at 40° of knee flexion. The same AP, compression, and VV loads were applied following AMR and PLR. The recorded kinematics from intact, AMT or PLT, and AMR or PLR states were repeated after removing the AM or PL bundle graft, followed by removal of the remaining intact PL or AM bundle.

AP tibial translation (APTT) under applied AP load, anterior tibial translation (ATT) under applied compression, and VV rotation under applied VV torques were calculated. Tissue forces were calculated using the principle of superposition. The difference in anterior load and varus/valgus resultant force contribution between the AM and PL bundle was calculated by (AM-PL)/(AM+PL). Joint laxity and tissue force contributions were compared between different states using one-way repeated measures ANOVA with Tukey's HSD. Paired t-test were utilized to compare differential joint laxity relative to intact state from different groups. Significance was set at 0.05.

RESULTS

AMT and PLT resulted in minor destabilization in the joint under AP drawer (Figure 1B). Both PL bundle injured and reconstructed joint showed AP joint laxity within 1 mm of intact state, which was more

stable than AM bundle injured and reconstructed joint (within 3 mm) (Figure 1C).

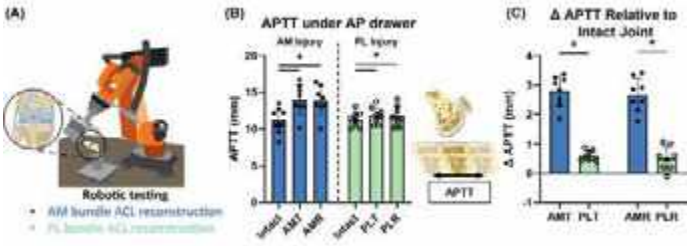

Figure 1: (A) Robotic testing system to assess selective ACL reconstruction. (B) Selective bundle reconstruction (AMR, PLR) did not significantly restore anterior-posterior tibial translation (APTT) relative to the bundle transected state (AMT, PLT). (C) PL bundle transected (PLT) and reconstructed (PLR) states showed better AP stability relative to the respective AM bundle groups. Data points presented with mean and 95% CI. Statistical significance ($p<0.05$) between states indicated (*).

AMT and AMR increased anterior instability under compression (ATT increased by 3.3 and 2.6 mm, respectively), while both PLT and PLR showed similar ATT as the intact joint (ΔATT relative to intact state was 0.5 and -0.7 mm, respectively) (Figure 2A). AMT and PLT resulted in joint destabilization under VV torque (VV increased by 1.1° and 0.4°, respectively) (Figure 2B). Varus-valgus stability was restored to intact state after both AM and PL bundle reconstruction (ΔVV relative to intact state was 0.3° and -0.3°, respectively) (Figure 2B).

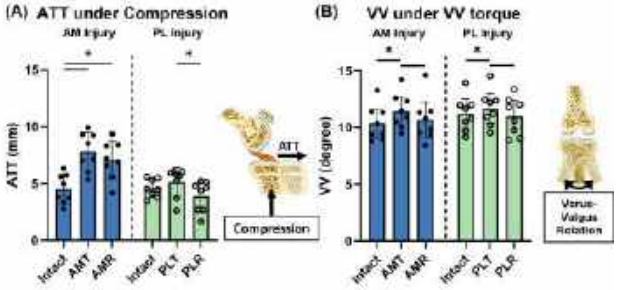

Figure 2: (A) Under compressive loading, both PL bundle transected (PLT) and reconstructed (PLR) states had similar anterior tibial translation (ATT) as the intact joint, but the AMT and AMR groups had increased ATT. (B) Varus-valgus rotation increased after AMT or PLT and was restored to levels similar to the intact state after AMR or PLR. Data points presented with mean and 95% CI. Statistical significance ($p<0.05$) between states indicated (*).

After AM bundle injury, the PL bundle bore higher forces under anterior tibial loading and varus-valgus moments (Figure 3). AM bundle reconstruction was able to restore the normal force distribution under varus-valgus loading (Figure 3B) but not anterior loading (Figure 3A). After PL bundle injury, the AM bundle also bore higher forces, though the forces in the intact state were already high (Figure 3). PLR partially returned these forces under anterior loading (Figure 3A). Under varus and valgus loading, PLR showed a dramatic shift such that the graft carried more force than the intact AM bundle (AM% - PL% = -47% and -25%, respectively) (Figure 3B).

DISCUSSION

In this study, selective bundle reconstruction showed the ability to partially restore the minor changes in joint laxity after partial ACL injury, but the force distribution within the graft and remaining ACL bundle did not fully restore the normal distribution within the intact

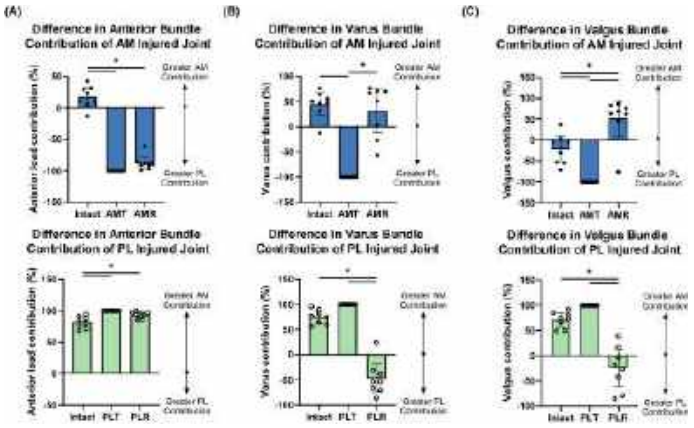

Figure 3: (A) The relative anterior force contribution of the bundles under anterior drawer shifted to PL bundle after AM bundle transection (AMT) and reconstruction (AMR), while stayed in the AM bundle after PLT and PLR in the PL groups. (B,C) The differences between groups in varus (B) and valgus (C) resultant force contribution were similar for both AM and PL groups. AMR restored VV resultant force back toward the AM bundle graft while PLR resulted in more VV resultant force in PL bundle graft relative to the intact PL bundle. Data points presented with mean and 95% CI. Statistical significance ($p<0.05$) between states indicated (*).

ACL bundles. The APTT kinematic data in the present work aligns with results reported in previous human cadaveric data and clinical data, indicating better initial and long-term joint stability following PL injury [7,8]. Additionally, the restoration of varus-valgus laxity through selective bundle reconstruction may be relevant in preventing secondary meniscus or medial collateral ligament (MCL) injuries. In terms of tissue-level forces, neither AM bundle nor PL bundle reconstruction could restore the normal ACL force distribution under all loading conditions tested. It is unclear how these initial imbalances in force distribution may change once the in-vivo graft remodeling process occurs [8]. Previous data from human patients revealed better ability to reduce anterior joint laxity after AM bundle reconstruction (0.8 mm side-to-side difference) compared to our work (2.7 mm) [9]. This difference may be impacted by the manner of testing: our study performed open surgery on cadaveric porcine joints, while clinical work performed arthroscopic surgery on human patients. Our data advances the understanding of selective bundle reconstruction in pediatric cases by providing biomechanical insights into the roles of AM and PL bundles. Ongoing and future in-vivo work will be needed to compare joint laxity and function after graft and intact bundle remodeling.

ACKNOWLEDGEMENTS

We would like to thank the NC State College of Veterinary Medicine and Laboratory Animal Resources for their contribution to this work. Funding provided by NIH (R01 AR071985).

REFERENCES

[1] Colombet, P et al., *Orthop Traumatol-Surg*, 96:S109-S118, 2010. [2] Mall, N et al., *Curr Rev Musculoskelet Med*, 6:132-140, 2013. [3] Sonnery-Cottet, B et al., *Knee Surg Sports Traumatol Art*, 18:47-51, 2010. [4] Ochi, M et al., *Arthrosc - J Arthrosc Relat Surg*, 22:463.e1-e5, 2006. [5] Mastro, A et al., *Eur J Orthop Surg Traumatol*, 23:471-80, 2013. [6] Ohsawa, T et al., *Arthroscopy*, 28:807-817, 2012. [7] Howe, D et al., *J Orthop Res*, 40:1853-1864, 2022. [8] Howe D et al., *bioRxiv*, 2022-11, 2023. [9] Sabat, D et al., *Indian J Orthop*, 49:129-135, 2015.

Multiscale Model Predicts Modulation of Cardiac Remodeling by Intrinsic Ventricular Contractility Before and After Mitral Valve Repair

JH. Bracamonte (1), LJ. Williams (2), BJ. Cooke (2), R. Xie (2), PN. Vardas (2), B. Pat (3), LJ. Dell'Italia (3), L. Watkins (4), JJ. Saucerman (4), JW. Holmes (1)

(1) Department of Biomedical Engineering, University of Alabama at Birmingham, Birmingham, AL, USA
(2) Division of Cardiothoracic Surgery, University of Alabama at Birmingham, Birmingham, AL, USA.
(3) Division of Cardiovascular Disease, University of Alabama at Birmingham, Birmingham, AL, USA.
(4) Department of Biomedical Engineering, University of Virginia, Charlottesville, VA, USA.

INTRODUCTION

Mitral valve repair (MVr) is a highly effective treatment for primary mitral valve regurgitation (MR), with survival rates equivalent to aged matched controls in clinical trials [1]. In some cases, MVr partially reverses hypertrophic remodeling of the left ventricle (LV) [2]. However, the timing of mitral valve surgical repair is critical: once patients develop dyspnea, orthopnea, LV ejection fraction (EF) below 60% or end-systolic ventricular diameter above 40 mm, clinical outcomes are worse [1]. Furthermore, 20% of the patients develop postoperative LV dysfunction even when pre-operative EF>60% [3]. These data suggest that more information is needed to improve the timely management of primary MR towards earlier intervention in some patients, before geometric, hormonal, and signaling changes associated with the gradual progression to heart failure become too entrenched. Recently, LV circumferential strain rate and LV end systolic dimension – both closely related to LV contractility – were identified as important predictors of post-operative ventricular dysfunction [3]. Previously, we developed a multiscale model of cardiovascular mechanics and cardiomyocyte hypertrophy and calibrated it to experimental data from experimental MR and volume overload. Here, we apply the calibrated multiscale model to explore how the ability to compensate for altered hemodynamic loading by increasing intrinsic contractility affects predicted ventricular growth and remodeling following MVr.

METHODS

Multiscale model

The mechanical model consists of a spherical compartment model of the ventricles with time-varying elastance $\left(E(t)\right)$ proposed by Santamore and Burkhoff, coupled to a lumped-parameter model of the circulation. We adjusted parameters previously calibrated to canine experiments to match human cardiovascular dimensions and dynamics by allometric scaling [4]. We added a mitral valve regurgitation resistance (MVRR) bypassing the one-directional valve element in the circulation model to provide an adjustable level of regurgitant flow. The mechanical model is coupled to a network model consisting of 109 nodes and 144 reactions representing established pathways for cardiac myocyte growth driven by various hormones as well as stretch [5]. The network model represents signaling interactions using a logic-based system of equations with variables normalized between 0 and 1, requiring no interspecies scaling [6].

Coupling of the multiscale model

At each growth step (i), the multicompartmental heart model and lumped-parameter circulation model simulated one cardiac cycle, solving iteratively until reaching steady-state. The calculated end-diastolic strains were passed to the stretch input of the signaling network model along with time-varying, data-driven estimates of circulating hormone levels and used to simulate 12 hours of cellular remodeling, producing a normalized Cell Area between 0 and 1. The Cell Area output was used to prescribe the remodeling of the left ventricle at organ scale. All growth was assumed to occur in the fiber direction [7].

Modeling adrenergic contractile reserve.

End-systolic elastance $\left(E_{sys}\right)$ measured at the chamber level from LV pressures and volumes depends both on the intrinsic contractility of the muscle and the geometry of the chamber. For a thin-walled sphere, these quantities are related by the equation:

$$E_{sys}^{i} = \frac{3}{2\pi}\frac{h_0^i}{\left(r_0^i\right)^4}\, e, \tag{1}$$

Where $\left(r_0^i\right)$ and $\left(h_0^i\right)$ are the radius and wall thickness of the unloaded ventricle at a given growth step, and (e) is the intrinsic contractility [7]. Notably, eccentric growth and dilation (increasing r_0^i) decrease E_{sys} even if (e) remains constant. Nagatsu et al observed that dogs with MR maintained normal pump function for several months but displayed systolic dysfunction under the effects of β blockers, suggesting that adrenergic compensation was preserving overall function by increasing

contractility [8]. To examine the remodeling implications of such compensation, we simulate two scenarios: a fully compensated case, where intrinsic contractility increases as much as needed to hold E_{sys} constant, and systolic dysfunction, where compensatory mechanisms are fully exhausted and contractility never increases above baseline.

Modeling chronic MR and Mitral Valve Repair

Simulation for both cases started from the same baseline, representing a healthy adult human. MR was simulated by setting MVRR to produce a regurgitant fraction of 30%. The neurohormonal response to MR was modeled by increasing the network inputs for ANG2, NE, ET1, ANP and BNP by fold changes of 3, 2, 3, and 10 respectively, based on reports from canine MR [9]. The model reached steady state after 6 simulated months. MVr was then simulated by increasing MVRR to prevent backflow. Following reports of partial normalization of neurohormone concentrations in blood following MVr in dogs and humans, ANG2, NE, ET1, ANP and BNP network inputs were decreased to 20% above the healthy baseline [10] following simulated repair in both simulation cases.

Comparisons to Clinical Data

The simulation results are compared to clinical reports of LV dimensions and function before and following mitral valve repair in primary MR patients with higher or lower pre-operative EF [11–13].

RESULTS

Chronic MR

During simulated MR, both model cases predict large increases in end-diastolic (EDV) and end-systolic (ESV) volumes (Fig. 1), accompanied by a drop in EF (Fig.2). The predicted changes are larger for the systolic dysfunction case, a finding that is consistent with the larger volumes and lower EF reported in primary MR patients with systolic dysfunction [11–13]. In the compensated model, increased contractility allows the LV to operate at lower EDP and EDV, reducing fiber strain and the stretch input to the network compared to the systolic dysfunction case. This results in less predicted dilation at steady state for the compensated model.

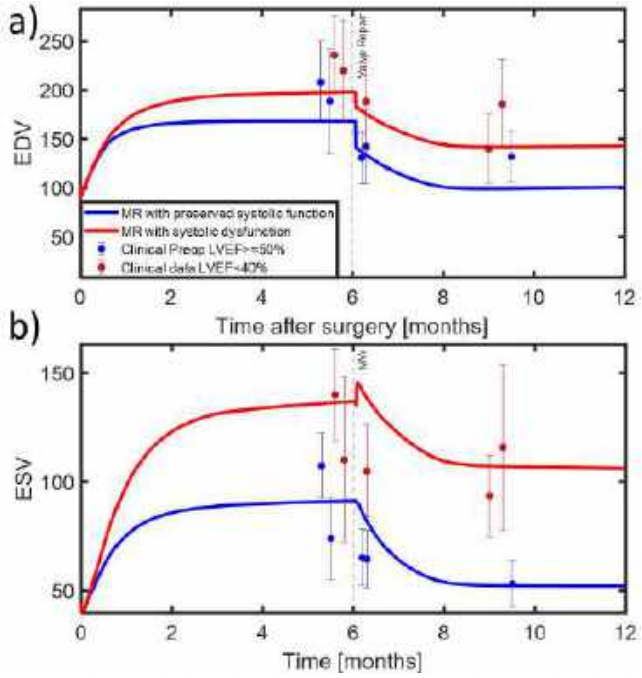

Figure 1. Time evolution of LV dimensions a)EDV, b) ESV for the fully compensated model (blue line), and dysfunctional model (red line) compared to data from patients with pre-op EF>50% (blue dots) and EF<40% (red dots).

Mitral Valve Repair

MVr produces an acute drop in EDV due to the relief of the MR-induced volume overload. The unloading of the LV decreases fiber strain and induces reverse remodeling, leading to further long-term decrease in EDV and ESV (Fig. 1). Without any calibration to the clinical data, the predicted volumes for our generic compensated and dysfunctional models matched reported post-MVr data from patients with higher and lower pre-operative EF (Fig. 1). As expected, simulated MVr initially reduces EF in both model cases, because the LV must eject all blood against the higher resistance of the aorta and systemic circulation (Fig.2) In the compensated model, reverse remodeling gradually restores EF to its preoperative baseline, while in the dysfunctional model EF never fully recovers

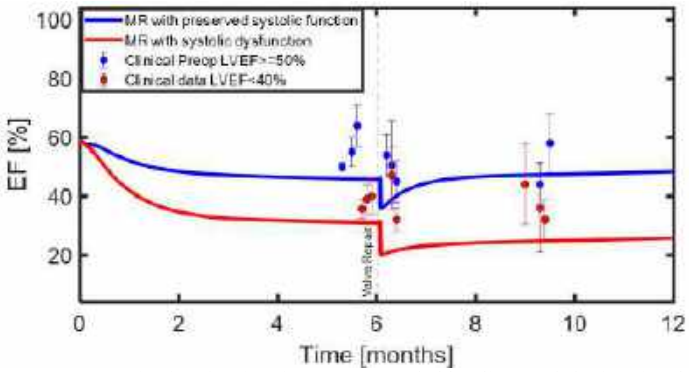

Figure 2. LV ejection fraction for compensated (blue line) and dysfunctional hearts (red line), plotted against clinical data from patients with pre-op EF>50% (blue dots) and EF<40% (red dots).

DISCUSSION

We explored the potential role of compensatory changes in myocardial contractility on ventricular remodeling due to MR and following MVr. Our model predicts that the inability to increase contractility exacerbates dilation in response to chronic MR and impairs reverse remodeling after MVr. This is driven by the higher EDP and EDV required to maintain cardiac output at lower levels of intrinsic contractility, which in turn produces more myocyte stretch and growth mechano-signaling. Systolic dysfunction also prevents the recovery of EF to pre-operatory levels following MVr. The match between reported clinical volumes and this preliminary model is encouraging. Future improvements could include collecting better data on neurohormonal activation post-MVr in patients with different levels of underlying systolic dysfunction and explicitly calibrating models to better match pre-operative states for individual patients or groups of patients.

ACKNOWLEDGEMENTS

This work is supported by the American Heart Association Grant 23POST1026645 (JB) and NIH/NHLBI Grant R01 HL159945 (JH).

REFERENCES

[1] Otto, C. M et al. (2021) Circulation, **143**(5), pp. E72–E227. **[2]** Le Tourneau, T. et al. (2019) Structural Heart, **3**(5), pp. 383–390. **[3]** Zheng, J. et al. (2023) Front Cardiovasc Med, **10**. **[4]** Caggiano, L. R. et al (2022) J Mol Cell Cardiol, **163**, pp. 156–166. **[5]** Khalilimeybodi, A.et al. (2020) PLoS Comput Biol, **16**(12), p. e1008490.**[6]** Clark, A. P.et al. (2024) bioRxiv, p. 2024.01.11.575227. **[7]**Witzenburg, C. et a; M.(2018) J Cardiovasc Transl Res, **11**(2), pp. 109–122. **[8]** Nagatsu, M. et al. (1994) Circulation, **89**(2), pp. 818–826.**[9]** Oyama, M. A., (2009) Journal of Small Animal Practice, **50**(SUPPL. 1), pp. 3–11.**[10]** Le Tourneau, T. et al (2000) J Am Coll Cardiol, **36**(7), pp. 2263–2269. **[11]** Joung, K. W. et al (2021) J Clin Med, **10**(13). **[12]** Zhou, T. et al. (2022) J Thorac Dis, **14**(12), pp. 4803–4814. **[13]**Marciniak, A. et al. (2011) European Journal of Cardio-Thoracic Surgery, **40**(5), pp. 1131–1137.

PHYSEAL-SPARING ACL RECONSTRUCTION PROVIDES BETTER INITIAL JOINT STABILITY AND FUNCTION THAN COMPLETE TRANSPHYSEAL ACL RECONSTRUCTION IN AN EARLY ADOLESCENT PORCINE MODEL

Yukun Zhang (1), Kaan Gurbuz (2), Jeffrey T. Spang (3), Matthew B. Fisher (1,3)

(1) Joint Department of Biomedical Engineering, North Carolina State University and University of North Carolina at Chapel Hill, Raleigh, NC, USA
(2) Kayseri State Education & Research Hospital, Kayseri, Turkey
(3) Department of Orthopaedics, University of North Carolina at Chapel Hill, Chapel Hill, NC, USA

INTRODUCTION

The incidence of pediatric anterior cruciate ligament (ACL) injuries has been increasing [1]. Current pediatric ACL reconstruction (ACLR) techniques include complete transphyseal, partial transphyseal, and physeal-sparing [2]. Complete transphyseal reconstruction is similar to the technique used for skeletally mature patients. Because of the higher risk of growth deformity in the femur, a partial transphyseal technique avoids disturbing the femoral physis for patients with some growth remaining [3, 4]. To further lower the risk of physis disturbance in young patients, physeal-sparing techniques have been developed with both femoral and tibial tunnels in the epiphyses [3]. Patient age is a major factor in technique selection; however, in the pre-adolescent/early adolescent age range (11-14 years old) all three techniques are commonly used [5]. Surgical technique is more associated with the surgeon's fellowship training rather than the joint and ACL function [5]. Yet, the porcine model has shown age-specific joint function during growth [6]. Thus, it is essential to compare ACLR techniques for specific ages using age-specific models. Therefore, the current work aims to compare initial joint stability and function following complete transphyseal, partial transphyseal, and physeal-sparing ACLR within an early adolescent porcine model.

METHODS

A total of 18 deep digital flexor tendons and 18 hindlimbs were collected from early adolescent (4.5 months old) pigs. The specimens were divided into three groups (n=6 each) with different pediatric ACLR techniques: complete transphyseal, partial transphyseal, and physeal-sparing (Figure 1A). A 6-degree-of-freedom robotic testing system with a universal force-moment sensor was used to test joint function (Kuka, simVITRO). The intact joint was first subjected to an 80 N anterior-posterior (AP) load, a 120 N compression, and a 4 N·m varus-valgus (VV) torque at 60° of flexion. Kinematics were recorded, then repeated while recording forces for the intact joint and after capsule removal. The same loading conditions were then applied after ACL transection (ACLT) while recording the kinematics. ACL reconstruction was then performed, using a 4.5-month-old porcine deep digital flexor tendon allograft. For each limb, one reconstruction technique (Fig. 1A) was performed through the tibial and femoral tunnels (8 mm diameter) placed between the anteromedial and posterolateral bundle footprints [6]. Femoral fixation was performed by a #2 FiberWire (Arthrex) with an ABS button (Arthrex), followed by 5 cycles of passive flexion-extension with 22 N pretension for precondition. Tibial fixation was then accomplished by a staple (Arthrex) with 100 N pretension applied to the graft at maximum posterior translation at 40° of knee flexion. The same AP, compression, and VV loads were applied following ACLR. The recorded kinematics were repeated after removing the graft. Then, kinematics from the intact, ACLT, and ACLR states were repeated after removal of the medial collateral ligament (MCL), lateral collateral ligament (LCL), medial meniscus (MMEN), lateral meniscus (LMEN), medial femoral condyle (MCON), and lateral femoral condyle (LCON).

AP tibial translation (APTT) under applied AP load, anterior tibial translation (ATT) under applied compression, and VV rotation under applied VV torques were calculated. Tissue forces were calculated using the principle of superposition. One-way ANOVA with Tukey's HSD was utilized to compare joint laxity between different states as well as tissue force contribution between different surgical techniques. Significance was set at 0.05.

RESULTS

ACL transection (ACLT) resulted in destabilization in the joint under AP drawer (13.4 – 15.1 mm increase). ACLR for all groups partially restored instability, but APTT remained 5.3 – 8.4 mm higher than intact (Figure 1B).

Anterior tibial translation (ATT) under compression increased after ACLT and was restored to intact state after ACLR with partial transphyseal and physeal-sparing (Figure 2A). Change in ATT relative to the intact state was greater in the complete transphyseal group relative to the other two techniques (Figure 2B). Varus-valgus laxity showed similar results, where the partial transphyseal and physeal-sparing

techniques restored the joint laxity to the intact state, but complete transphyseal did not (Figure 2C). No statistically significant difference was observed in the differential VV laxity relative to intact state across techniques, likely due to high variability (Figure 2D).

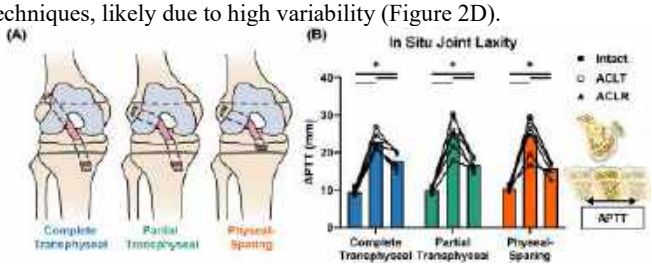

Figure 1: (A) Illustration of pediatric ACL reconstruction surgical techniques. (B) Anterior-posterior tibial translation (APTT) in response to anterior-posterior load was similar between intact, ACL transected (ACLT), and ACLR states. Data points presented with mean and 95% CI. Paired samples were connected. Statistical significance (p<0.05) between states indicated (*).

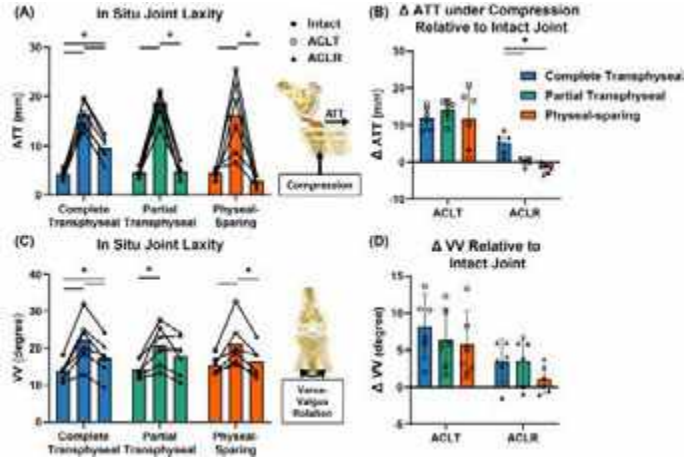

Figure 2: (A) Anterior tibial translation (ATT) under compression following ACLR was comparable to intact state only when using partial transphyseal and physeal-sparing technique. (B) Complete transphyseal led to greater increases in ATT under compression relative to intact state. (C) Varus-valgus (VV) rotation was restored to intact state when using partial transphyseal and physeal-sparing technique but not the complete transphyseal technique. (D) VV increases relative to intact state were variable across techniques. Data points presented with mean and 95% CI. Paired samples were connected. Statistical significance (p<0.05) between states indicated (*).

When performing ACLR with the complete transphyseal technique, the MCL had a greater anterior load contribution (55%) compared to partial transphyseal (33%) and physeal-sparing (28%) (Figure 3A). Under compression, loads shifted from the medial meniscus (MMEN) and medial femoral condyle (MCON) to the lateral structures (Figure 3B). No difference in varus resultant force was found across techniques (Figure 3C). The valgus resultant force taken by MCL increased after all techniques, while physeal-sparing showed the smallest increase in lateral meniscus (LMEN) (Figure 3D).

DISCUSSION

Partial transphyseal and physeal-sparing techniques revealed a superior ability to restore initial joint stability compared to the complete transphyseal technique in an early adolescent porcine joint. The results for anterior stability align with a previous human pediatric study, indicating that physeal-sparing technique resulted in better post-operative anterior joint laxity [7]. Additionally, varus-valgus laxity in

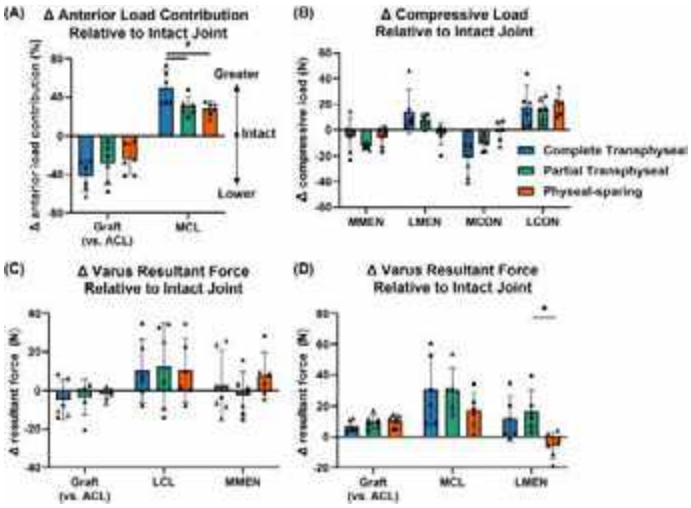

Figure 3: (A) MCL had a higher anterior force contribution under maximum anterior translation when using complete transphyseal technique for ACLR. (B) Compressive load under maximum compression shifted to lateral side following ACLR. (C) No difference in varus resultant force across techniques. (D) Physeal-sparing led to smaller valgus resultant force in the lateral meniscus (LMEN). Data points presented with mean and 95% CI. Statistical significance (p<0.05) between states indicated (*).

the current work was not reduced to the intact level after complete transphyseal ACLR. Tissue-level force data showed that more anterior forces shifted to MCL rather than reconstructed ACL graft following complete transphyseal technique. Femoral tunnel angle could be a factor for the differences between techniques, since the physeal-sparing and partial transphyseal techniques use a sharper angle to avoid crossing the physis. Previous biomechanical work indicated that 10 o'clock position showed better rotatory stability as well as smaller ATT when compared to 11 o'clock position [9]. A limitation of the model is that the differential AP laxity following ACLR ranged from 5.3 mm to 8.4 mm, which was higher than the joint laxity observed from a previous human pediatric patient work (within 2 mm) [5]. Yet, these data were comparable to a porcine biomechanical study with 89 N anterior tibial force after complete transphyseal ACLR (differential laxity of 7.3 mm) [8]. The difference relative to human studies may be due to larger native joint laxity of the porcine joints, along with differences in methods such as cadaveric testing versus clinical exams. A larger sample size may be able to detect additional statistical differences between groups. Identifying the impact of different pediatric ACL reconstruction techniques within age-appropriate joints can lead to a better understanding of operative treatments for ACL injuries in young patients. Future in-vivo work will compare the long-term degenerative outcomes following different pediatric ACLR techniques.

ACKNOWLEDGEMENTS

We would like to thank the NC State College of Veterinary Medicine and Laboratory Animal Resources for their contribution to this work. Funding provided by NIH (R01 AR071985).

REFERENCES

[1] James, E +, *Am J Sports Med*, 49: 4008-17, 2021. [2] McConkey, M +, *Curr Rev Musculoskelet Med*, 4: 37-44, 2011. [3] Ellis, H +, *JBJS Rev*, e22, 2023. [4] Chambers, C +, *Am J Sports Med*, 47: 1353-60, 2019. [5] Patel, N +, *Orthop J Sports Med*, 6(9), 2023. [6] Howe, D +, *J Orthop Res*, 40:1853-1864, 2022. [7] Pagliazzi, G +, *Knee Surg Sports Traumatol Arthrosc*, 31: 206-218, 2023. [8] Debandi, A +, *Knee Surg Sports Traumatol Arthrosc*, 19: 728-735, 2011. [9] Loh, J +, *Arthrosc - J Arthrosc Relat Surg*, 19:297-304, 2003.

SEX-RELATED VARIATIONS IN HEAD IMPACT KINEMATICS DURING CONTROLLED SOCCER HEADING

A. Abbasi Ghiri (1), M. Seidi (1,2), K. Cheever (2,3), M. Memar (2,4)

(1) Department of Mechanical Engineering, University of Texas at San Antonio, San Antonio, TX, USA
(2) Human Performance Research Interest Group, University of Texas at San Antonio, San Antonio, TX, UTSA
(3) Department of Kinesiology, University of Texas at San Antonio, San Antonio, TX, USA
(4) Department of Biomedical Engineering & Chemical Engineering, University of Texas at San Antonio, San Antonio, TX, USA

INTRODUCTION

In the context of sport-related concussions (SRC), soccer, which is one of the female-male comparable impact sports with high head impact rates, significantly contributes to the increasing incidents of SRC. Epidemiological evidence shows higher rates of SRC, longer recovery periods, and more severe post-concussive symptoms among females compared to males in comparable sports such as soccer [1, 2]; however, literature predominantly has focused on male athletes, creating a data gap in sport-related head impacts in females. Moreover, previous studies indicated that the risk and severity of brain damage are correlated with the severity of head impact kinematics and their characteristics such as magnitudes and directions of linear and angular accelerations, angular velocities and impact durations [3]. Despite these findings, there is limited research on the differences in head kinematics characteristics between male and female soccer athletes heading and their potential contributions to the rate of SRC. Therefore, this study aims to explore these differences and examine the role of head mass and impact location in these distinctions using a controlled laboratory experimental setup. The outcome of this study may inform sex-specific SRC prevention and protective strategies in soccer.

METHODS

Thirty-four healthy collegiate soccer players (18 females, 16 males) with an average of 8.2 years of soccer experience participated in this study. The head masses of participants were estimated as a percentage of their body weight (8.26% for males and 8.2% for females [4]). Participants underwent a soccer heading protocol, executing ten frontal head impacts, one minute apart, which is common in soccer heading practice, with a ball launched at 25 mph from 40 feet away [5]. The head kinematics during heading, including x-y-z direction (frontal-sagittal-transverse plane normal direction) and resultant peak angular accelerations (PAA), peak angular velocities (PAV), and peak linear accelerations (PLA), were accurately measured using validated sensor-embedded mouthguards (Prevent Biometrics, MN). Recorded video was utilized to confirm true impacts and identify the location of impacts on the head, including the front high and top front. Due to the frontal soccer heading protocol, the y-direction and resultant of peak angular accelerations and velocities (PAA-y, PAA-R, PAV-y, PAV-R) and resultant and x-z-direction of peak linear accelerations (PLA-x, PLA-z, PLA-R) were selected for further analyses. The effect of sex and head location of impacts on the kinematics parameters were analyzed using Multivariate Analysis of Variance (MANOVA). The sex, location and their interaction (sex*location) were considered as the main effects in full factorial MANOVA analysis with and without the head mass as a covariate to investigate its effect on the head kinematics. Additionally, pairwise comparison was implemented to explore the effect of the sex factor on each specific level of the location factor. Significance level: 0.05.

RESULTS

Peak Angular Accelerations: Sex had a significant effect on head peak angular accelerations (PAA-y and PAA-R), with greater magnitudes in females, especially for top front locations (Table 1, Figure 1a). However, this effect became insignificant when considering head mass as the covariate. Significant and marginally significant (p-value <0.1) effects of head mass were observed on PAA-R and PAA-y, respectively, in analysis with head mass as the covariate. While the location of impact did not significantly affect PAA-y and PAA-R in both MANOVA analyses, the interaction term (sex*location) showed a significant effect (Table 1).

Peak Angular Velocities: Head peak angular velocities (PAV-y and PAV-R) were not influenced by sex, but were significantly affected by impact location, with a higher magnitude for front high location regardless of adjusting for the head mass as a covariate (Table 1). Also, the interaction of sex and location factors showed a significant effect on PAV-y and a marginally significant effect on PAV-R (Table 1).

Peak Linear Accelerations: Sex did not significantly influence peak linear accelerations (PLA-x, PLA-z, PLA-R) in both MANOVA analyses; however, by including head mass as a covariate, a significant effect of head mass was observed on all three peak linear acceleration

parameters (Table 1, Figure 3a). Also, location and sex*location interaction terms significantly influenced PLA-x and PLA-z, and had no significant influence on PLA-R (Table 1), with or without the head mass as the covariate.

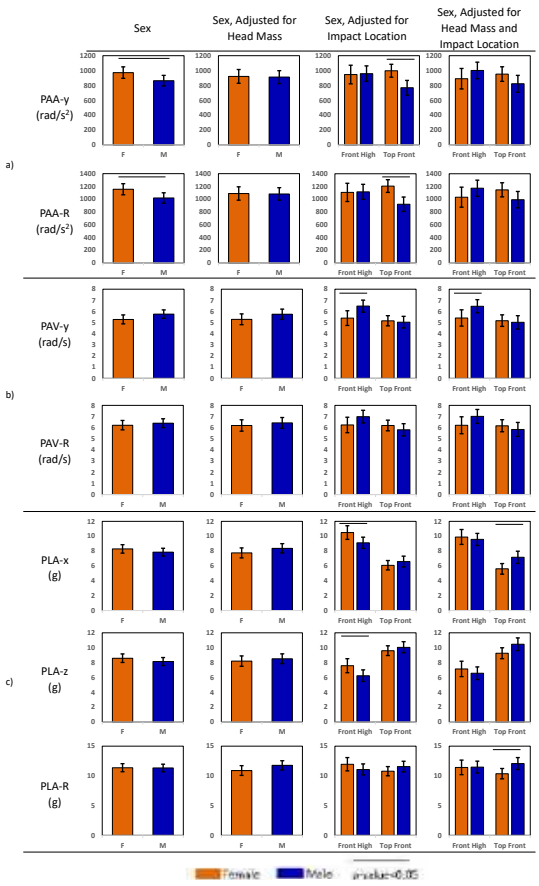

Figure 1: Mean and standard deviation of head kinematic parameters including a) PAA-y and PAA-R, b) PAV-y and PAV-R, and c) PLA-x, PLA-z and PLA-R. MANOVA results with (columns 2 and 4) and without (columns 1 and 3) adjustment for the head mass (as the covariate) are included.

Table 1: Comparison results (p-values) for all head kinematic parameters considering factors including sex, location, and their interactions with (b) and without (a) the head mass as a covariate

		parameter		PAA-y	PAA-R	PAV-y	PAV-R	PLA-x	PLA-z	PLA-R
a) Univariate tests without the head mass as covariate	Factors	Sex		**0.04**	**0.02**	0.09	0.54	0.27	0.27	0.92
		Location		0.19	0.44	**0.00**	**0.04**	**0.00**	**0.00**	0.47
		Sex*Location		**0.02**	**0.02**	**0.03**	0.06	**0.02**	**0.03**	0.08
	Pairwise Comparison	Sex comparison (adjusted location)	Front high	0.88	0.92	**0.01**	0.10	**0.02**	**0.03**	0.23
			Top front	**0.00**	**0.00**	0.73	0.30	0.31	0.37	0.20
b) Univariate tests with the head mass as covariate (Adjusted for the head mass)	Factors	Head mass		0.06	**0.03**	0.93	0.86	**0.01**	**0.05**	**0.04**
		Sex		0.89	0.93	0.25	0.57	0.25	0.57	0.19
		Location		0.28	0.59	**0.00**	**0.04**	**0.00**	**0.00**	0.62
		Sex*Location		**0.02**	**0.02**	**0.03**	0.05	**0.02**	**0.03**	0.08
	Pairwise Comparison	Sex comparison (adjusted location)	Front high	0.25	0.20	**0.04**	0.14	0.65	0.42	0.95
			Top front	0.12	0.11	0.74	0.47	**0.01**	0.06	**0.02**

DISCUSSION

Peak Angular Accelerations: The effect of sex on peak angular accelerations (PAAs) in soccer heading remains a subject of debate in the literature due to variations in the accuracy of head kinematic measuring systems and experimental set-ups employed. While some studies have reported that sex does not significantly affect PAAs [6], the majority of research, including our own, has observed significantly higher PAAs in females compared to males in soccer heading [7, 8]. This observation underscores the role of sex as a determinant in the brain injury outcomes of soccer heading, given the consistent reports of a strong correlation between PAAs and brain tissue deformations, as well as brain pathology [3]. This finding aligns with epidemiological studies indicating a greater incidence of concussions in high school and collegiate female soccer athletes compared to their male counterparts [9, 10]. Our results also indicated that the significant impact of sex on PAAs diminishes when accounting for head mass as a covariate, suggesting head mass serves as a mediating factor. This could explain why females, who typically have lower head mass, experience higher PAAs. This aligns with the previous studies that demonstrated head mass not only exhibits a significant adverse correlation with the peak angular and linear accelerations but also varies between sexes [7, 11].

Peak Angular Velocities: This study investigate PAVs of the head during soccer heading, a crucial parameter that is lacking in the literature and is highly correlated with the severity of brain injury [3]. No significant effect of sex and head mass was observed on PAVs. Logically, head mass primarily influences the rate of velocity change (accelerations); explaining why a significant effect of head mass was observed on PAAs and PLAs but not PAVs. Additionally, the higher PAVs for front-high impacts compared to top-front impacts may be attributed to the shorter moment arm in front-high head impacts.

Peak Linear Accelerations: Similar to PAAs and due to different experimental setups and sensor accuracy, literature regarding the effect of sex on the PLAs is inconsistent. While some studies suggested females may experience higher PLAs [8], our findings are in line with the majority of studies that reported no significant effect of sex on PLAs [6, 12, 13]. The significant effect of head mass on PLA parameters aligns with Newton's second law and is in agreement with the literature.

Conclusion: Our findings, showing that females experience higher PAAs, possibly due to their lower head mass, align with epidemiological evidence indicating a greater rate of SRC among female soccer players than males. Future research could investigate other factors such as hormonal dynamic, brain structure, neck stiffness, and heading techniques that contributes to the sex-based variations in the vulnerability, rate, and outcomes of SRC and identify potential interventions to reduce PAAs in female players, such as adjusting ball pressure, employing headgears, and enhancing heading techniques.

ACKNOWLEDGEMENTS

Funding support was provided by NSF-2138719 and the RIG, BHC, CONNECT program at the University of Texas at San Antonio

REFERENCES

1. McGroarty, N.K., et al. **8**(7): p. 2325967120932306, 2020.
2. Dave, U., et al.: p. 1-9, 2021.
3. Hajiaghamemar, M., et al., J Biomech Eng. **142**(3), 2020.
4. Plagenhoef, S., et al., Res Q Exerc Sport. **54**(2): p. 169-178, 1983.
5. Huibregtse, M.E., et al. **15**(10): p. e0239507, 2020.
6. Dezman, Z.D., et al., Sports Health. **5**(4): p. 320-6, 2013.
7. Bretzin, A.C., et al., Sports Health. **9**(2): p. 168-173, 2017.
8. Caccese, J.B., et al., Res Sports Med. **26**(1): p. 64-74, 2018.
9. Marar, M., et al., Am J Sports Med. **40**(4): p. 747-55, 2012.
10. Lincoln, A.E., et al., Am J Sports Med. **39**(5): p. 958-63, 2011.
11. Caccese, J.B., et al., Sports Biomech. **17**(4): p. 462-476, 2018.
12. Dorminy, M., et al., Brain Inj. **29**(10): p. 1158-1164, 2015.
13. Tierney, R.T., et al., J Athl Train. **43**(6): p. 578-84, 2008.

TEMPERATURE EFFECT ON IN-VITRO SINUS FLOW AFTER AORTIC VALVE REPLACEMENT

A. Bshennaty (1), B. Vogl (1), A. Sularz (2), M. Alkhouli (2) and H. Hatoum (1,3)

(1) Department of Biomedical Engineering, Michigan Technological University, Houghton, MI, USA
(2) Department of Cardiovascular Medicine, Mayo Clinic, Rochester, MN, USA
(3) Health Research Institute, Center of Biocomputing and Digital Health and Institute of Computing and Cybersystems, Michigan Technological University, Houghton, MI, USA

INTRODUCTION

Aortic valve replacement (AVR), whether surgically or percutaneously, is the standard procedure for patients suffering from aortic stenosis (AS) [1]. Leaflet thrombosis and calcification are common complications that arise following AVR due to the changes in the hemodynamics that are imposed by the non-native valve [2]. Therefore, it is imperative that the various commercially available valves are adequately assessed for their impact on the flow dynamics in the sinus and the aorta, which has been primarily performed through in-vitro experimentation based on the ISO standard [3]. Some research studies run their experiments with the blood analog solution at room temperature [4, 5]. Other studies have utilized the blood analog solution at body temperature [6].

It is known that temperature variations can impact the viscosity of fluids [7, 8]. Changes in viscosity may lead to different hemodynamics in the sinus that may impact the translationability of the results to clinical cases. Moreover, in the assessment of self-expanding valves, the complete expansion of the stent is expected to occur at the physiological temperature (37°C). However, Hatoum et al. have shown that the valve geometry exhibited no significant differences when at room temperature and when at body temperature [9]. To date, no comparative study has been performed to assess the impact of temperature in an experimental setting.

The aim of this study is to compare the in-vitro sinus hemodynamics after AVR between a blood analog at room temperature and at body temperature. This study may have implications on the translation of results obtained from experimental valve assessment.

METHODS

The blood analog used in this experiment is a mixture of 37.6% by weight glycerin and water, in line with previous experimental work. The assessment of the flow dynamics in the presence of a bioprosthetic aortic valve was carried out in a left heart simulator. The experimental setup, shown in **Fig.1**, consisted of a reservoir that feeds a bladder pump, which represents the left atrium and left ventricle, respectively.

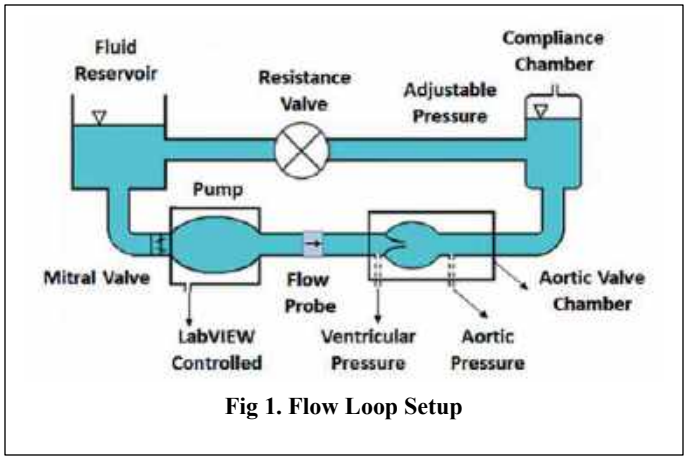

Fig 1. Flow Loop Setup

A mechanical valve is placed between them to prevent reverse flow, and a 23mm Edwards SAPIEN 3 Ultra valve is placed in an acrylic chamber downstream of the pump. The cardiac output was manipulated using a gate valve and a compliance chamber to achieve a flow rate of 5 L/min under a pressure of 120/80 mmHg. The experiment was run once with the solution at room temperature (24°C). Then, the solution was heated to body temperature (37°C), and its temperature was maintained throughout the experiment. In order to perform particle image velocimetry (PIV), the solution in the reservoir was seeded with Rhodamine B particles, which were illuminated using a Single Cavity Diode Pumped Solid State, High Repetition Rate Laser (Photonic Industries, NY, USA). The laser was reflected onto the acrylic chamber along the sinus to be captured by a high-speed CMOS camera (Photron, Inc). The timeseries images were collected at the rate of 4000 frames

per second and introduced to a multi-pass cross-correlation PIV algorithm in order to calculate the velocity field. The vorticity and shear stress data were obtained through the post-processing of the PIV frames.

RESULTS

Fig.2 shows the velocity vectors and vorticity contours in the sinus at peak systole and at deceleration at both temperatures. At peak systole, the sinus seems to exhibit slightly higher vorticities at body temperature. At deceleration, the sinus that is at body temperature seems to exhibit an elevated vorticity when compared with the one that is at body temperature, with no significant differences in the velocities. Overall, the sinus vortex was spotted in both cases rotating counterclockwise.

In order to better quantify the velocity differences, the magnitudes of the velocity and shear stress were extracted, and their probability density functions (PDF) over the full cardiac cycle were plotted in **Fig.3**. The plots indicate the presence of slightly elevated velocities and shear stress values in the sinus at body temperature compared to those at room temperature.

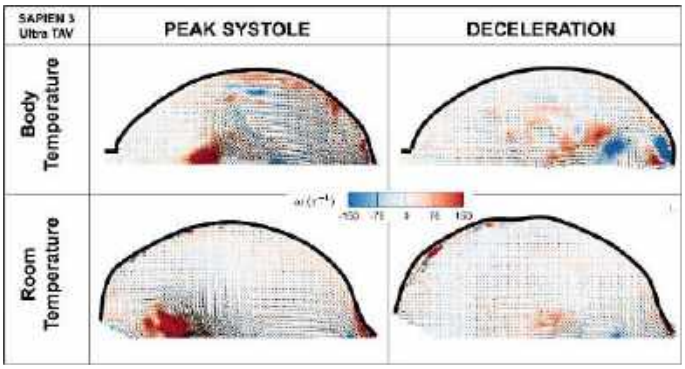

Fig 2. Peak Systole and Deceleration Frames

DISCUSSION

The results of this study have shown that the temperature of the solution has some implications for in-vitro studies assessing sinus flow. In particular, running similar experiments at room temperature may provide an underestimation of velocity and an overestimation of shear stress, albeit slightly. Typically, an increase in temperature correlates with a slight decrease in viscosity which may lead to higher velocities. This seems to be the case for the flow in the sinus, although the difference was not major (1.15 m/s vs. 1 m/s).

While differences are present, it seems that using room temperature in stasis-related diseases assessment such as leaflet thrombosis and calcification presents a more conservative approach compared to using body temperature. This means that an evaluation of blood stasis with a blood analog at room temperature does not necessarily guarantee the same evaluation at body temperature. However, because the difference is minor, studies that use blood analogs without maintaining the body temperature throughout the in-vitro assessment still have valuable information and insight on flow dynamics and disease relationship.

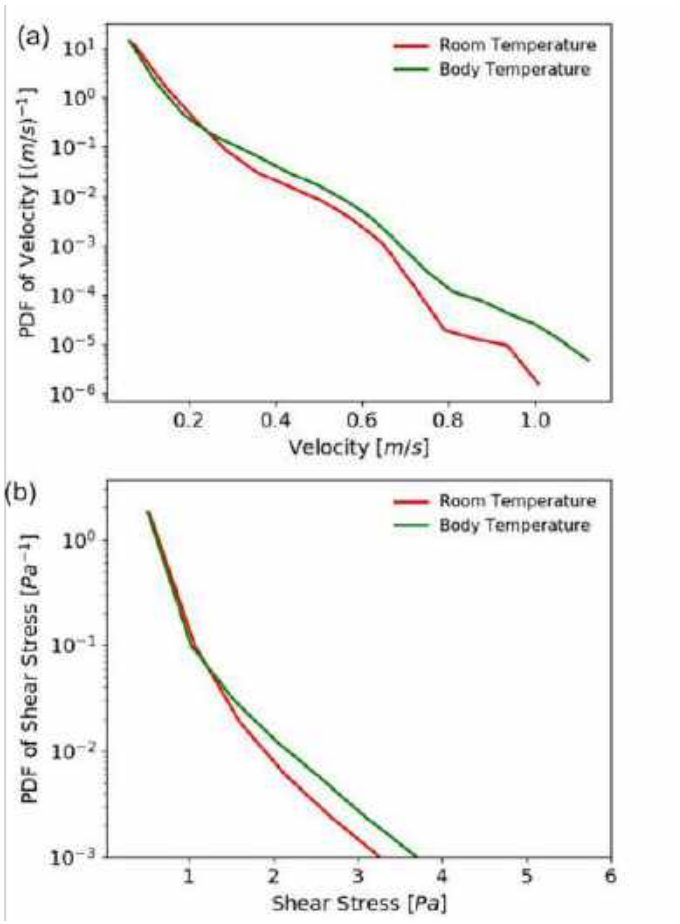

Fig 3. PDFs of (a) velocity and (b) shear stress in the sinus at room and body temperatures all over the cardiac cycle

REFERENCES

1. Spadaccio C et al., *F1000Research*, 8, 2019.
2. De Marchena E et al., *JACC CI*, 8(5):728- 39, 2015.
3. Standard AN. Cardiovascular implants: cardiac valve prostheses. ISO 5840-1, 2021.
4. Hatoum H et al.,*JTCS*, 154(1):32-43, 2017.
5. Trusty PM et al., *JACC:CI*, 12(13):1288-90, 2019.
6. Barannyk O et al., *JBP*, 43:279-96, 2017.
7. Inman BA et al., *IJH*, 29(3):206-10, 2013.
8. Pop GA et al., *NHJ*, 10(12):512, 2002.
9. Hatoum H et al., *JB*, 74:171-9, 2018.

BIOMECHANICAL ANALYSIS OF DUAL MOBILITY INTRAPROSTHETIC DISSOCIATION

Joshua T. Bland (1), Alexander W. Hooke (1), Allison M. Tanner (1), Katherine E. Mallett, M.D. (2), Sergio F. Guarin-Perez, M.D. (2), James S. Fitzsimmons (1,2), Chunfeng Zhao, MD (1,2) Michael J. Taunton, M.D. (2), Rafael J. Sierra, M.D. (2)

(1) Biomechanics Core, Mayo Clinic, Rochester, MN, USA
(2) Department of Orthopedic Surgery, Mayo Clinic, Rochester, MN, USA

INTRODUCTION

Dual-mobility hip implants were invented in France in the mid 1970's to increase range of motion.[1] Although, dual-mobility (DM) implants have been used in Europe since the 1970's, the adoption of their use in the United States is relatively recent. The FDA approved the use of DM implants in 2009.[1]

Rather than having a single bearing, a DM implant contains two bearing surfaces; a head that rotates within a polyethylene insert which subsequently rotates within an acetabular shell. This unique design reduces the risk of dislocation in total hip arthroplasty.[2-4] Although dislocations are rare for DM implants, there is a specific dislocation unique to DM implants called an intraprosthetic dissociation (IPD). During an IPD, the femoral head comes completely out of the polyethylene insert. While it remains unclear how an IPD happens *in-vivo*, there are documented accounts of IPDs occurring during the treatment of large-head dislocations.[5] A surgical intervention is necessary when an IPD occurs unlike a large-head dislocation which can be treated with manual manipulation.[5]

There is little knowledge on the torques and forces that cause IPDs in dual-mobility implants. The aim of this study was to investigate the forces, torques and energy that cause DM implants from various companies to dissociate.

METHODS

Samples

Polyethylene inserts from the dual mobility hip implants of five different companies were tested for this study.

- DePuy Synthes Pinnacle Dual Mobility, Crosslinked (n=3)
- Link Orthopedics E-Dur Dual Mobility System, Crosslinked (n=3)
- Smith & Nephew Polarcup Dual Mobility, Crosslinked (n=3)
- Stryker Modular Dual Mobility, Crosslinked (n=3)
- Zimmer Biomet G7 Dual Mobility, Crosslinked (n=3)
- Zimmer Biomet G7 Dual Mobility, Vitamin E Infused (n=2)

Testing Setup

All mechanical tests were executed on a servohydraulic test machine (MTS Systems, Eden Prairie, MN). A femoral stem (BioMet, Size 10, 130mm, Type 1 Taper) was attached to a custom fixture for all tests. In addition, a ceramic head (28mm diameter) was epoxied to the neck of the stem. The polyethylene inserts were attached to or resting on the bottom fixture for all tests. Below the bottom fixture was a 15000N capacity load cell that was used to measure loads during the tests.

Mechanical Tests

Three different procedures were used to test the polyethylene inserts (Figure 1). The first procedure was always an assembly force test. During the press-in test, the proximal side of the polyethylene insert rested in a short depression in the bottom fixture plate. The stem moved down at 1mm/s and stopped when the head was completely in the polyethylene insert.

Implants were disassembled using 2 different techniques: a pull-out and a lever-out. The pull-out procedure started with the head already in the polyethylene insert. A ring held the polyethylene insert against the bottom plate. The inner diameter of the ring was 1mm less than the insert's outer diameter. The stem moved up at 1mm/s and stopped when the head was completely out of the polyethylene insert.

The lever out procedure also started with the head already in the polyethylene insert. Similar to the pull-out procedure, a ring held the polyethylene insert against the bottom plate. In addition, the bottom plate was connected to a linear stage to prevent binding. The upper fixture applied a downward force to apply a torque to the stem. The upper fixture lowered at 9.75mm/s, which resulted in around 5 degrees/s of rotation at the impingement point, until the head was completely out of the polyethylene insert.

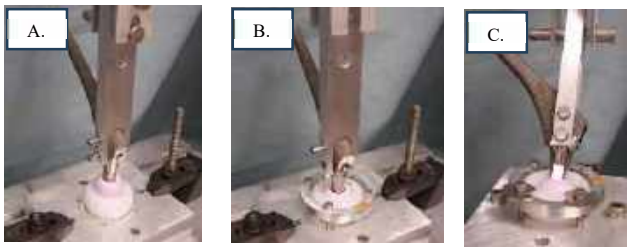

Figure 1: Test configuration for (a) press-in test (b) pull-out test and (c) lever-out tests.

Test Sequence

Each insert underwent a series of 6 total tests, 3 assemblies via press-in and 3 disassemblies via lever- and pull-out. Table 1 shows the testing sequence structure used for the insert models.

Table 1: Test Sequence for each vendor.

Sample #	Test Sequence	Trial # 1	2	3	4	5	6
1	A	Press-In	Lever-Out	Press-In	Pull-out	Press-In	Lever-Out
2	B	Press-In	Pull-Out	Press-In	Lever-Out	Press-In	Pull-Out
3	A	Press-In	Lever-Out	Press-In	Pull-out	Press-In	Lever-Out

*Zimmer Biomet ArCom had 2 samples with sequence B and 1 with sequence A

Data Analysis

For each trial a custom MATLAB script was used to determine the peak force. The component of the peak force normal the stem was used to calculate the dissociation torques for the lever-out trials. The energy values were determined by calculating the area underneath the load-displacement and torque-angle curves.

RESULTS

The maximum assembly force decreased for each repeated assembly (Figure 2). In addition, the maximum assembly force of the first assembly was statistically different between the companies ($p<0.01$). The Link E-Dur Dual Mobility System had the greatest maximum assembly force (1831.9±81.95N), maximum pull-out force (20589.89N), and dissociation torque (38.95±2.79Nm) as seen in Figure 2, Table 2, and Table 3. It should also be noted that when comparing the Zimmer Biomet crosslinked insert with the Zimmer Biomet vitamin E infused insert, the vitamin E infused insert had larger max assembly forces, and pull-out forces.

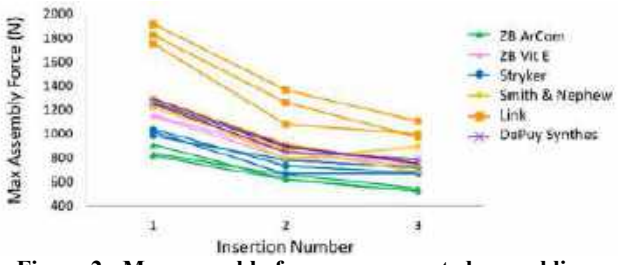

Figure 2: Max assembly force over repeated assemblies.

Table 2: Force and energy data for first pull-out trial.

Vendor	Pull-Out Force (N) Average	Std. Dev.	Sample Size	Pull-Out Energy (J) Average	Std. Dev	Sample Size
Zimmer Biomet ArCom	1167.03	55.14	N=2	5.35	0.46	N=2
Zimmer Biomet Vit E	1431.42	-	N=1	6.09	-	N=1
Stryker	1556.93	-	N=1	7.13	-	N=1
Smith & Nephew	1478.11	-	N=1	6.4	-	N=1
Link	2059.89	-	N=1	9.27	-	N=1
DePuy	1736.45	-	N=1	8.56	-	N=1

Table 3: Force and energy data for first lever-out trial.

Vendor	Lever-Out Force (N) Average	Std. Dev.	Sample Size	Lever-Out Energy (J) Average	Std. Dev	Sample Size
Zimmer Biomet ArCom	17.70	-	N=1	4.35	-	N=1
Zimmer Biomet Vit E	24.16	-	N=1	6.26	-	N=1
Stryker	27.53	-	N=1	*	-	N/A
Smith & Nephew	23.26	1.31	N=2	6.95	0.42	N=2
Link	38.95	2.79	N=2	11.05	1.2	N=2
DePuy	37.61	2.92	N=2	11.82	2.32	N=2

*Incomplete force-displacement curve

DISCUSSION

There is limited published data on assembly and dissociation forces for DM polyethylene inserts. Furthermore, not much is known about the differences in assembly and dissociation forces between DM implants from different companies. This study has shown that there are measurable differences between products lines which has potential implications for creating dissociation based mechanical testing standards. Any testing standards for dissociation should focus on the lever-out procedure as this is a more realistic simulation of *in-vivo* mechanics. This study also showed that the maximum assembly forces decreased after repeated assemblies. This finding indicates that polyethylene inserts should be replaced following dissociations.

The implant with the greatest resistance to dissociation was the Link E-Dur Dual Mobility System. This implant happens to have a vitamin E infused polyethylene liner. Interestingly, the Zimmer Biomet implant with vitamin E infused polyethylene had greater assembly, max pull-out, and max lever-out forces than the Zimmer Biomet crosslinked polyethylene insert. Vitamin E infused polyethylene liners were originally developed for their improved wear characteristics, but it has shown to improve strength as well.[6]

One of the limitations of this study is all testing was done at room temperature. Future studies should also conduct testing at body temperature to better simulate *in-vivo* conditions. Another way to better simulate *in-vivo* conditions would be induce wear of the insert before testing. Additionally, the confined number of samples from each company combined with the order effect of repeated assemblies, limited the number of data points we could use for analysis. The current experimental design makes it difficult to explore the contribution of individual design characteristics to the overall performance of the polyethylene inserts. It would be useful to know how different design and material choices such as diameter, retention ring shape, and polyethylene vitamin E infusion affect the performance independently. Future work should ultimately focus on determining what differences between manufacturers are clinically meaningful to inform minimum dissociation load standards.

ACKNOWLEDGEMENTS

This study was supported by the Mayo Clinic Biomechanics Core and a grant from The Hip Society.

REFERENCES

[1] De Martino I, et al., *World J Orthop* 2014, 5(3):180-187.
[2] Hartzler MA, et al., *Clinical orthopaedics and related research* 2018, 476(2):293-301.
[3] AAOS: American Joint Replacement Registry (AJRR): 2022 Annual Report. In: American Academy of Orthopedic Surgeons.
[4] Wright-Chisem J, et al., *Bone Joint J* 2022, 104-b(1):8-11.
[5] Mallett KE, et al., *JB JS Open Access* 2023, 8(3):e22.00108.
[6] Pletcher D., et al., Poster No. 1868, *ORS 2014 Meeting*.

COMPUTATIONAL AND MULTI-SCALE MECHANICAL ANALYSIS OF SOY GEL EXTRUSION PROCESS

Marco A. Fielder (1), Arun K. Nair (1)

(1) Mechanical Engineering, University of Arkansas, Fayetteville, AR, United States

INTRODUCTION

Evaluating the mechanical properties of soybean seeds and products derived from soy processed into gel for food applications is important for optimal storage [1]. For example, stress cracking of soybean seeds can occur during harvest, transport, or drying which impacts the quality of subsequent soy products and increases production costs [2]. Additionally, the molecular composition of the soybeans can affect different properties of the processed product. For example, oils with a higher linolenic acid content have improved shelf life [3]. Furthermore, the texture and firmness of food analogs derived from soybean should match that of the foods they substitute such as meats. For example, more cohesive meats like steak will have a different texture and firmness than meats like sausage or nuggets. The texture and firmness of foods can be quantified through measurements of microstructure and mechanical stress. Additionally, soy-based materials are also used in tissue scaffolds for applications in wound healing [4].

Extrusion is one preferred process for developing soy-based meat analogs. At the molecular level during extrusion, shearing promotes the stretching and orientation of unfolded protein along extrusion direction, forming layers like meat's fibrous structure. The shear and pressure expose reactive sites to enable intermolecular crosslinking and promotes protein aggregation. This aggregation forms continuous and dispersed phases that mimic meat texture. At high water levels, hydrogen bonds play a dominant role in extrudates' texture and stabilizing the structure.

This study thus develops a computational multi-scale model to correlate soybean seed composition to soy-based product mechanical properties which would be beneficial to quickly determine the optimal seed type. Furthermore, this study develops a model to understand the biomechanics of soybean and quantify how water content and pressure affect hydrogen bond formation, as well as quantifies the effect of extrusion on soy gel texture and firmness, which would be extremely beneficial in the identifying the optimal processing parameters for tuning the extrudate's texture, as well as tuning matrix texture for cell growth in tissue scaffolds.

METHODS

This study evaluates several experimental studies from literature to develop a regression model of predicted soy gel pore size and seed mechanical properties for different seed types [2, 5-7]. The mechanical properties are input into a finite element model with FEBio software to simulate compression of a soybean seed to quantify seed firmness (maximum stress). The properties are evaluated with machine learning (ML) classification models using Scikit Learn software to correlate different seed types with specific mechanical properties (Figure 1 (a)).

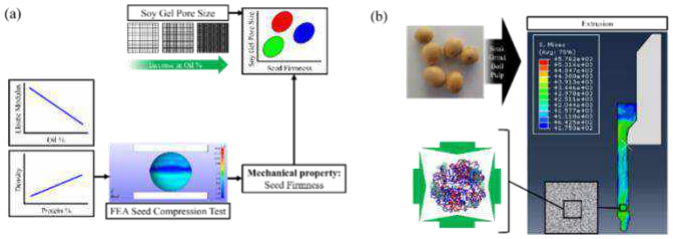

Figure 1: (a) Schematic correlating seed composition to mechanical properties, (b) Schematic of computational evaluation of soy gel micro and molecular structure, and mechanical extrusion tests.

Next, soy gel at the atomic scale is modeled with molecular dynamics (MD) using the 11S soy protein data bank (PDB) with code 3AUP and using OpenMM software and the CHARMM force field to simulate and quantify the formation of hydrogen bonds during compression and with different water contents. Lastly, we use Abaqus software [8] to simulate extrusion of soy gel and quantify the texture (change in dispersed phase aspect ratio), and firmness (maximum stress), as seen in Figure 1 (b) of the observed classes of soy gel for the evaluated seed types (Silken, Soft, and Firm). The gel is modeled as a

viscoelastic plastic material with associated coefficients. The geometry of the gel extrusion is of a cylindrical soy gel sample extruded through a conical steel nozzle. As the gel is extruded, the maximum stress, and overall stress distribution is calculated, and the mechanisms visualized.

RESULTS

From the evaluated mechanical properties of each seed type studied, we find three distinct clusters of seeds: seeds that produce softer gels, seeds that produce firmer gels, and strong seeds that are more resistant to stress cracking (Figure 2). We evaluate these clusters using four ML classification models: Random Forest (RF), Gradient Boost (GB), Support Vector (SV), and Multi-Layer Perceptron (MLP). The GB model was found to be the most accurate at 99%. The three observed classes are used in the soy gel extrusion models to accurately model the extrusion process with three different soy gel types: Silken (soft gels in Cluster A), Soft (strong seeds resistant to fracture in Cluster B), and Firm/Extra Firm (firm gels in Cluster C).

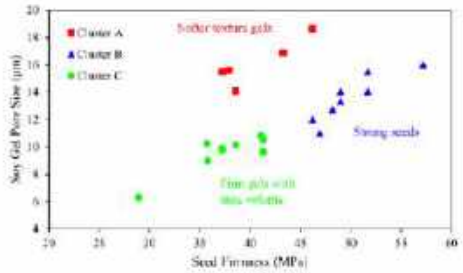

Figure 2: Seed Firmness vs. Soy Gel Pore Size.

Evaluation of the molecular dynamics models shows that hydrogen bonding increases for both increased pressure (1 atm to 1 MPa), and increased water content (6% to 80%) by 1.2% and 556% respectively. For the extrusion of the three soy gel classes, it is observed that the maximum stress increases as the gel elastic modulus increases but reaches a plateau in the Firm class (Figure 3 (a)). The stress also becomes more concentrated as the gel modulus increases (Figure 3 (b)).

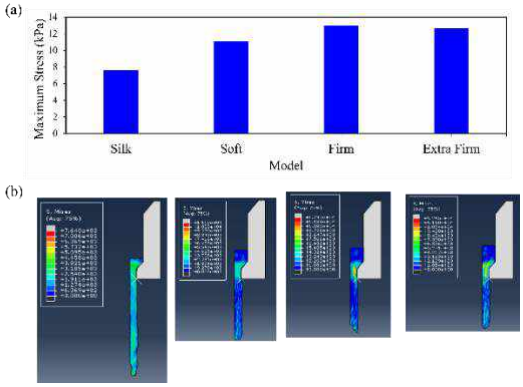

Figure 3: (a) Maximum Stress, and (b) stress distribution for three classes of soy gels

It is observed that as the soy gel becomes firmer, there is a decrease in the percent decrease in the Dispersed Phase Aspect Ratio (DPAR) due to extrusion. In Figure 4 (a) the Soft gel DPAR decreases by ~66%, while the Firm and Extra Firm DPAR decrease by ~33% and ~55% respectively. Figure 4 (b) shows the dispersed phase (not green) geometry before and after extrusion.

DISCUSSION

For the ML model, a higher weight value shows that a variable has a more significant effect on the output. Based on the value of the computed weights the components with the most effect on gel firmness were (in order): oil, linolenic, linoleic, and palmitic percentages. Our results agree with literature that a higher oil content leads to smaller pores (not novel), but linolenic, linoleic, and palmitic acids have the most effect on predicted pore size than the other fatty acids, and a higher percentage of any of these fatty acids results in larger pore sizes compared to the other fatty acids, which is novel. During extrusion, Silken gels extrude more linearly and with less defects, while once the gel is in the Firm class, and there is little change in the maximum stress as the elastic modulus increases.

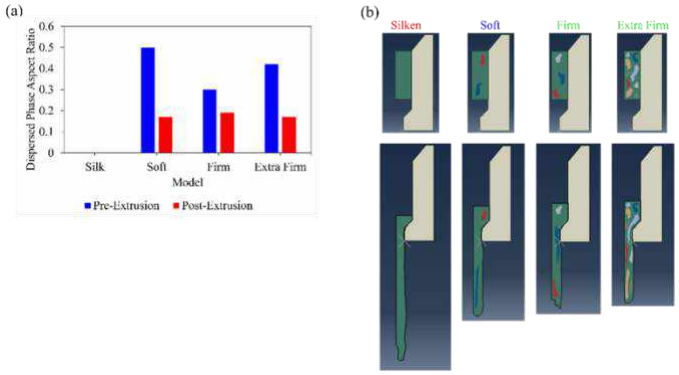

Figure 4: (a) Pre- and (b) post-extrusion dispersed phase aspect ratio for three classes of soy gels

There is also more change in the dispersed phase of softer gels than in firmer gels (66% vs. 33%) due to extrusion. These results are significant for quickly determining the optimal seed types to plant for desired characteristics, as well as for identifying the optimal processing parameters for tuning soy extrudate's texture and firmness for applications such as food analogs and tissue scaffolds for wound healing to match the mechanical properties of the materials they substitute such as meat in food applications, or bone and cartilage for wound healing applications.

ACKNOWLEDGEMENTS

We acknowledge the support from U.S. Soybean Farmers and Purdue University, West Lafayette, IN.

REFERENCES

[1] Kibar, H., and T. Ozturk. "Physical and mechanical properties of soybean." International Agrophysics 22.3 (2008): 239-244.

[2] Liu, M., et al. "Mechanical properties of the soybean cotyledon and failure strength of soybean kernels." Transactions of the ASAE 33.2 (1990): 559-0566

[3] Cao, Pan, et al. "Multi-omics techniques for soybean molecular breeding." International Journal of Molecular Sciences 23.9 (2022): 4994

[4] Ben-Arye T, at. al., 2020. Textured soy protein scaffolds enable the generation of three-dimensional bovine skeletal muscle tissue for cell-based meat. Nature Food. 1(4):210-220.

[5] Kuźniar, Piotr, et al. "Physical and chemical properties of soybean seeds determine their susceptibility to mechanical damage." 2016.

[6] Zemdirbyste-Agriculture 103.2 (2016): 183-192.

[7] Ningtyas, Dian W., et al. "Effect of different types and concentrations of fat on the physico-chemical properties of soy protein isolate gel." Food Hydrocolloids 111 (2021): 106226.

[8] ABAQUS (2023) Analysis User's Manual. Version 6.12, Dassault Systemes Simulia, Inc.

FEMTOSECOND LASER GENERATED MICRO-CUTS IN PARTIALLY RECRUITED COLLAGEN FIBERS SHOW MICRO-FORCES RELEVANT ON THE MICROSCALE

Miriam Bohlmann Kunz (1), Hannah Schilpp (1), Po-Yi Lee (2), Ian A. Sigal (1,2)

(1) Department of Ophthalmology, University of Pittsburgh, Pittsburgh, PA, USA
(2) Department of Bioengineering, University of Pittsburgh, Pittsburgh, PA, USA

INTRODUCTION

One important mechanical property of collagenous soft tissues is their non-linear stress-strain behavior curve (Figure 1). This curve demonstrates that very little force is required to stretch collagen (toe region), up to a certain point after which an increasing amount of force is required to further stretch the tissue and fibers. This nonlinearity is largely attributed to the morphological property crimp, where at the origin of this curve the fibers start crimped and are then straightened by the straining. Straightened fibers require larger forces to stretch, resulting in the increasing stress. This process of crimped fibers straightening is referred to as recruitment.[1] The force required to recruit fibers is small, and thus it is sometimes considered trivial and assumed to be zero.[1] We aim to better understand the process of collagen fiber recruitment. Towards this goal, we need a more refined characterization of the behavior of collagenous tissues in the low stress, high strain toe region of the curve. For this project we aimed to evaluate the effects of using micro-cuts to release the stresses on well-aligned collagen fibers. More specifically, we measured the changes in tortuosity in fibers that were cut compared with non-cut fibers.

METHODS

Chicken tendon was chosen because the collagen fibers are well aligned and uniform. Chicken legs were purchased from a local butcher, and the tendons were removed. A rectangular strip 10 x 2 mm was isolated and cryosectioned into 16 µm thick sections. The 2 mm on both ends of the tendon section were glued with a UV resin between two silicone sheets that were 3 x 3 mm in area and 0.125 mm thick. The ends were clamped with custom 3D printed clamps in a uniaxial micro vice (Micro Vice-Mini, PIKE Technologies). The tissue was immersed in water during testing and imaging. For the large stretch-low stress images, the tendon was stretched to the point that many of the fibers were recruited but stopped before the point of failure. This distance was different for each section.

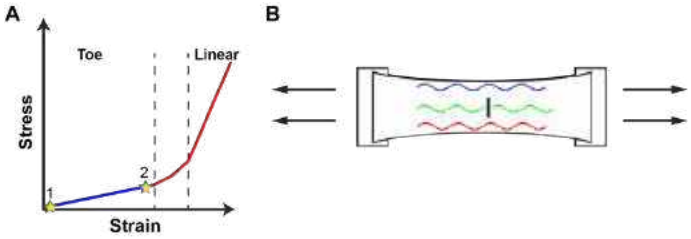

Figure 1. a) Example collagen stress-strain curve with toe region (blue), where little force is required to distort the collagen. Points 1 and 2 are the "no stretch" and "large stretch-low stress" scenarios respectively. b) The sectioned tendon was stretched, and micro-cuts were made (black line). Fiber tortuosities were measured and grouped into three regions relative to the cut: above (blue), within (green), and below (red).

A multiphoton microscope (Nikon) utilizing a femtosecond laser (Coherent) was used to visualize the collagen with second-harmonic generation (SHG) imaging and two-photon autofluorescence (TPF). We used a 25X water immersion objective (NA = 1.1). The femtosecond laser used for the multiphoton microscopy was also used to create the micro-cuts in the tendon sections. The method was adapted from Hovhannisyan et al.[2] The laser is tuned to 800 nm and powers between 25-40 mW are used. The laser continuously scans an area that is 128 x 4 µm. The diffraction limit of the 25X objective at 800 nm is 290 nm, and the laser scanning step-size was 250 nm. The collagen degradation is monitored during the laser exposure by simultaneously measuring the SHG and TPF signals. Photodegradation is marked by a decrease in the SHG signal and an initial increase in the autofluorescence from the creation of photoproducts. Femtosecond laser exposure continued until the SHG signal was zero in the micro-cut area.

Fiber tortuosity is defined as the ratio of the path length to the end-to-end distance. Crimped fibers have tortuosities greater than 1.00. The tortuosity of a perfectly straight fiber would be 1.00. Tortuosity decreases as fibers are recruited, but even when fully recruited the tortuosity can be greater than 1.00.[3] To calculate the tortuosity, the fiber paths were manually traced in the SHG maximum intensity projections, as demonstrated by the green path in Figure 2(c, d).

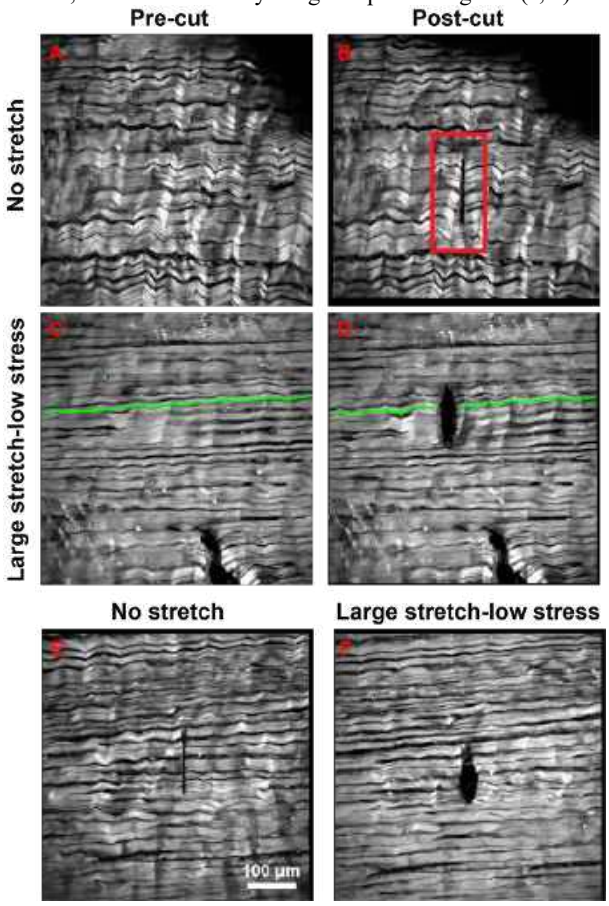

Figure 2. (a-d) show the same tendon section with no stretch (a-b) and with large stretch-low stress (c-d). In both scenarios, a micro-cut was made with a femtosecond laser (red box). The green line illustrates the manual marking to measure tortuosity. (e-f) shows a micro-cut that was made while the section was under no stretch (e), and after the cut was made the section was stretched (f).

RESULTS

We imaged the same tendon section before and after micro-cuts in two different environments: with no stretch, before there is any strain or stress (Fig.2 a-b) and with large stretch-low stress where the collagen fibers are beginning to be recruited (Fig.2 c-d). The "no stretch" corresponds to point 1 in the stress-strain curve, and "large stretch-low stress" corresponds to point 2 in the stress-strain curve. We observe a decrease in the tortuosity from the no stretch to the large stretch-low stress scenarios. The average fiber tortuosities of the section before any stretch or micro-cut was 1.08 and the average fiber tortuosities after stretch was 1.01. After the micro-cut in the no stretch scenario, there was no significant change in tortuosity, as shown by the flat lines in Fig. 3 left column. After the micro-cut while the fibers were in the large stretch-low stress scenario, the tortuosity increased for fibers within the cut (Fig. 3, center column, green lines), but was constant for fibers above and below the cut (Fig. 3, center column, red and blue lines). In addition, there was a greater increase in tortuosity in the center of the micro-cut versus the edges.

In a second tendon section, we made a micro-cut and then stretched the section (Fig. 2e-f). We measured the tortuosity before and after stretching. We observed a tortuosity decrease in fibers that were cut and fibers that were not cut, but observed a smaller decrease in tortuosity for the fibers that were cut (Fig. 3, right column, green lines).

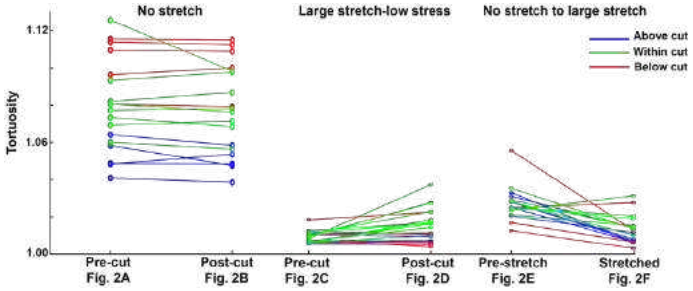

Figure 3. The tortuosity of the fibers in Fig.2 were measured and compared for each pair of images. The points connected by a line show how the tortuosity of a particular fiber changed between the images. The color corresponds to the location of the fiber: above the cut (blue), within the cut (green), or below the cut (red).

DISCUSSION

Our results lead to two points for discussion, the first related to the "toe" region of the stress-strain curve and the second related to the lateral strain in the tendon. The increase in tortuosity after the micro-cut in the large stretch-low stress fibers (Fig. 3 center column, green lines) indicates that there was some stress in the fibers before they were cut. However, we also note that the tortuosity does not increase to the pre-stretch values. These results show that although the stress is small before fibers have been recruited, the stress is not negligible, particularly at the microscale level of our experiments. Therefore, these forces will be important to consider as more research is done to understand the impact of collagen microarchitecture on macroscopic phenomena, as is being done in fiber-based modeling.[4]

For the second point of discussion, we highlight that after stretching the tendon with a micro-cut, even the fibers that were cut have a decrease in tortuosity (Fig. 3 right column, green lines). This is most likely due to the lateral strain in the tendon between the fascicles. The fascicles are connected by the interfascicular matrix leading to the lateral transfer of strain.[5] When the micro-cut is made in the large stretch-low stress scenario, the fiber segments on each side of the cut were pulled away from the cut creating the ellipse shape and an increase in the tortuosity of the cut fibers. This ellipse shape is also an indication of the lateral strain. The method of micro-cuts and uniaxial stretching can be used in the future to determine the spatial extent of the lateral strain and further characterize the contribution of the matrix to the tendon mechanical properties.

ACKNOWLEDGEMENTS

NIH R01-EY023966, P30-EY008098, 1S10RR028478-01, and T32-EY017271 (Bethesda, MD), the Eye and Ear Foundation (Pittsburgh, PA), and Research to Prevent Blindness (unrestricted grant to UPMC Ophthalmology, and Stein innovation award to Sigal IA).

REFERENCES

[1] Jan, N-J et al., *Acta Biomater.,* 72:295-305, 2018. [2] Hovannisyan, V et al., *Opt. Express*, 16:7958-7968, 2008. [3] Lee, P-Y et al., *Exp. Eye Res.,* 217:108967, 2022. [4] Ji, F et al., *Exp. Eye Res.*, 232:109510, 2023. [5] Haraldsson, BT et al., *Matrix Biol.,* 27:86-95, 2008.

TOWARDS VALIDATION OF KNEE-SPECIFIC FINITE ELEMENT MODELS IN A LOADED MRI CONDITION

Sean C. Letendre (1), Kalle L. Chastain (1), Joshua Leadem (3), Manuela Montes de Oca (3), Lila Pender (3), Madison Lang (3), Erin Leatherman (2), Thomas Santner (4), Kate Lindsey (3), Erin Argentieri (1), Amanda Wach (1), Ashley Pekmezian (1), Sara Sacher (1), Matthew F. Koff (1), Amy Lerner (3), Scott A. Rodeo (1), Suzanne A. Maher (1), Brett D. Steineman (1)

(1) Hospital for Special Surgery, New York, NY
(2) Kenyon College, Gambier, OH
(3) University of Rochester, Rochester, NY
(4) Ohio State University, Columbus, OH

INTRODUCTION

Finite element (FE) models have been used to estimate joint contact mechanics in healthy knees and to assess changes in various pathologies or treatment conditions.[1,2,3] Knee models are often developed from cadavers or open-source databases, such as the Open Knee(s) project, with extensive data derived from cadaveric knees, while others have created models based on clinical scans from patients.[4,5] Although models derived from patient scans can be informative, these models are limited since directly measuring and comparing contact mechanics is challenging and invasive. With an interest in developing applicable patient-based FE knee models without calibration, it is important to understand which contact outcomes are reliable. Therefore, the purpose of this study was to quantify the contact mechanics during simulations of a patient loading condition using a cadaver model and uncalibrated knee-specific FE models. We hypothesized that knee-specific FE models accounting for material property variability would exhibit contact area and pressure values similar to those measured by electronic pressure sensors in the simulated patient loading condition.

METHODS

Five cadaver knees (51-76 y.o.; 3M / 2F) were used to develop knee-specific FE models. None of these knees had soft tissue degeneration or prior knee surgery. The knees were dissected at the proximal femur and distal tibia and stripped of soft tissue for potting. Once potted, they were inserted into a loading mechanism designed to emulate a patient's knee position during an MRI equipped with a 6-degree-of-freedom load cell.[6,7] The mechanism was inserted into a clinical 3T MRI scanner (GE Healthcare, Waukeshau, WI) for imaging. Two image sets were acquired for each specimen: a 3D spoiled-gradient echo (SPGR) with frequency selective fat-supression and a 3D CUBE image, as described previously.[7] Images were acquired with the knee in a non-weight-bearing position at full extension to assess the non-deformed geometry of the soft tissue. Next, the gantry was displaced to compress the knee to achieve ½ of the donor's body weight (50-73 kg) to simulate standing in the MRI, similar to previous *in vivo* studies.[6,7] Images were acquired in this loaded configuration to determine the displacement of bones relative to each other for subsequent use in the FE models. Following scanning, the knee was unloaded for at least one hour, and an electronic pressure sensor (Model 4011, Tekscan, Norwood, MA) was inserted into the knee joint and placed across the articular surface of the tibial cartilage below the menisci. The loading protocol was repeated, and images of the loaded configuration were then re-acquired in parallel with data acquisition from the pressure sensor.

The bones and soft tissues were segmented from the unloaded and loaded scans using a combination of MeVisLab (MeVis Medical Solutions AG, Bremen, Germany) and Materialise Mimics (Materialise NV, Leuven, Belgium). The soft tissues were segmented from the unloaded scans. The bones were segmented from both the unloaded and loaded scans. The femoral and tibial cartilage and bones were segmented from the SPGR images, while the menisci were segmented from the CUBE scans due to better meniscal image contrast.

The FE knee models were developed from the scans and segmentations to replicate the loaded condition of each specimen. The soft tissues were meshed with hexahedral elements using TrueGrid (XYZ Scientific Applications, Inc., Pleasant Hill, CA). An iterative closest-point algorithm with Geomagic DesignX (3D Systems, Rock Hill, SC) was used to best-fit align the segmented bones to calculate a transformation matrix of the femur from the unloaded to loaded configuration relative to the tibia. The soft tissue meshes were transformed into the loaded position, and then the femoral cartilage was distracted from the joint to clear the menisci before the simulation. FE simulations were performed in Abaqus (Dassault Systèmes, Simulia Corp., Johnston, RI) by constraining the degrees of freedom of the knee to maintain the loaded orientation of the femur and tibia, except to allow

femoral varus-valgus rotation. A load was applied to mimic the resultant force in the axial direction measured during the loaded scan.

A maximin space-filling approach used ranges of cartilage and meniscal material properties from the literature to provide 70 iterations of material property scenarios. The following material properties were varied: cartilage (isotropic) Young's modulus and Poisson's ratio, menisci (transversely isotropic) circumferential and transverse Young's moduli and Poisson's ratios, and meniscal attachment spring stiffness.

Results, including compartment contact area, peak pressure, and mean pressure on the tibial cartilage, were compiled from the FE model and the electronic pressure sensors. Image intensity from the scans of the loaded knee joint provided an approximate location of the pressure sensor in each knee compartment. The location of the sensors was reconstructed with the FE data (Fig. 1). FE results outside of the sensor boundary were excluded for a more direct comparison.

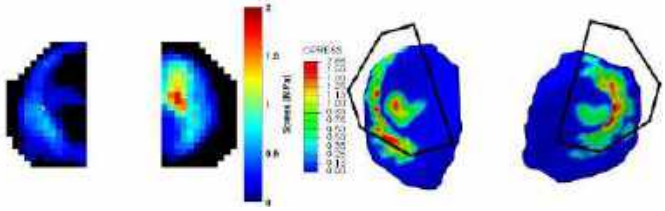

Figure 1: A comparison of pressure sensor data and FE pressure data with pressure sensor boundaries.

RESULTS

The compartment contact area was underestimated in the FE model when compared to the pressure sensor measurements (Fig. 2). In the cadaver models, the contact area varied from 319-563 mm^2 on the medial side and 236-454 mm^2 on the lateral side. The FE results ranged from 26-383 mm^2 on the medial side and 41-352 mm^2 on the lateral side. In the medial compartment, sensor measurements were greater than the FE predicted values by an average of 86±36 mm^2. In the lateral compartment, sensor measurements were greater than the FE model values by an average of 91±75 mm^2. Both models followed similar trends. For example, the knee with the highest contact area estimated by the FE model was also the knee with the highest contact area measured by the electronic pressure sensors in both compartments.

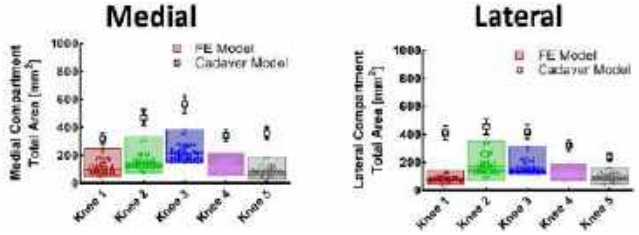

Figure 2: Medial and lateral compartment contact area values. Material property iterations are represented by individual dots with a full range shown by colored bars. Pressure sensor standard deviations were equal to 12% of measured values, based on an assessment of the sensors.

Mean and peak contact pressures measured from the FE knee models either overestimated or fell within the range of FE predictions (Fig. 3). For the mean pressure, sensor measurements fell within the FE model predictions for one of the five knees in the medial compartment and all five knees in the lateral compartment. In the cadaver models, the mean contact pressures varied from 0.19-0.34 MPa on the medial side and 0.34-0.59 MPa on the lateral side. The FE results ranged from 0.27-1.09 MPa on the medial side and 0.31-1.05 MPa on the lateral side. Of the four knees in the medial compartment that did not accurately predict pressure sensor values, the amount of deviation from the range for the mean pressure was 0.1 ± 0.1 MPa.

Peak pressure measurements fell within the FE model predictions for two of the five knees in the medial compartment and all five in the lateral compartment. In the cadaver models, the peak contact pressures varied from 0.6-0.9 MPa on the medial side and 0.8-1.8 MPa on the lateral side. The FE results ranged from 0.4-4.9 MPa on the medial side and 0.5-3.9 MPa on the lateral side. Of the three knees that did not overlap in the medial compartment, the amount of deviation from the range for the peak pressure was also 0.1 ± 0.1 MPa.

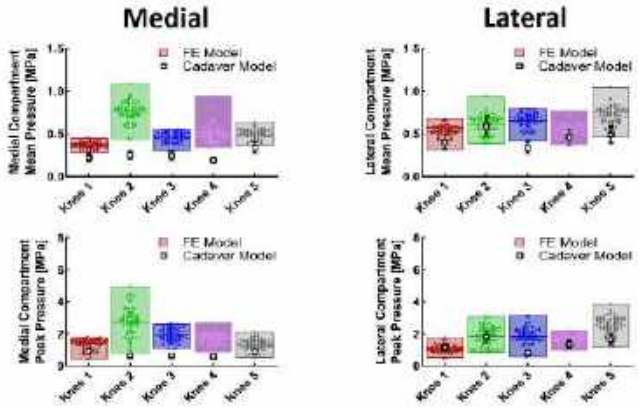

Figure 3: Mean and peak pressure in medial and lateral compartments. Material property iterations are represented by individual dots with a full range shown by colored bars. Pressure sensor standard deviations are equal to 20% of measured values based on an assessment of the sensors.

DISCUSSION

We found that uncalibrated FE knee models simulating a patient loading condition underestimated the compartment contact area but better estimated the mean and peak pressure measured in the physical cadaver model. This study took an uncalibrated modeling approach to evaluate contact mechanics, assuming the inability to obtain any data from patients that may be useful to calibrate the FE models. Future studies utilizing MRI may be used to calibrate the FE models as well as approximate contact area during the loaded portion of scanning by estimating the overlap of the articular soft tissue surfaces.[8] Predicted cartilage overlap maps derived from MR sequences could provide an insightful comparison to FE contact results and warrant investigation. Despite the limitations of uncalibrated FE models, contact pressure outcomes closely approximated values from the simulated loading condition.

ACKNOWLEDGEMENTS

We thank the following sources of support: The National Institutes of Health (AR075523), the Russell Warren Chair for Tissue Engineering and the HSS Surgeon-in-Chief Fund.

REFERENCES

[1] Mohamadi, A et al., *BMC Musculoskelet Disord*, 15;22(1):625, 2021
[2] Zielinska B, Haut Donahue TL, *J Biomech Eng*, 128(1): 115–123, 2006
[3] Zhang X et al., *BMC Musculoskeletal Disorders*, 22(1): 322, 2021
[4] Bae J et al., *Med Biol Eng Comput*., 50(1):53-60, 2011
[5] Erdemir A, *The Journal of Knee Surgery*, 29(2): 107–116, 2016
[6] Wang H et al., *J Biomech*, 48(12): 2934-2940, 2015
[7] Maher S et al., *J Orthop Res*, 35(3): 600-611, 2016
[8] Hosseini A et al., *J Orthop Res*, 30(11): 1781-1788, 2012

DEVELOPMENT AND ANALYSIS OF SCAFFOLD-FREE ADIPOSE SPHEROIDS

J. Liszewski (1,2), R. Behan-Bush (1,2), M. Schrodt (1,2), A. Klingelhutz (2), E. Sander (1), J. Ankrum (1,2)

(1)Department of Biomedical Engineering, University of Iowa, Iowa City, Iowa, United States
(2)Fraternal Order of Eagles Diabetes Research Center, University of Iowa, Iowa City, Iowa, United States

INTRODUCTION

With more than 2 in 5 adults in the US currently battling obesity, ongoing research strives to unravel the intricacies of adipose tissue and its role in metabolic syndromes[1], autoimmune diseases[2], cardiovascular diseases[3], and cancers[4]. To fully understand these diseases, it is critical to develop *in vitro* models that not only allow the study of how healthy adipocytes behave but also shed light on how dysfunctional cells may contribute to these pathologies.

Conventional monolayer models of adipogenic differentiation, while convenient, have significant limitations. Cells cultured in monolayers exhibit decreased efficiency in adipogenic differentiation, resulting in a heterogeneous population. Only a minority express the classic mature adipocyte phenotype, characterized by large, unilocular, lipid-rich droplets with substantially increased production of hormones such as adiponectin, along with decreased pro-inflammatory cytokine production [5]. Over the past decade, several 3D models of adipose tissue have been developed, progressively increasing in complexity. Protocols utilizing various scaffolding techniques, such as mechanically tunable 3D environments[6] and microfluidics chips[7] have been created. While these methods are fascinating, they often require specialized resources, expertise, and/or technologies that limit their applicability to a broader group of biomedical researchers.

We have distilled our methods for generating adipose spheroids into two formats that meet a wide range of experimental goals: a 96-well spheroid plate format and agarose micromold format. Both methods are relatively simple allowing their adoption across many biomedical research labs. We compared the two methods for experimental parameter design and use them to highlight the differences between monolayer and spheroid culture and the importance of characterizing donor variability.

METHODS

Adipogenic differentiation of adMSCs in monolayer: To stimulate adipogenesis, adMSCs were plated at 10k/well in a 96-well plate to achieve confluency. Cells were cultured within 150µL Preadipocyte Differentiation Medium (PDM-2) (Lonza) for the first week and changed to 150µL DMEM (25mM D-glucose) with 10% FBS and 1.9µM insulin the following week for achieving maturation. Media was collected for adipokine analysis via LegendPlex Adipokine Panel (BioLegend) according to manufacturer's protocols. Adipogenic differentiation of adMSCs in 96-well spheroid plates: adMSCs were seeded at either 5k, 10k, or 20k cells/well within 150µL PDM-2 (Lonza) for the first week and changed to 150µL DMEM (25mM D-glucose) with 10% FBS and 1.9µM insulin for the following week for adipocyte maturation. Adipogenic differentiation of adMSCs in agarose micromold format: A 4% w/v solution of agarose within PBS -/- was heated to 80°C to achieve a molten state. The solution was then transferred to either a Microtissues© 35-well micromold cast, or in-house printed 10-well micromold cast for 2 minutes until gelled. Micromolds were transferred to a 24-well plate and acclimated within PDM-2 for 1 hour, media was carefully aspirated, and cells were seeded within the cell seeding chamber in 75µL of media at various concentrations to achieve ~1k, 2k, 5k, 10k, or 17.5k cells/spheroid for another hour. Once formed, an additional 1mL of media was added and cells were differentiated as previously described.

Lipid staining and imaging: Cells cultured within monolayer were washed 2x with PBS -/-, fixed for 30 minutes with 10% Formalin, and stained for 30 minutes with 10 µM Hoechst 33342 and 2 µM BODIPY 493/502 within PBS followed by imaging via inverted fluorescent microscopy. Cells cultured within spheroid format followed the same procedure, with increased fixing and staining times of 1hr followed by imaging by confocal microscopy.

RESULTS

Study 1: Spheroid production and function via agarose micromold or spheroid plate. Spheroids formed within agarose micromolds have a greater size variability of 15 - 23 %CV compared to those formed within spheroid plates (Fig. 1C). For the spheroids formed within a 10- or 35-well micromold, increasing the number of cells per spheroids leads to a drastic decrease in adiponectin production, while increasing the overall number of spheroids leads to a further decrease (Fig. 1D).

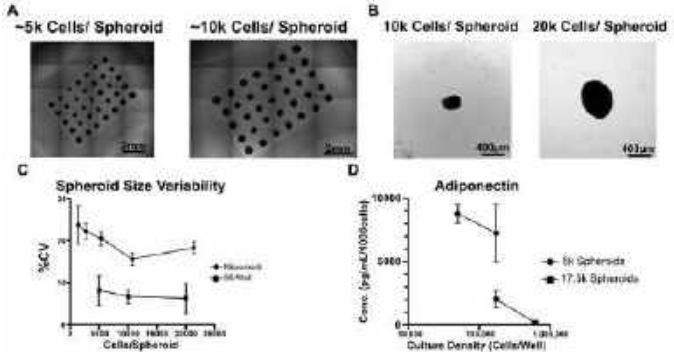

Figure 1: Representative images of spheroid production within (A) agarose micromolds and (B) spheroid plates. Spheroid size variability was compared between the two formats (C). Spheroid size variability depends on method of formation and not cells per spheroid. (D) Quantification of changes in adiponectin output per cell as a function of spheroid size and culture density. N = 3.

Study 2: Adipogenic differentiation in 2D monolayer and 3D spheroid culture formats. Cells differentiated within a 3D spheroid format at 10k cells/spheroid exhibited a 4.6x increase in adiponectin signaling in comparison to cells differentiated in monolayer (Fig. 2A). Pro-inflammatory cytokine production decreased across the board from 2D to 3D culture. Average concentrations decreased 116x for MCP-1 (Fig. 2B), 32x for IL-8 (Fig. 2C), and 65x for IL-6 (Fig. 2D) when switching from monolayer culture to spheroids. Cells differentiated within 3D also illustrated greater lipid droplet production compared to their 2D counterpart (Fig. 2E,F).

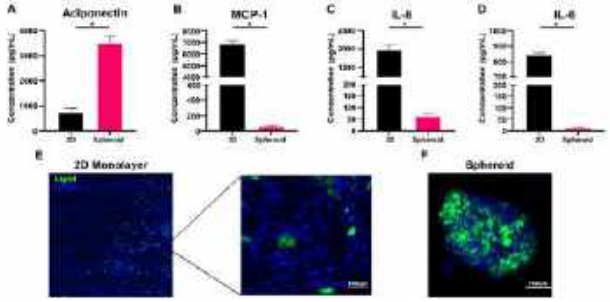

Figure 2: Comparison of adipokine signaling between monolayer- and spheroid differentiated adMSCs for (A) adiponectin, (B) MCP-1, (C) IL-8, and (D) IL-6. N=3 experimental replicates. Unpaired t-test, * designates significant difference of $p<0.05$. Representative fluorescent images of nuclei (blue) and lipid (green) stained cells in monolayer (E) and spheroid (F) formats.

Study 3: Donor-specific adipogenic variability within 3D culture format. After the 14-day spheroid differentiation at 10k cells/spheroid, Donors 2302 and 2414 had increased average lipid droplet counts of 714-814 compared to Donors 2334, 2220, and 11738 with counts of 174, 159 and 331 respectively (Fig. 3B). When analyzing adiponectin, donors 2414 and 11738 had 11x increased production compared to donors 2334, 2220 and 2302 (Fig. 3C). Donor 2334 had higher pro-inflammatory cytokine production across the board compared to the remaining four (Fig. 3D-F).

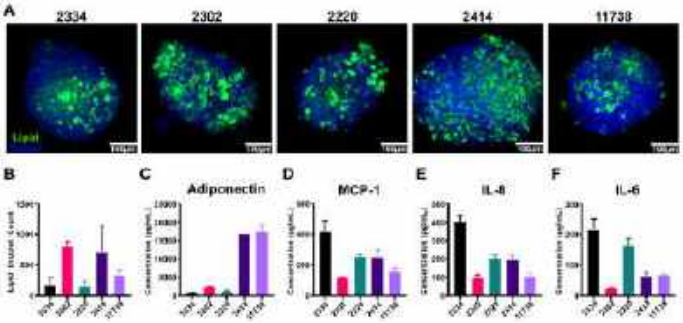

Figure 3: (A) Representative fluorescent confocal images of five separate donors. Total lipid droplet counts were quantified with ImageJ (B). Adiponectin (C), along with inflammatory cytokines: MCP-1 (D), IL-8 (E), and IL-6(F) were quantified via ELISA. n=3 experimental replicates.

DISCUSSION

These findings demonstrate the efficacy of using simple, scaffold-free techniques for adipogenic differentiation without the need for specialized scaffolding, machinery, or materials expertise. Both methods require minimal intervention after initial seeding, reducing user error and enhancing experimental reproducibility. Additionally, they provide full access to the spheroids, facilitating scaling up or increasing complexity. The spheroid plate format allows culturing on an individual spheroid basis, enabling screening experiments without consuming large quantities of reagents while preventing any opportunities for spheroid fusion. Agarose micromolds are well suited for generating spheroids in bulk, allowing experiments requiring 100s to 1000s of spheroids to generate biological material for RNA, conditioned media, or tissue engineering applications. We used these techniques to compare how 3D adipogenic differentiation leads to increased efficiency and decreased pro-inflammatory cytokine production compared to 2D as seen in prior work[5]. This is more in line with the low levels of inflammation expected within adipose tissue. We then directly compare spheroids from the methods showing the benefits and drawbacks of each. Finally, we use the 96-well plate method to highlight reveal donor variability. While all donors are capable of producing lipid droplets, adipokine profiles varied substantially. In conclusion, we have developed a highly reproducible method for generating functional adipose spheroids that is accessible to a broad range of researchers and experimental questions. With these two methods, any biomedical lab is capable of implementing and adapting these cost-effective techniques to achieve their specific goals.

ACKNOWLEDGEMENTS

This work was supported from NIGMS R01GM145626 (ES, JA), NIH P42 ES013661 (J.A. and A.K.), and a Diabetes Action Research and Education Grant (J.A.). Adipose supplied by the Tissue Procurement Core at the University of Iowa which is supported by an award from NIH (NCI award number P30CA086862) and the University of Iowa Carver College of Medicine.

REFERENCES

[1] Guilherme, A et al., *Nat Rev Mol Cell Biol* 9:367-77, 2008; [2] Neumann, E et al., *Cells* 10:216, 2021; [3] Patel, P et al., *J Obes* 2013:489187, 2013; [4] Yao, H et al., *Mol Med Rep* 24:866, 2021; [5] Klingelhutz, A et al., *Sci Rep-uk* 8:523, 2018; [6] Hu, W et al., *Nat Rev Endocrinol* :1-16, 2022; [7] Yang, F et al., *Lab on a chip* 21:435-46, 2021

ADAPTATION OF A MULTISCALE MODEL OF HEART GROWTH IN PREGNANCY FOR USE IN CANINES

Tiffany Corlin (1), Molly S. Kaissar (2), Kyoko Yoshida (2)

(1) Division of Maternal-Fetal Medicine, Department of Obstetrics, Gynecology and Women's Health, University of Minnesota, Minneapolis, MN, USA
(2) Department of Biomedical Engineering, University of Minnesota, Minneapolis, MN, USA

INTRODUCTION

Cardiovascular disease is the most common cause of maternal mortality in the United States [1]. Thus, an understanding of the physiologic cardiovascular changes that occur in pregnancy are paramount to manage the complications that may arise, such as hypertension and heart failure. It is established that there is cardiac growth in pregnancy, as well as changes in systemic vascular resistance and an increase in blood volume throughout gestation [1]. It is important to recognize however, that it is not only mechanical changes that influence the cardiovascular system in pregnancy. The hormonal changes that accompany advancing gestation also play a pivotal role in these physiologic changes [2].

Computational models are a useful tool in predicting the changes that occur during pregnancy, as real-time monitoring is often invasive or not practically feasible. The focus in a prior model was on the left ventricular (LV) mass, which grows, both in mass and in size, by 30% by the end of pregnancy and returns to a non-pregnant baseline within months postpartum [2,3]. These models have been applied to non-human species, such as the rat [2], and are applied here to the canine. Therefore, the aim was to scale the original rat model to a canine as a first step towards the objective of scaling to a human for clinical use.

METHODS

The MATLAB code for the previously developed multiscale model of heart growth in pregnancy in the rat is publicly available and was utilized [2]. The compartmental model was first reparametrized. The compartmental model uses time-varying elastance to simulate the ventricles, which are modeled as thin-walled spheres. The systemic and pulmonary vessels are modeled as capacitors in parallel with resistors. Allometric scaling was used to adapt the rat model's resistors and capacitors (represented by biological variable *Y*) to the canine [2,4-5]. The values were used for a canine based on a mass of 20 kg and a scaling coefficient of b=-3/4 for capacitors and b=1 for resistors [5] (Eq. 1):

$$Y_{canine} = Y_{rat}\left(\frac{M_{canine}}{M_{rat}}\right)^{b} \quad (1)$$

Once the compartmental model was altered to represent the canine hemodynamics, then the multiscale model was applied [2, 4, 6-7]. Hormone levels of estrogen (E2) and progesterone (P4) throughout canine pregnancy were input from published literature [8]. No published data on angiotensin II (AngII) levels in a canine pregnancy were available, thus it was assumed there was a 300% increase throughout pregnancy as is the case in the rat [9].

The relationship between the network and compartmental models involves using a linear transfer function to map the elastic stretch calculated by the compartmental model to the network Stretch input, and a separate transfer function to map the network CellArea output into a growth stretch [2] (Fig. 1). This relationship was not changed for the canine model from the rat model. At each growth step (8-hour increments), heartbeats were simulated until a steady state was reached (compartmental volumes at the start and end of each cardiac cycle differed by < 0.1 mL). We optimized the stressed blood volume at each growth step to match reported changes in end-diastolic diameter (EDD).

Figure 1: Multiscale cardiac growth model for pregnancy. The model couples a cell signaling network model (A) of hormones and stretch acting on the cell to a compartment growth model (B).

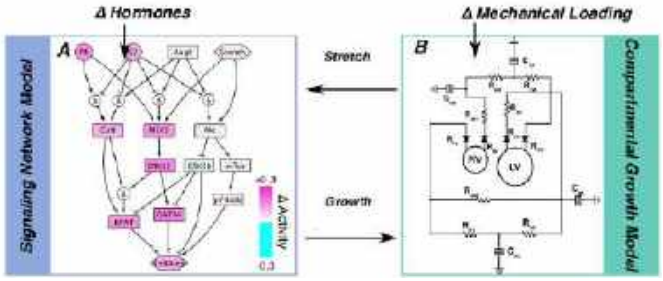

RESULTS

Using allometric scaling, the compartmental model demonstrated pressure-volume (PV) loop at baseline for the canine seen in previous studies [4]. From this baseline, we simulated heart growth throughout a 63-day gestation in canines (Fig. 2). The model captures an increase in stroke volume, as well as dropping mean arterial pressure (MAP) secondary to a decrease in peripheral vascular resistance that is known to occur during pregnancy [1] (Fig. 3).

Figure 2: PV loops during pregnancy-induced cardiac growth. Pressure-volume loops throughout 63 days of canine pregnancy. Baseline is in teal and the blue loop is at the end of pregnancy.

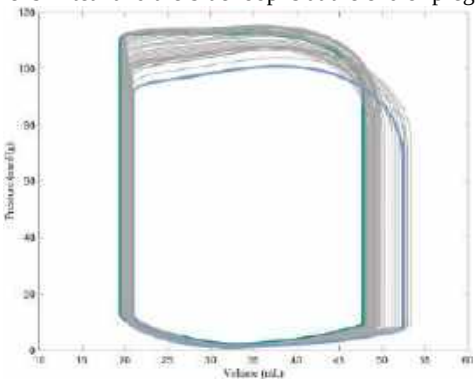

Figure 3: Model predictions for heart growth and hemodynamics. Relative changes in left ventricular mass (A), end-diastolic diameter (B), mean arterial pressure (C), and cardiac output (D) throughout canine pregnancy. Stars represent experimental data [6] and solid lines represent model predictions.

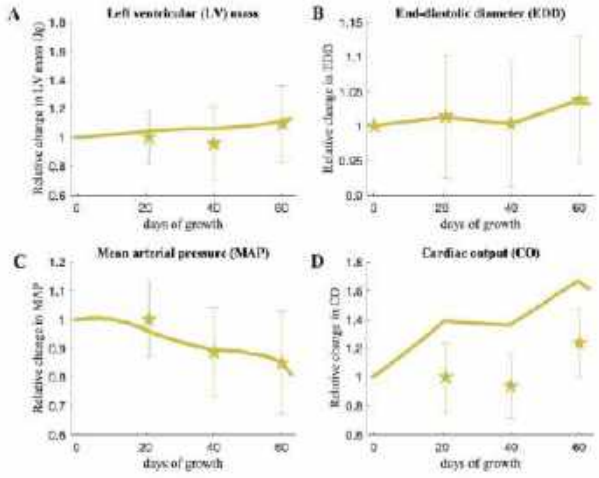

Experimental values of E2 and P4 from the literature demonstrate a slow increase in E2 throughout gestation with an early increase in P4. There were minimal changes in Stretch throughout pregnancy (Fig. 4). There is an increase in CellArea throughout pregnancy, which was primarily driven by the increasing hormones, P4 and AngII. At the organ-level, the model predicted a gradual increase in LV mass throughout pregnancy by nearly 20%, while changes in MAP followed the reported experimental trends (Fig. 4). However, the model overpredicted changes in cardiac output (CO) relative to experimental data [6].

Figure 4: Network model node activity during pregnancy. Values are normalized and range from 0 to 1. Each panel represents nodes in the signaling network.

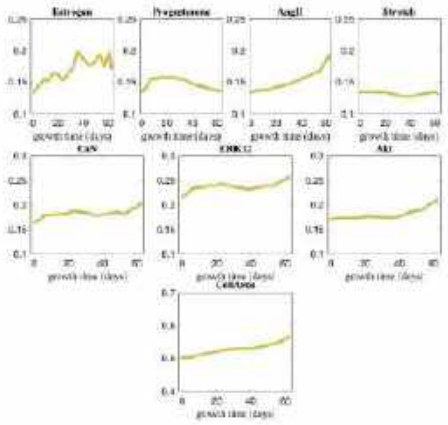

DISCUSSION

A multiscale model has been scaled from prior work in rats [2] to the hormonal and hemodynamic parameters of a canine, which is the first of its kind to model heart growth during a canine pregnancy. The application of this model to an additional species is novel because it demonstrates the multiscale model's ability to allometrically scale between species without recalibration. This suggests that the coupling framework is not species-specific. The model can predict appropriate growth when only given species-appropriate changes in hormones and hemodynamics, which could be feasibly measured by serum studies, monitoring, or echocardiograms in the clinical setting. Thus, this result has promising implications for real-world application.

We are currently addressing the overprediction of CO in our model by considering alternative hemodynamics measurements for model optimization. For example, we can optimize stressed blood volume to CO, instead of EDD. Understanding which non-invasive measurable hemodynamic parameters are appropriate for predicting growth is also important for future clinical applications.

While the experimental study used here reports no significant increase in LV mass as pregnancy progressed, other studies have reported significant LV growth in canines [6] and with human and rat pregnancies [1,2], thus the model demonstrates what was expected. Next steps will include scaling to the human species with validation from a database of echocardiographic data throughout pregnancy at different gestational ages and into the postpartum period.

In conclusion, we demonstrate that our multiscale model can be easily adapted to a new animal model, suggesting a promising next step towards its clinical application for pregnancy.

ACKNOWLEDGEMENTS

This work was supported by the UMN Cardiovascular Engineering Training Program (T32-HL139431), an AHA Career Development Award..

REFERENCES

[1] Presidential Task Force on Pregnancy and Heart Disease, *Obstet Gynecol*, 133:320-356, 2019. [2] Yoshida, K et al., *Biomech Model Mechanobiol*, 21:1267-1283, 2022. [3] Savu, O et al, *Circ Cardiovasc Imaging*, 5:289-297,2012. [4] Witzenburg, C et al. *J Cardiovasc Transl Res*, 11:109-122, 2018. [5] West, G et al. *Science*, 276:122-126, 1997. [6] Lobo, L, et al. *Vet Sci*, 8:1-10, 2021. [7] O'Rourk, R, et al. *Amer Heart J*, 81:55-60,1971. [8] Concannon, P, et al. *Biol Reprod*, 13:112-121, 1975. [9] Mishra, J et al. *Biol Reprod*, 99:1091-1099, 2018.

EFFECT OF IMPACT MAGNITUDE AND DIRECTION ON THE INJURY RISK OF NEURAL CELLS

Raisa. Akhtaruzzaman [(1)], Aurthur. Koster [(1)], Kamal. Awad [(2)], Venu. Varanasi [(2)], Marco. Brotto [(2)], Ashfaq. Adnan [(1)]

(1) Mechanical Engineering, University of Texas at Arlington, Arlington, Texas, United States of America
(2) Bone Muscle Collaborative Science, University of Texas at Arlington, Arlington, Texas, United States of America Brotto, Marco

INTRODUCTION

Recent studies suggest that neuronal cells change their morphology in response to mechanical stress. These morphological changes include junctions and cytoskeleton remodeling. Yet, the cells' responses to different mechanical loads are to be quantitatively understood [1]. While mechanical loads on cells can come from any directions, most of the lab-based studies are limited to shear-type or stretch-type loading [2, 3]. Here, the aim of this study is to quantify cellular response with application of different magnitudes of acceleration and identify the direction of mechanical loading that leads to a significant cell injury. To study these effects, we first carried out *in-vitro* cell culture studies using human neuronal cells. For the side mechanical load model (SL), we used a spring-loaded cylindrical bar to impart the desired acceleration. While drop tower was used for the top mechanical load model (TL). Cells morphological changes and induced injury were quantified using live-dead fluorescence stain. We tested for accelerations ranging from 5g to 300g as per the healthy to lethal transition range found in the literature [4] and tracked the cellular change over 30 minutes. Fluorescent images were captured and BZ Analyzer as well as ImageJ software were used to assess and quantify the results. The purpose of this study was to understand the biomechanics of brain injury using different mechanical loading mechanisms to fully understand and intervene traumatic brain injury and potentially limit undesirable complications.

METHODS

Human Neuroblastoma SHSY5Y cells were obtained from American Tissue Culture Collection (ATCC). The cells were cultured in DMEM culture medium supplemented with 10% FBS, 100 U/mL penicillin, 100 g/mL streptomycin (GIBCO) and 2 mM l-glutamine and maintained at 37˚C in a 5% CO_2 humidified atmosphere. Upon reaching 80% confluence, the cells were treated with 0.25% trypsin for 3 min to detach the cells. Cells were subsequently resuspended with DMEM culture medium containing 10% FBS. Following, cells were centrifuged at 100 x g for 5 min, the supernatant was removed, and cells were resuspended with fresh culture medium. The cells were counted, then density was adjusted to $5x10^5$ cells for each petri dish coated with Laminin. Subculturing was performed every two or three days, upon the cells reaching 80% confluence. Growth media was replaced every 48 hours. For staining, 10 ml phosphate buffer saline (PBS) containing 5 µL of Calcien AM and 20 µL of Ethidium Homodimer was used. To each 35mm petri dish, 400 µL of prepared stain is added and incubated for 20 minutes while covered with aluminum foil to avoid light exposure. Tri-axis accelerometer attached to the petri dish before impact and the analog signal is converted to digital signal in LabView and the acceleration versus time graph is plotted using MATLAB. A spring-loaded system and a drop tower were used to provide a linear force. In this setup we counted the number of cells and morphological changes (Spindle-like, polygonal, filipodia, etc.,) before and after impact. After impact, time-lapse recording was used for 30 minutes with 3 minutes interval by using BZ analyzer software. Keyence BZ-800X fluorescence microscope was used for imaging, post-processing, and quantification of cellular response.

RESULTS

As indicated in Figure 1, a spring-loaded bar is used to apply acceleration on a 35mm petri-dish and cells were monitored to study the morphological changes over time and with different accelerations. For each acceleration applied, the images after the impact were collected at the exact 3 locations as before and results are shown in figure 2. At accelerations of 30g there is changes in the cell morphology with time but very few or negligible cell death even after 30 minutes of the impact. At 210g, most of the cells are stained with red indicating that the death rate of the cells drastically increased. When impacted with higher acceleration the cells are not able to recover from there injury state. Another preliminary observation was that when insulted from the top by the drop tower for the same acceleration as of side load the injury to

the cells is much higher. Most of the cells were dead when the drop tower was used to insult the cells at a high acceleration (210g).

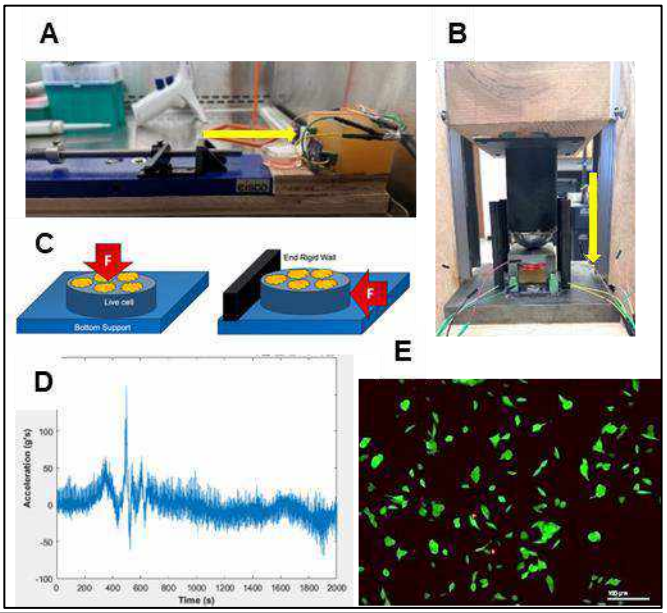

Figure 1: **Illustration of the model**. A) The spring is in compressed form and when release from the slot the bar hits the petri dish attached to the accelerometer. B) the top drop tower is release from a certain height to induce the insult. The line of action of impact is denoted by the yellow arrows in A & B. C) Schematical representation of A & B. D) Raw data display of acceleration response profile. E) Live cells stained with green/red fluorescence stain taken at 20X magnification before and every 3 minutes after the impact for 30 minutes. The red color indicates dead cells, and the green color indicates the live cells. The viability is calculated by dividing the total number of dead cells by the total number of cells.

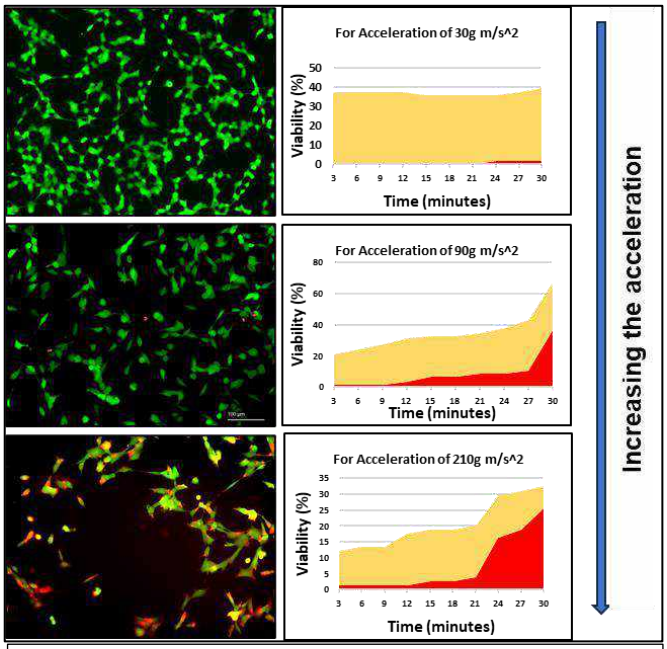

Figure 2: Cells viability at different acceleration. The yellow region in the graph represents unhealthy live cells and the red region represents dead cells. The number of cells is each of the 3 states (Normal cellular morphology, circular, and red) were identified and counted by BZ analyzer software.

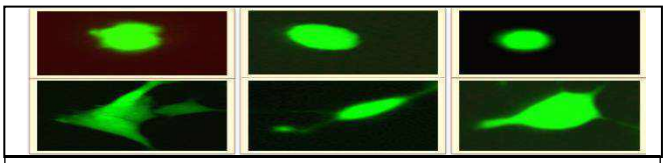

Figure 3: Cell morphology in healthy (top row) and unhealthy (bottom row) state.

DISCUSSION

As indicated in Figure 3, the cellular morphology changes indicate cell-damage as shown by the cells-shrinkage and circular shape. As the cell's stresses, they start to detach from the surface and forming a circular shape with minimal filipodia attachment. We hypothesize that these circular cells are an unhealthy state of the cells and as their concentration increase in the same region, their chances of survival reduce. In addition, in the group where TL is applied, the cell soma seems far more injured and beyond repair whereas for the SL group the cell soma is protected by the arms of the cells the dendrites and axons which when damaged can regrow and recover.

The healthy cells have extended filipodia and spindle-like shape whereas the round cells will either recover after certain amount of time or ultimately die. Axonal injury, loss of dendritic connections, loss of signal passage is known to recover after injury whereas cell soma cannot recover once dead leading to complex mechanical response of each cell. The reason for more dead cells in drop tower model may be due to the fact that cell soma is disrupted directly from surface of attachment with petri dish, whereas when impacted from the sides the axons and dendrites are more disrupted. This finding of directionality together with quantification of extent of cellular death with acceleration are our unique findings. In the case of high acceleration, we see that the whole structure has collapsed. We observe that the morphological change in the cell soma is minimal. But from this experiment we can clearly conclude that accelerations above 180g is fatal. This because some cells experienced spot death, whereas from literature we know it takes time for neuron cells to die due to their complex cellular structure. Thus, further investigation will be performed to fully understand this mechanism.

ACKNOWLEDGEMENTS

We sincerely acknowledge Dr. Timothy Bentley (Deputy, FHP Program) and ONR (N00014-21-1-2043) for supporting this work.

REFERENCES

[1]. J. Smith et al., "Placeholder Text: A Study," Citation Styles, vol. 3, Jul. 2021, doi: 10.10/X.

[2]. M. E. Edwards, S. S. S. Wang, and T. A. Good, "Role of viscoelastic properties of differentiated SH-SY5Y human neuroblastoma cells in cyclic shear stress injury," *Biotechnol Prog*, vol. 17, no. 4, pp. 760–767, 2001,

[3]. J B. Estrada et al. "Neural cell injury pathology due to high-rate mechanical loading", *Brain Multiphysics*, Volume 2, 2021, 100034

[4]. Rogers EA, Gross GW. Simultaneous electrophysiological and morphological assessment of functional damage to neural networks in vitro after 30–300 g impacts. Scientific Reports. 2019 Oct 18;9(1):14994.

LIVER INJURIES IN PORCINE DUE TO BEHIND ARMOR BLUNT TRAUMA

Parker R. Berthelson (1), Justin A. McMahon (1), Alexander V. Stotka (1), Barney J. McEntire (2), Robert S. Salzar (1)

(1) Mechanical and Aerospace Engineering, University of Virginia, Charlottesville, Virginia, USA
(2) Injury Biomechanics and Protection Group, U.S. Army Aeromedical Laboratory, Fort Novosel, Alabama, USA

INTRODUCTION

Body armor prevents ballistic munitions from penetrating the wearer's torso through the transfer and dissipation of ballistic energy into the deformation of the armor materials. However, this transfer results in a high-rate backface deformation that often leads to blunt injuries to the Warfighter [1-2]. This mechanism is referred to as behind armor blunt trauma (BABT).

The current design assessment methodology uses a clay surrogate (Roma Plastilina #1 [RP1]), clad with armor, to determine the backface deformation following impact loading [3]. A criterion of 44 millimeters (mm) of maximum deformation is then used to determine if the armor is sufficiently protective against BABT injuries [4]. While current armor designs have demonstrated success in BABT protection, there are key limitations to this design assessment criterion and methodology that lead to armors that are overdesigned, cumbersome, and heavy [5].

Primarily, there is limited medical basis for the 44 mm backface deformation criterion. This value was determined through concurrent caprine (clad with soft body armor) and ballistics gelatin testing where 44 mm was the average gelatin deformation [6]. This was later correlated to an overall 10% risk of mortality in the model [7]. Notably, no caprine test resulted in fatality in the original study at less than 44 mm of deformation [6-7]. Further, the current design assessment incorporates the 44 mm testing criterion for all regions of the armor and, in turn, all regions of the torso. It is likely, however, that different regions throughout the body have different levels of susceptibility to these BABT events and, thus, need different amounts of protection.

New criteria must be developed for localized body regions to inform and optimize future armor designs. To accomplish this, the physiological injury associated with impacts to varied body regions must be assessed using live animal surrogates. Previous studies have shown that porcine specimens are an ideal surrogate for the human torso as they have similar thoracic anatomy and physiological response [8-9]. By incorporating physiological injury, more discrete injury risk probabilities may be developed for various body regions that are susceptible to BABT-induced injury, such as the liver, lungs, and heart [10]. These probabilities may then be used to optimize the armor design through the reduction or addition of material depending on the regional injury risk. As such, this study focuses on quantifying the risk of inducing injuries to the liver through BABT.

METHODS

Impact tests were conducted to simulate BABT events using 15 Yorkshire porcine specimens with a target whole-body mass of 40 kilograms (kg) (mass = 45.6 ± 4.6 kg) to approximate the mass of a 50th percentile male human's torso sans extremities [11]. Prior to testing, all animal testing and handling protocols were approved by the University of Virginia (UVA) Animal Care and Use Committee (protocol: 4379-12-21) and the U.S. Army Animal Care and Use Review Office (protocol: MT21006.031.e002).

Upon arrival to the vivarium, each specimen was acclimated within the laboratory space for a minimum of three days prior to testing. On test day, each specimen was initially anesthetized with Telazol and maintained under anesthesia using 2% isoflurane with medical air. Throughout the anesthetized period, each specimen's vitals (blood oxygen, pulse rate, respiration rate, etc.) were monitored and recorded using a veterinary patient monitor (Avante Waveline VS) to ensure physiological stability. Prior to testing, bupivacaine, a local analgesic, was administered to the impact site.

Each impact test was conducted using a pneumatic linear-impactor system that propelled a 3D-printed indenter (mass = 0.245 kg, diameter = 10.2 centimeters [cm], nylon with carbon fiber reinforcement) into the specimen. The indenter's profile was modeled after the backface deformation of rigid body armor to represent a generic armor being impacted by a generic ballistic threat [2]. This indenter was equipped with an onboard single-axis accelerometer (Endevco 7270A) to allow for measurement of acceleration and acceleration-derived measures, such as velocity and displacement, throughout the impact event.

Each specimen was impacted a single time, with impacts conducted to the right side of the ribcage at the location of maximum liver surface area. This impact site was determined using B-Mode ultrasound imaging (Aixplorer Multiwave) to ensure that the liver would be sufficiently contacted by the indenter and to ensure that the more caudal organs, such as the bowels, were not significantly disrupted. Typically, this liver impact location overlapped with right ribs 8 through 12 and the caudal lobe of the right lung.

Following the completion of impact testing, the specimens were closely monitored until medical stability was determined, then they were recovered from anesthesia and returned to their housing area. The specimens were then closely supervised for approximately six hours post-impact (survival = 6.1 ± 0.6 hours) to observe the specimens' well-being over time. Following the survival window, specimens were imaged using computed tomography (CT) with contrast to document any structural or physiological injuries that may have been caused by the impact. Following imaging, the specimens were euthanized using Euthasol and a complete necropsy was conducted to confirm any injuries. The CT scans were then interpreted by a radiologist, who graded the injuries on the American Association for the Surgery of

Trauma (AAST) liver injury scale, which defines injury from grades 1-5 with 5 being the most severe [12].

In addition to the previously discussed measures, test metrics were calculated from the accelerometer data, including indenter velocity, impact energy, backface intrusion, impact force, and impulse. These metrics and injury diagnoses were then incorporated into the development of preliminary injury risk functions (IRF) using survival analysis. Here, data that resulted in induced injuries was considered left censored, while uninjured data was right censored. Predictor metrics and IRF distributions were assessed using the Briar Score (BS) and Akaike information criterion (AIC) [13].

RESULTS

Impact tests that simulate BABT events were conducted to the right side of the liver with resulting impact energies from 37.9 to 276.3 Joules (J). Figure 1 shows the distribution of AAST liver injury grades at each tested impact energy. Figure 2 presents the preliminary injury risk functions derived from this live porcine test data.

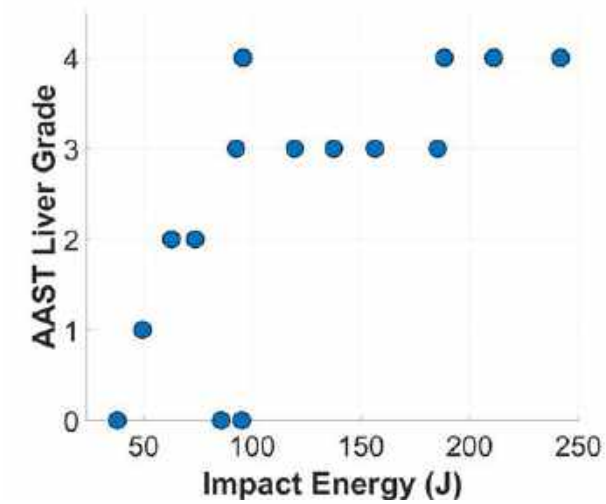

Figure 1: Observed injury outcomes across varied impact energy.

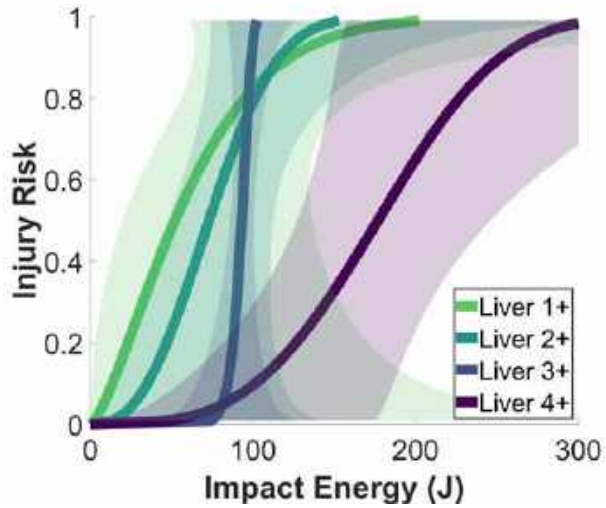

Figure 2: Preliminary injury risk functions that describe AAST grades 1+, 2+, 3+, and 4+ liver injury risk as a function of energy.

A wide array of liver injury severities was observed, ranging from non-injurious at low energies to AAST grade 4+ at high energies, as shown in Figure 1. The most severe of these resulted in large liver lacerations that caused significant active extravasation into the peritoneal cavity over time. In these severe cases, the liver injuries were often accompanied by severe lung contusions, as well as flail chest injuries (i.e., three or more flail rib segments) to the ribcage.

The preliminary IRFs, shown in Figure 2, used the impact energy as the predictor, due to its low BS (range: 0.1-4.5) compared to other metrics (i.e., backface intrusion BS range: 1.5-5.3), and were fit using the Weibull distribution, due to its relatively low AIC (range: 8.7-15.6). Here, the IRFs produced 50% risk levels for inducing AAST grade 1+ liver injuries at 52.0 J, grade 2+ at 72.9 J, grade 3+ at 93.0 J, and grade 4+ at 176.8 J.

DISCUSSION

The goal of this study was to investigate the liver's response to high-rate BABT impacts as a means of quantifying the susceptibility of the lower thoracic region to this injury mechanism. Tests resulted in both non-injurious and injurious outcomes, ranging from minor to very severe. Given the wide array of injury outcomes, IRFs were developed for AAST liver injury severity grades 1+, 2+, 3+, and 4+, illustrating the varied risk probabilities associated with low to high severity liver injuries across different impact energies. Despite current armor standards using backface intrusion as the sole criterion for assessing an armor's protective ability across all thoracic regions, the IRFs in this study produced lower BSs using impact energy as the predictor metric, rather than intrusion. These preliminary risk functions indicate that, generally, the greater severity injuries required increased input energy. However, some variation existed in the higher risk-regime, especially for the liver 3+ injury grades. The steep nature of this IRF was likely due to the data sampling, as only a single test with energy greater than 92.5 J resulted in an injury grade less than AAST level 3+. As testing is currently ongoing, these IRFs are preliminary, and future iterations will seek to improve the prediction at these key injury levels.

ACKNOWLEDGEMENTS

The authors would like to acknowledge Jeremy Gatesman, the UVA Center for Comparative Medicine, George Glass MD, Connor Sleeth MD, Kevin Kopp, Brian Overby, Joey White, and the UVA Center for Applied Biomechanics for their ongoing support throughout this study. The authors would also like to thank their consortium partners at the Medical College of Wisconsin, Duke University, Wayne State University, and the U.S. Army Aeromedical Research Laboratory. This project was supported by U.S. Army Medical Research and Development Command contract #W81XWH-15-9-001.

REFERENCES

[1] Cooper, G et al., *J Trauma*, 22(12), 994-1008, 1982.
[2] Bass, C et al., *Int J Occup Saf Ergon*, 12(4), 429-442, 2006.
[3] Prather, R et al., Report No. ARCSL-TR-77-55, 1977.
[4] NIJ Standard 0101.04, Report, 2000.
[5] National Research Council, 2012.
[6] Goldfarb, M et al., Report No. EB-TR-74073, 1975.
[7] Clare, V R et al., Report No. EB-TR-75016, 1975.
[8] Arborelius, U P et al., *Exp Lung Res*, 47(7), 323-333, 2021.
[9] Prat, N et al., *Forensic Sci Int*, 222(1-3), 179-185, 2012.
[10] Carroll A et al., *Ann Surg*, 188(6), 753-757, 1978.
[11] Clauser C et al., Report No. AMRL-TR-69-70, 1969.
[12] Kozar, R et al., *J Trauma Acute Care Surg*, 85(6), 1119-1122, 2018.
[13] Hostetler, Z et al., *Ann Biomed Eng*, 49, 3091-3098, 2021.

A REACTIVE VISCOELASTIC MODEL OF THE MACAQUE RHESUS CERVIX TO QUANTIFY CERVICAL REMODELING

Camilo A. Duarte-Cordon[1], Shuyang Fang[1], Ivan M. Rosado-Mendez[2,3], Timothy J. Hall[2], Helen Feltovich[4], Kristin M. Myers[1]

[1]Department of Mechanical Engineering, Columbia University, New York, NY, USA
[2]Department of Medical Physics, University of Wisconsin-Madison, Madison, WI, USA
[3]Department of Radiology, University of Wisconsin-Madison, Madison, WI, USA
[4]Department of Obstetrics & Gynecology, Mount Sinai, New York, NY, USA

INTRODUCTION

The cervix is a collagenous and hydrated tissue that plays a crucial mechanical role in pregnancy. During gestation, the cervix transforms from a rigid and closed structure that sustains the growing load of the fetus in the uterus to a soft and extensible structure that opens to allow birth at term.[1] This process, known as cervical remodeling, involves alterations in the cervix's extracellular matrix (ECM). Within the time scale of acute physiological loading, the cervix exhibits complex time-dependent mechanical behavior, including viscoelasticity, which is believed to be influenced by structural changes in its ECM. A fundamental understanding of the viscoelastic properties of the cervix is essential for developing quantitative ultrasound-based methods to predict cervical pathophysiologies, for instance, cervical insufficiency, which leads to preterm birth. Constitutive material models calibrated with *ex vivo* mechanical testing data from animal and human cervical tissue are valuable tools for quantifying changes in cervical ECM mechanical properties through pregnancy.[2,3] Nevertheless, most studies have focused on the mechanical properties of the cervix under equilibrium conditions. In a few studies examining the time-dependent response of cervical tissue, its viscoelastic properties were obtained only under compressive loading[4] and at two gestational points (pregnant and non-pregnant). Since the cervix exhibits tension–compression asymmetric mechanical response, quantifying the nonlinear time-dependent properties of the cervix under tensile loading will help us understand ECM remodeling, particularly the role of the collagen fiber network. Additionally, pregnancy is a protected environment, which is why studying the cervical viscoelastic response using experimental data from homologous human species, such as rhesus macaques (Fig. 1A), allows us to study the cervix viscoelasticity at multiple and relevant gestational time points.

METHODS

To study the time-dependent mechanical response of the cervix under tensile stress, we implemented a nonlinear viscoelastic model of the rhesus macaque cervical ECM based on the theory of reactive viscoelasticity.[5] In reactive viscoelasticity, biological tissue is modeled as a mixture of strong and weak

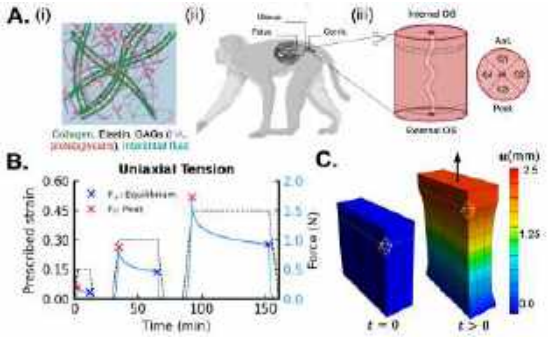

Figure 1: A. (i) Cervical extracellular matrix (ECM), (ii) rhesus macaque anatomy, and (iii) schematic of its cervix, showing the locations and quadrants from where specimens were dissected. B. Representative stress-relaxation curve showing peak F_0 and equilibrium forces F_∞, and C. finite element model built for IFEA.

bonds. Strong and weak bonds are responsible for the equilibrium and transient response of the material, respectively. Furthermore, due to the loading, weak bonds break and reform into a stress-free state. Inspired by the cervical ECM shown in Fig. 1A(i), cervical tissue is modeled as a continuous collagen fiber distribution embedded in a compressible neo-Hookean ground matrix. Only the fibers were assumed to be viscoelastic. The ground substance, which models the mechanical response of glycosaminoglycans (GAGs) and other proteins, only contributes to the equilibrium elastic response of the tissue. We used a continuous fiber distribution model for the strong and weak bonds of the reactive viscoelastic material. The constitutive model parameters were obtained by a three-step inverse finite element analysis (IFEA) using the software packages Dakota and FEBio. In IFEA, the material model parameters are estimated by maximizing the agreement between stress-relaxation curves obtained from simulations and uniaxial tension experiments. We used mechanical testing data from 30 cervical tissue samples collected from four rhesus macaques at the following gestational time points: non-pregnancy (NP), early second trimester (E2), early third trimester (E3), and late third trimester (L3).[6] In brief, cervical tissue samples were dissected from the cervix external os (EO) and internal os (IO) and in differ-

ent quadrants (Fig. 1A(ii) and (iii)). Quadrant 1 (Q1) corresponds to the anterior part of the cervix, quadrant 3 (Q3) is the posterior region, and quadrants 2 and 4 (Q2 and Q4) are the lateral right and left areas of the cervix, respectively. The uniaxial tension test consisted of three load-hold-unload cycles with prescribed displacements of 15%, 30%, and 45% of the grip-to-grip distance (Fig. 1B). A representative finite element (FE) model of the uniaxial tension specimen built for IFEA is shown in Fig. 1C. In total, nine material parameters were estimated from the IFEA, including the Young's modulus and Poisson's ratio of the ground matrix (E, ν), the initial fiber stiffness and stiffening effect constant for the strong (ξ_s, α_s) and weak bonds (ξ_w, α_w), and the exponential distortional relaxation function constants (τ_0, τ_1, α).

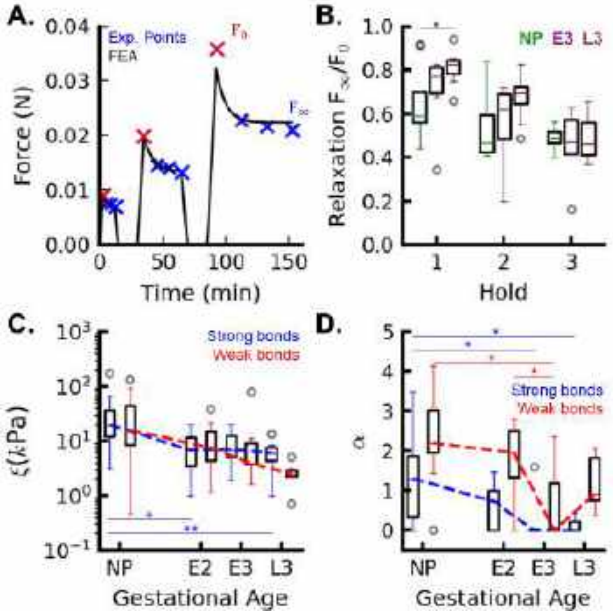

Figure 2: A. Representative force-relaxation curve obtained from finite element simulations (FEA), showing the experimental points used for IFEA. Summary results of material properties showing B. Relaxation ratio F_∞/F_0, C. fiber initial stiffness ξ, and D. stiffening effect constant α for weak and strong bonds (* $p \leq 0.05$, $p \leq 0.01$, and *** $p \leq 0.001$).**

RESULTS

Rhesus macaque cervical tissue exhibits nonlinear viscoelastic mechanical behavior under tensile loading. The reactive viscoelastic material model captures the equilibrium and time-dependent response of rhesus macaque cervical tissue subjected to uniaxial testing, where Fig. 2A shows a representative fitting result of an early second-trimester (E2) specimen dissected from the external os. A comparison of material properties (F_∞/F_0, ξ, and α) for different gestational ages is shown in Fig. 2B, C, and D. The relaxation ratios F_∞/F_0 for E3 and L3 pregnant tissue decrease from hold 1 to 3, with prescribed strains going from 15 % to 45% of the sample length. In contrast, the median value of F_∞/F_0 remains constant for NP. Furthermore, for hold 1 with a prescribed strain of 15%, the relaxation is lower for NP than for L3, suggesting that both samples have similar levels of viscoelasticity. For holds 2 and 3, no significant differences in the relaxation ratios were observed between samples from different gestational age groups. The median initial fiber stiffnesses ξ_s and ξ_w of the strong and weak bonds, respectively, decreased with gestational age, indicating that the cervix became more compliant as pregnancy progresses (Fig. 2C). The stiffening coefficients α_s and α_w also decreased during pregnancy, particularly after the second early trimester (E2), as shown in Fig. 2D. These results suggest that pregnant specimens are more extensible than nonpregnant samples, particularly during late pregnancy. No significant differences were found in other material parameters with the anatomical location and pregnancy status.

DISCUSSION

In this work, we present the implementation of a reactive viscoelastic constitutive model of the rhesus macaque cervix. The model also accounts for the different components of the cervical ECM microstructure, such as the collagen fiber network and ground substance, representing the contribution of GAGs. The model fits well with the multi-ramp uniaxial tension force-relaxation data of rhesus macaque cervical tissue. Notably, the constitutive model allows us to study cervical remodeling in terms of changes in its equilibrium and time-dependent mechanical properties at different gestational time points. We observed that the cervical collagen network plays a significant role in its mechanical response under tensile loading. The initial stiffness of the collagen fibers and stiffening effect coefficient decrease with gestational age, similar to findings from previous studies on cervical remodeling in mice and human tissue. Evidence has shown that this stiffness decrease correlates to a decrease in mature collagen crosslinking in pregnancy. Regarding the time-dependent mechanical properties of the cervix, we observed that the relaxation ratio decreases with prescribed strain for pregnant samples (E3 and L3), whereas for NP, it remains constant. Although the amount of relaxation is similar between pregnant and nonpregnant samples up to a deformation of 45 %, we hypothesize that as deformation increases over this strain value, pregnant samples will decrease their relaxation value and become more viscoelastic.

ACKNOWLEDGMENTS

This research was supported by the Eunice Kennedy Shriver National Institute Of Child Health & Human Development under Award Number R01HD091153 to KMM and R01HD072077 to KMM, HF, and TJH. The content is solely the responsibility of the authors and does not necessarily represent the official views of the National Institutes of Health.

REFERENCES

[1] B. Timmons, M. Akins, M. Mahendroo, *Trends in Endocrinology & Metabolism* **2010**, *21*, 353–361. [2] L. Shi, L. Hu, N. Lee, S. Fang, K. Myers, *Acta Biomaterialia* **2022**, *150*, 277–294. [3] K. Yoshida, H. Jiang, M. Kim, J. Vink, S. Cremers, D. Paik, R. Wapner, M. Mahendroo, K. Myers, *PLoS ONE* **2014**, *9*, (Ed.: L. Kreplak), e112391. [4] L. Shi, K. Myers, *Journal of the Mechanical Behavior of Biomedical Materials* **2023**, *143*, 105875. [5] G. A. Ateshian, *Journal of Biomechanics* **2015**, *48*, 941–947. [6] S. Fang, L. Shi, J.-S. Y. Vink, H. Feltovich, T. J. Hall, K. M. Myers, *in press*.

BIOMECHANICAL COMPARISON OF COMMONLY USED THREE DIFFERENT MATERIAL COMPOSITION USED IN CERVICAL DISC ARTHROPLASTY

Yuvaraj Purushothaman (1), Resetar Ethan (2), Hoon Choi (1) Abdulbaki Kozan (1) Narayan Yoganandan (3)

(1) Department of Neurological Surgery
Cleveland Clinic Florida
Weston, FL
(2) Department of Neurology
University of Michigan
Ann Arbor, MI
(3) Department of Neurosurgery
Medical College of Wisconsin
Milwaukee, WI

INTRODUCTION

Anterior cervical discectomy and fusion (ACDF) has traditionally been a widely employed procedure, providing relief from cervical myelopathy and radiculopathy by removing the degenerated disc and promoting fusion between adjacent vertebrae. However, concerns about adjacent segment degeneration and restricted motion have led to the rise of cervical disc arthroplasty (CDA) as an alternative which have been shown to reduce the incidence of adjacent segment disease and need for secondary surgery [1,2]. CDA involves the replacement of degenerated disc with an artificial one aiming to maintain natural spine biomechanics. There are currently several varieties of cervical disc arthroplasty device approved by the FDA and in use by orthopedic and neurosurgical physicians as an alternative to spinal arthrodesis [3]. Each of these devices vary in either material composition, number of moving parts, or both. The different materials composition is most important in their utilization as bearing surfaces which allow for articular motion at the disc space. One issue arising with the variety of CDA devices is a potential for variability in surgical outcomes. It is necessary to investigate how these subtle design and material variations in devices impact spine biomechanics in order to promote positive patient outcomes. The purpose of this study is to investigate the material construction of three different CDA devices (Prestige LP-metal on metal (MOM), Mobi-C- metal on polymer (MOP), Simplify- Polymer on ceramic (POC)) and their impact on cervical spine biomechanics in terms of range of motion (ROM) and facet joint loading.

METHODS

The validated three-dimensional finite element model was used for this study, representing the entire human cervical spinal column spanning from C2 to T1 [4]. The comprehensive intact spine model incorporated all structural components, including bony vertebrae, intervertebral discs, facet joints, and all soft tissue spinal ligaments. Each vertebral body was composed of cortical shell, cancellous bone, and superior and inferior endplates. The intervertebral disc within the model were represented as composite structures of the nucleus pulposus, annulus ground substance and annulus fibers securely attached to the vertebral endplates. The simulated discs were designed to accurately mirror the anteroposterior asymmetry of the human cervical spine. The annular fibers within the disc were structured with a crisscross pattern in the anterior region and oriented vertically in the posterior region to truly capture the nonlinear and orthotropic attributes of the annulus fibrosus. In addition, all ligaments integrated into the model were constructed based on their anatomical attachments and incorporated material properties drawn from well-established literature, aligning with standard practices in finite element modeling studies. The entire model was developed using a mapping block-based hexahedral meshing technique for solid elements and quadrilateral elements were used for soft tissue ligaments.

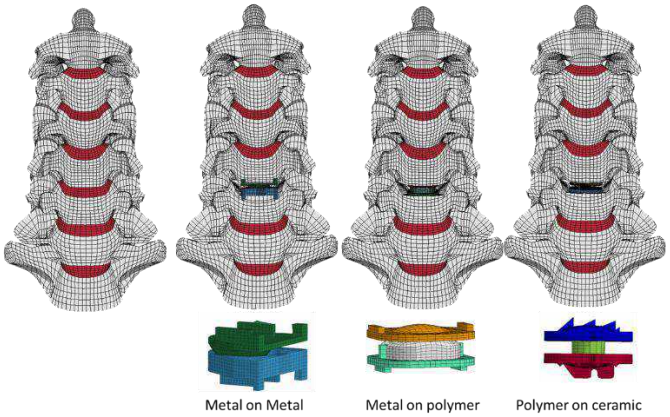

Figure 1: **coronal view of the spinal column (Intact), and the three US FDA approved discs (second (MOM), third (MOP), Fourth (POC) from left).**

The intact spine was modified at the C5-C6 functional spine unit level to simulate the biomechanics of three types of CDAs. The standard surgical procedure was used to simulate CDA at the C5-C6 level (Figure

1). The anterior longitudinal ligament was removed at the surgical level in both cases. In the case of ADR, a cavity was created at the implanted level for the placement of the disc prosthesis. All surgical procedures were executed under the close oversight and expertise of the lead author, a neurosurgeon with extensive clinical experience in cervical disc arthroplasty procedures.

All the finite element models were fixed at the T1 thoracic vertebra in all degrees of freedom, and the load was applied at the C2 superior endplate vertebra. Bending moment (2 Nm) combined with a follower load (75N) magnitude under flexion and extension and lateral bending was applied to the three groups (Prestige LP (MOM), Mobi-C (MOP) and Simplify (POC)). The range of motion was measured at each level and across the C3-C7 levels. The variable moment loading protocol (otherwise known as hybrid loading) was next applied [5]. The bending moment was varied until the MOM, and MOP and POC models displayed the same total range of motion across the C3-C7 levels (although individual segments could have different range of motion). The range of motion and facet force were obtained at the index and adjacent segments under the same loading mode.

RESULTS

FEM testing demonstrated polymer on ceramic to have less ROM, lower index level and both adjacent facet forces in inferior and superior level compared to the metal on metal and metal on polymer CDA's. The metal-on-metal CDA had an 8% inferior and 5% at the superior level decrease in ROM compared to the intact model in adjacent segment flexion. The CDA with metal on polymer had a 5.1% at inferior 13.9% at the superior level decrease compared to the intact. The polymer on ceramic CDA had an 10% inferior and 17.5% at the superior level decrease in ROM compared to the intact model in adjacent segment.

In extension inferior 7.2% and superior 4.5% decrease for MOM, 11.5% and superior 12.5% decrease for MOP and POC CDA at inferior 13% and inferior 16.2% decrease in compared to the intact. Similar decrease was observed in lateral bending with 7.9%, 15.1% and 16.5% in inferior and 5.4%, 15.5% and 12.7% at the superior level for MOM, MOP and POC respectively when compared to intact (Figure 2).

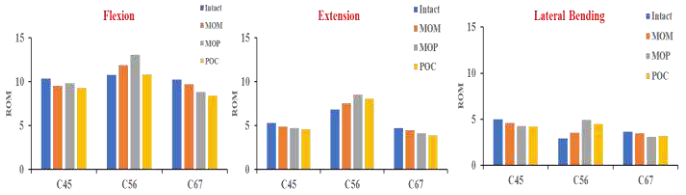

Figure 2: Range of motion at index level and adjacent segments

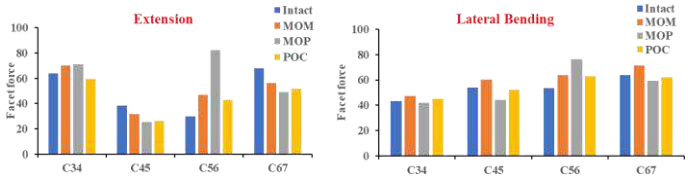

Figure 3: Facet force at index level and adjacent segments

This ROM at adjacent levels results in increased facet forces in MOM by 16.9% and 17% inferior and superior as compared to intact in extension and 11.3% inferior and 12.1% superior in lateral bending. The MOP exhibited 33.9% decrease inferiorly and 27.4% decrease superiorly when compared to intact in extension and 18.4% decrease inferiorly and 6.9 % decrease superiorly in lateral bending. In case of POC facet force decreased by 31.3% and 23.9% inferior and superior as compared to intact in extension and 3.8% Inferior and 2.6% superior in lateral bending. However, at the index level the MOM had a 56.21% and 19.6% increase in facet force at the index level compared to intact spine, similar increase of 174.3% and 43.1% in MOP and POC by 43.3% and 18.1% in extension and lateral bending respectively (Figure 3).

DISCUSSION

The objective of this research is to investigate how variations in the material composition of cervical disc arthroplasty device implanted at the C5-C6 vertebral level impact spinal biomechanics with respect to range of motion and facet joint loading forces. To evaluate this, a finite element (FE) model was used. Cadaveric studies are not as effective for this type of research as the variation of individual vertebral column morphologies lead to confounding variables that can only be overcome by large sample sizes.

The comprehensive biomechanical evaluation of three cervical disc arthroplasty devices- metal on metal (Prestige LP), metal on polymer (Mobi-C), and polymer on ceramic (Simplify)- revealed distinctive performance characteristics with potential clinical implications. Understanding these nuances is critical for informed decision making in spinal surgery. These three devices were compared to a model of an intact disc. It was found that the ceramic on polymer disc most closely matched the degree of spinal flexion seen in an intact model compared to the other material compositions. All three devices demonstrated a similar level of adjacent level flexion compared to the intact model. In extension and lateral bending, it was seen that the MOM most closely mimicked the intact model followed closely by the COP then the MOP device. Facet forces were calculated as a measure of the posterior portion of the vertebral column. During extension the facet forces at the level of implant were increased in all three material compositions with the greatest increases seen in the MOP followed by MOM devices. For the lateral bending the MOM exhibited an increase in force at the adjacent levels while the MOP displayed a large decrease in facet force. The simplify disc most closely mimicked the forces modeled by the intact disc. Adjacent segment disease (ASD) is characterized by degeneration of the intervertebral disc at spine segments that are adjacent to the site of spinal arthrodesis. This is typically accompanied by onset of symptoms reflecting radiculopathy or myelopathy. It has been shown that arthrodesis of a spinal segment leads to increased stress on the adjacent levels [6]. It believed that abnormal disc loading and increased forces on the intervertebral disc are applicable to the occurrence of ASD [7]. While all three of the material types demonstrate some deviation in biomechanical outcomes, the Simplify disc (polymer on ceramic) most closely matched the intact disc in terms of ROM and facet forces. This is important as reducing the strain on adjacent levels could lead to decreased incidence of ASD and necessity of reoperation.

ACKNOWLEDGEMENTS

This study was supported by the Office of the Assistant Secretary of Defense for Health Affairs, through the Broad Agency Announcement under Award No. W81XWH-16-1-0010 and the Department of Veterans Affairs Medical Center, Milwaukee.

REFERENCES

[1] Epstein NE et al., Surg Neurol Int., 2022
[2] Chang CJ, et al., J Neurosurg Spine, 2022.
[3] US FDA fda.gov
[4] John JD, et al., SB3C, 2017.
[5] Patwardhan A, et al., Spine 2001.
[6] Prasarn, M. L., et al., Journal of Neurosurgery: Spine, 2012.
[7] Tobert DG, et al., Clin Spine Surg. 2017

TRANSCATHETER AORTIC VALVE HEMODYNAMICS IN HALT POSITIVE AND NEGATIVE PATIENT COHORTS: AN FSI STUDY

Thangam Natarajan (1), Aniket Venkatesh (1), Stephanie L. Sellers (2), Janarthanan Sathananthan (2) and Lakshmi P. Dasi (1)

(1) Wallace H. Coulter Department of Biomedical Engineering, Georgia Institute of Technology, Atlanta, GA, USA
(2) Centre for Heart Valve Innovation, St. Paul's Hospital, University of British Columbia, Vancouver, Canada

INTRODUCTION

Transcatheter aortic valve replacement (TAVR) is a minimally invasive procedure involving the insertion of a (crimped) bioprosthetic valve via a catheter to replace a stenosed native aortic valve. Positioned as a successful treatment for high-surgical-risk patients with severe symptomatic aortic stenosis, TAVR saw approximately 72,000 procedures in the US in 2019 [1]. The 5-year PARTNER trial indicates comparable results between TAVR and SAVR, making TAVR the preferred treatment for high-risk patients, extending to a younger demographic [2]. However, the trial revealed a significant concern: Subclinical leaflet thrombosis, with up to 30% of patients exhibiting hypoattenuated leaflet thickening (HALT) and reduced leaflet motion (RLM) sometimes within the first year of implantation.

The etiology of leaflet thrombosis can be aligned with the Virchow's triad, where flow dynamics (flow-mediated shear, stasis), mechanical stresses of the TAV itself (over and under-expansion, alignment, and foreign materials), and biological factors (blood chemistry). [3]. Studies suggest that hemodynamics in the neo-sinus, the region between native and bioprosthetic leaflets, may trigger thrombus formation. Flow stasis or sustained low velocity in the neo-sinus could be key contributors [4, 5]. Despite oral anticoagulation (OAC) recommendations for thrombosis risk, it may not consistently benefit patients and can pose risks like thromboembolism and bleeding.

Therefore the objective of this study is to investigate the hemodynamics in regions around the Transcatheter aortic valve (TAV) using a loosely coupled fluid-structure interaction approach across four patient-specific anatomies with blinded HALT outcomes. The work involves the virtual deployment of a bioprosthetic valve using pre-TAVR CTs, followed by structural simulations for leaflet kinematics and fluid simulations for flow characteristics. First, we seek to establish a methodology where we use pre-TAVR CTs to segment and then deploy a bioprosthetic valve virtually. Then, we initiate a structural simulation to obtain the leaflet kinematics and integrate the displaced leaflets into a fluid simulation to obtain the flow characteristics. We initially validate our methodology against already published experiments and then present the hemodynamics of these four cases aiming to contribute to a deeper understanding of subclinical leaflet thrombosis and its links to hemodynamics in the neo-sinus.

METHODS

Patient anatomies were segmented, smoothed and converted to surface files from pre-TAVR CT scans. A bioprosthetic valve (SAPIEN 3) was deployed in these anatomies virtually using a reduced order method (ROM). This approach simulated the post-TAVR condition. Subsequently, patient-specific pressure waveforms were applied to the deployed valve leaflets, and their displacement and motion were obtained through finite element modeling (FEA) in Abaqus. The leaflet motion data were then integrated into fluid flow simulations under patient-specific conditions, conducted using the Open Field Operation and Manipulation (OpenFOAM) code.

The simulations involved solving the incompressible Navier-Stokes equations, assuming blood as Newtonian with a kinematic viscosity and density of 0.0036 Pa s and 1060 kg/m3, respectively. Aortic flow rate waveform was prescribed at the inlet and a generic pressure waveform was prescribed at the outlet and a no-slip boundary condition was applied to the walls. For each patient, the aortic flow waveform was scaled to match the patient's peak systolic flow rate, obtained from analysis of the left ventricular volume over the cardiac cycle. Parallel processing was implemented through the Message-passing interface (MPI) protocol, with grid partitioning facilitated by the SCOTCH algorithm [6]. Hexahedral control volumes discretized all grids, focusing on clustering cells around thin structures such as leaflets and stents. Each simulation ran for five cycles to mitigate initial transients, and results were extracted from the last cycle for presentation.The simulations were performed on Linux machines equipped with dual Intel Xeon 6226 @ 2.7 GHz CPUs on the PACE Phoenix cluster [7].

RESULTS

In fig. 1, a time-lapse top-down view illustrates leaflet motion from early systole (completely closed) to peak systole (completely open) for

one of the examined cases. The leaflet dynamics obtained from FEA simulations align closely with experimentally observed dynamics, validating our methodology to obtain the displaced leaflets. Figure 2 shows the instantaneous flow fields via velocity magnitude along the center slice of the anatomy at peak systole and late diastole. Inset figures indicate corresponding leaflet displacements. The centerline jet remains well-preserved, breaking down gradually upon impingement on the aortic arch before reaching the descending aorta. Notably, the flow around the sinus region exhibits greater persistence during diastole than the systolic phase. In fig. 3, vortex cores are presented via isosurfaces of Q-criterion (colored by vorticity) during various points in the cardiac cycle. Vortex cores break down, with a more prominent presence in the diastolic phase, particularly clustering around the sinus region.

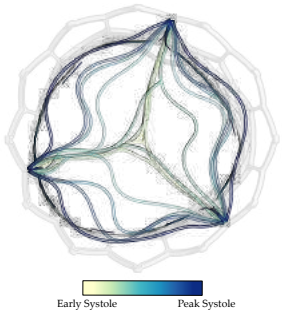

Figure 1: Top view of the bioprosthetic leaflet dynamics overlaid on top of each other from early systole to peak systole

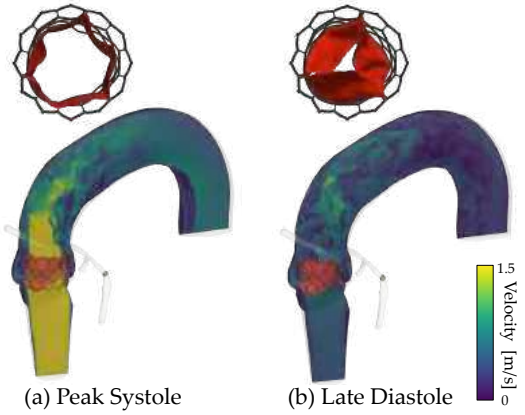

Figure 2: Velocity magnitude along the slice of the anatomy at (a) peak systole and (2) late diastole and the inset figures showing the opening area of the leaflets.

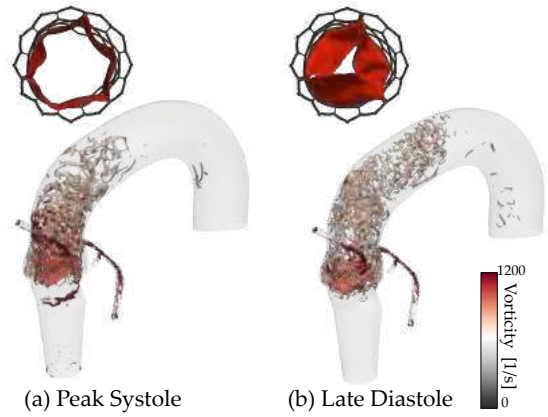

Figure 3: Isosurfaces of Q-criterion visualized at (a) peak systole and (2) late diastole and the inset figures showing the opening area of the leaflets.

DISCUSSION

Qualitative assessment of instantaneous flow fields reveals notable high-frequency flow fluctuations throughout the cardiac cycle. The impact of these fluctuations on degenerative changes, such as endothelial or mural cell remodeling and turnover, is well-documented [8, 9]. To investigate these flow fluctuations, we intend to analyze them spectrally using short-time Fourier transforms (STFT) represented via spectrograms [10].

Studies by Biasetti et al. [11] and Naim et al. [12] emphasize the significance of vortical structures and their interaction with the vessel wall or lumen. As a first step we investigate the evolution and interaction of vortical structures throughout the cardiac cycle by extracting the Q-criterion. Subsequently, given the known association of flow structures, particularly vortex cores, with thrombosis development and progression, we aim to assess the intensity of these vortex cores alongside wall shear stress in the relevant region.

Considering fluid dynamics, the hypothesized contribution of flow stasis to HALT prompts further investigation. We will analyze washout curves and identify flow stagnation regions around the sinus and neosinus, comparing outcomes between HALT-positive and HALT-negative cohorts. Steep washout curves, indicating efficient particle exit from the neo-sinus region in fewer cycles, generally suggest improved flow circulation. This comprehensive analysis aims to enhance our understanding of the hemodynamic factors contributing to HALT and further informs potential implications for patient outcomes.

In summary, our study intends to explore the fluid dynamics of TAVR, focusing on subclinical leaflet thrombosis. Through advanced simulations, we initially validate dynamic leaflet motion, revealing insights into flow fluctuations and vortex cores. Examining washout curves and flow stagnation regions in HALT-positive and HALT-negative cases could provide key perspectives on flow dynamics. These findings may offer valuable insights for better understanding HALT, contributing to improved patient care and informed clinical decisions in TAVR procedures.

REFERENCES

[1] Popma JJ et al. *New England Journal of Medicine* 380.18 (2019).

[2] Mack MJ et al. *New England Journal of Medicine* 389.21 (2023).

[3] Raghav V et al. *Journal of the Royal Society Interface* 18.184 (2021).

[4] Hatoum H et al. *The Journal of thoracic and cardiovascular surgery* 157.2 (2019).

[5] Trusty PM et al. *The Journal of thoracic and cardiovascular surgery* 164.3 (2022).

[6] Pellegrini F et al. *High-Performance Computing and Networking: International Conference and Exhibition HPCN EUROPE 1996 Brussels, Belgium, April 15–19, 1996 Proceedings 4*. Springer. 1996.

[7] PACE D (2017).

[8] Barakat AI. *Comptes Rendus Physique* 14.6 (2013).

[9] Davies PF et al. *Proceedings of the National Academy of Sciences* 83.7 (1986).

[10] Natarajan T et al. *Journal of Biomechanics* 110 (2020).

[11] Biasetti J et al. *Journal of The Royal Society Interface* 8.63 (2011).

[12] Ab Naim WNW et al. *Applied Mathematical Modelling* 40.4 (2016).

COMPUTATIONAL MODELING OF CAROTID ARTERY STENOSIS AND FIBROMUSCULAR DYSPLASIA FOR PREDICTION OF BIOMECHANICAL PLATELET ACTIVATION

James S. Malloy (1), Suman M. Guntupalli (2), Scott J. Cameron (2), Vitaliy L. Rayz (1,3)

(1) Biomedical Engineering, Purdue University, West Lafayette, IN, USA
(2) Vascular Medicine, Cleveland Clinic, Cleveland, OH, USA
(3) Mechanical Engineering, Purdue University, West Lafayette, IN, USA

INTRODUCTION

Fibromuscular dysplasia (FMD) is a non-inflammatory, non-atherosclerotic blood vessel disorder, most commonly affecting the carotid and renal arteries, that results in alternating regions of narrowed and dilated vasculature [1]. This so-called "string of beads" in multifocal FMD increases the risk of catastrophic vascular events including arterial dissection due to known weaknesses in the blood vessel well as well as platelet action as platelets and mechanically stimulated following exposure to disturbed blood flow (D-flow) in the ectatic artery. Both events increase the risk for thrombotic stroke. [2]. FMD often affects multiple regions of an artery, in contrast to carotid artery stenosis, which can be concentrated in a single location in the vessel. FMD is diagnosed via computed tomography angiography (CTA), MRA, or Carotid Duplex imaging but is not always easily distinguishable from other arterial diseases that cause arterial stenosis. Imaging-based diagnoses also make it challenging to determine which patients are at highest risk for stroke to properly manage medication. The purpose of this study is to analyze the hemodynamic environment in the carotid artery of patients with FMD compared with carotid artery stenosis to quantify the unique mechanical stress environment created from multifocal malformations. Comparisons are to be made against healthy arteries, as well as carotid artery stenosis (CAS) to determine any unique biomechanical patterns that can be found in patients with multifocal FMD for improved diagnostic decision making. Predictions of mechanical platelet activation will also be compared to platelet sensitivity to activation for patients with each respective disease to further characterize the effects of these diseases on platelet activation and clot formation. These findings will serve as the basis for incorporating quantitative metrics of platelet activation risk to clinical management of FMD patients.

METHODS

To quantify the hemodynamic conditions for FMD and stenotic carotid arteries, image-based models of diseased vasculature were imported into an open-source modeling software, Simvascular. Multiple cases, ranging severity of both FMD and CAS were used to characterize the biomechanical impact of each respective disease on blood flow and platelets. The flow was modeled as Newtonian and laminar and the arterial walls were assumed rigid. Generalized boundary conditions for inlet flow rates and outlet Windkessel conditions were assigned to the solver and the transient Navier-Stokes equations were numerically solved to obtain velocity fields. Computed velocity gradients were used to calculate the VonMises-like scalar stress at nodes according to (1):

$$\tau = \frac{1}{6}\left[(\sigma_x - \sigma_y)^2 + (\sigma_y - \sigma_z)^2 + (\sigma_x - \sigma_z)^2\right] + {\tau_{xy}}^2 + {\tau_{yz}}^2 + {\tau_{xz}}^2 \quad (1)$$

where, sigma and tau correspond to components of the rate of strain tensor. This evaluates the level of mechanical stress that the platelets experience as a result of the velocity field and has been used in the past to assess hemodynamic stress for red blood cells and platelets [3].

Biomechanical platelet activation is known to be a function of both platelet surface stress level and exposure time [3]. For each vascular geometry, the computed velocity field was used for Lagrangian particle tracking over multiple cardiac cycles, to represent the trajectories of platelets. This generates a stress history that discerns how long circulating platelets spend in different stress regions. A fourth order Runge-Kutta scheme, in combination with trilinear interpolation was utilized to advect particles as they travel through the vessel. The resulting stress history was then used to assess the levels of mechanical platelet activation, as defined by Soares et al. [4]. This three term model was solved using a fourth-order Runge-Kutta from the ordinary differential equation, shown below.

$$\frac{dPAS(t)}{dt} = [S(PAS, H_\tau) + F(PAS, \tau) + G(PAS, \dot{t})](1 - PAS) \quad (2)$$

In this equation, PAS is the platelet activation state at time t. S corresponds to the stress accumulation, where H is the integral of stress up to a time t. F is the contribution of the current level of stress. G is determined by the rate of stress loading.

$$S(PAS, H_\tau) = S_r * PAS * H_\tau \quad (3)$$

$$H_\tau = \int_0^t \tau(s)ds \quad (4)$$

$$F(PAS, \tau) = C^{\frac{1}{\beta}} * \beta * PAS^{\frac{\beta-1}{\beta}} * \tau^{\frac{\alpha}{\beta}} \quad (5)$$

$$G(PAS, \dot{\tau}) = C_r^{\frac{1}{\delta}} * PAS^{\frac{\delta-1}{\delta}} * |\dot{\tau}|^{\frac{\gamma}{\delta}} \quad (6)$$

The threshold for platelet activation which would increase the risk for stroke is also assessed in experiments, using platelets isolated from patients with FMD and CAS. These platelets are subjected to mechanical loading in rotating flow cones designed to produce varying levels of mechanical stress, especially resembling D-flow conditions. Platelet activation is then assessed via the appearance of surface biomarkers, such as CD62P (p-selectin), which is a widely accepted method to demonstrate increased expression in activated platelets [5].

RESULTS

Shown in Figure 1 is one representative case of FMD (1A), healthy (1B), and CAS (1C). Direct comparisons of hemodynamics within a single case of FMD in comparison to healthy vasculature, identified small regions of increased VonMises stress in multiple regions of the FMD patient, where there are noticeable beading patterns (1A). In contrast to this, the healthy case, has relatively uniform stress across straight segments of the artery (1B). The CAS model showed concentrated regions of elevated stress near to the stenosis (1C).

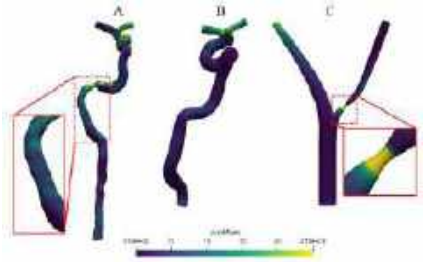

Figure 1: Stress Distribution in FMD, Healthy, and CAS Carotid

Initial results comparing single cases of FMD, and healthy arteries show increased levels of PAS in the left and right carotid of the FMD in comparison to the left and right healthy carotid artery respectively (2).

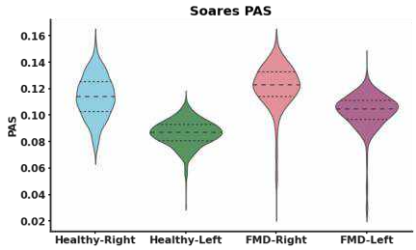

Figure 2: Predicted platelet activation in Healthy vs FMD Carotid

Platelets from FMD patients, healthy patients, and CAS patients showed differences in p-selectin expression after exposure to mechanical stress via rotating flow cones. Platelets isolated from FMD patients exhibited the highest amounts of p-selectin, demonstrating their increased reactivity to mechanical stress environments.

DISCUSSION

Stress distributions within the healthy, CAS, and FMD arteries show differences in the variations that may be seen in the stress history of platelets traveling through these patients. The major difference is the continuous pattern of elevated stresses along the wall of FMD patients. This continuous exposure to elevated levels of stress has the potential to induce activation, known to be a function of both stress and exposure time. This is a pattern that is unique to FMD and may present in a characteristic phenotype that can be used for more targeted diagnostic and therapeutic approaches to FMD. In comparison, CAS models show a focal region of higher shear, where platelets would likely reside in for a short period of time. The subsequent relaxation may create differences in activation characteristics of platelets highlighted in platelet activation state modeling and surface biomarker studies.

Initial comparisons identified minor elevation in PAS for the FMD patient carotid arteries compared to the healthy patient carotids. These results may be exemplified in further analysis of different arterial geometries and the platelet pathways. The initial results show promise in differentiating a case that does not have substantial regions of disturbed and recirculating flow or tortuous beading patterns observed in more severe cases of FMD. As such, looking at a broader range of FMD severity may lead to increased differences observed between the healthy and diseased cases. Additionally, the inclusion of patient outcomes will further validate findings by comparing numerically predicted activation levels to experimentally measured sensitivity of platelets to mechanical activation observed for the same patients.

Future analysis of stenotic in comparison to FMD and healthy vessels will provide confirmation of expected differences in stress history based on the stress distributions shown. The continuation of this calculation to platelet activation state will assess how effects of focal stenosis on platelets vary from multifocal FMD. The corresponding biomarker data from these cases will validate numerical predictions to determine characteristic phenotypes associated with FMD.

Large recirculating regions commonly observed distal to stenosis could also induce stroke due to increased flow residence time and reduced shear stresses which promote coagulation. Clots resulting from this phenomenon are rich in red-blood cells, distinguishable from the platelet-rich clots considered in this study.

This study aims to further understand how biomechanical environment in various arteriopathies affect platelet activation and risk of thrombosis. A quantifiable hemodynamic metric associated with the risk of stroke in FMD can help in creating patient-specific management plans for these patients.

ACKNOWLEDGEMENTS

None

REFERENCES

[1] Persu, Alexandre et al., *Cardiovascular Research*, 118(1):65-83, 2022. doi.org/10.1093/cvr/cvab086

[2] Rana, Akshita et al., *Frontiers in Cardiovascular Medicine*, 6:2019. doi.org/10.3389/fcvm.2019.00141

[3] Han, Dong et al., *J Biomech Eng*, 144(4):040801, April 2022. doi.org/10.1115/1.4052460

[4] Soares, João et al., *Biomech Model Mechanobiol*, 12(6):1127-1141, 2013. doi.org/10.1007/s10237-013-0469-0

[5] Morrell, Craig et al., *J Clin Invest.*, 132(9):e152373, 2022. doi.org/10.1172/JCI152373

SB^{3}C2024
Summer Biomechanics, Bioengineering and Biotransport Conference
June 11-14, Lake Geneva, WI, USA

STIFFENING OR SOFTENING? DECIPHERING THE ROLE OF MULTIPLE CONTRACTING INCLUSIONS IN MODULATING THE STIFFNESS OF A FIBROUS MATRIX

Mainak Sarkar (1), Brian M. Burkel (2,3), Suzanne M. Ponik (2,3), Jacob Notbohm (1,3)

(1) Department of Mechanical Engineering, University of Wisconsin-Madison, Madison, WI, USA
(2) Department of Cell and Regenerative Biology, University of Wisconsin-Madison, Madison, WI, USA
(3) University of Wisconsin Carbon Cancer Center, Madison, WI, USA

INTRODUCTION

In living tissues, cells mechanically interact with the surrounding fibrous extracellular matrix [1, 2]. Prior studies showed that the forces produced by a solitary contractile cell stiffens the matrix at the scale of tens of microns [3]. However, in many tissues, cells can interspersed within the same matrix. Owing to nonlinearity and complex force transmission within the matrix, it remains elusive how the collective contraction of many cells would alter the stiffness of the matrix and the subsequent effect on the cell sensing and response. To address this gap, we used mechanics-based models and experiments to quantify the stiffness of random fibrous matrices embedded with multiple contracting inclusions (which mimicked contracting cells) [4]. We also verified that the changes in the matrix stiffness due to contraction of inclusions were sufficient for the cells to sense and respond.

METHODS

We began by preparing models of random fibrous matrices embedded with multiple contracting inclusions, each of diameter $D = 2L_\mathrm{f}$ (L_f being the average fiber length in the matrix). The fibers in the matrix were modelled as beams highly susceptible to bending, similar to type I collagen fibers. Finite element simulations were performed with two load steps, wherein first load step induced contraction of the inclusions and a second load step was used to measure the stiffness of the matrix. While inducing contraction of the inclusions, free external boundaries were considered in the matrix which ensured global shrinkage of the matrix. To measure the stiffness of the matrix at cell scales, contracting dipoles of varying orientations were used.

To experimentally validate the simulation findings, we polymerized matrices of collagen type I and embedded contracting inclusions inside the matrices. These inclusions were active thermosensitive microspheres of poly(N-isopropylacrylamide) (PNIPAAm) [5], whose controlled contraction induced localized tension inside the matrix similarly to contracting cells. For matrices with free external boundaries, contraction of PNIPAAm microspheres induced global contraction of the matrices. The stiffness of these matrices was measured at the length scale of tens of microns using microscopic indentation experiments. To understand if the changes in the matrix stiffness due to the contraction of inclusions were sufficient for cells to sense, we seeded breast carcinoma cells (MDA-MB-231) on these matrices. Cell morphologies at 18 hr post-seeding were evaluated by analyzing microscopic images of cells.

RESULTS

To determine the effect of multiple contracting cells on the matrix stiffness, we used the computational model of fibrous matrix with contracting inclusions. Keeping the external matrix boundaries free, the embedded inclusions were radially contracted by 40% to induce localized tension in the matrix similar to the cell-generated forces (Fig. 1a,b), which also triggered global contraction of the matrix (Fig. 1b). The stiffness of the matrix was measured using contracting dipoles of length $2L_\mathrm{f}$ at various locations inside the matrix. Based on the prior literature [6, 7], the expectation was for the cell-induced local tension to stiffen the matrix. But, to our surprise, we noticed the stiffness of the matrix decreased due to the contraction of inclusions. For several independent random matrices, the ratio of the values of stiffness after and before the contraction of inclusions, k_s and $k_\mathrm{s,ref}$ respectively, were consistently less than one indicating softening in the matrix at all locations and in all directions (Fig. 1c).

To explain what might have caused this softening, we studied the evolving microstructure of the matrix due to the contraction of the inclusions. In the close vicinity of the contracting dipoles used to measure the stiffness of the matrix, we noticed the fibers to buckle strongly in response to the contraction of inclusions, as depicted in Fig. 2a, where fibers are color coded based on the extent of buckling. The extent of matrix softening measured by independent dipoles was correlated to the average buckling of fibers in the neighborhood of those dipoles (Fig. 2b), meaning that more fiber buckling corresponded to more softening in the matrix.

We experimentally validated these model predictions of softening using microscopic indentation tests on matrices of fibrous collagen embedded

with contracting PNIPAAm microspheres. With the outer boundaries of these matrices free, we induced contraction of the embedded microspheres and measured the stiffness of the matrix by indenting its surface with glass microspheres. Results showed that the matrices with contracted PNIPAAm microspheres softened in contrast to the control matrices with no microspheres, verifying model predictions (Fig. 3a). Lastly, in another series of experiments, we observed that cells could sense this buckling-induced softening in the matrix by altering their morphologies from being elongated to more rounded (Fig. 3b,c).

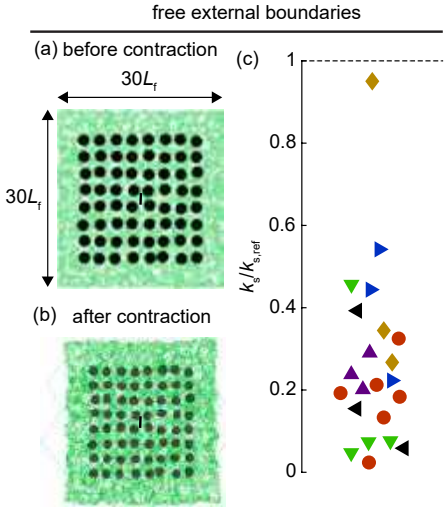

Figure 1: Contracting inclusions soften the matrix. (a) Undeformed matrix. (b) Deformed matrix (globally shrunk) after contraction of inclusions. Dipole used to measure the matrix stiffness is depicted by a black line in panels a and b. (c) For differently aligned dipoles and six independent matrices, $k_s/k_{s,ref} < 1$ indicates softening. Each marker type indicates a dipole from an independent model. Figure panels are adapted from ref. [4].

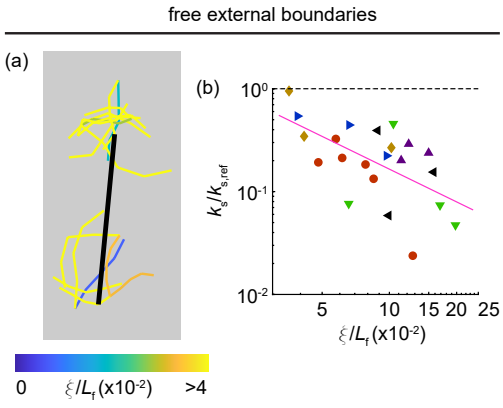

Figure 2: Fiber buckling is mapped to matrix softening. (a) Depiction of buckled fibers in the vicinity of contracting dipole, after the contraction of embedded inclusions. The extent of buckling of fibers were colored by measuring the difference between the contour length and the end-to-end distance of fibers (fiber excess length, ξ). (b) Scatter plot of normalized stiffness sensed by each dipole against the average excess length (ξ) in the vicinity of dipole. Each marker type indicates a dipole from an independent model. Figure panels are adapted from ref. [4].

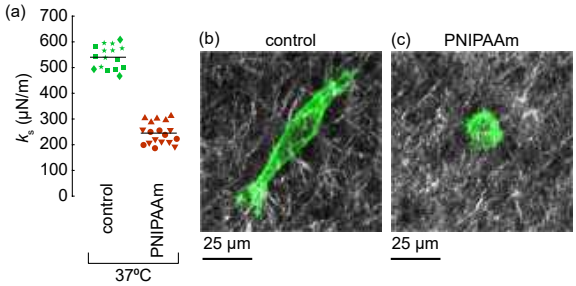

Figure 3: Cells sensed and responded to the changes in the stiffness of the matrix. (a) Stiffness of matrix at cell scales measured by different glass micro-indenters in control collagen matrices, and in globally contracted collagen matrices due to contracted PNIPAAm microspheres. Notice the drop in stiffness by a factor of 2 in the contracted matrices indicating softening by contracted inclusions. Markers with an identical shape and color indicate independent indenters from one sample. (b) Representative elongated morphology of MDA-MB-231 cell in control collagen matrix. (c) Representative rounded morphology of MDA-MB-231 cell in contracted collagen matrix, where contracting PNIPAAm microspheres triggered matrix contraction. Figure panels are adapted from ref. [4].

DISCUSSION

Our simulations and experiments reported softening under the boundary conditions different from prior studies. In contrast to the prior studies which showed softening in matrices under global compression [8], our study depicted a surprising phenomenon of matrix softening driven by the tensile forces generated by many contracting inclusions. Our observation of the occurrence of substantial fiber buckling in an unconstrained matrix with contracting inclusions is novel, and elucidates a new role of fiber buckling in modulating the mechanics of fibrous matrices that has not been reported before.

These findings have the potential to shift the paradigm in the field on how we interpret cell-matrix interactions in experiments on cell-embedded matrices. By revising the common notion that cells only stiffen the matrices, we introduced a new insight that the presence of many contracting cells can induce fiber buckling that triggers substantial mechanical softening in the matrix. For future work, it could be worth investigating to see if contracting myofibroblasts soften the fibrin matrix in wound healing. Such softening mechanism, if exists, can be speculated as a natural remedy against scar formation.

ACKNOWLEDGEMENTS

This work was supported by the National Science Foundation grant CMMI-1749400, National Cancer Institute of the National Institutes of Health awards R01CA179556 and U54CA268069, and University of Wisconsin Carbone Cancer Center Support Grant P30CA014520.

REFERENCES

[1] Hall MS et al. *P Natl Acad Sci USA* 113.49 (2016).

[2] Schlick SF et al. *Prog Biophys Mol Bio* 144 (2019).

[3] Yang H et al. *P Natl Acad Sci USA* 120.23 (2023).

[4] Sarkar M et al. *Acta Biomater* (2024). DOI: `https://doi.org/10.1016/j.actbio.2024.01.025`.

[5] Burkel B et al. *Soft Matter* 13.34 (2017).

[6] Sarkar M et al. *J Appl Mech* 89.11 (2022).

[7] Mann A et al. *J R Soc Interface* 16.159 (2019).

[8] Van Oosten AS et al. *Sci Rep* 6 (2016).

ROLE OF CALCIUM IN REGULATING MECHANICAL PHENOTYPE OF CELLS IN A 3D MICROTISSUE

Vaishali Bala (1), M.K. Sewell-Loftin (1,2)

(1) Department of Biomedical Engineering, University of Alabama at Birmingham, Birmingham, Alabama, USA
(2) O'Neal Comprehensive Cancer Center, University of Alabama at Birmingham, Birmingham, Alabama, USA

INTRODUCTION

Mechanical forces generated by stromal cells in the perivascular matrix play an essential role in controlling blood vessel growth and function [1]. Despite advances in tissue engineering, the ability to create larger, vascularized tissue scaffolds remains limited, largely due to the poor understanding of how mechanical cues promote and regulate angiogenesis. Our recent studies have provided some evidence suggesting that mechanical forces may drive angiogenesis through the activation of VEGFR-2 [2]. Previous work in our laboratory has enabled the characterization of mechanical fingerprints, or mechanical phenotypes, of various stromal cells by tracking matrix distortions generated by contractility events [3, 4]. Highly contractile cells generate more matrix distortions, and we refer to them as having a mechanically-active phenotype. Moreover, cadherins are recognized as mechanosensors responsible for sensing mechanical stimuli and maintaining cell-cell interactions and blood vessel stability [5]. Neural cadherin (N-Cad) in the vasculature, forming homotypic bonds, is responsible for polarity during cell migration, motility, and endothelial cell proliferation. [6]. Despite this knowledge, the role of mechanical crosstalk through cadherin signaling between different cell types in the perivascular matrix is still poorly understood. It could offer insight into regulating vascular function and growth through mechanical stimulation and whether it can be controlled while fabricating large, vascularized scaffolds.

Studies have indicated that lowering the calcium concentration available to the cells can deplete N-Cad due to reduction in binding affinity through mechanical cues [7]. Based on previous studies, we selected human microvascular endothelial cells (HMECs), normal breast fibroblasts (NBFs), normal human cardiac fibroblasts (NHCFs), and normal human lung fibroblasts (NHLFs) for our studies since they offer a diverse representation for investigation. HMECs, as endothelial cells, have the capability to grow blood vessels. NHLFs and NHCFs are pro-angiogenic fibroblasts, while NBFs are non-angiogenic. Our objective is to investigate the mechanical phenotype of these cells in 3D microtissue models with fluorophore beads. Additionally, we aim to quantify the amount of N-Cad present in these microtissues. Our studies explore whether N-Cad depletion can lead to mechanical phenotype changes, as measured by the ability to generate matrix distortions.

METHODS

HMECs, NBFs, NHCFs, and NHLFs were subjected to a bead displacement assay to track cellular movement and matrix distortions within a 3D microtissue model made of 10mg/mL fibrin using a polydimethylsiloxane ring to hold the tissues [3]. The microtissues received Dulbecco's Modified Eagle's Medium (DMEM) on Day 0. On Day 1, the control samples received DMEM media with physiological levels of Ca^{2+}, while the experimental samples received DMEM media with low Ca^{2+}.

The plates were imaged using live-cell imaging on Day 2 with an Olympus IX83 inverted epifluorescence microscope. A previously developed bead displacement algorithm was utilized to gather the data and analyze the mechanical phenotype of fibroblasts and endothelial cells [4]. The microtissues were then fixed and stained for N-Cad (Abcam, ab19348) at a 1:400 concentration. DAPI was used as a counterstain to calculate the total cell count. The samples were re-imaged after staining. All images collected were 100μm z-stacks with a step-size of 2.

RESULTS

The matrix distortion study was used to investigate the effects of N-Cad depletion on cell matrix distortions as measured by the ability of the cells to distort the matrix. Our data show that the 3D microtissue models with HMECs, NHCFs, and NHLFs showed significantly reduced average matrix distortion magnitudes compared to the control microtissues when cultured in low calcium conditions. At the same time, NBFs showed a significant increase in matrix distortion

magnitudes with low calcium levels (Figure 1). NHCFs displayed the highest matrix distortions, while NHLFs revealed the lowest matrix distortions amongst the cell lines. Staining for N-Cad indicates that HMECs, NHCFs, and NHLFs display a decrease in N-Cad expression levels in low calcium conditions (Figure 2). At the same time, no differences are seen in NBFs.

DISCUSSION

The perivascular matrix mechanics should regulate the formation, permeability, sustained growth of the vasculature since it is located in close proximity to the blood vessel network. Understanding the specific biomechanical cues, such as stromal cell mechanical phenotype in isolation from cytokine signaling, is difficult in *in vivo* models. Specifically, the link between stromal matrix distortion behaviors and cadherin signaling has been previously underexplored, prompting our studies to clarify how mechanical phenotype and cadherin levels regulate angiogenesis/vasculogenesis in 3D microtissue models. This pilot study was critical for identifying changes in mechanical phenotype and N-Cad in single cell cultures before future studies use co-cultures of HMECs with the stromal cells to investigate angiogenesis.

Our matrix distortion results suggest that even highly contractile cells are influenced by N-Cad depletion (Figure 1). These matrix distortions represent the movement of an individual bead caused by cell contracting events embedded within the fibrin matrices. The results also highlighted the heterogeneous nature of mechanical phenotype within a single cell line, as the magnitude of matrix distortion distributions varied in shape and range. While our prior work suggested that fibroblasts with higher matrix distortions can promote blood vessel growth, it is worth noting that NHLFs have long been recognized as pro-angiogenic stromal cells in various studies. Under normal cellular conditions, myosin, a motor protein that interacts with actin filaments to generate contraction, is activated by calcium ions. When calcium levels are reduced, this activation process is impeded, resulting in decreased matrix distortions. Conversely, high calcium conditions can relieve this inhibition, thereby allowing the contractile machinery to become more active, leading to an increase in matrix distortions. This phenomenon could partially explain the decreased matrix distortions in addition to the depletion of N-Cad. Furthermore, matrix distortions also vary depending on cell type as illustrated. Further studies are required to examine the direct influence of N-Cad on mechanical phenotype.

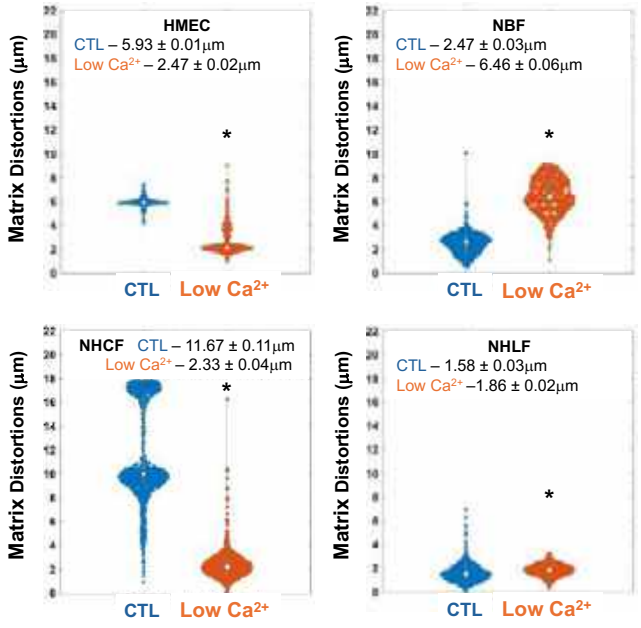

Figure 1 – Low Calcium Alters Fibroblast Generated Matrix Distortions. Violin plots representing bead displacement data from 3D cell cultures with different cell types. CTL is control media. Data is reported as magnitude of matrix distortions measured by bead tracing. Insets show average ± SEM. N = 3 microtissues per cell line with >500 beads per plot. Samples were compared using Student's t-tests with unequal variances. * p<0.0001.

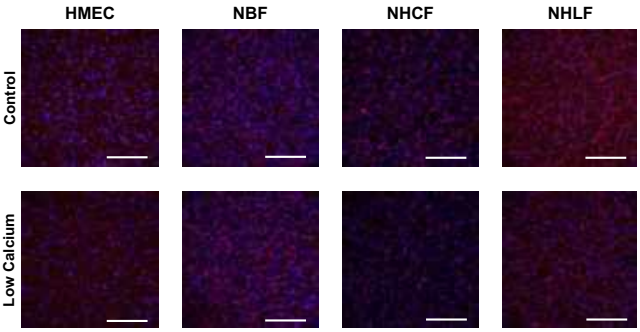

Figure 2 – Expression of N-Cad in 3D Microtissue Models. Representative immunofluorescence images of N-Cad in 3D microtissues cultured in normal (control) vs low calcium media for 24 hours. Scale bar = 200μm.

Upon visual inspection, it appears that the low calcium samples exhibit reduced N-Cad expression (Figure 2). HMECs do not exhibit spindle-like morphology when embedded in a microtissue; they are punctuated. The fibroblasts in 3D culture result in a spindle-like mesh network. The distinct response of NBFs compared to other cell types raises questions about the cell-type-specific regulation of N-Cad in relation to the ability of cells to generate matrix distortions. Such regulation may be influenced by the distinct functional roles of these cells and their particular interactions within the tissue microenvironment.

Together, this suggests that alterations in N-Cad in 3D *in vitro* systems may control how stromal cells interact with neighboring cells and the matrix partially through changes in mechanical phenotype. However, more work is needed to define the precise mechanism of these interactions. In the context of tissue engineering, mechanical forces promoted by cellular populations are a separate feature to include when developing vascularized scaffolds.

ACKNOWLEDGEMENTS

We wish to acknowledge funding for this project: R00-CA230202 (M.K.S.L.), IMPACT Award, O'Neal Comprehensive Cancer Center (M.K.S.L.), and Blazer Graduate Research Fellowship (V.B.).

REFERENCES

[1] Ruehle, M.A., et al., *Sci Adv*, 6(34), 2020. [2] Johnson, B.M., et al. *BMC Biol,* 21:290, 2023. [3] Sewell-Loftin, M.K., et al., *Sci Rep*, 7:12574, 2017. [4] Sewell-Loftin, M.K., et al., *Lab Chip*, 20:2776-2787, 2020. [5] Adil, M.S., et al., *Tissue Barriers*, 9:1848212, 2021. [6] Kruse, K., et al., *J Cell Biol*, 218:299-316, 2019. [7] Hutcheson, J.D. et al., *Arterioscler Thromb Vasc Biol*, 33:114-120, 2013.

CHARACTERIZATION OF BIOMATERIAL INTERFACES FOR CRANIAL PHANTOMS TO INVESTIGATE TRAUMATIC BRAIN INJURY

Anthony A.J. Baker (1), Natalie Smith (2), Suhas Vidhate (3), Ricardo Mejia-Alvarez (3), Zane R. Lybrand (2), Tony T. Yuan (4), Adam M. Willis (3,5), Michaelann S. Tartis (1)

(1) Department of Chemical Engineering, New Mexico Institute of Mining and Technology, Socorro, NM, USA
(2) Department of Biology, Texas Woman's University, Denton, TX, USA
(3) Department of Mechanical Engineering, Michigan State University, East Lansing, MI, USA
(4) Department of Radiology/Radiological Sciences, Uniformed Services University of Health Sciences, Bethesda, MD, USA
(5) Office of the Chief Scientist, 59th Medical Wing, Lackland AFB, TX, USA

INTRODUCTION

Traumatic brain injuries (TBIs) are a serious medical condition in military and civilian populations that can occur after a cranial impact. Long-term TBI effects are established, but damage mechanisms are less understood due to limited brain access during impacts. Thus, tissue surrogates model impact mechanics, and need to be characterized at the micro- and macroscale. In this study, Digital Image Correlation (DIC) characterizes tissue interfaces with embedded organoids, while Atomic Force Microscopy (AFM) probes microscale properties.

Fabricated tissue mimetics represent human brain components in cranial models [1,2]. Polyacrylamide (PAA) gels are employed for their transparency and easily tunable mechanical properties. Using PAA, a human-sized phantom, the Anthropomorphic Neurologic Gyrencephalic Unified Standard (ANGUS), was designed to mimic the bulk tissue deformation mechanics of TBIs [2]. Simplified models are established, but lack neural tissue. Neural organoids incorporate features that allow cellular-scale observations. Microscale characterization of features will show how varying mechanical properties affect neural organoid properties and how microscale and bulk properties relate.

Figure 1: Cranial phantom outline (a), 3D-printed skull (b), cranial phantom in skull (c), adapted from Knutsen, et al., 2023.

Gel-gel interfaces, where each gel has different mechanical properties, may capture properties similar to gray-white matter interfaces. Including these into the ANGUS phantom is crucial to understand shear transfer through an interface to study deformation in a living model. In the ANGUS phantom, blunt impact waves propagate through the gel. Therefore, shear transfer through a multi-layer gel with an embedded organoid needs to be characterized. To visualize shear transfer, DIC tracks unique subsets within an image to identify deformation and calculate strain.

AFM utilizes nanoindentation to obtain force-relaxation data to characterize soft materials, which after frequency analysis, can be compared to bulk rheological measurements, a comparison that is ambiguous [3]. This analysis is also performed on embedded neural organoids as substrate shape and stiffness are known to influence organoid and cell development [4,5]. Measuring neural organoids in physiological conditions is difficult with bulk rheology; however, physiologically favorable conditions are maintained in AFM

In this work, AFM characterizes the mechanical properties of hydrogels and how organoids adapt to them. Shear deformation measurements show shear transfer through gels to an organoid. This study aims to characterize these interfaces as a first step in introducing structural complexity and biological components into the ANGUS phantom to acquire changes in neural organoids after a blunt impact.

METHODS

Three PAA hydrogel formulations, 10% (w/v) 60-1, 7% (w/v) 60-1, and 7% (w/v) 15-1, are used to create various gel structures. The protocol for these gels is detailed in Baker, et al., 2023 [1]. The w/v percentage corresponds to the monomer content based on water volume followed by the monomer-to-crosslinker ratio. 10% (w/v) 60-1 and 7% (w/v) 60-1 gels were characterized and represent white and gray matter tissue [2]. A single layer gel is made for each formulation **Figure 2A**, the 60-1 formulations create double-layer gels **Figure 2B**, and the organoid chip consists of two 60-1 gels with a 15-1 gel microwell mimicking a neural organoid as those have not been embedded in this work **Figure 2C**.

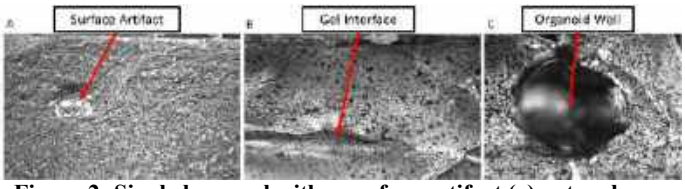

Figure 2: Single layer gel with a surface artifact (a), a two-layer gel (b), and a multi-layer organoid chip with an organoid well (c).

In AFM, super glue (Loctite Super Glue Ultra Gel Control) secures a 5 mm thick hydrogel to a 60 mm diameter x 15 mm deep petri dish (Kigley). The gel is covered with a 1% Pluronic F-127 solution (Sigma-Aldrich) to minimize adhesive interactions. A MLCT-SPH-10UM (Bruker) probe equilibrates in the solution and is then brought into contact with the gel and indented into the sample where that position is held for 30 to 60 seconds to obtain relaxation data.

Frequency analysis is performed on force-relaxation data with methods proposed by Chim, et al., 2018 [3]. The material instantaneous deformation value is calculated from the Hertz model in **Equation 1**, where R is the probe radius, ν is the Poisson ratio, estimated to be 0.5 for PAA, δ is probe displacement, and t is time. The material instantaneous deformation and force data are Fourier transformed and divided to obtain the complex shear modulus (G*) in **Equation 2**. Data is separated into real and imaginary components to exhibit the elastic (G') and loss (G") modulus of the material.

$$\Lambda\big(\delta(t)\big) = \frac{8}{3} * \frac{\sqrt{R}}{1-\nu} * \delta^{\frac{3}{2}}(t) \quad (1)$$

$$G^*(\omega) = \frac{\hat{F}}{\hat{\Lambda}} \quad (2)$$

A shear device developed in Vidhate, et al., 2021 is employed for shear transfer studies [6]. After the hydrogel samples equilibrate, the surface is dried with a Kimwipe to apply a speckle pattern of diluted black acrylic paint using a Master Performance Model 30 airbrush. Hydrogels (25 mm length and 8 mm height) are placed on a stage while a dynamic plate is lowered with enough force to prevent slipping. The dynamic plate is operated at shear rates of 10, 30, 50, and 70 Hz. High-speed images are captured with a Photron Fastcam SA-Z at 4000 FPS for 10 and 30 Hz and 5000 FPS for 50 and 70 Hz, with shutter speeds of 250 μsec and 198 μsec.

Images are analyzed in the VIC-2D (Correlated Solutions) software. Subsets from 25-45 px, step sizes from 5-7 px, and strain filters from 11-15 px are applied depending on speckle pattern quality. For single-layer gels, one area of interest (AOI) is placed from the top to the bottom of the gel. For multi-layer gels, one AOI is placed approximately equal distances from the gel interface and shear source for each gel. Strain values from the max applied shear were averaged in multi-layer gels to compare strain in two gels making up the interface.

RESULTS

Preliminary AFM data displays G' and G" values lower than expected due to measurements being on the surface where polymerization is suboptimal. Deeper indentations reveal a more representative crosslinking density, thus, probing deeper into the gel provides data closer to bulk measurements which will be performed [1].

DIC analysis of the starting versus max shear point are in **Figure 3**. Analysis shows when a two or one-layer gel is deformed, the softer gel experiences higher strain independent of its contact with the shear source. **Table 1** quantifies max shear strain at 30 and 50 Hz where condition one represents 7% (w/v) 60-1 in contact with the shear source, and condition two represents 10% (w/v) 60-1 in contact. **Table 2** quantifies max shear strain in single-layer gels at 30 and 50 Hz.

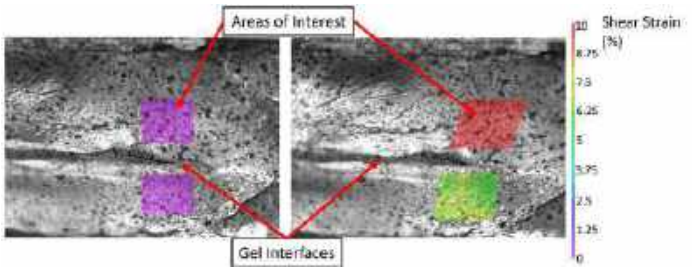

Figure 3: Starting frame (left) and max shear frame (right) of a 2-layer hydrogel from condition 1.

Table 1: Max shear strain in two-layer gels. Significance is shown between different gel formulations, *p<0.05.

	Condition 1		Condition 2	
PAA Gels	**30 Hz (n=6)**	**50 Hz (n=6)**	**30 Hz (n=5)**	**50 Hz (n=5)**
10% (w/v) 60-1	10 ± 0.3	7 ± 0.7	7 ± 0.1	6 ± 0.3
7% (w/v) 60-1	27 ± 0.8*	17 ± 1.8*	26 ± 0.2	27 ± 0.8*

Table 2: Max shear strain values in single-layer gels.

PAA Gels	30 Hz (n=6)	50 Hz (n=6)
10% (w/v) 60-1	7 ± 0.6	7 ± 0.9
7% (w/v) 60-1	11 ± 0.8	10 ± 1.0

DISCUSSION

AFM techniques will need to be optimized to compare bulk and local rheological measurements. Optimizing these measurements allows for force mapping across gel interfaces with a neural organoid. This data may present how organoids adapt to brain tissue mimetics.

DIC analysis shows softer gels experience more strain in shear deformation as expected. While 10% (w/v) 60-1 gels do not have a noticeable change in strain between single and double-layer conditions 7% (w/v) 60-1 gels do, supporting the claim that softer gels experience more shear strain in double-layer gels. Shear transfer will be further characterized to include a mimetic gray-white matter interface in the ANGUS phantom. The present experiments display shear transfer at gel interfaces and allow for correlation of applied shear force to neural organoid damage. This information will inform blunt impact parameters for the ANGUS phantom to induce trauma in embedded organoids.

DIC observations make it apparent that gel interfaces change the shear properties of the bulk material which could affect behavior of brain tissue mimetics. Characterizing these interfaces and neural organoids will help create a more accurate brain model for TBI research.

ACKNOWLEDGEMENTS

This work is supported by the DoD CDMRP Grant W81XWH2211117, Geneva Foundation award ID07200010-1201, DoD Newal Net Fund S-18007-02, NNSA Minority Serving Institution Partnership Program (MSIPP) award DE-NA0003988, and ONR DURIP N00014-19-1-2677 (Dr. Tim Bentley). The views expressed herein are those of the authors and do not necessarily reflect the official policy or position of the Defense Health Agency, Brooke Army Medical Center, the Uniformed Services University, the Department of Defense, nor any agencies under the U.S. government.

REFERENCES

[1] Baker, A.J., et al., *Data in Brief*, V 48, 109114, 2023.
[2] Knutsen, A.K., et al., *J. of the Mech. Beh. of Biom. Mat.* V 138, 2023.
[3] Chim, Y.H., et al., *Scientific Reports*, V 8, 2018.
[4] Pérez-Calixto, D., et al., *Polymers*, V 13, 1-28, 2021.
[5] Baptista, D., et al., *Trends in Biotechnology*, V 37, 838-854, 2019.
[6] Vidhate, S., *Doctoral Dissertation*, 2021.

EULERIAN-LAGRANGIAN FRAMEWORK FOR SIMULATIONS OF PARTICLE-LADEN BIOLOGICAL FLOWS IN COMPLEX GEOMETRIES

Abhilash Reddy Malipeddi(1), Jesse Capecelatro (1,2), C. Alberto Figueroa (3,4)

(1) Mechanical Engineering, University of Michigan, Ann Arbor, MI, USA
(2) Aerospace Engineering, University of Michigan, Ann Arbor, MI, USA
(3) Surgery, University of Michigan, Ann Arbor, MI, USA
(4) Biomedical Engineering, University of Michigan, Ann Arbor, MI, USA

INTRODUCTION

Fluid mechanics plays a crucial role in numerous physiological processes related to health and disease. Advances in medical imaging, computational power, and mathematical algorithms have made it possible to perform real-time, patient-specific computational fluid dynamics analyses. However, many problems involve complex interactions between fluids and particles of varying mass and size, which presents challenges in understanding and modeling their dynamics. Most of the development around particle-laden flows has been in the context of industrial applications such as gas-solid flows in fluidized beds using structured grids or process/industry applications for gas-solid flows[1, 2]. In contrast, biological flow applications often involve complex geometries and unstructured grids. The goal of this work is to develop a computationally efficient, scalable, physics-based framework for particle-laden biological flows in complex subject-specific geometries to enable the next generation of methods for computer-aided diagnostics and disease research. The present implementation is done within the `CRIMSON` framework [3] which specializes in simulation of blood flow within image-based geometries.

METHODS

The equation for the fluid phase are obtained by applying a spatial filtering operator on the incompressible Navier-Stokes equations, taking into account the volume occupied by the particles and the momentum exchange between the particles and fluid phase[4, 5]. Figure 1 illustrates the filtering procedure on a system of particles suspended in a fluid. The resulting continuity equation after filtering reads

$$\frac{\partial \phi_f}{\partial t} + \frac{\partial}{\partial x_i}\left(\phi_f u_i\right) = 0 \tag{1}$$

and the momentum equation is

$$\rho_f \phi_f \frac{\partial u_i}{\partial t} + \rho_f \phi_f u_j \frac{\partial u_i}{\partial x_j} = -\phi_f \frac{\partial p}{\partial x_i} + \phi_f \frac{\partial \tau_{ij}}{\partial x_j} + \phi_f \rho_f g_i + f_i^p \tag{2}$$

where $\tau_{ij} = \mu\left(u_{i,j} + u_{j,i}\right)$, μ is the fluid viscosity, ρ_f is the fluid density, g_i is the body force. The term f_i^p is the momentum feedback force from the particles acting on the fluid. ϕ_f is the volume fraction of the fluid phase.

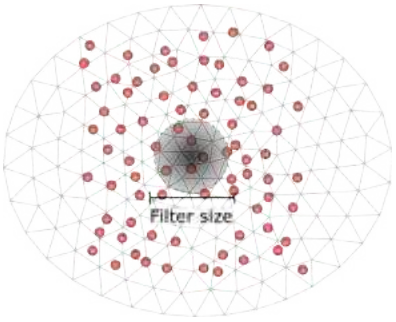

Figure 1: Schematic of Lagrangian particles inside a discretized fluid domain along with a representation of the filtering kernel

The particles are modeled as rigid spheres. Their motion is calculated according to Newtons second law for translation and rotation. The translational motion for particle p is given by

$$m_p \frac{\mathrm{d}v_i}{\mathrm{d}t} = f_i^h + f_i^{col} + (\rho_p - \rho_f) V_p g_i \tag{3}$$

where m_p, V_p and ρ_p are the mass, volume and density of the particle, f_i^h is the hydrodynamic force exerted on the particle by the fluid, which includes drag, added mass effects, Saffman lift forces, and f_i^{col} is the force due to particle-particle and particle-wall collisions.

RESULTS

Our method is applied to two particle-laden flow problems: pressure-driven flow in a pipe accounting for gravity, and flow in a bifurcation.

Pressure driven flow in a pipe: The first case considered is pressure driven flow in a cylindrical vessel (Figure 2). The Reynolds number based on the vessel diameter (5 mm) is 100. There are 10,000 particles ($d_p = 0.1$mm), which are initialized as a spherical bolus near the inlet boundary with a particle volume fraction $\phi_f = 0.3$. The domain is discretized using 25,000 linear tetrahedral elements. The inlet velocity is specified as parabolic flow profile. The outlet is a zero pressure boundary condition and the walls are no-slip boundaries. The particle are denser than the carrier fluid, $\rho_p = 5\rho_f$ and the effects of gravity are included.

Figure 2: In each frame, the figure on the left shows contour plots of the volume fraction of the particles on a vertical slice through the center of the cylinder. The figure on the right shows contour plots of the magnitude of the velocity field along with the particles themselves.

In Figure 2 we see that the particles are transported down the vessel by the fluid. The fully-coupled nature of the simulation is evident from the blocking effect of the particles, apparent in the velocity contours. Initially, the particles are at rest and block the fluid, which accelerates around the particles. This delays the development of the parabolic profile downstream of the particles. The particles slowly accelerate due to the fluid, gradually pick up speed and are carried out of the cylinder through the outlet. Due to the gravity effects, particles also settle along the bottom.

Flow in bifurcation: We present a comparison of particle-laden flows through two different bifurcating vessel geometries –one healthy and one stenosed, as shown in Figure 3. Each geometry is discretized using 220K tetrahedral elements. We initialize a bolus of 100,000 particles in the inlet with a mean volume fraction of 0.35. The particles and fluid are initially at rest. The inlet velocity is specified with a parabolic profile corresponding to a Reynolds number of 250 based on the inlet flowrate and vessel diameter. There is no gravity and the particles density is twice that of the fluid. The outlet vessels are coupled to three-element Windkessel models to represent the downstream vasculature.

Within each panel in Figure 3, the healthy geometry is on the right and the stenosed geometry is on the left. Up until $t = 15s$, the the particle distribution is largely similar for both cases. As the particles flow past the bifurcation (Figure 3(b), $t = 19s$) they split into both downstream vessels following complex trajectories. In figure 3(c) we see that the particles are accelerated through the constriction and reach the outlet much quicker than in the unconstricted case. Furthermore, in the stenosed case we see particles forming a spur-like shape and flowing backwards. This is due to a recirculation zone, a well-known feature of flow through stenosed vessels.

These examples are primarily meant to showcase the capabilities of our method. In the future, this work will be followed up with validation, performance evaluation, and scaling studies. We will also apply this method to larger and complex geometries derived from patient-specific medical images.

Figure 3: Comparison of particles flowing through a bifurcation with and without a stenosis. In (d) the particles can be seen to be flowing back away from the outlet in the stenosed branch. This is due to the formation of a circulating streamline topology caused by the stenosis.

DISCUSSION

We have presented a computational framework for modeling large scale particle-laden flows in complex geometries that enables subject-specific analysis. The framework is based on a volume-filtered Euler-Lagrange approach that uses a finite element method for the fluid phase and a discrete element method for the particle phase. The fluid phase is solved on a three-dimensional unstructured grid using a stabilized finite element method. The particle phase is modeled as rigid spheres and their motion is calculated according to Newton's second law for translation and rotation. The hydrodynamic force on the particles is calculated using a recently developed correlation for freely evolving suspensions of particles. The method is applied to a few different particle-laden flow cases. The results are of a qualitative nature and are not meant to be quantitative. The results demonstrate the capabilities of the implementation and the potential of the method for simulating large-scale particle-laden flows in complex geometries.

ACKNOWLEDGEMENTS

This work was supported by a Catalyst Grant from Michigan Institute for Computational Discovery and Engineering at University of Michigan.

REFERENCES

[1] Casagrande MVS et al. *Computational Particle Mechanics* 4.2 (2017).

[2] El Geitani T et al. *Industrial & Engineering Chemistry Research* 62.2 (2023). Publisher: American Chemical Society.

[3] Arthurs CJ et al. *PLOS Computational Biology* 17.5 (2021). Ed. by Schneidman-Duhovny D.

[4] Anderson TB et al. *Industrial & Engineering Chemistry Fundamentals* 6.4 (1967). Publisher: American Chemical Society.

[5] Capecelatro J et al. *Journal of Computational Physics* 238 (2013).

DEVICE DEPLOYMENT AND THE ONSET OF STRUCTURAL VALVE DEGENERATION: SIMULATION OF TRANSCATHETER AORTIC VALVE IMPLANTATION IN VITRO

Sam Boxwell (1), Dylan Armfield (2), William Hickey (3), Scott Cook (3), Patricia Kelly (3), Philip Cardiff (2), Laoise McNamara (1)

(1) Mechanobiology and Medical Device Research Group, Biomedical Engineering, College of Science and Engineering, University of Galway, Galway, Ireland
(2) School of Mechanical and Materials Engineering, University College Dublin, Dublin, Ireland
(3) Structural Heart, Boston Scientific Corporation, Galway, Ireland

INTRODUCTION:

Despite the rapid growth of transcatheter aortic valve implantation (TAVI) for the treatment of aortic stenosis, devices are prone to early failure due to structural valve degeneration (SVD). Recent standards define SVD as an acquired intrinsic bioprosthetic heart valve (BHV) abnormality, which may be identified as a change in device hemodynamics post-intervention [1]. Although SVD most commonly presents as leaflet calcification and tearing, other mechanisms have been identified including device asymmetry and stent fatigue [1,2]. It is suspected that TAVI deployment factors, including oversizing and eccentricity, may predispose TAVI devices to increased SVD when compared to surgical aortic valve replacements (SAVRs) [1,3,4]. TAVI devices are often oversized relative to the native annulus (between 5-35%) to prevent complications such as paravalvular leakage [5]. However, severe oversizing may result in device underexpansion. Recent clinical studies report optimal oversizing varies across self-expanding and balloon-expanding devices [5], yet the impact of such strategies on long-term device durability is unknown. Additionally, device and native anatomy interaction often results in severe device eccentricity upon deployment, which may impact device kinematics and physiological flow patterns [4,6]. Despite such concerns, recent clinical studies have reported a significantly lower rate of SVD at 8 years following TAVI when compared to SAVR, although TAVI cases of SVD were still substantial (13.9%) [2].

The mechanisms of SVD are intrinsically linked to biomechanical stresses experienced by devices in vivo [1,3]. Thus, computational approaches have been applied to assess and optimize the biomechanics of TAVI devices. Previous finite element (FE) studies report that underexpansion and eccentric deployment of TAVI devices results in increased leaflet stress [4,7], which may impact long-term durability. In a recent study, using a fluid-structure interaction (FSI) approach, Tsolaki et al. correlated biomechanical indicators to BHV calcification under idealized circular deployment, showing excellent agreement with calcification distribution across a sample of explanted SAVRs [8]. Yet due to complexities in simulating valve closure using FSI, this study excluded diastolic loading. Further, this study did not investigate the relationship between TAVI-specific deployment factors, including oversizing and eccentricity, and the onset of SVD, which remains poorly understood.

The objectives of this study are to (1) develop FE and CFD models of a commercial, self-expanding TAVI device, (2) validate the structural and hemodynamic performance of in silico models against in vitro testing, and (3) apply these models to investigate the occurrence of SVD across a range of clinically-relevant degrees of oversizing and eccentricity indices.

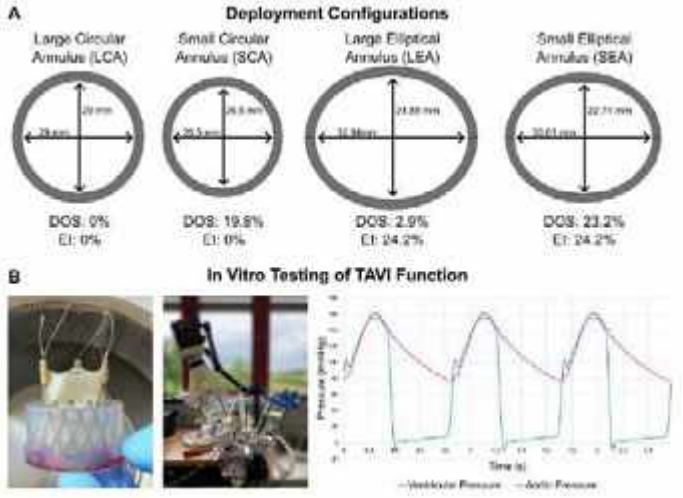

Figure 1: (A) Idealized Aortic Annulus Geometries with Degree of Oversizing (DOS) and Eccentricity Index (EI) and (B) In Vitro Testing Set-up with Moderate Hypertensive Pressure Waveform

METHODS:

The basis for this study was the self-expanding ACURATE Prime XL (Boston Scientific, USA), recommended for aortic annuli perimeter derived diameters ranging from 26.5 mm – 29 mm. This study sought to characterize the influence of annulus geometry by deploying the TAVI device within different annuli as shown in Fig. 1(A), which were characterized by degree of oversizing (DOS) and ellipticity index (EI), as given by [5,9] respectively.

In vitro testing of the TAVI device was performed using a ViVitro Pulse Duplicator (ViVitro Labs Inc., Canada). Briefly, the device was crimped, deployed within annuli geometries (Fig. 1(A)) and subject to moderate hypertensive pressure conditions (Fig. 1(B) – peak transvalvular pressure of 140 ± 3 mmHg at 70 BPM). Structural performance was assessed using a high-speed camera, mounted above the aortic chamber, which captured device dynamics during the cardiac cycle. Specifically, we measured the stent deflection (calculated as a function of the radial distance between the commissures posts at systole and diastole), the geometric orifice area (GOA) and the pinwheeling index (PI). Similarly, hemodynamic assessment captured peak velocities, effective orifice area (EOA) and transvalvular gradients across the various deployment configurations.

Computational models were developed to assess the structural and hemodynamic performance of the TAVI device across the various annuli geometries. FE models of the ACURATE Prime XL were developed using Abaqus/Explicit (Dassault Systemes, USA), with representative material properties for porcine pericardium and nitinol. We completed a parameter variation study examining the impact of various hyperelastic, isotropic leaflet tissue properties [7,11] on associated stent deflections. The FE framework simulated (1) crimping of the device (to numerical stability - 14 mm) using 12 rigid plates and (2) deployment of the complete TAVI device into the annulus. Deployment was simulated by unsheathing a rigid upper and lower catheter respectively, replicating the unique 'top-down' deployment mechanism of the ACURATE Prime XL. To simulate the cardiac cycle, moderate hypertensive pressure conditions were applied, whilst contact definitions comprised "hard" contact with a friction coefficient of 0.20. We validated the models by comparing device dynamics, GOA and PI to in vitro testing results. Following validation, we investigated the impact of both oversizing and eccentric deployment on the von Mises stress distribution throughout the device, a key biomechanical indicator of SVD. CFD simulations are in development, which will be validated using in vitro testing and used to obtain a prediction of shear stress, another biomechanical indicator of SVD [9].

RESULTS:

Fig. 2(B1) shows the deployed TAVI device at peak diastole in circular and elliptical annuli. Upon device deployment in the large circular annulus, the FE model predicts similar GOA (4.51 cm^2 vs 4.27 cm^2), PI (8.5% vs 3.6%) and TAVI stent deflections (1.92 mm vs 1.763 ± 0.275 mm) to in vitro testing data. Similar alignment was noted across the small circular and large elliptical annuli. Table 1 shows the stent deflection across each of the deployment configurations.

Table 1: In Silico TAVI Stent Deflections

Annulus	Commissure	Deflections (mm)
Large Circular	P1, P2, P3	1.92
Small Circular	P1, P2, P3	0.86
Large Elliptical	P1	2.63
	P2, P3	1.88

We predict that peak leaflet stress occurs at the commissure region across all deployment configurations. These magnitudes were decreased in the small circular deployment configuration, when compared to the large circular annulus (2.58 MPa vs. 3.36 MPa). Further, small circular deployment decreased pinwheeling (PI - 6.3% vs 8.5%), resulting in reduced von Mises stress on leaflet contact surfaces (0.20 vs 0.32 MPa). Coaptation mismatch and severe pinwheeling of non-dominant leaflets was observed in the elliptical deployment configuration, which was accompanied by increased von Mises stress on contact surfaces (3.40 MPa) and commissure region of non-dominant leaflets (2.91 MPa vs 3.42 MPa). As evident in Table 1 and Fig. 2(B2), leaflet deformation induced noticeable stent deflections (up to 2.63 mm). Despite this, stent maximum alternating strains were largely below adjusted alternating strain limits (0.215% vs 0.525% for large circular deployment).

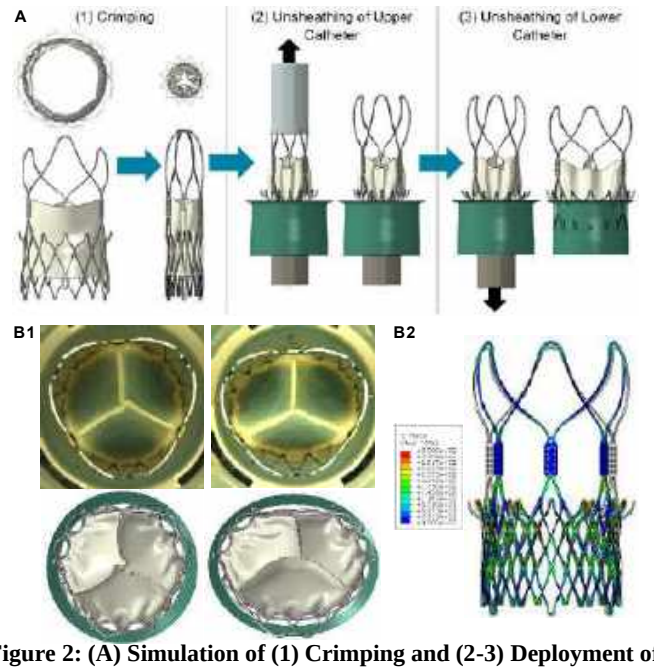

Figure 2: (A) Simulation of (1) Crimping and (2-3) Deployment of TAVI Device, (B1) Comparison of In Vitro and In Silico Circular and Elliptical Model at Peak Diastole, (B2) TAVI Stent Deflection between Systole and Diastole showing Von Mises Stress

DISCUSSION:

In this study, we investigated the influence of annulus geometry on TAVI deployment and function. We predicted that TAVI oversizing (up to 20%) is associated with reduced leaflet stress in regions prone to device failure in vivo [1]. Our ongoing work is assessing the impact of oversizing across a wider range of indices to capture oversizing ranges observed in vivo (5 – 35%) [5]. We also predicted that TAVI elliptical deployment resulted in coaptation mismatch, severe localized pinwheeling and altered device kinematics, which aligns with findings from previously published studies [4,7]. Our ongoing studies are developing CFD models to assess the impact of both oversizing and eccentricity on bulk flow and shear stress, to further investigate how valve oversizing may mitigate the occurrence of SVD in vivo.

ACKNOWLEDGEMENTS: Funded by the Irish Research Council Government of Ireland Postgraduate Scholarship (GOIPG/2022/2032).

REFERENCES: [1] Dvir, D et al., *Circulation*, 137:388-399, 2018. [2] Jørgensen, T et al., *Eur Heart J*, 42:2912-2919, 2021. [3] Whelan, A et al., *Acta Biomater*, 128:384-392, 2021. [4] Gunning, P et al., *Ann Biomed Eng*, 42:1989-2001, 2014. [5] Dvir, D et al., *Catheter Cardiovas Int*, 86:508-515, 2015. [6] Fuchs, A et al., *EIJ*, 13(9): e1067-e1075, 2017. [7] Martin, C et al., *Biomech Model Mechanobiol*, 13:759–70, 2014. [8] Tsolaki, E et al., *Acta Biomater*, 169:138-154, 2023. [9] Tchetche, D et al., *Circ Cardiovasc Int*, 12:e007107, 2019. [10] Li, K et al., *Ann Biomed Eng*, 38:2690-2701, 2010. [11] Caballero, A et al., *J Mech Behav Biomed Mater*, 75:486-494, 2017.

DIRECT QUANTIFICATION OF CANCER-ASSOCIATED EXOSOMES IN PLASMA ENABLES RAPID IDENTIFICATION OF CANCER USING ROTATIONAL DIFFUSOMETRY OF JANUS PARTICLES

John A Sinclair (1), Sonu Kumar (1), Tiger Shi (1), Satyajyoti Senapati (1), Han-Sheng Chuang (2), Hsueh-Chia Chang (1)

(1) Chemical and Biomolecular Engineering, University of Notre Dame, Notre Dame, IN, USA
(2) National Cheng Kung University, East District, Tainan City, Taiwan

INTRODUCTION

Unlike other diseases, cancer's intrinsic use of healthy cells allows it to grow and develop using pathways established within the human body. Perversion of the body's systems allows tumors to grow largely unchecked and without the knowledge of the individual. The disease only becomes apparent when the afflicted experiences signs of illness, typically indications of systemic toxicity. Naturally, this results in ~50% of cancers diagnosed in advanced stages and ~90% of cancer deaths caused ultimately by metastasis [1, 2]. An early diagnosis allows for more treatments and a more optimistic prognosis, with a number of cancers having 5-year survival rates of >80% and even >90% [2]. Exosomes, small lipid-bound extracellular vesicles, have shown diagnostic prowess in identifying cancer in a non-invasive screening manner [3-5].

Exosomes provide a communication highway for cells; their cargos contains a plethora of peptides, proteins, and RNA [6]. The cargos mediate roles including intercellular communication, immune modulation, cargo transportation, and communication across the blood brain barrier [6]. When a tumor develops, it has access to these powerful communication pathways, and abuses them for the survival of the tumor. This typically means exosomes induce immunosuppression, tumorigenesis, angiogenesis, and eventually metastasis [7].

While it is widely established that these exosomes are a good indicator of the presence of cancer, current isolation and purification methods prohibit the use of these techniques in high-throughput, sensitive detection methods. Ultracentrifugation (UC), the gold-standard in exosome isolation, can take 6 hours to extract unpurified exosomes from blood, and 2-3 days to extract purified exosomes from blood [8, 9]. Our lab has developed a technique to bypass this purification process and accurately quantify cancer-associated exosomes using a rapid, novel interference-resistant Janus Particle Technology[10].

METHODS

Our lab has developed a technique for quantifying plasma exosomes that employs rotational Brownian motion. The technology utilizes Janus Particles (JPs), one-micron fluorescent beads coated with a thin layer of gold on a singular hemisphere. Fundamental rotational Brownian motion produces a spin on the spheres with a frequency inversely proportional to the cubed particle diameter. The JPs appear to blink on account of the dissimilar halves, and any increase in the effective size, i.e. via exosome coupling, will slow the rotation with great sensitivity. These beads provide rapid (<60 minute) detection of exosomes due to a small ~100 um average separation of the JPs and exosomes in solution.

The JPs utilizes gold-conjugation to adhere antibodies onto the surface which will dock exosomes upon incubation. Our selected anti-active epidermal growth receptor (aEGFR), anti-carcinoembryonic antigen (CEA), and anti-glypican-1 (GPC1) antibodies due to their presence and upregulation in glioblastoma multiforme (GBM), Colorectal cancer (CRC), and pancreatic ductal adenocarcinoma (PDAC)[3-5].

We have developed a single particle tracking algorithm capable of decoupling translational Brownian motion from the rotational Brownian motion. The tracking records the brightness fluctuations of a JP across the duration of a video and applies a wavelet function to the signal in order to isolate the rotational frequency. The average value is calculated for the ensemble of JPs and compared against a sample where there are no exosomes present. The shift in rotational frequency can then be extrapolated to quantity the number of exosomes in solution.

RESULTS

To develop Janus Particles as a reliable nanoparticle biosensor, we first validated the platform using UC purified exosomes derived from healthy patients and quantified with Nanosight (Figure 1). Exosomes were serially diluted and incubated with Janus Particles that were

functionalized to detect exosomes containing the characteristic tetraspanin, CD63.

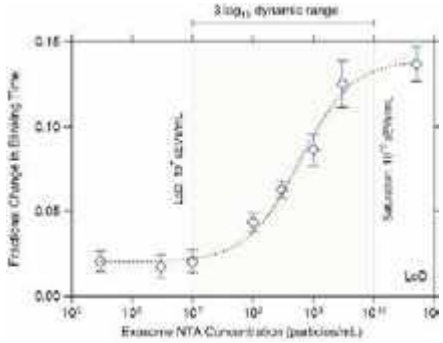

Figure 1: Janus Particle Calibration Curve using NTA benchmark

The first figure shows that they JPs have an impressive 3-log dynamic range and can detect as low as 1E7 exosomes/mL of plasma, which makes it ideal for quantifying low concentrations of exosomes. The initial experiment shows the potential to detect exosomes after purification, but our goal is to detect exosomes in complex media, such as plasma. We separated exosomes from the remainder of the plasma (flowthrough) using a tangential flow technique and recombined them in various ratios to see how well JPs respond to interference. JPs were then functionalized with an isotype antibody and subjected to the same exosome samples before being recorded. Both can be seen in Figure 2, below.

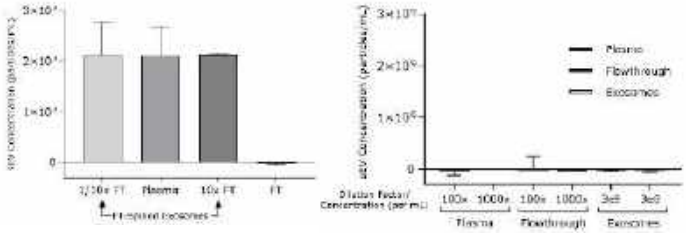

Figure 2: Janus Particle spiked protein incubation (left) and isotype control experiment (right)

Certain exosome characterization techniques respond poorly to the presence of interfering proteins. However, The Janus Particle response reveals it is sensitive only to exosomes containing the protein it is functionalized to detect and will not respond to non-target exosomes or soluble forms of protein in solution. This led us to believe that the JP platform would be ideal for selecting for cancer-associated exosomes while selecting against healthy exosomes which is tested in Figure 3.

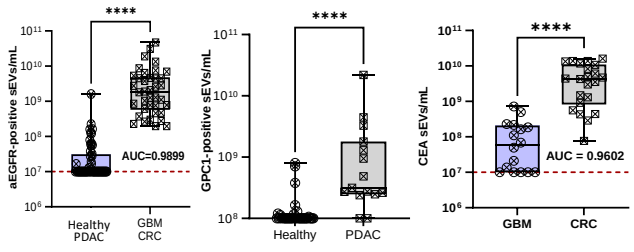

Figure 3: Glioblastoma, colorectal cancer, pancreatic cancer study using aEGFR, GPC1, and CEA functionalized Janus Particles.

The figure above represents the results acquired from our cancer trial. GBM and CRC to overexpress active EGFR while allows us to separate them from the healthy groups and those with pancreatic cancer. In the second graph, we are able to differentiate pancreatic cancer patients due to their upregulation of GPC-1 on their exosomes. In the final graph, we distinguish between the colorectal cancer patients from the glioblastoma patients due to the upregulation of CEA. Each individual point is a separate biological replicate with three technical replicates each.

DISCUSSION

Our results support our initial presumptions that the Janus Particle platform would be an ideal method for determing not just the presence of cancer, but the type of cancer as well. Previous screening techniques are isolated primarily to superficial organs of the body and are full of limitations. The rotational Brownian motion of Janus particles shows not only are we able to effectively able to screen for being positive or negative for cancer, but we are able to determine the origin of the exosomes and thus the type of cancer the patient likely has. This shows a potential for efficacious methods for screening complex, well-hidden cancers that would otherwise go completely unnoticed. The results of these experiments can be extrapolated to other cancers as well, if appropriate exosomal surface markers are readily detectable.

ACKNOWLEDGEMENTS

This work was supported in part by the Nation Institutes of Health Commons Fund, through the Office of Strategic Coordination/Office of the NIH Director, 1UG3CA241684-01, National Heart, Lung, and Blood Institute (NHLBI) under award number R01HL141909.

REFERENCES

1. Guan, X., Cancer metastases: challenges and opportunities. *Acta Pharm Sin B* **2015,** *5* (5), 402-18.
2. Crosby, D.; Bhatia, S.; Brindle, K. M.; Coussens, L. M.; Dive, C.; Emberton, M.; Esener, S.; Fitzgerald, R. C.; Gambhir, S. S.; Kuhn, P.; Rebbeck, T. R.; Balasubramanian, S., Early detection of cancer. *Science* **2022,** *375* (6586), eaay9040.
3. Cumba Garcia, L. M.; Peterson, T. E.; Cepeda, M. A.; Johnson, A. J.; Parney, I. F., Isolation and Analysis of Plasma-Derived Exosomes in Patients With Glioma. *Front Oncol* **2019,** *9*, 651.
4. Melo, S. A.; Luecke, L. B.; Kahlert, C.; Fernandez, A. F.; Gammon, S. T.; Kaye, J.; LeBleu, V. S.; Mittendorf, E. A.; Weitz, J.; Rahbari, N.; Reissfelder, C.; Pilarsky, C.; Fraga, M. F.; Piwnica-Worms, D.; Kalluri, R., Glypican-1 identifies cancer exosomes and detects early pancreatic cancer. *Nature* **2015,** *523* (7559), 177-82.
5. Xiao, Y.; Zhong, J.; Zhong, B.; Huang, J.; Jiang, L.; Jiang, Y.; Yuan, J.; Sun, J.; Dai, L.; Yang, C.; Li, Z.; Wang, J.; Zhong, T., Exosomes as potential sources of biomarkers in colorectal cancer. *Cancer Lett* **2020,** *476*, 13-22.
6. Tenchov, R.; Sasso, J. M.; Wang, X.; Liaw, W. S.; Chen, C. A.; Zhou, Q. A., Exosomes─Nature's Lipid Nanoparticles, a Rising Star in Drug Delivery and Diagnostics. *ACS Nano* **2022,** *16* (11), 17802-17846.
7. Yu, D.; Li, Y.; Wang, M.; Gu, J.; Xu, W.; Cai, H.; Fang, X.; Zhang, X., Exosomes as a new frontier of cancer liquid biopsy. *Mol Cancer* **2022,** *21* (1), 56.
8. Zhang, Q.; Jeppesen, D. K.; Higginbotham, J. N.; Franklin, J. L.; Coffey, R. J., Comprehensive isolation of extracellular vesicles and nanoparticles. *Nat Protoc* **2023,** *18* (5), 1462-1487.
9. Gao, J.; Li, A.; Hu, J.; Feng, L.; Liu, L.; Shen, Z., Recent developments in isolating methods for exosomes. *Front Bioeng Biotechnol* **2022,** *10*, 1100892.
10. Chen, W. L.; Chuang, H. S., Trace Biomolecule Detection with Functionalized Janus Particles by Rotational Diffusion. *Anal Chem* **2020,** *92* (19), 12996-13003.

DYNAMIC MICROMECHANICAL CHARACTERIZATION OF 3D PRINTED BONE IN VITRO MODELS MANUFACTURED VIA VAT PHOTOPOLYMERIZATION

Elizabeth A Hunt (1), S. Choi (2), E. Shangin (1), E. Nguyen (1), Dr. A. Whittington (3,4,5), Dr. C.J. Collins (1)

(1) Department of Biomedical Engineering and Sciences, Virginia Tech, Blacksburg, Virginia, USA
(2) Department of Biological Sciences, Virginia Tech, Blacksburg, Virginia, USA
(3) Department of Chemical Engineering, Virginia Tech, Blacksburg, Virginia, USA
(4) Department of Materials Science and Engineering, Virginia Tech, Blacksburg, Virginia, USA
(5) Department of Macromolecular Science & Engineering, Virginia Tech, Blacksburg, Virginia, USA

INTRODUCTION

Nonunion or delayed fracture healing is a prevalent clinical complication with a devastating impact on patient quality of life, leading to significant financial burden for patients[1]. Despite knowledge of the mechanobiology behind bone healing, we lack the ability to discern bone healing capacity in individual patients. Existing biomarkers for healing progression and clinical imaging modalities fail to discern which patients experience delayed fracture healing or proceed to nonunion. Current preclinical models for bone fracture healing rely on 2D cell culture and animal experiments, each with their own limitations regarding translation to patients[2]. Additionally, current detection strategies such as radiolucency in planar x-rays and reported pain by the patients do not account for the *in vivo* mechanical environment[3,4] though studies have shown a positive relationship between loading and bone healing[5]. 3D culture systems such as organoids provide an *in vitro* tissue culture platform that allow for the prolonged study of human cells in an environment that mimics *in vivo*[6]. To develop such a platform for assessing individual patient risk factors for non-union, this study aims to manufacture porous 3D scaffold geometries using a novel, osteoconductive resin via vat photopolymerization (VP) and analyze their ability to mimic the *in vivo* bone micromechanical environment.

METHODS

Resin Formulation: A mixture of 50 wt% epoxidized soybean oil acrylate (ESOA, Sigma-Aldrich) and 50 wt% polyethylene glycol diacrylate (PEGDA, Sigma-Aldrich, MW = 575) was used to formulate the resin for printing. To promote curing, 1 wt% diphenyl(2,4,6-trimethylbenzoyl)phosphine oxide photoinitiator (Sigma-Aldrich) and 0.20 wt% 2,5-bis(5-tert-butyl-benzoxazol-2-yl)thiophene UV absorber (TCI Chemicals) was added.

*Scaffold Printing & Sterilization***:** Three scaffold geometries (Voronoi, IsoTruss, and Truncated Octahedron (TO)) were designed (nTopology, Figure 1) with 489, 476, and 554 μm average pore diameters, respectively, and printed using a VP bottom-up platform (Autodesk Ember). Five burn-in layers underwent UV exposure (5 W, λ = 405 nm) for 25 s per layer, and the rest of the model layers were exposed for 2.5 s per layer. Every layer was 0.1 mm thick for a total of 10 mm for the entire scaffold. After printing, the burn-in layers were removed and the scaffolds were washed in 70% isopropyl alcohol (IPA) and UV cured for one minute.

Prior to cell seeding, scaffolds underwent sterilization using 70% ethanol for 1 hr, followed by 3 washes with phosphate buffered saline (PBS) and a final wash using media made of αMEM and supplemented with 10% fetal bovine serum (FBS) and 1% penicillin-streptomycin-amphotericin (Thermo-Fisher).

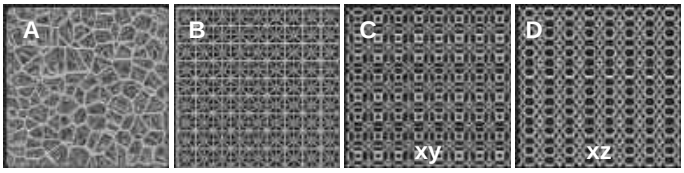

Figure 1: Voronoi (A), IsoTruss (B), and TO (C & D) lattices.

*Cell Seeding & Analysis***:** Murine fibroblasts (1 x 10^5 NIH 3T3) were seeded on each scaffold (n = 6/geometry) and cultured in media under static conditions for 4 and 7 days, with media exchange every 2-3 days. Subsequently, each sample was immersed for 5 minutes in 1 mL 10% formalin fixation solution, rinsed with PBS, and immersed in 1 mL of a post-fixation solution of 10% formalin. Scaffolds were then rinsed in PBS for 1 minute and stained with DAPI and Rhodamine Phalloidin dyes (Thermo-Fisher) for 1 hr in the dark before storage in deionized water at 4°C.

For assessment of the structural fidelity and biocompatibility, the scaffolds were cut in half and examined using a laser scanning confocal fluorescence microscope (Zeiss Axio Observer.Z1) with 10x objective (Plan-Apochromat 10x/0.45 M27, Zeiss) and 60 μm diameter pinhole.

Consistent processing and analysis of image stacks (voxel size 0.85x0.85x5.4 μm) were employed to assess cell nuclei spatial distribution within the scaffolds and the pore distribution within the scaffolds following image segmentation (ImageJ).

Dynamic Mechanical Analysis: Dynamic mechanical analysis (DMA, ElectroForce 3200) was performed on the seeded (n=6/geometry/day culture) and unseeded (n=1/geometry) scaffolds via cyclic compression using a strain sweep to analyze how microstructure impacts the organoid elastic modulus (E', storage modulus), viscous modulus (loss modulus), and damping coefficient (tanδ). The strain sweep was conducted at a frequency of 0.1 Hz starting with a dynamic amplitude of 0.2 mm (4% strain) and increasing by 0.1 mm until reaching 1 mm dynamic amplitude (10% strain). All testing was performed submerged in a 1x concentrated phosphate-buffered saline (PBS, pH 7.4) solution at 37 °C.

Statistical Analysis: Mechanical data was analyzed for descriptive statistics (python) using paired t-tests to determine significant differences between the 4-day and 7-day cultured scaffolds (α=0.05).

RESULTS

After 4 and 7 days of seeding, confocal microscopy confirmed successful cell adhesion and proliferation, with cells well distributed throughout all three scaffold geometries (Figure 2). Average pore diameters were 579, 397, 662 μm for the Voronoi, IsoTruss, and TO scaffolds, respectively, within range of the targeted print size.

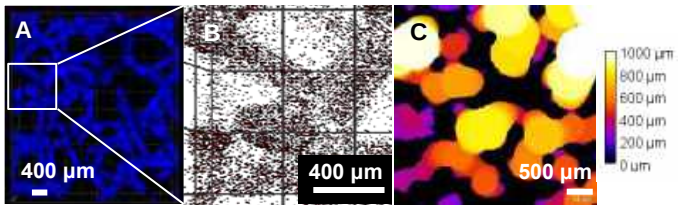

Figure 2: Voronoi structure (A, DAPI), cell nuclei distribution (B, Rhodamine), and pore thickness distribution map (C).

Some of the IsoTruss scaffolds (n=2) failed prematurely during the DMA testing due to inconsistencies in the printing, these were excluded from further analyses. For the remaining scaffolds, average storage modulus increased from day 4 to 7 of static culture (Table 1). The stiffest storage modulus achieved overall was reached by a 7-day cultured IsoTruss scaffold (2.70 MPa) Note, variation in the storage modulus for the 7-day IsoTruss scaffolds was the highest. The Voronoi scaffolds had the only significant and consistent increase in storage modulus between 4- and 7-day cultures (p=0.0293).

Table 1: Storage modulus (MPa) of the three scaffold geometries for 4- and 7-day cultures (mean ± SD).

Day	n	IsoTruss	TO	Voronoi
0	1	1.08	0.46	0.91
4	6	0.80±0.53*	0.64±0.40	0.55±0.25
7	6	0.81±1.27*	0.69±0.35	1.19±0.57
*n=4 for IsoTruss 4- and 7-day culture mechanical testing				

The peak storage modulus for the Voronoi 7-day cultured scaffolds is 2.26 MPa. Both of these peaks for IsoTruss and Voronoi are reached at the first strain sweep condition of 2% strain, or a dynamic amplitude of 2 mm. The peak storage modulus is achieved by a 4-day cultured scaffold for the TO geometry at 1.28 MPa at 2.14 % oscillation strain. Trends in loss modulus were consistent among the Voronoi and TO scaffolds, with a general increase with increased oscillation strain (Figure 3). On average, the loss modulus of IsoTruss scaffolds decreased at higher oscillation strains, leading to a tanδ of 0.0613, which is over 2x greater than Voronoi (0.0227) and TO (0.0297) at 2% strain.

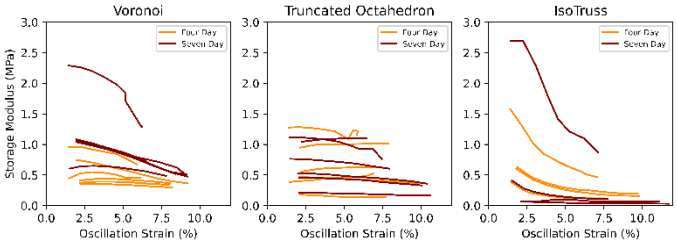

Figure 3: Storage modulus (MPa) vs. oscillation strain (%) for Voronoi, TO, and IsoTruss scaffolds.

DISCUSSION

Scaffold stiffness varied, with storage moduli on the order of soft fracture callus tissue after seeding (fracture callus moduli: 0.5-1000 MPa)[7]. Despite the limited number of samples available for testing, trends were observed on how seeding impacted scaffold stiffness. IsoTruss scaffolds achieved the maximum storage modulus of all 7-day seeded scaffolds; however, the rest of the 7-day IsoTruss seeded samples were significantly softer than the average TO and Voronoi scaffolds. Voronoi scaffolds had more consistent mechanical properties, while still achieving the second highest value for storage modulus. Further, Voronoi scaffolds had the most consistent increase in modulus with longer culture times, which may suggest the more consistent formation of extracellular matrix. Note, however, the range between 4- and 7-day seeded Voronoi scaffold storage moduli is limited. A portion of the IsoTruss scaffolds were too soft to perform DMA testing on, which could be due to inconsistencies in either the printing parameters or the curing process. As such, the remaining IsoTruss samples may have also been impacted by the same inconsistencies that prevented testing of the rest of the samples, contributing to the significantly higher damping detected in the IsoTruss specimens. Further spatial analysis of the cell distribution may also provide insight into the differences observed between scaffold geometries and culture time. The results of this study represent a successful first step at generating an organoid that recapitulates the micromechanical environment of healing bone. The investigated scaffold geometries 3DP via VP using the novel ESOA and PEGDA resin resulted in successful cell adhesion, proliferation, and extracellular matrix deposition, providing valuable insight into the structure/function relationship of pore shape and bone organoid mechanical properties.

ACKNOWLEDGEMENTS

We acknowledge support from the Beckman Scholar Foundation and the National Center for Advancing Translational Science of the NIH Award UL1TR003015/ KL2TR003016.

REFERENCES

[1] Hak, DJ et al., *Injury*, 45:S3-S7, 2014.
[2] Huang, J et al., *Cells*, 12:1590, 2023.
[3] Chen, JC, Jacobs, R, *Stem Cell Res Ther*, 4:107, 2013.
[4] Duan, ZW and H Lu, *Orthop Surg*, 13:369–375, 2021.
[5] Flowers, DW et al., *Bioeng*, 9:750, 2022.
[6] Lancaster, MA, Hutch, M, *Dis Model Mech*, 12:039347, 2017.
[7] Leong, PL, Morgan, EF, *Acta Biomater*, 4:1569-75, 2008.

CHARACTERIZATION OF A POLYMERIC DEVICE FOR LOCALIZED AND CONTROLLED DRUG DELIVERY TO CERVICAL CANCER

Jacob Provencio (1), Monica Elbjorn (2), Paige Phillips (3), David Di Rocco (2), R. Lyle Hood, PhD (1,2,4)

(1) Department of Biomedical Engineering, The University of Texas at San Antonio, San Antonio, TX, USA
(2) Department of Mechanical Engineering, The University of Texas at San Antonio, San Antonio, TX, USA
(3) Department of Biology, The University of Texas at San Antonio, San Antonio, TX, USA
(4) Department of Emergency Medicine, University of Texas Health Science Center at San Antonio, San Antonito, TX USA

INTRODUCTION

Cervical cancer ranks as the fourth most common cancer among women internationally, with 604,127 new cases reported annually (*1*). In 2020, over 300,000 deaths were attributed to this malignancy, making cervical cancer the fourth deadliest cancer among women (*2*). Individualized treatment plans depend on factors such as the patient's age, medical history, and stage of cancer. Traditionally, chemotherapy is administered either intravenously or through an ingestible pill. These forms of drug administration are suboptimal as they rely on systemic circulation, resulting in only a minor fraction reaching the malignant site (*3*). Consequently, higher dosages are required, leading to increased side effects and complications. A more effective form of administration would involve delivering medication locally to the target site, minimizing circulation elsewhere (*4*).

This work focused on an innovative localized implantable drug delivery system aimed to reduce the side effects and complications that arise from cervical cancer chemotherapy. The primary objective was to demonstrate loading and maintenance dosing protocol *in vitro*. A polymer injection mold was developed for manufacturing test implants. Implants produced from two different polymers and with four different geometries were loaded with Rhodamine B, acting as a drug analog. Subsequently, the implants underwent release testing over a 21-day period.

METHODS

Polycaprolactone (PCL) was chosen for this study due to its hydrophobicity and biocompatibility. Polylactic Acid (PLA) was selected for its versatility as a biopolymer, thermoplastic behavior, and biocompatibility (*5*). These polymers were combined with Rhodamine B, serving as a tracer dye and drug analog for cisplatin, a commonly used chemotherapeutic agent for localized cervical cancer treatment (*6*). Phosphate Buffered Saline (PBS) was chosen as a physiologically mimicking solvent due to its pH and isotonic nature.

Figure 1. shows the 12-bead injection mold which allowed for the mass production of polymeric devices, streamlining the creation through a highly repeatable batch process. Devices were manufactured using 2.00 grams of either PCL or PLA and 0.02 grams of Rhodamine B (1% of the mixture). The polymers were heated on a hot plate to their melting point, combined with Rhodamine B, and stirred for thorough mixing. The resulting mixture was then pressed into a hopper, leading into the 12-bead aluminum mold with interlocking channels to create the test devices. A post processing phase yielded four distinct devices: a Sphere, Sphere with a Through Hole, a Rod, and a Tube.

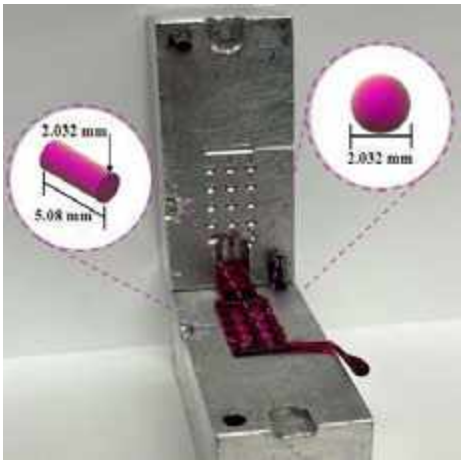

Figure 1. Mold for 12 Beads and Depiction of Polymeric Based Device Measurements

A 21-day release experiment assessed the release rate of the Rhodamine B devices. Batch produced devices were measured with

calipers to ensure that all selected test samples fell under a tolerance of ± 0.020 mm. Four implants were submerged in separate beakers, each containing 150 ml of PBS. A magnetic stir bar was added to maintain a well-mixed sink condition. A volume of 2.5 ml was withdrawn from the 150 ml sink solution and replaced with fresh PBS daily. The extracted sample was then pipetted into a cuvette for analysis using a UV-Vis Spectrophotometer. The sampling and analysis process was maintained for 21 days, with the final spectrophotometer analysis conducted at the conclusion of the experimentation period.

A secondary experiment aimed to ascertain the proper distribution of Rhodamine B within each individual implant during the batch-making process. Distribution was determined by splitting an implant into four equal pieces, with each piece then immersed in a 150 ml volume of PBS, sampled for 21-days, and analyzed as previously described. An additional split device was evaluated for homogeneity using the Scanning Electron Microscope (SEM) at resolutions of 300 µm, 10 µm, 5 µm, and 2 µm.

A third experiment was conducted to determine how varying the implant's geometry and surface area (SA) would impact the release rate. Four distinct geometries were tested: a Sphere (SA 12.97 mm^2), a Sphere with a Though Hole (SA 34.84 mm^2), a Rod (SA38.90 mm^2), and a Tube (SA 48.40 mm^2). Various geometrical patterns, including inner diameters of 0.635 mm, were achieved through post processing following the injection process. Each device was placed into a 150 ml volume of PBS, sampled, and analyzed as previously described.

RESULTS

Results exhibited a biphasic linear release pattern from PCL, characterized by an initial burst on the first day followed by a consistent linear release for the next 20 days. In contrast, PLA did not demonstrate any release in any of the experiments. For PCL, there was an initial surge of Rhodamine B release measuring 2.295 ± 0.40 µg on the first day of testing. The tracer dye continued to release incrementally at approximately 0.11 µg/ml daily throughout the 21-day experimentation period. After the initial week of testing, the average mass release form the PCL based devices were approximately 2.8 ± 0.3 µg. The initial burst of Rhodamine B accounted for 0.04% of the total release of tracer dye in a singular device. For the duration of the experimentation period, 3.8 µg was released from the device, representing 0.12% of the total amount of Rhodamine B per implant. After the initial burst, the incremental release of Rhodamine B exhibited an R^2 value of 0.9847 for the remaining days.

The experiment evaluating PCL implants being split into four pieces demonstrated similar biphasic linear release profiles with a percentage different of 4.2 ± 0.5%, establishing the fabrication process produced implants with Rhodamine B consistently mixed throughout the device. The images obtained using the SEM identified a smooth combination between Rhodamine B and PCL, with no clumping of tracer dye throughout the mixture.

The final experiment, shown in Figure 2., compared geometrical variability between each of the polymeric devices. The cylindrical tube achieved the highest initial and overall mass release of Rhodamine B, measuring 13.02 µg and 31.08 µg, respectively. The standard shaped sphere exhibited the least initial and final mass release, 3.68 µg and 8.02 µg, respectively. Changing the geometry of the sphere into a cylindrical rod increased the mass release by 22.48% ± 2%. Introducing a hole through the center of the cylindrical rod (tube), resulted in further increase in mass release by 35.064% ± 2%. As the surface area of the devices increased, the percentage of the total mass release increased congruently.

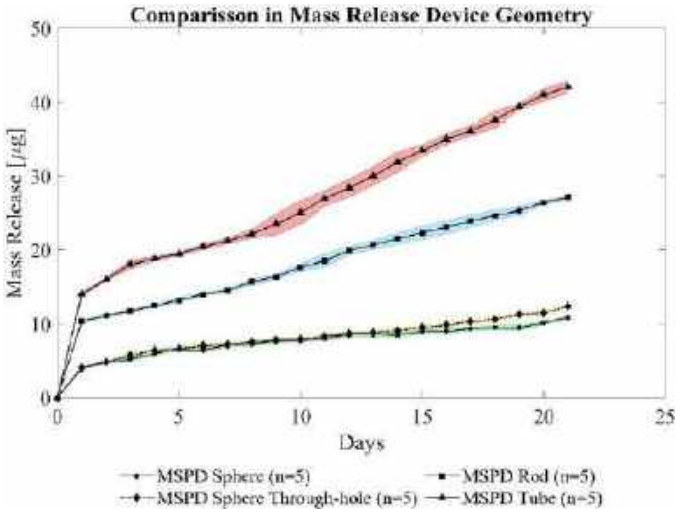

Figure 2. Mass Release profile comparison between a Sphere, Sphere with a Through Hole, Rod, and Tube

DISCUSSION

The implementation of a 12-bead polymer injection mold reduced the time needed for manufacturing experimental devices, ensuring consistent ratios of Rhodamine B to PCL and PLA. Results demonstrated that PLA was a poor choice as a drug release medium but may serve as a capping layer that could be leveraged in future composite geometries. Evaluation of four distinct geometries revealed a correlation between release rate and surface area, providing a tuning parameter for future dosage control. Future work is focused on controlling the initial burst release and refining dosage control through geometry and surface area. This study provides a foundation for future development of polymeric implantable for chemotherapeutic treatments.

ACKNOWLEDGEMENTS

The authors acknowledge the funding support from the University of Texas at San Antonio.

REFERENCES

1. M. Elbjorn *et al.*, An Innovative Polymeric Platform for Controlled and Localized Drug Delivery. *Pharmaceutics* **15**, 1795 (2023).
2. P. Poniewierza, G. Panek, Cervical Cancer Prophylaxis—State-of-the-Art and Perspectives. *Healthcare* **10**, 1325 (2022).
3. C. Federico *et al.*, Localized Delivery of Cisplatin to Cervical Cancer Improves Its Therapeutic Efficacy and Minimizes Its Side Effect Profile. *Int J Radiat Oncol Biol Phys* **109**, 1483-1494 (2021).
4. J. B. Wolinsky, Y. L. Colson, M. W. Grinstaff, Local drug delivery strategies for cancer treatment: gels, nanoparticles, polymeric films, rods, and wafers. *J Control Release* **159**, 14-26 (2012).
5. F. Akhter, G. N. W. Bascos, M. Canelas, B. Griffin, R. L. Hood, Mechanical characterization of a fiberoptic microneedle device for controlled delivery of fluids and photothermal excitation. *Journal of the Mechanical Behavior of Biomedical Materials* **112**, 104042 (2020).
6. J. Zhu *et al.*, Weekly versus triweekly cisplatin-based concurrent chemoradiotherapy in the treatment of locally advanced cervical carcinoma: An updated meta-analysis based on randomized controlled trials. *Medicine (Baltimore)* **99**, e18663 (2020).

A SYSTEMATIC ANALYSIS CONFIRMED THAT MECHANICAL AND STRUCTURAL ANISOTROPIES DO NOT CONCUR IN 37% OF EQUATORIAL SCLERA SAMPLES

Bangquan Liao (1), Yi Hua (2,3), Fengting Ji (1), Frederick Sebastian (4) Rouzbeh Amini (4) Ian Sigal (1,5)

(1) Department of Bioengineering, University of Pittsburgh, Pittsburgh, PA, USA
(2) Department of Biomedical Engineering, University of Mississippi, University, MS, USA
(3) Department of Mechanical Engineering, University of Mississippi, University, MS, USA
(4) Department of Bioengineering, Northeastern University, Boston, MA, USA
(5) Department of Ophthalmology, University of Pittsburgh, Pittsburgh, PA, USA

INTRODUCTION

Many soft tissues are mechanically anisotropic, meaning that their stiffness varies by orientation [1]. Collagen fibers are the main load-bearing components of soft tissues, and therefore the macro-scale mechanical anisotropy arises from micro-scale structural anisotropy in the collagen fibers [2,3]. Thus, it is frequently assumed that mechanical and structural anisotropies concur [4]. For instance, it is common to use fiber orientation information obtained from techniques such as polarized light microscopy (PLM) or small angle light scattering to derive constitutive models in which the mechanical anisotropy essentially matches the structural anisotropy [5].

Recently, we measured the mechanical and structural anisotropies of equatorial sclera using standard equibiaxial testing and PLM techniques [2,5]. To our surprise, we found that the mechanical and structural anisotropies did not always concur. Although we only analyzed four samples from one eye, and the mismatch only occurred in half of them, we reasoned that a discrepancy between mechanical and structural anisotropies would be crucial to understand, even if it only occurs sporadically.

Our goal in this study was to systematically replicate our previous study, increasing the number of eyes and carefully checking each and every step to ensure that there were no mistakes or artifacts that could have produced the observed mismatch in anisotropies.

METHODS

Equibiaxial tensile testing. Five pig eyes were dissected to isolate equatorial sclera samples (11mm × 11mm) for each anatomical quadrant: nasal (N), superior(S), temporal (T), and inferior(I). A small cut was made on the top right corner of the samples to indicate the meridional direction. Mechanical anisotropy was measured using equibiaxial tensile testing with loading axes aligned with the equatorial and meridional directions to a maximum stress of 120 kPa.[6] (**Figure 1**) The specimen subjected to ten cycles of loading/unloading, and the data from tenth cycle was used for further analysis. The specimens were immersed in PBS during testing and switched to formalin afterward.

Polarized light microscopy (PLM). The samples were cryosectioned (30μm thick) and all sections imaged by PLM using an MVX 10 microscope [7]. The images were registered into stacks and collagen orientations computed for each pixel and then for the whole tissue (**Figure 2**).

Mechanical anisotropy was quantified by the ratio of the stiffness (the stress-strain curve slope at the point of full fiber recruitment) in the meridional and equatorial directions. Structural anisotropy was quantified from the ratio of areas under the fiber distribution curves.

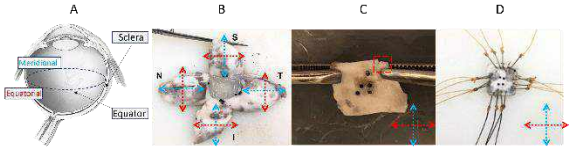

Figure 1: (A) Diagram of the eye with the location of the equator and the meridional and equatorial directions [6]. (B) Eye after dissection. (C) Excised quadrant with orientation mark. (D) Sample set for equibiaxial testing to measure mechanical anisotropy.

RESULTS

The equibiaxial test results show variable mechanical anisotropies between samples. Superior and inferior sectors had stiffer meridional directions (**Figure 3**). Nasal and

inferior sectors were closer to isotropic. The PLM measurements indicate substantial structural anisotropies, with a majority of the samples having the primary fiber alignment close to the meridional direction (**Figure 3**). Example cases with anisotropy match and mismatch are shown in **Figure 4**. One sample had problematic stretch tests and was excluded from further analysis. Overall, 7 of 19 samples (37%) had mismatched results between the mechanical and structural anisotropies (**Figure 5**).

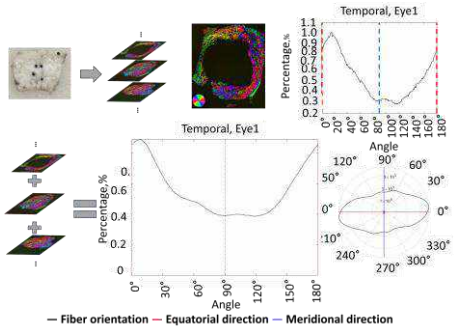

Figure 2: Structural anisotropy was measured from collagen orientation determined using PLM images of tissue cryosections. Shown are example images and orientation maps of a single section (top) and stack (bottom). This sample (T1) had clear anisotropy with fibers preferentially along the equatorial direction.

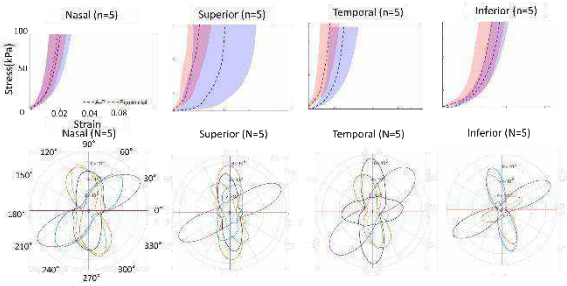

Figure 3: (top row) Arithmetic average (n=5) of 4 quadrants' strain at the same stress. Dashed curves represent the mean value of meridional and equatorial directions. The shaded regions are the standard error of the mean value. (bottom row) Polar plots of fiber orientations for all samples. Both tests show clear anisotropy and wide variations between samples.

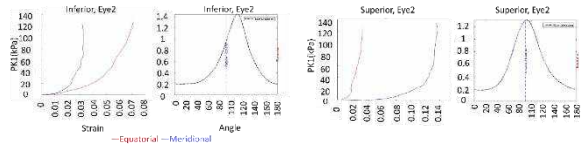

Figure 4: Matching (left pair) and mismatching (right pair) mechanical and structural anisotropies.

DISCUSSION

This study confirmed our previous finding that most equatorial sclera samples are mechanically and structurally anisotropic. Our observation that most equatorial sclera samples had collagen fibers preferentially aligned in the meridional direction is consistent with the literature [8]. Most importantly, our results confirmed that for 37% of the samples the mechanical and structural anisotropies do not concur.

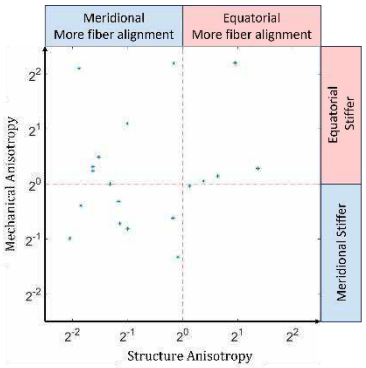

Figure 5. Scatter plot of R_{PLM} vs. R_{Mech}. The dashed line across the figure represents the mechanical and structure isotropic property. 7 samples are in mismatched regions. 12 samples are on the contrary.

The mismatch between anisotropies was not a surprise for this work. As we explained above, this study was motivated by the observation of the mismatch. In addition, in another study carried out independently by our group in collaboration with the Chen and Zhou labs in California we had observed anisotropy mismatches. Specifically, we had reported a mismatch between equatorial sclera mechanical and structural anisotropies. In those studies, however, mechanical anisotropies were not measured directly as we have done in this work. Tissue mechanics were instead inferred from measurements of wave propagation obtained from ultrasound and optical coherence tomography.

The causes underlying the mismatch between mechanical and structural anisotropies are not yet understood. This study cannot provide a definitive explanation for the mismatch phenomenon. But it is possible to speculate on some potential causes. One possible explanation could be differential collagen fiber crimp between orientations. This, however, seems unlikely as it would be discernible in the shape of the recruitment curve. It is also possible that the collagen fibers of the sclera vary in diameter [8], and thus in stiffness. It is also possible that there are directional variations in crosslinking [10], proteoglycan content or collagen type. Note that the PLM measurements are not perfect and do not account for the complex 3D nature of fibers that are interwoven. Fiber interweaving can also affect sample mechanics [11].

ACKNOWLEDGEMENTS

NIH R01-EY023966, P30-EY008098, and T32-EY017271; Eye and Ear Foundation (Pittsburgh, PA); Research to Prevent Blindness; (Stein Innovation Award).

REFERENCES

[1] Arnab C et al. *Appl Bionics Biomech*, 4838157–59,2018
[2] Fengting J et al. *Exp. Eye Res,* 10, 109510, 2022
[3] Boote, C et al., *Prog Retin Eye Res*, 74: 100773, 2020.
[4] Ramesh R et al. *J Biomech, 133*, 091011, 2011
[5] T. Christian G et al. *Acta Biomater,8*, 3091-3103, 2012
[6] Khoiy, K. A.et al. *J. Biomech*., 140, 094503, 2018
[7] Ningjiun J et al. *BOEx,* 6, 4705–4718, 2015
[8] Michaël J G et al., *IOVS*, 52, 9684-9693, 2011
[9] Komai, Y. et al, *IOVS,* 32, 2244–2258, 1991
[10] Lewis, P. N. et al., *Structure, 18, 239–245.* 2010
[11] Bingrui W et al, *Acta Biomater,* 113, 429-437, 2020

A MULTI-PHYSICS MODEL OF CONTRAST INJECTION IN THE CORONARY ARTERIES TO ASSESS INDEX OF MICROCIRCULATORY RESISTANCE

Haizhou Yang (1), Jiyang Zhang (2), Ismael Assi (3), Brahmajee K Nallamothu (4), Krishna Garikipati (5), C. Alberto Figueroa (1,6)

(1) Department of Biomedical Engineering, University of Michigan, Ann Arbor, MI, USA
(2) Department of Mechanical Science and Engineering, Sichuan University, Chengdu, Sichuan, China
(3) College of Medicine, University of Cincinnati, Cincinnati, OH, USA
(4) Department of Internal Medicine, University of Michigan, Ann Arbor, MI, USA
(5) Department of Aerospace and Mechanical Engineering, University of Southern California, Los Angeles, CA, USA
(6) Department of Surgery, University of Michigan, Ann Arbor, MI, USA

INTRODUCTION

Coronary microvascular dysfunction (CMD) is characterized by impaired blood flow and blood regulation in the microcirculation, and is a critical concern in the field of cardiology [1]. CMD encompasses a range of structural maladaptations in vessels and myocardium that disrupt the delicate balance between blood supply and demand, leading to adverse clinical outcomes. The index of microcirculatory resistance (IMR) is regarded as the current gold standard for evaluating coronary microcirculatory function [2]. IMR has reliably predicted myocardial viability after primary angioplasty following myocardial infarction as well as the extent and severity of myocardial infarction in patients [3], [4]. However, IMR assessment remains underused in many medical settings due to its invasive nature as it requires additional placement of a coronary wire in the vessel. Therefore, a non-invasive, data-driven approach for IMR assessment is highly desired. The primary goal of this study is to develop a data-driven framework capable of harnessing information encapsulated within angiography data, the most commonly used modality for coronary artery disease assessment, with multi-physics computational models to quantify IMR. Toward that goal, we have developed and calibrated a multi-physics computational fluid dynamics (CFD) model of contrast injection. This model provides a tool to: 1) interpret the computational angiography data, i.e. the dynamics of the contrast injection and washout within the coronary arteries, and 2) study the correlation between these dynamics and IMR.

METHODS

To provide an interpretation of the parameters that control the different scenarios of the contrast injection and washout, we developed a novel multi-physics CFD model of iodine contrast injection using CRIMSON [5]. Figure 1 shows an anatomical model of the aortic root and the main branches of the right coronary artery (RCA) built from a CT scan of a patient. The model includes the distal end of a catheter that will be used to simulate contrast injection. A key aspect of the model is the lumped parameter models (LPMs) for the left heart, right coronary arteries, and aortic outflow which are used as boundary conditions for the CFD simulation. The left heart model relies on a time-varying elastance function $E_{LV}(t)$, which represents ventricular contractility. The coronary models account for the systolic myocardial compression that produces the characteristic diastolic-dominated coronary flow patterns. The Navier–Stokes equations and the convection-diffusion transport equation are then solved in the 3D geometry to calculate velocity, pressure, and concentration of iodine contrast.

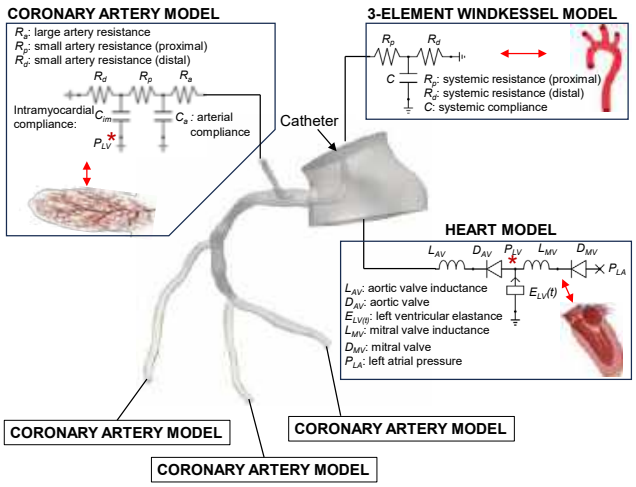

Figure 1: CFD model of contrast injection with LPMs as boundary conditions.

The computation of the transport of contrast within the coronary vessels provides a surrogate of the angiographic data, and the contrast

intensity curve can be extracted, as shown in Figure 2. The computed concentration of contrast within the RCA is projected onto 2D images using similar angles as in clinical X-ray angiograms. Segmentation is then performed via thresholding to generate binary images. Bright pixels for each frame are counted and an intensity curve representing the injection and washout of the contrast is produced. Similarly, AngioNet [6] was deployed to calculate contrast intensity curves through recursive segmentation of clinical angiograms in a cohort of 104 patients after successful percutaneous coronary intervention.

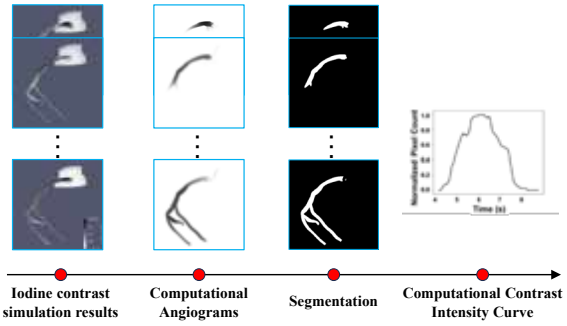

Figure 2: Contrast intensity curve generation from computational results.

RESULTS

Figure 3 depicts flow and pressure waveforms of a multi-physics simulation at aortic inlet, acute marginal and right posterior atrioventricular coronary outlets, as well as the 2-second iodine contrast injection through the catheter (denoted by light blue shade, **panel (b)**). Cardiac output (CO) is 4.88 L/min, and total RCA flow is 0.1 L/min (2% of CO). Coronary outlets present the typical diastolic-dominated profiles. Pressure ranges from 170-100 mmHg, without gradients through the RCA vessels, consistent with a lack of epicardial disease. **Panel (a)** shows a snapshot of pressure, velocity, and contrast agent concentration at time t=5.9 s. These hemodynamic results are therefore physiologically relevant and produce a solid foundation to study hemodynamics in these patients.

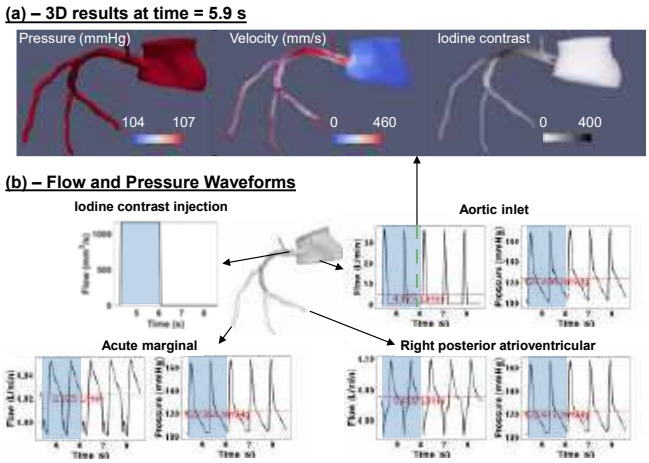

Figure 3: (a): 3D contours of pressure, velocity, and iodine contrast concentration at time t=5.9 s. (b): Representative flow and pressure waveforms.

To demonstrate the impact of altered microvascular resistances in the contrast injection curves, we conducted a study whereby the parameters governing coronary microvascular resistance (R_a, R_p, R_d in Figure 1) were gradually altered to simulate increased degrees of microvascular dysfunction. Figure 4 presents contrast intensity curves corresponding to three simulation scenarios: **1)** a healthy baseline (green line) with a total RCA flow of 0.15 L/min; **2)** a moderate disease (blue line) with a total RCA flow of 0.08 L/min, obtained by uniformly increasing R_a, R_p, R_d by 100% relative to the baseline case; **3)** a severe disease (orange line) with a total RCA flow of 0.05 L/min, obtained by further uniformly increasing R_a, R_p, R_d by 50% relative to the moderate disease case. The simulated contrast intensity curves matched the patterns from the patient cohort depicted in Figure 5, which demonstrates the substantial variability in the rising and falling slopes of the contrast intensity curves in a cohort of 104 patients. Slower rising and emptying patterns in the contrast intensity curves correspond to higher resistance values in the coronary microcirculation.

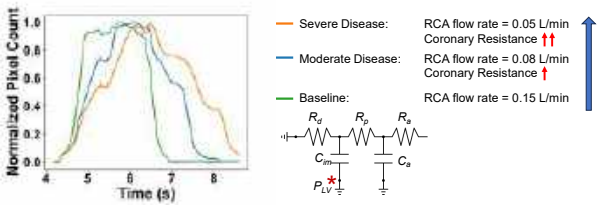

Figure 4: Contrast intensity curves of different simulations with increasing values of coronary resistance, indicative of coronary microvascular disease.

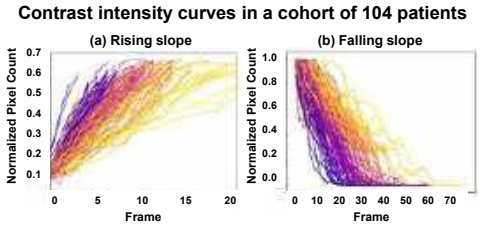

Figure 5: Intensity curves of RCA angiography data from 104 patients (warmer colors indicate greater disease severity).

DISCUSSION

This study developed a multi-physics CFD model to simulate the injection of iodine contrast into the coronary artery. The contract intensity curves are obtained from both computational angiograms and clinical angiograms to investigate the relationship between the dynamics of the contrast and microcirculatory resistance. Results show that the computational CFD model is a feasible surrogate for simulating the process of iodine contrast injection. Furthermore, both computational and clinical results prove that there is a strong correlation between the contrast intensity curve and microcirculatory resistance. Slower rising and emptying patterns in the contrast intensity curves correspond to higher resistance in the coronary microcirculation.

ACKNOWLEDGEMENTS

This work is supported by NSF Grant # 2151555.

REFERENCES

[1] Vancheri, F. et al., *J Clin Med*, 9:2880, 2020.
[2] Ford, T. J. et al., *European Heart Journal*, 38: 1990–1992, 2017.
[3] Fearon, W. F. et al., *Circulation*, 109: 2269–2272, 2004.
[4] McGeoch, R. et al., *JACC Cardiovasc Interv*, 3: 715–722, 2010.
[5] Arthurs, C. J. et al., *PLoS Comput Biol*, 17: e1008881, 2021.
[6] Iyer, K. et al., *Sci Rep*, 11: 18066, 2021.

IN VITRO, NETWORK-WIDE EXCITOTOXIC DISRUPTION FOLLOWING TRAUMATIC BRAIN INJURY MODEL TO ASSESS CRITICAL INJURY THRESHOLDS

J. Sergay (1), N. Schick (2), E. Blick (1), A. Hai (1), C. Franck (3)

(1) Department of Biomedical Engineering, University of Wisconsin Madison, Madison, WI, USA
(2) Department of Psychology, Rutgers, Piscataway, NJ, USA
(3) Department of Mechanical Engineering, University of Wisconsin Madison, Madison, WI, USA

INTRODUCTION

Traumatic brain injury (TBI) is a mechanically induced trauma to the head known to cause both short-term cognitive deficits and long-term neurodegeneration [1]. Even mild TBIs (mTBIs) present these effects and account for over 80% of TBI cases worldwide [1]. Despite the prevalence of mTBIs among athletes, soldiers, and civilians alike, so much is still unknown about the cellular consequences of the injury and targets for universally effective treatments.

One well-established molecular response is an increase in calcium (Ca^{2+}) ion concentration in neural cells after a TBI. This increased cytoplasmic concentration occurs through mechanosensitive channels, porated membranes, and some internal stores [2, 3]. In addition to the absolute change in internal Ca^{2+}, the Ca^{2+} dynamics associated with neuronal activity are altered [2, 4]. A study by Cramer et al. revealed that the overall functional connectivity of the neuronal network in the mouse dorsal cerebral cortex decreases post mTBI [4]. This study revealed a degradation of overall network health but was unable to calculate dynamics on the individual cell level. TBI literature assessing the effect of mechanical loading on neuronal signaling is scarce and often fails to look at both hyperacute and acute reactions.

Adverse disturbances of electrical activity have been found to impair executive functions at a lower strain threshold than is required to induce cell death [5]. The transmission of signals between individual neurons throughout the central nervous system (CNS) relies on complex causal relationships between ions, proteins, receptors, and other cell structures in the neurons and extracellular matrix. Abnormalities to any of the components can lead to catastrophic disruption to the signal and other secondary events. Excitotoxicity refers to the neurotoxic effects of dysregulated glutamate secretion and hyperactive N-methyl-D-aspartate (NMDA) glutamate receptors [6, 7]. Glutamate is recognized as the primary excitatory neurotransmitter responsible for neuronal depolarization within the mammalian CNS [6]. Excitotoxicity is hypothesized to be responsible for the Ca^{2+} dynamic response to TBI, but literature shows inconsistencies in the event timeline, relevant mechanisms, and biochemical and electrophysiological responses [8–10]. The presented project is needed to simulate cellular injury under controlled mechanical conditions while investigating more physiologically relevant in vitro models to study network activity via calcium dynamics.

METHODS

In vitro 2D cortical neural cell co-cultures are obtained from P0-P1 Sprague-Dawley rats. The dissected and dissociated cells are seeded on a stretchable polydimethylsiloxane dogbone-shaped substrate (SYLGARD 184, 10:1 base to curing agent), as seen in Fig. 1. Cells adhere to the substrate via a poly-d-lysine and laminin treatment before seeding. These cells are maintained for 20 days *in vitro* (DIV) by exchanging media (Neurobasal A Medium, Pen-Strep, DMEM, Glutamax, B-27 Plus) every 2-3 days.

Once a mature neural network has formed, the samples are stretched in a custom uniaxial tension device for precise strain and strain rate application relating to mTBI values [11]. Combinations of strains (0.1, 0.3, 0.5) and strain rates (1 s^{-1} and 50 s^{-1}) are tested as well as controls. The device sits atop the microscope for minimal handling during experiments.

Neural network activity is quantified by optically capturing the calcium dynamics during spontaneous network activities. Cultures are transfected with GCaMP6f at 10 DIV that is only expressed in neurons (AAV-hSyn1-GCaMP6f-P2A-nls-dTomato; from Dr. Jonathan Ting; Addgene plasmid #51085). Timelapse images are acquired at 25 frames per second using widefield microscopy (Nikon TiE; 10X objective NA 0.45; 2x2 bin; 12-bit). Samples are maintained at 37°C during the experiments. Fluorescent traces are extracted, corrected for photobleaching, and normalized via NeuroCa [12]. Two-minute timelapses are recorded immediately before (0^-) and after (0^+) stretch. Samples are incubated at 37°C for 24 hours and recorded one more time.

Cell viability is assessed using 5 μM Calcein UltraBlue in an imaging solution of Hibernate-A, Glutamax, and B-27 Plus. The dye is loaded right before the experiments and again at 24 hours.

Lastly, the role of glutamate is assessed in 20 DIV samples where extracellular glutamate is added in the place of stretching during the experiment. Varying glutamate concentrations are used: 0.5 μM, 1 μM, 5 μM, and 10 μM.

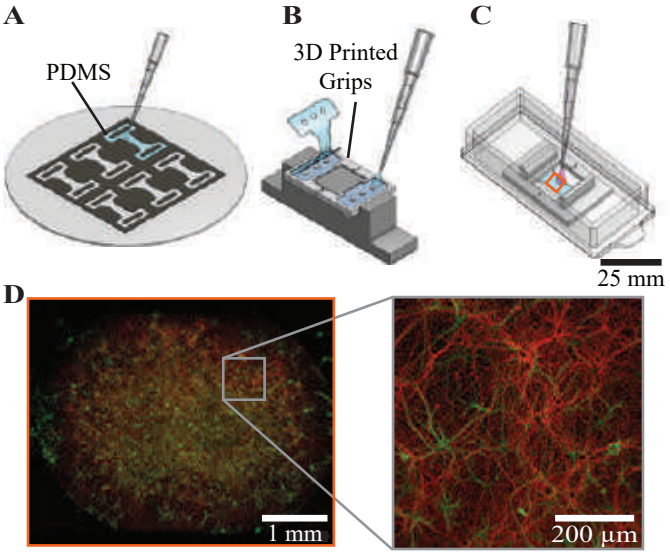

Figure 1: Preparation of 2D cortical co-culture. (A) PDMS cured into dogbone mold. (B) PDMS dogbones adhered to biocompatible grips. (C) Fully assembled sample with neural cells seeded in the gage region (orange). (D) Gage region at 20 DIV; immunostained for neurons (red: β-III-tubulin) and astrocytes (green: GFAP)

RESULTS

Preliminary data of samples stretched at 50 s^{-1} shows several noteworthy hyperacute post-injury events. Immediately after stretch, there is a global network increase in mean Ca^{2+} intensity and a network hyperexcitation that lasts between 10 to 20 seconds in all strain experimental groups. After this initial period, Ca^{2+} activity decreases compared to the 0^- data. This effect is not seen in sham samples. An example sample showing calcium activity before and after stretch can be seen in Fig. 2.

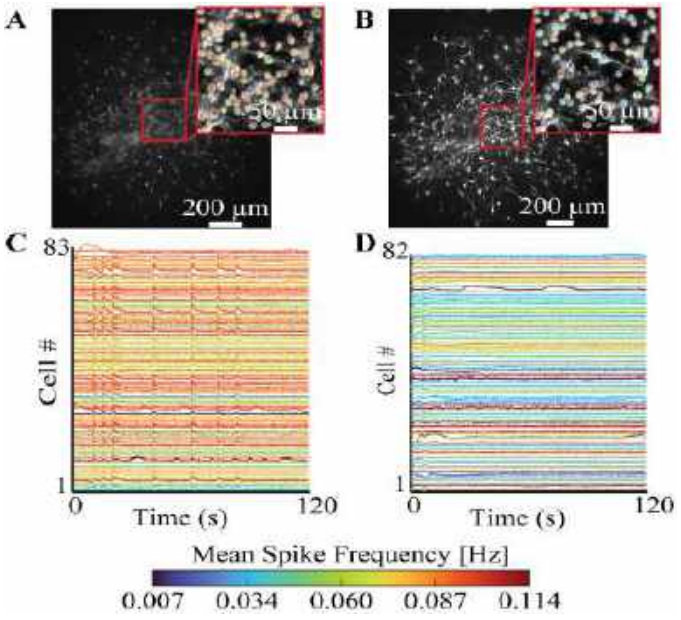

Figure 2: Preliminary data. (A) Neural co-culture stained with calcium probe immediately before applied stretch. (B) Frame of calcium image immediately after stretch (C,D) Normalized fluorescent traces from a subset of cells (respective red box) for the two-minute recording period

There is also an increase in the overall fluorescence after stretch, indicating increased overall intracellular Ca^{2+} concentration. This phenomenon is observed when comparing the unadjusted images in Fig. 2A and 2B.

DISCUSSION

The initial data is consistent with the excitotoxic timeline delineated in literature. After a neuronal stretch injury, studies observed prolonged calcium and sodium influx and potassium efflux into presynaptic neurites and synapses through over-active ion channels or porated membranes [8, 9]. This activates an abnormal depolarization cycle, possibly explaining the hyperpolarization period. This further triggers voltage-activated calcium channels which contributes to prolonged glutamate release [9]. Excitatory neurotransmitter receptors become over-activated, causing further excessive calcium influx into the postsynaptic neuron [8]. This also gives evidence to the overall calcium influx seen in the stretch experiments. The abnormal intracellular calcium levels have been shown to reduce action potentials down the line, lending to the hypo-polarization period [8, 10].

Excitotoxic disruption is believed to occur when extracellular glutamate reaches a concentration of 2 to 5 μM [6]. Blunt impact traumas have been established to release excessive amounts of glutamate into the extracellular space [6]. While the exact concentration is debated, some studies suggest a blunt mTBI may cause a release of up to 10 μM of glutamate [6, 13]. This study's glutamate experiments will clarify the involved mechanisms in the hyperacute network behavior after TBI.

A larger sample size is still needed for statistical analysis of all conditions. If the preliminary findings are consistent, this would indicate that low-level mTBI cases can still show damage to neural network functions even without undergoing significant apoptosis. The ability to collect quantifiable network dynamic measurements from over 200 cells in real time while simultaneously controlling cell deformation mechanics is unique to this experimental setup. The data will serve as the basis for determining a specific critical strain and strain rate threshold for Ca^{2+} signal dysfunction.

ACKNOWLEDGEMENTS

I would like to thank Jing Zhang for her support throughout this project.

This material is based upon research supported by the U. S. Office of Naval Research under PANTHER award numbers N000142112044 and N000142112855 through Dr. Timothy Bentley.

REFERENCES

[1] McKee AC et al. en. *Alzheimers. Dement.* 10.3 Suppl (2014).

[2] Weber JT. en. *Curr. Neurovasc. Res.* 1.2 (2004).

[3] Weber JT. en. *Front. Pharmacol.* 3 (2012).

[4] Cramer SW et al. en. *Neurobiol. Dis.* 176 (2022).

[5] Beamer M et al. en. *Exp. Neurol.* 283.Pt A (2016).

[6] Mark LP et al. en. *AJNR Am. J. Neuroradiol.* 22.10 (2001).

[7] Demirtas-Tatlidede A et al. en. *J. Head Trauma Rehabil.* 27.4 (2012).

[8] MacFarlane MP et al. en. *Brain Inj.* 29.2 (2015).

[9] Hoffe B et al. en. *Front. Mol. Neurosci.* 15 (2022).

[10] Magou GC et al. en. *Brain Res.* 1624 (2015).

[11] Summey L et al. *Exp. Mech.* 63.9 (2023).

[12] Jang MJ et al. en. *Neurophotonics* 2.3 (2015).

[13] Katayama Y et al. en. *J. Neurosurg.* 73.6 (1990).

VIGOR4D: VASCULAR IDEALIZED GEOMETRY OPEN-SOURCE REPOSITORY FOR 4D FLOW MRI DENOISING AND SUPER-RESOLUTION

Moses J. Hamm (1), Neal M. Patel (1), Vitaliy L. Rayz (1,2)

(1) Biomedical Engineering, Purdue University, West Lafayette, IN, USA
(2) Mechanical Engineering, Purdue University, West Lafayette, IN, USA

INTRODUCTION

Three-directional phase-contrast magnetic resonance imaging (4D flow MRI) is an emerging imaging technique which provides time-resolved *in vivo* measurements of blood flow velocities. Alterations in velocity-derived hemodynamic parameters such as wall shear stress (WSS) have been implicated in the pathogenesis of several vascular disorders [1]. However, the low resolutions (typically 0.75-3mm^3) and signal-to-noise ratios offered by 4D flow MRI limit accuracy in computation of these metrics, especially in smaller vessels such as the cerebral vasculature. Therefore, super-resolution and denoising of 4D flow MRI will enable more accurate characterization of flow changes in vascular disorders.

Recently, deep learning has become a popular tool to super-resolve and denoise 4D flow MRI data [2, 3]. However, training supervised convolutional neural networks requires large training datasets. While datasets, such as ImageNet [4], exist for many other applications, no such dataset exists for 4D flow MRI due to the prohibitive cost of running a large number of scans. A lack of benchmark data prevents performance comparison between models and forces researchers to curate their own data, negatively impacting sample size, data diversity, and study timelines.

In this work, we make the assumption that subject-specific physiological flows can be broken down into a combination of simpler flow structures. We aim to construct a dataset of these "building blocks" which can allow machine learning models to generalize to more complex subject-specific flow fields measured *in vivo* with 4D flow MRI. Accordingly, we use idealized, physiologically inspired geometries to construct a large dataset of paired high-resolution ground truth and low-resolution synthetic 4D flow MRI in diverse flow geometries and conditions.

METHODS

Idealized Model Generation. Here, we developed a Vascular Idealized Geometry Open-source Repository for 4D flow MRI denoising and super-resolution (VIGOR4D). Five classes of generalized vascular geometries were included in this dataset based on their ubiquity in healthy and diseased blood vessels and the range of secondary flow they cause. These classes include saccular and fusiform aneurysms, stenoses, T-junctions, and multifocal fibromuscular dysplasias (FMD). All geometries were generated in Fusion 360. For each class, nine distinct models were created by manipulating the vessel diameter, centerline curvature, branching pattern, and class-specific features. An example of the geometric variation scheme is shown in Figure 1.

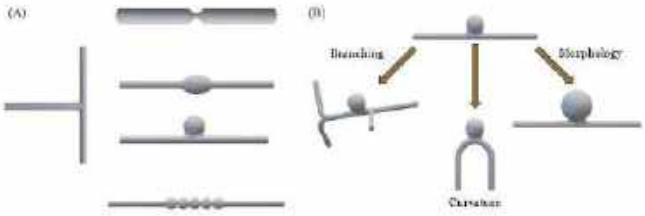

Figure 1: (A) Prototypical models for each class included in VIGOR4D. (B) Examples of additional geometric variations.

Three vessel sizes were represented in this dataset: primary branches of the aorta which typically have a diameter near 10mm, major systemic arteries which have diameters between 4-8mm, and small arteries such as those found near the Circle of Willis, with diameters of 2-4mm. Accordingly, generalized geometries were created with diameters of 3mm, 6.5mm, and 10mm. Models were constructed in straight pipe, semicircle, or 3D spline configurations to capture the interplay between secondary flow structures caused by the vessel's curvature and by the class-specific anatomical features representing vascular disorders. The variation of the branching pattern (e.g., symmetric bifurcations, small side branches, location relative to anatomy of interest) served a dual

purpose. First, it captured the effect of the vascular anatomy on the flow division between the distal branches. Second, it created flow disturbance which affects flow structures in the region of interest. Finally, morphological features such as aneurysm diameter and neck diameter, percent stenosis, and T-junction angle were manipulated to represent the variability among these lesions.

Inflow Waveforms. Because the geometries in this dataset do not correspond to specific arteries, generalized inflow waveforms which reasonably represent flow in any peripheral artery were generated. The reduced-order model presented in Musket et al. was used to generate whole-body population-based inflow boundary conditions [5]. The top three principal components were extracted and used in simulations. Each waveform component was randomly assigned a peak Reynolds number of 600, 1200, or 2000 ±10% considering both the nominal model diameter and any diametric change associated with the relevant pathology (e.g., stenosis).

Simulation. The open-source flow modeling software SimVascular was used to mesh and simulate blood flow in all geometries [6]. Due to the range of vessel sizes, maximum edge lengths were set at $0.1*D_{Nominal}$. A mesh independence study verified that this edge length was sufficient independent of model diameter. Blood was modeled as an incompressible, Newtonian fluid with a density of 1.06 g/mL and a viscosity of 4cP. Three simulations were conducted for each geometry corresponding to different inflow waveforms. Inflow waveforms were prescribed at the inlet using a Womersley velocity profile, and Windkessel RCR boundary conditions were prescribed at the model outlets. Three cardiac cycles were simulated with a time step less than or equal to 1E-4 seconds resulting in CFL << 1. Results from the final cycle were extracted and sampled at 50 time steps per cardiac cycle for further processing.

Synthetic 4D Flow MRI Data. The velocities resulting from simulations performed in SimVascular were used to generate synthetic 4D flow MRI at half the resolution of ground truth velocity fields using algorithms developed in prior work [7, 8]. The velocity fields computed with CFD on unstructured grids were interpolated on two structured isotropic grids with 0.5 mm and 0.33 mm element size respectively. The velocity field (u) over time (t) for all voxels (x_j) on the 0.33 mm isotropic grid is converted to a complex MR signal (ζ).

$$\zeta(x_j, t) = m(x_j) \cdot \exp\left[i \frac{\pi}{venc} u(x_j, t)\right] \quad (1)$$

This MR signal is convolved with a point spread function (h) and resampled Dirac comb function (ш) and a coefficient (c) to model the signal in the downsampled case. Spatial downsampling by a factor of three is performed using a sinc point spread function, and temporally downsampling by a factor of three is performed using a box point spread function. Complex gaussian noise (η) is also added to the complex MR signal:

$$Z = [(\zeta * h) \cdot (c \cdot ш_{4D})] + \eta \quad (2)$$

The complex signal, a reference signal derived by using a zero-vector velocity field, and the velocity encoding parameter (venc) of MRI acquisition are used to reconstruct the low-resolution velocity field (U).

$$U = \frac{venc}{\pi}\left(\angle \frac{Z}{Z_{ref}}\right) \quad (3)$$

Noise generation parameters (e.g., *venc*, noise magnitude, saturation ratio) are varied to simulate diverse data quality, resulting in three low-resolution velocity fields per high-resolution velocity field as shown in Figure 2.

RESULTS

The VIGOR4D dataset includes 135 high-resolution and 405 low-resolution synthetic 4D flow MRI cases in 45 distinct geometries. It is representative of the entire peripheral vasculature and its most common pathologies. In total, ten variables contribute to the overall diversity of the dataset. Geometric variables include the lesion type, diameter, curvature, branching, and morphological features. The boundary condition parameters include the waveform shape and peak Reynolds number. Lastly, simulated 4D flow MRI is generated using variable *vencs*, noise magnitudes, and saturation ratios.

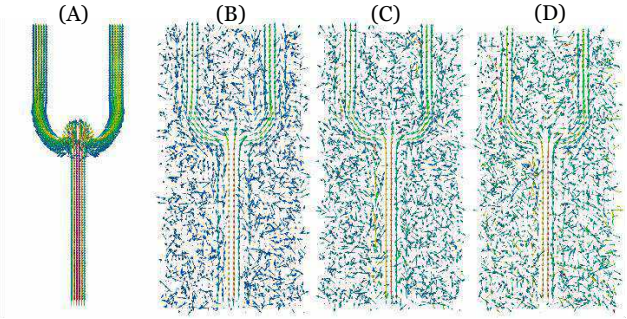

Figure 2: (A) High resolution ground-truth data. (B-D) Synthetic 4D flow MRI data with varied acquisition parameters and increasing noise magnitude.

DISCUSSION

To our knowledge, no training dataset of this scale or diversity has been generated or published in the domain of 4D flow MRI reconstruction. While CFD-derived data cannot fully replicate *in vivo* 4D flow MRI image artifacts and noise distributions, it does offer several benefits. First, the sample size of the dataset is not limited by the cost of imaging studies or difficulty in finding subjects. Second, the use of customized geometries enhances diversity and is assumed to improve generalizability of data-driven reconstruction methods. Finally, synthetic data negates the issue of patient privacy, allowing the dataset to be released publicly. One limitation, however, is that VIGOR4D is not representative of cardiac or aortic flows due to the complexity of turbulence modeling. We hope that VIGOR4D will accelerate development of deep learning algorithms for denoising and super-resolving 4D flow MRI.

REFERENCES

[1] G. Soulat *et al.*, "4D Flow with MRI," *Annu Rev Biomed Eng*, vol. 22, pp. 103-126, Jun 4 2020.

[2] E. Ferdian *et al.*, "4DFlowNet: Super-Resolution 4D Flow MRI Using Deep Learning and Computational Fluid Dynamics," *Frontiers in Physics*, vol. 8, 2020.

[3] D. R. Rutkowski *et al.* , "Enhancement of cerebrovascular 4D flow MRI velocity fields using machine learning and computational fluid dynamics simulation data," *Sci Rep*, vol. 11, no. 1, p. 10240, May 13 2021.

[4] J. Deng *et al.*, "ImageNet: A large-scale hierarchical image database," in *2009 IEEE Conference on Computer Vision and Pattern Recognition*, 20-25 June 2009 2009, pp. 248-255.

[5] J. C. Muskat *et al.*, "Hemodynamic modeling of the circle of Willis reveals unanticipated functions during cardiovascular stress," *J Appl Physiol (1985)*, vol. 131, no. 3, pp. 1020-1034, Sep 1 2021.

[6] A. Updegrove *et al.*, "SimVascular: An Open Source Pipeline for Cardiovascular Simulation," *Annals of Biomedical Engineering*, vol. 45, no. 3, pp. 525-541, 2017-03-01 2017.

[7] S. M. Rothenberger *et al.*, "Modeling Bias Error in 4D Flow MRI Velocity Measurements," *IEEE Transactions on Medical Imaging*, vol. 41, no. 7, pp. 1802-1812, 2022.

[8] J. Zhang *et al.*, "A multi-modality approach for enhancing 4D flow magnetic resonance imaging via sparse representation," *Journal of The Royal Society Interface*, vol. 19, 2022.

MYOSIN-FREE MOLECULAR CLUTCH MODEL PREDICTING MYOSIN-INDEPENDENT STIFFNESS SENSING

Nikhil Mittal (1), Sangyoon Han (1)

(1) Department of Biomedical Engineering
Michigan Technological University
Houghton, MI 49931, USA

INTRODUCTION

A number of studies have shown an increasing traction in response to increasing substrate stiffness (1-3). To explain this stiffness-dependent differential traction, a 'molecular clutch' model has been implemented (4). In the clutch model, F-actin's retrograde flow dynamically 'clutches' with the cell-matrix adhesion that transmits the force to the substrate. Myosin II contractility has been the main source of the retrograde flow where myosin's muscle-like behavior explains the stiffness-dependent differential traction (5, 6). However, evidence shows that even in the absence of myosin activity, cells transmit small but significant traction force with also increasing trend with increasing substrate stiffness (7). Given myosin as a 'result' of mechano-signaling, identifying how cells transmit differential force without myosin would shed light on the very initial stiffness sensing event by a cell without complication by myosin's effect. As an alternative power source, actin assembly at the barbed end of F-actin can contribute to the retrograde flow by pushing the membrane and being pushed by the membrane (8). Actin Related Protein 2/3 complex (Arp2/3) and formin homology protein are the two main actin nucleators (9, 10). In this abstract, we show experimental evidence that myosin-independent tractions are still stiffness-dependent and it comes from the actin retrograde flow powered by actin polymerization and its two main mediators. To predict this behavior, we develop a new molecular-clutch model which considers the role of polymerizing actin and its viscoelasticity in stiffness-dependent differential force transmission in a myosin-independent manner.

METHODS

In this model, the F-actin network unit was modeled as a mesoscale viscoelastic material with a length L with an individual spring constant of k_{actin} and viscosity of η. Rather than being controlled by a constant velocity determined by the force-velocity relationship (eq. 5), the flow in this model is driven by the force equilibrium between the F-actin filament, the clutches, and the substrate. The force generated in the purely elastic spring portion of the actin is generated by the force balance with the elastic clutch, and is found to be:

$$F_{\text{actin-k}} = \frac{N_{\text{n}}L - X_{\text{c}}}{N_{\text{o}} + N_{\text{n}}}\, k_{\text{actin}}, \quad (1)$$

where N_{n} is the number of new actin units added in that time step, and N_0 the number of units in the original filament at the start of the first time-step. N_{n} is modeled to be inversely related to the maximum force in any of the individual clutches denoted as F_{c}:

$$N_{\text{n}} = N_{\text{n,max}}\left(1 - \frac{F_{\text{c}}}{F_{\text{s,actin}}}\right) \quad (2)$$

where $F_{\text{s,actin}}$ is the stall force of actin addition, and $N_{\text{n,max}}$ is the maximum number of actin units that can be added in a single time step. The force in the substrate and clutch are described by following equations:

$$F_{\text{sub}} = k_{\text{s}} * x_{\text{sub}} \quad (3)$$

$$F_{\text{adh}} = N_{\text{c}}K_{\text{c}}(x_{\text{c}} - x_{\text{sub}}) \quad (4)$$

where F_{adh} is the force in the clutch, and N_{c} is the number of bound clutches. As the clutches are attached to the substrate, the force balance between the clutches and the substrate can be used to create the expression for the displacement of the substrate:

$$X_{\text{sub}} = \frac{N_{\text{c}}k_{\text{c}}X_{\text{c}}}{k_{\text{s}} + k_{\text{c}}N_{\text{c}}}. \quad (5)$$

The rate of change of the position of the clutch is derived using following equations:

$$\eta\dot{x}_{\text{c}} = F_{\text{actin-k}} - F_{\text{adh}} \quad (6)$$

$$\dot{x}_{\text{c}} = \frac{1}{\eta}\left(\frac{N_{\text{n}}L - X_{\text{c}}}{N_{\text{o}} + N_{\text{n}}}.\, k_{\text{actin}} - N_{\text{c}}k_{\text{c}}(X_{\text{c}} - X_{\text{sub}})\right). \quad (7)$$

The time derivative of the clutch position is explicitly integrated in the model using the Euler method to find the displacement following each time step of the simulation. The maximum rate of displacement of any of the clutches is considered to be the actin rearward speed. The displacement is used to calculate the force exerted on the substrate using equations (6) and (3), which is used to find the traction exerted on the substrate.

RESULTS

Through a series of experiments using traction force microscopy (TFM), we discovered that the traction of WT NIH 3T3 fibroblasts increases with increasing substrate stiffness, and this stiffness-dependent differential traction is also exhibited by cells treated with blebbistatin, a myosin ATPase inhibitor (11) (Fig. 1A). The myosin-independent, stiffness-dependent traction was significantly reduced with inhibition of either Arp2/3 (Fig. 1A) or formin in addition to myosin activity (11), but the stiffness-dependent differential traction was still observed, even with additional inhibition of actin polymerization itself in addition to myosin contractility (11). Imaging and quantifying F-actin deformation by quantitative fluorescence speckle microscopy (qFSM) revealed that the retrograde F-actin flow speed was differentially regulated by the ECM stiffness in WT cells as well as cells with myosin- or/and Arp2/3 inhibition (Fig. 1A). Such stiffness-dependent flow difference was abolished when formin activity was inhibited in addition to myosin inhibition. These results demonstrate that myosin-independent, stiffness-dependent differential traction depends on actin polymerization-powered actin retrograde flow.

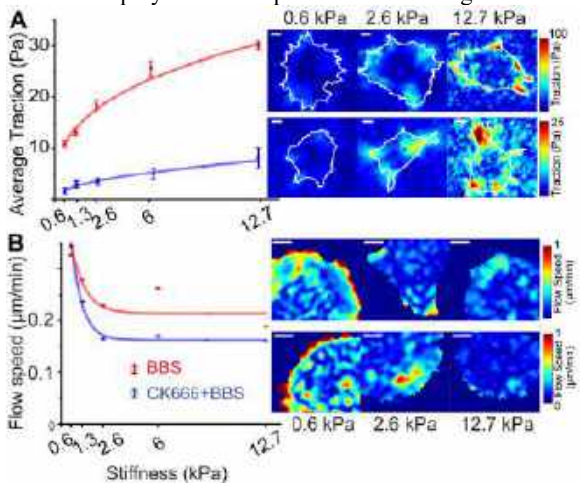

Figure 1: Myosin-independent traction is stiffness-dependent and it depends on the actin polymerization mediated by Arp2/3. (A,B) Average traction (A) and actin flow speed (B) as a function of the substrate stiffness with inhibition of myosin II and Arp2/3 + myosin.

From experiments, we found that Arp2/3 inhibition in addition to myosin reduced traction magnitude by ~4 fold (Fig. 1A) compared to the traction by cells with myosin-only inhibition while minimally reducing the F-actin flow (Fig. 1B). The original molecular clutch model has failed to explain this behavior because the actin filaments were assumed to be rigid (11). To resolve this difficulty, we developed a novel molecular clutch model where F-actin's own viscoelasticity contributes to the transfer of the actin motion to the traction force (Fig. 2). For example, an addition of a new F-actin unit network with higher rigidity (Fig. 2A) can push the clutch molecule harder than those with softer F-actin (Fig. 2B), thus transmitting larger traction while preserving similar actin flow velocity even when cells are on the substrates with the same ECM rigidity. Via collaboration with Dr. Alex Cartagena-Rivera (NIH, NIBIB), we found that indeed Arp2/3 and formin contribute to the elasticity of F-actin network (11). This model was able to explain the elevated traction with Arp2/3 (Fig. 2C) with the small difference in F-actin flow speed compared to myosin-only inhibition (Fig. 2D). Our finding also implies that this stiffness-dependent differential tension could be induced very early to the just-nucleated NAs independently of myosin and other mechano-signaling outputs.

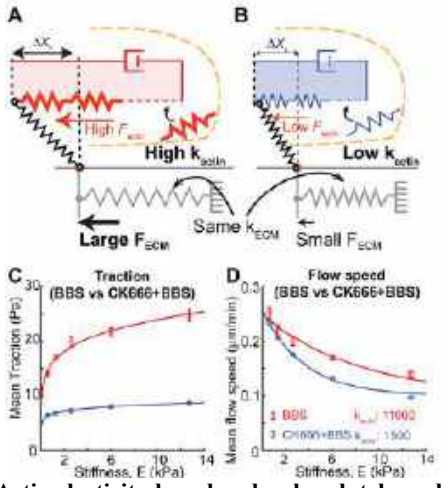

Figure 2: Actin elasticity-based molecular clutch model with high (A) or low (B) actin rigidity, k_{actin}, with the same substrate rigidity, k_{ECM}. Addition of high k_{actin} can push the clutch point more (by larger Dx_c) than the model with low k_{actin}. (C,D) Simulation results of traction (C) and actin flow speed (D) out of 5 independent stochastic simulations.

DISCUSSION

In this study, we provide a stiffness-sensing mechanism for adherent cells when myosin-II, a primary force generator in a cell, is not actively working. Our model suggests that actin nucleators control the sensitivity for stiffness-dependent differential force transmission by modulating the elasticity of the polymerizing actin. Our data demonstrate that the retrograde flow, which still exists in the absence of myosin-II activity via actin polymerization (12, 13), is able to induce the stiffness-dependent differential transmission. Previous molecular clutch models (6, 14) incorporated parameters for actin polymerization, but only they were not considered to be primary source of the retrograde flow and traction forces. Our model, for the first time to the best of our knowledge, uniquely integrates actin polymerization and viscoelasticity, serving as dual contributors to both actin flow and traction forces, which, in conjunction with clutch dynamics, are modulated by substrate stiffness. This approach delineates cellular mechanics without relying on myosin-II-driven forces.

ACKNOWLEDGEMENTS

This work was supported by NIH R15GM135806 and -02 grants.

REFERENCES

[1] Han SJ, *et al.* Biophys J 2012; 103(4): 640-8.
[2] Ghibaudo M, *et al.* Soft Matter 2008; 4(9): 1836-43.
[3] Oakes PW, *et al.* Biophys J 2014; 107(4): 825-33.
[4] Elosegui-Artola A, *et al.* Nat Cell Biol 2016; 18(5): 540-8.
[5] Mitrossilis D, *et al.* Proc Natl Acad Sci U S A 2009; 106(43): 18243-8.
[6] Chan CE,Odde DJ. Science 2008; 322(5908): 1687-91.
[7] Zhou DW, *et al.* Mol Biol Cell 2017; 28(14): 1901-11.
[8] Ji L, *et al.* Nat Cell Biol 2008; 10(12): 1393-400.
[9] Johnson HE, *et al.* J Cell Biol 2015; 208(4): 443-55.
[10] Pollard TD,Cooper JA. Science 2009; 326(5957): 1208-12.
[11] Mittal N, *et al.* Communications Materials 2024; 5(1): 6.
[12] Gardel ML, *et al.* J Cell Biol 2008; 183(6): 999-1005.
[13] Ponti A, *et al.* Science 2004; 305(5691): 1782-6.
[14] Elosegui-Artola A, *et al.* Nature materials 2014; 13(6): 631-7.

LONGITUDINAL MRI ANALYSIS OF INTRATISSUE CARTILAGE STRAIN AND RELAXOMETRY IN THE ACL RECONSTRUCTED KNEE: A CASE STUDY

Hongtian Zhu (1), Emily Y. Miller (2), Woowon Lee (1), Timothy W. Lowe (1), Corey P. Neu (1,2)

(1) Paul M. Rady Department of Mechanical Engineering, University of Colorado Boulder, Boulder, CO, USA

(2) Biomedical Engineering Program, University of Colorado Boulder, Boulder, CO, USA

INTRODUCTION

The anterior cruciate ligament (ACL) is a key stabilizing ligament in the human knee. It is also one of the most frequently injured structures by athletes and trauma victims [1]. Ever though ACL reconstruction is able to partially restore knee functionality, the damage to the articular cartilage, including microfracture and macromolecule breakdown, is irreversible, and those damages could eventually lead to post-traumatic osteoarthritis (PTOA) [2,3]. However, the whole picture of this pathological progression is still unknown. Here, with the help of modern magnetic resonance imaging (MRI) techniques, we have a unique opportunity to noninvasively probe the progression of biochemical and biomechanical changes of the tibiofemoral cartilage throughout PTOA pathogenesis.

The primary objective of this case study is to investigate the biochemical and biomechanical alterations of the tibiofemoral cartilage throughout the injury, repair, and recovery processes after ACL reconstruction (ACLR). We were able to collect full MRI analysis of one participant prior to ACL injury, and then again following ACLR and recovery. We were fortunate to acquire relaxometry maps (e.g., T2 [4], T2* [5], and T1ρ [6]), as well as the intratissue displacement and strain of knee cartilage [7] at four different imaging sessions, enabling tracking through time. All MRI metrics were acquired using the same 3 Tesla (T) MRI scanner. As far as we know, this study is the first to report longitudinal biochemical and biomechanical changes prior to injury and throughout the ACLR time course within human tibiofemoral cartilage *in vivo*.

METHODS

Patient recruitment: One 27-year-old Caucasian female with a previously healthy left knee was imaged as a healthy patient in one study [7], but was also enrolled in this continuation study after sustaining a complete ACL tear during a soccer game.

Experimental procedure: The scanning was done using a clinical 3T MRI system (SIEMENS Prisma^{fit} 3T, with QED 15-channel knee coil). For each scanning session, we first collected the proton density-weighted double echo steady state (DESS) images to establish a common plane for multi-contrast image acquisition. After DESS, T2-, T2*-, and T1ρ-weighted images were acquired before the spiral Displacement ENcoded Stimulated Echo MRI (spiral DENSE) sequence, which is capable of capturing the full-field displacement and strain map while the object of interest is under repetitive loading condition. For each set of weighted images, the corresponding relaxivity maps were calculated. Here, the T2 and T2* maps were directly output by the scanner (SIEMENS syngo MapIt; TEs for T2: 13, 26, 39, 52, 65, and 78ms; TEs for T2*: 4.87, 13.46, 22.05, 30.64, 39.23, 47.82, 56.41, and 65ms), while the T1ρ map (TEs: 0, 20, 40, 60, and 80ms) was calculated by fitting a monoexponential decay curve on each voxel of the weighted images using a customized software (MATLAB r2020a). Then, a set of high frame rate (27 frames/s) DENSE images were captured during a 0.5Hz cyclic loading (1s loading, 1s unloading) applied to the patient's ankle in the varus direction via a customized loading device (**Fig. 1A**) [8]. The force applied was equivalent to 0.5× body weight of the patient at the location of medial condyle [9].

To analyze the relaxometry data, the tibial and femoral cartilage areas were manually selected from the first echo of the weighted images as the regions of interest (ROIs), and the relaxivity values were averaged within each ROI. For T2 and T2*, we analyzed both medial and lateral sides, while for T1ρ we only did the medial side due to wrapping artifact. We also investigated cartilage zonal differences by splitting each ROI evenly into a superficial zone and a deep zone (**Fig. 1B**) [10], then averaging the relaxivity value. For the DENSE data, the tibial and femoral cartilage area at the medial condyle side were collectively selected as one ROI, and the displacement and 2D Green-Lagrange strain maps within the ROI were calculated on a pixel-by-pixel basis using customized software (MATLAB r2020a) [11]. The total scanning session was roughly 1.5h, and all images were acquired in the coronal plane.

Longitudinal study plan: This patient already participated in a research-based MRI scanning session before the left knee was injured, and the corresponding metrics were collected. After the injury, the patient returned for three more scans with identical MRI and data analysis protocol. The three scans were one week before the ACLR surgery, four months, and six months after the surgery. The ACLR was done using an autograft quadriceps tendon. The patient went through normal physical training after the surgery.

RESULTS

The average relaxometry data (**Fig. 1C, 1D**) showed a fluctuation in all three metrics throughout time. For T2, the value tended to peak at the before-surgery timepoint and dropped afterwards, while T2* had a similar trend. The lateral femoral cartilage had a maximum T2 value

of 53.25ms before surgery. When looking at the femoral/tibial differences, we noticed that the femur side would have a higher value than its counterpart on the tibia side. We observed the values of the superficial zone were generally higher than the deep zone, while the superficial zone values also peaked at the before-surgery timepoint (maximum 78.88ms at lateral femoral cartilage), then dropped at four-month and six-month timepoints. Meanwhile, the deep zone values gradually increased throughout the recovery process. For T1ρ, we found that the averaged value was lower at the before-surgery timepoint and recovered afterwards, while the femoral cartilage also showed a higher relaxivity value than tibial cartilage. Zonal analysis showed a similar trend except the medial tibial deep zone continued to increase through time. At the six-month timepoint, all three metrics resumed to similar values compared to the healthy timepoint.

The averaged displacement and strain data (**Fig. 2A, 2B**) showed that at before-surgery timepoint, the varus load induced low strains, with minimal *Exx*, *Eyy*, and *Exy* values. At four-month and six-month timepoints, the *x*-displacement would first decrease then increase while the *y*-displacement showed an opposite trend. Meanwhile, *Exx* became lower and *Eyy* became higher, while *Exy* continued to increase.

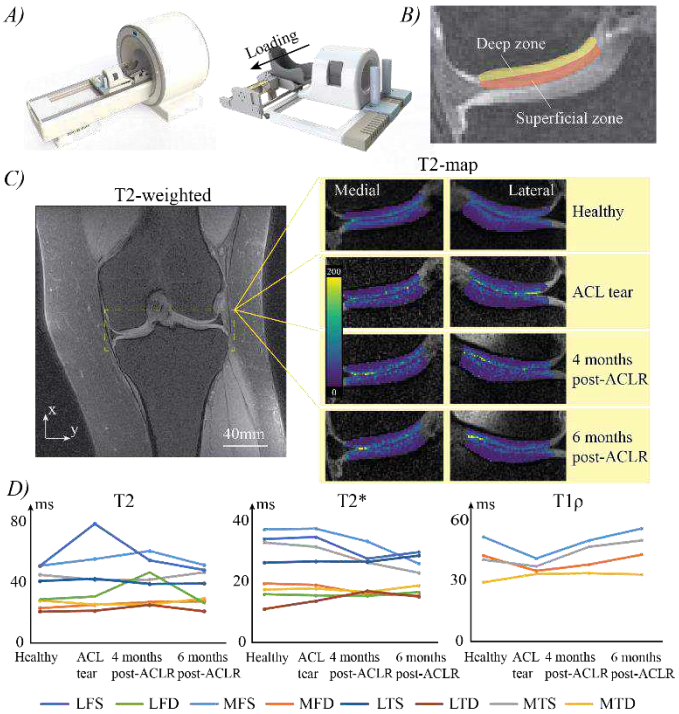

Figure 1: Experimental setup and averaged relaxometry values at 4 timepoints, with one example of the analysis. (A) Loading device in a 3T MRI system, the loading direction indicates varus loading. (B) Demonstration of superficial and deep zone. (C) T2 map at 4 different timepoints. T2* and T1ρ were analyzed similarly. (D) The averaged T2, T2*, and T1ρ values within 8 different ROIs at 4 timepoints. Maximum T2 was found within the lateral femoral cartilage (53.25ms, 78.88ms within its superficial zone) at before-surgery timepoint. Acronyms: LFS – Lateral femoral superficial zone; LFD - Lateral femoral deep zone; MFS – Medial femoral superficial zone; MFD - Medial femoral deep zone; LTS – Lateral tibial superficial zone; LTD - Lateral tibial deep zone; MTS – Medial tibial superficial zone; MTD – Medial tibial deep zone.

DISCUSSION

In this work, we recruited one patient and utilized MRI technology to track the biochemical and biomechanical alternations of the tibiofemoral cartilage at four different timepoints throughout the injury and recovery process of ACLR. The increased T2 and T2* values would suggest that the knee homeostasis had been disrupted and inflammation would occur due to the injury. This would also explain the decreased T1ρ value before surgery [12,13]. The recovery of those values through time would indicate that the restored knee functionality would be helpful to regain homeostasis of the knee and the inflammation was relieved throughout the healing process. Meanwhile, zonal analysis revealed that the superficial zone would be more prone to biochemical and biomechanical interruptions from the injury. The initial alternations will gradually convey through the depth of the cartilage resulting in decreased values of the superficial zone and increased values of the deep zone, and eventually, both zones will reach a new homeostasis. The peaked T2 value at the lateral femoral cartilage could indicate that the missing of the ACL could alternate the dynamics of the knee and would influence the lateral cartilage.

The displacement data demonstrated that the disturbed knee dynamics without ACL and ACLR could partially recover some of the knee functionality. However, the strain data revealed that even though the macroscopic dynamics of the knee was likely to resume back to normal, how the cartilage responded to loading would still be different. The elevated *Exy* could imply that early stage of cartilage degeneration had already occurred even with ACLR [9,14,15].

We believe this work is the first to track biochemical and biomechanical changes of knee cartilage before and after ACL injury in a clinical 3T MRI setup. Further research could involve in *ex vivo* testing of the tissue that collected during the ACLR surgery. Histological tests and omics analysis could be utilized to probe into the compositional alternations at tissue level. By doing so, we would establish a multiscale study which could provide a unique view of the pathogenesis of ACL injuries and lead to a better understanding of the onset of PTOA.

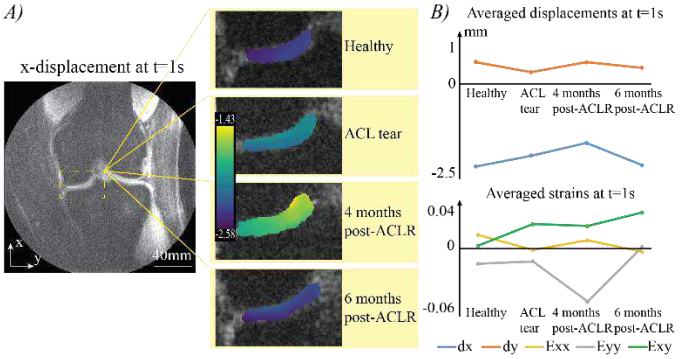

Figure 2: *In vivo* cartilage strain in the medial femoral condyle and tibial plateau was obtained during varus loading of the knee. (A) x-displacement map at 4 timepoints as an example of displacement and strain analysis. Here we only focus on the displacements and strains at t=1s, the raw value ranged from -1.43mm to -2.58mm. (B) The averaged x-displacement, y-displacement, *Exx*, *Eyy*, and *Exy* within ROI at 4 different timepoints.

ACKNOWLEDGEMENTS

This work was supported by NIH grant 2 R01 AR063712.

REFERENCE

[1] Evans+, *StatPearls. Treasure Island (FL)*: (2020). [2] Ferretti+, *Int. Orthop.* 15 (1991): 367-371. [3] Claes+, *KSSTA* 21 (2013): 1967-1976. [4] Dunn+ *Radiology* 232.2 (2004): 592-598. [5] Bittersohl+ *Osteo & Cart* 20 (2012): 653-660. [6] Wang+ Eur *J Rad* 81.9 (2012): 2329-2336. [7] Lee+ *Magn. Reason. Med.* (2023). [8] Zhu+, *SSRN*: (2023). [9] Chan+ *Sci Rep* 6 (2016): 1-14. [10] Waldenmeier+, *Cartilage* 10.3 (2019): 288-298. [11] Chan+ *Comp Methods Biomech Biomed Eng* 16.8 (2013): 852-860. [12] Souza+, *J Orthop Sports Phys Ther* 42.6 (2012): 511-520. [13] Le+, *Ann. N. Y. Acad. Sci.* 1383.1 (2016): 34-4. [14] Griebel+ *Magn. Reason. Med.* 71.2 (2014): 807-814. [15] Wilson+, *J. Magn. Reason. Imaging* 58.1 (2023): 189-197.

ENDOTHELIAL CELLS EXHIBIT A SIMILAR TEMPORAL RESPONSE TO ULTRASOUND AS NORMAL FLOW

Ian S. McCue, Adam R. Johnson, Joseph A. Turner, Ryan M. Pedrigi

Department of Mechanical and Materials Engineering, University of Nebraska-Lincoln, Lincoln, NE, USA

INTRODUCTION

Endothelial cells are exquisitely sensitive to flow. Disturbed flow promotes dysfunctional behaviors that can lead to the development of atherosclerosis, while unidirectional flow at a normal magnitude (i.e., normal flow) promotes all primary functions [1]. Importantly, normal flow also protects arteries from atherosclerosis. Moreover, our recent study demonstrated that restoring normal blood flow in atherosclerotic arteries promotes plaque stabilization [2]. This work demonstrates that the mechanobiological effects of normal flow are therapeutic. A remaining challenge is to develop a mechanism to activate the same beneficial mechanosensitive signaling in dysfunctional endothelial cells of diseased arteries in the body as normal flow.

Ultrasound can noninvasively deliver tunable mechanical stimuli into the body in a targeted manner for therapeutic applications such as thrombolysis in treating ischemic stroke [3]. In addition, it has been shown that endothelial cells exhibit angiogenic behaviors to low intensity pulsed ultrasound (LIPUS). An interesting feature of these studies is that cells are only exposed to LIPUS for 2-30 min [4-5]. This duration is much shorter than the 4-24+ h that is typically used in studies of endothelial cells under flow [6]. Short durations of flow have been shown to promote atherogenic behaviors [7-8]. No study has evaluated the endothelial response to longer durations of LIPUS. Therefore, in this study, we hypothesized that endothelial cells exposed to LIPUS for longer durations up to 24 h will exhibit a greater beneficial response than shorter durations (<1 h) and that the temporal response pattern will be similar to that seen under normal flow. We evaluated two well-established mechanosensitive genes related to a healthy endothelium, endothelial nitric oxide synthase (*eNOS*) and Kruppel-like factor 2 (*KLF-2*).

METHODS

Experimental setup. We developed two custom ultrasonic exposure tanks. The acoustic source consisted of 1 MHz unfocused immersion transducers of 13 mm diameter mounted to the bottom of the tanks and driven by a function generator and amplifier at 55 dB gain. 6-well cell culture plates were held within the tank by a mount that positioned the center of each culture well directly above the center of a transducer. The cavity of the bioreactor was filled with sterile degassed distilled water up to the sides of the culture plate.

Acoustic field measurements. We used a custom acoustic field characterization tank with a capsule hydrophone attached to a motorized three-axis gantry system to perform spatial mapping of the peak acoustic pressure field generated by the 1 MHz unfocused transducers in water. Axial mapping (0.5 mm resolution) was performed to determine and characterize the near-field-to-far-field transition. From this map, we set the culture plate position to 73 mm from the transducers. In-plane spatial mapping at this distance from the transducers was also performed (0.25 mm resolution). We also conducted acoustic field measurements within the wells of culture plates to directly evaluate the relationship between peak acoustic pressure versus voltage input to the transducers.

Cell culture. HUVECs pooled from 10 donors were used for all experiments at passages 3 to 7. Cells were seeded at 30,000 cells/cm^2 into 6-well culture plates coated with rat-tail type I collagen 18-24 h prior to the start. Each culture well was provided with 2.41 ml of medium to give a fluid height of 2.5 mm. Cells were visually inspected before and after each experiment to ensure a healthy appearance.

LIPUS experimental protocol. Two hours prior to experiments, the ultrasound exposure tank was sterilized, assembled, filled with degassed and pre-warmed distilled water, and placed in the incubator. Immediately prior to the start, a 1MHz ultrasound transducer (calibrated with the hydrophone) was used to set the acoustic pressure to 217 kPa within each well of a culture plate (without cells). Once set, the endothelial cell-seeded culture plates were placed within the exposure tank and visually inspected to ensure no air bubbles were present at the plate-water interface. A small weight was placed on top of the culture plate lid to prevent floating or other movement during the experiment.

Cell layers in these plates were exposed to a 1 MHz sine wave that was pulsed at 1 Hz (500,000 cycles per burst period) to simulate the cardiac cycle. Control cell layers were seeded into wells of the same culture plate that did not receive direct ultrasound stimulation. An acoustic pressure of 217 kPa was chosen based on preliminary experiments to identify the maximum acoustic pressure that could be applied to endothelial cells in the basal-to-apical direction without causing detachment. Experiments were conducted over five durations: 20 min, 1 h, 6 h, 9 h, and 24 h.

Flow experimental protocol. As a comparator, endothelial cells were exposed to normal flow within the wells of culture plates by using an orbital shaker that moved the plates in a horizontal circular orbit of 5 mm radius at 250 revolutions per minute (RPM) within an incubator. The outer periphery was subjected to unidirectional flow at a normal shear stress (mean of 1.4 Pa) and gene expression was evaluated in this region, following our previous work [1]. Flow experiments were conducted over six durations: 20 min, 1 h, 6 h, 24 h, 48 h, and 72 h.

RT-qPCR. At the end of each experiment, the well plates were removed from the incubator and cells were immediately lysed for total ribonucleic acid (RNA). We used a custom 3D-printed extractor to isolate RNA from the cell layers [1]. For the LIPUS-exposed cell layers, the spatial profile of the acoustic pressure field was used to guide the cell analysis. Therefore, the central 0-6 mm was isolated. For flow-exposed cell layers, the peripheral 11.0-17.4 mm was isolated. RT-qPCR was performed to evaluate *eNOS* and *KLF2* [1]. Data were analyzed with the delta-delta Ct method.

Statistics. Quantities are reported as mean ± standard deviation (SD). For normally distributed data, group comparisons were performed using a Welch's one-way analysis of variance (ANOVA) and pairwise comparisons were performed using an unpaired t-test with equal or unequal variances based on an F-test. Otherwise, a Kruskal-Wallis test and Mann Whitney U test with Levene's test for variances were used. Multiple comparisons were corrected using the Holm-Bonferroni method. A p-value of less than 0.05 was considered significant.

RESULTS

We evaluated the stability of our transducers over 24 h mock experiments (i.e., no cells) at a target peak pressure of 217 kPa (1 Hz pulsing). The mean peak pressure was 218±3 kPa. Thus, the signal deviated from the target by an average of only 0.5%. In-tank temperature measurements showed an increase in temperature from 33.5°C to a steady-state value of 38.2°C, which was achieved in approximately 12 h. Temperature measurements performed without powering the transducers demonstrated an increase from 33.4°C to 36.7°C. Thus, 24 h of pulsed ultrasound (pulsing at 1 Hz) at 217 kPa caused a temperature rise of only 1.5°C. Importantly, both experimental and control cell layers were exposed to this small temperature increase.

We evaluated the time-dependent response of endothelial cells to a peak acoustic pressure of 217 kPa after 20 min, 1 h, 6 h, 9 h, and 24 h of exposure. At 20 min, *eNOS* expression was slightly reduced to 0.77±0.10, in line with the known atherogenic effects of physiologic mechanical stimuli (e.g., normal flow) over short durations. At 1 h, expression increased to 1.14±0.07 and, at 6 h, it peaked with a maximum value of 2.69±0.45 (p<0.01 versus 20 min, 1 h, and 24 h). After, expression dropped off slightly at 9 h (2.24±0.53) and then declined considerably to 1.06±0.30 at 24 h. Similarly, *KLF2* exhibited a negligible response at 20 min (1.13±0.11) that then increased to a peak at 6 h of 1.94±0.35 (p<0.05 versus 20 min and 24 h), followed by a decline to 0.93±0.14 at 24 h. Remarkably, these expression patterns were qualitatively similar to those found for endothelial cell layers exposed to normal flow, but LIPUS induced peak beneficial signaling more rapidly than flow (**Figure 1**). However, peak expression of both genes was substantially higher for cells under flow for 24 h compared to LIPUS for 6 h with values of 6.67±1.78 (p<0.01) and 25.9±2.46 (p<0.001), respectively.

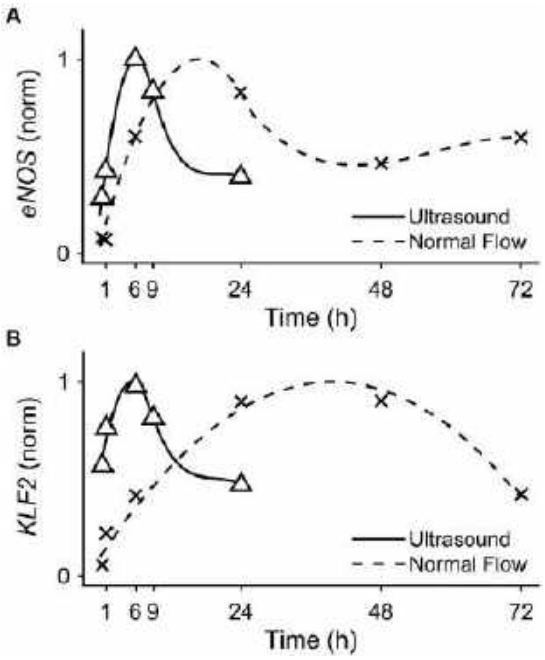

Figure 1. Normalized expression levels of *eNOS* and *KLF2* show qualitatively similar trends over exposure time between low-intensity pulsed ultrasound and normal flow. Normalized (A) *eNOS* and (B) *KLF2*. Points represent the mean expression at each time and lines are polynomial fits to illustrate the trend.

DISCUSSION

The few studies that have characterized the endothelial response to LIPUS have provided little rationale for the choice of parameters used [4-5]. In this study, we reasoned that longer continuous durations of LIPUS than has previously been used may exhibit stronger beneficial biological responses more comparable to those seen under normal flow. Our results demonstrated maximum expression of *eNOS* and *KLF2* after 6 h of LIPUS and similar temporal expression patterns as those seen under normal flow. This suggests that both mechanical stimuli are regulated by the same signaling pathways. However, flow promoted far greater expression of both atheroprotective genes compared to LIPUS, at least for the regimens used herein. Overall, this points to the need for more studies that characterize the endothelial response to the many LIPUS parameters over a broad range of values.

ACKNOWLEDGEMENTS

We gratefully acknowledge support from the NIBIB (grant#R21EB028960) and NSF (grant#CMMI-1944131).

REFERENCES

[1] Sahni, J et al., *J Mech Behav Biomed Mater*, 137:105545, 2023.
[2] Schake, M et al., *iScience*, 26:106760, 2023.
[3] Dalecki, D et al., *Annu Rev Biomed Eng*, 6:229-248, 2004.
[4] Shindo T et al., *ATVB*, 36:1220-1229, 2016.
[5] Altland, OD et al., *J Thromb Haemost*, 2:637-643, 2004.
[6] Chiu, JJ and Chien, S, *Physiol Rev*, 91:327-387, 2011.
[7] Warboys, CM et al., *Am J Physiol*, 298:H1850-1856, 2010.
[8] Dai, G et al., *Proc Natl Acad Sci USA*, 101:14871-14876, 2004.

OPTIMAL DESIGN OF EXPERIMENTS FOR NUCLEAR MEMBRANE STIFFNESS ESTIMATION

Emilio A. Mendiola (1), Rana Raza Mehdi (1), Jacques Ohayon (2,3), Roderic I. Pettigrew (1,3), Reza Avazmohammadi (1,3)

(1) Department of Biomedical Engineering, Texas A&M University, College Station, TX, USA
(2) Savoie Mont-Blanc University, Polytech Annecy-Chambéry, Le Bourget du Lac, France
(3) Department of Cardiovascular Sciences, Houston Methodist Research Center, Houston, TX, USA

INTRODUCTION

The ability of cells to sense and respond to mechanical forces is critical for various functions, including growth, motility, differentiation, and homeostasis. Recent work has indicated alterations in the mechanical properties of the cell compartments alter mechanosensing, possibly driving disease progression [1]. Thus, the accurate estimation of the mechanical stiffness of cellular components is critical to identifying novel mechanical mechanisms of disease. Currently, atomic force microscopy (AFM) is used to measure the force-displacement relationship and calculate the stiffness of cell compartments. However, many factors can affect the accuracy of AFM measurements, and AFM tests may not provide the most reliable calculation of cell stiffness. There is a need for a robust model-driven approach that can identify the "optimal" locations for AFM measurements, minimizing the effect of factors such as cell geometry and loading conditions on the estimation of the unknown material parameters. In this work, we combined experimental AFM measurements with the development of a cell-specific finite-element (FE) model to estimate the cytoplasmic and nucleus stiffness via an inverse problem approach. The validated FE model was then used to propose an optimal design of experiments approach and identify the locations for force application that provide parameter estimation that is least dependent on confounding factors, thus leading to the robust, unique, and accurate stiffness estimation. This optimal design approach was then used to identify the optimal testing sites and material stiffness for an extended cell model, which includes the nuclear membrane. Results indicated that the optimal design of such cellular experiments can enhance the characterization of the material parameters. This method will ultimately provide a means to reliably predict cell-scale mechanical changes, allowing for the improved investigation of longitudinal mechanical adaptation in the presence of disease.

METHODS

Cell preparation and AFM

Isogenic human umbilical vein endothelial cells (HUVECs) were obtained and cultured as per previously published [1]. Cells were seeded onto glass coverslips, and AFM was performed on the live cells using a Catalyst Biomicroscope (Bruker) with a spherical probe of radius 1.25 μm. Force-indentation measurements were taken at two locations: the cytoplasm and the nucleus. Cells were then fixed and stained. Super-resolution imaging was performed using a Nikon n-SIM Structured Illumination Super-Resolution Microscope System with Z-stack spacing set to 100nm.

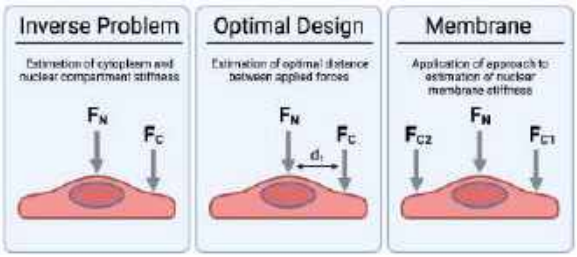

Figure 1: Material parameters were estimated via an inverse problem approach. An optimal design of experiments procedure was used to find the force application sites at which parameter estimation is most robust. The optimal design approach was applied to an extended cell model to accurately estimate the stiffness of the nuclear membrane.

Model development and parameter estimation

The 3-D reconstructed geometries of the cytoplasm and nucleus were used to develop an FE model of the cell. The cytoplasm and nucleus geometries were meshed with linear tetrahedral elements, and the nuclear membrane was modeled using triangular shell elements with a prescribed thickness of

35 nm. The components were modeled as isotropic, hyperelastic, nearly incompressible materials with a constitutive model of the form

$$W(\mathbf{E}) = \frac{a_i}{2b_i} e^{b_i(I_1-3)}; \quad i = c, m, n, \tag{1}$$

where a_c, b_c, a_m, b_m, a_n, and b_n are positive material constants governing the contribution of the cytoplasm (c), nuclear membrane (m), and nucleus (n), respectively. The kinematic variables I_1 is defined as $I_1 = tr\ \mathbf{C}$, where $\mathbf{C}$ is the right Green deformation tensor. The AFM probe was modeled as a thick-walled rigid sphere with an outer radius of 1.25 mm and a thickness of 0.15 mm.

An inverse modeling approach was used to estimate the material parameters. A least-squares optimization routine was used to estimate the material parameters that minimized the squared error between the measured and simulated reaction cellular force at each probe location. The parameter set was estimated simultaneously.

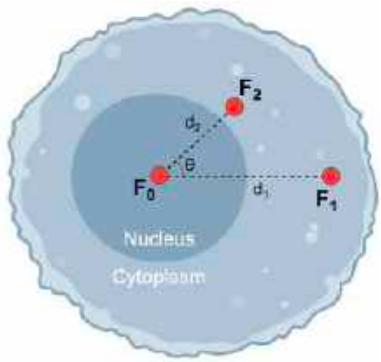

Figure 2: Schematic indicating the variation in locations at which the two cytoplasmic forces will be applied.

Optimal design of experiments

Identifying the optimal locations on the cell surface to conduct the simulated force-indentation measurements results in the best determinability and minimum covariance of the unknown parameters. This identification problem was set up as a parametric optimization of three parameters: d_1, d_2, and θ. The distance d_i is the distance of the applied force from the center of the nucleus, and the angle θ is formed by the two lines connecting the location of the applied cytoplasmic forces to the center of the nucleus (Fig. 2). A set of these parameters was chosen, and the optimal location was determined by minimizing the confidence region of the parameter set, effectively minimizing the covariance of the unknown parameters. This process was accomplished by defining an information matrix $\mathbf{M} = \mathbf{J}^T\mathbf{J}$, where $\mathbf{J}$ is the sensitivity matrix defined as the derivative of the model relative to the parameters. The confidence region was minimized by maximizing the D-optimality of the information matrix $\mathbf{M}$. This optimal design approach is described in detail by Avaz et al. [2].

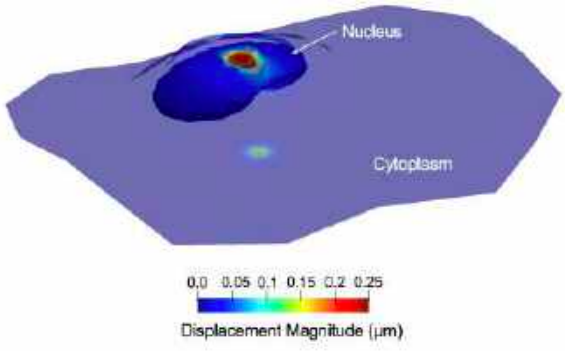

Figure 3: Representative FE simulation results visualizing the displacements in the cell upon application of forces on cytoplasm and nucleus.

RESULTS

Our approach for the optimal design of the experiment was initially conducted with a two-compartment (nucleus and cytoplasm) FE cell model for simplicity. Thus, only one factor was optimized, namely, the distance of the force application from the nucleus.

Table 1: Material parameters estimated by the inverse problem for the cytoplasm and nuclear compartments.

Cytoplasm		Nucleus	
a_c (kPa)	b_c	a_n (kPa)	b_n
7.37	1.08	4.05	1.00

Estimated material parameters

The estimated material parameters for the cytoplasm and nucleus compartments are presented in Table 1. Estimated material parameters indicated the nucleus is softer in comparison to the cytoplasm. The simulated displacement field is presented in Figure 3.

Optimal testing sites

Three locations of force application were compared using the two-compartment model and will be referred to as: near nucleus, middle, and near border. The results of the numerical comparisons between different force application sites are presented in Table 2. Recalling that the maximization of the D-optimality (Δ_D) coincides with the minimization of the confidence region, the results indicate the force application site nearest the cell border (furthest from the nucleus) is the most optimal.

Table 2: The D-optimality criteria for each force application site. Maximizing the D-optimality implies minimization of the confidence region of the parametric optimization.

	Near Nucleus	Middle	Near Border
Δ_D (10^2)	0.317	2.42	5.71

Future work will involve applying our approach to an extended model that includes the nuclear membrane.

DISCUSSION

This study aimed to present a novel integrated experimental-computational method to improve the process of cell-scale mechanical analysis. The accurate estimation of the material behavior of the cell is essential to the improved understanding of diseases that affect cellular mechanobiology.

Our results indicated that, indeed, there exist certain "optimal" sites at which the application of forces for parameter identification improves the identifiability and robustness of the estimation. Previous studies regarding the optimal design of experiments have indicated that the use of optimal sites additionally improves the predictive accuracy of the estimated parameters [2], and we expect to observe a similar improvement in future analysis of our approach. The stiffness of the nuclear membrane, although integral to the mechanical behavior of the cell, is an elusive measurement. The presented pipeline will be applied to similar cells to accurately estimate, for the first time, the stiffness of the nuclear membrane. These results will drive the use of such approaches in the design of cellular AFM experiments and, ultimately, improve the accuracy of the analysis of cellular mechanical properties and the mechanical adaptations of cells in disease.

REFERENCES

[1] Walther BK et al. *Matter* 6.10 (2023).

[2] Avazmohammadi R et al. *Biomechanics and modeling in mechanobiology* 17.1 (2018).

INVESTIGATING THE PARACRINE EFFECTS OF BREAST CANCER CELLS ON OSTEOBLAST DIFFERENTATION, PROLIFERATION, AND MINERAL DEPOSITION

Sarah Nano(1), Laurie E. Littlepage(2), Laoise M. McNamara(3), Glen L. Niebur(1)

(1) Bioengineering Graduate Program, Department of Aerospace and Mechanical Engineering, University of Notre Dame, Notre Dame, IN, USA
(2) Department of Chemistry and Biochemistry, University of Notre Dame, Notre Dame, IN, USA
(3) Department of Biomedical Engineering, University of Galway, Galway, Ireland

INTRODUCTION

The incidence of breast cancer is increasing, accounting for 1 in 8 cancer diagnoses globally, with a 20-30% mortality rate associated with metastatic disease [1,2]. Bone is the most common site of breast cancer metastasis, where cancer cells can disseminate to bone even before the primary tumor is diagnosed [3]. Once established, metastatic tumors alter the normal bone physiology, resulting in uncontrolled bone resorption or formation and hyperplasia [4]. Biochemical factors (IL-6, PTHrP, TNFα) produced by cancer cells trigger bone resorption by osteoclasts, which drives the tumor metastatic progression in a vicious cycle.

Mechanical stimulation has been shown to both inhibit tumor progression and prevent bone destruction [5,6,7] and to increase tumor burden in a dose dependent manner [8]. Our group has created an engineered model of bone metastasis showing increased osteoblast-secreted proteins DMP1 and BSP2 in response to mechanical stimulation in mineralized cancer mimetic constructs [9]. Cancer cells have also been shown to induce an osteoblast inflammatory response [10] and disrupt osteoblast arrangement when in physical contact [11]. This indicates a phenotypic change in osteoblasts is partially responsible for the altered bone physiology during metastasis.

Alterations of osteoblast proliferation and viability, differentiation into osteocytes, and mineral deposition in the metastatic environment are not well understood, especially in the presence of mechanical stimulation. Additionally, crosstalk between osteoblasts and osteoclasts in the metastatic environment has not been well characterized. As such, the objectives of this study are to investigate 1) how osteoblast differentiation, proliferation, and mineral deposition is altered in the presence of cancer cells, 2) whether osteoclast resorption alters cancer cell mediated osteoblast activity and 3) if mechanical stimulation mitigates the cancer-induced phenotypic changes of osteoblasts.

METHODS

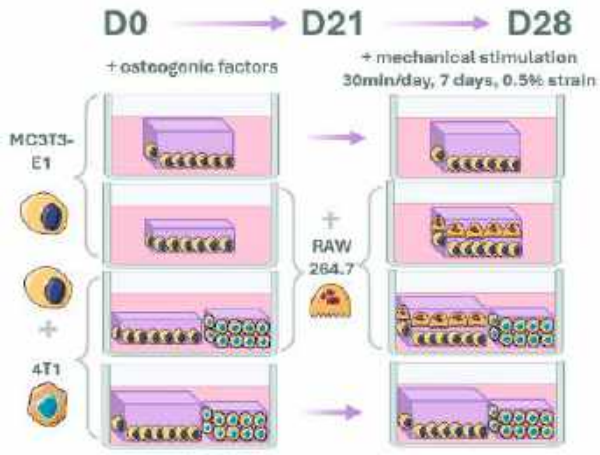

Figure 1: Experimental setup.

We engineered a segregated co-culture hydrogel model to isolate the paracrine effects of cancer cells on osteoblasts (Fig.1). Briefly, MC3T3-E1 murine osteoblastic cells (MC3) are cultured in standard conditions and embedded at 2×10^6 cells/mL in 3% w/v gelatin, 5.5% v/v nano-hydroxyapatite (nHA) and cross-linked with 0.3% w/w microbial transglutaminase. Triple negative murine mammary cancer cells (4T1) are cultured and embedded in a separate hydrogel under the same conditions.

MC3T3 hydrogels are either cultured alone or in the same well as 4T1 hydrogels as segregated co-cultures. All culture conditions are supplemented with osteogenic media (50 μM ascorbic acid, 10 mM β-glycerophosphate, and 100 nM dexamethasone) for 21 days to allow for mineralization of gels. On day 21, RAW264.7 osteoclast precursor cells (RAW) are added to MC3T3 gels in monoculture and co-culture with 4T1 gels. Unloaded controls remain in culture for an additional 7 days. Mechanical stimulation is applied to loaded groups for 30 minutes at 0.5% strain for 7 days. Live-dead staining is performed on day 21 to validate cell viability and quantify apoptotic rates in culture conditions. FITC, DAPI, and DMP1 staining is performed at days 7, 14, 21, and 28 to analyze MC3T3 morphology and differentiation. DNA, calcium, and ALP assays are performed at days 21 and 28 to analyze cell number and bone formation.

RESULTS

Live-dead staining on day 21 confirmed viability of MC3 cells in long-term hydrogel culture (Fig. 2A,E). Cell viability was higher in MC3 monoculture, with a live-dead ratio of 1.47 compared to 0.98 for MC3+4T1 co-culture. There was evidence of increased cell spreading in MC3 monoculture compared to MC3+4T1 coculture in confocal images of actin/nuclear on day 21 (Fig. 2B-C, F-G). Higher levels of visible mineral were found in MC3 monoculture gels (Fig. 2D) compared to MC3+4T1 co-culture (Fig. 2H).

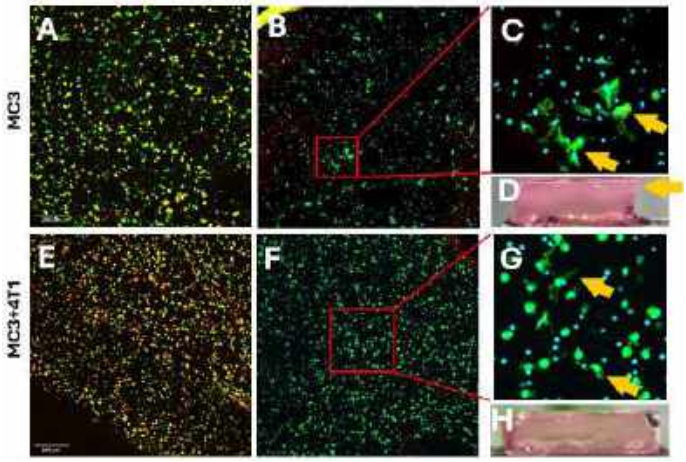

Figure 2: Live dead stain indicated greater cell viability in monoculture (A) than MC3+4T1 coculture (E). More cell spreading was seen in actin/nuclear staining of monoculture (B,C) than co-culture (F,G). Mineral deposition was visually apparent on day 21 in monoculture (D), but not co-culture (H).

DNA assays confirmed similar cell populations in all culture conditions at both time points ($p > 0.05$; not shown). Calcium content was elevated in MC3 monoculture and MC3+RAW co-culture conditions compared to cancer co-cultures, MC3+4T1 and MC3+4T1+RAW, at both 21 and 28 d ($p < 0.0001$; Fig. 3A). Interestingly, calcium content in MC3+RAW co-culture was lower at day 28 compared to day 21 ($p < 0.0001$), but unchanged in MC3+4T1+RAW tri-culture. Extracellular ALP activity was similar between culture conditions at day 21 ($p > 0.05$), except between MC3+RAW and MC3+4T1+RAW co-culture conditions (Fig. 3B). On day 28, the ALP level was highest in MC3+4T1 coculture ($p < 0.005$), and the MC3 monoculture levels were higher than the RAW cell groups ($p < 0.05$). Only the non-loading condition has been analyzed to date.

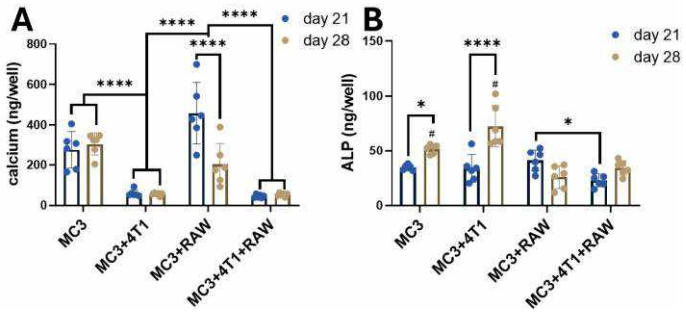

Figure 3: Calcium (A), and extracellular ALP (B) content measured after 21 and 28 d (* $p < 0.05$; **** $p < 0.0001$; # $p < 0.05$ vs +RAW groups at 28 d; N=6; bars are ±1 S.D.).

DISCUSSION

We developed a novel model of the breast cancer metastatic niche in bone to quantify the phenotypic changes of osteoblasts due to paracrine signaling with cancer cells in this environment. Our results demonstrate that osteoblast viability, morphology, mineral deposition and calcium content, and ALP expression are altered through crosstalk with tumor cells in this engineered metastatic niche. Notably, osteoblast mineral deposition and calcium content was greater in the absence of cancer cells. Osteoblasts similarly exhibited a more spread morphology in monoculture compared to co-culture with cancer cells. In contrast, ALP expression was highest in osteoblasts and cancer co-culture, consistent with elevated serum ALP levels in metastatic patients [12], but osteoclasts partially suppress this effect.

Overall, we have shown that triple negative mammary cancer cells alter the morphology of osteoblasts in a 3-D model, suggesting that cancer-associated osteoblasts (CAO) may contribute to altered bone physiology in the presence of metastasis. Future work in this project will further characterize how mechanical stimulation alters osteoblast phenotypic changes in co-culture with breast cancer cells.

ACKNOWLEDGEMENTS

Naughton Accelerator Grant, NIH RO1CA252878, DOD BCRP W81XWH2110432.

REFERENCES

[1] Giaquinto, AN et al. *CA Cancer J Clin*, 72:524-541, 2022. [2] Riggio, AI et al., *British J of Cancer*, 124:13-26, 2020. [3] Braun, S et al., *N Engl J Med*, 342:525-533, 2000. [4] Breuer, EK et al., *Cell Death & Dise*, 10:1-15, 2019. [5] Yang, S et al., *The FASEB Journal*, 33:10742-10752, 2019. [6] Lynch, ME et al., *JBMR*, 28:2357-2367, 2013. [7] Wang, S et al., *Bone*, 153:116100-116112, 2021. [8] Fan, Y et al., *Bone Research*, 8:1-11, 2020. [9] Kumar, V et al., *BioRxiv*, 09-19, 2022. [10] Kinder, M et al., *Experimental Cell Research*, 314:173–183, 2008. [11] Kimura Y et al. *Scientific Reports*, 7: 1–11, 2017. [12] Singh, AK et al., *3 Biotech*, 3:517-520, 2013.

UNIAXIAL BIOMECHANICAL RESPONSE OF MURINE UTERINE TISSUE AFTER SURGERY-INDUCED SCARRING

S. Chatman (1), A. Fisk (2), N. Karbasion (2), P. Brody (2), M.R. Bersi (1,2)

(1) Department of Biomedical Engineering, Washington University in St. Louis, St. Louis, MO, USA
(2) Department of Mechanical Engineering and Materials Science, Washington University in St. Louis, St. Louis, MO, USA

INTRODUCTION

During pregnancy, the uterus undergoes structural and mechanical transformations to withstand the demands of a successful delivery [1]. In cases where vaginal birth is not feasible, a Cesarean section (c-section), which involves a transverse abdominal incision, is used to facilitate delivery of the fetus and placenta [2]. Following the procedure, the uterus and abdominal tissue are carefully sutured to support postpartum recovery, leading to uterine scarring at the incision site.

However, women who have undergone a c-section face an increased risk of uterine rupture when attempting vaginal birth in subsequent pregnancies. Uterine rupture is a rare peripartum complication that involves mechanical failure of the uterine wall during gestation or delivery [2]. While a history of vaginal delivery and successful vaginal birth after c-section may reduce the overall risk, factors such as multiple prior c-sections and single-layer uterine closure can elevate the likelihood of uterine rupture [3]. However, the effects of postpartum remodeling and involution on uterine scar integrity and the associated uterine biomechanical properties is not well understood.

Understanding the relationship between uterine scar integrity and biomechanical properties in non-pregnant tissue is a first step toward better understanding the biomechanics of postpartum involution and is essential to predict the risk of uterine rupture during future labor events. To this end, the aim of this project is to utilize ex-vivo mechanical testing to investigate the relationship between uterine scar structure and composition using a surgical model of uterine hysterotomy in nulliparous female mice. This project utilizes mouse uterine ring samples to assess the structural and mechanical properties of the uterus with the goal of quantifying the change in biomechanical properties throughout the healing process. The study will measure the strength of scarred uterus tissue through cyclic loading and extension to failure. Imaging via Optical Coherence Tomography (OCT) will provide insights into tissue structure. Ultimately, this project aims to unveil the connection between uterine scar healing and uterine tensile strength.

METHODS

Surgical Model of Uterine Scarring. Non-pregnant female wild-type mice (C57BL/6J) were anesthetized using sterile surgical technique prior to midline incision and externalization of one uterine horn. A 3-5 mm longitudinal uterine incision was introduced and subsequently closed with 6/0 absorbable suture prior to sterile washing and closure of the abdominal cavity. After closure of the uterus and abdomen, animals were allowed to recover for either 1, 2, or 3 weeks prior to euthanasia.

Mechanical Testing. Uniaxial loading of murine uterine samples was conducted using an ElectroForce 3200 Series III test instrument (TA Instruments). Figure 1a illustrates the comprehensive experimental setup, including two cameras to track tissue deformation and a saline bath for sample hydration. Figure 1b details the sample mounting fixture and is based on a setup previously published for use in mechanical testing of mouse reproductive tissues [1].

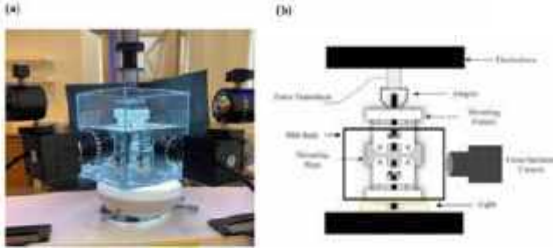

Figure 1: a) Complete experimental setup to test mouse uterine ring samples using the ElectroForce 3200 system. b) Detailed schematic outlining all components needed for proper mounting, imaging, and testing of uterine ring samples.

Uterine horn samples were submerged in PBS, gently cleaned of excess connective tissue, and cut into 2.5-3.5 mm sections (including any scars) to form the ring for mechanical testing. Prepared samples

were then mounted on the fixtures, illustrated in Figure 1b, by threading 2-0 silk suture through the inner lumen of the sample. The sample and mounting plate were then immersed in a PBS bath at 4°C for a minimum of 2 hours before testing to allow for tissue equilibration.

To execute the mechanical test on the ElectroForce 3200 machine, an adapter was added to the top adjustable fixture and secured to the force transducer (max: 45 N). After setting up the sample apparatus in an empty PBS bath and adjusting the actuator height, 400 mL of PBS were added to the bath to submerge the tissue. Finally, two high-resolution cameras were attached to the stage with one camera facing the tissue and the other positioned at a 90° angle from the front.

A preload of 0.01 N was established before testing to set a reference position. Four cyclical loads (0.1 N, 0.3 N, 0.5 N, and 0.7 N) were applied, each with a dwell time of 400 seconds between cycles to allow for tissue recovery toward an equilibrium state. The applied displacement rate was 0.1 mm/s, and each load level was repeated in duplicate. Following completion of the load cycles, samples were ramped until failure. Throughout the testing procedure, the output force-displacement data was recorded in a .csv file. A calibration tool was used to establish video scaling based on the camera lens settings. This allowed for real-time recording of sample geometry during testing for analysis of tissue mechanical properties and the generation of stress-strain curves for each load cycle until failure.

Estimating the geometry of the sample as a rectangular prism, the stress experienced by the uterine ring was calculated using the Cauchy Stress described in Equation (1).

$$\sigma = \frac{F}{A} \quad (1)$$

where F is the experimental force collected by the ElectroForce software and A is the current deformed cross-sectional area measured by the cameras. The cross-sectional area was defined to be that of a rectangular prism, referenced in Equation 2, where W and L are the width and length of the tissue sample as it deformed.

$$A = W \times L \quad (2)$$

To analyze the mechanical behavior of the tissue, the stress was plotted with respect to the stretch described in Equation (3).

$$\lambda = \frac{h}{H} \quad (3)$$

where H is the original height of the sample and h is the current height as measured by via LabView recordings. When testing to failure, the failure point was defined as the maximum stress experienced by the sample prior to a persistent decrease in measured force.

All of the force, geometric behavior, displacement, stress, and strain data was analyzed using Matlab. For statistical comparison, one-way ANOVA was performed with a Dunnett post-hoc comparison to determine differences from control with $p < 0.05$ considered significant.

RESULTS

After a longitudinal scar is introduced to the uterine horn, the uniaxial behavior of the tissue evolves throughout the healing process. Initially, the force required to rupture the tissue, as well as the Cauchy stress and stretch, decreases with respect to un-scarred control tissue ($p < 0.05$ at 1 week post-surgery; **Fig.2A**). The scarred uterine horn samples at each time point, however, can be displaced more prior to rupture than the control with the most prominent increase at 3 weeks after surgery (**Fig.2B**). Over time, the stress-stretch responses begin to resemble that of a normal murine uterine horn. However, the maximum Cauchy stress and stretch at rupture is still less than that of the control, suggesting some persistent tissue remodeling (larger cross-sectional area) that remains at 3 weeks post-surgery ($P< 0.05$, 0.01 at 1 and 3 weeks post-surgery; **Fig.3A,B**). OCT imaging at the location of uterine scarring confirmed the changes in tissue structure and geometry associated with post-surgical healing (**Fig.4**).

DISCUSSION .

The initial findings of this project provide insight into the uniaxial behavior of murine uterine tissue as it recovers from longitudinal scar placement. Despite the maximum rupture force returning to levels similar to the control after three weeks, the Cauchy stress and stretch remained lower than the control for all time points.

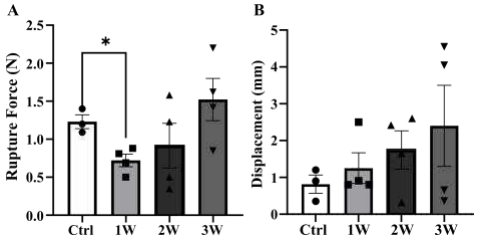

Figure 2: Maximum rupture force (a) and displacement (b) of murine uterine tissue after scar formation. * p < 0.05; one-way ANOVA with post-hoc Dunnett comparison to control.

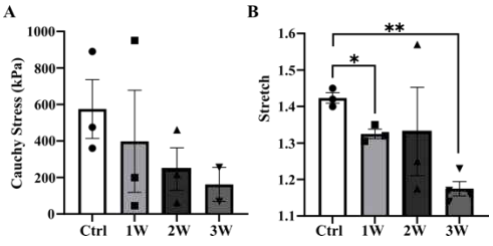

Figure 3: Cauchy stress (a) and strain behavior (b) at failure of murine uterine tissue after scar formation. *, p < 0.05, 0.01; one-way ANOVA with post-hoc Dunnett comparison to control.**

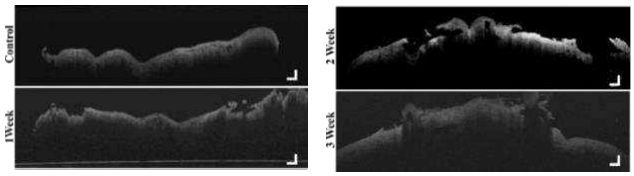

Figure 4: OCT imaging of scarred murine uterine tissue over time

Throughout the healing process, the microstructural composition of the scarred uterine wall must remodel to accommodate the biomechanical demands of the tissue. Thus, it is expected that scarring will affect the uniaxial biomechanical behavior due an increase in scar-related fibrosis. While our findings suggest uterine scar affects the uniaxial behavior of the uterus, additional mechanical testing approaches, such as biaxial testing, could further quantify how scar integrity impacts the likelihood of rupture. Our initial findings show that despite the longitudinal scar changing the tissue composition (see **Fig.4**), the biomechanical response of the uterus begins to return to the baseline values after three weeks of healing. Understanding the mechanobiology of this healing process in non-pregnant animals may also provide insight into the factors regulating c-section scar integrity.

ACKNOWLEDGEMENTS

This work was supported by an internal seed grant through the WashU Centers for Women's Health Engineering and Regenerative Medicine.

REFERENCES

[1] Jayyosi, C., et al, *Acta Biomaterialia*, 308:319, 2018. [2] Al-Zirqi I, et al, *BJOG*, 117:809–820, 2010. [3] Landon M., et al., *Seminars in Perinatology*, 267:271, e34-4, 2010.

ENHANCING THE TARGETING EFFICACY OF ENDOTHELIAL COLONY FORMING CELLS FOR RENAL REGENERATION VIA KIDNEY-TARGETED LIPOSOMAL NANOPARTICLES

B. Cruz Gonzalez (1), F. Fan (2), E. Hall (3), S. Saha (4). D. Hanjaya-Putra (1,3,4)

(1) Aerospace and Mechanical Engineering, University of Notre Dame, South Bend, IN, USA
(2) Chemistry, Michigan State University, East Lansing, MI, USA
(3) Aerospace and Mechanical Engineering, University of Notre Dame, South Bend, IN, USA
(4) Aerospace and Mechanical Engineering, University of Notre Dame, South Bend, IN, USA

INTRODUCTION

Stem cell engineering has been one of the most promising approaches for precision health nowadays. The Endothelial Colony Forming Cells (ECFCs) have demonstrated to exhibit a high proliferative potential have the unique ability to create *de novo* blood vessels *in-vivo*, indicating a higher angiogenic potential compared to mature endothelial cells like Human Umbilical Vein Endothelial Cells (HUVECs). As a result of these distinctive traits, ECFCs have shown promising therapeutic potential for various vascular disorders [1, 2, 3]. Acute renal failure, also known as AKI (Acute Kidney Injury), is characterized by a sudden decline in renal function primarily caused by ischemia/reperfusion (I/R) injury. This type of injury results in significant vascular damage, leading to capillary loss. Considering these challenges, researchers have explored the administration of exogenous endothelial cells as a potential strategy for treating AKI [4, 5]. Upon immediate injection, ECFCs were detected predominantly in the lungs, with an occasional presence in the kidney, liver, spleen, and heart. However, after 1 hour, ECFC density in the lungs decreased, and their presence in other tissues became scarce. By the 24-hour mark, ECFCs were barely detectable in any tissues [6]. This highlights the need to engineer a solution that can enhance the retention of ECFCs in the kidney, thereby improving their performance in promoting kidney regeneration. In this project, our goal is to utilize Liposome Nanoparticles (LNPs) not as conventional drug carriers but as vehicles to facilitate cell homing and create what it is refereed as the “backpack molecule”. To achieve this, a lipid formulation containing thiol-reactive maleimide headgroups is employed. This reaction is made possible by the presence of free thiol groups on the surface of ECFCs, which readily interact with the maleimide groups in the LNPs [7]. However, it is important to note that this interaction offers specificity.

While LNPs have demonstrated specificity, they lack selectivity, apart from their size, which is a crucial factor to cross organ barriers. To overcome this limitation, it is essential to identify a specific marker capable of target either the kidney or an AKI marker. Kidney-targeted Nanoparticles (NPs) designed for drug delivery have demonstrated great promise as an emerging strategy for AKI therapy. The Kidney Targeting Peptide (KTP) has demonstrated an enhance binding and high accumulation in proximal tubules and vascular endothelium of the kidney. These findings highlight the exceptional renal selectivity of KTP and support the notion that the construct is not species-specific, demonstrating its lack of acute renal toxicity [8]. Therefore, our general hypothesis is that our unique backpack molecule KTP-nanoparticle design will enhance the targeting efficacy of the ECFCs leading to vascular renal regeneration.

METHODS

Synthesis, Conjugation, and Characterization of LNPs with the KTP Peptide.

To facilitate the attachment of KTP to the LNPs, a free thiol group on the KTP peptide, referred to as KTP-SH is introduced. This modification can be achieved using Traut's reagent in a two-pot reaction. Subsequently, the KTP-SH can be attached to the LNPs via a click chemistry reaction, as the LNPs possess a maleimide group that can readily react with free thiol groups. Ellman's assay was employed to detect the successful modification of the KTP peptide after a 24h of incubation period. PEGylation was performed to block possible maleimide groups (MAE) promoting a non-specific interaction in the future with different thiol groups within the cell lines. Dynamic light scattering was performed to show the size distribution and Z-potential of the different sets of LNPs, before and after PEGylation. Absorbance measurements were done in a FITC-SH peptide to show the interaction of the thiol groups with the LNPs.

In-vitro Evaluation of the KTP-nanoparticle design.

The incorporation of the KTP peptide into LNPs (LNPs@KTP) is expected to enhance the selectivity of these nanoparticles for HRPTEpC cells compared to the ECFCs cell line. To establish this selectivity, flow cytometry studies was performed. This was done since a comparison of the behavior of the KTP with different kidney cell lines was previously described [8], therefore the same behavior is expected for our nanoparticle design.

RESULTS & DISCUSSION

The click-chemistry approach is suitable to decorate LNPs.

The modification of the KTP peptide was achieved as described in **Figure 1 A.** Free thiol groups can be detected by Ellman's absorbance assay few minutes after starting the reaction. **Figure 1 B.** Shows the difference between the free thiol groups on the Traut's reagent and the KTP-SH, demonstrating that the KTP after reaction do express free thiol groups which are suitable for the conjugation with the LNPs.

A. B.

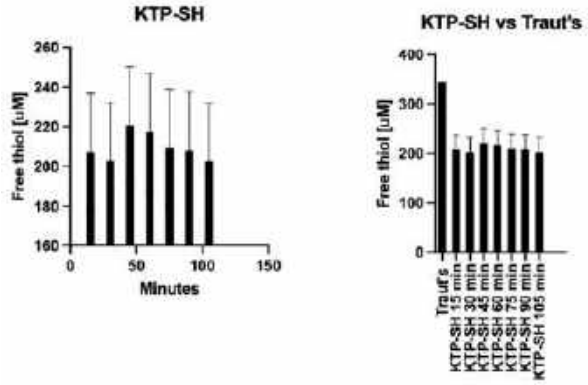

Figure 1. Time Course Analysis of Thiol Group Formation in KTP Peptide (KTP-SH) Reaction and it is a comparison with Traut's reagent. A. Kinetics of thiol group formation on the KTP peptide through a reaction with Traut's reagent. The experiment involves performing Ellman's assay readings at regular intervals (every 15 minutes) for a total of 105 minutes after initiating the KTP-SH reaction. B. Kinetics of thiol group formation on the KTP peptide vs Traut's reagent.

The decoration of the LNPs with the KTP was performed by a click chemistry reaction between the KTP-SH and MAE group on the LNPs (Figures 2, A and B), therefore a change in size and Z-potential is expected. The DLS characterization showed that the size of the LNPs is (141.8±5.6) nm and LNPs@KTP is (164.2±2.9) nm. Moreover, the Z-potential is -28.9 mV and, -30 mV for LNPs and LNPs@KTP respectively. Figure 2C shows the interaction of FITC-SH with the LNPs, where a positive FITC signal suggests that the decoration of the LNPs has been achieved. Those results suggest that the KTP has been successfully attached to the LNPs.

KTP peptide can attach to the preferentially with HRPTEpCs than the ECFCs.

The unique backpack molecule KTP-nanoparticle design showed to provide the expected selectivity for the Human Renal Proximal Tubular Epithelial Cells rather than the control cell line (ECFCs). Figure 4 displays the flow cytometry analysis for the binding studies were in quadrant 2 (Q2) is expected to have positive signal if the binding of the LNPs@KTP@PEG has been achieved, showing that with HRPTEPc (Fig 4A), a 91.3% of the cells are binding to the cell line and ECFCs (Fig. 4B), a 42.0% of cells are being positive for the binding. Those results show that the KTP has demonstrated an enhance binding and high accumulation on the HRPTEPc cell line.

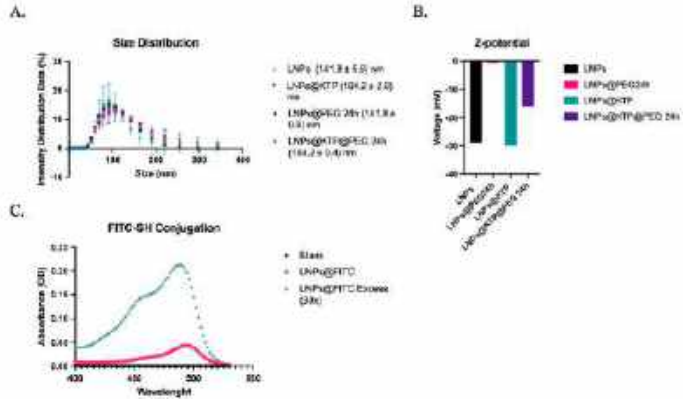

Figure 2. Verification of LNPs@KTP conjugation. A. Size Distribution Analysis for four different sets of LNPs designs. According to our measurements, the size range is (141.8±5.6) nm, (164.2±2.9) nm, (141.8±0.8) nm, and (164.2±0.4) nm for LNPs, LNPs@KTP, LNPs@PEG24h, LNPs@KTP@PEG24h respectively. B. The obtained Z-potential data set is -28.9 mV, -0.635 mV, -30 mV, and -16.1 mV for LNPs, LNPs@PEG24h, LNPs@KTP and LNPs@KTP@PEG24h respectively. C. LNPs showed to be positive for the FITC signal, which suggests that the click chemistry between the FITC-**SH** and the LNPs has been achieved with an excess of the reagent and with our synthesis conditions.

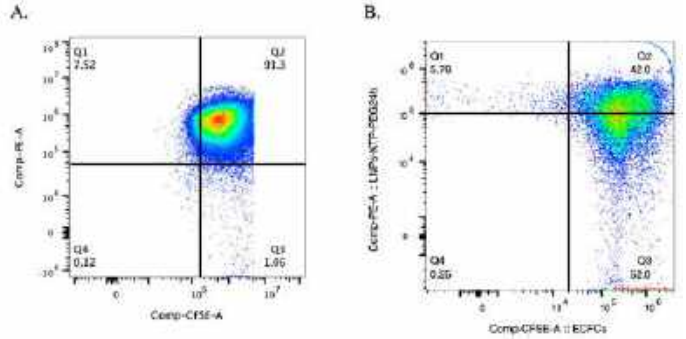

Figure 4. Binding studies for LNPs@KTP@PEG24h on different cell lines. Q4. Displays the double negative staining for PE (LNPs) and CFSE (cell line). Q2. Exhibits the double positive staining for PE and CFSE. Q1. Shows PE positive signal. Q3 Displays CFSE positive signal. A. Flow cytometry assay for the conjugation of HRPTEPc with LNPs@KTP@PEG24h where in Q2 can be appreciated that 91.3% of the cells are successfully binding with the nanoparticle design. B. Conjugation of the ECFCs where Q2 shows that just 42.0% of the cells are attaching to the nanoparticle design.

REFERENCES

[1] David A Ingram, Laura E Mead, Hiromi Tanaka, Virginia Meade, Amy Fenoglio, Kelly Mortell, Karen Pollok, Michael J Ferkowicz, David Gilley, and Mervin C Yoder. Identification of a novel hierarchy of endothelial progenitor cells using human peripheral and umbilical cord blood. Blood, 104(9):2752–2760, 2004.

[2] Mervin C Yoder, Laura E Mead, Daniel Prater, Theresa R Krier, Karim N Mroueh, Fang Li, Rachel Krasich, Constance J Temm, Josef T Prchal, and David A Ingram. Redefining endothelial progenitor cells via clonal analysis and hematopoietic stem/progenitor cell principals. Blood, 109(5):1801–1809, 2007.

[3] Paul J Critser and Mervin C Yoder. Endothelial colony forming cell role in neoangiogenesis and tissue repair. Current opinion in organ transplantation, 15(1):68, 2010.
[4] Kimihiko Banno and Mervin C Yoder. Tissue regeneration using endothelial colony-forming cells: promising cells for vascular repair. Pediatric research, 83(1):283–290, 2018.
[5] Joseph V Bonventre, Li Yang, et al. Cellular pathophysiology of ischemic acute kidney injury. The Journal of clinical investigation, 121(11):4210–4221, 2011.
[6] Dylan Burger, Jose L Vin˜as, Shareef Akbari, Hajira Dehak, William Knoll, Alex Gutsol, Anthony Carter, Rhian M Touyz, David S Allan, and Kevin D Burns. Human endothelial colony-forming cells protect against acute kidney injury: role of exosomes. The American journal of pathology, 185(8):2309–2323, 2015.
[7] Loan Bui, Shanique Edwards, Eva Hall, Laura Alderfer, Kellen Round, Madeline Owen, Pietro Sainaghi, Siyuan Zhang, Prakash D Nallathamby, Laura S Haneline, et al. Engineering bioactive nanoparticles to rejuvenate vascular progenitor cells. Communications Biology, 5(1):635, 2022.
[8] Gene L Bidwell III, Fakhri Mahdi, Qingmei Shao, Omar C Logue, Jamarius P Waller, Caleb Reese, and Alejan- dro R Chade. A kidney-selective biopolymer for targeted drug delivery. American Journal of Physiology-Renal Physiology, 312(1):F54–F64, 2017.

CARTILAGE STRAIN PREDICTS PATIENT-REPORTED OUTCOMES SIX MONTHS POST-ACL RECONSTRUCTION

Emily Y. Miller (1), Timothy Lowe (2), Hongtian Zhu (2), Woowon Lee (2), Daniel Stokes (3), Rachel Frank (3), Jonathan Bravman (3), Eric McCarty (3), Nancy Emery (4), Corey P. Neu (1,2)

(1) Biomedical Engineering Program, University of Colorado Boulder, Boulder, CO, USA
(2) Paul M. Rady Department of Mechanical Engineering, University of Colorado Boulder, Boulder, CO USA
(3) Department of Orthopedics, University of Colorado Anschutz Medical campus, Aurora, CO, USA
(4) Ecology and Evolutionary Biology, University of Colorado Boulder, Boulder, CO, USA

INTRODUCTION

Knee Osteoarthritis (OA) is a major source of pain for 86 million adults worldwide that lacks both approved therapeutic interventions and disease-modifying treatments. As OA progresses, cartilage composition and material property alterations can contribute to knee pain, joint instability, and biomechanical alterations, ultimately leading to joint destruction and impaired quality of life. Alterations to cartilage can be associated with a traumatic injury such as ligament rupture or can progress over time due to cell- and inflammation-related factors [1]. As nearly one half of individuals with an ACL tear develop post-traumatic OA within 10 years, joint injury cohorts provide an opportunity to study and characterize the development of OA at its earliest stages. Post-traumatic OA may progress from an initial injury in the superficial zone of cartilage to more widespread biochemical and mechanical changes throughout the zonal tissue cartilage, therefore quantifying changes to cartilage mechanical and biochemical properties non-invasively *in vivo* is of substantial interest.

MRI is unique among imaging tools as it can characterize tissues with high contrast and spatial detail and has a deep penetration depth [2]. Recent work supports that quantitative MRI mapping (T2, T2*, T1rho), can discriminate between subjects with mild OA and controls [1]. In other works, dualMRI has been used to calculate pixel level full field displacement maps of cartilage under repetitive motion [2]. In this study, we utilized both dualMRI and qMRI techniques to predict patient outcomes and cartilage function *in vivo* at 6 months post ACL-reconstructive surgery.

METHODS

Participant Recruitment: 32 participants were identified in the orthopedic clinic following unilateral ACL surgery 6±2 months prior to the MRI scan date. Participants ranged from 18 to 40 years of age, having received either a bone-patella tendon-bone autograft or quadriceps tendon autograft at the recommendation of one of three collaborating orthopedic surgeons. All subjects had ligament reconstructive surgery within 3 months of injury. All subjects had no prior history of concomitant, symptomatic knee pathologies on their ACLR knee and no injury or surgery to their contralateral knee. While supervised therapeutic exercise was generally prescribed following ACLR, rehabilitation was not standardized across the cohort. We obtained demographic information on all subjects, including age, sex, body mass index (BMI) and race at the time of recruitment. At the time of the scan, we also collected standardized patient reported outcomes (WOMAC score) to assess pain, knee stiffness, quality of life, and physical activity levels (Figure 1A).

Overview of MRI Method: An MRI-compatible loading apparatus capable of providing a varus load to the tibiofemoral cartilage of the knee, leading to compression of the medial femoral condyle was used to load the cartilage during scanning (Figure 1B) [3-5]. Moment conservation was used to calculate the load applied on the foot to be equivalent to 0.5 times body weight of load applied at the medial condyle. Patients were subjected to a 0.5 Hz cyclic loading regime (i.e., pneumatic, 1s load,1s unload) to mimic a walking cadence. The knee imaging protocol consisted of 3D double echo steady state (DESS) acquisition, quantitative T1ρ, T2 and T2* measurements, and DENSE MRI during cyclic varus loading on the knee joint (Figure 1A). All imaging was performed using a clinical MRI system (3 T; Siemens Prismafit) with a 15-channel quadrature knee coil (Tx/Rx Knee 15 Flare Coil, QED, LLC). For T1ρ images the spin-lock frequency was 500 Hz and the spin-lock durations was 20, 40, 60, 80 ms. T1ρ relaxation maps were calculated by fitting the four MR intensity images to a monoexponential relaxation model using non-linear least squares. T2 measurements were made using a multi-echo spin echo sequence with the following acquisition parameters: TEs = 13, 26, 39, 52, 65, 78 ms, TR = 1290 ms, flip angle = 180°, image average = 2 [3]. Spiral DENSE MRI was collected following preconditioning to a quasi-steady-state

load-displacement response. A steady-state response was achieved by applying 8 minutes of cyclic loading to minimize the viscoelastic response of articular cartilage [4,5]. 10 spiral interleaves were used to collect data on k-space and the temporal resolution was 40ms. Displacement encoding gradient was 0.64cycles/mm.

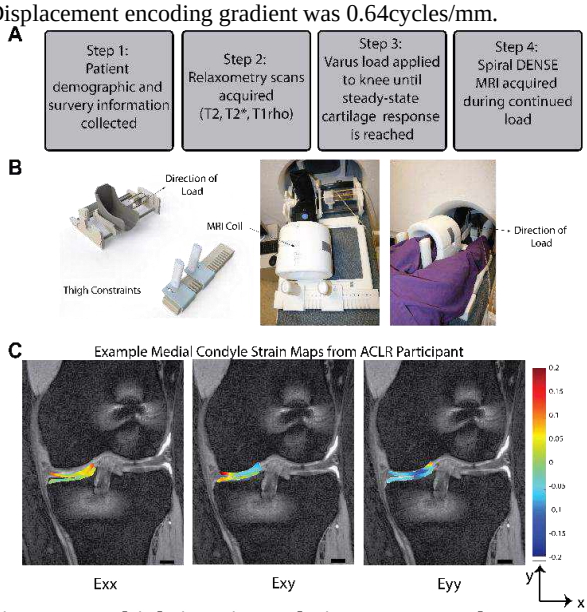

Figure 1: Multiple imaging techniques were used to assess cartilage response to load an ACLR cohort. (A) MRI scanning session workflow. (B) Varus-valgus MRI compatible loading device. (C) Example strain maps from DENSE MRI. Scale bars indicate 10mm.

MRI Data Processing and Statistical Analysis: DENSE MRI Data analysis was processed prior to qMRI processing. The articular cartilage was segmented via a semi-automatic segmentation algorithm into two regions of interest (ROI) based on the anatomical regions of the knee (i.e., medial femur, medial tibia). This was repeated on all 27 time frames. Locally weighted scatterplot smoothing (LOWESS) using a span of 10 and for 30 cycles was applied to raw displacement data to smooth the displacements. In-plane Green-Lagrange strains (Exx, Exy, Eyy) were then calculated on the ROIs from the smoothed displacement using the deformation gradient tensor (Figure 1C) [2]. On the T2, T2*, T1ρ maps, ROIs were selected analogous with the DENSE ROIs. The mean value for each MRI metric within each ROI (femoral and tibial) was then calculated. Correlations were then calculated among MRI metrics and the WOMAC score using a linear mixed-effects model, with patient treated as a random effect and multiple fixed effects accounting for potential covariates (Figure 2). [1]. A mixed effects linear prediction model of patient-reported outcome severity with variable inclusion based upon the previous models was developed (Figure 3).

RESULTS

We found that femoral shear strain best predicted patient-reported outcomes at six months ($p = 0.032$, $R^2=0.41$). We observed that increased shear strains were correlated with worse patient reported outcomes as quantified by higher WOMAC score. This is supported by our previous work demonstrating shear in cartilage explants as a potential biomarker for cartilage degeneration [1]. We also found that axial strain (Exx) was correlated with increased WOMAC score ($p = 0.031$, $R^2=0.42$). No significant correlations were found between WOMAC score and average T2 or T1ρ values. T2* was additionally correlated with WOMAC score with higher T2* indicating a higher WOMAC score, and therefore a worse outcome ($p = 0.005$, $R^2=0.53$).

We also found that the combined use of multiple MRI metrics (multiparametric analysis) may predict patient reported outcomes better than any single MRI metric (Figure 3). The predicted OA scores of a statistical model that contains Exy, T2, T2*, age, surgeon, and graft type were compared to measured scores. This combined model matches the actual data better than either dualMRI or relaxometry individually.

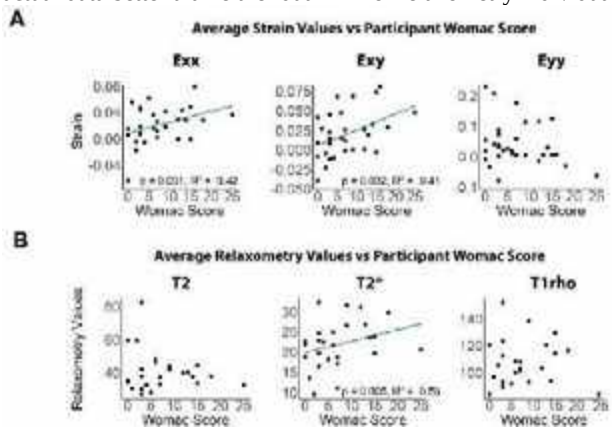

Figure 2: Average strain (A) values and relaxometry (B) values regressed against participant WOMAC score in the medial femoral cartilage region of interest.

DISCUSSION

While previous work has linked macro-scale whole joint mechanical changes post-ACLR, to our knowledge no other studies have quantified tissue level mechanical changes in cartilage *in vivo* in a post-ACLR population. This work provides a small cohort proof-of-concept of an MRI framework to non-invasively determine cartilage strains in a clinical setting. The results support the use of DENSE MRI, in particular shear strain [1,2], as a potential diagnostic tool to evaluate early cartilage degeneration. There is a clinical need for a noninvasive imaging method that can detect and measure articular cartilage changes before cartilage loss occurs. This data demonstrates the potential of dualMRI, particularly in conjunction with other imaging biomarkers, to fulfill that need.

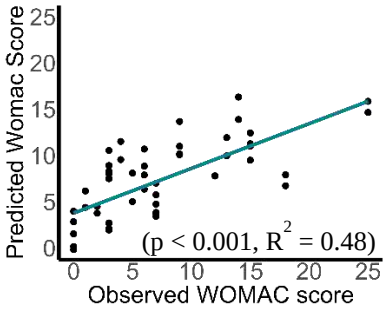

Figure 3: Multicontrast MRI improves results over either dualMRI or qMRI in an ACLR cohort.

ACKNOWLEDGEMENTS

This work was supported by NIH grant 2 R01 AR063712.

REFERENCES

[1] Griebel A. et al. *MRM*, 2014. [2]. Chan D. et al., *Sci. Rep*. 2016. [3] Lee W. et al., *MRM* 90(3), 2023. [4] Lee W. et al., *MRM* 89(2), 2023. [5]. Zhu H. et al., *SSRN 4569548*

WALKING RECOVERS CARTILAGE STRAIN: AN ANALYSIS OF MEASUREMENT REPEATABILITY

JiYeon A. Hong (1), Tejus Surendran (1), Shu-Jin Kust (2), Dana Voinier (3), Kyle D. Meadows (2), Dawn M. Elliott (2), Daniel K. White (3), Axel C. Moore (1)

(1) Department of Biomedical Engineering, Carnegie Mellon University, Pittsburgh, PA, USA
(2) Department of Biomedical Engineering, University of Delaware, Newark, DE, USA
(3) Department of Physical Therapy, University of Delaware, Newark, DE, USA

INTRODUCTION

Articular cartilage lines the ends of long bones in synovial joints and provides load-bearing and low-friction articulation. These biomechanical functions are largely driven by the poroelastic mechanics of the articular cartilage [1]. Unfortunately, the same poroelastic pressure that leads to load-bearing and lubrication also drives fluid exudation and concurrent tissue consolidation (strain). Static loading in vivo (e.g., standing) produces as much as -30% strain in 60 min. Active loading (e.g., walking, knee bends, cycling, running) in vivo also produces an initial period of fluid exudation and strain (~ -5%) [2]. Interestingly, active loading beyond this initial period leads to a maintenance of tissue hydration and strain unlike static loading [3]. While static and active loading drive fluid exudation and cartilage strain, static unloading (e.g., lying down) provides recovery, and to date, is the only in vivo mechanism that has been shown to restore hydration and strain.

We hypothesize that active loading is actually a hydration and strain recovery mechanism that has yet to be observed. In this study, we investigate whether active loading (walking) is only an exudation and arresting mechanism or whether it is also capable of recovery. We use magnetic resonance (MR) imaging to evaluate the in vivo strain of articular cartilage in human knees following: (1) standing (static loading), (2) lying down (static unloading), and (3) walking (active loading). Furthermore, we evaluate measurement repeatability within and between raters, and with and without blinding.

METHODS

Participants. Following IRB approval, we recruited N=8 asymptomatic young adults to participate in the study. Participant age (29 ± 3 years of age, mean ± 95% confidence interval), biological gender (4 male, 4 female), and BMI (23 ± 2) were recorded. Up to 5 days prior to MR scanning, participants were given a wrist worn activity monitor to track the number of steps taken each day (13 ± 5k steps/day). Knee joint health was assessed using the self-reported Knee Injury and Osteoarthritis Outcome Score (KOOS).

MR Scanning. Participants arrived at the MR facility on the day of scanning and were positioned within the scanner (3T MAGNETOM Prisma, Siemens) with a 15 channel Tx/Rx knee coil around their right knee. Participants were scanned in the following fixed order: (1) baseline, and immediately after (2) 30 min of standing, (3) walking for 10 min at 110 steps per min, (4) 30 min of standing, and (5-8) 12, 24, 36, and 48 min of lying down (**Fig 1**). A proton density weighted turbo spin echo (PD-TSE) was used to assess the morphology and thickness of the articular cartilage. The in-plane resolution and slice thickness were 0.3 and 1.5 mm respectively.

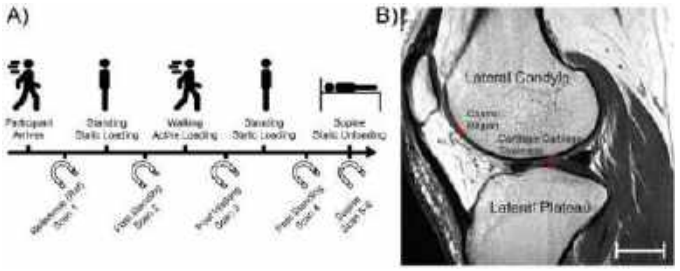

Figure 1: (A) Order of activities. MR scanning is indicated with the magnet symbol, and the numbering corresponds to the scan number, see section *MR Scanning*. (B) Representative measurement locations on a PD-TSE MR image.

Data Analysis. We calculate cartilage thickness as the tibiofemoral bone-to-bone distance within the medial and lateral compartments, measured within the region of contact. MR scans were registered to the baseline scan to ensure the same region was measured. We calculate cartilage strain as the change in cartilage thickness divided

by the baseline thickness. All values are reported as the mean ± 95% confidence interval unless stated otherwise.

Repeatability Analysis. Repeatability was determined through intra-rater and inter-rater assessments. Rater 1 measured the strain in all conditions and then repeated this analysis on a separate day without reference to the original measurement locations. Rater 2 measured the strain in all conditions without reference to Rater 1's measurement locations. In a final test, Rater 2 was blinded to the scan order and performed the same analysis without reference to the original measurement locations.

RESULTS

The average strain in the medial and lateral compartments for 8 participants are shown in **Fig 2 A&B**. The baseline strain is set at 0%. After 30 min of static loading (standing), there is a clear thinning of the articular cartilage to an average -5.0 ± 0.4 and -5.3 ± 0.6% strain in the lateral and medial compartments. Following a 10 min walk (active loading), the cartilage thickness recovers 2.3 ± 0.3 and 2.6 ± 0.6% strain, which directly agrees with our hypothesis that active loading is capable of recovery. Following another bout of static loading to approximately the same strain (-5.4 ± 0.3 lateral and -5.1 ± 0.5% medial) the participant lies supine (static unloading), and the cartilage thickness and strain progressively recover. Following the first scan (12 min post standing), the cartilage recovered 1.5 ± 0.6 and 1.1 ± 1.0% strain in the lateral and medial compartments. Following 48 minutes of unloaded recovery the cartilage recovered 3.8 and 3.6% strain in the lateral and medial compartments.

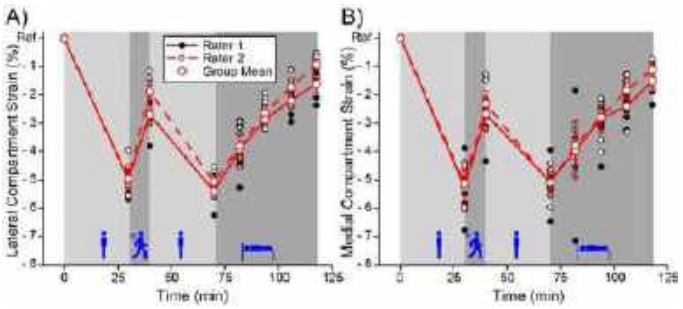

Figure 2: Cartilage strain in the central region of contact for all 8 participants in both the (A) lateral and (B) medial compartments. Individual and mean measures are shown for both Rater 1 and Rater 2.

Repeatability was assessed by quantifying the bias (mean difference) and the ± 95% confidence interval. Intra-rater repeatability was found to be -0.2 ± 0.1% strain. Inter-rater repeatability was found to be -0.3 ± 0.2% strain, see **Fig 2 A&B**.

DISCUSSION

While epidemiological studies have documented the chondroprotective nature of joint activity, we have yet to identify the mechanism that provides chondroprotection. The observation that in vivo active loading recovers cartilage strain, and possibly hydration, opens new opportunities for understanding the long term biomechanical and cellular responses to active loading. Furthermore, the simplicity and repeatability of the analysis method demonstrates methodological robustness and potential for translation.

ACKNOWLEDGEMENTS

This work was supported by NIH COBRE 2P20GM 103653-06.

REFERENCES

[1] G.A. Ateshian et al, *J. Biomech*. (2009).
[2] F. Eckstein et al, *J. Anat*. (2006).
[3] F. Eckstein et al, *Anat. Embryol*. (1999).

A COMPUTATIONAL MODELING APPROACH FOR THE FORENSIC ANALYSIS OF INFANT SHORT HEIGHT FALLS

Keith D. Button (1), Yun Cai (1), Luis A. Nolasco (1), Brian T. Weaver (1)

(1) Explico Inc., Novi, MI, USA

INTRODUCTION

Intracranial bleeding, such as subdural and subarachnoid hemorrhaging, represents a serious and potentially life-threatening medical condition. In infants, the presence of intracranial bleeding can potentially be the result of non-accidental trauma. As such, it is especially important to utilize forensic biomechanics techniques to investigate the etiology of infant intracranial bleeding to determine if the scenario presented by the caretaker provides the requisite biomechanical environment to cause these injuries.

Biomechanically, intracranial bleeding occurs as a result of injurious levels of rotational head acceleration [1,2]. Since rotational head acceleration can be imparted as a result of direct impact or inertial loading, biomechanical studies have investigated rotational acceleration induced by both loading environments [3,4]. The first study to investigate this was conducted by Duhaime and colleagues[3]. The authors crafted a model of a 1-month-old infant and exposed it to violent shaking and impact by both male and female experimenters, finding that direct impact produced significantly higher magnitudes of rotational head acceleration. A subsequent study by Prange et al. utilized an anthropomorphic surrogate of a 1.5 month old to simulate falls from short heights (0.3, 0.9, and 1.5 m), vigorous shaking, and inflicted head impact [4]. In a more recent study by Ibrahim et al., the authors developed an updated anthropometric test device and performed drops at 0.3, 0.6, and 0.9 [5]. Results from the Ibrahim and Prange studies showed substantially lower magnitudes of angular acceleration produced by shaking when compared with short-height falls onto both concrete and carpeted surfaces. The next logical step would be to present an approach that allowed for the subject-specific analysis of short-height fall scenarios for the investigation of real-world accidents.

Physical testing has previously been conducted documenting the impact characteristics between the head and various household surfaces. These studies demonstrate that the duration of head impact for more rigid surfaces such as concrete and hardwood typically range between 5 and 7 ms and 7 to 13 ms for more compliant surfaces such as carpet [5–7]. The purpose of the current study was to develop a computational approach to investigate the angular head accelerations experienced during short-height falls allowing for variable drop heights, infant anthropometry, and impact duration for comparison with an applied aggressive shake using MADYMO (MAthematical DYnamic Models). The authors hypothesized that simulated short-height falls would produce greater magnitudes of angular head acceleration than simulated shaking events.

METHODS

Part 1: Simulated Falls/Shakes Using HIII Crash Test Dummy

In order to develop a methodology applicable to the investigation of real-world accidents, it is important to utilize a subject-specific model, scaled to the height and weight of the subject being analyzed. As such, simulations were conducted using the Hybrid III 6-year-old Anthropomorphic Test Device (HIII 6YO ATD), which is a scalable ATD. The HIII 6YO ATD has been validated using component-level tests at the neck, neck/head, and thorax. The HIII 6YO ATD was scaled to the height and weight of a 1 year-old ATD (0.740 m and 9.6 kg).

In MADYMO, the ATD was positioned at heights of 0.3, 0.6, 0.9, and 1.5 m and dropped to the surface (Figure 1). The interaction between the ATD and surface was modulated by adjusting the friction, damping, and impact characterization function to produce impacts with durations of 5, 7, 10, and 13 ms to represent the range of impact characteristics most commonly encountered during household falls. The influence of contact duration and drop height was evaluated using an ANOVA.

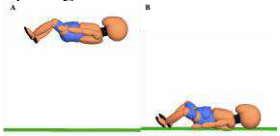

Figure 1: Initial (A) and final positions (B) of drop simulation (0.2 m).

In addition to simulated falls, an aggressive shake was simulated (Figure 2). For this analysis, the ATD was suspended in the air and the torso was accelerated and decelerated based on data provided by Wolfson et al. [8]. In this study, ten volunteers were asked to shake an infant ATD as long and hard as they could. The torso-acceleration trace provided by the authors was applied to the ATD torso and had a maximum linear acceleration of 9 g's.

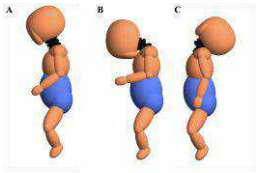

Figure 2: Initial (A), max flexion (B), and max extension of shaking simulations

Part 2: Simulated Falls/Shakes Using HIII 6 Y/O

RESULTS

The maximum linear acceleration and angular head accelerations for the simulated impacts and shakes are depicted in Figure 1 and Figure 2, respectively. Maximum linear (211 g) and angular (46,642 rad/s^2) head accelerations occurred at a drop height of 1.5 m and pulse duration of 5 ms. Minimum linear (22 g) and angular (5,044 rad/s^2) head accelerations occurred at a drop height of 0.3 m and pulse duration of 13 ms. All impacts produced greater linear and angular head accelerations than the shaking simulations (14 g and 1,457 rad/s^2, respectively). A 2-factorial ANOVA (height and duration) found an increase in height and decrease in contact duration to significantly increase the angular ($p < 0.05$) and linear ($p<0.01$) head acceleration.

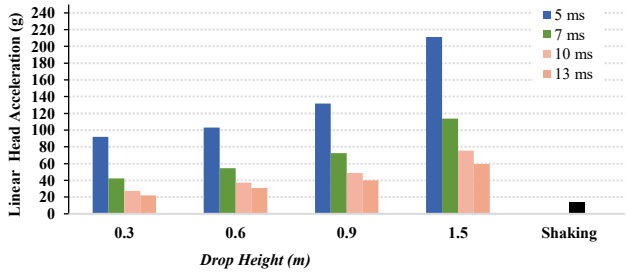

Figure 2: Linear Head Acceleration Resulting from Simulated Short-Height Falls and Shakes

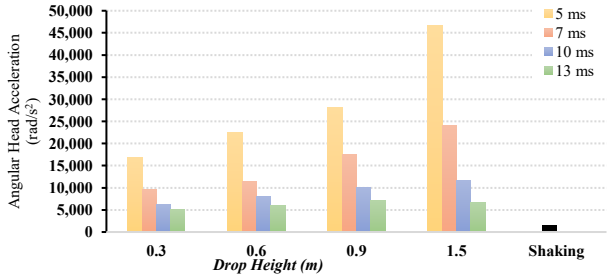

Figure 2: Angular Head Acceleration Resulting from Simulated Short-Height Falls and Shakes

DISCUSSION

Biomechanical work conducted over the last three decades has repeatedly demonstrated the risk of serious and sometimes fatal injuries occurring from short-height falls in infants. The current study presented a computational approach to analyze short height falls with subject-specific inputs for infant anthropometry, fall height, and impact duration.

Results of the simulations were closer to the experimental work done Ibrahim et al. than the work done by Prange et al. [4, 5]. Specially, Ibrahim documented angular head accelerations on carpet (contact durations of 7 ms) of 5,000, 18,000, and 15,000 rad/s^2 at drop heights of 0.3, 0.6, and 0.9 m, respectively. For comparison, the angular head accelerations calculated in the current model at the same heights and duration were 9,536, 11,312, and 17,568 rad/s^2. Prange, however, documented angular head accelerations of between 28,000 and 70,000 rad/s^2 for carpeted drops and between 39,000 and 85,000 rad/s^2 for concrete drops between 0.3 and 1.5 m. It is noteworthy that the Ibrahim neck model was validated based on adult humans and pediatric caprine and primate models, while the Prange neck model utilized a custom-built resistance-free hinge joint. The general agreement between the computational modeling results and the Ibrahim study demonstrates the potential for the use of MADYMO to analyze real-world infant falls using subject-specific modelling. Furthermore, the modeling indicates that short-height falls produce larger head angular head acceleration than aggressive shaking for all impact conditions. These computational results are in agreement with previously-conducted biomechanical studies using various ATDs.

Traumatic acute subdural hemorrhaging occurs as a result of bridging vein rupture. Bridging vein rupture has been produced in adult cadavers at rotational head accelerations between 5,267 and 13,411 rad/ s^2, with a proposed threshold of 10,000 rad/s^2 [1]. All the head accelerations for the 5 ms simulations, the 7 ms simulations at 0.6, 0.9, and 1.5 m, and the 10 ms simulation at 1.5 m exceeded this threshold. While there is currently no accepted threshold to produce bridging vein rupture in infants, the literature reports several videotaped incidents which resulted in bridging vein rupture in infants. One such study documented an incident in which a two-year old child suffered a fall from 71 cm onto a 95 mm thick piece of plush carpet remnant covering a concrete floor, striking first with outstretched hands, then with the right front side of her forehead. The child was diagnosed with a subdural hematoma and bilateral retinal hemorrhaging and the fall was witnessed by the child's grandmother and was videotaped [9]. Another study documented a case in which a 5-month old infant fell from a 5-year old's lap who was seated on an office swivel chair [10]. The infant fell less than 1 m onto a wooden deck and suffered subdural hemorrhages and multilayered retinal hemorrhages. The fall was captured via a home security camera. By utilizing the subject-specific modeling techniques outlined above, there exists the potential to develop thresholds to produce intracranial bleeding in infants based on the information provided by these real-world incidents. These thresholds can be instrumental in the forensic analysis of infant head injury. Additionally, these thresholds could provide valuable information to assist with the design of a safer household environment to protect infants from serious head injury.

REFERENCES

[1] Depreitere, B et al. *J Neurosurg*, 104:950–6. 2006.
[2] Ommaya, A et al., *J Neurosurg,* 16: 220-42, 2002.
[3] Duhaime, A et al., *J Neurosurg,* 66:409–15, 1987.
[4] Prange, M, et al. *Neurosurg* 99:143–50, 2003.
[5] Ibrahim N, et al. *PED*, 6:57–68, 2010.
[6] Goldsmith, W., et al. *Am J For Med Pathol,* 25:89–100, 2004.
[7] Deland, T et al. *J For Sci,* 61:54-59, 2016.
[8] Wolfson, D et al., *Proc Inst Mech Eng H*, 219:63–70, 2005.
[9] Plunkett, J et al., *Am J For Med Pathol* 22: 433–5, 2001.
[10] Geoghegan, A et al. *J Am Assoc Ped Ophth Strab*, 27: 222-224, 2023.

FIBER ALIGNMENT AND TORTUOSITY INFLUENCE THE LOAD-CARRYING PERFORMANCE OF THE LAMINA CRIBROSA COLLAGEN BEAMS

Yi Hua (1,2,3), Lindee Wilson (1), Ian A. Sigal (3)

(1) Department of Biomedical Engineering, University of Mississippi, University, MS, United States
(2) Department of Mechanical Engineering, University of Mississippi, University, MS, United States
(3) Department of Ophthalmology, University of Pittsburgh, Pittsburgh, PA, United States

INTRODUCTION

The lamina cribrosa (LC) is a trabecular structure consisting of an intricate network of collagen beams that support the delicate retinal ganglion cell axons passing through the pores. [1] The mechanical strength of a beam, vital for its load-carrying performance, is largely determined by its mechanical properties, such as anisotropy (directional stiffness) and nonlinearity (strain-dependent stiffness). [2, 3] Using polarized light microscopy, we observed that collagen fibers align along the beam direction and exhibit a natural crimp with quantifiable tortuosity (path length divided by end-to-end length). [4, 5] However, the influence of fiber alignment and tortuosity on the load-carrying performance of collagen beams remains unclear.

In this study, we developed a specimen-specific model of the LC collagen beams. Following that, we generated three variations of this model by assigning distinct beam mechanical properties: isotropic, anisotropic, and anisotropic with tortuosity. Subsequently, we compared the stress/strain responses of these models under uniaxial stretch to identify the roles of fiber alignment and tortuosity in the load-carrying performance of the collagen beams in the LC.

METHODS

A coronal section of the sheep LC, with a thickness of 16 μm, was imaged using polarized light microscopy (**Figure 1**). The energy information obtained from the image was used to segment the collagen beams in the LC. Based on the segmentation, we reconstructed the model geometry in SolidWorks. We then generated three variations of this model by assigning distinct beam mechanical properties: isotropic, anisotropic, and anisotropic with tortuosity. Specifically, we employed an anisotropic hyperelastic constitutive equation developed in our previous study. [6] This equation allows for incorporating fiber orientations and tortuosities measured by polarized light microscopy. We set the 1st Mooney-Rivlin constant at 150 kPa, and the modulus of straightened fibers at 30 MPa. A concentration parameter, denoted as k, was introduced to regulate the distribution of collagen fibers. For isotropic properties, k was assumed to be zero, while for anisotropic properties, k was set to 2. In addition, we defined a bulk modulus of 0.1 GPa to ensure tissue incompressibility. [7] All models were subjected to uniaxial stretch. Two in-plane loading conditions were considered at the right boundary of the model to simulate a 'pull' from the peripapillary sclera: a pressure of 3 kPa and a displacement of 200 μm (equivalent to 10% stretch). All models were solved in FEBio v2.9.1 with eight-noded hexahedral elements. Convergence tests were performed, and adequate accuracy was achieved with an average element length of 25 μm. We quantified the maximum principal strain (a measure of stretch) and the von Mises stress (a measure of force).

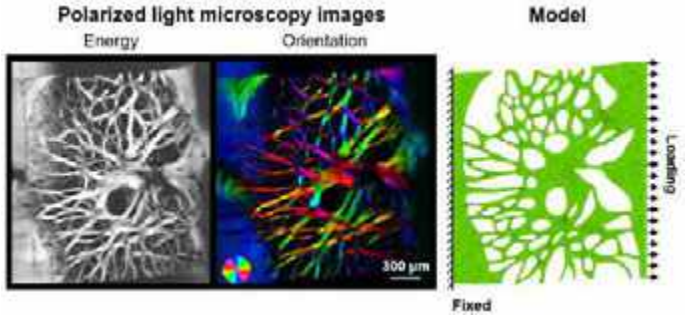

Figure 1. Illustration of the modeling approach. A coronal section (thickness: 16 μm) of the sheep LC was imaged using polarized light microscopy. The energy image represents collagen density, while the orientation image utilizes colors to indicate fiber orientations. The model geometry was reconstructed based on the energy information, and the anisotropic mechanical properties of the model were defined using the orientation information. To simulate uniaxial stretch, full constraint was applied to the left boundary of the model, and in-plane loading was exerted on the right boundary.

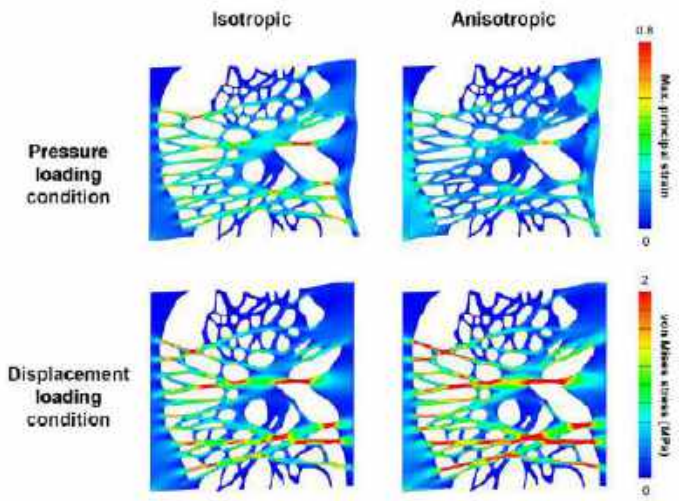

Figure 2. Model-predicted maximum principal strain (top row) and von Mises stress (bottom row) under the pressure and displacement loading conditions, respectively. When subjected to the pressure loading condition, the model with anisotropic mechanical properties demonstrated lower strain compared to the model with isotropic mechanical properties. Conversely, under the displacement loading condition, the model with anisotropic mechanical properties exhibited higher stress than the model with isotropic mechanical properties. These observations collectively indicate that fiber alignment enhances the stiffness and load-carrying performance of the collagen beams.

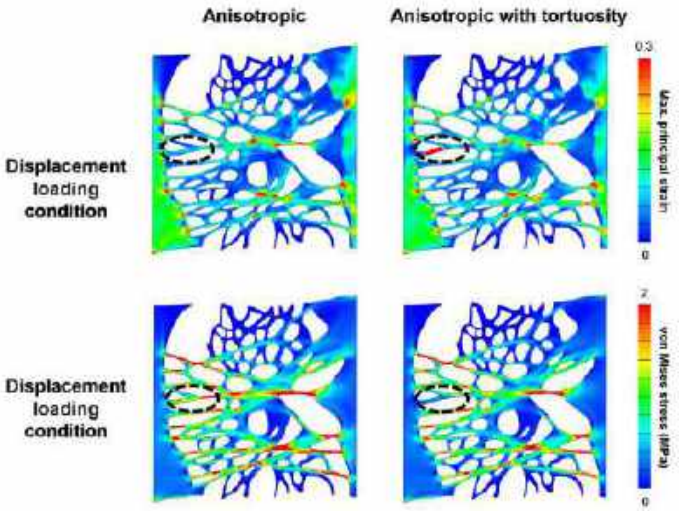

Figure 3. Model-predicted maximum principal strain (top row) and von Mises stress (bottom row) under the displacement loading condition. In the model incorporating anisotropic mechanical properties with tortuosity, the stress of the collagen beams decreases, while the strain increases compared to the model with anisotropic mechanical properties alone. This trend is particularly pronounced in collagen beams exhibiting relatively large tortuosity, as indicated by the dotted ellipse. These results imply that fiber tortuosity reduces the load carried by the collagen beams at the expense of increasing their elongation.

RESULTS

In our analysis, we first examined the impact of fiber alignment by comparing the maximum principal strain and von Mises stress between the models with isotropic and anisotropic mechanical properties (**Figure 2**). Subsequently, we investigated the effects of fiber tortuosity by comparing the maximum principal strain and von Mises stress between the models with anisotropic mechanical properties without and with tortuosity information (**Figure 3**).

DISCUSSION

Our goal was to study the roles of fiber alignment and tortuosity on the load-carrying performance of the LC collagen beams. Two main findings arise from this study: 1) fiber alignment enhances the stiffness and load-carrying performance of the collagen beams, and 2) fiber tortuosity reduces the load carried by the collagen beams at the expense of increasing their elongation. Below we discuss each finding in detail.

In comparison to the model incorporating isotropic mechanical properties, the model incorporating anisotropic mechanical properties exhibited increased stresses during uniaxial stretch. This implies that fiber alignment plays an important role in enhancing the stiffness and load-carrying performance of the LC collagen beams, which is of paramount significance when considering the impact of elevated intraocular pressure. The increased stiffness of collagen beams, resulting from fiber alignment, may serve as a protective mechanism for the delicate neural tissues and intricate vascular network within the LC, by bearing more of the load imposed by increased intraocular pressure.

In the model incorporating anisotropic mechanical properties with tortuosity, the stress of the collagen beams decreases, while the strain increases in comparison to the model with anisotropic mechanical properties alone. This trend is particularly pronounced in collagen beams exhibiting relatively large tortuosity. Our findings indicate that fiber tortuosity acts to reduce the load borne by the collagen beams, albeit at the expense of increasing their elongation. Our earlier study has demonstrated distinctions in fiber tortuosity between thin and thick beams in the LC. [8] Specifically, the thicker beams exhibited greater tortuosity compared to their thinner counterparts, implying that these thicker beams may only stiffen under higher intraocular pressure when subjected to substantial deformation.

In conclusion, our models predict that the load-carrying performance of the LC collagen beams depends on fiber alignment and tortuosity. This understanding of the interplay between fiber alignment, fiber tortuosity, and load-carrying performance offers valuable insights into the biomechanics of the LC, particularly concerning elevated intraocular pressure and its potential implications for retinal ganglion cell axon damage in glaucoma.

ACKNOWLEDGEMENTS

NIH R01-EY023966, P30-EY008098 and T32-EY017271 (Bethesda, MD), Brightfocus, Research to Prevent Blindness (unrestricted grant to UPMC Ophthalmology, and Stein innovation award to Sigal IA), and REU Development Grants for UM Faculty.

REFERENCES

[1] Jan, N.J. et al., *IOVS*, 58:735-744, 2017.
[2] Fratzl, P., *Springer*, 1-13, 2008.
[3] Voorhees, A.P. et al., *Acta Biomater*, 58: 278-290, 2017.
[4] Jan, N.J. et al., *IOVS*, 58:3378-3388, 2017.
[5] Jan, N.J. et al., *Acta Biomater*, 72:295-305, 2018.
[6] Foong, T.Y. et al., *Exp Eye Res*, 230:109446, 2023.
[7] Girard, M.J. et al., *J Biomech Eng*, 131:051011, 2009.
[8] Brazile, B.L. et al., *IOVS*, 59:4653-4661, 2018.

INVESTIGATING THE EFFECTS OF AN INCREASED ADIPOCYTE DENSITY ON A 3D HUMAN BREAST TUMOR SPHEROID MODEL

Jensen N. Amens (1), Gökhan Bahçecioglu (2), Pinar Zorlutuna (1,2,3,4)

(1) Department of Aerospace and Mechanical Engineering, University of Notre Dame, Notre Dame, IN, USA
(2) Bioengineering Graduate Program, University of Notre Dame, Notre Dame, IN, USA
(3) Department of Chemical and Biomolecular Engineering, University of Notre Dame, Notre Dame, IN, USA
(4) Harper Cancer Research Institute, University of Notre Dame, Notre Dame, IN, USA

INTRODUCTION

Obesity has been reported to increase the risk of breast cancer. Those with obesity who have breast cancer also have a poor prognosis with increased rates of metastasis and decreased rates of cancer-free survival. Current obesity models [1, 2] do not use adipocytes and instead utilize adipose-derived stem cells or are 2D models that don't recapitulate the 3D environment of the human body. Mice are often used to model obesity but lack human physiology. While the impact of obesity on breast cancer risk is clinically clear, the effect of an increased adipocyte density within the breast tissue, which occurs in the case of severe obesity, has not yet been investigated.

METHODS

Adipocytes were detached using trypsin and strained to remove any remaining stem cells. Adipocytes were then mixed into a 6.6 mg/mL solution of human collagen at low (4 million cells/mL) or high (16 million cells/mL) densities, loaded into a bioprinter, and droplet printed into a 96-well plate to form low- or high-density adipocyte stromal compartments.

Tumor spheroids were immediately collected by aspirating with a micropipette, loaded into the bioprinter cartridge, and printed into the stromal compartments (adipocyte-laden collagen). The low- and high-density adipocyte-collagen systems were allowed to gel at 37 °C before being cultured in basal medium (Fig. 1).

Models were then cultured and imaged for live/dead analysis and nile red stained. Alamar blue assays were performed every four days. After two weeks of culture, models were fixed and sectioned and stained for Ki67, MMP-2, MMP-9, ZEB2, and E-Cadherin.

Data were analyzed for statistical significance using GraphPad Prism 6. Welch's t-test was performed to compare the results. Data are presented as the mean ± standard deviation (SD).

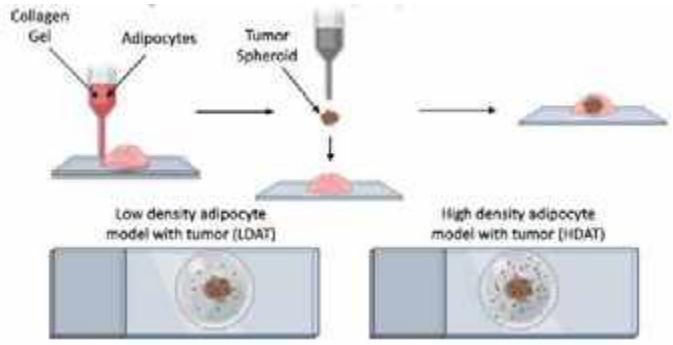

Figure 1: Depiction of 3D model printing schematic and final model configurations.

RESULTS

After 3D bioprinting the models, we first characterized it through brightfield imaging, live/dead staining, and Nile red staining to confirm its viability. We showed through live/dead staining that the bioprinting process did not kill the cells or disintegrate the spheroids and that we had an intact model with cell viability in the range of 66%-88% (mean: 78% ± 9.2%). We also stained the models with Nile red stain to show that the adipocytes were still intact within the gel. The Nile red stain confirmed the presence of two different adipocyte density models.

Next, we wanted to study the effects of the increased adipocyte density within the model on the tumor spheroid. We first investigated its effects on proliferation of the tumor spheroid. We cultured our models for two weeks and performed an Alamar blue assay on days 1, 4, 7, 10, and 14 to study the effect of high adipocyte density on metabolic activity of the tumor cells (Fig. 2A). We found an overall increase in signal, which corresponds to increase in metabolic activity, over the course of the culture time for the high-density adipocyte with

tumor (HDAT) model. Models without tumors were used as negative controls and the unchanged signal with the tumor-free gels over the culture period signifies that the tumor spheroid is what is causing the increase in signal. The HDAT model showed the highest increase in signal, with an increase of 127% over the 14-day period. The increase in signal for the low-density adipocyte with tumor (LDAT) model was lower than that of the HDAT model, with only an increase of 47% over the 14-day period. To confirm that this increase in metabolic activity within the tumor spheroid was due to an increase in proliferation, we stained sections of the tumor models after the culture period with Ki67, which stains for actively dividing cells. We imaged the tumor cells within the model to see if these cells were positive for Ki67. The HDAT model again contained a higher number of Ki67-positive tumor cells (63.0% ± 16.1%) than the LDAT model (21.2% ± 8.2%) (Fig. 2B).

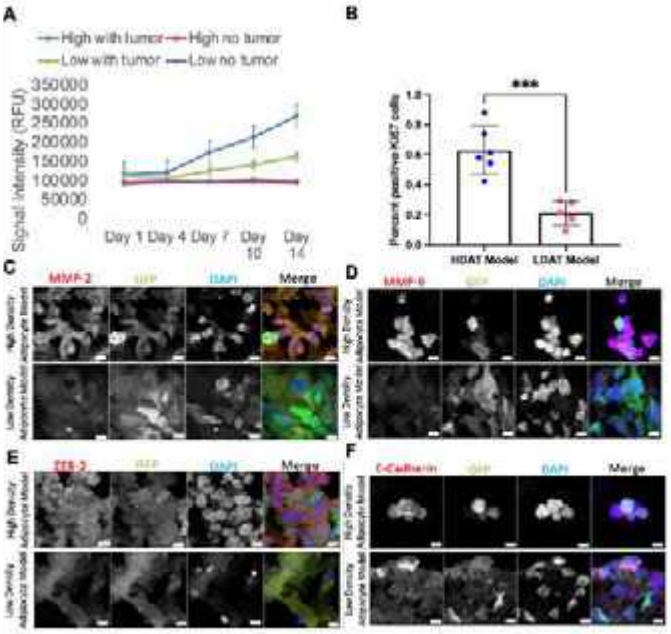

Figure 2: A) Alamar blue assay results over the course of the 14-day culture period (n=3). B) Quantification of the Ki67 stain. n=3, and 5 images were used for each sample to quantify signal intensity. Immunofluorescent images of the tumor spheroid stained for (C) MMP-2, (D) MMP-9, (E) ZEB-2, and (F) E-Cadherin. Scale bars: 10 µm. For statistical significance, Welch's t-test was performed for (B) * denotes statistical significance with P<0.001.**

Finally, we showed that the tumor spheroid (expressing GFP) within the higher density adipocyte model has an increase in tumor progression factors MMP-2 (Fig. 2C), MMP-9 (Fig. 2D), and ZEB2 (Fig. 2E), and a decrease in tumor suppression factor E-Cadherin (Fig. 2F). Through the staining, we showed 86%, 112%, and 171% increase in MMP-2, MMP-9, and ZEB2 expression, respectively, within the tumor spheroid of the HDAT model compared to LDAT model. E-Cadherin, conversely, decreased by 45% in the case of the HDAT model as compared to the LDAT model. Even though the MMP-2 quantification is the only statistically significant difference, we can still see a large change between the two models for E-Cadherin, ZEB2, and MMP-9.

DISCUSSION

Through this investigation, we were able to create a 3D bioprinted obese breast cancer model. This 3D bioprinted obesity model is the first printed fat tissue model related to investigating the progression of breast cancer. This model is also more biomimetic than previous obesity models in that it utilizes hASCs differentiated into adipocytes and human collagen to compose the model. Severe obesity within the breast tissue was modeled using an increase in adipocyte density throughout the collagen gel within the model.

. Over the course of the culture period (14 days), both models containing tumors increased their Alamar blue signal. Our results showed an increase in Alamar blue assay signal over the course of the 14-day culture period and a significant increase in Ki67 positively stained tumor cells within the HDAT model. Previous studies confirm our findings [3, 4]. It has been shown that adipose tissue causes an increase in proliferation for both melanoma cell lines and breast cancer cell lines with adipose tissue grafts even causing an increase in growth of residual cancer cells that remain in the body after treatment.

Next, we wanted to study how the increase in adipocyte density affects the expression of specific tumor progression and tumor suppression factors. After the 14-day culture period, the models were fixed, cryosectioned, then immunostained for common tumor progression factors MMP-2, MMP-9, and ZEB2, as well as tumor suppression factor E-Cadherin. Previous literature [5-7] has consistently shown an increase in expression of MMP-2, MMP-9, and ZEB2, and a decrease in E-Cadherin expression for those cancer cells affected by surrounding adipocytes, which confirm our immunostaining results from our 3D models.

Our study shows that increasing adipocyte density within our obese model causes an increase in proliferation and tumor progression factors and a decrease in a tumor suppression factor. These results suggest that the increased adipocyte density is another contributing factor to how obesity supports breast cancer progression. This work is the first of its kind to utilize 3D bioprinting of fat tissue for breast cancer research. This model will allow for the recapitulation of a more human replicative environment, through utilizing human cells and collagen, and can contribute to the field of breast cancer research through testing novel breast cancer drugs on the model in the future. The 3D bioprinted obese breast cancer model better replicates the severe obese microenvironment and helps to solve issues of previous models.

ACKNOWLEDGEMENTS

This study was funded by NIH award number 5R01EB027660-02 and Walther Cancer Foundation, Harper Cancer Research Institute Cancer Cure Ventures Award number 0184.01. We would also like to acknowledge Dr. Siyuan Zhang for the gift of the MDA-MB-231 cells used in this study and Dr. Harikrishna Nakshatri of Indiana University for the gift of the hASCs used in this study.

REFERENCES

[1] Springer NL, et al. *Am J Pathol*; 2019, Vol. 189, Iss. 10, Pages 2019-2035
[2] Fischbach C, et al. *Exp Cell Res*; 2004, Vol. 300, Iss. 1, Pages 54-64
[3] Pallua, N, et al. *J Craniofac Surg.*, 2015, 26(4):1403-1407.
[4] Massa M, et al. *Aesthet Surg J*. 2016;36(3):358-363.
[5] Chu DT, et al. *Cells*. 2019;8(8):857.
[6] Wang C, et al. *PLOS ONE*. 2015;10(3):e0119348.
[7] Zhou W, et al. *J Biomed Sci*. 2014;21(1):97.

IN VIVO PULMONARY AND THORACIC WALL INJURY RISK FROM BEHIND ARMOR BLUNT TRAUMA

Justin A. McMahon (1), Parker R. Berthelson (1), Alexander V. Stotka (1), Barney J. McEntire (2), Robert S. Salzar (1)

(1) Mechanical and Aerospace Engineering, University of Virginia, Charlottesville, Virginia, USA
(2) Injury Biomechanics and Protection Group, U.S. Army Aeromedical Laboratory, Fort Novosel, Alabama, USA

INTRODUCTION

Body armor is designed to protect military personnel from penetrating injuries and the blunt energy resulting from backface armor intrusions. However, the deformations of some armor designs result in high-rate loading to the wearer's torso. This loading may result in skeletal and physiological damage through an injury modality known as behind armor blunt trauma (BABT) [1-3].

Current body armor design standards are based upon experimental testing from the 1970s in which matched-pair experiments were performed on goats clad with soft body armor and blocks of 20% ballistic gelatin [4]. From these experiments, an armor design criterion of 44 millimeters (mm) of backface deformation (BFD) was developed, and this level of BFD was correlated with a 10% risk of lethality in the goats [5]. However, the elastic nature of the ballistic gelatin caused difficulties in quantifying the BFD following the impact, resulting in the adoption of Roma Plastalina No. 1 (a modeling clay with a similar observed response to the ballistic gelatin) as an armor backing [6]. The 44 mm clay standard has since been adopted by the National Institutes of Justice (NIJ) for use in ballistic body armor performance standards, with its scope being expanded to include both hard and soft body armor evaluations. Although there has been apparent success using the 44 mm standard and clay testing methodology, the standard has limited or no correlation to physiological injury, and the resulting armor designs are heavy, with the potential of being overly conservative in protection [7].

Biological models must be used to assess the underlying injuries associated with BABT to develop body armor based on standards equated to physiological injury. Specifically, live animal models must be used to study the physiological response of the body at BABT levels of impact. Previous biomechanical studies have used the porcine model to represent the human thorax, as it approximates the thoracoabdominal anatomy, physiology, and biomedical responses of a human [8-11]. It is expected that pulmonary injuries due to BABT, such as pulmonary contusion and pneumothorax, will be a focus of study due to the association of these injuries with severe morbidity and mortality [12]. This study aimed to quantify pulmonary and chest wall injury risk from BABT by varying impact energies to produce a range of injury severities.

METHODS

A custom pneumatic impactor was designed to simulate impacts that would cause BABT by accelerating a 0.245 kilogram (kg) indenter into a porcine thorax at velocities ranging from 10 to 50 meters per second (m/s). The indenter was 3D printed using carbon fiber-reinforced nylon (Onyx, Markforged) and its impact surface contour was designed to approximate the BFD profile of rigid body armor protecting against a generic ballistic threat. The indenter was equipped with a single-axis accelerometer (Endevco 7270A) sampled at 500 kilohertz (kHz) with a 100 kHz antialiasing filter. Accelerometer data were further filtered using a four-pole phaseless lowpass Butterworth filter with a cutoff frequency of 2 kHz.

The 27 adult Yorkshire porcine specimens (average mass = 45.0 ± 3.6 kg) tested in this study were selected to approximate the effective mass of the 50th percentile male human torso (approximately 39.6 kg [13]). Before testing, all animal testing and handling protocols were approved by the University of Virginia (UVA) Animal Care and Use Committee (protocol: 4379-12-21) and the U.S. Army Animal Care and Use Review Office (protocol: MT21006.031.e002). Porcine specimens were then procured and allowed to acclimate for a three-day period upon arrival. On the day of the experiment, the specimen was induced using Telazol, and maintenance anesthesia was applied using 2% isoflurane in medical air under positive end expiratory pressure. Specimens were injected with a local analgesic (bupivacaine) subcutaneously at the impact location and were placed on a heating pad during experimentation to maintain thermoregulation. Each specimen was connected to a patient monitor to monitor heart rate, blood oxygen (SpO_2), respiratory rate, and body temperature, with at least 15 minutes of baseline vitals collected prior to the impact event. The specimen was then positioned under the impactor with the impact location flush against the barrel and orthogonal to the indenter. Twelve specimens were impacted over the cranial lobe of the right lung (around ribs 6 through 8), and 15 were impacted over the caudal lobe (around ribs 9 through 11).

Post-impact, the specimens' heart rate and SpO_2 were monitored for at least 15 minutes to ensure vitals returned to a stable condition. Once the specimen was determined to be stable, it was removed from anesthesia and returned to its housing, where continuous monitoring for well-being continued for 6 hours. If the animal was determined to not be recoverable at any time post-impact, the specimen was humanely euthanized with Euthasol via an ear catheter. After approximately 6 hours, the specimen was reinduced for computed tomography (CT) imaging. Specimens were humanely euthanized after CT, and a comprehensive necropsy was performed to determine the extent of the injuries from the impact event. Lung and chest wall injuries were recorded for each specimen and were then assigned a severity score based on the American Association for the Surgery of

Trauma (AAST) Injury Scoring Scale [14-15] with input from the necropsy and radiology.

Preliminary injury risk functions (IRFs) were developed based on the injury data from impact testing. The indenter accelerometer was used to calculate impact energy, which was selected as the most favorable predictive metric for a variety of observed injuries. These values were then used as left and right censored inputs into a survival analysis where IRFs were generated using a Weibull distribution.

RESULTS

Impact energies ranged from 21.9 to 247.5 joules (J), and injury results ranged from no injury up to a grade 4 on the AAST injury scale for both lung and chest wall injuries. The distribution of injury severities can be seen in Table 1, with a grade of 4 being the most severe.

Table 1. AAST Injury Severity Distributions.

	Uninjured	AAST 1	AAST 2	AAST 3	AAST 4
Chest Wall	1	3	10	10	3
Lung	6	10	4	6	1

The most severe injury case seen in the chest wall was a flail chest in which eight rib fractures were observed in total. A large expanding hematoma was seen in the most severe lung injury case. Preliminary IRFs were generated using indenter energy as the predictor metric to assess injury risk for AAST injury severities and are presented in Figures 1 and 2. Impact energy was chosen as an exemplary metric to compare the injury risk across different anatomical structures. The 50% injury risk for Chest Wall 2+, 3+, and 4+ were 40.32 J, 104.29 J, and 228.85 J, respectively. The risk of Lung Injury 2+ and 3+ were 121.64 J and 163.48 J, respectively. A Lung Injury 4+ was not generated due to only having one 4+ injury case.

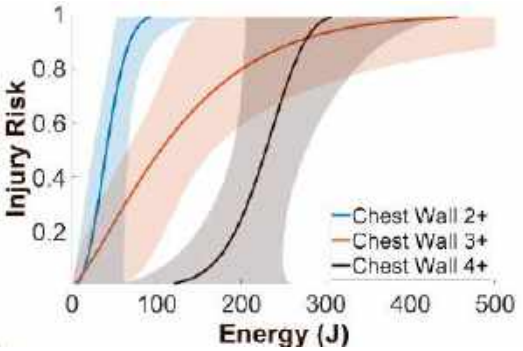

Figure 1: Injury risk across AAST Chest Wall Injuries 2+, 3+, and 4+ with 95% confidence intervals.

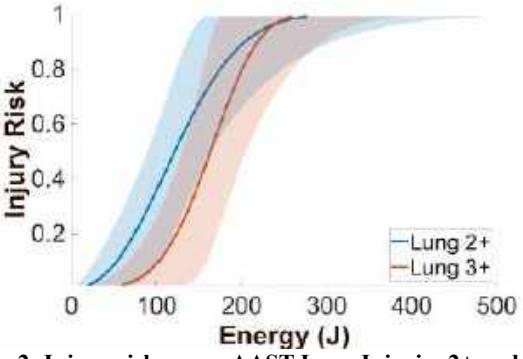

Figure 2: Injury risk across AAST Lung Injuries 2+ and 3+ with 95% confidence intervals.

DISCUSSION

There have been limited studies on the physiological injuries that result from BABT to the thorax. This study adds insight to the existing literature on BABT by conducting live porcine experiments that can be used to quantify the risk of physiological injuries and lead to body armor optimized for weight and performance. Regarding the observed chest wall injuries, only a relatively low amount of energy was required to cause three or more rib fractures graded at AAST level 2+. However, it took much more energy to induce injuries that would be classified at the more severe grades of 3+ and 4+. Looking at the lung injuries, more energy was needed to produce similar severity lung injuries as compared to the chest wall. This is most likely due to the ribcage absorbing much of the energy from impacts at lower severities. As the impact energy increased, flail rib fractures were induced, and more of the impact energy transferred through to the lung, causing more severe pulmonary injuries.

These results are comparable to findings observed by Gryth et al. and Günther et al. [11, 9], whose experiments used body armor and live munitions. In the study by Gryth et al., a large hematoma and contusion were observed on the impacted lung during the post-test necropsy of one of their specimens. Similarly, the highest severity lung injury observed in this study resulted in a hematoma of comparable size to that seen by Gryth et al. Also, multiple specimens in this study had pulmonary contusions similar to the one shown in Günther et al. These results indicate that the generic indenter is capable of reproducing injuries comparable to those found in tests with body armor and live munitions.

Further work is ongoing to understand the injury tolerance of different thoracic regions to BABT. Current body armor designs do not account for regional variations in anatomical stiffness, criticality of underlying organs, and physiological response of the torso. Due to the complex nature of the human thorax, regional variations in anatomy could result in varying injury tolerance during BABT. These local variations in injury tolerance would allow body armor design to be optimized for weight based on the local injury criteria associated with each thoracic region.

ACKNOWLEDGEMENTS

The authors would like to thank Jeremy Gatesman and the UVA Center for Comparative Medicine staff for their assistance on this project. George Glass MD, Connor Sleeth MD, Kevin Kopp, Brian Overby, and Joey White from the UVA Center for Applied Biomechanics were of utmost importance to the success of this study. The authors would also like to thank their consortium partners at the Medical College of Wisconsin, Duke University, Wayne State University, and the U.S. Army Aeromedical Research Laboratory. This project was supported by U.S. Army Medical Research and Development Command contract #W81XWH-15-9-001.

REFERENCES

[1] Carr, D et al., *BMJ Mil Health*, 162(1), 8-11, 2016.
[2] Cooper, G et al., *J Trauma*, 22(12), 994-1008, 1982.
[3] Bass, C et al., *Int J Occup Saf Ergon*, 12(4), 429-442, 2006.
[4] Goldfarb, M et al., Report No. EB-TR-74073, 1975.
[5] Clare, V. R et al., Report No. EB-TR-75016, 1975.
[6] Prather, R et al., Report No. ARCSL-TR-77-55, 1977.
[7] National Research Council, 2012.
[8] Arborelius, U. P et al., *Exp Lung Res*, 47(7), 323-333, 2021.
[9] Günther, M et al., *Exp Lung Res*, 46(5), 117-127, 2020.
[10] Prat, N et al., *Forensic Sci Int*, 222(1-3), 179-185, 2012.
[11] Gryth, D et al., *Mil Med*, 172(10), 1110-1116, 2007.
[12] Eaton, M et al., *ASME IMECE*, 84522, V005T05A050, 2021.
[13] Clauser C et al., Report No. AMRL-TR-69-70 1969.
[14] Moore, E et al., *J Trauma Acute Care Surg*, 36(3), 229-300, 1994.
[15] Moore, E et al., *J Trauma Acute Care Surg*, 33(3), 337-339, 1992.

STRUCTURE AND FUNCTION OF THE MURINE GREATER THORACIC VESSELS

Abhay B. Ramachandra (1,2), Cristina Cavinato (1,3), Jay D. Humphrey (1,4)

(1) Department of Biomedical Engineering, Yale University, New Haven, CT, USA
(2) Department of Mechanical Engineering, Iowa State University, Ames, IA, USA
(3) Laboratoire de Mécanique et Génie Civile, Université Montpellier, Montpellier, France
(4) Vascular Biology and Therapeutics Program, Yale School of Medicine, New Haven, CT, USA

INTRODUCTION

The greater thoracic vessels are targeted in multiple cardiovascular surgeries and are central to a well-functioning circulatory system. They undergo remodeling under altered hemodynamic conditions which can either improve outcomes or drive comorbidities and complications. A necessary first step in understanding their remodeling process is quantifying their structure and function in the native circulation. Here we use consistent methods to quantify and compare microstructural features and biaxial biomechanical properties of the following six greater thoracic vessels in a wild-type mice: ascending thoracic aorta (ATA), descending thoracic aorta (DTA), right subclavian artery (RSA), right pulmonary artery (RPA), thoracic inferior vena cava (TIVC), and superior vena cava (SVC). We report similarities and differences in structure and mechanics of these vessels.

METHODS

Mechanical testing: All live animal protocols were approved by the Institutional Animal Care and Use Committee of Yale University. Adult male mice (C57BL/6J from Jackson Labs, ME) between 14 and 20 weeks of age were euthanized with an intraperitoneal injection of Beuthanasia-D (150 mg/kg), with death confirmed upon exsanguination. Vessels were harvested, perivascular tissue and fat gently removed, and small branch vessels were ligated with suture. Each vessel was then cannulated on custom glass micro-pipettes and secured with 6-0 sutures, then mounted in our custom biaxial device [1] and subjected to active and passive testing. For active testing, specimens (n = 5–6 per group) were immersed within a buffered Krebs-Ringer solution that was maintained at 37 °C and bubbled with 95% O_2 and 5% CO_2 to maintain pH 7.4. Active preconditioning consisted of two sets of vasoconstriction with 100 mM KCl (50 mM for SVC) at a fixed pressure and axial stretch below *in vivo* conditions. Following preconditioning, the vessels were contracted with 100 mM KCl at a pressure P_{active} (Table 1) and specimen-specific *in vivo* axial stretch. This protocol consisted of 5 min of equilibration, 15 min of contraction with 100 mM KCl, and 10 min of relaxation following washout of KCl with a fresh Krebs-Ringer solution.

Table 1: Summary of group-specific mechanical testing parameters used in biaxial quantification of active and passive mechanics

Vessel	Pressure active test (mmHg)	P_{min}-P_{max} (mmHg)	~f_{max} (mN)	Pressure force-length tests (mmHg)
ATA	90	10-140	58.8	10,60,100,140
DTA	90	10-140	44.1	10,60,100,140
RSA	90	10-140	19.6	10,60,100,140
RPA	15	5-40	9.8	5,15,25,40
TIVC	3.5	1-30	3.4	3.5,5,10,30
SVC	1	1-30	1.5	1.5,5,10,30

Active tests were followed immediately by passive tests upon replacement of the Krebs-Ringer solution with a Hanks buffered physiologic solution at room temperature. Preconditioning involved six pressure cycles from P_{min} to P_{max} at the specimen-specific value of *in vivo* stretch (Table 1) to elicit a pseudoelastic behavior. Testing consisted of seven protocols: cyclic pressure distension from P_{min} to P_{max} at three different fixed axial stretches (0.95, 1.00 and 1.05 times the *in vivo* axial stretch) and axial force extension from ~ 0 mN to f_{max} at four different fixed pressures (P_{fl}). Region-specific mechanical testing parameters are summarized in Table 1. Passive mechanical data was fit to a pseudo strain energy function which included a neo-Hookean term for elastin-dominated amorphous behaviors and four families of fibers (along axial, circumferential, and two symmetric

diagonal directions) described by a Fung-type exponential relation to model passive smooth muscle and collagen-dominated behaviors. Mechanobiologically relevant quantities such as mean biaxial wall stress and material stiffness were computed from the energy function at pressures and axial stretches of physiological relevance. Details of these calculations can be found in our prior work [2,3,5].

2 Photon Imaging: Following mechanical testing, samples (n = 3–6 per group) were incubated in a fluorescent nucleic acid stain (SYTO™ 61 at 2 μM) for 1 h, then stored overnight at 4 °C in a buffered physiological solution. For imaging, they were mounted on a fixed biaxial loading frame to simulate the *in vivo* condition and placed within the field-of-view of a two-photon microscope (LaVision Biotec TriMScope) operated with a Titanium-Sapphire Laser (Chameleon Vision II, Coherent). The excitation wavelength was tuned to 840 nm, and signal detection was set at 390–425 nm for second harmonic generation (SHG) from collagen structures, 500–550 nm for auto-fluorescent signals of elastin structures, and above 550 nm for fluorescence of cell nuclei. For samples containing cardiomyocytes (namely, the SVC), the signal from these cells were detected between 500 and 550 nm and above 550 nm. All imaging was completed within 48 h following sample harvest. An Olympus 20X water immersion objective lens (NA 0.95) allowed acquisition of 3D image stacks with a x, y-plane (i.e., axial-circumferential plane) field-of-view of 500 μm × 500 μm and a z-step in the radial direction of 2 μm. Samples were imaged under comparable load conditions, which were *ex vivo* equivalent vessel-specific *in vivo* axial stretch and representative pressure. 3D images were post-processed using ImageJ v1.53 and MATLAB R2020a as described in our previous work [4].

Volume fractions (VFs) were defined as the average black and white pixel ratio for all components between boundaries defined by thresholding and segmenting using constant thresholds, defined using the Otsu method on a training set [4].

RESULTS

Note that all results are reported as mean± standard error of mean and in order as ATA, DTA, RSA, RPA, TIVC and SVC. Vasoconstriction in response to 100 mM KCl at *in vivo* conditions was -16.80±1.354,-20.55±2.051,-9.316±0.7258,-31.15±2.547,-9.672±0.4944 and -9.006±0.9139% for the ATA, DTA, RSA, RPA, TIVC and SVC, respectively; computed with respect to basal outer diameter pre-contraction. Vasoconstriction was the highest in RPA, and similar between the ATA and DTA. RSA contractility was low, despite being a systemic artery, and was similar to the thoracic veins. Passive mechanics for all six regions were computed at subject-specific axial *in vivo* stretch and representative group-specific physiologically relevant pressures. Stored energy (92.52±3.88, 63.98±3.61, 46.09±3.28, 10.96±1.01, 9.45±2.35 and 0.59±0.07 kPa) and circumferential stress (257.22±7.22, 210.80±8.14, 147.62±4.42, 27.72±1.67, 19.13±1.88 and 4.27±0.42 kPa) tended to lessen down the vascular tree but reductions in circumferential stiffness (1.24±0.05, 1.03±0.06, 0.87±0.03, 0.09±0.01,0.76 ±2.12 and 0.06±0.01) were non-monotonic. Stored energy and circumferential stress were similar only between the RPA and the veins.

Quantification of the multiphoton images confirmed a decreasing elastin volume fraction (49.95± 3.737, 40.58± 3.810, 31.32± 3.554, 29.14 ±5.509, 9.198± 2.545, 1.243± 1.068) and increasing collagen volume fraction (23.29±1.912, 38.16±2.957,42.71±2.005, 49.41±3.354, 62.71±3.776 and 63.02±6.207) down the vascular tree. The overall fraction of cells was relatively constant across (26.77± 2.871, 21.27±2.251, 23.62 ± 2.967, 21.45± 3.063, 35.74± 7.257 and 28.10 ± 4.121) all six regions. Noticeable differences in orientation of collagen and cells were observed across different regions (data not shown).

DISCUSSION

Similarities and differences across systemic, pulmonary, and venous circulations highlight underlying design principles of the vascular system. We submit that the protocols and results from this study will help pave a way forward for a similar study in human vessels, which will be needed to predict evolving changes during a surgical correction.

ACKNOWLEDGEMENTS

This work was funded in part by grants from Additional Ventures (SVRF and AVCC).

REFERENCES

[1] Gleason, R., S. et al., *J. Biomech. Eng.* 126:787–795, 2004.
[2] Ferruzzi, J., et al., *Ann. Biomed. Eng*. 41:1311–1330, 2013.
[3] Ramachandra, A. B., et al., *J. Biomech.* 84:18–26,2019.
[4] Cavinato, C., et al., *Mech Ageing Dev.*, 196:111471, 2021.
[5] Ramachandra, A.B., et al., *Ann. Biomed. Eng*., 1:9, 2024

DEVELOPMENT AND IMPLEMENTATION OF NOVEL FRAMEWORK FOR THERMOFLUID ANALYSES IN FEBIO

Raphael J. Kepecs (1), Steve A. Maas (2), Jeffrey A. Weiss (2), Gerard A. Ateshian (1,3)

(1) Mechanical Engineering, Columbia University, New York, NY, USA
(2) Biomedical Engineering, University of Utah, Salt Lake City, UT, USA
(3) Biomedical Engineering, Columbia University, New York, NY, USA

INTRODUCTION

While many processes in mammalian physiology may be suitably modeled to take place under isothermal and isobaric conditions, there are important cases where spatiotemporal variations in temperature and pressure must be allowed. Moreover, biological tissues and cells may interact with an environment at a different temperature or pressure, such as ambient air flowing in the lungs, injurious heating (e.g., burning) or cooling (freezing) of skin by external fluids, or potentially detrimental thermal effects of medical procedures, such as laser ablation or cryotherapy. A recent expert review article illustrates how modeling can improve our understanding of soft tissue injuries resulting from pressure and temperature [1]. To better understand how to model such processes, it becomes necessary to expand the open-source finite element software FEBio [2] to include variations in temperature in its fluid mechanics module. By expanding standard thermodynamics methodologies, we propose novel methods for assessing energy exchanges during reactive and thermal processes involving biological fluids.

METHODS

Currently, FEBio models fluid dynamics assuming isothermal conditions (uniform and constant temperature) [3]. In this study we introduce thermal effects in the existing fluid dynamics module to analyze thermofluid processes. In practice, this task involves adding the axiom of energy balance to the governing equations, to incorporate temperature changes and various sources of heat, as outlined below. The detailed theoretical developments underlying the FEBio fluid solver have been reported previously [3], where we adopted a function of state for the fluid pressure, relating it to the fluid dilatation. For isothermal applications it is common to model fluids that are in liquid form, where the function of state for the pressure involves the liquid's bulk modulus. In thermofluid analyses however, it makes sense to also model compressible fluids, such as ideal and real gases, whose pressure depends on dilatation and temperature. In this presentation, we expand this concept by incorporating a dependence of the pressure function of state on temperature. Below, we provide an overview of the governing equations for this thermofluid framework, along with results from a FEBio finite element implementation.

In our fluid dynamics framework [3], the governing equations include the kinematic constraint of eq.(1) between the fluid volume ratio J^f and the fluid velocity $\boldsymbol{v}^f$, which produces an exact solution for the fluid mass density,

$$\dot{J}^f = J^f \operatorname{div} \boldsymbol{v}^f \,,\ \rho^f = \frac{\rho_r^f}{J^f}. \tag{1}$$

Here, ρ^f is the fluid mass density in the current configuration while ρ_r^f is the fluid mass density in the reference configuration, when $J^f = 1$. The fluid volume ratio is related to the fluid dilatation e^f via $e^f = J^f - 1$. The other governing equation is the linear momentum balance,

$$\rho^f \dot{\boldsymbol{v}}^f = \operatorname{div} \boldsymbol{\sigma}^f + \rho^f \boldsymbol{b}^f \tag{2}$$

where $\boldsymbol{\sigma}^f$ is the fluid stress tensor and $\boldsymbol{b}^f$ is a user-specified specific body force acting on the fluid, such as gravity. For thermofluid analyses, these equations are supplemented with the axiom of energy balance,

$$\rho^f \dot{u}^f = \boldsymbol{\sigma}^f : \operatorname{grad} \boldsymbol{v}^f - \operatorname{div} \boldsymbol{q} + \rho^f r \tag{3}$$

where u^f is the fluid's specific internal energy, $\boldsymbol{q}$ is the heat flux, and r is the specific heat supply from user-specified sources (such as microwave heating or Joule heating). The fluid stress $\boldsymbol{\sigma}^f = -p^f \boldsymbol{I} + \boldsymbol{\tau}^f$ can be separated into a gauge pressure term p^f and a viscous shear stress $\boldsymbol{\tau}^f$, where $\boldsymbol{I}$ is the identity tensor. From basic thermodynamics it can be shown that p^f depends on the absolute temperature T and J^f (or e^f), thus $p^f = p^f(T, J^f)$. Note that fluid viscosities, such as the shear viscosity η^f appearing in $\boldsymbol{\tau}^f$, may also vary with temperature and volume. Using the decomposition of the stress into pressure and viscous contributions, we may rewrite the energy balance as

$$\rho^f c_v^f \dot{T} = (\boldsymbol{\tau}^f - T\frac{\partial p^f}{\partial T}\boldsymbol{I}) : \boldsymbol{D}^f - \operatorname{div}\boldsymbol{q} + \rho^f r, \qquad (4)$$

where $c_v^f \equiv \partial u^f/\partial T$ is the specific isochoric heat capacity of the fluid and $\boldsymbol{D}^f$ is the fluid rate of deformation tensor. This form of the energy balance shows how we can solve for the temperature T in a finite element formulation, by adding the energy balance to the virtual work statement used in a standard isothermal formulation.

One of the challenges is to formulate suitable constitutive models for the functions of state $p^f(T,J^f)$ and $c_v^f(T,J^f)$. Here we adopt ideal gas law for illustrations. For the heat flux $\boldsymbol{q}$ we use Fourier's law of heat conduction, $\boldsymbol{q} = -k^f(T,J^f)\operatorname{grad} T$ where $k^f(T,J^f)$ is the thermal conductivity. Since p^f depends on the nodal degrees of freedom T and e^f, the finite element implementation allows users to prescribe a desired pressure on a boundary by modeling it as a constraint between T and e^f.

RESULTS

Numerically, the most challenging aspect of thermofluid analyses is the ability to model convective heat transfer, especially when using high Peclet numbers. Therefore, we illustrated our implementation of the thermofluid framework of FEBio using two representative problems, one for free convection and the other for forced convection.

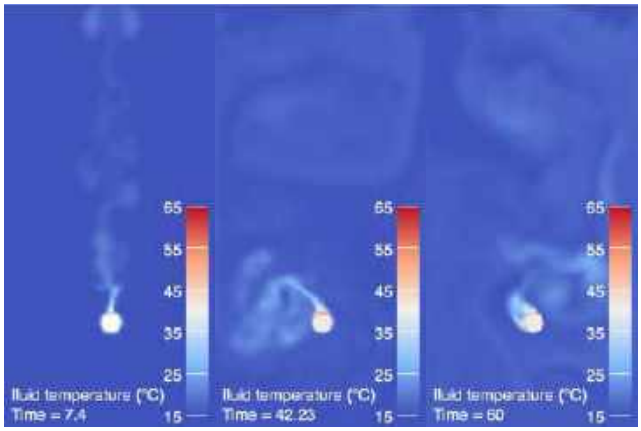

Fig. 1: Thermofluid solver example showing free convection of air modeled as an ideal gas in a 0.7 m × 1.4 m domain, under the action of gravity, around a ∅ 6 cm cylinder heated to 65 °C, in a closed container. Initial air temperature was 15 °C.

For free convection, we modeled a rectangular 2D fluid domain, 0.7 m × 1.4 m × 0.01 m, under the action of gravity g, with zero fluid velocity and normal heat flux along all lateral sides. The initial, uniform, fluid temperature was 15 °C, whereas the initial fluid gauge pressure increased linearly from zero at the top surface, according to $p^f = \rho_r^f gy$, where y was the vertical downward coordinate. A cylindrical surface (∅ 0.06 m) located at the center of the bottom half was assigned zero fluid velocity, and a prescribed temperature of 65 °C at time $t = 0^+$. The analysis was modeled to run for 60 s. The fluid used the properties of air as an ideal gas with constant specific heat capacity. The mesh had 10720 nodes and 5204 hex8 elements, biased near all no-slip boundaries. Temperature variations in this free convection problem are displayed in Fig. 1, at three representative time points.

The second example employed planar Poiseuille flow in a rectangular domain, 0.1 m × 0.06 m × 0.002 m, with a prescribed pressure drop of 1 Pa along the length. No-slip conditions were prescribed on the top and bottom faces. The fluid was modeled as gaseous O_2, using ideal gas law with temperature-dependent specific heat capacity and constant thermal conductivity. The initial uniform fluid temperature was set to 50 °C and the inlet temperature (left face) was set to 60 °C at time $t = 0^+$. The mesh had 16482 nodes and 8000 hex8 elements, with mesh biases near the no-slip boundaries. The analysis was run for a modeled duration of 0.5 s, during which the fluid accelerated from 0 to 1.3 m/s. The flow distribution evolved from plug profile to parabolic profile with increasing time. The peak Peclet number achieved at the highest velocity was $Pe \approx 4500$.

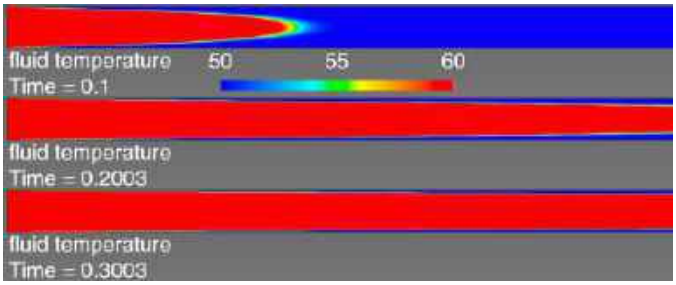

Fig. 2: Forced convection of gaseous oxygen in 10 cm × 0.6 cm rectangular domain, under a prescribed pressure drop of 1 Pa (left to right). Initial gas temperature was 50 °C and the prescribed inlet temperature was 60 °C. At 0.5 s the velocity reached 1.3 m/s, producing a Peclet number of 4500.

Snapshots of the temperature distribution at three representative time points (Fig. 2) demonstrated that there was negligible heat conduction in this problem, which was dominated by heat convection, as could be assessed from the very sharp temperature profile flowing through the domain. Most notably, the solver could handle outward flow of this sharp temperature profile across the downstream face.

DISCUSSION

Results demonstrated that the code could properly combine large variations in temperature with gravitational or convective effects, to model the flow of a heated gas in closed or open domains, optionally in the presence of buoyancy forces leading to unsteady flow and vortex shedding. The ability to model convective heat transfer across open boundaries, at high Peclet numbers, may be particularly helpful for realistic modeling applications. The development and implementation of a novel thermofluid solver in FEBio, as well as its successful application in simulating free and forced convection, highlights its potential for a wide range of biomedical applications.

To complete this framework, we plan to introduce constitutive models for real gases and real liquids, which can reproduce p^f, c_v^f, k^f and η^f reported in standard thermodynamics tables [4].

ACKNOWLEDGEMENTS

This study was supported by NIH GM083925.

REFERENCES

[1] McGregor GL, Rego BV, Diller KR: Mathematical Model for Combined Effects of Temperature and Pressure in Causing Soft Tissue Injury. J Heat Trans-T Asme, 144(3), 2022, PMCID.

[2] Maas SA, Ellis BJ, Ateshian GA, Weiss JA. FEBio: finite elements for biomechanics. J Biomech Eng 2012;134(1):011005.

[3] Ateshian GA, Shim JJ, Maas SA, Weiss JA. Finite Element Framework for Computational Fluid Dynamics in FEBio. J Biomech Eng 2018;140(2).

[4] Commerce USSo, 2023, "Thermophysical Properties of Fluid Systems," https://webbook.nist.gov/chemistry/fluid/.

EVALUATION OF TRANSCATHETER EDGE-TO-EDGE REPAIR CLIP SELECTION VIA AN OPEN-SOURCE FINITE ELEMENT SIMULATION FRAMEWORK

Patricia M. Sabin (1), Devin W. Laurence (1,2), Wensi Wu (1,2), Christian Herz (1), Steve A. Maas (3,4), Jeffrey A. Weiss (3,4), Matthew A. Jolley (1,2)

(1) Department of Anesthesiology and Critical Care Medicine, Children's Hospital of Philadelphia, Philadelphia, PA, USA
(2) Division of Pediatric Cardiology, Children's Hospital of Philadelphia, Philadelphia, PA, USA
(3) Department of Biomedical Engineering, University of Utah, Salt Lake City, UT, USA
(4) Scientific Computing and Imaging Institute, University of Utah, Salt Lake City, UT, USA

INTRODUCTION

Atrioventricular valve regurgitation (AVVR) is a leading cause of morbidity and mortality. Transcatheter edge-to-edge repair (TEER) is an effective and minimally invasive intervention for the treatment of AVVR in adults that avoids the increased risks associated with open heart surgery [1,2]. AVVR is also a serious complication in children and young adults with congenital heart disease (CHD). However, to date, application of TEER in CHD has been limited and the effect of TEER on leaflet function and mechanics in CHD is unknown [3].

Successful application of TEER therapy relies on the delivery of a clip to a precise location on the atrioventricular (AV) valve leaflets. In this setting, patient-specific modeling and simulation has facilitated successful TEER interventions in CHD [4]. However, simple image-derived modeling does not allow the clinician to preoperatively evaluate the effect of TEER on valve function or the effect of intervention on leaflet mechanics [5]. Further, the effect of clip size and shape on the resulting valve mechanics is unknown. 3D image-derived finite element (FE) modeling has begun to provide a method for "virtual valve repair", and several studies have simulated TEER intervention in AV valves [6]. This study aims to understand the effect of clip selection on a pediatric mitral valve model exhibiting posterior leaflet prolapse using an open-source pipeline as a foundation for further development of computational pre-intervention planning and assessment in CHD.

METHODS

Model Geometry: An existing image-informed regurgitant mitral valve model exhibiting posterior leaflet prolapse was discretized with 4-node linear quadrilateral shell elements [7]. Models for the base and arms of four MitraClip G4 clips (Abbott Cardiovascular, Plymouth, MN, sizes NT, NTW, XT, XTW) were adapted from the ValveClip Device Simulator module in the SlicerHeart extension for 3D Slicer (www.slicer.org) and meshed with 4-node tetrahedral elements in FEBio Studio. Valve and clip models are shown in **Figure 1**.

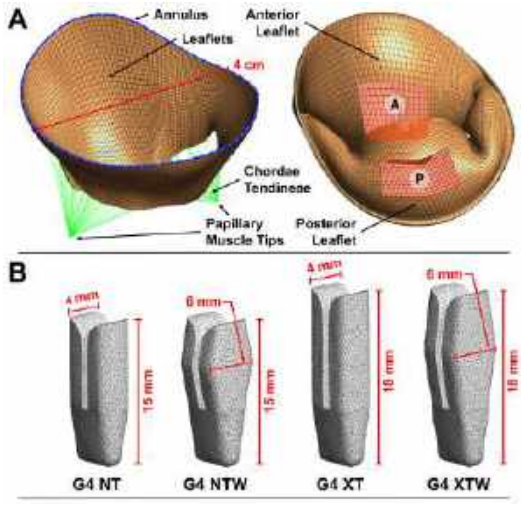

Figure 1: Models of (A) mitral valve and (B) MitraClip G4 clip

Initial Valve Simulation: FE simulation of the prolapsed mitral valve was performed using the FEBio dynamic solver (V2.4.0, University of Utah) as previously described [8]. Briefly, fixed displacement boundary conditions were assigned to the valve anulus and papillary muscle tips. Leaflet tissue was represented with an isotropic Lee-Sacks constitutive model:

$$\psi = \frac{c_0}{2}(I_1 - 3) + \frac{c_1}{2}\left[e^{c_2(I_1-3)^2} - 1\right] + \frac{1}{2}K(\ln J)^2 \qquad (1)$$

where c_0, c_1, and c_2 are material coefficients, I_1 is the first invariant of the right Cauchy-Green deformation tensor, K is the bulk modulus, and J is the Jacobian of the deformation gradient. Chordae tendineae were represented as tension-only 2-node springs with a nonlinear force-

displacement response. A 100 mmHg ventricular pressure was applied to the ventricular surface of the valve until the valve reached steady state, and the closed valve geometry was exported.

Valve Clip Simulation: The base and arms of the clip were represented as separate rigid bodies. The closed valve geometry was used as a reference to position the valve and clip for ideal leaflet capture. FE analysis was performed in steps (**Figure 2**). In analysis step 1, the valve was closed as described in the initial valve simulation, and clip arms were opened via a rigid rotation. In analysis step 2, the ventricular pressure was released to allow the valve leaflets to fall onto the clip arms, and a sticky contact was initiated between the leaflets and clip. In analysis step 3, the clip was closed via a rigid rotation, and the ventricular pressure was re-applied to close the clipped valve until it reached steady state.

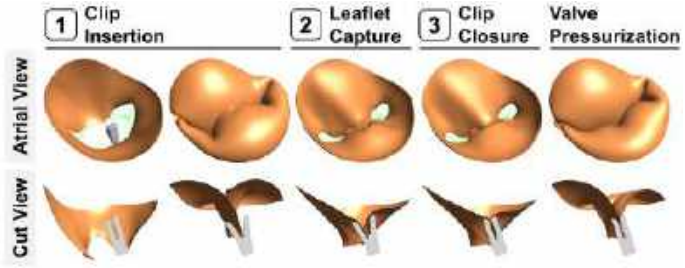

Figure 2: FE pipeline. Boxed numbers indicate analysis steps.

RESULTS

Outcome results of the FE TEER simulations are summarized in **Table 1** and **Figure 3**. Average 1st principal stress over the full valve model was slightly lower for all four clip types compared to the non-clipped valve, and average 1st principal strain remained relatively consistent. When isolating the belly regions of the anterior and posterior leaflets (A and P as defined in **Figure 1**), there was little change in average stress and strain in the A region, but stress and strain were higher in the P region for all clip types versus the non-clipped valve. Valves clipped with the taller XT and XTW clips showed the highest stress and strain in the P region.

Contact area (CA) increased for all clip types compared to the non-clipped valve, with the largest contact area in the wider NTW and XTW clips. The posterior leaflet capture gap (PCG), or the distance of the posterior leaflet free edge from the clip base (used to quantify the quality of leaflet capture), was larger for the taller XT and XTW clip models.

Table 1: Summary of outcome metrics after valve closure.
CA = contact area; PCG = posterior leaflet capture gap.

Clip Type	Avg. 1st Principal Stress (kPa)			Avg. 1st Principal Strain			CA (mm^2)	PCG (mm)
	Full	A	P	Full	A	P		
No Clip	282.2	570.8	330.2	0.231	0.274	0.192	89.2	--
G4 NT	261.5	570.0	346.9	0.234	0.285	0.294	256.3	2.56
G4 NTW	261.9	571.0	348.7	0.234	0.283	0.297	270.9	2.22
G4 XT	251.8	571.9	423.3	0.228	0.285	0.321	257.2	4.00
G4 XTW	252.3	575.4	425.7	0.228	0.286	0.323	267.3	3.67

DISCUSSION

This study provides a foundation for TEER simulation through the comparison of valve mechanics across MitraClip G4 clip types via an open-source FE modeling pipeline. These methods can be extended to further aspects of pre-intervention decision making, such as clip placement and number of clips, offering an approach to TEER planning that is valuable in pediatric populations with heterogeneous anatomy.

The differing trends in average stress and strain across the full valve model and targeted A and P regions highlight the importance of studying regional metrics for a full understanding of post-clip leaflet mechanics. Here, while average strain in the full valve remained relatively constant across clip types, the increased strain in the P region with taller clips suggests that clip selection may impact long-term valve durability. The increased PCG with the taller XT and XTW clips suggests clip selection could also impact the quality of the repair. If modeling indicates a large leaflet capture gap on either leaflet, a "staged leaflet capture" technique could be considered, wherein leaflets are grasped sequentially and the clip is repositioned between the capture of the first and second leaflets [9].

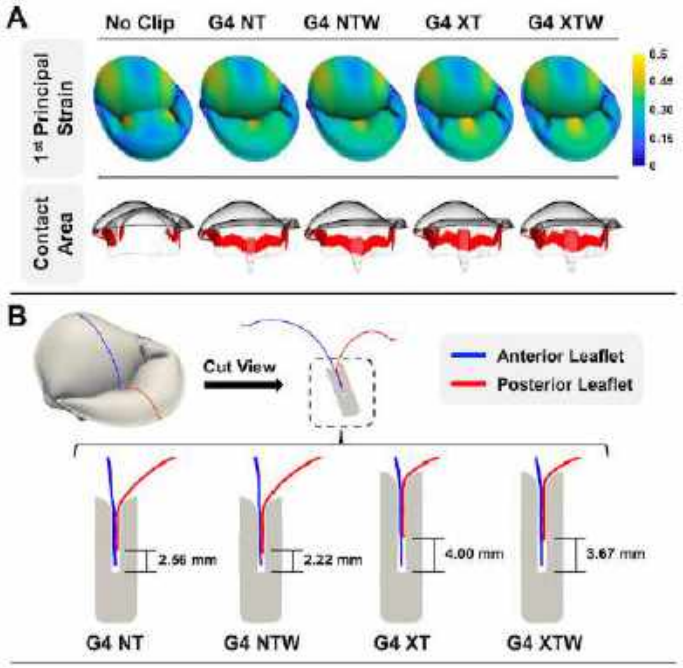

Figure 3: (A) Mechanical and functional outcome metrics, and (B) posterior leaflet capture gap (PCG). Results suggest increased posterior belly region strain and larger PCG with taller clips.

As a foundational study, there are opportunities to improve this simulation pipeline for more accurate image-derived TEER modeling. The existing prolapsed mitral valve model has several limitations, as previously discussed [7], and future models will include dynamic annulus and papillary muscle movement. In addition, the clip was applied to the leaflets in a fixed position, which may have limited the movement of the leaflets during the final valve pressurization. Future work will implement the release of this fixed constraint as well as include clip displacement to achieve sequential, independent leaflet capture for more comprehensive TEER simulation.

ACKNOWLEDGEMENTS

Supported by The Cora Topolewski Pediatric Valve Center at CHOP, an Additional Ventures Single Ventricle Research Fund Grant, NIH R01 HL153166, R01 GM083925 (SAM, JAW), T32 HL007915 (DWL), and K25 HL168235 (WW).

REFERENCES

[1] Stone, GW et al., *N Engl J Med*, 379:2307-2318, 2018. [2] Nickenig, G et al., *Circulation*, 135:1802-1814, 2017. [3] Guerin, P et al., *J Am Heart Assoc*, 11:e025628, 2022. [4] Jolley, MA et al., *Catheter Cardiovasc Interv*, 1-9, 2023. [5] Narang, H et al., *Ann Biomed Eng*, 49(12):3711-23, 2021. [6] Kong, F et al., *J Biomech*, 104:109730, 2020. [7] Wu, W et al., *J Mech Behav Biomed Mater*, 142(6):105858, 2023. [8] Wu, W et al., *J Biomech Eng*, 144(10):101012, 2022. [9] Silva, I et al., *Struct Heart*, 7(2):100114, 2022.

A PARAMETRIC ANALYSIS OF CHORDAE TENDINEAE DENSITY AND BRANCHING IN FINITE ELEMENT SIMULATIONS OF MITRAL VALVE CLOSURE

Nicolas R. Mangine B.S. (1), Patricia M. Sabin M.S. (1), Devin W. Laurence Ph.D. (1,2), Wensi Wu Ph.D. (1,2), Christian Herz M.S. (1), Christopher N. Zelonis M.S. (1), Csaba Pinter Ph.D. (3), Andras Lasso Ph.D. (4), Stephen Ching B.S. (1), Steve Maas Ph.D (5), Jeff Weiss Ph.D. (5), Matthew Jolley M.D. (1,2)

(1) Jolley Lab, Department of Anesthesia and Critical Care Medicine, Children's Hospital of Philadelphia, Philadelphia, PA, USA
(2) Division of Cardiology, Children's Hospital of Philadelphia, Philadelphia, PA, USA
(3) EBATINCA, Las Palmas de Gran Canaria, Las Palmas, Spain
(4) Queens University, Ontario, CA
(5) University of Utah, Salt Lake City, UT, USA

INTRODUCTION

Atrioventricular valve regurgitation is the most prevalent form of valve disease in developed countries. The purpose of the mitral valve is to regulate blood flow from the left atrium into the left ventricle. This is achieved by two leaflets supported by chordae tendineae. The chordae tendineae are string-like tissues composed of collagen fiber that anchor the valve leaflets to papillary muscles in the ventricle and support the valve leaflets during ventricular contraction. During mitral valve closure the free edge of the leaflets come together to create a coaptation zone and prevent the regurgitation of blood from the left ventricle into the left atrium. [1,2]

Finite element (FE) models are emerging as a tool to understand valve function, dysfunction, and inform valve repair [3,4]. This abstract explores use of linear trussses, specifically chordae density, in our FE simulations relative to an established open-source workflow using spring elements [3,5].

METHODS

Image-Informed Mitral Valve Creation: To create the FE simulations of mitral heart valves, the open-source platforms 3D Slicer (www.slicer.org) and FEBio (V2.4.0 University of Utah) were used. An existing image-informed mitral valve model was meshed into 4-node linear quadrilateral (Quad4) shell elements [3,5]. The chordae tendineae in this model were assumed to be 2-node springs with a nonlinear force displacement response [6]. Spring models are simple to implement however, truss elements offer the advantage of being able to be assigned material properties and structured into a branching configuration to present a more accurate physiology.

Chord Generation: We implemented custom code in the SlicerHeart Valve FEM Export module to generate chordae insertion points on the leaflets from papillary muscle nodes. The region of chordae generation was defined as 1/3 the leaflet starting from the free edge. Chordae density was varied from 6 chords/cm^2 to 25 chords/cm^2 with branch lengths of 4.5 mm and radials of 4. Valve and chordae are shown in **Fig 1**.

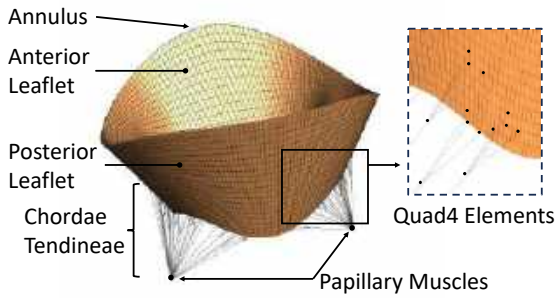

Figure 1. Finite Element Simulation

Finite Element Simulations: FE analysis was completed via dynamic simulation in FEBio. The mitral valve leaflets were modeled with the Lee-Sacks constitutive model [3] and assumed to have a thickness of 0.36 mm. The chordae were considered as linear truss elements with a stiffness of 40,000 Pa, and a cross-sectional area of 0.05 mm^2. The leaflet annulus and papillary muscles were fixed to prevent rigid body motion. A linearly ramped 13.3 kPa (100 mmHg) pressure surface load was applied to the ventricular leaflet surface over 0.0005 s and maintained until 0.01 s to achieve steady state [7]. A Kamensky contact was considered for the valve leaflets to model valve closure [8].

Analysis: Each valve was flattened to 2-dimensions and separated into anterior and posterior leaflets with the chordae insertion points identified (**Figs. 1-5**). Next, the first, second, and third principal strain on the flattened models were extracted from the FEBio simulation. Finally, using our existing spring model as the reference [3,5], the

element centroid error and first principal strain error were computed using an in-house python script.

RESULTS

The surface-to-surface error, strain, and strain error are shown in **Figs. 2-5**. Surface-to-surface error analysis identifies 10 chords/cm^2 as the most accurate, however there is a larger discrepancy in the commissure region (**Fig. 2**) and in the body of the posterior leaflet (**Fig. 3**). Interestingly, the first principal strain is similar for all chordae densities (**Figs. 4,5**).

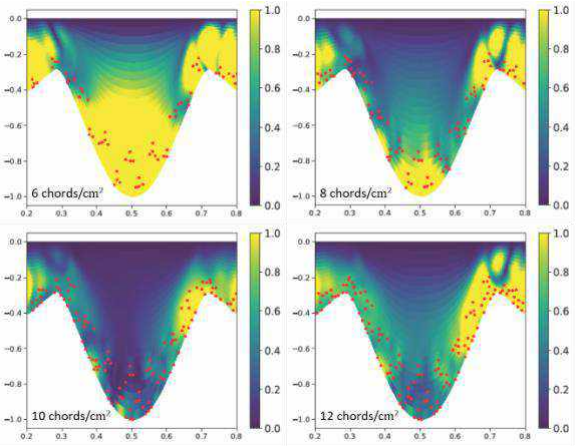

Figure 2. Surface-to-surface error: anterior leaflet

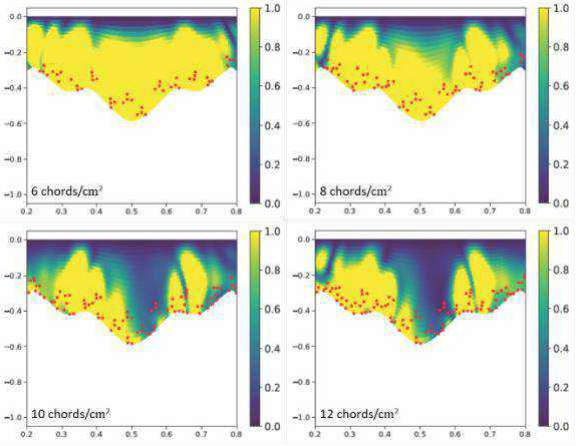

Figure 3. Surface-to-surface error: posterior leaflet

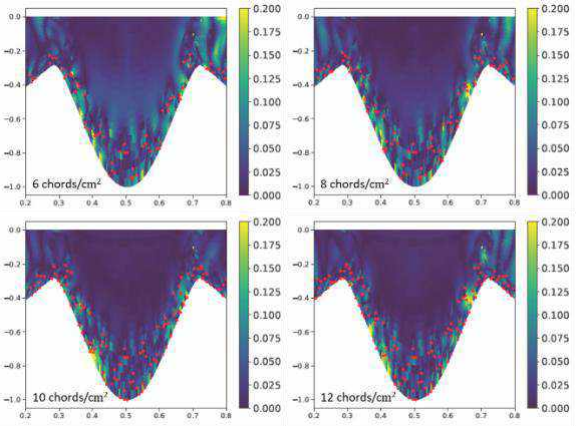

Figure 4. First principal strain error: anterior leaflet

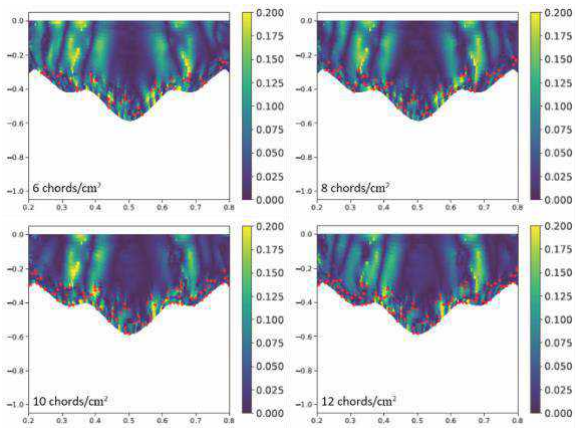

Figure 5. First principal strain error: posterior leaflet

DISCUSSION

We contribute a framework for investigating the effect of chordae model type and density on mitral valve dynamics. We found that the chordae properties primarily influence valve closure with minimal impact on the leaflet strains (**Figs. 4,5**). This suggests that chordae properties may primarily alter the valve function with minimal impact on the leaflet mechanics. The results further demonstrated that the chordae density influences the mitral valve closure with an optimal density of 10 chords/cm^2. Interestingly, we observed non-uniformities in the surface-to-surface error that may suggest the commissures and posterior leaflet require different chordae densities to appropriately capture valve function (**Figs. 2,3**). In our experimental experience, these regions may have larger chordae densities and require further refinement to appropriately capture valve closure.

Several limitations should be acknowledged for this study. This model assumes chordae tendineae as linear truss elements with uniform material properties, cross sectional area, and branching. In reality these chordae exhibit nonlinear behavior with varying geometries. Also, in these simulations the annulus and papillary muscles were fixed rather than dynamic as observed *in vivo*.

We can build upon this study to increase our understanding of mitral valve closure. In the future we can explore additional variables including chordae insertion area, branching length, number of branches, and heterogenous chordae structure. Also, in FE simulations optimizing the linear truss element material properties could provide more accurate valve closure. Additionally, future integration of image-derived models could bridge the gap between computational FE modeling and valve function. In summary, linear truss elements can produce similar valve closure to springs with notable differences in the commissures and posterior leaflet that can be addressed in future exploration.

ACKNOWLEDGEMENT

Supported by The Cora Topolewski Pediatric Valve Center at CHOP, an Additional Ventures Single Ventricle Research Fund Grant, NIH R01 HL153166, R01 GM083925 (SAM, JAW), T32 HL007915 (DWL) and K25 HL168235 (WW).

REFERENCES

[1] Khalighi, A *et al*., *ABME*, 45: 378–393, 2017.
[2] Drach, A *et al*., *IJNBME*, 34, 2017.
[3] Wu, W *et al*., *JBME*, 144(10):101012, 2022.
[4] Laurence, D.W. *et al*., *IJNMBE*, 36(7):e3346, 2020.
[5] Wu, W *et al*., *JMBBM*, 142(6):105858, 2023.
[6] Ross, C.J. *et al*., *ABME*, 48:1463-1474, 2020.
[7] Jett, S *et al*., *JMBBM*, 87:155-171, 2018.
[8] Kamensky, D *et al*., *CMAM*, 330: 522-546.

OPTIMIZATION OF IPSC DIFFERENTIATION TO LYMPHATIC ENDOTHELIAL CELLS THROUGH METABOLITES AND MACHINE LEARNING

D. Jeong (1), S. Saha (1), M. Zarodniuk (1), D. Hanjaya-Putra (1,2,3)

(1) Aerospace and Mechanical Engineering, University of Notre Dame, Notre Dame, IN, USA
(2) Chemical and Biomolecular Engineering, University of Notre Dame, Notre Dame, IN, USA
(3) Harper Cancer Research Institute, University of Notre Dame, Notre Dame, IN, USA

INTRODUCTION

Induced pluripotent stem cell (iPSC)-derived endothelial cells (dEC) are crucial for developing vascularized tissues and modeling vascular diseases, but the existing differentiation protocols suffer from two major challenges. First, the protocols yield high percentage of undesired cell lines that share the mesodermal lineage such as fibroblasts, reducing the yield of dEC and necessitating removal of these cell lines to prevent fibroblast overgrowth. Second, there is a lack of efficient protocols that target specific subvariants of dECs, namely into lymphatic endothelial cells (LEC), which are useful for developing lymphatic organoids and promoting wound healing. iPSCs undergo changes to membrane potential as they differentiate, suggesting that a potential method to improve the yield of dEC may be to target membrane polarization of iPSC.[1]

Another method to improve the specificity of differentiation protocols into LEC may be to take advantage of its unique metabolic characteristics. LECs rely heavily on fatty acid oxidation for its metabolic needs and for generation of acetyl-CoA used for activation of VEGFR3, an LEC-specific marker with a positive feedback loop to a master lymphatic regulator gene, Prox1.[2] Therefore, in this study, we explore the use of polarizing molecules and acetyl-CoA precursor molecule to improve both the yield of total dECs and specifically the LECs. Additionally, we explore the use of convolutional neural network coupled with machine-learning based segmentation algorithm to identify the desired dECs and LECs from imaging data without relying on immunofluorescence or flow cytometry data.

METHODS

Based on the existing differentiation protocol for dEC published by Harding and colleagues, we developed the following modified protocol (Fig 1A). We induce mesodermal identity through 2 days of treatment with 6μM of CHIR99021, a Wnt-pathway activator. Then we induce endothelial progenitor characteristics through 2 days of treatment with 50ng/mL of VEGF-A, FGF2, and BMP4 along with 10nM of ouabain, a small molecule that causes depolarization. Cells are passaged and replated to density of 50,000 cells/cm^2. Lastly, we treat the cells with 100ng/mL of VEGF-C and up to 50mM of sodium acetate (NaAc) for 4 days to induce LEC markers. To analyze the effects of our treatments, cells were passaged either after the endothelial progenitor induction stage or the LEC maturation stage.

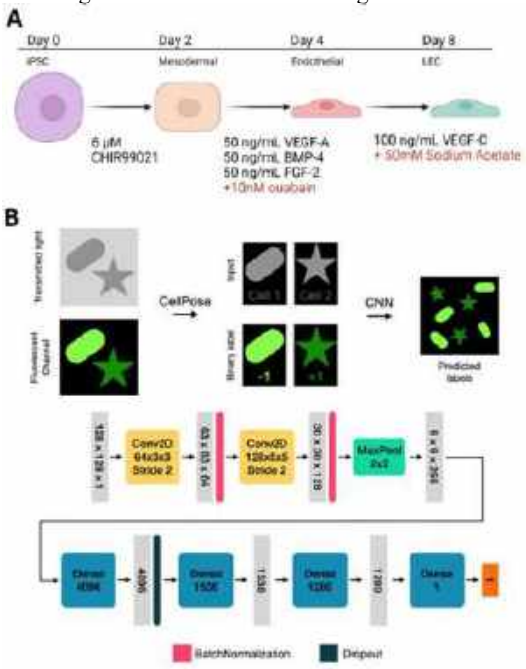

Figure 1. A) Schematic for the proposed differentiation protocol. B) Overview of the machine learning algorithm design.

We also created a deep learning model using Keras library in Python to distinguish between endothelial cells and fibroblasts (Fig 1B). The model first processes the image into smaller segments centered around each cell identified using Cellpose library, which uses backbone U-net based neural network to accurately segment non-circular cells such as ECs. We then use each of the segments to train a network consisting of three convolutional layers and four dense layers, whose depth are optimized using Keras-tuner library. We pre-stained the ECs with fluorescent dye and re-plated stained ECs with unstained fibroblasts in 1:1 mixture at approximately 20,000 cells/cm^2 immediately before imaging. Each segment generated by the algorithm was labeled as either EC or fibroblast based on the presence of fluorescent signals within the cell boundary.

RESULTS

After 4 days, following the endothelial induction and treatment with ouabain, we performed flow cytometry for CD144, an endothelial marker, and Tra-1-60, a pluripotency marker. We observed a significant increase in the yield of CD144+ endothelial cells from approximately 50% to 70% when the iPSCs were treated with 10nM of ouabain during the endothelial progenitor induction stage (Fig 2A). All cells were Tra-1-60 negative and ouabain treatment during the mesodermal stage did not affect CD144+ yield, indicating that ouabain specifically affects cells in the mesodermal-endothelial state rather than drive iPSC in general towards differentiation.

After 8 days, we performed qPCR and flow cytometry for various LEC markers and CD31, a mature endothelial marker and found a significant increase in lymphatic markers PDPN and Prox1 when treated with 50mM NaAc (Fig 2B-C). We replicated the method across three iPSC cell lines and saw an increase in PDPN+/CD31+ LECs from approximately 5-10% to 40-60% with NaAc treatment (Fig 2D). The differentiated cells also produced comparable levels of reelin and retained the ability to form networks on a Matrigel surface (Fig 2E-F).

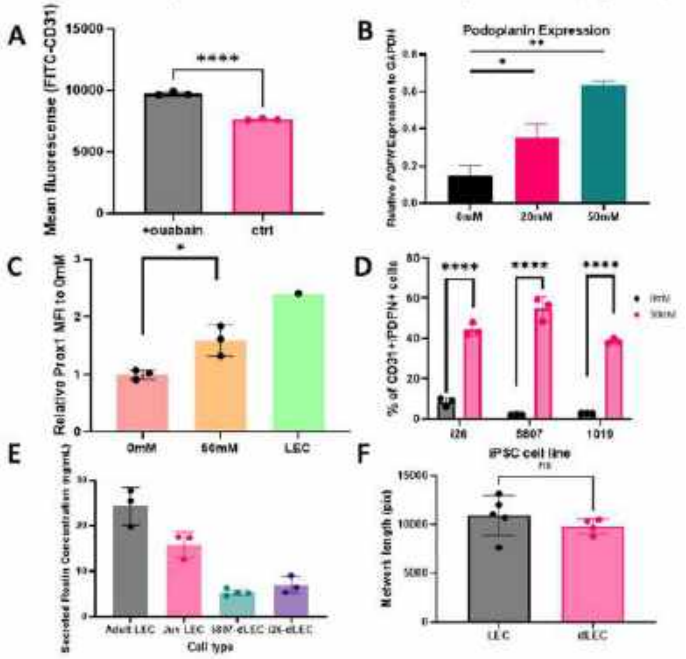

Figure 2. A) Mean expression of CD31 in cells differentiated with and without ouabain. B) qPCR results showing an increase in PDPN expression with higher NaAc treatment. C) Average Prox1 expression increased with treatment with NaAc. D) Percentage of CD31/PDPN+ cells following differentiation. E) ELISA results showing Reelin secretion. F) Network length quantification after network formation assay.

Using the optimal model, we confirmed that the accuracy of the model reaches approximately 80% (Fig 3A). The dataset was approximately 60% fibroblasts and 40% endothelial cells. We observed that the model begins to overfit by 200 epochs, which is when the validation loss reaches similar value to the training loss. We tested the optimized model on a testing image and generated the output image based on the predictions of the model (Fig 3B-C). We observe that the model accurately predicts most cells, but it misclassifies cells that are closely packed due to difficulties in segmenting dense cell clusters.

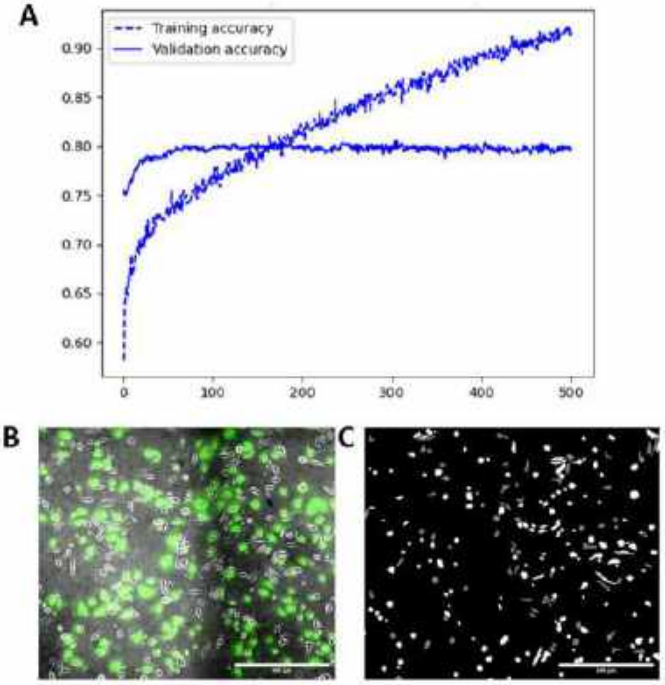

Figure 3. A) Training and validation accuracy curves for model trained on dataset of 10000 cells. B) Input image to the machine learning algorithm. Green fluorescence is overlaid and indicates VEcad+ population. C) Output image from the network indicating VEcad+ cells as white.

DISCUSSION

Our differentiation protocol improves both the yield of CD144+ dECs and PDPN+/CD31+ mature LECs, which will be useful lymphatic and vascular tissue engineering research. We also developed a potential tool that can be used to distinguish dECs from the byproducts such as fibroblasts and fibroblast-like cells, which will help researchers quickly determine the efficacy of their differentiation protocols.

ACKNOWLEDGEMENTS

We are grateful for the funding from the NSF, NIH, and the AHA. Fund number: NSF-RECODE-2225601, NSF-CAREER-2047903, NIH-R35GM143055, AHA-CDA-34630012.

REFERENCES

[1] Sundelacruz, S et al. *Plos One.* 3(11):e3737, 2008.
[2] Wong, BW et al. *Nature*. 542(7639):49-54, 2017.

OSTEOTOMY HAS VARIABLE EFFECTS ON CONSTRUCT STIFFNESS OF CADAVERIC TIBIAE: IMPLICATIONS FOR FUNCTIONAL EVALUATIONS

Luke T. Mattar (1), M. Enes Kayaalp (1,3), Tianyu Chen (1), Ron Curelaru (2), Volker Musahl (1,2), Richard E. Debski (1,2)

(1) Department of Orthopaedic Surgery, University of Pittsburgh, Pittsburgh, PA, USA
(2) Department of Bioengineering, University of Pittsburgh, Pittsburgh, PA, USA
(3) Department for Orthopaedics and Traumatology, Istanbul Kartal Dr. Lutfi Kirdar Training and Research Hospital, Istanbul, Turkey

INTRODUCTION

Osteotomies are a surgical technique utilized by orthopaedic surgeons to alter and reshape bony morphology. For example, slope reducing osteotomies cut and remove a wedge of bone on the anterior side of tibia to reduce the posterior tibial slope. Individuals with tibial slopes ≥12.0° are at an increased risk for failure following anterior cruciate ligament reconstruction (i.e., graft failure) [1]. Therefore, surgeons may perform a slope reducing osteotomy in combination with a ligament reconstruction depending on the individual's tibial slope to reduce the risk of rupture [2]. However, the time zero effects of performing osteotomy cuts on the tibial construct's stiffness may be altered which influences the deformation of the complex. Changes in stiffness have implications for osteotomies in patients, material testing protocols, and functional evaluations utilizing the assumption of rigid bodies. Therefore, the objective was to quantify the stiffness of Intact, Osteotomized Native Slope, and Osteotomized Increased Slope states.

METHODS

Seven fresh frozen cadaveric tibiae (61.5 ± 12.6 years, 6 females and 1 male) were dissected and all soft tissue removed. The tibia was potted in an epoxy compound (Bondo; 3M) and secured with a custom aluminum clamp to the base of a uniaxial material testing machine (Figure 1). Three tibial construct states (Intact, Osteotomized Native Slope, and Osteotomized Increased Slope) underwent a non-destructive cyclic compression testing protocol. All surgical procedures including the osteotomy and external fixation were performed by a fellowship trained orthopaedic surgeon with five years of experience. The tibial complex was preloaded to 5.0N and then preconditioned for 30 cycles between 5.0 and 125.0N. Thirty cycles were chosen for preconditioning based on preliminary testing to determine the number of cycles required to minimize hysteresis. Finally, the construct was cyclically loaded between 5.0N and 250.0N. The construct was allowed to rest for thirty minutes in between states and continuously hydrated with saline.

For each construct, the secant stiffness was quantified during the 50th loading cycle. In the Osteotomized Native Slope state, the osteotomy cut was made and the bone removed during the cutting process was replaced with a thin PLA 3D printed wedge to account for the blade thickness of the oscillating saw and maintain the native slope value (Figure 1). The wedge was approximately 1.0mm thick. Similarly, when the slope was increased, a larger wedge printed from PLA was inserted and the construct was fixed with an external fixator (three carbon rods and four Schanz pins). The external fixation configuration was determined based on preliminary testing to maximize rigidity. The slope was increased by approximately 12.0° (the same wedge was inserted to each specimen) to ensure each tibia would hit the slope threshold where osteotomy is indicated [3]. Secant stiffness was chosen due to the complex loading condition (i.e., compression, tension, shear) that occurs when cuts are made to the bone and multiple materials are in the construct. Thus, due to the varying materials in the system, the modified secant stiffness is most appropriate as it provides an average response of the entire complex (calculated as the slope of line connecting first and last point of loading cycle) [4].

Since the data was not normally distributed, the Friedman test was utilized to determine if any differences existed between the secant stiffness of the three states. If the Friedman test was significant, Wilcoxon Sign Ranked tests were used to compare all states. Then, a Bonferroni correction would be utilized to correct for multiple comparisons. Since the current study assessed all pair-wise comparisons, significance was set at $p<0.017$ for post-hoc testing based on the correction for multiple comparisons.

RESULTS

The median and interquartile ranges (25th percentile, 75th percentile) for the Intact, Osteotomized Native Slope, and Osteotomized Increased Slope stiffnesses were 546.5 N/mm (501.5, 602.7), 520.3 N/mm (465.6, 638.0), and 456.1 N/mm (339.8, 490.4), respectively.

Specimen specific data for each construct state are shown in Table 1. Utilizing the quartile-based coefficient of variation (interquartile range/median), the interquartile range was 18.5%, 33.1%, and 33.0% of the median stiffness for the Intact, Osteotomized Native Slope, and Osteotomized Increased Slope. Thus, variability in the data increased following the osteotomy and increased slope.

Overall, the median stiffness for the Osteotomized Native Slope was 4.8% smaller compared to the Intact state. The Osteotomized Increased Slope median stiffness was 12.3% smaller compared to the Osteotomized Native Slope state, and the Osteotomized Increased Slope state median stiffness was 16.5% smaller compared to the Intact state. All specimens experienced decreased secant stiffness following each change in construct state, with the exception of specimen 1 and 4 (essentially no change between Osteotomized Native Slope and Increased Slope states). No statistically significant differences in secant stiffness at the 50th cycle between states were found. Specifically, following post-hoc tests with Bonferroni correction, there was no difference in stiffness between the Intact state and Osteotomized Increased Slope state ($p=0.043$). No difference in stiffness was observed between the Osteotomized Native Slope state compared to the Osteotomized Increased Slope state ($p=0.028$). No difference was found between the Intact and Osteotomized Native Slope states ($p=0.176$).

DISCUSSION

The major findings from the current study were: 1) Performing an osteotomy and increasing the slope did not significantly decrease the tibial construct stiffness, and 2) based on the interquartile ranges for each state, there is large variability in stiffness changes for different tibial construct states. The first finding suggests that performing the osteotomy cut in isolation or in combination with increasing the slope does not significantly affect the tibial constructs' stiffness. However, all specimens experienced decreased or no change in secant stiffness following each change in construct state, with the exception of specimen 1. Furthermore, specimen 3's secant stiffness for the Intact and Osteotomized Native Slope states were much higher and could be due to better bone quality observed while handling the specimen.

Based on the large interquartile ranges, quartile-based coefficient of variation, and limited sample size, assuming the stiffness does not change may be inappropriate on a case-by-case basis. The finding has implications for surgery in older individuals and experimental studies utilizing robotic testing systems to evaluate knee function following osteotomy. Osteotomies in the coronal plane (e.g., medial closing or lateral opening wedge) are often used in older patients to relieve symptoms associated with lateral compartment degeneration [5]. Thus, surgeons should consider the variable time-zero effects of performing osteotomies on the bony construct's stiffness. Furthermore, during experiments utilizing robotic testing systems to evaluate knee function and in-situ forces in ligaments, researchers should establish quantitative checks to ensure the principle of superposition [6] is not violated (i.e., rigid body assumption holds). For example, the magnitude and direction of the in-situ force should be checked to ensure the magnitude and direction (tensile force) are reasonable. Care should be taken when applying external fixation to ensure rigidity of the construct is maximized.

The primary limitation of the current study is that an increased slope was simulated by performing an osteotomy and inserting a plastic wedge to maintain the increased slope. However, this methodology has been utilized in peer-reviewed published literature with cadaveric specimens [7]. Thus, the current work has implications for surgical procedures and future experimental work evaluating the effects of osteotomy on knee function. Future work will quantify the bone quality of cadaveric tibiae and determine the association with secant stiffness.

ACKNOWLEDGEMENTS

We gratefully acknowledge support from the Departments of Orthopaedic Surgery and Bioengineering at the University of Pittsburgh.

REFERENCES

[1] Webb, JM et al., *AJSM*, 41:2800-2804, 2013.
[2] Vivacqua, T et al., *Orthop J Sports Med.*, 11: 2023.
[3] Dejour, H and Bonnin M., *J Bone Joint Surg Br*., 76:745-749, 1994
[4] Reul, ON et al., *J. Vis. Exp.*, 199:2023.
[5] Duerr, RA et al., *Arthrosc Tech., 9:925-933, 2020.*
[6] Rudy, TW et al., *J Biomech*, 29:1357-1360, 1996.
[7] Winkler, PW et al., *J Orthop Res*., 41:1430-1438, 2023.

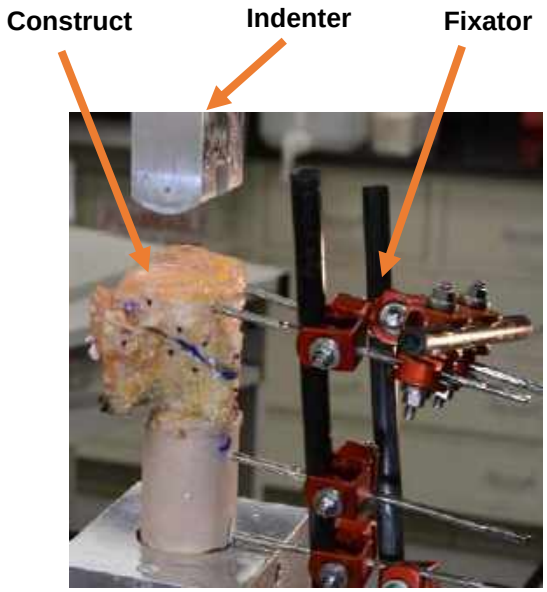

Figure 1: Osteotomized Native Slope construct mounted in material testing machine with bicondylar indenter mimicking the femoral condyles and external fixator.

Table 1: Secant stiffness for Intact, Osteotomized Native Slope, and Osteotomized Increased Slope for each specimen.

Specimen	Intact	Osteotomized Native Slope	Osteotomized Increased Slope
1	546.5	638.0	585.1
2	405.1	371.9	339.8
3	1143.9	986.8	302.3
4	501.5	465.6	469.5
5	575.7	520.3	450.5
6	602.7	566.4	490.4
7	544.6	495.2	456.1

INTERPLAY BETWEEN INTERSTITIAL FLOW AND EXTRACELLULAR MATRIX PHYSICAL PROPERTIES IN THE INITIATION AND CONTROL OF ANGIOGENESIS AND LYMPHANGIOGENESIS

Jacob C. Holter (1), Shashwat S. Agarwal (2), Chia-Wen Chang (3), Joseph W. Tinapple (1), Marcos G. Cortes-Medina (1), Travis H. Jones, (3), Joseph Barlage (1), Jonathan W. Song (2,4) (1,2,3)

(1) Biomedical Engineering, Ohio State University, Columbus, OH, USA
(2) Mechanical and Aerospace Engineering, Ohio State University, Columbus, OH, USA
(3) Chemical and Biomolecular Engineering, Ohio State University, Columbus, OH, USA
(4) Comprehensive Cancer Center, Ohio State University, Columbus, OH, USA

INTRODUCTION

Tumor microenvironments undergo marked changes in extracellular matrix (ECM) and vascularity that affect cancer cell signaling, drug delivery, and effects of therapy (*1*). Tumors also contain an abundance of leaky blood vessels combined with a compromised drainage system due to poorly functioning lymphatic vessels, resulting in elevated interstitial fluid pressure. These aberrations in ECM composition and vascular function manifest in biophysical changes in tissue stiffness, ECM pore size, and interstitial diffusive and convective transport. Perfusion, interstitial pressure, and altered ECM composition comprise specific cancer phenomena that are difficult to examine *in vivo*. Here, we used several biomimetic 3-D microfluidic systems that couple systematic evaluation of interstitial flow-potentiated angiogenesis and lymphangiogenesis with detailed characterization of ECM physical properties determined by the ECM composition. The focus of these studies are the effects of glycosaminoglycans (GAGs), such as hyaluronic acid (HA), in modulating the bioactivity of the ECM by altering the structural properties of fibrillar collagen, in controlling angiogenesis in the presence of interstitial flow.

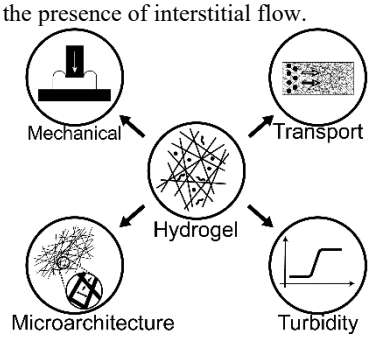

Figure 1. Biophysical characterization scheme for hydrogels. We assay collagen supplemented with GAGs for indentation stiffness (mechanical), hydraulic permeability (transport), confocal reflectance microscopy (microarchitecture), and turbidity (aggregate formation) (*2-4*).

METHODS

We have developed a characterization scheme for fibrillar collagen-based hydrogels (Figure 1) (*2-4*), which measures coupling between ECM mechanics and transport properties mediated by different GAGs (*5*). These methods uniquely position us to define interrelationships among physical properties of the ECM and interstitial flow. We have also developed several microfabricated microvessel models described below.

RESULTS

We recently reported that endothelial cells integrate physical cues derived from matrix HA during angiogenesis induced by interstitial flow (*5*) (Figure 2). A novel finding was that HA enhances interstitial flow-mediated angiogenic sprouting through its alterations to ECM stiffness and pore size. We have also developed a microtissue-engineered model that mimics the microanatomy of initial lymphatic capillaries and enables quantification of lymphangiogenesis and lymphatic vessel permeability (Figure 3). We show that interstitial flow is maximum at the blind-ended region (Fig 3D), thereby mimicking the fluid absorption characteristics of lymphatic capillaries (*6*). We demonstrate that interstitial flow (5 μm/s) alone, and in absence of a pro-lymphangiogenic molecule (e.g., CXCL12 or VEGF), preferentially induces lymphangiogenesis at the blind-ended region of the lymphatic vessel (Fig 3G).

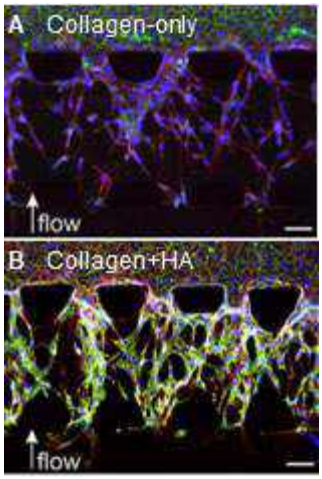

Figure 2. HA enhances interstitial flow-mediated sprouting angiogenesis. Human umbilical vein endothelial cell (HUVEC) sprouting induced by interstitial flow (~10 μm/s) in A) 3 mg/ml collagen-only and B) 3 mg/ml collagen and 1 mg/ml HA matrices(*5*).

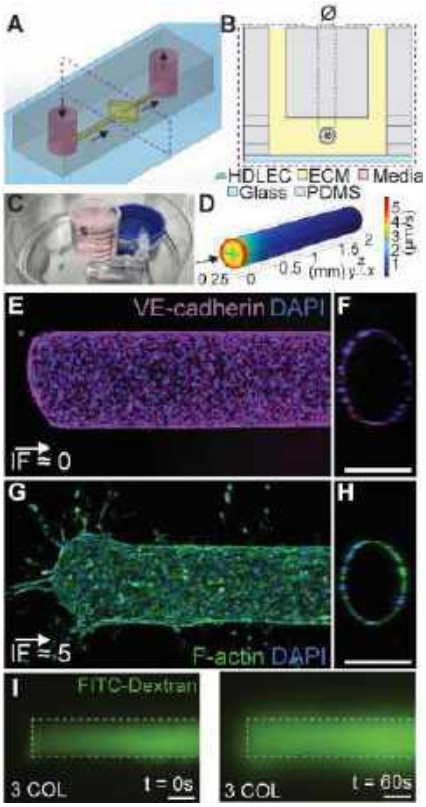

Figure 3. Micro-engineered and perfusable blind-ended lymphatic vessel. A) Schematic of a PDMS-based microfluidic device containing human dermal lymphatic endothelial cells (HDLECs) assembled into a patent lymphatic vessel. **B**) Transverse cross section of vessel surrounded by ECM. The microvessel absorbs fluid into its lumen originating from the upstream media port. ⊗ denotes fluid flow into the vessel. **C**) Photograph of vessel-containing microfluidic device setup. **D**) COMSOL analysis of interstitial flow. **E**) Confocal projection and **F**) cross section of a blind-ended and quiescent HDLEC-lined microvessel stained at day 4 for endothelial junctions (VE-cadherin, magenta) and nuclei (DAPI, blue) in a 3 mg/mL collagen gel under static flow conditions. **G**) Confocal projection and **H**) cross section of a blind-ended microvessel stained at day 4 for F-actin (Phalloidin, green) and nuclei (DAPI, blue) in a 3 mg/mL collagen gel under interstitial flow potentiated by an interstitial fluid pressure gradient. **I**) Measurement of lymphatic microvessel permeability using 20 kDa FITC-Dextran as a fluorescent tracer. Images were recorded at t = 0 and 60 s after loading of the dye. Dashed box outlines engineered lymphatic vessel. Scale bars are 200 μm.

DISCUSSION

Using 3D microfluidic biomimicry with detailed characterization of hydrogel scaffolds, we investigated how ECM physical properties influence interstitial flow-mediated sprouting angiogenesis and lymphangiogenesis. Key observations include the addition of HA to collagen-based hydrogels significantly enhances the initial extension and sustained elongation of endothelial sprouting in response to interstitial flow. Moreover, in a blind-ended lymphatic vessel, sprouting preferentially occurred at the leading edge where interstitial flow was highest or a local maximum. Taken together, these novel findings comprise important advancements toward refining our understanding of angiogenesis and lymphangiogenesis that is mediated by the biophysical microenvironment. Moreover, these results will help inform future developments in pro-angiogenic biomaterials and *in vitro* disease models (e.g., organs-on-a-chip) for interrogating mechanisms of vessel outgrowth and remodeling.

ACKNOWLEDGEMENTS

NSF CAREER Award (CBET-1752106), the American Heart Association (15SDG25480000), R01HL141941, and Pelotonia. Facility research support from DMR-1420451 and P30 CA016058 from the National Cancer Institute. We also acknowledge the laboratory of Dr. Yi-Chung Tung for their collaboration.

REFERENCES

1. H. T. Nia, L. L. Munn, R. K. Jain, Physical traits of cancer. *Science* **370**, eaaz0868 (2020).
2. A. Avendano *et al.*, Integrated Biophysical Characterization of Fibrillar Collagen-Based Hydrogels. *ACS Biomater Sci Eng* **6**, 1408-1417 (2020).
3. M. Cortes-Medina *et al.*, Chondroitin sulfate, dermatan sulfate, and hyaluronic acid differentially modify the biophysical properties of collagen-based hydrogels. *bioRxiv*, 2023.2005.2022.541626 (2023).
4. M. Cortes-Medina *et al.*, Chondroitin sulfate, dermatan sulfate, and hyaluronic acid differentially modify the biophysical properties of collagen-based hydrogels. *Acta Biomaterialia*, (2023).
5. C. W. Chang *et al.*, Extracellular Matrix-Derived Biophysical Cues Mediate Interstitial Flow-Induced Sprouting Angiogenesis. *ACS Appl Mater Interfaces* **15**, 15047-15058 (2023).
6. G. W. Schmid-Schonbein, Microlymphatics and lymph flow. *Physiol Rev* **70**, 987-1028 (1990).

ESTABLISHING A COMPREHENSIVE COLLECTION OF ETHICS RESOURCES FOR BMES AT THE ONLINE ETHICS CENTER: ASSESSING AND STRUCTURING MENTORING RESOURCES

Anjelyka T. Fasci (1), Sanjana Prashanth (2), Andrew O. Brightman, Ph.D. (2), Robert L. Hood, Ph.D. (1)

(1) Department of Biomedical Engineering, University of Texas at San Antonio, San Antonio, TX, USA
(2) Weldon School of Biomedical Engineering, Purdue University, West Lafayette, IN, USA

INTRODUCTION

In the dynamic landscape of Biomedical Engineering, the ethical considerations surrounding research, teaching, and training play a pivotal role in shaping the character and impact of the biomedical engineering community[1], [2]. Ethics, in this context, refers to the principles and standards that guide professionals in making morally sound decisions, ensuring responsible conduct in every aspect of their work. The commitment to ethical practices is fundamental in engineering, fostering trust, accountability, and integrity within the Biomedical Engineering Society (BMES). Recognizing the evolving ethical dimensions, the BMES Ethics Committee undertakes the crucial task of aggregating resources to equip members with the necessary knowledge and insights.

The impetus for this initiative stems from the Ethics Committee's dedication to addressing the multifaceted challenges posed by ethical considerations in all aspects of professional life and practice. This study was focused on the realm of mentoring within Biomedical Engineering. Mentorship, a cornerstone in the development of future engineers, involves a symbiotic relationship that extends beyond technical proficiency. It encompasses the transmission of ethical values, instilling a sense of responsibility and integrity in the mentees[3]. This emphasis on ethical mentorship aligned with the special session at the 2023 Annual BMES Conference, focusing on "Establishing and Sustaining Effective Mentor/Mentee Relationships."

Moreover, drawing inspiration from the 2022 paper on "Ethical Practices and Tips for Improving Engineering Faculty-Student Research Relationships," the committee acknowledges the evolving nature of ethical considerations, particularly in the academic and research spheres, resulting in the 2022 revision of the BMES ethics code of conduct[4]. Mentorship and leadership, integral components of scientific endeavors, take on added significance when viewed through the ethical lens. Mentorship goes beyond the mere transfer of technical knowledge; it becomes a guiding force that shapes the ethical compass of future scientists and engineers[3].

In recognizing the critical role of mentorship, our study aims to evaluate the available resources, identify gaps, and lay the groundwork for enhancing ethical discourse. Through a thorough examination, we seek to contribute valuable insights to the ongoing conversation on mentorship ethics, aligning with our commitment to cultivating responsible and ethical practices within the realm of scientific mentorship.

METHODS

In systematically organizing ethical resources, the student research team collaborated with mentors to formulate a comprehensive plan, aiming not only to accumulate but critically evaluate and categorize existing resources on the Online Ethics Center for Engineering and Science (OEC). Virtual brainstorming sessions facilitated nuanced discussions on potential categories addressing diverse ethical challenges in Biomedical Engineering. Using an organic approach, the team identified foundational terms for mentorship discussions, exploring OEC resources and uncovering new categories.

With a deliberate focus on the "Mentors and Trainees" section, the team centralized addressing the ethical minutiae of mentorship. This was a trial-by-trial process, in which the team read each individual resource and placed them in the appropriate categories, which then lead to the creation of new categories if there was a trend that required such action. This resulted in 14 categories for the resources to be organized.

RESULTS

As shown in Figure 1, the 14 categories have a variety of wealth. Critical gaps in mentorship coverage surfaced, notably in various mentoring types like Community, Team, or Reciprocal mentoring. These omissions highlight an oversight, leaving potential guidance gaps for those engaging in these dynamics.

Additionally, the analysis revealed a lack of discussion on negligence within the mentor-mentee relationship, a crucial aspect needing attention and direction. This gap raises considerations for enhancing ethical discourse, emphasizing the need for comprehensive insights on recognizing and addressing negligence from both mentor and mentee perspectives. Of particular significance is the identified diversity gap, including age, sexual identity, race, and gender.

Figure 1 Mentorship Category Resources

The age distribution, depicted in Figure 2 (1989-2022), reveals a shortage of recent materials, suggesting a potential gap in addressing contemporary ethical challenges. While historical context is rich, the limited representation of recent perspectives underscores the need to incorporate modern viewpoints. This consists of inclusion, diversity, and boundary setting, items which are vital for guiding the next generation of biomedical engineers in navigating the ethical complexities inherent in their roles as mentors and leaders.

On a positive note, abundant resources were available for protocols, training, boundaries, and power dynamics prove invaluable for those entering mentorship. These serve as foundational guidance for navigating mentor-mentee complexities. Despite strengths, identified gaps emphasize the continuous need for refining resources in mentorship ethics within Biomedical Engineering's diverse and evolving challenges[4].

DISCUSSION

This finding underscores the dynamic nature of the ethical landscape in Biomedical Engineering, shaped by evolving societal norms, technological advancements, and interdisciplinary collaborations. While historical perspectives offer valuable insights, relying exclusively on past materials may inadvertently neglect the unique ethical dilemmas emerging in the rapidly changing discipline. The scarcity of materials from the last two decades emphasizes the urgency of infusing the ethical discourse surrounding mentorship and leadership with contemporary perspectives. This infusion is vital for addressing novel challenges presented by advancements in technology, changes in research methodologies, and evolving expectations within academic and professional settings.

In light of these observations, broadening the scope of ethical considerations gains added significance. Actively incorporating modern perspectives ensures alignment with current standards, resonating with challenges in today's rapidly evolving landscape. Recognizing the importance of not only filling resource gaps but also adopting a forward-looking, inclusive approach is essential. As the field advances, an adaptive and contemporary ethical framework becomes indispensable for fostering responsible conduct, integrity, and ethical leadership within the engineering community.

Figure 2 Mentorship Resource Ages

Acknowledging the wealth in the "Mentors and Trainees" resources, the study identifies three critical areas for improvement. Firstly, recognizing the need to address content scarcity, especially in diversity-related categories like age, sexual identity, race, and gender, underscores the imperative of fostering a more inclusive ethical framework in the engineering community. Secondly, a recommendation is made for the reorganization of OEC resources to enhance usability, aiming for a more accessible platform that fosters responsible conduct.

Lastly, the study emphasizes the pressing need for expanding contemporary ethical mentoring resources that engage with the evolving landscape of the scientific and engineering community. Ethical considerations in mentorship and leadership should not be static; they should evolve to address contemporary issues, ensuring that future engineers are equipped to navigate the ethical complexities of their profession. This research serves as a foundational step towards a broader initiative, collecting and organizing pertinent materials for the changing landscape of mentoring ethics in bioengineering and biomedical engineering.

ACKNOWLEDGEMENTS

Dr. Andrew O. Brightman, OEC Fellow for Ethics in Biomedical Engineering, and Dr. R. Lyle Hood, BMES Ethics Committee Chair, led the team using OEC resources. Each professor mentored a student in identifying, evaluating, and organizing materials for the Biomedical Engineering Society. Some authors were supported by the AFWERX Direct to Phase II SBIR contract number FA864922P0928.

REFERENCES

[1] B. J. Franklin, “Biomedical Ethics for Engineers: Ethics and Decision Making in Biomedical and Biosystem Engineering,” *Biomed Instrum Technol*, vol. 43, no. 3, 2009, doi: 10.2345/0899-8205-43.3.196.

[2] P. Saha, “Ethical Challenges for the Biomedical Engineer of the Future,” *Ethics in Biology, Engineering and Medicine: An International Journal*, vol. 11, no. 1, 2020, doi: 10.1615/ethicsbiologyengmed.2021037458.

[3] S. Kaul, “Development of a Mentorship Program in Engineering and Engineering Tech-nology DEVELOPMENT OF A MENTORSHIP PROGRAM IN ENGINEERING AND ENGINEERING TECHNOLOGY.”

[4] I. Villanueva Alarcon, “Ethical Practices and Tips for Improving Engineering Faculty-Student Research Relationships,” in *Proceedings - Frontiers in Education Conference, FIE*, Institute of Electrical and Electronics Engineers Inc., 2022. doi: 10.1109/FIE56618.2022.9962431.

COMPARING REGIONAL VARIATIONS IN RADIODENSITY WITH STIFFNESS IN AN ATHEROSCLEROTIC HUMAN AORTA

Carly L. Donahue (1), Victor H. Barocas (1)

(1) Department of Biomedical Engineering, University of Minnesota, Minneapolis, MN, USA

INTRODUCTION

Atherosclerosis is a vascular disease characterized by the buildup of plaque in the arterial wall and local tissue remodeling in response to both biological and mechanical cues [1]. Atherosclerotic lesions can be visualized *in vivo* by computed tomography (CT)-based technologies, which are often used to calculate local tissue density for the detection and assessment of atherosclerotic plaques in the clinical setting [2].

In the aorta, atherosclerotic lesions are associated with several life-threatening conditions, such as the formation and failure of aneurysms, pseudoaneurysms, and aortic plaque rupture [3]. Notably, each of these complications is largely mechanical in nature. While many studies have sought to characterize the mechanical properties of plaque lesions [4]; few [5] have focused on the mechanical changes to the nearby vessel wall. Understanding these alterations is crucial, as they play an important role in the formation, progression, and failure of the aforementioned complications.

The current work assessed the correlation between local tissue radiodensity from micro-CT analysis and the heterogeneous local stiffness obtained from biaxial testing of human cadaveric aortic tissue samples. We tested the hypothesis that higher tissue radiodensity indicates a larger local stiffness.

METHODS

Sample Preparation: A total of 8 cruciform-shaped samples (example in Fig. 1A) were dissected from a fresh human cadaveric aorta (75M, Anatomy Bequest Program, U of Minnesota), 4 from the ascending thoracic aorta and 4 descending thoracic aorta. The samples had widths of 20-25 mm and an average thickness of 2.0 mm.

Mechanical Testing: The samples were speckled and mounted into the grips of a planar biaxial system (Instron-Sacks, Norwood, MA, Fig. 1B). Samples were submerged in 1XPBS throughout the experiment. A 0.1 N preload was applied to each arm before testing. The Generalized Anisotropic Inverse Mechanics (GAIM) protocol [6] consisting of 15 different deformations was applied. All extensions were to 15% grip strain at a displacement rate of 10 mm/min. All tests were video-recorded for subsequent DIC analysis.

Micro-CT Analysis: Samples were laid flat on a foam stage, sprayed with 1XPBS for hydration, and scanned with an average resolution of 85.1 μm (NSI, Rogers, MN, Fig. 1C). Scan times were ~7 minutes. Regional values for radiodensity were reported in Hounsfield units (HU).

Inverse Mechanical Analysis: Regional differences in CT radiodensity were used to partition the sample into 10 homogeneous sub-regions as described in [7]. Using the surface deformation determined from DIC analysis and the forces on the boundary, the 2-D linear stiffness tensor C was determined for each partition [6]. The largest eigenvalue of C, the Kelvin Modulus, is a measure of the material stiffness of the partition.

Comparisons and Statistical Analysis: The local material stiffness was mapped to the average through-thickness radiodensity for each partition. Linear regression was used to assess their correlation.

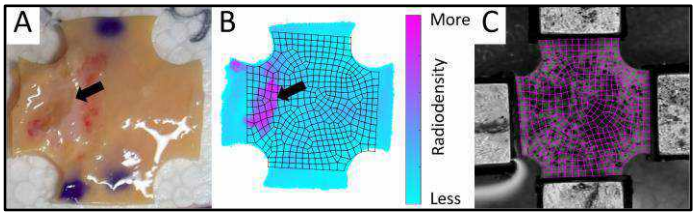

Figure 1: A) Aortic sample with atherosclerotic plaque lesion (arrow). B) Average through-thickness radiodensity measured via micro-CT. The arrow points to the denser plaque region. C) Biaxial tensile test. The overlaid mesh shown in B and C was used to map radiodensity to mechanical results.

RESULTS

Six of the eight samples had at least one calcified plaque lesion (HU >300, Fig. 2A). The other two samples showed early signs of atherosclerosis, but the micro-CT did not show a calcified lesion. The partitioning algorithm segmented the calcified regions from the surrounding aortic media. In most cases, this was determined to be the stiffest part of the sample (e.g., Fig. 2B).

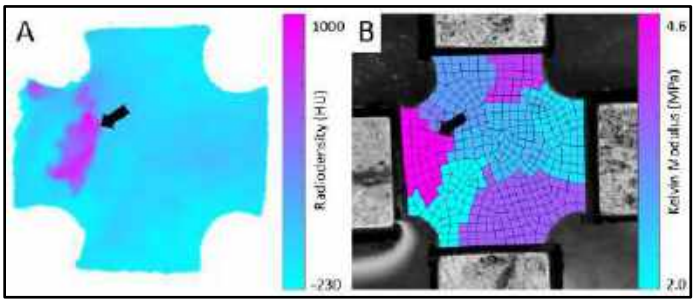

Figure 2: A representative sample. Average through-thickness radiodensity (HU) measured via Micro-CT. The arrow points to the calcification. B) Stiffness of each homogeneous partition (Kelvin Modulus, MPa) measured via inverse mechanical analysis. The stiffest region (arrow) corresponds to the calcification.

Figure 3 shows the correlation between the average partition radiodensity (HU) and the partition stiffness (Kelvin Modulus, MPa) for all partitions of all eight samples. Overall, stiffness is positively correlated with tissue radiodensity, as shown by the positive slope of the linear regression ($p < 0.0001$). The highest densities showed high Kelvin moduli, and there were many low-radiodensity, low-modulus partitions. However, there were also some low-radiodensity, high-modulus partitions, and many partitions fell outside of the confidence bounds demonstrating a rather weak fit of the data ($R^2 = 0.173$).

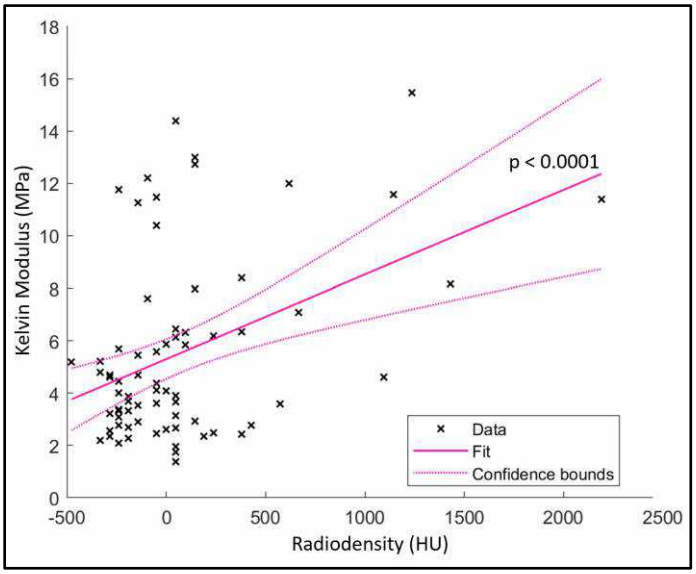

Figure 3: Radiodensity measured via micro-CT (Hounsfield units, HU) vs. Kelvin modulus (MPa) measured via inverse mechanical analysis for each partition. The solid red line shows the linear regression, and the dotted lines show the confidence bounds.

DISCUSSION

The present study investigates the biomechanical interplay between calcified plaque lesions, as identified by increased local tissue radiodensity, and the local stiffness of a human aortic wall measured via biaxial testing. The stiffest regions, identified through inverse mechanical analysis, consistently coincided with calcified areas, emphasizing the impact of advanced atherosclerotic disease on tissue stiffness. Overall, the results reveal a positive correlation between tissue radiodensity, assessed through micro-CT, and local stiffness measured via biaxial testing, corroborating the existing body of literature that associates atherosclerosis with augmented vessel wall stiffness [8,9].

The prominence of partitions with low radiodensity but high stiffness introduces complexity to the relationship between radiodensity and stiffness. As a result, there is a weak fit of the data to the linear model, as indicated by the modest R^2 value, suggesting that factors that go undetected by micro-CT, such as non-calcified components, different stages of plaque development, or tissue crosslinking, may contribute to the stiffness of the tissue [10]. Further investigations into the compositional diversity of atherosclerotic plaques and the adjacent medial tissue as well as their biomechanical implications are warranted to comprehensively understand the observed variations.

This study is one of the few that establish a correlation between micro-CT-derived radiodensity and the mechanical properties of blood vessels [11]. However, it is important to acknowledge the inherent limitations associated with our methodology, particularly in the assumptions made during the Generalized Anisotropic Inverse Mechanics (GAIM) analysis. First, the use of a 2D mesh assumes uniform sample thickness and material properties through the thickness, introducing potential inaccuracies. Second, the material behavior of each partition is assumed to be linear, oversimplifying the complex nature of arterial tissue behavior. While these limitations may introduce quantitative errors, they do not take away from our overall conclusions.

In conclusion, the observed correlation between tissue radiodensity and stiffness, despite its nuances, underscores the potential of utilizing CT imaging to assess the biomechanical implications of plaque lesions. Since CT is non-invasive and is routinely used to monitor many patients with vascular disease, especially many aortopathies, a CT-based mechanical assessment could potentially improve our ability to evaluate clinical risk and manage atherosclerosis-related conditions.

ACKNOWLEDGEMENTS

We would like to thank Amanda Devos, John Brigham, and the Visible Heart Lab for their expertise and aid in micro-CT scanning and the anonymous organ donors of the Anatomy Bequest Program for making this work possible. This work was supported by AHA Predoctoral Fellowship 23PRE1019931 and NIH grants R01-HL164800, and U01-HL139471.

REFERENCES

[1] Ma, Z et al., Am. J. Physiol. Cell Physiol., 319:481-499, 2020.
[2] Papazoglu, A et al., *Hellenic J. Cardiol*, 62: 399-407, 2021.
[3] Ikeda, Y, *Ann Vasc Dis*, 2:73-79, 2016.
[4] Akyildiz, A et al., *J. Biomech*, 47: 773-783, 2014.
[5] Holzapfel, G et al., *J. Biomech Eng*, 126: 657-65, 2004.
[6] Raghupathy, R. & Barocas, *J. Biomech Eng*, 132, 081006, 2010.
[7] Witzenburg, C et al., *IEEE Trans Med Imaging*, 35:29-41, 2026.
[8] Hooglugt, A et al., Curr Opin Lipidol, 33(6): 353–363, 2022.
[9] Van Popele, M et al., *JAHA Stroke*, 32:454–460 (2001).
[10] Lacolley, P et al., *ATVB*, 40:1055–1062, 2020.
[11] Fortunado, R et al., *Exp Mech*, 65:5-18, 2021.

CONCENTRIC CONTRACTION DURING UNLOADING PREVENTS STRAIN SOFTENING IN THE MOUSE URINARY BLADDER

Tyler G. Tuttle (1), Daniel Deuel (1), Sara Roccabianca (2), Sarah Calve (1)

(1) Paul M. Rady Department of Mechanical Engineering, University of Colorado Boulder, Boulder, CO, United States
(2) Mechanical Engineering, Michigan State University, East Lansing, MI, United States

INTRODUCTION

Current methods of *ex vivo* bladder mechanical testing employ techniques used to test passive tissues (*e.g.* skin and tendons), where the tissue is loaded and unloaded passively in tension [1]. During passive-only testing, bladder tissue does not fully return to the original configuration and subsequent loading shows increased tissue compliance, which is called strain-softening. In passive tissues like skin and tendon, strain-softening does not occur either *in vitro* or *in vivo*; in the bladder, strain-softening is prevented via detrusor contraction [2]. It is thought that strain softening in the bladder occurs due to slippage of actomyosin cross-bridges during passive distension and is reversed via cyclical contraction of detrusor smooth muscle cells during emptying [3]. Here we present a novel mechanical testing method that incorporates passive distention and optogenetic contraction to prevent strain-softening and enable us to accurately measure the material properties of bladder tissue.

METHODS

To induce contractility *ex vivo*, we crossed *ChR2(H134R)-EYFP* mice (JAX, #024109), with *SM22-Cre^{tg}* mice (JAX, #017491), in which Cre recombinase is under the control of the mouse smooth muscle protein 22α promoter. SM22-*Cre^{tg};ChR2(H134R)-EYFP* mice express channelrhodopsin-2 and enhanced yellow fluorescent protein (EYFP) in smooth muscle cells (SMCs), enabling contraction of the bladder via blue-light stimulation (450-490 nm) and visualization of SMCs via EYFP. We utilized a floating platform mechanical testing system (Fig 1) that allows for mechanical testing and imaging while submerged in phosphate buffered saline (PBS). Optogenetic contraction was induced via a 500 mW, 455 nm diode laser (Opto Engine) and optical fiber patch cable (RWD Life Science), with a circular spot size of 50 mm^2 to generate an approximate irradiance of 10 mW/mm^2.

Two mechanical testing protocols were used. First, a passive-only protocol was used to demonstrate an example of field-standard mechanical testing. In this protocol, circumferential bladder rings were excised, mounted onto the testing system, and stretched using a force-mediated approach where a 100 µN tare load is added. Then the tissue was cycled between 0-20 mN of tension for 5 cycles. Following this protocol, the load cell was detached from the mechanical testing setup to allow unconstrained sample movement. The bladder was then contracted via the addition of acetylcholine chloride, to a final bath concentration of 0.1 mM, to allow the bladder to freely contract.

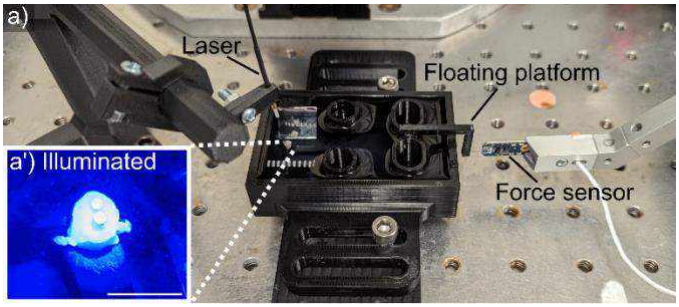

Figure 1: Mechanical testing setup used for both methods of mechanical testing. (a') For optogenetic contraction tests, the bladder was stimulated via the 455 nm laser.

The second protocol utilized optogenetic contraction during the unloading stage to recapitulate the active contraction that occurs during micturition *in vivo*. After a 100 µN tare load was added, the tissue was loaded to 10 mN, unloaded to 0 mN, then contracted via optogenetic stimulation while the tissue was returned to the original unloaded length. This cycle was repeated 5 times.

RESULTS

Passive-only testing (Fig. 1) resulted in substantial strain-softening. This is revealed by the increase in unloaded tissue length at zero force (Fig 1a, the unloading phase stops at displacements greater than 0), and

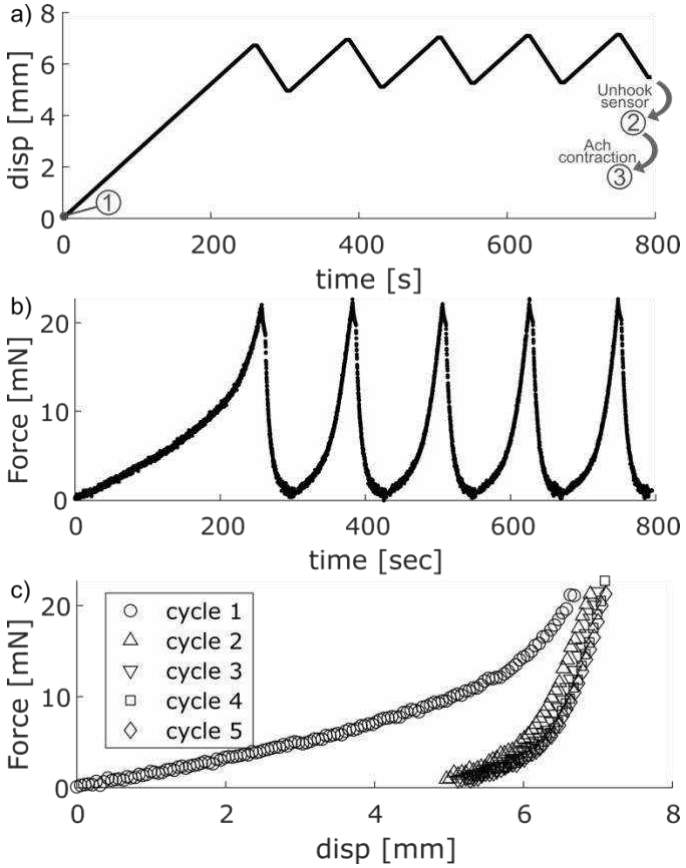

Figure 2: Mouse bladder ring mechanical data collected using the field-standard passive-only deformation method. a) Displacement history, b) force history, and c) force-displacement loading curves.

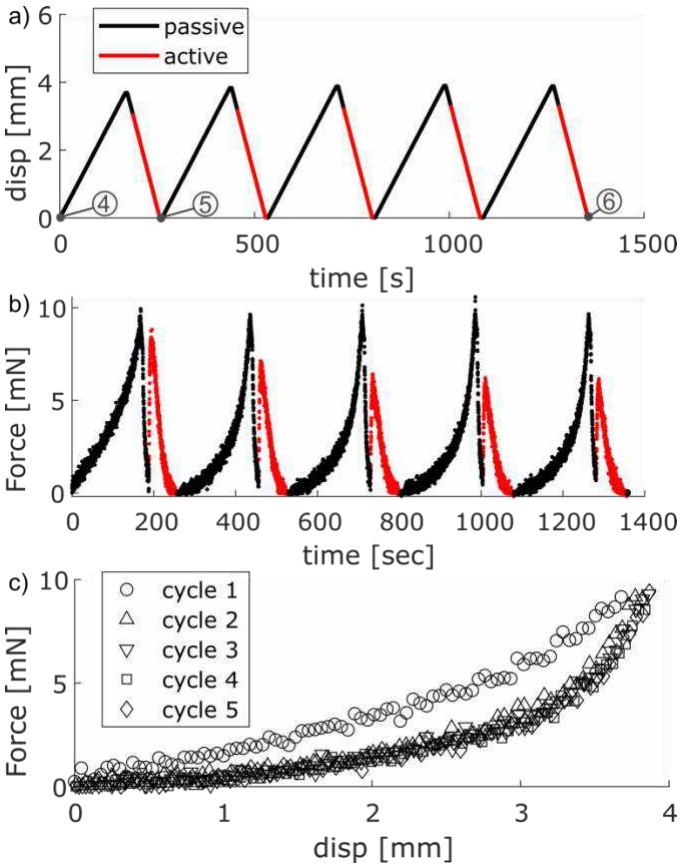

Figure 3: Mouse bladder ring mechanical data collected with an optogenetic concentric contraction protocol. a) Displacement history, b) force history, and c) force-displacement loading curves.

increased tissue compliance (Fig 1c, rightward shifted force-displacement loading curves). When the concentric contraction protocol was used, the tissue was able to return to its original unloaded length (Fig 2a, active contraction during unloading returns displacement to zero). After this contraction, subsequent passive loading curves (Fig 2c) were repeatable and not rightward shifted.

Following mechanical testing with the passive-only protocol, unloaded bladder rings remained in a deformed state (Fig 4, top row). Subsequent contraction of the unloaded bladder via addition of acetylcholine allowed the bladder to return to its original unloaded configuration (Fig 4). Using the optogenetic concentric contraction mechanical testing protocol, the bladder configuration returned to the unloaded configuration after all 5 cycles (Fig 4, bottom row).

DISCUSSION

Current field-standard methods of *ex vivo* bladder mechanical testing lead to strain softening that is not recovered until contraction is applied. This limits the ability to translate *ex vivo* mechanical data to *in vivo* mechanics. Applying contraction during the concentric phase of deformation prevents strain softening. We are working to combine the optogenetic-induced contraction with multiphoton imaging to uncover the effect of detrusor contraction on ECM configuration. Ultimately, we plan on implementing the morphological and mechanical data in an FE model that will be used to evaluate the importance of ECM organization on the mechanical response. The combination of experimental and computational methods will be useful in evaluating bladder dysfunction and improve predictions of pathological changes in bladder function.

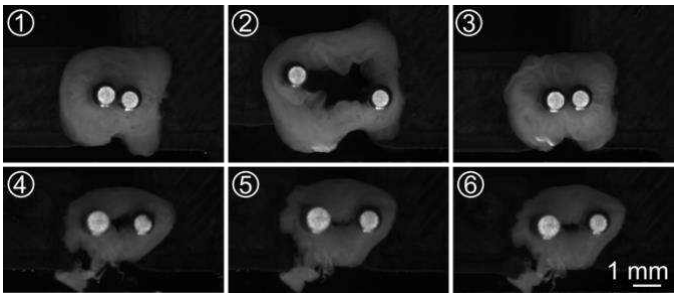

Figure 4: Top row shows ring from control mouse (1) before testing, (2) after testing, and (3) after contracting with acetylcholine. Second row shows ring from SM22-*Cre^{tg};ChR2 mouse* (4) before testing, (5) after cycle 1 + active contraction and (6) after cycle 5 + active contraction. Numbers indicate when brightfield images of rings were acquired at different stages of loading as illustrated in Figs 2 and 3.

ACKNOWLEDGEMENTS

This work was supported by NIH R21AG085874 to SC and SR and NIH T32AG000279 to TT.

REFERENCES

[1] Tuttle, T.G., et al. *Acta Biomater*141 (2022): 280-289. [2] Cullingsworth, Z.E., et al. *Neurourol and Urodynam* 39, 2 (2020): 707-714. [3] Neal, C.J., et al. *Am J Physiol-Renal Physiolog* 313, no. 1 (2017): F126-F134.

WALL SHEAR STRESS IN INTRACRANIAL ANEURYSMS COMPUTED FROM CFD AND 4D FLOW MRI AUGMENTED WITH FLOW PHYSICS PRINCIPLES

Farshid Goudarzian (1), Mohammadreza Balouchestani Asl (1), Neal Patel (1), Abhishek Singh (2) Jiacheng Zhang (2), Pavlos P. Vlachos (1,2), Vitaliy L. Rayz (1,2)

(1) Weldon School of Biomedical Engineering, Purdue University, West Lafayette, IN 47907, USA
(2) School of Mechanical Engineering, Purdue University, West Lafayette, IN 47907, USA

INTRODUCTION

While most cerebral aneurysms remain stable over the years, their rupture results in 50% mortality and morbidity, thus necessitating comprehensive methodologies for their risk stratification. Variations of Wall Shear Stress (WSS) have been established to correlate with the growth and rupture of an aneurysm[4]. Subject-specific computational fluid dynamics (CFD) models can provide high-resolution WSS distribution for aneurysmal arteries[1], however numerical results depend on multiple modeling assumptions. Alternatively, 3-directional phase-contrast Magnetic Resonance Imaging (4D flow MRI) can capture velocity fields over the cardiac cycle, enabling non-invasive *in vivo* assessment of cerebral blood flow dynamics[2]. However, the spatiotemporal resolution and image noise can limit the accuracy of 4D flow measurements, affecting in turn the accuracy of MRI-based WSS estimates. These limitations hindered the adaptation of 4D flow MRI in both research and clinical settings. Recent studies demonstrated that 4D flow MRI data can be enhanced by using fluid dynamics principles to estimate and reduce the error of measured velocity fields[3,5]. This study aims to compare WSS distribution based on velocity fields derived from CFD simulations and from 4D Flow MRI in cerebral aneurysms. By evaluating similarities and discrepancies in WSS obtained from these alternative approaches, we provide the groundwork for examining the capabilities of 4D flow MRI in providing hemodynamic factors discriminating between stable and unstable cerebral aneurysms.

METHODS

The aneurysms used for this study were scanned on a 3T Siemens Skyra scanner at Northwestern Memorial Hospital with prospective ECG gating and during free breathing. Cerebral arteries were imaged using dual-*venc* 4D flow MRI using a high *venc* of 100 $^{cm}/_{s}$ and a low *venc* of 50 $^{cm}/_{s}$ (1x1x1 mm, TR/TE/flip-angle = 6.3 ms/3.47 ms/15°).

A two-step process was used for image segmentation. Initially, an automated segmentation approach based on the Standardized Difference of Means of the measured velocities was applied to identify MRI voxels with statistically significant net flow effects. Subsequently, a higher-resolution flow mask was obtained from a Time-of- Flight (TOF) MR angiography, using the open-source tool ITK-SNAP. The resulting flow segmentations were coregistered using the Coherent Point Drift algorithm to apply the TOF-based mask to the 4D Flow data. The Universal Outlier Detection method was then applied to the 4D flow data to eliminate spurious velocity measurements. Additionally, in-house phase unwrapping algorithm was applied, and conservation of mass was enforced through a least squares-based global optimization approach.

Vascular geometries and inflow waveforms obtained from MRI data were also used for numerical simulations of the flow using open-source SimVascular software. Blood flow was assumed laminar, and Newtonian and the vessel walls were assumed rigid. The Womersley profile was prescribed at the inlet and RCR boundary conditions were used for each of the outlets. Iterative adjustments were made to the resistance and capacitance parameters by performing several simulations to obtain physiological range of the pressure waveform. Mesh independence of the numerical solution was achieved by obtaining solution on grids with different resolution.

The resulting velocity fields from CFD and 4D flow MRI were used as the starting point for calculating WSS distribution. The WSS is calculated using the radial basis function-generated finite difference method (RBF-FD) a "mesh-free" method based on the localized RBF-interpolant in a compact finite-difference mode. This method can approximate the differential operator at the center node x_1 with a linear combination of the values of a function of $u(x_i)$ of n surrounding nodes:

$$\mathcal{L}u(x_1) \approx \sum_{k=1}^{n} w_{1,k}\, u(x_i) \qquad (1)$$

In this expression, $\mathcal{L}$ represents the derivative operator and $w_{1,k}$ denotes the RBF-FD weights obtained by solving the system below:

$$\begin{bmatrix} \phi & e \\ e^T & 0 \end{bmatrix} \begin{bmatrix} w \\ \mu \end{bmatrix} = \begin{bmatrix} \mathcal{L}\phi \\ 0 \end{bmatrix} \quad (2)$$

where the $\phi_{k,l} = \phi(\|.\|)$ is the RBF function, e is an identity column vector with n entries, $\mathcal{L}\phi$ is the column vector of derivative values of RBF, and μ is constant that ensures the summation of all RBF-FD is zero. Subsequently, the 4D flow-based velocity field was augmented by applying the pressure-gradient induced velocity gradient correction (PG-VGC) method[3] which corrects the velocity gradient based on the reconstructed pressure field gradient to improve the WSS estimation. The conservation laws of mass and linear momentum are incorporated to formulate a linear system. This linear system is used to estimate the velocity-gradient errors with a least-squares approach. The error is then subtracted from the velocity gradient to improve the assessment of WSS. In order to use consistent methods for WSS calculations from both modalities, the same RBF-FD method was applied to obtain WSS from the velocities computed with SimVascular. The resulting WSS distributions were then compared to assess whether physics-based 4D flow MRI reconstruction improves the agreement between the image-based and CFD-based results[3].

RESULTS

Here we show a representative case of an internal carotid artery (ICA) aneurysm. The time-averaged WSS (TAWSS) was calculated for each method and the results were normalized by the TAWSS spatially averaged over a healthy segment of the vessel. The TAWSS obtained directly from SimVascular and calculated from SimVascular-computed velocities with the RBF-FD method were in close agreement as shown in Figure 1 (a) and (b). However, these distributions were noticeably different from TAWSS computed from 4D flow MRI data processed by both RBF-FD and PG-VGC in Figure 1 (c) and (d). Despite that, there are regions of high TAWSS and low TAWSS just before the flow enters the aneurysm, over its wall, and after the flow exits the aneurysm, that are shared across the distributions, obtained with alternative methods.

Figure 2 shows the violin plots for the TAWSS distribution over the aneurysm wall obtained with each method. Both CFD-based TAWSS distributions are similar, while the RBF-FD applied to 4D flow MRI results are different from those obtained with the PG-VGC method.

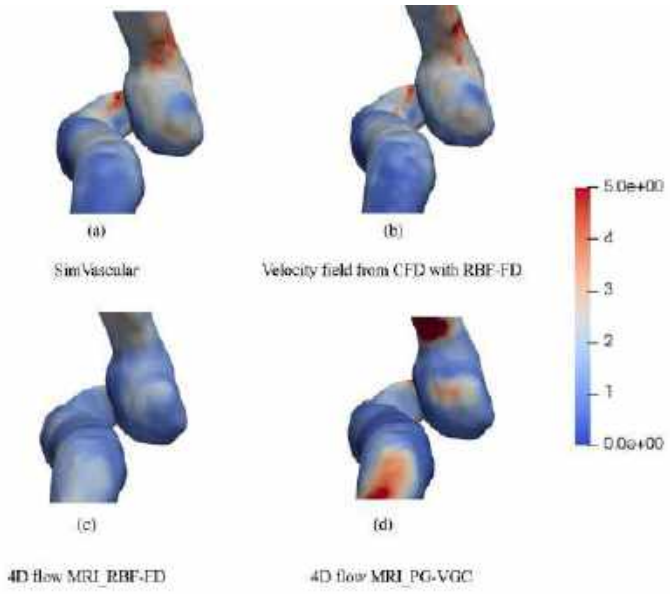

Figure 1: Normalized TAWSS obtained from CFD and 4D flow MRI for an ICA aneurysm.

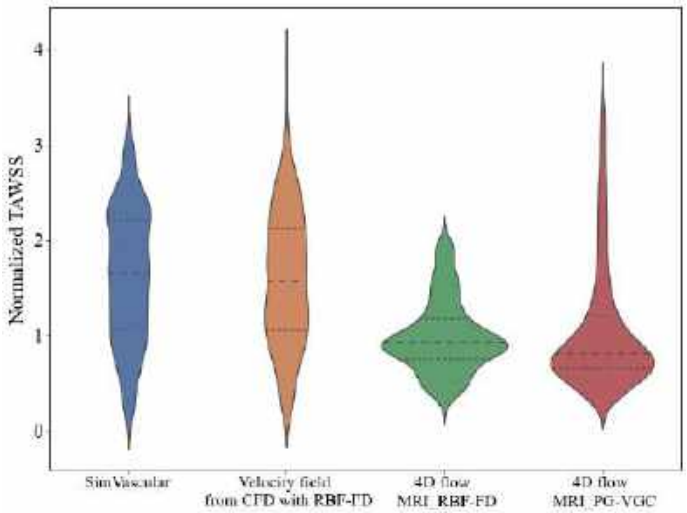

Figure 2: Distribution of normalized TAWSS over the ICA aneurysm obtained from CFD and 4D flow MRI.

DISCUSSION

In this study we compare WSS distributions in an ICA aneurysm computed from CFD and from *in vivo* 4D flow MRI data augmented with PG-VGC method. The WSS was computed from the numerical and MRI-based velocity distributions using the same numerical schemes. This study demonstrates the effect of spatial and temporal resolution on velocity measurements and the resulting discrepancy in the WSS distribution. Additional studies where the same methods are applied to more aneurysmal geometries will allow us to better understand 4D flow limitations in measuring near-wall velocities and improve the accuracy of image-based WSS estimates.

ACKNOWLEDGEMENTS

The authors would like to acknowledge Dr. M. Markl, and Dr. S. A. Ansari for providing the 4D flow MRI data. This work was supported by the R01 HL115267 award.

REFERENCES

[1] Schnell, S., Ansari, S. A. et al., *Journal of magnetic resonance imaging : JMRI*, *46*(1), 102–114, 2017. https://doi.org/10.1002/jmri.25595

[2] Xiang, J., Tutino, V. M. et al., *American Journal of Neuroradiology*, *35*(10), 1849-1857,2014.

[3] Zhang, Jiacheng, Sean M. Rothenberger et al., *Annals of Biomedical Engineering* 50(12):1810–25, 2022. doi: 10.1007/s10439-022-02993-2.

[4] Detmer, F. J., Chung, B. J. et al., International journal of computer assisted radiology and surgery, 13(11), 1767–1779, 2018. https://doi.org/10.1007/s11548-018-1837-0

[5] Rothenberger, S. M., Patel et al., (2023). Automatic 4D flow MRI Segmentation Using the Standardized Difference of Means Velocity. *IEEE Transactions on Medical Imaging, 2023*.

A CASE STUDY: COMPUTATIONAL MODELING OF HEMODYNAMICS IN A PATIENT WITH END STAGE RENAL DISEASE UNDER HEMODIALYSIS VIA ARTERIOVENOUS FISTULA WITH PULMONARY HYPERTENSION

Fatemeh Bahmani (1), Kaitlin Southern (1), Alex Vadati (1), Veeranna Maddipati (2), Stephanie M. George (1)

(1) Department of Engineering, East Carolina University, Greenville, NC, USA
(2) Internal Medicine, Brody School of Medicine, East Carolina University, Greenville, NC, USA

INTRODUCTION

Arteriovenous fistula (AVF) hemodialysis in end stage renal disease (ESRD) patients may lead to pulmonary hypertension (PH), left ventricle dysfunction and heart failure. Cardiovascular problems are the main cause of high mortality rates among ESRD patients who undergo hemodialysis via a surgically created AVF [1]. Understanding the role of arteriovenous fistula creation and characteristics on pulmonary artery (PA) hemodynamics and cardiac output could assist in managing treatment plans and performing kidney transplant before cardiac failure occurs. It is suggested to monitor fistula flow, pulmonary artery pressure and ejection fraction at least six months after the fistula creation to diagnose pulmonary hypertension and intervene to prevent heart failure [1, 2].

Several studies have investigated the increased incidence of pulmonary hypertension in ESRD patients who undergo hemodialysis via arteriovenous fistula and examined the relationship between the fistula blood flow volume, pulmonary artery pressure (PAP) and cardiac output (CO). A fistula with flow rates greater than 1-1.5 L/min is considered a high flow fistula [1]. The prevalence of PH in hemodialysis patients has been reported to be 14% - 43.7% [2-4]. However, these studies defined PH using doppler echocardiography and different diagnostic criteria: sPAP ≥30 mm Hg [2], mPAP≥25 mm Hg [3], sPAP ≥35 mm Hg [4]. No PH was reported in patients who received peritoneal hemodialysis. It is observed that temporary fistula closure or kidney transplant will return the cardiac output and pulmonary pressure to their normal range [4]. The mechanism of PH incidence in ESRD patients who undergo AVF hemodialysis is still ambiguous. Several hypotheses are mentioned in the literature as potential explanations of PH prevalence in ESRD patients. The potential causes might be excessive cardiac output, anemia, and fluid overload. Also, the change in hormones and metabolism may lead to artery constriction and increase the pulmonary artery resistance which may cause pulmonary hypertension. Yilga et al. suggested that increased cardiac output may not be the primary reason for PH incidence in ESRD patients, but increased resistance of vessel wall and decreased response of the pulmonary vasculature could be the main cause. The arteriovenous access for hemodialysis causes an excessive cardiac output and the pulmonary vasculature with increased resistance has lower response to the increased cardiac output to maintain the blood pressure [4].

The goal of our study is to use computational fluid dynamics (CFD) to model the subject-specific blood flow in the pulmonary artery and arteriovenous fistula in a single ESRD patient who was undergoing hemodialysis and developed pulmonary hypertension. This is a unique case study as the imaging data used to create both models were acquired at the same time from the same patient. The results will be compared with findings from the literature.

METHODS

The data acquisition from the patient was approved by East Carolina University Internal Review Board (UMCIRB 19-000708). Here we report the complete results for one subject. This individual was an African American male, 41 years of age at the time of imaging, had been diagnosed with PH via right heart catheterization (RHC) several months before the time of imaging and was undergoing hemodialysis through a mature surgically created arteriovenous fistula. Data measured by RHC of pulmonary artery is listed in table 1.

Table 1. Right heart catheterization data of the patient

mPAP (mm Hg)	PCWP (mm Hg)	PVR (Wood units)	Cardiac Output (L/min)
54	35	2.07	8.2

The MR imaging was performed using a Siemens Aera 1.5 T scanner which uses a gradient echo (GR) imaging sequence. The subject's pulmonary artery geometry was reconstructed using 22 slices with 8 mm thickness from short axis cine scan. The transient velocity waveform of the cardiac cycle just past the leaflets of the pulmonary

artery was obtained using phase-contrast magnetic resonance imaging (PCMRI). For imaging of the fistula, the patient was in the supine position in the MR machine. This allowed for the brachial AVF to be captured in the images. The PCMRI images were processed with an in-house MATLAB code to obtain the PA and AVF data included in table 2.

Table 2. Mean PA and AVF data from PCMRI image processing over one cardiac cycle

	Vessel area (cm^2)	Velocity cm/s	Flow rate (mL/min)	PA diameter (cm)
PA	10.243	6.756	4146.751	3.611
AVF	0.075	17.609	1967.494	0.308

The patient specific pulmonary artery and fistula geometries were reconstructed using the segmentation techniques in Mimics 20.0 (Materialise, Inc., Plymouth, MI). The models were then imported into ANSYS Workbench (ANSYS, Inc., Canonsburg, PA) where the computational mesh was generated, and fluid flow simulations were set up using ANSYS Fluent. Blood was taken to be a non-Newtonian fluid with Carreau viscosity model and a density of 1060 kg/m^3. The transient velocity waveform was implemented at the inlet boundary and the outlets were taken to be zero pressure gradient outlets for pulmonary artery and an 84% proximal vein (PV) and 16% distal artery (DA) split flow outlet for fistula.

RESULTS

Here we report on both pulmonary artery and arteriovenous fistula hemodynamics from the same patient based on data acquired at the same time. The volume rendering of blood velocity and contour of wall shear stress in pulmonary artery at peak systole are shown in figure 1. Volume rendering of blood flow velocity in arteriovenous fistula at peak systole and the velocity waveform implemented at the inlet of proximal artery are shown in figure 2. Pulmonary artery and fistula parameters obtained from CFD simulations are included in table 3.

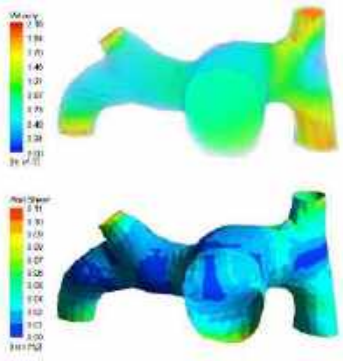

Figure 1. PA volume rendering of velocity (top) and contour of wall shear stress at peak systole (bottom)

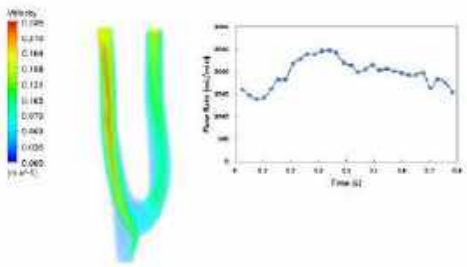

Figure 2. AVF volume rendering of velocity at peak systole (left) and AVF inlet volume flow rate across one cardiac cycle (right)

Table 3. Summary of PA and AVF results from CFD simulation

	Volume Weighted Average Velocity at Peak Systole	Max WSS at Peak Systole (mm Hg)	Max time-Averaged WSS (mm Hg)	Mean of Time Averaged WSS (mm Hg)
PA	0.847 (m/s)	0.114	0.039	0.008
AVF	7.89 (cm/s)	0.131	0.112	0.004

DISCUSSION

Pulmonary hypertension has a prevalence of up to 43% in ESRD patients who receive hemodialysis via AVF [2-4]. The summary of data obtained from echocardiography to study the relationship between AVF flow rate and PA pressure reported in literature is listed in table 4.

Table 4. Literature data of ESRD patients under hemodialysis

Study	No. of patients	PH criteria	% w/ PH	PAP range (mm Hg)	PAP mean±SD (mm Hg)	CO	Fistula flow rate
Beigi 2009	34	sPAP>30 mm Hg	14	11.4-45 (all patients)	19.9±9.17 (all patients)	5500 mL/min before fistula vs 5680 ml/min after fistula	2750 mL/min w/PH 1322 mL wo/PH
Acarturk 2008	32	mPAP≥25 mm Hg	43.7	8-39 all patients 25-39 w/PH patients	32.2±4.7 w/PH va 14.4±4.4 wo/PH	No data	Median 978.0 mL/min (Interquartile range 762.0–1584.5)
Yilga 2003	58	sPAP>35 mm Hg	39.7	37-65 (w/PH patients)	44±7	6.9 L/min w/PH vs 5.5 L/min wo/ PH	No data

As seen in table 6 higher AVF blood flow rates are observed in ESRD patients with PH which is correlated with high cardiac output (p=0.017) [4] and cardiac index (r=0.453, p=0.014) [3]. Our AVF flow rate of 1967.494 mL/min obtained from PCMRI is relatively high compared to normal.

While echocardiography is a useful tool for initial screening of PH, it is reported to be of moderate accuracy. RHC is the gold standard to diagnose pulmonary hypertension and we have used RHC for PH diagnosis. Also other studies have focused on the CFD of PA while we have included CFD of both PA and AVF. Using MRI and CFD provides better insight into the hemodynamics of PA and AVF.

We have obtained an mPAP value of 54 mm Hg from RHC, mean wall shear stress of 0.008 mm Hg for PA and 0.004 mm Hg for AVF from CFD. Our results and data from other studies [5] show lower values of WSS in PH patients compared to normal which could be used as a measure for PH diagnosis.

It is claimed that diminished vasodilatory capacity of pulmonary artery due to calcification and increased resistance may play a role in developing PH in ESRD patients [4]. Endothelin 1 (ET-1) which is a vasoconstrictor is increased in chronic renal patients [6]. Our future goal is to recruit more patients to study the effect of AVF alterations on pulmonary artery hemodynamics.

ACKNOWLEDGEMENTS

The authors would like to thank Constantin B. Marcu, MD for image acquisition. This work was supported in part by the Division of Research, Economic Development, and Engagement, East Carolina University

REFERENCES

[1] Warner, Eric D, et al., J Card Fail., 29(6), 979-981, 2023.
[2] Beigi AA, et al., J Vasc Access.,10(3), 160-6, 2009.
[3] Acarturk ,Gursel, et al., Int Urol Nephrol, 40(2), 509-13, 2008.
[4] Yigla, Mordechai, et al., Chest, 123(5), 1577-82, 2003.
[5] Tang, Beverly T et al., Pulmonary circulation 2.4: 470-476, 2012.
[6] Brooks DP, Clin Exp Pharmacol Physiol, Apr, 23(4), 1996.

EFFECTS OF SOAKING SOLUTION ON ANTERIOR CRUCIATE LIGAMENT HYDRATION, MECHANICS, AND MAGNETIC RESONANCE IMAGING

Charlotte Andreasen (1), Peter Kuetzing (1), Hassan Siddiqui (2), Audrey McManus (3), Ulrich Scheven (1), Ellen M. Arruda (1,3,4)

(1) Mechanical Engineering, University of Michigan, Ann Arbor, MI, USA
(2) Premedicine, Pennsylvania State University, State College, PA, USA
(3) Biomedical Engineering, University of Michigan, Ann Arbor, MI, USA
(4) Macromolecular Science and Engineering, University of Michigan, Ann Arbor, MI, USA

INTRODUCTION

The anterior cruciate ligament (ACL) connects the femur and tibia, preventing anterior tibial translation and helping to limit rotation of the tibia relative to the femur. It is vital in maintaining proper mechanics of the joint [1]. ACL tears are very common, especially in athletes, with more than 200,000 of these injuries happening annually in the US alone. More than half of these injuries are non-contact, meaning further research into the mechanics of the ligament could help prevent these injuries occurring [2].

Studies have examined the mechanics of isolated ACLs in a variety of ways, including repeated submaximal loading and collecting full field strain data for constitutive modeling using magnetic resonance (MR) imaging [3, 4]. Protocols like these often require testing over a period of time or lag time between tissue extraction and testing. Once the ligament is removed from its natural environment, it begins to dehydrate, which causes the tissue to stiffen, making tissue hydration a primary concern in mechanical testing. Often, tissues are frozen so that they do not have to be used immediately, but this also affects the mechanical properties of the tissue and causes the water in the tissue to leave, causing lower MR visibility [5]. While phosphate buffered saline is often used to combat tissue dehydration, studies have shown that many tissues will become oversaturated with fluid if soaked in PBS and that the best buffer to maintain the physiologic level of hydration is tissue dependent [6, 7].

Therefore, this study aims to determine what storage solution will maintain the physiological hydration level of the ACL; and how this solution affects the mechanical properties and MR imaging capabilities of the ACL.

METHODS

Ovine tibiofemoral joints were purchased from a local abattoir and the anteromedial (AM) bundles of the ACL were extracted. We utilized the following solutions to test the hydration level of the ACL after soaking for either 2 or 12 hours:

- phosphate buffered saline (PBS): PBS is commonly used to maintain the hydration of tissues.
- bovine synovial fluid: The ACL is contained in synovial fluid in its natural environment.
- polyethylene glycol (PEG): PEG 20000 was used so that the molecule was large enough not to absorb into the ACL. A range of concentrations were tested.
- ophthalmic gel: Ophthalmic gel is a non-newtonian fluid commonly used to maintain hydration of canine eyes.
- unsoaked tissue contained in nitrile glove: Nitrile gloves were used to create a climate chamber around the ACL because of their low permeation rate.

For mechanical testing, ACLs were soaked in PBS, synovial fluid, ophthalmic gel, or PEG 8% weight/volume for 0, 2, or 12 hours. Then the ligaments underwent loading in the main fiber direction with a 5% strain at 1 Hz for 60 cycles. The peak force of each loading cycle was then plotted against the natural log of time (or cycle number) to identify a change in material properties by soaking time and solution. Finally, separate ACLs were segmented and soaked in PBS, ophthalmic gel, and PEG 8% to determine the effect of these solutions on MR signal amplitude.

RESULTS

The relationship between swelling ratio, soaking solution, and soaking time is shown in Figure 1.a. PEG 8% w/v had a swelling ratio with no significant difference from zero. This indicates the hydration level did not significantly change after soaking.

The rate of force decay shown in Figure 1.b was compared between samples using Student's T tests. None of the samples in buffers at time 0

differed significantly from the unsoaked samples. All of the buffers led to a significantly larger rate of force decay after 12 hours, though PEG 8% w/v had the smallest change. A linear regression was performed to determine the effect of swelling ratio, soak time, and initial peak force on the rate of force decay. When the rate of force decay was normalized by the initial peak force, both soak time and swelling ratio were significant predictors of the rate of force decay.

Soaking in all of the tested buffers led to an increase in signal amplitude and T_2^* during MR imaging as shown in Figure 2. These changes were not significantly different between solutions, so changing the soaking solution does not affect the capabilities of MR imaging.

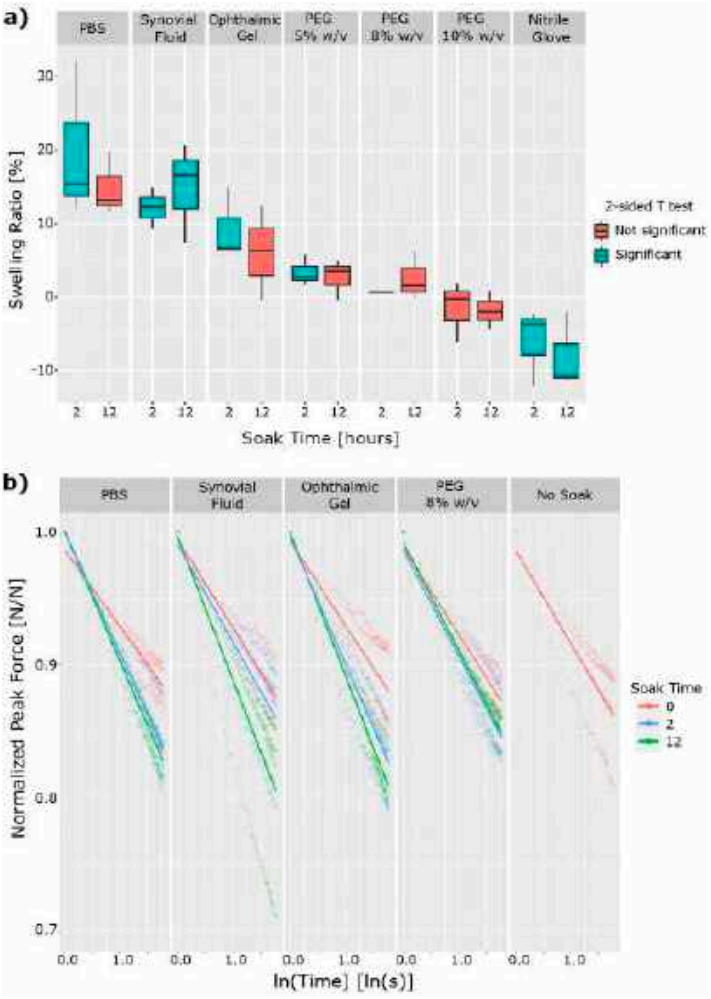

Figure 1: a) The swelling ratios for AM bundles of ovine ACLs, by soaking solution, after 2 or 12 hours of soaking at room temperature. A two-sided T-test determined whether each group was significantly different from a swelling ratio of 0 (i.e. no fluid uptake). b) The peak force from each loading cycle was plotted on a semi-log plot with time and we define the slope of these plots as the rate of force decay.

DISCUSSION

As mechanical testing of ligaments becomes more complex and nuanced, maintaining the physiological conditions of the ligaments becomes more important. These results suggest that there is some level of degradation occurring in the ligaments after 12 hours and that the ingress of water "softens" the materials. Maintaining the physiological hydration level helps to reduce the changes in mechanical behavior over time. Moreover, we see that soaking ACLs in synovial fluid causes an uptake in fluid, which leads us to believe that the boundary conditions and connective tissue in the joint play a more important role in the hydration and mechanics than previously thought. Future work will investigate this.

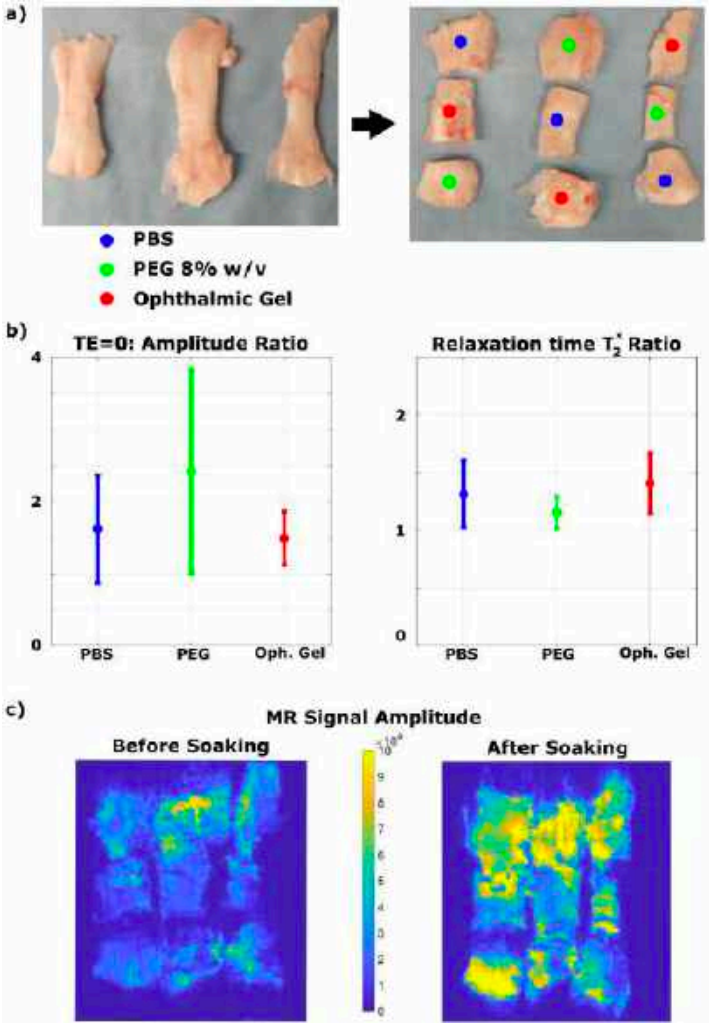

Figure 2: a) Three ovine ACLs were segmented into approximately equal length sections. One section from each was soaked in PBS, PEG 8% w/v and Ophthalmic Gel. b) The per voxel signal amplitude increased by a factor of 1.5-2.5 after soaking overnight and the relaxation time increased by a factor of 1-1.5. c) The scaled signal amplitude shows where fluid was taken up into the tissue.

ACKNOWLEDGEMENTS

This material is based upon work supported by the National Science Foundation Graduate Research Fellowship under Grant No. DGE-1841052. Any opinion, findings, and conclusions or recommendations expressed in this material are those of the authors and do not necessarily reflect the views of the National Science Foundation.

REFERENCES

[1] H Y et al. Treasure Island (FL): StatPearls Publishing, 2023.

[2] Chia L et al. *Sports Med* 52 (2022).

[3] Kim J et al. *J Exp Orthop* 9.1 (2022). DOI: 10.1186/s40634-022-00507-6.

[4] Luetkemeyer CM et al. *Journal of the Mechanics and Physics of Solids* 156 (2021). DOI: 10.1016/j.jmps.2021.104577.

[5] Venkatasubramanian R et al. *Annals of Biomedical Engineering* 34 (2006). DOI: 10.1007/s10439-005-9044.

[6] Safa B et al. *J Biomech* 61 (2017). DOI: 10.1016/j.jbiomech.2017.06.045.

[7] Werbner B et al. *J Mech Behav Biomed Mater* 125 (2022). DOI: 10.1016/j.jmbbm.2021.104951.

ON THE MARGINATION OF WHITE BLOOD CELLS

Thien-Tam Nguyen (1), Trung B. Le (1)

(1) Department of Civil, Construction, and Environmental Engineering
North Dakota State University Fargo ND, United States

INTRODUCTION

The margination of white blood cells (WBCs) has been the focus of extensive experimental and numerical studies [1, 2] due to its importance in bio-engineering[3]. Although the exact mechanism of this phenomenon is yet to be fully understood, it has inspired the development of a new generation of micro-carriers for targeted drug delivery. These carriers, mimicking the margination behavior of WBCs, could address the challenges in drug delivery [4]. Therefore, identifying important factors in WBC margination could be valuable in designing and advancing the development of next-generation micro-carriers. A deeper understanding of phenomena such as the margination of WBCs could open up new avenues for targeted drug delivery systems and further advance the field of biomedical engineering.

In this work, a series of numerical experiments using a hybrid dissipative particle dynamics (DPD)-computational fluid dynamics (CFD) solver is used elucidate the role of the WBC membrane stiffness in the deformability and trajectory of WBCs in microchannel flows.

METHODS

The White Blood Cell is modeled in two parts, namely the membrane and the cytoplasm. Our method of choice for the latter component is the Dissipative Particle Dynamics (DPD) method. The cytoplasm is a gel-type fluid that mediates all chemical transportation and signaling processes. While different cytoplasmic organelles exist, the DPD method allows the grouping of atoms and particles that make up these ”little organs” into particle-like entities through a coarse-grained representational process.

The membrane of WBC is also modeled with DPD (Table 1). However, for this particular component, an initial configuration is required to generate the network of DPD particles into the shape of the desired cell. We have used an equation for a sphere to achieve the initial shape of all the WBCs. A standard calibration procedure for the DPD method calls for testing the membrane configurations in the equilibrium and the stretching tests. We have carried out these tests with five configurations of the WBC membrane having from 200 to 4000 particles. The stretch test mimics a pair of microbeads pulling the WBCs in opposite directions with a total force of 15 micro-Newton.

Our study of leukocyte membrane stiffness consists of a series of numerical experiments using the calibrated model of the cell from the above step in a microchannel flow. The interaction between the cell and the fluid is a two-way interaction. To achieve this goal, the DPD method is two-way coupled with a CFD solver with the implementation of the curvilinear immersed boundary (CURVIB) method. The CFD solver utilizes three-dimensional, unsteady incompressible continuity and Navier-Stokes equations in a discrete form [5]. The discrete equations are integrated over time using a fractional step method. For solving the momentum equations, we use a Newton-Krylov solver in the momentum step, and a GMRES solver with a multigrid pre-conditioner is used for the Poisson equation.

We used Pointwise software to generate a rectangular microchannel whose width and height are five times the cell’s diameter, while the length is 20 times. The WBC configuration has the same number of particles for both the cytoplasm and the membrane for all the simulations, which are 65 and 660, respectively. We come to decide on these numbers based on the results of the calibration tests. The location of the cell is at the center of the crosswise plane of the blood plasma grid while being at a distance of 5 times the cell diameter from the left wall to minimize the impact of prescribed conditions at the inlet. The total number of grid points is 3 million. Uniform velocity is prescribed at the inlet while a fully developed profile is prescribed at the outlet. No-slip wall is prescribed for other faces to complete the boundary conditions. We fixed the WBCs in place and disabled two-way coupling (FSI) for the first 1000 time steps. During this time, the CFD solver would reach a steady-state solution, and an equilibrium state should be reached for the cells. Only then, the FSI module was enabled.

Table 1: Cell parameters of the DPD method for modeling the White Blood Cell.

Cell Diameter (μm)	Shear Modulus ($pN/\mu m$)	Persistence Length (μm)	Maximum Extension Length (μm)	Bending Stiffness (Nm^2)	Force Coefficient (J)
7.0	$4.7E+3$	$1.8E-3$	0.59	$1.5E-24$	$2.4E-18$

RESULTS

Figures (1) and (2) show the continuum mesh adaptively changed according to the movement of the cell. As the result of the CURVIB method, the Navier-Stokes solver only solved for flow solutions in the volume without the occupy of the cell's volume. A trace of the WBC (region with zero velocity submerged within the flow field) can be tracked in many cut planes without visualizing the DPD particles. Our method allows the hemodynamics outside the cell to be captured in high fidelity.

By tracking the top and bottom DPD points and plotting them in tandem with the cell's displacement, Figure (2) clearly shows that the WBC was rolling when migrating downstream. The traces of immersed nodes on vertical and horizontal middle-cut planes further tell the direction of the movement, which is upward and toward the right wall.

In DPD formulation, the shear modulus μ_0 characterizes the stiffness of the cell's membrane. Thus, we test the shear modulus from the range of Red Blood Cells (RBCs) ($10^1 pN/\mu m$) to 2 orders of magnitude greater range ($10^3 pN/\mu m$). In a similar implementation of the DPD method for the case of RBCs, it has been reported [6] that the membrane requires at least 500 DPD particles to behave accurately in the numerical experiments. This explains the 660-particle configurations in our setup.

The behavior of circulatory cells to their membrane stiffness has been studied in detail, as evidenced by the results presented in Figure (3). It was found that the spherical cell with the RBC membrane's stiffness behaved similarly to this type of circulatory cell. The cell membrane deformed quickly and attained an equilibrium shape, which propagated along the flow in a straight line, with no visible rolling during the maneuver.

However, when the membrane stiffness doubled within the first order of magnitude, the cell's trajectory became more chaotic and sensitive to instantaneous changes in the flow. Observing the tracers' paths, it was noted that the trajectory had multiple sudden changes, but no visible rolling occurred during the cell's maneuver. This was the case where the cell executed the quickest displacement toward the right wall.

From the latter half of the second order of magnitude to the WBC range, rolling became a stable behavior. As depicted in Figure (3), the cases of $750pN/\mu m$ and $5000pN/\mu m$ had almost identical trajectories despite a significant leap in membrane stiffness value. These findings shed light on the behavior of circulatory cells in different membrane stiffness conditions and can inform future research in the field.

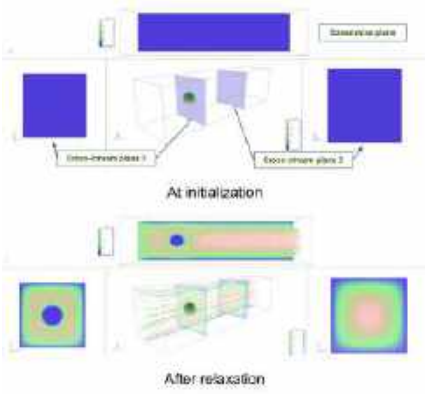

Figure 1: The flow fields at initial condition (up) and fully converged (bottom) are the results of the relaxation step by the 3D incompressible Navier-Stokes solver.

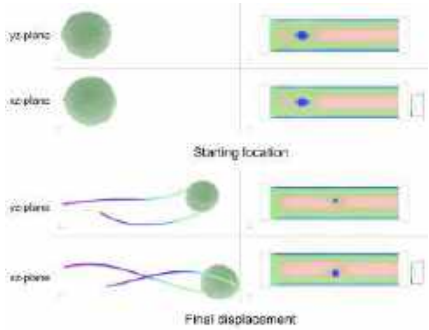

Figure 2: Displacement of the WBC (in green) from the starting location to the last snapshot of the simulation. The rolling behavior is highlighted by tracking two particles in the membrane (left). CFD-DFD coupling allows two-way interaction between the fluid and the cell (right).

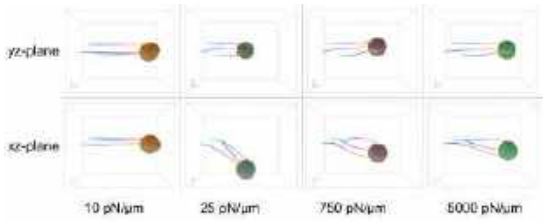

Figure 3: Differences in rolling behavior of circulatory cells where the membrane stiffness differs.

DISCUSSION

Our findings could have significant implications for the development of micro-carriers for targeted drug delivery. By mimicking the stiffness of the WBC membrane, these carriers could potentially navigate through the bloodstream with greater precision and efficiency, ultimately leading to more effective drug delivery. Further research in this area is necessary to fully understand the potential applications of these findings in the field of biomedical engineering.

ACKNOWLEDGEMENTS

We acknowledge the financial support from the ND-EPSCoR via the ND-ACES grant (NSF Grant number 1946202). Our computational simulations in this study were performed using the computational resources of the Center for Computationally Assisted Science and Technology (CCAST) at North Dakota State University. We want to express our deepest gratitude toward Dr. Amit Joshi of the Medical College of Wisconsin for providing us with an excellent experiment movie and professional insights that led us to the subject of this study.

REFERENCES

[1] Fedosov DA et al. *Microcirculation* 17.8 (2010).

[2] Fedosov DA et al. *Physical review letters* 108.2 (2012).

[3] Takeishi N et al. *Physiological reports* 2.6 (2014).

[4] Qi X et al. *Physics of Fluids* 33.12 (2021).

[5] Le TB et al. (2010).

[6] Akerkouch L et al. *Fluids* 6.4 (2021).

STENT RETRIEVER REMOVAL FORCES IN AN EXPERIMENTAL STROKE MODEL WITH PORCINE CAROTID ARTERIES

Demitria A. Poulos (1), Michael T. Froehler (2), Bryan C. Good (1)

(1) Mechanical, Aerospace, and Biomedical Engineering
University of Tennessee
Knoxville, TN, USA

(2) Vanderbilt Cerebrovascular Program
Vanderbilt University Medical Center
Nashville, TN, USA

INTRODUCTION

In the United States nearly 800,000 strokes occur each year, 87% of which are classified as an acute ischemic stroke (AIS) [1]. AIS, a result of the sudden occlusion of a cerebral artery, is typically treated by a mechanical thrombectomy (MT), either through aspiration or stent retriever (SR) techniques. MT is a transfemoral endovascular approach used to achieve recanalization and can increase the treatment window up to 24 hours [2]. While SR MT is the predominantly used method, a meta-analysis comparing the efficacy outcomes of direct aspiration and SR MT identified no significant difference in good clinical outcomes [3]. Despite its clinical success, adverse outcomes including hemorrhage and thrombus embolization can also still occur [4]. To improve the degree of revascularization and limit the risk of complications, experimental circulatory flow systems are used to assess various parameters of SR MT.

Previous studies conducted in our lab used an experimental flow loop to identify the forces required to achieve thrombus dislodgement by the SR (i.e., removal force) in various cerebral artery models made of PVC tubing [5]. These *in-vitro* models offer a more practical approach for testing devices but, in many cases, do not capture the frictional and adhesive forces that occur between SRs and vessel walls. To more accurately mimic *in-vivo* conditions, and to assess the influence of the vessel wall material on thrombus removal force, experiments were conducted using commercial SRs and porcine carotid arteries (CAs) and compared to data collected previously in PVC models.

METHODS

A circulatory flow system (**Fig. 1**) was developed using a peristaltic pump (VWR 3300), fluid reservoir, and a cerebral artery model. Water was circulated at a flowrate of 300 mL/min within the system to mimic typical cerebral artery conditions. To perform an SR MT procedure, a 6x30 mm Solitaire2 SR (Medtronic) within a Phenom27 microcatheter (Medtronic) was passed through a hemostatic valve into the flow loop (**Fig. 1**). The SR was then deployed within the arterial model and connected to a force gauge (MXmoonfree) attached to a stepper motor (kdScientific) which ensured the SR was pulled at a constant speed for 15 seconds and the maximum removal force was recorded.

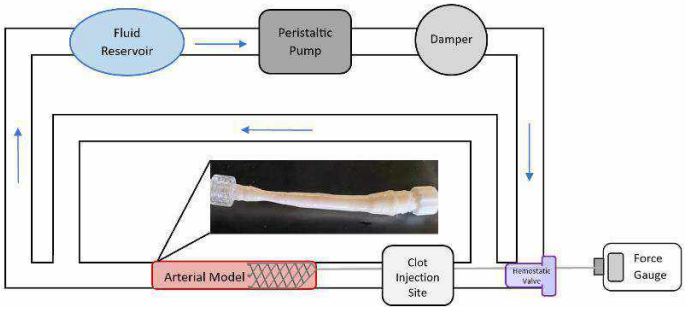

Figure 1: Schematic of experimental circulatory flow loop used to evaluate SR MT removal forces.

For these experiments, two different cerebral artery models were incorporated into the flow loop: porcine CAs and straight PVC tubing that tapered from 5.5 to 3.3 mm in diameter to represent naturally constricting cerebral arteries. Porcine CAs were obtained from Lampire Biologics and were stored in PBS at 4 °C until experimental testing. To ensure the CAs did not dry out between testing, one CA was prepared and tested, while the other CAs were kept stored in PBS. Prior to testing, the tunica

adventitia layer was carefully removed from the CA, and it was cut to be approximately 3 inches in length. The porcine CAs naturally taper, as seen in **Fig.1**, and therefore the inner diameters at each end were measured with digital calipers before proceeding to the next preparation stage. Each CA end was then stretched over a male plug to socket connecter and adhered with Loctite super glue to ensure its attachment to the flow loop without fluid leakage. Care was taken throughout the entire CA preparation process so as to not damage the inner endothelium of the vessel samples. Prior to testing each CA, a marker was made on the SR and catheter devices so that the length of the SR deployed within the system and the distance it is pulled during each MT trial could be controlled across all trials.

RESULTS

The maximum SR removal force for each experimental test parameter is summarized in **Table 1**. For these experiments, 3 different porcine CAs were used to create a sample size of n=20, 8 SR MTs were performed with CAs #1 and #2 and 4 SR MTs were performed with CA #3.

Table 1: SR removal force for each model material

Test Parameter	Sample (n)	Average Removal Force (N)
PVC	20	0.25 ± 0.01
Porcine	20	0.31 ± 0.05

A comparison of the PVC tubing and porcine artery model materials is displayed in **Fig. 2**. From this, a greater SR removal force is observed with the porcine CAs. A one-way ANOVA with significance at $p < 0.05$ was performed on the resultant data and indicated a significant difference in the SR MT removal forces between the two arterial model materials ($p = 5.69E-7$).

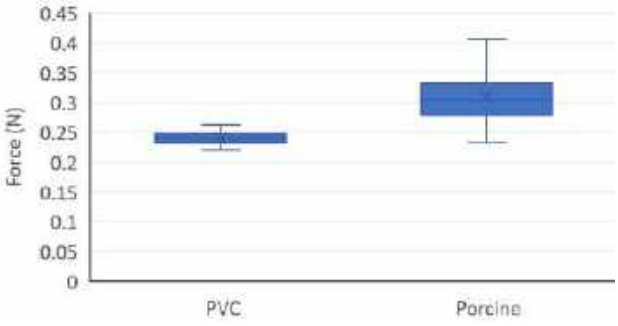

Figure 2: Maximum SR removal forces from PVC and porcine arterial model materials.

DISCUSSION

Experimental circulatory flow loops modeling AIS are typically used to evaluate the performance of SRs, and EA fracture and embolization [6]. These *in vitro* flow loops include either patient specific or simplified cerebral artery geometries, usually composed of silicon, glass, or plastic materials [6]. Many of these models, however, do not take into consideration the interaction between the SR and vessel wall, which can influence the SR performance and overall MT outcome [7]. Pulling the SR during the thrombus retrieval process can also lead to SR elongation or collapse, and the friction between the SR and endothelium can cause the vessel to stretch or tear [7].

Studies have also indicated that the SR to vessel wall interaction is a key component of successful recanalization [8]. These results have led us to the hypothesis that the vessel wall material influences the SR removal force (i.e., pulling of the SR to dislodge the thrombus), and should be a factor considered in the development of any experimental model of AIS.

This study compares the SR removal forces in a benchtop experimental model of MT performed using both porcine CAs and PVC tubing arterial models. The porcine CAs used in these experiments tapered from approximately 4.9 to 3mm in diameter, which was similar to the tapering in the PVC tube models (~5.5 to 3.3mm). A comparison of the average SR removal forces indicates that a higher force was required in the porcine CAs (0.31 ± 0.05 N) than in the PVC tube (0.25 ± 0.01 N). These results indicate that accurately representing the interaction between the vessel endothelium and nitinol SRs in *in-vitro* models can lead to higher removal forces than previously expected.

The coefficients of kinetic friction between SRs and various AIS model materials were previously investigated in our lab [9]. The results, presented in **Table 2**, provide further evidence that the higher removal forces found in this study may be due to the higher friction coefficients between SRs and carotid artery materials compared to PVC and other non-biological materials.

Table 2: Coefficients of kinetic friction between nitinol SRs and common arterial model materials [9]

Test Material	Coefficient of Kinetic Friction
glass	0.18 ± 0.05
PVC	0.61 ± 0.06
silicone	0.78 ± 0.06
bovine CA	0.73 ± 0.17

Future work will focus on incorporating embolus analogs (EAs) into the flow loop to mimic an AIS. EAs will be lodged within the arterial models, both PVC tubing and porcine CAs, and previously stated flow loop protocols will be repeated to measure the SR removal forces. Higher SR removal forces are expected in both the PVC and porcine models with the presence of an EA when compared to the results collected without an EA. Therefore, we hypothesize that greater SR removal forces will be observed with porcine CAs, since we predict that the EAs will also have greater adhesion and friction with vessel walls.

REFERENCES

[1] Benjamin EJ, et al. *Circulation* 2019; 139.
[2] Inoue M, et al., *JAHA* 2021; 10.
[3] Primiani CT, et al., *Journal of Stroke and Cerebrovascular Diseases* 2019; 28:1329-1337.
[4] Luraghi G, et al., *Interface Focus* 2020; 11.
[5] Poulos DA, et al., *SB3 Conference* 2023.
[6] Luraghi G, et al., *Journal of Biomechanics* 2021; 127.
[7] Kwak Y, et al., *Frontiers* 2022; 13.
[8] Machi P, et al., *JNIS* 2017;9:257-263.
[9] Elkhayyat O, et al., SB3 Conference 2023.

FLEXIBLE ROTOR BLADES IN LVADS: INVESTIGATING IMPLICATIONS FOR HEMOCOMPATIBILITY

Shweta Karnik (1), Shobana Santhanam (1), Charles Federico (1), Huang Chen (1), Lakshmi Prasad Dasi (1)

(1) Department of Biomedical Engineering, Georgia Institute of Technology and Emory University, Atlanta, GA, USA

INTRODUCTION

Heart failure (HF) is one of the leading causes of death, affecting nearly 6.2 million people in the United States (US)[1]. The preferred surgical therapy for end stage HF is heart transplantation; however, this therapeutic option is progressively limited due to the limited availability of donor hearts.

Left Ventricular Assist Devices (LVADs) have emerged as a standard of care for patients suffering from end stage HF as both bridge-to-transplantation and destination therapy[2,3]. After the discontinuation of two prominent LVADs in the last few years, namely Thoratec HeartMate II (now Abbott lab) and HeartWare HVAD (now Medtronic), Abbott's HeartMate III remains as the only implantable LVAD on the market.

Despite its clinical success, LVAD therapy is associated with serious morbidities and mortality[4,5]. Complications such as thrombosis can result in LVAD failure, requiring a potential second open-heart surgery for device replacement in the patient. Hemocompatibility plays a critical role in determining the long-term operation of the device.

Conventionally, LVADs have been designed to operate efficiently at a single operating condition i.e 5 L/min, 90mmHg. However, while implanting an LVAD, the operating speeds are often modified to match the device output with the patient's cardiac output. This would result in device operating at off design points, potentially compromising both hemocompatibility and longevity of the device.

To address this, we have developed a novel LVAD prototype with flexible rotor blades. Our hypothesis is that the mechanoresponsive behavior of flexible blades will enable them to deform as a response to the complex inflow conditions. With an optimized geometry and flexibility, this would not only improve the hemocompatibility of the LVAD but also offer a wider range of operation with optimal efficiencies.

In this study, we investigate the hemocompatibility implications of deploying flexible rotor blades in a centrifugal LVAD under adult physiological conditions (5L/min, 90mmHg). We will also explore the hydrodynamic performance of these LVAD prototypes at adult physiological condition i.e 5L/min,90 mmHg.

METHODS

Design and Manufacturing

Three designs were chosen for producing rigid and flexible rotor blade LVAD prototypes each. The blade thickness and height were fixed at 1.2mm and 7mm respectively. The inlet angle of the blades was set at 20º whereas the outlet angle was varied from 30º to 70º with 20º increments as shown in Figure 1. The rigid rotor blades were 3D printed using a J850 Pro (Stratasys Ltd, MN, USA) whereas the flexible rotor blades were casted using polyurethane resin of shore hardness 60A.

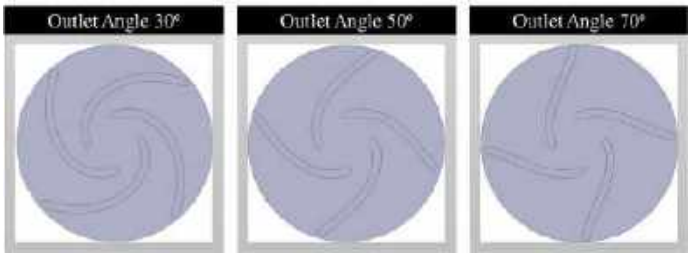

Figure 1: Novel LVAD Prototype Designs.

In vitro Hemocompatibility Assessment

The blood damage caused by both rigid and flexible blade LVAD prototypes was evaluated using porcine blood in a blood circulation loop (Figure 2). It consisted of a motor to drive the rotor, a flow probe, pressure transducers upstream and downstream of the rotor and a pinch valve to vary the downstream resistance.

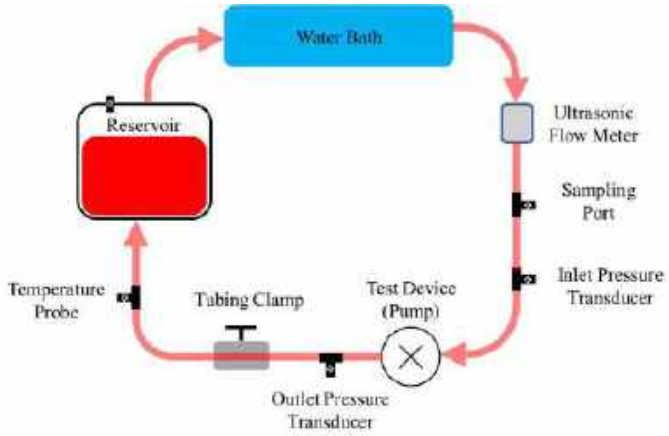

Figure 2: Blood Circulation Loop Schematic.

The blood circulation loop (BCL) was tuned to the adult physiological condition and blood samples were collected every 60 minutes over a period of 6 hours. The blood samples were centrifuged to prepare plasma. Hemolysis and platelet activities were quantified using commercially available enzyme-linked immunoassays (ELISA).

Hydrodynamic Performance Evaluation

The hydrodynamic performance of the LVAD prototypes was evaluated on a benchtop setup like the BCL. A blood mimicking 40% wt glycerin solution was used as the working fluid. The mounted rotor was driven at 3000 RPM, and the flow produced by the rotor was measured as the pinch valve incrementally increases downstream resistance. To characterize hydrodynamic performance, the gradient of the pressure-flow curve and the efficiency were measured.

$$gradient = \frac{P_4 - P_6}{4-6} \frac{mmHg}{L/min} \quad (1)$$

RESULTS

For a rigid rotor blade with an outlet angle of 30º, the gradient at adult operating conditions was – 11.52 mmHg/ (L/min)$^{-1}$ whereas its flexible counterpart had the gradient of – 11.12 mmHg/ (L/min)$^{-1}$. As the outlet angle increased, the pressure/flow gradient decreased for rigid rotor blade prototypes.

Results for the remaining hydrodynamic evaluation and hemocompatibility assessment is currently being generated and will be presented at the conference.

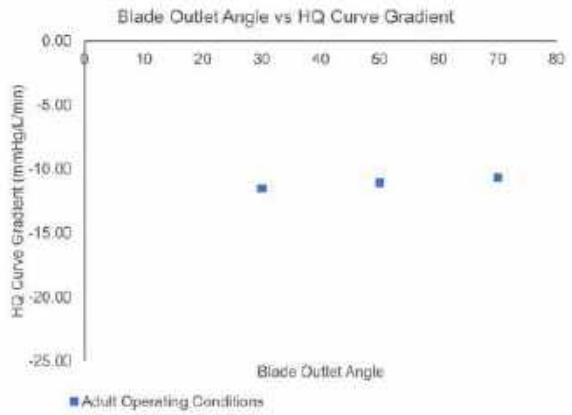

Figure 3: Effect of Outlet Angle of HQ curve gradient for Rigid Rotor Blade LVAD Prototypes.

DISCUSSION

The flexible rotor blade LVAD prototypes proposed in this study will be a positive step towards enhancing hemocompatibility of LVADs and thereby increasing device longevity. Preliminary results show that flexible rotor blades can generate a 'flatter' pressure-flow curve, a characteristic that is desirable. This would not only improve the preload sensitivity of the LVAD but also offer a wider range of operation with optimal efficiencies.

ACKNOWLEDGEMENTS

Research supported by the National Institute of Biomedical Imaging and Bioengineering of the National Institute of Health under Award Number 5R21EB033960.

REFERENCES

[1] Tsao, Connie W., et al. "Heart disease and stroke statistics—2022 update: a report from the American Heart Association." *Circulation* 145.8 (2022): e153-e639.

[2] Drakos, Stavros G., et al. "Bridge to recovery: understanding the disconnect between clinical and biological outcomes." *Circulation* 126.2 (2012): 230-241.

[3] Trivedi, Jaimin R., et al. "Survival on the heart transplant waiting list: impact of continuous flow left ventricular assist device as bridge to transplant." *The Annals of thoracic surgery* 98.3 (2014): 830-834.

[4] Kilic, Arman, Michael A. Acker, and Pavan Atluri. "Dealing with surgical left ventricular assist device complications." *Journal of thoracic disease* 7.12 (2015): 2158.

[5] Piccione Jr, William. "Left ventricular assist device implantation: short and long-term surgical complications." *The Journal of heart and lung transplantation* 19.8 (2000): S89-S94.

CHARACTERIZATION OF THE BASAL ENDOTHELIAL GLYCOCALYX

Zoe L. Vittum (1), Solomon A. Mensah (1,2)

(1) Biomedical Engineering, Worcester Polytechnic Institute, Worcester, MA, United States
(2) Mechanical Engineering, Worcester Polytechnic Institute, Worcester, MA, United States

INTRODUCTION

The endothelial glycocalyx is a transmembrane grass-like structure that encompasses endothelial cells serving to transduce extracellular signals, regulate vascular permeability, and inhibit the adhesion of leukocytes [1,2,3]. Glycoproteins and proteoglycans are the core proteins of the glycocalyx [1]. Glycoproteins have short carbohydrate chains attached while proteoglycans are glycoproteins that have glycosaminoglycan (GAG) chains attached [1,4]. GAGs are long repeating chains, the main GAG chains are hyaluronan, chondroitin sulfate (CS), various moieties of sialic acids (SA), dermatan sulfate, and heparan sulfate (HS) [1].

The glycocalyx along the lumen of the vessel is referred to as the apical glycocalyx which is directly exposed to shear due to blood flow. The basal glycocalyx is present at the smooth muscle cell interface. Historically, the apical and basal glycocalyx have been independently investigated due to the differences in their local environment and stimuli. The apical glycocalyx has been at the forefront of research efforts due to its direct role in mechanotransduction of shear forces due to flow [5,6]. The basal glycocalyx has also demonstrated sensitivity to shear forces [5,7]. Shear forces due to flow are transmitted from the apical glycocalyx through the cell cytoskeleton to basal glycocalyx components promoting alternate signaling pathways and influencing cell migration and morphology [7,8,9]. For example, Beayens et al. found that the mechanisms that instigate elongation and directional alignment may be independently regulated by apical and basal glycocalyx elements through investigation of core protein knockdown [7]. Their results suggest the apical and basal glycocalyx may play differing roles in sensing the magnitude and direction of shear stress [7].

Syndecan-4 is a predominantly basal proteoglycan that is colocalized with adhesion molecules, integrins, and cytoskeletal elements to form focal adhesions [1,5,7]. Evidence of the basal glycocalyx's shear response has been gathered through investigating syndecan-4 and attached heparan sulfate chains as little to no evidence of other proteoglycans and glycoproteins and their function in the basal cell membrane have been presented in literature [5,7]. Yet, investigation of endothelial cell shear force transmission often ends with probing cytoskeleton and focal adhesion structure for morphological differences leaving the basal glycocalyx's response to shear largely unknown.

Here we begin characterizing the basal glycocalyx through visualization of both the apical and basal glycocalyx encompassing the endothelial cell in static culture. Future experiments will include probing the basal glycocalyx after exposure to physiologically normal shear forces. Positive glycocalyx signal in both experiments indicates the presence of glycocalyx core proteins attaching extracellular glycocalyx components to the cell. Deviations observed in coverage and thickness of the basal glycocalyx signal between the static and flow cell's basal will indicate a remodeling response of the basal glycocalyx in response to shear. The observed response will shed light on how the basal core proteins and attached chains are adapting to shear on the basal surface of endothelial cells. Results of this study will aid in developing a deeper understanding of how the endothelial cell wholistically senses and responds to shear.

METHODS

Human lung microvascular endothelial cells (HUVECs) were maintained in Microvascular Endothelial Cell Growth Medium (Signma Aldrich) at 37 °C and passaged using 0.05% trypsin-EDTA at 70–80% confluence. Passage five HLMVECs were plated at 100,000 cells/mL on 24 mm x 24 mm fibronectin coated glass cover slips (Fisher Scientific) and allowed to adhere and remain in static culture for 18 hours after plating.

Slides were fixed with 0.4% paraformaldehyde and experimental groups were permeabilized with a series of 0.3% Triton X-100 (Thermo Fisher Scientific) treatments. The Triton X-100 treatment included a series of three 5-minutes exposures to 0.3% Triton X-100 and 5-minute PBS washes. Immunostaining using Wheat Germ Agglutinin (WGA)

(Thermo Fisher Scientific) as primary antibody and Alexa-flour 488 conjugated anti biotin (Thermo Fisher Scientific) as secondary antibody was used to label the overall glycocalyx. The slides were mounted with Flouromount DAPI Mounting Media (Thermo Fisher Scientific) for nuclei visualization. Confocal Z-stack images were taken with a 3 µm slice thickness. Image J was used to develop Z-direction orthogonal views of the to visualize the glycocalyx expression encapsulating the cell.

RESULTS

Preliminary results of staining of the apical glycocalyx, and both apical and basal glycocalyx are shown in Figure 1A and Figure 1B respectively. The HLMVECs were stained with WGA which targets all glycocalyx components (Fig. 1A, 1B). The glycocalyx signal is shown as green and the nucleus as blue. Figure 1A shows the nonpermeabilized result where only the apical glycocalyx is exposed to the immunofluorescent antibodies. In Figure 1A cell boundaries can be easily distinguished and the orthogonal view distinctly shows the apical glycocalyx coverage over the nuclei of the HLMVECs. Figure 1B shows the permeabilized result where Triton-X100 treatment was used to expose the basal glycocalyx to immunofluorescent antibodies. In the permeabilized group (Figure 1B) the glycocalyx signal is localized around nuclei structures, cell boundaries are not visualized as in Figure 1A. The orthogonal view of Figure 1B shows glycocalyx signal throughout the area that is expected to be occupied by the cell. This effect can be seen in the overlap of glycocalyx (green) and nuclei (blue) signal in the orthogonal view that is not present in Figure 1A. Finally, nuclei signal was observed at Z planes above and below the expected regions. This can be seen through observation of the orthogonal nuclei signal in Figure 1B and comparison to Figure 1A.

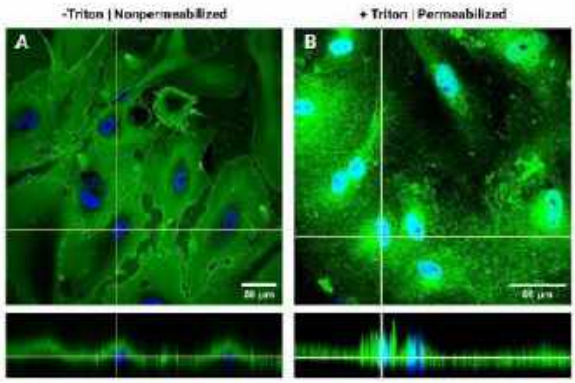

Figure 1: Glycocalyx coverage in static cultured HLMVECs in the apical (A) and apical and basal (B) cell.

DISCUSSION

An extensive literature review was conducted to understand how the basal glycocalyx has been previously investigated and characterized. Unfortunately, limited literature is present describing the basal glycocalyx. Existing literature and knowledge roots from select studies investigating Syndecan-4 signaling mechanism and recent studies of syndecan-4 knockdown and expression levels [7,10]. Therefore, limited data is present to compare the results presented here and future experiments. Visualizing and localizing basal glycocalyx structures, akin to the studies conducted on apical glycocalyx elements such as syndecna-1, would fill this gap in our understanding of the basal glycocalyx [11].

The preliminary results presented display positive staining for the glycocalyx with good visualization of the apical glycocalyx as seen in Figure 1A. The orthogonal view of Figure 1A also clearly depicts the glycocalyx coverage of cell bodies as seen by the coverage undisrupted signal over the nuclei. The preliminary attempt of visualization of the apical and basal glycocalyx, as shown in Figure 1B, was disrupted due to the permeabilization treatment utilized. The glycocalyx signal seen overlapping with the nuclei signal throughout the anticipated cell body area is hypothesized to be due to a collapse of the cell membrane as a result of permeabilization. The permeabilization protocol will be optimized for visualization of both the apical and basal glycocalyx without compromising the structure of the cell. This will be achieved by altering the Triton-X100 concentration and exposure time. Confocal Z-stack images will also be taken with 0.5 µm slice thickness for increased sensitivity in orthogonal visualization.

In future experiments, the presence of specific GAGs including HS, CS, and SA will be probed. Evidence of other GAGs in the basal glycocalyx is limited in literature, findings will not only shed light on the distribution and presence of specific GAGs in the basal glycocalyx but also the presence of core proteins. While WGA signal in the basal cell also implies the presence of core proteins, the roles and binding patterns of the individual GAG chains will provide more insight on the possible core proteins and their function in the basal glycocalyx.

Once static visualization is achieved future experiments will probe the basal glycocalyx signal after 30 minutes and 24 hours of shear exposure. In the basal cell we expect to observe an increase in glycocalyx expression and coverage at 30 minutes with expression decreasing to static levels at 24 hours. This is due to findings presented by Zeng et al. in 2016 where syndecan-4 expression was measured at multiple time points [10]. It was found that at physiologically normal shear rates the expression of syndecan-4 increases rapidly after onset of shear peaking at 30 minutes [10]. This timeline corresponds to the timeline of cytoskeleton and focal adhesion remodeling which syndecan-4 has been shown to regulate [5,6,7,10]. The cumulative knowledge from this study will be used to further complete existing models of endothelial cell force transduction and eventually shed light on how different components of the basal glycocalyx contribute to and modulate crucial endothelial cell signaling pathways.

ACKNOWLEDGEMENTS

This research was supported with startup funds from Worcester Polytechnic Institute awarded to Dr. Mensah. The authors would like to thank Natasha Calderon for her help with training and protocol development.

REFERENCES

[1] Foote, C.A. et al., *Comprehensive Physiology*, *12*(4), 3781–3811. 2022.
[2] Jin J. et al., *Frontiers in Cellular Neuroscience*, 15, 2021.
[3] Reitsma, S. et al. *Pflugers Archiv European Journal of Physiology*, *454*(3), 345–359. 1999.
[4] Merry, C. L. R. et al., *Essentials of Glycobiology.* 2022.
[5] Ebong, E. E. et al., 2014 *Integrative Biology: Quantitative Biosciences from Nano to Macro Vol.*, *6*, 338–347, 2014.
[6] Chronopoulos, A. et al., *Nature Materials*, *19*(6), 669–678. 2020.
[7] Baeyens, N. et al., *Proceedings of the National Academy of Sciences of the United States of America*, *111*(48), 17308–17313, 2014.
[8] Thi, M. M. et. al., *PNAS November*, *23*, 16483–16488. 2004.
[9] Elfenbein, A. et al., *Journal of Cell Science*, *126*(17), 3799–3804, 2013.
[10] Zeng, Y. et al., *Cellular and Molecular Biology*, 62(8), 28-34, 2016.
[11] Zeng, Y. et al., *PLoS ONE*, 9(1), 2014

MACHINING LIVING OSTEOCHONDRAL ALLOGRAFTS FOR JOINT RESURFACING IN A CANINE PATELLOFEMORAL JOINT MODEL

Katherine A. Spack (1), Chantelle C. Bozynski (2), Courtney A. Petersen (3), Joseph E. Viola (1), Peter T. Shyu (1), X. Edward Guo (1), Clark T. Hung (1,4), James L. Cook (2), Gerard A. Ateshian (1,3)

(1) Department of Biomedical Engineering, Columbia University, New York, NY, United States
(2) Department of Orthopaedic Surgery, University of Missouri, Columbia, MO, United States
(3) Department of Mechanical Engineering, Columbia University, New York, NY, United States
(4) Department of Orthopedic Surgery, Columbia University, New York, NY, United States

INTRODUCTION

Osteochondral allograft (OCA) transplantation has been used with increasing frequency and success to resurface joints and treat defects in articular cartilage. Despite the increased use of OCA transplantation and improvement in live tissue preservation methods, limitations in the application of OCAs persist. When selecting donor tissue, matching the size and curvature of the transplanted allografts to the native joint is crucial, as allografts that are incongruent with the native joint locally increase contact stresses and can instigate a cascade of negative repercussions.[1-3] Bendable osteochondral allografts (BOCAs) were developed to address this need, allowing surgeons to augment the articular curvature of allograft explants by machining grooves in the underlying bone.[4] Live OCAs show superior functional outcomes when compared to nonliving tissues, as attempts to transplant frozen, decellularized, or lyophilized tissues have yielded significantly worse functional outcomes than live OCAs.[5,6] Since clinical standards recommend that only allograft samples with >70% chondrocyte viability should be considered candidates for transplantation as OCAs,[6] it is important to verify that the process of creating bendable osteochondral allografts does not induce chondrocyte apoptosis or increase the risk of surgical complications by introducing pathogens.

In this study, we used an established canine patellofemoral joint model to analyze a method of machining live osteochondral tissue for transplantation in accordance with federal regulations. We hypothesized that this novel method would enable us to ship live (viable) OCAs from the donation site to the machining site, then store, image, machine, and ship again for transplantation, without compromising chondrocyte viability or tissue aseptic status.

METHODS

With IACUC approval (#16680), whole patellae (n=16) were harvested from adult purpose-bred canines at the University of Missouri at Columbia. Samples were procured within 24 hours of euthanasia and preserved in Missouri Osteochondral Preservation System (MOPS) media at room temperature for overnight shipping to Columbia University in the city of New York.[3,8]

Six patellae were used for ex-vivo testing of the impact of machining and reshaping the articular surface on chondrocyte viability. Whole patellae were transferred under aseptic conditions into custom-built polysulfone fixation rigs. Samples were secured into sterile single-use PLA inserts with Adafruit low-temperature fixation thermoplastic (Fig. 1). Patellae were scanned in a VivaCT 80 μCT scanner with an isotropic 78 μm voxel resolution. Resultant DICOM files were processed in 3D Slicer to create models of the patellae within the fixation rigs (www.slicer.org). Sample-specific CNC milling machine cutting paths were generated in the HSMworks application (autodesk.com) incorporated within SOLIDWORKS 2022 (solidworks.com). Machining was performed in a purpose-built laminar airflow machining cabinet with UV sterilization cycles run between samples. All patellae were planed on their anterior surface, creating shell allografts, then 1.6 mm wide grooves were milled through the subchondral bone to the tidemark to enable bending of the articular surface in BOCAs.[9]

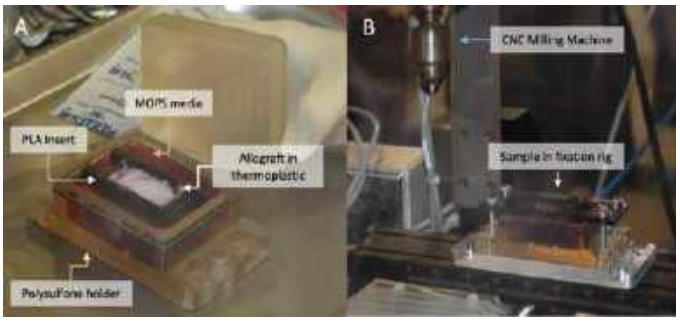

Fig. 1: Aseptic allograft machining process. A: Patella fixed in in removable insert in MOPS bath for scanning and machining. B: Patella cut in sterile enclosure to create bendable allograft.

Following grooving, BOCAs were stored in polystyrene culture dishes with MOPS media at 20 °C. After 14 days, sterilized rubber strips were placed in the machined grooves of three BOCAs (expanded treatment group) to increase the surface radius of curvature along the medio-lateral direction. Expanded samples were maintained thusly for 24H, 48H, and 72H while control samples (remaining three BOCAs) were maintained without expansion for the same period (Fig. 2). The articular cartilage of the BOCA samples was resected and assessed for cell viability using an assay kit (Invitrogen).

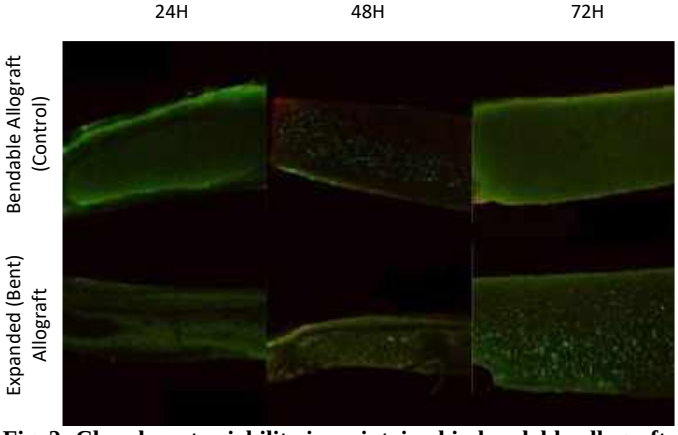

Fig. 2: Chondrocyte viability is maintained in bendable allografts following aseptic machining and sustained alteration of medio-lateral articular surface curvature in BOCAS.

Once the ability to create live machined allografts was established, remaining canine patellae (n=10) were fixed in machining rigs as described above and machined to create a shell allograft group (OCAs, n=5) and a grooved BOCA group (n=5) for shipping and in-vivo surgical transplantation in the canine model. Live OCAs and BOCAs were shipped back to the University of Missouri. Upon reception, media samples and allograft tissue samples were sent for aerobic and anaerobic culture before transplantation, to check for clinically relevant microbial growth. After aseptic conditions were confirmed in all samples, allograft bone was treated with saline pulse lavage and autologous bone marrow concentrate before being fixed in the contralateral stifle joints of five purpose-bred research hounds using bioresorbable pins (Figure 3) with IACUC approval (#16680). The total time between retrieval of patellae from the dogs and transplantation as allografts was 33 days. Donor patellae were not size-matched to the recipients such that BOCAs were expanded or compressed, while OCAs were anatomically positioned for best fit. Dogs were recovered from surgery, provided analgesics and antibiotics, and restricted in activity for 1 month, then provided leash walking, socialization, and enrichment activities.

RESULTS

Cell viability tests on the first batch of machined patellae (n=6, Fig. 2) indicated high levels of chondrocyte viability in the BOCA (88%) and expanded allograft groups (93%) across the measured timepoints.[10]

In the second batch (n=10), clinically relevant microbial growth was absent in the cultures of the patellar allografts and media at the time of transplantation. At three months post transplantation radiographic and gross assessments of canine knees revealed mechanical failure of the BOCAs. The 1.6 mm wide grooves in the BOCA group were too wide for maintaining canine patella structural integrity, resulting in fissuring, fragmentation, and resorption with corresponding trochlear erosions (Fig. 3). The canine study was terminated, and allograft ground tissue and synovial fluid were analyzed using aerobic and anaerobic culture. No microbial growth developed in the retrieved allografts or was measured in the synovial fluid. Viable chondrocytes were present

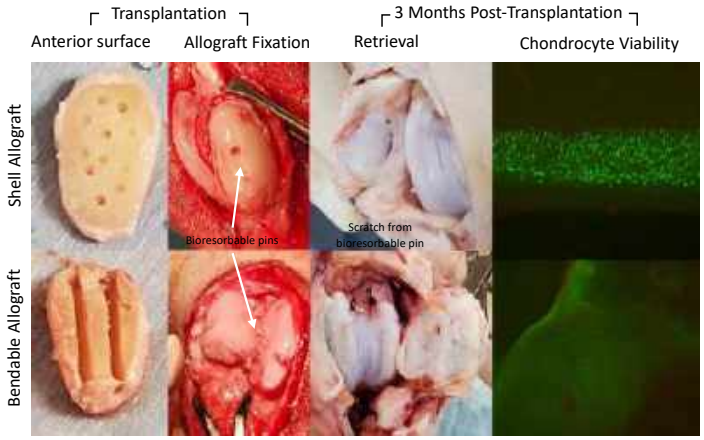

Fig. 3: Canine shell and bendable allograft implanted in canine stifle joint. Allografts were fixed in the patellofemoral joint with a single resorbable pin. Chondrocyte viability was sustained in shell and bendable BOCA allografts, but damage to bendable allografts resulted in changes in hyaline tissue morphology.

in both bendable and shell allografts and shell OCAs maintained hyaline cartilage morphology following 3 months of transplantation (Fig. 3). The BOCAs showed changes in cell phenotype and tissue remodeling in the articular cartilage in response to the tissue fracture.

DISCUSSION

This study establishes the clinical viability of live sterile tissue machining to modify the shape of extant living osteochondral allografts. BOCAs machined from living osteochondral tissue explants demonstrated clinically acceptable levels of cell viability ex vivo (>70%, Fig. 2) following machining, storage in culture media, and sustained bending.[11] This study also demonstrated the successful ability to perform high-precision aseptic machining of live osteochondral tissue, shipping back-and-forth between two states, without inducing apoptosis in the tissue chondrocyte population or introducing foreign pathogens, leading to successful transplantation of allografts in dogs. However, allograft fissuring, fragmentation, and resorption with corresponding trochlear erosions was noted in BOCAs (Fig. 3), attributable to weakening the strength of these allografts by using a groove width better suited for human allografts.

Results confirm that machining of grooves in live osteochondral allografts can be achieved successfully in a practical setting involving shipping of tissue samples between locations and transplantation into animals. However, the specific width of grooves adopted for this canine study, originally intended for human-sized tissue samples, showed that there exists a risk of compromising structural integrity in grooved allografts. A study is currently underway to optimize the width of machined grooves for further preclinical testing in a dog model, so that BOCAs can safely be used without compromising allograft strength.

ACKNOWLEDGEMENTS

U.S Department of Defense (W81XWH-18-1-0361/PR171360).

REFERENCES

[1] Latt L. et al., *America J Sports Med*. 39(12):2662-9, 2011. [2] Du P., et al., *Am J Sports Med*, 46(9):2122-2127, 2018. [3] Buyuk A. et al., *Arthrosc J Arthrosc Relat Surg*. 39(3):650-659, 2023. [4] Rosenwasser, M. et. al., U.S. Patent 10,251,751 B2, 2019. [5] Arnoczky S. et al., *J Knee Surg*. 19(3):207-214, 2006. [6] Ball S.et al., *Clin Orthop Relat Res*. Jan:(418):246-252, 2004. [7] Stannard J. et al., *Orthop J Sport Med*. 44(5):1260-8, 2015. [8] Stoker A.M. et al., *Am J Sports Med*. 46(1):58-65, 2018. [9] Spack K. et al., SB3C, 2021 [10] Spack K.A. et. al, *ORS*, 2023.

IMPACT OF NOVEL ELASTOMERIC MEMBRANE ON VAGINAL SMOOTH MUSCLE STRUCTURE AND FUNCTION

Sophya Breedlove, BS (1), Gabrielle King, MS (2), Pamela Moalli, MD, PhD (1-3), Katrina Knight, PhD (1,3)

(1) Department of Bioengineering, University of Pittsburgh, Pittsburgh, PA, USA
(2) Magee-Womens Research Institute, Pittsburgh, PA, USA
(3) Department of Obstetrics, Gynecology and Reproductive Sciences, University of Pittsburgh, Pittsburgh, PA, USA

INTRODUCTION

Pelvic organ prolapse (prolapse) is a common gynecologic condition characterized by the descent of pelvic organs from their normal anatomic position. Women have a 12.6% risk of undergoing prolapse surgery by the age of 80[1]. Prolapse can be treated via a sacrocolpopexy, in which synthetic mesh is attached to the anterior and posterior walls of the vagina. Around 300,000 women undergo prolapse surgery each year, with direct costs exceeding 1 billion dollars annually[2]. The economic burden of prolapse is expected to increase as the population ages[3].

Surgical procedures involving synthetic mesh are limited by significant complication[4-7]. Pain and exposure of the mesh through the vaginal epithelium are the most reported complications[8]. Studies indicate that these complications are a result of two primary factors: 1) a mismatch of the stiffness between the mesh and vaginal tissue resulting in a stress shielding phenomenon, and 2) mesh deformation (pore collapse and mesh wrinkling)[9]. The surgical meshes used in prolapse procedures are manufactured primarily from polypropylene, which is orders of magnitude stiffer than vaginal tissue; therefore, it must be extruded into thin fibers and then knitted. Studies demonstrate that stiffer meshes are associated with a maladaptive remodeling response characterized by degeneration and atrophy[10].

Polycarbonate urethane (PCU) is a promising alternative to polypropylene. It is a biocompatible medical grade polymer that has been used in long-term medical implants[11]. PCU can be tuned to match the stiffness of the vagina and it is tough enough to withstand the physiologic loads involved in sacrocolpopexy procedures. Additionally, instead of being knitted, PCU membranes (devices that are like meshes but have no knots) can be readily 3D printed[12-14].

In this study, we hypothesized that PCU membranes would result in a more favorable host response, characterized by the preservation of vaginal smooth muscle structure and function, as compared to polypropylene mesh. To test this hypothesis, we evaluated the effects of polypropylene meshes and PCU membranes on the smooth muscle layer of the vagina in a rabbit model.

METHODS

Meshes: PCU membranes (PCU EMs) were 3D printed from a lower stiffness grade of PCU (EM low) and a higher stiffness grade of PCU (EM high) that are within the range of the stiffness of the vagina. Commercially available polypropylene meshes, Restorelle (Coloplast, USA) and Gynemesh PS (Ethicon, USA) were chosen for comparison. Prior to implantation, the PCU EMs and polypropylene meshes were cut to a size of 1cm x 2cm.

Animals and Surgical Procedures: New Zealand White Rabbits (n=22) were used in this study according to the University of Pittsburgh Institutional Animal Care and Use Committee (IACUC #22030732). All rabbits were retired breeders and housed in standard cages with access to food and water *ad libitum*. PCU EMs and meshes were implanted in a total of 12 animals, with six constructs (membranes and/or meshes) implanted per rabbit (three on the anterior wall and three on the posterior wall). The membranes and meshes were not placed on tension, so that the effects of the material could be evaluated in the absence of tension. Sham animals in which no construct was implanted served as controls (n=10). Sample size for the constructs were as follows: EM low (n=24), EM high (n=24), Restorelle (n=12), and Gynemesh (n=12). Membrane and mesh-vagina complexes were explanted after 12 weeks.

Smooth Muscle Morphology and Thickness Quantification: Explanted complexes were fresh frozen in optimal cutting temperature compound, cryosectioned at 7um, and stained with Masson's Trichrome. Tissue sections were imaged at 4X with a Nikon Ni-E microscope. The smooth muscle layer of each tissue section was digitally outlined, and a custom Python script was used to calculate the average thickness of the smooth muscle layer.

Vaginal Contractile Function: Membrane and mesh-vagina complexes, 2mm x 7mm, were clamped along the circumferential

direction, attached to a force transducer, and submerged in oxygenated Krebs solution at 37ºC. Complexes were treated with a 120 mM KCl solution to evaluate muscle-mediated contraction (a direct measure of smooth muscle contraction). To account for differences in sample dimensions, the responses were normalized by tissue volume.

Statistical Analysis: ANOVAs, Kruskal-Wallis tests, and post hoc tests were performed as appropriate. Statistical significance was set to $p<0.05$ unless specified otherwise.

RESULTS

Qualitatively, the organization and density of the vaginal smooth muscle bundles in the PCU EM low group most closely resembled Sham (Figure 1). Implantation of PCU EM high and the polypropylene meshes appeared to have reduced the density of the smooth muscle bundles.

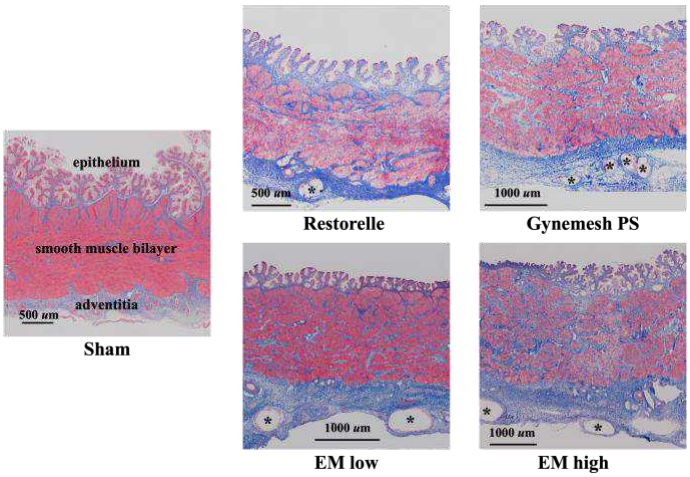

Figure 1: Masson's trichrome stain of membrane and mesh-vagina complex tissue sections. *indicates membrane/mesh fiber.

The thickness of the smooth muscle layer was not significantly impacted by the implantation of the PCU EMs compared to Sham and Restorelle (p-values>0.05, Figure 2). However, relative to Gynemesh PS, the smooth muscle layer was 28% ($p<0.005$) and 34% ($p=0.005$) thicker for EM low and EM high, respectively.

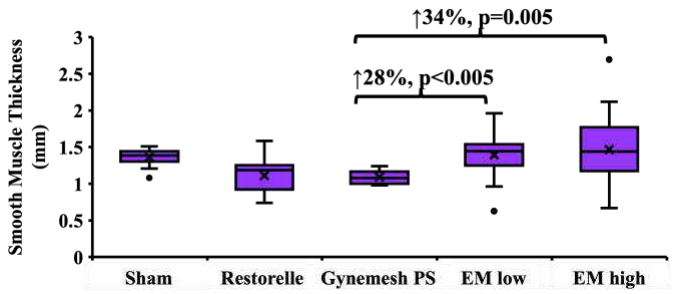

Figure 2: Vaginal smooth muscle layer thickness was not significantly impacted by EM implantation.

The contractile function of the vagina significantly decreased following implantation of the PCU membranes and polypropylene meshes relative to Sham ($p<0.001$, Figure 3). However, vaginal contractile function was not significantly different between the PCU EMs and the polypropylene meshes (all p-values>0.05).

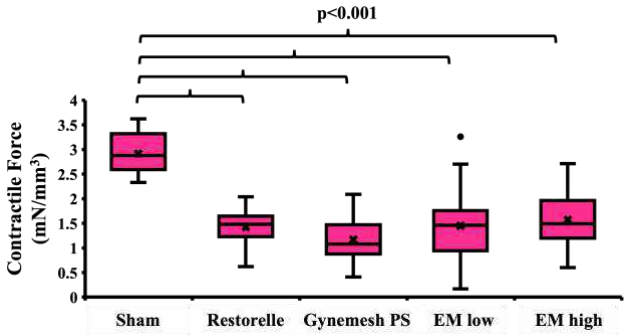

Figure 3: Vaginal contractile function in response to 120 mM KCl.

DISCUSSION

Overall, the structure of the smooth muscle layer was preserved after implantation with PCU EM low. However, the PCU EMs and polypropylene meshes had a similar effect on the function of the vagina. The observed decline in vaginal contractile function for the PCU EMs is likely due to the relative thinness and low stiffness of the rabbit vagina compared to human and non-human primate vaginal tissue. Future studies will use the non-human primate model to overcome the thickness and stiffness limitations of the rabbit vagina. Additionally, the small size of the constructs (1cm x 2cm) and the absence of tension may have minimized differences between the EMs and meshes. Thus, studies using the full-length (3cm x 12cm) membranes and meshes implanted on the rabbit vagina are ongoing.

The low stiffness of the EMs required that they be constructed of more material to meet physiologic loading demands, making them substantially heavier than polypropylene meshes (169 g/m^2 vs 42 g/m^2). The results of this study suggest that heavier devices, if manufactured from a low stiffness polymer, are still associated with a favorable host response. This is contrary to polypropylene meshes in which heavyweight meshes lead to poor outcomes[10]. These findings also suggest that the impact of a lower weight PCU EM should be explored.

Overall, the results of this study support the use of PCU as an alternative to polypropylene for prolapse repair devices, and additional studies are underway to further evaluate the PCU EMs.

ACKNOWLEDGEMENTS

We are grateful for the financial support provided by the National Institute of Health HD097187 and K12 HD043441, as well as the T32 Biomechanics in Regenerative Medicine (BiRM) Training Program.

REFERENCES

[1] Wu JM et al., *Obstet. Gynecol.*, 123(6):1201-6, 2014.
[2] Subak LL et al., *Obstet. Gynecol.*, 98(4):646-51, 2001.
[3] Wu JM et al., *Obstet. Gynecol.*, 114(6):1278-83, 2009.
[4] Gupta P et al., *Female Pelvic Med. Reconstr. Surg.*, 24(6) 2018.
[5] Manodoro et al., *An International Journal of Obstetrics and Gynaecology*, 120(2):244-50, 2013
[6] Nygaard I et al., *Jama*, 309(19):2016-24, 2013.
[7] Osmundsen BC et al., *Female Pelvic Med. Reconstr. Surg.*, 18(2):86-8, 2012.
[8] FDA, Urogynecological Surgical Mesh, 2011.
[9] Knight KM et al., *Acta Biomaterialia*, 148:323-35, 2022.
[10] Liang R et al., *Curr. Opin. Obstet. Gynecol.*, 28(5):413-19, 2016
[11] Abela D et al., *Xjenza Online*, 10(1):48-60, 2022.
[12] Miller AT et al., *Polymer (United Kingdom)*, 108:121-34, 2017.
[13] Bachtier EO et al., *J. Biomech. Eng.*, 145(9), 2023.
[14] Bickhaus JA et al., *Urogynecology*. 27(2), 2021.

EVALUATING MECHANICAL PROPERTIES AND EXTRACELLULAR MATRIX COMPOSITION OF ANTERIOR AND POSTERIOR MURINE VAGINAL WALLS

Qinhan Zhou (1), Triniti N. Vanoven (1,2), Maria Florian-Rodriguez (3), Isaac J. Pence (1,2), Kristin S. Miller (1,2,3,4)

(1) Department of Bioengineering, University of Texas at Dallas, Dallas, TX, United States
(2) Department of Biomedical Engineering, University of Texas Southwestern Medical Center, TX, United States
(3) Department of Obstetrics and Gynecology, University of Texas Southwestern Medical Center, Dallas, TX, United States
(4) Department of Mechanical Engineering, University of Texas at Dallas, Dallas, TX, United States

INTRODUCTION

The vagina is a fibromuscular organ involved in pelvic organ support. Vaginal structural integrity is dictated by the underlying extracellular matrix (ECM) composition. Changes in the vaginal composition alter the vaginal mechanical properties, such as stiffness and extensibility. The loss of structural integrity of the vaginal fibromuscular layer may contribute to clinical problems such as pelvic organ prolapse (POP). POP develops more frequently in the anterior vaginal wall (34.3%) compared to the posterior (18.6%) [1]. Studies in human tissues suggest that local differences in vaginal wall mechanical properties may contribute, however, local vaginal structure-function relationships are not fully understood, nor are vaginal dynamics with POP risk factors such as age and injury [2,3]. Towards this end, and due to limited access to human vaginal tissue, mouse models are widely used in reproductive and POP studies to elucidate fundamental structure-function relationships and potential evolving structural mechanisms of pelvic floor stability [4-6]. To evaluate regional tissue composition, Raman spectroscopy (RS), a light-based technique that measures the photons scattered by the interaction between laser light and molecular bonds, can measure tissue components at a small scale. RS has previously been employed to quantify cervical composition such as total collagen, elastin, and actin and demonstrated its ability in regional composition assessment [7]. Furthermore, noninvasive measurements of cervical tissue composition based on RS correlate with biomechanical changes [7], yet this approach has not yet been extended to the assessment of the vaginal wall. Herein we proposed to leverage RS and biaxial testing to elucidate local vaginal structure-function relationships in the murine anterior and posterior walls. We hypothesized that posterior murine vaginal wall would be stiffer than the anterior, and that Raman coefficients of total collagen, elastin, and actin would be higher in the posterior wall compared to the anterior. Potential correlations between mechanical properties and ECM components were also evaluated.

METHODS

10 vaginas were collected from wild-type C57BL/6 mice (IACUC UTSW approved, 10-11 months of age) and stored at -20 °C. Before the testing, specimens were thawed at 4°C overnight. The anterior and posterior walls were separated by cutting longitudinally along the midlines of two sides and tested individually (Fig 1A). The unloaded thickness was measured by laser scale. The sample was speckle coated by airbrush with black alcohol ink (Fig 1B). Then the tissue was mounted on BioTester 5000 (CellScale, Waterloo, ON, Canada) and recorded unloaded grip-to-grip length in circumferential and axial direction. The displacement-controlled equibiaxial tensile testing was performed with a preload of 10mN, a stretching rate of 0.25%/s, and a target displacement of 15% of the original length, and test settings were based previous biaxial studies [8,9]. The tissue was preconditioned with 5 rounds of tests of 5 cycles followed by 10-minute equilibration. Then 8 cycles of equibiaxial tests were performed, and the last loading cycle was used for analysis. A MATLAB program adopted AL-DIC algorithm was applied to track the deformation and calculate the Green-Lagaragian strain and first Piola–Kirchhoff stress. A bilinear function fit strain-stress data to determine toe and linear moduli, which were calculated as the slopes of the toe and linear regions and served as metrics of material stiffness at low and high strain (Fig 1C).

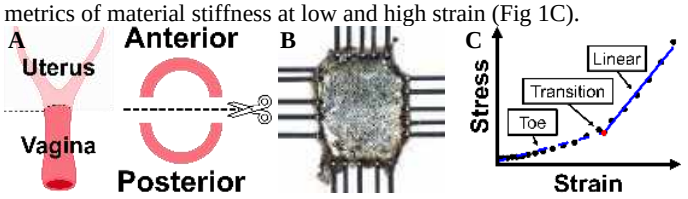

Figure 1. (A) Vaginal wall isolation. (B) Speckle-coated tissue. (C) Bilinear fitting of strain and stress.

After mechanical testing, anterior and posterior samples of 6 mice were subjected to RS to evaluate the Raman coefficients of total collagen, actin, and elastin. A 785nm laser (Innovative Photonic

Solutions, Plainsboro, NJ, USA) and fiber optic probe (EmVision, Loxahatchee FL, USA) in conjunction with an imaging Raman spectrograph (EmVision) equipped with a thermoelectrically cooled back-illuminated CCD (Teledyne PI, Trenton NJ, USA) was utilized to acquire ten spectral repetitions of the sample at 6 regions of interest. Standard protocols and materials were used for system calibration and data preprocessing, including Savitzky-Golay smoothing, and background subtraction as previously outlined (Fig 2) [10]. A non-negative least squares analysis of the data against a database of pure sample spectra was conducted to calculate regional Raman coefficients of total collagen, elastin, and action. The coefficients of 6 regions from the same sample were averaged for each vaginal wall sample. The normality and homogeneity of variance of moduli and regional Raman coefficients were evaluated by Shapiro-Wilk and Levene's tests. Paired sample t-tests or nonparametric alternative, Wilcoxon tests, evaluated potential differences between anterior and posterior walls in biomechanical properties and regional Raman coefficients of each protein. Pearson correlations were calculated between moduli and averaged Ramen coefficients.

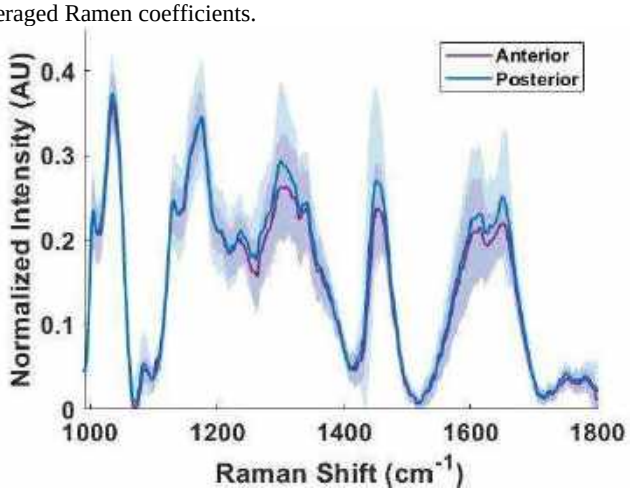

Figure 2. Normalized Raman spectra (mean +/- standard deviation) per group showing the differences in signature between the anterior (purple) and posterior (blue).

RESULTS

The moduli were normally distributed with equal variance. When comparing circumferential linear moduli between anterior and posterior vaginal walls, the linear modulus was significantly lower in the anterior wall compared to the posterior (Fig 3A, p=0.04). No other significant differences were identified in moduli between vaginal walls.

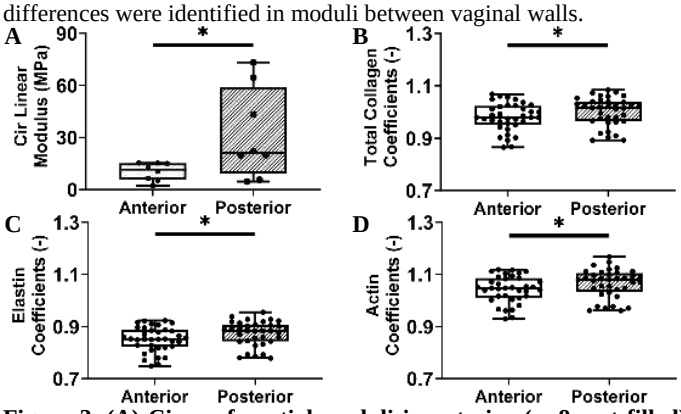

Figure 3. (A) Circumferential moduli in anterior (n=8, not filled) and posterior (n=8, shadow) walls. Comparison of regional Raman coefficients of total collagen (B), elastin (C), and actin (D) between anterior (n=36, not filled) and posterior (n=36, shadow) walls.

For composition, total collagen coefficient was significantly lower in the anterior wall compared to the posterior (Fig 3B, p=0.03). The elastin coefficient (Fig 3C, p=0.01) and the actin coefficient were significantly lower in the anterior wall compared to the posterior (Fig 3D, p=0.01). Circumferential linear modulus of the posterior wall strongly negatively correlated to averaged coefficients of total collagen (R=-0.92, p<0.01), elastin (R=-0.96, p<0.01), and actin (R=-0.98, p<0.01). No other significant correlations were identified.

DISCUSSION

Herein, the circumferential stiffness was significantly higher in the posterior vaginal wall compared to the anterior, which is consistent with observations in the human vagina [2]. The increased stiffness coincided with a higher regional Raman coefficient of total collagen in the posterior wall compared to the anterior. Collagen fibers are largely responsible for providing tensile strength and stiffness in soft tissues. Additionally, high regional Raman coefficients of elastin and actin were identified, suggesting that the posterior wall has higher collagen, elastic fiber, and smooth muscle cell content. The higher stiffness in the posterior wall may potentially contribute to the lower incidence rate of POP involving the posterior compartment compared to the anterior compartment [1]. Additionally, strong negative correlations were identified between posterior circumferential stiffness and regional Raman coefficients of total collagen, elastin, and actin. This may suggest that circumferential stiffness of the posterior vagina decreases when ECM fibers and smooth muscle cells become less dense in the tissue, which may be due to aged mice used in this study. However, further study is needed to address the underlying microstructural mechanisms, as well as the processes of remodeling in each wall with age and other POP risk factors such as vaginal delivery and injury. Interestingly, anterior and posterior vaginal wall stiffness in the axial direction was not statistically significant, which may be due to anisotropic distribution and alignment of elastic and collagen fibers and merits further investigation [5].

One limitation of this study was the lack of quantification of collagen and elastic fiber microstructure, such as orientation and undulation. Additional work employing RS analysis would permit quantification of fiber orientations providing additional information on vaginal structure-function relationships [11]. It is also necessary to quantify other ECM components such as fibulin-5 [4]. This study used only aged mice, and future comparison between age groups is needed to understand vaginal dynamics. Overall, this study observed that murine vaginal walls were significantly stiffer in the circumferential direction in the posterior wall, highlighting the importance of quantifying local vaginal function and composition to develop more therapeutic regimes for POP.

ACKNOWLEDGEMENTS

The authors would like to acknowledge Haolin Shi for animal husbandry. This work was supported by UTD CoBRA (KSM 2023), AAOGF/Wellcome Boroughs Career Development Award (MFR), and UT Rising STARs award (IJP).

REFERENCES

[1] Hendrix, S+, *Am. J. Obstet. Gynecol.*, 186(6): 1160-1166, 2002; [2] Martins, P+, *Gynecol. Obstet. Invest.*, 75(2): 85-92, 2013; [3] Ulrich, D+, *PloS one*, 9(8): e104972, 2014; [4] Clark-Patterson, G+, *Sci. Rep.*, 11(1): 20956, 2021; [5] Clark-Patterson, G+, *Interface Focus*, 9, no. 4 (2019): 20190025, 2019; [6] White, S+, *J. Biomech. Eng.*, 144(6): 061010, 2022; [7] O'Brien+, *Sci. Rep.*, 7(1): 6835, 2017; [8] Danso, E+, Sci. Rep., 10(1):1-14, 2020; [9] Huntington, A+, *Ann. Biomed. Eng.*, 47(1): 272-281, 2019; [10] Lieber, C+, *Appl. Spectrosc.*, 57(11): 1363-

1367, 2003; [11] Masic, A+, *Biomacromolecules*, 12(11): 3989-3996, 2011.

BIOMECHANICAL AND COMPOSITIONAL CHANGES IN THE MURINE UTERUS WITH AGE

Mari J.E. Domingo (1), Triniti N. Vanoven (1,2), Raffaella De Vita (3), Maria Florian-Rodriguez (4), Isaac J. Pence (1,2), Kristin S. Miller (1,2,4,5)

(1) Department of Bioengineering, University of Texas at Dallas, Richardson, TX, USA
(2) Department of Biomedical Engineering, University of Texas Southwestern Medical Center, Dallas, TX, USA
(3) Department of Biomedical Engineering and Mechanics, Virginia Tech, Blacksburg, VA, USA
(4) Department of Obstetrics and Gynecology, University of Texas Southwestern Medical Center, Dallas, TX, USA
(5) Department of Mechanical Engineering, University of Texas at Dallas, Richardson, TX, USA

INTRODUCTION

Advanced maternal age is correlated with adverse outcomes in pregnancy and parturition such as spontaneous abortion, prolonged labor, and postpartum hemorrhaging [1]. While the etiology of these risks are not fully understood, changes in the uterine extracellular matrix (ECM) with age may contribute. The uterus is principally composed of collagen fibers, elastic fibers, and smooth muscle cells (SMC). Collagen fibers impart the uterus with native tensile strength while elastic fibers provide the ability to stretch and recover. Collectively, the passive mechanical properties of soft tissues are primarily attributed to fibrous components such as collagen and elastic fibers as well as non-fibrous components such as glycosaminoglycans. For successful pregnancy and parturition, the contractile active behavior of the SMC work in conjunction with the passive components of the matrix. Prior mouse models have been employed to understand the relationship between uterine contractility and age[2], [3], however the changes in passive mechanical properties and underlying composition of the uterus with age remain unknown. Further, the passive material stiffness and amount of elastic fibers increases in the murine vagina with reproductive age[4], [5]. Biaxial extension-inflation protocols are useful methods to quantify multiaxial mechanical properties while maintaining native tissue geometry, while Raman spectroscopy provides a molecular signature of tissue that is sensitive to the types and amounts of multiple ECM proteins and components. Therefore, the objective of this study was to quantify the passive mechanical properties and composition of the nulliparous murine uterus with age using biaxial extension-inflation protocols and Raman spectroscopy. We hypothesize that there will be an increase in stiffness and ECM components with reproductive aging.

METHODS

Animal Care. 9 female nulliparous wildtype C57BL/6 mice were used (UTSW IACUC approved). Mice were divided into three groups: 2-3 months, 4-6 months, and 10-11 months of age (n=3/group). **Specimen Preparation**. Mice were euthanized via cervical dislocation and uterine horns were dissected from the reproductive tract (Fig 1). One uterine horn was randomly allocated to mechanical testing while the other was used for Raman Spectroscopy. The tissue was frozen at -20°C. Prior to testing, the tissue was defrosted for one hour at 4°C. **Biomechanics**. The uterus was cannulated onto a biaxial extension inflation device (Danish MyoTechnologies, Aarhus, Denmark) in calcium free Kreb's Ringer Buffer and equilibrated at 37°C (Fig 1). The physiologic length was restored by extending the tissue to the length where force remained constant over a range of increasing pressure [6]. To achieve consistent and repeatable measurements, five cycles of preconditioning was performed [7], [8]. Following, three cycles of pressure-inflation testing were performed at the physiologic length, -2% and +2% of the physiologic length. Force length testing was performed by cycling between -2% and +2% of the physiologic length at pressures of 10, 67, 133, and 200 mmHg [7], [9]. **Raman Spectroscopy**. Compositional analysis was conducted on the opposite uterine horn in the 2-3 month and 10-11 month uterus (n=3/group). The tissue was opened longitudinally. Ten spectra were acquired at each of six regions of interest (Fig 1) using a 785nm laser (Innovative Photonic Solutions, Plainsboro, NJ, USA) and fiber optic probe (EmVision, Loxahatchee FL, USA) in conjunction with an imaging Raman spectrograph (EmVision) equipped with a thermoelectrically cooled back-illuminated CCD (Teledyne PI, Trenton NJ, USA). Data was preprocessed for analysis through Savitzky-Golay smoothing and background subtracting as previously described[10]. **Data Analysis.** First Piola-Kirchhoff stress-stretch curves were calculated in the circumferential and longitudinal direction. To determine the toe and linear moduli, a bilinear function fitted the stress-stretch curves. Material stiffness at low strain was determined as the slope of the toe region while material stiffness at high strain was determined as the slope of the linear region. A non-negative least squares (NNLS) fitting analysis was performed against a database of pure sample spectra to determine the concentration

of total collagen, elastin, cholesterol, and lipids [11]. **Statistical Analysis.** Lilliefors and Levene's test evaluated if the mechanical data was normally distributed and met the assumption of homogeneity of variance, respectively. To determine if age and direction influenced material stiffness, the Scheirer Ray Hare (SRH) test was performed followed by Dunn's test if appropriate for the toe and linear moduli. The Shapiro-Wilks test evaluated the normal distribution of the NNLS coefficients in each group. To determine if age affected ECM composition, a Kruskal-Wallis test was performed for each component of interest.

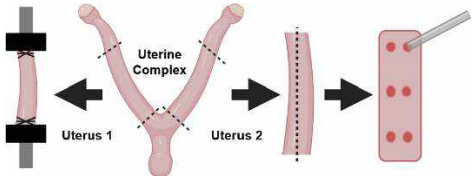

Figure 1. Dissection of the murine uterus. One uterine horn was randomly allocated to mechanical testing and cannulated onto an extension-inflation device. The other uterine horn was randomly allocated for Raman Spectroscopy wherein the tissue was rolled out by a singular longitudinal cut. A fiber optic probe assessed six regions.

RESULTS

Biomechanics. An increase in age increased distensibility demonstrated by the rightward shift in both the circumferential and longitudinal directions. For the toe moduli, significant differences were identified in material stiffness with respect to age ($p=0.003$) while direction ($p=0.15$) and interactions ($p=0.80$) were not significant. When compared to the 2-3 month uterus, material stiffness significantly decreased in the 4-6 month ($p=0.02$) and 10-11 month ($p=0.003$) uterus. A SRH test identified significant differences in the linear moduli with respect to age ($p=0.008$) and direction ($p=0.03$). The interactions were not significant ($p=0.80$). When compared to the 2-3 months, material stiffness significantly decreased in the 4-6 month ($p=0.04$) and 10-11 month ($p=0.009$) uterus (Fig 2A). Within each age group, material stiffness was significantly greater in the circumferential direction than the longitudinal direction ($p<0.05$). **Raman Spectroscopy.** The four NNLS coefficients of interest (total collagen, elastin, lipid, and cholesterol concentrations) saw a significant increase in the 10-11 month uterus ($p < 0.001$) as opposed to the younger group (Fig 2B).

DISCUSSION

This study quantified passive mechanical properties and composition in the uterus with respect to reproductive age. The uterus displayed an increase in distensibility and a decrease in material stiffness with age. While aging is largely associated with an increased in stiffening of soft tissues, the observed trends are in agreement with previous work in the murine cervix [2]. The increase in distensibility in the uterus may be the result of 10-11 months characterizing reproductive aging but not fully aged or menopausal tissue. The 10-14 month old C57 mouse is correlated to 38-47 human years while 18-24 months is correlated to 56-69 human years [12]. In this intermediary aging process, it is possible that immature collagen fibers are being produced without the degradation of elastic fibers, thus resulting in increased distensibility and decreased material stiffening. Additionally, a significant increase in total collagen was found in the older age group. This finding is in agreement with previous studies wherein insoluble collagen deposition increased with age [13]. While an increase in collagen is typically associated with an increase in material stiffness, Raman Spectroscopy can only detect the total collagen signal, which is not able to distinguish mature and immature collagen content or changes in the type I: III collagen ratio.

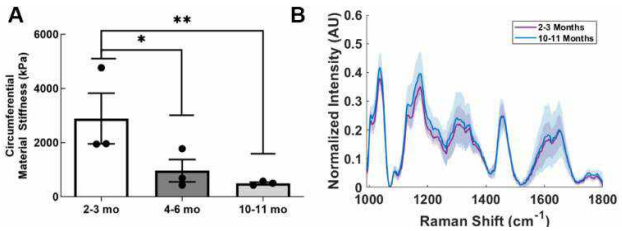

Figure 2. (A) The circumferential material stiffness of the murine uterus aged 2-3 (white), 4-6 (grey), and 10-11 (light grey) months (n=3/group) at high strain. An SRH test showed significant differences between direction ($p=0.03$) and age ($p=0.008$) with no significant interactions. Compared to 2-3 months, material stiffness significantly decreased in the 4-6 month ($p=0.03$) and 10-11 month ($p=0.009$) uterus. (B) The average of the post-processed 2–3-month (purple) and 10–11-month (blue) spectra ± standard deviation plotted against the Raman shift in inverse centimeters.

A significant increase in elastin signal with age was also identified. Prior work in the vagina detected a larger amount of elastic fibers in older age groups but a decrease in fiber length and width [5].This may suggest a decrease in functional elastic fibers resulting in altered mechanics. Finally, cholesterol and lipids increased in the older uterus. Elevated cholesterol levels are detrimental to uterine SMC contractile potential, which may correlate with prolonged labor [14]. Further, lipids associated with decreased tissue distensibility were identified in the cervix of mouse models with delayed parturition [11]. Future studies are needed to investigate how these changes in cholesterol and lipids affect uterine function with age. Taken together, the decrease in material stiffness correlated with an increase in ECM components may suggest fiber-specific remodeling rates of the uterus with age.

This study is not without limitations. The uterus is responsible for exhibiting contractile behavior to facilitate processes such as pregnancy, and parturition. Prior studies demonstrate an important relationship between SMC and ECM properties [5]. While investigating active contractile behavior of the uterus with age and pregnancy is of interest, initial studies in the passive, nulliparous state are critical to establishing a fundamental baseline of uterine mechanical behavior with age. Quantifying the uterine mechanical and compositional properties with age may provide key insights to improve outcomes related to advanced maternal age.

ACKNOWLEDGEMENTS

The authors would like to acknowledge Haolin Shi for animal husbandry. This work is funded, in part, by NSF CMMI 2053851 (De Vita, Abramowitch, Miller, Myers), UT Rising STARs Award (Pence) and AAOGF/Wellcome Boroughs Career Development Award (Florian-Rodriguez).

REFERENCES

[1] Correa-de-Araujo & Yoon, *J. Women's Health*, 30: 160–167, 2021. [2] Patel+, *Physiol. J.,* 595: 2065–2084, 2017. [3] Elmes+, *Physiol Rep*, 3: e12305, 2015. [4] White+, *J.Biomech. Eng.*, 144: 061010, 2022. [5] White+, *Acta Biomaterialia*, 175: 186–198, 2024. [6] Van Loon, *Biorheology*, 14: 181–201, 1977. [7] Robison+, *J.Biomech. Eng*, 139: 104504, 2017. [8] Ferruzzi+, *Ann Biomed Eng*, 41: 1311–1330, 2013. [9] Conway+, *J. Biomech.*, 94: 39–48, 2019. [10] Lieber & Mahadevan-Jansen, *Appl Spectrosc*, 57: 1363–1367, 2003. [11] O'Brien+, *Sci Rep*, 7: 6835, 2017.[12] Fox+, *The Mouse in biomedical research*. New York: Academic Press, 1981. [13] Mulholland & Jones, *Microscopy Res & Technique*, 25: 148–168, 1993. [14] Zhang+, *Reprod. Sci.*, 14: 456–466, 2007.

INVESTIGATING THE INFLUENCE OF GAG DIGESTION AND CORNEAL CROSSLINKING ON COLLAGEN FIBRIL ORGANIZATION

M.E. Emu (1), H. Hatami-Marbini (1)

(1) Mechanical and Industrial Engineering, University of Illinois Chicago, Chicago, IL USA
Email: hatami@uic.edu

INTRODUCTION

The cornea, a transparent tissue at the front of the eye, plays a crucial role in refraction and protection. Its mechanical and optical properties are governed by the extracellular matrix (ECM), specifically the stroma, which comprises 90% of the corneal thickness. Collagen fibrils within the stroma, arranged in pseudo-hexagonal arrays, interact with proteoglycans (PGs), forming a lattice-like structure. Glycosaminoglycan (GAG) side chains of PGs, including chondroitin sulphates (CS), dermatan sulphates (DS), and keratan sulphates (KS), contribute to interfibrillar GAG duplexes, maintaining collagen fibril organization [1]. Studies reveal diverse models for PG-collagen interactions, emphasizing the significance of GAG-GAG interactions. It has been observed that genetic mutations affecting PG lumican lead to disrupted collagenous matrix, impacting corneal transparency [2]. Microstructural changes are expected to influence corneal mechanical properties. For example, in keratoconus, KS GAG chains have been observed to reduce significantly. Thus, in order to clarify the role of GAGs in the structural properties of the cornea, it is important to investigate the relation between KS GAGs and corneal stromal microstructure.

Corneal crosslinking (CXL) treatment enhances corneal mechanical properties, particularly in keratoconus. Previous studies showed conflicting results regarding collagen fibril diameter changes post-CXL [3, 4]. This research employs transmission electron microscopy (TEM) to investigate GAG effects on corneal ECM organization before and after CXL. The hypothesis posits GAGs as being crucial in defining corneal microstructure, prompting the use of keratanase enzyme for GAG depletion and subsequent characterization of CXL-treated samples.

METHODS

Porcine eye globes were collected from a slaughterhouse and brought to the laboratory on ice. Samples were divided into four groups: control, control CXL, enzyme, and enzyme CXL. For GAG depletion, corneal strips were immersed in a keratanase II enzyme solution (0.1 U/ml) with 100 mM sodium acetate buffer for 20 hours at 37°C and pH 6.0. The corneal strips in CXL groups underwent a conventional CXL protocol, involving soaking in a 20% dextran 0.1% riboflavin solution for 30 minutes, followed by irradiation with UVA light (3 mW/cm2, 370 nm) for an additional 30 minutes [5]. For the transmission electron microscopy, corneal tissue blocks (Figure 1) from each group were fixed in 2.5% phosphate-buffered glutaraldehyde, washed, and post-fixed in osmium tetroxide [6]. After staining, dehydration, and resin embedding, semi-thin sections were cut, stained with Toluidine blue, and examined under a light microscope for tissue preservation. Ultra-thin sections were contrasted and examined using a JEOL JEM-1400 Flash transmission electron microscope, and images were captured at various magnifications for detailed analysis of fibril diameter & interfibrillar spacing using Image J software.

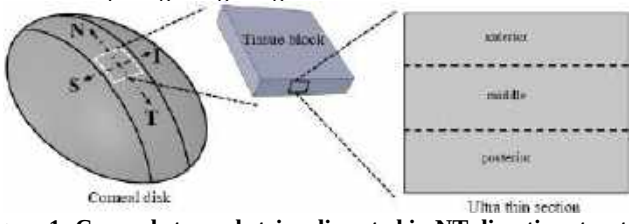

Figure 1: Corneal stromal strips dissected in NT direction, treated, and analyzed with TEM.

RESULTS

Figures 2 and 3 show electron micrographs of the anterior cornea at various magnifications for control, control CXL, enzyme, and enzyme CXL conditions. Keratocytes, collagen lamellae, and individual collagen fibrils are visible. Grey regions between fibrils, seen in control samples, suggest PGs/GAGs, confirmed by their reduction in GAG-

depleted samples. Micrographs for middle and posterior regions were similarly obtained to assess microstructural changes due to enzymatic digestion and CXL treatment (results not shown).

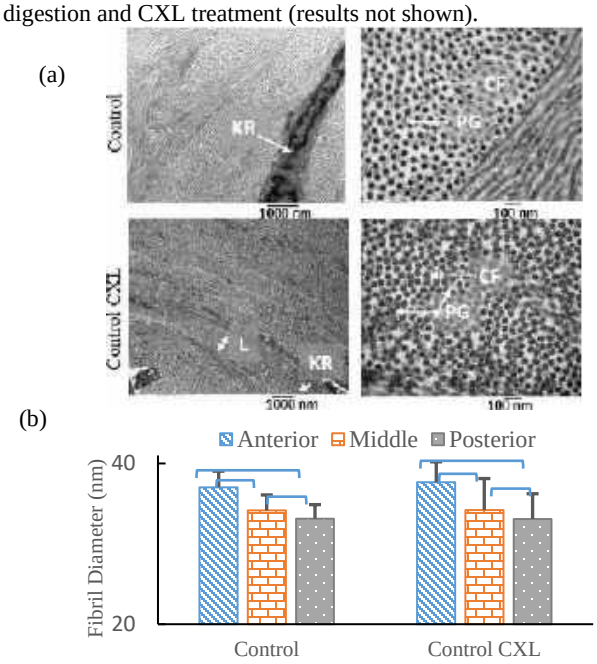

Figure 2: (a) Typical Electron micrographs of anterior corneal stroma for control and control CXL specimens. Marked features include keratocytes (KR), collagen lamellae (L), and collagen fibrils (CF) with white arrows. (b) The effect of CXL treatment on regional variation of collagen fibril diameter. Vertical bars indicate one standard deviation, and horizontal brackets denote significance.

Collagen fibril diameter analyses (Fig. 2-3) revealed no significant changes due to CXL or enzymatic digestion. However, a notable regional difference was observed, with anterior collagen fibrils significantly larger than posterior ones in control samples ($P < 0.05$). Center-to-center distances showed no significant regional differences, except in control CXL samples (data is not shown here). CXL treatment significantly reduced interfibrillar spacing in the anterior and middle parts of the control and GAG-depleted samples ($P < 0.05$). Enzymatic GAG removal increased interfibrillar spacing in anterior and posterior regions ($p < 0.05$), indicating loosely packed collagen fibrils in enzyme-treated specimens.

DISCUSSION

The primary objective of this work was to investigate the impact of GAGs and CXL on the arrangement of corneal collagen fibrils using transmission electron microscopy (TEM). Notably, the anterior porcine corneal stroma displayed larger collagen fibril diameters compared to the posterior region (Fig. 2). Interestingly, the fibril diameter exhibited a reduction through the thickness of control samples, measuring ~37 nm in the anterior, ~34 nm in the middle, and ~33 nm in the posterior regions. Neither CXL nor enzymatic digestion showed a significant impact on collagen fibril diameter. This observation was contrary to previous TEM findings but in agreement with X-ray scattering studies [3, 4]. The consistent results between TEM and X-ray diffraction point towards species-dependent effects of CXL on fibril diameter, as seen in rabbit cornea studies that reported increased fibril diameter post-CXL, highlighting variability across species. Additionally, Keratanase digestion followed by crosslinking demonstrated no significant effect on collagen fibril diameter.

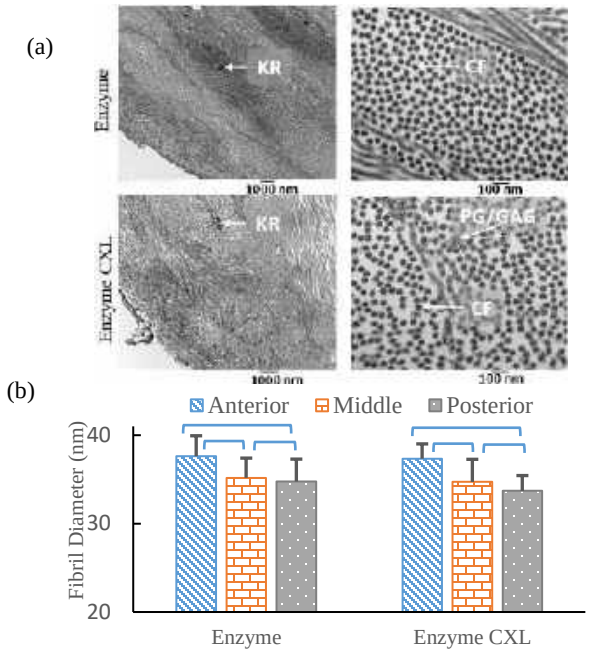

Figure 3: (a) Typical electron micrographs of anterior corneal stroma for enzyme and enzyme CXL specimens. Marked features include keratocytes (KR), collagen lamellae (L), and collagen fibrils (CF) with white arrows. (b) The effect of enzyme and CXL treatment on regional variation of collagen fibril diameter. Vertical bars indicate one standard deviation, and horizontal brackets denote significance.

Center-to-center distances between adjacent collagen fibrils were also calculated. Control samples showed no significant through-the-thickness center-to-center distance variation, averaging about 55 nm. CXL treatment significantly reduced this distance in anterior and middle layers ($P < 0.05$), aligning with previous reports on pig and human corneas. The posterior region remained unaffected. Enzyme-treated samples had significantly larger values than controls ($P < 0.05$), and CXL treatment decreased center-center distances significantly ($P < 0.05$). GAG removal led to loosely packed collagen lamellae, increasing this distance, while CXL treatment added crosslinks, stiffening the interfibrillar domain and compacting collagen lamellae.

The study used porcine corneas because of human donor tissue scarcity; however, it provided valuable insights into microstructural changes in corneal mechanical properties resulting from cross-linking (CXL) and GAG removal. Our ongoing research involves human corneas to identify potential microstructural differences contributing to a deeper understanding of corneal biomechanics.

ACKNOWLEDGEMENTS

Authors thank NIH-R21EY030264 for partial support and express gratitude to staff at UIC's Electron Microscopy Core.

REFERENCES

[1] Bettelheim, F.A. and B. Plessy, Biochimica et Biophysica Acta (BBA) - General Subjects, 1975. 381(1): p. 203-214.
[2] Chakravarti, S., et al., Investigative Ophthalmology & Visual Science, 2000. 41(11): p. 3365-3373.
[3] Wollensak, G., et al., Cornea, 23 (2004), pp. 503-507
[4] Hayes, S., et al., PLoS One, 2013. 8(1): p. e52860.
[5] Hatami-Marbini, H. and M.E. Emu, Experimental Eye Research, 2023. 234: p. 109570.
[6] Hatami-Marbini, H. and M.E. Emu, Experimental Eye Research, 2023: p. 109476.

IMAGE-BASED PATIENT-SPECIFIC MODELING OF HUMAN STOMACH ELECTROMECHANICS

Lei Shi (1), Qi Zhao (2), Yurui Chen (3)

(1) Department of Mechanical Engineering, Kennesaw State University, Marietta, GA, USA
(2) Department of Gastroenterology, Shandong Provincial Hospital, Jinan, China
(3) Department of Mechanical Engineering, Columbia University, NY, USA

INTRODUCTION

The stomach is a muscular organ located in the upper abdomen, between the esophagus and the small intesline. Responsible for functions like food storage, mechanical and chemical digestion, and the production of gastric juices, its motility is controlled by electrical signals. Any electrophysiological or mechanical dysfunction in the stomach may contribute to various gastrointestinal conditions, including gastric motility disorders, gastroesophageal reflux disease, functional gastrointestinal disorders, among others. Therefore, both electrophysiology and mechanics are indispensable factors in comprehensively studying the physiology and pathology of the stomach.

The personalized electromechanics modeling for the stomach is crucial, providing a more precise, individualized approach to diagnosing, treating, and understanding gastrointestinal conditions. This advancement holds the promise of improving patient outcomes and driving progress in medical knowledge and technology. Despite being in its early stages, efforts are underway to develop this field [1]. Remarkable improvement in the medical imaging technology now enables high-resolution and real-time imaging of the stomach, enhancing the accuracy of stomach modeling.

In this work, we present a comprehensive workflow tailored to model the electromechanics of patient-specific stomachs. Within this workflow, we study the segmentation methodology, stomach mechanics, fiber generation, and electromechanics coupling. The goal is to extend this workflow to more patients (~15) to get more generalized characteristics of the human stomach. This initiative aims to establish a foundational understanding of the physiology and pathology of the stomach.

METHODS

The entire workflow is shown in **Fig. 1**. We acquire the 3D CT data of the abdomen of a healthy male patient. Using the open-source software – Simvascular (https://simvascular.github.io/), we segment the 3D CT data to construct a finite element analysis (FEA) model of the human stomach. The model spans from the lower esophageal sphincter (LES) to the pyloric sphincter (PS) plane. Considering the small thickness of the stomach wall, we segment the lumen of the stomach and assume the thickness based on literature [2].

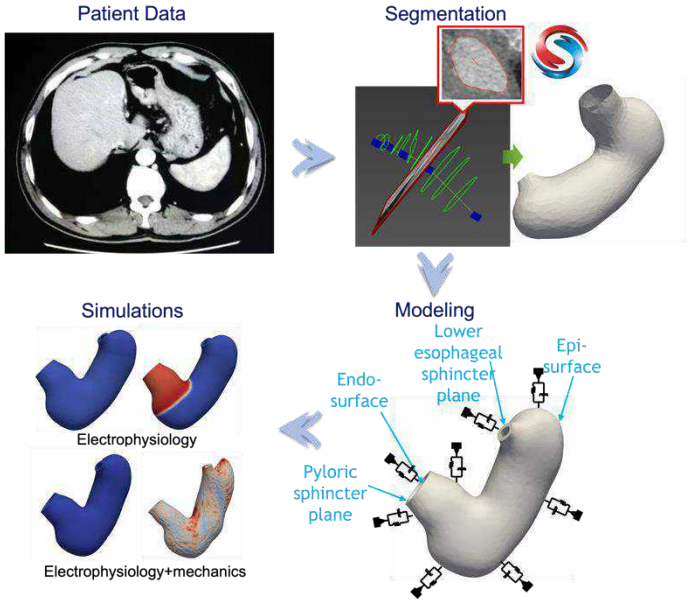

Figure 1: The workflow for stomach electromechanics modeling. FEA model is segmented from the patient CT data. The fiber orientation is generated on the 3D stomach model using a rule-based method, and subsequently, electrophysiology and solid mechanics coupling simulation is conducted and analyzed.

After that, we develop a rule-based fiber assignment algorithm, inspired by myocardium fiber orientation work [3], to assign the muscle fiber orientations to different locations within the stomach model (**Fig. 2**). By solving three Laplace-Dirichlet problems with distinct Dirichlet boundary conditions, we obtain the transmural distance ψ_{EPI}, and two other distances ψ_{LP} (LES-PS) and ψ_{LA} (LES-Apex). Adapting the method from [3], we calculate the local coordinate system and establish the orthotropic fiber orientation. Stomach muscle fibers exhibit distinct orientations in different layers: oblique in the innermost layer, circularly in the mid-layer, and longitudinally in the outermost layer. To determine the orientation angle of the fibers, a series of threshold values are defined and applied across the transmural distance.

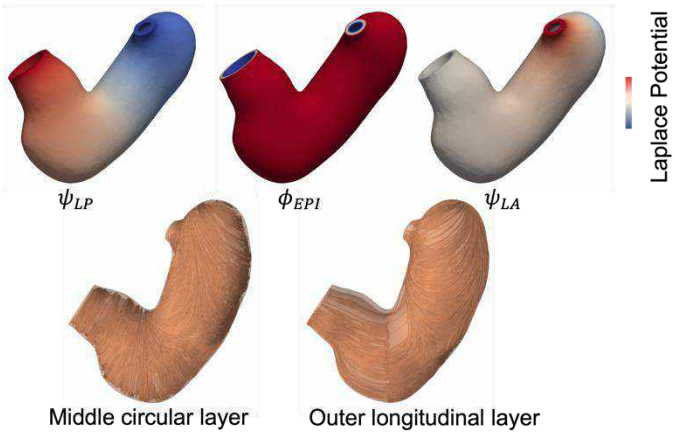

Figure 2: Top: The solutions to 3 Laplace boundary problems. Bottom: Generated fiber orientations for different muscle layers.

To account for tissue support at the lower esophageal sphincter plane, pyloric sphincter plane, and the effects of the epi-surface serosa, Robin boundary conditions are implemented with appropriate stiffness and viscosity. The unified variational multiscale formulation [4] is employed to solve the domain problem. The constitutive model comprises a passive component, described by a Holzapfel-Ogden (HO) model with a viscous part [5], and an active component driven by electromechanics coupling. The electrophysiology model involves simulating the monodomain equation for transmembrane potential and the Sathar ionic model [6]. Pacemaker cells are defined as elements at the pyloric sphincter plane, while non-pacemaker conducting cells extend through the stomach body to the fundus. Elements in the fundus are designated as insulators, as the fundus does not contract.

RESULTS

In **Fig. 3**, the results of electrophysiology simulations are presented. The top panel illustrates stimulus and potential changes over time for pacemaker cells, replicating the typical depolarization-repolarization curve of potential vs. time with the stimulus. The bottom panel displays corresponding potential maps for the 3D stomach model, revealing the clear travel of electrical signals activating the entire stomach body except for the fundus. The signals then gradually repolarize to the resting state.

In **Fig. 4**, the results of the active contraction simulation are illustrated. The dominant factor in active contraction is the active stress induced by electromechanics, as shown. The volume undergoes a significant reduction during contraction and subsequently relaxes to the resting state, accompanied by a decrease in active stress.

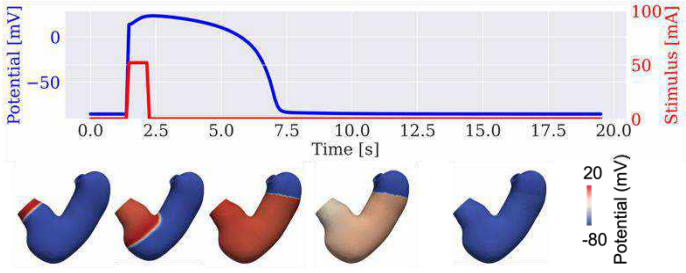

Figure 3: Results of electrophysiology simulations. Top: The stimulus and potential changes with time for pacemaker cells. Bottom: Corresponding potential maps for the 3D stomach model.

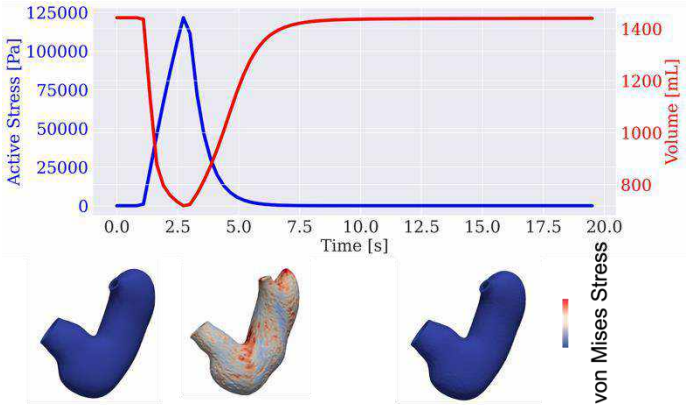

Figure 4: Top: Active stress and volume changes with time during the active contraction simulation. Bottom: Corresponding deformation and stress field for the 3D stomach model.

DISCUSSION

This work demonstrates a proof-of-concept application of a personalized modeling framework to simulate the electrophysiology and solid mechanics coupling for a 3D stomach model derived from the patient CT image. By laying this groundwork, the research paves the way for developing more sophisticated computational models to quantify the electromechanical properties of the digestive track under various conditions, including those with defects or diseases

To move forward, we will study the coupling of the current electromechanics model with fluid to account for the effects of food and water. We will then extend this framework to all of our available patient data, thereby obtaining statistically meaningful electromechanics characteristics of the stomach. The final goal is to establish a mature workflow to predict and design treatments for the stomach-related defects and diseases. This initiative is geared towards enhancing patient outcomes through informed and tailored treatment strategies.

ACKNOWLEDGEMENTS

We acknowledge meaningful discussions about tissue modeling with Dr. Vijay Vedula from Columbia University.

REFERENCES

[1] Acharya S., et al. *Com Bio and Med* 143, 104948 (2022)
[2] Akbas, A., et al. Journal of Oncology 2019 (2019).
[3] Bayer, J.D. et al., *Annals Bio Eng* 40, 2243-2254 (2012).
[4] Liu J., et al., *CMAME*, (2018)
[5] Shi L. et al. Manuscript preparation. (2024)
[6] Sathar S., et al., *Ann Biomed Eng.* 82, 63-81 (2014)

ROTARY PIVOT SHIFT: A NEW LOADING PROFILE FOR QUANTIFYING ROTATIONAL STABILITY IN THE KNEE

Elizabeth B. Pace (1), Robb W. Colbrunn (1), Vincent Lizzio (2), Paul Saluan (2), Tara F. Nagle (1)

(1) Lerner Research Institute, Cleveland Clinic Foundation, Cleveland, Ohio, USA
(2) Dept. of Orthopedic Surgery, Cleveland Clinic, Cleveland, Ohio, USA

INTRODUCTION

The anterior cruciate ligament (ACL) provides stability to the knee, primarily by limiting anterior tibial translation. ACL injuries are common amongst athletes. The anterolateral ligament (ALL) is also believed to provide rotational stability to the knee. During an ACL reconstruction, the ALL may also be reconstructed if there is concern for residual rotational instability.

A common clinical technique to diagnose ACL injuries is called the pivot shift. During a typical pivot shift, the physician applies a valgus torque to the tibia while flexing the knee from 0° (fully extended) to 90° [1]. However, the pivot shift is a binary diagnostic – a "clunk" indicates injury, while no "clunk" indicates no injury.

During *in vitro* testing, loading profiles are applied to the joint under different surgical conditions and the resulting kinematic responses are used to assess the biomechanical effects and to ultimately make surgical recommendations. To assess surgical conditions relating to the ACL and other ligaments in the knee, quasistatic and dynamic loading profiles that aim to replicate clinical exams like the Lachman and Pivot Shift are often utilized [2,3]. While quasistatic loading profiles have been successful in evaluating anterior stability, rotational stability is not often reported. Dynamic loading profiles have shown to engage the joint rotationally, but they are complex as commanded loads dynamically change in all degrees of freedom (DOF).

The novel *rotary pivot shift* presented in this study aims to reduce the variables that can produce a positive pivot shift and as such, does not involve dynamic flexing of the knee. All commanded loads and flexion angle are constant throughout except for external rotation (ER) torque. Initial loads position the joint in a subluxed state and ER torque is increased until reduction occurs.

The goal of this study was to verify that the *rotary pivot shift* loading profile can produce a positive pivot shift in an ACL deficient knee and that it could be used to assess and quantify rotary stability in the knee joint under varying ligamentous injury and surgical conditions.

METHODS

Rotary Pivot Shift Loading Profile

The rotary pivot shift loading profile consisted of four static loads:

- 50 N Medial Drawer
- 50 N Anterior Drawer
- 150 N Compression Force
- 15 Nm Valgus Torque

ER torque was increased from -0.5 to 11 Nm until reduction occurred.

ACL Deficient Verification

One ACL deficient fresh-frozen cadaver knee specimen was procured and tested using a simVITRO® Universal Musculoskeletal Simulator (Cleveland Clinic, Cleveland, OH) and a 6-axis force/torque (FT) sensor (Omega160, ATI, Apex, NC). During setup, each specimen was rigidly mounted to the robot in full extension. Coordinate systems were established for the tibia and femur and spatial relationships between the knee, robot, and FT sensor were quantified and established. Kinematics and kinetics were calculated based on these spatial relationships and FT sensor measurements.

The rotary shift loading profile was executed on the specimen at four (4) flexion angles (15°, 20°, 25°, and 30°). Anterior tibial translation (ATT) and External tibial rotation (ETR) were evaluated at each flexion angle to determine whether a shift had occurred.

.

ALL Rotary Stability Evaluation

One fresh-frozen cadaver was prepared and tested using the same lab setup as in the ACL deficient validation. This specimen underwent testing at three surgical conditions:

- Intact
- ALL injured
- ALL reconstructed

The ALL injured state was created by transecting the ALL near its tibial insertion with a scalpel. The ALL was reconstructed using a hamstring allograft that was secured using suture anchors at the anatomic origin on the femur and insertion on the tibia. The graft was tensioned with the knee in full extension and neutral rotation In each condition, the ACL was kept intact in order to eliminate variables surrounding surgical effectiveness of an ACL reconstruction.

For each of these conditions, the rotary shift loading profile was executed at 30° flexion.

ETR difference between a common ER torque value that occurred after reduction for all surgical conditions and 0 Nm was calculated. The ETR differences were normalized to intact to easily compare the relative rotational stability of the surgical conditions to intact.

RESULTS

ACL Deficient Evaluation

A positive shift occurred at each of the four flexion angles (15°, 20°, 25°, and 30°). Figures 1 and 2 display the ATT and ETR as a function of ER torque and were shifted to 0 mm and 0° at 0 Nm ER torque, respectively, to better display differences. These results indicate that the rotary pivot shift can be performed at any flexion angle from 15° to 30°. 30° was selected for simplicity, as this flexion angle is the prescribed angle for the Lachman test. A positive shift in an ACL-deficient knee confirmed that the rotary pivot shift loading profile performed as intended.

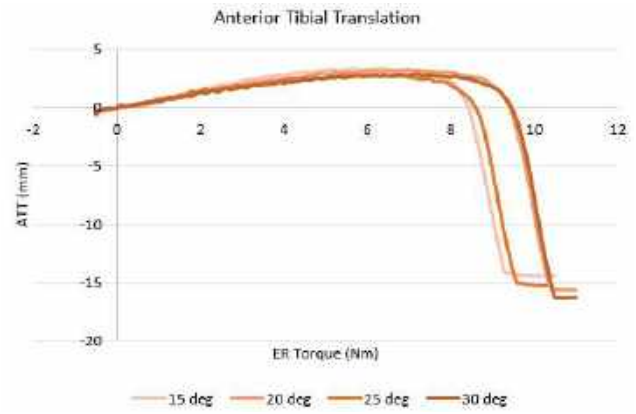

Figure 1: Anterior tibial translation at 15°, 20°, 25°, and 30° of flexion

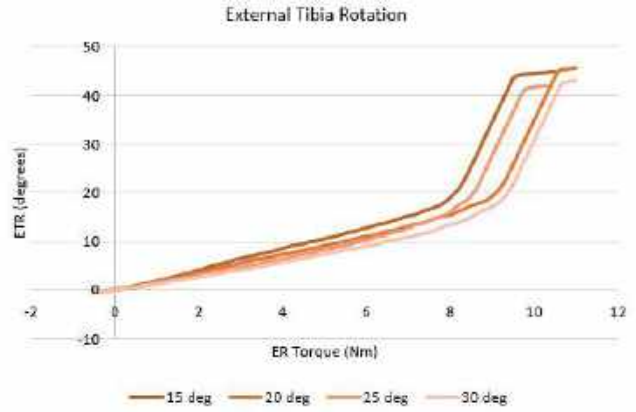

Figure 2: External tibial rotation at 15°, 20°, 25°, and 30° of flexion

ALL Rotary Stability Evaluation

Figure 3 displays ETR for the three surgical conditions. The ETR plots were shifted to 0° at 0 Nm ER torque to better display differences. For all surgical conditions, the knee reduction occurred before 4 Nm ER torque and so the ETR difference between 0 and 4 Nm was calculated for comparison. The intact knee rotated 19.1°, while the ALL injured knee rotated 20.7° (108.4% of intact), and the ALL reconstructed knee rotated 12.1° (63.2% of intact). This data indicates that differences in rotational stability can be detected with the rotary pivot shift.

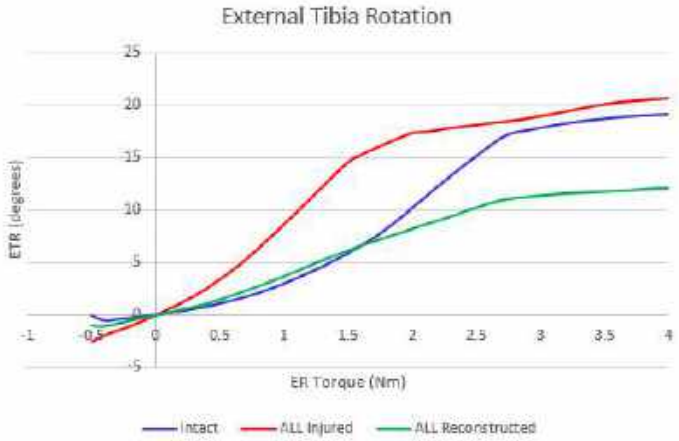

Figure 3: External tibial rotation of the intact, ALL injured, and ALL reconstructed conditions

DISCUSSION

This study evaluated the effectiveness of a new loading profile, called the rotary pivot shift, in measuring rotary stability of the knee joint. The results demonstrate success using the rotary pivot shift for one specimen. Further, the rotary pivot shift was able to demonstrate that minor differences in tibial rotation can be induced under different surgical conditions.

Another advantage of the rotary pivot shift is that it is only dynamic in one DOF, which means it does not require a multi-DOF simulator and can be performed with a single axis machine and deadweights.

Future work will include application of this loading profile to a statistically significant number of specimens to ensure the ramp pivot shift can be validated. Additionally, we want to consider scaled down loads to see if positive shifts can be induced while reducing the stress on the joint to make it more effective when used in a larger testing suite to evaluate time-zero surgical repairs.

REFERENCES

[1] Musahl, V et al., *Knee Surg Sports Traumatol Arthrosc*, 20:724-731, 2012.

[2] Kim, S et al., *Clin Orthop Relat Res*, 317: 237–242, 1995.

[3] Colbrunn, R et al., *J Orthop Res*, 37(12):2601-2608, 2019.

REGIONAL CORRELATION OF STIFFNESS AND PERFUSION IN THE HUMAN BRAIN AT 7T MRI THROUGH MR ELASTOGRAPHY AND ARTERIAL SPIN LABELING TECHNIQUES

Caitlin M. Neher[1], Em R. Triolo[1], Mehmet Kurt[1]

[1]Mechanical Engineering Department, University of Washington, Seattle, WA, USA

INTRODUCTION

The mechanical properties of the brain give us insight into disease states and open avenues for new methods of medical diagnosis[1]. It is known that brain tissue gets softer as we age[2], but it is unknown whether and how tissue property changes are related to the branched cerebral vascular system in health and disease. Research suggests that changes in cerebral blood flow may be correlated with cognitive deficits in mild cognitive impairment[3], amyloid-beta deposits in Alzheimer's disease (AD)[4], and even diseased liver tissue[5]. However, there is limited research investigating the relationship between perfusion and tissue stiffness in the healthy human brain. In Alzheimer's disease it is unknown how the cascade of associated events contributes to its pathogenesis, but amyloid-deposits, tau tangles, tissue softening, hypoperfusion, and metabolic changes are disease correlates. It has been shown in one preliminary study that perfusion, stiffness, and flux rate are connected in the brain due to higher intravascular pressure that is present in small vessels, coupled with the constriction of vessels in non-compliant tissue[6]. This suggests that perfusion, an indicator of cell metabolic activity and blood volume, will have an impact on the measurable mechanical properties of brain tissue and can be used as a biomarker of underlying pathology. In this study, we utilized the advanced neuroimaging tools of Magnetic Resonance Elastography (MRE) and Arterial Spin Labeling (ASL) to quantify brain stiffness and perfusion non-invasively by voxel. First, a modular pipeline for the post processing and correlation of stiffness and perfusion was developed and used to analyze the collected data from a young control cohort with no known disease. This preliminary dataset serves as a proof-of-concept investigation into how these two metrics may be related in health and disease states of the human brain. Accordingly, the objective of this study was to collect, process, and compare stiffness and perfusion MRI data in a healthy cohort to determine whether these two factors may be correlated.

METHODS

In this study, we obtained pulsed ASL and MRE data from eight healthy volunteers aged 20-35 on a Siemens Magnetom 7T MRI scanner with a 32-channel head coil. The MRE sequence was an echo-planar spin-echo 2D pulse sequence with 3D motion-encoding gradients (TE=70ms, TR=5600ms, GRAPPA=3, 1.1mm isotropic resolution)[7] and a custom pneumatic actuator applied vibrations at 50Hz[8]. The MRE phase magnitude images were masked using SPM12[9], denoised using a MP-PCA algorithm[10] and unwrapped using Segue Phase Unwrapping[11]. The resulting unwrapped displacement data was used to calculate the magnitude of the complex shear modulus (|G*|) using an iterative nonlinear viscoelastic inversion of the time-harmonic Navier's equation[12]. Also acquired at 7T, a PASL sequence was used with EPI readout (TE=39ms, TR=5000ms, 25 repeats, 3.5mm isotropic resolution). Arterial spins were labeled by a 10cm inversion slab proximal to the image slices, with the labeling method Q2TIPS[13]. Subtraction, Bayesian Inference, inversion of the kinetic model of label inflow, and equilibrium magnetization calculations from a proton density weighted (M0) image were used to acquire quantified cerebral blood flow (CBF) in ml/100g/min in accordance with the recommended ASL whitepaper implementation summarized by equation (1) below[14].

$$CBF = \frac{6000*\lambda*(SI_{control}-SI_{label})*e^{\frac{TI}{T_{1,blood}}}}{2*\alpha*TI_1*SI_{PD}} \quad (1)$$

FreeSurfer[15] segmentation was used with a custom MATLAB script to calculate the correlation coefficient of stiffness and perfusion in gray and white matter regions across subjects. Only whole brain white matter was analyzed based on its low SNR due to high arterial transit time and relatively low perfusion[16]. During analysis, images were visually checked and regionally evaluated based on mean, standard deviation,

and volume to determine inconsistencies; no subjects were removed as outliers.

RESULTS

After all subject data was processed and co-registered to the matrix space of each respective T1 image, 3D perfusion maps and elastograms were obtained for each subject; an example of these can be seen in **Figure 1**. As expected, gray matter regions, when averaged across subjects, had higher perfusion and lower stiffness than white matter regions (44.8 ± 4.86 vs. 34.2 ± 8.73 ml/100g/min and 1.57 ± 0.25 vs. 2.42 ± 0.29 kPa, respectively). These findings are consistent with brain stiffness as measured by the magnitude of the complex shear modulus (|G*|) and perfusion values in existing literature.

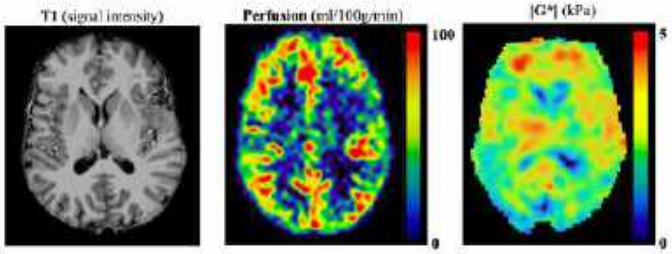

Figure 1: Exemplary axial slice of T1-weighted signal intensity image, perfusion map in ml/100g/min, and elastogram in kPa.

Furthermore, our analysis showed varying strengths of inverse correlation between stiffness and perfusion in some gray matter regions of the brain. Within a cortical gray matter mask, stiffness and perfusion show a strong inverse correlation across subjects (p-value=0.0121, correlation coefficient=-0.823, **Figure 2**). The frontal lobe showed a similar result, with a p-value of 0.0206 and correlation coefficient of -0.787. The white matter across subjects showed a similar, though not statistically significant trend (p-value=0.119, corr. coefficient=-0.596).

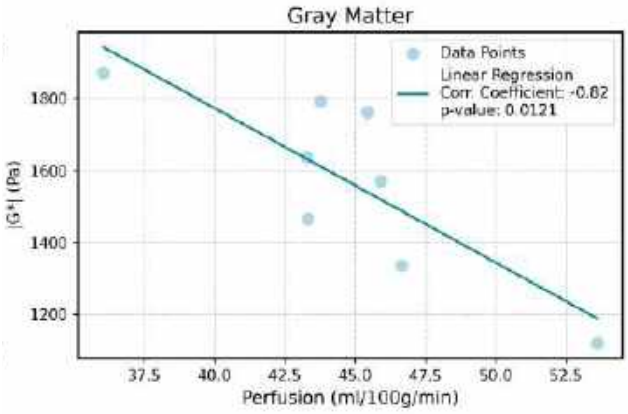

Figure 2: Inverse correlation of stiffness and perfusion in the cortical gray matter, across subjects.

DISCUSSION

Our results showed a strong inverse correlation between stiffness and cerebral blood flow (perfusion) in the healthy human cortex. This result supports our hypothesis that increased blood flow is related to reduced stiffness due to an increase in the relative size of vascular structures[6], a trend that is also consistent with existing research showing reduced whole-brain stiffness following exercise[17], and therefore increased perfusion[18].

These preliminary results, suggesting that there is a measurable correlation between stiffness, a mechanical property of tissue, and perfusion, a measure of blood delivery within tissue, may indicate an underlying biological mechanism that must be investigated further. ASL is unique in the respect that by measuring the delivery of blood to the brain tissue, it is a metric of brain health at the capillary bed level[19]. Unlike other vasculature scans, such as time of flight (TOF) angiography, ASL measures blood delivery rather than blood vessel characteristics. The establishment of correlations between stiffness and perfusion could enhance our understanding of disease pathology in Alzheimer's Disease and other neurodegenerative diseases by highlighting the interplay between tissue mechanics and metabolic and neuroinflammatory changes. To do so, further investigation of this relationship is needed to establish a baseline in the healthy brain. Future work on this study will be accomplished by increasing the pool of healthy controls, acquiring higher resolution and enhanced SNR perfusion data with a pseudo-continuous ASL sequence, and investigating smaller brain regions of interest with different levels of vascularity.

ACKNOWLEDGEMENTS

This work was supported by the National Science Foundation (NSF CMMI 1953323).

REFERENCES

[1]Bokkers et al. Whole-brain arterial spin labeling perfusion MRI in patients with acute stroke. *Stroke*, 2012.
[2]Arani et al., *NeuroImage*, 2015.
[3]Johnson et al. Pattern of Cerebral Hypoperfusion in Alzheimer Disease and Mild Cognitive Impairment Measured with Arterial Spin-labeling MR Imaging: Initial Experience. *Radiology,* 2005.
[4]Mattsson et al. Association of brain amyloid-β with cerebral perfusion and structure in Alzheimer's disease and mild cognitive impairment. *Brain*, 2014.
[5]Chouhan et al. Vascular assessment of liver disease–towards a new frontier in MRI. *The British Institute of Radiology*, 2016.
[6]Sack et. al., Journal of Cerebral Blood Flow and Metabolism, 2017.
[7]Johnson et al. 3D multislab, multishot acquisition for fast, whole-brain MR elastography with high signal-to-noise efficiency. *Magn. Reson. Med.*, 2013.
[8]Triolo et al., *Current Protocols*, 2022.
[9]Penny et al. Statistical Parametric Mapping: The Analysis of Functional Brain Images. *Psychology*, 2011.
[10]Veraart et al. Denoising of diffusion MRI using random matrix theory. *NeuroImage*, 2016.
[11]Karsa, A., Shmueli, K., *IEEE Transactions on Medical Imaging*, 2018.
[12]McGarry MD, Van Houten EE, Johnson CL, Georgiadis JG, Sutton BP, Weaver JB, Paulsen KD., *Med Phys.* 39(10):6388-96, 2012.
[13]Luh et al. QUIPSS II with Thin-Slice TI1 Periodic Saturation. *Magn. Reson. Med.*, 1999.
[14]Alsop et al., *Magn. Reson. Med.*, 73(1): 102-16, 2015
[15]Fischl B., FreeSurfer. *NeuroImage*, *62*(2), 774–781, 2012.
[16]van Gelderen, P., de Zwart, J.A. and Duyn, J.H, *Magn. Reson. Med.*, 59: 788-795, 2008.
[17]McIlvain, G. Acute Effects of High-Intensity Exercise on Brain Mechanical Properties and Cognitive Function. *ISMRM*, 2022.
[18]Ogoh, S., Ainslie, P., Cerebral blood flow during exercise: mechanisms of regulation. *Journal of Applied Physiology*, 2009.
[19]Jezzard et al. Arterial Spin Labeling for the Measurement of Cerebral Perfusion and Angiography. *Journal of Cerebral Blood Flow & Metabolism*, 2017.

COMPUTATIONAL MODELING OF A HUMAN PLACENTONE

Armita Najmi (1), Noelia Grande Gutiérrez (1)

(1) Department of Mechanical Engineering, Carnegie Mellon University, Pittsburgh, Pennsylvania, USA

INTRODUCTION

The placenta is a vital organ facilitating the exchange of oxygen and nutrients between the mother and fetus. During pregnancy, the maternal uterine vasculature undergoes significant changes, including the remodeling of the spiral arteries (SAs) to establish uteroplacental circulation. A better understanding of placenta formation and the factors affecting its function is essential for detecting and predicting pregnancy disorders. While placentation remains understudied due to limitations in imaging modalities and diagnostic tools that can safely be utilized during pregnancy, computational modeling can provide valuable insights. Previous placental blood flow numerical studies have focused on modeling the placentone [1]–[4], which is the basic functional structure of the placenta. These models have typically employed a porous media approach to model the intervillous space (IVS). A common limitation among these studies is their lack of validation against experimental data. Also, there has been insufficient attention to IVS pressure, which is sensitive to the imposed boundary conditions (BCs). Our computational model aims to address these issues. Due to the limited *in vivo* imaging data and the lack of experimental studies, there is still uncertainty regarding the placentone structure. In addition, the effect of modeling assumptions and parameter values in simulation results has yet to be systematically evaluated. In this project, we assessed the sensitivity of uteroplacental hemodynamics to model parameters and examined necessary conditions to ensure physiological simulation results. We used Doppler ultrasound measurements from clinical studies in the literature [5], such as jet length and fluid velocity measured at the SA opening, as targets to tune the model parameters.

METHODS

We constructed a three-dimensional idealized model of a plancentone informed by histology and MRI literature data [6]–[8]. The model consisted of the spiral artery (SA), two veins, and the placentone lobule with a free-of-villi cavity (Figure 1). We simulated variations in the placentone structure including 1) veins location, 2) cavity length, 3) SA remodeling and its remodeling length. We employed a porous medium approach to model the IVS as proposed by prior studies. We assigned two different porosity values to the lobule periphery and its central region (Figure 1) to represent differences in villi density as reported by histology [7] and *in vivo* MRI studies [8].

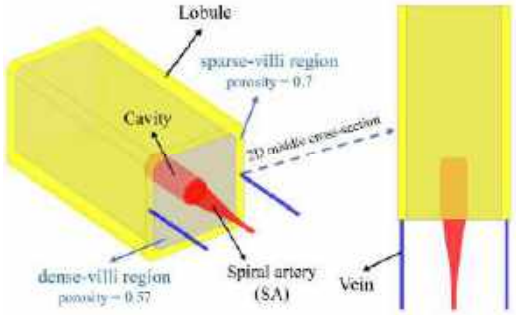

Figure 1: Idealized 3D placentone model including the lobule and the maternal vasculature and its 2D middle cross-section.

We solved the continuity and Navier-Stokes equations that govern blood flow inside the non-porous regions of the placentone (SA, veins, and cavity). The governing equations in the porous region (lobule except cavity), were the Continuity and Darcy-Brinkman equations.

The numerical simulation was performed in SimVascular [9]. We modified SimVascular multiphysics finite element solver, svFSI, to include a porous medium model.

We applied zero pressure BC on the veins outlet surfaces and utilized an at-term inflow BC ($145\ mm^3/s$) on the inlet surface. We set no-slip rigid wall BC on the rest of the surfaces. Most of the previous works in placentone modeling have applied a no-slip wall BC on the lobule side surfaces representing the septa. However, the septa do not extend to the end of the placentone [1]. Therefore, we also simulated the

case of two distinct BCs for the placentone side surfaces: a no-slip rigid wall proximal to the maternal side and a pressure BC on the wall proximal to the fetal side. For the later, a pressure value of 12 mmHg was imposed according to the reported data in the literature [10]–[12].

RESULTS

We validated our implementation of a porous media model in SimVascular against the commercial software COMSOL and obtained good agreement in our simulation results (<4% difference).

Based on measured jet lengths, veins draining the placentone are likely to be in the lobule periphery. Figure 2 shows the velocity contour for the veins located close to the SA and in the lobule periphery.

Fixing the location of the veins to the lobule periphery, we studied the effect of cavity length on the jet length. We observed an increase in jet length with cavity length. However, the rate of increase is reduced for longer cavities. In this case, a cavity length of 7 mm resulted in a jet length of 5.285 mm, comparable to the mean value for a normal, healthy pregnancy as reported via ultrasound (5.3 mm). Figure 3A shows the velocity contour when there is no cavity at the SA opening.

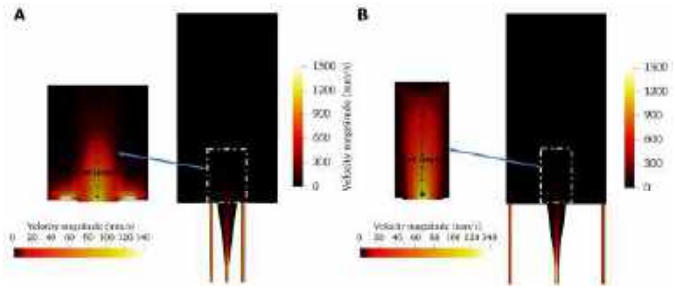

Figure 2: Velocity contour when A) veins are located close to the SA, and B) veins are located in the lobule periphery.

We observed prescribing a rigid wall BC on the entire placentone lateral surface resulted in pressure inside the lobule > 40 mmHg, which is higher than the expected physiological pressure of 12 mmHg [10]–[12]. When we applied a pressure of 12 mmHg on the side surfaces more proximal to the fetus, we obtained physiological pressures inside the IVS. Also, we observed a shorter cavity (6.5 mm) was enough to produce a jet length comparable to the mean jet length for a normal, healthy pregnancy.

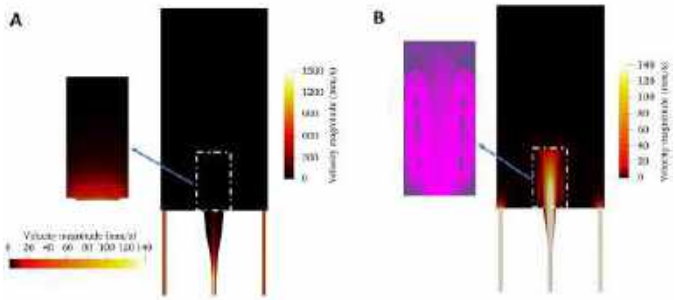

Figure 3: Velocity contour when A) no free-of-villi cavity is considered, and B) remodeling of the SA is incomplete.

Changing the periphery porosity, we observed a slight increase in the jet length (<8%) when the periphery was a sparser villi region.

Computational experiments considering partial remodeling for the SA (60%), representing a diseased case, show higher shear rates (x2.6 healthy case on the cavity side surface), higher velocities (x1.22 healthy case velocity on the upper cavity surface) and strong flow recirculation inside the cavity. Figure 3B shows velocity magnitude and streamlines for the incomplete SA remodeling case.

DISCUSSION

Our simulation results suggest that uteroplacental hemodynamics are sensitive to the structure of the placentone model, and BCs that capture placental physiology are critical to the success of these models.

First, we had to define the SA remodeled part length. We conducted simulations with different remodeling lengths for the SA. We observed that when the remodeled length is too short, there is flow separation inside the SA, which is not expected in a completely remodeled SA. Therefore, we gradually increased the remodeling length to achieve no flow separation and, at the same time, meet the maximum velocities at the SA opening reported from Doppler ultrasound data [5].

Our numerical results show a physiological jet length does not form unless veins are located far enough from the SA opening. Veins must be located in the lobule periphery (Figure 2) to achieve the mean jet length reported for a normal, healthy pregnancy.

We demonstrated the existence of a villi-free cavity at the SA opening is critical to obtaining physiological uteroplacental flow. In the absence of a cavity, no jet at the entry of the IVS is formed (Figure 3A).

The extension length of the septa separating adjacent placentones may significantly affect IVS pressure. When we considered the septa on the entire placentone side surface, we obtained non-physiological IVS pressure values.

Both histology and MRI studies have shown that the lobule peripheral region is a sparser villi region compared to its central part [7], [8]. Increasing the porosity to simulate a less dense peripheral region slightly increased the jet length. This small effect could be biased to selecting a small region as the peripheral region.

Studies suggest incomplete remodeling of the SA is the underlying cause of some pregnancy disorders. For a case of 60% remodeling of the SA, we observe strong flow recirculation inside the cavity and higher shear rates compared to the normal case. These high shear rates can be detrimental to the delicate structure of the villi, and the higher velocities can limit the diffusion of biomolecules between the mother and baby. Moreover, the pressure drop along the SA is three times higher than that of the normal case, suggesting a potential correlation with high blood pressure in preeclampsia.

In conclusion, we have successfully developed a model to simulate uteroplacental hemodynamics, and we have identified optimal model parameters to represent physiological placental blood flow conditions. In our first attempt at modeling uteroplacental hemodynamics, we modeled the SA as a straight conduit along the penetration depth. Our Ongoing work is focused on analyzing the effect of SA tortuosity.

ACKNOWLEDGEMENTS

We acknowledge CMU's start-up fund for support.

REFERENCES

[1] Chernyavsky *et al.*, *Placenta*, 31: 44–52, 2010.
[2] Lecarpentier *et al.*, *PLOS ONE*, 11: e0147262, 2016.
[3] Roth *et al.*, *Scientific Reports*, 7: 40771, 2017.
[4] Mekler *et al.*, *Placenta*, 129: 15–22, 2022.
[5] Collins *et al.*, *Placenta*, 33: 782–787, 2012.
[6] Burton *et al.*, *Placenta*, 30: 473–482, 2009.
[7] Baergen *et al.*, *Benirschke's Pathology of the Human Placenta*. Springer Nature, 2021.
[8] Kliewer *et al.*, *Placenta*, 131: 104–110, 2023.
[9] Updegrove *et al.*, *Ann Biomed Eng*, 45: 525–541, 2017.
[10] Yartsev, "Uteroplacental blood flow | Deranged Physiology."
[11] Clark *et al.*, *Placenta*, 66: 74–81, 2018.
[12] Moll *et al.*, *Pflugers Arch.*, 377: 225–228, 1978.

IN VITRO ASSESSMENT OF METFORMIN TREATMENTS FOR CARTILAGE INJURY

Hessam Noori-Dokht (1,2), Taylor Williams (3), Sogol Younesi (4), Diane R. Wagner (1,2,3,4)

(1) Department of Mechanical Engineering, Indiana University-Purdue University Indianapolis, Indianapolis, IN, USA
(2) School of Mechanical Engineering, Purdue University, West Lafayette, IN, USA
(3) Department of Biomedical Engineering, Indiana University-Purdue University Indianapolis, Indianapolis, IN, USA
(4) School of Biomedical Engineering, Purdue University, West Lafayette, IN, USA

INTRODUCTION

A single traumatic impact to cartilage triggers a chondrocyte injury response that includes mitochondrial dysfunction, cell death, and eventual breakdown of cartilage tissue, resulting in post-traumatic osteoarthritis (PTOA).[1-3] Due to the limited natural repair abilities of cartilage, there is a clinical need for new approaches to treat cartilage injuries and prevent PTOA progression. The objective of this study was to investigate metformin as a potential treatment for impact-induced cartilage injuries. Metformin, a well-established oral antidiabetic medication,[4] also prevents the onset of osteoarthritis (OA) in various animal models.[5-8] However, these models lack a mechanical overload of cartilage that is usually seen in joint trauma. Therefore, this study aimed to assess the effective dose and timing of metformin treatment for impact-induced chondrocyte injury in cartilage explants.

METHODS

Osteochondral cores were harvested from fresh bovine metacarpophalangeal joints and were cultured.[9] Specimens were impacted with a drop tower instrumented with a load cell and accelerometer (**Fig. 1**) and were treated with 0, 10 or 50 mM metformin.[9] Mitochondrial dysfunction (TMRM and MitoTracker Green, both Molecular Probes) and cell viability (LIVE/DEAD viability kit) were determined via confocal microscopy 24 h post-impact.

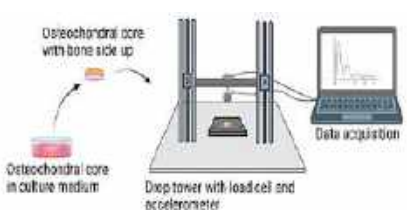

Figure 1: Schematic of drop tower impact model.[9]

Impacted cartilage explants were untreated as controls or were treated with either 1 mM metformin for 28 d or with 50 mM metformin for 24 h post-impact (**Fig. 2**). These treatments were designed to mimic daily oral administration and a single intraarticular injection, respectively. Stress-relaxation indentation was performed before impact and at 1, 7 and 28 d post-impact and was analyzed with a Standard Linear Solid model. Instantaneous (E_0) and equilibrium (E_{eq}) moduli, and time constant (τ) were reported. At 28 d post-impact, GAG content of the tissue was determined with the DMMB assay and in histological sections stained with Safranin-O. Similarly, hydroxyproline (HYP) was quantified with the Chloramine-T assay to determine tissue collagen content. Finally, pyridinoline crosslinks (PYD) were quantified in tissue hydrolysates (Quidel MicroVue PYD ELISA). In addition, medium for each specimen was assayed for GAG and HYP to assess matrix degradation during culture. Significance was set at $p<0.05$ in one-way ANOVAs.

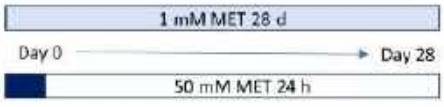

Figure 2: Metformin (MET) treatments representing daily oral administration (1 mM for 28 days) or intraarticular injection (50 mM for the first 24 hours).

RESULTS

Cartilage was impacted with peak stress of 374 ± 33 MPa, impact duration of 0.86 ± 0.08 ms and impact energy density of 22.2 ± 7.9 mJ/mm^3. Mitochondrial polarity was significantly decreased in cartilage explants 24 h post-impact and was rescued with 50 mM metformin but

not the 10 mM dose (**Fig. 3**). Similarly, treatment with 50 mM metformin preserved cell viability at 24 h post-impact significantly better than 10 mM metformin (data not shown).

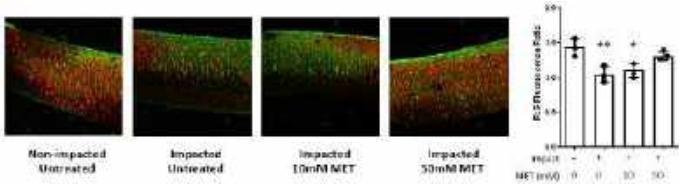

Figure 3: Red:green fluorescent ratio in cartilage treated with metformin (MET) and co-stained with MitoTracker Green (all mitochondria) and TMRM (functional mitochondria stained red) 24 h post-impact. *, ** indicates significant differences from non-impacted control, $p<0.05$.

With the mechanical overload, both E_0 and E_{eq} were maintained at days 1 and 7 (data not shown) but were lower than non-impacted tissue by d 28 (**Fig. 4**). The time constant τ was not altered at any time post-impact (d 28 in **Fig. 4**). Viscoelastic material properties of impacted cartilage did not significantly improve when 1 mM metformin was applied for the entire 28 d culture period but were improved by a single day (24 h) of 50 mM metformin (**Fig. 4**).

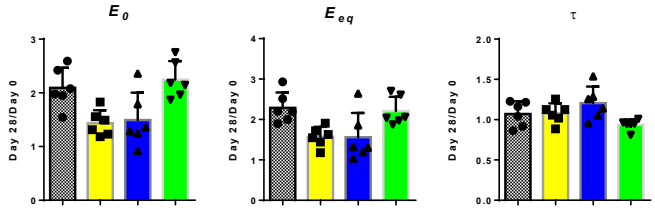

Figure 4: Ratio of material properties of cartilage explants at day 28/day 0. From left to right: instantaneous modulus (E_0), equilibrium modulus (E_{eq}) and time constant (τ). * indicates significant difference from nonimpacted control, $p < 0.05$.

Neither GAG nor HYP content of the tissue were significantly changed by impact or metformin treatments (**Fig 5**), and these results were confirmed with histological sections stained with Safranin-O (**Fig. 6**). Similarly, no differences were detected in the GAG and HYP released to the media (data not shown). However, PYD crosslink density was lower in the impacted tissue, was not significantly changed by exposure to 1 mM metformin for 28 d, and was rescued by 50 mM metformin treatment for 24 h (**Fig 5**).

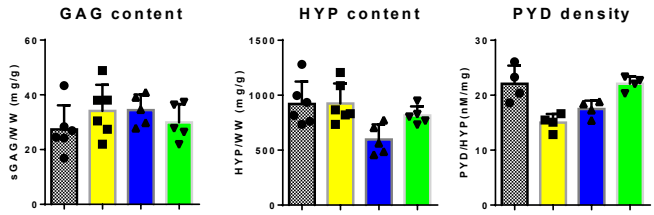

Figure 5: Tissue content of cartilage explants 28 days post-impact. From left to right: glycosaminoglycan (GAG) content per tissue wet weight (WW), hydroxyproline (HYP) content per tissue WW, and pyridinoline (PYD) normalized to HYP. * indicates significant difference from nonimpacted control, $p < 0.05$.

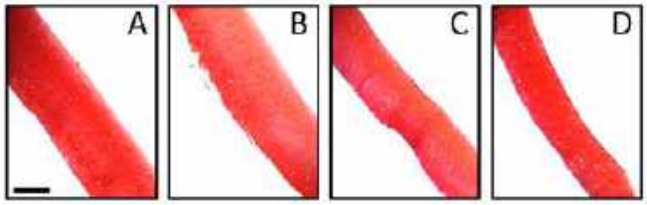

Figure 6: Cartilage sections stained with Safranin-O. A) nonimpacted control, B) impacted control, C) impacted treated with 1mM metformin for 28 d, D) impacted treated with 50 mM metformin for 24 h. Scale bar = 500 µm.

DISCUSSION

This study revealed that a concentration of 50 mM metformin was necessary to rescue mitochondrial dysfunction and cell viability in chondrocytes 24 h post-impact. This concentration is orders of magnitude higher than what is expected in the joint with oral delivery, suggesting that intraarticular injection of metformin may be necessary for effective cartilage injury treatment. To investigate this, we evaluated the viscoelastic properties and biochemical composition of impacted cartilage under two metformin treatment conditions: a lower 1 mM dose of metformin maintained for the entire 28 d culture period, simulating daily oral administration, and a higher 50 mM concentration applied for the first 24 h after impact, representing a single intraarticular injection of metformin. Only the higher concentration maintained viscoelastic material properties of cartilage 28 d post-impact, even though the treatment was limited to the 24 h period following the mechanical overload. These results suggest that rescuing chondrocyte viability and metabolic function during the acute injury phase is required for the long-term preservation of cartilage mechanics.

No significant changes in GAG or collagen content of the tissue were detected with mechanical impact or metformin treatments, nor did biochemical analyses indicate significant tissue degradation during culture. However, impacted tissue exhibited lower PYD density. This decrease in enzymatic collagen crosslinking was rescued with the 50 mM metformin treatment. PYD density was the only biochemical measure that correlated with the changes in material moduli. These findings underscore the sensitivity of cartilage material properties to collagen crosslinking and identify a new mechanism by which a mechanical overload can influence the material behavior of cartilage. Given that increased PYD density is linked to enhanced cartilage wear resistance,[10] these data also indicate that effective metformin treatments may improve functional properties of cartilage following impact injury.

In conclusion, this study demonstrated that 50 mM metformin prevents or delays impact-induced markers of chondrocyte injury and degeneration of cartilage mechanics, suggesting that it may be an effective treatment for cartilage overload injury. Extension of the current findings to an animal model of cartilage trauma may advance intraarticular metformin as a treatment for cartilage injury and the prevention of PTOA.

ACKNOWLEDGEMENTS

Supported by NIH/NIAMS R21AR080255.

REFERENCES

1) Kurz B. et al., *Arthritis and Rheumatol* 2004; 2) Wolff K.J. et al., *J Orthop Res* 2013; 3) Coleman M.C. et al., *Sci Trans Med* 2018; 4) Drzewoski J. and Hanefeld M., *Pharm* 2021; 5) Feng X. et al., *Aging* 2020; 6) Li J. et al., *Ann Rheum Dis* 2020; 7) Li H. et al., *Arthritis Res Ther* 2020; 8) Sik Na H. et al., *Cells* 2021; 9) Karnik S. et al., *IJMS* 2023; 10) Joukar A. et al., *JMBBM* 2023.

FUNCTIONAL-AGGREGATE METHOD FOR OBJECTIVE DETERMINATION OF VERTEBRAL COORDINATE SYSTEMS

Tara F. Nagle (1,2), Jeremy G. Loss (1), Robb W. Colbrunn (1,2)

(1) Lerner Research Institute, Cleveland Clinic Foundation, Cleveland, Ohio, USA
(2) Dept. of Applied Biomedical Engineering, Cleveland State University, Cleveland, Ohio, USA

INTRODUCTION

Spine biomechanics research examines how pathologies, injury, and surgical intervention affects the mechanics of the spine. To examine how different surgical interventions affect spine biomechanics, i*n vitro* testing using a 6 degree of freedom (6-DOF) joint simulator allows for straightforward comparisons. Testing multilevel spines is most often required as interventions commonly bridge multiple functional spinal units (FSU)s and understanding the effects of intervention on adjacent level biomechanics is clinically relevant.

During *in vitro* spine testing, local coordinate systems (CS) must be assigned to individual vertebrae to measure intervertebral motion of individual FSUs. Anatomical CS that only rely on landmarks collected on individual vertebrae are subject to observer variability and are not easily reproduced. Functional CS have been shown to reduce variability in some joints [1]. However, since the spine does not have a unique passive movement path, these methods cannot be used independently to objectively determined vertebral CS.

This study aims to present a Functional-Aggregate method for establishing coordinate systems in the spine using an aggregate of anatomical landmarks from the whole spine to define axis orientations, and kinematics from pure moment motion to optimize origins. We hypothesize that CS variability and resulting kinematic response variation would be reduced with the newly presented Functional-Aggregate CS compared to Anatomical CS.

METHODS

The Functional-Aggregate Method

The Functional-Aggregate method for establishing vertebral CS include the following four steps:

a. Establish Anatomical CS. Anatomical CS are defined from 4 anatomical landmarks (left and right transverse processes, and anterior-rostral and anterior-caudal endplates) displayed in Figure 1.

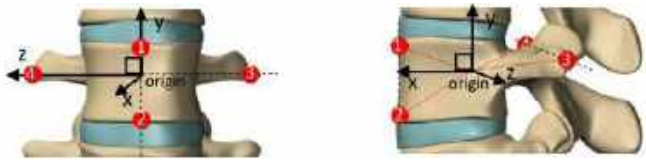

Figure 1: Anatomical Coordinate System

b. Data Collection. Pure-moment testing in the three primary directions must be performed while collecting motion data for each vertebra, and a snapshot of all vertebral kinematics must be collected at the spine's neutral pose.

c. Establish Aggregated Orientations (Figure 2)

Step. 1. At neutral pose, the average z-axis (FE axis) of all included vertebrae is calculated and applied to each vertebra, ensuring a consistent sagittal plane.

Step 2. The anterior-rostral endplate and anterior-caudal endplate points are projected onto the common sagittal plane. A 4th degree polynomial is fit onto the points using the "least absolute residual" method.

Step 3. A vector (pointed rostrally), corresponding to the tangent of the polynomial at the midpoint of the anterior-caudal and anterior-rostral endplate points is the y-axis (AR axis) for each vertebra.

Step 4. The x-axis (LB axis) is the cross-product of the y-axis and z-axis (not pictured).

d. Optimize Functional Origins. Collected kinematic data from pure moment testing is used to redefine origins using the LLS optimization approach for calculating the hip origin [2].

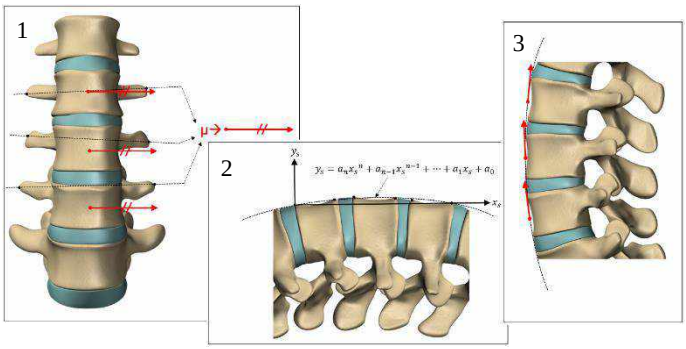

Figure 2: Aggregated Orientation Method

Full Spine Validation

Three observers collected anatomical landmarks from C2-L5 vertebrae on a plastic anatomical spine model. For each observer, Anatomical vertebral CS were established, and Aggregate CS orientation were established across different spinal regions, including Cervical (C2-C7), Thoracic (T1-T12), Lumbar (L1-L5), Cervical + Thoracic, Thoracic + Lumbar, and the Full Spine (C2-L5).

Maximum and average Anatomical and Aggregate CS variation was calculated for each vertebra across the three observers. Paired t-tests compared the variation between Anatomical and Aggregate axis orientations for LB, AR, and FE axes across all vertebrae.

Lumbar Spine Validation

Three human cadaveric spines, T9-Sacrum were secured caudally to a fixed 6-axis force/torque sensor (Delta, ATI, Apex, NC) and rostrally to a 6-DOF robotic manipulator (KR16, Kuka, Augsburg, Germany). Optotrak motion tracking sensors (Northern Digital Inc., Waterloo, ON, Canada) were secured to T12-L5 vertebrae. Three observers collected anatomical landmarks for each instrumented vertebra relative to its respective motion capture sensor. Robotic testing was performed using simVITRO® software (Cleveland Clinic, Cleveland, OH).

To establish Functional-Aggregate CS, motion tracking sensor data was collected during pure moment loading and with the spine in neutral pose. 18 quasistatic pure moment loading conditions (6 uniaxial and 12 combined) were executed to compare kinematic response based on CS definitions.

Anatomical landmarks relative to their respective motion tracking sensor were used to establish Anatomical-CS for each level (Figure 1), and the aggregated landmarks at the spine's neutral pose were used to redefine the CS axes for each level (Fig. 2). Kinematic data from the pure moment testing was used in the optimization for redefining the CS origins, establishing a Functional-Aggregate CS for each level.

Motion capture sensor data from the 18 loading conditions was used to calculate FSU kinematics with Anatomical and Function-Aggregate CS definitions. Average variation of kinematic response across all observers was calculated for each specimen, FSU level, and loading condition combination. Paired t-tests compared the variation between Anatomical and Functional-Aggregate kinematic response for each DOF across all specimens, FSUs, and loading conditions.

RESULTS

Full Spine Validation

Across all levels, average Aggregate CS variation, compared to Anatomical, significantly reduced by 1.35° ± 2.12° (p=0.006), 1.50° ± 2.00° (p=0.002), and 0.87° ± 0.85° (p<0.001), for LB, AR and FE axes, respectively (Figure 3).

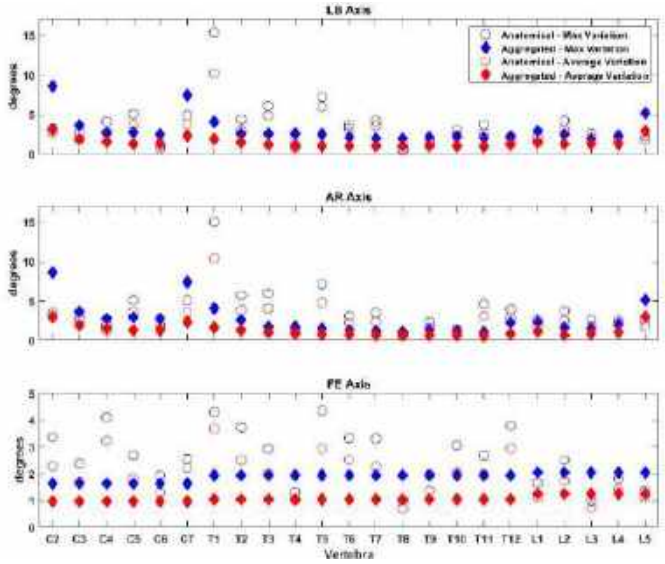

Figure 3: Maximum and average axis orientation variation

Lumbar Spine Validation

Overall, the use of Functional-Aggregate CS significantly reduced FSU kinematic variation compared to Anatomical CS for all DOF (p<0.001) (Figure 4).

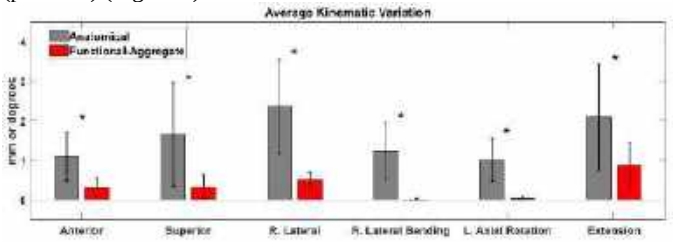

Figure 4: Average FSU kinematic variation and standard deviation. *Significance determined for p-value < 0.05

DISCUSSION

This study examined the variation attributed to CS definition, comparing traditional methods of using anatomical landmarks from a single vertebra to a newly proposed Functional-Aggregate method where aggregation of anatomical landmarks from the entire spine region was used to establish CS orientations and optimization of functional motion was used to establish CS origins.

The method was validated on a full spine model, where average CS axis orientation variation was significantly reduced across all levels compared to Anatomical (Figure 3).

Significant reductions in average kinematic response variation were observed in all DOF during *in vitro* lumbar spine pure moment testing with Functional-Aggregate CS compared to Anatomical. Furthermore, Figure 4 displays *clinically* significant reductions in average kinematic variations for right lateral bending (1.22° ± 0.72°), left axial rotation (0.97° ± 0.53°) and extension (1.20° ± 1.26°), as reported FSU rotations are typically within these orders of magnitude.

We have demonstrated that using Functional-Aggregate CS significantly reduces kinematic response variation. We recommend that Functional-Aggregate CS be used in *in vitro* spine testing.

REFERENCES

[1] Nagle, T et al., *J Biomech*, 127:110664, 2021.
[2] Piazza, S et al., *J Biomech*, 37(3):349-56, 2004

DIFFERENTIATING BETWEEN THE EFFECT OF DAMAGE TO TENOCYTES AND EXTRACELLULAR MATRIX USING PRECISE LASER ABLATION

Diane M. Stonestreet (1), Robert F. Hawkins (2), Nozomi Nishimura (2), Nelly Andarawis-Puri (1,3)

(1) Sibley School of Mechanical and Aerospace Engineering, Cornell University, Ithaca, New York, United States
(2) Meinig School of Biomedical Engineering, Cornell University, Ithaca, New York, United States
(3) Biomechanics, Hospital for Special Surgery, New York City, New York, United States

INTRODUCTION

Tendinopathy is a common and debilitating musculoskeletal condition typically resulting from overuse or accumulation of sub-rupture matrix damage.[1] Although tendon injuries account for over 40% of all musculoskeletal injuries yearly,[2] the limited insight into the pathogenesis of tendinopathy hinders the development of therapeutics aiming to halt or reverse the progression of damage. Sub-rupture tendon injuries are characterized by an increase in apoptosis (programmed cell death),[3] presence of microtears and isolated ruptures in the extracellular matrix (ECM),[4,5] and formation of damage kinks due to plastic deformation of collagen fibers.[6] This pervasive damage to the ECM creates an aberrant loading environment for surviving cells, increasing cell stress and driving them to a catabolic state which promotes degeneration.[3,7] Sub-rupture injuries fail to mount the canonical biological healing response, preventing healing and leaving the tendon subject to further damage accumulation and ultimately rupture.[8]

In contrast, acute tendon ruptures and lacerations induce the canonical biological healing cascade beginning with inflammatory cell infiltration, followed by heightened cell activity and matrix deposition, albeit through scar formation and without reconstitution of the aligned pre-injury tissue structure.[9,10] One likely explanation for the disparate healing responses in acute versus sub-rupture injury types is the presence of cell necrosis, which occurs in laceration and rupture injuries. However, this is notably absent in sub-rupture damaged tendons.[11,12] During necrosis, damage-associated molecular patterns (DAMPs) are released from the injured cell, which activate nearby immune cells and initiate the inflammatory cascade that is critical for tissue repair.[13,14]

To recreate the inflammatory environment that stimulates repair of acute tendon injuries, recent work has examined the use of dry needling in sub-rupture damaged tendon. Dry needling is a clinical intervention wherein the tissue is punctured multiple times with a needle to incite an inflammatory response and disrupt the cycle of chronic degeneration in sub-rupture injuries. However, there is no standard technique for implementing dry needling in tendon. Study designs vary widely and thus so do healing outcomes, with little commentary on what makes this procedure successful in some cases and harmful in others.[15]

As dry needling is an imprecise technique, we expect that the punctures to the tendon cause both cell necrosis and micro-ruptures to the collagen matrix. While ECM micro-ruptures and damage kinks are present in sub-rupture injuries, these types of damage do not trigger inflammation. We believe that this is due to the absence of cell necrosis, which drives inflammation and the subsequent healing cascade in acute injuries. It is possible that sub-rupture injuries do not accumulate enough ECM damage to mount an inflammatory response prior to rupture, however ECM disruption may also be contributing to a catabolic response that prevents effective healing from taking place. The competing effects of cell necrosis and ECM damage could be responsible for the variable healing responses seen in tendon dry needling. This could also explain why both acute and overuse tendon injuries do not heal effectively, whether cell necrosis and inflammation are present or not. Thus, it is critical to develop a precise method for isolating cell necrosis and ECM damage *in vivo* to examine the effects of these two types of damage on inflammation and subsequent healing outcomes in sub-rupture damaged tendons.

To address this, we have developed methods for precise amplified femtosecond laser (AFL) ablation of tenocytes or tendon ECM. This technique uses amplified laser pulses to cause damage to the targeted tissue with sub-micron precision without disrupting the surrounding area. AFL ablation has been used in many biological tissues, such as the cornea and the brain,[16] though this technology has yet to be used in tendon. This study will describe our methodology for *in vivo* imaging of the patellar tendon (PT) in mice and assess the efficacy of AFL ablation at isolating damage to either tenocytes or tendon ECM. Future work will utilize these methods to interrogate mechanisms that drive inflammation and promote effective healing of tendon injuries.

METHODS

Fifteen C57BL/6 mice (16-32wk) were used to optimize *in vivo* cell staining, imaging, and ablation parameters. Cells were labeled by injecting Hoechst 33342 (100µL, 0.1mg/mL), a nuclear-binding dye, into the joint space above the left patellar tendon 2-4 hours prior to imaging. Animals were anesthetized, placed in a stereotax to reduce motion artifacts, and the PT was exposed for imaging. A custom multiphoton imaging setup was used to simultaneously visualize cells labeled with Hoechst and aligned collagen via Second Harmonic Generation (SHG) microscopy. The Ti:Sapphire ablation laser (800-nm, 50-fs, 1-kHz pulses) was then aligned on top of the imaging lasers and the ablation laser energy and number of pulses were gradually increased until successful damage was observed. Laser pulse energies ranged from 200-500nJ with 1-10 pulses. Animals received ablation to cells to induce cell necrosis or ablation to ECM to cause matrix micro-ruptures. Z-stack images (1µm per step for 30µm) were collected immediately before and after ablation, as well as 10 minutes following ablation, and the average intensity of each stack was found using a z-projection in ImageJ. Representative images demonstrate proof of concept for the use of laser ablation to isolate damage to tendon cells and ECM.

RESULTS

Tenocyte nuclei were clearly labeled with Hoechst up to a depth of 40-50µm (Figure 1). Positive Hoechst staining allowed for tenocytes to be precisely ablated without damaging surrounding ECM. Following cell ablation, the damaged region was distinctly contained within the cell nucleus and remained visible 10 minutes post-injury without significant photobleaching (Figure 2B, 2C). Ablation altered the overall shape of the nucleus and decreased nuclear size by over 10%. Similarly, micro-ruptures created in the ECM resulted in an absence of SHG signal which was sustained 10 minutes after ablation (Figure 2E, 2F).

Figure 1: Second Harmonic Generation (gray) and Hoechst-labeled cell nuclei (blue) 0, 20, and 40µm below tendon surface.

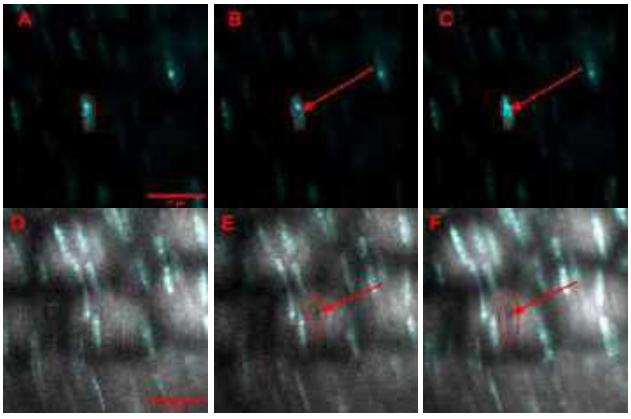

Figure 2: Tenocytes and extracellular matrix immediately before (A,D), after (B,E), and 10 minutes after ablation (C,F). Arrows point to ablated areas showing decreased Hoechst or SHG signal.

DISCUSSION

This study serves as proof of concept for the use of amplified femtosecond laser ablation in tendon. In summary, we have developed a method for marking tenocyte nuclei *in vivo* and precisely targeting cells or extracellular matrix with the ablation laser. Preliminary results provide convincing evidence that this method can isolate damage to cells or matrix.

Interestingly, Hoechst signal of cells was not found to fade 10 minutes following ablation of the nucleus. However, previous work has shown that cells undergoing ablation-induced necrosis do not exhibit an immediate decrease in Hoechst signal, and instead this signal fades gradually over time.[17] To verify that ablation is inducing cell necrosis, we will use propidium iodide in conjunction with Hoechst, allowing us to confirm cell death following ablation. In areas of ECM ablation, the absence of SHG signal represents a disruption to the highly aligned structure of collagen, likely due to unraveling of the triple helix in ablation-damaged fibrils.[18] We suspect that in response to this loss of structure at the injury site, adjacent intact collagen fibers are able to reorganize to bear the load, as has been previously observed in other collagen rich tissues such as the cornea.[19]

One major challenge when using laser ablation *in vivo* is locating and tracking ablated areas across multiple timepoints. Therefore, our next step is to use reporter mice and live cell dyes to examine the effects of ablation on whole tendon cell populations, rather than examining the local response surrounding the ablated region. Specifically, we are using CX3CR1-CCR2 reporter mice to quantify the impact of cell necrosis and ECM micro-rupture on the immune response and subsequent healing outcomes.

Overall, the present study represents an important step towards interrogating the damage component that drives inflammation in tendon. Isolating the effect of cell and matrix damage will allow us to examine their individual and combined impacts on the inflammatory and overall healing response in sub-rupture tendon injuries. We will be able to determine if ECM damage stifles or enhances the healing response and test our hypothesis that cell necrosis drives inflammation in tendon injuries. Our data will inform future work which seeks to modulate inflammation and promote repair in sub-rupture injured tendons to halt or reverse the progression of damage accumulation into ruptures.

ACKNOWLEDGEMENTS

This research was supported by the Cornell Sprout Award and the HSS Cameo T32 Training Grant.

REFERENCES

[1] Fung, D et al., *J Biomech*, 43:274-279, 2010. [2] Wu, F et al., *EFORT Open Rev*, 2:332-342, 2017. [3] Egerbacher, M et al., *Clin Orthop Relat Res*, 466:1562-1568, 2008. [4] Nakama, L et al., *J Orthop Res*, 23(5):1199-1205, 2005. [5] Fung, D et al., *J Orthop Res*, 27:264-273, 2009. [6] Neviaser, A et al., *J Shoulder Elbow Surg*, 21:158-163, 2012. [7] Chatterjee, M et al., *Connect Tissue Res*, 63:28-42, 2021. [8] Andres, B et al., *Clin Orthop Relat Res*, 466:1539-1554, 2008. [9] Ackerman, J et al., *Cell Rep*, 41:111706, 2022. [10] Noah, A et al., *J Appl Physiol*, 128:473-482, 2020. [11] Kondratko-Mittnacht, J et al., *J Biomech*, 48:3299-3305, 2015. [12] Andarawis-Puri, N et al., *J Musculoskelet Neuronal Interact*, 11:106-114, 2011. [13] Davidovich, P et al., *Biol Chem*, 395:1163-1171, 2014. [14] Arvind, V et al., *Front Bioeng Biotechnol*, 9:719047, 2021. [15] Stoychev, V et al., *Curr Rev Musculoskelet Med*, 13:133-140, 2020. [16] Nishimura, N et al., *Proc SPIE*, 6261:62611J, 2006. [17] Cheng, Z et al., *Optica*, 8:1559-1572, 2021. [18] Manickavasagam, A et al., *Analyst*, 139:6135-6143, 2014. [19] Han, M et al., *J Biomed Opt*, 9:760-766, 2004.

POPULATION-SPECIFIC BIOMECHANICAL RESPONSE OF THE BRAIN BY AGE AND SEX

Ahmed A. Alshareef (1), Aaron Carass (2), Yuan-Chiao Lu (3), Joy Mojumder (4), Ruth J. Okamoto (5), Alexa M. Diano (6), Curtis L. Johnson (6), Dzung L. Pham (3,7), Jerry L. Prince (2), Philip V. Bayly (5)

(1) Department of Biomedical Engineering, University of South Carolina, Columbia, SC, USA
(2) Department of Electrical and Computer Engineering, Johns Hopkins University, Baltimore, MD, USA
(3) The Military Traumatic Brain Injury Initiative, The Henry M. Jackson Foundation, Bethesda, MD, USA
(4) Department of Radiology and Imaging Sciences, National Institute of Health, Bethesda, MD, USA
(5) Department of Mechanical Engineering, Washington University in St. Louis, St. Louis, MO, USA
(6) Department of Biomedical Engineering, University of Delaware, Newark, DE, USA
(7) Radiology and Radiological Sciences, Uniformed Services University, Bethesda, MD, US

INTRODUCTION

Traumatic brain injuries (TBI) remain a serious societal concern, with over 1.7 million injuries occurring yearly in the United States[1]. TBIs typically occur due to sudden head motion resulting from impacts in sports, automotive vehicle crashes, and falls[2]. The mechanical forces transmitted from the head to the brain have been a focus of research that aims to quantify the relationship between input loading and brain tissue mechanics[3,4]. Anatomically-detailed finite element (FE) models or physical surrogates of the brain that predict tissue mechanical response are crucial for understanding brain injury and developing injury mitigation countermeasures. A challenge in brain model development is validation against experimental brain deformation data, especially average response within different demographic groups, such as sex and age stratified cohorts. These average data responses are commonly computed in injury biomechanics to represent a population mean from a set of experimental tests[5]. Recently, we have collected data on the *in vivo* biomechanical response of the brain under harmonic head motion using magnetic resonance elastography (MRE) and impulsive head motion using tagged magnetic resonance imaging (tMRI)[4]. The objective of this study is to compute and compare group average anatomical templates, material properties, and maximum strain templates for the young, mid-age, and older adult brains for male and female populations.

METHODS

Scans from 135 volunteers (68M/67F; 18–73 yrs) were collected using anatomical MRI sequences, and either MRE or tMRI, at three acquisition sites (Table 1). All processed data are publicly available[6]. Structural MRI data was collected at all sites. High-resolution MRE data were acquired at the University of Delaware. tMRI data were collected at the NIH Clinical Center through the Henry M. Jackson Foundation. All subjects provided informed consent under a protocol approved by the Institutional Review Boards of the respective institutions. The structural anatomical images included T1-weighted and T2-weighted MRI scans. MRE data were with a 3D multiband, multishot spiral MRE sequence with OSCILLATE acceleration[7] at 1.5 mm isotropic imaging resolution. Vibration was applied using the Resoundant with pillow actuator at 30, 50, and 70 Hz. The brain tissue material properties from MRE were estimated using the nonlinear inversion algorithm (NLI)[8]. tMRI was acquired using a custom-built MRI-safe device[4,9] that facilitates a repeatable mild axial head rotation of 3-4 rad/s and 200-350 rad/s[2]. Data were acquired using 1:1 SPAMM tagging at a 2 mm spatial resolution with a 20 ms temporal resolution[9]. All tMRI data were processed using HARP-FE to generate strain fields[10]. Details on acquisition and processing have been previously presented[4].

Table 1: Number of subjects within each population.

Age	Sex	MRI	MRE	tMRI
Young (18-21)	Female	9	7	6
	Male	10	6	3
Mid-age (22-49)	Female	38	11	7
	Male	40	9	8
Older (50+)	Female	20	12	1
	Male	18	9	4

Anatomical Template: The ANTs[11] template creation script with multimodal input was used to create average T1w and T2w images. All images were preprocessed by rigidly registering to MNI space, followed by N4 bias correction[12]. The template script calculates an average anatomical template through iterative nonlinear registrations and averaging, followed by a sharpening filter to enhance edges.

MRE Material Property Template: For each population, all subjects were nonlinearly registered using ANTs to the T2w anatomical template using the MRE magnitude images. The spatial transformations were then applied to the shear stiffness and damping ratio maps of each subject at all three MRE frequencies (30, 50, 70 Hz) using linear interpolation. The average response was calculated using an average with a majority vote mask to remove edge voxels.

tMRI Strain Template: tMRI experiments result in 4D data (3D voxels and time) for each of the 6 strain components. To simplify this analysis to a scalar value, the peak maximum principal strain (MPS) across all time for each voxel was chosen. For each population, all subjects were nonlinearly registered using ANTs to the T1w anatomical template using each subject's T1w image. The spatial transformations were then applied to the peak MPS maps of each subject using linear interpolation.

The average response was calculated using an average with a majority mask to remove edge voxels.

RESULTS

The generated anatomical templates are presented in Fig. 1. The templates were qualitatively checked by running the SLANT-CRUISE segmentation algorithm[13] to quantify the brain volumes and ensure consistency with the individual subjects. Features of the aging brain, such as enlarged ventricles, are clearly visible in the older group. Quantitatively, the template brain volumes are larger in males than females and are within 10% of the average brain volumes of individual subject brain volumes within each population.

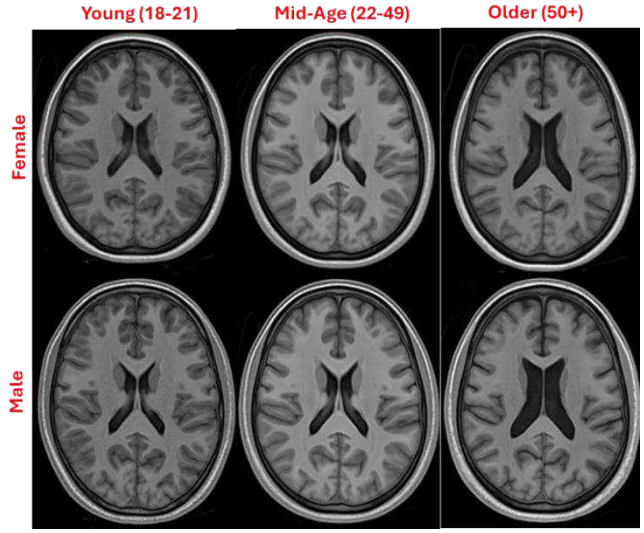

Figure 1: Anatomical T1w templates of all population groups.

The generated MRE material property templates were computed for each population. The templates were similar in the spatial distribution of the stiffness measurements, with the older groups resulting in higher standard deviation and lower magnitudes of stiffness than the younger groups. There were no significant differences in average stiffness magnitude with sex. Cumulative distributions of the 50 Hz stiffness are presented in Fig. 2. The damping ratio averages showed slight differences across population, but no clear trend with sex or age. These observations were similar for templates at 30 and 70 Hz.

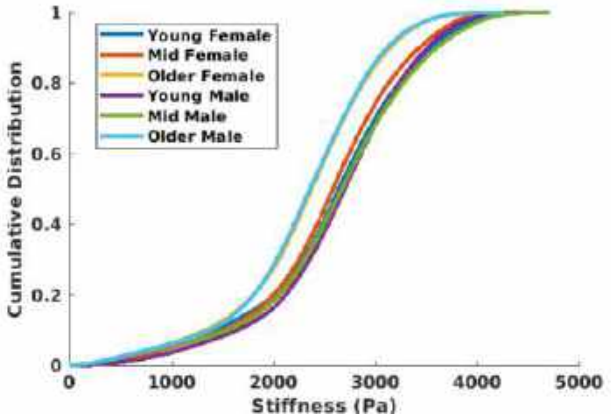

Figure 2: Cumulative distribution of 50 Hz stiffness of the MRE templates for all populations.

The generated tMRI MPS templates are shown in Fig. 3. The older population templates are not shown since the older female group only had 1 subject, and the older male group had two subjects with incomplete field of view during data acquisition, which explains the missing portions of this cross-section. The templates were similar in the distribution and magnitude of MPS, except for the mid-age female group, which had lower magnitudes. There was no significant difference of MPS distributions with sex. There was a slight decrease in peak MPS with age, but the applied head rotational velocities were also smaller in the older groups. More data is needed to draw conclusions for the effect of age on MPS.

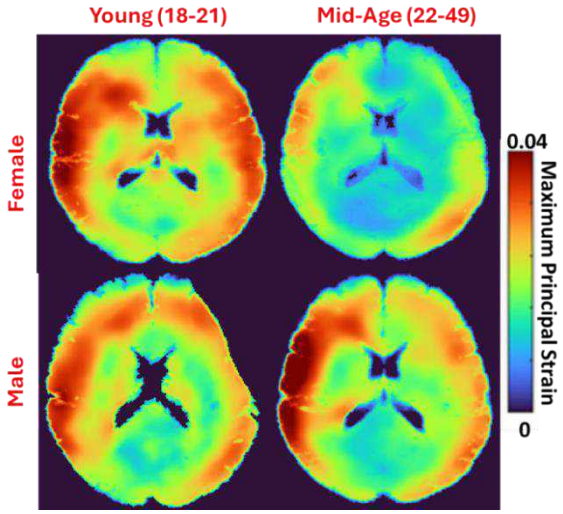

Figure 3: Population-specific peak MPS templates from tMRI.

DISCUSSION

Datasets of brain biomechanics are scarce and usually include a limited number of subjects, hindering group average analysis and FE model validation. Using recent datasets of in vivo biomechanical MRI measurements, this study created population average templates by age and sex for brain anatomy, material properties, and maximum strain. Our results indicate that age is an important consideration in model development. While templates have been created previously for a mix of subjects, this is the first study to generate population-specific templates. The resulting templates, once refined with more subjects, can be used to create population-specific injury prediction tools, such as FE models or physical surrogates.

ACKNOWLEDGEMENTS

Research reported in this abstract was supported by the National Institute of Neurological Disorders and Stroke of the National Institutes of Health under Award Number U01NS112120. The opinions and assertions expressed herein are those of the authors and do not reflect the official policy or position of the Henry M. Jackson Foundation, Uniformed Services University, or the Department of Defense

REFERENCES

[1] Taylor, C. A., et al. MMWR Surveill. Summ. 66, 1 (2017).
[2] Coronado, V. G. et al. J. Safety Res. 43, 299–307 (2012).
[3] Alshareef, A. et al. J. Neurotrauma (2020).
[4] Bayly, P. V. et al. Ann. Biomed. Eng. 49, 2677-92 (2021).
[5] Bir, C., et al. (2004). Journal of biomechanics, 37(1), 73-79.
[6] https://www.nitrc.org/projects/bbir/
[7] McIlvain, G., et al. Magn. Reson. Med. 88, 1659-72 (2022).
[8] McGarry, M. D. J. et al. Med. Phys. 39, 6388–6396 (2012).
[9] Knutsen, A. K., et al. (2020). Brain Multiphysics, 1, 100015.
[10] Gomez, A. D., et al. (2018). IEEE TBME, 66(5), 1456-1467.
[11] Avants, B. B., et al (2009). ANTS. Insight j, 2(365), 1-35.
[12] Tustison, N. J., et al. (2010). IEEE TMI, 29(6), 1310-1320.
[13] Huo, Y., et al. (2019). NeuroImage, 194, 105-119.

MECHANICS OF COBALT SUBSTITUTION IN BIOMMETIC APATITES

Abigail Eaton (1), Stephanie Wong (2), Kennedy Drake (2), Alix Deymier(2), Arun Nair (1)

(1) Mechanical Engineering, University of Arkansas, Fayetteville, AR, USA
(2) Department of Biomedical Engineering, University of Connecticut, Farmington, CT, USA

INTRODUCTION

Millions of people have cobalt-chrome prosthetics with more than a million having metal-on-metal (MoM) hip implants in North America[1]. These types of prosthetics have been shown to release large amounts of metal particles that can oxidize and release toxic heavy metals into the body. As a result, patients can develop cobalturia leading to cardiac and brain disfunction[1]. In addition to the systemic effects of metal release, there is also evidence that the presence of metal implants has led to unintended and sudden hip/femur fracture thus defeating the purpose of the implant. This leaves millions of individuals at risk of complex fractures with few alternatives for treatment due to the unclear cause of these fractures. Increased inflammation leading to bone resorption and cell death due to metal toxicity have both been suggested as possible causes of this increased fracture risk. We hypothesize that metal ion absorption into bone mineral may also play a critical role in controlling bone mechanics and fracture risk.

Bone is primarily composed of biological apatite which has a strong tendency of substituting cations and anions into the lattice. As a result, bone mineral is expected to have a propensity for absorbing heavy metal ions released from the MoM implants. Due to the composite nature of bone, these nanoscale changes can lead to whole tissue mechanical failure. It is therefore essential that we examine that fundamental ways in which metal ions interact with the apatite crystals to unravel the mechanisms associated with the apatite crystal substitutions, change in its mechanical properties and how that leads to fracture initiation under mechanical loading. Here we propose to couple development of an *ab initio*-based model of apatite crystals with Co substitutions, which can capture the interactions at the nanoscale, with x-ray diffraction-based experiments on biomimetic apatites to predict the change in crystallographic properties of apatite crystals exposed to Co. This combined in vitro and in silico approach will allow for a full elucidation of the role that Co substitutions play in modifying apatites and in turn bone health.

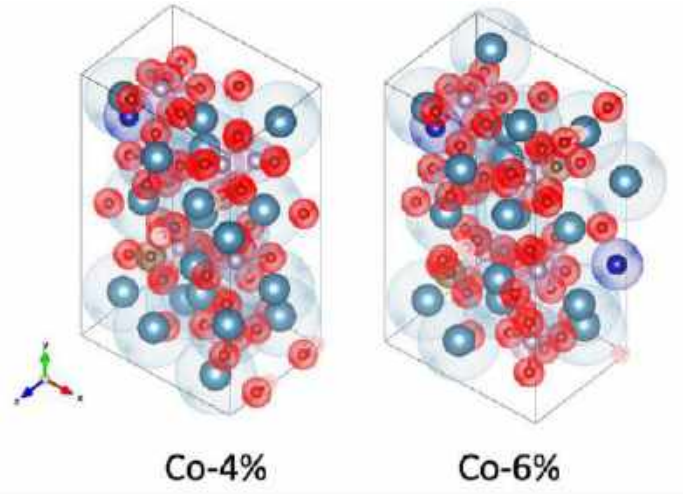

Figure 1: Co apatite samples with 4% and 6% carbonate substitutions, with x-axis corresponds to *a*-axis and z-axis corresponds to *c*-axis.

METHODS

Experimental

Biomimetic apatites with increasing levels of Co were made via one of two aqueous precipitation techniques. First, a solution of calcium nitrate and cobalt nitrate as well as a solution of ammonium phosphate were added to dropwise to sodium bicarbonate in a round bottom flask. The reaction was digested for 2 hours at pH 9 and 65°C. In the second technique, a solution of calcium nitrate and cobalt nitrate was directly mixed with a solution of sodium bicarbonate and ammonium phosphate and allowed to mature for 3 days. Cobalt nitrate levels were varied to the 2nd technique to create apatites with varying levels of Co. In all

cases, the solutions were filtered and rinsed to collect the apatite crystals, which were then dried at 60°C overnight.

Crystals from technique 1 were examined via X-ray Diffraction (XRD) to determine the crystal lattice spacing. Crystals from technique 2 were examined Inductively Couples Plasma-Mass Spectroscopy (ICP-MS) and Carbon-Hydrogen-Nitrogen Analysis to obtain the cobalt and carbonate (CO_3^{2-}) content of the crystals. Raman spectroscopy was used to confirm the apatite phase.

Computational

For studying mechanical properties of apatite crystals, it is more practical to transform it into an orthorhombic cell (*x*, *y* and *z* axes see Fig.1) with the *z*-axis parallel to the *c*-axis. However, it is necessary to double the *b*-axis direction to maintain the periodicity of the lattice in the orthorhombic description. Due to this the unit cell is twice as large as the unit cell and contains 88 atoms for the hydroxyapatite (HAP sample. We use this 88-atom unit cell to substitute Ca atom with Co and add carbonate group to form the 4% and 6% samples.

One of the widely used *ab inito* modeling method is Density Functional Theory (DFT) [2]. There are several previous studies using DFT on biomaterials. The feasibility of using DFT as a tool to predict material property has been widely accepted among the scientific community [3]. The DFT model is used to compute the lattice strains after introducing the Co ion in the HAP crystal.

RESULTS

Apatites containing Co-substitutions were successfully created using both techniques as determined by Raman spectroscopy and XRD. The Co content of the low and high Co apatites made with technique 2 were 0.09 and 0.26 mmol respectively. This increase in Co content was associated with an increase in carbonate content suggesting that there is concomitant substitution of the Co cation with CO_3^{2-}, Fig 2. This is also accompanied by a decrease in mineral calcium (Ca^{2+}) content. Thus, we decided to investigate the combined effect of Co and CO_3^{2-} using DFT.

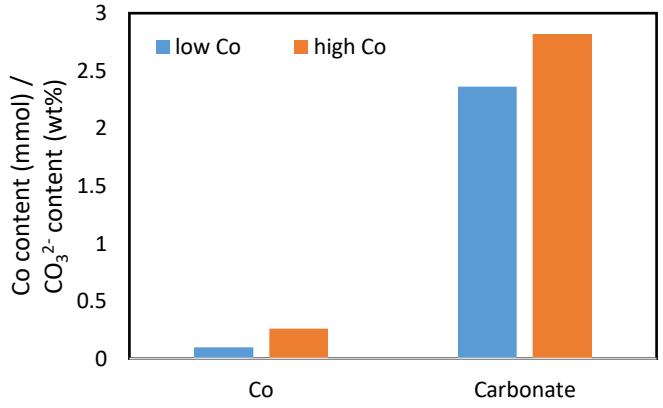

Figure 2: Plot of Co and CO_3^{2-} content showing the concomitant increase in carbonate with increasing Co.

We first calculate the lattice properties of hydroxyapatite crystal using DFT and then use that as a reference point to calculate the difference in the lattice properties when Co substitution occurs. Figure 3 shows the lattice change when Co is substituted along with carbonate ions with concentrations of 4% and 6%. The *a*-axis change of negative value indicates that the Co-4% a-axis is decreasing in length. We observe that as the carbonate concentration changes from 4% and 6%, the decrease in *a*-axis is ~50% smaller. Similarly for c-axis, the trend is same with 4% case having an increase in lattice and 6% case has ~12% lower lattice expansion.

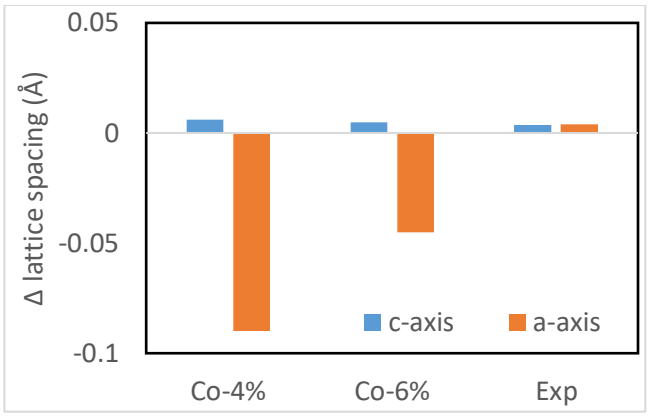

Figure 3: Plot of lattice changes as a function of Co and CO_3^{2-} substitutions. Co-4% and Co-6% represent computational Co apatites with 4 and 6% CO_3 respectively. Exp shows the experimental lattice spacing.

When XRD was performed on the Co-containing apatites made with technique 1, we found that there was a small expansion of the *c*-axis compared to stoichiometric hydroxyapatite in agreement with the DFT models. However, unlike the DFT model, the *a*-axis exhibited expansion of the *a*-axis with Co and CO_3^{2-} substitutions.

DISCUSSION

The addition of Co into solution during apatite precipitation successfully led to the formation of Co-substituted apatites. This suggests that free Co from implant materials could easily substitute into bone mineral during bone deposition. The presence of Co is also associated with increased CO_3^{2-} substitutions. Paired substitutions of anions and cations in apatites is common [4]. This usually occurs to establish charge balance when molecules of differing charge are substituted. Co is expected to exchange with Ca^{2+} in lattice meaning that it could be charge neutral if it carries a valence of +2. However, the apatites exhibit a decrease in Ca^{2+} larger than the uptake of Co pointing to vacancy formation and charge imbalances. DFT was able to successfully model concomitant Co and CO_3^{2-} substitution in apatites. We believe that the difference in the a-axis trend between DFT and experiments could be (a) due to the location of carbonate substitution, as CO_3^{2-} group is planar in nature, (b) the Co substitution location, which is either Ca (1) or Ca (2) sites. Further study is required to determine this.

ACKNOWLEDGEMENTS

We acknowledge funding support from NSF grant# 2323499 #107141 and #2044870.

REFERENCES

1. Tower, S.S., et al., *Prevalence of Cobalturia Among Adults With Joint Replacements.* JAMA Network Open, 2021. **4**(8): p. e2121758-e2121758.
2. Giannozzi, P., et al., *QUANTUM ESPRESSO: a modular and open-source software project for quantum simulations of materials.* Journal of Physics: Condensed Matter, 2009. **21**(39): p. 395502.
3. Deymier, A.C., et al., *Protein-free formation of bone-like apatite: New insights into the key role of carbonation.* Biomaterials, 2017. **127**: p. 75-88.
4. Wopenka, B. and J.D. Pasteris, *A mineralogical perspective on the apatite in bone.* Materials Science and Engineering: C, 2005. **25**(2): p. 131-143.

TOWARDS 3D-3C VELOCITY MAPS FROM SINGLE CAMERA 2D-2C PTV USING PHYSICS INFORMED NEURAL NETWORKS

Amin Pashaei Kalajahi (1), Zayeed Bin Mamun (1), Forouzan Naderi (1), Sangeeta Yadav (1), Roshan M D'Souza (1)

(1) Department of Mechanical Engineering, University of Wisconsin-Milwaukee, Milwaukee, Wisconsin, USA

INTRODUCTION

Particle Tracking Velocimetry (PTV) is an experimental method for analyzing complex fluid flows. It involves seeding fluid flows with micron-scale tracer particles, illumination by a pulsed laser sheet, and cameras capturing successive time-resolved snap shots. Fluid velocities are then estimated from displacements of particle images between successive snapshots [1].

PTV relies on low particle density for effective particle correspondence, resulting in sparse spatial velocity data [2]. Recent attempts to improve spatial resolution through physics-constrained machine learning use costly 3D3C PTV data obtained from elaborate PTV hardware configurations [2, 3]. This poses a significant burden on experimental cost and complexity for flow estimations.

We present a novel method utilizing physics-informed neural networks with geometric optics to generate dense 3D3C velocities and relative pressure from sparse 2D2C PTV data. Experiments on synthetic data demonstrate the method's remarkable accuracy in recovering time-resolved 3D velocity fields from sparse 2D inputs.

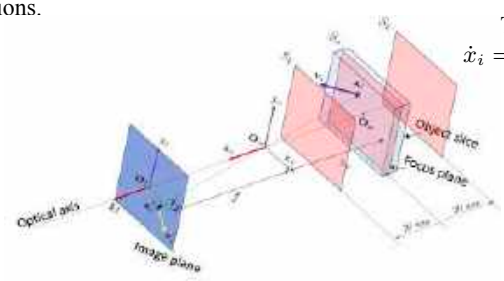

Figure 1: PTV optical setup. S_o is the focus plane in the middle of the object slice. S_1, S_2 are planes where the prediction of the algorithm is tested.

METHODS

Without loss in generality,we model a pinhole camera setup for our image capture process (Fig. 1). A thin sheet (object slice) with thickness Δ of a particle laden flow is illuminated by a laser. The focus plane and image distance from the pinhole are z_o, f, respectively. The location of a particle $\mathbf{x}_i$ at time t is give by Eq. 1.

$$\mathbf{x}_i = \begin{bmatrix} x_i \\ y_i \\ z_i \end{bmatrix} = \begin{bmatrix} x_i \\ y_i \\ z_o \pm \delta_i \end{bmatrix} \approx \begin{bmatrix} x_i \\ y_i \\ z_o \end{bmatrix} \tag{1}$$

Here $\delta_i < \frac{\Delta}{2} << z_o$. This location is mapped to an image location $\bar{\mathbf{x}}_i$ given by

$$\bar{\mathbf{x}}_i = \begin{bmatrix} \bar{x}_i \\ \bar{y}_i \end{bmatrix} = -\frac{f}{z_i}\begin{bmatrix} x_i \\ y_i \end{bmatrix} = -\frac{f}{z_o \pm \delta_i}\begin{bmatrix} x_i \\ y_i \end{bmatrix} \approx -\frac{f}{z_o}\begin{bmatrix} x_i \\ y_i \end{bmatrix} \tag{2}$$

The velocity of the particle in the image is given by Eq. 3 where $\dot{x}_i = u_i, \dot{y}_i = v_i, \dot{z}_i = w_i$.

$$\bar{\mathbf{v}}_i \approx -\frac{f}{z_o^2}\begin{bmatrix} u_i z_o + w_i \dfrac{\bar{x}_i}{f} \\ \\ v_i z_o + w_i \dfrac{\bar{y}_i}{f} \end{bmatrix} \tag{3}$$

We assume that 2D2C velocities and locations with time stamp $(\bar{\mathbf{x}}_i^o, \bar{\mathbf{v}}_i^o, t_i)$ are available through 2D PTV experiments. Given $\bar{\mathbf{x}}_i^o$, we derive the approximate 3D locations $\mathbf{x}_i^o$ using Eq. 1, 2. The locations $\mathbf{x}_i^o$ are the inputs to a multilayer percepteron (MLP) (Fig. 2) which generates as output the predicted 3D velocity $\mathbf{v}_i^{pred}$ and relative pressure p. Using Eq. 3, we then compute the predicted velocity in the image $\bar{\mathbf{v}}_i^{pred}$. The MLP is trained with the loss function given by

$$\mathcal{L} = \alpha \frac{1}{N}\sum_{i=1}^{N} \|\bar{\mathbf{v}}_i^{pred} - \bar{\mathbf{v}}_i^o\|^2 + (1-\alpha)\mathcal{L}_P \tag{4}$$

.

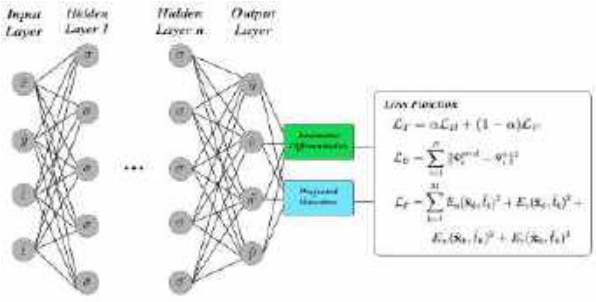

Figure 2: Multilayer perceptron model to represent velocity and relative pressure

Here α is a weighting factor and $\mathcal{L}_P$ is the physics regularizer that penalizes the deviation of the solution from Navier-Stokes and mass conservation equations at a user-defined number of collocation points in object space.

RESULTS

To generate test data, we simulated blood flow with pulsatile boundary conditions in a scaled brain aneurysm geometry using computational fluid dynamics (CFD). We collected velocity snapshots at time intervals of $\Delta t = 15ms$. The unstructured velocity data was interpolated into a regular grid of 2 mm voxels. Within an 107 × 165 × 1 voxels object slice, we picked 800 voxels at random (corresponding to a particle density of 0.05 ppp). 2D projected position and velocity images were constructed based on Eq. 2,3. This approximates the process of generating 2D-2C velocity components from particle image data. Velocity component-wise zero mean Gaussian noise with an SNR of 30 dB was added.

Figures 3 and 4 show the results of our tests. We evaluated the velocity predictions of our algorithm at planes S_1 and S_2 which are 20 mm away from the focus plane S_o, showcasing our algorithm's ability to accurately estimate a dense 3D3C velocity field from the sparse input $\bar{u}$ and $\bar{v}$ shown in the first column of Fig. 3. The following columns of Fig. 3 illustrates a good match between the predictions u^{pred}, v^{pred}, and w^{pred} and the ground truths of u^{gt}, v^{gt}, and w^{gt}.

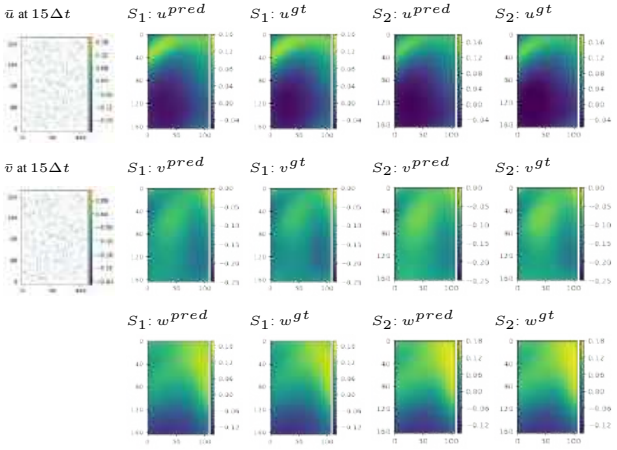

Figure 3: Illustration of predictions $(\cdot)^{pred}$ against ground truth $(\cdot)^{gt}$ for each velocity component and the sparse input data at $15\Delta t$.

Fig. 4 highlights the error metrics for our evaluation. The first column displays strong directional agreement between the predicted and the ground truth vectors through the cosine distance between the vectors at S_1 and S_2. We present minimal absolute error for each velocity component at S_1 and S_2 in the following columns, along with a strong alignment between predictions and ground truth for the entire velocity range in the scatter plots.

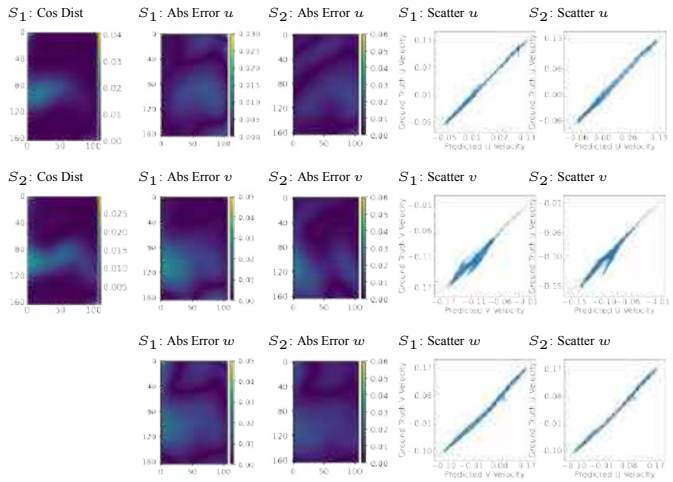

Figure 4: Illustration of error metrics for predictions at S_1 and S_2 at $15\Delta t$.

Table 1 provides a numerical representation of our algorithm's performance at S_1 and S_2. We report the coefficient of determination (R^2) and the root mean squared error (RMSE) for each velocity component. These results prove that our methodology can accurately predict three-dimensional velocity fields with sparse, two-dimensional input.

Table 1: Table of numerical error metrics at $15\Delta t$.

Velocity Component	S_1: R^2	S_2: R^2	S_1: RMSE	S_2: RMSE
u	0.995	0.989	0.00327	0.00587
v	0.889	0.908	0.00803	0.00705
w	0.989	0.991	0.00769	0.00732

DISCUSSION

We have introduced an innovative deep learning approach for estimating 3D3C velocity fields from sparse 2D2C Particle Tracking Velocimetry (PTV) data. In this method, we incorporate the effects of perspective projection using a pinhole camera model into flow physics constrained Multilayer Perceptron (MLP) training to estimate the time resolved 3D velocities. Our approach achieves a highly accurate three-dimensional flow field using only the two-dimensional input from a single camera.

Unlike traditional PTV practices that necessitate a complex experimental arrangement involving three or more cameras for tomographic estimation of three-dimensional velocity maps, our approach is able to accomplish this task with a single camera. This has the potential to reduce experimental costs significantly and enhance accessibility. Currently, our model utilizes a straightforward pinhole camera setup, and future work aims to replace the pinhole with a lens configuration for a more precise representation of modern image acquisition mechanics.

ACKNOWLEDGEMENTS

This work was partly supported by National Science Foundation (NSF) Grants 2205265, 2103560. The views expressed in this abstract are the authors' alone and are not necessarily endorsed by the NSF.

REFERENCES

[1] Adrian R. *Applied optics* 23 (1984). DOI: 10.1364/AO.23.001690.

[2] Leoni P et al. *Experiments in Fluids* 64 (2023). DOI: 10.1007/s00348-023-03629-4.

[3] Hasanuzzaman G et al. *Measurement Science and Technology* 34 (2022). DOI: 10.1088/1361-6501/aca9eb.

Hydrogel Phantom System as Mechanical Placental Tissue Mimics

Samyuktha Kolluru [1], Adrienne Scott [2], Patrick Yang [2], Michelle Oyen [1,2]

Institute of Material Science and Engineering [1], Biomedical Engineering Department[2], Washington University in St Louis, MO, USA

INTRODUCTION

Pathological complications of the placenta have been linked to alterations in the tissue microscale structure, resulting in changes in mechanical properties. One such complication is fetal growth restriction (FGR), in which an underdeveloped placenta is unable to provide sufficient oxygen and nutrients to the fetus, affects roughly 5-10% of all pregnancies and is a primary cause of stillbirth [1]. From prior literature, it is understood that FGR gives rise to modifications in placental microstructure. However current methods allow detection using clinical US imaging of FGR only later in the gestational period [2]. As FGR affects the transport of nutrients, it is important to study placental properties related to nutrient exchange, including diffusion and porosity. These characteristics are linked to time dependent phenomenon such as viscoelasticity and poroelasticity. Therefore, this project aims to establish a hydrogel system with independently tunable time dependent and independent properties. The variance in mechanical properties is an effect of variable microstructure and the creation of a controllable gel phantom system will allow biomimicking placental tissue microstructure. Further, correlating mechanical properties with raw frequency (RF) data acquired through Quantitative Ultrasound (QUS) lead to the development of a predictive model. This model can be employed to quantify placental microstructure in vivo, enabling earlier detection of deviations from a healthy placenta.

METHODS

Gelatin (300 g bloom) and agar were obtained from Sigma–Aldrich (St. Louis, MO). Gelatin (Gel; 7.5% and 30% w/w) and agar (1% and 3% w/w) gel solutions were prepared by soaking granules in distilled water at room temperature. The stock solutions were stirred in a water bath at 65°C (gelatin) or 90°C (agar) until dissolved. Solutions were left in the warm room without stirring until trapped gas had been released. Composite gelatin- agar gel solutions were mixed by volume fraction of melt solution. Mixtures were moderately stirred at 75°C for 5 min. Single phase solutions and composite gel mixtures were poured into molds to cool for one hour before being placed in a refrigerator to set for 48 hours. Next, the gels were swollen in PBS for 48 hours to achieve gels in equilibrium state prior to mechanical testing. Patients were recruited and a placenta was obtained for indentation testing under an IRB approved protocol. Mechanical testing of all hydrogels and placenta was performed on an Instron with a 5 N load cell. Tests were performed in displacement control using a ramp- hold profile: the displacement (h) is ramped at a constant rate to a fixed level and then held at the peak displacement (h_{max}) for a 300 sec hold time. The load (P) is recorded for the duration of the test. Indentation tests were carried out using a stainless-steel spherical tip with a radius (R) of 12.7 mm. Strain was kept at 5% during indentation, to stay within the linear regime. Thus, peak displacement was set to 1.14 mm according to equation 1. Three indents were performed on each sample, spaced at least 15 mm apart. Data was processed through a poroviscoelastic analysis, and values of stiffness, permeability (κ) and diffusion coefficient (D) were obtained. Pore size (ζ) was calculated as the square root of permeability. Poroelastic response is calculated according to an empirical solution published by [3]. The viscoelastic response is calculated using a generalized Maxwell model, consisting of a linear spring connected in parallel with n number of Maxwell units, containing a linear spring and dashpot connected in series. The poroviscoelastic model involves the coupled effect of poroelastic (PE) and viscoelastic (VE) behaviors as shown in equation 2, where P_∞ is the equilibrium load.

$$\varepsilon = 0.2\ (h_{\max}/\mathrm{R})^{1/2} \quad \text{Eq. 1}$$

$$P_{PVE} = \frac{P_{\mathrm{PE}}(t) \cdot P_{\mathrm{VE}}(t)}{P_\infty} \quad \text{Eq. 2}$$

RESULTS

Pure agar gels did not swell at all, while gelatin gels demonstrated substantial swelling [4]. Therefore, gelatin gels were tested on consecutive days to establish the time required for equilibrium swelling as 48 hours. Stiffness and viscoelastic ratio (measure of the degree of relaxation) were chosen as the metrics for time independent and time dependent properties respectively. The viscoelastic ratio of the material denotes the elastic portion of the material's response. When this ratio equals unity, it indicates time-independent mechanical behavior and a purely elastic material. In contrast, a ratio of zero indicates complete relaxation, signifying a purely viscous material response. Five conditions were targeted, spanning a wide range of low and high stiffness and relaxation levels, with an additional medium variation. Two gelatin-agar systems were defined to create the hydrogel phantom system: 7.5% Gel–3% Agar and 30% Gel–1% Agar system. When agar was the stiff phase (7.5%Gel–3%Agar system), its non- swelling response dominated the single phase and composite gels and gave rise to more relaxation. For gels

based on the stiff gelatin system (30%Gel–1%Agar system), the swelling was directly proportional to gelatin content and thus gave rise to less relaxation. Thus, making single phase and composite hydrogels with varying volume fractions of gelatin and agar created a hydrogel system that successfully encompasses a wide range of stiffness levels and relaxation characteristics (figure 2). The placenta shows substantial relaxation behavior and very small stiffness values.

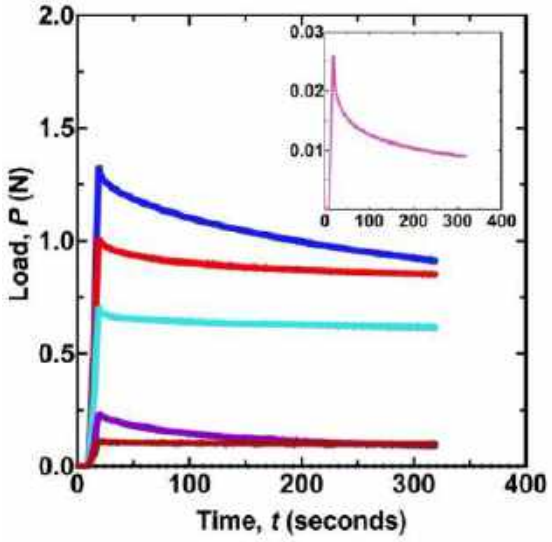

Figure 1: Load (*P*) versus time (*t*) curves of different hydrogel phantoms and placenta (inset) during indentation

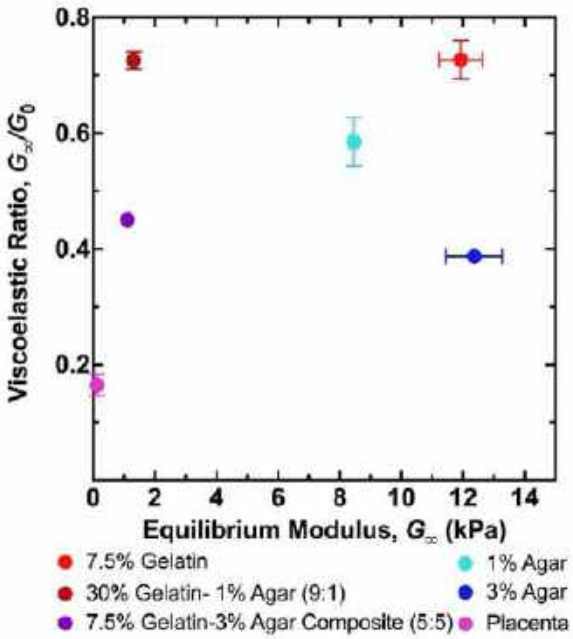

Figure 2: Viscoelastic ratio (G_∞/G_0) versus equilibrium stiffness (G_∞) plot of 5- point system consisting of single phase and composite gels

The diffusion coefficient (*D*) and hydraulic (Darcy) permeability (κ) values showed variation between each gel (table 1) indicating changes in the microstructure.

Table 1- Comparison of diffusion coefficient (*D*), permeability (κ) and pore size (ζ) between gel phantoms

Gel	*D* (mm^2s^{-1})	κ (nm^2)	ζ (nm)
1% Agar	0.0791	5,390	73.4
3%Agar	0.058	418	20.4
7.5%Gelatin	0.0365	1,160	34.1
30%Gelatin- 1% Agar (9:1)	0.119	443	21.0
7.5%Gelatin- 3%Agar (5:5)	0.108	417	20.4
Placenta	0.188	99,720	315

DISCUSSION

Gelatin-agar systems have been used here to demonstrate the wide range of mechanical properties and, more importantly, mechanical property combinations that can be engineered into hydrogels. Change in these mechanical properties results in hydrogels of different microstructures validated by variation in structural properties such as pore size. Indentation testing, with its ease of implementation and established analytical framework, facilitated the identification of individual property transitions in single phase gels and composites, opening a space for design of unique gels ideally suited for mimicking a wide range of microstructure that can be exhibited by placental tissue. Placenta tested in this study shows mechanical properties that fall into this wide range previously reported in literature [5]. Future work involves testing of different placentas acquired from the patients in this study. With more placental tissue data, the gel phantom system can be expanded to fully capture an array of placental properties. Permeability and diffusion data shows variation indicating a change in the microstructure of gels. Through QUS analysis of gels, we can establish a relationship between the gel mechanical properties established here and the effect that they have on RF data, thus enabling a model that can use US for detecting alterations in placental microstructure in vivo. Overall, a predictive model that can identify changes at small length scales using US allows earlier detection of Fetal Growth Restriction (FGR).

REFERENCES

(1) Nardozza, L.M. + *Arch. Gynecol. Obstet.* 295:1061-1077, 2017.
(2) Odibo A., + *Am J Perinatol* 31(02): 139-144, 2014.
(3) Hu Y,. + *Applied Physics Letters* 96.12 (2010).
(4) Strange D., + *Journal of the mechanical behavior of biomedical materials* 11:16-26, 2012.
(5) Lau J.S., + *J Biomech*. 49(2):173-84, 2016.

INDUCED PLURIPOTENT STEM-CELL DERIVED CARDIOMYOCYTE AGED TISSUE MODEL

Hatice S. Emanet (1), Frances E. Dipietro (2), Sneha Philip (2) Dr. Aylin Acun (1)

(1) Department of Biomedical Engineering, Widener University, Chester, PA, United States of America
(2) Biology Department, Widener University, Chester, PA, United States of America

INTRODUCTION

As living beings grow older, their cells undergo significant transformations. These cell transformations are a part of the natural aging process and may significantly impact cellular health and functionality. For tissues with high metabolic requirements such as the heart, these alterations may even result in abnormal functionality or complete loss of function, leading to various age-related illnesses or even mortality.

Cardiovascular diseases (CVD) are predominant among the elderly population and are an increasingly frequent global problem that goes beyond national borders. Systematic analyses of worldwide epidemiological data consistently identify CVDs as the primary cause of death worldwide - thus emphasizing its significance to public health agendas by necessitating multifaceted approaches for prevention, management, and treatment [1]. In most cases, CVD research utilizes young animal models despite prevalence of CVDs increases significantly with age. In addition, there are inherent differences in the cardiovascular systems of animals and humans which limits the translatability of findings from these studies into the clinical setting [2].

Effective cardiovascular therapies and interventions depend on having a reliable knowledge of its pathology. An aged human-heart tissue model can provide a means of studying the mechanistic intricacies of cardiac aging as they relate to CVD pathogenesis. This understanding forms a basis for therapeutics that may help decrease negative consequences associated with age on cardiovascular health.

Current studies in cellular aging mechanisms have shown that cells experience increased apoptosis, cellular senescence, and waste accumulation [3,4,5] with age however there is a gap in knowledge regarding the development of aged tissue models in a short period of time that accurately replicate the complexities of age-related cardiovascular diseases. This research seeks to bridge this gap by establishing an induced pluripotent stem-cell (iPSC) derived cardiomyocyte (CM) aged tissue model, induced by oxidative stress to accelerate the aging process. This will provide a way for readily available physiologically relevant tissue models that can be used for enhanced drug discovery and therapeutic interventions in cardiovascular medicine.

METHODS

iPSC Differentiation into Cardiomyocytes: First the iPSCs are differentiated into cardiomyocytes (iCMs) utilizing established protocols [6]. This differentiation process ensures the generation of functional cardiomyocytes that mimic the properties of native heart tissue. Additionally, we implemented an approach that enabled a comprehensive examination of the impact of oxidative stress on cells at varying stages of differentiation, adding a nuanced layer to our understanding of the aging process in iCMs. For each experiment, we evaluated how the cells responded to oxidative stress in two distinct states: immature and mature iCMs. The immature state corresponds to iCMs that started receiving treatment on day 9 of the differentiation process, allowing minimal time for maturation. In contrast, the mature iCMs initiated treatment on day 21, which gave an extended period for maturation and growth.

Inducing Aging Through Oxidative Stress: Following successful differentiation, iCMs were subjected to varying concentrations of hydrogen peroxide (H_2O_2) to induce in vitro aging. Four concentrations—50 μM, 100 μM, 200 μM, 300 μM —were used to represent low, moderate, and high oxidative stress levels. Additionally, short, medium, and long exposure durations, specifically, 7, 15, and 21 days, were implemented to assess the impact of oxidative stress exposure times on the aging process.

Assessment of Aging: The degree of aging induced by oxidative stress was assessed in aged cells where non-aged cells at the same day of differentiation were used as controls. Apoptotic cell percentage was determined using CellEvent™ Caspase-3/7 Green dye

and performing image analysis. Senescent cell percentage was determined using a senescence-associated β-galactosidase (SA-β-gal) staining kit. Sudan Black B (SBB) staining was utilized to assess cellular waste accumulation patterns which increases with aging. Quantification of the results were performed through image analysis using ImageJ and 5-10 images were used for quantification of each sample.

Statistical Analysis: Statistical analysis of the collected data was conducted using student's t-test to compare the effects of different oxidative stress levels and exposure durations on aging markers. The sample number was 3 for each experiment and significance where ** represents $p<0.001$ and *** represents $p<0.0001$.

RESULTS

The study revealed a notable increase in apoptotic cells, waste accumulation, and senescence with increasing H_2O_2 concentrations (Figure 1, 2) and showed differences between the mature and immature cell groups.

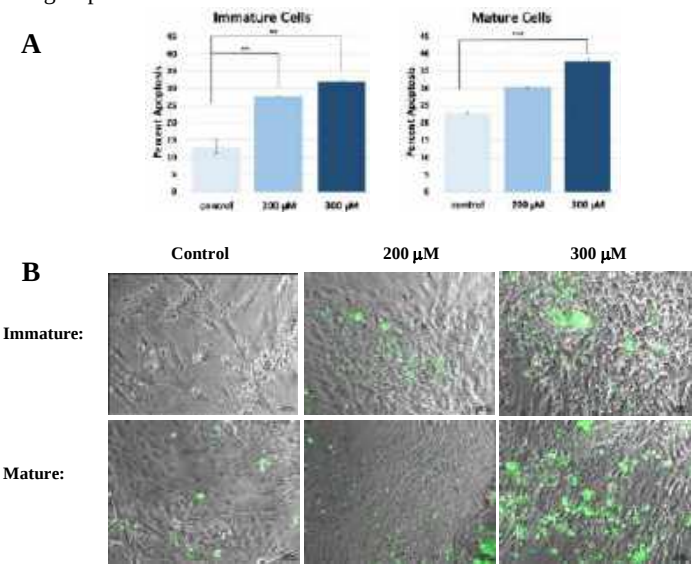

Figure 1. (A) Percentage of apoptotic cells in immature and mature iCMs aged for 7 days exposed to 200 and 300 µM H_2O_2. (B) Bright-field and fluorescence images of iCMs showing apoptotic cells (green) after different aging treatments.

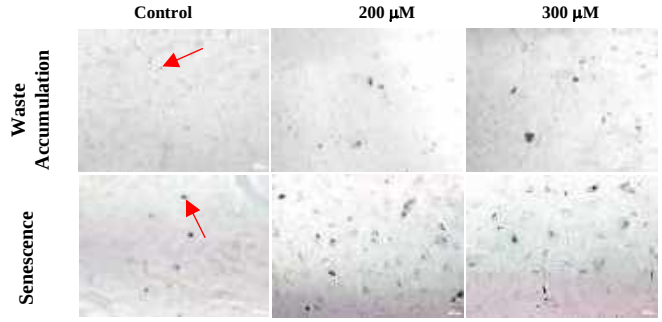

Figure 2. Bright-field images of iCMs show an accumulation of lipofuscin granules (top row) and senescent cells (bottom row) after different aging treatments, examples shown with red arrows.

As can be seen in Figure 1, for immature cells aged for 7 days in control, 200 µM, and 300 µM concentrations, apoptosis rates were 13.1%, 27.7%, and 31.9%, respectively, while mature cells displayed higher rates of apoptosis at 22.9%, 30.3%, and 37.8% for the same conditions, respectively. We also showed when exposed to 50 µM and 100 µM concentrations for 15 days, immature cells exhibited apoptosis rates of 7.4%, 15%, and 18.4%, and mature cells showed rates of 10.3%, 18.8%, and 24%, respectively (data not shown).

In addition to apoptosis levels, we also determined lipofuscin accumulation and senescence in iCMs after in vitro aging. Figure 2 shows qualitatively that with increased H_2O_2 concentration an increase in lipofuscin granules and senescent cells is achieved.

DISCUSSION

Our results align with the current understanding that cellular aging mechanisms in the heart involve increased apoptosis, cellular senescence, and waste accumulation. We observed a trend of increase in these aging markers, notably apoptosis, with added oxidative stress, which concurs with the current understanding that oxidative stress accelerates and greatly contributes to cellular aging mechanisms [7], thus can be used for developing readily available aged cardiac tissue models.

Investigating the rate of apoptosis revealed that the optimal treatment condition for achieving accelerated in vitro aging is exposing immature iCMs to 200 µM or 300 µM H_2O_2. Even though exposing the mature iCMs yielded similar or higher rates of apoptosis, our goal of achieving accelerated aging within the shortest possible duration is satisfied using immature iCMs. The 15-day treatment group exposed to 50 µM and 100 µM H_2O_2 exhibited lower rates of apoptosis for both immature and mature iCMs but additional testing currently being performed will be needed to help comprehensively understand the impact of these concentrations on cellular behavior and response.

This information offers a novel contribution to the field. Our results show that elevated apoptosis levels, along with lipofuscin accumulation and senescence can be induced within a short duration (7 days) and a high concentration of H_2O_2 when compared to the control. This presents a potential way for aging cells in an efficient time frame to create aged tissue models. While our study provides valuable insights into iCMs aging, ongoing analyses focusing on other aging markers such as p21 expression and contractility abnormalities that are more prevalent in the aged population are in progress. Such additional data will further strengthen our conclusions based on the presented findings.

The observed differences in aging markers between immature and mature cells highlight an additional factor in the experiment. Future studies could delve deeper into the molecular mechanisms underlying these observations and test various differentiation timeframes.

In conclusion, this research provides a foundation for advancing our understanding of iCM aging and offers potential implications for pathologically relevant, age-appropriate tissue model development to be used in drug discovery of cardiovascular medicine. By researching the interplay between oxidative stress, cell maturity, and aging markers, this study contributes to the broader topic of CVDs and sets the stage for further exploration into therapeutic paths for cardiovascular health in aging populations in more realistic model platforms. The challenges emphasize the need for ongoing refinement of further tests to enhance result reproducibility and reliability.

REFERENCES

[1] Tang X et al., *Front Endocrinol (Lausanne)* 11:280, 2020.
[2] Cesarovic N et al., *European Heart Journal* 41(2):200-203, 2020.
[3] Pollack M et al., *Ann NY Acad Sci*, 959: 93-107, 2002.
[4]Calcinotto A et al., *Physiological Reviews* 99(2):1047-1078, 2019.
[5] Li WW et al., *Exp Cell Res* 403(1):112585, 2021.
[6] Lian X et al., *Nat Protoc* 8:162–175, 2013.
[7] Forman HJ et al., *Nat Rev Drug Discov* 20(8):652, 2021.

COUPLING SYSTEMS BIOLOGY AND KINEMATIC GROWTH IN OPEN-SOURCE FINITE ELEMENT SOFTWARE

Steven A. LaBelle (1,2), Mohammadreza S. Sadrabadi (3), Seungik Baek (4), Mohammad R. K. Mofrad (5), Jeffrey A. Weiss (1,2), Amirhossein Arzani (1,6)

(1) Scientific Computing and Imaging Institute, University of Utah, Salt Lake City, UT, USA
(2) Department of Biomedical Engineering, University of Utah, Salt Lake City, UT, USA
(3) Department of Mechanical Engineering, Northern Arizona University, Flagstaff, AZ, USA
(4) Department of Mechanical Engineering, Michigan State University, East Lansing, ME, USA
(5) Departments of Bioengineering and Mechanical Engineering, University of California Berkley, Berkley, CA, USA
(6) Department of Mechanical Engineering, University of Utah, Salt Lake City, UT, USA

INTRODUCTION

Tissue-level growth and remodeling accompany development, wound healing, adaptation, and aging. Growth processes depend on extrinsic (environmental) and intrinsic (genetic, metabolic) stimuli. As such, substantial effort has been directed to mathematically relate tissue growth with various stimuli. Kinematic growth is a popular approach where the local growth is defined exclusively as a change in shape resulting from kinematic assumptions [1-2], rather than via the axiom of balance in the context of constrained mixture theory [3]. This approach has been applied to predict growth in musculoskeletal and cardiovascular applications, cancer, development, and wound healing.

Despite the popularity of kinematic growth theory, accessibility via open-source software and reproducibility are lacking. The simple intuition behind kinematic growth belies its complicated implementation. Prior studies have been implemented in commercial software as user subroutines (that generally are not publicly available). Further, there are several strategies available for implementing coupling kinematic growth with reaction-diffusion equations to provide an explicit, physiological growth signal. Our objective was to implement and cross-validate kinematic growth coupled with chemical kinetics in the open-source software frameworks Finite Elements for Biomechanics (FEBio) and FEniCS [4-5]. FEBio solves biomechanics and biotransport problems and includes a user-friendly GUI (FEBio Studio). FEniCS is an open-source program for solving PDEs from user-defined variational forms in Python or C++. It requires proficiency in numerical methods and software development. We generated test problems that defined growth in response to chemical species (c^α, 1-way coupling), or additionally allowed chemical kinetics to respond to feedback from the growth-driven stress (**σ,** 2-way coupling).

METHODS

Kinematics: The motion of a particle is denoted $\mathbf{x} = \chi(\mathbf{X}, t)$ where $\mathbf{X}$ is position in the reference frame and $\mathbf{x}$ is in the current frame. The deformation gradient is $\mathbf{F} = \partial\mathbf{x}/\partial\mathbf{X}$. Kinematic growth theory postulates an intermediate configuration due to growth that facilitates a multiplicative split of $\mathbf{F}$ [1-2,6]:

$$\mathbf{F} = \mathbf{F}_e\mathbf{F}_g, \qquad \mathbf{F}_g = \mathbf{I} + \sum_{i=1} \vartheta_i \mathbf{n}_{0,\mathrm{i}} \otimes \mathbf{n}_{0,\mathrm{i}}\,. \tag{1}$$

Here, $\mathbf{F}_e$ is the (short-time) elastic contribution and $\mathbf{F}_g$ is the (long-time) growth contribution. During growth, each orthogonal material orientation $\mathbf{n}_{0,i}$ has an associated stretch ϑ_i due to growth. The rate of this stretch is given by $\dot{\vartheta}_i = k(\vartheta_i)\phi$, where $k(\vartheta_i)$ is a bandpass function that prohibits uncontrolled growth/resorption, and ϕ relates hypothesized changes of mass or microstructure to stimuli by kinematic constitutive assumption(s).

Chemical kinetics: Chemical kinetics for each species α were governed by conservation of mass including diffusion and reactions:

$$\frac{dc^\alpha}{dt} = D\nabla^2 c^\alpha + \sum_i \nu_i^\alpha \hat{\zeta}_i\,, \tag{2}$$

where c^α is concentration of species α, D is diffusivity, ν_i^α is the net stoichiometric change of α for a given reaction i (note: $\nu_i^\alpha = 0$ for reactions not involving α) and $\hat{\zeta}_i$ is total molar supply of all species associated with reaction i [7]. For 1st order mass-action reactions with reaction rate k_i, the molar supply was the product $\hat{\zeta}_i = k_i\Pi_\alpha c^\alpha$. For biochemical signaling networks, production rates were formulated as normalized Hill activation/inhibition functions with interactions modeled via Boolean logical operators [8-9].

Hyperelastic Mechanics: The Cauchy stress $\boldsymbol{\sigma_e}$ was evaluated relative to the intermediate configuration. Materials were represented as neo-Hookean solids:

$$W(\mathbf{C}_e) = c_1(I_1 - 3) - 2c_1 \ln J_e + K(\ln J_e)^2, \tag{4}$$

$$\boldsymbol{\sigma_e} = \frac{1}{J}\mathbf{F}_e\mathbf{S}_e\mathbf{F}_e^T = \frac{1}{J}\mathbf{F}_e\left(2\frac{\partial W(\mathbf{C}^e)}{\partial \mathbf{C}^e}\right)\mathbf{F}_e^T, \quad (5)$$

where $J_e = \det(\mathbf{F}_e)$, $\mathbf{C}_e = \mathbf{F}_e^T\mathbf{F}_e$.

Test Case 1: We first introduced a "toy-model" to highlight features of kinematic growth coupled with spatially varying chemical kinetics. The growth of a cubic tissue specimen was simulated along the z-axis ($\vartheta_1 = \vartheta_2 = 0$) for 10 years. The mass-action chemical system studied was $\mathrm{A} + \mathrm{B} \rightarrow \mathrm{C}$. Growth was related to c^{C} via $\phi(c^{\mathrm{C}}) = \mathrm{d}c^{\mathrm{C}}/\mathrm{d}t$. We first investigated 1-way coupling of growth to chemical kinetics. Here, the production of A was given by $\hat{\zeta}_q^{\mathrm{A}}(\mathbf{X})$ (Fig 1). We next investigated 2-way coupling of growth to mechanosensitive chemical kinetics. Here, the production of A ($\hat{\zeta}_q^{\mathrm{A}}(\mathbf{X}, I_1)$) increased w.r.t $I_1 = \mathrm{tr}(\boldsymbol{\sigma})$. The source $\hat{\zeta}_q^{\mathrm{B}}$ and decays $\hat{\zeta}_d^{\mathrm{A}}$, $\hat{\zeta}_d^{\mathrm{B}}$, and $\hat{\zeta}_d^{\mathrm{C}}$ were constant.

Test Case 2: An aneurysm was modeled to grow for 8 years in response to matrix metalloproteinase (MMP) downstream of transforming growth factor-β (TGFβ) and intermediate signaling members MAPK, Smad, and TIMP (Fig 1) [8]. The chemical system was modeled as a network of normalized Hill activation/inhibition functions. Growth was related to c^{MMP} via $\phi(c^{\mathrm{MMP}}) = 2.5\ \mathrm{d}c^{\mathrm{MMP}}/\mathrm{d}t$, $\vartheta_1 = \vartheta_2, \vartheta_3 = 0$. For 1-way and 2-way cases, $c^{\mathrm{TGF\beta}}$ was given as $c^{\mathrm{TGF\beta}}(\mathbf{X})$ or $c^{\mathrm{TGF\beta}}(\mathbf{X}, I_1)$ respectively (Fig 1). The decay for each species $\hat{\zeta}_q^{\alpha \neq TGF\beta}$ was constant. Prescribed $c^{\mathrm{TGF\beta}}$ increased w.r.t I_1.

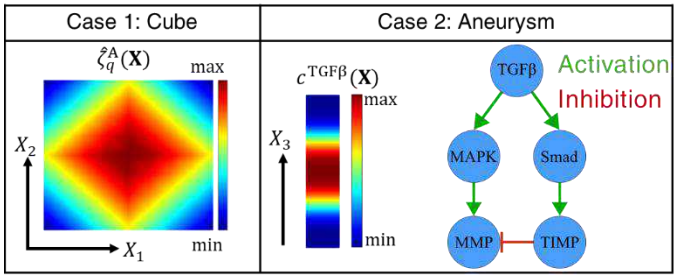

Figure 1: Cube) Spatial variation in $\hat{\zeta}_q^{\mathrm{A}}(\mathbf{X})$. Aneurysm) Left: Spatial variation in $c^{\mathrm{TGF\beta}}(\mathbf{X})$. Right: Signaling networks.

RESULTS

Case 1: Globally 3D growth emerged from locally 1D growth. Qualitative agreement is shown between FEBio and FEniCS (Fig 2). Values of I_1 were greatest along the edges of the specimen and smallest on the interior. Max stresses, deformation, $\hat{\zeta}_q^{\mathrm{A}}$, and c^{C} were reduced by 2-way coupling. Introducing diffusivity to the 1-way case yielded similar trends but with less differential growth and spatial variation.

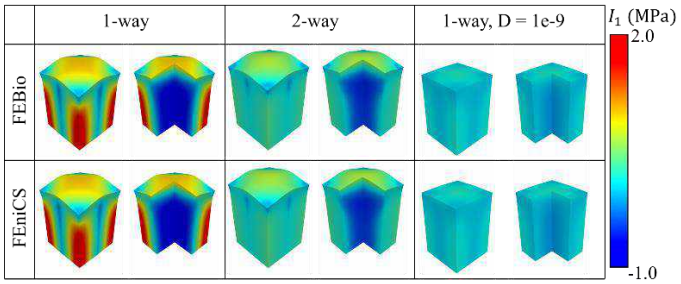

Figure 2: Results for vertical growth after 8 years are displayed for each growth rule alongside a ¾ cut view. Different growth formulations resulted in different solutions of similar problems.

Case 2: Growth occurred primarily in the radial directions (X_1, X_2) with qualitative agreement between FEBio and FEniCS (Fig 3). High stress gradients formed within the lumen near the edges of the aneurysms. Again, stresses decreased for the 2-way and diffusing formulations. Diffusivity delocalized growth, resulting only in vessel dilation. A double-aneurysm was produced by increasing the max value of $c^{\mathrm{TGF\beta}}$.

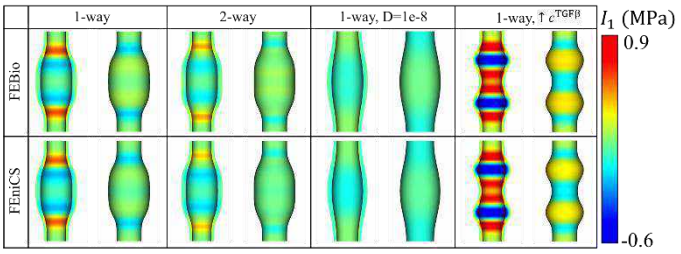

Figure 3: Comparison of aneurysm growth with luminal and abluminal views for each case. 2-way coupling and diffusion facilitated stress dissipation. Increasing $c^{\mathrm{TGF\beta}}$ resulted in a double aneurysm.

DISCUSSION

We implemented and cross-validated kinematic growth coupled to systems biology in FEBio and FEniCS. Our results demonstrate the variability of kinematic growth formulations, reiterating the need for reproducibility and careful selection of constitutive assumptions. Improved accessibility was achieved by implementing these features in FEBio, which allows user-friendly model development in a GUI. Similarly, FEniCS has modern features such as auto-differentiation and just-in-time compilation of C++ code from user-supplied Python scripts. The source code and input files will be available on GitHub and FEBio's online model repository.

FEBio models were limited to formulations of $\mathbf{F}_g$ where ϑ depends directly on chemical concentration (which may evolve via mechanosensitive kinetics). Formulations of $\mathbf{F}_g$ where ϑ depends directly on stress or strain would require modifications to the code and new linearizations. In contrast, the FEniCS implementation could easily be adapted for other stimuli by modifying a few lines in the Python script. Such changes could be linearized via auto-differentiation which would automatically be recompiled at runtime. In the future, we may incorporate similar features in FEBio to support user-defined kinematic growth without requiring code changes or separate software releases.

The test cases we developed are phenomenological examples that may be used to explore growth mechanisms. For instance, double aneurysms emerged in our model since the equilibrium MMP distribution was not monotonic with respect to the TGFβ distribution. This suggests that localized biological processes may produce delocalized downstream effects.

ACKNOWLEDGEMENTS

Funding through NSF grant 2246911 (AA) and NIH grants R01GM083925 and U24EB029007 (JAW) are appreciated.

REFERENCES

[1] Eskandari, M, & Kuhl, E, *Wiley Interdiscip Rev Syst Biol Med*, 7(6):401-12, 2015. [2] Rodriguez, E et al., *J Biomech*, 27(4):455-67, 1994. [3] Humphrey, J D, & Rajagopal, K R., Math Models Methods Appl Sci, 12(03):407-30, 2002. [4] Maas, S A, et al., *J Biomech Eng*, 134(1):011005, 2012. [5] Logg, A, et al., Automated Solution of Differential Equations by the Finite Element Method, Springer, 2012. [6] Göktepe, S, et al., *J Theor Biol*, 265(3):433-42, 2010. [7] Ateshian, G A, et al., *Biomech Model Mechanobiol*, 13:1105-1120, 2014. [8] Irons, L, & Humphrey, J D, *PLoS Comput Biol*, 16(8): e1008161, 2020. [9] Kraeutler M J, et al., *BMC Syst Biol*, 4(1):157, 2010.

STABILITY OF THE C2-C3/C3-C4 LEVEL DURING C4-C6 LAMINOPLASTY WITH AND WITHOUT C3 LAMINECTOMY IN CADAVERIC BIOMECHANICAL MODELS

John J Francis (1), Jeremy Loss (2), Derrick Obiri-Yeboah (3), Orlando Martinez (1), Bilal Butt (2), Michael Steinmetz (2)

(1) School of Medicine, Case Western Reserve University, Cleveland, OH, USA
(2) Center for Spine Health, Cleveland Clinic Foundation, Cleveland, OH, USA
(3) Cleveland Clinic Lerner College of Medicine, Cleveland, OH, USA

INTRODUCTION

Cervical spondylotic myelopathy (CSM) is a progressive neurological disorder that reduces patient quality-of-life and functional ability. C3 laminectomy, as part of a cervical laminoplasty, may improve decompression and reduce postoperative morbidity, such as pain. Despite the benefit, complete laminectomy may result in instability. We performed an analysis of cadaveric spines to determine the effects of C3 laminectomy on C2-C3 stability and range of motion during C4-C6 laminoplasty.

METHODS

Eight human-cadaveric spines (C1-T2) were mounted to a six degree-of-freedom robotic testing system (simVITRO®) and underwent preconditioning with pure moment loading of ±1.5 Nm in flexion/extension (FE), axial rotation (AR), and lateral bending (LB) to minimize viscoelastic effects. For testing, a 30 N head compressive force was maintained as a head load while ±1.5 Nm moments were applied to the native spine in FE, LB, AR, and in the coupled directions of flexion with axial rotation (FE±AR) and extension with axial rotation (E±AR). Total Spine, C2-C3, and C3-C4 range of motion (ROM) was collected during each applied moment test. After testing, left sided open door laminoplasties were performed at C4, C5, and C6 (Stryker). The specimens were tested again with the above approach. A complete C3 laminectomy was then performed and testing was repeated.

RESULTS

At C2-C3, there were statistically-significant differences in ROM during left-axial rotation ($p = 0.030$) and combined A-flexion and left-axial rotation ($p = 0.009$) between surgical states. At C3-C4, there were statistically-significant differences in ROM during right-axial rotation ($p=0.007$), overall flexion ($p<0.001$), combined A-flexion and right-axial rotation ($p = 0.011$), and combined F-flexion and right-axial rotation ($p=0.042$). On quaternion difference analysis, at C2-C3, there were no statistically-significant differences in ROM between the two surgical states. At C3-C4, ROM during overall flexion ($p<0.001$), combined flexion and left-axial rotation ($p=0.016$), combined flexion and right-axial rotation ($p=0.021$), and right lateral bending ($p=0.011$) were significantly different.

Figure 1: C2-C3 Primary Axis Differences

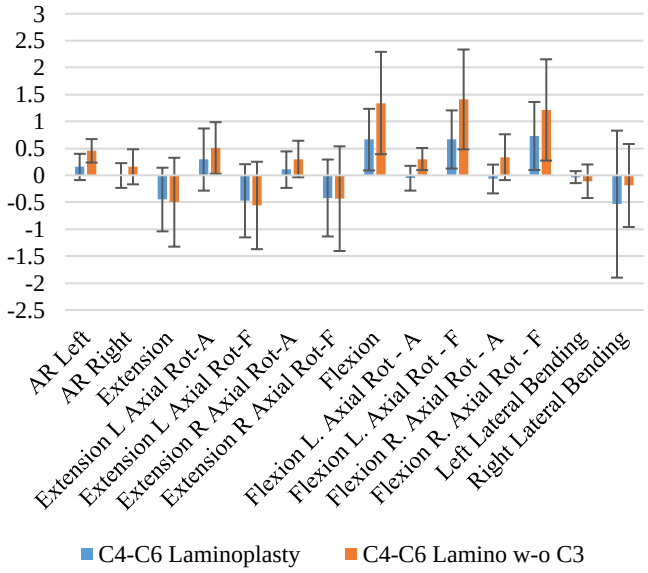

Primary Axis Differences in ROM at C2-C3 Between Surgical States

Figure 2: C3-C4 Primary Axis Differences

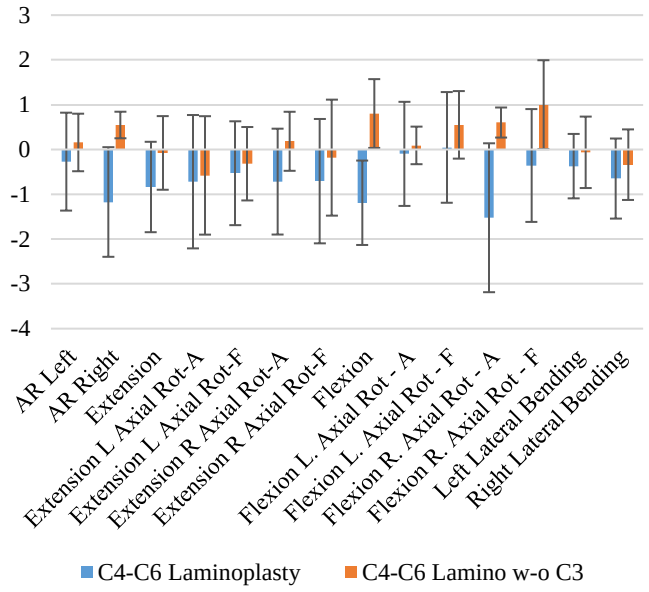

Primary Axis Differences in ROM at C3-C4 Between Surgical States

Figure 4: C3-C4 Quaternion Differences

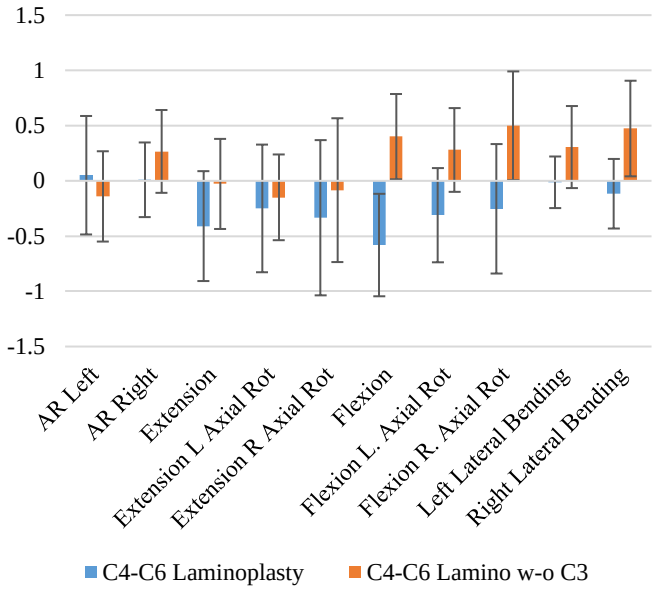

Quaternion Differences in ROM at C3-C4 Between Surgical States

Figure 3: C2-C3 Quaternion Differences

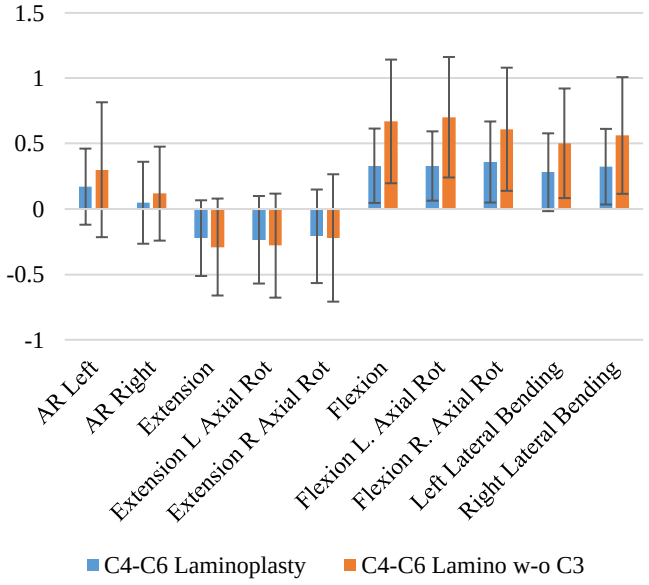

Quaternion Differences in ROM at C2-C3 Between Surgical States

DISCUSSION

Augmenting standard C4-C6 laminoplasty with C3 laminectomy significantly alters the biomechanics at C3-4. Further studies are necessary to determine the clinical correlations of these findings.

ACKNOWLEDGEMENTS

We would like to acknowledge the Cleveland Clinic Foundation Spine Center Clinical Outcomes Research Group for helping make this project possible.

REFERENCES

[1] Gibson, J et al., *Yale J Biol Med.* 2018 Mar 28;91(1):43-48.

[2] Weinberg DS et al., *J Spine Surg.* 2020 Mar;6(1):290-301.

PATIENT-SPECIFIC LONG-TERM PREDICTION OF TRANSCATHETER EDGE-TO-EDGE MITRAL VALVE REPAIR

Natalie T. Simonian (1), Sneha Vakamudi (2), Mark J. Pirwitz (2), Michael S. Sacks (1)

(1) James T. Willerson Center for Cardiovascular Modeling and Simulation, The Oden Institute and the Department of Biomedical Engineering, University of Texas at Austin, Austin, TX, USA
(2) Ascension Texas Cardiovascular, Austin, TX, USA

INTRODUCTION

Mitral regurgitation (MR) is the most common valvular disease in the United States affecting over 2% of the population and is expected to double by 2030 due to population aging. The etiologies of MR span a wide range including primary degeneration of the mitral valve (MV) leaflet tissue (DMR), or secondary causes, such ischemia or non-ischemic cardiomyopathy (FMR). However, MR of any type is a major prognostic factor of mortality: the risk of mortality with severe MR at five years is 36% and even moderate MR nearly doubles the risk of mortality in patients with multiple cardiac comorbidities [1].

Recently, transcatheter MV repair methods such as the MitraClip have been of great interest as the technique is generally safe and improves patient outcomes. However, its efficacy compared to other treatment options (replacement, undersized ring annuloplasty, and pharmacological management) has been unclear, with the outcomes largely dependent on MR etiology, MR severity, and existing comorbidities. The landmark MITRA-FR and COAPT studies found diametrically opposite outcomes in terms of mortality and unplanned hospitalization when comparing MitraClip to pharmacological management [2,3]. Though the precise cause for this discrepancy remains unclear, generally it can be attributed to differences in left ventricle size relative to MR severity between the two study cohorts [4]. Despite updated guidelines, TEER recurrence rates remain inferior to those for surgical MV repair. Moreover, 49% of patients with severe MR are denied surgical intervention [5], and up to 50% of patients with FMR are excluded from the current AHA/ACC criteria [6]. These critical limitations coupled with contradictory clinical trial findings strongly emphasize the need for a patient-specific approach to MR treatment planning.

Furthermore, the MV has the capability to remodel in response to sustained changes in equilibrium. The long-term consequence of permanently stretching the leaflets together and restricting their motion has also never been studied and is likely a key mechanism that drives MitraClip failure. We have previously demonstrated that the MV *plastically* deforms after myocardial infarction, with permanent distortions in annular dimensions, leaflet size, and leaflet stretch [7]. Moreover, we have also shown that altered mechanical loading stimulates changes in MV biosynthesis on the cellular and molecular levels [8]. Therefore, as the MitraClip constitutes a particularly exaggerated shift in homeostasis, we hypothesize that the MV leaflets will undergo a substantial plastic deformation in response to the device.

Standard-of-care real-time 3D echocardiography has advanced to the point that high-resolution images of the patient's MV can be acquired over multiple cardiac cycles. By integrating our previous work on MV plasticity models with the wealth of patient-specific data contained in these preoperative clinical images, we aim to develop a *long-term predictive MV repair model* to quantitatively optimize treatment strategies and achieve maximum repair durability.

METHODS

First, we developed a finite-element model of the full, patient-specific MV apparatus using our previously published methods [9]. As the MV chordae tendinae (MVCT) are not typically visible on standard-of-care rt-3DE imaging, we quantified the MVCT insertions and origins from 5 CT-imaged excised human hearts. Then, we segmented the MV leaflet geometries and papillary muscle (PM) positions for 5 patients from their *preoperative* rt-3DE images. By mapping the population-averaged MVCT insertion density map onto the patient leaflet geometries, we were able to generate patient-specific full MV apparatus models that incorporated both the leaflets and MVCT network.

For preoperative leaflet closure, we defined the segmented end-diastolic (ED) to end-systolic (ES) annular and PM displacements as Dirichlet boundary conditions and applied a ventricular pressurization. Given that patient-specific material properties are impossible to obtain from rt-3DE imaging, we calibrated the tissue material model by iteratively adjusting MV leaflet and MVCT prestrains such that the

Figure 1: Predictive TEER simulation progression with full patient-specific MV apparatus.

change in l^2-norm between the simulated and segmented preoperative ES geometries was less than 5%. We then utilized this fully calibrated MV model to simulate MV repair scenarios by implementing 3D MitraClip models directly onto the MV leaflets (Fig. 1).

Next, we built on our previous work on MV plasticity in response to myocardial infarction to model the long-term consequences of the MitraClip on the MV leaflets [10]. The MV tissue is modeled as an incompressible composite of collagen fibers and an isotropic matrix, and we assume all time-dependent behaviors are constrained to the matrix phase, where bond scission and healing continually alters the stress-free configuration of the matrix according to first-order kinetics. We also assume that the time-scale required to induce a plastic response in the MV leaflets is sufficiently large that only *sustained* changes in leaflet strain would affect leaflet geometry and function e.g. the permanent approximation of the MV leaflets by a MitraClip device. The matrix component of the second Piola-Kirchoff stress tensor, $\boldsymbol{S}_m$, can be defined as follows:

$$\boldsymbol{S}_m = \mu_m \left[e^{-kt}(\boldsymbol{I} - C_{33}\boldsymbol{C}^{-1}) + \int_0^t k e^{-k(t-\tau)} (\tilde{\boldsymbol{C}}^{-1} - C_{33}\tilde{C}_{33}^{-1}\boldsymbol{C}^{-1} d\tau \right] \quad (1)$$

We fit the plasticity rate constant k using additional rt-3DE imaging taken 3-months post-TEER in a subset of consented patients.

RESULTS

With the fully calibrated preoperative MV apparatus model, we were able to *predict* the post-TEER ES geometry to within a millimeter and closely match the leaflet strain patterns when compared to simulations that directly applied postoperative boundary conditions. We also found notable stress concentrations on the MV leaflets at the locations where the MitraClip devices were placed (Fig. 2A). This stress concentration was accompanied by a local change in MV leaflet strain (Fig. 2B). It is this sustained change in MV leaflet deformation that we hypothesize results in the MV plasticity response.

In the follow-up simulations, we were able to reproduce key effects of TEER repair at the 3-month time point using our plasticity model. We noted substantial changes in the MV functional state over time in the ED configuration, where strains are principally induced by permanent distortions in geometry. Specifically, we observed highly compressive circumferential strain on both leaflets in the region of the clip, and slight radial extension in the same region (Fig. 3).

DISCUSSION

Given the persistent challenges and controversies surrounding optimum MR treatment strategies, there is an urgent need for patient-specific methods for predicting treatment outcomes, specifically with a focus on long-term repair durability. Here, we have presented an approach for *predicting* the postoperative state of the MV apparatus both immediately after TEER repair and at 3 months post-repair using standard-of-care, preoperative clinical imaging alone. This pipeline allows us to quantitatively interrogate the impact of the TEER procedure on MV behavior, such as shifts in deformation and nonphsyiological

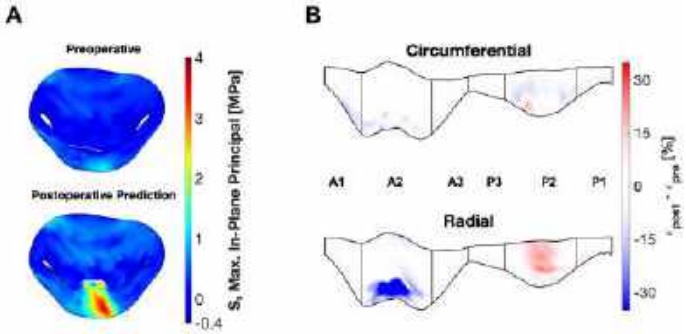

Figure 2: A. Pre- and postoperative maximum in-plane principal Cauchy leaflet stress. The MitraClip induces a notable stress concentration on the posterior leaflet. B. Differences in leaflet strain from pre- to post-TEER, in the circumferential and radial directions. The Carpentier segment where the MitraClip is placed undergoes substantial changes in deformation due to the leaflet approximation.

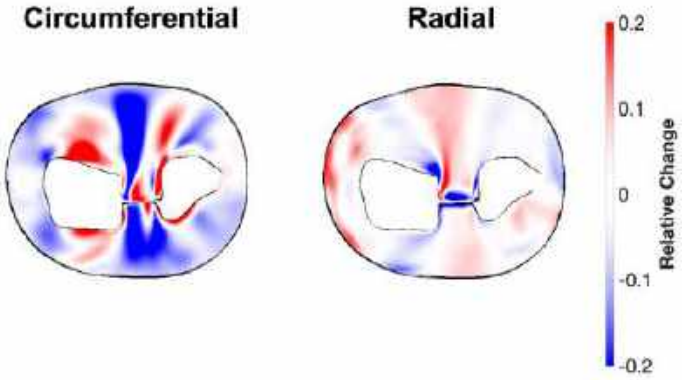

Figure 3: Relative change in leaflet strain from immediately post-repair to 3 months after the procedure. There is notable compression in the circumferential direction, as well as some extension radially locally in the region of the MitraClip.

stress concentrations, as well as the consequences of this permanently altered state on *long-term MV function*. Thus, we can elucidate mechanistic drivers of repair failure, which constitute key targets for optimized treatment durability and efficacy. Our results, which reveal continued MV remodeling in response to the MitraClip, underscore the importance of a long-term view of repair success in the context of MV function, rather than a reductive focus on immediate MR reduction.

ACKNOWLEDGEMENTS

The authors gratefully acknowledge funding from National Institutes of Health grant no. R01 HL073021 to MSS and NIH/NHLBI F31 Predoctoral Fellowship no. 1F31HL170754-01 to NTS.

REFERENCES

[1] Enriquez-Sarano, M, et al., *New Engl J Med*, 352(9):875-83, 2005.
[2] Obadia, JF, et al., *New Engl J Med*, 379(24):2297-306, 2018.
[3] Stone, GW, et al., *New Engl J Med*, 379(24): 2307-18, 2018.
[4] Grayburn, PA, et al., *JACC Cardiovasc Imaging*., 14(4):726-9, 2020
[5] Mirabel, M, et al., *Eur Heart J*., 28(11):1358-65, 2007.
[6] Scotti, A, et al., *Can J Cardiol*, 38(3):320-9, 2022.
[7] Rego, BV, et al., *Ann Biomed Eng*, 51(1):71-87, 2023.
[8] Ayoub, S, et al. *J Roy Soc Interface*, 14(135):21070580, 2017.
[9] Liu, H, et al. *J Biomech Eng*, 145(11):111002, 2023.
[10] Rego, BV et al., *Sci Rep*, 12(1):18012, 2022.

ALTERATIONS OF THE MECHANICAL AND FAILURE PROPERTIES OF AGING HUMAN DESCENDING THORACIC AORTA WITH TYPE-II DIABETES

Ruizhi Wang (1), Katherine Yanhang Zhang (1,2,3)

(1) Department of Mechanical Engineering, Boston University, Boston, MA, USA
(2) Department of Biomedical Engineering, Boston University, Boston, MA, USA
(3) Division of Material Science and Engineering, Boston University, Boston, MA, USA

INTRODUCTION

Diabetes has an increasing prevalence and currently affects over 400 million people worldwide [1], exerting a massive socioeconomical burden to the healthcare system of most countries. As an important risk factor for a broad range of cardiovascular comorbidities, diabetes plays a multifaceted role in the mechanical functions and pathologies of the aortic wall. Diabetes patients show signs of accelerated age associated aortic stiffening [2]. On the other hand, several nationwide statistical investigations demonstrated a negative association between diabetes and the risk of aortic dissection [3,4]. Correspondingly, studies based on animal [5] and *in vitro* [6,7] models of diabetes have provided biomechanical evidence supporting the clinically observed effects of diabetes on the stiffness and dissection propensity of aorta. However, there lacks a comparison of the mechanical and failure behavior between diabetic and nondiabetic human aortic tissues. Such data will not only shed light on the pathological development of diabetic aorta from a mechanistic perspective, but also may provide a foundation for creating high-fidelity computational models that could ultimately lead to the establishment of novel metrics for aorta health assessment and prediction for diabetic patients. In this study, using biomechanical testing approaches, we aim to demonstrate the effect of type-II diabetes on the mechanical and failure properties of human descending thoracic aorta (DTA).

METHODS

Planar biaxial tensile test

Human proximal DTAs with type-II diabetes ranging from 30 to 81 years of age were collected and divided into three age groups: <40 (n=2), 40-60 (n=8) and >60 (n=5) years. Planar biaxial tensile tests were conducted to characterize the mechanical properties of aorta. Briefly, square samples with a size of approximately 2.5 × 2.5 cm were biaxially preloaded with 5 N/m tension and preconditioned with 40 N/m cyclic tension. Samples were subsequently subjected to 200:200 N/m equibiaxial loading, from which the peak stretches were obtained to evaluate the stiffness of each sample as well as the degree of anisotropy defined as $(\lambda_L - \lambda_C)/[0.5\ (\lambda_L + \lambda_C)]$, where λ_L and λ_C are the peak stretches in the longitudinal and circumferential directions of the sample, respectively. A positive degree of anisotropy corresponds to a higher circumferential stiffness, whereas a negative degree of anisotropy corresponds to a higher longitudinal stiffness. In addition, the areal strain under 200:200 N/m equibiaxial tension, obtained as $\lambda_L\lambda_C$-1, was used to evaluate the overall stiffness of each sample [8]. Two samples were obtained from each aorta for biaxial tensile testing except for two aortas due to limited tissue size.

Peeling test

Peeling tests were conducted to characterize the failure properties of aorta. Briefly, two rectangular samples with a size of approximately 15 × 6 mm were obtained from each aorta. The long edge of one sample was oriented in the circumferential direction of the aorta while that of the other sample was oriented in the longitudinal direction. The adventitial and intimal layers of each sample were removed. The medial layer of each sample with an incision was peeled apart with an extension rate of 0.2 mm/s. The peeling force and displacement was recorded until complete delamination. The interlamellar toughness is calculated as $F_m[1+(l/L)]/w$, where F_m is the mean peeling force, w is width of the sample, and l and L are bonded length of the sample in the deformed and initial states, respectively [9].

Statistical data analysis

Experimental data including the peak stretch, areal strain, degree of anisotropy, mean peeling force/width and interlamellar toughness are summarized using bar graphs for each age group and are presented as mean ± standard error of the mean. Biomechanical testing results from diabetic human DTAs were compared to those from their age group-matched nondiabetic counterparts from our previous study [10].

Unpaired t – tests were performed to compare results between the diabetic and nondiabetic samples. Across different age groups, one-way analysis of variance (ANOVA) was used with Bonferroni correction to evaluate the effect of aging on the mechanical and failure properties of both nondiabetic and diabetic samples. $p<0.05$ was considered statistically significant.

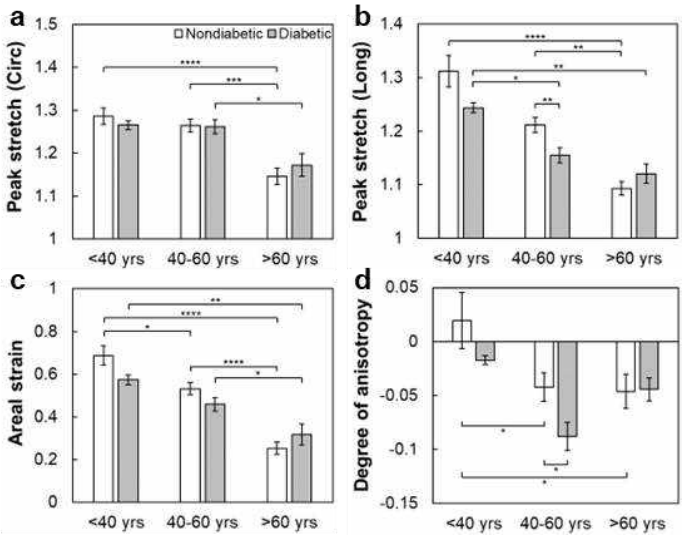

Figure 1: Effect of type-II diabetes on the planar biaxial tensile properties of aging human DTA. Data were obtained under 200:200 N/m equibiaxial tension. Error bars represent standard error of the mean. (*p<0.05, **p<0.01, ***p<0.001, ****p<0.0001).

RESULTS

Results of planar biaxial tensile tests are presented in Fig. 1. A stiffening effect of aging on the biaxial mechanical behavior of the aorta can be observed for both nondiabetic and diabetic samples. No significant difference was observed in the circumferential peak stretch and areal strain between nondiabetic and diabetic aortas of all age groups. However, diabetes was found to accelerate aging-associated aortic stiffening in the longitudinal direction between 40-60 years of age, as revealed by the significantly lower peak stretch as well as degree of anisotropy ($p<0.05$) in the diabetic samples of the 40-60 years group (Figs. 1b and 1d). In addition, for diabetic samples, no significant difference in the degree of anisotropy was found across three age groups, as opposed to the significant decrease in the degree of anisotropy after 40 years of age exhibited in nondiabetic samples ($p<0.05$) (Fig. 1d). Therefore, diabetes expedites the reverse of anisotropy of the aorta with aging. In fact, higher longitudinal stiffness exhibited in all diabetic samples examined regardless of age.

Results of peeling tests are presented in Fig. 2. Diabetes enhances the dissection resistance capability of the aortic wall. Such effect is more prominent after 60 years of age. Compared with nondiabetic samples, in the >60 years group, diabetic samples demonstrated significantly higher longitudinal peeling force/width ($p<0.05$) and circumferential interlamellar toughness ($p<0.05$) (Figs. 2b and 2c). Also, for diabetic aortas, the same level of dissection resistance capability was sustained as the patient passes 60 years of age, as opposed to the significant decrease of longitudinal interlamellar toughness between 40-60 and >60 years groups ($p<0.05$) (Fig. 2d). Furthermore, diabetes has a more prominent effect on the failure behavior of the aorta along the circumferential direction than the longitudinal direction, as circumferentially no significant difference was found in the peeling force/width and interlamellar toughness across three age groups, while longitudinally both the peeling force/width and interlamellar toughness decreases significantly after 40 years of age.

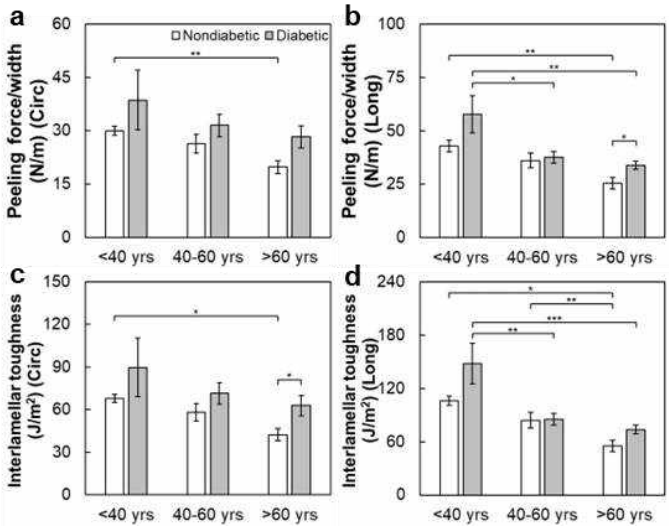

Figure 2: Effect of type-II diabetes on the dissection properties of aging human DTA. Error bars represent standard error of the mean. (*p<0.05, **p<0.01, ***p<0.001).

DISCUSSION

The current study provides, to the best of our knowledge, the first experimental results illustrating changes of human aorta mechanics under the effect of type-II diabetes. Diabetes results in complex multifaceted alterations in the mechanical and failure behavior of the aging aorta (Figs. 1 and 2). The increase of stiffness and interlamellar toughness found in aortas of diabetic patients (Figs. 1 and 2) is consistent with clinical observations [2-4]. Through a combination of chemical and biological pathways, diabetes could have a comprehensive impact on the compositional and structural properties of the aortic wall. In particular, excessive glucose molecules react with amino groups of extracellular matrix proteins to form advanced glycation end-products, which cause nonenzymatic crosslinking of extracellular matrix fibers and could elevate tissue stiffness and toughness [7].

In conclusion, diabetes accelerates aging-associated stiffening in the longitudinal direction of human DTA under 60 years of age and increases the dissection resistance capability of human DTA with a more drastic effect after 60 years of age. Quantitative microscopic imaging and biochemical analysis is needed to resolve the structural mechanisms underlying the altered mechanical and failure properties of the aorta and to gain a better understanding of diabetes-induced aortic remodeling and pathology.

ACKNOWLEDGEMENTS

National Institute of Health (2R01HL098028).

REFERENCES

[1] Saeedi, P et al., *Diabetes Res Clin Pract*, 157:107843, 2019.
[2] Cruickshank, K et al., *Circulation*, 106(16):2085-2090, 2002.
[3] Prakash, SK et al., *J Am Heart Assoc*, 1(2):e000323, 2012.
[4] Avdic, T et al., *J Am Heart Assoc*, 7(3):e007618, 2018.
[5] Tong, J et al., *Ann Biomed Eng*, 46:429-442, 2018.
[6] Wang, Y et al., *J Mech Behav Biomed Mater*, 49:244-254, 2015.
[7] Wang, R et al., *Exp Mech*, 61:81-94, 2021.
[8] Geest, JPV et al., *J Biomech Eng*, 126(6):815-822, 2004.
[9] Sommer, G et al., *J Biomech Eng*, 130:021007, 2008.
[10] Wang, R et al., *J Mech Behav Biomed Mater*, 140:105705, 2023.

UMBILICAL ARTERIAL DEVELOPMENT AND MECHANICS IN GESTATIONAL DIABETES MELLITUS

Kara E. Peak (1), Sarah A. Wernimont (2), Victor H. Barocas (1)

(1) Department of Biomedical Engineering, University of Minnesota, Minneapolis, MN, USA
(2) Department of Obstetrics, Gynecology and Women's Health (OBGYN), University of Minnesota, Minneapolis, MN, USA

INTRODUCTION

During pregnancy, the vasculature of the placenta and umbilical cord connects the pregnant individual and fetus. The importance of this connection is demonstrated by the increased risk of negative outcomes when the umbilical and placental vasculature are malformed. The risk of developing cardiovascular disease increases for both parent and fetus [1], and the risk of stillbirth is also elevated [2]. Of particular interest in the current study is vascular abnormality associated with gestational diabetes mellitus (GDM) [3]. Gestational diabetes occurs solely during pregnancy and results in increased blood glucose levels due to insulin resistance. Within the United States, GDM is becoming more prevalent, increasing 37% from 2016 to 2021 to impact approximately 8% of pregnancies [4]. Therefore, it is necessary to better understand how GDM influences umbilical and placental vascular development.

In utero ultrasound measurements show GDM causes increased umbilical arterial wall thickness [5]. Additionally, *in utero* shear-wave elastography measurements have shown placental stiffening due to GDM [6]. While these differences have been observed, the mechanisms that underlie anomalous remodeling and possible stiffening of the umbilical vasculature in GDM remain unclear. Here, we used complementary morphological quantification and mechanical testing to investigate how GDM impacts the development and mechanical properties of umbilical arteries.

METHODS

Human umbilical cords from either healthy or GDM full-term pregnancies were collected after delivery. The two umbilical arteries (UAs) were dissected from the cord (Fig. 1A-B). Dissected UA segments (1-3 cm long) were cut transversely into small (~2 mm long) explants to create 2 replicate rings (Fig. 1B). All cords analyzed were from female fetuses and the reported n represents the number of vessels studied.

To quantify changes in morphology, the vessel wall thickness (h) and inner (lumen) diameter (d_o) were measured and the wall-to-lumen ratio (h/d_0) was calculated (Fig. 1C). Values for wall thickness for an individual explant were measured and averaged across 4 locations using ImageJ [FIJI]. The inner diameter was taken as the initial pin distance of mounted explants at its pre-stretched state for circumferential mechanical testing (Fig. 1D). A one-sided, two-sample Students' t-test was used to determine significance for morphological quantification.

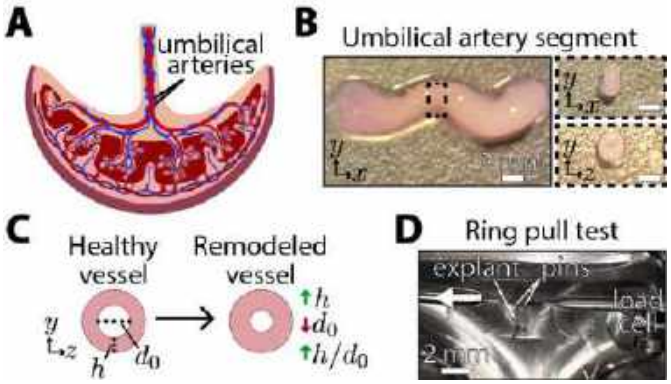

Figure 1: UA Dissection and Quantification Methods. (A) Schematic of umbilical and placental vasculature. Umbilical arteries are noted. (B) Representative dissected umbilical artery segment and explant (inset). Insets show longitudinal (top) and transverse (bottom) view. (C) Schematic of inward remodeling. Wall thickness (h) increases, inner diameter (d_0) decreases, and the wall-to-lumen ratio (h/d_0) increases. (D) Representative UA explant mounted for ring pull testing.

To investigate the mechanics of these same vessels, the explants underwent circumferential testing using a ring pull test [DMT Organ

Bath System 820MO]. Explants were stretched by 10%, 15%, 20%, 30%, and 40% ($\lambda = 1.1, 1.15, 1.2, 1.3, and\ 1.4$) and allowed to equilibrate for 5 minutes following each applied stretch. The resulting force exerted by the tissue was recorded, at a rate of 1000 Hz. The equilibrium force (F_{eq}) at each stretch was calculated for each individual explant. The viscoelastic response was quantified by taking the ratio of the equilibrium force to the peak force (F_{eq}/F_p). Next, the Cauchy stress in the circumferential direction ($\sigma_{\theta\theta}$) for each explant was calculated:

$$\sigma_{\theta\theta} = \frac{F_{eq}}{2A} \quad (1)$$

where A is the deformed cross-sectional area of the explant. Finally, the Young's modulus (E) of each explant was calculated:

$$E = \frac{\sigma_{\theta\theta}}{\epsilon} \quad (2)$$

where ϵ is the strain. A two-way ANOVA with a Tukey post-hoc test or a two-sided, two-sample Students' t-test were used to determine significance for mechanical analysis.

RESULTS

Umbilical arteries from GDM pregnancies had significantly increased vessel wall thickness (h) and decreased lumen diameter (d_0) as compared to healthy pregnancies (Fig. 2A-B). These changes due to GDM were suggestive of inward remodeling (Fig. 1B). Indeed, the morphological changes result in a significant increase in the wall-to-lumen ratio of UAs from GDM pregnancies as compared to healthy pregnancies (Fig. 2C).

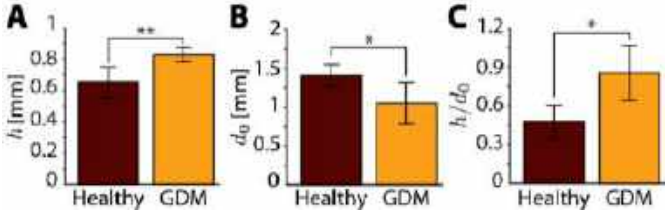

Figure 2: Morphology of Umbilical Arteries. (A-C) Average wall thickness (h) (A), inner diameter (d_0) (B), and wall-to-lumen ratio (h/d_0) (C) for healthy and GDM UAs. Error bars are standard deviation. Healthy: n = 4, GDM: n = 6. *p<0.05, **p<0.01.

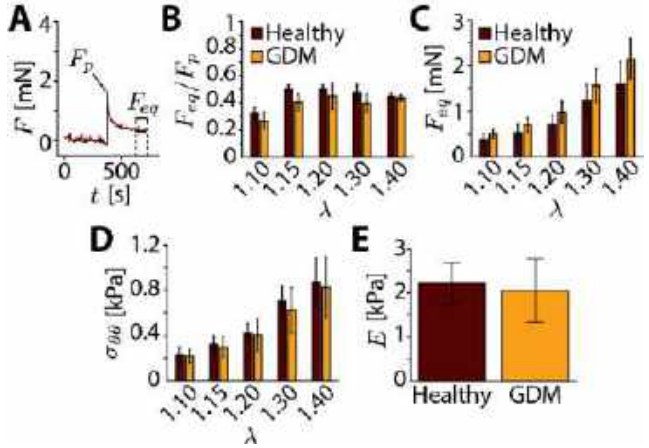

Figure 3: Mechanics of Umbilical Arteries. (A) Representative force (F) vs. time (t) curve shown for 10% stretch ($\lambda = 1.10$). The peak force (F_p) and equilibrium force (F_{eq}) are shown. (B-D) Mean ratio of equilibrium force to peak force (B), equilibrium force (C), and Cauchy stress ($\sigma_{\theta\theta}$) (D) vs. stretch for healthy and GDM UAs. (E) Mean Young's modulus (E) for healthy and GDM UAs. Error bars are standard deviation. Healthy: n = 4, GDM: n = 6.

The viscoelastic response of the vessels was observed when the applied stretch resulted in an initial peak force (F_p) that relaxed to an equilibrium force (F_{eq}, Fig. 3A-B). The relaxation was slightly greater (i.e. F_{eq}/F_p was slightly lower) for the GDM UAs, but the result was not significant. The measured equilibrium forces were slightly higher, although not statistically significant, in GDM UAs as compared to healthy UAs (Fig. 3C). However, there was no difference between GDM and healthy UAs when comparing the Cauchy stress values (Fig. 3D). The Young's modulus for each condition were also similar amongst both groups (Fig. 3E).

DISCUSSION

These data suggest GDM can cause morphological differences in umbilical arteries that do not impact the material behavior of the tissue. Vessel morphology is connected to hemodynamics, which has been shown to be altered in fetuses of GDM pregnancies [7]. Specifically, the resistive index, which is inversely related to lumen diameter, has been shown to increase in GDM pregnancies [7]. The morphological changes quantified here could explain why differences in fetal hemodynamics arise in GDM.

The similar material properties of the UAs from healthy versus GDM pregnancies is counterintuitive to the well-established arterial stiffening observed within adults with diabetes [8,9]. Unlike the adult vasculature, umbilical arteries are undergoing rapid changes as they develop over the course of pregnancy. Despite this growth, UAs from healthy pregnancies maintain constant material properties that do not change with gestational age [10]. Therefore, it is possible the UAs from GDM pregnancies similarly seek to maintain these same material properties but must adapt their vessel morphology and/or structure as they develop to counteract diabetes-related vessel stiffening.

The umbilical cords used for this analysis were obtained from pregnancies of female fetuses to eliminate possible differences due to fetal sex. Future studies to investigate how GDM impacts the morphology and mechanics of the umbilical vasculature within male fetuses as well as any sex-dependent differences are needed.

ACKNOWLEDGEMENTS

This work was supported by the University of Minnesota Obstetric Measures: Gestational Outcomes and Pediatric Health Repository (UMOMS:GOPHER) and NIH grant R01 HL164800. Additionally, this research was supported by the National Institutes of Health's National Center for Advancing Translational Sciences, grant UL1TR002494. The content is solely the responsibility of the authors and does not necessarily represent the official views of the National Institutes of Health's National Center for Advancing Translational Sciences.

REFERENCES

[1] Thornburg, KL et al., *Placenta*, 31:S54–S59, 2010.
[2] Silver, RM et al., *Am J Obstet Gynecol*, 196(5):433–444, 2007.
[3] Singh, SD, *Early Hum Dev*, 14(2):89–98, 1986.
[4] Martin, JA et al., *NVSS Morb Mortal Wkly Rep*, 72(1):16, 2023.
[5] Sarikabadayi, YU et al., *Neonatology*, 102(2):157–162, 2012.
[6] Lai, H et al., *Placenta*, 101:147–153, 2020.
[7] Wei, Z et al., *Am J Trans Res*, 13(4):3330-3336, 2021.
[8] Hayden, MR et al., *Cardiovasc Diabetol*, 4:9, 2005.
[9] Prenner, SB et al., *Atherosclerosis*, 238:370–379, 2014.
[10] Nye, KS et al., *Am J Perinatol*, 32(3):263-269, 2015.

INTRATUMORAL COMPRESSION PROMOTES PRONEURAL TO MESENCHYMAL TRANSITIONS IN GLIOBLASTOMA

Allison McKenzie Johnson (1), Lylah Cox (2,3), Joseph Chen (1)

(1) Department of Bioengineering, University of Louisville, Louisville, KY USA
(2) Department of Biology, University of Louisville, Louisville, KY, USA
(3) Department of Anatomical Sciences and Neurobiology, University of Louisville, Louisville, KY, USA

INTRODUCTION

Glioblastoma (GBM) is the most prevalent and malignant brain cancer, accounting for over half of all brain cancer diagnoses and carrying an average life expectancy of 14 months after diagnosis [1,2]. The lethal nature of this cancer is due to the rapid invasion and recurrence despite multimodal, aggressive treatment [3]. Reports suggest that a critical driver of this progression is proneural to mesenchymal transition (PMT), a phenotypic switch that cause cells to become increasingly migratory and therapy resistant [4]. Current therapies target this phenomenon through biochemical avenues, which has not been effective [5]. However, emerging studies have suggested that PMT is highly sensitive to biophysical cues, which drugs currently do not target, and thus new investigations into the biophysical axis is warranted [6]. The tumor microenvironment is mechanically complex, with varied ECM stiffness, elevated shear stress from fluid flow, and increased compressive stress all mediating cancer progression and invasion [7]. Although ECM stiffness and shear stress are well studied, Intratumoral compression is much less understood. Intratumoral compressive stress is experienced by the tumor as it rapidly expands against the surrounding tissue, experiencing a normal force back against the tumor [8]. Due to the dense nature of the brain ECM, the normal force pushing back is expected to be high, therefore increasing the compressive stress on the tumor [8]. Compressive stress is shown to increase invasive potential in epithelial cancer, but the mechanism by is still poorly understood [9]. This research aims to elucidate the mechanism by which compression activates PMT to identify novel therapeutic targets for pharmacological intervention.

METHODS

The compression device was designed to allow for varying amounts of compression while maintaining sterility and cells' access to cell culture media (Figure 1). The design utilizes a 24 mm diameter with 0.4 µm pores to allow for nutrient exchange with the media below but inhibit migration through the transwell. Atop the cell monolayer is a 2% agarose gel and a 3D printed cup containing tungsten carbide discs to induce compression.

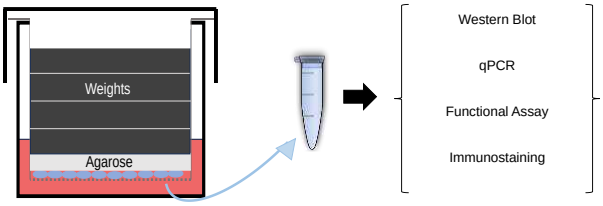

Figure 1. Compression Device design and intended use.

U251s were cultured then seeded for 24 hours before being compressed under 1 kPa pressure. After 72 hours, the cells were lysed, fixed, or replated. Cells were lysed in RIPPA with a Protease inhibitor then a BCA was done. Protein levels were normalized, and a Western Blot was run on a 14% acrylamide gel. The blot was stained for CD44 before being imaged via an Odyssey-XF. Densitometry was done via ImageJ. For Immunostaining, cells were fixed in 10% Formalin with Triton. Cell monolayers were stained for Ki-67, Zeb1, and DAPI. Cells were imaged via an Olympus BX51M. Nuclear localization and fluorescent intensity were quantified via ImageJ. For the functional assay, the cells were lifted with Trypsin EDTA, and replated on tissue culture plastic. After 24 hours, the cells were imaged every 15 minutes for 24 hours at 10x on a Nikon Eclipse TE2000-U. Quantification of cell speed and persistence were done via ImageJ.

RESULTS

To confirm that our system is applying compression to the cells, we assessed nuclear shape and circularity. We found that compressed cells showed appeared flattened and how a significant decrease in

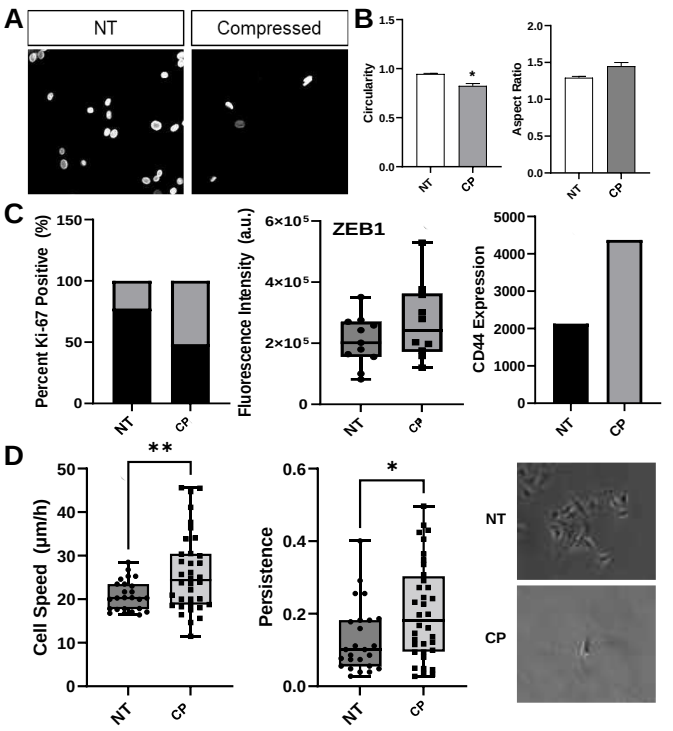

Figure 2. DAPI staining shows significant changes in nuclear size and shape in response to compression (A). Proliferation decreases due to compression but ZEB1 and CD44 both increase (B), indicating a mesenchymal shift. Functional assessment shows significant increase in cell speed and persistence after compression (C).

circularity and an increase in aspect ratio, indicating an elongated morphology (Figure 2 A,B). To determine the effect of compression on cell proliferation, we stained both conditions with Ki-67 and evaluated nuclear localization. We found that the compressed condition showed less Ki-67 nuclear localization than the non-treated cells (Figure 2C). To assess the potential PMT shift, compressed and non-compressed cells were stained for ZEB1, a mesenchymal transcription factor seen in the early stages of PMT, and CD44, a marker of the mesenchymal phenotype. For ZEB1, the fluorescent intensity was higher in the compressed population than the non-compressed, providing evidence of a shift to a mesenchymal phenotype (Figure 2C). CD44 staining revealed higher CD44 levels in the compressed condition, supporting a shift towards a mesenchymal phenotype (Figure 2C).

To test whether there was a functional effect in compressed cells, a 2D motility assay was conducted. The non-treated condition showed proliferative cells that maintained cell-cell contact with little migration. However, the compressed cells exhibited large lamellipodial protrusions and were more migratory and persistent (Figure 2D).

DISCUSSION

In this study, we developed a compression platform to investigate the effect of increased compressive stress on PMT in U251 GBM lines. We confirm that our compression platform is capable of squeezing cells by showing that compressed cultures displayed elongated nuclear shape. Using this platform, we found that compressed cells proliferated less, which may point to a more migratory phenotype. Additionally, we observed an increase in mesenchymal markers ZEB1 and CD44 in the compressed population. The upregulation of these markers is significant because they were activated in the absence of any other stimulus, providing evidence of the pro-malignant effect of elevated compressive stress. Through a 2D motility assay, we show that compressed cells migrated faster and more persistently regardless of any chemotactic cue. This indicates an innate increase in migration potential after compression. Compressed cells also had much larger cell area with extended lamellipodial protrusions, which supports a migratory phenotype.

Collectively, these results show that intratumoral compressive stress alone can promote the shift towards a more mesenchymal and malignant phenotype. In patients, this compressive stress may increase the likelihood of tumor cell invasion into the surrounding tissue, which may help it evade the initial surgical recission and propagate new tumors. Future work will examine the mechanism by which compression promotes a mesenchymal shift in GBM by interrogating the nuclear mechanotransductive axis. The identification of new targets in this axis may lead to the development of novel therapies for this deadly disease.

ACKNOWLEDGEMENTS

This work is supported by NIH Grant P20GM135004.

REFERENCES

[1] Rock, K., et al. The British journal of radiology, 85(1017), e729–e733, 2012.
[2] Omuro, A. and DeAngelis, L.M., JAMA, 310(17): 1842-50, 2013.
[3] Weil, S., et al. Neuro-oncology, 19(10), 1316–1326, 2017.
[4] Fedele, M., et al. Int. J. Mol. Sci., 20, 2746, 2019.
[5] Yalamarty, S. S. K., et al. Cancers, 15(7), 2116, 2023.
[6] Wang, C., et al. Tissue engineering. Part A, 27(5-6), 390–401, 2021.
[7] Zhu, P., et al. Cancer biology & medicine, 20(1), 44–55. 2023.
[8] Stylianopoulos, T. Journal of Biomechanical Engineering 139(2), 2017.
[9] Tse, J. M., et al. Proceedings of the National Academy of Sciences of the United States of America, 109(3), 911–916, 2012.

DEVELOPING MOUSE-TUMOR MODEL FOR HIGH INTENSITY FOUCSED ULTRASOUND (HIFU) ABLATION PROCEDURES

Nabin Khanal (1), Victoria Summey (2), Jeffrey Bailey (2), Xin Duan (3), Liang Zhu (4) Rupak K. Banerjee (5)

(1) Department of Mechanical and Materials Engineering, College of Engineering and Applied Science, University of Cincinnati, Cincinnati, Ohio, USA
(2) The Comprehensive Rodent and Radiation Facility, Cincinnati Children's Hospital Medical Center, Cincinnati, Ohio, USA
(3) Experimental Hematology and Cancer Biology, Cincinnati Children's Hospital Medical Center, Cincinnati, Ohio, USA
(4) Department of Mechanical Engineering, University of Maryland Baltimore County (UMBC), Baltimore, USA
(5) Department of Biomedical Engineering, College of Engineering and Applied Science, University of Cincinnati, Cincinnati, Ohio, USA

INTRODUCTION

High Intensity Focused Ultrasound (HIFU) stands out as a non-invasive modality gaining prominence for the localized treatment of deep-seated malignant tumors. To enhance the effectiveness and validate the applicability of HIFU procedures, researchers have devised diverse *in vitro* [1, 2] and *in vivo* models [2, 3]. The literature reveals a spectrum of experiments involving *in vitro* models employing tissue mimicking materials (TMM) and turkey/chicken breasts, progressing to *in vivo* models featuring mice. Currently, the majority of HIFU research revolves around mouse tumor models.

In the area of cancer research, an array of mouse strains is readily available, primarily sourced from Jackson Laboratory in Bar Harbor, ME. The judicious selection of mouse strain is important for seamless experimental flow in tumor studies. Cincinnati Children's Hospital and Medical Center (CCHMC) locally houses three mouse strains, all originating from Jackson Laboratory: NOD/SCID GammaC-/- (NSG), NSG-SGM3 (NSGS), and Homozygote J:NU (Nude). These three types of mice were assessed in this study for developing a mouse tumor model.

The NSG mice, with their severe immunodeficiency due to scid and IL2rgnull mutations, have become pivotal in cancer research. Their compromised immune system allows efficient engraftment of human cells, facilitating studies on tumor biology and the testing of potential cancer therapies. The NSGS mice, an advancement in cancer research models, express human IL3, GM-CSF, and SCF. This modification enhances engraftment of myeloid lineages and regulatory T cells, making them particularly relevant for immuno-oncology studies. These mice provide a superior platform for investigating complex interactions between the immune system and cancer. Nude mice, characterized by athymia and immunodeficiency, have been fundamental in cancer research for decades. Their lack of T cells enables successful transplants of tumor cell xenografts, contributing to studies on tumor growth and drug testing in oncology. While not capturing full immune complexity, Nude mice remain relevant in specific contexts, offering insights into tumor biology and early-stage drug evaluations.

A human PC3 (CRL-1435) prostate cancer cell line used for developing the tumor model in mice is provided by American Type Culture Corporation (ATCC). The PC3 cell line is initiated from a bone metastasis of grade IV prostatic adenocarcinoma from a 62-year-old, White, male.

METHODS

The experimental cohort was comprised of two male mice from each of the three selected strains, totaling six mice. All animal studies were approved by the internal ethics and the local government committees. To establish the cell line-derived xenograft model, 6 to 8 weeks old male mice with a bodyweight around 30 g were engrafted subcutaneously with 1×10^7 PC3 cells into the right flank. Mice were group-housed under pathogen-free and controlled environmental conditions (21 ± 1.5 °C temperature, $55 \pm 10\%$ humidity and a 12 h light–dark cycle).

The PC3 cells were procured from ATCC, and the thawed contents of the vial were transferred to a 75 cm^2 tissue culture flask. A growth medium was formulated using F-12K as the base medium, supplemented with 10% fetal bovine serum (FBS) and 1% Penicillin-Streptomycin (Pen-Strep). Rigorous filtration was employed to eliminate potential contaminants. The cells were cryopreserved using DMT solution.

For cell culture, a mixture of 9 ml of the prepared medium and approximately 1 ml of frozen cells were placed in a 50 ml centrifuge tube and spun at room temperature. Cell counting, facilitated by a cell counter, revealed a visible white cell pellet at the tube's base. The culture was then incubated at 37°C, with a waiting period of 2-3 days for confluence. Subsequently, subculturing ensued to attain the desired cell quantity. Ethanol was used to sterilize all equipment before subculturing, and 0.25% (w/v) Trypsin-0.53 mM EDTA solution aided

in cell detachment. The cells were observed under an inverted microscope until the cell layer dispersed, typically within 5 to 15 minutes. The addition of 6 to 8 ml of complete growth medium facilitated aspiration, and sub cultivation was carried out from 1 culture vessel to 3 culture vessels. Medium renewal occurred 2 to 3 times per week, maintaining consistency across subsequent passages.

For the injection procedure, PBS served as the medium, and a 0.2 ml solution containing the requisite cell count was injected using a 27-gauge needle. Post-injection, all mice underwent observation for abnormal behavior. Tumor monitoring involved regular measurements 2 to 3 times weekly over a 5 to 7 week growth period. The area surrounding the tumor was consistently shaved to facilitate clear observation. The tumor measurement was done using digital calipers.

The tumor was assumed as an ellipsoid and the following formula was used to calculate the surface area of the ellipsoid.

$$SA = \left(\frac{4\pi((ab)^{1.6}+(ac)^{1.6}+(bc)^{1.6})}{3}\right)^{1/1.6} \quad (1)$$

The following formula was used to calculate the volume of ellipsoid.

$$V = \frac{4}{3}\pi abc \quad (2)$$

where a, b and c are the three dimensions of the ellipsoid.

RESULTS

Figure 1 illustrates the temporal progression of *tumor surface area* growth. Data collection commenced on the tenth day post-tumor cell injection, considering the initial small size of the tumors. This figure depicts the mice's tumor surface growth fitted to a parabolic profile. The initial tumor growth is characterized by a slow pace. Notably, NSGS mice exhibit a larger tumor surface area until approximately day 26, after which NSG mice surpass them, and the gap in surface area widens over time. Beyond day 40, NSG mice demonstrate a surface area of approximately 17 cm², NSGS mice exhibit around 13 cm², and Nude mice present approximately 11 cm². This highlights that, by the end of day 40, NSG mice possess a tumor surface area: about 31% larger than NSGS mice and 55% larger than Nude mice.

Figure 2 illustrates the temporal evolution of *tumor volume* growth. Similar to the surface area data, the figure displays the tumor surface area growth of mice fitted to a parabolic profile. Until approximately day 24, NSGS mice exhibit the largest tumors among the three strains; however, from that point onward, NSG mice surpass the others in tumor size. By day 40, a discernible distinction in tumor size emerged, with NSG mice boasting the largest tumor volume, Nude mice presenting the smallest, and NSGS mice fell in between the two. Specifically, the tumor volumes at day 40 are approximately 0.8 cm² for NSG mice, 0.52 cm² for NSGS mice, and 0.4 cm² for Nude mice. This indicates that, by the end of day 40, NSG mice have a tumor volume about 54% larger than NSGS mice and 100% larger than Nude mice.

In summary, both the tumor surface area and volume results consistently indicate that NSG mice exhibit the most robust tumor growth among the three experimental groups. This is evident from their larger tumor volume and surface area.

DISCUSSION

This research establishes that the NSG mice are better suited for tumor research based on tumor growth. NSG mice have the larger tumor surface area and volume compared to the other two over the established growth period. One can select this strain for HIFU research involving mice. One secondary factor that could have been considered is the Nude mice having no fur. They are very easy to handle as one must shave the tumor area of NSG and NSGS mice. As the most important parameter for developing a model is tumor size, the tumor surface area and volume of Nude mice is extremely low compared to the other two strains. Hence, they were not considered suitable for development of mouse tumor model.

Limitations: There are other strains of mice provided by Jackson Laboratory and those could be considered as well. This research only focuses on the three strains that are available at CCHMC. Only two mice of each category were taken for observation. More mice from each category can be observed in the future to strengthen the current results. Digital calipers were used for tumor measurement. While it is relatively easy to measure the two dimensions of the tumors with calipers, it was somewhat complex to accurately measure the depth of the tumor.

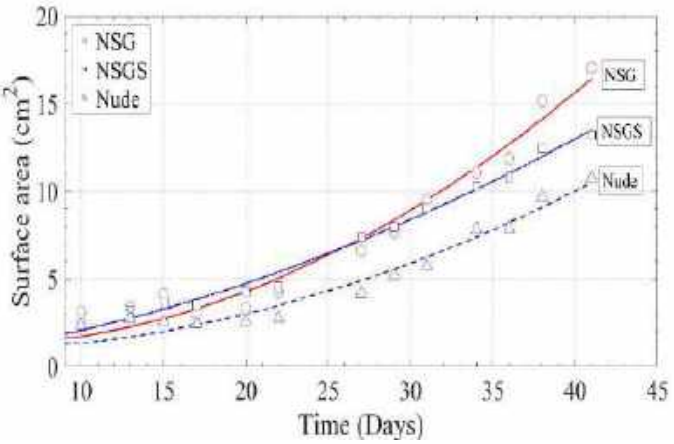

Figure 1: Tumor surface area growth with time

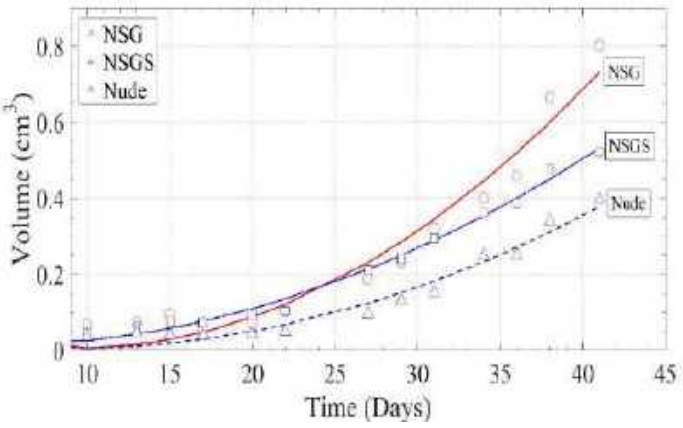

Figure 2: Tumor volume growth with time

ACKNOWLEDGEMENTS

This research was supported by the National Science Foundation through Grant #NSF CBET 2045234.

REFERENCES

[1] Dibaji et. al., J. of Nanotechnol. Eng. Med. Nov 2013, 4(4): 040902.
[2] Devarakonda et. al., Nano Lett. 2017, 17, 4, 2532-2538.
[3] Devarakonda et. al., ACS Biomater. Sci. Eng. 2019, 5, 8, 4102-4111.

EXPERIMENTAL AND COMPUTATIONAL MODELING OF BRAIN SHUNT PERFORMANCE

Bryan C. Good (1), Ashley Handy (1), Alyson Matushek (1), Stephanie C. TerMaath (1)

(1) Mechanical, Aerospace, and Biomedical Engineering
University of Tennessee
Knoxville, TN, USA

INTRODUCTION

Hydrocephalus is a condition in which an excess amount of cerebrospinal fluid (CSF) accumulates within the ventricles of the brain, leading to elevated intracranial pressure. Approximately 1 of every 500 infants is born with hydrocephalus, making it the highest cause of brain surgery in children [1]. The most common treatment for this condition is the surgical placement of a brain shunt to drain CSF from the ventricles to other parts of body. However, brain shunts have extremely high failure rates, with a majority of patients needing a device repair or replacement within 10 years [2]. Therefore, the objective of this research is to develop experimental and computational models of brain shunts (both catheter and valve) that capture *in vivo* conditions and to characterize CSF transport under normal and shunt failure operation.

METHODS

Ventricle Parameter Study on VP Catheter Performance

Computational models of VP catheters inside ventricles of varying size, geometry, and choroid plexus (CP) location were created using SolidWorks. Additional patient-specific ventricle models were reconstructed from CT images using the open-source Slicer. The VP catheter has 4 rows with 4 tapered drainage holes (0.8mm diameter) in each row. The catheter is 200 mm long with 1.2 and 2.5mm inner and outer diameters, respectively.

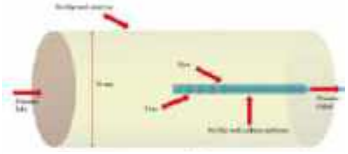

Fig 1: Baseline computational model.

The baseline fluid chamber was modeled as a cylinder (30mm diameter and 60mm length) to represent a simplified ventricle (**Fig. 1**). Additional 'small' and 'larger' cylindrical models were created (**Fig. 2**) to investigate the role of ventricle size on catheter performance.

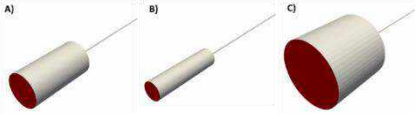

Fig 2: Ventricle size on catheter performance.

Patient-specific ventricle models (**Fig. 3**) were reconstructed from healthy 10-year-old patients (LV1, LV2, and LV3), a hydrocephalus patient (LV4), and a patient with a slit ventricle anatomy (LV5). For each of the five models, three different catheter locations were also considered: Kocher point, and normal and pushed Frazier points.

Fig 3: Patient-specific ventricle geometry on VP catheter performance.

The CP is the main source of CSF production, and its size, shape, and location can be unique for each patient. Therefore, the effect of CP geometry and location on catheter performance was studied (**Fig. 4**).

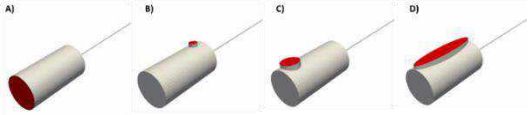

Fig 4: Choroid plexus (red) shape and location on VP catheter performance.

Steady vs. Pulsatile Pressures on VP Catheter Performance

Prior CFD simulations were run with fixed pressure boundary conditions (BCs), with static intracranial pressures (ICP) from 5-20 mmHg. The pulsatile effects of varying ICPs were also investigated using two ICP waveforms (**Fig. 7A**); a simplified periodic waveform adapted from [3] and a hydrocephalus patient pressure waveform. Following each CFD simulation, postprocessing was performed to analyze ventricle flow patterns, CSF flow through the catheter, and wall shear stresses (WSS) as parameters of shunt performance.

Experimental Models of Brain Shunt Valve Performance

Static and dynamic experimental flow models were developed to evaluate the performance of brain shunt valves. Two commercial valves were evaluated statically (**Fig. 6A**) (Medtronic Strata II and Codman Programmable Valve) and one evaluated dynamically (Delta 2.0, Medtronic). For static testing, both explanted failed valves and new

valves of each type were connected to a hydrostatic water column (where "ICP" was controlled by varying the height of water) and an electronic balance used to measure the resultant flow rates over time. For dynamic testing (**Fig. 6B**), the catheters were placed into a water-filled balloon to represent the ventricle's elastic properties. Surrounding the balloon was a 1:1 mixture of ultrasound gel and water that closely mimicked the properties of brain matter. A plastic skull surrogate enclosed the gel and balloon to limit the expansion of the ventricle, as occurs in vivo. CSF production and flow into the model was controlled with an IV infusion pump at a rate of 21 ml/hr. A pressure transducer (Grainger) and flow sensor (Sensirion) were inserted into the model to measure the resultant ICP and shunt drainage, respectively

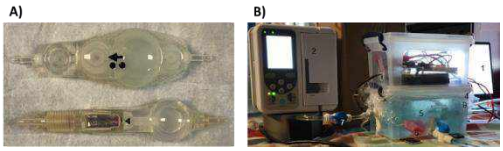

Fig 5: A) Strata II and Codman valves used for static testing. **B)** Delta 2.0 valve used for dynamic testing.

RESULTS

Parameter studies were performed to determine the individual effects of ventricle size and shape, CP size and location, and pressure BCs on CSF flow and WSS distribution (both known to correlate with shunt obstruction).

With regards to CSF flow through the catheter (**Fig. 6A**), no significant differences were observed with changing ventricle size (left), CP shape and location (middle), and in patient-specific ventricles (right). In all cases, approximately 43% of the total CSF flow exited through catheter hole #1, with the % flow splits decreasing exponentially with hole distance. Differences of 1-2% were observed between the small and large cylinder models, <1% between the different CP models, and < 1% between the different patient-specific models.

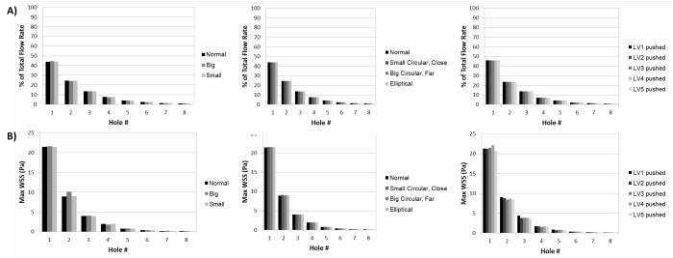

Fig 6: Ventricle size (left), CP (middle), and patient-specific effects on catheter **A)** flow rate and **B)** WSS.

For WSS (**Fig. 6B**), the highest values occurred in drainage hole #1 in all cases (~22 Pa) and decreased with additional hole distance. WSS differences of 1-12% were observed between the medium and large cylinders (right), with the greatest difference at drainage hole #2, 1-2% differences between the different CP models (middle), and <10% differences between the different patient-specific models (right).

Two pulsatile pressure waveforms (simplified periodic and hydrocephalus patient) were also applied as inlet BCs (**Fig. 7A**). The periodic waveform lead to flow rates ranging from 10-30 ml/min, while the hydrocephalus patient waveform generated smaller flow rates variations (13-17 ml/min). Comparing parameters for drainage hole #1, flow rates behaved similarly but with less pulsatility overall (**Fig. 7B**). However, when normalized against total catheter flow (**Fig. 7C**), the % flow split in each hole did not vary with time and was not significantly different from static ICP cases. The same trends were also observed with WSS over time (**Fig. 7D**), with fluctuations between 6-38 Pa with the simplified waveform and 11-16 Pa with the hydrocephalus waveform.

Experimental testing of the Strata II valve (**Fig. 8A**) confirmed the new valve followed pressure-flow curves from Medtronic (black) at a 1.0 performance setting, while the failed valve exhibited significant over drainage (red). The Codman valve (**Fig. 8B**) displayed unique pressure-flow behaviors due to its secondary SiphonGuard valve that maintained a ~20mL flowrate at excess ICPs. The new Codman valve

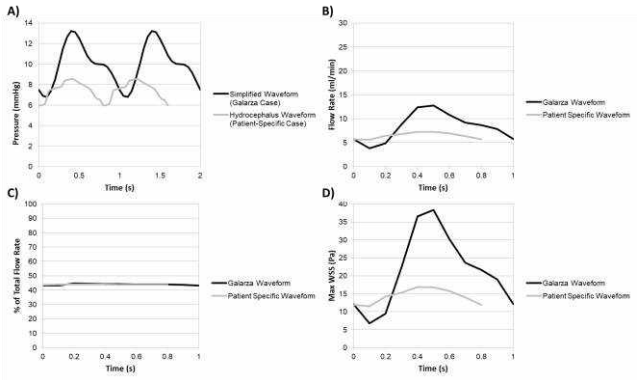

Fig 7: A) Simplified and hydrocephalus pressure waveforms [3]. Comparison of drainage hole #1 **B)** flow, **C)** normalized flow, and **D)** WSS.

displayed a linear pressure-flow relationship up to 100mHg, while the explanted valve had a lower flow rate and stayed open until 150mmHg. For dynamic testing, the Delta valve demonstrated varying drainage behaviors depending on increases in ICP, as CSF filled the ventricle model over time (**Fig. 8C**). ICP built up linearly, causing the valve to open between 8-16mmH,g depending on the valve setting, and quickly returned to a baseline ICP of approximately 5mmHg.

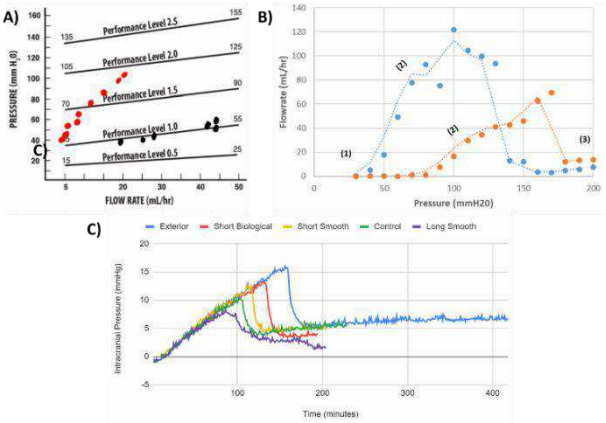

Fig 7: Static testing of new and explanted **A)** Strata II and **B)** Codman shunt valves. **C)** Dynamic testing of a new Delta 2.0 shunt valve.

DISCUSSION

Computational models of brain shunt catheters were developed, and ventricle and CP parameters varied, to determine that they do not play a significant role in catheter performance. Specifically, we determined that a simplified ventricle model will achieve the same catheter outcomes as patient-specific models. It was also determined that catheter flow rates, as well as WSSs, scaled linearly with increasing static ICP but not with pulsatile ICP. Further experimental testing of commercial brain shunt valves displayed significantly different pressure-flow behaviors between new and explanted valves and valves of different types. While the CFD studies did not include valves, future simulations will incorporate their opening and closing behaviors and be validated against the presented experimental data.

REFERENCES

[1] National Hydrocephalus Foundation. http://nhfonline.org/MoreHydrocephalusFacts.pdf
[2] Paff et al. Ventriculoperitoneal shunt complications: a review. Interdisciplinary Neurosurgery. 2018; 13:66–70.
[3] Giménez et al. Pulsatile flow in ventricular catheters for hydrocephalus. Philosophical Transactions of the Royal Society. 2017.

EVALUATION OF SPINE BIOMECHANICS USING MICRO-COMPUTED TOMOGRAPHY

Hutomo Tanoto (1), Yuxiao Zhou (1)

(1) Department of Mechanical Engineering, Texas A&M University, College Station, Texas, USA

INTRODUCTION

The overall prevalence of spine fracture is approximately 30.5% [1]. Due to the complicated structure of spine, its intricate biomechanical function remains inadequately understood. This study focuses on studying the biomechanics of healthy and osteoporosis human spines using a combination of micro-computed tomography and image correlation method, to characterize the 3D (three-dimensional) mechanical deformation inside the vertebrae under axial compressive loads. Investigating the biomechanics of the spine is fundamental to understanding its health and function and provides significant implications for the pathological fragility of the spine affected by various diseases such as osteoporosis.

METHODS

Mechanical testing coupled with micro X-ray computed tomography (**micro-CT**) and digital volume correlation (**DVC**) is a non-contact method that can measure both the structures and 3D full-field internal mechanical deformation vector field in bone under external forces at sub-millimeter resolution. It has been used to measure mechanical strain in engineering materials [2], [3], trabecular bone [4]–[7], knee [8], spine, and shoulder bone [9]. In the PI's prior work, this method was used to study the biomechanics of human shoulder bones [10], bones with rheumatoid arthritis [11], human jaws [12], and to numerically optimize oral surgery procedure [13], [14].

In this study, *ex vivo* mechanical tests were performed on healthy and osteoporosis human cadaveric vertebrae. Each spine was placed inside a loading device (CT5000TEC, Deben, Suffolk, UK), and the loading device was placed inside a micro-CT chamber (NSI Micro-CT System, North Star Imaging Inc., Rogers, MN) (**Figure 1**). A multi-step axial mechanical loading procedure was performed multiple CT scans were collected: no-load (Scan#1)---1000 N---hold---(Scan#2)---2000 N (or fracture)---hold---(Scan#3)---Fracture---hold---(Scan#4). Prior to each scan, the sample will be held in position for 50-minutes to relax bone from viscoelastic effect. A 30-minutes scan with 160 kV, 0.175 mA and aluminum filter will give images with isometric resolution of 25.4 µm. Image segmentation was performed on the micro-CT images using the watershed tool in Avizo 3D analysis software (Thermal Fisher Scientific, Burlington, MA) to digitally remove background and extract only the spine volume in the images. The 3D full-field mechanical deformation in spine was calculated by correlating the corresponding loaded images with images at no-load state (Scan#1) in DaVis software (LaVision Inc., Germany). Mechanical strain was calculated by taking partial derivative of the 3D deformation vector field.

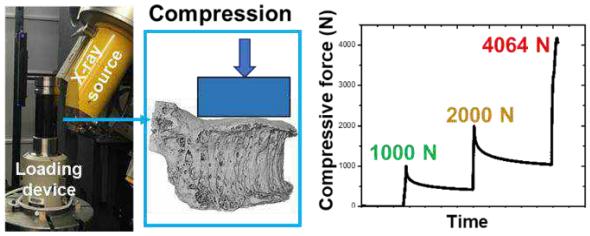

Figure 1: Experiment setup and loading profile.

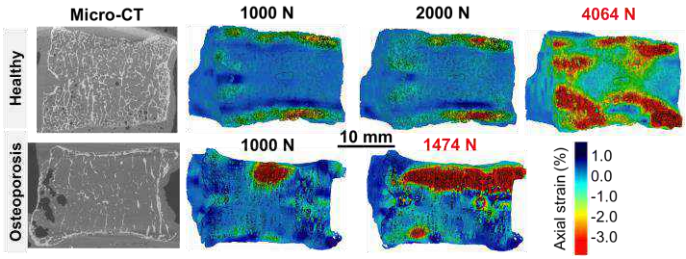

Figure 2: Axial strain distribution in healthy (T9) and osteoporosis (T10) spines.

RESULTS

The axial strain in healthy (T9) and osteoporosis (T10) vertebrae under different mechanical forces were shown in **Figure 2**. Micro-CT image shows reduced thickness and number of trabeculae in osteoporosis bone. The results indicate that under axial compressive loads, strain concentration appeared close to the endplate in both healthy and osteoporosis spine. Both healthy and osteoporosis vertebrae failed in endplate region. In osteoporosis spine, the strain range was much higher than that in healthy spine.

DISCUSSION

The complicated mechanical strain distribution in spine observed in this study is consistent with results in literature [15]–[17]. This is due to the nonhomogeneous distribution of trabeculae structure inside vertebra. This study has some limitations. First, only one vertebra was studied in each group, and a larger number of specimens should be included in future study. Second, we only added compressive mechanical forces to a single vertebra. The physiologically realistic mechanical forces experienced by spine are complicated, and the mechanical reaction in an isolated vertebra is different without the presence of surrounding vertebrae and the intervertebral disc. A more comprehensive study including more vertebrae and multi-axial mechanical loading will help understand the pathological fragility in spine with osteoporosis.

ACKNOWLEDGEMENTS

This research is supported by the J. Mike Walker'66 Department of Mechanical Engineering and the Texas A&M Engineering Experiment Station (TEES). We would also like to thank Dr. Jessie Maisano, Dr. Matthew Colbert, and Mr. David Edey at the Department of Geological Sciences, University of Texas at Austin for their help with micro-CT imaging, and the support from the NSF Division of Earth Science Instrumentation and Facilities Program (NSF EAR-1762458) and NASA (80NSSC23K0199).

REFERENCES

[1] M. T. Löffler *et al.*, "Epidemiology and reporting of osteoporotic vertebral fractures in patients with long-term hospital records based on routine clinical CT imaging," *Osteoporos. Int.*, vol. 33, no. 3, p. 685, Mar. 2022, doi: 10.1007/S00198-021-06169-X.

[2] B. P. Croom *et al.*, "Damage mechanisms in elastomeric foam composites: Multiscale X-ray computed tomography and finite element analyses," *Compos. Sci. Technol.*, vol. 169, no. November 2018, pp. 195–202, Jan. 2019, doi: 10.1016/j.compscitech.2018.11.025.

[3] M. Mehdikhani *et al.*, "Digital volume correlation for meso/micro in-situ damage analysis in carbon fiber reinforced composites," *Compos. Sci. Technol.*, vol. 213, p. 108944, Sep. 2021, doi: 10.1016/J.COMPSCITECH.2021.108944.

[4] O. Jiroušek, I. Jandejsek, and D. Vavřík, "Evaluation of strain field in microstructures using micro-CT and digital volume correlation," *J. Instrum.*, vol. 6, no. 01, pp. C01039–C01039, Jan. 2011, doi: 10.1088/1748-0221/6/01/C01039.

[5] B. K. Bay, T. S. Smith, D. P. Fyhrie, and M. Saad, "Digital Volume Correlation : Three-dimensional Strain Mapping Using X-ray Tomography," *Exp. Mech.*, vol. 39, no. 3, pp. 217–226, 1999, doi: https://doi.org/10.1007/BF02323555.

[6] E. Verhulp, B. Van Rietbergen, and R. Huiskes, "A three-dimensional digital image correlation technique for strain measurements in microstructures," *Exp. Mech.*, vol. 37, pp. 1313–1320, 2004, doi: 10.1016/j.jbiomech.2003.12.036.

[7] R. Zauel, Y. N. Yeni, B. K. Bay, X. N. Dong, and D. P. Fyhrie, "Comparison of the linear finite element prediction of deformation and strain of human cancellous bone to 3D digital volume correlation measurements.," *J. Biomech. Eng.*, vol. 128, no. 1, pp. 1–6, Feb. 2006, doi: 10.1115/1.2146001.

[8] S. Rapagna *et al.*, "Quantification of human bone microarchitecture damage in press-fit femoral knee implantation using HR-pQCT and digital volume correlation," *J. Mech. Behav. Biomed. Mater.*, vol. 97, pp. 278–287, Sep. 2019, doi: 10.1016/J.JMBBM.2019.04.054.

[9] J. Kusins, N. Knowles, M. Ryan, E. Dall'Ara, and L. Ferreira, "Performance of QCT-Derived scapula finite element models in predicting local displacements using digital volume correlation," *J. Mech. Behav. Biomed. Mater.*, vol. 97, pp. 339–345, Sep. 2019, doi: 10.1016/j.jmbbm.2019.05.021.

[10] Y. Zhou, C. Gong, G. S. Lewis, A. D. Armstrong, and J. Du, "3D full-field biomechanical testing of a glenoid before and after implant placement," *Extrem. Mech. Lett.*, vol. 35, p. 100614, Feb. 2020, doi: 10.1016/j.eml.2019.100614.

[11] Y. Zhou, J. Dang, Y. Chen, S. G. Zheng, and J. Du, "Microstructure and mechanical behaviors of tibia for collagen-induced arthritic mice treated with gingiva-derived mesenchymal stem cells," *J. Mech. Behav. Biomed. Mater.*, vol. 124, p. 104719, Dec. 2021, doi: 10.1016/J.JMBBM.2021.104719.

[12] Y. Zhou, C. Gong, M. Hossaini-Zadeh, and J. Du, "3D full-field strain in bone-implant and bone-tooth constructs and their morphological influential factors," *J. Mech. Behav. Biomed. Mater.*, vol. 110, p. 103858, Oct. 2020, doi: 10.1016/j.jmbbm.2020.103858.

[13] Q. Mao, K. Su, Y. Zhou, M. Hossaini-Zadeh, G. S. Lewis, and J. Du, "Voxel-based micro-finite element analysis of dental implants in a human cadaveric mandible: Tissue modulus assignment and sensitivity analyses," *J. Mech. Behav. Biomed. Mater.*, vol. 94, pp. 229–237, Jun. 2019, doi: 10.1016/j.jmbbm.2019.03.008.

[14] K. Su, Y. Zhou, M. Hossaini-Zadeh, and J. Du, "Effects of implant buccal distance on peri-implant strain: A Micro-CT based finite element analysis," *J. Mech. Behav. Biomed. Mater.*, 2021, doi: 10.1016/j.jmbbm.2021.104325.

[15] A. I. Hussein, P. E. Barbone, and E. F. Morgan, "Digital Volume Correlation for Study of the Mechanics of Whole Bones," *Procedia IUTAM*, vol. 4, pp. 116–125, 2012, doi: 10.1016/j.piutam.2012.05.013.

[16] M. Palanca *et al.*, "Digital volume correlation can be used to estimate local strains in natural and augmented vertebrae: An organ-level study," *J. Biomech.*, vol. 49, no. 16, pp. 3882–3890, Dec. 2016, doi: 10.1016/J.JBIOMECH.2016.10.018.

[17] M. Palanca, G. Cavazzoni, and E. Dall'Ara, "The role of bone metastases on the mechanical competence of human vertebrae," *Bone*, vol. 173, p. 116814, Aug. 2023, doi: 10.1016/J.BONE.2023.116814.

NOVEL MRI PHANTOMS FOR INVESTIGATING SKULL-BRAIN MECHANICS USING MAGNETIC RESONANCE ELASTOGRAPHY

J. Mojumder (1), S. Vidhate (2), Y.-C. Lu (1,3), A. Diano (4), A. Alshareef (5), C. Johnson (4), M. Tartis, (6), J. Butman (1), D. Pham (1,7)

(1) Department of Radiology and Imaging Sciences, National Institutes of Health, Bethesda, MD, US
(2) Intuitive Surgical, Inc., Sunnyvale, CA, US
(3) Military Traumatic Brain Injury Initiative, The Henry M. Jackson Foundation, Bethesda, MD, USA
(4) Department of Biomedical Engineering, University of Delaware, Newark, DE, US
(5) Department of Mechanical Engineering, University of South Carolina, Columbia, SC, US
(6) Department of Chemical Engineering, New Mexico Institute of Mining and Technology, Socorro, NM, US
(7) Radiology and Radiological Sciences, Uniformed Services University, Bethesda, MD, US

INTRODUCTION

Traumatic brain injury (TBI) is a leading cause of death and disability worldwide, affecting an estimated 10 million people annually, including both civilians and military personnel. TBI results from rapid brain tissue deformation, typically in response to an impact applied to the head. Recent research employing magnetic resonance imaging (MRI) has revealed that damage to the interface between the brain and skull occurs frequently because of TBI [1]. However, the precise transmission of motion from the skull through the interface to the brain during an impact remains unknown. This is primarily due to the challenges in simultaneously quantifying brain and skull motion in vivo [2]. Recent studies have indicated that the bone marrow of the skull provides excellent signal during non-invasive magnetic resonance elastography (MRE), suggesting its potential utility in quantifying skull-brain motion [3]. However, validation and optimization of MRI and MRE methods for skull-brain measurement is difficult since the motion is not known. Physical phantoms offer one approach to validate the methods, but most existing phantom models have been used to simulate only the brain [4]. Because understanding the specific role of boundary conditions between the marrow and brain layers is essential to validate the accuracy in characterizing the biomechanical relationship between the skull and brain, we created two phantom models to assess MRI investigations related to the mechanics of the skull-brain interface.

METHODS

Our biofidelic MRI brain phantom, namely, the skull-brain phantom (SBP), was developed using a cylindrical container, where the inside of the mold represents the brain region and the cavities inside the wall represent marrow within the skull (**Fig. 1a**). Because the amount of marrow is not uniform throughout the medullar cavity region of skull, the cavities representing marrow in the phantom were divided into eight slots. The inner brain region was filled with polyacrylamide (PAA) gel and the skull slots were filled with 100% fat and 50% fat solution at adjacent slots in alternating fashion. Two different boundary conditions were implemented in the brain region: 1) attached boundary condition, where the PAA gel sticks to the container wall ("SBPa") and 2) unattached boundary wall, where the gel had a smaller diameter and the container wall was covered with Teflon tape, preventing the gel from adhering with container wall ("SBPu"). In the mold fabrication process, two identical cylindrical molds (outer diameter: 12.2cm; inner diameter: 10.16cm; length: 20.32cm) were 3D printed using Acrylonitrile butadiene styrene (ABS) plastic for both SBP models. The bottom end caps had protrusions to fix the gel in the mold at that end, while the gel was kept free at the top end. To make it air-tight, the mold end was covered with a silicone gasket followed with an acrylic endcap tightened by nylon screws. A complete fabricated mold is shown in **Fig. 1b**.

The process of gel fabrication for these phantom models was modified from methods previously reported in the literature [4] to prevent swelling. PAA gel was used as a brain tissue simulant due to its easily tunable material properties at room temperature fabrication. PAA was the product of the cross-linking of two monomers, Acrylamide and Methylene-bis-Acrylamide (MBA). Briefly, 150.0 g of acrylamide (purity ≥ 98.0%) was dissolved in 1500 mL deionized water in a vacuum flask at room temperature to generate a 10% (weight/volume) solution. After the acrylamide was fully dissolved, 10 g of *N,N′*-methylene-bis-acrylamide (MBA, purity 99%) was added. Once the solution was homogenized, 1.30 g of ammonium persulfate was added to initiate the crosslinking of the two monomers of acrylamide. At these steps, the air was vacuumed inside the flask before and during stirring the solution. Finally, upon the addition of 2.667 ml of *N,N,N′,N′*-tetramethylethylenediamine (TEMED, purity 99%), the solution was poured immediately into the brain region of the molds following the addition of TEMED.

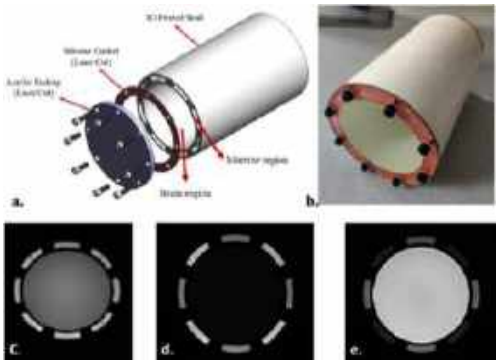

Figure 1: a) Schematic of SBP mold, b) Fabricated mold, c) T1-weighted image, d) and e) Dixon image showing fat and water in the mold correspondingly.

For the marrow, we used 100% fat and a 50% fat-water emulsion in alternating slots for both phantoms. For 100% fat, we used Crisco (Proctor and Gamble, Cincinnati, OH) vegetable shortening. The recipe of 50% fat-water emulsion was modified from previous methods [5]. For the water component, we used 10% (weight/volume) PAA solution with 200 mL deionized water and respective proportion of chemicals, as described above. For the fat component, 2 ml of Span80 (Polyoxyethylene (80) sorbitan monooleate) was added with 200 ml of peanut oil and stirred at 150°C 1100 rpm for 5 minutes. The oil solution was slowly added to the PAA solution (50 – 50 fat water mixture) at room temperature. Finally, 3.6 ml of TEMED was added to the solution while it was stirred at 200rpm. After homogenizing through stirring, the mixture was poured in the marrow slots of the SBPs.

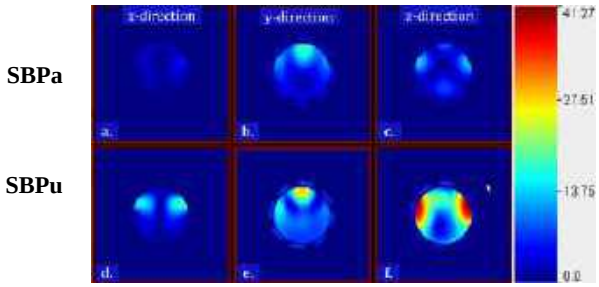

Figure 2: Displacement (μm) in x, y, z direction shown for SBPa phantom l (a-c) and SBPu (d-f) for 50 Hz.

MRE experiments were employed for preliminary testing. The phantoms were placed on a soft "pillow" driver attached to a pneumatic actuator system (Resoundant Inc., Rochester, MN, USA) with the long axis approximately parallel to the bore of the scanner. The pillow applied an excitation in the "anterior-posterior" (AP) direction, which was orthogonal to the long-axis, represented as the y-axis in all images. Using a multi-shot spiral imaging sequence designed for fat-water analysis [6], MRE displacement data were acquired in five slices for three separate scans at 30, 50, and 70 Hz, with 2.5 mm isotropic imaging resolution and the following acquisition parameters: FOV = 120×120 mm, slice thickness = 5mm, phase offset = 4, motion encoding gradient = 21.5mT/m, 2mT/m. All imaging data were acquired on a Siemens 3T Prisma MRI scanner with a 20-channel head/neck coil. MRI data processing was performed in MATLAB R2020a (MathWorks, MA, USA) to compute pixel-wise total displacements from the phase of one period of motion across the phase offsets for the simulated brain and marrow compartments. To investigate the effect of boundary conditions, *motion transmission* was computed as the ratio of average displacement in marrow regions to the average displacement in the brain.

RESULTS

A T1-weighted image for a SBPa is shown in **Fig. 1c**. A Dixon MRI sequence [7], which separates fat and water components, was also applied to visualize the brain and marrow simulants (**Fig. 1d, 1e**). As expected, the marrow slots containing 100% fat exhibited a brighter signal in the fat component images, and the fat-water emulsion slots were visible on both fat and water images. The displacement components at 50Hz (**Fig. 2)** showed a similar pattern in both phantoms with an increase magnitude in SBPu compared to SBPa. **Fig. 3** shows the total displacement in both phantoms at different frequencies for a central slice. Minimal displacement was also observed in regions with fat. The motion transmission was plotted along different frequencies in **Fig. 4**. While there is a reduction in relative displacement with increasing frequencies is shown in SBPa (from 30 Hz to 70 Hz) and SBPu (from 30 Hz to 50 Hz), the relative displacement increased at 70 Hz for SBPu, likely due to the lack of time to transmit motion at higher frequencies.

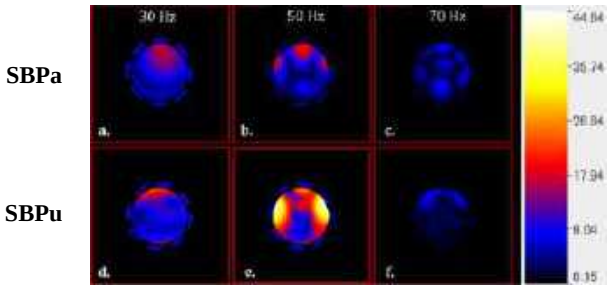

Figure 3: Displacement (μm) shown for SBPa (a-c) and SBPu (d-f) in a central slice for 30, 50 and 70 Hz.

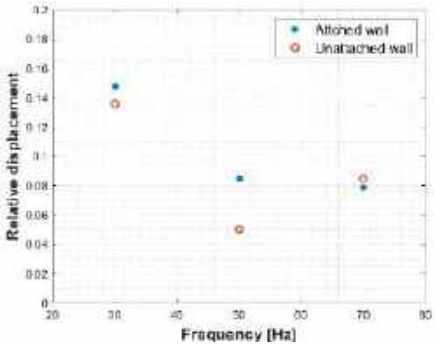

Figure 4: Relative displacement between marrow and brain region showing the effect of boundary conditions at 30, 50 and 70 Hz.

DISCUSSION

The transmission of harmonic motion was studied using two different phantom models for different frequencies, and the results suggest that the relative transmission of motion was higher with an attached wall compared to the unattached wall. Due to the lack of attachment to the container wall, the oscillation imparted more motion in the SBPu model at lower frequencies. In addition, the pattern of displacement was different at different harmonic frequencies, suggesting a frequency dependency in the motion of the PAA gel representing brain. The developed phantoms will allow investigations into alternative metrics and acquisition techniques to maximize sensitivity to changes in skull-brain interface that can subsequently be used for clinical research. In addition, these data could be further used to investigate the change in viscoelastic properties of the material.

ACKNOWLEDGEMENTS

This work was partially supported by grant NIH U01 NS112120, the Department of Defense in the Center for Neuroscience and Regenerative Medicine, and the intramural research program of the NIH Clinical Center through the Bench-to-Bedside program. The opinions and assertions expressed herein are those of the authors and do not reflect the official policy or position of the Uniformed Services University of the Health Sciences or the Department of Defense.

REFERENCES

1. Turtzo, LC et al, Brain Commun, 2(2): fcaa143, 2020.
2. Feng Y, et al J R Soc Interface, 7(53):1677-88, 2010.
3. Yin Z, et al Magn Reson Med, 80(6):2573-2585, 2018.
4. Knutsen, A.K. et al, J of Mec Beh of Bio Mat, V 138, 2023.
5. Bush, E. C., et al *J. Vis. Exp.* (139), (2018).
6. Diano, AM et al. ISMRM 2023. Toronto, ON
7. Van Vucht, N., et al. Skeletal Radiol **48**, 1861–1874 (2019).

METHOD FOR EXTRACTING INTACT SKULL-BRAIN SAMPLES FOR EX-VIVO MECHANICAL TESTING

Brandon P. Chelstrom (1), Corinne R. Henak (1,2,3)

(1) Department of Biomedical Engineering, University of Wisconsin-Madison, Madison, WI
(2) Department of Mechanical Engineering, University of Wisconsin-Madison, Madison, WI
(3) Department of Orthopedics and Rehabilitation, University of Wisconsin-Madison, Madison, WI

INTRODUCTION

Traumatic brain injury (TBI) results from trauma to the head causing mechanical damage to the brain tissue. While TBI fatalities have remained constant at 18.5 per 100,000 since 2010, TBI hospitalization rates have tripled from roughly 70,000 in 2006[1] to over 210,000 in 2020[2], disproportionally affecting youth athletes (largely unreported[3]), elderly populations (32% of hospitalizations in 2020[2]), and military personal (40-60% of deployed service members[4]). Therefore, while the efforts to reduce TBI related deaths have been largely successful, further research is required to understand nonfatal injuries. A range of complex physical symptoms including loss of consciousness, headache, nausea, and dizziness[5] require coupling head-level mechanical loading, tissue-level mechanics, and ultimately cellular-level (axonal) strains to understand TBI[6].

A critical tool in this process is finite element (FE) modeling, which predicts cellular-level strains by accurately modeling the organ- and tissue-level response of the brain to load. Boundaries and interfaces, including connections between adjacent tissue types, dramatically affect model prediction accuracy. The complex anatomy of the brain gives rise to multiple interfaces between adjacent types of thin, interfacial tissues, such as the meninges (Fig 1). Previous FE models have focused on the cortex and skull, often neglecting[7,8] or treating the meninges as a simple, uniform tissue[6,9,10] with material behavior based on isolated tissues.

However, obtaining intact samples of the skull-brain interface for *ex-vivo* mechanical testing has proved difficult[11] due to the immense stiffness gradient from the skull (G = 1.38 GPa[12]) to the cortex (G = 1.43 kPa[13]). During dissection, the outer most layer of the meninges (dura mater) tends to separate from the skull due highly organized collagenous sheets[14], while the inner most layer (pia mater) tends to separate from the cortex since it is often only a single cell thick[14] (Fig. 1). The challenge in maintaining intact tissues is exacerbated by an average meningeal thickness of 500 µm in humans (300 µm in pigs) and a significant amount of fluid flow through the arachnoid mater.

Therefore, the objective of this study was to demonstrate a method for obtaining intact samples of the skull-brain interface for *ex-vivo* mechanical testing.

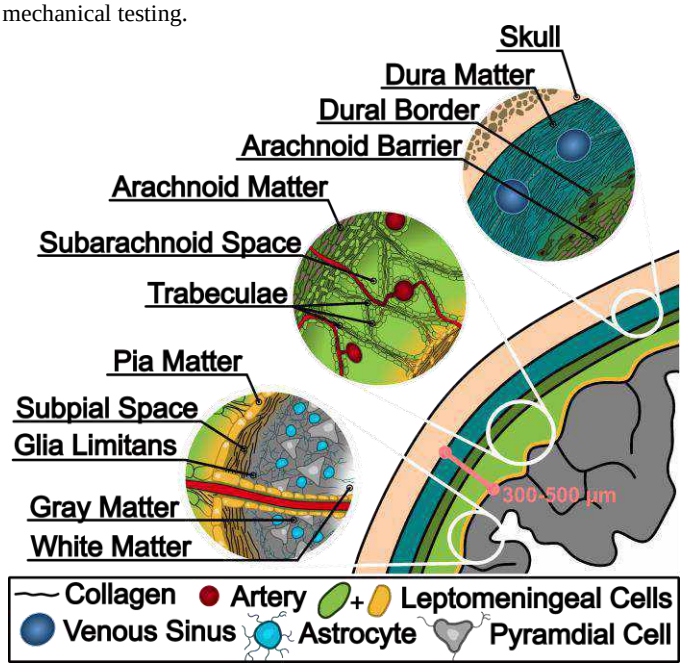

Figure 1: Skull-brain interface anatomy highlighting the dura mater, arachnoid mater, and pia mater that make up the meninges.

METHODS

Porcine heads were collected from the Swine Research and Teaching Center (SRTC), Arlington, WI. Tissue was collected from skeletally mature animals (n = 2, Female, 2.5 and 4 years) from another

study (IACUC #A006267-R01-A01) and were sacrificed via penetrating captive bolt. The most superior portion of the brain was not affected by the bolt. The porcine heads were separated between the occipital bone and first cervical vertebra, creating an access plane at the most caudal part of the mandibles and occipital bone (Fig 2A). Tissue was collected within 1 hr of sacrifice, transported (1 hr) on ice, and stored at -20°C before sample collection. While the effect of post-mortem stiffening[15] and temperature[16] on cortex and meningeal mechanics have been thoroughly investigated, the tissue was used to demonstrate a sample collection procedure, and the freezing step can be eliminated in future testing.

The skull was exposed by cutting through the soft tissue starting lateral to the caudal occipital bone and cutting to the dorsorostral parietal bone (Fig 2B). Using an 18 TPI reciprocating saw, part of the mandible, temporal bone, and zygomatic bone were removed with a horizontal cut parallel with the most ventral point of the eye socket. The outer periosteum of the remaining temporal bone and parietal bone was removed with scalpel and forceps to reduce potential clogging of the bone saw blade. Using a 36 TPI stainless steel bone saw at 100-200 RPM, the temporal and parietal bones were gently ground away until the dura was exposed (Fig 2B).

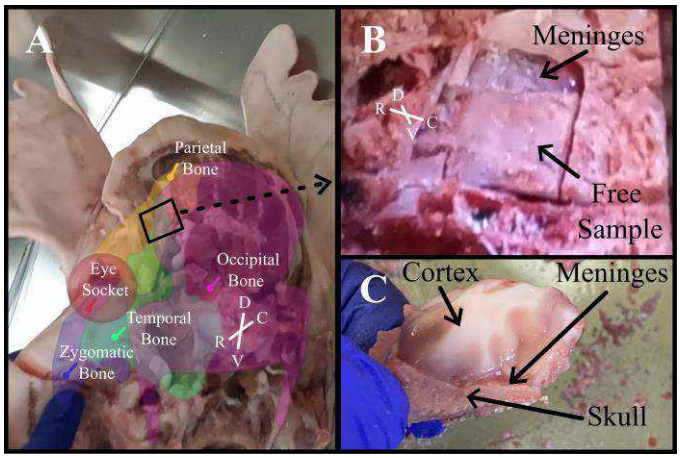

Figure 2: Diagram of (A) cut plane with bones indicated for reference, (B) separated skull, and (C) final removed sample (marked as the box in A). Dorsal (D)-Ventral (V) and Caudal (C)-Rostral (R) axes are shown for reference.

Two sets of orthogonal parallel cuts were made ~30 mm apart next to the exposed dura (Fig 2B), using the thickness of the skull as a reference for cut depth. The dura directly below the cuts often separated from the skull; therefore, the disconnected portions of the freed skull were slowly ground away until only the connected portions remained. The meninges and cortex were cut using a scalpel beginning ~10 mm away from the sample and moving towards the sample area to avoid skull-dura separation. A scalpel was inserted in the occipital bone spinal column entrance to make a horizonal cut ~20 mm inferior to the most dorsal surface of the cortex. To remove the sample from the head, forceps grasped the free skull end to gentle pull upwards while the inserted scalpel gentle pressed upwards on the cortex.

The weight of the cortex was enough to cause separation at the skull-dura and pia-cortex interface (Fig 3C). Therefore, a simple proof-of-concept separation test was captured via highspeed camera (Phantom V211 at 100 FPS). The sample was gripped with the skull superior to the cortex, allowing the weight of the cortex to naturally separate the interface.

RESULTS

After development of the extraction method, 2 of 3 attempts resulted in samples. Throughout the separation test, multiple portions of the skull-dura and pia-cortex interface failed. An isolated portion of the pia-cortex interface is shown in Figure 3 where a clear separation was visible over 600 ms. Separation began at the most superior portion of the interface (Fig. 3B) and continued downwards (Fig. 3C) until a new equilibrium was established (Fig. 3D).

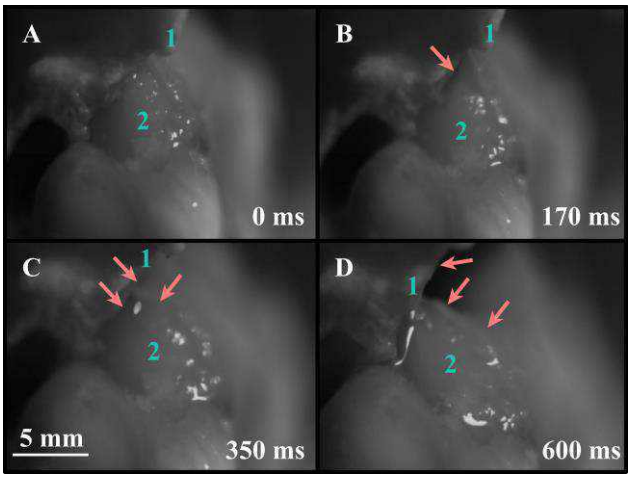

Figure 3: Separation between meninges (1) and cortex (2). (A) Intact boundary, (B) initiation of separation at red arrow, (C) progression of separation at red arrows, and (D) final equilibrium after separation.

DISCUSSION

This study provides a method for extracting intact skull-brain interface samples for *ex-vivo* mechanical testing. Preliminary mechanical tests indicate that adjacent layers were connected upon extraction and separated after an applied load (Fig. 3). The sample tended to separate at the dura-skull interface compared to the pia-cortex interface. Internal separation of the meninges could not be observed.

Future research will develop steps to obtain smaller samples (10 mm x 10 mm) with less cortical tissue (~10 mm) to reduce natural separation due to the weight of the cortex. Once separated, a phosphate-buffered saline (PBS) drip will be used to maintain cortical tissue hydration and minimize adhesion of the cortical tissue and scalpel. Finally, a wider paddle instead of a scalpel will be used to support the bottom of the sample during the final removal step. In conclusion, this study presents a novel method for extracting intact samples of the skull-brain interface that can be used for *ex-vivo* mechanical testing.

ACKNOWLEDGEMENTS: This material is based upon research supported by the U. S. Office of Naval Research under PANTHER award number N000423SB001 through Dr. Timothy Bentley. Tissue from the SRTC is gratefully acknowledged.

REFERENCES: [1] CDC, *Surveillance Report*, 2010. [2] CDC, *TBI Data*, 2023. [3] Bell+, *J. Safety Research*, 2017. [4] Ling+, *Neurotrauma, 2009.* [5] VA/DoD, *J. Rehabil. Res. Dev.*, 2009. [6] Wright+, *J. Neurotrauma*, 2013. [7] Al-Bsharat+, *43rd Stapp Car Crash Conf. Prec.*, 1999. [8] Brands, *Technische Universiteit Eindhoven*, 2002. [9] Calrsen+, *Brain Multiphysics*, 2021. [10] MacManus+, *Acta Biomater*, 2017. [11] Agrawal+, *Comp Biomech Med*, 2015. [12] Lillie+, *J. Bone. & Min.*, 2016. [13] Budday+, *J. Mech. Behav. Biomed. Mat.*, 2015. [14] Gray+, *Gray's Anatomy*, 1995. [15] Exton+, *Sci. Reports*, 2023. [16] Peter+, *Biorheology*, 1997.

INJECTABLE SYNTHETIC PLATELET-BASED THERAPY ENHANCES CLOT FORMATION IN SYNOVIAL FLUID JOINT INJURY MODEL

Melika Osareh (1), Grant Scull (1), Jacob Thompson (1), Ashley C. Brown (1), Matthew B. Fisher (1,2)

(1) Joint Department of Biomedical Engineering, North Carolina State University and University of North Carolina at Chapel Hill, Raleigh, NC, USA
(2) Department of Orthopaedics, University of North Carolina at Chapel Hill, Chapel Hill, NC, USA

INTRODUCTION

Anterior cruciate ligament (ACL) injuries can occur due to sports or other activities and constitute a major clinical problem, affecting about 200,000 people annually in the United States.[1] While extra-articular injuries of the joint, such as medial collateral ligament (MCL) injuries, are able to heal, intra-articular injuries, such as ACL injuries, have a limited healing capacity. This is believed to be due, in part, to the proteolytic environment of the synovial fluid (SF) surrounding the ligament and the low presence of necessary clotting factors such as fibrinogen and thrombin hindering the healing process by not allowing fibrin scaffolds to form (Fig. 1A).[2, 3] During early healing, platelets interact with fibrin to form a clot at the injury site and to attract cells (Fig. 1B).[4] Fibrin-based therapies have been investigated to enhance healing in the joint but lack the ability to maintain stable clots for cell infiltration in proteolytic environments like SF.[2] Additionally, SF is known to become less viscous due to overproduction of proteases upon joint injury which may further reduce the ability of clots to form and healing ability to occur.[5] Novel synthetic platelet-like-particles (PLPs), made with fibrin-binding motifs coupled to ultra-low crosslinked (ULC) poly(N-isopropylacrylamide) microgels, are highly deformable and have been shown to induce stable fibrin clotting and fibrin scaffold retraction by mimicking natural activated platelets in plasma.[6] Prior work has indicated that incorporation of PLPs in addition to fibrinogen and thrombin into synovial fluid can induce ideal levels of clotting and can further promote fibrin stability.[7] **The objective of this study is to assess clot-forming ability of PLPs in a low-viscosity SF joint injury model and a high viscosity healthy SF model. We hypothesized that PLPs can improve mature and stable clotting in low viscosity SF.**

METHODS

Pooled porcine synovial fluid collected from 6-9-month old male and female pigs (Innovative Research, Inc) were used to assess clot formation. Clots were formed on glass slides using a solution of 70% (v/v) synovial fluid, 1X HEPES buffer, 2 mg/mL purified fibrinogen, and 0.5 U/ml of thrombin. In PLP treatment groups, 0.5 mg/mL PLPs were added to the clot mixture. As previously described, ULC poly-NIPAM-co-acrylic acid particles were coupled to a fibrin fragment-E-targeting antibody to synthesize PLPs.[6] After 2 and 24 hours of polymerization, z-stack images of clots were taken by confocal microscopy (Zeiss 880). Images were analyzed for fibrin density and fibrin branching using ImageJ by quantifying black to white pixel ratio and maximum number of branches per fiber, respectively, as compared to a SF + fibrinogen-thrombin (FT) clot control. The clot mechanics of each group was assessed under oscillation using an Anton-Paar MCR 92 rheometer (1% shear strain, 1 Hz frequency, 25°C, 15 hours). Low viscosity (LV) SF, representative of an injured joint, and high viscosity (HV) SF, modeling a healthy joint, with clotting factors were compared to those with added PLPs at various concentrations.

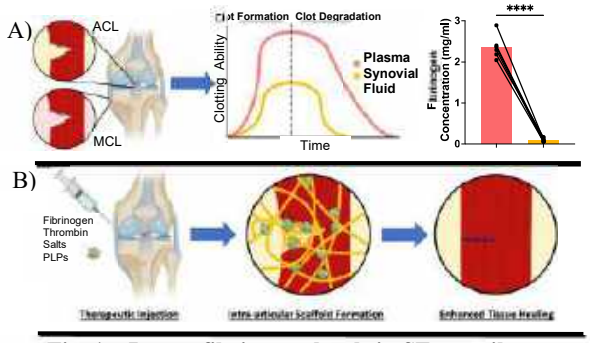

Fig. 1 – Lower fibrinogen levels in SF contribute to improper clotting (A). The therapeutic mechanism of action of PLPs combined with clotting factors are shown for ACL injury healing (B). ****=p<0.0001

To create low viscosity SF (injury model), 10 μg/ml of

hyaluronidase was mixed into high viscosity (healthy) SF and incubated in a water bath (37°C) for 1 hour. Afterwards, the same procedure as non-treated SF was used for inducing clotting and performing analyses comparing naturally low and high viscosity SF to the treated SF with and without PLPs.

To check if the studied FT matrix allows prolonged cell retention and activity, bovine fetal mesenchymal stem cells (MSCs) were seeded onto FT and FT+PLP clots at 0.5 mg/ml PLPs. Confocal z-stack images were taken after day 1 and 6. An alamarBlue metabolic activity assay was performed after 21 days.

A one or two-way ANOVA test (depending on groups), followed by Tukey's multiple comparison's test, was used to determine statistical significance between groups (alpha=0.05).

RESULTS

The addition of clotting factors (fibrinogen and thrombin) induced clotting in synovial fluid within 2 hours as determined by significantly higher scaffold density analysis (Fig. 2A). Notably, the addition of at least 1.0 mg/ml PLPs resulted in significantly higher scaffold density and branching in LV SF compared to SF+FT. However, adding PLPs to high viscosity (HV) SF showed no further significant clotting after the addition of clotting factors. Rheological testing also indicated significantly higher maximum shear storage modulus achieved by adding PLPs to LV SF + FT and lower overall time to reach maximum stiffness and clot degradation in LV SF than HV SF (Fig. 2B).

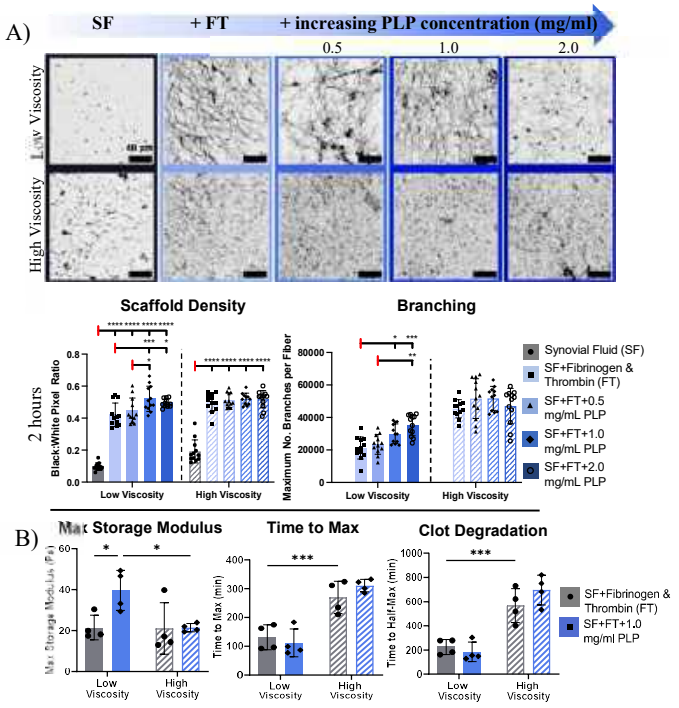

Fig. 2 – Effect of fibrinogen and thrombin (FT) with doses of PLPs on clot formation within low and high viscosity SF. Confocal z-stack images of clots taken 2 after polymerization with scaffold density and fibrin branching analyzed (A). Rheological analysis of clots +/- PLPs over 15 hours (B). *=p<0.05; **=p<0.01, ***=p<0.001; ****=p<0.0001

The addition of hyaluronidase to high viscosity SF achieved similar scaffold density to naturally LV SF and significantly lower maximum storage modulus than before treatment (Fig. 3A). Treated SF with clotting factors FT was visibly less dense than non-treated HV SF, more similar to LV SF (Fig. 3B). Scaffold density and branching analysis showed the significant effect of PLPs in increasing scaffold density and branching in hyaluronidase-treated SF but not in naturally HV SF (Fig. 3C.) Additionally, FT and FT PLP clots were shown to support cell retention and metabolic activity for the length of the cell study (21 days, data not shown).

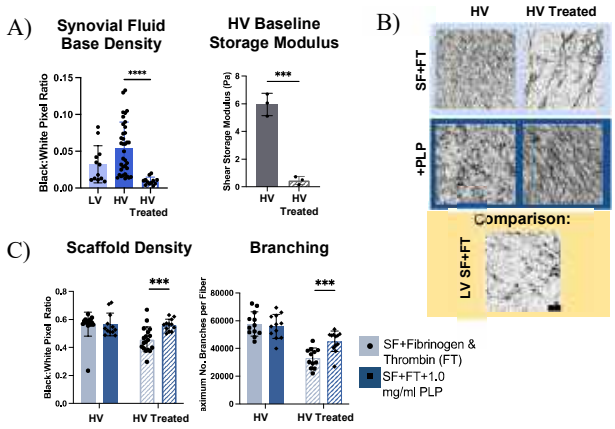

Fig. 3: Hyaluronidase (HAase) treated HV SF acts as a joint injury model comparable to LV SF. Characterization compared treated SF to LV and HV SF by confocal scaffold density analysis and rheology (A). Confocal images (2hrs) of clots within HV and treated HV SF with clotting factors and 1.0 mg/ml PLPs is compared to LV SF +FT (B) and analyzed (C). ***=p<0.001

DISCUSSION

PLPs, along with clotting factors fibrinogen and thrombin, were able to successfully establish stable fibrin clots in LV SF, simulating a joint injury environment. These results support our hypothesis. PLPs allowed stable fibrin network formation, required to withstand the fibrinolytic environment of the surrounding SF, whereas non-PLP groups were less stiff. Specifically, the addition of at least 1 mg/ml of PLPs was shown to promote denser, highly branched, and more stable clotting in both LV SF and HAase treated SF via scaffold density, branching, and rheological analyses, respectively, within 2 hours of polymerization. Consistent with literature on PLPs in dermal applications[6], it allows initial local stiffness and maintained structure of the scaffold, important in the healing process to allow for cell-infiltration and tissue remodeling. A limitation is that the presence of enzymatic activity within the SF was not measured. However, even for the same SF, lowering the viscosity was able to recreate the experimental findings for the naturally LV SF environment, indicating the potential of the model to simulate some aspects of the joint injury environment. Future studies will explore cell viability and migration rates of cells embedded in a PLP-laden FT scaffold and the ability of this injectable therapeutic to enhance ACL healing in-vivo.

ACKNOWLEDGEMENTS

We acknowledge the funding support of the NIH-T32 (T32GM133366) Molecular Biotechnology Program training grant for Melika Osareh, NIH-T32 Comparative Molecular Medicine training grant (T32GM133393) to Grant Scull and the NSF Graduate Research Fellowship Award to Jacob Thompson in support of this research.

REFERENCES

[1] Herzog, M. M. et al., *Sports Heal.*, 10(6):523–531, 2018. [2] Scull, G. et al., *Med Devices Sens,* 4(1): e10147, 2021. [3] Murray M. M. et al., *J Bone Joint Surg Am*, 82(10):1387-97, 2000. [4] Hou, Y. et al., *J Biomed Res*, 29(6):437-444, 2015. [5] Freeney, E. et al., *J Orthop Res*, 37(5):1071-1079, 2019. [6] Nandi, S. et al., *Biomater Sci,* 7(2): 669–682, 2019. [7] Thompson, J. D. et al., [abstract]. In: *Ortho Res Soc Annual Conf*; 2023 Feb 10-14; Dallas, TX.

EVALUATING THE PERFORMANCE OF EXTENDED KALMAN FILTER VS. UNSCENTED KALMAN FILTER FOR DISPLACEMENT ESTIMATION

N. Mohammadianaftah (1), S. Wilson (1), N. Sharma (2)

(1) Mechanical Engineering, University of Kansas, Lawrence, Kansas, United States
(2) Physical Therapy, Rehabilitation Science, and Athletic Training, University of Kansas Medical Center, Kansas City, Kansas, United States

INTRODUCTION

Lumbar mobilization is a technique that has been used by physical therapists as a standard intervention for lower back pain [1]. It involves a clinician (such as a physical therapist) applying small oscillatory motion to the lumbar spine. These motions are categorized into four grades [2]. The levels of mobilization are distinguished by both the range of oscillation amplitudes and the maximum displacement [3]. The therapist places the pisiform surface of their hand or both thumbs over the selected spinous process of the patient's lumbar spine. The double-handed grip used for manual manipulation provides better control and precision during mobilization. While spinal mobilization is pivotal in the realm of physical therapy, it relies on subjective assessment of the motion by the clinician. This can result in variability that can impact the effectiveness of the treatment and make it difficult to train students in the techniques.

An inertial measurement unit (IMU) is a small and inexpensive device that can be used to quantify lumbar mobilization [4]. IMUs contain a 3-axis of an accelerometer, a 3-axis of a gyroscope, and a 3-axis of a magnetometer that can capture the small, oscillatory, hand motions. To determine hand orientation and displacement fusion of the data from these sensors is required using different filtering techniques such as a Kalman Filter [5]. In this research, the use of an Extended Kalman Filter and an Unscented Kalman Filter were compared to Bias-corrected Integrated Acceleration for sensor fusion of the IMU data.

METHODS

For this study, an Arduino Nano BLE Sense microcontroller connected to the inertial measurement unit (Adafruit Absolute Orientation Sensor, BNO055). A circuit board is designed to integrate with the hand wrap device shown in Figure 1. The IMU's displacement can be determined by double integrating of the acceleration data over time. However, this integration process is susceptible to signal drift owing to signal noise. To mitigate this issue, filtering techniques such as Kalman Filter are employed on the IMU data. The Kalman Filter leverages a mathematical model and IMU sensor measurements to real-time estimate the system's state. For these calculations, the rotation around three axes of a Cartesian frame $R_x(\varphi), R_y(\theta), R_z(\Psi)$ are defined in the body frame of the hand in local North-East-Down (NED) coordinate system.

Figure 1: Hand wrap prototype

Extended Kalman Filter (EKF)

The Kalman estimator is designed to determine the position vector in a two-dimensional Cartesian coordinate by updating the Kalman state vector recursively. The state vector, denoted as X, is represented as a 6-by-1 column vector, encompassing position components (x and y), velocity components (V_x and V_y), and acceleration components (a_x and a_y).

$$X = \begin{bmatrix} x \\ y \\ V_x \\ V_y \\ a_x \\ a_y \end{bmatrix} \quad (1)$$

The state model is based on the classical laws of motion.

$$x = x_0 + V_x.dt \quad (1)$$
$$y = y_0 + V_y.dt \quad (3)$$
$$V_x = V_{x0} + a_x.dt \quad (4)$$
$$V_y = V_{y0} + a_y.dt \quad (5)$$

The filter algorithm is assumed to be a discrete time linear dynamic system that can be represented by the state space model:

$$x_k = F_k x_{k-1} + B_k u_{k-1} + w_k \quad (6)$$

where F_k is the state matrix, B_k is the input matrix, u_k is the control vector and w_k is a zero-mean, gaussian distributed process noise. Please note that since the system is time variant F, B depend on the time k and for LTI systems, they can be assumed to be a constant matrix. The measurement assumed to be a linear function of the state variable shown as:

$$y_k = H_k x_k + v_k \quad (7)$$

where H_k is the measurement matrix and v_k is a zero-mean, gaussian distributed measurement noise and w_k and v_k are mutually independent. A fundamental constraint of the Kalman filter lies in its dependency on both the dynamic system and measurement functions being linear with respect to the state variables. To address this limitation, the extended Kalman filter (EKF) acts as a modified version of the standard Kalman filter, specifically designed to accommodate nonlinearities in either the system or measurement models. The state variable can be written as:

$$x_{k+1} \approx f(\bar{x}_k, u_k) + \frac{\partial f}{\partial x} . (x - \bar{x}_k) + w_k \quad (8)$$

$$y_k \approx h(\bar{x}_k) + \frac{\partial h}{\partial x} . (x - \bar{x}_k) + v_k \quad (9)$$

where $\frac{\partial f}{\partial x}$ is the Jacobian at the current estimate in real time which defines F_k and $\frac{\partial h}{\partial x}$ is the Jacobian which update the covariance estimate.

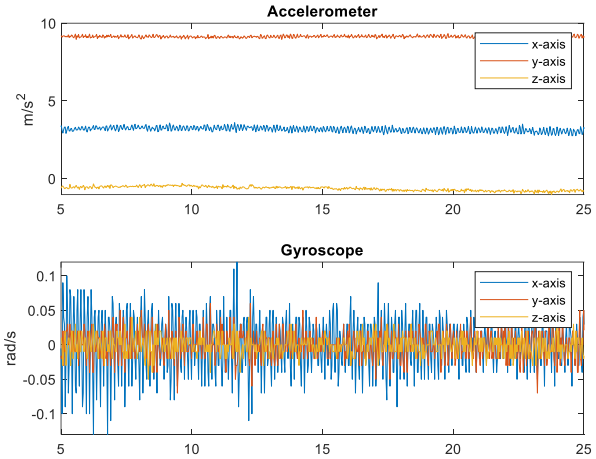

Figure 2 Raw accelerometer and gyroscope data from the IMU during grade III lumbar mobilization. Oscillation is primarily observed in the x axis while some rotation is also observed.

Unscented Kalman Filter (UKF)

An Unscented transform tracks the characteristics of a nonlinear distribution and Unscented Kalman Filter is chosen to find the propagation of the sigma points through the assigned nonlinear functions. The unscented transform is applied at prediction and update steps. The number of sigma points are 2L +1 where L shows the number of the states, and the scaling factors are assumed to be $\lambda = \alpha^2(L + \kappa) - L, \alpha = 10^{-3}, \beta = 2, \kappa = 0.$

The mean and covariance can be computed as

$$\hat{x}_{k|k-1} = \sum_{i=0}^{2n} W_i^{(m)} \hat{x}_{k|k-1}^i \quad (10)$$

$$p_{k|k-1}^x = \sum_{i=0}^{2n} W_i^{(c)} (\hat{x}_{k|k-1}^i - \hat{x}_{k|k-1})(\hat{x}_{k|k-1}^i - \hat{x}_{k|k-1})^T + Q \quad (11)$$

where $W_i^{(m)}, W_i^{(c)}$ are the weights can be found as a function of the scaling factors which contain some prior information about the states. The UKF is derivative-free and gives us second order accuracy.

Integrated Acceleration Data

The two filters were compared to the displacement obtained by the double integration of the raw accelerometer data.

Data Collection and Assessment

Motion data was collected during the grade III lumbar manipulation motions performed by an experienced physical therapist. This data was part of a pilot study on measuring hand movement during lumbar mobilization and was approved by the University of Kansas Medical Center Human Subjects Committee.

RESULTS

The estimation problem was implemented in MATLAB. The sampling frequency of the wearable device was calculated to be 41.25 Hz. Figure 2 shows the raw accelerometer and gyroscope readings from the IMU sensor. Looking at the estimated displacement from these signals, significant drift was observed in the integrated acceleration data after 50 seconds. The UKF filter was found to have some initial large oscillations before obtaining a stable, drift free, assessment of the displacement oscillations. The EKF filter was also found to be largely drift free but appears to have some error in estimating oscillations relative to the integrated accelerometer data over short time windows.

DISCUSSION

While IMUs have the advantage of small size and low cost relative to other motion capture technology, IMUs may not be the first choice for position estimation. Apart from addressing the displacement estimation drift due to integration of acceleration, there are challenges with removing gravitational acceleration readings. These obstacles can be overcome by using high pass filtering and sensor fusion algorithms such as complementary filters, Madgwick filters, or Kalman filters to mitigate the effects of gravitational acceleration and integration drift. This study found that both the Extended Kalman Filter (EKF) and Unscented Kalman Filter (UKF) algorithms can be employed for position estimation. UKF's superior ability to track mean and covariance through a method known as the unscented transform appears to be beneficial in comparison to EKF. Future research will examine the performance of these filters against other of displacement such as motion capture systems.

REFERENCES

[1] Mehyar, F., et al., J of Allied Health, 49(1):20-28, 2020.
[2] Maitland, G.D., Vertebral Manipulation. 1986: Elsevier Health Sciences.
[3] Snodgrass, S.J., J of Manipulative and Physiological Therapeutics, 2006. 29(4): p. 316-329.
[4] Mehyar, F., et al., J of Manipulative and Physiological Therapeutics, 43(2):114-122, 2020.
[5] Jeon, H., et al., IEEE Sensors Journal, 22(23):23188-23199, 2022.

BUBBLER SYSTEM DESIGN FOR REMOVAL OF OXYGEN FROM MEDIA IN AN OPEN TESTING ENVIRONMENT

Margaret H. Capalbo (1), Spencer E. Szczesny (1,2)

(1) Biomedical Engineering, The Pennsylvania State University, University Park, PA, USA
(2) Orthopaedics and Rehabilitation, The Pennsylvania State University, Hershey, PA, USA

INTRODUCTION

Tendinopathy affects approximately 5% of people at some point during their lifetime, but little is known about what causes the disease [1]. Recent data suggest that hypoxia is associated with early tendon degeneration [2]. Additionally, our own recent data from a tendon explant model show that tendon degeneration is induced with fatigue loading only under hypoxic conditions. However, understanding the mechanism linking hypoxia and tendon degeneration is difficult since adjusting oxygen levels for in vitro experiments is usually limited to closed environments (e.g., incubator, microscope enclosure). Specifically in the case of studying tendon degeneration in an explant model, there is a need for a system that can deoxygenate an open in vitro environment to study the relationship between hypoxia, mechanical loading, calcium signaling, etc. This requires a gas bubbler system that is capable of driving oxygen levels in the media bath down from 21% (typical atmospheric concentration) to 8% or even 3%, which are physiologic and hypoxic oxygen levels, respectively, for rodent Achilles tendons [3]. Therefore, the objective of this study was to build and optimize a bubbler system that will bring oxygen levels of the tendon explant environment to 3%.

METHODS

Bubbler System Design: The bubbler consisted of a 1000 ml glass reservoir, two peristaltic pumps, two potentiometers, tubing, and a basin (Fig. 1). A QWORK 1/4" Flare Inlet and Outlet Connection Nitrogen Flow Indicator was used to control the rate of nitrogen flow from a nitrogen gas tank into an opening in the lid of the reservoir to deoxygenate the bottle. The reservoir's lid had a total of four ports; the two with tubing from the pumps and the free port were sealed, while the port with the nitrogen tube was unsealed to allow extracted oxygen and excess nitrogen out of the reservoir. Each pump had the capability of a flow rate up to 150 ml/min and was connected to a 100 Ω potentiometer to control the flow. Tubing with an inner diameter of 3/16" and a length of 30.5" was attached to the inlet and outlet of each pump. The inlet of one pump and the outlet of the other pump were placed in the reservoir with the opposite configuration placed in the basin to create a closed loop system. The Creality Ender-3 3D printer and PLA filament were used for the printing of the testing basin.

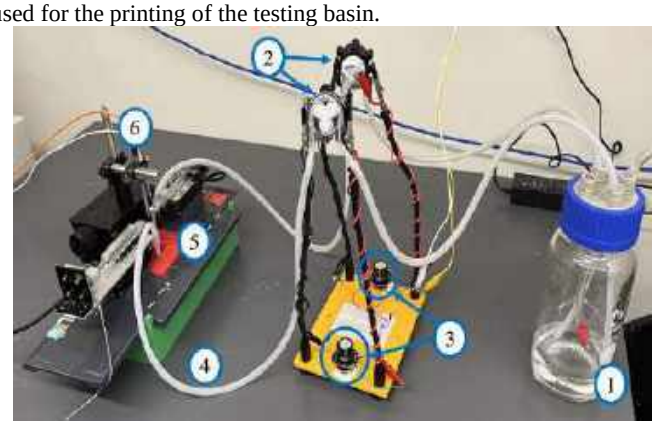

Figure 1: Schematic of the bubbler design: reservoir (1), peristaltic pumps (2), potentiometers (3), tubing (4), basin (5), oxygen and temperature sensors (6). Not pictured: nitrogen tank and flow rate indicator.

Design Optimization: Three flow rates (35, 55, 80 ml/min), three total media volumes (100, 200, 300 ml), and three basin designs were tested to determine the optimal bubbler design. Basin designs were adjusted to provide three different combinations of surface area-to-basin volume ratio and basin-to-total volume ratio (Table 1). A constant flow rate of nitrogen into the reservoir was maintained at 65 cubic feet per hour. Water was added to the reservoir, which was primed for 20 minutes for the water to reach a deoxygenated state at room temperature. A PyroScience OXF1100 oxygen sensor and Pt100 temperature sensor were connected to a FireSting-O2 oxygen meter and placed in the basin to measure the oxygen saturation. The pumps were turned on and

oxygen saturation was collected over 15 min. Between each combination of testing parameters, all water was returned to the reservoir and primed.

Table 1: Properties of experimental basins

	V (ml)	SA (cm^2)	SA:V (cm^2/ml)	V_b:V_t (100 ml)	V_b:V_t (200 ml)	V_b:V_t (300 ml)
1	4.80	6.40	1.33	0.048	0.024	0.016
2	8.80	17.60	2.00	0.088	0.044	0.029
3	6.48	8.10	1.25	0.065	0.032	0.022

Data Analysis and Statistics: Two time points (5 min and 15 min) were chosen to measure the stability of the oxygen concentration in the basin. To account for signal noise, the last 15 sec of data prior to each time point were averaged. Since the measurements received from the oxygen sensor were in terms of oxygen saturation (0 – 100), these values were converted to the percentage partial pressure of oxygen (P) using,

$$P = 21s/100 \quad (1)$$

where s is the oxygen saturation. The effect of the basin volume-to-total system volume (Vb:Vt) on the oxygen levels was tested via a linear regression. All other parameters were tested for significance with a one-way ANOVA followed by Tukey's post-hoc test. Significance was set to $p<0.05$.

RESULTS

Oxygen levels were only significantly affected by the total system media volume (Fig. 2). While oxygen levels were inversely proportional to the basin volume-to-total system media volume ratio (Vb:Vt), the effect was not statistically significant (p=0.12) (Fig. 2A). The oxygen levels with a 200 ml total system volume was significantly lower than 100 ml and 300 ml (Fig. 2C). There was no effect of surface area-to-volume ratio of the basin or pump flow rate on oxygen levels. The lowest oxygen level after 15 min was 2.84%, which was achieved using 200 ml with Basin 1 at a pump flow rate of 80 ml/min (Table 2). In general, the oxygen level increased over time from 5 to 15 min, with a significance difference between the time points.

Table 2: O_2% for Basin 1 in relation to all other parameters

Basin 1	100 (ml)		200 (ml)		300 (ml)	
	5 min	15 min	5 min	15 min	5 min	15 min
35 (ml/min)	7.858	7.273	2.896	4.758	4.281	6.383
55 (ml/min)	4.956	7.551	2.597	3.228	3.792	5.271
80 (ml/min)	7.375	7.344	2.294	2.836	4.576	6.532

Table 3: O_2% for Basin 2 in relation to all other parameters

Basin 2	100 (ml)		200 (ml)		300 (ml)	
	5 min	15 min	5 min	15 min	5 min	15 min
35 (ml/min)	4.938	5.945	3.332	4.124	4.492	6.814
55 (ml/min)	6.976	14.235	3.543	4.390	6.896	9.019
80 (ml/min)	5.890	6.409	3.713	4.421	11.973	11.776

Table 4: O_2% for Basin 3 in relation to all other parameters

Basin 3	100 (ml)		200 (ml)		300 (ml)	
	5 min	15 min	5 min	15 min	5 min	15 min
35 (ml/min)	4.755	5.484	4.911	5.472	5.143	6.426
55 (ml/min)	4.823	5.983	4.970	4.934	7.455	9.685
80 (ml/min)	6.905	8.519	3.772	4.209	4.127	4.448

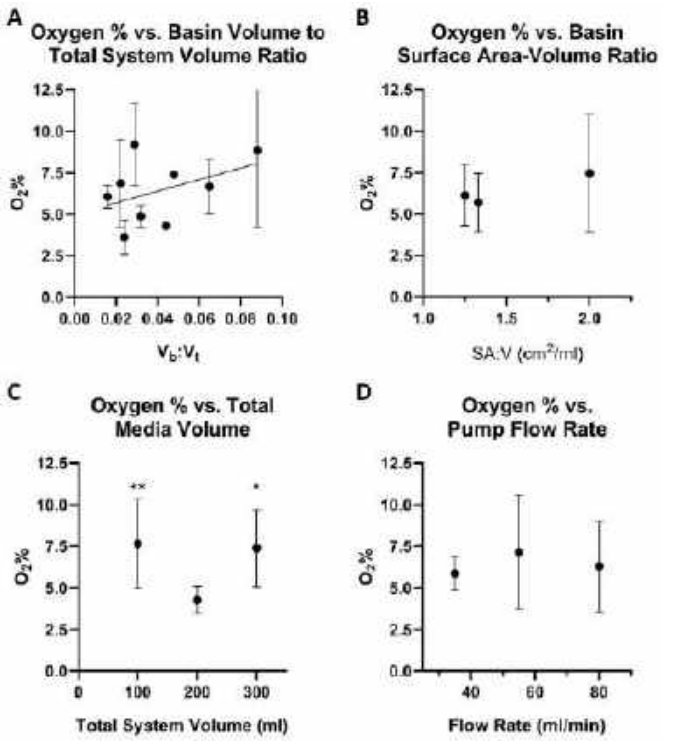

Figure 2: Graphs with means of all data points in relation to a single parameter. A) Basin volume to total system volume ratio. B) Basin surface area to volume ratio. C) Total media volume. (*p<0.05, **p<0.01) D) Pump flow rate.

DISCUSSION

This study presents a simple bubbler system to deoxygenate media in an open environment. The bubbler can reach a minimum oxygen level of 2.84%, which is a hypoxic state for rodent Achilles tendons [3]. Additionally, many combinations grant 8% oxygen, which will enable comparison to physiologic oxygen responses of rodent Achilles tendons [3]. The only factors significantly impacting the oxygen level were total system media volume and time. The optimal total system media volume is 200 ml likely because it is small enough to be easily deoxygenated but large enough to provide a stable reservoir of deoxygenated water. While not statistically significant, the trend toward lower oxygen levels with lower Vb:Vt makes sense since a small basin volume lowers the amount of media exposed to air and allows for reoxygenation. However, it was surprising that the basin surface area-to-volume ratio was not significant, which suggests that the surface area exposed to the atmosphere did not cause enough of an oxygen exchange to alter the oxygen percentage. Still, the fact that the oxygen level increased over time suggests that oxygen was reentering the media. It is unclear if 15 min is sufficient for the system to reach equilibrium, which is important for long experiments. Still, this system will enable experiments requiring oxygen control in an open environment. Therefore, the role of oxygen in tendinopathy as well as possible oxygen treatments can be further investigated with this system.

ACKNOWLEDGEMENTS

This work was supported by funding from the National Science Foundation (CAREER 2142627).

REFERENCES

[1] Kaux, J et al., *J Sports Sci and Med*, 10:238-253, 2010.
[2] Millar, N et al., *Ann Rheum Dis*, 71:302–310, 2012.
[3] Gray, L et al., *J Physiol*, 175:161–171, 1964.

A NOVEL METHOD FOR STUDYING MECHANOTRANSDUCTION: COMPLEX FORCE FREQUENCY APPLICATION USING MAGNETIC VORTEX MICRODISCS

Matthew J. Holler (1), Elena A. Rozhkova (2), Valentine Novosad (3), Scott T. Wood (1)

(1) Nanoscience and Biomedical Engineering, South Dakota Mines, Rapid City, SD, USA
(2) Center for Nanoscale Materials – Argonne National Laboratory, Lemont, IL, USA
(3) Materials Science Division – Argonne National Laboratory, Lemont, IL, USA

INTRODUCTION

The current understanding of how cells respond to static and dynamic mechanical forces, particularly as it relates to mechanotransduction, is limited by the lack of an accurate and reliable way to precisely apply mechanical forces using complex frequency profiles in a research environment.

The primary challenge for this type of research lies in the empirical approach that is widely adopted for determining discrete frequencies of applied forces in mechanotransduction studies. This fails to accurately determine the optimal frequencies for force application and is made even less reliable due to the complex nature of cellular motions and intracellular responses to mechanical stimulation.

A method to precisely apply mechanical forces using physiological frequency profiles would deeply enhance the study of mechanotransduction. This would not only provide further tools to grow the fundamental understanding of cellular biology, but also lay a framework for innovative new therapeutic strategies, particularly in diseases where mechanotransduction plays a key role in the pathophysiology [1].

To gain a deeper understanding into the mechanotransduction mechanisms of chondrocytes, we have proposed the use of biofunctionalized magnetic vortex microdiscs for the purpose of applying tensile forces to specific cellular integrins. Magnetic vortex microdiscs, when exposed to an alternating magnetic field, can induce measurable and specific mechanical forces at complex frequency profiles to a single cell. They can provide the specificity needed to appropriately observe changes in cellular behavior such as the catabolic force or frequency thresholds for specific integrins. To accomplish this goal, we will employ the use of a very simple electromagnet built and validated in-house. An example of an application of these disks would be to track α5β1 and α1β1 integrins by measuring downstream a myriad of appropriate markers to answer questions such as: How do different levels of static and dynamic tensile forces affect the cellular stress response?

METHODS

It was important to select the optimal design of the magnet system in accordance with the experimental requirements that were posed. The magnet and disk system would be required to apply a controlled force in the range of 5 to 210 pN across the sample. Any magnetic field should be confined to the experimental area and uniform throughout the sample. It was decided that the disks would provide a much higher threshold of control when applying dynamic motion when compared to magnetic beads that have been previously used for similar applications [2].

To properly validate the relationship between the coil voltage (V) and the resulting magnetic field (H), we employed the use of COMSOL for all pre and post construction modeling. This modeling was corroborated using a handheld magnetometer. The force applied to the integrins by the disks will be calculated according to equation 1.

The described process for disk manufacturing involves fabricating magnetic disks (MDs) on a silicon wafer. It begins with the application of photoresist on the wafer, followed by UV exposure through a mask to create a pattern. An organic solvent removes unexposed photoresist. Then, a 5 nm gold underlayer, 60 nm of permalloy, and another 5 nm gold layer are deposited using magnetron sputtering. The MDs are released from the wafer in acetone using a lift-off process. This process enables cost-effective production of uniformly sized MDs with a specific magnetic spin state for use in magnetic storage applications.

The disks are manufactured in conjunction with collaborators from the Center for Nanoscale Materials (CNM) located within Argonne National Laboratory. The final part of disks manufacturing is application of a 5 nm gold coat for the enhancement of biocompatibility and functionalization [3].

Equations

$$(1) \quad F(t) = \frac{2m(t)*H(V,t)}{\pi\beta(t)E}$$

RESULTS

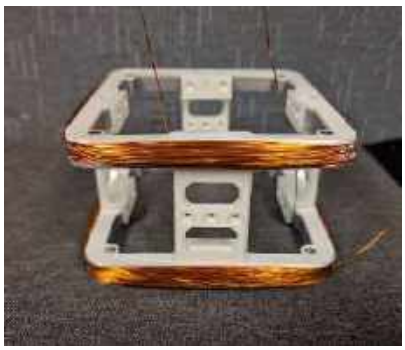

Figure 1: 3D printed Helmholtz Coil

The production and validation of a suitable electromagnet resulted in the development of a small-scale Helmholtz coil that was able to distribute a uniform magnetic field across the sample. The field strength was shown to match the simulation at the lower current that is available without the use of a dedicated benchtop power supply. Upon the arrival of the benchtop power supply, this will be validated again under higher current conditions that still fit the constraints of the wire that is used. Currently, the wire in question is 24 AWG and is rated for use up to 3.5 amps. This amount of current should be suitable to reach past the desired magnetic field strength of 100 Oe.

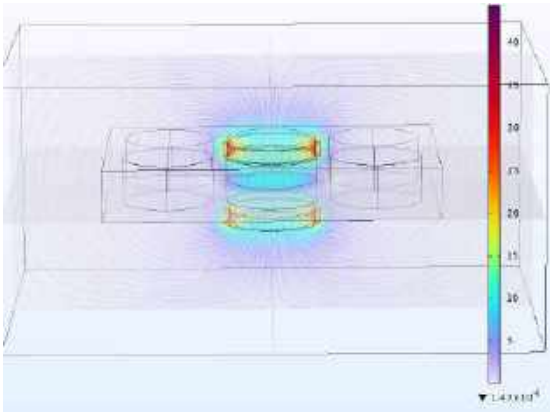

Figure 2: Representative Model of the Electromagnet with a 6-well Plate

The production of wafers during the pre-manufacturing process was completed under direct supervision of experts in the field of nanofabrication at the CNM. Each wafer was observed through optical microscopy to ensure that the shape and size of the disk diameter was ±0.5 µm from the desired size of 3 µm. Through ImageJ analysis, the average disk diameter was found to be 2.903 µm with a standard deviation of 0.048 µm.

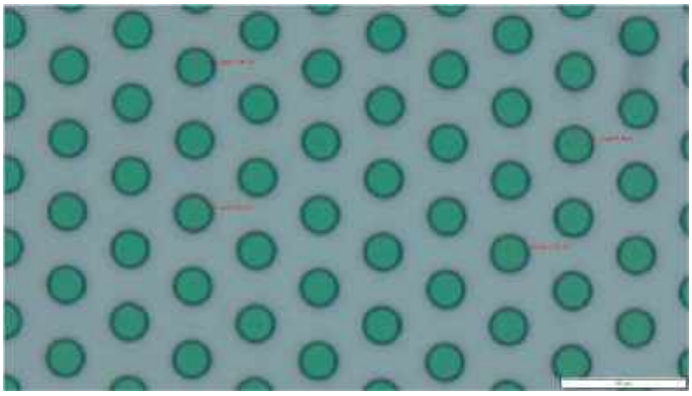

Figure 3: 3 µm Feature Wafer Produced at the Center for Nanoscale Materials

DISCUSSION

Mechanotransduction, the process by which cells sense and respond to mechanical forces, is a fundamental aspect of cellular biology with broad implications for health and disease. However, the current understanding of mechanotransduction is hampered by the lack of precise methods to apply mechanical forces at physiological frequencies in research settings. The commonly utilized empirical approach to selecting frequencies for force application that is commonly used has limitations, as it relies on trial-and-error methods to determine force frequencies, that are almost always discrete in nature. However, that approach fails to recapitulate the complex motions of cells that drive many mechanotransduction processes. The research presented here directly addresses this problem and bridges the existing gap by introducing a new method for applying complex frequency profiles to targeted cell surface mechanoreceptors. The significance of this methodology opens doors to a wide range of mechanotransduction studies in different biological contexts and cell types, which will provide valuable insights into how cells respond to mechanical cues in their native environments. These insights could pave the way for a more complete understanding of disease phenotypes and novel therapeutic options.

ACKNOWLEDGEMENTS

This material is based upon work supported by the National Science Foundation award #2144240. Any opinions, findings, and conclusions or recommendations expressed in this material are those of the author(s) and do not necessarily reflect the views of the National Science Foundation.

Work performed at the Center for Nanoscale Materials, a U.S. Department of Energy Office of Science User Facility, was supported by the U.S. DOE, Office of Basic Energy Sciences, under Contract No. DE-AC02-06CH11357. Additional thanks are extended to Dr. Volodymyr Yefremenko and Dr. Ralu Divan, who were instrumental in the training procedures that occurred pertaining to clean room use and nanofabrication.

REFERENCES

[1] Nix, Z et. al., *Progress in Biophysics and Molecular Biology*, *176*, 3–15. (2022)
[2] Marjoram, R. J. et. al., *Methods*, *94,* 19–26. (2016)
[3] Dong-Hyun Kim et. al., *Nature Materials*, *9 (2)*, 165–171. (2010)

MODULATING IN VIVO COMPLIANCE AND REMODELING OF A POLYURETHANE BASED, ANTITHROMBOGENIC TISSUE ENGINEERED VASCULAR GRAFT VIA GELATIN INCORPORATION

Katarina M. Martinet (1), David R. Maestas (1), Keishi Kohyama (1), William R. Wagner (1,2,3,4), Jonathan P. Vande Geest (1,4,5)

(1) Department of Bioengineering, University of Pittsburgh, Pittsburgh, PA, USA
(2) Department of Surgery, University of Pittsburgh, Pittsburgh, PA, USA
(3) Department of Chemical Engineering, University of Pittsburgh, Pittsburgh, PA, USA
(4) McGowan Institute of Regenerative Medicine, University of Pittsburgh, Pittsburgh, PA, USA
(5) Vascular Medicine Institute, University of Pittsburgh, Pittsburgh, PA, USA

INTRODUCTION

Coronary artery disease (CAD) is one of the leading causes of mortality, contributing to approximately 360,000 deaths per year [1] . In response, over 400,000 coronary artery bypass grafting procedures are performed every year [2]. Current bypass grafts have up to a 42.8% failure rate at two years after implanting due to blockage by thrombosis or the formation of intimal hyperplasia (IH) [3].

Failure via thrombosis has two major causes. First, interactions between the blood and the graft biomaterial leading to increased platelet deposition and clot formation [4]. Additionally, compliance mismatch between the native artery and the graft has a similar platelet activating effect. Compliance mismatch leads to changes in artery hemodynamics including oscillating sheer stress and sheer stress gradients. Disruption of these stresses facilitates clot formation [5]. Additionally, this disruption causes intimal hyperplasia (IH). IH is characterized by an abnormal migration of smooth muscle cells into the intimal layer of the artery that deposit excess ECM and constrict the inner diameter of the graft [6].

In this study we aim to create a tissue engineered vascular graft (TEVG) that decreases failure via thrombosis by using polyester sulfobetaine urethane urea (PESBUU) - a novel antithrombogenic polyurethane that has been shown to decrease palette aggregation and clot formation *in vitro* [7]. In response to *in vivo* PESBUU TEVG data, this study also looks at using gelatin to create compliance matched PESBUU based TEVGs. Our lab has previously developed CM TEVGs by layering varying computationally optimized ratios of gelatin and polycaprolactone (PCL) [8,9]. During 28 days of remodeling, CM TEVGs showed increased abluminal vascular smooth muscle cell (VSMC) counts and decreased markers of inflammation compared to hypocompliant grafts [10]. Polyester urethane urea (PEUU) was used as a substitute for PESBUU in non-blood contacting surfaces. PEUU is a well-established biomaterial with near identical mechanics to PESBUU and increased cellular infiltration potential.

METHODS

All TEVGs were fabricated via electrospinning. Pure PESBUU grafts were fabricated by spinning 350µL of PESBUU. Compliance matched TEVGs (CM TEVGs) were spun in three layers: a 35 µL inner layer of 100% PESBUU, a 65 µL middle layer of 80:20 PEUU:gelatin layer, and a 125 µL outer layer of 20:80 PEUU:gelatin. All materials were spun out of a 10% (w/v) solution made in HFP onto a 0.1mm mandrel. Gelatin containing grafts were then crosslinked in a genepin solution for 24 hours before being thoroughly rinsed in ethanol. *In vitro* mechanical testing was performed using a custom tubular biaxial mechanical testing device from Cell Scale Inc (Waterloo, Canada). Graft compliance was calculated using outer diameter measurements at the intraluminal pressures seen in *Equation 1*.

$$Compliance = \frac{(OD_{120} - OD_{80}) \,/\, OD_{80}}{120\ mmHg - 70\ mmHg} \quad (1)$$

Grafts were then implanted interpositionally into the abdominal aorta of Sprague Dawley rats for either 28 days (CM TEVGs) or 6 months (PESBUU). During implantation, doppler ultrasound was used to confirm patency and measure inner diameter and hemodynamics. CM TEVGs were scanned weekly and PESBUU grafts were scanned weekly for the first four weeks and then monthly until the end of the study. To calculate *in vivo* compliance a population pulse pressure was used (*Equation 2*).

$$Compliance = \frac{(ID_{systolic} - ID_{diastolic}) \,/\, ID_{diastolic}}{Pulse\ Pressure} \quad (2)$$

After explant, grafts were frozen in OCT, sectioned, and evaluated for cellular makeup via immunofluorescent staining. All results are presented as mean ± standard deviation. Compliance comparisons were performed via one-way ANOVA with a Tukey post-hoc.

RESULTS

The average wall thickness of the PESBUU and CM TEVGs grafts were 95 µm and 165 µm, respectively. To calculate *in vitro* native aortic compliance, 3 male and 2 female rats were used. Compliance of CM TEVGs was not significantly different than that of native rat aorta. PESBUU grafts were hypocompliant when compared to native rat aorta **(Figure 1)**.

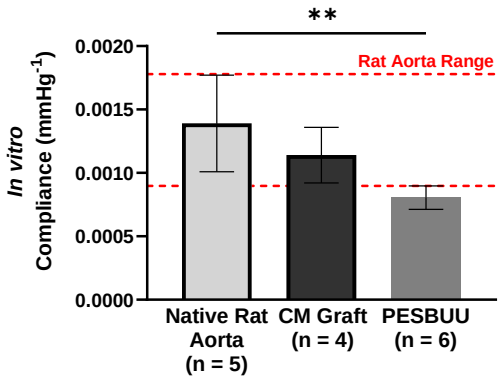

Figure 1: *In vitro* mechanical characterization of electrospun grafts compared to native rat aorta. *, p<0.05

No significant decrease in inner diameters was noted *in vivo* over the 6 month implant period **(Figure 2)**. Ultrasound measurements were taken on 10 rats (6M, 4F) and no differences were noted between sexes. Cells staining positive for α – SMA and CD31 were seen on the inner lumen of the graft. No cell nuclei were present within the graft or abluminally.

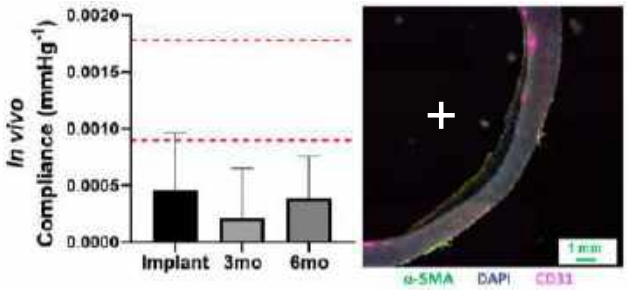

Figure 2: (Left) *In vivo* compliance values of PESBUU grafts over 6 months (n = 11). (Right) Fluorescent image of a representative explanted graft. Plus denotes the inner lumen. Scale bar = 1mm.

Compliance measurements were taken on 6 rats (3M, 3F). Grafts were shown to remain compliance matched post implant but were shown to have a significant decrease in compliance after 28 days of remodeling **(Figure 2).** At 28 days the gelatin dense outermost layer of the CM TEVG appeared to be fully degraded in all samples. Some rats (2/6) degradation of the middle layer was also noted. The presence of VSMCs (α – SMA) and small amounts of endothelial cells (CD31) was noted. There was little to no cellular infiltration into the inner and middle layers **(Figure 2).**

Hemodynamically, the average peak systolic velocity in the CM TEVG after 4 weeks of remodeling was 636.9 ± 288.3 mm/s in females and 1154.1 ± 315.6 mm/s in males. In PESBUU grafts females measured an average 903.9 ± 157.2 mm/s and males measured 891.9 ± 258.8 mm/s.

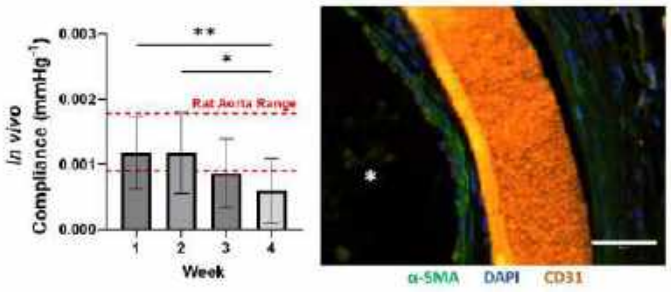

Figure 3: (Left) *In vivo* compliance values of CM TEVGs over 28 days (n = 6). *, p<0.05 **(Right) Fluorescent image of a representative explanted graft.** Asterisk denotes the inner lumen. Scale bar = 50µm.

DISCUSSION

In this study we were able to successfully create CM TEVGs utilizing the antithrombogenic polymer PESBUU by including gelatin into the graft matrix. PESBUU alone was hypocompliant and though we saw no signs of IH in our model (no significant diameter decrease or VSMC buildup) we believe that this is model specific. Additionally, PESBUU showed little to no signs of infiltration nor degradation on its own. There were no shifts in graft compliance, nor material loss.

In response, we successfully modulated the compliance and cellular interaction of PESBUU grafts through gelatin inclusion in out CM TEVGs. These grafts were compliance matched both *in vitro* and *in vivo*, robust enough for implantation, and remained patent over 28 days of remodeling. Unexpectedly, grafts did not remain compliance matched over 28 days of remodeling. We noted an increase in TEVG inner diameter (dilation) in some female rats that likely contributed to decreased compliance numbers. Ultrasound revealed that the hemodynamics within these dilations were abnormal and not fully pulsatile. This may explain why we see sex specific hemodynamic differences in CM TEVGs but not PESBUU grafts. Explant data from these dilated grafts showed advanced graft degradation in PEUU containing layers.

While these initial results are encouraging, there were some limitations within this study. For example, the rat model is not able to capture human hemodynamics and has starkly different clotting dynamics. Additionally, using a population pressure for compliance calculations is less desirable than subject specific pressures. That being said, our initial results are still promising.

As we continue this work we plan to study longer timepoints for CM TEVGs, incorporate growth factors to encourage cellular infiltration, understand sex differences seen in compliance shifts, and move to a larger animal model.

ACKNOWLEDGEMENTS

This research was funded by NIH R01 (HL157017) and NIH T32 (T32HL076124) Cardiovascular Bioengineering Training Program.

REFERENCES

[1] Tsao C.W., et al., *Circulation,* 145:e153–639, 2022.
[2] Gaudino M, et al., *Circulation,* **136**:1749–64, 2017
[3] Hess C.N., et al., *Circulation,* **130**:1445–51, 2014
[4] Alexander, et. al..N *Engl J Med,* 375:e22, 2016
[5] Salacinski H.J., et al., *J Biomater Appl* **15**:241–78, 2001
[6] Lemson M.S., et al., *Eur J Vasc Endovasc* **19**:336–50, 2000
[7] Ye S-H., et al., *ACS Appl Mater Interfaces* **6**:22796–806, 2014
[8] Harrison S., et al., *J Biomechanical Eng* **138**:014505, 2016
[9] Tamimi E.A., et al.,*J Biomechanical Eng* **141**, 2014
[10] Furdella K.J., et al., *Acta Biomater* **123**:298–311, 2021

PORCINE THORACIC AORTIC TISSUE FAILURE STRENGTH IS ASSOCIATED WITH BULK DENSITY WHICH MAY BE DETECTABLE FROM DIFFUSION TENSOR IMAGING

Pete H. Gueldner (1), Cyrus J. Darvish (1), Timothy K. Chung (1), Chandler C. Benjamin (2), Keshava Rajagopal (3), T. Kevin Hitchens (4), Spandan Maiti (1), Kumbakonam R. Rajagopal (1,2), and David A. Vorp (1,5-9)

(1) Department of Bioengineering, University of Pittsburgh, Pittsburgh, Pennsylvania, USA
(2) Department of Mechanical Engineering, Texas A&M University, College Station, Texas, USA
(3) Division of Cardiac Surgery, Department of Surgery, Thomas Jefferson University, Philadelphia, Pennsylvania, USA
(4) Advanced Imaging Center, University of Pittsburgh, Pittsburgh, Pennsylvania, USA
(5) Department of Mechanical Engineering and Materials Science, University of Pittsburgh, Pittsburgh, Pennsylvania, USA
(6) McGowan Institute for Regenerative Medicine, University of Pittsburgh, Pittsburgh, Pennsylvania, USA
(7) Department of Surgery, University of Pittsburgh, Pittsburgh, Pennsylvania, USA
(8) Department of Chemical and Petroleum Engineering, University of Pittsburgh, Pittsburgh, Pennsylvania, USA
(9) Department of Cardiothoracic Surgery, University of Pittsburgh, Pittsburgh, Pennsylvania, USA
(10) Clinical and Translational Sciences Institute, University of Pittsburgh, Pittsburgh, Pennsylvania, USA

INTRODUCTION

An aortic aneurysm occurs when the aortic wall, either in the thoracic or abdominal segment, weakens and irreversibly dilates. This expansion results from a gradual degradation of the extracellular matrix, especially elastin [1]. Aortic aneurysm ruptures, which happen when the wall stress surpasses the wall strength, resulted in 9,923 deaths in the United States in 2018 [2] and are thus a significant health concern. Understanding and predicting aortic wall tissue strength in aneurysms could have substantial clinical benefits.

To study the effects on mechanical tissue properties, vascular extracellular matrix (ECM) has been modified using protease treatments [4,5]. Correlations have been observed relating the density of concrete and polymers its failure point [6], leading us to hypothesize a parallel behavior in aortic tissue; that is, tissue strength is directly linked to its density. Generally, a diminished extracellular matrix correlates with weaker tissue. We propose that a reduction in wall tissue density may lead to decreased aortic tissue strength.

Diffusion tensor (DT) imaging, a magnetic resonance imaging technique, visualizes the movement of protons across surfaces. Commonly applied in brain imaging to map fibers, it provides measures of anisotropy and diffusivity, which may be indicative of the tissue's local density. This pilot study aims to explore the potential link between proteolytically altered density using diffusion coefficients derived from DT imaging and experimentally measured mechanical properties of porcine thoracic aortic tissue.

METHODS

Porcine Specimen Treatment: Freshly harvested porcine thoracic aortas, sourced from a local abattoir, were prepared into longitudinal rectangular specimens (80mm x 4mm) and immersed in phosphate buffered saline for 12 hours. The initial (untreated) saturated mass and volume were measured for each specimen and initial density calculated as described below. The samples were then submerged in a collagenase (50 mg/mL, n=7) or elastase (0.01 mg/mL, n=7) solution to selectively degrade collagen or elastin, respectively. Sham/control specimens were submerged in pure PBS (n=7). Submerged specimens were then incubated with end-over-end rotation at 37° C for 24 hours. Post-treatment density was calculated (described below) for each specimen following incubation and then uniaxially tensile tested to failure. The stress-stretch curve was used to calculate nominal ultimate tensile strength (UTS) and tangent modulus, and all statistical analysis was performed using an ANOVA with Tukey's post-hoc.

Specimen Density Measurements: Mass (m) of all porcine specimens was measured using a precision balance (PR503, Mettler Toledo, Columbus, OH). The width-length surface area and average thickness were determined from images of the specimens prior to testing. Solid volume (V) was calculated from the measured surface area (SA) and average thickness (t) across the specimen (**Equation 1**).

$$V = SA * t \quad (1)$$

Bulk tissue density (ρ) was determined for each specimen before and after enzymatic degradation (**Equation 2**).

$$\rho = \frac{m}{V} \quad (2)$$

Percent density change (before vs. after treatment) for each specimen was calculated.

Diffusion Tensor Imaging: DT imaging was conducted on a single sample at the University of Pittsburgh Advanced Imaging Center using

an 11.7T/89 Bruker Avance AV3 HD microimaging scanner. The sample was maintained at 37° C inside a 15 mm diameter tube filled with phosphate buffer saline. The scanning process took approximately two hours. Post-scanning, the DT images were processed using DSI Studio (High-Definition Fiber Tractography Lab, University of Pittsburgh, Pittsburgh, PA). We reconstructed the DT images through eigenvector analysis applied to the calculated tensors. For analysis, we focused on the central region of the tissue. The number of voxels analyzed varied by treatment: 56 for the sham tissue, 48 for collagenase-treated samples, and 65 for those treated with elastase. Voxels refer to the three dimensional 'points' and represent the diffusion tensors measured. Voxel count varied by selecting a rectangular region along the center of the tissue and the size of the tissue's central region. Mean and standard deviation of each variable was taken for each voxel in the region of interest and compared between the specimens.

RESULTS

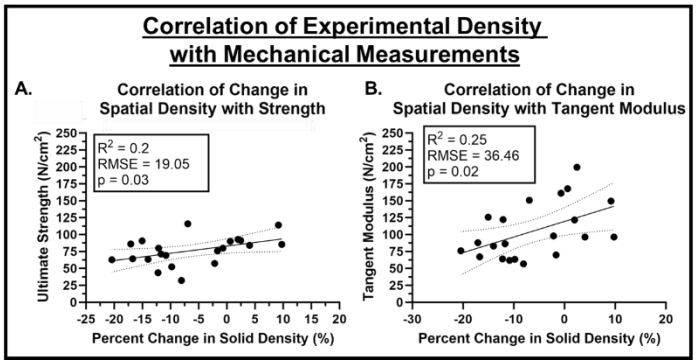

Figure 1: A) Correlation of comparing UTS and experimental density, and B) Correlation of porcine samples comparing UTS and sample density

The results for the porcine aortic tissue show a significant difference in % change in solid density between sham (2.3±5.3%) and both collagenase-treated (-11.8±5.7%, p=0.005) and elastase-treated (-9.2±6.9%, p=0.011) tissue. Parallel differences were also seen for the UTS for the sham (95.70±12.8 N/cm^2) and the collagenase (63.5±16.2 N/cm^2, p=0.024) and the elastase groups (69.9±15.2 N/cm^2, p=0.03). The tangent modulus also showed similar differences between the sham (149.5 ± 30.7 N/cm^2), collagenase (74.8±11.1 N/cm^2, p=0.007) and the elastase groups (90.8±25.0 N/cm^2, p=0.025). Linear regression revealed that density is a significant predictor of UTS for porcine thoracic aorta (R^2=0.2, p=0.03) (Figure 1A). Additionally, density is a significant predictor of tangent modulus (R^2=0.25, p=0.02) (Figure 1B).

Table 1: Diffusion parameters statistically compared from collagenase and elastase groups and compared to the sham group.

	Sham	Collagenase	Elastase
Mean Diffusion	0.073±0.13	0.85±0.08 (p=0.01)	0.77±0.05 (p=0.04)
Axial Diffusion	1.14±0.11	1.23±0.06 (p=0.01)	1.12±0.05 (ns)
Radial Diffusion	0.52±0.16	0.66±0.17 (0.03)	0.60±0.11 (ns)

The DT imaging shows significant differences in calculated parameters from the images. The fractional anisotropy, which is purely isotropic at a value of 0 and more anisotropic as it approaches 1, was significantly different in the collagenase (0.40±0.15, p=0.02) and elastase (0.40±0.04, p=0.01) groups compared to the sham group (0.47±0.08). Additionally for the diffusion parameters, see **Table 1** for statistical comparisons. As diffusion parameters increase, hydrogen ions are more easily able to pass through the tissue. Additionally, **Figure 2** has qualitative images showing each voxel's primary diffusion tensor in color.

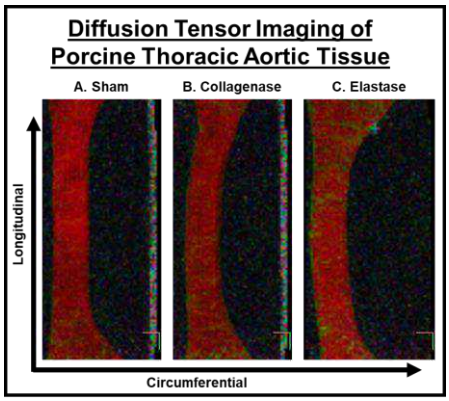

Figure 2: Magnetic resonance Image of diffusion tensors of 3 separately treated specimens (A. Sham, B. Collagenase, and C. Elastase) from the same porcine thoracic aorta. The red color suggests that the primary tensors for tissue microstructure are in the circumferential orientation, blue would be radial, and green longitudinal.

DISCUSSION

Experiments performed in this study revealed that through proteolytic treatments we can manually manipulate (decrease) the bulk tissue density of aortic tissue, which in turn can alter the UTS and tangent modulus (**Figure 1**). The reduction of fractional anisotropy in the elastase and collagenase specimen compared to the sham specimen is consistent with previously presented results that have shown this effect mechanically[8]. Very recently DT imaging has revealed increases in mean diffusivity in proteolytically degraded porcine aorta[9]. To our knowledge, axial diffusivity (circumferential in respect to the porcine anatomy) has not been explored. It is expected that the elastase group would remain unchanged from the sham, as elastase would not remove collagen fibers which are primarily circumferentially oriented. While radial diffusion was significantly different in the collagenase group from the sham treatment, the elastase group was not different than the sham group. The lower density tissues (collagenase and elastase treated) have lower fractional anisotropies (more isotropic), are more diffusive (more porous), and have lower mechanical strength and stiffness than higher density tissue (sham).

This study is limited by assuming that collagenase only reduces the collagen content of the tissue and that elastase only reduces the elastin content. Future work will include histology of the specimens to compare the effect of the degradation on the extracellular matrix. We will also expand our work to relate diffusion values and fractional anisotropy to bulk density values to relative strength determinations in order to explore the potential of DT imaging as a tool to assess bulk tissue density.

ACKNOWLEDGMENTS

PG was supported by the National Science Foundation Graduate Research Fellowship under Grant #1747452.

REFERENCES

[1] Dobrin, P, et al., *Surgery*, (1988). [2] C.f.D Control, WISQARS. 2017. [3] Vorp, D, *J. Biomech.*, 2007. [4] Berman, A, et al., *Scientific Reports*, 2022. [5] Noble, C, et al., *J Mech Behav Biomed Mater*, 2016. [6] Murru, P, et al., *Int. J. Pavement Eng.*, 2020. [7] Alagappan, P., *Proc. R. Soc. A: Math. Phys. Eng. Sci.*., 472(2192), 2015. [8] Gundiah, N., et al., *Physiological Measurement*, 2013. [9] Wang, M., et al, *Eur Heart J Open*, 2024.

DISSECTING YAP/TAZ MECHANOTRANSDUCTIVE MECHANISMS IN VASCULAR MORPHOGENESIS

Paula Camacho (1), Brendan Tobin (2), Devon E. Mason (1,3), Jason A. Burdick (4), Amber N. Stratman (5), Levi Wood (2), Joel D. Boerckel (1,3)

(1) Department of Orthopaedic Surgery, University of Pennsylvania, Philadelphia, PA, USA
(2) George W. Woodruff School of Mechanical Engineering, Georgia Institute of Technology, Atlanta, GA, USA
(3) Department of Bioengineering, University of Pennsylvania, Philadelphia, PA, USA
(4) BioFrontiers Institute and Department of Chemical and Biological Engineering, College of Engineering and Applied Science, University of Colorado Boulder, Boulder, CO, USA
(5) Department of Cell Biology and Physiology, Washington University in St. Louis, St. Louis, MO, USA

INTRODUCTION

Mechanical stimuli and endothelial cell (EC) mechanotransduction are critical for proper vascular morphogenesis.[1,2] We can study this by perturbing the mechanical environment in the endothelium or by manipulating specific mechanosensors and mechanotransducers. However, ECs perceive and transduce mechanical signals through a variety of signaling pathways.[3] Additionally, mechanotransducers may be regulated by multiple upstream inputs and regulate diverse downstream outcomes, not all related to mechanotransduction. It is challenging to dissect which cell behavior and gene expression profiles are regulated by a specific mechanotransducer in response to mechanical cues, especially *in vivo*.

Here we investigate which mechanotransductive pathways are specifically regulated by the transcriptional coactivators Yes-associated protein (YAP) and transcriptional-coactivator with PDZ-binding motif (TAZ) during endothelial mechanosignaling and vascular morphogenesis. We previously identified YAP/TAZ as mechanosensitive mediators of a feedback loop that modulates cytoskeletal tension and focal adhesion (FA) formation to regulate EC motility and vascular morphogenesis.[4,5] These observations position YAP and TAZ as potential key mediators of cytoskeletal-induced transcriptional programs.

METHODS

We performed two types of studies, one in zebrafish larval vessel morphogenesis and one in human EC adhesion adaptation to substrates of different rigidities. In the two experimental models, we perturbed mechanical environment and YAP/TAZ signaling and evaluated transcriptional changes. The parallel structure of this study allowed us to identify mechanotransductive genes and pathways that are specifically regulated by YAP and TAZ *in vitro* and *in vivo*.

We used small molecule inhibitors 2,3-butanedione monoxime (BDM) and Verteporfin (VP) to block heart beat-induced mechanical cues and YAP/TAZ signaling, respectively, during vascular morphogenesis in transgenic zebrafish Tg*(fli:egfp)*^{y1} [6] embryos beginning at 28-29 hours postfertilization (hpf). Fluorescent images were collected using a spinning disk confocal microscope between 28-48 hpf to measure intersegmental vessel (ISV) length.

Sequencing-based gene expression assays were performed in both ECs and zebrafish models. Endothelial colony forming cells (ECFCs) received either YAP/TAZ-silencing siRNA, or scrambled control, and were seeded onto 1kPa or 18kPA methacrylated hyaluronic acid (MeHa) hydrogels at 48 hours post-transfection.[5] Cells were collected for RNA-sequencing at 4 hours after seeding to identify the immediate transcriptional targets of mechanotransduction[5]. In parallel, 'AngioTag' zebrafish embryos[7] were treated with BDM starting at 24 hpf, and collected at 36 hpf for Translating Ribosome Affinity Purification (TRAP). This technique enables collection of actively translating mRNA species via sequencing of mRNAs trapped in ribosomes, pulled down by immunoprecipitation.[7]

Transcriptional changes were analyzed using Gene Set Variation Analysis (GSVA), in R. GSVA is a generalized gene set enrichment method that detects variations of pathway activity over a sample population in an unsupervised manner.[8] We quantitatively compared gene sets expression in the experimental conditions and defined cellular behaviors and signaling pathways regulated by YAP/TAZ mechanotransduction. GSVA was computed using annotations from the Molecular Signatures Database C2 [v7] gene sets (MSigDB). Gene sets with FDR adjusted p-value qFDR < 0.05 were considered significant. Statistically significant differences and fold changes in individual genes were computed via DESEq2 v. 1.36.0.

RESULTS

Pharmacological disruption of heart beat using BDM arrested zebrafish ISV morphogenesis by 35 hpf compared to DMSO controls (Fig. 1A, B). Washing out the inhibitor after 3 hours restored vessel

growth. These data indicate that mechanical cues induced by the heartbeat dynamically regulate ISV morphogenesis. Next, to test for a role of YAP/TAZ signaling in ISV morphogenesis, we repeated this experiment using the YAP/TAZ inhibitor, verteporfin (VP). Like BDM, YAP/TAZ inhibition slowed vessel morphogenesis but could be rescued by inhibitor washout (Fig 1C, D). Together, these data indicate that dynamic mechanical stimulation and YAP/TAZ signaling regulate ISV morphogenesis. However, we need to determine the extent and mechanisms of YAP/TAZ mechanotransduction, per se.

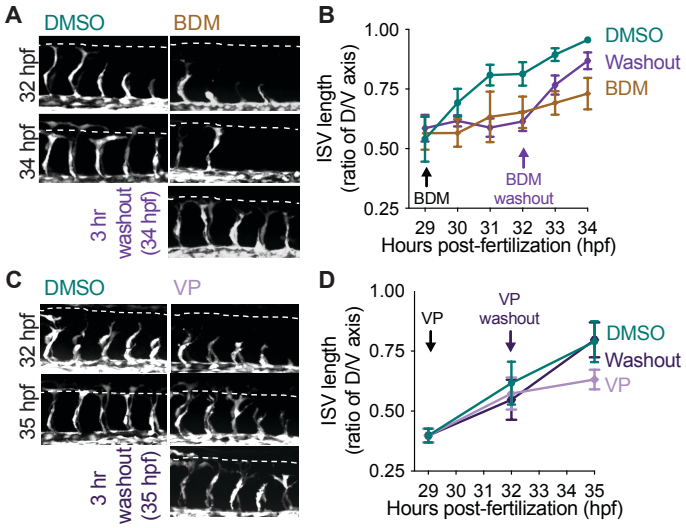

Figure 1. Dynamic mechanical stimulation and YAP/TAZ signaling regulate zebrafish ISV morphogenesis. Representative confocal images of DMSO and BDM (**A**) or VP (**C**) treated zebrafish embryos at 32 hpf (top), 34/35 hpf (middle), or at 34/35 hpf 3 hours of compound washout (bottom). Quantification of ISV length of embryos continuously incubated in BDM (**B**) or VP (**D**) versus the associated washout condition.

To dissect the cellular pathways and genes that are specifically regulated by mechanotransduction through YAP and TAZ, we evaluated changes in gene expression of control and YAP/TAZ depleted ECs cultured on soft (1 kPA) or stiff (18 kPA) matrices (Fig 2A). Because of the duration of YAP/TAZ depletion prior to adhesion and the potential non-mechanotransductive roles of YAP and TAZ, YAP/TAZ knockdown had a greater impact on transcription compared to substrate stiffness adhesion after 4 hrs (Fig 2B). YAP/TAZ depletion of cells cultured on the stiff matrix differentially regulated 989 gene sets (Fig 2B, dark blue panel). From this large list, we extracted 61 gene sets specifically regulated by YAP/TAZ mechanotransduction (Fig 2B, dashed circle, C). Combining gene sets by biological function elucidated several altered pathways, including Wnt/B-catenin signaling (Fig 2D), focal adhesions, mRNA processing, hypoxia response, EGF signaling, and Notch signaling.

To test the extent to which the identified YAP/TAZ-regulated genes and pathways mediate mechanosignaling in vivo, we treated zebrafish with BDM for 3 hours and used TRAP-seq to analyze translating mRNAs in the ECs. Comparing treated versus control conditions, 1194 gene sets were differentially regulated by mechanical cues. We cross-referenced these to the YAP/TAZ-regulated mechanosensitive gene sets identified *in vitro,* and found 39 overlapping. After combining the gene sets by function, we identified 4 pathways of particular interest and regulated specifically by YAP/TAZ mechanotransduction: Wnt/B-catenin signaling, focal adhesions, mRNA processing, and EGF signaling.

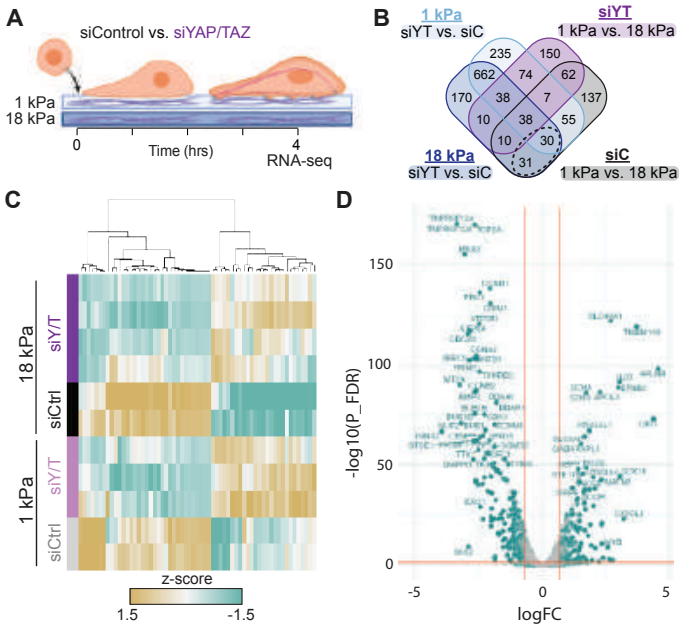

Figure 2. Transcriptional profiling reveals genes and pathways regulated by substrate stiffness through YAP/TAZ signaling. **A.** Experiment schematic: Control or YAP/TAZ depleted ECFCs were cultured on 1 or 18 kPa MeHA matrices. **B.** Differentially expressed gene sets in the four experimental conditions. Those driven by YAP/TAZ mechanotransduction identified in the dashed circle**. C.** Enrichment scores and **D.** example of a pathway (Wnt/B-catenin) of YAP/TAZ regulated mechanosensitive gene sets. Volcano plot shows differentially expressed genes from siControl vs siYAP/TAZ on 18 kPa comparison.

DISCUSSION

Here, we sought to dissect mechanosignaling pathways to identify gene expression profiles that are specifically regulated by YAP/TAZ mechanotransduction in ECs in culture and during vascular morphogenesis. This parallel approach allowed us to identify YAP/TAZ mechanotransductive mechanisms in vascular morphogenesis. Our data suggest that, YAP and TAZ play important roles in endothelial cell motility and mechanosensing through diverse transcriptional programs, including genes and pathways directly controlled by YAP/TAZ mechanotransductive transcription. Future studies will explore how changes in cytoskeletal tension drive the identified pathways, with *in vivo* dissection, using novel optogenetic tools.

ACKNOWLEDGEMENTS

This work was funded by the NIH/NIGMS (R01 GM143400) and the Center for Engineering MechanoBiology (CEMB), an NSF Science and Technology Center, under grant agreement CMMI: 15-48571.

REFERENCES

[1] S. Barrasa-Ramos, el at., *J R Soc Interface*, 19:20220360, 2022. [2] L.-K. Phng & H.-G. Belting, *Semin Cell Dev Biol,* 120:32-43, 2021. [3] K. Tanaka, et el., *Cytoskeleton*, 78:217-231, 2021. [4] D.E. Mason, et al., *JCB*, 218:1369-1389, 2019. [5] D.E. Mason, et al., *eLife,* 12, 2023. [6] N.D. Lawson & B.M. Weinstein, *Dev Biol* 248;307-318, 2002. [7] M. Miller, et al., *bioRxiv*, 815696, 2019. [8] S. Hänzelmann, et al., *BMC Bioinform*, 14:7, 2013.

ENHANCING PREDICTIVE ACCURACY IN CEREBRAL ANEURYSM HEMODYNAMICS: INSIGHTS FROM MACHINE-LEARNING EVALUATION AND PARAMETER INFLUENCE ANALYSIS

N. Kamaei Asl, M. Sharbatdar

(1) Department of Mechanical Engineering, University of Tehran, Tehran, Tehran, Iran
(2) Department of Mechanical Engineering, K. N. Toosi University of Technology, Tehran, Tehran, Iran

INTRODUCTION

Cerebral aneurysms are dilations of the cerebral arteries and, in most cases, patients with cerebral aneurysms do not have any early symptoms. Nevertheless, it is a severe pathology, with a high mortality rate after rupture [1]. Several studies have focused only on the hemodynamics of the flow within the cerebral aneurysm [2]. However, the development and rupture of the cerebral aneurysm are also associated with a combination of other factors such as the geometrical properties of cerebral aneurysm [3].

Computational fluid dynamics (CFD) has been used to assess the development of cerebral aneurysms, with a focus on hemodynamic parameters like wall shear stress to understand rupture status, risk, and growth. While various parameters have been developed, their contributions to cerebral aneurysm dynamics are not fully explored. The association between aneurysm morphology and rupture status is acknowledged, but the specific contribution of each morphologic variable remains unclear [4].

Machine learning (ML) has rapidly advanced and applied in various fields, including clinical medicine. In clinical medicine, the application of ML holds significant potential for enhancing diagnostic capabilities and improving overall medical practices [5].

This research endeavors to predict hemodynamic parameters crucial for assessing the proper treatment for each patient based on hemodynamic parameters. However, recent studies faced challenges due to insufficient data, leading to less reliable results in evaluating these parameters. The ability to determine appropriate patient treatments based on hemodynamic factors has been limited by the inadequacy of data in these studies.

METHODS

In this study, numerical simulations were conducted using Ansys to analyze blood flow and various geometric characteristics of a cerebral artery vessel featuring a saccular aneurysm, as illustrated in Figure 1.

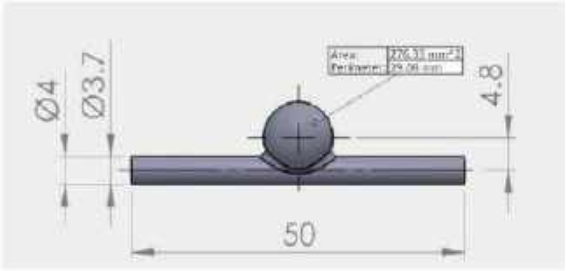

Figure 1 sample cerebral aneurysm

The geometry of the cerebral aneurysm model is based on the work of Souza [1]. Key geometric parameters encompass the vessel length, vessel diameter, distance of the aneurysm center from the vessel axis, distance of the aneurysm center from the origin of the vessel, aneurysm diameter, and vessel curvature, with their respective ranges detailed in Table 1. Also, curvature and radius angle have been considered for some cases.

Table 1 Geometrical parameters ranges

Vessel length	Vessel diameter	Distance from axis	Aneurysm diameter	Distance from origin
5-25 mm	3.4-8.6 mm	3.9-17 mm	5-30 mm	2.5-12.2 mm

The governing equations are the continuity and Navier-Stokes equations solved by utilizing the finite volume commercial software CFX, Ansys 2021 R2. The Newtonian blood flow is considered to be a Steady and incompressible regime, with rigid walls and zero outlet pressure. The investigated blood flow parameters including blood

density, blood viscosity, and blood inlet velocity, each with its specified range are detailed in Table 2.

Table 2 Blood flow parameters range

Blood Velocity	Blood Viscosity	Blood Density
0.14-0.85 $^{m}/_{s}$	0.00345-0.05345 $Pa.s$	1050-1056 $^{kg}/_{m^3}$

For each case, the computational domain includes a mesh with an average of 360,000 control volumes, with a residual error set at 10^{-4}. The convergence rate of 30 seconds per case on average, has been assessed. Output hemodynamic parameters include inlet pressure, maximum wall shear stress (WSS), average wall shear stress, maximum velocity, average velocity, and maximum vorticity inside the aneurysm dome.

Subsequently, machine learning models were employed to predict these output parameters based on input parameters. The predictive models encompassed random forest regressor (RFR), gradient boosting regressor (GBR), support vector regressor (SVR), linear regressor (LR), decision tree regressor (DTR), artificial neural network (ANN), k-nearest neighbors (KNN), and Bayesian Ridge (BR).

RESULTS

A total of 1846 distinct simulations were generated using CFD simulation. Similar to the prior research, the available data proved insufficient for yielding robust results; however, machine learning models require ample data for achieving high accuracy. Subsequently, we normalized all the data and then applied each machine-learning method to predict individual outputs for both normalized and denormalized data and evaluated each model using two metrics: Mean Squared Error (MSE) and R square (R2). The results are presented in Table 3.

Table 3 Results from machine learning models for each output normalized and denormalized

output	Best model	MSE (scaled)	MSE	R2
Inlet pressure	RFR	8.90×10^{-5}	$1.57 \times 10^{+5}$	0.9771
Maximum WSS	RFR	7.01×10^{-5}	$6.23 \times 10^{+1}$	0.9738
Average WSS	GBR	2.44×10^{-4}	1.75	0.9619
Maximum velocity	DTR	3.81×10^{-5}	3.58×10^{-3}	0.9934
Average velocity	DTR	4.37×10^{-5}	3.1×10^{-4}	0.9946
Maximum vorticity	DTR	1.81×10^{-5}	$5.09 \times 10^{+3}$	0.9885

The correlation matrix in Figure 2 illustrates the pairwise correlations among the variables considered in our machine-learning analysis. The values in the matrix range from -1 to 1, where -1 indicates a perfect negative correlation, 1 indicates a perfect positive correlation, and 0 indicates no correlation.

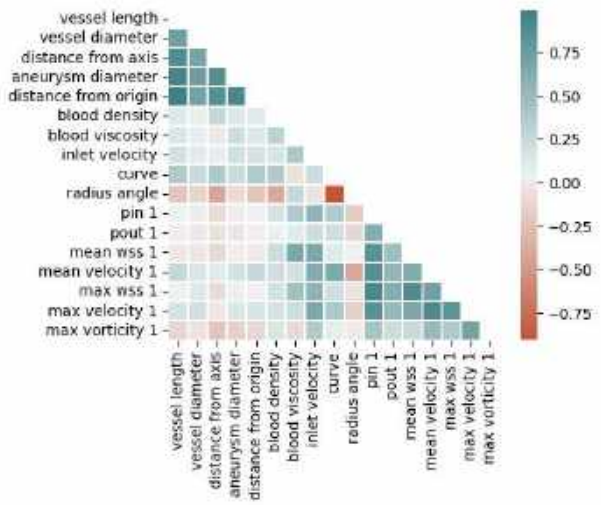

Figure 2 correlation matrix of input and output parameters data

DISCUSSION

Upon applying various machine-learning methods The outcomes, as described in Table 3, provide valuable insights into the efficacy of each machine-learning method in assessing and predicting the intricate hemodynamic parameters under investigation.

As you can see in Figure 2 which shows the correlation between parameters we can conclude that if we consider maximum wall shear stress as one of the critical hemodynamic parameters in cerebral aneurysms it shows that between input parameters blood viscosity and inlet velocity have the most effect on the results that haven't been investigated in previous research. between geometrical input parameters and blood flow input parameters, blood flow parameters show more influence on the output parameters.

These results not only contribute to the understanding of predictive capabilities in hemodynamic modeling but also prompt further considerations for refining methodologies, expanding datasets, and exploring novel approaches to enhance the accuracy of machine-learning predictions in the context of cerebral artery vessel simulations. Future research endeavors may benefit from addressing the challenges posed by limited data availability, thereby advancing the applicability and reliability of machine-learning models in predicting complex hemodynamic phenomena. By calculating hemodynamic parameters you can decide which approach of treatment will be appropriate for each patient.

REFERENCES

[1] Souza, MS et al. Fluid Flow and Structural Numerical Analysis of a Cerebral Aneurysm Model. Fluids. 2022; 7(3):100.

[2] Rayz, VL et al. AA. Hemodynamics of Cerebral Aneurysms: Connecting Medical Imaging and Biomechanical Analysis. Annu Rev Biomed Eng. 2020;22:231-256.

[3] Zanaty M et al Aneurysm geometry in predicting the risk of rupture. A review of the literature. Neurol Res. 2014;36(4):308-313.

[4] Aranda, A et al. STUDY ON CEREBRAL ANEURYSMS: RUPTURE RISK PREDICTION USING GEOMETRICAL PARAMETERS AND WALL SHEAR STRESS WITH CFD AND MACHINE LEARNING TOOLS. Machine Learning and Applications: An International Journal. 5. 2018; 15(2):200-204.

[5] Tanioka, S et al. Machine Learning Classification of Cerebral Aneurysm Rupture Status with Morphologic Variables and Hemodynamic Parameters. Radiol Artif Intell. 2020;2(1):e190077

TOWARDS THE ESTIMATION OF TUMOR STIFFNESS USING B-MODE ULTRASOUND IMAGING

Tanmay Mukherjee (1), Adarsh Shree (2), Reza Avazmohammadi (1,2)

(1) Department of Biomedical Engineering, Texas A&M University, College Station, TX, USA
(2) Department of Mechanical Engineering, Texas A&M University, College Station, TX, USA

INTRODUCTION

Cancer is a major cause of mortality and morbidity worldwide, with diagnosis relying heavily on ultrasound (US) imaging [1]. Recent advances in imaging techniques have evidenced the stiffening of tumors as early signs of malignancy. The lateral and axial strains of the tumor microenvironment have been identified as key indicators of malignancy, with mechanical properties such as Young's modulus and Poisson's ratio proposed as potential biomarkers [2]. Regional changes in these markers are mapped using brightness mode (B-mode) in conjunction with elastography. However, B-mode images are often susceptible to motion artifacts, with any subsequent calculations also heavily dependent on the abilities of the operator. Additionally, a majority of current research models the tumor as a linear elastic solid, thus providing a confounded representation of the tumor microenvironment [3]. Most biological tissues are known to behave as incompressible hyperelastic materials, thus necessitating an improvement in the characterization of the mechanical properties of the tumor. We propose an inverse model that uses synthetic images derived from in-silico finite element simulations of a tumor-healthy tissue assembly under compression to estimate a regional map of tumor stiffness.

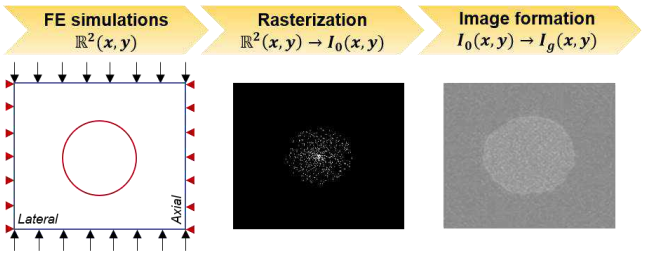

Figure 1: Schematic representation of the in-silico simulations comprising the steps involved in forming the synthetic B-mode images.

METHODS

The proposed methodology comprises the generation of synthetic US images of tumor cells included in healthy tissue (Fig. 1). Images are generated from two-dimensional plane stress finite element simulations of the tumor-tissue geometry under varying degrees of compression. Finally, we use a speckle tracking algorithm to calculate strains and displacements from the deforming geometry to facilitate an inverse model of the same geometry to estimate the mechanical properties of the tumor. *Finite element simulations*: The tumor is modeled as an irregular circle-like structure embedded in the background tissue. Both the tumor and the tissue were modeled as Neo-Hookean Hyperelastic materials of varying properties such that the strain energy function (ψ) was formulated as: $\psi = C(I_1 - 3)$, where C is a material parameter, and I_1 is the first invariant of the right Green deformation tensor. The tissue was axially compressed to 10%, 20%, and 30% of its length, with the lateral boundaries of the tissue assembly fixed in all directions. *Image generation*: The nodal positions of the deforming tissue assembly were estimated through the displacement vectors at each loading step, and were rasterized onto a 2D grid of pre-defined size and spacing. Each node on this grid ($G_0(x,y)$) can be considered as an object in space, and the subsequent US image (I_0) formation can be modeled as a linear system,

$$I_0 = G_0(x,y)H(x,y) + \eta,$$

here I_0 is obtained via the convolution of G_0 with a wave function, H and adding Gaussian noise, η. In this study, H is formulated as a sine kernel of size 5 and frequency of 3 mm to obtain an I_0 of size 256 x 256 with a resolution of 1 mm. *Speckle tracking*: A speckle tracking algorithm implementing normalized cross-correlation between successive image frames was used to calculate cartesian displacements [4]. The displacements between each frame were used to build the deformation gradient, with each tensor projected over all the frames to derive the total deformation gradient. The mean squared errors in

displacements and strains calculated were evaluated between speckle tracking and FE simulations.

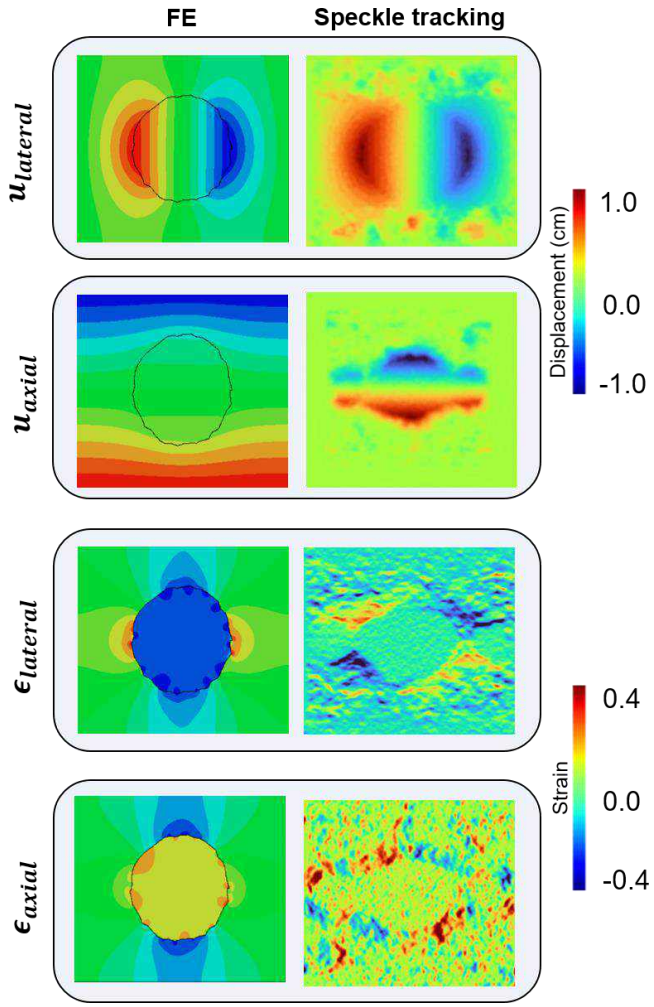

Figure 2: Representative heat maps of the (top) displacement and (bottom) strain calculations at 20% compression through finite element simulations and speckle tracking. ϵ_{axial} and u_{axial} are the axial strain and displacements, respectively. $\epsilon_{lateral}$ and $u_{lateral}$ are the lateral strains and displacements, respectively.

RESULTS

While minimal deformation was observed in both the healthy tissue and tumor at 10% compression, the lateral strains were significantly higher under 20% and 30% compression. Whereas the healthy tissue was observed to expand under compression, the tumor tissue was seen to contract with a mean lateral strain of -0.1245 ± 0.044 at 20% compression (Fig. 2). This transition was especially significant at the boundary between the two tissue classes. Despite the spatial heterogeneity in the deformation patterns under compression, realistic US images were produced through rasterization. As expected, the spatial distinction between the two tissue classes was very minimal. However, the cartesian displacement patterns were qualitatively recapitulated for all loading conditions through speckle tracking. In addition to qualitatively similar displacement patterns, there was good agreement in the mean strain values obtained within the tumor and at the interface at 20% (lateral: -0.1386 ± 0.066, longitudinal: -0.1511 ± 0.056). In contrast, spurious strains were observed at 30% compression, with both lateral and axial strains presenting over 40% error at the interface between the tumor and the healthy tissue. This is indicative of a common limitation in the spatiotemporal description of tissue-tissue interfaces seen in most B-mode US imaging.

DISCUSSION

In this study, we presented a pipeline to facilitate the estimation of the mechanical properties of tumors using standard B-mode US images via inverse modeling. In approaches such as US elastography, the tissue under consideration is compressed prior to the estimation of its mechanical properties. Subsequently, prolonged exposure to such mechanical loading may introduce motion-blur artifacts that may compromise the accuracy of the estimated properties. Indeed, such artifacts are known to compromise image quality and the resulting motion calculations using US imaging. To address such limitations, a well-established material model of tissue biomechanics was incorporated to create a library of varying tumor tissue properties. The ground-truth motion was subsequently estimated to create their corresponding synthetic US images. Realistic images were obtained by using the standard image formation principles of wave-based imaging methods. We presented a series of spatially heterogeneous deformation patterns of tumor inclusion in healthy tissue, with the proposed methodology successfully recapitulating FE simulations at 20% compression. However, at higher levels of compression, spurious strain values were obtained at the interface of the tumor inclusion. We suspect the image quality in capturing the more rapid deformation affects the resulting strain calculations. Sub-pixel motion estimation via speckle tracking is often challenged by rapid deformation, thus necessitating more robust image resolution. We expect these improvements can be facilitated by updating the image formation process through rectification and interpolation to improve the spatiotemporal resolution. However, the aim of this study was to establish the potential inverse relationship between the image-derived strains and stresses to estimate the tumor stiffness effectively. Despite minimal regions of spurious strains, an overall qualitative agreement between the FE- and image-derived strains was obtained. We will conduct a least-squares optimization-based inverse model to estimate tissue stiffness to characterize the mechanical properties of the tumor. We expect our findings to improve the structural characterization of tumors to estimate tumor malignancy effectively through standard B-mode US imaging.

ACKNOWLEDGEMENTS

This work was supported by the NIH (R00HL138288 to R.A).

REFERENCES

[1] Ophir, J.,et al. (1999). Elastography: ultrasonic estimation and imaging of the elastic properties of tissues. Proceedings of the Institution of Mechanical Engineers, Part H: Journal of Engineering in Medicine, 213(3), 203-233.

[2] Islam, M. T., et al. (2018). A new method for estimating the effective Poisson's ratio in ultrasound poroelastography. IEEE transactions on medical imaging, 37(5), 1178-1191.

[3] Islam, M.T., et al. Non-invasive imaging of Young's modulus and Poisson's ratio in cancers in vivo. Sci Rep 10, 7266 (2020).

[4] Mukherjee, T., et al. (2023). Improved right ventricular strain estimation in rats using anisotropic diffusion filtering. In Proc. of SPIE Vol (Vol. 12470, pp. 124700Y-1).

IMPACT OF GAGS REMOVAL AND CXL THERAPY ON CORNEAL STROMAL PROPERTIES

H. Hatami-Marbini (1), M.E. Emu (1)

(1) Department of Mechanical and Industrial Engineering, University of Illinois Chicago, Chicago, IL USA Email. Hatami@uic.edu

INTRODUCTION

The cornea, a transparent tissue at the front of the eye, serves as the protective layer for the internal contents of the eye by resisting external stresses. The mechanical properties of the cornea primarily stem from its extracellular matrix, which is known as the stroma. The stroma is the thickness layer of the cornea and is mainly composed of collagen fibrils and proteoglycans (PGs). PGs are macromolecules that are composed of a core protein to which glycosaminoglycan (GAG) chains are attached. They are important in maintaining the almost uniform collagen diameter in addition to regulating the arrangement of collagen fibrils inside the corneal stroma. The uniform diameter and hexagonal arrangement of collagen fibrils are necessary for corneal transparency. GAGs define the hydration of the stroma because they are negatively charged attract water molecules inside the stroma. They also generate osmotic swelling pressure and contribute to corneal mechanical strength. In addition, they bridge the collagen fibrils and could be important in transferring load among them. The primary GAGs inside the cornea are Keratan Sulfate (KS) and Chondroitin/Dermatan Sulfate (CS/DS). The composition and density of GAGs change due to diseased conditions.

Various eye diseases impact the composition, microstructure, and biomechanics of the corneal stroma. For example, keratoconus is a progressive ectatic disorder in which the cornea loses its mechanical strength and becomes cone-shape. The corneal crosslinking (CXL) treatment has been shown to slow down the progress of keratoconus. The CXL therapy uses UVA light and riboflavin solution to create crosslinks in the corneal stroma [1]. The CXL efficacy is usually assessed by investigating its effects on healthy corneas, i.e. the effects of altered composition and structure of keratoconus cornea are not considered. The purpose of this research was to assess how any reduction of KS GAG content affects the efficacy of CXL treatment. KS GAGs have been shown to decrease in keratoconus; thus, they might explain the significant reduction of tensile strength due to this diseased state [2,3]. For this purpose, we removed enzymatically GAGs from the cornea and used the CXL therapy to strengthen the GAG-depleted samples. We performed uniaxial tensile experiments and pepsin digestion studies to assess the structural integrity and tensile properties of samples before and after the CXL treatment. The findings were compared with the properties of control samples before and after the CXL therapy.

METHODS

Fresh porcine eyeballs were obtained and brought to the laboratory from a local slaughterhouse. The eyeballs were used on the same day by first removing excess tissues and then excising corneal rings with a 2 mm scleral rim. From corneal rims, strips were cut in the nasal-temporal direction. Random assignment was used to place strips into Control, Control CXL, KS II, and KS II CXL groups. Additionally, 8 mm full-thickness corneal discs were prepared for biochemical analysis and pepsin digestion. For GAG depletion (KS II group), corneal strips were immersed in an enzyme solution (0.1 U/ml keratanase II, 100 mM sodium acetate buffer) for 20 h at 37° C and pH 6.0. The thickness of incubated samples was measured and they were washed in PBS before being used in the experiments.

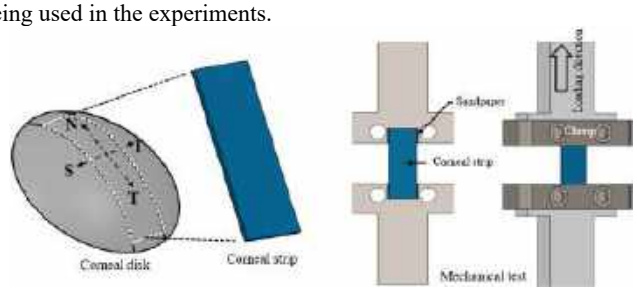

Figure 1: A schematic plot that shows the direction of the corneal strips and the mechanical grip of the uniaxial tensile testing machine.

Corneal strips underwent the conventional CXL protocol, i.e. they were soaked in 20% dextran - 0.1% riboflavin solution for 30 minutes and were then irradiated with UVA light (3 mW/cm^2, 370 nm) for another 30 minutes. Irradiance level was controlled with a UVA meter, and riboflavin solution was replenished at regular intervals during the UV irradiation. Uniaxial tensile tests were performed by an RSA-G2 testing machine (TA Instruments, MD). The samples were mounted into the testing machine using sandpaper to prevent slippage, Figure 1. The mechanical tests began by applying a preload in order to straighten the strips and remove any slack. Then, the initial length of the samples was used to calculate the displacement required to stretch the samples upto 20%. A displacement rate of 3 mm/min was used and the experiments were done without any bathing solution. The duration of the experiments was short and pre- and post-test thickness comparison showed no significant changes in the hydration of samples. The pepsin digestion study used five corneal disks from each group. For this purpose, the corneal samples were placed in 1 g $\geq$ 400 U/mg pepsin in 0.1 M hydrochloric acid (pH 1.2) solution and their diameter was measured. Like previous studies, we did not use any thickness measurement of pepsin digested samples as samples became significantly swollen. Data analysis, performed with the SAS analytic tool, involved Shapiro–Wilk tests for checking normality of the experimental data. ANOVA and t-tests with P value of 0.05 were also done to identify statistically significant differences.

RESULTS

The histological evaluation done by Alcian blue stain (results not shown) confirmed that the keratanase II enzyme treatment significantly reduced staining in GAG-depleted samples, confirming the successful GAG removal in these samples. Figure 2 depicts the tensile response of various groups. Tensile stress and tangent modulus at different strains were calculated from the stress-strain curves. It was found that the CXL procedure increased maximum tensile stress in control samples significantly and GAG depletion reduced the maximum tensile stress significantly ($P < 0.05$). Additionally, the CXL treatment of GAG-depleted samples significantly increased maximum tensile stress ($P < 0.05$). Finally, no significant difference was observed between KS II CXL and Control samples.

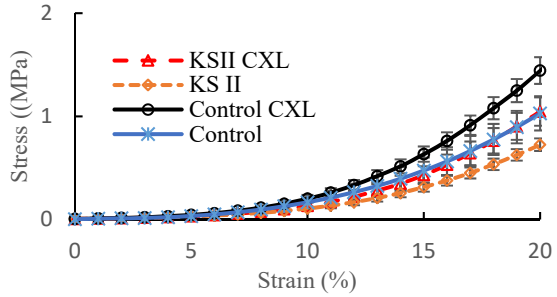

Figure 2: Effect of GAG removal and CXL therapy on tensile stress-strain curves.

Figure 3 shows the variation of the cornea diameter because of the pepsin digestion. Except for CXL-treated Control samples, all other samples were fully digested. GAG-depleted samples were digested significantly faster (average time: 6 days) than Control samples (average time: 9 days, $P < 0.05$). The CXL treatment increased the average digestion time of GAG-depleted disks from 6 to 8 days, which was a significant increase ($P < 0.05$). Figure 3 also shows that the reduction in the average diameter of Control and Enzyme CXL groups did not significantly differ between until day 7.

DISCUSSION

It is known that the CXL treatment is effective in enhancing corneal structural integrity, and thus it could stabilize and halt the keratoconus progression [4]. Extensive research has aimed at improving the original CXL protocol [5]. However, the stiffening effect of this procedure has commonly been assessed in vitro and by using healthy corneal samples. The keratoconus-induced changes in the corneal extracellular matrix were considered in the present work by using KS II GAG-depleted samples. We found that in agreement with previous studies, the CXL therapy significantly increased tensile properties of control samples. Furthermore, we found that removing KS GAGs significantly reduced corneal tensile properties, consistent with a recent finding from our laboratory [2-3]. GAG-depleted samples exhibited marked softening, contrasting with the CXL-induced stiffening in control samples. KS GAGs, forming duplex structures, act as bridges in the corneal stroma, contributing to collagen fibril stability and organization. GAG depletion led to reduced density and softening.

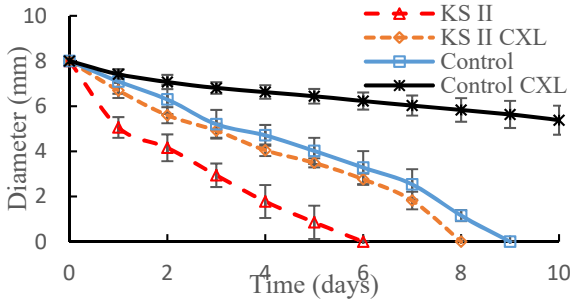

Figure 3: The sample diameter variation over time which was conducted to assess the resistance of samples from various groups to pepsin digestion.

The CXL procedure enhances mechanical properties of keratoconus cornea and halts the disease progression by creating additional crosslinks within PG core proteins and/or between collagen molecules [6]. These additional crosslinks are believed to be responsible for stiffening the tensile response. The present study found that the CXL treatment improved tensile properties of GAG-depleted samples. The CXL treatment also improved corneal resistance to enzymatic degradation, crucial for halting keratoconus progression [7]. We observed decreased enzymatic degradation rates in the CXL-treated Control samples and enhanced resistance in CXL-treated GAG-depleted samples. In conclusion, the present work gave unique insights into the role of KS GAGs in the efficacy of the CXL treatment, highlighting their substantial influence on corneal tensile properties. In continuation of this investigation, we are now comparing the mechanical properties of human and porcine corneas. Expanding upon the foundational knowledge acquired here, our subsequent research delves into the distinctions and similarities between porcine and human cornea, enriching our understanding of corneal biomechanics across species.

ACKNOWLEDGEMENTS

This work has been supported in part by grants from the National Institutes of Health (R21EY030264).

REFERENCES

[1] Spoerl, E., et al., Experimental Eye Research, 1998. 66(1): 97-103.
[2] Hatami-Marbini, H., Investigative Ophthalmology & Visual Science, 2023. 64(4): 3-3.
[3] Hatami-Marbini, H., M.E. Emu, Experimental Eye Research, 2023, 234: 109570.
[3] Raiskup, F., et al., American Journal of Ophthalmology, 2023. 250: 95-102.
[4] Wollensak, G., E. Spoerl, and T. Seiler, Journal of Cataract and Refractive Surgery, 2003. 29(9): 1780-1785.
[5] Hayes, S., et al., PLoS One, 2013. 8(1): e52860.
[6] Spoerl, E., et al., Current Eye Research, 2004. 29(1): 35-40.

USING FIBER MODELING TO UNDERSTAND THE EFFECTS OF MODULATING TISSUE MECHANICAL PROPERTIES AS A PREVENTATIVE TREATMENT FOR GLAUCOMA

Yingzhe Han (1), Bingrui Wang (1), Xuehuan He (1), Yuankai Lu (1) Ian A. Sigal (1,2)

(1) Department of Ophthalmology, University of Pittsburgh, Pittsburgh, PA, USA
(2) Department of Bioengineering, University of Pittsburgh, Pittsburgh, PA, USA

INTRODUCTION

Glaucoma is one of the top causes of blindness worldwide. Vision loss in glaucoma is due to damage to the retinal ganglion cell axons that carry visual information from the retina to the brain [1]. The damage initiates in the lamina cribrosa (LC) a region in the posterior pole of the eye. Although the mechanisms lading to neural tissue damage are not yet fully understood, elevated intraocular pressure (IOP) is the main risk factor [2]. Moreover, all current treatments to slow down or stop the progression of glaucoma are based on lowering IOP. However, the treatments to lower IOP have side effects and are not equally effective for every patient [1].

An alternative to lowering IOP has been discussed in the glaucoma community: instead of lowering IOP, perhaps it is possible to reduce the sensitivity of an eye to IOP [3]. Underlying this hypothesis is the idea that some eyes have characteristics that make them more robust, and therefore able to sustain levels of IOP that would hurt other eyes. Thus has surfaced the idea of modulating the mechanical properties of the eye to reduce its sensitivity to IOP [4]. Several approaches have been suggested to achieve this goal, including the use of chemical crosslinkers with or without photoactivation. Proposals of tissue modulation aim at stiffening the sclera with the intent that this translates into lower insult at the LC [3,4].

We propose that it may be possible to modulate the mechanical properties of the LC, with the advantage of acting directly on the region where the effect is desired. Furthermore, we believe that it may be advantageous to modulate LC properties both through stiffening or softening [5].

Our goal in this study was to simulate hypothetical treatments based on local tissue modulation and evaluate their effects on LC mechanics. We hypothesized that the effects of tissue modulation will depend on whether the modulation was done within the LC or in the adjacent sclera, and whether the modulation was done for softening or stiffening the tissues. Finally, we postulate that the effects of the tissue modulation will depend on how the collagen fibers of the LC and sclera bear and transmit the forces over long distances or to other fibers [6].

METHODS

Because of the complexity of the LC it is convenient to use numerical techniques to evaluate and personalize the tissue modulation process to obtain optimal interventions. A section through the LC of a sheep eye was imaged using polarized light microscopy to reveal the collagen density and fiber architecture. Based on this image, two specimen-specific computational models were built representing extremes of the fiber behavior: a highly dissipative conventional continuum model (CC) and a novel direct fiber model (DF). In the CC model, the tissue mechanical properties are simulated according to a constitutive formulation with a functional representation of fiber orientation and anisotropy. In this model, the fibers and forces are "smeared" within the elements and their boundaries. In the DF, the fiber bundles carry forces over long distances (Fig 1). The actual properties of the fibers themselves are modeled in the same way, but the models differ in how they are integrated and how the fibers interact and transfer forces. Both models were used to simulate a canal expansion of 10%. Regions of the LC and sclera were selected for stiffening or softening.

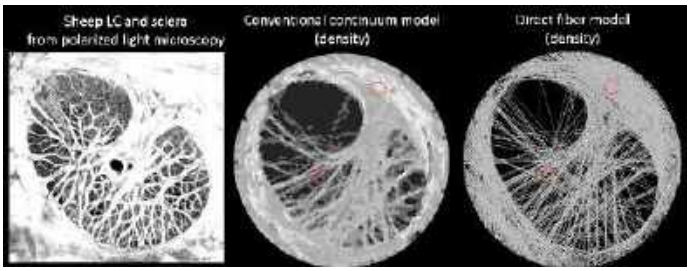

Figure 1: Based on an image of a sheep LC (left) two models were constructed (middle and right). Shown are density maps overlaid with circles indicating the location of tissue modulation, one in the LC and another in the sclera.

RESULTS

Tissue modulation had significant effects on the response of the whole region (Fig 2), with effects that were different for softening and stiffening.

The force dissipation process had large effects on the effects of the modulation. In the CC models, the changes were confined primarily within the area where tissue properties changed, with changes in the LC spreading farther than those in the sclera. In the DF models, the largest effects of the modulation were also localized to the place of change, but some substantial differences extended far from the change.

Figure 2 (below): Contour level plots of displacement, stretch and stress for the models as reconstructed (top row), and of the differences due to stiffening or softening of the LC or sclera. All modulations had clearly discernable effects on all three outcomes, but with different magnitudes and distribution.

DISCUSSION

The collagen fibers of the LC and sclera form complex interweaving bundles spanning mm-scale distances in the optic nerve head. On the one hand interweaving suggests that forces are easily transferred between the fibers and thus dissipated in the close vicinity of a tissue property change. On the other hand, long fibers can carry forces over long distances, suggesting that the effects of changes can spread far. Our modeling results indicate that accurately predicting how LC and sclera respond to tissue modulation requires a more detailed understanding of how fibers transmit the forces in actual tissues. We suspect that none of the two modeling approaches we used is entirely appropriate as both imply assumptions that are known to be violated in actual tissues, and thus cannot be considered fully reliable. However, we posit that by considering both modeling approaches it is possible to gain a more comprehensive understanding of how tissues may respond to modulating their mechanical properties.

Our results suggest that modulating the LC properties, including for softening, has the potential to improve the LC mechanical environment as much as modulating the sclera.

ACKNOWLEDGEMENTS

NIH R01-EY023966, P30-EY008098 and T32-EY017271 (Bethesda, MD), and Research to Prevent Blindness (unrestricted grant to UPMC Ophthalmology, and Stein innovation award to Sigal IA)

REFERENCES

[1] Quigley HA, IOVS, 2005. [2] Burgoyne CF, Exp Eye Res. 2011. [3] Strouthidis NG, et al. Curr Opin Pharmacol. 2013 [4] Gerberich BG, et al. Biomaterials. 2021 [5] Voorhees AP, et al. IOVS 2020
[6] Wang B, et al. Acta Biomater. 2020

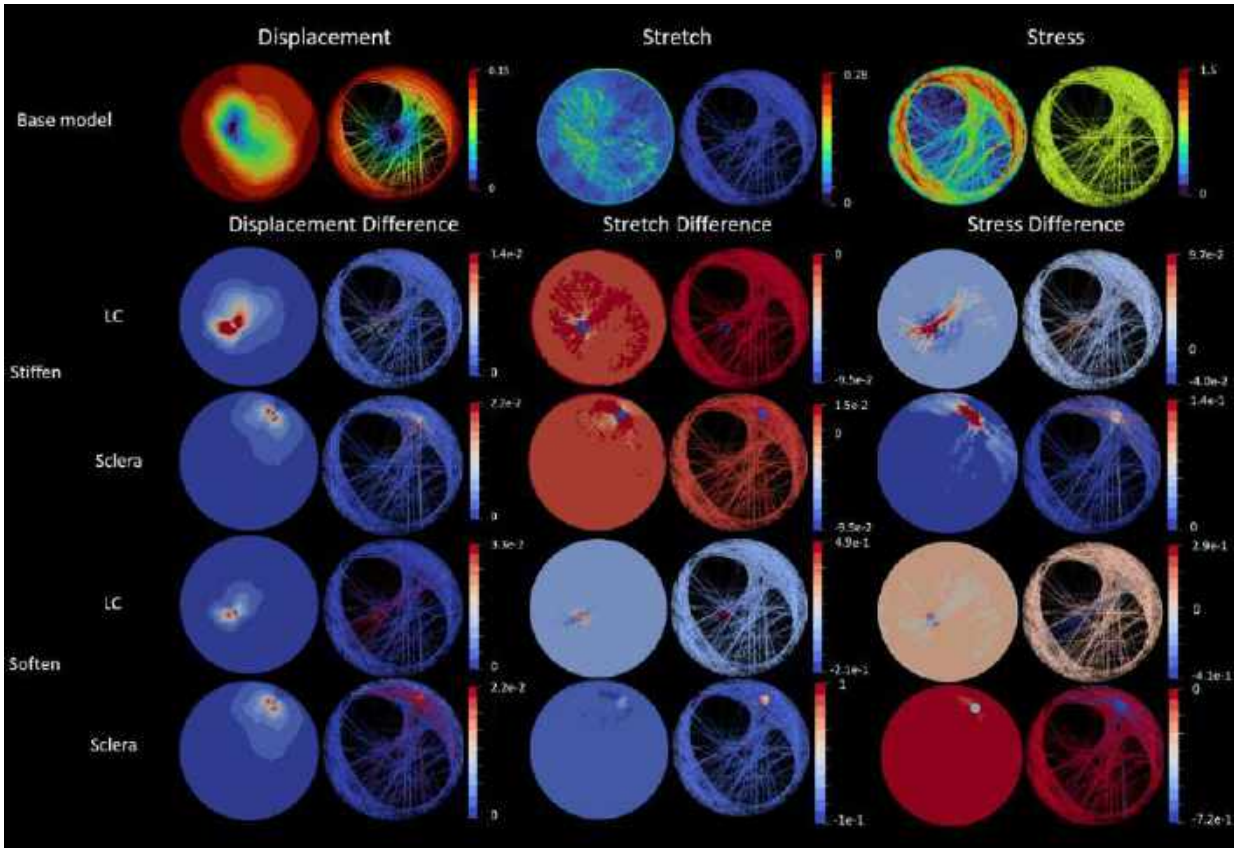

NUMERICAL ANALYSIS OF PULMONARY ARTERY BEHAVIOR: INVESTIGATING THE EFFECTS OF WALL COMPLEXITY, MODEL PARAMETERS, AND PRESTRAIN

Seda Aslan (1), Tianyi Xu (1), Enze Chen (2), Miya Mese-Jones (3), Xiaolong Liu (4), Bryan Gonzalez (5), Ryan O'Hara (5), Yue-Hin Loke (5,6), Narutoshi Hibino (7), Laura Olivieri (8), Axel Krieger (1), Thao D. Nguyen (1)

(1) Department of Mechanical Engineering, Johns Hopkins University, Baltimore, MD, U.S.A.
(2) Department of Civil and Systems Engineering, Johns University, Baltimore, MD, U.S.A.
(3) Baltimore Polytechnic Institute, Baltimore, MD, U.S.A.
(4) Department of Mechanical Engineering, Texas Tech University, Lubbock, TX, U.S.A.
(5) Sheikh Zayed Institute of Pediatric Surgical Innovation, Children's National Hospital, Washington DC, U.S.A.
(6) Division of Cardiology, Children's National Hospital, Washington DC, U.S.A
(7) Section of Cardiac Surgery, Department of Surgery, The University of Chicago Medicine, Chicago, IL, USA
(8) Division of Pediatric Cardiology, University of Pittsburgh Medical Center, Pittsburgh, PA, U.S.A.

INTRODUCTION

Computational models are pivotal in the progress of cardiovascular applications enabling the creation of patient-specific designs of stents, grafts, and patches [1-5] for virtual surgical planning, the visualization of surgical outcomes, and the prediction of the mechanical behavior of the repaired or reconstructed arteries [5,6]. However, the precision of these models is often challenged by patient-specific factors including variations in arterial wall thickness and the specific parameters that define the material properties of the arteries. Another complex factor is the pre-stretch of arteries, which refers to their natural tension without any external forces. Recognizing and integrating these individual factors is crucial to refine the precision of computational models, which in turn, can significantly improve the effectiveness of surgical planning for cardiovascular conditions.

METHODS

In this research, the deformation response of a porcine pulmonary artery (PA) under a pressure increase of 13 mmHg from diastolic to systolic phase [7], was analyzed using finite element software FeBio [8]. The study conducted a thorough analysis to understand how changes in material properties and arterial wall thickness impact the artery's deformation. The established Holzapfel-Gasser-Ogden (HGO) [9] model provided the framework for characterizing the stress-strain relationship of the arterial wall. Different model complexities were considered as shown in Fig. 1. To investigate the effect of wall thickness, the arterial wall was modeled in two ways: as a single-layer structure (intima-media, IM) and as a dual-layer structure (IM and adventitia, ADV) with constant and varying wall thicknesses (t). To study the influence of the heterogeneity of material properties across the PA, HGO parameters were varied based on ex-vivo data derived from the literature [10] in different regions of the PA, namely main PA (MPA), bifurcation region (B), left PA (LPA), and right PA (RPA), as illustrated in Fig. 1(d). The material constants used in each PA region are listed in Table 1. The circumferential strain as a result of pressure increase on the luminal wall was calculated [11]. To assess the influence of t and HGO parameters on the circumferential strains, a sensitivity analysis was carried out by varying the parameters within their standard variation [10,11]. Adjustments to model parameters and t were made to match the observed circumferential strains in vivo [11]. Furthermore, a pre-stretch state [12] was added to the model at the end-diastolic phase to examine its impact on both stress and circumferential strain outcomes using the prestrain gradient available in FeBio [8].

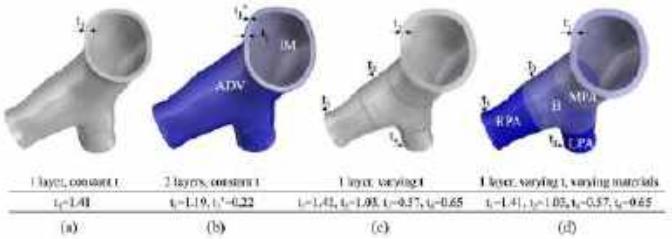

Figure 1: Computational model of PA walls with different wall layers and thicknesses. The unit of thickness is mm [11].

Table 1: HGO model parameters in different regions of PAs [10]

	MPA	B	LPA	RPA
C (kPa)	40	30	43	82
k_1 (kPa)	66	80	247	473
k_2	0.53	0.67	0.61	0.78
β (degrees)	18.9	55.24	39.96	15.14

RESULTS

The circumferential strains along the MPA and B regions obtained using different models are shown in Fig.2a. The results revealed that to replicate the strain response measured in-vivo by magnetic resonance imaging (MRI), it is necessary to incorporate a variation in wall thickness across different regions, and a single-layer model sufficed for this purpose. The sensitivity analysis showed that the strain response was most sensitive to variations in thickness, *t*, and isotropic shear modulus, *C*, of the artery wall (Fig. 2b).

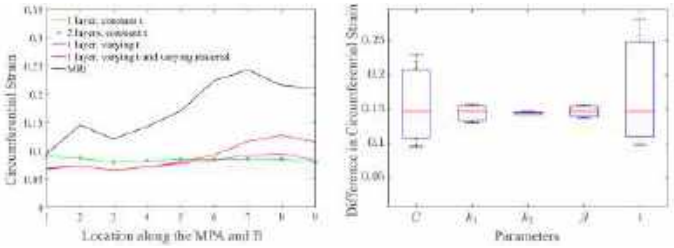

(a) (b)

Figure 2: a) Circumferential strain outcomes of various models. The x-axis shows the PA centerline locations where circumferential strains were measured. b) The difference in circumferential strain resulting from varying parameters [11].

Using this knowledge, we tuned the model parameters for the porcine model until the deformation results were within 10% of the MRI-measured deformations. The initial and tuned *t* along the PAs are shown in Fig. 3a. On the x-axis, positions 1 to 9, 10 to 15, and 16 to 21 correspond to MPA, LPA, and RPA, respectively. Below the figure, the table presents both the initial and tuned values of C in each region of the PA, alongside the range of the values specified in the literature [10]. Initial, tuned, and MRI-measured circumferential strains were presented in Fig. 3b.

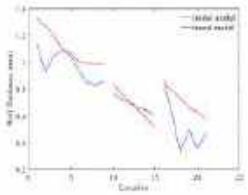

(a)

C			
	initial	tuned	range
MPA	40	35	40.77±11.02
B	30	21	30.03±11.52
LPA	45	60	45.24±71.72
RPA	82	80	82.61±90.54

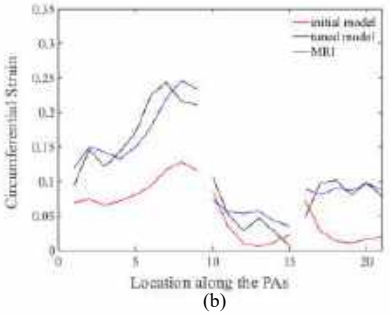

(b)

Figure 3: a) Wall thickness variation of initial and tuned models b) Initial, tuned, and MRI-measured circumferential strains [11].

In the final part of our analysis, as depicted in Fig. 4, we plotted the displacement magnitude (Fig.4a) on the PA walls and examined the impact of varying the pre-stretch value, G. By focusing on a specific node in region B, where the displacements are relatively higher, we noted that an increase in G resulted in a decrease in displacement magnitude (Fig. 4b, top) and an increase in the first principal stress (Fig. 4b, bottom). To further understand the influence of pre-stretch on deformation across the entire PA walls, circumferential strains were plotted for G values of 1.01, 1.014, and 1.018 in Fig.4c. We observed that in the proximal MPA and the distal RPA, deformations increased with an increase in G. In contrast, the LPA exhibited a decrease in circumferential strain. This pattern suggests that pre-stretch may be influenced by geometric factors. Similarities in circumferential strain trends in the LPA and RPA, were observed. It is important to note that the RPA has a larger diameter (approximately 11.66 mm) compared to the LPA (around 10 mm), and a thinner wall (0.57 mm versus 0.65 mm). Additionally, the LPA and RPA do not branch off from the MPA in a perfectly symmetrical manner. Consequently, the large deformation observed in region B, near the LPA and RPA, might contribute to different deformation effects in these areas.

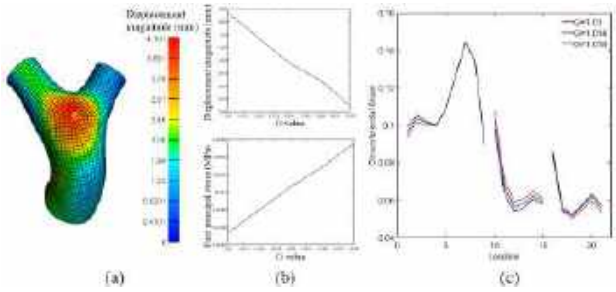

(a) (b) (c)

Figure 4: a) Displacement magnitude on the PA walls at a pre-stretch value of G=1.01. b) Displacement magnitude (top) and first principal stress (bottom) for a selected node in region B with increased G. c) Circumferential strains at different G values.

DISCUSSION

Our modeling framework aims to deepen insights into the influence of arterial wall parameters and to predict the biomechanical response of arteries. For procedures like artery reconstruction, understanding post-surgical shape deformations is crucial, as they can lead to suboptimal outcomes. Our model offers the capability to anticipate these shape changes before surgery. In our upcoming research, we plan to validate this model against the actual post-surgical results of reconstructed arteries. Furthermore, we intend to refine the pre-stretch input of our model by experimentally measuring residual stresses, which will allow us to derive a prestrain gradient using ex vivo porcine PAs. As we acquire more comprehensive data from human arteries, it will become possible to convert these animal models into patient-specific ones.

ACKNOWLEDGEMENTS

This work was supported by the National Science Foundation under Award NSF FRR CAREER 2144348.

REFERENCES

[1] Caimi, A et al. *Journal of Biomechanics*, 79:135–146, 2018.
[2] He, R et al. *Procedia Structural Integrity*, 15:28–32, 2019.
[3] Razaghi, R et al. *Current pharmaceutical design*, 24(37):4492–4502, 2018.
[4] Fegan, K et al. *Frontiers in cardiovascular medicine*, 9:883179, 2022.
[5] Lashkarinia, S et al. *Annals of biomedical engineering*, 46:1292–1308, 2018.
[6] Lashkarinia, S et al. *Journal of Biomechanics*, 117:110274, 2021.
[7] Mueller-Graf, F et al. *Biomedicines*, 9(9):1212, 2021.
[8] Maas, SA et al. *Journal of Biomechanical Engineering*, 134(1) 2012.
[9] Gasser, T et al. *Journal of the royal society interface*, 3(6):15–35, 2006.
[10] Pillalamarri, N et al. *Experimental mechanics*, 61:285–303, 2021.
[11] Aslan, S et al. *In Proceedings of the 17th International Joint Conference on Biomedical Engineering Systems and Technologies (BIOSTEC2024)*
[12] Pourmodheji, R et al. *Journal of the mechanical behavior of biomedical materials*, 119:104448, 2021.

A NOVEL DIFFUSION TENSOR MYOCARDIAL MATERIAL MODEL USING NEURAL NETWORKS FOR FORM DETERMINATION

Benjamin J. Thomas (1), Christian L. Goodbrake (1), Michael S. Sacks (1)

(1) James T. Willerson Center for Cardiovascular Modeling and Simulation, Oden Institute for Computational Engineering and Sciences and the Department of Biomedical Engineering, University of Texas, Austin, Texas, USA

INTRODUCTION

Cardiac tissue is a very complex structure made up of myocytes, blood vessels, and extracellular matrix. The structure also exhibits changes in orientation that can be seen throughout the heart. Determining the effects of structural changes is critical to improving the treatment of cardiac pathologies. Due to these large variations in structure, the tissue is modeled as a nearly incompressible, anisotropic material, where anisotropy is typically modeled through the use of pseudo-invariants giving a measure of strain in certain directions.

Diffusion Tensor Magnetic Resonance Imaging (DTMRI) is an established non-invasive method to obtain the structural properties of fibrous tissue. The diffusion tensor itself has not been fully incorporated in these models, but rather only used to determine the local material orientation. As the diffusion tensor **D** contains much structural information, it seems logical that **D** should be fully incorporated into the material model. However, one ongoing problem in developing new material models is that of determining its form. This is typically done by trial and error and often results in sub-optimal results. By utilizing a machine learning approach, one can give a generic form of the model, with very little prior knowledge, dependent on the diffusion tensor and see which terms are important through the training process.

Neural networks are universal function approximators, allowing them to achieve a good fit to a broad range of problems. By constraining the architecture in a specific way, one can obtain an architecture of neural network that fits most material models dubbed Constitutive Artificial Neural Networks [1]. Extending this idea, the neural network can be inserted into an inverse modeling framework for anisotropic materials, leveraging automatic differentiation to obtain the gradients required to train the system. The method can then be used to determine how the diffusion tensor plays a role in the material model.

METHODS

Given each force-displacement pair, we want to obtain the material parameters for the strain energy function without knowing the exact form it takes. The neural network will represent the arbitrary forms of strain energy functions possible through compositions of functions. Creating the neural network is straightforward since it is a composition of functions beginning with the deformation gradient **F**.

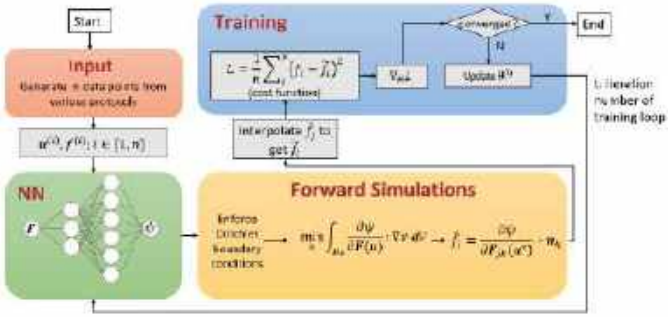

Figure 1: The inverse modeling pipeline from input data until convergence.

Extending the idea to anisotropic materials, the strain energy is no longer a constant scalar field since **F** now has dependence on position, **x**. Thus, a finite element framework is required to solve for the material parameters to capture the variation. The software JAX-FEM was used to incorporate the neural network structure in a finite element package. Now, incompressibility must be enforced weakly through a nearly incompressible formulation depending on det(**F**),

$$\psi_J(\boldsymbol{F}) = \alpha(J(J-1) - \ln(J)) \tag{1}$$

The final strain energy has contributions from the neural network and the incompressible term where α is increased until J ≈ 1 for all elements. The final strain energy is thermodynamically consistent, so the First

Piola-Kirchoff Tensor, **P**, can be found by automatic differentiation with respect to **F** which can give of the force on the respective face.

As seen in Figure 1, an initial model form is chosen, can be with extra terms. The displacements are used as boundary conditions dependent on the protocol. The nodal displacements are solved for, which are then used to calculate the forces from the neural network. The loss, the mean squared error of forces, is now minimized to achieve the desired parameters.

With this method of determining form, one can also add structural information into the form of ψ. For cardiac tissue, the diffusion tensor gives the structural data we desire by distinguishing fiber and sheet directions of the tissue. The diffusion tensor is sampled on a 1 cm^3 grid, so the values used are interpolated onto the mesh are normalized, so integrating ρ in (2) will equal 1. The spatial variation of the diffusion will account for the anisotropy of the material giving us a structural model of the form:

$$\rho(\theta,\phi) = n(\theta,\phi)^T \boldsymbol{D} n(\theta,\phi) \tag{2}$$

$$\psi(\boldsymbol{F}) = \int_{-\frac{\pi}{2}}^{\frac{\pi}{2}} \int_{0}^{\pi} \rho(\theta,\phi)\hat{\psi}(\boldsymbol{F},\theta,\phi)\sin(\phi)\, d\theta d\phi \tag{3}$$

Where the total strain energy $\psi(\boldsymbol{F})$ is calculated from $n(\theta,\phi)$, the normal vector in spherical coordinates, **D,** the diffusion tensor, and $\hat{\psi}(\boldsymbol{F},\theta,\phi)$, the function made from the network mentioned previously.

RESULTS

Testing our inverse modeling method, we used the model and diffusion tensor data described in [2] by Li. The Li dataset comes from 5 specimens of ovine ventricular myocardium with various degrees of anisotropy. Synthetic data was generated to know the true parameters, where the Li model contains 6 pseudo-invariants to cover the ranges of stress seen in the different specimens. An initial guess was determined by finding parameters under the assumption of a homogeneous material model. These initial estimates were then used to determine the anisotropic parameters to obtain the desired fit seen in Figure 3 with the corresponding loss in Figure 2.

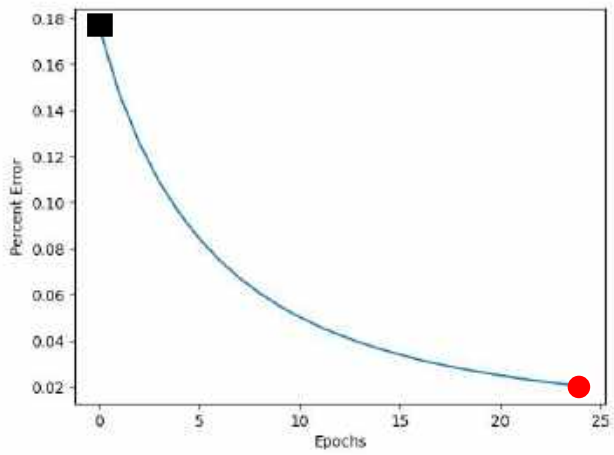

Figure 2: Training curve for learning the Li Model where the black square and red circle corresponds to points in Figure 3 taking roughly 1.5 hours to train.

Using the same data as above along with the force-displacement pairs, the new structural model described in (3) was tested using a strain energy function as follows:

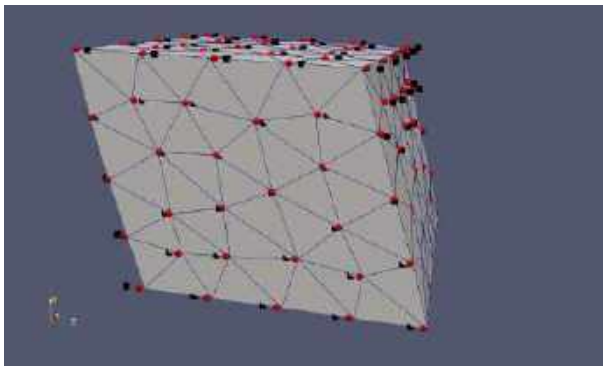

Figure 3: Specimen after pure shear in X1/X2 direction. Black squares represent prediction with initial estimate, red spheres are the prediction after training, and the wireframe is the true solution.

$$\hat{\psi}(\boldsymbol{F},\theta,\phi) = \sum_{i=1}^{5} c_i (I_4 - 1)^{2i} + \sum_{j=1}^{5} d_i (I_5 - 1)^{2i} \tag{4}$$

The specific strain energy was chosen for its ability to capture anisotropy as well as the ease of implementation. The same process of the initial guess was done as before to determine an estimate of the parameters c_i and d_i. Then the inverse method was used to determine the anisotropic parameters for the material where we only needed the first three terms of I_4 with results shown in Figure 4.

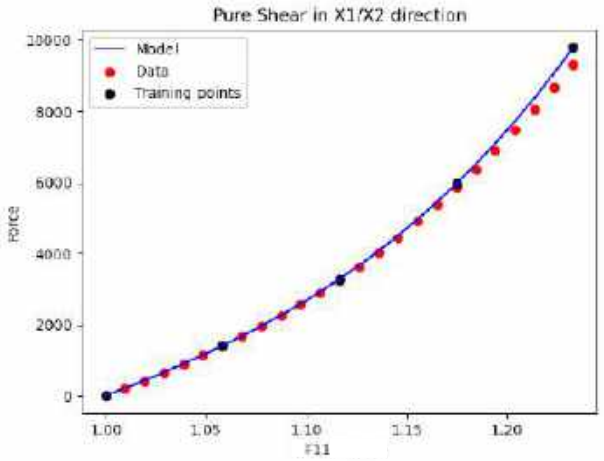

Figure 4: **Force vs. displacement curve for pure shear in the tensile direction.**

DISCUSSION

The framework provided allows us to determine the material model form from the given data, by seeing which parameters go to 0, eliminating guess work in form determination. We can incorporate structural information into the model through diffusion tensor data. Moreover, the models are no longer locally homogeneous because the diffusion tensor varies spatially. This culminates into a simple material model given by (3) and (4) fully describing the anisotropy of the myocardial tissue.

ACKNOWLEDGMENTS

NIH R01 HL073021

REFERENCES

[1] Linke K. et al., Acta Biomaterialia, 160:134-151, 2023

[2] Li, DS et al., J Mech Behav Biomed Mater, 2020, 103, 10350

FUNCTIONALIZED NANOPARTICLES MEDIATED HIGH INTENSITY FOCUSED ULTRASOUND (HIFU) ABLATION IN MICE

Nabin Khanal (1), Michael Marciniak (2), Marie-Christine Daniel (2), Liang Zhu (3), Matthew Lanier (4), Charles Dumoulin (4,5), Rupak K. Banerjee (5)

(1) Department of Mechanical and Materials Engineering, College of Engineering and Applied Science, University of Cincinnati, Cincinnati, Ohio, USA
(2) Department of Chemistry and Biochemistry, University of Maryland Baltimore County (UMBC), Baltimore, USA
(3) Department of Mechanical Engineering, University of Maryland Baltimore County (UMBC), Baltimore, USA
(4) Imaging Research Center (IRC), Cincinnati Children's Hospital Medical Center, Cincinnati, Ohio, USA
(5) Department of Biomedical Engineering, College of Engineering and Applied Science, University of Cincinnati, Cincinnati, Ohio, USA

INTRODUCTION

High Intensity Focused Ultrasound (HIFU) is a non-invasive procedure that has gathered clinical interest for tumor ablation. Its effectiveness has been demonstrated through *in vitro* and *in vivo* models. The key to treating tumors lies in applying sufficient acoustic power to induce necrosis. However, the challenge arises as high acoustic power may inadvertently cause collateral damage to neighboring tissues, resulting in issues like skin burns, and damage to blood vessels and nerve cells. To address this, external heat absorbers such as nanoparticles have been employed to reduce power requirements and exposure durations.

Numerous researchers have explored the use of nanoparticles to enhance thermal effects and decrease power requirements. For instance, Dibaji et. al. [1] utilized magnetic nanoparticles (mNPs) in tissue-mimicking materials (TMM), while recent studies have shown the efficacy of gold nanoparticles (gNPs) in achieving enhanced thermal effects, both *in vitro* and *in vivo* [2].

In a study by Devarakonda et al. [3], the impact of gNPs during HIFU procedures was investigated for 0% gNPs concentration and 0.125% gNPs concentration. However, there is a possibility of injected gNPs being washed away by the bloodstream, diminishing their presence around the tumor, and hindering the intended temperature enhancement. Considering this, the current study emphasizes the use of gNPs functionalized with antibody fragments (Fab) to ensure they adhere to the tumor after injection.

Ouyang et al. [4] discovered that over 15% of functionalized nanoparticles reach the tumor when administered via tail vein injection, provided the number of injected nanoparticles exceeds 1 trillion, a condition met in the present study. In a previous study from our lab [3], a 0.125% concentration (maximum) of non-functionalized gNPs was used. The current research, however, utilizes 15% of the 0.125% concentration, resulting in a required tumor domain concentration of 0.01875%, considering the use of functionalized nanoparticles.

METHODS

Each NSG mouse in the experiment was injected with 1×10^7 PC3 tumor cells. Mice were then housed and monitored at Cincinnati Children's Hospital and Medical Center (Cincinnati, Ohio). The tumor growth was monitored for 4 – 6 weeks. The size of the tumor was measured regularly 2-3 days per week. Once the tumor was roughly above 10 cm in both transverse and longitudinal direction, it was deemed suitable for treatment. This was done to ensure that the treatment can be done in at least two zones of a particular tumor.

The functionalized gNPs construct was prepared following several steps reported by Dockery et. al. [5]. A solution of gNP-CO2H/N3 (81 mL, 2.14×10^{13} gNPs/mL) in filtered, pH8 1X PBS was stirred at room temperature in a freshly cleaned 250 mL round bottom flask. 501 mg Fab-DBCO (~10 Fab/gNP from 1 mg/mL stock) was added to this stirring solution. The reactants were stirred for 1 hour at room temperature. After 1 hour the reaction was stopped. The solution was centrifuged (45k x g, 2 hours, 4˚C), and resuspended in 40 mL filtered pH8 1X PBS. This was followed by another centrifugation (45k x g, 2 hours, 4˚C) with resuspension in 6 mL filtered pH8 1X PBS. Subsequently, a final centrifugation step (21 k x g, 1 hour, 4˚C) followed by resuspension in 2 mL (0.62×10^{15} gNP/mL) filtered, pH8 1X PBS was done.

Figure 1: Schematic representation of functionalization of dendronized gNPs with cancer specific targeting antibody fragment, Fab, starting from citrate gNPs.

The resulting concentrated solution was characterized using DLS and UV-Vis spectroscopy. The Z-average of the particle size was 27.49 nm and the maximum absorbance wavelength was 525 nm. The synthesis of intermediate dendrons and materials is described in the literature [6].

Gold nanoparticles (gNPs) were injected 24 h before the treatment. Mice were put in an incubator at 40˚C for 1 h before gNPs injection. The solution containing gNPs had a distinct purple color, such that it can be visible around the tumor after the injection.

A clinical MR-HIFU system (Sonalleve V2, Philips Medical Systems, Vantaa, Finland), integrated into 1.5 T (T) whole body scanner (Philips Ingenia, Healthcare, Best the Netherlands) was used for the scanning of the mouse tumors. The MR-HIFU system contains a 256-element phased array HIFU transducer that can be used to focus energy to small volumes within the tumor. The diameter of the array transducer and the operating frequency are 140 mm and 1.2 MHz. The focal spot of the HIFU bean was ~2 mm in radial direction. Further details about the MR-HIFU system can be found in Devarakonda et. al. [2].

On the treatment day, the mice were prepared by shaving around the tumor, applying Nair, and injecting with anesthesia. A set of two mice were placed under the HIFU transducer for the treatment. They were covered with acoustic gel to avoid the formation of bubbles and cavitation. MR images were taken before and after the treatment. The treatment was done first by locating the tumor with test sonication and then applying the assigned power with therapy sonication. The temperature rise using MR Thermometry was observed and recorded for analysis. The mice were kept for 4 h after the treatment under analgesia and then euthanized.

RESULTS

The reference body temperature was taken as 37 °C to calculate the temperature rise in all cases. Figure 2 shows the temperature rise data fitted to a linear profile for two cases: 0 % gNPs and 0.01875 % gNPs concentration cases. It illustrates the temperature rise (°C) using acoustic powers of 30 W and 40 W for gNPs concentration of 0% (hashed blue line) considered as the baseline case. Notably, the temperature rise was approximately 10°C and 17°C for 30 W and 40 W acoustic powers, respectively. When the acoustic power was elevated from 30 W to 40 W with 0% gNPs concentration, the temperature rise increased by 70%. A discernible linear trend is evident, characterized by a slope of 0.41 with R^2 value of 0.99.

Figure 2 also illustrates the temperature rise (°C) at acoustic powers of 40 W and 50 W for gNPs concentration of 0.01875% indicated by solid red line. The temperature rise was around 21°C and 30°C for 40 W and 50 W acoustic powers, respectively. An increase from 40 W to 50 W with 0.01875% gNPs concentration resulted in an increase in temperature rise of 42.8%. A linear trend is observed, featuring a slope of 0.58 with R^2 value of ~ 1. Therefore, the slope of temperature rise is higher in the 0.01875 % gNPs case than in the 0 % gNPs case (Figure 2).

In Figure 3, the temperature rise (°C) is presented for the same acoustic powers of 40 W, but with two different gNPs concentrations: 0% and 0.01875%. Notably, the temperature rose to approximately 18°C with 0% gNPs concentration and 21°C with 0.01875% gNPs concentration at the same 40 W acoustic power. This indicates that the temperature rise at 0.01875% gNPs concentration was 17.3% higher than the 0% gNPs concentration (or baseline case). Figure 3 also shows the temperature map around the focal pixels at acoustic power 40 W for both 0 % and 0.01875 % gNPs concentration.

DISCUSSION

The findings of this study highlight that the temperature rise increases with or without the use of gNPs as acoustic power increases. Also, most importantly, it shows that the temperature rise is higher for the case with gNPs in comparison to the case without gNPs for the same acoustic power. This underscores the significant impact of using functionalized gNPs in enhancing thermal effects at the same acoustic power.

Limitations: The study currently provides results for the 0% gNPs case at acoustic powers of 30 W and 40 W, and for the 0.01875% gNPs case at acoustic powers of 40 W and 50 W. Notably, data for the 0% gNPs with 50 W acoustic power and 0.01875% gNPs with 30 W acoustic power are not presented as these aspects are part of an ongoing study, and their findings will be shared in future presentations. Additionally, the current results are based on two mice in each category, and a more extensive study involving four mice in each category is part of an ongoing study.

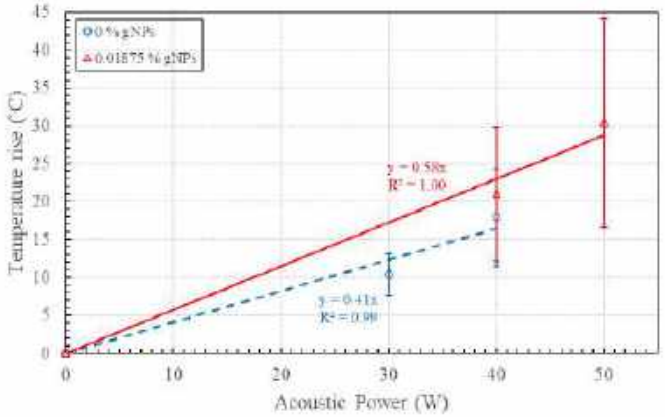

Figure 2: Temperature rise (˚C) with a) 0 % gNPs concentration for acoustic power 30 W and 40 W b) 0.01875 % gNPs concentration for acoustic power 40 W and 50 W

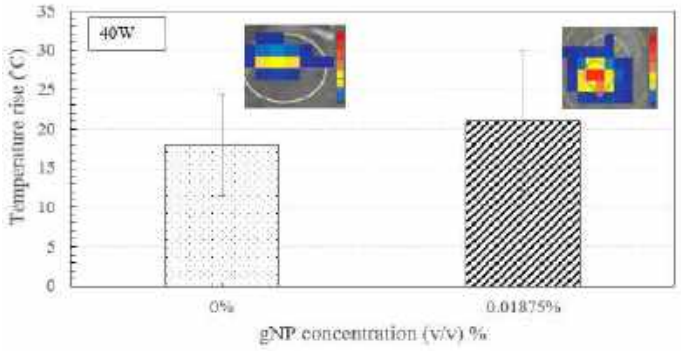

Figure 3: Temperature rise (˚C) for 0 % and 0.01875 % gNPs concentration for acoustic power of 40 W with respective temperature maps

ACKNOWLEDGEMENTS

This research was supported by the National Science Foundation through Grant #NSF CBET 2045234.

REFERENCES

[1] Dibaji et. al., J. of Nanotechnol. Eng. Med. Nov 2013, 4(4): 040902.
[2] Devarakonda et. al., Nano Lett. 2017, 17, 4, 2532-2538.
[3] Devarakonda et. al., ACS Biomater. Sci. Eng. 2019, 5, 8, 4102-4111.
[4] Ouyang et. al., Nat. Mater. 2020, 19, 1362-1371.
[5] Dockery et. al., Pharmaceutics 2023, 15(8), 2103.
[6] Dockery et. al., Tetrahedron 2022, 125, 133044.

INCREASING STUDENTS' EXPOSURE TO RESEARCH VIA APPLIED HOMEWORK PROBLEMS INTEGRATED IN RESEARCH MANUSCRIPTS

Sean Harrington (1), Turner Jennings (1), Ana I. Vargas (2), Frederick Sebastian (2), Rouzbeh Amini (1,2)

(1) Department of Mechanical and Industrial Engineering, Northeastern University, Boston, MA, USA
(2) Department of Bioengineering, Northeastern University, Boston, MA, USA

INTRODUCTION

Experiential learning, the process of integrating real-world problems and academics to create broadly applicable learning outcomes, is a pillar of the Northeastern University learning model. The experiential learning program provides an opportunity for students to apply the models learned in a classroom setting to real-world examples. While pathways to apply the same techniques to research opportunities exist, fewer students participate in research opportunities.

High school and undergraduate education coursework focuses predominantly on design-focused industry applications for the knowledge developed. As a result, for many undergraduate students, the concepts of academic research remain opaque. Integration of research into coursework mostly begins at a graduate level, artificially limiting the population of students engaged with research to those who are already demonstrating an interest in continued education. While lower undergraduate participation in research compared to industry opportunities is at least partially due to the student's anticipated career trajectory (Fig. 1), it is possible that the lower student participation in research is partially due to fewer opportunities to see how to use classroom knowledge in a research setting.

Existing research has shown that exposure to research through classwork increases undergraduate participation and performance in research [1, 2]. Such experiences have been shown to increase student GPA and reduce time to graduate [3]. While the value of participation is well known to the research community, the added value can be unclear to students who may not be able to relate fundamental STEM concepts to cutting-edge, modern scientific inquiry.

We share a framework herein for increasing undergraduate exposure to research through writing research manuscripts with integrated homework problems [4–8]. Examples of our existing papers published using the framework are included to highlight how undergraduate-level concepts can be extracted from complex papers in a way that encourages students to contextualize the course material in terms of potential applications to recent research. The methods discussed herein encourage researchers to broaden the reach of their manuscripts, with benefits to the research community, teaching community, and to the general efficacy of STEM graduates.

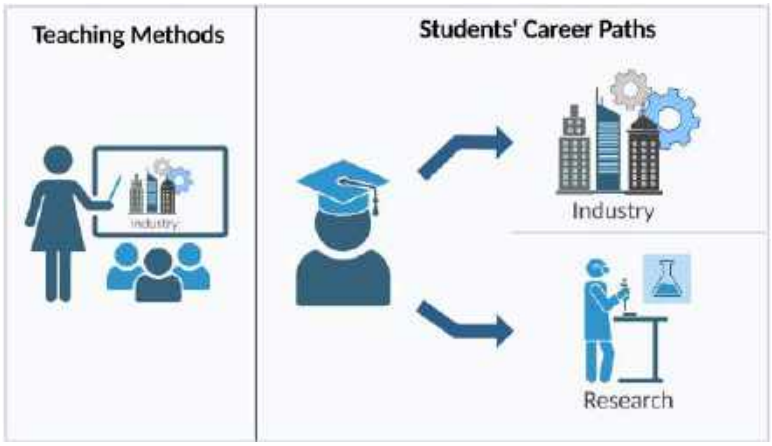

Figure 1: While conventional applications of engineering education often revolve around industry-centric design, research has increasingly emerged as a significant career avenue for numerous biomedical engineering students.

FRAMEWORK

To create a homework problem which encourages students to contextualize their classroom learning in terms of possible research applications, the following criteria have been defined:

1. The problem should be developed with a concept or course in the relevant field in mind.

2. The problem should directly align with the key theoretical concepts or findings presented in the research manuscript. It should serve as a practical application or extension of the research.

3. The problem should require the student to read the manuscript to understand the theoretical framework relevant to the problem.

Existing problems using this framework, examples of which are included hereunder, were developed by adapting existing classroom example problems to describe the core mechanics of the research performed in the related manuscript. Such an approach requires students to read the contents of the manuscript to understand how the simplified problem is foundational to the research performed, while encouraging the student to identify relationships between the simplified models and methods taught in undergraduate coursework and the more complex concepts derived from them used in cutting edge research.

While adhering to the same structural framework, our approach to conceptualizing problems for each paper took diverse paths. On one occasion, the problem originated from discussions among co-authors even before the paper was written. In another instance, a graduate student, serving as the primary author, independently crafted the problem. Additionally, on a separate occasion, the problem arose as a response to a reviewer's inquiry, prompting the authors to delve into and elucidate a fundamental concept.

EXAMPLES

The following "homework problem" examples were included in research manuscripts to bridge theoretical classroom concepts with practical research applications aiming to enhance students' critical thinking skills and comprehension of the research showcased in the specific manuscript.

1. *Undergraduate level biomechanics course—Using kinematics of rigid bodies [7]*: This research manuscript centers around an experimental phantom setup aimed at determining the accuracy of strain measurement in a magnetic resonance imaging (MRI) device. The homework problem posed a straightforward question, intending to establish connections between concepts such as angular velocity and the motion of the phantom. The calculations were mandated to be performed within the imaging plane, in accordance with the specifications of the MRI machine. Within this study, the experimental phantom setup serves as a crucial component, acting as a testing ground to assess the precision of strain measurements within the unique environment of an MRI device. The homework problem, designed to bridge theoretical concepts with practical research applications. The necessity to conduct calculations within the specific imaging plane prescribed by the MRI machine adds an additional layer of complexity and relevance to the research. This careful consideration ensures that the homework problem not only explores the theoretical aspects but also aligns with the practical constraints and requirements imposed by the imaging technology.

2. *Undergraduate level biomechanics course—Using the Law of Laplace to study aortic remodeling during pregnancy [4]*: In the homework problem presented in this manuscript, students are tasked with computing the percentage change in circumferential wall stress within a tubal tissue (specifically, the aorta) between late-gestation and control groups. They should utilize the data provided in the manuscript and apply the Law of Laplace to calculate the stress. Additionally, students are required to investigate the influence of hypertension by incorporating various blood pressures into the analysis of vessel wall stress. This problem provides insights into the biomechanical adaptation of the aorta during pregnancy and how these adaptations are modified in the presence of hypertension.

3. *Undergraduate engineering statistics course—Applying qualitative and quantitative analysis of metadata [5]*: This problem involves data analysis from the most recent SB^3C abstracts or an equivalent conference. A table is provided that outlines abstract counts categorized by the availability of ex-related data, including both sexes, balanced representation, only males, and only females. Students are assigned the responsibility of filling out the table and subsequently comparing their gathered data with the provided information. This exercise offers a practical application of statistical concepts within the realm of metadata analysis.

4. *Higher-level biomechanics or continuum mechanics course—Biaxial data analysis of hyper-elastic materials [6]*: This problem guides students through calculations of stresses and strains in a hyperelastic material using a provided dataset. The first part involves deriving the deformation gradient tensor and subsequently calculating the right Cauchy-Green deformation tensor and Green-Lagrangian strain tensor. In the second part, students have to determine the first Piola-Kirchhoff stress, considering sample thickness and applied loads. The students then have to create stress-strain plots. This problem provides a hands-on, comprehensive analysis of the mechanical responses of planar tissues under biaxial extension.

APPLICATIONS IN TEACHING

In most undergraduate engineering curriculum, homework problems resemble problems that the students would see in industry. Mechanical Engineering students receive countless truss bridge and transverse beam problems in Statics, Mechanics of Materials, and Finite Element Analysis, and while this exposure is great for someone who makes a career in building bridges, it has much less relevance to someone who aims to make a career in academia or research.

For example, a student in Mechanical Engineering will see many examples of pressurized pipes, and learn the Law of Laplace through many variations of the same problem. We propose that instead of assigning the students 3 homework problems with 3 pressurized pipes, the instructor instead assigns one research paper, such as a paper on the structural remodeling of the aorta in pregnancy [4], and assign the problem at the end of the paper for homework. The students would get the same amount of practice with pressurized pipes, but see a real-world application of the topic.

In this example, the students use what they've learned in class to calculate the stress in the walls of the aorta. They would be able to see how the aorta remodels during pregnancy to accommodate the higher volumetric output of the mother's heart during pregnancy. This method of instruction gives the students the same practice as the normal textbook problems, while showing the students a unique application of the topics they are learning in class.

CONCLUSIONS

The proposed framework aims to enhance undergraduate exposure to research by incorporating research manuscripts with integrated homework problems. The criteria for creating these problems involve aligning them with relevant field concepts, directly connecting to key theoretical concepts in the research, and necessitating manuscript reading for understanding. We aimed to illustrate how undergraduate-level concepts could be extracted from complex papers, encouraging students to contextualize course material in terms of potential applications to recent research.

ACKNOWLEDGEMENTS

Support for this work was provided in part by the National Science Foundation (CAREER 2049088).

REFERENCES

[1] Gilmore J et al. *J High Educ* 86.6 (2015).

[2] Lindsay HA et al. *J Chem Educ* 77.9 (2000).

[3] Chamely-Wiik D et al. *J-SoTL* 23.1 (2023).

[4] Vargas AI et al. *Curr Res Physiol* (2023).

[5] Sebastian F et al. *J Biomech* (2023).

[6] Clarin J et al. *ASME J Eng* 2 (2023).

[7] Nwotchouang BST et al. *Magnetic resonance in medicine* 85.3 (2021).

[8] Thomas VS et al. *Acta biomaterialia* 94 (2019).

FIBER SHORTENING AND LAMINAR THICKENING STRAIN ATTRIBUTES REVEAL GREATER TRANSMURAL HETEROGENEITY IN MYOCARDIAL DEFORMATION THAN GREEN STRAINS VIA DENSE MRI

Tawfik M. Hussein (1), John N. Oshinski (1,2)

(1) Wallace H. Coulter Department of Biomedical Engineering, Georgia Institute of Technology and Emory University School of Medicine, Atlanta, GA, USA
(2) Department of Radiology and Imaging Sciences, Emory University School of Medicine, Atlanta, GA, USA

INTRODUCTION

Heart failure with preserved ejection fraction (HFpEF) is a complex clinical syndrome that is characterized by a stiffened myocardium. However, little is known about the local myocardial deformation pattern [1–4]. In HFpEF, global indices of ventricular function, such as ejection fraction (EF), and echocardiographic indices of stiffness fail to capture the local adaptive remodeling that occurs in the myocardium [4]. Local indices, however, such as strain could provide insights into early changes in myocardial deformation. Current imaging-based measures of strain, which rely on the quantification of the circumferential and radial Green strains (E_{CC} and E_{RR}, respectively), do not qualify changes in the myocardial microstructure, and therefore lack clinical intuition and utility. Furthermore, the Green strains are not physically meaningful when the deformation is finite, which may compromise the reproducibility of the computed stiffness in finite element formulations [5, 6]. Due to the variation of the fiber orientation across the myocardial wall, the Green strains also do not capture the known transmural heterogeneity (i.e., subendocardial to subepicardial) of the deformation in relation to the myocardial microstructure [10].

To address the limitations of the Green strain, Criscione et al. developed a set of strain attributes that are optimized for one-fiber family materials, such as the myocardium. These strain attributes relate to the deformation of the myocardial microstructure [1–5]. Additionally, Srinivasa formalized a method, known as QR decomposition, to decompose the deformation into an orthogonal rotation tensor and an upper triangular stretch tensor. The components of the upper triangular stretch tensor are physically meaningful and mathematically tractable and are directly related to Criscione et al's strain attributes and have other major advantages [7]. Hussein et al. then utilized both QR decomposition and the strain attributes proposed by Criscione et al. to develop the Criscione–Hussein model for the myocardium, a constitutive model that was shown to represent the biomechanical behavior of the myocardium better than the Fung and the Holzapfel–Ogden models [6].

Because the strain attributes have yet to be quantified in humans, the goal of this work was to thus quantify the local changes in *fiber shortening and laminar thickening strain attributes* (α_2 and α_3, respectively) in human myocardium, which relate directly to the myocardial microstructure. Laminar thickening is defined as the deformation of the radial–cross-fiber plane along the radial and cross-fiber directions. Strain measurements were based on in-vivo displacement measurements acquired using displacement encoding with stimulated echoes (DENSE) MRI [8]. We hypothesized that fiber shortening and laminar thickening strains will capture greater transmural heterogeneity in myocardial deformation compared to the standard measurements of circumferential and radial Green strains.

METHODS

In 10 healthy humans (6 males ages 25-59 years and 4 females ages 22-31 years), ECG-gated cine DENSE MRI was used to measure pixel displacement in the basal, mid, and apical short axis (SA) orientations of the left ventricular (LV) myocardium [8]. (1) For each SA orientation, the mean and standard deviation of α_2, α_3, E_{CC}, and E_{RR} were calculated globally over the cardiac cycle. (2) Subsequently, to display the transmural variation in strain, the LV myocardium was represented by an AHA 16-segment model, and each segment was divided into 3 layers: subendocardial, midmyocardial, and subepicardial. α_2 and α_3 were calculated by assuming a transmural variation in the fiber orientation from -70° (outer wall) to +80° (inner wall) [9]. Finally, a paired *t*-test was used to assess if the difference between the mean E_{CC} and α_2 as well as the E_{RR} and α_3 per SA region were significant.

RESULTS

In the basal, mid, and apical myocardium, α_2 and α_3 revealed greater insights into the changes in the myocardial microstructure than

E_{CC} and E_{RR}. To illustrate, while the mean E_{CC} and mean E_{RR} were comparable, the mean α_2 was found to be greater than the mean α_3 by two-fold, indicating that *each myocardial region underwent more global fiber shortening than laminar thickening* (**Figure 1**).

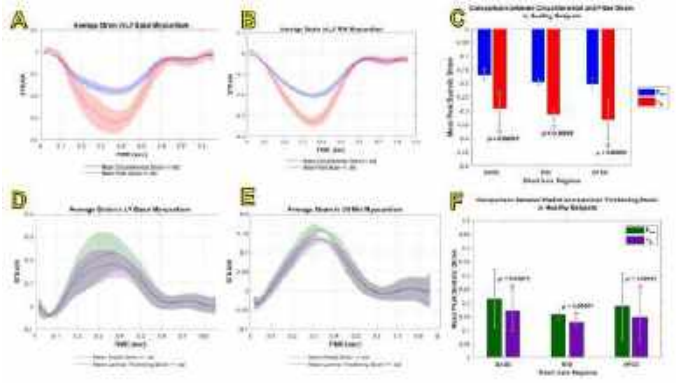

Figure 1: Mean E_{CC} (blue) & α_2 (red) and standard deviation for (A) basal and (B) mid SA view. (C) Mean peak systolic E_{CC} & α_2 for all 3 SA regions. Mean E_{RR} (green) & α_3 (purple) and standard deviation for (D) basal and (E) mid SA view. (F) Mean peak systolic E_{RR} & α_3 for all 3 SA regions.

There were significant differences between both peak systolic α_2 and E_{CC} in the basal ($p = 1.7\times10^{-9}$), mid ($p = 7\times10^{-8}$), and apical regions ($p = 9.9\times10^{-9}$). Likewise, there were significant differences between both peak systolic α_3 and E_{RR} in the basal ($p = 1.1\times10^{-9}$), mid ($p = 1.1\times10^{-9}$), and apical regions ($p = 1.9\times10^{-9}$). See **Table 1**.

Table 1: Measured mean peak systolic E_{CC}, E_{RR}, α_2, and α_3 in the basal, mid, and apical myocardium.

	E_{CC}	α_2	E_{RR}	α_3
Base	– 0.17 ± 0.002	– 0.29 ± 0.002	0.21 ± 0.006	0.17 ± 0.008
Mid	– 0.20 ± 0.002	– 0.31 ± 0.005	0.16 ± 0.007	0.13 ± 0.006
Apex	– 0.20 ± 0.004	– 0.33 ± 0.003	0.19 ± 0.003	0.15 ± 0.001

Figure 2 shows the transmural strain distribution across the myocardium for the mid SA image in peak systole.

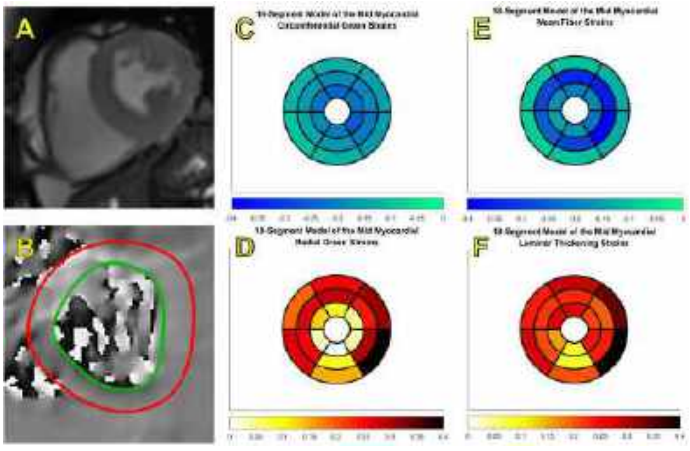

Figure 2: (A) Cine image for orientational reference. (B) Phase SA image of DENSE. Transmural distribution of (C) E_{CC}, (D) E_{RR}, (E) α_2, and (F) α_3 in mid SA region.

DISCUSSION

The goal of this study was to quantify the fiber shortening and laminar thickening strains *in vivo* and compare them to the more commonly used circumferential and radial strains. This study is the first that quantifies Criscione et al.'s strain attributes in the human myocardium. In our data (see **Table 1**), both α_2 and E_{CC} increase from base to apex in peak systole. Likewise, both α_3 and E_{RR} show a reduction in strain from base to mid and an increase from mid to apex in peak systole. Our results show the magnitudes of E_{CC} and E_{RR} were comparable; however, α_2 was double that of α_3 (**Figure 1**). This indicates that the strain attributes show greater transmural heterogeneity compared to the Green strains (**Figure 2**).

One of the seminal studies that sought to quantify the peak systolic Green strains was that of Costa et al., where the transmural variation in the peak systolic myocardial strain was quantified [10]. Our results agree with Costa et al.'s where E_{CC} increased from base to apex, which also agrees with other tagged MRI studies in humans [10–12]. Costa et al. also reported increasing radial thickening from base to apex and uniform fiber shortening (which were both based on Green strains) [10]. However, our work shows that the mean fiber shortening increases from base to apex whereas the laminar thickening decreases from base to mid but increases again from mid to apex. Thus, it appears that the choice of strain (Green vs Criscione et al.) reveals different conclusions about the myocardial microstructure, and thus care should be taken as such conclusions would prove significant for predicting and elucidating patient-specific pathophysiology in disease states such as HFpEF.

Our study is limited in that it needs histological data and/or diffusion tensor MRI data to validate our conclusions about changes in the myocardial microstructure. Additionally, we utilized 2D DENSE data when 3D DENSE would reveal a more complete picture. 3D DENSE would measure all 9 components of the strain tensor as opposed to just 4, producing a more robust means of comparison.

In conclusion, fiber and laminar thickening strain provide deeper insights into the myocardial microstructure compared to the circumferential and radial strains. Furthermore, measurements of such strains could provide clinicians with more mechanistic insights into the LV remodeling process and may serve as predictive markers of adverse remodeling in HFpEF.

ACKNOWLEDGEMENTS

The authors would like to acknowledge the NIH/NHLBI training grant T32HL166146.

REFERENCES

[1] Borlaug, BA et al., *Eur Heart J.*, 32:670–679, 2011.
[2] Shah, SJ et al., *Circulation*, 1001–1026 , 2020.
[3] Zile, MR et al., *Circulation*, 131: 1247–1259, 2015.
[4] Mitter, SS et al., *J. Am. Coll. Cardiol,* 69:1451–1464, 2017.
[5] Srinivasa, A., *Int. J. Eng. Sci.*, 60: 1–12, 2012.
[6] Hussein, TM et al., *J. Biomech. Eng.*, 145: 1–42, 2023.
[7] Criscione, JC et al., *J. Phys. Solids*, 50: 1681–1702, 2002.
[8] Kim, D et al., *Journal of Radiology*, 2004, 230(3):862–71.
[9] Wong, J et al., *Comp. Meth. Biomed. Eng.*, 17:11, 1217-1226, 2014.
[10] Costa, K et al., *Am. J. Physiol*. 276:H595–H607, 1999.
[11] Clark, NR et al., *Circulation*. 84: 67–74, 1991.
[12] Palmon, L et al., *Circulation*,89: 122–131, 1994.

EMPLOYING MICRO-COMPUTED TOMOGRAPHY TO ELUCIDATE HYPOXANTHINE-INDUCED ALTERATIONS IN BLADDER WALL GEOMETRY

F. Azari (1), L.A. Birder (2)(3), A.S. Wolf-Johnson (2), R. Cardoza (1), A.M. Robertson (1)(4)

(1) Department of Mechanical Engineering and Materials Science, University of Pittsburgh, Pittsburgh, PA, U.S.A.
(2) Department of Medicine, University of Pittsburgh, Pittsburgh, PA, U.S.A.
(3) Department of Pharmacology and Chemical Biology, University of Pittsburgh, Pittsburgh, PA, U.S.A.
(4) Department of Bioengineering, University of Pittsburgh, Pittsburgh, PA, U.S.A.

INTRODUCTION

The urinary bladder, a structurally intricate organ, is characterized by its remarkable distensibility and capacity for muscular contraction, integral to its primary function of urine storage and expulsion. The bladder's multi-layered architecture, incorporating a transitional epithelium known as urothelium, high compliance lamina propria, contractile detrusor muscle layer and mechanically protective adventitia, enables it to fill under low pressures and generate sufficient intravesical pressure for near complete emptying, as evidenced in studies [1-6]. However, the advent of senescence introduces a spectrum of structural and functional impairments, significantly attenuating bladder function, a phenomenon extensively documented in gerontological literature [7,8].

In the domain of gerontological research, elucidating these age-associated morphological and functional transformations within the bladder is crucial for developing effective treatments for age related changes including incontinence and increased residual urine. Animal models of aging are needed for investigations of the multifaceted aspects of age-related bladder pathophysiology and provide a platform for developing therapeutic modalities [9]. Hypoxanthine, a purine metabolite that can be a source of potent reactive oxygen species (ROS) has shown great promise in addressing this need as it has a demonstrated ability to generate senescence related structural and functional changes in the murine bladder [9].

Here, we use this murine model of aging to explore one aspect of age-related changes– bladder geometry. While changes to the mechanical properties of rat bladder wall during aging have been studied [10], little attention has been given to age related changes in bladder geometry. The shape and wall thickness of the bladder directly impact the ability of the SMC in the wall to generate pressure in the bladder lumen and therefore have a primary impact on voiding effectiveness.

METHODS

Changes to bladder geometry were assessed in intact, unfixed bladders harvested from control and hypoxanthine treated 3-4-month-old female Sprague-Dawley rats. 3D data sets on bladder geometry including wall thickness were obtained at multiple states of inflation using high resolution micro-CT imaging (Skyscan 1272, Bruker) **Figure 1.** Briefly, following extraction and urine evacuation from control (N=5) and from animals treated with hypoxanthine in their drinking water for 10 mg/kg/day for 3 weeks (N=5), the bladders were placed in Hank's buffer solution containing inhibitors of muscle contraction. The bladders were then mounted on a custom inflation

Figure 1: Skyscan 1272 benchtop device (left) Traditional X-ray micro-CT depiction of internal Image Processing(right) [11]

system and preconditioned for 4 cycles of inflation from 5 to 35 mmHg, controlled using a programmable pump (BS-8000, Braintree Scientific). The intact bladders were then scanned under high resolution micro-CT at a fixed pressure of 7 mmHg and 35 mmHg within a 15 mL humidity-controlled chamber. The micro-CT scans were conducted at settings of 50 kV and 200 μA, 20 μm resolution, and 0.25-degree rotations over the complete 180° rotation, generating data that was post-processed to create 3D STL models of each bladder. Bladder volume and wall thickness were quantified using software tools including Simpleware ScanIP and Materialize 3-matic. Additionally, the bladder compliance was calculated as the change in volume divided by change in pressure from 7mmHg to 35mmHg. To assess asymmetry in wall thickness, four lines were drawn across the bladder lumen, orthogonal to the

longitudinal axis, **Figure 2**. Asymmetry was assessed using a wall uniformity index (WUI), defined as the ratio of maximum to minimum wall thickness across each line with WUI = 1 for perfectly uniformity (equal thickness) and tending to zero with increasing nonuniformity. Data were averaged from the mid lumen (WUI from two middle lines). Data are presented as mean ± standard deviation, with statistical validation using an ordinary one-way ANOVA, significance ($P<0.05$).

RESULTS

The asymmetry of the dome walls was significantly greater in the treated animals than controls (WUI $=0.85 \pm 0.11$ for control, WUI $= 0.48 \pm 0.18$ for treated, $P < 0.01$) [9]. This difference in symmetry is visible, for example, in Figure 2, where the bisected cross sections are shown for representative (A) control and (B) treated bladders. It is striking that despite these significant differences, the average wall thickness was maintained (control 0.65 ± 0.28, treated $0.64 \pm 0.20, P < 0.01$) [9]. The asymmetry can be seen in the deviation about this average. For example, in Figure 2(B), the average wall thickness for the treated bladder is 0.47 ± 0.25 mm. In contrast, the control bladder (A), demonstrates a relatively uniform thickness. 0.27 ± 0.03 mm.

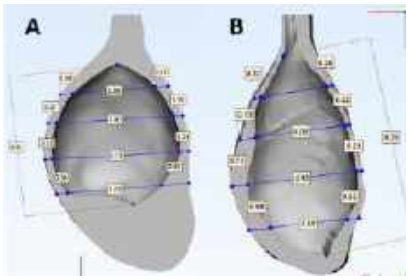

Figure 2: Bisected bladder geometries for control and treated bladders held at 7 mmHg (units in mm)

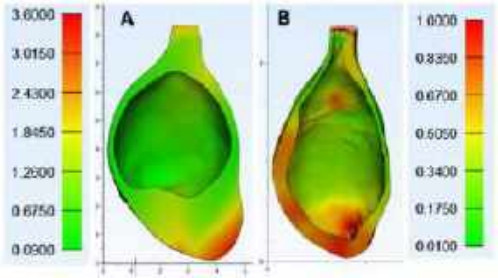

Figure 3: Visualization of Bladder Wall Thickness Variability in Rat Models at 7mmHg.

Figure 3 provides an alternate visualization of the spatially varying wall thickness in these same bladders, where wall thickness is visible as color contours. The control bladder (A) has nearly a uniform wall thickness in the mid lumen region, consistent with a value of WUI close to one. In contrast, the hypoxanthine-treated bladder displays a varied coloration, with red zones signifying areas of greatest thickness.

Moreover, the bladder compliance is decreased in treated versus control animals (4.7 mm^3/mmHg and 5.3 mm^3/mmHg, respectively). Additionally, the average luminal volume at 7mmHg is increased in treated bladders compared with control bladders (42.9 ± 36.5 mm^3 versus 22.4 ± 10.9 mm^3.

DISCUSSION

Several aspects of the geometry of hypoxanthine-treated bladders are substantially different than those of controls. The lumen volume of treated bladders at low pressure is nearly double those of controls. Moreover, the compliance was substantially reduced in the treated bladders. Namely, a larger change in pressure would be required for the same change in volume, suggesting voiding will be impaired. Both trends were also seen in bladders of older rats [10], though different methods were used in this earlier study.

In addition, the current study found the dome walls of treated bladders are less uniform than controls, with a WUI nearly half that of controls. The homogeneity in wall thickness across the control bladder dome would be expected to be associated with a more uniform mechanical stress distribution during micturition cycles, likley important for optimized voiding and filling.

In stark contrast, hypoxanthine-treated bladders exhibited pronounced wall thickness asymmetry, despite having an average wall thickness close to that of controls. This variation would, in turn, lead to a more heterogeneous stress distribution across the bladder dome. Moreover, thickened regions may be susceptible to hypoxia injury unless there is a concomitant increase in feeding vessels.

FUTURE WORK

The current work is an important step toward understanding ROS driven changes to the bladder geometry. Future studies are needed to understand the causes of these changes. It is possible that the urethral resistance increases in treated animals, which would be expected to drive an increase in bladder size, based on prior studies of bladder outlet obstruction [12]. Wall heterogeneity could follow if ROS-damaged bladders had impaired ability to maintain a constant wall thickness during this period of growth. Alternatively, abnormalities in bladder thickness due to heterogeneities in ROS driven changes could result in diminished bladder function, that in turn could drive remodeling changes that increase the bladder size.

An additional key area for future research involves examining the structural alterations linked to variations in bladder wall thickness. It's crucial to ascertain whether thicker areas are caused by fibrosis or smooth muscle cell hypertrophy. In contrast, it remains unclear which components are reduced in thinner sections of the wall. Such knowledge is not only scientifically fundamental but will also contribute to the development of computational models that assess how these structural changes affect bladder functionality and adaptation. Furthermore, upcoming studies will investigate the applicability of this ROS and oxidative stress-based animal model to human conditions and potentially other illnesses. This line of inquiry becomes even more relevant considering findings that show an increase in bladder wall thickness, underscoring the importance of understanding the wider effects of reactive oxygen species on bladder dynamics.

ACKNOWLEDGEMENTS

The author appreciates the support from NIH-1R01AG056944-01A1 Bladder Mucosal Dysfunction During Aging.

REFERENCES

[1] Hanczar, M., et al. (2021). *Int J Mol Sci*, 22(23): 12657.
[2] Trostorf, R., et al. (2022). *JMBBM*, 133, 105347.
[3] Hennig, G., et al. (2023). *Biomech Model Mechanobiol*, 1-11.
[4] Parekh, A., et al. (2010). *J biomechanics*, *43*(9), 1708-1716.
[5] Trostorf, R., et al. (2021). *JMBBM*, 115, 104275.
[6] Ajalloueian, F., et al. (2018). *Nat Rev Urol*, 15(3), 155-174.
[7] Damaser, M. S. (1999). *Scand J Urol Nephrol*, 33(201), 51-58.
[8] Miftahof, R. N., et al. (2013). Springer Science & Business Media.
[9] Birder, L. A., et al. (2023). *J Gerontology: Series A*, glad171.
[10] Cheng, F., et al. (2018). *Biomech Model Mechanobiol*,17(2),403-417.
[11] *X-ray Micro-CT Analysis*. (n.d.). DigiM Solution. https://digimsolution.com/services/imaging/x-ray-micro-ct-analysis/
[12] Cheng, F., et al. (2022). *JMBBM,134*, 105337.

INVESTIGATING NONLINEAR INTRINSIC VISCOELASTICITY OF COLLAGEN TYPE II IN IMMATURE BOVINE ARTICULAR CARTILAGE

Kimberly R. Kroupa (1), Jeffrey A. Weiss (2,3) Gerard A. Ateshian (1,4)

(1) Department of Mechanical Engineering, Columbia University, New York, NY, USA
(2) Department of Biomedical Engineering, University of Utah, Salt Lake City, UT, USA
(3) Department of Orthopaedic Surgery, University of Utah, Salt Lake City, UT, USA
(4) Department of Biomedical Engineering, Columbia University, New York, NY, USA

INTRODUCTION

The mechanical behavior of articular cartilage is conferred by its extracellular matrix (ECM) structure. Composed primarily of proteoglycans (PGs), collagen (COL), and interstitial water, each component plays both independent and cooperative roles in sustaining articular contact. The bulk of PGs are aggregates, i.e. chondroitin sulfate and keratin sulfate, which hold a strong negative charge, producing Donnan osmotic pressure and contributing to the compressive stiffness of the tissue [1-3]. The interwoven type II collagen network counteracts this swelling and provides tensile strength. Together, crowding of these constituents creates the permeable ECM.

Under loading, interstitial fluid will pressurize in the ECM [4]. As the fluid flows through the porous matrix, friction between fluid molecules and the solid matrix dissipates energy, producing flow-*dependent* viscoelasticity. Flow-*independent* viscoelasticity, or intrinsic viscoelasticity, arises instead from the friction between molecules of the solid itself. In compressive loading, the creep and stress relaxation responses of cartilage are dominated by the flow-dependent effect. [2,3, 5,6]. In tensile loading, due to the large ratio of tension to compression nonlinearity of collagen, the response is instead dominated by the intrinsic viscoelasticity [7, 8]. Thus, modeling or isolating the contribution of intrinsic viscoelasticity in compressive loading responses of cartilage is difficult to achieve in the native tissue.

In 1990, Schmidt et al. [9] developed a sequential digestion protocol to remove more than 90% of PGs from cartilage, leaving a nearly pure collagen type II matrix. They measured the tensile response of the digested tissue and compared to native tissue. Under tensile creep testing, PGs were found to limit sudden stretching of the tissue, suggesting a protective role over the collagen matrix during sudden load application. However, the presence of PGs did not affect the equilibrium response of cartilage in any significant way. This method of isolating cartilage constituents overcame the limitations of confounding flow-dependent and intrinsic viscoelasticity in tension.

Similarly, we postulate that by removing nearly all PGs from the cartilage tissue, using this same digestion protocol, the flow-dependent response and fluid pressurization of cartilage under confined compression becomes negligible, producing a response dominated by the intrinsic type II collagen properties. As such, we propose to investigate the intrinsic viscoelasticity of immature bovine articular cartilage by 1) measuring the response of near-completely PG-depleted cartilage tissue under compression, and 2) performing parameter optimization to develop a suitable viscoelastic material model.

METHODS

Sample Preparation: Cylindrical cartilage explants were harvested from the condyles of 8 immature bovine knee joints (∅ 5 mm). Middle and deep zones were retained, with a thickness of 2.23 ± 0.3 mm. To date, 150 explants have been digested of proteoglycans (PGs) using the protocol in [9], as verified with a DMMB assay. Mechanical Testing: Samples underwent stress relaxation testing in unconfined compression. A 10 g tare load was applied to mitigate a toe region response. Then, 10% strain was applied at a rate of 1 μm/s and held for 1800s while the sample relaxed. Young's modulus E_Y was estimated from equilibrium load, displacement, and sample geometry [10]. Samples were allowed to relax for several hours, then retested at 40% strain, and held until an equilibrium load was reached, up to 2 hours (n=2).

Modeling: A finite element model was generated in the open-source FE software FEBio (www.febio.org) to replicate the experimental data. A unit cube (one hex8 element) was aligned with the XYZ-coordinate axes (Fig. 1). Fixed displacement boundary conditions were prescribed normal to each of the coordinate planes, resulting in a homogeneous state of strain and stress in the model. On the Z-face, the displacement profile of experimental strain was prescribed using a rigid 'platen'.

Material Model: Collagen was modeled using reactive viscoelasticity [13], with Type I bond kinetics, and elastic neo-Hookean models for strong and weak bonds, with modulus E and Poisson ratio $\nu = 0$.

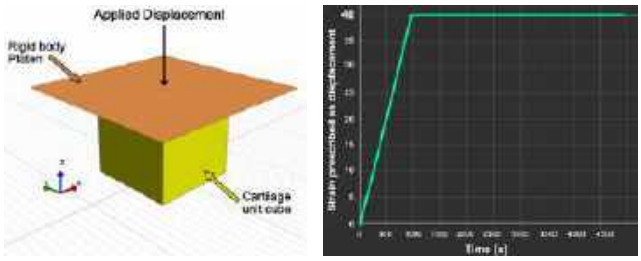

Figure 1: (A) Model geometry showing unit cube of cartilage and rigid body platen in contact with Z+ face. The load response on the platen represents stress (Figure 2, yellow) (B) Displacement profile from experimental data, prescribed on the platen

due to the lack of radial expansion (bulging) noted during experimentation [11]. A reduced relaxation function was selected by trial and error [15], landing on the continuous relaxation spectrum [12]:

$$g(t) = \frac{\tau_2 e^{\frac{-t}{\tau_2}} - \tau_1 e^{\frac{-t}{\tau_1}} + t\left[Ei\left(-\frac{t}{\tau_1}\right) - Ei\left(-\frac{t}{\tau_2}\right)\right]}{\tau_2 - \tau_1} \quad (1)$$

where Ei is the exponential integral function. Here, shortest time constant for relaxation is τ_1 and longest is τ_2. A power-law cumulative distribution function (CDF) was used to account for recruitment of weak bonds with increasing strain [15], with the form:

$$F(\Xi) = \mu_0 + \mu_1 \left(\frac{\Xi}{\Xi_0}\right)^{\alpha} \quad (2)$$

This function starts at μ_0=1, and rises with exponent $\alpha = 2$ and coefficient μ_1, increasing with a measure of strain Ξ, scaled by Ξ_0, where $\Xi = \|\boldsymbol{E}\|$ and $\boldsymbol{E}$ is the Lagrange strain tensor. A parameter optimization was performed to fit for E_e, E_b, τ_1, τ_2, μ_1, Ξ_0 from stress data of 40% strain tests, where e and b refer to strong and weak bonds, respectively.

RESULTS

The fitted values of the six material constants for two representative samples are listed in Table 1. Parameter optimization on the experimental 40% strain transient stress response data (Fig. 2) resulted in the fits shown, with $R^2 = 0.99$ for samples 1 and 2. The model exhibited slight undershoot at the peak stress (~900 s), reaching 90% of the experimental maximum, and slightly faster relaxation than observed.

Table 1: Material parameters fit for samples S1 and S2

Param.	Value	
	S1	S2
E_e (kPa)	18.8	19.8
E_b (kPa)	551	946
τ_1 (s)	10^{-3}	1.2×10^{-3}
τ_2 (s)	65.9	66.4
μ_1	27.8	21.8
Ξ_0	0.854	0.991

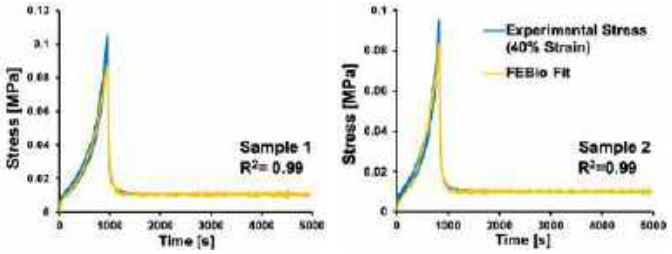

Figure 2: FEBio fit of 40% strain stress response (yellow), compared to experimental data (blue). S1 $R^2 = 0.99$, S2 $R^2 = 0.99$

These fitted values were then used to predict the response to the experimental stress response data at 10% strain (Fig. 3). These predictions consistently undershoot the experimental response over the duration of testing, but they maintain the profile of the experimental data well (R^2 =?). Here also, the model relaxed slightly faster than experimental data. Noise in the experimental data was due to the actuating stepper motor's resolution (~0.5 μm per step).

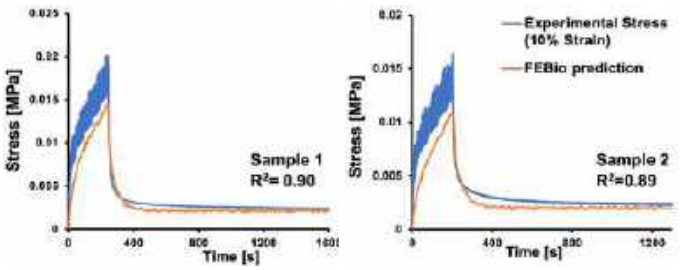

Figure 3: FEBio prediction of 10% strain stress response (orange), compared to experimental data (blue). S1 $R^2 = 0.90$, S2 $R^2 = 0.89$

DISCUSSION

This study demonstrates that near complete digestion of PGs allows us to characterize the intrinsic viscoelasticity of the porous type II collagen matrix of articular cartilage. Two samples were tested preliminarily, producing reasonable fits (Fig. 2) and predictions (Fig. 3). The fact that the prediction at 10% strain underestimates the experimental response suggests that the viscoelastic response is strain-dependent (thus, collagen is nonlinearly viscoelastic). These preliminary findings suggest that we may need to fit data from multiple ramp-and-hold stress relaxation tests (e.g., four times 10% strain, instead of a single 40% strain test). This refinement in the testing protocol will be explored next.

In 2015, we proposed [13] to model nonlinear viscoelasticity using the reactive viscoelasticity framework, where strain energy density in a material depends on the stored energy of strong and weak bonds in the tissue [14]. *Strong bonds,* such as covalent bonds [15], bind collagen together, and make up the elastic part of a load response (Figs. 2&3, see stress plateau >1500 s). *Weak bonds,* such as hydrogen bonds (formed by electrostatic attraction of local electrical charge variations along the length of collagen fibrils), become stressed under loading, then break and reform in a stress-free state. This time-dependent reaction produces the viscous contribution to the tissue load response (Figs. 2&3, see stress peak, which decreases rapidly according to τ_2 as bonds break and reform <1000 s). As the tissue is compressed, it is sensible that more local charges come into proximity to one another, giving rise to the need for weak bond recruitment, represented by the power CDF [14].

As expected, the values fitted for E_e (Table 1, n=2) agree with the average equilibrium modulus of PG-depleted cartilage explants, 18.9 ± 3.7 kPa (n=30). The fitted values for E_b (Table 1) were far greater than E_e, in accordance with observations of a large increase in stress with strain (Fig. 2), implying that intrinsic viscoelasticity is very significant in the type II collagen matrix of immature bovine articular cartilage, potentially playing a major role in the protection of the tissue against damage under loading, as explained in our recent theoretical study [14]. In our ongoing studies we will continue to investigate the best model to fit to experimental unconfined compression stress-relaxation data on PG-depleted cartilage samples, to acquire more insights into cartilage structure-function relations.

ACKNOWLEDGEMENTS

The authors acknowledge support from NIH GM083925.

REFERENCES: [1] Maroudas+ *Adult Art Cart*, *215-90,* 1979. [2] Mow+ *J Biomech*, 17:377-94, 1984. [3] Mow+ *Trans Orthop Res*, 9:262, 1984. [4] Ateshian+ *J Biomech*, 42(9): 1163-1176, 2009. [5] Edwards+ *J Physiol*, 183:5P-6P, 1966. [6] Mow+ *J Biomech Eng*, 102:73-84, 1980. [7] Huang+ *J Biomech*, 123:410-17, 2001. [8] Huang+ *J Biomech*, 125:84-93, 2003. [9] Schmidt+ *J Orthop Res*, 8(3):353-53, 1990. [10] Cigan+ *J Biomech*, 47(16): 3845-3854, 2014. [11] Park+ *J Biomech Eng,* 128(4):623-30, 2006. [12] Fung+ *Prentice-Hall*, 1972. [13] Ateshian+ *J Biomech*, 48(6):941-7, 2015. [14] Ateshian+ *J Biomech Eng,* 2023.

DISPLACEMENT PROPAGATION IN PRESTRESSED TWO-DIMENSIONAL FIBROUS NETWORKS

Ashutosh Mishra (1), Hamed Hatami-Marbini (1)

(1) Department of Mechanical and Industrial Engineering, University of Illinois at Chicago, Chicago, Illinois, USA, Email: hatami@uic.edu

INTRODUCTION

Fibrous networks, serving as fundamental structural components in numerous materials such as paper, fabric, rubber, cytoskeleton, and soft tissues, have captured the interest of researchers for a long time [1]. The intriguing aspect lies in how these network structures not only contribute to the structural integrity of materials they compose but also influence their characteristics and functions. For instance, studies show that non-woven fabric benefits from fiber networks in holding and absorption, while rubber's cross-linking network structure provides its distinctive elasticity. Likewise, fibrous networks play a vital role in biological materials, with one such notable example being the Extracellular Matrix (ECM). Ubiquitous in all tissues, ECM primarily consists of various macromolecules, with collagen as the predominant fibrous protein organizing into networks. The ECM, with its network structure, plays a central role in various physiological processes, including cell growth, homeostasis, cell migration, differentiation, and morphogenesis [2].

A distinct feature of biological materials like the ECM, is nonlinear strain stiffening. This characteristic enables these materials to stiffen as per the applied strain, setting them apart from the non-biological materials [3]. Recent studies have also highlighted another interesting aspect of biological fibrous networks— the presence of residual stresses. These residual stresses play a crucial role in biological materials, such as supporting the mechanics of heart functioning in cardiovascular tissues and alveolar ducts in lung tissues [4][5]. These residual stresses, or prestress emerge from different factors like fluctuations in water concentration within the interstitial fluid, contraction in embedded fibroblast cells, or even from the early stages of development in the ECM [6]. These prestresses are known to induce anisotropy in collagen fibrous networks, even altering stiffness and modifying the onset of strain stiffening in these structures [7][8]. Therefore, it is evident that prestress is a fundamental aspect of fibrous networks and recognizing prestress as a fundamental influence on fibrous networks, its consideration becomes vital in their modeling and analysis.

The ECM also plays a crucial role in cell-cell communication, where cells within the ECM perceive and respond to their environment and neighboring cells. Previous studies have shown that contracting cells within fibrous ECMs can transmit displacement and forces over considerable distances relative to their size. However, previous studies often overlook the presence of residual stresses when analyzing networks subjected to local contraction. As highlighted earlier, prestresses are significant and should be considered when modeling and analyzing ECM network structures. Therefore, the aim of this study is to investigate the propagation of displacement through ECM generated due to cellular contractions in the presence of residual stresses.

METHODS

To simulate a fibrous network, a 2D regular network consisting of triangular unit cells is generated, with dimensions L in both directions. Each fiber, with a length of l_0, crosslinks at nodes with a local connectivity of 6. As known, biological fibrous networks exhibit a random and sub-isostatic nature, where the average connectivity falls between 3 and 4. To achieve this randomness and desired network connectivity, fibers within the network are removed with a probability of 1-q, where q is the probability of retaining fibers, until the desired connectivity is reached. To simulate a contracting cell embedded in the network, fibers inside a circular inclusion at the center of the network are removed. The inclusion's radius, R_c, is carefully chosen to maintain a ratio of $l_0/R_c \geq 0.4$. Network dimensions are selected to be at least 40 times greater than R_c to minimize any boundary effects.

The fibers in the network are modelled as athermal planar beam elements with a circular cross-section having area A, Elastic Modulus E, and Moment of Inertia I. These fibers have an axial modulus $\mu=EA$ and bending modulus $\kappa=EI$. A dimensionless bending rigidity, denoted as $\bar{\kappa} = \kappa/\mu l_0^2$, is set at 10^{-3} for this study unless otherwise specified.

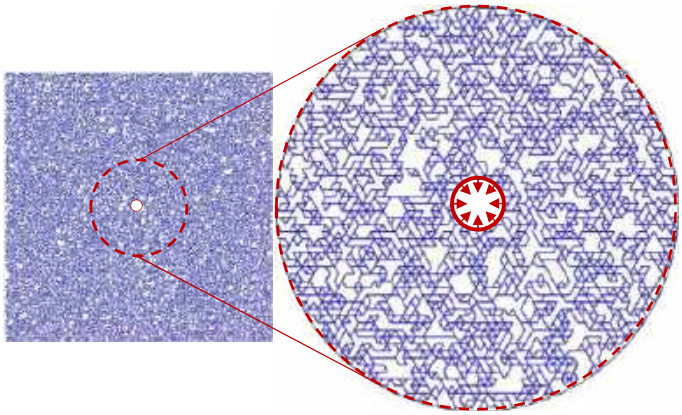

Figure 1: The diluted fibrous network with the center inclusion region where isotropic contraction is applied

Additionally, to accurately capture fiber deformation, the fibers in the network are subdivided into multiple elements. Figure 1 shows the diluted fibrous network with central inclusion where isotropic contraction is applied to mimic the cellular contraction.

To introduce residual stress to the network, nodes along the top boundary are either moved towards or away from the bottom boundary, while the bottom nodes remain fixed. The nodes along the vertical boundaries are subject to periodic boundary conditions. After applying prestress, the center inclusion undergoes isotropic contraction towards the network center, while ensuring the nodes at the network boundary remain fixed in their positions. The contraction is incrementally applied till 30%, resulting in localized contractile deformation.

RESULTS

The random networks were subjected to various levels of prestress in both tensile (away from the bottom or postive) and compressive (towards the bottom or negative) directions. In figure 2(a-c), the displacement propagation within the random network is illustrated under +5%, 0%, and -5% uniaxial prestress, respectively, due to 30% isotropic cell contraction at the center inclusion. The results clearly shows that the magnitude of displacement is most pronounced in the vicinity of the network center, diminishing gradually with increased distanceas observed in previous studies [9]. The propagation of displacement through the network also depends on the direction of prestress applied. When -5% prestress is applied, the displacement spreads further compared to the non-prestressed network. In contrast, +5% prestress results in a quicker reduction in displacement spread, concentrating nearer to the center of the network.

To quantify the observations the normalized radial displacement ($\hat{U}$) and normalized radial distance ($\hat{R}$) were obtained by dividing radial displacement (Ur) and radial distance (R) by the radius of the inclusion center (R_c), respectively. The findigs, shown in figure 2(a-c), were then fitted to the following mathematical expression

$$\hat{U} = A\hat{R}^{-n} + B\hat{R}^{n} \quad (1)$$

where A, B, and n are fitting coefficients. The coefficient n indicates the rate of displacement decay. A lower value n suggesta a more spreadout displacement field. Figure 2d illustrates the average normalized radial displacement with respect to the normalized radial distance of the nodes for different applied uniaxial prestress values.

DISCUSSION

The deviation in displacement propagation behavior in random networks, compared to a linear elastic continuum, can be attributed to compression weakening and fiber reorientation mechanisms. Previous

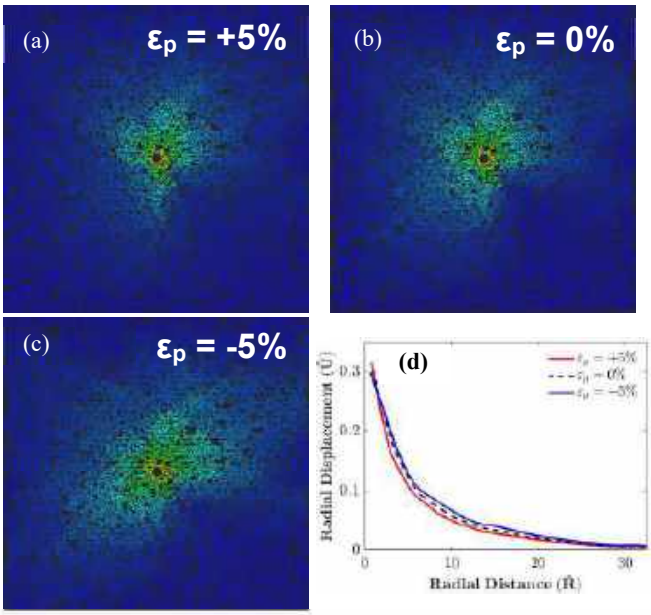

Figure 2: The propagation of displacement within random fibrous networks under (a) +5%, (b) 0% and (c) -5% uniaxial prestress subjected to 30% local contraction; (d) The smoothened average normalized radial displacement with respect to the normalized radial distance of the nodes for multiple values of the applied uniaxial prestress obtained using expression (1)

studies emphasize the crucial role of prestress in altering matrix stiffness. Negative prestress reduces overall network stiffness, allowing lower-energy deformations like bending and buckling when subjected to isotropic contraction, intensifying these mechanisms. Reduced stiffness enhances fiber reorientation, allowing fibers more easily align in response to applied forces, contributing to increased displacement propagation. Conversely, positive prestress increases stiffness, making fibers less prone to bending and favoring stretching, thus restricting displacement spread, and leading to reduced propagation.

In summary, this study highlights the impact of prestress on the extent of the displacement field in fibrous networks. Positive prestress led to a higher n-value compared to the non-prestressed network. Networks with greater stiffness showed decreased transmission of displacement compared to less stiff networks. Future investigations should delve into the influence of fiber bending rigidity and average network connectivity. Additionally, considering the composite nature of ECM, as suggested by recent studies, could be a valuable aspect for exploration in future research.

ACKNOWLEDGEMENTS

The authors would like to acknowledge the computational resources provided by ACER group at UIC.

REFERENCES

[1] Broedersz C. P., *Rev. Mod. Phys.*, 86, no. 3, 995–1036, 2014
[2] Frantz C., *J. Cell Sci.*, 123, no. Pt 24, 4195–4200, 2010
[3] Storm C., *Nature*, vol. 435, no. 7039, 191–194, 2005
[4] Fomovsky G. M., *Spec. Is Extracell. Mat*, 48, no. 3, 490–496, 2010
[5] Knudsen L., *Histochem. Cell Biol.*, 150, no. 6, 661–676, 2018
[6] Masic A., *Nat. Commun.*, 6, no. 1, 5942, 2015
[7] Thomopoulos S., *J. Biomech. Eng.*, 129, 5, 642–650, 2007
[8] Hatami-Marbini H., Biophys. *J.*, 120, no. 3, 527–538, 2021
[9] Hatami-Marbini H., *Int. J. Solids Struct.,* 228, p. 111045, 2021

DIGITAL TWIN DEVELOPMENT AND FATIGUE OPTIMIZATION OF NOVEL POLYMERIC TAVR DEVICES TAILORED FOR PATIENT-SPECIFIC NEEDS

Brandon J. Kovarovic (1), Kyle J. Baylous (1), Ryan T. Helbock (1), Oren M. Rotman (1), Marvin J. Slepian (2), Danny Bluestein (1)

(1) Department of Biomedical Engineering, Stony Brook University, Stony Brook, NY, USA
(2) Department of Medicine and Biomedical Engineering, Sarver Heart Center, University of Arizona, Tucson, AZ, USA

INTRODUCTION

Transcatheter aortic valve replacement (TAVR) has emerged as a minimally invasive alternative to high-risk surgical procedures, deploying a stented bioprosthetic valve within the aortic valve. Despite its rapid adoption and surpassing surgical valve procedures in 2019 [1], TAVR is associated with persistent clinical complications, primarily stemming from the limitations of chemically-fixed tissue bioprosthetic valve material.

The unknown *in vivo* durability of the leaflet structures poses a significant challenge, with structural valve degeneration (SVD) and wear leading to valve failure [2]. TAVR, originally intended for high-risk patients, now includes lower-risk and younger patients, further emphasizing the need for durable alternatives. Complications such as leaflet tissue damage during crimping and deployment phases, as well as thrombosis-related issues, remain prevalent. Testing and prediction of device fatigue (both leaflet and stent frame durability) has been limited to complex and costly *in vitro* accelerated wear testing that does not capture psychological motion/interaction of the device.

To overcome these challenges, polymeric valve alternatives are being explored. Polymeric technology offers the flexibility to design optimal valve configurations, considering ease, cost-effectiveness, and control of polymer manufacturing. While attempts at polymeric valve devices date back to the 1950s, limitations in available materials hindered progress. Key requirements for polymeric TAVR devices include hemocompatibility, flexibility, and exceptional durability (25 years in vivo). However, challenges arise in compressibility compared to tissue materials, necessitating design modifications to facilitate crimping into reasonable delivery catheter sizes.

This study presents the development of a polymeric TAVR device, from the concept surgical valve and progressing through material refinement and *in silico* optimization of the device performance and fatigue life prediction. Digital twin modeling utilizing patient models and complex beating heart model (Living Heart Model, Dassault Systemes, Vélizy-Villacoublay, France) allowed the optimization of

Figure 1 - Timeline for PolyV-2, and the PolyV-B device for BAV patients.

both devices for trileaflet and bileaflet patient anatomies. The latest generation, PolyV-2 27 mm (PolyNova Cardiovascular Inc, Stony Brook, NY), showcases advancements in polymeric TAVR technology, addressing key limitations and offering a promising solution to enhance durability and mitigate clinical complications associated with tissue valves (Fig1). The PolyV-B is the latest concept optimized polymer valve specifically designed to address the special needs of bileaflet aortic valve (BAV) patients, who are currently treated with commercial TAVR devices that are intended to restore the typical trileaflet aortic valve circular orifice configuration. When deployed in BAV patients whose valve's orifice is eccentric, such devices may perform poorly.

METHODS

The PolyV-2 device builds upon the advancements and success of the cross-linked styrene-isobutylene-styrene (xSIBS) based thermoset material known as "Flexamer." This material has recently demonstrated anti-thrombotic characteristics [3] and remarkable durability, enduring the equivalent of 25 in vivo years through 1 billion accelerated wear cycles [4]. The development and optimization of PolyV-2 aimed to achieve several key objectives, including the generation of larger valve sizes, establishment of suitable radial anchoring forces, targeting an 18F delivery catheter, enhancing valve performance, and implementing a

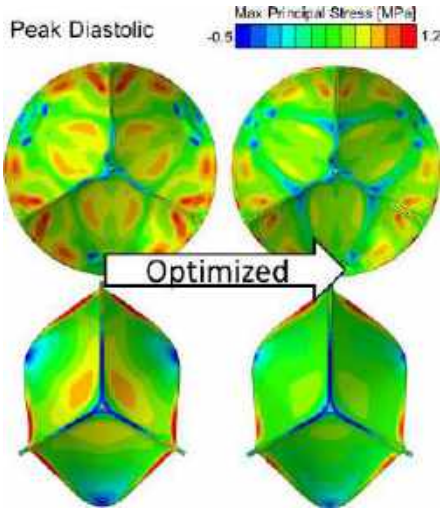

Figure 2 - Max principal stresses during peak diastole of the PolyV-2 (top) and PolyV-B (bottom) and the impact of the variable thickness optimized design.

"sutureless" molding approach. The primary focus was on designing for sutureless molding, allowing for the casting of both the leaflets and sleeve onto the stent frame in a single operation. This innovative approach eliminates a significant source of manufacturing error associated with the multi-day hand suturing of tissue to the stent frame. The design process involved in silico trials, leveraging finite element analysis (FEA) with Abaqus 2022 by Dassault Systemes. The optimization sequence included refining the stent frame design, followed by optimizing the leaflet profile, and finally fine-tuning the leaflet thickness (Fig 2). These steps were crucial in achieving the desired goals of larger sizes, effective anchoring, catheter compatibility, improved performance, and sutureless molding. The PolyV-B was optimized with a similar methodology [5], but with the assumption that the final stent will be eccentrically deployed, and asymmetrical leaflets will be used to achieve the highest device performance in the non-ideal deployment.

The PolyV-2 was compared to commercial tissue valve alternatives in the Living Heart Model v.2019 (The Living Heart Project, Simulia, Dassault Systemes) and simulated using ABAQUS Explicit. The simulation involved crimping the stents to the appropriate diameter and retracting the outer sheath, simulating the deployment procedure within the native aortic valve. Following stabilization, the heart was allowed to beat, and the stent deformation was tracked over three cycles until repeatability was achieved.

FEA was employed to assess the fatigue resistance of the stent models, utilizing the nitinol material properties as defined by Pelton et al [6]. Given the unique hyperelastic characteristics of self-expanding nitinol stents, the analysis tracked both the mean strain (over the loading cycle) and the strain amplitude (change in strain over the cycle) of each element node. Pelton's defined curve (Fig 3) established limits, with mean absolute principal strains over 8% and strain amplitudes over 0.4% indicating a risk of fatigue failure. Conversely, values below the curve were considered indicative of no risk of fatigue failure. This approach provided a comprehensive evaluation of the fatigue resistance of the stent models, contributing valuable insights into their performance under dynamic conditions.

RESULTS

The PolyV-2 design (Fig 3) was iterated to optimize achieving the highest radial force with a lower crimping volume of the stent (total volume must be reduced due to the incompressiblity of the polymer). The PolyV-2 prototypes were evaluated for hydrodynamic performance (ISO 5840 2021) and achieved greater performance (Effective orifice area >2.0 cm^2) compared to commercial tissue valves of similar size. Hydrodynamic testing also confirmed the adequate anchoring force with the larger (>120mmHg) diastolic back pressures, confirming the success of in depth *in silico* testing prior to manufacturing.

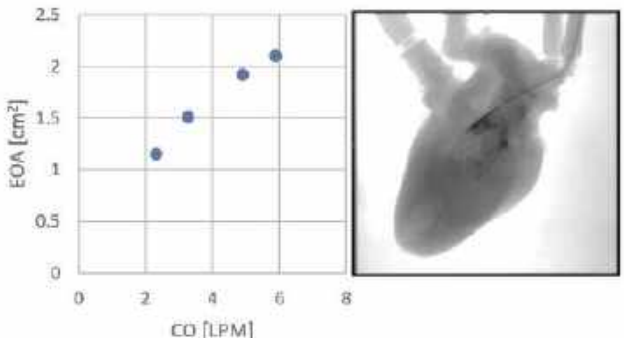

Figure 3 - (Left) Hydrodynamic performance (EOA) vs the cardiac output of the PolyV-2, (Right) Angiogram of the deployed PolyV-2 in an ex vivo ovine heart.

The PolyV-B was evaluated in patient-specific models and compared to commercial tissue valves [5], and with the optimization process achieved *in silico* performance 10-50% larger than the commercial alternative. The beating heart fatigue analysis demonstrated (Fig 3) the PolyV-2 struts were optimized to reduce the strain in stent joints and thus achieving better fatigue resistance in the top and mid element compared to the commercial stent and similar fatigue in the annulus region.

DISCUSSION

This study demonstrates the utility of digital twin modeling for cardiovascular device optimization, design to address specific anatomies and to help predict fatigue life of the device *in vivo*. By placing more effort in the design of the device, the PolyV-2 is able to mitigate the common pitfalls of previous polymeric valves failures [4]. The PolyV-2 is currently ongoing acute and chronic ovine trials. The initial *in silico* evaluation of the PolyV-B demonstrated superior performance and ability to design a device to address a currently neglected patient population with a unique anatomy.

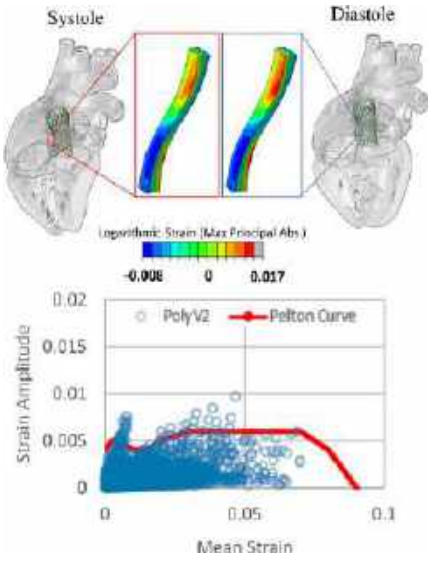

Figure 4 - (Top) TAVR stent deployed in the Living Heart Model tracking the stent strain over the cardiac cycle, (Bottom) is the Goodman analysis of the fatigue resistance of the PolyV-2 stent.

ACKNOWLEDGEMENTS

Funding provided by NIH-NIBIB Phase II-U01EB012487 (DB); NIH-NIBIB 1U01EB026414-01 (DB). Industry Partners: ANSYS, Dassault Systèmes.

REFERENCES

[1] Carroll J, et al. (2020). J Am Coll Cardiol, 24;76(21):2492-2516.
[2] Rotman O, et al. (2018). Ex Review of Med Devices, 15:11, 771-79.
[3] Rotman O, et al. (2019). Ann Biomed Eng 47, 113–125.
[4] Kovarovic B, et al. (2022). JBME. 144(6): 061008.
[5] Helbock R, et al. (2023). ABME. Jan;51(1):58-70.
[6] Baylous K, et al. (2024). CMPB. Jan:243:107886.

COMPUTATIONAL ANALYSIS OF THE EFFECT OF TYPE B AORTIC DISSECTION ON PULSE WAVE VELOCITY AND PULSE WAVEFORM SHAPE

Marisa S. Bazzi (1), Hadi Wiputra (2), Rumi Faizer (3), Victor H. Barocas (2)

(1) Department of Chemical Engineering and Materials Science, University of Minnesota, Minneapolis, MN, USA
(2) Department of Biomedical Engineering, University of Minnesota, Minneapolis, MN, USA
(3) Division of Vascular Surgery, UP Medical, Culver City, CA, USA

INTRODUCTION

Aortic dissection (AD) is a severe condition associated with high morbidity and mortality [1]. AD is often managed using medical therapy alone when showing no complication and confined to the descending region of the aorta (type B dissection). However, the 3-year survival rate for those cases is only 78%. The prognosis of patients surviving an acute type B dissection is uncertain, and frequent imaging and clinical follow-up are recommended to identify signs of the progression of the disease such as severe aortic dilation (diameter > 60 mm), rapid aortic dilation (> 10 mm/year)[1, 2].

Diagnosis based on geometrical quantities such as diameter and growth rate often fails to provide a comprehensive diagnosis, resulting in inadequate prediction of the actual risk [3]. In order to address this issue, the exploration of alternative diagnostic measures has become popular. One promising avenue involves leveraging pulse wave velocity (PWV) or extracting diagnostic insights from pressure waveforms. Carotid-femoral PWV is a standard technique to measure arterial stiffness [4], and it has numerous advantages over, e.g., MRI or contrast CT, in terms of examination time, cost, and lack of contrast agent. In addition to PWV, pressure tonometry can provide a full waveform, which may be informative regarding the health of the aorta.

Here, we tested the hypothesis that the PWV or pressure waveform is altered by the presence of a type B dissection. To isolate the effect of dissection on the PWV and the pulse waveform, we used a patient-based geometry, and removed the dissection to create a non-dissection case. Both geometries were used as the basis for fluid-solid-interaction simulations with the same boundary conditions, so the effects on the pulse wave, and PWV were only based on presence of the dissections.

METHODS

We used a patient-based geometry with a type B dissection [5] as shown in Fig 1A, and manually removed the dissection using Meshmixer to create a similar model, but without dissection, as shown in Fig. 1B. For both geometries, we solved the unsteady blood flow problem using the svFSI solver [6]. Resistor-capacitor-resistor boundary conditions were used for the outlets, and a flow waveform was imposed in the inlet, with boundary conditions kept the same for both the dissection and no dissection cases. Wall mechanics were described as neo-Hookean, and a Robin type boundary condition was imposed in the outer surface of the wall to account for the viscoelastic support of the outer arterial wall. All simulations were run for ten cardiac cycles. Other computational details followed Baumler [5].

The pulse waveforms were then extracted from the inlet (before the dissection) and outlet. PWV was calculated by the time lag between the wave foot [7]. The waveforms were analyzed by the metrics of [8] (shown in Figure 1C) to obtain a broad measure of change in wave shape. In addition, the waveforms were compared in the frequency domain to identify any finer-scale changes induced by the presence of the dissection.

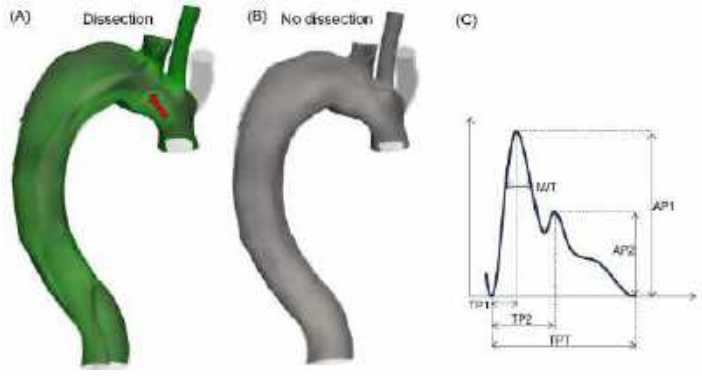

Figure 1: Patient-based geometry with a (A) type B dissection starting in the aortic arch (red arrow), and a (B) no-dissection geometry, by manually removing the dissection in (A). (C) Pulse waveform with shape metrics [8].

We also performed analysis of the pulse wave, treating the aorta as linear time-invariant system [9] using the formula:

$$H = F(h, f) = \frac{F(aa, f)}{F(da, f)}$$

Where F is the Fourier function, H is the Fourier transform of the transfer function h, f is the frequency, aa and da and the ascending and descending aorta pressure waveforms, respectively.

RESULTS

Figure 2 shows the inlet and outlet pressure waveforms for both non-dissection (A) and dissection (B) cases. The most striking effect is that the inlet and outlet waveform shapes were both altered by the dissection. For example, the dicrotic notch (red arrows) was at a higher pressure in both the inlet and outlet waveforms for the dissection case, and it occurred slightly later in the cardiac cycle. Additionally, there was a decrease of about 15% in the PWV for the dissection case relative to the no dissection case. These effects are summarized in Table 1.

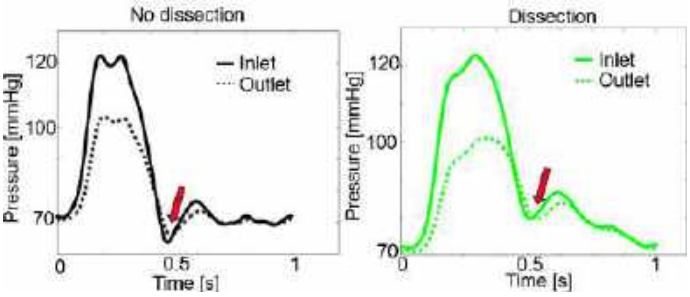

Figure 2: Pulse waveform for (A) no dissection and (B) dissection, solid lines are inlet pressure waveform and dotted lines are outlet waveform. Red arrows point to the dicrotic notch.

When analyzing the shape metrics (Table 1), we observe that the time metrics such as crest time (TP1), dicrotic wave time (TP2) and interwave time (IWT) were slightly larger for the dissection model, although the significance of the small changes, if any, is not clear. In contrast, we observe that measurements associated with pressure difference throughout the cardiac cycle, such as systolic amplitude (AP1) and dicrotic wave amplitude (AP2) had larger vales for the dissection case, with the AP1 difference quite pronounced.

As the pulse pressure travel from the ascending to the descending aorta, there is attenuation in pressure (|H| < 1, Fig. 3) across all frequencies. On average across the frequencies, the attenuation was more severe in models in dissection (mean: 0.54) than in those without dissection (mean: 0.61).

Table 1: Waveform measurements.

	Dissection	No dissection
PWV [m/s]	9.2	10.9
Dicrotic notch inlet [mmHg]	79	64
Dicrotic notch outlet [mmHg]	79	66
TP1 [s]	0.22	0.21
TP2 [s]	0.57	0.55
TPT [s]	0.95	0.96
IWT [s]	0.27	0.24
AP2 [mmHg]	14	3.6
AP1 [mmHg]	50	48

DISCUSSION

The most important result of this study is the observable changes in the pulse characteristics when a dissection is added to an otherwise unchanged aorta. Although this result is not surprising, it suggests the potential for pulse wave measurements to contribute to risk assessment in patients with chronic aortic dissection.

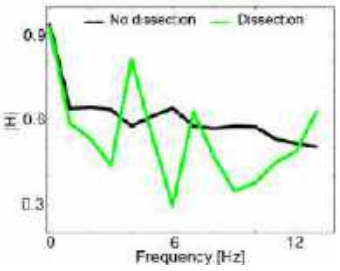

Figure 3: Amplitude of the pulsed pressure transfer function (H) for no dissection and dissection case.

The change in PWV is potentially significant since PWV is often used as an assessment of aortic health [10]. While the aortic stiffness is routinely estimated from PWV, we found in our computational model that the PWV was altered considerably even though the mechanical properties of the aortic wall were not changed, serving as a reminder that both aortic geometry and aortic wall stiffness contribute to PWV.

Similarly, we observed that the shape of the pulse waveform changed between the non-dissection and dissection cases despite the same inlet flow profile and the same outlet boundary conditions. Shape changes were also seen in the frequency domain. Since the difference between the inlet and outlet pressure waveforms would be expected to correlate roughly with clinically measured differences between the carotid and femoral pressure waveforms, these results suggest that PWV, in conjunction with more detailed analysis of waveform features in different locations, may be able to provide insight into the status of a chronic dissection.

It must be emphasized that this study used only one geometry and only imposed one change (+/- dissection), whereas every patient is different in many ways. The results here suggest numerous potential pathways for future study but should be taken as suggestive, not conclusive.

ACKNOWLEDGEMENTS

The study was supported by the National Institutes of Health under the grants R01 NS126762 and R01 HL164800. MSB and HW acknowledge support by the America Heart Association Predoctoral Fellowship and Postdoctoral Fellowship programs. Computations were made possible by resources grant from the Minnesota Supercomputing Institute.

REFERENCES

[1]R. Erbel *et al.*, *Eur Heart J*, vol. 35, no. 41, pp. 2873–2926, Nov. 2014, doi: 10.1093/eurheartj/ehu281. [2] *Eur J Vasc Endovasc Surg*, vol. 53, no. 1, pp. 4–52, Jan. 2017, doi: 10.1016/j.ejvs.2016.06.005. [3] M. A. Coady, J. A. Rizzo, G. L. Hammond, G. S. Kopf, and J. A. Elefteriades, *Annals Thor Surg*, vol. 67, no. 6, pp. 1922–1928, Jun. 1999, doi: 10.1016/s0003-4975(99)00431-2. [4] A. Milan *et al.*, *J Hypertension*, vol. 37, no. 8, p. 1547, Aug. 2019, doi: 10.1097/HJH.0000000000002081. [5] K. Bäumler *et al.*, *Biomech Modeling Mechanobiol*, vol. 19, no. 5, pp. 1607–1628, 2020, doi: 10.1007/s10237-020-01294-8. [6] A. Updegrove, N. M. Wilson, J. Merkow, H. Lan, A. L. Marsden, and S. C. Shadden, *Annals BME*, vol. 45, no. 3, pp. 525–541, 2017, doi: 10.1007/s10439-016-1762-8. [7] P. Salvi *et al.*, *J Hum Hypertens*, vol. 22, no. 10, Art. no. 10, Oct. 2008, doi: 10.1038/jhh.2008.42. [8] D. Korpas, J. Hálek, and L. Dolezal, *Physiol Res*, vol. 58, no. 4, pp. 473–479, 2009, doi: 10.33549/physiolres.931468. [9] Hotek, J.C.. et al., *J Pharmacol Toxicol Methods, 124:107476, 2023. [10] Eur Heart J, vol. 31, no. 19, pp. 2338–2350, Oct. 2010.*

THE IMPACT OF SEX AND HORMONE-DIFFERENCES ON HEART VALVE DISEASE

Colton J. Kostelnik (1), Chien-Yu Lin (1), Magda L. Piekarska (2), Gaweda Boguslaw (2), Austin J. Goodyke (2), Tomasz A. Timek (2), Manuel K. Rausch (1,3,4)

(1) Biomedical Engineering, The University of Texas at Austin, Austin, TX, USA
(2) Cardiothoracic Surgery, Corewell Health, Grand Rapids, MI, USA
(3) Aerospace Engineering, The University of Texas at Austin, Austin, TX, USA
(4) Mechanical Engineering, The University of Texas at Austin, Austin, TX, USA

INTRODUCTION

Tricuspid valve disease is an extremely common disease that can lead to high morbidity and mortality [1]. In fact, in more than 1 million Americans, tricuspid valve disease is severe enough that it requires treatment [2]. In more than 75% of those cases, tricuspid valve disease is considered functional [3]. That is, the valve itself is considered intact, while other causes are to be blamed for the dysfunction of the valve; for example, left-sided heart disease or pulmonary hypertension. We recently discovered that functional tricuspid valve disease may not be so functional after all [4]. In fact, we found that sheep with "functional tricuspid regurgitation" had valves that were maladapted. That is, their valves remodeled by changing their microstructural organization and composition, and showed cellular markers of inflammation. As a consequence, those leaflets also became larger, thicker, and stiffer. We also showed in a computational study that this change in thickness and stiffness contributes to valvular dysfunction, putting into question the concept of "functional tricuspid regurgitation." [5] Thus, tricuspid valve maladaptation may be a novel treatment target. Specifically, pharmacologically suppressing the observed maladaptative changes may relieve millions of patients suffering from tricuspid valve disease.

In the next step toward understanding tricuspid maladaptation as a cause of valvular dysfunction, we are investigating sex-dependent differences in the severity and frequency of maladaptive markers. This is an exciting question, as valvular disease is observed more frequently in women than men [6]. Thus, should we discover that maladaptation is more pronounced in female subjects than male subjects, we may contribute a first explanation for the cause of sex differences in heart valve disease. In addition to investigating the impact of sex on heart valve maladaptation, we are also interested in investigating the impact of hormonal differences within a sex. To this end, we also compare castrated and non-castrated male sheep. Thus, the overall objective of this study is to compare the severity of tricuspid valve maladaptation in female, castrated male, and non-castrated male sheep.

METHODS

We will base this study, as our previous ones, on a large animal model of pulmonary hypertension. To this end, we sedate female and male (both castrated and non-castrated) sheep, perform a mini-sternotomy, and band their pulmonary arteries. We then tighten the snare around the pulmonary artery just short of hemodynamic collapse. Afterward, we recover the animals for approximately 12 weeks, at which point we sacrifice them, excise their valves, and quantify three maladaptive markers. First, we quantify leaflet area based on images taken of the flattened-out valve on a calibrated grid. Next, we quantify thickness. To this end, we image the valve using an optical profilometry technique [7]. Finally, we remove 7x7 mm leaflet samples from each leaflet and test those samples biaxially using standard planar biaxial protocols [8]. We compare those metrics to control animals that did not undergo banding but are matched to the disease subjects in terms of age, weight, and sex.

We compare all data using a linear mixed model as implemented in the R package afex. We consider $p \leq 0.05$ as statistically significant.

RESULTS

We have analyzed the data for 30 animals of the planned total of 100 animals for this study. Thus, the results presented below are preliminary but will be finalized by the time we present this work at SB3C. Moreover, we show data in Figures 1, 2, and 3 representatively for the anterior leaflets only.

Specifically, in **Figure 1**, we representatively show the total anterior leaflet area for castrated male and female sheep for both the control and the disease groups. We found that leaflet area depends on disease ($p<0.01$). That is, in this study, too, tricuspid valve leaflets maladapted due to pulmonary hypertension by increasing the leaflet area. Additionally, we found that the three leaflets differed from each other, i.e., the anterior, posterior, and septal leaflets had differing areas

(p<0.001). Additionally, we found that leaflet size depended on sex (p<0.001). Noteworthily, in our limited preliminary study, we did not find any significant interaction effects.

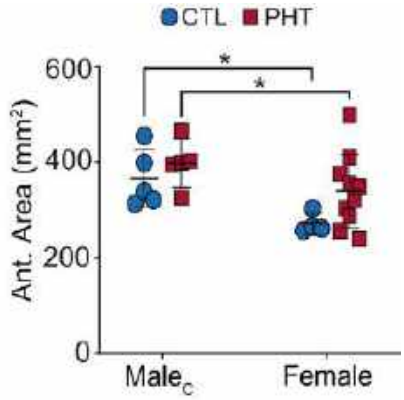

Figure 1: Leaflet area representative of the anterior leaflet of both castrated male and female sheep from the control and disease groups. Each data point represents one subject. CTL = Control, PHT = Pulmonary hypertension (i.e., disease). * p<0.05, **p<0.01

In **Figure 2**, we show both an example thickness map leaflet as well as our preliminary data comparing the mean leaflet thickness between male castrated and female sheep (representatively for the anterior leaflet only). Here, we find that leaflets also maladapted by thickening (p=0.013), as we have found in our previous work. We also found that thickness differed between leaflets (p<0.001) but did not find any differences due to sex or hormones (p=0.69).

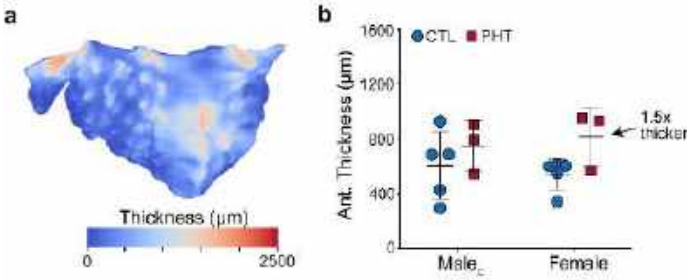

Figure 2: (a) Leaflet thickness map representatively shown for a control, female, anterior leaflet. (b) A comparison between the thickness of the anterior leaflets for castrated male and female sheep of the control and disease group. Note that we reduced the full-thickness maps as shown in (a) to scalar values by averaging the thickness maps across each leaflet center. Each data point represents one leaflet. CTL = Control, PHT = Pulmonary hypertension (i.e., disease).

Finally, in **Figure 3**, we representatively show the biaxial tension-stretch curves for a female anterior leaflet, comparing the disease and the control group. We also show stiffness at large strain (calf stiffness) and stiffness at small strain (toe stiffness) in both radial and circumferential directions. While the mean curves appear different between the control and disease groups, a statistical comparison between the leaflet stiffness at both large strain (p=0.74) and small strain (p=0.22) failed to show differences between them. Similarly, a comparison between castrated males and females also fails to show differences for both metrics (p=0.73 and p=0.77, respectively).

DISCUSSION

Our preliminary data of this very large study supports our prior findings in that we see that sheep with pulmonary hypertension have large leaflets, thicker leaflets, and may (albeit currently unsupported) have stiffer leaflets. Importantly, the objective of this current study was to investigate sex differences. Here, we found the first evidence that tricuspid valve leaflets, in general, may show some sex-dependence. That is, we found that leaflet size depended on sex. A first suspicion may be that animals of different sexes may be of different weight. However, even when corrected for weight, our observed difference persists. At this point, we did not find sex-dependent differences in leaflet thickness or stiffness. Additionally, we did not find any interaction effects between sex and disease. In other words, we have not yet found evidence that maladaptation is more or less prevalent in female sheep. Lack of evidence may be due to underpowering or due to lack of effect. Given the preliminary nature of our data, we are confident that including our additional animals (~70) will further power our study and provide a confident answer to the question as to whether heart valve disease, specifically maladaptation, depends on animal sex and hormones.

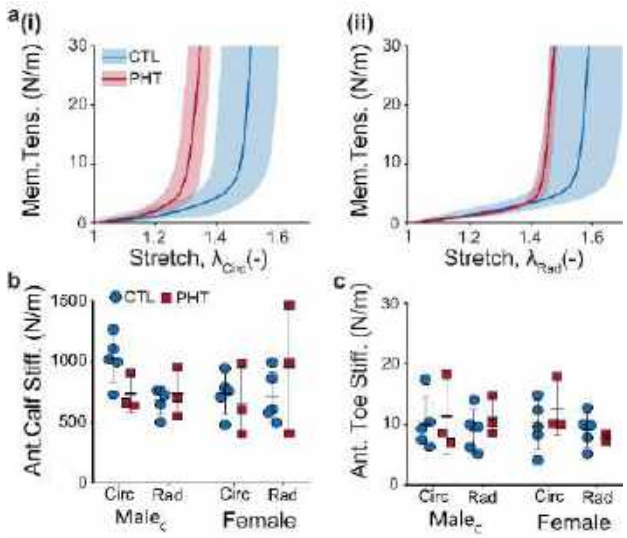

Figure 3: (a) Biaxial tension-stretch curves representatively shown for a female anterior leaflet in circumferential (i) and radial (ii) directions. (b) Calf stiffness (i.e., at high strain) and (c) toe stiffness (i.e., at low strain). Each data point represents one leaflet. CTL = Control, PHT = Pulmonary hypertension (i.e., disease).

ACKNOWLEDGEMENTS

Support from the National Institutes of Health via grants X and Y are greatly appreciated.

REFERENCES

[1] Rodes-Cabau, J et al., *The Lancet*, 288:2431-2442, 2016.
[2] Sarano-Enriquez, M et al., *Prg Cardiovasc Dis*, 62: 447-451, 2019.
[3] Adler, D, *Ann Cardiothorac Surg*, 6: 204-213, 2017.
[4] Meador, W et al., *eLife*, 9:e63855, 2020.
[5] Mathur, M et al., *J Mech Behav Biomed Mat*, submitted.
[6] DesJardin, J et al., *Circ Research*, 130:455-473, 2022.
[7] Lin, G et al., *C-Y*, *Biomech Mod Mechanobiol*, 22:1487-1498, 2023.
[8] Meador, W et al., *Acta Biomat*, 102:100-113, 2020.

UNIFORM GROWTH LAWS RECAPITULATE SOME ASPECTS OF ASCENDING AORTIC ANEURYSM PROGRESSION IN THE FBLN^{SMKO} MOUSE

Marisa S. Bazzi (1), Hadi Wiputra (2), Victor H. Barocas (1,2)

(1) Department of Chemical Engineering and Materials Science, University of Minnesota, Minneapolis, MN, USA
(2) Department of Biomedical Engineering, University of Minnesota, Minneapolis, MN, USA

INTRODUCTION

Arterial growth and remodeling (G&R) is the process by which living tissues adapt their physical and mechanical properties in response to biomechanical stimuli, aiming to maintain a homeostatic stress level in the vessel walls [1]. This process is generally balanced in healthy arteries but can become disrupted in the presence of diseases such as aneurysm and atherosclerosis. In the case of ascending thoracic aortic aneurysm (ATAA), disrupted homeostasis leads to continuous growth and weakening of the vessel wall, significantly increasing the risk of rupture [2]. A major challenge in managing ATAA involves accurately predicting which patients are at high risk of a ruptured aneurysm, since traditional measurements like aneurysm diameter and growth rate often provide insufficient diagnostic accuracy [3].

Recent research suggests that alternative biomarkers, especially those linked to blood flow dynamics, might offer additional insights into the disease [4]. Yet, these biomarkers, whether they are simple and geometrical or more complex and related to blood flow dynamics, tend to only indicate the likelihood of a rupture, without providing much insight into the disease's progression over time.

In this study, we investigated progressive G&R of aortic tissue using a subject-specific approach based on previous work by our collaborator on the *Fbln^{SMKO}* mouse model [4] . The data set used included longitudinal CT imaging and mechanical testing. The computational model used a simplified G&R model in conjunction with fluid-solid-interaction (FSI) simulations tailored to individual mice.

METHODS

We used a synergistic combination of FSI and G&R models. The model is split into tuning and validation stages. For the tuning stage, information for two-month-old and four-month-old mice was used to fit the growth parameters. For the validation stage, the tunned parameters are used to predict the 6-month growth and compare the resulting geometry to the CT image.

Subject-specific FSI simulation: The unsteady blood flow simulation was solved for a subject-specific geometry using the svFSI solver [10]. RCR boundary conditions were used for the outlets, and a waveform was imposed in the inlet. Wall mechanics were described as neo-Hookean, with the neo-Hookean constant adjusted for each mouse based on postmortem mechanical testing. A Robin-type boundary condition was used to account for the viscoelastic support of the outer arterial wall [14]. The time average wall stresses were extracted for each element and used as input for the growth and remodeling (G&R) model.

G&R model: Aortic wall growth was modeled as kinematic growth in response to chronic changes in the hemodynamics. The growth laws were based on Alford et al. [17]. To account for tissue remodeling, we assume that material property changes follow the total growth.

$$W_{Total} = J_g(t) W_{NH} \quad (1)$$

where $J_g(t)$=det(F_g) is the total growth for each element. To solve for the growth over the full vessel, we used the prestrain framework in FEBio2.9.1 [20].

Fitting growth parameters: During the tuning stage, the time constants associated to circumferential (T_θ) and axial (T_s) growth were used as fitting parameters. The choice was based on our ability to calculate both change in radius, and axial growth from the images. Measurements of circumferential growth and axial lengthening were used for the optimization of the growth parameters. For the circumferential growth, equally spaced rings from the heart to brachycephalic trunk were created as shown on Fig 2A. For the axial lengthening, the distance between two consecutives centroids was calculated. Optimization was conducted by comparing the grown-based geometry to the medical-based geometry at 4 months. A set of parameters was fitted for each of ten mice.

Model performance assessment: To evaluate the radial performance of the growth model for both tuning and validation, we used percentage error given by:

$$\Delta r\% = \frac{r^m - r^p}{r^m} \times 100 \quad (2)$$

where r^m is the image-based measured radius and r^p is the model prediction radius

RESULTS

Detailed analysis of a representative case: To begin, we examine the performance in both the tuning and the validation stage of a specific mouse, mouse 2. This mouse was selected due to its development of severe aneurysm, showcasing significant growth from the 2-month to 6-month mark, with an approximate 90% increase in the maximum diameter. Figure 1 depicts the 2-month geometry (A) and the contrast between the geometry projected from the model (B) and the geometry extracted from CT scans (C). Figure 1D displays the temporal evolution of the average radius of the predicted geometry (green) compared to the in-vivo measurements (blue). The model slightly underestimates the average radius at 4mo and overestimates it at 6mo.

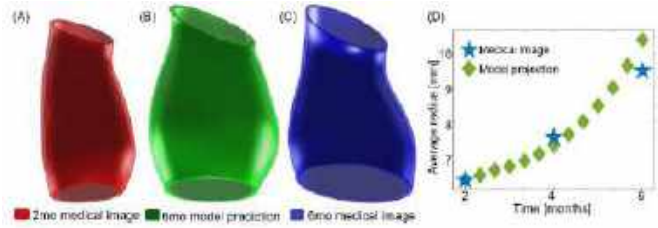

Figure 1: (A) 2mo medical image obtained in vivo and used as the initial geometry for the growth model, (B) 6mo projected geometry from the growth model and (C) 6mo in-vivo geometry obtained from medical images. (D) time evolution of the average radius of the model (green) compared to in vivo measurements (blue).

Model Performancee: Model performance was assessed as described in Eq. 2. The proximity of Δr to 0% indicates the effectiveness of the model fit. The analysis was performed in 4 rings along the geometry, named R2 (blue), R3 (red) R4 (yellow) and R5 (purple), as shown in Figure 2A. Rings R1 and R4 were the rings at inlet and outlet and were excluded from the analysis to avoid bias from the boundary conditions. Figure 2B shows the performance results for the tuning stage. Negative Δr% means the model geometry exceeded the in vivo measurement. Conversely, positive Δr% means the model geometry was narrower than the in vivo measurement. The average results show that the model was effective in capturing the 4-month geometry, with the minimum Δr% being -0.26% for mice 7 and 9 and the maximum Δr% of 9% for mouse 10. Most of the mouse models showed local errors between -8.5% (ring 4, mouse 5) to 11.8% (ring 4, mouse 2).

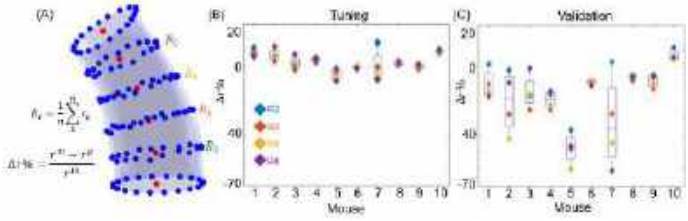

Figure 2:Performance analysis for the tunning data set (B) and validation data set (C). The tuning captures how well the model can tune the projected 4-month to the observed 4-month growth using the G&R time constants. The validation data set used the fitted parameters found in the tuning stage and compared the model-projected growth for 6mo to the observed 6-month geometry.

Figure 2C displays the analysis conducted on the validation dataset, using the parameters derived in the tuning stage to predict the 6-month geometry. Notably, the model's radial performance varied across different mice within this stage. Mouse 8 had the best performance, exhibiting minimal discrepancies across the rings with and a Δr=-5%. Conversely, mice 5 and 7 demonstrate poor performance. Despite these variations, the model's overall performance on the validation dataset showed a positive outcome. Eight out of ten mice showed an |Δr|<=20%,

DISCUSSION

This study applied a combination of (1) subject-specific modeling (2) fluid-solid-interaction FSI simulations, and (3) a simple growth and remodeling law to maladaptive growth and remodeling of the ascending thoracic aorta in the *Fbln*^{SMKO} mouse. All three aspects of the simulations were important. The subject-specific models allowed mouse-specific analysis including comparison to longitudinal data. The FSI simulations provided accurate estimates of pressure-induced wall stress and wall shear stress. The growth and remodeling model predicted the time evolution of aortic growth in response to calculated stresses. The validation step showed highly encouraging results: 80% of the models demonstrated an error less than 20% when compared to in-vivo measurements, with 40% of cases exhibiting errors less than 10%.

The computational model successfully captured the overall growth of the aorta in the *Fbln*^{SMKO} mouse and provided insights into the local growth patterns. However, some limitations need to be addressed for the model to be more widely applicable. Currently, the model primarily considers hemodynamic factors, yet substantial evidence points to the critical role of biochemical factors such as inflammatory markers and matrix metalloproteinases in growth and remodeling [5]. Incorporating these elements into the model framework could significantly heighten its predictive accuracy. This study also focused on a relatively small number of mice. While the results are encouraging, validating the model with a larger dataset is essential to confirm its generalizability. Additionally, investigating the model's performance across different mouse models of ATAA would further strengthen its applicability, and perhaps provide insights into how different genetics challenges drive aneurysm formation and growth.

Despite its limitations, this study has made significant contributions to the understanding of ATAA progression. The development of hemodynamics-driven G&R models offers a promising approach for personalized risk assessment and treatment planning for patients with ATAA.

ACKNOWLEDGEMENTS

The study was supported by the National Institutes of Health under the grants R01 NS126762 and R01 HL164800. MSB acknowledges support by the America Heart Association Predoctoral Fellowship Award # 916587. Special thanks to Casey Hokanson for the help with the segmentation of the mice data. Computations were made possible by resources grant from the Minnesota Supercomputing Institute.

REFERENCES

[1] E. K. Rodriguez, A. Hoger, and A. D. McCulloch, "Stress-dependent finite growth in soft elastic tissues," *Journal of Biomechanics*, vol. 27, no. 4, pp. 455–467, 1994, doi: 10.1016/0021-9290(94)90021-3. [2] J. D. Humphrey and M. A. Schwartz, "Vascular Mechanobiology: Homeostasis, Adaptation, and Disease," *Annu. Rev. Biomed. Eng.*, vol. 23, no. 1, pp. 1–27, Jul. 2021, doi: 10.1146/annurev-bioeng-092419-060810. [3] T. W. Raaymakers, G. J. Rinkel, M. Limburg, and A. Algra, "Mortality and morbidity of surgery for unruptured intracranial aneurysms: a meta-analysis.," *Stroke*, vol. 29, no. 8, pp. 1531–1538, Aug. 1998, doi: 10.1161/01.str.29.8.1531. [4] V. H. ; Bazzi, M.S.; Balouchzadeh, R.; Pavey, S.N.; Quirk, J.D.; Yanagisawa, H.; Vedula, V.; Wagenseil, J.E.; Barocas, "Experimental and mouse-specific computational models of the Fbln4SMKO mouse to identify potential biomarkers for ascending thoracic aortic aneurysm," *Cardiovascular Engineering and Technology*. [5] E. Hadler-Olsen, B. Fadnes, I. Sylte, L. Uhlin-Hansen, and J.-O. Winberg, "Regulation of matrix metalloproteinase activity in health and disease," *FEBS J*, vol. 278, no. 1, pp. 28–45, Jan. 2011, doi: 10.1111/j.1742-4658.2010.07920.x.

A SEX-BASED BIOMECHANICAL ANALYSIS AND NORMALIZATION FOR IMPROVED PREDICTION OF ABDOMINAL AORTIC ANEURYSM RUPTURE

Katherine E. Kerr[1], Pete H. Gueldner[1], Indrani Sen[2], Tiziano Tallarita[2], Joseph C. Wildenberg[2], Nathan L. Liang[3], David A. Vorp[1, 4-8], Timothy K. Chung[1]

(1) Department of Bioengineering, University of Pittsburgh, Pittsburgh, PA, USA
(2) Division of Cardiovascular Surgery, Mayo Clinic Health Systems, Eau Claire, Wisconsin, USA
(3) Division of Vascular Surgery, University of Pittsburgh Medical Center, Pittsburgh, PA, USA
(4) Department of Surgery, University of Pittsburgh, Pittsburgh, PA, USA
(5) Department of Cardiothoracic Surgery, University of Pittsburgh, Pittsburgh, PA, USA
(6) Department of Chemical and Petroleum Engineering, University of Pittsburgh, Pittsburgh, PA, USA
(7) McGowan Institute for Regenerative Medicine, University of Pittsburgh, Pittsburgh, PA, USA
(8) Center for Vascular Remodeling and Regeneration, University of Pittsburgh, Pittsburgh, PA, USA

INTRODUCTION

Abdominal aortic aneurysm (AAA) is a localized dilation of the abdominal aorta that can be devastating when ruptured, with up to a 90% fatality rate reported in the literature[1,2]. Due to this high mortality rate, it is important to determine the likelihood of rupture as accurately as possible. Currently this is guided by the size of the AAA, with the threshold for determining whether to surgically intervene being 5.0 cm for female patients and 5.5 cm for male patients[3]. However, studies have reported that 7 - 23.4% of aneurysms between 4.1 and 5.5 cm rupture[4,5].

Female patients specifically suffer from the unsuitability of the size criterion to guide surgical intervention, with a rupture rate between three and four times higher that of their male counterparts[1,6]. Literature investigating potential causes of this difference in AAA rupture rates between sexes has been conflicting, with factors including intraluminal thrombus (ILT)[7], differences in elastin and collagen concentrations[8], and stiffness of tissue[9] being just a few potential points of interest. Previous attempts to improve on the diameter threshold specifically for female patients, such as aortic size index[10], have not been widely adopted into clinical practice.

Our lab and others have established the importance of biomechanical considerations in predicting AAA rupture risk.[11,12] Historically, however, biomechanical analysis of AAAs has focused largely on male patients, likely due to the higher prevalence of AAAs in males, and have not considered sex differences. Understanding sex-based differences in AAA biomechanics is important for creating models that can accurately assess rupture likelihood in both male and female patients.

In this study we present a sex-based analysis on the abilities of various morphological and biomechanical parameters, both alone and normalized to patient-specific diameter, to predict aneurysm rupture.

METHODS

A multicenter study was conducted between the University of Pittsburgh Medical Center (UPMC) and the Mayo Clinic on AAA patients identified using ICD 9/10 and CPT codes with chart review to confirm diagnosis. Patients were identified from a retrospective database from the Health Record Research Request, a service of the University of Pittsburgh Department of Bioinformatics in partnership with UPMC, for cases between 2004-2019 and all patients within the Mayo Health system between 2021-2023. Medical images from Mayo Clinic were extracted and delivered through a material transfer agreement #DUA00004445 to the University of Pittsburgh team. The images were processed using a well-established computational pipeline to extract the region of interest, perform 3D surface reconstruction, and apply material properties to the AAA wall and ILT[12]. The wall stress analysis was performed by constraining the proximal and distal boundaries of the AAA and pressurizing to an ideal systolic pressure of 120 mmHg. A custom in-house MATLAB (MathWorks Inc., Natick, MA, USA) script was used to extract additional one-, two-, three-, and higher dimensional morphological indices[12].

This study consisted of a total of 381 patients, 108 of which were female. Of the 273 male patients, 12 underwent surgical repair and 10 experienced rupture. Of the female patients, 3 patients underwent surgical repair and 3 experienced a rupture event. Due to a limited sample size, the repair and rupture groups were pooled into one "unstable" group for this study. All AAA not in the unstable group were put into the "stable" group. Statistical comparisons of various clinical variables, biomechanical, and morphological indices were performed using a two-tailed Mann-Whitney non-parametric test. These comparisons were performed between sexes, but also within sexes to investigate differences in parameters between groups with and without ILT as well as above and below the respective threshold for each sex.

Previous literature has investigated using normalization techniques as predictors of aneurysm rupture, specifically for women[10]. To investigate the predictive capabilities of the biomechanical and morphological indices, each patient's maximum diameter was divided by each metric. Cumulative distribution curves representing ruptured

and repaired aneurysms as a function of each metric were created as previously described[10]. Thresholds for each metric were established by determining the inflection point of the cumulative distribution curve for female and males. The known outcome of stable or unstable AAA was then predicted based on this threshold and the predictive capability of that metric was evaluated using a confusion matrix.

RESULTS

Female patients were found to have significantly different morphological and biomechanical metrics than their male counterparts (**Table 1**). Additionally, significant differences were found when comparing patients above and below the diameter threshold as well as when comparing patients with and without ILT. Specifically, female patients in the unstable group had significantly lower lumen surface area values. Stable female patients had significantly lower wall volume, ILT volume, and asymmetry values than male patients in these groups. Comparing female patients above and below the 5 cm threshold, patients above the 5 cm threshold had significantly higher ILT volume and peak wall stress than those under the 5 cm threshold.

Table 1: Comparison of male and female biomechanical and morphological indices for stable and unstable groups

	Stable			Unstable		
	Female (n=102)	Male (n=251)	p-value	Female (n=6)	Male (n=22)	p-value
Maximum Diameter (cm)	3.89 ± 1.6	4.59 ± 1.4	<.001	4.67 ± 0.8	5.42 ± 1.0	0.131
Wall Volume (mL)	59.6 ± 62.3	77.9 ± 66.2	<.001	88.1 ± 47.4	119.4 ± 52.5	0.104
Lumen Volume (mL)	33.7 ± 27.3	47.2 ± 31.6	<.001	45.7 ± 21.9	64.1 ± 33.8	0.198
Mean Wall Asymmetry	30.0 ± 25.9	37.67 ± 25.8	.002	53.1 ± 13.0	60.4 ± 12.3	0.287
Max Wall Asymmetry	57.2 ± 50.4	73.4 ± 51.5	<.001	103.27 ± 24.1	117.09 ± 24.4	0.240
ILT Volume (ml)	25.9 ± 44.0	30.7 ± 42.5	.067	42.4 ± 35.9	55.3 ± 30.0	0.218
Asymmetry Factor cm^2	0.29 ± 0.61	0.51 ± 0.68	<.001	0.98 ± 0.01	0.95 ± 0.03	0.314
Lumen Surface Area cm^2	75.7 ± 33.3	94.6 ± 33.1	<.001	87.2 ± 26.5	126.3 ± 36.0	0.025
Peak Wall Stress N/cm^2	16.1 ± 6.3	19.7 ± 6.6	<.001	19.5 ± 4.8	23.4 ± 6.9	0.287
Mean Wall Stress N/cm^2	8.8 ± 3.0	10.1 ± 2.8	<.001	9.4 ± 3.8	10.4 ± 3.0	0.911

Thirty-two different biomechanical and morphological parameters were evaluated for predictive capability. An example of the cumulative distribution plot and confusion matrices can be seen in **Figure 1**.

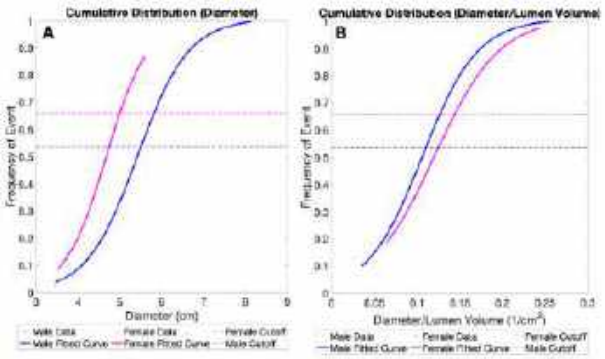

Figure 1: Cumulative distributions for (A) diameter and (B) diameter/lumen volume demonstrating cutoffs at 5 cm and 5.5 cm for female patients and male patients, respectively.

Of the thirty-two different metrics evaluated, there were several parameters that outperformed diameter in predicting unstable aneurysms. For female patients, six parameters (asymmetry[4], lumen volume, diameter/mean wall stress, diameter/peak wall stress, diameter/neck height, and diameter/asymmetry) predicted the same outcomes as maximum diameter. The parameters predicted more stable outcomes for males as compared to females, with 74% of metrics predicting stable outcomes more often for male patients and only 43% of metrics leaning towards stable predictions for female patients. The parameters that best predicted the unstable group, are shown in **Table 2**. For male patients, the maximum diameter criterion ranked among the highest accuracy rate for unstable prediction, while it ranked among the lowest for unstable prediction for female patients.

Table 2: Morphological and biomechanical parameters as ranked by true unstable percent accuracy

	Sex	Diameter Cut Off (cm)	True Stable	False Unstable	False Stable	True Unstable	Percent Accuracy
Maximum Diameter Criterion	M	5.50	67.8%	24.2%	3.3%	4.8%	72.5%
	F	5.00	78.7%	15.7%	3.7%	1.9%	80.6%
Maximum Lumen Asymmetry	M	4.72 ± 0.88	54.2%	37.7%	1.1%	7.0%	61.2%
Maximum Wall Asymmetry	M	4.72 ± 0.88	54.2%	37.7%	1.1%	7.0%	61.2%
Diameter/Lumen Volume	M	4.82 ± 0.50	57.9%	34.1%	1.1%	7.0%	64.8%
Diameter/Wall Volume	M	4.98 ± 1.05	63.0%	28.9%	1.5%	6.6%	69.6%
Diameter/Peak Wall Stress	M	5.11 ± 0.56	66.7%	25.3%	2.6%	5.5%	72.2%
Lumen Surface Area	M	5.17 ± 0.24	67.4%	24.5%	3.3%	4.8%	72.2%
Diameter/Mean Wall Stress	M	5.21 ± 0.21	67.8%	24.2%	3.3%	4.8%	72.5%
Mean Wall Stress	M	5.23 ± 0.19	67.8%	24.2%	4.0%	4.0%	71.8%
Diameter/Lumen Volume	F	4.28 ± 0.49	67.6%	26.9%	1.9%	3.7%	71.3%
Diameter/Maximum Lumen Asymmetry	F	3.93 ± 0.00	59.3%	35.2%	1.9%	3.7%	63.0%
Diameter/Mean Lumen Asymmetry	F	4.32 ± 1.04	70.4%	24.1%	1.9%	3.7%	74.1%
Diameter/Maximum Wall Asymmetry	F	3.93 ± 0.00	59.3%	35.2%	1.9%	3.7%	63.0%
Diameter/Mean Wall Asymmetry	F	4.32 ± 1.04	70.4%	24.1%	1.9%	3.7%	74.1%
Diameter/Wall Surface Area	F	4.51 ± 1.40	73.1%	21.3%	1.9%	3.7%	76.9%

DISCUSSION

Maximum AAA diameter, the current threshold for surgical intervention of AAAs, does not always accurately predict AAA rupture, particularly for female patients. We identified several parameters that were able to predict unstable aneurysms better than maximum aortic diameter for female patients, including diameter/lumen volume, diameter/maximum lumen asymmetry, and diameter/mean lumen asymmetry. For male patients, maximum aortic diameter was among the top predictors of unstable aneurysm.

Previous literature has suggested differences in ILT characteristics between female and male patients[7]. The findings in this abstract support this idea, as female patients in the stable and repair groups both had significantly smaller ILT volume as compared to their male peers. Additionally, female patients with AAAs above the clinical threshold had significantly larger ILT volume as compared to those below the clinical threshold. Asymmetry was also statistically significant between females and males. While asymmetry has been previously investigated as a diagnostic tool[4], sex-based differences have not been previously demonstrated. In the future, ILT and asymmetry could be interesting metrics to further investigate.

Due to the small sample size of female patients, the repair and rupture groups were pooled for this study and not all metrics were able to be evaluated. Female patients have been historically underrepresented in AAA biomechanics studies, likely due to decreased prevalence rate as compared to male patients but despite an increased rate of rupture among female patients[1,6]. The current study provides a biomechanical and morphological sex-based analysis. Widening understanding of the biomechanical differences between female and male patients could better inform both clinical decision making and prediction models, leading to improved outcomes for female patients.

ACKNOWLEDGMENTS

PG and KK were supported by the National Science Foundation Graduate Research Fellowship under Grant #1747452.

REFERENCES

[1] Brown L, et al., *Ann. Surg.*, 1999. [2] Powell J, et al., *N. Engl. J. Med.* 2003. [3] Chaikof, E.L. et al., *J. Vasc. Surg*. 2018. [4] Doyle, B.J. et al., J. Vasc. Surg. 2009. [5] RC, D., Circulation 1977. [6] Brown, P.M. et al., *J. Vasc. Surg.* 2003. [7] Tong, J. et al., *Eur. J. Vasc. Endovasc. Surg.* 2013. [8] Villard, C.M.D.P. et al., *J. Vasc. Surg.* 2017. [9] Sonesson, B. et al., *Eur. J. Vasc. Endovasc. Surg.* 1999. [10] Lo, R.C. et al., *J. Vasc. Surg.* 2014. [11] Raghavan, M. & Vorp, D.A., *J. Biomech.* 2000. [12] Chung, T.K. et al., *Bioengineering* 2022.

MRC2 IS NECESSARY FOR TYPICAL CERVICAL REMODELING IN RODENT PREGNANCY

Serena R. Russell (1), Bex Pendrak (1), Mariano Colon-Caraballo (2), Mala Mahendroo (2), Kristin M. Myers (1)

(1) Mechanical Engineering, Columbia University, New York, New York, USA
(2) Department of Obstetrics and Gynecology and Green Center for Reproductive Biology Sciences, University of Texas Southwestern Medical Center, Dallas, Texas, USA

INTRODUCTION

In pregnancy, the cervix must undergo dramatic remodeling to allow for a healthy, full-term pregnancy and successful delivery [1]. Defects in cervical remodeling contribute to preterm birth (PTB), defined as birth before 37 weeks. PTB is a serious pregnancy complication leading to detrimental health effects for the mother and offspring [2]. In mice, pregnancy spans a 19-day period in which the cervix softens during the first 17 days and ripens on days 18-19. This process is possible because the complex structure of the cervix is comprised of muti-scale components including collagen [3, 4]. Fibrillar collagen I is the main constituent of the extracellular matrix (ECM), significantly influencing the cervix's tissue mechanical properties [5]. Our prior studies demonstrate continuous collagen turnover suggesting a balance between collagen synthesis and degradation in the cervix of pregnant and non-pregnant mice. However, how collagen degradation is achieved during physiological cervical remodeling is not yet defined. One route for collagen degradation is through intracellular pathways, which involve the uptake of cleaved collagen fragments. The mannose receptor C type 2 (MRC2) expressed in fibroblast cells plays a role in ECM remodeling via receptor-mediated endocytic action [6].

This study uses mice lacking MRC2 expression to determine if loss of the MRC2 intracellular endocytic pathway compromises collagen turnover efficiency to impact the mechanical properties of the cervix. Utilizing the whole cervix of wild-type (MRC2 +/+) and knockout (MRC2 -/-) mice at non-pregnant (NP), mid-pregnancy (d12), and late-pregnancy (d18) time points, this work aims to better understand the mechanical behavior of the cervix in pregnancy.

METHODS

Mouse cervix samples were collected from three time points in pregnancy, NP, d12, and d18. For each time point, 1 MRC2 -/- and 1 genetically matched MRC2 +/+ were collected. Samples were prepared for whole specimen tensile loading using an Instron universal material tester, as previously described [7]. The sample was first allowed to swell for 2 hours in phosphate buffered saline (PBS) with 2 mM ethylenediaminetetraacetic acid. A preload of ~0.001 N was applied to ensure the sample was in contact with threaded sutures. The loading protocol consists of 2 main sections: 1) 3 cyclic load-unloads and 2) stress relaxation ramp- holds followed by a load to break (Fig. 1).

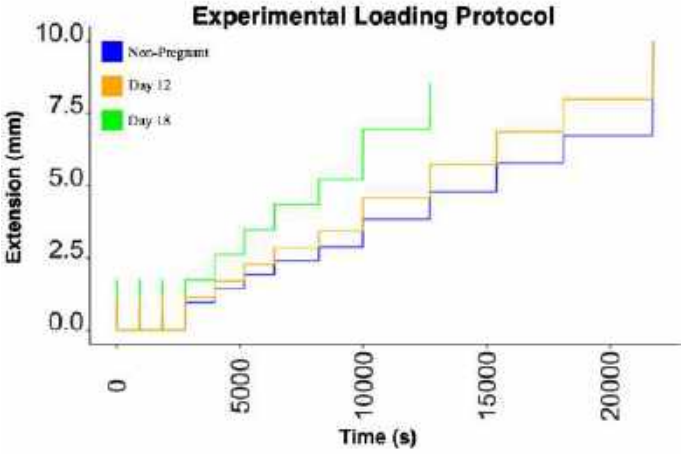

Figure 1: Mechanical testing profiles for Instron tensile testing of non-pregnant, mid-gestation, and late-gestation murine cervix.

Tests were performed at a strain rate of 10% of the cervical opening per second (mm/s) determined for each cervix individually. The sample was held at zero displacement between each cyclic load for 20 minutes to recover and equilibrate. For each ramp-hold, the cervix is stretched vertically via the regimen in Fig. 1. Measurements were taken at 1/s and 1/120s while holding to record deformation of the sample. For this initial mechanical analysis, we compared force-displacement

curves of the cyclic loading section and force-time curves of the stress relaxation section between MRC2+/+ and MRC2-/- samples.

RESULTS

The engineering stress-stretch curves of the 3rd, 4th, and 5th load cycle for MRC2+/+ and MRC2-/- mice at NP, mid, and late-gestation time points are shown in Fig.2. At the NP time point, the MRC2+/+ cervix was stiffer than the MRC2-/- cervix. At the d12 and d18 time points, the MRC2-/- cervix reaches higher stresses and steeper slopes than the d18 MRC2+/+ cervix indicating that the MRC2-/- cervixes are stiffer at these time points (Fig. 2).

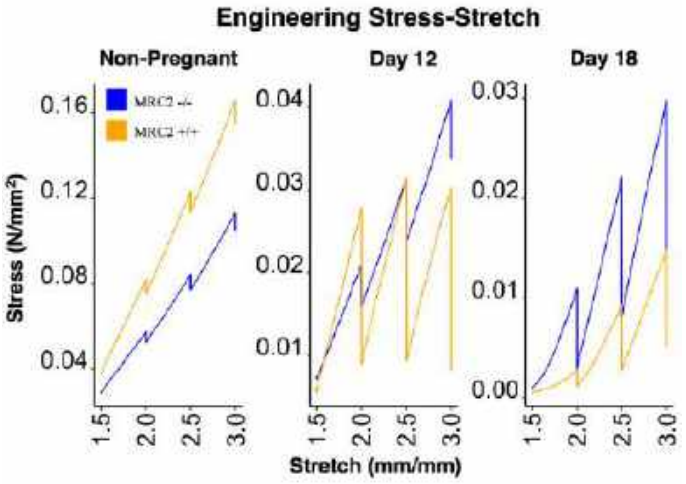

Figure 2: Engineering stress (force divided by initial cervical area) versus engineering stretch (current cervical opening divided by initial cervical opening) of non-pregnant, mid-gestation, and late-gestation cervixes in both MRC2 -/- and MRC2 +/+ mice.

For the NP samples, there is no apparent difference between MRC2 -/- and MRC2 +/+ cervixes in their force-relaxation patterns (Fig. 3). Equilibrium forces are similar for NP samples as well. However, MRC2 -/- tissue displays higher peak and equilibrium forces at d12 and d18 gestation time points (Fig. 3). This indicates a difference in mechanical function at mid and late-stage pregnancy in MRC2 -/- mice versus their MRC2 +/+ counterparts.

DISCUSSION

These preliminary results are a portion of what will be explored in this study, focusing on MRC2-/- murine cervical biomechanics over the course of pregnancy. Overall, the MRC2-/- cervixes do not function differently from their MRC2+/+ counterparts in non-pregnancy. There is a shift, however, in both mid and late-pregnancy, as MRC2-/- and MRC2+/+ samples differ in their equilibrium forces at d12 and d18. Higher forces and steeper slopes as seen in the MRC2-/- mice in Fig. 2, indicate that without the uptake of collagen by MRC2, the murine cervix has a stiffer modulus. The extensibility of MRC2-/- cervixes in NP, d12, and d18 mice is not altered, as these cervixes can still deform to the same level as MRC2+/+ cervixes. This hints at dysfunctional turnover of cervical collagen in MRC2-/- mice during pregnancy. Despite the increase in stiffness, MRC2-/- have normal parturition timing. This is supported by our observation that even though the cervix is stiffer, it can still stretch to levels beyond what would be observed in typical pup delivery. Collectively these studies suggest that the MRC2-mediated intracellular pathway of collagen degradation is necessary for optimal collagen turnover during cervical remodeling.

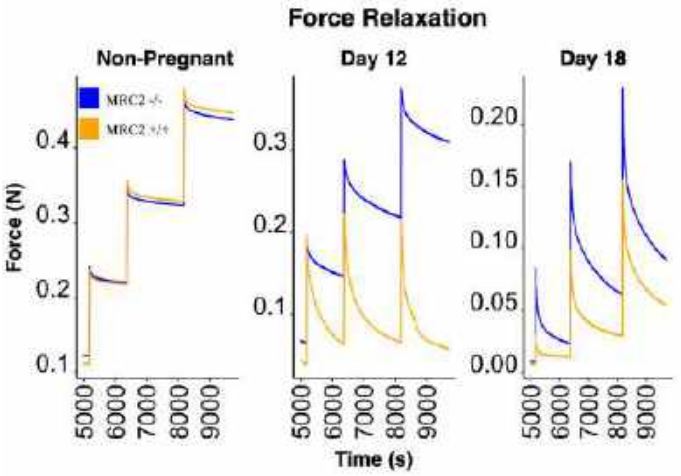

Figure 3: Force on MRC2 -/- and MRC2 +/+ murine cervix at non-pregnant, mid-gestation, and late-gestation time points over the course of three ramp-holds to display tissue relaxation behavior.

The effect of knocking out MRC2 on viscoelasticity and how it manifests structurally needs to be explored further by increasing sample size of this study and performing inverse finite element analysis to determine material properties of MRC2-/- cervical tissue and then comparing to MRC2+/+ tissue. Currently, this study is limited in its sample size and does not capture early pregnancy effects. Additional samples are currently being tested, and further analysis will be conducted on this dataset. Rupture stress, locking stress, initial stiffness, equilibrium stress, and model fit will be calculated using inverse finite element analysis to tease out more nuanced differences between MRC2-/- and MRC2+/+ mice. These initial results provide evidence to support a functional role of intracellular collagen degradation via MRC2 in physiologic cervical remodeling. This framework of understanding is necessary to define pathways of abnormal cervical remodeling associated with preterm birth.

ACKNOWLEDGEMENTS

Research was funded by the Eunice Kennedy Shriver National Institute of Child Health & Human Development Grant (R01HD113224 to KM and MM). The content is solely the responsibility of the authors and does not necessarily represent the official views of the National Institutes of Health.

REFERENCES

[1] Timmons, B. et al., *Trends in Endocrinology & Metabolism*, 21(6): 353-361, 2010.
[2] Vink, J. et al., *Seminars in Perinatology*, 41:427-437, 2017.
[3] Yoshida K. et al. *PLOS One,* 9(11): e112391, 2014.
[4] House M. et al. *Seminars in Perinatology*, 33(5): 300-307, 2009.
[5] Kadler KE. et al. *Biomech J,* 316:1-11, 1997.
[6] *MRC2 protein expression summary*. The Human Protein Atlas.
[7] Jayyosi C. et al., *Acta Biomaterialia*, 78:308-319, 2018.

EFFECT OF CORTICAL FOLDS ON HEAD ACCELERATION-INDUCED BRAIN DEFORMATION: A COMPUTATIONAL STUDY

A. Tripathi (1), J. G. Gonzalez (2), P. Ferrazzano (2), C. Franck (3), R. Carlsen (1)

(1) Department of Engineering, Robert Morris University, Moon Township, PA, USA
(2) Waisman Center, University of Wisconsin Madison, Madison, WI, USA
(3) Mechanical Engineering Department, University of Wisconsin Madison, Madison, WI, USA

INTRODUCTION

Risk of concussion or mild traumatic brain injury (mTBI) is significantly variable across different individuals. For patient-specific risk assessment using computational models, we need to incorporate the anatomical details that contribute to variabilities in the predicted injury response (such as brain tissue maximum strain and strain rates). Currently, some FE models used to study mTBI incorporate cortical folds [1-4], while some don't [5].

Previous studies have investigated the effects of cortical folds on strain distributions on single subjects [1]. This study aims to investigate the contribution of variations in cortical folds across 20 individuals on the variability in the risk of concussion under a given loading through subject-specific finite element (FE) modeling.

METHODS

We created detailed gyrencephalic (with cortical folds) and smoothed lissencephalic (without cortical folds) models of 20 individuals. The cohort consisted of 11 males and 9 females with ages ranging from 9 to18 years old (head volume 1.09×10^6 mm^3 – 1.31×10^6 mm^3). Comparing the peak strains and strain rates from the models with and without cortical folds provides insight into the role of gyri-sulci on the brain deformation mechanics. The strain and strain rate variability between the two types of models also provides insight into the contribution of cortical folds on the variability of the strain response found between individuals.

The detailed subject-specific gyrencephalic 3D FE models were developed from each individual's MRI scans: T1-weighted (T1w), T2-weighted (T2w), and diffusion tensor imaging (DTI). Models included the brain parenchyma, cerebrospinal fluid (CSF), meninges (dura, falx, and tentorium), and skull. An automated brain segmentation was performed on FreeSurfer to segment different parts of the brain. The skull was segmented using FSL. The meninges and sub-arachnoid CSF were added manually in 3D Slicer after combing the FreeSurfer and FSL segmentations.

The lissencephalic (without cortical folds) models were generated by modifying the detailed gyrencephalic models. The heterogenous subarachnoid CSF was replaced by a uniform 1 mm layer of CSF lining the meninges (dura, falx, and tentorium). The cerebral segments were replaced by one segment 'cerebrum' filling between the subarachnoid CSF and the deep brain structures.

The axonal tract orientations were incorporated from DTI through an anisotropic hyper-viscoelastic material model [6]. The models used a voxel-based mesh of 1 mm size that allowed the capturing of fine anatomical details (gyri and sulci), numerical mesh convergence, and led to faster model generation times.

Simulations were conducted in an explicit time scheme on Abaqus software. A sinusoidal half-wave rotational acceleration 10 krad/sec^2 resulting in angular velocity of 60 rad/sec (10 ms pulse width) was applied to the skull in the three principal anatomical planes (axial, sagittal, and coronal) in separate simulations. The injury metrics, such as 95th percentile maximum principal strain (MPS95) and maximum principal strain rate (MPSR95), were calculated for the entire brain. The 95th percentile strains are generally chosen so that numerical outliers in highly complex FE mesh will be excluded. The results

from the axial rotations are shown in this abstract and discussed to understand the contribution of cortical folds on brain mechanics and on the variability of the injury response across individuals.

RESULTS

We observed peak strains on the outer surface of the brain in both models (with and without cortical folds), as shown for four representative subjects in Figure 1. However, higher strain concentrations are found in the deeper brain regions, specifically between the lateral ventricles and the lateral sulcus, in the model with the cortical folds under axial rotation. This was not pronounced in the lissencephalic models without the cortical folds (Figure 1).

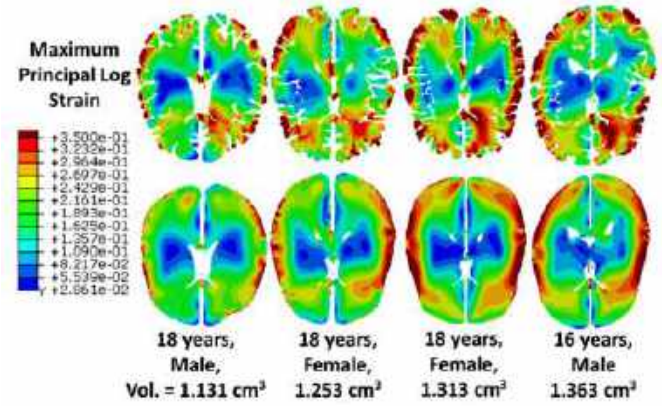

Figure 1 Maximum principal strain distribution in models with (top) and without (bottom) cortical folds for 4 representative subjects

We also calculated the MPS95 and MPSR95 over the duration of the simulation. Figure 2a shows the average (solid line) and minimum-maximum range (shaded region) of the MPS95 for 20 subjects for the models with cortical folds (red) and the models without cortical folds (blue). Figure 2b shows the average and range of the MPSR95 for both types of models.

There was a variability of 35% in MPS95 and as well as in MPSR95 among the gyrencephalic models. For the same subjects, the smooth lissencephalic models had a variability of 33% in MPS as well as MPSR. We found reductions of 18% and 19% in the peak value of the average MPS95 and average MPSR95, respectively after smoothing out the cortical folds.

DISCUSSION

We observe high strains in the outer surface of the brain under rotational boundary conditions typical of head impacts. As the skull starts to rotate, it starts to shear the tissue next to it and sends down a shear wave to the center of the brain. As the wave travels to the deeper brain regions, it quickly gets dissipated due to the viscous nature of the brain tissue and CSF, resulting in larger strains on the outer surface of the brain.

In the models with cortical folds, we also capture strain concentrations, especially between the lateral ventricles and lateral sulcus, which are caused by the sharper geometrical features. Smoothing out the folds and fissures reduces strain localizations and thus reduces the MPS95 and MPSR95. Adding the cortical folds also introduces CSF in between gyri, effectively making the region softer than in the lissencephalic model, also contributing to a higher deformation. This result is in contrast with the previous study that found a 12% increase in the strains by removing cortical folds from the model [1]. Multiple modeling parameters including material properties can result in these differences, and we are currently exploring them in detail.

The variability in the peak MPS95 and MPSR95 results directly from the anatomical differences. The variability in the models with a smooth cortical surface stems from the head shape and size. On the other hand, in the models with cortical folds, differences in the cortical folding pattern and a more heterogeneous skull-brain interface also contribute to the brain injury mechanics.

Our simulations demonstrate the importance of incorporating cortical folds in subject-specific head models for the assessment of brain deformation and mTBI risk under rotational loading.

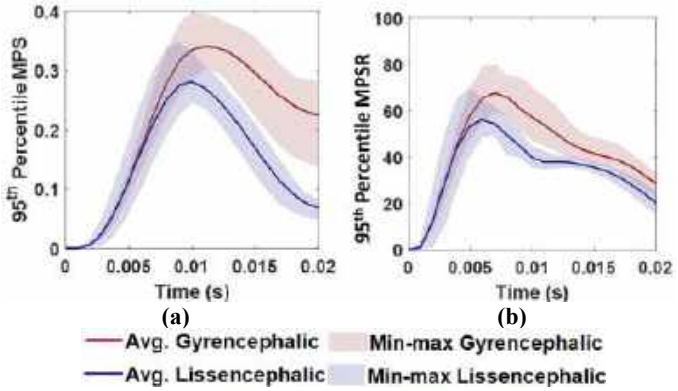

Figure 2 Average (solid line) and range (shaded region) of (a) MPS95 and (b) MPSR95 for 20 subjects using models with (red) and without (blue) cortical folds.

ACKNOWLEDGEMENTS

We gratefully acknowledge the support by the U. S. Office of Naval Research under awards N000142112044 (PANTHER) and grant from the University of Wisconsin Madison Office of Vice Chancellor for research and graduate Education (136-AAI3375, 136-AAI3376, 136-AAI3377, 136-AAI3378).

REFERENCES

[1] Ho, Johnson, and Svein Kleiven. *J Biomech* 42.13: 2074-2080, 2009.

[2] Li, Xiaogai, Zhou Zhou, and Svein Kleiven. *BMMB* 20: 403-431, 2021.

[3] Giudice, J. Sebastian, et al. *Ann Biomed Eng.* 48: 2412-2424, 2020.

[4] Reynier, Kristen A., et al. *Ann Biomed Eng.* 50.11 (2022): 1510-1519.

[5] Ji, Songbai, et al. *Ann Biomed Eng.* 50.11: 1389-1408, 2022.

[6] Wright, Rika M., et al. J. *Neurotrauma* 30.2 (): 102-118, 2013.

REVISITING MURRAY'S LAW IN PULMONARY ARTERIES: EXPLORING BRANCHING PATTERNS AND PRINCIPLES

Sofia Altieri Correa (1), Amirreza Kachabi (1) Mitchel J. Colebank (1), Naomi C. Chesler (1)

(1) Edwards Lifesciences Foundation Cardiovascular Innovation and Research Center, and Department of Biomedical Engineering, University of California, Irvine, Irvine, CA, USA

INTRODUCTION

Nearly 100 years ago, Murray [1] formulated the most well-recognized structure-function relation for the optimal branching pattern of vascular networks based on a minimum energy principle. He introduced a cost function that balanced the pressure-flow energy required to pump blood with the metabolic energy required to maintain blood temperature. Assuming steady, fully-developed laminar flow in all vessels, and that metabolic energy is proportional to blood volume, Murray predicted that volumetric blood flow rate in any branching vessel (parent or child) is proportional to the cube of its diameter. A corollary prediction is that the parent diameter cubed is equal to the sum of the daughter branch diameters cubed.

Experimental studies to test the validity of these relationships have predominantly been conducted in systemic blood vessels and different optimization models has been proposed [2][3][4][5]. However, fewer studies have investigated if these principles hold in the pulmonary circulation. The present work experimentally examines the relationships between parent and child diameters in pulmonary arterial networks. Our results show that the cubed relationship does not hold and that blood flow rate proportional to diameter raised to the power ≈1.88 is observed in our data. We consider principles that may govern these branching patterns following Murray's approach.

METHODS

We generated and analyzed arterial networks for five healthy canines from magnetic resonance angiography images that were obtained previously [6], as depicted in Fig. 1. First, we created three-dimensional (3D) segmentations of pulmonary artery (PA) geometries through the application of 3DSlicer [7]. Subsequently, the Vascular Modeling Toolkit was employed to convert these 3D segmentations into centerline networks [8]. Finally, we post-processed the specific networks using custom MATLAB software, extracting length, radius, and connectivity data for each network [9].

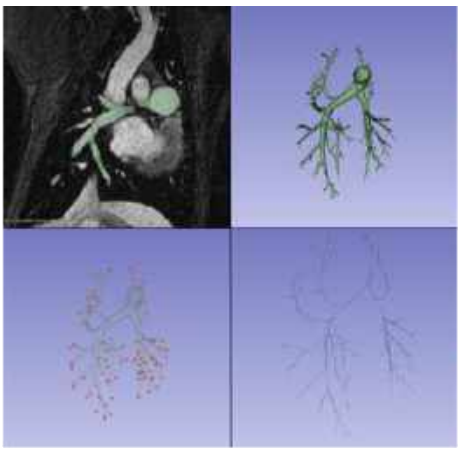

Figure 1: 1D arterial network extraction for one subject from MRI images.

Murray was the first to establish a link between the radius and flow rate of a vessel segment. He introduced an energetic cost function, denoted as E, which sums the energy required to pump blood (flow, Q, multiplied by pressure drop, ΔP) with the metabolic cost to maintain body temperature (assumed to be proportional to blood volume) for a single vessel of radius r and length L (Eq. (1)), where K_1 is an unknown constant. Additionally, he assumed fully developed laminar flow within the vessel and a fluid viscosity μ (Eq. (2)).

$$E = Q\Delta P + K_1\,\pi\,r^2 L \quad (1)$$

$$E = \frac{8\mu L}{\pi r^4} Q^2 + K_1\,\pi\,r^2 L \quad (2)$$

In accordance with Murray's minimum principle, when this relationship is differentiated with respect to radius and minimized (i.e., set to zero), an optimal condition exists (Eq. (3)) and for these assumptions flow rate Q is proportional to the cube of radius (Eq. (4)):

$$r = \left(\frac{16\mu}{k_1\pi^2}\right)^{\frac{1}{6}} Q^{\frac{1}{3}} \quad (3)$$

$$\Rightarrow Q \propto r^3 \quad (4)$$

Because flow is conserved at any branching, $Q_0 = Q_1 + Q_2$, where Q_0 is the flow in the parent vessel and Q_1, Q_2 are the flows in the daughters, hence:

$$r_0^3 = r_1^3 + r_2^3, \quad (5)$$

where r_0 represents the radius of the parent vessel, and r_1 and r_2 denote the radii of the daughter vessels of the bifurcation.

Following the acquisition of radius values for all branches from the healthy canine data, we proceeded to solve the following equation for the exponent (x) in Eq. (6) at each bifurcation for each subject using MATLAB software.

$$r_0^x = r_1^x + r_2^x \quad (6)$$

RESULTS

Figure 2 shows the optimal exponent for each bifurcation across all subjects. Overall, the resulting mean exponent value is 1.88 (±0.62).

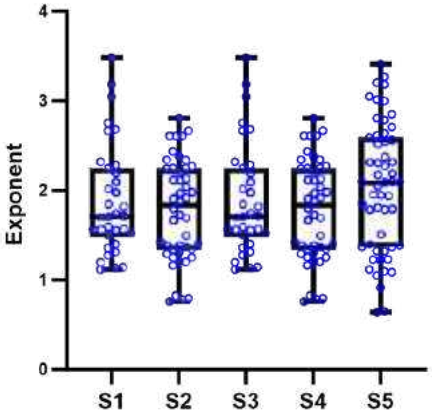

Figure 2: Exponent values for the bifurcations for each subject (S).

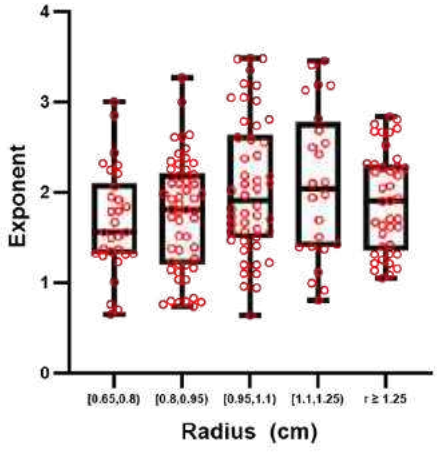

Figure 3: Exponent values grouped in terms of the radius size.

In Fig. (3), the exponent values are presented, organized based on the size of the radius of the smaller daughter in the bifurcation, including all bifurcations and subjects. The values of the exponent are observed to lack a direct dependence on the radius of the bifurcation vessels and, consequently, on the generation within the PA branching tree.

Given that pulmonary arteries are much shorter than systemic arteries, we explored replacing the Poiseuille flow assumption with a Bernoulli (blunt profile) flow assumption as in Eq. (7), where B is an unknown constant.

$$E = B\frac{Q^3}{r^4} + K_1\,\pi\,r^2 L \quad (7)$$

Differentiating this expression with respect to r, we obtain:

$$\frac{dE}{dr} = (-4)B\frac{Q^3}{r^5} + 2K_1\pi r L \quad (8)$$

And, setting this to zero, we obtain:

$$Q \propto r^2 \quad (9)$$

In addition, we explored balancing the energy required to pump blood with the need to have a large surface area to facilitate gas exchange in the lungs. In that case, a new cost function, Eq. (10) can be written where the second term is not proportional to the volume of the vessel but to its surface area:

$$E = B\frac{Q^3}{r^4} + K_2 2\pi r L \quad (10)$$

where K_2 is an unknown constant. By optimizing Eq. (10) with respect to r we obtain

$$\frac{dE}{dr} = (-4)B\frac{Q^3}{r^5} + K_2 2\pi L \quad (12)$$

$$Q \propto r^{5/3} \quad (13)$$

such that the flow rate is proportional to the radius raised to the power of 1.67.

DISCUSSION

The mean exponent value for pulmonary artery branches in this sample of healthy canines was 1.88±0.62, which is much lower than 3.0 expected for Murrays' Law. The assumptions of blunt flow and a principle governing branching based on surface area instead of flow yielded improved predictions of the exponent. In addition, our results show a relatively consistent pattern in exponent values across PA subjects' bifurcations and different generations. The observed variation in results may be attributed to manual MRI image segmentation. Further analysis downstream in the PA branching tree is needed to explore whether the exponent value increases as branching radius decreases. Additionally, studies in other species including humans are necessary to support our measurement of patterns and interpretation of branching principles in pulmonary arteries.

ACKNOWLEDGEMENT

SAC received funding support from Balsells Fellowship. MJC was funded by TL1TR001415. NCC was funded through R01HL154624 and R01HL147590.

REFERENCES

[1] Murray CD, Proc. Natl. Acad. Sci., 12(3):207-14, 1926.
[2] Uylings HB., Bull Math Biol., 39(5):509-20, 1977.
[3] Olufsen MS et al., Ann Biomed Eng., 28(11):1281-99, 2000.
[4] Taber LA., Biophys J., 74(1):109-14, 1998.
[5] Kassab GS, Comput. Methods Appl. Mech. Eng, 196, 2007.
[6] Mulchrone et al., Front Cardiovasc Med., 5:189, 2019.
[7] Fedorov A, et al., Magn Reson Imaging 30:1323–1341., 2012.
[8] Antiga L, et al. Med Biol Eng Comput 46:1097-1112, 2008.
[9] Colebank MJ et al., Am J Physiol Heart Circ Physiol, 2021.

SENSOR FUSION ALGORITHM TO IMPROVE ACCURACY OF ROBOTIC SUPERPOSITION TESTING USING A 6-DOF POSITION SENSOR

Callan M. Gillespie (1,2), Lesley R. Arant (3), Tara F. Nagle (1,2), Joshua D. Roth (4, 5), Robb W. Colbrunn (1,2)

(1) Lerner Research Institute, Cleveland Clinic Foundation, Cleveland, Ohio, USA
(2) Dept. of Applied Biomedical Engineering, Cleveland State University, Cleveland, Ohio, USA
(3) Department of Biomedical Engineering, University of Wisconsin-Madison, Madison, WI, USA
(4) Department of Orthopedics and Rehabilitation, University of Wisconsin-Madison, Madison, WI, USA
(5) Department of Mechanical Engineering, University of Wisconsin-Madison, Madison, WI, USA

To quantify the contribution of specific ligaments to overall biological joint movement, the principle of superposition has been used for nearly 30 years [1]. This principle relies on using a robotic test system to move a human joint to the same position before and after transecting a specific ligament. The difference in force at the same position is assumed to be the transected ligament's contribution to passive joint stability. However, the test system's ability to accurately return the joint to the commanded position is dependent on the compliance of the system's various components, which is often neglected [2]. Errors in position of only 100-200 microns can result in -25% error in computed ligament tension in a relatively compliant artificial knee joint. In stiffer cadaver knees, computed ligament tension at peak load can be underestimated by more than 50% [3].

Optical 6-DOF motion capture sensors can be more accurate than robot encoders to measure joint position because their signal is able to account for system compliance. However, they can have 10-100 times more noise than a robot encoder position signal. By fusing low-noise robot position data with a higher accuracy motion capture system (i.e. an optical 6-DOF position sensor), this combined signal can be placed into the control loop of a cadaveric biomechanical test system to greatly reduce the commonly overlooked historical accuracy challenges of superposition testing [2,4].

This study has two aims. First, to develop a sensor fusion algorithm that safely and effectively fuses robot position with 6-DOF position sensor data so in can be used within a real-time control loop. Second, to demonstrate the accuracy of the sensor fusion technique by validating that superposition computed ligament tension in an artificial knee joint matches directly measured tension and comparing these results to traditional techniques.

METHODS

The Sensor Fusion Algorithm

In typical testing systems (**Figure 1A**) the relative relationship of Rigid Body 1 secured to the base and Rigid Body 2, secured to the robot end-effector (for example the tibia and femur, respectively) can be described with the following kinematic chain:

$$T_{RB1\_RB2} = T_{RB1\_w1} T_{w1\_w2} T_{w2\_Robot} T_{Robot_0\_RB2} \quad (1)$$

Where the two dynamically changing 4x4 homogenous transformation matrices are the robot position relative to its base (T_{w2_Robot}), and the relative 6-DOF position of rigid body 2 relative to rigid body 1 (T_{RB1_RB}). Robot$_0$ refers to the initial position of the end effector at digitization. Robot refers to the end effector's position throughout time.

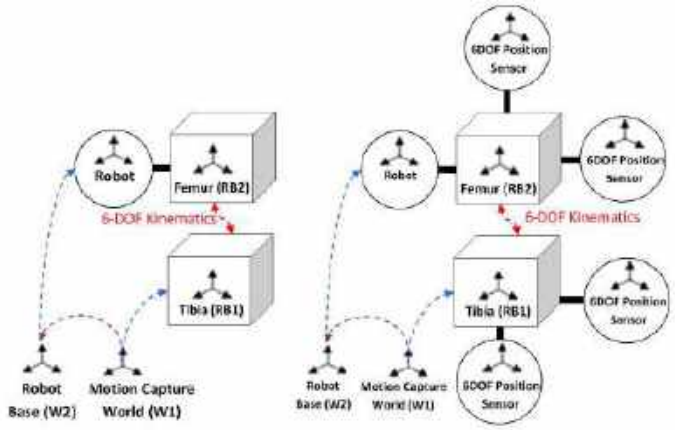

A: Traditional **B: Sensor Fusion**

Figure 1: Kinematic Chains with Varying Control Schemes

To minimize inaccuracies due to compliance in the system control loop, 6-DOF position sensors must be added to the kinematic chain (**Figure 1B**). These sensors are represented by $T_{Robot\_Robot_0}$, a dynamically changing matrix that is highlighted in blue below.

$$T_{RB1\_RB2} = T_{RB1\_w1} T_{w1\_w2} T_{w2\_Robot} T_{Robot\_Robot_0} T_{Robot_0\_RB2} \quad (2)$$

$T_{Robot\_Robot_0}$ is the spatial relationship between where the position sensors calculate the robot to be and where the robot was relative to the sensors when first digitized. In eq. (2), the precision and bias are directly dependent on the noise, accuracy, and placement of the motion capture markers. Filtering may be done on the motion capture marker data to decrease noise injected into the control signal.

It should be noted that eq. (2) is simplified for ease of reading, and the algorithm used within the validation software was generalized to also compensate for base compliance. In addition, multiple 6-DOF position sensors could be added to a given rigid body to add measurement redundancy. The algorithm was used to compensate for compliance in biological joint pose, gravity compensation, and load transformations. These abilities differentiate this sensor fusion algorithm from other similar visual servoing algorithms used in robotics literature [5].

Most importantly, safety parameters were also added to the sensor fusion algorithm. Motion capture markers may be occluded, passive markers might be mislabeled by a tracking system, or a marker might suddenly come back into view causing an instantaneous kinematic correction. Therefore, the algorithm also included a sensor integrity handler that performs various safety checks to reduce the risk of dangerous system motion. The sensor fusion algorithm that performs compliance compensation with a sensor integrity handler to make the system safe is collectively called eXactoPOSE®. More details on eq. (2) are included in patent US 11,745,341 B2.

Validation of the Sensor Fusion Algorithm

To validate the algorithm, a ligament phantom spanning an artificial knee joint was used [6]. A single axis load cell (Futek LCM300) was mounted on a spherical rod end pin and directly measured force through the ligament phantom during superposition testing. Similarly, a motion capture system (OptiTrack, Corvalis Oregon) served as the 6-DOF position sensor and the markers were placed close to the artificial knee joint. These measurements were collected at the same time as the 6-DOF kinetics & kinematics measured by a 6 axis force/torque sensor (Omega, ATI, Apex, NC), and a 6-DOF robot (KR 300, KUKA, Augsburg, Germany).

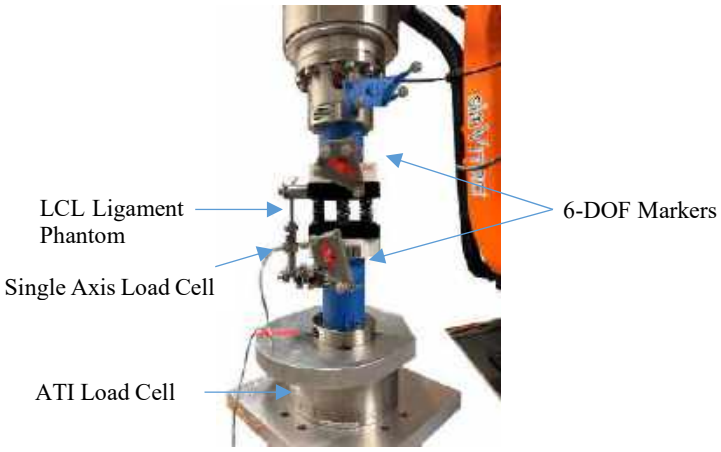

Figure 2: Artificial Knee with LCL Ligament Phantom

A force control test was performed by personnel at the University of Wisconsin-Madison while using a simVITRO® test system (Cleveland Clinic, Cleveland, OH). The test consisted of a ramp to 15 Nm of Varus torque, while maintaining a constant compression force of 50 N. All other DOF were initially in force control and prescribed 0 N or 0 Nm, except flexion angle, which was prescribed a 0° rotation angle. This testing protocol was used to maximize force going through the LCL during testing. After the force control test, the resulting 6-DOF kinematics were played back in position control while changing 2 independent variables: LCL (intact or deficient) and robot control methodology (traditional or sensor fusion). Superposition computed LCL tension was calculated as the vector difference in force measured by the 6 axis force/torque sensor during LCL intact and deficient trajectories. Superposition computed LCL tension was compared to tension directly measured by the load cell for both robot control methodologies.

RESULTS

There was a notable difference between the traditional superposition tests and those fusing an optical 6-DOF position sensor. In particular, the difference in red and blue lines in **Figure 3A** show that the traditional control technique underestimated ligament stiffness by about 25%. In contrast, tension values in **Figure 3B** track similarly, indicating that sensor fusion does not underestimate ligament contribution. The sensor fusion superposition computed force data was filtered to reduce motion capture induced noise in the data.

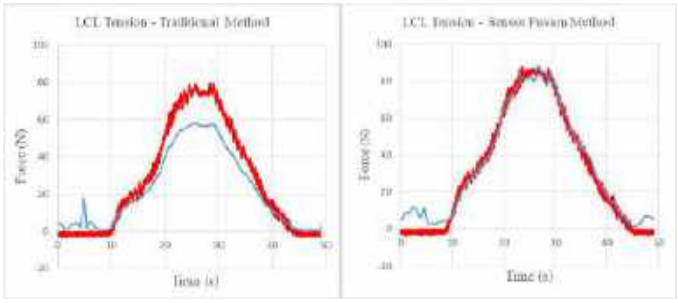

Figure 3: Superposition Computed LCL Tension using Traditional and Sensor Fusion Methods for Kinematic Control.

DISCUSSION

This study demonstrates the effectiveness of using 6-DOF position sensors within a sensor fusion algorithm for mitigate errors in ligament tensions computed using superposition testing. The errors shown in Figure 3 may in fact underestimate the magnitude of commonly overlooked errors in estimating ligament tension when using traditional superposition techniques because the artificial knee is less stiff in compression than a cadaveric knee [3]. In future superposition testing, the compliance of various equipment should be measured and reported or 6-DOF position sensors should be used to improve the accuracy of controlling joint motion. The stiffness of the system components is less important if using position sensors in the control loop. Ultimately, better estimates of ligament contribution to passive joint stability should enable researchers and device manufacturers to better design and refine medical devices and surgical techniques in the future.

REFERENCES

[1] Fujie, H et al., *J Biomech Eng*, 117:1-7, 1995, [2] Haas, J et al., *SB3C*, 2017, [3] Arant, LR et al., *ORS*, 2024, [4] Gillespie, M et al., *SB3C*, 2019, [5] Chaumette, C et al., *Handbook of Robotics*, 841-866, 2016. [6] Arant, L et al. *J Mech Behav Biomed Mat*, 126: 1-10, 2021

EFFECTS OF RESIDUAL STRESS ON THE BUCKLING AND TWISTING BEHAVIOR OF ARTERIES

Qin Liu (1, 2), Alejandro W. Cisneros (1), Hai-Chao Han (1)

(1) Department of Mechanical Engineering, University of Texas at San Antonio, San Antonio, TX 78249, United States
(2) Department of Mechanical Engineering, New York Institute of Technology, Old Westbury, NY 11568, United States

INTRODUCTION

Residual stress exists in arteries and significantly affects the stress distribution in the arterial wall, thus affecting the growth and remodeling of the arterial wall [1-3].

However, it is unclear how residual stress would affect certain mechanical behaviors of arteries such as pressurized inflation (P-V curve), torsion (axial twisting) and buckling [4-5].

Accordingly, the objective of this study was to evaluate the effects of residual stress (opening angle) on the mechanical behavior of arteries.

METHODS

The arterial wall was assumed to be a homogenous nonlinear elastic material described by the Holzapfel-Gasser-Ogden two-fiber strain energy functions [6]:

$$\psi = \frac{c}{2}(\bar{I}_1 - 3) + \frac{b_1}{b_2}[exp(b_2(\bar{I}_4 - 1)^2) - 1] \quad (1)$$

where b_1, b_2, and c are positive material constants. $I_1 = tr\ (F^T F)$ is the first invariant. $I_4 = \lambda_\theta^2 \sin^2 \alpha + \lambda_0^2 \cos^2 \alpha$ is the invariant that reflects the stretch ratio in the two diagonal fiber directions, with α denoting their alignment angle. The Cauchy stress can be expressed in terms of the strain energy

$$\boldsymbol{\sigma} = \mathrm{p}\mathbf{I} + \mathbf{F} \cdot \frac{\partial \mathrm{W}}{\partial \mathbf{E}} \cdot \mathbf{F}^{\mathrm{T}} \quad (2)$$

The lumen pressure and axial tension in arterial segments under lumen pressure can be expressed as [4,5]:

$$p_i = \int_{r_i}^{r_e} (\sigma_{\theta\theta} - \sigma_{rr}) \frac{dr}{r} \quad (3)$$

$$N = \pi \int_{r_i}^{r_e} (2\sigma_{zz} - \sigma_{rr} - \sigma_{\theta\theta}) r dr + \pi r_i^2 p_i \quad (4)$$

wherein r_i and r_e represent the lumen and outer radius, and subscripts r, θ, z represent the radial, circumferential and axial directions, respectively. The mechanical properties were determined by free-end pressurized inflation testing [4,5]. The experimental data were fitted with these equations to determine the material constants by minimizing the error function using the nonlinear least square function in Matlab. Considering the effect of residual stress (opening angle), the material properties of the arteries were obtained in two approaches – including and ignoring the opening angles.

These material constants were then used in buckling analysis and torsion analysis to determine the effect of residual stress on the bent buckling and twisting behavior of the arteries, respectively. The critical pressure of the arteries buckling at different axial stretch ratios were obtained using the buckling equation previously developed [7]:

$$p_{cr} = \frac{N + (\frac{n\pi}{l})^2 H}{\pi {r_i}^2} \quad (5)$$

The torque-rotation angle relationship of the arteries were determined using the torque equation [5]

$$T = 2\pi \int_{r_i}^{r_e} \sigma_{\theta z} r^2\, dr \quad (6)$$

We simulated the buckling and torsion of porcine carotid arteries using experimental data obtained from our previous studies [4]. Numerical simulations were done using a custom code in Excel.

RESULTS

Our simulations demonstrated that fitting the pressure-diameter-length curves obtained from pressurized inflation experiment data with and without considering the opening angle leads to different set of material constants. For a given set of material parameters, ignoring or including the opening angle leads to different pressure-diameter relationships. The vessel is less stiffer when including the opening angle as compared to the inflation curve ignoring the opening angle (Fig. 1).

The residual stress slightly increases the critical pressure of arteries, mainly in the higher axial stretch ratio range (Fig. 2).

When subject to torsion at given pressure and axial stretch ratio, the arterial wall is stiffer against twisting deformation when opening angle is considered compared to the twisting when the opening angle is ignored (Fig. 3).

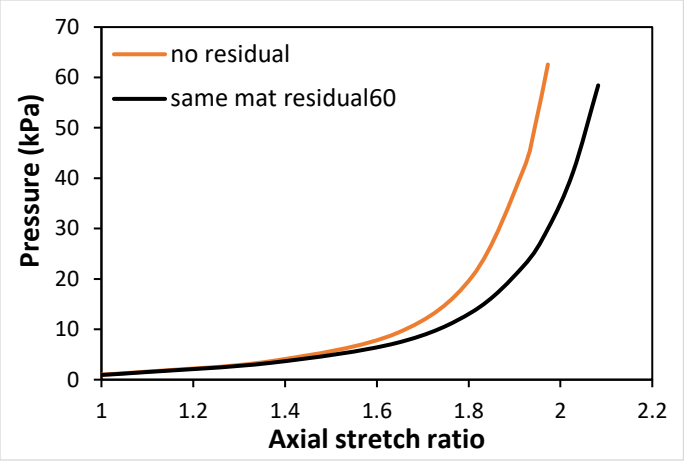

Figure 1: Pressure-diameter relationships of an artery subject to pressurized inflation at a fix axial stretch ratio of 1.3. The black curve, "same mat residual60" refers to the case an opening angle of 60 degrees is considered.

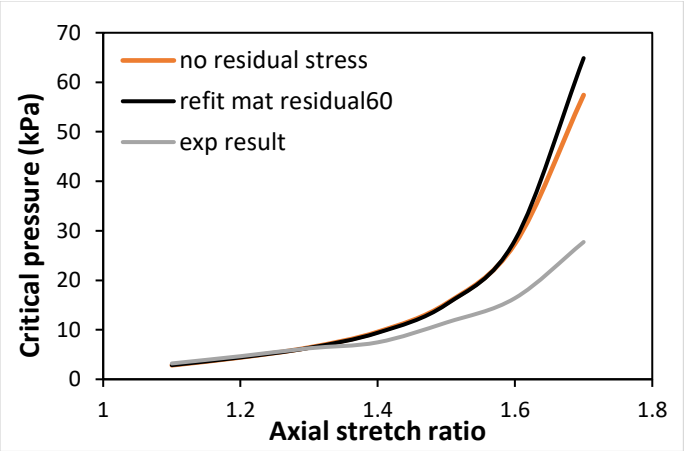

Figure 2. Critical pressure as a function of axial stretch ratio. The black curve, "refit mat residual60" refers to using material constants obtained with an opening angle of 60 degrees.

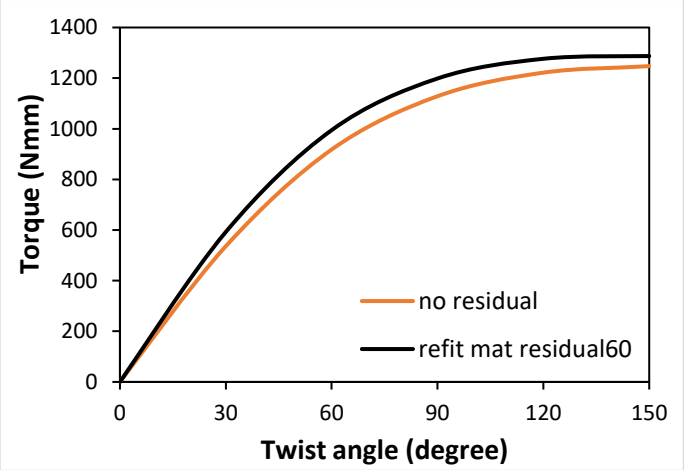

Figure 3. Torque-twisting angle relationship of an artery subjected to torsion at a given lumen pressure (10kPa) and axial stretch ratio (1.3).

DISCUSSION

Our results demonstrated that residual stress affects the pressurized inflation, torsion, and the bent buckling behavior of arteries. In mechanical analysis of arteries, it is necessary to include residual stress as it not only affects the stress distribution in the arterial wall, but also affects deformation behaviors of the artery. It is also necessary to consider the residual stress when determining the material constants.

REFERENCES

[1] Fung YC. What are the residual stresses doing in our blood vessels? Ann Biomed Eng, 1991. 19(3): 237-49.

[2] Chuong CJ and YC Fung, On residual stresses in arteries. J Biomech Eng, 1986. 108(2): 189-92.

[3] Du Y, C Lü, M Destrade, and W Chen, Influence of Initial Residual Stress on Growth and Pattern Creation for a Layered Aorta. Scientific reports, 2019. 9(1): 8232-32.

[4] Liu Q, Q Wen, M Mottahedi, and HC Han. Artery buckling analysis using a four-fiber wall model. J Biomech, 2014. 47(11): 2790-6.

[5] HC Han, S Sultan, M Xiang. The effects of axial twisting and material non-symmetry on arterial bent buckling. J Biomech 2023, 157: 111735.

[6] Holzapfel GA, TC Gasser, and RW Ogden. A new constitutive framework for arterial wall mechanics and a comparative study of material models. Journal of Elasticity, 2000. 61(1-3): 1-48.

[7] Han HC. Nonlinear buckling of blood vessels: a theoretical study. J Biomech, 2008. 41(12): 2708-13.

PREDICTION OF TEARING IN VAGINAL TISSUE USING MACHNIE LEARNING

Mostafa Zakeri (1), William D. Snyder (1), Justin A. Krometis (2), Traian Iliescu (2), Raffaella De Vita (1)

(1) Biomedical Engineering and Mechanics, Virginia Tech, Blacksburg, Virginia, USA
(2) Mathematics, Virginia Tech, Blacksburg, Virginia, USA

INTRODUCTION

Approximately 80% of women undergoing vaginal delivery experience some degree of perineal lacerations [1]. To predict the likelihood and severity of such lacerations, prescribe preparatory measures, or recommend an alternative mode of delivery (i.e., cesarean section), computational tools that can simulate vaginal delivery in real-time are needed. While experimental investigations have explored the mechanisms of vaginal lacerations in rats [2, 3], computational methods have yet to be employed for modeling and predicting such lacerations. Regrettably, sophisticated finite element (FE) models of the reproductive system prove to be computationally intensive, rendering them impractical for real-time interventions [4,5].

We have recently applied reduced order modeling techniques, including a feed-forward neural network model, to describe the deformations of a rat vaginal canal with and without a tear [4,5]. In this study, we implement a variety of machine learning (ML) models and compare them to determine which model most effectively captures the deformations of vaginal canals with tears. Our analysis demonstrates the potential of these ML techniques as valuable real-time predictive tools for anticipating maternal birth trauma.

METHODS

We conducted FE simulations reproducing experimentally observed deformations of rat vaginal tissue subjected to inflation testing to generate data for this ML study. The geometry, boundary conditions, and material model parameters for the FE simulations are reported in our recent investigation of projection-based and data-driven reduced order modeling techniques [4]. Specifically, we considered eight unique combinations of mean preferred fiber orientations in three equally sized anatomical regions of the vagina (distal, mid, and proximal region). Each combination was utilized to simulate the response to 30 intraluminal pressures, ranging from 2.5 to 75 kPa, in equal increments. This generated a total of 240(=8x30)

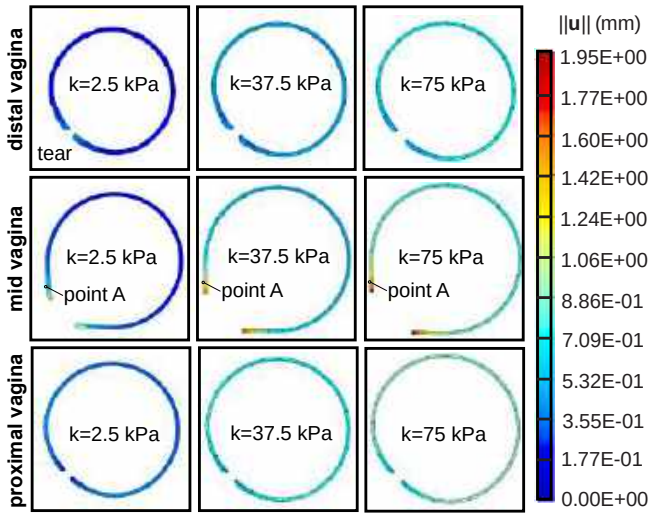

Figure 1: Magnitude of the displacement vector u at different cross-sections of a vaginal canal with a tear at increasing intraluminal pressures. Point A is an arbitrary node at which ML models are compared in Figure 3.

simulations that formed our snapshots, each with 10,257 degrees of freedom. Figure 1 displays the magnitude of the displacement vector in the proximal, mid, and distal vagina (cross-sectional views), under minimum, medium, and maximum pressure values for one combination of mean preferred fiber orientations.

We then compared four distinct ML algorithms: support vector machine (SVM), stochastic gradient descent (SGD), random forest (RF) and extreme gradient boosting (XGBoost). We chose the SVM

technique for its well-known power to capture complex relationships in data, its ability to maximize the margin between data points of different classes, and its superior performance in high-dimensional spaces. The SGD technique was chosen for its versatility as an optimization algorithm for linear regression problems, demonstrating computational efficiency and suitability for large datasets owing to its stochastic nature. We selected the RF ensemble learning method which combines multiple decision trees to enhance accuracy and robustness due to its effectiveness in capturing non-linear relationships between input features and the target variable. Lastly, the XGBoost method, which is an optimized implementation of gradient boosting, was employed for its suitability in handling large datasets and complex regression tasks. It incorporates regularization techniques to prevent overfitting, thereby improving generalization to new data.

We utilized four input parameters, three mean fiber orientation values, one for each anatomical region, and one intraluminal pressure value. The outputs were the components of the displacement vectors at the nodal points. Concerning data splitting, we partitioned our FE snapshots into training and test data with an 80% to 20% ratio, respectively. Prior to the split, random shuffling of the snapshots was applied. Additionally, we employed the grid search method to optimize hyperparameters during the model training process. Then, in order to compare the performance of the different ML models, we computed R^2 scores for each model as follows:

$$R^2 = 1 - \frac{\sum_{i=1}^{n}(u_i - \hat{u}_i)^2}{\sum_{i=1}^{n}(u_i - \overline{u}_i)^2} \quad (1)$$

where u_i is the displacement component associated with the i^{th} snapshot, $\overline{u}_i$ is the mean of displacement components for the i^{th} snapshot, $\hat{u}_i$ is the predicted value of displacement component for the i^{th} snapshot for a given ML model, and n is the total number the FE snapshots (n=240). Averages of R^2 scores were computed for all ML models that were trained using each algorithm for all the degrees of freedom.

RESULTS

The R^2 scores for each model are illustrated in Figure 2 for both the training and test datasets. SVM exhibited the highest performance, achieving a score exceeding 0.99. Subsequently, SGD, RF, and XGBoost follow as the next best-performing models.

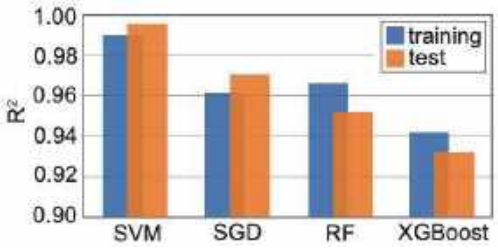

Figure 2: R^2 scores of each ML model for predictions of both training and test data for the entire dataset containing 240 snapshots, each with 10,257 degrees of freedom.

The predicted values generated by each model are compared to the actual values from the FE simulations at an arbitrary point A shown in Figure 1 and are visually presented for the test dataset in Figure 3. Each point on the graph represents a snapshot with a unique set of inputs corresponding to point A. The gray line represents the ideal case scenario, and points aligning with this line indicate superior model performance.

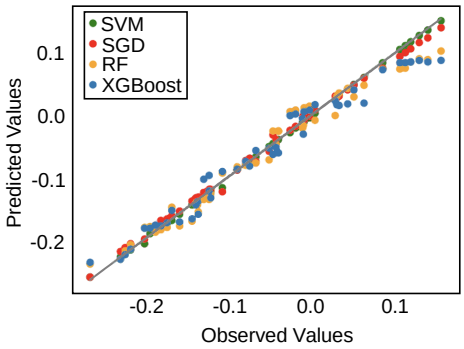

Figure 3: ML model predicted vs. observed values at point A reported in Figure 1.

We utilized *Google Colab's* CPU runtime with 12.7 GB of accessible RAM for training the models. Table 1 displays the necessary time for both the training and prediction phases of each model.

Table 1: Training and prediction time for each model for all snapshots and degrees of freedom

Model	Training Time (s)	Prediction Time (s)
SVM	68.42	2.51
SGD	17.74	2.59
RF	399.97	28.84
XGBoost	1671.99	13.10

DISCUSSION

We successfully employed four ML algorithms to predict the effect of a tear on the mechanical behavior of vaginal tissue by training data obtained from FE simulations. The SVM model demonstrated superior performance, exhibiting the highest R^2 score. Its predictions for various sets of inputs were remarkably accurate, closely aligning with the ideal line (Figure 3). Additionally, it ranks as the second fastest model in terms of training time and the fastest in prediction time with 2.51 seconds. Among the considered models, XGBoost exhibited the lowest performance and longest training time. However, it still achieved an R^2 score exceeding 0.93 for both the training and test datasets. SGD and RF demonstrated intermediate performance, with SGD slightly outperforming RF and being the fastest model with a training time of 17.74 seconds. This study shows that ML techniques can generate rapid and real-time simulations of vaginal deformations, decreasing the computational time required for FE based simulations and expediting their integration into clinical settings.

ACKNOWLEDGEMENTS

This research is supported by the National Science Foundation (NSF) under grant number 2227614.

REFERENCES

[1] Samuelsson, E., et al., Acta Obstetricia et Gynecologica Scandinavica, vol. 81, no.1, p. 44-49, 2002.
[2] McGuire, J.A., et al., Interface Focus, vol. 9, no.4, p. 20190029, 2019.
[3] McGuire, J.A., et al., Acta Biomaterialia, vol.127, p. 193-204, 2021.
[4] Snyder, W., et al., International Journal for Numerical Methods in Biomedical Engineering, vol. 39, p. e3660, 2023.
[5] Snyder, W., et al., Computers & Mathematics with Applications, vol. 152, p. 168-180, 2023.

SB^{3}C2024
Summer Biomechanics, Bioengineering and Biotransport Conference
June 11-14, Lake Geneva, WI, USA

THE MECHANICAL LOADING OF THE MURINE UTERUS AND CERVIX IN EARLY PREGNANCY

Abigail W. Laughlin (1), Joy Y. Vink, MD (2), Steven D. Abramowitch (3), Kristin S. Miller (4), Raffaella De Vita (5), Kristin M. Myers (1)

(1) Department of Mechanical Engineering, Columbia University, New York, New York, USA
(2) Department of Obstetrics and Gynecology, Hawaii Pacific Health Medical Group, University of Hawaii John A. Burns School of Medicine, Honolulu, HI, USA
(3) Department of Bioengineering, University of Pittsburgh, Pittsburgh, PA, USA
(4) Department of Bioengineering and Mechanical Engineering, University of Texas Dallas, Richardson, TX, USA
(5) Department of Biomedical Engineering and Mechanics, Virginia Tech, Blacksburg, VA, USA

INTRODUCTION

During pregnancy, maternal anatomic structures undergo vast remodeling to accommodate the load of the growing fetus. Insufficient tissue remodeling can lead to serious pregnancy complications such as preterm birth (PTB, delivery before 37 weeks gestation), which affects 10% of deliveries worldwide and is the leading cause of infant mortality [1]. Due to inherent risks and complexities associated with studying pregnancy *in utero*, computational modeling, coupled with experimental data, has emerged as an invaluable tool for studying the biomechanics of pregnancy and has enabled the quantification of tissue stress and stretch throughout gestation. In previous studies, computational models of human pregnancy have enabled us to better understand loading patterns on the proximal cervix for different patient anatomies [2-3].

To understand the growth and remodeling during pregnancy, the murine model has been widely utilized to characterize the mechanical behavior of the cervix. However, there are distinct differences between human anatomy and mouse models, as mice have a gestational period that is 12 times faster, bicornate uterine horns, large litter size, and placental structural and physiological differences [4]. To evaluate the mouse as a mechanical model for pregnancy, the goal of this research is to compare the pattern and magnitude of mechanical loading of the murine cervix and uterus with human pregnancy. Using finite element analysis (FEA) and histological sections of the whole murine reproductive track, this study quantified the stretch of the mouse uterus from the non-pregnant state until early pregnancy (day 6 of an 18.5-day gestation). Future studies will include quantifying the mechanical environment of the murine uterus and cervix for the full gestation.

METHODS

Uterine and cervical tissue samples were collected from wild-type mice at nonpregnant (NP, n=5), mid-pregnancy (d6, n=3) and late-pregnancy (d18, n=2) timepoints. Samples were acquired from the coronal plane and included entire cervical and uterine geometries. Slices were fixed in 10% formalin for 24 hours, transferred to 70% ethanol, and paraffin embedded. To appreciate the general tissue structure (collagen, mucin, muscle distribution), 5-μm sections were stained with Movat pentachrome. Using stained images, dimensions were measured and recorded in ImageJ for maximum right and left uterine horn diameters, cervical length, cervical diameter, and cervical canal diameter for all samples. Membrane thickness was also measured on d6 samples.

Three-dimensional models of murine reproductive anatomy were generated for each of the five nonpregnant samples. To build these models, the uterus and cervix were identified and traced using a spline in Solidworks (Dassault Systemes, Vélizy-Villacoublay, France). By assuming symmetry about the coronal plane, the cervical and uterine diameters were used to create a lofted circular profile, following the direction of the outer spline and creating an appropriately scaled and anatomically accurate geometry (Fig. 1). The uterine cavity was then traced and generated for each model, and a membrane and cervical canal was added using previously measured thicknesses. Each model was then embedded in an abdomen. The posterior half of each geometry was used for computational efficiency, and models were discretized into elements using Hypermesh (Altair Engineering Inc., Troy, MI). The meshed geometry was imported into FEBio Studio (v1.3.0) where finite element analysis (FEA) was performed.

Material properties, boundary conditions, and contacts were defined within FEBio Studio. For preliminary model development, material parameters were used based on experimental values obtained in human pregnancy computational model [5-7]. Neo-Hookean material properties were assigned to the uterus, membrane, and abdomen. The cervix was modeled as a passive fiber composite material with a compressible neo-Hookean ground substance and a mid-pregnancy cervical fiber stiffness value [8]. The uterus and cervix were tied together, and both structures were tied

to the abdomen. The membrane was tied to the uterus and cervix, and a uniform pressure was applied to the intrauterine membrane for each non-pregnant anatomy. The x,y, and z planes of the abdomen were fixed.

All models were loaded to 0.6 kPa. The cervix and uterus were then examined to understand how the magnitude and pattern of tissue stretch and stress begin to evolve in a murine pregnancy.

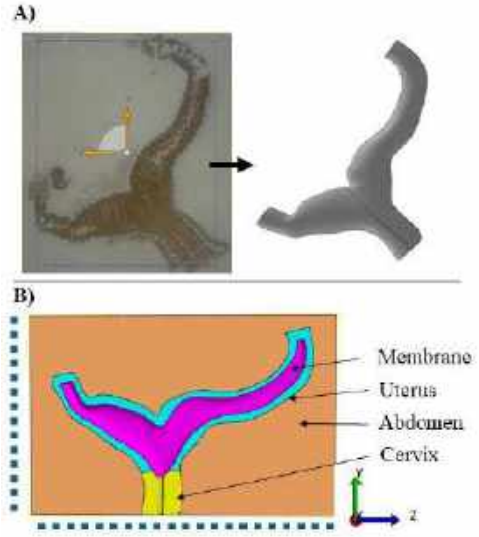

Figure 1: (A) Build process for mouse geometry involves tracing stained images and using a loft to create 3 dimensional CAD model. (B) FEBio geometry generated from CAD model.

RESULTS

Average caliper measurements recorded from tissue samples for each gestational timepoint are shown in Table 1. Left uterine diameter (Left UD) and right uterine diameter (Right UD) were recorded for n=5 NP, n=3 d6, and n=2 d18 samples. For two samples, the cervix boundaries were unclear. Cervical Length (CL), cervical diameter (CD1) and cervical canal diameter (CD2) were recorded for n=5 NP, n=2 d6, and n=1 d18 samples. Table results show increasing uterine diameters for later gestational time points. While uterine diameters show a clear trend, there is no clear trend amongst gestational groups for cervical measurements.

For each mouse anatomy, deformed configurations were examined and compared to the reference configuration (Fig. 2). All samples had increased left and right UD in response to the applied load.

Using the deformed anatomies, the pattern and directionality of the first principal Lagrange strain and Von Mises stress were examined for each model (Fig. 3) by mirroring the proximal cervix about the coronal plane. We notice higher stress and stretch occur around the cervical canal, which is more concentrated on the left and right sides of the canal than the anterior and posterior.

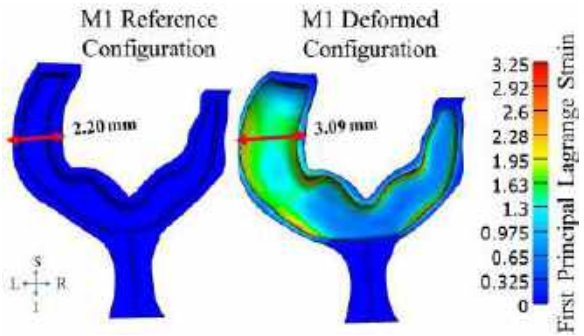

Figure 2: Reference and Deformed Configuration for Mouse 1

Table 1: Caliper Dimensions from Tissue Samples (mm)

	Left UD	Right UD	CL	CD1	CD2
Nonpregnant	2.25	1.91	1.66	1.63	0.23
D6	3.46	3.74	1.82	1.41	0.15
D18	9.64	12.23	2.52	2.32	0.25

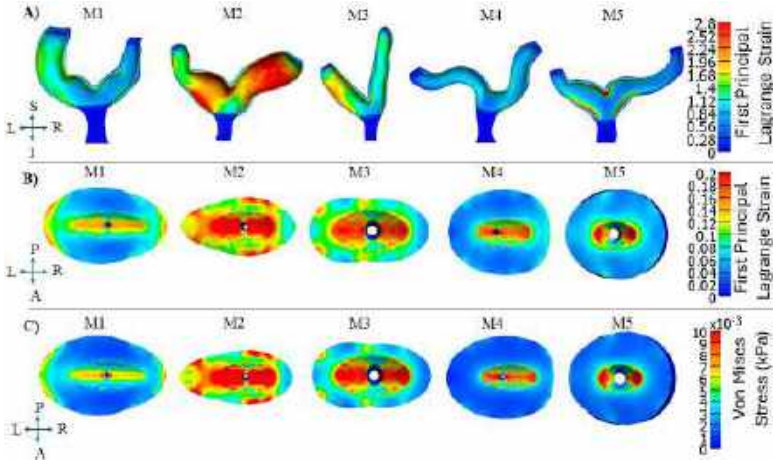

Figure 3: (A) First principal strain. (B) First principal cervical strain (C) Von Mises cervical stress. Anatomical directions are provided.

DISCUSSION

These computational results show the feasibility of modeling the murine reproductive tract during pregnancy. Here, initial proximal cervix loading maps were generated from this study. Moving forward, further work is needed to characterize loading patterns in the mouse model and compare them to other species. For example, in the human model, the fetal membrane is tied to the uterus and allowed to slide on the cervix. To create a direct comparison between mouse and human proximal cervix loading, this contact condition will be replicated in a future version of the mouse FEA model. Additionally, physiologically relevant mouse material properties will be incorporated into the model. Mouse cervical properties have previously been measured and reported from tensile stress-relaxation tests [9]. Uterine properties will be obtained by replicating this testing protocol on recently acquired mouse uterus samples.

The limitations of this study are not trivial. Although tissue samples included samples from different gestational time points, the sample size was small. It did not provide insight into the relative changes each mouse's anatomy undergoes as a longitudinal study would. Additionally, although this model shows promise in replicating the strain experienced during the first trimester of mouse pregnancy, it is not yet able to replicate the large amount of deformation that this anatomy experiences at a late pregnancy timepoint (day 18).

ACKNOWLEDGEMENTS

This work was funded by the National Science Foundation under grant 2053851 to RD, SA, KM, and KM.

REFERENCES

[1] Chawanpaiboon S, et al., *Lancet Glob Health*: :e37-e46, 2019, [2] Westervelt, AR et al., *J Biomech*, 139: 0510041–05100411, 2017, [3] Louwagie, E et al., *PLOS ONE*, 16(1): e0242118, 2021, [4] Carter, A. M, *Reproduction*, 160: R129-R143, 2020, [5] Myers, K et al., *J Biomech,* 48: 1533-1540, 2015, [6] Conrad, J et al., *Am J Ob Gynecol*, 96: 1055-1059, 1966, [7] Bürzle, W and Mazza, E., *J Biomech*, 46: 1777-1783, 2013, [8] Badir, S et al., *Prenat Diagn*, 33:737-741, 2013, [9] Yoshida, K et al., *Acta Biomat* 36: 195-209, 2016

DEVELOPMENT OF A MICROFLUIDIC DUAL-GEL CELL CULTURE MODEL

Malgorzata Dwulat (1), Sihong Wang (1), Jing Fan (2)

(1) Department of Biomedical Engineering, City College of New York, New York City, NY, USA
(2) Department of Mechanical Engineering, City College of New York, New York City, NY, USA

INTRODUCTION

Metastatic breast cancer is one of the leading causes of deaths in women worldwide [1].Therefore, it is crucial to focus on the study of its mechanism and treatment. Imitating the tumor microenvironment, including the extracellular matrix (ECM), in metastatic breast cancer research is of utmost significance. This approach enables to create a more accurate representation of the conditions in which cancer cells grow and spread, shedding light on the intricate process of metastasis. It also plays a pivotal role in drug development, as it allows for testing the efficacy of anticancer drugs under conditions that closely resemble those found in the body. The stiffness and permeability of the ECM can significantly influence the behavior of cancer cells. Increased ECM stiffness is often associated with enhanced cancer cell migration and invasion, contributing to tumor progression. This is because stiffer ECMs can enhance the mechanical signals that are transduced into the cells, promoting more aggressive behaviors in cancer cells [2].On the other hand, ECM permeability affects how nutrients, signaling molecules, and cells themselves move through the tumor environment, impacting tumor growth and metastasis [3].Moreover, understanding how cancer cells interact with the ECM and other microenvironmental factors is crucial in identifying resistance mechanisms and developing novel therapeutic strategies to combat drug resistance. Additionally, the study of interstitial flow within the tumor microenvironment is gaining increasing importance in metastatic cancer research. Interstitial flow influences various aspects of tumor behavior, including cell migration and the transport of nutrients and signaling molecules. Its role in metastatic cancer cannot be understated, as it affects the ability of cancer cells to invade surrounding tissues and disseminate to distant organs [4]. Investigating interstitial flow dynamics provides valuable insights into the mechanics of metastasis and offers potential targets for therapeutic intervention. Therefore, comprehending the interplay between interstitial flow and metastatic breast cancer progression is a critical avenue of research in advancing our understanding and treatment of this disease. Most previous methods of studying migration involve a monolayer cell culture system together with hydrogels, which is unable to either recreate the tumor migration nor to sufficiently mimic tumor microenvironment [5]. Lack of interstitial flow and usage of only single gel-based cell culture limits control of matrix properties therefore impedes structural imitation of the extracellular matrix as well as tumor microenvironment. To overcome this limitation, we have developed a microfluidic dual-gel cell culture model, which can better mimic the heterogeneous nature of the tumor ECM, providing a more accurate model for studying cancer cell migration and behavior. By incorporating varying stiffness and permeability characteristics in different gel regions, we can more effectively study how these ECM properties influence cancer progression and response to therapies, while controlling the interstitial flow. The current results represent an initial phase in developing the final dual-gel system. Currently our focus has been on encapsulation cells within GelMA microbeads. Moving forward, the dual-gel system will be enhanced by incorporating collagen between the microbeads.

METHODS

The dual-gel cell culture model was manufactured through standard soft lithography using a single-layered structure of PDMS (polydimethylsiloxane). Gelatin Methacryloyl (GelMA) was chosen as the primary gel due to its unique properties and characteristics. GelMA is biocompatible and provides a natural microenvironment that closely mimics the extracellular matrix of tissues, making it highly suitable for cell culture. 7 million/mL GFP-tagged MB-MDA 231 were encapsulated in 7.5% GelMA using a PDMS microfluidic droplet device and packed to another PDMS microfluidic device (Figure 1) through inlet, where they were trapped in a chamber by the pillars and

cultured using continuous flow at 0.5ul/min for 7 days via a syringe pump in a 5% CO_2/37°C incubator. Live-dead assay was performed after 7 days using ethidium homodimer staining. Prior to the experiment, all cells were stained with CellTracker Green, a fluorescent dye making living cells appear green under fluorescence microscopy. Additionally, dead cells were identified using ethidium homodimer, a compound that penetrates only dead cells and makes them appear red under fluorescence. Images were captured, showing cells in two colors: green for live cells and red for dead cells. To determine cell viability, the images were analyzed by counting the total number of cells (green-stained) and the number of dead cells (red-stained). Cell viability was calculated by subtracting the number of dead (red) cells from the total number of cells (green) and then multiplied by 100 to obtain the cell viability percentage. Experiments to study metastasis will be performed using the same chip design (Figure 1), but encapsulated in 7.5% GelMA will be cancer Associated Fibroblast (CAFs) and MB-MDA 231 will be seeded around the beads. Second gel will also be introduced.

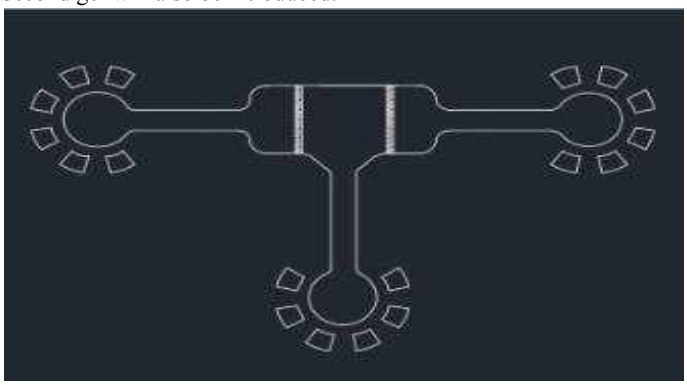

Figure 1: CAD design of microfluidic device used for culturing of GelMA microbeads. The chamber is 1mmx1mmx200um.

RESULTS

Micropillars were able to successfully trap microbeads inside of the chamber during the constant flow creating a two-layer packing as shown in Figure 2.

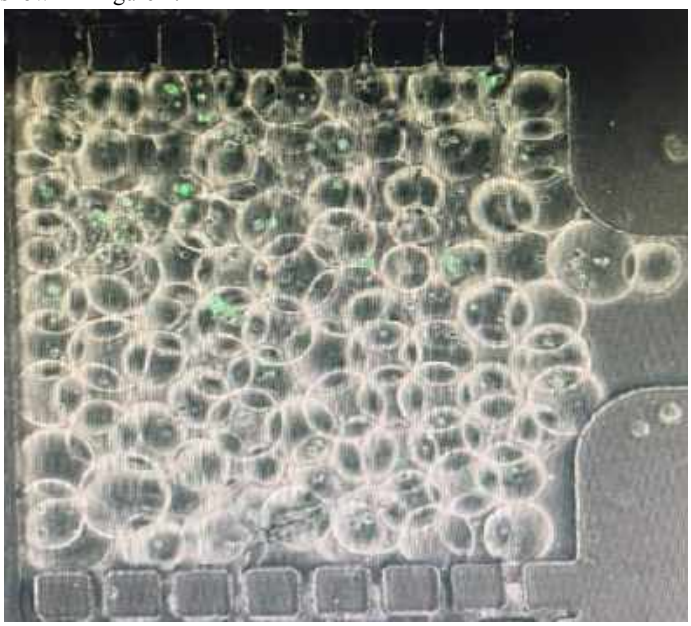

Figure 2: PDMS microfluidic device packed with encapsulated in GelMA GFP MB-MDA 231.

Live-dead assay of encapsulated in GelMA GFP MB-MDA 231 cells after 7 days of continuous flow at 0.5ul/min showed over 95% viability, as shown below on the Figure 3.

A)

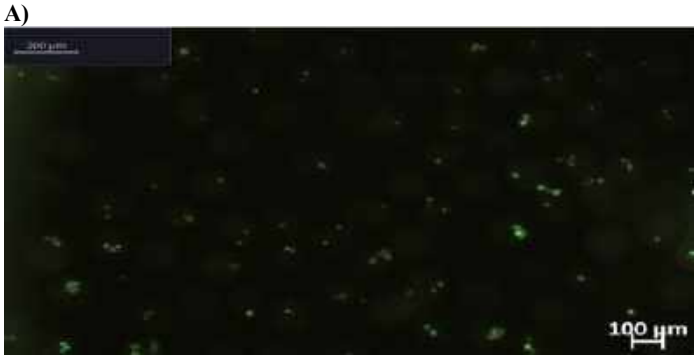

B)

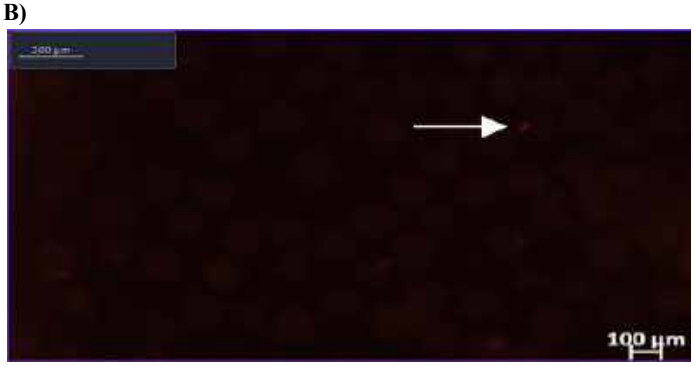

Figure 3: Pictures of live-dead assay made by fluorescent microscope.
A) Image representing live population of MB-MDA 231-green.
B) Image representing dead population of MB-MDA 231- 2 red cells shown with an arrow.

DISCUSSION

The novel dual-gel cell culture model combines the encapsulation of cells within GelMA via a droplet device and their subsequent cultivation in a continuous flow system. This approach has maintained high cell viability, with over 90% viability observed after seven days, which hold big hopes and potential for future research applications. By introducing a secondary gel and incorporating an additional cell line, it will more accurately replicate the complex interactions within the tumor microenvironment,which is crucial for understanding the dynamics of cancer progression and metastasis.The potential of this dual-gel system extends beyond basic research and holds significant promise for informing the development of targeted cancer therapies.

ACKNOWLEDGEMENTS

Funding for this project was provided by National Science Foundation (NSF), project 40K09-00 01.

REFERENCES

[1]Globocan Database, *gco.iarc.fr,* access date: 01/22/2023

[2] Butcher, D. T et al., *Nature Reviews Cancer*, 9(2), 108-122 (2009)

[3] Egeblad, M et al., *Current Opinion in Cell Biology*, 22(5), 697-70 (2010)

[4] Evje, S et al.,*Cel.Mol. Bioeng,* 12, 227-254 (2019).

[5] Bouchalova, P et al., Cancer *Cell Int* 22, 394 (2022)

PRESSURE OVERLOAD DURING MURINE PREGNANCY AND ITS EFFECTS ON ACUTE CARDIAC REMODELING

Adalyn M. Meeks (1), Elnaz Ghajar-Rahimi (1), Molly S. Kaissar (2), Kyoko Yoshida (2), Craig J. Goergen (1)

(1) Weldon School of Biomedical Engineering, Purdue University, West Lafayette, IN, USA
(2) Department of Biomedical Engineering, University of Minnesota, Minneapolis, MN, USA

INTRODUCTION

The American College of Obstetrics and Gynecology's diagnostic criteria for chronic pre-existing hypertension is having either a systolic pressure ≥ 140 mmHg or diastolic pressure ≥ 90 mmHg before pregnancy [1]. Chronic hypertension affects approximately 1 in 20 pregnancies and its prevalence in pregnancies continues to increase. Blood pressure typically decreases by 5-10 mmHg near the end of the first trimester and starts to return to pre-pregnancy values around the start of the third trimester [1]. This decrease is seen in normotensive pregnancies and chronic hypertension pregnancies, but not in preeclamptic patients [2].

The maternal cardiovascular system goes through dynamic changes during pregnancy to meet the demands of perfusing the gestation, especially during the exponential growth seen later in pregnancy. Studies on C57BL/6J mice demonstrate comparable cardiovascular changes during pregnancy to those observed in humans [3]. Additional studies utilizing pressure overload models, such as the transverse aortic constriction model, have found that pregnancy had a positive effect on cardiac remodeling compared to non-pregnant controls [4].

In this study, our objective was to non-invasively characterize cardiac remodeling in a small animal model of chronic hypertension with pregnancy. We used a combination of ultrasound imaging and non-invasive blood pressure measurements to longitudinally monitor the physiological adaptations that occur during chronic hypertension in pregnancy.

METHODS

Nine nulliparous female mice (C57BL/6J; 10 weeks old) were used in this study. Cardiovascular health was assessed using a non-invasive blood pressure monitoring system (CODA, Kent Scientific Corporation, Torrington, USA) and high-frequency ultrasound for echocardiography (Vevo3100 Imaging system, FUJIFILM VisualSonics, Inc., Toronto, ON, Canada).

A subset of five mice were randomly assigned to be in the hypertensive cohort (AngII cohort). The remaining four mice were assigned as the normotensive-pregnant cohort (control cohort). After baseline assessment, a mini-osmotic pump (Azlet 2006, Durect) was implanted subcutaneously to dose 1000 ng/kg/min angiotensin II (AngII) for 6 weeks [5]. The mice were re-evaluated via ultrasound to establish a hypertensive baseline (HT baseline). The mice were then paired 2:1 with male mice (C57BL/6J; 2-6 months old) to induce pregnancy. Mice from the control cohort were immediately paired after the initial assessment. After pairing, the mice were assessed every 3-4 days using high-frequency ultrasound to identify gestation [6].

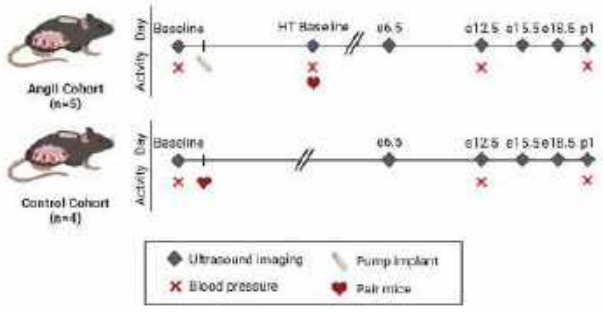

Figure 1: Experimental timeline for AngII and control cohort. Created with BioRender.com.

Mice from both cohorts were imaged at embryonic day 6.5 (e6.5), e15.5, e18.5, and the first day postpartum (p1) using a 40 MHz central frequency transducer. The experimental timeline for both cohorts is outlined in Figure 1. ECG-gated Kilohertz Visualization images of the long axis of the left ventricle were analyzed using Vevo Lab software

(Figure 2). After segmentation of the endocardium of the left ventricle, we can estimate the volume of the ventricle throughout the cardiac cycle, stroke volume (SV), ejection fraction (EF), and cardiac output (CO). Blood pressure was also acquired on e12.5 and p1.

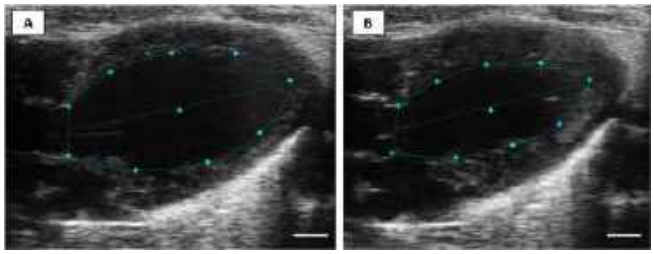

Figure 2: Representative long axis B-mode images of the left ventricle at (A) diastole and (B) systole with segmentation points shown in cyan. Scale bar = 1 mm.

The normality assumption was assessed under a Shapiro-Wilk test and homoscedasticity was assessed under a Levene's test. The parameters were analyzed using a two-way ANOVA with post-hoc Tukey pairwise comparisons. Parameters were considered significant when the p-value(*p) was less than 0.05.

RESULTS

Mice were considered hypertensive if there was at least a 10 mmHg increase from baseline mean arterial pressure (MAP). For the AngII cohort, this occurred approximately two weeks after mini osmotic pump implantation. There was a significant decrease in MAP in the AngII cohort compared to their hypertensive baseline and control group at e12.5 (Figure 3).

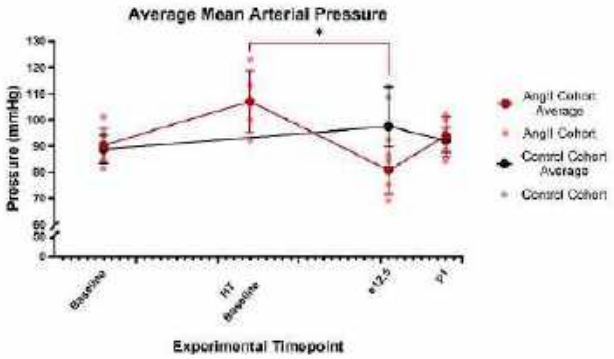

Figure 3: Longitudinal average mean arterial pressure displayed as average ± standard deviation. *p<0.05.

Mice in the AngII cohort had a significant decrease in EF from their baseline to HT baseline (Figure 4A). They also had a significant increase in diastolic volume on days e12.5 and e15.5 compared to their HT baseline (Figure 4B). Similar increases were seen in CO on e15.5 and SV on e15.5 and p1 for the AngII cohort (Figures 4C and 4D).

DISCUSSION

The relationship between systemic hypertension, pregnancy, and acute cardiac remodeling is multi-faceted and complex. Our murine results suggest potential counteracting effects of pregnancy-induced volume overload and hypertension-induced pressure overload. The AngII cohort of mice had blood pressure data that followed similar trends compared to a human study which reported a decrease in blood pressure during the beginning of pregnancy, followed by an increase in the later stages [1]. The SV and CO results of the control cohort were similar to previously reported values at their respective embryonic days for our control mice [3].

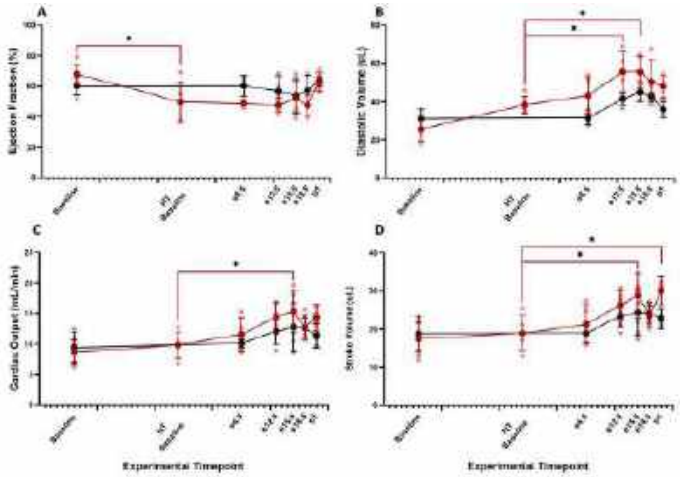

Figure 4: Longitudinal average (A) ejection fraction, (B) diastolic volume, (C) cardiac output, and (D) stroke volume displayed as average ± standard deviation. *p<0.05.

We observed similar trends in diastolic volume throughout pregnancy in both cohorts, as diastolic volume continued to increase from baseline to e15.5, followed by a slight decrease. However, we see on average a higher diastolic volume in the AngII cohort compared to the control cohort on corresponding embryonic days. This suggests that the AngII-induced pressure overload leads to more pronounced eccentric hypertrophy. AngII also significantly decreased the EF after the mice became hypertensive. This was expected as AngII is known to stimulate collagen formation in the extracellular matrix of cardiovascular tissue, which leads to hypertrophy and ventricular stiffening [7]. The similarities that we observed in SV and diastolic volume trends could explain why EF remains relatively similar throughout pregnancy.

Ongoing histological analysis will provide insight into the composition of the extracellular matrix and compositional differences between cohorts. Altogether, this study using mini osmotic pumps to subcutaneously infuse AngII in pregnant mice has provided key insights into how chronic hypertension influences cardiac remodeling during pregnancy. Additional work is needed to translate these findings into therapeutics aimed at helping patients with pre-existing hypertension, pregnancy-induced hypertension, and/or preeclampsia.

ACKNOWLEDGEMENTS

This work was funded by the Charles C. Chappelle Fellowship (AM), the NIH through the Cardiovascular Engineering Training Program at the University of Minnesota (MK; T32-HL139431), an AHA Career Development Award (KY), and the Purdue University Women's Global Health Institute (CG).

REFERENCES

[1] Seely, E et al., *AHA Circulation*, 129:1254–1261, 2014. [2] Hermida, R et al., *AHA Hypertension*, 36:149-158, 2000. [3] Kulandavelu, S et al., *AHA Hypertension*, 47:1175-1182, 2006. [4] Xu, H et al., *AJP Heart*, 311:807-814. [5] Okuno, K et al., *AHA Hypertension,* 80:668-677, 2023. [6] Greco, A et al., *PLOS ONE*, 8(10):e77205. [7] Zieman, S et al., *AHA Arteriosclerosis, Thrombosis, and Vascular Biology*, 25:932–943, 2005.

OPTICAL COHERENCE ELASTOGRAPHY MEASUREMENT OF CEREBRAL ARTERY STIFFNESS

Mykyta Ananchenko (1), Xu Feng (2), Samuel C. Halvorsen (1), Guoyang Li (3), Seok-Hyun A. Yun (2, 4), Katherine Y. Zhang (1, 5, 6)

(1) Mechanical Engineering, Boston University, Boston, Massachusetts, United States
(2) Harvard Medical School and Wellman Center for Photomedicine, Massachusetts General Hospital, Boston, Massachusetts, United States
(3) Department of Mechanics and Engineering Science, Peking University, Beijing, China
(4) Harvard-MIT Division of Health Sciences and Technology, Cambridge, Massachusetts, United States
(5) Biomedical Engineering, Boston University, Boston, Massachusetts, United States
(6) Division of Materials Science & Engineering, Boston University, Boston, Massachusetts, United States

INTRODUCTION

Elastography is a medical imaging modality that is used to determine mechanical properties of biological tissues. There exist various elastography techniques that use ultrasound [1] or magnetic resonance imaging. Optical coherence elastography (OCE) is a more recently developed technique that applies optical coherence tomography (OCT) imaging modality. Wave-based OCE is based on excitation of elastic waves in tissues. Wave velocity obtained from the OCT images is related to the shear modulus of the probed material, using elastic wave theory. Wave-based OCE has been used to infer stiffness of various soft biological tissues.

Previous research mainly focused on the application and validation of elastography technique on the phantoms [2]. Recently, OCE has been applied to determine stiffness of biological tissues such as eye cornea [3] and skin [4]. Ultrasound elastography has been used to determine mechanical properties of arteries *in vivo*, such as sheep and human common carotid artery [5]. In this study, OCE was applied to determine local shear modulus of human anterior cerebral arteries (ACAs), which was then compared with tissue properties from mechanical test.

METHODS

OCE measurement

ACA samples, approximately 1.5 cm long and 2 mm in diameter, were mounted on a custom device and placed under the OCE setup (Fig. 1). The ACA samples were then pressurized up to 120 mmHg using 1×phosphate-buffered saline (PBS) solution with OCE measurements made every 20 mmHg. The elastic waves were excited by a piezoelectric actuator with frequencies range from 1 kHz to 100 kHz. The OCE system is operated in a M-B scan mode to acquire traveling waves data along the longitudinal direction of the ACA.

Figure 1: OCE measurement of ACA cannulated on a custom device and pressurized up to 120 mmHg.

The propagation of the guided wave was analyzed from arterial wall displacements using the method previously described [3]. Briefly, to calculate wave speeds, at each frequency, Fourier transformation was performed on the displacements in the wavenumber k domain. An experimental dispersion curve was then plotted.

Shear modulus from OCE measurement

Lamb wave theory was used to describe the wave guided by the arterial wall [6] allowing a dispersion relation to be obtained. Fluid-solid-fluid interface interactions were considered while deriving the dispersion relation as the following [1]:

$$4k_L^2\eta\beta\cosh(\eta h)\sinh(\beta h) - (2k_L^2 - k_s^2)\cosh(\beta h)\sinh(\eta h) = \eta/\eta_f * k_s^4\cosh(\eta h)\cosh(\beta h) \quad (1)$$

where h is the artery thickness. The Lamb wavenumber $k_L = \omega/c$ is calculated from experimental data, where ω is the angular frequency of excited wave, and c is the experimentally obtained wave speed. The

shear wave number $k_s = \omega\sqrt{\rho/\mu}$ that depends on shear modulus μ, and the material density ρ. Other parameters $\eta \approx k_L$ and $\beta = \sqrt{{k_L}^2 - {k_s}^2}$.

To determine shear modulus μ, the dispersion relation in Eqn. 1 was fitted to the dispersion curves obtained from OCE experiments.

Artery stiffness from mechanical testing

Biaxial inflation-extension testing was performed on ACAs using a pressure myograph [7]. Briefly, samples were stretched to their *in vivo* stretch ratio and inflated up to 120 mmHg pressure, while the axial force, transmural pressure and outer diameter were recorded. Circumferential stretch and stresses were calculated. Tangent modulus was then determined as the slope of the circumferential stress-stretch curve for all tested pressure values [7].

Local shear modulus obtained using the OCE method was then compared to the tangent modulus from mechanical testing.

RESULTS

Displacement maps were generated for all samples at every pressure value. For each tested frequency ranging from 1 kHz to 100 kHz, images of arterial wall displacements that caused by traveling waves were generated (Fig. 2). The alternating red and blue pattern represent the positive and negative vertical displacements, respectively. At higher frequencies the distance between the minimum and maximum vertical displacements is smaller due to smaller wavelength.

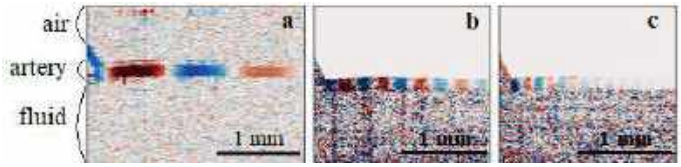

Figure 2: Displacement maps at frequencies of (a) 10 kHz, (b) 30 kHz, (c) 50 kHz in an ACA wall pressurized to 80 mmHg.

We introduced a cutoff frequency that ranges between 15-30 kHz, after which Lamb wave theory is applicable to describe the guided elastic wave in the artery [6]. At frequencies higher than the cutoff frequency, the dispersion relation from Eqn. 1 fits the experimental data well (Fig. 3).

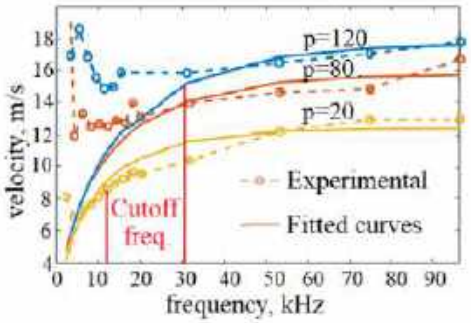

Figure 3: Experimental data (dotted lines) and fitted with Eq. 1 dispersion curves (solid lines) for given sample at 20 mmHg , 80 mmHg and 120 mmHg pressure.

From the fitted curve the local shear modulus of the ACA was obtained at each tested pressure. Figure 4 shows the comparison of shear modulus from OCE and tangent stiffness from mechanical test for an ACA sample. The local shear modulus increases from 0.22 to 0.44 MPa as pressure increases from 20 to 120 mmHg, while the tangent modulus obtained from mechanical test increases from 0.34 MPa to 4.6 MPa.

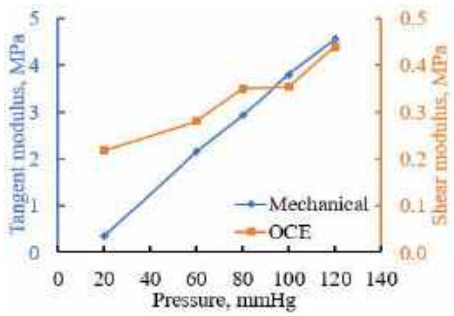

Figure 4: Comparison of shear modulus from OCE to tangent modulus from mechanical testing of an ACA sample at pressures from 20 to 120 mmHg.

DISCUSSION

Both local shear modulus and tangent modulus increase with pressure due to stiffening of the artery. The ratio between local shear modulus and tangent stiffness obtained from biaxial extension-inflation mechanical test decreases from 0.6 to 0.1 as the pressure increases (Fig. 4). While further studies are still needed to understand such discrepancy, it is important to point out the differences in the two testing modalities. Firstly, shear modulus measured with OCE is local, and limited by 5-10 wavelength or scan length (typically < 3 mm), while the mechanical test measures the averaged tissue level properties of the whole artery. Secondly, the mechanical test is a quasi-static experiment, while OCE is a dynamic test, therefore viscoelasticity will play an important role. Finally, shear modulus from OCE experiment is measured in the longitudinal direction, whereas tangent stiffness was obtained in the circumferential direction, which is important to consider for such an anisotropic material as ACA.

A cutoff frequency was specified when interpreting the experimental data using Lamb wave theory (Fig. 3). Our results show that at low frequencies the wavelength is comparable to the arterial radius. In this range Eqn. 1 derived from the Lamb wave theory that assumes wave propagation in a flat plate, will not be applicable to describe guided wave propagation in curved artery.

In this study, Lamb wave model was used under the assumption of fluid-solid-fluid interface interaction. Similar assumption was made in a previous study that applied dynamic wave elastography *in vivo* [5], assuming the connective tissue around the artery is significantly softer than the arterial wall. Study is underway to develop a Lamb model with air-solid-fluid interface interaction, which may describe the experiments more accurately.

In this research OCE was successfully applied to determine local shear modulus of ACA samples. Further studies are underway to understand the comparison of measurements from different modalities, and the mechanical properties of ACAs with the progression of neurodegenerative disease, such as Alzheimer's disease.

ACKNOWLEDGEMENTS

National Institutes of Health (R01AG075876)

REFERENCES

[1] Bernal, M et al., *J Acoust Soc Am.*, 129(3):1344-54, 2011.
[2] Maksuti, E. et al., *Ultrasound in Med. & Bio.*, 42(1):308-321, 2016.
[3] Ramier, A. et al., *Sci Rep*, 10:17366, 2020.
[4] Feng, X. et al., *Acta Biomaterialia*, 146:295-305, 2022.
[5] Couade, M. et al., *Ultrasound Med Biol.*, 36(10):1662-76, 2010.
[6] Li, G-Y. et al., *Ultrasound in Med. & Bio.*, 43(2): 505-516, 2017.
[7] Liu, X. et al., *Alz Res Therapy*, 15:185, 2023.

FINITE DEFORMATIONS OF THE ENTIRE MURINE REPRODUCTIVE TRACT UNDER INFLATION

Aileen C. Suarez (1), Steven D. Abramowitch (2), Kristin M. Myers (3), Kristin S. Miller (4), Raffaella De Vita (1)

(1) Department of Biomedical Engineering and Mechanics, Virginia Tech, Blacksburg, VA, USA
(2) Department of Bioengineering, University of Pittsburgh, Pittsburgh, PA, USA
(3) Department of Mechanical Engineering, Columbia University, New York City, NY, USA
(4) Department of Bioengineering and Mechanical Engineering, University of Texas Dallas, Richardson, TX, USA

INTRODUCTION

The female reproductive tract is unique in its ability to undergo significant remodeling and large deformations during pregnancy. Due to ethical considerations, these remarkable changes have been understudied in human subjects, limiting our understanding of the effects of pregnancy on women's health. For example, there are still many unknowns about the reversible and irreversible alterations in the mechanical properties of reproductive tissues that occur in women with pregnancy. Researchers have relied on animal models such as rodents, ewes, swine, and primates to investigate the mechanical properties of the reproductive organs throughout pregnancy [1]. *Ex vivo* reproductive tissues from mice and rats have been used to quantify the biaxial mechanical properties of the vagina and uterine body using inflation testing [3-7]. In these studies, each reproductive organ was either tested in isolation [3-6] or its deformations were characterized only partially [5-7], providing an incomplete picture of the *in vivo* mechanical behavior of the organ. Rodents can be adopted as a model for pregnancy research as long as differences between mice and humans are well understood. By using advanced magnetic resonance imaging (MRI) technology, we have recently documented pregnancy-induced *in-vivo* remodeling of the reproductive organs in mice, taking advantage of mice's short gestation period, ease of animal husbandry, and low cost [2]. In this study, to better simulate the *in vivo* physiological conditions, we performed *ex vivo* inflation testing of the entire murine reproductive tracts with full-field deformation measurements of the main component of the tracts.

METHODS

The current study was conducted with the approval of the Institutional Animal Care and Use Committee (IACUC) at Virginia Tech. Sexually mature 3-4 months old nulliparous (virgin) CD1 mice (Charles River Laboratories Inc., Wilmington, MA) were sacrificed using CO_2 asphyxiation, followed by cervical dislocation. The reproductive tract (from introitus to ovarian fat pads) were isolated from each mouse. Extraneous connective tissue and fat were removed, without compromising the integrity of the reproductive tract. The intact reproductive tract was connected to a stainless-steel dispensing needle via the introitus. The ovaries, oviducts, and the tips of the uterine horns were occluded in methyl 2-cyanoacrylate before being loosely tied with sutures at the ends of the uterine horn. This allowed the reproductive tract to freely extend and shift during testing while maintaining an upright orientation. Specimens were speckled with an aerosol fast dry gloss black paint for non-contact strain measurement (Figure 1).

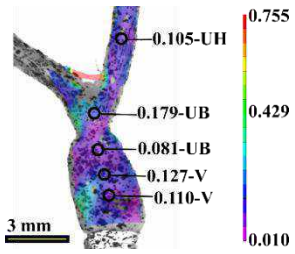

Figure 1: Hoop strain maps of one representative murine reproductive tract at 88 kPa luminal pressure.

Testing was performed on a custom-built inflation set up described elsewhere [3,4]. Briefly, specimens were immersed in a phosphate buffered saline (PBS) filled tank at room temperature, connected to a pressure transducer (Max capacity: 345 kPa, Omega Engineering Inc., Norwalk, CT) and computer-controlled syringe pump (New Era Pump Systems Inc., Farmingdale, NY) via plastic tubing. Each tract was preconditioned by 20 cycles of infusion and withdrawal of PBS to a pressure of 0 to 10 kPa at a flow rate of 2 ml min^{-1} using a closed-loop analog control sensor interface (ANABOX-11, New Era Pump Systems Inc., Farmingdale, NY) [4], followed by 40 cycles of a fixed 0.11 ml volume at a rate of 4.7 ml min^{-1}. It was then unloaded to 0 kPa and infused with PBS (flow rate of 0.47 ml min^{-1}) until rupture. Images were collected at 4 Hz during testing via two CMOS cameras (Basler ace A2440-75 um, Basler Inc., Exton, PA) equipped with c-mount lenses (Xenoplan 2.8/50, Schneider Optics Inc., Hauppauge, NY). Non-contact strain measurements were computed on the dorsal side of the reproductive tract using a calibrated 3D digital image correlation system (Vic-3D 9, Correlated Solutions, Columbia, SC). The average Lagrangian normal strains in the hoop and axial directions were collected over small circular regions at the vagina, uterine body (connection of the uterine horns to the cervix and vaginal fornix), and uterine horns (Figure 1).

RESULTS

The average pressure at rupture and average volume infused in the reproductive tract (n=5) was 73.95 ± 19.67 kPa and 0.673 ± 0.155 ml. Tissue rupture occurred away from the introitus, the clamped end, at seemingly random locations within the uterine horn wall. Deformations in the hoop direction were larger than those in the axial direction in each region of the reproductive tract; at times, almost double (Figures 2 and 3). Both strains were non-linearly correlated with the applied pressure; the uterine horns and uterine body had a more variable pressure-strain relationship across specimens (Figure 3 depicts change in regions for n=1).

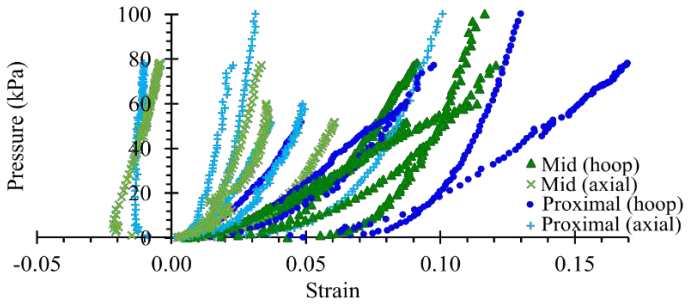

Figure 2: Hoop and axial strain versus pressure for the mid and proximal vagina (n=5 specimens).

For the vagina, the maximum strain in the hoop direction was consistently larger (0.129 ± 0.032, mean ± standard deviation) than the maximum strain in the axial direction (0.060 ± 0.060) (Figure 2). At the uterine body, the maximum hoop strain was 0.284 ± 0.264 with the maximum axial strain equal to 0.123 ± 0.045. Regions of the uterine horns had more variations in strain along both directions, with strains in the hoop and axial yielding a maximum value of 0.200 ± 0.125, and 0.105 ± 0.041, respectively.

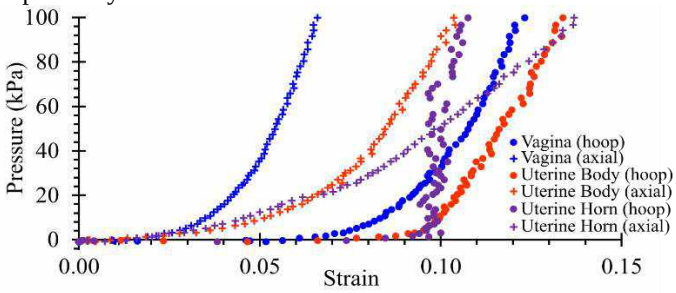

Figure 3: Hoop and axial strain versus pressure for the vagina, uterine body, and uterine horns of one reproductive tract (same as in Figure 1).

DISCUSSION

To our knowledge, this is the first study that reported the full-field deformations of the entire reproductive tract simultaneously without isolating the vagina, uterine body, and uterine horns in response to increasing intraluminal pressure, up to failure. Differences in magnitude of hoop and axial strains in the vagina (Figure 2) align with previous inflation studies of the *ex-vivo* rat [3,4] and mouse vagina [5,6]. Measurements of local strains in multiple anatomical regions suggest mechanical differences between the proximal and the mid vagina (Figure 2). These findings could be also determined by geometric differences of the organs as quantified *in vivo* in our recent MRI study [2]. Direction-dependent differences in strains (e.g., the hoop strain being greater than the axial strain) are not consistent in the uterine body and uterine horns (see, e.g., pressure-strain data for the uterine horn in Figure 3). This may be the result of their overall irregular geometry and variations in wall thickness. Our strain values are higher than those reported in published studies on murine reproductive tissues likely due to differences in testing modality and applied pressures [6,7]. We plan to conduct additional tests on entire murine reproductive tracts, including from mice at different time points during gestation. This research represents an important first step in evaluating mice as an animal model for examining reproductive tissue deformations during pregnancy. In addition to enhancing our understanding of mouse physiology, this work can provide valuable insights into human pregnancy and contribute to the generation of research hypotheses in the field of women's health.

ACKNOWLEDGEMENTS

This work was funded by the National Science Foundation under grant # 2053851.

REFERENCES

[1] Baah-Dwomoh, A, *App Mech Rev*, 68(6), 2016. [2] Suarez, AC, *Sci Rep*, 14(586), 2024. [3] McGuire, JA, *Interface Focus*, 9(4), 2019. [4] Dubik, J, *Integr Comp Biol*, 62(3), 625-640, 2022. [5] Robison, KM, *J Biomech Eng*, 139(10), 2017. [6] White, SE, *J Biomech Eng*, 144(6), 2022. [7] Conway CK, *J Biomech*, 94, 39-48, 2019.

AUTOMATIC SEGMENTATION OF ABDOMINAL AORTIC ANEURYSM FROM COMPUTED TOMOGRAPHY ANGIOGRAPHY USING A PATCH-BASED DILATED U-NET MODEL

Merjulah Roby (1), Juan C. Restrepo (1), Haehwan Park (1), Satish C. Muluk (2), Mark K. Eskandari (3), Ender A. Finol (1)

(1) Department of Mechanical Engineering, University of Texas at San Antonio, San Antonio, TX
(2) Department of Cardiothoracic Surgery, Allegheny Health Network, Pittsburgh, PA
(3) Division of Vascular Surgery, Northwestern University School of Medicine, Chicago, IL

INTRODUCTION

Abdominal Aortic Aneurysm (AAA) is a serious condition where the distal end of the body's main blood vessel, the aorta, dilates abnormally. This dilation can be life threatening if the vessel ruptures. Various factors contribute to its development, including aging, smoking, high blood pressure, plaque buildup in arteries (atherosclerosis), and male gender [1]. At its early stages, an AAA often shows no symptoms, making it challenging to detect without proper screening. However, as the aneurysm grows larger, it can cause severe abdominal or back pain. A ruptured aneurysm is a medical emergency and can be fatal. Doctors typically diagnose AAA using imaging methods such as ultrasound, computed tomography (CT), or magnetic resonance imaging exams.

AAA clinical images can be segmented semi-automatically or automatically to identify specific regions of interest (ROI). Semi-automatic methods often require initial guidance through seed points and commonly use deformable models or active shape models [2]. Our study introduces an innovative automated segmentation technique to identify the AAA lumen and outer wall boundaries. The method does not require specialized AAA knowledge or specific segmentation software. What makes it unique is its high accuracy and reliability due to a carefully crafted diverse training dataset, ensuring precise results. The segmentation methodology not only establishes a robust foundation for comprehensive biomechanical assessment of AAAs, but also exceeds the speed of conventional segmentation methods.

METHODS

We used the patch-based dilated U-Net architecture for segmentation and identification of the AAA lumen and outer wall boundaries, evolving from Ronneberger *et al.'s* U-Net model [3]. In the U-Net architecture, dilation rates play a crucial role in how the network sees the image through its convolutional layers. In addition to its architectural components, our methodology integrates patch-based processing, which is a technique that subdivides large image stacks into smaller, manageable patches. These patches undergo individual processing, enabling efficient analysis and segmentation of extensive datasets. Furthermore, data augmentation strategies are employed to expand the training dataset and enhance model generalization.

Overall, the 2D U-Net's patch-based dilated model efficacy for AAA segmentation lies not only in its architectural intricacies, incorporating dilation rates for enhanced feature extraction, but also in its practical approach leveraging patch-based processing and data augmentation to handle extensive image datasets effectively. These methodological aspects collectively contribute to the model's precision and scalability in medical imaging tasks. Figure 1(a) shows the patch-based dilated U-Net model, 1(b) illustrates the overlaid binary mask, while 1(c) and 1(d) provide a visual representation of the coronal and sagittal planes, respectively.

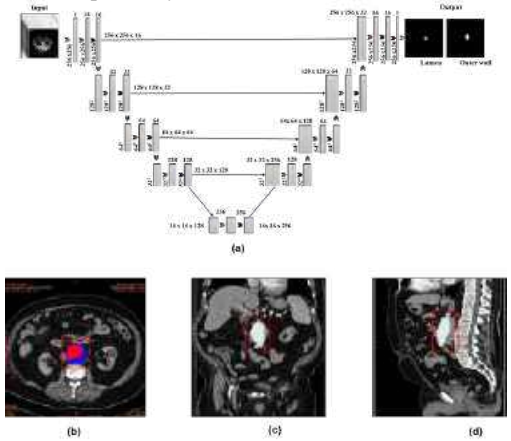

Figure 1. The overall model architecture for AAA segmentation and visualization of the reconstruction.

The dataset utilized in this study is a compilation of 2D high-resolution CT images acquired from screenings conducted at Allegheny General Hospital (Pittsburgh, PA) and Northwestern Memorial Hospital (Chicago, IL). To ensure ethical compliance and data integrity, this study received approval from the Institutional Review Board (IRB) at each medical center. The images in the dataset exhibit variation in slice thickness, ranging from 1 mm to 3 mm, and possess a resolution of 512 x 512 pixels. They were carefully annotated using a specialized script called AAAVASC (v.0168, The University of Texas at San Antonio), enabling a semi-automated approach for vessel wall detection [2].

RESULTS

Utilizing a patch-based dilated U-Net model, trained with 4268 CT contrast-enhanced images, and tested with 1385 images, accurate boundaries for the lumen and outer wall were identified. Figure 2 illustrates the segmentation protocol followed in our approach, outlining the anatomical components, and leading to the 3D reconstruction of the AAA geometry. The results shown in Table 1 indicate a substantial overlap between the predicted result segmented by the model and the ground truth.

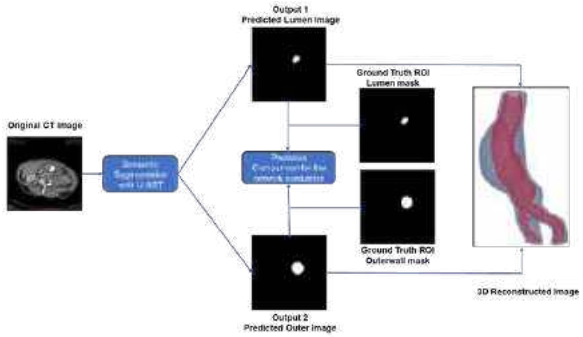

Figure 2. Image segmentation, identification of the lumen and outer wall ROIs, followed by 3D reconstruction.

Table 1. Performance evaluation based on image segmentation of 18 AAAs and 4 complex AAAs with high tortuosity.

Metric	Lumen	Outer wall	Complex AAA 1	Complex AAA 2
Accuracy	0.9995	0.9992	0.9995	0.9994
Sensitivity	0.9482	0.9666	0.9587	0.9695
Precision	0.9667	0.9674	0.9660	0.9785
MCC	0.9566	0.9660	0.9617	0.9736
Dice Coefficient	0.9562	0.9658	0.9616	0.9737
Specificity	0.9998	0.9996	0.9998	0.9997
IOU-Score	**0.9175**	**0.9354**	**0.9269**	**0.9492**

We observed small differences between the original ground truth measurements (L1, O1) and our model's predictions (L2, O2) for the left common iliac artery (Area_1) and right common iliac artery (Area_2) regions. For example, for Area_1, the original lumen area (L1) was 0.7244 mm², while the predicted lumen area (L2) was 0.7265 mm², yielding a difference of 0.0021 mm². Similar subtle variations were noticed in the outer wall area measurements. Despite these differences, the overall discrepancies between the original and predicted ROIs appear to be small. Conversely, the differences between the original measurements (L1, O1) and those obtained by different observers (I1, I2) are more noticeable. This underscores the greater level of variability in the segmentation results amongst human observers than between the original measurements (made by clinical experts) and our model's predictions. In evaluating diameter and normalized diameter of the common iliac arteries, the differences between original and predicted values are acceptable. For Diameter_1, the original and predicted diameters differed by 0.052 cm, while Diameter_2 showed a 0.0624 cm difference. Normalized diameter differences were 0.0032 cm for Diameter_1 (Norm) and 0.0005 cm for Diameter_2 (Norm).

Table 2. Statistical measures of the model.

	L1	L2	O1	O2	I1	I2
Area_1	0.7244	0.7265	1.0834	1.0878	0.7533	1.1217
Area_2	0.7237	0.7272	1.0830	1.0876	0.7514	1.0989
Diameter_1	4.4366	4.4886	6.7379	6.7120	4.4424	6.7693
Diameter_1 (Norm)	1.2447	1.2415	1.4552	1.4587	1.2347	1.4537
Diameter_2	1.2430	1.2425	1.4540	1.4589	1.2357	1.4376
Diameter_2 (Norm)	4.4279	4.4903	6.7283	6.7072	4.4345	6.6854

DISCUSSION

In routine clinical practice, determining the size of an AAA often involves manual measurement of the maximum diameter, which is often susceptible to substantial inter-observer variability. Our fully automated model excels in AAA segmentation, outperforming other deep learning methods with exceptional DICE scores of 0.9616 and 0.9737 for the lumen and outer wall ROIs, respectively. The model's accuracy is evident, particularly in cases with complex tortuosity, when compared to other lumen [4–6] and outer wall [7, 8] ROI methods. It also has exceptional speed, measured at 17 ± 0.02 milliseconds per frame to generate the final segmented output.

An inherent limitation of our study lies in the model's dependency on contrast-enhanced CT images. To moderate this constraint, our future roadmap includes integrating unenhanced images into the training dataset once an adequate volume of patient data becomes available. This prospective addition of unenhanced images is pivotal, given that a subset of AAA patients experience delayed adverse reactions to radiographic contrast media, ranging from 1% to 23%, occasionally escalating to moderate or severe levels [9]. Moreover, future enhancements will augment our dataset with diverse CT images. This expansion in training data holds promise for refining the model's performance across varying clinical scenarios and anatomical presentations.

ACKNOWLEDGEMENTS

This work was partially supported in part by the National Institutes of Health award R01HL159300.

REFERENCES

[1] Jennifer L., et al., *J Cardiovasc Dev Dis*, 6(2):19, 2019.
[2] Shum, J. et al., *Medical Physics*, 37(2): 638-648, 2010.
[3] Ronneberger, O. et al., *MICCAI*, 234–241, 2015.
[4] Jirik, M. et al., *International Conference on Pattern Recognition and Image Analysis*, 201–204, 2013.
[5] Badrinarayanan, V. et al., *IEEE Transactions on Pattern Analysis and Machine Intelligence*, 39: 2481–2495, 2017.
[6] Bhalerao, M., & Thakur, S., *MICCAI Brainlesion Workshop*, 218–225, 2019.
[7] Siriapisith, T. et al., *Review Journal of Digital Imaging*, 31(4):490-504, 2018.
[8] Li, C. et al., *IEEE Transactions on Image Processing*, 19(12):3243–3254, 2010.
[9] Loh, S. et al., *Radiology*, 255(3):764–771, 2010.

ANALYSIS OF REGIONAL HEMODYNAMIC CHANGES IN TYPE A AORTIC DISSECTION REPAIR USING 4D FLOW MRI

H. Cebull (1), H. Dong (2,3), M. Liu (2,4) J. Elefteriades (5), R. Gleason Jr (2,3) J. Oshinski (1,2), M. Piccinelli (1), B. Leshnower (3)

(1) Department of Radiology and Imaging Sciences, Emory University School of Medicine, Atlanta, GA, USA
(2) Department of Biomedical Engineering, Georgia Institute of Technology, Atlanta, GA, USA
(3) Division of Cardiothoracic Surgery, Department of Surgery, Emory University School of Medicine, Atlanta, GA, USA
(4) Department of Mechanical Engineering, Texas Tech University, Lubbock, TA
(5) Aortic Institute at Yale-New Haven Hospital, Yale University School of Medicine, New Haven, CT

INTRODUCTION

Residual aortic dissections (RAD) commonly occur (43-77% of cases) following the surgical repair of a Stanford Type A aortic dissection.[1] They are characterized by a residual patent false lumen (FL) occurring along the aortic arch and/or descending aorta. RADs increase the risk for aortic growth and rupture and therefore require frequent monitoring including computed tomography angiography (CTA) scans. CTAs can help determine risk of rupture based on diameters and growth rate. CTA scans have high spatial resolution and excellent image quality but cannot reveal hemodynamic changes or assess hemodynamic features in the FL. Establishing a method that incorporates the characterization of the complex blood flow in RADs may improve the identification and treatment of high-risk patients.

Many studies have aimed to identify specific hemodynamic metrics that can predict thrombus or growth rate in aortic dissections, such as pulse wave velocity (PWV), entry tear flow, and wall shear stress (WSS).[2-4] However, due to the geometric and hemodynamic complexity, it can be challenging to consistently detect patterns, particularly in RAD cases. These cases often have entry tears in the arch and have undergone varying degrees of aortic repair, causing unique blood flow patterns in each individual subject.

4D flow magnetic resonance imaging (MRI) combined with CTA analysis enables a regional assessment of both geometric and hemodynamic differences to better understand the effect of Type A aortic repair. Here, we present a preliminary investigation of local, *in vivo* hemodynamic and geometric changes in RAD cases of varying severity.

METHODS

Patient Demographics and Data Collection. RAD patients who were outpatients at Emory University Hospital were enrolled in this study under approval from the Institutional Ethics Committee. Patients signed a written informed consent before undergoing testing. 4D flow MRI was acquired one-month post-Type A repair on three subjects (P1-3; 2 male) with residual Type A aortic dissections and one control (male) using a 3T scanner (Siemens PrismaFit) at Emory University Hospital. We used the following imaging parameters: Retrospective ECG gating, *VENC* = 150 cm/s, *TE* = 2.39 ms, flip angle = 7°, and 25 time frames. Post-processing included eddy current and anti-alias correction and noise masking using previously developed methods (Mathworks, Natick, MA).[5,6]

CTA-derived 3D model. CTAs were clinically acquired pre- and post-Type A repair. We segmented the image volumes using VMTK and Slicer for visualization and characterization of the geometry.

4D Flow MRI data. 3D true (TL) and false lumens (FL) were also segmented from 4D flow MRI magnitude images (Materialise Mimics, Belgium) to guide 4D flow MRI data analysis. The following quantifications were performed.

Streamlines visualization in TL/FL. A main advantage of 4D flow MRI is the quantification and visualization of blood flow velocity. We used the 3D lumen segmentations in Ensight (v.2021 Ansys, PA, USA) to visualize streamlines and observe patterns such as vortical and reverse flow as well as the extent of flow in the FL.

Wall shear stress (WSS). WSS estimates drag caused by blood flow on the aortic wall. WSS has been associated with changes in the FL growth and thrombus formation. Using a previously established method (van Ooji, P., GitHub Repository, 2017), WSS vectors were calculated using Equation 1:

$$\overrightarrow{WSS} = \mu \dot{\varepsilon} \vec{n} \qquad (1)$$

where μ is the blood viscosity ($3.2 \cdot 10^{-3}$ Pa·s) and ε and n are the rate of deformation tensor and normal vector, respectively.

Pulse wave velocity. Used as a proxy for arterial stiffness, PWV measures the velocity at which the blood flow waveform propagates through the arteries. Using the 3D true lumens extracted from the

magnitude image, PWV was estimated by measuring planes placed perpendicular to flow direction throughout the aorta and calculating the time delay between flow waveforms at each point calculated using cross correlation to provide a mean estimate of PWV [2].

RESULTS

CTA models revealed varying size and extent of dissections in RAD cases both before and after surgical repair of the ascending aorta, as shown in Figure 1. We observed that P1 had the smallest false lumen that fully thrombosed before the 4D flow MRI acquisition, while P3 had the largest and exhibited a patent FL along the entire descending aorta.

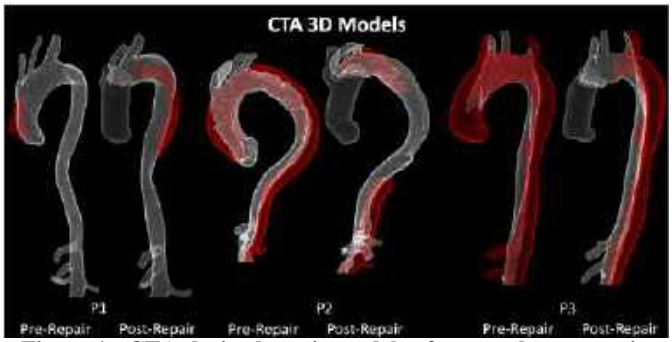

Figure 1: CTA-derived aortic models of pre- and post-repair Type A aortic dissection patients with residual false lumens (red).

Wall shear stress revealed regions of high stress in the RAD cases, particularly on the outer curvature in the ascending aorta, where the graft is located (Figure 2). However, low WSS was found in the false lumens. The estimated WSS in the control case had less heterogeneity and distribution of values compared to the RAD cases. This observation was helpful for confirming the abnormal WSS patterns found in the RAD cases.

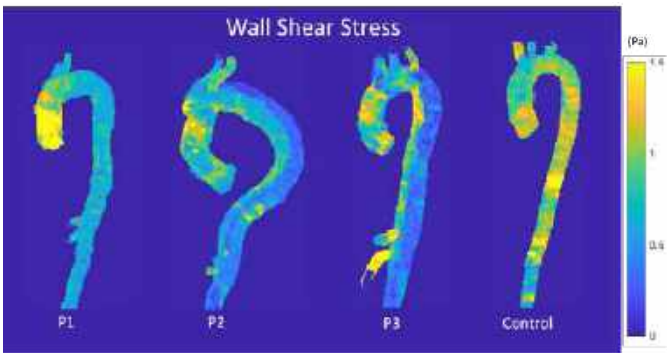

Figure 2: Mean intensity projections of wall shear stress in three RAD cases and one control subject.

Pulse wave velocity was measured in all cases in the true lumen or whole aorta. With the control PWV of 6.1 m/s, we found that P1 with no patent false lumen was higher than the control (13.7 m/s) and P2 and P3 were lower (3.2 and 2.6 m/s). Waveforms at each plane were also plotted in both true and false lumens (Figure 3A). From the velocity streamline estimation, slow and recirculating flow was observed in the false lumens (Figure 3B).

DISCUSSION

While most studies have investigated mean or peak systolic hemodynamic metrics in RAD cases [2-4], this study focused on detecting regional differences within and between cases. In the case of P2, the localized TL region of high velocity and WSS near the brachiocephalic artery (Figure 3B,C). Interestingly at the 3-month follow-up CTA, a leak between the graft and the native tissue was detected at the level of max WSS. PWV varied greatly between cases with P1 (thrombosed false lumen) having a higher than normal PWV and P2 and P3, lower.

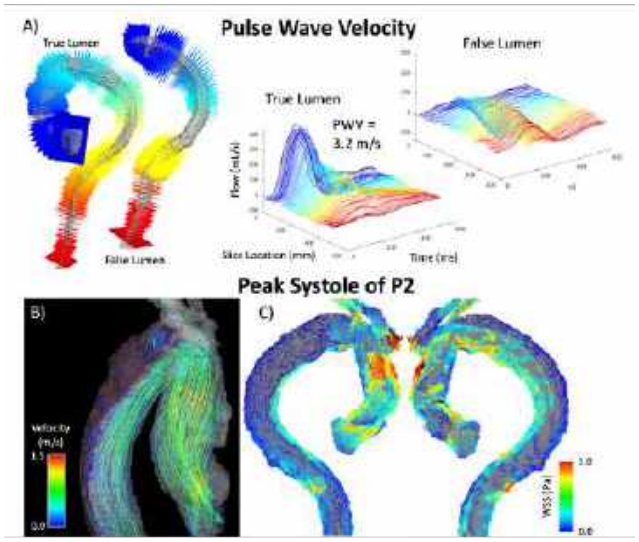

Figure 3: A) peak systolic velocity streamlines in the true and false lumen of P2 and B) WSS vectors; C) planes and flow waveforms used in PWV estimation

There are a few limitations to note within this study. With a limited sample size, this preliminary investigation cannot reveal any significant trends from the properties measured but can highlight the high variability in presentation and results from follow-up of Type A repairs. In addition, WSS values may be unreliable when derived from 4D flow MRI because of partial volume effects and segmentation errors.[7] However, when the analysis is performed in a consistent way, intra- and inter-subject differences can still be appreciated.

This study established the feasibility of measuring hemodynamic metrics using 4D flow MRI and its clinical value in the study of RAD. It also demonstrates the importance of regional analysis, where localized high WSS correlated with the location of a leak found in a follow up CTA. This type of regional analysis may be useful for improving the ability to monitor and treat patients. Future work will include the enrollment of more subjects and investigation of additional hemodynamic metrics.

ACKNOWLEDGEMENTS

We would like to acknowledge the effort of the healthcare team that acquired the images and performed the procedures and the patients willing to participate in this study. We would also like to acknowledge Dr. Michael Markl and his team for sharing their 4D flow post-processing procedure. This study is supported by NIH R01HL155537 and the National Center for Advancing Translational Sciences under Award Numbers UL1TR002378 and TL1R002382.

REFERENCES

[1] Kimura, N et al., *J Thorac Cardiovasc Surg*, 149:91-98, 2025.
[2] Maroun, A et al. *Circulation*, 146:A14815, 2022.
[3] Muñoz et al. *Eur Radiol*, 1-10, 2024.
[4] Muñoz et al. *Eur Heart J*, 42:1-10, 2021.
[5] Bernstein M, et al. *Magn Reson Med*, 39:300-8, 1998.
[6] Walker, et al. *J Magn Reson Img*, 3:521-530, 1993.
[7] Zhang J, et al. *Ann Biomed Eng*, 50:1810-1825, 2022.

OSCILLATORY SHEAR STRESS MODULATES LYMPHATIC PROGENITOR CELLS MATURATION INTO LYMPHATIC VESSELS WITH ANTI-CANCER PHENOTYPES

N. Keilany Lightsey (1), Eva Hall (1), Sanjoy Saha (1), D. Paul Jeong (1), Donny Hanjaya-Putra (1,2)

(1) Department of Aerospace and Mechanical Engineering – Bioengineering Graduate Program, University of Notre Dame, Notre Dame, IN, USA
(2) Department of Chemical and Biomolecular Engineering, University of Notre Dame, Notre Dame, IN, USA

INTRODUCTION

Lymphedema is a chronic condition characterized by the swelling of tissues caused by the failure lymphatic valves which can be congenital or caused by diseases. Lymphatic valves provide a one-way flow of lymph that aids intrinsic pumping in the lymphatic system. Our research group have previously reported that human pluripotent stem cells (hPSCs) can be differentiated into lymphatic endothelial cells (LECs) to form lymphatic capillaries [1]. However, these lymphatic vessels lack lymphatic valve that is required for lymphatic pumping. Since oscillatory shear stress (OSS) has been shown to regulate lymphatic valve morphogenesis in vivo [1-2], we hypothesize that physiological OSS can induce LECs maturation and morphogenesis into lymphatic valves.

METHODS

Juvenile LECs and hiPSC-derived LECs (differentiated using our previously reported step-wise protocols) were cultured onto *ibidi* µ-Slide I 0.6 Luer channel slides. Slides were coated with 40-60 µg/mL fibronectin. OSS (at 0.5 dyne/cm^2 and 10 dyne/cm^2) were applied to all LECs with the *ibidi* Pump System for 48 hours. For oscillatory flow, the pump changed flow directions every 4 seconds. Immunostaining was conducted and imaging was done on revolve fluorescence microscope and confocal microscope. Image analysis was conducted on ImageJ utilizing the directionality and circularity plugins. Real-time PCR was conducted with human angiogenesis array panels. Statistical analyses were unpaired *t*-tests with P = 0.05 conducted on GraphPad Prism V10.

RESULTS

OSS Induces Mature Lymphatic Cell Morphology in hiPSC-Derived LECs In response to the two differing physiological OSS flow rates, both juvenile and dLECs demonstrated a cellular alignment in response to the flow direction (**Figure 1A-B**). Furthermore, the presence of 'zipper-like' junctions between individual cells increased in the high OSS flow rate condition compared to the low OSS flow rate (**Figure 1A**). These cells also demonstrated a transformation to a more cuboidal-shape cell morphology in response to the OSS flow rate, especially at the high OSS flow (**Figure 1C-D**).

The static juvenile and dLECs did not demonstrate similar flow alignment to cells under OSS (**Figure 1A-B**). There was also a lack of 'zipper-like' junctions between the cells and an elliptic-shape cellular morphology which is expected in cells that are not lymphatic-valve forming (**Figure 1C-D**).

OSS-Dependent Expression of Lymphatic-Valve Forming Markers in hiPSC-Derived LECs In response to OSS, dLECs demonstrated previously observed patterns of genetic expressions in genes known to play significant roles in lymphatic valve development *in vivo*. A major finding was the increase in *Prox1* expression under low OSS flow rates and the expected decrease in *Prox1* expression at high OSS flow rates that occurs to maintain the longevity and functionality of lymphatic valves. The dLECs also had an upregulation of *FOXC2,* which is an important upstream transcription factor to *Prox1*, that has been highly associated with lymphatic valve development. *CDH5*, which encodes a required adherens junction protein VE-cadherin for lymphatic valve development and maintenance, was increasingly upregulated as OSS flow rates increased. Confocal images obtained demonstrates these varying trends in lymphatic markers **(Figure 2A-B)**.

An increase in other genes relating to lymphatic maturation as OSS flow rate increases was also observed demonstrating its capability to display favorable lymphatic-valve forming properties (**Figure 2C**).

Cancer-Related Gene Expression Dependence on Varying OSS Flow Rates Real-time PCR results from the array panel demonstrated OSS flow rate dependent expression of multiple genes in the hiPSC-derived LECs, especially at the high OSS flow rate (**Figure 3A**). Three genes (*NRP2, CXCL12,* and *ITGAV*) that were upregulated in response to the high OSS flow rate were identified to be previously associated with tumor growth and anti-tumor immunity within the lymphatic

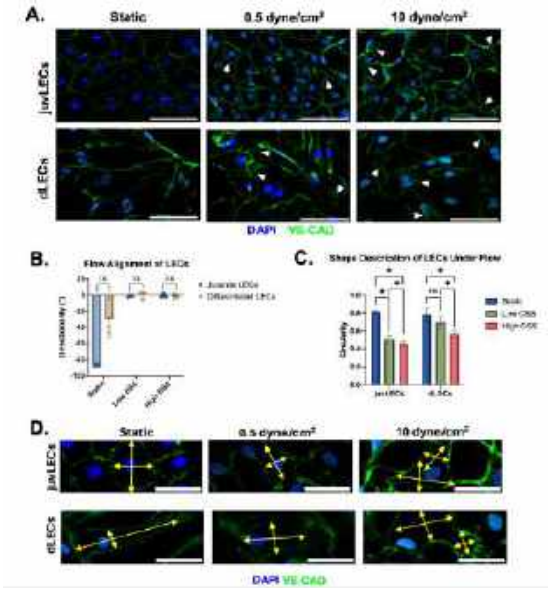

Figure 1: dLECs undergo the same alignment as LECs and transform into a cuboidal shape under OSS. A) VE-CAD (green). DAPI (blue). "Zipper-like" junctions are identified by the white arrowhead. Scale bar is at 100 µm. **B)** Mean directionality of LECs (n=3) Error bars are s.d. **C)** Circularity values (1 = perfect circle, 0 = elongated polygon). Error bars are 95% c.i. **D)** Yellow arrows indicate the areas measured. VE-CAD (green). DAPI (blue). Scale bar is 50 µm.

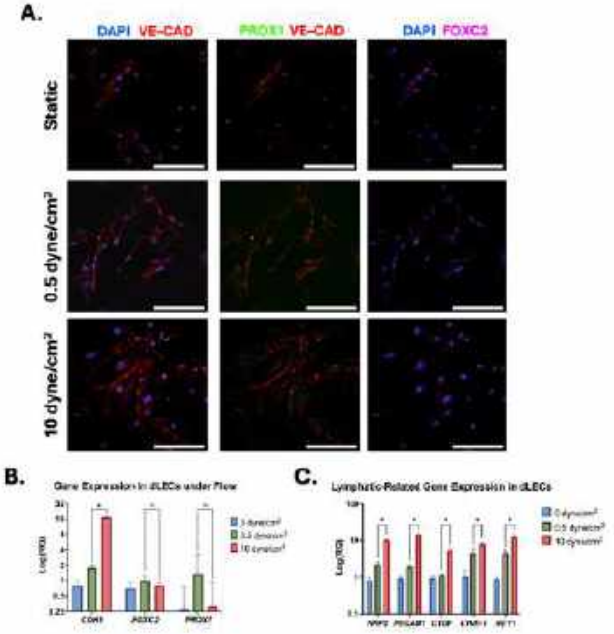

Figure 2: dLECs demonstrates an upregulation of VE-cadherin and FOXC2 in both low and high OSS while also demonstrating a decrease in Prox1 at high OSS. A) DAPI (blue), Prox1 (green), VE-CAD (red), FOXC2 (pink). Scale bar is 200 µm. **B)** Relative quantification of relevant lymphatic-valve forming genes (n=4). **C)** Relative quantification of other mature lymphatic related genes (n=4). Error bars are s.d.

system [3-5]. **Figure 3B** demonstrates the OSS flow rate dependent expression of these genes in dLECs.

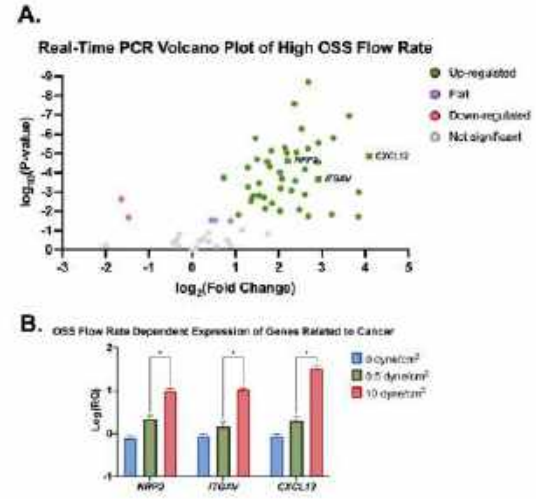

Figure 3: OSS Induces Anti-Tumor Phenotypes in dLECs. A) Each dot represents a gene. Labelled genes of interest. **B)** Relative quantification of cancer-related genes (n=4).

DISCUSSION

The morphological properties and genetic expressions obtained from exposing hiPSC-derived LECs to low and high OSS flow rates demonstrates its efficiency in maturing into lymphatic-valve forming cells. The dLECs were able to respond to OSS and remodel its shape similarly to juvenile LECs as well as demonstrate the unique 'zipper-like' junctions in mature LECs. Moreover, the dLECs demonstrated a favorable change in the expression of genes primarily responsible for lymphatic valve development in response to different physiological OSS flow rates. Overall, it was demonstrated that the hiPSC-derived LECs were able to mimic the mechanotransduction responses that are crucial during lymphatic valve development. Furthermore, it was identified that the OSS flow rate significantly decreased or increased the expression of genes that can promote tumor growth and T-cell decumulation. Other sources of LECs have been extensively studied and was considered when assessing our findings. Nevertheless, these findings support the use of hiPSC-derived LECs in the regeneration of biomimetic lymphatic vessels to provide treatment opportunities for lymphedema as well as provide preliminary understanding of the lymphatic system's role in cancer.

ACKNOWLEDGEMENTS

We acknowledge support from the University of Notre Dame through "Advancing Our Vision" Initiative in Stem Cell Research, Harper Cancer Research Institute – American Cancer Society Institutional Research Grant (IRG-17-182-04), American Heart Association through Career Development Award (19-CDA-34630012 to D.H.-P), National Science Foundation (2047903 to D.H-P.), National Institutes of Health (1R35-GM-143055-01 to D.H.-P.), and GEM Fellowship to N.K.L.

REFERENCES

[1] Alderfer, L et al., *FASEB J*, 35:e21498, 2021.
[2] Sabine, A et al., *Development Cell*, 22:430-445, 2012.
[3] Wang, J. et al., *Cancer Letters*, 418:176-184, 2018.
[4] Loeser, H. et al., *Sci Rep*, 10:1, 2020.
[5] Steele, M. et al., *Nat Immunol*, 24:4, 2023.

DEVELOPMENT OF AN ACOUSTICALLY AUGMENTED UNIAXIAL EXTENSION TESTING APPARATUS TO DETECT THE PROPORTIONAL LIMIT IN BIOLOGICAL SOFT TISSUES

Cyrus J. Darvish (1), Peter Jacobs (2), Elias C. Mignonga (2), Yuqi Cai (2), Pete H. Gueldner (1), David A. Vorp (1-7), Timothy K. Chung (1)

(1) Department of Bioengineering, University of Pittsburgh, Pittsburgh, Pennsylvania, USA
(2) Department of Mechanical Engineering and Materials Science, University of Pittsburgh, Pittsburgh, Pennsylvania, USA
(3) McGowan Institute for Regenerative Medicine, University of Pittsburgh, Pittsburgh, Pennsylvania, USA
(4) Department of Surgery, University of Pittsburgh, Pittsburgh, Pennsylvania, USA
(5) Department of Chemical and Petroleum Engineering, University of Pittsburgh, Pittsburgh, Pennsylvania, USA
(6) Department of Cardiothoracic Surgery, University of Pittsburgh, Pittsburgh, Pennsylvania, USA
(7) Clinical and Translational Sciences Institute, University of Pittsburgh, Pittsburgh, Pennsylvania, USA

INTRODUCTION

Mechanical testing and characterization of vascular tissues has been a key tool in developing material models and measuring failure properties. Uniaxial extension testing of biological soft tissues has allowed for a basic understanding of the strength of material and mechanical behavior when stretched to failure. For engineering materials such as ductile metals, the concept of a yield point or proportional limit exists when transitioning from elastic to plastic deformation. This is problematic for nonlinear materials such as biological soft tissues, as there is no clear demarcation of where a potential proportional limit may exist.

The current method for engineering materials relies on a 0.2% offset method, in which a parallel line for the linear elastic region is drawn. However, there is no clear method for identifying the proportional limit in biological soft tissues other than to manually choose a point where the stress decreases. Christensen introduced a modified offset method to identify the stress-strain curve for Hookean materials [1]. The modified yield point occurs when a linearly extrapolated stress value exceeded the actual observed stress by 5%.

Acoustic signals have been used in the past to measure various aspects of engineering materials and biological soft tissues. The more pertinent being acoustoelastic behavior using ultrasonic waves to recover nonlinear strains of materials during extension testing or compression testing (where the elastic wave velocities are a function of stress). In this study, we investigate whether an audible acoustic signal can be detected during uniaxial extension testing. To achieve this, an acoustically augmented testing apparatus that records audible noises from XPS silicone (Silicones Inc., High Point, NC, USA) and porcine during uniaxial extension testing was designed and manufactured.

METHODS

Uniaxial Extension Testing Apparatus – The apparatus was designed and manufactured to be modular using a linear rail, stepper motor, and an aluminum double t-slot frame (**Figure 1**). A custom mount was CNC milled out of aluminum to mount a stainless-steel rod that connected to a clamping mechanism. The stepper motor was attached to a 3D printed top mount that could be sealed to an acrylic base.

Electronic Components, microcontrollers, load cell, and stepper motor – Two Arduino Uno (Arduino, Somerville, MA, USA) microcontrollers were used in parallel with a custom printed circuit board (PCB). The PCB allowed for a coupled approach to perform precision microstepping for the stepper motor (at a rate of 3 mm/min) while synchronously recording data from a 3 kg load cell. A HX711 (Sparkfun Electronics, Niwot, CO, USA) load amplifier was used to rescale the analog sensor values. Precision weights were used to calibrate the

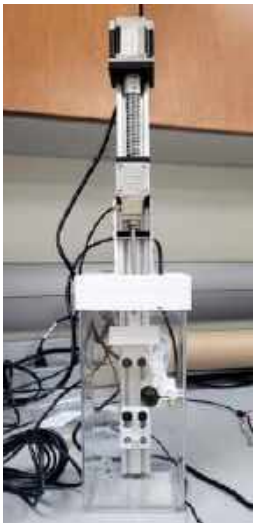

Figure 1: Uniaxial extension testing apparatus with stepper motor and hydrophone.

load cell (1, 10, 50, 100-, 500-, 1000-, and 3000-gram weights).

Python Graphical User Interface and Firmware – A custom C++ script was uploaded to an Arduino board to read the raw load cell sensor values in real time. A separate script was loaded to control a stepper motor that communicates with a custom python graphical user interface (GUI) to control the movements of the stepper motor. The python GUI was built to plot the load/displacement curve in real-time while recording acoustic signals from the hydrophone.

Experimental testing of XPS silicone and porcine aorta – A composite material was created by molding a paper towel in between two layers of XPS silicone. The test specimen was cut into a rectangular strip (30 x 4 mm). The composite material was used for feasibility testing whether the hydrophone could hear audible tearing during experimentation. Additionally, porcine aorta was procured from a local butcher and cut into rectangular strips (30 x 4 mm). The uniaxial extension tests were performed using an extension rate of 3 mm/min. Custom disposable laser-cut clamps were mounted onto the uniaxial extension testing device. Sound deadening foam was placed around the acrylic base to remove ambient noise. Lastly, the acrylic base was filled with water, and the experimental test was performed while 'listening' to the specimen via the hydrophone.

RESULTS

A custom uniaxial extension testing apparatus with hydrophone was successfully designed and manufactured (**Figure 1**). Tearing of the composite silicone and paper towel material was audible during feasibility testing, providing a basis to continue with the porcine aorta. **Figure 2A** is an example of a force-displacement curve of a test with porcine aorta. A small audible tear was detected (green oval) in **Figure 2B** prior to a drop in force (0.2 N). **Figure 2C** shows a center tear of the specimen at failure.

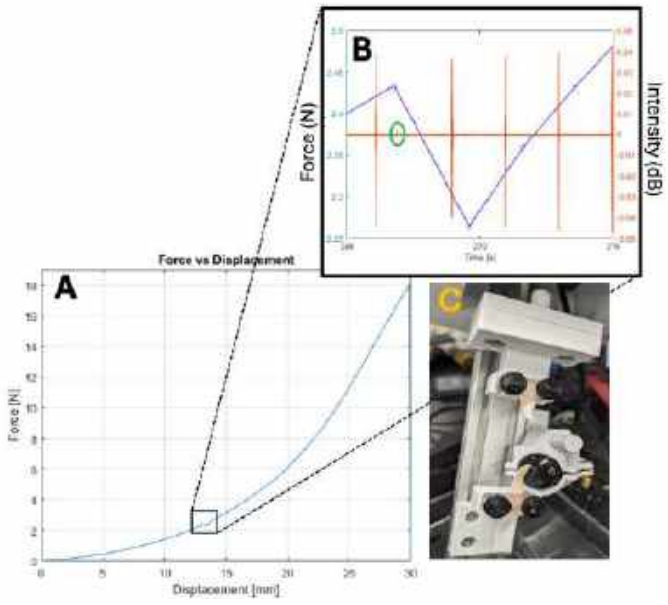

Figure 2: A) Force-displacement curve of a porcine aorta test, B) is a small audible noise (0.1 dB) that precedes a drop of force (0.2 N), C) a center tear of the porcine specimen.

DISCUSSION

In this study we performed a pilot study to determine whether acoustic signals could be detected during uniaxial extension testing. The tearing of the composite material indicated that the audible noise was directly related to a pre-failure force. An audible noise was present in porcine aorta that preceded a drop in force prior to failure. However, it cannot be definitively stated that this reduction in force is indicative of the proportional limit or yield point.

Typically, material models are fit to a theoretical proportional limit that is visually inspected after uniaxial or biaxial extension testing. The point that is chosen is much higher than the range of strain than the initial tear from our apparatus detected. Additional studies have performed uniaxial extension testing with concurrent multiphoton imaging [2] that allows for visualization of collagen and elastin fibers in real time. In addition, the concept of rupture potential index or the ratio of stress to strength has been used to assess risk based on biomechanical factors [3]. The current study may provide a basis for using a theoretical proportional limit rather than strength as it may possibly indicate where vascular dysfunction may occur [4]. Although the preliminary results from the testing apparatus are interesting, there are limitations to the study. There is no visual confirmation of damage to collagen or elastin fibers that were paired with the initial results. Future studies will utilize multiphoton imaging after stopping the test when the first audible tear is detected. The stepper motor provided additional noise within the system, creating periodic noise (**Figure 2**). It is possible that a tear may have been overridden by the noise from the stepper motor. The apparatus could be redesigned by introducing a damper to the stepper motor or decouple the load cell from the aluminum frame to reduce noise.

The overall study provided a method to listen to tissue specimens during mechanical testing. The potential for understanding a potential proportional limit in biological soft tissues could lead to new discoveries regarding fatigue and pre-failure limits of tissues that progress to a diseased state.

ACKNOWLEDGEMENTS

We would like to acknowledge the University of Pittsburgh Swanson School of Engineering Mechanical Engineering and Materials Science Department senior design instructor, David Schmidt, PhD for providing an effect project management plan.

REFERENCES

1. Christensen, R.M., Observations on the definition of yield stress. Acta Mechanica, 2008. 196(3): p. 239-244.
2. Haskett, D.G., et al., 2-Photon Characterization of Optical Proteolytic Beacons for Imaging Changes in Matrix-Metalloprotease Activity in a Mouse Model of Aneurysm. Microscopy and Microanalysis, 2016. 22(2): p. 349-360.
3. Vande Geest, J.P., et al., A biomechanics-based rupture potential index for abdominal aortic aneurysm risk assessment: Demonstrative application. Annals of the New York Academy of Sciences, 2006. 1085: p. 11-21.
4. Chung, T.K., et al., A Comparative Study of a Generalizable Machine Learning and Algorithmic Approach to Automatically Identify the Yield Point in Normal and Aneurysmal Human Aortic Tissues. Journal of Biomechanical Engineering, 2023.

CLINICAL VALIDATION OF THE PSCOPE HYBRID FRAMEWORK FOR CARDIOVASCULAR PREDICTIVE MODELING

Abraham, E. Umo (1), Brett, A. Welch (2), Arman Kilic (2), Ethan, O. Kung (1,3)

(1) Bioengineering, Clemson University, Clemson, SC, USA
(2) Cardiothoracic Surgery, Medical University of South Carolina, Charleston, USA
(3) Mechanical engineering, Clemson University, Clemson, SC, USA

INTRODUCTION

Various Cardiovascular predictive modeling (CPM) approaches have been developed to aid clinicians in diagnosing, prognosticating, and treating cardiovascular diseases but there has been a shortage of efforts to clinically validate their accuracy.[1,2,3,4,5,6,7]

The Physiology Simulation Coupled Experiment (PSCOPE) is a hybrid modeling framework that can be implemented as a mechanistic CPM tool. It couples a physical fluid experiment to a lumped parameter network (LPN) simulation to model the closed-loop feedback between simulated cardiovascular physiology and fluid dynamics in a physical experiment. Previous studies verified the modeling capabilities of the PSOCPE framework by demonstrating its correspondence with a multiscale computational standard when both approaches were used to model a Fontan graft obstruction in the cavopulmonary pathway.[8] In this study, we validate the PSCOPE framework by comparing its predictions directly against clinical data. The study is designed to validate the CPM capabilities of PSCOPE in predicting the post-surgical physiology of a patient after implantation of the HeartMate 3 LVAD. We will also offer context on how these predictions can potentially assist clinicians in achieving favorable post-surgical outcomes.

METHODS

We obtained ICU health records for three adult patients implanted with the HeartMate 3; this data includes at least 3 days of continuous (high volume) pre-surgical and post-surgical acquisition of various flow rate and pressure measurements. A dynamic moving variance analysis was applied to the pre-surgical time series data of each flow rate and pressure parameter. The evaluated variance in each window of this analysis quantifies the data precision of the corresponding pre-surgical timeframe. We used the median of each parameter in the most precise timeframe (minimal variance) as the reference value to characterize the pre-surgical physiology of each patient (Table 1). We then tune an LPN model to match the derived median values, thereby constructing a virtual patient replicating the pre-surgical physiology of each patient. The PSCOPE framework models the LVAD implantation by coupling the virtual patient to a physical HeartMate 3 device flow experiment (Fig 1). The resulting hybrid model produces an estimation of flow rate and pressure parameters that characterize the post-surgical physiology of the virtual patient. We characterize the real-world post-surgical physiology of each patient by the median value of ICU measurements acquired in the first 12 hours after implantation. To quantify the CPM performance of the PSCOPE framework, we evaluate the difference between the PSCOPE predictions and the corresponding post-surgical clinical measurements.

RESULTS

The percentage difference (1.3% - 44.9%) between the PSCOPE predictions and the post-surgical clinical data across the three patients reveal variability in the performance of PSCOPE as a CPM tool. PSCOPE accurately predicted an increase in cardiac output for two of the three patients but was unsuccessful in predicting a non-intuitive decrease in cardiac output for one of the patients. Notably, PSCOPE demonstrates significantly better estimations of mean pressure values (4.5% - 25.7%) compared to their systolic and diastolic counterparts (3.5% - 44.9%). (Table 2).

DISCUSSION

This work assesses the accuracy of PSCOPE in modeling the surgical implantation of a HeartMate 3 device via a virtual patient. The PSCOPE estimations correctly predicted the observed clinical trends of increase/decrease in critical parameters—including mean/diastolic aortic pressure and mean pulmonary artery pressure—between pre-surgical and post-surgical physiology for all three patients. Lastly, the results suggest that PSCOPE can more accurately predict mean pressure values and may have limitations in capturing the pulsatility of the patient's hemodynamics after LVAD implantation. Overall, these

findings provide context on how PSCOPE physiology estimates can be interpreted to potentially guide patient-specific decision making in the surgical planning process.

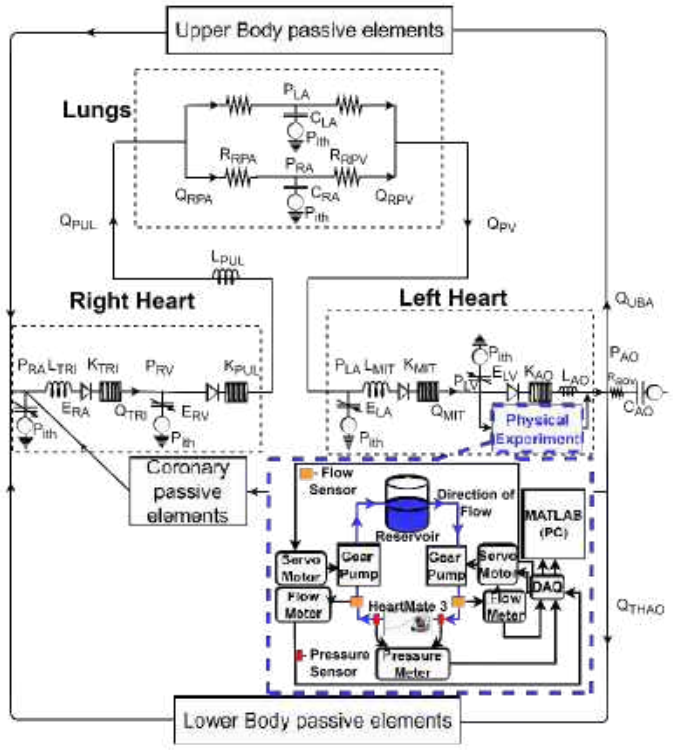

Fig. 1 PSCOPE hybrid model of the physical HeartMate 3 implantation in the virtual patient represented by an LPN.

Table 1
Clinical Pre-surgical median values. CO - Cardiac Output; CVP - Central Venous Pressure; $P_{ao,(s;m;d)}$ - Aortic Pressure (systolic; mean; diastolic); $P_{pul,(s;m;d)}$ - Pulmonary Arterial Pressure (systolic; mean; diastolic).

Parameter	Patient 1	Patient 2	Patient 3
CO (l/min)	**2.9**	**3.8**	**5.6**
CVP (mmHg)	**9.0**	**8.0**	**7.0**
$P_{ao,s}$ (mmHg)	**94.0**	**111.0**	**103.0**
$P_{ao,m}$ (mmHg)	**68.0**	**76.0**	**80.0**
$P_{ao,d}$ (mmHg)	**53.0**	**50.0**	**66.0**
PAWP (mmHg)	**25.0**	**23.0**	**19.0**
$P_{pul,s}$ (mmHg)	**55.0**	**59.0**	**57.0**
$P_{pul,m}$(mmHg)	**38.0**	**34.0**	**33.0**
$P_{pul,d}$ (mmHg)	**23.0**	**23.0**	**22.0**

Table 2
PSCOPE predictions vs clinical post-surgical medians.

	P_{PSCOPE}; $P_{Clinical}$ (% difference)		
Parameter	**Patient 1**	**Patient 2**	**Patient 3**
CO (l/min)	3.7; 3.2 (16.6%)	4.6; 4.2 (9.1%)	5.8; 4.6 (23.1%)
CVP (mmHg)	8.5; 11.0 (25.8%)	9.1; 9.0 (1.4%)	7.0; 9.0 (25.2%)
$P_{ao,s}$ (mmHg)	94.8; 84.0 (12.1%)	111.5; 87.0 (24.7%)	90.7; 94.0 (3.5%)
$P_{ao,m}$ (mmHg)	84.1; 77.0 (8.8%)	90.7; 79.0 (13.8%)	82.2; 86.0 (4.5)
$P_{ao,d}$ (mmHg)	59.8; 66.0 (9.9%)	51.5; 70.0 (30.5%)	69.2; 78.0 (11.9%)
PAWP (mmHg)	12.2; 18.0 (38.3%)	20.39; N/A	16.8; N/A
$P_{pul,s}$ (mmHg)	48.2; 34.0 (34.5%)	61.0; 57.0 (6.8%)	55.2; 35.0 (44.9%)
$P_{pul,m}$(mmHg)	28.8; 24.0 (18.3%)	33.6; 34.0 (1.3%)	31.1; 24.0 (25.7%)
$P_{pul,d}$ (mmHg)	13.3; 18.0 (30.0%)	19.9; 24.0 (18.9%)	19.7; 18.0 (9.1%)

ACKNOWLEDGEMENTS

This work was supported in part by Clemson University and in part by an award from the National Science Foundation under Grant 1749017.

REFERENCES

[1] Wessler, BS et al., Circ Cardiovasc Qual Outcomes. 2015 Jul;8(4):368-75.

[2] Wessler, B.S. et al., Tufts PACE Clinical Predictive Model Registry: update 1990 through 2015. *Diagn Progn Res* 1, 20 (2017).

[3] Luraghi, G et al., Cardiovasc Eng Technol. 2019 Sep;10(3):437-455.

[4] Zhao, S et al., *Sci Rep* 11, 16486 (2021).

[5] Tomov, et al., J Am Heart Assoc. 2019 Dec 17;8(24):e014490.

[6] Madero, R et al., J Biomech. 2017 Mar 21;54:111-116.

[7] Bonfanti, M et al., Ann Biomed Eng. 2020 Dec;48(12):2950-2964.

[8] Kung. E et al. (2019). *Journal of Biomechanical Engineering*. 10.1115/1.4042665.

SIMULATED TAVR LIFETIME MANAGEMENT TO ASSESS CORONARY OBSTRUCTION RISK FOR VARIED DEPLOYMENTS OF BALLOON-EXPANDABLE AND SELF-EXPANDING VALVES

Courtney E. Ream (1), Taylor N. Becker (2), Venkateshwar Polsani (3), Pradeep K. Yadav (3), Vinod H. Thourani (3), Lakshmi P. Dasi (1)

(1) Wallace H. Coulter Department of Biomedical Engineering, Georgia Institute of Technology, Atlanta, GA, USA
(2) Department of Medicine, The Ohio State University, Columbus, OH, USA
(3) Department of Cardiology, Piedmont Hospital, Atlanta, GA, USA

INTRODUCTION

Transcatheter Aortic Valve Replacement (TAVR) has become a popular therapy for aortic stenosis patients over the past twenty years as a minimally invasive alternative to open heart surgery. It has primarily been performed in older, high surgical risk patients, but is now becoming standard of care even for younger patients (life expectancy > 10 years) with low surgical risk. Current research indicates that transcatheter heart valves (THVs) last about ten years and fail even earlier in chronic renal failure patients [1]. Therefore, it is more likely that TAVR candidates may face degradation or failure of their first THV in their lifetime. Consequently, clinicians must consider future interventions, such as redo-TAVR, to adequately provide lifetime management for TAVR patients.

Redo-TAVR poses risks that can lead to further complications if not properly considered at the time of index valve implantation. Namely, coronary obstruction (CO) is a potentially fatal complication that is nearly twice as common in redo-TAVRs than a primary TAVR [2]. A patient's risk for CO may vary based on the type and deployment depth of THVs as they interact with the patient's unique native anatomy. One emerging methodology of pre-procedural planning is the use of computational modeling to digitally reconstruct patient specific anatomy and visualize its interaction with the THV during TAVR, thus aiding the prediction of possible adverse outcomes. In this study, we aimed to assess CO risk for a variety of redo-TAVR combinations using DASI Simulations' *PrecisionTAVI*, a predictive modeling software which implements reduced-order modeling to simulate TAVR. These combinations included balloon-expandable and self-expanding valves as well as variation in deployment depth.

METHODS

Pre-procedure computed tomography (CT) scans were obtained for TAVR patients who fit the following criteria (n=7): 1) low-to-intermediate surgical risk; 2) were less than 80 years old; 3) have a tricuspid native aortic valve. *PrecisionTAVI* predictive modeling software was used to simulate 4 deployment variations of the index TAVR in the 3D reconstructed models from the pre-CTs; the balloon-expandable (BE) and self-expanding (SE) THVs were deployed at annular and sub-annular depths to achieve "high" and "deep" deployments, respectively. A subsequent second TAVR was then simulated at both high and deep deployments for the following combinations: BE-in-BE, SE-in-BE, BE-in-SE (Figure 1).

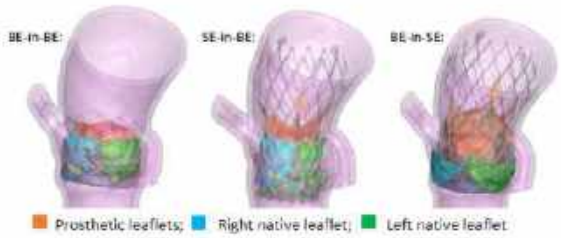

Figure 1: Main treatment pathways investigated.

A total of 112 simulations were executed (Figure 2). CO risk for the left and right coronaries was assessed after both the first and second TAVR using a previously validated biomarker shown in Figure 3 [3].

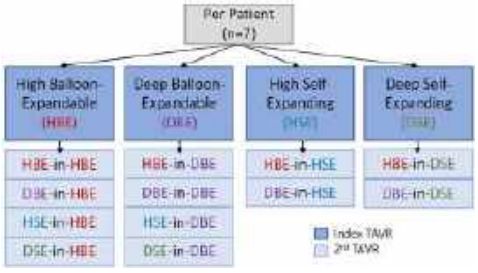

Figure 2: Deployment combinations simulated per case.

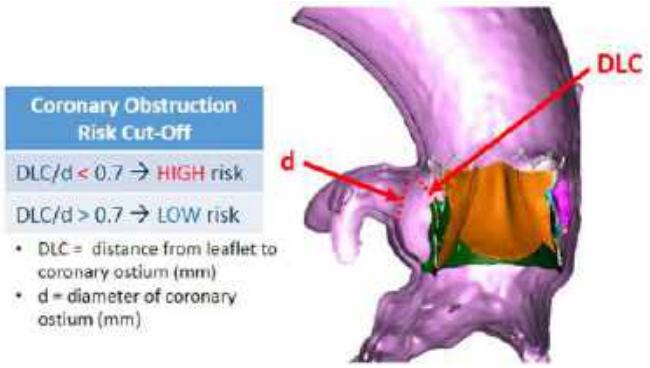

Figure 3: CO risk biomarker from Heitkemper et al.

Then, for both the first and second TAVR simulations, the average DLC/d values for the left and right coronaries were obtained for each THV type and deployment depth as well as their standard deviations. T-tests were performed to determine the statistical significance of CO risk in both coronaries as it changed from first to second implantation for all combinations.

RESULTS

For the first TAVR, deep deployment of the BE THV yielded the highest DLC/d averages of 1.82 and 2.38 for the left and right coronaries, respectively, as shown in the top chart in Figure 4.

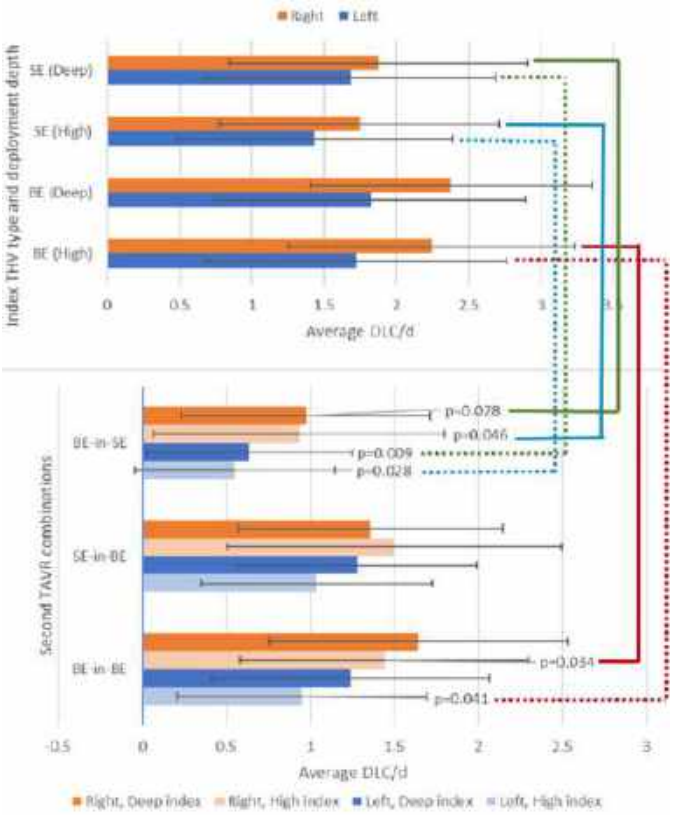

Figure 4: Average DLC/d for first and second TAVR*
***p-values applicable to high second deployments.**

It is important to note that the bottom chart in Figure 4 displays values averaged from both high and deep second THV deployments for visual simplification, though all combinations were statistically analyzed. For the second TAVR, high deployment of a BE THV in an SE index THV, regardless of index valve deployment depth, had the lowest DLC/d averages, ranging from 0.55-0.63 and 0.93-0.97 for the left and right coronaries. This deployment scenario also displayed a significant decrease in DLC/d from first to second THV ($p<0.05$ for left and right coronaries). Additionally, the HBE-in-HBE scenario exhibited a large decrease in DLC/d values from first to second deployment ($p<0.05$ for left and right coronaries).

DISCUSSION

High DLC/d averages in both coronaries for a deep index BE THV indicates that this THV type and deployment depth minimizes CO risk the most for this patient cohort. In contrast, the low DLC/d averages found for a high SE index THV indicates higher risk for CO in both coronaries upon the first TAVR. The statistically significant reduction in DLC/d average from first to second TAVR suggests that a high index THV deployment may not be most optimal from the standpoint of CO during a second TAVR.

Changes in DLC/d averages from first to second TAVR were calculated for each combination, but most were not found to be statistically significant. This can likely be attributed to the large standard deviations that arose from variation in coronary ostia diameters, coronary heights, and varying degrees of calcification in the leaflet and coronary regions.

Although this study included a limited number of cases, the initial findings propose that this novel method of computational modeling can be implemented to analyze trends in larger patient cohorts and enhance patient specific TAVR lifetime management, which is currently non-standardized.

ACKNOWLEDGMENTS

Not applicable.

REFERENCES

[1] Richter, I et al, *J Clin Med*, 10(18):4180, 2021.
[2] Prandi, FR et al., *J Cardiovasc Dev Dis*, 10(5):187, 2023.
[3] Heitkemper, M et al., *J Thorac Cardiovasc Surg*, 159:829-838, 2020.

INCUBATION IN PHYSIOLOGICALLY RELEVANT OXYGEN CONDITIONS CHANGES LYMPHATIC ENDOTHELIAL CELL GENE EXPRESSION AND VESSEL MORPHOLOGY

E. Johandes (1), D. Hanjaya-Putra (2)

(1) Bioengineering, University of Notre Dame, Notre Dame, Indiana, United States
(2) Bioengineering, University of Notre Dame, Notre Dame, Indiana, United States

INTRODUCTION

Lymphatic Endothelial Cells (LECs) exist *in situ* in an environment which contains 3-5% oxygen [1]. Their behavior is regulated by Hypoxia Inducible Factors (HIFs), which stabilize at oxygen levels below 6% [2]. HIFs influence LEC proliferation, migration, metabolism, and extracellular matrix remodeling [3]. Hif2α is associated with daily cellular function at physiological oxygen levels [4]. Meanwhile, Hif1α has been linked to hypoxia, inflammation, and fibrosis [5]. While Hif1α is necessary in wound healing and adapting to sudden hypoxia (as in the case of a heart attack or stroke), overexpression of Hif1α and downregulation of Hif2α has been shown to exacerbate lymphatic disorders such as lymphedema [6].

LECs are typically cultured *in vitro* at 21% O_2. By doing so, an inaccurate model of lymphatic behavior is created, which can lead to difficulties when trying to replicate *in vitro* results *in vivo* [7].

Successful tissue engineering relies on an accurate representation of the *in situ* environment of the target tissue. In this study, LECs are cultured at 3-5% to examine changes in gene expression over the course of seven days, as well as changes in vessel formation.

Over the course of incubation at 3-5% oxygen, *Hif2α*, *Lyve1*, *Prox1*, and *VEGFR3* gene expression were increased. Furthermore, vessels grown in 3-5% oxygen appeared thicker and better developed than those grown in 21%. As such, culturing LECs in physiologically relevant oxygen may lead to the more efficient engineering of lymphatic tissues, as well as create *in vitro* models that more accurately reflect native LEC behavior.

METHODS

LECs were seeded and allowed to attach for 24 hours in 21% O_2. After changing their media, the cells were placed in an incubator containing 5% CO_2, 92% N_2, and 3% O_2. O2 concentration in cell media was measured using a 6-well PreSens Optical Oxygen Sensor (PreSens, Regensburg, Germany). Media changes were performed on day 3 and day 6 with media that had been pre-acclimated in the 3% O_2 incubator overnight. Changes in gene expression were evaluated using RT-PCR relative quantification (RQ). For this assay, LECs cultured in 21% O_2 for 24 hours were used as a control. A vessel formation assay compared the tube-forming ability of LECs cultured 3 days in 21% O_2 and kept in 21% to form vessels, LECs cultured for 3 days in 21% O_2 but moved to 3-5% O_2 to form vessels ("no conditioning"), and LECs that had been previously cultured in 3-5% O_2 for 3 days ("pre-conditioned") and left in 3-5% to form vessels. To facilitate vessel formation, LECs were seeded on Matrigel with 50ng/mL VEGF-C. All experiments were completed in triplicate. Statistical analysis of PCR RQ was performed with GraphPad Prism Version 10 (La Jolla, CA). Student's t-tests were performed to analyze differences between timepoints, with significance levels set to $P \leq 0.05$.

RESULTS

An increase in *HIF* transcription as a response to physiological oxygen was confirmed over the course of 7 days (Figure 1).

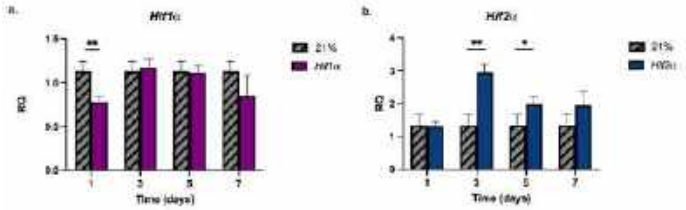

Figure 1. Physiological oxygen increases *Hif2a* expression but not *Hif1α*. * P<0.05, **P<0.01.

While *Hif1α* decreased on day 1 and then recovered to similar levels expressed by LECs in 21% oxygen, *Hif2α* significantly increased by day 3 to 3-fold its initial expression.

To observe the impact of increased *Hif2α* on LECs long-term, the expression levels of *Lyve1*, *Podoplanin*, *Prox1*, and *VEGFR3* were measured. These genes were chosen for their involvement in hyaluronic acid binding and motility, cytoskeleton remodeling, maintenance of LEC identity, and lymphangiogenic growth factor binding, respectively [8–11]. Compared to cells cultured at 21% oxygen, cells cultured in 3-5% oxygen, after an initial decrease, had significant increases in *Lyve1*, *Prox1*, and *VEGFR3* that peaked on day 5 (Figure 2).

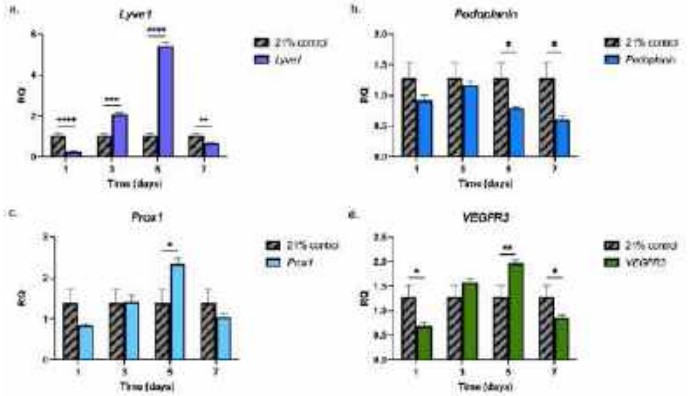

Figure 2. LEC characteristic gene expression. * P<0.05, **P<0.01, ***P<0.001, ****P<0.0001.

By day 5, *Lyve1* expression increased 5.5-fold, while *Prox1* and *VEGFR3* increased 2-fold. *Podoplanin* expression never reached its 21% oxygen expression level and decreased significantly on days 5 and 7.

Changes in LEC gene expression when incubated at physiologically relevant oxygen conditions also influenced LEC vessel formation ability. Qualitatively, LECs cultured in 3-5% oxygen formed thicker vessels than LECs cultured in 21% oxygen (Figure 3).

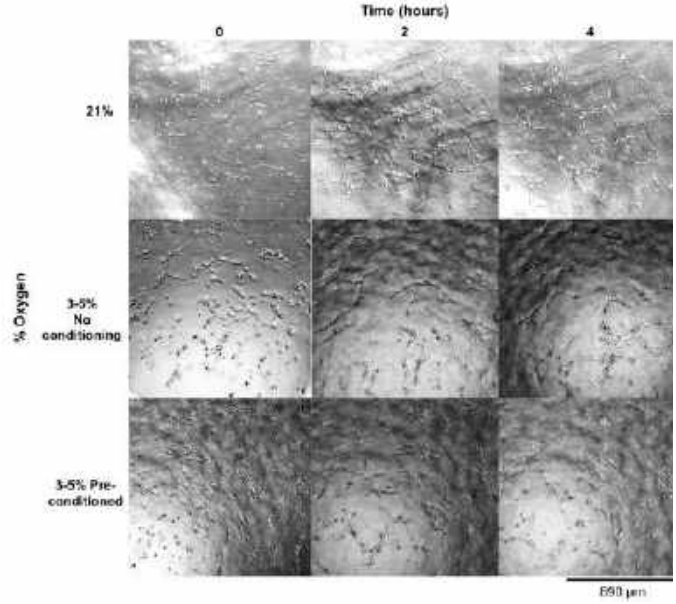

Figure 2. Influence of 3-5% oxygen on LEC vessel formation.

This was true for both LECs that had been previously cultured in 21% oxygen and moved to 3-5% oxygen for vessel formation (no conditioning) as well as LECs that were grown for three days in 3-5% oxygen and then kept in 3-5% oxygen for vessel formation. Although it appears that the pre-conditioned vessels are more numerous than vessels grown with non-conditioned cells, a quantitative analysis needs to be performed to verify this conclusion.

DISCUSSION

This study examined the impact of long-term culture at physiologically relevant conditions on LEC gene expression and vessel formation. In line with previous studies conducted on cells in 3-5% oxygen, *Hif2α* expression was increased (Figure 1) [5]. Increases in LEC markers *Prox1* and *VEGFR3* also matched previous literature, as *Prox1* has a known hypoxia response element which binds HIFs, and low oxygen concentration is known to upregulate general *VEGFR* expression [11], [12] (Figure 2). The decrease in *Podoplanin* was unexpected, as it is typically upregulated under hypoxic conditions [13]. However, these experiments were conducted under 1% oxygen, indicating that *Podoplanin* is not upregulated by *Hif2α*, which is the HIF upregulated at 3-5% oxygen. The gene that showed the largest increase in gene expression, *Lyve1,* has been found to be upregulated in macrophages under hypoxic conditions [14]. However, its role is understudied. Although it has been correlated with wound healing and migration, it is not essential for lymphatic development and therefore has not been focused on in the field [15, 16] . Its large upregulation suggests that it has an additional, unknown role in the body that is missed when cultured *in vitro* at 21% oxygen.

Preliminary results suggest that the changes in gene expression caused by physiological oxygen result in morphological changes in vessels formed *in vitro* (Figure 3). Although a quantitative analysis is still needed, it appears that vessels formed in 3-5% oxygen are not only thicker than those developed in 21%, but appear more organized than vessels grown with cells that overexpress *Hif1α*, which mimics a hypoxic environment [17]. As *Hif2a* contributes to lymphatic vessel stabilization, culturing LECs in physiologically relevant oxygen concentrations may lead to more accurate lymphatic models for research, as well as more robust vessels for applications in tissue engineering.

ACKNOWLEDGEMENTS

I would like to thank the Indiana Clinical and Translational Sciences Institute, National Science Foundation, Notre Dame Research, and The American Heart Association for their generous funding. A special thanks to Francine Graham, Natalee Hutchinson, Tomasz Harbut, and Eva Hall for their assistance in these experiments.

REFERENCES

[1] Schito, L. et al., *Trends Cancer*. **8**, 771–784 (2022)
[2] Jiang, B. H. et al., *Am. J. Physiol.-Cell Physiol.* **271**, C1172–C1180 (1996)
[3] Dengler, V. L. et al., *Crit. Rev. Biochem. Mol. Biol.* **49**, 1–15 (2014)
[4] Koh, M. Y. et al., *Trends Biochem. Sci.* **37**, 364–372 (2012)
[5] Jiang, X. et al., *Front. Pharmacol.* **13** (2022)
[6] Jiang, X. et al., *J. Clin. Invest.* **130**, 5562–5575 (2020)
[7] Zenewicz, L. A., *Front. Immunol.* **8** (2017)
[8] Alderfer, L. et al., *Acta Biomater.* **133**, 34–45 (2021)
[9] Wicki, A. et al., *Cancer Cell*. **9**, 261–272 (2006)
[10] Zhou, B. et al., *FEBS Lett.* **587**, 724–731 (2013)
[11] Kukk, E. et al., *Development*. **122**, 3829–3837 (1996)
[12] Tang, N. et al., *Cancer Cell*. **6**, 485–495 (2004)
[13] Tejchman, A., *Universitéd'Orléans Thesis*. (2018)
[14] Cho, C.-H. et al., *Circ. Res.* **100**, e47–e57 (2007)
[15] Chiu, A. et al., *Bioengineering*. **10**, 149 (2023)
[16] Gale, N. W. et al., *Mol. Cell. Biol.* **27**, 595–604 (2007)
[17] Han, T. et al., *Int. J. Oncol.* **54**, 139–151 (2019)

MAPPING NONLINEAR MECHANICAL PROPERTIES OF EX VIVO BRAIN TISSUE USING MR ELASTOGRAPHY WITH APPLIED PRE-STRAIN

Olivia M. Bailey (1), Alexa M. Diano (1), Ali H. Lateef (1), Elise A. Corbin (1), Curtis L. Johnson (1)

(1) Department of Biomedical Engineering, University of Delaware, Newark, DE, USA

INTRODUCTION

Traumatic brain injury (TBI) is defined as a disruption in typical brain function, or other evidence of brain pathology, caused by an external force such as blast or blunt impact[1]. Computational modeling is a promising method used to investigate TBI because it enables the understanding and analysis of human brain tissue behavior during injury across a continuum of applied impacts[2]. These models require advanced experimental data on mechanical properties of the brain, which can be acquired using magnetic resonance elastography (MRE)[3–5]. However, MRE only returns linear mechanical properties in the small strain regime, and brain tissue has been shown to exhibit nonlinearity, specifically with compressive strain, which is critical for modeling high strain and strain-rate injuries[6,7]. Here, we perform MRE with incremental compressive pre-strain on *ex vivo* bovine brain tissue samples to provide insight into the nonlinear behavior that brain tissue may exhibit during injury. This experimental data was fit using a two-term Mooney-Rivlin model to extract relevant nonlinear parameters that can be incorporated into computational TBI models.

METHODS

Samples: Fresh calf bovine brain samples were purchased from a local butcher, cut into approximately 8 x 8 x 3 cm^3 sections, and encapsulated in a 0.65 wt.% agarose phantom to minimize boundary interference and assist with wave penetration. The phantoms were stored at 4°C to gel and brought to room temperature prior to scanning.

Imaging: Using a Siemens 3T Prisma MRI scanner with a 20-channel head/neck coil, MRE data was collected on the tissue-agar phantoms using a 2.5 mm^3 resolution echo-planar imaging sequence. The Resoundant pneumatic actuation system (Rochester, MN) was used to induce 75 Hz vibrations with four phase offsets.

Pre-Strain: Axial pre-strain was applied using a custom-made MR-compatible incremental compression device (Figure 1) that allowed us to control strain and strain-rate. Turning the top knob lowers the plate onto the sample (0.98mm/360° turn). MRE and T1-weighted magnitude images were collected at baseline and each sequential compression state. A nonlinear inversion algorithm was used to determine the voxel-specific mechanical properties at each compression state[8].

Figure 1. CAD model illustrating the incremental compression device at various levels of applied compression.

Experimental Analysis: To evaluate voxel-specific strain, we used nonlinear registration between the magnitude images at each compression state compared to baseline. The resulting registration warp field was used to calculate deformation gradient tensor, $\boldsymbol{F}$, which in turn was used to define the left Cauchy Green strain tensor, $\boldsymbol{B}$. The component of $\boldsymbol{B}$ corresponding to uniaxial strain equates to $\boldsymbol{a}^2$, where $\boldsymbol{a}$ refers to the applied strain and is used as a model input parameter.

$$\boldsymbol{B} = \boldsymbol{F}\boldsymbol{F}^T = \begin{bmatrix} 1/\boldsymbol{a} & 0 & 0 \\ 0 & \boldsymbol{a}^2 & 0 \\ 0 & 0 & 1/\boldsymbol{a} \end{bmatrix} \quad (1)$$

Modeling: The voxel-wise experimental data (i.e. stiffness and strain at each compression state) was fit to a two-parameter Mooney-Rivlin hyperelastic model, below, that has been shown to appropriately capture tissue nonlinearity in compression[9]. For this analysis, we modeled the bovine tissue-agar phantom as a homogeneous, isotropic, and incompressible, hyperelastic material.

$$\mu_0 = C_1 + C_2 e^{-b} \quad (2)$$

Here, μ_0 is the voxel stiffness for each compression state (kPa), and the two material coefficients determined from the model are C_1 and C_2. The first coefficient, C_1, corresponds to baseline stiffness (kPa), while C_2 relates to the nonlinear parameter ($kPa * mm/mm$) of the material. The voxel strain, b (mm/mm) is calculated as ln(**a**).

RESULTS

One representative phantom was used for this analysis where nine compression states were achieved, starting at baseline and ending at approximately 6% global strain. Figure 2, below, depicts the relationship between apparent stiffness and applied pre-strain, where we saw a 28% increase in apparent stiffness from 2.6 kPa to 3.4 kPa as pre-strain was applied. The highly spatially varying strain sensitivity of brain tissue, displayed in the strain fields shown in Figure 2, emphasizes the importance of a voxel-specific analysis rather than whole-phantom viscoelastic property and strain estimation.

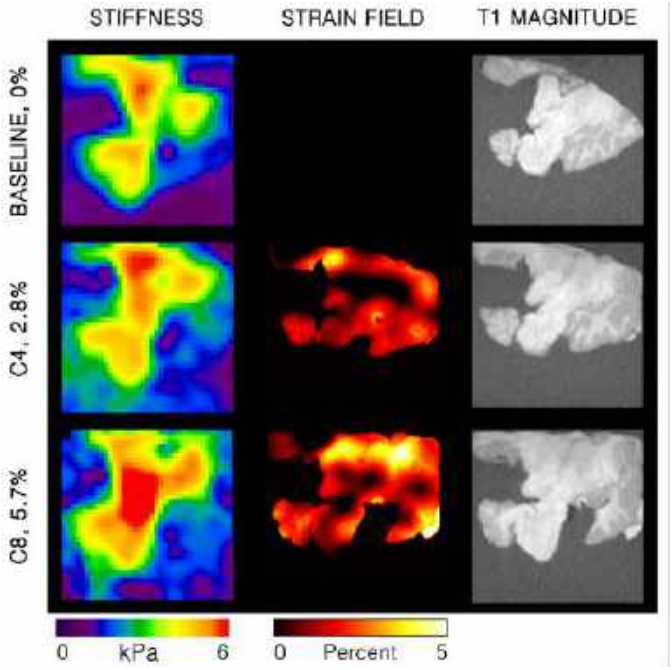

Figure 2: Apparent stiffness (left), strain field (middle), and a T1-weighted magnitude image (right) displayed across three states of compression (baseline, middle, and final compression).

Using the two-term Mooney-Rivlin model, outlined above, material coefficients, C_1 and C_2, were fit at each voxel across all compression states. Figure 3, below, illustrates these masked tissue property maps overlayed on the baseline T1-weighted magnitude image.

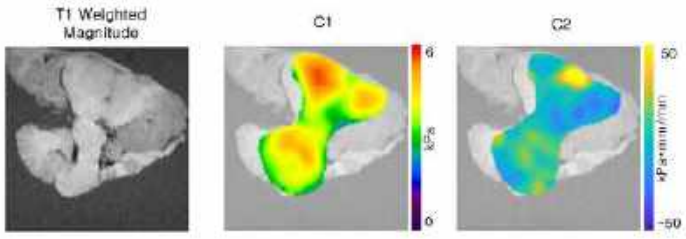

Figure 3: Model coefficients, C1 and C2, calculated at each voxel independently across all compression states.

C_1 is the model coefficient corresponding to baseline tissue stiffness and appears to be an appropriate estimate of the bovine brain stiffness. C_2, which is the material property related to tissue nonlinearity, further highlights the spatial variance within the brain tissue section. Figure 4, below, shows the relationship between applied pre-strain and apparent stiffness fit with the Mooney-Rivlin model for one representative voxel.

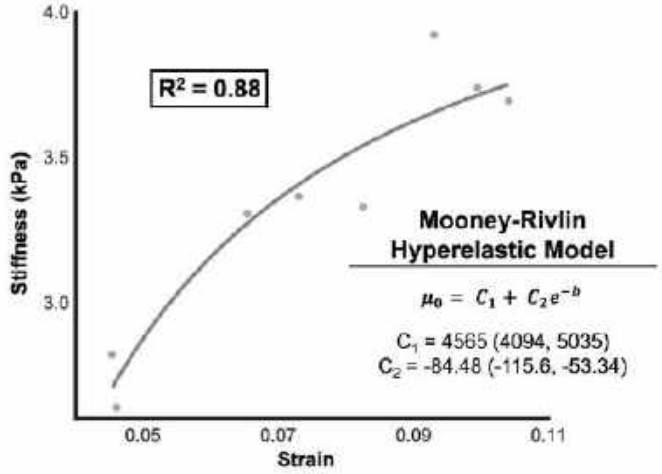

Figure 4: Plot depicting the Mooney-Rivlin model fit at one representative voxel across each compression state.

The model proved to successfully fit the experimental data with an R^2 value of 0.88 for this voxel. Across a randomly selected 200 voxels, the average R^2 value was 0.80, further indicating a satisfactory fit between the model and our collected MRE with pre-strain experimental data.

DISCUSSION

For this analysis, MRE was used to obtain experimental results of the relationship between viscoelastic properties and applied pre-strain through incremental compression. We fit this data to a two-term Mooney-Rivlin hyperelastic model to characterize the material nonlinearity exhibited by the increase in apparent tissue stiffness from applied compression. Our preliminary results show adequate agreement between the model and our experimental results. This experiment serves as proof-of-concept for capturing tissue nonlinearity, and subsequent investigations will ensure that proper mechanical testing guidelines for appropriate sample preparation are followed. Future work seeks to test the fit of multiple models to investigate which best captures the nonlinear viscoelastic properties of bovine and human cadaveric brain tissue measured from pre-strain MRE experiments. Long term applications of this study will use nonlinear property values from MRE to supplement computational TBI models.

ACKNOWLEDGEMENTS

This project was supported by the NIH grant U01-NS112120 and an NIH Bench-to-Bedside grant.

REFERENCES

[1] Khellaf, A et al., *J Neurol,* 266(11):2878-2889, 2019. [2] Budday, S et al., *Acta Biomater,* 48:319-340, 2017. [3] Bayly, P et al., *Ann Biomed Eng,* 49(10):2677-2692, 2021. [4] Alshareef, A et al., *Brain Multiphysics,* 2:100038, 2021. [5] Upadhyay, K et al., *J R Soc Interface,* 1-27, 2022. [6] Capilnasiu, A et al., *Biomech Model Mechanobiol,* 18(1):111-135, 2019. [7] Clarke, E et al., *J Biomech,* 44(13):2461-2465, 2011. [8] McGarry, M et al., *Med Phys,* 39(10):6388-6396, 2012. [9] Mendis, K et al., *J Biomech Eng,* 117(3):279-285, 1995.

BIPHASIC MODELING OF 9L GLIOMA: RADIATION TREATED VERSUS UNTREATED

I.N. Rivera Santiago (1), M. Sarntinoranont (1), P. Acharya (2, 5), J.R. Ewing (2, 3, 4, 5, 6), G. Cabral (2) T.N. Nagaraja (3,4), S.L. Brown (4, 7)

(1) Department of Mechanical and Aerospace Engineering, University of Florida, Gainesville, FL, US
(2) Department of Neurology, Henry Ford Hospital, Detroit, MI, US.
(3) Department of Neurosurgery, Henry Ford Hospital, Detroit, MI, US.
(4) Department of Radiology, Michigan State University, East Lansing, MI, US.
(5) Department of Physics, Oakland University, Rochester, MI, US.
(6) Department of Neurology, Wayne State University, Detroit, MI, US.
(7) Department of Radiation Oncology, Henry Ford Hospital, Detroit, MI.

INTRODUCTION

Glioblastomas (GBMs) are tumors that originate in astrocytes, a type of glial cell found in the brain. Gliomas are physically and molecularly heterogeneous among the patient population. This leads to the vast differences in patient response to treatment and the poor long-term outcomes observed. The brain is a difficult tissue to study and model due to the complex cell differentiation, the diverse loads it experiences, and its low stiffness [1, 2].

A subset of major mechanical models are biphasic continuum models which treat the brain as a complete solid-fluid mixture. In this framework, the cells, vessels, and extracellular matrix are defined as solid while the fluid medium is composed of interstitial fluid. These models can account for the forces imparted by both states. Tumor interstitial fluid pressure (TIFP) is an important feature of the fluid state which greatly impacts the stresses felt in the peritumoral region [3]. A limitation of many brain tumor models is the lack of clinically relevant tumor data. These models often embed in-silico tumors of a spherical shape [4]. In practice, gliomas are highly variable and do not always take on a spherical shape. In-silico models lack experimental data regarding tumor properties and structure.

The objective of this project is to create patient-specific image-based computational models. Individualized brain models allow for a personalized treatment plan to improve patient response and long-term outcomes. For example, mechanical fields–velocity, stress fields, and pressure maps–within and around tumors can inform injection site selection for drug delivery or paths of tumor invasion.

The present study utilizes experimental data from rats implanted with 9L tumors. Dynamic Contrast-Enhanced Magnetic Resonance Imaging (DCE-MRI) techniques are employed *in vivo* to quantify key features of the tumors. In this study, the methods are applied to radiation-treated 9L rat models and untreated 9L rat models to predict the mechanical fields.

METHODS

Mechanical Model. The present model is an application of previous work by Rey et al., [5, 6]. The model is a biphasic model which accounts for the solid and fluid components of the brain. The continuum-based approach treats the tissue as a continuous medium containing an equal mixture of solid and pore space at every point in the material. In the model, the solid phase is defined as the cells, extracellular matrix, and vessels with non-linear neo-Hookean behavior, as described by equation 1.

$$\boldsymbol{\sigma}_s = \lambda J^{-1} \ln(J)\, \boldsymbol{I} + \mu J^{-1}(\boldsymbol{b} - \boldsymbol{I}) \qquad (1)$$

$\boldsymbol{\sigma}_s$ is the solid Cauchy stress tensor, $\boldsymbol{b}$ is the left Cauchy-Green tensor, and $\boldsymbol{I}$ is the identity tensor. The Jacobian, J, is the determinant of the deformation gradient tensor, $\boldsymbol{F}$. The Lamé parameters, λ and μ, are tissue-specific constants related to Young's Modulus and Poisson's ratio. The fluid phase is the interstitial fluid described by Darcy's law and Starling's equation. The equations account for the fluid production at every source and govern the flow of fluid in the pore space. Isotropic tumor growth was modeled with the FEBio Prestrain plug-in. The implementation of the plug-in and specific material properties is described by previous models [5, 6].

Animal Model. Animal studies were conducted at Henry Ford Hospital according to the Institutional Animal Care and Use Committee standards. The 9L cell line is a Fischer rat-derived gliosarcoma immunogenic line. Tumor cells were embedded in the right hemisphere and allowed to grow (n=8). A subset of the animals (n=3) was radiation treated with 25Gy. TIFP measurements are taken via wick-in-needle (WIN) methods [7].

DCE-MRI. A novel component of this approach comes from the use of DCE-MRI techniques. DCE-MRI along with pharmacokinetic compartmental modeling theories are used to acquire important

information on tumors of interest [8]. These parameters include heterogenous maps of the volume transfer constant (K_{trans}), plasma volume fraction, and extravascular extracellular volume fraction. The extravascular extracellular volume fraction represents the porosity of the tissue and is used in this study to scale the hydraulic conductivity of the tumor. The K_{trans} map represents vascular permeability and is used to scale the vessel wall hydraulic conductivity, a component of Starling's law.

Computation. Each mesh element is considered a source, and each element corresponds to one MR voxel. The resolution of the mesh is 58x68x20 (x, y, z) for a total of 78,880 hexahedral elements corresponding to the MR voxel dimensions. Voxel models have been described by our lab in the past [5, 6]. The model was solved via finite element analysis using FEBio (FEBio.org, version 2.0) and conducted in MATLAB (MathWorks Inc., MATLAB, version R2023a) using the GIBBON add-On (gibboncode.org, version 2018).

RESULTS

Overall, we see similar trends shown by our previous models for the U251 orthotropic cell line [5,6]. For both treated and untreated 9Ls we observe elevated fluid pressure in the tumor center (Figure 1) Currently, the model utilizes an average TIFP value from WIN measurements to scale the vascular pressure when applying Starling's law. With this, the model is generally able to predict trends in TIFP along the centerline of the tumor (Figure 2).

Further, the initial findings of the WIN experiments reveal differences in pressure between the irradiated and unirradiated animals: the irradiated animals have a higher TIFP. The increase in pressure leads to elevated velocities at the tumor rim. Similarly, there is an increase in bulk stress at the tumor center and rim (Figures 3 and 4).

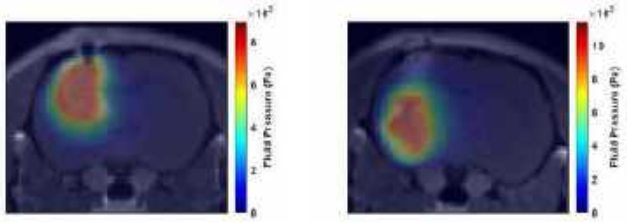

Figure 1: Fluid pressure (Pa). Left: FL221 irradiated animal. Right: FL223 unirradiated animal.

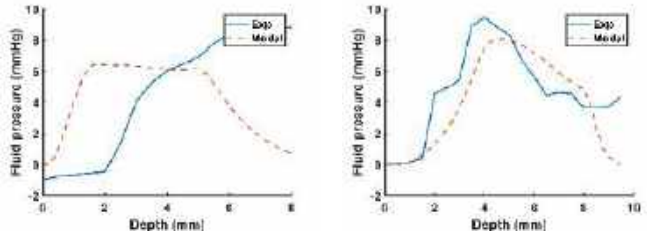

Figure 2: Modeled pressure versus WIN measurements. Left: FL221 irradiated animal. Right: FL223 unirradiated animal.

Further, the initial findings of the WIN experiments reveal differences in pressure between the irradiated and unirradiated animals: the irradiated animals have a higher TIFP. The increase in pressure leads to elevated velocities at the tumor rim. Similarly, there is an increase in bulk stress at the tumor center and rim (Figures 3 and 4). Additionally, there is an impact on the principal solid stresses. In all three principal directions, the model predicts tension (radial stress) within the tumor: with the irradiated animal having higher levels of tension. In contrast to the tumor center, the first principal stress produced hoop stress at the tumor boundary in both treated and untreated animals.

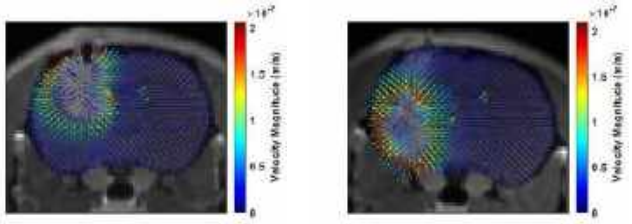

Figure 3: 10% maximum velocity magnitude in (m/s). Left: FL221 irradiated animal. Right: FL223 unirradiated animal.

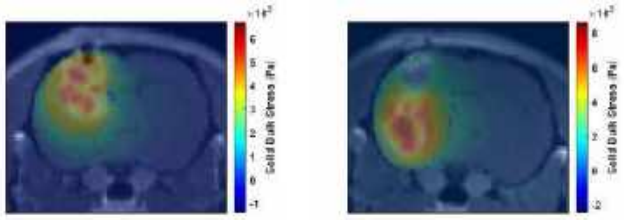

Figure 4: Predicted bulk stress maps. Left: FL221 irradiated animal. Right: FL223 unirradiated animal.

DISCUSSION

The model presented depicts elevated pressure and stress due to tumor growth and vascular leakiness. The elevated pressure leads to higher velocity magnitudes in and around fluid-filled spaces such as the CSF-filled ventricle spaces and at the brain surface. Previous have quantified interstitial fluid flows within regions of interest, such as the white matter tracts [9]. However, further work is required to validate the predicted solid stress fields.

The purpose of our computational model is to contribute to the understanding of the mechanical environment created by gliomas. A future application, the impact on drug distribution and metastasis. In addition, this model can be adapted to model human brains as the input parameters are based on constituent properties scalable to humans. This will allow for the formation of a unique treatment plan.

ACKNOWLEDGEMENTS

Acknowledge grant or other funding support or the assistance of others as appropriate.

REFERENCES

[1] Bergmann, G et al., *J Biomech*, 34:859-871, 2001.
[1] Budday, S et al.,*Arch Computat Methods Eng*, 27: 1187–1230, 2020.
[2] Goriely, A et al., *Biomech Model Mechanobiol*, 14:931-965, 2016.
[3] Hofmann, M et al., *Neoplasia*, 8,2:89-95, 2006.
[4] Angeli, S et al., *NeuroImage. Clinical*, 20:664-673, 2018.
[5] Rey, J et al., *Biomech Model Mechanobiol*, 20:1981-2000, 2021.
[6] Rey, J, University of Florida, 2022. Print
[7] Elmghirbi, R et al., *Magn Reson Med*, 80,5:2040-2052, 2018.
[8] Ewing, J et al., *NMR in biomedicine*, 28,11:1557-1569, 2013.
[9] Chatterjee, K et al., *J Neurosci Methods*, 333: 108541, 2020.

SYNTHETIC HYALURONIC ACID COATING PRESERVES THE PHENOTYPES OF LYMPHATIC ENDOTHELIAL CELLS

S. Saha (1), F. Fan (1), L. Alderfer (1), F. Graham (2), E. Hall (1), D. Hanjaya-Putra (1,2,3)

(1) Department of Aerospace and Mechanical Engineering, Bioengineering Graduate Program, University of Notre Dame, IN 46556, USA.
(2) Department of Chemical and Biomolecular Engineering, University of Notre Dame, IN 46556, USA.
(3) Harper Cancer Research Institute, University of Notre Dame, IN 46556, USA.

INTRODUCTION

Lymphatic endothelial cells (LECs) play a critical role in the formation and maintenance of the lymphatic vasculature, which is essential for the immune system, fluid balance, and tissue repair. However, LECs are often difficult to study in vivo and in vitro models that accurately mimic their behaviors and phenotypes are limited. In a variety of diseases, such as cancer and chronic inflammation, the integrity of LECs is disrupted, leading to lymphatic dysfunction and immune suppression[1,2]. To understand many of these mechanisms and pathophysiology, it is imperative to have a reliable in vitro culture system that can preserve the phenotype and characteristics of LECs. Another important aspect of having a robust in vitro culture system for LECs is tissue engineering. Nowadays there have been tremendous efforts to generate lymphatic vessels using functional biomaterials like hydrogels[3,4]. Often it is not realized that just having a more complex and physiologically relevant 3D system will not result in better tissue engineering unless the rudimentary 2D culture is optimized as well. Therefore, it is important to culture LECs on a coating that supports their proliferation, survival, and functional activity over extended periods of time. Currently, LECs are cultured mostly on treated plastics or conventional coatings like fibronectin or collagen. Compared to other ECM proteins, the use of Hyaluronan (HA) has been shown to hold promise in the culture of vascular endothelial cells. Here, we describe the development of a novel synthetic coating based on HA to preserve the phenotypes and characteristics of LECs.

METHODS

Dopamine-modified HA (HA-DP) is generated by causing a reaction between sodium hyaluronate solution and dopamine in presence of DMTMM and MES buffer. Conjugation of dopamine group to HA was confirmed using 1H-NMR. HA-DP was coated on tissue culture plates through polymerization of dopamine under basic conditions. HA-DP was dissolved in deionized water at 5 mg/ml. Prior to adding HA-DP to wells for coating, 20 μL of 10 M NaOH was added per 1 mL of HA-DP. After incubating at 37 °C overnight, the wells were vigorously washed with deionized water before cell culture. HA-DP coating was characterized and quantified using toluidine blue assay, as previously described[5].Briefly, HA-DP coated plate were incubated with 1 ml Toluidine blue O (TBO, Sigma 198161-5G), supernatant was aspirated, and samples were washed properly with 10mM NaOH. At this stage, a picture was taken to show TBO staining of coated wells compared to non-coated ones. Human adult and juvenile lymphatic endothelial cells (PromoCell, Heidelberg, Germany) were expanded and used for experiments between passages 4 and 8, as previously described[6,7]. Briefly, LECs were maintained at 37C with 5 CO2 in Endothelial Cell Growth Medium (EGM-MV2, C-22022, PromoCell). For phenotypic expression, flow cytometry, PCR and immunofluorescence assay were utilized. Prox1, Podoplanin, LYVE-1, VEGFR3 were selected as LEC characteristic markers throughout the experiments. To visualize focal adhesion kinase and F Actin distribution FAK antibody (Abcam, 1:20) and phalloidin (Abcam, 1:50) were used. Conjugated YAP and TAZ antibodies were used to visualize and quantify spatial distribution of YAP/TAZ.

RESULTS

While it is a common practice to culture LEC on tissue culture plastic according to established protocols, we noticed difference in cell morphology and proliferation over different passages. Our FACS data shows that both adult and juvenile LECs lose their characteristic expression and surprisingly fast (Fig.1). This led us to think consider alternatives to traditional coatings.

Though HA is one of the most abundant components of the extracellular matrix (ECM), a naturally occurring HA based matrix is not commercially available, unlike many other constituents like fibronectin and collagen. One top of that as HA itself is negatively charged, just solution of HA is incapable of forming any type of coating on tissue

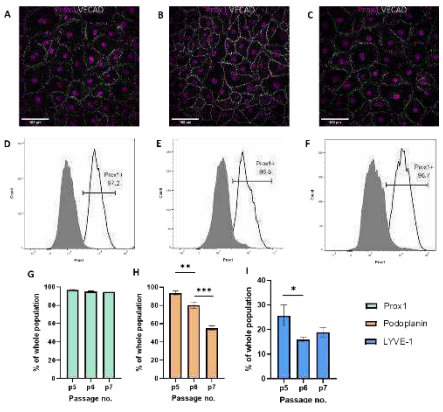

Figure 1. In spite of having similar Prox1 expression LECs exhibit reduced LYVE-1 and podoplanin expression over time.

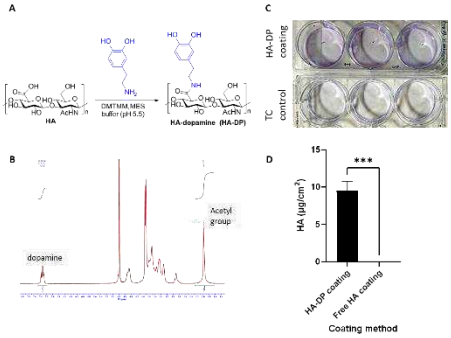

Figure 2. Synthesis and characterization of Ha-Dp polymer

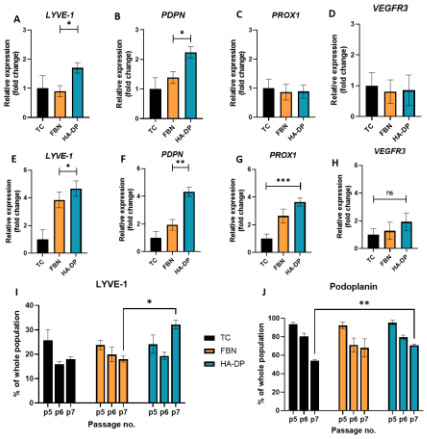

Figure 3. Protein and gene expression of cells over three passages, cultured on different coatings.

culture plastic. To resolve the issue, we synthesized a dopamine conjugated functional HA polymer (HA-DP). After coating the TC plate with the described method, we utilized toluidine blue, a reagent widely used for negative polymer staining, for quantification (Fig.2). Many of the regulatory proteins LYVE-1, podoplanin, VEGFR3 and transcription factor Prox1 collectively control LEC identity, characteristics, proliferation, and migration. Among the known receptors, LYVE-1 interacts with HA and that suggests that we can modulate this aspect and control LEC phenotype. We started culturing LEC on HA coated surface over different passages and found that interaction of LYVE-1- HA not only facilitates better expression of LYVE-1 but other characteristics of LECs like podoplanin and Prox1 as well (Fig.3).

Difference in ECM component often induces different mechanical force on the cells independent of stiffness. Though there is no difference in stiffness between fibronectin and HA-DP coating, we found that late passage LECs showed significantly higher mechanotransduction on fibronectin compared to HA-DP (Fig.4).

It is evident that stress-mediated mechanotransducers YAP/TAZ are critically involved in maintaining lymphatic integrity during adulthood8. Strikingly, lymphatic YAP/TAZ directly but negatively regulates Prox1 transcription and modulates Prox1 activity and lymphatic plasticity[8]. This suggests that comparatively reduced mechanotransduction on HA-DP coating causes suppressed YAP/TAZ activity in LEC (Fig.5) which inversely translates to better Prox1 expression.

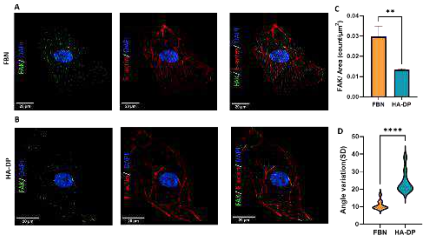

Figure 4. Focal Adhesion Kinase (FAK) Expression of LECs Cultured on Fibronectin and HA-DP Coated Plates.

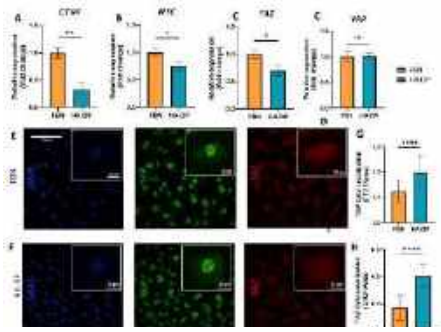

Figure 1. YAP/TAZ Expression for LECs Cultured on HA-DP and Fibronectin Coated Plates.

Collectively, HA-DP is a promising biomaterial to culture LECs in vitro toward their applications in basic lymphatic biology and lymphatic regeneration.

DISCUSSION

While there is no agreement on the best culture condition to culture LECs in vitro, it has been recognized that LECs may start to lose their lymphatic expression overtime during culture. We demonstrated that a simple coating with HA-DP can effectively preserve key lymphatic markers over several passages in vitro. In fact, key lymphatic makers were maintained on high passage (P.7) of LECs cultured on HA-DP, compared to LECs cultured on fibronectin coated plates. Mechanistically, HA-DP caused downregulation of YAP/TAZ, which upregulate Prox1 and therefore maintain lymphatic phenotypes, consistent with previous findings.

ACKNOWLEDGEMENTS

We acknowledge support from the University of Notre Dame through "Advancing Our Vision" Initiative in stem cell research, Harper Cancer Research Institute – American Cancer Society Institutional Research Grant (IRG-17-182-04), American Heart Association through Career Development Award (19-CDA-35630012 to D.H.-P.), National Science Foundation (2047903 to D.H-P.), and National Institute of Health (R35-GM-143055 to D.H.-P.).

REFERENCES

[1] Y. Wang and G. Oliver, Genes Dev, 2010, 24, 2115-2126.
[2] S. Liao and T. P. Padera, Lymphat Res Biol, 2013, 11, 136-143.
[3] L. Alderfer, E. Hall and D. Hanjaya-Putra, Acta Biomater, 2021, 133, 34-45.
[4] L. Alderfer, A. Wei and D. Hanjaya-Putra, J Biol Eng, 2018, 12, 32.
[5] S. Lee, S. Kim, J. Park and J. Y. Lee, International Journal of Biological Macromolecules, 2020, 151, 1314-1321.
[6] D. P. Jeong, E. Hall, E. Neu and D. Hanjaya-Putra, Cellular and Molecular Bioengineering, 2022, 15, 467-478.
[7] L. Alderfer, E. Russo, A. Archilla, B. Coe and D. Hanjaya-Putra, FASEB J, 2021, 35, e21498.
[8] H. Cho, J. Kim, J. H. Ahn, Y.-K. Hong, T. Mäkinen, D.-S. Lim and G. Y. Koh, Circulation Research, 2019, 124, 225-242.

LIM-NEBULETTE REGULATES PODOCYTE MECHANORESPONSE AND FOCAL ADHESION REMODELING

Jacob M. Wright (1), Yixin Hu (1), Anthony Mendoza (1), Nanditha Anandakrishnan (1), Anika Hudson (1), Alan Stern (1), Eric G. Lima (2), Evren U. Azeloglu (1,3)

(1) Division of Nephrology, Department of Medicine, Icahn School of Medicine, NY, NY, USA
(2) Mechanical Engineering, The Cooper Union, NY, NY, USA
(3) Department of Pharmacological Sciences, Icahn School of Medicine, NY, NY, USA

INTRODUCTION

Glomeruli, highly organized segments of the kidney that control full circulatory hemodynamics and respond to fluctuations in blood pressure, are one of the most biophysically complex organs in the body [1]. The glomerulus and its unique cytoarchitecture respond to the properties of an altered biomechanical environment that are governed by, among other factors, cyclic fluid flow. A prime example of a stressful condition the glomeruli face is glomerular hypertension. Due to high capillary tensile stress caused by high pressures, the glomerular basement membrane (GBM) increases in thickness and surface area[2]. Podocytes, visceral epithelial cells, are one of the main regulators that maintain glomerular cytoarchitecture[3]. In response to the expansion of the GBM, podocytes try to adapt and remodel to maintain coverage of the GBM[2]. The podocyte cytoskeleton is mechanosensitive, and its filaments remodel as a result of the feedback from biomechanical changes in the glomerular microenvironment[4]. Our understanding of the mechanosensitive characteristics of the actin cytoskeleton is therefore integral to our ability to counter the pathophysiology of foot process effacement and overall podocyte loss. LIM-nebulette, which is specific to podocytes within the glomerulus, is an actin-associated protein that has been shown to localize to actin stress fibers and focal adhesions in other cell types. Among other cell biological roles that have been previously explored, it has been shown to be a key actin binding partner in podocytes, particularly under Adriamycin induced stress[5]. We have previously shown that LIM-nebulette controls cytoskeletal resilience and impacts calcium dynamics.[5]. Here we investigate LIM-nebulette's mechanosensitive role in glomerular podocytes under biomechanical stress.

METHODS

We have developed a large-scale automated biaxial cyclic stretcher (Figure 1) equipped for six 10 cm stretchable dishes and can fit in a standard incubator. The dishes consist of a silicone membrane between two stainless steel rings. When loaded on the stretcher, the stage moves the dishes down a set displacement, corresponding to calibrated strain over a Teflon cup indenter. The device was calibrated by tracking dots drawn onto a membrane undergoing indentation. The stretcher is programmable via a graphical user interface (GUI) to adjust strain, frequency of motion, and duration of experiment. Differentiated mClover-LIM-nebulette and mScarlet-LifeAct expressing immortalized podocytes were seeded onto stretcher dishes and stretched at 10% Eulerian strain for 30 minutes. Three conditions were tested on these dishes: unstretched (control), stretched, and unstretched 10 μM blebbistatin, a myosin IIA inhibitor, treatment. After 30 minutes, 12 mm cut outs were taken from the dishes for confocal microscopy. Separately, the cells were seeded and differentiated on glass coverslips. Live cell total internal reflection fluorescence (TIRF) imaging was performed on cells with and without 1 μM cytochalasin D, an actin repolymerization inhibitor, and 200 μM blebbistatin.

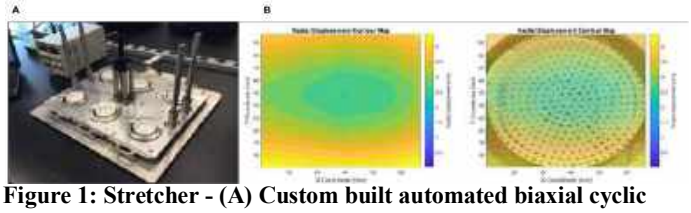

Figure 1: Stretcher - (A) Custom built automated biaxial cyclic stretcher. (B) Strain field of calibrated deformable silicone surface that cells are seeded onto for stretching.

RESULTS

Differentiated immortalized human podocytes that stably express mClover-LIM-nebulette and mScarlet-LifeAct cyclically stretched at 10% strain and a frequency of 1 Hz for 30 minutes were observed to have a change in the spatial expression of LIM-nebulette. At 30 minutes of stretch nebulette localizes to the periphery of the cell when

compared to control as measured via LIM-nebulette intensity distribution across 4 radial bins extending from the center of the cells. Bin 1 was established as closest to the nuclear region and bin 4 closest to the cell periphery (Figure 2). In control and blebbistatin conditions nebulette localizes more at the nucleus and perinuclear regions of the cells; however, the blebbistatin treated podocytes have higher perinuclear LIM-nebulette distribution.

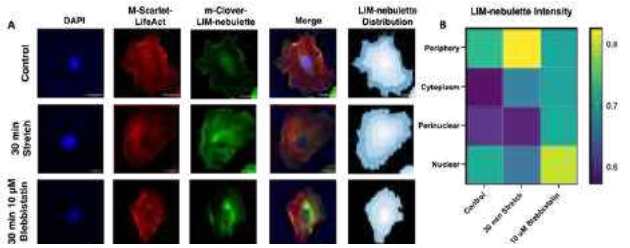

Figure 2: Stretched Podocytes - (A) 20x magnification 3x zoom confocal images of m-Clover-LIM-nebulette and m-Scarlet-LifeAct differentiated human podocytes seeded on silicone membranes and cyclically stretched at 10% strain, 1Hz for 30 min (n=1012) or treated with 10 µM Blebbistatin for 30 min (n=687) or control (n=896). (B) Heat map of LIM-nebulette intensity distribution in subcellular regions for each condition. Scale bar = 50 µm.

LIM-nebulette mediates stress fiber repair after acute injury in cytochalasin D model. At T = 0 minutes of TIRF microscopy on the cells, nebulette appears to localize to the focal adhesions (FA) and stress fibers (SF). After 10 minutes of 1μM Cytochalasin D treatment, disruption of SF and nebulette was observed. The cells were then washed, and at T = 30-60 minutes, post wash, nebulette returns in a wave like pattern (Figure 3) to the vicinity it was before, and SF start reforming.

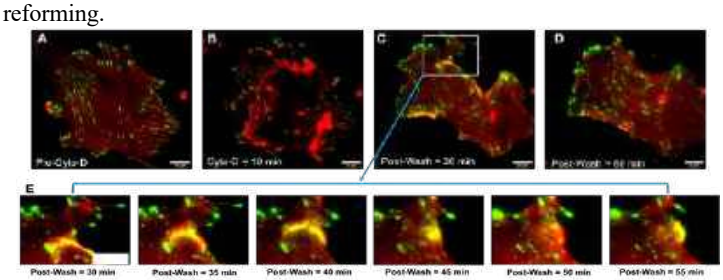

Figure 3: Actin injury model. Nebulette (green) LifeAct (red). (A) Before treatment with 1μM cytochalasin D. (E) Inset of 30-60 min sequence between C and D in 5 min intervals. Scale bar = 25 µm.

Recruitment of LIM-nebulette into focal adhesions (FA) depends on intracellular tension. Contraction was inhibited using 200 μM blebbistatin (Figure 4). 10 minutes after blebbistatin addition, contraction was fully inhibited and nebulette expression decreased at the FA, while the actin SF remained intact. After washing, contraction resumed and nebulette returned to the FA upon recovery **(**Figure 4).

DISCUSSION

Differentiated mClover-nebulette and mScarlet-LifeAct expressing immortalized podocytes were seeded onto dishes. After a 24-hours, the dishes were placed onto the stretcher overnight at 1% pre-strain to allow the cells time to adapt. Next, the stretcher was programed to run for 30 minutes at 10% biaxial Eulerian strain, which was determined prior to seeding cells (Figure 1). When compared to the control cells, the stretched podocytes displayed increased intensity at the cell periphery, which suggest increased expression of nebulette at the edges of the cell. This localization to the periphery could suggest that nebulette goes to the leading and lagging edges of the cells to stabilize attachment to the underlying extracellular matrix during mechanical stretch. In the control, nebulette intensity at the periphery is lower and appears to localize near the nucleus, most likely in the endoplasmic reticulum near the nuclei, where it is being translated. In the contraction inhibited condition, there was increased intensity of nebulette in the nuclear and perinuclear regions when compared to the other conditions. This suggests that nebulette localization throughout the cell has a dependence on myosin IIA contractility. Contraction provides less tension than our external stretch model. We have previously shown that LIM-nebulette crosslinks vimentin filaments with the actin cytoskeleton[5]. It is noteworthy that under reduced cytoskeletal tension conditions with blebbistatin, the distribution of nebulette is more perinuclear and filamentous suggesting increased affinity with intermediate filaments. We hypothesize that inhibited contractility, will leave cryptic binding sites in a closed or inactive conformation and therefore, not exposed. This in turn would leave nebulette with less binding sites at the FA.

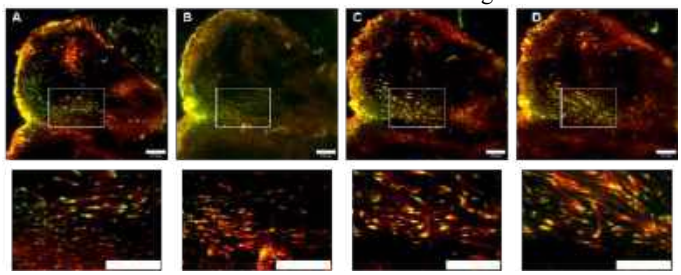

Figure 4: Myosin IIA inhibition (A) Control, nebulette is expressed at focal adhesions. (B) Blebbistatin induced contraction inhibition, nebulette expression at the FA is reduced. Upon washing, contraction is no longer inhibited and nebulette expression increases at (C) 30 and (D) 60 min. Scale bar = 25 µm.

To assess nebulette's role in a cytochalasin D induced acute injury model and recovery, the cells were observed using a TIRF microscope under incubated conditions to see real time dynamics of nebulette. After about 5 – 10 minutes of imaging the control state, 1 μM cytochalasin D doped media was added for 10 minutes. During treatment actin dysregulation and aberrant cell morphology occurred. Nebulette remains at focal adhesions. Following the 10 minutes treatment, cells were washed and imaged for recovery for an hour. Nebulette returned to anchor actin fibers in a wave like pattern and fibers and cell shape returned to resemble that of the control. For the blebbistatin treated cells, after 10 minutes of blebbistatin exposure, present actin fibers remained intact, but nebulette expression decreased (Figure 10B). The blebbistatin treatment was washed and replaced with fresh media and after 30 minutes (Figure 10C) and 60 minutes (Figure 10D) of recovery, nebulette expression increased as it returned to the focal adhesions. These observations suggest that nebulette plays a mechanistic role in podocytes' response to biomechanical stress.

ACKNOWLEDGEMENTS

NIH (R01 DK11822). JMW was supported in part by T32 GM062754.

REFERENCES

[1] Martin, The Glomerulus: The Sphere of Influence. JASN 2014

[2] Endlich, The Challenge and Response of Podocytes to Glom. Hypertension. Seminars in Nephrology. 2012

[3] Meyrier, FSGS: Multiple Pathways Are Involved. Sem. Nephrology. 2011

[4] Endlich, Podocytes Respond to Mechanical Stress In Vitro. JASN 2001

[5] Ge. LIM-Nebulette Reinforces Podocyte Structural Integrity by Linking Actin & Vimentin Filaments. JASN 2020

INFLUENCE OF GLENOHUMERAL JOINT ANGLE ON *IN SITU* SUPRASPINATUS STRAIN BEHAVIOR

Aaron R. Hellem (1), John P. Liffrig (1,2), Allison J. Rao (3), Matthew MacEwen (2), Victor H. Barocas (2), Paula M. Ludewig (1), Arin M. Ellingson (1)

(1) Department of Family Medicine and Community Health, University of Minnesota, Minneapolis, MN, U.S.A.
(2) Department of Biomedical Engineering, University of Minnesota, Minneapolis, MN, U.S.A.
(3) Department of Orthopedic Surgery, University of Minnesota, Minneapolis, MN, U.S.A.

INTRODUCTION

Shoulder pain accounts for millions of physician visits annually and is associated with enormous healthcare costs [1,2]. Rotator cuff (RC) tears are found in more than 20% of the population, increase with age, and contribute to shoulder pain [3,4] with the supraspinatus tendon (SST) the most involved component [5]. Treatment for RC tears typically involves conservative care (i.e. rehabilitation) and/or surgical repair with a shared goal to decrease pain and improve function.

Rehabilitation aims to guide progressive mechanical loading via exercise to drive tissue adaptation [6] while surgery repairs torn tissue to restore anatomy and replicate biomechanical properties. Thus, both pathways are informed by underlying mechanical function. However, pain recurrence is common and RC repair failure rates remain high [7,8]. Taken together, this suggests a lack of understanding of the complex loading of the RC within the glenohumeral joint (GHJ).

Our current understanding of RC mechanics is based on *ex vivo*, uniaxial tensile tests despite evidence suggesting regional-dependent, inhomogeneous material properties of the SST [9,10]. These studies are limited in that they rely on static imaging to assess strain or have not explored clinically relevant end ranges of motion. End ranges of elevation and rotation place the GHJ, and SST, into vulnerable positions and are of high clinical interest. However, dynamic, *in vivo* study of RC strain would be highly invasive and is currently infeasible.

A better understanding of the mechanical behavior could lead to improved management of RC tears while also contributing valuable tissue properties/boundary conditions for future modeling studies. Thus, the purpose of this work was to determine the influence of GHJ position and SST load on sub-failure strain behavior of the SST *in situ*.

METHODS

A single fresh-frozen osteoligamentous cadaveric right shoulder specimen (Age: 71, Male) with no history of GHJ pathology was used. Soft tissue was removed to expose the RC tendons without violating the capsule. The lateral acromion was removed to visualize the intact SST. The medial aspect of the RC muscles was removed leaving 1-2 cm proximal to the muscle-tendon junction where Krackow stitches were placed in the (1) supraspinatus, (2) subscapularis, and (3) infraspinatus/teres minor for the application of load.

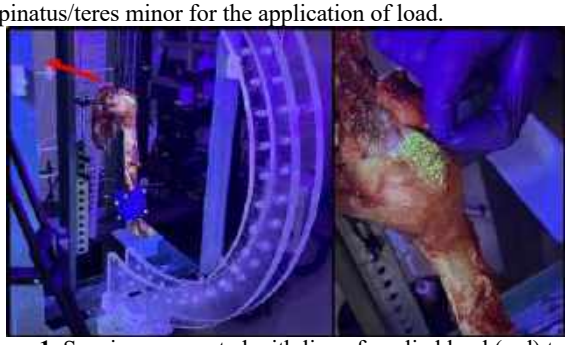

Figure 1. Specimen mounted with line of applied load (red) to SST (A). Speckled SST with identification of footprint (B).

The scapula was mounted to a custom jig (**Fig.1**) and the RC tendons loaded along their line of action [11] to seat the humeral head within the glenoid: subscapularis = 41 N, infraspinatus/teres minor = 40 N, and supraspinatus = 21 N. The SST was speckled using dried UV-reactive paint in conjunction with UV light emitters. Two Nikon D7500 cameras were used for surface strain tracking (F-stop: 5.6, ISO- 1250, 4k resolution, 30 FPS). Five infra-red motion capture cameras were used to quantify glenohumeral kinematics using retroreflective markers and provide real-time feedback of GH position (**Fig. 1**). The initial position was recorded, and the system was bore-sighted with the humeral epicondyles perpendicular to the plane of the scapula.

Preconditioning was performed via cyclic passive motion and tensile SST loading prior to each trial. Sevel trials were performed: 1) neutral position (neutralGH); 2) constrained elevation preventing axial rotation (constrainedElev); 3) elevation with natural axial rotation

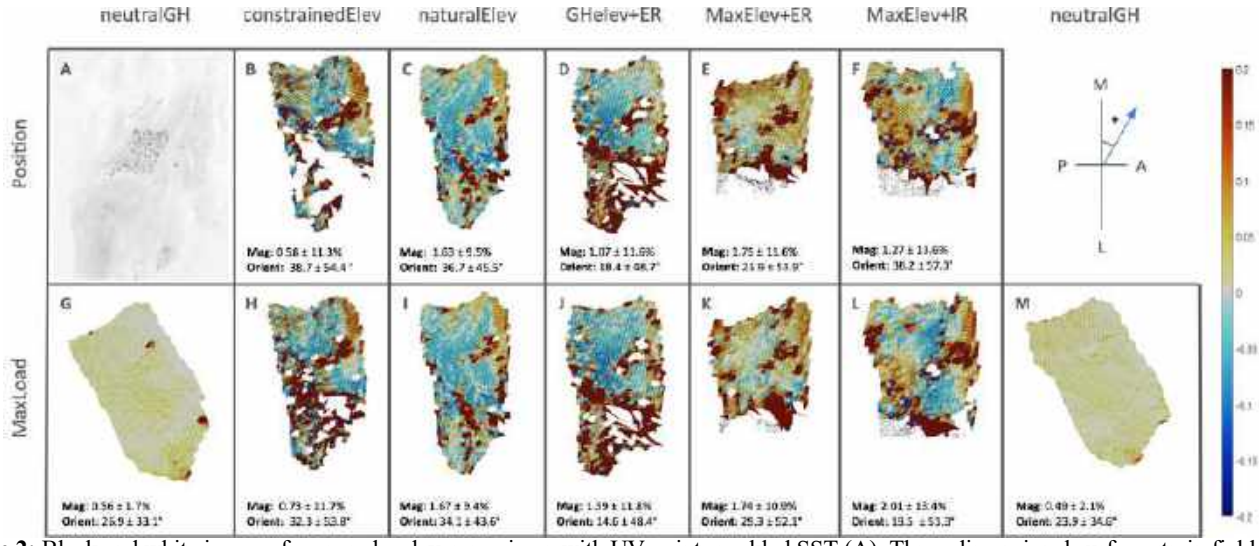

Figure 2: Black and white image of prepared cadaver specimen with UV-paint speckled SST (A). Three-dimensional surface strain fields of SST at GHJ 'Position' [top row] and 'MaxLoad' [bottom row] for trials 1 through 6 with additional neutral GH trial (B-M). Mean strain magnitude and orientation shown for each trial. Anatomical directions (M: medial, L: lateral, A: anterior, P: posterior) and sample orientation direction shown.

(naturalElev); 4) elevation with max external rotation (GHelev+ER); 5) maximum GH elevation with max external rotation (MaxElev+ER); 6) max elevation with max internal rotation (MaxElev+IR); and 7) retest neural position (staticGH). All trials began in the neutral position. The humerus was manually moved into the test position and SST was loaded to 100N (Tindeq, Norway), ~15% of ultimate tensile strength [12].

Strain was calculated during arm positioning and application of SST load, with the neutral position as reference for all trials. Mean 1st principal Lagrangian strain magnitude (% strain) and orientation (°) relative to the long axis of the SST, along with their respective standard deviations. Two discrete instances were investigated: 1) test position ('Position') and 2) test position with additional SST load ('MaxLoad').

RESULTS

No structural damage was observed throughout testing (**Fig. 2 G&M)**. Qualitatively, SST faces were most visible in neutral position and natural GH elevation (**Fig. 2G, 2C, 2I**). The tissue demonstrated buckling on itself near the tendon footprint when approaching 90° of GH elevation as evidenced by holes in the strain maps, this improved following the application of load (**Fig. 2B vs 2H**). Buckling was also observed during max elevation trials with the addition of internal and external rotation that did not resolve with the application of additional load resulting in no data for that area of the tendon (**Fig. 2E-F, 2K-L**).

Mean strain magnitude increased from the neutral position to each of the test positions and further after the application of additional load. Approximately 68% of the surface strain vector orientation was distributed between 6° posteromedial and 60° anteromedial with a mean orientation of 27° anteromedial in the staticGH position (where 0° is perfectly medial approximating the tendon's long axis). Mean strain orientation became more off-axis moving from the neutral position to each test position with exception of trials 4 and 5 where the application of ER resulted in a more medial mean vector orientation (**Fig. 2D-E**). The application of additional load to the SST resulted in mean vector orientation more in line with the tendon's long axis (**Fig. 2 Bottom)**.

DISCUSSION

These results suggest that GHJ position has a greater influence on mean SST strain than uniaxial loads, up to 100 N. This finding is consistent with previous work demonstrating the influence of testing angle on surface and intra-tendinous SST strain behavior of excised tissue [9,10]. Inhomogeneous strain was observed across the tendon surface with strain near the tendon footprint (i.e. more lateral) appearing higher than the mid-tendon in all elevated GH angles where the footprint was visible which has been reported previously [9]. Thus, the mean magnitude % strain may be a poor representation of the environment.

The orientation of mean strain across the tendinous surface becomes more aligned with the long axis of the tendon between 'Position' and 'MaxLoad' time points in all but 1 dynamic trial, evidence that GHJ position impacts SST line of action.

Reproducing clinically relevant joint orientations revealed challenges when collecting surface strain of the SST. There were several instances of observed 'buckling' at ≥ 90° GH elevation angles, where the border between tendon insertion and midsubstance appeared to collapse on itself. Interestingly, the application of additional load seemed to reduce the buckling in the pureElev trial as exhibited by an increase in the number of faces represented in the MaxLoad panel. The complex nature of tendon behavior from neutral to each trial's 'Position' also resulted in holes across the face of the tendon with exception of naturalElev where non-tensile strain appeared in greater proportion hinting at a protective role of typical GH elevation kinematics. Large rigid body translations of the tendon made it difficult to track each point through the duration of the motion. However, it was critical that the strain measurements for each trial were based upon the same neutral (i.e. bore-sighted) position. These challenges are most starkly reflected in the trials with drastic GH elevation and axial rotation in which the insertion site of the tendon did not produce any data.

ACKNOWLEDGEMENTS

This study was supported by UMF Grant (AP-0323-02), OACA (FRD #21.25), and the University of Minnesota Anatomy Bequest Program. Thanks to the Mayo Biomechanics Lab for equipment assistance.

REFERENCES

[1] Oh, LS., *Clin Orthop Relat Res*, 2007. [2] Dieleman, JL., *JAMA*, 2020. [3] Yamamoto, A., *J Shoulder Elbow Surg*, 2010. [4] Teunis, T., *J Shoulder Elbow Surg*, 2014. [5] Redondo-Alonso, L. *BMC Musc Disord*, 2014. [6] Heinemeier, KM., *J Musc Neur Interact*, 2011. [7] Kuijpers, T., *BMC Musc Disord*, 2006. [8] Plachel, F., *AJSM*, 2023. [9] Huang, CY., *J Orthop Res*. 2005. [10] Bey, MJ., *J Orthop Res,* 2002. [11] Ackland, DC., *J of Anat*, 2009. [12] Takatani, KC., *Theor Iss Ergo Sci*, 2017.

TIBIAL SLOPE AFFECTS ACL FORCE AND COUPLED INTERNAL TIBIAL ROTATION UNDER A SIMULATED CLINICAL PIVOT SHIFT EXAM: A COMPUTATIONAL STUDY

Reza Pourmodheji (1), Mitchell GH Wheatley (1), Julien Lulec (3), Jacob M. Hirth (1), Mark J. Amirtharaj (2), Thomas L. Wickiewicz (2), Matthieu Olivier (3), Andrew D. Pearle (2), Danyal H. Nawabi (2), Carl W. Imhauser (1)

(1) Department of Biomechanics, Hospital for Special Surgery, New York, NY
(2) Sports Medicine Institute, Hospital for Special Surgery, New York, NY
(3) Department of Orthopedics and Traumatology, Aix-Marseille University, Marseille, France

INTRODUCTION

Increased posterior-distal directed slope of the tibial plateau (i.e., tibial slope) is associated with increased risk of first-time, noncontact anterior cruciate ligament (ACL) injury [1] and ACL graft failure after surgical reconstruction of this ligament [2]. While tibial slope is often thought of as a non-modifiable risk factor for ACL injury, performing a slope-correcting, sagittal-plane, high tibial osteotomy (HTO) is thought to reduce the risk of ACL and ACL graft failure by reducing force on the ACL [3].

The biomechanical effects of tibial slope on both ACL force and knee kinematics remain poorly understood. Previous in vitro biomechanical models have several limitations. One study assessed two extreme increments of tibial slope, which does not quantify the biomechanical effect of tibial slope increments that are common in the natural knee [4]. Another cadaveric model included more refined increments of tibial slope; however, they utilized a loading system with limited degrees of freedom that did not allow coupled rotations, an important determinant of ACL force [2]. Finally, another cadaveric model correlated tibial slope measured in healthy knees to ACL strain under loads simulating a drop jump [5]. This study did not isolate tibial slope as a controlled, independent variable. Therefore, the observed relationship may have been influenced by other anatomical factors that impact knee mechanics including laxity, volume of the tibial spine, and femoral notch width.

To overcome these limitations, we developed a computational model to allow controlled changes of tibial slope in well-defined increments and motion of the tibiofemoral joint in all anatomical planes. We addressed the following research question: What is the effect of simulated slope changing HTO on ACL force, anterior tibial translation (ATT) and coupled internal tibial rotation (ITR) under serially applied compressive and valgus loads?

METHODS

Computational models of the tibiofemoral joint were developed from ten cadaveric, right knees (five male, five female; age: 33.0±6.9 years) in four major steps [6]. In the first step, each knee underwent MRI and CT scanning; then, 3D geometries of the bones, cartilage, and menisci were reconstructed using image processing software (Mimics Materialise, Inc., Leuven, Belgium). Then, using the 3D rendering of the tibia, the native tibial slope was measured using a previously published method [7]. Second, each of the ten tibial bony geometries were imported into reverse engineering software (Geomagic Wrap, Morrisville, NC) to conduct a virtual anterior closing wedge HTO (Fig 1a). To simulate the HTO procedure a medial-lateral axis was first identified. This axis was parallel to the line connecting the center of the medial and lateral tibial plateau passing through the tibial insertion of the posterior cruciate ligament. The proximal tibia was then rotated about this axis from +15° (posterior tibial slope) to -3° (anterior tibial slope) in increments of 3° (Fig. 1b). In the third step, bony geometries of all seven increments of tibial slope and the associated meniscal, and cartilage geometries for each of the ten knees were integrated with the insertions of the cruciates, collaterals, capsule, and peripheral and root attachments of the menisci and imported into a multi-body dynamics (MBD) software package (MSC software; ADAMS, 2021-4, Newport Beach, CA) (Fig. 1c) [8]. In the MBD software, tissue stiffnesses were standardized via population mean values from the literature, and ligament slack lengths were standardized using a previously published optimization algorithm [8]. Fourth, loads were applied to the computational models simulating a clinical pivot shift maneuver, which consisted of serially applied compression (100 N) and valgus (4 Nm) at 15° of flexion (Fig. 1d). Outcome measures were force carried by the ACL at the peak applied loads, and ATT and coupled ITR. Outcome measures were not normally distributed; therefore, medians and quartiles were reported. Outcome measures were compared among all seven levels of tibial slope (15° to -3° in 3° increment) using a

nonparametric Kruskal-Wallis test with Least Significant Difference (LSD) post-hoc correction for multiple comparisons (α=0.05).

RESULTS

Decreasing lateral tibial slope from +15° to -3° reduced ACL force by a median of 82.5 [60.6 107.7] N ($p<0.01$) and reduced coupled ITR by 16.5° [15.0° 21.0°] ($p<0.01$) (Fig.2). The effect of each 3° increment of slope on coupled ITR was not the same. Specifically, the decrease in coupled ITR from +15° to +6° of tibial slope was not statistically significant, while this decrease from +6° to -3° of lateral tibial slope was a median of 10.2° [8.1° 12.0°] ($p<0.01$). Finally, the effect of the tibial slope on ATT was not statistically significant.

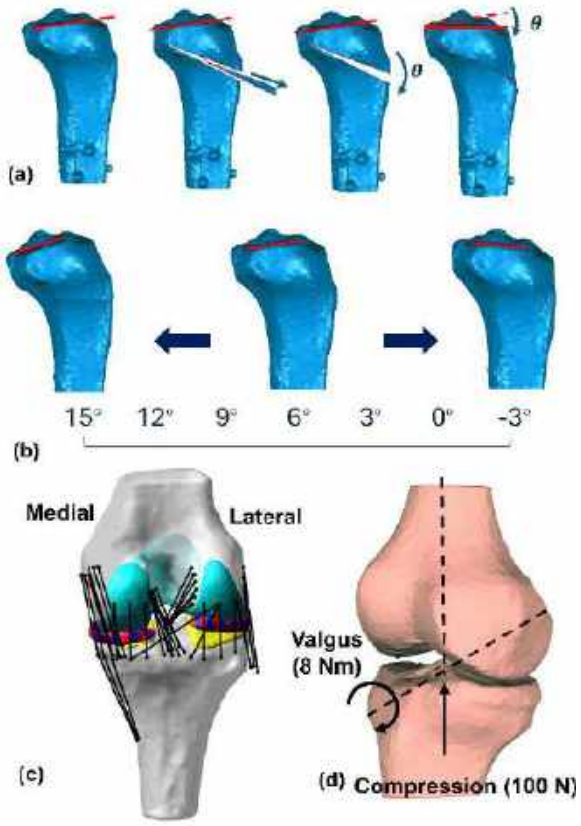

Figure 1: Computational modeling workflow consisted of performing simulated anterior closing wedge HTO (a); in increments of 3° from +15° to -3° (b); assembling the multibody computational model (c); and applying loads at 15° of flexion (d).

DISCUSSION

Our most important finding was that changing tibial slope via HTO influences both coupled ITR and ACL force under combined compression and valgus loads. Our findings suggest that reducing tibial slope via HTO decreases ACL force by decreasing coupled ITR.

Model predictions of decreased ACL force and coupled ITR with reduced tibial slope corroborates previous cadaveric studies [2, 3]. For example, Yamaguchi et al. [4] found that under applied compression and valgus loads, decreasing the tibial slope from +8° to -3° reduced both ACL force and ITR by 30 N and 9°, respectively. This previous work assessed a 10° change in tibial slope.

By also assessing tibial slope at intermediate increments of 3°, we found that the ability of HTO to reduce coupled ITR and ACL force varied among knees, especially, with tibial slopes between 0° and 9° (Fig. 2). For example, ACL force in knees with 6° of tibial slope ranged from 12.3 to 119 N. This finding suggests that additional geometric features like notch width and tibial spine height and offset may act in combination with tibial slope to either magnify or counteract the biomechanical impact of this surgery. Therefore, our modeling approach may be used to help identify those patients who may benefit most from HTO. This speculation requires further investigation.

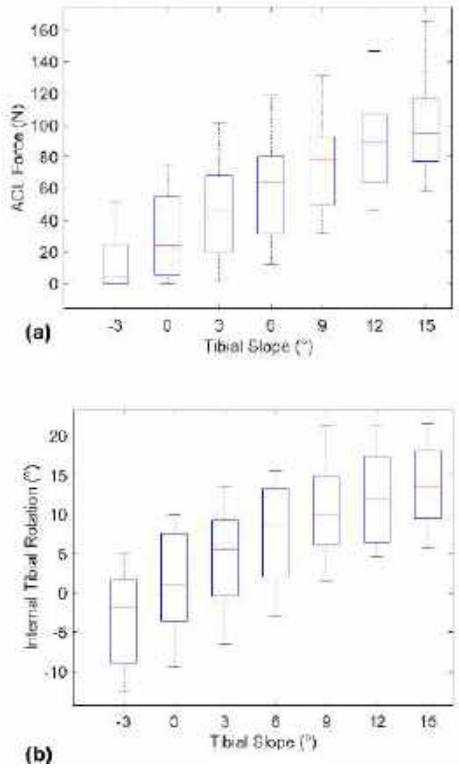

Figure 2: Boxplots of (a) resultant ACL force and (b) coupled ITR vs. tibial slope. Red lines are medians. The whiskers extend to the most extreme data points not considered outliers.

In conclusion, we developed an efficient workflow for studying the biomechanical impact of HTO via computational modeling. Our study confirmed that tibial slope modulates coupled ITR to reduce ACL force. This computational workflow may ultimately be used to identify those individuals who may most benefit from this surgical treatment.

ACKNOWLEDGEMENTS

Steers Family, Ludwig Family, R21AR073388, Gosnell Family, Clark Foundation, Kirby Foundation

REFERENCES

[1] Beynnon, BD et al., *Am J Sports Med*, 42(5):1039-1048, 2014.
[2] Bernhardson, AS et al., *Am J Sports Med*, 47(5):1168-1174, 2019.
[3] Bernhardson, AS et al., *Am J Sports Med*, 47(2):296-302, 2019.
[4] Yamaguchi, KT et al., *Am J Sports Med*, 46(2):370-377, 2017.
[5] McLean, SG et al., *J Bone Joint Surg*, *93:*1310-7, 2011.
[6] Razu, SS et al., *J Biomech Eng*, *145(5):*071003, 2023
[7] Amirtharaj, MJ et al., *J Biomechanics*, *79:*212-217, 2018
[8] Kia, M et al., *J Biomech Eng*, *138(5):*051010, 2016.

SIMULATION OF SELF-EXPANDING TRANSCATHETER PULMONARY VALVE DEPLOYMENT IN THE RIGHT VENTRICULAR OUTFLOW TRACT

Christopher Zelonis M.S. (1), Nicolas Mangine B.S. (1), Kyle Sunderland M.S. (2), Steve Maas Ph.D. (3), Stephen Ching B.S. (1), Yuval Barak-Corren M.D. (4), Devin W. Laurence Ph.D. (1,4), Wensi Wu Ph.D. (1,4), Patricia M. Sabin M.S. (1), Andras Lasso Ph.D. (2), Matthew Gillespie M.D. (4), Jeff Weiss, Ph.D. (3), Matthew A. Jolley M.D. (1,4)

(1) Department of Anesthesiology and Critical Care Medicine, Children's Hospital of Philadelphia, Philadelphia, PA, USA
(2) Laboratory for Percutaneous Surgery, Queen's University, Kingston, ON, Canada
(3) University of Utah, Salt Lake City, Utah, USA
(4) Division of Cardiology, Children's Hospital of Philadelphia, Philadelphia, PA, USA

INTRODUCTION

In patients with some forms of congenital heart disease, such as Tetralogy of Fallot (TOF), surgical relief of right ventricular outflow tract (RVOT) obstruction and RVOT reconstruction often result in severe pulmonary insufficiency and the need for pulmonary valve replacement [1-5]. Transcatheter pulmonary valve replacement (TPVR) has evolved over two decades and is increasingly utilized in patients with deteriorating right ventricle to pulmonary artery conduits and surgically implanted bioprosthetic valves, in addition to use in native or surgically repaired RVOT [3,4,6]. Designed as a less invasive alternative to surgery, TPVR is the preferred intervention today, overtaking conventional surgical methods [2,4,6].

Unfortunately, over 70% of patients with native (non-conduit) RVOT are not candidates for traditional balloon-expandable transcatheter pulmonary valves (TPV) [1,3,6]. As such, self-expanding TPV which conform to the heterogenous RVOT are increasingly applied to this complex population but require precise matching of the optimal TPV to an individual patient [3,4,6]. While finite element (FE) simulations to inform TPV placement are emerging, these simulations are not yet routinely applied to determine patient candidacy or inform device selection in TPVR.

In order to meet this need, we developed a workflow for the image-derived FE simulation of TPV deployment into simplified and image-derived models of the RVOT.

METHODS

This workflow utilizes four open-source programs: 3D Slicer (www.slicer.org), SlicerHeart [7], Tetwild [8], and FEBio [9]. The Institutional Review Board at the Children's Hospital of Philadelphia approved this study.

TPV Models: We focused on three widely available TPV device options for TPVR in pediatric patients: the Alterra (Edwards Lifesciences, Irvine, CA), and two Harmony TPV devices, the TPV-22 and TPV-25 (Medtronic, Minneapolis, MN). All three are made of self-expanding nitinol wire. TPV dimensions were obtained from micro-CT of the devices in their expanded state. The TPVs were fabricated Fusion 360 (Autodesk, San Francisco, CA) and re-meshed as tetrahedral elements with TetWild.

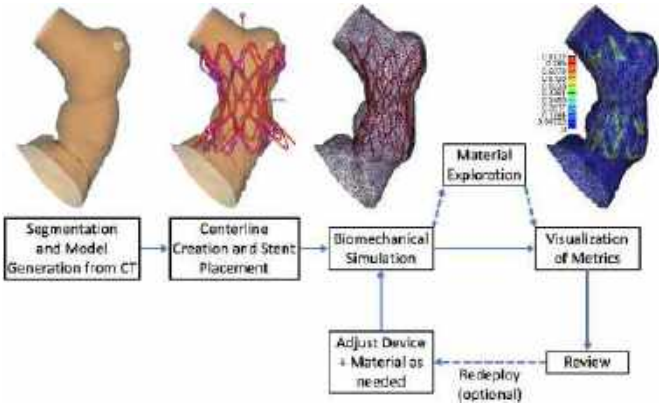

Figure 1: Modeling workflow.

TPV Placement: We created the TPVR Simulation module in SlicerHeart. The module allows the TPV device to be placed along a defined centerline and adjusting its location based on imaging or user preferences.

Vessel Geometry: The three idealized vessel models of varying complexities were constructed using the tube creation part of the TPVR Simulation module. The patient-specific RVOT model was segmented in 3D Slicer from previously acquired CT images.

FE Simulation: Our dynamic FE simulations are carried out in FEBio. The TPV must be constrained within a ~8 mm (25 Fr) catheter system. We apply a normal displacement to the tube that surrounds the

device to compress it uniformly from 28mm to 8 mm and push the TPV into the vessel, simulating release from the delivery catheter system.

A Neo-Hookean model is introduced for the TPV and the tube. We use an uncoupled Mooney Rivlin constitutive model for the vessel. A single node in the TPV is given a zero-displacement condition along the Z axis to prevent the TPV from sliding during compression. Potential-based contacts are instituted between the geometries. In the second analysis step, the tube is expanded at the same rate at which it was compressed, allowing the TPV to self-expand. Contact area between the vessel and the TPV was visualized and exported from FEBio at the last time step.

RESULTS

First, we virtually implanted three TPV into a simple, cylindrical vessel. Our simulations showed device-specific contact with the vessel, with the TPV-22 having the least amount of contact. The TPV-25 and Alterra demonstrated similar contact in the most proximal and distal rows of cells. The TPV-22 would not be ideal in a vessel of this size because its radius is too small relative to the vessel, evidenced by the limited amount of contact between the vessel and the TPV (**Fig. 2**).

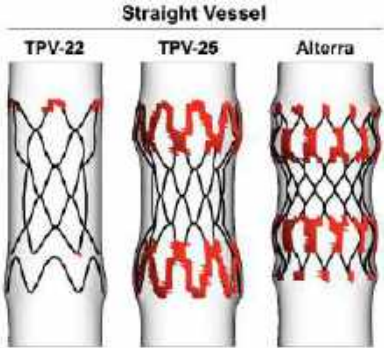

Figure 2: Contact area for the TPV-22, TPV-25, and Alterra, respectively, in the idealized 30 mm tube-like vessel.

Next, we deployed the TPV-25 in four different vessel geometries of increasing curvature and complexity. All simulations successfully converged. All four experienced similar contact at the end of the TPV devices, around the farthest rows of cells. No contact was made near the central part of the TPV for our straight, idealized vessel (**Fig. 3**). The vessel with minor curvature (Vessel A) exhibited some contact along the inside of the curve, while the more curved vessel (Vessel B) saw higher contact in this area. The patient-specific vessel has mild curvature on either side of the TPV with respect to the centerline; consequently, small areas of contact coexist with these features. Contact in Vessel A appeared most similar to the patient-specific model. Higher contact was found in areas of higher curvature.

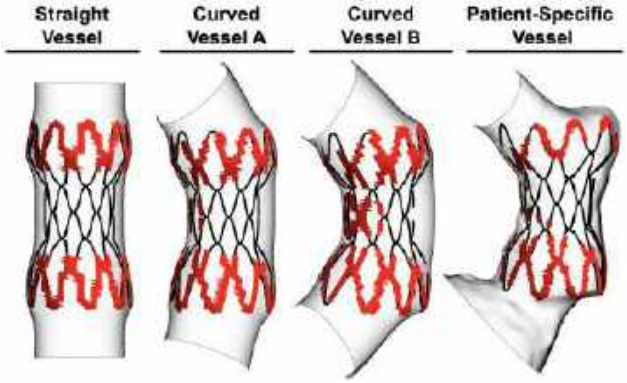

Figure 3: Contact area for the TPV-25 in the curved vessels and patient-specific vessel.

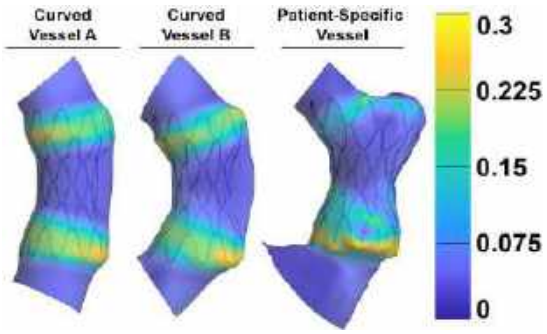

Figure 4: First Principal Strain for the TPV-25

DISCUSSION

We demonstrate initial application of an integrated open-source workflow for simulation of self-expanding TPV deployment in both simplified and image-derived, patient-specific RVOT geometry. We show realistic behavior for the three existing commercially available devices, as well as early visualizations of vessel and device contact. While our initial driving application is TPVR, this open-source framework is fundamentally applicable to any self-expanding device across a range of cardiovascular applications.

Current limitations include modeling of complex TPV structure in a simplified form and capturing contacts in our simulations with many degrees of freedom. Specifically, the TPV-22 and TPV-25 consist of individual nitinol wire rings sutured together rather than a solid metal structure. This may influence our computational results and is difficult to capture mechanically. In addition, our current TPV model utilizes volumetric tet elements, which are computationally expensive relative to beam elements. We will incorporate beam elements in the future. Finally, patient-specific RVOT material properties will be challenging to obtain, and further parameter estimation and sensitivity analysis are needed before reliable clinical application can be considered.

In the future we will continue to explore the range of material properties seen in the RVOT using parameter estimation and sensitivity analysis. We will utilize a new material model for the TPV to better reproduce the known superelasticity and shape-memory capabilities of the nitinol wire [10]. In addition, we will build from these initial results to create an integrated image to simulation workflow. This will consist of machine learning based-segmentation of the RVOT from CT and MRI images, and easy selection and placement of the desired TPV in the RVOT within SlicerHeart with export for simulation in FEBio. Results of simulation will then be displayed in an intuitive form within SlicerHeart to inform patient candidacy and optimal device selection.

ACKNOWLEDGEMENTS

This work was supported by the Cora Topolewski Pediatric Valve Center at the Children's Hospital of Philadelphia, a CHOP Cardiac Center Innovation Award, the Topolewski Endowed Chair, NIH R01 HL153166, R01 GM083925 (SAM, JAW), T32 HL007915 (DWL) and K25 HL168235 (WW).

REFERENCES

[1] Gillespie, MJ et al., *JACC Interv*, 16:1917-1928, 2023.
[2] Crago, M., et al., *Bioeng Transl Med*, 8, 2023.
[3] Jolley, MA et al., *Cath Cardiovasc Interv*, 93:E143-152, 2019.
[4] Gartenberg, AJ et al., *Semin Thorac CV Surg*, 35:333-338, 2022.
[5] Law, MA, Chatterjee, A, *World J Cardiol*, 13:117-129, 2021.
[6] Kenny, DP et al., *Circ Res*, 120:1015-1026, 2017.
[7] Lasso, A et al., *Front CV Med*, 9, 2022.
[8] Hu, Y et al., *ACM Trans Graph*, 37:1-14, 2018.
[9] Maas, SA et al., *J Biomech Eng*., 134, 2012.
[10] Stoeckel, D et al., *Eur Radiol*, 14:292-301, 2004.

NUMERICAL MODELLING OF LOW-LEVEL BLAST SCENARIOS TO QUANTIFY LIKELIHOOD OF CAVITATION-INDUCED TRAUMATIC BRAIN INJURY

Manik Bansal (1), Baudouin Fonkwa (2), Eric Johnsen (2), Christian Franck (3), Rika Carlsen (1)

(1) Injury Biomechanics Laboratory, Department of Engineering, Robert Morris University, Moon Township, PA
(2) Mechanical Engineering Department, University of Michigan, Ann Arbor, MI
(3) Department of Mechanical Engineering, University of Wisconsin-Madison, Madison, WI

INTRODUCTION

Blast-induced traumatic brain injury (bTBI) is the most common and concerning injury for warfighters during the ongoing era of asymmetric warfare. Traumatic brain injury (TBI) involves diffused microscopic injuries at the cellular level which are invisible to non-invasive standard imaging methods like computer tomography (CT) and magnetic resonance imaging (MRI). A recent post-mortem study [1] indicates the occurrence of chronic traumatic encephalopathy (CTE) is low for bTBI compared to impact TBI. CTE may not result from bTBI because brain tissue strains tend to be low (1% to 1.5%) even for relatively high blast exposures of 30 psi [2]. The primary cause of neuronal injury in the brain tissue due to blast wave interaction is still not completely understood.

Both numerical and experimental studies [3], observe high intracranial pressure due to blast wave interaction with the brain tissue. This study hypothesizes that the occurrence of high negative intracranial pressure leads to cavitation-induced primary neuronal injury in the brain tissue for overpressure magnitudes of blast waves ranging from 15 kPa (2 psi) to 105 kPa (15 psi). The warfighters are repetitively exposed to low-level blasts during handheld weapon system training [4]. The key objectives of the study are,

1. To develop a high fidelity framework to numerically predict high-resolution intracranial pressure field maps in the human brain tissue due to low-level blast waves
2. To understand the relationship between incident low-level blast wave parameters, cavitation bubble size, and risk of bTBI

METHODS

The high-fidelity cavitation-induced neuronal injury framework is performed in three steps as follows,

1. Predict intracranial pressure (ICP) field map of the brain by numerically modeling the blast wave interaction with a high-fidelity human body model (GHBMC-M50-Pv5.3.4)
2. Calculate maximum bubble size at the element level using ICP history data as input to a cavitation bubble growth model
3. Quantify primary neuronal injury based on estimates from cavitation growth model and in-vitro micro-cavitation experiments on neuronal tissue cultures

Modelling of Blast Wave Interaction

Blast wave interaction experiments on human surrogates or animals are challenging and limited to low spatial-temporal resolution. Various computational techniques and high-fidelity human brain models were developed in the past decade to understand the biomechanics of bTBI. The majority of the computational techniques consist of blast wave generation and Fluid-Structure interaction (FSI) capabilities. In this study, we implemented the Prescribed Inflow-Arbitrary Eulerian-Lagrangian (PIF-ALE) approach [5] using LS-Dyna to model ideal Friedlander blast wave interaction with the high-fidelity GHBMC (Global Human Body Models Consortium) model as shown in Figure1. The PIF-ALE approach models the ideal Friedlander blast pressure wave ($P(t)$) in Eq.(1) more accurately compared to the ConWep (Conventional Weapon System)-ALE approach.

$$P(t) = P_a + P_i = P_a + P_o(1 - \frac{t}{t_o})e^{-\frac{t}{t_o}} \tag{1}$$

where P_a(101.3 kPa) is the atmospheric pressure. P_o and t_o is the positive blast wave overpressure magnitude and duration, respectively.
The frontal blast wave was generated by defining temporal curves of volume change ($V(t)$), temperature change ($T(t)$), and particle velocity ($V_r(t)$) at the front surface (as shown in blue in Figure1) of the cuboid domain using the expression below [5],

$$V(t) = \left(\frac{P_a}{P(t)}\right)^{1/\gamma} \tag{2}$$

$$T(t) = T_0 V(t)^{1-\gamma} \tag{3}$$

$$V_r(t) = \frac{5P_i}{7P_a} \times \frac{a}{\sqrt{1 + 6P_i/7P_a}} \tag{4}$$

where a is the ambient speed of sound (340 m/s), T_0 (293 K) is the initial temperature, and γ is the ratio of specific heat (for air, $\gamma = 1.4$). The rear surface (as shown in black in Figure1) of the cuboid ALE domain was assigned as a non-reflecting boundary condition. All the remaining surfaces (as shown in red in Figure1) were assigned as slip boundary conditions.

Cavitation Bubble Growth Model

Inertial cavitation is characterized by explosive bubble growth and collapse due to negative pressure, which is known to cause neuronal tissue injury. Past research has related the extent of neuronal injury to the maximum bubble size. We implement a cavitation model based on the Keller-Miksis equation [6] for spherical bubble dynamics assuming isothermal conditions, incorporating the neuronal tissue properties (shear modulus, density, viscosity, and sound speed) and incorporating the effect of the local intracranial pressure-time profile. The neuronal tissue is modeled using a non-linear Kelvin-Voigt material model with Neo-Hookean elasticity. Our model is solved numerically using an explicit multi-stage time marching technique. The model predicts the maximum bubble radius due to the elemental intracranial pressure history of the brain tissue. A reduced model is being developed, which we plan to incorporate into the FE model.

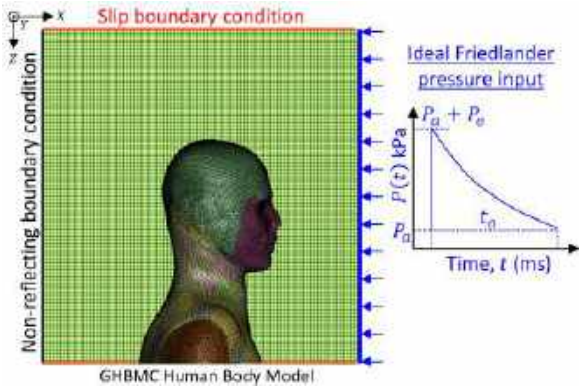

Figure 1: Boundary conditions applied over 3D cuboid ALE domain (in green). a) Non-reflecting boundary condition (in black) on the rear surface, b) slip boundary on all side surfaces (in red), and c) temporal input curve (volume, temperature, and particle velocity) on the front surface (in blue) to model an ideal Friedlander blast pressure wave. No constraint is applied to the Lagrangian elements of the GHBMC-M50-P v5.3.4 model. Dimension of the cuboid Eulerian domain is 570 mm (in X-axis) $\times$ 600 mm (in Y-axis) $\times$ 600 mm (in Z-axis). Eulerian domain is modeled with a total of 950,000 elements (each hexahedral element with an edge length of 6 mm). GHBMC-M50-P v5.3.4 consists of a total of 2.2 million elements.

Cavitation-Induced Neuronal Injury Estimate

We estimate neuronal injury based on our recently established injury thresholds for primary injury under high strain-rate loading as occurs during cavitation. Here, critical injury thresholds are detailed for several structural neuronal biomarkers as well as complete cell loss derived from an established 3D in-vitro neuronal tissue TBI model [7]. The experimental study establishes a non-linear relationship between the cumulative probability of neuronal injury and the threshold value of critical hoop stretch experienced by neuronal cells during a cavitation loading event. As an example, at hoop stretch values equal to 1.2 and 2, the cumulative probability of neuronal tissue injury is 10% and 100%, respectively. The hoop stretch, which can also be expressed in terms of tissue strain, depends upon the ratio of the equilibrium and the maximum radius of the cavitation bubble estimated using the bubble growth model.

RESULTS

We have demonstrated our proposed framework by performing a preliminary study for three cases based on measured blast over-pressures from heavy weapon training [4]. The details of the frontal blast characteristics i.e. overpressure magnitude and duration for each case are tabulated in Table 1. The percentage volume of cavitation-induced neuronal injury in grey and white matter are tabulated in Table1. The percentage neuronal injury volume for a particular tissue (white or grey matter) is the ratio of the sum of elemental volume with the likelihood of injury and the total volume of the tissue. It is observed from blast wave interaction simulation that the effect of overpressure duration is insignificant because the blast wave reflected from the human body attenuates the temporal effect of the on-coming blast wave. For the blast exposures of 2 psi and 4 psi, the volumetric estimates for neuronal injury are negligible compared to blast exposure of 15 psi.

DISCUSSION

We developed a high-fidelity numerical framework with the capability to model low-level blast wave interaction with the human brain tissue for quantifying cavitation-induced neuronal injury. Using this framework we can better understand the biomechanics of TBI and the risk of injury in warfighters exposed to low-level blasts during the handheld weapon system training. The analysis shows that the blast overpressure magnitude has a significant effect on the risk of cavitation-induced neuronal injury compared to overpressure duration. One of the main limitations of the current study is that cavitation injury likelihood results are highly sensitive to the choice of initial cavitation bubble size. We plan to explore the experimental evidence of initial cavitation bubble size for brain tissue in our future work.

Table 1: Percentage of white and grey matter volume with 50% likelihood of cavitation-induced neuronal injury for three different low-level blast exposures.

Case number	Blast wave characteristics	Percentage volume with 50% likelihood of neuronal injury	
		White matter	Grey matter
1	104 kPa (15 psi) & 6 ms	3.2%	2.8%
2	13.8 kPa (2 psi) & 1 ms	0.02%	0.33%
3	27.5 kPa (4 psi) & 1 ms	0.03%	0.36%

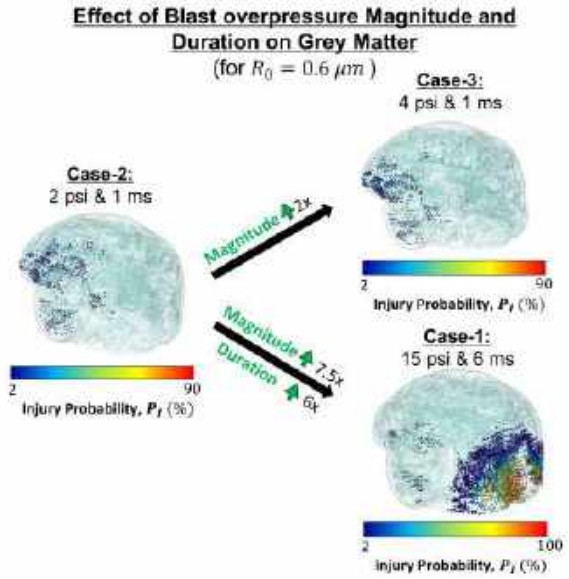

Figure 2: Discrete contour plots for three different frontal blast exposures illustrating the effect of a blast overpressure magnitude and duration on the likelihood of cavitation injury in grey matter region of the brain tissue. Each spatial point illustrates the centroid of the element colored (rainbow spectrum from blue to red) based on the value of the neuronal injury probability ranging from 2% to 100 %. R_0 is the initial cavitation bubble size with a value equal to 0.6 μm.

ACKNOWLEDGEMENTS

This material is based upon research supported by the U.S. Office of Naval Research under PANTHER award number N00014-21-1-2855, N00014-21-1-2044, and N00014-22-1-2828 through Dr. Timothy Bentley.

REFERENCES

[1] Priemer DS et al. *New England Journal of Medicine* 386.23 (2022).

[2] Petr K et al. *Journal of Computational and Nonlinear Dynamics* 7.3 (2012).

[3] Bir C et al. U.S. Army Medical Research and Materiel Command Fort Detrick, Maryland 21702-5012, Annual Report. Award number: W81XWH-09-1-0498. 2010.

[4] Wiri S et al. *Frontiers in neurology* 14 (2023).

[5] Yu X et al. *International journal for numerical methods in biomedical engineering* 35.12 (2019).

[6] Gaudron R et al. *Journal of Fluid Mechanics* 766 (2015).

[7] Estrada JB et al. *Brain Multiphysics* 2 (2021).

MODELING PHARYNGEAL AIRWAY PRESSURE DISTRIBUTIONS WITH NEURAL NETWORKS

Jun Tao Cui (1), Kok Ren Choy (1), Sanghun Sin (2), Mark E. Wagshul (3), Jayaram K. Udupa (4), Ranaan Arens (2), David M. Wootton (1)

(1) Dept. of Mechanical Engineering, The Cooper Union, New York, NY, USA
(2) Division of Respiratory and Sleep Medicine, Children's Hospital at Montefiore, Bronx, NY, USA
(3) Gruss MR Research Institute, Albert Einstein College of Medicine, Bronx, NY, USA
(4) Medical Image Processing Group, Dept. of Radiology, University of Pennsylvania, Philadelphia, PA, USA

INTRODUCTION

Obstructive sleep apnea syndrome (OSAS) is a prevalent condition characterized by repeated episodes of airway collapse during sleep, with negative long-term health effects. A better understanding of OSAS may improve diagnosis and treatment [1], [2], [3]. E*ffective compliance* (EC) is a potential biomarker that includes tissue compliance and airway muscle activity in the pharyngeal airway, and has been shown to correlate with OSAS severity [4], [5]. Calculating EC requires dynamic airway geometry and pressures. Previous papers calculated EC over brief moments in time by simulating airway pressures with computational fluid dynamics (CFD). However, it would be infeasible to use the same methods to calculate EC over longer periods of time due to long simulation run times [4], [5]. This is not ideal because OSAS patients exhibit different breathing behavior over the course of sleep, all of which may reveal a fuller picture of OSAS. As an alternative to CFD, we explored using a neural network (NN) to estimate airway pressures.

METHODS

Image-based CFD: Dynamic volume MR imaging and physiologic data from 5 OSAS subjects was used to train and evaluate the performance of a NN. Data from each subject included airway geometry and synchronized flow for 960 frames in time over ~8 minutes. A semi-automated machine learning algorithm [6] segmented the airway volume for each fame. The airway pressure field was calculated with a custom semiautomated CFD system (Altair HyperMesh, ANSYS Fluent, Python), with a low-resolution mesh. The simulation method was verified using high-resolution CFD of sample frames, and had run times much shorter than the ones in [4], [5]. Following CFD, airway centerlines were found using the *Vascular Modeling Toolkit* [7]. Area and average pressure distributions vs. the airway centerline position (Fig. 1) were extracted for each frame.

The goal was for the NN to predict airway pressures, given information on airway geometry and flow rate. Inputs to the NN were 32-point arrays for centerline section areas, change in centerline coordinates, and flow rate (ex. [a1, a2, a3, ...]). The output (dp) was an array for the change in centerline section pressures. Elements in arrays corresponded to locations along centerlines, and were ordered from inlet to outlet (Fig. 1). The "change" description for arrays refers to a change of quantity between adjacent centerline locations. Pressures relative to the inlet (p) were calculated from a cumulative sum of dp.

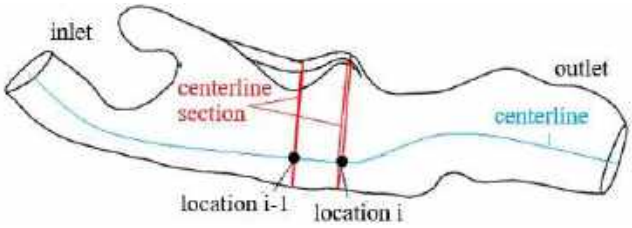

Figure 1: Airway geometry, centerline, and sections, for a single inhalation frame. (Centerline direction reversed for exhalation.)

Several considerations based on fluid mechanics were made when designing the NN. The architecture was inspired by *WaveNet*, a NN for generating audio waveforms [8]. dp was calculated from 1D causal convolutions that prevented elements of dp from being affected by input elements corresponding to downstream centerline location. Dilated convolutions ensured that the receptive field for calculating elements of dp was large enough to include all upstream inputs, so that flow details can be implicitly accounted for in the hidden layers.

Mean squared error loss was used for training. Models were trained with data from 4 of the 5 subjects, and tested on data from the remaining subject. A model was trained to test on each of the 5 subjects. Training was done on a commercially available 32-processor, *AMD Ryzen Threadripper PRO 5975WX @ 3.59 GHz* (Lenovo).

RESULTS

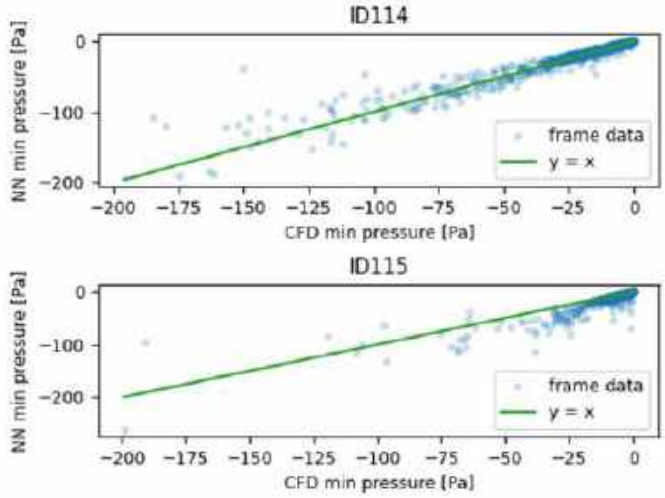

Figure 2: NN Predicted vs. CFD minimum p (symbol) across all test frames, compared to identity line, for two sample subjects.

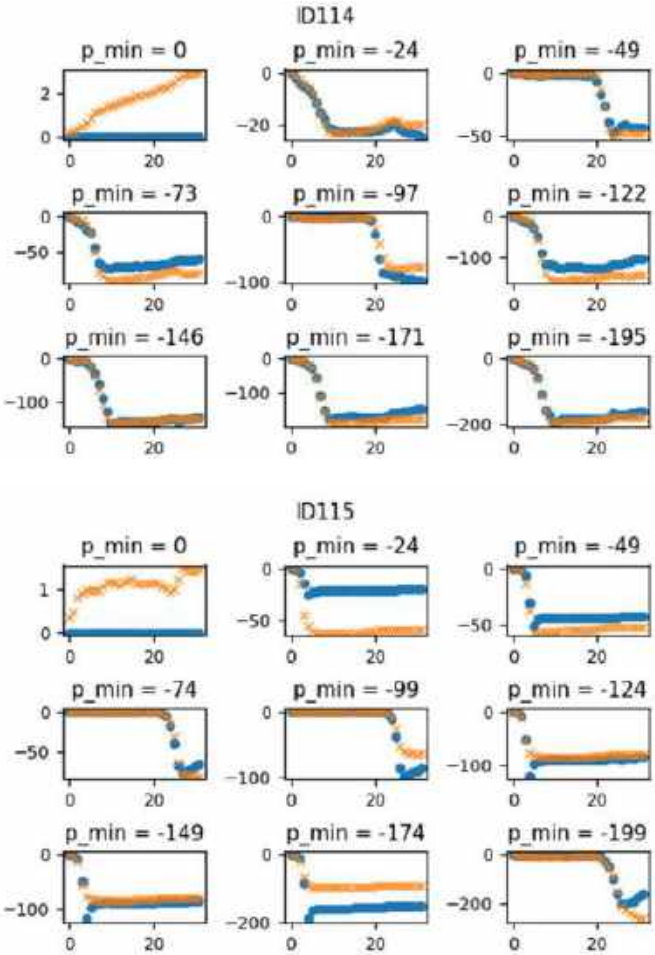

Figure 3: Samples of frame $p(x)$ (x = distance from inlet, y: p [Pa]) by CFD (●) and NN (×); CFD minimum p also shown.

Low resolution CFD run times were ~5 minutes per frame. The training time for each NN model was < 1 hour. Once trained, the NN models predicted dp for their respective test data in < 1 minute.

Results are shown for two sample subjects. In some subjects, e.g. ID114, CFD minimum p was predicted well by the NN, while predictions for subject ID115 strayed from the identity line, with the NN often predicting more extreme pressure drop (Fig. 2).

Figure 3 shows p distribution along the airway centerline for samples of both inspiratory and expiratory frames. Except for when p is negligible (order 1 Pa), NN and CFD resolved the same p trends along airway. Relatively high percent errors resulted from a small number of bad dp predictions near the velopharynx, indicated by narrowest region of the airway in Figure 1, and the highest slopes in Figure 3.

DISCUSSION

Extrapolation of low-resolution CFD run times gives ~3 days to process 960 frames, a significant improvement in through-put compared to the estimated years it would take high-resolution CFD to do the same. The NN is faster still, being able to model airway pressures almost instantly once trained.

Based on [9], [10], and our own comparisons of low to high-resolution CFD, we estimate that the NN has potential to predict p with errors as low as 10-20%, compared to the 15-37% from a simple Bernoulli's estimate. The main advantage of the NN model over other 1D or lumped parameter models is its robustness to the complexity and variety in airway shapes. In addition to instant predictions, another advantage of the NN over CFD is the simplicity with which it represents the relationship between airway geometry and pressures. Whereas 3D airway geometries are required for CFD, the NN works only with simple arrays. These arrays are easier to manipulate, making them more suitable for developing Fluid-Structure Interaction or other dynamic simulations.

Subjects where the NN model performed poorly seem related to problems with the training dataset. For example, the training set used to predict on ID115 had cross-section areas consistently larger than in the test set. Plots for ID114 and 2 other subjects (not shown) suggest that this NN can model pharyngeal airway pressures from airway geometry as well as low-resolution CFD can, when the airway size is represented in the training data.

Future work will include adding subjects to the training and testing datasets, revisiting high-through-put CFD model postprocessing methods to improve training data quality, and exploring the use of scaling to create synthetic data with a wider range of cross-section area. Ultimately the models will be used to dynamically visualize the distribution of effective compliance in patients with OSAS.

ACKNOWLEDGEMENTS

We are grateful for funding from The Cooper Union (Bioengineering Research Fellowship) and NIH (R01 HL130468), and the advice of Professor Christopher Curro (The Cooper Union).

REFERENCES

[1] Eckert D. J. et al., *J Appl Physiol*, 116(3):302-313, 2014.
[2] Senaratna C. V. et al., *Sleep Medicine Reviews*, vol. 34:70-81, 2017.
[3] Knauert, M et al., *WJOHNS*, 1(1):17-27, 2015.
[4] Choy K et al., *J Appl Physiol,* 131(2):532-543, 2021.
[5] Wootton, D. M. et al., *J Appl Physiol*, 121(4):925–931, 2016.
[6] Xie, L et al., *Medical Physics*, 49(1):324-342, 2022.
[7] The Vascular Modeling Toolkit, http://www.vmtk.org/.
[8] van den Oord, A. et al., *arXiv*, arXiv:1609.03499, 2016.
[9] Young, D et al., *J Biomech*, 6(4):395-410, 1973.
[10] Warran, J et al., *The Cooper Union*, 2014.

MODIFICATION OF POLYACRYLAMIDE USING DEXTRAN AND LINEAR ACRYLAMIDE CHAINS TO MIMIC HUMAN BRAIN TISSUE

James D. Angelos (1), Adam M. Willis (2,3), Michaelann S. Tartis (1)

(1) Department of Chemical Engineering, New Mexico Institute of Mining and Technology, Socorro, NM, USA
(2) Department of Mechanical Engineering, Michigan State University, East Lansing, MI, USA
(3) Office of the Chief Scientist, 59th Medical Wing, Lackland AFB, TX, USA

INTRODUCTION

Traumatic brain injuries (TBI) are caused by impacts to the head resulting in brain dysfunction and lifelong complications. According to the defense health agency, the department of defense has reported 485,000 TBIs for military service members worldwide [1]. To study which impact parameters cause damage, it becomes necessary to develop a surrogate model for human tissue due to the limitations in observing *in vivo* impact. Polyacrylamide (PAA) hydrogel is used to emulate the material properties of human brain tissue [2,3]. To measure shear properties in a living human volunteer, shear waves are propagated from a passive driver into a volunteer's head while being scanned with magnetic resonance imaging (MRI) [2]. The data collected is reconstructed through the use magnetic resonance elastography (MRE) to display shear properties. **Figure 1** shows agreement with healthy human volunteer data in terms of shear stiffness (μ) but is inadequate in terms of the damping ratio (ξ).

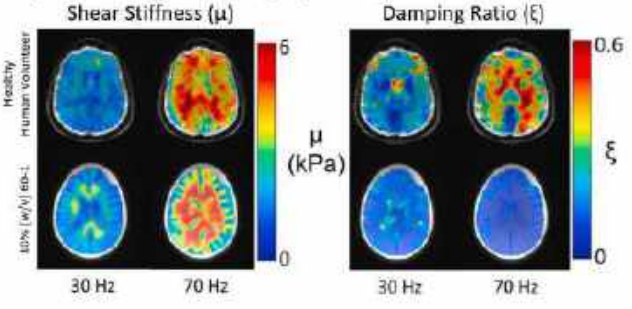

Figure 1: Measurements of shear stiffness and damping ratio of human tissue and 10% (w/v) 60-1 obtained from MRE. Adapted from [2]

The 10% (w/v) 60-1 formulation demonstrates an elastic component or storage modulus (G') of 1-3 kPa which is comparable to brain tissue; however, the viscous component or loss modulus (G") is deficient as seen in **Table 1**. The tangent of the phase angle (tan(δ)) is used to compare the value of G" to G', a ratio of the viscous and elastic contributions, as seen in **Eq. 1**. The complex modulus is a Pythagorean relationship that combines G' and G" into a singular value as seen in **Eq. 2**. The rheological properties of the PAA hydrogel can be converted to MRE material properties as shown in **Eq. 3** and **4** allowing comparison to in-vivo human tissue. According to **Figure 1**, since the shear stiffness is on par with brain tissue, the damping ratio needs to be increased.

$$\tan(\delta) = \frac{G''}{G'} \quad (1)$$

$$G^* = \sqrt{G'^2 + G''^2} \quad (2)$$

$$\mu = \frac{2|G''|^2}{G' + |G^*|} \quad (3)$$

$$\xi = \frac{G''}{2G'} \quad (4)$$

The objective of this research is to increase the viscous component of the PAA hydrogel while maintaining its stiffness, to accurately replicate human brain tissue. Previous findings suggest that increasing crosslinker present in the PAA hydrogel increases the G" value [3]. Additionally, two other methods were attempted: the addition of linear acrylamide chains (LAC) to produce a semi-interpenetrating polymer network and the addition of dextran to increase the amount of free water [4,5]. LACs are shown to help increase the viscous component of a hydrogel by acting as damping pockets; the LACs are not crosslinked with the overall gel network. Dextran is a polysaccharide that can interact with the water present in a material to limit the amount of water bound to the acrylamide backbone chain. Water affected by dextran effectively becomes free water and able to flow about the gel matrix freely due to the non-interaction between dextran and the acrylamide backbone.

Table 1: Material properties of human brain tissue vs 10% (w/v) 60-1 PAA formulation [2]

	Rheological Properties			MRE	
Material	G' (kPa)	G" (kPa)	Tan(δ)	μ (kPa)	ξ
Human Brain Tissue	1 - 2	0.2 - 0.4	0.3	1 - 3	0.1
10% (w/v) 60-1 PAA	1 - 2	0.05 - 0.1	0.05	1 - 3	0.025

METHODS

Acrylamide (purity 98%), Methylenebisacrylamide (MBA, purity 99%), Ammonium persulfate (APS, ACS, purity 98%), N,N,N',N'-Tetramethylethylenediamine (TEMED, ReagentPlus, purity 99%), and Molecular Weight 450,000 – 600,000 (450k MW) and Molecular Weight 40,000 (40k MW) Dextran from Leuconostoc mesenteroides was purchased from Sigma-Aldrich USA.

To synthesize a PAA hydrogel with the formulation of 10% (w/v) 30-1 is as follows: 10.0 g of acrylamide and 0.333 g of MBA are mixed into 100 mL of degassed DI water. 0.086 g APS and 0.177 mL of TEMED mixed in to initiate and catalyze the reaction. The solution is transferred to a 25 mm disc mold and allowed to polymerize for 24 hours and is then placed in an isotonic solution to swell for 24 hours.

LACs length can affect material properties, two lengths of LACs were produced, the formulations outlined in **Table 2**. The length of the LACs is directly affected by the amount of APS present in the solution, and APS signifies the quantity of chains. Synthesis of LAC stock solution uses the chemical amounts outlined in **Table 2** mixed into DI water. The solution is heated to 37°C for 2 hours to allow for polymerization of the acrylamide monomers. Once polymerized, the LAC stock solution is stored at 4°C until needed.

Table 2: Long and short LAC formulation

Material	Long	Short
DI Water (mL)	200	200
Acrylamide (g)	14	14
APS (g)	0.1	1
TEMED (mL)	0.01	0.01

To modify the PAA hydrogel to incorporate LACs: 20 g of LAC of desired length is added to a graduated cylinder. Water is added and gradually stirred until 100 mL is reached and the mixture is homogeneous. The diluted LACs are degassed for 10 minutes and the acrylamide, MBA, APS and TEMED are added. Modifying the PAA hydrogel to incorporate dextran is as follows, 1.4 grams of dextran mixed into 100 mL of DI water. The dextran water mixture is then degassed, and components are added as stated previously. The same molecular weight of dextran is added to DI water to swell the dextran PAA gels. To test the effects of dextran and LACs and any combinational effects of the two on PAA hydrogels, an experimental matrix was developed outlined in **Table 3**.

Table 3: Experimental matrix, 10% (w/v) 30-1 PAA hydrogel base for each formulation with LAC and/or dextran.

10% (w/v) 30-1 PAA (Control)	Short LAC	Long LAC
40k MW	40k MW Short LAC	40k MW Long LAC
450k MW	450k MW Short LAC	450k MW Long LAC

Each PAA hydrogel was tested on a strain-controlled rheometer, ARES, with 25 mm parallel plate geometry. A frequency sweep was performed at 1% strain from 1 to 81 Hz. The G', G" and tan(δ) values were collected for each formulation and averaged together (n=9) to analyze the trend.

RESULTS

As seen in **Figure 2** the G' tends to be roughly 1 kPa for each formulation, LAC containing formulations being slightly lower. LACs work counterproductively and undermines the goal of increasing the loss modulus. Notably, at frequencies lower than 10 Hz the 450k MW shows an increase in G" compared to the control, but at the higher frequencies this trend begins to diminish. High frequency damping is desired as seen in **Figure 1** when comparing PAA to the human brain tissue. Though there is a slight increase in the viscous nature of the PAA using dextran, the change did not result in the desired 0.2 tan(δ).

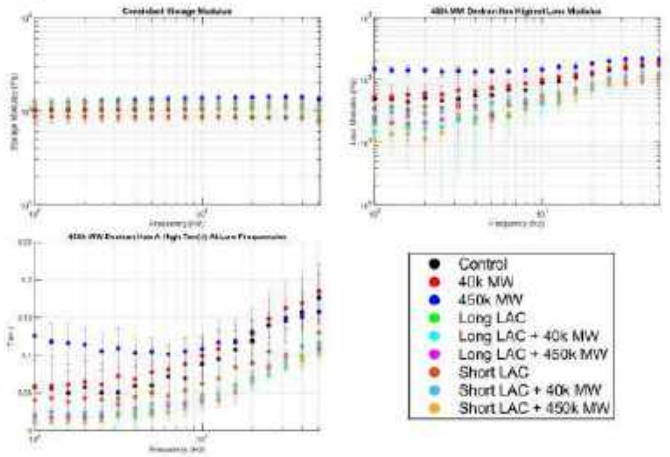

Figure 2: The storage modulus, loss modulus, and tan(δ) of various formulations outlined in Table 3.

DISCUSSION

LACs are undesirable for the project's objectives and there are no advantageous combinational effects of combining LACs and dextran. Though the dextran does appear to increase the G", at higher frequencies the prevalence of free water diminishes compared to the properties of the hydrogel matrix itself. Next steps would be to experiment with larger quantities of dextran. An issue with dextran is the scale up cost, synthesizing small batches using dextran is reasonable, but should a full-sized brain phantom gel be synthesized, dextran would quickly become the costliest reagent. Though the experiments did not yield the desired results, it has demonstrated that increasing the loss modulus is possible.

ACKNOWLEDGEMENTS

This work is supported by the DoD CDMRP Grant W81XWH2211117, NNSA Minority Serving Institution Partnership Program (MSIPP) award DE-NA0003988, and ONR DURIP N00014-19-1-2677 (Dr. Tim Bentley). The views expressed herein are those of the authors and do not necessarily reflect the official policy or position of the Defense Health Agency, Brooke Army Medical Center, the Uniformed Services University, the Department of Defense, nor any agencies under the U.S. government.

REFERENCES

[1] DOD TBI Worldwide Numbers. *Military Health System*, 2023
[2] Knutsen, A. et al., *J of Mec Beh of Bio Mat*, V138, 2023
[3] Baker, A.J.A. et al., *Data in Brief,* V48, 109114, 2023
[4] Charrier, E. E., *APL Bioengineering*, 4(3), 036104, 2020
[5] Dinu, M.v. et al., *Cen Euro J of Chem*, 11(2), 248-258, 2013

A 3D TISSUE MODEL OF THE ENDOTHELIAL GLYCOCALYX POST-PNEUMONECTOMY

Camden T. Holm (1), Jacob Elliot (1), Mia Long (1), Solomon A. Mensah (1,2)

(1) Department of Biomedical Engineering, Worcester Polytechnic Institute, Worcester, Massachusetts, United States
(2) Department of Mechanical and Materials Engineering, Worcester Polytechnic Institute, Worcester, Massachusetts, United States

INTRODUCTION

The endothelial glycocalyx (GCX) plays a crucial role in determining vascular permeability and maintaining endothelial integrity [1]. Despite being studied for over four decades, its functions have only recently become the subject of in-depth research. The GCX is a layer of proteins that coats the luminal surface of endothelial cells (ECs), comprising various transmembrane proteins serving as mechanotransducers for cellular responses [1,3]. One of its primary functions is to regulate the contraction or dilation of blood vessels in response to changes in blood flow [4]. Studies indicate that the proteins constituting the GCX, connected to the cytoskeleton, can influence the reorganization of cytoskeletal proteins and other biochemical activities [5]. Diseases like atherosclerosis or invasive procedures such as pneumonectomies can lead to damage to the GCX, adversely affecting vasculature [2].

A pneumonectomy involves the removal of either the right or left lung, typically due to conditions like cancer or traumatic injury. This highly invasive and high-risk procedure is associated with elevated morbidity and mortality rates. The redirection of blood to one lung and its associated vasculature during a pneumonectomy increases pressures, velocity, and shear stress throughout, with shear stress post-pneumonectomy being double the magnitude observed in arteries under normal conditions [6,7,8].

While the direct relationship between pneumonectomy and GCX is not well understood, there is a potential link between the redirection of blood flow and GCX health. It is hypothesized that the changes in blood flow and the increase in shear stress detrimentally affect GCX and, consequently, endothelial cell health [9].

To better comprehend the relationship between GCX and endothelial cell health, an in vitro pneumonectomy model was developed. Although literature on actual in vivo shear stress changes is limited, precise values were calculated using computer simulations in SolidWorks and COMSOL based on a pneumonectomy scenario.

METHODS

Using SolidWorks, a model of a vascular system was developed as a control no-pneumonectomy (NP) model and a left pneumonectomy (LP) model. Average right and left pulmonary artery (PA) diameter for this model was determined by available literature to be 19.8mm and 22.1mm, respectively [10]. This value was used to set the scale and measure CT scans of pulmonary vasculature in ImageJ Fiji to obtain diameters for selected segments, and branches in the system. These values were used to create a 3D model that represents the PA and its branches in SolidWorks, as shown in Figure 1.

Figure 1: CT Scan of right pulmonary artery, measured and used to develop complete NP (right) SolidWorks model

Both models underwent fluid simulation in COMSOL to analyze and observe areas of high shear stress and to calculate require flow rates during testing (Figure 3). Several sections of interest in the model were selected by notable differences in shear stress between NP and LP models. Average shear stress was calculated for each of these areas of interest using MATLAB and was used to show the fold change of the shear stress between the NP and LP models (Figure 4).

Once vessels of interest were chosen, they were individually replicated in SolidWorks to create a positive mold for PDMS casting

(Figure 2). A plexiglass enclosure (Figure 2) was machined to secure the mold and to attach tubing for media flow through the model.

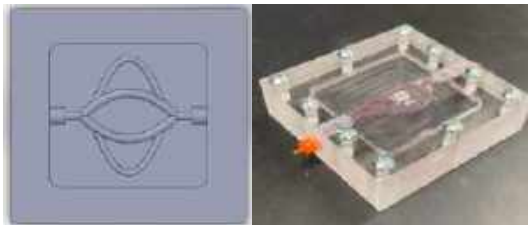

Figure 2: 3D model (left) of PDMS mold that can be modified to simulate a pneumonectomy. The mold is inserted into the flow case and secured (right)

Once cast, each half of the PDMS mold was coated with fibronectin to promote cell adhesion and seeded with $1x10^6$ human lung microvascular endothelial cells (HLMVECs), in endothelial growth medium (Sigma Aldrich) at 37°C and allowed to attach and proliferate for 24 hours. The molds were then placed in the plexiglass enclosure and clamped together (Figure 2) and connected to the flow system. Media was pumped through the system to expose the cells to 10-12 dyn/cm^2 of shear stress due to fluid flow for 24 hours. and connected to the flow system.

Immunostaining was used to quantify differences in expression of GCX. Following exposure to flow, cells were fixed in 4% PFA and stained using Wheat Germ Agglutinin (Thermo Fisher Scientific) primary antibody and AF-488 conjugated anti-biotin (Thermo Fisher Scientific) as secondary antibody (Figure 5). DAPI was used to display cell nuclei.

RESULTS

COMSOL simulation showed shear stress due to fluid flow to be significantly increased in certain areas in the LP model, as shown in Figure 3 by the color map. These areas of greater shear stress were selected as areas of interest.

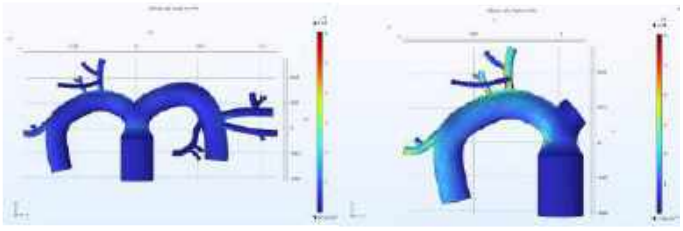

Figure 3: COMSOL shear stress simulation results for NP (left) and LP (right) models. Red areas show high shear stress

The change in shear stress in the selected areas was calculated to be more than 6 fold as shown in Figure 4.

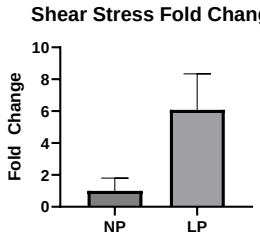

Figure 4: Fold change in shear stress calculated from COMSOL simulations

Preliminary testing of the seeded molds in the flow system for 24 hours revealed successful adherence and confluence of human lung microvascular endothelial cells on coated PDMS surface, forming a lumen. This was visualized via brightfield imaging as well as immunocytochemistry (ICC) with WGA and DAPI (Figure 4). In Figure 4, the green represents the WGA staining for GCX components, and the blue represents cell nuclei.

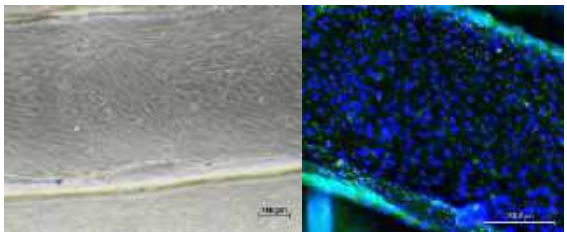

Figure 5: Brightfield image of cell coverage and alignment after exposure to flow (left). ICC results in NP model (right) stained for WGA (green) and DAPI (blue)

DISCUSSION

While our current knowledge of shear stress changes following pneumonectomy is limited, initial tests using this model suggest its capability to simulate post-pneumonectomy conditions. The digital simulation effectively highlighted significant variations in shear stress after the invasive procedure, pinpointing bifurcations as potential sites for increased damage to the glycocalyx.

Despite limitations in the molding process, including low surface resolution and frequent irregularities, preliminary immunofluorescence results indicated a healthy glycocalyx and a complete lumen after 24 hours of flow exposure. Future experiments will involve analyzing COMSOL results in MATLAB to quantify shear stress, closely examining and quantifying glycocalyx staining. Mold refinement and immunostaining will be conducted to confirm the formation of physiologically accurate lumens. Additionally, diverse pneumonectomy and bifurcation models will be developed and validated.

This study demonstrates the potential accuracy of our model as a vascular representation, with ongoing refinement and validation efforts. Future research will explore various vascular shapes, bifurcation types, use a more physiologically relevant matrix like collagen, and conduct quantitative analysis of glycocalyx health. Understanding the glycocalyx's role in vascular health post-pneumonectomy may provide insights into reducing morbidity and mortality rates after surgery.

ACKNOWLEDGEMENTS

The authors would like to thank Dr. Solomon Mensah for valuable direction, support and discussions, and WPI for providing laboratory space and funding for the project through the startup package provided to Dr. Solomon Mensah.

REFERENCES

[1] Reitsma, S et al., *Pflugers Arch*. 454:345-359. 2007.
[2] Ebong, E et al., *Integr Biol (Camb)*, 6:338-347, 2014.
[3] Bartosch, A et al., *Sci Rep*, 11:11386, 2021.
[4] Haroon, M et al., *Experimental Cell Research*, 417(1):113204, 2022.
[5] Thi, M et al., *Proc Natl Acad Sci U S A*, 101:16483-16488, 2004.
[6] Algar, F et al., *EACTS*, 23(2):201-208, 2003.
[7] Chiu, J et al., *Phyisiol Rev*, 91(1):327-87, 2011.
[8] Katz, M et al., *J Vis Exp*, 145, 2019, doi: 10.3791/59050.
[9] Dietz, N et al., *SCVA*, 4(1):31-35, 2000.
[10]Bozlar, U et al., *Acta Radiologica*, 48(10):1086–1091, 2017.

The Impact of Natural Estrogen and Progesterone Cycling on Cardiac Function in Mice

Thaotho H. Nguyen (1), Cassandra K. Conway-O'Donnell (1), Naomi C. Chesler (1)

(1) Edwards Lifesciences Foundation Cardiovascular Innovation and Research Center, and Department of Biomedical Engineering, University of California, Irvine, Irvine, CA, USA

INTRODUCTION

Heart disease is the leading cause of death for all sexes and most racial and ethnic groups in the United States [1]. Prior to menopause females are less likely to develop overt cardiovascular disease (CVD) compared to age matched males [2]. However, post-menopause CVD onset increases substantially until the incidence of CVD in females surpasses that in males [3]. This disparity in heart disease is attributed to decreasing levels of estrogen and progesterone after menopause, however, the roles of female sex hormones in heart function are not well understood. Estrogen and progesterone cyclically rise and fall during the menstrual cycle with the highest amount of estrogen occurring immediately prior to ovulation and rising levels of progesterone occurring in the luteal phase [4]. In women just prior to ovulation, systolic blood pressure and soft tissue compliance increases [5][6]. In contrast, in women during the luteal phase, in which progesterone is rising and estrogen levels are falling, heart rate increases, and systolic blood pressure decreases [5].

The 28-day (on average) human menstrual cycle and the 4-day (on average) mouse estrous cycle share some similarities. In both cases, the cycles consist of distinct phases. The mouse estrous cycle includes four phases: proestrus, estrus, metestrus, and diestrus. Proestrus is characterized by the preparation of the reproductive system for mating, similar to the human follicular phase. The estrus phase, often referred to as the "heat" period in animals, aligns with human ovulation when the egg is released. Metestrus and diestrus in mice correspond to the luteal phase in humans, involving changes in the uterus and hormonal fluctuations [7]. Despite species differences, understanding the impact of these cycles in mice is crucial for reproductive research and can provide valuable insights into the effects of the menstrual cycle in women.

The goal of this study was to quantify the impact of the estrus cycle on cardiac function in mice to better understand the heart function of women in the premenopausal state. Knowledge of natural fluctuations in heart function that occur due to natural variations in sex hormones in females could help inform cardiovascular research and limit variability in data that results from those natural variations.

METHODS

All animal procedures were approved by the University of California, Irvine Institutional Animal Care and Use Committee (IACUC).

Transthoracic Echocardiography: Daily transthoracic echocardiography using a Vevo 3100 ultrasound system was conducted for five days to assess the morphology and function of the left ventricle, aorta, and pulmonary artery in a group of five (5) C57BL/6 female mice at 6-weeks-old using a 40Mhz probe. The mice were initially anesthetized with 5% isoflurane and maintained at 2% isoflurane during the entire procedure. A heated platform was used to maintain the body temperature at 37°C. Imaging was conducted daily at the same time and for 5 consecutive days. B-mode and M-mode images were taken of the left ventricle. B-mode and pulse wave doppler were used to measure geometry and blood flow velocity in the aorta and pulmonary artery.

Visual Assessment of Estrous Cycle: After performing echocardiography, a visual examination of the vaginal cavity was performed to ascertain the phase of the estrous cycle. Estrous cycle phase was assessed visually by observing the color, moistness, and aperture of the vaginal opening [7]. Whereas proestrus is characterized by swollen, pink, and moist tissue, the vagina in estrus loses some pinkness and moistness but remains open. Metestrus can be identified by the slight closure of the vaginal canal, pale color, and presence of white cellular debris; in diestrus the vaginal canal is closed, has a pale color, no swelling, and no debris [7].

Data Analysis: Vevolab 5.8.0 software was used to analyze the echocardiogram images. Echocardiographic parameters including left ventricle anterior wall (LVAW) and posterior wall (LVPW) thickness in systole and diastole, left ventricle internal dimensions

(LVID) at diastole and systole (LVIDd and LVIDs respectively) were evaluated in M-mode by averaging measurements obtained over a minimum of three consecutive cardiac cycles. LV ejection fraction (EF), LV fractional shortening (FS), and LV posterior wall thickness (PW) were calculated in Vevolab software by using the following formulas:

$$EF\ (\%) = 100 \times [(LVEDV - LVESV)/LVEDV] \quad (1)$$
$$FS(\%) = 100 \times [(LVID_d - LVID_s)/LVID_d] \quad (2)$$
$$LVPW = 100 \times [(LVPW_s - LVPW_d)/LVPW_d] \quad (3)$$

EKG was also measured using surface electrodes and heart rate was determined with Vevolab software.

After analysis, parameters were categorized into one of the four stages of the estrous cycle as determined by the visual assessment. In total, 23 echocardiograms were analyzed. Subsequently, a normality and logistic regression were conducted on all parameters. If all tests yielded normal results, ANOVA was performed to compare serial measurements within the groups with P values < 0.05 were considered statistically significant. All statistics were performed using GraphPad Prism. Repeated measured statistics were not performed since not all animals cycled through all four phases. Diestrus was observed and reported but omitted from the statistical analysis, as the diestrus phase was only observed twice in the 5 mice during the 5-day testing period. One mouse was excluded from the data starting on day 3 due to an adverse reaction to anesthesia.

RESULTS

As shown in **Table 1**, heart rate (HR) did not vary over the course of the estrus cycle. Stroke volume (SV) tended to be higher in metestrus and diestrus than proestrus or estrus, but the differences were not significant. Cardiac output (CO), calculated as the product of HR and SV, also was not significantly different between cycle phases. Both fractional shortening (FS) and ejection fractioning (EF) showed a significant change with natural fluctuations in estrogen and progesterone in the female mice in this sample. As shown in **Figure 1**, FS and EF were significantly lower in mice in metestrus compared to mice in proestrus.

Table 1: Heat rate (HR), stroke volume (SV), ejection fraction (EF), fractioning shortening (FS), and cardiac output (CO) expressed as mean ± standard error.

Parameters	Proestrus N=7	Estrus N=5	Metestrus N=8	Diestrus N=2
HR (BPM)	532.0 ± 36.0	506.9 ± 48.0	480.4 ± 36.2	506.3 ± 4.6
SV (µL)	26.8 ± 5.0	26.3 ± 8.1	30.4 ± 4.7	36.8 ± 8.6
CO (mL/min)	14.2 ± 3.0	13.2 ± 4.0	14.7 ± 3.1	18.6 ± 4.5

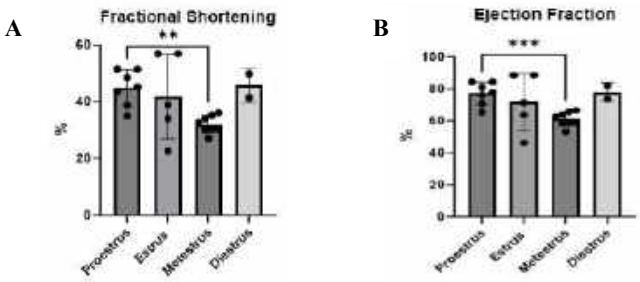

Figure 1. Mice in metestrus exhibited a significant decrease in fractional shortening (FS) and ejection fraction (EF) in compared to mice in proestrus (**P < 0.001 and ***P < 0.0001).

DISCUSSION

Female sex hormones, specifically estrogen, have been considered cardioprotective [8]. However, research on the role of female sex hormones on cardiac function in premenopausal women is lacking. Historically, female sex was excluded from clinical studies and animal research prompting the NIH Policy on Sex as a Biological Variable in 2015. This study sought to better understand the impact of hormonal fluctuations in the mouse estrous cycle on cardiac function using echocardiograms. Our investigation found increased fractional shortening and ejection fraction during proestrus compared to metestrus. Overall, we found that increasing estrogen levels in the estrous cycle can influence cardiac contractility.

Kwissa et al. found a significantly shorter left ventricle ejection times in the mid-luteal phase compared to the late follicular phase of the menstrual cycle in human women [9]. Similarly, our findings show that cardiac contractility (fractional shortening) increased at proestrus, a phase characterized by high estrogen levels. These findings underscore the necessity of not only including females in cardiovascular research but also accounting for the specific phase of the estrous cycle.

One limitation of our study was that the mice did not reliably cycle through all phases of the estrous cycle during a five-day data collection window. The limited data points for the diestrus phase prohibited quantifying cardiac function for all estrous phases. Also, the visual assessment method of determining estrus cycle phase can be complemented by employing vaginal cytology [7].

In conclusion, our investigation sheds light on the intricate relationship between the estrous cycle and cardiac dynamics. By connecting our major findings to existing literature and emphasizing the role of estrogen, we advocate for a refined approach to cardiovascular research that considers both sex and estrous cycle phases which may help improve timing for medical interventions in premenopausal women and prompt animal researchers to report estrous phase as a variable within the study. Future work to expand the findings of this study could include taking serial blood pressure measurements and including mitral and tricuspid valve jet velocities in the analysis.

ACKNOWLEDGEMENTS

The authors would like to acknowledge Tim Hacker and Leticia Charco for their contributions.

REFERENCES

[1] Heather et al. *Am J Physiol Heart Circ Physiol*, 323 (1), H176-H200. 2022.
[2] Stanhewicz et al. *Am J Physiol Heart Circ Physiol*, 315(6), H1569-H1588. 2018.
[3] Ryczkowska et al. *Arch Med Sci*. 2022; 19(2):458-466. 2022.
[4] Carr. *Harrison's Principles of Internal Medicine. 11th ed. New*
[5] Martin et al. *Front Sports Act Living*, 3, 616999
[6] Moran et al. *Wiley*, 20(6), P496-504. 2008.
[7] Byers et al. *PLoS One*, 7(4), e35538. 2012.
[8] Aryan et al. *Int. J. Mol. Sci.* 21(12), 4314. 2020.
[9] Kwissa et al. *J Clin Med.* 2022.
[10] Kehmeier et al. *Am J Physiol Heart Circ Physiol,* 323 (6), H1057-H1067. 2022.

DECIPHERING WOUND HEALING COMPLIEXITY: NEAR-INFRARED SPECTROSCOPY ANALYSIS OF MAMMALIAN SKIN

P. Kim (1), C. Juntunen (2), J. Niezgoda (3), A. Alonso (4) S. Gopalakrishnan (5), M. Dabagh (6), Y. Sung (7)

(1) Biomedical Engineering, University of Wisconsin-Milwaukee, Milwaukee, WI, U.S.A.
(2) Mechanical Engineering, University of Wisconsin-Milwaukee, Milwaukee, WI, U.S.A.
(3) College of Letters and Science, University of Wisconsin-Milwaukee, Milwaukee, WI, U.S.A.
(4) Biomedical Engineering, University of Wisconsin-Milwaukee, Milwaukee, WI, U.S.A.
(5) College of Nursing, University of Wisconsin-Milwaukee, Milwaukee, WI, U.S.A.
(6) Biomedical Engineering, University of Wisconsin-Milwaukee, Milwaukee, WI, U.S.A.
(7) Mechanical Engineering, University of Wisconsin-Milwaukee, Milwaukee, WI, U.S.A.

INTRODUCTION

Wound healing is a critical biological process essential for the restoration of skin integrity following injury. Understanding the mechanisms underlying the healing process in chronic wounds has an immense clinical significance, as it enables us to predict the efficiency of clinical interventions and improve both current healing time and patient outcomes. Having the capability to quantify wound tissue's characteristics and identify its chemical structure will advance our understanding on mechanisms involved in the healing process. Clinical studies have reported that the structure of tissue surrounding a healing wound changes significantly during the healing process. Based on these findings, the tissue surrounding a chronic wound and the peri wound area have gained significant clinical attention where application of particular treatments is expected to promote the healing by stimulating the tissue [1-6]. In contrast, the role of chemical modification and its interplay with structural changes during the healing process, which can greatly improve the design of intervention strategies and patient outcome, have been elusive. This study introduces innovative methods for observing and quantifying wound healing in mammalian models, specifically through detailed microscopic examination of mice skin.

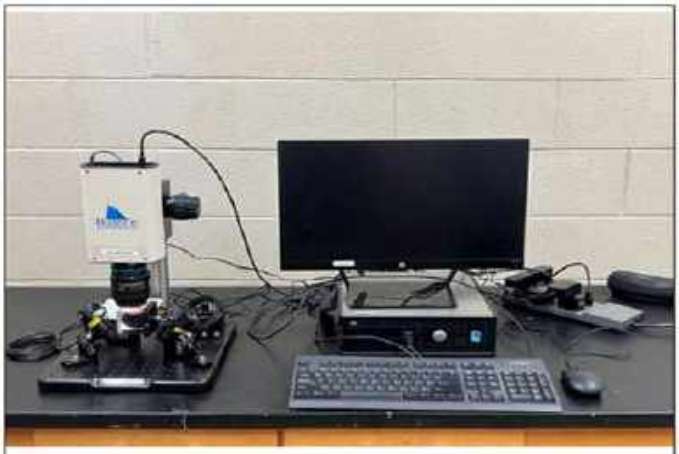

Fig1. Our in-house developed microscope.

METHODS

We use near-infrared (NIR) spectroscopy imaging to acquire the structural and chemical characteristics of wound tissues. We have already developed a microscope using NIR to explore how the measured tissue characteristics corelate with the healing trajectory of old and young mice (Figure 1). We focused on the absorption and reduced scattering coefficients of the skin surface as key parameters indicative of structural and biochemical changes during tissue repair.

RESULTS

Present results chronologically or in order of importance. Describe the major results in the text, referencing the figures and tables parenthetically as appropriate. Our data revealed notable differences in skin surface characteristics. The examined areas showed variation in the absorption coefficient, correlating with increased vascular activity and cellular proliferation. Additionally, the reduced scattering coefficient demonstrated variations, suggesting alterations in the skin's collagen structure.

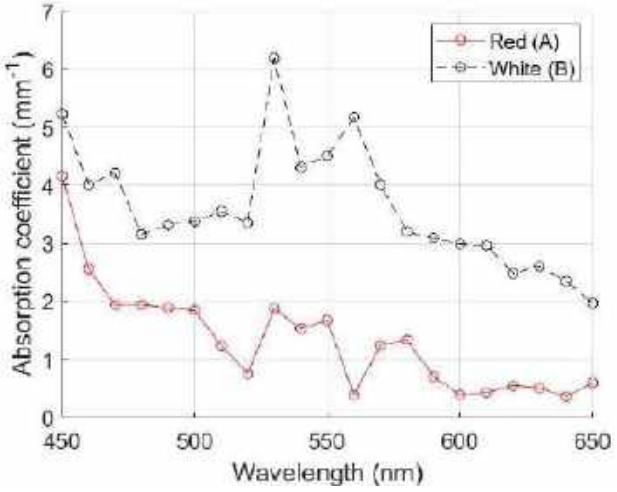

Figure 2: Absorption Coefficients Variability within same Mice Tissue Samples at Various Wavelengths. This graph displays the absorption coefficient (mm^-1) across wavelengths ranging from 450 nm to 650 nm for two distinct areas of the same tissue sample. Area Red (a) and White (B) demonstrate significant variability in absorption, indicating heterogeneity in biological processes such as vascularization. This intra-sample variation underlines the complexity of the wound healing process and may inform the development of localized treatment strategies.

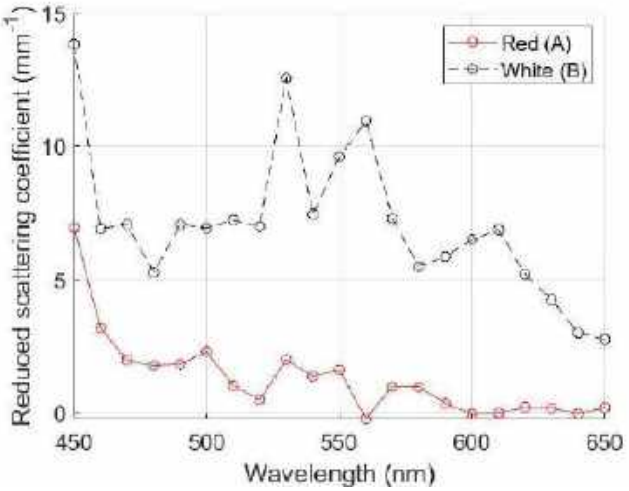

Figure 3: Intra-sample Variance in Reduced Scattering Coefficients of Healing Tissue. The graph depicts the reduced scattering coefficient (mm^-1) across wavelengths from 450 nm to 650 nm for two different areas within the same tissue sample undergoing wound healing. The Red (A) area shows a markedly lower scattering coefficient compared to the White (B) area, suggesting a denser and possibly more organized tissue structure in Red (A). The disparity between the two areas underscores the non-uniform nature of tissue regeneration and could be indicative of different stages or qualities of healing within the tissue sample.

DISCUSSION

The observed variability in the absorption and reduced scattering coefficients within distinct areas of the same tissue sample elucidates the heterogeneous nature of wound healing. The Red (A) area's lower scattering coefficient suggests a more orderly tissue matrix, likely indicative of advanced healing stages characterized by organized collagen deposition. Conversely, the White (B) area exhibits higher scattering, potentially reflecting an earlier healing phase with less organized tissue structure.

The absorption coefficient differences signal varying degrees of chromophore presence, such as hemoglobin, within the tissue, hinting at differential vascularization levels. The Red (A) area's increased absorption could correlate with heightened vascular activity, a vital component of the proliferative phase of healing, supplying the wound with necessary nutrients and oxygen. These distinctions emphasize the complexity of the wound healing continuum, where multiple phases co-exist within a single wound milieu.

These findings underscore the need for a nuanced understanding of wound healing, advocating for a tailored approach to treatment. Current therapeutic strategies may benefit from being adapted to the localized conditions of wound sites, aligning interventions with the specific healing stage evident in each area.

Future investigations should focus on a longitudinal analysis to track these biophysical parameters over time, providing insight into the temporal dynamics of wound healing. Correlating these optical characteristics with histological and molecular markers will also be paramount to confirm the physiological processes driving the observed data. Such multidimensional analysis might reveal critical insights, potentially translating into more effective, personalized wound management strategies.

ACKNOWLEDGEMENTS

Authors acknowledge the UWM Discovery and Innovation Grant (101-199821-4-101X433), UWM-College of Engineering and Applied Science, and the University of Wisconsin-Milwaukee Office of Undergraduate Research (OUR).

REFERENCES

[1] *Kuehlmann B, et al. Mechanotransduction in Wound Healing and Fibrosis. J Cli Med 2020; 9: 1-19.*

[2] *Wilkinson H, et al. Wound healing: cellular mechanisms. Open Bio 2020; 10: 1-14.*

[3] *Silver F, Gravity S. Mechanotransduction and Healing: How Mechanical Forces Promote Tissue Repair. SM J Biomedical Engineering 2017; 3: 1023.*

[4] *Tonnesen M, et al. Angiogenesis in Wound Healing. J Invest Derm Sym Proc 2000; 5: 40-46.*

[5] *Collaboration, N.C.D.R.F., Worldwide trends in diabetes since 1980. Lancet 2016; 387: 1513-30.*

[6] *Klister J, Ebben A, McElvain K, Gopalakrishnan S, Dabagh M. Impact of wound dressing stiffness on force transmission within tissues of chronic wounds. Wound Week 2022, Philadelphia, PA*

LOW BACK PAIN TREATMENT OPTIONS BASED ON STATISTICAL SHAPE MODELS: SPINAL DECOMPRESSION SURGERY VERSUS NON-OPERATIVE

Mary Foltz (1), Alexandra Seidenstein (2), Amit Jain (2), Jill Middendorf (1)

(1) Department of Mechanical Engineering, The Johns Hopkins University, Baltimore, MD, USA
(2) Department of Orthopaedic Surgery, The Johns Hopkins University, Baltimore, MD, USA

INTRODUCTION

Low back pain is a pervasive issue affecting approximately 28.9% of the US adult population [1]. A significant portion of these individuals have compression of the neural structures. The precise compression of these neural structures is not well understood. Treatment options to decrease pain include spinal decompression surgery and non-operative options, with subjective clinical guidelines. Patient-specific indicators may help to inform on optimal treatment. Current evidence points to patient-specific factors such as smaller spinal cord cross-sectional areas and facet joint angles that may occur in patients with spinal stenosis [2,3]. However, these factors as well as other standard clinical measures do not fully explain the differences.

Previously, statistical shape models (SSMs) have been used to identify patient-specific variations within the lumbar spine [4]. These models have identified and shown variations in curvature and vertebral body sizes that are difficult to identify. To our knowledge, the SSMs have not been used to distinguish between patients indicated for spinal decompression surgery and non-operative treatment options.

Additionally, the shape variations identified from SSMs can be incorporated into finite element models of spinal decompression surgeries. Finite element analysis can assess how patient-specific geometries affect the biomechanical factors contributing to adverse post-surgical outcomes. Targeting the patient-specific geometries could help to determine the best treatment option based on key patient-specific variations.

Therefore, this study aims to determine differences between patient-specific geometries associated with individuals recommended for spinal decompression surgery compared to non-operative treatment.

METHODS

In this study, we used a sample of an open-access Lumbar Spine MRI dataset collected from 515 patients with symptomatic back pain [5]. We analyzed two MRI slices (mid-axial and mid-sagittal planes), from 21 randomly selected vertebral regions. Each axial MRI slice was chosen such that the slice passed through the center of the facet joint and the intervertebral disc. Then, an orthopaedic spine surgeon (AJ) used axial and sagittal MRIs to classify a patient as recommended for a spinal decompression surgery or a non-operative approach.

We used a previously published customized SegNet algorithm for lumbar spinal anatomy to automatically segment out the 21 images [5]. Specifically, we extracted the disc and posterior elements in the axial images and used a custom code to extract mathematical (automatically) and anatomical (manually) landmarks (Figure 1). Mathematical and anatomical landmark points were then used to compare the regions.

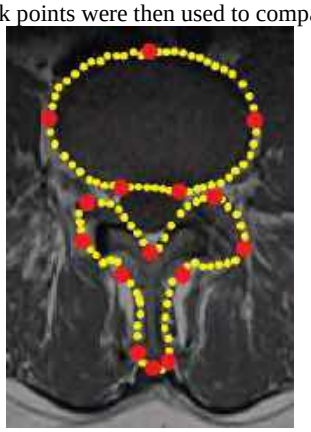

Figure 1: Sample axial MRI with anatomical (red, large circles) and mathematical (yellow, small circles) landmark points.

Two anatomical landmark points (posterior left disc and spinous process tip) were used to align regions. We calculated the average shape and covariance matrix. From the covariance matrix, we calculated the eigenvectors, eigenvalues (λ), and weighted matrix. The principal components (PCs), variance (λ), and weights were extracted and

evaluated for the 95% explained variance to ensure a comprehensive representation. Square-root of the variance represented the standard deviation for each PC. The percent of total image explained by a given principal component was determined by dividing a PC's standard deviation by the sum of all standard deviations. The number of standard deviations away from the average was then calculated by normalizing an image's weight by the standard deviation of the PC. Differences between these normalized weights were separated into surgically indicated and non-operative groups for comparison.

RESULTS

The statistical shape model can be used to understand variations in the shapes. This model discovered a total of 20 PCs shapes. The first 13 PCs represented over 95% of the shape variance, therefore consistent with other SSM approaches only the first 13 PCs were considered in this analysis. Of these 13 PCs, the first 4 PCs account for 55% of the total standard deviation (Figure 2). PCs with lower numbers always account for a higher percentage of the total shape variation.

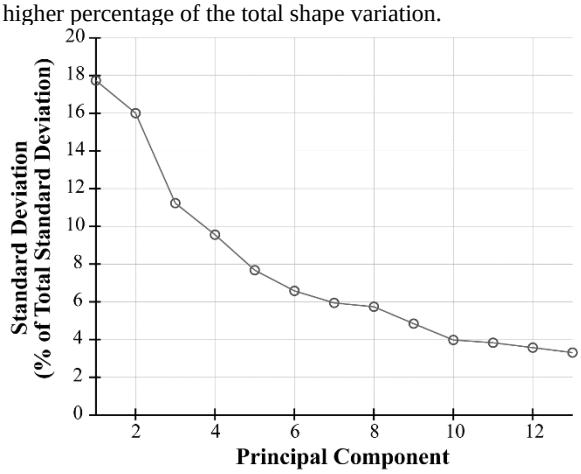

Figure 2: Percent of Total Shape Standard Deviation accounted for by a given Principal Component.

When the weights of each PC are split between surgically indicated and non-operative groups, there was no difference observed for most PCs (Figure 3). However, PC4 shows a trend toward a difference between surgically indicated and non-operative groups. PC5 through PC13 were analyzed but the data was not shown for clarity.

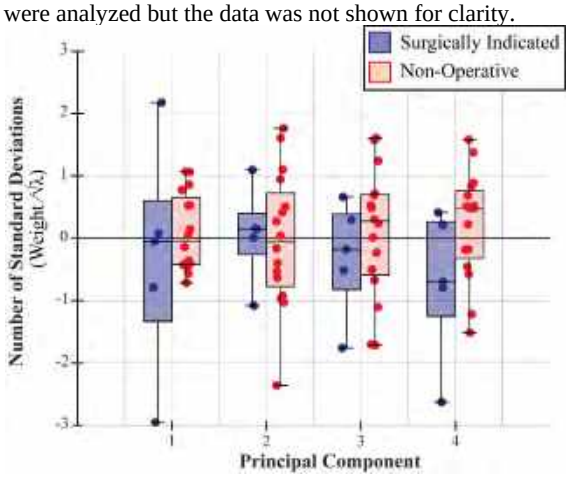

Figure 3: Principal Components for those surgically indicated (blue) and non-operative (red) treatment options.

A visual representation of the standard deviation of a PC can help indicate how the spinal shape varies (Figure 4). An increase in PC1 appears to increase the size of the intervertebral disc region and narrow the posterior elements. PC4 has a subtle change that appears in the gap between the facet joint and the intervertebral disc. This gap decreases slightly in the surgically indicated group.

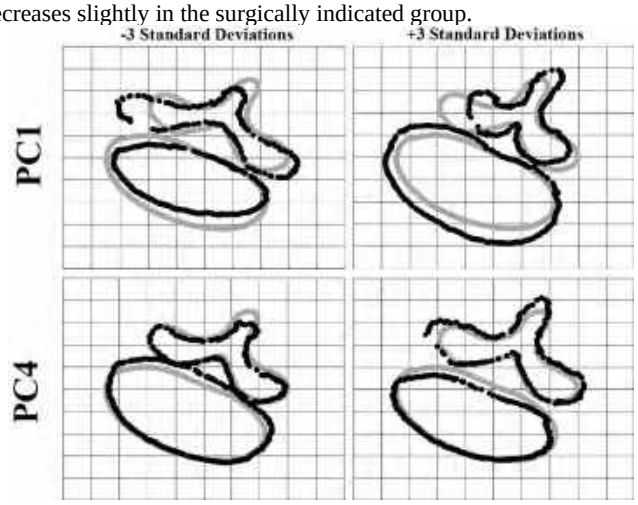

Figure 4: Average Statistical Shape (in gray) with -3 and +3 standard deviations on the left and right, respectively: PC1 (top row, black), PC4 (bottom row, black).

DISCUSSION

In our current analysis, a comprehensive examination of spinal element shapes revealed no discernible differences between those surgically indicated and non-operative groups. This lack of differences most likely means that all spinal variations in patients with low back pain must be considered for biomechanics analysis of spinal decompression surgeries. However, there did appear to be a trend with PC4, which visually indicated a decrease in the gap between the intervertebral discs and facet joint regions. This decrease in gap space is to be expected since foraminal space decreases during stenosis [2].

This study provides an initial dive into studying these axial images, and there are some limitations. First, we took an overarching look at the images, and we need to reveal additional patterns (i.e., spinal level, region specifics, anatomical structures). Second, only 5 surgically indicated cases were included. This underscores the need for continued research and refinement of our analytical approaches to capture the intricacies of patient-specific geometry that may relate to biomechanics and patient-specific treatment options.

Nevertheless, the results shown here provide evidence to support the use of SSM in identifying differences between spinal shapes associated with lumbar spinal decompression surgeries and non-operative treatments. Applying this approach could prove useful for developing a more comprehensive understanding of spinal element shapes and their potential impact on biomechanics.

ACKNOWLEDGEMENTS

This study was supported in part by the National Institute of Arthritis and Musculoskeletal and Skin Diseases (NIAMS) of the National Institutes of Health under award number T32 AR07708-06.

REFERENCES

1. Ma, V et al., *Archives of Physical Medicine and Rehabilitation*, 95(5), 986-95, 2014.
2. Yang, J et al., *Korean J. Spine*, 10(3):149-54, 2013.
3. Zileli, M et al., *World Neurosurgery: X*, 7, 2020.
4. Alimohamadi Gilakjan, S et al., *Int. J. Med. Robot. Comput. Assist. Surg.*, 16(3):1-9, 2020.
5. Sudirman, S et al., *Mendeley Data*, "Lumbar Spine MRI Dataset", V2, DOI: 10.17632/k57fr854j2.2, 2019.

THE EFFECTS OF PREECLAMPTIC MILIEU ON CORD BLOOD DERIVED ENDOTHELIAL COLONY-FORMING CELLS

Eva M. Hall (1), Laura M. Alderfer (1), Sanjoy Saha (1), Ellie Johandes (1), Laura S. Haneline (2,3,4), and Donny Hanjaya-Putra (1,5)

(1) Aerospace and Mechanical Engineering, Bioengineering Graduate Program, University of Notre Dame, Notre Dame, IN, USA
(2) Herman B Wells Center for Pediatric Research, Department of Pediatrics, Indiana University School of Medicine, Riley Hospital for Children at Indiana University Health, Indianapolis, IN, USA
(3) Department of Microbiology and Immunology, Indiana University School of Medicine, Indianapolis, IN, USA
(4) Department of Anatomy, Cell Biology, and Physiology, Indiana University School of Medicine, Indianapolis, IN, USA
(5) Chemical and Biomolecular Engineering, University of Notre Dame, Notre Dame, IN, USA

INTRODUCTION

Preeclampsia (PE), a hypertensive disorder of pregnancy, is one of the leading causes of infant and maternal death worldwide [1]. Currently, most treatments focus on mitigating maternal symptoms, including increased blood pressure and seizures [1]. However, the only definitive treatment is delivery, but even that is not perfect. PE causes increased long term risk of hypertension, stroke, and heart disease for both the mother and the child [2]. Preterm delivery causes increased likelihood of other complications for the infant, including diabetes and neurodevelopmental impairments [3]. Despite the dangers of this disorder, the root cause is not fully understood due to it being a complex multi-system pathology.

One of the hallmarks of PE is angiogenic dysfunction. One cell line affected by PE that may play a role in this dysfunction is Endothelial Colony Forming Cells (ECFCs), a type of endothelial progenitor cell that supports new vessel development and homeostasis. ECFCs have been seen to be influenced by *in utero* diseases and have therapeutic potential with vascular disorders [4, 5]. In this study, ECFCs isolated from umbilical cord blood were used to understand the phenotypic and genetic differences between healthy and preeclamptic ECFCs (PRECs).

METHODS

Human ECFCs and PRECs were isolated from cord blood samples with a variety of gestational ages. These cells were provided through clinical trials by members of the Indiana University School of Medicine, Dr. Laura Haneline and Dr. David Haas. ECFCs and PRECs were stained for endothelial markers including CD31, CD144, and Von Willebrand factor (vWF).

Angiogenic potential was assessed using a Matrigel tube formation assay and quantified using the plugin Kinetic Analysis Vasculogenesis (KAV) [6]. Flow cytometry and FlowJo were used to quantify EdU and DNA content stains for cell cycle analysis. To assess migration, a wound healing assay was imaged every hour for 24 hours with changes in area calculated using a protocol by BioTek Instruments. For senescence, passage 12 cells were fixed and stained based on Abcam's protocol for the Senescence Detection Kit. Cytokine secretion was assessed using R&D Systems Proteome Profiler Human Angiogenesis Array Kit and Proteome Profiler Human Cytokine Array Kit. The samples were quantified using ImageJ.

Four biological replicates selected for preeclamptic and healthy ECFCs (n=3) Real-time qPCR was performed for *LYVE-1, Prox-1,* and *GAPDH* in addition to the TaqMan Array Human Angiogenesis Panel. Statistical analysis was done with GraphPad Prism. Student's t-test or ANOVA was used to compare ECFCs and PRECs.

RESULTS

To better understand how PE affects tube formation, cells were seeded onto Matrigel and allowed to grow for 9 hours. The ECFCs formed clear, organized networks **(Fig. 1A)**, while the PRECs tended to have more cells clumping together and incomplete loops **(Fig 1B)**. When quantified using KAV, network area, an indicator of morphological shifts, was decreased in PRECs compared to their healthy counterparts **(Fig. 1C)**. Together, this indicates that the PRECs exhibit lower angiogenic potential than ECFCs.

Proliferation was assessed through cell cycle analysis. Cells were stained with EdU to identify cells in the S-phase and PI/RNAse for DNA content. The PRECs have less cells in the G0/G1 phase and more cells in the S-phase, indicating that they are more proliferative **(Fig 2A)**. Other *in utero* diseases affect migration indicating PE may also have an effect [4]. Therefore, migration was assessed using a wound healing

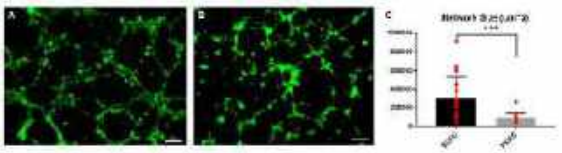

Figure 1: Angiogenic potential of (A) ECFCs and (B) PRECs. KAV was used to quantify the (C) network size ***p < 0.001. Scale bar = 250 µm.

assay. ECFCs closed the wound sooner than the PRECs **(Fig. 2B)**. Finally, passage 12 cells were stained for senescence. While passage 12 is higher than was used for other experiments, it is a lower passage than when a more senescent population is expected. PRECs had a higher percentage of senescent cells compared to the ECFCs **(Fig. 2C)**.

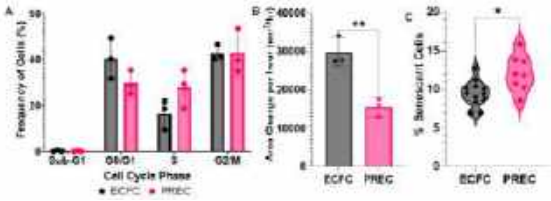

Figure 2: (A) Proliferation was examined using cell cycle analysis. (B) A wound healing assay was used to quantify migration. (C) Senescence was investigated using a β-gal assay. *p<0.05, **p<0.01. Scale bar = 1000 µm

Since PE is a hypoxic disorder, inflammatory cytokines were evaluated. A proteomics assay showed that PRECs see an increase in CXCL1/GROa, IL-8, and MIF and a decrease in Serpin E1 **(Fig. 3A)**. These were not significant due to high variability between biological replicates. PRECs cause a noticeable dysregulation of angiogenesis associated proteins **(Fig. 3B)**. Serpin E1 and IL-8 followed the same pattern as previously seen. Urokinase plasminogen activator (uPA) was downregulated as expected as it is inhibited by Serpin E1. FGF basic and MCP-1 were noticeably upregulated and Pentraxin 3 was downregulated, but there was no statistical significance due to high variability between biological replicates.

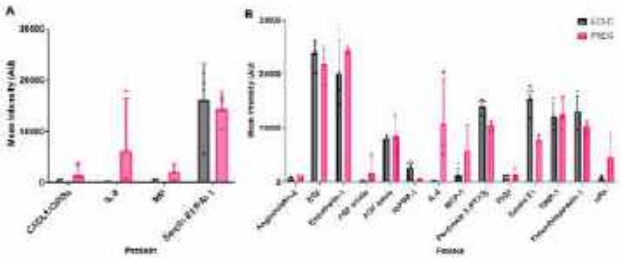

Figure 3: Proteomic analysis of ECFCs and PRECs for (A) inflammatory and (B) angiogenesis associated proteins.

To better understand this functional shift, a 94 gene angiogenesis PCR panel was run with four ECFC and PREC cell lines. Fibulin 5 (*FBLN5*) and proto-oncogene, receptor tyrosine kinase (*KIT*) were significantly upregulated with fold change greater than 2 **(Fig. 4A)**. These genes influence vessel sprouting, proliferation, and migration. In addition, some lymphatic associated genes were upregulated in PRECs compared to ECFCs. Lymphatic vessel endothelial hyaluronan receptor 1 (*LYVE-1*) was increased in PRECs compared to ECFCs and lymphatic endothelial cells (LECs). However, it was not statistically significant due to high variability between biological samples. Prospero homeobox protein 1 (*Prox-1*), the "master regulator" for lymphatic markers, was seen to be significantly upregulated as well **(Fig. 4D)**.

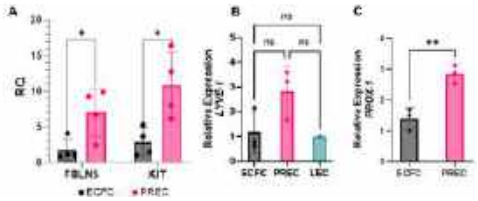

Figure 4: (A) Fold change for *FBLN5* and *KIT*. Four biological replicates were used for ECFCs and PRECs (n=3). PCR was for (C) *LYVE-1* and (D) *Prox-1*. GAPDH was used as an endogenous control. Three biological replicates were used for PRECs, ECFCs, and LECs (n=3). **p<0.01, and *p<0.05

DISCUSSION

As a result of PE, PRECs exhibit increased proliferation and senescence while tube forming ability and migration are decreased. The increased proliferation may be compensatory for the premature senescence. While functional changes are to be expected, ours do not align exactly with other studies as no additional growth factors were added during our experiments. These functional changes indicate what genetic pathways should be explored.

Therefore, angiogenesis associated genes and proteins were investigated. Serpin E1 was decreased and IL-8 and uPA were increased in PRECs compared to ECFCs. Serpin E1 and uPA play a role in extracellular matrix degradation, which could cause changes in soluble factors. *FBLN5* and *KIT* were also found to be upregulated in PE. These genes play a role in proliferation, angiogenic sprouting, and migration [7,8]. Together these findings support the functional changes previously seen. In addition, inflammatory proteins production was primarily increased in PRECs. Higher inflammatory response could lead to excessive activation of the immune system. Lymphatic associated genes *LYVE-1* and *Prox-1* were also increased in PRECs. This may mean that the PRECs are experiencing lymphatic mimicry.

Overall, these experiments indicate specific genes and pathways to explore further. One limitation of this study is that PRECs were from more mild PE cases based on gestational age. More severe cases may see other genes or proteins dysregulated.

Collectively, these results provide insight into PE at the cellular level and provide potential biomarkers. In addition, these genes and proteins could be targeted to restore angiogenic potential in PE and improve the health of infants born from preeclamptic pregnancies.

ACKNOWLEDGEMENTS

We acknowledge support from the University of Notre Dame, Harper Cancer Research, American Heart Association, Indiana Clinical and Translational Science Institute, and National Institutes of Health. We would like to thank the Notre Dame Bioinformatic Core and AngioBioCore at Indiana University for isolating and characterizing cord blood samples. ECFCs were kindly provided by Dr. Laura Haneline and Dr. David Haas at IUSM.

REFERENCES

[1] Rana, S. et al., *Circ Res*. **124**, 1094–1112 (2019)
[2] Uzan, J. et al., *VHRM*, 467 (2011)
[3] Cosmi, E. et al., *Journal of Pregnancy*. **2011**, 1–6 (2011)
[4] Bui, L. et al., *Commun Biol*. **5**, 635 (2022)
[5] Alphonse, R. S. et al., *Circulation*. **129**, 2144–2157 (2014)
[6] Varberg, K. M. et al., *JoVE*, 57044 (2018)
[7] Matsui, J. et al., *JBC*. **279**, 18600–18607 (2004)
[8] Albig, A. R. et al., *DNA and Cell Biology*. **23**, 367–379 (2004)

LOW STRAIN RATE CYCLIC LOADING AND RECOVERY EFFECT ON THE FATIGUE PROPERTIES OF THE ANTERIOR CRUCIATE LIGAMENT

Peter M. Kuetzing (1), Ulrich M. Scheven (1), Ellen M. Arruda (1,2,3)

(1) Mechanical Engineering, University of Michigan, Ann Arbor, MI, USA
(2) Biomedical Engineering, University of Michigan, Ann Arbor, MI, USA
(3) Macromolecular Science and Engineering, University of Michigan, Ann Arbor, MI, USA

INTRODUCTION

Anterior Cruciate Ligament (ACL) injury affects a wide demographic of athletes, spanning from professional to youth sports, plaguing an estimated 34 per 100,000 residents in the United States alone each year and disproportionately affecting females aged 12 to 17 [1]. Progress in understanding ACL failure mechanics is slowed by the hierarchical structure of collagen, complex ligament-bone insertion site, and non-uniform cross-section. Recent advancements in full-field methods and constitutive modeling have provided insight into static loading conditions [2]. However, the mechanism of fatigue and its role in ACL failure has remained illusive.

During gait, the ACL is loaded in tension when counteracting anterior tibial translation (ATT) and internal rotation brought on by contact between the femoral condyles and tibial slope. The estimated physiological strain that resembles walking is approximately 5% at 1 Hz [3]. The ACL may see considerably higher strain rates through actions like jumping. Repeated heal striking on cadaveric knees at forces 4 times body weight have been shown to cause ACL failure in under 70 cycles [4]. However, ACL failure often occurs from a single high strain event. This may be attributed to a reduction in the ACL failure criterion threshold caused by the culmination of many smaller fatigue cycles. Our goal was to probe the effects of low strain rate fatigue, akin to walking, the effect of recovery times between sets of loading cycles, and the loading history on ACL mechanics.

METHODS

Ovine knee morphology is anatomically comparable to that of a human knee and has widely been used to study ACL mechanics [5]. We procured ovine legs (n=24) which encompassed the intact knee joint, tibia, and femur from 12 separate animals. The left and right legs of each animal were purchased from a local butcher at the same time. Dissection of a randomly selected knee, left or right, was completed the same day the animal was slaughtered. During dissection, the ACL was split into the anteromedial (AM) and posterolateral (PL) bundles. The bone beyond the entheses were cut to a create an AM bundle and bone complex. The isolated AM complex was soaked in 7 mL of either Polyethylene Glycol (PEG) 8% w/v (n=8), Ophthalmic Gel (OG) (n=8), or Bovine Synovial Fluid (SF) (n=8) for 12 hours and stored at 4°C during that time. The following morning, the complementary leg was dissected, its AM complex extracted and soaked in the same solution type in an identical manner.

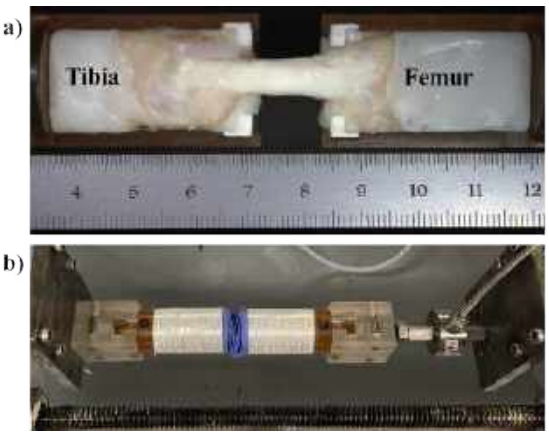

Figure 1: Experimental Setup: a) AM bundle and bone complex in the bottom half of the custom clam shell pots, b) Enclosed sample, hermetically sealed with nitrile sleeve and fiber reinforced tape.

The AM bundle and bone complex was affixed in custom clam shell pots which held the bone fixed and allowed the ligament to expand freely (Figure 1a). The gauge length, defined as the central region of straight fibers before splay into the enthesis occurs, was determined using ImageJ which became the basis for calculating 5% strain. The AM bundle was then covered with a nitrile sleeve and the edges sealed with fiber reinforced tape to create a hermetically sealed environment to reduce drying out (Figure

1b). The nitrile sleeve was left empty (n=12) or filled with 5 mL of the same soak solution type (n=12) for the duration of mechanical testing.

Each AM bundle was fatigued by displacement controlled uniaxial tension for 8 sets of 60 cycles, each at 5% strain and 1 Hz, for a total of 480 cycles in an ADMET Micro Tester. Breaks, referred to as recovery times, of varying duration were taken between fatigue sets while the AM complex remained unloaded. After an initial baseline experiment of 60 cycles, the duration of recovery times of the first of the animal's AM bundles increased from 1, 2, 4, 8, 15, 30, to 60 minutes between sets. Conversely, the duration of recovery times of the second of the animal's AM bundles decreased from 60, 30, 15, 8, 4, 2 to 1 minute between sets. Ultimately, a total of 192 sets of 60 cycles were measured. At the onset of each set, the ligament was loaded to 0.5 N to ensure fiber engagement prior to loading. Load and displacement data was analyzed in MATLAB.

RESULTS

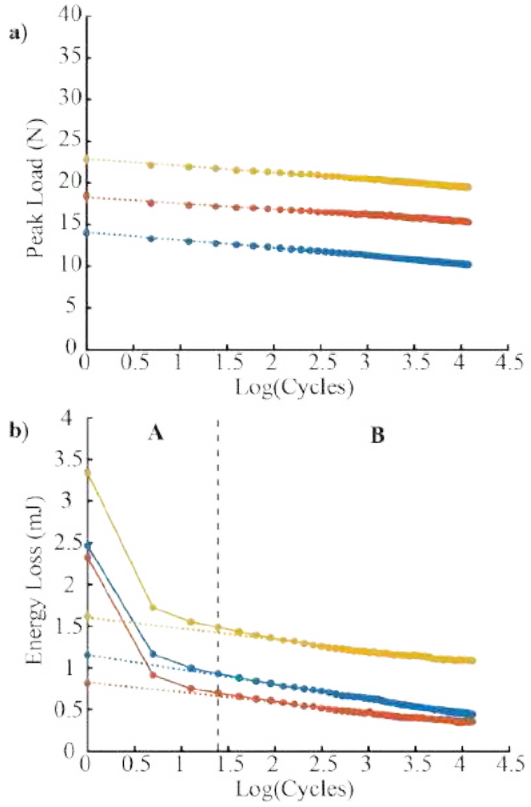

Figure 2: Data from three representative samples. a) Peak Load versus Log(Cycles) with linear fit of cycles 1 through 60, b) Energy Loss versus Log(Cycles) with linear fit of cycles 4 through 60 and two regions, labeled A and B.

The peak loads of each cycle per 60-cycle set were linear when visualized on a semi-log plot (Figure 2a). This was further confirmed by a chi-squared statistic close to one. The energy loss of each cycle per 60-cycle set fell into two distinct linear regions, A and B (Figure 2b). The first region was marked by a significant energy loss drop over the first three cycles. The second region began by the fourth cycle and continued to the end of the test. Moreover, this dual region phenomenon was present in each 60-cycle set irrespective of recovery time duration. As expected, the greatest energy loss occurred in the first cycle and decreased due to the viscoelastic nature of collagen [6]. This energy loss was often two and half times greater than the energy loss of the fourth cycle while the difference between the fourth and 60th cycle's energy loss is considerably less. The energy loss increased as the AM complex was subjected to more cycles, although the difference between the energy loss from the 1st and 4th remained roughly the same. These results were consistent and observed for all samples (n=192).

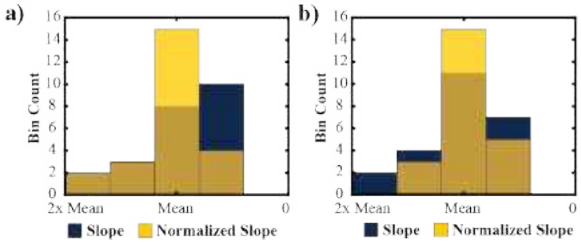

Figure 3: Histograms from baseline fatigue sets (n=24) of the linear fit slopes and normalized slopes for a) Peak Load vs. Log(Cycles), cycles 1 through 60, and b) Energy Loss vs. Log(Cycles), cycles 4 through 60.

The distributions of measured slopes (n=24) for peak force and energy loss are plotted (Figure 3a, 3b). The width of these distributions is affected by intrinsic materials properties and by the geometric variability of our samples. In order to separate the two, the values of the slopes were divided by the back extrapolated y-intercept (symbol ⧫ in figure 2). Figure 3 shows the distribution of slopes before division and after. The distributions of slopes normalized by the intercepts ⧫ are observed to be narrower and more uniformly distributed than those found in the raw data.

DISCUSSION

There are two distinct linear regions of energy loss, A and B (Figure 2b), which persist with all independent variables. The large energy dissipation seen in Region A may indicate the presence of a macroscale injury prevention mechanism through collagen fibril uncrimping during tensile deformation [6].

The ACL has a highly irregular geometry, is anisotropic, and may have nonuniform fiber engagement during loading. Furthermore there is considerable variability in the overall geometry of samples used in this study. Therefore, a dimensionless fatigue parameter was calculated by dividing the slopes of linear fits in figure 2 by the y-intercept of those fits. This enabled a quantitative comparison of fatigue parameters of samples having variable geometries. Previous data published from this lab indicated that the MCL, whose splay is less severe than the ACL, has greater energy loss in the entheses as opposed to the mid-section [7]. Future work will leverage the optical images of each specimen (n=24) to further explore the effects of geometrical factors on normalization.

ACKNOWLEDGEMENTS

This study was funded through internal grants from the University of Michigan and the National Science Foundation Graduate Research Fellowship Program.

REFERENCES

[1] Huston LJ Greenfield ML WE. *Clin Orthop Relat Res* 372 (2000). DOI: 10.1097/00003086-200003000-00007.

[2] Luetkemeyer CM et al. *Journal of the Mechanics and Physics of Solids* 156 (2021). DOI: 10.1016/j.jmps.2021.104577.

[3] Nagai K et al. *Journal of Orthopaedic Research* 37.9 (2019). DOI: 10.1002/jor.24330.

[4] Wojtys EM et al. *Journal of Orthopaedic Research* 34.12 (2016). DOI: 10.1002/jor.23441.

[5] Proffen BL et al. *The Knee* 19.4 (2012). DOI: 10.1016/j.knee.2011.07.005.

[6] Fratzl P et al. *Progress in Materials Science* 52.8 (2007). DOI: 10.1016/j.pmatsci.2007.06.001.

[7] Ma J et al. *IUTAM Symposium on Cellular, Molecular and Tissue Mechanics* 16 (2010). DOI: 10.1007/978-90-481-3348-2_1.

PATIENT-SPECIFIC MODELING OF LEFT ATRIAL ELECTROMECHANICS

Lei Shi (1), Aaron L. Brown (2), Fanwei Kong (2), Chen Zhang (3), Hannah Haider (3), Vijay Vedula (3)

(1) Department of Mechanical Engineering, Kennesaw State University, Marietta, GA, USA
(2) Department of Mechanical Engineering, Stanford University, Stanford, CA, USA
(3) Department of Mechanical Engineering, Columbia University, New York, NY, USA

INTRODUCTION

Atrial fibrillation (AFib) is an irregular rhythm disorder in the upper chambers of the heart, affecting millions of people worldwide, and has a high risk of stroke [1]. While personalized modeling of the electrical activity in the left atrium (LA) has been instrumental in targeted ablation [1], a personalized electromechanical model of LA plays a vital role in understanding the mechanisms for clot development, assessing the risk of stroke, and planning treatment. However, unlike the left ventricular myocardium, the LA myocardial electromechanics remains relatively less studied. This is partly attributed to the scarcity of data on atrial thickness, myofiber orientation, and robust cellular activation models. Here, we introduce a workflow to model the electromechanical interactions in an LA model derived from time-dependent image data. Our robust workflow incorporates machine learning-based segmentation and model creation, an efficient optimization framework to extract passive mechanical parameters, and a recently developed implicit modular approach to couple the 3D LA myocardium model with a zero-dimensional (0D) lumped parameter network (LPN) model of the circulatory system. This workflow will be a stepping stone toward developing a multiphysics model of LA, coupling electromechanics and blood flow, to study AFib and stroke.

METHODS

Our workflow begins with constructing an LA myocardium from a patient's time-resolved 3D CT data (**Fig. 1**). Clinical data acquired include cuff blood pressures and electrocardiogram (ECG) waveforms (**Table 1**). Subsequently, we employ a deep neural network-based whole-heart mesh reconstruction framework [2] to segment the LA blood pool, and extract lumen volumes and nodal displacements at select landmarks during the cardiac cycle. We then choose the segmented LA during its relaxed state (early systole, ~20%R-R) and prescribe a uniform thickness (~2mm) to construct the LA myocardium [3]. Further, we follow a Laplace-Dirichlet rule-based approach to prescribe myocardial fiber directions [4].

Table 1: Clinical characteristics of a healthy subject

Item	Blood pressure	Heart rate	PR interval	QRS duration	QT (ms)
Value	98/53 mmHg	87 BPM	182 ms	88 ms	384 ms

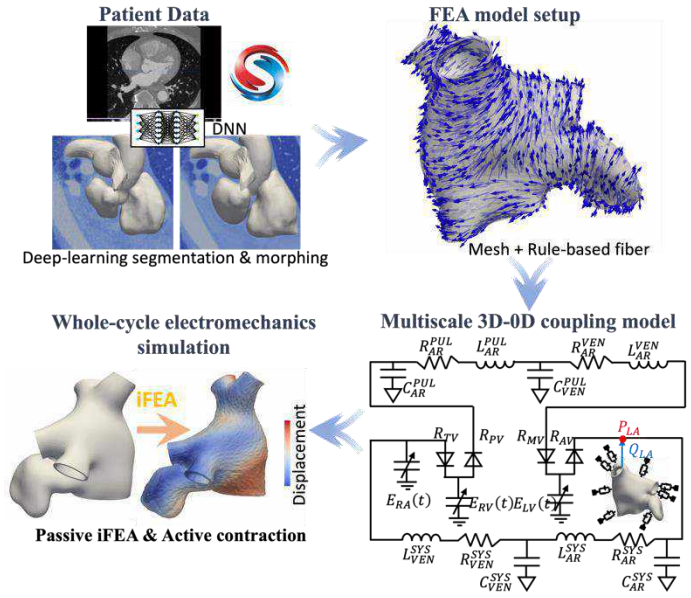

Figure 1: Workflow for LA electromechanics modeling. FEA model is segmented from the patient CT data using neural newtorks. A multiscale coupled 0D/3D model is personalized to simulate LA electromechanics.

Subsequently, we employ a differential evolution algorithm to estimate the parameters of the closed-loop LPN model [5] to match the clinical targets, including the min/max aortic pressures and the four-chamber volumes. The LPN incorporates a surrogate model of the LA with time-varying elastances to model the pressure-volume (PV) relations of all the four chambers (left/right ventricle/atrium), assemblies of capacitor-resistor-inductor to model the circulatory system, and diodes to model the cardiac valves.

We conduct inverse finite element analysis (iFEA) with a novel multilevel optimization scheme to extract passive material properties of the LA myocardium. Our iFEA scheme [6] includes an outer loop iterating on constitutive model parameters to match image-based LA volumes and local nodal displacements during passive expansion. The inner loop estimates a reference stress-free configuration using Sellier's algorithm, considering a set of material parameters and pressure load set by the outer loop. The pressure profile during LA passive expansion is obtained from the tuned LPN model. This process enables extraction of patient-specific LA material properties fitting time-dependent, image-based LA topology under personalized pressure loads.

In each forward FEA simulation during iFEA iterations, we apply physiologically relevant boundary conditions, including Robin boundary conditions, to model tissue support on pulmonary veins, the mitral valve plane, and the epicardial surface, and LPN-based hemodynamic pressures. We employ the Holzapfel-Ogden (HO) material model with a viscous component as the constitutive model for the passive myocardium, and a stabilized FEA solver to simulate the passive nonlinear elastodynamics equations [7].

We now focus on tuning the active component of the myocardium. We replace the tuned surrogate model of the LA with the 3D model, coupled to the rest of the 0D LPN model. The coupling between the 3D and 0D models is achieved using our recently developed, modular, implicit method [8]. Briefly, at each time step, the pressure and flow rates are iteratively exchanged between the 3D and 0D solvers until convergence, taking into account the resistance induced by the 0D fluid on the 3D solid model. This additional resistance is critical to ensure smooth convergence and resolve isovolumic phases (for ventricles). We assume an active stress model to couple the atrial myocyte excitation with the tissue deformation. We then adjust the active stress parameter to fit the volume change during atrial contraction. We employ the Nygren model [9] to simulate the local myocyte dynamics, coupled to an anisotropic diffusion-based monodomain model to simulate the propagation of the transmembrane potential across the myocardium. An efficiently implemented implicit-explicit (imex) scheme with operator-splitting is employed for time integration, while FEA is used to resolve spatial diffusion. Numerics for mechanics and electrophysiology are implemented in our multi-physics FEA solver, svFSI [10].

RESULTS

Table 2 shows the best-fit passive material parameters of the LA myocardium.

Table 2: Best-fit passive material parameters of the LA.

Parameter	a **(Pa)**	b	a_f **(Pa)**	b_f
Value	25.3	8.24	41400	17.9
Parameter	a_s **(Pa)**	b_s	a_{fs} **(Pa)**	b_{fs}
Value	287	15.9	216	11.4

Fig. 2 shows the results of iFEA (**Fig. 2A**) and the simulated 3D-0D coupled LA model across six cardiac cycles (**Fig. 2B-C**). Notably, both the LA and LA appendage (LAA) experience substantial contraction and expansion during the heart cycle (**Fig. 2B**), along with physiological pressure-volume (PV) loops and the activation map (**Fig. 2C**). Our model captures the classic "8"-shaped atrial PV loop, comprising the active "booster" pump, reservoir, and conduit functions.

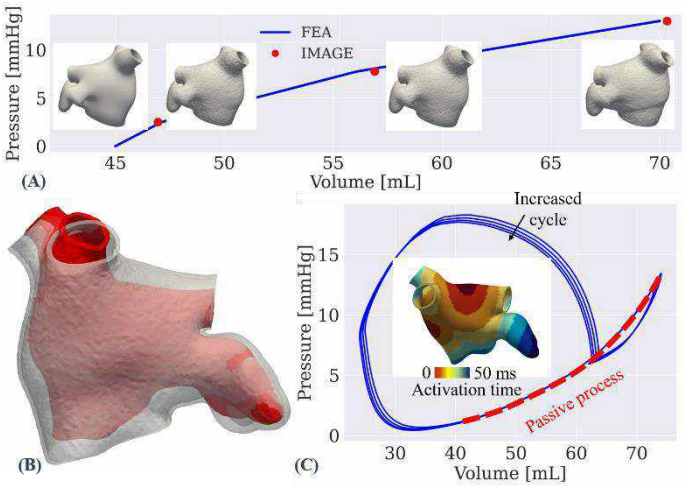

Figure 2: Results of (A) iFEA optimized PV-relation during passive atrial filling and comparison against image-based measurements and (B-C) the 3D-0D coupled simulation for six cardiac cycles. (B) LA model at the most contracted (red) and fully expanded (gray and transparent) states. (C) PV loops for the LA.

DISCUSSION

This work demonstrates a proof-of-concept development of a personalized modeling framework that tightly integrates phase-resolved image data and other clinical measurements with a comprehensive electromechanical model of LA , coupled to a closed-loop LPN model of the cardiovascular system. Our robust framework employs machine learning to automate segmentation, versatile optimization methods for characterizing passive mechanical properties, and efficient and modular coupling between the 3D and 0D models. The method was demonstrated to resolve the physiological mechanical response of the left atrium.

To assess the senstitivity of certain assumptions in our model, we will compare the effects of different fiber generation methods, the assumption of uniform thickness, and extend the analysis to multiple patients. We will explore using machine learning methods such as the graph neural network to design emulators that can substantially accelerate iFEA for characterizing LA passive mechanics.

By laying this groundwork, the research paves the way for developing comprehensive multiphysics computational models integrating myocyte dynamics with tissue deformation, blood flow, and potentially, the blood coagulation cascade. This enables us to quantify the role of electromechanical disruptions during AFib on the changes in blood flow, leading to clot development. Ultimately, this may lead to better assessment of the risk of stroke in AFib patients, and develop individual treatment strategies.

ACKNOWLEDGEMENTS

We acknowledge computing resources from CU Ginsburg HPC.

REFERENCES

[1] Vilalba G et al., *Front Phys J* 12, 596596. (2021)
[2] Kong F., et al., *Med Im Ana* 74, 102222 (2021)
[3] Ho, S.Y. et al., *Circulation* 1 220-228 (2012)
[4] Piersanti R. et al., CMAME 373 113468 (2021).
[5] Regazzoni F., et al., *J Comp Phys* 457, 111083 (2022)
[6] Shi L., et al., (2024), manuscript in preparation
[7] Liu J., et al., *CMAME*, (2018)
[8] Brown A., et al., *CMAME*, (2024)
[9] Nygren A., et al., *Circulation research* 82, 63-81 (1998)
[10] Zhu C. et al *JOSS* 7 (78), 4118

CO-MAPPING OF SMOOTH MUSCLE CELL ACTIN AND HEMODYNAMICS IN INTACT HUMAN INTRACRANIAL ANEURYSM

Yasutaka Tobe[1], Anne M. Robertson[1], Mehdi Ramezanpour [1], Juan R. Cebral[2], Simon C. Watkins [3], Fady T. Charbel [4], Sepideh Amin-Hanjani[5], Alexander K. Yu[6], Boyle C. Cheng[7], Henry H. Woo[8]

[1]Department of Mechanical Engineering and Materials Science, University of Pittsburgh, Pittsburgh, PA, 15261, USA
[2]Department of Bioengineering, George Mason University, Fairfax, VA, 22030, USA
[3]Department of Cell Biology, University of Pittsburgh, PA, 15261, USA
[4]Department of Neurosurgery, University of Illinois at Chicago, Chicago, IL, 60612, USA
[5]Department of Neurological Surgery, University Hospital Cleveland Medical Center, Cleveland, OH, 44106, USA
[6]Department of Neurological Surgery, Allegheny Health Network, Pittsburgh, PA, 15212, USA
[7]Director of Translational Research, Neuroscience and Orthopedic Institutes, Allegheny Health Network, Pittsburgh, PA, 15212, USA
[8]Department of Neurosurgery, Donald and Barbara Zucker School of Medicine at Hofstra Northwell, Manhasset, NY, 11549, USA

INTRODUCTION

Intracranial aneurysms (IAs) are known to have a strong correlation with hemodynamic stress[1, 2]. Previous studies have considered the associations between fluid dynamic parameters and rupture status. However, failure is a local phenomenon and it is known that even ruptured aneurysms can have regions of "healthy wall"[3, **?**]. There is a need for studies that consider local flow and local wall conditions. In this regard, local collagen architecture and local flow have been previously co-mapped [4, 5]. Recently, we have introduced a new imaging pipeline that makes it possible to compare local wall pathology and hemodynamics of IA[6]. The current study utilizes this platform to compare SMC actin and hemodynamics, providing novel insights into the relationship between local IA pathology and blood flow.

METHODS

Two IA dome specimens (one unruptured and one ruptured) were harvested during surgery at Allegheny General Hospital (Pittsburgh, PA) and fixed in 4% paraformaldehyde. The patients were a 61-year-old female and a 60-year-old male with IAs of 7 mm and 8.9 mm, respectively. The specimens were stained with monoclonal mouse anti-human smooth muscle actin clone 1A4 IgG2a antibody (Dako, Denmark) and Alexa Fluor 488 goat anti-mouse IgG2a (Invitrogen, USA), both diluted to a 1:100 ratio with 1% normal goat serum. The stained samples were scanned with a multiphoton microscope (Nikon A1R MP HD, Tokyo, Japan) and reconstructed with IMARIS 10.1.0 (BitPlane AG Zurich, Switzerland). The scanned SMA images were analyzed and categorized into three types: high density (Type 1), low density (Type 2), and no signal (Type 3) using cluster analysis presented previously [6]. Hemodynamic analysis was performed using the techniques described in [7]. The simulation was performed for 2 cardiac cycles with a timestep of 0.01 seconds. The volumetric meshes were composed of tetrahedral elements with a minimum resolution of 200 um. Critical points within the wall shear stress (WSS) vector field were detected, counted, and averaged over the cardiac cycle. The vortex core line was derived using the previously described technique [8].

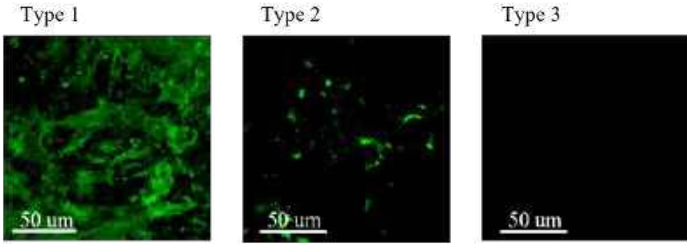

Figure 1: Categories of wall region based on smooth muscle cell actin density

RESULTS

Figure 2 presents the results of the SMA signals from MPM, cluster analysis, and hemodynamic analysis for Case 1 and Case 2. The MPM results reveal that the αSMA signals appear as two large islands in Case 1 and as small scattered islands in Case 2. The distribution of SMA Types 1, 2, and 3 are 59%, 15%, and 26% in Case 1, and 17%, 53%, and 30% in Case 2, respectively. In Case 1, the sample is segmented into four regions: Region A, the top left quadrant with Type 1 SMC; Region B, the right half of the sample with Type 1 SMC; Region C, the left bottom quadrant with Type 3 SMC; and Region D, the area between Regions A and B with Type 3 SMC (as shown in Fig.1(b-i)). In Case 2, the sample is divided into three regions: Region A, the left bottom area with Type 2 SMC; Region B, the top right area with Type 2 SMC; and Region C, the middle strip with Type 3 SMC (as shown in Fig. 1(b-ii)). In terms of hemodynamics in Case 1, region A was exposed to very high WSS (>100 dynes/cm^2) with zero OSI. Region B experienced high WSS (>35 dynes/cm^2) with high OSI.

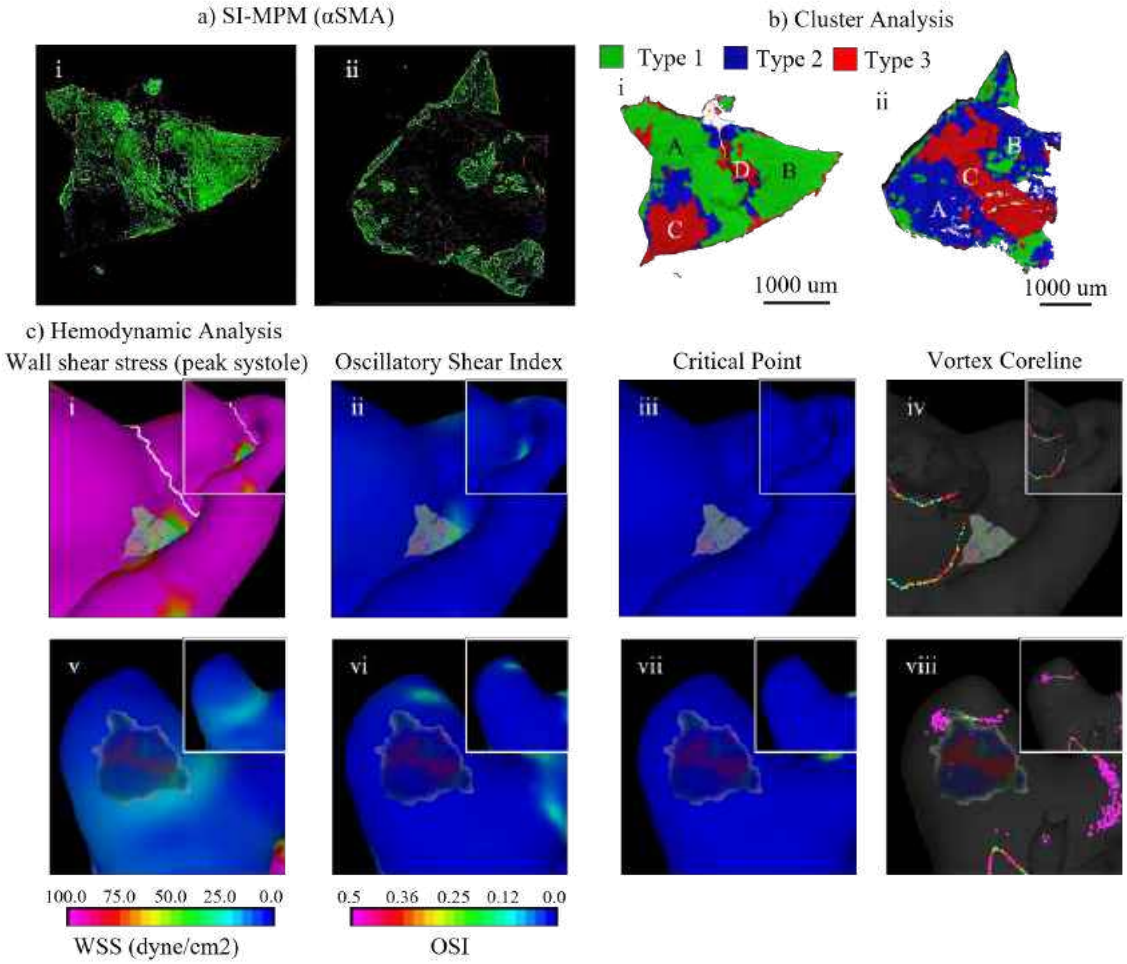

Figure 2: Comparison of smooth muscle cell actin types and hemodynamic parameters

Region C was exposed to very high WSS with zero OSI, similar to Region A. Region D was exposed to a high spatial WSS gradient. In Case 2, region A experienced normal WSS (15-20 dynes/cm^2). Region B was exposed to low WSS (<15 dynes/cm^2), and region C had normal WSS (around 15 dynes/cm^2). All three regions had zero OSI. No critical point or vortex core line was present in either Case 1 or Case 2.

DISCUSSION

Previous hemodynamic studies have proposed that both high and low WSS, along with OSI can instigate maladaptive remodeling of IA wall [9, 1]. Here we explore one crucial feature needed for remodeling, namely, viable SMCs. In Case 1, despite regions A and C having similar hemodynamic characteristics, we observed SMC of two extreme types: high density and no signal. Interestingly, region B, which was exposed to high WSS and OSI, only displayed high-density SMC. These observations imply that the majority of the IA wall in Case 1 was robust to extreme flow conditions, aligning with the fact that this case remains unruptured. In Case 2, despite flow conditions being close to those observed in non-pathological cerebral arteries, the SMC types were relatively sparse across the sample. Collectively, these two cases demonstrate some IA walls can have dense SMCs despite flow conditions that have been associated with increased rupture risk (high WSS and high OSI). A possible explanation for increased risk is that other components of the wall, such as collagen fibers, are degraded. We also demonstrated SMCs can be greatly diminished even under flow conditions that are considered "healthy". This suggests other flow parameters or mechanical factors, such as intramural stress, may be important. To draw definitive conclusions about the relationship between flow and SMCs, further studies with larger sample sizes are necessary. It is also important to consider other cell types, such as endothelial and inflammatory cells, to fully understand wall remodeling.

ACKNOWLEDGMENTS

We acknowledge support for this work through grants 2R01NS097457 and 1S10OD025041.

REFERENCES

[1] H Meng et al. *Am J Neuroradiol*, 35(7):1254, 2014.

[2] J Frösen et al. *Acta Neuropathol*, 123(17):773, 2012.

[3] J Frösen et al. *Stroke*, 35(10):2287, 2004.

[4] JR Cebral et al. *Am J Neuroradiol*, 36(9):1695, 2015.

[5] JR Cebral et al. *Ann Biomed Eng*, 44(12):3553, 2016.

[6] Y Tobe et al. *Microsc. Microanal.*, 2023 in revision.

[7] JR Cebral et al. *Am J Neuroradiol*, 26(10):2550, 2005.

[8] G Byrne et al. *Am J Neuroradiol*, 35(2):333, 2014.

[9] J Frösen et al. *Neurosurg. Focus*, 47(1):E21, 2019.

ANISOTROPIC MECHANICAL PROPERTIES IN SCALED LATTICE COMPOSITES ESTIMATED BY MAGNETIC RESONANCE ELASTOGRAPHY

Kevin N. Eckstein (1), Daniel J. Yoon (1), Margrethe Ruding (1), Ramin Balouchzadeh (1), Aaliyah Thompson-Mazzeo (1), Ruth J. Okamoto (1), Curtis L. Johnson (2), Matthew D. J. McGarry (3), Philip V. Bayly (1,4)

(1) Mechanical Engineering and Materials Science, Washington University, St. Louis, MO, USA
(2) Biomedical Engineering, University of Delaware, Newark, DE, USA
(3) Thayer School of Engineering, Dartmouth College, Hanover, NH, USA
(4) Biomedical Engineering, Washington University, St. Louis, MO, USA

INTRODUCTION

Accurate anisotropic material properties of the brain are needed to improve computational models of traumatic brain injury [1]. Brain tissue is difficult to mechanically characterize, however, because it is encased within the skull and stiffens after death [2]. Magnetic resonance elastography (MRE) can noninvasively map brain material properties in humans. Furthermore, anisotropic properties can be extracted from MRE data through a new inverse-finite element (FE) method called transversely isotropic nonlinear inversion (TI-NLI) [3]. Anisotropic properties characterized by TI-NLI include shear and elastic moduli in the fiber direction (μ_1, E_1, respectively), shear and elastic moduli transverse to the fiber direction (μ_2, E_2, respectively), and degrees of shear and tensile anisotropy ($\phi = \mu_1/\mu_2 - 1$ and $\zeta = E_1/E_2 - 1$, respectively). TI-NLI has accurately mapped simulated MRE data while demonstrating reproducibility on human data [3]. However, further evaluation of the accuracy of TI-NLI is needed using phantoms with known anisotropic mechanical properties.

The purpose of this study was to design a phantom with known anisotropic properties and then test if TI-NLI can detect these properties. We designed scaled 3D printed lattices (Fig. 1a) such that, when embedded in a soft gel (Fig. 1c), the resulting composite mimics anisotropy in brain white matter ($\phi \cong$ 0–0.6, $\zeta \cong$ 0.1–1.6) [3,4]. We mechanically tested lattices and modeled composite behavior to predict phantom mechanical properties, and finally performed MRE on a phantom (Fig. 1c) and mapped anisotropic properties with TI-NLI.

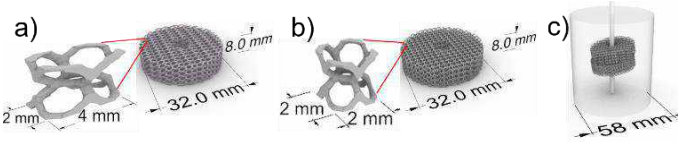

Fig. 1 a) Scaled unit cell and macrostructure; b) unscaled unit cell and macrostructure; c) illustration of phantom with actuator rod in middle.

METHODS

Design and fabrication of lattices and phantom: Previous work demonstrated that vintile unit-cell based structures with directional scaling achieve anisotropy [4]. Both scaled (anisotropic) and unscaled (isotropic) designs were tested and included in the MRE phantom. Macrostructures with 300μm strut diameters were generated in Rhino3D (TLM, Inc.) and printed with a LumenX+ DLP printer (CELLINK) using PEGDA Start PhotoInk™. Macrostructure discs of 15mm diameter × 4mm height and 10×10×10mm cubes were tested in shear and compression, respectively. The MRE phantom contained two 32mm diameter discs: one with a scaled lattice (Fig 1.a) and one with an unscaled lattice (Fig 1.b). To make the phantom, a plastic container was filled with 11 wt% gelatin (Knox) at 30°C, into which two lattices were submerged at a slight angle with a 3.2mm diameter Delrin actuator rod positioned in the middle (Fig 1.c).

Mechanical testing: Shear moduli of 3D printed lattices were determined in directions parallel (μ_1) and transverse (μ_2) to scaling direction through shear testing on a custom apparatus [4]. Elastic moduli in the principal directions E_1 and E_2 were determined from unconfined compression at 10% strain (HR 20, TA Instruments). *FE modeling:* FE models (Abaqus) simulated shear and unconfined compression in 14 separate cases to predict shear and elastic moduli for lattices and lattice-gel composites, using experimentally determined linear elastic E = 3 MPa for the 3D printed material, a range of stiffnesses for the gelatin matrix (E_{gel} = 11–24 kPa) and assuming ν = 0.499 for all materials. Prescribed displacement boundary condition (BC) of 1% compressive or shear strain was performed in a single linear step, assuming infinitesimal strain. Meshes used hybrid quadratic tetrahedral (C3D10H) elements; mesh refinements determined an appropriate mesh density. One symmetry BC was used in shear models while three symmetry BCs were used in compression models.

MRE experiments: MRE was performed at 400 Hz and 600 Hz on a 9.4T Bruker MRI scanner using a modified EPI sequence [5] with the

following parameters: 60x60x36 mm field-of-view; 1mm^3 isotropic voxels; motion-encoding gradients (MEG) 5 cycles at 66 mT/m for 400 Hz and 8 cycles at 132 mT/m for 600 Hz; 8 time points/period; TE/TR = 40/3600ms. Harmonic waves were induced by a central rod driven by piezo actuator (APA150NM, Cedrat) with sinusoidal voltage (LA75C amplifier, Cedrat; 40V amplitude). T1 and T2 images were collected. Sample temperatures ranged from 20–24°C before and after testing.

MRE analysis: Masks were applied to isolate the phantom volume. Phase wrapping was removed from displacement data (FSL PRELUDE, FMRIB). T1 images visualized lattices and ITK-SNAP software was used to identify the principal fiber direction of the scaled lattice for input to TI-NLI. TI-NLI mapped anisotropic properties μ_2, ϕ, and ζ on the 600 Hz dataset (μ_1, E_1, and E_2 are computed from these). Distributions of properties were taken from a circular region of interest (ROI) containing lattice (or pure gelatin) within 2D slices.

RESULTS

Mechanical testing and FE modeling found that $\mu_1 > \mu_2$ and $E_1 > E_2$ for scaled lattices (Fig. 2). Simulation of composite behavior of scaled lattices predicted that as gelatin matrix stiffness increases, ϕ and ζ decreases (Fig. 3).

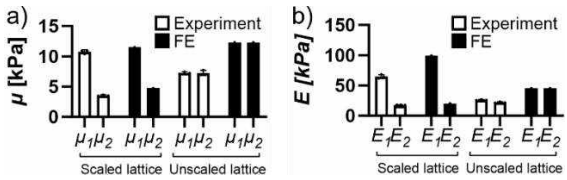

Fig. 2 Experimental results and FE predictions for a) shear modulus μ and b) compressive elastic modulus E in directions 1 (axial) and 2 (transverse) for scaled and unscaled lattices.

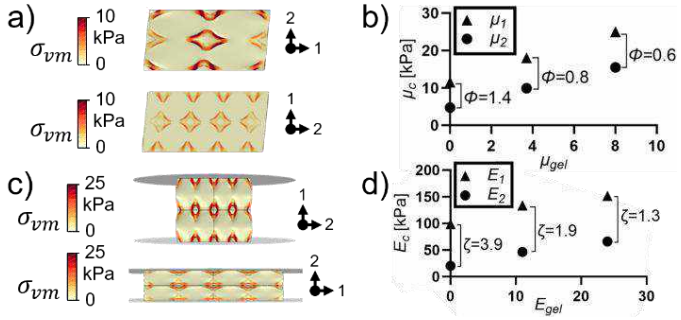

Fig. 3 FE predictions of composite behavior; a) von Mises stress (σ_{vm}) fields during shear in 1-direction (top) and 2-direction (bottom). b) Composite shear moduli μ_c for 1- and 2-directions, and resultant ϕ, for a range of gelatin stiffness μ_{gel}. c) σ_{vm} fields during compression in 1-direction (top) and 2-direction (bottom). d) Composite elastic moduli E_c for 1- and 2-directions, and resultant ζ, for a range of gelatin stiffness E_{gel}. 10× deformation scale factor shown in models.

In the MRE phantom, lattice geometries were visible in T1 images (Fig. 4.a). MRE images of displacement fields visualized elliptical waves in the scaled lattice region (Fig. 4.b). TI-NLI mapped properties in both lattice regions, which were 60–80% stiffer than the gelatin region (Fig. 4.c,f), and both lattice regions exhibited positive ϕ and ζ values, with the scaled region having the highest median ϕ and ζ of 0.7 and 0.6, respectively. Between FE composite predictions (Fig. 3) and TI-NLI results (Fig. 4) for the scaled lattice region, when assuming μ_{gel} = 8 kPa, the median properties fitted by TI-NLI had 3% difference for μ_2 (15.5 kPa (FE) vs. 16 kPa (TI-NLI)), 14% difference for ϕ (0.7 (FE) vs 0.6 (TI-NLI)), and ζ had 50% difference (1.3 (FE) vs 0.6 (TI-NLI)).

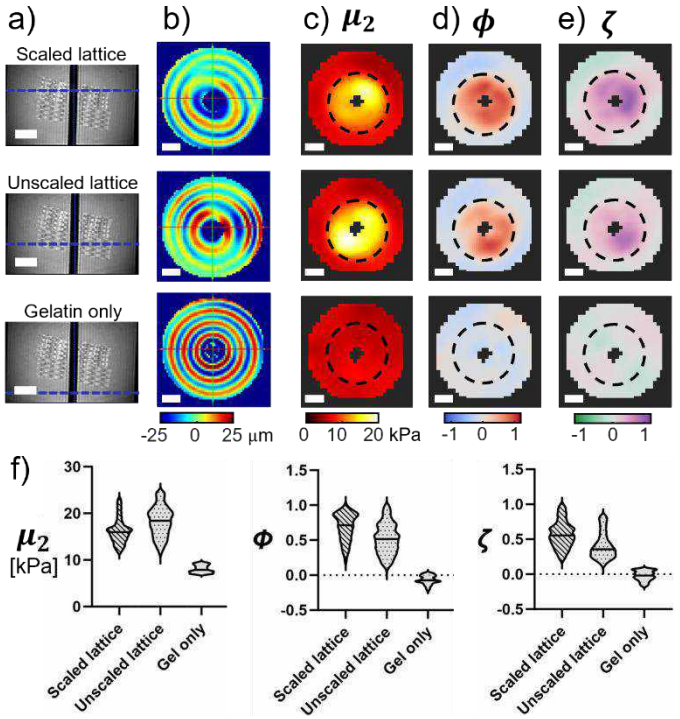

Fig 4 (a-e) MRE imaging results for scaled lattice region (top row), unscaled lattice region (middle row), and gelatin only (bottom row). a) T1 side view images; blue line indicates slice for corresponding row of images. b) Displacement field at one time point; c) transverse shear modulus μ_2; d) shear anisotropy, ϕ; e) tensile anisotropy, ζ. Scale bars = 1 cm. f) distribution of anisotropic properties within each ROI.

DISCUSSION

Our transversely anisotropic lattices demonstrated anisotropy through mechanical testing, while the TI-NLI algorithm successfully detected anisotropic material properties from MRE data. To evaluate TI-NLI, we sought to understand the behavior of our lattice composites through testing and FE modeling. Agreement between scaled lattice mechanical test data and FE models provided a foundation from which FE models could then predict composite behavior. Composite FE model predictions were useful for evaluating TI-NLI and suggested that TI-NLI was accurate for μ_2 and ϕ estimates but less sensitive to ζ. The unscaled lattice region was determined by TI-NLI to have non-zero ϕ and ζ; this may be the blurring of results from the adjacent scaled region, as the effective resolution of TI-NLI is limited by wavelength (~7 mm).

Successful detection of anisotropic properties improves our confidence in TI-NLI, which may enable more accurate models of traumatic brain injury. Controlling anisotropic properties in gel composites may also be useful to evaluate new anisotropic ultrasound elastography techniques [6] and in tissue engineering applications like spinal cord regeneration where anisotropic scaffolds are desired [7].

ACKNOWLEDGEMENTS

NIH R01 EB025875, T32 EB028092, ONR N00014-22-1-2198

REFERENCES

[1] Hajiaghamemar, M et al., *J. Neurotrauma*, **38**:144-157, 2021.
[2] Wang, S et al. *NeuroImage* **277:**120234, 2023.
[3] McGarry, M et al. *Med. Image Anal.* **78**:102432, 2022.
[4] Yoon, D, & Ruding, M et al., *JMBBM.* **138**:105652, 2023.
[5] Milbocker, KA et al., *Alcohol Clin. Exp. Res.* **00:**1–12, 2024.
[6] Knight, AE et al. *IEEE Trans. Med. Imaging* **41**:133–144, 2022.
[7] Xue, W *et al.*, *Bioact. Mater.* **6:**4141–4160, 2021.

CONNEXIN-43 POSITIVE CELL RATIO IS NOT MODULATED BY SEVERITY OF DAMAGE OR CHANGE IN CYCLE NUMBER IN TENDON FATIGUE INJURY MODEL

Benjamin B. Johnston (1), Nelly Andarawis-Puri (2,3)

(1) Meinig School of Biomedical Engineering, Cornell University, Ithaca, New York, United States
(2) Sibley School of Mechanical and Aerospace Engineering, Cornell University, Ithaca, New York, United States
(3) Biomechanics, Hospital for Special Surgery, New York City, New York, United States

INTRODUCTION

Tendinopathy is a common chronic musculoskeletal disorder, frequently resulting from accumulation of sub-rupture fatigue damage. These injuries disrupt the structure of the tendon, and do not innately repair, worsening mechanical properties and ultimately increasing risk of rupture. Development of therapeutics to halt or reverse the progression of sub-rupture induced tendinopathy is hindered by the paucity of data regarding onset and progression of the disease. To fill this gap in knowledge, our lab has developed a tunable fatigue loading injury model in the rat patellar tendon (PT) to examine changes in cellular and biological markers that are associated with onset and pathogenesis of tendinopathy.[1] In this injury model, diagnostic non-damaging mechanical tests are performed immediately before and after a cyclical fatigue loading protocol to allow calculation of four parameters that are established as effective metrics of the damage induced by the fatigue loading cycles.[2] Accordingly, our model allows us to evaluate biological outcomes in the context of this induced damage, in addition to the applied number of damaging cycles.

We have previously shown that apoptosis and expression of matrix remodeling genes are directly regulated by the severity of induced damage, but not cycle number, and were ultimately associated with a lack of repair.[3,4] Accordingly, we evaluated the effect of blocking apoptosis via pan-caspase inhibition to determine whether an effective repair response could be induced by increasing the number of healthy cells available to repair the damage. Surprisingly, this intervention further worsened mechanical properties and increased cellular markers of stress.[5] The removal of damaged cells via apoptosis is a necessary part of the response to any injury, but the lack of repair following fatigue loading leads us to suspect that the intense apoptotic response is not limited to catabolic cells. The heterogeneous nature of matrix damage induced by fatigue loading suggests there may be a population of otherwise healthy cells residing in less damaged regions in which apoptosis is induced by the unchecked spread of apoptotic signals from catabolic cells in more highly damaged regions. Broad inhibition of apoptosis does not differentiate between these cell populations, and forces survival of catabolic cells, furthering tendon degeneration. We therefore seek to identify how apoptotic signals may be spread from damaged to otherwise healthy cells to identify potential targets by which apoptosis could be more specifically limited.

Connexin-43 (Cx43) gap junctions (GJ) are a mechanosensitive communication mechanism present between tendon cells which play an important role in coordinating the tissue level response to loading during homeostasis via transmission of secondary messengers.[6] Cx43 gene expression and GJ communication transiently increase following application of physiological levels of strain to tenocytes in vitro.[7] Importantly, Cx43 has been implicated in the spread of apoptotic signals in other cell types, including osteoarthritic chondrocytes.[8] Given the knowledge from these in vitro studies that Cx43 is mechanosensitive and can spread apoptotic signals, we suspect that fatigue loading facilitates changes in Cx43 presence and function which contribute to increased apoptosis and further disease progression.

The objective of this study is to quantify changes in Cx43 positive (Cx43+) cell ratio following fatigue loading and correlate these changes with mechanical damage parameters and cycle number to investigate how the presence and role of Cx43 may impact tendinopathic disease progression. We hypothesize that time, damage, and cycle number are modulators of Cx43+ cell ratio following fatigue injury.

METHODS

Twenty-four 9-month-old female Sprague Dawley rats underwent cyclic fatigue loading of the PT to either 100- or 7200-cycles at 1-40N, 1 Hz per our established protocol.[1] Pre- and post-load diagnostic data were collected as previously described and four damage parameters (elongation, change in hysteresis, change in loading stiffness, and change in unloading stiffness) were calculated using custom MATLAB code.[2] Animals were cage active until sacrifice 3- or 7-days post injury, when injured and contralateral hindlimbs were processed for histology.

Samples were sectioned at 6µm thickness and stained for Cx43 (1:500; abcam11370) with a NucRed counterstain. Fluorescent images were collected and Cx43+ cell ratio was quantified using ImageJ FIJI.

Following data collection, Cx43+ cell ratios were normalized against the mean of naïve samples collected during the same week to account for seasonal effects that commonly impact rodents.[9] 3-day 100-cycle, 7-day 100-cycle, 3-day 7200-cycle, and 7-day 7200-cycle groups were then compared to naïve using a Wilcoxon rank sum test. Subsequently, damage parameter data for both days were categorically split into "high" and "low" damage groups via sum of squares minimization. Mann-Whitney tests and Kruskal-Wallis tests with Dunn's posthoc were used to compare data with two groups or three or more groups, respectively. Data analysis and statistics were performed using R and GraphPad Prism; * $p<0.05$, # $p<0.1$.

RESULTS

Cx43+ cell ratio significantly increased for all loaded samples vs. naïve (Fig. 1A). Comparing the effect of cycle number across time showed that Cx43+ cell ratio significantly increased for 3-day 100-cycle and 7-day 100-cycle groups compared to naïve and trended similarly for 3-day 7200-cycle and 7-day 7200-cycle groups (Fig. 1B).

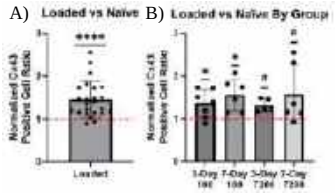

Figure 1: (A) Normalized Cx43+ cell ratio increased in loaded tendons vs. naïve. (B) Normalized Cx43+ cell ratio increased vs. naïve for 100-cycles of loading at 3- and 7-days and trended the same for 7200-cycles of loading at both days. Red dashed lines indicate naïve levels. **** $p<0.0001$

We next divided the data into "high" and "low" damage groups for a given day, independent of the number of loading cycles. Comparison of induced damage confirmed that change in hysteresis, elongation, and change in unloading stiffness are significantly greater for high than low damage groups at both days (Fig 2A-C). Change in loading stiffness increased for high compared to low damage at 3-days and trended towards the same at 7-days (Fig. 2D). Change in Cx43+ cell ratio was not different between high and low damage groups for any of the four parameters at either day (not shown).

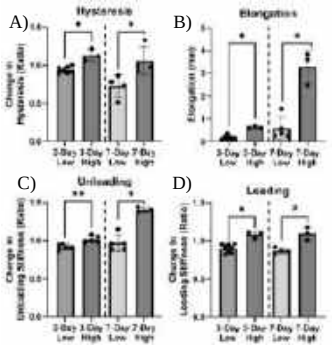

Figure 2: (A) Change in hysteresis, (B) elongation, and (C) change in unloading stiffness were significantly greater in high than low damage groups at both 3- and 7-days. (D) Change in loading stiffness was significantly greater in the high than low damage group at 3-days with a trend towards the same at 7-days. ** $p<0.01$

We then assessed the data for differences between the 3- and 7-days groups of each parameter in a given damage tier. Induced damage did not differ between 3- and 7-day groups with high change in hysteresis, low change in unloading stiffness, and low and high change in loading stiffness; subsequently, change in Cx43+ cell ratio did not differ between 3- and 7-day groups in any of these cases (Fig. 3A, C, D). If the amount of induced damage was different for 3- and 7-day groups in the same damage tier of the parameter in question, we did not compare change in Cx43+ cell as we would be unable to determine if any difference was correlated with time or the difference in damage.

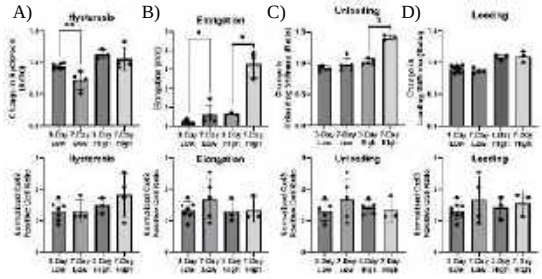

Figure 3: The high damage groups at 3- vs. 7-days were not different for change in (A) hysteresis and (D) loading stiffness, and the low damage groups at 3- vs. 7-days were not different for change in (C) unloading stiffness and (D) loading stiffness. Change in Cx43+ cell ratio was not different between 3- and 7-day groups at either damage severity for any parameter. ** $p<0.01$

DISCUSSION

Contrary to our hypothesis, we did not observe a correlation between changes in Cx43 and changes in induced damage. This suggests that the damage parameters evaluated here do not regulate changes in Cx43+ cell ratio in tendon following fatigue loading. This finding also highlights some potential limitations of this study. First, Cx43 can localize to the cytoplasm, cell membrane, or cellular protrusions, with location dictating function. While not quantified in this study, Cx43 localization has been observed to change in a load dependent manner in vitro, and more work is necessary to determine if Cx43 localization, and thus function, vary following loading in our model.[7] Second, this study does not evaluate Cx43+ cell ratio on a regional basis. The different loading environments of the insertion, midsubstance, and origin regions of the PT affect the molecular response to loading, and future work will include additional analysis to determine if changes in Cx43+ cell ratio are also region dependent.[3,4]

While the increase in Cx43+ cell ratio was surprisingly not cycle dependent, these findings are consistent with our previous data showing that the increase in apoptosis post loading is also independent of cycle number.[3] We have observed ECM disruptions, including damage kinks and widening of interfibrillar spaces, sustained for 7 or more days following any number of fatigue loading cycles.[1] Additionally, Cx43 expression is increased by underloading of tendon cells.[10] It is plausible that these ECM disruptions could lead to underloading of individual cells despite macroscale physiological loading, increasing Cx43+ cell ratio regardless of the number of loading cycles. The sustained ECM disruptions could also explain the surprising lack of time dependency of change in Cx43+ cell ratio seen here, as the effects of stress deprivation on tenocyte Cx43 expression were similarly observed out to 7- days.[10]

This work demonstrates that Cx43+ cell ratio is not correlated with induced mechanical damage parameters following fatigue loading, but it remains to be evaluated whether the role of Cx43 changes independent of positive cell ratio to contribute to disease progression.

ACKNOWLEDGEMENTS

Cornell-HSS T32 NIAMS AR078751, NIH R56AR077239, NIH R21AR074602, NSF/CCMI 2038057

REFERENCES

[1] Fung, D.T. et al., *J Biomech*, 43:274-279, 2010. [2] Andarawis-Puri, N. et al., *J Biomech*, 45:59-65, 2012. [3] Andarawis-Puri, N. et al., *J Orthop Res*, 32:1097-1103, 2014. [4] Andarawis-Prui, N. et al., *J Orthop Res*, 30:1327-1334, 2012. [5] Bell, R. et al., *Eur Cell Mater*, 36:44-56, 2018. [6] Wall, M.E. & Banes, A.J., *J Musculoskelet Neuronal Interact*, 5:70-84, 2005. [7] Maeda, E. et al., *Biochem Biophys Res Commun*, 482:1170-1175, 2017. [8] Li, s. et al. *Tissue Cell* 73, 2021. [9] Ferguson, S.A. & Maier, K.L., *Physiol Behav*, 119:130-136, 2013. [10] Egerbacher, M. et al., *Connect Tissue Res* 63:43-52, 2022.

COMBINED EFFECTS OF PROTEOGLYCAN AND COLLAGEN ON THE LUBRICATION PROPERTIES OF A POLYVINYL ALCOHOL HYDROGEL

M. Maeda (1), H. Chiba (2) and H. Fujie (1)

(1) Graduate School of Systems Design, Tokyo Metropolitan University, Hachioji, Tokyo, Japan
(2) Faculty of Systems Design, Tokyo Metropolitan University, Hachioji, Tokyo, Japan

INTRODUCTION

Biphasic lubrication theory [1] is one of the major joint lubrication theories in which the interstitial fluid supports the majority of loads applied to joint surfaces. Proteoglycans (PGs) are thought to be important constituent material that improves the lubrication property of ground substances by attracting water molecules. However, it is impossible to quantitatively determine the effect of PG on the lubrication properties using articular cartilage specimens. Our previous study revealed that the addition of PG powder to polyvinyl alcohol (PVA) hydrogels improves lubrication properties, but that an excessive addition of PG powder conversely increases friction [2]. The reason for this was considered to be ploughing friction occurred due to the softening of PVA hydrogel. In the present study, PG/COL hydrogels were developed by adding PG with either type I collagen (COL1) or type II collagen (COL2) to PVA hydrogels, and their frictional properties were investigated.

METHODS

PVA powder of 6.0 g (P0469, Tokyo Kasei Kogyo Co., Ltd., degree of polymerization: about 1700, degree of saponification: 97.0-100.0 mol%) was dissolved in ultrapure water (approximately 19.93-23.60 g depending on the amount added and the type of COL) to prepare a PVA solution of 40.0 g (Fig. 1). PG powder including dextrin (DEX) (Proteoglycan F, ICHIMARU PHARCOS Co., Ltd.) was dissolved in either 10.86 g of COL1 solution or 9.00 g of COL2 solution with 10 x phosphate buffered saline, to prepare PG/COL solution. The mixture of these solutions was poured into Petri dishes (10 g each) and preserved at 8°C, 50%RH until the weight change of the solution settled down, and cast dry films were produced. The films were then immersed in 333 mL of ultrapure water for more than 72 hours to produce PG/COL hydrogels. Percentage of PG of the solid elements in the hydrogels was 1.2 wt% (PG/COL (I)), 3.3 wt% (PG/COL (II)) and 5.0 wt% (PG/COL (III)). For comparison, hydrogels consisting of only COL1 (COL1) or COL2 (COL2), and PG hydrogels without collagen (PG(I), PG(II), PG(III)) were prepared. The composition of the solid elements in each gel is shown in Fig. 2.

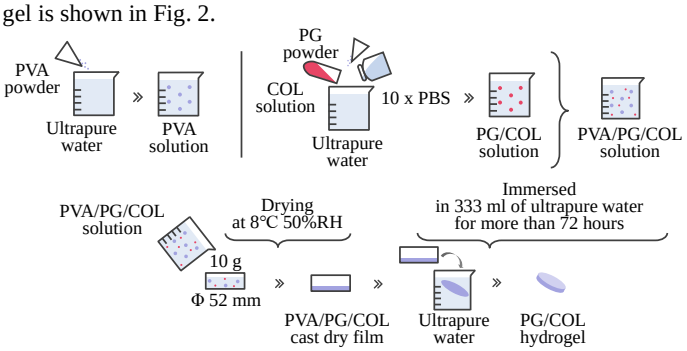

Fig.1 Preparation of PG/COL hydrogels, and COL and PG hydrogels

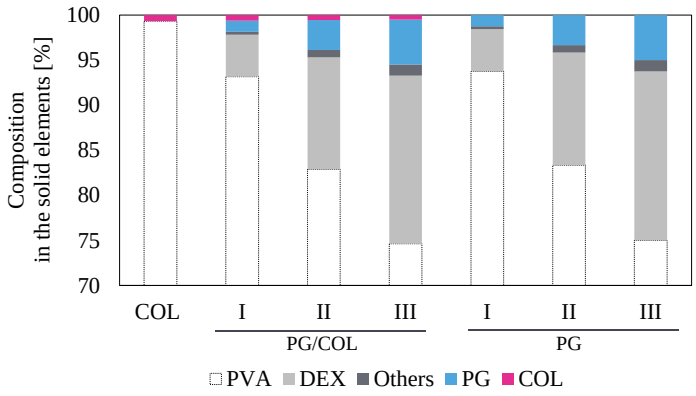

Fig. 2 Composition of the solid elements in hydrogels

Scanning electron microscopic (SEM) observation was performed for the cross section of the hydrogels using a SEM (VE-8800, KEYENCE Co.). The hydrogels were punched to 18 mm long × 10 mm wide specimens and fixed in a fluid bath filled with 37°C saline solution. A dynamic mechanical analysis was first performed for the hydrogels using a dynamic viscoelasticity tester (Electro Force 5500, TA Instrument) to determine the storage and loss moduli of the hydrogels. A reciprocating friction test was then performed for the hydrogels against an alumina ceramic sphere of 6.00 mm in diameter at the condition of a vertical load of 0.9 N (maximum surface pressure 1.51 MPa), preload time of 5 s, friction velocity of 10.0 mm/s, and friction stroke of 10 mm for 50 cycles trips (total friction distance 1,000 mm).

RESULTS

SEM images of the hydrogels are shown in Fig. 3. Laterally aligned many pores of approximately 200 μm in lateral length are included in PG/COL1 and PG/COL2 hydrogels, with the largest member observed in PG/COL2 hydrogels.

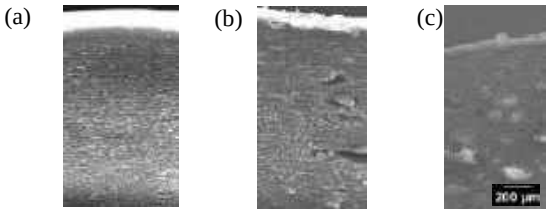

Fig.3 Cross-sectional SEM images of
(a) PG, (b) PG/COL1 and (c) PG/COL2 hydrogels

The storage moduli of COL hydrogels were approximately 0.4 MPa (Fig.4). The addition of PG increased the moduli with the significant increases observed in PG/COL1 (I) and PG/COL2 (I) hydrogels, although the moduli decreased with the increase of PG. Note that the modulus was significantly lower in PG (III) hydrogels than in PG/COL (III) hydrogels.

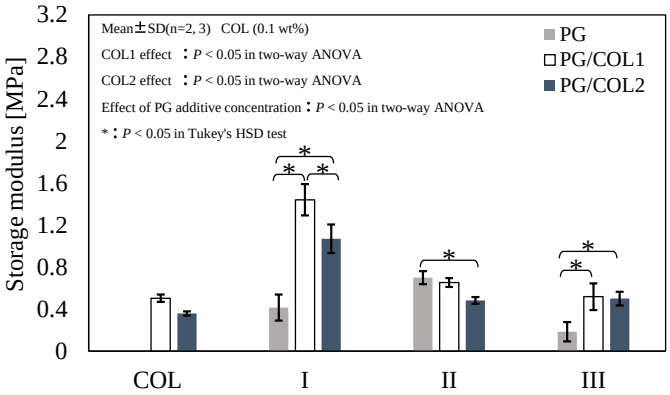

Fig.4 Storage modulus of COL,
PG/COL1 and PG/COL2, and PG hydrogels

The coefficients of dynamic friction at the beginning (distances 0-200 mm) and the end (distances 800-1000 mm) of friction were indicated in Fig. 5. In COL hydrogels, the coefficient of dynamic friction was the highest (0.035-0.050) among all the specimens at the beginning of friction, and significantly decreased during friction. In PG hydrogels, the coefficient of dynamic friction remained lower level (0.016) when the percentage of PG in the solid elements was 1.2 wt% and 3.3 wt%, but significantly increased (0.035) when the percentage was 5.0 wt%, with a significant increase observed during friction. In contrast to these comparison groups, the coefficient of dynamic friction in PG/COL groups remained lower level (0.015-0.023) during entire friction, with the lowest observed in PG/COL1 group.

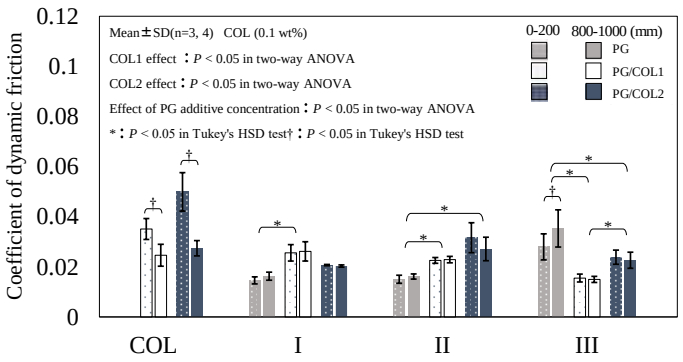

Fig. 5 Coefficient of dynamic friction of COL,
PG/COL1 and PG/COL2, and PG hydrogels

DISCUSSION

The coefficient of dynamic friction was higher in COL hydrogels than in other hydrogel, in particular, at the beginning of friction. It is suggested that friction increased due to the lack of water retention ability in the hydrogels. The coefficient of dynamic friction increased with the increase of PG in PG hydrogels. Based on the biphasic lubrication theory, gels retaining much water exhibit excellent lubrication properties when fluid load support ratio of water increases. However, it is thought that the high-water retention of PG caused the PG hydrogels to soften as indicated in the dynamic mechanical analysis test, and resulted in friction increases due to ploughing.

The coefficient of dynamic friction was significantly higher in PG/COL hydrogels than in PG hydrogels when the percentage of PG in the solid elements was 1.2 wt% and 3.3 wt%. However, the trend became opposite when the percentage of PG was 5.0 wt% in those hydrogels. Note that the storage modulus was significantly higher in the PG/COL hydrogels than in PG hydrogels at the condition. It is suggested that better lubrication properties and adequate moduli can be achieved with the increase of PG in collagen-included PVA hydrogels.

REFERENCES

[1] Ateshian GA, Wang H, Lai WM, “The role of interstitial fluid pressurization and surface porosities on the boundary friction of articular cartilage”, *Journal of Tribology*. 1998; 120 (2): 241-248.
[2] Maeda M, Yarimitsu S, Fujie H, “Relationship between lubrication properties and proteoglycan content in articular cartilage”, *Proceeding of Biotribology Fukuoka 2023*. 2023; G13.
[3] Yarimitsu S, Nakashima K, Sawae Y, Murakami T, “Influence of phospholipid and protein constituents on tribological properties of artificial hydrogel cartilage material”, *Journal of Biomechanical Science and Engineering*. 2013; 8 (3): 257-267.
[4] Tatara Y, Kakizaki I, Suto S, Ishioka H, Negishi M, Endo M, “Chondroitin sulfate cluster of epiphycan from salmon nasal cartilage defines binding specificity to collagens”, *Glycobiology*. 2015; 25: 557-569.

BUILDING HOME-MADE OPTICAL TWEEZERS TO STUDY THE MECHANICAL FORCES OF THE CHONDROCYTE CYTOSKELETON IN THE CONTEXT OF OSTEOARTHRITIS

Samantha L. Smith (1) and Scott T. Wood (1)

(1) Department of Nanoscience and Biomedical Engineering, South Dakota School of Mines, Rapid City, South Dakota, United States

INTRODUCTION

One way to measure forces in cells is by using optical tweezers. Commercially available optical tweezers are very expensive, costing around $200,000, which makes utilizing this technique inaccessible for many laboratories. Luckily, a low-cost version can be made using parts from a DVD burner. Using the optical pickups of a DVD burner, we can build an optical tweezer assembly that is capable of single cell isolation [1]. In this study, home-made optical tweezers will be built for future use in characterizing integrin motion in chondrocytes for research on osteoarthritis (OA).

OA is a debilitating disease of the cartilage that results in pain, deformity, and loss of function for those who suffer from the disease. OA is the most common form of arthritis and is a major cause of disability in older adults. It is typically referred to as degenerative joint disease, which can be misleading because it is not simply a process of wear and tear, but an abnormal remodeling of joint tissues driven by inflammation. Pathologic changes seen in OA include degradation of cartilage, growth of painful bone spurs, inflammation, and degeneration of ligaments, all leading to joint failure [2]. Surprisingly little is known about the mechanisms that result in the degeneration of the joint that occurs in osteoarthritis.

Chondrocytes are highly specialized, metabolically active cells in articular cartilage that play a major role in the development of OA. These cells work constantly to regulate the surrounding extracellular matrix (ECM) but have a limited potential for replication which contributes to their poor intrinsic healing capacity. Chondrocyte survival depends on an optimal chemical and mechanical environment. Their homeostasis is regulated by mechanotransducers called integrins that respond to mechanical stimulation from the surrounding ECM [3]. In previous experiments integrin motion of chondrocytes was characterized using Atomic Force Microscopy (AFM) force measurement [4]. The AFM experiments on chondrocytes produced exciting results, but there were difficulties differentiating the signal from thermal noise. Because of this we decided to use optical tweezers for validation and to provide more information on chondrocyte integrin motion.

Optical tweezers can be used to directly measure forces that are applied to optically trapped objects. The basic principle behind optical tweezers is the momentum transfer associated with bending light. Light carries momentum that is proportional to its energy in the direction of propagation. Because of this, any change in the direction of light, by either reflection or refraction, will result in a change of the momentum of the light. If an object bends the light, changing its momentum, conservation of momentum requires that the object must undergo an equal and opposite momentum change. This change in momentum is what creates the force that traps the object [5]. By attaching specific molecules to polystyrene microspheres, we can study the forces acting on the molecules under various conditions and use these results to model their physical behavior.

In this study, a home made optical tweezer assembly is built for the future investigation of the movement of the actin cytoskeleton of chondrocytes in the context of OA. The proposed optical tweezer assembly is made from the optical pickups of a DVD-RW drive that is integrated into an inverted microscope with the help of a 3D printed stand and light filters to protect the microscope's camera. The total cost of this assembly is estimated to be about $700. Utilizing this optical pickup build increases the accessibility of this technique by providing a method for optical tweezer experiments at a significantly lower cost.

METHODS

Optical traps behave like linear springs because the trap exerts a linear restoring force on the object. The force of the optical trap can be described as shown in Equation 1, where k is the trap stiffness and Δx is the radial displacement of the bead in the trap. The trap stiffness can be determined experimentally by the application of viscous drag.

$$F = -k\Delta x \quad (1)$$

At low Reynold's number, Stoke's law gives the force on a sphere in a uniform velocity flow field in Equation 2, where η is the viscosity of the fluid, d is the diameter of the microsphere, c is the correction factor for proximity to the glass surface, and V is the velocity of fluid flow [5].

$$F = 3\pi\eta dcV \quad (2)$$

In order to define the trap stiffness, a controlled viscous drag force must be applied to a trapped microsphere. Stoke's law, which describes the motion of spheres through a viscous medium, can be used to determine the applied force. This applied force, along with the experimentally measured displacement of the sphere within the trap, can then be used to determine the trap stiffness.

Using the optical tweezer setup shown in Figure 1, we can measure the basal integrin forces that are present in the chondrocyte cytoskeleton. By functionalizing the beads with fibronectin, we can form a bond between the bead and a chondrocyte that is adhered to a glass surface. By optically trapping the bead and tracking the movement of the bead within the trap we can record the basal forces that are being exerted by the cell on the bead. This information can then be used to validate the results of the AFM experiments and provide more information on the dynamic movement of the chondrocyte cytoskeleton.

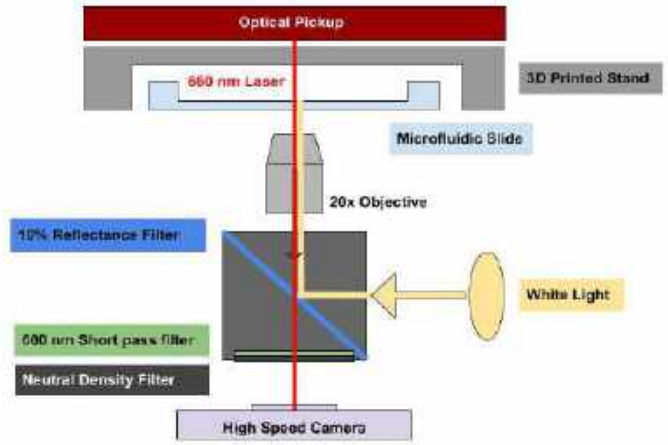

Figure 1: DVD optical tweezer assembly.

RESULTS

To build the optical trap, the optical pickup assembly of a DVD RW drive is integrated into an upright microscope without compromising its imaging modalities. As typically employed, the optical pickup is an electronically steered and stabilized microscope that extracts information from DVD discs. The DVD burner's laser diode is capable of providing the necessary power and focusing optics needed for optically trapping micron-sized particles and cells [1]. The mechanical components from the DVD burner can be used to control the focus of the laser and steer the optical trap to target and capture cells.

The optical pickup assembly used in this project is pictured in Figure 2. Using these optical tweezers, we were able to successfully trap and move a 4 μm glass bead. Unfortunately, soon after trapping the bead the laser diode unexpectedly burned out. Although the laser diode still produced the expected spectrum, the laser power was measured to be less than 10 μW rather than the expected 60 mW, and the laser was no longer capable of forming an optical trap. We initially suspected that the damage was due to electrostatic discharge, as no procedures to prevent this were in place. After sourcing a new optical pickup, we used an antistatic wrist strap when handling the optical pickups to prevent this type of damage, but the measured power of the new laser was still less than 10 μW. Because of this, we plan to investigate the wiring and operating specifications of the pickups as well as exploring other optical pickup sources. Once operational, we plan to measure the optical tweezer's trap strength, as well as the trap strength as a function of voltage. Then, we can begin working on extending its use to cells and developing a protocol for measuring the dynamic motion of the actin cytoskeleton in chondrocytes.

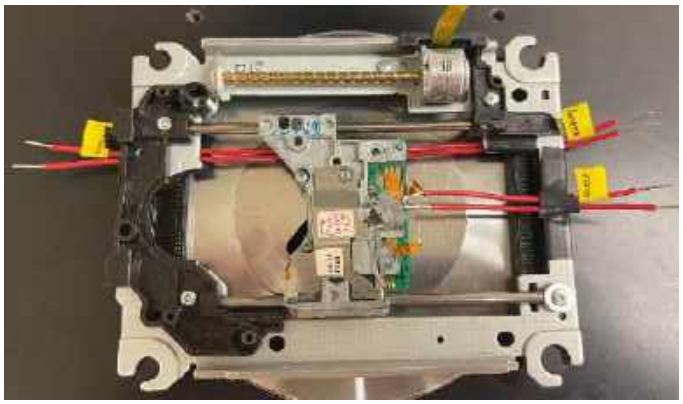

Figure 2: DVD optical pickups.

DISCUSSION

Surprisingly little is known regarding the cellular forces that are present in chondrocytes This project aims to provide a method to unveil the mechanical forces that are necessary for regulating chondrocyte homeostasis. The hypothesis driving this experiment is that the dynamic motion of the actin cytoskeleton, which influences homeostasis in chondrocytes, can be measured using a low-cost optical pickup setup. The project's outcomes will supplement the current understanding of why chondrocytes respond differently to static and dynamic forces. The success of this project will not only provide a path to advance the understanding of OA pathogenesis but also provide a foundation for developing strategies to combat the disease.

OA stands as a leading cause of disability in the developed world, affecting over 32.5 million US adults [6]. Clinical treatments for OA are often limited to pain management and joint replacement due to an incomplete understanding of how this highly complex disease develops. This research will help reveal the intracellular mechanisms for regulation of chondrocyte homeostasis, providing much needed background for advancements in tissue engineering and OA-related healthcare. Additionally, the use of the optical pickup setup for measuring cellular forces in chondrocytes enhances the accessibility of this technique, making optical tweezer experiments more feasible at a significantly lower cost. The affordability of this setup makes it an optimal tool for teaching applications across diverse communities, including those with limited resources.

ACKNOWLEDGEMENTS

This material is based upon work supported by the National Science Foundation award #2144240. Any opinions, findings, and conclusions or recommendations expressed in this material are those of the author(s) and do not necessarily reflect the views of the National Science Foundation.

REFERENCES

[1] Kasukurti, A. et al., *Optics Express*, 19(11): 10377-10386, 2011.
[2] Loser, R.F. et al., *Arthritis & Rheumatism*, 64(6): 1697-1707, 2012.
[3] Fox, A.J.S. et al., *Sports Health*, 1(6): 461-468, 2009.
[4] Nix, Z. et al., *Prog Biophys Mol Biol*, 176:3-15, 2022.
[5] Brouhard, G.J. et al., *IEEE Trans Biomed Eng*, 50(1):121-5, 2003.
[6] CDC, *Centers for Disease Control and Prevention*, 2020.

TACKLING HETEROGENEITY IN CANINE OSTEOSARCOMA- A BIOMECHANICAL ANALYSIS OF HISTOTRIPSY-TREATED AND UNTREATED BONE

Preeya F. Achari (1), Elliana Vickers (1, 2, 3), Lauren Ruger (1), Eli Vlaisavljevich (1), Joanne Tuohy (3), Caitlyn J. Collins (1)

(1) Department of Biomedical Engineering and Mechanics, Virginia Tech, Blacksburg, VA, USA
(2) Translational Biology, Medicine, and Health, Virginia Tech, Roanoke, VA, USA
(3) Virginia-Maryland College of Veterinary Medicine, Blacksburg, VA, USA

INTRODUCTION

Osteosarcoma (OS) is a rare, aggressive bone cancer and one of the most common malignancies in children and adolescents.[1] The survival rate for OS has not improved in decades due to the refractoriness of metastatic disease to therapy.[1] The combination of chemotherapy, surgical resection, and radiotherapy has improved patient outcomes; however, some patients may not qualify for surgical resection due to tumor characteristics or disease progression.[2] Many patients who do continue with treatment suffer from metastasis, infection and reduced limb mobility and function post-treatment.[2] Non-surgical options for primary tumor treatment remain extremely limited.

Recently, canines are being explored as a comparative oncology model for the development of effective clinical OS treatments. Canine OS shares several biological characteristics with human OS (e.g. disease presentation, genetic complexity, and histological characteristics) rendering it an ideal model to explore comparative and translational OS research.[3,4] OS accounts for over 85% of bone tumors in canines, with 95% of patients presenting with spontaneous micrometastases and high levels of pain at time of diagnosis. Current treatment options for canine OS are limited, the most common involving tumor resection via limb-salvage or limb-amputation surgery and adjuvant chemotherapy. Some dogs may not qualify for limb amputation, and serious complications after limb-salvage surgery such as implant failure and infection occur.[3,5]

Histotripsy is a noninvasive, non-thermal ablation technique that uses ultrasound to mechanically destroy tissue. Previous histological *ex vivo* studies on canine bone have demonstrated that histotripsy effectively ablates primary OS tumor tissue without causing cell death or damage to normal surrounding bone.[6,7] Although the effects of histotripsy on OS bone have been explored histologically, its biomechanical effects on the structural integrity of bone and tumor tissue have yet to be determined. The objective of the current study is to determine the biomechanical effects of histotripsy on OS tumor and adjacent grossly normal bone tissue as a crucial next step in developing a non-invasive limb-salvage treatment option for canine osteosarcoma. We hypothesize that histotripsy does not significantly alter the biomechanical properties of treated bone and can safely be used without altering the biomechanics of surrounding, normal bone.

METHODS

Ten amputated limbs from canine patients with primary OS tumors undergoing standard-of-care limb amputation were acquired under an approved institutional IACUC protocol (22-091). *Ex vivo* histotripsy ablation with a dosage of 1000 pulses/point was applied to the OS tumor and a matching volume of grossly normal bone with a custom setup utilizing 1-2 cycle histotripsy pulses at a pulse repetition frequency of 500 Hz. Bone tissue from a treated tumor (AT), treated grossly normal bone (AN), an untreated tumor (UT), and untreated grossly normal bone (UN) were extracted for biomechanical testing (**Figure 1**).

Figure 1: Canine forelimb with an OS tumor in the distal ulna. Representative locations from which specimens were extracted are highlighted.

Cubic specimens (7.5mm x 7.5mm x 7.5mm) were cut from the trabecular bone sections and subjected to repeat (n=3) compressive loading with a 20N preload in three anatomical directions (medial-lateral, anterior-posterior, and superior-inferior) until just below the yield point to assess potential differences in anisotropy and to determine the elastic modulus of each sample. A final compression test to failure along the primary axis of loading (superior-inferior axis), was performed to determine the yield and ultimate compressive stresses of each tissue. UT specimens (n=7) were microCT scanned prior to testing at a 17.5x17.5x17.5 μm voxel resolution for qualitative assessment.

Rectangular beam specimens (15mm x 2mm x 1mm) of cortical bone were cut from each specimen along the longitudinal bone axis and subjected to 3-point bending until failure.

Compressive and bending moduli, calculated from the slope of the linear region of the stress-strain curves, and maximum stresses were determined to assess the impact of histotripsy on tissue stiffness and strength, respectively.

A linear mixed effects model was used to assess the impact of loading direction and tissue on the compressive moduli of the trabecular bone specimens. A Kruskal-Wallis test was used to assess elastic and post-yield behavior of the cortical bone specimens and post-yield behavior of the trabecular bone specimens. Where necessary, Dunn's test was performed as a post-hoc measure to compare data between groups. The alpha value was set 0.05 and p-values were adjusted for multiple comparisons.

RESULTS

The material properties of a total of 67 cortical beams and 36 trabecular cubes were analyzed. For the cortical bone specimens, elastic modulus was significantly higher in grossly normal bone (UN and AN) groups than in tumor tissue (UT and AT) groups (**Figure 2, Table 1**). No significant differences were found between untreated and treated grossly normal bone or between untreated and treated tumor tissue groups. Maximum stress followed a similar trend; normal bone specimens were significantly stiffer than tumor tissue specimens, and no differences were found between treated and untreated specimens in either the normal bone or tumor tissue groups (**Table 1**). No significant differences were found in the mechanical properties for the trabecular bone specimens; however, UT specimens exhibited both a higher value and range regarding elastic modulus, maximum stress, and yield stress/strain than the other groups (**Figure 2,3**).

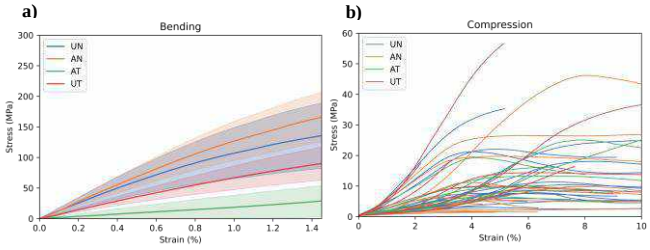

Figure 2: Failure mechanics for (a) cortical bone under 3-pt bending (b) trabecular bone under compression

Table 1: Mechanical properties of UN, AN, UT, and AT cortical bone specimens for 3-pt bending tests. Data reported as median (IQR).

		Condition				
Compression	Property	UN	AN	UT	AT	(p)
	Maximum stress (MPa)	14.7 (12.8)	8.42 (12.8)	17.4 (12.0)	13.3 (9.65)	0.262
	Elastic modulus (MPa)	363 (328)	224 (255)	631 (451)	185 (186)	0.312
	Yield strength (MPa)	8.80 (10.8)	3.13 (12.03)	11.8 (9.46)	9.58 (9.24)	0.162
	Yield strain (%)	2.12 (1.45)	1.94 (1.26)	2.18 (1.28)	2.88 (0.485)	0.104
Bending	Property	UN	AN	UT	AT	(p)
	Maximum stress (MPa)	189 (99.1)	214 (63.6)	116 (109)	115 (114)	<**0.001***
	Elastic modulus (GPa)	12.2 (6.85)	12.9 (4.91)	6.57 (6.47)	4.95 (7.07)	<**0.001***
	Elastic work (J)	1.05 (0.401)	1.11 (0.341)	1.05 (0.766)	0.902 (1.07)	0.956
	Toughness (MJ/m³)	3.93 (1.97)	8.35 (5.79)	2.80 (2.27)	2.23 (3.22)	<**0.001***

Differences in UT composition were qualitatively analyzed via micro-CT, showing a wide range in densities (**Figure 3**). Regarding anisotropy, stiffness was often higher in the primary loading direction, but no significant differences were found within the three loading directions between groups. As such, data was grouped by tissue type for the remainder of the statistical analyses.

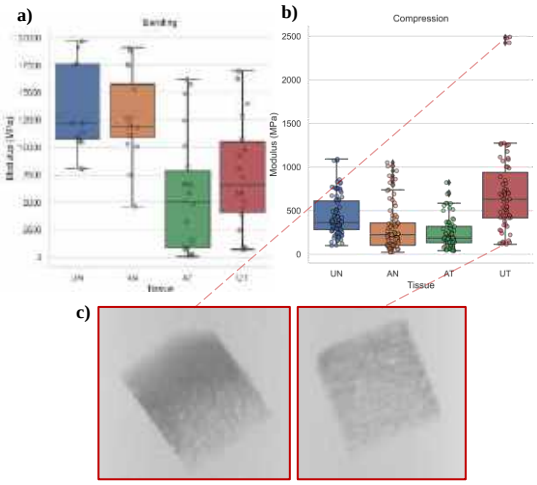

Figure 3: Elastic modulus distribution for a) cortical bone b) trabecular bone specimens. MicroCT projections of Selected UT specimens, demonstrating the range in density of the trabecular network.

DISCUSSION

The similarities between the biomechanical properties of untreated and treated normal bone specimens support our hypothesis that histotripsy tumor ablation does not detrimentally affect the biomechanical properties of grossly normal bone. Similarities between untreated and treated tumor tissue specimens carry the same implication. However, the clinical nature of this pilot study prevented complete control over key variables such as tissue donor characteristics (age, weight, breed, etc.), the anatomical location from which sample tissue was extracted (i.e., radius, ulna, tibia, femur), and sample size. As such, the detected differences between groups may have been influenced by the anatomical location of each of the samples as well as donor demographics. Furthermore, significant differences may be masked by the high variation shown in the calculated properties. To address these limitations, future controlled studies on the biomechanical effects of histotripsy dose on healthy and OS tumor tissue should be performed to establish treatment guidelines. Further exploration into the properties and composition of untreated OS tumor tissue, which shows a high degree of heterogeneity, using density calibrated imaging will also be imperative in understanding and refining the relationship between histotripsy dose and tumor tissue mechanics. Ultimately, the results of the current work will aid in the development and advancement of effective, non-invasive, patient-specific treatments for clinical OS.

ACKNOWLEDGEMENTS

The authors gratefully acknowledge the support of the Veterinary Memorial Foundation, the Focused Ultrasound Foundation, and the Virginia Tech COE EFO-O program.

REFERENCES

1. Luu, A.K. & Viloria-Petit, A.M., *Int. J. Mol. Sci.* **21**, (2020).
2. Xu, M. et al., *Orthop. Surg.* **12**, 1021–1029 (2020).
3. Lazarides, A.L. et al., Osteosarcoma--Biology, behavior and mechanisms (2017).
4. Makielski, K. M. et al., *Vet. Sci. China* **6**, (2019).
5. Kuhn, J. L. et al., *J. Biomech.* **22**, 95–107 (1989).
6. Arnold, L. et al., *Ultrasound Med. Biol.* **47**, 3435–3446 (2021).
7. Ruger, L. N. et al., *IEEE Trans. Biomed. Eng.* **PP**, (2022).

COMPUTATIONAL MODELING OF LEFT VENTRICULAR FLOW USING MRI-DERIVED FOUR-DIMENSIONAL WALL MOTION

Seyed Babak Peighambari (1), Tanmay Mukherjee (1), Amr Darwish (2), Roderic Pettigrew (1,3), Dipan Shah (2), Reza Avazmohammadi (1,3)

(1) Department of Biomedical Engineering, Texas A&M University, College Station, TX, USA

(2) Houston Methodist DeBakey Heart & Vascular Center, Houston, TX, United States

(3) School of Engineering Medicine, Texas A&M University, Houston, TX 77030, USA

*rezaavaz@tamu.edu

INTRODUCTION

Intracardiac hemodynamics plays a crucial role in cardiac efficiency, yet the intricate patterns of atrioventricular blood flow are not fully understood. While deviations in wall motion serve as direct evidence of an apparent clinical ailment, exploring intracardiac hemodynamics shifts the emphasis from diagnosing diseases to predicting their onset and progression [1]. The estimation of vortical flow structures in the left ventricle (LV) has recently emerged as a potential hemodynamic marker for various pathologies. Specifically, aberrant vortices and vortex rings are found to be associated with an increase in viscous energy loss during LV filling (diastole) which then necessitates an increase in mechanical energy to preserve the cardiac output during LV contraction (systole) [2]. Hemodynamic analysis of atrioventricular flow is necessary for valvular diseases such as mitral valve prolapse (MVP). MVP is characterized by the incursion of one or both mitral valve leaflets into the left atrium by more than 2 mm. Affecting approximately 2-3% of the adult population in the United States, the only definitive treatment for MVP is surgical intervention, which may involve repair or replacement with mechanical or biological prosthetic valves [3]. Therefore, understanding the hemodynamic factors influencing cardiac remodeling before and after mitral valve surgery is essential.

In this work, using magnetic resonance imaging (MRI), we introduce a novel patient-specific fluid-structure-interaction (FSI) modeling to characterize the LV hemodynamics in a patient with MVP. Our method extends upon previous MRI-based methods, with our approach leveraging non-rigid estimation of myocardial deformation and phase contrast (PC-)MRI images to create a four-dimensional (4D) map of intraventricular flow in the LV. We analyze traditional hemodynamic markers, such as kinetic energy and flow velocities, in addition to vortex analysis.

METHODS

An in-house non-rigid image registration framework was implemented over the short-axis (SA) MR image stack of a post-surgery MVP patient (n=1) to evaluate deformation. The framework extends upon the optimization-based registration problem introduced by [4] to find the best transformation in aligning a reference frame.

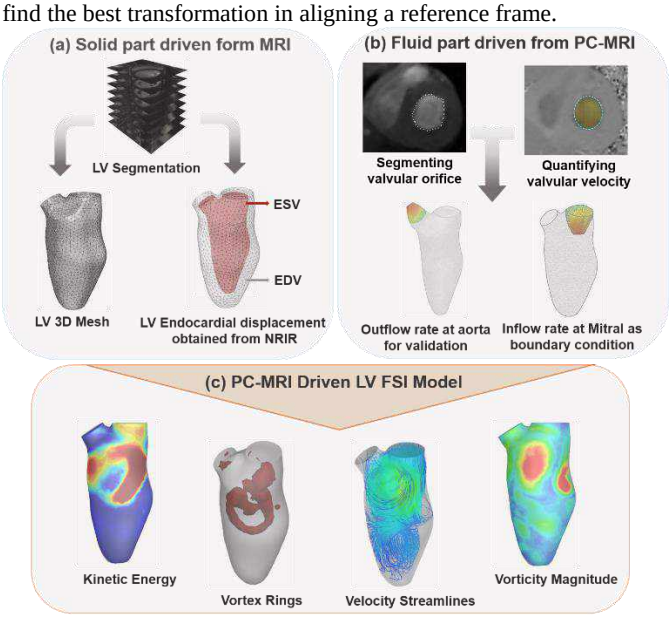

Figure 1: (a) Reconstruction of LV geometry using short-axis MR images and implementation of the NRIR method to obtain the endocardial wall displacement from end-diastolic and end-systolic volumes. (b) The flow rate using PC-MRI velocity measurements over the mitral and aortic orifices. (c) The LV hemodynamic characterizations, derived from the FSI modeling.

In this study, the LV endocardium in SA MRI images was segmented over all slices. This process involved creating endocardial contours at each time point, followed by resampling and smoothing through Delaunay triangulation and radial basis functions to enhance 3D segmentation quality. The LV wall for analysis was reconstructed at end-diastole (ED), mapping displacements from subsequent time points onto it with a least-squares method(Figure 2a).

Using PC-MRI, a non-invasive imaging method capable of assessing the velocity of blood flow in all three directions, the blood flow velocity field was calculated at the deforming mitral and aortic orifices. The integrated mitral flow rate was implemented in the model and the aortic flow rate was used for further validation (Figure 3b). For the governing equation, the incompressible Navier–Stokes equations with the arbitrary Lagrangian-Eulerian (ALE) formulation were used, and the continuity and the momentum equations were solved to assess the LV hemodynamics (Figure 4c).

RESULTS

Following the FSI modeling, the LV vorticity magnitude was calculated in a cardiac cycle(Figure 2). At early diastole, the inflow jet of the E-wave enters the LV and creates two counter-rotating vortex formations, while the dominant vortex forms close to the aortic outflow tract and extends through the intraventricular septal wall. The two vortices reach their maximum size in the diastasis phase. With the onset of systole, the two remaining vortices shrink and get ejected out of the LV as the contraction proceeds to the peak systole.

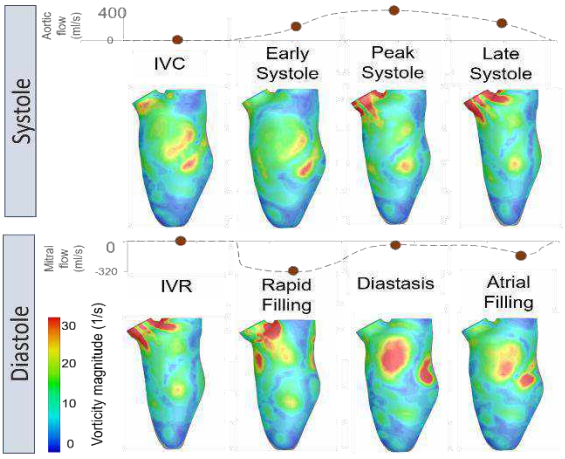

Figure 2: Vorticity magnitude in the transversal plane, crossing the mitral and aortic orifices. The top row illustrates the vorticity magnitude in the systole while the bottom row depicts the vortices in the diastole.

Furhermore, the iso-surface vortex rings in a cardiac cycle were acquired (Figure 3). As depicted, there are three main vortex rings formed in a cardiac cycle. One surrounding aortic outflow track in early systole, and two main vortex rings formed with E-wave and A-wave inflow jets at the mitral valve.

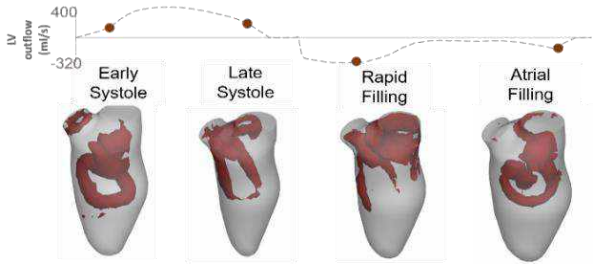

Figure 3: Iso-surface vortex rings illustrated in a cardiac cycle. Three main vortex rings were detected corresponding to the early systolic outflow jet, E-wave, and A-wave of diastolic inflow jets.

For validation, the flow velocity at the aortic orifice was measured from PC-MRI (Figure 4a), and the integrated volumetric flow rate was compared with the FSI model(Figure 4b). As no boundary conditions were imposed to model at the aortic orifice, the ejection curve of the flow at the aortic orifice is mainly implied by the moving wall, reinforcing the accuracy and robustness of the method.

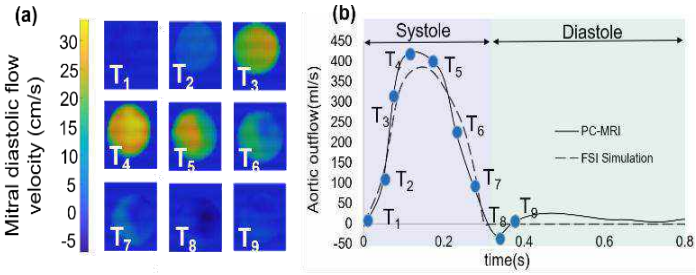

Figure 5: (a) 2D-PC-MRI-derived flow velocity at the short axis view of the aorta during the systole. (b) The aortic volumetric outflow rate captured from PC-MRI compared to the aortic flow assessed by the FSI modeling in a cardiac cycle.

DISCUSSION

In this study, we introduced an innovative patient-specific modeling approach to characterize LV hemodynamics. Our approach focused on integrating standard MRI and phase contrast images with moving boundary modeling obviating the need for complex electromechanical models of the myocardium to mimic LV hemodynamics. Hence, using MRI scans, a patient-specific LV model was introduced with a dynamic endocardium wall motion with a patient-specific flow boundary condition at the mitral valves to improve the fidelity of the model.

Per literature, under normal conditions, one vortex fills the entire LV chamber during diastole to minimize the kinetic energy loss and maximize the LV function[5]. In contrast, in cases of impaired flow due to MVP, two main vortices are typically reported in the LV; which is consistent with our results [6]. Although our model did not include a valve construct, all vortical properties, such as the position and circulation of the vortex rings, agreed with previous studies [7]. This highlights the utility of our approach in describing the impact of potential LV pathologies and, consequently, characterizing the association between LV wall motion and intracardiac hemodynamics. This study was carried out on a patient with MVP prior to mitral valve surgery. We are currently extending our research to include post-surgery data from the same patient, aiming to explore the changes in the formation of vortices within the LV post-surgery.

ACKNOWLEDGEMENTS

This work was supported by the NIH (R00HL138288 to R.A)

REFERENCES

[1] Chnafa C, et.al. Annals of biomedical engineering.2016;44:3346-58.
[2] Pedrizzetti G, et al. Annals of biomedical engineering.2010; 38:769-73.
[3] Delling FN, et al. Circulation. 2016;133(17):1688-95.
[4] Vercauteren T, et al. InBiennial International Conference on Information Processing in Medical Imaging 2007 ; (pp. 495-506).
[5] Pedrizzetti G. Nature Reviews Cardiology. 2014; 11(9):545-53.
[6] Faludi R, et al.The Journal of thoracic and cardiovascular surgery. 2010; 139(6):1501-10.
[7] Elbaz MS, et al. Journal of Cardiovascular Magnetic Resonance. 2014; 16(1):1-2.

SB³C2024
Summer Biomechanics, Bioengineering and Biotransport Conference
June 11-14, Lake Geneva, WI, USA

IMPROVING GLIOMA SEGMENTATION FAIRNESS IN LOW-RESOLUTION DOMAINS WITH TRANSFER LEARNING

Juampablo E. Heras Rivera (1), Tianyi Ren (1), Harshitha Rebala (2), Ethan Honey (1), Abhishek Sharma (1), Mehmet Kurt (1,2)

(1) Mechanical Engineering, University of Washington, Seattle, WA, USA
(2) Computer Science, University of Washington, Seattle, WA, USA

INTRODUCTION

Gliomas, which include glioblastomas and a subtype known as diffuse astrocytic glioma that shares molecular characteristics with glioblastoma (categorized as WHO Grade 4 astrocytoma), are the most frequently occurring and most severe type of malignant primary brain tumors found in adults [1]. Unfortunately, glioblastoma patients have a poor prognosis, with survival times typically being short despite aggressive treatment. The standard approach to treating glioblastoma involves surgical removal followed by radiotherapy and chemotherapy. Moreover, the likelihood of long-term survival with glioblastoma is increased by precise identification of pathological features through brain MRI, with subsequent confirmation by histopathology.

Glioblastomas present a challenge for diagnosis and treatment as they are highly variable in appearance, shape, and histology. Given the crucial nature of the pathological feature segmentation, the task is typically performed manually by experienced neuroradiologists. However, the segmentation process is time-consuming, tedious, and error prone as evidenced by variations in assessments among different radiologists (inter-rater variability) and the same radiologist over time (intra-rate variability) [2]. To address these challenges, computational segmentation algorithms have been developed that streamline the labeling process and minimize variability. Deep learning algorithms have recently become the primary choice in this context, largely due to advances in the computational power of modern graphic processing units (GPU), and algorithms. However, effectively training these models requires large amounts of data.

The Brain Tumor Segmentation Challenge (BraTS) is an annual international competition that aims to evaluate the state-of-the-art models by providing an ample dataset of fully labeled, multi-institutional images of patients with varying degrees of gliomas. The BraTS Challenge is divided into tasks; in this work, we use the datasets from Task 1 and Task 2. Task 1 data includes images of gliomas and labels of their sub-regions, namely: the enhancing tumor, the peritumoral edema, and the necrotic and non-enhancing tumor core. The annotations are combined into 3 nested subregions: whole tumor (WT), tumor core (TC) and enhancing tumor (ET). Task 2 provides similar images taken from patients in Sub-Saharan Africa (SSA).

What distinguishes the Task 1 (US) and Task 2 (SSA) datasets? In the US, 3T MRI machines are widespread in clinics and are commonly used to image brain tumors, while in SSA, 1.5T MRI is most used due to financial constraints. The lower MRI magnetization results in a significant drop in imaging contrast and resolution, which reduces the accuracy of segmentations and consequently the quality of medical care for patients in SSA. Additionally, there is limited internet connectivity throughout clinics in SSA, so acquiring and uploading imaging data to a cloud for dissemination to research institutions is very difficult. Clinic availability, transportation costs, among other systemic issues limit the accessibility to tumor treatment in SSA, and this manifests as patients typically being imaged at more severe tumor stages. As a result of these disparities, the available BraTS SSA Glioblastoma dataset is significantly smaller and of lower resolution than the USA dataset (60 subjects vs. 1126 subjects, respectively).

Machine learning methods in the field of transfer learning provide a way to bridge the gap in segmentation quality between models trained on US and SSA datasets by "transferring" insights gained from a larger domain (or dataset in this instance) to a smaller one. In this work, we experiment with two distinct transfer learning approaches. Our first approach consists of fine-tuning a well-performing model trained on Task 1 data by "freezing" components of the model and training the unfrozen components of the model on Task 2. Our second approach is directly inspired by the theory of domain adaptation, which suggests that for effective domain transfer, predictions should be based solely on features

that are domain-invariant. To this end, we adapt the concept of Domain Adversarial Neural Networks (DANN) [3], which explicitly removes domain dependent features during parameter optimization. We compare the results of the two approaches to baseline neural networks trained on the independent domains and demonstrate improvement in transfer learning.

METHODS

Data: The BraTS 2023 Task 1 Glioma training dataset includes 1126 samples of multiparametric MRI (mpMRI) scans for each patient comprising a native T1, post-contrast T1-weighted, T2-weighted, and T2 Fluid Attenuated Inversion Recovery (T2-FLAIR) volumes. The dataset was preprocessed by applying DICOM to NIfTI file conversions, and coregistration to the same SRI24 anatomical template. Additionally, the images were resampled to a uniform isotropic resolution (1mm3) and skull-stripped to maintain anonymity.

Approach 1—Fine-tuning by freezing layers: For this approach, we begin with the Optimized U-Net [4] neural network architecture proposed by NVIDIA, which took first place at the BraTS 2021 challenge in the validation phase. The Optimized U-Net was found by extensively searching for the optimal depth of the U-Net encoder, the number of convolutional channels and post-processing strategy. The model was then trained on the Task 1 Glioma dataset using the Adam optimizer with no weight decay and am exponentially decaying learning rate with initial value of $6e\text{-}5$. The official training dataset was divided into a 90:10 training-validation split. After each epoch, the model was evaluated on the validation hold by calculating the Dice and HD95 score between the model prediction and the ground truth for regions of ET, TC, and WT, and then averaging these scores for each subject. The validation scores are then collectively averaged after each epoch, and the model with the highest score was used.

Upon training the original model, we then experimented by freezing various combinations of model components, including the encoder, decoder, and bottleneck layers. Freezing in this context of transfer learning refers to the designated layer's weights and biases being prevented from updating during training. After freezing, the models were fine-tuned by training on the Task 2 dataset. The models were compared using the average Dice and HD95 scores for the three regions (ET, TC, WT).

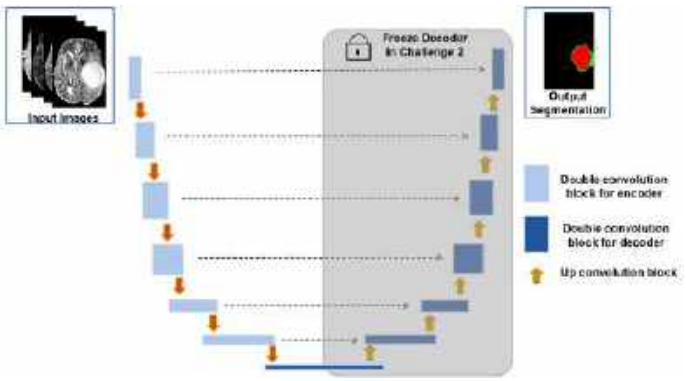

Example Figure 1: Figure caption centered below the graphic.

Approach 2—Deep Adversarial Neural Network (DANN): DANN [3] aims to learn features that are both discriminative and domain-invariant by optimizing a neural network comprising two classifiers: a label predictor, which provides segmentations and is used both during training and testing, and a domain classifier that discriminates between domains during training. The optimization process minimizes the label classifier loss while maximizing the domain classifier loss, promoting the emergence of domain-invariant features through an adversarial optimization.

Our implementation of the DANN approach consists of a backbone convolutional encoder-bottleneck-decoder architecture (such as U-Net [5] in this case) for segmentation, with an additional domain classifier the bottleneck layer. By embedding domain adaptation into the process of representation learning, the final classifications are made based on features that are both discriminative and invariant to domain changes. In the context of transfer learning between Task 1 and Task 2, we expect the model to leverage domain-invariant features common across domains for segmentation.

RESULTS

The results presented in Table 1 indicate that the freezing decoder approach resulted in the most improvement in Dice Score over the baseline Challenge 2 model which was trained only on the Task 2 dataset. Additionally, the results indicate that the model trained only on the Task 1 dataset (under "Challenge 1 model" in Table 1) produced the largest improvements in HD95 score.

Example Table 1: Lesion-wise scores for the Freezing Layers Experiment.

Experiments	Dice				HD95			
	ET	TC	WT	mean	ET	TC	WT	mean
Challenge 2 model	0.6524	0.6925	0.5972	0.6474	81.96	70.49	120.81	91.09
Challenge 1 model	0.7188	0.7424	0.6433	0.7015	**52.35**	**48.16**	101.58	**67.36**
Freeze encoder layers	0.6745	0.7143	0.5810	0.6566	80.40	69.80	142.55	97.58
Freeze middle layers	**0.7392**	**0.7533**	0.6484	0.7136	57.27	55.10	114.41	75.59
Freeze decoder layers	0.7200	0.7358	**0.7039**	**0.7199**	59.21	60.21	**86.48**	68.63
Freeze nothing	0.7159	0.7214	0.6764	0.7046	68.72	67.43	103.55	79.90

DISCUSSION

The presented approach provides a systematic procedure to improve fairness in segmentation in the low-resolution Task 2 domain by training a model with data from another domain. The results of the freezing layers approach indicate that freezing the network's decoder improves segmentation fairness. This result is different from what is expected, since typical transfer learning approaches involve freezing the encoder. This discrepancy between the theory and results is potentially a byproduct of the small Task 2 dataset being nonrepresentative of the distribution of images in its domain. The DANN approach is presently being explored for transfer learning and the preliminary results are encouraging.

ACKNOWLEDGEMENTS

This material is based upon work supported by the U.S. Department of Energy, Office of Science, Office of Advanced Scientific Computing Research, Department of Energy Computational Science Graduate Fellowship under Award Number(s) DE-SC0024386

REFERENCES

[1] Hanif, F et al., Asian Pac J Cancer Prev, 18 (1): 3-9, 2017.
[2] Visser, M et al., Neuroimage Clin 22, 101727, 2019.
[3] Ganin, Y et al., JMLR 17:1-35, 2016.
[4] Futrega, M et al., Itnl. MICCAI Brainlesion Workshop, 15-29, 2021.
[5] Cicek, O et al., MICCAI 2016, Part II 19:424-432, 2016.

GROWTH PLATE AND ITS ROLE IN PEDIATRIC ACL INJURIES

Isaac. Woodward (1), Antonis. Stylianou (1)

(1) Department of Mechanical Engineering, University of Missouri – Kansas City, Kansas City, MO, USA

INTRODUCTION

Over the last few decades, as competitive youth athletic activity has become more common, anterior cruciate ligament (ACL) injuries have become more common in the pediatric and adolescent populations [1,2]. ACL injuries are much more likely to occur in adolescent females than males [3,4] with injury incidence rate reaching its peak in males between 19-25 years old whereas in females the incidence rate is highest at 14-18 years old [5]. Understanding the reasons behind the incidence rate discrepancy between males and females can help us in treatment and prevention of the injury. Anatomical, muscular and hormonal differences have been correlated to ACL injury risk but no studies have looked into the role of the growth plate (physis) in ACL injury mechanics.

Novaretti et al (2018) speculated that the presence of an open physis may play a role in bone bruising patterns after an acute ACL injury as the energy dissipates across the physis. Data from this study demonstrated that patients with an open physis at the occurrence of an ACL rupture have unique bruise patterns compared to those with a closed physis. In skeletally immature patients the bone bruise pattern is less frequently observed in the tibial and femoral metaphysis [6]. Since closure of the physis occurs in females much earlier than males, it is possible that the physis plays a protective role in relation to the ACL and may explain part of the discrepancy in ACL injuries between the sexes in the adolescent population.

The purpose of this pilot study was to investigate the effect of the open physis in ACL strains under different loading scenarios using a finite element model of the knee joint.

METHODS

The finite element models were created from a de-identified MRI dataset of a pediatric knee joint with an open physis. Geometries for the femur, tibia, fibula, anterior and posterior cruciate ligaments and medial and lateral collateral ligaments, tibial and femoral cartilages, and the tibial and femoral growth plates were segmented using 3d Slicer (www.slicer.org). Two models were created: model 1 included the growth plates and model 2, where the growth plates were fused by removing the growth plates and then filling the resulting space thus fusing the proximal and distal parts of the tibia and the femur (Figure 1).

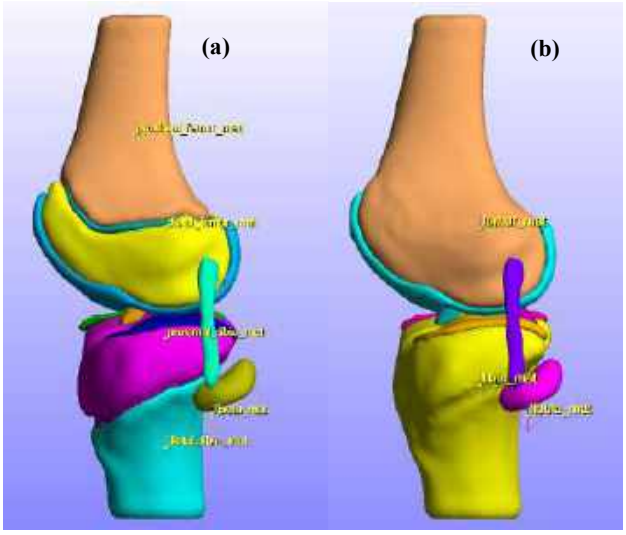

Figure 1: Model 1 with open growth plates (a), Model 2 with fused growth plates (b).

Finite element models were built in FEBio [7]. All bones were modeled as rigid bodies and cartilages, growth plates and ligaments

were meshed with linear tetrahedral elements. Cartilage and growth plates were modeled as nearly incompressible Neo-Hookean materials and all ligaments were modeled as nearly incompressible, transversely isotropic hyperelastic Neo-Hookean materials [8]. Rigid contacts were used for connecting ligaments, cartilage and growth plates to bones and frictionless sliding elastic contacts were created between femoral and tibial cartilages.

Four simulations were run on each of the two models. An unloaded 7mm anterior tibial translation, an unloaded 5-degree internal tibial rotation, a 250 N axial compression with a 7mm anterior tibial translation, and a 250 N axial compression with a 5-degree internal tibial rotation.

RESULTS

Average Lagrange strain and effective stress in the same central region of the ACL ligament (Figure 2) were computed and the results are tabulated in Table 1.

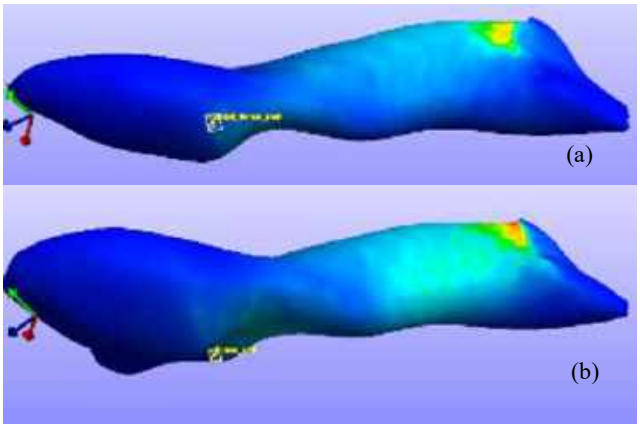

Figure 2: Effective stress maps for the case of loaded internal tibial rotation, model 1 (a), model 2 (b).

	Unloaded Translation		Unloaded Rotation	
	Model 1	**Model 2**	**Model 1**	**Model 2**
Stress(MPa)	15.635	16.575	0.128	0.243
Strain	0.471	0.470	0.016	0.031
	Loaded Translation		**Loaded Rotation**	
Stress(MPa)	20.320	20.980	0.088	0.136
Strain	0.539	0.545	0.011	0.015

Table 1: Stress and strain calculated in the central region of the ACL.

During anterior tibial translation, effective stress is 5.67% and 3.15% lower in model 1 (model that has the open growth plate) for the unloaded and loaded cases, respectively. For internal tibial rotation, effective stress is 47.23% and 35.47% lower in model 1 for the unloaded and loaded cases, respectively.

DISCUSSION

The main finding of this preliminary study is that the open physis can have a protective role on the ACL during loading. Both stress and strain are significantly lower in the model with the open physis especially in the case of internal tibial rotation. The reduction is more moderate in the case of anterior tibial translation however there is still a decrease in stress and strain when the physis is present.

Since closure of the physis happens at different ages between males and females, this result may explain part of the differences seen in ACL injury incidence rates between the sexes during adolescence.

This study has several limitations. Both models were created by a single knee MRI and only two simple loading conditions were investigated. The study needs to be conducted on a much larger sample of knee geometries to establish the validity of the results. In addition, the loading conditions investigated are fairly simple and done in isolation. Simulations should be conducted in cases where anterior tibial translation happens simultaneously with internal tibial rotation and in cases where knee adduction is present.

ACKNOWLEDGEMENTS

Support for this study was provided by the University of Missouri – Kansas City Summer Research Opportunity Grant.

REFERENCES

[1] Nogaro, MC et al., *Bone Joint J*, 102-B:239-245, 2020.
[2] Fabricant PD and Kocher MS, *Orthop Clin North Am,* 47(4):777-788, 2016.
[3] Powell JW and Barber-Foss KD, *Am J Sports Med,* 28(3):385-391, 2000.
[4] Bram Jt et al., *Am J Sports Med,* 49(7):1962-1972, 2021.
[5] Sanders TL et al., *Am J Sports Med,* 44(6):1502-1507, 2016.
[6] Novaretti JV et al., *Am J Sports Med,* 46(9):2128-2132, 2018.
[7] Maas SA et al., *J Biomech Eng,* 134(1): 011005, 2012.
[8] Erdemir A, *J Knee Surg,* 29(2):107-116, 2016.

A NEURAL-NETWORK FINITE-ELEMENT APPROACH TO MODELING OF MULTIBODY CONTACT OF TRILEAFLET HEART VALVES

Kenneth L. Meyer (1), Christian Goodbrake (1), Shruti Motiwale (1), Michael S. Sacks (1)

(1) Oden Institute for Computational Engineering and Sciences, The University of Texas at Austin, Austin, Texas, USA

INTRODUCTION

Computational modeling in directing patient-specific therapies has great potential to provide accurate predictions and determine optimal treatments. This is especially true for the treatment of heart valve disease due to the complexity of heart valve function, geometry, and highly nonlinear leaflet tissue behaviors. Solving the partial differential equations governing heart valve closure using the Finite Element Method (FEM) has been achieved on a patient-specific level but remains too slow to implement in clinically relevant timeframes. To simulate heart valve closure in clinically relevant timeframes, we have begun development of a Neural-Network Finite Element (NNFE) approach [1]. The NNFE approach has been shown to simulate the deformation of a single leaflet with no constraints subjected to a pressure load with error of 0.1% when compared to traditional FEM simulations [1]. The advantage of this method is its speed and scalability; for fine meshes, speedups of 100x are observed for forward simulations [1]. The functionality required to simulate contact between a deformable and rigid body has been recently implemented in the NNFE framework [2]. In this work, our goal is to extend this to implement full multi-body contact in the NNFE approach for a full tri-leaflet heart valve. We achieve this by first implementing contact with a single leaflet against frictionless symmetry planes, followed by implementing full multi-body contact simulations of the closure of a tri-leaflet heart valve.

METHODS

First, we select a material model to predict heart valve leaflet deformation. Heart valve leaflets undergo relatively large deformations and exhibit highly non-linear behavior. Thus, a hyper-elastic material model is used to accurately capture this behavior. Our choice of strain energy density function Ψ is:

$$\Psi = \Psi_{int} + \Psi_{vol} \tag{1}$$

where

$$\Psi_{int} = C_{10}(\bar{I}_1 - 3) + \frac{c_0}{2}\{\exp[c_1(\bar{I}_1 - 3)^2] - 1\} \tag{2}$$

$$\Psi_{vol} = \kappa J_{ref}(J(J - 2 + D_1) - D_1\, log(J) - D_1 + 1). \tag{3}$$

Ψ_{int} describes the internal hyperelastic strain energy of the system, and Ψ_{vol} describes the volumetric energy that is zero when $\mathrm{J} = 1$, i.e. when there is no change in volume. $C_{10}, c_0,$ and c_1 are constants determined in [3] and κ and D_1 are parameters tuned to determine the strength of the volumetric energy term; they determine the compressibility of the material. Additionally, $I_1 = \mathrm{tr}(C)$ and $\bar{I}_1 = J^{-2/3} I_1$ where C is the right Cauchy-Green deformation tensor. $\bar{I}_1$ is used in place of I_1 because we discretize the leaflets with solid finite elements. Scaling I_1 by a factor of $\mathrm{J} = \det \mathrm{F}$ accounts for distortion during deformation, as we are using solid elements.

The leaflets used during NNFE training in this work had a fixed basal attachment and commissure attachments and deviatoric constants of $\kappa = 1\mathrm{E}4$ kPa and $\mathrm{D} = 1\mathrm{E}9$ were used. In the NNFE framework, *our objective function is the gradient of potential energy* Π:

$$\mathcal{L}(\theta, p) = \nabla\Pi(u, p) \tag{6}$$

During NN training within the NNFE framework we train over all admissible ranges of boundary conditions. Once the network is trained, it can be used to compute the displacement field of a body subjected to a specific boundary condition within this admissible range. In this work, we use the NNFE approach to train a NN that learns the displacement field of tri-leaflet heart valve for the range of pressures they experience during closure. During training, we minimize our objective function for a range of pressures $\mathrm{p} = \{\mathrm{p_i} \in [0.0, \mathrm{p_{max}}]\}_{\mathrm{i=1}}^{\mathrm{n}}$, where the sample $\mathrm{p_i}$ are generated using a Halton Sequence. These pressures are inputs to the NN, as shown in the flow chart below.

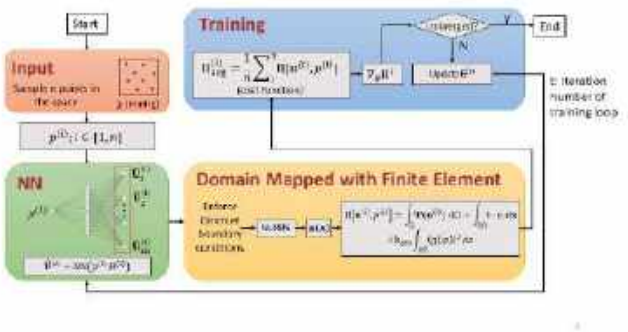

Figure 1: NNFE Training Pipeline (with Contact)

The NNFE approach uses Finite Elements to discretize our domain, so during each epoch, we use this discretization to enforce boundary conditions and compute the gradient of the total potential energy of the system. This process is shown below, note that it does *not* involve training on data.

This work adds contact to a structural model of heart valve leaflets within the NNFE framework. An energy penalty term is used to discourage penetration between a leaflet and a plane, and later a leaflet with another leaflet to simulate contact [2]:

$$\Pi = \int_\Omega \Psi \, d\Omega + \int_{\partial\Omega} t \cdot n \, ds + k_{pen} \int_{\partial\Omega} \langle -g(\varphi) \rangle^2 \, ds \qquad (7)$$

This term computes the signed distance from a body to another body using a gap function g to check for penetration, where $\langle x \rangle = min(x, 0)$. In the multi-body setting, we can integrate multiple gap functions g^{ij}, the signed distance from the i^{th} to the j^{th} leaflet. The distance from a point on one leaflet to another leaflet is defined as $min\, d\left(x_i, x_j\right)$, where x_i and x_j are nodes on the meshes for the i^{th} and j^{th} leaflets. A contact penalty $k_{pen} = 20.0$ was used to penalize penetration in this study.

RESULTS

Contact between a single leaflet of a tri-leaflet heart valve and a frictionless symmetry plane was simulated first. Below, the FEM simulation of this leaflet under a 30mmHg pressure load in FEniCS is shown, where the frictionless symmetry plane is shown in the background in grey, where u is the displacement field:

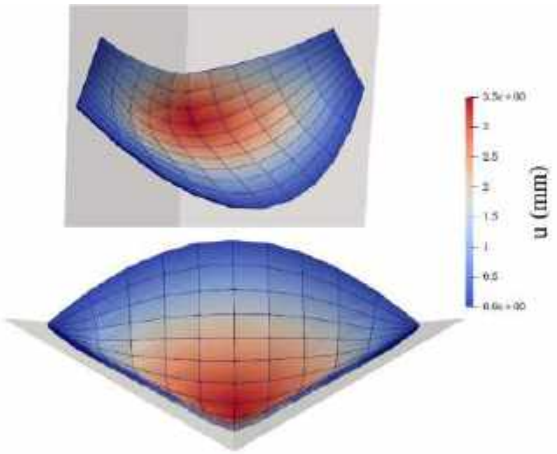

Figure 2: A Single-leaflet Contact Result Using FEM (Side/Top)

This shows that the contact energy penalty term succeeds in capturing the deformation of a heart valve leaflet with solid elements. The L_∞ error of the NNFE solution and a FEniCS is 0.9mm, which will be improved upon with further NN training and debugging. The speedup of the NNFE method remains with the implementation of contact, which is advantageous as it allows high-fidelity simulations to be run cheaply, which is a requirement to use this method in a clinical setting:

	Runtimes	
# control points	**NNFE**	**FEniCS (FEM)**
147	5.34s	89.36s
720	5.75s	788.53s

Table 1: NNFE Runtimes Scale Better than FEM

A result using the NNFE approach was obtained for multi-body contact for a tri-leaflet heart valve. A NN was trained to predict the closure of a tri-leaflet heart valve, and below is the displacement produced by the network for a tri-leaflet valve under a pressure load of 30mmHg:

Figure 3: Multi-body Contact, Open and Closed States

This demonstrates that full multi-body contact in the NNFE framework is achievable as a physiologically accurate deformation of a tri-leaflet heart valve with contact between each leaflet pair is observed. This is the first successful multi-body contact simulation achieved in the NNFE framework.

DISCUSSION

Our findings are consistent with results seen while studying the deformation of a flat plate with the NNFE approach – the NNFE simulations are significantly faster without a large loss in accuracy [1]. The convergence of the solution with mesh refinement has not yet been rigorously studied. Additionally, the scalability of the NNFE approach needs to be verified in the multi-body contact setting. Lastly, there is a small orifice in the center of the valve; this can likely be eliminated by improvements to the NN training process. Once these are improved upon, different types of boundary conditions can be trained over. This includes geometry; we hope to use the NNFE approach to train a NN over ranges of admissible geometric parameters - including leaflet height and tilt angle – to predict displacement fields under a given load.

ACKNOWLEDGEMENTS

Sarofim Fellowship, NIH R01 HL073021

REFERENCES

[1] Sacks, MS et al. Neural Network Approaches for Soft Biological Tissue and Organ Simulations. *J Biomech Eng*. 2022

[2] Goodbrake, Christian et al. A Neural Network Finite Element Method for Contact Mechanics. *CMCMA* 2023

[3] Lee, Chung-Hao et al. An Inverse Modeling Approach For Stress Estimation In Mitral Valve Anterior Leaflet Valvuloplasty For In-Vivo Valvular Biomaterial Assessment. *J. of Biomech.* 47(9):2055–63 2014

A TALE OF TWO TISSUES: EFFECTS OF COLLAGEN III DYSYFUNCTION ON DETERMINANTS OF MECHANICAL PROPERTIES IN TENDON AND CERVIX

Amir Ostadi Moghaddam (1), Matthew P. Confer (2), Roberto Pineda Guzman (3), Kelechi Uhegbu (4), Rohit Bhargava (2,5), Bruce Damon (2,3,5), Sanmi Koyejo (4), Christina Laukaitis (3,6,7), Amy Wagoner Johnson (2,6,7,8), Mariana E. Kersh (2,7,8)

(1) Dept. of Mechanical and Materials Engineering, University of Nebraska-Lincoln, Lincoln, Nebraska, USA
(2) Beckman Institute for Advanced Science and Technology, University of Illinois at Urbana-Champaign, Urbana, Illinois, USA
(3) Carle Clinical Imaging Research Program, Carle Health, Urbana, IL, USA
(4) Dept. of Computer Science, Stanford University, Stanford, California, USA
(5) Dept. of Bioengineering, University of Illinois at Urbana-Champaign, Urbana, Illinois, USA
(6) Institute for Genomic Biology, University of Illinois at Urbana-Champaign, Urbana, Illinois, USA
(7) Carle Illinois College of Medicine, University of Illinois at Urbana-Champaign, Urbana, Illinois, USA
(8) Dept Mechanical Science and Engineering, University of Illinois at Urbana-Champaign, Urbana, Illinois, USA

INTRODUCTION

Local disruptions in collagen quality can result in aberrant tissue properties leading to bulk scale failure [1]. It is unclear if disruptions to tissue structure and composition manifest similarly in all tissues. Moreover, the early detection of collagen dysfunction is complicated by the inherent variability within tissues that is challenging to account for with standard statistical methods. Finally, a non-invasive method to detect tissue dysfunction continues to be an urgent need. Therefore, the objectives of this study were to (1) assess the effect of systemic collagen dysfunction on tissue microstructure and composition, (2) develop a machine learning model for predicting collagen dysfunction based on microstructure, and (3) evaluate the capacity for diffusion tensor magnetic resonance imaging to quantify tissue dysfunction.

METHODS

Animal model: A transgenic missense mutation Col3a1^{G938D} [2] that mimics the collagen dysfunction of vascular Ehlers-Danlos Syndrome was used. Pairs of Achilles tendon and cervix from a 61 day-old Col3a1$^{G938D/+}$ female and a littermate control (WT) were harvested.

Diffusion tensor MRI: DT-MRI was used to providing non-invasive inferred measures of microstructure [3]. DT-MRI data of the cervices were obtained using a 9.4T MRI scanner (Bruker). Following calibration procedures and structural imaging, DTI data were acquired using a spin-echo sequence (repetition time, 2000 ms; echo time, 20 ms; b-value, 500 s/mm^2; 12 diffusion-encoding directions; slice thickness, 1 mm; in-plane resolution, 0.1x0.1 mm^2). The diffusion tensor was estimated by regressing the signals on the b-value and diffusion-encoding matrix using a weighted least squares method. The eigenvalues and eigenvectors were estimated using singular value decomposition. The longitudinal and perpendicular diffusivities and fractional anisotropy were calculated.

Tissue sectioning: Tissues were embedded in optimal cutting temperature media for cryosectioning (sagittal, tendon; transverse, cervix) at -20ºC. Adjacent sets of 50 and 5 μm thick sections were used for microstructural and compositional measurements, respectively.

Microstructural measurements: Second harmonic generation (SHG) imaging was used to quantify collagen microstructure. A femtosecond laser (MaiTai DeepSee, Spectraphysics) producing 70-fs centered at 780 nm was used to illuminate the sample while a confocal microscope (Zeiss LSM 710, Oberkochen) imaged the tissue sections using a 40 × 1.2 NA water-immersion objective lens. Backward SHG signals were collected from each image volume (80x80x50 μm). The out-of-plane collagen fiber orientation (ϕ) and the three-dimensional dispersion of the collagen fibers (SV: spherical variance) according to previous work [4]. Analyses were performed in Matlab (Mathworks).

Compositional measurements: High-definition Fourier transform infrared (HD-FTIR) spectroscopic imaging [5] was used to quantify changes in protein secondary structure. HD-FTIR images were obtained on a Cary 670 spectrometer (Agilent) coupled to a Cary 620 microscope (Agilent) using a 15x reflective objective in high-magnification mode with a 128x128 element focal plane array (FPA) Mercury-Cadmium-Telluride liquid nitrogen cooled detector providing 1.1 μm square pixels. Background spectrum was acquired at 128 coadditions per pixel on a clean area of the slide. Each spectrum was baseline corrected to account for scattering and truncated to the lower noise spectral range of 900 to 3800 cm^{-1}. Initial data was processed in Python with further data processing and analysis occurring in either ENVI (L3Harris Geospatial) or Matlab.

Specifically, we spectroscopically quantified the components of the Amide I band (sensitive to protein secondary structure [6]), glycosaminoglycans and two of the major collagen cross-links (pyr and deH-DHLN) and mapped their spatial distribution as a function of anatomical location.

Predictions of tissue origin and dysfunction using microstructure: We evaluated two prediction tasks using machine learning: (1) WT tissue origin (inner cervix, outer cervix, or tendon) and (2) detection of

missense mutation using SHG images. For classification settings, we used stratified cross-validation, i.e., where each split of train and test is proportional to the distribution of class labels of the whole dataset. Results were evaluated using 5-fold cross-validation and compared against a random performance baseline of 25% accuracy.

RESULTS

The morphological effect of a collagen III missense mutation was more clearly seen in the cervix than tendon. The cervix in TM mice was smaller in diameter and had a smaller cervical canal than WT (Fig 1E).

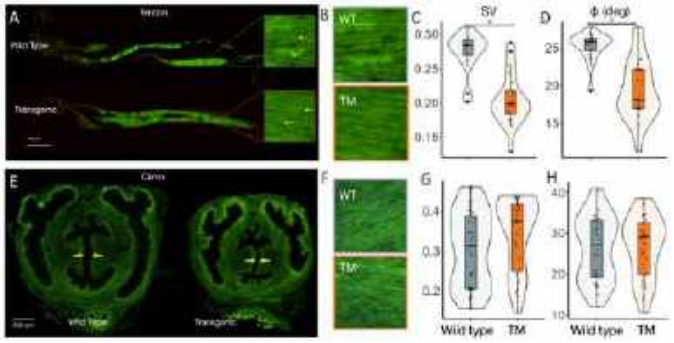

Figure 1: Tissue specific changes from Col3a1 mutation (TM)

Collagen III missense mutation disrupted tendon, but not cervix, collagen microstructure. There were distinct and measurable microstructural differences in tendon with the Col3a1 mutation. Fibers were more heterogeneous in the WT group (Fig 1B) and measured as a decrease in SV (Fig 1C) in contrast to the trend of the cervix. The Col3a1 mutation markedly decreased the degree of alignment (ϕ, Fig 1D) in tendon but had no effect in the cervix.

Collagen missense mutation affects more than collagen content. On average there were significant spectral differences between the WT and TM samples including absorbance at 1336 cm^{-1}, 1392 cm^{-1}, 1452 cm^{-1}, and line shape differences in the Amide I (1640 cm^{-1}) and Amide II (1536 cm^{-1}) bands and are indicative of differences in protein composition and secondary structure. The spatial variation in Amide III (collagen) normalized intensity at 1240 cm^{-1} (Fig 2A) highlights collagen content across the tendon with increased heterogeneity in WT. Spectral differences in tendon were also found at 1080 cm^{-1} (phosphate stretch), Amide I and II, and 1744 cm^{-1} (C=O stretch). Similar variations were found in the cervix but at different spectral values. The spatial distribution of the Amide I normalized intensity (1516 cm^{-1}) was increased between the IZ and OZ of the cervix and the vaginal wall (Fig 2C,E) and decreased intensity in WT (Fig 2D).

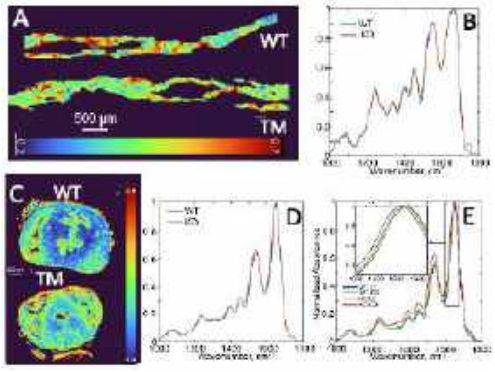

Figure 2: Missense mutation changed Coll III distribution in tendon (A,B) and cervix (C-E).

Predicting tissue origin and missense mutation: The machine learning model accuracy for predicting WT tissue origin (tendon, inner cervix, or outer cervix) was 96.4 (± 0.03)% (Fig 3A). This model was also able to differentiate TM from WT tendon with 94.4 (± 0.06) % accuracy (Fig 3B).

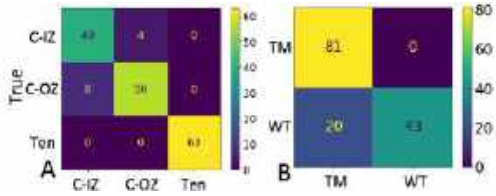

Figure 3: Accuracy of prediction of WT tissue origin (A); between WT and TM (B).

DT-MRI measurements were sensitive to the effects of collagen III mutation. Longitudinal diffusivities and fractional anisotropy decreased in cervix with missense mutations (Fig 4). There was no effect on diffusion in the perpendicular direction. FA maps reveal spatial heterogeneity.

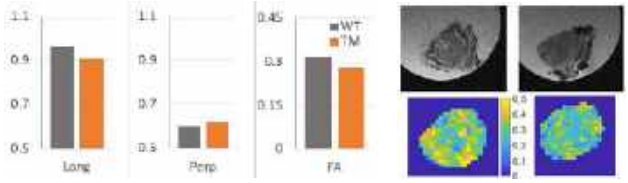

Figure 4: Diffusion tensor metrics of inner zone in cervix indicative of tissue microstructure. Spatial map of FA (bottom

DISCUSSION

The effects of collagen III on structural determinants of tissue quality were tissue specific. The overall size of the cervix was affected by the missense mutation but only subtle changes in fiber dispersion. In contrast there were clear differences in tendon fiber dispersion and orientation between the WT and TM; however there was overlap in SV values. Some of the WT mice had portions of tendon with similar structural phenotypes as those with the collagen mutation indicating that genetic mutations in collagen manifest heterogeneously.

Accordingly, the missense mutation altered the spatial distribution of the Amide bands in both tendon and cervix. The missense mutation decreased collagen III heterogeneity along the tendon length. Similar radial changes were found in the cervix: the outer zone became enriched in type III collagen whereas the inner zone in type I. Changes in Amide I may be due to increased triple helix (1637 cm^{-1}) and α-helix vibrations (1658 cm^{-1}) [6]. The variation in C=O stretch in tendon between WT and missense mutations may indicate differences in glycosaminoglycan (GAG) content and composition [7].

DT-MRI diffusion metrics complemented the microscopy results providing additional evidence of subtle changes in cervix microstructure wherein the longitudinal diffusion was most sensitive. Importantly, these data indicate the potential of DT-MRI as a non-invasive imaging modality to detect the effect of collagen dysfunction.

We were successful in using machine learning to develop a predictive model of tissue origin and dysfunction with high accuracy. The capacity to distinguish tissues using a single model suggests that a single principle of structure-function may be possible - even for tissues with clearly distinct biological functions such as tendon, cervix. Future work by our group aims to confirm and expand upon these results to provide novel, clinically viable metrics of tissue function.

ACKNOWLEDGEMENTS

We are grateful to the lab of H Dietz for donating the tissues.

REFERENCES

[1] Zitnay J et al Sci Adv 6.35 (2020). [2] Bower C et al J Clin Inv 130.2 (2020) [3] Pineda Guzman R et al A Biomed Eng (2023) [4] Rao R et al Optics Express (2009) [5] Bhargava R et al Ann Rev Analy Chem 16 (2023) . 2023 Jun 14;16:205-30. [6] Belbachir K et al A& Bioanaly Chem 395.3 (2009) [7] Lettow et al A&Bioanaly Chem 412.3 (2020).

PROFIBROTIC AND MYOFIBROBLAST ACTIVATION GENE EXPRESSION IN RIGHT VENTRICULAR CARDIAC FIBROBLASTS IN PULMONARY ARTERIAL HYPERTENSION

Giuditta Monti (1), Yufan Li (1), Daniela Valdez-Jasso (1)

Department of Bioengineering, University of California, San Diego
La Jolla, California, United States

INTRODUCTION

Pulmonary arterial hypertension (PAH) is a vascular disease characterized by a sustained rise in mean pulmonary arterial pressure exceeding 20 mmHg [1]. Despite being 4 times more predominant in women, men have worse outcomes and lower survival rates [2]. In PAH the right ventricle (RV) can adapt to the pressure overload. However, if left untreated, this often results in right heart failure. Thus, RV function is an important predictor of morbidity and mortality in PAH patients [3].

Clinical data have shown RV diastolic stiffening in PAH patients [4]. Our group and others have used the well-established rat model of PAH (sugen-hypoxia) and found RV myocardium diastolic stiffening to be a mechanism to compensate for the sustained pressure [4]. When examining the passive tissue properties of the intact and decellularized myocardium via planar biaxial mechanical testing, our group found significant remodeling of the collagen extracellular matrix (ECM) [5]. However, in this same study, the collagen concentration did not appear to be significantly different [5]. When we measured profibrotic and myofibroblast gene expression in RV tissues, we found them to be upregulated. Thus, we inferred that RV cardio fibroblasts (CFs) have a role in RV remodeling and investigated their response to mechanical stimuli (i.e. substrate stiffness and stretching). We thus hypothesize that in PAH these RVCFs get activated, leading to an increase in myofibroblast population, collagen production, and ECM remodeling, which leads to progressive RV diastolic stiffening.

METHODS

Adult cardiac fibroblasts were isolated from right ventricular (RV) free wall harvested from normotensive male Sprague–Dawley rats (Charles River Laboratories, Wilmington, MA, USA) and cultured in two T75 flasks per animal. After reaching confluency, cells were detached and platted onto collagen-coated circular hydrogels (12 mm diameter) on a PDMS membrane (200,000 to 300,000 cells were plated on each hydrogel). The remaining cells were platted back in a T75 flask and used in following experiments, up to 3 passages. Thus, up to six experiments can be completed with the cells isolated from one RV. The hydrogels were designed and produced to be at 7 kPa or 40 kPa, the approximate stiffness experienced by cells in healthy or pathological conditions, as reported by Jang et al [6]. To account for the strain experienced by the fibroblasts in pathological conditions due to the changes in pressure, and thus vessel diameter, the PDMS membranes were biaxially stretched by 10% in a custom-made 3D-printed polycarbonate circular stretcher. The control group was plated on 7kPa hydrogels on unstretched membranes [7]. To exclude the role of animal serum from our data, the cells were fed serum-free DMEM media at the time of stretch, 24 hours before being harvested and lysed. The isolated RNA was then used to synthetize cDNA and run qPCR to determine the changes in gene expression due to both changes in stiffness and stretching. The cells cultured on each gel constitute one analyzed sample. The mRNA of Collagen 1a1 (*Col1a1*), Collagen 3a1 (*Col3a1*), Elastin (*Eln*), lysyl oxidase-like 1 (*Loxl1*), α-smooth muscle actin (Acta), fibronectin 1 (Fib1), and muscleblind-like protein 1 (*MBNL1*) were measured and normalized to the housekeeping gene 18S ribosomal (Figure 1). The data was analyzed using two-way ANOVA, with stiffness and stretch being the fixed factors.

RESULTS

Profibrotic and Myofibroblast Activation Gene Results:

QPCR analysis of RVCFs harvested from male rats and cultured on hydrogels of different stiffnesses (7 kPa and 40 kPa) and with different stretch (none or 10%) showed that all the analyzed genes changed under these conditions. More specifically, the profibrotic genes *Col1a1*, *Col3a1*, and *Fn1* genes were upregulated on a stiffer substrate in cells derived from male rats. The myofibroblast activation genes *Loxl1* and *Acta* were also upregulated when the samples were stretched (**Figure 1)**. Each dot in Figure 1 represents one sample (cells cultured on one single hydrogel).

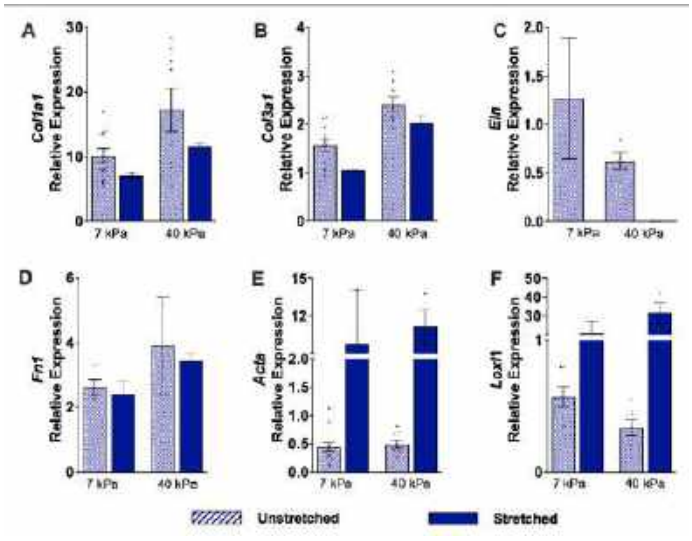

Figure 1: Relative expression of profibrotic genes (A) *Col1a1* (B) *Col3a1,* (C) *Eln,* (D) *Acta,* (E) *Fn1,* (F) *Loxl*1 in RV cardiac

fibroblasts isolated from male rats and cultured on different substrate stiffness (7 kPa and 40 kPa representing normotensive and PAH conditions) and stretch (10% or none). The expression is relative to the housekeeping gene 18S and plotted as mean ± standard errors of the mean of mRNA levels. *p<0.05 stiffness and # p<0.05 stretch.

DISCUSSION

Our studies on male derived RV fibroblasts show a significant upregulation of profibrotic genes due to increased substrate stiffness (*Col1a1, Col3a1, Fn1*) (**Figure 1**). The myofibroblast activation genes *Acta* and *Loxl1* were significantly upregulated by stretch, but not by stiffness (**Figure 1**). Thus RV male-derived cardiac fibroblasts respond more to changes in substrate stiffness and myofibroblast activation genes to stretch. While our preliminary data are limited to male rats, we are expanding our study to include fibroblasts collected from female rats. Based on our mechanobiology studies on PAAFs, we have observed significant differences in profibrotic gene expression between male and female derived cells [7].

Based on the findings from a detailed literature review, we found that MBNL1 is crucial to myofibroblast activation in myocardial hypertrophy [8]. Since myofibroblast activation also occurs in PAH, we hypothesized that the RNA-binding protein *MBNL1* plays a role in myofibroblast activation in PAH [9]. Preliminary qPCR results on a control sample (male RVCFs on a 7 kPa gel, with no stretch) showed that the *MBNL1* primers we designed can detect the gene with high specificity, and that this gene is expressed in rat RVCFs (**Figure 2A**). In addition, *MBNL1* expression increased when samples were stretched (10%) and on a stiffer substrate (40 kPa) (**Figure 2B**).

A study by Elhasnaoui et al. on primary tumor cells showed that estrogen is a key modulator of *MBNL1* concentration [10]. Thus, we hypothesize that *MBNL1* relative expression is upregulated in the RV and modulated by estrogen, making *MBNL1* one of the intermediaries in the pathways that make PAH sex dependent. As a further step in understanding the role of sex hormones in PAH, we will incorporate estrogen studies to study its potential role in upregulating or downregulating the analyzed genes.

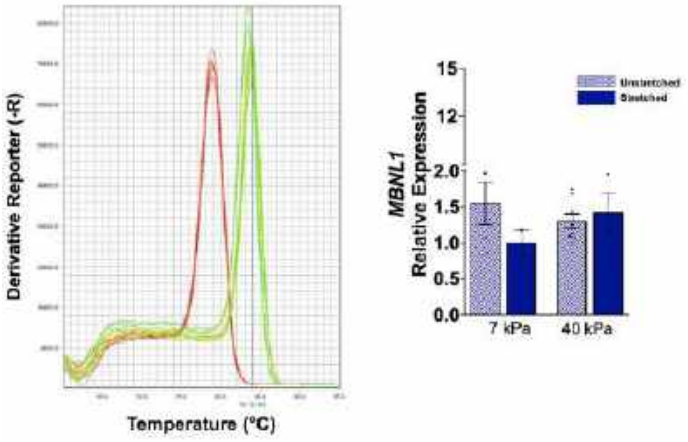

Figure 2: (A) The red peak in the melt curve represents the housekeeping gene 18s as control. The green peak represents *MBNL1*. This plot shows that the primers were designed correctly and *MBNL1* is in fact expressed in RV cardiac fibroblasts. (B): *MBNL1* relative expression in male rats changes as fibroblasts are stretched and on a stiffer substrate.

Finally, our experimental data will be employed to expand the biochemical model developed by Saucerman et al. [11] This model maps the cellular pathways of cardiac fibroblasts to provide quantitative predictions of the biomechanical outputs using normalized Hill-type ordinary differential equations [11].

ACKNOWLEDGEMENTS

This work was funded by National Heart, Lung, and Blood Institute Grants 1R01HL155945-01 (to D. Valdez-Jasso) and National Science Foundation CAREER Award 2046259 (to D. Valdez-Jasso).

REFERENCES

[1] Montani, D et al., *Orphanet J. Rare Dis.*, 8(97), 2013.
[2] Morris, H. et al., *Clin. Chest Med.*, 42(1):217–228, 20215.
[3] Chalise, U. et al., *Am. J. Physiol.-Heart Circ. Physiol.*, 326(1): H223–H237, 2024.
[4] Kwan, E. D. et al., *Am. J. Physiol.-Heart Circ. Physiol.*, 321(4): H702–H715, 2021.
[5] Vélez-Rendón, D. et al, *J. Biomech. Eng.*, 141(091011), 2019.
[6] Jang, S. et al., *J. Am. Heart Assoc. Cardiovasc. Cerebrovasc. Dis.*, 6(9): e006084, 2017.
[7] Wang, A. et al., *Cells*, 10(5):1000, 2021.
[8] Xu, Y. et al., *J. Cell. Mol. Med.*, 25(2): 1100–1115, 2021.
[9] Bugg, D. et al., *Cell Stem Cell*, 29(3): 419-433.e10, 2022.
[10] Elhasnaoui, J. et al., *Cancers*, 13(24), 2021.
[11] Zeigler, A. C. et al., *J. Mol. Cell. Cardiol.*, 94:72–81, 2016.

HEMODYNAMIC ANALYSIS OF SINOTUBULAR JUNCTION PLICATION TECHNIQUES DURING ASCENDING AORTIC REPLACEMENT

Hannah Zhai (1), Yurui Chen (1), Yu Hohri (2), Hiroo Takayama (2), Vijay Vedula (1)

(1) Department of Mechanical Engineering, Columbia University, New York, NY, USA
(2) Department of Surgery, Columbia University Medical Center, New York, NY, USA

INTRODUCTION

The sinotubular junction (STJ) plays an important role in the function and motion of the aortic valve. [1] In some cases of STJ dilation, it is coupled with an aortic root aneurysm, for which current guidelines recommend aortic root surgery if the root diameter is >4.5cm. [2] However, root surgery is not recommended if the STJ dilation occurs without a root aneurysm, as the longer operative time introduces unnecessary risks. [3] These patients with STJ dilation, but without root aneurysms (see Fig 1a), are treated by ascending aortic replacement surgery.

The typical replacement surgical procedure is a secure proximal anastomosis technique, in which a prosthetic graft is secured to the native aorta using a simple suture technique to shrink the STJ diameter, shown in Fig. 1(b). In this work, we aim to evaluate the hemodynamic performance of a new technique, which utilizes a Hegar dilator to tighten the graft in the STJ region to a specific optimal size based on preoperative computerized tomography (CT) imaging. After tightening, the graft is anastomosed with the primary prosthetic graft.

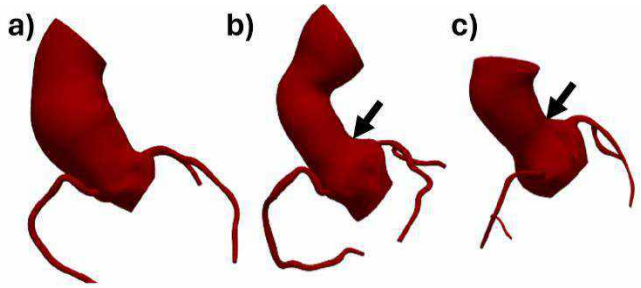

Figure 1: Patient-specific models of ascending aorta. a) before surgery; b) Patient A: after surgery, old surgical method; c) Patient B: after surgery, new method.

In this preliminary analysis, we evaluate the hemodynamic patterns in the ascending aorta for two patients, one from each surgical method. We aim to visualize the blood flow in the STJ region after both surgeries using personalized multiscale computational hemodynamics modeling, and examine if the new technique restores 'normal' flow patterns.

METHODS

We use SimVascular's workflow to perform multiscale patient-specific blood flow modeling in ascending aorta with coronary circulation (Fig. 2).[4,5]

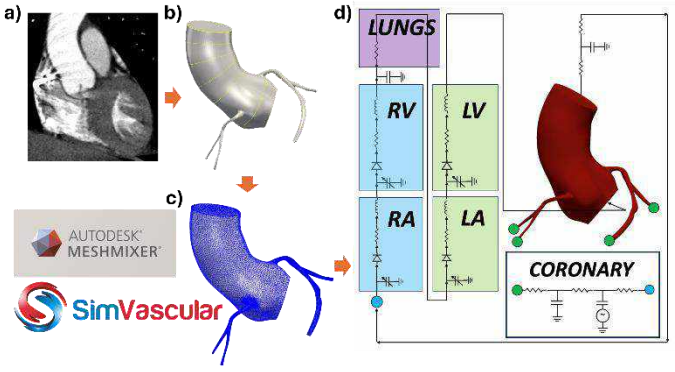

Figure 2: Workflow for multiscale patient-specific blood flow modeling. a) CT images of the ascending aorta. b) Segmentation and model creation pipeline. c) Mesh using boundary layers and local refinement. d) Schematic of the closed loop 0D/3D model used for multiscale blood flow simulation.

The image-to-flow pipeline (Fig. 2) to evaluate the hemodynamic patterns for each case begins with the CT images, where segmentation was performed using SimVascular to extract the aorta, starting from the aortic root through a short portion of the ascending aorta, with major

coronaries (Figs 2a,b). [4] The surface was then exported as a triangulated surface and was smoothed at the vessel bifurcations and refined in Meshmixer (Autodesk Inc.). The refined model was then reimported back into SimVascular, where the surface and volumetric meshes were generated, employing regional refinement for the coronaries, with a boundary layer mesh in the ascending aorta (Fig. 2c). The total number of tetrahedral elements for each model was ~1M. The 3D model was coupled to a 0D lumped parameter network (LPN) model of the circulatory system to apply physiologically relevant boundary conditions (Fig. 2d). The parameters of the LPN model were tuned manually to fit clinical data (Table 1).

Table 1: Patient Clinical Data

	Patient A (old method)		Patient B (new method)	
	Pre	Post	Pre	Post
BP (mmHg)	120/70	129/79	146/96	130/88
HR (bpm)	59	74	70	85
Height (in)	65		67	
Weight (lb)	175		179	

We modeled blood as an incompressible Newtonian fluid and assumed the walls to be rigid. We employed stabilized finite element methods to simulate blood flow with the implicit, second-order accurate, generalized-α time integration method, implemented in a validated open-source solver, *svFSI*.[6] The coupling between the 0D and 3D flow solvers is achieved using a modular, implicit coupling approach to resolve the multiscale interactions between the 3D and 0D flow solvers. [7] The resulting nonlinear equations are solved using the bi-partitioned method for incompressible flows with backflow stabilization. [8] Blood flow simulations were performed for pre- and post-operative models for each patient, from each surgical method, and the resulting hemodynamics were compared.

RESULTS

The resulting velocity and pressure fields, flow rates, and wall shear stresses were simulated for each case, for six cardiac cycles until the LPN flow rates and pressures were equilibrated. A representative flow field and flow rate waveforms at the inlet and various outlets are shown in Fig. 3 for the preop model (Patient B).

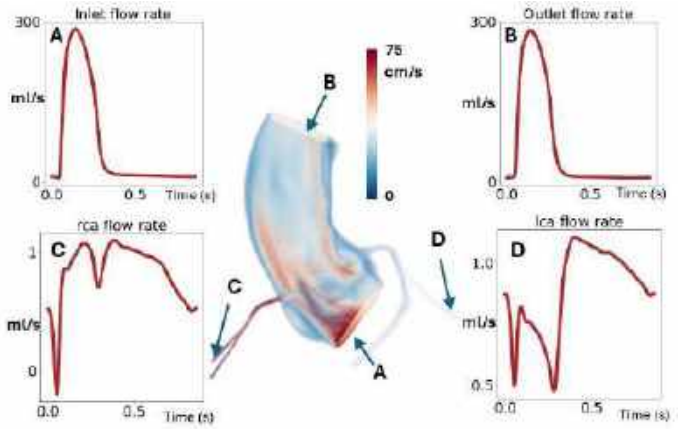

Figure 3: Flow field during peak systole and time-varying flow rates at various boundary faces (A-D) for Patient B, pre-surgery.

Additionally, the time-averaged wall shear stress (TAWSS) was computed for each of the four models and is shown in Fig. 4. We note that the TAWSS appears to be generally elevated in the STJ region in the postoperative models, with the newer method (Patient B) demonstrating a higher degree of elevation.

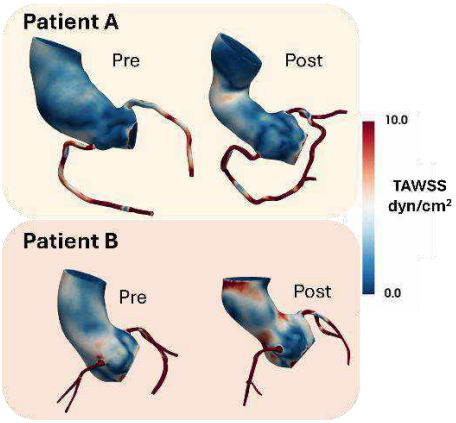

Figure 4: Comparison of TAWSS between the two surgical methods, pre- and post-surgery. (top, Patient A) old; (bottom, Patient B) new method.

DISCUSSION

Here, we performed patient-specific blood flow modeling for two patients with STJ dilation and compared two surgical techniques to address it. Our preliminary analysis found that the TAWSS increased in postoperative models, with a marked increase in the newer method, where the dimensions of the aorta are closer to a normal value, compared to the older method. However, further analysis is required against healthy subjects to understand the hemodynamic implications of the newer surgical reconstruction technique.

One of the limitations of the current model is that the boundary conditions for the pre/postop simulations for both patients were different, tuned to match the patient's blood pressure at the time of CT imaging. This resulted in changes in the LPN parameters, including cardiac output. To perform a fair comparison between the two methods, we plan to virtually apply the new surgical technique to patients who underwent the old surgical method, by morphing the STJ diameter to the size of the Hegar dilator that the new technique would have used. Additionally, we plan on simulating both surgical methods with the same boundary conditions tuned to the preoperative model, to determine the differences between the two procedures independent of variations such as the patient's blood pressure at the time of measurement.

Further, to address the current limitations of the preliminary analysis, we additionally plan to include fluid-structure interaction (FSI) with the aortic valve to measure aortic insufficiency, a major health concern in these patients, and perform blood flow modeling without a rigid wall assumption. We will employ the material properties of the prosthetic graft while performing FSI simulations to capture realistic deformations and hemodynamic stresses. We will perform this analysis on multiple patients to demonstrate statistical significance.

ACKNOWLEDGEMENTS

We acknowledge computing resources from Columbia University's Shared Research Computing Facility - Ginsburg high performance computing cluster.

REFERENCES

[1] El Khoury, G et al., *Curr Opin Cardiol*, 20(2):115-121 (2005)
[2] Isselbacher, E et al., *J Am Coll Cardiol*, 146(24):344-482 (2022)
[3] Conzelmann, LO et al., *Eur J Cadiothorac Surg*, 49(2):44-52 (2016)
[4] Updegrove, A et al., *ABME*, 45.3 (2017)
[5] Sankaran, S et al., *ABME*, 40.10 (2012)
[6] Zhu, C et al., *JOSS*, 7.78 (2022)
[7] Esmaily-Moghadam, M et al., *JCP* 244 (2013)
[8] Esmaily-Moghadam, M et al., *CMAME* 286 (2015)

SB³C2024
Summer Biomechanics, Bioengineering and Biotransport Conference
June 11-14, Lake Geneva, WI, USA

MICROFLUIDIC DUAL-GEL CELL CULTURE MODEL: STUDYING CELL MIGRATION UNDER CONTROLLED INTERSTITIAL FLOW

Rossana Iturbide (1), Alimohammad Anbari (1), Sihong Wang (2), Jing Fan (1)

(1) Mechanical Engineering Department, The City College of New York, New York, NY, USA
(2) Biomedical Engineering Department, The City College of New York, New York, NY, USA

INTRODUCTION

Breast cancer is the most common cancer type among women in the United States [1]. The American Cancer Society estimates that the number of new cases will reach 310,720 and the number of deaths will reach 42,250 in 2024 [2]. These prognostics highlight a need for the early detection and treatment of breast cancer. Furthermore, breast cancer development can lead to metastasis. Metastasis causes high mortality in most cancers because cells migrate from the primary site and spread to lymph nodes or distant organs [3]. During the initial stages of metastasis, cancer cells migrate by degrading and moving through the ECM (extracellular matrix) of the surrounding tissue. Studies postulate that metastasis is driven by cell invasion and migration through the ECM during those initial stages. Therefore, a deeper understanding of the cell-matrix dynamics is necessary to identify the necessary steps towards metastasis prevention.

Cell migration is affected by interstitial flow through individual and collective contributions of various biological phenomena. The connection between interstitial flow and cell migration is of key interest because interstitial flow is linked to extracellular matrix permeability and provides direct mechanical cues via shear and normal stress. To identify the mechanisms that regulate cell migration, it is necessary to manipulate interstitial flow velocity and extracellular matrix permeability independent of parameters such as stiffness and cell-binding site density. Previous studies have used single gel-based cell culture models to study cell migration, but these models are limited by the interconnection between various properties of a hydrogel. To improve traditional single gel-based cell culture models used to observe cell migration, we propose a dual-gel dual-porosity 3D cell culture matrix that enables independent control of key matrix properties that retains and mimics the structural heterogeneity of the extracellular matrix. We study the morphology and migration of GFP MDA-MB 231 breast cancer cells under controlled interstitial flow in a dual-gel matrix consisting of stiffer primary GelMA-PEGDA (gelatin methacryloyl-polyethylene glycol diacrylate) microgels, acting as the main cell adhesive, and a secondary softer alginate hydrogel in the interstitial spacing of the primary matrix, acting as a control mechanism for permeability and directly compare with our previous study that used collagen as a secondary gel. Our results confirm that the microfluidic dual-gel cell culture model improves the single gel-based cell culture model and allows quantitative studies on interstitial flow effects on cell behaviors.

METHODS

The microfluidic dual-gel dual-porosity cell culture model is manufactured through standard soft lithography using a layer of PDMS (polydimethylsiloxane). The cell culture model shown in Figure 1 consists of: (1) four culture chambers measuring 1000 μm × 1000 μm × 200 μm that are surrounded by 30 μm square filters, (2) two microgel injection inlets labeled A1 and A2, (3) four outlets labeled C1, C2, C3, and C4, (4) two cell injection inlets labeled B1 and B2, and (5) a central inlet used for medium injection labeled D. The PDMS layer is bonded to a coverslip via oxygen plasma treatment.

The 100 μm diameter GelMA-PEGDA microgels are made by crosslinking monodisperse droplets generated by a PDMS droplet generating device. The microgels consist of an aqueous solution of: *20 wt.%* PEGDA, *8 wt%* GelMA, and *0.5 wt.%* Irgacure 2959 as the dispersed phase, and HFE oil with *2 wt%* Fluorosurfactant as the continuous phase. The sodium alginate solution consists of an aqueous solution of *1.5 wt%* sodium alginate, 15 mM $CaCl_2$, and 7.5 mM DM-Nitrophen.

Following the microfluidic model fabrication is degassing and microgel injection. The densely packed microfluidic devices, shown in Figure 2, are placed under the biological hood for UV sterilization. After sterilization, cells are seeded at a 8×10^6 *cells/mL* cell density. We allow 24 hours for the cells to adhere to the microgels before we fill the interstitial space between the microgels by the softer secondary alginate

gel. The migration behavior of the cancer cells can be compared to the dual gel system we previously studied using collagen as the secondary gel. In both studies, the cells are cultured under interstitial flow of 5 μm/s. After 24 hours of live cell imaging, we assess cell viability using ethidium homodimer staining.

The study using collagen as the secondary gel uses Collagen Type I 1.5 *mg/mL* collagen concentration and 5×10^6 *cells/mL* cell density. The collagen solution is kept below 4°C to avoid gelation. After cell seeding the microfluidic device is placed in an incubator at 37°C and 5% CO_2 for two hours for gelation. The collagen study uses RFP MDA-MB 231 cells and as a result cell viability tests use Calcein AM. The collagen iteration of the study computed 4D tomographs using Imaris software. Using Imaris allows spot tracking to automatically capture and track cell migration over the length of the 24-hour imaging with the appropriate modifications. Live cell imaging is captured using confocal microscopy (Zeiss LSM 800).

RESULTS

First, the microfluidic dual-gel cell culture model is characterized using: (1) volume fraction of the primary gel matrix, (2) confining pore size, (3) interstitial fluid velocity, (4) stiffness, and (5) permeability. Interstitial flow promotes amoeboid mobility. The collagen study showed a 90% viability over three days, shown in Figure 3, verifying the feasibility of our 3D invitro cell culture model. Experiments were conducted multiple times to confirm reproducibility. Cell migration behavior is quantified by analyzing: (1) motility, (2) migration speed, (3) persistence, and (4) cells aspect ratio. The primary gel matrix promotes cancer cell motility with mesenchymal-like morphology. The presence of the GelMA-PEGDA microgels caused a high percentage of mesenchymal-like cells due to the microgels' strong cell binding surface. At a 8 *wt%* concentration, GelMA offers more cell binding sites than collagen at 1.5 *mg/mL* concentration.

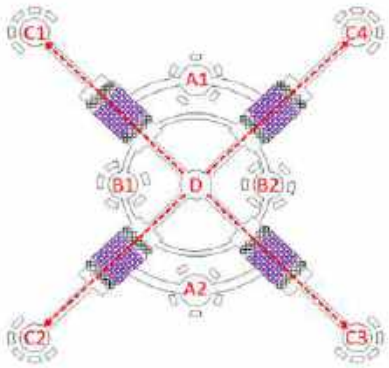

Figure 1: Schematic of the microfluidic cell culture chip. The red dashed arrow shows the direction of the fluid flow.

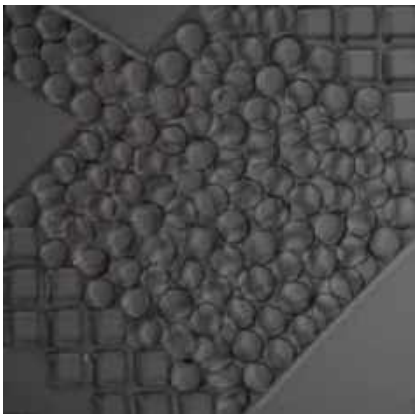

Figure 2: Confocal image of densely packed GelMA-PEGDA microgels in microfluidic device.

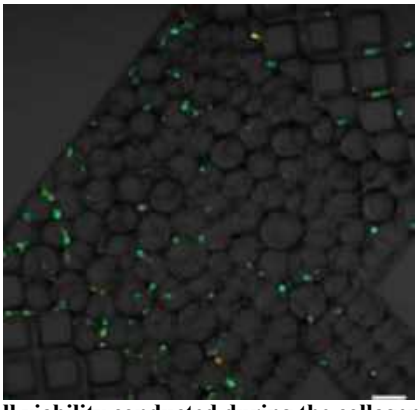

Figure 3: Cell viability conducted during the collagen study using 2 μM Calcein.

DISCUSSION

Our results and observations are consistent with previous studies that state interstitial flow promotes MDA-MB 231 cells in 3D cell culture towards the amoeboid cell morphology and motility. This is explained by low adhesion molecules present such as fibronectin during flow, as flow takes away the cell-secreted adhesion molecules. This phenomenon prevents fibril assembling which further prevents durable adhesion formation with ECM fibers. Our proposal to replace collagen with alginate will corroborate our findings because alginate has no cell-binding sites. Our dual-gel dual-porosity cell culture chamber effectively demonstrates that the stiffness of the primary gel is the dominant local mechanical property that regulates cell migration behaviors. With the substitution of collagen with alginate, we will eliminate all the cell-binding sites of the secondary gel and open the platform to a range of other studies.

ACKNOWLEDGEMENTS

Funding support is provided by the National Science Foundation (NSF), project 2047072.

REFERENCES

[1] Breast Cancer Statistics. Division of Cancer Prevention and Control, Centers for Disease Control and Prevention. *cdc.gov.*2023.
[2] Breast Cancer Facts & Figures 2022-2024. American Cancer Society. *cancer.org.* 2022.
[3] Park, M et al., *Int J Mol Sci,* 23:6806, 2022.

A THERMODYNAMICS-BASED APPROACH FOR ESTIMATING VENTRICULAR EFFICIENCY: APPLICATION IN PATIENTS WITH SINGLE VENTRICLE PHYSIOLOGY

S. Gurung (1), A. Pogosyan (2), G.S. Perens (3), K.L. Nguyen (1,2), J.P. Finn (1,2)

(1) Department of Radiological Sciences, University of California, Los Angeles, California, USA
(2) Department of Medicine, University of California, Los Angeles, California, USA
(3) Department of Pediatric Cardiology, University of California, Los Angeles, California, USA

INTRODUCTION

Patients with congenital heart disease (CHD) have complex cardiovascular malformations and compromised blood circulation. One method for assessing energetics in complex CHD is through the estimation of ventricular mechanical efficiency (VE). Current approaches for VE estimation require invasive cardiac catheterization-based pressure-volume loops and inferior vena cava (IVC) occlusion, which makes it unsuitable for routine clinical exams. A new model for VE estimation is developed based on thermodynamic principles that eliminates the need for IVC occlusion and could be estimated using radiographic and hemodynamic metrics obtained during routine clinical exams. The developed model aims to provide additional information about ventricular performance, which may aid in clinical diagnosis and surgical treatment planning.

METHODS

The ventricular efficiency model VE_{Thermo} was developed based on the thermodynamic analysis of energy exchange occurring during each cardiac phase W_{1-2}, W_{2-3}, W_{3-4} and W_{4-1} (Figure 1). VE_{Thermo} is defined as the ratio of energy in blood flowing out of the ventricle to the total energy expected to be consumed by the ventricle during a complete cardiac cycle (Eq. 1). VE_{Thermo} is then compared with ventricular efficiency approximated from the pressure-volume area (PVA), VE_{PVA} (Eq. 2) [1]. In this work, VE_{Thermo} and VE_{PVA} are used to assess the ventricular performance of patients with single ventricle physiology (SVP) at different stages of single ventricular palliation.

This study was approved by the UCLA Institutional Review Board and utilized retrospective clinical data from 17 SVP patients who had undergone clinical cardiovascular magnetic resonance imaging (MRI) exams at 1.5T or 3.0T. The data included in the simulations consisted of 4D MUSIC and cine MRI, 2D and 4D flow MRI, cardiac catheterization-based aortic (P_{aortic}) and ventricular pressures ($P1$, $P2$, $P3$, and $P4$), and vital signs (heart rate, blood pressure, pulse oximetry). MRI DICOMs were analyzed in Circle cvi42 and 3D Slicer to obtain ventricular end-systolic volume (ESV), end-diastolic volume (EDV), and aortic flow rate (Q_{aortic}). Baseline data for 19 healthy female volunteers aged 20 to 50 years, denoted by 'Left Ventricle (LV) in 4-chamber heart' were used for comparison. Student's t-test was used to compare the difference between the mean VE of each SV palliation stage and healthy LV. Next, errors for estimation of VE_{Thermo} based on non-invasive blood pressure (NIBP) versus cardiac catheterization-based pressure in SVP patients were analyzed.

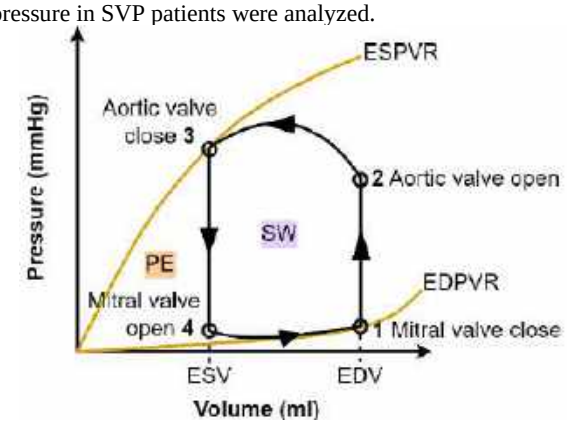

Figure 1: Pressure-Volume loop for left ventricle. EDV, end-diastolic volume; ESV, end-systolic volume; EDPVR, end-diastolic pressure-volume relationship; ESPVR, end-systolic pressure-volume relationship; PE, potential energy; SW, stroke work

$$VE_{Thermo} = \frac{P_{aortic} * Q_{aortic}}{HR * (W_{1-2} + W_{2-3} + W_{3-4} + W_{4-1})} \quad (1)$$

$$VE_{PVA} = \frac{P_{aortic} * Stroke\ volume}{Stroke\ work + \frac{1}{2} * ESV * P_3} \quad (2)$$

RESULTS

Ventricular energy expended in each cardiac phase as a percent of total energy consumed by the ventricle per cardiac cycle (E_{in}) for SVP patients is shown in Table 1. Figure 2 shows the variation of stroke work (SW) and VE_{Thermo} for SVP patients and healthy volunteers across a spectrum of age range. SVP patients had a SW range of 0.05 J to 0.86J, an ejection fraction (EF) range of 46 % to 77 %, and VE_{Thermo} range of 11.8 % to 35.3%. For healthy volunteers, the SW range was 0.47 J to 1.33 J, the EF range was 51.62 % to 78.15 %, and the VE_{Thermo} range was 25.97 % to 40.47 %.

Table 1: Ventricular energy expended during each cardiac phase

Process	Cardiac phase	(% of E_{in}) Mean	(% of E_{in}) Std. dev	Sample size
1 - 2	Isovolumic contraction	31%	4%	17
2 - 3	Systolic ejection	41%	6%	17
3 - 4	Isovolumic relaxation	24%	5%	17
4 - 1	Diastolic filling	4%	1%	14

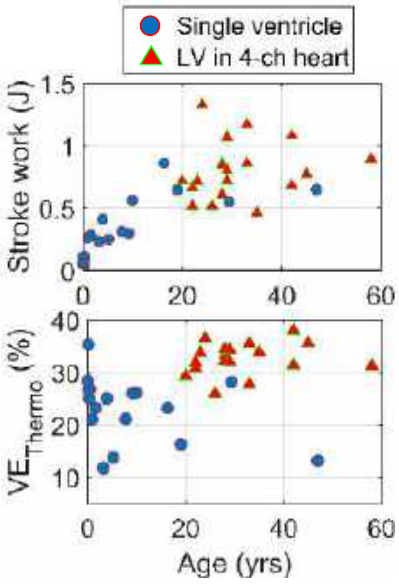

Figure 2: Stroke work and VE_{Thermo} vs age.

Figure 3 shows the variation of VE_{PVA} and VE_{Thermo} in healthy volunteers (LV in 4-ch heart) and in patients with SVP palliation. VE_{PVA} and VE_{Thermo} models in patients with SVP palliation showed a decreasing trend in mean ventricular efficiency (denoted as ×). A significant difference was found between the mean VE_{PVA} of pre-SVP and post-Fontan stages and also between healthy LV and post-Fontan (marked by * in Figure 3). A moderate correlation ($r = 0.57$, $p < 0.5$) was found between VE_{Thermo} and VE_{PVA}. NIBP for SVP patients differed from cath aortic pressure by up to 24 mmHg, but VE_{Thermo} based on NIBP differed by only 1.4 % to -3.2 % compared to VE_{Thermo} based on cardiac catheterization pressure.

DISCUSSION

First, this study demonstrates the potential of VE_{Thermo} for assessing ventricular performance in complex CHD based on themodynamic principles. Next, VE_{Thermo} and VE_{PVA} show that the ventricle's pressure-volume cycle may be less efficient as SV palliation progresses (Figure 3). Reduced ventricular efficiency observed in this study may explain the reduced performance of Fontan patients in exercise tests compared to healthy subjects [2][3]. While previous literature reports reduced cardiac function in SVP patients due to abnormal circulatory physiology, this study facilitates quantification of the change in ventricular efficiency. Reduced ventricular function in SVP patients is also evident by the lower SW for SVP patients relative to the SW of healthy volunteers, who have a typical 4-chamber heart circulatory system (Figure 2).

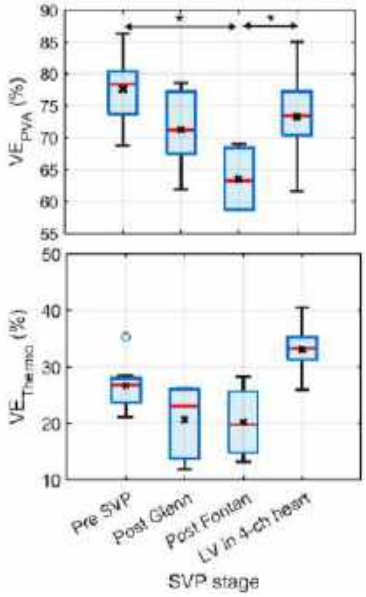

Figure 3: VE_{PVA} and VE_{Thermo} vs SVP stage.

In addition, VE_{Thermo} is expected to be sensitive to losses in the setting of ventricular systolic failure and valve regurgitation but less sensitive to diastolic failure. Using hemodynamic data from published articles, VE_{Thermo} was lower for heart failure with reduced ejection fraction patients than the normal values (~30 %). In contrast, VE_{Thermo} was near to normal or greater than normal for heart failure with preserved ejection fraction and hypertensive patients. Similar observations of near-normal or even increased ventricular efficiency in pressure overloading conditions have also been noted[4].

Strengths of this model include the simplicity and omission of the requirement for invasive IVC occlusion. VE_{Thermo} could also be estimated using NIBP (with limited accuracy) as an approximation to aortic pressure and ventricular diastolic pressures (P_1 and P_4), which were estimated analytically using the energy distribution in Table 1. Such approximations can facilitate computation of VE_{Thermo} non-invasively using routine cardiac MRI or echocardiograms in combination with data from routine vital signs. Limitations from the current work include accuracy with which the input parameters were estimated, and the small sample size used in deriving model parameters.

In conclusion, VE_{Thermo} serves as a direct metric for cardiac performance and may provide additional diagnostic information but is less invasive for patients with CHD.

ACKNOWLEDGEMENTS

We thank Dr. Takegawa Yoshida, Dr. Ihab Ayad and Dr. Daniel Levi. Funding was provided by NIH grant R01HL127153.

REFERENCES

[1] Suga, H, *Am J Physiol Heart Circ Physiol*, 236(3), H498-505, 1979.
[2] Haley, J.E.; Davis, C., *J. Cardiovasc. Dev. Dis.*, 9, 167, 2022.
[3] Pajak, L et al., *Acta Cardiologica*, 69(2), 155-160, 2014.
[4] Schipke, J.D., *Basic Res Cardiol* 89, 207–240, 1994.

SB³C2024
Summer Biomechanics, Bioengineering and Biotransport Conference
June 11-14, Lake Geneva, WI, USA

INVESTIGATING THE RANGE OF CELL CLUSTER BIOMECHANICAL BEHAVIOR WITH CLUSTER SIZE

Sara Ghanbarpour Mamaghani (1), Ethan Wagner (2), Jonathan P. Celli (2), Joanna B. Dahl (1)

(1) Engineering Department, University of Massachusetts Boston, Boston, MA, USA
(2) Physics Department, University of Massachusetts Boston, Boston, MA, USA

INTRODUCTION

Successful tissue engineering requires that biomaterials survive implantation and mechanically mimic the native tissue. Better predictive modeling and rationale design of engineered biomaterials would help advance the field. An important step for understanding the complex biomechanics of natural and engineered tissues is understanding the mechanical behavior of simpler multicellular systems. 3D cell clusters up to ~1 mm diameter (e.g., spheroids) are model systems in between single cells and tissues that are useful for understanding tissue mechanics [1]. These multicellular aggregates contain cell-cell junctions with paracrine signaling and partially recapitulate the adherent state that most human cells experience.

Cell cluster biomechanics has been studied using many of the same techniques used for single cell biomechanics. This includes bulk techniques that deform the whole cell cluster (e.g., parallel-plat compression), localized techniques that contact a small area (e.g., AFM), and interior perturbations (e.g., cavitation) [2]. From these studies, we know that the mechanical behavior of cell clusters is determined by the interaction of intercellular junctions, cell contractility, and the ECM, with some mechanical models proposed [1].

Other aspects of cell cluster biomechanics remain underexplored. All measurements have been performed on cell clusters from a narrow size range. At most, cluster size differs by a factor of 2 in a single study. *How does cell cluster biomechanics change across a wide range of sizes?* As a viscoelastic biomaterial, how fast a cell cluster is deformed and where the force is applied will affect its biomechanical response. The timescales of most spheroid mechanics measurements are on the order of seconds to several minutes to days [1, 2]. *How do cell clusters behave at millisecond timescales?* We are aware of only one study using microfluidics that probed clusters on a millisecond scale [3], compared to tens of studies with timescales on the order of seconds and longer. This timescale is important for clinical applications. For cancer metastasis, there is increasing recognition that invasive progression of cancer is not only driven by single invading cells but also by collective invasion of multicellular clusters [4]. It follows that the biomechanics of these clusters—including in circulation as they flow through vessels and capillaries—will be important factors for understanding metastasis and treating cancer.

In this work, we begin to address the questions of cluster biomechanics variation with size and millisecond timescales. Here we measure and compare the deformations of single cells and cell clusters of 2 sizes in non-contact flow conditions using microfluidics.

METHODS

PANC1 pancreatic cells (ATCC) were used. Suspensions of 3 million cells/mL containing mostly clusters with some single cells were created by gently and non-vigorously resuspending trypsinized cells. The cell clusters were suspended in aqueous 0.8% w/v methyl cellulose in phosphate buffered saline (viscosity $\mu = 110$ m·Pa).

Cell clusters were stretched in a microfluidic extensional flow device (300 µm wide, 200 µm deep), commonly called a cross-slot, consisting of two channels that intersect at 90 degrees and generate a linear extensional flow field (**Figure 1**). The cell cluster suspension and buffer solution were infused at flow rate of 4 mL/hr from two opposite inlets (extensional strain rate $\Omega = 123\ s^{-1}$). Flow focusing with a buffer sheathing flow is used to center clusters on the central streamline. Videos were captured of single cells and clusters entering the straight inlet channel (Poiseuille flow) and stretching in the central extensional flow region using brightfield microscopy at 10x (Zeiss Axiovert 200M) and a high-speed camera (KAYA Instruments JetCam, 1,300 fps). Image processing was done in MATLAB (MathWorks). Contours of the deformed cells and clusters in each movie frame were detected using the level set method [5]. From each contour, the shape metrics used to quantify deformation were the contour bounding box (width, height) and strain $\varepsilon = (a–b)/(a+b)$ where the a and b are the major and minor axes of the best-fit ellipse, respectively (**Figure 1**). The equivalent

diameter is calculated from the contour's 2D projected area: d = sqrt($4A/\pi$). For single cells that achieved quasi-static strain near the stagnation point, the cell shear elastic modulus G was calculated using the mechanical model $\varepsilon = (5/2)\mu\Omega/G$ from our previous work [6]. For this study, the deformations of single cells (average d ~ 20 µm, N = 3), smaller clusters (7 – 10 cells, d ~ 50 um, N = 3), and larger clusters (> 30 cells, d ~ 70 um, N = 3) were analyzed and compared.

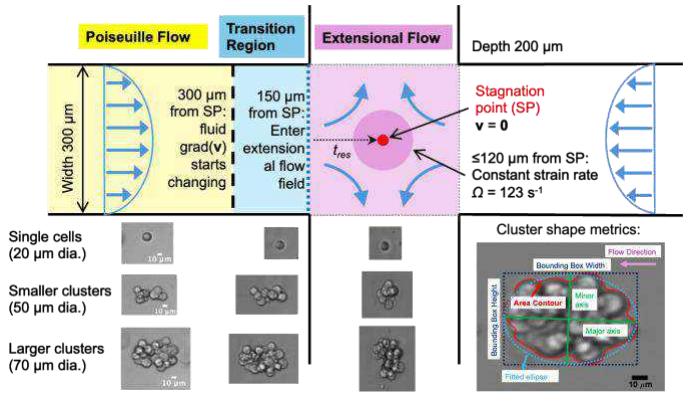

Figure 1: Schematic of the experimental set up, cluster shape metrics, and representative single cell and cluster images from the three major fluid flow regions.

RESULTS

Similar deformation trends arose for all sizes as the objects passed through the different flow zones, though the amount and rate of change of deformation varied with cluster size. In the Poiseuille flow region, objects were elongated in the flow direction. The clusters were more deformed away from a sphere shape than single cells, as seen in images (**Figure 1**) and with bounding box Δ(width) (**Figure 2A**, **Table 1**). In the transition region where the velocity gradient as measured by PIV (data not shown) began to change, objects started to compress to a spherical shape followed by elongation in the perpendicular outlet flow direction within the extensional flow region. The clusters stretched more than the single cells, as seen in bounding box Δ(height) and strain magnitudes (**Figure 2**, **Table 1**). Taken together, this indicates that single cells were stiffer than multicellular cluster sizes even for the smaller 7-10 cell clusters.

The softer clusters more rapidly deformed in response to changing hydrodynamic forces (t_{AR}, **Table 1**) and did not reach a quasi-static deformation like the single cells (**Figure 2B**). The larger clusters changed shape more than twice as fast as the smaller clusters in the extensional flow region (slope in **Table 1**, **Figure 2B**). The larger the cell or cluster, the less time it dwelled in the extensional flow region due to the lack of active trapping at the stagnation point (t_{res}, **Table 1**).

Table 1: Average shape metrics ± standard deviation for single cells and two cluster sizes (N =3 for all). Figures 1 & 2 explain table quantities.

	d [µm]	BB Δ(W) [px]	BB Δ(H) [px]	t_{AR} [ms]	t_{res} [ms]	Slope Δ strain/ ms
Single Cells	21±4	3.3±1.5	3.7±1.5	31±6	30±11	---
Smaller Clusters	48±6	21±12	16±13	17±3	20±10	0.0064± 0.0009
Larger Clusters	71±5	21±6	25±11	14±1	16±8	0.017± 0.008

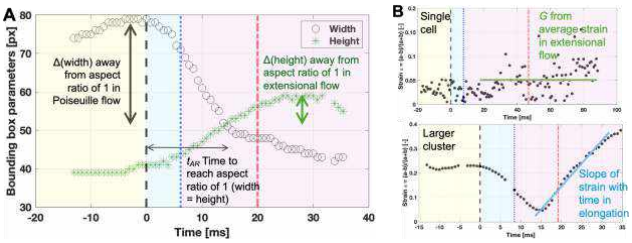

Figure 2: A) Representative bounding box width and height history for a cell cluster. B) Representative strain histories of a single cell (top) and larger cell cluster (bottom). Larger clusters deform more than single cells even though they dwell for a shorter time in extensional flow. Axes shading reflects flow region.

DISCUSSION

Cluster mechanical behavior in our experiments is reminiscent of droplet deformation behavior in linear flow fields [7]. In future work, we will use inverse finite element methods applied to our cell cluster stretching data to test which proposed spheroid mechanical model– an elastic or viscoelastic solids or a liquid with an apparent surface tension [1] – is more valid in different size ranges. Application of a model would also disentangle cluster size from amount of deformation, a limitation of the current study, by providing intrinsic mechanical properties.

Our finding that single cells are stiffer than clusters made of the same cell is consistent with a previous study that found 130-µm-diameter spheroids to be 10 times softer than single cells [3]. The single cell shear elastic modulus G = 630 ± 120 (average ± std. dev.) is similar to previous measurements of suspended cells in microfluidic devices (~ 1 kPa [8]. The large variation in G can be attributed to the small magnitude of the single cell strains that resulted in noise and scatter. Higher flow rates and stronger hydrodynamic forces would improve the signal-to-noise ratio for the single cells. Though more study is needed, we observed individual cells within clusters visibly stretching, sometimes more than the single cells studied here. Further study into the deformation of individual cells within clusters could provide helpful insights that link single cell to cluster mechanical behaviors.

Our future work includes greatly expanding the size range of spheroids from single cells up to about 1 mm diameters using agarose micro-molds (Microtissues). Based on the study presented here that explores a narrow range of cluster sizes yet seems to indicate deformation differences between 10-cell clusters and >30- cell clusters, we anticipate changes to both the elastic and viscous parts of cluster viscoelastic behavior with size.

ACKNOWLEDGEMENTS

This is supported by the National Science Foundation (CMMI Award No. 2301804). Thank you to Dr. Eric Ibarra (IRPHÉ) for discussions on implementing the level set method for edge detection.

REFERENCES

[1] Y. M. Efremov, Y.M. et al, *Biophysical Rev.* 13, 541–561 (2021).
[2] Boot, R.C., et al., *Adv. Phys. X* 6, 1978316 (2021).
[3] Panhwar, M.H., et al. *Nat. Commun.* 11, 2190 (2020).
[4] K. J. Cheung, A. J. Ewald, *Science* 352, 167–169 (2016).
[5] Wan, M., et al., *Remote Sens.* 10, 1039 (2018).
[6] Jeong, M.H., et al., *Adv. Mater. Technol.* 8, 2201412 (2023).
[7] Stone, H.A. *Annu. Rev. Fluid Mech.* 26, 65–102 (1994).
[8] Darling, E.M., et al., *Annu. Rev. Biomed. Eng.* 17:35–62 (2015).

RE-DIFFINET: MODELING DISCREPANCY IN TUMOR SEGMENTATION USING DIFFUSION MODELS

T. Ren (1), A. Sharma (1), J. Heras Rivera (1), H. Rebela (2), A. Chopra (1), E. Honey (1), M. Kurt (1)

(1) Department of Mechanical Engineering, University of Washington, Seattle, WA, USA
(2) Department of Computer Science, University of Washington, Seattle, WA, USA

INTRODUCTION

The Gliomas are the most common primary malignancies in the central nervous system (CNS). This heterogeneous group of tumors is characterized by their resemblance to glia that perform a variety of important functions including support to neurons.[1] The treatment for gliomas patient generally consists of surgery, radiotherapy, and chemotherapy and the outcomes of patients with gliomas vary widely according to the glioma type and prognostic factors. Due to the superior soft tissue contrast, multimodal MRI images, which allow the complexity and the heterogeneity of the tumor lesion to be better visualized than a CT scan, have become the golden standard for surgical decision-making for glioma patients. However, visual identification of tumor margins in CT or MRI remains a challenge for neurosurgeons and researchers. Clinically, brain tumor masks are often obtained through Magnetic Resonance Imaging (MRI) scans, which require experienced radiologists to manually segment tumor sub-regions. This is a long process that is unscalable to the needs of all patients. Thus, the recent growth of machine learning technologies holds promise to provide a reliable and automated solution to segmentation to save time and help medical professionals with this process.

Deep learning techniques have been widely used in brain tumor segmentation. UNet model is the state of art for tumor segmentation.[2] UNet architecture confirm the shortcomings of traditional training frameworks, as the predicted segmented masks do not capture the high spatial variation or physically realistic structures of the diffused tumor structure, making them unreliable for clinical use. A novel architecture is needed to tackle this challenge. Generative modeling techniques have seen great improvements in recent times.[3] Specifically, Generative Adversarial Networks and Denoising-Diffusion based models have been used to generate desired images of greater quality and with greater control over the specifics of images. Also, the Diffusion model has been applied to medical image segmentation successfully. However, the model performance still has room for improvement when compared to previous UNet models.[4][5]

In this work, we introduce a framework called Re-Diffinet, for modeling discrepancy between the outputs of a segmentation model like UNet and the ground truth, using the advantages from Denoising Diffusion Probabilistic Models and UNet model. By explicitly modeling the discrepancy, we intend to improve over the previous segmentation model, and exploit diffusion models' ability to generate finer details.

METHODS

Dataset: The training dataset provided for the BraTS23 challenge [4] consists of 1,251 brain MRI scans along with segmentation annotations of tumorous regions. The 3D volumes were skull-stripped and resampled to 1 mm^3 isotropic resolution, with dimensions of (240, 240, 155) voxels. For each example, four modalities were given: native (T1), post-contrast T1-weighted (T1Gd), T2-weighted (T2), and T2 Fluid Attenuated Inversion Recovery (T2-FLAIR). Example images of each modality are presented in Figure 1. Segmentation labels were annotated manually by one to four experts. Annotations consist of four classes: enhancing tumor (ET), peritumoral edematous tissue (ED), necrotic tumor core (NCR), and background (voxels that are not part of the tumor).[6]

Training details: Our network is implemented in Pytorch and MONAI on 4 NVIDIA A40 GPUs. The baseline UNet model was trained using an optimized UNet model.[7] The diffusion model architecture is shown in **Figure 1a**. The model was trained using a compound loss function includes DICE loss, BCE loss, and MSE loss for diffusion model. The model was trained for 200 epochs using the Adam optimizer with a learning rate of 0.0001 and a weight decay equal to 0.0001. To generalize the network's performance and evaluate its reliability, a 5-

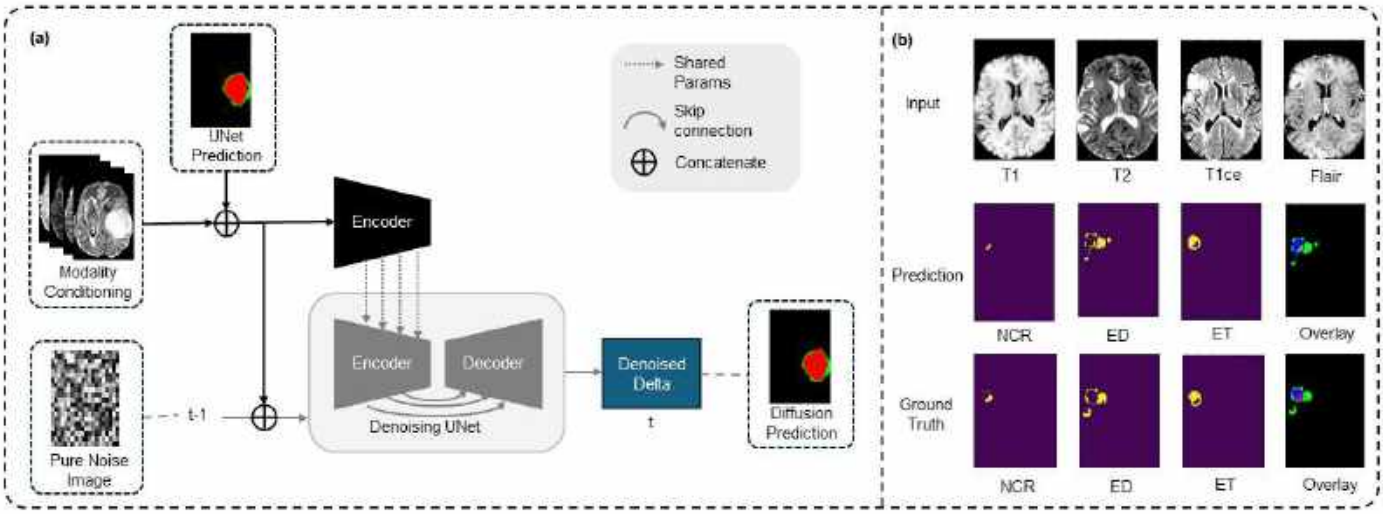

Figure 1: (a) Model architecture of Re-DiffiNet which aims to model the discrepancy using Diffusion. (b) Model predictions of segmentation results of three segmented labels produced by our network and on BraTS2020 dataset. First row shows the four input contrasts, second row shows our model predictions, and the third row shows the ground truth labels.

fold cross validation was performed. The data were randomly shuffled and equally split into 5 groups as training validation.

RESULTS

The results of 5-fold cross validation are shown in **Table 1**, which reports the Dice Score (DICE) and 95 percentile Hausdorff distance (HD95) and the average scores of all methods on the three overlapping regions whole tumor (WT), tumor core (TC) and Enhancing tumor (ET) for the BraTS2023 dataset (**Figure 1b**). We found that while using the diffusion model to directly output the tumor segmentation mask does lead to improvements over the UNet model, the improvements are modest: 0.12% improvement in Dice, and 5.61% improvement in HD95 score.

On the other hand, with Re-DiffiNet we found a 16.28% improvement in HD95 score, indicating the benefits of modeling discrepancy using diffusion models. The improvement in Dice score was again marginal: 0.55%.

DISCUSSION

In this research, we proposed a 3D medical image segmentation framework, named Re-DiffiNet, based on the diffusion model, which models medical image segmentation as a discrete data generation task. The proposed algorithm could predict the difference between the UNet prediction and ground truth labels, leveraging the advantages of the diffusion model to improve segmentation robustness.

The results also show that the diffusion probabilities model has the potential to refine the medical image segmentation model by appropriately conditioning the MRI contrast. Future research could investigate the behavior of the diffusion model to better quantify the uncertainty introduced in the segmentation label inference stage of the model.

Overall, our work presents an important contribution to the field of medical image segmentation, demonstrating the effectiveness of the Diffusion model in the 3D medical image segmentation task. The proposed method has the potential to facilitate more precise and accurate diagnosis and treatment of medical conditions, ultimately leading to improved patient outcomes.

ACKNOWLEDGEMENTS

There is no funding source to declare.

REFERENCES

[1] Alcantara Llaguno SR et al., *Br J Cancer*, 115(12):1445-1450, 2016
[2] Isensee, F et al., *Nat Methods* , 203–211, 2021.
[3] Ho, J et al., *arXiv:2006.11239*, 2020
[4] Xing, Z et al., *arXiv:2303.10326*, 2023
[5] Wolleb, J et al., *arXiv:2112.03145*, 2021
[6] Baid, U et al., *arXiv:2107.02314*, 2021
[7] Futrega, M et al., *arXiv:2110.03352*, 2021

Table 1: Results of average dice score and HD95 score from three model architecture.

Model	Dice (-)				HD95(mm)			
	WT	ET	TC	Average	WT	ET	TC	Average
UNet	92.03%	87.14%	93.09%	90.51%	1.3218	1.7250	1.3472	1.4647
Diffusion - baseline	92.20%	87.02%	93.48%	90.62%	1.25	1.63	1.26	1.38
Diffusion - delta	92.72%	87.27%	93.76%	91.02%	1.1284	1.5125	1.1331	1.2262

SB^{3}C2024
Summer Biomechanics, Bioengineering and Biotransport Conference
June 11-14, Lake Geneva, WI, USA

VASCULAR MODEL GENERATION WITH THE SPACE COLONIZATION ALGORITHM

Daniel Emerson (1), Yoed Rabin (1), Levent Burak Kara (1)

(1) Department of Mechanical Engineering, Carnegie Mellon University, Pittsburgh, Pennsylvania, USA

INTRODUCTION

Vascular models are a valuable tool for understanding fluid flow through the vasculature in organs. Vascular models have been used to inform surgical procedures such as coronary artery bypass graft surgery [1] in the heart, partial liver resection surgery [2], and superior cavopulmonary connection surgery in the lungs [3]. In each of these cases it is important for clinicians to understand the effects that surgical intervention has on the behavior of flow, including wall shear stresses, pressure drops, and distribution of flow throughout the organ.

Patient specific models can be obtained through medical imaging techniques like computed tomography (CT) scans and magnetic resonance imaging (MRI), however the level of detail and depth of the images is often limited, and does not capture the small scale vessels. Researchers have developed algorithms capable of generating vessels to greater levels of detail [4, 5]. Some algorithms are initialized with patient specific geometries containing the higher level vessels [6, 7], while others generate completely synthetic models [5]. For medical applications requiring large amounts of data such as training machine learning models it can be difficult to obtain a sufficient amount of patient specific models. Therefore, algorithms capable of generating high quality synthetic data with high degrees of variability similar to that of the patient population are highly desirable [8].

The most common algorithm for generating vascular models is constrained constructive optimization (CCO) [4]. The CCO algorithm iteratively generates new vessels within a specified domain, optimizing the local structure at each bifurcation with each added vessel. The primary limitation of the CCO algorithm is that it does not allow for explicit control of the trajectory or terminal location of vessels. This is a desirable property when modeling organs such that arteries and veins connect at a common location and flow can be simulated through the entire vasculature.

In pursuit of this objective, we implement the space colonization algorithm which was initially developed to model botanical trees [9]. With the addition of target attractor concept from [10] we are able to explicitly control the location of terminal vessels to create fully connected models of vasculature in organs. Our algorithm simply requires a mesh of the organ, and allows for a high degree of customization through algorithmic parameters to generate vascular models which closely match anatomical data, or to generate models of varying levels of depth and topological variability.

METHODS

Point Sampling: Starting with a triangle mesh of the organ, we utilize the Möller-Trumbore ray-triangle intersection algorithm to efficiently sample random points inside the mesh. These points are used as the attractors for the space colonization algorithm. The number of points sampled can affect the topology of the generated model and is detailed in the discussion section. We also perform k-means clustering with on this point cloud to obtain k target attractors that are spaced evenly throughout the domain. The number of target attractors, k, directly corresponds to the level of detail in the generated model.

Space Colonization Algorithm: The space colonization algorithm is an attractor based growth method, meaning that the vasculature is generated by adding new vessels (growth) towards points (attractors) in the domain. There are three parameters which must be defined in the algorithm: step distance (D), kill distance (d_k), and sphere of influence (d_i). These parameters have a strong influence on the topology of the generated model as detailed in the discussion. We represent the generated vasculature with "nodes" and "vessel". A vessel connects any two nodes, and a node can have any number of vessels entering and exiting it. At each iteration of the algorithm we look for attractors within d_i of the existing nodes, referred to as "active attractors". A new node is added at a distance D in the average normal direction of the active attractors from their respective node. Once all new nodes have been added for a given iteration, we look for attractors within d_k of existing nodes, and eliminate those attractors from the point set. In this way, the model is incentivized to grow towards regions of the domain which have no existing nodes.

Target Attractors: The addition of the target attractor concept stipulates that a target attractor cannot be removed from the point set until it is explicitly reached by a node. When the only active attractor for a node is a target attractor and is within a distance D, the target attractor is grown directly to and subsequently removed from the point set. The algorithm terminates once all target attractors are reached.

Pruning: Since we aim to create a fully connected model, we want our model to only terminate at the location of target attractors. Thus, it is necessary to prune our model, or trim off the unnecessary vessels. We start at the terminal vessels and traverse the model in reverse to the root vessel. All vessels which are not traversed are pruned from the model.

Radius Assignment: At this point, we have generated all the vessels in our model, but we have not assigned radii to any vessels. We simply need to specify the radius of the root vessel, and then all subsequent radii are assigned according to Murray's law. Murray's law has been shown to closely model the relationship of radii at junctions in biological vascular networks as detailed in [11].

RESULTS

Morphological Validation: We demonstrate the ability of our algorithm to generate models which agree well with morphological data from real human livers as detailed in Fig. 1 and Tab. 1. We determine the generation a vessel belongs to using the Strahler ordering method which considers the topological connectivity of the vessels in the model.

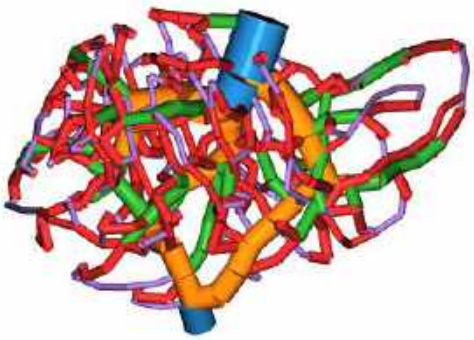

Figure 1: Lung vasculature model of portal and hepatic veins with vessels colored according to Strahler generation.

For organs with well known primary vessels like the liver, we can perform a staged approach to the space colonization algorithm where we run the algorithm twice. First, to initialize the primary vessels, namely the left and right portal veins, and the left, middle and right hepatic veins. These initialized vessels can be seen in orange in Fig. 1. Then, the full space colonization algorithm can be run from this initialized model to obtain better agreement to real human models.

Table 1: Morphological statistics by Strahler generation for portal vein (PV) and hepatic vein (HV) from space colonization model depicted in Fig. 1, as well as from anatomical corrosion cast of real human liver from [12]. Lengths and radii in mm.

	Space Colonization			Anatomical		
Generation	Count	Length	Radius	Count	Length	Radius
PV1	1	34.38	6.71	1	35	7.3
PV2	2	35.00	4.82	2	35	6.3
PV3	5	30.95	3.35	7	33	4.0
PV4	25	36.80	2.28	27	32	2.1
PV5	80	28.08	1.67	80	27	1.5
HV5	80	27.29	2.72	76	19	1.1
HV4	22	27.99	3.68	33	28	1.7
HV3	5	23.18	5.06	18	33	2.4
HV2	3	40.00	6.99	3	74	5.0
HV1	1	91.37	11.54	1	68	13

Topological Variability: We also highlight the ability to vary the topology of generated models by changing various parameters within the space colonization algorithm. Smaller values of D, d_k, and d_i lead to vessels that have more tortuosity, while larger values lead to more direct vessels as illustrated in Fig. 2. The density of the attractor point cloud can also have an effect on the topology of the generated model. For the same set of space colonization parameters, sparse point clouds will result in more tortuous models, while dense point clouds result in smoother, more direct models at increased computational cost.

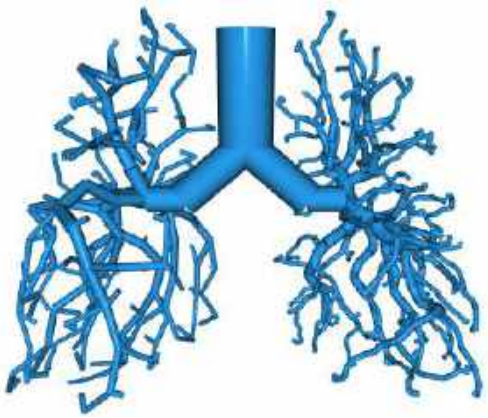

Figure 2: Pulmonary artery model where each lung is generated with unique space colonization parameters. The left lung (reader's view) is generated with $D = 20$, $d_k = 22.5$, $d_i = 25$, while the right lung is generated with $D = 5$, $d_k = 10$, $d_i = 15$. Units in mm.

These results illustrate the ability of the space colonization algorithm to generate models which agree with known morphological data, as well as the ability to generate highly customizable models with large degrees of variability. Currently we do not generate models to the full level of depth seen in biological organs [12] or some published algorithms [5]. The space colonization algorithm is uniquely able to create fully connected models that allow for flow throughout the entire organ by controlling the trajectory of terminal points with the target attractor concept. This target attractor concept also lends itself well to a staged approach where primary vessels can be accurately initialized as discussed in the morphological validation section, and could be extended to create even more complex models as mentioned in the discussion.

DISCUSSION

This work illustrates a novel approach to algorithmically generate vascular models in a variety of organs. We demonstrate the capability of the approach to generate realistic models that agree well with morphological data, in the case of the liver. We also demonstrate how models with varying topologies can be generated by varying parameters of the algorithm, in the case of the lung. Future works can further develop on the space colonization algorithm by implementing a staged approach which varies space colonization parameters as the vasculature is grown, such that primary vessels appear more direct, and later vessels are more tortuous as is the case in the pulmonary vasculature. The fully connected models can be used to simulate flow throughout whole organs to investigate the global distribution of flow, as well as local flow effects caused by morphological and topological variations. Overall, we see this algorithm as an enabling technology for researchers and clinicians to rapidly develop models of vasculature that can be used for a multitude of applications.

REFERENCES

[1] Sankaran S et al. *Annals of Biomedical Eng.* 40.10 (2012).
[2] Tithof J et al. *Journal of The Royal Society Interface* 20.207 (2023).
[3] Schiavazzi DE et al. *J. Thorac. Cardiovasc. Surg.* 149.3 (2015).
[4] Karch R et al. *Computers in biology and medicine* 29.1 (1999).
[5] Jessen E et al. *Journal of The Royal Society Interface* 19.191 (2022).
[6] Kannan R et al. *Journal of Comp. Design and Eng.* 8.2 (2021).
[7] Abadi E et al. *IEEE Transactions on Medical Imaging* 37.3 (2018).
[8] Tucker A et al. *npj Digital Medicine* 3.1 (2020).
[9] Runions A et al. *NPH* 7.63-70 (2007).
[10] Ulu NG et al. *Journal of Visual Lang. & Computing* 31 (2015).
[11] Sherman TF. *The Journal of general physiology* 78.4 (1981).
[12] Debbaut C et al. *IEEE Transactions on Bio.l Eng.* 58.1 (2011).

CHARACTERIZING THE INFLUENCE OF PROTEOGLYCANS ON PASSIVE AND VISCOELASTIC MATERIAL PROPERTIES OF FEMALE PELVIC FLOOR SKELETAL MUSCLES

Megan R. Routzong (1), Francesca B. Sesillo (1), John B. Rudell (1), Marianna Alperin (1,2)

(1) Department of Obstetrics, Gynecology & Reproductive Sciences, University of California, San Diego, La Jolla, CA, USA
(2) Sanford Consortium for Regenerative Medicine, La Jolla, CA, USA

INTRODUCTION

The skeletal muscles of the pelvic floor are critical to the mechanical support of pelvic organs and tissues and maintenance of their continence and sexual function. In females, the pelvic floor muscles (PFMs) are impacted by pregnancy and vaginal childbirth. Pregnancy-induced remodeling of the PFMs must take place in response to the loads imposed by the growing fetus and uterus. Then, during vaginal delivery, they must stretch considerably, often to the point of mechanical failure, to allow passage of the fetus through the birth canal. Such injuries predispose women to the development of pelvic floor disorders later in life, with vaginal parity (the number of times one has given birth vaginally) being their greatest epidemiologic risk factor.

Studies have shown that pregnancy significantly impacts the mechanical behavior and structure of the pelvic floor muscles.[1,2] However, the mechanisms underlying these changes are poorly understood. It has been shown that the extracellular matrix (ECM) contributes significantly to passive tensile stiffness and load-bearing capacity of skeletal muscle.[3] The structure of skeletal muscle ECM is primarily established by collagen fibrils. Proteoglycans (proteins linked to glycosaminoglycans (GAGs)) also make up a large component of the ECM and are known to regulate multiple cellular processes.

We aimed to characterize the contributions of PFM ECM and GAGs (specifically chondroitin sulfate (CS)) to passive mechanics and viscoelastic properties via multi-step stress-relaxation tests of PFMs with and without decellularization and enzymatic degradation of CS. We hypothesized that decellularization would impact elastic moduli, particularly at peak stresses, while CS degradation would impact relaxation time constants.

METHODS

PFMs (specifically the pubocaudalis (PCa) portion) were harvested from three-month-old, nulligravid, female Sprague-Dawley rats (Envigo, Indianapolis, IN) immediately after sacrifice. All procedures were carried out with the approval of and in compliance with the University of California San Diego IACUC.

Samples were dissected under a dissecting microscope to form muscle bundles approximately one third the width of the entire muscle and then divided into three experimental groups: non-perturbed (control muscle group), decellularized (decell group), and Chondroitinase ABC treated after decellularization (decell+ABC group). Muscles were decellularized by incubation in Latrunculin B to disrupt actin filaments followed by alternating osmotic stress via potassium iodide, potassium chloride, and water. Samples underwent a final incubation in DNAse I, were washed in water for two days and stored at 4°C. Samples undergoing CS degradation via Chondroitinase ABC were then incubated at 37°C for 1 hour prior to mechanical testing.

Mechanical testing consisted of multi-step stress-relaxation tests using a microscope mountable isolated muscle system with a 50mN load cell (1530A and 400C, Aurora Scientific, ON, Canada). One end of each sample was sutured to the lever arm of the load cell while the other was a fixed post via small magnets. Initial lengths, widths, and thicknesses were measured and the displacements required to created 9 steps in 11% strain increments were determined. Nine steps at 11% strain were chosen instead of 10 steps at 10% strain due to a limit in the software's maximum number of step inputs. Displacements were controlled and resulting forces measured via LabChart (ADInstruments, Dunedin, NZ). Each step consisted of a 0.05s ramp up to the desired strain followed by 120s of relaxation at constant strain. Samples were tested to 99% strain or failure in a bath of relaxing solution.

To characterize the mechanical behavior across the entire strain range tested, a straight line was fit to the peak (obtained at end of the 0.5s ramp up) and equilibrium (obtained 1s before the next ramp up) stress-strain curves (**Figure 1**). A straight line was chosen after initial observations of the first few datasets. The coefficient of the linear equations served as the peak and equilibrium elastic moduli (E). All calculations were done in Matlab (MathWorks, Natick, MA).

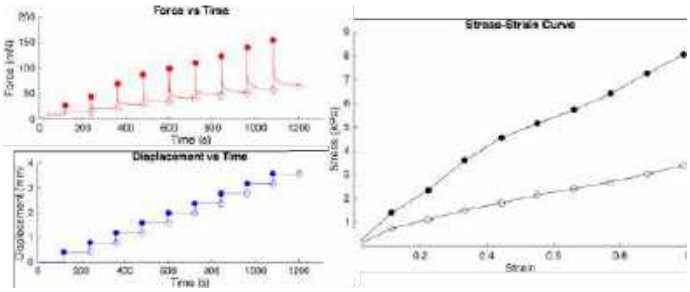

Figure 1: An illustrative example of the multi-step stress-relaxation protocol and generation of peak (filled circles) and equilibrium (empty circles) stress-strain curves.

A viscoelastic analysis was carried out using only the first stress-relaxation step. A 3 Maxwell unit generalized Maxwell Model (3mGMM) was used. This spring-dashpot model equation, simplified based on assumptions specific to stress-relaxation testing, was fit to our data using a linear algebra approach. The stress relaxation curves were smoothed with a second order Savitzky-Golay finite impulse response smoothing filter to reduce noise and then numerical integrations were performed using the trapezoidal rule over 1s intervals. First, second, and third order integrations were performed. By expressing stress in terms of its integrals (or derivatives), the problem is reduced to solving a system of linear equations, allowing the parameters of the 3mGMM equation to be solved for. The negative reciprocal of the determined exponential values was computed to determine the relaxation time constants ($\tau_{1\text{-}3}$). The coefficients were converted to elastic moduli ($E_{0\text{-}3}$) by dividing by the constant strain value. In this format, the subscripts of τ and E denote which Maxwell unit they belong to while E_0 is the lone spring. Mechanical parameters were compared between control, decellularized, and decellularized+ABC groups.

RESULTS

The decellularized muscle group exhibited the largest average peak and equilibrium elastic moduli, while the decell+ABC group exhibited values smaller than the decell group (**Figure 2**).

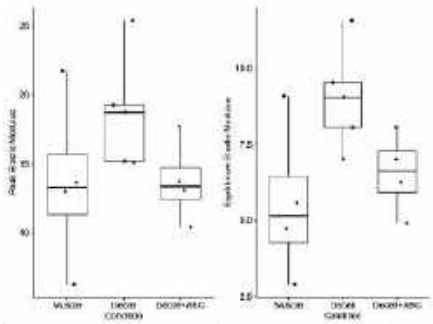

Figure 2: Peak and Equilibrium Elastic Moduli for Each Group

The control muscle group exhibited the smallest $E_{1\text{-}4}$ values, on average (**Figure 3**). The decell group exhibited the largest E_2 values. Considering the fastest time constants (τ_1), the decell group's was faster than the other two. For slower time constants ($\tau_{1\text{-}2}$), the decell+ABC group exhibited the fastest values on average.

Decellularization generally increased elastic moduli, both those fit linearly and using the 3mGMM, compared to control muscle samples. Meanwhile, CS degradation increased τ_1 but decreased τ_3 on average compared to the decell group. The decell and decell+ABC groups only demonstrated meaningful differences in elastic moduli within the linear analysis, not those fit by the 3mGMM.

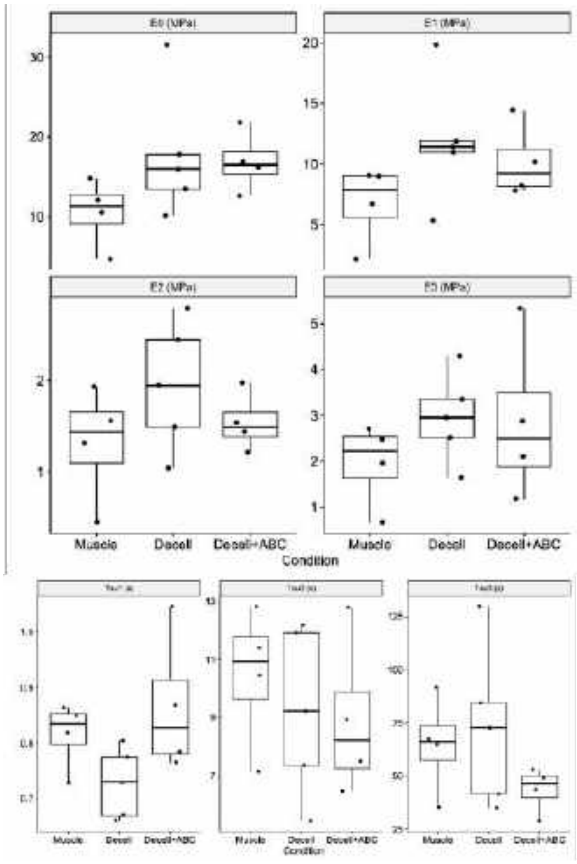

Figure 3: 3mGMM Parameter Values for Each Group

DISCUSSION

Corresponding with our original hypothesis, our findings show that decellularization increases the elastic moduli (though both peak and equilibrium values comparably) compared to control muscle while CS degradation impacts the relaxation time constants; increasing τ_1 and decreasing τ_2 compared to the decell group. This supports that CS (and GAGs in general) significantly contribute to the passive mechanics and viscoelastic properties of PFMs and the ECM specifically, by increasing relaxation times at short scales and decreasing them at longer scales. Future directions will involve evaluating mid- and late-pregnant PFMs to quantify these relationships in pregnancy and hind limb muscles to serve as non-pelvic controls.

ACKNOWLEDGEMENTS

The project described was supported by NICHD T32 HD007203 (M. Routzong), NHLBI DK128639 (F. Sesillo), and R01 HD102184 and 2R01 HD092515 (M. Alperin) from the NIH. Its contents are solely the responsibility of the authors and do not necessarily represent the official views of the NIH.

REFERENCES

[1] Catanzarite, T et al., *Am J Obstet Gynecol*, 218(5):512.e1-512.e9, 2018.
[2] Rieger, M et al., *Am J Obstet Gynecol*, 226(5):708.e1-708.e13, 2022.
[3] Meyer, G et al., *J Biomech*, 44(4):771-773, 2011.

SIMULATION OF THE VISCOELASTICITY OF CLOTS CONSIDERING RED BLOOD CELLS AND FIBRIN NETWORK

Ryan C. Mueller (1), Jifu Tan (1)

(1) Mechanical Engineering, Northern Illinois University, Dekalb, IL, USA

INTRODUCTION

About 30 people die every minute because of heart attack or stroke in the world[1], which is about 30% of the total mortality. Clots play a major role in these cardiovascular diseases. Decades of research have made great advances in biochemistry and cell biology of clot formation, however, how does clot respond to applied force, i.e., the constitutive law, remained largely unknown. As a heterogeneous material, clot is mainly made of red blood cells (RBCs), platelets, fibrin network, plasma and other components such as leukocytes, neutrophil extracellular traps, von Willebrand factor (vWF), etc[2]. The interplay between those components determines the mechanical response of clots. RBCs were assumed to play a passive and minor role in clot mechanics previously, however, they started to gain attention recently[3]. As an important component of clots, RBCs' volume fraction can be as high as 63%[4]. In this paper, we will develop a computational model considering the venous clot with trapped red blood cells and fibrin network to investigate the viscoelastic properties of clots.

METHODS

Venous blood clots are modeled as a mixture of red blood cells and fibrin. Red blood cells are modeled as coarse-grained cell membranes[5–9], The potential energy for an RBC is given by, $U(\boldsymbol{X}_i) = U_{stretch} + U_{bending} + U_{area} + U_{volume}$ where $U_{stretch}, U_{bending}$ are the stretching and bending potentials, respectively. They are given by

$$U_{stretch} = \sum_{j\in 1\ldots N_s} \left[\frac{k_B T l_m}{4 l_p}\frac{3x_j^2 - 2x_j^3}{1-x_j} + \frac{k_p}{l_j}\right], \quad (1)$$

$$U_{bending} = \sum_{j=1\ldots N_s} k_b(1 - cos(\theta_j - \theta_0)) \quad (2)$$

where $U_{stretch}$ is based on the worm-like chain (WLC) model[10]. Other parameters can be found in Ref.[11]. Individual fibrin fiber is modeled as worm-like chains using the same potential format as $U_{stretch}$ but with different parameters that are taken from Ref.[12]. Both the cell and fibrin models are implemented in LAMMPS (Large-scale Atomic/Molecular Massively Parallel Simulator) [13], with further simulations extending to Palabos (Parallel Lattice Boltzmann Solver)[14] to handle the simulations relevant to shear flow. The cells and fibrin are coupled with fluid flow through the Immersed Boundary Method (IBM)[11, 15].

RESULTS

Separate simulations were carried out to calculate the mechanical and dynamic properties of blood clots. To find the equivalent Young's Modulus for the clot, a random clot structure was generated in a 20 μm^3 box. The clot is composed of 6 red blood cells and 151 fibrin fibers. Each red blood cells and fibrin structure are made up of 2562 and 15 particles, respectively. The interaction between particles are modeled as Morse potential. The clot is then compressed by a plate (Fig. 1a) with a velocity of 4.8 mm/s. The forces acting on the plate were measured, then the stress was computed and compared against linear strain to calculate the modulus of elasticity. Shear modulus and viscosity was calculated through a shear flow experiment. The blood clot structure was immersed in a fluid under Couette flow conditions (Fig. 1b) with a shear rate of 600 s^{-1}. The shear stress on the clot was compared against the shear rate or shear strain to compute the viscosity and shear modulus, respectively.

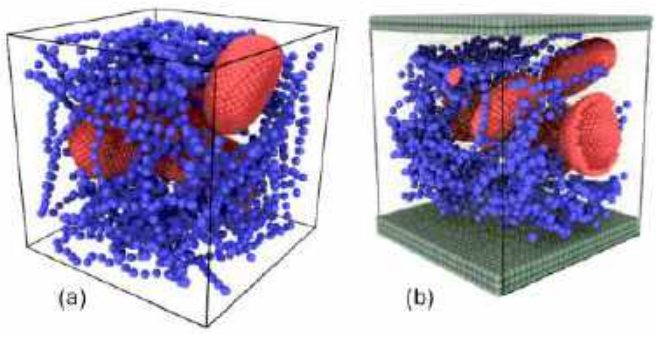

Figure 1: Simulation snapshots of clots under (a) vertical compression and (b) pure shearing flow.

Storage and loss modulus, the two main properties defining a rheological material, were found through a shear flow simulation with oscillating wall velocities. In the simulation, the shear strain oscillated between positive and negative values, resembling a torsional viscometer. The results were then verified in an equilibrium stress autocorrelation simulation.

Property	Value	Experimental	Ref
Elastic modulus	157 mPa	0.1-1500 Pa	[16]
Shear modulus	600 Pa	150-700 Pa	[17]
Storage modulus	100-1000 Pa	800-1200 Pa	[18]
Loss modulus	100-1000 Pa	200-500 Pa	[18]

Table 1: Simulation results for clot mechanical properties

Through the clot compression simulation, an elastic modulus of 157 mPa was calculated. A shear modulus of 600 Pa was found from the shear flow simulations, as shown in Table 1. The rheological properties, storage and loss modulus, were found through the stress autocorrelation simulation with the help of Green-Kubo formulations. The storage and loss moduli were both in the range of $10^2 - 10^3$ Pa. Most of the simulation results are within the range of experimental measurement, as shown in Table 1. Further detailed analysis will be reported in the full paper.

DISCUSSION

Clot mechanical properties such as Young's modulus and shear modulus strongly depend on clot composition, the structure of fibrin (e.g., branching or cross-linking), and the adhesion between fibrin and cells. The complete understanding of the mechanical and dynamic properties of blood clots remains elusive. This paper presents some preliminary studies for the viscoelasticity of clots, demonstrating the feasibility of numerical models to characterize clot mechanics based on the composition of clots. Such a model potentially has the ability to predict the mechanical strength, toughness, and viscoelasticity of the clot with given composition.

ACKNOWLEDGEMENTS

The authors would like to acknowledge the funding support from NSF through grant #2301736

REFERENCES

[1] Organization TWH (2020). URL: `https://www.who.int/news-room/fact-sheets/detail/the-top-10-causes-of-death`.

[2] Alkarithi G et al. *Arteriosclerosis, thrombosis, and vascular biology* 41.9 (2021).

[3] Litvinov RI et al. *ISBT science series* 12.1 (2017).

[4] Chernysh IN et al. *Scientific reports* 10.1 (2020).

[5] Pivkin IV et al. *Physical review letters* 101.11 (2008).

[6] Reasor DA et al. *International Journal for Numerical Methods in Fluids* 68.6 (2012).

[7] Dao M et al. *Materials Science and Engineering: C* 26.8 (2006).

[8] Tan J et al. *Proceedings of the Institution of Mechanical Engineers, Part C: Journal of Mechanical Engineering Science* (2017).

[9] Yu X et al. *Journal of Thrombosis and Haemostasis* 16.2 (2018).

[10] Marantan A et al. *American Journal of Physics* 86.2 (2018).

[11] Tan J et al. *Journal of Computational Science* 25 (2018).

[12] Houser J et al. *Biophys J. 2010;99(9):3038-3047* (2010).

[13] Thompson AP et al. *Computer Physics Communications* 271 (2022).

[14] Latt J et al. *Computers & Mathematics with Applications* (2009).

[15] Peskin CS. *Acta numerica* 11 (2002).

[16] Weisel JW. *Biophysical chemistry* 112.2-3 (2004).

[17] Huang CC et al. *Medical physics* 40.4 (2013).

[18] Schmitt C et al. *Journal of biomechanics* 44.4 (2011).

EXPLORING THE POTENTIAL ROLE OF SEX-BASED BRAIN STRUCTURAL VARIATIONS IN SUSCEPTIBILITY TO TRAUMATIC BRAIN INJURY FROM A BIOMECHANICS PERSPECTIVE

B. Jafari (1), M. Memar (1)

(1) Department of Biomedical Engineering and Chemical Engineering, University of Texas at San Antonio, San Antonio, TX, USA

INTRODUCTION

Sex differences in the human brain neuro-structure are increasingly recognized as one of the underlying factors contributing to the sex variations in the prevalent incidence, onset, and development of neurological disorders and brain injuries [1]. In particular, when it comes to traumatic brain injury (TBI), studies using finite element models (FEM) of brain have shown that the overall and regional differences in brain structure can directly or indirectly affect how the brain deforms under head biomechanical loadings during traumatic events [3, 4]. Furthermore, the brain deformation is proven to be correlated with the occurrence and pathology of TBI [2]. For instance, a brain FEM study showed that applying the same impact kinematics to head models with different sizes, or the same size but a different shape, resulted in different peaks and distributions of strain especially in the corpus callosum (CC), a critical location for traumatic axonal injury [3]. Another FEM study investigated the mitigating role of cerebrospinal fluid (CSF) under head injuries and showed that CSF reduces maximum brain strains and provides a protective buffer against impacts [4].

Although there are evident sex-related differences in various brain regions, research exploring these differences at both the macro- and meso-scale levels remains limited and all the previously developed FEMs of brain have been biased toward males. Moreover, we have previously shown that these sex-based structural differences cannot be addressed by global and uniform scaling [1]. Therefore, in this study, we aim to investigate the anatomical features and volumetric measurements of brain (macroscale), along with diffusion tensor imaging (DTI) metrics and the connections between brain regions (mesoscale), to explore sex-specific variations in the brain structure from biomechanics perspective. Such information is crucial for future studies involving FEMs in the field of brain biomechanics particularly when examining the impact of sex-specific differences on the onset and outcomes of TBI.

METHODS

In this study, subcortical brain segmentation was performed on magnetic resonance images (MRI) from 500 females and 500 males using the FreeSurfer software. The details about dataset used herein can be found in [1]. The final brain masks had the size of 256×256×256 with a voxel size of 1.0 mm×1.0 mm×1.0 mm. The total brain volume (TBV) along with the volume of several regions including CC and CSF were calculated for all subjects. The absolute volumes of the segmented regions were normalized by the TBV of each subject to obtain the fractional volumes and investigate whether the sex variations are proportional to the TBV. The sex-based structural differences were evaluated by the Mann-Whitney test with a significance level of $p=0.05$.

The diffusion-weighted MRIs of the same dataset underwent DTI analysis and fiber tractography using DSI-Studio software. The orientation distribution functions for images were aligned using subject-specific frameworks, employing Q-space diffeomorphic reconstruction technique. These frameworks were generated by a nonlinear registration of widely-used ICBM-152 T1-common space to T1-MRI head from each subject image. “FreeSurferSeg” atlas in DSI-Studio was adapted to optimize the best selection of regions in brain tractography resulting in the 23 regions of interest (ROIs). These regions include Corpus callosum (CC), Left Cortex (L-Co), Left Cerebral white matter (L-Cr-WM), Left Cerebellum white matter (L-Cb-WM), Left Cerebellum grey matter (L-Cb-GM), Left Thalamus (L-Th), Left Putamen (L-Pu), Left Pallidum (L-P), Left Hippocampus (L-Hi), Left Amygdala (L-Amg), Left Accumbens (L-Ac), Brainstem (BS), Optic chiasm (OX), Right Cortex (R-Co), Right Cerebral white matter (R-Cr-WM), Right Cerebellum white matter (R-Cb-WM), Right Cerebellum grey matter (R-Cb-GM), Right Thalamus (R-Th), Right Putamen (R-Pu), Right Pallidum (R-P), Right Hippocampus (R-Hi), Right Amygdala (R-Amg), Right Accumbens (R-Ac), Cerebrospinal fluid (CSF). We also mapped the refined atlas to the common space of each individual subject. Fiber tracking was then conducted on each subject in DSI-Studio, employing

Euler tracking algorithm [5]. For each subject, scaler metrics including fiber anisotropy (FA) and mean diffusivity (MD) were derived and the brain connectivity matrix was calculated using 1000000 fiber tracts. The matrix cells (count*FA) were calculated using the count of connecting tracts passing through pairs of regions multiplied by the mean FA values measured on those tracts as a quantification of connection strength between the two ROIs. Independent-samples Mann-Whitney U tests were performed on DTI metrics and the pair-wise connections to examine the distribution of these metrics for all 23 brain regions across the two categories of sex.

RESULTS

Significant difference was observed in the distribution of TBV between male and females with males having larger values and wider distribution compared to females (Figure 1). In addition, the distribution of both the absolute and the fractional volume of CC was significantly different across sexes, and female population was observed to have a larger CC, proportional to their brain. Regarding CSF, while the fractional volume distributions were mostly similar across sexes, the absolute values were noticeably higher in males.

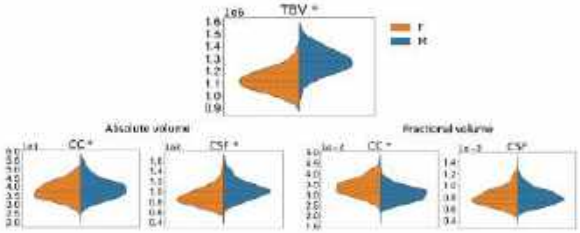

Figure 1: Sex-based comparison of the distribution of volumes for TBV, CC, and CSF. The asterisk * symbol shows a statistically significant difference

The difference values between mean regional FA and MD in females and males (Figure 2) shows that FA values are significantly larger in majority of regions with highest difference in CC which is known as the largest white matter structure. This trend was the opposite for MD values. These significant differences were observed in 70% and 91% of the regions for the FA and MD values, respectively.

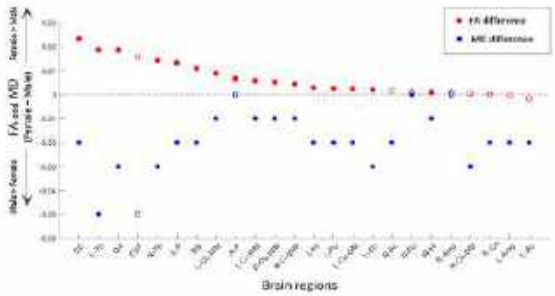

Figure 2: Sex differences in the FA and MD values (median of population) across brain regions. Filled markers denote regions with statistically significant differences ($p < 0.05$)

The heatmap shown in Figure3-a indicates that in 70% of the region pairs, there is a significant sex difference in the brain connectivity (count*FA). The strength connectivity difference matrix between female and male populations (Figure3-b), obtained by subtracting their respective median connectivity matrices (count* FA), shows stronger connections, including interhemispheric white matter and those from left and right cortical regions, passing through CC, in females compared to males.

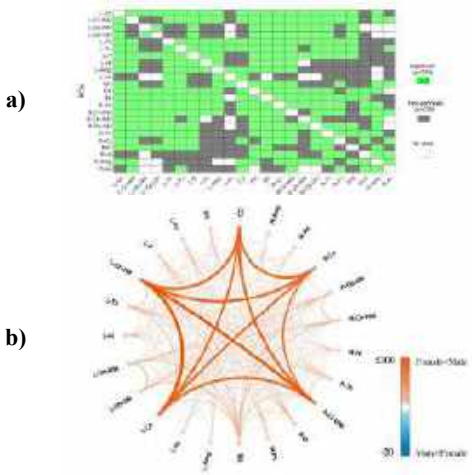

Figure 3: a) Statistical comparison of the component of brain connectivity matrix between female and male subjects (green shows significant difference), and b) the median female-male connectivity difference matrix (count* FA)

DISCUSSION

The distribution of volumetric parameters as well as the DTI metrics and the strength of connections were significantly different for most of the brain regions across males and females. Due to such intricate sex-based structural variations at macro- and meso-scales, and the inaccuracy of global linear scaling [1], developing separate brain templates and FEMs for males and females are highly encouraged to investigate sex-specific TBI mechanisms and protection interventions.

Exploring sex-specific brain vulnerability to TBI reveals different patterns at both macroscale and mesoscale levels. From the macroscale perspective, males have a larger brain volume potentially leading to greater deformations during impacts, making them more susceptible to TBI. This is further supported by the smaller fractional volume of CC, indicating higher vulnerability in males. However, the larger absolute volume of CSF in males may provide better cushioning, mitigating the risk of TBI in males. On the mesoscale, females exhibited higher FA values for most ROIs and stronger inter-hemispheric connections which could influence their TBI exposure differently. Furthermore, larger volume and higher FA for CC as well as its stronger connections in females may suggest a lower susceptibility to TBI in CC in females.

All in all, our findings may suggest a possible higher TBI vulnerability in males compared to females undergoing same head kinematic accelerations from brain structure perspective. However, this possibility may be counterbalanced by the sex-based variations in head kinematic severity and hormonal dynamics. The interaction of sex-specific brain FEMs with further biological research is promising to unravel such complex interplay of factors influencing TBI vulnerability in males and females.

ACKNOWLEDGEMENTS

Funding support was provided by NSF-2138719. The authors would like to thank Dr. Mohammadreza Ramzanpour for his helps.

REFERENCES

1. Ramzanpour, M., et al., Brain Multiphysics: p. 100077, 2023.
2. Hajiaghamemar, M., et al., Biomech Model Mechanobiol. **19**: p. 1109-1130, 2020.
3. Kleiven, S., et al., J Biomech. **35**(2): p. 153-160, 2002.
4. Luo, Y., et al., Proc Inst Mech Eng H. **226**(7): p. 499-509, 2012.
5. Yeh, F.-C., et al., Neuroimage. **178**: p. 57-68, 2018.

YAP/TAZ ACTIVIY REGULATES A MECHANO-METABOLIC CROSSTALK DURING 3D BREAST CANCER INVASION

Haider Ali (1), Hrishika Rai (1), Adil Khan (1), Jacopo Ferruzzi (1,2)

(1) Department of Bioengineering, University of Texas at Dallas, Richardson, TX, USA
(2) Department of Biomedical Engineering, University of Texas Southwestern Medical Center, Dallas, TX, USA

INTRODUCTION

Breast cancer invasion is driven by both cell autonomous and micro-environmental factors. Among the intracellular programs that sustain malignancy, the transcriptional coactivators yes-associated protein (YAP) and transcriptional coactivator with PDZ-binding motif (TAZ) regulate gene expression as part of the Hippo pathway [1]. In terms of micro-environmental effects, the role played by a collagen-rich extracellular matrix (ECM) is particularly acute in breast cancer, where collagen densification and alignment impact tumor progression [2]. YAP and TAZ are known to respond to biomechanical cues, through the process of mechanotransduction [3], and to metabolic pathways [4]. As oncoproteins, YAP/TAZ are localized in the nucleus of cancerous epithelial cells with elevated rates of malignancy. Therefore, YAP/TAZ activity is expected to enhance cancer cell invasion, cell-ECM interactions, and metabolic plasticity. However, it is yet unknown how YAP/TAZ activity impacts ECM mechanics and metabolism during breast cancer invasion. Hence, in this study we used tumor spheroids to investigate how nuclear activation of YAP/TAZ regulate a mechano-metabolic crosstalk between ECM mechanics and cell metabolism, thereby influencing invasion in complex 3D micro-environments.

METHODS

Control MCF-10A cells and the doxycycline-inducible nuclear mutants TAZ(4SA) and YAP(5SA) [5] were used to form multicellular spheroids (~10^3 cells/spheroid). Such spheroids were embedded into a 3D network of rat-tail collagen I via established methods [6]. Control, TAZ(4SA), and YAP(5SA) spheroids were cultured for 4 days in graded collagen concentrations (1, 2, 3, and 4 mg/mL), supplemented with MCF-10A growth media [7] with (+Doxy) or without (-Doxy) doxycycline. Each spheroid was imaged immediately after embedding (day 0) and at days 2 and 4 to characterize the dynamics of invasion. For each day, time-lapse imaging (every 10 minutes for 8 hours) was conducted using a Nikon AX confocal microscope equipped with an environmental chamber (37°C, 5% CO2) and a 10× objective. Bright field (DIC) images were acquired to quantify the dynamics of invasion, while confocal reflection images were collected using an excitation wavelength of 488nm to capture the structural effects of collagen remodeling. Matrix displacements due to spheroid-generated traction forces were measured from time-lapse movies [8] as a measure of collective contractility. Micro-mechanical changes due to permanent remodeling of the collagenous ECM by invading cancer cells were measured using 3D Magnetic Twisting Rheometry (3D-MTR), a novel method developed in our laboratory. Briefly, iron oxide beads were embedded in the collagen matrix surrounding each tumor spheroid. At days 0, 2, and 4, a homogenous torque was applied to all beads through the application of coordinated magnetic fields (via two orthogonal sets of coils mounted on a custom microscope insert). Confocal image stacks were acquired both before and after magnetic stimulation and compared using digital image correlation algorithm. The magnitude of the 3D displacement field around each bead was compared with that produced by a finite element model and the difference was minimized to estimate the unknown material properties of the local collagen network. For the sake of simplicity, collagen was modeled as a neo-Hookean material $W = c/2\,(I_c - 3)$ and the associated Young's modulus $E = 2c(1 + \nu)$ was used to report local material properties, where the Poisson's ratio ν was determined in preliminary experiments by means of uniaxial unconfined compression.

In terms of metabolic activity, we cultured each cell type as a 2D monolayer and used a Seahorse Assay followed by a Click-iT EdU cell proliferation assay to measure differences in cell metabolism and proliferation. Spatio-temporal heterogenities in cell metabolism associated with 3D invasion were mapped out using Fluorescence Lifetime Imaging (FLIM) of the metabolic cofactor NAD(P)H. FLIM image stacks were acquired at days 0, 2, and 4 using a multiphoton microscope (Olympus FVMPE-RS) and analyzed using published methods [9]

RESULTS

The mutant cell lines TAZ(4SA) and YAP(5SA) formed larger spheroids and displayed increased EdU nuclear incorporation, thus indicating an increased rate of proliferation. After embedding, Control MCF-10A spheroids invaded collectively in low and intermediate density collagen, with modest remodeling of the collagen network. Conversely, MCF-10A TAZ(4SA) and YAP(5SA) spheroids cultured in low density collagen generated higher displacements in the ECM, aligned collagen fibers radially and invaded more aggressively, both as continuous multicellular protrusions and as single cells (Figure 1). A Seahorse Assay performed on 2D monolayers shows that activation of TAZ leads to an increased respiratory capacity and a higher glycolytic activity while activation of YAP leads primarily to a higher glycolytic activity. FLIM on 3D TAZ(4SA) spheroids shows a consistent reduction in the ratio of free (α1) to bound (α2) NAD(P)H. With invasion, metabolic heterogeneities arise within the spheroid core, which shows an optical signature consistent with glycolysis while the spheroid periphery displays a shift towards oxidative phosphorylation (Figure 2a). Quantification of spheroid-generated contractile forces (Figure 2b) shows that matrix displacements at the end of day 4 are modest in control MCF-10A spheroids while the TAZ(4SA) mutants display the largest extent of matrix remodeling and invasion. Such differences in contractile forces translate into a heterogeneous material stiffening of the collagen matrix, as measured by 3D-MTR (Figure 2c).

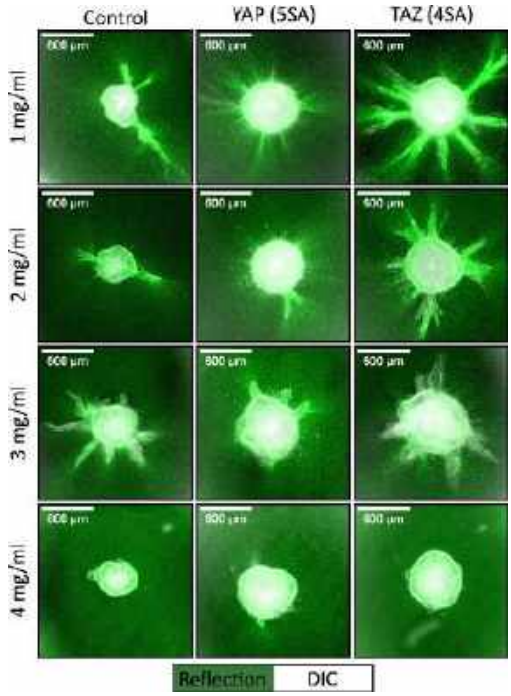

Figure 1: YAP/TAZ activation results in increased proliferation, as indicated by larger spheroid size. Control MCF-10A spheroids invade collectively, with modest remodeling of the collagen network. In comparison, YAP(5SA) and TAZ(4SA) spheroids in low collagen densities align radially the surrounding matrix and invade more as individualized cells.

DISCUSSION

Tumor invasion is known to depend on the physical properties of both cells and the ECM and is fueled by metabolism. Here, we show that activation of nuclear YAP/TAZ impacts breast cancer spheroid proliferation regardless of the extracellular micro-environment, while migration, generation of contractile forces, and collagen remodeling are favored especially in low collagen density. We also show that activation of YAP/TAZ alters the metabolic profile of tumor spheroids in a spatially and temporally heterogeneous manner, with a metabolic shift towards glycolysis in the spheroid core while the invasive edge shifts towards oxidative phosphorylation. Future work will investigate the mechanistic links between YAP/TAZ, ECM mechanics, and cell metabolism and explore how they impact breast cancer invasion.

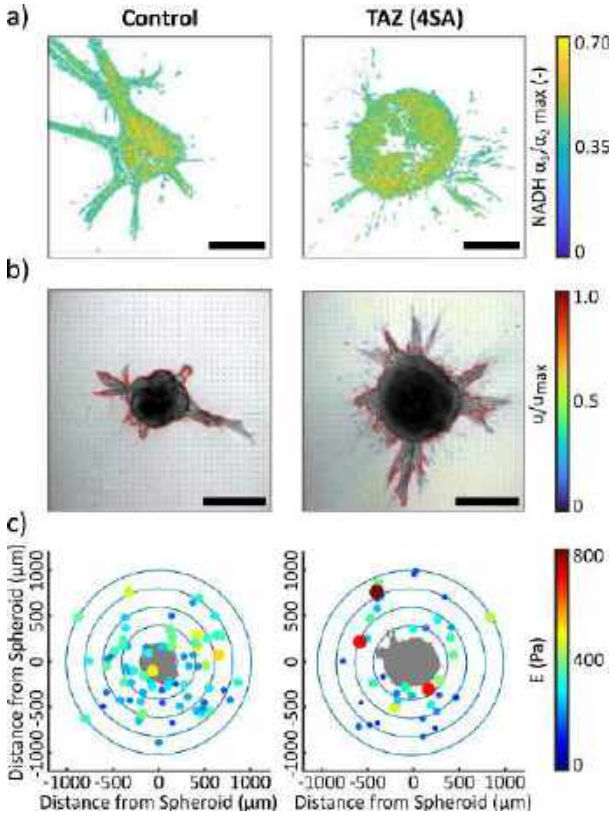

Figure 2: Comparison of the (a) glycolytic activity, as measured by Fluorescence Lifetime Imaging (FLIM), (b) 3D matrix displacements, as measured from timelapse images of invading spheroids, and (c) mechanical remodeling of the ECM, as measured by 3D-magnetic twisting rheometry, between MCF-10A control (left) and TAZ-activated (right) spheroids. TAZ activation results in altered metabolism and in increased structural remodeling and mechanical stiffening of the surrounding ECM. Scale bar: (a) 250μm, (b) 500μm.

ACKNOWLEDGEMENTS

We acknowledge Professor Xaralabos Varelas (Boston University) for providing the cell lines MCF-10A TAZ(4SA) and YAP(5SA). This project was funded in part by The University of Texas at Dallas Office of Research and Innovation through the SPIRe program.

REFERENCES

[1] Zanconato F. et al., *Cancer Cell*, 29: 783-803, 2016.
[2] Provenzano P.P. et al., *BMC Med*, 4:38, 2006.
[3] Dupont S. et al., *Nature*, 474: 179-183, 2011.
[4] Enzo E. et al., *EMBO J*, 34: 1349-1370, 2015.
[5] Hiemer S.E. et al., *J Biol Chem*, 289: 13461-13474, 2014.
[6] Kang W., Ferruzzi J. et al., *iScience*, 24: 103252, 2021.
[7] Debnath J. et al., *Methods*, 30: 256-268, 2003.
[8] Mark C. et al., *Elife*, 9: e51912, 2020.
[9] DeCamp S.J. et al., *Sci Rep*, 10: 18302, 2020.

STRUCTURAL AND BIOMECHANICAL HALLMARKS OF EARLY-ONSET COLORECTAL CANCER

Nicole Huning (1), Munir H. Buhaya (2), Adil Khan (1), Haider Ali (1), Sara Roccabianca (3), Emina Huang (2), Jacopo Ferruzzi (1,4)

(1) Department of Bioengineering, University of Texas at Dallas, Richardson, TX, USA
(2) Department of Surgery, University of Texas Southwestern Medical Center, Dallas, TX, USA
(3) Department of Mechanical Engineering, Michigan State University, East Lansing, MI, USA
(4) Department of Biomedical Engineering, University of Texas Southwestern Medical Center, Dallas, TX, USA

INTRODUCTION

Colorectal cancer (CRC) remains one of the most common causes of cancer-related deaths in the United States [1]. Over the past decades, public awareness has led to increased rates of routine colonoscopy screening, thereby causing a decline in the incidence of average onset colorectal cancer (AO CRC), which affects patients above 65 years of age. Meanwhile, early onset colorectal cancer (EO CRC), which affects patients under 50 years of age, has been rising at an alarming 2% per year and is expected to increase by 124% by the year 2030 [2]. The precise etiology of EO CRC remains unknown, with no unique mutational drivers. Epidemiological studies have indicated that chronic, low-grade inflammation could represent a pathogenic mechanism in the EO CRC patient cohort [3]. It is well established that collagen remodeling and overall tissue stiffening are hallmarks of fibrosis and inflammation. However, there is a lack of biomechanical data on EO CRC. Therefore, we hypothesized that fibrotic stiffening could represent a quantifiable hallmark of EO CRC. To test this hypothesis, we investigated the structural and biomechanical properties of colonic tissue specimens harvested from patients undergoing surgical resection. The objectives of this work are threefold: 1) to compare, for the very first time, the biomechanics of tissues from AO and EO CRC; 2) to quantify properties from matched cancerous and normal tissues; 3) to investigate both local (mesoscale) and global (macroscale) mechanical properties of the human colon.

METHODS

We investigated both cancerous and matched normal samples harvested from patients undergoing surgical resection. For each sample we punched two cylindrical specimens (4 mm in diameter) and subjected them to four local indentation tests and to one global unconfined compression test to determine its material properties. Indentation was performed in 5 incremental steps, each with a magnitude equal to 1% of the original height of the sample and interspersed with 1-minute hold phases. Steady state force values from the hold phases (F) were graphed versus displacement (δ) and fitted using a solution from linear elasticity [4],

$$F = E\left(\frac{2R}{1-\nu^2}\right)\delta, \tag{1}$$

where E represents the unknown Young's modulus, R = 35 μm is the radius of the cylindrical indenter and ν = 0.5 is the Poisson's ratio for an incompressible linear material. Instead, unconfined compression was performed in 8 incremental steps, each with a magnitude equal to 2.5% of the original height interspersed with 2-minute hold phases. The Poisson's ratio ν was calculated by finding the best fit line between the axial and radial strain. Steady state values of the equilibrium Cauchy stress were fitted using a neo-Hookean strain energy density function,

$$W = \frac{c}{2}\left(I_C - 3\right), \tag{2}$$

where c represents an unknown material parameter and I_C represents the first invariant of the Cauchy-Green tensor. To allow for comparisons, the global Young's modulus was determined as $E=2c(1+\nu)$. Histological examination was conducted using Hematoxylin and Eosin (H&E) and Picrosirius Red (PSR) staining from formalin fixed and paraffin embedded (FFPE) blocks. To determine the underlying content and organization of fibrillar collagen, H&E stained slides were imaged using second harmonic generation (SHG) imaging, while PSR stained slides were imaged under polarized light (PSR) microscopy. Collagen fiber length, width, and orientation from SHG images were analyzed using the ImageJ plugin Ridge Detection [5], while the percentage of the tissue area occupied by thick (red–orange) and thin (yellow–green) birefringent collagen fibers from PSR images was determined using an established Matlab code for quantitative histology [6]. Statistical comparisons were conducted using a two-way ANOVA to assess

differences between normal and cancerous samples and between AO and EO tissues. Post-hoc pairwise comparisons were performed using the Bonferroni correction, and $p < 0.05$ was considered significant.

RESULTS

We collected biomechanical data from 21 AO CRC patients and 15 EO CRC patients. Local indentation data (Figure 1a-b) indicates that cancerous tissues from EO are materially stiffer than their AO counterparts. Intriguingly, we observed the same trend in matched normal tissues, with EO tissues revealing a stiffer behavior than AO tissues. Global compression data (Figure 1c-d) confirm our findings from indentation and reveal that, under 20% compression, these tissues display a mild but noticeable nonlinearity, which becomes more pronounced when looking at individual stress-strain curves. Interestingly, under the assumption of linear elastic behavior and using a Poisson's ratios measured from each specimen, we calculate Young's moduli that are comparable to those obtained using local indentation. These results are limited to the analysis of steady-state equilibrium data and do not incorporate time-dependent behaviors. Ongoing efforts are aimed towards the analysis of stress-relaxation data from global compression using a Maxwell-Wiechert model [7]. Regardless, the observed mechanical trends are corroborated by trends in the collagenous microstructure. Analysis of PSR stained slides (Figure 2a) reveal that EO normal tissues display an increased fraction of thick (red) collagen fibers with respect to AO normal tissues (Figure 2b). Instead, both AO and EO cancers reveal an increase in thin (yellow-green) collagen fibers with respect to normal. Analysis of H&E slides imaged via SHG (Figure 2c) confirms these trends by showing that collagen fibers in cancer samples are thinner than collagen fibers in normal samples. In addition, collagen fibers from EO cancers are thicker (Figure 2d) and more aligned (not shown) than collagen fibers from AO cancers. This finding correlates with the fact that EO cancers display a highly invasive and metastatic behavior [2].

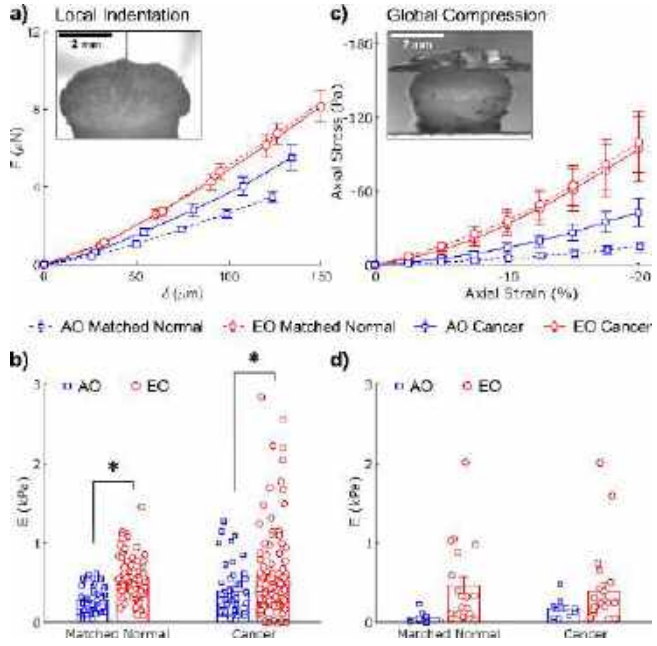

Figure 1: (a) Average force-indentation (*F-δ*) data from local indentation tests. (b) Young's modulus *E* quantified from indentation data. (c) Average axial stress-axial strain data from global compression. (d) Young's modulus quantified from compression data. Insets in both (a) and (c) show representative tissue specimens undergoing mechanical testing.

DISCUSSION

Fibrotic stiffening of tumors is known to impact cancer progression and metastasis. In this work we combined local and global mechanical testing to investigate the biomechanical hallmarks of human EO CRC. Using these methods, we found that differences between normal and cancer tissues are not as pronounced as previously reported [8]. Instead, we find that not only cancerous but also normal tissues from EO patients are stiffer than those from AO patients, thereby suggesting that mechanical stiffening may play a role in the development of colorectal cancer early in life. Future work will be aimed at quantifying the presence of markers associated with chronic inflammation in the stroma, and with increased mechanosensing in the colonic epithelium.

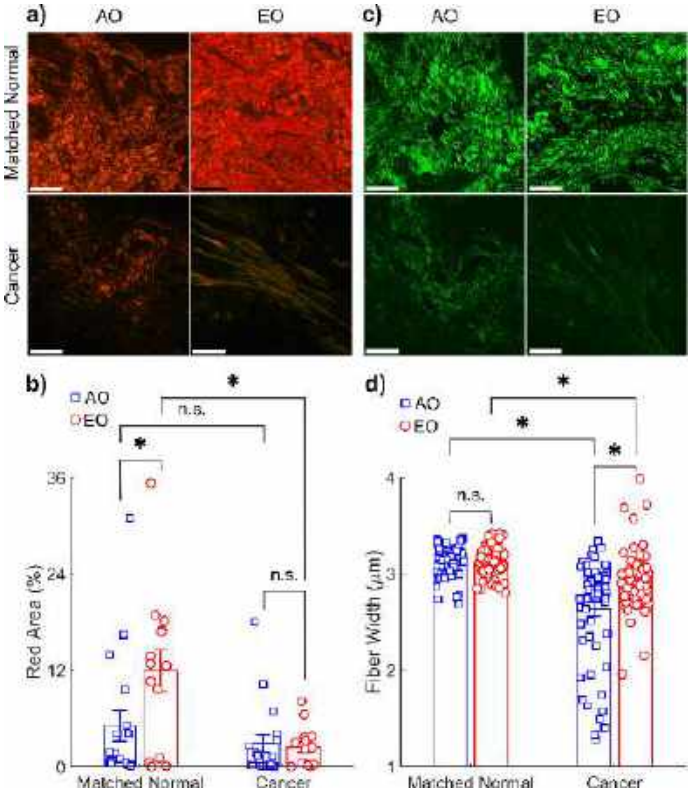

Figure 2: (a) Representative PSR images acquired using polarized light and (b) associated quantifications of thick (red) collagen fibers. (c) Representative SHG images and (d) associated quantifications of fiber width. Scale bars indicate 200 μm.

ACKNOWLEDGEMENTS

We thank Dr. Robert Fisher, Dr. Dan Zhao, Ms. Manal Ali, and Mr. Yaroslav Bisikalo (University of Texas Southwestern) for providing human tissues collected under IRB #STU-2021-0161 via MTA #MMTA220202-0120. This project was funded (or partially funded) by The University of Texas at Dallas Office of Research and Innovation through the CoBRA program.

REFERENCES

[1] Siegel R.L. et al., *CA Cancer J Clin*, 73: 233-254, 2023.
[2] Hofseth L.J.H. et al., *Nat Rev Gastroenterol Hep*, 17: 352-364, 2020.
[3] Murphy C.C. et al., Gastroenterology, 156: 958-965, 2019.
[4] McKee C.T. et al., *Tissue Eng Part B Rev*, 17: 155-164, 2011.
[5] Steger C., *IEEE Trans PAMI*, 20: 113-115, 1998.
[6] Bersi M.R. et al., *Int J Adv Eng Sci Appl Math*, 4: 228-240, 2013.
[7] Tuttle T. et al., *J Mech Behav Biomed Mater*, 143: 105926, 2023.
[7] Brauchle E. et al., *Matrix Biol*, 68-69: 180-193, 2018.

SB^{3}C2024
Summer Biomechanics, Bioengineering and Biotransport Conference
June 11-14, Lake Geneva, WI, USA

PHYSICS BASED MACHINE LEARNED CONSTITUTIVE MODELS FOR FIBROUS MATERIALS

Jacob S. Merson (1), Nishan Parvez (1)

(1) Department of Mechanical, Aerospace, and Nuclear Engineering, Rensselaer Polytechnic Institute, Troy, NY, USA

INTRODUCTION

Fibrous biological materials are exceedingly difficult to model with relevant length and timescale spanning more than nine orders of magnitude. Accurate modeling of fibrous structures continues to be a key issue driving the emergence of new analytical material models that can account for more detailed micro-structural information and non-locality [1, 2]. Another area of growing interest is to use multiscale methods to capture the material behavior across three orders of magnitude [3]. Although these methods provide a substantial increase accuracy, they are astoundingly expensive when using RVEs that are large enough to eliminate size effects requiring use of supercomputers and specialized numerical methods [4, 5].

Another recent trend in biomechanical modeling is to use machine learning methods to predict the solution of boundary value problems or material properties. Amazing progress has been made in predicting solution fields, however these methods are typically sensitive to boundary conditions and require re-training for applications to novel geometries as one might see in patient specific geometry. Here, we consider developing surrogate models for the constitutive response of fibrous materials. Previous works have shown the importance of incorporating constitutive constraints such as frame indifference, and polyconvexity into the machine learned models which aids in the training performance and ensures that the model will be usable for a finite element analysis [6–8].

Here, we investigate the use of a novel neural network architecture and a large library of constitutive data that has been generated by the MuMFiM, a multiscale finite analysis code for fiberous materials [5]. For hyperelastic materials, much of the literature focuses on training the energy response with a high degree of accuracy, however we have found that due to the high problem dimensionality, the derivatives (i.e., stress and stiffness) are not capture well if they are not included in the training process. To that end, we use H2 Sobolev minimization.

METHODS

Fiber Networks. Random fiber network structures are created by seeding a box with points sampled from a uniform random distribution. A Delaunay triangulation is constructed based on the seed points and fibers are placed along the edges of the triangulation. The fiber generation box is then trimmed by placing new nodes fiber nodes along the trimming surfaces and removing the outer portions of any fibers. The edge length of the generation box is three times the trimmed edge length of the Representative Volume Element (RVE) which minimized any impact in boundary effects which are present in the triangulation procedures.

Training Data Generation. Homogeneous displacement boundary conditions are applied to the RVE through a prescribed deformation gradient F_appp. And, the RVEs are solved to static equilibrium using the dynamic relaxation methods described in [5]. The material stiffness are constructed using a finite difference method described in [5]. The use of dynamic relaxation and finite difference allows the method to solve for a static equilibrium state even when the system may have a non-invertable Jacobian at some points in the load path due to sub-isostaticity, or non linearity such as snap-through and buckling.

When constructing the range of deformation gradients to sample, we are interested in controlling the minimum and maximum stretches so that when using the constitutive models in a real analysis we can detect if they are outside of the applicable training ranges. Since we measure the second Piola-Kirchoff stress, we use the Green Lagrange strain as a work conjugate measure. Thus, we can construct our prescribed deformations from the positive definite set of stretch tensors. To this end, our routines start with the principle stretches as this allows control over the fitting range.

We construct the principle stretches using latin hypercube sampling and sample a rotation matrix R from a uniform distribution. To construct the right stretch tensor U we perform a change of basis by finding $U^* = RUR^T$

Neural Network Structure. The network architecture is based on the Input Convex Neural Network [9]. This architecture requires that all activation functions are convex and that only positive weights are used. This ensures that the network outputs will be convex with respect to the inputs. In this work, the inputs are the scaled invariants of the deformation gradient and the output is the energy. The architecture has two hidden layers each with four nodes. We found that layer pass-through improve the training performance. A mean squared error loss function was used. We used an 80/20 test/train protocol. The network architechture is shown in figure 1.

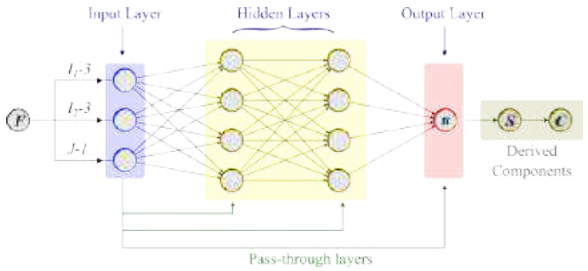

Figure 1: Neural network architecture.

The loss functions included the energy only ($H0$), energy and stress ($H1$, first derivatives), and energy, stress, and stiffness ($H2$, first and second derivatives). The derivatives were computed using autodifferentiation in PyTorch.

RESULTS

Figure 2 shows the loss function for the energy, stress and stiffness over 50 epochs for the $H0$, $H1$, and $H2$ training protocols. Here we see that the stress and stiffness loss are significantly reduced by including the derivatives in the loss function during training.

Figure 3 shows the truth plots for the six independent components of the stress tensor. Here we see exceptional agreement between the true and predicted values of the stress.

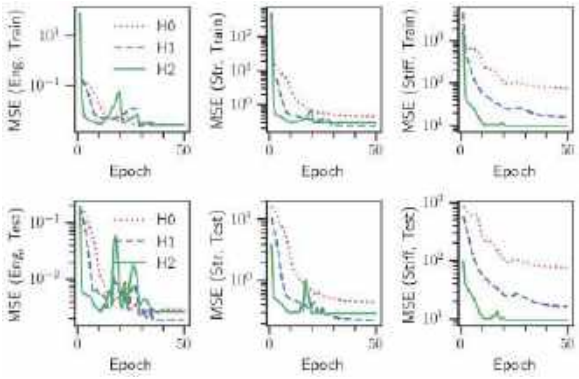

Figure 2: Mean squared error loss function for energy, stress, and stiffness for $H0$, $H1$, and $H2$ training protocols.

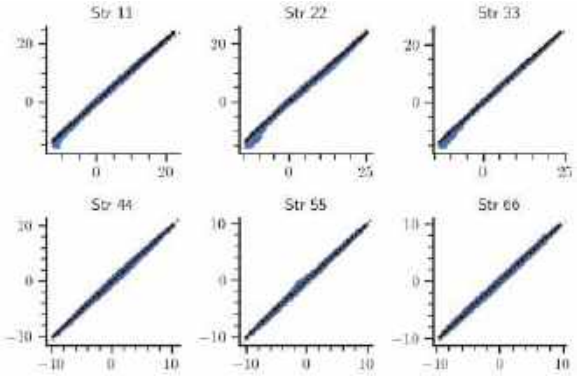

Figure 3: Truth plots for the stress.

DISCUSSION

We developed a novel neural network architecture and used Sobolev training to obtain excellent material predictions for biological materials. Our methods use the network architecture to enforce both polyconvexity through the use of the Input Convex Neural Network, and frame-indifference through the use of the invariants as network inputs.

The resulting material models have been deployed into a multiscale finite element code (results not shown here) and the overall results closely matched those of the full multiscale analysis. And reduced the solution time such that problems of interest could be solved on a laptop rather than a supercomputer. Further work is needed to include fiber anisotropy and damage.

ACKNOWLEDGEMENTS

This research used resources of the Center for Computational Innovation at Rensselaer Polytechnic Institute.

REFERENCES

[1] Holzapfel GA et al. *Journal of Elasticity* 61.1 (2000).
[2] Notbohm J et al. *Journal of The Royal Society Interface* 12.108 (2015).
[3] Mahutga RR et al. *Journal of the Mechanical Behavior of Biomedical Materials* 144 (2023).
[4] Merson J et al. *International Journal of Solids and Structures* 206 (2020).
[5] Merson J et al. *Engineering with Computers* (2024). Accepted.
[6] Thakolkaran P et al. *Journal of the Mechanics and Physics of Solids* 169 (2022).
[7] Linka K et al. *Computer Methods in Applied Mechanics and Engineering* 403 (2023).
[8] Tac V et al. *Engineering with Computers* 38.5 (2022).
[9] Amos B et al. *Proceedings of the 34th International Conference on Machine Learning*. PMLR, 2017.

SB³C2024
Summer Biomechanics, Bioengineering and Biotransport Conference
June 11-14, Lake Geneva, WI, USA

A COMPUTATIONAL MODEL TO SIMULATE THE ROUGHNESS OF NARROWED CORONARY AND CEREBRAL ARTERIES IN DIABETES MELLITUS PATIENTS AND TO DESIGN EFFECTIVE TREATMENT STRATEGIES

S. Piskin (1)

(1) Department of Mechanical Engineering,
Faculty of Engineering and Natural Sciences,
Istinye University
Istanbul, Turkey

INTRODUCTION

Cardiovascular diseases (CVD) pose a significant threat to human health, ranking as the leading cause of death in many Western countries. Atherosclerosis, a prevalent type of CVD, primarily affects the carotid and coronary arteries and is associated with various risk factors, including hypertension, diabetes, high cholesterol levels, smoking, oxidative stress, and age [1]. Treatment options for atherosclerosis in coronary artery disease (CAD) or carotid artery disease include stent implantation through interventional cardiology or open-heart surgery with bypass grafting. Diabetes mellitus (DM) is a common comorbidity in CAD patients, significantly influencing disease severity, treatment strategy, and patient prognosis [2].

Computational hemodynamics (CH) is an innovative in-vitro method to design coronary artery bypass grafting (CABG) procedures or anticipate the short-term and long-term impacts of treatment. Wall shear stress (WSS), a critical biomarker that CH can predict, is linked to the patency of the graft or the narrowed artery following revascularization surgery. However, whether high, low, oscillating or any other WSS derivative causes artery restenosis or CABG closure remains a topic of debate. Numerous clinical and computational studies are ongoing to identify potential correlations. Despite the vast number of patient populations, the computational hemodynamics of CABG for DM patients is not a well-established field. Another crucial aspect of hemodynamics is the roughness of the artery surface [9] or the graft. Recent research has characterized surface roughness in the healthy left anterior descending (LAD) coronary artery [3-4]. However, the effect of roughness on hemodynamics is not fully understood. It can significantly alter the WSS distribution. In this study, we employ a computational model to analyze and compare the flow dynamics of DM patients with healthy controls. We also investigate the effects of wall roughness on WSS in the DM patient model.

METHODS

Two computer-aided models were constructed and simulated using computational fluid dynamics (CFD) techniques. To isolate the geometric influence on hemodynamics, simplified models of coronary arteries were developed. Figure 1 depicts the geometry of a coronary artery with mild stenosis. The wall roughness is set to zero (0) for the smooth artery surface and 0.001 meters (height) for the rough wall.

The three-dimensional (3D) continuity and steady-state Navier-Stokes (NS) equations (Equations 1 and 2) were solved using ANSYS Fluent (ANSYS Inc, PA, USA), a commercially available computational fluid flow solver. The inlet boundary was assigned a velocity profile, and the outlet boundary was assigned a pressure outlet. The artery geometry was based on the typical size of a coronary artery [5], with a length of 30 millimeters and a diameter of 5 millimeters. The wall roughness height was set to 0.5 micrometers, and the roughness coefficient was set to 0.5, assuming uniform roughness.

$$\boldsymbol{\nabla} \cdot \boldsymbol{u} = 0 \tag{1}$$

$$\rho \boldsymbol{u} \cdot \boldsymbol{\nabla} \boldsymbol{u} = -\boldsymbol{\nabla} p + \boldsymbol{\nabla} \cdot [\mu(\boldsymbol{\nabla} \boldsymbol{u} + (\boldsymbol{\nabla} \boldsymbol{u})^T)] \tag{2}$$

where $\boldsymbol{u}$ is the velocity vector, p the pressure, t the time, ρ and μ the density and the dynamic viscosity of the blood, respectively. In addition to the Navier-Stokes equations, the standard k-ε turbulence model was incorporated to account for turbulent flow conditions. The transport equations for the k-ε model are presented in Equations 3 and 4.

$$\frac{\partial}{\partial t}(\rho k) + \frac{\partial}{\partial x_i}(\rho k u_i) = \frac{\partial}{\partial x_j}\left[\left(\mu + \frac{\mu_t}{\sigma_k}\right)\frac{\partial k}{\partial x_j}\right] + G_k - \rho\epsilon \tag{3}$$

$$\frac{\partial}{\partial t}(\rho \epsilon) + \frac{\partial}{\partial x_i}(\rho \epsilon u_i) = \frac{\partial}{\partial x_j}\left[\left(\mu + \frac{\mu_t}{\sigma_\epsilon}\right)\frac{\partial \epsilon}{\partial x_j}\right] + C_{1\epsilon}\frac{\epsilon}{k}G_k - C_{2\epsilon}\rho\frac{\epsilon^2}{k} \tag{4}$$

where x_i and are the spatial coordinates, k the turbulence kinetic energy, ϵ the rate of dissipation of turbulence kinetic energy, μ_t the turbulence viscosity, σ_k (=1.0) and σ_ϵ (=1.3) the turbulent Prandtl numbers for k and ϵ, respectively, G_k the generation of turbulence kinetic energy due to the mean velocity gradients, and $C_{1\epsilon}$ (=1.44) and $C_{2\epsilon}$ (=1.92) are constants. μ_t and G_k are computed by Equations 5 and 6, respectively.

$$\mu_t = \rho C_\mu \frac{k^2}{\epsilon} \tag{5}$$

where C_μ (=0.09) is a constant, and

$$G_k = \mu_t S^2 \tag{6}$$

where S is the modulus of the mean rate-of-strain tensor, defined as $S = \sqrt{2S_{ij}S_{ij}}$. Viscosities are taken $3.5{\cdot}10^{-3}$ Pa·s and $6.8{\cdot}10^{-3}$ Pa·s [6-7] for healthy subject and diabetes mellitus patient, respectively. Densities are assigned 1060 kg/m^3 for both groups.

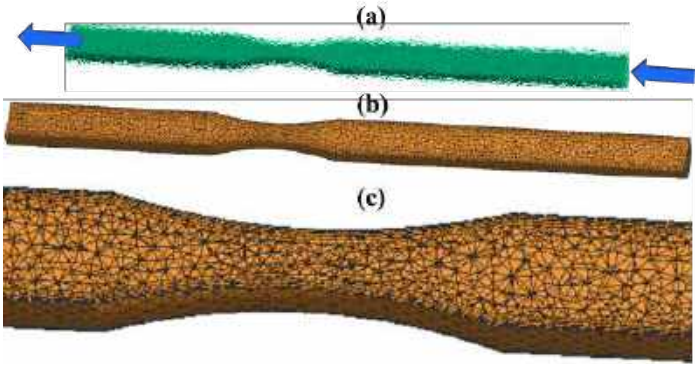

Figure 1: (a) Coronary artery model geometry with representative wall roughness and inlet and outlet boundary conditions, (b) Three-dimensional mesh with boundary layer at the proximity of the wall (c) Zoomed-in view of the mesh around the stenosis zone.

CFD simulations were conducted until the variables u_x, u_y, u_z, p, k, and ϵ reached a convergence criterion of an iteration difference of 10^{-5}.

RESULTS

The WSS distribution across the artery for all three cases was generated: healthy control, DM patient, and rough and smooth wall. Wall shear stress is consistently higher near the artery wall compared to the center of the lumen. This trend is consistent across all conditions, regardless of the presence of diabetes or the roughness of the vessel wall (not shown in the figure). Figure 2 illustrates the pressure distribution pattern which aligns with the expected physiological behavior of a linear pressure drop along the length of the artery except the stenosis region.

Table 1 summarizes the spatially averaged WSS (SAWSS) for all cases: healthy control, DM patient under rough and smooth wall conditions. The wall roughness (height) has been varied to assess its impact on SAWSS. The nominal roughness value is based on literature data, while the other two heights represent hypothetical scenarios of diseased arteries or medical device surfaces. These simulations provide insights into the design of potential treatments or medical devices.

Figure 2: Pressure distribution for the healthy case

Table 1: Spatially averaged wall shear stress (SAWSS) values

SAWSS	Healthy (Pa)	Diabetes Mellitus (Pa)
Smooth wall	107	175
Rough wall (=$3{\cdot}10^{-6}$ m) [3]	107	175
Rough wall (=$3{\cdot}10^{-5}$ m)	108	176
Rough wall (=$3{\cdot}10^{-4}$ m)	92	157

DISCUSSION

Individuals with diabetes mellitus often present with blood viscosity levels that differ significantly from healthy individuals. If they also have coronary artery or carotid artery stenosis, additional caution is necessary when selecting cardiovascular disease treatment options. To address this issue, we have developed an in-silico model to analyze the hemodynamic effects of lumen or medical device roughness in patients with diabetes mellitus. Our preliminary study found that natural wall roughness does not significantly alter spatially averaged wall shear stress (SAWSS) in either healthy individuals or patients with diabetes mellitus (DM). However, when wall roughness increased to approximately 3 × 10^-4 meters, SAWSS decreased moderately, by approximately 15% for healthy subjects and 10% for DM patients. This reduction in SAWSS is consistent with the observed roughness of deployed stents [8].

The study's preliminary results suggest that engineered roughness in novel stents or bypass grafts could be used to modulate wall shear stress (WSS) in patients with diabetes mellitus (DM). This could potentially improve the outcomes of interventional or surgical procedures. However, further research is needed to validate these findings and refine the simulations using real coronary or carotid artery geometries and real-world surgical scenarios.

ACKNOWLEDGEMENTS

We acknowledge the following two fundings that supported this research: the Istinye University BAP project with an ID of 2019B1 and the Marie-Sklodowska Curie Actions Individual Fellowship funded by the European Research Executive Agency with an ID of 101038096. This project has received funding from the European Union's Horizon 2020 research and innovation programme.

REFERENCES

[1] Avgerinos, NA et al, *Ann. Biomed. Eng.,* 47:1764–1785, (2019).
[2] Alexandrovna BN et al, *Coronary Artery Bypass Grafting in Patients with Diabetes Mellitus: A Cardiologist's View*, 2017.
[3] Burton HE et al, *Cardiovasc. Eng. Technol.*, 8:41-56, 2017.
[4] Burton HE et al, *Appl. Bionics. Biomech.*, 2019.
[5] Dodge JT Jr et al, *Circulation,* 86:232-46, 1992.
[6] Hochmuth RM et al, *Annu. Rev. Physiol*., 49:209–219, 1987.
[7] Irace C et al, *Diabetes Care*, 37: 488-492, 2014.
[8] Syaifudin A et al, *Bio-Med Mater. Eng.*, 25: 189-202, 2015.
[9] Owen DG. et al, *J. R. Soc. Interface*., 17:20200327-20200327, 2020

DEVELOPMENT OF CELL-LADEN GELATIN METHACRYLATE (GELMA) HYDROGELS WITH TUNABLE MECHANICAL PROPERTIES FOR CARDIOVASCULAR TISSUE ENGINEERING

Caitlin Westgate (1), Josh Vecchio (2), James Babcock (3), Ludovic Robinson (1) and Jason W. Nichol (1,2)

(1) Dept of Bioengineering, Endicott College, Beverly, MA ,USA
(2) Dept of Biotechnology, Endicott College, Beverly, MA ,USA
(3) Dept of Engineering, Endicott College, Beverly, MA ,USA

INTRODUCTION

Tissue engineering as a field holds great promise for both repairing damaged or diseased tissues as well as correcting congenital defects. While use in clinical applications is of critical importance to improve human health, engineered tissues also hold great value in other important areas, such as drug discovery and study of disease mechanisms. The ability to create tissues with controllable mechanical properties is of the utmost importance in reliably creating tissues with known properties, and often is an elusive goal for many tissue engineering systems.

We have been using Gelatin Methacrylate (GelMA) in our lab to investigate the role of the mechanical environment on cellular behaviors in many systems, such as cancer cell transformation and migration as well as stem cell differentiation[1,2]. GelMA is easily remodeled by a variety of cell types having abundant binding and degradable domains, and the mechanical properties are easily tunable within soft (100-1000 Pa) to moderate stiffness (1000 – 5000 Pa) ranges, however reliably achieving stiffer properties (10 – 15 kPa) has been difficult for us to achieve using GelMA alone. We have previously demonstrated the ability to increase the stiffness of GelMA hydrogels by creating a co-polymer with PEGDA (up to 100 kPa), however the handling and encapsulation techniques are more complicated, and less tolerated by cells [3].

In this study we will investigate which system, cells encapsulated in pure GelMA or PEG-GelMA, is a better hydrogel platform for creating model cardiac tissues using C2C12 myoblast cells. The goals will be to achieve a physiological stiffness range of 5 – 15 kPa, while not sacrificing cell health, morphology or remodeling capacity. Results of these studies will be used in parallel studies of creating engineered cardiac tissues using a contractile bioreactor system with electrical stimulus using both C2C12 and human mesenchymal stem cells.

METHODS

Gelatin methacrylate was created as previously described, by reacting aqueous gelatin (300 bloom from porcine skin) in PBS (10% w/vol) with varying amounts of methacrylic anhydride (0.25 ml, 1.25 ml, 5 ml, 10 ml) to create a group of GelMA precursors with varying degree of methacrylation (low, medium, medium-high, high). The resultant mixture was reacted at 50°C for 2-3 hours under agitation, then quenched with 2-3x volume of PBS and then dialyzed for roughly 1 week to remove the excess methacrylic acid from the reactant. The resultant mixture was then lyophilized until dried and stored at -20°C until further use.

Hydrogels were created by mixing GelMA precursor at concentrations of 7.5-15% w/vol with 0.1% w/vol Irgacure 2959 in PBS and irradiating 2 ml of the mixture for 1-3 minutes with 365nm UV light. Cell laden gels were made similarly by adding the above mixture to a cell pellet, mixing, then polymerizing as described and immediately being placed in a well plate with 1-2 ml growth media. Cells were cultured using standard techniques and flasks using standard DMEM with 10% fetal bovine serum (FBS), 1% penicillin-streptomycin-neomycin and 2% L-Glutamine.

For mechanical tests, polymerized GelMA from all 4 groups will be created at 5%, 7.5%, 10%, 12.5% and 15% concentrations, then incubated for 24-48 hours at 4°C in PBS to achieve maximal swelling. Roughly 4-6 samples from each gel will be created with a 5mm biopsy punch and compressed at a fixed strain rate to determine the stress-strain properties. Elastic modulus will be determined using a Matlab script which finds the slope of the 0-5% strain range from the stress-strain curve. Similar studies will be attempted with pure PEGDA (1000 Da) in similar concentrations, as well as GelMA-PEGDA copolymers of various combination keeping the overall gel concentration at 15%.

Candidates with stiffnesses in the ranges of 5 – 15 kPa will then be evaluated with C2C12 cells in static 7 day cultures to determine cellular phenotype. Cell proliferation, alignment and cell-cell interconnectivity

will be evaluated using microscopy at 2-3 points in the 7 day culture period to evaluated cell behavior in response to stiffness. Live/Dead stain will also be performed according to manufacturer directions to assess cell viability at similar time points.

RESULTS & DISCUSSION

In general, the stiffness increases both with gel concentration as well as the degree of methacrylation. However handling GelMA of concentrations 7.5% and above becomes more complicated as it reversibly gels at room temperature and must be kept at 37°C to prevent this. Similar concerns for co-polymers are ensuring complete mixing and miscibility, while also maintaining cell viability. We expect that several combinations of co-polymers will yield appropriate stiffness ranges, but that cell viability & migratory properties will be inversely proportional to the PEGDA concentration.

REFERENCES

[1] Nichol, JW et al., *Biomaterials*, 31(21):5536-44. 2010.
[2] Aubin, H et al., *Biomaterials*, 31(27):6941-6951. 2010.
[3] Huston, CB et al., *Tissue Engr Part A,* 17(13-14): 1713-23. 2011

PITCH COMPETITION: A RAPID NOVEL ASSAY FOR MEASURING HEMOGLOBIN-OXYGEN AFFINITY

Rucha Natu[1], Zoe Sekyonda[2], Yuxuan Du[1],John Hinshaw[3], Peter Galen[3], Umut Gurkan[1,2,3]

(1) Department of Mechanical and Aerospace Engineering, Case Western Reserve University, Cleveland, Ohio, USA
(2) Department of Biomedical Engineering, Case Western Reserve University, Cleveland, Ohio, USA
(3) Hemex Health Inc, Portland, Oregon, USA

PROBLEM STATEMENT

Hemoglobin (Hb) delivers Oxygen (O_2) to the tissues through binding, transport and dissociation. Modifying the Hb-O_2 affinity is a promising approach for treatments developed for hemoglobinopathies like sickle cell disease (SCD), hypoxemia related to pulmonary diseases, wound healing and ischemia among others [1] [2] [3]. After US FDA's approval for Voxelotor in 2019 [4] which improves Hb-O_2 affinity for treatment of SCD, new interest has spawned in modification of Hb-O_2 affinity for SCD treatment [5] [6]. In this context, measuring Hb-O_2 affinity quantitatively reported as p50 (the partial pressure of oxygen at which Hb is half-saturated with oxygen) has gained importance.

Currently p50 is determined using complex instruments like tonometers, Hem-O-Scans, and TCS Hemox Analyzers. However, these are not ideal for point of care (POC) screening due to high cost, complex operation, bulky equipment (including nitrogen cylinders), long testing time and limited throughput [7]. Globally, an estimated 400,000 babies are annually born with hemoglobinopathies. In the USA, SCD affects more than 100,000 individuals and reduces life expectancy by approximately 30 years [8]. Most of the affected population resides in underserved areas with limited access to high rescource facilities. p50 measurement is important for treatment monitoring but is underutilized due to technical and operational limitations. Our technology-Rapid Hemoglobin Oxygen Dissociation Assay (RHODA) provides a rapid measurement of Hb-O_2 affinity, to screen for Hb-O_2 affinity disorders, determine cellular oxygen availability, and monitor the effectiveness of O_2-modifying therapies for SCD patients. Translation of this laboratory-based technology to a commercial device by integration with a platform for HB variant screening will enable rapid screening and therapy monitoring in one place.

TECHNOLOGY/SOLUTION DESCRIPTION

Hb-O_2 affinity is determined via measuring Hb-O_2 saturation level (SO_2, %) and oxygen partial pressure (pO_2, mmHg) [9]. RHODA uses the principle that when hemoglobin binds with oxygen, it changes its conformation and this affects the pattern of light absorption in the specific range of wavelengths. In the RHODA test, a small sample of blood (few µl) is mixed with a buffer to adjust the pH for rapid deoxygenation of blood. A fluorescent dye is used as the marker to indicate dissolved oxygen. Assay is run in two steps: 1) it uses chemically induced deoxygenation and measures the absorption and amount of spectral shift. Using the spectral shift, we determine the rate of oxygen dissociation as an oxygen affinity index. Then 2) we measure the emission intensity of fluorescent dye to determine pO_2 and SO_2 which are used to calculate p50.

We plan to integrate the laboratory-based RHODA technology with an existing commercial platform- Gazelle developed by Hemex Health Inc. The Gazelle reader includes a cuvette based optical system designed for malaria diagnosis. The two-part cuvette used for malaria testing will be modified to be used as a one-step cartridge for RHODA. The bottom part of the cartridge will be used to perform fingerstick and absorb blood using capillary interface. Absorbed blood will be collected in the bottom part. The bottom part will also incorporate fluorescent markers for oxygen sensing. The top part of the cuvette will be modified to contain the buffer and chemical components for inducing deoxygenation. On locking the two parts, the contents from the top will mix with the blood and will deoxygenate the blood. The cartridge will be inserted into the Gazelle platform. Gazelle optical system will be modified to use two light sources 1) Broad-spectrum light and 2) Fluorescent excitation light. A compact spectrometer will collect transmitted light from the cuvette to determine the absorption spectrum of the blood sample over time as it is deoxygenated. The fluorescent emission will be measured with the same spectrometer. The Gazelle software will be programmed to calculate the pO2 and SO2 and display the values on the Gazelle screen. The Gazelle platform is already equipped for POC Hb variant testing. RHODA will complement the

application of the platform. Figure 1 details the proposed setup for RHODA and the modified cuvette to act as a one-step cartridge.

BUSINESS CASE

More than 7% of the world's population carry hemoglobin gene mutations resulting in Hb variants resulting in sickle cell disease among other blood disorders [10]. Most of this population lives in the underserved areas around the world. HPLC is the gold standard in Hb Variant testing, however, is suited for high resource laboratories. POC diagnostic testing provided by the Gazelle Hb Variant test invented at CWRU and commercialized by Hemex Health Inc has been distributed in over 27 countries with more than 400,000 tests conducted on Gazelle. The Gazelle Hb variant test has proven to be game-changing in POC settings for Hb variant diagnosis, but Gazelle currently doesn't support therapy monitoring that improves Hb-O_2 affinity. A diagnostic system that can be used for screening and Hb-O_2 affinity treatment monitoring is urgently needed. Addition of RHODA will complement the Gazelle Hb Variant test. Optimal management of SCD requires early diagnosis and treatment monitoring. Treatment monitoring and management will benefit from rapid and affordable POC testing, which RHODA will enable.

On incorporating the RHODA technology, the upgraded Gazelle RHODA will be marketed as a device. RHODA test kits containing single use two-piece cartridges will be sold to use with the platform. With a few simple steps, the platform will display results for oxygen affinity measurement from a few µl of blood within minutes. Based on the prior progress and preliminary results, we do not anticipate major challenges in technology. The approach of determining oxygen affinity by measuring spectral shifts during desaturation has been clearly demonstrated in preliminary work. We anticipate some challenges in adapting the laboratory sample preparation technique-including the fingerstick, blood collection and mixing with buffer to one step cartridge for users with minimal laboratory skills. Making this process reproducible and consistent among different users provides an engineering challenge. To solve this challenge, we are experimenting with different cartridge designs and attachments. In case of failure to addressing these challenges, the cuvette design will be modified.

Analytical and clinical validation for the device will be conducted according to FDA "Bioanalytical method validation guidelines" [11]. Following FDA guidelines and consultations from regulatory experts will enable us to engage with FDA in the early stage of device development. Unlike the current analyzers, Gazelle based RHODA is advantageous as it is compact, portable, easy to use, does not require additional training and allows rapid analysis of oxygen affinity in POC settings using few µl of blood. Due to these advantages, RHODA will target low to moderate resource clinical labs and hematology clinics in, and outside USA. The existing market base for Gazelle will prove advantageous for marketing the upgraded platform.

ACKNOWLEDGEMENTS

Authors acknowledge the National Institute of Health Small Business Technology Transfer Grant (RES601405)

REFERENCES

[1] M. K. Safo, M. H. Ahmed, M. S. Ghatge and T. Boyiri, "Hemoglobin–ligand binding: Understanding Hb function and allostery on atomic level," *Biochimica et Biophysica Acta,* vol. 1814, no. 6, pp. 797-809, 2011.

[2] X. Geng, K. Dufu, A. Hutchaleelaha, Q. Xu, Z. Li, C.-M. Li, M. P. Patel, N. Vlahakis, J. Lehrer-Graiwer and D. Oksenberg, "Increased hemoglobin–oxygen affinity ameliorates bleomycin-induced hypoxemia and pulmonary fibrosis," *Physiological Reports,* vol. 4, no. 17, 2016.

[3] G. J. Kato, F. B. Piel, C. D. Reid, M. H. Gaston, K. Ohene-Frempong, L. Krishnamurti, W. R. Smith, J. A. Panepinto, D. J. Weatherall, F. F. Costa and E. P. Vichinsky, "Sickle Cell Disease," *Nature Reviews,* 2018.

[4] E. V. C. Hoppe, K. I. Ataga, R. E. Ware, V. Nduba, A. El-Beshlawy, M. Hoda Hassab, M. M. Achebe, S. Alkindi and R. C. Bro, "A Phase 3 Randomized Trial of Voxelotor in Sickle Cell Disease," *New England Journal of Medicine* , vol. 381, no. 6, pp. 509-519, 2019.

[5] W. A. Eaton, "Hemoglobin S polymerization and sickle cell disease: A retrospective on the occasion of the 70th anniversary of Pauling's Science paper," *American Journal of Hematology,* pp. 205-211, 2019.

[6] E. R. Henry, B. Metaferia, Q. Li, J. Harper, R. B. Best, K. E. Glass, T. Cellmer, E. B. Dunkelberger, A. Conrey, S. L. Thein, H. F. Bunn and W. A. Eaton, "Treatment of sickle cell disease by increasing oxygen affinity of hemoglobin," *Blood,* pp. 1172-1181, 2021.

[7] M. P. Patel, V. Siu, A. Silva-Garcia, Q. Xu, Z. Li and D. Oksenberg, "Development and validation of an oxygen dissociation assay, a screening platform for discovering, and characterizing hemoglobin–oxygen affinity modifiers," *Drug Design, Development and Therapy,* pp. 1599-1607, 2018.

[8] F. B. Piel, M. H. Steinberg and D. C. Rees, "Sickle Cell Disease," *New England Journal of Medicine* , vol. 376, no. 16, pp. 1561-1573, 2017.

[9] A. J. Srinivasan, C. Morkane, D. S. Martin and I. J. Welsby, "Should modulation of p50 be a therapeutic target in the critically ill?," *Expert Review of Hematology,* pp. 449-458, 2017.

[10] B. Modell and M. Darlison, "Global epidemiology of haemoglobin disorders and derived service indicators," Bulletin of the World Health Organization, 2008.

[11] U. FDA, "Bioanalytical Method Validation Guidance for Industry," 2018. [Online]. Available: https://www.fda.gov/regulatory-information/search-fda-guidance-documents/bioanalytical-method-validation-guidance-industry.

FROM LIGHT TO RELIEF: REVOLUTIONIZING PAIN MANAGEMENT WITH OPTICAL BLOOD-SPINAL CORD BARRIER MODULATION

H. Dave(1), T. Leong(1), E. David(4), T. Price(4,5), Z. Qin(1,2,3,5)

(1) Department of Bioengineering, The University of Texas at Dallas, Richardson, Texas, USA
(2) Department of Mechanical Engineering, The University of Texas at Dallas, Richardson, Texas, USA
(3) Department of Biomedical Engineering, University of Texas Southwestern Medical Center, Dallas, Texas, USA
(4) Department of Neuroscience, The University of Texas at Dallas, Richardson, Texas, USA
(5) Center for Advanced Pain Studies, The University of Texas at Dallas, Richardson, Texas, USA

PROBLEM STATEMENT

Spinal cord diseases encompass a range of conditions, such as multiple sclerosis, spinal stenosis, spinal tumors, and chronic pain. High-impact chronic pain is a concept that incorporates the pain burden and disability in the chronic pain population, can be inflammatory or neuropathic, and impacts about 5-8% of the United States population. Individuals suffering from high-impact chronic pain frequently find minimal relief from oral medications and may undergo invasive procedures and rely on spinal drug pumps or stimulators for pain relief, all of which contribute to higher health expenditures. The development of effective therapies is notably hindered by the blood-spinal cord barrier (BSCB), which poses a significant challenge in delivering treatments directly to the affected areas. [1-5]

Conventional treatment options, including surgical interventions and systemic drug administrations, face limitations due to the presence of the BSCB. Innovations such as focused ultrasound with gas-filled microbubbles aim to open the blood-brain barrier to transiently improve therapeutic delivery. However, this method faces challenges, including the potential for acoustic-thermal deposition in surrounding bones and the complexity of spinal geometry, which have impeded its application to the spinal cord.[6] Consequently, there is an urgent need for a robust, reliable, and minimally invasive technique to breach the BSCB and increase the availability of therapeutics via systemic administration with minimal side effects.

TECHNOLOGY/SOLUTION DESCRIPTION

Leveraging the pioneering OptoBBB technology developed in our lab, [7,8] this current technology (Opto-BSCB) focuses on using short-pulsed laser light to stimulate vascular-targeted gold nanoparticles (AuNPs) in the spinal cord as an efficient mechanism for enhancing the permeability of the BSCB. **(Fig. 1A&B)**. This cutting-edge method facilitates the direct delivery of pain-relief medications to the spinal cord, representing a significant advancement from the current invasive surgical procedures.

As a proof of concept, our Opto-BSCB technology works efficiently in modulating the permeability of the BSCB in the spinal cord. The innovative optical approach facilitated the delivery of a peptide, inducing itch behavior, within a specific 24-hour window. **(Figure 1C & Figure 2)** This successful proof-of-concept validates the technology's ability to modulate neural responses and showcases its potential for targeted drug delivery in the spinal cord.

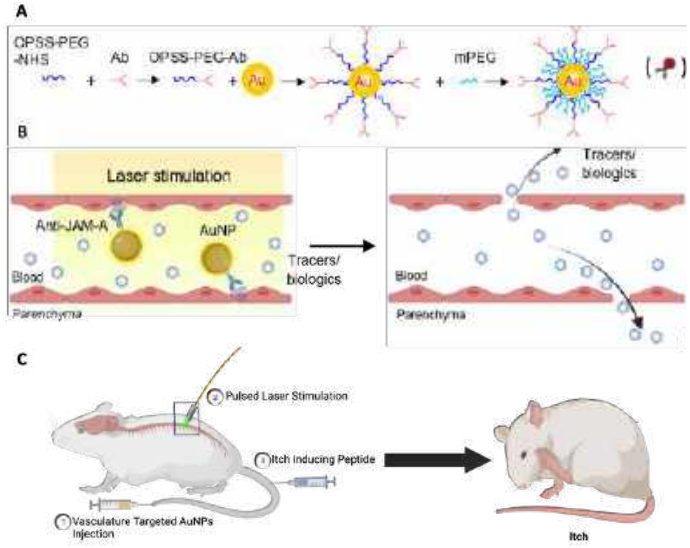

Figure 1. Schematic of (A) Synthesis method for brain vasculature targeting nanoparticles. (B) Mechanism of enhanced BSCB permeability. (C) Method of BSCB modulation and peptide/therapeutic delivery.[9]

Crucial technical steps to bring current Opto-BSCB to market include optimizing delivery parameters, conducting comprehensive safety and efficacy studies, and scaling up manufacturing processes for AuNPs. Preclinical trials with larger animal models like porcine and non-human primates are vital for validation. Navigating regulatory pathways and cost optimization are essential for market entry. We are currently validating our Opto-BSCB technology in porcine models. **(Figure 3A)**

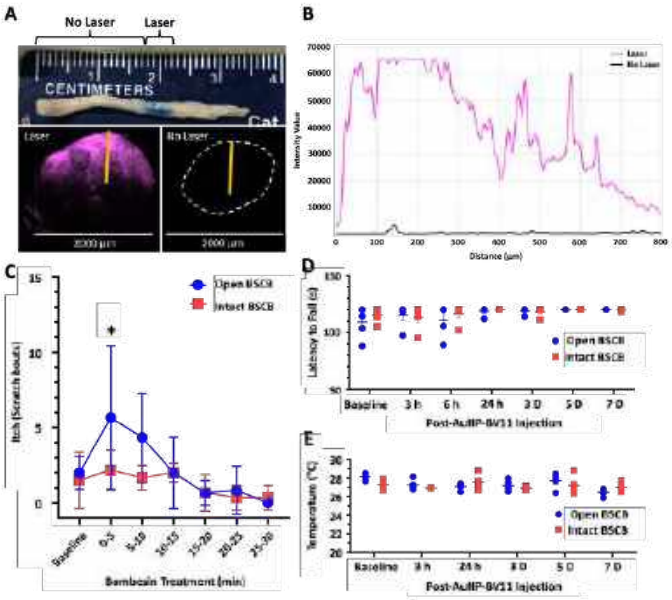

Figure 2: (A) External and fluorescent cross-sectional views of mouse spine, showing enhanced Evans Blue dye penetration in laser-stimulated regions (blue) versus unstimulated areas (natural color). (B) Fluorescent intensity difference between the two regions. (C) Elevated itching activity was observed in mice with an open BSCB compared to control mice with an intact BSCB. (C and D) Effects of BSCB modulation on motor skills and temperature in the hind paws.

BUSINESS CASE

1. **Identification of Patients, End Users, and Payers:**
   - **a.** Patients: The primary focus of this technology is on individuals experiencing high-impact chronic pain. It aims to significantly alleviate the discomfort and improve the quality of life for patients.
   - **b.** End Users: Clinicians specializing in neurology, neurosurgery, and pain management will be crucial in facilitating the adoption of OptoBSCB. Their acceptance would be essential for adopting and administering this innovative treatment.
   - **c.** Payers: Entities in the healthcare system responsible for financing medical treatments, such as insurance companies, healthcare institutions, and government health agencies, would eventually be responsible for funding the expenses related to OptoBSCB treatment.

2. **Potential Hurdles to Market:**
   - **a.** Manufacturing Challenge: This involves setting up a dependable manufacturing process for the components of OptoBSCB, including the AuNPs and vascular targeting protein. Ensuring consistent product quality is critical, and scalability may pose a challenge. Also, precisely controlling the laser parameters would be crucial.
   - **b.** Regulatory Strategy: In the United States, the FDA, specifically its Center for Devices and Radiological Health (CDRH), would oversee the approval and regulation of medical devices and technologies like OptoBSCB. This would involve comprehensively evaluating safety, efficacy, and quality before approving medical use.
   - **c.** Marketing Strategy: Our marketing strategy for OptoBSCB revolves around understanding patient and doctor needs, educating healthcare professionals, and building credibility. We'll engage with experts, conduct clinical trials, and work on reimbursement agreements. Online presence and patient advocacy will play a significant role in increasing awareness and adoption.

3. **Anticipated Risks:** As we plan to commercialize OptoBSCB technology to improve spinal cord disease treatment, we acknowledge potential challenges. These include regulatory hurdles, competition, proving OptoBSCB's effectiveness, gaining healthcare professional support, scaling up production, and addressing legal matters. Successful risk management is crucial for our research to benefit spinal cord disease patients through OptoBSCB. (Detailed Strategy - **Figure 3B**)

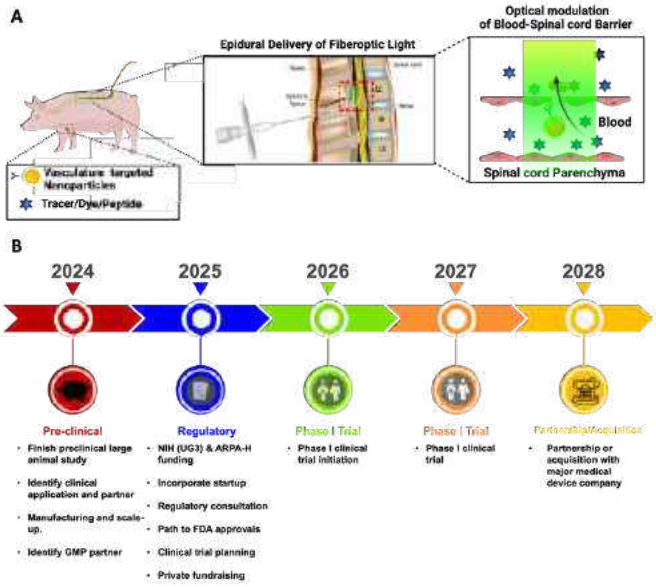

Figure 3: (A) Schematic showing Opto-BSCB modulation in porcine model. (B) Commercialization Strategy for Opto-BSCB technology.

ACKNOWLEDGEMENTS

We acknowledge funding support from the Department of Defense (DOD: W81XWH2110219).

REFERENCES

[1] Bartanusz, V. et al., *Annals of Neurology*, 70(2), 194-206, 2011.
[2] Rossi, F. et al., *Expert Opinion on Drug Delivery*, 10, 385-396, 2013.
[3] Daneman, R., *Annals of Neurology*, 72(5), 648-672, 2012.
[4] Wolka, A.M. et al., *Adv Drug Deliv Rev*, 55(8), 987-1006, 2003.
[5] Schaefer, C.P. et al., *Fluids and Barriers of the CNS*, 14(1), 32, 2017.
[6] Gross, C.G. et al., *Med Phy,* 48, 4395-4401, 2021.
[7] Li, X et. al., *Nano Lett,* 21, 22, 9805–9815, 2021.
[8] Cai, Q et. al., *Nat Commun,* 14:4934, 2023
[9] Gao, Z et. al., *bioRxiv*, 2022.

PITCH COMPETITION: DELTA CUFF

Cyrus J. Darvish (1), Pete H. Gueldner (1), Rabih A. Chaer (2), David A. Vorp (1-8), and Timothy K. Chung (1)

(1) Bioengineering, University of Pittsburgh, Pittsburgh, Pennsylvania, USA
(2) Division of Surgery, University of Pittsburgh Medical Center, Pittsburgh, Pennsylvania, USA
(3) Mechanical Engineering and Materials Science, University of Pittsburgh, Pittsburgh, Pennsylvania, USA
(4) McGowan Institute for Regenerative Medicine, University of Pittsburgh, Pittsburgh, Pennsylvania, USA
(5) Surgery, University of Pittsburgh, Pittsburgh, Pennsylvania, USA
(6) Chemical and Petroleum Engineering, University of Pittsburgh, Pittsburgh, Pennsylvania, USA
(7) Cardiothoracic Surgery, University of Pittsburgh, Pittsburgh, Pennsylvania, USA
(8) Clinical and Translational Sciences Institute, University of Pittsburgh, Pittsburgh, Pennsylvania, USA

PROBLEM STATEMENT

Deep vein thrombosis (DVT) occurs when a blood clot forms in the deep veins, typically in the legs (**Figure 1**). The clot reduces return blood flow to the heart, resulting in pain and swelling. Each year, as many as 900,000 people are affected by DVT and associated pulmonary embolisms [1]. Post-thrombotic syndrome (PTS) is a condition that can occur after DVT. It involves long-term symptoms of pain, swelling, and skin discoloration. This chronic condition occurs because the blood clot damages the vein and valves permanently, diminishing the vein's normal function. PTS affects up to 50% of patients who have experienced acute DVT [2]. PTS is not fatal to the patient, but it results in a significant decrease in quality of life and bears significant healthcare costs of up to $22,445 per patient per year in addition to DVT costs [3].

There is a significant challenge in the medical community when it comes to understanding the progression from acute DVT to PTS. It is understood that the damage to the vein walls and valves causes regurgitation of blood past the valve, leading to pooling and ultimately resulting in chronic symptoms. The clinical problem is that a patient's diagnosis is delayed up to six months from the onset of the blood clot. This delay exists because there is no method to detect PTS until after the treatment of DVT. Clinical evaluation is the primary method of diagnosing PTS. A separate clinical survey and ultrasound imaging offer supplemental confirmation. None of these methods provide a risk assessment for preventing the disease or offer discernability between an acute blood clot and PTS. This problem is exacerbated further in Black individuals, where the prevalence of thrombosis and blood clot-related diseases is higher [4, 5].

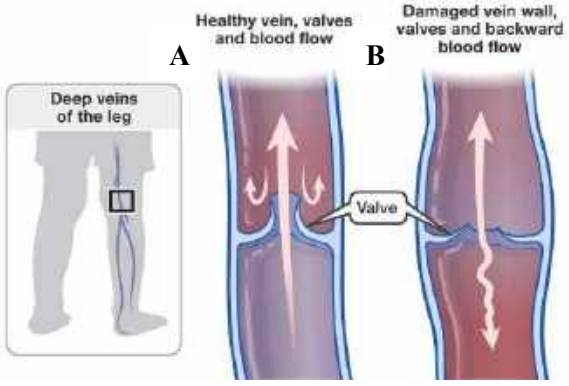

Figure 1: A) Shows a healthy vein with normal blood flow through the deep vein. **B)** Depicts a deep vein that has been afflicted by a blood clot and the valve has been damaged, resulting in backward blood flow.

Providing a method to predict the risk of a patient developing PTS could help clinicians pre-emptively treat high-risk patients to halt or eliminate the progression to PTS using more extensive compression therapy, aggressive anticoagulation therapy, or surgical intervention. This change in the clinical timeline would result in improved quality of life, reduced healthcare costs, and improved long-term patient outcomes.

TECHNOLOGY/SOLUTION DESCRIPTION

Our team has invented the Delta Cuff to address the problem of predicting the transition of acute DVT to PTS. The Delta Cuff combines hardware innovation with machine learning (ML) to

help clinicians create a care plan tailored to the patient. The first part of our strategy is a non-invasive compression cuff embedded with arrays of specially chosen sensors that will be placed on patients' thighs or calves to measure the bruit-like acoustics of venous flow as an indicator of vein flexibility or compliance. The cuff temporarily occludes venous flow with pressurization and then releases the pressure to observe the waveforms gathered from the sensors (**Figure 2**). This device complements the current standard of care for treating DVT, which is compression therapy.

The second portion of our approach includes creating an ML model that will utilize various data inputs, such as the compliance measured via vibration/audio waveform metrics and patient-specific survey and clinical data. This model will identify patients at risk of transitioning to PTS, enabling clinicians to design a care plan to potentially prevent chronic complications. The Delta Cuff, therefore, addresses the problem through early identification and medical prevention. By combining a pneumatically driven cuff with an intelligent ML model, the system can pre-emptively identify DVT patients at elevated risk of developing PTS. Patients deemed high-risk can be offered more intense surveillance, an extended regimen of anticoagulation therapy, optimized compression therapy, and surgical intervention. All of which can hopefully prevent chronic conditions from forming.

Our team has developed an initial bench-level prototype of the Delta Cuff. A pressure cuff was designed with three separate three (3x3) sensor arrays to record flexibility at different locations around a patient's leg (**Figure 2A)**. A separate box was intended to house all the related electronic and power components (**Figure 2B**). An initial test was conducted to determine whether our bench-level prototype could identify a human subject sitting or standing. The cuff was wrapped around the person's leg, and data collection was performed while they were standing and then while they were seated using the nine sensors, as shown in **Figure 2A**. A pooled average and polynomial fitting of the nine signals were performed. The signal for the person standing was noticeably greater than while seated, indicating our device can discern between different hemodynamic situations or potentially different patient groups.

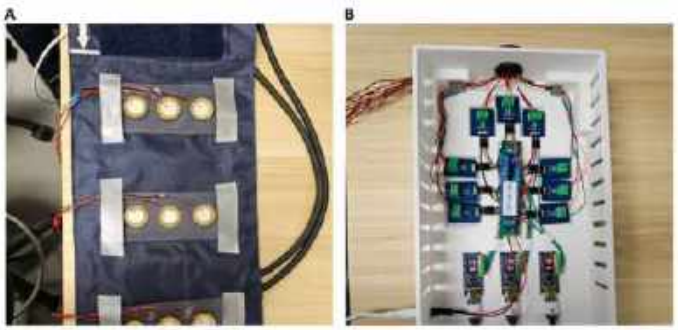

Figure 2: Hardware prototype of Delta Cuff. **A)** PDMS-embedded pressure sensor arrays attached to the pressure cuff. **B)** 3-D printed housing unit for the electronic components of Delta Cuff including Arduino Nano boards, amplifiers, and power distribution block. Not shown in the image are the constant 5V power brick and USB hub.

Moving our technology closer to commercialization will require further prototype development, testing, and validation. We will perform rigorous validation of the Delta Cuff signals and how they relate to disease prediction. This validation will require obtaining IRB approval, gathering data from healthy, DVT, and PTS patients, and determining any distinguishing waveforms in the signal. We will also have to validate our ML model using a training data set and testing data set. The training data set will be used to create the model. Some of the data, the testing data set, will be intentionally held out of the training to validate how well the model performs.

BUSINESS CASE

There is a significant market opportunity for a device that can identify patients at high risk of PTS. With roughly 900,000 cases of DVT each year, each patient would be required to have further testing to see whether they will develop PTS (as it is unknown whether the disease will progress in an individual). To estimate the market size, we researched the compression therapy market, which is closely related to our device. The total global market of compression therapy for vascular diseases such as DVT, leg ulcers, and varicose vein treatment is $3.7 billion and is projected to reach $4.9 billion by 2027. The U.S. has the highest market share, about 50%. We intend to enter this market by partnering with an existing compression therapy vendor. This strategy would allow us to use already established distribution channels to the hospitals, who will be our primary customers. Operating with an established company provides clinical familiarity, making adopting our technology easier.

The primary stakeholder is the physician providing care. After conducting customer discovery interviews with vascular surgeons, we determined that the most effective time to implement the Delta Cuff is in the acute stage of the DVT, immediately at the time of diagnosis. We plan on selling the device directly to doctors' offices and hospitals, with the end-user primarily being primary care physicians, who typically see the patient immediately at the onset of DVT. There would be certain situations where a vascular surgeon may use the Delta Cuff.

The Delta Cuff will follow the 510k pathway with a predicate device, such as doppler ultrasound, which evaluates changes in blood flow through compression. In future design iterations, we will ensure that our sensors do not cause discomfort or pain for the patient. We hope to create various sizes and spacings to accommodate different anatomies. Our long-term development plan includes bolstering our bench-level prototype, conducting testing, determining a potential partner, pre-clinical validation, FDA approval and clinical studies, and reference studies with end users.

REFERENCES

[1] Caprini, J.A., Amer J Surg, 199(1): p.S3-S10, '10. [2] Kahn, S.R., Amer Soc Hemat Ed Prog, p. 413-418, '16. [3] Ashrani, A.A., J.A. Heit, J Thromb Thrombolysis, 28: p. 465-476, '09. [4] White, R.H., C.R. Keenan, Thromb Res, 123: p. S11-S17, '09. [5] Weze, K.O., et al., Amer J Prev Med, 63(1): p. e11-e20, '22.

PITCH COMPETITION: YOUNGHEARTVALVE – NEXT GENERATION HEART VALVE TECHNOLOGY

Lakshmi Prasad Dasi (1), Srujana J. Joshi (1), Justin Gangwish (2), Nipa Khair (2), Susan P. James (2)

(1) The Wallace H. Coulter Department of Biomedical Engineering, Georgia Institute of Technology, Atlanta, GA, USA
(2) Department of Mechanical Engineering, Colorado State University, Fort Collins, CO, USA

PROBLEM STATEMENT

In the United States alone, heart disease remains a leading cause of death for both men and women. Aortic stenosis, characterized by the narrowing of the aortic valve opening, is one of the most common heart valve diseases, impacting over 800,000 Americans over the age of 75 in 2019 [1]. While the standard treatment for severe aortic stenosis is surgical aortic valve replacement (SAVR), transcatheter aortic valve replacement (TAVR) has become the preferred approach for the oldest and most frail patients at high risk for open heart surgery. TAVR is a minimally less invasive procedure wherein the replacement valve is delivered to the site of the diseased valve through a catheter. However, not all individuals with severe aortic stenosis are at high risk for surgery. Globally, many patients present with an intermediate or low risk, and would therefore tolerate a SAVR approach. Despite this, many, including a growing number of trained interventional cardiologists, prefer TAVR due to its less invasive nature, lack of need for in-procedure full sedation, shorter hospital stay, faster recovery time, and potential avoidance of long-term anticoagulation therapy. Following the Food and Drug Administration (FDA) approval for the use of TAVR in patients with intermediate risk, the landscape of TAVR in the United States has evolved. Initially approved only for patients aged 80 and above, TAVR is now used to treat patients with aortic stenosis with an average age of 73. However, the current technology limitations continue to preclude younger, more active patients from receiving this option – thereby limiting the full potential and benefits offered by the TAVR method.

Current commercial TAVRs predominantly utilize animal-derived tissue, such as bovine or porcine pericardium, for their leaflets. However, these tissue-based valves face durability challenges, marked by calcification and structural valve degeneration (SVD)[2]. Hypoattenuated leaflet thickening (HALT), resulting from thrombosis, is linked to valve dysfunction and mortality in 10% of commercial TAVRs [3]. Paravalvular leakage (PVL), affecting 8-18% of TAVR patients despite newer designs, can lead to stroke and silent death post-treatment [4]. These concerns not only limit device longevity but also necessitate reinterventions. Beyond performance issues, the manufacturing process for these valves is intricate, involving manual leaflet sewing with thousands of sutures, relying on an animal tissue-dependent supply chain. This complexity increases production costs and restricts global device availability. Thus, there is a pressing need for a synthetic TAVR with superior biocompatibility, hemodynamics, and durability, suitable for patients of all ages and varying aortic stenosis severities.

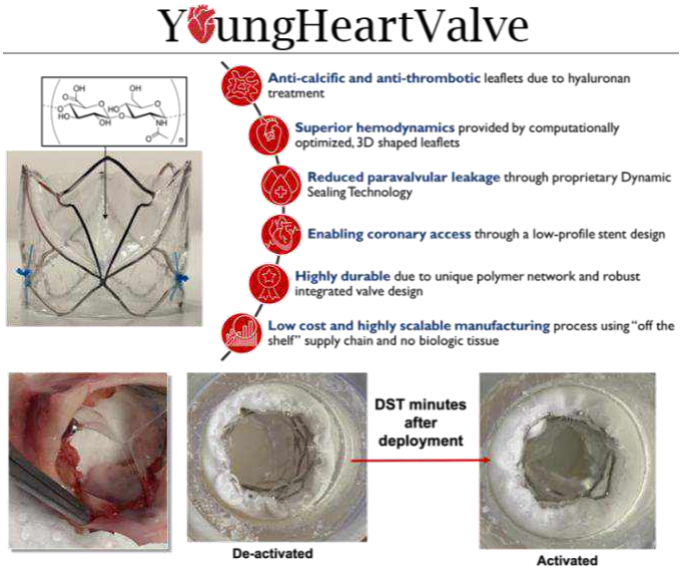

Figure 1: YoungHeartValve's Rejuvenate™ Valve preclinical testing

TECHNOLOGY/SOLUTION DESCRIPTION

YoungHeartValve, Inc. (YHV) distinguishes itself in the competitive landscape of TAVR development by offering a polymeric device that not only overcomes the biocompatibility challenges associated with bioprosthetic tissue but also provides a more cost-effective solution. While several organizations in the market are working on polymeric heart valves, our technological solution stands out by addressing a comprehensive set of market needs, including the prevention of the need for anti-coagulation therapy.

Our commitment at YHV is to commercialize the next generation of heart valves, introducing novelty in polymer material, valve design and manufacturing. The proprietary polymer used is an interpenetrating network of hyaluronan (HA) and linear-low density polyethylene (LLDPE), creating hydrophilic leaflets that are thrombosis and calcification resistant, durable, and precisely 3D-shaped for superior hemodynamic performance [5, 6]. Our first product, the Rejuvenate™ Valve, is a 26 mm balloon-expandable TAVR that incorporates dynamic sealing technology for a reliable annular seal to prevent PVL, which is yet another feature that sets us apart from any competitor. In addition to the material benefits, our "no tissue/no farm" manufacturing automation and supply chain significantly reduce the cost and complexity associated with pericardial-based TAVR systems. This approach opens possibilities for the widespread adoption of this life-saving technology globally. YHV aims to define the next "technology curve" in the evolution of prosthetic aortic heart valves, with the potential paradigm shift for all other heart valve positions treating a multitude of valvular diseases across patient age groups.

The Rejuvenate™ Valve is currently in the pre-clinical developmental stage (Figure 1). The material has successfully undergone in vitro biocompatibility and hemocompatibility tests, meeting ISO 5840 durability requirements. Prototype valves, subjected to acute and chronic animal studies, have shown promising results, especially in a 6-month juvenile sheep model where HA-LLDPE leaflets remained pristine without thrombosis or calcification. The valve design, optimized through computational modeling, ensures excellent hemodynamic performance (pressure gradient of 4.77 mmHg and effective orifice area of 2.33 cm^2) and increased durability by minimizing stresses on the stent and leaflets. Our current focus is on completing detailed ISO 5840 hemodynamic and durability studies on the current valve design with dynamic sealing technology to achieve design freeze. Subsequently, we plan to conduct longer chronic and acute animal studies, with the collected data forming the basis for our FDA presubmission. Furthermore, the 3D shaping, and HA treatment processes are established but not yet automated. Our next objective is to automate these steps for manufacturing reproducibility, collaborating with Contract Manufacturing Organizations (CMOs) to streamline the process. Upon reaching manufacturing freeze, our goal is to initiate first-in-man clinical trials, a crucial step towards obtaining FDA approval.

BUSINESS CASE

Despite the impressive global adoption of TAVR in recent years, with a CAGR of 16-20% and a projected $5 billion for 2023, the forecast indicates a continued growth at a 14% CAGR through 2030. Our strategic timeline involves achieving design and manufacturing freeze, as well as FDA pre-submission by 2026, with enrollment in first-in-human clinical trials in subsequent years. We aim to launch our Rejuvenate™ Valve by 2032-33 (Figure 2).

Regulatory oversight falls under the purview of the US FDA and Center for Devices and Radiological Health (CDRH) for the Rejuvenate™ Valve. It will classify as a Class III device and will require Premarket Approval (PMA), contingent on the FDA's determination of sufficient valid scientific evidence affirming the device's safety and efficacy. We will leverage our manufacturing partner's Quality System, adhering to Design Control practices, and conducting testing in compliance with ISO 5840-3:2021 and ISO 10993:2009 standards at GLP facilities. Additionally, we will also engage with an experience Regulatory Consultant.

Globally, TAVR adoption is supported by reimbursement mechanisms. Hospitals, facilitated by Current Procedural Terminology (CPT) codes, can attain reimbursement from insurance companies for TAVR procedures. Our business model includes estimating annual TAVR procedures in partnering hospitals and supplying TAVRs in bulk. Key stakeholders for Rejuvenate™ valve include interventional cardiologists, cardiothoracic surgeons, and approved patients. Our marketing strategy involves showcasing technological developments at targeted conferences, digital marketing on professional platforms, and an aggressive approach post-preclinical testing, expanding presence at clinical conferences and leveraging connections of advisory board members.

The main challenge for YHV in commercializing the Rejuvenate™ Valve is securing funding and recruiting skilled engineers and project managers for expediting the FDA pre-submission process. Strategic partnerships or collaborations for developing the valve's delivery system, a critical aspect of the device ecosystem, will also be explored. Further steps involve leveraging the platform for diverse devices targeting various valvular heart diseases across patient groups, including pediatrics. Establishments of necessary expertise and clinical connections is imperative for these endeavors.

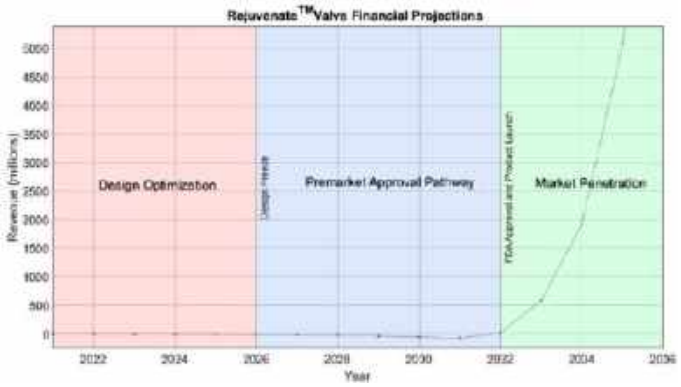

Figure 2: Financial projections for YHV's Rejuvenate™ Valve

ACKNOWLEDGEMENTS

We would like to acknowledge NIH SBIR I and Georgia Research Alliance for funding support for the development of the device.

REFERENCES

1.Leon, M.B., et al.,. *N Engl J Med*, 2010. 363(17): p. 1597-607.
2. Richter, I., et al., *J Clin Med*, 2021. 10(18).
3. Hein, M., et al.,. *JACC Cardiovasc Interv*, 2022. 15(11): p. 1113-22.
4. Lerakis, S., et al., *Circ*, 2013. 127(3): p. 397-407.
5. Simon-Walker, R., et al., *J Biomed Mater Res B Appl Biomater*, 2018. 106(5): p. 1964-75.
6. Heitkemper, M.,et al. *J Mech Behav Biomed Mater*, 2019. 98: p. 163-71.

PITCH COMPETITION: PULSE ELECTRIC FIELD TREATMENT INDUCED ANGIOGENESIS AS A PROMISING THERAPY FOR DIABETIC FOOT ULCERS.

Neeraj Raghuraman Rajagopalan (1), Govindarajan Srimathveeravalli (1,2)

(1) Department of Mechanical and Industrial Engineering, University of Massachusetts, Amherst, MA, USA.
(2) Institute of Applied Life Sciences, University of Massachusetts Amherst, MA, USA.

PROBLEM STATEMENT

Non-healing diabetic foot ulcer (**DFU**) is a severe consequence of uncontrolled and prolonged diabetes mellitus (*DM*, 422 million cases worldwide) manifesting as chronic ulceration at the bottom of the foot in 15% of cases affected with DM. Currently, 15-25% of DFU patients undergo amputation of the foot due to severity of the infection and more than 50% of patients who recovered have had recurrence within 1-3 years, resulting in diminished quality of life (**QoL**) and increased morbidity rate. DFU occurs as a sequelae to insufficient angiogenesis where inadequate blood supply to the affected area results in severe infection coupled with neuropathy and neuronal dysfunction. Current treatment modalities for DFU are either non-invasive (wound dressing, antibiotics & cell therapy) or invasive (skin grafting, debridement or revascularization) focusing primarily on controlling the infection and topical wound care. Despite such clinical significance, *there are no effective treatment methods in the market that can vascularize the wound area to reverse and prevent the recurrence of these ulcerations.* Our proposed treatment modality is designed to address the important problem in the disease model using an existing device with an entirely different set of inputs.

TECHNOLOGY/SOLUTION DESCRIPTION

Our technology uses an existing clinical technique - pulsed electric fields (**PEF**) that is used for solid tumor ablation where microsecond long pulses are delivered at very high electric field strength (**EFS**). Treatment with PEF induces actin cytoskeletal remodeling, loss of tight junction proteins and transient blood-brain barrier (BBB) disruption resulting in increased blood vessel permeability (**Fig. 1A & 1B**), recapitulating the important mechanical cues that play a pivotal role in angiogenesis where endothelial cells (**EC**) and mural cells collectively remodel the matrix. This remodeling facilitates cell migration and proliferation, onsetting of a series of canonical biochemical signaling cascades that are central to induce angiogenesis.

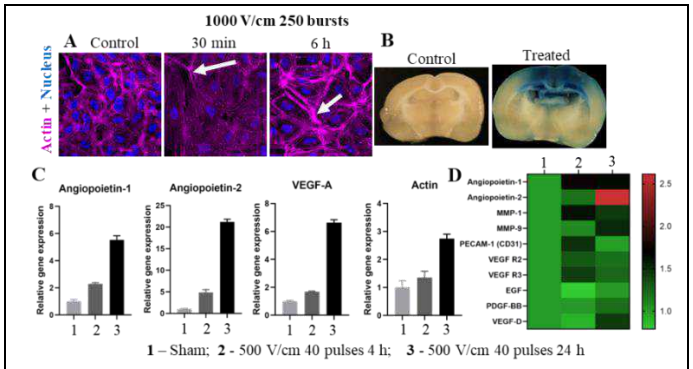

Fig. 1A. PEF applied on a confluent monolayer of HUVECs showed drastic changes in actin cytoskeleton as early as 30 min post treatment and peaks at 6 h where stress fibers are highly concentrated at the junctions between cells. **B.** PEF treated rat brains showed uptake of Evans blue dye injected intravenously at 4 h post treatment. PEF treated cells showed significant upregulation of genes (**C**) and proteins (**D**) attributed to having pro-angiogenic effects at 4 h and 24 h post treatment.

Innovation: Firstly, the application of PEF for reproducing an effect similar to mechanical stimulus opens up a new treatment

modality for therapeutic angiogenesis (**TA**) that is previously unexplored. While it is established that mechanical cues are essential for the initiation of the biomechanical pathways for angiogenesis, currently there is no product or treatment modality in clinics that can be used for such in vivo applications. *Due to the lack of an in vivo mechanical stimulation device for angiogenesis, careful optimization of PEF parameters will present us with a new paradigm for therapeutic angiogenesis in vivo while recapitulating effects similar to mechanical stimulation.* Secondly, PEF is an existing treatment option for tumor ablation therapy and drug delivery and we will be identifying a new set of parameters and waveform for an entirely new set of application.

Our treatment strategy involves the use of a conductive patch that will be placed on the site of the wound (**Fig. 2B**). High frequency low voltage electric pulses will be used with a biphasic waveform that will deliver energy to stimulate the region but not kill the cells. This will avoid muscle and neuronal excitation while stimulating the ECs alone. The region of stimulation can be predicted using established computational models which will help clinicians optimize the treatment strategy specific to individual patients.

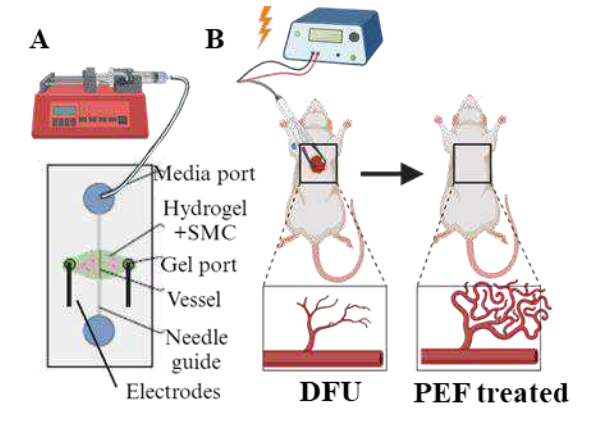

Fig. 2A. Microfluidic model of a blood vessel on a chip. **B.** Rat model of DFU showing PEF induced angiogenesis in wound healing.

The safety of this technology has been validated using in vitro 2-D and 3-D microfluidic models (**Fig. 2A**) and preclinical models across multiple treatment parameter domains used for drug delivery. PEF treated cells have been analyzed for expression of pro-angiogenic factors at different time points at protein and gene levels. Data from PCR and Elispot assays showed increased expression of angiogenic factors like VEGF-A, Angiopoietin 1 & 2 at 4 and 24 h post treatment (**Fig. 2C & 2D**).

The next steps would involve the testing of high frequency biphasic parameters on DFU induced rat models to assess the efficacy of the treatment before it can be translated to clinical trials. We are currently working on optimizing the PEF parameters that can be used on animal models which would give us the desired pro-angiogenic effect on wounds.

BUSINESS CASE

Our promising PEF based technology will impact the therapeutic angiogenesis domain which is currently in the process of finding a simple and reliable solution for diseases pertaining to lack of angiogenesis like DFU, coronary artery disease, Ischemic stroke and retinopathy. Our first clinical target will be towards patients with DFU and this benefit podiatrists who would otherwise treat it with conventional topical wound treatment methods or perform surgery to amputate the leg depending on the severity. This treatment modality may require multiple doses at regular intervals but offers a non-invasive solution.

Patients with DM are prone to DFU and have a poor QoL leading to social, psychological and financial stress. DFU related limb amputation affects African American people who are in a rural setting the most compared to others. Existing treatment methods offer relief to some extent where in most cases, it can only be managed but not completely cured. *PEF treatment offers a simple, inexpensive, highly localized, non-pharmaceutical, non-surgical alternative that can be easily translated to clinic.* This technology will tremendously benefit people in rural areas where an initial training to use the commercially available FDA approved pulse generator will suffice. At present, there is no product in the market that offers a non-invasive treatment method which addresses the core of the problem – angiogenesis and has the potential to treat without involving the need for a surgery. Our product is based on FDA approved predicates that are already in clinical use for over a decade, providing a clear pathway to regulatory approval and this technology is positioned as a non-invasive topical treatment method, thereby qualifying as a Class II device eligible for 510k approval with limited clinical trials documenting safety.

ACKNOWLEDGEMENTS

G.S. acknowledges grant and funding support from the National Cancer Institute and the National Institute of Diabetes, and Digestive and Kidney Diseases of the National Institutes of Health under Award Number R01CA236615 and R01DK129990, and the Dept. of Defense CDMRP PRCRP Award CA170630 and CA190888.

PITCH COMPETITION: TAPPING INTO LIGAMENT TENSION WITH OUR LIGAMENT TENSIOMETER TO ENHANCE OUTCOMES FOLLOWING TOTAL KNEE ARTHROPLASTY

Lesley R. Arant (1), Kai M. Heineman (1), Josh D. Roth (2, 3)

(1) Department of Biomedical Engineering, University of Wisconsin-Madison, Madison, WI, USA
(2) Department of Orthopedics and Rehabilitation, University of Wisconsin-Madison, Madison, WI, USA
(3) Department of Mechanical Engineering, University of Wisconsin-Madison, Madison, WI, USA

PROBLEM STATEMENT

Complications associated with either over- or under-tensioned ligaments following total knee arthroplasty (TKA) have a large public health burden. Under-tensioned ligaments can lead to instability and pain, and over-tensioned ligaments can lead to stiffness and pain[1]. Symptoms associated with over-/under-tensioned ligaments are commonly self-reported as reasons that up to 20% of patients are not satisfied following TKA[2]. With up to 3.8 million patients projected to receive TKA annually by 2033[3], this equates to up to 760,000 patients per year who are not satisfied. Improving rates of patient satisfaction is becoming an important consideration for healthcare systems to maximize their reimbursements in a value-based payment model[4]. Additionally, post-operative complications associated with over-/under-tensioned ligaments are responsible for up to 64% of revision procedures[5]. Assuming a conservative revision rate of 2% and a cost per revision procedure of $37,000[5,6], the economic burden is around $1.8 billion per year, which does not account for other economic burdens (e.g., lost wages).

Despite the well-documented importance of proper ligament tensioning, existing solutions to gauge ligament tension intraoperatively are either subjective or fail to assess tension in an individual ligament. One common technique is a laxity assessment, in which ligament tension is indirectly inferred from joint motion and stiffness[7]. Since this assessment is commonly subjective, its outcomes vary according to a particular surgeon's training and experience[8]. Although distraction devices[9] and contact force sensors[10] provide quantitative measurements, they are unable to assess tension in an individual ligament. Thus, given the lack of adequate devices available, there is no consensus on the proper target or method of assessing ligament tension.

Accordingly, a sensor that provides direct and objective measurements of ligament tension would give orthopedic surgeons the information needed to (1) improve patient function and satisfaction after TKA, and (2) alleviate the economic burden of revision TKAs.

TECHNOLOGY/SOLUTION DESCRIPTION

Our technology, termed a ligament tensiometer, shows promise for filling this gap in a surgeon's toolbox because it provides direct and quantitative measurements of ligament tension. The ligament tensiometer is a handheld device placed in contact with the ligament of interest. It consists of two main components (***Figure 1***): (1) a voice coil actuator that excites low amplitude shear waves in the ligament, and (2) a piezoelectric load cell that tracks the shear wave propagation along the ligament's length. The tensiometer software computes the shear wave speed in the ligament using the time delay between the voice coil actuator and load cell signal (***Figure 1***). The tensiometer software then calibrates measured shear wave speeds to ligament tension using the linear relationship between shear wave speed squared and tension[11,12]. Thus, the tensiometer has the competitive advantage of direct and objective measurements of tension in a specific ligament.

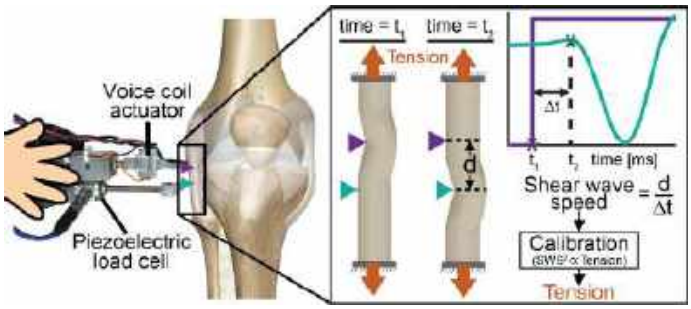

Figure 1: Our ligament tensiometer is a handheld device that uses shear wave speed to measure tension in a particular ligament.

We performed a preliminary error analysis of our tensiometer prototype to assess its accuracy of measuring collateral ligament tension (***Figure 2***). We chose these ligaments to study because their tension is routinely manipulated by surgeons during TKA[13]. We used our ligament tensiometer to measure shear wave speeds in the medial and lateral

collateral ligaments of human cadaveric knees (n = 3) under manually applied loads (***Figure 2a***). We used a calibration algorithm to compute the tensiometer-measured tensions from measured shear wave speeds. We computed the errors between the tensiometer-measured tensions and the gold standard tensions measured using a six degree-of-freedom robot and the principle of superposition[14]. We found that the tensiometer can directly measure ligament tension with low bias errors (***Figure 2b***). Additionally, when we coupled the tensiometer with optical motion capture to track ligament length, the tensiometer could accurately measure ligament engagement length (i.e., length at transition from toe to linear region) (***Figure 2c***). Thus, the tensiometer could be used with existing surgical navigation tools to measure other key metrics of ligament mechanics.

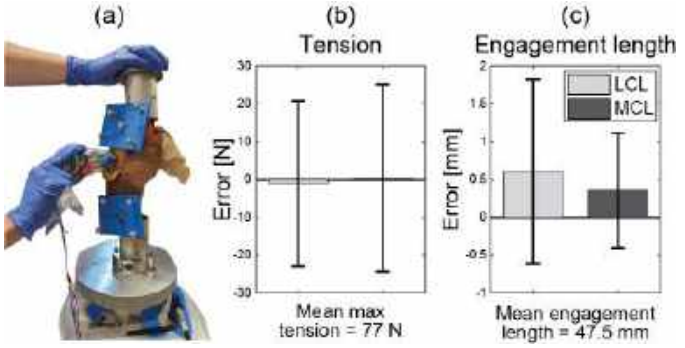

Figure 2: (a) We used the tensiometer to measure lateral and medial collateral ligament (LCL and MCL, respectively) tension during laxity assessments in three cadaveric knees. (b) The tensiometer measured ligament tension with low bias errors. (c) When coupled with optical motion capture, the tensiometer accurately measured ligament engagement length.

The key technical advancement required to take our tensiometer to market is to increase its precision through design optimization. Preliminary data suggests that tensiometer-measured tension is sensitive to tensiometer design factors (e.g., tip spacing, excitation frequency[15]) and use factors (e.g., application force[16], positioning of the tensiometer on the ligament[17]). Thus, our current work is focused on identifying the optimal combinations of these design and use factors that yield repeatable and precise measures of ligament tension, while maintaining the tensiometer's ease-of-use and low bias errors. With this key technical advancement, the ligament tensiometer will be a strong candidate for a marketable product to meet a critical unmet need in orthopedics.

BUSINESS CASE

We validated our initial product-market fit in TKA by completing over 150 discovery interviews through regional and national NSF I-Corps programs (NSF Award #: 2323033). Our total available market will reach 3.8 million TKAs annually by 2033[3]. Even if we conservatively limit this to technology-enhanced TKAs (currently 14.7% of TKAs), the serviceable obtainable market remains 559,000 TKAs annually. In the TKA market, the end users are orthopedic surgeons and their operating room staff who treat TKA patients. The payers are the hospitals, insurance agencies, and the patients who receive the surgery.

Once marketed, we envision the cost structure of the tensiometer to be a one-time payment for the device, followed by the purchasing of disposables and software licenses as needed. At our validated effective cost of $500 per case, a conservative projection of our serviceable obtainable market for TKA applications is $280 million per year. Considering that the tensiometer has potential use in many other procedures, joints, and ligaments (e.g., unicompartmental arthroplasty, ligament reconstruction, and tendon repair), this should be considered a conservative estimate of the patient market size.

Our marketing strategy involves three stages (***Figure 3***). In stage 1, our collaborating "champion" surgeon will test the tensiometer on a small subset of patients at the UW-Madison Hospital. This stage requires IRB approval before the tensiometer can be used in live patients. To fund stage 1, we plan on seeking Small Business Technology Transfer (STTR) phase I and II funds totaling $2.3 million. In stage 2, we will continue to use STTR funding streams to complete a randomized control trial in which we fabricate at least ten tensiometers and send each to a different institution for use by surgeons. This stage will require FDA Investigational Device Exemption. In stage 3, we plan to acquire FDA Premarket Notification 510(k) clearance to enable widespread tensiometer use as a Class II device.

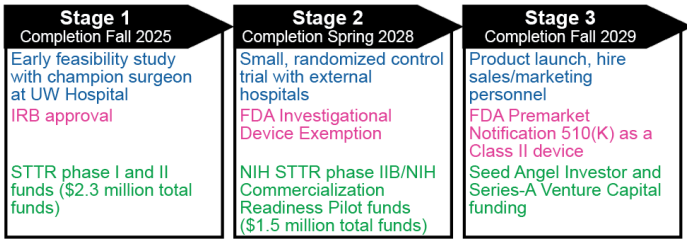

Figure 3: Pathway to market for the ligament tensiometer.

The main hurdle to market is translating our tensiometer from a prototype to a clinically usable device. In particular, the tensiometer components must be either sterilizable or disposable so that the tensiometer can be reused in different patients. Additionally, to decrease manufacturing cost and time and to increase product robustness, the tensiometer housing must not be made of 3D-printed polymers.

The main risk to the developmental pathway of the tensiometer is the reluctance of surgeons to incorporate a new technology into their surgical procedure. If this challenge presents, then we will lean on the support of the existing early adopters to generate more data that supports the benefit of tensiometer measurements to improving patient outcomes. This may lengthen the time to commercialization, but we do not believe this will be a permanent roadblock to translation of our device.

In summary, our three-stage marketing plan aims to recruit surgeons who will fuel the generation of supporting data, which in turn will fuel market expansion. Once commercialized, the ligament tensiometer has great potential to enhance the process of ligament tensioning during orthopedic procedures, leading to more consistent, predictable, and positive surgical outcomes for patients suffering from debilitating orthopedic injuries and diseases like osteoarthritis.

ACKNOWLEDGEMENTS

This work was supported by the Draper Technology Innovation Fund (TIF), administered by Discovery to Product (D2P) at UW–Madison.

REFERENCES

[1] Babazadeh, S et al., *Orthop Rev (Pavia)*, 1:e26, 2009. [2] Bourne, RB et al., *Clin Orthop Relat Res*, 468:57-63, 2010. [3] Singh, JA et al., *J Rheumatol*, 46:1134-1140, 2019. [4] Lin, E et al., *Clin Orthop Relat Res*, 479:674-678, 2021. [5] Paxton, EW et al., *JBJS*, 93:20-30, 2011. [6] Lavernia, C et al., *Clin Orthop Relat Res*, 446:221-226, 2006. [7] Casino, D et al., *Knee Surg Sports Traumatol Arthrosc*, 17:369-373, 2009. [8] Järvelin, J et al., *Acta Orthopaedica*, 83:190-196, 2012. [9] Takashima, Y et al., *Knee*, 27:1071-1077, 2020. [10] Park, C et al., *Clin Orthop Surg*, 13:1-9, 2021. [11] Martin, J et al., *Nat Commun*, 9:1592, 2018. [12] Blank, J et al., *J Mech Behav Biomed Mater*, 105:103704, 2020. [13] Whiteside, LA, *J Arthroplasty*, 17:23-27, 2002. [14] Fujie, H et al., *J Biomech Eng*, 117:1-7, 1995. [15] Arant, L et al., *ORS*, 2022. [16] Arant, L et al., *SB3C*, 2022. [17] Blank, J et al., *ORS*, 2020.

BIOMEDICAL APPLICATIONS OF NOVEL MAGNETOSTRICTIVE COMPOSITE

Aaron L. Brandner (1), Chiu Tai Law (2), Rani Elhajjar (3), Priyatha Premnath (4)

(1) Department of Biomedical Engineering, University of Wisconsin Milwaukee, Milwaukee, Wisconsin, United States
(2) Electrical Engineering, University of Wisconsin Milwaukee, Milwaukee, Wisconsin, United States
(3) Civil and Environmental Engineering, University of Wisconsin Milwaukee, Milwaukee, Wisconsin, United States

INTRODUCTION

There is an increasing demand for biomaterials with characteristics that can be altered *in vivo* to enhance tissue properties. One such branch of materials is smart biomaterials that can respond to cues *in vivo* and alter their properties. It is estimated that by 2030 the market size for these kinds of smart polymers will be 8.15 billion US dollars [1]. The primary aim for smart biomaterials is to provide mechanical support, mimic, guide, or induce a tissue or natural process, and/or act as a vehicle for drug delivery [2], [3].

Magnetostrictive materials are a group of smart materials that respond to a magnetic field by altering their domain [2], [4], [5]. The human body is constantly encountering external forces and internal chemical reactions. Some dynamic tissues and processes such as bone, muscle, neurons, and cardiomyocytes may benefit from magnetostrictive materials that produce a strain response. An example of a magnetostrictive material is Terfenol-D, an iron alloy containing terbium and dysprosium [2],[6]. This alloy has a high saturation strain compared to other magnetoactive materials. A magnetic field will induce the Terfenol-D to change orientation, causing strains to be generated [3], [4], [5], [7].

In this context, a novel composite was developed combining Polymethyl methacrylate (PMMA) commonly known as Bone Cement and a particulate form of Terfenol-D (TD). This study delves into the micro-morphology, mechanical properties, and biocompatibility characteristics of this composite material. The combination of PMMA and Terfenol-D opens avenues for innovative materials that could play a significant role in advancing technology and addressing the evolving needs of the health industry.

METHODS

1. Preparation of PMMA and TD Magnetostrictive Composite

1.1 Material Processing To prepare the TD (Nalgene) and PMMA composite, 75mg of Terfenol-D particles (maximum particle size ~300μm) 7.5%w/v was combined with 1g of PMMA and 5mL of Monomer liquid. To effectively mix into a homogenous solution, a Sonicator (QSonica Q55) was used. Control samples were prepared with only PMMA and no terfenol-D. The liquified mixtures were aspirated and dispensed on a glass slide and left under a fume hood until the polymers had completely polymerized and dried.

2. Cell Viability Assays.

1.2.1 MTT Assay. Composites were placed in 96 well plates. 5,000 murine fibroblasts (NIH 3T3, ATCC) were cultured on each sample including a positive and negative control and left in the incubator at 37^0C for 3 days. Then a stock solution was prepared by combining Thiazolyl Blue Tetrazolium Bromide 98% (Acros Organics) (0.5%w/v) to corning phosphate buffer saline (PBS). The media from the wells were aspirated. 10 microliters of stock solution were added to each sample along with 100 microliters of PBS keeping the volume across all wells equal. It was incubated again for 4 hours at 37^oC. Next, all but 25 microliters were removed from the wells and 50 microliters of dimethyl sulfoxide (DMSO, Sigma Aldrich) was added and left to incubate for 10 minutes at 37^oC and measured at a wavelength of 540nm on a spectrophotometer. MTT assay was conducted in triplicates. Kruskal-Wallis is one way analysis of variance was used to determine significance between PMMA/PMMA+TD and positive control (no material).

3. Mechanical Testing

3.1 Dynamic Mechanical Analysis (DMA). Both the PMMA and the PMMA with Terfenol-D composite were cut into rectangles and their dimensions were measured. PMMA was cut to dimensions of 10.15mm x 9.2mm x 0.48mm and the PMMA-TD composite was cut to 16.29mm x 8.82mm x 0.74mm. They were then fastened to the DMA Q800

machine (TA Instruments). The test was conducted at a frequency of 1 Hz, under a tension of 1 newton, and temperature ramp rate of 10^0C per minute with a max temperature of 200^0C. Data was analyzed using TA Instruments software.

RESULTS

During polymerization PMMA gained magnetostrictive properties owing to the addition of TD particles. SEM imaging revealed that this material is relatively nonporous and is embedded with TD particles.

DMA testing was conducted to determine mechanical properties of the samples. TA analysis of the PMMA polymer provided a glass transition temperature of 115^0C and that the PMMA+TD composite was 97^0C, based on Tan Delta. This shows that the composite has a lowered glass transition temperature than that of the PMMA, yet since the glass temperature is still within range, the composite material can be used for in vivo applications.

The biocompatibility of this novel composite was evaluated by MTT assay to measure the materials' cytotoxicity for biomedical applications. After seeding the cells onto the composite for both tests, the samples were incubated for 3 days till cells adhered to the sample. The results from the MTT assay demonstrated high biocompatibility of the composite and polymer compared to the culture-plate only control. Significantly higher live cells were observed in the polymer and composite samples. Overall, the composites' structure and chemical composition provided a basis for rapid cell adhesion and proliferation.

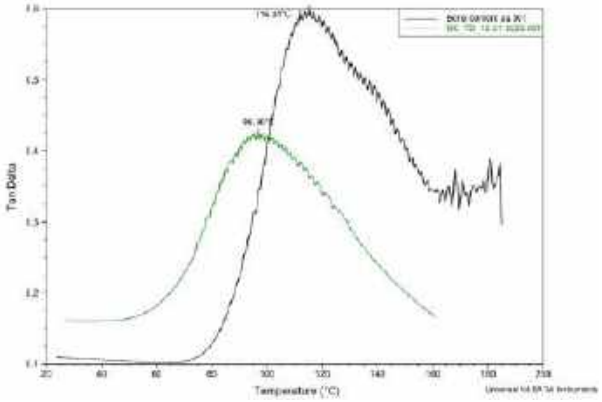

Figure 1. Mechanical Characterization. DMA analysis of composite material

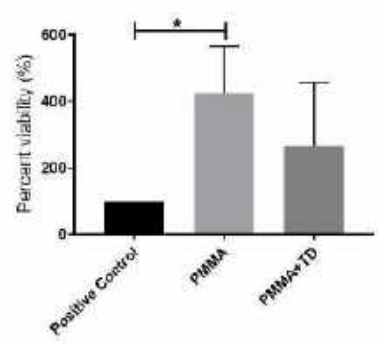

Figure 2. Viability of fibroblasts. Fibroblasts were cultured on PMMA and PMMA+TD samples and cell viability was assessed via MTT assay. N=3

DISCUSSION

These findings demonstrate the potential for this material to be used as a smart biomaterial for humans and animals. The composite's biocompatibility, along with its high melting temperature, and durability shows promise. PMMA is an FDA approved polymer that is already in use clinically. The addition of TD can significantly enhance PMMA's properties. It can be employed in a wide variety of applications such as neural, cardiovascular, and musculoskeletal regeneration. In addition, the materials ability to change shape allows it to be used for diagnostics, drug delivery, and influence tissue and cellular functions. Overall, its behavior makes it an ideal smart material for biomedical applications.

ACKNOWLEDGEMENTS

We thank Dr. Hardcastle at the Advanced Analysis Facility for help with mechanical analysis. Aaron Brandner was provided funding through the SURF program at UWM.

REFERENCES

[1] "Smart polymers market size, industry share: Forecast, 2030," Smart Polymers Market Size, Industry Share | Forecast, 2030, https://www.fortunebusinessinsights.com/smart-polymers-market-106860 (accessed Jan. 21, 2024).

[2] Author links open overlay panelChengde Gao a et al., "Magnetostrictive Alloys: Promising Materials for Biomedical Applications," Bioactive Materials, https://www.sciencedirect.com/science/article/pii/S2452199X2100311X (accessed June 21, 2023).

[3] C. M. Wells, M. Harris, L. Choi, V. P. Murali, F. D. Guerra, and J. A. Jennings, "Stimuli-Responsive Drug Release from Smart 2019, (accessed July 15, 2023)

[4] Author links open overlay panelA.G. Olabi et al., "Design and application of Magnetostrictive Materials," Materials & Design, https://www.sciencedirect.com/science/article/abs/pii/S0261306907000027#! (accessed Sept. 29, 2023).

[5] G. P. McKnight and G. P. Carman, "[112] oriented terfenol-D composites," MATERIALS TRANSACTIONS, https://www.jstage.jst.go.jp/article/matertrans/43/5/43_5_1008/_article/-char/en (accessed Jan. 21, 2024).

[6] "Terfenol-D - Materials - Materials Library," Institute of Making, https://www.instituteofmaking.org.uk/materials-library/material/terfenol-d (accessed Jan. 29, 2024).

[7] C. Gao, Z. Zeng, S. Peng, and C. Shuai, "Magnetostrictive alloys: Promising materials for biomedical applications," *Bioactive Materials*, vol. 8, pp. 177–195, Feb. 2022, (accessed Dec. 2, 2023)

SB³C2024
Summer Biomechanics, Bioengineering and Biotransport Conference
June 11-14, Lake Geneva, WI, USA

COMPREHENSIVE ASSESSMENT OF COMMUNITY MOBILITY AND PARTICIPATION OF WHEELCHAIR USERS USING WEARABLES.

Madisyn R. Adelman (1), Maja Goršič (1,2), Grace Fasipe (1), Jacob R. Rammer (1)

(1) Department of Biomedical Engineering, University of Wisconsin-Milwaukee, Milwaukee, Wisconsin, USA
(2) Department of Biomedical Engineering, Marquette University, Milwaukee, Wisconsin, USA

INTRODUCTION

According to the United Nations approximately 65 million people worldwide require a wheelchair for their daily mobility [1]. Wheelchair use can negatively impact community mobility (the ability to move independently) and participation (interaction with peers outside the home) [2]. An individual's community mobility and participation has demonstrated a direct relationship to well-being, overall health, and quality of life [3], making it critical for rehabilitation specialists to monitor patients' mobility to better assign treatments and therapies for recovery. Monitoring these parameters is increasingly important for manual wheelchair users (MWUs) as they present a higher risk of injury [4]. Traditionally, a patient's community mobility and participation is monitored during in-clinic testing [4]. Even though in clinic testing is accurate, it does not completely represent the user's daily mobility.

Alternatively, a user's community mobility and participation can be observed remotely through self-surveys, activity journals and questionnaires. Evaluations like the Life Space Assessment [5] and Wheelchair Use Confidence Scale [6] are commonly used. Information such as the participant's activity level and distance traveled from home is captured in the Life Space Assessment, and confidence utilizing their wheelchair in various situations along with personal assurance is reflected in the Wheelchair Use Confidence Scale. Still, such evaluations are seen as unreliable because of subjective observation.

Similarly, GPS devices have been used as a mode of remote assessment, with increasing promise for delivering explicit results tracking human activity. However, limitations of standalone GPS connectivity result in inaccurate activity detection and insufficient information for community participation [7].

This study illustrates an innovative technique of remote community mobility and participation measurement employing activity journals, GPS, and questionnaires. The technique accounts for weaknesses of established methods, providing comprehensive measurements of the participant's mobility and necessary context regarding their community participation. Data of a wheelchair user over a course of a week is presented in this feasibility study.

METHODS

This study was approved by the University of Wisconsin – Milwaukee International Review Board (protocol #24.059). The participant, a 39-year-old male with a T-8 complete spinal cord injury met with the research team in the University of Wisconsin – Milwaukee Advanced Mobility Biomechanics Lab in August. The participant signed a written consent form and was provided with a paper-based activity journal, commercially available Garmin Forerunner 753XT GPS wristwatch, and instructions of use.

The participant was instructed to wear the Garmin watch and utilize its recording function for the entire duration he was out of home. Upon arrival home, the participant was advised to fill out the day's journal entry entirely. After a week, the participant filled out the Life Space Assessment [5] and Wheelchair Use Confidence Scale (short form) [6]. The Garmin watch recorded the participant's position and heart rate daily. Once returned, the watch data was saved to the Garmin Connect app and the activity journal was transcribed into an Excel File.

The participants' activity journal was organized using a Microsoft Excel spreadsheet to classify the interactions, locations, and barriers. The recorded interactions were categorized based on varying interpersonal relationship types and social group size.

The GPS data was processed using MATLAB R2022b software, where the participants geographical points were mapped out. The locations visited each day were quantified based on the participants journal entries and compared with GPS locational points for further clarification. For example, the journal entry on the third day listed the locations visited as "everywhere" but the GPS data showed that the participant visited 8 locations. Additionally, the watch recorded the participants heart rate and speed that was used for further analysis of their physical activity.

RESULTS

The participant recorded six daily entries in his provided activity journal, while the Garmin watch collected GPS data for five days due to an uncharged battery on the sixth day.

Figure 1 shows the overall route of one trip made by the participant on day three. Table 1 shows the information entered by the participant in the activity journal. Notably, the number of locations visited, barriers encountered, and types of interactions he had each day.

Figure 2 shows the speed and heart rate of the participant for the entire trip presented in Figure 1. At the top, the type of location and wheeling vs driving is displayed, determined based on the participants heart rate, speed, and activity journal.

The participant scored 202 out of 210 possible points on the Wheelchair Use Confidence Scale indicating a lack of comfortability maneuvering imperfect conditions and self-confidence socially. The Life Space Assessment indicated that he has been active around his and surrounding cities but has not recently traveled out of the state.

DISCUSSION

The results from the participant's activity journal (Table 1) and corresponding GPS data (Figure 1) validate that the participant maintained frequent community engagement throughout the week. The participant visited several locations, maintained a higher heart rate when wheeling themselves (Figure 2) and had interactions of varying interpersonal relationships daily. Moreover, the participant faced barriers during the week (Table 1) that could have impacted their community mobility and participation and should be taken into consideration [3].

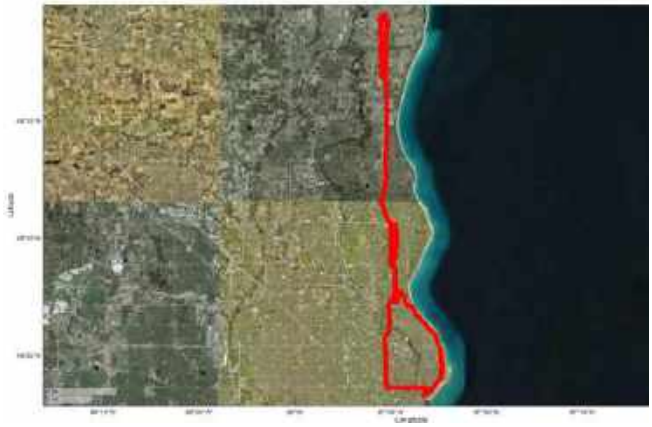

Figure 1: GPS data for one trip on day 3.

Table 1: Activity Journal Data of a Wheelchair User for a Week. Pro: Professional, Rom: Romantic, Fam: Familial (including pets), Plat: Platonic, Txn: Transactional, G: Group (3 or more), P: Personal (1-2 People), E: Exchange.

	Day 1	Day 2	Day 3	Day 4	Day 5	Day 6
# of Location	4	2	8	5	3	3
Barriers	None	Stairs	Big Hill	Tight Space	None	None
Interactions	Pro, Fam	Pro	Rom, Fam, Txn	Plat, Txn	Pro, Plat	Plat, Rom, Fam
Interaction Types	G, P	P	P, E	P, G, E	G	P, G

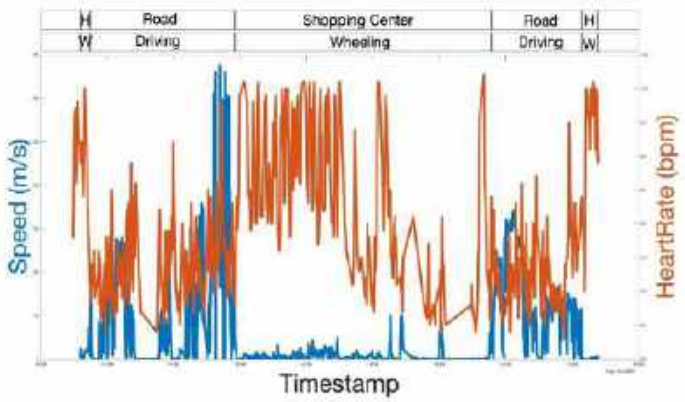

Figure 2: Participant speed, heart rate and activities. W: wheeling, H: home.

Additionally, the results of both the Life Space Assessment and Wheelchair Use Confidence Scale scores reinforce the results from the activity journal and GPS data. Attributing to the participants confidence outside of their home and in different social situations, which is indicative of their community mobility and participation [3].

Furthermore, the methods limitations should be addressed in future studies. This includes the loss of GPS data which is a common occurrence in similar studies [7] and ambiguity of an activity journal, which shows the importance of clear instruction with the participant.

Our combined technique results in more comprehensive information for rehabilitation specialists than activity journals, GPS data, or questionnaires alone. This approach provides both qualitative and quantitative data about the participants' activities and confidence within their community. Overall, the combination of these three methods provides rehabilitation specialists with a comprehensive understanding of their patients' community mobility and participation, allowing for greater patient specific care. Future work will expand this technique to larger populations to better understand optimal rehabilitation and activity promotion strategies for manual wheelchair users.

ACKNOWLEDGEMENTS

The authors would like to acknowledge the UWM Office of Undergraduate Research for the Support from Undergraduate Research Fellows (SURF) funding.

REFERENCES

[1] Robertson, B et al., *Archives of Rehabilitation Research and Clinical Translation*, 5(1):100249, 2023.
[2] Loyd, C et al., *Journal of the American Geriatrics Society*, 66(7):1399–1403, 2018.
[3] Fasipe, G et al., *Frontiers in Human Neuroscience*, 17, 2024.
[4] Rice L. A et al., *American Journal of Physical Medicine & Rehabilitation*, 98(8):649–656, 2019.
[5] Taylor, J. K et al., *Aging Clinical and Experimental Research*, 31(4):439–445, 2018.
[6] Rushton P. W et al., *Disability and Rehabilitation: Assistive Technology*, 6(1):57–66, 2011.
[7] Allahbakhshi, H et al., *Sensors*, 20(3):588, 2020.

DEVELOPMENT OF AN AUTOMATED BONE TRANSPORT DEVICE FOR USE IN DISTRACTION OSTEOGENESIS

Chloe R. Brekhus (1)

Faculty Advisor(s)

Benjamin C. Gadomski (1), Christian M. Puttlitz (1)

(1) Department of Mechanical Engineering, Colorado State University, Fort Collins, CO, USA

INTRODUCTION

Distraction osteogenesis is a procedure used to heal severe bone defects, commonly in the long bones of the leg and arm. Large segmental bone defects can result from high energy trauma injuries (like combat-related blast injuries) or surgical bone tumor excision in cancer patients [1], and occur in about 150,000 patients in the US annually [2]. These defects are considered "critical-sized" if nonunion is imminent (i.e., the bone cannot heal on its own), which happens in up to 17% of open tibial fractures [3]. In these cases, distraction osteogenesis is often necessary to regenerate bone.

This procedure involves placing an external fixator around the limb and moving a segment of healthy bone across the defect (Figure 1). The external fixator frame is attached to the limb via pins drilled into the bone, and the middle ring (connected to the transport bone segment) is moved (i.e., distracted) across the gap by manual hardware manipulation. This bone transport process creates tension in the defect, providing mechanical signals to induce bone growth via osteoblast activity and other ossification pathways.

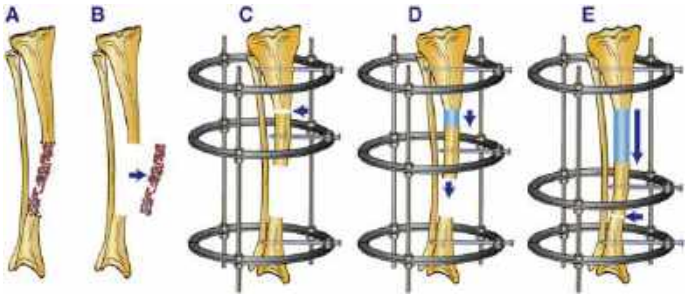

Figure 1: Distraction osteogenesis process [2]: defect removal (A and B), external fixator placement (C), distraction of transport segment (D), and bone regeneration (E).

It has been shown that distracting the bone in smaller increments more frequently optimizes bone regeneration [4], which is difficult to achieve with the current method of manual distraction. Furthermore, manual distraction requires a high-level of patient compliance, as the patient has to manually turn nuts on the external fixator at a specific time each day. The proposed solution is to develop a device that can automatically distract the bone in a nearly continuous fashion to improve bone growth and minimize patient input to the external fixator.

PRODUCT DESIGN

The proposed "auto-distractor" is based on a circular ring external fixation system (Figure 2). Bone transport will be driven by two stepper motors fixed to the middle ring, which is in turn attached to the transport bone segment. This ring slides along the connecting rods via linear ball bearings so that the distraction increment is limited only by the step size of the motor lead screws. Bone transport has been found to be optimized using a rate of 1 mm/day, with at least 60 increments per mm being considered continuous [5]. The selected motors are specified to have a linear travel of 0.0015875 mm/step, allowing for continuous distraction.

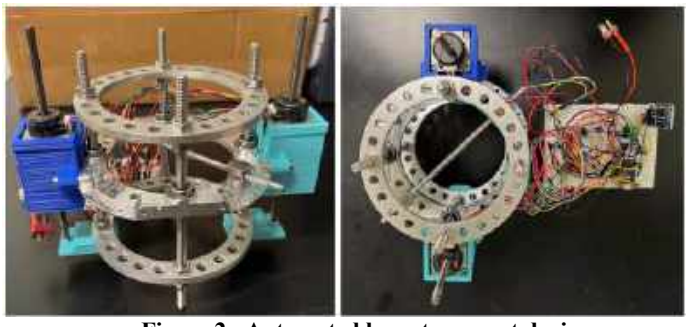

Figure 2: Automated bone transport device.

The motors will be controlled by a circuit (Figure 3) and Arduino code that specifies the time and distance of distraction. The circuit is powered by a 14.8V lithium-ion battery, which directly supplies voltage to the Arduino and motors, and a voltage regulator is used to drop this to 5V going into the stepper motors and encoders. The stepper motor drivers limit the motor current and receive signals from the Arduino to control motor movement. Each motor has an encoder that can sense the position of the motors; when the motors move the expected distance, the Arduino connects to Wi-Fi and emails the user to confirm that distraction has occurred. The motors are coded to automatically move at specific times so distraction happens at regular intervals. Time is kept by the real time clock (RTC) component, which runs on a separate 3V lithium cell battery and continuously sends the updated time to the Arduino.

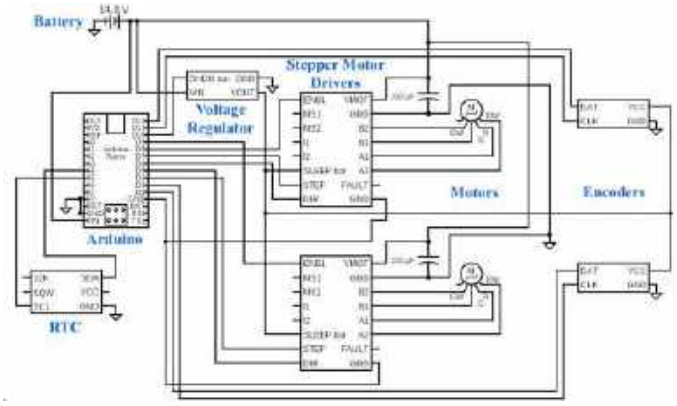

Figure 3: Circuit diagram for the auto-distractor.

This device will be used on patients with large segmental bone defects to improve healing. The surgical process will be essentially the same as current external fixator placement surgeries, with the motors and electronics being placed on the device one week after surgery when the distraction process begins. The novel aspects of the device are the sliding middle ring and motor construct, as well as the use of motor encoders to provide email feedback when distraction occurs. This device should be technically feasible, as the initial prototype was able to complete a successful bone transport in an ovine cadaver metatarsal.

BUDGET & MARKET ANALYSIS

The design budget for this project was $3,000 to cover the cost of components. The prototype shown in Figure 1 cost approximately $2,400, with the largest costs being the custom-machined transport ring ($700) and the customized motors with encoders ($786 for both). This is in comparison to the approximate cost of a manually driven device ("Ilizarov frame") of $730. A study in 2023 found the average total cost of an Ilizarov distraction osteogenesis procedure to be £26,126 (about $33,015) including surgery and hospital stay [6]. Using the auto-distractor would add $1,670 based on the prototype cost, which is only a 5% increase in price. The benefits of this device, including a potentially lower rate of nonunion, fewer overall revision surgeries, and decreased healing time, will likely offset this slightly higher cost. Furthermore, implementing the auto-distractor will not increase surgery time, as the electronic components of the device can be added later when the distraction period starts (usually 1-week post-op).

About 150,000 large segmental bone defects are reported each year in the US [2], and about 37% of critical-sized defects are treated using bone transport [7]. Based on these statistics, it is estimated that 55,500 bone transport procedures are done in the US each year. With only one other automated long bone distractor on the market (the Maxframe Autostrut™) [8], we estimate that 20,000-30,000 devices could be sold each year. At this volume, the expected cost per device is approximately $2,000 due to decreases in the manufacturing cost of the customized parts (motors and transport ring). The projected sales price will then be $3,000, resulting in a profit margin of 50%.

Investment costs in tooling are expected to be minimal for this device. Almost all components of the device are either 3D printed or available off-the-shelf; the only exceptions are the motors and transport ring, for which the manufacture will continue to be outsourced to reduce unnecessary tooling costs. The only machines needed for in-house manufacturing would be a 3D printer and basic soldering equipment, adding up to approximately $1,400. Assuming 25,000 units can be sold, this results in a return on investment of 49.9%.

ACKNOWLEDGEMENTS

This project received no external funding.

REFERENCES

[1] Lasanianos, N et al., *Orthopaedics and Trauma*, 24:149-163, 2010.
[2] Makhdom, A et al., *Nanomedicine*, 11:1-18, 2015.
[3] Kuhn, S et al., *European Journal of Trauma and Emergency Surgery*, 13:159-169, 2007.
[4] Kessler, P et al., *British Journal of Oral and Maxillofacial Surgery*, 43:392-398, 2005.
[5] Ilizarov, G, *Clinical Orthopaedics and Related Research*, 239:263-285, 1989.
[6] Kanakaris, N et al., *European Journal of Trauma and Emergency Surgery*, 49:951-964, 2023.
[7] Bezstarosti, H et al., *Trauma Surgery*, 141:1215-1230, 2021.
[8] Gigi, R et al., *Journal of Children's Orthopaedics*, 15:130-136, 2021.

INVESTIGATING THE EFFECTS OF SURFACE STIFFNESS AND VISCOELASTICITY ON HUMAN MESENCHYMAL STEM CELL IMMUNOMODULATION

Sara J. Olsen (1), Rose E. Leader, (2), Bethany M. Almeida (1)

(1) Department of Chemical and Biomolecular Engineering, Clarkson University, Potsdam, NY, USA
(2) Department of Mechanical and Aerospace Engineering, Clarkson University, Potsdam, NY, USA

INTRODUCTION

Chronic, non-healing wounds are a growing financial and medical burden, with the global wound care market valued at approximately $20B in 2022.[1] Human mesenchymal stem cells (hMSCs) implanted at the wound site are an attractive therapy for chronic, non-healing wounds due to their immunomodulatory behavior.[2] However, hMSCs have low viability, poor engraftment, and a risk of eliciting an immune response, thereby reducing therapeutic potential.[3] Additionally, variability in donor, age, and tissue source results in hMSC heterogeneity.[4] Prior studies have demonstrated that substrate stiffness and viscoelasticity have been shown to modulate hMSC differentiation.[5,6] For example, Engler et al demonstrated that hMSCs commit to different lineages as a function of the elasticity of their culture substrate.[7] They demonstrated that soft matrices mimicking the elasticity of brain tissue yielded neurogenic differentiation, stiffer matrices mimicking muscle induced myogenesis, and rigid matrices that mimic bone resulted in osteogenesis.[7] In addition to substrate elasticity, researchers have looked at the effect of viscoelasticity on hMSC fate, as human tissues are naturally viscoelastic. Chaudhuri et al found that cell spreading, proliferation, and osteogenic differentiation were all enhanced on hydrogels with faster matrix stress relaxation.[8] However, the effects of stiffness and viscoelasticity on hMSC immunomodulation remain largely unknown. Few studies in the literature have examined this; the literature thus far suggests that a soft,[9] more viscous (ie, higher stress relaxation)[10] extracellular matrix maximizes the production of paracrine factors by hMSCs that are indicative of immunomodulation, however other studies suggest that 3D culture of hMSCs is more important than matrix stiffness and viscoelasticity in expressing key immunomodulatory genes.[11] These studies clearly demonstrate the impact that biophysical properties have on the immunomodulatory potential of hMSCs. However, the mechanisms by which these biophysical cues affect immunomodulation have yet to be elucidated. In addition, there is missing from the literature a comprehensive study that seeks to demonstrate the synergistic relationship between matrix stiffness and viscoelasticity on hMSC immunomodulatory for a range of elastic, storage, and loss moduli. Thus, we seek to elucidate the synergistic effects of substrate stiffness and viscoelasticity on hMSC immunomodulatory behavior using highly tunable polyacrylamide (PAAm) gels for a range of biophysical properties towards elucidating the mechanisms by which immunomodulation is affected.

METHODS

PAAm gels were fabricated as described in the literature.[12] Briefly, three gels were fabricated, a low-stiffness gel, a medium-stiffness gel, and a high-stiffness gel. To impart viscoelastic properties to the gels, linear acrylamide was fabricated and mixed with the acrylamide and bis-acrylamide monomer mixture prior to gelation.[6,13] Young's (elastic) modulus (E) was characterized using dynamic mechanical analysis at 37 °C (DMA; DMA850, TA Instruments, New Castle, DE). Viscoelasticity, defined as shear stress-mediated storage and loss moduli, G' and G'', was characterized using a rheometer (AR2000, TA Instruments, New Castle, DE) using a frequency sweep from 0.05 to 50 Hz at 37 °C, a controlled 2% strain rate, and 0.1 N normal force. Values at 0.16 Hz were reported; these values were selected due to their biological relevance.[14] The PAAm gels were coated in fibronectin (Sigma, Billerica, MA) via sulfo-SANPAH to aid cell attachment and bone marrow-derived hMSCs (Lonza, Hopkinton, MA) were seeded at 5,000 cells/cm^2 on the fibronectin-coated PAAm gels. Viability was assessed using a live/dead assay (Fisher Scientific, Hampton, NH), and cellular morphology was characterized by fluorescently staining F-actin using Alexa Fluor 488 Phalloidin (Fisher Scientific, Hampton, NH) and nuclei using DAPI (Sigma, Billerica, MA) and imaging on a Nikon Ti2E inverted epifluorescence microscope (Nikon, Tokyo, Japan).

RESULTS

Table 1 shows the fabrication parameters of each gel formulation, including the expected Young's modulus (E), as well as the measured E, storage modulus (G'), loss modulus (G"), and tanδ.

Table 1. Mechanical characterization of the PAAm gels

	Low (-)	Low (+)	Med (-)	Med (+)	High (-)	High (+)
Expected Values						
% Acryl.	4	4	5	5	5	5
% Bis-Acryl.	0.06	0.06	0.15	0.15	0.30	0.30
% Linear Acryl.	0	4	0	4	0	4
E (kPa)	1.16 ± 0.54	1.16 ± 0.54	4.47 ± 1.19	4.47 ± 1.19	8.73 ± 0.79	8.73 ± 0.79
Measured Values						
E (kPa)	1.44 ± 0.11	1.15 ± 0.08	4.13 ± 0.51	4.99 ± 0.34	8.54 ± 0.55	8.82 ± 0.22
G' (Pa)	164	175	347	329	599	600
G" (Pa)	40.1	110	109	190	237	217
Tanδ	0.25	0.63	0.31	0.58	0.396	0.361

Abbreviations: Acryl, acrylamide; Bis-acryl., N-N' methylene bisacrylamide; high, high stiffness; low, low stiffness; med, medium stiffness; -, without linear acrylamide; +, with linear acrylamide.
Note: n=3 for E, n=1 for G', G", Tanδ

Live/Dead assay confirmed the viability of the hMSCs on these gels (Figure 1A). It is notable that there are fewer cells overall, as well as more dead cells, on the low- and high-stiffness gels in comparison with the medium gels. In addition, morphological analysis demonstrated that cells on low-stiffness gels were rounder and smaller, cells on medium-stiffness gels were larger and more 'spindle-like', and cells on high-stiffness gels were larger and more spread out (Figure 1B).

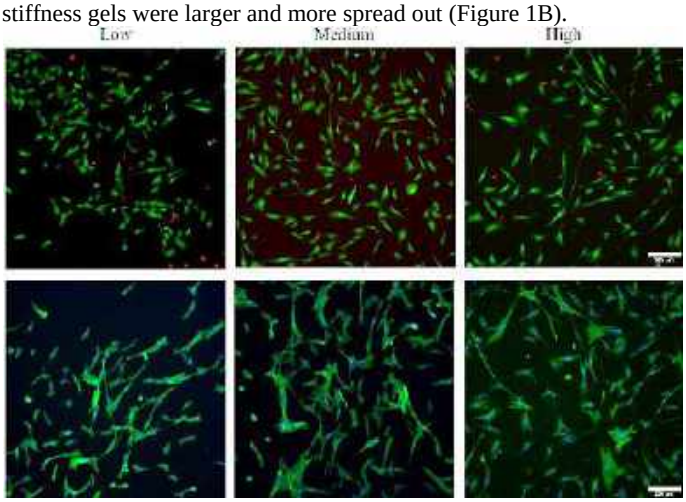

Figure 1: Viability (top) and morphology (bottom) of hMSCs cultured on non-viscoelastic low (left), medium (middle), and high (right) stiffness PAAm gels. Top: Live cells = green, dead cells = red, scale bar = 200 µm; Bottom: F-actin = green, nuclei = blue, scale bar = 200 µm.

DISCUSSION

Mechanical characterization of the gels (Table 1) shows that for low-, medium-, and high-stiffness non-viscoelastic and viscoelastic gels, the measured Young's modulus matched the expected values. Additionally, the storage modulus, which relates to the elastic behavior of materials, increases proportionally with Young's modulus. The loss modulus, related to the viscous behavior of materials, and Tanδ, a ratio measurement indicative of elastic:viscous components with larger Tanδ suggesting increased viscous components, increases as expected from the non-viscoelastic to viscoelastic low- and medium-stiffness PAAm gels. However, the high stiffness gels demonstrate no change in G" or Tanδ. This may be related to the increased concentration of bis-acrylamide yielding a higher chance of the linear acrylamide crosslinking to the acrylamide matrix at its terminal ends. However, these results are from an n=1, and more investigation is required. To investigate differences in crosslinking due to the presence of acrylamide and bis-acrylamide concentrations, a very high-stiffness non-viscoelastic and viscoelastic PAAm gel were also made, with an expected Young's modulus of ~19.66 kPa (8% acrylamide, 0.26% bis-acrylamide, data not shown in Table 1). The measured Young's modulus of these gels was found to be 9.50 ± 0.99, and 20.1 ± 0.94 kPa for the very high-stiffness non-viscoelastic and viscoelastic PAAm gel, respectively. Interestingly, the very high-stiffness gel did show an increase in Young's modulus when linear acrylamide was added. As suggested before, this may be a result of the increase in acrylamide and bis-acrylamide monomer concentration resulting in a greater chance for the linear acrylamide to crosslink at its terminal ends, decreasing the dissipative effects and increasing stiffness.

The viability assay showed a greater number of cells on the medium-stiffness gel compared to low- and high-stiffness gels. The decreased number of cells is likely due to a decrease in focal adhesion formation on these gels. Despite this, all stiffness gels were found to be cytocompatible, with few dead cells present. F-actin and nuclei staining also demonstrated noticeable differences in cell shape between the hMSCs cultured on different stiffness PAAm gels. As differences in hMSC morphology are known to affect hMSC behavior, this demonstrates the potential for variations in immunomodulatory potential as a result of differences in hMSC interactions with the different PAAm gels. Current work is focused on quantifying viscoelastic properties, viability, focal adhesion formation, morphology changes over time, and immunomodulatory potential changes over time by investigating the production of immunomodulatory cytokines by hMSCs cultured on these gels.

ACKNOWLEDGEMENTS

We acknowledge funding from the NSF #2138587. We also acknowledge support from Hubert Bilan with DMA and Rheology.

REFERENCES

[1] Sen C. et al., Adv Wound Care, 12(12):657-670, 2023.
[2] Keshavarz R. et al., Bioeng. & Trans. Med., 9(1):e10598, 2023.
[3] Im G. et al., Int J Mol Sci., 20(19):4835, 2019.
[4] Chen S. et al., Colloids Surf B Biointerfaces, 140:574-582, 2016.
[5] Wang S. et al., Advanced Healthcare Materials, 10(3):2001244, 2020.
[6] Charrier E. et al., Nat. Comm., 9(1):449, 2018.
[7] Engler A. et al., Cell, 126(4): 677-689, 2006.
[8] Chaudhuri et al., Nature Materials 15: 326-334, 2016.
[9] Wong S. et al., Science Advances, 6(15): eaaw0158, 2020.
[10] Phuagkhaopong et al., ACS Appl. Mater. Interfaces, 13(26): 30420-20433, 2021.
[11] Gonzales-Pujana et al., Biomaterials, 257: 120266, 2020.
[12] Tse J. and Engler A., Cur. Prot. in Cell Bio., 47(1):10.16.1-10.16.16; 2010.
[13] Pogoda K. et al., Bio-protocol, 11(16):e4131, 2021.

MECHANICAL RESPONSE TO COMPRESSION OF THE PIG OPTIC NERVE

K. Metrey (1), A. Korneva (1)

(1) Biomedical Engineering, Virginia Tech, Blacksburg, VA, USA

INTRODUCTION

The optic nerve is a crucial component of the visual system that transmits signals from the eye to the brain. A damaged nerve results in a partial or a complete loss of vision and leads to a significant decrease in the quality of life. Nearly 900,000 individuals are hospitalized after experiencing head trauma, and 50-65% of patients at rehabilitation facilities reported traumatic brain injury impacting their vision.[1] By studying the mechanical behavior of the optic nerve, we can better understand how mechanical trauma affects vision and eventually improve the quality of life of injured individuals. The optic nerve is small, ranging from 2.46 to 5.19 mm in diameter [2] and a soft tissue. This presents a challenge when designing a mechanical testing system to measure the material properties of optic nerves. The compressive properties of the optic nerve have been investigated in just two studies, reporting the elastic moduli, 1.895 and 3.05 kPa.[3, 4] The aim of this study was to measure the mechanical response of pig optic nerves to uniaxial compression. The pig optic nerves showed creep behavior, which can be described by a viscoelastic model.

METHODS

Healthy pig eyes were obtained from the Virginia Tech Meat Center (Blacksburg, VA). The eyes were dissected leaving only the optic nerve and optic nerve head. The outer layer of the optic nerve sheath, the dura mater, was removed leaving intact the inner layer of the sheath surrounding the optic nerve. The specimen was stored in phosphate buffered saline solution at 4°C until testing. The optic nerve was cut to an axial length of 3-4mm using two razor blades separated by a spacer.

Unconfined compression tests and creep tests were performed. Optic nerve samples were weighed before and after testing. Compression was applied to the top of the specimen using cellophane, with weights ranging between 30 to 50 mg. Top-view images were taken using a camera and side-view images using a second camera mounted on an Olympus MVX10 microscope. Photographs were taken by both cameras every 30 seconds for 10 minutes. The images were traced using FIJI (U.S. National Institutes of Health, Bethesda, MD, USA) to measure the height and the diameter of the specimen. An average of the major and minor axes was used for each diameter.

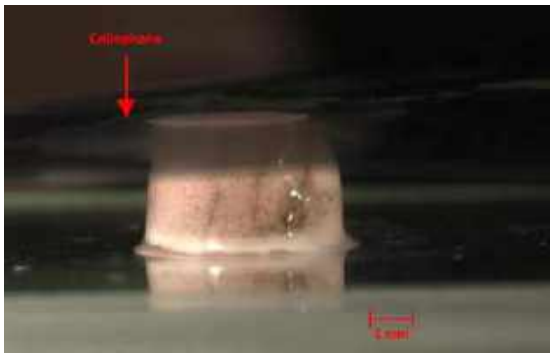

Figure 1: A pig optic nerve sample under compression. Applied load was the weight of a cellophane square. Scalebar 1mm.

Axial strain was calculated as the change in the height of the specimen divided by the initial height. The stress was calculated as the applied force divided by the initial cross-sectional area. The axial strain over time of the creep experiment was fit to the Kelvin-Voigt model for a spring and a dashpot,

$$\varepsilon(t) = \frac{\sigma_o}{E}\left(1 - e^{-\frac{Et}{\mu}}\right) \quad (1)$$

where σ_o was initial stress, E/μ was the time constant, E was the Young's modulus, and μ was the shear modulus. The axial strain over time data was fit to the model with two constants, σ_o/E and E/μ, using the nonlinear least-squares solver (*lsqcurvefit*) in MATLAB

(MathWorks, Natick, MA, USA) and the squared norm of the residuals reported. The initial stress, σ_o, was equal to the force of the applied weight divided by the initial cross-sectional area. The Young's modulus, E, and the shear modulus, μ, were found from the initial stress and the fitted constants.

RESULTS

Pig optic nerves were subjected to unconfined uniaxial compression and found to exhibit creep behavior. The behavior was fit to a simple viscoelastic model, the Kelvin-Voigt model of a spring and a dashpot. Norm of the residuals of the fit to Eq. 1 were 0.0016, 0.00055, and 0.00051, indicating a good fit. The volume of the specimen was measured from images acquired during the creep test. Volume was conserved over time, as seen by the average slope of 0.068 mm^3/min in Figure 2. As the height of the specimen decreased, the diameter increa-
\

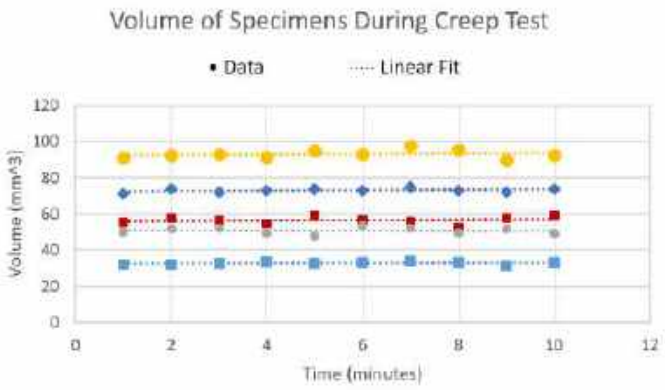

Figure 2: Volume of the pig optic nerve specimens during the creep experiment. Data for 5 specimens and their linear fits.

sed. There was a decrease in the weight of the specimen during the experiment. This was due to an observed loss of fluid from the open ends of the optic nerve.

The compressive creep behavior was similar between the three specimens (Figure 3). The estimated time constants, E/μ, were 0.57, 1.14, and 0.22 minutes. From the time constants of the specimens, the

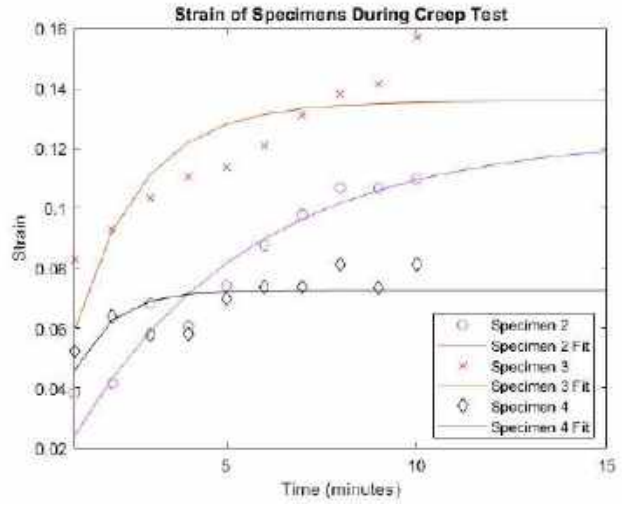

Figure 3: Axial compressive strain of pig optic nerves during the creep experiment. The data for three specimens were fitted to the Kelvin-Voigt viscoelastic model.

steady state equal to 99% of the asymptotic value would be reached in 11 ± 3.51 minutes. Young's Moduli, E, were of the same order of magnitude, with values 144, 321, and 154 Pascals (Pa). The shear moduli, μ, were also of the same order of magnitude, 252, 282, and 718 Pa.

DISCUSSION

Pig optic nerves exhibited creep behavior when subjected to uniaxial compression. This was likely due to fluid loss from the open ends of the nerves. However, fluid loss did not significantly affect the volume of the specimen, which was conserved over time. Fluid did not escape through the layer of the optic nerve sheath, but only through the open top and bottom ends.

The Kelvin-Voigt model for a viscoelastic material was used to fit the preliminary data. The pig optic nerves had an average Young's modulus of 206.3 ± 99 Pa. The steady-state strain was estimated to be reached in 11 ± 3.51 minutes in the creep experiment. Safa et al. performed a similar experiment on pig optic nerve heads, except between two stiff plates with four increasing loads for creep periods of five minutes.[3] The group also found the specimens behaved as viscoelastic materials, like the results of this study. They found that the volume was compressible, in contrast to the results of this study (Fig. 2). Safa et al. also reported that fluid may have escaped during the experiment. Studies by Safa et al. and Boazak et al. reported values for the elastic modulus, 1.895 and 3.05 kPa.[3, 4] These numbers are an order of magnitude higher than the mean elastic modulus of 206.3 Pa found herein.

Limitations during testing included the leaning of specimen when under compression and bending of cellophane due to its dimensions. Both limitations can impact the measurement of the specimen height, affecting the calculated strain and stress values. The material parameters, E and μ, may therefore be affected in those specimens. Hence only data collected on specimens where these limitations were not observed is presented. Future testing will address these challenges.

Additional experiments will be conducted to increase the sample size of the work. To determine if the creep behavior is due to fluid loss, future compression tests will be conducted with specimens where the open ends are sealed. In conclusion, the material properties reported in this study can be used to advance knowledge of the mechanics of the optic nerve and to determine how the tissue responds to impact during traumatic brain injury.

ACKNOWLEDGEMENTS

Funding for this project was from the Virginia Tech Department of Biomedical Engineering and Mechanics.

REFERENCES

[1] M. Yanoff and J. Duker, Ophthalmology, 6th ed. Elsevier, 2023.
[2] S. S. Mncube and M. D. Goodier, "Normal measurements of the optic nerve, optic nerve sheath and optic chiasm in the adult population," South African Journal of Radiology, vol. 23, no. 1, Nov. 2019, doi: https://doi.org/10.4102/sajr.v23i1.1772.
[3] B. N. Safa, A. T. Read, and C. R. Ethier, "Assessment of the viscoelastic mechanical properties of the porcine optic nerve head using micromechanical testing and finite element modeling," Acta Biomaterialia, vol. 134, pp. 379–387, Oct. 2021, doi: https://doi.org/10.1016/j.actbio.2021.07.022.
[4] E. M. Boazak, J. d'Humières, A. T. Read, and C. R. Ethier, "Compressive mechanical properties of rat and pig optic nerve head," Journal of Biomechanics, vol. 93, pp. 204–208, Aug. 2019, doi: https://doi.org/10.1016/j.jbiomech.2019.06.014.

ADAPTIVE SPORT SOLUTIONS: ASSISTIVE KAYAK MOUNT DEVICE FOR MOBILITY IMPAIRED USERS

Alexander B. Britton (1), Megan P. Parker (1), Douglas T. Wingert (1)

Faculty Advisor
Christine Walck Ph.D. (1)

(1) Mechanical Engineering, Embry-Riddle Aeronautical University, Daytona Beach, FL, USA

INTRODUCTION

In the United States, 12.1% of individuals live with a serious mobility disability impacting their day-to-day lives [1]. In addition, 71% of surveyed people with a mobility impairment reported feelings of emotional stress and isolation. Today, participating in adaptive sports is said to enhance physical well-being and enrich life by fostering meaningful social connections [2]. Recreational kayaking, a versatile adaptive activity, caters to diverse users like stroke victims, paraplegics, and those with mobility impairments. Tailored to individual needs, it fosters inclusivity, promotes equality, and builds community.

Adaptive kayaking products assist the user by securing the paddle in a self-stabilizing mounting device like the one seen in Fig. 1 featuring the most common assistive device used in para-kayaking, the Gamut Paddle Holder by Angle Oar Inc. [7]

Fig. 1: The Gamut Paddle Holder by Angle Oar Inc.

The Gamut Paddle Holder incorporates a ball-in-socket mechanism that, while intended for versatility, unfortunately, restricts its functionality, leading to a more limited rotational range than is ideally desired. This restriction negatively impacts the user's movement patterns, steering them away from optimal performance and efficiency. More specifically steering them toward a teeter-tooter movement pattern versus a forward stroke pattern. Moreover, instances of the design coming apart during use have been reported, further highlighting the need for improvements. Such constraints not only limit the effectiveness of movements but also hinder the development of strength in users. In addition, this device ranges from $315 to $500 per unit [7]. Such a cost can be a hardship for this community. On average, accommodating a disability requires an extra 28% of one's annual income to maintain the same standard of living which leaves little left for extracurricular activities or rehabilitation not covered by insurance.

Therefore, our goal is to develop an assistive device that accurately mimics the natural forward stroke movement in kayaking and securely attaches to the kayak to prevent detachment. Additionally, we aim to make this device affordable, ensuring it is accessible to a wider range of users.

PRODUCT DESIGN

This project aims to improve the common Gamut Paddle Holder by introducing an assistive device featuring a four-bar linkage mechanism. Drawing on motion capture technology, this device is designed to closely replicate the natural path of a forward kayak stroke. The design's motion profile is informed by an analysis of 15 total strokes, indicating dimensions of 768 mm across the mediolateral axis (y), 473 mm in the superior-inferior axis (z), and 502 mm in the anterior-posterior axis (x), as depicted in Fig. 2. This analysis reveals a semi-ellipsoidal motion pattern that emphasizes efficient water slicing during the paddle's down strokes, aiming for a more effective and natural paddling experience.

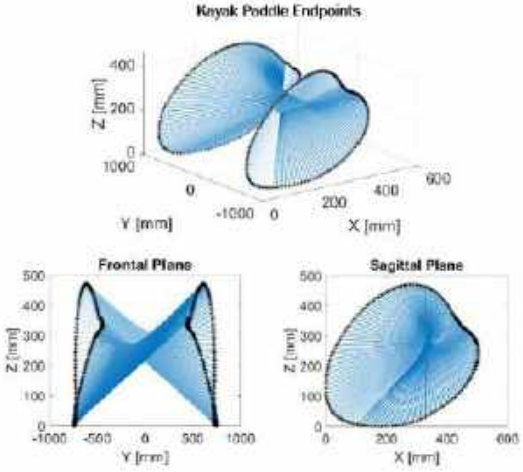

Fig. 2: Full Motion Capture Kayak Stroke Paddle Profile

Central to our redesign was the extrapolation of the kayak's theoretical center point from motion capture data, serving as a foundation for a 3D motion profile in space (Fig. 3a). This critical step accurately accommodates the kayaking stroke's required degrees of freedom, supporting complex, multi-directional movements.

To replicate the 3D motion profile, a crank-rocker mechanism was incorporated, which includes a rotating crank, an oscillating rocker, two stationary ground points, and a connecting coupler. The critical point of the coupler, labeled as "C" in Fig. 3b, aligns with the sagittal plane On-Stroke Position (OSP), where the paddle's center point is attached. To enhance adaptability, boots are fitted on the lower pin joints, offering flexibility in the frontal plane. This allows the device to accommodate

different kayak widths and individual stroke variations. The dimensions of the linkage were finalized after optimizing the stroke profile based on motion capture data in MATLAB. The optimization process ensured that the coupler point "C"'s output profile closely matches the OSP, with a maximum relative error of 3.7%.

Our device focuses on accurately replicating a kayak's forward stroke, targeting the limitations of existing mounts. It goes beyond enhancing the paddling experience, offering a design that supports correct paddling techniques, promotes rehabilitation for joint and muscle strength, and provides a sense of normalcy. Our solution avoids the inefficiency and fragility of "teeter-totter" movements found in traditional mounts. This helps mitigate issues related to mobility impairments, such as mental anxiety and stress, enhancing participation and well-being.[7].

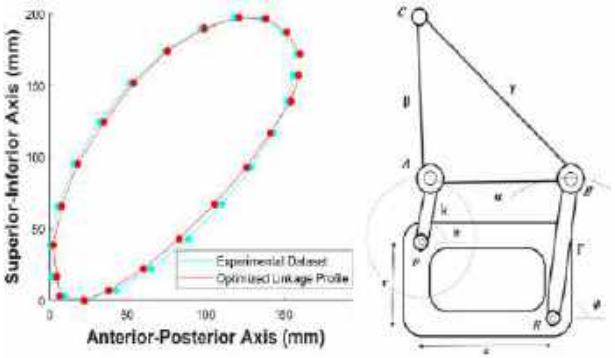

Fig. 3a: Optimized Profiles (left) and 3b) Model Side View (right)

BUDGET & MARKET ANALYSIS

The development of a functional device and the creation of an initial inventory of 90 units are projected to cost approximately $22,000, as shown in Fig. 4. This estimate encompasses the overhead expenses related to the operation of 3D printers, electricity consumption, and the procurement of initial stock materials. Figure 4 breaks down the costs into Year 1 Overhead Costs (left) and Material Costs (right). The expense for producing a single device is estimated at around $105, factoring in the costs for the 3D printing filament necessary for the linkage and the materials required for the base's fabrication.

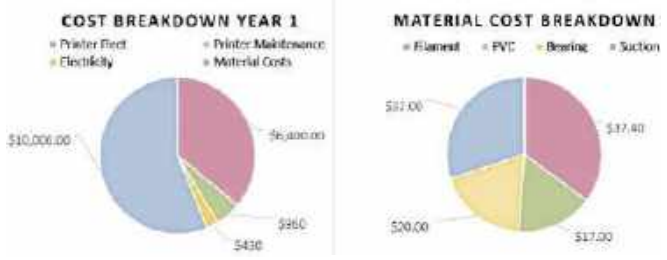

Fig. 4a: Overhead Year 1 Costs (left) and 4b) Material Costs (right)

By setting the retail price at $259.99, we aim to achieve a profitable margin that will allow us to recoup the initial outlay from our starting inventory while offering a price advantage over our competitors, whose products range from $315 to $375. This pricing strategy is particularly relevant considering our survey findings, which indicate that nearly half (44%) of Americans with serious illnesses and long-term disabilities have exhausted their savings, compared to about a quarter (24%) of individuals without disabilities. This stark contrast highlights the critical importance of maintaining a competitive retail price to make our device accessible to those in need.

Our project has entered a partnership with the Oceans of Hope Foundation (OOHF), to sell an initial 40 units at a 10% discount, aiding our financial targets. We are also negotiating with other organizations, including Team River Runner in Orlando and Selkie Ability Inc. in Boca Grande, FL, which both have high annual participation rates, boosting future sustainability and market demand. According to our break-even analysis, shown in Fig. 5, we need to sell 73 devices from our initial inventory of 90 units to start generating a profit. The agreement with OOHF, along with the prospective deals with other organizations, positions us well to achieve and surpass this break-even point. By securing this initial bulk order, we are significantly closer to reaching our sales target, ensuring that every additional unit sold beyond this point contributes to the profitability of our project. This strategic approach highlights the project's financial viability.

Fig. 5: Break-Even Cost Analysis of Overhead and Inventory

The kayaking and canoeing equipment market valuation is currently at $1.3 billion and is projected to grow to around $1.4 billion by 2029 [8]. Adaptive kayaking is a niche market in comparison to the broader paddle sports equipment market, with a smaller total addressable target market of 3.6 million individuals. In addition, the field of adaptive sports is growing as access to technological innovation benefiting those with mobility impairments is increasing. Research shows that the percentage of individuals using adaptive kayaking devices increased from 36% to 68% from 2020 to 2021 [10]. As adaptive kayaking's popularity grows, it is reasonable to expect growth in the addressable market.

In the competitive landscape of adaptive kayaking devices, two standout features distinguish this product: Optimal Stroke Profile Path and Detachability. Unlike competitors such as the Gamut Paddle, which primarily offers stability, our device enhances the kayaking experience by enabling the ideal stroke. Additionally, its detachable design avoids permanent modifications to the kayak, distinguishing it as a significant innovation in the market.

REFERENCES

[1] Disability impacts all of us Infographic | CDC. (2023, May 15). Centers for Disease Control and Prevention.

[2] Côté-Leclerc, F., Duchesne, G. B. (2017). How does playing adapted sports affect quality of life of people with mobility limitations?

[3] Pickard, J. K., Carretero, J. A., & Merlet, J. (2019). Appropriate analysis of the four-bar linkage. Mechanism and Machine Theory.

[4] H., & Reinholtz, C. (1987). Mechanisms and Dynamics of Machinery (4th Edition). Wiley.

[6] Goodman, Morris, Mc, & McGarity. (2020, October). The extra costs of living with a disability in the U.S.

[7] Gamut Paddle Holder for Sit-on-Top Kayaks. (2023). AngleOar.com.

[8] Industry Expert Research (2024, January 4) Canoeing and Kayaking Equipment Market Share Trend and Industry Share 2030 LinkedIn.

[9] Disability impacts all of us Infographic | CDC. (2023, May 15). Centers for Disease Control and Prevention.

EXOSKELETON FOR SURGERY TRAINING

Jeremy K. Varughese, Andres J. Miramontes (1), Jesse A. Gomez, Andrew K. Gonzales Alayo, Anissa D. Cantu, Luis A. Morales (2)

Faculty Advisors
Dr. Todd Polk (1), Dr. Robert Hart (2)

(1) Biomedical Engineering, University of Texas at Dallas, Richardson, TX, United States
(2) Mechanical Engineering, University of Texas at Dallas, Richardson, TX, United States

INTRODUCTION.

The current method of surgical training relies heavily on in-person instruction and physical guidance by experienced surgeons to convey proper technique to surgeons in training. However, this approach is resource-intensive, time-consuming, and limited in scalability, as it requires a surgeon to dedicate significant time to each individual student. To modernize and enhance the efficiency of surgical education, there is a critical need for the development of an innovative exoskeleton system. This system should provide a streamlined and effective means of training residents in surgical techniques, reducing the dependency on in-person instruction and physical guidance while maintaining the quality of training. Our challenge is to design and implement an exoskeleton solution that can accurately mimic the guidance and feedback provided remotely by experienced surgeons, ultimately improving the proficiency of surgical trainees.

PRODUCT DESIGN

To simplify the project, two subgroups were identified: the *Exoskeleton Glove* and the *Trainer Glove*. Both subgroups utilized an Arduino Nano 33 BLE to communicate with each other, with the Trainer Glove sending data to the Exoskeleton Glove exclusively. Additionally, both gloves are powered by a 9V battery. Further details in the design will be specified in their respective sections under *RESULTS*. The designs settled upon lend themselves from many inspirations in the rehabilitation field, along with novel ideas from the team.

The finger portion of the Exoskeleton Glove was inspired by work done by B. Kang et al. [1] By using fishing line, we can articulate the fingers, and utilizing silicone allows the device to be flexible and lightweight in the portion of the hand that articulates the most, as seen in **Figure 1A**. A passive thumb body, showcased in **Figure 1B**, will provide extra support on the trainee's palm. Our design diverges from the original in that the portions surrounding the fingertips are left open as seen in **Figure 1C.** This is to accommodate a more tactile feel for users, ensuring a more accurate representation of how tools will feel without the Exoskeleton Glove.

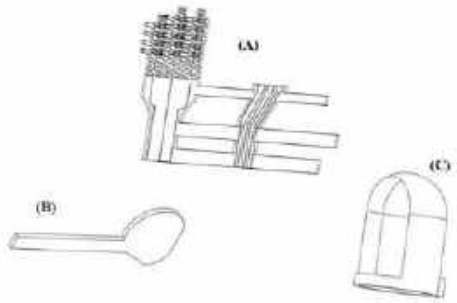

Figure 1: Exoskeleton Glove finger portion components. (A) Main Body (B) Thumb Body (C) Open Fingertip Thimble.

The wrist portion of the Exoskeleton Glove possesses an original design from our team. The wrist assembly, as seen in **Figure 2**, is structured with two stationary red bracelet plates holding a beige slider in between. The blue blocks represent the placements of the motors for the hand actuation. The silver plate is the hand attachment to place on top of the trainee's hand and kept strapped along the palm. Two rods that extrude outside of the red bracelet plates are utilized for mechanical stops to keep from overexerting the trainee wrist. These rods are placed precisely at the 135° angle mark, as surgeons typically do not exceed a wrist rotation of 135° in suturing tasks. The beige slider piece allows the device to move and guide the direction of the wrist, while the two red bracelet plates contain extruding spring clamps in the interior ring for wrist size adjustments. Assessing the necessary spring constant, and relation to the wrist force, we considered **Equation 1** below.

$$F = kx \qquad (1)$$

The *F* denotes the applied force, *x* denotes the distance that the spring is compressed or stretched away from its equilibrium state, and the *k* variable denotes the spring constant.

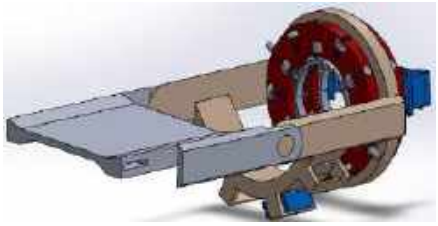

Figure 2: Exoskeleton Glove Wrist Assembly.

Lastly the Trainer Glove, which draws inspiration from Gordon Ng, alumni to UBC [2]. The initial design featured a more open structure, prompting our team to take liberty in designing a case to house the components. A power switch was added along with a toggle switch to allow the user to control the Exoskeleton Glove remotely.

The team selected continuous rotation micro servo motors to facilitate movement with the wrist and fingers on the Exoskeleton Glove. Two of the servo motors will be simultaneously operating to move the wrist portion of the device, while four others will be operating for each the thumb, index, middle, and ring fingers. Assessing the necessary peak stall torque and motor output force, we considered **Equation 2** below.

$$\tau = rF \sin \Theta \qquad (2)$$

The peak stall torque is denoted by τ, radius from axis of rotation to the point of application force is denoted by r, and Θ denotes the control angle from the axis of rotation. The control angle in the wrist portion is 135° as the mechanical stopping rod in our wrist device is set at a 135° point, and the fingers contain a control angle of 90°.

As mentioned before, two Arduino Nano 33 BLE devices are utilized to facilitate Bluetooth communication between the Exoskeleton Glove and the Trainer Glove. The Trainer Glove, specifically, utilizes flex sensors and the MPU-6050 accelerometer to track finger actuation and wrist orientation. These devices are placed in a case that sits behind the gloves respectively. A model of the Trainer Glove is shown in **Figure 3**.

Figure 3: Trainer Glove with devices case and case interior.

To begin remote controlling, the Exoskeleton Glove must be in a predetermined neutral position before allowing the Trainer Glove to toggle on "Trainer Mode". When Trainer Mode is active, the Arduino sends the mapped datapoints from the Trainer Glove to the Exoskeleton Glove via BLE (Bluetooth Low Energy), which is then translated to servo actuation accordingly.

A finite element analysis test was conducted with the theoretical results expressed in **Figure 4**. The top portion represents the wrist slider, and the bottom portion represents the mechanical stop rod. The purple arrows indicate how force is applied onto the device and the green arrows indicate stationary components. The tests indicated how little-to-some deformation would be experienced due to the stress experienced, especially on the body of the rod, though our experimental results have shown no deformation to any component of our device.

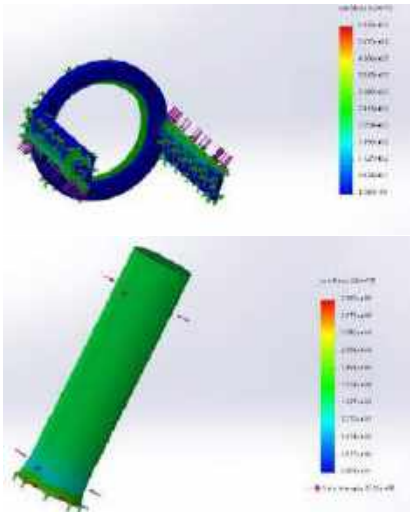

Figure 4: Finite Element Analysis for wrist slider and rods.

Limitations of this study include how we focused our scope on just the dominant arm as the other is used for pressing and holding down, though we understand there could still be learning opportunities there. Another is how Bluetooth communication is somewhat susceptible to external signal noise based on our testing. Bluetooth was still the best choice compared to a Wi-Fi device, as there is far less reliability in that area. Overall, we found that creating two light wearable gloves that communicate via Bluetooth are effective in surgical training remotely.

BUDGET & MARKET ANALYSIS

We were able to build a prototype for $381.36, excluding the price of 3D printed materials and molds as they were provided by the university. Accounting for this and labor costs, the estimated total for a single unit is $391.44.

As the device is targeted towards surgical residents, we can expect a reasonable market size of over 7,650 units per year by the end of the third year with the total resident number totaled over 150,000 as of 2023 [3]. This rate would assume that a 5% market share is captured after three years. The expected manufacturing cost for this volume per unit would be $150 and adding 25% for General and Administrative costs would bring the total manufacturing cost per unit to $187.50. The projected sales price, at a 50% margin level, would be about $375. Assuming investment costs of around $2,000,000, leaving a return of 112.5%. This return would indicate a promising potential for a profitable venture in the medical training device market.

ACKNOWLEDGEMENTS

We express our sincere gratitude to our directors Dr. Robert Hart and Dr. Todd Polk, for their invaluable guidance and support throughout this endeavor. Additionally, we extend our appreciation to Dr. Caroline Park of UT Southwestern Medical Center, and Gene Woten and the UTDesign staff for their insightful collaboration, resources, and funding. Furthermore, our sincere thanks to Senior Robotics Engineer Husam Wadi of Daifuku Intralogistics America, whose expertise contributed greatly to the success of this project.

REFERENCES

[1] Kang, B et al., *Soft Robotics*, 6(2):214–227, 2019.
[2] Ng, G et al., *Flex Sensor Glove*, 2019.
[3] AAMC, *Report on Residents Executive Summary*, 2023.

EPILOG: RAPID EEG DETECTION OF STATUS EPILEPTICUS

R. Chhaya (1), C. Flynn (1), E. Grajales (1), P. Shah (1), D. Xu (1)

Faculty Advisor(s)

D. Adewole (1), E. Berlew (1), D. Dlugos (2), D. Meaney (1)

(1) Bioengineering, University of Pennsylvania, Philadelphia, Pennsylvania, USA
(2) Pediatric Neurology, Childrens Hospital of Pennsylvania, Philadelphia, Pennsylvania, USA

INTRODUCTION

Status epilepticus (SE) is a medical emergency defined as an enduring seizure or a series of rapidly recurring seizures without a return to baseline neurological activity and stands as the most prevalent neurological emergency during childhood [1]. In some children, the transition into this state, characterized by a decrease in outward movement, can be easily confused with the tiredness and unresponsiveness associated with the comedown from a convulsive seizure. These similarities often cause a delayed response, or no response at all, in the event of SE, leading to a mortality rate of up to 30% [2]. Current seizure detection devices on the market are largely designed to detect the onset of seizures, with little to no emphasis dedicated to seizure termination. Motion-based devices, such as accelerometer-based bracelets and wristwatches, provide no insight into seizure activity once outward movements have ceased, rendering them useless during cases of SE. Current EEG-based devices, such as helmets and caps, either require trained hospital technicians for placement or involve a full-head system that are uncomfortable and inconvenient for rapid application during the seizure comedown period. These shortcomings inhibit the rapid recognition of SE, which is critical for successful treatment. The Epilog EEG headband represents a significant advancement in assistive technology for epilepsy management. Designed for rapid, at-home detection of status epilepticus in children, it provides a vital tool for caregivers, facilitating early intervention and potentially mitigating long-term neurological damage. This innovation enhances the quality of life for individuals with epilepsy by enabling more immediate and effective responses to seizures, thus embodying the essence of rehabilitation science and assistive technologies in supporting individuals with challenging medical conditions.

PRODUCT DESIGN

Our proposed device, Epilog, is an EEG headband designed to be rapidly secured around a child's head during the seizure comedown period after outward movements have ended (Fig. 1). This device will provide a convenient, comfortable, at-home solution for parents to check for SE in their children, leading to greater peace of mind and providing necessary urgency in emergencies. After the visual signs of a seizure have stopped, the caregiver secures Epilog to the child's head (Fig. 2). Epilog immediately begins recording EEG data and feeds it into a machine learning model via Bluetooth for extraction of relevant features for SE diagnosis. Based on the diagnosis, Epilog will alert the caregiver if the child remains in a state of seizure for further medical intervention.

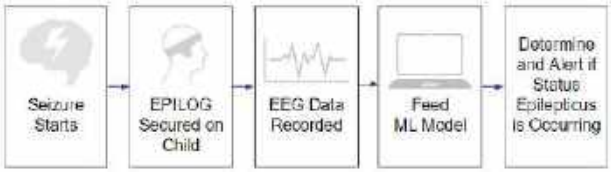

Figure 1. Epilog Use Flow Diagram

Our need specifications for this device include a specificity and sensitivity of at least 85% and 90%, respectively. The false negative rate must be extremely low: the device reporting a seizure is over when it is still occurring may be fatal to the user. For peace of mind and reliable use of the product, the false alarm rate must also be minimized. Furthermore, Epilog offers clinical-level seizure monitoring with the use of eight hospital-grade silver chloride electrodes, ensuring quality signal collection and providing enough channels for accurate seizure detection while maximizing patient comfort and ease of application. Our headband has been designed for at-home use and can be easily applied by a caregiver with minimal training. The addition of attached combs encircling each electrode on the headband allows for EEG collection through diverse hair types.

To achieve the signal resolution necessary for seizure detection, we have built a data acquisition system to collect EEG data that amplifies the signal with a gain of 2,500 and filters it using a bandpass filter selecting from 1.5 - 30 Hz. These frequencies capture the most relevant frequencies for seizure detection while discarding 60 Hz electronic noise from the surroundings. Features are selected by converting data to

the wavelet domain one second at a time and calculating the mean, standard deviation, and power of each relevant EEG frequency band. These features were fed into a machine learning classifier (balanced random forest) to detect the presence of a seizure at each second. We trained, cross-validated and tuned hyperparameters, and tested the model using the CHB-MIT Scalp EEG Database [3], which consists of 22 subjects of various ages and medical backgrounds. The final model is hosted on the cloud and can be accessed using an API and via the Epilog app, which provides an easy-to-use user interface that connects to the headband via Bluetooth and the machine learning model via network requests.

Our proof of concept consisted of three components: the physical headband with the electrodes, the electrical data acquisition and transmission system, and the seizure detection algorithm. We constructed a prototype of the fabric headband to confirm rapid application, with rendering shown in Fig 2. To allow for rapid application of Epilog, we developed a method for simultaneously applying gel to all of the electrodes on the headband, which reduces application time. When not in use, the headband is stored in a dual compartment case wherein the headband lays flat in the upper compartment (Fig. 2). The lower compartment contains tubing that connects the upper and lower compartments through holes that align with the EEG electrodes on the headband. When EEG gel is applied through the tubing, the electrodes are concurrently gelled, and Epilog is ready for use. To test our design's functionality, we inserted the EEG electrodes and wiring into the fabric of the headband and confirmed clear EEG readings.

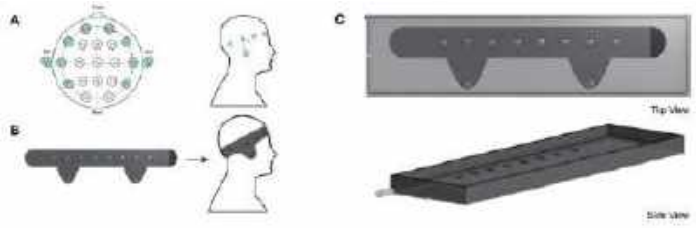

Figure 2. Epilog physical design. **A.** Standard EEG electrode placements and selection. **B.** Epilog headband. **C.** Epilog gel case for rapid application.

For our data acquisition system, we demonstrated that we could read blink artifacts from four electrodes and wirelessly transmit data from eight channels. To test the recording of blink artifacts, we placed four electrodes on the forehead of one subject, who blinked once per 5 seconds for 30 seconds, and repeated this process 5 times. Each blink was successfully captured. To test the transmission of 8 channels of data, which is the final amount for seizure detection, we input eight different sinusoids. Our system was successfully able to record and transmit each of the sinusoids without signal distortion. The technical feasibility of Epilog is firmly established through rigorous engineering and validation processes, highlighted by the development of a machine learning classifier with remarkable performance metrics. In testing with the CHB-MIT Scalp EEG Database, our device achieved a specificity of 0.883 and sensitivity of 0.946, with a ROC value of 0.95, demonstrating its capability for real-time, accurate seizure detection. Despite potential delays from Bluetooth transmission and network requests, Epilog's prediction time remains under 1 second, ensuring continuous, real-time detection. This comprehensive validation process confirms Epilog as a practical, reliable solution, with great potential for real-world deployment in the management of SE.

BUDGET AND MARKET ANALYSIS

We have secured a $600 design budget from the Bioengineering Department at Penn to design, build, and test our EEG headband prototype. This funding, along with access to the department's facilities and materials, will cover many of our initial expenses, enabling us to develop a full prototype within this budget.

For the intellectual property strategy, we would plan to apply for a utility (non-provisional) patent to secure the technology. Currently, related existing patents include US 2021/0267539 A1 for Systems and Methods for Processing Sonified Brain Signals, US 11,471,088 B1 for a Handheld or Wearable Device for Recording or Sonifying Brain Signals, and US 2023/0000416 A1 for Adjustable Geometry Wearable Electrodes.

In analyzing the potential market and financial viability for the EEG headband designed to detect Status Epilepticus, the market size within the United States, focusing on children with epilepsy, is estimated at 470,000 as reported by the CDC [4]. Assuming a conservative market penetration of 10% in the first year, we would expect to sell around 47,000 units. With a projected sales price of $500 per unit, the revenue would be $23.5 million. The strategy to capitalize on this market includes a recommendation from a clinical mentor at the Hospital of the University of Pennsylvania to all applicable patients, and the establishment of partnerships with medical research centers, with initial efforts focused on Penn Medicine.

The estimated manufacturing cost per unit is $150, leading to a total manufacturing cost of $7.05 million for the projected sales volume. Additional investments, including engineering, tooling, and intellectual property costs, are estimated at $2.5 million. Marketing and distribution costs, estimated at 15% of total revenue, would amount to $3.525 million. Therefore, the total costs would sum to $13.075 million. Subtracting the total costs from the projected revenue, we anticipate a profit before taxes and other expenses of $10.425 million. Given the total initial investment of $2.5 million, the return on investment (ROI) is calculated at an impressive 417%. This positive ROI demonstrates the significant profit potential for the EEG headband in the market, even with conservative estimates of market penetration and initial costs.

We also consider several potential risks that could impact our project's success. Regulatory approval presents a significant hurdle, as medical devices must undergo rigorous FDA scrutiny to ensure safety and efficacy. We plan to engage with regulatory consultants early to navigate the approval process efficiently. Our market entry strategy includes highlighting Epilog's unique value proposition of rapid, at-home detection and the potential to reduce long-term healthcare costs, making a compelling case for insurance coverage. Technological adoption by our target demographic is another risk. We plan to address this through comprehensive user education and support, ensuring that the benefits of Epilog are communicated clearly and effectively. By preemptively identifying and strategizing around these risks, we aim to position Epilog for a successful market introduction and sustained impact in epilepsy management.

ACKNOWLEDGEMENTS

We extend our gratitude to the Bioengineering Department at Penn for their financial support and to our faculty advisors for their invaluable guidance and expertise, which was instrumental in the development of Epilog. We also thank collaborators from Penn Bioengineering and Penn Neurology. Their perspectives have significantly enriched our project, highlighting the value of collaboration across fields in creating innovative healthcare solutions.

REFERENCES

[1] Glauser, T et al., Epilepsy Currents, 16(1), 48-61, 2016.
[2] Trinka, E et al., Frontiers in Epidemiology, 3, 1081757, 2022.
[3] Guttag, J, CHB-MIT Scalp EEG Database. PhysioNet, 2010
[4] Zack et al., MMWR. 2017;66:821–825, 2015.

SEX DIFFERENCES IN IRIS STIFFNESS IN PATIENTS WITH A HISTORY OF ANGLE-CLOSURE GLAUCOMA: AN IN-VIVO IMAGE-BASED INVERSE MODELING ANALYSIS

Hayden DelCiello (1), Frederick Sebastian (2), Anup Dev Pant (3), Vanita Pathak-Ray (4), Syril K. Dorairaj (5), Rouzbeh Amini (2,6)

(1) Khoury College of Computer Sciences, Northeastern University, Boston, MA, USA
(2) Department of Bioengineering, Northeastern University, Boston, MA, USA
(3) Department of Biomedical Engineering, The University of Akron, Akron, Ohio, USA
(4) LV Prasad Eye Institute, Hydrebad, India
(5) Department of Ophthalmology, Mayo Clinic, Jacksonville, Florida, USA
(6) Department of Mechanical and Industrial Engineering, Northeastern University, Boston, MA, USA

INTRODUCTION

Glaucoma is characterized as a group of diseases that cause damage to the optic nerve. Such damage is usually —not always—associated with an increase in the intra-ocular pressure (IOP). The profile of the iris and its interaction with the flow of the aqueous humor (AH) in the anterior eye could affect IOP. The AH flows from the posterior chamber of the eye, around the iris into the anterior chamber, and then out through a drainage pathway between the iris and the cornea (Fig. 1). Primary angle-closure glaucoma (PACG), affecting over 17 million people worldwide [1] and a leading cause of blindness [2, 3], is generally caused by pupillary block. During pupillary block, the iris bows toward the anterior, reducing the anterior chamber angle (ACA), the angle between the iris and the cornea (Fig. 1), and subsequently obstructing AH outflow, and increasing IOP [4].

Early diagnosis of PACG improves outcomes, but current diagnostic methods are susceptible to misdiagnosis [5]. In recent years, researchers have studied iris biomechanics and found evidence that higher iris stiffness contributes to the narrowing of the ACA [4, 6–8]. In this study, we aimed to identify the relationship between iris biomechanics and biological sex, a known PACG risk factor [9]. Since PACG is more prevalent among women, we hypothesized that the iris would be stiffer in women, both in a control group and a in group with a history of PACG.

METHODS

This study had 27 total subjects of an Indian population at the LV Prasad Eye Institute in Hyderabad: 14 female (7 healthy; 7 PACG) and 13 male (7 healthy; 6 PACG). Males and females each had healthy group and a group who had undergone laser peripheral iridotomy (LPI) as treatment for the pupillary block associated with PACG. All patients included in this study continued to suffer from occludable ACAs following LPI procedure. The tenets of the Declaration of Helsinki were followed for this study.

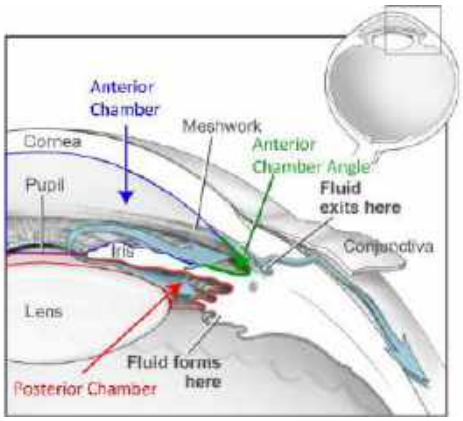

Figure 1: Anterior segment anatomy and aqueous humor flow (image modified from National Eye institute, NIH, Bethesda, MD)

Iris Imaging and Meshing-Our methods have been described in detail previously [4]. Briefly, two anterior segment optical coherence tomography (AS-OCT) cross-sectional images (Fig. 2) were associated with each subject, one in dark conditions (dilated) and one in light conditions (contracted). The image from the light conditions was measured between the iris root and tip to obtain a target distance to be used for the inverse modeling. One side of the dilated iris was traced and meshed, using SOLIDWORKS (Dassault Systèmes, Vélizy-Villacoublay, France) and Abaqus (Dassault Systèmes, Vélizy-Villacoublay, France). Within the pupillary portion of the iris, a region on the mesh of an estimated 7% volume was chosen as the sphincter region. All S8R elements from Abaqus were then converted to 9-node biquadratic quadrilateral elements, using Python.

Numerical Model-The iris was modeled as a two-dimensional (axisym-

metric), isotropic, nearly incompressible (Poisson's ratio $\nu = 0.49$) neo-Hookean solid [4], governed by a stress balance equation:

$$\nabla \cdot \boldsymbol{\sigma} = \mathbf{0} \tag{1}$$

$$\boldsymbol{\sigma} = \boldsymbol{\sigma}_{\text{NH}} + \boldsymbol{\sigma}_{\text{Sph}} \tag{2}$$

where $\boldsymbol{\sigma}$ is the Cauchy stress tensor, defined as the sum of the neo-Hookean stress $\boldsymbol{\sigma}_{\text{NH}}$ and the active sphincter stress $\boldsymbol{\sigma}_{\text{Sph}}$, applied only in the sphincter region of the domain. The magnitude of the sphincter stress was unknown for each subject, so it was fixed to 40 kPa for all subjects, and the resulting elastic modulus E from computations (see the next section) was divided by 40 kPa to obtain E', the so-called normalized elastic modulus [4].

Inverse Finite Element Model-The inverse model in this project was developed by combining the Galerkin finite element method for discretization over a mesh and differential evolution [10] for efficient solution convergence. All programs were developed internally using C and used MUMPS [11, 12] as a sparse solver. All simulations were run using 11 processes on Intel CPUs from Northeastern University's Discovery Cluster in the Massachusetts Green High Performance Computing Center. The shear modulus G was the target of computation, and each trial value for G resulted in a different iris model which deformed uniquely with the same sphincter contraction. We defined a cost function as the absolute difference between the measured distance in the AS-OCT light condition image d_{exp} and that same distance in the simulated deformation d_{sim}.

$$Error = |d_{\text{sim}} - d_{\text{exp}}| \tag{3}$$

Differential evolution minimized the cost function over multiple generations of a population of shear modulus values. When the population converged to a narrow distribution, the shear modulus associated with the lowest error was taken as the computed shear modulus for a particular subject. From there, the elastic modulus was computed as:

$$E = 2G(1 + \nu) \tag{4}$$

and then normalized by division over 40 kPa.

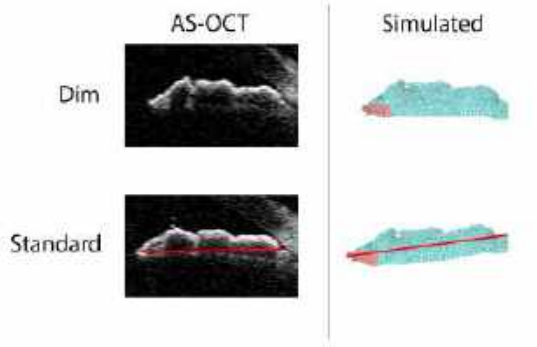

Figure 2: Relationship between AS-OCT images and in-silico model. Red lines indicate measurements of d_{exp} and d_{sim}

Statistical Analysis-A one-tailed Student's t-test was used for comparisons of the normalized elastic moduli between groups, where $p < 0.05$ is considered significant.

RESULTS

Simulations for each subject typically completed between 10 and 20 minutes. In the group of subjects with a history of angle-closure glaucoma, female subjects exhibited a significantly higher normalized elastic modulus E', as compared to males ($p < 0.05$, Fig. 3). In contrast, in the healthy cohorts, no significant difference existed between female and male individuals.

When comparing E' between healthy and post-LPI groups for males and females separately, the female post-LPI group has a significantly higher E' than the female healthy group ($p < 0.05$), though E' is not significantly higher for the same comparison between healthy and post-LPI male groups.

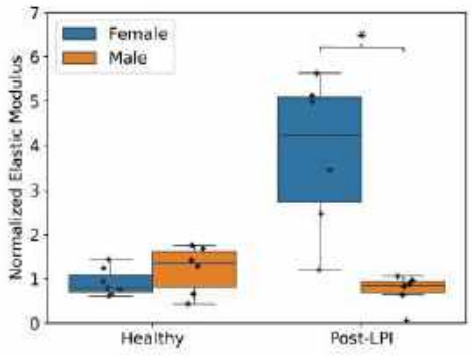

Figure 3: Comparison of normalized elastic modulus sexes in healthy and post-LPI groups

DISCUSSION

Consistent with our proposed hypothesis, we found out that in the cohort with a history of angle-closure glaucoma, the iris was stiffer in female subjects as compared to their male counterpart. Our results, however, were inconsistent with our hypothesis in the healthy group, where female and male iris stiffness were not significantly different. Past research using similar methods has shown a significant increase in iris stiffness among post-LPI subjects, compared to healthy subjects, without distinguishing among sexes [4]. In-vivo image-based modeling in mice has shown a significant difference between iris stiffness in healthy male versus female mice [13]. Since the human tissue has larger variation as compared to animal tissues, we suspect that by increasing our sample size we may be able to identify sex-based differences in healthy human iris, as well. Perhaps since the magnitude of stiffness was much larger in post-LPI female group detection of differences was easier in that cohort with our current small sample size. Conversely, one could also argue that either the biomechanical factors behind PACG are uniquely different between female and male, or females have a higher prevalence of an increased iris stiffness leading to development of PACG.

Quantifying iris stiffness in-vivo comes with difficulties and limitations. The iris model used in this study was isotropic and homogeneous, significantly decreasing the actual complexity of the iris, which consists of multiple layered materials with varying mechanical properties, such as the stroma and the dilator muscle. Additionally, iris contraction was simplified from a combined contraction and relaxation of the dilator and sphincter muscles to just a contraction of the sphincter muscle, which was assumed to have a similar magnitude in all subjects. Despite the limitations of our study, we have, to our knowledge, demonstrated for the first time that in-vivo iris stiffness is significantly greater in female subjects with a history of angle-closure glaucoma. Further research is essential to identify the underlying mechanism of the increased iris stiffness and its correlation with the sex of the individual.

ACKNOWLEDGEMENTS

Acknowledgement is made to the donors of the National Glaucoma Research, a program of The BrightFocus Foundation, for support of this research (grant numbers G2018177).

REFERENCES

[1] Zhang N et al. en. *Front Med (Lausanne)* 7 (2021).
[2] Sun X et al. *Prog Retin Eye Res* 57 (2017).
[3] Medeiros FA et al. *Ophth* 122.2 (2015).
[4] Pant AD et al. *Inv Ophth & Vis Sci* 59.10 (2018).
[5] Wright C et al. *Acta Ophth* 94.3 (2016).
[6] Jouzdani S et al. *Inv Ophth & Vis Sci* 54.4 (2013).
[7] Seet LF et al. *Clin & Exp Ophth* 44.8 (2016).
[8] Safa BN et al. *J Roy Soc Int* 19.192 (2022).
[9] Tehrani S. *Cur Eye Res* 40.2 (2015).
[10] Storn R et al. *J Global Opt* 11.4 (1997).
[11] Amestoy PR et al. *SIAM J Mat Anal & Apps* 23.1 (2001).
[12] Amestoy PR et al. *ACM Trans Math Soft* 45.1 (2019).
[13] Lee C et al. *Exp Eye Res* 202 (2021).

SISTANCE: A TWO-WAY BASE COMMUNICATION SYSTEM FOR DEAF-BLIND STUDENTS

Mackenzie L. Hunt (1), K. Maxim Hansen (1,2), Souleymane Cissokho (1), Timothy G. Johnson (1, 2)

Faculty Advisor(s)

J. Miles Canino (1)
(1) Department of Mechanical Engineering, Rose-Hulman Institute of Technology, Terre Haute, Indiana, United States
(2) Department of Engineering Management, Rose-Hulman Institute of Technology, Terre Haute, Indiana, United States

INTRODUCTION

Children with vocal, visual, and/or auditory deficits are constantly faced with communication barriers. They often show signs of frustration because of their limited capacity to interact with the world and meaningfully engage with their surroundings. Because of these restrictions, fundamental learning concepts can take a longer time to develop. A concept that is crucial to the development of basic communication is the ability to simply convey "yes" or "no." Unfortunately, assistive technology for this stage of development is commercially lacking for this target audience.

The most common form of communication education for these students is through a process called associative learning. Associative learning starts with giving a child an object and taking a corresponding action. For example, giving the child a basketball and associating that object with going to the gym. The next step would be introducing the ability to physically communicate preference. This communication process demonstrates a distinction between the desire to take the action or not take the action. To teach a child this process, the object is presented to the child and a decision is conveyed via some physical indication - regardless of what the child actually wants. This physical indication will then produce a corresponding action. After an understanding of the choice communication system is demonstrated, more complex topics can be introduced.

Our team identified features missing from current market products to develop a solution focused on incorporating communication in both the classroom and home environments. Incorporating multisensory learning in a portable device enhances the learning process and establishes independence faster. Once a child is able to communicate if they are sick, hurt, or hungry via a yes/no base communication, the whole world opens up to them. They are newly able to connect to others in a way never experienced before.

Product design

Run by a standard 9V battery, the device's two buttons work to express the two base concepts, "yes" and "no." The blue button, when pressed, plays a low tone, vibrates in quick pulses, and lights shine blue. The red button, when pressed, plays a high tone, vibrates continuously, and lights shine red. If both buttons are pressed, no outputs are triggered. The size of the device allows students of various ages to interact with the system while held in the hand or while resting on a flat surface. In this way, the association of object, choice, and action can be learned in an intuitive way, aided by the tactile features of the system.

A physically distinguishable orientation, proficient dexterity support, size/portability, and two consistent visual, auditory, and tactile stimulations are all required for a successful product. The choice indicators are colored red and blue which are correlated to the color lights that display when the choice is selected. Different sound pitches and vibration patterns also play depending on the button pressed.

It is very rare that a child is both completely deaf and blind and the quality of these senses can vary by day. This means that our device's attempt to stimulate three senses can prove valuable in system and concept discrimination. Similarly, the decision to utilize red and blue are based on the research that red and yellow are most documented to stimulate those that are cortically visually impaired [1]. Having one color more likely to elicit a response, while the other color is less likely, is another important factor when creating two clearly discernible choices. Similarly, few auditory deficiencies cater to higher frequencies while most favor low frequency sound [2], thus the two inputs trigger opposing tones for enhanced distinguishability. The differing vibration patterns also assist in the tactile differentiation of the two choices in cases where there are no other meaningful stimuli for the user. The device in one of the active states is shown in Figure 1.

Figure 1: The Sistance device with the red input button activated - the red LEDs, buzzer and vibrational motor running.

The overall physical design of the device was made to enforce distinguishability. The hemispherical indent on the bottom of the device indicates the directionality of the system while it is in use. The device also utilizes a tactile band that encompasses the outside shell.

Tactile bumps have been added to half of this band to further differentiate one side from the other. Rubber feet are included to increase viability of table play - these rubber feet are also designed with different shapes, indicating device orientation. The overall design allows the child to associate physical features of the product with the button inputs regardless of how the child chooses to hold and interact with the system. As shown in Figure 1, there is ample space between the buttons so children can interact with the device in any way that is comfortable to them, such as using their whole hand or a single finger. Overall, the device is intended for children with no visual or auditory ability, however, the inclusion of light and sound stimulation increases accessibility for those children with basic lingual challenges or nonverbal tendencies..

Budget & Market Analysis

For this project, our team had a budget of $240. Table 1 shows a cost breakdown of each item used to create our prototype, as well as a production cost estimation.

Table 1: Items used to create the prototype with production costs

Item Name	Quantity	Prototype USD/Unit	Production USD/Unit
TPU Filament	1	$29.99	$2.28
Micrcontroller	1	$14.95	$0.45
Button	2	$5.95	$0.38
Vibration Motor	1	$1.95	$1.56
Resistors	4	$0.00	$0.02
RGB LED	4	$0.00	$0.04
Glue	1	$0.00	$0.59
Active Buzzer	1	$0.00	$0.23
Screws	4	$0.00	$0.01
Wires	~	$0.00	$0.02
PLA Filament	1	$0.00	$0.97
Total	-	$58.79	$7.19

This low cost is extremely advantageous in the current market. Table 2 provides details on the costs of possible solutions. Many of these products have extremely high prices due to low competition in the market. This clearly demonstrates how our more reasonably priced product has a competitive advantage in the market. Our device poses as a viable, affordable and portable solution to fill a significant gap in the market for students with deaf blindness.

Table 2: The Cost of other multisensory stimulation devices designed to aid the learning of students with deaf blindness

Assistive Device	Description	Cost
All That Glitters [3]	A multi-dome device that utilizes light, sound and vibration	$299.95
4 Plate Communicator [4]	Switch device with 4 recorded messages and light	$209.95
Tactile Communicator[5]	Tactile switch device with 4 recorded messages	$189.95
Sistance	Out portable tactile device with light sound and vibration	$~30

Our device provides portable multisensory stimulation solutions at a comparatively low price point. We expect to invest around $150,000 in tooling, material and labor. $~60,000 for a plastic injection molding machine[6] as well as $~10,000 for a PCB printer and materials[7]. The remaining will be used to purchase materials at scale and pay for labor. In 2021-2022 over 7.3 million students received special education with ~.5% of these being students with deaf-blindness.[8] This works out to ~35,000 students from this we assume yearly sales of 5,000 to 10,000 units per year. The simple payback of our initial investment would be 1 year or less assuming we sell at least 5,000 units. Ultimately we believe our device is a feasible and valuable portable tool for multisensory associative learning to accelerate the learning process for students living with deaf-blindness.

ACKNOWLEDGEMENTS

We thank Jennie Lee, an educator having extensive experience in this specific form of deaf-blind education for over 20 years, for her insights into the user experience within associative learning. We also thank Karry Hunt, a Physical Therapist with over 20 years of experience working with visually and auditorily impaired persons, for her commentary and consultation on the mobility and dexterity accessably of the interface. Lastly, Carrie Owens, the administrative assistant and SW lending library manager in Warrick County for over 10 years, who helped inform the group of current market products.

References

[1] S. H. Swift, R. C. Davidson and L. J. Weems, “Cortical Visual Impariment in Children: Presentation Intervention and Prognosis in Educational Settings”

[2]"National Library of Medicine: National Center for Biotechnology Information," 30 November 2017.

[3]“AllThatGlitters,”*EnablingDevices*.https://enablingdevices.com/product/all-that-glitters/ Feb.11,2024

[4]“4 Plate Communicator Say It Play It,” *Enabling Devices*. https://enablingdevices.com/product/4-plate-communicator/

[5]“Tactile Communicator Say It Play It!,” *Enabling Devices*. https://enablingdevices.com/product/4210-tactile-communicator-say-it-play-it/ Feb. 11, 2024

[6]“How Much Does Injection Molding Cost? | Rex Plastics Mold Manufacturer,” *Rex Plastics*, Jul. 15, 2013.

[7]“V-One - A Desktop PCB Printer | Voltera,”

[8]National Center for Education Statistics, “Students with disabilities,”

ERIAS: A Bluetooth Cardiac Monitoring System for Pediatric Inpatient Use

Angela Song, Daphne Nie, Samir A. Maarouf, Georgia Georgostathi and Alexandra A Dumas

(1) School of Engineering and Applied Sciences, University of Pennsylvania, Philadelphia, PA, USA
(2) Cardiology, Children's Hospital of Philadelphia, Philadelphia, PA, USA

Dr. Tania Khanna (1) and Dr. Maully Shah (2)

INTRODUCTION

Electrocardiogram (ECG) systems are commonly used to measure the electrical activity of the heart in inpatient clinical settings[1]. Despite their prevalence, the numerous wires on standard ECG systems pose challenges to pediatricians and children. Wires are easily disconnected or removed, limiting the usefulness of wired ECG systems for continuous cardiac monitoring[2]. Additionally, wired cardiac monitoring systems limit patient mobility and often become entangled causing frustration to healthcare providers.

While portable ECG telemetry boxes exist, they must be carried around by the patient. To address these challenges, Erias aims to create a wireless ECG monitor that interfaces with a physician computer app for extended trouble-free inpatient heart activity monitoring and detection of cardiac irregularities[3].

To date, our team has developed a core hardware system that uses five leads and a Bluetooth low energy (BLE) chip to seamlessly record and transmit electrophysiological data to our physician interface. Once the data is recorded and transmitted, this information can be visualized on our desktop interface (GUI). Our software system allows a user to access and input patient observations and personal information, visualize live cardiac signals from five leads, and observe live calculations of heart rate as well as ventricular and atrial contraction rate.

Moving forward, we plan to scale down the size of our device using a printed circuit board (PCB), integrate lithium-ion batteries, and work towards additional cardiac parameters for arrhythmia detection on our physician interface. Together, these improvements will help us improve patient mobility and the current standards for cardiac data analysis to redefine the standard of care for inpatient pediatric cardiac monitoring.

Product design

Erias aims to fulfill three main needs: reduce the wires present on pediatric patients for enhanced patient comfort, implement Bluetooth data transmission for improved patient mobility, and integrate arrhythmia detection for streamlined real-time, continuous monitoring of patient conditions. Moreover, to adhere to the current gold standards utilized in pediatric cardiac intensive care units (CICU), we designed our device to derive 5 leads simultaneously from 5 electrodes. Based on these needs, we aimed to fulfill the corresponding design specifications. For the device bulk reduction and mobility, the device was designed to be small and portable, with dimensions of at most 6 cm (diameter) x 2 cm (height) as presented in Figure 1.A Bluetooth low energy (BLE) chip was incorporated into our compact chest pod to fulfill the need for continuous, real-time wireless data transmission, and the data was displayed in our graphical user interface for seamless end-user (clinician) access. Here, physicians can observe five cardiac signals and cardiac metrics (heart rate, atrial rate, ventricular rate, QT interval, and QRS interval) to visualize potential arrhythmias in pediatric patients. The proposed device is designed to not only improve patient experience but also to provide physicians with the required reliable data monitoring and parameters. This approach ensures that the device meets the ethical and quality standards required in engineering medical devices. Our system aims to revolutionize cardiac monitoring by improving patient mobility and comfort and by furthering techniques for accurate cardiac data analysis.

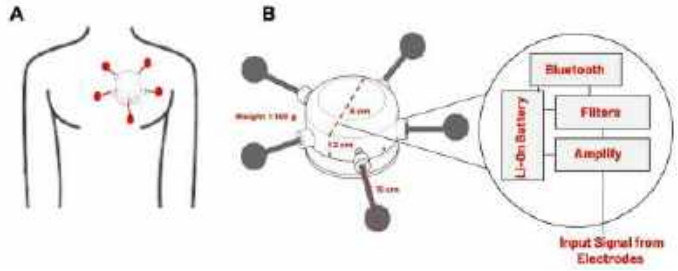

Figure 1. A. Diagram of Erias on chest with extending lead B. Final device schematic with major hardware components.

For the proof of concept, we successfully built a Bluetooth-enabled electrocardiogram device that displays a single lead on an interactive GUI. Next, for the minimum viable product (MVP), we achieved the collection and transmission of five leads from a compact, mobile device for display in an integrated GUI. Upon testing the device on ourselves as users, we saw continuous ECG data streaming on our Bluetooth device, therefore validating our hardware and software design. However, we were unable to fulfill our goal of device compactness as the device itself was measured to be 30 x 30 x 5 cm. For our next prototype (Fig. 2A-E), we continued working on improving the device and adding additional leads. To realize our goals of device compactness and a five-lead ECG system and add to our proof of concept design, we realized that signal filtration needed to be accomplished by software filtering to reduce the number of hardware components. For this prototype, the hardware component aimed to accomplish three main tasks: amplification, derivation of the differential signal, and transmission by an embedded system. The heart, atrial, and ventricular rates were calculated by performing peak

detection for the R peaks and P waves of the ECG signal. The peak detection threshold is defined relative to the patient's baseline to ensure generalizability. The effectiveness and accuracy of the calculations were performed by comparing with the published parameters associated with an online database (Chapman University & Shaoxing People's Hospital) on patients with normal and abnormal ECG signals. From these leads we were able to successfully measure non-sinus rhythms to a 95% accuracy and we are currently working towards detecting non-sinus cardiac parameters to an accuracy of 55%.

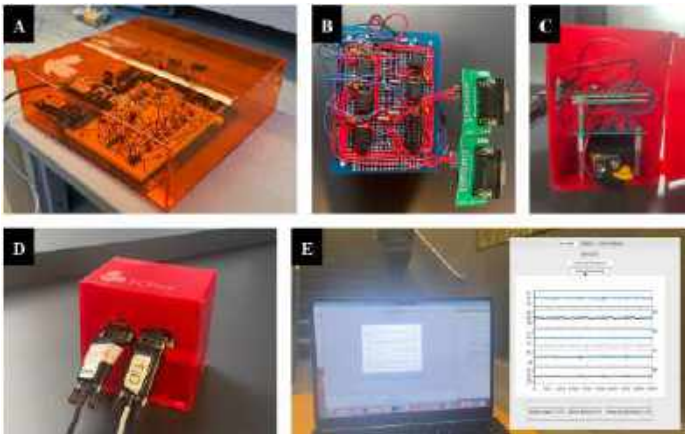

Figure 2. Erias Minimum Viable Product. A. First Iteration of breadboarded 5 lead ECG hardware. B. Protoboarded 5 lead ECG hardware components. C. Image of hardware inside final encasing. D. Image of final MVP device with outer casing containing protoboarded hardware and Bluetooth transmission chip. E. Device being used by an Erias team member to demonstrate patient mobility during live transmission of 5 lead ECG data to a desktop interface.

As we move toward our final product, we still have several specifications to address on both the hardware and software sides of our device. We hope to shrink the scale of our device so it rests on the chest more easily, explore recharging and backup data storage, expand our backend algorithm to include additional cardiac metrics, and explore software compatibility with Epic. Together these improvements will enable us to create a device that is compact and simple to use for clinicians and nursing staff.

Budget & Market Analysis

At present our team has been supplied with $1200 through the Penn Bioengineering (BE) Department's allotment for senior design. In addition to this funding the Stephenson Biomarker Space and Detkin Electrical Engineering Lab has supplied us with free basic circuit components and 3D printing materials for our product development. Our current spending plan has been outlined below in Table 1. As we move forward and begin implementing our PCB we anticipate exploring professional manufacturing costs for our device's circuitry, main body casing and electrodes. However, whilst optimizing our system we have focused upon minimizing costs by collaborating with maker spaces and instructional labs within the Penn Engineering ecosystem.

ECG systems are essential devices across all spheres of medicine, especially inpatient clinics and emergency medicine. Expanding the purview of this technology to a wireless cardiac monitoring allows for improved continuous monitoring for pediatric patients whilst simultaneously transforming the standard of care for all clinical settings. The cardiac electrophysiology market was evaluated at 5.6 billion USD in 2022 and is expected to grow an additional 12% CAGR by 2032. Additionally, it is believed that the rising prevalence of cardiac arrhythmias will only further increase demand for cardiac monitoring technologies. This coupled with the knowledge gained from 20 clinician interviews through Penn iCORPs demonstrated the niche our device would be filling in this enormous market.

Table 1: Budget Breakdown for Erias Development

Item	Price ($)	Quantity	Total ($)
XIAO NRF 52840 Bluetooth Chip	16	1	16
Adafruit Feather	33	1	33
5 Electrode leads and circuit connector	150	2	300
3D Printed CAD design	0 (provided by Penn BE)	N/A	0
Passive filters, Op-amps and other circuit components	0 (Provided by Penn BE or ESE)	N/A	0
5 Electrode single leads	10	5	50
Kardia Mobile ECG system (for studying data collection and processing)	150	1	150
Permanent Circuit Board	50	2	100
Kendall 530 Monitoring Foam Electrodes for Skin Connection	32	4 packs	128
Conductive Gel	10	5	50
Lithium-Ion batteries	6	8 packs	48
Lithium-Ion battery holder (Coin cell)	7	1 pack	7
Pediatric / Neonatal Electrodes	118	1 pack	118
TOTAL			$1000

ACKNOWLEDGEMENTS

We would like to acknowledge Penn's Stephenson Bioengineering Maker Space and the Senior Design teaching staff for their technical support of our project.

References

1. Mumford, J et al (2023) BJPsych Bulletin, 47(2), 116-116.
2. Wang, L.-H. et al (2019). Sensors, 19(22), 4996.
3. Chen, M.-Y et al (2018). Morbidity and Mortality Weekly Report, 67(38), 1045-1049.

A MACHINE LEARNING APPROACH TO MINING HEMODYNAMIC DATA FROM PULMONARY ARTERIAL HYPERTENSION RATS

Jingwen Hui (1), Ethan D. Kwan (1), Daniela Valdez-Jasso (1)

(1) Shu Chien – Gene Lay Department of Bioengineering, University of California San Diego, La Jolla, California, USA

INTRODUCTION

Pulmonary arterial hypertension (PAH) is characterized by sustained elevated blood pressure in the pulmonary arteries, causing a pressure overload on the right ventricle (RV). The classification and management of PAH is challenging because highly invasive procedures such as cardiac catheterization are required to confirm and track disease progression. Recent studies have described distinct patient remodeling phenotypes and therapy responses, revealing important differences in cardiac structure and function despite hemodynamic similarities [1],[2]. However, patient studies often face limitations in feasibility, invasiveness, and experimental design resulting in insufficient data relative to animal studies.

Our research team has previously obtained invasive measurements of cardiac structure and function involving large cohorts of PAH-induced male, female, and ovariectomized rats. Employing machine learning (ML), we leverage its predictive features and capabilities to explore underlying patterns challenging to discern through traditional methods. To that end, we 1) develop a predictive model using a support vector machine (SVM) with principal component analysis (PCA) for dimensionality reduction, 2) apply SVM and permutation importance analysis to understand quantitative differences across categories, and 3) investigate unexplored parameter relationships relevant to PAH through bivariate data visualization.

METHODS

Data acquisition. Hemodynamic and morphological data were collected from sugen-hypoxia (SuHx) treated rats as previously described [3]. Right-ventricular (RV) and left-ventricular (LV) blood pressure and volume were collected during an open chest procedure using a 1.9F admittance catheter (Transonic, Ithaca, NY) during steady state and vena cava occlusion. All additional hemodynamics metrics (stroke volume, end-diastolic volume, end-systolic volume, ejection fraction, cardiac output, dp/dt max, dp/dt min, pulmonary vascular resistance, end-diastolic elastance, end-systolic elastance, arterial elastance, ventricular vascular coupling) were derived from these timeseries. Morphological measurements (RV thickness, RV mass, Fulton index, animal mass, right/left atrial mass, septal hypertrophy index, liver mass) were collected immediately post hemodynamic studies. Septal Hypertrophy Index is calculated as LV mass divided by the sum of LV mass and septum mass, expressing the relative proportions of the LV chamber wall that make up the septum.

Numerical methods. SuHx animals were categorized as hypertensive if the mean pulmonary arterial pressure (mPAP) exceeds 20mmHg. If mPAP is unavailable, we defined hypertensive subjects as those that exceed 30mmHg for RV end-systolic pressure. Supervised ML, unsupervised ML, permutation importance analysis, and exploratory data visualizations were performed on the dataset comprising nearly equal proportions of male, female, and ovariectomized rats after 4, 8, 12, and 15 weeks of SuHx. Control group is referred to as week 0.

Weeks of SuHx/PAH Predictor

To investigate defining variables from this dataset, we performed PCA and fitted our dataset with a SVM model of Radial Basis Function (RBF) kernel. This model was chosen due to its effectiveness for handling high dimensional data with non-linear boundaries. Data was split into training and testing datasets (80%, 20%). Due to data imputation challenges, we only include RV hemodynamics and morphology data for this task.

Quantitative Categorical Analyzer

Of the rats treated with SuHx, some did not develop PAH. We define this group as non-hypertensive SuHx rats. First, we compared non-hypertensive SuHx *vs.* control rats using SVM and permutation importance analysis. Then we compared non-hypertensive SuHx to

hypertensive SuHx rats (i.e., treated *vs.* untreated SuHx). Through permutation importance analysis, we identify quantitative distinctions among these groups. Permutation importance coefficients quantify the change in our model's performance when the value of a variable is randomly shuffled, indicating the variable's contribution to the model's predictive power.

PAH Parameter Exploration

Leveraging pair plots, we explore correlations between morphological and hemodynamics parameters.

RESULTS

Weeks of SuHx/PAH Predictor

The model predicted PAH stage with 70% accuracy based on the weeks of SuHx. PC1, the most significant component, explains ~30% of the variance, which is more than double to that of PC2. The three variables with the greatest positive loadings of PC1 are RV mass, pulmonary vascular resistance (PVR), and end-systolic pressure (ESP). Conversely, the variables with the highest negative loadings are dp/dt min, ejection fraction, and cardiac output.

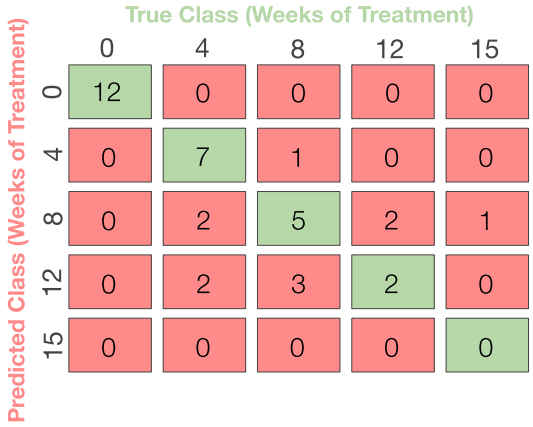

Figure 1: Confusion matrix of SVM shows significant accuracy in early-stage rats (week 4).

Quantitative Categorical Analyzer

The SVM model identifies control rats from non-hypertensive SuHx rats with a 92% accuracy level. The feature permutation analysis shows that the right atrial mass, left atrial mass, and ESP are the most significant indicators with permutation importance of 0.133, 0.075, and 0.036, respectively. On the other hand, SVM distinguishes hypertensive SuHx rats from the non-hypertensive SuHx ones with 100% accuracy. Feature permutation importance identified Fulton index, RV thickness, and RV mass as the key variables with permutation importance of 0.066, 0.039, 0.027, respectively.

$$\text{Permutation Importance} = \text{Original Accuracy} - \text{Permutated Accuracy} \quad (1)$$

$$\text{Accuracy} = \#\text{ of Correct Predictions} / \text{Total } \#\text{ of Predictions} \quad (2)$$

PAH Parameter Exploration

Pair plot visualizations showed previously unidentified relationships between Fulton index and three hemodynamics variables (dp/dt max, PVR, and end-systolic elastance (Ees)). When the Fulton index is low, these metrics tend to remain low. However, when the Fulton index is high, these parameters can vary across a range from low to high. The Pearson coefficients for the Fulton Index with dp/dt max, PVR, and Ees are 0.5878, 0.6033, and 0.4321, respectively.

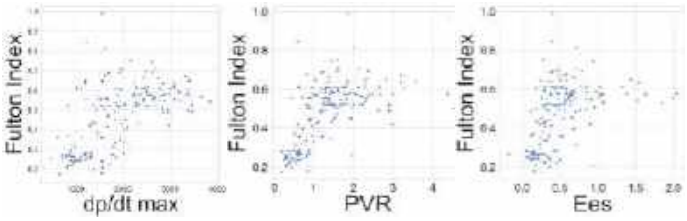

Figure 2: Strong linear correlations between hemodynamics parameters dp/dt max (left), PVR (middle), and Ees (right) and Fulton Index.

DISCUSSION

This study employed ML and data visualization tools to identify defining variables specific to different groups and uncover inter-categorical correlations. The SVM demonstrated exceptional accuracy in the early weeks, needing further fine-tuning to enhance prediction at the later weeks (weeks 8 and 12). Despite the limitations of a dataset with diverse y variables (weeks of treatment), the 70% accuracy achieved is noteworthy, particularly given previous SVM work mainly addressed binary y variables (hypertensive *vs.* normotensive).

The model also revealed distinctive characteristics of non-hypertensive SuHx rats. The right and left atrial masses were lower in non-hypertensive SuHx rats relative to hypertensive SuHx rats. Also, hypertensive SuHx animals displayed elevated values for the Fulton index and RV thickness compared to non-hypertensive SuHx rats, confirming increased right ventricular remodeling as hypothesized.

Also, the metric exploration study revealed correlations between non-invasive measurement of the Fulton Index with key hemodynamics metrics such as dp/dt max, PVR, and Ees. These three parameters are clinically collected invasively through cardiac catheterization. PVR is used as a PAH disease indicator while dp/dt max and Ees are informative variables that help physicians understand chamber stiffness. This finding holds significance by potentially mitigating the invasiveness associated with clinical PAH diagnosis. However, further research is required to unravel the underlying mechanisms and explain the medical relevance of these relationships.

Recent studies of PAH have found success leveraging SVM to perform gene expression categorization and screening for early-stage PAH diagnosis [4]. While this ML-oriented study highlights key correlations and defining parameters within our animal dataset, future improvements are required. These include acquiring and expanding our dataset to eliminate imputations and allowing the implementation of multilayer perceptron (MLP) neural networks that provide flexibility of capturing complex relationships through advanced feature learning and nonlinear transformations.

ACKNOWLEDGEMENTS

Funding provided by NHLBI 1R01HL155945-01 and NSF CAREER Award 2046259.

REFERENCES

[1] M. M. Hoeper *et al.*, *J Heart Lung Transplantation*, 39(12), 2020.
[2] P. Rambarat *et al.*, *PLoS One*, 18(8), 2023.
[3] ED Kwan et al., Am J Physiol Heart Circ Physiol, 321(4), 2021.
[4] Z. Shang *et al.*, *Front Genet*, 2021.

REGIONAL, ADJUSTABLE PRESSURE PROSTHETIC SOCKETS FOR TRANS-FEMORAL AMPUTEES

C. Rodriguez Rozas (1), K. Bindas (2), K. LeClaire (3), M. Viteri (4), S. Waymer (5)

Faculty Advisor(s)

G. Fiedler (1), M. Gartner (2)

(1) Bioengineering, University of Pittsburgh, Pittsburgh, Pennsylvania, United States of America
(2) Department of Rehabilitation Science and Technology, University of Pittsburgh, Pittsburgh, Pennsylvania, United States of America

INTRODUCTION

Lower-limb loss, whether resulting from trauma, disease, or conditions like diabetes, poses significant challenges for individuals. A key determinant of post-amputation quality of life and independence is the acceptance or rejection of the prosthesis. A primary factor influencing rejection rates is the promptness of prosthetic fitting, notwithstanding immediate concerns such as surgical risks and wound healing. In addition to typical surgical risks like infection and anesthesia complications, amputation technique lacks standardization. Surgeons not specialized in limb preservation and prosthetic optimization may differ in their choices for factors like nerve reinnervation, tendon balancing, or residual limb length. A poorly executed amputation can lead to pain, discomfort, and impeded healing, which delays rehabilitation.

The critical recovery period spans the initial six weeks post-surgery, where recovery emphasizes infection prevention, pain management, and early rehabilitation. Fitting a prosthetic limb during this phase is pivotal and correlates with a higher acceptance rate of the device [1]. The use of a shrinker, which reduces swelling and assists in shaping the limb, is standard during this phase. While 17-35% muscle volume will decrease in the initial six months, amputees will face daily and lifelong limb volume fluctuations, impacting prosthetic fit and comfort [2].

Prosthetic fit is further complicated by rigid, static sockets conflicting with dynamic body properties. Developing an interface that supports the rigid socket while allowing dynamic volume and pressure variations in the residual limb would enhance prosthetic comfort and has long been an objective of respective development efforts [3]. However, current adjustable sockets hold inherent problems such as unequal pressure distribution, increased discomfort, improper fit, and mechanical malfunctions persist and are pervasive across all current available sockets on the market. Creating an adjustable socket that allows the user to adjust the device based on current discomfort and fit could reduce rejection rates, necessitating fewer adjustments and increasing prosthetic longevity.

PRODUCT DESIGN

Our innovative socket design is characterized by two distinct sub-systems (Figure 1). The first is a rigid outer shell made in the conventional lamination technique, providing enhanced support and stability. Second, the inner liner consisting of four air cells made of double walled vinyl plastic, encased by a nylon sheath, lining the inside of the shell, each individualized for independent control of air inflow/outflow.

Figure 1: Prosthetic Socket with Inner Liner

To create the air flow, an air valve was placed to the exterior of each airbag, establishing a closed system for air inflow/outflow. For best user interaction, holes were created in the outer shell such that the valve protrudes through the thickness of the socket. Each valve can be individually affixed to a miniature electric air pump, which is light enough for the user to easily attach/deattach to each valve.

We evaluated the capacity of three customizable designs to distribute air most effectively towards the bottom of separate airbags. This was imperative due to our observation of a higher concentration of soft tissue towards the proximal end of the residual limb as opposed to the distal

end. Following informal tests, a zig-zag design presented itself as the optimal choice, with triangular shaped slits along each side of the cell, demonstrating superior air redistribution capabilities (Figure 2).

Figure 2: Zig-Zag Air Bag Pattern

Following the selection of an effective air redistribution method, we transitioned from positioning the air tubing at the top of the bag to a configuration where valves are placed at the bottom of the bag (Figures 3,4). This allows for a better user interaction with the adjustability features.

To minimize direct contact between airbags and human skin, we introduced a nylon sheath casing around the airbags, enhancing durability. Differing from figure 3, in our updated design, the air cells are no longer attached to each other, instead, the nylon casing lines the socket. The casing includes four pockets, that can be opened and closed, designed for individual insertion and extraction of an air bag in each pocket, designed in the event of an airbag malfunction.

Figures 3 (left) and 4 (right): Air Bags Within Nylon Casing

Current adjustable sockets hold inherent problems such as unequal pressure distribution, increased discomfort, improper fit, and mechanical malfunctions persist and are pervasive across all current available sockets on the market. Our socket poses to avoid these issues by completing mechanical testing on the air bags for design strength and ensuring that there is ideal quality control on the seals of the air bags

Technical feasibility of our devices includes qualification testing to account for all of our design specifications to meet the pre-determined acceptance criteria that has been established by the design team. Examples of verification tests include testing the pressure strength of the air bags, testing the mobility, usability, and cleanability of the socket system.

BUDGET & MARKET ANALYSIS

Our allocated budget for this project, spanning across our two-semester Senior Design course, amounted to $1500. As we near the completion of our design, our expenditure stands at a modest $600, covering all design ideations and prototypes thus far.

In terms of market potential, our target audience comprises individuals who are current trans-femoral amputees. Within the United States, this demographic represents approximately 18.5% of the 1.9 million individuals with limb loss, totaling around 350,000 people [4]. From a market perspective, the cost per unit in small-scale production ranges between $8 and $12, contingent upon the precise fitting for the individual's residual limb size. However, in larger-scale production, the cost per unit decreases significantly to between $4 and $8 due to economies of scale. The production process necessitates heat sealing and sewing, with an estimated investment of approximately $100 for efficient equipment on a smaller scale.

Each unit has the potential to add a value of $75, exclusive of the molded hard socket and liner. Estimating our return on investment, with an initial investment of $300 and a projected return of $500 over the course of a year, yields a potential return of approximately 67%.

ACKNOWLEDGEMENTS

We would like to thank Dr. Fielder (Dept. Rehabilitation Science and Technology) for providing valuable support and advice, Dr. Mark Gartner (Dept. Bioengineering), Sarah Frazier-Kim, The Pittsburgh Amputee Support group, University of Pittsburgh's SHRS Orthotics & Prosthetics School, and the Swanson Center for Product Innovation for their gracious contributions and support throughout our design.

REFERENCES

[1] Sanders, JE et al., *J Rehabil Res Dev,* 48(8):9449-9986, 2015.
[2] Ding, Z. et al., *J Biomech*, 149:111484, 2023.
[3] Abd Razak, N.A. et al., *Biomed Res Int,* 2022:9, 2022.
[4] Liu, Hangsheng et al., *Rand Corp,* 2017.

LAPPI: THE LIP AND PALATE PROSTHETIC INTERFACE

Serena Carson, Ryan Lim, Ravikiran Ramjee, Andrea Urdaneta, Camilla Whitesel

Faculty Advisor(s)

Dr. Eugene Ko (1), Stefanie Modri (2)

(1) Penn Dental Medicine, Philadelphia, PA, USA
(2) Children's Hospital of Philadelphia, Philadelphia, PA, USA

INTRODUCTION

Cleft lip and/or palate (CLP) is an orofacial birth defect that occurs when a baby's lip and hard palate tissue do not fuse. The manifestation of a cleft lip is an opening in the upper lip, characterized by either one gap in the tissue (unilateral) or two gaps in the tissue (bilateral). The manifestation of a cleft palate is an opening in the roof of the mouth from gaps in the tissue of the hard palate.[1] An immediate concern of CLP in infants is feeding, with CLP infants often unable to breastfeed or traditionally bottle feed.[2] Specifically, CLP infants are unable to create the pressure necessary for breastfeeding (4 psi) and cannot create a true seal around the tip of a baby bottle. CLP causes nasal regurgitation and swallowing of air during feeding.

To treat CLP, reconstructive surgeries can be performed once infants meet certain biomarker thresholds, including age and weight. However, CLP infants are consistently below the 50th percentile for weight up to 5 months of age from inadequate nutrition uptake, which can delay surgery.[3] Current feeding solutions seek to improve feeding efficacy for CLP infants. These include specialized bottles, notably Dr. Brown's 'Specialty Feeding System' and the 'Pigeon Feeder Bottle'. These bottles feature a one-way valve to prevent milk from flowing back into the bottle and allow infants to bite the bottle nipple to receive milk. However, Dr. Brown's bottles are not made specifically for CLP and babies still experience significant regurgitation.[4] With the 'Pigeon Feeder Bottle,' infants experience regurgitation and caretakers must often squeeze the bottle to feed with force. Caretakers are thus forced to resort to feeding techniques to hold the cleft closed while feeding, an inconsistent and ineffective solution. While there are products marketed to allow for bottle feeding, there is no solution that allows CLP infants to breastfeed, preventing them from capitalizing on benefits of immunity, self-regulation, and bonding.[5]

PRODUCT DESIGN

LAPPI, the Lip and Palate Prosthetic Interface, aims to enable a variety of feeding options for infants with CLP, allowing for proper suction and minimal fluid loss to regurgitation. LAPPI is a set of two products to allow infants with CLP to feed with regular bottles and to breastfeed. LAPPI's design consists of a lip cover that occludes the cleft lip and a palate cover that occludes the hard palate (Figure 1). The design of the palate cover intentionally covers a large portion of the roof of the mouth to account for most palate defects. This design choice reflects LAPPI's goal of accessibility, with a generic shape that caregivers can use for most infants within a certain size range. The lip and palate covers are not designed for specific cleft openings or manifestations but will be adjusted in size to fit most presentations of CLP in infants. LAPPI for bottle-feeding (Figure 1A) includes a one-way valve to reduce backflow whereas LAPPI for breastfeeding (Figure 1B) has an open bottom to allow for movement of the mandible. During feeding, caregivers will place LAPPI into the infant's mouth and can use any standard bottle or breast shield product to feed. LAPPI will be made of BPA-Free and FDA-approved food-grade silicone, allowing for s sterilization.

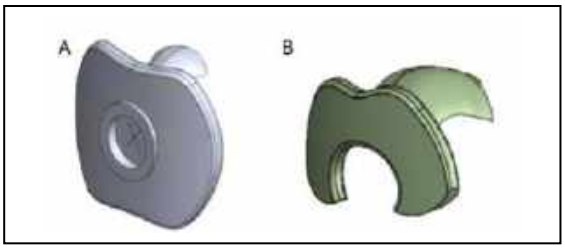

Figure 1: (A) LAPPI for bottle-feeding (B) LAPPI for breastfeeding

LAPPI's Minimum Viable Product (MVP) included a lip and palate cover that was printed in elastic resin. Elastic resin mimicked food grade silicone's flexibility and heat resistance. A 1:1 scale bilateral CLP infant head model was 3D printed in elastic resin and used to create a pressurized bottle-feeding model (Figure 2).

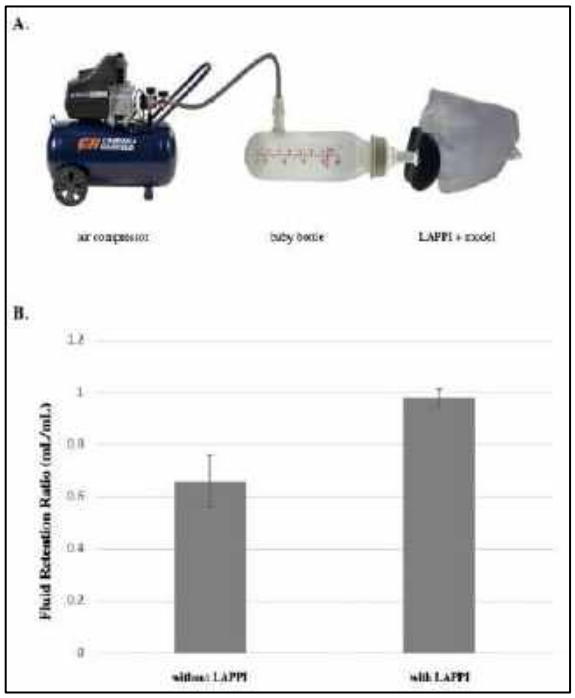

Figure 2: (A) LAPPI for bottle-feeding MVP testing setup (B) LAPPI fluid retention data (n=5, error bars represent standard deviation.

An air compressor was used to create pressure in a standard baby bottle to indirectly create the pressure difference in the oral phase of feeding. The CLP model had two pathways for fluid travel: one representing retained liquid through the esophagus and another representing fluid lost to regurgitation/leakage. The MVP performance was evaluated by analyzing the fluid retention ratio, or the amount of fluid down the esophageal pathway compared to the total amount of fluid through the model. The ratio with LAPPI was significantly higher than without LAPPI, demonstrating its efficacy in occluding the CLP. To preliminarily test LAPPI's efficacy with breastfeeding, a testing setup with a breast model and a syringe pump was made to replicate the pulsatile movement of milk through the breast duct (Figure 3). The fluid retention ratio was calculated with and without LAPPI. Again, LAPPI significantly increased fluid retention.

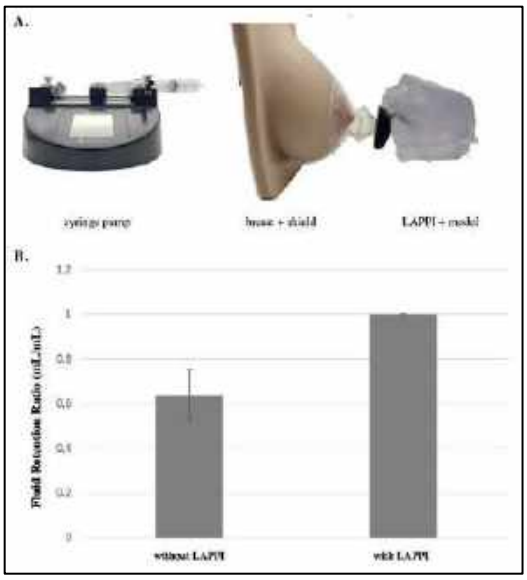

Figure 3: (A) LAPPI for breastfeeding MVP testing setup (B) LAPPI fluid retention data (n=5, error bars represent standard deviation.)

BUDGET & MARKET ANALYSIS

Through the bioengineering department at the University of Pennsylvania, LAPPI has been given a flexible budget of a minimum of $600. To date, LAPPI has spent $210 on equipment used to validate the solution. Current versions of LAPPI have been 3D printed in polylactic acid (PLA) and elastic resin which have been provided by the University of Pennsylvania.

Given the monetary and logistical burden of caring for a CLP infant before and during reconstructive surgery, a solution to occlude CLP defects and allow for stable breast and bottle feeding at a minimal resource burden is paramount. There is a clear place for such a solution in the market, as the current global CLP surgery market is valued at around $408.4 million USD and is expected to grow at a compound annual growth rate of 5% by 2030.[6] To facilitate the feeding of CLP infants, the solution must be compatible with both breast and bottle feeding and be an inexpensive device. The devices must be sterilizable and able to withstand temperatures above 235 ℃. To implement this device, it must be biocompatible and made with FDA approved materials.

Production costs rely on the current price of food-grade silicone that can be used in the molds to create LAPPI. Currently, we aim to have 10 bottle-feeding and 10 breastfeeding-compatible LAPPI devices by mid-March with an initial expense of $200 (estimated from the cost to rent the space and tools required). Once the first several casts and molds are completed, LAPPI production can be scaled up with additional varying costs being food-grade silicone. This limited overhead allows LAPPI to sell for less than $20.

The LAPPI solution will relieve caregivers of the burden of implementing specific CLP feeding techniques as well as increasing feeding efficiency and allowing for more fluid retention. This will enable reconstructive surgery with minimal delay, alleviating CLP for infants without complication and achieving less frequent medical and lactation consultant visits and expenses.

ACKNOWLEDGEMENTS

We thank the Stephenson Foundation BioMaker Space and the University of Pennsylvania Rapid Prototyping Laboratory for allowing us to use their space and resources. We thank Jacqueline Baselier for sharing their CLP infant head model and the University of Pennsylvania Education Commons for 3D printing for us in elastic resin. We thank the Children's Hospital of Philadelphia (CHOP) for providing pacifiers and as a source for CLP clinicians and caregivers.

REFERENCES

[1] Kosowski,, T. R., Weathers, W. M., Wolfswinkel, E. M., & Ridgway, E. B. (2012, November). Cleft Palate - PMC. NCBI. Retrieved December 17, 2023, from https://www.ncbi.nlm.nih.gov/pmc/articles/PMC3706041/

[2] Riley, J. W. (2011, February 16). Feeding interventions for growth and development in infants with cleft lip, cleft palate or cleft lip and palate. NCBI. https://www.ncbi.nlm.nih.gov/pmc/articles/PMC7144736/

[3] Da Silva Freitas, Renato, et al. "Weight gain in children with cleft lip and palate without use of palatal plates." *Plastic Surgery International*, vol. 2012, 2012, pp. 1–4, https://doi.org/10.1155/2012/973240.

[4] Danelz, A. (n.d.). Cleft Lip/Cleft Palate: Feeding Your Child (for Parents) - Nemours KidsHealth. Kids Health. https://kidshealth.org/en/parents/clefts-feeding.html

[5] Dieterich, C. M. (2014, February 1). Breastfeeding and Health Outcomes for the Mother-Infant Dyad. NCBI. https://www.ncbi.nlm.nih.gov/pmc/articles/PMC3508512/

[6] Cleft Lip Surgery Market Size, Share & Trends Report, 2030. (n.d.). Grand View Research. https://www.grandviewresearch.com/industry-analysis/cleft-lip-surgery-market-report

EASY-O: LOW-COST OXYGEN THERAPY UNIT

E. Kim (1), K. Hara-Lee (2), A. Gammage (3), D. Gaw (4), S. Packer (5), M. Jones (6), A. Donoso (7)

Faculty Advisor(s)

X. Wang (1)

(1) Department of Chemical Engineering, Queen's University, Kingston, ON, Canada
(2) Department of Mathematics and Statistics, Queen's University, Kingston, ON, Canada
(3) Department of Mechanical and Materials Engineering, Queen's University, Kingston, ON, Canada
(4) Department of Electrical and Computer Engineering, Queen's University, Kingston, ON, Canada

INTRODUCTION

In sub-Saharan Africa's low-resource healthcare centers, intermittent electricity supply restricts medical interventions, particularly oxygen therapy for patients, during crucial evening hours. The generator only operates during surgeries, leaving hospitals without power most nights. After 13 hours, the generator cannot be restarted, endangering patients experiencing respiratory distress [1]. The prohibitive costs of battery-powered oxygenators exacerbate the issue. These challenges underscore the urgent need for affordable and sustainable solutions to ensure consistent access to crucial medical treatments in areas with unreliable power sources.

Oxygen concentrators draw room air through filters to produce oxygen-rich air, which is then delivered to patients. These units cost approximately USD 2,000, and require constant electrical connection, as well as frequent filter replacements and regular servicing [2]. In low-resource settings, maintenance may be unavailable or improper. A study in southwest Nigeria found that out of 57 concentrators within a facility, only 2 were fit for use, with many blowing room air rather than medical oxygen [3]. Compressed gas cylinders are also used for oxygen therapy; these systems can function without an electrical connection. Compressed gas cylinders also offer the benefit of minimal maintenance being required [2]. This method of oxygen therapy administers a single flow rate of oxygen which must be manually set.

The creation of an oxygen therapy unit that implements the most advantageous features of oxygen concentrators and compressed gas cylinders would benefit low-resource healthcare centers worldwide. The focus of this design is to ensure that it is low-cost, compact, and user-friendly. These criteria aim the project toward low-resource healthcare centers, specifically those with unreliable power sources.

PRODUCT DESIGN

The proposed solution aims to address the needs of stakeholders through the development of a low-cost, battery-operated oxygenator capable of operating for 14 hours without requiring an electrical connection. This is greater than the maximum continuous operating time of oxygen concentrators, which is 12 hours [2]. Healthcare workers can interact with the oxygenator via an app presented on a digital display mounted onto the unit. The app, running on a Raspberry Pi, offers two modes: manual, allowing healthcare workers to set the desired oxygen flow rate, and automatic, utilizing PID control. Real-time patient data, including oxygen saturation [%] as a plot, pulse [bpm], and oxygen flow rate [L/min], are displayed on the interface. A pulse oximeter gathers oxygen saturation data from the patient and sends the raw data to an Arduino, which then communicates it to the Raspberry Pi.

Oxygen is delivered from a pressurized tank through medical-grade tubing to a Venturi mask or nasal cannula for patient administration. The flow regulator being used to control the oxygen stream allows for flow rates between 4 and 15 L/min, as required for in-hospital use. A solenoid valve then regulates oxygen delivery for PID control and is monitored by an in-line gas flow sensor. A humidifier will be implemented to reduce the risk of respiratory mucosa lesions, caused by the dry properties of oxygen gas [4]. The system is battery-powered, using switching voltage regulators for different component voltages. Components are housed in a Meijia case using 3D printed mounts, designed to ensure airflow and prevent overheating, aided by a two-fan system. This compact design facilitates easy transportation within the healthcare center.

The mounts for all components have been modeled utilizing Fusion360 software and a full model of the oxygenator layout is being assembled. The waterproof Meijia case can be seen in Figure 1.

Figure 1: Meijia case with dimensions of 25 x 19.41 x 8.61 inches.

The app's skeleton code, created using CustomTkinter in Python, can update values live via a PySerial connection with the Arduino and can run on the Raspberry Pi. The electrical system design and schematic have also been created. The graphical user interface (GUI) can be seen in Figure 2.

Figure 2: GUI displaying the layout of all live data and limiting values, manual mode is not displayed.

The pulse oximeter module circuit is fully implemented, with other modules and code development ongoing. Key verification metrics for oxygen delivery have also been identified to check key performance indicators such as humidity levels and verification of flow rates. A schematic of the oxygenator system can be seen in Figure 3.

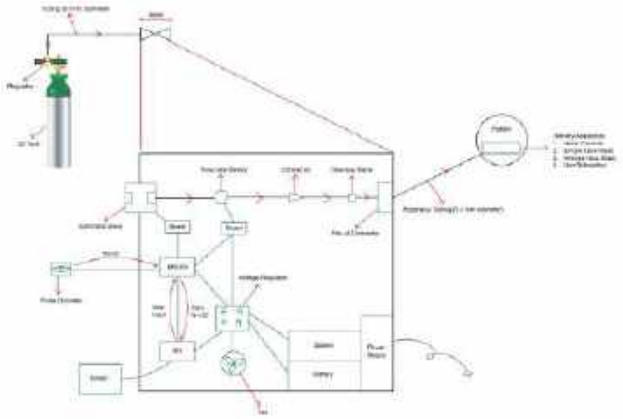

Figure 3: Schematic of the oxygenator system, indicating the flow of oxygen and interactions between all components.

BUDGET & MARKET ANALYSIS

The total design budget for the oxygen therapy unit is CAD 1,000. The cost of materials for the prototype is CAD 800, which accounts for all parts needed for assembly. CAD 100 has been allocated to the assembly of the prototype, and an additional CAD 100 accounts for any costs associated with testing. To remain accessible to low-resource healthcare centers, a markup of 15% will be implemented, or a total of CAD 1,150.

The COVID-19 pandemic highlighted the continual inequity in access to medical oxygen therapy, especially in resource-limited settings, and the need for improvements to prevent unnecessary deaths [3]. The World Health Organization reported that only 28% of health facilities and 34% of hospitals in sub-Saharan Africa have access to reliable electricity [3]. Oxygen-requiring diseases and conditions also account for 1.75 million annual deaths in these locations [3]. There is a major need for accessible oxygen therapy within the target market of low-resource healthcare centers in sub-Saharan Africa. There is also a worldwide need for the product, emphasized by the global market for medical oxygen concentrators being valued at USD 1.75 billion in 2018 [2]. This value was projected to expand at an annual growth rate of 7.4% from 2019 to 2025 [2].

NEXT STEPS

The pathway forward for this project includes a multi-faceted approach aimed at creating an impactful solution for providing consistent access to medical oxygen therapy in resource-constrained settings. First and foremost, we will continue to refine and test the prototype, focusing on optimizing individual components and integrating them into a functional unit. A component of interest is the pulse oximeter, and the accuracy of the oxygen saturation readings depending on a patient's ethnicity and existing health conditions. The oxygen saturation of patients with dark skin tones can be overestimated by up to 2%, increasing the risk of unrecognized hypoxemia [5]. Falsely elevated readings can also occur in cases involving conditions such as anemia [6]. Throughout rigorous testing, we aim to ensure the reliability and efficiency of the system under various conditions.

By exploring innovative design strategies and sourcing cost-effective materials, we aim to make a solution that is affordable for healthcare facilities in low-resource settings, without compromising performance standards. The goal of this project is to have it brought to market and implemented in low-resource healthcare centers throughout sub-Saharan Africa.

ACKNOWLEDGEMENTS

We thank the members of the QBiT for their work on this project and review of this abstract. We are grateful for funding from Dean Kevin Deluzio, and the Sci'73 Foundation.

REFERENCES

[1] F.N. Jaeger, M. Bechir, M. Harouna, D.D. Moto, J. Utzinger, Challenges and opportunities for healthcare workers in a rural district of Chad, BMC Health Services Research 18 (2018) 7. https://doi.org/10.1186/s12913-017-2799-6.

[2] G. Hardavella, I. Karampinis, A. Frille, K. Sreter, I. Rousalova, Oxygen devices and delivery systems, Breathe (Sheff) 15 (2019) e108–e116. https://doi.org/10.1183/20734735.0204-2019.

[3] M. Ross, S.K. Wendel, Oxygen Inequity in the COVID-19 Pandemic and Beyond, Glob Health Sci Pract 11 (2023) e2200360. https://doi.org/10.9745/GHSP-D-22-00360.

[4] V. La Fauci, G.B. Costa, A. Facciolà, A. Conti, R. Riso, R. Squeri, Humidifiers for oxygen therapy: what risk for reusable and disposable devices? J Prev Med Hyg 58 (2017) E161–E165.

[5] K.D. Torp, P. Modi, E.J. Pollard, L.V. Simon, Pulse Oximetry, in: StatPearls, StatPearls Publishing, Treasure Island (FL), 2024. http://www.ncbi.nlm.nih.gov/books/NBK470348/ (accessed February 13, 2024).

[6] M.S. Weekley, L.E. Bland, Oxygen Administration, in: StatPearls, StatPearls Publishing, Treasure Island (FL), 2024. http://www.ncbi.nlm.nih.gov/books/NBK551617/ (accessed February 13, 2024).

REINFORCING SAFE WALKER USE: A UNIVERSAL 2-WHEEL WALKER MONITORING DEVICE

Ashwin V. Gadiraju (1), Pradnesh C. Kolluru (1), Sunggun Lee (1), Cecelia J. Rodriguez (1), Nick G. Tsintolas (1)

Faculty Advisor(s)

Dr. Aaron Kyle (1), Dr. Eric Richardson (1), Matt Brown (1)

(1) Biomedical Engineering Department, Duke University, Durham, NC, USA

INTRODUCTION

In the United States, falls are the leading cause of injury-related death among adults ages 65 and older [1]. Despite their goal of assisting with senior mobility, walkers have been implicated with the vast majority (87%) of the nearly 50,000 mobility-aid related falls treated in US emergency departments annually [2]. Of the various forms of walkers available, 2-wheeled (2W) walkers (aka 'front wheeled walkers') are some of the most commonly prescribed mobility aids for users who lack upper body strength but still require adequate stability and support [3]. Despite their prevalence in hospitals and residences across the country, these 2W walkers have proven to be highly susceptible to misuse, consequently increasing the risk of falls and injury for a population that is already vulnerable [4], [5].

Confirmed by previous studies and dozens of interviews with physical therapists (PTs), nurses, walker users, and caretakers, it was found that there are three primary cases in which these 2W walkers are misused: 1. Lifting the walker (instead of gliding at all times) [4], 2. Standing too far back from the walker [6], and 3. Turning the walker too rapidly. See Figure 1 for a diagram of these failure modes. While this misuse can easily be observed and corrected in an in-patient setting, the issue arises when considering that the majority (60.9%) of these walker-related falls occur at home [2].

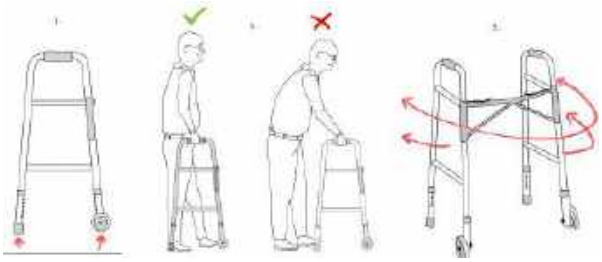

Figure 1. Common Cases of Improper 2W Walker Use

When examining the potential causes of this misuse, a gap in user training and follow-up regarding proper 2W walker use becomes apparent. One study indicated that out of 158 rolling walker users surveyed at a senior living community, only 20% of them were provided with instructions on how to use their devices. Moreover, only 1% of these users were provided with walker reassessment following initial prescription/use [7]. This lack of sufficient training becomes particularly relevant in the context of our conversations with community stakeholders. Multiple PTs and walker-users noted that the prevalence of lifting 2W walkers may be due to confusion between standard 4-legged walker guidance (to lift between every step) and 2W walker guidance (to maintain contact with the floor at all times). The general lack of training and feedback coupled with user confusion between walker-types has likely resulted in the widespread misuse in 2W walkers that is observed today.

In the past decade, a range of advanced walker sensing systems have been developed [8]. Despite their immense potential, these devices either target to replace rollators (4-wheels) as opposed to 2W walkers, attempt to reinvent the walker through expensive, bulky, over-engineered 'smart-walker systems' (that may require entirely new training protocols to use), and/or regularly fail to make it out of research phases due to their inability to integrate with current products. This lack of integration creates an immediate barrier to commercialization. Hospitals and users are less likely to purchase entirely new sets of expensive 'smart walkers' as compared to a mere attachment to existing 2W walkers. More importantly, there are no existing devices that monitor 2W walker lifts, user positioning, and rapid turns.

The prevalence of hospitalizations, misuse, and lack of training related to 2W walker use, particularly in home environments, warrants an immediate solution. With this, there is a strong need for a universally mounting device to continuously monitor and provide feedback for improper 2W walker use to facilitate tailored training interventions and ultimately reduce the risk of falls for patients.

PRODUCT DESIGN

We propose a novel monitoring device that incorporates sensing, feedback, and evaluation of improper 2W walker use. The device utilizes a combination of sensors that can be readily added to the walker to detect lifts, improper positioning, and rapid turns. The mechanical design of the device allows for secure, snap-on mounting to any existing 2W walker design (see Figure 2.) Finally, all monitoring data can be wirelessly transmitted to a secure database for easy mobile phone visualization (for users, caretakers, or healthcare workers).

Figure 2: 2W Walker Monitoring Device Design

To detect lifting of the 2W walker, an ultrasonic (US) sensor is positioned to monitor the height of the walker from the ground and sense when there is an acute increase in distance from the calibrated baseline height. For positioning, an infrared (IR) proximity sensor is placed along the back leg of the walker to face the user at mid-thigh level. Here, it can detect when users are within an appropriate range to quickly diagnose and inform users of unsafe postures. Lastly, an inertial motion unit is used to identify rapid walker turns.

The device also incorporates auditory, visual, and haptic feedback. Auditory feedback is provided with a speaker within the center module. Visual feedback is in the form of an OLED display and LED lights. Finally, haptic cells are mounted onto the aluminum framing of the walker to allow for subtle, yet noticeable vibrations when incorrect use is detected. In addition to the immediate feedback provided to users, historical usage data can be paired with a mobile app for easy visualization by healthcare personnel or users.

This design includes two primary modules that house and securely tether all the electronic components to a user's previously purchased or prescribed 2W walker. The center module (module 1 as annotated in Figures 2 and 3) contains a microcontroller, two US sensors, a centrally mounted gyroscope/accelerometer, and all the feedback methods described previously. Module 2 houses the IR proximity sensor to monitor proper user positioning. These two casings are tethered with a single cable that can be tied to the aluminum framing of the 2W walker.

Figure 3: Isolated Views of Design Modules

BUDGET & MARKET ANALYSIS

Table 1 below summarizes the anticipated budget required to complete the design, manufacturing, and testing of our device to prepare for commercialization. These numbers are calculated based on individual component prices and estimations provided by our faculty advisors.

Table 1: Anticipated Design Budget

DESIGN PHASES	*ESTIMATED COST*
Total Material Cost	$4,000
Contract Manufacturing	$5,000
Testing & Regulatory Approval	$5,000
	$14,000

The market for 2W walkers accounts for 20-30% of the total assistive walking device market, with a valuation of roughly $380M and servicing 320M people [9]. The rising geriatric population indicates this market is expected to grow at a compounded annual growth rate (CAGR) of 7.1% [10]. Since this is a reusable device, annual sales will be limited by a lack of repeat customers. As such, annual sales can be estimated at 500,000 units sold per year.

In bulk, the expected fabrication costs will be approximately $60 per unit. The medical device business model includes high margins of around 60-80%, so the device could reasonably be priced at $200, which is similar to other "smart" walkers. Medicare Part B covers walkers and other assistive devices under its durable medical equipment (DME) policy. Elderly patients will pay 20% of the Medicare-approved amount [11].

The expected return on investment for each unit is $100-$140, which could be reinvested into manufacturing, engineering, or market expansion.

ACKNOWLEDGEMENTS

We would like to thank our senior design teaching assistants Paris Brown, and Lokesh Kumar Manivannan for their guidance. Prototyping funding and resources were graciously provided by the Duke Pratt School of Engineering Biomedical Engineering Department

REFERENCES

[1] R. S. Kakara, et al., Public Health Rep., 139:54–58, 2024.
[2] J. A. Stevens, et al., *J. Am. Geriatr. Soc.*, 57:1464–1469, 2009.
[3] C. Sadowski, et al., *Pharm. Pract.*, 1:24–31, 2014.
[4] S. B. Thies et al. *BMC Geriatr.*, 20:90, 2020
[5] S. Thomas *et al.*, *J. Physiother.*, 56:267–272, 2010
[6] Mayo Clinic, "Tips for choosing and using walkers"
[7] H. (Howe) Liu, *Geriatr. Gerontol. Int.*, 9:124–130, 2009
[8] X. Zhao et al., *Front. Neurorobotics*, 14, 2020
[9] World Health Organization, "Ageing and health."
[10] GWR, "Walking Aids Market Size & Share Report, 2022 - 2030."
[11] Medicare.gov, "Walkers For Seniors Coverage."

KINEMATIC SENSITIVITY STUDY OF TOTAL KNEE REPLACEMENT FEA MODEL TO LIGAMENT ATTACHMENT SITE

Elizabeth A. Wynn (1,2), Takayuki Koya (1,3), Markus A. Wimmer (1), Hannah J. Lundberg (1), Steven P. Mell (1)

(1) Rush University, Chicago, IL, USA
(2) University of Illinois at Chicago, Chicago, IL, USA
(3) Showa University Koto Toyosu Hospital, Tokyo, Japan

INTRODUCTION

The demand for total knee replacements (TKRs) has increased significantly in the past decade as the number of TKR procedures has grown from 402,100 to 1.38 million [1]. As the number of TKRs performed each year increases, long-term failure due to mechanical failure, polyethylene wear, and instability remains a prominent concern [2]. In addition, the influence of ligament properties on knee kinematics is not well understood. Computational modeling and finite element analysis (FEA) can be used to better understand TKR failure and instability. To design such a model, a previously published and validated model of TKR contact was modified to include the LCL, MCL, and PCL ligaments [1]. However, it is important to characterize computational models by performing sensitivity studies to reduce the number of parameters required to be varied in future studies. Therefore, the goal of this study was to determine how changing the ligament attachment sites of the LCL, MCL, and PCL impacts knee translation and rotation during flexion, in a computational model of a TKR with realistic ligament properties. To accomplish this goal, a sensitivity study was performed by varying ligament attachment sites using Latin Hypercube Sampling Design of Experiments (LHS DOE), and multiple linear regression analysis was done to understand the sensitivity of attachment site on the maximum anterior-posterior (AP) translation and minimum internal-external (IE) rotation during flexion.

METHODS

FEA Model. A previously published and validated FEA cruciate retaining TKR model was modified to include three ligaments that are kept intact after TKR surgery: the LCL, MCL, and PCL (Figure 1). The tibial component was modeled using 78,108 linear hexahedral elements (C3D8R). The femoral component was modeled using a combination of 4080 quadratic quadrilateral elements (SFM3D8) and 547 quadratic triangular elements (SFM3D6). Contact between these components was modeled using surface-to-surface contact with a 0.04 coefficient of friction. The ISO 14243-1 force control standard was applied as boundary conditions to the FEA model. Flexion was applied to the femur which was otherwise fixed. AP force, axial force, and IE moment was applied to the tibial component. Abduction-adduction and medial-lateral translation of the tibial component were left free.

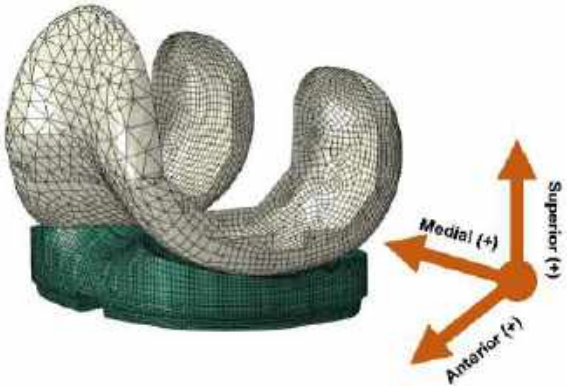

Figure 1: Finite element model. Left-side NexGen CR TKR (Zimmer Biomet).

Parametric Study. To determine the sensitivity of the model kinematics to ligament attachment site, a parametric study was performed. First, the approximate radius of each ligament attachment site was calculated from the average attachment site area and was used as the parameter bounds for a LHS DOE approach [5,8,9,11]. The starting location for each ligament was determined from previous literature [5-11] and confirmed by a trained orthopaedic surgeon. Attachment site locations were then varied parametrically within the determined attachment stie area. Parameters included the superior and inferior attachment points of each of the 3 ligaments, along 3 translational directions, for a total of 18 parameters. The outputs of the

study included the maximum AP translation and maximum IE rotation of the tibial component. A total of 274 simulations were performed.

Ligament Properties. Ligaments were modeled as linear connector elements with a stiffness defined according to previous literature: LCL 59 N/mm, MCL 63 N/mm, and PCL 198.9 N/mm [3-4]. The average length and attachment site areas for each ligament were also obtained from previous literature [5-11]. The LCL had an average length of 69.6 mm, an average femoral attachment site area of 48 mm^2, and an average fibular attachment site area of 43 mm^2 [5]. The PCL had an average length of 37.1 mm, which was calculated by taking the average length between the anterolateral and posteromedial bundles of the PCL, 35.5 and 38.7 mm, respectively [6]. The PCL had an average femoral attachment site area of 209 mm^2 and an average tibial attachment site area of 243.9 mm^2 [8,9]. The MCL had an average length of 94.8 mm, an average femoral attachment site area of 79.7 mm^2, and an average tibial attachment site of 348.6 mm^2 [10,11].

Statistical Analysis. Multiple linear regression analysis was performed using MATLAB v2022b on the total AP translation and total IE rotation throughout the gait cycle. Sensitivity of ligament attachment site on the resulting kinematic parameter was defined as the maximum change in the resulting kinematic parameter due to the change in attachment site parameter.

RESULTS

226 out of 274 FEA simulations successfully converged. Failed jobs had the femoral component fall off the edge of the tibial insert. AP translation was sensitive to six ligament attachment site parameters, five of which were related to the PCL attachment points (R^2 = 0.794, p<<0.001, Figure 2). IE rotation was sensitive to thirteen attachment site parameters across all ligaments (R^2 = 0.842, p<<0.001, Figure 3).

DISCUSSION

The purpose of this study was to modify an existing FEA TKR model to incorporate the LCL, MCL, and PCL ligaments with realistic ligament properties, with the long-term goal of understanding the influence of ligament attachment sites, and properties on knee kinematics. It is important to understand the influence of ligament properties on knee kinematics in order to address TKR failure and instability. In this study, LHS DOE techniques followed by multiple linear regression analysis was performed to determine model sensitivity to ligament attachment site parameters. Our results indicate that TKR predicted AP translation is highly sensitive to the location of the PCL ligament. TKR predicted IE rotation was highly sensitive to the location of the attachment points of several ligaments, with the highest effect due to the location of the PCL. A total of 14 out of 18 parameters achieved statistical significance for at least one of the outputs investigated, indicating that not all ligament attachment site degrees of freedom need to be accounted for in future studies. Depending on the needs of future studies, the effect sizes determined here (some of which are small) could be used to reduce this number further. Limitations of this work include the use of tension-only linear connector elements, that do not account for wrapping, and standardized loading. For future work, we will perform additional statistical analysis on the significance of our results using more jobs and with larger parameter bounds. In addition, we will also investigate sensitivity to additional ligament properties (slack length, material properties), and modeling approach (non-linear material definition, inclusion of wrapping, and area of influence). Future studies will also implement population-specific loading and kinematics to increase clinical relevance. The results of this study demonstrate the impact of ligament attachment on predicted knee kinematics in a finite element model of a TKR, which is important for TKR alignment and ultimately understanding TKR surgery outcomes.

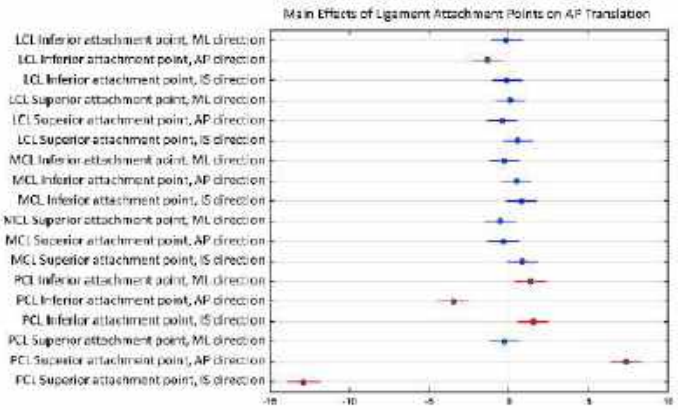

Figure 2: Predicted maximum effect (black circles) on motion due to a change in the corresponding parameter (ligament, location, direction of change). Lines represent 95% confidence intervals for regression models. AP translation was sensitive to six ligament attachment site parameters (shown in red) (R^2 = 0.794, p<<0.001).

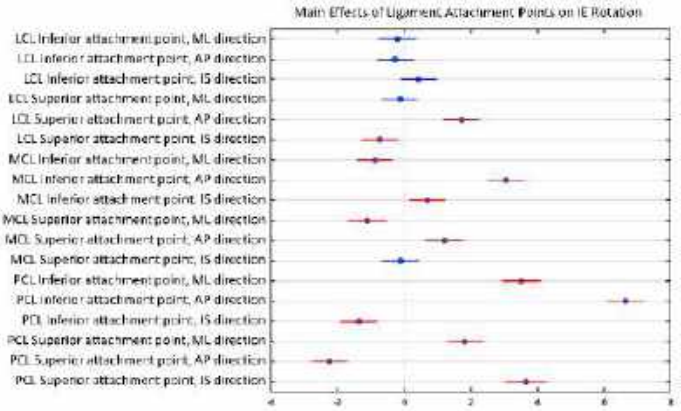

Figure 3: Predicted maximum effect (black circles) on motion due to a change in the corresponding parameter (ligament, location, direction of change). Lines represent 95% confidence intervals for regression models. IE rotation was sensitive to thirteen ligament attachment site parameters (shown in red) (R^2 = 0.842, p<<0.001).

ACKNOWLEDGEMENTS

Philanthropic funding (to SPM) is acknowledged. Thanks to Zimmer for providing CAD models of the NexGen CR TKR.

REFERENCES

[1] Mell, SP et al., *J Orthop Res*, 38:1538-1549, 2020.
[2] Shah, A et al., *J Am Acad Orthop Surg Glob Res Rev*, 6, 2022.
[3] Wilson, WT et al., *J Orthop Sports Phys Ther*, 42:345-351, 2012.
[4] Levy, BA et al., *Orthop J Sports Med*, 9, 2021.
[5] Kennedy, MI et al., *Clin Sports Med*, 38:261-274, 2019.
[6] Ahmad, CS et al., *Am J Sports Med*, 31:221-225, 2003.
[7] Papannagari, R et al., *Am J Sports Med*, 35:1507-1512, 2007.
[8] Lopes, OV et al., *J Bone Joint Surg Am*, 90:249-255, 2008.
[9] Tajima, G et al., *J Bone Joint Surg Am*, 91:859-866, 2009.
[10] LaPrade, RF et al., *J Bone Joint Surg Am*, 89:2000-2010, 2007.
[11] Liu, F et al., *J Orthop Surg Res*, 5, 2010.

SB³C2024
Summer Biomechanics, Bioengineering and Biotransport Conference
June 11-14, Lake Geneva, WI, USA

SEE-RYNGE: A VISUALLY ACCESSIBLE LIQUID MEASUREMENT DEVICE

Chiadika N. Eleh (1), Isaac Kim (1), Liam Y. Pharr (1), Venkatesh S. Shenoy (1), Joey Wei (1)

Faculty Advisors
David F. Meaney, PhD (1), Erin Berlew, PhD (1, 2), Oledayo O. Adewole, PhD (1, 2)

(1) Department of Bioengineering, University of Pennsylvania, Philadelphia, Pennsylvania, U.S.A.
(2) Perelman School of Medicine, University of Pennsylvania, Philadelphia, Pennsylvania, U.S.A.

INTRODUCTION

Liquid measurement, a daily task for many, is effortlessly carried out by a significant portion of the American population in activities like medication administration and meal preparation. However, for the majority of visually impaired individuals globally, this common practice is challenging due to the strong emphasis on visual ability. This challenge is further exacerbated by the absence of visually accessible liquid measuring devices, forcing visually impaired individuals to estimate measurements themselves or seek daily assistance, undermining their autonomy. In our user research, one poignant instance that deeply resonated with our group involves a blind mother whose child had contracted retinoblastoma. This mother faced the serious risk of having her child taken away because several professionals believed she wouldn't be able to accurately measure her child's necessary medication. This heartbreaking narrative not only underscores the severity of this issue but also serves as the driving force propelling our project forward.

Presently, the market lacks a comprehensive solution that fully tackles the challenge of precise liquid measurement for the visually impaired. The existing options either fall short in providing genuine independence, lack versatility for general-purpose use, or fail to meet the required accuracy standards. Among these alternatives is a makeshift DIY tactile syringe, consisting of makeshift bump dots or knife markings.[1] However, a DIY syringe is a crude, often imprecise alternative and its creation often requires aid from a sighted individual. Another alternative is a syringe specifically designed for diabetes applications (i.e., Count-A-Dose).[2] Although this is a more tactile and refined alternative, it only supports insulin dosage in very small volume ranges. In addition, measuring cups with large text can be helpful for moderately visually impaired individuals who retain some vision. However, such cups lack tactility and precision, and are not a viable option for completely blind users. The final options available are talking measuring cups or kitchen scales that audibly announce the weight or volume being measured. Although the audio feedback is helpful, these devices lack the critical tactility and precision required for precise measurements, particularly in applications such as medical dosage.

After examining these solutions, it was clear to us that the current options available to the visually impaired do not sufficiently nor completely solve the problem of liquid medication measurement for the visually impaired population. Thus, there is a substantial need for a solution that not only addresses the existing accessibility concerns regarding liquid measurement tasks but also empowers the visually impaired population with the tools required to perform activities confidently and autonomously.

PRODUCT DESIGN

See-Rynge is a handheld liquid measurement device for the visually impaired. Our device uses a lightweight stepper motor to draw precise volumes of liquid into a disposable syringe, which can then be easily detached from the device for flexible and immediate use. To accommodate visually impaired users, See-Rynge features tactile buttons for its user inputs, each of which is also associated with a distinct sound cue to provide audio feedback (shown in Fig. 1). These buttons are an On/Off switch, volume increase and decrease buttons, a volume gauge button, and a "Go" button. The user may adjust their desired volume via these buttons or an accessible Bluetooth-enabled phone application. This streamlined workflow ensures that our device empowers users to measure volumes with precision, completely eliminating the reliance on visual feedback. See-Rynge is currently powered by a 9-volt battery, uses a small limit switch as a positional sensor, and is encased within a custom 3D printed housing to ensure that it is lightweight, portable, and comfortable to use.

When compared to current accessible liquid measurement alternatives, See-Rynge offers significant advantages in accuracy and precision while ensuring user independence. See-Rynge is mechanically precise, demonstrating an average volumetric error of only 1.05% in quantitative trials (see Fig. 2). This more than meets ISO standards for syringe accuracy, which range from 3% to 5% error depending on nominal and expelled syringe volumes.[3] Additionally, See-Rynge has been observed to work with no noticeable differences in performance along a wide range of viscosities–testing liquids with poise values of 1E-2 to 1E5–ensuring reliable and versatile use for users. Finally and most importantly, See-Rynge promotes the user's autonomy by allowing them to independently measure liquids.

The minimum viable product version of See-Rynge consists of a functional iteration of our device enclosed within a 3D printed housing with its companion app in a functional, early development phase. At the culmination of the undergraduate senior design curriculum, See-Rynge will utilize injection-molded housing, allowing easier

scaling to mass production–which is accounted for in the following budget and market analysis.

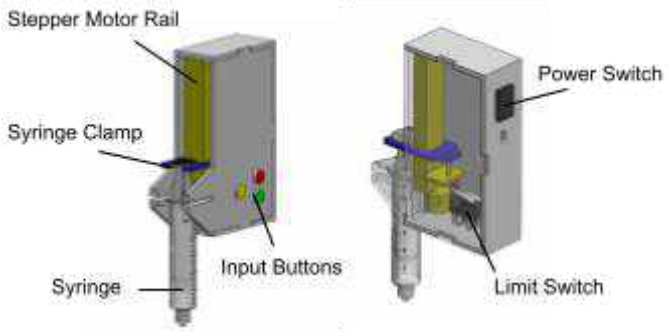

Figure 1: CAD Render of device prototype, with functional components labeled. Microprocessor, battery, and speaker not shown. Housing is composed of 3D printed PLA.

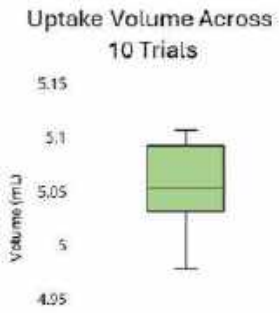

Figure 2. Average volume intaken for a 5 mL test volume. Over 10 trials See-Rynge demonstrated an average volumetric error of 1.05% ± 0.81%.

BUDGET & MARKET ANALYSIS

One million Americans are blind and six million Americans have vision loss.[4] At a National Federation of the Blind Keystone Chapter meeting in December following a hands-on demonstration, blind users were polled on their need for our device. 8 of 12 members responded "Very High Need," while the remaining four members raised concerns about our prototype's design–which has since been modified according to their feedback–whilst acknowledging potential usefulness of an assistive liquid measuring device. At a conservative 60% of the total one million blind individuals, we are able to address a significant need for ~600,000 people immediately. In discussion with primary care providers at Bucks County Blind, they estimated that ~25% of non-blind individuals with vision loss would significantly benefit from an assistive liquid measurement device. These estimates result in a total serviceable available market of ~1.1 million Americans.

As seen in the accompanying budget pro forma (Table 1), we are targeting an initial 1,000 sales for 2025 and 5,000 sales in 2026 at a retail price of $50. Electronics components, including an Arduino Nano microchip, Piezo Speaker, and Lithium-Ion battery are expected to cost approximately $15 per device based on bulk order retail prices. Injection-molded plastic housing is expected to cost an additional $5 per device while product assembly is expected to cost an initial $20 per device in 2025 which will decrease to $15 per device as volume increases in 2026. This provides a total margin of $10 per device in 2025 and $15 per device in 2026. We are anticipating needing $15,000 to complete device development, including the production of 10 working devices for use in demonstrations at trade shows and expos. Our marketing and sales budget will allow our team to visit conferences and trade shows over the next three years, while our general and administrative will cover any additional expenses. Finally, we are forecasting requiring approximately $35,000 for legal fees as we file for a patent and go through FDA trials. We are forecasting a net income of $47,200 by 2026, nearly covering all costs, at only 1% market penetration.

	2024	2025	2026
# of Sales	0	3,000	8,000
Sales	**$0**	**$150,000**	**$400,000**
COGS	$0	$135,000	$320,000
Electronic Components	$0	$60,000	$160,000
Non-Electronic Components	$0	$15,000	$40,000
Labor/Assembly/Packaging	$0	$60,000	$120,000
Gross Margin	$0	$15,000	$80,000
Opex			
Research and Development	$10,000	$5,000	$0
Marketing and Sales	$1,000	$5,000	$15,000
General and Administrative	$1,000	$1,000	$1,000
Legal	$30,000	$10,000	$5,000
Total Opex	$42,000	$21,000	$21,000
EBITDA	-$42,000	-$6,000	$59,000
Depreciation & Amortization	$0	$0	$0
Interest Expense	$0	$0	$0
Pre-Tax Income	-$42,000	-$6,000	$59,000
Taxes	$0	$0	$11,800
Net Income	-$42,000	-$6,000	$47,200

Table 1: See-Rynge budget pro forma projecting 2024-2026.

ACKNOWLEDGEMENTS

We would like to thank the University of Pennsylvania School of Engineering and Applied Science Bioengineering Senior Design Program for their funding and guidance. Additionally, we would like to thank the National Federation of the Blind Pennsylvania (NFB PA), as well as the NFB PA Keystone Chapter in specific, for their constant support and feedback throughout the development of See-Rynge.

REFERENCES

[1] Julie Ann Nastasi. (2023). The strategies used by adults with visual impairment. British Journal of Occupational Therapy. https://doi.org/10.1177/03080226231214369

[2] Count-A-Dose. (n.d.). Medicool. https://medicool.com/products/count-a-dose

[3] ISO 7886-1:2017(E). Sterile Hypodermic Syringes for Single Use—Part 1: Syringes for Manual Use. 2nd ed. Geneva, Switzerland: ISO; 2017.

[4] CDC. (2021, September 27). Protect Your Vision. Centers for Disease Control and Prevention. https://www.cdc.gov/visionhealth/resources/features/vision-loss-mental-health.html#:~:text=More%20than%207%20million%20Americans%20have%20vision%20impairment%2C

IV TUTOR: IV INSERTION TRAINING MODULE

K. Hara-Lee (1), E. Kim (2), N. Duncan (3), G. Nyhof (4), M. Goodman (4), A. Kim (5)

Faculty Advisor(s)

X. Wang (3), R. Hisey (5)

(1) Department of Mathematics & Statistics, Queen's University, Kingston, ON, Canada
(2) Department of Chemical Engineering, Queen's University, Kingston, ON, Canada
(3) Department of Mechanical & Materials Engineering, Queen's University, Kingston, ON, Canada
(4) Department of Electrical & Computer Engineering, Queen's University, Kingston, ON, Canada
(5) School Of Computing, Queen's University, Kingston, ON, Canada

INTRODUCTION

Intravenous (IV) insertion is vital for up to 80% of hospital inpatients worldwide [1]. Despite its ubiquity, the procedure is plagued by a substantial failure rate ranging from 30% to 50% [2]. Insertion failure can lead to complications, including arterial or nerve damage, hematoma, and bleeding at the insertion site. Of the successfully placed IV lines, up to 50% may eventually fail before reaching clinical obsolescence [1]. The pervasive failure not only impacts patients and caregivers but also imposes substantial economic burdens on the healthcare systems, necessitating urgent strategies for improvement.

Current techniques for IV insertion training are insufficient in bridging the gap between theory and practice. Online training modules for IV insertion exist but lack the physical aspect, like skin texture and resistance felt during needle insertion. On the other hand, physical models designed to mimic human arms offer a more hands-on experience but come with significant drawbacks. These models can cost up to $3,000, making them less accessible to many healthcare institutions, especially in resource-limited settings [3].

Our solution addresses these shortcomings by providing a training method that is both realistic and cost-effective. By closely simulating the tactile experience of IV insertion at a low cost, we aim to enhance skill acquisition, reduce the rate of insertion failures, and alleviate the associated economic and health burdens.

PRODUCT DESIGN

IV Tutor combines a physical 3D-printed arm model with a virtual guidance system to help the user improve their IV insertion techniques. IV Tutor uses the webcam and ArUco markers for precise 3D tracking to display the needle movement in real-time in 3D Slicer, a user-friendly, free medical software [4]. This software is linked with the webcam through PLUS software to accurately capture the needle's position, offering immediate visual feedback and instructional guidance. The model arm is designed with a neoprene fabric to imitate skin at the insertion site and incorporates anatomically correct vein simulation. This is achieved through a conductive mechanism inside the arm, which mimics a vein's response by altering electrical potential upon needle contact, signaling successful insertion via a microcontroller. The system is enhanced with accelerometers and force-sensitive resistors that deliver precise feedback on needle trajectory and technique. This improves learning outcomes by allowing students to see and adjust their methods in real-time.

The IV Tutor project comprises four sub-teams: Phantom, electrical, software, and research. The phantom team has designed a lifelike arm model using SOLIDWORKS, as seen in Figure 1. The model includes a removable forearm to allow easy access for installing electrical components. The arm is ready for 3D printing, with efforts underway to refine the adhesion of the neoprene fabric to the model for realistic IV insertion simulations[5].

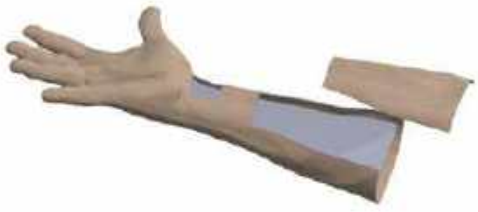

Figure 1: A CAD model of the phantom arm with a removable forearm.

The electrical team has developed a prototype of the vein simulator, which will be integrated into the arm phantom. The simulator utilizes a

Monel wire mesh for the vein due to its puncture-friendly characteristics that maintain electrical conductivity. A 3V3 direct current is sent through the mesh to simulate blood flow. The complete prototype is shown in Figure 2 (a). This configuration incorporates a visual feedback system featuring an LED that illuminates upon needle contact with the vein, as seen in Figure 2 (b).

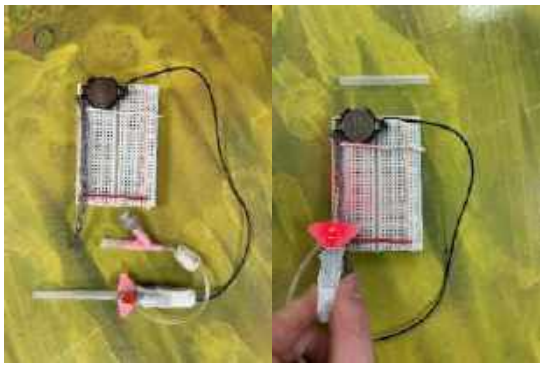

Figure 2: (a) illustrates the entire electrical system of the simulated vein, and IV needle (b) illustrates when the needle touches the simulated vein, an LED flashback is triggered.

The software team has connected the webcam to 3D Slicer, initiating the calibration process for the needle tracking. A GUI is being developed for 3D Slicer to provide information on object tracking and offer instructional notes on system usage and IV insertion methods. In parallel, the size limitations of ArUco Markers are being tested to achieve precise needle calibration.

BUDGET & MARKET ANALYSIS

The IV Tutor project, set at a $760 budget, develops a cost-efficient IV insertion training tool. It allocates $650 towards 3D printing the arm phantom and assembling the vein simulation system. The Software team was budgeted $80 to purchase a webcam, tripod, print AruCo markers, and additional camera setup equipment. 3D Slicer is free and open source, so software costs only come from the setup. The Research team does not require a budget; however, a $30 contingency was added. A 10% markup was added for a sale value of $836.

The nursing education market, which stood at USD 7.85 billion in 2021, is projected to ascend to USD 11.5 billion by 2029, growing at a 4.88% compound annual growth rate (CAGR) [6]. This trajectory underscores an excellent demand for training solutions such as the IV Tutor. With its substantial investment in nursing education, the North American market stands out as a primary market with new technology adoption capacity. Amidst an increasing emphasis on practical skills and the escalating complexity of healthcare challenges, the IV Tutor is positioned to address the dynamic requirements of nursing programs and healthcare institutions.

With over 2,600 colleges or universities in the United States offering nursing degree programs, the opportunities for the IV Tutor in this educational landscape are substantial [7]. This provides a broad avenue for annual sales, highlighting the potential for a favourable return on investment. The IV Tutor is well-positioned to impact the market significantly, enhancing healthcare training standards and contributing to improved clinical outcomes.

NEXT STEPS

The immediate next steps for the IV Tutor project focus on integrating the vein simulator into the 3D-printed arm and refining the navigation system. Enhancements to the arm include improving visibility under the neoprene fabric through structural modifications or LED backlighting. The project also plans to simulate vein movement by employing actuators or nitinol alloys and incorporating a microcontroller for electronics management and PC connectivity. The next steps for the navigation system include attaching AruCo markers to the needle and arm for tracking and investigating various object calibration methods for accurate 3D position display.

IMPLEMENTATION

The IV Tutor project implementation is guided by accessibility, effectiveness, and continuous improvement. With a focus on low-cost considerations, we aim to make the IV Tutor accessible to healthcare institutions worldwide, including those in resource-constrained settings. We plan to collaborate with hospitals, and schools to integrate our training tool into existing educational programs, providing hands-on learning opportunities for nurses and physicians. The research team will gather quantitative and qualitative data involving key metrics such as insertion time and an error rate that can be tracked by the device, allowing for identifying trends that indicate effectiveness. Current plans are to collaborate with Queen's University School of Medicine to integrate the prototype into a cohort of medical students and extend collaborations with local hospitals, enabling comprehensive testing and feedback to improve our solution further.

ACKNOWLEDGEMENTS

We thank the Queen's University class of Applied Science '73 for their financial support towards the Queen's Biomedical Innovation Team. We thank Rebecca Hisey for her support with surgical navigation technology and 3D Slicer. We thank Taylor Sweet from YGK3D for printing our arm phantom.

REFERENCES

[1] G. B. Beecham and G. Tackling, ‘Peripheral Line Placement’, in *StatPearls*, Treasure Island (FL): StatPearls Publishing, 2024. Accessed: Feb. 09, 2024. [Online]. Available: http://www.ncbi.nlm.nih.gov/books/NBK539795/

[2] R. E. Helm, J. D. Klausner, J. D. Klemperer, L. M. Flint, and E. Huang, ‘Accepted but unacceptable: peripheral IV catheter failure’, *J. Infus. Nurs. Off. Publ. Infus. Nurses Soc.*, vol. 38, no. 3, pp. 189–203, 2015, doi: 10.1097/NAN.0000000000000100.

[3] ‘Life/form Complete IV Arm and Pump Set - AED4Life’. Accessed: Feb. 13, 2024. [Online]. Available: https://aed4life.ca/injection-iv-training/life-form-complete-IV-arm-pump-set

[4] ‘3D Slicer image computing platform’, 3D Slicer. Accessed: Nov. 20, 2023. [Online]. Available: https://slicer.org/

[5] ‘Anatomy model - Hand | 3D CAD Model Library | GrabCAD’. Accessed: Feb. 16, 2024. [Online]. Available: https://grabcad.com/library/anatomy-model-hand-1

[6] ‘Nursing Education Market Size, Scope, Report & Future Trends By 2029’. Accessed: Feb. 13, 2024. [Online]. Available: https://www.databridgemarketresearch.com/reports/global-nursing-education-market

[7] ‘Nursing School 411 Welcomes You’, Nursing School 411. Accessed: Feb. 13, 2024. [Online]. Available: https://www.nursingschool411.com/

NON-INVASIVE, QUANTITATIVE ANTERIOR CRUCIATE LIGAMENT INTEGRITY MEASUREMENT SYSTEM

L. Phillips (1), D. Lounsbery (2), J. Ritchie (3), A. Ropars (4) (1,2,3,4)

G. German (1), T. Hookway (2), Q. Wang (3) (1,2,3)

INTRODUCTION

Anterior cruciate ligament (ACL) rupture is a devastating injury that often takes up to a year of rehabilitation before a return to activity. This recovery process suffers from a reliance on indirect milestones such as hamstring:quadriceps strength ratio, patient reported outcome measures, and range of motion. Quantitative assessment of ACL integrity is a promising supplement to current rehabilitation protocols to monitor improvements in ACL function and enable physical therapists to make informed adjustments to treatment plans to reduce reoperation rates. The ACL serves primarily as a stabilizer against anterior movement of the lower leg past the knee; therefore, its integrity can be quantified by measuring linear tibial displacement caused by a force imparted upon the lower leg anteriorly. This is the principle underlying the Lachman test, a physical assessment of ACL integrity performed by orthopedic specialists in diagnosis of ACL rupture.

The main goal of the device is to record anterior tibial displacement while the Lachman test is conducted. The reconstructed ACL's data can then be directly compared to a patient's healthy leg. Cost, safety, performance, and integrability were highly prioritized to select a user-friendly solution for physical therapists and orthopedic surgeons. A device that can assign numerical values to rehabilitation monitoring is relevant in professional sports as well as in research settings to better understand ACL mechanics. Finite element analysis, weight calculations, and conversations with various experts in the field were conducted to verify the design's safety and feasibility. Continuing work during the Spring 2024 semester will involve iterative prototyping and testing prior to presenting the device at a competition in May.

PRODUCT DESIGN

There exists an unmet niche in the rehabilitation of ACL tears for a measuring device to track rehabilitation progress quantifiably. A device for measuring the anterior displacement of the tibia during a Lachman test has the potential to overcome the shortcomings of the current approaches used in the evaluation of ACL integrity. The linear motion of the Lachman test and the isolation of the ACL in resisting this motion both lend themselves well to quantification and consistency in results. The device follows a similar principle to arthrometers, but it has a more simple, affordable design for measuring anterior tibial displacement under 10 lbf at 30° of knee flexion. Displacement measurements are recorded using a gear rack fastened to a sensor tip in contact with the proximal tibia. As the tibia is displaced anteriorly, the gear rack translates along with it, turning a gear fastened to a potentiometer. This potentiometer is part of a Wheatstone bridge circuit, so the changing resistance of the potentiometer changes the voltage output. Voltage readings are collected via DAQ systems such as Arduino. The data collected by this device is plotted in the time domain using MATLAB and stored between measuring sessions periodically throughout the rehabilitation process to evaluate improvements in knee integrity. This plot could be compared against the healthy leg of the patient as well as thresholds formed from a database of measuring sessions to determine the integrity of the ACL in question. The apparatus attaches around the lower leg inferior to the proximal tibia via a neoprene strap passed through 3D-printed PLA clamps situated medially and laterally. Brackets secured to these clamps with screws hold the displacement sensor in place with its point of contact at the proximal tibia. At the start of each data collection session, the sensor tip is calibrated in contact with the proximal tibia without any force being imparted by the orthopedic specialist performing the Lachman test. Future iterations of this device may include robust force measurement to plot force-displacement curves during the Lachman test. Additionally, alterations to the displacement measurement system based on precision, comfort, and cost may be in order using such alternative methods as an inductive transducer or a laser sensor.

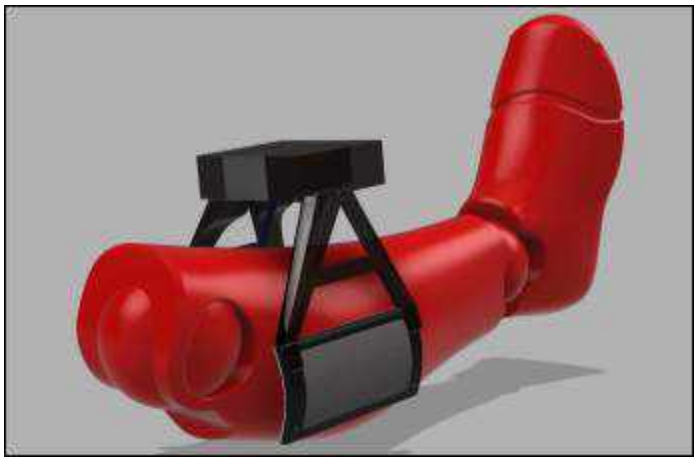

Figure 1: Render of device from Fusion360 displaying lateral clamp placement and displacement probe tip placement on model right leg.

Budget & Market Analysis

The total budget for design and building of the prototype is $2200; the majority of the budget will be used to purchase components. This will include parts such as the iGaging digital indicator to act as a baseline comparison, Arduino Uno Rev3, neoprene velcro straps, etc. This budget will also account for multiple iterations of 3D printed parts through the Watson Fabrication Laboratory.

Interviews for the potential customers of a conceptual prototype of this project were conducted from September 2023 through December 2023, revealing an initial market potential on a small scale. Interviewees included physical therapists, orthopedic surgeons, and athletic trainers, and they stated that a device capable of noninvasively assessing ACL integrity could be incredibly valuable. Individuals in the field of physical therapy and athlete management can work with patients who are largely sedentary, or they can be in charge of ensuring a professional athlete's longevity and health throughout a season.

As a result, there is a vast potential market for this form of device. However, as this device is in early development, a realistic financial manufacturing analysis cannot be performed at this time. Additionally, a return on investment is unable to be determined as this project will be advanced through several more iterations before being finalized and marketed.

While final production costs are not known at this time, one of the most important considerations for this design is to minimize cost while maintaining a high degree of precision and accuracy. ACL injuries are devastating to individuals at all levels of athletic performance, not exclusively professionals. As such, it is imperative that the price of the device is not a limiting factor for anyone to be able to purchase it, regardless of their level within their respective sport.

ACKNOWLEDGEMENTS

This project is supported by United Health Services I-Corp additional funding. Thanks to UHS doctors Stanley Hunter and Max Kammerman for representing UHS's interests and their contributions to the project.

SMARTSLEEVE+

J. Moni, G. Nair, P. Raghupathy, A. Saran

Department of Bioengineering, University of Pennsylvania, Philadelphia, PA, USA

Faculty Advisor(s)
Dr. John Kelly

INTRODUCTION

Open fractures are serious injuries that occur when a high-energy trauma causes a bone to break and puncture the skin.[1,2] The immediate exposure of the wound area along with the soft tissue and vascular damage that occurs fosters an environment for bacterial growth and infection.[3] The risk of infection is due to a range of factors, the principal cause being severity of the wound. Following an open fracture, patients will be taken to the emergency room where their bone is set, however, it is in this hospital setting where the majority of infections are acquired.[5]

There is a clear clinical need for a simple and effective solution to monitor a patient's wound area post-operation as infections significantly impact the prognosis of an open fracture due to complications such as non-union or lack of healing overall.[1] This contributes to patients having increased length of stay in the hospital and may even lead to amputation of the limb.[3,6] Additionally, fracture related infections (FRIs) are shown to significantly deteriorate a patient's quality of life as they report decreased physical function, increased bodily pain, and worse mental health.[6] The economic impact of these complications is also a significant burden for both hospitals and patients. Patients with an FRI directly increase hospital-related costs by eight times and FRI patients are out of work longer which has been shown to significantly decrease their annual income up to 6 years post-discharge.[6]

PRODUCT DESIGN

In order for our device to achieve its maximum potential there are a few key factors that must be taken into consideration: accessibility, portability, and form factor. Our product needs to be light, flexible, and thin enough to fit under a standard cas while being relatively low cost. To achieve this, a comprehensive leg model has been developed to fully test and integrate each separate component of our device. By using different solutions of various pH and temperature, we are able to simulate an infected environment and achieve an accuracy rate of over 90%. Furthermore, to increase the portability we will be moving to RFID technology powered by lithium ion batteries to make our device as energy efficient as possible. The other aspect of our device is centered around the end-user, through the use of an app. This app will be available for both Android and iOS and will display current sensor readings in real time and send messages to patient providers. To ensure patient safety and address circuit shorting concerns, a moisture wicking barrier in contact with the skin will be added. Ultimately we will be testing various 3D printed housing for our Raspberry Pi for efficient form factor and function.

Category	Specification	Target	Justification
Cast Compatibility	Size	< 2cm	Space under fiberglass layer of a cast
	Biocompatible	No interference with wound healing, use non toxic materials	Should not affect the wound healing
	Moisture Wicking	Use Moisture Wicking fabric	Moisture should not add to the infection, or interfere with electronics
Data Collection	pH Sensing	Sense range between 4.0 - 9.0 pH, and incremental changes of 0.5	Range for healthy/infection and incremental change that may occur
	Temperature Sensing	Detect 0.1°C - 2.5°C difference between baseline and wound sensors	Range for healthy/infection and incremental change that may occur
	Impedance Sensing	Sense range between 0-200 mΩ, and incremental changes of 5 mΩ	Range for healthy/infection and incremental change that may occur
	Cast functionality	Sensors stay consistent accurately under cast	Must function under cast or product is useless
Data Transmission	Real Time Tracking	Continuous tracking of data	Need to alert to the onset of infection rapidly
	Algorithm	95% Accuracy 95% Specificity 85% Sensitivity	Matches existing disease detection devices on market
	GUI	Provide real time readings on smartphone	Patient and doctor needs to get alerted of infection

Table 1: Need Specifications for the SmartSleeve+ Device

Studies have demonstrated that growth of bacteria is more optimal in alkaline environments with pH of up to 10. Thus, monitoring the pH of the wound can be a good option to determine the

presence of bacterial colonization within the injury site.[7] Additionally, there has been a strong positive correlation observed between the wound site temperature and the presence of infection, with infected wounds often displaying around a 1.5-2.2$^{\circ}C$ increase[8] compared to stable body temperature. Finally, skin impedance has also been proven to be an effective tool for wound monitoring, as resistance of the skin has been shown to decrease in an infected wound as opposed to a healthy wound.[8]

For ease-of-access for the patient being treated for an open-fracture, sensor data will be wirelessly transmitted to the patients' smartphone via WiFi and warning notices will appear alongside the sensor reading when the readings reach concerning levels so that the patient can easily understand when to consult a doctor.

Our device would fit in seamlessly with current casting procedure workflow, as the device is designed to be compact, so that it can easily fit within the layers of the cast. The physician would just need to replace the stockinette base that is currently used with the modified stockinette base that we fabricated, and then attach the padded layer that contains our temperature sensor to the outside of the stockinette base.

Initially, the product would be targeted towards patients being treated for open fractures, post-operation. With the initial release and integration of our product into the hospital workflow, we hope to decrease the rate of undiagnosed and untreated infections in the United States, and to subsequently reduce the rate of catastrophic outcomes such as limb amputation due to infection.

Long term, we hope to launch our product globally, so as to reduce the impact of open fractures and related traumas on a larger scale. SmartSleeve+ can have a positive economic impact on patients, as our product is fabricated using relatively low-cost materials, and can prevent further complications from the injury that may lead to increased medical treatment down the road. SmartSleeve+ also hopes to bridge socioeconomic gaps and be accessible to impoverished and resource-limited populations as it is reproducible and can very easily be integrated into the existing casting methods and workflow of any hospital quickly.

Figure 1: Prototype of the product (shown left) and smartphone application (shown right).

Budget & Market Analysis

The approximate design budget for this project was around $1,000. However, the cost of materials totalled approximately $400. Money was spent primarily on the temperature sensors, materials to fabricate the pH sensor, and the environment and housing for the device.

As mentioned above, the breadth of this issue is quite large, with around 101,000 people suffering from this trauma annually. The potential market size would include this entire population. At this volume, the manufacturing cost per unit would approximately be $10, and the product would approximately be sold for $12 per unit. The return on the investment using these numbers would be approximately $2 per unit.

ACKNOWLEDGEMENTS

We acknowledge the Penn Bioengineering department for all financial support in procuring the parts for this product. We also would like to acknowledge the Orthopedic Department of Penn Medicine for supplying the casting materials to help us design and model the product.

References

[1] Sop, Jessica L. & Sop, Aaron. (2023). Open Fracture Management. StatPearls. https://www.ncbi.nlm.nih.gov/books/NBK448083/

[2] Kim, P. H., & Leopold, S. S. (2012). Gustilo-Anderson Classification. Clinical Orthopaedics and Related Research. https://doi.org/10.1007/s11999-012-2376-6

[3] Coombs, J. et al. (2022). Current Concept Review: Risk factors for infection following open fractures. Orthopedic Research and Reviews. https://doi.org/10.2147/orr.s384845

[4] Carsenti-Etesse, H., Doyon, F., Desplaces, N. et al. (1999). Epidemiology of Bacterial Infection During Management of Open Leg Fractures. European Journal of Clinical Microbiology and Infectious Diseases. https://doi.org/10.1007/PL00015012

[5] Kortram, K., Bezstarosti, H., Metsemakers, W., Raschke, M. J., Van Lieshout, E. M., & Verhofstad, M. H. (2017). Risk factors for infectious complications after open fractures; a systematic review and meta-analysis. International Orthopaedics. https://doi.org/10.1007/s00264-017-3556-5

[6]Youssef, K., Ullah, A., Rezai, P., Hasan, A., & Amirfazli, A. (2023). Recent advances in biosensors for real time monitoring of pH, temperature, and oxygen in chronic wounds. Materials Today Bio. https://doi.org/10.1016/j.mtbio.2023.100764

[7]Chanmugam, Arjun et al. (2017). Relative Temperature Maximum in Wound Infection and Inflammation as Compared with a Control Subject Using Long-Wave Infrared Thermography. Advances in Skin & Wound Care. https://journals.lww.com/aswcjournal/fulltext/2017/09000/relative_temperature_maximum_in_wound_infection.4.aspx

[8]Lukaski, H. C., & Moore, M. (2012). Bioelectrical impedance assessment of wound healing. Journal of diabetes science and technology. https://doi.org/10.1177/193229681200600126

HOME UNWEIGHTING EXERCISE DEVICE FOR PATIENTS WITH DIABETIC FOOT ULCERS

Victoria J. Moore (1), Miles W. Yoshinobu (2), Mirabella A. Herrera (2), Tanveer Ahmed (2), Rachel N. Porter (2),

Faculty Advisor(s)
Robert Hart (2), Todd Polk (1), Gu E. Kang (1)

(1) Biomedical Engineering, The University of Texas at Dallas, Richardson, Texas, United States
(2) Mechanical Engineering, The University of Texas at Dallas, Richardson, Texas, United States

INTRODUCTION

An estimated 29.2% of Americans over the age of 65 have diabetes [1]. An additional 97.6 million adults were estimated to have prediabetes in the same year, with a significant increase seen over the last two decades [1]. The economic cost of diabetes was found to be about $327 billion in 2017 through reduced productivity and medical costs [2]. Along with diabetes comes the risk of Diabetic Foot Ulcers (DFUs). Diabetic polyneuropathy, one of the main causes of neuropathy in this population, has a prevalence rate of 50% for diabetic patients across their lifetimes [3]. Those with diabetic foot neuropathy have altered gaits that can result in the formation of ulcerations on the feet [4]. Additionally, diabetic individuals with neuropathy are only one-third as active as diabetic individuals that have not lost sensation in their feet [5]. Frequent exercise has been shown to decrease mortality rates by 39% for diabetic individuals [6]. Furthermore, exercise is especially important for those with DFUs as exercise dramatically improves wound healing times [7]. Improving healing for DFUs is of clinical importance. As many as 24% of ulcers lead to amputation, and 85% of amputations in diabetic patients are preceded by ulcers [8]. The 5-year survival rate for patients post-amputation is only 50% [9].

The most effective treatment method of DFUs is off-loading of the affected area. The gold-standard for this is the Total Contact Cast, and there are also Removable Cast Walkers that are removable off-loading boots [8]. While these treatment options are effective at removing pressure from the ulcerated area, they restrict movement, further alter their gaits, and make exercise even more of a difficulty. Therefore, a device that allows individuals to safely offload a portion of their weight so they can safely exercise in their own homes is needed to improve healing times and allow for better outcomes for individuals with DFUs.

PRODUCT DESIGN

This product is intended to safely offload weight from patients with DFUs so that they can exercise within their homes. The device itself is mainly comprised of an aluminum frame that supports an unweighting system. A CAD rendering of the completed device can be seen in **Figure 1**. In this depiction, the box at the center represents the harness that is meant to support the user's weight.

The frame is made from two sizes of aluminum tubing, 1.5-inch square tubing and 1.25-inch square tubing. The 1.5-inch square acts as the base portion of the device, and the 1.25-inch square tubing makes up the upper portion of the device and telescopes into the larger tubing to allow the device to accommodate a range of user heights. Aligned holes in the tubing are used to select the correct height with clevis pins.

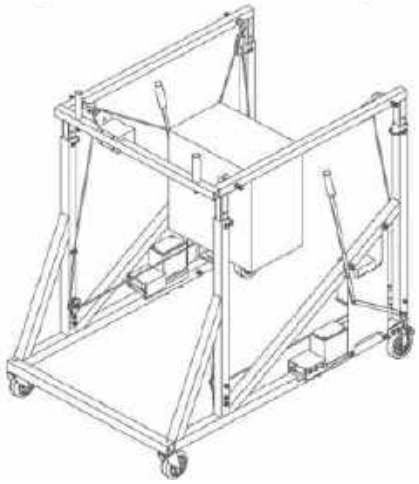

Figure 1: CAD overview of device

The aluminum frame supports the unweighting system of this device. Two electric winches, with a 2000-lb rated load, are used to lift the user and offload a portion of their weight. These winches are each powered by a 12V battery, and three relays are used to control the polarity and power supply to each winch. Each winch operates two separate cables, one that runs to the front of the device, and another that goes towards the back. The winches sit on the bottom of the frame on either side of the device. These cables are then run through a series of pulleys and rope guides around the device. At the center of the device is the harness which the patient dons while using the device. This harness has three aluminum rings that can support a lifting force, one in the front and one on each side. The cables each end in a loop, and carabiners are used to attach the cables to the rings on the harness. The front ring of the harness is connected to the two front cables, and each side ring is connected to the associated cable coming from the rear of the device.

This lifting system is operated by a control panel situated at the

front of this device. A spring-loaded rocker switch with a default off position is used to control the winches' movement. In its default position, the winches are stationary. When pressed upwards, the winches will begin winding the cables in and lifting the harness to offload the user's weight. When pressed down, the winches will unwind and lower the harness.

To first begin using the device, the height must be adjusted using the telescoping portion of the frame so that the top of the frame stands about 4 inches above the hips of the user. This is the ideal positioning of the frame according to analysis performed on the tension in the cables as seen in **Figure 2**. To enter the device, the user may put on the harness first in a seating position or stand in the center of the device where the harness is. The rocker switch is used to control the movement of the harness. Once in the device, the user can begin walking as the device will move on its wheels. As they walk, they can rest their arms on the frame, holding the handlebars shown on the front crossbar of the device. The brakes are easily accessible from extended handles, as seen on either side of the device in **Figure 1**, should the user feel the need to control the device's movement at any time. Once finished, the rocker switch is used to lower the harness so that the user can doff the harness and exit the device.

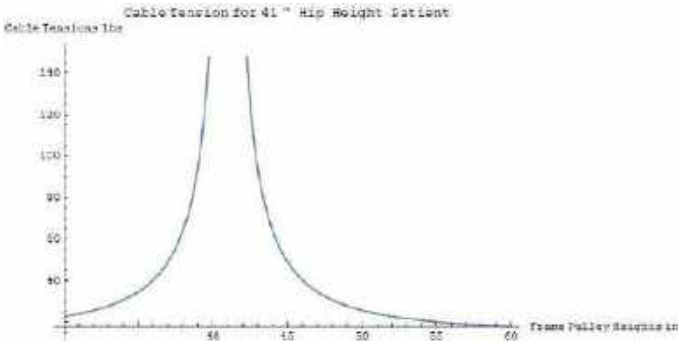

Figure 2: Cable tension as a function of frame height. A hip height of 41 inches requires a frame height of 45 inches to reduce tension.

A beam stress analysis was performed assuming a case of extreme loading, and all calculated stresses were within acceptable ranges for the tubing. Deflection analysis was also performed with an increased loading of 50lb of tension of each of the 4 cables, as seen in **Figure 3**. Even with these high tensions, the beam stresses are not catastrophic and the resulting deflection is minimal. The maximum deflection shown is 0.1 inches and is exaggerated in the rendering.

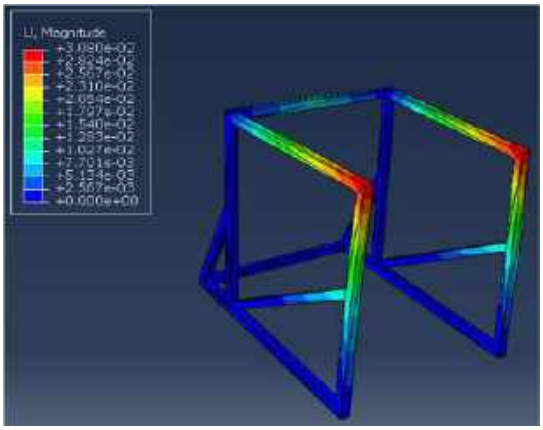

Figure 3: Color-coded results of deflection analysis performed on the frame of the device assuming 50lb of tension on all cables

BUDGET & MARKET ANALYSIS

The expected cost to build this prototype is $3,437.54, which represents $2593.54 in materials cost and an additional $844 in manufacturing costs. The current design budget is $4500, which covers the cost of creating the prototype as well as contingency funds.

The potential market for this device includes all individuals experiencing DFUs. In 2021, 38.4 million Americans had diabetes, and the annual incidence rate of DFUs for those with diabetes can be up to 4% [1] [10]. Assuming this product will reach 5% of this market over the course of a year, approximately 76,800 units may be purchased or rented annually. Each unit will have an estimated price of $2500 to match the current market for relevant products.

To manufacture this product at this scale, materials costs are expected to decrease as items will be purchased in bulk. These costs could reasonably drop to $1500 per product. Labor would be approximated at $200 per assembly, and overhead costs would follow at about $500. This means that each product would have an estimated manufacturing cost of $2200, allowing for a $300 profit margin.

However, there will be investment costs for welding the frame. To employ the use of a robotic welding systems for this product, costs start at $90,000 per system. To create two welding systems, one for each portion of the welded frame, it would cost $180,000. Again, assuming that 76,800 units are sold per year, with a profit of $300 per unit, there stands to be a great return on investment for this product.

ACKNOWLEDGEMENTS

Funding was provided by Dr. Kang's Biomechanics Lab at the University of Texas at Dallas in collaboration with UTSW. This project was performed as a part of UT Design.

REFERENCES

[1] "National Diabetes Statistics Report." *Centers for Disease Control and Prevention*, 29 Nov. 2023.

[2] "Economic Costs of Diabetes in the U.S. in 2017." *American Diabetes Association*, 22 Mar. 2018.

[3] Juster-Switlyk, Kelsey, and A Gordon Smith. "Updates in diabetic peripheral neuropathy." *F1000Research*, vol. 5 F1000 Faculty Rev-738. 25 Apr. 2016.

[4] Alam, U et al. "Diabetic Neuropathy and Gait: A Review." *Diabetes therapy: research, treatment and education of diabetes and related disorders* vol. 8,6 (2017): 1253-1264.

[5] Lemaster, J W et al. "Effect of weight-bearing activity on foot ulcer incidence in people with diabetic peripheral neuropathy: feet first randomized controlled trial." *Physical therapy* vol. 88,11 (2008): 1385-98

[6] Gregg EW, Gerzoff RB, Caspersen CJ, Williamson DF, Narayan KMV. "Relationship of Walking to Mortality Among US Adults with Diabetes". *Arch Intern Med.* 2003; 163(12):1440–1447.

[7] Emery, C. F et al. "Exercise accelerates wound healing among healthy older adults: a preliminary investigation." *The journals of gerontology. Series A, Biological sciences and medical sciences* vol. 60,11 (2005): 1432-6.

[8] Alexiadou K, and Doupis J. "Management of diabetic foot ulcers." *Diabetes therapy: research, treatment and education of diabetes and related disorders* vol. 3,1 (2012): 4.

[9] Turan Y, Ertugrul BM, Lipsky BA, Bayraktar K. "Does physical therapy and rehabilitation improve outcomes for diabetic foot ulcers?" *World Journal of Experimental Medicine*. 2015 May 20; 5(2):130-9.

[10] Edmonds M, Manu C, Vas P. "The current burden of diabetic foot disease". *Journal of clinical orthopaedics and trauma*. 2021 Feb 8; 17:88-93.

KneeVive: At-Home Osteoarthritis Symptom Mitigation

A. Chaudhary (1), A. Gautam (2), Y. Lemus (3), D. Yarberry (4), Z. Haque (5), A. Kuraszkiewicz (6), A. Kulkarni (7), I. Miller (8), A. Lin (9), B. Goldblatt (10), B. Oberlee (11), C. Gerety (12), D. Asawa (13), D. Yee (14), J. Tao (15), K. Touserkani (16), K. Gami (17), L. Morrison (18), M. Leacoma (19), N. Parseghian (20), S. Uddin (21), S. Goryachev (22), V. Villalonga (23), W. Hanson (24), Z. Khalil (25)

Faculty Advisor(s)

S. Wojda (1), G. Srimathveeravalli (2)
(1) Biomedical Engineering, UMass Amherst, Amherst, MA, USA
(2) Mechanical and Industrial Engineering, UMass Amherst, Amherst, MA, USA

INTRODUCTION

Over 32.5 million people in the United States suffer from osteoarthritis [2]. This disease is characterized by the deterioration of the protective cartilage surrounding the affected joint, causing pain and decreased mobility [1]. The joints most commonly affected include the fingers, the hips, the neck, the lower back, and the knee [2]. Rehabilitation treatments for osteoarthritis consist mainly of regular exercise, maintaining a healthy weight, stretching, and physical therapy [3]. A recent study has shown that applying vertical traction on the patient's knee joint daily for ten minutes over a period of six months reduces pain and discomfort from 7.979±0.3503 out of 10 to 3.189±1.468 out of 10, whereas using traditional techniques, the patients' pain went from a 7.979±0.3503 to a 5.253±0.0751 [4]. Since traction mimics the slight separation of the knee joint, this treatment increases blood flow and promotes hyaline cartilage growth [4, 5].

Traditional knee traction therapy is performed by physical therapists in clinical settings. However, traction therapy currently consists of a cumbersome pulley system which both takes up a lot of space and makes the therapy inaccessible to patients outside of a clinical setting. Currently, there are no medical devices that can perform knee traction therapy and are accessible to home-bound patients. These patients, recovering from knee replacement surgery, have limited mobility and may be unable to complete daily tasks. Thus, seeing a physical therapist multiple times a week may cause unnecessary stress. Our team designed an osteoarthritis symptom mitigation device that makes osteoarthritis therapy accessible from the patient's home. A typical course of physical therapy costs anywhere from $557 to $919, where our at-home therapy would have a cost of $130 and would be cheaper than glucocorticoid injections, where a single injection can cost anywhere from $99 to $172 [6].

Figure 1: Side view of the device attached to a patient's leg

PRODUCT DESIGN

The boot serves as the anchor, keeping the foot planted to the ground with the knee at a 90-degree angle (See Figure 1). The boot also contains inflatable airbags for a more snug fit and anchoring the foot within the boot. Mounted to the boot is a linear actuator that can bear a load of up to 330 lbs. The linear actuator applies an upward force on the underside of the thigh, at the distal end near the knee. This pressure is applied through a 3D-printed leg cradle attached to the linear actuator. Velcro straps secure the thigh to the leg cradle.

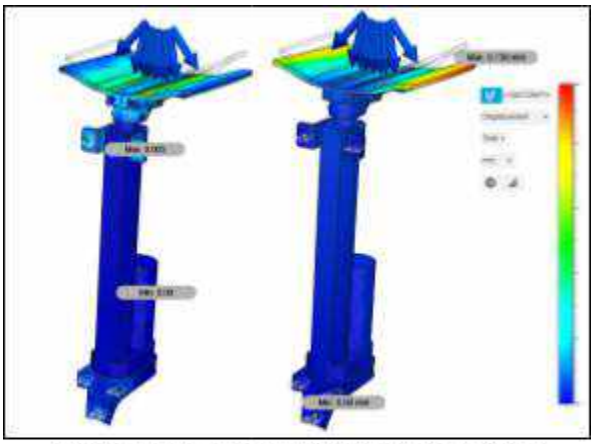

Figure 2: FEA Analysis of force placed on device

Our thigh plate has been engineered to provide structural stability to deliver the force at a 90 degree angle in the y direction while also providing comfort based elasticity for the patient's convenience. After doing an FEA analysis of force loaded on our device, we can verify that there is no deformation in the motion system. However, there is deformation in the socket where we expect it to be present.

The electrical components of the device are wired through an Arduino UNO. A set of relays allows us to change the direction of the linear actuator, which is powered by a 12-volt DC motor. We can measure the pressure applied to the leg with a 50kg load cell force sensor. Our user interface consists of a potentiometer and OLED I2C display. This system allows users to select their weight and then determine how much pressure to apply.

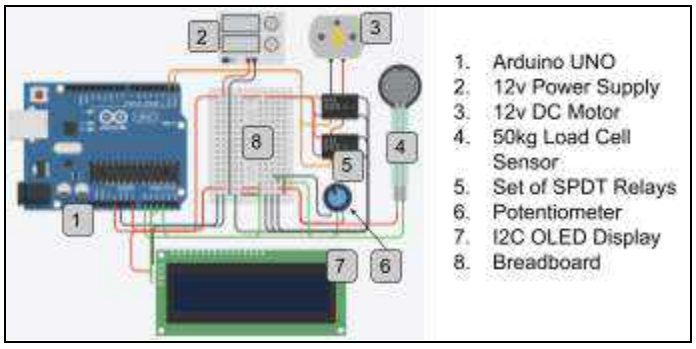

Figure 3: Electrical schematic of the device.

The device includes a failsafe system that utilizes the force sensors. The maximum applied force allowed on the user is 6% of their body weight. When the force sensors detect a force induced on the user that exceeds this maximum force, the linear actuator will retract and the device will turn off. Additionally, the current from the power source will be monitored, and the device will be shut off if the current exceeds 2 amps.

BUDGET & MARKET ANALYSIS

The global market for general osteoarthritis products is expected to grow with a Compound Annual Growth Rate of 8.5% from 2022-2030, forecasting $15 billion in revenue. [8] Our team spent $152.90 on developing the prototype. If brought to market, economics of scale would reduce the cost of production to $83. This is due to theoretical discounts from the individual manufacturers to order 1 million units of all components. After applying a 50% profit margin on the manufacturing cost, the proposed MSRP is $170. This price can be further discounted to patients as the device falls under general traction devices covered by US medical insurance companies. In the long-term, the cost of the electronic components would be significantly reduced due to the capacity of internal production.

Table 1: KneeVive's market price compared to competitors

Traction Device	Description	Cost
Knee Works 300	Wooden static stretcher	$379
KneeVive	Personalized traction therapy	$170
KneeSled PLUS	Locks knee within range of motion	$150
IdealKnee One Pad	Metal bar brace for knee extension	$105

As depicted in Table 1, our device fills a significant gap in the market as it provides an automated traction-based brace therapy at a reasonable price. Unlike other products that rely on a less user-friendly pulley system or stiff brace, our product is easy to use and individualized to fit every knee osteoarthritis patient's needs.

ACKNOWLEDGEMENTS

Funding was provided by the University of Massachusetts Amherst Biomedical Engineering Department and through an award from the Berthiaume Center for Entrepreneurship Tech Challenge. We thank our faculty advisors S. Wojda and G. Srimathveeravalli, as well as staff members of the University of Massachusetts Amherst Maker Space for their guidance and support of this project.

REFERENCES

[1] Chief Editor Pruthi, S., Mayo Foundation for Medical Education and Research. (June 16, 2021). Osteoarthritis. Mayo Clinic.
[2] Chief Editor Jack, L., Centers for Disease Control and Prevention. (2023, June 12). Osteoarthritis. Centers for Disease Control and Prevention.
[3] Chief Editor Pritchard, A., Osteoarthritis - Treatment and support. (2017, October 23). Retrieved from nhs.uk website.
[4] Kamble, M, Chettinad Health City Med J. 12(2):15-20, 2023.
[5] Hsu, H, "Knee Osteoarthritis", StatPearls [Internet], NIH NCBI.
[6] Rhon D et al,. JAMA Network Open, 5(1):e2142709, 2022.
[7] "3 Knee Flexion Anatomy Artwork." [Online Image]. Fine Art America. https://images.fineartamerica.com/images-medium-large-5/3-knee-flexion-anatomy-artwork-science-photo-library.jpg (accessed February 14, 2024).
[8] "Osteoarthritis Market Size Global Report, 2022 - 2030." Polaris, ABIOGEN Pharma, Oct. 2022.
[9] Deshpande, BR et al., Arthritis Care Res (Hoboken). 68(12):1743-1750, 2016.
[10] Yao, Q et al., Signal Transduction and Targeted Therapy, 8(1):56, 2023.

ENHANCING LABOR COMFORT: DEVELOPMENT OF AN ADAPTIVE PRESSURE CLAMP FOR DOUBLE HIP SQUEEZE

C. Beck[1], N. Kibler[2], S. Korah[1]

Faculty Advisor

O. Sayginer[1]

(1) Department of Mechanical Engineering, Temple University, Philadelphia, PA, USA
(2) Department of Electrical and Computer Engineering, Drexel University, Philadelphia, PA, USA

Labor is a challenging and painful process that impacts pregnant individuals both physically and emotionally. The counter pressure double hip squeeze technique is commonly employed by support individuals during labor to alleviate back pain and enhance overall comfort. We introduce an innovative device designed to perform the counter pressure double hip squeeze and tailor its functionality to meet the individual needs of birthing individuals.

INTRODUCTION

Labor is an exhaustive and painful process that affects pregnant people physically and emotionally. Counter pressure double hip squeeze (CPDHS) is an exercise performed during the labor process, aiming to alleviate lower-back pain [2]. This technique applies pressure to the hips to provide pain relief during labor [1]. To achieve this technique, both sides of the hips need pressure that pushes vertically towards the torso [2].

Figure 1: Illustration of CPDHS technique
Illustration by Shanna Dela Cruz. © 1994, 1999, 2005 Ruth S. Ancheta. Reproduced with permission from The Labor Progress Handbook: Early Interventions to Prevent and Treat Dystocia, 1st and 2nd Editions, by Penny Simkin and Ruth Ancheta (Ox- ford: Blackwell Publishing, 1999, 2005)

CPDHS is typically performed by a support person including patient's partner, midwife, or the attending doula [3]. However, manual fatigue can diminish the effectiveness of this technique over time, even with alternating support [3]. Some studies suggest that synchronizing the hip squeeze with the birthing person's breathing can enhance pain relief [4]. Nonetheless, maintaining periodic pressure for extended periods poses a significant challenge.

In this study, we introduce an innovative and low-cost device known as the Adaptive Pressure Clamp (ADAC), designed specifically for performing the double hip squeeze technique during labor. The ADAC offers versatility, as it can be effortlessly attached to the lower back of any pregnant person, regardless of body size. One of the devices' key features is its ability to mimic and replicate the motions applied initially by a support person. Moreover, the ADAC can adjust its motion in synchronization with the respiratory activity of the pregnant person in labor, providing tailored support throughout the birthing process.

PRODUCT DESIGN

ADAC is an electromechanical device comprising of mechanical and electronic components. Some of its key components and their functions are as follows:
Contact Pads: Constructed from medical-grade silicone materials, these pads are suitable for both direct skin contact and cloth/textile contact. They provide excellent grip in both scenarios and feature touch sensors on both sides. These sensors detect the support person, initiate the learning mode, and automatically record motions.
Control Unit: This unit controls all functions of the ADAC. Includes a gearbox, microcontroller, power supply unit, DC motor, encoder, digital display, and an emergency button.

ADAC offers simple installation and removal, requiring no fasteners or straps for secure attachment. Installation involves placing the handles on the patient's hips, ensuring straightforward and hassle-free use. Additionally, in emergency situations, the device is equipped with an emergency button (a physical kill switch) located on the control unit. This switch can be pressed to immediately shut off the device, ensuring rapid response and safety. Preliminary design of the ADAC is shown in Fig. 2.

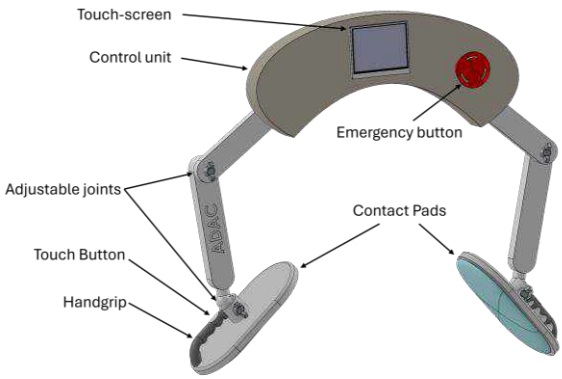

Figure 2: 3D Model of Preliminary Design

ADAC offers three modes to accommodate varying needs and preferences:

Learning Mode: In this mode, the device learns from a support person's application, capturing and storing the applied pattern. Subsequently, it accurately repeats the learned pattern, ensuring consistent and effective performance. To use this mode, the support person must apply pressure to the devices handles in the pattern that is desired. Once finished, the user can simply let go and the device will begin repeating the pattern.

Adaptive Mode: This mode is specifically designed to recognize and synchronize with the patient's breathing patterns, allowing the device to dynamically adjust its operation accordingly. Initially, the user will manually enter the breathing frequency. However, in subsequent stages of device development, a respiratory sensor will automatically gather respiratory information. To activate this mode, simply select the "Adaptive" button."

Manual Mode: For users seeking greater control over the device's operation, the manual mode allows for the manual selection of both the frequency and power of the pressure. This flexibility enables customization to suit individual patient requirements and preferences. To use this mode, the desired motion profile must first be uploaded to the device. The support person can then select the “Manual” menu which will allow them to select their desired profile.

BUDGET & MARKET ANALYSIS

We propose a device that prioritizes affordability, recognizing the significant financial burdens associated with expecting a child. By ensuring affordability, our device can be accessible to expecting families worldwide, particularly in regions with limited access to medical care. Our goal is to achieve a unit cost of $ 50 at large manufacturing scale.

ADAC could be purchased by expecting families or doulas looking to enhance their support services for birthing individuals. According to a price analysis conducted using [5], ADAC offers a relatively affordable option compared to its price and performance with commonly used birthing products such as birthing balls and Doppler fetal monitors.

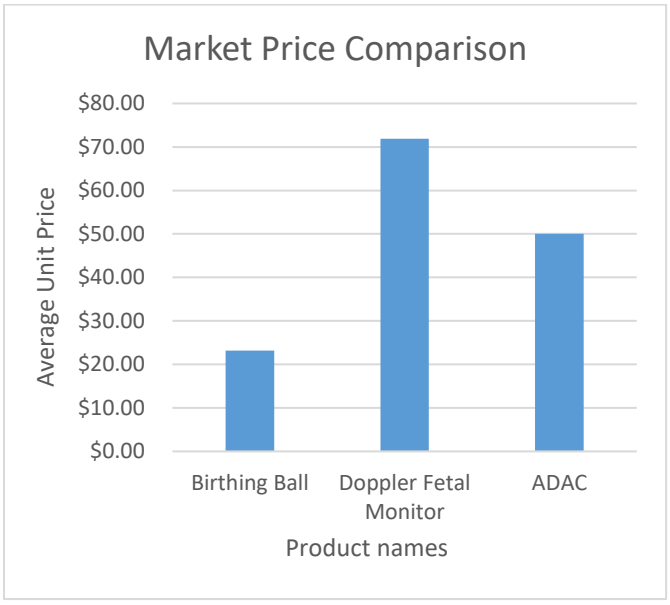

Figure 3: Market price analysis of ADAC vs Similar Products

REFERENCES

[1] Adams, E., Bianchi, A. A Practical Approach to Labor Support, 2008
[2] Osborne, C., Kolakowski, M., Lobenstine, D. Gluteal Double Squeeze or Double Hip Squeeze and Pelvic Press Techniques, 2021.
[3] Paterno, M., Van Zandt, S., Murphy, J., Jordan, E. Evaluation of a Student-Nurse Doula Program: An Analysis of Doula Interventions and Their Impact on Labor Analgesia and Cesarean Birth, 2012.
[4] Issac A, Nayak SG, T P, Balakrishnan D, Halemani K, Mishra P, P I, Vr V, Jacob J, Stephen S. Effectiveness of breathing exercise on the duration of labour: A systematic review and meta-analysis. J Glob Health. 2023
[5] Amazon Product Research Tool & FBA Sellers Software. AMZScout. (n.d.). https://amzscout.net/

CARDIOFORECASTER - AN AI-DRIVEN CARDIOVASCULAR DISEASE FORECASTING PLATFORM

Krysta L. Bernold, Kylie G. Herbert, Valerie S. Balas, James Evangelisto III, Mathieu L. Colon

Faculty Advisor(s)

Ria Mazumder (1), Daniel Roozbahani (2)

(1) Biomedical Engineering Department, Widener University, Chester, PA, USA
(2) Robotics Engineering Department, Widener University, Chester, PA, USA

INTRODUCTION

Cardiovascular disease, particularly myocardial infarction (commonly known as heart attack), remains a leading cause of mortality worldwide, claiming millions of lives annually [1]. Early identification of myocardial infarction remains a challenge due to limited resources. This project proposes an innovative approach, aiming to develop an AI-driven platform for forecasting cardiovascular disease. The system leverages two key components: a trained AI algorithm and a deformable 3D simulation of the human heart and cardiovascular system. The AI algorithm is trained on pre-processed, segmented, and sliced CT scans of de-identified myocardial infarction patients obtained from the SegMed medical image database. During training, the algorithm focuses on identifying blockages in the Left Anterior Descending (LAD) artery, which is the most commonly affected site in heart attacks [2]. Python is utilized for image processing and segmentation, preparing the data for optimal AI training. Following training, the algorithm undergoes validation, troubleshooting, and testing to ensure accuracy and reliability.

Phase two of the project revolves around constructing a simulation platform of blood flow within a detailed 3D model of the heart and cardiovascular system, with specific emphasis on LAD artery blockages using platforms such as Autodesk Inventor, 3D MAX, and ANSYS Fluent software. Blood is modeled as a non-Newtonian fluid, reflecting its complex properties to enable analysis of blood flow dynamics to analyze the consequences of arterial blockages on heart function on each specific patient. The platform allows for replicating specific blockages observed in patient CT scans to provide a tool for validating the accuracy of the AI-based diagnostic algorithm.

PRODUCT DESIGN

The CardioForecaster system is an AI-driven cardiovascular disease forecasting platform designed to predict the risk of heart attacks in patients using cardiac CT scans and 3D heart models.

CardioForecaster is classified as an FDA class 1 medical device and is aligned with regulatory standards for medical devices impacting cardiac disease diagnosis and treatment. As Software as a Medical Device (SaMD), it operates independently of physical medical devices. The platform utilizes open-sourced, de-identified CT scans to justify exemption from Institutional Review Board (IRB) approval.

The design process involved careful consideration of alternative methods and technologies, including imaging types, modeling software, and coding languages. The selection of cardiac CT scans as the primary imaging modality was based on its prevalence in heart attack diagnosis, cost-effectiveness, and ability to visualize the coronary arteries and any plaque buildup present.

Initially, the utilized methodology in this project involves an image segmentation step, where image processing techniques are applied to delineate the areas of interest within the CT scans. This step is essential for isolating the heart muscle and associated arterial structures. Then, each DICOM image undergoes a slicing procedure, being divided into 256 distinct slices with a resolution of 786×786 pixels. The slices are then fed into a combined Convolutional Neural Network (CNN) and Recurrent Neural Network (RNN) model. The CNN component is adept at extracting and learning spatial hierarchies of features from the sliced images, capturing the nuanced patterns and textures indicative of potential arterial blockages. The RNN layer, on the other hand, processes these features over sequential slices, allowing the model to understand the temporal and spatial progression of arterial conditions.

In the second part of the project, CardioForecaster employs a multi-software approach to investigate the hemodynamics within a simulated heart and cardiovascular system, focusing on the effects of Left Anterior Descending (LAD) artery blockages. Initially, a detailed 3D representation of the heart and cardiovascular system is crafted using Autodesk Inventor. Subsequently, these designed models are seamlessly integrated using 3D MAX software, a process that involves the fusion of the heart and cardiovascular system into a singular model.

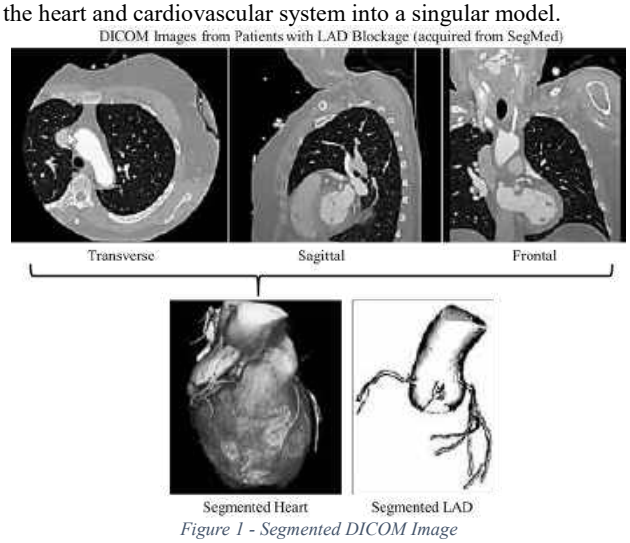

Figure 1 - Segmented DICOM Image

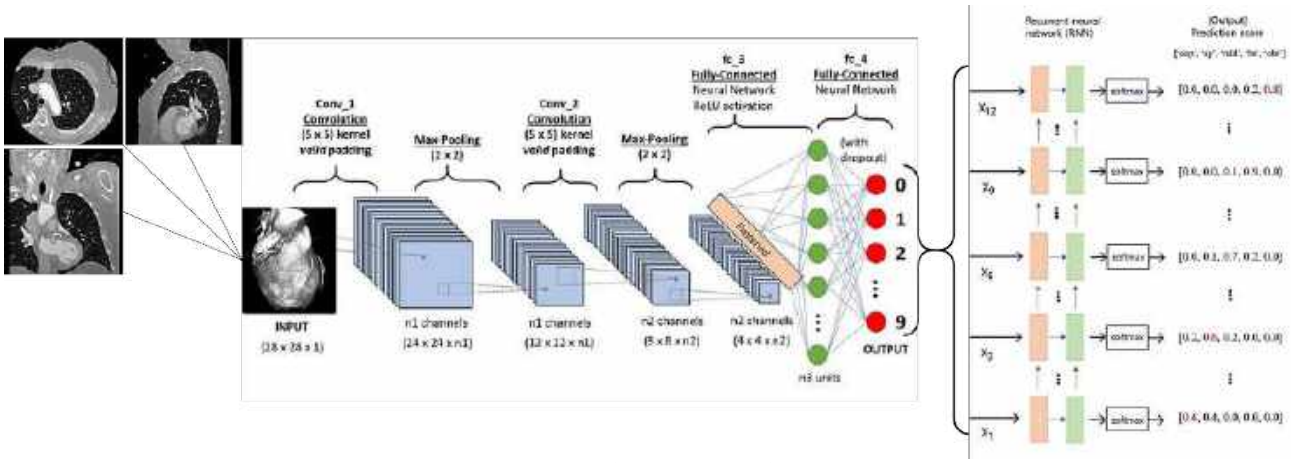

Figure 2 - The employed CNN + RNN algorithm

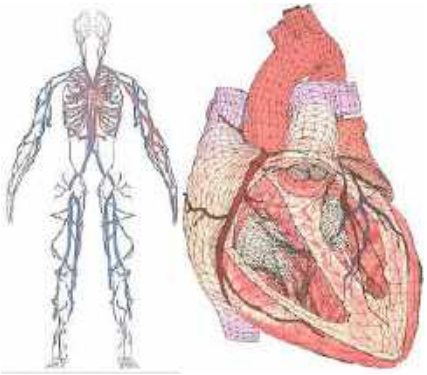

Figure 3 - The Under Study Cardiovascular System in 3DMax

This integration is crucial for maintaining the continuity of the cardiovascular structure and closed-circuit blood flow, which is essential for accurate simulation of simulation of the blood flow dynamics. Following the integration, a mesh of the entire system is generated and imported into ANSYS Fluent, a Computational Fluid Dynamics (CFD) software. ANSYS Fluent is utilized to simulate the blood flow within this system, using fluid dynamics algorithms to model the blood as a non-Newtonian fluid, mirroring its real-life rheological properties. This step enables the detailed analysis of blood flow patterns, velocity fields, and pressure distributions throughout the cardiovascular system under normal and pathological conditions. The simulation further uses the specific blockages identified in the LAD artery, mirroring the obstructions observed in CT scans used in the project's first phase. These blockages are modeled to replicate the exact conditions leading to myocardial infarction, thereby allowing for an in-depth exploration of the resultant hemodynamic alterations. This congruence between the simulated blockages and those identified in CT scans ensures that the model serves as both a predictive tool and a verifiable method to assess the AI algorithm's diagnostic accuracy developed in the project's initial phase.

BUDGET & MARKET ANALYSIS

This project has been completed with approximately $2300 in funding, alongside hardware donations, valued at approximately $300. All software used in this project are open-source or free for educational usage.

The CardioForecaster platform has the potential for broad implementation across 6,120 U.S. hospitals, private clinics, research facilities, and international markets [4]. The project entails an initial investment, notably a $100 million data center and $100,000 for further development. Financial projections, assuming full U.S. hospital adoption, suggest a one-year break-even with $125 million in revenue and a $20,000 license fee, yielding a $100 million annual ROI. Over five years, achieving break-even requires $225 million in revenue with a $7,000 license fee and anticipates a $20 million annual ROI. For a ten-year plan, the revenue need is $350 million with a $5,000 license fee, aiming for a $10 million annual ROI. This simplified financial outlook underscores the platform's market opportunity and economic potential.

CONCLUSION

In summary, the CardioForecaster project marks an advancement in the field of cardiovascular health, using the synergy between artificial intelligence, 3D modeling, and fluid simulation technologies to offer an approach to heart attack risk assessment. By analyzing the dynamics of blood flow and arterial blockages, particularly in the Left Anterior Descending (LAD) artery, this platform sets a new standard in predictive healthcare. The integration of AI with detailed heart models and simulations not only enhances the accuracy of heart attack predictions but also provides insights into the physiological impacts of arterial obstructions, thereby improving patient care and preventive measures.

ACKNOWLEDGEMENTS

We would like to acknowledge Mr. Theodore M. Hogan for his contributions.

REFERENCES

[1] Department of Health. (n.d.). Heart Disease and Stroke Prevention. https://www.health.ny.gov/diseases/cardiovascular/heart_disease

[2] Novant Health. (n.d.). The “widow-maker” heart attack hits women, too. Healthy Headlines. https://www.novanthealth.org/healthy-headlines/how-to-check-your-heart-health

[3] Author, G. (2023, August 9). Deep learning for medical imaging: Use cases and network types. Healthcare IT Today. https://www.healthcareittoday.com/2023/08/18/deep-learning-for-medical-imaging-use-cases-and-network-types/

[4] American Hospital Association. (n.d.). Fast facts on U.S. hospitals, 2024. https://www.aha.org/statistics/fast-facts-us-hospitals

[5] Jones, H. (2023, September 27). What does it cost to build a data center? Go-to-Market and Webinar-Led Growth for Data Center Industry. https://www.dcsmi.com/data-center-sales-and-marketing-blog/what-does-it-cost-to-build-a-data-center

DEVELOPMENT OF TAILORED FINITE ELEMENT HEAD MODELS FOR FREE VIBRATIONAL ANALYSIS ACROSS SUBJECT SPECIFIC GEOMETRY

Diego Acosta (1), Turner Jennings (1), Sinan Müftü (1), Rouzbeh Amini (1,2)

(1) Department of Mechanical and Industrial Engineering, Northeastern University, Boston, MA, USA
(2) Department of Bioengineering, Northeastern University, Boston, MA, USA

INTRODUCTION

Vibration analysis is a critical tool for evaluating potential harmful effects on the body from our daily environment. However, experimental testing methods impose a risk on human subjects. As a result, computational modeling is used to evaluate how vibrations impact the human brain without risking subject health. Though the use of finite element head models (FEHMs) has been employed previously [1,2], limitations arise from the geometric bio-fidelity of the meshes used. We hypothesize that the adoption of anatomically accurate meshes that encompass several layers of the human head (skin, skull, cerebrospinal fluid (CSF), grey matter, and white matter) will yield a novel calculation of the free vibration behavior of the brain. Additionally, previous researchers have described the vibration behavior of the head from a single subject-specific or population-averaged model [1,3,4]. We hypothesize that incorporating a range of ages and head geometries will result in varying resonance responses of the brain meshes not currently predicted by existing single models.

To address the need for more population-representative models of brain vibration behavior, we have developed a library of subject-specific FEHMs. Within a MATLAB script, the original meshes were optimized for vibration analysis within LS-DYNA by eliminating elements with poor aspect ratios. With the meshes loaded into the Finite element Analysis (FEA) software, material properties adapted from Iwamoto et al. [5] for the different tissues were applied. Lastly, modal analysis of the skull and brain for the first 50 modes were compared to current literature [1,3, 4, 6-8] for validation.

METHODS

Twenty subject-specific meshes originally derived from MRI images were used [9]. The meshes provided a highly detailed representation of the human head, and all its modeled layers (scalp, skull, CSF, grey matter, and white matter). Development of the tetrahedral element meshes used can be found in the literature [9]. For the scope of our study, a new method of translating the subject-specific meshes into a format for mechanical vibration simulation was developed. Conversion of the meshes to a compatible format was achieved through an internally developed MATLAB script in which the brain mashes were converted from the original file format into keyword input files for the LS-DYNA commercial FEA software. In addition to format conversion, volumetric checks and optimizations were implemented to correct elements with zero or near zero volume. By employing this conversion approach, the meshes became compatible with FEA software, enabling comprehensive modal analysis and determination of the natural frequencies of the human brain, along with the resulting resonant deformations. Once the original files were loaded in, both element and nodal data were extracted and organized within the MATLAB script. Two methodologies for volumetric calculations were employed. Element volume was calculated using Gaussian integration, to align with the volume calculation in LS-DYNA and also using geometric vector operations shown in Eq. 1.

$$V_{exact} = \frac{|(P_1) \cdot (P_2 \times P_3)|}{6} \tag{1}$$

Where $P_{1,2,\&3}$ represent three nodes from a reference node P_4. Calculating each element volume through numerical integration, began by defining Gaussian points and weights for a unit element in isoperimetric space. The shape functions, partial derivatives, and Jacobian matrix were computed. The sum of the Jacobian determinant evaluated at the Gauss points was used to calculate the volume, according to Eq. 2:

$$V_{gauss} = \sum_{i,j,k=1}^{n} w_i w_j w_k \, |J_{jkl}(x, y, z, \xi, \eta, \zeta)| \tag{2}$$

where w_i, w_j, w_k are the weights associated with the Gauss points in the parameter space ξ, η, ζ, and x, y, z are the coordinates of the corresponding points in the physical space.

Both methods of volume calculation were checked for zero-volume elements. To correct zero-volume elements, one node was displaced normal to the plane formed by the other 3 to recover a sufficient aspect ratio. The overall workflow of the described MATLAB script is illustrated in Figure 1.

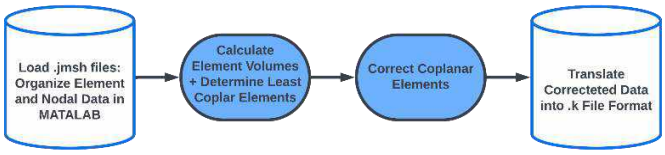

Figure 1. General Workflow of Developed MATLAB Script

Within LS-DYNA, material properties were assigned to the five layers of the model as linear elastic for the scalp and skull (MAT-001), and viscoelastic for the brain and CSF (MAT-061 and MAT-006, respectively). The material properties used were adapted from an existing FEHM [5].

With the 20 subject-specific models fully defined within LS-DYNA, modal analysis of the first 50 eigenvalues of subjections of the model (skull and brain) was conducted. The resulting natural frequencies were compared with the results from existing literature [1,3,4,6-8] for validation.

RESULTS

The natural frequencies associated with modes 1, 5, and 10 of the 20 skull and brain models are shown in Figure 3A and 3B, respectively. The data generated by the newly developed brain meshes are compared to three other studies that used different skull and brain models.

Figure 4 shows similar vibration modes in three typical subject-specific models. While the vibration modes are the same for all three, the natural frequencies are unique in each subject, explaining the variance seen in Figure 3.

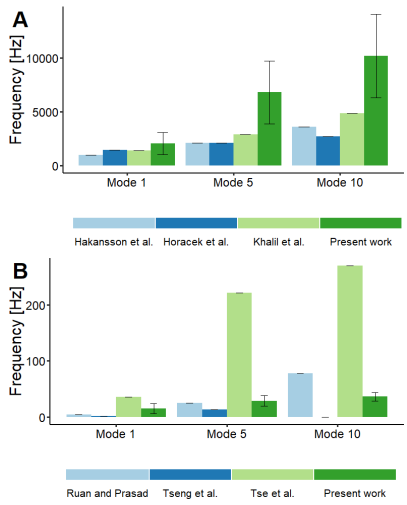

Figure 3. Comparison of (A) calculated natural frequencies of the 20 skull models with validation cases [6-8], (B) calculated natural frequencies of the 20 brain models with validation cases [1,3,4]

DISCUSSION

The original hypothesis was that the introduction of subject-specific head models of diverse geometries would result in varying natural frequencies that are not currently predicted by existing single-averaged models. The results from our initial work support this claim given the evident spread of natural frequencies presented in Figure 3.

As shown in Figure 3A, we observed significant variation in skull frequencies across the different meshes especially in modes 5 and 10. Figure 3B displays the resulting natural frequencies of the 20 brain models. When comparing the results of Figure 3, we observed that the use of the 20 subject-specific models produced a range of natural frequencies both in the skull and brain models. The range of natural frequencies captures the variability in biological geometry. Demonstrating how using subject-specific models as opposed to a single averaged model can provide a more comprehensive characterization of natural frequencies of the human skull and brain.

Figure 3 also shows that calculated natural frequencies can vary with head geometry. However, such disparities could also arise from the distinct methodologies employed in each study. More importantly, our research aligns closely with most of the studies presented in Figure 3, indicating that the newly formulated models maintain consistency with prior calculations.

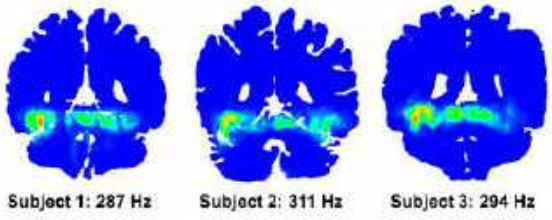

Figure 4. Coronal sections of similar vibration modes across three subject-specific brain models.

With further investigation of the modal analysis of the newly developed meshes, variation between the natural frequency and resulting excitement at the same mode of subject-specific models are shown in Figure 4. Such differences reiterate the contribution of individualized anatomical nuances in the brain, which the subject-specific models feature. The observed variation demonstrates the necessity of using subject-specific models in vibrational biomechanical analysis, as averaged models may not adequately represent unique characteristics that influence the natural frequencies of the human brain.

The tool developed herein has provided a comprehensive subject-specific model of the human head and demonstrated the impact of considering subject-specific models when conducting modal analysis. While this study focused on the natural frequencies of the first 50 modes of subject-specific models, the next steps include the calculation of higher modes and analysis of age-specific models to draw a correlation to variation in skull and brain size and natural frequency. Our framework lays the foundation for impact simulations and the study of general human system interactions.

ACKNOWLEDGEMENTS

We would like to thank Northeastern University's Project-Based Exploration for the Advancement of Knowledge (PEAK) Awards for their support of the authors. Funding for this project was provided in part by the United States Army Research Lab Soldier Protection Program (#W911NF2120208). The views presented in this research are those of the authors and not necessarily the views of the sponsors.

REFERENCES

[1] Tse, K et al., *Comp Meth Biomech Biomed Eng,* 18(9):961-973, 2015. [2] Fereydoonpour M et al., *Biomedical and Biotech*, 18 2022. [3] Ruan, J, Prasad P, *Stapp Car Crash J,* 45, 2001. [4] Tseng, J et al., *Bioengineered,* 7(4):219-225, 2016. [5] Iwamoto, M et al., Traffic Inj. Prev., 16: S36-S48, 2015. [6] Khalil, T et al., *J Sound Vib,* 63(3) :351-376,1979. [7] Horáček, J et al., *Nat Conf Int Part Eng Mech,* 2003. [8] Hakansson, B et al., *J Acoust Soc Am,* 95(3):1474-1481, 1994. [9] Tran, A et al., *Neurophotonics*, 7(1), 2020

TrueDose, AN ADOLESCENT MEDICATION COMPLIANCE IOS APPLICATIONS

N. Cilenti (1), E. Ferguson (1), S. Ford (1), M. Jester (1)
Faculty Advisor(s)
E. Berlew (1)
1. Department of Bioengineering, University of Pennsylvania, Philadelphia, PA

INTRODUCTION

1.a) Use Case

Medication non-adherence is a pervasive and multifaceted problem in adolescents. Core drivers for non-adherence include a desire for autonomy, a lack of parental support, and a sense of invincibility (S. Foster, personal communication, October 3, 2023). TrueDose aims to increase adherence by connecting patients, parents, and physicians; incorporating positive reinforcement; and promoting patient autonomy. TrueDose is designed for all adolescents, with a focus on adolescents required to take complex medication regimens.

1.b) Problem Impact

70% of adolescents are non-adherent to their medications, contributing to 50% of treatment failures, 25% of hospitalizations, and 125,000 patient deaths annually in the US.[1,2] Existing solutions, including pill boxes and reminder apps, target forgetfulness, but are limited as they neglect the complex nature of adolescent non-adherence. Current solutions fail to address the desire for independence, the impacts of incentivization, and the customizable nature of an app that can adapt to adolescents changing medication regimes.

1.c) Scope (Objective)

TrueDose aims to increase medication adherence by targeting the core drivers of non-adherence. TrueDose integrates reminder capabilities, a pill identifier, data analytics, and patient incentives to improve adherence by balancing external support with patient autonomy. TrueDose is designed with patients in mind, but functions with three interfaces to serve as a support network for patients, their parents, and physicians alike, bringing all medication questions to one singular application.

Product design

TrueDose consists of 3 unique interfaces, one for the patient, one for the physician, and one for the parents or guardians. Physicians may create an account as a physician and once logged in are able to register their patients by email. They can then input the medication type, quantity, timing and any other pertinent information for the patient to have.

From the patient perspective, once registered they will be able to view a calendar dashboard of all of their required medications and other general information. At the time they are required to take their medications they will receive a push notification, and if they click on it it will bring them to their camera. They will then take a photograph of their medication on a plain background and the pill algorithm will detect if it is the correct medication. If it is correct the app will instruct the patient to take X number of the medication. If the app detects the wrong medication, it will instruct the patient to try again.

The third interface, the parents interface, allows guardians to monitor their child's medication compliance from afar. They will have the option to enable a two-factor authentication feature or remain in view-only mode. In two-factor authentication mode the parents have the option to approve the medication that was taken. They will get a push notification when their child takes a photo of the medication and then can confirm or deny if this is true. Further they can input incentives based on what makes sense for their family. The goal of the parents interface is to provide a sense of supervision while still giving as much autonomy as possible.

Figure 1: A sample interface for each of the three interfaces of the application.

Budget & Market Analysis

The design budget allotted to TrueDose was $600 per semester of the academic year, resulting in $1200 through the course of the entire design project. The budget has supported design and development of the software and launch onto the apple store.

On its largest scale the market size for our product is adolescents in America. Currently there are approximately 21 million Americans aged 15-19.[3] Within the population of American adolescents, our product is more suitable for adolescents with chronic diseases or complex medication regimes. According to the CDC, nearly 40% of children and teenagers have chronic illness, making the target population closer to 9M adolescents[4]. The population is large and sadly ever growing as more adolescents continue to develop chronic diseases annually.

Within this target population we estimate that we can penetrate 0.01% of this population in the first year, leading to approximately 90,000 adolescents, however when multiplied by 3 as a physician, and guardian is needed for each patient the total number of users is around 270,000 users.

Once launched on the app store, the application is easily accessible to anyone with a smartphone, which is assumed to be the majority of the adolescent population. We aim to charge $5 for the application, keeping the cost low and accessible to all populations. The development costs are very low as the product is fully software. The development costs however fall on the data scientist and software engineers holding the back end of the application together. The cost per unit can be expected to be very low, and the majority of expenses will relate to updating and keeping the software running.

We plan to include advertising and other potential revenue streams later on, but initially are looking to make the app accessible for all and want to keep the cost low. Often people have an aversion to paying for apps, especially when they are more expensive.

Ultimately, TrueDose aims to increase medication adherence in adolescents with the hopes of improving health outcomes in this population.

ACKNOWLEDGEMENTS

We gratefully acknowledge the support provided by the University of Pennsylvania throughout the completion of this project. Additionally, we extend our sincere appreciation to the Bioengineering Senior Design faculty for the mentorship and assistance.

References

1. DTB. 2016;54:6-9.
2. Kim, J. US Pharm. 2018;43(1)30-34.
3. Bureau, U. C. (2022, August 18). *The U.S. adult and under-age-18 populations: 2020 census*. Census.gov. https://www.census.gov/library/visualizations/interactive/adult-and-under-the-age-of-18-populations-2020-census.html
4. Pavilonis, V. (2022, February 10). *Fact check: More than 40% of children have chronic illness, CDC says*. USA Today. https://www.usatoday.com/story/news/factcheck/2022/02/10/fact-check-more-than-40-children-have-chronic-illness-cdc-says/6639320001/

THE SMALLER, THE BETTER?: STUDYING THE IMPACT OF MINIATURIZING LVADS ON HYDRODYNAMICS AND HEMOCOMPATIBILITY

Shobana Santhanam (1), Shweta Karnik (1), Charles Federico (1), Lakshmi P. Dasi (1)

(1) Department of Biomedical Engineering, Georgia Institute of Technology and Emory University, Atlanta, GA, USA

INTRODUCTION

There are approximately 960,000 new cases of heart failure (HF) in the United States every year[1]. While many of these cases are addressed with non-invasive treatment such as medication, severe cases of heart failure require either a heart transplant or a left ventricular assist device (LVAD). While heart transplantation is the gold standard of treatment for extreme HF, the longer waiting periods for donor hearts make it unfeasible for the patients to receive timely and appropriate care. Thus, LVADs have become the new standard of care for HF patients.

An LVAD is a mechanical pump that assists in pumping blood from the heart to the body. It can restore heart function, and prolong and improve patients' lives; however, it is associated with significant complications that can affect its long-term operation [2,3].

Currently, Heartmate 3 LVAD (Abbott Lab, Illinois) is the only FDA-approved implantable device on the market. Approved for long-term usage in adults in 2018, this device aims to minimize blood trauma and eliminate the wear and tear caused by contact bearings using magnetic levitation technology. However, issues such as inlet flow disruptions, material deformations, and halted pumps have been reported by users worldwide[4].

Studies have found that women are at a higher risk of post-LVAD mortality and right-ventricular failure. In a 2-year outcome study of the MOMENTUM 3 (Multicenter Study of MagLev Technology in Patients Undergoing Mechanical Circulatory Support Therapy With HeartMate 3) trial, it was found that women had an increased rate of stroke (adjusted incidence rate ratio [aIRR]: 1.52), major bleeding (aIRR: 1.28) and infection (aIRR 1.14)[5]. One measurable factor that has been connected to these morbidities is the patient's preoperative left-ventricular end-diastolic diameter (LVEDD). Smaller LVEDD, usually defined as less than 60 mm, is independently predictive of worse outcomes after LVAD implantation[6].

Currently, there is only one size of the Heartmate 3 available on the market. A possible solution to higher mortality among smaller patients is to reduce LVAD size based on the LVEDD. This study aims to determine the potential of miniaturizing LVADs and explore its effect on the pump performance and the hemocompatibility.

METHODS

Design and Manufacturing

Three LVAD sizes with rotor outer diameter (OD) of 15 mm, 30 mm, and 45 mm were created. The blade inlet and outlet angles were set at 20º and 30º respectively. Each blade had a set thickness of 1.2 mm and a height of 7 mm. The volute sizes were adjusted to the rotor ODs to ensure design consistency. These prototypes were then 3D printed using a J850 Pro (Stratasys Ltd, MN, USA).

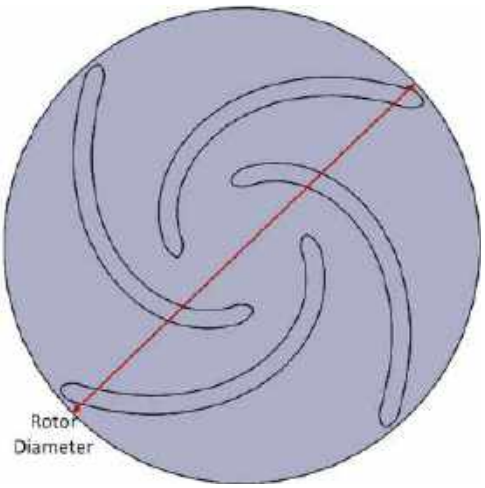

Figure 1: LVAD Prototype with 30 mm Rotor Diameter.

Hydrodynamic Performance Analysis

A bench top loop was set up with a 40% wt glycerin solution that imitates the viscosity of blood. The bench top loop consisted of a reservoir, a motor to drive the rotor, an ultrasonic flow probe to measure the volumetric flow rate, a resistance clamp on the outlet of the device to vary the resistance to flow and produce required pressure and two pressure transducers to measure the inlet and outlet device pressures.

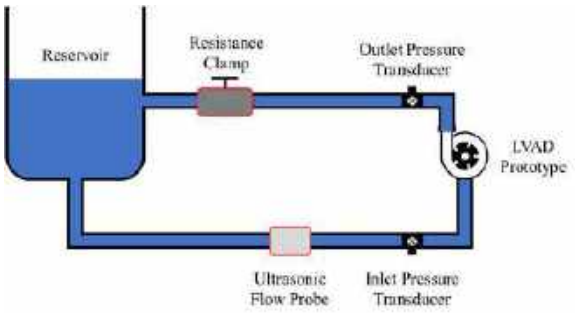

Figure 2: Hydrodynamic Performance Testing Bench-Top Loop Schematic.

The pump was driven at 3000 RPM, the downstream resistance was increased incrementally, and the pressures and flowrates were measured. To analyze the hydrodynamic performance, the hydrodynamic efficiency (η_h) and the gradient of the pressure-flow curve were calculated.

$$\eta_h = \frac{Hydraulic\ Power}{Mechanica\ \ Power} \times 100 \quad (1)$$

$$Gradient_{4-6} = \frac{P_4 - P_6}{4-6} \quad (2)$$

Hemocompatibility Testing

A similar testing setup was used to measure the hemocompatibility of each of the three LVAD prototypes. The experimental procedure included collecting data over a six-hour period and performing each test five times. The loop is adjusted to simulate the pressure and flow conditions of an average adult heart (5 L/min, 90 mmHg). The loop temperature, the operating speed and power consumption of the LVAD prototypes were measured and maintained for each experiment.

The blood samples were collected every 30 to 60 minutes for six hours, following the standard practice recommended by ASTM F1841-19. The collected samples were then centrifuged to obtain plasma for further analysis. Platelet activation and hemolysis were measured using enzyme-linked immunoassays (ELISA) kits.

RESULTS

For the LVAD prototype with a rotor diameter of 30mm, the gradient at adult operating conditions was – 11.52 mmHg/ $(L/min)^{-1}$. The pressure-flow curve is as shown in Figure 3.

Results for the remaining hydrodynamic performance analysis and hemocompatibility testing is currently being generated and will be presented at the conference.

DISCUSSION

The miniaturization of LVAD prototypes proposed in this study will lay a solid foundation to understand its effect on the hydrodynamic performance and the hemocompatibility of LVADs. This knowledge, in turn, will aid in designing the next generation of size appropriate LVADs based on LVEDD.

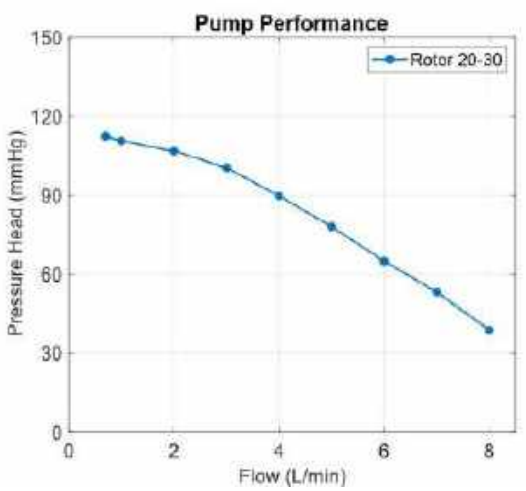

Figure 3: Pressure-Flow Curve for LVAD Prototype with 30 mm Rotor Diameter.

ACKNOWLEDGEMENTS

Research supported by the National Institute of Biomedical Imaging and Bioengineering of the National Institute of Health under Award Number 5R21EB033960.

REFERENCES

[1] Virani SS. et al. *Circulation.* 141(9):e139-596. 2022
[2] Rogers JG, et al. *Journal of the American College of Cardiology* 55.17 (2010): 1826-1834.
[3] Kato TS, et al. *The Journal of heart and lung transplantation* 31.1 (2012): 1-8.
[4] Heaton, J. N. et al. *Indian Heart Journal*, 73(6), 765–767. 2021
[5] Ramu B. et al. *JACC. Heart failure* vol. 11,12 (2023): 1692-1704.
[6] Anne Dual, S., et al. *ASAIO journal,* 68(1), 21–27. 2022.

SB³C2024
Summer Biomechanics, Bioengineering and Biotransport Conference
June 11-14, Lake Geneva, WI, USA

THERMAL CONTROL OF CIRCADIAN FUNCTION FOR ENHANCED SLEEP ONSET AND BLOOD PRESSURE MODULATION

Kenneth R. Diller, Laura H. Namisnak, Sepideh Khoshnevis (1)

(1) Biomedical Engineering Department, University of Texas at Austin, Austin, TX, USA

INTRODUCTION

Thermoregulatory function is governed very strongly by blood flow between the body core tissues and organs and glabrous skin, particularly in the hands and feet. This vascular network constitutes the heat transfer component of the circulatory system, having its own dedicated control function. The terminal vessels of this flow network are arteriovenous anastomoses (AVAs) which have the capability of vasodilating to a diameter more than an order of magnitude larger than the capillaries that terminate the parallel nutritional network. The heat exchange and nutritional networks have independent control functions, but operate under a single pumping source, the heart. Distribution of blood flow throughout the complete vascular system is regulated primarily by the local flow resistance which, according to Poiseuille's law, is proportional the inverse of the vessel diameter to the fourth power.

Given its key function in thermoregulation, the ability to upregulate AVA blood flow on demand has numerous important clinical and life advantages. Increasing nutritional blood flow is as easy as applying a capsaicin cream that is ubiquitously available over the counter to treat muscle pain. However, AVA blood perfusion is stubbornly resistant to flow enhancement by capsaicin or any other commonly known means to cause an increase in local blood flow in nonglabrous skin.

Several years ago our lab discovered a technique that we have termed Selective Thermal Stimulation (STS) to intervene in the control of blood flow to AVAs on demand [1]. STS may be practiced by simple and safe surface heating along the cervical spine to warm receptors that have key inputs into thermoregulatory control, and specifically to cause parasympathetic relaxation of vasoconstriction of AVAs. The objective is to increase glabrous skin blood flow (GSBF) on demand to access physiological and medical benefits.

METHODS

Since discovering STS the Diller lab has conducted hundreds of exploratory experiments to characterize this phenomenon. Healthy human subjects are placed in a supine position on a comfortable surface in a thermoneutral environment. The clothing ensemble such as shorts and a tee shirt minimize thermal insulation to heat transfer convection with quiescent room air. These experiments are approved by the university of Texas IRB. Instrumentation consists of laser Doppler flow sensors placed on the pad of a middle finger and on the volar forearm. Beat-by-beat blood pressure is monitored via pulse transit time technology. STS is practiced by applying mild warming along the cervical spine either by surface heating or by using a penetrating heat source. In all cases the STS protocol design must adhere to a strict balance between achieving efficacy for increasing GSBF, which in general is proportion to the stimulation temperature [1], and safety, which requires that the temperature within deep tissues not exceed the threshold for thermal injury. This threshold is generally held to be 43°C [2] so that our protocols limit the applied temperature to no higher than 43°C and as the technology has evolved to no more than 41°C. This practice has been worked well since heat applied at the surface would need to diffuse to deeper neurological structures before damage could occur where the temperature would be less than at the surface.

During testing regimens subjects are initially exposed to a thermal accommodation period of about 20 minutes to adjust to the room environment. Next, STS warming is initiated on the skin overlying the cervical spine and maintained for a minimum of 10 to 15 minutes and sometimes as long as one hour. This procedure is practiced by either a flexible polymeric bladder through which warm water is circulated or by direct application of an electrical resistance heater. Sometimes the electric heater is cycled on and off to provide a dynamic stimulus although this method provided no measurable benefit.

Primary instrumentation applied to subjects consists of thermocouples on the skin at the site of STS and at representative glabrous and nonglabrous skin locations and laser Doppler blood flow probes also at glabrous and nonglabrous locations.

RESULTS

Data from an exemplar STS trial is shown in Fig. 1. Following an initial benchmark period of 10 min, an electric heating pad was placed over the cervical spine for 25 min and then physically removed.

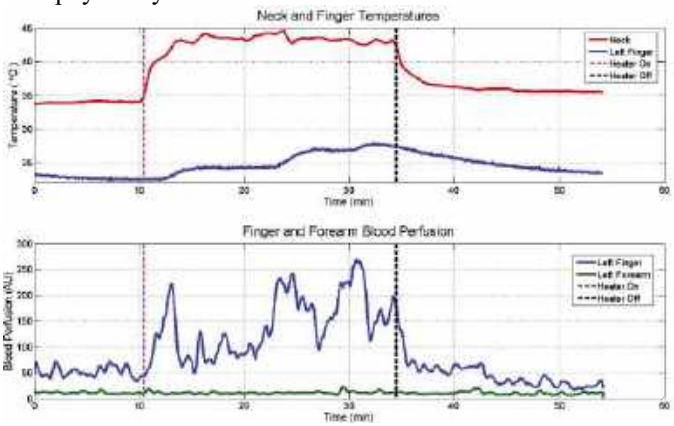

Figure 1. Temperature and blood flow data for an exemplar STS trial. The top panel shows skin temperatures on the cervical spine (red) and a middle finger pad (blue). The bottom panel shows laser Doppler blood flow at a finger pad (blue) and corresponding forearm (green).

The data demonstrate that the subject was vasoconstricted at the start of the trial. There is a strong correlation between the upregulation and downregulation of GSBF in conjunction with the application and removal of STS. The alteration of GSBF begins approximately when the cervical skin temperature rises to the range of 39-40°C. The surface temperature on the finger pad follows the level of blood perfusion measured in the adjacent finger with an approximate 2 min delay as heat diffuses outward from the warm perfused blood to the skin surface. STS has no effect whatsoever on blood flow in the volar forearm.

DISCUSSION

Although STS has important clinical implications for manipulating core temperature to induce or remove a hyper- or hypo-thermic state, the focus of the present study is to enhance the role of glabrous skin blood flow in achieving effective sleep. Opportunities having the greatest potential impact are to enable more rapid sleep onset, to adjust the sleep onset time, and to lower the blood pressure during sleep. Subjects are instrumented with skin thermal sensors on the calf and sole to measure the distal – proximal gradient (DPG) as an indication of GSBF. Trials consist of spending a night in our sleep lab using our prototype bed equipped with STS plus differential mattress temperature zones between the body core and peripheral areas. Fig. 2 presents data for DPG difference of 9 subjects sleeping on the bed on nights for control and for the thermal system activated. The horizontal line indicates the lights out period. [3]

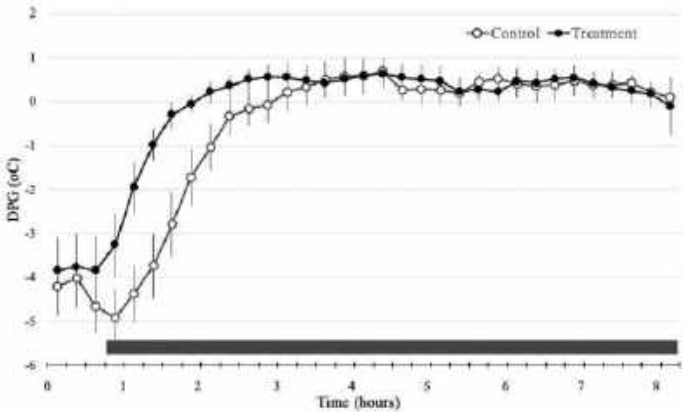

Figure 2. DPG temperature between treatment and control nights for nine subjects. Enhanced GSBF prevails through the first 3+ hours of sleep following initial STS period. Sleep onset latency decreased from 83 to 35 min with the thermal system activated causing greater GSBF ($p = 0.012$).

Data has been gathered from some 90 STS trials in which blood pressure was measured on a beat-by-beat basis to assess whether STS induces a dip in blood pressure in conjunction with AVA vasodilation. A large longitudinal trial by Hermida, et al has documented that sleep time dipping of blood pressure leads to a 43% reduction in the five-year probability of experiencing major cardiovascular events such as an arrest or stroke [4]. Thus, we are engaged in a large-scale statistical analysis of our STS data so identify the efficacy for inducing BP dipping. Initial data indicates a promising outcome.

ACKNOWLEDGEMENTS

This research was sponsored in part by NIH Small Business Technology Transfer (STTR) grant 2R42GM119871 awarded to Mercury Biomed, LLC (Cleveland, OH) and subcontracted to The University of Texas at Austin, and by the Robert and Prudie Leibrock Professorship in Engineering at the University of Texas at Austin. Kenneth Diller has an equity position in Mercury Biomedical, LLC, a corporation that holds a license from the University of Texas for STS technology. Dr. Diller has never received financial compensation from Mercury Biomedical.

REFERENCES

[1] Diller, KR, *Adv Heat Trans*, 47:341-396, 2015.
[2] Henriques, FC, *Arch Pathol*, 43:489-502, 1947.
[3] Haghayegh, S, et al, *J Sleep Res*, 31:e12662, 2022.
[4] Hermida, RC, et al, *Chronobiol Internat*, 40(1):63-82, 2023.

COLLABORATIVE PATHWAYS: EMPOWERING PREGNANT AND PARENTING TEENS THROUGH STEM ENGAGEMENT

Oluwatomisin O. Ajayi (1), Emily A. Hoffmann (1), Paige R. Nielsen (1), Lauren E. Tolbert (2), Kyoko Yoshida (1)

(1) Department of Biomedical Engineering, University of Minnesota, Minneapolis, MN, USA
(2) Longfellow Alternative High School, Minneapolis, MN, USA

INTRODUCTION

The Pregnancy Research Engineering Group (PREG) at the University of Minnesota (UMN) seeks to understand the mechanics of maternal soft tissue growth and remodeling during pregnancy and discover how and why complications occur [1]. Since research alone cannot help pregnant patients, PREG strongly seeks to not only fill scientific knowledge gaps in pregnancy and women's health, but also uplift and support women through other venues, including by sharing our research with populations affected by pregnancy. Here, we address the need for educational support and resources for the underserved population of pregnant and parenting (P&P) teen girls, who face many obstacles and are at high risk for preterm birth [2]. With only 50% high school and 2% college completion rates, it is evident that P&P girls do not get all the support they need. Among existing college pathway programs available to P&P teens, less than 50% provide opportunities to visit universities, and only 12% pair them with college mentors. These statistics culminate with the reality that although 59% of pregnant and parenting teens aspire to careers that require college education, only 20% enroll, and even fewer finish [3].

To address this issue in our community, we created an outreach program to introduce high school P&P girls to STEM careers, provide them with resources, and encourage them to follow their aspirations. We partnered with Longfellow Alternative High School for pregnant and parenting teens in Minneapolis, Minnesota that provides an Early Learning Center for the students' children and a clinic to support P&P girls (ages 13-21) in finishing high school. In addition to visiting and inviting the students to the research lab on campus during the 2022-2023 school year, we had the opportunity to visit the students this past October and are planning for future visits and campus tours at UMN. Here, we present an outreach activity we developed, which introduced P&P girls to pregnancy biomechanics and research at PREG, an interactive problem-solving activity demonstrating uterine contractions during labor, and post-secondary education opportunities and resources. As a lab that specializes in pregnancy biomechanics, we strive to use our research as a tool to ignite a passion for STEM in P&P students through their personal pregnancy experience with the ultimate goal to provide them with the confidence to pursue STEM education and careers.

PROGRAM DESCRIPTION

We began the outreach activity with an introduction to engineering and PREG. To encourage participation from the P&P girls, we asked them to share their impressions of engineering and STEM. We introduced the concept of engineers as creative problem-solvers and followed with a brief overview of the research goals of PREG to demonstrate how STEM careers contribute to increasing knowledge about their shared experience of pregnancy. Our introduction also included an icebreaker, during which we asked the P&P girls and teachers to share weird or interesting things that happened during their pregnancies. It was a valuable opportunity for the students to connect with each other.

We then introduced the students to the anatomy and physiology of pregnancy and the uterus, which we further contextualized with a realistic, three-dimensional anatomical model (Fig. 1). The crux of our activity was a hands-on learning and problem-solving activity to demonstrate labor contractions (Fig. 2). The students were asked to inflate balloons containing a ping-pong ball which sealed the air. Here, the balloon and ball represented the uterus and fetus, respectively. Working in pairs, we tasked the P&P girls with figuring out the best way to get the ping-pong ball out of the balloon. They were given time to experiment and problem solve, reflecting what engineers would do to overcome a challenge. Finally, we came together as a group to demonstrate that squeezing at the top of the balloon was the best way to extract the ping-pong ball, mimicking how the uterus contracts for labor. The balloon activity concluded with an explanation of the science behind uterine contractions during pregnancy. We demonstrated a finite

element model simulation of the activity, developed in our lab (using FEBio v2.4, Fig. 3), and a video of the first birth captured in an MRI to further contextualize the connection between pregnancy and technology [4].

Our visit to Longfellow concluded with a Q&A session for the P&P girls to ask about the activity and careers in STEM. We had a range of backgrounds and experiences on the panel, including our research advisor, 2 graduate researchers, and 2 undergraduates to provide input from women in different career and life stages. The P&P girls asked questions including, 'Is engineering hard?', 'Are any of you mothers or plan to have children?', 'What is college like?', 'How did you create the FEA model?', and 'Have you found the best ways to recover from pregnancy through your research?' Overall, this provided an intimate opportunity to share personal experiences and challenges in STEM.

Figure 1. Exploring the anatomy of pregnancy.

Figure 2. Thinking like engineers during the balloon contractions activity.

Figure 3. Contextualizing the connection between pregnancy and technology.

STUDENT FEEDBACK AND FUTURE DIRECTIONS

The students were incredibly receptive towards the balloon activity, demonstrating curiosity and engagement throughout the session. We followed up with an interview with Longfellow's science teacher, Ms. Lauren Tolbert, to evaluate the presentation and receive feedback. The teachers felt that the concepts covered were fully explained without making the experience too passive and lecture-heavy. The students' enthusiasm reinforced the importance of providing accessible STEM education opportunities to P&P girls. In addition to asking questions, the P&P girls shared their career interests and we found that many are now more interested in pursuing STEM careers. Here are some direct comments from the students and teachers at Longfellow:

> *"I appreciated how friendly and outgoing all the presenters were, and how flexible the lesson was. You all made time for the students to play and explore."*
>
> *"I never saw a visual of how the muscles in our uterus make contractions happen until that presentation."*
>
> *"The lesson was lively and engaging, students enjoyed it and continued talking about it for quite a while afterwards."*
>
> *"I never thought I wanted to be an engineer. If I can study pregnancy and birth, I'm more interested in it!"*
>
> *"It was inspiring for them to see successful students excited about their education, and to hear about the various paths that brought them to PREG."*
>
> *"It was cool to see how the way we pushed on the balloon is the same way our baby is pushed out!"*

Moving forward, we plan to include more visuals, small group work, focusing on think-pair-share and other active learning strategies, and introduce other technical skills, such as programming and engineering design. We also plan to improve on our demonstrations of the FE model and give the P&P girls a behind-the-scenes look at what goes into building a simulation. We will complement our activity with an on-campus tour at UMN for the Longfellow students in the Spring. Overall, we succeeded in sparking curiosity for STEM and engineering in P&P girls, highlighting the transformative impact of targeted outreach initiatives. We will continue to improve and expand this outreach activity to increase access to resources and support for pregnant and parenting students with the long-term goal of diversifying the future generation of engineers and STEM professionals.

ACKNOWLEDGEMENTS

This work was supported by the NSF CAREER Award. We also acknowledge and thank the University of Minnesota's Student Parent HELP center for gifts for the students, Emi Gaçaj for her help with the activity, and the Longfellow High school students and teachers.

REFERENCES

[1] "Pregnancy Research and Engineering Group (PREG)." Online, yoshida.bme.umn.edu/research, 2023.
[2] Marvin-Dowle et al., *BMJ Open,* 8(3):e016258, 2018.
[3] Costello, C. B. "Pathways to Postsecondary Education for Pregnant and Parenting Teens: Working Paper. *Institute for Women's Policy Research*, 2014.
[4] Bamberg, et al., *Am. J. Obstet. Gynecol*, 206(6):505, 2012.

CONTROLLING NEURAL CULTURE DENSITY AND ORIENTATION FOR ENHANCED ANALYSIS OF TRAUMATIC BRAIN INJURY ELECTROPHYSIOLOGY

G. Radtke (1), J. Sergay (2), J. Park (1), J. Zhang (1), C. Franck (1)

(1) Department of Mechanical Engineering, University of Wisconsin - Madison, Madison, WI, USA
(2) Department of Biomedical Engineering, University of Wisconsin - Madison, Madison, WI, USA

INTRODUCTION

Approximately sixty-nine million people worldwide suffer a traumatic brain injury (TBI) each year, leading to potentially permanent neural damage and a severe decline in quality of life [1]. For mild TBIs, there is evidence that significant, irregular signal activation and propagation among neural networks within the brain tissue occurs after impact [2]. Nonetheless, quantitative descriptions of the relationship between neural network activity and specific injury mechanics, such as the strain and strain rate of brain tissue deformation, are still largely lacking at the cellular level. A current noninvasive technique to characterize the mechanical threshold for significant electrophysiological disruption utilizes large-scale imaging of fluorescent calcium probes in 2D in vitro neural cell cultures in conjunction with applying strain to the cells. Current computational tools to differentiate calcium signals in individual neurons can only deconvolve fluorescent signals retrieved from the cell somas due to the challenge of soma-neurite overlap within dense 2D cultures. However, signal propagation through neurites and synapses also provides vital network information relevant to altered electrophysiology post-TBI uncaptured by current methods.

To address this gap in knowledge, this study spatially controls the 2D geometric arrangement of in vitro neural networks to better trace intracellular calcium dynamics throughout all neural cell structures. This is achieved via the development of a protocol to micro-contact print (μCP) a cell-adherent protein layer capable of confining single cells directly on stretchable polydimethylsiloxane (PDMS) substrates [3]. Alongside protocol refinement, this study investigates the influence of varying spatial distributions, cell densities, and network branching on functional neural networks and their response to TBI-like loading. Ultimately, the various μCP networks will be subjected to uniaxial tensile stresses to simulate mild TBIs while collecting fast-rate calcium images pre- and post- stretch. This enables comparison between μCP and unpatterned culture electrophysiology and offers insight into potential dysregulation in calcium dynamics [4]. Here, we outline this methodology enabling enhanced spatial and temporal resolution to analyze the effect of physical network parameters on the altered network activity propagation following TBI.

METHODS

Stamp master-molds were fabricated through traditional UV lithography techniques via a PRIMO system (Alvéole), with pattern designs within the master-molds iteratively optimized to confine a single cell to a single unit space (12.5 μm central nodes connected to 7.5 μm wide and 50 μm long extensions) (**Fig. 1a**). To produce stamps, master-molds were coated with 10:1 PDMS (Sylgard 184), cured overnight at 60°C, and cut into stamps (**Fig. 1b**). As partially described in previous work and illustrated in **Fig. 1d**, stamps were then treated with oxygen plasma, coated with a 1 μg/mL laminin/Poly-D-Lysine (PDL) solution, cleaned of excess solution via nitrogen gas, and pressed into contact with an 80 μm thick polyvinyl alcohol (PVA) film [5].

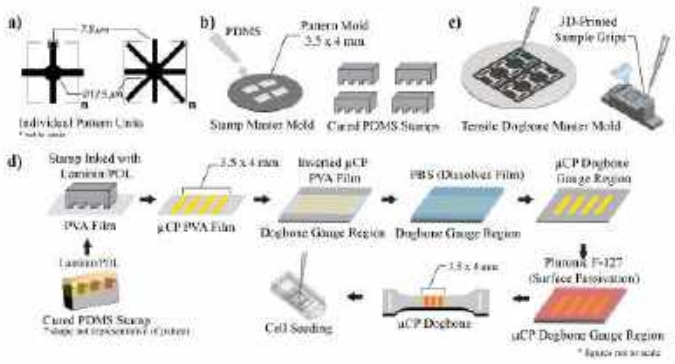

Figure 1: Preparation of μCP neural co-culture. a) Depiction of grid and hexagonal pattern geometry, respectively. Preparation via soft lithography of b) stamps for extracellular matrix patterning and c) tensile dogbone samples within biocompatible grips. d) Overview of sample substrate patterning.

The sacrificial PVA film, as shown in **Figure 1d**, was trans-printed and placed into contact with a prepared PDMS tensile sample (10:1; Syl-

gard 184) within 3D-printed, biocompatible constructs (**Figure 1c**). Subsequent phosphate-buffered saline (PBS) washes dissolved away the sacrificial film. The substrate was, lastly, passivated with 1% Pluronic F-127 to minimize off-pattern adherence and migration and further washed with PBS. Cortical cells from postnatal day P0-P1 Sprague-Dawley rat pups were then dissected and seeded onto the substrate (at a density of 575 $\frac{cells}{mm^2}$) and maintained until maturation at 10 days in vitro (DIV) via media exchange every two days.

Following culture maturation, network activity was captured via optical measurement of fluorescence using the calcium indicator Fluo-4 AM, wherein fluorescence indicates relative intracellular Ca^{2+} concentration. μCP and unpatterned (i.e., wherein the laminin/PDL is applied non-specifically to the sample substrate) culture activity is compared. Timelapse images of network activity within both culture types were acquired at 25 frames per second via epifluorescence microscopy (Nikon Ti2E; 20x objective) at 37°C. Image sequences were binarized within ImageJ, and fluorescent traces were extracted and processed within the NeuroCA application, outputting raster plots of network activity as previously described [6].

RESULTS

Preliminary data are promising, with μCP samples maintaining pattern fidelity and exhibiting electrophysiological activity at 10 DIV. Moreover, μCP cultures exhibit, albeit on a less drastic scale, relatively equivalent global activity to unpatterned cultures. **Figure 2a,c** juxtapose unpatterned and patterned density, orientation, and resolution. That is, the unpatterned culture (**Figure 2a**), while allowing for deconvolution of activity within the cell body, lacks visualization of individual neurites; the patterned culture (**Figure 2c**), however, consistently enables deconvolution of fluorescent signals throughout all intracellular structures. **Figure 2b,d** demonstrates the mentioned coordination in global activity, an indication of network maturity, with coordinated firing observed past 60 second time-mark in the unpatterned sample (**Figure 2b**). In the patterned sample (**Figure 2d**), the network bursts are seen within the first quintile of the timelapse. Thus, we developed and validated a consistent method for control and confinement of neural co-culture growth on a stretchable PDMS substrate.

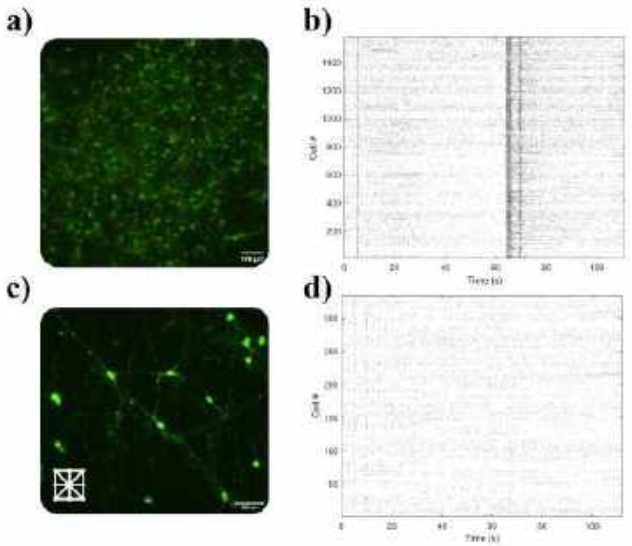

Figure 2: Sample baseline comparison at 10 DIV of electrophysiological activity. a) Unpatterned neural co-culture, seeded at a density of 1,750 $\frac{cells}{mm^2}$ and imaged at 20x magnification (green: Fluo-4 AM). b) Raster plot of unpatterned culture activity. c) Patterned neural co-culture, seeded at a density of 575 $\frac{cells}{mm^2}$ and imaged at 20x magnification, enlarged (green: Fluo-4 AM). d) Raster plot of patterned culture activity.

DISCUSSION

These results are exciting, particularly given their novelty. Numerous examples of μCP single-cell resolution cultures on both rigid and flexible substrates exist within the literature; however, full (2D) control of cell density and neurite orientation – consistently resolving the electrophysiological dynamics of a single cell and its respective protrusions – atop a stretch-ready substrate has yet to be reported. The significance of both variables (i.e., density and orientation) should be noted, as neural culture density is known to influence both culture maturity and global electrophysiological activity, while neurite orientation is heavily implicated in injury susceptibility during mechanical deformation [7, 8].

Braun et al., for instance, report confinement of neurite orientation along one axis atop a PDMS substrate; however, this study lacks control of both density and full neurite confinement. Further, the electrophysiological data extraction from single cells instead relies upon patch clamp methods – lacking global activity resolution [8]. Likewise, the methods outlined by Nagamine et al., while enabling full control of cell density and orientation, lack particular application to the TBI-relevant stretch injury that the methods described in this abstract aim to ultimately model [9].

With method refinement complete, we proceed to the next aim of subjecting μCP cultures to controlled mechanical loading, with the goal of extracting electrophysiological dysregulation within all intracellular structures following loading.

ACKNOWLEDGEMENTS

This research is supported by the U. S. Office of Naval Research under PANTHER award numbers N000142112044 and N000142112855 through Dr. Timothy Bentley.

REFERENCES

[1] Meaney, D. F., Morrison, B., & Dale Bass, C. (2014). The mechanics of traumatic brain injury: a review of what we know and what we need to know for reducing its societal burden. *Journal of biomechanical engineering*, *136*(2), 021008.

[2] Weber J. T. (2012). Altered calcium signaling following traumatic brain injury. *Frontiers in pharmacology*, *3*, 60.

[3] Kane, R. S., Takayama, S., Ostuni, E., Ingber, D. E., & Whitesides, G. M. (1999). Patterning proteins and cells using soft lithography. In D. F. Williams (Ed.), *The Biomaterials: Silver Jubilee Compendium* (pp. 161–174). Elsevier Science.

[4] Summey, L., Zhang, J., Landauer, A. K., Sergay, J., Yang, J., Daul, A., Tao, J., Park, J., McGhee, A., & Franck, C. (2023). Open Source, In-Situ, Intermediate Strain-Rate Tensile Impact Device for Soft Materials and Cell Culture Systems. *Experimental Mechanics*, *63*(9), 1445–1460.

[5] Yu, H., Xiong, S., Tay, C. Y., Leong, W. S., & Tan, L. P. (2012). A novel and simple microcontact printing technique for tacky, soft substrates and/or complex surfaces in soft tissue engineering. *Acta Biomaterialia*, *8*(3), 1267–1272.

[6] Jang, M. J., & Nam, Y. (2015). NeuroCa: integrated framework for systematic analysis of spatiotemporal neuronal activity patterns from large-scale optical recording data. *Neurophotonics*, *2*(3), 035003.

[7] Biffi, E., Regalia, G., Menegon, A., Ferrigno, G., & Pedrocchi, A. (2013). The influence of neuronal density and maturation on network activity of hippocampal cell cultures: a methodological study. *PloS one*, *8*(12), e83899.

[8] Braun, N. J., Liao, D., & Alford, P. W. (2021). Orientation of neurites influences severity of mechanically induced tau pathology. *Biophysical Journal*, *120*(16), 3272–3282.

[9] Nagamine, K., Hirata, T., Okamoto, K., Abe, Y., Kaji, H., & Nishizawa, M. (2015). Portable Micropatterns of Neuronal Cells Supported by Thin Hydrogel Films. *ACS Biomaterials Science & Engineering*, *1*(5), 329–334.

COMPLIANCE MATCHING A POLYURETHANE AND PLCL BIOHYBRID TISSUE ENGINEERED VASCULAR GRAFT

Trin Murphy (1,2), David R. Maestas Jr. (1,2), Katarina Martinet (1,2), William R. Wagner (1,2), Sang-Ho Ye (1,2), Jonathan P. Vande Geest (1,2,3)

(1) Bioengineering, University of Pittsburgh, Pittsburgh, PA, USA
(2) McGowan Institute for Regenerative Medicine, University of Pittsburgh, Pittsburgh, PA, USA
(3) Vascular Medicine Institute, University of Pittsburgh, Pittsburgh, PA, USA

INTRODUCTION

Heart disease remains the leading cause of mortality in the United States, with coronary artery disease (CAD) resulting in 928,741 deaths in 2020 [1]. One treatment option for CAD is a coronary artery bypass graft (CABG). Approximately 400,000 patients undergo CABG each year [2], though these have a high failure rate, of 42.8% [3]. It is hypothesized that this is due to a biomechanical compliance mismatch between the native blood vessel and the CABG, resulting in intimal hyperplasia and thrombosis [4]. To improve patient outcomes, it is crucial to develop a small diameter tissue engineered vascular graft (TEVG) that matches the compliance of the native blood vessel. This study aimed to develop small diameter compliance matched TEVGs and vary their compliances. Two TEVG designs were developed: a poly(ester urethane)urea (PEUU) based graft containing PEUU and gelatin, and a poly(Lactide-co-caprolactone) (PLCL) based graft containing PLCL and gelatin. The inner layer of the PEUU graft utilized a modified PEUU with sulfobetaine groups (PESBUU-50) known for its anti-thrombogenic properties [5]. PLCL was selected as the primary material for the second graft due to its high elasticity and lack of toxic byproducts. Both grafts incorporated a significant amount of gelatin in the outer layer to promote cellular infiltration and remodeling. The production of the grafts involved a trial-and-error approach to ensure they fell within the compliance range. Once compliance matched grafts were achieved the wall thickness was adjusted to create hypocompliant or hypercompliant grafts. Four TEVG designs were developed: thin and thick PEUU-based TEVGs and thin and thick PLCL-based TEVGs.

METHODS

The TEVG polymer mixtures consisted of gelatin isolated from porcine skin (MilliporeSigma), PEUU, PESBUU-50, PLCL (MilliporeSigma). Trilayered PEUU grafts were created by electrospinning solutions of 8% PESBUU-50, 10% 80:20 PEUU:Gelatin, then 10% 20:80 PEUU:Gelatin. All solutions were dissolved in 1,1,1,3,3,3-Hexafluoro-2-propanol (HFP). The solutions were electrospun at a voltage difference of +20 kV, and -4 kV, at a working distance of 10 cm. Trilayered PLCL grafts were fabricated by electrospinning solutions of 10% PLCL, 10% 80:20 PLCL:Gelatin, then 10% 20:80 PLCL:Gelatin. The solutions were electrospun at a voltage difference of +15 kV and -0.5 kV, at a working distance of 10 cm. Both grafts solutions were dispensed onto a rotating target mandrel of 1.1 mm diameter at 1000 rpm at a rate of 10 µl/min. Both trilayered grafts were crosslinked for 24 hours in 0.5% genipin in 200 proof ethanol at 37°C. After crosslinking, the grafts were washed 3 times using 200 proof ethanol.

Four TEVG design groups were tested: thin and thick PEUU based TEVGs, and thin and thick PLCL based TEVGs. The grafts were mechanically tested using a custom microbiaxial mechanical device (CellScale, Waterloo, Canada) (**Figure 1**) that pressurized the samples from 5 mmHg to 120 mmHg in a 37°C heated water bath across 10 cycles, imaging the TEVG outer diameters at a frequency of 5 Hz.

Figure 1: Microbiaxial mechanical device.

Throughout the mechanical tests the captured images were utilized to monitor the outer diameter of the TEVG. The first 9 cycles of the testing were used to pre-condition the graft, and the 10th cycle was the

testing phase. Compliance was calculated using the outer diameters at 70 mmHg and 120 mmHg [4] (**1**). To assess compliance the obtained values were compared to the range of compliance values observed in native rat aortas. Compliance matched values were those that fell within the range of native aortas. Values that fell within this range were considered compliance matched. Grafts with values exceeding this range were classified as hypercompliant indicating excessive elasticity while grafts with values below this range were categorized as hypocompliant indicating excessive stiffness. Compliance values were evaluated in relation to native rat aorta explants. Graft diameters and thicknesses were measured by cutting a cross section and measuring using an Olympus Surgical Microscope. Statistical significances were assessed using ordinary one-way ANOVA with a post-hoc Tukey test for multiple comparisons.

$$\text{Compliance} = \frac{(OD_{120} - OD_{70})/OD_{70}}{50\ \text{mmHg}} \quad (1)$$

RESULTS

The average compliance values of both thick and thin PLCL trilayers were lower than native rat aortas and PEUU trilayers. The average compliance value of thin PEUU trilayers was higher than native rat aortas (**Table 1**). There was a statistical difference ($p<0.05$) in the compliance of the thin PEUU trilayer compared to the thick PEUU trilayer, thin PLCL trilayer, and thick PLCL trilayer. (**Figure 2**). All TEVG designs had a higher average wall thickness than native rat aortas. There was a statistical difference ($p<0.05$) between the native rat aorta wall thickness and the wall thickness of all other designs (**Figure 3**).

Table 1: Average TEVG compliance and wall thickness measurements

Graft Design	Average Compliance ($mmHg^{-1}$)	Average Wall Thickness (μm)
Native Rat Aorta	0.00139	89
PEUU Thin	0.00196	126**
PEUU Thick	0.00114	167***
PLCL Thin	0.00136	159***
PLCL Thick	0.000741*	175***

*/**/*** indicate statistical significance at the 5%/1%/<0.01% in comparison to native rat aortas

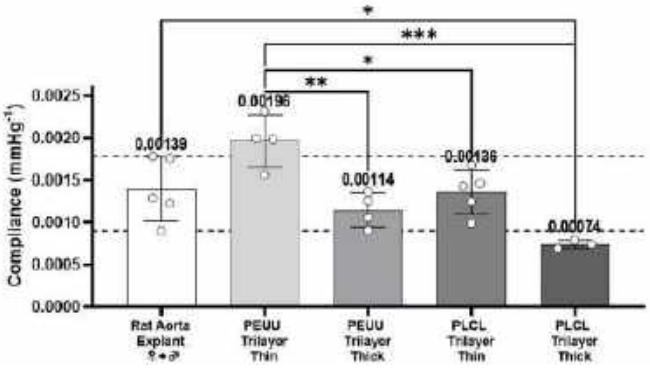

Figure 2: Compliance values of native rat aorta explants in comparison to trilayered TEVG designs, n = 3-5.

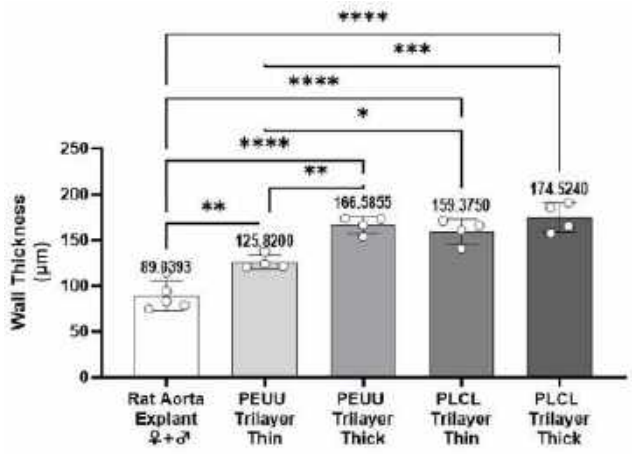

Figure 3: Wall thickness values of native rat aorta explants in comparison to trilayered TEVG designs, n = 4-5.

DISCUSSION

The objective of the study was to develop two compliance matched TEVG designs with tunable compliance. Both the thick PEUU trilayers and thin PLCL trilayers have average values that fall within the compliance range of native rat aortas indicating they are compliance matched. The average compliance value of the thin walled PEUU based trilayers falls above the range of compliance values of native rat aortas, making it hypercompliant, while the average compliance value of the thick walled PLCL based trilayer falls below the range of native rat aorta compliance, making it hypocompliant. The same applies to PLCL trilayers where the average compliance value of thin trilayers matches compliance compared to the average compliance of thick trilayers which are hypocompliant. The difference in average compliance values between thick and thin graft designs of both PEUU and PLCL trilayers suggests that compliance can be modulated by varying the wall thicknesses. All trilayered wall designs were thicker than the native rat aorta wall thickness. The thick PEUU, thin PLCL, and thick PLCL grafts all have relatively similar wall thickness but different compliance values. Compliance is not only impacted by the wall thickness of the grafts but the materials used in the grafts as well. In the future, computational analysis can be utilized to quantify the relationship between wall thickness, biomaterial mixture ratios, and compliance. Future work will also include both *in vitro* and *in vivo* studies to verify the anti-thrombogenicity of PESBUU-50 in TEVGs, as well as the extent of cellular infiltration and remodeling when utilized as an interpositional vascular graft. Trilayered TEVGs can be compliance matched to native rat aortas, and compliance can be modified by changing the graft thickness or materials in the grafts.

ACKNOWLEDGEMENTS

This research was funded by NIH award R01HL157017 to JPVG.

REFERENCES

[1] Tsao C.W. et al., Circulation, 147, 2023.
[2] Bachar B.J. et al., *StatPearls*, 2023.
[3] Hess C.N. et al., *Circulation*, 13, 2014.
[4] Jeong, Y et al., *Biomaterials Science,* 8.16, 2020.
[5] Ye, S.H., Hong, Y., Sakaguchi, H., Shankarraman, V., Luketich, S., D'Amore, A., and Wagner, W.R., *ACS Applied Mat. & Int*, 6.24, 2014.

SB3C2024
Summer Biomechanics, Bioengineering and Biotransport Conference
June 11-14, Lake Geneva, WI, USA

NEURAGAME: INTEGRATING APP-BASED & PHYSICAL THERAPY FOR AT HOME STROKE REHABILITATION

J. Basu (1), S. Kabbur (1), A. Nair (1), D. Kaneria (2), R. Virkar (3), R. Muppala (3)

Faculty Advisor(s):
Dr. Dan Puperi (2)

1. Chandra Dept. of Electrical & Computer Engineering, University of Texas at Austin, Texas, United States
2. Dept. of Biomedical Engineering, University of Texas at Austin, Texas, United States
3. Dept. of Computer Science, University of Texas at Austin, Texas, United States

INTRODUCTION

Every day, more than 2,100 people in the United States suffer from stroke.[1] 70% of stroke survivors are left with upper extremity impairments leaving them unable to carry out everyday tasks.[2] Physical rehab within the first 3 months post-stroke is critical for maximizing recovery for these patients, but unfortunately 35% of stroke survivors do not receive any physical therapy.[3,4]

Given over 70% of stroke patients are discharged to their homes, the lack of rehabilitative care can be attributed to low participation in outpatient care programs.[5] Reasons for this include transportation issues and limited insurance coverage resulting in high out-of-pocket costs.[6] Without any other option, family members are forced to become the primary source of care for stroke survivors without any training or support system.[7] This responsibility creates enormous physical, psychological, and economic strain for families.

In response to this challenge, mobile health apps utilize widespread smartphone ownership to establish an at-home therapy environment. However, research indicates optimal recovery of hand functionality in stroke patients requires a combination of physical and app-based therapy.[8] Existing app-based therapies lack integrated physical components to simulate conventional physical therapy methods. On the other hand, home rehabilitation tools simulating physical therapy can cost thousands of dollars, more than most patients can afford.

Given these shortcomings in current outpatient and at-home rehabilitation care, there exists a pressing need for a smart device integrating mobile health and physical therapy for at-home use. The most important stakeholder requirements for such a device come from the patients and caregivers themselves. Any product must minimize cost given the already high financial burden placed on families from stroke-related expenses. The smart device must also be user-friendly, require minimal training, and be usable without help from medical professionals given how transportation is a critical barrier to rehab access. Additionally, the device should provide a user experience that is engaging and serves as a source of motivation for patients throughout their rehabilitation process.

PRODUCT DESIGN

Neuragame is an affordable smart home rehabilitation aid integrating physical and app-based components to facilitate recovery from the physical and neurological effects of stroke. Designed for recovering individuals with limited upper limb dexterity, Neuragame allows patients to improve motor skills, memory, and reaction time through gamified exercises. No professional help is required to use the device. All a caregiver has to do is log into the app, connect the device via USB, and simply help the patient navigate the app. Caregivers no longer have to worry about providing rehabilitative care for their dependents.

Figure 1: Neuragame Physical Interface

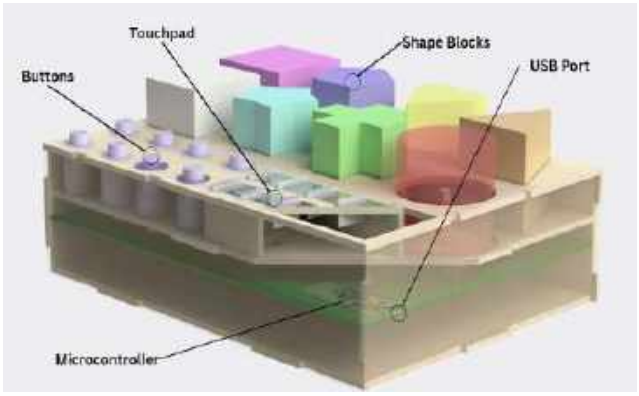

Caregivers/patients interact with the app to start activities and track progress. Exercises fitting the needs of the patient can be selected with personalized recommendations also being generated based on patient progress. A tutorial video is included in the app to show users how to complete each activity. A patient's progress is recorded offline in an authenticated database with infrastructure available to upload it for a medical professional to view, as requested.

The physical interface is composed of a plastic casing that houses the main printed circuit board (PCB). The encasing is a box-like structure incorporating shape blocks, buttons, and a touchpad (embedded as a separate, smaller PCB in the encasing) for use in the games. The main PCB connects sensors that can detect shape rotations, button presses, and touchpad selections to the microcontroller, which is responsible for communication with the app via USB.

Each part of the board is used in multiple games emulating clinically proven rehab exercises to target distinct aspects of stroke recovery. Modeled after the clinically-validated Nine Hole Peg Test, the blocks can be removed and rotated in games such as "Shape Rotation" for patients to practice hand-eye coordination and improve grip strength. The touchpad promotes stimulus-response, memory, and finger dexterity by simulating piano keys and teaching users to repeat simple patterns through a clinically-proven exercise called finger-tapping. The buttons can be used in a variety of games such as Whack-A-Mole to improve stimulus-response and reaction time by having users press specified buttons in an allotted amount of time. These are just a few examples of games inspired by exercises used in conventional therapy that are integrated in Neuragame. Performance on these clinically-proven exercises are used as recovery markers in providing tailored recommendations.

The technical design takes into account several challenges. One key issue was the app-device communication method. Although wireless communication has become more prevalent, compatibility issues across different smartphone hardware can arise. Instead, USB communication was chosen because of its reliability independent of smartphone hardware and its convenience as a power source for the physical interface. Additionally, connecting the touchpad PCB to the main PCB posed a challenge. Since manually adding wires does not create a reliable connection, a ribbon cable is used instead, similar to the internal connections of a smartphone.

All parts have been designed with manufacturing feasibility in mind. The plastic housing, buttons, and shape blocks of the physical interface can all be produced at high volumes through plastic injection molding, a commonly employed method in commercial manufacturing. For the touchpad and main PCB, the PCB production can be outsourced with a manufacturing facility completing the final assembly of the PCBs and the housing.

BUDGET AND MARKET ANALYSIS

Considering the initial target market of stroke survivors with upper extremity impairments unable to afford traditional physical rehabilitation, the potential US market size is approximately 155,000 individuals annually.[1,2,4] The product, estimated to cost $30 for mass manufacturing, incurs an initial expense of $170,000 for injection molding (for initial production capacity of 100,000 units annually) with no other major investment costs required. Accounting for Neuragame's projected sales price of $70 and $60 expenses per unit (including manufacturing costs & related expenses), there is a 14% net profit margin. Assuming a 20% adoption rate within the US market, Neuragame could generate approximately $2.17 million in revenue annually. With a net profit of about $310,000 annually and the mentioned expenses, the ROI is estimated to be 17%. These projections are specific to the mentioned US market and do not take into account opportunities in other countries. Thus, they should be viewed as highly conservative. The below design budget would allow for complete preliminary engineering testing prior to clinical trials and patent filings.

Table 1: Estimated Design Budget Calculation

Item	Cost
Raspberry Pi Pico H	$30.00
Capacitive Touch 12-Key Sensor	$40.00
Hall Effect Sensors	$10.00
I2C Multiplexer	$17.00
Logic Analyzer	$26.00
Magnets	$20.00
PCB	$200.00
Buttons	$20.00
Wood	$50.00
Assorted Resistors	$30.00
Assorted Capacitors	$30.00
iPhone X (Used)	$200.00
Tecno Smartphone (Used)	$175.00
Vivo Smartphone (Used)	$150.00
Total	$998.00

ACKNOWLEDGMENTS

We would like to acknowledge James Degnan for his contributions to the revisions of this paper. We would also like to thank our advisor, Dr. Dan Puperi in the Department of Biomedical Engineering at the University of Texas at Austin, for his advice during the design development phase.

REFERENCES

[1] Centers for Disease and Control Prevention, *Stroke Facts*, Last Reviewed May 4, 2023.
[2] Dutta, D et al., *Smart Health*, 23, 2022
[3] Raghavan, P, *Johns Hopkins Medicine*, 2024.
[4] Brittany, M et al., *Stroke*, 54:831-839, 2023.
[5] Reeves, M et al., *BMC Neurol*, 7:115, 2017.
[6] Ayala, C et al., *MMWR Morbidity and Mortality Weekly Report*, 67:575-578, 2018.
[7] Prvu Bettger, J et al., *Stroke*, 50:3307-3313, 2019.
[8] Sawant, N et al., *Journal of Enabling Technologies,* 14:221-231, 2020.

4D FLOW MRI REVEALS THAT CAROTID ARTERY BIFURCATION GEOMETRY IMPACTS HEMODYNAMICS ASSOCIATED WITH ATHEROSCLEROSIS

C. Lucas (1), B. Anderson (2), R. El Sayed (1), J. Allen (3,4), J. Oshinski (1,3)

(1) The Wallace H. Coulter Department of Biomedical Engineering at Georgia Institute of Technology and Emory University, Atlanta, Georgia, USA
(2) Medical College of Georgia at Augusta University, Augusta, Georgia, USA
(3) Department of Radiology and Imaging Sciences, Emory University, Atlanta, GA, USA
(4) Department of Radiology and Imaging Sciences, Indiana University, Indianapolis, IN, USA

INTRODUCTION

The development of atherosclerosis tends to occur at branches within the arterial tree, such as the carotid artery bifurcation. The geometric features of the carotid artery bifurcation have been linked to an increased risk factor for atherosclerosis disease, due to the impact of particular geometries on hemodynamic disturbances[1]. These hemodynamic factors include increased complex flow, reduced time-average wall shear stress (TAWSS), and increased oscillatory wall shear index (OSI)- leading to local vasculature endothelial cell dysfunction.[2] Due to the potential relationship between atherosclerotic plaque development and variations in carotid geometries, previous studies have investigated how carotid bifurcation geometry may serve as a predictor of complex flow and vessel wall thickening.[3,4] *This study aimed to analyze the influence of geometric features of the carotid bifurcation on the development of atherosclerosis by comparing 4D Flow MRI analysis in healthy carotid bifurcations and carotid bifurcations in patients with atherosclerosis.*

METHODS

Patient Population and Image Acquisition: All subjects were imaged on a 3T system (MAGNETOM Prismafit, Siemens Medical Solutions). The study population includes subjects with mild atherosclerosis disease (ICA n=10 from 8 patients, 4F, age 72±10, mean stenosis of 40±10%), and healthy volunteers (ICA n=12 from 8 patients, 7F, age 42±13). 4D flow MRI images were acquired for each carotid (FOV=162*200mm^2, resolution=1mm^3; flip-angle=7°; TR=45ms; TE=5ms). Additionally, Multi-slab, transverse, 3D time of flight (TOF) images were acquired to cover the bifurcation (0.5mm, TR=23ms, TE=3.1ms). The carotid artery was segmented from the TOF images using the open-source 3D Slicer Software.

Geometric Analysis: Geometric analysis of the segmented vessels was accomplished using the Vascular Modeling Toolkit (VMTK), an open-source software that has previously been used in the literature for the geometric analysis of 3D vascular segments.[4] The VMTK extension within the 3D Slicer application was utilized to calculate and provide further geometric analysis of the vessels when the centerline is generated within the 3D Slicer (Figure 1). Using the geometric data acquired from VMTK, the bifurcation angle and the internal carotid artery (ICA) angles were determined by using methods described by Thomas et al.[4] The carotid bifurcation angle was determined by taking the difference between the in-plane angles of the ICA and the external carotid artery (ECA). The ICA angle was determined by taking the supplementary angle of the difference between in-plane angles of the common carotid artery (CCA) and ICA.

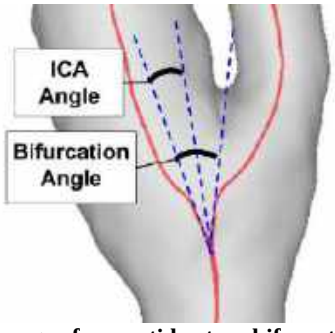

Figure 1. An image of a carotid artery bifurcation centerline visualization from 3D Slicer with the measured bifurcation angle and ICA angle labeled.

4D Flow Analysis: Processing was performed using a custom-written MATLAB code to correct for eddy currents and aliasing, perform noise filtering, and create a 3D magnetic resonance angiogram (MRA)[5]. MRA images were segmented using Mimics and

imported into EnSight (ANSYS Inc, 2019) for streamline visualization and extracting 2D planes. Four planes were placed perpendicular to the centerline: the CCA plane at one CCA diameter (D) below the carotid bifurcation, and the ICA planes at 0.5D, 1D, and 1.5D (ICA 1, 2, and 3 respectively) downstream from the maximum stenosis in subjects with atherosclerosis or from the bifurcation in healthy subjects. TAWSS and OSI have been linked to vascular dysfunction. Therefore, TAWSS and OSI were quantified using MATLAB allowing manual lumen contours as vessel walls for all time frames[6].

Statistical Analysis: The geometric factors were plotted versus TAWSS and OSI data from each vessel, and then a line of best fit was computed and an R^2 value was acquired. The geometric factors and flow data were then divided into healthy and atherosclerotic subjects and t-tests were performed to determine significant differences. The significant factors were then analyzed through 2x2 contingency tables. These factors were given cut offs that gave a minimum sensitivity of 0.7 and then maximized both specificity and sensitivity, giving the bifurcation angle a cutoff of 50°, ICA angle a cutoff of 30°, TAWSS at ICA 1 and ICA 2 a cutoff of 0.3 Pa, and OSI a cutoff of 3%.

RESULTS

Geometric Factors and 4D Flow MRI: TAWSS showed a positive correlation to bifurcation angle (R^2 = 0.39) at ICA 1 (Figure 2). This relationship was not significant between TAWSS and bifurcation angle at CCA (R^2 = 0.1932), ICA 2 (R^2 = 0.1179), and ICA 3 (R^2 = 0.06). No significant correlation was found between any OSI data points and geometric factors.

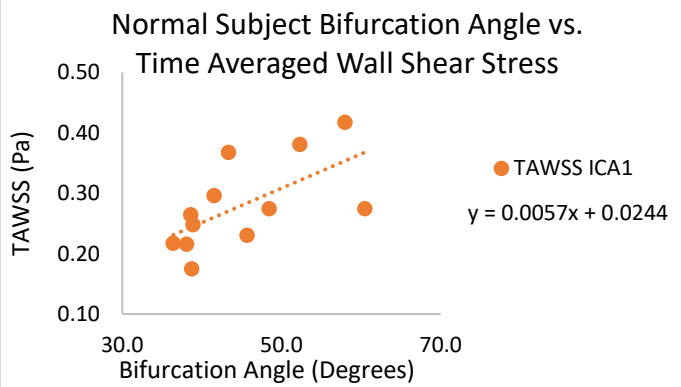

Figure 2. TAWSS ICA 1 plotted against bifurcation angle.

Geometric Risk Factors in Healthy Subjects versus Atherosclerosis Subjects: Several factors were found to be significantly different between the healthy and atherosclerotic subjects including: the bifurcation angle, ICA angle, TAWSS ICA 1, TAWSS ICA 2, and OSI ICA 1. The contingency tables were analyzed for sensitivity, specificity, positive predictive value, and negative predictive value (Table 1).

Table 1. Predictive analysis of geometric and hemodynamic factors on atherosclerosis diagnosis. Equality symbols are used to indicate criteria for higher atherosclerosis risk.

Factor (Cutoff)	Sensitivity	Specificity	Positive Predictive Value	Negative Predictive Value
Bifurcation Angle (>=50°)	0.700	0.750	0.700	0.750
ICA Angle (>=30°)	0.800	0.833	0.800	0.833
TAWSS ICA 1 (>=0.3 Pa)	0.900	0.750	0.750	0.900
TAWSS ICA 2 (>=0.3 Pa)	0.900	0.583	0.643	0.875
OSI ICA 1 (<3%)	0.700	0.833	0.778	0.769

DISCUSSION

The major findings of this study were that 4D Flow MRI showed a significant correlation between the bifurcation angle and TAWSS in ICA 1. It also showed bifurcation angle, ICA Angle, TAWSS at ICA 1 & 2, and OSI at ICA 1 were significantly different between healthy subjects and subjects with atherosclerosis.

Geometric Factor Influence on Wall Shear Stress and Atherosclerosis Risk: Higher bifurcation angles corresponded to higher wall shear stress values in the ICA 1. Furthermore, the bifurcation angle provided a 0.700 sensitivity and 0.750 specificity in separating atherosclerosis subjects from healthy subjects. Larger bifurcation angles were found in atherosclerosis patients, and large bifurcation angles were also associated with higher TAWSS in the healthy subjects. Low WSS is associated with the development of plaque that leads to atherosclerosis, and high WSS develops after the disease has progressed.[7] Higher bifurcation and ICA angles also appear to be good predictors of flow patterns associated with atherosclerosis. Finally, key hemodynamic markers of atherosclerosis such as high TAWSS at ICA 1 and ICA 2 and low OSI at ICA.

In conclusion, geometric factors could be used as one factor in the prediction of atherosclerosis, and the hemodynamics of atherosclerosis seen in this 4D flow MRI study was consistent with previous literature.[7]

ACKNOWLEDGEMENTS

This work was funded by National Institutes of Health Grant Numbers: R21NS114603 (Allen and Oshinski) and R01EB027774 (Oshinski); and the American Heart Association Innovative Project Award No. 19IPLOI34760670 (Allen).

REFERENCES

[1] Phan TG, et al. Carotid artery anatomy and geometry as risk factors for carotid atherosclerotic disease. *Stroke*. 2012;43(6):1596-1601.

[2] Davies PF. Hemodynamic shear stress and the endothelium in cardiovascular pathophysiology. *Nat Clin Pract Cardiovasc Med*. 2009;6(1):16-26.

[3] Lee S, et al. Geometry of the Carotid Bifurcation Predicts Its Exposure to Disturbed Flow. *Stroke*. 2008; 39:2341-2347.

[4] Thomas JB, et al. Variation in the carotid bifurcation geometry of young versus older adults: implications for geometric risk of atherosclerosis. *Stroke*. 2005;36(11):2450-2456.

[5] Wu SP, et al. Three-dimensional phase contrast velocity mapping acquisition improves wall shear stress estimation in vivo. *J Magn Reson Imaging*. 2004;22(3):345-351.

[6] El Sayed R, et al. Assessment of complex flow patterns in patients with carotid webs, patients with carotid atherosclerosis, and healthy subjects using 4D flow MRI. *Journal of Magnetic Resonance Imaging*. 2023.

[7] Zhou M, et al. Wall shear stress and its role in atherosclerosis. *Front Cardiovasc Med*. 2023;10:1083547.

Advancing cardiac metrics: computational CMR methods for ejection fraction evaluation

E. Lyon (1); I. Essafri (1); M. Zhang (1); M. Lucero (1); K, Ichimura (2); KR, Stenmark (1); E, Spiekerkoetter (2); VO, Kheyfets (1)

(1) Cardiovascular Pulmonary Research Laboratories, Division of Pediatrics-Critical Care, Department of Medicine and Pediatrics, University of Colorado Anschutz Medical Campus, Aurora, CO, USA.

(2) Department of Medicine, Division of Pulmonary, Allergy and Critical Care Medicine, Stanford University, Stanford, CA, USA.

I. Introduction

The ejection fraction (EF, see Eq. 1) is a measure of systolic function that is commonly used in the clinic [1]. Precise EF calculations require accurate right ventricle (RV) and left ventricle (LV) volume measurements. Segmenting the heart cavities from cardiac magnetic resonance (CMR) images is considered the widely accepted, non-invasive, method to acquire LV and RV volumes [2].

$$EF = \frac{End\ Diastolic\ Volume - End\ Systolic\ Volume}{End\ Diastolic\ Volume} \quad (1)$$

For research application, EF is also a commonly used metric to evaluate systolic function in rodent models. A typical CMR image includes multiple short-axis slices (see Fig. 1a), which are acquired along the length of the heart ("transverse plane"), and a single long-axis slice where both ventricles can be seen (see Fig. 1b). Because traditional volume segmentation techniques only rely on the short-axis slices, the accuracy of a volume calculation is limited by the number of short-axis (SA) slices that can be acquired along the transverse plane and the total coverage of those slices.When the 5 short-axis slices fail to cover the entire base-to-apex span (as can be seen in the example Fig. 1b), we suspect it results in omitted volume and an erroneous EF calculation.

The objective of this study was to develop and evaluate different post-processing algorithms that find volume by either only utilizing short-axis slices or combing short-and-long axis slices.

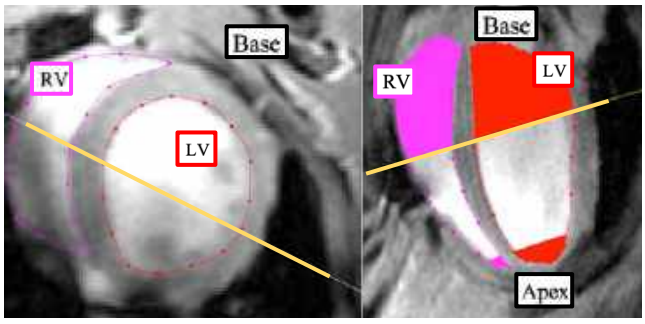

1a. 1b.

Fig. 1. (a) Manually delineated CMR SA slice of the RV and LV (b) LA Slice intersecting the SA slice, showing omitted volume due to SA slice limitations.

II. Methods

Balanced steady state free precession (bSSFP) cine CMR was gathered on nine mice, five Sham (control) and four Pulmonary-Artery-Banded (PAB). Four imaging scans (3 RV, 1 LV) were excluded from the α-shape estimation due to subject movement disrupting acquisition.

A. Segmentation Methods:

CMR segmentation involved the manual endocardium delineation of all required SA slices and one LA slice [3]. The software's intersection of LA and SA slices provided context for segmentation of area with unclear endocardial boundaries.

B. Three Methods for Reconstructing Ventricular Cavity:

We evaluated 3 methods for finding RV and LV cavity volume in rodent CMR images:

1) **Simpson's Disk Summation [4]:** Multiplies the area within the delineated contour by the slice thickness (see Fig. 2a).
2) **SA α-shape estimation:** Estimates cavity volume using short-axis (SA) slices. First, the geometry was aligned so that each short axis slice is parallel to the x-y plane and is stacked from the apex to the base along the z-axis (see Fig. 2a). The most apical point from the long axis view is positioned at the (0,0,0) origin. To create 3D model of the ventricular cavity, an α-shape was created from the short axis slices where each SA slice has 80 known coordinates along the circumference of the cavity (see Fig. 2b).
3) **LA + SA α-shape estimation:** Combines one long-axis (LA) and all available SA slices for volume estimation. After applying model realignment (described in SA α-shape estimation), shape-preserving piecewise cubic interpolation is used to create a 3-dimensional point cloud (See Fig. 2c). An α-shape is then created from the resulting point cloud, which can be used to compute the shape volume.

Standard rodent CMR is acquired with 5 SA slices and assumes the slices will cover most of the volume. This assumption may not be true. We aimed to evaluate how these 3 methods withstand the limitations of data acquisition. Therefore, we segmented each CMR image under two conditions: (1) Using all available short-axis slices (*Non-Truncated*) and (2) removing the most apical and basal slice (*Truncated*). Non-Truncated segmentations incorporate data from more slices to provide a more precise volume estimate. The agreement between Non-Truncated and Truncated was evaluated with linear regression and Bland-Altman analysis. Greater agreement across truncation status indicates higher accuracy in volume measurement.

Fig. 2 compared methods for volume calculation: (a) Simpson's Disc Summation; (b) SA α-shape estimation; (c) LA + SA α-shape estimation

C. Numerical Volume Calculation of an α-shape:

The CMR segmentation for the SA α-shape estimation and LA + SA α-shape estimation were post-processed using our in-house software (MATLAB, MathWorks, MA). There are multiple methods for computing an α-shape volume, but many can result in error when there are holes on the surface. To avoid this issue, we utilized a Monte Carlo technique that randomly assigns the domain 1e6 points while keeping track of the number of points that landed within the α-shape. The ratio of points that landed within the α-shape versus the total number of points assigned to the domain is directly proportional to the cavity volume.

III. Results

Stronger agreement between Non-Truncated and Truncated segmentations is observed with α-shape estimations (SA and SA+LA) compared to Simpson Disc Summation.

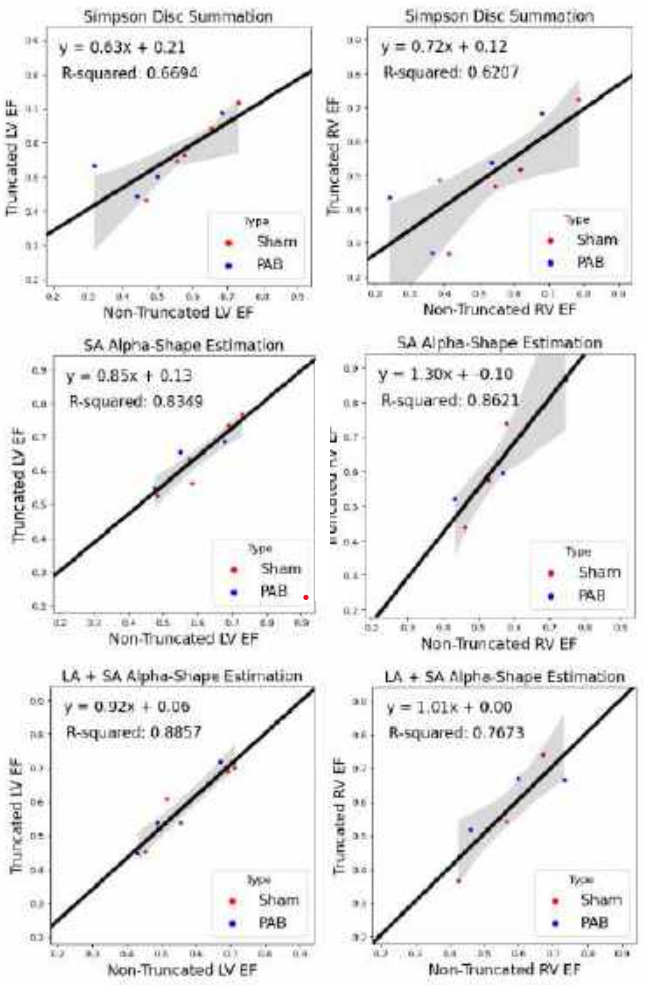

Fig. 3: Linear regression of Non-Truncated vs. Truncated EF estiamtes for LV and RV using three methods.

While correlation analysis offers the degree of covariance, Bland-Altman (BA) analysis measures the agreement between the Non-Truncated and Truncated segmentations. Our findings revealed the LA + SA α-shape method to be the most accurate method of volume acquisition considering BA analysis (see Table 1) and correlation (see Fig. 3).

TABLE I. Bland Altman Analysis

Volume Assessment Method	LV		RV	
	Mean Difference	*±1.96 SD (mL)*	*Mean Difference*	*±1.96 SD (mL)*
Simpson Disc Summation Non-Truncated vs. Truncated	-0.01	± 0.14	0.02	± 0.20
SA α-shape estimation Non-Truncated vs. Truncated	-0.04	± 0.07	-0.07	± 0.12
LA + SA α-shape estimation Non-Truncated vs. Truncated	-0.02	± 0.07	-0.01	± 0.11

IV. Discussion

Given the technical limitations of acquiring CMR images in rodents, our study compared 3 methods for computing ventricular cavity volume in healthy and PAB mice. The Simpson method uses Euler's method for volume integration along the transverse plane with global truncation error on the order of the slice thickness (h). This reveals drastically different EF calculations based on the number of short-axis slices acquired. Discrepancies were more pronounced in the RV due to its unique shape and CMR imaging alignment favoring the LV, resulting in a substantial amount of RV volume being omitted during acquisition. When we improved longitudinal integration along the SA slices using α-shape SA boundary reconstruction of the cavity volume (with global truncation error on the order of h^2), this improved the accuracy of the integration but does not account for omitted RV volume at the base and apex. Finally, when we combined the SA and LA segmentation with α-shape integration, this resulted in the most consistent estimate of RV EF.

Our study's limitations stem from the constraints of rodent CMR images that lack the clear pixel contrast seen in human cardiac imaging so automatic segmentation was not possible. Incorporating additional LA views could further enhance accuracy but is not a routine practice in CMR. Ongoing studies in our lab are cross-referencing CMR with CT-derived cardiac volumes. We are also performing an inter/intra-observer variability study, alongside exploring machine learning techniques for automated segmentation to account for the complexities of rodent imaging.

Acknowledgement

This work was supported by NIH R01HL152250.

References

[1] M. J. Dufva *et al.*, *Journal of Cardiovascular Magnetic Resonance,* vol. 23, no. 1, 2021-12-01 2021.

[2] J. Schulz-Menger, Bluemke, D.A., Bremerich, J. et al., *J Cardiovasc Magn Reson 22, 19 (2020).* 2020.

[3] *Design and Validation of Segment – a Freely Available Software for Cardiovascular Image Analysis,* (2010). BMC Medical Imaging.

[4] G. Reiter, Reiter, U., Rienmüller, R., Gagarina, N., & Ryabikin, A., *European Journal of Radiology,* vol. 52, no. 2, pp. 110-118, 2004.

FULL-FIELD COMPARISON OF PORCINE PULMONARY AND AORTIC VALVE LEAFLET COLLAGENOUS ARCHITECTURE USING QUANTITATIVE POLARIZED LIGHT IMAGING

Shreya Sreedhar (1), Daniel P. Pearce (1), Connor Link (1), Colleen M. Witzenburg (1)

(1) Department of Biomedical Engineering
University of Wisconsin-Madison
Madison, Wisconsin, USA

INTRODUCTION

Aortic and pulmonary valve leaflets play a crucial role in regulating blood flow from the heart to the body and lungs, respectively. Although similar in shape and physiological function, aortic and pulmonary valve leaflets are subject to vastly different loading conditions [1]. The normal transvalvular pressure at rest for the pulmonary valve is 10 mmHg, and 80 mmHg for the aortic valve. Although aortic valves experience pressures 5-8 fold higher than pulmonary valves, they are only about 2 times thicker than the pulmonary valves [2].

Mechanical testing indicates material properties also differ between leaflets from the semi-lunar valves. Uniaxial mechanical testing indicated that pulmonary valve leaflets exhibited a greater degree of mechanical anisotropy than aortic valve leaflets [3]. Similarly, a biaxial comparison of semi-lunar valves revealed greater anisotropy and lower stiffnesses in pulmonary valve leaflets [4]. Although efforts have been made to characterize the full-field structure of aortic and pulmonary valve leaflets individually, there are few studies comparing their full-field collagenous architectures.

Quantitative polarized light imaging (QPLI) is a technique that capitalizes on the birefringent properties of collagen fibers to quantify full-field anisotropy of thin connective tissues. It provides overall incident light intensity (S0), the angle of linear polarization (AoP), and the degree of linear polarization (DoLP) [5]. Our objective was to apply QPLI to porcine pulmonary and aortic valve leaflets to evaluate and compare their heterogeneous structures. We hypothesized that pulmonary valve leaflets would exhibit similar spatial patterns in AoP and DoLP to aortic valve leaflets but would exhibit higher levels of collagen organization.

METHODS

Sample preparation. Aortic and pulmonary heart valves were excised from the hearts of 5–6-month-old pigs obtained from a local butcher (Hoesly's Meats, New Glarus, WI). Leaflets were stored in phosphate-buffered saline (PBS) and frozen at -80 degrees C. Following thawing, leaflets were carefully placed on a black platform and scanned by the LJ-V7080 laser micrometer (Keyence) at 200 Hz to obtain a 3D thickness profile. A sample aortic leaflet is shown in Fig. 1.

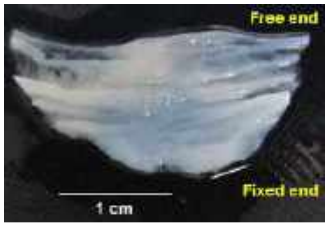

Fig. 1: Sample aortic leaflet

Imaging. Each sample was transferred to a glass platform for QPLI such that its orientation remained the same. The sample was lit by an LED light with a circularly polarized filter and imaged using the Polarization GUI (SpinView) at 20 Hz and the "Polarized8" pixel format.

Data Analysis. For all leaflets imaged S0, DoLP, and AoP were computed from the raw data as done previously [3,5]. Briefly, S0 indicates the overall intensity of incident light. AoP indicates the angle of linear polarization and is a measure of the preferred collagen fiber angle. DoLP indicates the degree of linear polarization and is a measure of fiber angle preference, with a value of 0 indicating no alignment and 1 indicating total alignment. Spatial values of thickness, S0, and DoLP were plotted against one another for each leaflet. A Pearson's correlation coefficient (r) was calculated to quantify the correlation and an α-value of less than 0.05 was considered significant. A Welch's t-test was then applied to determine if there was a significant difference

between the correlation coefficients for the aortic and pulmonary samples.

RESULTS

Fig. 2 includes the raw thickness and S0 values from laser micrometry and QPLI, respectively, for a representative pulmonary leaflet. A visual comparison suggests an inverse relationship between thickness and intensity: in regions of high thickness, S0 was low, and in regions of low thickness, S0 was high. To quantitatively compare the spatial distributions of each metric, a rotational matrix was used to warp the values of thickness to fit the shape of the S0 plot for each leaflet. Aortic valve leaflets had a significantly larger mean spatial thickness (0.80 ± 0.10 mm) than pulmonary valve leaflets (0.67 ± 0.08 mm) (Fig. 4A).

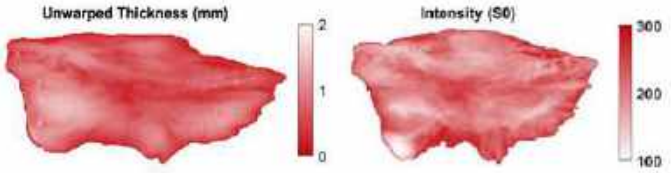

Fig. 2: Unwarped Thickness (left) and S0 (right) for a representative pulmonary valve leaflet.

Fig. 3 includes the S0, warped thickness in mm, DoLP, and AoP in degrees for representative aortic and pulmonary leaflets. In both the representative aortic and pulmonary valve leaflets, S0 and warped thickness follow correlated spatial patterns – in regions of high thickness, there was lower S0. There is also a larger region of low DoLP in the aortic leaflet in comparison to the pulmonary leaflet. AoP is a useful metric when DoLP is high since it provides directionality to the collagen fibers. In the representative leaflets below, the pulmonary leaflet displays more variation in fiber angle than the aortic leaflet.

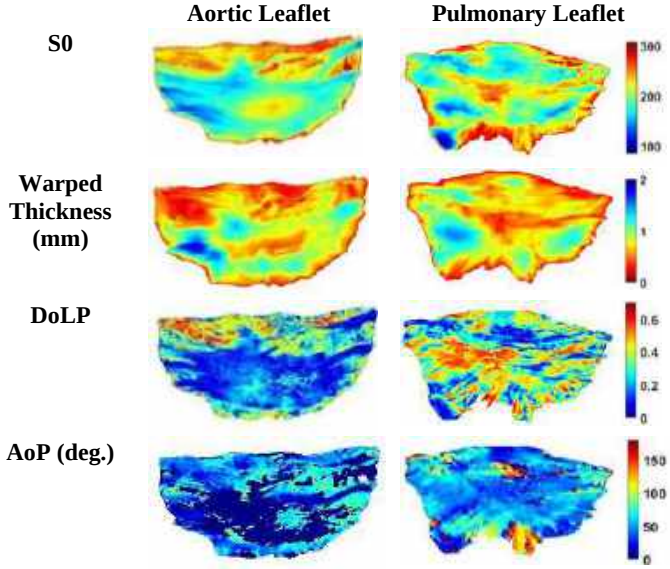

Fig. 3: S0, Warped Thickness (mm), DoLP, and AoP (deg.) for representative aortic and pulmonary valve leaflets.

Fig. 4B-C displays a DoLP comparison, and the correlation coefficient (r) values for DoLP and warped thickness, for aortic and pulmonary valve leaflets. Each metric was computed using a pixel-to-pixel correlation and *p*-values for every sample were below 1e-10. The mean DoLP values were 0.24 ± 0.04 and 0.31 ± 0.04 for aortic and pulmonary leaflets respectively, indicating that DoLP was significantly lower in the aortic leaflets than the pulmonary leaflets. Correlations between DoLP and warped thickness, and S0 and DoLP were more pronounced in aortic valve leaflets. A t-test for S0 and warped thickness was also performed. They were negatively correlated for both aortic and pulmonary leaflets, but there was no difference in correlation between the two groups.

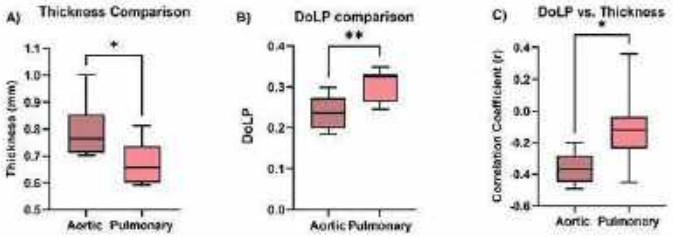

Fig. 4: Box and whisker plot of the A) Thickness comparison, B) DoLP comparison, and correlation coefficient (r) for C) DoLP vs. Thickness. **Indicates statistical significance (α < 0.01). * Indicates statistical significance (α < 0.05).

DISCUSSION

We obtained spatial distributions of S0, AoP, and DoLP for both aortic and pulmonary porcine valve leaflets. All samples showed patterns of low alignment in the belly region, similar to previous studies [6], however, there was a more distinct belly region of disorganized collagen in aortic leaflets. The mean DoLP values were significantly higher for the pulmonary leaflets, indicating a higher level of organization in the pulmonary leaflets. Clinically, heart valve failure is more likely to occur on the left side of the heart, so comparing the ECM organization between valve types can further our understanding of their reason for failure [7]. Furthermore, the aortic valve leaflets exhibited a significantly higher mean thickness than the pulmonary leaflets. However, the observed 15% difference between means is considerably lower than the 5-8 times greater pressure gradient experienced by the aortic valve compared to the pulmonary valve [2]. This disproportionality in thickness and *in vivo* pressure warrants further exploration of the ECM structure in both leaflet types. In addition, both the aortic and pulmonary leaflets exhibited a strong negative correlation between light intensity and thickness, while thickness and DoLP exhibited a much weaker negative correlation, indicating that DoLP provides separate information from S0. Additionally, amongst the various valve leaflets, there appeared to be disparate relationships linking ECM organization and thickness (Fig. 4C); the reason for this remains a mystery and warrants further exploration.

Future work will include a quantitative regional analysis between aortic and pulmonary leaflets to determine differences in spatial trends between the two tissues, as well as dynamic imaging of leaflets during biaxial loading. Dynamic imaging will provide more information on collagen fiber alignment and rotation during alternative loading conditions, which can reveal more about the function of the tissue's ECM. We will also conduct further investigation into the effects of warping and reducing the error involved in warping the thickness scan. Ultimately, studying the full-field organization of each valve leaflet's heterogenous ECM can give insight into how their *in vivo* function relates to their structure and inform therapies and prosthetics seeking to mimic this relationship.

ACKNOWLEDGEMENTS

This work was funded by a grant from the NSF to C.M.W (2030173).

REFERENCES

[1] Pragt, H et al., Thorac. and Cardio. Surg., 159:1051-1059.e1, 2020 [2] Sacks MS, et al., J Biomech, 42(12):1804-24, 2009 [3] Gorczynski, A. et al. Thorax 37, 535–539, 1982 [4] Christie, G. W. & Barratt-Boyes, B. G, Ann. Thorac. Surg. 60, S195–S199, 1995 [5] Perkins, R et al., Opt. Exp., 18:25815-25824, 2010 [6] Sacks, MS et al., Ann Biomed Eng., 25:678-89, 1997 [7] Cleveland Clinic., Heart Valves, 2022

IN-SILICO MODELS OF IN-VIVO CERVICAL STIFFNESS MEASUREMENTS FOR IMPROVING PRETERM BIRTH PREDICTION

Adriana Delagarza (1), Erin M. Louwagie (1), Abigail W. Laughlin (1), Jacqueline C. Hairston (2), Mirella Mourad (3), Michael House (4), Kristin M. Myers (1)

(1) Mechanical Engineering, Columbia University, New York, New York, USA
(2) Obstetrics and Gynecology, Northwestern Medicine, Chicago, IL, USA
(3) Obstetrics and Gynecology, Columbia University Irving Medical Center, New York, NY, USA
(4) Obstetrics and Gynecology, Tufts Medical Center, Boston, MA, USA

INTRODUCTION

Complications due to preterm birth (PTB, delivery <37 weeks) were the most common cause of death for children under 5 in 2019 [1]. Globally, PTB occurs in about 10% of live births [1]. Despite its clinical importance, PTB is difficult to predict. Current prediction methods are based upon measurements of cervical length (CL) using transvaginal ultrasound, with a shorter cervix associated with increased risk. However, the positive predictive value of a short cervix for predicting preterm birth is only 15-33% for singleton pregnancies [2]. It is known that cervical mechanical integrity is important for term delivery, thus mechanical assessment methods may improve PTB prediction [3].

A novel device for PTB prediction is the Pregnolia system, which tests the stiffness of the cervix via aspiration [4]. The device consists of a vacuum pump connected to a probe placed on the anterior cervical face. Once the probe makes full tissue contact, a negative pressure is applied, pulling the cervical tissue 4 mm into the probe. After this deformation, the vacuum stops, and the final pressure is recorded. Three measurements are taken, and the average is reported as aspirated cervical stiffness (aCS, [mbar]). Recent work has shown that patients with a short cervix and no PTB history who delivered <30 weeks have a significantly lower aCS value than patients with a short cervix who delivered >30 weeks [5]. We believe PTB prediction could be further improved with *in-silico* simulation of this *in-vivo* mechanical test.

The goal of this study is to determine patient-specific cervical material properties using numerical simulation of cervical aspiration efficiently and accurately, which could be used to enhance PTB prediction. Using transvaginal ultrasound images of patient cervices and their corresponding aCS values, inverse finite element analysis (IFEA) was performed on models of patients at low- and high-risk for PTB to find computed cervical stiffness values (cCS). Each patient was modeled with three different levels of cervical geometry fidelity. The resulting material properties were compared to determine the necessary level of geometric detail for application to PTB prediction.

METHODS

To create three-dimensional patient specific cervix models, transvaginal ultrasound images of three low risk for PTB (screened against known PTB risk factors) and three high risk for PTB (CL < 20 mm, no PTB history) pregnant patients were examined and measured. Patients were selected to cover a range of cervical sizes and aCS values. For each patient, three different cervix models were created in SolidWorks: a high-fidelity (HF, ~60 measurements), a medium-fidelity (MF, ~20 measurements), and a low-fidelity (LF, 3 measurements) model. The LF model parameters were identical to those used to model the cervix in previous patient-specific parametric cervical models [6]. MF and HF models were developed for this study.

The boundary of the cervix was labelled in transvaginal ultrasound images by a clinician as previously described (Fig. 1a) [7]. Images were then imported to ImageJ software for measurement. An approximate boundary separating the uterus and cervix was drawn by extending the outer edge of the uterus across the cervix. The cervical canal was used to find the cervical length. The outside lengths of the anterior and posterior regions of the cervix were measured and split into ten percent intervals. At each interval, the cervical diameter (CD) was recorded. Lines collinear with the CD were drawn between the anterior cervical boundary and the cervical canal, as well as between the posterior cervical boundary and the cervical canal to measure the anterior and posterior cervical radii, respectively. Cervical canal measurements were calculated by taking the difference between each CD measurement and its corresponding cervical radii measurements. For HF models, CD angle was recorded as the angle between each CD and the cervical base.

After measurements were recorded, a baseline sketch was made in SolidWorks. In the HF and MF models, CD measurements were incorporated as circles and connected with a spline. Sketched circles were lofted to create the outer boundary of cervical tissue, with the HF incorporating angles between CD measurements. To create the cervical canal, canal diameters were drawn in SolidWorks and connected with a

spline, and a lofted cut was used. To improve computational efficiency, only the left half of the cervix was used (Fig. 1b,c). The LF was modeled as a quarter cylinder, with a radius of half the CD and length of CL (Fig. 1d). To model the aspiration probe, a 4 mm long cylindrical tube was added to the top anterior edge of the cervix. The placement of the probe was based on the clinical instructions for device placement [8].

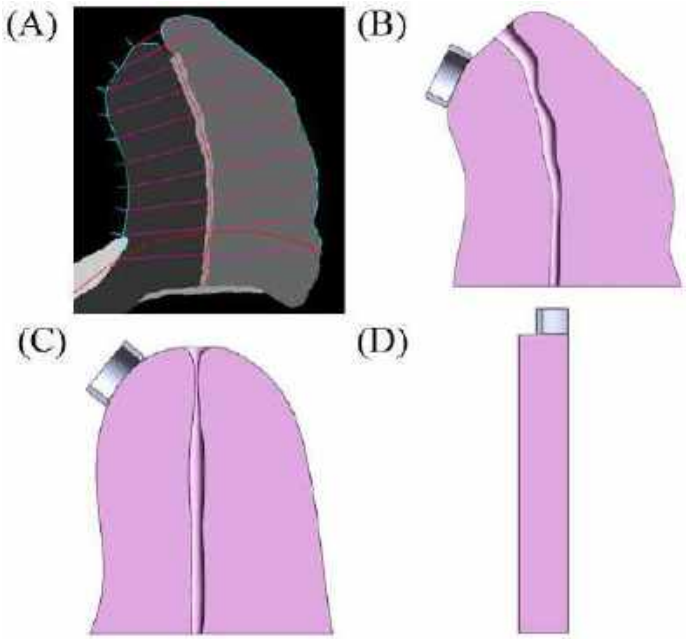

Figure 1: (A) Masked ultrasound image of low risk for PTB patient with parametric measurements. Corresponding (B) HF, (C) MF and (D) LF parametric solid cervical models.

All models were imported to Hypermesh (Altair Engineering Inc., Troy, MI) and meshed with quadratic tetrahedral elements. Models were then imported to FEBio Studio (v1.3.0) for finite element analysis (FEA). Material properties, boundary conditions, and contacts were defined within FEBio Studio. The cervix was modeled as a passive fiber composite material with a compressible neo-Hookean ground substance fit to existing mechanical tissue tests [9]. To simulate the placement of the aspirator in the HF and MF models, the probe was translated in the xy-plane until it made full contact with the cervix while minimizing tissue strain. Once full contact was reached, negative pressure was applied to the section of tissue directly beneath the aspirator to simulate the suction of cervical tissue into the aspirator. Inverse finite element analysis was then performed to find the exact fiber stiffness (cCS) value necessary for the tissue to be deformed by 4 mm (within 1%). cCS values for HF, MF, and LF models were compared to understand how geometric fidelity affected the numerical outcomes of the simulations. Simulation run time was also considered in the analysis.

RESULTS

The LF, MF, and HF models varied in simulation run time and cCS values across all patients. On average, simulation run time was 0.7 hours for LF, 6 hours for MF, and 7 hours for HF models. No clear trend in cCS values were found, with some high cCS values correlating with lower aCS values, etc. (Tab. 1). Additionally, there was no direct correlation between CL, aCS, and cCS values. In future work, birthing outcomes (pre- vs. at-term) will be incorporated into these analyses to understand whether any of the parameters alone or combined accurately predict PTB.

Table 1: CL, aCS, and LF, MF, and HF cCS values for patients at low and high risk for PTB.

Patient #	CL (mm)	aCS (mbar)	cCS (kPa)		
			LF	MF	HF
Low Risk					
P7	48	113	42	33	18
P16	42	89	32	36	20
P32	40	59	14.1	8.3	9
High Risk					
P1	18	81	6	9	7
P2	7	129	9	0.2	0.3
P6	8	23	0.2	1.47	2.6

DISCUSSION

This study analyzed three parametric methods of patient-specific cervical modeling in aspiration simulations. No clear trends between models were found, with differences between fidelities ranging from 0.1-24 kPa. However, it was clear that the LF model had the fastest simulation time, being 4-24 times faster than the MF and HF models. Ideally, the modeling approach for widespread implementation would maintain the trends of the highest-fidelity model but also take the least amount of time to measure and simulate. Ultimately, the HF and MF models presumably display more accurate cCS values (because their geometries bear more resemblance to ultrasound images), but their slow run times make them impractical candidates for population-level analyses. Therefore, in the future, we plan to implement the LF approach in large cohorts of patients at low and high risk for PTB to determine if it alone can improve PTB prediction.

There are several limitations to this study. First, the small sample size limits the conclusions that can be drawn about the best modeling approach, and delivery outcome analysis is necessary. The strain-minimizing approach for probe placement was also a source of inter-model error, as it was geometry-dependent, so different strains were applied to MF and HF models of the same patient. Thus, the difference in cCS values may be partially attributed to discrepancies in tissue strain prior to pressure application. This is one reason that LF models are preferred for future iterations; they do not require any applied strain. It must also be noted that the cervix position during a speculum exam may not be an exact match to the ultrasonic image, potentially making the HF model inconsistent with *in-vivo* conditions. Lastly, a mesh-size convergence study was not performed, though a conservatively fine mesh was used for all models. A coarser meshing scheme may yield faster simulation runtimes with the same resulting cCS value.

ACKNOWLEDGEMENTS

This work is supported by the Columbia University Egleston Scholars Program and Eunice Kennedy Shriver National Institute of Child Health & Human Development of the National Institutes of Health under award number 1R01HD091153-01. The content is solely the responsibility of the authors and does not necessarily represent the official views of the National Institutes of Health.

REFERENCES

[1] World Health Organization, “Preterm Birth”, 2023.
[2] *Obstet & Gynecol*, 138(2):e65-e90, 2021.
[3] Vink, J et al., *Best Pract Res Clin Obstet Gynaecol*, 52:88-102, 2018.
[4] Kyvernitakis, I et al., *PLOS One*, 18(4):e0283944, 2023.
[5] Hairston, J et al., *Reprod Sci*, 30(S1):127A, 2023.
[6] Louwagie, E et al., *PLOS One*, 16(1): e0242118, 2021.
[7] Dagle, A et al., *PIPPI 2022,* LNCS 13575:48–59, 2022.
[8] Pregnolia, “Instructions”, 2023.
[9] Shi, L et al., *J Biomech Eng*, 141(9): 0910171–09101713, 2019.

3D GEOMETRIC RECONSTRUCTION OF ELECTROSPUN FIBERS

Evan He (1), Shruti Motiwale (2), Elizabeth Cosgriff-Hernandez (1), Michael S. Sacks (1,2)

(1) Biomedical Engineering, The University of Texas at Austin, Austin, Texas, United States
(2) Mechanical Engineering, The University of Texas at Austin, Austin, Texas, United States

INTRODUCTION

Electrospun fibrous meshes serve as excellent biomaterial scaffolds owing to their structural similarities to extracellular matrices and their tunable material properties due to the electrospinning process. In a previous study modeling the complex biaxial and shear mechanical behavior of these meshes, presence of novel fiber-fiber interactions was observed [1]. Present understanding of electrospun meshes is limited to 2D statistical fibrous network models using a theoretical fiber density, fiber intersection density, and orientation distribution function [2]. This study presents the first accurate 3D reconstruction and structural analysis of electrospun fiber geometry with the goal of understanding how fiber-fiber interactions at the microscale level may impact the bulk mechanical properties of electrospun fibrous meshes.

METHODS

A randomly oriented electrospun polycarbonate urethane fiber mesh was imaged into 3D nanoCT images with a cubic voxel resolution of $(180\ nm)^3$ (Figure 1). Parameters, such as fiber diameter and fiber volume fraction, were collected in ImageJ. Fiber diameter was averaged across 10 randomly chosen fibers within a resliced image. Total fiber volume fraction was calculated by binarizing the nanoCT images and computing the fraction of voxels corresponding to a fiber to the total number of voxels. A grayscale binarization value of 170 minimized image noise. A representative volume element (RVE) size was determined using a convergence analysis for fiber volume fractions; incrementally larger children cubic volume subsets originating from the vertices of the largest possible cubic parent volume $(200\ \mu m)^3$ were created from the nanoCT images. Convergence is reached when the fiber volume fractions for all children subsets converge to a single value.

Custom Python scripts were also written to analyze and model fiber segment lengths and fiber intersection points within the electrospun fiber mesh. First, resliced nanoCT images were imported and cropped to provide smaller cubic subsets of data to analyze. Next, the images were binarized, denoised, and 3D skeletonized to demarcate all fiber centerlines. Using the fiber centerline data, a connectivity plot was created to identify fiber intersections (nodes) and individual fiber segments between fiber intersections (vertices) in a 3D graph structure. Finally, residual image artifacts were removed, fiber segment lengths and the number of fibers per fiber intersection point from the 3D connectivity graphs were extracted, and 3D fiber connectivity was visualized (Figure 2).

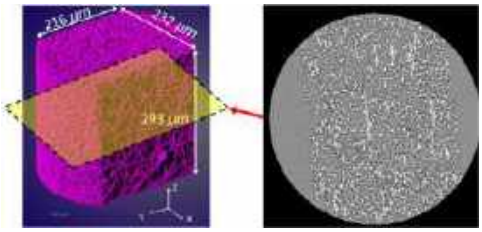

Figure 1: 3D rendering of full electrospun fiber mesh. A cut section depicts one of 1628 original image slices stacked across Z. Image resolution: 345 µm x 361 µm. Voxel resolution: $(180\ nm)^3$.

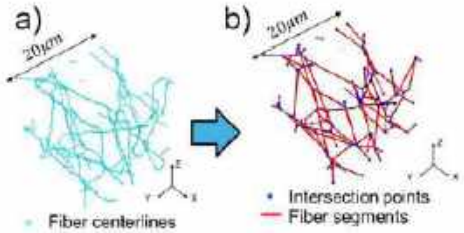

Figure 2: (a) Fiber centerlines and (b) fiber connectivity for a $(20\ \mu m)^3$ cubic volume.

Convergence of fiber segment lengths and convergence of the number of fibers per fiber intersection point were also considered for determining the RVE size. The largest possible cubic parent volume from the 3D connectivity graph (150 μm)^3 was used to create incrementally larger children cubic volume subsets from each of the vertices of this parent volume. Convergence is reached when the fiber segment lengths and number of fibers per fiber intersection point for all children subsets each converge to a single value.

In the next phase of analysis, the established RVE size was used to create a volume mesh for the finite element simulation. The nanoCT images were imported into ORS Dragonfly to generate a surface mesh with triangle elements using the marching cubes algorithm. The surface mesh was then imported into GMSH to create a volume mesh with linear tetrahedral elements using the Delaunay algorithm (Figure 3). The resulting volume mesh for the RVE contained 1,113,547 nodes and 3,465,484 elements. As a preliminary test, a linear ramping uniaxial planar displacement test was simulated using an implicit finite element analysis with Abaqus/Standard for a 20% displacement. The mechanical properties of the RVE mesh were approximated using an isotropic Neo-Hookean material model (C1 = 2.5 Pa, D1 = 0.005 Pa^{-1}).

$$\Psi^{sf} = \begin{cases} c_1(I_1 - 3) + D_1(J-1)^2, & \lambda_f \geq 1 \\ 0, & \lambda_f < 1 \end{cases} \quad (1)$$

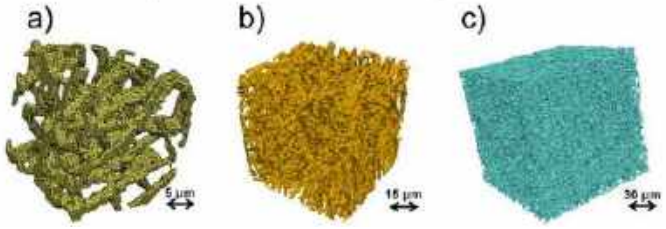

Figure 3: Cubic volume meshes for sizes (a) (25 μm)^3, (b) (90 μm)^3, and (c) (180 μm)^3.

RESULTS

The total fiber volume fraction of the electrospun polycarbonate urethane mesh was 22.14%. The convergence analyses found the RVE size to be a (100 μm)^3 cubic volume because fiber volume fractions from children volume subsets across all parent vertices consolidated at 21.34%; and fiber segment lengths and the number of fibers per fiber intersection point converged to 4.710 ± 2.411 μm and 3.811 ± 1.609, respectively (Figures 4 and 5). Preliminary results for a 20% uniaxial finite element displacement simulation of the RVE demonstrated thinning at the center of the mesh (Figure 6). A nearly linear relationship is found when plotting the sum of forces experienced by the displacement plane with the prescribed displacement (Figure 7).

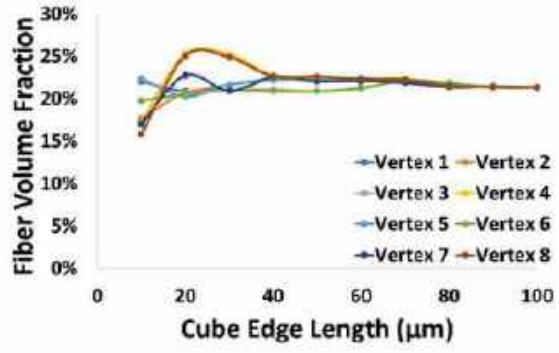

Figure 4: Fiber volume fractions for children volumes converge at 21.34%.

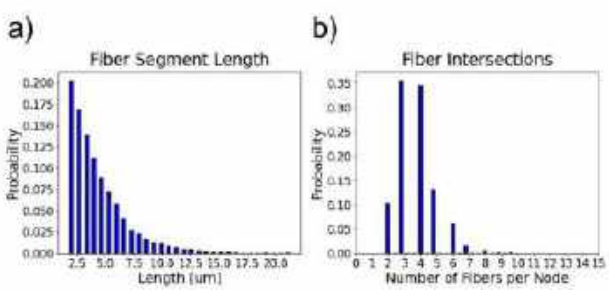

Figure 5: (a) Fiber segment length and (b) fiber intersection distributions for a (100 μm)^3 volume.

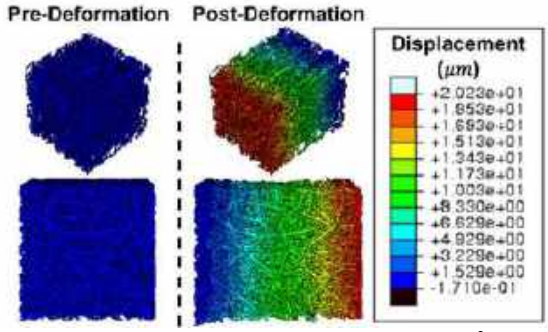

Figure 6: Uniaxial displacement test for (100 μm)^3 fiber mesh. Linear displacement ranges between 0 μm (blue) and 20 μm (red).

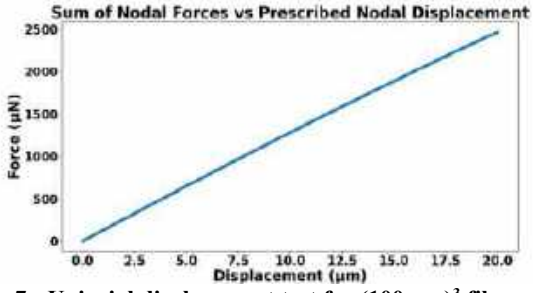

Figure 7: Uniaxial displacement test for (100 μm)^3 fiber mesh. Net force on displaced mesh plane is plot against its linear displacement.

DISCUSSION

This study presents a computational pipeline to develop an accurate and detailed 3D computational model of an electrospun fibrous mesh. Parameters like fiber volume fraction, fiber segment length and number of fibers per fiber intersection point can be extracted to characterize the geometric properties of an electrospun mesh. The linear relationship found from the uniaxial displacement simulation matches the stress-strain trends found in our previous study [2]. Consequent simulations will be performed on the RVE according to the planar biaxial test setup found in [2] and results will be presented at the meeting. Although this study is still in progress, it can grant valuable insight into the bulk mechanics of electrospun fiber meshes based on microscale geometric interactions.

ACKNOWLEDGEMENTS

R01 HL129077 and R01 HL142504

REFERENCES

[1] Motiwale, S. et al. Journal of the mechanical behavior of biomedical materials vol. 125 (2022)

[2] Carleton, J. et al. Acta biomaterialia vol. 12 (2015): 93-101.

PERSONALIZED FINITE ELEMENT MODELS OF TISSUE EXPANSION FOR BREAST RECONSTRUCTION AFTER MASTECTOMY

Joel Laudo (1), Tianhong Han (1), Ariel Figueroa Baker (2), Arun Gosain (2), Taeksang Lee (3), Adrian Buganza Tepole (1)

(1) Mechanical Engineering, Purdue University, West Lafayette, Indiana, United States
(2) Feinberg Medical School, Northwestern University, Chicago, Illinois, United States
(3) Mechanical Engineering, Myongji University, Yongin, Korea

INTRODUCTION

Tissue Expansion is a common medical procedure that induces new skin growth to repair large skin defects. It is especially useful in the early stages of breast reconstruction because it can create new skin *in situ* to make space for a permanent breast implant. This method is used in 65% of all breast reconstructions in the United States [1]. However, the current inability to predict the precise amount and location of new skin growth can lead to undesirable cosmetic results and complications, including skin tearing and necrosis, at a frequency of 16% or higher [1]. Our past work has developed and calibrated a mechanical model that predicts local skin growth based on stretch [2]. In this work, we build finite element models of a patient undergoing bilateral breast reconstruction and predict total skin growth in each breast using our computational skin growth model.

METHODS

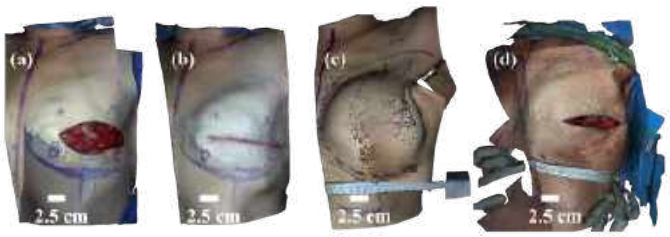

Figure 1: Patient breast scans taken (a) before expander insertion, (b) after expander insertion, (c) after completing the inflation protocol, and (d) immediately after expander removal.

Finite Element Model

Data was collected from a patient undergoing bilateral breast reconstruction (Figure 1 shows the cancerous left breast). To build the finite element models in the software package Abaqus, the surface scans of each breast taken immediately after expander insertion were discretized with 58,260 C3D8 elements for the cancerous breast, and 31,254 elements for the contra-lateral breast. A 14 cm diameter circular expander geometry was created using S4R shell and F3D4 fluid cavity elements. The patient inflation volume protocol (Table 1) was simulated in both breasts.

Table 1: Bilateral Inflation Protocol of Patient

Date [MM/DD]	Volume [ml]	Time [Days]
11/23/21	60	0
11/30/21	180	7
12/16/21	300	23
03/22/22	360	120
09/13/22	450	296

The finite element skin growth model is based on our previous work [2]. Briefly, skin is modeled as a neo-Hookean solid with shear modulus μ. Skin local area deformation is split into growth and elastic parts,

$$\boldsymbol{\theta} = \boldsymbol{\theta}^g \boldsymbol{\theta}^e \quad , \tag{1}$$

with the local area growth rate proportional to the elastic deformation

$$\dot{\theta^g} = k(\theta^e - \theta^{\text{crit}}) \quad , \tag{2}$$

with growth rate parameter k, and critical area stretch θ^{crit}.

Uncertainty Analysis

To account for uncertainty between simulation conditions and the patient treatment, influential simulation design parameters were varied in a design of experiments (Figure 2a). Due to the long time between inflations, we confirmed that the growth parameter had no effect on the final

skin growth and held it constant at $k = 0.48day^{-1}$ based on prior work [2]. The skin shear modulus was also held constant to a realistic value of $\mu = 900kPa$ [3] [4]. θ^{crit} was unknown so a value of $\theta^{\text{crit}} = 1.1567$ from previous work [2] was used initially. Four geometric parameters of interest were sampled, the region of loose skin around the expander tol, the expander offset h, the subcutaneous expander rotation φ, and the expander profile S_x. Their sampling ranges are shown in Table 2. A total of 296 simulations were run between both breasts by sampling the parameters in Table 2 using Latin hypercube sampling.

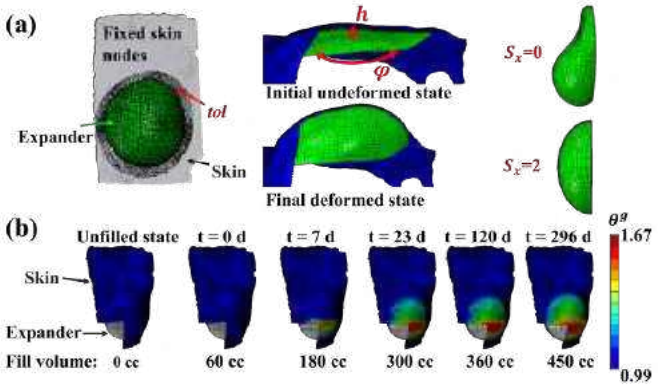

Figure 2: (a) Geometric design parameters varied using LHS and (b) growth θ^g field over time for a single simulation.

Table 2: Ranges for Boundary Conditions

Parameter	Range
tol [mm]	[15, 25]
h [mm]	[2, 10]
φ [deg]	[-15, 15]
S_x	[0, 2]

RESULTS

A representative simulation is illustrated in Figure 2b. As the expander inflates, the skin stretches, deforming more at the apex. Eventually, the stretch surpasses θ^{crit} and skin growth accumulates. The growth field θ^g measures the relative area gain. Contours in Figure 2b show greater growth at the apex. A more useful metric of growth is the integration of the area gain over the entire expanded skin surface, $A^g = \sum A_i^0 \cdot \theta_i^g$ where A_i^0 is the initial element area and θ_i^g is the final growth for each element i on the skin surface.

Simulation nodal coordinates at the final time point were compared against the observed geometry (e.g. Figure 1c for the cancerous breast). The mean distance errors were computed (Figure 3a), resulting in error distributions due to design parameter sampling (Figure 3b, gray). Minimum error thresholds (maximum likelihood) were selected to filter out the simulations that best match the data (Figure 3b, red). By filtering out these best fitting simulations from the overall distribution, the uncertainty in the growth distribution is reduced. The uncalibrated growth prediction distribution $p(A^g)$ is shown in Figure 3c, in gray. After considering only simulations that best match the observed geometry just prior to expander removal, the growth prediction distribution is narrowed (Figure 3c, in red). Since we had access to the relaxed skin geometry after expander removal but before implant placement and the initial geometry before expander insertion (see Figure 1d, Figure 1a), we were able to obtain the experimental values for A^g (Figure 3c, in green). It can be seen that the calibrated area growth predictions based on only *in vivo* data match well the underlying growth value, which can only be measured by removing the expander and measuring the relaxed skin area.

The assumption of the critical stretch $\theta^{\text{crit}} = 1.15$ from previous work is strong, based on porcine experiments [2]. From the results in Figure 3c it appears that this critical stretch is also applicable to human breast skin. However, considering uncertainty in θ^{crit}, greater uncertainty in A^g is shown in Figure 3d.

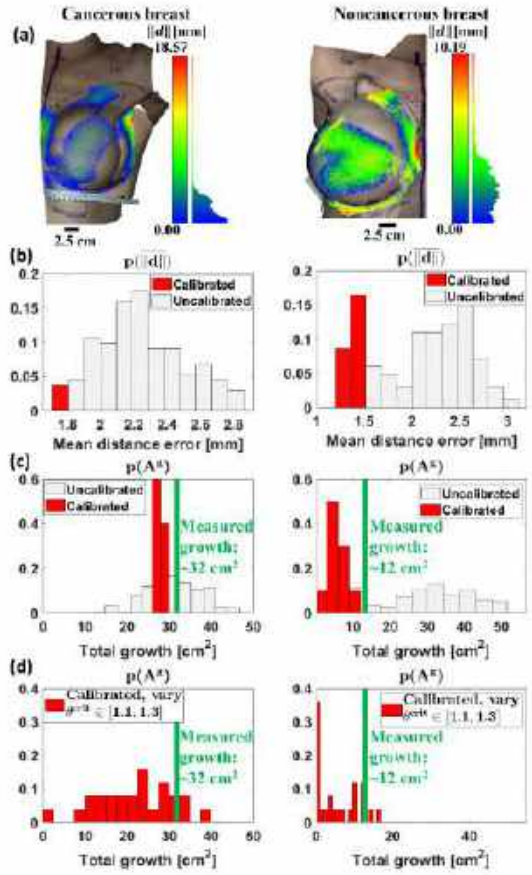

Figure 3: (a) Simulation results aligned with the final surface scan. Mean distance error (b) and total growth (c) distributions for all simulations (grey) and high likelihood results (red) assuming $\theta^{\text{crit}} = 1.15$ align with experimental measurement (green). (d) Growth distribution with additional uncertainty by removing the assumption $\theta^{\text{crit}} = 1.15$ and instead sampling $\theta^{crit} \sim U([1.1, 1.3])$.

DISCUSSION

Our results demonstrate for the first time how tissue expansion can be simulated to make patient-specific predictions in the setting of breast reconstruction. The current simulations are based on extensive prior work validating the model with tissue expansion data in a porcine model [2]. Leveraging that prior knowledge and minimizing the uncertainty with respect to the final deformation observed in-patient, we were able to accurately predict the true skin growth (Figure 3d). More data must be collected to fully characterize the distribution of the growth model parameters in the context of human patients. We anticipate that our model can eventually be used by physicians to inform patient-specific protocols to reduce complication risks, increase the precision of results, and standardize the procedure.

ACKNOWLEDGEMENTS

This work was supported by NIAMS R01AR074525

REFERENCES

[1] Bertozzi N et al. *Annals of medicine and surgery* 21 (2017).

[2] Han T et al. *Acta Biomaterialia* 137 (2022).

[3] Luebberding S et al. *Skin Research and Technology* 20.2 (2014).

[4] Mueller B et al. *Journal of Biomechanical Engineering* 143.2 (2020). ISSN: 0148-0731. DOI: 10.1115/1.4047661.

BUILDING ASGR1-OVEREXPRESSED FLUORESCENT REPORTER CELL MODEL FOR OPTIMIZATION OF CRISPR DELIVERY

Yun-I Sang, Morgan Clay, Chun-Wei Chi, Yeh-Hsing Lao

Department of Pharmaceutical Science, University at Buffalo, The State University of New York, Buffalo, New York, USA 14214

INTRODUCTION

CRISPR/Cas9 technology enables precise manipulation at a specific locus of target cell genome through the guidance of its corresponding RNA guide (gRNA). Since the first Cas9 system was reported in 2015, advances in CRISPR/Cas9-mediated genome editing have revolutionized the gene therapy field and led to recent approvals of somatic gene editing therapies with more than 90 ongoing clinical trials and a significant number of different applications in preclinical pipelines,[1] indicating the massive race in the translation of gene editing technologies is currently underway.

Effective delivery is the key to realizing the full potential of this emerging technology. As an exogenous component, CRISPR machinery needs a delivery carrier to reach the target tissue and then enter the target cell. Seeing the recent approval of small interference RNA product applying Asialoglycoprotein Receptor 1 (ASGR1)/N-acetylgalactosamine (GalNac) interaction for in vivo hepatocyte targeting,[2] we are developing new CRISPR delivery approaches adopting this delivery mechanism. As part of this effort, we built an in vitro reporter model to characterize the effectiveness of our designed CRISPR delivery systems, thereby facilitating our screening and optimization processes. Here we present our HEK293T/Ai9-ASGR1 reporter cell model. Integrating both Ai9 (CAG-LoxP-STOP-LoxP-TdTomato) and ASGR1 expression cassettes to the HEK293T cell line, we demonstrate that this reporter cell can be used to screen CRISPR delivery systems and overexpress the ASGR1 receptor on the cell membrane. This in vitro toolkit allows us to screen different GalNac-conjugated CRISPR delivery systems in the downstream pipeline.

METHODS

The Ai9 (CAG-LoxP-STOP-LoxP-TdTomato) expression cassette was first retrieved from the parental plasmid from Addgene (#22799) and cloned to a transposon system then transfected to HEK293T cells. HEK293T/Ai9 stable line was then selected through selection, and TdTomato signal was confirmed by CRE- and Cas9-activation.

The cDNA encoding ASGR1 variant 1 or 2 was then cloned to the lentiviral backbone with a puromycin resistant gene expression cassette. ASGR1-carrying lentiviruses were then generated through co-transfection of ASGR1-trasfer plasmid and packaging plasmids (psPAX2 and pMD2.G) using Calfectin. Media containing lenviruses were collected at 48h and 72h post-transfection and purified using a column method. Viral titer was determined by RT-qPCR using the quantification kit from Abm.

HEK293T/Ai9 cell line was then transduced with ASGR1-lentiviruses (MOI=10). Afterwards, three rounds of puromycin selection were carried out to obtain the final HEK293T/Ai9-ASGR1 reporter line. The level ASGR1 expression for both variants was confirmed by qPCR, while location of ASGR1 confirmed by confocal microscopy.

RESULTS

We first confirmed whether the Ai9 expression cassette was integrated to HEK293T genome. We transfected our generated

HEK293T/Ai9 line with a CRE-encoding plasmid using Lipofectamine 3000. At 48h post-transfection, we were able to detect CRE-activated TdTomato signals and could use this to quantify the efficiency of delivery carrier (Lipofectamine 3000, 35.6 ± 3.5%, **Figure 1A**). To test whether it could be also activated by Cas9, we used our published *Staphylococcus aureus* Cas9 plasmid (Addgene# 207878)[3] encoding Ai9-targeting gRNA to transfect the cell line. Similarly, at 48h post-transfection, we detected Cas9-induced TdTomato signals (**Figure 1B**). These confirm the success of Ai9 cassette integration in the HEK293T cell.

After the second step in generating HEK293T/Ai9-ASGR1 line, we quantified the ASGR1 expression by RT-qPCR. As shown in **Figure 2**, The ASGR1 expression level in the both HEK293T/Ai9-ASGR1 variant 1 and 2 lines was >1,000 times higher than that in the parental HEK293T/Ai9 (ASGR1 variant 1: 1409±119.4 folds; ASGR1 variant 2: 1131±514.5 folds). This confirms the overexpression at the mRNA level in our generated HEK293T/Ai9-ASGR1.

To confirm the location of our overexpressed ASGR1 variant 1 and 2, we carried out immunostaining with ASGR1-specific antibody. The confocal microscope results confirmed that ASGR1 variant 1 is expressed on the cellular membrane, while the parental HEK293T/Ai9 expressed very minimal ASGR1 on membrane as expected (**Figure 3A**). As ASGR1 variant 2 is secreted protein, our immunostaining was therefore not able to visualize it. We also quantified the level using ImageJ. As shown in **Figure 3B**, ASGR1 variant 1-expressing line showed higher intensity than its counterparts (parental HEK293T/Ai9 and HEK293T/Ai9-ASGR1 variant 2), consistent with the results shown in **Figure 3A**. Both qPCR and confocal microscopy results confirm the overexpression of ASGR1 protein in our established cell line model at both mRNA and protein level, and the location of the protein is expected.

DISCUSSION

ASGR1/GalNac interaction has been widely used for small RNA delivery to hepatocyte. Two recent works have also shown the feasibility of using this interaction for CRISPR delivery.[4,5] Our goal here is to establish a cell line model to help our downstream design and optimization of our GalNac-conjugated CRISPR delivery systems for liver targeting. Through two steps of the reporter (Ai9) and ASGR1 expression cassettes, we have successfully established the HEK293T/Ai9-ASGR1 cell model for this purpose. This in vitro reporter model can be used for quantification of gene editing performance (**Figure 1**). The overexpression of ASGR1 variant 1 protein can be used to screen the GalNac-conjugated nanocarriers (**Figure 2**), while two counterparts (HEK293T/Ai9 and HEK293T/Ai9-ASGR1 variant 2) can serve as controls for specificity optimization of the CRISPR delivery carriers (**Figure 3**). Our work here demonstrates a new in vitro model that allows to benchmark the performance of CRISPR delivery systems.

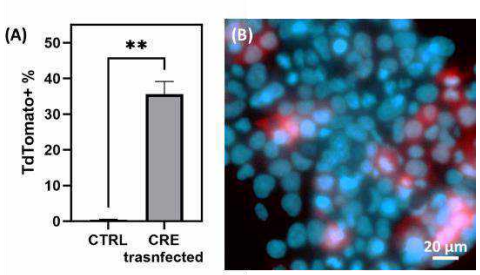

Figure 1: TdTomato activation on HEK293T/Ai9. (A) CRE-induced and (B) Cas9-induced TdTomato activation on our generated HEK293T/Ai9 cell line.

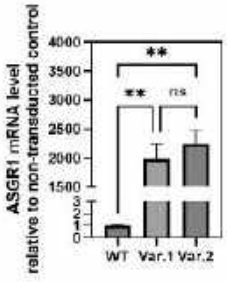

Figure 2: ASGR1 overexpression in our HEK293T/Ai9-ASGR1 at the mRNA level. Relative ASGR1 level was determined through normalization to the house-keeping gene GAPDH.

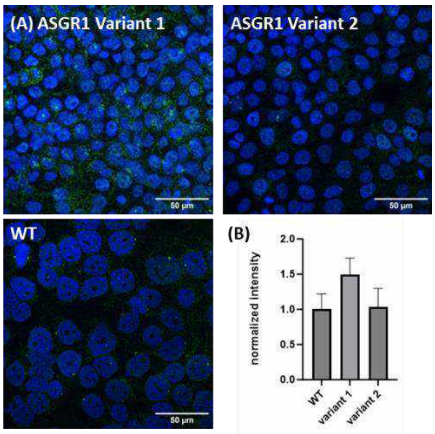

Figure 3: ASGR1 overexpression in our HEK293T/Ai9-ASGR1 at the protein level. (A) Representative confocal images to confirm the location of overexpressed ASGR1 in our established cell line. (B) Quantification of ASGR1 protein level.

ACKNOWLEDGEMENTS

We acknowledge the instrument support from the Optical Imaging and Analysis Facility at UB School of Dental Medicine. This work is supported by NIH (R21NS133635) and UB Center for Protein Therapeutics.

REFERENCES

[1] Morshedzadeh et al., *Mol Biotechnol* (**2023**) *66*: 179-197.
[2] Zimmermann et al., *Mol Ther* (**2017**) *25*: 71-78.
[3] Lao et al., *PNAS* (**2023**) *120*: e2302910120.
[4] Rouet et al., *JACS* (**2018**) *140*: 6596-6603.
[5] Zhang et al., bioRxiv (2023), DOI: 10.1101/2023.03.20.533459.

REGIONAL MECHANICAL PROPERTIES ON THE MACROSCALE AND MICROSCALE ARE NOT ASSOCIATED FOR THE EQUINE SUPERFICIAL DIGIAL FLEXOR TENDON

Samantha L. Watson (1), Zachary G. Davis (1,2), Shannon S. Connard (3), Lauren V. Schnabel (3), Matthew B. Fisher (1,2,4)

(1) Joint Department of Biomedical Engineering, North Carolina State University & University of North Carolina – Chapel Hill, Raleigh, NC, USA
(2) Comparative Medicine Institute, North Carolina State University, Raleigh, NC, USA
(3) College of Veterinary Medicine, North Carolina State University, Raleigh, NC, USA
(4) Department of Orthopaedics, University of North Carolina – Chapel Hill, Chapel Hill, NC, USA

INTRODUCTION

Tendon injuries are one of the most common musculoskeletal injuries in humans[1]. Such injuries can also occur in animals. For example, the superficial digital flexor tendon (SDFT) of the horse is prone to tendonitis[2]. Thus, the SDFT can also serve as a model to study human tendon injuries[3]. SDFT injuries commonly occur in the midsubstance of the tendon, in part due to its smaller cross-sectional area[4]. However, variations in the intrinsic mechanical properties of the tendon could also play a role. Mechanical properties can be studied macroscopically and microscopically, to probe different levels of the hierarchical collagenous extracellular matrix[5]. This can allow mechanics at different scales to be studied independently and determine if a relationship exists between them. The objective of this study was to look at the regional mechanical differences of equine SDFT on the macroscale and microscale and determine if a relationship exists across the length scales.

METHODS

Equine SDFTs were obtained from 3 horses. Subject 1 was a 12-year-old warmblood (WB) mare, Subject 2 was a 4-year-old American quarter horse (QH) and WB filly, and Subject 3 was a 3-year-old QH stallion. The sheath was removed from the outside of the tendon. The tendon was divided into three sections: proximal, middle, and distal. The sections were embedded in Celluclay and sliced into 1 mm thick slices (5-7 slices per section)[6]. From each slice, longitudinal and transverse dog bone punches were taken relative to the long-axis of the tendon using a 10 mm Print-A-Punch[7] and a 1 cm x 1 cm square was taken from the center of the slice for atomic force microscopy (AFM, Asylum Research). Macroscale samples were tested using an Instron (model 5944) with pneumatic clamps to record the elongation and force. The longitudinal and transverse macroscopic samples were pulled to failure at a rate of 1 mm/s. ImageJ was used to measure the gauge length, width, and thickness of the dog bone sample from images taken prior to testing. Stress was calculated by dividing the force by the cross-sectional area, while strain was calculated by dividing the displacement by the length of each sample. The elastic modulus was found by calculating the slope of the linear section of the stress-strain curve using MATLAB. Microscale sections (AFM) were cryosectioned into 10 µm slices. The modulus was found at four points on each sample using a colloidal tip on contact force mode masked and converted to stiffness values using the Hertz model. A one-way ANOVA with Tukey's test (α=0.05) was used for statistical comparisons between subjects and regions separately. Linear regression analysis was done between data for the AFM and longitudinal and transverse testing. Data is presented graphically as mean ± standard deviation.

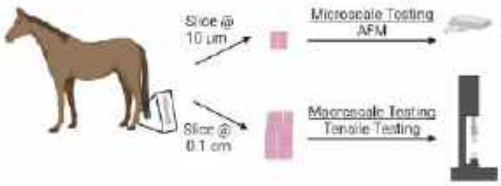

Figure 1: Methodology for testing of equine superficial digital flexor tendon (n=3, age 3-12 yrs. old) at multiple scales

RESULTS

Between subjects, for the macroscale longitudinal modulus, mean values were roughly similar (Fig. 2A). For the macroscale transverse modulus, the mean value for Subject 3 was found to be 2 times larger than Subject 1 and 4 times larger than Subject 2 (Fig. 2B). For the microscale modulus, mean values for Subjects 1 and 2 were 2 times larger than Subject 3. However, no significant differences were found between any subjects for macroscale or microscale testing ($p>0.05$).

Between regions, for macroscale longitudinal samples, the mean values for the proximal and middle sections were about 1.6 times larger than the distal section. For microscale samples, the mean modulus values of the proximal section were about 1.4 times larger than the middle and distal regions. However, for both longitudinal and AFM samples, the differences between regions were not statistically different

(Fig. 3A-B).

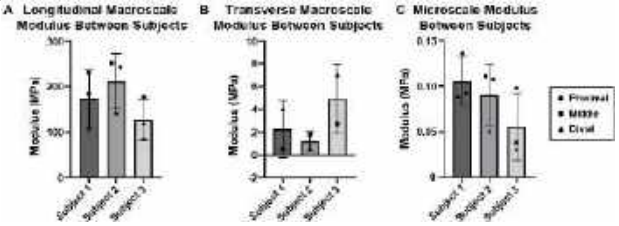

Figure 2: A. Longitudinal macroscale (tensile) modulus for each subject B. Transverse macroscale modulus for each subject C. Microscale (AFM) modulus for each subject

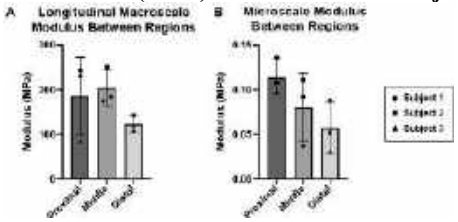

Figure 3: A. Longitudinal macroscale testing data for each region B. Microscale data for each region

Across scales, longitudinal modulus values (170.9 ± 42.6 MPa) were found to be 3 orders of magnitude larger than AFM (0.083 ± 0.025 MPa, $p<0.05$), while transverse macroscale modulus values (2.8 ± 1.9 MPa) were approximately 1 order of magnitude larger than microscale values (Fig. 4A, $p<0.05$). No associations were found between the moduli obtained from microscale and macroscale longitudinal samples ($R^2 = 0.07$, $p = 0.06$), microscale and macroscale transverse samples ($R^2 = 0.02$, $p = 0.50$) and macroscale longitudinal and transverse samples ($R^2 = 0.01$, $p = 0.69$) (Fig. 4B-D).

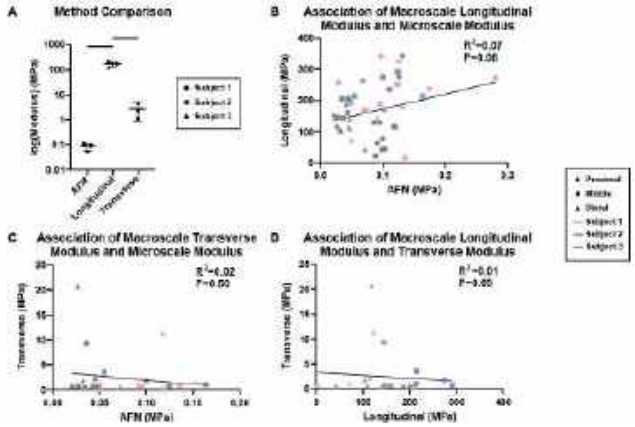

Figure 4: A. Macroscale and microscale method comparison (bar represents $p<0.05$) B. Associations between macroscale longitudinal tensile testing and microscale C. Associations between macroscale transverse tensile testing and microscale D. Associations between macroscale longitudinal and transverse tensile testing

DISCUSSION

This study showed that mechanical properties for the equine SDFT obtained from the microscale are not strongly associated with properties obtained from macroscale testing. Between subjects, there was no consistent rank-order in terms of modulus values.

When looking at the different regions, values were again not consistent in terms of rank-order across the different testing methods. wed by the proximal and distal region. Subject 3 did have an unusually low moduli for the proximal region for the longitudinal testing which may partially explain the difference between the longitudinal macroscale and microscale testing methods. These differences were not studied for transverse samples as the proximal region was too narrow to obtain samples.

Across scales, longitudinal macroscale testing was found to be 3 orders of magnitude larger than microscale testing. Meanwhile, the transverse macroscale testing was only 1 order of magnitude larger than microscale testing. No significant associations were found between either longitudinal or transverse macroscale testing and microscale testing. When looking at the macroscale directionality, no significant association was found between the longitudinal and transverse direction. The lack of association between the longitudinal and transverse directions highlights the anisotropic properties of tendon, in which collagen fibers align along the longitudinal direction. Testing in the longitudinal and transverse directions gives information about the macroscale mechanical properties due to the collagen fibers and the non-collagenous matrix, respectively. The lack of association between macroscale and microscale length-scales highlights the difference in mechanical properties obtained when using different methods to test matrix at different scales.

Previous studies found the longitudinal moduli of equine SDFT to be approximately 1000 MPa; however, those studies looked at the whole tendon rather than thin samples, which may disrupt some of the collagen fibers or introduce clamping effects[8-9]. A similar study for sheep flexor tendon and human MCL found the transverse moduli to be 2 orders of magnitudes smaller than the longitudinal moduli, which was consistent with the results of this study[10-11]. When comparing this to previous data, it can be seen that the AFM modulus found for equine tendon (0.083 ± 0.025 MPa) had similar values to the mean modulus found for wild-type mice tendon of 0.053 MPa[12].

One limitation of this study was a lack of samples, as well as a lack of knowledge on the subject's injury history. It was unknown if any of the subjects used had previous tendon injuries that may have impacted the results of this study. In addition, the loading conditions varied across the scales with macroscale testing being conducted in tension and microscale testing being conducted in compression through indentation.

Overall, this study found that regional differences of the SDFT tendon are not replicated between different length-scales, this may be due to the lack of association found between both longitudinal and transverse macroscale testing and microscale moduli values. This implies that macroscale and microscale mechanical properties of the tendon may differ with respect to age and region of the tendon. Future work will be done to increase the number of samples to help combat the differences caused by subject variability. We also plan to study the multiscale mechanical differences between healthy versus diseased samples.

ACKNOWLEDGEMENTS

We would like to acknowledge the NC State Office of Undergraduate Research and the NC State Abrams Scholars Program for their support.

REFERENCES

[1] Wu, F et al., *EFORT Open Rev.,* 2:332–342, 2017.
[2] O'Brien, C et al., *Equine Vet. J.*, 53:417-430, 2020.
[3] Lui, P et al., *Scand. J. Med. Sci. Sports,* 21:3-17, 2011.
[4] Anoushepour, A et al., *Vet. Res. Forum,* 14:579-582, 2023.
[5] O'Brien, C et al., *Equine Vet. J.*, 53:417-430, 2020.
[6] Wale, M et al., *J Biomech. Eng.,* 143, 2021.
[7] Nelson, S et al., *J Biomech.,* 112, 2020.
[8] Birch, H et al., *Int. J. Exp. Pathol.,* 88:241-248, 2007.
[9] Dowling, B et al., *Vet. J.,* 170:184-192, 2005.
[10] Lynch, H et al., *J Biomech. Eng.,* 125:726-31, 2003.
[11] Quapp, K et al., *J Biomech. Eng*., 120:757-763, 1998.
[12] Kammoun M et al., *Sci. Rep.,* 9:7733, 2019.

PREVENTING AND DETECTING NASOGASTRIC TUBE DISLODGEMENT IN INFANT PATIENTS

Jeffrey J. Huang (1), Katherine H. Han (2), Dahin I. Song (1), Suh Kyung Yoon (1)

Faculty Advisor(s)

David F. Meaney (1), Nicolas Bamat (2), Megan Snyder (3)

(1) Bioengineering, University of Pennsylvania, Philadelphia, Pennsylvania, United States
(2) Division of Neonatology, Children's Hospital of Philadelphia, Philadelphia, Pennsylvania
(3) Pediatric Intensive Care Unit, Children's Hospital of Philadelphia, Philadelphia, Pennsylvania

INTRODUCTION

Nasogastric (NG) tubes are vital for delivering sustenance and medications to patients unable to swallow normally. Annually utilized by over 1.2 million patients in the United States, NG tubes are prone to dislodgement, which occurs when the tip of the tube becomes significantly displaced from its intended position within the stomach[1]. Tube dislodgement is particularly dangerous if pulled into the esophagus, leading to severe or fatal pneumonia[2]. Dislodgement impacts up to 50% of patients, incurring replacement costs of up to $500 and frequently necessitating additional support from interventional radiology[3]. Notably, infant patients face a disproportionate risk, with over 60% experiencing tube dislodgement. This vulnerability is accentuated by their smaller fingers, increasing the likelihood of unintentional tugging[4]. Even a slight displacement of a few centimeters can pose life-threatening risks, due to their shorter stomach. There is no continuous monitoring system for NG tubes, necessitating caregivers – parents, physicians, and bedside nurses – to manually inspect for dislodgement every four hours.

Tools designed to address NG tube dislodgement must fulfill crucial criteria, including effective detection, prevention, and a straightforward, non-invasive setup approach. Unfortunately, current solutions are inadequate, especially when it comes to addressing this issue in infant patients Internal bridles (AMT bridle and CORGRIP retention system) offer partial prevention of dislodgement by looping a rigid tube through the nasal cavity and around the nasal septum[6]. However, this invasive approach is unsuitable for administering to infant patients due to the delicate nature of their nasal epithelia. In fact, the AMT bridle was initially recalled during clinical trials due to an incident where the bridle tore through a patient's nasal septum and became wedged between the torn septum[5]. None of the current standards of practice are capable of both detecting dislodgement and preventing resulting complications.

PRODUCT DESIGN

NG-LOOP, designed for both hospital and home use, addresses the critical need for increased safety and quick detection of NG tube dislodgement events in infants. The core mechanism includes an external bridle for secure tube attachment and an integrated alert system with a magnetic sensor setup, allowing real-time response to dislodgement (Figure 1). The system automatically halts the feeding pump through a Wi-Fi-connected smart plug, preventing aspiration pneumonia. At the same time, caregivers also receive instant notifications via email-to-SMS for prompt intervention. NG-LOOP distinguishes itself in NG tube management, showcasing a unique combination of dislodgement prevention, detection, and complication management with a noninvasive setup.

This system's innovation lies in its ability to promptly alert caregivers and automatically stop the feeding pump upon dislodgement detection. This not only mitigates the potential for harm but also alleviates the burden on healthcare staff, allowing for immediate intervention. The ease of NG-LOOP's application and its non-invasive nature further distinguish it from current practices, offering a proactive solution that prioritizes patient safety and caregiver efficiency.

The retention and alarm system seamlessly integrates into current workflows in hospital and home care settings. The attachment process of the external bridle is designed to be easily incorporated into routine procedures, ensuring a smooth and efficient user experience for healthcare professionals and caregivers. The system modifies existing workflows by automating the detection of dislodgement events, reducing the need for constant visual monitoring. Overall, the device improves the feeding experience for infant patients undergoing NG tube feeding, minimizing disruptions, and promoting stability and comfort, potentially enhancing patient compliance with feeding regimens.

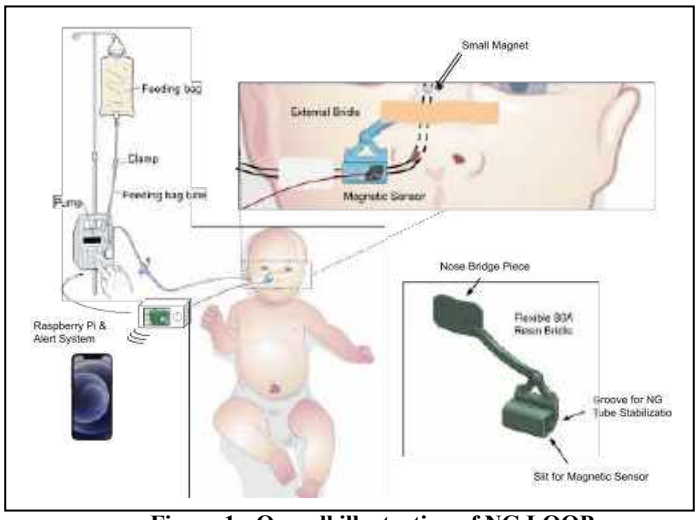

Figure 1: Overall illustration of NG LOOP

The effectiveness of the bridle was assessed using various hanging weights to simulate tube dislodgement, both with and without the bridle. This approach was selected to closely mimic the pull force experienced by infant patients. Tube dislodgement was defined as the displacement of the tube by more than 5cm from its original position within the nostril; this threshold was determined upon discussion with various NICU clinicians at the Children's Hospital of Philadelphia. It was observed that the bridle successfully prevented tube dislodgement 100% of the time, and the average displacement length of the tube with the bridle was significantly lower ($p = 0.00004$) than without the bridle. To ensure magnet security on the NG tube inside the nostril, we simulated an intranasal mucous environment with intense mechanical stimulation for over 2 weeks. For all 5 trials, the magnet stayed completely dry and was not displaced. The performance of the magnetic sensor was assessed by measuring the absolute voltage change at different lengths of magnet/tube displacement. This simulation aimed to replicate the conditions of an actual event where a tube gets dislodged and pulled to the exterior of the nostril. A true positive was defined as when the displacement of the tube by 5cm (as defined above) led to a *change* in sensor voltage reading above the predetermined threshold. The system demonstrated an 85% true positive accuracy rate in detecting tube dislodgement, with both (SMS alert and feeding pump termination) feedback mechanisms being activated in 100% of trials where the difference threshold was met.

BUDGET & MARKET ANALYSIS

While accurate metrics are scarce, one firm, Grand View Research estimates that the global nasogastric tube market was valued at USD 505.1 million in 2022 and is anticipated to grow at a CAGR of 5.3% from 2023 to 2030[6]. This growth is driven by the essential role of nasogastric tubes in medical care, including enteral feeding, medication administration, and diagnostic purposes, particularly for preterm infants. With preterm birth rates ranging from 5% to 18% across 184 countries, the demand for nasogastric tubes is expected to surge, given their critical application in providing necessary nutrition to premature babies. This increasing demand, coupled with the market's expected growth, presents a significant opportunity for investment in engineering and tooling to support the manufacturing of nasogastric tubes.

The development and testing phase of the NG-LOOP prototype incurred a total cost of $3,992.37, encompassing electronic components, development tools, 3D printing materials, and testing equipment. This initial investment provides invaluable insights into the potential manufacturing costs at scale. We estimate further physical device development costs to be $20k and software development costs to be $10K. Assuming economies of scale, which will reduce costs with increased production volume, we can project a more cost-effective manufacturing process for NG-LOOP. If the per-unit production cost could be reduced to around $40-$80 through mass production, it suggests a feasible path to affordability and profitability.

Table 1: Design budget for building prototype

Item	Cost Per Unit ($)	Number of Units	Total Cost ($)
3D printing material and services	68	1	68
Raspberry Pi 4	75	1	75
Smart plug	13	1	13
USB dongle	35	1	35
Pi prototyping HAT	13	1	13
Waterproof wire connectors	1	1	1
Laser cut enclosure	20	1	20
DRV5055 sensor	10	1	10
Medical wrapping	2	1	2
Magnet	5	3	15
		Total Cost =	**$252**

Considering the market's potential size, if we conservatively estimate that a fraction of the global nasogastric tube demand could shift towards the NG-LOOP system for its added safety and efficiency benefits, the unit sales could be significant. Assuming the global market requires millions of nasogastric tubes annually, capturing even a small percentage of this market with NG-LOOP could translate into hundreds of thousands of units sold per year.

Given the manufacturing cost and the added value NG-LOOP provides—including enhanced safety features, automatic feeding pump shutdown, and real-time caregiver alerts—a sales price ranging between $150-$200 per unit could be justifiable. This pricing strategy not only ensures a healthy margin to cover operational costs and reinvestment into further product development but also aligns with the device's innovative benefits and the critical healthcare need it addresses.

NG LOOP revolutionizes NG tube care for infants, delivering safety and peace of mind. This product is essential for any facility or home using NG tubes, offering a new standard in safety and caregiver reassurance.

ACKNOWLEDGEMENTS

We are grateful to Dr. Dayo Adewole, Dr. Erin Berlew, Riya Mathur, and the team at Penn Bioengineering Department for their guidance. Special thanks to the Stephenson Foundation Educational Laboratory & Bio-MakerSpace for their resources and funding.

REFERENCES

[1] Bloom, L et al., *AACN Adv Crit Care*, 33:68–84, 2022.
[2] Gomes, G F et al., *Curr Opin Clin Nutr Metab Care*, 6:327–333, 2003.
[3] Pancorbo-Hidalgo, P L et al., *J Clin Nurs,* 10:482-490, 2001.
[4] Quandt, D et al., *J Pediatr Gastroenterol Nutr*, 48:608–611, 2009.
[5] U.S. Food and Drug Administration, *Class 3 device recall amt bridle nasal tube retaining system*. 2017.
[6] Grand View Research, *Nasogastric Tube Market Size, Share & Trends Analysis Report*, 2023.

MRI-BASED MEASUREMENTS OF STRAIN IN THE AORTA: DOES CARDIAC DISEASE IMPACT AORTIC DEFORMATION?

Petra Alsahwi (1), Alice Guest (1), Rylan Marianchuk (2), Dina Labib (2), James A. White (2,3)
Elena S. Di Martino (1,3)

(1) Department of Biomedical Engineering, University of Calgary, Calgary, Alberta, Canada
(2) Stephenson Cardiac Imaging Centre, University of Calgary, Calgary, Alberta, Canada
(3) Libin Cardiovascular Institute of Alberta, University of Calgary, Calgary, Alberta, Canada

INTRODUCTION

Heart disease referral populations have been shown to have a high prevalence of abnormal aortic distensibility [1]. Altered aortic function may serve as a systemic indicator of global cardiovascular health in these populations. However, many factors – such as age and sex and vascular disease – contribute to changes in aortic diameter and strain across each patient's lifespan. Despite a significant amount of research and studies focusing on aortic deformation and strain [2,3], there exists a gap in understanding how these changes manifest in healthy and diseased patients. Knowledge of normal ranges and regional variability in aortic strain from cardiac MRI-based techniques are lacking. Another limitation of current studies on aortic strain is the use of indirect measurement techniques [2]. While indirect measurements can provide a global measure of stiffness, direct measurements of strain can be far more precise allowing for better tracking of strain changes over time. Moreover, a direct measurement technique enables a more localized and complete understanding of aortic deformation [3]. The main objectives of this study were to use direct measurement techniques from cine MRI to determine strain in the descending aorta: both to establish health reference values and evaluate regional differences observed in cardiovascular disease.

METHODS

Two cohorts of patients were studied. The cohort of healthy subjects had 64 studies and the cohort of cardiovascular patients had 84 studies. This cohort consisted of 58% healed myocardial infarction (MI), 20% hypertrophic cardiomyopathy (HCM), 8% non-ischemic cardiomyopathy (NICM), 5% left ventricular non compaction (LVNC), 4% cardiac amyloid, 4% acute myocardial infarction (MI acute), and 1% hypertensive cardiomyopathy (HTNcm). A Cine-MRI sequence was used to capture motion of the aorta over the cardiac cycle. All images were obtained from 4-chambers cardiac MRI studies that capture the descending aorta. Each patient had 30 DICOM images representing time steps in the cardiac cycle. Semi-automated Python code was used to isolate and track the aorta for each patient. The three main techniques used are region growing, convex hull, and optical flow. First, the code focuses on the isolation of the descending aorta from its surroundings by converting the image to grey scale and applying automatic thresholding. If the automatic threshold does not isolate the aorta well enough, the user can enter a threshold repeatedly until the aorta is isolated. The convex hull section then places a contour around the aorta which allows for the tracking of the aortic wall. The tracking is achieved for all time steps by an optical flow function.

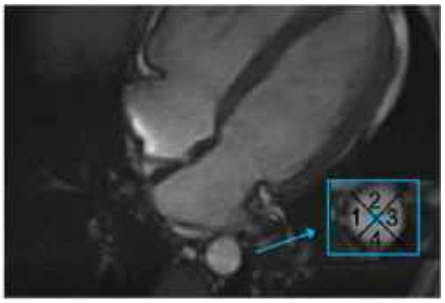

Figure 1: Position of the aorta relative to the heart on MRI image, strain quadrants magnified in the blue inset.

For all 30 phases of the cardiac cycle, the contour coordinates of the aorta were saved and used to determine strain. Equation (1) was used to express changes of the aortic area as strain percentage. Furthermore, the changes along the contour are related to the original contour and quantified as an average for each of the four quadrants as shown in Figure 1.

$$Aortic\ Strain\ Percentage = \frac{(Maximum\ aortic\ area - minimum\ aortic\ area)}{minimum\ aortic\ area} \times 100\% \quad (1)$$

The same code and methodology were utilized for both cohorts.

RESULTS

The healthy cohort comprised subjects of age 46±14. The cardiovascular cohort comprised patients age 60±13. Figure 2 shows aortic area increased with age for both cohorts of patients. The patients with cardiovascular disease showed higher variability in the aortic area while healthy patients followed a tight linear trend.

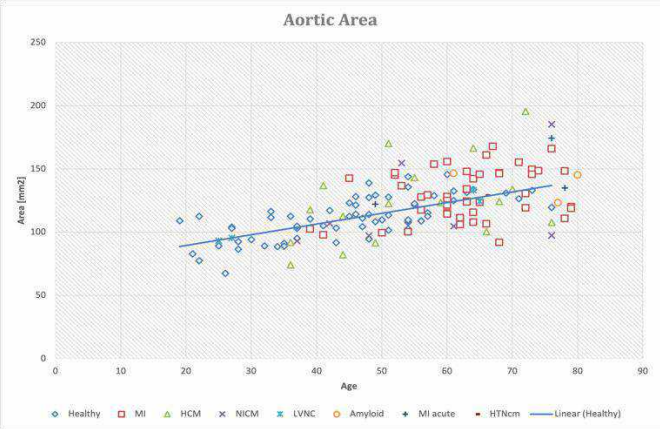

Figure 2: Aortic Area versus Age for two cohorts of patients. Patient cohorts and their cardiovascular diseases are distinguished by color and symbol. The blue line shows a trend for healthy patients.

Figure 3 shows the distribution of circumferential strain in the four quadrants Q1-Q4 for healthy subjects (upper graphs) and cardiovascular patients (lower graphs). The quadrants position is shown in Figure 1. As evident from the box plots and the pie plots, the deformations present in aortas of patients with cardiovascular disease differed from those in healthy aortas, which reached higher strains in all quadrants but Q3 (circumf_strain healthy median 11% IQR7.7%, circumf_strain cardiovascular patients median 9% IQR7.2%). Healthy aortas showed the maximum strain distribution mainly in quadrants one and two; aortas of diseased patients showed maximum strain in quadrants one, two, and three.

Statistical t-tests between the strain in the quadrants for healthy and non-healthy patients showed significant differences between quadrants Q1 ($p=0.003$), Q2 ($p=0.001$), and Q4 ($p=0.0008$). Anova test restricting age to >40 showed that in both cohorts the quadrants had different strain ($p=1.e\text{-}7$).

DISCUSSION

Overall, deformation markers of the aorta were heterogeneously distributed with respect to quadrant location in both healthy volunteers and patients with cardiovascular disease. Quadrants one and two are adjacent to the heart while the other two quadrants are posterior and adjacent to the spine. Considering the effect of the surrounding structures, it would make sense that the healthy aorta deforms more in the direction towards the heart as heart tissues are softer than the spine. Our results showed that for cohorts with cardiovascular diseases, the aorta becomes progressively stiffer limiting its maximum deformation. Moreover, the deformation is more evenly spread across quadrants. This conclusion was also valid when the young patients (< 40 years old) were removed from the cohort of healthy patients to correct for possible age effects. The lower strain in cardiac patients may also indicate a lower stroke volume than in healthy patients. In order to better differentiate the effects of disease versus aging, future analysis will include multivariate statistics to assess whether older healthy aortas deviate from the trend. The differences in distribution of strain across quadrants, however, could not be justified simply by lower overall strain in the diseased aortas. In conclusion, our study showed a unique trend for healthy subjects versus cardiovascular patients with respect to strain distribution in the descending aorta assessed via cardiac MRI. These differences point to altered deformations beyond those explained by aging alone.

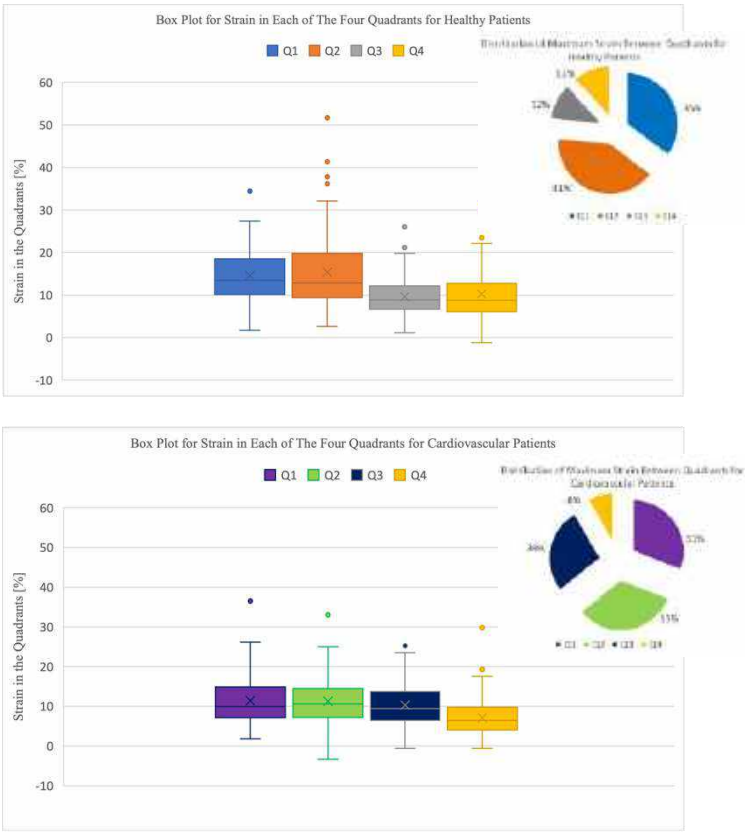

Figure 3: Boxplots of strain and pie plots of maximum strain in four quadrants for both cohorts.

ACKNOWLEDGEMENTS

We gratefully acknowledge funding from National Science and Engineering Research Council of Canada and Biomedical Engineering (U of C) Summer Research Studentship.

REFERENCES

[1] Groenewegen, A et al. Epidemiology of heart failure. Eur J Heart Fail, 22: 1342-1356, 2020.

[2] Jadidi, M et al., *Acta Biomaterialia*, 103:172-188, 2020.

[3] Ohyama, Y et al., *Circ Cardiovasc Imaging*, 11:e005617, 2018

OPTIMIZATION OF OBJECTIVE MEASUREMENTS FOR EVALUATING SAGITTAL SYNOSTOSIS DETECTION AND TREATMENT EFFICACY

Tim Dixon (1), Jason A. Ramsey (2), Phillip M. Stevens (2), Brittany Coats (1)

(1) Department of Mechanical Engineering, University of Utah, Salt Lake City, UT, USA
(2) Hanger Clinic, Austin, TX

INTRODUCTION

Sagittal synostosis, the premature fusion of the sagittal suture, occurs in 2-3 per 10,000 live births, and results in cranial malformations that can have severe consequences on brain growth and development.[1] Successful outcomes can be achieved through early diagnosis, surgical treatment, and post-operative cranial orthotics.[2]

Cephalic index (CI), the percent ratio of cranial width to length, is a common metric used to monitor post-operative correction but can be subjective because measurements are made using handheld calipers at the estimated largest equator of the skull (**Fig. 1**). Optical surface scanning, now common at orthotics facilities, provides an opportunity to develop metrics that are more sensitive to cranial correction [3] and that can be automated to remove subjectivity.

The objective of this study was to automate calculation of additional craniometrics and optimize the definitions of those metrics to improve sensitivity.

METHODS

Optical surface scans were performed as a point of standard care in 2-4 months old (n=25, 2.5±0.7 months) infants treated for sagittal synostosis.

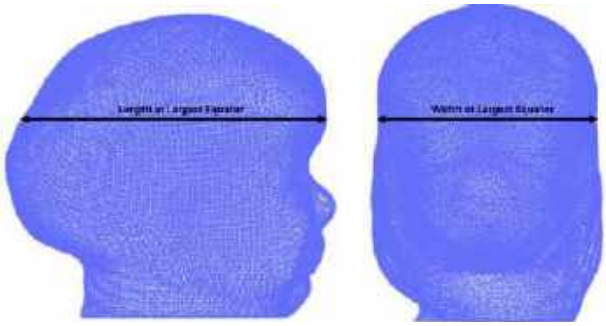

Figure 1. Length and width of a 2-month-old female with sagittal synostosis. Cephalic index is the ratio of width to length multiplied by 100 at the largest cranial equator.

Follow-up scans were obtained 3-13 months later (6.5±2.3 months). Scans from infants without cranial abnormalities were obtained from ages 4-13 months of age (n=33, 6.7±2.6 months).

A custom python script was created to evaluate 3 metrics from the three-dimensional normal and abnormal point cloud data (**Fig. 2**): (1) *Occipital Contour Angle* (OCA): angle created by mirrored lines drawn from the center point of the skull at the sellion level to the occipital bone at an angle, θ. (2) *Vertex Proportionality Index* (VPI): percent ratio of posterior radius r_P to anterior radius r_A, which are drawn from the center point at the sellion level to the

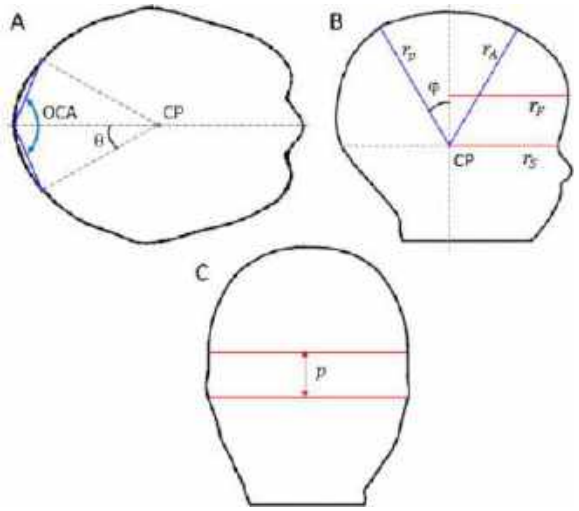

Figure 2. Craniometrics included (A) OCA, (B) VPI and (C) PTI. Optimized values were θ, φ, and *p*.

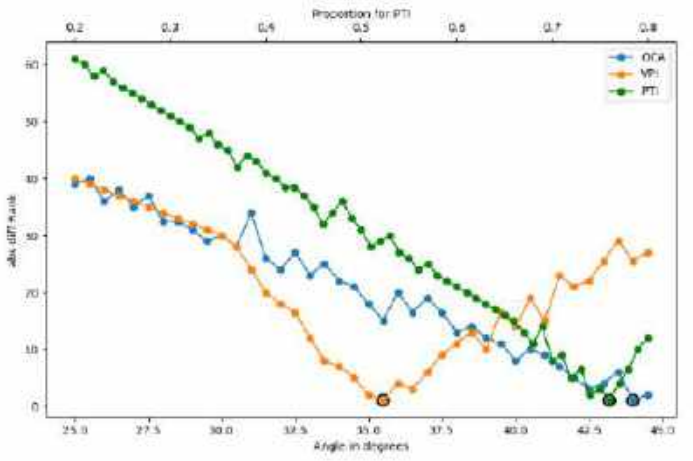

Figure 3. Optimal parameters for each metric were identified with a cumulative ranking of largest differences across all pathological cases. A rank of 1 was the most ideal parameter.

surface of the skull at an angle, φ. (3) *Parietal-Temporal Index* (PTI): percent ratio of the coronal width at the sellion level to the coronal width at a proportion, *p* between the sellion level and the top of the head.

An optimization script was created to identify the most sensitive angle/proportion values for each metric. Angles were varied from 25° to 45° in 0.5° increments for OCA and VPI, and proportions were varied from 20% to 80% in 1% increments for PTI measurements. FSI had no parameters to optimize but was still calculated for each infant. Sensitivity of the metric was evaluated using a cumulative rank-sum on the difference of each metric between initial and final scans within pathological subjects. Measurements with a z-score greater than 1.96 (a 95% confidence interval) relative to the mean of the control group, were marked as pathological, while measurements falling inside the range were marked as normative.

RESULTS

Optimization identified θ=35.5°, φ=44°, and *p*=76% as the most sensitive angle/proportion for quantifying differences between initial and final scans (**Fig. 3**). Use of these optimal metrics identified 6 infants in the control group that may have minor abnormalities not identified by CI, but were determined not to require orthotics. In the confirmed pathological group OCA, VPI, and PTI accurately identified cranial abnormalities in 80%, 88%, and 64%. If all 3 optimized metrics (OCA, VPI, and PTI) were considered, 96% (24/25) of confirmed pathological cases were identified compared to only 80% (20/25) identified by CI. There were no cases identified by CI that were not identified by either OCA, VPI, or PTI.

DISCUSSION

This study automated and optimized 3 cranial metrics as a tool to help identify cranial abnormalities as well as to monitor progress during treatment of sagittal synostosis. The inability of any single metric to identify cranial abnormalities with high accuracy highlights the variability of the infant skull response to sagittal synostosis, and strongly suggests a multi-metric approach is needed, as presented in this study.

The confirmed pathological group consisted of 20 males and 5 females, most of whom were diagnosed around 2 months of age. In other ongoing work in our lab, we find the 0-2 month female infant skull is significantly thicker than the male skull, and may be less immediately responsive to sagittal fusion. Evaluation of sex- and age-specific thresholds for identifying abnormalities may be warranted.

ACKNOWLEDGEMENTS

We'd like to thank James Kyeh for pre-processing and aligning the point cloud data for the study.

REFERENCES

[1] Schlobin, NA *World Neurosurg*, 164:413-423, 2022.

[2] Jimenez, DF et al. *JNS*, 100(5):407-417, 2004.

[3] Ramsey JA et al. *J Craniofacial Surg*, 32(5):1727-1733, 2021

DEVELOPMENT OF IN-SILICO MODEL OF CANCEROUS TISSUE

Nathanael E. Sovitzky (1), Mahsa Dabagh (1,2,3)

(1) Biomedical Engineering, University of Wisconsin-Milwaukee, Milwaukee, WI, USA
(2) Biomedical Engineering, University of Wisconsin-Milwaukee, Milwaukee, WI, USA

INTRODUCTION

Agent-based modeling (ABM) combined with coarse-grained modeling offers a powerful approach to simulate complex systems like cancerous tissue [1]. ABM focuses on individual agents, such as cells or drug particles, each following predefined rules and interacting with neighboring agents. Coarse-grained modeling, on the other hand, simplifies the system by grouping multiple agents into coarse-grained entities, reducing computational complexity while retaining essential features.

In this study, the ABM component represents individual fibroblasts, collagen fibers, and drug particles, each with specific behaviors and interactions. These agents collectively form the extracellular matrix (ECM) of the tissue. By simulating the behavior of these agents, researchers can analyze properties such as ECM stiffness and the effects of drugs on it.

Combining ABM with coarse-grained modeling allows for a multiscale approach, capturing both microscopic details and mesoscopic behaviors. While ABM provides insights into the dynamics of individual agents, coarse-grained modeling enables the study of emergent phenomena at a higher level of abstraction. This synergy facilitates the analysis of complex interactions within the tissue microenvironment and the effects of interventions such as drug treatments.

Among the various software platforms available for such modeling, LAMMPS MD software stands out for its versatility and usability across scales [2]. Its ability to handle both mesoscopic and microscopic simulations make it well-suited for this project, enabling researchers to explore the mechanical properties of cancerous tissues and evaluate the efficacy of drug therapies in silico. By leveraging the capabilities of LAMMPS MD software, this study aims to advance our understanding of cancer progression and treatment response, ultimately guiding the development of more effective therapeutic strategies.

METHODS

A combination of agent based modeling and coarse grain modeling are being used to drive the project. In order to build the model from ground up, the properties of each component must be validated independently testing the parameters of each component.

In the simulation setup, cells and collagen fibers were coarse-grained to accurately represent their mechanical properties within the range accepted in literature. Coarse-graining involves simplifying complex structures by grouping multiple atoms or particles into larger entities while preserving essential characteristics. For cells, this coarse-graining approach ensures that their mechanical behavior, particularly their Young's modulus, falls within the expected range observed in experimental studies. By coarse-graining cells in this manner, the model strikes a balance between computational efficiency and fidelity to biological reality, enabling simulations that capture relevant biomechanical phenomena.

Similarly, collagen fibers were coarse-grained to ensure that their mechanical properties align with experimental observations. Collagen, as a major component of the extracellular matrix, plays a crucial role in determining tissue stiffness and mechanical integrity. Coarse-graining collagen fibers allows the model to represent their structural and mechanical characteristics while minimizing computational complexity. By incorporating collagen with appropriate mechanical properties, the simulation can accurately capture the interactions between cells and their microenvironment, providing insights into tissue-level behaviors such as deformation and remodeling.

The internal energy of the system was primarily governed by harmonic bonds, reflecting the interactions between coarse-grained

entities such as cells and collagen fibers. Harmonic bonds represent a simplified yet effective model for describing the elastic properties of materials, where the energy of deformation is proportional to the displacement from equilibrium. By employing harmonic bonds as the basis of internal energy, the simulation captures the mechanical responses of cells and collagen to external forces and interactions within the tissue microenvironment. This approach facilitates the exploration of various mechanical phenomena, including tissue deformation, stress distribution, and response to mechanical stimuli, contributing to a deeper understanding of cancer biomechanics and the effects of therapeutic interventions. The energy contained between one harmonic bond is shown in equation (1).

$$E = k(x - x_o) \qquad (1)$$

The young's modulus was calculated by performing a tensile test of a subject and computing the stress tensor corresponding to the axis of deformation. Strain is easily calculated by taking the deformation.

RESULTS

The main results of the project are that tensile tests for fibroblasts and for collagen show promising fidelity to results reported in literature [3], [4].

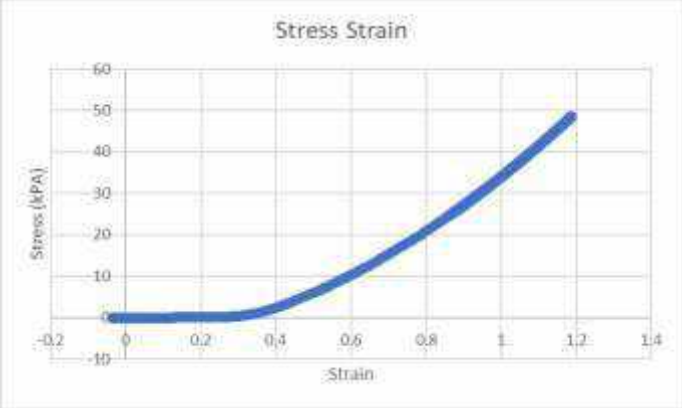

Figure 1: Stress-Strain Curve in (kPa) representing a fibroblast cell.

Figure 2: Visualization of the fibroblast under uniaxial tension.

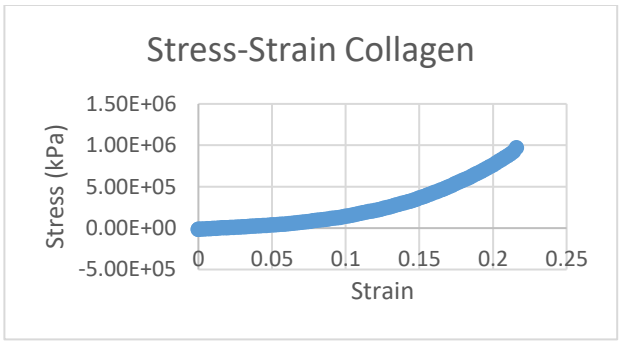

Figure 3: Stress-Strain Curve in (kPa) representing the collagen layer.

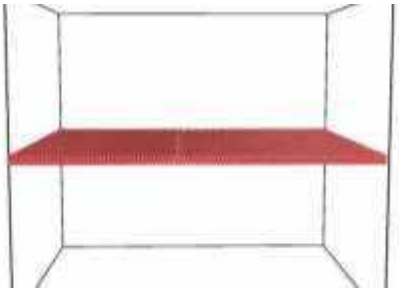

Figure 4: Layer of collagen undergoing uniaxial tension.

DISCUSSION

This research project is under development with progress being made in accurately modelling individual objects, such as cells or drug particles. Future plans are to run simulations with layers of cells and extracellular matrix. representing tissue layers of a tumor microenvironment, while simulating diffusion of drug particles, using random placement of drug particles to study the penetration depth and adherence of the drugs, given their mechanical properties. Extensions for this project are to adapt this model to the patient specific imaging data to tie the model to real-life patient data. The key to the project is its flexibility in defining parameters, since material properties can be adjusted by changing the value of the

ACKNOWLEDGEMENTS

The authors would like to thank the UW-Milwaukee Undergraduate Research Fellows (SURF) for supporting the project.

REFERENCES

References should be arranged in numerical order according to the citation sequence in the text. Each reference should include the last name of at least the first author followed by his/her initials, the journal name, volume, pages and year. You may include more detailed reference information if space allows.

Sample Reference:

[1] Liedekerke, P, et al., *Comp. Part. Mech.*, 2:401–444, 2015
[2] LAMMPS Documentation
[3] Quan, F. S., et al., *Acta Biochim Biophys Sim*, 48(10), 865-871, 2016
[4] Salvatore, L, et. al., *Front. Bioeng. Biotechnol.* 9:644595, 2021

ENDOTHELIAL CELL RESPONSE TO HYPERTENSIVE PRESSURE CHANGES

Ashlyn N. Terasaki (1), Mahsa Dabagh (2), Woo-Jin Chang (3)

(1) Department of Biomedical Engineering, University of Wisconsin-Milwaukee, Wisconsin, United States
(2) Department of Mechanical Engineering, University of Wisconsin-Milwaukee, Wisconsin, United States

INTRODUCTION

Hypertension is impacting endothelial cells (ECs) and their health. Our objective is to monitor how ECs response to hypertension and change their shape and interactions with neighboring ECs. For this purpose, we are designing in-house microfluidic devices that will allow the application of fluids with different pressures on ECs. Microfluidic devices are widely used to study various applications. In biomedical engineering research fields, these devices allow for integration of cells, particles, and other substances to observe their behavior under various conditions over time [1]. Polydimethylsiloxane (PDMS) is often used for the fabrication of microfluidic devices, and this is due to the material being inexpensive, transparent, bio-compatible, deformable, and permeable to gas [2].

Although there are many advantages to using PDMS, a drawback for this material when being used with biological samples is its inherent hydrophobicity. This poses a problem when working with cell culture because hydrophobicity impedes the adherence of cells to surfaces. Many methods have been used to make the PDMS more hydrophilic, including the use of extracellular matrix (ECM) proteins as a coating material [3]. By doing this, the PDMS channels of microfluidic devices are made hydrophilic and supports cell culture. Fibronectin has been commonly used as a coating for microchannels in experiments with endothelial cells and it has been shown to encourage cell adhesion to the PDMS surface. A layer of fibronectin or other ECM proteins provides a substrate for cells to adhere and proliferate on if the device is being used for cell culture studies.

In this study, the effects of hypertensive conditions on the vascular integrity will be evaluated using pressurized microfluidic ECs culture device. For experiments that use perfusion culture under pressurized conditions, a pressure pump will be used with microfluidic devices, which allows for control over the flow and pressure that are being introduced into the microchannels [4].

METHODS

1. Microfluidic Device: A three-channel microfluidic device made of PDMS will be fabricated with varying diameters for each channel. There will be an inlet and an outlet for each separate channel to allow for controlled pressure. The pressure will be determined based on physiological hypertension and normal blood pressure, which is relevant to the vessel size. A pressure pump will be used to create the pressure through the microchannels.

2. Fibronectin Coating and Endothelialization of Microfluidic Channels: To create a hydrophilic layer on the PDMS, fibronectin solution will be perfused through the three separate channels and left to incubate to adsorb on the PDMS. PBS will be used to wash away excess fibronectin solution. ECs (HUVECs) will be perfused through the channels at varying pressures for each channel. The cell solution will be incubated to form a monolayer of ECs around the microchannels.

3. Immunofluorescence Detection of the Fibronectin Coating, EC adhesion, and EC Nuclei: To confirm coating efficiency of the Fibronectin layer, fluorescent microscopy will be used. An Alexa Fluor dye that is conjugated with an anti-FN antibody will be introduced into the channels and incubated. The excess dye will be rinsed with PBS. A nuclear stain will be used with the ECs and to visualize the adherence of the cells to the fibronectin coated surface, an anti-human VE-Cadherin antibody (primary antibody) will be added to the channels and incubated. Excess will be washed with PBS. An anti-mouse secondary antibody with Alexa fluor dye will then be added in the channels and incubated. Cells will then be washed with PBS. Images of the channels will then be taken and analyzed.

RESULTS

The effect that hypertensive conditions have on the vascular integrity will be evaluated based on the amount of VE-cadherin that is

stained ECs. A fluorescent microscope will be used to view the proteins and cells that are stained with the dyes and pictures will be obtained and analyzed for each sample. The results of the normal pressure conditions will then be compared to the hypertensive conditions to see how much of an impact hypertension has on the endothelium wall leakage.

Figure 1:

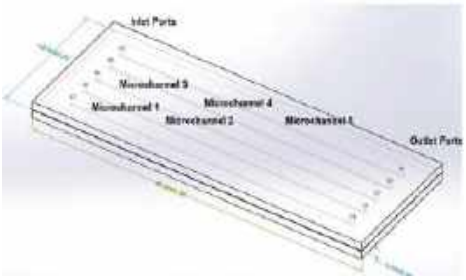

This schematic represents the microfluidic design that will be used in the experiment. The various sized channels will be aligned parallel to each other.

Figure 2:

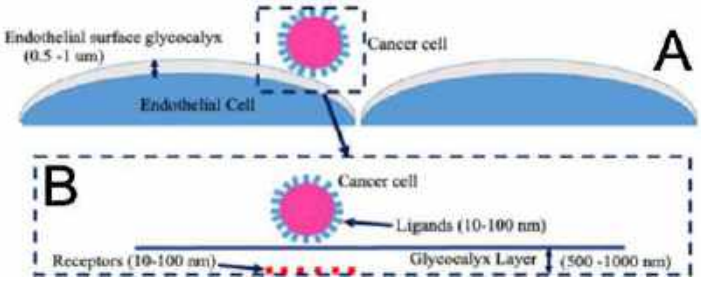

This schematic demonstrates how cancer cells adhere to the endothelial cells through their ligands and the receptors on the cell surface. The deformation of ECs exposed to hypertensive condition will impact ECs interactions with cancer cells.

DISCUSSION

By conducting this experiment, the role that hypertension plays in the integrity of the endothelium can be better understood. In cancer metastasis studies, the state of the endothelium affects the behavior of the cancer cell by either promoting or impeding its extravasation out of the vessel [5],[6]. Alterations and compromised integrity of the endothelium can promote the transmigration of cancer cells by providing them with a way in and out of the vessel [7]. Assessing the role that hypertension plays in creating these dysfunctions in the microvasculature is a first step into understanding the effect it has on cancer metastasis, specifically extravasation. Using microfluidics, this scenario can be modeled with endothelial cells, tumor cells, and controlled pressure through the microchannels. Other structures or different types of cells can also be combined with the microfluidic device to further replicate the *in vivo* conditions for metastasis studies [8]. Data obtained from these experiments can contribute to other areas of cancer research such as drug development or diagnostics.

REFERENCES

[1] Team, E. (2022, December 2). *Microfluidics: A general overview of microfluidics - Elveflow*. Elveflow.
[2] Miranda, I., Souza, A., Sousa, P., Ribeiro, J., Castanheira, E. M. S., Lima, R., & Minas, G. (2021). Properties and Applications of PDMS for Biomedical Engineering: A Review. *Journal of functional biomaterials*, *13*(1), 2.
[3] Akther, F., Yakob, S. B., Nguyen, N. T., & Ta, H. T. (2020). Surface Modification Techniques for Endothelial Cell Seeding in PDMS Microfluidic Devices. *Biosensors*, *10*(11), 182.
[4] Ma, Q., Ma, H., Xu, F., Wang, X., & Sun, W. (2021). Microfluidics in cardiovascular disease research: state of the art and future outlook. *Microsystems & Nanoengineering*, *7*(1).
[5] Azzi, S., Hebda, J. K., & Gavard, J. (2013). Vascular permeability and drug delivery in cancers. *Frontiers in oncology*, *3*, 211.
[6] Reymond, N., D'água, B. B., & Ridley, A. J. (2013). Crossing the endothelial barrier during metastasis. *Nature Reviews Cancer*, *13*(12), 858–870.
[7] Escribano, J., Chen, M. B., Moeendarbary, E., Cao, X., Shenoy, V. B., Aznar, J. M. G., Kamm, R. D., & Spill, F. (2019). Balance of mechanical forces drives endothelial gap formation and may facilitate cancer and immune-cell extravasation. *PLOS Computational Biology*, *15*(5), e1006395.
[8] Xu, H., Liu, X., & Le, W. (2018). Recent advances in microfluidic models for cancer metastasis research. *TrAC Trends in Analytical Chemistry*, *105*, 1–6.

ENGINEERING MESENCHYMAL STROMAL CELLS TO FACILITATE MUSCLE REGENERATION BY CORRECTING OXIDATIVE STRESS

Ali A. Eldeiry (1), Sing-Wan Wong (1,2)

(1) Department of Mechanical Engineering, Colorado State University, Fort Collins, CO, USA
(2) School of Biomedical Engineering, Colorado State University, Fort Collins, CO, USA

INTRODUCTION

Muscle injuries frequently occur as a result of daily activities. The human body is capable of regenerating injured muscle to an extent. However, regeneration often can be compromised when the injury is too severe or underlying complications such as muscular dystrophy exist[1]. While the pathological mechanism is unique between muscle injury cases, there is one main factor commonly contributes to the inhibition of muscle regeneration, the oxidative stress. Oxidative stress is a result from accumulation of reactive oxygen species (ROS), which are mostly generated during post-injury inflammation[2]. These highly reactive molecules are naturalized by anti-oxidative enzymes under normal conditions. Unfortunately, the production of anti-oxidative enzymes often becomes insufficient depending on one's body health or underlying conditions. This imposes the need of providing additional anti-oxidative support to correct the oxidative stress, hence, facilitating muscle regeneration. One way to fulfill the extra antioxidative demand is to intake antioxidative supplements. However, multiple antioxidants are necessary to provide a full spectrum antioxidation as oxidative stress is a result of a collection of varied ROS and different antioxidants are required to neutralize specific ROS. With this consideration, mesenchymal stromal/stem cells (MSCs) can serve as a suitable therapeutic candidate for the purpose because of their multiaxial regulatory role[3]. In this study, we aim to harness the therapeutic potential of MSCs and engineer them through a mechanobiology approach, as it has been shown that the secretome profile of MSCs is sensitive to the mechanical properties of the microenvironment they reside in [4]. We hypothesize that an optimum biomaterials system can be made to enhance the production of antioxidative enzymes from MSCs, then we will apply this novel technology to promote muscle regeneration by correcting the post-injury oxidative environment.

METHODS

One possible approach to engineer the phenotype of the MSCs is by regulating the stiffness of the surrounding microenvironment. For this purpose, we employed alginate hydrogels with Ca^{2+} ionic crosslinking. By altering the concentration of Ca^{2+}, we can consequently adjust the mechanical properties of the hydrogel. The complex modulus, a measurement that can represent both elastic and viscous behaviors of the hydrogels, was then analyzed by an amplitude frequency sweep from 0.1% to 100% strain. To perform this, an HR20 rheometer (TA instruments) was used with an 8mm geometry at 37°C. Hydrogels crosslinked with 15mM-40mM [Ca^{2+}] in 5mM increments were tested.

Once the mechanical properties of the hydrogel were characterized, Murine bone marrow derived MSCs, D1 cells, were encapsulated within the hydrogels and subjected to 1nM, 10nM, and 1μM of hydrogen peroxide (H_2O_2) treatment to mimic the post-injury oxidative environment. Three days after the treatment, RNA from the MSCs was extracted, purified and underwent reverse transcription, then was followed by a quantitative PCR (qPCR) analysis on the expression of three antioxidative enzymes: catalase (CAT), Glutathione Peroxidase (GPX1), and Superoxide Dismutase (SOD1).

RESULTS

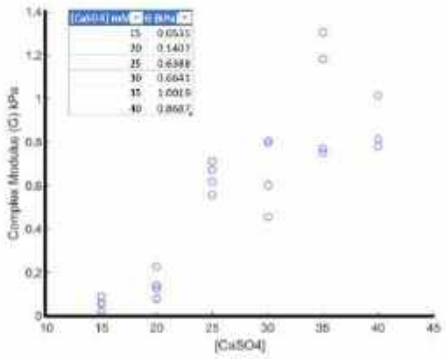

Figure 1: Complex modulus of alginate hydrogels crosslinked with varied [Ca^{2+}]

2)

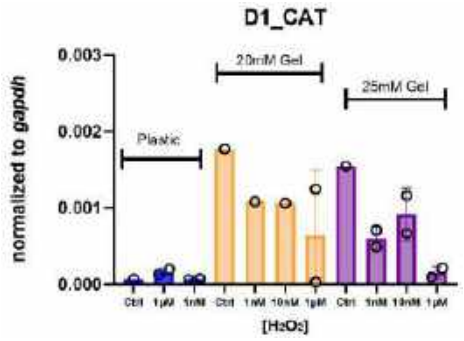

3)

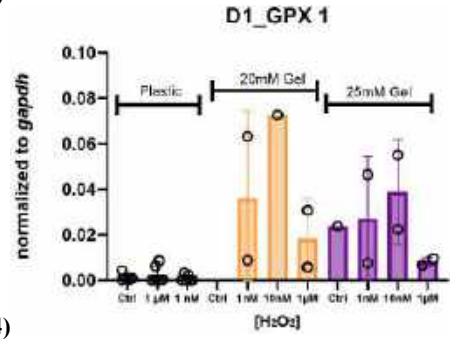

4)

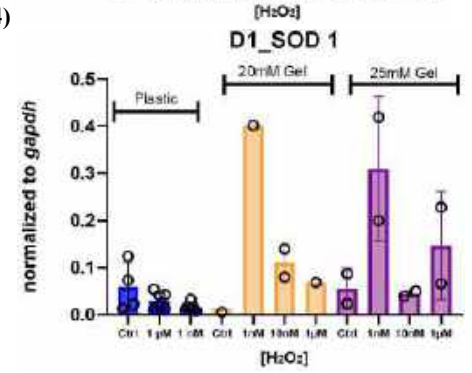

Figure 2-4: Antioxidative enzyme expression of D1 cells encapsulated in hydrogels with H_2O_2 treatments

DISCUSSION

As expected, the complex modulus of the hydrogel is proportionally correlated with the Ca^{2+} concentration. The key observation is that between 20mM and 25mM Ca^{2+} crosslinking, the complex modulus shows a shape jump from 0.1407 to 0.6388 kPa. Due to this large difference, these hydrogel formulations were chosen for the gel encapsulations experiments.

The expression of antioxidative enzymes CAT, GPX1 and SOD1 were reported in figures 2-4. Each enzyme behaves and reacts uniquely to the treatments and conditions. In regard to the H_2O_2 influence on the CAT gene, the control group appeared to have the highest expression and was at its lowest at 1µM. For the GPX1 gene, expression was greatest at the 10nM followed by 1nM, then 1µM, and finally lowest at the control. The trend remains similar between 20 and 25mM gel, but GPX1 expression is not detectable in 20mM gel without H_2O_2 stimulation. Interestingly, the SOD1 featured a separate behavior between the 20mM and 25mM. For the 20mM gel, 1nM H_2O_2 treatment leads to the highest expression of SOD1, followed by the 10nM, 1µM, and lowest in the control group. For the 25mM, the 1nM treatment results in the highest expression, followed by the 1µM, the 10nM, and finally the control. Overall, SOD1 expression is the highest among all three enzymes.

Universally, it is evident that culturing MSCs in gels increases the expression of the antioxidative enzymes. This is related back to the soft nature of the gels compared to the stiff environment a plastic well plate provides. This supports our claim that softer environments will emulate physiological conditions thus facilitating improved enzyme production. Although the findings differ between each enzyme, one conclusion can be made which suggests manufacturing of the enzymes is highest when under conditions closest to H_2O_2 physiological conditions which is 0 to 10nM [5]. Once the ROS content rises too high at 1µM, the enzyme production, on the other hand, is inhibited.

The next phrase of this study is to test our hydrogel-stem cell approach on promoting skeletal muscle regeneration. A C2C12 cell line, mouse satellite muscle cells, will be subjected to a physical scratch injury. Then we will co-culture the engineered D1 cells with the highest antioxidative expression with the injured muscle cell, followed by quantification of muscle regeneration through the expression of biomarkers including MyoD, myogenin, and pac7, which signifying successful muscle regeneration. We will also analyze muscle regeneration through image analysis by measuring the size of the induced scratch over time. Our goal is to demonstrate that engineered MSCs can be an effective method for muscle regeneration.

REFERENCES

[1] M. C. Rodriguez and M. A. Tarnopolsky, "Patients with dystrophinopathy show evidence of increased oxidative stress," *Free Radic. Biol. Med.*, vol. 34, no. 9, pp. 1217–1220, May 2003, doi: 10.1016/S0891-5849(03)00141-2.

[2] M. Kozakowska, K. Pietraszek-Gremplewicz, A. Jozkowicz, and J. Dulak, "The role of oxidative stress in skeletal muscle injury and regeneration: focus on antioxidant enzymes," *J. Muscle Res. Cell Motil.*, vol. 36, pp. 377–393, 2015, doi: 10.1007/s10974-015-9438-9.

[3] R. Stavely and K. Nurgali, "The emerging antioxidant paradigm of mesenchymal stem cell therapy," *Stem Cells Transl. Med.*, vol. 9, no. 9, pp. 985–1006, Jun. 2020, doi: 10.1002/sctm.19-0446.

[4] X. Zhang, S. Zhang, and T. Wang, "How the mechanical microenvironment of stem cell growth affects their differentiation: a review," *Stem Cell Res. Ther.*, vol. 13, no. 1, p. 415, Aug. 2022, doi: 10.1186/s13287-022-03070-0.

[5] "Oxidative eustress: On constant alert for redox homeostasis - PMC." Accessed: Feb. 11, 2024. [Online]. Available: https://www.ncbi.nlm.nih.gov/pmc/articles/PMC7930632/

UNIVERSAL HITCH ATTACHMENT FOR BLIND VETERAN

Christopher Iuliucci (1), Marvin Moreno (1), Joshua Perry (1), Alexa Warren (1), Anna Sasse (2), Bailey Erickson (3)

(1) Biomedical Engineering Department, Rowan University, Glassboro, New Jersey, USA
(2) Mechanical Engineering Department, Rowan University, Glassboro, New Jersey, USA
(3) Experiential Engineering Education Department, Rowan University, Glassboro, New Jersey, USA

Faculty Advisor
Dr. Erik Brewer (1)

INTRODUCTION

Mike Nelson is a United States Army veteran who sustained life-changing injuries during his service that caused him to lose his vision. With the loss of his vision, Mr. Nelson experiences many daily challenges that individuals of standard eyesight do not encounter. One of these issues includes transporting his five children in their strollers. Mr. Nelson expressed challenges in navigating strollers and his cane simultaneously and thus has difficulty navigating both. Together with Quality of Life Plus (QL+), a non-profit that pairs wounded veterans with engineering capstone teams, he has tasked Rowan engineers to design a stroller attachment that allows him to pull his children behind him without burdening the use of his cane in front of him, or his ability to navigate outside. The engineering team must ensure that any modifications to the stroller won't impact criteria established in ASTM F833-21, which outlines safety standards for strollers, including their weight-bearing capacity and braking ability.

PRODUCT DESIGN

The veteran requested specific user criteria for a design, including that it must be lightweight, compactable for storage purposes, be comfortable for his children and not interfere with their use of the stroller, and compatible with many varying stroller and cart models while still being able to attach/detach independently. In addition, safety standards established by ASTM F833-21, which all strollers must adhere to, give guidance on certain safety specifications that our design may impact: Strollers and their modifications must accommodate 40kg in loaded weight, and brakes must be able to prevent unwanted rolling of the stroller. To accommodate for this, twist lock wheels were added to the mechanism to give Mr. Nelson a way to lock the wheels in place if needed. For example, if taking a stroller with the hitch on public transportation, Mr. Nelson will have a way to lock the brakes in place.

The final design integrates criteria outlined by Mr. Nelson, QL+, and additional parameters identified by seasoned advisors across physical therapy, occupational therapy, and mechanical design domains. Occupational therapist Darick Wright, mobility specialist Allie Futty of UMass Boston and Mike Mulligan of Blind on the Move were three mobility specialists who provided insight into the daily challenges experienced by someone with a visual impairment. They discussed the importance of maintaining alignment of the body and the white cane when designing the mechanism, which would be a major design criterion to make the design usable, would be to have Mr. Nelson push the hitch instead of pull. Melanie Amadoro of Rowan University, Dr. Smitesh Bakrania of Rowan University, and Barry Hulce of the University of Vermont were both mechanical engineers who provided insight into the mechanical design of the mechanism. Dr. Bakrania initiated the idea of manipulating the stroller wheels with our design rather than implementing a simple clamp onto a bar on the stroller to avoid interference from the children in the stroller. Amadoro expressed the importance of suspension in the tires and choosing a material that is lightweight, inexpensive, and strong. Hulce urged us to seek out the minimum viable product to satisfy the design criteria. The attachment was designed to extend up to 28.5" to accommodate most strollers with varying widths while also being able to contract to fit through any door. Positioned ahead of the mechanism is a pivotal main wheel, synchronized with a user-initiated pulling action by Mr. Nelson. This way he's able to have complete control over the mechanism while also providing safety aspects to prevent possible injuries to the children inside the stroller. The extending platform functions akin to drawer movement facilitated by sliding tracks affixed to the platforms.

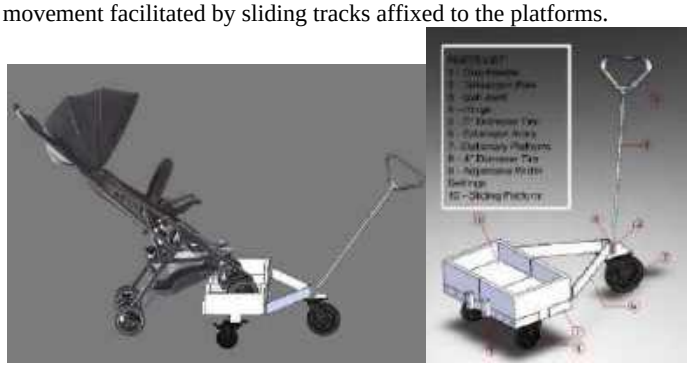

Figure 1. SOLIDWORKS Prototype with Stroller Attached.

The following engineering standards were referenced from ASTM F833-21 [2] to facilitate design and conduct testing for this device:

- 6.1.1 - A parking brake shall be provided on the unit. Each parking brake shall remain engaged during the test as specified in 7.6. Each parking brake shall prevent the braked wheel(s) from rotating more than 90° during the 5th test cycle specified in 7.6.
- 6.2.2 - A stroller shall support a static load of 100 lb (45.4 kg) or 2.5 times the manufacturer's recommended maximum weight, whichever is greater, per individual seating area, when placed in the approximate center of the area intended to support the child occupant.

Since the design utilizes wheels intended to replace the stroller wheels, ASTM standard 6.1.1 was followed to test the parking brakes on the design's wheels. To ensure that the design will not break in compliance with the safety constraints, ASTM standard 6.2.2 was followed when designing for a maximum weight load of the stroller weight plus the weight inside of the stroller.

The prototype that was developed was optimized for testing purposes; however, we look to simplify the design after basic functionality is achieved. We would like to eliminate the boxiness of the platform and condense the overall length of the device so that it is not so difficult to make turns with. We would also like to ensure that the device is as low to the ground as possible to avoid the stroller sitting on a large degree of incline when strapped on top of the platform and putting the child at risk.

BUDGET & MARKET ANALYSIS

The mission statement for Quality of Life+, is to provide custom engineered solutions to veterans whose unique disabilities are not met with commercially available or viable products. Therefore, the initial scope of this project is to design unique accommodation for Mr. Nelson. The sponsor of this project, Quality of Life + provided a budget of $1,500 for the entirety of the project. This sum of money was used to purchase materials to create a physical rendition and prototype of our design as seen in ***Figure 1***. The hope is to spend about $150 on our first prototype, budgeting ourselves to be able to spend the money on the best quality material for the final design. We hope to need no more than two prototypes before being able to send the final design to Mr. Nelson. The local community was generous and donated strollers for us to test our design to make sure it functions correctly and safely for the children and Mr. Nelson.

Despite the narrow scope of the project, we believe this design would be beneficial to all people who utilize a white cane: about 8% of people with vision loss, or roughly 480,000 people in the U.S. utilize a white cane. If we were to attain 10% of our serviceable obtainable market, which would be parents that utilize white canes (~192,000 people), we would be able to satisfy a market size of 19,200 users. Since people with limited vision use a white cane, they cannot use both the stroller and cane at the same time. This design allows both to be comfortably used at once. The costs of our materials for our final prototype total are approximately $80. To stay profitable and to accommodate for the labor needed to complete each attachment, we estimate this universal hitch attachment to cost $124.99.

ACKNOWLEDGMENTS

We would like to acknowledge Quality of Life + who sponsored this project, along with Rowan University and Dr. Erik Brewer for providing us with the necessary resources to succeed. Additionally, the team would like to extend our gratitude to Mike Mulligan of Blind on the Move, Ally Futty, Jen Kaldenberg, and Derrick Wright from the University of Massachusetts – Boston, Barry Hulce from the University of Vermont, Dr. Smitesh Bakrania of Rowan University, and Melanie Amadoro of Rowan University. These individuals allowed us access not only to their time but also to their vast skills and knowledge, allowing this project to move forward at a successful rate.

REFERENCES

[1] Flaxman, A. D., Wittenborn, J. S., Robalik, T., Gulia, R., Gerzoff, R. B., Lundeen, E. A., Saaddine, J., & Rein, D. B. (2021). Prevalence of Visual Acuity Loss or Blindness in the US: A Bayesian Meta-analysis. In JAMA Ophthalmology (Vol. 139, Issue 7, pp. 717–723). American Medical Association. https://doi.org/10.1001/jamaophthalmol.2021.0527

[2] ASTM International. (2021). Standard consumer safety performance specification for carriages and strollers (ASTM F833-21). Retrieved from ASTM International website: https://www.astm.org/f0833-21.html

[3] Blindness statistics | National Federation of the blind. (n.d.-b). https://nfb.org/resources/blindness-statistics

EFFECT OF INTERMOLECULAR CROSSLINKING ON THE MULTISCALE MECHANICAL BEHAVIOR OF TENDONS

Madeline K. Wagner (1,2), Rachel K. Klink (1,2), Steven J. Eppell (3), Allen H. Lin (4), Jeffrey A. Weiss (1,2,5)

(1) Scientific Computing and Imaging Institute, University of Utah, Salt Lake City, UT, USA
(2) Department of Biomedical Engineering, University of Utah, Salt Lake City, UT, USA
(3) Department of Bioengineering, Case Western Reserve University, Cleveland, OH, USA
(4) Revvity, Boston, MA, USA
(5) Department of Orthopaedics, University of Utah, Salt Lake City, UT, USA

INTRODUCTION: The collagen molecule is the main building block of connective tissues. Molecules are connected laterally by intermolecular crosslinks [1]. When collagenous tissues are overloaded in tension, collagen molecules can unravel, resulting in molecular denaturation. However, the role of crosslinks in resisting tissue damage is unclear [2]. Molecular dynamics simulations have shown that crosslinks can transfer load between adjacent collagen molecules during axial extension [3]. However, this load transfer mechanism and its role in the damage of collagen molecule assemblies has not been experimentally demonstrated. Hierarchical levels of organization between the collagen molecule and whole tissue further complicate the cascade of load transfer, so multiple organizational levels need to be tested. The objective of this study was to discover the mechanical effect of increased crosslinking during tensile overload of both tendon fascicles and fibrils to explore the role of crosslinks in tendon mechanics. We hypothesized that increased crosslinking would increase the strength and stiffness at both the fibril and fascicle level of tendons thus altering the damage and yield behavior.

METHODS:

Crosslinking: To increase crosslinking in tendon, the low-toxicity chemical genipin was used to form covalent intermolecular crosslinks with amine groups in collagen residues [4]. Rat tail tendon fascicles (RTTFs) were isolated from 12-16 week old male Sprague-Dawley rats. Fascicles were divided into two groups. The Control group was soaked in 1X PBS, while the Genipin group was soaked in 0.25% w/v genipin solution in 1X PBS. Both groups were soaked for 1 hour at room temperature.

Fascicle Differential Scanning Calorimetry: Differential scanning calorimetry (DSC) was performed to confirm increased thermal stability (n=3 in both groups). Hermetically sealed pans with dry-blotted RTTFs were heated from 20-90°C and cooled back to 20°C at 10°C/min. Temperature at onset of denaturation and peak temperature were quantified, along with curve width and curve area.

Fascicle Tensile Testing: Uniaxial tensile testing was performed on RTTFs using a TA Electroforce 3300 (n=8 control, n=6 treated). Cross-sectional area (CSA) was measured using a laser micrometer. Three measurements were taken and averaged. A 0.03 N tare load was applied to each RTTF. The sample was stretched at 0.5 %/s to 20% strain.

Fibril Tensile Testing: Fascicles were soaked for an additional hour and then mechanically agitated to isolate individual collagen fibrils (n=6 control, n=7 treated) [5]. Custom MEMS devices were used to stretch individual fibrils to failure (**Fig. 1**). Each MEMS device was attached

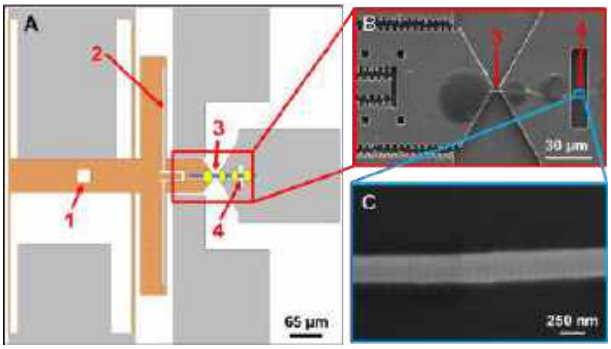

Figure 1: A: The MEMS device. Orange: moveable pad. Gray: anchored pads. Blue line: collagen fibril. Yellow ovals: epoxy droplets. (1) Pinhole. (2) Force gauge beam. (3) Test region. (4) Control region. B: SEM image of the (3) test and (4) control regions. C: SEM image of a collagen fibril.

to a piezoelectric actuator and immersed in PBS. Fibrils were mounted on custom MEMS devices and adhered using UV-curing epoxy drops. A tungsten probe was placed in a pinhole to hold the moveable pad.

Elongation was applied at a constant strain rate of 0.5-1%/s until failure and images of the MEMS device and fibril were acquired at 1 Hz. Images were processed to obtain the displacement of a force-gauge beam integrated with the MEMS device. Beam displacement was converted to applied force using the results of a finite element model of the MEMS device. To calculate fibril CSA, scanning electron microscopy was used to measure diameter of the unstretched region of each fibril. Line tracking was used to measure fibril elongation in the test region and deflection of the force gauge beam. A finite element model of the MEMS device was analyzed to calculate the force applied to the fibril based on the force gauge beam displacement.

Data Analysis: For both fascicle and fibril tensile testing, CSA and gauge length were used to obtain stress-strain curves from force-elongation curves. The yield point was identified as the strain where modulus was reduced by 50%. Data were analyzed using independent t-tests (α=0.05). Green asterisks (*) indicate significant differences.

RESULTS: For DSC, onset temperature (p=0.003), area (p=0.002), and width (p<0.001) were significantly higher for treated samples. Peak temperature trended higher for treated samples but was not significantly different (**Fig. 2**).

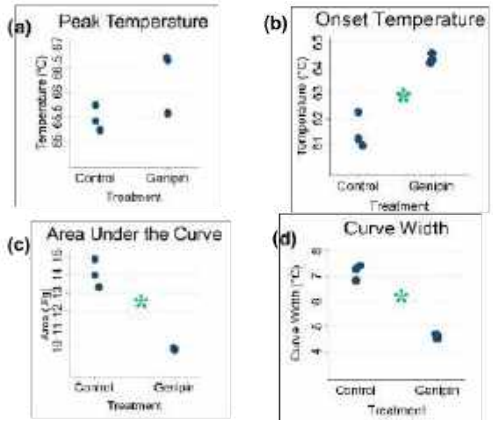

Figure 2: Results of DSC analysis. Peak and onset temperatures (a,b) are measures of thermal stability, while AUC and curve width (c,d) are measures of tissue homogeneity [6].

Genipin treatment produced qualitatively similar changes in the stress-strain curves at both the fascicle and fibril levels, but the changes were much more pronounced at the fibril level (**Fig. 3**).

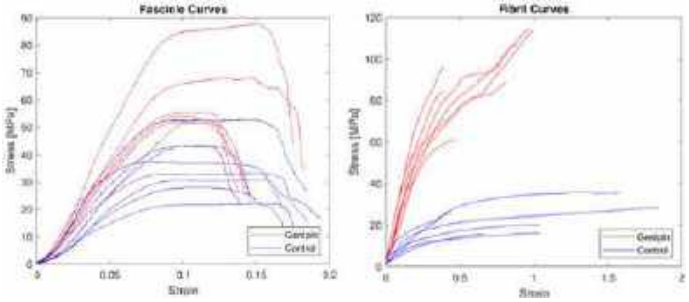

Figure 3: Stress-strain curves for fascicle (left) and fibril (right) tensile tests.

Fascicles treated with genipin sustained significantly higher yield stress (p<0.001), yield strain (p=0.006) and peak stress (p=0.002) (**Fig. 4**). At the fibril level, genipin treatment resulted in higher yield stress and peak stress than control fascicles (p<0.001), but there was no effect of treatment on yield strain. Unlike fascicle level tests, treated fibrils

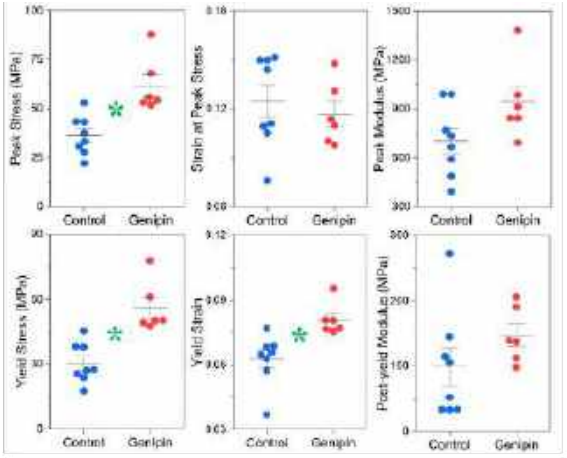

Figure 4: Results for fascicle tensile testing. Peak stress, yield stress, and yield strain were significantly higher for genipin group.

sustained higher peak modulus (p<0.001) but did not differ in peak strain or yield strain (**Fig. 5**).

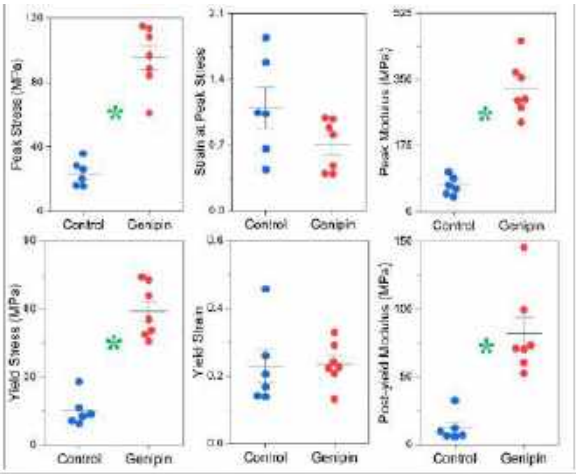

Figure 5: Results for fibril tensile testing. Peak stress, peak modulus, yield stress, and post-yield modulus were significantly higher for genipin group.

DISCUSSION: Increased onset temperature, area, and width confirmed that genipin crosslinking produced a more thermally stable, structurally uniform tissue. At the fascicle level, increased yield stress and yield strain due to genipin treatment resulted in an increase in toughness, but the treatment did not affect peak modulus. This is likely due to sliding between fibers and fibrils. The lateral distance between these structures is too large to be affected by chemical crosslinking. At the fibril level, genipin treatment produced a dramatic increase in yield stress, pre-yield modulus, and post-yield modulus, while the yield strain was unaffected. These results indicate that genipin intermolecular crosslinking increases lateral load transfer between collagen molecules in the fibril.

ACKNOWLEDGEMENTS: NIH grant R01AR071358.

REFERENCES: [1] Ahsan, T et al., *Osteoarth. Cartil.*, 13:709-715, 2005. [2] Zitnay, J et al., *Sci. Adv.*, 6, 2020. [3] Zitnay, J et al., *Nat. Commun.*, 8:1-12, 2017. [4] Uquillas, J et al., *JMBBM*, 15:176-189, 2012. [5] Lin, A et al., *Acta Biomater.*, 155:461-470, 2023. [6] Herod, T et al. *Acta Biomater.*, 42:296-307, 2016.

MECHANICAL AND DAMAGE PROPERTIES OF PRETERM AND ADULT SHEEP MIDDLE CEREBRAL ARTERIES FOLLOWING MECHANICAL DAMAGE

Kerrigan B. Denham (1), Joseph D. Bail (1), Andrew J. Rebentisch (2), Kurt H. Albertine (2), Kenneth L. Monson (1,3)

(1) Department of Mechanical Engineering, University of Utah, Salt Lake City, Utah, USA
(2) Division of Neonatology, Department of Pediatrics, University of Utah, Salt Lake City, Utah, USA
(3) Department of Biomedical Engineering, University of Utah, Salt Lake City, Utah, USA

INTRODUCTION

In 2020, 13.4 million infants were born premature, accounting for over 10% of all births that year [1]. A full-term, human pregnancy is 40 weeks. If an infant is born at less than 28 (70% gestation), between 28 to 32 (70 to 80%), or between 32 to 37 weeks (80% to 92.5%), it is classified as extremely preterm, very preterm, or moderately preterm, respectively [1]. Of the infants that are born before 32 weeks (80% gestation) and weigh less than 1.5 kg, 32% will experience intraventricular hemorrhage (IVH); 75% of these cases will experience long-term neurodevelopmental impairments [2].

Structural deficiencies in the developing cerebral vasculature may play a significant role in the occurrence of IVH [2]. The structural integrity of blood vessels is largely defined by the extracellular matrix proteins elastin and collagen. Elastin is relatively mature by late gestational periods, although collagen components are developing significantly up until the juvenile period [3]. Computational models predict that failure strain and strength of collagen fibrils increase as the collagen triple-helix develops enzymatic cross-links as part of development [4]. Consistent with this, experiments show dramatic increases in sheep cerebral artery mechanical and failure properties with age, although lamb vessels from the earlier preterm ranges have not yet been studied [5]. Recent work from our laboratory further shows that cerebral vessels are damaged with overstretch [6]. Deformations associated with even mild brain motion in premature neonates may therefore disrupt cerebral vessels and lead to IVH. The objective of this preliminary study was to characterize the mechanical properties and damage characteristics of preterm lamb cerebral arteries in comparison to those from adults.

METHODS

Tissue Collection and Preparation: Dissections used procedures previously reported by the Monson group [5]. In short, lamb middle cerebral arteries (MCAs) were received from the Lamb Intensive Care Unit at the University of Utah. Adult sheep MCAs were collected from a local slaughterhouse. For both cases, the head and the top of the skull were removed following euthanasia. The brain was freed from internal attachments, separated from the dura, and placed in a petri dish. The MCAs were removed, starting at the Circle of Willis, using micro scissors and then placed into cold, calcium-free, phosphate-buffered saline (PBS; KH_2PO_4 1.54, $NaCl$ 155.2, $Na_2HPO_4 - 7H_2O$ 2.7 concentration in mM). Using a dissection microscope, surrounding pia-arachnoid tissue was carefully removed with forceps, and branches were ligated using unwound 6-0 silk sutures. Finally, cross sections of proximal and distal ends of the vessel were imaged.

Mechanical Testing: Mechanical tests used procedures previously reported by the Monson group [5]. In short, MCAs were mounted to cannulas using 6-0 suture and a small amount of cyanoacrylate. Using a custom testing system, MCAs were subjected to preconditioning by cycling the pressure from 6.7 to 20 kPa, during which in vivo length (L_{iv}) was determined. MCAs were characterized by a baseline response test by axially stretching MCAs to $1.1 * L_{iv}$ at a quasi-static rate. The MCAs were then axially overstretched to $1.3 * L_{iv}$. The same quasi-static baseline test was subsequentially repeated to evaluate the changes in the baseline stress response as a result of being overstretched. The MCAs were then carefully removed from the cannulas.

Data Processing and Analysis: Consistent with our previous work, MCAs were assumed to be incompressible, homogeneous, circular cylinders with uniform wall thickness [5]. Using cross-sectional images obtained prior to mechanical testing, cross-sectional area and unloaded diameter were determined for each MCA. Data were filtered with a 4th-order, Butterworth, low-pass filter. First Piola-Kirchhoff stress was calculated, and stretch was normalized by the in vivo length (L_{iv}) of each specimen. In vivo stiffness was found by fitting an exponential function to the in vivo portion of the stress-stretch curve and by calculating the value of its derivative at L_{iv}. Softening values (i.e., reduction in stiffness) were calculated by comparing the stiffness values

pre- and post-overstretch. A t-test was used to determine if there was a statistical difference ($p < 0.05$) between the softening values of the adult and preterm samples.

RESULTS

Eight preterm MCAs were tested, with seven within the moderately preterm (80 to 92.5% gestation) range, and one within the very preterm (70 to 80%) range. In a sheep model, a full-term pregnancy is 148 days. Three preterm lambs were born at 128 days (86.5% gestation), two at 120 days (81.1%), two at 119 days (80.4%), and one at 118 days (79.7%). Eight adult MCAs were tested for comparison, all over the age of 12 months.

The stretch-stress curves, pre- and post-overstretch, demonstrated a nonlinear response, typical of soft, biological tissues (Figure 1). The toe regions of the adult and preterm stretch-stress curves were relatively similar, suggesting that there is little difference between the tissues at physiological loads. However, higher stress values were found in adult samples compared to preterm samples at similar stretch values during large deformations. Interestingly, the difference in pre- and post-overstretch values appeared to result in a higher mean softening value in preterm compared to adult samples although this difference was not statistically significant (Figure 2).

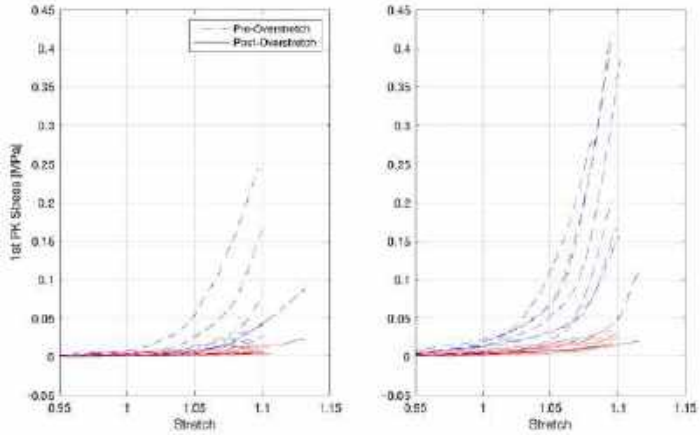

Figure 1: Baseline axial stretch-stress responses pre- and post-overstretch (blue and red, respectively) for preterm sheep born from 118 to 128 days gestation (left) and for adult sheep of at least 12 months (right).

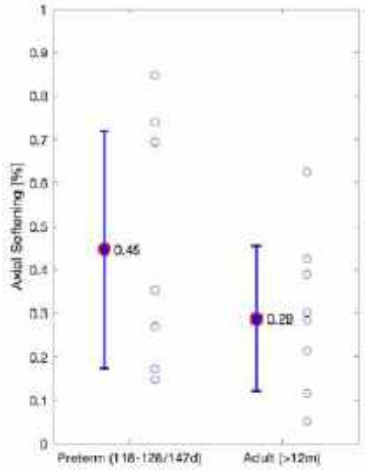

Figure 2: Individual softening values for both preterm and adult samples (blue circles), accompanied with mean (red) and standard deviations (blue lines) for each group.

DISCUSSION

The objective of this preliminary study was to investigate cerebral blood vessel mechanical properties and damage characteristics of preterm lamb cerebral arteries in comparison to those from adults. While samples from the moderately preterm lambs were qualitatively different from adult samples, results unexpectedly show no statistical differences in the reduction of stiffness between the two groups following mechanical deformation.

Consistent with previous results, at low deformations, no significant difference was detected between age groups. This is likely because elastin is the dominant mechanical fiber during low-stretch deformation. Previous work shows that elastin is finished maturing by late gestational periods [3]. All but one of the samples tested were classified as moderately preterm, meaning they correspond with the oldest gestational ages that are considered to be premature. For larger deformations, collagen is the main load carrying mechanical element. Therefore. the difference in stiffness and softening values, although not statistically significant, could be an indication of the underdeveloped enzymatic collagen cross-linking.

The primary motivations of this preliminary work were to better understand the mechanical changes in the cerebrovasculature at different developmental ages following large deformations and to predict how this may contribute to IVH. However, this study mainly included a range of samples from moderately preterm cases; therefore, further mechanical testing will need to be done to include more samples from other preterm classifications, including extremely preterm (less than 70% gestation) and very preterm (70 to 80% gestation). Further research is also needed to link mechanical damage to IVH, specifically how microstructural damage impacts the permeability of the vessel wall.

ACKNOWLEDGEMENTS

Financial support was provided in part by the NSF (CMMI 2027367) as well as the University of Utah's Office of Undergraduate Research. Research support and guidance was provided by the University of Utah's Laboratory of Head Injury and Vessel Biomechanics in the Department of Mechanical Engineering as well as from the University of Utah's School of Medicine in the Department of Pediatric Medicine in the Neonatology Division.

REFERENCES

[1] 'Preterm birth', World Health Organization (2023).
[2] Nye, K. et al., American Journal of Perinatology, 32:263-260, 2015.
[3] Wagenseil, J. et al., Physiological Reviews, 89: 957-989, 2009.
[4] Depalle, B. et al., Journal of the Mechanical Behavior of Biomedical Materials, 52:1-13, 2015.
[5] Nye, K. et al., Annals of Biomedical Engineering, 45:1101-1110, 2016.
[6] Converse, M. et al., Annals of Biomedical Engineering, 49:3540-3549, 2021.

VITAFLOW - Future of Heart Preservation

J. Jung, N. Newby, S. Tuohy, T. McGoldrick
University of Pennsylvania

Faculty Advisors:
D. Meaney PhD, E. BerlewPhD, D. Adewole PhD, M. Hilman MSE
Bioengineering, University of Pennsylvania, Philadelphia PA, USA

User Need

Historically, the limited availability of hearts for donation has created a large supply-demand disparity. Recently, advances enabling the usage of "donation after circulatory determination of death" (DCD) hearts, rather than just "donation after brain death" (DBD), show promise in significantly increasing the supply of available organs. Ischemia, or heart damage, limits the distance across which donor hearts can be transported. Ischemia reduces the total available donor hearts, as such engineering a preventative measure to address ischemia is a clear need. To reduce ex vivo heart damage, perfusion is necessary to provide nutrients to the heart during transport and reduce ischemia. With only two platforms achieving clinical success in ex-vivo heart preservation, and high price points of $20,000 - $80,000 per use, there is a clear need for a disruptive, effective, and affordable technology within this field to address the persisting supply-demand gap. Our proposed solution, VITAFLOW, seeks to integrate successful techniques and technologies from ex-vivo preservation and perfusion theory, maintaining efficacy, monitoring, and patient outcomes while drastically reducing costs using sub-normothermic temperature.

Design Inputs

Some of Vitaflow's strictest constraints and requirements are cost of design, temperature regulation, sterility, supply chain issues, and portability. We designed our own parts instead of buying existing solutions and the outcome of our own design efforts allowed us to attain greater user affordability. To address sterility, we plan to incorporate UV light and design our organ transport device for one time use to reduce contamination. For portability, we plan to make a compact carrying structure with wheels and handles to facilitate easy transportation of the donor heart.

Solution

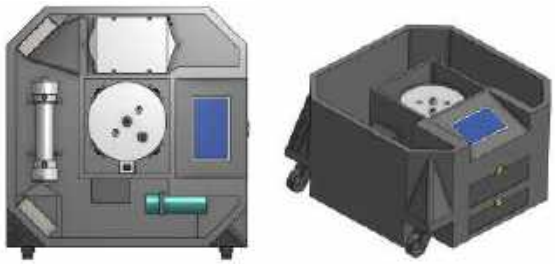

Figure 1. *3D rendering of VITAFLOW*

Our solution contains an oxygenator, , a central heart chamber which will house the donor organ, a temperature regulator module, a pump, sensors, a touch screen, and an Arduino. Our engineered solution addresses our problem. We have developed a system that continuously perfuses and oxygenates normothermic blood through a donor heart. The system is intended to provide an optimal environment for heart preservation. We have real-time sensor data of Sp02, Pressure, pH, and temperature which feed information back into an Arduino microcontroller to regulate the system's environment based on set parameters of the user on the touchscreen.

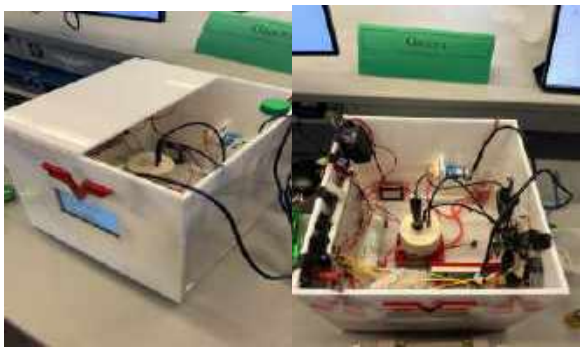

Figure 2. *Minimal Viable Product of VITAFLOW*

The minimum viable product contained a pump, pH sensor and temperature sensors, an oxygenator, a central chamber, a heating and cooling module, and an Arduino with a touchscreen.

Verification of Results

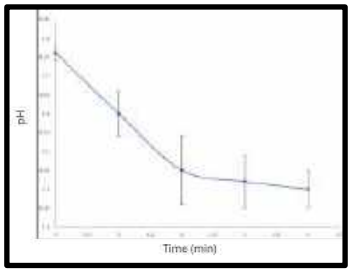

Figure 3. *Time and pH graph for CO2 gas exchange*

Measuring pH showed an initial reading that CO2 could be effectively perfused into our system which indicates effective gas exchange. We used bicarbonate to show that if there was gas exchange pH would be lowered (Figure 3).

Budget & Market Analysis

We have allocated a budget of $600 for the development of a functional prototype. Additionally, we have secured access to a makerspace, which is well-equipped with the necessary tools for the fabrication and testing of components.

We estimate that the manufacturing cost at scale will approximate our initial budget of $600. This is achievable through our decision to fabricate cost-effective parts, thereby ensuring overall affordability. Our pricing strategy positions the product in the retail market at a competitive range of $1000 to $2000, significantly undercutting current market rates.

The annual rate of transplants currently stands at nearly 4,000, a figure we anticipate will rise markedly with the advent of medical device innovations that prolong organ viability. Our product is expected to contribute to and benefit from this upward trend in transplant numbers.

Conclusion

We have been able to meet our requirements without violating our constraints. By fabricating most of our own parts and creating a functioning system that successfully changes the perfusing fluid, we are optimistic about our product design. Potential revisions include automatic injections potential nutrients into the perfusing blood to further decrease ischemic damage and prolong viability. Prolonged viability of donor hearts would contribute to closing the supply demand disparity. Furthermore, our low-cost transport device could potentially expand supply to lower-income parts of the world.

Acknowledgements:

Ayyaz Ali, MD, PhD, Erin Berlew, PhD, Dave Meaney, PhD, Dayo Adewole, PhD, Melanie Hilman, MSE

References:

Alomari, Mohammad et al. doi:10.7759/cureus.26281, Bryner, Benjamin S et al. doi:10.1016/j.xjon.2021.04.020, "Heart Disease" Facts."www.cdc.gov/heartdisease/facts.htm.

SENSITIVITY OF CONTACT MECHANICS TO FE MODEL GENERATION DECISIONS COMPARED TO VARIATIONS BETWEEN KNEES AND DUE TO PARTIAL MENISCECTOMY

Joshua Leadem (1), Sean C. Letendre (2), Mitchell Kershner (1), Manuela Montes de Oca (1), Lila Pender (1), Erin R. Leatherman (3), Matthew F. Koff (2), Suzanne A. Maher (2), Brett D. Steineman (2), Amy Lerner (1)

(1) University of Rochester, Rochester, NY
(2) Hospital for Special Surgery, New York, NY
(3) Kenyon College, Gambier, OH

INTRODUCTION

Finite Element (FE) Analysis is useful for understanding the complex contact mechanics of the tibial plateau. FE Models have been used to quantify the difference in joint mechanics between knees with different geometries, as well as between knees with different conditions, such as meniscectomy[1]. Typically, these models are developed from medical imaging of either cadaver knees or patients[2]. For use in clinical applications, it is important to verify that the model is not overly sensitive to uncertainties in modeling inputs. The ASME V&V 40 standard emphasizes this need and presents a framework for completed verification and validation in credible computational models[3]. Many steps in the model generation procedure are automated, however segmentations and model refinement may involve subjective inter-operator decisions related to tissue identification in images. Therefore, the goal of this study was to test the sensitivity of the model to variations in 1.) cartilage thickness, 2.) meniscal attachments and 3.) boundary conditions related to load application location. The effects of these variations were then compared to differences in contact patterns between knees, due to variations in material properties, and resulting from 2 sizes of partial meniscectomy. Based on the incidence of injury, our study focuses on the contact mechanics in the medial compartment.

METHODS

Finite Element models were created from MR Images of four cadaveric knees, potted in a loading fixture designed to apply axial loading during imaging. SPGR (Spoiled-gradient echo) and CUBE image sets were obtained in the non-weight-bearing position, and then again in a loaded configuration, equivalent to 50% body weight. The unloaded images were used for segmentation of soft tissue, and bones were segmented in both positions to determine the movement due to loading. This protocol is based on similar *in vivo* studies[4]. A variety of programs were used in segmentation such as MeVisLab, Amira, and ITK Snap. FE models were created from the segmentations with meshes of hexahedral elements generated using TrueGrid, and simulations were run in Abaqus. Loading conditions for this simulation were based on a transformation matrix from unloaded to loaded position and fixing all degrees of freedom of the knee other than varus-valgus rotation. A load was applied in the axial direction at a femoral reference point to reflect loading during the scan (Fig. 1)[5]. The direction and location of the load was applied to a femoral reference point determined from an automated MATLAB code that established the coordinate systems of the femur and tibia[6]. The cartilage was assigned isotropic properties, and the menisci were transversely isotropic, with stiffer modulus in the circumferential direction. Meniscal attachments were assigned spring stiffnesses to a shared reference point. To evaluate possible variations in material properties, each model was run with 70 different combinations of Young's moduli and Poisson's ratio for the cartilage and menisci. In addition to these baseline conditions, we explored variations in three categories as defined below for the boundary conditions, meniscal boundaries, and cartilage thickness, with each case run through a range of material properties.

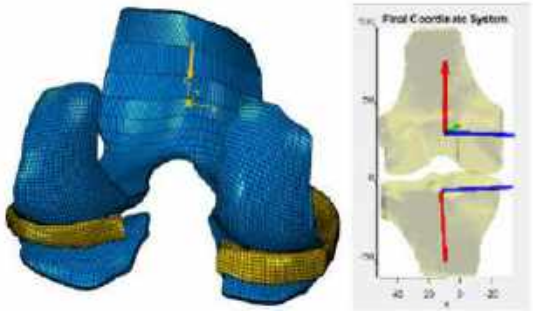

Figure 1: FE Model of the knee represented by tissues, with displayed femur reference point and axial load (left) from tibiofemoral coordinate system (right)

Boundary Condition Modification:

Because the coordinate system is sensitive to changes in bone geometry, segmentation and smoothing can impact the location and orientation of the load. To determine the effect of this variation, the femoral reference point was moved +/-1.3mm in the ML and AP directions, a magnitude equivalent to 1 slice thickness in the MR image sets used for segmentation. Next, the same cadaver images were segmented using two different software tools, Amira and MeVisLab. To account for the difference between resulting segmentations, the rotations of the model were modified by 1 degree in I/E and F/E directions.

Meniscus Modification:

Identifying boundaries between the meniscus and its attachments is challenging during segmentation and sharp edges in the model may impact successful convergence in FE simulations. Therefore, to determine the effect of the length of the anterior horn, the medial meniscus was modified by deleting a region of elements and shortening the meniscus by approximately 7.5mm, effectively lengthening the spring attachments. To study the effect of the geometry of the meniscus, each of the meniscal edges were tapered to reduce high concentrations of contact pressure with the tibial cartilage. For comparison, two sizes of partial meniscectomies were modeled in the posterior medial compartment (Fig. 2).

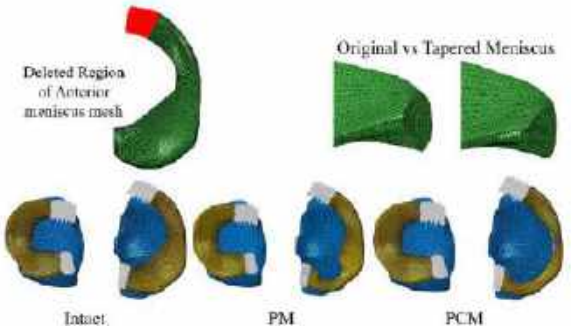

Figure 2: Medial Meniscus Shortening, Tapering, Intact and Meniscectomy Conditions

Tibial Cartilage Modification:

Uncertainty in segmentation may lead to variations in cartilage thickness of approximately one image voxel. Therefore, we modified each model to investigate increases in cartilage thickness of 0.3 mm (Fig. 3). Additionally, the cartilage at the periphery of the knee gradually tapers down, but this could result in distorted hexahedral elements. Therefore, the mesh is often shortened to allow a vertical edge. A different way to model this geometry with hexahedral elements could include a "staircase effect," where rows of elements are removed along the edge of the tibial cartilage. These conditions were run for a representative sample of 25 material property combinations.

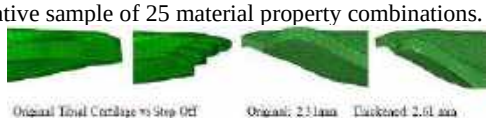

Figure 3: Tibial Cartilage Step Off and Thickening

To evaluate the variations described above, 1355 FE models were run. Our primary interest relates to the role of the meniscus in contact mechanics; thus, we calculated the total contact area on the medial plateau and the fraction of force supported by the meniscus.

RESULTS

The role of the meniscus in carrying contact forces varied greatly between knees, due to partial meniscectomy and due to uncertainty in material properties, with the ~25% of the force through the meniscus in one knee and nearly 100% of the load in two other knees. In contrast, thickening the cartilage resulted in minimal difference in the mean or distribution of the fraction of force through the meniscus for any of the four knee models tested (Fig. 4). Focusing on one knee, creation of the partial meniscectomies greatly reduced the role of the meniscus, with modeling variations related to the boundary conditions or meniscal ends having minimal effect.

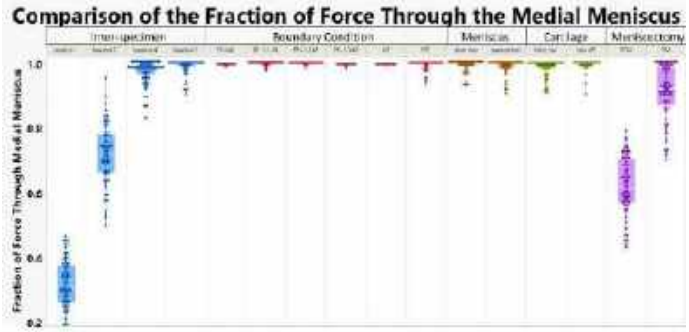

Figure 4: Fraction of Force Through Medial Meniscus between different knees and in one knee

The effects of our modeling variations on contact areas were similar, with differences between knees and differences due to modeling modifications much smaller than differences due to material property variations.

DISCUSSION

Model-generation variations in the FE models did not result in large effect on the outputs of interest. The small variability in outputs relative to variability between knees and meniscectomy conditions demonstrates that the FE model is robust enough to handle small, expected variability in the model making process. There is a larger effect on contact area from the range in material properties than from modification to the models. Our study contributes to further understanding the sensitivity of contact mechanics to model inputs[7,8,9] by focusing on variations resulting from uncertainties in segmentations. This preliminary work focused on variations made on only one cadaveric model, which had a very large fraction of force through the medial meniscus. Future studies will confirm this finding for multiple knee geometries and other model outputs such as locations and magnitudes of peak pressure. Four cadaver models make up a small sample size, and verification analysis should continue with more knees with varying geometries and outputs. Despite these limitations, our sensitivity study showed that the modification of models had a small influence on the primary outcomes of interest relative to the difference between knees and due to meniscectomy.

ACKNOWLEDGEMENTS

We thank the following sources of support: The National Institutes of Health (AR075523), the Russell Warren Chair for Tissue Engineering and the HSS Surgeon-in-Chief Fund

REFERENCES

[1] Zielinska, B., et al., *J Biomech Eng*, 128(1): 115–123, 2006
[2] Bae, J et al., *Med Biol Eng Comput*., 50(1):53-60, 2011
[3] *ASME V&V 40*, 2018
[4] Maher, S et al., *J of Orthopaedic Research*, 35(3), 600-611, 2016
[5] Steineman, B.D. et al, Paper No. 214, ORS 2023 Annual Meeting
[6] Miranda, DL et al., *J Biomech*, 43(8):1623-1626, 2010
[7] Yao et al., *Biomechanics and Modeling in Mechanobiology*, 2024
[8] Yao, J. et al., *J Biomech*, 41(2): 390-398, 2008
[9] Guo H. et al., *J of Orthopaedic Research*, 35(10): 2233-2242, 2017

DESIGN AND OPTIMIZATION OF A 3D-PRINTED TESTING PLATFORM FOR EVALUATING THE EFFECTS OF VOLUNTARY WHEEL RUNNING ON THE BIOMECHANICAL PROPERTIES OF MURINE ACHILLES TENDONS

Elsa Lecaj[1,2], Samantha Muscat[2,3], Nolan Sparks[2], Mark Buckley Ph.D[1,2] and Anne E.C. Nichols Ph.D.[2]

(1) Department of Biomedical Engineering, University of Rochester, Rochester, NY, USA
(2) Department of Orthopaedics and Rehabilitation, Center for Musculoskeletal Research, University of Rochester Medical Center, Rochester, NY, USA
(3) Department of Pathology and Laboratory Medicine, University of Rochester Medical Center, Rochester, NY, USA

INTRODUCTION

The Achilles tendon is an integral biomechanical structure that connects the gastrocnemius and soleus muscles of the calf to the calcaneal insertion, facilitating planar flexion of the foot, shock absorption, and storage and release of energy. It is composed of a complex, largely collagenous, matrix that can be analyzed using mechanical properties such as nonlinearity, modulus of elasticity, stress, strain, and viscoelasticity. These mechanical properties allow the tendon to efficiently transmit force which is fundamental to locomotion and injury prevention.[1] Optimal levels of mechanical loading facilitates the growth of a healthy tendon, yet excessive or insufficient loading can lead to damage and give rise to injury.[2] While mechanical load is critically important to maintaining tendon mechanical properties, how this process is coordinated at a cellular level is currently unknown. The overarching goal of this project is to establish voluntary wheel running (VWR) as a model for studying the cellular and molecular regulators of physiological tendon adaptation. We hypothesized that physiological loading through VWR would result in altered tendon material properties that will allow tendons to transfer energy more efficiently (e.g. increased peak stress, elastic modulus, and stress relaxation). In order to assess changes in tendon mechanical properties due to VWR, we developed a customizable 3D printed testing platform and robust protocol.

METHODS

The University Committee on Animal Resources approved all animal studies. 10-week-old male C57BL/6J mice (n=40) engaged in VWR using a slanted saucer shaped wheel, with all run activity being recorded continuously electronically. Control mice were provided with a locked wheel. Mice were sacrificed after 8 or 12 weeks of running, and the right hind limbs were harvested at the knee for testing.

Samples were kept hydrated in phosphate buffered saline (PBS). The plantaris tendon was removed, and the Achilles tendon was isolated while keeping intact the calcaneal insertion. Preserving the insertion point and bone ensured that the distal end of the tendon could be effectively gripped without compromising the tendon mid-substance. The proximal end of the tendon was dissected from the gastrocnemius muscle to maximize gripping surface and increase gauge length.

Custom 3D printed grips were developed through multiple iterations using CAD software (SOLIDWORKS® 3D CAD) and printed using an Original Prusa i3 MK3 3D Printer with 1.75mm polylactic acid (HATCHBOX 3D). To reinforce grip stability and tendon clamping, thread holes for steel screws were created using a T-handle tap wrench. 3M coarse 60-grit sandpaper was affixed to the grips using cyanoacrylate glue to enhance traction and prevent slippage.

Dissected tendons were placed on the prepared grips using a 3D designed alignment tool (Fig. 1A) ensuring a consistent gauge length of 4.35 mm. Tendons were bonded with the grips using cyanoacrylate glue then fastened with steel screws and allowed to cure overnight at 4°C in PBS to ensure polymerization of the cyanoacrylate glue. A 3D-printed PBS bath was designed to fit within the tensile tester (Fig. 1B) ensuring tendon hydration during mechanical testing.

Mechanical testing was conducted using a semi-customized uniaxial microtester (eXpert 4000 MicroTester, ADMET, Inc.). Data was collected using MTESTQuattro®. The cross-sectional area (CSA) of the Achilles tendon was measured using ImageJ from images acquired prior to testing.

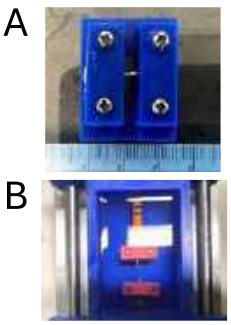

Figure 1: (A) Prepared grip in alignment tool. (B) PBS bath in tensile tester.

The test procedure included an initial preload to a load of 0.1N followed by 10 cycles of loading at 6% strain. Displacement required to reach defined strain percentages was calculated from the gauge length under a preload of 0.1N for each tendon. Tendons underwent stress relaxation phases at both 8% and 16% strain, allowing for a 500-second recovery period at each stage. Finally, a ramp-to-failure test at a rate of 1mm/s was conducted to determine the ultimate tensile strength, stiffness, and elastic modulus of each tendon. Change in stress was calculated by subtracting the equilibrium stress from the peak stress for each phase of stress relaxation. Differences in biomechanical outcomes were assessed by Two-way ANOVA with Tukey's multiple comparisons test (GraphPad Prism 10.1.1).

RESULTS

Following a 4-week acclimatization period, running behavior stabilized at 5 weeks, with an average weekly distance of 123.8 ± 13.5 km (Fig. 2). The average weekly distance from weeks 8 to 12 was 91.59 ± 5.1 km. Throughout the experiment, the 8-week VWR cohort recorded a total run distance of 783.09 ± 49.0 km, while the 12-week VWR cohort averaged 1111.0 ± 131.1 km.

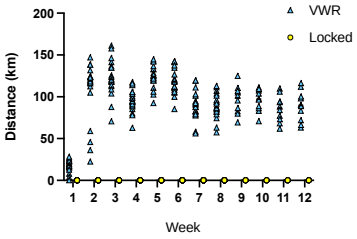

Figure 2: Running distance of mice for 12 weeks of VWR (blue) compared to control (yellow).

There was a significant increase in stress relaxation of VWR tendons compared to locked controls during the 8% stress relaxation phase at 8 weeks, which returned to baseline by 12 weeks (Fig. 3A). We observed no differences in stress relaxation between VWR and control tendons at either timepoint during the 16% phase (Fig. 3B); however, there was a significant decrease in stress from 8 to 12 weeks in the VWR group. At 8 weeks, both peak stress (Fig. 3C) and elastic modulus (Fig. 3D) were significantly increased in VWR tendons compared to controls (~55% and ~44% increased, respectively). Neither difference persisted to 12 weeks. No significant changes were found in peak load or stiffness between VWR and control tendons at either time point (Figs. 3E-F); however, we observed a significant decrease in the stiffness of control tendons from 8 to 12 weeks (Fig. 3F). No significant differences were observed in the CSA of VWR tendons compared to control at either timepoint (Fig. 4).

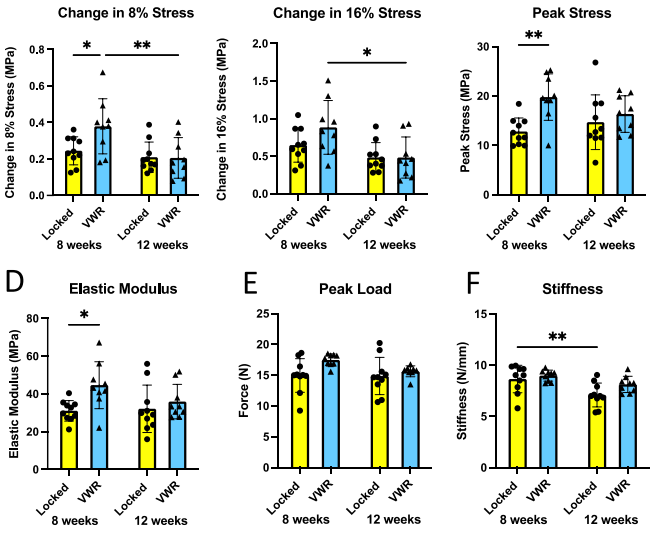

Figure 3: Biomechanical properties of Achilles tendons after 8 and 12 weeks of VWR (blue) compared to locked controls (yellow). Graphs depict (A) Change in 8% Stress, (B) Change in 16% Stress, (C) Peak Stress, (D) Elastic Modulus, (E) Peak Load (F) Stiffness. n=9-10 per group. *p≤ 0.05, **p ≤0.01.

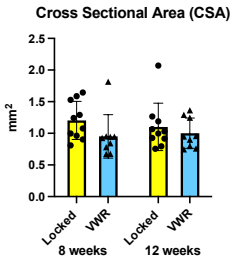

Figure 4: CSA of tendons

DISCUSSION

The strengths of this study lie in the reproducibility of the testing procedure and the physiological relevance of VWR as a model. Results demonstrate that mice have a natural inclination to run without additional stress, and that, in line with our hypothesis, VWR resulted in significant changes in the mechanical properties of Achilles tendons after 8 weeks. Furthermore, a notable achievement of this study was the 100% success rate in the mechanical testing of the tendons by effectively eliminating tendon slippage. Adjusting the tendon dissection method and gripping techniques also ensured that all tendons broke at the mid-substance, facilitating reproducible examination of the major region exposed to physiological loads during locomotion, thus demonstrating that our customized platform provides an accurate analysis of in vivo mechanical properties and adaptation.

In this study, VWR did not induce significant changes in the CSA of tendons. This outcome suggests that 8 to 12 weeks of VWR may not significantly influence tendon morphometry. It is possible that tendon hypertrophy may necessitate a longer duration or a different intensity of mechanical loading. The change in stress relaxation at 8% stress, peak stress, and elastic modulus of tendons were significantly increased after 8 weeks of VWR. These results demonstrate an increase of tendon strength and resilience against applied forces, suggestive of an adaptive response to mechanical load. The lack of significant changes in tendon stiffness at 8 weeks combined with the change in modulus suggests that while no large structural changes occurred, VWR induces changes in tendon material quality. These findings have important implications for understanding the biomechanics of tendons and how exercise may affect tendon mechanics. Interestingly, these differences in 8% stress, peak stress, and elastic modulus did not persist at the 12-week mark, with no notable changes between the locked and VWR groups. This plateau may point to a time-dependent response in tendon adaptation, suggesting that there might be a limit to the extent of change achievable within this timeframe. Future work will examine time-dependent nature of tendon response to mechanical loading and the potential for adaptation over longer periods.

In the future, we aim to tailor the grip design to accommodate anatomically different tendons. This will increase the platform's versatility and broader application in tendon research, potentially being applied across different animal models and tendon structures. This testing platform will also be used to evaluate how genetically altering important mechanosensitive pathways affects the biomechanical properties of tendons, with the ultimate goal of determining how tendons adapt to mechanical load.

ACKNOWLEDGEMENTS

This work was supported by NIH/NIAMS K99 AR080757 (to AECN)

REFERENCES

[1] Freedman, BR et al., *Muscles, Ligaments and Tendons Journal*, 4(2):245-255, 14 Jul. 2014.

[2] Wang, JH-C et al., *Journal of Hand Therapy*, 25(2):133-140, 2012.

ASSESSMENT OF A TUMOR'S MALIGNANCY USING IN SILICO MODEL OF BREAST TUMOR TISSUE

Hannah Vincent, Morgan Connaughton [1], Kianoush Falahkheirkhah[2], Erik Robert Hansen[1], Rohit Bhargava [2], Mahsa Dabagh[1]

(1) Department of Biomedical Engineering, University of Wisconsin-Milwaukee, Milwaukee, WI, United States
(2) Department of Biomedical Engineering, University of Illinois at Urbana-Champaign, Illinois, United States

INTRODUCTION

The complexity of tumor microenvironments remains a significant challenge in cancer research. Specifically, the differences and interactions between cancerous and noncancerous tissues present numerous obstacles, varying case by case and dependent on the location (e.g., breast, pancreas, etc.). This demonstrates the importance of *in-silico* experimentation built based on patient-specific images to enable more accurate modeling of tissue environments, including the tumor microenvironment. The current study aimed to develop an *in-silico* model of a patient-specific breast tumor tissue which will then be applied to assess the tumor's malignancy through quantifying the forces within the breast tumor tissues.

METHODS

We used the standard and high-definition Fourier Transform Infrared (FTIR) imaging to image and classify to forty tissues to four distinct breast tissue pathology types: "Normal Breast Tissue," "Hyperplasia," "Invasive Carcinoma of No Special Type (NST)," and "Invasive Lobular Carcinoma." Using an FTIR imaging microscope, we will first record high-definition data and apply numerical noise reduction methods to provide high spectral signal-to-noise ratio (SNR). Standard definition data then will be recorded on the same breast tissue samples (tissue arrays from US Biomax) [1-4]. Each image contained six tissue components, including noncancerous epithelial tissue, cancerous epithelial tissue, dense stroma, loose stroma, reactive stroma, and other (e.g., blood vessels).

Image Processing: The FTIR images were received in MATLAB file format and were subsequently processed to extract individual tissue components. For instance, in the case of the malignant tissue images, a separate image was extracted specifically for each noncancerous epithelial tissue, cancerous epithelial tissue, dense stroma, loose stroma, reactive stroma, and other. In total, 31 FTIR files were processed.

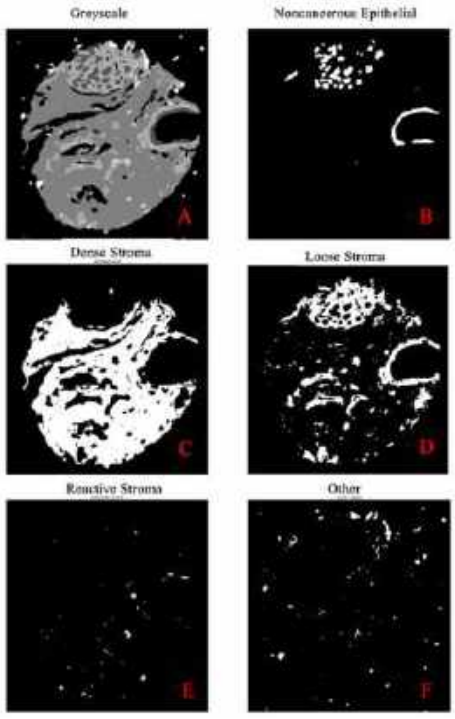

Figure 1. Hyperplasia sample processed in MATLAB. Figure 1A depicts a complete hyperplasia sample in grayscale, with all tissue types of present. Figures 1B-1G depict the individual tissue types extracted from the FTIR images as B) Noncancerous Epithelium C) Dense Stroma; D) Loose Stroma; E) Reactive Stroma; F) Other Tissue. In this sample, no malignant tissue was present.

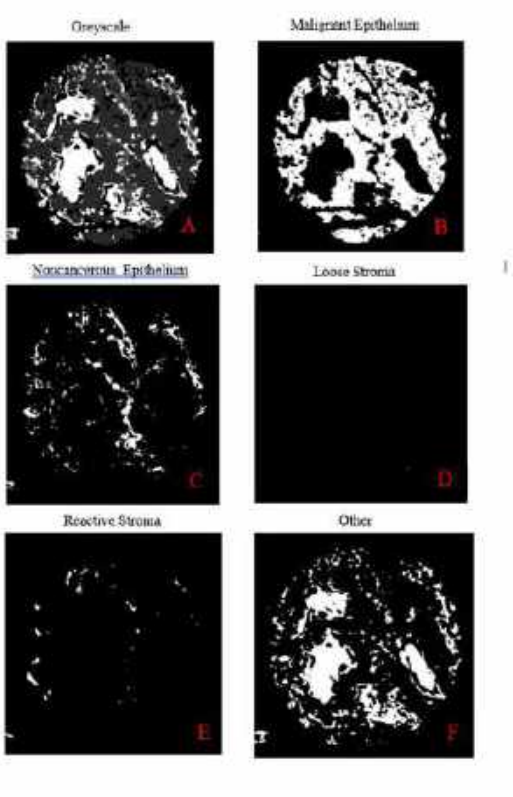

Figure 2. Invasive carcinoma sample processed in MATLAB.
Figure 2A depicts sample in grayscale, with all tissue types present , Figures 2B_G depict the individual tissue types extracted from the FTIR images as B) Malignant tissue; C) Noncancerous Epithelium; D) Dense Stroma; E) Loose Stroma; F) Reactive Stroma; G) Other Tissue.

Image Segmentation: The extracted tissue types were then imported into Mimics, a software application for medical image processing. Segmentation was performed within Mimics to generate three-dimensional representations of each tissue type. These segmented images were then exported in STL format for further analysis.

Discussion:
Our ongoing study focuses on developing in-silico models of breast tumor tissues, leveraging patient-specific data acquired through FTIR imaging. We are planning to the segmented image files exported from Mimics into LAMMPS (Large-scale Molecular Dynamics Massively Parallel Simulator) to build three-dimensional *in-silico* model of breast tumor tissue. Figure 4 depicts our *in-silico* models of four breast tumor tissues as A) Hyperplasia; B) Invasive Carcinoma NST; C) Invasive Lobular Carcinoma; D) Normal Breast. It is clear that the different pathology types display different variations of the tissue, for example, dense stroma tissue (depicted in orange) varies patient to patient [5-6]. These models aim to quantify the von Mises stress magnitude and distribution within breast tumor tissues, considering diverse pathology types. Understanding the mechanical properties is paramount for accurate *in silico* modeling, as these properties are recognized hallmarks in cancer initiation and progression. This study plays a critical role in developing targeted interventions and advancing our understanding of the biomechanical factors influencing cancer progression.

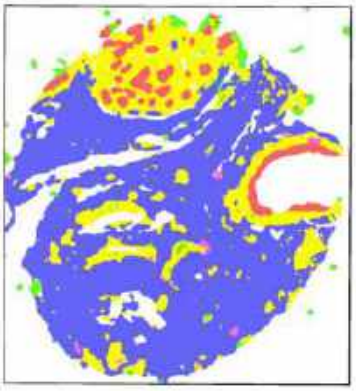

Figure 4. In silico model of Hyperplasia loaded into a Molecular Dynamics Software (LAMMPs)

REFERENCES

[1] Bhargava R, Madabhushi A. Emerging Themes in Image Informatics and Molecular Analysis for Digital Pathology. Annu. Rev. Biomed. Eng. 2016, 18:387–412. Doi:10.1146/annurev-bioeng-112415-114722.
[2] Bhargava R, Mittal S. Tissue microenvironment analysis based on tiered classification and clustering analysis of digital pathology images**.** 2022, 04-07, US20220108123A1(pending).
[3] Tiwari S, Falahkheirkhah K, Cheng G, Bhargava R. Colon Cancer Grading Using Infrared Spectroscopic Imaging-Based Deep Learning. Appl. Spectrosc 2022, 76: 475-484.
[4]. Mittal S, Wrobel T, Walsh M, Kajdacsy-Balla A, Bhargava R. Breast cancer histopathology using infrared spectroscopic imaging: The impact of instrumental configurations. Clinical Spectroscopy 2021, 3:100006. Doi.org/10.1016/j.clispe.2021.100006.

DEVELOPMENT OF A BENCHTOP MODEL FOR CEREBRAL COLLATERAL CIRCULATION

Argudit Chauhan (1), Alena Tucker (1), Debanjan Mukherjee (2)

(1) Biomedical Engineering Program, University of Colorado Boulder, Boulder, CO, USA
(2) Paul M. Rady Department of Mechanical Engineering, University of Colorado Boulder, Boulder, CO, USA

INTRODUCTION

Blood flow in the brain occurs through a highly complex vessel network originating from the ring-like network of supplying arteries named the Circle of Willis (CoW). During arterial insufficiency due to occlusive events such as ischemic stroke, a subsidiary vessel network complements and stabilizes the flow, thereby enabling redundancy [1]. This is referred to as collateral circulation. While the CoW itself enables proximal collateral flow routes, additional smaller distal (leptomeningeal) vessels play a significant role in supporting collateral flow [2]. Collateral flow is recognized to be a key determinant of cerebral tissue damage during stroke, and strongly influences stroke therapy outcome and recanalization success [3]. Despite their importance, collateral circulation remains poorly understood, due to several factors. Distal collateral pathways are small and difficult to image or experimentally study in vivo. Furthermore, the hemodynamic interplay between proximal and distal collateral pathways is poorly understood. Current efforts in collateral assessment are based on imaging, such as the ASPECTS score based on CT imaging [4], and the Perfusion Collateral Index. These metrics are derived solely based on image pixel intensities, and often the underlying hemodynamic patterns remain unclear. Thus, there is a need to develop techniques to characterize cerebral collateral flow. Here, we outline an in vitro benchtop model for a comprehensive understanding of cerebral hemodynamics with collateral flow, that can: (a) incorporate patient anatomy features; (b) identify simple flow descriptors; (c) illustrate proximal-distal collateral pathway interaction.

METHODS

Image-based 3D printing of Circle of Willis: We devised a custom in house workflow to create a 3D printed phantom of the arterial network at the level of the CoW, as illustrated in Figure 1. Specifically, we segment the arterial network upto the cerebral arteries in the CoW to generate a 3D model of the vascular network (SimVascular). Thereafter, we extract centerlines and obtain morphometric features of the CoW network (3DSlicer); which is used to generate a planar projected model of the CoW network (Solidworks). The network is then printed into a physical model using SLA 3D printing with a rigid clear resin.

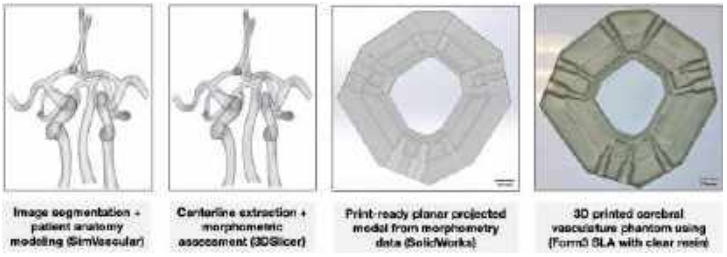

Figure 1: Illustration of the steps in the workflow for obtaining the 3D printed arterial network model for the Circle of Willis (CoW).

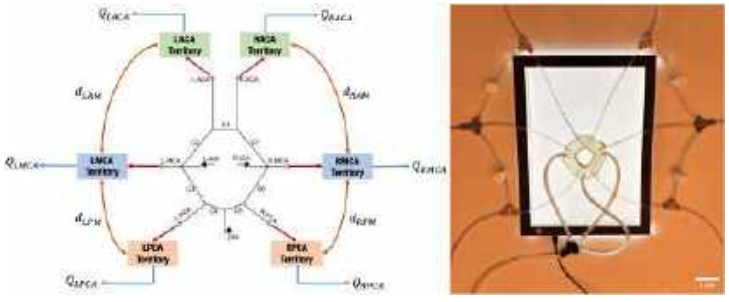

Figure 2: Network model demonstrating the flow pathways (left) and the benchtop implementation of the flow network connections (right).

Flow-loop design: The 3D printed CoW model was incorporated into an in vitro flow loop with distilled water as working fluid. A peristaltic pump was set to deliver total inflow of 650 ml/min, split into the 3 inlets into the model - L+R internal carotid (ICA) and basilar arteries (BA). A custom 3D printed trifurcating flow splitter was designed to map 230.57 ml/min to LICA; 277.95 ml/min to RICA; and 140.16 ml/min to BA. This mimics cervical vessel flow distributions reported in prior works [5]. Hydraulic pathways representing distal collateral circulation were incorpo-

rated via silicone tubing of 3/16 in. inner diameter connected to the outflows between the 6 cerebral arteries as shown in Figure 2, leading to 4 labelled distal collateral routes. Non-contact precision flow control valves were used to control patency/flow for each distal tubing. Finally, a stroke was simulated in the flow-loop by identifying the vessel to be occluded (right or left M1, A1, P1 segment), and 3D printing a solid cylindrical pellet fitted to the inner diameter of that vessel in the model.

Design of experiments: We conducted a set of experiments with a CoW model that had a complete ring anastomosis of the CoW connecting vessels. 6 stroke events were modeled at each of left and right M1, A1, and P1 vessels. Each of the four distal routes were either kept fully open or fully closed. This led to a sum-total of 96 different experiments, and one additional control case with no stroke. For all experiments, the peristaltic pump flow-rate was kept fixed; and volumetric outflow at each of the 6 CoW outlets were measured. Mass balance relation was used to identify measurement errors. Finally, a simplified hemodynamic descriptor was developed by quantifying the proportion of flow into the occluded vessel that was recovered by activating a collateral pathway combination. This is referred to as a collateral recovery ratio in this study.

RESULTS

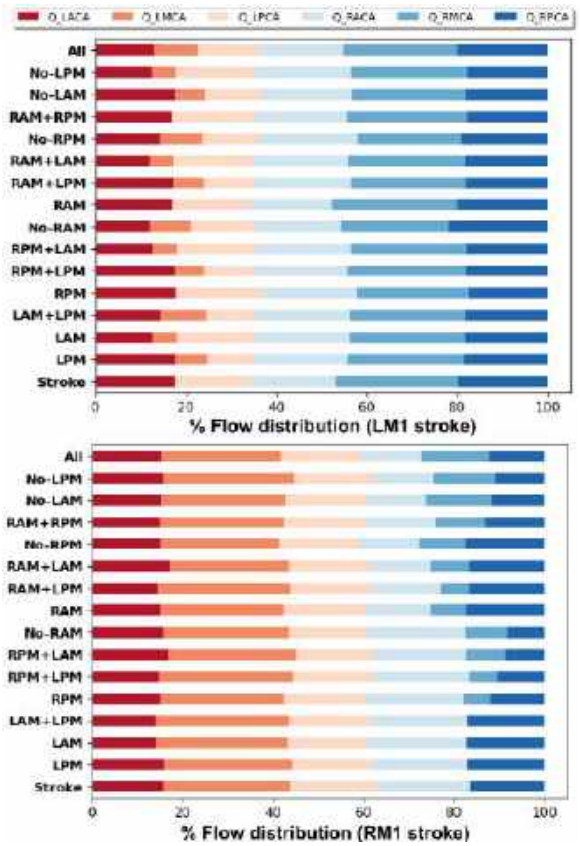

Figure 3: Flow distribution in terms of percentage of cerebral blood flow input for LM1 stroke (top) and RM1 stroke (bottom) as a function of varying distal pathways.

For each stroke location, we computed and compared the volumetric flow distribution across all 6 cerebral artery outlets as function of varying distal collateral pathways. For brevity, here we illustrate these results for the two MCA stroke scenarios (occluded left and right M1 respectively). The distribution patterns, represented in percentage of total cerebral blood flow input, across the 6 cerebral arteries for these two cases are presented in Figure 3. The cases labelled *Stroke* are the scenarios with no distal collateral - hence zero flow recovery onto the occluded vessel outlet. Likewise, cases labelled *All* denote the scenario where all 4 distal pathways were fully open. The measurement error for each of these experiments was less than 3%. The recovery ratio for these left and right M1 stroke scenarios are subsequently computed, and illustrated as a function of distal collateral pathways in Figure 4. The results clearly indicate a fractional or partial flow recovery distal to the occlusion site for both stroke scenarios. We also observe that, for the two MCA stroke scenarios shown here, if neither of the ipsilateral distal pathways are active, no recovery will occur - which is expected from vascular anatomy considerations. However, the findings indicate that the presence of collateral activity in the contralateral hemisphere may influence the amount of recovery; while maximum recovery for the RM1 stroke is noted when all distal routes are active, for the LM1 stroke it is instead observed when only ipsilateral distal routes are open. Additionally, we note that owing to inherent asymmetries in real vascular anastomoses, the flow distributions and recovery ratios are not symmetric between left and right.

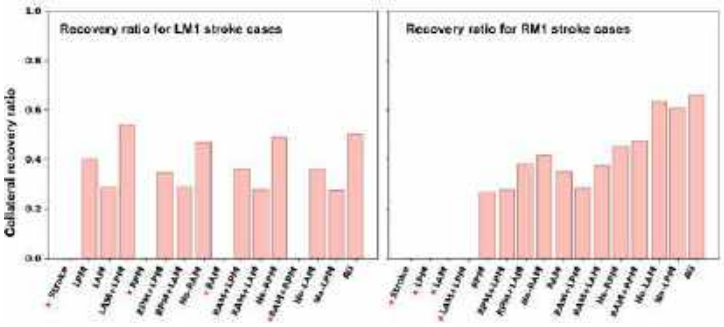

Figure 4: Illustration of computed collateral recovery ratio for LM1 (left) and RM1 (right) stroke cases as a function of distal collateral pathways. zero recovery cases are indicated with a red asterisk.

DISCUSSION

Here we have demonstrated a novel in vitro benchtop model for studying cerebral collateral circulation. To the best of our knowledge this is amongst the first attempts to create an in vitro model of cerebral collateral circulation. The model enables key insights into the collateral circulatory pathways, the hydraulic network type effects, and the extent of flow recovery in an occluded vessel region; as demonstrated in this contribution. The design is flexible to support further advancements. For instance, CoW anatomical variations, as studied extensively in our prior works, can be integrated to study how flow recovery patterns vary with CoW network topology. While the present study only considered distal vessels to be open or closed off, the use of flow control valves enables us to further regulate and vary the extent of distal flow route patency, allowing the recreation of several scenarios for collateral activity. These will inform continuing investigations using our proposed model. Additionally, this contribution presents a framework for quantifying collateral circulation using a fluid dynamics basis; indicating an extent of flow recovery in an occluded vessel as function of distal collateral routes. This has significant clinical implications in enabling better understanding of current metrics for collaterals that are based on imaging alone; and also complement existing image-based methodologies towards advancements in collateral flow characterization techniques in standard-of-care for stroke and ischemic disorders.

ACKNOWLEDGEMENTS

We acknowledge support from Oak Ridge Associated Universities for a Ralph Powe Junior Faculty Enhancement Award (DM), and the CU Undergraduate Research Opportunities Program (AC).

REFERENCES

[1] Bang OY et al. *Stroke* 46.11 (2015).

[2] Liebeskind DS. *Stroke* 34.9 (2003).

[3] Nambiar V et al. *American journal of neuroradiology* 35.5 (2014).

[4] Mokin M et al. *Stroke* 48.6 (2017).

[5] Mukherjee D et al. *Annals of biomedical engineering* 46 (2018).

TOWARD THE DETECTION OF CEREBRAL VESSEL SOFTENING USING MAGNETIC RESONANCE ELASTOGRAPHY

L. Bolster (1), H. Odeen (2), A. Payne (2), K. Monson (1, 3)

(1) Department of Mechanical Engineering, University of Utah, Salt Lake City, Utah
(2) Department of Radiology and Imaging Sciences, University of Utah, Salt Lake City, Utah
(3) Department of Biomedical Engineering, University of Utah, Salt Lake City, Utah

INTRODUCTION

Cerebral blood vessels have stiffness values orders of magnitude larger than brain tissue [1] yet when studying the dynamic response of the brain in traumatic brain injury (TBI), the cerebrovasculature is often not accounted for. Additionally, recent studies have suggested that even mild deformations can damage, and soften, cerebral arteries [2]. Significant in vitro testing has been done to characterize isolated vessel softening [2,3], but to meaningfully utilize this information in clinical and research settings, it is necessary to contextualize it and understand the interactions between the vascular structure and other brain tissue. Recent computational studies have found significant differences in brain mechanics with and without major cerebral vessels [4], so it is important to study these discrepancies to ensure dynamic models of the brain are accurate.

A promising method for this characterization is magnetic resonance elastography (MRE). Through the use of specialized phase-contrast MRI sequences and the propagation of mechanical shear waves through tissue, MRE generates stiffness maps based on measured displacements in a material. However, resolutions, which are dependent on the frequency of mechanical vibrations applied to a tissue, are only reliable down to approximately 2 mm^3, with some experimental techniques reaching accurate resolutions of approximately 1-mm^3 voxels in cortical brain tissue (although not vessel structures) with ultra-high field scanners [5]. To begin using MRE to characterize cerebral vessel softening, we aimed to investigate resolution thresholds as a function of the size and stiffness of inclusions, as well as the frequencies used in the imaging.

METHODS

Two MRE phantoms were fabricated to study MRE resolution thresholds: one gel-only phantom acted as a control for comparison to the second phantom. The second inclusion phantom contained three evenly spaced layers of silicone and plastic tubing, ranging from 4 to 10 mm in diameter, to gauge the resolution thresholds of MRE with high-stiffness elements and their effect on the surrounding tissue. Phantoms were made with 50% diluted 125-bloom gelatin, which is typical in brain MRE studies. Stiffness data was acquired using an MRE research pulse sequence on a 3T scanner (MAGNETOM PrismaFit, Siemens Healthineers, Erlangen, DE). Phantoms were strapped to a pneumatic drum actuator and placed in the head coil. MRE data were acquired at mechanical frequencies of 60, 80, 100, and 120 Hz. More precise geometry of the phantoms was obtained from a high-resolution T1-weighted MRI acquisition, for comparison with the MRE data. A tensile test to 1.2 times the original length of the tube was performed on the smallest (4 mm diameter) inclusion to determine its shear modulus for comparison to MRE elastogram data.

A finite element (FE) model corresponding to the gel-only phantom was constructed in FEBio, and MRE was simulated at the same scan frequencies used in the experimental MRE. The FE model used a 1-term Ogden model with a 2-term Prony series to model the gel, and model parameters were extracted from previously reported mechanical tests on minipig brain [6]. The model was constructed as a cylindrical mesh matching the phantom geometry, with rigid boundary conditions on the outer layer of the cylinder (Figure 1). Mesh convergence tests were run on phantom simulations to ensure accuracy. Typically, displacement and point stress values are used to test convergence, but the oscillating nature of the model prevented this. Instead, maximum stress values and distance between shear wave fronts were used as convergence criteria.

RESULTS

In the inclusion phantom, even the smallest inclusion (4 mm diameter) was visible in the elastograms of all four frequencies at an approximate resolution of 1.64x1.64x3 mm. This tubing had an experimentally determined elastic modulus of 3713.2 kPa, and Poisson's ratio of nearly 0.5, giving a shear modulus of 1237.7 kPa for

an isotropic material. While the elastograms provided drastically smaller values of shear modulus in the region of the smallest inclusion, the moduli were notably higher than those associated with the control phantom across all four frequencies (Figure 2). For example, in the 80-Hz scans a maximum stiffness of 4.04 kPa was observed around the 4-mm inclusion compared with the median gelatin stiffness of 3.08 kPa observed in the gelatin-only control phantom. This difference only increased around the regions of larger inclusions. Vessel detection was also observed to be frequency-dependent (Table 1).

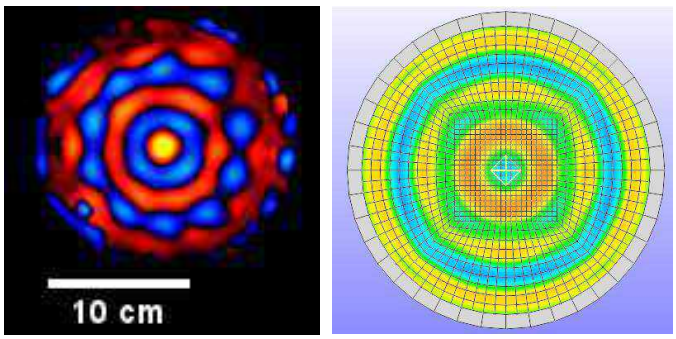

Figure 1: Example of wave similarities in control phantom MRE wave data (left) and FEBio simulation shear waves represented by stress magnitude (right).

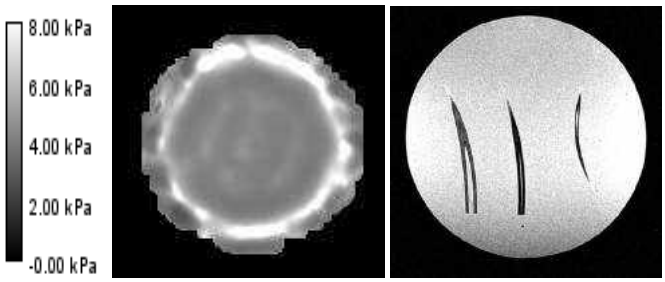

Figure 2: MRE elastogram at 80 Hz (left) and T1-weighted MRI (right) acquisitions of the inclusion phantom at approximately the same slice depth containing the smallest (4 mm) inclusion (rightmost of the three seen in both MRI image and areas of slightly elevated stiffness in elastogram). The color bar on the left corresponds only to the elastogram.

Scan frequency	4-mm Inclusion Stiffness % Difference
60 Hz	6.72%
80 Hz	26.97%
100 Hz	13.70%
120Hz	14.98%

Table 1: Percent difference between measured MRE stiffness values surrounding the 4 mm inclusion and control phantom median stiffness values at same frequencies.

DISCUSSION

The purpose of this study was to explore the use of MRE as a method to potentially measure cerebral vessel stiffness and softening given the affect TBI has been shown to have on the mechanics of the cerebral vasculature. Considering that the tubing used in the test phantoms does not give off any MR signal yet had an impact on the stiffness readings of the surrounding gelatin, the results demonstrate that MRE can detect stiffness inclusions near or below its intrinsic resolution. The notion that vessel stiffness can be detected from their influence on surrounding tissue, despite not generating any signal, is especially promising given that real vessels will contribute MR-detectable signal. Although the inclusions used in this study lack the viscoelasticity of cerebral vessels, the low strains produced in MRE would negate differences between real vessels and the materials used here. With the observed dependence of the surrounding tissue signal on frequency, further work should be done to correlate inclusion shear modulus readings to optimal scan frequency.

Additionally, the FE model predicted the same number of wavefronts and similar wave spacing once steady state had been reached for all four frequencies. Based on similarities between the control scan and FE model predictions, the accuracy of MRE for detecting below-resolution shear modulus changes could be further improved and applied to even smaller vessels. As a continuation of this investigation, an FE model is currently being created with a single tubing element for comparison with single-inclusion MRE phantoms. Ultimately, findings indicate that MRE is certainly a suitable candidate for detecting softening of larger vessels such as the middle cerebral artery, and possibly for smaller vessels as well. This information could be key to establishing more quantitative criteria of vessel softening for further study of TBI.

ACKNOWLEDGEMENTS

Financial support was provided by an award from the Department of Radiology and Imaging Sciences and by the Office of Undergraduate Research, both at the University of Utah. We would also like to acknowledge Brad Bolster, PhD, of Siemens Healthineers for access to the prototype MRE sequence and assistance acquiring data.

REFERENCES

[1] Monson KL *et al.*, Journal of Biomechanical Engineering 125(2):288-94 2014.
[2] Bell, E. D *et al.* Frontiers in Bioengineering and Biotechnology 3:2 2015.
[3] Anderl, W. *et al.* Acta Biomaterialia, 164:282-292. 2023
[4] Zhao, W. *et al.* Journal of Biomechanics, 104:109732. 2020
[5] Braun, J. *et al.* NeuroImage, 90:308-314. 2014
[6] Sundaramurthy, A. *et al.* Frontiers in Bioengineering and Biotechnology, 9:757755. 2021

TRACHEOSTOMY HUMIDIFICATION DEVICE

E. Enciso Pelayo (1), J. Balsano (1), M. Fong (1)

Faculty Advisor(s)

A. Vahabzadeh-Hagh (2), A. Taylor (1)

(1) Bioengineering, University of California – San Diego, United States
(2) UCSD Health, San Diego, California, United States

INTRODUCTION

Tracheostomy is a surgical procedure that involves the opening of the trachea from the outside of the neck of patients dealing with severe respiratory conditions to maintain a durable airway. [1] Tracheostomy tubes permit air to enter directly into the trachea. The entering air bypasses the upper respiratory airway, causing cold and dry air to enter the lungs, which causes irritation of the lining of the trachea. This leads to complications that can be life threatening.
Current humidification devices used in hospitals have tethering and wasteful setups, usually requiring the use of oxygen tanks.

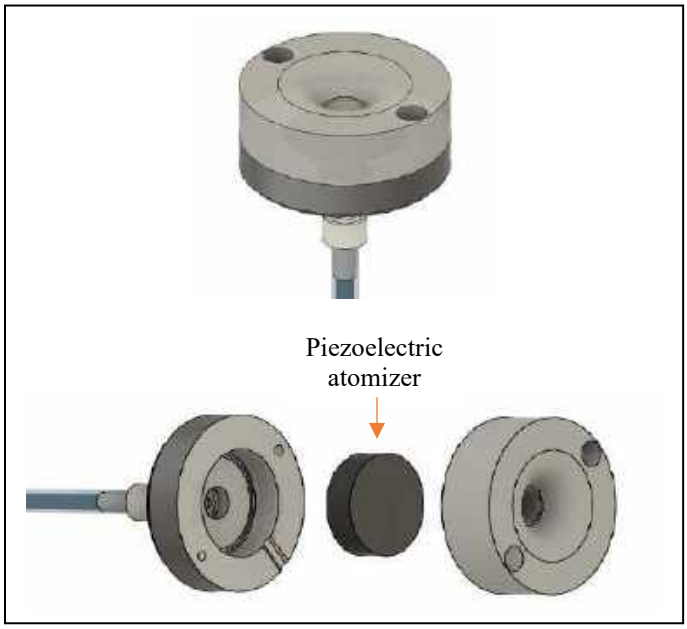

Figure 1: Piezoelectric atomizer holder with attached water tube with luer lock connector. Front view (top) and exploded view (bottom).

Our goal is to reduce the scale of the setup with a portable and efficient humidification device that will untether these patients as to increase their comfort levels and reduce energy and water consumption. Moreover, a device like this one is crucial during natural disasters when patients need to be transported out of the hospital and/or when there is a shortage of resources like oxygen tanks.

The market potential of this product is promising since more than 100,00 patients receive tracheostomies each year, which results in hospital costs of almost 11 billion dollars in the United States alone. [2]

PRODUCT DESIGN

Our proposed design solution is to place a piezoelectric atomizer in an encased holder (Figure 1) near the opening of the trachea. One side of the holder feeds water to the piezo through a tube. On the other side there is an opening through where the atomized water exits. The water tube is connected to a water reservoir encased in a fanny pack that the patient will be wearing (Figure 2). The water reservoir bag uses a step motor that compresses the bag as needed to maintain constant contact between the water in the tube and the piezoelectric atomizer.

BUDGET & MARKET ANALYSIS

The budget allotted for our project was 1000 dollars. We have spent a total of 156 dollars to build and test the prototype. The budget does not include the 3D printed resin components that our project mentor provided us with.

The potential market size of our tracheostomy humidification device is approximately 5,000 units if 3% of tracheostomy patients buy the device, and hospitals acquire 2,000 units every year.

The expected manufacturing cost per unit is approximately 45 dollars. The projected sales price is 120 dollars. The investment cost would be approximately 2500 dollars for a Formlabs 3D resin printer package. The return of investment for the first year could be up to 35,000 dollars if at least 500 units are sold.

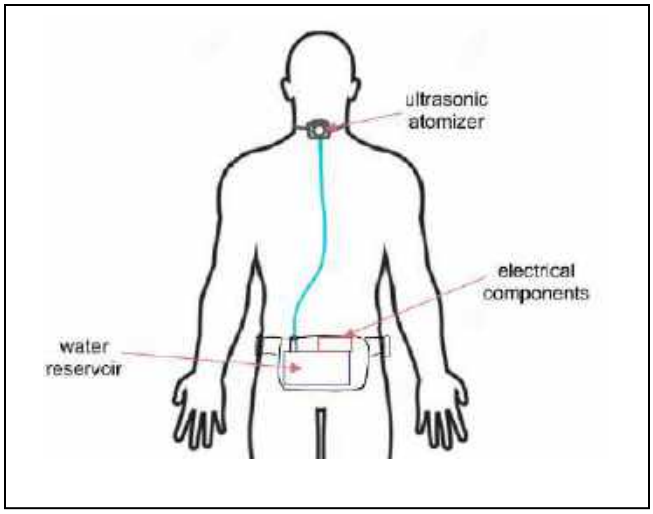

Figure 2: Diagram of the tracheostomy humidification device design solution.

ACKNOWLEDGEMENTS

We would like to thank the following people for their assistance with this project.

Course Instructor: Dr. Taylor
Course TA: Ananya Rajan
Project Mentor: Andrew Vahabzadeh-Hagh, MD

Jaycee Custodio
Lorenzo Balsano
UCSD Bioengineering Department

REFERENCES

[1] Raimonde AJ, Westhoven N, Winters R. Tracheostomy. [Updated 2023 Jul 24]. In: StatPearls [Internet]. Treasure Island (FL): StatPearls Publishing; 2024 Jan-. Available from: https://www.ncbi.nlm.nih.gov/books/NBK559124/

[2] Mehta AB, Walkey AJ, Curran-Everett D, Douglas IS. One-Year Outcomes Following Tracheostomy for Acute Respiratory Failure. Crit Care Med. 2019 Nov;47(11):1572-1581. doi: 10.1097/CCM.0000000000003959. PMID: 31397716; PMCID: PMC7262790.

[3] Transparency Market Research, 2023

FIREFIGHTER COOLING DEVICE

Emanuel Guzman (1), Wade T. Coons (1), Brady A. Killham (1)

Faculty Advisors

Dr. Oguz Yetkin (1), Dr. Cheng-Jen Chuong (1)

(1) Department of Bioengineering, University of Texas-Arlington, Arlington, Texas, USA

INTRODUCTION

When dealing with fires, firefighters put their bodies through extreme heat stress which can lead to serious issues that have an impact on their health and their ability to react efficiently. Our group is designing and developing a cooling system that can be worn with the current firefighter's gear without impacting the wearer's motion while maintaining a cooler environment inside the suit to tackle this issue. Wearable cooling systems already exist with many of them centered around helping first responders. These systems utilize cooling methods including fans, desiccants, and phase change materials. From reviewing the current market and the literature about these cooling systems our team decided to design a cooling system that utilizes drone motors and propellors to cool air across an array of ice packs that would potentially be cooled by dry ice. The device our group is designing is required to have a total weight below 10 pounds, operate up to 50°C for up to 4 hours, and maintain an internal temperature of 37°C inside the suit.

In today's market, common cooling methods for devices include phase change materials, liquid cooling, evaporation, and fan-based ventilation. Researching cooling vest designs revealed: **Compressed air cooling:** average power 41 W/m2, max power 44 W/m2, unlimited cooling time, capacity 331 W*hr/m2. **Liquid cooling vests:** average power 17 W/m2, max power 60 W/m2, cooling time 151 minutes, capacity 118 W*hr/m2. **Evaporative cooling vests**: average power 4-22 W/m2, max power 6-43 W/m2, cooling time 0-210 minutes, capacity 0-113 W*hr/m2. **PCM cooling vests:** average power 5-23 W/m2, max power 16-92 W/m2, cooling time 0-210 minutes, capacity 0-164 W*hr/m2**. Evaporative and PCM hybrid:** average power 20-22 W/m2, max power 57-88 W/m2, cooling time 194-224 minutes, capacity 127-146 W*hr/m2**. Dry ice at 45°C:** average power 36.6-168.4 W/m2. [1][2]. While dry ice was determined to be the best method in terms of cooling capacity, the difficulty in handling and the hazard from the CO_2 in a confined space make it problematic for the current application. A system based on commercial ice packs and a drone motor was chosen instead.

PRODUCT DESIGN

The inner housing for the cool gel packs, made of ABS filament, has slots that fit 2 to 3 cooling packs (each at 10.8 cm x 2 cm x 13.3 cm) as shown in Fig. 1b. The front of the housing unit has a nozzle-shaped outlet for the flow of air cooled by the cooling packs. Two Arduino Uno R3 boards control the drone motor operated (capable of 5,000 rpm) for a 3-blade 3-in diameter propeller. Two DHT11 temperature and humidity sensors monitor the changes in air temperature and humidity of the system from inlet to exit. A cage attached to the housing holds the drone motor, propeller that protects the firefighters when wearing it as shown in Fig. 1d.

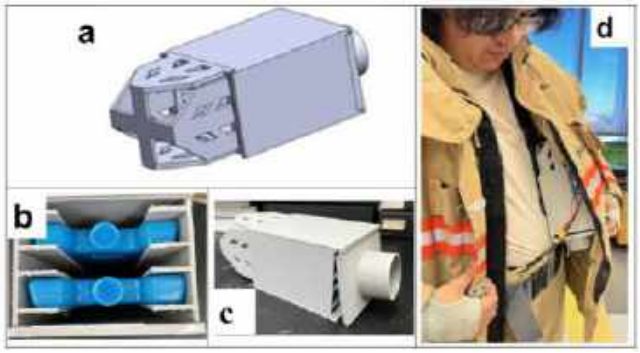

Figure 1: a). SolidWorks assembly of the cooling system, b). Bird's eye view of the inside of the cooling system with cool gel packs, c). Fully assembled model of the cooling system, & d). Cooling device inside of firefighter jacket.

The device is designed to help cool firefighters while wearing bunker suits executing firefighting missions. The device will be attached to the firefighter's overalls with the nozzle end pointing downward. The fan will blow the cool air from the cooled gel packs out through the nozzle end to inside the bunker suit. The attributes making this device unique include: 1) using a combination of ventilation and gel packs to cool the users, 2) as an independent lightweight, low-cost device (not a jacket), 3) providing the users with the option to cool the ice packs to dry ice or liquid nitrogen temperatures, increasing the cooling power, if these materials are accessible.

When planning on what type of pathways for our design, we looked at different variations of on-the-market products, which are shown below in Table 1.

Table 1: Possible Pathways for Project Design

	Design 1	Design 2	Design 3	**Design 4 (chosen)**

Description	Liquid Cooling + Ventilation	Evaporative cooling + Desiccant + Ventilation	Ventilation + Desiccant	Ventilation + Ice pack cooled with Dry ice
Pros	Remove moisture and heat simultaneously. Large coverage of body area.	Desiccant aids sweat evaporation. More effective cooling power.	Great for moisture absorption.	Easy to deploy. Uses readily available parts.
Cons	Bulkiness Low cooling time.	Higher cost Adds moisture into the system.	No direct cooling method. Less cooling power.	Requires freezer or cooler with dry ice.

The pathway that our team agreed on for our project design was ventilation with ice packs or dry ice, which was design pathway four.

When coming up with a design for our device the team bought two on-the-market cooling vests the "Venture Heat Wearable Cooling Fan Vest" and the "NJDGF Unisex-Adult Work Cooling Vest". Tests were run with the vests and how they functioned inside a firefighter bunker suit. The test was conducted by a member going up two floors in a building and testing what area of the body is affected by the cooled air. The team then decided to move away from vests and agreed to build a singular device that could be lightweight and easily removable. The team tested the device in an external and internal environment to assess its affect on the cooling rate of gel packs. The Elegoo Uno R3 boards were programmed using Arduino IDE.

RESULTS

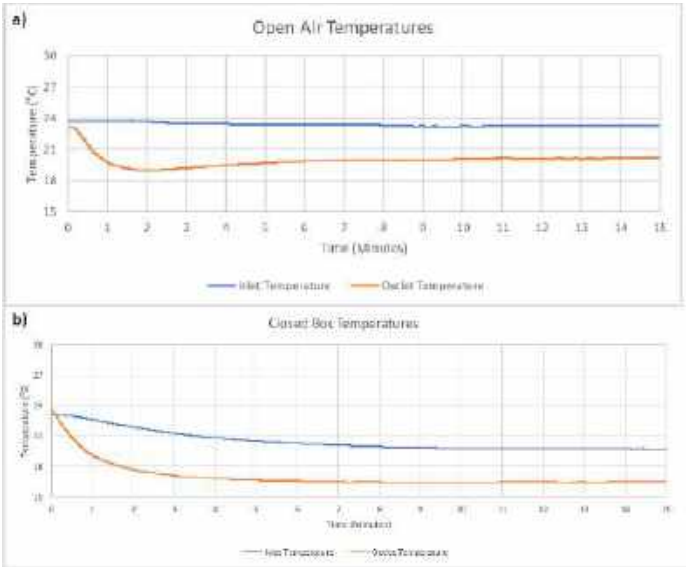

Figure 2: Recorded temperature data at inlet and outlet in an open-air environment (a) and a closed box environment (b).

For testing of our device we performed 2 tests: one with the device in an open-air environment and one with the device in a closed box environment. For each test, the temperature at the inlet and outlet of the device were monitored. The maximum temperature drop was calculated as the difference between the average inlet temperature and the minimum outlet temperature. The ice packs used in each test were frozen to a temperature of -18°C.

The first test (open air, Fig. 2a) resulted in a maximum temperature drop of 4.4°C and a final temperature difference of 3.1°C. The second test (closed air, Fig. 2b) resulted in a maximum temperature drop of 4.1°C and a final temperature difference of 3.2°C.

DISCUSSION & FUTURE WORK

The data from these tests show that our device does create a measurable drop in temperature as air is pushed across the ice packs. Even in a closed box, the device was able to provide a similar drop in temperature as compared to the open-air test and the temperature difference was sustained for the 15-minute duration of each test. In addition to this, the inlet temperature of the closed box test steadily decreased over the duration of the test showing that the device is capable of cooling the entire environment in which it is contained not just cooling intake air.

In the future we would like to implement data collection on humidity to assess its effect on the system as the ice packs melt inside the device. We would also like to test the effect of motor speed on the cooling rate of the device to understand the effect of heat coming off the motor into the system. We will also perform a longevity test to assess for what duration our device can sustain its temperature difference.

BUDGET & MARKET ANALYSIS

The budget for the cooling device was calculated to be $133.68. A breakdown of this budget was $44.60 for the two (2) Arduino boards, $2.62 for the two (2) DHT11 temperature and humidity sensors, $11 for a packet of drone propellors, $22 for the drone motor, $8.46 for eight (8) packs of cool gel packs, $36 for the 5200 mAh battery, and $9 for the ABS printed housing unit. The breakdown of the budget is shown below in Table 2.

Table 2: Breakdown of Budget & Weight of Components

Materials	Weight (g)	Price ($)
Arduino Uno R3 (2)	50	44.60
DHT11 Sensors (2)	44	2.62
Drone Fan (1)	2.56	11
Drone Motor (1)	198	22
Cool Gel Packs (2)	454	8.46
5200 mAh Batter (1)	380	36
Cooling Pack Housing	225.94	9
Total	1354.5 ≈ 3 lbs	133.68

When observing the cost of cooling devices that are on the market shows that the average for the least expensive cooling device was $53.40 and the average for the most expensive cooling device was $556.40. Our device costs $133.68 to manufacture and produce. The number of units that could be sold in a year would be approximately 50,000 to 75,000 units a year. The expected manufacturing cost would be approximately $135. The projected sales price of the device would be $235. The investment costs in engineering this device would be approximately $ 337,500 or a 2% annual fee. The return on the investment would be an annual rate of return of approximately 10 %.

ACKNOWLEDGEMENTS.

We would like to thank Dr. Oguz Yetkin for his guidance and for allowing our team to use some of his materials and Dr. Cheng-Jen Chuong for his guidance and for allowing the team to have access to his lab room.

REFERENCES

1) Ciuha U. Cooling Efficiency of Vests with Different Cooling Concepts Over 8 Hour Trials. 5. 625-629. 2021
2) Duncan, J. R. Design Of A Personal Dry-ice Cooling Garment: Its Physiological And Heat Transfer Aspects. 1975

GONIOTAPE: CREATING A WEARABLE ALERT SYSTEM FOR POST OPERATIVE PATIENTS AND COMMUNICATION TO HEALTHCARE PROFESSIONALS

V. Addanki, C. Shorr, M. Plone

Faculty Advisor(s)

E. Brewer

(1) Biomedical Engineering, Rowan University, Glassboro, NJ, USA

INTRODUCTION

In 2022, there were 2.8 million hip and knee arthroplasties in the United States alone[1]. It can also be noted that around 30% of knee and hip arthroplasty patients from ages 65-74 required total revision[2]. These numbers show that joint arthroplasties can affect much of the population. Not only this, but these procedures also require an extensive recovery, with some patients even requiring follow-up procedures.

Revision surgery involves correcting complications that arise after total joint arthroplasty, such as implant loosening, infection, or component failure. Lack of patient compliance with post-operative care, including activity restrictions and follow-up appointments, can exacerbate these issues and increase the likelihood of requiring revision surgery. Non-compliance may lead to delayed detection of complications and more severe problems necessitating surgical intervention. Studies show that up to 65% of patients can be non-compliant with post-surgical precautions[3]. Therefore, patient education and clear communication from healthcare providers are crucial to ensure adherence to post-operative care guidelines and minimize the risk of complications.

Occupational therapists will provide guidelines to their patients that pertain to range of motion. In a clinical setting, they will practice moving within these guidelines, or precautions, that are provided to them. However, there is no way for the patient or healthcare provider to monitor their compliance outside of this setting. Therefore, there is a need to improve patient compliance to post-operative precautions in order to improve patient outcomes.

Goniotape, a company started by occupational therapists, has teamed up with Rowan University engineering students to develop a solution to this problem. Our solution is a wearable device that aims to improve compliance by monitoring patient movement and providing alerts when a patient is non-compliant. By providing these alerts and allowing the patient to self-correct, we predict a lower rate of revision surgeries in those wearing the device compared to control patients.

In order to success, our device must be able to track the movement of the post-operative patient, including the angle at which the surgical joint is bent for several different planes of motion. Based on this data, the patient will be alerted if they are breaking their precautions. It must be able to detect any shoulder flexion beyond 90°, shoulder abduction beyond °90 hip flexion beyond 90°, hip extension beyond 0°, or hip adduction beyond 0°. These measurements must have an error of <5°, to maintain accurate patient feedback. The targeted prototype will have a localized, wireless communication ability, and in initial stages, intended for a clinical site for preliminary clinical trials that demonstrate the ability the correct failures to patient precaution compliance. Once initial efficacy is determined, the goal will be to develop at-home wearable sensors that communicate to the patients via a mobile phone app.

Creating a device that can closely monitor post-surgical precautions would be largely beneficial to help patients lower their risk of surgical revisions. This would allow patients to recover faster and with better peace of mind that they are not hurting themselves. Furthermore, we believe that there are multiple stakeholders in lower risk of re-surgery – such as benefits for healthcare providers and insurance providers.

PRODUCT DESIGN

In order to achieve this goal, we needed to create a system that could be worn by a patient, can calculate joint movements in real-time, and notify them of potential deviations for post-surgical precaution limitations. The prototype must be able to accurately measure the range of motion of a given joint, initially targeted to be within ±5° of the actual rotational movement. Furthermore, it must be designed in a way that it can be easily worn by a patient, meaning it must be somewhat compact. Our design uses Inertial Measurement Units (IMUs) to track and store patients' movements. The inertial measurement units used for this product are MPU6050s, as shown in Figure 1A, which can track a variety of movements and data using 6-axis degrees of freedoms. This module contains an accelerometer, gyroscope, and magnetometer. Using a microcontroller and the Arduino IDE (Figure 1D), our team has worked to develop a proof-of-concept interface that outputs the angle between the IMUs by monitoring the acceleration of the sensors in the X, Y, and Z axes. The sensors, labeled "A" are connected to printed control boards (C), which allow them to be connected to a multiplexer (Figure 1B), the Arduino board (Figure 1D), and to each other via the connective wires (Figure 1D). There are a total of four sensors, with two on each end of the system. Adjacent sensors will have their data averaged together to mitigate any error caused by sensor drift and ensure

that the data is as accurate as possible.

As the patient moves with the device, multiple accelerometers measure the level of acceleration relative to earth's gravimetric pull in multiple coordinates. By comparing the pull of gravity with respect to each sensor in different coordinate and finding the dot product between them, the relative angle between the sensors can be found. Based on the specific precautions for each individual, this angle output will be accompanied by an alert to the patient with their compliance status. This device will help the patient to adhere to their precautions without the presence of their occupational therapist.

We are currently working with a proof of concept on a printed control board to use in testing. This printed control board plugs into our microcontroller and sensors and is connected to additional modules which can be placed along a patients' body at key joints to better understand their movements. As shown in the figure below, this design will take the form of a medical tape that can be directly adhered to the patient in the future.

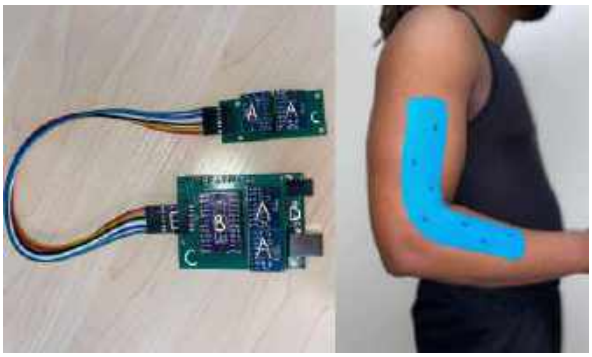

Figure 1: Left side shows current prototype design and right side shows final "tape" design to be implemented in the future. A: IMU Sensors, B: Multiplexer, C: Printed Control Board, D: Arduino Board, E: Connecting wires

BUDGET & MARKET ANALYSIS

There were 50,220 total hip arthroplasty revisions performed in 2014, and incidence rates are expected to increase between 78% and 182% through 2030[2]. The current US market for total hip revisions is $2.7B annually[4], and Medicare estimates that revisions account for 20% of direct costs associated with hip revisions[5]. Our device aims to reduce the incidence rates of revisions for wearers by at least 20%, reducing total health care costs by approximately $110M, which represents our potential market.

Our design budget includes hardware components to create our device. We need sensors, microcontrollers, and other materials (wires, headers, etc) to create more versions of our devices. Additionally, we are looking to upgrade our model to a fully wireless device using Bluetooth modules and a microcontroller with WiFi and Bluetooth capability. Our initial prototype built for clinical testing costs approximately $100. Scaled for manufacturing, and accommodating anticipated changes, we estimate that our final prototype will cost $70 per unit, with bulk ordering and production.

Studies have shown that over a third of users from sixteen different countries use wearables or health apps to record fitness and health, proving that this business model will not only work domestically, but also overseas[6]. Insurance companies are already taking note of tracking in wearable devices. For example, UnitedHealthcare will reimburse Fitbit users as much as $1,500 depending on how much they walk, and users can use this credit towards out-of-pocket medical expenses, such as copays and deductibles[7]. This creates mutual value for the insurance companies, and the patient. This market is relatively untapped, as only 1% of users have worn wearables sponsored by health insurance providers[8]. A key disadvantage of this market is the lack of understanding and cost of these devices. Our device uses inexpensive, very accessible, materials that can easily manufacture devices. With proper documentation, we believe that we can penetrate the market for wearables and create value for multiple parties.

ACKNOWLEDGEMENTS

We would like to thank Sarah Rothenberger, Antonia Trupio, and Cecilia Roling of Goniotape, LLC for assistance in providing market research, design input, information about surgical precautions, funding, and other feedback for the development of this product.

REFERENCES

[1] Hegde, V., Stambough, J. B., Levine, B. R., & Springer, B. D. (2023). Highlights of the 2022 American Joint Replacement Registry Annual Report. *Arthroplasty today*, *21*, 101137. https://doi.org/10.1016/j.artd.2023.101137

[2] Schwartz, A. M., Farley, K. X., Guild, G. N., & Bradbury, T. L., Jr (2020). Projections and Epidemiology of Revision Hip and Knee Arthroplasty in the United States to 2030. *The Journal of arthroplasty*, *35*(6S), S79–S85. https://doi.org/10.1016/j.arth.2020.02.030

[3] Badge, H. M., Churches, T., Naylor, J. M., Xuan, W., Armstrong, E., Gray, L., Fletcher, J., Gosbell, I., Lin, C., & Harris, I. A. (2021). Non-compliance with clinical guidelines increases the risk of complications after primary total hip and knee joint replacement surgery. *PloS one*, *16*(11), e0260146. https://doi.org/10.1371/journal.pone.0260146

[4] Bhandari M, Smith J, Miller LE, Block JE. Clinical and Economic Burden of Revision Knee Arthroplasty. *Clinical Medicine Insights: Arthritisand Musculoskeletal Disorders*. 2012;5. doi:10.4137/CMAMD.S10859

[5] Ong, K L; Mowat, F S; Chan, N; Lau, E; Halpern, M T; Kurtz, S M. Economic Burden of Revision Hip and Knee Arthroplasty in Medicare Enrollees. Clinical Orthopaedics and Related Research 446():p 22-28, May 2006. | DOI: 10.1097/01.blo.0000214439.95268.59

[6] Neumann, D., Tiberius, V., & Biendarra, F. (2022, April 27). Adopting wearables to customize health insurance contributions: A ranking-type Delphi - BMC Medical Informatics and Decision making. BioMed Central. https://bmcmedinformdecismak.biomedcentral.com/articles/10.1186/s12911-022-01851-4

[7] Vincent, Ryan (2022, March 15). *Wearable tech: The future of your health (and health insurance)*. Insurance Quotes - Get Multiple Auto Rates - Insurance Quotes. https://www.insurancequotes.com/health/health-insurance-and-wearable-tech

[8] Caplan, Z. (2023, May 25). U.S. older population grew from 2010 to 2020 at fastest rate since 1880 to 1890. Census.gov. https://www.census.gov/library/stories/2023/05/2020-census-united-states-older-population-grew.html#:~:text=The%20older%20population%20reached%2055.8,were%20age%2065%20and%20over

IN VITRO STRETCH INJURY AFFECTS MITOCHONDRIAL MEMBRANE POTENTIAL, CALCIUM CONCENTRATION, AND NUCLEAR MORPHOLOGY IN RAT ASTROCYTES

C. Santacruz (1), A. Yufa (2), S. Shiravi (1), J. Finan (1)

(1) Department of Mechanical and Industrial Engineering, University of Illinois Chicago, Chicago, IL, USA
(2) Department of Biomedical Engineering, University of Illinois Chicago, Chicago, IL, USA

INTRODUCTION

Traumatic brain injury (TBI) arises from external forces acting on the head in a range of scenarios, including falls, assault, sports-related accidents, and high-risk occupations. Globally, an estimated 69 million individuals suffer from TBI annually [1]. TBI is not a static condition but rather a progressive process. TBI increases the risk of neurodegenerative disorders such as Alzheimer's disease [2]. However, the pathological processes influencing TBI outcomes are still not fully understood and there are no proven treatments for TBI patients. *In vitro* modeling of neurotrauma provides a valuable opportunity to investigate cellular responses, offering insights into pathophysiological mechanisms and possible therapeutic targets. *In vitro* stretch injury reproduces important pathologies of clinical neurotrauma. Ellis et al. developed a stretched-induced injury model using air pressure to deform flexible substrates with rat cortical astrocytes cultured on them [3]. Our objective is to establish an *in vitro* model of stretch-injury in astrocytes by deforming flexible cell culture substrates using rigid, indenting posts. This approach stretches the cell culture substrate more rapidly and with a more uniform spatial distribution than air pressure. We have already demonstrated this approach in a 96 well format. The goal of this work was to implement it in a 6 well format that would provide more cells per well for assays that require large cell numbers and more readily accommodate indentation experiments to measure cell stiffness.

METHODS

We adapted our custom-built device previously used for a 96-well stretch-injury model [4] to create this 6-well stretch injury model. We designed and built a new 6-well array of indenting posts to stretch flexible bottom 6-well plates. Briefly, we laser cut and stacked layers of acrylic to create a block with an array of holes on the top surface, aligning with the hole positions of the 6-well plate. We turned 1.2" diameter indenting posts from Delrin on a lathe and attached them to the block using screws. We fitted food-safe, dry-running thrust bearings around a boss at the top of the Delrin posts to minimize friction and eliminate the need for lubrication. To quantify the membrane stretch caused by a 4 mm deep indentation, we spray painted cell-free dry plates and indented them while imaging the well bottoms with a high-speed camera. We quantified the resulting strains using the digital image correlation software GOM.

We used an E18 Rat Astrocyte Cortex Culturing kit (BrainBits) to isolate astrocytes according to manufacturer's instructions. We attached sheets of polydimethylsiloxane (PDMS) to 6 well plate bodies using biocompatible double-sided tape and sterilized the resulting plates by immersing them in ethanol for 15 minutes. Then, we coated the cell culture surfaces with poly-D-lysine. We plated the astrocytes onto the PDMS 6-well plates and maintained them for 17 days. On day 17, we traumatized only 2 wells with a 4 mm deep indentation with a duration of 60 ms, leaving 2 wells untraumatized on the same plate. We incubated the astrocytes for 24 hours post-injury at 37°C. We stained our cell cultures with TMRM, Calbryte 520 AM, and Hoechst to assess mitochondrial membrane potential, intracellular calcium concentration, and nuclear morphology respectively. We imaged the cultures with a FV3000 Olympus confocal microscope. We quantified nuclear morphology using area, form factor ($4*\pi*Area/Perimeter^2$) and eccentricity (the ratio of the distance between foci and the major axis

length for an ellipse with the same second moments of area as the region).

RESULTS

The strain was uniformly distributed across most of the well bottom (see Fig. 1A). The average strain trace in a single well during an indentation event peaked near 7% and returned to 0% with a duration of approximately 55 ms, indicating a transient mechanical deformation (see Fig. 1B).

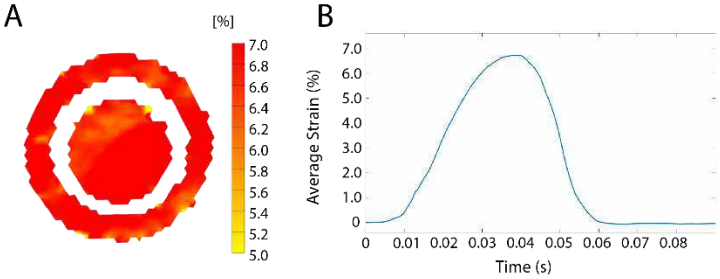

Figure 1: A) Spatial distribution of strain across cell culture membrane at peak indentation depth. The white ring in the distribution occurs because the edge of the washer disrupts the background during digital image correlation. B) Average strain over time during an indentation in a single well.

Injury reduced the intensity of TMRM and Calbryte fluorescence. Additionally, injury reduced the number of visible nuclei, suggesting that some cells detached (see Fig. 2).

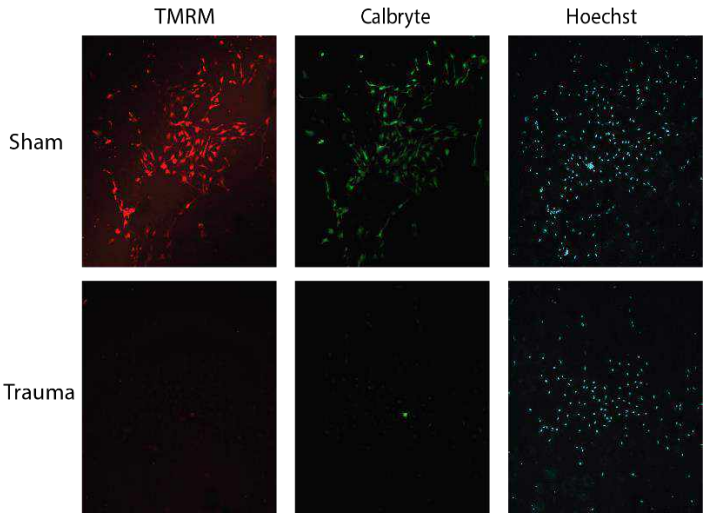

Figure 2: Fluorescent images of sham-treated and trauma cultures.

Trauma created a downward trend in nuclear area (see Fig. 3A). It also created trends in form factor and eccentricity, suggesting that it changed nuclear shape as well as nuclear size. However, the trend in form factor suggests nuclei became less round while the trend in eccentricity suggests nuclei became more round.

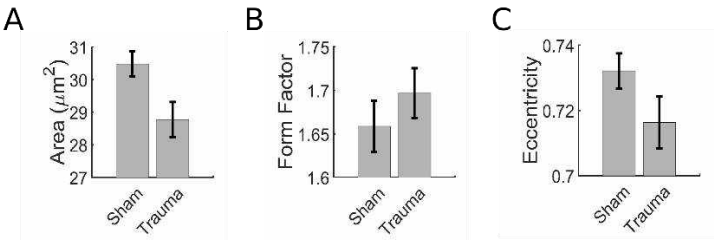

Figure 3: Quantification of nuclear morphology with and with out trauma (error bars = 1 standard error, n=1428 for sham, n = 689 trauma).

DISCUSSION

Our 6-well plate adaptation of our 96 well model achieved a uniform strain distribution with 60 ms pulse duration that is on the same time scale as brain deformations during clinical head impact events [5]. Trauma impairs mitochondrial membrane potential, crucial for cellular energetics, indicating mitochondrial dysfunction (see Fig. 2). These changes are consistent with previously published results from *in vitro* stretch injury models [6]. Reduced Calbryte 520 AM intensity post-trauma indicates a decline in intracellular calcium concentration. Current literature implicates dysregulated calcium signaling in TBI-induced neuronal damage, with excessive calcium influx intensifying cellular injury [7]. Surprisingly, our results point to a post-trauma calcium efflux. Further investigations are necessary to understand the precise mechanisms underlying calcium homeostasis disruption following TBI. Nuclear area trended downwards and nuclear shape parameters changed after trauma. These findings are consistent with a model in which actin stress fibers pull the nucleus into a flattened shape under normal conditions and trauma disrupts these fibers, allowing the nucleus to rebound into a taller shape with a smaller horizontal cross-sectional area. However, the nuclear shape results are contradictory, possibly because our pixel size was too large to allow precise shape quantification. Our *in vitro* model of stretch injury provides valuable information about the cellular responses to traumatic brain injury. In particular, it creates an opportunity to investigate the biomechanical origins of changes in nuclear morphology after trauma.

ACKNOWLEDGEMENTS

This work was supported by the NIH R01NS113935.

REFERENCES

[1] Dewan, M.C. et al., J Neurosurg, 130(4), 1080-1097, 2018.

[2] Barnes, D.E. et al., JAMA Neurol, 75(9), 1055-1061, 2018.

[3] Ellis, E.F. et al., J Neurotrauma, 12(3), 325-339, 1995.

[4] Phillips, J.K. et al., JoVE (Journal of Visualized Experiments), (134), e57305, 2018.

[5] Hardy, W.N. et al, Stapp Car Crash Journal, 51, 17–80, 2007.

[6] Ahmed, S.M. et al., Neurochem, 74(5), 1951-1960, 2000.

[7] Rzigalinski, B.A. et al., J Neurochem, 68(1), 289-296, 1997.

EXOFLEX: AN ACCESSIBLE EXOSKELETON GLOVE FOR GROSS HAND FUNCTION REHABILITATION

N. Meng (1), H. Morgenstern (1), A. Saldutti (1), S. Zheng (1)

Faculty Advisors

D. Meaney (1), E. Berlew (2), L. Levin (3)

(1,2) Bioengineering Department, University of Pennsylvania, Philadelphia, PA, USA
(3) Department of Orthopedic Surgery, University of Pennsylvania, Philadelphia, PA, USA

INTRODUCTION

Every year, there are over 10 million new stroke survivors around the world. Over 7 million will experience upper limb dysfunction while 5 million will go on to develop a permanent disability. One of the main upper limb functions lost is the ability to contract and extend the fingers in a grasping motion. Stroke survivors often experience spasticity of the hand muscles that develop into contractures - a permanent shortening and hardening of the muscle fibers (1). The loss of the gross hand function prevents the patient from performing everyday tasks and living independently which leads to high rates of job loss and depression (2). An effective post stroke rehabilitation plan - characterized by controlled repetitive movements and a personalized, accessible routine - is crucial in regaining as much function as possible and preventing permanent muscle damage (3). Exoskeletons are proven to be significantly beneficial in improving limb function post stroke since they allow for both mechanical support and high control over functionality (4). However, current exoskeleton gloves for gross hand function rehabilitation such as SaeboGlove, Emovo Grasp, IpsiHand, and SYREBO do not meet patient needs in affordability, usability, or functional integration. Our team has therefore developed ExoFlex, an effective and accessible exoskeleton glove for gross hand function rehabilitation.

PRODUCT DESIGN

ExoFlex is an adjustable exoskeleton glove that assists in gross hand function recovery. ExoFlex has a passive extension and active contraction mechanisms to assist with different levels of hand spasticity as well as open fingertips and a portable design to ensure usability. An adjustable 3D printed wrist guard functions to support the wrist to prevent its over-contraction (Figure 1). Additionally, the grasping motion is actuated by EMG signals taken from the flexor digitorum profundus muscle in the forearm which allows for direct motor cognitive control over the glove's functionality (Figure 2).

The passive extension mechanism consists of rubber bands on the dorsal side of the hand (Figure 1D) that extend the fingers away from the palm. The contraction mechanism is actuated by a series of fishing wires anchored by rings around each phalange. When the muscle of the forearm is contracted, the EMG signal triggers the motor to reel in the fishing wires which mimic the function of finger tendons by pulling the fingers into a grasping motion (Figure 1C). When the muscle is not activated, the motor unwinds the fishing wires, allowing for the passive extension mechanism to pull the fingers into a relaxed position. The EMG signal analysis is completed through hardware and software processing. The hardware processing amplifies, rectifies, and filters the EMG signal between 50 Hz and 160 Hz and sends the signal to an Arduino Uno that calibrates, thresholds, and processes the signal. Five seconds of calibration data is taken on startup to adjust to the specific signal strength of the user and encoders are implemented to track and limit the number of motor rotations to prevent over contraction of the fingers.

ExoFlex was evaluated on four fronts: motor response accuracy, contraction aid, and extension aid. The motor response was characterized by the response accuracy to the flexing of the muscles at the EMG placement where 100% accuracy would be the correct motor response in the clockwise or counterclockwise direction in response to each contraction and relaxation respectively 100% of the time. Over 100 trials, final accuracy was determined to be 95%. Another testing factor was the delay time between the muscle contraction to the motor response where the average response time was 1.3 seconds with a range of .4 - 3.5 seconds. The longer delay times were due to the subject flexing the forearm by mistake while the hand had been relaxed.

The contraction aid was analyzed by measuring the phalange angles of the fingers during full motor contraction (Figure 3). This was compared to the angles of the phalanges in fist formation. Overall, ExoFlex was able to perform a rounded grasping motion sufficient in retraining the contraction of the hand. It was found that the contraction of the hand was partially limited by the overall design including the thickness of the rings and the shape of the wrist guard, causing the phalange angles to be smaller than the unhindered hand (Figure 3).

To assess the efficacy of the extension aid, a spring scale was used to quantify the force exerted by the elastic bands on each phalange of the hand. The measurements were conducted under different levels of tightness, achieved by wrapping the bands multiple times around each anchoring peg ranging from 0 loops to 6 loops around each peg. The force exerted by the rubber bands was measured to be 1.5N-6N from the lowest to highest tightness levels.

ExoFlex was designed with the patient's needs at the forefront. Our team spoke to occupational therapists, patients, and doctors in the rehabilitation field to receive insight on design and usability. ExoFlex is therefore more effective and accessible to those who would benefit from the product compared to other exoskeleton gloves (Table 1). First, ExoFlex has significantly cheaper price point, making it more accessible to lower income patients. Additionally, ExoFlex aids in both contraction and extension to account for patients that are hindered in both motions vs. devices that only provide a passive extension mechanism. ExoFlex integrates an EMG control system that allows the user to cognitively activate the grasping function which is crucial in rebuilding the motor cognitive link. The integration of EMG develops the neuroplasticity crucial to successful rehabilitation compared to other gloves on the market that often use a push button to trigger a contraction. ExoFlex is also designed for long-term use with open fingertips that also allow for stroke patients to recover their sense of touch. ExoFlex is lightweight, washable, and portable with a rechargeable battery pack and minimal wires for increased comfort. The overall accessibility and the unique inclusion of both rehabilitation and functionality design features make ExoFlex the preferred choice for stroke survivors going through gross hand function rehabilitation.

Table 1: Product Comparison: *N/A is not available for sale.

	SYREBO	Saebo Glove	Emovo Grasp	Ipsi-Hand	ExoFlex
Cost	$550	$399	N/A*	N/A*	< $150
Open Fingertips	No	No	Yes	Yes	Yes
Integrative Control	No	N/A	No	Yes (EEG)	Yes (EMG)
Portable	No	Yes	No	Yes	Yes

Figure 1: Images of ExoFlex Prototype. Palmar View (A), Dorsal View (B), Grasping Proximal View (C), Grasping Dorsal View (D)

Figure 2: Summary Diagram. The EMG signal is taken from the forearm, processed by an Arduino Uno and sent to the motor which then activates a contraction or releases to allow extension.

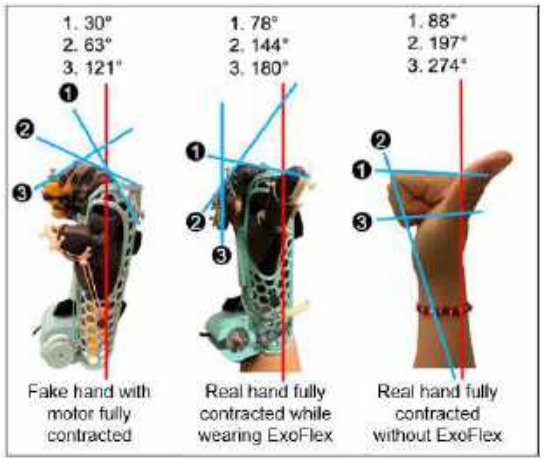

Figure 3: Contraction Analysis. Contraction angle is compared between motor contracted fake hand in ExoFlex, fully contracted real hand in ExoFlex, and the standard - fully contracted hand.

BUDGET & MARKET ANALYSIS

Every year, there are around 600,000 new stroke survivors in the US. With one out of three stroke survivors losing gross hand functionality, there would be a market of around 200,000 new users annually [5]. Additionally, many rehabilitation centers look to purchase assistive devices for both inpatient and outpatient purposes. There are around 2400 stroke rehabilitation centers across the US, further expanding the market for ExoFlex [6]. Current clinically approved exoskeleton gloves on the market such as the Saebo Glove cost $399 with other brands ranging over $500. The cost of ExoFlex at $250 is therefore well below the standard price of similar products on the market. ExoFlex is predicted to have an ROI of approximately 16.7% at the predicted sales price and manufacturing costs. With a net return of $100 per unit and a total available market of 200,000 annually, it is estimated to have a net annual return of $20,000,000 (Table 2).

Table 2: Market Analysis

	Cost per unit ($)	Cost per year ($)
Manufacturing Cost	$150	30,000,000
Projected Sales Price	$250	50,000,000
Value of Investment	$60	20,000,000

ACKNOWLEDGEMENTS

Materials, engineering equipment, and 3D printing services provided by George H. Stephenson Foundation Educational Laboratory & Bio-MakerSpace. A $600 fund was provided by the Department of Bioengineering at Penn Engineering.

REFERENCES

[1] Harrison, R. et al.,Cerebrovascular Diseases, 39:190-201, 2015
[2[Robinson, R. , American Journal of Psychiatry, 173:221-231, 2016
[3] Wade, D. et al., Sage Journals, 34:571–583, 2020
[4] Singh, N., Journal of NeuroEngineering and Rehab, 18:37, 2021
[5] Dobkin, B., Current Atherosclerosis Reports, 15:33, 2014
[6] Boggs, K. et al. JACEP OPEN, 3: 22, 2013

A BENCHTOP STUDY OF PHYSIOLOGICAL RESPONSE FOR THE NOVEL SELF-POWERED FONTAN CIRCULATION

Purdy Clayton[1*], Anthony Damon[2], Levi Blumer[1], Keyu Vadaliya[2], Martin Cinelli[2], Megan Parker[1], Ray Prather[1,3], Arka Das[1], Eduardo Divo[1], Alain Kassab[3], and William DeCampli[4]

(1) Department of Mechanical Engineering, Embry-Riddle Aeronautical University, Daytona Beach, FL, USA
(2) Department of Aerospace Engineering, Embry-Riddle Aeronautical University, Daytona Beach, FL, USA
(3) Department of Mechanical and Aerospace Engineering, University of Central Florida, Orlando, FL, USA
(4) The Heart Center, Orlando Health Arnold Palmer Hospital for Children, Orlando, FL, USA

ABSTRACT

Around 8% of all newborns with a congenital heart defect have only a single functioning ventricle (SV). The Fontan circulation is a result of the third stage surgical procedure to correct the SV anatomy in these patients. Despite successful implementation over the years, this altered circulation is prone to failure, with survival rates of only 50-80% to adulthood. Increased inferior vena caval (IVC) pressure plays a significant role in "Fontan failure." We propose to augment energy in the Fontan circulation with an injection jet shunt (IJS) drawing flow directly from the aortic arch, balanced by a conduit-to-atrial fenestration to approximately preserve the ratio of pulmonary flow (Qp) to systemic flow (Qs). The basic concept involves the injection of a high-velocity jet in the direction of flow, causing flow entrainment, leading to a significant reduction of upstream (i.e., IVC) pressure and enhancement of downstream flow. The "Hardware-in-the-Loop" (HIL) technique has been utilized to embed the supervisory controller into the mock flow loop (MFL) setup on a real-time basis. This automated controller has been developed to maintain the Qs constant by modulating the ventricular preload and the systemic vascular resistance to mimic circulatory response in the presence of shunting IJS flow.

A supervisory control algorithm (SCA) is developed based on the results of system identification and the "Software-in-the-Loop" (SIL) approach, in which the behavior of the Harvard Apparatus Pulsatile pump was characterized. Dynamic real-time adjustments are calculated based on error calculation methods derived from the SIL technique. An error is calculated by comparing the 0D Lump Parameter Model (LPM) of the Fontan circulation in which the ideal biological conditions were generated and measured against experimental output. Error estimations are converted into input signals and sent to a central control module utilizing conversions found during system identification. HIL techniques incorporate the SCA and SIL findings to interface directly with hardware components to manipulate systemic flow in real time. The SCA received corrections to controller input parameters through the usage of the SCA to determine precise corrections to both the Harvard Apparatus and resistance valves located within the testing loop, providing appropriate correction to variations in systemic flow caused by the introduction of the IJS. Supervisory control within the HIL receives input from computational fluid dynamics (CFD) calculations compared with measured Qs output from the Harvard Apparatus to determine correction amounts corresponding to biological conditions.

The MFL replicates a reduced four-compartmental LPM of the Fontan circulation, and it is integrated with a patient generic 3D phantom of the IJS-assisted Fontan with average dimensions matching those of a 2–4-year-old patient. Experimental results are presented and compared to the computational findings on the hemodynamic results and oxygen saturations for various total cavopulmonary configurations.

TITLE – FUNCTIONAL CHANGES IN HYPOXIC NEONATAL BRACHIAL PLEXUS AFTER STRETCH

Dario Duran (1), Meredith Dunbar (1), Anita Singh (1)

(1) Bioengineering Department, Temple University, Philadelphia, PA, USA

INTRODUCTION

Neonatal Brachial Plexus Palsy (NBPP) is a serious condition affecting infants during their delivery and often accompanied by hypoxia. It is characterized by either a stretch or rupture of the brachial plexus [1-7]. Brachial Plexus comprises of C5-T1 spinal roots and depending on the root injured is classified into different types of palsy; Erb's Palsy being the most common one affecting C5 and C6 roots. *In vivo* electrophysiology data of hypoxic neonatal brachial plexus and its association to the stretch response does not exist. This study focuses on reporting the normal, post-stretch and one-hour post stretch latency in the compound action potentials of hypoxic brachial plexus nerves (ulnar and median) in a neonatal piglet.

METHODS

Four neonatal brachial plexus nerves were put through mechanical stretching by clamping the nerve and pulling it to a fixed strain as shown in Fig.1. All procedures were according to the approved IACUC protocol, Drexel University.

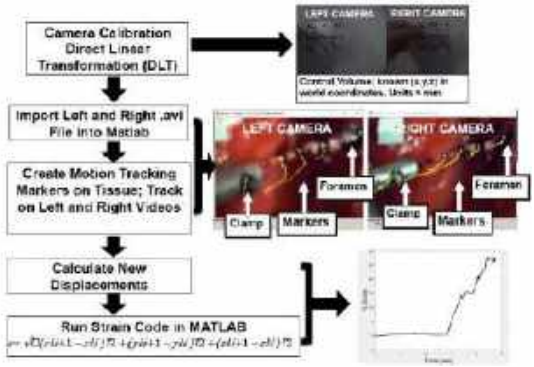

Figure 1: Biomechanical Data Analysis

The electrophysiology and data acquisition set up consisted of an amplifier, stimulator, DAQ system, bipolar stimulating and recording cuff electrodes, ground electrode and a laptop with LabView software as shown in Fig.2.

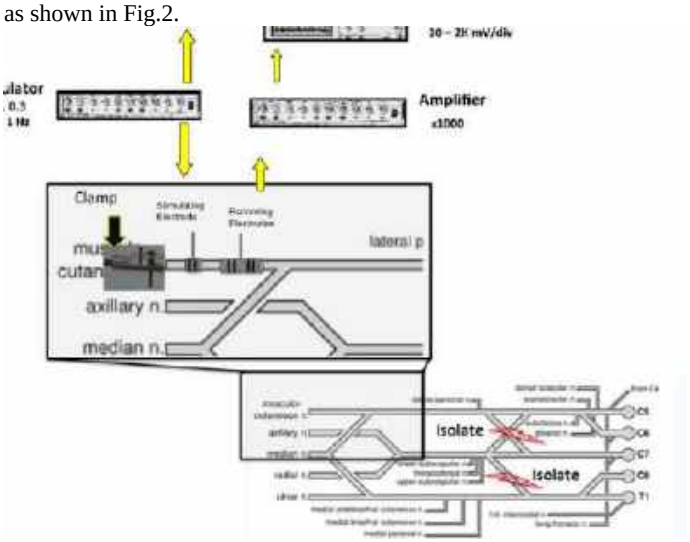

Figure 2: Details of Electrophysiology Recordings

The brachial plexus segment was stretched at known strains and compound action potential was acquired at sampling rate of 20,000 Hz, acquisition time of 1 sec, gain of 10K and duration of 0.1 msec before, after and one-hour post stretch. The stimulus applied was 0-2V with increments of 0.5V. A ZED camera was placed over the nerve being tested to capture the distance between the stimulating and recording electrodes to determine the conduction velocity (CV) and amplitude of

the compound action potentials. Eq. 1 show how to calculate percentage change in latency post-stretch.

% change in latency post-stretch = [latency before stretch – latency after stretch] / [latency before stretch] Eq(1)

A customized MATLAB code was used to determine the latency of compound action potentials recorded for before stretch, post-stretch and one-hour post stretch conditions to check for recovery or conduction block.

RESULTS

Electrophysiological recordings reported immediate conduction block when subjected to a 20% strain (Fig.3). No spontaneous recovery was observed at 1 Hr or 3 Hr. At a 15% strain, the nerve continued to conduct however, a 100% increase in latency immediately post stretch, which did not recover.

Nerves	Before	After	1-hr	3-hr
Median (Strain: 20±10% Load:14.7N)				
Ulnar Secondary Nerve		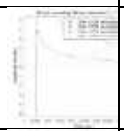		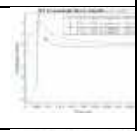
Median (Strain: 15±8% Load:11.0N)				

Figure 3: Nerve Conduction Data obtained from Stretched Nerve

DISCUSSION

No data is available on the mechanical, and related functional changes in the hypoxic neonatal BP subjected to stretch. This study is the first to a direct correlation between subjected strain and observed functional changes. Data from the study confirms that the extent of stretch directly affects the injury outcomes and spontaneous recovery responses. Strains of 20% or more leads to significant conduction block in hypoxic tissues. Obtained data helps better understand the mechanism of NBPP and can help with prognosis and identification of optimal treatment options., especially in complicated cases including hypoxia.

ACKNOWLEDGEMENTS

This research was supported by funding from the Eunice Kennedy Shriver National Institute of Child Health and Human Development of the National Institutes of Health under Award Number R15HD093024 and R01HD104910A and NSF CAREER Award Number 1752513.

References:

1. CR D'Andrea et al., 2021, Journal of Orthopaedic Research 39 (5), 907-918
2. Singh et al., A Singh, R Magee, S Balasubramanian
3. JoVE (Journal of Visualized Experiments), e59860
4. CR D'Andrea et al., 2021, Journal of Orthopaedic Research® 39 (5), 919-928
5. Singh et al., 2019, Journal of biomechanical engineering 141 (12), 121011
6. Singh et al., 2018, Journal of brachial plexus and peripheral nerve injury 13 (1), e8
7. Tom et al., 2018, Experimental brain research 236, 3077-3084

IMPACT OF A COGNITIVE DUAL TASK ON OLDER ADULT MOTOR PERFORMANCE AND STRATEGIES

Erin C. Kreis (1), Mitchell Tillman (2), Jun Liu (2), Zahava Hirsch (2), Antonia Zaferiou (2)

(1) Mechanical Engineering, Stevens Institute of Technology, Hoboken, NJ, United States
(2) Biomedical Engineering, Stevens Institute of Technology, Hoboken, NJ, United States

INTRODUCTION

Falls are the leading cause of fatalities and nonfatal injuries among older adults, impacting over fourteen million older adults annually [1]. The impact of falls can extend beyond physical harm, threatening a person's independence and overall quality of life. Situations involving the simultaneous execution of a motor and cognitive task may lead to falls. These dual task scenarios arise in everyday life (e.g., walking while talking) and pose a significant threat to older adults due to aging-related physical and cognitive changes. Studies have shown that dual task gait is a valuable marker of cognitive impairment and fall risk [2] that replicates the daily-living gait of older adults more closely than single task gait in a lab setting [3].

The current body of literature regarding dual tasks primarily focuses on straight-line gait [2]; however, motor tasks involving postural control and transfers, such as turns, are also common movements. The Timed Up and Go (TUG) test is a validated mobility assessment that combines multiple everyday movements, including straight-line gait, turns, and sit-to-stand tasks. A significant decrease in gait speed or cognitive performance when a dual task (DT) is introduced has been associated with higher fall risk [2].

In a traditional TUG DT assessment, a physical therapist records completion time and cognitive task performance. Wearable sensors, like inertial measurement units and accelerometers, and optical motion capture technology allow for the extraction of more specific gait features beyond the completion time and cognitive task performance. The addition of a DT typically increases number of steps, decreases step length, and decrease step duration among older adults during straight-line gait [2]. The analysis of gait parameters during TUG DT has been minimal, but one study utilized optical motion capture to focus on turn-specific parameters, including time to turn, number of steps taken to turn, and axial segment reorientation [4]. There is little existing information about the impact of a DT on the median step duration of the full TUG motion. We will investigate the effects of a DT on TUG motor performance and kinematic gait parameters with the goal of better understanding realistic fall risk scenarios and informing future DT interventions for the older adult population.

We hypothesized that the TUG performed with a DT would be associated with decreased motor performance (e.g., increased completion time) and altered movement strategies (e.g., more, shorter steps) vs. the TUG without the DT.

METHODS

Healthy older adults (n=8, mean age 70.9 ± 6.0 years) volunteered to participate in this research, in accordance with the IRB. The TUG consists of standing up from a chair, walking three meters forward, making a 180° turn, walking three meters back, and returning to a seated position in the chair (**Figure 1**). Each older adult performed the TUG twice: once without any additional cognitive load, followed by once with a dual task (TUG DT). The cognitive dual task was serial-3 subtraction, where older adults were instructed to count backward aloud starting from a specified number. A physical therapist administered the test.

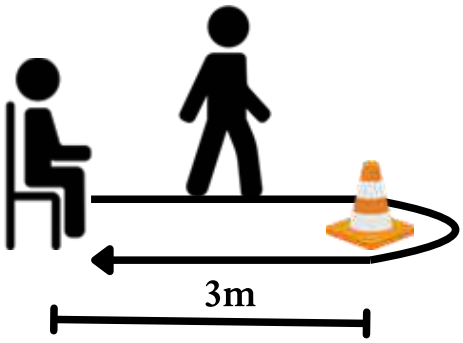

Figure 1: Illustration of the Timed Up and Go (TUG) Assessment.

Optical motion capture (Optitrack, 250 fps) was used to measure movement and a data processing program (MATLAB) was used to compute measures of interest. Measures of interest included: (1) the completion time of the test, measured by the Physical Therapist, (2) the number of steps used, (3) the step length, and (4) the step duration. Measures 2-4 required heel strike events, which were determined using motion capture software to observe the beginning of the foot's rotation in the sagittal plane after the heel contacted the ground. Heel strike times were confirmed with a video review.

Heel strike events were recorded during the straight-line gait and turning motions and did not include sit-to-stand tasks. The end of sit-to-stand and initiation of stand-to-sit movements were observationally identified by continuous increases or decreases in height of any point on the pelvis. This approach accommodated various sit-to-stand task techniques, including tilting the pelvis to initiate the motion and keeping the pelvis relatively flat. By removing sit-to-stand and stand-to-sit subphases from the analysis of walking measures of interest, there were more consistent computations of the measures of interest across participants.

A two-tailed paired sign test was used to evaluate the direction of possible differences between TUG and TUG DT for each measure of interest (α=0.05).

RESULTS

Between the TUG and TUG DT trials, there were increases in completion time (p=0.0078) and total steps (p=0.0156) (**Figure 2**). Median step length (p=0.0703) and median step duration (p=0.2891) were not significantly different across TUG and TUG DT trials (**Figure 2**).

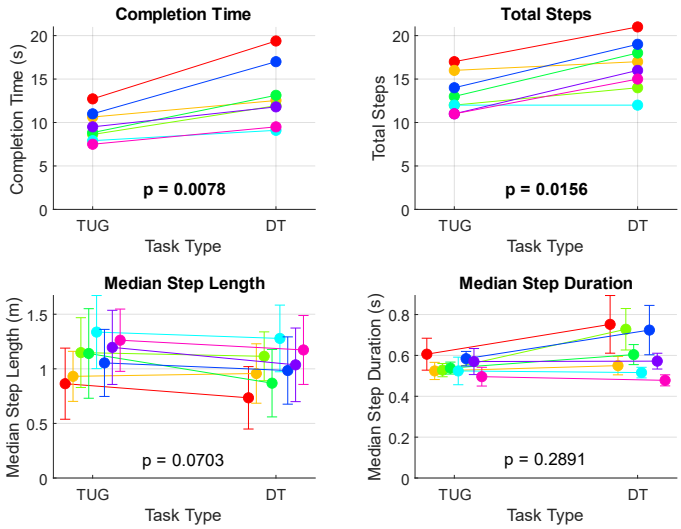

Figure 2: Comparison of Timed Up and Go (TUG) and Dual Task TUG (DT) across outcome measures. Each participant's data are distinct colors; group p-values are included.

DISCUSSION

Our finding that total steps and completion time of the TUG increased with the addition of the DT is consistent with our hypothesis and with the results of previous studies [2]. Though not significant in this small cohort, **Figure 2** shows that median step length during the TUG decreased with the addition of a DT for most older adults. This trend may be significant with a greater sample size.

There was not a clear trend in median step duration during the TUG with the addition of a DT. Most current literature that suggests a DT increases step duration is based on straight-line gait. By using optical motion capture or other biomechanical sensors during the TUG, future work could evaluate the impact of the DT on median step duration during the straight-line gait and turn TUG sub-phases separately.

The findings of this study are limited by the small sample size, which may introduce variability in the results. These results are also limited by the lack of data on the cognitive task performance during DT. The prioritization of either the cognitive or motor task could impact performance. These limitations suggest the need for further research with larger cohorts of older adults to validate and expand these preliminary findings.

The use of optical motion capture to evaluate specific kinematic measures of interest has exciting potential for future research. Future research could build on these results by focusing on the turn phase of TUG or investigating measures like gait variability and path length.

The TUG test with a DT replicates complex daily scenarios that may pose additional fall risk for older adults. Future research that focuses on how the addition of a DT impacts other kinematic parameters and specific phases of the TUG test could expand our understanding of how DT impacts a variety of motions, leading to the development of more specific and effective DT training interventions.

ACKNOWLEDGEMENTS

This study uses existing data from a larger ongoing study (NSF Award#1944207). We thank the volunteer participants.

REFERENCES

[1] Kakara R. et al., *CDC*, 72(35):938–943, 2023.
[2] Bayot M. et al., *NCCN*, 50(6):401-440, 2020.
[3] Hillel, I. et al., *EURAPA*, 16(6), 2019.
[4] Hollands K.L. et al., *NNR*, 24(4):358-67, 2010.

COMPARATIVE STUDY OF IMAGE-BASED MODELING USING A NOVEL MEDICAL-IMAGE-TO-REDUCED-ORDER-SIMULATION FRAMEWORK

Boyang Gan (1), Numi Sveinsson Cepero (1), Shawn C. Shadden (1)

(1) Department of Mechanical Engineering, University of California, Berkeley, Berkeley, California, USA

INTRODUCTION

Cardiovascular disease (CVD) remains the global leading cause of death. Recent developments in image-based modeling and patient-specific hemodynamic simulation have proven effective in enabling virtual personalized diagnosis, preventive care, and treatment planning without the risks of invasive measures. Despite the growth of such technologies, creating an image-based simulation from medical image (CT or MRI) scans is labor-intensive [1], and performing accurate computational fluid dynamics (CFD) simulations generally requires extensive technical knowledge of numerical methods and supercomputing resources [2].

Developing automated and efficient capabilities to go directly from medical images to simulation results, even if those results are approximate, can be highly informative in several scenarios including timely decision support, screening, boundary condition tuning, uncertainty quantification, treatment design, etc. With this in mind, we have been developing a streamlined process to produce reduced-order model (ROM) simulations of patient-specific hemodynamics from volumetric angiography. This framework leverages lumped-parameter and 1D Navier-Stokes solvers built into our SimVascular software [3, 4] coupled with recent machine learning (ML) model construction we have developed to automate the segmentation of vascular models from medical images. Work towards a medical-image-to-reduced-order-simulation (MIROS) framework we are developing is presented here and used to conduct a comparative study that examines the impact of machine learning models versus traditionally constructed models on ROM simulation results.

METHODS

The MIROS framework relies on automation of the vascular model construction and setting up and running a ROM flow solver to compute flow rate and pressure through each vessel. To verify our implementation, we compared the output of MIROS (i.e. flow and pressure calculations) to ROM flow and pressure calculations using traditional model construction for a series of cases in the Vascular Model Repository (VMR) (http://vascularmodel.org) – herein referred to as the VMR model/results. The main difference between MIROS and VMR is that we employ ML automated vascular segmentation, whereas the VMR models were manually constructed. We also automate the simulation process, but the flow solvers are the same. Also, to ensure consistent comparison of flow and pressure results, we use the same boundary conditions and solver parameters in MIROS as was used to generate the VMR results.

Segmentation. MIROS relies on a novel method called Sequential Segmentation (SegSeg) for automated segmentation of the vasculature. SeqSeg requires a seed point for initialization (chosen at the inlet) and automatically traces the vasculature based on local vessel segments. The method captures bifurcations automatically and traces down branches as long as image resolution and segmentation quality allow. The local vessel segments are averaged together into a global segmentation that is returned as a binary segmentation map, where pixels labeled 1 represent blood vessel and 0 represent background. These segmentation maps are converted to surface meshes using marching cubes and smoothed using Laplacian smoothing to remove pixel artifacts.

Outlet Definition. SeqSeg can capture more vasculature than contained in the manually segmented VMR models. To apply boundary conditions consistently, we generally needed to truncate the MIROS models to terminate at the same approximate location as in the VMR models. We automatically compute the coordinates, radius, and unit tangent vector of each endpoint in each VMR model and then orient and scale clipping boxes to trim the corresponding MIROS model. We also keep the largest contiguous volume, which is then remeshed to produce our desired surface. This workflow is shown in Figure 1 for two representative models (an aortic arch model and an abdominal aorta model).

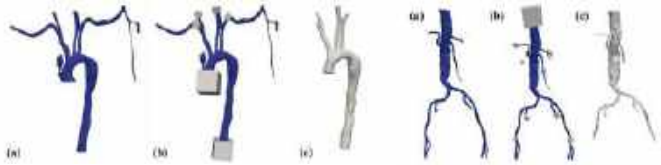

Figure 1: Creating consistent boundaries. (a) ML generated discrete surface (b) clipping boxes on ML surface (c) trimmed and filtered surface

Branch-matching. Because the ML method might capture a different number of branches than existing manually segmented surfaces in the VMR, we must match the branches and apply consistent boundary conditions to only outlets that are in common. Thus, the number of matching branches was determined, and any additional branches were merged into the vessel wall, which then become ignored during centerline extraction.

Centerline extraction. The MIROS and VMR 3D image-based models were used to generate a discrete centerline representation. The centerline extraction was performed using Vascular Modelling Toolkit (VMTK) functions that generated centerlines paths as well as vessel radius information along each vessel path. Both the discrete centerlines paths and associated areas along the paths were required for the ROM flow solver.

Boundary condition file preparation. We applied RCR boundary conditions at all outlets with RCR values tuned to clinical measurements and provided in the VMR [4]. In cases where the VMR contained a branch not included in the MIROS model, we ignore that boundary. Although this does not preserve the global consistency of the boundary conditions, we do this to keep the simulation consistent between MIROS and VMR models.

Solver. ROM simulation of flow and pressure was performed by solving the 1D Navier-Stokes equations using the SimVascular's 1D solver. Blood flow is assumed to be a Newtonian, incompressible fluid in a deforming and elastic domain. The governing equations consist of the continuity equation, a single axial momentum balance equation, a constitutive equation, and suitable initial and boundary conditions [5]. The overall workflow that MIROS models undergo is shown in Figure 2 for a representative model.

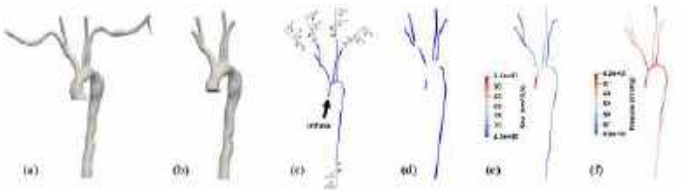

Figure 2: Pipeline workflow. (a) ML based surface (b) trimmed surface (c) centerline extraction (d) 1D model generation with boundary conditions (e)&(f) simulated flow and pressure mapped to centerline

RESULTS

Averaged relative error over time. Each simulation was run for more than 7 cardiac cycles to reach a periodic solution. We compared relative error in mean flow and pressure of the last simulated cardiac cycle. We took the average of relative errors of each branch to get the relative error of the entire model. The results are shown in Table 1.

Table 1: Relative error averaged over the last cardiac cycle.

Surface Name	Relative Error: mean flow	Relative Error: mean pressure
0063_1001	3.575%	7.658%
0090_0001	0.6245%	0.2769%
0131_0000	0.2834%	0.2820%
0146_1001	1.002%	0.7106%
0174_0000	0.3172%	0.1566%
0176_0000	0.3306%	0.1925%
Average	1.022%	1.850%

Qualitative plots of flow and pressure over time. For qualitative comparison, we plotted the average flow and pressure of the same branches between the MIROS and VMR simulations over time to visualize the differences in simulation outcomes between the two modeling methods. As an example, Figure 3 below shows the plots of 0176_0000, whose overall mean relative error in flow was 0.3306% and overall mean relative error in pressure was 0.1925%.

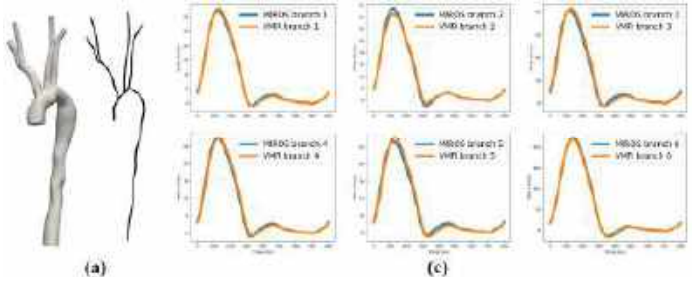

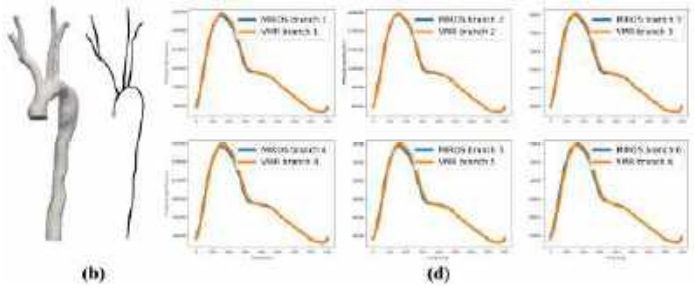

Figure 3. Qualitative comparison of flow and pressure result for each branch. (a) VMR model and its centerline (b) MIROS model and its centerline (c) flow comparison of each branch (d) pressure comparison of each branch.

DISCUSSION

We developed and automated a process for generating patient-specific, reduced-order model simulations of hemodynamics from volumetric angiography, culminating in a Medical-Image-to-Reduced-Order-Simulation (MIROS) framework. This framework significantly accelerates the traditionally hours-long tasks of vascular segmentation and the subsequent setup and execution of flow solvers, reducing overall time to a matter of minutes. Utilizing MIROS, we conducted a comparative analysis to evaluate the impact of different modeling approaches—manual segmentation versus machine learning segmentation—on simulation outcomes. Results indicate relatively modest errors of 1.022% for mean flow and 1.850% for mean pressure when averaged across all models and vessels. Given that consistent boundary conditions were used, these differences reflect errors in geometric reconstruction and are expected to be far less than errors typically associated with uncertainty of boundary conditions. This study demonstrates the efficiency and advantages of employing ML for automated vascular segmentation and highlights MIROS's capability to facilitate rapid hemodynamic simulations.

Limitations and Future Work. There are two noteworthy limitations that arise largely based on the nature of performing a comparative study. First, for some images, there were vessels captured by MIROS not captured by the VMR and vice-a-versa. Our analysis here focused only on models that contained vessels both methods captured. We plan to study this trade-off in future studies. Second, the boundary conditions for the MIROS model were the same as used for the VMR model. While this was necessary for consistent comparison, typical applications of modeling would require generation of de novo boundary conditions. We plan to study the application of MIROS to de novo analysis requiring generation of boundary conditions. Lastly, SimVascular has the ability to perform so-called 0D (also known as lumped-parameter) simulation based on a 3D model. We plan to connect such 0D ROM with MIROS, and to potentially consider more complex boundary conditions, such as used for coronary flow.

ACKNOWLEDGEMENTS

We acknowledge support from the NIH, Award No. 5R01LM013120 the NSF, Award No. 2310910 and 1663747.

REFERENCES

[1] Maher, G et al., *Cardiovasc Eng* Technol, 11(6):621-635, 2020.
[2] Randles, A et al., *Journal of Computational Science,* 9:70-75, 2015
[3] Updegrove, A et al., *Ann Biomed Eng*, 45, 525-541, 2017.
[4] Pfaller, M et al., *Int J Numer Method Biomed Eng*, 38(10):e3639, 2022.
[5] Hughes, T et al., *Mathematical Bioscience,* 18(1-2): 161-170, 1973.

EFFECTS OF DETRUSOR CONTRACTION ON URINARY BLADDER EXTRACELLULAR MATRIX ORGANIZATION

Daniel O. Deuel (1, 2), Tyler G. Tuttle (1), Sara Roccabianca (3), Sarah Calve(1)

(1) Paul M. Rady Department of Mechanical Engineering
University of Colorado Boulder, Boulder, CO, United States

(2) Department of Chemical and Biological Engineering
University of Colorado Boulder, Boulder, CO, United States

(3) Department of Mechanical Engineering
Michigan State University, East Lansing, MI, United States

INTRODUCTION

The urinary bladder is a hollow organ that stores urine through passive filling and voids urine through active concentric contraction. The bladder undergoes strain softening, a phenomenon where the compliance of a material increases after repeated stretching. This occurs following passive emptying where the bladder is voided without proper detrusor contraction [1]. *In vivo*, strain softening is mitigated by contraction of the detrusor during voiding [2], which we have replicated *ex vivo* using optogenetic stimulation. Current *ex vivo* bladder passive mechanical testing methods are based on protocols for tissues that do not require contraction as part of their normal use (*e.g.* tendon, ligament, skin) and fail to prevent strain softening [3]. Although research has gone into understanding possible causes of this mechanical change, like slippage of actin-myosin cross-bridges [4], the organizational response of the extracellular matrix (ECM) to this change has not been studied. This is important to investigate because the smooth muscle cells of the detrusor are intertwined with the ECM, and the composition and organization of the ECM governs bladder passive mechanical properties. Here we describe a method of quantifying changes in the organization of fibrillar collagen in the bladder using multiphoton microscopy. We will use this method to quantify strain softening during passive mechanical testing, and prevention of strain softening via active concentric contraction using optogenetic stimulation.

METHODS

Loading cycles were carried out using a floating platform mechanical testing system (Fig, 1). The mechanical testing system was comprised of a bath containing a floating platform which was attached to a bladder and a micromechanical testing system (FemtoTools, Furtbachstrasse CH) [5]. Above the bladder, a movable pulsed blue light laser was mounted, allowing imaging and optogenetic stimulation to be quickly swapped between. *Ex vivo* mouse urinary bladders were tested with two mechanical testing protocols, one which utilized passive loading and unloading and one which utilized passive loading and active unloading via optogenetic contraction. After the samples were attached to the floating platform and pulled to a 0.5 mN preload, they were imaged, stretched to a stress of 5 kPa, imaged again, and unloaded. This was repeated five times per sample.

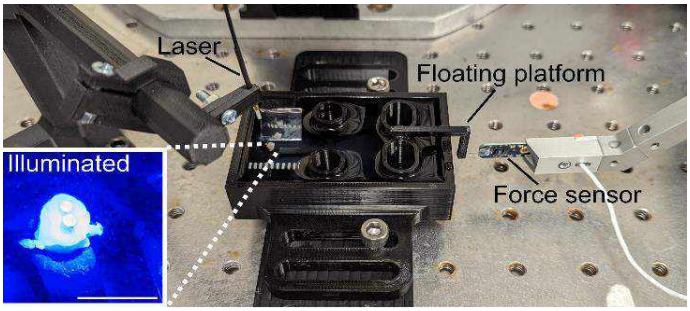

Figure 1: Mechanical testing setup. Stimulation of bladder with blue light laser shown in zoomed in square.

For the active unloading group**,** on demand contraction of the bladder was achieved using a cross of *ChR2(H134R)-EYFP* mice (JAX, #024109), with *SM22-Cre^{tg}* mice (JAX, #017491). These mice express the light sensitive ion channel channelrhodopsin-2 and Enhanced Yellow Fluorescent Protein (EYFP) in smooth muscle cells. This method allowed for the stimulation of detrusor contraction using a 500 mW, 450 nm blue light laser (Opto Engine), pulsed at 100 Hz with 10% duty cycle [6].

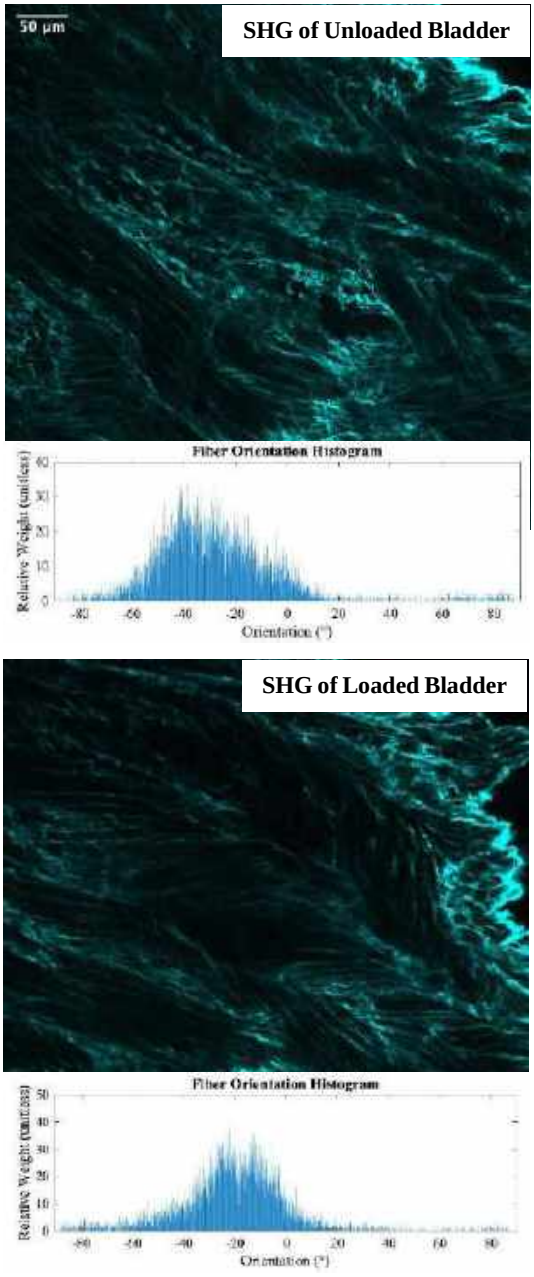

Figure 2: Comparison of loaded vs unloaded orientation distributions.

Imaging of the bladders was conducted from the adventitia to the lamina propria using a 25x objective on an Olympus FVMPE-RS Twin Laser Multiphoton microscope. Second harmonic generation (SHG) of fibrillar collagen and EYFP were exited simultaneously using a wavelength of 920 nm.

The organization of fibrillar collagen was quantified using orientation, coherency, and energy data from the ImageJ plugin OrientationJ [7]. This allowed for the calculation of weighted orientation distributions to represent organization. Furthermore, this data was used in the creation of streamlines that trace groups of fibers to approximate fiber waviness [8].

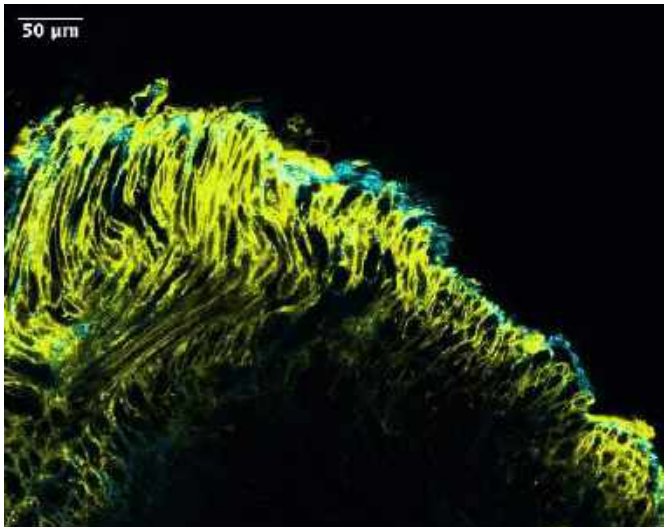

Figure 3: Colocalization of smooth muscle cells (EYFP, yellow) and fibrillar collagen (SHG, cyan)

RESULTS

Qualitatively, fibrillar collagen was wavier in unloaded vs loaded bladders, which was seen quantitatively in the fiber orientation distributions (Fig, 2) where the unloaded bladder had an orientation standard deviation of 24.47° while the loaded bladder had an orientation standard deviation of 21.71°. Furthermore, fibers became more aligned in the direction of applied stretch. Lastly, EYFP and SHG imaging displays the interconnectedness of smooth muscle cells and fibular collagen in the detrusor.

DISCUSSION

Narrowing of the fiber orientation distributions coinciding with a qualitative straightening of fibers indicates that our methods can capture changes in the organization of the ECM. Additional data collection will elucidate differences in the fibrillar collagen organization between the passive and active unloading groups. Additionally, future work will more clearly visualize the structure of the lamina propria and urothelium as the current method of imaging starting at the adventitia leads to minimal to zero signal in these layers. How the aspect ratio of smooth muscle cells responds to loading and unloading will also be investigated to further understand the interplay between mechanical loading, the ECM, and smooth muscle cells. Our long-term goal is to use orientation distributions and fiber waviness from this imaging to inform computational modeling of strain softening and prevention of strain softening via contraction in the bladder.

REFERENCES

[1] Balthazar, A., et al. *Neurourol and Urodynam* 38, 5 (2019): 1222-1228.
[2] Tuttle, T.G., et al. *Acta Biomater* 141 (2022): 280-289.
[3] Cullingsworth, Z.E., et al. *Neurourol and Urodynam* 39, 2 (2020): 707-714.
[4] Neal, C.J., et al. *Am J Physiol-Renal Physiolog* 313, no. 1 (2017): F126-F134.
[5] Acuna, A., et al. *Acta Biomater* 134 (2021): 466-476.
[6] Park, J. H., et al. *Scientif Reports* 7, 1 (2017): 40872
[7] Püspöki, Z., et al. *Bio-image informat* (2016): 69-93.
[8] Salazar C., et al. *Biomed Optics* 27, 1 (2022): 016503-016503.

EXTENT OF VASCULAR DAMAGE AT VARYING DEGREES OF STRETCH IN HYPOXIC NEONATAL BRACHIAL PLEXUS

S. Srinivasan (1), V. Orozco (1), S. Nair (2), M. Sahni (3), S. Balasubramanian (1), A. Singh (2)

(1) School of Biomedical Engineering, Science and Health Systems, Drexel University, Philadelphia, Pennsylvania, United States of America
(2) Bioengineering, Temple University, Philadelphia, Pennsylvania, United States of America
(3) Sunrise Children's Hospital, Las Vegas, Nevada, United States of America

INTRODUCTION

Neonatal brachial plexus palsy (NBPP) is defined as an injury to brachial plexus (BP) nerves due to over-stretching during complex birthing scenarios. Despite advancements in obstetric care, NBPP has an incidence of 1-4 cases per 1000 live births [1, 2]. Neonatal hypoxia can also occur as a result of obstetric complications, such as disrupted blood supply to the fetus due to umbilical cord compression and can significantly impact the tissues and other organ functions [3]. Characterizing the extent of vascular damage of hypoxic neonatal BP at varying degrees of stretch can further the understanding of the injury thresholds of NBPP.

METHODS

All procedures were approved by the Institutional Animal Care and Use Committee. 15 neonatal piglets (3-5 days old) were anesthetized and exposed to FiO2 of 7% for 1 hour to induce hypoxia and re-perfused to FiO2 of 21%. Using an axillary approach, the BP was exposed, and BP nerves were stretched at a rate of 500 mm/min to predetermined low- (<15%) and high- (>15%) strains. Post-stretch, BP nerves were harvested and OCT-embedded. Ten-µm-thick serial longitudinal sections were stained with Hematoxylin-Eosin (H&E). Using the Olympus BX53 motorized microscope, stained slides were imaged at 10x magnification along the nerve length. Each stitched image was split along its nerve length into regions of interest (ROIs) using a custom MATLAB script [4-5]. An independent-blinded observer scored each ROI for vascular damage on a scale of 0-2 (0-no damage, 1-torn vessel, 2-scattered blood cells, **Fig. 1**).

RESULTS

Based on our modified scoring system, preliminary results show that vascular damage increased with increasing stretch injury **(Fig. 2)**, and similar degrees of damage were observed in the central and peripheral regions of the nerve **(Fig. 3)**.

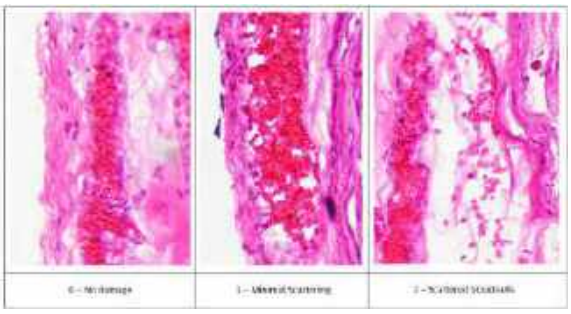

Figure 1: Vascular damage scoring system.

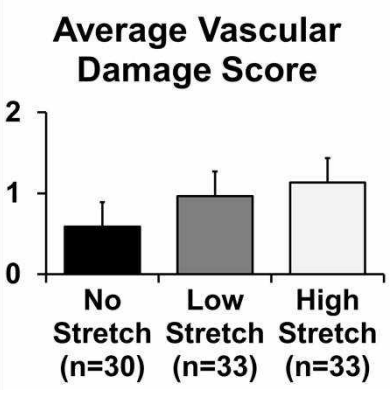

Figure 2: Bar graph of increasing vascular damage with increasing stretch

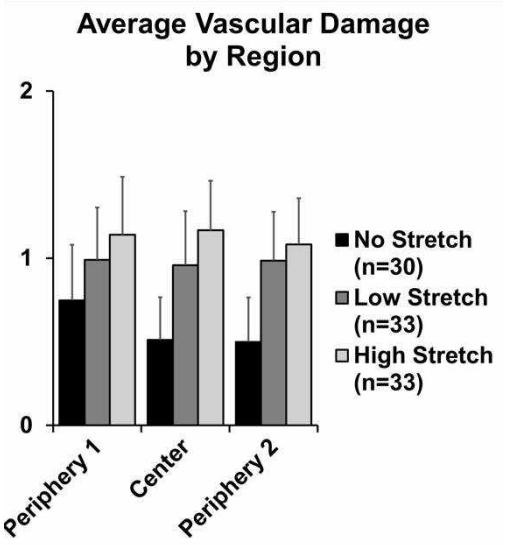

Figure 3: Bar graph of vascular damage by nerve region.

Control	<15 %	>15%
0	8.9 ± 4.0	21.2 ± 6.8

Table 1: Average strain reported for each group.

DISCUSSION

This ongoing study is the first to characterize vascular damage of hypoxic neonatal BP nerves with respect to varying degrees of stretch. Determining the depth of vascular damage of the BP by analyzing the three regions presented in conjunction with the overall vascular damage will provide a more detailed characterization of the injury [7-9]. Due to the anatomical similarities between neonatal piglets and neonatal human BP, this study will help further the understanding of injury thresholds of NBPP.

ACKNOWLEDGEMENTS

This project was funded by the Eunice Kennedy Shriver National Institute of Child Health and Human Development of the National Institutes of Health R15HD093024; R01HD104910-01A1 and NSF CAREER grant Award #1752513.

REFERENCES

1. Abzug, J.M. Orthopedics 33: 430-435 (2010).
2. Johnson, E.O. Injury 44(3), 293-298 (2013).
3. Piešová, M, Mach, M. Impact of perinatal hypoxia on the developing brain. (2020)
4. CR D'Andrea et al., 2021, Journal of Orthopaedic Research 39 (5), 907-918
5. Singh et al., JoVE (Journal of Visualized Experiments), e59860
6. CR D'Andrea et al., 2021, Journal of Orthopaedic Research® 39 (5), 919-928
7. Singh et al., 2019, Journal of biomechanical engineering 141 (12), 121011
8. Singh et al., 2018, Journal of brachial plexus and peripheral nerve injury 13 (1), e8
9. Tom et al., 2018, Experimental brain research 236, 3077-3084

ROBOGRIPPER: EMG-CONTROLLED, WRIST BRACE-MOUNTED, ROBOTIC MANIPULATOR FOR HAND PARALYSIS PATIENTS

Shaiv Y. Mehra (1), Tyler D. Merrill (1)

Faculty Advisor(s)

Brad S. Duerstock (1)

(1) Weldon School of Biomedical Engineering, Purdue University, West Lafayette, Indiana, United States of America

INTRODUCTION

Hand paralysis is a life changing disability, leading to loss of functionality to grasp objects. This disability typically stems from medical conditions such as stroke, cerebral palsy, or spinal cord injuries (SCI), the last of which can cause incomplete tetraplegia, partial functionality loss in the extremities [1]. According to the National Spinal Cord Injury Statistical Center as of 2023, approximately 302,000 people in the US alone suffer from traumatic SCI, where 47.1%, 142,242 people, have incomplete tetraplegia [2].

Patients living with this disability lose their independence and often require assistance with daily tasks. They must develop new ways to manipulate the objects around them; however, patients experience hand weakness and are forced to use unnatural wrist positions, known as tenodesis grip. Restoring hand functionality would improve their independence and quality of life. Many therapeutic procedures and a few robotic orthotics have been studied but they are high in cost, fail to produce enough hand functionality, or are unintuitive to use, resulting in continued research in advanced orthotics [3]. An EMG-controlled robotic gripper mounted to a wrist brace would allow patients to manipulate everyday objects, leading to an increased quality of life and reduce harmful grips like tenodesis.

PRODUCT DESIGN

Traditional manipulator devices can be expensive, cumbersome to use, and/or large and bulky. To combat these shortcomings, this proposed design is lightweight and inexpensive (< $5,000.00) due to the 3D printed components, and easy to operate by flexing a bicep via electromyography (EMG). Additionally, this device aims to solve a common issue in manipulator devices, range of usage, by making use of flexible, compliant grippers to conform to complex shapes and sizes with improved grip. Furthermore, it can be attached to wrist braces with a dovetail fitting, allowing the device to work alongside assistive devices already in use by patients (Figure 1).

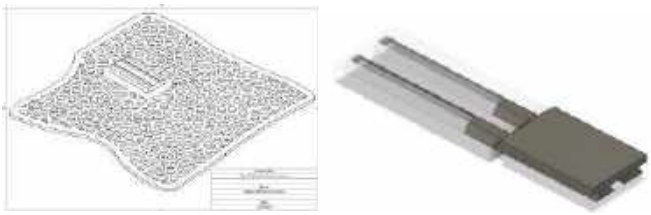

Figure 1: Mount on flexible, 3D printed wrist brace (left) and proposed dovetail attachment mechanism (right).

The gripper drive system is composed of a motor, lead screw, rack and pinion gears with claws (Figure 2). If the gripper was driven directly by the motor, the motor would need to maintain torque to grip an object, wearing down the motor and consuming battery power. The single-start trapezoidal lead screw is self-locking, meaning that the slide friction and flank angle maintains the grip without motor torque. The rack translates the linear motion produced by the screw to rotational by rotating the gears attached to grippers, allowing them to open and close.

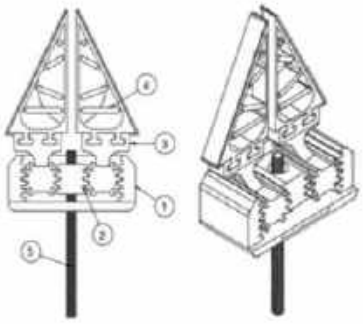

Parts List		
Part Number	Description	Material
1	Drive System Base	PLA
2	Gear Rack	PLA
3	Gripper Support System	PLA
4	Compliant Gripper Body	TPU
5	Lead Screw	Steel

Figure 2: Gripper Drive System CAD Assembly with Parts List

The triangular grippers consist of two main parts: the compliant gripper body and the support system (Figure 2). The body is flexible, allowing for improved grip and range of applications by conforming to the shape of different objects. Various infill designs and densities for NinjaFlex Thermoplastic Polyurethane (TPU) were tested to determine the most optimal geometry, measured by its overall ability to deform while providing adequate torque. The support system provides backbone along the length and base of the triangle, allowing for maximum torque and maintaining grip alignment.

The EMG circuit is comprised of an instrumentation amplifier (INA), notch filter, and bandpass filter (Figure 3). The INA amplifies low-level EMG signals from around 1 mV to roughly 1 V, while maintaining a large common-mode rejection ratio (CMRR) to reject common mode noise, and high input impedance, ensuring accurate measurement of the low-voltage EMG signal. Two inputs measure the voltage difference across the bicep via skin electrodes. The notch filter removes 60 Hz noise introduced from the transmission line. The active bandpass filter captures signals from 20 Hz to 450 Hz and further amplifies the signal to about 4.3 V. This signal is input to the analog pin of an Arduino, which can only measure up to 5V. When the bicep is flexed, the EMG signal is spiked triggering a Parallax continuous servo motor from the Arduino. With a torque output of 2736 oz-in, the servo motor allows the gripper mechanism to grasp a variety of objects.

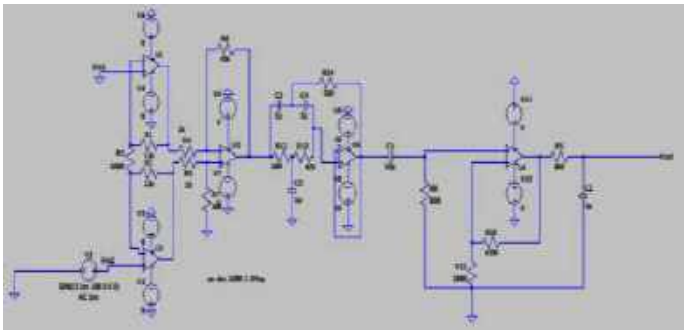

Figure 3: LTSpice schematic diagram for EMG circuit.

BUDGET & MARKET ANALYSIS

About 142,242 people in the US suffer from SCI-induced incomplete tetraplegia with an increase of about 8,478 people each year [2]. Therefore, the first year has a potential market of about 142,242 product sales domestically, with an additional 8,478 sales annually.

The total design cost is $771.80, and the single unit material cost is $114.90 as determined in Table 1.

Table 1: Design Budget

Component	Need	Cost per unit ($)	Quantity used	Total cost ($)
Arduino Teensy	Microcontroller	9.60	1	9.60
Parallax Continuous Servo Motor	Motor	19.95	1	19.95
Lead screw	Gripper drive system	1.05	1	1.05
Threaded fitting	Fits lead screw into Drive system	0.22	1	0.22
Shaft collar	Attached screw to motor	0.49	1	0.49
PLA material	Hard 3D print material	24.99 per kg	11.47 grams	0.29
TPU material	Soft 3D print material & testing	64.00 per kg	290 grams	18.56
Operational amplifier (LM741)	EMG circuit	0.48	5	2.40
Capacitor Set	EMG circuit	9.99	1	9.99
Resistor Set	EMG circuit	9.99	1	9.99
Wire Set	EMG circuit	13.99	1	13.99
Breadboard	EMG circuit	2.95	1	2.95
Electrode Wires	Measure bicep EMG	10.81	1	10.81
EMG pad pack	Electrode-bicep connection	19.99	1	19.99
Unit Material Sub-Cost				114.90
3D printer - Prusa MK3S+	Manufacturing	649.00	1	649.00
Force Sensors	Force testing	3.95	2	7.90
Total Cost				771.80

An additional engineering cost of about $1000.00 is required to improve the design by making it smaller and expanding its performance. Based on materials, development, and labor costs, an approximate sales cost is $500.00 with a manufacturing cost of $250.00 per unit. The developers' return on investment (ROI) is $250.00 for the first unit, $35,560,500.00 for the first year, and $2,119,500.00 each following year. Also, the product could be beneficial for all hand paralysis patients, in addition to those with incomplete tetraplegia, and the product availability can be expanded globally, both increasing the potential for profit. In turn, the profits would fund more printers, materials, and labor for larger production. For the users, the sales price is much lower than the cost of current products on the market, such as robotic hand orthotics which can be priced at $5,000.00. Their ROI relative to similar products is high, as the gripper device provides a light, convenient solution to everyday problems patients may face, while being low in cost.

ACKNOWLEDGEMENTS

We acknowledge the guidance and preliminary funding provided to this project by Professor Brad Duerstock and Mitchell Sanchez from the Purdue University Duerstock Institute of Accessible Science research lab.

REFERENCES

[1] H. In, B. B. Kang, M. Sin, and K.-J. Cho, "Exo-Glove: A Wearable Robot for the Hand with a Soft Tendon Routing System," IEEE Robotics & Automation Magazine, vol. 22, no. 1, pp. 97–105, 2015. doi: 10.1109/mra.2014.2362863.

[2] "Traumatic Spinal Cord Injury Facts and Figures at a Glance 2023 SCI Data Sheet." Available: https://www.nscisc.uab.edu/public/Facts%20and%20Figures%202023%20-%20Final.pdf

[3] E. Y. Chang, R. Mardini, Y. Andrew, Y. Gloumakov, and H. Stuart, "Tenodesis Grasp Emulator: Kinematic Assessment of Wrist-Driven Orthotic Control," in Proceedings of the IEEE International Conference on Robotics and Automation (ICRA), 2022. doi: 10.1109/icra46639.2022.9812175.

A FRAMEWORK FOR SLICE-WISE MOTION CORRECTION IN MAGNETIC RESONANCE ELASTOGRAPHY OF THE HUMAN BRAIN

Tyson Lam[1], Emily R. Triolo[1], Mehmet Kurt[1]

[1]Mechanical Engineering, University of Washington, Seattle, WA, USA

INTRODUCTION

Magnetic Resonance Elastography (MRE) is an advanced MR imaging technique that enables the non-invasive measurement of tissue stiffness[1], with emerging applications in the evaluation of brain disorders[2]. Despite its significant potential, MRE is challenged by motion-related artifacts such as non-uniform "Z-striping" (Fig. 1), which can obscure the accurate representation of tissue properties and compromise diagnostic efficacy. These artifacts are often exacerbated by involuntary subject movement during scanning, introducing errors in MRE phase images that can compromise the solution to the inverse problem of viscoelastic inversion and mislead clinical interpretations. Because MRE is a motion-sensitive phase-contrast sequence, any involuntary subject motion will slightly alter the reference phase in the volume during which the subject motion occurred. In MRE sequences with interleaved slice acquisition (often used in EPI-based sequences to reduce volume distortion[3]), these errors therefore affect alternating slices in the volume, and even minute motions can propagate through multiple slice acquisitions.

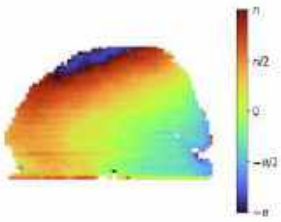

Figure 1: Sagittal view of the brain with "Z-striping" in the lower half of the image (Axial slice acquisition direction).

The current landscape of MRE technology lacks robust solutions for correcting these artifacts, particularly in the context of brain imaging where precision is paramount. Outside of alternative readout gradient structures (e.g. spiral acquisitions[4]), existing methodologies predominantly rely on low-pass filtering (for small motions that propagate through an entire volume) or manual intervention, wherein researchers are tasked with meticulously identifying and rectifying outlier slices on a slide-by-slice and volume-by-volume basis through adjustments in the phase angle. However, considering larger, expansive datasets, enhanced resolution imaging, and the potential for researcher-induced bias, this approach may be deemed highly suboptimal and inefficient.

As such, there is a current need for advanced and automated processing methods capable of mitigating the impact of motion-induced errors and improving the robustness and reliability of MRE scans. This abstract introduces a novel approach using inspired by techniques used in correcting artifacts in standard MRI sequences, specifically repurposing the principles of FSL's Eddy current correction[5]. The proposed method adapts these principles to the unique context of MRE, aiming to effectively identify and compensate for the motion-induced inconsistencies across the Z-axis of the brain scans. By integrating this approach with advanced image processing algorithms, we anticipate a substantial reduction in the presence of Z-striping artifacts during the MRE inversion process.

This work serves as a potential method for enhancing MRE image processing, tackling a widespread and complex challenge in brain imaging. The ambition of this research is to improve the diagnostic accuracy of MRE, potentially impacting the study and treatment of neurological disorders significantly.

METHODS

Ultra-high field MRE data was obtained from healthy volunteers aged 20-35 on a 7T MRI whole body scanner (Magnetom 7T, Siemens Healthineers, Germany) with a 32-channel head coil (Nova Medical, Wakefield, MA). The MRE sequence used was an echo-planar spin-echo 2D multi-slice pulse sequence with 3D motion-encoding gradients (TE=65 ms, TR=4800 ms, GRAPPA = 2, 2.5 mm isotropic resolution)[6]

and a custom pneumatic actuator by *Triolo et al* described applied vibrations at 50 Hz[7].

After each MRE scan, we collected raw data and DICOM images. We used the Gadgetron framework[8] for post-hoc reconstruction to remove artifacts caused by scanner reconstruction error, such as inaccurate value assignment in pixels along phase wrapping lines, by employing advanced coil combination based on a non-linear optimization scheme[9].

Utilizing custom Python scripts, the magnitude images were derived from the complex images reconstructed by Gadgetron and subsequently processed through FSL's Eddy tool[5]. In addition to performing automated motion correction on magnitude images, Eddy also generates a subject motion report map that outlines the standard deviation displacement from the mean for every slice in each volume in an acquisition. It's important to note that while Eddy is not explicitly designed for motion correction in MRE datasets and cannot directly correct phase data, the motion reports it produces were useful in identifying significant phase shifts attributable to extensive subject movement.

Further refinement was achieved through additional custom Python scripts, leveraging Eddy's motion report standard deviation outputs to pinpoint slices of compromised quality (mean slice deviation threshold above 0.5). These identified slices were then subjected to a phase adjustment process, utilizing their adjacent 'good' slices to estimate the approximate phase in these slices as if the subject had not moved.

After Eddy correction, we applied Marchenko-Pasteur Principal Component Analysis (MP-PCA)[10] denoising in a 5×5×5 sliding window for noise reduction without losing anatomical detail or resolution, leveraging MRE acquisition redundancies (48 volumes acquired per slice) to remove noise-only principal components. The difference was then taken between the two sets of phase images acquired with reversed MEGs to acquire wrapped displacement (in radians), and the displacement was then unwrapped using 3D SEGUE unwrapping[11]. We also employed a simple low-pass Butterworth filter to remove the high-frequency striping effect that occurs due to small, irregular subject motions.

The derived unwrapped displacement data was then used to calculate the storage modulus (G'), loss modulus (G"), and therefore the complex shear modulus (G' + iG" = G*) through an iterative, nonlinear viscoelastic inversion of the time-harmonic Navier-Stokes equation[12]. The nonlinear inversion algorithm additionally output reports of G' and G" in the volume as a function of iteration number to assess how the simulation converged.

RESULTS

After processing the subjects, it was observed that, absent any of any corrections beyond the standard pre-unwrapping procedures (Gadgetron, MP-PCA and Butterworth lowpass filtering), our example subject demonstrated difficulty in convergence during nonlinear inversion (Fig. 2), favoring stiffer and unrealistic parameters.

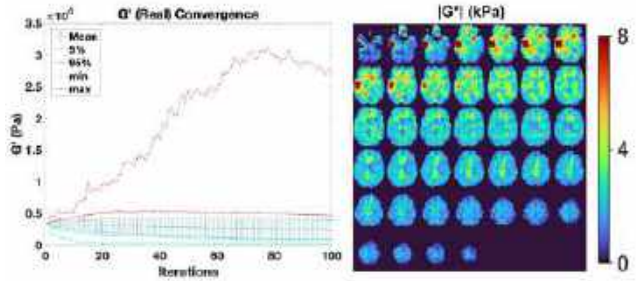

Figure 2. Poor convergence of example subject.

The real component of the complex shear modulus is considered here as it diverges more significantly when there are phase errors from subject motion. In contrast, when Eddy motion correction was performed, by adjusting slices, convergence was achieved with greater consistency with each iteration during the nonlinear inversion process (Fig. 3).

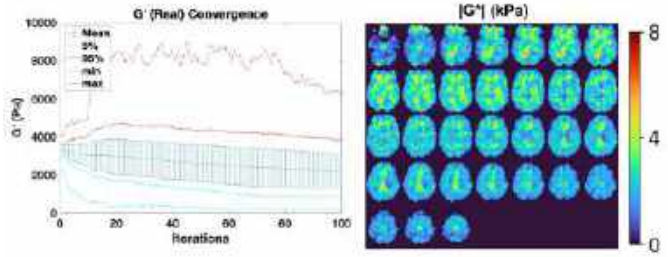

Figure 3. Good convergence of the same example subject when correction is applied.

DISCUSSION

The findings demonstrate the potential of streamlining the QC process, by identifying outliers from phase distortion using FSL's Eddy toolkit and applying correction to outlier slices. While a prior investigation proposed using FSL's Eddy toolkit for motion correction of MRE data, correction was only applied to the magnitude images for segmentation purposes and therefore had no effect on the viscoelastic inversion result[13]. Applying this post-hoc motion correction in phase as well as magnitude is imperative for generating accurate elastograms of subject populations that are more likely to shift during scans (e.g., pediatric population, patients with neurodegenerative disorders).

The subject population described in this study additionally underwent MRE scans at higher resolutions, so future work will involve application of motion correction on, and comparisons to, these higher resolution scans. Further parameter optimization to better suit FSL's Eddy for each of these resolutions will also be investigated.

ACKNOWLEDGEMENTS

This work was supported by NSF CMMI 1953323. The authors would like to thank Ms. Aislinn Diaz for assistance in volunteer recruitment and coordination, Dr. Alex Khegai for his work on the 7T MRE sequence and Gadgetron reconstruction, and Dr. Matt McGarry for providing the nonlinear inversion algorithm and technical support.

REFERENCES

[1] Muthupillai, PJ, *et al., Magn Reson Med*, 36(2): 266-274. [2] Clayton EH, Genin GM, Bayly PV., *J R Soc Interface*. 2012; 76: 2899-2910. [3] Chang, H., *et al., PLOS ONE*. 2014; 9(12): e116378. [4] C. L. Johnson *et al., Magn Reson Med*, 2013; 70(2):404–412 [5] Andersson JLR, Sotiropoulos SN., *Neuroimage*. 2016; 125: 1063-78. [6] Triolo, E., *et al., Proc. ISMRM-ESMRMB 31st Annual Meeting*, 2022. [7] Triolo, E. *et al.*, *Current Protocols*. 2022;2: e379. [8] Hansen, MS & Sørensen, TS, *Magn Reson Med*. 2013; 69(6): 1768-1776. [9] S. J. Inati, M. S. Hansen, and P. Kellman, *Proc. Intl. Soc. Meg. Reson. Med*. 2014; 4407. [10] Veraart, J., *et al., Neuroimage*. 2014; 142: 394-406. [11] A. Karsa and K. Shmueli, *IEEE Trans Med Imaging*. 2019; 38(6): 1347-1357. [12] McGarry, M., *et al., Med Phys*, 39(10): 6388-6396. [13] Fehlner, A., *et al., Journal of Magnetic Resonance Imaging*. 2017; 46(1): 134-141.

OPTICAL COHERENCE TOMOGRAPHY AND VIBROMETRY ENDOSCOPE

C. Clark (1), S. Gandarilla (1), B. Marquez (1), M.H. Tran (1), A. Valencia (1)

Faculty Advisors
Dr. H. Park (1), Dr. W. Dong (2)

(1) Department of Bioengineering, University of California-Riverside, Riverside, CA, United States of America
(2) Veterans Affairs Loma Linda Health Care, Loma Linda, CA, United States of America

INTRODUCTION

Approximately 5% of the world's population suffers from disabling hearing loss.[1] One category in this statistic is conductive hearing loss, which is characterized by damage to the middle ear structures. Although several methods exist to diagnose conductive hearing loss, each has its limitations. Audiometer tests are readily available but only provide a subjective account of the severity of hearing loss with no insight into what structures of the hearing pathway are compromised.[2] On the other hand, CT imaging can indicate what structures are compromised but cannot measure the extent to which sound conduction in the middle ear is affected and exposes the patient to high levels of ionizing radiation.

Beyond diagnostics, a few methods exist to treat conductive hearing loss. The current standard of treatment is exploratory surgery of the middle ear, a procedure with a risk of damage to the ossicle bones and facial nerves.[3] Even with successful surgery, no standard diagnostic test quantifies treatment efficacy.

Optical Coherence Tomography (OCT) is a known diagnostic imaging technology capable of addressing the limitations of current diagnostic tools in a single device, potentially positioning this device as the gold standard for conductive hearing loss diagnosis. OCT imaging data is acquired using broadband near-infrared (NIR) laser light, which enables the system to capture images with a resolution between 10-15 microns. This means the system can resolve the tiny structures of the ear and is sensitive enough to measure the frequency and amplitude of vibrations in those structures in response to a sound of known frequency and sound pressure. An additional use case, enabled by the live imaging data and high resolution, is guidance of surgical instruments during a procedure on the middle ear, which could reduce the risk of permanent anatomical damage from accidental misplacement of surgical tools. The use of infrared light also means patients are not exposed to ionizing radiation during an imaging study.

Our device is an OCT imaging probe that can be inserted into the ear to facilitate imaging and vibrometry of middle ear structures in the sound conduction pathway on *ex vivo* human ear samples. These structures include the Tympanic Membrane, Umbo, Manubrium, and Incus in order of sound propagation.[3] When developed, the proposed device can be used by otolaryngologists, family doctors, and educational hospitals that require gold standard diagnostic technology. Additional users would include researchers studying the middle ear or hearing loss. Ultimately, we seek to create an OCT device that is not only suitable for clinical medical practice but also one that will be an improvement upon current hearing loss diagnostics and treatments.

PRODUCT DESIGN

The challenges with utilizing OCT for endoscopy of the ear are positioning the system near a patient's head, introducing the laser through the ear canal unobstructed, and focusing on the structures of interest. This device addresses these challenges by utilizing a gradient index of refraction (GRIN) lens that is long and narrow enough to pass through the ear canal and focus the NIR laser at the right depth. The GRIN lens will be protected using an otoscope speculum. The lens will be advanced with the assistance of a fiber optic endoscope with a live video of the area surrounding the lens. Our design also utilizes lightweight materials that a single person can easily utilize.

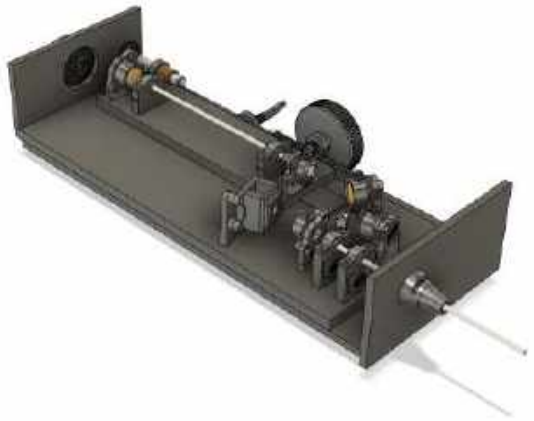

Figure 1. The CAD assembly of the device design was generated in Solidworks. The assembly contains all components of the device design without the case walls to enable easy visibility of internal mechanisms within the device.

Front Assembly

The front assembly of our design serves as the main interface between the internal optics, notably the GRIN lens being inserted into the ear and the patient. The following components all form part of the front assembly: case front panel, otoscope speculum, disposable speculum tip, GRIN lens, GRIN lens sleeve, microphone, speaker, and fiberoptic endoscope. The speculum protects the GRIN lens as it protrudes from the case. The fiberoptic endoscope is attached to the GRIN lens via an elastic resin sleeve, allowing both components to move in unison so that the user can see where the GRIN lens is positioned in relation to the ear canal. The microphone and speaker is designed to sit inside the case near the opening of the speculum to enable vibrometry.

Case

The casing we have designed for our device is fabricated of acrylic panels and includes the stage base, side walls, and front panel. Each panel is designed to interlock with its neighboring panel via teeth-like cutouts. This case serves as a protective barrier between the user and the delicate optical components.

Two-tier Linear Stage

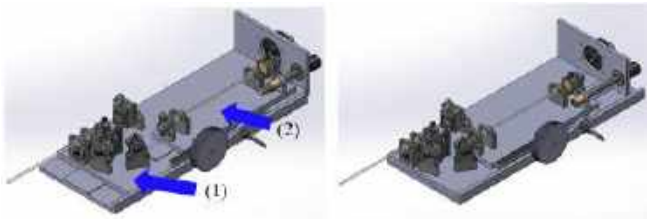

Figure 2: The stage is constructed from acrylic and consists of two portions: the main stage (1) and the reference arm stage (2).

These stages serve three purposes: Provide a stable platform for the optical assembly, allow for calibration of the system, and enable the GRIN lens to be advanced into the ear canal without misaligning the optics. Both stages utilize a dovetail mechanism that allows the user to carefully slide the main stage inside the case, moving the Gradient Index (GRIN) lens into the ear canal. Each acrylic stage is laser cut with post holes to place the optic holders in their ideal positions calculated in the CAD model.

Optomechanics

We designed custom optic holders with the minimum necessary range of adjustability and fabricated them with resin. This allows us to significantly reduce the size and weight of the overall system while maintaining enough rigidity to withstand external disruptions like sudden impacts to the case that would otherwise disrupt the optical alignment. Our optic holder designs are limited to 3 degrees of freedom adjusted via the compression of elastomer bushings. They have a thick base with two prongs to fit perpendicular to and tightly with the stage mechanism.

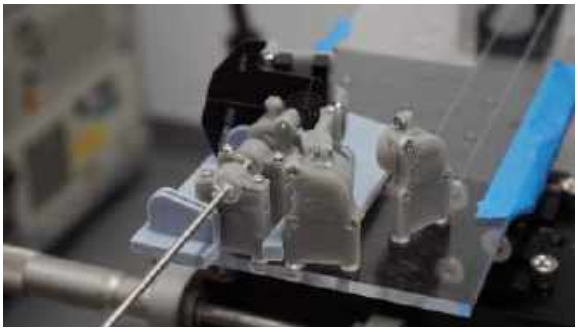

Figure 3. This photo contains the main stage resin optomechanics slotted into our acrylic laser cut panel/stage for a preliminary prototype. In this photo, we have placed the device's true lenses and mirrors into the optic holders and began alignment with a collimated beam.

BUDGET & MARKET ANALYSIS

If OCT becomes the gold standard for diagnosing and testing conductive hearing loss, the total addressable market of our device includes all hospitals that provide inpatient otolaryngology services, any outpatient clinics specializing in otolaryngology, primary care clinics in populations where conductive hearing loss is prevalent, and researchers studying the middle ear. There are 6,120 total hospitals in the United States and about 1,483 practicing otolaryngologists, 97% of whom work in some form of private practice as of 2022.[4] Therefore, we estimate about 7000 total sales of the initial device.

Long-term service of the device, such as replacement of cracked GRIN lenses, sale of proprietary speculum tips, and other accessories and consumables relating to the use of the device will provide additional revenue after the initial sale of the probe.

The material cost to produce one probe is approximately $1,400. Fabrication of the final device from scratch is expected to take about 40 man-hours of labor by a trained professional, so labor costs are estimated to be $1,600 per device. Running costs such as electricity, servicing of tooling machines, and accidental damaging of components during manufacturing is estimated to be $500 per device at a maximum. The total cost estimate is $3,500 per device.

OCT probes in the current market sell for about $9,000. However, our device would be one of the only on the market to be inserted into an ear. Considering the novelty of our probe and current probe pricing, we determined a sale price of $12,500.

Yearly sales will be limited by production time. With a small production team of about 20 employees, we estimate a production of 700 to 1000 units annually. This would equate to an approximate yearly revenue of 8,750,000 to 10,000,000 over the course of 7 to 9 years. A yearly profit estimate would be $6,300,000 to $9,000,000 per year from device sales alone.

Our device is only a probe and cannot capture data unless it is connected to an OCT base unit. A base unit supplying broadband light with a center frequency of 1310 nm would cost about $80,000. Additional components, such as the microphone and data acquisition card, will cost an additional $50,000. This upfront cost would negatively impact the initial adoption of our device but will likely improve over time.

ACKNOWLEDGMENTS

We would like to acknowledge our faculty advisors, Dr. H. Park and Dr. W. Dong, for sponsoring this project and guiding us throughout the design process.

REFERENCES

1. World Health Organization. *Addressing the Rising Prevalence of Hearing Loss,* 2018

2. Dong, W & Meenderink, S. *Seminars in Hearing*, (0734-0451). 2023

3. MIDDLE EAR EXPLORATION (OSSICULOPLASTY) for HEARING LOSS. Subent.com, Accessed 18 Nov. 2023

4. American Academy of Otolaryngology. *The 2022 Otolaryngology Workforce.* 2022.

THE FUTURE OF INTRAVENOUS THERAPY INSERTIONS BY USING VEIN FINDER TECHNOLOGY IN EMERGENCY SCENARIOS TO IMPROVE PATIENT SAFETY

U. Akpati, R. Flores, T. Pham

Faculty Advisor(s)

B. Yuan

Biomedical Engineering, University of Texas at Arlington, Arlington, Texas, USA

INTRODUCTION

•First time IV success rates in medical & trauma patients are 80-95%
•IV access is needed in emergency scenarios such as heart attacks to administer medications such as epinephrine or nitroglycerin
•Products such as the Accuvein av500 exist in a hospital setting but there are no options available for use by first responders.
•The av500 uses near-infrared light to penetrate the skin for providing contrast by absorption from de-oxygenated blood in veins.
•The remaining near-infrared is captured by a photodiode then processed to display a negative space in a projection onto the skin.
•A limitation of this product for first responder is that it needs one hand to operate, is dependent on the stability of the operator, and is bulky at 5 x 6 x 20 cm.
•The prototype being developed would allow for a handsfree vein finder that would be affixed to the first responders head to provide a hands-free and reliable way to detect and project vein locations.
•This advancement would incorporate existing technology in a unique design to help in emergency scenarios to provide a stable image on the patient's skin to improve care to those with hypotension or high BMI.
•Utilizing this new scheme, we aim to increase the accuracy for IV placement as well as decrease the time needed to place an IV.

PRODUCT DESIGN

•The enclosure of our portable version of the vein finder was designed in discussion with first responders and has undergone multiple iterations in terms of button placement, charging ports, and sensor positioning.
•Surveys were conducted for 10 individuals on the comfort of the head mounted device.
•For the working principle, a photodetector (FDS1010 - Si Photodiode with 65ns rise time) receives the reflected near-IR signal from the targeted skin region after passing through a 760nm bandpass filter and amplitudes greater than a threshold level will be distinguish as surrounding tissue versus veins.
•A laser that projects at 760nm is ideal as it has high absorbance by deoxygenated blood in veins.
•The laser that will be used to project the mapping onto the skin will have a wavelength of 520nm for maximum visibility in all environments and will be a class 1 laser to ensure patient safety.
•The device will be tested for water resistivity through exposure to moisture and water droplets by spraying water onto the surface to simulate sterilization and it will also be tested for durability by undergoing simulated drop tests.

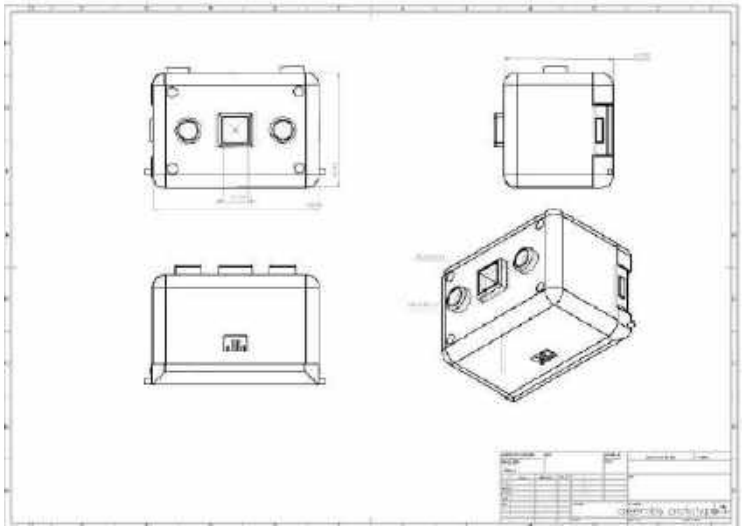

Figure 1: SolidWorks Drawing of Wearable Vein Finder Design

Figure 2: SolidWorks Model of Wearable Vein Finder Design

BUDGET & MARKET ANALYSIS

The design budget for this product is $1000, which has been provided by the University.

The market analysis has been produced based on a $500,000 budget.

Table 1: Market Analysis of Proposed Vein Finder Product

Requested Budget	$500,000
Engineering/Marketing	$100,000
Manufacturing Cost/Unit	$800
Projected Sales Price/Unit	$1,200

With this model, about 500 units would be produced within a year with a $600,000 revenue and a $100,000 profit.
and any investments costs in engineering or tooling.

ACKNOWLEDGEMENTS

This design project was identified and developed from my experience in the Clinical Immersion Program led by Dr. Justyn Jaworski and Dr. Michael Cho. Research and programs reported in this presentation were supported by NIBIB (National Institute of Biomedical Imaging and Bioengineering) of the National Institutes of Health under Award Number R25EB032766. The content is solely the responsibility of the authors and does not necessarily represent the official views of the National Institutes of Health. •We would like to thank the medical professionals and staff at the Arlington Fire Department for sharing their knowledge and for discussions during the program to help better define the clinical need for the project.

References

Evidence | AccuVein, Inc. (2023b, September 1). AccuVein, Inc. https://www.accuvein.com/why-accuvein-evidence/

Rahman, A. B. A., Juhim, F., Chee, F. P., Bade, A., & Kadir, F. (2022). Near infrared illumination Optimization for vein detection: Hardware and software approaches. *Applied Sciences*, *12*(21), 11173. https://doi.org/10.3390/app122111173

RPI camera module - eLinux.org. (n.d.). https://elinux.org/Rpi_Camera_Module

SOFT ROBOTICS FOR PROGRESSIVE VERTEBRAE REHABILITATION

Charmaine Z. Tan (1), Rachel G. Yu (1,6), Michelle P. Haung (1), Thomas Ho (1), Jesse M. Kimie-Brylka (2), Nathan Ou (1,3), Amber Q. Kashay (2), Ian N. Morales (1), Allison Cheng (4), Carissa Ott (5,6) , Evan Y. Zhao (6), Sina Ghadimi (4)

Faculty Advisor(s)

S. Sangiorgio (1)

(1) Department of Bioengineering, UCLA, Los Angeles, CA, USA
(2) Department of Mechanical Engineering, UCLA, Los Angeles, CA, USA
(3) Department of Computational Biology, UCLA, Los Angeles, CA, USA
(4) Department of Electrical Engineering, UCLA, Los Angeles, CA, USA
(5) Department of Psychology, UCLA, Los Angeles, CA, USA
(6) Department of Computer Science, UCLA, Los Angeles, CA, USA

INTRODUCTION

The spine stands as the central support for the human body, essential for our everyday movement and stability. However, the spine's pivotal role in our daily lives underscores its susceptibility to injury and degeneration, accelerated by factors such as poor posture, sedentary lifestyles, repetitive movements (such as those in occupations requiring frequent physical exertion), and aging.

Epidemiological trends reveal a significant increase in both acute and chronic lower back pain (LBP), as well as more severe spinal conditions, on a global scale in recent decades. LBP not only stands as a leading cause of disability in the United States but also imposes a substantial economic burden, with the annual cost of treatment reaching $50 billion in the US alone [1, 2]. Globally, back pain has taken the world by storm, growing from 377.5 million confirmed cases to over 577 million in the span of just 3 decades (1990-2017) [3]. Moreover, projections indicate a substantial rise in spinal procedures like lumbar spinal fusions, particularly in larger, industrialized European populations with aging demographics [4].

Despite the concerning rate of growth in global LBP, contemporary industry has been inadequate in fully satisfying the demands of an ever-growing total addressable market (TAM). For example, NeuroMD Medical Technologies - an incumbent in the field - offers a corrective therapy device for back pain that utilizes electrical stimulation to pinpoint and correct the source of LBP. While impressive, they fall short for customers with preexisting medical conditions who are in need of a more traditional solution since previous treatments may respond unfavorably to external electrical signals - i.e. pacemakers. Additionally, traditional lumbar orthosis has also been scrutinized for potentially weakening lower back muscles due to "oversupport," further exacerbating LBP issues in the future [5].

In this paper, the design and development of Vertiflex, a soft robotic based orthosis (Fig. 1) targeting the thoracic and lumbar spinal regions in prevention of lower back pain, capable of tracking and correcting patient posture and movement, is presented. VertiFlex provides just the right amount of somatosensory feedback to the wearer, promoting a conscious awareness of good posture without doing the "heavy-lifting" that a traditional lumbar orthosis would do. With comfort in mind, VertiFlex digs deep into the contemporary criticisms of current, state-of-the-art LBP devices, searching to provide a much-needed service that has the potential to revolutionize the space of lumbar-focused orthotic devices.

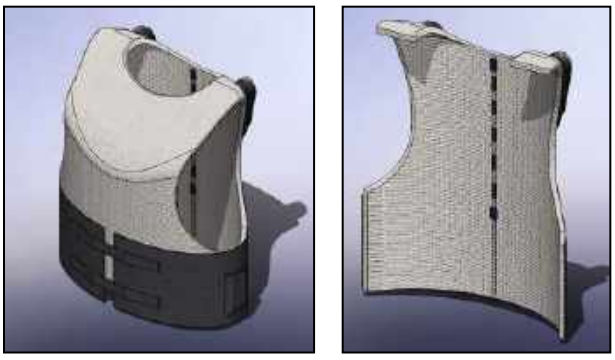

Figure 1. VertiFlex vest exterior with dual-layered canvas and semi-rigid lumbar support

PRODUCT DESIGN

VertiFlex is engineered to address the shortcomings of traditional back braces and at-home posture rehabilitation methods. Its design focuses on providing real-time feedback for spinal strain through an intuitive interface, empowering users with personalized rehabilitation and efficient recovery trajectories. With an emphasis on the thoracic and lumbar spinal regions, VertiFlex combines advanced hardware components with innovative software integration to offer unparalleled

support and correction for spinal health.

VertiFlex's hardware components form the foundation of its functionality, ensuring precise monitoring and effective posture correction. The device incorporates a dual-layered canvas vest designed to house essential hardware, including circuitry, a rechargeable battery pack, and specialized components such as inertial measurement units (IMUs), flex sensors, and pressure sensors, all of which are controlled by a Raspberry Pi. The canvas vest offers durability and flexibility, providing a comfortable fit for users while seamlessly integrating all components for optimal functionality. Positioned strategically at the cervical and thoracic spine regions, IMUs and flex sensors work in tandem to monitor user posture and back movement. IMUs leverage accelerometer and gyroscope data to assess head and neck alignment relative to the thoracic spine, while a band of six flex sensors spanning 30cm along the spine delivers accurate measurements of back flexion and bending. Calibration of IMUs for each user ensures accurate posture positioning, serving as a reference point for evaluating posture alignment.

VertiFlex employs soft robotics technology to actively correct posture deviations detected by the IMUs and flex sensors. The soft robotic component, crafted from silicone (Ecoflex A and Ecoflex B), inflates upon detection of poor posture, exerting gentle pressure to realign the user's spine. Control of air pumped into the soft robotic pouches is managed by PCB circuits based on data obtained from flex sensors. While inflated, pressure sensors are used to offer insight into the internal dynamics of the soft robotics, revealing precise pressure gradients from the air inflation. A dual-pump setup is implemented for each portion of the soft robotic system. With this, each silicone pouch has 2 inputs for tubing connected to the motors and a single output to a solenoid valve. This valve opens as needed to alleviate air pressure during inflation as well as at the conclusion of patient use. To further stabilize the lumbar spine, VertiFlex incorporates a semi-rigid lumbar back brace composed of neoprene for flexibility and high-density polyethylene for enhanced stability. The brace offers support during extension, flexion, and rotation while incorporating velcro fasteners for secure placement. This component ensures optimal spinal alignment and support, further enhancing the device's effectiveness.

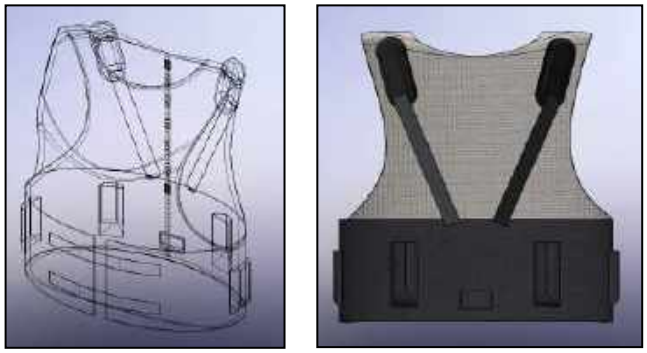

Figure 2. VertiFlex vest outline showcasing incorporated soft robotic silicone pouches, pneumatic air pumps, and semi-rigid lumbar support

VertiFlex seamlessly integrates hardware functionality with a user-friendly software interface, providing users and healthcare providers with valuable insights and tools for effective rehabilitation. The web app interface offers calibration, charts, statistics, and an avatar model for visualizing posture corrections. Real-time data collection and analysis enable the device to track user progress and offer personalized recommendations for posture improvement and pain relief. Machine learning algorithms then utilize this data to offer predictive solutions for strain relief and posture correction. Users can view calibration results, posture charts, and statistics, as well as receive personalized recommendations for posture improvement and pain relief in a user-friendly web app. Seamless communication between users and healthcare providers enables proactive monitoring of progress and adjustment of treatment plans as needed.

BUDGET & MARKET ANALYSIS

Substantial resources will be allocated towards establishing a streamlined production process, targeting an approximate unit cost of $750. These investments encompass materials procurement, initial manufacturing process design, and labor costs. With an estimated 10% of the global population (approximately 770 million) experiencing chronic back pain or conditions necessitating vertebrae rehabilitation, along with moderate market competition and anticipated consumer adoption, the potential market size is projected to range from tens of millions to potentially over a hundred million units annually. The product is meticulously tailored to address this demand, positioning it within a distinct niche market segment.

The company will adopt a business-to-business (B2B) approach, forging direct collaborations with healthcare clinics and physicians to provide the product for prescription to patients. The pricing strategy has been carefully crafted to ensure competitiveness while maintaining sustainable profit margins. With a profit margin of 20% to 30% per unit, the pricing model is set between $999 to $1299 per unit. This pricing structure not only reflects the value proposition of the solution but also offers flexibility to cater to various market segments.

The return on investment (ROI) strategy revolves around enhancing patient communication and engagement, leveraging the product's effectiveness in preventive back pain management. Through targeted marketing initiatives and strategic partnerships, the aim is to capitalize on this ROI while upholding regulatory compliance and industry standards. By adeptly navigating the interplay of budgetary considerations and market dynamics, the product is poised to secure a robust foothold in the market, presenting a compelling solution to individuals grappling with the debilitating effects of back pain.

ACKNOWLEDGEMENTS

This work was supported by the Biomedical Engineering Society (BMES) chapter of University of California, Los Angeles (UCLA); funding from the UCLA Samueli Engineering Alumni Association; and funding from a UCLA Spark campaign.

REFERENCES

[1] Druss, B.G. et. al., *Health Affairs*, 21(4):105-111, 2002.
[2] Pai, S et al., *Orthop Clin North Am.* 35(1):1-5, 2004.
[3] Wu, A et al., *Ann Transl Med.*, 8(6):299, 2020.
[4] Heck, V et al., *Clin Orthop Relat Res.*, 481(8):1610-1619, 2023.
[5] Eisinger, D et al., *Am J Phys Med Rehab.*, 75(3):194-197, 1996.

RAPID THERMAL CONTROL OF LIQUIDS (REALCOOL): DEVELOPMENT OF A FOUR-COMPARTMENT TRANSIENT HEAT TRANSFER MODEL

N.M. Hannon, M.N. Rylander, C.G. Rylander

Walker Department of Mechanical Engineering, The University of Texas, Austin, TX, USA

INTRODUCTION

Existing methods for heating or cooling liquids often rely on conduction of heat through a vessel wall which is time consuming, especially when the vessel is constructed of thermally insulating materials like thermoplastic or glass. Additionally, these methods often do not monitor or control liquid temperature, resulting in final temperature above or below what is desired. For example, most commercially available human milk warmers used to prepare milk for babies consist of a simple water bath and immersion heater. They require the user to wait over 5 minutes to heat a plastic bottle containing 240 mL of pumped and refrigerated milk from ~4-10°C to a serving temperature of ~37°C, and they do not notify the user when the milk has reached the desired temperature.

RealCooL (Rapid Thermal Control of Liquids) is a novel technology and device that can rapidly heat or cool many liquids to a desired user-input temperature. The liquid temperature can be quickly and accurately controlled through a closed loop system which monitors temperature at multiple sites and actuates fluid pumps, valves, and a high-powered heater. The current RealCooL prototype utilizes a 10-plate heat exchanger (HX), two diaphragm pumps, two solenoid valves (to switch between heating and cooling mode), a cartridge heater, and food safe silicone tubing as shown in Figure 1. While this prototype has shown feasibility of rapid and accurate heating and cooling of several liquids, further refinement is necessary to optimize the design for specific applications.

Through extensive interviews conducted during the National Science Foundation National I-Corps™ program, we found a need for a device such as RealCooL to warm human milk for babies, which is the primary use case in this study. In particular, the design should accommodate volumes of milk up to the size of a full bottle (typically 240 mL), and accommodate the unique material properties of milk (*i.e.*; density, thermal conductivity, and specific heat). The system components should be sized appropriately to warm milk from refrigerator to serving temperature in under 2 minutes.

In order to refine the design of RealCooL for the milk warming use case, including optimal selection of components such as heater, HX, and fluid pumps, we needed to better understand the heat transfer processes involved in this system. To do so, we developed a four-compartment transient heat transfer model and compared model results with experimental results generated from our current RealCooL prototype.

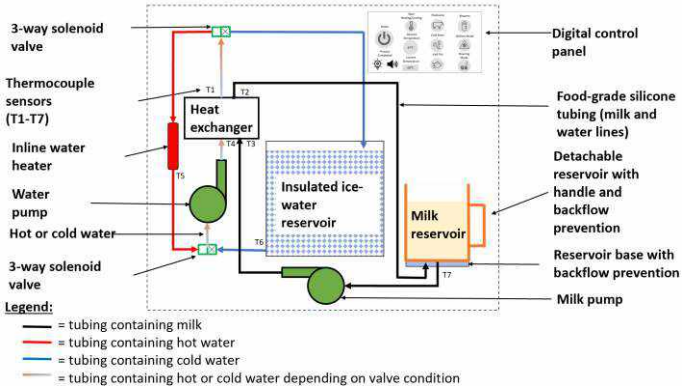

Figure 1: Schematic of RealCooL Prototype

METHODS

We developed a four-compartment transient heat transfer model to represent the RealCooL system and serve as a future tool for design optimization for specific use cases including human milk warming. The system was simplified into four linearly-adjacent compartments: 1) heater, 2) water, 3) HX, and 4) milk. Each compartment was assumed to have spatially uniform temperature throughout, as verified by a low Biot number for the solids and a well-mixed condition for the liquids.

The overall system was insulated from the surrounding environment. An energy balance on each of the compartments was used to determine the governing equation relating the change of temperature with respect to time of the compartment with respect to heat storage (capacitance) of the compartment and heat transfer (resistance) between adjacent compartments. The additional constitutive equations related the convective heat fluxes between adjacent compartments to the temperatures of each compartment [1]. Uniform volumetric heat generation was assumed within the heater. The initial temperature of the heater, water, and HX was 20℃, and the initial temperature of the milk was 10℃. A numerical method (ode45, MATLAB™, USA) was used to solve the system of four coupled ordinary differential equations, resulting in the transient temperature of each compartment.

The model required geometric and material properties for each of the four compartments in order to calculate their respective thermal capacitance as well as resistance to heat flow between them. Values used in the model correspond as closely as possible to the actual manufacturer-specified or measured components in the current RealCooL prototype. The heater is a 304 stainless steel 1500 W cartridge heater (DERNORD, China). The HX is a 10-plate 304 stainless steel HX (B3-5A-10, Duda Diesel, USA). Water and human milk volumes and material properties were obtained from published sources [2]. The heat transfer convection coefficients on interfaces between compartments were calculated based on diaphragm pump (SFDP1-012-035-21, SEAFLO, China) measured flow rates and geometry of contact surfaces via intermediate calculations of dimensionless parameters including Reynolds and Nusselt numbers.

Results of the mathematical model were compared with experimental data collected from RealCooL. 240 mL of fresh dairy milk was warmed from 10℃ to 37℃, and 6 T-type thermocouples were placed throughout the system to gather transient temperature data using a data logger (S220-T8, HUATO, China). The first thermocouple was placed in the milk reservoir. The second thermocouple was placed directly downstream of the cartridge heater, measuring the maximum temperature of the water. Four more thermocouples were placed on each of the four ports of the heat exchanger: milk inlet, milk exit, water inlet, and water exit. The water and milk pumps and heater were all energized at t=0.

RESULTS

The model predicted that RealCooL should take about 52 s to heat 240 mL of milk from 10℃ to 37℃ (Figure 2). All four compartments show a nonlinear temperature dependence on time, with more nonlinearity at earlier times. A small dip in HX and water temperature is observed at the beginning of the simulation, which is caused by the transfer of heat from these components to the cold milk. At later times, as the heater temperature is much greater, the transient temperature of each compartment appears more linearly related to time.

Experimental data gathered with the RealCooL prototype showed it took 72 s to warm 240 mL of dairy milk from 10℃ to 37℃ (Figure 3). Results demonstrated a linear temperature vs. time dependence for all thermocouples. Temperature variation was observed across the four HX ports, with a 5℃ difference in temperature between the water inlet and outlet ports on the HX, and about 3℃ difference in temperature between the milk inlet and outlet ports. The milk outlet temperature is about 3℃ less than the water outlet temperature at all times.

DISCUSSION

The transient heat transfer model demonstrates some of the characteristics experimentally observed with the RealCooL prototype. In particular, at later times, all transient temperatures have a linear time dependence. Additionally, at around 1 minute into both the simulation and experiment, the difference in temperature between water and milk was about 15℃. These similarities provide a level confidence that the assumptions built into the simulation are appropriate.

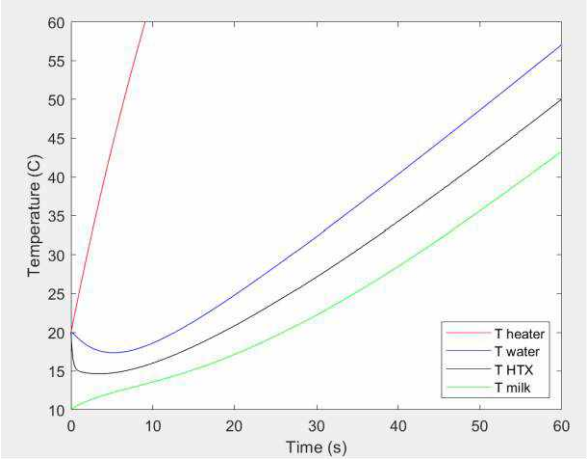

Figure 2: Mathematical Model Data

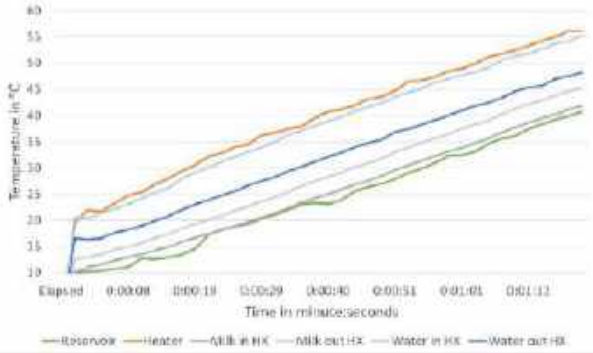

Figure 3: Experimental Data

Unfortunately, there are some discrepancies in the time for the milk to reach the desired final temperature (52 s in the model vs. 72 s in the experiment). The model accuracy may benefit in the future by including a fouling factor on one or both sides of the HX which is an additional realistic resistance to heat transfer and will more closely align the model with experimental results. Additionally, we assumed that there was no spatial variation of temperatures within the HX compartment, which is not accurate based on the four different temperatures experimentally recorded on each port of the HX. However, it may still be acceptable to model the HX as a single compartment with a temperature equivalent to the average of the temperatures at the four ports for purpose of predicting transient milk temperature.

ACKNOWLEDGEMENTS

We would like to acknowledge the National Science Foundation I-Corps™ program for partially funding this project under NSF award #2228384. Additionally, authors MNR and CGR are co-inventors on PCT application WO/2023/240034 related to RealCooL technology.

REFERENCES

[1] Bergman, G.L. et al., *Fundamentals of Heat and Mass Transfer Seventh Edition*, 978-0470-50197-9, 2011

[2] More, G. R., & Prasad, S. (1988). *Thermal conductivity of concentrated whole milk.* Journal of Food Process Engineering, 10(2), 105–112. https://doi.org/10.1111/j.1745-4530.1988.tb00007.x

EFFECTS OF SEMI-OCCLUDED VOCAL TRACT EXERCISE ON VOCAL FOLD BIOMECHANICS AS OBSERVED DURING HIGH-SPEED VIDEOENDOSCOPY

David S. Ford (1), Dimitar D. Deliyski (2)

(1) Department of Speech-Language Pathology, John G. Rangos Sr. School of Health Sciences, Duquesne University, Pittsburgh, PA, USA

(2) Department of Communicative Sciences & Disorders, Michigan State University, East Lansing, MI, USA

INTRODUCTION

Semi-occluded vocal tract exercise (SOVT) is a common technique/posture used in both habilitation and rehabilitation of the voice. By narrowing, but not completely occluding, the vocal tract at one end (e.g. the lips), a backpressure is created, which assists in coupling the source (vocal fold vibration) and the filter (vocal tract) of voicing. This coupling results in various physiologic changes which collectively have a profound impact on voice production. Physiologic changes include: maximized impedance matching by increasing vocal tract inertance [1], better distribution of acoustic energy [2], decreased phonation threshold pressure [3], increased maximum flow declination rate and increased strength of high harmonics [4], a "squaring up" shape of the vocal folds [5], reduced collision pressure during vocal fold adduction [6], increased thyroarytenoid muscle to cricothyroid muscle ratio resulting in thicker vocal folds with a more pliable cover, decreased vertical position of the larynx [7], and relaxation of intrinsic and extrinsic laryngeal musculature during phonation [8].

While the effects of SOVTs are well represented throughout the literature with regard to acoustic and aerodynamic effects, vocal economy and efficiency, and laryngeal biomechanics, most findings were the result of modeling and theoretical constructs. Few studies have investigated SOVTs experimentally and even fewer have explored the effects of the technique *during* SOVT production. This study aims to elucidate these gaps in knowledge by exploring the effect of SOVT exercise on vibratory characteristics of the vocal folds, using objective measures derived from high-speed videoendoscopy.

METHODS

Given the pioneering nature of this study and the timing of data collection occurring at the height of the COVID-19 pandemic, results were treated more as a qualitative proof-of-concept, than a study of statistical significance. There were only two participants (one male and one female) in this study, but the robustness of the collected measures was generated by the large number of "frames" of video data. Neither participant reported current voice, speech, medical, or behavioral impairments that may impact phonatory function, nor a history of voice rehabilitation or habilitation.

A custom-designed high-speed videoendoscopy (HSV) system was used, consisting of a FASTCAM Mini AX200, M4 32GB high-speed camera (Photron USA, Inc., San Diego, CA), controlled by MSI GL63 8SE laptop camera control system, coupled with a 45-mm endoscope lens adapter Model 9117 (Pentax Medical, Montvale, NJ), a 3.5-mm flexible fiberoptic endoscope FNL-10RP3 (Pentax Medical), an audio recording interface (Focusrite Scarlett 2i2 2nd Gen), and an AKG C420 headset condenser microphone for simultaneous capturing of the acoustic signals. The HSV system was used to record sustained /i/ vowel phonation productions from the two vocally healthy adults before, during, and immediately after SOVT exercises at the speed of 4,000 frames per second (fps). The image analysis and measurements were performed using a video viewing software (PFV4 Photron FASTCAM Viewer, Photron USA, Inc., San Diego, CA), which allowed for variable playback speed. The SOVT exercises were phonation into a 19.7 cm plastic straw with a 5.59 mm diameter and submerging the straw into an 8 oz cup filled with 4 oz of water. The protocol amounted to 20 seconds of total recording time, which allowed for partitioning of the camera's memory into two, 10-second partitions as seen in **Figure 1**.

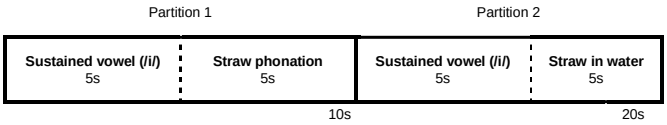

Figure 1: Schematic of memory partitioning of the HSV examination protocol

The specific variables of vocal fold vibratory behavior analyzed were glottal attack time (GAT), which is defined as the time between

the first vocal fold oscillation modulating the airflow and the first vocal fold contact [9], glottal offset time (GOT), which is the time between the final vocal fold contact and the final vocal fold oscillation, and glottal contact closed quotient (GCCQ), which is referring to the intra-cycle ratio (%) the vocal folds spend in the closed phase, relative to the period.

RESULTS

The values for GAT, GOT, and GCCQ are presented in **Table 1**. While complete normative values are not readily available for all measures, reference values for GAT have been reported as follows [9]: in "comfortable" glottal onsets, attack times ranged from -1.4 to 9.6 ms, in breathy glottal onsets, they ranged from 7.6 to 38.0 ms, and in hard glottal onsets, they ranged from -9.5 to -1.7 ms. Perhaps more important than the actual values is the concept that comfortable onsets are generally short and positive, breathy onsets are long and positive, and hard onsets are negative. The two unreported GOT values are because of offsets which were not captured due to anatomical structures obscuring the view of the glottis.

Table 1: Objective vocal fold vibratory measures collected using HSV for each participant

Variable	Participant 1 (M)			Participant 2 (F)		
	GAT	GOT	GCCQ	GAT	GOT	GCCQ
Straw phonation into water	8.8	8.8	.205	35.0	64.0	.023
Straw phonation	8.0	15.0	.019	12.0	26.0	.008
Pre-SOVT /i/	-13.0	7.7	.014	-12.0	-	.014
Post-SOVT /i/	14.0	15.5	.022	24.0	-	.011

*All values in milliseconds

In general, both participants' GAT values trended toward longer, positive values during SOVT exercises, compared to sustained phonation pre-SOVT. This trend was more pronounced for straw phonation into a cup of water than for straw phonation alone. Both participants demonstrated negative GAT values consistent with hard glottal onsets, prior to SOVT production, and with breathy glottal onsets following SOVT production. GOT values cannot be interpreted due to missing data, but it appears the trend would be similar to GAT. The results for GCCQ were more variable with a sizable increase in time spent in the closed phase for participant 1 during straw phonation into a cup of water and a modest increase for straw phonation alone. A similar increase in GCCQ was noted for participant 2, but a decrease in GCCQ was noted for straw phonation alone. **Figure 2** illustrates participant 2's increase in GCCQ from sustained phonation to straw phonation into a cup. It also demonstrates additional descriptive information that was consistent across both participants, the existence of supraglottic activity.

Although not objectively measured, visual inspection of the HSV data revealed anterior-posterior squeezing of the supraglottic structures during participant 2's sustained vowel phonation. This squeeze behavior was not present during either SOVT exercise. There was also lateral squeezing of the false vocal folds during participant 1's sustained vowel phonation, which was not present during the SOVT trials. The extent of the supraglottic activity was much less significant for participant 1 compared to participant 2.

DISCUSSION

The trend of increased GAT across both participants, during SOVT, was expected and supports the notion that that there is a "cushioning" effect on vocal fold contact pressure during SOVT postures. It was somewhat surprising that GAT was longer during straw phonation into water than during straw phonation alone, but this can be explained by the density of the water providing more resistance than the air, therefore requiring more vocal fold collision pressure to overcome the resistance.

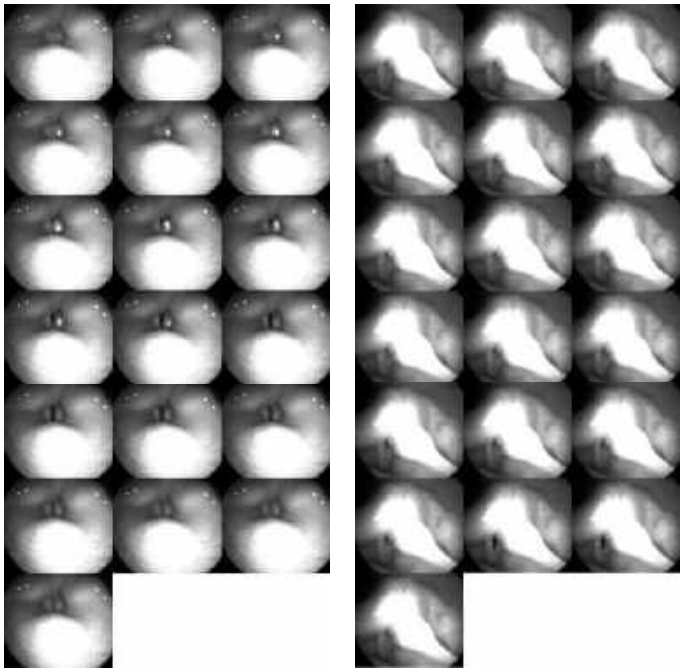

Figure 2: HSV images depicting GCCQ over 19 frames (one glottal cycle in this case) for sustained /i/ (left) and straw phonation into a cup of water (right)

The variability of the GCCQ measure across the participants was somehow both expected and surprising. While it was hypothesized that GCCQ would decrease, due to less "pressing" of the vocal folds during SOVT exercise, paradoxical results were found. GCCQ increased during straw phonation into a cup of water for both participants and during straw phonation for participant 1. The only decrease in GCCQ was observed during straw phonation for participant 2. Perhaps the reason for the increased GCCQ is similar to the previously referenced assumption that the increased resistance provided by the SOVT required additional muscle recruitment to overcome, contributing to a more "pressed" vocal fold posture. This explanation makes more sense for GAT and other measures of glottal onset, since any additional effort required to overcome the SOVT resistance is unlikely to have an impact on vocal fold vibration that persists cycle-after-cycle.

ACKNOWLEDGEMENTS

Data collection for this project was completed entirely at Mayo Clinic Arizona with the assistance of Dr. Stephanie Zacharias and Dr. David Lott.

REFERENCES

[1] Story, B.H. et al., *J Voice*, 14(4):455-469, 2000.
[2] Bickley, S. et al., *Vocal Fold Phys*, Singular: 239-253, 1991.
[3] Kang, J. et al., *J Voice*, 33(5): 810e5-810e11, 2019.
[4] Titze, I.R., *J Speech, Lang, Hear Res.*, 49(2): 448-459, 2006
[5] Titze, I.R., *J Acoust Soc. Of America.*, 135: 2091–2101, 2014
[6] Laukkanen, A.M., *Folia Phon et Logop*, 60(6): 298-311, 2008
[7] Titze, I., *Journal of Singing*, 74(3): 311-312, 2018.
[8] Bele, I.V., *Logopedics Phoniatrics Vocology*, 30(1): 34-40, 2005.
[9] Orlikoff, R.F. et al., *J Voice*, 23(2): 164-168, 2009.

IN VITRO PLATFORMS TO ASSESS THE SPATIAL RESPONSE TO BURN INJURY AND THERMOEMBOLIZATION

S. Brocklehurst (1), A. Sabaghan (1), M. N. Rylander (1)

(1) Department of Mechanical Engineering, The University of Texas at Austin, Austin, Texas, USA

INTRODUCTION

The capability to characterize the spatial and temporal thermal and mass transport and biological response to a diverse range of stimuli within physiologically representative experimental systems is of profound importance. Applications for which this would be meaningful include prediction of burn injury response, assessment of treatment efficacy of thermal and chemical based treatments, and measurement of transport of diagnostic and therapeutic agents.

Experimental systems for measuring biological response include *in vitro* and *in vivo* models and *ex vivo* tissue. Existing *in vitro* models fail to capture sufficient physiological complexity while *in vivo* models lack spatial and temporal precision in a cost-effective manner. Computational models exist, but are frequently based on limited experimental data necessary for validation. *In vitro* microfluidic platforms have emerged as an attractive option for mimicking appropriate physiological complexity while enabling the spatial and temporal response to be measured in a high throughput manner.

Our team has been developing advanced, biologically representative *in vitro* tissue platforms for the past 15 years [1-3]. Our platforms model the cellular complexity of the system of interest, mimic the extracellular matrix (ECM) of the respective tissue, and incorporate fully functional blood vessels and lymphatics with physiological flow. This abstract will focus on the development and utilization of these platforms for modeling contact burn injury and thermoembolization.

METHODS

In vitro platforms were created as we have previously published to predict the spatial and temporal response to burn injury [1]. For this application, human dermal keratinocytes and fibroblasts were embedded in collagen type 1 hydrogels in a multilayer structure recreating the epidermis and dermis. Buffer solutions for creating the collagen ECM were prepared by mixing 1X DMEM, 10X DMEM, and 1 M NaOH. The buffer was combined with 6 mg/mL collagen containing fibroblasts at 100,000 cells/mL stock solution in a 1:1 ratio. Two parallel vascular channels were embedded within the dermis and enabled perfusion of physiological flow. To create the vascular channels two shortened 22-gauge blunt tip needles were inserted into the platform and polymerized within the collagen ECM as previously published [2,3]. Keratinocytes were mixed into collagen gels in the same fashion as above, then 120 µL of the keratinocyte-bearing mixture was pipetted onto the top of the platform. Both layers were polymerized together to create a multi-layer structure. After the lower layers were created and placed in an incubator, fibroblast media was added to the platform for culture in the incubator for 24 hours before burn exposure. Platforms were exposed to contact burns for 3 seconds using a 3 mm diameter cylindrical copper tip heated to 50, 65, 75, 85, or 100 °C. Different platforms were exposed to varied vascular flow regimes: no flow, parallel, and opposing endothelial media flow of 520.5 µL/minute in each channel to induce a wall shear stress of 2 dyn/cm^2 for at least 3 seconds before applying the contact burn, and at least 5 seconds afterwards during the cooling phase. The spatial cell viability was measured 24 hours following contact burns for varied flow regimes by means of staining with calcein (stains live cells green) and propidium iodide (stains dead cells red) and imaged with confocal microscopy. Horizontal cross-sections of the platforms were analyzed in 90 µm thick sections and the area of the ablated region was measured for each section using ImageJ. COMSOL Multiphysics (6.1) was used to determine the spatial and temporal distributions of temperature within skin platforms during and immediately after exposure to contact burns similar to our published work [1]. Experimentally measured contact burn ablated volumes were analyzed with computationally predicted spatial and temporal temperature distributions to determine the process coefficients A and E_a for burn injury that best describe the results.

We also used our *in vitro* platforms to characterize the response to thermoembolization treatments that foster changes in ph, temperature, and oxygen concentration and for which the spatial and temporal

distribution can be characterized. For these experiments, *in vitro* platforms consisted of a similar type 1 collagen hydrogel of identical concentration with a single embedded vascular channel. To simulate thermoembolization, 150 µl of 3M and 1M dichloroacetyl chloride (DCACl) solutions dissolved in poppy seed oil were loaded into syringes. These solutions were then injected into the microchannel using a 24-gauge needle and perfused at 10 µL/minute with a syringe pump. A high-resolution infrared thermal camera (model: FLIR T62101) was utilized to monitor temperature distribution in the gel over time, offering a top-view perspective. A K-type thermocouple and ph probe were also used to measure temperature and ph respectively.

RESULTS

Contact Burns: Figure 1 shows the spatial cell viability a function of contact burn tip temperature and model predicted temperature based on the Penne's equation for countercurrent vascular flow in the skin platforms. It is evident that for increasing tip temperatures, the ablated tissue volume increase (Figs. 1A and 2) and temperature elevations are more significant (Fig 1B).

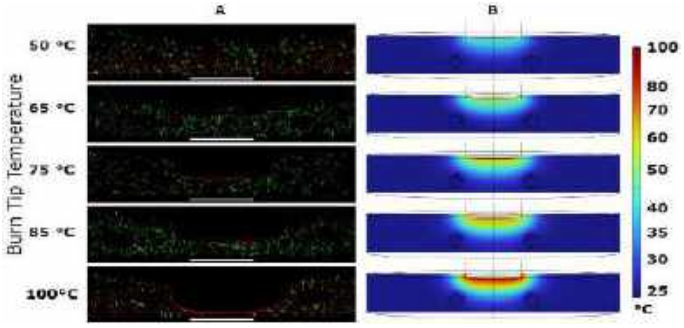

Figure 1- Experimentally measured cell viability distribution and model predicted temperature with varied tip temperatures - A: Cell viability determined with calcein/propidium iodide staining with live cells in green and dead cells in red showing cross sections of skin platforms 24 hours after contact burns. Scale bar = 3 mm. B: Computational model predicted temperature distributions of skin platforms after 3 seconds of contact burn exposure.

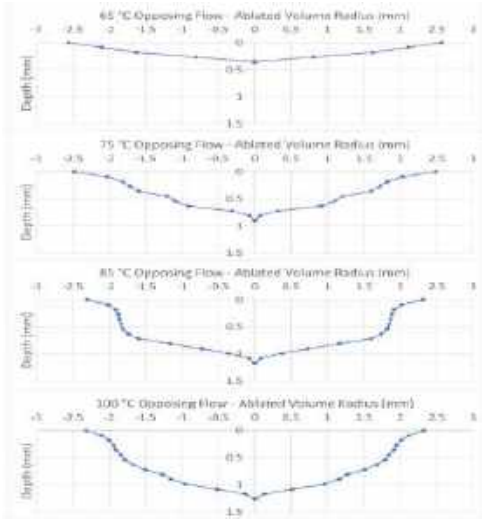

Figure 2- Average cross-sectional profiles of ablated regions of contact burns from contact tips of varied temperature for opposing flow, mm units.

Thermoembolization Results: Figure 3 illustrates the temperature distribution immediately after and 60 seconds following the injection of DCACl solutions (3M and 1M) into the platform vessel microchannel. The interaction of the DCACl solution with the collagen surrounding the microchannel resulted in an exothermic reaction, causing a temperature increase in the injection vicinity. Moreover, the data demonstrates that the higher concentration of DCACl (3M) induces a more pronounced temperature elevation in the platform compared to the lower concentration (1M). This effect extends over a larger spatial area and persists for a longer duration. Additionally, regarding the images taken with the visible light camera, given the use of phenol red in the gel (as a component of DMEM) and knowing the fact that its color shifts to yellow in acidic pH conditions, a notable pH decrease around the injection area is observed over time following the administration of DCACl (3M) which is greater than DCACl (1M). Figure 4 (A) depicts the maximum temperature increase, while Figure 4 (B) displays the pH following the addition of 150 µl of DCACl at concentrations of 1, 3, and 10.4 M to the collagen platform within a 24-well plate, encompassing gel concentrations of 4 and 7 mg/ml. Notably, while the variations in gel concentration does not show a meaningful impact on both temperature and pH, elevating the DCACl concentration from 1 to 10.4 M reduces the pH level. In addition, a slight increase in temperature rise is observed when raising the DCACl concentration from 1 to 3 M. However, temperature rise substantially escalates upon further increase in the DCACl concentration from 3 to 10.4 M.

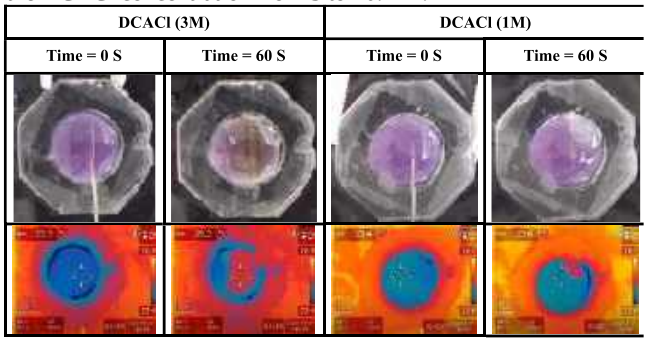

Figure 3- Images of the microfluidic platform taken by visible light camera (1st row) and infrared thermal camera (2nd row) 0 and 60 seconds after injection of DCACl with concentrations of 1 and 3M.

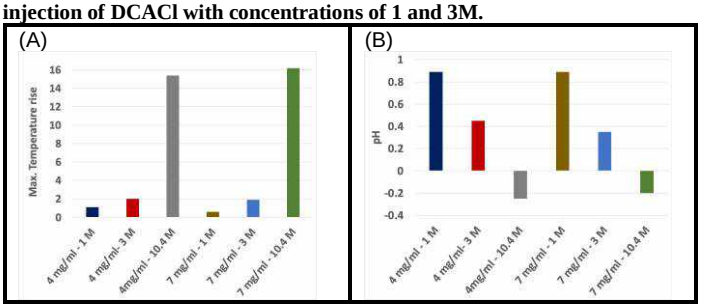

Figure 4- Maximum temperature rise (A) and pH (B) after adding 150 µl of DCACl solutions (1, 3, 10.4 M) to 1.5 ml of collagen gel (4 and 7 mg/ml).

DISCUSSION

The *in vitro* platforms used in this study enabled measurement of pH and spatial temperature and cell viability for varying treatments. This type of quantitative information was not previously possible with animal models or existing *in vitro* systems and will permit prediction of the tissue response critical for treatment planning.

ACKNOWLEDGEMENTS

We would like to acknowledge funding from the joint Texas Advanced Computing Center, Oden Institute, and MD Anderson Cancer Center.

REFERENCES

[1] Brocklehurst S. et al., *Bioengineering*, 17;10(2): 265, 2023.

[2] Gadde M. et al., *Cancers*, 15(19): 4883, 2023.

[3] M. Gadde, et al., *Biotechnology and Bioengineering*, 117(11):3572-3590, 2020.

SYNERGETIC EFFECTS OF PERIODICALLY MILD HYPERTHERMIA AND ULTRASOUND TREATMENT ON OSTEOGENESIS IN AGED HUMAN MESENCHYMAL STEM CELLS

D. Dawkins and S. Wang

Biomedical Engineering Department, City University of New York/City College, New York, NY, USA

INTRODUCTION

With a growing, longer lived elderly population, osteoarthritis (OA) is the most common form of chronic arthritis and affects millions of people annually with an inevitable joint degeneration including joint cartilage and subchondral bone [1]. The almost ubiquitous presence of OA amongst this population limits their mobility and increases demand for specialized health care workers, leading to a heavy burden on the financial portion of the healthcare system as a whole [2,3]. During 2019 to 2021, 21.2% of U.S. adults (53.2 million) reported diagnosed arthritis [2], wherein 32.5 million adults are OA patients [3]. Furthermore, OA was the second most costly health condition treated at US hospitals in 2013 [4]. In that year, it accounted for $16.5 billion, or 4.3%, of the combined costs for all hospitalizations [4]. OA has long been viewed and labeled as an inevitable disease due to wear and tear of the joint (articular) cartilage and is seen as synonymous with aging. Cells that compose articular cartilage, chondrocytes, are mostly tasked to maintenance of the cartilage structure and cartilage is not vascularized or innervated, and does not have the capacity to regenerate or repair itself [1]. Articular cartilage is nourished via the surrounding synovial fluid, whose nutrition/biological activities is supported and regulated by subchondral bone. Inflammation is not obviously detectable in the early stage of OA, but become evidential in synovial membrane/joint capsule, leading to thick and cloudy synovial fluid, swelling joint, degeneration of cartilage and subchondral bone, and then subchondral bone spur and pain along the timeline of worsening of the OA development [5, 6, 7]. There is no effective cure for OA currently except whole joint replacement for patients with the late stage of OA and usually over 60 years-old. Pain and inflammation mitigation methods, such as NSAIDs (nonsteroidal anti-inflammation drugs), hyaluronic acid injection, braces/orthotics, and minor invasive arthroscopic surgery to trim off teared cartilage debris [8], are not effective to prevent the progress of OA or tissue repair, especially in mid-aged and old adults [9].

Prevention and tissue regeneration approaches were chosen in our study of this challenge. Targeted therapeutic ultrasound has been proven to heal non-union fractures bone in rat models [10], and has been utilized in physical therapy of muscular skeletal injury due to its portability and non-invasive properties [11]. On the other hand, the previous study from our lab shows that periodically mild hyperthermia (i.e., 1 hour at 39°C for every other day over a couple of weeks) facilitates osteo- and chondrogenic differentiation of human mesenchymal stem cells by ~30% via the regulation of heat shock protein 70 [12-15]. A study into the regenerative and anti-inflammation properties of human mesenchymal stem cells (hMSCs) combined with therapeutic ultrasound to perform thermal and mechanical loading stimulations simultaneously may deliver a different OA mitigation and treatment strategy.

METHODS

In order to investigate the synergetic effects of mild hyperthermia and ultrasound treatment on osteogenesis in old human mesenchymal stem cells, two types of ultrasound (US) transducers were used, plane-wave one to provide ultrasound (US) wave for mechanical loading while focused US transducer to provide heating at 39±0.5°C and mechanical loading. As shown in Figure 1, hMSCs were seeded in 12-well plates at 5,000 cells/cm^2 and US transducers were located under the plate with US coupling get in-between. To produce the waveform required for LIPUS, a single channel function generator (Tektronix, Inc., AFG3251) set to pulse burst mode was used to generate the pulses. LIPUS dictates that the signal must have a 20% duty cycle, with a 1 kHz repetition rate. The focused transducer is a 1 MHz custom cubic immersion transducer constructed specifically for this purpose by NDT Systems Inc. (IEMF0.18) that features a 2-inch focal length with a spherical focus, with an 1-inch diameter element. The 1 MHz cubic plane wave transducer also constructed by NDT Systems Inc., (IEMF0.13) is also

custom made, cubic and features a 0.375-inch diameter element. The pulsing voltage profile was based primarily around the focused transducer: 90 mVrms out to the amplifier for 6 minutes, followed by a drop in voltage to 45 mVrms for 42 minutes, accompanied by one more drop to 40 mVrms for 18 minutes for a total of 1 hour and 6 minutes of exposure to ultrasound pulses. Plates were pulsed every other day for an hour each. To emulate indirect heating conditions as used in the prior experiment, an incubator at 39°C was utilized, and cells were placed into the incubator for 1 hour plus the time taken to maintain a 39°C temperature for at least one hour, once every other day.

To mimic the MSCs coming from mid-to-old people, hMSCs of passage 5 (P5) and 6 (P6) were used in the experiments instead of passage 3 or 4. The standard hMSC growth medium, Dulbecco's modified Eagle's medium, low glucose with 10% fetal bovine serum and 1% penicillin-streptomycin were used. For osteogenic medium, hMSC growth medium was supplemented with 50 µM L-ascorbic acid phosphate magnesium salt n-hydrate, 0.1 µM dexamethasone, and 10 µM β-glycerophosphate disodium salt hydrate. Assays of ALP activity and calcium deposition were performed to evaluate hMSC osteogenesis. Total DNA content of samples was used to normalize the data. ANOVA was used for statistical analysis.

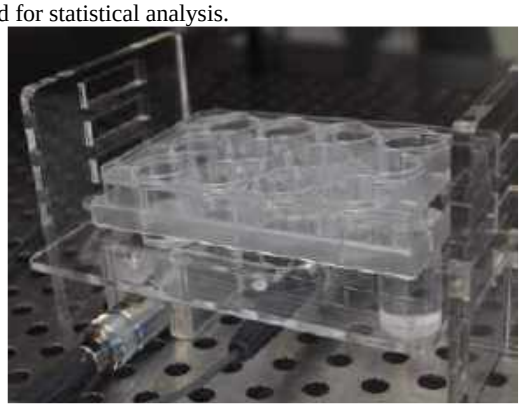

Figure 1: Device set-up to host ultrasound transducers below the 12-well culture plate.

RESULTS

As shown in Figure 2, P5 MSCs undergoing osteogenesis show significantly higher values of ALP activity at both time points (Day 6 and 12) for the US pulsed conditions than that of the incubator 37°C control ($p < 0.01$) condition. Interestingly, for P5 MSCs, there is no significant difference between the incubator 39°C condition and the incubator 37°C control.

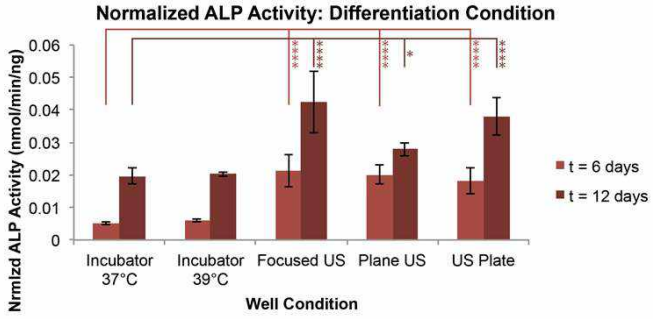

Figure 2: ALP activity normalized with DNA content at 6 days and 12 days for the differentiated P5 MSCs. Error bars denote standard deviation. Lines indicate a comparison to the incubator 37°C control. Statistical significance denoted by ** is equivalent to $p \leq 0.0001$, * is equivalent to $p \leq 0.05$.**

Osteogenic P6 hMSCs on Day 19 of differentiation were used in the calcium deposition assays. Calcium deposition is significantly higher in both US stimulated conditions than that of the incubator 37°C control or incubator 39°C condition (Data not shown here). However, there is no significant difference between the samples of two types of US conditions.

DISCUSSION

The results demonstrate that the synergetic stimulation of thermal and mechanical loading using focused ultrasound can rescue the function of heat-enhanced osteogenesis in older hMSCs. If this synergetic effect exists for chondrogenic differentiation in old hMSCs needs to be further investigated. In addition, separation of the focused transducer and the plane wave transducer in different culture plates should be paramount. In this study, we kind of artificially generated aged hMSCs by passage cells for more than 4 generations using in vitro subculture methods. The same experiments should be repeated using hMSCS isolated directly from aged mammals (e.g. mice) since obtaining hMSCs from aged human being is probably not possible. In terms of mechanism studies of the synergetic effects, mechano-sensing signaling pathways (e.g. TRPV receptors) will be investigated.

ACKNOWLEDGEMENTS

The study was supported by NIH/NIA grant to S.W. and Louis Stokes Alliances for Minority Participation (LSAMP) scholarship to D.D.

REFERENCES

[1] Berenbaum, F., Osteoarthritis Cartilage, 2013. 21(1): p. 16-21.
[2] Fallon, E.A., et al., MMWR Morb Mortal Wkly Rep. 2023 Oct 13; 72(41): 1101–1107.
[3] US Bone and Joint Initiative: The Burden of Musculoskeletal Diseases in the United States (BMUS), Fourth Edition. Rosemont, IL.
[4] Torio C.M, Moore B.J. National Inpatient Hospital Costs: The Most Expensive Conditions by Payer, 2013. Rockville, MD., 2016.
[5] Nalbant, S., et al., Osteoarthritis and Cartilage, 2003. 11(1): p. 50-54.
[6] Reimann, I., Clin Orthop Relat Res, 1976(119): p. 237-41.
[7] Goldring, M.B. et al., Ann N Y Acad Sci, 2010. 1192(1749-6632).
[8] Crawford, D.C., et al., Orthop Rev (Pavia), 2013. 5(1): p. e2.
[9] Jackson, R.W. et al., J Bone Joint Surg Br, 1982. 64(4).
[10] Takikawa, S., et al., J Ultrasound Med, 2001. 20(3): p. 197-205.
[11] Miller, D.L., et al., J Ultrasound Med, 2012. 31(4): p. 623-34.
[12] Chen, J., et al., Tissue Engineering Part A, 2013 Mar;19(5-6):716-28.
[13] Chen, J., et al., PLUS One, March 14, 2014; 9(3): e91561.
[14] Li, C., et al., Sci. Rept., January 18, 2018.
[15] Sunderic, K., et al., J Biomech Eng. 2021 Jan 1;143(1):011006.

SB³C2024
Summer Biomechanics, Bioengineering and Biotransport Conference
June 11-14, Lake Geneva, WI, USA

KEN DILLER AND BIOHEAT TRANSFER

J. Bischof

Mechanical Engineering Department, University of Minnesota Twin Cities, Minneapolis, MN, USA

ABSTRACT

This talk will celebrate Dr. Ken Diller's retirement by highlighting some of his lasting impact on the field of bioheat transfer. Ken is known not only as an excellent engineering scientist, but also a caring and thoughtful educator, mentor and historian of the field. His contributions range from the first micro-processor controlled cryomicroscope (the prototype of which is shown in Figure 1 (1), to some of the first biophysical studies of islets, blood cells and others during freezing (2-5). As a result of these efforts he also traced the history of the field, especially early cryobiologists which can be seen on his library shelves and led to separate review monographs on Maximov and Sachs (6, 7). He is also a world expert in burn injury having studied and carefully documented and consulted on both cellular and vascular effects of elevated temperature over time effects on tissues (8, 9).

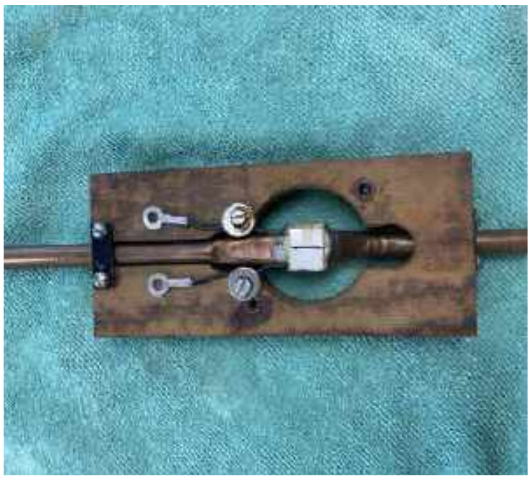

Figure 1: The original Diller cryomicroscope. This device was engineered to observe live cells during freezing processes under the microscope. Note the copper tube to deliver cryogen and electrical leads to provide differential heating to the optical stage in the middle.

During the course of these studies he trained many excellent students in bioheat transfer who are now leaders in both academia and biomedical industry and has been selfless in making time for others not specifically trained in his lab. He also published many chapters including his most comprehensive entitled "Bioheat transfer" in the CRC Thermal Engineering Handbook that I continually return to (10). He also was one of the inaugural editors of the Annual Review of Biomedical Engineering which is one of the top cited journals in the field of biomedical engineering. One impactful outgrowth of his training and mentorship is his leadership in the NSF ERC VaNTH (Vanderbilt-Northwestern-Texas-Harvard/MIT) which revolutionized biomedical educational technologies and led to a biotransport textbook, and dramatic changes in how he and others teach the field biomedical engineering (11). Indeed, his mentorship and support also helped propel my team towards our own National Science Foundation Engineering Research Center (ERC) for Advanced Technologies for the Preservation of Biological Systems (ATP-Bio). In summary, this talk demonstrates the many ways that Ken Diller has substantively contributed to the field of bioheat transfer.

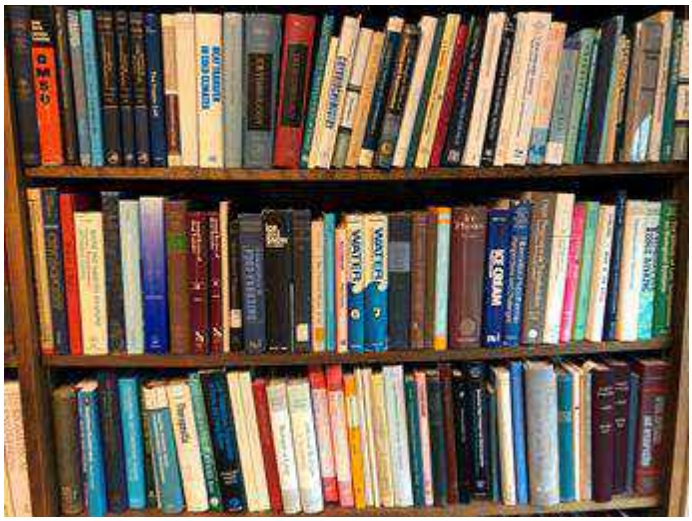

Figure 2: The Diller bioheat library includes many cryobiology classics including a full set of Biodynamica, many bound volumes of Cryo-Letters and Cryobiology. Many of the early works in cryobiology are also present including some of the early German writings from the 19th century. Many of these are still available thanks to Ken Diller's generous gift of this library to the NSF ERC ATP-Bio at the University of Minnesota (ATP-bio.org).

REFERENCES

1. Diller KR, Cravalho EG. 1970. A cryomicroscope for the study of freezing and thawing processes in biological cells. *Cryobiology* 7:191-9
2. Diller KR, Cravalho EG, Huggins CE. 1972. Intracellular freezing in biomaterials. *Cryobiology* 9:429-40
3. Schwartz GJ, Diller KR. 1983. Analysis of the water permeability of human granulocytes at subzero temperatures in the presence of extracellular ice. *J Biomech Eng* 105:360-6
4. de Freitas RC, Diller KR, Lakey JR, Rajotte RV. 1997. Osmotic behavior and transport properties of human islets in a dimethyl sulfoxide solution. *Cryobiology* 35:230-9
5. McCaa C, Diller KR, Aggarwal SJ, Takahashi T. 1991. Cryomicroscopic determination of the membrane osmotic properties of human monocytes at subfreezing temperatures. *Cryobiology* 28:391-9
6. Diller KR. 1996. Pioneers in Cryobiology: Julius von Sachs (1832-1897). *Cryo-Letters* 17:201-12
7. Diller KR. 1997. Pioneers in Cryobiology: Nikolay Aleksandorvich Maximov (Maksimov) (1880-1952),. *Cryo-Letters* 18:81-92.
8. Diller KR. 1994. The mechanisms and kinetics of heat injury accumulation. *Ann N Y Acad Sci* 720:38-55
9. Evans CD, Diller KR. 1982. A programmable, microprocessor-controlled temperature stage for burn and freezing studies in the microcirculation. *Microvasc Res* 24:314-25
10. Diller KR. 2000. Bioheat Transfer. In *Thermal Engineering Handbook*, ed. F Kreith: CRC. Number of.
11. Roselli RJ, Diller KR. 2011. *Biotransport : principles and applications*. New York: Springer. xx, 1286 p. pp.

PROFESSOR KEN DILLER'S IMPACT IN CRYOBIOLOGY AND BIOMEDICAL ENGINEERING

M. Toner

Massachusetts General Hospital & Harvard Medical School
Harvard-MIT Health Sciences & Technology
Boston, MA, USA

ABSTRACT

The field of biomedical engineering has been at the forefront of applying quantitative approaches to biology and medicine to advance healthcare. Professor Kenneth Diller's early contributions in low-temperature biology stand out as prime examples of integrating quantitative sciences into biology, significantly shaping the entire field of biomedical engineering. In 1970, he pioneered the development of the modern cryomicroscope (1, 2), a pivotal tool for monitoring thermodynamics, heat, and mass transport phenomena. This innovation provided critical insights into the complex physicochemical processes governing water's fate within biological cells during freezing (3-5). Today, the cryomicroscope is indispensable in every cryobiologist's laboratory. Diller's seminal work also encompasses the development of mathematical models to predict cellular responses to cryopreservation protocols. These models not only enhanced our understanding of the biophysics of cryopreservation but also facilitated the optimization of protocols. The impact of Diller's work extends broadly, from the storage of red blood cells and other blood components for transfusion medicine to the establishment of biobanks for cells and tissues in regenerative medicine. His pioneering efforts have inspired multiple generations of scientists, laying the foundation for advancements in cryobiology and biomedical engineering. This presentation will delve into the profound influence of Diller's early work, particularly in cryobiology, and its broader implications for biomedical engineering.

REFERENCES

1. Diller KR, Cravalho EG. 1970. A cryomicroscope for the study of freezing and thawing processes in biological cells. *Cryobiology* 7:191-9
2. Diller KR, Cravalho EG, Huggins CE. 1972. Intracellular freezing in biomaterials. *Cryobiology* 9:429-40
3. Schwartz GJ, Diller KR. 1983. Analysis of the water permeability of human granulocytes at subzero temperatures in the presence of extracellular ice. *J Biomech Eng* 105:360-6
4. de Freitas RC, Diller KR, Lakey JR, Rajotte RV. 1997. Osmotic behavior and transport properties of human islets in a dimethyl sulfoxide solution. *Cryobiology* 35:230-9
5. McCaa C, Diller KR, Aggarwal SJ, Takahashi T. 1991. Cryomicroscopic determination of the membrane osmotic properties of human monocytes at subfreezing temperatures. *Cryobiology* 28:391-9